Available online at www.sciencedirect.com
ScienceDirect
Polyhedron 26 (2007) 2703–2712
POLYHEDRON
www.elsevier.com/locate/poly

1D and 3D coordination polymers with the $M(\mu_1,\mu_1\text{-}X)_2M$ motif (M = Na, Zn, Cd): Observation of a linear $[Na(H_2O)_4]_n^{n+}$ cation and a five-connected **sqp**-net

Franz A. Mautner [a,*], Mohamed A.S. Goher [b], Hanna'a E. Moustafa [b], Morsy A.M. Abu-Youssef [b], Lars Öhrström [c]

[a] *Institut für Physikalische und Theoretische Chemie, Technische Universität Graz, A-8010 Graz, Austria*
[b] *Department of Chemistry, Faculty of Science, Alexandria University, P.O. Box 426, Ibrahimia, 21321 Alexandria, Egypt*
[c] *Department of Chemical and Biological Engineering, Physical Chemistry, Chalmers Tekniska Högskola, SE-412 96 Göteborg, Sweden*

Received 15 December 2006; accepted 12 January 2007
Available online 21 January 2007

Abstract

Three polymeric complexes $[Zn(pydz)(N_3)(SO_4)]_n[Na(H_2O)_4]_n(H_2O)_{4n}$ (**1**), $[Cd(3\text{-ampy})(N_3)Cl]_n$ (**2**), and $[Cd(DENA)Cl_2(H_2O)]_n$ (**3**), (pydz = pyridazine or 1,2-diazine, 3-ampy = 3-aminopyridine, DENA = *N*,*N*-diethylnicotineamide) have been synthesized and characterized by spectral and structural methods and their network topologies analysed. Complex **1** crystallizes in monoclinic C-centred space group *C*2/*m*, the Zn(1) center is octahedrally coordinated; and simultaneously bridged by EO-azido, *N*,*N*′-pydz, and *O*,*O*′-sulphato ligands. The ZnN_4O_2-octahedra form a 1D anionic chain along *b*-axis. The $Na(OH_2)_6$-octahedra have also common water molecules, thus also forming a 1D chain along *b*-axis. The cationic and anionic chains are connected via hydrogen bonds of type O–H···O including lattice water molecules to form a supramolecular 3D network structure. In complex **2**, the Cd(1) is six-coordinated by two EE-bridging azide groups, and two nitrogen atoms of bridging *N*,*N*′, 3-ampy ligand, and two bridging chloro ligands. The three different bridging ligands connect the distorted octahedra of the Cd(II) centres to form a 3D network structure with the topology of a square pyramidal net ($4^3 \cdot 6^6$-**sqp**). The centrosymmetric Cd_2Cl_2-rings are planar and the NH_2- of the 3-ampy groups forms additional hydrogen bonds of type N–H···N to the adjacent azido groups. In complex **3**, the octahedrally coordinated Cd(1) centres are occupied by alternating monodentate DENA ligand and a water molecule and the other four sites are occupied by four bridging chloro ligands. Thus the Cd_2Cl_2-rings form common edges to form 1D chains of Cd(II) octahedra along the *b*-axis of the monoclinic unit cell. 2D supramolecular sheets extended along the *bc*-planes of the unit cell are formed by the O–H···O hydrogen bond. The IR spectra of the three complexes were measured and they confirm the X-ray structural data.
© 2007 Elsevier Ltd. All rights reserved.

Keywords: Azide; Cadmium(II); Synthesis; Crystal structures; Zinc(II); 3D-net

1. Introduction

The pursuit of polymeric crystalline assemblies extending across a wide variety of organic–inorganic hybrid compounds has been motivated by creating structures with new topologies, cavities and channels of potential use in gas adsorption and storage, ion exchange, non-linear optical and magnetic materials [1,2]. Synthesis and studies of hybrid architecture via combination of organic bridging ligands and metallic nodes provides complexes with systematically tunable properties of interest [3]. In this context, the μ-aqua and azido-bridged complexes have became of high interest, due to the coordination versatility of the aqua and azido bridging modes. We have focused on

* Corresponding author.
E-mail address: mautner@ptc.tu-graz.ac.at (F.A. Mautner).

0277-5387/$ - see front matter © 2007 Elsevier Ltd. All rights reserved.
doi:10.1016/j.poly.2007.01.009

the magnetic diversity of the complexes where azide ion can link two or more metal ions in various modes and mediate magnetic exchange of different nature and magnitude [4–6] (Scheme 1).

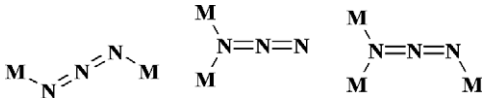
These modes may simultaneously exist in the same compound in various alternating sequences or coexist with other bridging groups. An increasing number of 2D and sometimes 3D systems have been obtained by this strategy, and the second bridging ligands used thus far have been pyridyl-based ditopic ligands such as pyrazine, 4,4′-bipy and their analogues, with some exceptions that contain carboxylate groups [7].

On the other hand, although the ligands used in this work (see Scheme 2) are interesting from the structural point of view and can exhibit novel bridging networks different from other pyridine derivatives, and there are only a few known crystal structures. Pyridazine is well known as a *N*,*N*′-bridging ligand with Co(II), Ni(II), Cu(II), Pt(II), However, only one Zn(II) compound has been reported and then with pyridazine as a monodentate ligand [8]. Also bridging *N*,*N*′-3-ampy is seldom found in coordination chemistry [9].

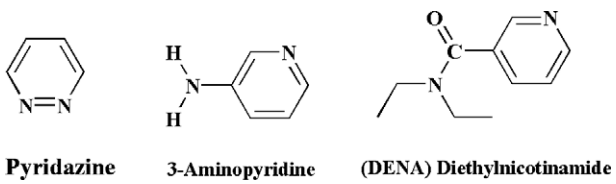
Therefore, we extend our work to explore the different possible systems arising with these ligands. As part of our investigation on metal azides, we have recently reported a number of cadmium(II) azido and thiocyanato coordination polymers with some pyridine derivative ligands containing different bridging modes of $[Cd(N_3)_2]_n$ and $[Cd(NCS)_2]_n$ chains to construct coordination supramolecular frameworks [10–12]. Compared to the relatively large number of the azido-bridged polymers with Mn(II), Ni(II) and Cu(II) reported in the literature, the Cd(II) polymers are still very rare. Although diamagnetic, the cadmium and zinc systems are interesting from the structural point of view, since the systems can exhibit novel bridging networks different from other metal complexes [13]. From an applications point of view it can be noted that Cd(II) and Zn(II) coordination polymers forming 3D-nets have shown excellent non-linear optical properties [14].

Recently, such 3D-nets have been subject of renewed efforts of classification [15,2d], a very timely endeavour since such compounds may have important technological applications, as stated above.

Here, we present the reactions of zinc(II) ions with pyridazine and cadmium(II) ions with 3-aminopyridine and diethylnicotinamide in presence of azide ions, and the structure and network analysis of the three compounds; 1:1:1:1 for Zn:pyridazine:azide:sulphate (**1**) and Cd: 3-aminopyridine:azide:chloride (**2**) and 1:1:2:1 for Cd:diethylnicotinamide:Cl:H_2O (**3**).



Scheme 1.



Scheme 2.

2. Experimental

2.1. Materials and instrumentation

Infrared spectra were recorded in a Bruker IFS-125 model FT-IR spectrophotometer as KBr pellets [10]. C,H,N analyses were carried out using a Perkin–Elmer analyzer [12], Cd and Zn were analysed by a Perkin–Elmer Analyst 300, AAS atomic absorption spectrometer. Pyridazine, 3-aminopyridine and diethylnicotinamide ligands have been purchased from Aldrich Company and other chemicals were of analytical grade quality and used without further purification.

Caution: Metal azide complexes are potentially explosives. Only a small amount of material should be prepared and should be handled with caution.

2.2. Synthesis

2.2.1. $[Zn(pydz)(N_3)(SO_4)]_n[Na(H_2O)_4]_n(H_2O)_{4n}$

To an aqueous solution (20 cm^3) of $ZnSO_4 \cdot 7H_2O$ (0.57 g, ~2.0 mmol) and (0.32 g, 4 mmol) of pyridazine in ethanol (15 cm^3) were added, followed by a drop-wise addition of aqueous solution of NaN_3 (0.65 g, 10 mmol) with continuous stirring. The final clear mixture was allowed to stand at room temperature for several days. Colourless crystals suitable for X-ray measurement were collected, dried in air, with a yield 0.45 g, ~50.4% with respect to the metal. *Anal*. Calc. data: C, 10.66; H, 4.47; N, 15.54; Zn, 14.50, S, 7.11, Na, 5.10. Found: C, 10.50; H, 4.35; N, 15.60; Zn, 14.69; S, 7.09, Na, 5.15%. IR, KBr (cm^{-1}) (v, very; s, strong; m, medium; w, weak; br, broad): 3361 br, 3078 m, 2624 w, 2565 w, 2089 vs, 1643 w, 1629 br, 1575 s, 1450 m, 1422 s, 1408 w, 1356 m, 1291 s, 1195 br, 1110 br, 990 s, 972 w, 769 vs, 674 s, 655 w, 620 vs, 594 vs, 445 br, 395 m, 366 m, 345 m, 316 m, 293 m, 270 s.

2.2.2. $[Cd(3\text{-}ampy)(N_3)Cl]_n$

To an aqueous/methanolic solution (20 cm^3) of $CdCl_2 \cdot H_2O$ (0.2 g, ~1.0 mmol) and (0.2 g, 2.0 mmol) of 3-aminopyridine in (15 cm^3) methanol were added, then drops of a mixture of L-Asc (0.1 g., 0.6 mmol) and NaN_3 (0.5 g, 7.7 mmol) were added to the metal–ligand mixture. A white precipitate was formed, dissolved upon heating and stirring for 10 min. The clear solution was allowed to stand for few days, yellowish powder was obtained. Recrystallization of the precipitated powder in distilled

water gave deep yellow crystals suitable for X-rays measurements after four days with yield 0.23 g, ~82% with respect to the metal. *Anal*. Calc. data: C, 21.14; H, 2.12; N, 24.66; Cd, 39.57. Found: C, 21.32; H, 2.25; N, 24.48; Cd, 39.39%. IR, KBr (cm^{-1}) (v, very; s, strong; m, medium; w, weak; br, broad): 3405 m, 3313 s, 3254 s, 3160 s, 3058 m br, 2065 vs, 1585 vs, 1486 vs, 1447 vs, 1265 vs, 1195 s, 1145 m, 1099 m, 1055 s, 1031 s, 949 vs, 929 vs, 899 s, 827 s, 807 s, 698 s, 645 s, 627 m. 601 m, 534 m, 412 m, 385 m, 344 w, 316 w, 294 w, 270 m.

2.2.3. *[Cd(pyridine-N,N-diethylnicotinamide)Cl_2(H_2O)]$_n$*

To an aqueous mixture (15 cm^3) of L-ascorbic acid (0.1 g., 0.6 mmol) and NaN_3 (0.5 g, 7.7 mmol) an ethanolic solution (15 cm^3) of (0.35 g, 2.0 mmol) of pyridine-*N*,*N*-diethylnicotinamide (DENA) were added. Followed by the drop-wise addition of an aqueous solution (10 cm^3) of oxalic acid (0.2 g, 2.2 mmol), with continuous stirring and heating until clear solution was obtained. Further, an aqueous solution of $CdCl_2 \cdot H_2O$ (0.2 g, ~1.0 mmol) were added. The final clear mixture was allowed to stand for several weeks, white crystals suitable for X-rays measurements were collected, dried in air with yield 0.21 g, ~55.7% with respect to the metal. *Anal*. Calc. data: C, 31.64; H, 4.24; N, 7.38; Cd, 29.61. Found: C, 31.70; H, 4.33; N, 7.29; Cd, 29.47%. IR, KBr (cm^{-1}) (v, very; s, strong; m, medium; w, weak; br, broad): 3431 vs br, 3345 vs br, 3247 vs, 3097 s, 3069 s, 2996 s, 2978 s, 2935 m, 1635 vs, 1604 vs, 1585 vs br, 1500 s, 1455 vs br, 1424 vs, 1392 s, 1359 s, 1317 vs, 1289 vs, 1211 s, 1194 s, 1104 vs, 1075 s, 1048 s, 1032 s, 1005 m, 947 m, 880 s, 828 vs, 794 m, 748 s, 731 m, 707 s, 646 vs, 593 vs br, 503 s, 433 m, 404 m, 371 m, 344 w, 316 w, 295 w, 270 w.

2.3. X-ray crystallography

Single crystal X-ray data were measured at 100(2) K on a modified STOE four circle diffractometer using graphite crystal-monochromatized Mo Kα radiation ($\lambda = 0.71069$ Å). The intensities were corrected for Lorentz-polarisation effects and for absorption. Crystallographic data and processing parameters are given in Table 1. The structures were solved by direct methods and subsequent Fourier analyses. Programs used for computations: DIFABS [16], SHELXTL/PC program package [17] and MERCURY [18]. Analytical expressions of neutral-atom scattering factors were employed, and anomalous dispersion corrections were incorporated. Anisotropic displacement parameters were applied to non-hydrogen atoms in full-matrix least-squares refinements based on F^2. All hydrogen atoms were located from difference Fourier maps assigned with isotropic displacement factors and included in the final refinement cycles as follows: (a) pyrazine hydrogen atoms bonded to carbon by geometrical restraints using the HFIX utility of SHELXTL/PC package; (b) water hydrogens by use of O–H distance restraints. Split occupancy of 0.5 was applied to the disordered lattice water molecule O(9) of **1** . Selected bond distances and bond angles are given in Tables 2–4, for complexes **1**–**3**, respectively. Hydrogen bonds are listed in Table 5.

2.3.1. Network analysis

Abbreviations (three-letter codes) for 3D nets were taken from the web-based Reticular Chemistry Structure Resource, where crystallographic coordinates and other useful details for 3D-nets can be obtained [19]. For the less common nets we recommend adding the short (Schläfli) symbol before the three-letter code for clarity, as in

Table 1
Crystallographic data and processing parameters

Compound	**1**	**2**	**3**
Empirical formula	$C_4H_{20}N_5NaO_{12}SZn$	$C_5H_6CdClN_5$	$C_{10}H_{16}CdCl_2N_2O_2$
Formula mass	450.70	284.01	379.56
System	monoclinic	monoclinic	monoclinic
Space group	*C*2/*m*	$P2_1/n$	$P2_1/c$
a (Å)	16.127(4)	6.511(2)	9.539(2)
b (Å)	7.067(2)	10.197(3)	7.975(2)
c (Å)	15.078(6)	12.367(4)	17.302(5)
α (°)	90	90	90
β (°)	105.08(3)	97.53(3)	99.76(2)
γ (°)	90	90	90
V (Å^3)	1659.2(9)	814.0(4)	1297.2(6)
Z	4	4	4
μ (Mo Kα) (mm^{-1})	1.701	2.957	2.086
D_{calc} (Mg/m^3)	1.804	2.318	1.944
Crystal size (mm)	0.26 × 0.20 × 0.12	0.26 × 0.21 × 0.14	0.22 × 0.14 × 0.08
θ Range (°)	2.80–27.00	3.32–25.99	2.82–26.00
Reflections collected	3156	1999	2864
Independent reflections/R_{int}	1960/0.0507	1593/0.0338	2541/0.0206
Parameters	159	116	157
Goodness-of-fit on F^2	1.206	1.113	1.072
R_1/wR_2 (all data)	0.0427/0.1076	0.0414/0.0976	0.0210/0.0542
Residual extrema (e/Å^3)	0.629/−0.616	0.858/−0.871	0.358/−0.473

Table 2
Selected bond lengths (Å) and angles (°) for (**1**)

Zn(1)–N(11)	2.095(2)	Zn(1)–O(1)	2.120(2)
Zn(1)–N(1)	2.201(3)	N(1)–C(1)	1.323(4)
N(1)–N(1A)	1.352(6)	C(1)–C(2)	1.401(5)
C(2)–C(2A)	1.357(7)	N(11)–N(12)	1.214(6)
N(12)–N(13)	1.149(6)	Na(1)–O(6D)	2.397(3)
Na(1)–O(5E)	2.410(3)	Na(1)–O(4F)	2.447(3)
N(11)–Zn(1)–O(1)	91.75(12)	N(11)–Zn(1)–N(1B)	92.80(12)
O(1)–Zn(1)–N(1)	90.26(10)	N(12)–N(11)–Zn(1)	119.48(12)
Zn(1C)–N(11)–Zn(1)	115.0(2)	N(13)–N(12)–N(11)	178.5(5)

Symmetry codes: (A) $x, -y, z$; (B) $-x+1/2, -y+1/2, -z+1$; (C) $-x+1/2, y-1/2, -z+1$; (D) $-x, -y+1, -z$; (E) $-x, -y, -z$; (F) $-x, y, -z$.

Table 3
Selected bond lengths (Å) and angles (°) for (**2**)

Cd(1)–N(1)	2.310(5)	Cd(1)–N(11)	2.341(6)
Cd(1)–N(13A)	2.347(6)	Cd(1)–N(2B)	2.440(5)
Cd(1)–Cl(1C)	2.590(2)	Cd(1)–Cl(1)	2.665(2)
N(11)–N(12)	1.166(8)	N(12)–N(13)	1.184(8)
N(1)–Cd(1)–N(11)	89.3(2)	N(1)–Cd(1)–N(13A)	94.0(2)
N(11)–Cd(1)–N(13A)	94.1(2)	N(1)–Cd(1)–N(2B)	90.8(2)
N(11)–Cd(1)–N(2B)	90.7(2)	N(13A)–Cd(1)–N(2B)	173.2(2)
N(1)–Cd(1)–Cl(1C)	177.08(13)	N(11)–Cd(1)–Cl(1C)	93.1(2)
N(13A)–Cd(1)–Cl(1C)	87.5(2)	N(2B)–Cd(1)–Cl(1C)	87.47(13)
N(1)–Cd(1)–Cl(1)	88.41(13)	N(11)–Cd(1)–Cl(1)	172.4(2)
N(13A)–Cd(1)–Cl(1)	93.2(2)	N(2B)–Cd(1)–Cl(1)	82.15(14)
Cl(1C)–Cd(1)–Cl(1)	89.01(5)	Cd(1C)–Cl(1)–Cd(1)	90.99(5)
N(12)–N(11)–Cd(1)	167.6(5)	N(11)–N(12)–N(13)	178.6(7)
N(12)–N(13)–Cd(1D)	121.3(5)		

Symmetry codes: (A) $-x+3/2, y+1/2, -z+1/2$; (B) $-x+1/2, y-1/2, -z+1/2$; (C) $-x+1, -y+1, -z$; (D) $-x+3/2, y-1/2, -z+1/2$.

Table 4
Selected bond distances (Å) and angles (°) for (**3**)

Cd(1)–O(1)	2.354(2)	Cd(1)–N(1)	2.360(3)
Cd(1)–Cl(2A)	2.6203(8)	Cd(1)–Cl(1B)	2.6438(8)
Cd(1)–Cl(2)	2.6633(9)	Cd(1)–Cl(1)	2.6698(8)
O(1)–Cd(1)–N(1)	160.73(8)	O(1)–Cd(1)–Cl(2A)	96.50(6)
N(1)–Cd(1)–Cl(2A)	96.64(6)	O(1)–Cd(1)–Cl(1B)	98.89(5)
N(1)–Cd(1)–Cl(1B)	95.63(6)	Cl(2A)–Cd(1)–Cl(1B)	87.84(3)
O(1)–Cd(1)–Cl(2)	82.87(6)	N(1)–Cd(1)–Cl(2)	86.83(6)
Cl(2A)–Cd(1)–Cl(2)	169.13(2)	Cl(1B)–Cd(1)–Cl(2)	81.55(3)
O(1)–Cd(1)–Cl(1)	80.77(5)	N(1)–Cd(1)–Cl(1)	87.21(6)
Cl(2A)–Cd(1)–Cl(1)	81.86(3)	Cl(1B)–Cd(1)–Cl(1)	169.58(2)
Cl(2)–Cd(1)–Cl(1)	108.66(3)	Cd(1A)–Cl(1)–Cd(1)	97.77(3)
Cd(1B)–Cl(2)–Cd(1)	98.52(3)		

Symmetry codes: (A) $-x+1, y+1/2, -z+1/2$; (B) $-x+1, y-1/2, -z+1/2$.

$4^3 \cdot 6^6$-**sqp** [3e]. This notation tells us the number of smallest rings found in the net, and, for nets with more than two nodes, also tells us the stoichiometry of the nodes, and thus gives a rough idea of the type of network in question. The topology of this net was established by computing the vertex symbol (extended Schläfli or long symbol) [20] giving $4 \cdot 4 \cdot 4 \cdot 4 \cdot 6 \cdot 6 \cdot 6_5 \cdot 6_5 \cdot 6_5 \cdot 6_5$ and comparing both the symbol and the experimental net with the ideal net. The computation was performed using the OLEX program [21], a good alternative is the TOPOS program [22].

Table 5
Hydrogen bond systems

Donor–H...A [Symmetry of A]	D–H (Å)	H...A (Å)	D...A (Å)	D–H...A (°)
Compound ***1***				
O(4)–H(41)···O(3)	0.82	2.09	2.875(4)	159
O(4)–H(42)···O(7) [$-1/2+x, 1/2-y, z$]	0.82	2.03	2.807(5)	157
O(5)–H(51)···O(9) [$1/2-x, -1/2+y, -z$]	0.83	2.01	2.796(7)	158
O(5)–H(51)···O(9) [$1/2-x, 1/2-y, -z$]	0.83	2.01	2.796(7)	158
O(5)–H(52)···O(3)	0.82	1.99	2.803(5)	170
O(6)–H(61)···O(8)	0.82	2.02	2.843(6)	177
O(6)–H(62)···O(9)	0.82	2.03	2.795(7)	154
O(6)–H(62)···O(9) [$x, 1-y, z$]	0.82	2.03	2.795(7)	154
O(7)–H(71)···O(2)	0.81	2.09	2.880(4)	163
O(7)–H(72)···O(4) [$1/2+x, 1/2-y, z$]	0.82	2.03	2.807(5)	157
O(8)–H(81)···O(1)	0.82	2.10	2.908(4)	172
O(9)–H(91)···O(7)	0.82	1.96	2.731(7)	157
O(9)–H(92)···O(7) [$1/2-x, 1/2-y, -z$]	0.82	1.96	2.758(7)	165
Compound ***2***				
N(2)–H(6)···N(13) [$x, 1+y, z$]	0.90	2.384	3.245(8)	160
N(2)–H(7)···N(13) [$1-x, 1-y, 1-z$]	0.90	2.568	3.461(8)	174
Compound ***3***				
O(1)–H(11)···O(2) [$1-x, -1/2+y, 1/2-z$]	0.83	1.954	2.780(3)	179
O(1)–H(12)···O(2) [$x, 3/2-y, -1/2+z$]	0.82	1.986	2.810(3)	179

D, donor, A, acceptor.

3. Results and discussion

3.1. Structures

$[Zn(pydz)(N_3)(SO_4)]_n[Na(H_2O)_4]_n(H_2O)_{4n}$ (**1**) crystallizes in monoclinic C-centred space group $C2/m$ (no. 12) with 9iZ = 4; with following special positions: Zn(1) on inversion centre; pydz, azide, sulphato group, as well as water molecules O(5), O(6) and O(8) on mirror planes; Na(1) on diad. Water molecule O(9) is disordered with split occupancy of 0.5!

The Zn(1) centre is octahedrally coordinated; and simultaneously bridged by EO-azido, *N*,*N*′-pydz, and *O*,*O*′-sulphato ligands (Fig. 1). The ZnN_4O_2-octahedra are elongated, with Zn(1)–N(1) apical bond distances of 2.201(3) Å to pydz ligands, whereas Zn(1)–N(11) and Zn(1)–O(1) basal bond distances to N atoms of azide and O atoms of sulphato bridges are 2.095(2) and 2.120(2) Å, respectively. The Zn-octahedra form a 1D anionic chain (Fig. 2) along *b*-axis of monoclinic unit cell, with a Zn(1)...Zn(1′) separation of 3.5353(14) Å.

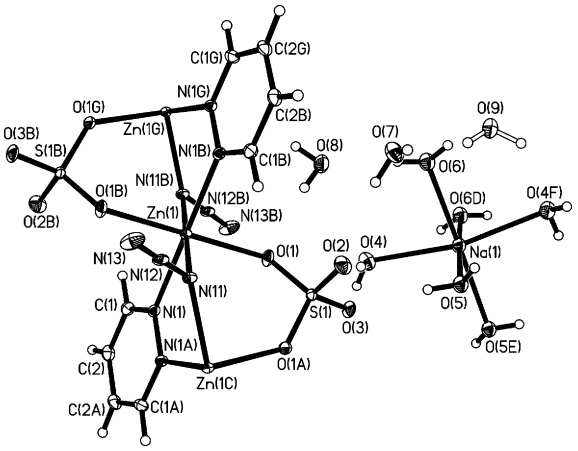


Fig. 1. Perspective view with atom labelling scheme of **1**.

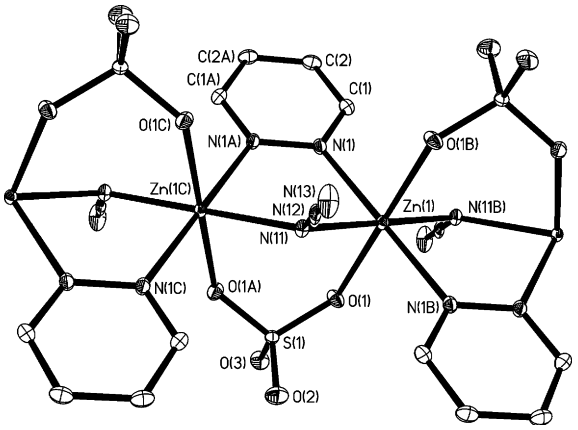


Fig. 2. Part of the chain structure of **1**.

The $Na(OH_2)_6$-octahedra have also common water molecules [O(4) and O(5)], thus also forming a 1D chain along *b*-axis [Na(1)...Na(1′) are 3.426(4) and 3.641(4) Å]. The Na–O distances are in the range from 2.397(3) to 2.447(3) Å. The cationic and anionic chains are connected via hydrogen bonds of type O–H···O including lattice water molecules [O(7), O(8) and O(9)] to form a supramolecular 3D network structure (Fig. 3, Table 5). The moiety of **1** may be formulated: $[Zn(pydz)(N_3)(SO_4)]_n$-$[Na(H_2O)_4]_n(H_2O)_{4n}$.

A picture of the asymmetric unit of [Cd(3-aminopyridine)$(N_3)Cl]_n$, compound **2**, is given in Fig. 4, and selected bond parameters are listed in Table 3. Cd(1) is six-coordinated by N(11) and N(13A) of EE-bridging azide group, N(1) and N(2B) of bridging 3-ampy ligand, and Cl(1) and Cl(1C) of bridging chloro ligands. The Cd(1)–N bond distances are in the range from 2.310(5) to 2.440(5) Å, whereas the Cd(1)–Cl bond distances are 2.590(2) and 2.665(2) Å. The three different bridging ligands connect the distorted octahedra of Cd(II) centers to form a 3D network structure (Fig. 5a and b). The Cd···Cd separations within the network structure are 3.7482(13) Å (via chloro-bridges), 6.310(2) Å (via azido), and 6.883(2) Å, (via 3-ampy), respectively. The centrosymmetric Cd_2Cl_2-rings are planar, with a Cd(1)–Cl(1)–Cd(1C) bond angle of 90.99(5)°. The EE-azido bridges are almost symmetric [N(11)–N(12) = 1.166(8) Å, N(12)–N(13) = 1.184(8) Å, N(11)–N(12)–N(13) = 178.6(7)°]. The Cd(1)–N(11)–N(12) bond angle is almost linear [167.6(5)°], while the Cd(1D)–N(13)–N(12) bond angle is close to 120° [121.3(5)°]. The Cd(1)–N(11)···N(13)–Cd(1D) torsion angle is 129.6(6)°. The 3-ampy ligand form a torsion angle of C(1)–C(2)–N(2)–Cd(1E) of 97.3(6)°. The NH_2-groups form additional hydrogen bonds of type N–H···N to N(13) atoms of adjacent azido groups.

A perspective view of [Cd(pyridine-*N*,*N*-diethylnicotinamide)$Cl_2(H_2O)]_n$ (**3**) is given in Fig. 6, selected bond parameters are summarized in Table 4. The apical positions of the octahedrally coordinated Cd(1) centers are occupied by N(1) of a monodentate DENA ligand [Cd(1)–N(1) = 2.360(3) Å], and by O(1) of a water molecule with Cd(1)–O(1) bond distance of 2.354(2) Å. The other four sites are occupied by bridging chloro ligands with Cd(1)–Cl bond distances in the range from 2.6203(8) to 2.6698(6) Å. Thus the Cl(1) and Cl(2) bridges form common edges to form 1D chains of Cd(II) octahedra along the *b*-axis of the monoclinic unit cell (Fig. 7). The Cd_2Cl_2-rings have similar Cd–Cl–Cd bridge angles of 97.77(3)° and 98.52(3)°. 2D

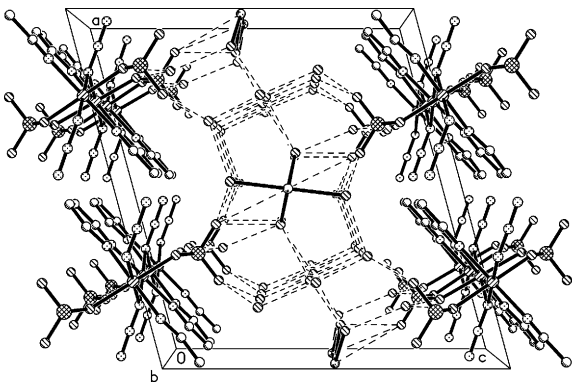


Fig. 3. Packing plot of **1**. Broken lines indicate hydrogen bonds.

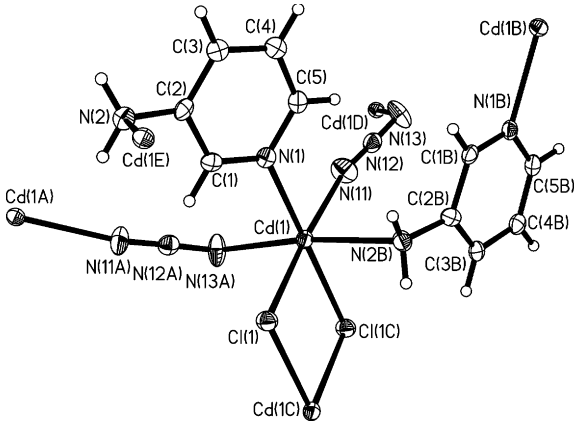


Fig. 4. ORTEP view of **2** with the atom labelling scheme.

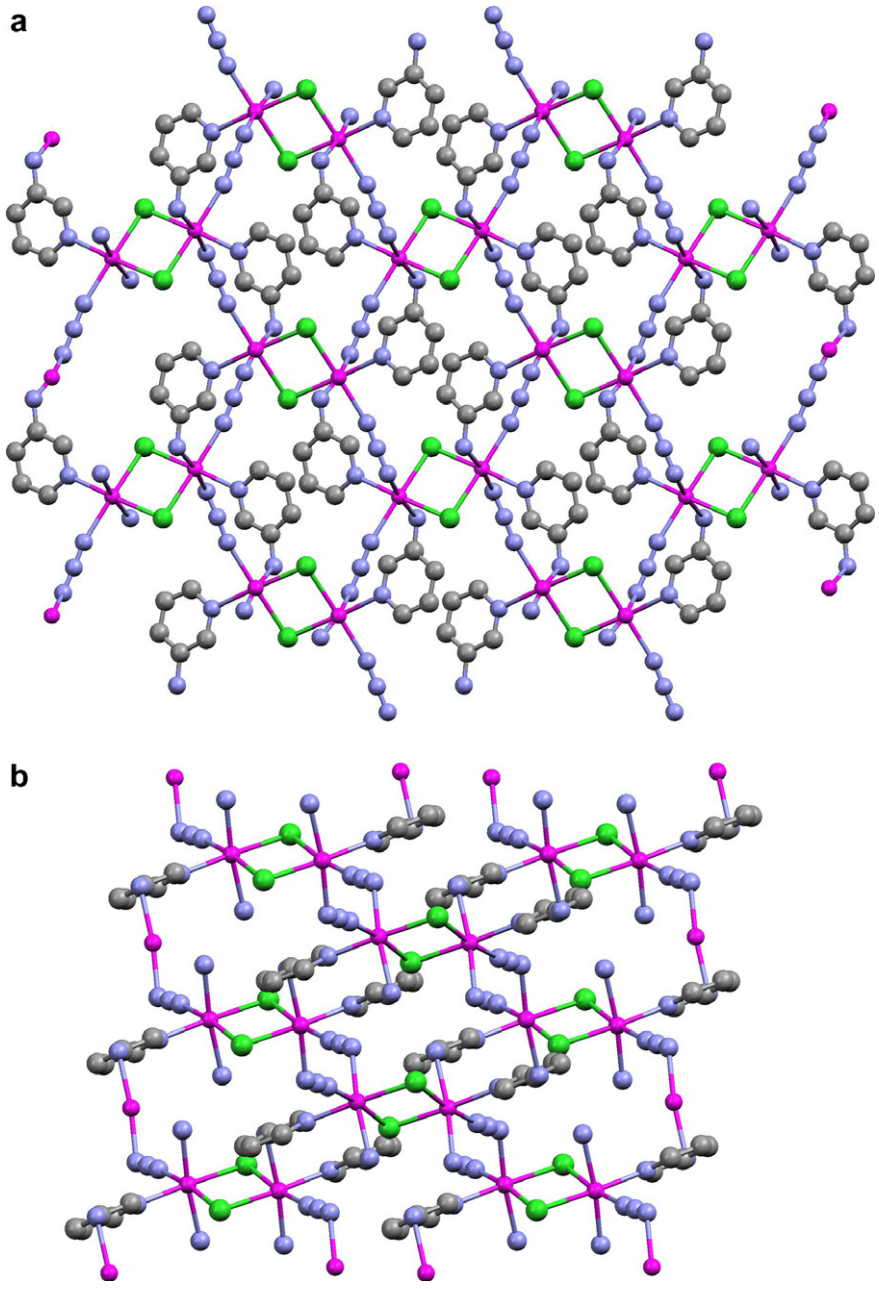


Fig. 5. Packing plots of **2** viewed along *a*- and *b*-axis of the unit cell.

supramolecular sheets extended along the *bc*-planes of the unit cell are formed by the O(1)–H(12)···O(2) $[x, 3/2 - y, -1/2 - z]$ hydrogen bond, whereas O(1)–H(11)···O(2) $[1 - x, -1/2 + y, 1/2 - z]$ is forming an intra-chain hydrogen bond.

The aromatic 6-membered rings in all three compounds show π–π stacking with the following Cg(ring)···Cg(ring) (Cg = centre of gravity) separations; (a) pyridazine ring(1) of complex **1**: [ring(1): N(1), C(1), C(2), N(1A), C(1A), C(2)]; Cg(1)···Cg(1)#1 and Cg(1)···Cg(1)#2 = 3.733(2) Å [#1: $-x, y, 1 - z$; #2 $-x, -y, 1 - z$]; (b) pyridine ring (2) of 3-aminopyridine ligand of complex **2**: [ring(2): N(1), C(1)–C(5)]; Cg(2)···Cg(2)#3 = 3.715(4) Å [#3: $1 - x, 1 - y, 1 - z$]; (c) pyridine ring(3) of *N*,*N*-diethylnicotinamide ligand of complex **3**: [ring(3): N(1), C(1)–C(5)]; Cg(3)···Cg(3)#4 = 3.601(2) Å [#4: $1 - x, 1 - y, 1 - z$].

3.2. Network analysis

All crystals are of course three-dimensional, and therefore a common misunderstanding is that any crystal will consist of a 3D-net, you just need to look hard enough. The three compounds in this report adequately illustrates that this is not the case.

First, we note that they are all built around a common structural theme, double (or triple) M–Y–M bridge (Y = O, N, N = N, Cl; M = Zn, Na, Cd) giving –M–Y–M–Y-rings.

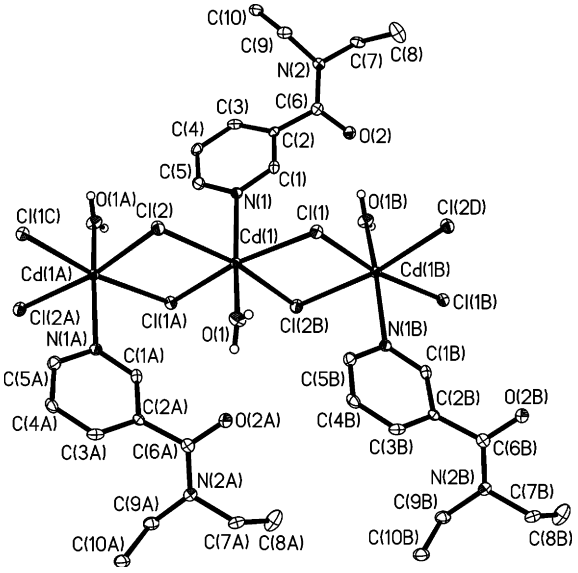


Fig. 6. ORTEP view of **3** with the atom labelling scheme.

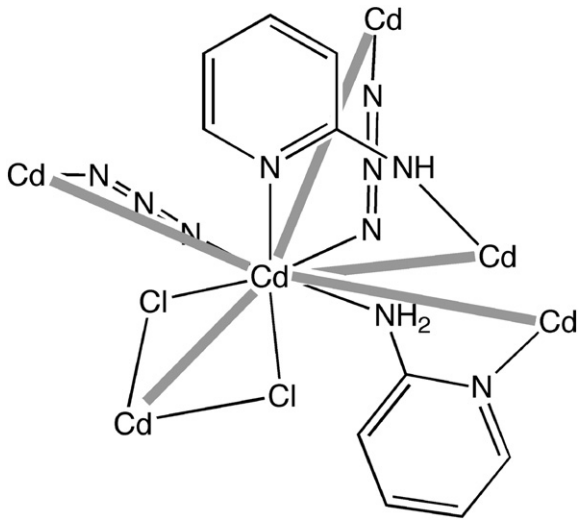


Fig. 8. Node assignment in **2**.

In compound **1** these bridges are directly connected giving both Na(I) and Zn(II) 1D coordination polymers extending along the *b*-axis. An intricate pattern of hydrogen bonds is then interconnecting these chains to give a three-dimensional crystal. However, as each Na(I) chain connects to four Zn(II) chains and two Na(I) chains with numerous attachment points using all the solvent water molecules and the coordinated waters as intermediates, there is no obvious way to single out some of these as network links and to assign nodes at specific atoms or groups of atoms. Instead, it seems much more profitable to view this structure as a parallel packing of anionic and cationic coordination polymers, a rare feature as coordination polymers are normally neutral or cationic (see Fig. 3).

Moreover, the linear $[Na(H_2O)_4]_n^{n+}$ ion is an archetypical precursor to the gel-type precipitates often formed when pH is raised in solutions of $[M(H_2O)_6]^{n+}$ although such species are rarely isolated in the solid state. Indeed, a zig-zag chain was recently found in tetradecaaquatetrasodium hexaaquanickel(II) decavanadate(V) trihydrate (see Fig. 8) [23].

In compound **2** we have a very different situation. Clearly this compound extends via covalent (dative) bonds in all three dimensions. Moreover, there is an obvious directionality of these links making node assignment easy: all links branch from the metal ions. Thus, we made the node assignment shown in Fig. 9. This results in a 3D-net comprising interconnected square pyramidal nodes with the $Cd(Cl)_2Cd$ short link in the apical position. It is rela-

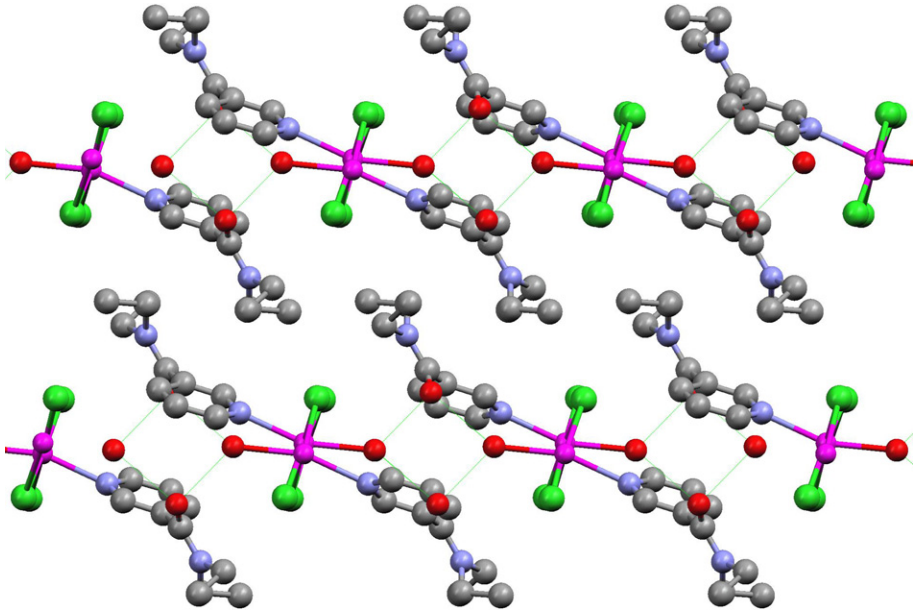


Fig. 7. Packing plot of **3** viewed along *b*-axis of the unit cell.

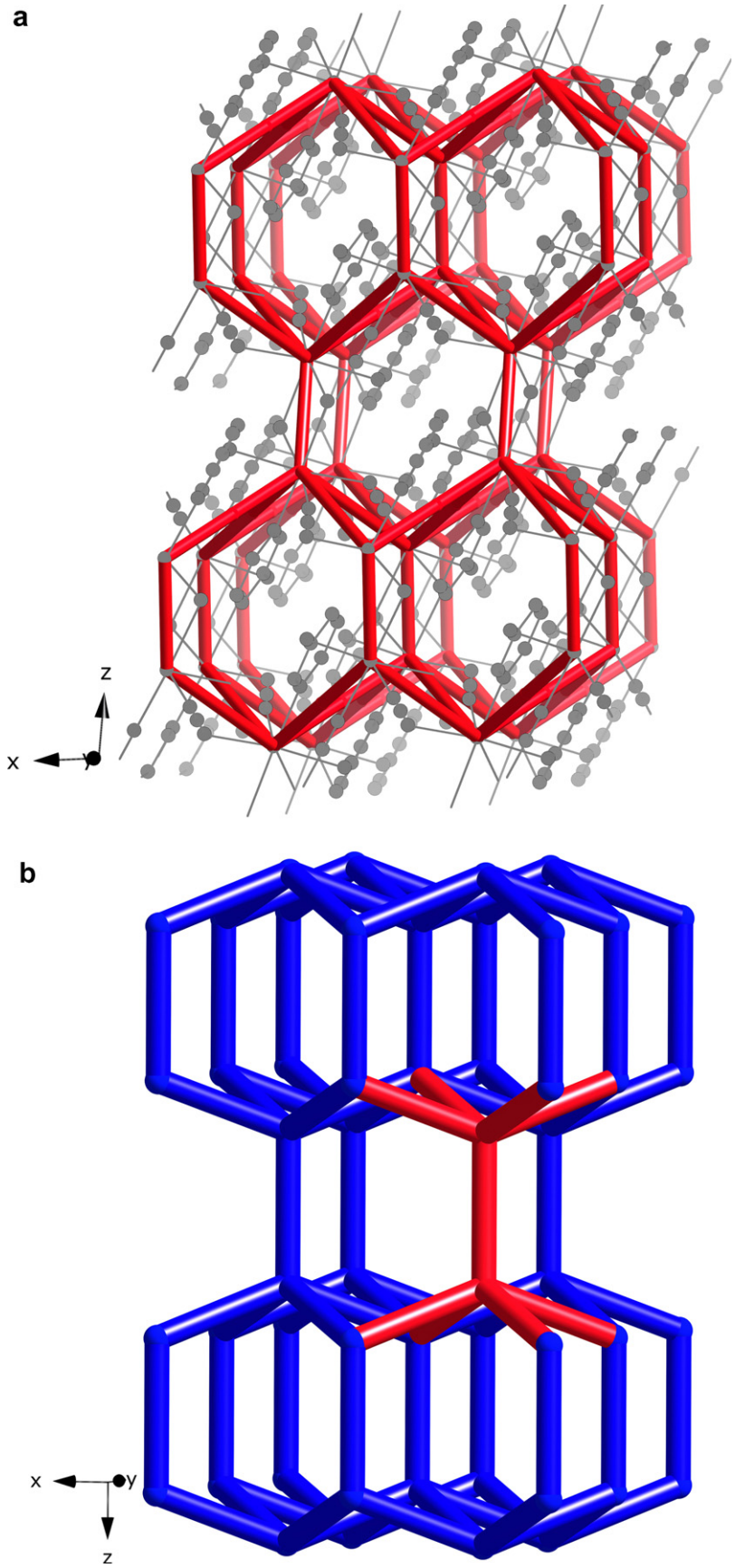


Fig. 9. (a) The $4^3 \cdot 6^6$-**sqp** net formed by compound **2**. (b) Idealized $4^3 \cdot 6^6$-**sqp** net with the characteristic staggered square pyramidal dimer highlighted in red. (For interpretation of the references to colour in this figure legend, the reader is referred to the web version of this article.)

tively easy (although please refer also to Section 2) to visibly identify this net as the $4^4 \cdot 6^6$-**sqp** net (according to the new three-letter codes proposed by O'Keeffe and Yaghi [2f]. The figure preceding the code is the short (Schläfli) symbol telling us that this is a five-connected net with four and six membered rings as the smallest entities.). This is not all that surprising since this is the second most common net found with five-connected nodes, the most common being the $4^6 \cdot 6^4$-**bnn** (or boron nitride) net based on trigonal bipyramidal nodes [24]. The net superimposed on all atoms in the structure is shown in Fig. 9 together with its idealized form. We note that this might be a gemerla way to build these types of nets, a $M(Cl)_2M$ unit leaving four sites on an octahedral M^{n+} ion to propagate the net in four new directions, with an approximate square pyramidal geometry for the entire node.

Finally, compound **3** is a straightforward neutral 1D coordination polymer where parallel chains are hydrogen bonded to sheets where also ''π-stacking'' males a contribution. The ethyl groups of neighbouring sheets interdigitate each other. Thus it is difficult, and to no profit to try to impose a network on this structure.

Acknowledgements

This work was funded by the Swedish International Development Cooperation Agency under the Swedish Research Links program (Grants Nos. 348-2002-6879 and 348-2004-5473). F.A.M. thanks Prof. Kratky and Prof. Belaj (Univ. Graz) for the use of the STOE 4-circle diffractometer.

Appendix A. Supplementary material

CCDC 631081, 631082 and 631083 contain the supplementary crystallographic data for this paper. These data can be obtained free of charge via http://www.ccdc.cam.ac.uk/conts/retrieving.html, or from the Cambridge Crystallographic Data Centre, 12 Union Road, Cambridge CB2 1EZ, UK; fax: (+44) 1223-336-033; or e-mail: deposit@ccdc.cam.ac.uk. Supplementary data associated with this article can be found, in the online version, at doi:10.1016/j.poly.2007.01.009.

References

[1] (a) B.F. Hoskins, R. Robson, J. Am. Chem. Soc. 112 (1990) 1546;
(b) M. Fujita, Y.J. Kwan, S. Washizu, K. Ogurs, J. Am. Chem. Soc. 116 (1994) 1151;
(c) O.M. Yaghi, H.L. Li, J. Am. Chem. Soc. 117 (1995) 10401;
(d) P.J. Hagrman, D. Hagrman, J. Zubieta, Angew. Chem., Int. Ed. Engl. 38 (1999) 2638.

[2] (a) C. Janiak, J. Chem. Soc., Chem. Commun. (1994) 545;
(b) C. Janiak, T.G. Charmann, W. Gunter, F. Girgsdies, H. Hemling, W. Hinrichs, D. Lentz, Chem. Eur. J. 1 (1995) 637;
(c) J.L.C. Rowsell, O.M. Yaghi, Angew. Chem., Int. Ed. Engl. 44 (2005) 4670;
(d) M. O'Keeffe, O.M. Yaghi, J. Solid State Chem. 178 (2005) V;
(e) J.L.C. Rowsell, O.M. Yaghi, Microporous Mesoporous Mater. 73 (2004) 3;
(f) O.M. Yaghi, M. O'Keeffe, N.W. Ockwig, H.K. Chae, M. Eddaoudi, J. Kim, Nature 423 (2003) 705;
(g) X.B. Zhao, B. Xiao, A.J. Fletcher, K.M. Thomas, D. Bradshaw, M.J. Rosseinsky, Science 306 (2004) 1012;
(h) D. Bradshaw, J.B. Claridge, E.J. Cussen, T.J. Prior, M.J. Rosseinsky, Acc. Chem. Res. 38 (2005) 273.

[3] (a) J.M. Lehn, Supramolecular Chemistry, VCH, Weinheim, 1985;
(b) R. Robin, B.F. Abrahams, R.R. Barten, R.W. Gable, B.F. Huskiness, J. Lieu, Supramolecular Architecture, American Chemical Society, Washington, DC, 1992;
(c) O. Kahn (Ed.), Molecular Magnetism, a Supramolecular Function, Kluwer, Dordrecht, 1996;
(d) J. Ribas, A. Escuer, M. Monfort, R. Vicente, R. Cortés, L. Lezama, T. Rojo, Coord. Chem. Rev. 193–195 (1999) 1027 (and references therein);
(e) L. Öhrström, K. Larsson, Molecule-Based Materials: The Structural Network Approach, Elsevier, Amsterdam, 2005.

[4] (a) A. Escuer, R. Vicente, M.A.M. Abu-Youssef, F.A. Mautner, M.A.S. Goher, L. Öhrstrom, Polyhedron 24 (2005) 557;
(b) J. Cano, Y. Journaux, M.A.S. Goher, M.A.M. Abu-Youssef, F.A. Mautner, G.J. Reiß, A. Escuer, R. Vicente, New J. Chem. 2 (2005) 306;
(c) A. Escuer, F.A. Mautner, M.A.S. Goher, M.A.M. Abu-Youssef, R. Vicente, J. Chem. Soc., Chem. Commun. (2005) 605.

[5] (a) A. Escuer, R. Vicente, F.A. Mautner, M.A.S. Goher, M.A.M. Abu-Youssef, J. Chem. Soc., Chem. Commun. (2002) 64;
(b) M.A.M. Abu-Youssef, M. Drillon, A. Escuer, M.A.S. Goher, F.A. Mautner, R. Vicente, Inorg. Chem. 39 (2000) 5022;
(c) M.A.M. Abu-Youssef, A. Escuer, M.A.S. Goher, F.A. Mautner, G.J. Reiß, R. Vicente, Angew. Chem., Int. Ed. Engl. 39 (2000) 1624;
(d) M.A.M. Abu-Youssef, A. Escuer, D. Gatteschi, M.A.S. Goher, F.A. Mautner, R. Vicente, Inorg. Chem. 38 (1999) 5716.

[6] (a) M.A.S. Goher, J. Cano, Y. Journaux, M.A.M. Abu-Youssef, F.A. Mautner, A. Escuer, R. Vicente, Chem. Eur. J. 6 (2000) 774;
(b) M.A.S. Goher, M.A.M. Abu-Youssef, F.A. Mautner, R. Vicente, A. Escuer, Eur. J. Inorg. Chem. (2000) 1819;
(c) M.A.M. Abu-Youssef, A. Escuer, M.A.S. Goher, F.A. Mautner, R. Vicente, J. Chem. Soc., Dalton Trans. (2000) 413.

[7] (a) E.-Q. Gao, Z.-M. Wang, C.-H. Yan, J. Chem. Soc., Chem. Commun. (2003) 1748;
(b) E.-Q. Gao, S.-Q. Bai, Z.-M. Wang, C.-H. Yan, J. Chem. Soc., Dalton Trans. (2003) 1759;
(c) E.-Q. Gao, Z.-M. Wang, C.-S. Liao, C.-H. Yan, New J. Chem. 26 (2002) 1096.

[8] L. Pazdreski, E. Szlyk, A. Wojtczak, L. Kozerski, J. Sitkowsky, Acta Crystallogr., Sect. E 60 (2004) m1270.

[9] M.A.S. Goher, A.K. Hafez, M.A.M. Abu-Youssef, A.M.A. Badr, C. Gspan, F.A. Mautner, Polyhedron 23 (2004) 2349.

[10] (a) F.A. Mautner, M.A.M. Abu-Youssef, M.A.S. Goher, Polyhedron 16 (1997) 235;
(b) M.A.S. Goher, F.A. Mautner, M.A.M. Abu-Youssef, A.K. Hafez, A.M.A. Badr, J. Chem. Soc., Dalton Trans. (2002) 3309;
(c) M.A.S. Goher, F.A. Mautner, A.K. Hafez, M.A.M. Abu-Youssef, C. Gspan, A.M.A. Badr, Polyhedron 22 (2003) 975;
(d) S. Hanna, F.A. Mautner, B. Koppelhuber-Bitschnau, M.A.M. Abu-Youssef, Mater Sci Forum 321–325 (2000) 1098.

[11] (a) F.A. Mautner, C. Gspan, M.A.S. Goher, M.A.M. Abu-Youssef, Monatsh. Chem. 134 (2003) 1311;
(b) M.A.S. Goher, F.A. Mautner, M.A.M. Abu-Youssef, A.K. Hafez, A.M.A. Badr, C. Gspan, Polyhedron 22 (2003) 3137;
(c) F.A. Mautner, C. Gspan, K. Gatterer, M.A.S. Goher, M.A.M. Abu-Youssef, E. Bucher, W. Sitte, Polyhedron 23 (2004) 1217.

[12] (a) F.A. Mautner, C. Gspan, M.A.M. Abu-Youssef, M.A.S. Goher, Monatsh. Chem. 136 (2004) 107;
(b) M.A.M. Abu-Youssef, Polyhedron 24 (2005) 1829;
(c) M.A.M. Abu-Youssef, J. Coord. Chem. 58 (2005) 1377;
(d) M.A.M. Abu-Youssef, V. Langer, Polyhedron 25 (2005) 1187.

[13] (a) Y.-F. Yue, E.-Q. Gao, S.-Q. Bai, Z. He, C.-H. Yan, CrystEngComm 6 (2004) 549;
(b) S.-Q. Bai, E.-Q. Gao, Z. He, C.-J. Fang, C.-H. Yan, CrystEngComm 6 (2004) 606.
[14] W. Lin, L. Ma, O.R. Evans, J. Chem. Soc., Chem. Commun. (2000) 2263.
[15] (a) N.W. Ockwig, O. Delgado-Friedrichs, M. O'Keeffe, O.M. Yaghi, Acc. Chem. Res. 38 (2005) 176;
(b) O. Delgado-Friedrichs, M.D. Foster, M. O'Keeffe, D.M. Proserpio, M.M.J. Treacy, O.M. Yaghi, J. Solid State Chem. 178 (2005) 2533;
(c) I.A. Baburin, V.A. Blatov, L. Carlucci, G. Ciani, D.M. Proserpio, J. Solid State Chem. 178 (2005) 2452;
(d) V.A. Blatov, L. Carlucci, G. Ciani, D.M. Proserpio, CrystEngComm 6 (2004) 377;
(e) O. Delgado-Friedrichs, M. O'Keeffe, O.M. Yaghi, Acta Crystallogr., Sect. A 59 (2003) 22.
[16] H. Walker, D. Stuart, Acta Crystallogr., Sect. A 39 (1983) 158.
[17] SHELXTL/PC Version 5.03, Siemens Analytical Automation Inc., Madison, WI, 1995.
[18] MERCURY Version 1.4.1, Software from the Cambridge Crystallographic Data Centre, http://www.ccdc.cam.ac.uk/mercury/.
[19] M. O'Keeffe, O.M. Yaghi, Reticular Chemistry Structure Resource, Arizona State University, Tempe, 2005. http://okeeffe-ws1.la.asu.edu/rcsr/home.htm.
[20] M. O'Keeffe, M. Eddaoudi, H.L. Li, T. Reineke, O.M. Yaghi, J. Solid State Chem. 152 (2000) 3.
[21] (a) O.V. Dolomanov, A.J. Blake, N.R. Champness, M. Schroder, J. Appl. Cryst. 36 (2003) 1283;
(b) O.V. Dolomanov, OLEX, http://www.ccp14.ac.uk/ccp/web-mirrors/lcells/index.htm.
[22] (a) V.A. Blatov, A.P. Shevchenko, V.N. Serezhkin, J. Appl. Cryst. 33 (2000) 1193;
(b) V.A. Blatov, http://www.topos.ssu.samara.ru/, 2004.
[23] Z.G. Sun, L.S. Long, Y.P. Ren, R.B. Huang, L.S. Zheng, S.W. Ng, Acta Crystallogr., Sect. E 58 (2002) i34.
[24] N.W. Ockwig, O. Delgado-Friedrichs, M. O'Keeffe, O.M. Yaghi, Acc. Chem. Res. 38 (2005) 176.

Available online at www.sciencedirect.com
ScienceDirect
Polyhedron 26 (2007) 2713–2718
POLYHEDRON
www.elsevier.com/locate/poly

Synthesis, spectroscopic studies and crystal structures of two new vanadium complexes of 2-benzoylpyridine containing hydrazone ligands

Mini Kuriakose [a], M.R. Prathapachandra Kurup [a,*], E. Suresh [b]

[a] Department of Applied Chemistry, Cochin University of Science and Technology, Kochi 682 022, Kerala, India
[b] Analytical Sciences Division, Central Salt and Marine Chemicals Research Institute, Bhavnagar, Gujarat 364 002, India

Received 12 October 2006; accepted 12 January 2007
Available online 20 January 2007

Abstract

The reaction of $VO(acac)_2$ with 2-benzoylpyridine substituted aroylhydrazones is studied. Oxovanadium(IV) and (V) complexes are obtained, indicating the binding of ligands to the metal ion through the imine nitrogen, enolate oxygen and pyridyl nitrogen. The oxovanadium(IV) compound $[VOL^1(OCH_3)]\cdot 0.14H_2O$ (**1a**) gets oxidized to dioxovanadium(V) species $[VO_2L^1]$ (**1b**) upon crystal formation. The crystal structures of the ligand and the two vanadium complexes are reported. Single crystal X-ray diffraction studies of the compound $[VO(HL^2)(\mu_2\text{-}O)]_2$ (**2**) revealed a centrosymmetric dimer.
© 2007 Elsevier Ltd. All rights reserved.

Keywords: 2-Benzoylpyridine; Aroylhydrazone; Crystal structures; Vanadium complexes; Dimer

1. Introduction

Hydrazones and their metal complexes are widely studied due to their versatile applications in the field of analytical and medicinal chemistry [1–11]. Compounds containing hydrazide and acylhydrazone moieties and their complexes possess biological activity, especially as potential inhibitors for many enzymes [12,13]. Hydrazone ligands can act as bidentate, tridentate or tetradentate ligands depending on the nature of heterocyclic ring substituents attached to the hydrazone unit. These ligands due to their facile keto–enol tautomerization and the availability of several potential donor sites can coordinate with metals. Hydrazides and hydrazones have interesting ligation properties due to presence of several coordination sites.

The vanadium coordination compounds play an important role in nitrogen activation, fixation and other biologically important reactions [14–16]. The role of vanadium complexes in catalytically conducted redox reactions [17], potential pharmaceutical applications [18–20], studies on the metabolism and detoxification of vanadium compounds under physiological conditions [21] have stimulated the interest in the stereochemistry and reactivity of its coordination compounds.

As part of our research in the study of coordinating capabilities of aroyl hydrazones and their coordination compounds [22–26], we now report a new aroyl hydrazone ligand 2-benzoylpyridine 4-hydroxy benzoylhydrazone (H_2L^2) and two new vanadium compounds $[VOL^1(OCH_3)]$ and $[VO(HL^2)(\mu_2\text{-}O)]_2$.

2. Experimental

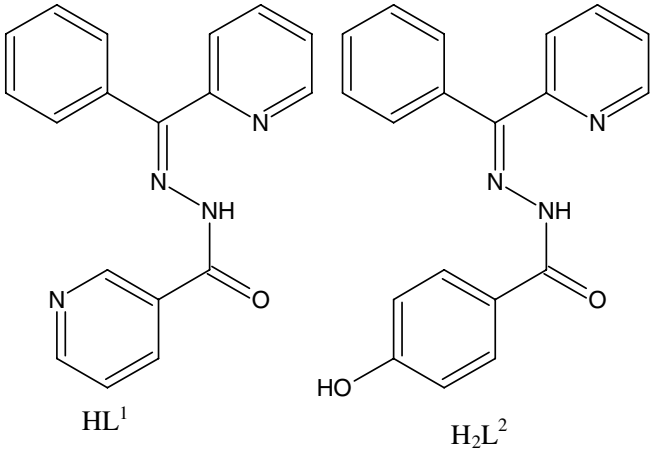
The chemicals 2-benzoylpyridine (Aldrich), 4-hydroxybenzhydrazide (Fluka), nicotinic acid hydrazide (Fluka) $VO(acac)_2$ (Merck) was of Analar grade and used without further purification.

* Corresponding author. Tel.: +91 484 575 804; fax: +91 484 577 595.
E-mail address: mrp@cusat.ac.in (M.R. Prathapachandra Kurup).

0277-5387/$ - see front matter © 2007 Elsevier Ltd. All rights reserved.
doi:10.1016/j.poly.2007.01.008

2.1. Synthesis of ligands

The structures of the ligands are given in Fig. 1. The ligand HL^1 was synthesized as described in the literature [22]. For the preparation of H_2L^2, a mixture of 2-benzoylpyridine (0.3664 g, 2 mmol) dissolved in ethanol containing a few drops of glacial acetic acid and 4-hydroxybenzhydrazide (0.3043 g, 2 mmol) in DMF was refluxed for 6 h. The white shining crystalline precipitate obtained on cooling the reaction media was filtered, washed with ethanol and dried over P_4O_{10} in vacuo. Yield (0.415 g, 65.5%). The elemental *Anal.* Calc. for the compound: C, 71.91; H, 4.76; N, 13.24. Found: C, 70.93; H, 4.93; N, 13.13%.



HL^1 H_2L^2

Fig. 1. Structure of ligands.

2.2. Synthesis of vanadium complexes

$[VO(L^1)(OCH_3)]$ 0.14 H_2O (**1a**): A mixture of HL^1 (0.302 g, 1 mmol) in methanol and a solution of $VO(acac)_2$ (0.265 g, 1 mmol) in dimethylformamide was refluxed for 6 h. Reddish orange crystalline product separated out, which was filtered, washed with methanol, followed by ether and dried over P_4O_{10} in vacuo. Yield: 0.27 g (68.8%). Elemental *Anal.* Calc.: C, 56.72; H, 4.09; N, 13.93. Found: C, 56.05; H, 3.46; N, 13.98%.

$[VO(HL^2)(\mu_2\text{-}O)]_2$ (**2**): To a solution of H_2L^2 (0.317 g, 1 mmol) in DMF–methanol mixture, the metal salt VO $(acac)_2$ (0.265 g, 1 mmol) dissolved in dimethylformamide was added and refluxed for 6 h. The resulting deep brown solution was concentrated to half its volume and kept for evaporation. Reddish brown needle like product separated out, which was filtered, washed by ether and dried over P_4O_{10} in vacuo. Yield: 0.20 g (51%). Light yellow block shaped crystals suitable for diffraction were grown from a solution of the compound in methanol–DMF (1:1 v/v). Elemental *Anal.* Calc.: C, 57.15; H, 3.53; N, 10.52. Found: C, 57.05; H, 3.46; N, 10.66%.

2.3. X-ray crystallographic studies

Structural measurements for H_2L^2, compound **2** were performed on a Bruker Smart Apex CCD diffractometer and for compound **1b** on a Nonius MACH3 diffractometer, both equipped with fine-focused sealed tube. Crystallo-

Table 1
Crystal data for H_2L^2, $VO_2(L^1)$ and $[VO(HL^2)(\mu_2\text{-}O)]_2 \cdot 2H_2O$

	H_2L^2	VO_2L^1 (**1b**)	$[VO(HL^2)(\mu_2\text{-}O)]_2 \cdot 2H_2O$ (**2**)
Formula	$C_{19}H_{15}N_3O_2$	$C_{18}H_{13}N_4O_3V$	$C_{38}H_{32}N_6O_{10}V_2$
Formula weight	317.34	384.26	834.58
Crystal system	monoclinic	monoclinic	triclinic
Space group	$P2_1/n$	$P2_1/c$	$P\bar{1}$
Unit cell dimensions			
a (Å)	9.1294(15)	8.6580(6)	8.246(5)
b (Å)	12.081(2)	8.9000(7)	8.468(5)
c (Å)	14.760(2)	21.105(3)	13.793(8)
α (°)	90.00	90.00	85.537(9)
β (°)	99.095(3)	91.163(8)	74.352(8)
γ (°)	90.00	90.00	83.260(9)
Volume Z	1607.5(5), 4	1625.9(3), 4	919.9(9), 1
Calculated density	1.311	1.570	1.506
Absorption coefficient	0.088	0.637	0.576
$F(000)$	664	784	428
Crystal size	$0.22 \times 0.18 \times 0.16$	$0.35 \times 0.20 \times 0.15$	$0.28 \times 0.14 \times 0.08$
θ range for data collection	2.19–28.21	1.93–24.98	1.54–28.24
Index ranges	$-11 \leqslant h \leqslant 11$, $-13 \leqslant k \leqslant 15$, $-19 \leqslant l \leqslant 14$	$-10 \leqslant h \leqslant 10$, $0 \leqslant k \leqslant 10$, $-25 \leqslant l \leqslant 0$	$-10 \leqslant h \leqslant 10$, $-10 \leqslant k \leqslant 10$, $-18 \leqslant l \leqslant 17$
Reflections collected/unique $[R_{int}]$	9483/3731 [0.0148]	2947/2862 [0.0206]	6801/3801 [0.0342]
Refinement method	full-matrix least-squares on F^2	full-matrix least-squares on F^2	full-matrix least-squares on F^2
Data/restraints/parameters	3731/0/222	2862/0/235	3801/0/317
Goodness-of-fit on F^2	1.052	1.041	0.956
Final R indices $[I > 2\sigma(I)]$	$R_1 = 0.0428$, $wR_2 = 0.1125$	$R_1 = 0.0384$, $wR_2 = 0.0828$	$R_1 = 0.0487$, $wR_2 = 0.1101$
R indices (all data)	$R_1 = 0.0520$, $wR_2 = 0.1192$	$R_1 = 0.0766$, $wR_2 = 0.0925$	$R_1 = 0.0687$, $wR_2 = 0.1213$

Table 2
Selected bond lengths (Å) of H_2L^2, VO_2L^1 and $[VO(HL^2)(\mu_2\text{-}O)]_2 \cdot 2H_2O$

	H_2L^2	VO_2L^1	$[VO(HL^2)(\mu_2\text{-}O)]_2 \cdot 2H_2O$
O1–C13	1.2239(15)	1.307(3)	1.316(3)
C6–N2	1.2956(15)	1.292(3)	1.298(3)
N2–N3	1.3658(14)	1.381(3)	1.381(3)
C13–N3	1.3616(15)	1.315(3)	1.316(3)
C13–C14	1.4777(17)	1.477(4)	1.462(4)
C6–C5	1.4883(17)	1.474(4)	1.480(4)
C6–C7	1.4889(16)	1.484(3)	1.478(3)
V1–O2		1.606(2)	
V1–O4			1.673(2)
V1–O4(a)			2.329(2)
V1–O3		1.6495(19)	1.610(2)
V1–O1		1.969(2)	1.955(2)
V1–N1		2.109(2)	2.134(2)
V1–N2		2.127(2)	2.119(2)

Table 3
Selected bond angles (°) of H_2L^2, VO_2L^1 and $[VO(HL^2)(\mu_2\text{-}O)]_2 \cdot 2H_2O$

	H_2L^2	VO_2L^1	$[VO(HL^2)(\mu_2\text{-}O)]_2 \cdot 2H_2O$
C6–N2–N3	118.50(10)	120.3(2)	120.9(2)
N2–N3–C13	118.94(10)	107.4(2)	108.1(2)
N3–C13–O1	122.49(12)	124.3(3)	123.0(2)
C5–C6–N2	126.94(11)	112.4(2)	111.8(2)
N3–C13–C14	115.07(10)	117.3(2)	118.1(2)
O2–V1–O3		107.33(11)	
O3–V1–O4			105.52(10)
O3–V1–O4(a)			177.74(8)
O2–V1–O1		99.97(11)	
O4–V1–O1			106.26(8)
O4(a)–V1–O1			80.91(8)
O3–V1–O1		105.11(9)	99.31(11)
O2–V1–N1		96.59(11)	
O4–V1–N1			99.26(9)
O4(a)–V1–N1			84.53(8)
O3–V1–N1		97.89(10)	94.14(10)
O1–V1–N1		145.99(8)	146.59(8)
O2–V1–N2		103.93(10)	
O4–V1–N2			152.75(10)
O4(a)–V1–N2			76.77(8)
O3–V1–N2		148.27(10)	101.11(10)
O1–V1–N2		74.28(8)	74.58(7)
N1–V1–N2		73.00(8)	72.87(8)

graphic data for H_2L^2, **1b** and **2** are listed in Table 1. The unit cell parameters were determined and the data collections were performed using a graphite-monochromated Mo Kα ($\lambda = 0.71073$ Å) radiation. The data collected were reduced using SAINT [27] and MAXUS [28] programs correspondingly. The trial structure was obtained by direct methods [29] using SHELXS-97, which revealed the position of all non-hydrogen atoms and refined by full-matrix least squares on F^2 (SHELXL-97) [30] and the graphics tool used include DIAMOND (Version 3.0) [31] and ORTEP. Selected bond lengths and angles are listed in Tables 2 and 3.

3. Results and discussion

The ligand was synthesized by refluxing equimolar ratios of the corresponding hydrazide with the ketone. Complexes **1a** and **2** were synthesized in a straightforward fashion from solutions of the respective ligands and the metal salt. Oxovanadium(IV) compound **1a** oxidized to dioxovanadium(V) in the solution of the compound in DMF upon crystal formation.

3.1. Electronic spectra

The electronic spectrum of the ligand in DMF showed the $n \rightarrow \pi^*$ and $\pi \rightarrow \pi^*$ transitions as a band as a shoulder at 327 and 282 nm respectively. For the dimeric oxovanadium(V) compound **2**, no d–d bands are expected as there are no d electrons. In compound **1a** the d–d bands observed in the higher frequency region are very weak. The shoulder viewed at 443 nm can be assigned to the d–d transition (Fig. 2). Compounds **1a** and **2** display an intense electronic spectral band with shoulders in the near-UV region. This band originates due to ligand to metal charge transfer transition. The values are 415 nm for **1a** and 420 nm for **2**. The other bands observed at 315 (sh) and 289 nm for **1a** and 244 and 216 nm **2** corresponds to intraligand transitions.

3.2. Infrared spectra

In the IR spectrum of the ligand H_2L^2, the bands at 3318 and 3197 cm^{-1} are assigned to O–H and N–H stretching frequencies. The carbonyl and azomethine spectral bands are observed at 1620 and 1590 cm^{-1} respectively. The band at 1537 cm^{-1} corresponds to amide II band. The bands in the range 1570–1325 cm^{-1} are difficult to assign due to crowding of bands. The IR spectra of the compounds exhibit significant alterations due to coordination of the tridentate ligand with the metal. The assignments done are tentative due to crowding of peaks. In compound $VOL^1(OCH_3)$, a medium intensity band observed with splittings at 1597 cm^{-1} is due to newly formed —C=N—N=C— moiety. The shifting of the $C{=}N_{azo}$ band,

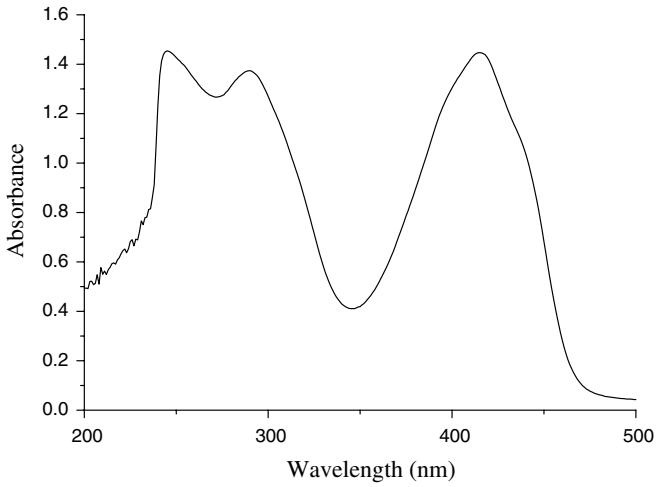


Fig. 2. Electronic spectrum of compound **1a.**

due to complexation is comparatively less when compared to that of the ligand and is found at 1580 cm^{-1}. A strong band observed at 1368 cm^{-1} is assigned to the amide III band. Strong bands are observed in the range 1510–1420 cm^{-1}. These are attributed to the aromatic ring vibrations. The band at 939 cm^{-1} is assigned to ν(V=O).

In the compound **2**, the —C=N—N=C— moiety is observed as a medium band at 1650 cm^{-1}. In the present compound, the band corresponding to the azomethine C=N bond is found to be shifted to higher frequency. The band was viewed as a strong band at 1607 cm^{-1}. Such shifting of the C=N band to higher frequencies are reported [32,33]. The amide III band is assigned for the band at 1365 cm^{-1} [34–36]. The dimeric compound exhibits the ν(V=O) band at 934 and the ν(V—(μ-O)—V) band at 898 cm^{-1} [37].

3.3. Electron paramagnetic studies

The EPR spectrum of the compound **1a** was recorded in polycrystalline state and in DMF solution at 77 K. The absence of a forbidden $\Delta M_s = \pm 2$ transition, at half the field of the allowed $\Delta M_s = \pm 1$, transition excludes the possibility for the dimeric species which would also split the resonant absorptions into 15 lines [$2nI + 1$; $n = 2$; $I = 7/2$]. In DMF solution at 77 K (Fig. 3), the compound displayed an axial spectrum. The g values calculated are $g_{\|} = 1.937$ and $g_{\perp} = 2.008$. The corresponding coupling constants are found to be 197.1 and 62.5 Gauss respectively.

3.4. Description of the structures

Colorless block shaped crystals suitable for X-ray diffraction study were grown from a solution of H_2L^2 in DMF–ethanol (1:1 v/v) media. The lattice is monoclinic in nature with $P2_1/n$ symmetry. The unit cell comprises of four molecules. The configuration along the C(6)–N(2) bond is *cis* thereby forming the intramolecular hydrogen bonded molecular structure (Fig. 4) given below. The torsion angle 2.61(19) perceived by C(5)–C(6)–N(2)–N(3) supports this. The presence of three aromatic rings and the steric requirements for the centroids Cg(1) and Cg(2) defined by atoms, N(1), C(1), C(2), C(3), C(4), C(5) and C(7), C(8), C(9), C(10), C(11), C(12) makes the molecule nonplanar. The dihedral angle value of 61.22° between these centroids supports this nonplanarity. The centroid Cg(1) makes a dihedral angle separation of 18.71° with the centroid Cg(3) defined by C(14), C(15), C(16), C(17), C(18), C(19). However, the central core of the molecule constituted by atoms C(6), N(2), N(3) and C(13) is planar as suggested by the torsion angle of −179.05° due to extensive conjugation. The C(6)–N(2) and C(13)–O(1) bond distances are within the usual range of double bonds, augmenting the fact that the molecule exists in keto form. The N(3)–N(2) bond length of 1.3658(14) is similar to the earlier reported benzoylhydrazone ligands [38,39].

In the unit cell, sets of two molecules are well arranged in an offset fashion. Each such set consisting of two molecules are then self assembled in a perpendicular fashion with the neighbouring set, which repeats to form a 3D network, by making use of intermolecular hydrogen bonding interactions. Table 4 lists the intermolecular interaction

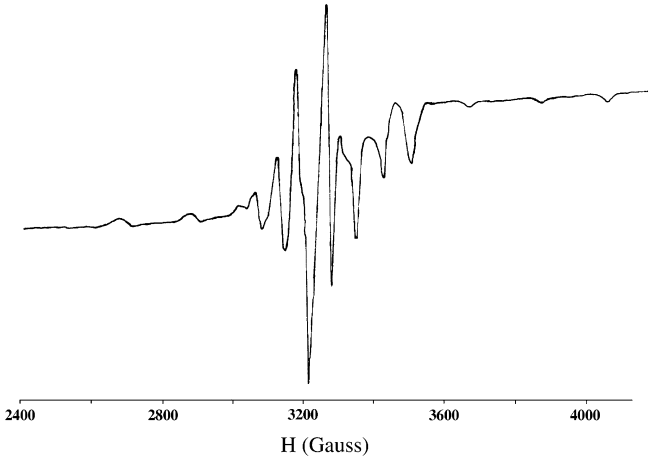


Fig. 3. EPR spectrum of compound **1a** in solution at 77 K.

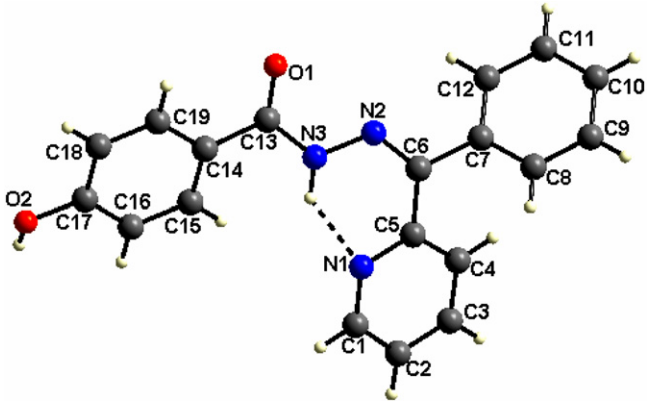


Fig. 4. Molecular structure of HL^2 with intramolecular hydrogen bonding interaction.

Table 4
H-bonding and C–H···π interaction parameters of H_2L^2

H-bonding interaction				
D–H···A	D–H (Å)	H···A (Å)	D···A (Å)	D–H···A (°)
O(2)–H···O(1)[a]	0.82	1.97	2.6998(15)	148
C(2)–H···O(1)[b]	0.93	2.58	3.2985(19)	135
C–H···π interaction				
X–H(I)···Cg(J)	H···Cg (Å)	X–H···Cg (°)	X···Cg (Å)	
C(18)–H(18)···Cg(3)[c]	3.393	114.52	3.873	

Equivalent position code a: $-1/2 + x, 3/2 - y, -1/2 + z$, b: $1/2 + x, 3/2 - y, -1/2 + z$, c: $1 - x, 1 - y, -z$ Cg(3) = C(14), C(15), C(16), C(17), C(18), C(19).

existing in the molecule. These intermolecular interactions perceived between the adjacent molecules in two layers leads to the tight packing of molecules in the unit cell.

The compound $VOL^1(OCH_3)$ crystallized as a dioxovanadium species **1b** due to aerial oxidation into a monoclinic lattice with $P2_1/c$ symmetry. Yellow block shaped crystals suitable for X-ray diffraction were grown from a solution of compound **1a** in a mixture of methanol and DMF (1:1 v/v). The ligand deprotonates and acts as a tridentate chelating species forming two 5-membered chelate rings surrounding the vanadium atom (Fig. 5). The oxygen atoms satisfy the other two sites of the square pyramid. Thus the compound exists in the VO_2^+ state. Comparing the bond angles, it is evident that the geometry is considerably distorted, with the axial site taken up by one of the terminal oxo atom O(2) of the VO_2 core. The $V{=}O_{apical}$ distance 1.606(2) is not exceptional [40,41]. The C(13)–O(1) bond length due to deprotonation extends to 1.307(3) Å in the complex from 1.2158(15) Å in the ligand, making the V(1)–O(1) distance, 1.969(2) Å. The V(1)=O(3) distance corresponds to 1.6495(19) Å. The *trans* angles O(3)–V(1)–N(2) 148.27(10)° and O(1)–V(1)–N(1) 145.99(8)° are reasonably compressed. As a result the basal plane constituted by atoms O(3), O(1), N(1), N(2) deviates significantly from planarity with the central vanadium atom shifted by 0.7041 Å from this plane towards the apical oxygen atom O(2).

The X-ray crystal structure of the dimeric compound $[VO(HL^2)(\mu_2\text{-}O)]_2$ **2** (Fig. 6) revealed that the one half of the molecule is related to the other half by an inversion centre [symmetry code: $2-x, -y, -z$]. The lattice is triclinic in nature with $P\bar{1}$ symmetry and the unit cell consists of one molecule and two water molecules. Our group has reported [42] a similar compound with a thiosemicarbazone derived from 2-benzoylpyridine. The centrosymmetric dimer is formed via the bridging oxygens connecting two vanadium atoms. Hence the vanadium atom adopts a distorted octahedral geometry. For dimeric vanadium chelates with an oxo bridging core, five configurations are possible in accordance with the orientation of the vanadyl groups with respect to the plane defined by the vanadium centers and the bridging oxygen atoms [43]. The configurations are *syn*-orthogonal, *anti*-orthogonal, *syn*-coplanar, *anti*-coplanar and twist. The present compound with the inversion centre, reveals that the disposition of the oxovanadium groups is *anti*-coplanar, a configuration usually found in dimeric oxovandium compounds [44,45]. The atoms O3, N2 and the bridging oxygen atoms constitute the equatorial plane, while the axial positions are occupied by the pyridyl nitrogen and enolic oxygen. Prominent deviations from the regular octahedron is evident from the bond angles O(1)–V(1)–N(1) 146.59(8)°, O(4)–V(1)–N(2) 152.75(10)°. The two 5-membered rings *viz.* V(1)–N(1)–C(5)–C(6)–N(2) (1) and V(1)–O(1)–C(13)–N(3)–N(2) (2) formed as a result of chelation exist with a dihedral angle of 6.38°. The planar central plane V(1)–O(4)–V(1a)–O(4a) consisting the inversion center, makes dihedral angles of 88.55° and 85.40° with the chelate rings (1) and (2). The

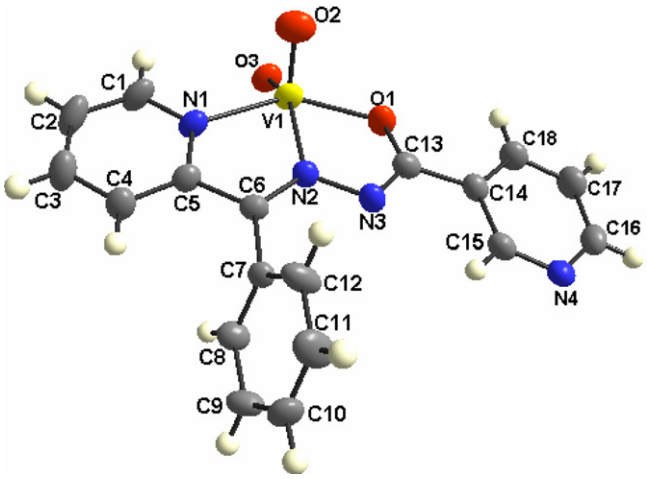


Fig. 5. Molecular structure of $VO_2(L^1)$.

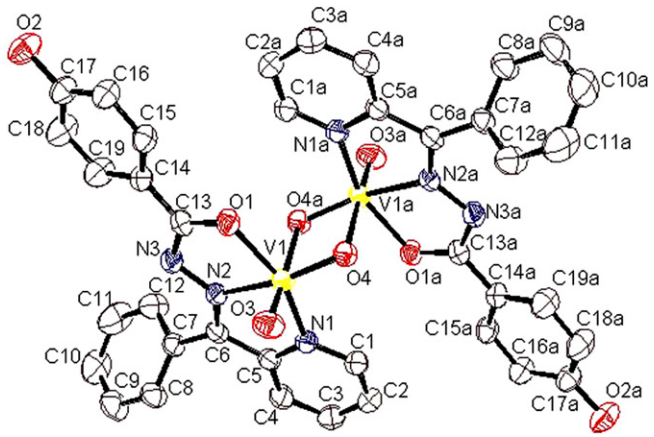


Fig. 6. Molecular structure of $[VO(HL^2)(\mu_2\text{-}O)]_2 \cdot 2H_2O$. Hydrogen atoms and water molecules are omitted for clarity.

Table 5
H-bonding and π–π interaction parameters of the compound $[VO(HL^2)(\mu_2\text{-}O)]_2 \cdot 2H_2O$

H-bonding				
D–H···A	D–H (Å)	H···A (Å)	D···A (Å)	D–H···A (°)
O(2)–H···O5	0.813	1.889	2.701	178.09
O(5)–H···O(4)	0.793	2.076	2.866	173.08
O(5)–H···O(3)	0.800	1.977	2.776	176.86
π–π interactions				
Cg(I)–Res(1)···Cg(J)	Cg–Cg (Å)	α°	β°	
Cg(2)–[1]···Cg(1)[a]	2.6323	85.39	55.46	
Cg(3)–[1]···Cg(1)[a]	2.6956	88.55	57.36	
Cg(1)–[1]···Cg(4)[a]	3.8959	86.34	28.41	

Equivalent position code a: x, y, z.
Cg(1) = V1, O4, V1A, O4A; Cg(2) = V1, O1, C13, N3, N2; Cg(3) = V1, N1, C5, C6, N2; Cg(4) = N1, C1, C2, C3, C4, C5.
D, donor; A, acceptor; Cg, centroid; α, dihedral angles between planes I and J; β, angle Cg(I) and Cg(J).

dihedral angle between the pyridyl ring and the phenyl ring bearing the hydroxyl substituent O(2)–H is 18.12(1).

The packing in the unit cell is stabilized by short ring interactions (Table 5) and by a ring metal interaction between Cg(2) [V(1), O(1), C(13), N(3), N(2)] and V(1) at a ring metal distance of 3.962 Å. It is found that considerable π–π interactions exist between the centroids Cg(1) [V(1), O(4), V(1a), O(4a)] and Cg(2) [V(1), O(1), C(13), N(3), N(2)] and between Cg(1) and Cg(4) [N(1), C(1), C(2), C(3), C(4), C(5)] at distances of 2.6323 and 3.8959 Å respectively. The presence of water molecule leads to intermolecular hydrogen bonding. The oxygen atom O(5) of the water molecule is hydrogen bonded to O(2)–H. Also the hydrogen atoms attached to O(5) are involved in hydrogen bonding with O(4) and O(3).

Acknowledgements

The authors are thankful to the Sophisticated Analytical Instrumentation Facility, Cochin University of Science and Technology, Kochi 22, India for elemental analyses and for recording IR spectra and Sophisticated Instruments Facility, IISc Bangalore, India for NMR measurements. M.R.P. Kurup is also thankful to CSIR (No: 01(1963)/05/EMR-II) New Delhi, India for financial support.

Appendix A. Supplementary material

CCDC 263196, 618557 and 618556 contain the supplementary crystallographic data for ligand HL^2, compound **1b** and compound **2**. These data can be obtained free of charge via http://www.ccdc.cam.ac.uk/conts/retrieving.html, or from the Cambridge Crystallographic Data Centre, 12 Union Road, Cambridge CB2 1EZ, UK; fax: (+44) 1223-336-033; or e-mail: deposit@ccdc.cam.ac.uk. Supplementary data associated with this article can be found, in the online version, at doi:10.1016/j.poly.2007.01.008.

References

[1] M.F. Iskander, L. Sayed, A.F.M. Hefny, S.E. Zayan, J. Inorg. Nucl. Chem. 38 (1976) 2209.
[2] G.H. Havanur, V.B. Mahale, Indian J. Chem. 26A (1987) 1063.
[3] H. Adams, D.E. Fenton, G. Minardi, E. Mura, M. Angelo, Inorg. Chem. Commun. 3 (2000) 4.
[4] Z.Y. Yang, R.D. Yang, F.S. Li, K.B. Yu, Polyhedron 19 (2000) 2599.
[5] S.S. Katiyar, S.N. Tandon, Talanta 11 (1964) 892.
[6] G.S. Vasilikiotis, J.A. Tossidis, J. Microchem. 14 (1969) 380.
[7] M. Gallego, M.G. Vargas, M. Valcarcel, Analyst 104 (1979) 613.
[8] R.L. Dutta, M.M. Hossain, J. Sci. Ind. Res. 44 (1985) 635.
[9] M.L. Vitolo, J. Webb, J. Inorg. Biochem. 20 (1984) 255.
[10] E. Baker, M.L. Vitolo, J. Webb, Biochim. Pharmacol. 34 (1985) 3011.
[11] P. Ponka, D. Richardson, E. Baker, H.M. Schulman, J.T. Edward, Biochim. Biophys. Acta 967 (1988) 122.
[12] G. Tamasi, L. Chiasserini, L. Savini, A. Sega, R. Cini, J. Inorg. Biochem. 99 (2005) 1347.
[13] Y.-X. Ma, Z.-L. Lu, Q.-B. Song, X.-L. Wu, J. Coord. Chem. 32 (1994) 353.
[14] A. Butler, C.J. Carrano, Coord. Chem. Rev. 109 (1991) 61.
[15] I. Cavaco, J.C. Pessoa, M. Duarte, R.D. Gillard, P. Matias, Chem. Commun. (1996) 1365.
[16] D. Rehder, Angew. Chem., Int. Ed. 30 (1991) 148.
[17] A.G.J. Ligtenbarg, R. Hage, B.L. Feringa, Coord. Chem. Rev. 237 (2003) 89.
[18] D. Rehder, Inorg. Chem. Commun. 6 (2003) 604.
[19] H. Sakurai, Y. Kojima, Y. Yoshikawa, K. Kawabe, H. Yasui, Coord. Chem. Rev. 226 (2002) 187.
[20] D. Rehder, J.C. Pessoa, C.F.G.C. Geraldes, M.M.C.A. Castro, T. Kabanos, T. Kiss, B. Meier, G. Micera, L. Pettersson, M. Rangel, A. Salifoglou, I. Turel, D. Wang, J. Biol. Inorg. Chem. 7 (2002) 384.
[21] E.J. Baran, J. Inorg. Biochem. 80 (2000) 1.
[22] M. Kuriakose, M.R.P. Kurup, E. Suresh, Spectrochim. Acta A 66 (2007) 353.
[23] B.N.B. Raj, M.R.P. Kurup, E. Suresh, Struct. Chem. 17 (2006) 201.
[24] B.N.B. Raj et al., Spectrochim. Acta (2007), doi:10.1016/j.saa.2006.05.006.
[25] P.B. Sreeja, M.R.P. Kurup, A. Kishore, C. Jasmin, Polyhedron 23 (2004) 575.
[26] P.B. Sreeja, M.R.P. Kurup, Spectrochim. Acta 61 (2005) 331.
[27] Siemens, SMART and SAINT, Area Detector Control and Integration Software, Siemens Analytical X-ray Instruments Inc., Madison, WI, USA, 1996.
[28] S. Mackay, C.J. Gilmore, C. Edwards, N. Stewart, K. Shankland, MAXUS Computer Program for the Solution and Refinement of Crystal Structures. Nonius, The Netherlands, MacScience, Japan and The University of Glasgow, 1999.
[29] G.M. Sheldrick, Acta Crystallogr., Sect. A 46 (1990) 467.
[30] G.M. Sheldrick, SHELXS-97 Program for the Solution of Crystal Structures, University of Göttingen, Göttingen, Germany, 1997.
[31] K. Bradenburg, H. Putz, DIAMOND Version 3.0, Crystal Impact, GbR, Postfach 1251, D-53002 Bonn, Germany, 2004.
[32] D. Demertzi, D. Nicholls, Inorg. Chim. Acta 73 (1983) 37.
[33] C.N. Elgy, D. Nicholls, J. Inorg. Chem. Nuclear Chem. 43 (1981) 2025.
[34] P.K. Singh, D.N. Kumar, Spectrochim. Acta 64A (2006) 853.
[35] V.R. Rao, K.G. Reddy, U.V. Seshaiah, Transit. Met. Chem. 18 (1993) 258.
[36] S. Srinivasan, J. Annaraj, P.R. Athappan, J. Inorg. Biochem. 99 (2005) 876.
[37] M.R. Maurya, S. Khurana, C. Schulzke, D. Rehder, Eur. J. Inorg. Chem. (2001) 779.
[38] A. Lyubchova, A.C. Barbi, J.P. Doucet, Acta Crystallogr., Sect. C 51 (1995) 1893.
[39] S.S.S. Raj, H.K. Fun, Z.L. Lu, W. Xiao, Y.X. Tong, B.S. Kang, Acta Crystallogr., Sect. C 55 (1999) 942.
[40] S. Samanta, D. Ghosh, S. Mukhopadhyay, A. Endo, T.J.R. Weakley, M. Chaudhury, Inorg. Chem. 42 (2003) 1508.
[41] M.R. Maurya, A. Kumar, A.R. Bhat, A. Azam, C. Bader, D. Rehder, Inorg. Chem. 45 (2006) 1260.
[42] A. Sreekanth, H.-K. Fun, R.P. John, M.R.P. Kurup, S. Chantrapromma, Acta Crystallogr., Sect. E 62 (2006) 1919.
[43] W. Plass, Angew. Chem., Int. Ed. Engl. 35 (1996) 627.
[44] T. Carofiglio, E. Solari, C. Floriani, A. Chiesi-Villa, C. Rizzoli, Polyhedron 15 (1996) 4435.
[45] J. Salta, J. Zubieta, Inorg. Chim. Acta 257 (1997) 83.

Available online at www.sciencedirect.com
ScienceDirect
Polyhedron 26 (2007) 2719–2727
POLYHEDRON
www.elsevier.com/locate/poly

Monomer, dimer, tetramer and salt: Structural variations in Zn(II) complexes of 4,4′-bipyridine-*N*,*N*′-dioxide

Susan A. Bourne *, Lesego J. Moitsheki

Department of Chemistry, University of Cape Town, Rondebosch 7701, South Africa

Received 20 October 2006; accepted 12 January 2007
Available online 20 January 2007

Abstract

Complexes of Zn^{II} salts with 4,4′-bipyridine-*N*,*N*′-dioxide (bpdo) have been prepared by solvathermal and solvent layering methods. Three complexes were obtained from $ZnBr_2$: **1** is a 2D coordination polymer $[Zn_2Br_4(bpdo)_2]_n$, (**2**) a discrete trimetallic molecule $[Zn_3Br_6(H_2O)_2(bpdo)_4]$ and **3** a salt $[ZnBr_4][Zn(H_2O)_5(bpdo)]$. Complexes **2** and **3** contain Zn^{II} ions in both octahedral and tetrahedral coordination geometry. While in **2**, these are covalently linked by bridging bpdo ligands forming zwitterionic trimetallic molecules, in **3** there is complete charge separation into $[ZnBr_4]^{2-}$ anions and $[Zn(H_2O)_5(bpdo)]^{2+}$ cations. When $Zn(NCS)_2$ is used as starting material, a 1D coordination polymer $[Zn(H_2O)_2(bpdo)(NCS)_2]_n$ is obtained.
© 2007 Elsevier Ltd. All rights reserved.

Keywords: Crystal structures; 4,4′-bipyridine-*N*,*N*′-dioxide; Zinc(II) ions

1. Introduction

Synthesis of metal-organic compounds attracts interest due their extensive structural diversity and potential functional properties [1–3]. A considerable amount of research has exploited bridging ligands which offer two or more donor units, such as 4,4′-bipyridine and its analogues, bound to different metals [4–8]. The metal-organic networks designed form a variety of network structures, including diamondoid [9], grids [4], honeycomb [9,10], helix [11] and brickwall [7] frameworks as well as other topological architectures. These complexes usually comprise building blocks held together by supramolecular interactions such as hydrogen bonding, van der Waals forces or π–π interactions, all of which play a role in the self-assembly process [12,13]. A number of coordination compounds of 4,4′-bipyridine-*N*,*N*′-dioxide (bpdo) with transition metals have recently been reported [14–20]. We have previously demonstrated that the topology and dimensionality of crystal structures is strongly dependent on the counteranion, while using the same metal, Co^{II} and spacer ligand, bpdo [21]. We have also undertaken studies on the effect of crystallisation conditions, including temperature and solvent systems, on the metal coordination complexes obtained. In this regard, we report here the effect of varying solvent mixtures on the complexation of Zn^{II} with bpdo. Four novel network solids $[Zn_2Br_4(bpdo)_2]_n$ (**1**), $[Zn_3Br_6(H_2O)_2(bpdo)_4]\cdot(bpdo)$ (**2**), $[ZnBr_4][Zn(H_2O)_5(bpdo)]\cdot 2(bpdo)\cdot(H_2O)$ (**3**) and $[Zn(H_2O)_2(bpdo)(NCS)_2]_n\cdot nH_2O$ (**4**) have been prepared using different crystallisation methods. Remarkably, three of these were prepared from the same salt, $ZnBr_2$. X-ray crystallographic characterisation of these products showed a diversity of structural types, including mono-, di- and tetrameric species with 0D, 1D and 2D-topologies.

2. Experimental

2.1. Compound synthesis and crystal growth

Reagents were purchased from commercial sources and were used without further purification. Differential Scanning

* Corresponding author. Tel.: +27 21 650 2563; fax: +27 21 689 7499.
E-mail address: susan.bourne@uct.ac.za (S.A. Bourne).

0277-5387/$ - see front matter © 2007 Elsevier Ltd. All rights reserved.
doi:10.1016/j.poly.2007.01.007

Calorimetry was performed using a Perkin–Elmer DSC7 and Thermogravimetry on a Mettler Toledo TGA/sDTA 851[e], both using a heating rate of 10 °C min^{-1} under an atmosphere of dry N_2 flowing at 30 cm^3 min^{-1}.

Compound **1** was prepared by solvent layering of an ethanolic or methanolic solution of bpdo (28.23 mg, 0.15 mmol) on top of a layer of 5 mL $CHCl_3$ or CH_2Cl_2 in which $ZnBr_2$ (22.52 mg, 0.10 mmol) had been placed, but not fully dissolved. Compounds **2**–**4** were prepared by slow evaporation of a solution containing bpdo and the metal salt. In a typical preparation of **2**, 22.40 mg (0.10 mmol) $ZnBr_2$ was dissolved in 1.5 mL methanol. 27.53 mg (0.15 mmol) bpdo was dissolved in 3 mL methanol and added to the metal salt solution. The solvent was allowed to evaporate slowly at ambient temperatures and colourless crystals were achieved within a week. Similar preparations using same chemical quantities as above were done by replacing methanol with ethanol to acquire compound **3**. For compound **4**, ethanolic solutions of $Zn(NCS)_2$ (19.10 mg, 0.10 mmol, 2 mL) and bpdo (28.60 mg, 0.15 mmol, 4 mL) were mixed. The mixture was filtered through a 0.5 μm filter and the solvent was allowed to evaporate slowly at room temperature. Colourless crystals were afforded in two weeks.

Compound **1** was unstable to atmospheric conditions when removed from the mother liquor, while compound **4** was very hygroscopic making preparatory measures for microanalysis or powder X-ray diffraction (for **4**) impossible. PXRD (HUBER Guinier 670 Imaging Plate diffractometer with Cu Kα radiation, 1.542 Å) established that the bulk material of compounds **1**, **2** and **3** had the same crystal phase as the crystals selected for single-crystal analysis. Elemental analysis confirmed this: Compound **2**: Found: C, 36.62; H, 2.67; N, 8.39%, $[Zn_3Br_6(C_{10}H_8N_2O_2)_4(H_2O)_2]\cdot(C_{10}H_8N_2O_2)$ requires C, 36.34; H, 2.68; N, 8.48%; Compound **3**: Found: C, 32.39; H, 2.90; N, 6.99%, $[ZnBr_4][Zn(H_2O)_5(C_{10}H_8N\ {}_2O_2)]\cdot 2(C_{10}H_8\ N_2O_2)\cdot(H_2O)$ requires C, 32.09; H, 3.23; N, 7.48%. Thermal analysis of compounds **1**–**4** showed that all four begin to decompose at temperatures above 70 °C and decomposition is complete just above 300 °C. The mechanism of decomposition is complex, but seems to involve the loss of coordinated and guest water molecules in each case.

Table 1
Summary of crystallographic data for compounds **1**–**4**

	1	**2**	**3**	**4**
Empirical formula	$[Zn_2Br_4(C_{10}H_8N_2O_2)_2]$	$[Zn_3Br_6(C_{10}H_8N_2O_2)_4(H_2O)_2]\cdot(C_{10}H_8N_2O_2)$	$[ZnBr_4][Zn(H_2O)_5(C_{10}H_8N_2O_2)]\cdot 2(C_{10}H_8N_2O_2)\cdot(H_2O)$	$[Zn(NCS)_2(C_{10}H_8N_2O_2)(H_2O)_2]\cdot H_2O$
Formula weight (g mol^{-1})	826.74	1652.52	1123.03	423.78
Temperature (K)	113	113	113	113
Crystal system	triclinic	triclinic	triclinic	triclinic
Space group	$P\bar{1}$	$P\bar{1}$	$P\bar{1}$	$P\bar{1}$
Unit cell dimensions				
a (Å)	8.236 (2)	7.244 (1)	7.712 (2)	7.311 (2)
b (Å)	9.322 (2)	12.017 (2)	15.768 (3)	9.863 (2)
c (Å)	9.471 (3)	16.630 (3)	16.639 (3)	12.013 (2)
α (°)	66.603 (1)	99.90 (3)	70.99 (3)	77.29 (3)
β (°)	84.578 (1)	95.97 (3)	87.77 (3)	79.67 (3)
γ (°)	66.673 (2)	95.21 (3)	85.63 (3)	88.12 (3)
Volume (Å^3)	611.1 (3)	1409.60 (5)	1907.3 (7)	831.3 (3)
Z	1	1	2	2
D_{calc} (g cm^{-3})	2.247	1.947	1.955	1.693
μ (mm^{-1})	8.537	5.588	5.515	1.759
F(000)	396	810	1108	432
Crystal size (mm)	0.05 × 0.10 × 0.15	0.25 × 0.25 × 0.35	0.04 × 0.08 × 0.12	0.09 × 0.15 × 0.20
θ Range scanned (°)	2.70–27.90	2.32–27.91	2.65–25.68	2.83–26.31
Index range	−10,10; −12,12; −12,12	−9,9; −15,15; −21,21	−9,9; −19,19; −20,20	−9,9; −12,12; −14,14
Reflections collected/ unique	16797/2917	39535/6747	49973/7211	32479/3356
Goodness of fit on F^2	1.038	1.014	0.951	1.096
Final *R* indices $[I \geqslant 2\sigma I]$ [a,b]	$R_1 = 0.0267$, $wR_2 = 0.0503$	$R_1 = 0.0308$, $wR_2 = 0.0611$	$R_1 = 0.0326$, $wR_2 = 0.0691$	$R_1 = 0.0232$, $wR_2 = 0.0575$
R indices (all data)	$R_1 = 0.0429$, $wR_2 = 0.0542$	$R_1 = 0.0496$, $wR_2 = 0.0662$	$R_1 = 0.0553$, $wR_2 = 0.0784$	$R_1 = 0.0283$, $wR_2 = 0.0595$
Largest difference in peak and hole (e Å^{-3})	0.67, −0.58	1.16, −0.58	0.96, −0.62	0.33, −0.40

[a] $R_1 = \sum(|F_o| - |F_c|)/|F_o|$.
[b] $wR_2 = \left\{\sum[w(F_o^2 - F_c^2)^2/\sum w(F_o^2)^2]\right\}^{1/2}$.

2.2. Crystal structure and refinement

All data for crystal and molecular structure determination were measured on a Nonius KappaCCD diffractometer using graphite-monochromated Mo Kα radiation (0.7107 Å) at 113 K. In each case, a series of frames were recorded with width ranging from 1° to 1.5° in ϕ or in ω (with $\kappa \neq 0$) to ensure completeness of the data collected to $\theta > 25°$. The unit cell was indexed from the first twenty frames and positional data were refined along with diffractometer constants to give the final cell parameters. Integration and scaling correction (DENZO, scalepack) [22] resulted in unique data sets corrected for Lorentz-polarization effects and for the effects of crystal decay and absorption by a combination of averaging of equivalence reflections and an overall volume and scaling correction. The structures were solved using SHELXS-97 and refined using the full-matrix least squares methods in SHELXL-97 [23], with the aid of the program XSEED [24].

Crystal structure refinement data are given in Table 1. Non-hydrogen atoms were modeled anisotropically. Hydrogens attached to water molecules were located in the difference electron density maps where possible and refined with a distance restraint for compounds **1**–**3** and independently in compound **4**. Other hydrogen atoms were assigned an isotropic thermal parameter 1.2 times that of their parent atom and refined using a 'riding' model. Images of crystal and molecular structures were rendered using the program POV-Ray [25].

3. Results and discussion

Crystals isolated from layered solutions of $ZnBr_2$ in chloroform and bpdo in alcohol were characterised as the 2D coordination polymer $[Zn_2Br_4(bpdo)_2]_n$ (**1**) in which both Zn^{II} metal centres are coordinated to two bromide ions and three bpdo ligands (Fig. 1). The Zn–Br bond lengths are 2.373 and 2.382 Å, respectively corresponding well with the literature value of 2.390 Å [26]. The metal ion adopts a distorted trigonal bipyramidal coordination geometry (O1–Zn1–O8 154.9°) with oxygen atoms in the equatorial plane and bromide ions in the axial positions. The bridging bpdo ligand is asymmetrically placed relative to the Zn ions, with Zn–O bond lengths of 2.039 and 2.353 Å. The third Zn–O length, to a third bpdo ligand is 2.100 Å. Compound **1** forms a planar layer with metal centres bridged by the bpdo ligands *via* terminal oxygen atoms forming double strand polymer chains (Fig. 2a). The bridged zinc metals are separated from each other by a distance of 3.659 Å and the bridging oxygen terminals are 2.449 Å apart. The bridging angle Zn1–O8–Zn1 is 112.66°. There are no classic hydrogen bonds in **1**, but there are $\pi\cdots\pi$ interactions between aromatic rings within each layer and adjacent layers are linked through weak C–H···O and C–H···Br hydrogen bonds (Fig. 2b, Table 2).

By contrast, slow evaporation of a methanol solution of $ZnBr_2$ and bpdo produced $[Zn_3Br_6(H_2O)_2(bpdo)_4]\cdot(bpdo)$ (**2**), while an ethanolic solution of the same stoichiometry produced $[ZnBr_4][Zn(H_2O)_5(bpdo)]\cdot 2(bpdo)\cdot(H_2O)$ **(3)** (Fig. 3). There are two zinc environments present in both **2** and **3**: one octahedral and one tetrahedral. In **2**, a centrosymmetric molecule is formed with a metal:ligand ratio of 3:4. This acts as host to a further bpdo molecule included as a guest. The octahedral Zn(1) ion is coordinated to two water molecules and four *trans*-bpdo's. Two of the latter form the bridges to two end groups consisting of tetrahedrally coordinated $[ZnBr_3]^-$ groups. At Zn(1), the Zn(1)–O(aqua) bond length is 2.080 Å, while the Zn(1)–O(bpdo) bond lengths are 2.072 Å and 2.110 Å. These values correspond well with literature values [26]. Bond angles around Zn(1) range from 86.85° to 93.15°. At the tetrahedral centre, Zn(2)–Br lengths average 2.397 Å and Zn(2)–O(bpdo) is 2.011 Å. Bond angles around Zn(2) range from 100.49° to −117.11°, a distortion from ideal tetrahedral geometry. The coordinated bpdo rings are twisted by between 15.2° and 27.8° while the guest bpdo rings are coplanar. The discrete molecules are connected by O–H···O hydrogen bonding (Fig. 4; Table 2) through coordinated water molecules and the oxygens of the coordinated bpdo

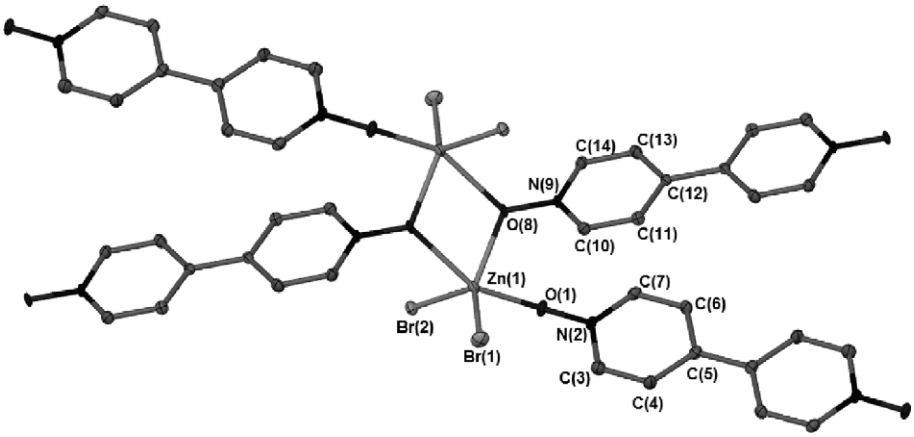


Fig. 1. Molecular structure of **1**. Ellipsoids shown at 50% probability.

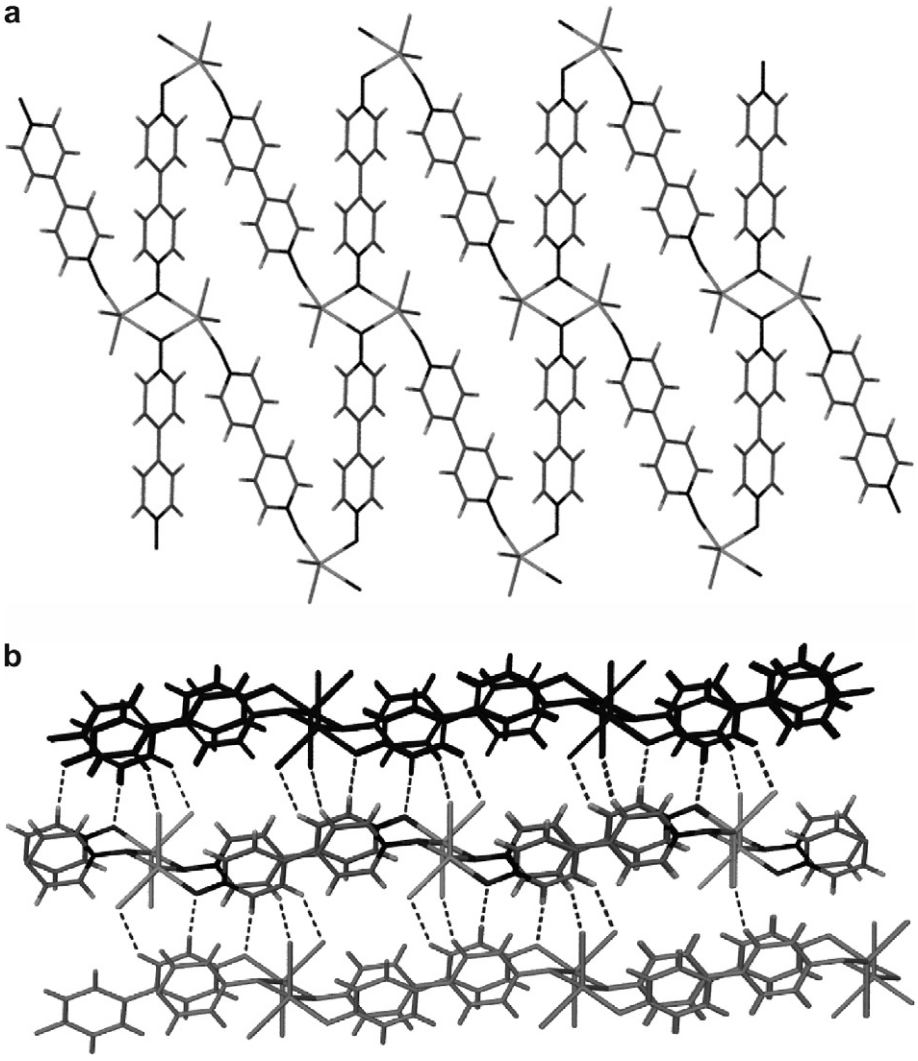


Fig. 2. (a) Two-dimensional polymer chains form a planar layer in **1** and (b) packing of layers in **1**, showing weak hydrogen bonds between layers.

ligands. Extensive weak C–H···O and C–H···Br interactions as well as π···π interactions between aromatic rings, contribute to the packing of the X-shaped molecules into a host framework which forms channels to accommodate bpdo guest molecules. These are held in place by π···π interactions between guest and host aromatic rings.

Interestingly a different compound, **3**, was formed when the components were crystallised from ethanol rather than methanol. Like **2**, **3** has two independent zinc ions with octahedral and tetrahedral coordination geometries, this time in separate entities. In **3**, the Zn(1) ion is coordinated to one bpdo ligand and five water molecules forming an octahedral cation $[Zn(bpdo)(H_2O)_5]^{2+}$ while Zn(2) is coordinated to four bromide counterions adopting a tetrahedral coordination geometry $[ZnBr_4]^{2-}$. A further two bpdo ligands are included without coordinating. Both guest and coordinated bpdo rings are twisted by between 15.3° and 17.9°. The Zn(1)–O(aqua) bond lengths range from 2.044 to 2.129 Å while Zn(1)–O(bpdo) is 2.092 Å. The bond angles deviate slightly from the expected value of 90° being between 84.75° and 93.06°. Around Zn(2), Zn–Br bond lengths are 2.414–2.424 Å (literature value 2.39 Å). Br–Zn–Br bond angles are between 108.29° and 110.35°. Discrete $[Zn(bpdo)(H_2O)_5]^{2+}$ are linked by a network of hydrogen bonding through coordinated water molecules, bpdo and guest water molecule (Fig. 5). These "host" molecules pack into layers parallel to the *c*-axis. Intercalated between these layers are the $[ZnBr_4]^{2-}$ anions as well as layers of bpdo guest molecules, packed in herringbone fashion, and hydrogen bonded to the host framework. The crystal structure is stabilized by extensive C–H···O, C–H···Br and π interactions (summarized in Table 2).

A search of the Cambridge Crystallographic Database (Version 5.27, May 2006) [27] found several examples of octahedral zinc complexes containing an associated $[ZnX_4]^-$ (X = Cl or Br) anion [28], but only one example of a zwitterionic trimetallic molecule [29]. In that case,

Table 2
Hydrogen bonding and π interactions

	D–H (Å)	D···A (Å)	D–H···A (°)	Symmetry operator
1				
C(13)–H(13)···Br(1)	0.95	3.650 (3)	156	$1+x, -1+y, z$
C(7)–H(7)···O(1)	0.95	3.326 (3)	174	$1-x, -y, 2-z$
C(6)–H(6)···Br(2)	0.95	3.670 (3)	141	$1-x, -y, 2-z$
Cg(N2–C7)···Cg(N9–C14)		3.846 (1)		x, y, z
C(7)–H(7)···Cg(N9–C14)	0.95	3.190	91	x, y, z
2				
O(2)–(H2W1)···O(22)	0.84	2.730 (3)	170	$x, y-1, z$
O(2)–(H2W2)···O(22)	0.89	2.663 (3)	162	$2-x, 2-y, -z$
C(3)–H(3)···O(22)	0.95	3.249 (4)	157	$-1+x, -1+y, z$
C(4)–H(4)···O(29)	0.95	3.173 (4)	132	$-1+x, y, z$
C(6)–H(6)···Br(3)	0.95	3.698 (3)	142	$2-x, 2-y, 1-z$
Cg(N2–C7)···Cg(N30–C35)		3.633 (2)		x, y, z
Cg(N9–C14)···Cg(N9–C14)		3.932 (2)		$1-x, 2-y, 1-z$
Cg(N16–C21)···Cg(N23–C28)		3.979 (2)		$1-x, 2-y, -z$
Cg(N30–C35)···Cg(N2–C7)		3.633 (2)		x, y, z
C(17)–H(17)···Cg(N2–C7)	0.95	3.613	123	x, y, z
C(20)–H(20)···Cg(4)	0.95	3.851	118	$2-x, 2-y, -z$
C(25)–H(25)···Cg(3)	0.95	3.310	91	$1-x, 2-y, -z$
C(35)–H(35)···Cg(N30–C35)	0.95	3.502	104	$2-x, 1-y, 1-z$
3				
O(2)–(H2W2)···O(1W)	0.81	2.780 (4)	165	$1-x, 1-y, 1-z$
O(2)–H(2W1)···O(8)	0.86	2.762 (4)	165	$1-x, 1-y, 2-z$
O(3)–H(3W2)···O(8B)	0.91	2.668 (5)	176	$x, y-1, z$
O(3)–H(3W1)···O(8)	0.75	2.690 (4)	167	$1-x, 1-y, 2-z$
O(4)–H(4W1)···O(8A)	0.83	2.746 (4)	164	$1-x, -y, 1-z$
O(4)–H(4W2)···O(1B)	0.95	2.685 (4)	176	$1-x, 1-y, 2-z$
O(5)–H(5W2)···O(1A)	0.90	2.664 (4)	177	x, y, z
O(5)–H(5W1)···O(1B)	0.88	2.683 (4)	167	$-x, 1-y, 2-z$
O(6)–H(6W1)···O(8A)	0.88	2.733 (5)	158	$x, 1+y, z$
O(6)–H(6W2)···O(1W)	0.78	2.784 (4)	161	x, y, z
O(1W)···O(1)		2.765		$-x, 1-y, 1-z$
C(3A)–H(3A)···O(8B)	0.95	3.306 (6)	148	$x, -1+y, z$
C(3B)–H(3B)···O(3)	0.95	3.142 (5)	126	$-x, 1-y, 2-z$
C(10A)–H(10A)···O(1B)	0.95	3.321 (6)	155	$x, -1+y, -1+z$
C(4)–H(4)···Br(3)	0.95	3.561 (5)	126	$x, y, 1+z$
C(4B)–H(4B)···Br(3)	0.95	3.726 (5)	165	$-x, 1-y, 1-z$
C(6B)–H(6B)···Br(4)	0.95	3.642 (5)	145	$x, y, 1+z$
C(14B)–H(14B)···Br(2)	0.95	3.572 (5)	145	$-x, 1-y, 1-z$
C(14A)–H(14A)···Br(1)	0.95	3.772 (5)	170	$1-x, -y, 1-z$
C(13A)–H(13A)···Br(4)	0.95	3.840 (5)	162	$1-x, -y, 1-z$
C(6B)–H(6B)···Cg(N9B–C14B)	0.95	3.806	124	$1-x, 2-y, 2-z$
C(11A)–H(33)···Cg(N2A–C7A)	0.95	3.398	103	$-x, -y, 1-z$
Cg(N2A–C7A)···Cg(9A–C14A)		3.677 (2)		$1-x, -y, 1-z$
Cg(9A–C14A)···Cg(N2A–C7A)		3.677 (2)		$1-x, -y, 1-z$
4				
O(1W)–H(1W1)···O(8)	0.77 (3)	2.793 (2)	175(3)	$1-x, 1-y, 1-z$
O(1W)–H(1W2)···O(1)	0.82 (3)	2.847 (2)	176(3)	$-x, 1-y, 1-z$
O(15)–H(15B)···O(1W)	0.78	2.662 (2)	170	x, y, z
O(16)–H(16A)···O(1)	0.84	2.839 (2)	175	$-x, 2-y, 1-z$
O(16)–H(16B)···O(8)	0.78	2.853 (2)	178	$1-x, 2-y, 1-z$
C(3)–H(3)···O(1W)	0.95	3.089 (2)	134	x, y, z
C(7)–H(7)···N(20)	0.95	3.468 (2)	163	$-x, 2-y, 1-z$
C(10)–H(10)···N(17)	0.95	3.439 (2)	160	$1-x, 2-y, 1-z$

the Zn^{II} ions were coordinated to an ethylenediamine derivative of adenine. In **2**, the $[ZnBr_3]^-$ end moieties of the zwitterionic molecule are tucked into pockets between the aromatic rings of coordinated and guest bpdo molecules. As may be expected, there are several C–H···Br contacts holding these ends in place (Table 2, Fig. 4). In **3**, the individual cation complex interdigitates, forming chains running parallel to the *c*-axis with strong inter-ion O–H···O interactions. Hydrogen bonds crosslink these chains with water and bpdo guest molecules (Fig. 5, Table 2). The

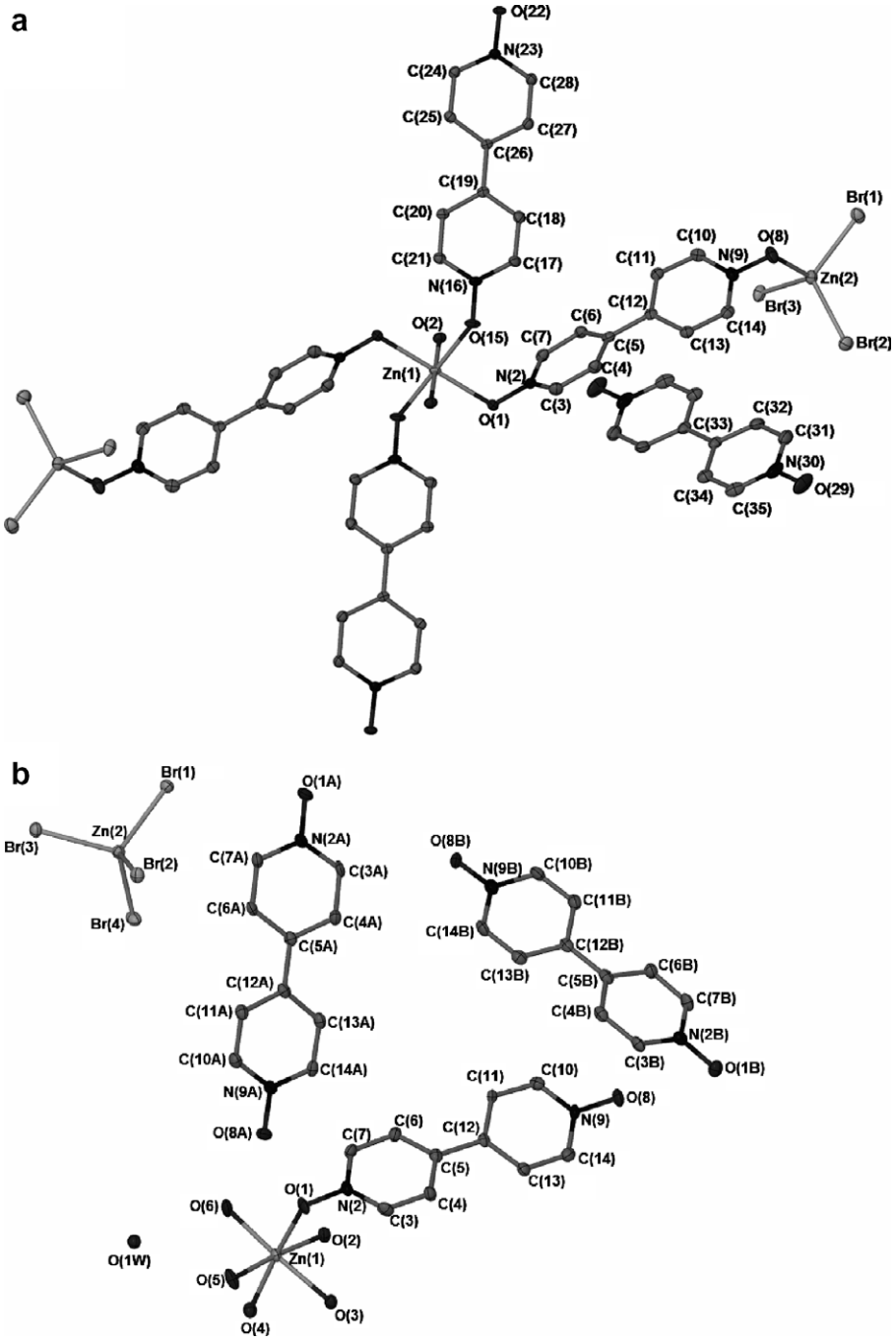


Fig. 3. X-ray structures of (a) **2** and (b) **3**. Ellipsoids shown at 50% probability.

environment around the $[ZnBr_4]^{2-}$ anions is similar to that in **2**. They are also surrounded by aromatic rings, with several C–H···Br contacts.

Changing the counterion, in **4**, gives rise to the formation of a 1D coordination polymer. Previous work [30] had suggested that using these starting materials in a similar method produced a coordination polymer characterised as $[Zn_2(bpdo)_3(NCS)_4]$. No crystal structure of this material was available but the infrared spectrum was consistent with a polymeric structure having terminal NCS groups. In this study we obtained material which is polymeric and has terminal NCS groups but has a metal:ligand ratio of 1:1, rather than 2:3. The central Zn ion is coordinated by two NCS^- counterions in the axial positions, while the equatorial positions are occupied by two water molecules and two bpdo ligands, resulting in octahedral coordination geometry (Fig. 6). All bond lengths and angles were within the expected ranges [26]. The Zn–N bond length is 2.034 Å, while Zn–O(bpdo) and Zn–O(aqua) are 2.154 Å and 2.169 Å respectively. Adjacent polymer chains are linked by a network of hydrogen bonds between the aqua and bpdo ligands (Fig. 7a). Coordinated water (O16)

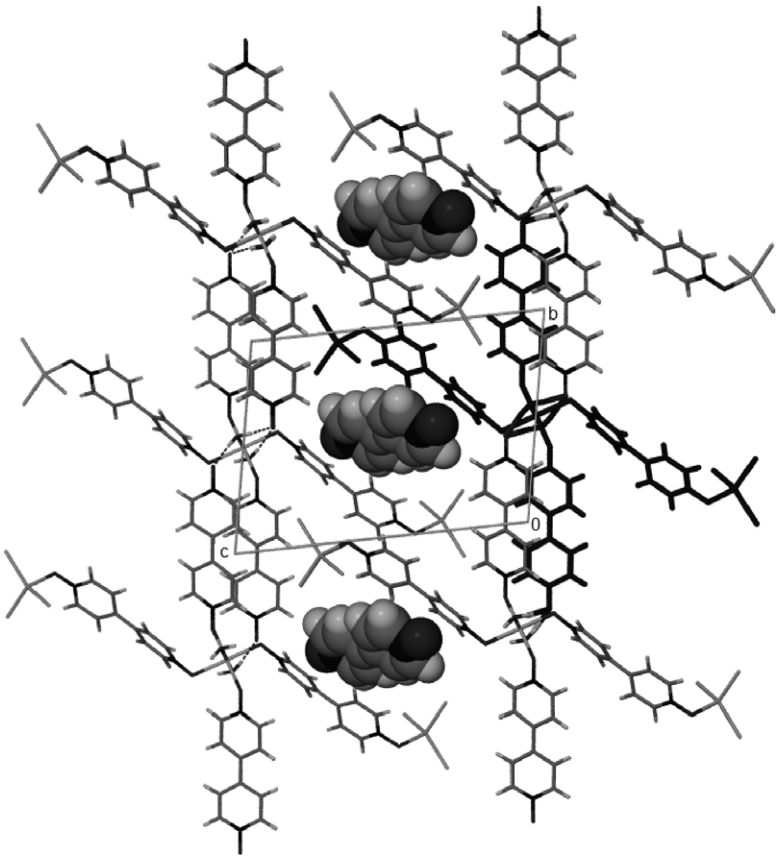


Fig. 4. Packing diagram of **2**, viewed along [1 0 0]. One X-shaped trimeric molecule is highlighted in dark grey and guest bpdo molecules are shown with van der Waals radii. Only O–H···O hydrogen bonds are shown.

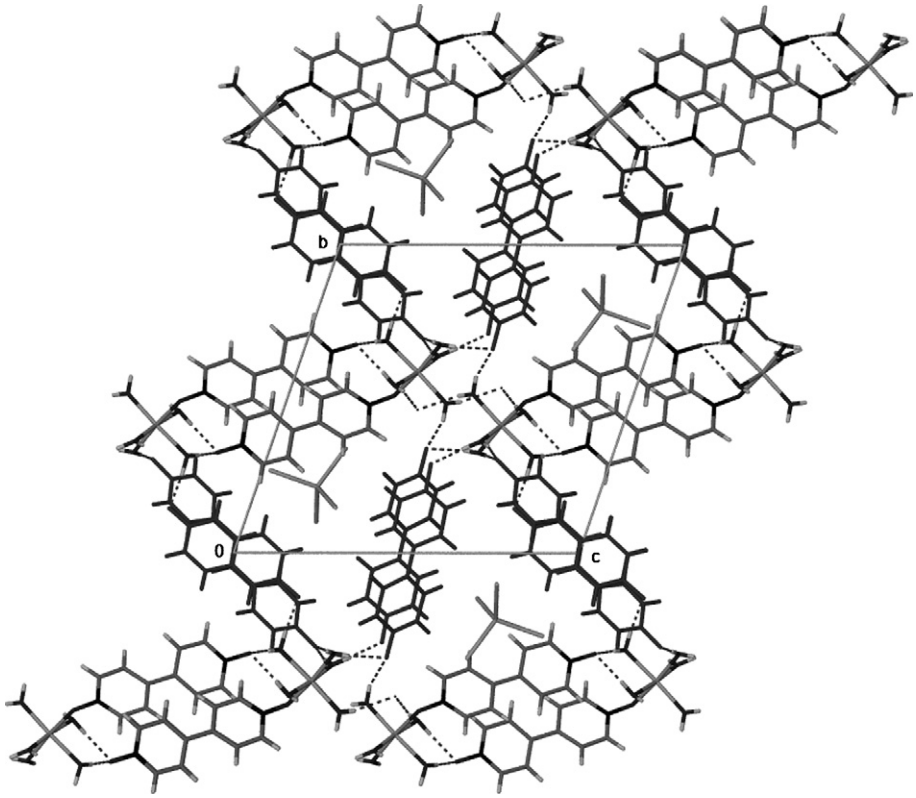


Fig. 5. Layers of $[Zn(bpdo)(H_2O)_5]^{2+}$ and bpdo guests in **3**. The latter are depicted in darker grey. Only O–H···O hydrogen bonds are shown.

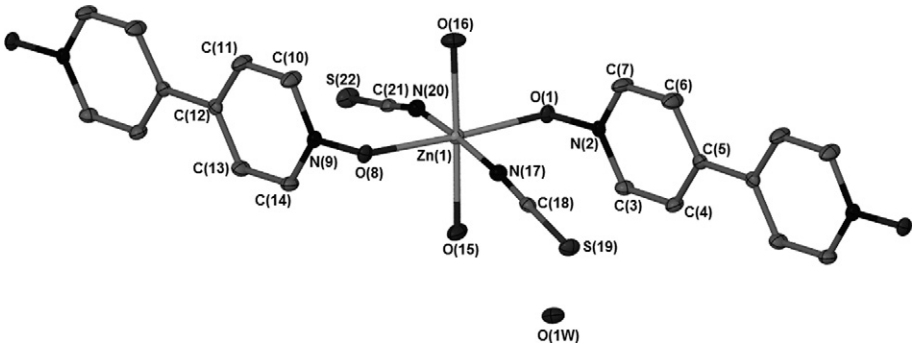


Fig. 6. Molecular structure of **4**. Ellipsoids shown at 50% probability.

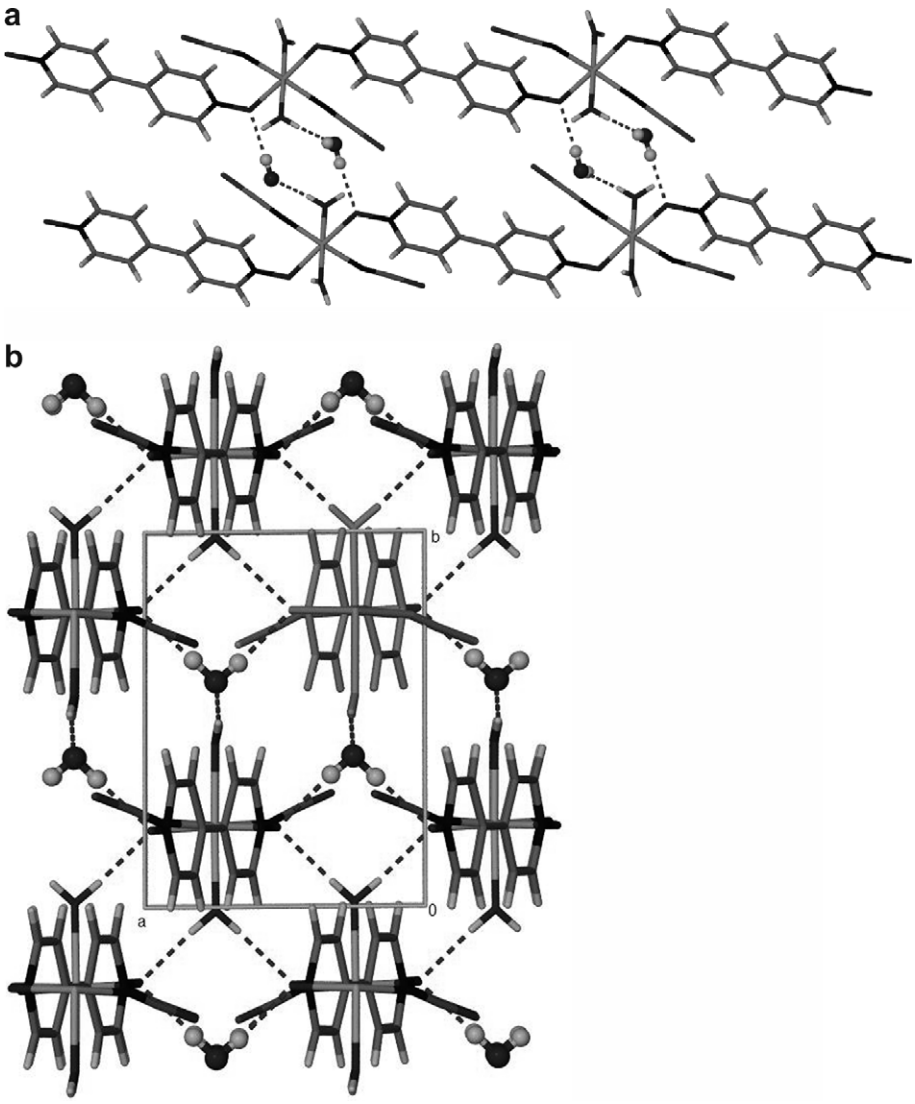


Fig. 7. (a) Hydrogen bonding interactions link adjacent 1D coordination polymers in **4** and (b) guest water molecules are located in channels between the 1D chains.

donates hydrogen bonds {O(16)–H(16A)···$O(1)_{bpdo}$ and O(16)–H(16B)···$O(8)_{bpdo}$} to the terminal oxygens of the coordinated bpdo ligand with the $O(16)_{aqua}$···$O(1)_{bpdo}$ distances of 2.839 Å and 2.853 Å, respectively. The *trans*-coordinated water molecule donates hydrogen bonds (O(15)–H(15B)···O(1W)) to guest water molecule with the O(15)···O(1W) guest distance of 2.662 Å. The guest water molecule in return donates hydrogen bonds, O(1W)–

H(1W1)···O(8) and O(1W)–H(1W2)···O(1), to two coordinated bpdo ligands linking the adjacent chains with the O···O distance of 2.793 Å for $O(1W)_{aqua}\cdots O(8)_{bpdo}$ and 2.848 Å for $O(1W)_{aqua}\cdots O(1)_{bpdo}$. A summary of hydrogen bonding and π interactions is given in Table 2. The water molecules are found in channels running parallel to [0 0 1] as shown in Fig. 7b.

4. Conclusion

4,4′-Bipyridine-*N*,*N*′-dioxide forms a neutral 1:1 metal to ligand 1D coordination polymer **4** with $Zn(NCS)_2$ but a trimeric molecule **2** and a monomeric cationic complex **3** with $ZnBr_2$ under the same conditions. When crystallisation conditions are altered, the neutral 2D coordination polymer (metal to ligand 1:2) **1** is obtained, also from $ZnBr_2$.

Complexes **2** and **3** contain both octahedral and tetrahedral Zn(II) ions: in **2** these are covalently linked by bridging bpdo ligands forming zwitterionic trimetallic molecules while in **3** there is complete charge separation into $[ZnBr_4]^{2-}$ anions and $[Zn(H_2O)_5(bpdo)]^{2+}$ cations. Although the packing of these two compounds is quite different, the $[ZnBr_3]^-$ entities are located in similar chemical environments and both compounds have included guest bpdo molecules in channels which run through the crystal structure. Complexes **1** and **4** are both coordination polymers which form layered structures. In **1**, planar layers are linked by weak hydrogen bonding but **4** consists of zigzag polymer layers which are linked by strong O–H···O hydrogen bonding through bridging water molecules.

While bpdo is often cited as a bidentate ligand which may be expected to form a bridge between metal centres, this work illustrates that this is not always the case. Bpdo serves as a bridging ligand in **1**, **2** and **4**, but there are also terminal bpdo ligands in **2** and **3**. A CSD search identified 50 structures with bpdo present: in 24 cases the bpdo acts as a bridging ligand, there are seven structures in which it is coordinated via only one end, eight structures in which it is not coordinated, even in the presence of a metal ion and eleven structures which contain bpdo but no metal species.

Acknowledgements

We thank the National Research Foundation (FA2004032500017), the University of Cape Town Research Committee and the CSIR (LJM) for financial support.

Appendix A. Supplementary material

CCDC 623177, 623178, 623179 and 623180 contain the supplementary crystallographic data for this paper. These data can be obtained free of charge from the Cambridge Crystallographic Data Centre via www.ccdc.cam.ac.uk/data_request/cif. Supplementary data associated with this article can be found, in the online version, at doi:10.1016/j.poly.2007.01.007.

References

[1] T.M. Reineke, M. Eddaoudi, D. Moler, M. O' Keeffe, O.M. Yaghi, J. Am. Chem. Soc. 122 (2000) 4843.
[2] C-B. Liu, S-S. Tan, Z-S. Wu, H-L. Wen, Acta Crystallogr. E62 (2006) m1496.
[3] N. Lah, I. Leban, Inorg. Chem. Commun. 9 (2006) 42.
[4] K. Biradha, M. Fujita, J. Chem. Soc., Dalton Trans. (2000) 3805.
[5] S.A. Bourne, J. Lu, B. Moulton, M.J. Zawarokto, Chem. Commun. (2001) 861.
[6] L.J. Moitsheki, S.A. Bourne, L.R. Nassimbeni, Acta Crystallogr. E62 (2006) m542.
[7] S.J. Dalgarno, M.D. Hardie, J.L. Atwood, J.E. Warren, C.L. Raston, New J. Chem. 29 (2005) 649.
[8] D.L. Long, A.J. Blake, N.R. Champness, M. Schröder, Chem. Eur. J. 8 (2002) 2026.
[9] L.R. MacGillvray, S. Subramanian, M.J. Zaworokto, J. Chem. Soc., Chem. Commun. (1994) 1325.
[10] G.B. Gardner, D. Venkataraman, J.S. Moore, S. Lee, Nature 374 (1995) 792.
[11] K. Biradha, C. Seward, M.J. Zaworokto, Angew. Chem., Int. Ed. 38 (1999) 492.
[12] G.R. Desiraju, Acc. Chem. Res. 35 (2002) 565.
[13] T. Steiner, Cryst. Rev. 6 (1996) 1.
[14] D.L. Long, A.J. Blake, N.R. Champness, M. Schröder, Chem. Commun. (2000) 2273.
[15] A.J. Blake, M.T. Brett, N.R. Champness, A.N. Khlobystov, D.L. Long, C. Wilson, M. Schröder, Chem. Commun. (2001) 2258.
[16] B.Q. Ma, H.L. Sun, S. Gao, G.X. Xu, Inorg. Chem. 40 (2001) 6247.
[17] B.Q. Ma, S. Gao, H.L. Sun, G.X. Xu, J. Chem. Soc., Dalton Trans. (2001).
[18] B.Q. Ma, S. Gao, H.L. Sun, G.X. Xu, Cryst. Eng. Comm. 35 (2001) 1.
[19] B.Q. Ma, H.L. Sun, S. Gao, Inorg. Chem. 44 (2005) 837.
[20] Y. Xu, D. Yuan, Y. Xu, W. Bi, Y. Zhou, M. Hong, Acta Crystallogr. E 60 (2004) m713.
[21] S.A. Bourne, L.J. Moitsheki, CrystEngComm 7 (2005) 674.
[22] Z. Otwinowski, W. Minor, DENZO and SCALEPACK, in: M.G. Rossman, E. Arnold (Eds.), International Tables for Crystallography, Vol. F, Kluwer, Dordrecht, 2000.
[23] G.M. Sheldrick, SHELXS97 and SHELXL97, Suite of programs for crystal structure determination and refinement, University of Göttingen, 1997.
[24] L.J. Barbour, J. Supramol. Chem. 1 (2003) 189.
[25] Pov-Ray for Windows, Version 3.1e.watcom.win32, The Persistence of Vision Development Team, ©1991–1999.
[26] F.H. Allen, O. Kennard, D.G. Watson, L. Brammer, A.G. Orpen, R. Taylor, J. Chem. Soc. Perkin Trans. (1989) S1.
[27] F.H. Allen, Acta Crystallogr. B 58 (2002) 380.
[28] (a) A. Bekaert, P. Lemoine, J.D. Brion, B. Viossat, Acta Crystallogr. C 61 (2005) m76;
(b) C.R. Rice, S. Onions, N. Vidal, J.D. Wallis, M.C. Senna, M. Pilkington, H. Stoeckli-Evans, Eur. J. Inorg. Chem. (2002) 1985.
[29] M.A. Shipman, C. Price, A.E. Gibson, M.R.J. Elsegood, W. Clegg, A. Houlton, Chem. Eur. J. 6 (2000) 4371.
[30] I.S. Ahuja, R. Singh, L. Sriramulu, Trans. Met. Chem. 5 (1980) 373.

Available online at www.sciencedirect.com
ScienceDirect
Polyhedron 26 (2007) 2728–2732
POLYHEDRON
www.elsevier.com/locate/poly

Crystal structure, spectroscopy and magnetism of a dinuclear strongly antiferromagnetically coupled *N*-oxido-bridged Cu(II) compound with 2,2′-bipyridine-1,1′-dioxide (bpdo) as a ligand; $[Cu_2(bpdo)_2Br_4]$

Gerard A. van Albada [a], Ilpo Mutikainen [b], Urho Turpeinen [b], Jan Reedijk [a,*]

[a] *Leiden Institute of Chemistry, Gorlaeus Laboratories, Leiden University, P.O. Box 9502, 2300 RA Leiden, The Netherlands*
[b] *Laboratory of Inorganic Chemistry, Department of Chemistry, P.O. Box 55 (A.I.Virtasen aukio 1), 00014 University of Helsinki, Finland*

Received 17 November 2006; accepted 12 January 2007
Available online 26 January 2007

Abstract

A new dinuclear compound, $[Cu_2(bpdo)_2Br_4]$, (in which bpdo = 2,2′-Bipyridine-1,1′-dioxide), has been synthesized and fully characterized, including the X-ray and the magnetic susceptibility. Each copper(II) ion in the dinuclear compound has a distorted square pyramidal geometry with the basal plane formed by two oxygen atoms of two ligand molecules which are bridging between the Cu ions with Cu–O distances of 2.021(2) and 2.039(2) Å and two bromide atoms with Cu–Br distances of 2.3577(6) and 2.3665(7) Å. The fifth position is occupied by a non bridging oxygen atom of a ligand with a Cu–O distance of 2.197(2) Å. The distance between the Cu ions is 3.334 Å, while the Cu–O–Cu angle is 110.37(9)°. The magnetic susceptibility measurements (from 5 to 350 K) agree with a very strong antiferromagnetic interaction with a large singlet–triplet splitting (J) of $-905\ cm^{-1}$. At high T (above 250 K) a triplet powder EPR is observed.
© 2007 Elsevier Ltd. All rights reserved.

Keywords: Copper(II); Crystal structure; Magnetism; *N*-Oxido-bridged

1. Introduction

2,2′-Bipyridine-1,1′-dioxide (hereafter abbreviated as bpdo) is a useful tool in crystal engineering [1] and synthesizing new electroactive materials [2]. Also the chelating properties of this heterocyclic NO-donor ligand have been studied especially with copper(II) [3–6], however, without obtaining X-ray crystal structures. So far one X-ray crystal structure with Fe(III) [7] and only a few X-ray structures with Cu(II) and the bpdo ligand have been reported [8–13].

Baran and co-workers [8] published two isomeric structures with the general formula $[Cu_2(bpdo)_2Cl_4]$, a green isomer which contains a chloride bridge and an yellow-orange isomer containing an *N*-oxido-bridge. The magnetic susceptibility reveals a very weak antiferromagnetic interaction (with $J = -0.8\ cm^{-1}$) for the green isomer and a very strong antiferromagnetic interaction ($J = -730\ cm^{-1}$) for the yellow-orange isomer. To investigate the influence of the anion on the magnetism, we synthesize the bromide compound with bpdo, $[Cu_2(bpdo)_2Br_4]$. It appeared that in this case only one isomer can be obtained. In this paper we present the synthesis, spectroscopic measurements, X-ray crystal structure, as well as the magnetic susceptibility measurements of the bromide compound $[Cu_2(bpdo)_2Br_4]$, a dinuclear compound with 2*N*-oxido-bridges, in a comparable geometry as for the yellow-orange isomer of the corresponding chloride [8].

* Corresponding author.
E-mail address: reedijk@chem.leidenuniv.nl (J. Reedijk).

0277-5387/$ - see front matter © 2007 Elsevier Ltd. All rights reserved.
doi:10.1016/j.poly.2007.01.017

2. Experimental

2.1. General

C,H,N determinations were performed on a Perkin–Elmer 2400 Series II analyzer. Ligand field spectra were obtained on a Perkin–Elmer Lambda900 spectrophotometer using the diffuse reflectance technique, with MgO as a reference. X-band powder EPR spectra were obtained on a Jeol RE2x electron spin resonance spectrometer using DPPH ($g = 2.0036$) as a standard. FTIR spectra were obtained on a Perkin Elmer Paragon 1000 FTIR spectrophotometer equipped with a Golden Gate ATR device, using the reflectance technique (4000–300 cm^{-1}, res. 4 cm^{-1}). Magnetic susceptibility measurement (5–350 K) were carried out (at 0.1 T) using a Quantum Design MPMS-5S SQUID magnetometer. Data were corrected for the magnetisation of the sample holder and for diamagnetic contributions, which were estimated from Pascal constants.

2.2. Synthesis of the coordination compound

The ligand bpdo was used as commercially available and handled without additional purification. 1.2 mmol of $CuBr_2$ and 1.2 mmol of the ligand bpdo were each dissolved in 10 ml of methanol. The Cu(II) salt solution was then added slowly to the ligand solution and filtered to remove any undissolved material. After a few days crystalline brown-red products separate. The were isolated by filtration and dried in air.

Yield about 72%, Elemental *Anal.* Calc. for $C_{20}H_{16}Br_4Cu_2N_4O_4$: C, 29.2; H, 2.0; N, 6.8. Found: C, 29.0; H, 2.1; N, 6.8%. No other compounds were isolated from this solution, irrespective of the M:L ratio, and/or changing the solvent or temperature.

Table 1
Crystallographic data for $[Cu_2(bpdo)_2Br_4]$

Formula	$C_{20}H_{16}Br_4Cu_2N_4O_4$
Molecular weight	823.09
Crystal system	orthorhombic
Temperature (K)	173(2)
Space group	*Pbca*
a (Å)	10.790(2)
b (Å)	14.366(3)
c (Å)	15.946(3)
V (Å^3)	2471.8(8)
Z	4
D_{calc} (g cm^{-3})	2.212
$F(000)$	1576
μ (mm^{-1})	8.222
Crystal size (mm)	$0.20 \times 0.20 \times 0.20$
Colour, shape	darkred, block
θ_{min}, θ_{max} (°)	3.11–27.56
Total reflection	28 143
Total unique reflection [R_{int}]	2818 [0.0566]
Number of refined parameters	154
R^a, $wR_2{}^b$, S	0.029, 0.069, 1.10
Minimum and maximum residual density (e Å^{-3})	−0.78; 0.70

[a] $R_1 = \sum\|F_o| - |F_c|/\sum|F_o|$.
[b] $wR_2 = [\sum[w(F_o^2 - F_c^2)^2]/\sum[w(F_o^2)^2]]^{1/2}$.

2.3. Crystal structure determination and refinement

A suitable crystal was selected from the mother liquid and mounted to a glass fibre using the oil-drop method; data were collected on a Nonius KappaCCD diffractometer (graphite-monochromated Mo Kα radiation). The intensity data were corrected for Lorentz and polarization effects, for absorption and extinction. The structures were solved by direct methods. The programs COLLECT [14], SHELXS-97 [15], SHELXL-97 [16] were used for data reduction, structure solution and structure refinement, respectively. Refinement of F^2 was done against all reflections. All non-hydrogen atoms were refined anisotropically. All H atoms were introduced in calculated positions and refined with fixed geometry with respect to their carrier atoms. Crystallographic data are presented in Table 1.

3. Results and discussion

3.1. Description of the crystal structure

A thermal ellipsoid plot, together with the numbering scheme is shown in Fig. 1, with selected bond lengths and bond angles given in Table 2. The centrosymmetric dinuclear unit has a centre of symmetry located between the Cu(II) ions. The basal plane of the 5-coordinated Cu ion is occupied by two oxygen atoms of two ligand molecules which are bridging between two Cu ions with Cu–O distances of 2.021(2) and 2.039(2) Å and two bromide atoms with Cu–Br distances of 2.3577(6) and 2.3665(7) Å. The fifth position is occupied by a non-bridging oxygen atom of a ligand with a Cu–O distance of 2.197(2) Å. The geometry of 5-coordinated compounds can be described by the

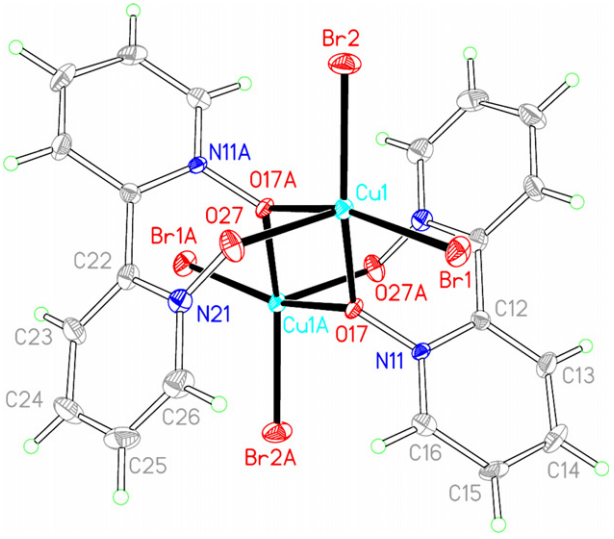


Fig. 1. Atomic displacement plot (50% probability level) of the molecular structure of $[Cu_2(bpdo)_2Br_4]$.

Table 2
Selected bond lengths (Å) and angles (°) for $[Cu_2(bpdo)_2Br_4]$

Cu(1)–O(17)A	2.021(2)	Cu(1)–O(17)	2.039(2)
Cu(1)–O(27)	2.197(2)	Cu(1)–Br(2)	2.3577(6)
Cu(1)–Br(1)	2.3665(7)	Cu(1)–Cu(1)A	3.3339(9)
O(17)A–Cu(1)–O(17)	69.63(9)	O(17)A–Cu(1)–O(27)	82.98(9)
O(17)–Cu(1)–O(27)	98.97(9)	O(17)A–Cu(1)–Br(2)	94.28(6)
O(17)–Cu(1)–Br(2)	151.76(7)	O(27)–Cu(1)–Br(2)	101.96(7)
O(17)A–Cu(1)–Br(1)	162.00(6)	O(17)–Cu(1)–Br(1)	92.38(6)
O(27)–Cu(1)–Br(1)	101.06(6)	Br(2)–Cu(1)–Br(1)	101.91(2)
Cu(1)–O(17)–Cu(1)A	110.37(9)		

A = symmetry operation $-x, -y, -z+1$.

parameter τ ($\tau = (\beta - \alpha)/60$, where β and α are the largest coordination angles, $\tau = 0$ for square pyramidal (SP) and $\tau = 1$ for trigonal bipyramidal (TBP) geometry) [17]. The two largest angles in this case are 162.00(6)° and 151.76(7)°, so the τ value is 0.17, agreeing with a distorted square-pyramidal geometry for the Cu ions. The distance between the Cu ions is 3.3339(9) Å, while the Cu–O–Cu angle is 110.37(9)°. The related yellow-orange chloride isomer [8] has a slightly smaller distortion, in that case the τ value = 0.13, a comparable Cu–Cu distance of 3.333(1) Å and a slightly smaller Cu–O–Cu angle of 109.2°.

3.2. Spectroscopy and EPR

The ligand-field transition measured as a solid with the diffuse reflectance technique is observed as a very broad band with a maximum at about 10.0×10^3 cm^{-1}. This is a normal ligand field transition for (distorted) square pyramidal geometries and weak ligands [18]. In the IR spectra the N–O stretching vibrations were observed at 1221 and 1204 cm^{-1} and the N–O bending vibrations at 844 and 833 cm^{-1}. The Cu–O vibration was observed at 408 cm^{-1}. These vibrations are in agreement with the vibrations found for the chloride isomer [8].

The EPR spectra of the compound was recorded as a polycrystalline powder at RT and 77 K from 0 to 800 mT at X-band frequency ($h\nu = 0.325$ cm^{-1}). The spectrum at RT reveals a typical $S = 1$ triplet spectrum with transitions observed at 140, 225, 340 mT as broad bands and a split broad band at 430, 470 and 525 mT (see Fig. 2). The signal at 140 mT can be assigned to the forbidden half-field signal ($\Delta M_s = \pm 2$), while the band at 340 mT is the $S = 1/2$ resonance from a mononuclear impurity, which usually is present in dinuclear Cu(II) compounds. The broad unresolved bands at 225 mT and the more or less split band at 430, 470, 525 mT can tentatively be assigned to the H_{x1y1z1} and the H_{x2}, H_{y2} and H_{z2}, respectively [24,25] The zero-field splitting parameter D can be estimated as 0.2 cm^{-1} (with $g_{av} = 2.19$) [26]. At 77 K the solid changed from red brown colour to yellow ochre and no signals were observed any more, only the $S = 1/2$ resonance at 340 mT from the monomeric impurity is present. These features are in agreement with the magnetic susceptibility measured (vide infra), as no triplet state is occupied any more at this low T. After re-synthesizing the yellow-orange chloride bridged isomer[1] also the same type of EPR spectrum was observed (see Fig. S1), with very similar parameters.

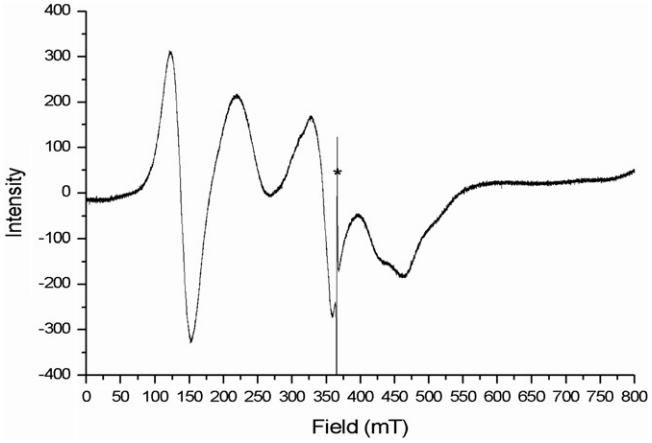


Fig. 2. EPR spectrum of the title compound at RT. A star denotes DPPH.

3.3. Magnetic properties

The magnetic susceptibility of a powdered sample was measured from 5 to 350 K. The magnetic properties of the title compound are depicted in Fig. 3 in the form of $\chi_m T$ versus T for two Cu(II) ions. At 350 K the $\chi_m T$ product has a value of 0.097 cm^3 mol^{-1} K (0.81 μ_B), which is far below the spin-only value for two non-interacting Cu(II) ions (0.75 cm^3 mol^{-1} K, 2.83 μ_B, at RT). From 350 K the $\chi_m T$ product decreases gradually to a value of 0.005 cm^3 mol^{-1} K (0.21 μ_B) at 5 K. This magnetic behaviour agrees with a very strong antiferromagnetic interaction.

The theoretical expression for the magnetic susceptibility for two interacting $S = 1/2$ centres, which is based on the general Hamiltonian [19] is: $H_{ex} = -JS_1S_2$, in which the exchange parameter J, is negative for antiferromagnetic and positive for ferromagnetic interaction. The magnetic data were fitted to the equation given in the literature [19] for dinuclear copper compounds:

$$X_m = (2Ng^2\beta^2)[kT - (2zJ'/(3 + \exp(-J/kT)))]^{-1} [3 + \exp(-J/kT)]^{-1}(1 - p) + X_p p,$$

in which N, g, β, k and T have their usual meanings [19]. The parameter p denotes the fraction of paramagnetic impurity in the sample and zJ' the interaction between neighbouring dinuclear identities. The fit was accomplished by minimisation of $R = (\chi_m \cdot T_{calc} - \chi_m \cdot T_{obs})^2/(\chi_m \cdot T_{obs})^2$ by a least-squares procedure. The best fit for the title

[1] The yellow-orange isomer $[Cu_2(bpdo)_2Cl_4]$ (from Ref. [8]) was resynthesized as described by Baran et al., although it appears that the solution had to be refluxed for at least 16 h in stead of the earlier reported 2.5 h to obtain the yellow-orange product. In the original article [8] only a broad peak at around 50 mT with no splitting was observed in the EPR spectrum at RT.

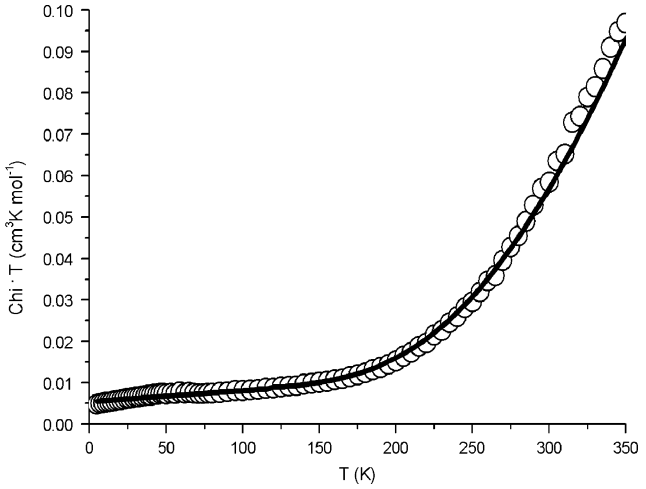


Fig. 3. A plot of the temperature dependence of $\chi_m T$ vs. T for $[Cu_2(bpdo)_2Br_4]$. The solid line represents the calculated curve for the parameters $J = -905$ cm^{-1}, $g = 2.15$ (see text).

compound, depicted in Fig. 3 as a solid line, was obtained for $J = -905$ cm^{-1}, $g = 2.15$, $zJ' = 0.02$ cm^{-1}, $p = 0.01$, with a final R of 2×10^{-2}. The R value appears a bit high, but that is ascribed to the fact that susceptibility measurements above 300 K are less accurate due to a reduced accuracy in temperature.

4. Conclusion

In this paper a new dinuclear compound with formula $[Cu_2(bpdo)_2Br_4]$ has been synthesized, characterized by infrared spectroscopy, EPR and also the X-ray structure and the magnetic susceptibility have been investigated. The compound has a double bridge consisting of the oxygen atom of the bpdo ligand and is isostructural with the related chloride compound $[Cu_2(bpdo)_2Cl_4]$ [8]. Unlike the case for the earlier reported chloride compound, no other isomer could be isolated for the bromide. Hatfield and Hodgson proposed a correlation between the Cu–O–Cu angle and the magnetic interaction for dinuclear planar hydroxido-bridged compounds [20,21]. This correlation considers the fact that for Cu–O–Cu angles greater then 97.6° the overall magnetic behaviour is antiferromagnetic and for smaller ones a ferromagnetic coupling is observed. Later the same type of correlations were also established for alkoxido-bridged compounds [22,23]. Hatfield and Hodgson [20,21] deduced a linear correlation between J and α (α = Cu–O–Cu angle) as $J = -74\alpha + 7270$. In our case the Cu–[O–O]–Cu chromophore is also planar, a good overlap of the magnetic orbitals can be proposed, even though the bridging ligands are N-oxides instead of hydroxide. The Cu–O–Cu angle for the bromide compound is 110.37° and according to the correlation formula a value of -897 cm^{-1} would be predicted, which fits well the observed value of -905 cm^{-1}. The analogues chloride compound [8] has a Cu–O–Cu angle of 109.2°, which would give a calculated value of -811 cm^{-1}, compared to an observed value of -730 cm^{-1} in the literature [8] and of -777 cm^{-1} by re-measuring of the chloride adduct [Ref. 1 and Fig. S2]. The difference in magnetic interaction is most probably related to the change in the Cu–O–Cu angle. The Cl and Br anions appear to play only a minor role in this, as e.g. the Cl–Cu–Cl and Br–Cu–Br angles are 102.2(1)° and 101.9(2)°, respectively.

Acknowledgements

The work described in the present paper has been supported by the Leiden University Study group WFMO (Werkgroep Fundamenteel Materialen Onderzoek).

Financial support and coordination by the FP6 Network of Excellence "Magmanet" (contract number 515767) is kindly acknowledged.

Appendix A. Supplementary material

The EPR spectrum and the magnetic susceptibility measurement of the chloride isomer[1] [8] are submitted as supplementary material.

CCDC 614553 contains the supplementary crystallographic data for this paper. These data can be obtained free of charge via http://www.ccdc.cam.ac.uk/conts/retrieving.html, or from the Cambridge Crystallographic Data Centre, 12 Union Road, Cambridge CB2 1EZ, UK; fax: (+44) 1223-336-033; or e-mail: deposit@ccdc.cam.ac.uk. Supplementary data associated with this article can be found, in the online version, at doi:10.1016/j.poly.2007.01.017.

References

[1] S.G. Bodige, M.A. Zottola, S.E. McKay, S.C. Blackstock, Cryst. Eng. 1 (1998) 243.
[2] J.C. Panigrahi, R.K. Panda, Mater. Sci. Eng. B14 (1992) 5.
[3] P.G. Simpson, A. Vinciguerra, J.V. Quagliano, Inorg. Chem. 2 (1963) 282.
[4] A. Vinciguerra, P.G. Simpson, Y. Kakiuti, J.V. Quagliano, Inorg. Chem. 2 (1963) 286.
[5] S.K. Madan, W.E. Bull, J. Inorg. Nucl. Chem. 26 (1964) 2211.
[6] E.J. Halbert, C.M. Harris, E. Sinn, G.J. Sutton, Aust. J. Chem. 26 (1973) 951.
[7] G.A. van Albada, I. Mutikainen, U. Turpeinen, J. Reedijk, J. Chem. Cryst. 31 (2002) 75.
[8] P. Baran, M. Koman, D. Valigura, J. Mroziński, J. Chem. Soc., Dalton Trans. (1991) 1385.
[9] P. Baran, D. Valigura, I. Svoboda, H. Fuess, Z. Kristallogr. 203 (1993) 279.
[10] M. Koman, P. Baran, D. Valigura, Acta Crystallogr. C47 (1991) 2529.
[11] H. Paulus, H. Fuess, P. Baran, D. Valigura, Z. Kristallogr. 202 (1992) 134.
[12] H. Paulus, H. Fuess, P. Baran, D. Valigura, Z. Kristallogr. 202 (1992) 140.
[13] G.A. van Albada, I. Mutikainen, U. Turpeinen, J. Reedijk, Acta Cryst. E59 (2003) m889.

[14] Nonius (2002), COLLECT, Nonius BV, Delft, The Netherlands.
[15] G.M. Sheldrick, SHELXS-97, Program for Crystal Structure Determination, University of Göttingen, Germany, 1997.
[16] G.M. Sheldrick, SHELXL-97, Program for the Refinement of Crystal Structures, University of Göttingen, Germany, 1997.
[17] A.W. Addison, T.N. Rao, J. Reedijk, J. van Rijn, G.C. Verschoor, J. Chem. Soc., Dalton Trans. (1984) 1349.
[18] B.J. Hathaway, in: G. Wilkinson, R.D. Gill, J.A. McCleverty (Eds.), Comprehensive Coordination Chemistry, vol. 5, Pergamon Press, Oxford, 1987 (Chapter 53).
[19] O. Kahn, Molecular Magnetism, VCH Publ., NY, 1993.
[20] D.J. Hodgson, Prog. Inorg. Chem. 19 (1975) 173.
[21] V.H. Crawford, H.W. Richardson, J.R. Wasson, D.J. Hodgson, W.E. Hatfield, Inorg. Chem. 15 (1976) 2107.
[22] E. Merz, W. Haase, J. Chem. Soc., Dalton Trans. (1980) 875.
[23] H. Astheimer, W. Haase, J. Chem. Phys. 85 (1986) 1427.
[24] J.R. Wasson, C.-I. Shyr, C. Trapp, Inorg. Chem. 7 (1968) 469.
[25] R. Cejudo-Marin, G. Alzuet, S. Ferrer, J. Borràs, A. Castiñeiras, E. Monzani, L. Casella, Inorg. Chem. 43 (2004) 6805.
[26] J. Reedijk, B. Nieuwenhuijse, Rec. Trav. Chim. 91 (1972) 533.

Available online at www.sciencedirect.com
ScienceDirect
Polyhedron 26 (2007) 2733–2740
POLYHEDRON
www.elsevier.com/locate/poly

First hybrid oximehydrazonate phthalocyaninoclathrochelates: The synthesis and properties of lutetium phthalocyanine-capped cage iron(II) complexes

Yan Z. Voloshin [a,*], Oleg A. Varzatskii [c], Larisa G. Tomilova [b], Marya O. Breusova [b], Tatiana V. Magdesieva [b], Yurii N. Bubnov [a], Roland Krämer [d]

[a] *Nesmeyanov Institute of Organoelement Compounds, 119991 Moscow, Russian Federation*
[b] *Lomonosov Moscow State University, 119992 Moscow, Russian Federation*
[c] *Vernadskii Institute of General and Inorganic Chemistry, Kiev-142, 03680, Ukraine*
[d] *Anorganisch-Chemisches Institut, Universität Heidelberg, Im Neuenheimer Feld 270, 69120 Heidelberg, Germany*

Received 29 September 2006; accepted 15 January 2007
Available online 7 February 2007

Abstract

Ditopic oximehydrazonate iron(II) phthalocyaninoclathrochelates were synthesized by a transmetallation (a capping group exchange) reaction of the initial labile triethylantimony-capped clathrochelate iron(II) oximehydrazonates with lutetium(III) phthalocyanine as a Lewis acid. The complexes obtained were characterized using elemental analysis, PD and MALDI-TOF mass spectrometries, IR, UV–Vis, ^{57}Fe Mössbauer, and ^{1}H, ^{13}C{^{1}H} NMR spectroscopies. An encapsulated iron(II) ion was found to be in a low-spin state. The cyclic voltammograms show oxidation and reduction waves assignable to $Fe^{2+/3+}$ couples of macrobicyclic framework and to phthalocyanine macrocycles.
© 2007 Elsevier Ltd. All rights reserved.

Keywords: Iron complexes; Clathrochelates; Macrocyclic compounds; Phthalocyanines

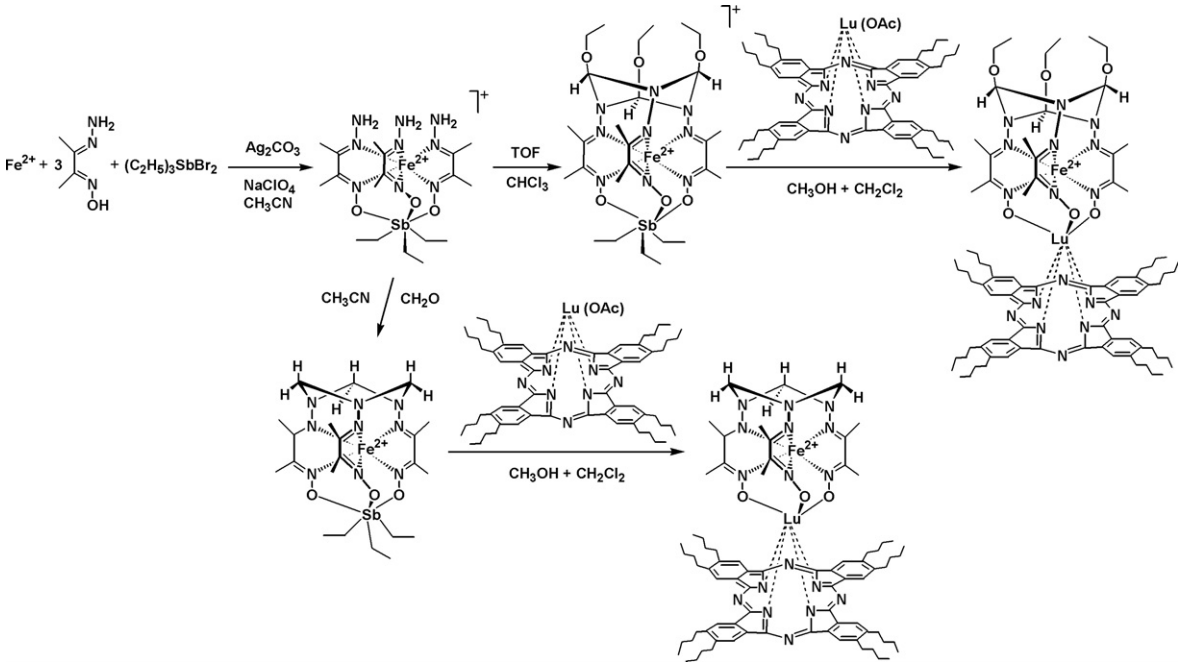
1. Introduction

The hybrid polytopic transition metal complexes, which molecules contain the distal and isolated fragments with relatively independent π- and σ-electronic systems, are the most promising precursors for molecular electronic devices [1–6] and the artificial photoexcited long-lived donor–acceptor charge separation systems with photosynthetic properties [7–13]. The recently synthesized tris-dioximate iron(II) phthalocyaninoclathrochelates belong to the type of ditopic complexes with highly intensive visible absorption bands of both the macrocyclic (phthalocyanine) and macrobicyclic (clathrochelate) fragments of the hybride molecule [14].

Unlike the clathrochelate tris-dioximate precursor, both capping fragments of which are reasonably labile in the transmetallation reactions [15,16], in case of the oximehydrazonate clathrochelates [16–23] only trioximate capping fragment may undergo transmetallation. However, the intramolecular rearrangements without destruction of the cage framework have been observed for clathrochelates with 1,3,5-triazacyclohexane hydrazonate capping fragment only (in particular, to give a tripodal methine fragment in case of triethyl orthoformate derivatives) [20]. The iron(II) ion has proved to be the most efficient template in the synthesis of such compounds. Moreover, among the synthesized earlier boron-, tin-, germanium- and antimony-capped iron(II) clathrochelates, the triorganylantimony-capped complexes undergo the

* Corresponding author.
E-mail address: voloshin@ineos.ac.ru (Y.Z. Voloshin).

0277-5387/$ - see front matter © 2007 Elsevier Ltd. All rights reserved.
doi:10.1016/j.poly.2007.01.044



Scheme 1.

transmetallation reactions only. Therefore, we proposed the following strategy for the synthesis of the hybrid oximehydrazonate phthalocyaninoclathrochelates (Scheme 1): the initially obtained triethylantimony-capped clathrochelate iron(II) oximehydrazonates undergo transmetallation reactions with Lewis-acidic rare-earth metal(III) phthalocyanines (in particular, with diamagnetic lutetium(III) phthalocyanines). This allowed us to obtain intracomplex hybrid oximehydrazonate phthalocyaninoclathrochelates (the formal positive 2+ charge of the encapsulated iron(II) ion is compensated by the formal negative 2− charge of the capping O_3LuN_4 fragment). The formation of this intracomplex facilitated the isolation and purification of the resulting hybrid clathrochelate. On the other hand, the nature of this compound increases its solubility in aprotonic polar and apolar organic solvents (chloroform, methylene dichloride and benzene). Eight *n*-butyl substituents in the phthalocyanine fragment enhance significantly the solubility of both the initial lutetium(III) phthalocyanine and the target hybrid clathrochelate in these solvents as well. The use of the diamagnetic lutetium(III) ion as a capping one allowed us to control the course of the reactions by ^{1}H and ^{13}C NMR spectroscopies.

2. Experimental

2.1. General procedures

The reagents used, $NaClO_4$, paraformaldehyde, triethyl ortoformate (TOF), $CaCO_3$, sorbents, organic bases, and solvents were obtained commercially (Fluka). Complex $Fe(CH_3CN)_4Cl_2$ was prepared as described elsewhere [24]. The triethylantimony(V) dibromide and diacetylmonoxime hydrazone (HDXO) were synthesized by known procedures [25,26].

Analytical data (C, H, N content) were obtained with a Carlo Erba model 1106 microanalyzer. Iron content was determined spectrophotometrically.

The plasma desorption (PD) mass spectrum of $[FeDXO_3(HCOC_2H_5)_3(Sb(C_2H_5)_3)](ClO_4)$ complex was recorded in the positive spectral region using a BC MS SELMI time-of-flight mass spectrometer and an accelerating voltage of 20 kV. The ionization was induced by ^{252}Cf spontaneous decay fragments, and typically 20 000 decay acts were registered. The sample (approximately 1–2 mg) was applied to a gilded disk.

The MALDI-TOF mass spectra were recorded using a MALDI-TOF-MS Bruker Autoflex mass spectrometer in reflecto-mol mode. The ionization was induced by UV-laser with wavelength 336 nm. The samples were applied to a nickel plate, 2,5-dihydroxybenzoic acid was used as a matrix. The accuracy of measurements was 0.1%.

The IR spectra of solid samples (KBr tablets) in the range of 400–4000 cm^{-1} were recorded with a IR200 Thermo Nicolet FT-spectrophotometer.

The UV–Vis spectra of solutions in methylene dichloride were recorded in the range of 230–900 nm with a Lambda 9 Perkin–Elmer spectrophotometer. The individual Gauss components of these spectra were calculated using the SPECTRA program.

The ^{1}H and ^{13}C NMR spectra were recorded from CD_2Cl_2, DMSO-d_6 and $CDCl_3$ solutions with a Bruker AC-200 FT-spectrometer.

The ^{57}Fe Mössbauer spectra were obtained with a YGRS-4M spectrometer with a constant acceleration mode. The spectra were collected with a 256-multichannel

amplitude analyzer. The isomer shift was measured relative to sodium nitroprusside, and an α-Fe foil was used for the velocity scale calibration. ^{57}Co in a chromium matrix was used as the source, which was always kept at room temperature. The minimal absorption line-width in the spectrum of a standard sample of sodium nitroprusside was 0.24 mm/s.

Voltammetric experiments were performed with a potentiostat–galvanostat IPC-Win in a conventional one-compartment three-electrode cell. Working electrode was either platinum (Pt) or glassy carbon (GC) disk electrode with an active surface area of 0.085 cm^2. The electrodes were thoroughly polished and rinsed before measurements. A platinum wire counter electrode and Ag/AgCl/KCl with a salt bridge filled with 0.15 M $(Bu_4N)BF_4$ solution in *o*-dichlorobenzene as a reference electrode were used. The formal potential of the ferrocene Fc/Fc^+ couple versus RE is about 600 mV in *o*-dichlorobenzene. The scan rate was varied from 20 to 200 mV/s. All solutions in *o*-dichlorobenzene (10 ml) were thoroughly deaerated before the experiments and all measurements were made under argon.

2.2. Synthesis

Complex [Lu(Bu$_8$Pc)(CH$_3$COO)] was prepared as described in Ref. [27]. ^{1}H NMR ($CDCl_3$/DMSO-d_6 (3:1)): δ (ppm) 1.10 (t, 24H, CH_3(Bu)), 1.65 (m, 16H, γ-CH_2), 1.95 (m, 19H, CH_3 (acetate)+β-CH_2), 3.15 (m, 16H, α-CH_2), 9.20 (s, 8H, HAr). ^{13}C{^{1}H} NMR (CD_2Cl_2): δ (ppm) 14.3 (s, CH_3(Bu)), 23.3 (br s, CH_3(acetate)), 23.6 (s, CH_2(Bu)), 34.0 (s, CH_2(Bu)), 34.5 (s, CH_2(Bu)), 122.9 (br s, Pc), 137.1 (s, Pc), 142.8 (s, Pc), 155.3 (s, Pc). UV–Vis (CH_2Cl_2): λ_{max}/nm ($\varepsilon \times 10^{-3}$, mol^{-1} l cm^{-1}) 253 (48), 273 (37), 289 (27), 316 (28), 350 (80), 387 (15), 422 (8.2), 584 (4.9), 623 (27), 654 (20), 686 (145).

2.2.1. *[FeDXO$_3$ (Sb(C$_2$H$_5$)$_3$)](ClO$_4$)*

Complex $Fe(CH_3CN)_4Cl_2$ (2.9 g, 10 mmol), diacetylmonooxime hydrazone (3.4 g, 30 mmol), $CaCO_3$ (2 g) and $NaClO_4$ (6 g) were dissolved/suspended in acetonitrile (70 ml) under argon and the solution/suspension of $(C_2H_5)_3SbCO_3$, obtained by reaction of $(C_2H_5)_3SbBr_2$ (7.72 g, 20 mmol) with Ag_2CO_3 (8.27 g, 30 mmol) in acetonitrile (20 ml), was added. The reaction mixture was stirred for 1 h, heated to boiling and the solvent (~40 ml) was evaporated for 1.5 h. The reaction mixture was diluted with methylene dichloride (50 ml) and filtered. The filtrate was rotary evaporated to dryness and extracted with chloroform–acetonitrile 10:1 mixture. The extract was evaporated to a half-volume and precipitated with hexane. The precipitate was filtrated, washed with hexane and dried in vacuo (yield: 1.06 g, 15%). *Anal.* Calc. for $C_{18}H_{39}N_9O_7ClFeSb$: C, 30.59; H, 5.57; N, 17.84; Fe, 7.90. Found: C, 30.45; H, 5.49; N, 17.81; Fe, 7.95%. MS (MALDI-TOF): *m*/*z* 607 $[M - ClO_4^-]^+$. ^{1}H NMR ($CDCl_3$): δ (ppm): 1.35 (t, 9H, CH_3(Et)), 1.74 (m, 6H, CH_2(Et)), 2.32 (br s, 18H, CH_3(DXO)), 6.03 (br s, 6H, NH_2). ^{13}C{^{1}H} NMR ($CDCl_3$): δ (ppm): 10.0 (s, CH_3(Et)), 13.3 (s, CH_3(DXO)), 13.6 (s, CH_3(DXO)), 23.4 (s, CH_2(Et)), 152.6 (s, C=N(oxime)), 156.6 (s, C=N(hydrazone)). IR (cm^{-1}, KBr): 1550sh, 1576 *ν*(C=N), 966, 987, 1016 sh, 1083 m *ν*(N – O). UV–Vis (CH_2Cl_2): λ_{max}/nm ($\varepsilon \times 10^{-3}$, mol^{-1} l cm^{-1}) 247 (6.5), 290 (13), 328 (3.3), 357 (1.2), 409 (1.3), 462 (3.3), 511 (3.1), 540 (1.4).

2.2.2. *[FeDXO$_3$ (HCOC$_2$H$_5$)$_3$(Sb(C$_2$H$_5$)$_3$)] (ClO$_4$)*

Complex $[FeDXO_3(Sb(C_2H_5)_3)](ClO_4)$ (1.6 g, 2.26 mmol) was dissolved in chloroform (50 ml) and an excess of OIF (2 ml) was added. The reaction mixture was refluxed under argon with drier for 3 h, cooled to room temperature and left overnight. Then the reaction mixture was evaporated to ~20 ml, diluted with diethyl ether (100 ml) and filtered. The filtrate was evaporated to dryness, washed with hexane and extracted with methylene dichloride–hexane 1:2 mixture. The extract was evaporated to dryness, the solid residue was washed with hexane and dried in vacuo (yield: 0.40 g, 20%). *Anal.* Calc. for $C_{27}H_{51}N_9O_{10}ClFeSb$: C, 37.06; H, 5.89; N, 14.41; Fe, 6.38. Found: C, 37.22; H, 5.99; N, 14.27; Fe, 6.53%. MS (MALDI-TOF): *m*/*z* (I, %) 775(20) $[M - ClO_4^-]^+$, 746(25) $[M - Et - ClO_4^-]^+$, 730(100) $[M - OEt - ClO_4^-]^+$, 717(10) $[M - 2Et - ClO_4^-]^+$. MS (PD): *m*/*z* (I, %): 875(30) $[M]^{+\bullet}$, 775(100) $[M - ClO_4^-]^+$; 730(65) $[M - OEt - ClO_4^-]^+$; 701(55) $[M - OEt - Et - ClO_4^-]^+$, 630(35) $[M - 5Et - ClO_4^-]^+$. ^{1}H NMR (CD_2Cl_2): δ (ppm) 1.23/1.44 (m, 18H, CH_3(SbEt + OEt)), 1.65 (m, 6H, CH_2(SbEt)), 2.12/2.20 (two s, 18H, CH_3(DXO)), 4.07 (m, 6H, CH_2(OEt)), 7.03 (br s, 3H, HC(methine)). ^{13}C{^{1}H} NMR (CD_2Cl_2): δ (ppm) 9.8 (s, CH_3(SbEt)), 13.3 (s, CH_3(DXO)), 13.6 (s, CH_3(DXO)), 15.9 (s, CH_3(OEt)), 24.0 (s, CH_2(SbEt)), 63.5 (s, CH_2(OEt)), 155.3 (s, HC(methine)), 157.2 (s, C=N(oxime)), 164.4 (s, C=N(hydrazone)). IR (cm^{-1}, KBr): 1567, 1580 *ν*(C=N), 928 sh, 994/1008 m, 1104 m *ν*(N – O). UV–Vis (CH_2Cl_2): λ_{max}/nm ($\varepsilon \times 10^{-3}$, mol^{-1} l cm^{-1}) 255 (25), 292 (21), 323 (12), 359 (6.0), 403 (4.0), 446 (3.1), 477 (4.3), 503 (5.0), 536 (5.0), 566 (4.5).

2.2.3. *[FeDXO$_3$ (CH$_2$)$_3$(Sb(C$_2$H$_5$)$_3$)](ClO$_4$)*

The dry freshly-distilled acetonitrile (10 ml) was saturated with gaseous formaldehyde, obtained by distillation of paraform (0.5 g), and 3 Å molecular sieves (2 g) were added. Then the solution of complex $[FeDXO_3(Sb(C_2H_5)_3)](ClO_4)$ (0.17 g, 0.24 mmol) in acetonitrile (5 ml) was added. The reaction mixture was left for 3 days, and then filtered. The filtrate was rotary evaporated to dryness, the solid residue was washed with methanol, hexane and dried in vacuo. The product was extracted with a small amount of methylene dichloride and the extract filtered was evaporated to dryness. The dark-violet product was reprecipitated from methylene dichloride solution with hexane, washed with hexane and dried in vacuo (yield: 0.12 g, 67%). *Anal.* Calc. for $C_{24}H_{39}N_9O_7ClFeSb$: C, 33.96; H, 5.30; N, 16.97; Fe, 7.52. Found: C, 33.94; H, 5.15; N, 16.98; Fe, 7.43%. MS (MALDI-TOF): *m*/*z*: 643

$[M{-}ClO_4^-]^+$. ^1H NMR (CD_2Cl_2): δ (ppm) 1.28 (t, 9H, CH_3(Et)), 1.75 (quartet, 6H, CH_2(Et)), 2.22 (s, 9H, CH_3-(DXO)), 2.30 (s, 9H, CH_3(DXO)), 3.41 (d ($J_{^1H-^1H} = 23$ Hz), 3H, $CH_2(NCH_2)$), 5.13 (d ($J_{^1H-^1H} = 23$ Hz), 3H, $CH_2(NCH_2)$). $^{13}C\{^1H\}$ NMR (CD_2Cl_2): δ (ppm): 10.4 (s, CH_3(Et)), 13.7 (s, CH_3(DXO)), 17.4 (s, CH_3(DXO)), 25.0 (s, CH_2(Et)), 76.5 (s, $CH_2(NCH_2)$), 154.2 (s, C=N(oxime)), 167.7 (s, C=N(hydrazone)). IR (cm^{-1}, KBr): 1560, 1599, 1628 ν(C=N), 924, 972, 995, 1092, 1109 ν(N – O). UV–Vis (CH_2Cl_2): λ_{max}/nm ($\varepsilon \times 10^{-3}$, $mol^{-1}\,l\,cm^{-1}$) 253 (8.8), 283 (5.2), 313 (3.6), 334 (1.3), 441 (1.1), 490 (2.6), 524 (2.6), 576 (2.4), 618 (1.9), 655 (0.9).

2.2.4. [FeDXO$_3$(CH$_2$)$_3$(Lu(Bu$_8$Pc))]

$CaCO_3$ (0.2 g), silica gel Silasorb SPH-300 (0.1 g), complex $[FeDXO_3(CH_2)_3(Sb(C_2H_5))_3](ClO_4)$ (0.035 g, 0.047 mmol) and complex $[Lu(Bu_8Pc)(CH_3COO)]$ (0.053 g, 0.044 mmol) were dissolved/suspended in methanol–methylene dichloride 3:1 mixture (13 ml). The reaction mixture was stirred for 2 h, and then evaporated to dryness. The solid residue was washed with methanol and extracted with methylene dichloride (5 ml). The extract was filtered through a Silasorb SPH-300 layer (5 mm) and evaporated to dryness. The solid was washed with hexane and dried in vacuo (yield: 0.045 g, 56%). *Anal.* Calc. for $C_{79}H_{104}N_{17}O_3FeLu$: C, 60.41; H, 6.68; N, 15.16; Fe, 3.55. Found: C, 60.39; H, 6.83; N, 15.08; Fe, 3.48%. MS (MALDI-TOF): m/z 1571 $[M]^{+\bullet}$. ^1H NMR (CD_2Cl_2): δ (ppm) 0.77 (s, 9H, CH_3(DXO, oxime)), 1.03 (t, 21H, CH_3(Bu)), 1.55 (m, 16H, γ-CH_2(Bu)), 1.61 (s, 9H, CH_3(DXO, hydrazone)), 1.92 (m, 16H, β-CH_2(Bu)), 2.59 (d, 3H, $CH_2(NCH_2)$), 3.13 (m, 16H, α-CH_2(Bu)), 4.27 (d, 3H, $CH_2(NCH_2)$), 9.16 (s, 8H, HAr). $^{13}C\{^1H\}$ NMR (CD_2Cl_2): δ (ppm) 11.6 (s, CH_3(DXO)), 14.3 (s, CH_3(Bu)), 15.9 (s, CH_3(DXO)), 23.5 (s, CH_2(Bu)), 30.0 (s, CH_2(Bu)), 33.9 (br s, CH_2(Bu)), 75.2 (s, $CH_2(NCH_2)$), 142.8 (br s, Pc), 151.5 (s, Pc), 166.1 (s, Pc). IR (cm^{-1}, KBr): 1543, 1577, 1618 ν(C=N), 972, 993, 1018, 1070, 1092 ν(N – O). UV–Vis (CH_2Cl_2): λ_{max}/nm ($\varepsilon \times 10^{-3}$, $mol^{-1}\,l\,cm^{-1}$) 246 (58), 270 (38), 287 (38), 325 (36), 351 (77), 378 (18), 504 (7.0), 531 (8.5), 563 (8.3), 587 (9.1), 620 (37), 656 (33), 688 (246).

2.2.5. [FeDXO$_3$(HCOC$_2$H$_5$)$_3$(Lu(Bu$_8$Pc))]

This complex was synthesized like the previous one except that complex $[FeDXO_3(HCOC_2H_5)_3(Sb(C_2H_5)_3)](ClO_4)$ (0.035 g, 0.040 mmol) was used instead of clathrochelate $[FeDXO_3(CH_2)_3(Sb(C_2H_5)_3)](ClO_4)$ (yield: 0.030 g, 48%). *Anal.* Calc. for $C_{85}H_{116}N_{17}O_6FeLu$: C, 59.95; H, 6.88; N, 13.98; Fe, 3.28. Found: C, 60.11; H, 6.74; N, 13.90; Fe, 3.14%. MS (MALDI-TOF): m/z (I, %): 1703(100) $[M]^{+\bullet}$, 1674(15) $[M - Et]^+$, 1550(7) $[M - 3OEt - Bu + K^+]^+$, 1534(25) $[M - 3OEt - Bu + Na^+]^+$, 1511(35) $[M - 3OEt - Bu]^+$, 1340(20) $[M - 3OEt - 4Bu]^+$, 1283(45) $[M - 3OEt - 5Bu]^+$. ^1H NMR (CD_2Cl_2): δ (ppm) 0.79 (s, 9H, CH_3(DXO, oxime)), 0.89 (t, 9H, CH_3(OEt)), 1.04 (t, 24H, CH_3(Bu)), 1.15 (m, 16H, CH_2(Bu)), 1.39 (s, 9H, CH_3(DXO, hydrazone)), 1.62 (m, 16H, γ-CH_2(Bu)), 1.93 (m, 16H, β-CH_2(Bu)), 3.64 (quartet, 6H, CH_2(OEt)), 6.14 (s, 3H, HC(methine)), 9.16 (s, 8H, HAr). $^{13}C\{^1H\}$ NMR (CD_2Cl_2): δ (ppm) 11.6 (s, CH_3(DXO)), 14.0 (s, CH_3(OEt)), 14.3 (s, CH_3(Bu)), 15.6 (s, CH_3(DXO)), 23.5 (s, CH_2(Bu)), 30.0 (s, CH_2(Bu)), 33.7 (br s, CH_2(Bu)), 62.9 (s, CH_2(OEt)), 142.8 (br s, Pc), 153.2 (s, Pc), 155.0 (s, HC(methine)), 163.5 (s, Pc). IR (cm^{-1}, KBr): 1558, 1580 sh, 1618 ν(C=N), 960, 995, 1018, 1070, 1092 ν(N – O). UV–Vis (CH_2Cl_2): λ_{max}/nm ($\varepsilon \times 10^{-3}$, $mol^{-1}\,l\,cm^{-1}$) 247 (52), 274 (32), 294 (28), 326 (38), 351 (60), 372 (19), 402 (7.8), 486 (4.4), 527 (7.7), 561 (6.3), 591 (4.6), 621 (25), 655 (25), 688 (183).

3. Results and discussion

3.1. Synthesis

The synthesis of the ditopic complexes is limited by several factors: the macrobicyclic tris-diiminates can be obtained by a template synthesis with cross-linking Lewis acids, which form the apical groups with a target geometry and a given size of the capping atoms (~0.25/0.8 Å). This is accounted for by the requirement of the geometrical complimentarity of an apical capping group and a target rigid macrobicyclic framework. Moreover, the successful self-organization in multicomponent template reaction is caused by the geometrical complimentarity of a template metal ion and the fragments of this macrobicycle. The deviations of the geometrical parameters of the initial entities of a macrobicyclic ligand from ideal ones direct this template reaction to the differ pathways and result in nonmacrocyclic by-products. Nevertheless, we have obtained relatively sterically strained clathrochelates via the modification reactions of the initially synthesized "regular" macrobicyclic precursors [14,16,28]. In particular, the complexes with an encapsulated cobalt(I) ion have been obtained by chemical reduction of the parent cobalt(II) clathrochelates [28].

We used successfully the transmetallation (exchange of the capping fragments) reaction of the triorganylantimony-capped clathrochelates, obtained by a direct template synthesis, in order to change apical capping groups. These clathrochelates undergo the unique (in the series of clathrochelate complexes) transmetallation reaction under mild conditions without destruction of the macrobicyclic framework. This approach allowed to obtain a series of the ditopic tris-dioximate phthalocyaninoclathrochelates one of the two apical capping groups of which contains the sevencoordinate Hf^{4+} and Zn^{4+} ions ($r_i \sim 0.9$ Å) [14].

In the present study this pathway (Scheme 1), using an antimony-capped clathrochelate as a macrobicyclic precursor (synthon), allows us to synthesize the ditopic oximehydrazonate clathrochelates whereas we failed to obtain these complexes by a direct template reaction. Our attempts to use the described earlier [21] triphenylantimony-capped oximehydrazonate iron(II) clathrochelate as

a precursor also gave no desired product: this clathrochelate is insufficiently labile in the transmetallation reactions with the weak Lewis-acidic rare-earth metal phthalocyanines. Additionally, the Shannon ionic radii of the apical rare-earth metal ions are essentially greater than the optimal ones (in particular, in case of the Lu^{3+} ion $r_i \sim 1.1$ Å). Therefore, we obtained much more labile oximehydrazonate clathrochelate synthon with triethylantimony capping group, the transmetallation reactions of which proceeded readily and in relatively high yields (~50–60%). It should be emphasized that a greater lability of the triethylantimony-capped clathrochelates is accounted for by a lower Lewis acidity of the trialkylantimony(V) compounds when compared with that of the triarylantimony(V) derivatives. This causes difficulties in the synthesis of such more labile clathrochelates. In particular, trying to obtain the triethylantimony-capped oximehydrazonate iron(II) semiclathrochelate, one should remove water in the course of reaction, which results in the equilibrium shift in the direction of the target complexes. In contrast, triphenylantimony-capped clathrochelate complexes are formed in high yields in aqueous solutions [21]. The synthesis of labile clathrochelates is also complicated by side reactions (in particular, by the reduction of antimony(V) to antimony(III)). These side reactions may be caused by a low equilibrium concentration of the triethylantimony-capped iron(II) semi- and clathrochelates in the reaction mixture and essentially decrease the yield of the target products. The high lability of triethylantimony capped fragment is the reason of relatively low (~20%) yield in the macrocyclization reaction of triethylantimony-capped semiclathrochelate with TOF. On the other hand, there are some difficulties in using of column chromatography on SiO_2 and Al_2O_3 for purification of the triethylantimony-capped complexes since they undergo the transmetallation reactions on surface of these Lewis-acidic sorbents.

3.2. Structure and spectra

The formation of the ditopic clathrochelate complexes was confirmed both by elemental analysis and MALDI-TOF mass spectra, which contained highly intensive peaks of the molecular ions of the hybrid oximehydrazonate phthalocyaninoclathrochelates. The relative intensities of the isotope peaks of molecular and fragment ions were calculated from the data on the abundance of natural isotopes of all elements forming a part of these ions. The composition of molecular or fragment ions in the experimental mass spectra was confirmed by comparing the isotope peak series of these ions with the calculated ones.

The ^1H and ^{13}C NMR spectra of hybrid compounds obtained were appreciably different from those for their clathrochelate and phthalocyanine precursors: these spectra contained no characteristic signals assigned to the triethylantimony capping fragment and the acetate counter ion, respectively. The ^{13}C NMR spectra showed the significant (by 20 ppm) lowfield shift of the signals of the carbon atoms of phthalocyanine macroring. In the ^1H NMR spectra the significant shift was also observed for the signals assigned to the methyl substituents of the oximehydrazonate fragments because of the magnetic field of the π-electron current in the conjugated phthalocyanine macrocycle. The formation of hybrid complexes has a more dramatic effect on ^{13}C NMR signals of both oxime and hydrazonate carbon azomethine atoms of the cage ligand donor groups. These signals are widened drastically due to the effects of the lutetium phthalocyanine-containing capping fragment and, therefore, were not observed in the spectra. In contrast, the ^1H and ^{13}C NMR signals of hydrazonate fragments, which shifted essentially after the transmetallation reaction, remained narrow. In particular, in the case of the formaldehyde derivative, the spin–spin interaction between nonequivalent axial and equatorial hydrogen atoms of the methylene fragment with characteristic constant $J_{^1H-^1H} \sim 20$ Hz was distinctly observed in the ^1H NMR spectrum. The ^{13}C NMR chemical shift of the signal of carbon methine atom ($\delta_{^{13}C} \sim 155$ ppm) of triethoxy-substituted 1,3,5-triazacyclohexane ring remains practically unchanged after transmetallation and is similar to those for tin-, germanium- and antimony-capped clathrochelate oximehydrazonates [16,20–22]. Such value of the chemical shift differs significantly from the chemical shift ($\delta_{^{13}C} \sim 90$ ppm) of this type carbon atoms in the ^{13}C NMR spectra of the boron-capped clathrochelate oximehydrazonates with *syn*, *syn*, *syn*-orientation of the ethoxy substituents at the 1,3,5-triazacyclohexane ring relative to the clathrochelate framework [20]. Thus, both the clathrochelate $[FeDXO_3(HOC_2H_5)_3(Sb(C_2H_5)_3)]^+$ precursor and the hybrid $[FeDXO_3(HCOC_2H_5)_3(Lu(Bu_8Pc))]$ complex are *anti*-, *anti*-, *anti*-isomers of the corresponding clathrochelates: all of the ethoxy groups and the clathrochelate framework are located on the different sides of the plane passing through the nitrogen atoms of the 1,3,5-triazacyclohexane fragment.

The isomeric shift (IS) values in the ^{57}Fe Mössbauer spectra (Table 1) of the triethylantimony-capped semiclathrochelate complex and the clathrochelate precursor as well as the hybrid oximehydrazonate phthalocyaninoclathrochelates obtained are typical for the low-spin iron(II) complexes. The quadrupole splitting (QS) values in these spectra have been used for deducing of a geometry of the low-spin iron(II) complexes in cases, when the direct X-ray crystallography data cannot be obtained (in particular, we failed to obtain the monocrystals of the complexes synthesized, suitable for X-ray crystallography, because of low symmetry of their molecules and, in case of hybrid compounds, due to their intracomplex character and high number of the aliphatic substituents in the macrocyclic fragment). As shown earlier [15,29], QS has a positive sign (level e_1 is higher than level a_1 in energy) in trigonal prismatic complexes (TP, $\varphi = 0°$) and decreases with an increase of the distortion angle φ of a coordination N_6-polyhedron up to ~30°. Then the inversion of the levels takes place (level a_1 becomes higher in energy than e_1 level;

Table 1
Parameters of ^{57}Fe Mössbauer spectra (mm/s) and electrochemical data (mV) for clathrochelate iron(II) oximehydrazonates and α-dioximates

Complex	IS	QS (sign of QS)	φ obtained (deduced) (°)	E_p^{Ox}	E_p^{Red}
$[FeDXO_3(HCOC_2H_5)_3(Sb(C_2H_5)_3)](ClO_4)$	0.39	(−) 0.51	(40–45)	1190	−1000
$[FeDXO_3(CH_2)_3(Sb(C_2H_5)_3)](ClO_4)$	0.36	(−) 0.52	(40–45)	1180	−1130
$[FeDXO_3(HCOC_2H_5)_3(Lu(Bu_8Pc))]$				650, 1010, 1390	−1020, −1680
$[FeDXO_3(CH_2)_3(Lu(Bu_8Pc))]$	0.38	(−) 0.64	(45–50)	610, 990, 1420	−1090, −1690
$FeNx_3(BBu)(HfPc)$ [14]	0.33	(+) 0.24	29.9[a]	1030, 1260, 1700	−650, −180, −1860
$FeNx_3(BBu)(ZrPc)$ [14]	0.31	(+) 0.21	30.2[a]	1030, 1270, 1680	−640, −1700, −1870
$FeNx_3(BBu)(Sb(C_2H_5)_3)$ [16]	0.32	0.00	(27–32)	950, 1900	−1800
$[FeDXO_3(HCOC_2H_5)_3(Sb(C_6H_5)_3)](B\ F_4)$ [21]	0.41	(−) 0.49	(40–45)	505	
$FeNx_3(Sb(C_2H_5)_3)_2$ [21]	0.36	(−) 0.27	35.7[a]	−65	
$[FeDXO_3(HCOC_2H_5)_3(BC_6H_5)](BF_4)$ [20]	0.35	(+) 0.34	18.2[a]	780	
$[FeDXO_3(Sb(C_6H_5)_3)](BF_4)$ [21]	0.42	(−) 0.36	(35–40)	420	

[a] X-ray data.

QS has a negative sign) and QS increases in absolute value with an increase of the φ value up to 60° (trigonal antiprism, TAP). As mentioned above, the passing from boron-capped iron(II) clathrochelates (TP geometry) to antimony-, tin- and germanium-containing analogues with a greater size of a capping atom leads, as a rule, to an increase of the φ value (TAP geometry). In all cases, QSs for complexes obtained are greater in absolute value than QS for their X-ray crystallographically characterized TP boron-capped $[FeDXO_3(HCOC_2H_5)_3(BC_6H_5)](BF_4)$ analog [20]. It is clear, that QSs for all complexes synthesized have a negative sign. This allowed us to deduce TAP geometry for all complexes obtained as well as to deduce the distortion angle φ values from 40° to 50°, listed in Table 1.

The solution UV–Vis spectra of the hybrid clathrochelates obtained (Fig. 1) contain bands of both chromophoric centers of the ditopic molecule. The intense ($\varepsilon \sim 3-8\times10^4\ mol^{-1}\ l\ cm^{-1}$) bands of the π,π*-transitions both in the dioximate fragments of the clathrochelate framework and in the phthalocyanine macrocycle are overlapped

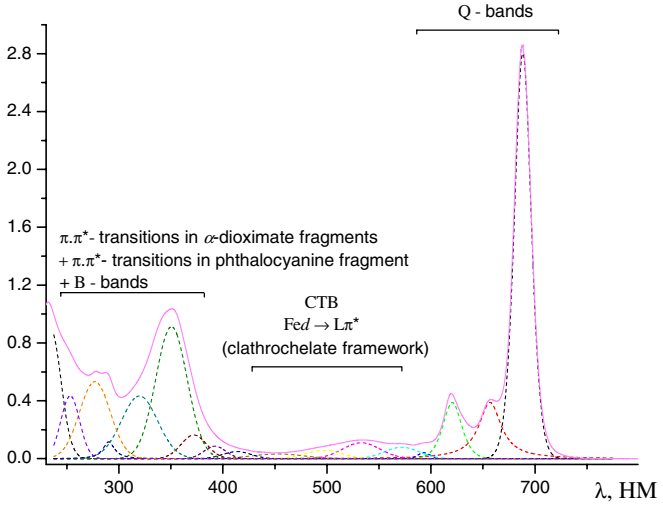


Fig. 1. UV–Vis spectrum of the methylene dichloride solution of $[FeDXO_3(HCOC_2H_5)_3(Lu(Bu_8Pc))]$ phthalocyaninoclathrochelate (—) and Gauss components of this spectrum (—).

with the phthalocyanine B-bands. The observed four intense ($\varepsilon \sim 5-9\times10^3 mol^{-1}\ l\ cm^{-1}$) bands at 500–600 nm in visible region were assigned to the Fed → Lπ* charge transfer bands in the clathrochelate fragment [15]. These bands are overlapped slightly with the most intensive ($\varepsilon \approx 2\times10^5\ mol^{-1}\ l\ cm^{-1}$) characteristic Q-bands of a phthalocyanine fragment.

3.3. Electrochemistry

The cyclic voltammetry data present the information concerning the stability of electrochemically generated cationic and anionic forms of iron(II) clathrochelates, which is important for the estimation of the influence of structural functionalization on the stability of the cage molecules and their photophysical and redox properties [14,15]. Electrochemical study of the new hybrid complexes with luthetium phthalocyanine as one of the capping groups as well as their antimony-capped precursors was performed. Due to the presence of two redox active centers (the encapsulated iron(II) ion and the luthetium phthalocyanine-containing capping group, which is well known as "electron sponge"), several redox transitions could be expected for these compounds.

The $[FeDXO_3(HCOC_2H_5)_3(Lu(Bu_8Pc))]$ and $[FeDXO_3(CH_2)_3(Lu(Bu_8Pc))]$ phthalocyaninoclathrochelates differ by the structure of hydrazonate capping group, hence, the difference in their electrochemical behavior can be explained by the variation of stabilizing effect of these apical fragments. In both cases three oxidation and two reduction peaks were observed in the potential range from −2.0 to 2.0 V (Fig. 2). First two oxidation processes are quasi-reversible, ΔEp is equal to 60–90 mV and the ratio of peak currents for direct (anodic) and reverse (cathodic) waves is close to 1. The most anodic third peak is irreversible at all scan rates investigated (up to 1 V/s) and this process is more likely accompanied by the chemical destruction of the clathrochelate framework. In the reverse scan after the third oxidation peak one can observe the additional reduction peak at a potential of −0.05 V which probably corresponds to the reduction of the products of chemical destruction. The first reduction process is quasi-

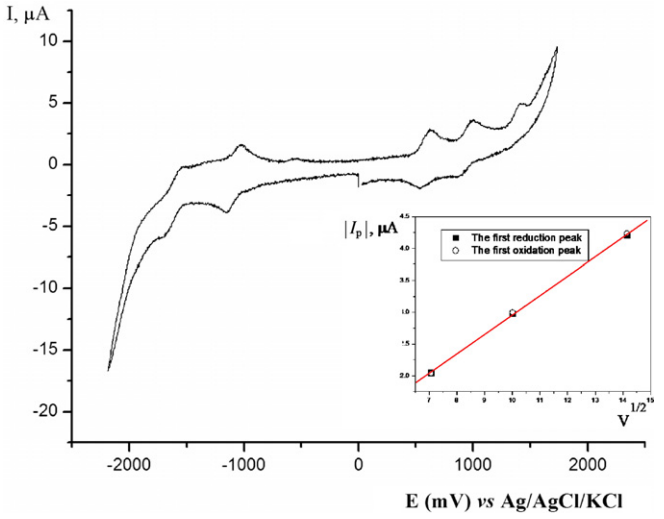


Fig. 2. Cyclic voltammogram for 0.52 mM solution of $[FeDXO_3(CH_2)_3(Lu(Bu_8Pc))]$ clathrochelate in *o*-dichlorobenzene (Pt, 0.15 M $(Bu_4N)BF_4$, 50 mV/s). In the insert: the linear $|I_p|$ vs. $v^{1/2}$ dependences for the first reduction and oxidation peaks.

reversible in case of $[FeDXO_3(CH_2)_3(Lu(Bu_8Pc))]$ clathrochelate and irreversible for $[FeDXO_3(HCOC_2H_5)_3(Lu(Bu_8Pc))]$ complex. This indicates that ditopic $[FeDXO_3(CH_2)_3(Lu(Bu_8Pc))]$ complex is more stable than $[FeDXO_3(HCOC_2H_5)_3(Lu(Bu_8Pc))]$ clathrochelate. As a seen from Table 1, the potentials of redox transitions for $[FeDXO_3(HCOC_2H_5)_3(Lu(Bu_8Pc))]$ phthalocyaninoclathrochelate are only slightly anodically shifted, respectively, to $[FeDXO_3(CH_2)_3(Lu(Bu_8Pc))]$ complex due to the presence of electron-withdrawing ethoxyl substituents in the capping 1,3,5-triazacyclohexane fragment. These data are in good agreement with previously obtained results [24,27] indicating that the redox potentials are much more sensitive to the structural changes in the chelate ribbed fragments than to the substituents in the capping groups.

Antimony-capped formaldehyde $[FeDXO_3(CH_2)_3(Sb(C_2H_5)_3)](ClO_4)$ precursor is more stable than triethyl ortoformate $[FeDXO_3(HCOC_2H_5)_3(Sb(C_2H_5)_3)](ClO_4)$ derivative: the former complex can be oxidized and reduced reversibly, the cation radical and anion radical species produced are sufficiently stable in cyclic voltammetry time scale at scan rates more than 50 mV/s. In contrast, the oxidation and reduction of $[FeDXO_3(HCOC_2H_5)_3(Sb(C_2H_5)_3)](ClO_4)$ clathrochelate are irreversible and followed by the destruction of the clathrochelate framework. However, the oxidized species are more stable than reduced ones because of the fact that at the reverse scan the corresponding reduction peak can be observed, though $I_c/I_a < 1$.

Trying to assign the redox transitions observed to the redox active centers of the hybrid phthalocyaninoclathrochelates, we compared their E_p values with those for their clathrochelate precursors. The first reduction and oxidation processes are more likely phthalocyanine-based. The differences between E_p values are typical for redox processes localized on the phthalocyanine macrocycle (1680 mV [30]). The second oxidation peaks for phthalocyaninochlatrochelates might be assigned to the encapsulated $Fe^{2+/3+}$ redox couples. Their potentials are cathodically shifted (see Table 1) relatively to the values for the antimony-capped precursors. This indicates that the stability of the clathrochelate oxidized form increase in the presence of rather polarizable phthalocyanine fragment with formal charge −2 of the capping group.

The first reduction and oxidation peaks for both clathrochelates are diffusionally controlled as follows from the linear I_p versus $v^{1/2}$ dependence (where v is the scan rate). As a seen from Fig. 2, the correlation is good enough ($r = 0.9998$ and 0.9997 for reduction and oxidation, respectively). Second and third oxidation peaks show a different kinetic behaviour. This may be an additional proof for the involvement of the different redox sites in the various electrochemical steps.

The simple comparison of the redox behavior of lutetium phthalocyanine-capped cage iron(II) complexes with obtained earlier [14] data for hafnium- and zirconium-containing phthalocyaninoclathrochelates (Table 1) is rather complicated since too many parameters are varied (the nature of both the capping groups and the chelate fragments). Nevertheless, the characteristic potential difference of the first oxidation and first reduction waves, which is equal to 1680–1700 mV, is the same for all four hybride clathrochelates. This supports our idea to assign these waves to phthalocyanine-based redox processes.

Acknowledgements

The authors gratefully acknowledge support of the RFBR (Grants 05-03-33184, 05-03-33202, 05-03-32759 and 06-03-32626), RAS (programme 7) and INTAS (Project 04-83-4012).

Appendix A. Supplementary material

Supplementary data associated with this article can be found, in the online version, at doi:10.1016/j.poly.2007.01.044.

References

[1] P.J. Low, Dalton Trans. (2005) 2821.
[2] C.S. Lent, B. Isaksen, M. Lieberman, J. Am. Chem. Soc. 125 (2003) 1056.
[3] M. Koepf, A. Trabolsi, M. Elhabiri, J.A. Wytko, D. Paul, A.M. Albrecht-Gary, J. Weiss, Org. Lett. 7 (2005) 1279.
[4] P.-N. Cheng, P.-T. Chiang, S.-H. Chiu, Chem. Commun. (2005) 1285.
[5] D.W. Steuerman, H.-R. Tseng, A.J. Peters, A.H. Flood, J.O. Jeppesen, K.A. Nielsen, J.F. Stoddart, J.R. Heath, Angew. Chem., Int. Ed. 43 (2004) 6486.
[6] D.A. Leigh, M.A.F. Morales, E.M. Perez, J.K.Y. Wong, C.G. Saiz, A.M.Z. Slawin, A.J. Carmichael, D.M. Haddleton, A.M. Brouwer, W.J. Buma, G.W.H. Wurpel, S. Leon, F. Zerbetto, Angew. Chem., Int. Ed. 44 (2005) 3062.

[7] K. Ohkubo, H. Kotani, J. Shao, Z. Ou, K.M. Kadish, G. Li, R.K. Pandey, M. Fujitsuka, O. Ito, H. Imahori, S. Fukuzumi, Angew. Chem., Int. Ed. 43 (2004) 853.
[8] F. D'Souza, R. Chitta, S. Gadde, M.E. Zandler, A.S.D. Sandanayaka, Y. Araki, O. Ito, Chem. Commun. (2005) 1279.
[9] L.R. Sutton, M. Scheloske, K.S. Pirner, A. Hirsch, D.M. Guldi, J.-P. Gisselbrecht, J. Am. Chem. Soc. 126 (2004) 10370.
[10] P.S. Baran, R.R. Monaco, A.U. Khan, D.I. Schuster, S.R. Wilson, J. Am. Chem. Soc. 119 (1997) 8363.
[11] D. Balbinot, S. Atalick, D.M. Guldi, M. Hatzimarinaki, A. Hirsch, N. Jux, J. Phys. Chem. B 107 (2003) 13273.
[12] T.-G. Zhang, Y. Zhao, I. Asselberghs, A. Persoons, K. Clays, M.J. Therien, J. Am. Chem. Soc. 127 (2005) 9710.
[13] M. Isosomppi, N.V. Tkachenko, A. Efimov, H. Lemmetyinen, J. Phys. Chem. A 109 (2005) 4881.
[14] Y.Z. Voloshin, O.A. Varzatskii, S.V. Korobko, V.Y. Chernii, S.V. Volkov, L.A. Tomachynski, V.I. Pehn'o, M.Y. Antipin, Z.A. Starikova, Inorg. Chem. 44 (2005) 822.
[15] Y.Z. Voloshin, N.A. Kostromina, R. Krämer, Clathrochelates: Synthesis, Structure and Properties, Elsevier, Amsterdam, 2002.
[16] Y.Z. Voloshin, O.A. Varzatskii, S.V. Korobko, M.Y. Antipin, I.I. Vorontsov, K.A. Lyssenko, D.I. Kochubey, S.G. Nikitenko, N.G. Strizhakova, Inorg. Chim. Acta 357 (2004) 3187.
[17] J.A. Belinski, M.E. Squires, J.M. Kuchna, B.A. Bennet, J.J. Grzybowski, J. Coord. Chem. 19 (1988) 159.
[18] J.J. Grzybowski, R.D. Alien, J.A. Belinski, K.L. Bieda, T.A. Bish, P.A. Finnegan, M.L. Hartenstein, G.S. Regitz, D.M. Ryalls, M.E. Squires, H.J. Thomas, Inorg. Chem. 32 (1993) 5266.
[19] K.L. Bieda, A.L. Kranitz, J.J. Grzybowski, Inorg. Chem. 32 (1993) 4209.
[20] Y.Z. Voloshin, A.I. Stash, O.A. Varzatskii, V.K. Belsky, Y.A. Maletin, N.G. Strizhakova, Inorg. Chim. Acta 284 (1999) 180.
[21] Y.Z. Voloshin, O.A. Varzatskii, S.V. Korobko, Y.A. Maletin, Inorg. Chem. Commun. 1 (1998) 328.
[22] Y.Z. Voloshin, O.A. Varzatskii, N.G. Strizhakova, E.Y. Tkachenko, Inorg. Chim. Acta 299 (2000) 104.
[23] Y.Z. Voloshin, O.A. Varzatskii, A.I. Stash, V.K. Belsky, Y.N. Bubnov, I.I. Vorontsov, K.A. Potekhin, M.Y. Antipin, E.V. Polshin, Polyhedron 20 (2001) 2721.
[24] Y.Z. Voloshin, O.A. Varzatskii, T.E. Kron, V.K. Belsky, V.E. Zavodnik, A.V. Palchik, Inorg. Chem. 39 (2000) 1907.
[25] K. Issleib, B. Hamann, Z. Anorg. Allg. Chem. 339 (1965) 289.
[26] M.O. Forster, B.B. Dey, J. Chem. Soc. 101 (1912) 2234.
[27] V.E. Pushkarev, M.O. Breusova, E.V. Shulishov, Y.V. Tomilov, Russ. Chem. Bull. Int. Ed. 54 (2005) 2087.
[28] Y.Z. Voloshin, O.A. Varzatskii, I.I. Vorontsov, M.Y. Antipin, Angew. Chem., Int. Ed. 117 (2005) 3466.
[29] Y.Z. Voloshin, E.V. Polshin, A.Y. Nazarenko, Hyperfine Interact. 141/142 (2002) 309.
[30] C.C. Leznoff, A.B.P. Lever (Eds.), Phthalocyanines: Properties and Applications, Wiley, New York, 1989.

Available online at www.sciencedirect.com
ScienceDirect
Polyhedron 26 (2007) 2741–2748
POLYHEDRON
www.elsevier.com/locate/poly

Synthesis, structure and spectroscopic properties of some thiosemicarbazone complexes of platinum

Sarmistha Halder [a], Ray J. Butcher [b], Samaresh Bhattacharya [a,*]

[a] Department of Chemistry, Inorganic Chemistry Section, Jadavpur University, Kolkata 700 032, India
[b] Department of Chemistry, Howard University, Washington DC 20059, USA

Received 8 December 2006; accepted 16 January 2007
Available online 9 February 2007

Abstract

Reaction of salicyldehyde thiosemicarbazone (H_2L^1), 2-hydroxyacetophenone thiosemicarbazone (H_2L^2) and 2-hydroxynapthaldehyde thiosemicarbazone (H_2L^3) (general abbreviation H_2L, where H_2 stands for the two dissociable protons, one phenolic proton and one hydrazinic proton) with $K_2[PtCl_4]$ afforded a family of polymeric complexes of type $[\{Pt(L)\}_n]$. Reaction of the polymeric species with two monodentate ligands (D), viz. triphenylphosphine (PPh_3) and 4-picoline (pic), yielded complexes of the type [Pt(L)(D)]. These mixed-ligand complexes were also obtained from the reaction of the thiosemicarbazones with $[Pt(PPh_3)_2Cl_2]$ and $[Pt(pic)_2Cl_2]$. The crystal structure of $[Pt(PPh_3)(L^2)]$ has been determined. The thiosemicarbazone ligands are coordinated, via dissociation of the two protons, as dianionic tridentate O,N,S-donors. The [Pt(L)(D)] complexes show characteristic ^1H NMR spectra and intense absorptions in the visible and ultraviolet region. They also fluoresce in the visible region at ambient temperature.
© 2007 Elsevier Ltd. All rights reserved.

Keywords: Thiosemicarbazones; Platinum complexes; Crystal structure; Spectral properties

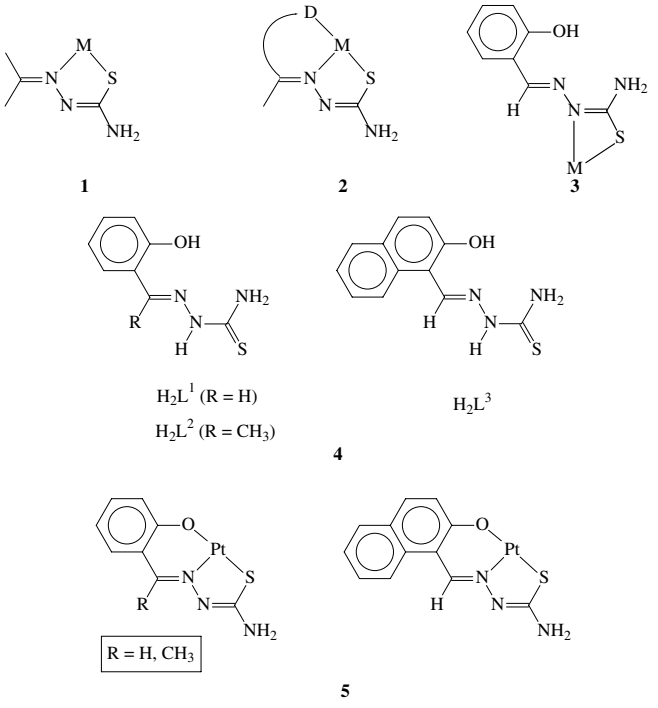
1. Introduction

The chemistry of transition metal complexes of thiosemicarbazones has been receiving considerable attention, largely because of their bioinorganic relevance [1]. Such complexes are of particular importance due to their potentially beneficial biological (viz. antibacterial, antimalarial, antiviral and antitumor) activities [2]. Thiosemicarbazones usually bind to a metal ion, via dissociation of the hydrazinic proton, as a bidentate N,S-donor forming a five-membered chelate ring (**1**) [3]. If a third donor site (D) is incorporated in such ligands, linked to the carbonylic carbon via one or two intervening atoms, then D,N,S-tricoordination (**2**) normally takes place [4]. In addition to displaying D,N,S-tricoordination, such ligands are also known to bridge a second metal ion through the sulfur [5]. It has also been observed that salicylaldehyde thiosemicarbazone, in spite of having the phenolic oxygen as a potential third donor site, coordinates as a bidentate N,S-donor forming a rather unusual four-membered chelate ring (**3**) [6]. This mode of binding (**3**) has also been displayed by some other thiosemicarbazones [7]. Formation of such a chelate ring (**3**) by salicylaldehyde thiosemicarbazone, leaving some potential donor sites unused, has been successfully utilized for the synthesis of interesting polynuclear complexes [8]. This variable binding mode of thiosemicarbazones has encouraged us to explore their coordination chemistry further [6,8,9], and the present work has originated from this exploration. Herein we have chosen three potentially tridentate thiosemicarbazones, viz. thiosemicarbazones of salicylaldehyde, 2-hydroxyacetophenone and 2-hydroxynaphthaldehyde. These thiosemicarbazones are abbreviated in general as H_2L, where H_2 stands for the two dissociable protons, the phenolic proton and the hydrazinic proton. Individual ligand abbreviations

* Corresponding author. Tel.: +91 33 2414 6223; fax: +91 33 2414 6584.
E-mail address: samaresh_b@hotmail.com (S. Bhattacharya).

0277-5387/$ - see front matter © 2007 Elsevier Ltd. All rights reserved.
doi:10.1016/j.poly.2007.01.048

are shown in **4**. To interact with the chosen thiosemicarbazones platinum has been selected as the metal. It may be mentioned here that although the chemistry of platinum complexes of some thiosemicarbazones has been studied [1,10], that of the chosen thiosemicarbazones (**4**) appears to have remained unexplored. Reaction of the three selected thiosemicarbazones (**4**) has been carried out with three platinum starting materials, viz. $K_2[PtCl_4]$, $[Pt(PPh_3)_2Cl_2]$ and $[Pt(pic)_2Cl_2]$ (pic = 4-picoline), which has afforded a family of interesting complexes containing the thiosemicarbazones coordinated in the tridentate fashion (**5**). The chemistry of these complexes is reported in this paper with special reference to their synthesis, structure and spectral properties.



2. Experimental

2.1. Materials

Chloroplatinic acid was purchased from Arora Matthey, Kolkata, India, and was converted to $K_2[PtCl_4]$ [11]. Salicylaldehyde, 2-hydroxyacetophenone and 2-hydroxynaphthaldehyde were obtained from S.D. Fine-chem, Mumbai, India. Thiosemicarbazide was procured from Loba Chemie, Mumbai, India. All other chemicals and solvents were reagent grade commercial materials and were used as received. $[Pt(PPh_3)_2Cl_2]$ and $[Pt(pic)_2Cl_2]$ were prepared from $K_2[PtCl_4]$ by following reported procedures [12,13]. The thiosemicarbazone ligands (H_2L^1, H_2L^2 and H_2L^3) were prepared by condensing the respective aldehyde or ketone with thiosemicarbazide in hot ethanol.

2.2. Synthesis

2.2.1. $[\{Pt(L^1)\}_n]$

To a solution of H_2L^1 (47 mg, 0.24 mmol) in hot methanol (30 mL) triethylamine (48 mg, 0.48 mmol) was added followed by $K_2[PtCl_4]$ (100 mg, 0.24 mmol). The mixture was heated at reflux for 24 h. A brown precipitate settled down on cooling, which was collected by filtration, washed with methanol and dried in air to afford $[\{Pt(L^1)\}_n]$ as a brown powder. Yield: 67 mg. *Anal.* Calc. for $(C_8H_7N_3SOPt)_n$: C, 24.67; H, 1.80; N, 10.79. Found: C, 24.78; H, 1.93; N, 10.82%.

The $[\{Pt(L^2)\}_n]$ and $[\{Pt(L^3)\}_n]$ complexes were prepared by following the same above procedure using HL^2 and HL^3 instead of HL^1.

$[\{Pt(L^2)\}_n]$: *Anal.* Calc. for $(C_9H_9N_3SOPt)_n$: C, 26.87; H, 2.24; N, 10.45. Found: C, 27.38; H, 2.32; N, 10.49%.

$[\{Pt(L^3)\}_n]$: *Anal.* Calc. for $(C_{12}H_9N_3SOPt)_n$: C, 32.88; H, 2.06; N, 9.59. Found: C, 32.14; H, 2.14; N, 9.63%.

2.2.2. $[Pt(PPh_3)(L^1)]$

Method A: The polymeric $[\{Pt(L^1)\}_n]$ species (100 mg) and triphenylphosphine (68 mg) were taken together in ethanol (30 mL) and the solution was refluxed for 24 h to yield a lemon yellow solution. Evaporation of this solution gave a yellow solid, which was subjected to purification by thin layer chromatography on a silica plate. With 1:40 acetonitrile–benzene as the eluant, a major yellow band separated, which was extracted with acetonitrile. Upon evaporation of the acetonitrile extract $[Pt(PPh_3)(L^1)]$ was obtained as a crystalline yellow solid. Yield: 95 mg (57%).

Method B: To a solution of H_2L^1 (20 mg, 0.10 mmol) in hot ethanol (30 mL) triethylamine (20 mg, 0.20 mmol) was added followed by *cis*-$[Pt(PPh_3)_2Cl_2]$ (100 mg, 0.13 mmol). The mixture was heated at reflux for 6 h to yield a lemon yellow solution. Evaporation of this solution gave a yellow solid, which was subjected to purification by thin layer chromatography on a silica plate. With 1:40 acetonitrile–benzene as the eluant, a major yellow band separated, which was extracted with acetonitrile. Upon evaporation of the acetonitrile extract $[Pt(PPh_3)(L^1)]$ was obtained as a crystalline yellow solid. Yield: 49 mg (60%). *Anal.* Calc. for $C_{26}H_{22}N_3SOPt$: C, 47.92; H, 3.38; N, 6.45. Found: C, 47.88; H, 3.42; N, 6.49%. ^1H NMR in $CDCl_3$, δ ppm: 4.87 (s, 2H), 6.86 (t, 1H, $J = 7.4$ Hz), 6.75 (d, 1H, $J = 8.5$ Hz), 7.20–7.32* (2H), 7.39–7.77* (PPh_3), 8.55 (d, 1H, $J = 11.8$ Hz).

The $[Pt(PPh_3)(L^2)]$ and $[Pt(PPh_3)(L^3)]$ complexes were prepared by following the same above procedure using H_2L^2 and H_2L^3 instead of H_2L^1.

$[Pt(PPh_3)(L^2)]$: *Anal.* Calc. for $C_{27}H_{24}N_3SOPt$: C, 48.71; H, 3.61; N, 6.31. Found: C, 48.74; H, 3.66; N, 6.33%. ^1H NMR in $CDCl_3$, δ ppm: 2.86 (s, 3H), 4.84 (s, 2H), 6.67–6.72* (2H), 7.17 (t, 1H, $J = 7.5$ Hz), 7.40–7.80 ($PPh_3 + 1H$).

$[Pt(PPh_3)(L^3)]$: *Anal.* Calc. for $C_{27}H_{24}N_3SOPt$: C, 51.20; H, 3.41; N, 5.97. Found: C, 51.23; H, 3.88; N,

6.92%. ^{1}H NMR in $CDCl_3$, δ ppm: 4.87 (s, 2H), 6.86 (d, 1H, $J = 9.1$ Hz), 7.26 (t, 1H, $J = 7.4$ Hz), 7.61 (d, 1H, $J = 9.2$ Hz), 7.67 (d, 1H, $J = 7.9$ Hz), 7.42–7-.78* (PPh_3 + 1H), 8.17 (d, 1H, $J = 8.6$ Hz), 9.57 (d, 1H, $J = 11.8$ Hz).

2.2.3. [Pt(pic)(L^1)]

Method A: The polymeric [{Pt(L^1)}$_n$] species (100 mg) and 4-picoline (24 mg) were taken in ethanol (30 mL) and the solution was refluxed for 24 h to yield a yellow solution. Evaporation of this solution gave a yellow solid, which was subjected to purification by thin layer chromatography on a silica plate. With 1:20 acetonitrile–benzene as the eluant, a prominent yellow band separated, which was extracted with acetonitrile. Upon evaporation of the acetonitrile extract [Pt(pic)(L^1)] was obtained as a crystalline yellow solid. Yield: 70 mg (56%).

Method B: To a solution of H_2L^1 (44 mg, 0.22 mmol) in hot ethanol (30 mL) triethylamine (45 mg, 0.44 mmol) was added followed by [Pt(pic)$_2$Cl$_2$] (100 mg, 0.22 mmol). The mixture was heated at reflux for 24 h to yield a yellow solution. Evaporation of this solution gave a yellow solid, which was subjected to purification by thin layer chromatography on a silica plate. With 1:20 acetonitrile–benzene as the eluant, a major yellow band separated, which was extracted with acetonitrile. Upon evaporation of the acetonitrile extract [Pt(pic)(L^1)] was obtained as a crystalline yellow solid. Yield: 54 mg (50%). *Anal.* Calc. for $C_{14}H_{14}N_4SOPt$: C, 34.63; H, 2.89; N, 11.54. Found: C, 34.45; H, 2.74; N, 11.34%. ^{1}H NMR in $CDCl_3$, δ ppm: 2.45 (s, 3H), 5.05 (s, 2H), 6.70–6.80* (2H), 7.13 (d, 1H, $J = 6.2$ Hz), 7.33–7.46* (3H), 8.30 (s, 1H), 8.81 (d, 2H, $J = 6.2$ Hz).

The [Pt(pic)(L^2)] and [Pt(pic)(L^3)] complexes were prepared by following the same above procedure using H_2L^2 and H_2L^3 instead of H_2L^1.

[Pt(pic)(L^2)]: *Anal.* Calc. for $C_{15}H_{16}N_4SOPt$: C, 36.36; H, 3.23; N, 11.32. Found: C, 36.54; H, 3.46; N, 11.13%. ^{1}H NMR in $CDCl_3$, δ ppm: 2.43 (s, 3H), 2.81 (s, 3H), 4.93 (s, 2H), 6.74 (t, 1H, $J = 7.5$ Hz), 7.14 (d, 1H, $J = 8.3$ Hz), 7.22 (d, 2H, $J = 5.6$ Hz), 7.30 (t, 1H, $J = 8.9$ Hz), 7.81 (d, 1H, $J = 8.3$ Hz), 8.78 (d, 2H, $J = 9.0$ Hz).

[Pt(pic)(L^3)]: *Anal.* Calc. for $C_{18}H_{16}N_4SOPt$: C, 40.67; H, 3.01; N, 10.54. Found: C, 40.43; H, 3.20; N, 10.32%. ^{1}H NMR in $CDCl_3$, δ ppm: 2.47 (s, 3H), 4.94 (s, 2H), 7.24–7.33* (4H), 7.53 (t, 1H, $J = 7.5$ Hz), 7.71–7.80* (2H), 8.14 (d, 1H, $J = 8.5$ Hz), 8.86 (d, 2H, $J = 6.1$ Hz), 9.30 (s, 1H).

2.3. Physical measurements

Microanalyses (C, H, N) were performed using a Heraeus Carlo Erba 1108 elemental analyzer. IR spectra were obtained on a Shimadzu FTIR-8300 spectrometer with samples prepared as KBr pellets. Electronic spectra were recorded on a JASCO V-570 spectrophotometer. Emission spectra were recorded on a Perkin–Elmer LS55 Luminescence Spectrometer. ^{1}H NMR spectra were recorded in $CDCl_3$ solutions on a Bruker Avance DPX 300 NMR spectrometer using TMS as the internal standard.

2.4. X-ray crystallography

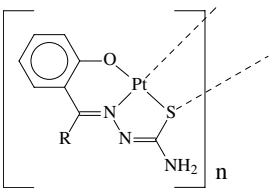
Single crystals of [Pt(PPh$_3$)(L^2)] were grown by slow evaporation of a solution of the complex in 1:1 dichloromethane–acetonitrile. Selected Crystal data and a summary of the data collection appear below, the full details are provided in Table S1. Data were collected on a Bruker SMART CCD diffractometer using graphite-monochromated Mo Kα radiation ($\lambda = 0.71073$ Å) by ϕ and ω scans. X-ray data reduction, structure solution and refinement were done using the SHELXS-97 and SHELXL-97 packages [14]. The structure was solved by direct methods.

Crystal data for $C_{27}H_{24}N_3OPSPt$, $M = 664.61$, $0.55 \times 0.35 \times 0.12$ mm^3, monoclinic, space group $P2_1/c$, $a = 15.7537(12)$ Å, $b = 9.0719(6)$ Å, $c = 17.1657(13)$ Å, $\beta = 94.61(10)°$, $V = 2445.3(3)$ Å^3, $Z = 4$, $D_{calc} = 1.805$ Mg m^{-3}, $F(000) = 1296$, $\lambda = 0.71073$ Å, $T = 103$ K, $\mu = 5.915$ mm^{-1}, 17316 reflections collected, 5901 unique ($R_{int} = 0.049$). Final goodness-of-fit = 1.03, $R_1 = 0.0273$, $wR_2 = 0.0625$, R indices based on 4607 reflections with $[I > 2\sigma(I)]$.

3. Results and discussion

3.1. Syntheses and crystal structure

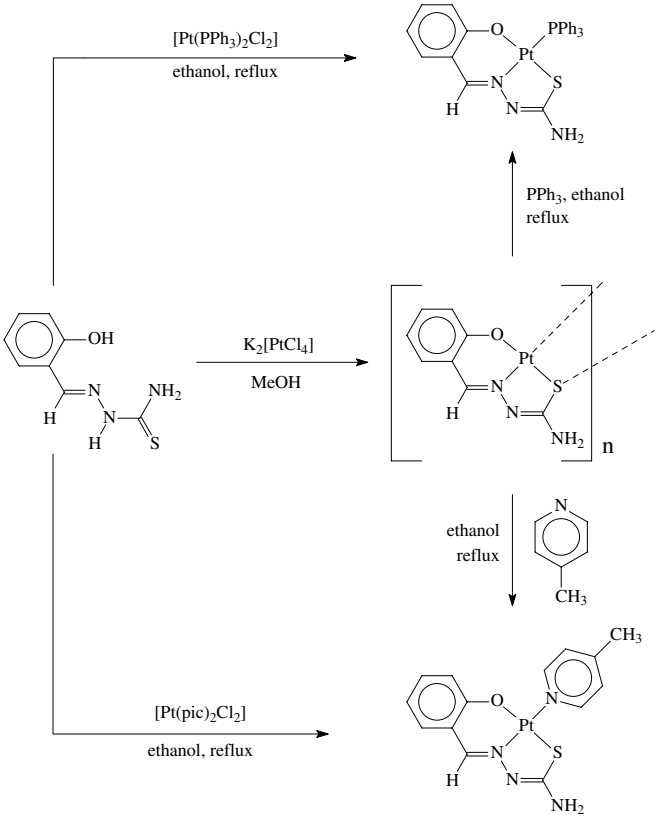
The reaction of the selected thiosemicarbazones (H_2L, **4**) has been first carried out with $K_2[PtCl_4]$ in refluxing methanol in the presence of triethylamine to afford a family of polymeric complexes of the type {Pt(L)}$_n$ in decent yields. Based on the composition of these complexes, as well as the +2 oxidation state of platinum in them, the thiosemicarbazones are believed to coordinate the metal center in the expected dianionic O,N,S-fashion (**5**). The fourth coordination position on platinum in the Pt(L) fragment is assumed to be taken up by the sulfur of a coordinated thiosemicarbazone belonging to another Pt(L) fragment (**6**). This bridging action of the thiosemicarbazone–sulfur, which is well documented in the literature [5], appears to be responsible for the formation of the polymeric species.



6

In order to explore the possibility of forming monomeric complexes by splitting the sulfur bridge in the {Pt(L)}$_n$ complexes, their reaction has been carried out with two

monodentate ligands (**D**), viz. 4-picoline (pic) and triphenylphosphine (PPh_3). From each of these reactions a monomeric complex of type [Pt(L)(D)] (D = pic or PPh_3) has been obtained. The same monomeric complexes have also been synthesized, in better yields, by the reaction of the thiosemicarbazones (**4**) with $[Pt(PPh_3)_2Cl_2]$ and $[Pt(pic)_2Cl_2]$ in refluxing ethanol in the presence of triethylamine. The synthetic methods of all the complexes are illustrated in Scheme 1. The observed elemental (C, H, N) analytical data of all the complexes are consistent with their compositions. It appears from the formulation of the monomeric complexes that the thiosemicarbazones are serving as tridentate ligands in them. In order to authenticate the coordination mode of the thiosemicarbazones in these complexes, the structure of a representative member of this family of monomeric complexes, viz. $[Pt(PPh_3)(L^2)]$, has been determined by X-ray crystallography. A selected view of the complex molecule is shown in Fig. 1 and some relevant bond parameters are listed in Table 1. The structure shows that the thiosemicarbazone ligand (L^2) is coordinated to platinum in the expected tridentate fashion (**5**), forming a six- and a five-membered chelate ring with O–Pt–N and N–Pt–S bite angles of 92.48(12)° and 85.09(9)°, respectively. A triphenylphosphine is coordinated to the metal center, which is trans to the nitrogen atom. Platinum is thus nested in a NOSP core, which is slightly distorted from an ideal square-planar geometry, as reflected in the bond parameters around the metal center. The Pt–N, Pt–O, Pt–P and Pt–S distances



Scheme 1.

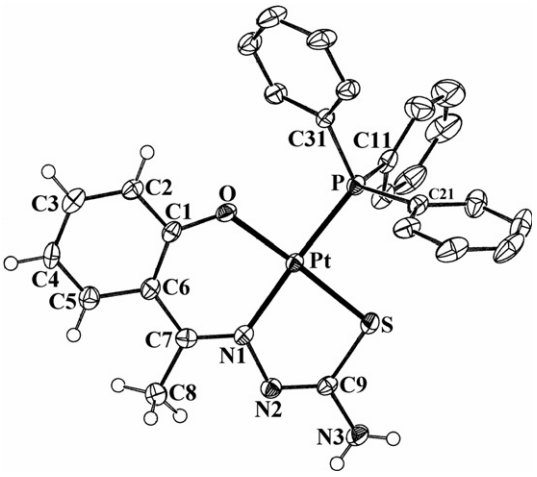


Fig. 1. Structure of the $[Pt(PPh_3)(L^2)]$ complex.

Table 1
Selected bond distances (Å) and angles (°) for $[Pt(PPh_3)(L^2)]$

Bond distances (Å)			
Pt–N(1)	2.038(3)	C(7)–N(1)	1.320(5)
Pt–P	2.2598(11)	C(9)–N(3)	1.386(5)
Pt–S	2.2575(10)	C(1)–O	1.325(5)
Pt–O	2.006(3)	N(1)–N(2)	1.403(5)
		C(9)–S	1.742(4)
Bond angles (°)			
N(1)–Pt–P	175.57(9)	N(1)–Pt–O	92.48(12)
O–Pt–S	175.71(8)	N(1)–Pt–S	85.09(9)

are normal, as observed in other structurally characterized complexes of platinum containing these bonds [10,15]. Bond distances within the coordinated thiosemicarbazone are also usual [9c]. The absence of any solvent of crystallization in the crystal lattice indicates possible existence of non-covalent interaction(s) between the individual complex molecules. A closer look at the packing pattern of the crystal reveals that non-covalent interactions of two types, viz. C–H···S and N–H···π interactions, are active in the lattice,

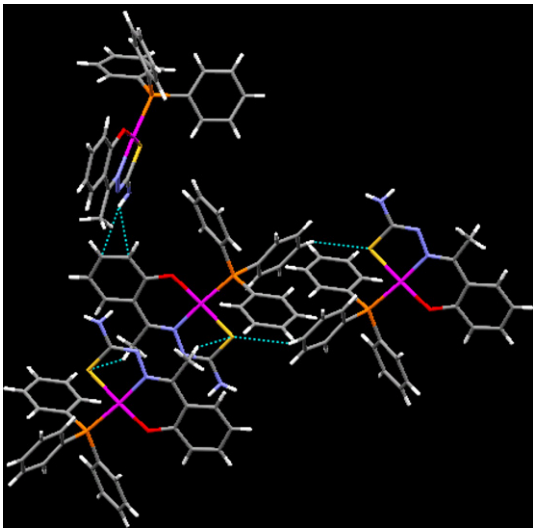


Fig. 2. Packing pattern in the lattice of the $[Pt(PPh_3)(L^2)]$ complex.

which is illustrated in Fig. 2. The sulfur of each coordinated thiosemicarbazone is hydrogen-bonded to two C–H fragments, a phenyl C–H of the PPh_3 and a methyl C–H of the thiosemicarbazone belonging to two different neighboring complex molecules. One N–H fragment of the thiosemicarbazone is involved in hydrogen-bonding with the π-cloud over a C–C bond of the phenol fragment of an adjacent complex molecule in a η^2-fashion. Each complex molecule is thus linked with three surrounding complex molecules through C–H···S and N–H···π interactions (Fig. 2), and this extended intermolecular hydrogen-bonding is responsible for holding the crystal together. All the monomeric [Pt(L)(D)] complexes are assumed to have similar structures to $[Pt(PPh_3)(L^2)]$.

3.2. Spectral properties

^1H NMR spectra of the $[Pt(PPh_3)(L)]$ complexes, recorded in $CDCl_3$ solutions, show all the expected signals. The phenyl protons of the PPh_3 ligands show broad signals within the range δ 7.39–7.80 ppm. In the $[Pt(PPh_3)(L^1)]$ and $[Pt(PPh_3)(L^3)]$ complexes the azomethine proton signal of the coordinated thiosemicarbazone is observed at δ 8.55 and 9.57 ppm, respectively. The methyl signal from the coordinated thiosemicarbazone in the $[Pt(PPh_3)(L^2)]$ complex is observed at δ 2.86 ppm. The NH_2 signal of the coordinated thiosemicarbazone is observed around δ 4.8 ppm. Most of the expected signals from the phenyl ring of the coordinated thiosemicarbazone are clearly observed in the aromatic region, whilst a few could not be detected due to their overlap with other signals. In the ^1H NMR spectra of the [Pt(pic)(L)] complexes, the methyl signal of the coordinated picoline is observed around δ 2.4 ppm. The NH_2 signal of the coordinated thiosemicarbazone is observed around δ 5.0 ppm and the azomethine proton signal (for $L = L^1$ and L^3) is observed between δ 8.3–9.3 ppm. The methyl signal from the coordinated thiosemicarbazone in the $[Pt(pic)(L^2)]$ complex is observed at δ 2.81 ppm. A distinct doublet observed near δ 8.8 ppm in all the three [Pt(pic)(L)] complexes is attributable to the α-proton of picoline. The other aromatic proton signals are observed in the expected region as overlapping signals. The ^1H NMR spectral data of the $[Pt(PPh_3)(L)]$ and [Pt(pic)(L)] complexes are therefore in well accordance with their compositions.

Infrared spectra of all the $[Pt(PPh_3)(L)]$ complexes show many vibrations of different intensities in the 1600–400 cm^{-1} region. Assignment of each individual band to a specific vibration has not been attempted. However, three strong bands displayed near 513, 694 and 743 cm^{-1} by each of these complexes are attributed to the coordinated PPh_3 ligands. Comparison with the spectrum of the *cis*-$[Pt(PPh_3)_2Cl_2]$ complex shows the presence of several new bands (e.g. near 1130, 1226, 1292, 1334, 1352, 1423, 1508, 1541 and 1560 cm^{-1}) in the spectra of the $[Pt(PPh_3)(L)]$ complexes, which must be due to the presence of the coordinated thiosemicarbazone ligands. Besides an absence of the three diagnostic bands for the PPh_3 ligands near 513, 694 and 743 cm^{-1}, the infrared spectral properties of the [Pt(pic)(L)] complexes are qualitatively similar to that of the $[Pt(PPh_3)(L)]$ complexes.

The $[Pt(PPh_3)(L)]$ and [Pt(pic)(L)] complexes are readily soluble in methanol, ethanol, acetone, acetonitrile, dichloromethane, chloroform, etc., producing intense lemon yellow solutions. Electronic spectra of these complexes have been recorded in dichloromethane solution. A selected spectrum is shown in Fig. 3 and spectral data are presented in Table 2. Each complex shows several intense absorptions in the visible and ultraviolet regions. The absorptions in the ultraviolet region are assignable to transitions within the ligand orbitals. To have an understanding of the nature of the transitions in the visible region, qualitative EHMO calculations have been performed [16] on computer generated models of the $[Pt(PPh_3)(L)]$ and [Pt(pic)(L)] complexes. The composition of selected molecular orbitals is given in Table 3 and a partial MO diagram for a representative $[Pt(PPh_3)(L)]$ complex is shown in Fig. 4. The partial

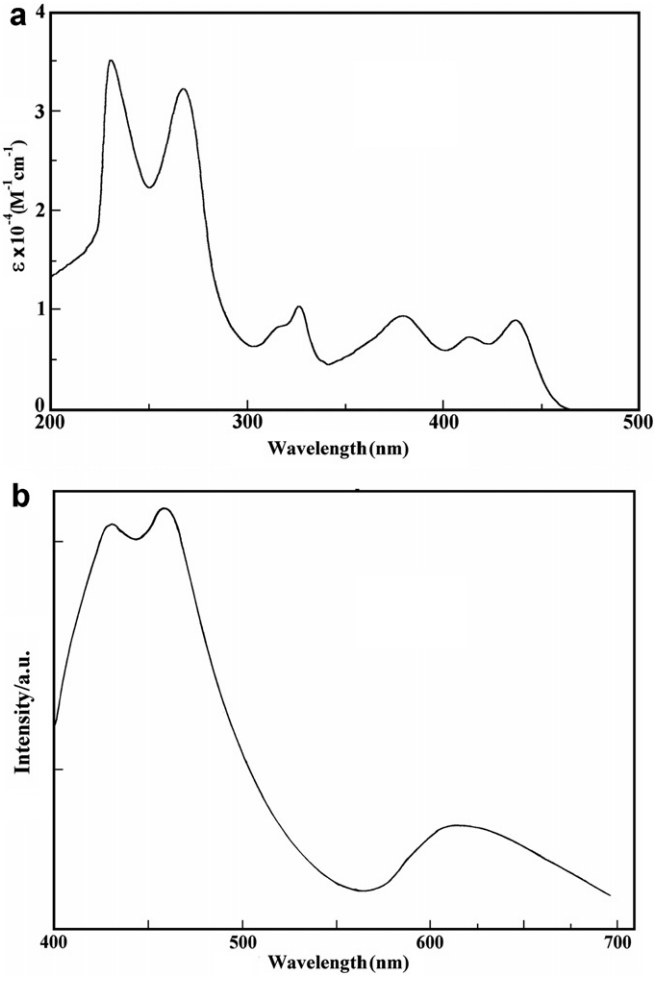


Fig. 3. (a) Electronic spectrum and (b) emission spectrum of $[Pt(PPh_3)(L^3)]$ in dichloromethane solution.

Table 2
Electronic spectral data in dichloromethane solution

Compound	λ_{max}/nm (ε/M^{-1} cm^{-1})
[Pt(PPh$_3$)(L^1)]	416 (4800), 364 (9000), 306 (6500), 294 (7200), 262 (18300)[a]
[Pt(PPh$_3$)(L^2)]	412 (4600), 364 (8300), 306 (6700)^s, 292 (8300), 256 (21300)
[Pt(PPh$_3$)(L^3)]	436 (9100), 413 (7400), 379 (9500), 327 (10400), 317 (8400)^s, 267 (32300)
[Pt(pic)(L^1)]	411^s (2000), 364 (3800), 338 (3400), 310 (3500), 299 (3400), 253 (9100)^s
[Pt(pic)(L^2)]	417^s (4500), 364 (10100), 349^s (8500)^s, 311^s (7300), 299 (7700) 245 (25400)
[Pt(pic)(L^3)]	438 (3600), 415 (3200), 380 (5200), 328 (4500), 317^s (3800)^s, 267 (15800)

[a] s, shoulder.

Table 3
Composition of selected molecular orbitals of the complexes

Compound	Contributing fragments	% Contribution of fragments to	
		HOMO	LUMO
[Pt(PPh$_3$)(L^1)]	Pt	64	
	L^1	32	95 (C=N, 52)
[Pt(PPh$_3$)(L^2)]	Pt	64	
	L^2	29	92 (C=N, 47)
[Pt(PPh$_3$)(L^3)][a]	Pt	11	
	L^3	84	95 (C=N, 33)
[Pt(pic)(L^1)]	Pt	64	2
	L^1	32	73 (C=N, 43)
	pic		21
[Pt(pic)(L^2)]	Pt	55	2
	L^2	34	44 (C=N, 24)
	pic	2	46
[Pt(pic)(L^3)][b]	Pt	19	
	L^3	72	90 (C=N, 31)
	pic		2

[a] The HOMO − 1 has 68% contribution from the metal.
[b] The HOMO − 1 has 67% contribution from the metal.

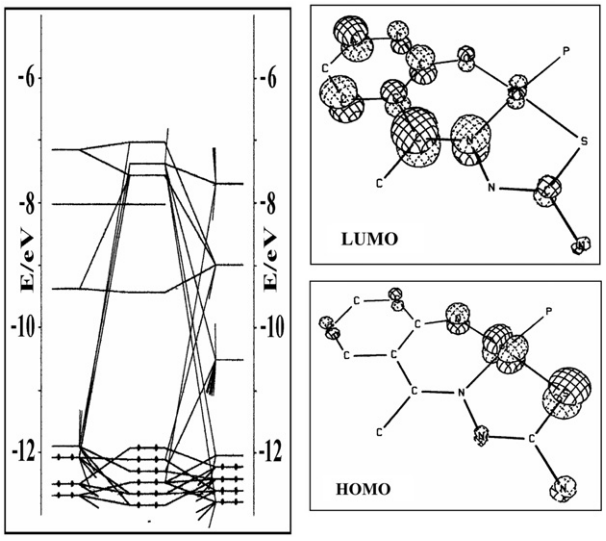


Fig. 4. Partial molecular orbital diagram of the [Pt(PPh$_3$)(L^2)] complex.

Table 4
Emission spectral data for the complexes

Compound	Emission data		
	λ_{max} (nm)		Quantum yield (φ)
	Excitation	Emission	
[Pt(PPh$_3$)(L^1)]	364	595, 570, 445, 415^s	1.82×10^{-3}
[Pt(PPh$_3$)(L^2)]	364	432, 415^s	1.13×10^{-3}
[Pt(PPh$_3$)(L^3)]	379	610, 460, 422	0.42×10^{-3}
[Pt(pic)(L^1)]	363	600, 565^s, 430, 408	2.39×10^{-3}
[Pt(pic)(L^2)]	364	610, 562, 432^s, 415	0.59×10^{-3}
[Pt(pic)(L^3)]	380	610, 432, 416	0.73×10^{-3}

s, shoulder.

MO diagram for a representative [Pt(pic)(L)] complex is deposited as Fig. S1. In the case of the [Pt(PPh$_3$)(L^1)] and [Pt(PPh$_3$)(L^2)] complexes the highest occupied molecular orbital (HOMO) has major contributions from the platinum d orbitals. The lowest unoccupied molecular orbital (LUMO) is delocalized almost entirely on the thiosemicarbazone ligand, and is largely concentrated on the imine fragment. Therefore the lowest energy absorption near 410 nm is assignable to a charge-transfer transition taking place from the filled metal orbital (HOMO) to the vacant π^*-orbital of the thiosemicarbazone ligand (LUMO). However, in case of the [Pt(PPh$_3$)(L^3)] complex the HOMO has only 11% metal character, while the LUMO is similar in nature as before. Hence the lowest energy absorption at 436 nm in this complex is assignable to a transition within the orbitals belonging primarily to L^3. It may be mentioned in this context that this absorption is much more intense compared to the lowest energy transition in the earlier two complexes. It may also be noted here that there is a second absorption at 413 nm, which may be assigned to a charge-transfer transition taking place from the filled metal orbital (HOMO − 1) to the vacant π^*-orbital of the thiosemicarbazone ligand (LUMO). The electronic spectral properties, as well as features of the molecular orbitals, of the [Pt(pic)(L)] complexes are similar to those of the [Pt(PPh$_3$)(L)] analogues.

The intensities of the charge-transfer transitions in the visible region have tempted us to explore the luminescence properties of these complexes and this has been carried out in dichloromethane solution at ambient temperature (298 K). All six complexes display emission in the visible region using an excitation wavelength of ~350 nm (Fig. 3). Quantum yields (ϕ) of these emissions have been evaluated (Table 4) with reference to [Ru(bpy)$_3$]Cl$_2$ ($\phi = 0.028$ at 298 K) [17].

4. Conclusion

The present study shows that salicylaldehyde thiosemicarbazones and similar ligands can smoothly bind to platinum as tridentate O,N,S-donors yielding stable complexes, which not only show intense absorptions in the visible region but also fluoresce at room temperature.

Acknowledgements

Financial assistance received from the Council of Scientific and Industrial Research, New Delhi, India [Grant No. 01(1952)/04/EMR-II] is gratefully acknowledged. The authors thank Prof. Chittaranjan Sinha and Dr. Asok Nath Mandal of the Department of Chemistry, Jadavpur University, for their help with the florescence and NMR spectral measurements, respectively. Sarmistha Halder thanks the University Grants Commission, New Delhi, India, for her fellowship [Grant No. 10-2(5)2004(1)-E.U.II].

Appendix A. Supplementary material

CCDC 626762 contains the supplementary crystallographic data for [Pt(PPh_3)(L^2)]. These data can be obtained free of charge via http://www.ccdc.cam.ac.uk/conts/retrieving.html, or from the Cambridge Crystallographic Data Centre, 12 Union Road, Cambridge CB2 1EZ, UK; fax: (+44) 1223-336-033; or e-mail: deposit@ccdc.cam.ac.uk. Full details of data collection are provided in Table S1. A partial MO diagram of the [Pt(pic)(L^1)] complex has been deposited as Fig. S1. Supplementary data associated with this article can be found, in the online version, at doi:10.1016/j.poly.2007.01.048.

References

[1] (a) M.J.M. Campbell, Coord. Chem. Rev. 15 (1975) 279;
(b) S.B. Padhye, G.B. Kaffman, Coord. Chem. Rev. 63 (1985) 127;
(c) I. Haiduc, C. Silvestru, Coord. Chem. Rev. 99 (1990) 253;
(d) D.X. West, S.B. Padhye, P.B. Sonawane, Struct. Bond. 76 (1992) 1;
(e) D.X. West, A.E. Liberta, S.B. Padhye, R.C. Chikate, P.B. Sonawane, A.S. Kumbhar, R.G. Yerande, Coord. Chem. Rev. 123 (1993) 49;
(f) J.R. Dilwarth, P. Amold, D. Morales, Y.L. Wong, Y. Zheng, Modern Coord. Chem. (2002) 217;
(g) A.G. Quiroga, C.N. Raninger, Coord. Chem. Rev. 248 (2004) 119.
[2] (a) F.A. French, E. Blanz Jr., J. Med. Chem. 13 (1970) 1117;
(b) A.C. Sartorellic, K.C. Agrawal, A.S. Tsiftsoglou, A.C. Moore, Adv. Enzyme Regul. 15 (1977) 117;
(c) K.C. Agrawal, A.C. Sartorelli, Prog. Med. Chem. 15 (1978) 321;
(d) J.P. Scovill, D.L. Klayman, C.F. Franchino, J. Med. Chem. 25 (1982) 1261;
(e) A. Kraker, S. Krezoski, J. Schneider, D. Mingel, D.H. Petering, J. Biol. Chem. 260 (1985) 13710;
(f) A.E. Liberta, D.X. West, Biometals 5 (1992) 121;
(g) D. Kovala-Demertzi, A. Domopoulou, M.A. Demertzis, C.P. Raptopoulou, A. Terzis, Polyhedron 13 (1994) 1917;
(h) A. Papageorgiou, Z. Iakovidou, D. Mourelatos, E. Mioglou, L. Boutis, A. Kotsis, D. Kovala-Demertzi, A. Domopoulou, D.X. West, M.A. Demertzis, Anticancer Res. 17 (1997) 247;
(i) M.C. Miller III, C.N. Stineman, J.R. Vance, D.X. West, I.H. Hall, Anticancer Res. 18 (1998) 4131;
(j) D. Kovala-Demertzi, J.R. Miller, N. Kourkoumelis, S.K. Hadjikakou, M.A. Demertzis, Polyhedron 18 (1999) 1005;
(k) Z. Iakovidou, A. Papageorgiou, M.A. Demertzis, E. Mioglou, D. Mourelatos, A. Kotsis, P.N. Yadav, D. Kovala-Demertzi, Anticancer Drugs 12 (2001) 65;
(l) J. Patole, S. Dutta, S. Padhye, E. Sinn, Inorg. Chim. Acta 318 (2001) 207;
(m) R.I. Maurer, P.J. Blower, J.R. Dilworth, C.A. Reynolds, Y. Zheng, G.E.D. Mullen, J. Med. Chem. 45 (2002) 1420;
(n) A.R. Cowly, J.R. Dilworth, P.S. Donnely, E. Labisbal, A. Sousa, J. Am. Chem. Soc. 124 (2002) 5270;
(o) M.B. Ferrari, F. Bisceglie, G. Pelosi, M. Sassi, P. Tarasconi, M. Cornia, S. Capacchi, R. Albertini, S. Pinelli, J. Inorg. Biochem. 90 (2002) 113;
(p) E.M. Jouad, X.D. Thanh, G. Bouet, S. Bonneau, M.A. Khan, Anticancer Res. 22 (2002) 1713;
(q) S. Padhye, Z. Afrasiabi, E. Sinn, J. Fok, K. Mehta, N. Rath, Inorg. Chem. 44 (2005) 1154;
(r) J. Ruiz, N. Cutillas, C. Vicente, M.D. Villa, G. López, J. Lorenzo, F.X. Avilés, V. Moreno, D. Bautista, Inorg. Chem. 44 (2005) 7365.
[3] Y.P. Tion, C.Y. Duan, Z.L. Lu, X.Z. You, H.K. Fun, S. Kandasamy, Polyhedron 15 (1996) 2263.
[4] (a) A. De Bolfo, T.D. Smith, J.F. Boas, J.R. Pilbrow, Aust. J. Chem. 29 (1976) 2583;
(b) Z. Lu, C. White, A.L. Rheingold, R.H. Crabtree, Inorg. Chem. 32 (1993) 3991;
(c) D.X. West, Y.-H. Yang, T.L. Klein, K.I. Goldberg, A.E. Liberta, J. Valdés-Martínez, R.A. Toscano, Polyhedron 14 (1995) 1681;
(d) D.X. West, Y.-H. Yang, T.L. Klein, K.I. Goldberg, A.E. Liberta, J. Valdés-Martínez, S. Hernández-Ortega, Polyhedron 14 (1995) 3051;
(e) P. Souza, I.A. Matesanz, V. Fernandez, J. Chem. Soc., Dalton Trans. (1996) 3011;
(f) D. Kovala-Demertzi, A. Domopoulou, M.A. Demertzis, J. Valdés-Martínez, S. Hernández-Ortega, G. Espinosa-Pérez, D.X. West, M.M. Salberg, G.A. Bain, P.D. Bloom, Polyhedron 15 (1996) 2587;
(g) M.A. Ali, K.K. Dey, M. Nazimuddin, F.E. Smith, R.J. Butcher, J.P. Jasinski, J.M. Jasinski, Polyhedron 15 (1996) 3331.
[5] (a) D. Kovala-Demertzi, N. Kourkoumelis, M.A. Demertzis, J.R. Miller, C.S. Frampton, J.K. Swearingen, D.X. West, Eur. J. Inorg. Chem. (2000) 727;
(b) P.N. Yadav, M.A. Demertzis, D. Kovala-Demertzi, A. Castiñeiras, D.X. West, Inorg. Chim. Acta 332 (2002) 204.
[6] F. Basuli, S.-M. Peng, S. Bhattacharya, Inorg. Chem. 36 (1997) 5645.
[7] (a) A. Castiñeiras, E. Bermejo, D.X. West, A.K. EI-Sawaf, J.K. Swearingen, Polyhedron 17 (1998) 2751;
(b) A. Castiñeiras, M. Gil, E. Bermejo, D.X. West, Z. Naturforsch. B 55 (2000) 863;
(c) E. Bermejo, A. Castiñeiras, L.J. Ackerman, M.D. Owens, D.X. West, Z. Anorg. Allg. Chem. 627 (2001);
(d) C.A. Brown, W. Kaminsky, K.A. Claborn, K.I. Goldberg, D.X. West, J. Braz. Chem. Soc. 13 (2002) 10.
[8] I. Pal, F. Basuli, T.C.W. Mak, S. Bhattacharya, Angew. Chem., Int. Ed. 40 (2001) 2923.
[9] (a) F. Basuli, M. Ruf, C.G. Pierpont, S. Bhattacharya, Inorg. Chem. 39 (1998) 6113;
(b) F. Basuli, S.-M. Peng, S. Bhattacharya, Inorg. Chem. 39 (2000) 1120;
(c) S. Dutta, F. Basuli, S.M. Peng, G.H. Lee, S. Bhattacharya, New J. Chem. 26 (2002) 1607;
(d) R. Acharyya, S. Dutta, F. Basuli, S.M. Peng, G.H. Lee, L.R. Falvello, S. Bhattacharya, Inorg. Chem. 45 (2006) 1252;
(e) S. Basu, R. Acharyya, W.S. Sheldrick, H. Mayer-Figge, S. Bhattacharya, Struct. Chem. 18 (2007) (in press).
[10] (a) I. Pal, F. Basuli, S. Bhattacharya, Proc. Indian Acad. Sci. 114 (2002) 255;
(b) D. Kovala-Demertzi, M.A. Demertzis, E. Filiou, A.A. Pantazaki, P.N. Yadav, J.R. Miller, Y. Zheng, D.A. Kyriakidis, Biometals 16 (2003) 411;
(c) M.S. Bakkar, M. Yamin Siddiqi, M.S. Monshi, Synth. React. Inorg. Met-Org. Chem. 33 (2003) 1157;
(d) D. Kovala-Demertzi, C. Vidjeluc, M.A. Demertzis, E. Siapi, T. Mayromoustakos, Thermochim. Acta 424 (2004) 53;
(e) N. Fahmi, M.K. Biyala, R.V. Singh, Transition Met. Chem. 29 (2004) 681;
(f) M.K. Biyala, N. Fahmi, R.V. Singh, Indian J. Chem. A 43 (2004) 2536;

(g) L. Papathanasis, M.A. Demertzis, P.N. Yadav, D. Kovala-Demertzi, C. Prentjas, A. Castineiras, S. Skoulika, D.X. West, Inorg. Chim. Acta 357 (2004) 4113;
(h) R.K. Agarwal, S. Prasad, Turk. J. Chem. 29 (2005) 289;
(i) J.L. Neto, G.M. De Lima, H. Beraldo, Spectrochim. Acta A 63 (2006) 669;
(j) J. Patole, S. Padhye, M.S. Moodbidri, N. Shirsat, Eur. J. Med. Chem. 40 (2006) 1052;
(k) N.I. Dodoff, D. Kovala-Demertzi, M. Kubiak, J. Kuduk-Jaworska, A. Kochel, G.A. Gorneva, Z. Naturforsch. B 61 (2006) 1110;
(l) R.V. Singh, M.K. Biyala, Phosphorus Sulfur Silicon Relat. Elem. 181 (2006) 1477;
(m) M.K. Biyala, N. Fahmi, R.V. Singh, Indian J. Chem. A 45 (2006) 1999.

[11] F.R. Hertley, in: P.L. Robinson (Ed.), The Chemistry of Palladium and Platinum, vol. 14, Applied Science, London, 1973, p. 458.

[12] L. Malatesta, M. Angoletta, J. Chem. Soc. (1957) 1186.

[13] (a) G.B. Kauffman, Inorg. Synth. 7 (1963) 249;
(b) C. Tessier, F.D. Rochon, Inorg. Chim. Acta 295 (1999) 25.

[14] G.M. Sheldrick, SHELXS-97 and SHELXL-97: Fortran Programs for Crystal Structure Solution and Refinement, University of Göttingen, Göttingen, Germany, 1997.

[15] (a) Y. Shimazaki, M. Tashiro, T. Motoyama, S. Iwatsuki, T. Yajima, Y. Nakabayashi, Y. Naruta, O. Yamauchi, Inorg. Chem. 44 (2005) 6044;
(b) N.D. Jones, P. Meessen, U. Losehand, B.O. Patrick, B.R. James, Inorg. Chem. 44 (2005) 3290.

[16] (a) C. Mealli, D.M. Proserpio, CACAO Version 4.0, July 1994, Firenze, Italy;
(b) C. Mealli, D.M. Proserpio, J. Chem. Educ. 67 (1990) 399.

[17] (a) G.A. Crosby, W.H. Elfring Jr., J. Phys. Chem. 80 (1976) 2206;
(b) M.J. Cook, A.P. Lewis, G.S.J. Thomson, J.L. Glasper, D.J. Robbins, J. Chem. Soc., Perkin Trans. (1984) 293.

Available online at www.sciencedirect.com
ScienceDirect
Polyhedron 26 (2007) 2749–2760
POLYHEDRON
www.elsevier.com/locate/poly

Effects of counter anions on stereospecific interactions through π-conjugated systems of sulfur-bridged dinuclear cobalt(III)–platinum(II) complexes with optically active penicillaminates: Synthetic, structural, and spectroscopic studies

Yasunori Yamada [a,*], Masahiko Inoue [a], Yoshitaro Miyashita [b], Ken-ichi Okamoto [b], Masayuki Koikawa [a], Tadashi Tokii [a]

[a] Department of Chemistry and Applied Chemistry, Faculty of Science and Engineering, Saga University, 1 Honjo-machi, Saga 840-8502, Japan
[b] Department of Chemistry, Graduate School of Pure and Applied Science, University of Tsukuba, 1-1-1 Tennodai, Tsukuba, Ibaraki 305-8571, Japan

Received 17 November 2006; accepted 16 January 2007
Available online 30 January 2007

Abstract

The optically active S-bridged dinuclear complex, [Pt(bpy){Co(D-pen)$_2$}]X (**1X**: bpy = 2,2′-bipyridine; pen = penicillaminate; X = NO_3^-, ClO_4^-, Br^-, or I^-), and its enantiomer, [Pt(bpy){Co(L-pen)$_2$}]X (**2X**), were prepared by the reactions of [$PtCl_2$(bpy)] with K[Co(D-pen)$_2$] and K[Co(L-pen)$_2$], respectively. The racemates, [Pt(bpy){Co(D-pen)$_2$}]$_{0.5}$[Pt(bpy){Co(L-pen)$_2$}]$_{0.5}$X (**3X**), were also obtained by the slow evaporation of aqueous solutions containing equimolar amounts of **1X** and **2X**. The crystal structures of **3**$NO_3 \cdot 3H_2O$, **3**$ClO_4 \cdot 2H_2O$, **3**$Br \cdot 2H_2O$ and **3**$I \cdot 5.5H_2O$ were determined by X-ray crystallography, and compared with those of **1**$ClO_4 \cdot H_2O$, **1**$Br \cdot 2H_2O$, **1**$I \cdot 2H_2O$, **2**$ClO_4 \cdot H_2O$, **2**$Br \cdot 2H_2O$ and **2**$I \cdot 2H_2O$. The optically active complexes **1X** and **2X** exist as monomers, accompanied by no intermolecular interactions in the π-electronic systems of the bpy moieties. In the crystals of **3**$Br \cdot 2H_2O$, on the other hand, the enantiomeric complex cations, [Pt(bpy){Co(D-pen)$_2$}]$^+$ (***D***) and [Pt(bpy){Co(L-pen)$_2$}]$^+$ (***L***), are arranged alternately with overlapping bpy planes along the *c* axis, and the π electronic system of the bpy framework in ***D*** interacts with those in ***L***. The remaining three racemates, **3**$NO_3 \cdot 3H_2O$, **3**$ClO_4 \cdot 2H_2O$ and **3**$I \cdot 5.5H_2O$, afford dimeric structures with π–π stacking contacts between the enantiomeric ***D*** and ***L*** complex cations. Differences in the crystal structures between the optically active complexes and the racemates significantly mirror the diffuse reflectance spectral behaviors.
© 2007 Elsevier Ltd. All rights reserved.

Keywords: Stereospecific interactions; Dinuclear Co(III)–Pt(II) complexes; 2,2′-Bipyridine complexes; Penicillaminate complexes; Crystal structures; Spectrochemistry

1. Introduction

It has been shown so far that an octahedral metal chelated by plural β-aminoalkylthiolates acts as an S-donating bidentate metalloligand toward [MX_2(bpy)] (M = Pd(II) or Pt(II), X = Cl^- or NO_3^-, bpy = 2,2′-bipyridine), in which the two X^- ligands are susceptible to substitutions by other ligands, resulting in the formation of a dinuclear complex composed of a [M(μ-S)$_2$(bpy)] framework and an octahedral metal unit [1–5]. In the reaction of *fac*(*S*)-[Co(aet)$_3$] (aet = 2-aminoethanethiolate) with [$PtCl_2$(bpy)], for instance, a dinuclear complex, [Pt(bpy){Co(aet)$_3$}]$^{2+}$, is formed [1]. A similar reaction of [Ni{Co(aet)$_2$(en)}$_2$]$^{4+}$ (en = ethylenediamine), in which the two terminal *cis*(*S*)-[Co(aet)$_2$(en)]$^+$ units can be regarded as bidentate S-donors, with [$PtCl_2$(bpy)] gives [Pt(bpy){Co(aet)$_2$(en)}]$^{3+}$ [1]. Two absolute configurations, Δ and Λ, are possible for such octahedral S-donating metal units, and hence these dinuclear complexes are obtained as racemic crystals.

* Corresponding author. Tel./fax: +81 952 28 8806.
E-mail address: yyamada@cc.saga-u.ac.jp (Y. Yamada).

0277-5387/$ - see front matter © 2007 Elsevier Ltd. All rights reserved.
doi:10.1016/j.poly.2007.01.024

On the other hand, an optically active trinuclear analog, ΔΔ-[Ni{Co(aet)$_2$(*R*-pn)}$_2$]$^{4+}$ (pn = 1,2-propanediamine), reacts with [MX$_2$(bpy)] to form Δ-[M(bpy){Co(aet)$_2$(*R*-pn)}]$^{3+}$ stereoselectively [2,3]. A similar optically active S-bridged dinuclear complex, [M(bpy){Co(D-pen)$_2$}]$^+$ (pen = penicillaminate), is preferentially derived from the bidentate metalloligand, *trans*(*N*)-[Co(D-pen)$_2$]$^-$ [3]. While these optically active complexes exist as monomers in the crystalline states, the racemic complexes afford dimeric or higher dimensional linear-chain structures due to π–π stacking of the bpy frameworks in the dinuclear units [1–3]. This implies some enantioselective interaction between the π frameworks, which are rather distant from the chiral center of the octahedral metal unit, in these dinuclear complexes. In fact, a mixture of equimolar amounts of [Pt(bpy){Co(D-pen)$_2$}]Cl and [Pt(bpy){Co(L-pen)$_2$}]Cl in H$_2$O crystallizes as the racemic [Pt(bpy){Co(D-pen)$_2$}]$_{0.5}$[Pt(bpy){Co(L-pen)$_2$}]$_{0.5}$Cl with a linear-chained π–π stacking structure, in which two enantiomeric complex cations are arranged alternately [4]. In the racemic crystal of [Pt(bpy){Co(aet)$_2$(*R*-pn)}]$_{0.5}$[Pt(bpy){Co(aet)$_2$(*S*-pn)}]$_{0.5}$ (ClO$_4$)$_3$, which is grown from an aqueous solution containing equimolar amounts of Δ-[Pt(bpy){Co(aet)$_2$(*R*-pn)}](ClO$_4$)$_3$ and Λ-[Pt(bpy){Co(aet)$_2$(*S*-pn)}](ClO$_4$)$_3$, in addition, two enantiomers exist as a dimer through π–π interactions between the bpy frameworks [5]. Although dimers or linear-chains can be formed by π–π stackings between enantiomers in these dinuclear complexes, as remarked above, the factors governing such structures are still uncertain. In many cases of S-bridged polynuclear complexes with aromatic ligands, the counter ions and/or solvents of crystallizations hold control over π–π stacking structures [6]. It seems therefore that the counter anions exert some influence on the structures of such dinuclear complexes. In the present investigation, at the first onset, we have examined the effects of monovalent counter anions on the stereo- and spectrochemical characteristics for optically active [Pt(bpy){Co(D-pen)$_2$}]X (X = NO$_3^-$, ClO$_4^-$, Br$^-$, or I$^-$) and the enantiomeric [Pt(bpy){Co(L-pen)$_2$}]X, together with racemic [Pt(bpy){Co(D-pen)$_2$}]$_{0.5}$[Pt(bpy){Co(L-pen)$_2$}]$_{0.5}$X.

2. Experimental

2.1. Materials

2,2′-Bipyridine, K$_2$PtCl$_4$, CoCl$_2\cdot$6H$_2$O, NaNO$_3$, NaClO$_4\cdot$H$_2$O, NaBr, and KI were obtained from Wako Pure Chemical Ind. Co., Ltd. The optically active D- and L-penicillamines were purchased from Tokyo Chemical Co., Ltd. and Aldrich Chemical Co., Inc., respectively. K[Co(D-pen)$_2$]$\cdot$2.5H$_2$O, K[Co(L-pen)$_2$]$\cdot$2.5H$_2$O and [PtCl$_2$(bpy)] were prepared by modified methods from the literature [7–9]. The other chemicals were obtained from Wako Pure Chemical Ind. Co., Ltd. or Tokyo Chemical Co., Ltd. All of the chemicals were of reagent grade and were used without further purification.

2.2. Preparation of [Pt(bpy){Co(D-pen)}]NO$_3\cdot$6H$_2$O (**1**NO$_3\cdot$6H$_2$O)

To a brown solution containing K[Co(D-pen)$_2$]$\cdot$2.5H$_2$O (0.13 g, 0.25 mmol) in 20 ml H$_2$O was added [PtCl$_2$(bpy)] (0.10 g, 0.25 mmol). After the mixture was stirred at 55 °C for 1 h, NaNO$_3$ (0.85 g, 10 mmol) in 5 ml H$_2$O was added to the resulting dark green solution. The whole was allowed to stand at 25 °C for several days, and the resulting green-brown crystals were collected by filtration. Yield: 0.15 g (68% based on Co). *Anal.* Calc. for C$_{20}$H$_{38}$N$_5$O$_{13}$S$_2$CoPt (**1**NO$_3\cdot$6H$_2$O): C, 27.46; H, 4.38; N, 8.01. Found: C, 27.50; H, 4.34; N, 7.96%. ^{1}H NMR (600 MHz, D$_2$O), δ = 1.55 (s, 6H, pen), 1.74 (s, 6H, pen), 3.96 (s, 2H, pen), 7.93 (t, 2H, bpy), 8.44 (t, 2H, bpy), 8.49 (d, 2H, bpy), 9.14 (d, 2H, bpy). ^{13}C NMR (150 MHz, D$_2$O), δ = 31.02 (pen), 34.56 (pen), 54.90 (pen), 75.85 (pen), 127.07 (bpy), 131.19 (bpy), 144.87 (bpy), 150.16 (bpy), 159.44 (bpy), 183.58 (pen). UV–Vis spectrum in H$_2$O [ν_{max}, 10^3 cm^{-1} (log ε/mol^{-1} dm^3 cm^{-1})]: 16.23 (2.09), 19.46 (2.11), 25.4 (3.3)^{sh}, 28.5 (3.7)^{sh}, 31.25 (4.27), 32.36 (4.26), 37.4 (4.2)^{sh}, 41.49 (4.43), 49.26 (4.69). CD spectrum in H$_2$O [ν_{max}, 10^3 cm^{-1} ($\Delta\varepsilon$)]: 16.26 (−5.02), 19.46 (+8.12), 22.5 (+0.2)^{sh}, 25.58 (−5.85), 29.4 (+14.5)^{sh}, 30.96 (+16.67), 37.59 (+25.15), 44.64 (+36.25). Diffuse reflectance spectrum [ν_{max}, 10^3 cm^{-1}]: 16.00, 18.90, 25.2^{sh}, 28.3^{sh}, 30.52, 31.7^{sh}, 40.1^{sh}.

2.3. Preparation of [Pt(bpy){Co(D-pen)}]ClO$_4\cdot$H$_2$O (**1**ClO$_4\cdot$H$_2$O)

This complex was prepared by a similar method to that for **1**NO$_3\cdot$6H$_2$O, using NaClO$_4\cdot$H$_2$O instead of NaNO$_3$. Yield: 0.17 g (83% based on Co). *Anal.* Calc. for C$_{20}$H$_{28}$N$_4$O$_9$S$_2$ClCoPt (**1**ClO$_4\cdot$H$_2$O): C, 29.22; H, 3.43; N, 6.82. Found: C, 29.19; H, 3.40; N, 6.75%. ^{1}H NMR (600 MHz, 1:1 mixed solved of CD$_3$CN and D$_2$O), δ = 1.52 (s, 6H, pen), 1.68 (s, 6H, pen), 3.85 (s, 2H, pen), 7.97 (t, 2H, bpy), 8.46 (t, 2H, bpy), 8.51 (d, 2H, bpy), 9.10 (d, 2H, bpy). ^{13}C NMR (150 MHz, 1:1 mixed solved of CD$_3$CN and D$_2$O), δ = 31.02 (pen), 34.66 (pen), 54.96 (pen), 75.69 (pen), 127.28 (bpy), 131.54 (bpy), 145.06 (bpy), 150.12 (bpy), 159.06 (bpy), 182.49 (pen). UV–Vis spectrum in H$_2$O [ν_{max}, 10^3 cm^{-1} (log ε/mol^{-1} dm^3 cm^{-1})]: 16.16 (2.04), 19.38 (2.05), 25.3 (3.2)^{sh}, 28.5 (3.7)^{sh}, 31.25 (4.27), 32.47 (4.26), 37.2 (4.2)^{sh}, 41.32 (4.42), 49.0 (4.6)^{sh}. CD spectrum in H$_2$O [ν_{max}, 10^3 cm^{-1} ($\Delta\varepsilon$)]: 16.21 (−4.03), 19.46 (+8.02), 22.5 (+0.2)^{sh}, 25.51 (−6.06), 29.4 (+15.0)^{sh}, 30.86 (+16.89), 37.74 (+25.53), 44.84 (+35.97). Diffuse reflectance spectrum [ν_{max}, 10^3 cm^{-1}]: 16.02, 18.92, 25.2^{sh}, 28.3^{sh}, 30.82, 32.0^{sh}, 40.0^{sh}.

2.4. Preparation of [Pt(bpy){Co(D-pen)}]Br$\cdot$2H$_2$O (**1**Br$\cdot$2H$_2$O)

This complex was prepared by a similar method to that for **1**ClO$_4\cdot$H$_2$O, using NaBr instead of

$NaClO_4 \cdot H_2O$. Yield: 0.14 g (68% based on Co). *Anal.* Calc. for $C_{20}H_{30}N_4O_6S_2CoBrPt$ (**1**Br · $2H_2O$): C, 29.28; H, 3.68; N, 6.83. Found: C, 29.32; H, 3.66; N, 6.78%. ^{1}H NMR (600 MHz, D_2O), $\delta = 1.55$ (s, 6H, pen), 1.75 (s, 6H, pen), 3.96 (s, 2H, pen), 7.94 (t, 2H, bpy), 8.45 (t, 2H, bpy), 8.50 (d, 2H, bpy), 9.15 (d, 2H, bpy). ^{13}C NMR (150 MHz, D_2O), $\delta = 31.03$ (pen), 34.60 (pen), 54.89 (pen), 75.84 (pen), 127.09 (bpy), 131.21 (bpy), 144.87 (bpy), 150.16 (bpy), 159.46 (bpy), 183.60 (pen). UV–Vis spectrum in H_2O [ν_{max}, 10^3 cm^{-1} ($\log\varepsilon$/mol^{-1} dm^3 cm^{-1})]: 16.16 (2.03), 19.38 (2.04), 25.4 (3.2)^{sh}, 28.4 (3.7)^{sh}, 31.25 (4.27), 32.36 (4.25), 37.2 (4.2)^{sh}, 41.32 (4.42), 49.2 (4.7)^{sh}. CD spectrum in H_2O [ν_{max}, 10^3 cm^{-1} ($\Delta\varepsilon$)]: 16.21 (−4.85), 19.46 (+7.82), 22.5 (+0.2)^{sh}, 25.51 (−5.56), 29.3 (+14.3)^{sh}, 30.96 (+16.25), 37.74 (+24.56), 44.64 (+35.39). Diffuse reflectance spectrum [ν_{max}, 10^3 cm^{-1}]: 16.00, 18.92, 25.3^{sh}, 28.5^{sh}, 30.63, 31.9^{sh}, 40.0^{sh}.

2.5. Preparation of [Pt(bpy){Co(D-pen)}]I · $2H_2O$ (**1**I · $2H_2O$)

This complex was prepared by a similar method to that for **1**Br · $2H_2O$, using KI instead of NaBr. Yield: 0.18 g (83% based on Co). *Anal.* Calc. for $C_{20}H_{30}N_4O_6S_2CoIPt$ (**1**I · $2H_2O$): C, 27.69; H, 3.48; N, 6.46. Found: C, 27.70; H, 3.46; N, 6.47%. ^{1}H NMR (600 MHz, D_2O), $\delta = 1.52$ (s, 6H, pen), 1.72 (s, 6H, pen), 3.93 (s, 2H, pen), 7.90 (t, 2H, bpy), 8.41 (t, 2H, bpy), 8.46 (d, 2H, bpy), 9.12 (d, 2H, bpy). ^{13}C NMR (150 MHz, D_2O), $\delta = 31.03$ (pen), 34.59 (pen), 54.91 (pen), 75.85 (pen), 127.09 (bpy), 131.21 (bpy), 144.87 (bpy), 150.18 (bpy), 159.50 (bpy), 183.62 (pen). UV–Vis spectrum in H_2O [ν_{max}, 10^3 cm^{-1} ($\log\varepsilon$/mol^{-1} dm^3 cm^{-1})]: 16.13 (2.05), 19.38 (2.05), 25.3 (3.2)^{sh}, 28.5 (3.7)^{sh}, 31.25 (4.28), 32.36 (4.26), 37.4 (4.2)^{sh}, 41.3 (4.5)^{sh}, 45.25 (4.62). CD spectrum in H_2O [ν_{max}, 10^3 cm^{-1} ($\Delta\varepsilon$)]: 16.21 (−5.08), 19.46 (+8.19), 22.5 (+0.2)^{sh}, 25.51 (−5.85), 29.3 (+14.0)^{sh}, 30.86 (+17.26), 37.74 (+25.96), 44.64 (+36.94). Diffuse reflectance spectrum [ν_{max}, 10^3 cm^{-1}]: 16.06, 18.96, 25.2^{sh}, 28.3^{sh}, 30.63, 31.9^{sh}, 40.2^{sh}.

2.6. Preparation of [Pt(bpy){Co(L-pen)}]NO_3 · $6H_2O$ (**2**NO_3 · $6H_2O$)

This complex was prepared by a similar method to that for **1**NO_3 · $6H_2O$, using K[Co(L-pen)$_2$] · $2.5H_2O$ instead of K[Co(D-pen)$_2$] · $2.5H_2O$. Yield: 0.14 g (64% based on Co). *Anal.* Calc. for $C_{20}H_{38}N_5O_{13}S_2CoPt$ (**2**NO_3 · $6H_2O$): C, 27.46; H, 4.38; N, 8.01. Found: C, 27.48; H, 4.35; N, 8.03%. ^{1}H NMR (600 MHz, D_2O), $\delta = 1.54$ (s, 6H, pen), 1.73 (s, 6H, pen), 3.95 (s, 2H, pen), 7.92 (t, 2H, bpy), 8.43 (t, 2H, bpy), 8.48 (d, 2H, bpy), 9.14 (d, 2H, bpy). ^{13}C NMR (150 MHz, D_2O), $\delta = 31.02$ (pen), 34.56 (pen), 54.91 (pen), 75.85 (pen), 127.07 (bpy), 131.20 (bpy), 144.87 (bpy), 150.16 (bpy), 159.45 (bpy), 183.58 (pen). UV–Vis spectrum in H_2O [ν_{max}, 10^3 cm^{-1} ($\log\varepsilon$/mol^{-1} dm^3 cm^{-1})]: 16.18 (2.04), 19.42 (2.05), 25.3 (3.2)^{sh}, 28.6 (3.7)^{sh}, 31.25 (4.28), 32.47 (4.26), 37.4 (4.2)^{sh}, 41.49 (4.43), 49.02 (4.72). CD spectrum in H_2O [ν_{max}, 10^3 cm^{-1} ($\Delta\varepsilon$)]: 16.21 (+5.02), 19.46 (−8.13), 22.5 (−0.2)^{sh}, 25.51 (+5.81), 29.4 (−14.1)^{sh}, 30.96 (−15.97), 37.59 (−23.90), 44.64 (−35.26). Diffuse reflectance spectrum [ν_{max}, 10^3 cm^{-1}]: 16.13, 18.89, 25.2^{sh}, 28.2^{sh}, 30.49, 31.7^{sh}, 40.1^{sh}.

2.7. Preparation of [Pt(bpy){Co(L-pen)}]ClO_4 · H_2O (**2**ClO_4 · H_2O)

This complex was prepared by a similar method to that for **1**ClO_4 · H_2O, using K[Co(L-pen)$_2$] · $2.5H_2O$ instead of K[Co(D-pen)$_2$] · $2.5H_2O$. Yield: 0.16 g (78% based on Co). *Anal.* Calc. for $C_{20}H_{28}N_4O_9S_2ClCoPt$ (**2**ClO_4 · H_2O): C, 29.22; H, 3.43; N, 6.82. Found: C, 29.21; H, 3.42; N, 6.76%. ^{1}H NMR (600 MHz, 1:1 mixed solved of CD_3CN and D_2O), $\delta = 1.51$ (s, 6H, pen), 1.67 (s, 6H, pen), 3.84 (s, 2H, pen), 7.97 (t, 2H, bpy), 8.46 (t, 2H, bpy), 8.51 (d, 2H, bpy), 9.09 (d, 2H, bpy). ^{13}C NMR (150 MHz, 1:1 mixed solved of CD_3CN and D_2O), $\delta = 31.04$ (pen), 34.67 (pen), 54.98 (pen), 75.72 (pen), 127.30 (bpy), 131.55 (bpy), 145.06 (bpy), 150.12 (bpy), 159.06 (bpy), 182.33 (pen). UV–Vis spectrum in H_2O [ν_{max}, 10^3 cm^{-1} ($\log\varepsilon$/mol^{-1} dm^3 cm^{-1})]: 16.21 (1.99), 19.31 (2.00), 25.4 (3.2)^{sh}, 28.7 (3.7)^{sh}, 31.15 (4.22), 32.47 (4.21), 37.5 (4.2)^{sh}, 41.32 (4.38), 49.0 (4.6)^{sh}. CD spectrum in H_2O [ν_{max}, 10^3 cm^{-1} ($\Delta\varepsilon$)]: 16.21 (+4.44), 19.46 (−7.17), 22.5 (−0.2)^{sh}, 25.51 (+5.12), 29.5 (−13.2)^{sh}, 30.86 (−14.82), 37.59 (−22.44), 44.64 (−32.00). Diffuse reflectance spectrum [ν_{max}, 10^3 cm^{-1}]: 15.97, 18.94, 25.2^{sh}, 28.3^{sh}, 30.82, 32.0^{sh}, 40.0^{sh}.

2.8. Preparation of [Pt(bpy){Co(L-pen)}]Br · $2H_2O$ (**2**Br · $2H_2O$)

This complex was prepared by a similar method to that for **1**Br · $2H_2O$, using K[Co(L-pen)$_2$] · $2.5H_2O$ instead of K[Co(D-pen)$_2$] · $2.5H_2O$. Yield: 0.13 g (63% based on Co). *Anal.* Calc. for $C_{20}H_{30}N_4O_6S_2CoBrPt$ (**2**Br · $2H_2O$): C, 29.28; H, 3.68; N, 6.83. Found: C, 29.29; H, 3.69; N, 6.80%. ^{1}H NMR (600 MHz, D_2O), $\delta = 1.55$ (s, 6H, pen), 1.75 (s, 6H, pen), 3.96 (s, 2H, pen), 7.94 (t, 2H, bpy), 8.45 (t, 2H, bpy), 8.50 (d, 2H, bpy), 9.16 (d, 2H, bpy). ^{13}C NMR (150 MHz, D_2O), $\delta = 31.04$ (pen), 34.60 (pen), 54.90 (pen), 75.85 (pen), 127.09 (bpy), 131.21 (bpy), 144.87 (bpy), 150.17 (bpy), 159.47 (bpy), 183.61 (pen). UV–Vis spectrum in H_2O [ν_{max}, 10^3 cm^{-1} ($\log\varepsilon$/mol^{-1} dm^3 cm^{-1})]: 16.23 (2.04), 19.34 (2.04), 25.4 (3.2)^{sh}, 28.5 (3.7)^{sh}, 31.25 (4.27), 32.36 (4.26), 37.4 (4.2)^{sh}, 41.49 (4.42), 49.0 (4.7)^{sh}. CD spectrum in H_2O [ν_{max}, 10^3 cm^{-1} ($\Delta\varepsilon$)]: 16.26 (+4.95), 19.49 (−8.00), 22.5 (−0.2)^{sh}, 25.51 (+5.71), 29.4 (−14.8)^{sh}, 30.86 (−16.83), 37.74 (−25.56), 44.84 (−36.29). Diffuse reflectance spectrum [ν_{max}, 10^3 cm^{-1}]: 16.04, 18.94, 25.3^{sh}, 28.5^{sh}, 30.68, 31.9^{sh}, 40.0^{sh}.

2.9. Preparation of [Pt(bpy){Co(L-pen)}]I · 2H$_2$O (2I · 2H$_2$O)

This complex was prepared by a similar method to that for **1**I · 2H$_2$O, using K[Co(L-pen)$_2$] · 2.5H$_2$O instead of K[Co(D-pen)$_2$] · 2.5H$_2$O. Yield: 0.17 g (78% based on Co). *Anal.* Calc. for $C_{20}H_{30}N_4O_6S_2CoIPt$ (**2**I · 2H$_2$O): C, 27.69; H, 3.48; N, 6.46. Found: C, 27.66; H, 3.48; N, 6.42%. ^{1}H NMR (600 MHz, D$_2$O), $\delta = 1.52$ (s, 6H, pen), 1.72 (s, 6H, pen), 3.93 (s, 2H, pen), 7.90 (t, 2H, bpy), 8.42 (t, 2H, bpy), 8.46 (d, 2H, bpy), 9.12 (d, 2H, bpy). ^{13}C NMR (150 MHz, D$_2$O), $\delta = 31.03$ (pen), 34.59 (pen), 54.90 (pen), 75.85 (pen), 127.09 (bpy), 131.21 (bpy), 144.87 (bpy), 150.18 (bpy), 159.50 (bpy), 183.62 (pen). UV–Vis spectrum in H$_2$O [ν_{max}, 10^3 cm^{-1} ($\log\varepsilon$/mol^{-1} dm^3 cm^{-1})]: 16.18 (2.05), 19.42 (2.05), 25.3 (3.2)^{sh}, 28.5 (3.7)^{sh}, 31.25 (4.28), 32.36 (4.26), 37.3 (4.2)^{sh}, 41.3 (4.5)^{sh}, 45.25 (4.62). CD spectrum in H$_2$O [ν_{max}, 10^3 cm^{-1} ($\Delta\varepsilon$)]: 16.21 (+5.06), 19.46 (−8.19), 22.5 (−0.2)^{sh}, 25.51 (+5.84), 29.3 (−15.0)^{sh}, 30.86 (−17.17), 37.59 (−26.03), 44.84 (−37.23). Diffuse reflectance spectrum [ν_{max}, 10^3 cm^{-1}]: 16.06, 18.96, 25.2^{sh}, 28.2^{sh}, 30.63, 31.8^{sh}, 40.2^{sh}.

2.10. Preparation of [Pt(bpy){Co(D-pen)}]$_{0.5}$[Pt(bpy)-{Co(L-pen)}]$_{0.5}$NO$_3$ · 3H$_2$O (3NO$_3$ · 3H$_2$O)

To a green solution containing **1**NO$_3$ · 6H$_2$O (0.10 g, 0.11 mmol) in 20 ml H$_2$O was added **2**NO$_3$ · 6H$_2$O (0.10 g, 0.11 mmol) in 20 ml H$_2$O. After the mixture was allowed to stand at 25 °C for several days, the resulting green-brown crystals were collected by filtration. Yield: 0.14 g (78% based on Co). *Anal.* Calc. for $C_{20}H_{32}N_5O_{10}S_2CoPt$ (**3**NO$_3$ · 3H$_2$O): C, 29.27; H, 3.93; N, 8.53. Found: C, 29.30; H, 4.00; N, 8.45%. ^{1}H NMR (600 MHz, D$_2$O), $\delta = 1.53$ (s, 6H, pen), 1.73 (s, 6H, pen), 3.94 (s, 2H, pen), 7.92 (t, 2H, bpy), 8.43 (t, 2H, bpy), 8.48 (d, 2H, bpy), 9.14 (d, 2H, bpy). ^{13}C NMR (150 MHz, D$_2$O), $\delta = 31.02$ (pen), 34.56 (pen), 54.91 (pen), 75.86 (pen), 127.08 (bpy), 131.20 (bpy), 144.87 (bpy), 150.17 (bpy), 159.45 (bpy), 183.58 (pen). UV–Vis spectrum in H$_2$O [ν_{max}, 10^3 cm^{-1} ($\log\varepsilon$/mol^{-1} dm^3 cm^{-1})]: 16.18 (2.06), 19.27 (2.07), 25.4 (3.3)^{sh}, 28.5 (3.7)^{sh}, 31.25 (4.29), 32.47 (4.27), 37.4 (4.2)^{sh}, 41.49 (4.44), 49.26 (4.70). Diffuse reflectance spectrum [ν_{max}, 10^3 cm^{-1}]: 16.04, 19.07, 27.3^{sh}, 30.49, 31.7^{sh}, 40.2^{sh}.

2.11. Preparation of [Pt(bpy){Co(D-pen)}]$_{0.5}$[Pt(bpy)-{Co(L-pen)}]$_{0.5}$ClO$_4$ · 2H$_2$O (3ClO$_4$ · 2H$_2$O)

This complex was prepared by a similar method to that for **3**NO$_3$ · 3H$_2$O, using 0.11 mmol of **1**ClO$_4$ · H$_2$O and **2**ClO$_4$ · H$_2$O instead of **1**NO$_3$ · 6H$_2$O and **2**NO$_3$ · 6H$_2$O. Yield: 0.16 g (86% based on Co). *Anal.* Calc. for $C_{20}H_{30}N_4O_{10}S_2ClCoPt$ (**3**ClO$_4$ · 2H$_2$O): C, 28.59; H, 3.60; N, 6.67. Found: C, 28.61; H, 3.64; N, 6.58%. ^{1}H NMR (600 MHz, 1:1 mixed solved of CD$_3$CN and D$_2$O), $\delta = 1.50$ (s, 6H, pen), 1.66 (s, 6H, pen), 3.83 (s, 2H, pen), 7.95 (t, 2H, bpy), 8.45 (t, 2H, bpy), 8.50 (d, 2H, bpy), 9.09 (d, 2H, bpy). ^{13}C NMR (150 MHz, 1:1 mixed solved of CD$_3$CN and D$_2$O), $\delta = 31.02$ (pen), 34.66 (pen), 54.97 (pen), 75.71 (pen), 127.28 (bpy), 131.55 (bpy), 145.06 (bpy), 150.14 (bpy), 159.06 (bpy), 182.41 (pen). UV–Vis spectrum in H$_2$O [ν_{max}, 10^3 cm^{-1} ($\log\varepsilon$/mol^{-1} dm^3 cm^{-1})]: 16.21 (2.05), 19.34 (2.05), 25.4 (3.2)^{sh}, 28.5 (3.7)^{sh}, 31.55 (4.24), 32.36 (4.25), 37.4 (4.2)^{sh}, 41.32 (4.42), 49.0 (4.6)^{sh}. Diffuse reflectance spectrum [ν_{max}, 10^3 cm^{-1}]: 16.01, 18.98, 26.9^{sh}, 30.72, 31.9^{sh}, 40.2^{sh}.

2.12. Preparation of [Pt(bpy){Co(D-pen)}]$_{0.5}$[Pt(bpy)-{Co(L-pen)}]$_{0.5}$Br · 2H$_2$O (3Br · 2H$_2$O)

This complex was prepared by a similar method to that for **3**ClO$_4$ · 2H$_2$O, using 0.11 mmol of **1**Br · 2H$_2$O and **2**Br · 2H$_2$O instead of **1**ClO$_4$ · H$_2$O and **2**ClO$_4$ · H$_2$O. Yield: 0.13 g (72% based on Co). *Anal.* Calc. for $C_{20}H_{30}N_4O_6S_2CoBrPt$ (**3**Br · 2H$_2$O): C, 29.28; H, 3.68; N, 6.83. Found: C, 29.26; H, 3.70; N, 6.72%. ^{1}H NMR (600 MHz, D$_2$O), $\delta = 1.54$ (s, 6H, pen), 1.74 (s, 6H, pen), 3.95 (s, 2H, pen), 7.92 (t, 2H, bpy), 8.44 (t, 2H, bpy), 8.49 (d, 2H, bpy), 9.14 (d, 2H, bpy). ^{13}C NMR (150 MHz, D$_2$O), $\delta = 31.03$ (pen), 34.58 (pen), 54.90 (pen), 75.85 (pen), 127.08 (bpy), 131.20 (bpy), 144.87 (bpy), 150.17 (bpy), 159.48 (bpy), 183.61 (pen). UV–Vis spectrum in H$_2$O [ν_{max}, 10^3 cm^{-1} ($\log\varepsilon$/mol^{-1} dm^3 cm^{-1})]: 16.21 (2.07), 19.46 (2.07), 25.4 (3.3)^{sh}, 28.5 (3.8)^{sh}, 31.25 (4.30), 32.36 (4.28), 37.4 (4.2)^{sh}, 41.67 (4.45), 49.0 (4.7)^{sh}. Diffuse reflectance spectrum [ν_{max}, 10^3 cm^{-1}]: 15.92, 19.07, 27.0^{sh}, 30.53, 31.7^{sh}, 40.2^{sh}.

2.13. Preparation of [Pt(bpy){Co(D-pen)}]$_{0.5}$[Pt(bpy)-{Co(L-pen)}]$_{0.5}$I · 2H$_2$O (3I · 5.5H$_2$O)

This complex was prepared by a similar method to that for **3**Br · 2H$_2$O, using 0.11 mmol of **1**I · 2H$_2$O and **2**I · 2H$_2$O instead of **1**Br · 2H$_2$O and **2**Br · 2H$_2$O. Yield: 0.18 g (88% based on Co). *Anal.* Calc. for $C_{20}H_{37}N_4O_{9.5}S_2CoIPt$ (**3**I · 2H$_2$O): C, 25.81; H, 4.01; N, 6.02. Found: C, 25.85; H, 4.03; N, 5.92%. ^{1}H NMR (600 MHz, D$_2$O), $\delta = 1.52$ (s, 6H, pen), 1.72 (s, 6H, pen), 3.93 (s, 2H, pen), 7.90 (t, 2H, bpy), 8.41 (t, 2H, bpy), 8.46 (d, 2H, bpy), 9.12 (d, 2H, bpy). ^{13}C NMR (150 MHz, D$_2$O), $\delta = 31.03$ (pen), 34.59 (pen), 54.91 (pen), 75.85 (pen), 127.09 (bpy), 131.21 (bpy), 144.87 (bpy), 150.18 (bpy), 159.50 (bpy), 183.62 (pen). UV–Vis spectrum in H$_2$O [ν_{max}, 10^3 cm^{-1} ($\log\varepsilon$/mol^{-1} dm^3 cm^{-1})]: 16.21 (2.07), 19.46 (2.07), 25.4 (3.3)^{sh}, 28.5 (3.8)^{sh}, 31.25 (4.30), 32.36 (4.28), 37.4 (4.2)^{sh}, 41.67 (4.45), 45.25 (4.66). Diffuse reflectance spectrum [ν_{max}, 10^3 cm^{-1}]: 16.14, 19.01, 25.4^{sh}, 30.62, 31.8^{sh}, 40.2^{sh}.

2.14. Measurements

Electronic absorption spectra were recorded with a Perkin–Elmer Lambda 19 spectrophotometer, and the CD spectra with a JASCO J-600 spectropolarimeter. These measurements were carried out in aqueous solu-

tions at room temperature. Diffuse reflectance spectra were measured with a JASCO Ubest V-570 spectrophotometer equipped with an integrating sphere apparatus JASCO ISN-470, using powder samples diluted with MgO. ^{1}H and ^{13}C NMR spectra were recorded with a Bruker AVANCE-600 NMR spectrometer in a 1:1 mixed solvent of CD_3CN and D_2O for **1**$ClO_4 \cdot H_2O$, **2**$ClO_4 \cdot H_2O$ and **3**$ClO_4 \cdot 2H_2O$, or in D_2O for **1**$NO_3 \cdot 6H_2O$, **1**$Br \cdot 2H_2O$, **1**$I \cdot 2H_2O$, **2**$NO_3 \cdot 6H_2O$, **2**$Br \cdot 2H_2O$, **2**$I \cdot 2H_2O$, **3**$NO_3 \cdot 3H_2O$, **3**$Br \cdot 2H_2O$ and **3**$I \cdot 5.5H_2O$, using sodium 4,4-dimethyl-4-silapentane-1-sulfonate (DSS) as an internal reference. Elemental analyses (C, H, N) were performed with a Perkin–Elmer 2400 CHN Elemental Analyzer.

2.15. X-ray structure determination

Single crystals of **1**$ClO_4 \cdot H_2O$, **1**$Br \cdot 2H_2O$, **1**$I \cdot 2H_2O$, **2**$ClO_4 \cdot H_2O$, **2**$Br \cdot 2H_2O$, **2**$I \cdot 2H_2O$, **3**$NO_3 \cdot 3H_2O$, **3**$ClO_4 \cdot 2H_2O$, **3**$Br \cdot 2H_2O$ and **3**$I \cdot 5.5H_2O$ were used for data collection on a Rigaku AFC5S automated four-circle diffractometer with graphite-monochromatized Mo Kα ($\lambda = 0.71069$ Å) radiation. Cell constants and an orientation matrix for data collection were obtained from a least-squares refinement using the setting angles of 25 carefully centered reflections in the range $14° < \theta < 15°$ for **1**$ClO_4 \cdot H_2O$, **1**$Br \cdot 2H_2O$, **1**$I \cdot 2H_2O$, **2**$ClO_4 \cdot H_2O$, **2**$Br \cdot 2H_2O$, **2**$I \cdot 2H_2O$, **3**$NO_3 \cdot 3H_2O$, **3**$ClO_4 \cdot 2H_2O$, **3**$Br \cdot 2H_2O$ and **3**$I \cdot 5.5H_2O$. The data were collected at a

Table 1
Crystallographic data of **1**$ClO_4 \cdot H_2O$, **1**$Br \cdot 2H_2O$, **1**$I \cdot 2H_2O$, **2**$ClO_4 \cdot H_2O$, **2**$Br \cdot 2H_2O$, **2**$I \cdot 2H_2O$, **3**$NO_3 \cdot 3H_2O$, **3**$ClO_4 \cdot 2H_2O$, **3**$Br \cdot 2H_2O$, and **3**$I \cdot 5.5H_2O$

	1$ClO_4 \cdot H_2O$	**1**$Br \cdot 2H_2O$	**1**$I \cdot 2H_2O$	**2**$ClO_4 \cdot H_2O$	**2**$Br \cdot 2H_2O$
Formula	$C_{20}H_{28}N_4O_9S_2ClCoPt$	$C_{20}H_{30}N_4O_6S_2CoBrPt$	$C_{20}H_{30}N_4O_6S_2CoIPt$	$C_{20}H_{28}N_4O_9S_2ClCoPt$	$C_{20}H_{30}N_4O_6S_2CoBrPt$
Formula weight	822.06	820.53	867.53	822.06	820.53
Crystal dimensions (mm)	$0.50 \times 0.50 \times 0.50$	$0.30 \times 0.30 \times 0.50$	$0.20 \times 0.30 \times 0.50$	$0.40 \times 0.40 \times 0.60$	$0.50 \times 0.50 \times 0.50$
Space group	$P3_2$	$P6_2$	$P6_2$	$P3_1$	$P6_4$
a (Å)	14.561(1)	14.454(1)	14.542(3)	14.563(3)	14.446(1)
b (Å)	14.561(1)	14.454(1)	14.542(3)	14.563(3)	14.446(1)
c (Å)	11.835(1)	11.827(1)	11.854(3)	11.840(4)	11.823(1)
α (°)	90	90	90	90	90
β (°)	90	90	90	90	90
γ (°)	120	120	120	120	120
V (Å^3)	2173.0(3)	2139.7(3)	2171.0(8)	2174.8(9)	2137.0(4)
Z	3	3	3	3	3
D_{calcd} (g cm^{-3})	1.884	1.910	1.991	1.883	1.913
μ (cm^{-1})	56.65	70.51	66.32	56.60	70.60
Transmission factor	0.66–1.00	0.62–1.00	0.70–1.00	0.76–1.00	0.88–1.00
Number of reflections measured	3681	1922	1945	3680	1922
Number of reflections used	3298	1554	1451	3397	1589
Number of variables used	351	179	179	351	174
R (R_w)	0.042 (0.057)	0.045 (0.063)	0.054 (0.066)	0.041 (0.058)	0.047 (0.065)
Goodness-of fit on F^2	1.01	1.01	1.01	1.00	1.00
	2$I \cdot 2H_2O$	**3**$NO_3 \cdot 3H_2O$	**3**$ClO_4 \cdot 2H_2O$	**3**$Br \cdot 2H_2O$	**3**$I \cdot 5.5H_2O$
Formula	$C_{20}H_{30}N_4O_6S_2CoIPt$	$C_{20}H_{32}N_5O_{10}S_2CoPt$	$C_{20}H_{30}N_4O_{10}S_2ClCoPt$	$C_{20}H_{30}N_4O_6S_2CoBrPt$	$C_{20}H_{37}N_4O_{9.5}S_2CoIPt$
Formula weight	867.53	820.64	840.07	820.53	930.58
Crystal dimensions (mm)	$0.30 \times 0.30 \times 0.40$	$0.20 \times 0.30 \times 0.40$	$0.10 \times 0.20 \times 0.50$	$0.10 \times 0.30 \times 0.40$	$0.20 \times 0.50 \times 0.50$
Space group	$P6_4$	$P2_1/n$	$P\bar{1}$	$C2/c$	$P\bar{1}$
a (Å)	14.548(2)	13.848(2)	9.898(2)	18.577(2)	10.087(2)
b (Å)	14.548(2)	11.255(3)	10.434(2)	16.918(1)	10.264(1)
c (Å)	11.855(2)	17.464(2)	15.916(4)	8.121(2)	15.782(2)
α (°)	90	90	72.57(1)	90	72.66(1)
β (°)	90	98.28(1)	76.26(1)	92.84(2)	76.534(8)
γ (°)	120	90	72.88(1)	90	74.15(1)
V (Å^3)	2172.7(5)	2693.5(9)	1478.6(5)	2549.3(6)	1479.8(3)
Z	3	4	2	4	2
D_{calcd} (g cm^{-3})	1.989	2.024	1.887	2.138	2.088
μ (cm^{-1})	66.26	60.01	55.54	78.90	65.02
Transmission factor	0.68–1.00	0.55–1.00	0.42–1.00	0.31–1.00	0.30–1.00
Number of reflections measured	1944	6758	7164	3121	7265
Number of reflections used	1652	4178	5985	2505	6066
Number of variables used	179	379	379	174	379
R (R_w)	0.042 (0.055)	0.054 (0.068)	0.056 (0.090)	0.036 (0.046)	0.039 (0.053)
Goodness-of fit on F^2	1.01	1.00	1.00	1.01	1.00

temperature of 296 ± 1 K using the ω–2θ scan technique to a maximum 2θ value of 55°. The weak reflections ($I < 10.0\sigma(I)$) were rescanned (maximum of 3 scans) and the counts were accumulated to ensure good counting statistics. Stationary background counts were recorded on each side of the reflection. The ratio of peak counting time to background counting time was 2:1. The intensities of three representative reflections were measured after every 150 reflections. Over the course of the data collection, the standards decreased by 0.0–8.2%. Polynomial correction factors were applied to the data to account for this phenomenon. Empirical absorption corrections based on azimuthal scans of several reflections were applied. The data were corrected for Lorentz and polarization effects. Corrections for secondary extinctions were applied [10]. The crystal data and experimental parameters are summarized in Table 1.

The structures were solved by direct methods for $\mathbf{1}ClO_4 \cdot H_2O$, $\mathbf{1}Br \cdot 2H_2O$, $\mathbf{1}I \cdot 2H_2O$, $\mathbf{2}ClO_4 \cdot H_2O$, $\mathbf{2}Br \cdot 2H_2O$, $\mathbf{2}I \cdot 2H_2O$, $\mathbf{3}NO_3 \cdot 3H_2O$, $\mathbf{3}ClO_4 \cdot 2H_2O$ and $\mathbf{3}Br \cdot 2H_2O$, and heavy-atom Patterson methods for $\mathbf{3}I \cdot 5.5H_2O$, and expanded using Fourier techniques [11–13]. In the hexagonal structures of $\mathbf{1}X \cdot 2H_2O$ and $\mathbf{2}X \cdot 2H_2O$ (X = Br or I), Co and Pt lie on a crystallographic twofold axis and for these compounds the asymmetric unit comprises, in addition to the metal atoms, exactly one half of the bpy ligand, a single complete pen ligand, the oxygen atom of one water molecule and a halide counter anion, X, with occupancy of 0.5 due to its disorder over a pair of symmetry related sites. The non-hydrogen atoms were refined anisotropically, except for oxygen atoms of perchlorate anions in $\mathbf{1}ClO_4 \cdot H_2O$ and $\mathbf{2}ClO_4 \cdot H_2O$, which were refined isotropically. All the hydrogen atoms, except those of the water molecules which were not included in any of the structural models, were placed in calculated positions and refined with a riding model. The final cycle of full-matrix least-squares refinement on F was based on observed reflections ($I > 2.00\sigma(I)$) and variable parameters, and converged with unweighted and weighted agreement factors of R $(=\sum||F_o| - |F_c||/\sum|F_o|)$ and Rw $(= [\sum w(|F_o| - |F_c|)^2 / \sum wF_o^2]^{1/2})$. Neutral atom scattering factors were taken from Cromer and Waber [14]. Anomalous dispersion effects were included in F_c; the values for $\Delta f'$ and $\Delta f''$ were those of Creagh and McAuley [15–17]. The absolute configurations for $\mathbf{1}ClO_4 \cdot H_2O$, $\mathbf{1}Br \cdot 2H_2O$, $\mathbf{1}I \cdot 2H_2O$, $\mathbf{2}ClO_4 \cdot H_2O$, $\mathbf{2}Br \cdot 2H_2O$ and $\mathbf{2}I \cdot 2H_2O$ were determined on the basis of the known S and R configurations of the asymmetric carbon atoms in the D- and L-pen ligands, respectively, and the structures were supported by the Flack parameters (0.03(2) for $\mathbf{1}ClO_4 \cdot H_2O$, 0.20(5) for $\mathbf{1}Br \cdot 2H_2O$, 0.04(5) for $\mathbf{1}I \cdot 2H_2O$, 0.10(2) for $\mathbf{2}ClO_4 \cdot H_2O$, 0.22(5) for $\mathbf{2}Br \cdot 2H_2O$ and −0.02(4) for $\mathbf{2}I \cdot 2H_2O$) [18]. All calculations were performed using the CrystalStructure crystallographic software package of the Molecular Structure Corporation [19].

3. Results and discussion

3.1. Crystal structures

An X-ray structural analysis for $\mathbf{1}ClO_4 \cdot H_2O$ revealed the presence of a discrete monovalent complex cation, one perchlorate anions and one water molecule. A perspective drawing of the complex cation **1** is given in Fig. 1a, and selected bond distances and angles are listed in Table 2. As shown in Fig. 1a, **1** is composed of one Co atom and one Pt atom to form an S-bridged dinuclear structure. Although two chiral configurations, R and S, are possible for each of the two bridging S atoms in **1**, both S atoms are stereoselectively unified to the S configuration. These structural features for $\mathbf{1}ClO_4 \cdot H_2O$ are essentially consistent with those for $\mathbf{1}Cl \cdot 3H_2O$, $\mathbf{1}Br \cdot 2H_2O$ and $\mathbf{1}I \cdot 2H_2O$, being independent of the nat-

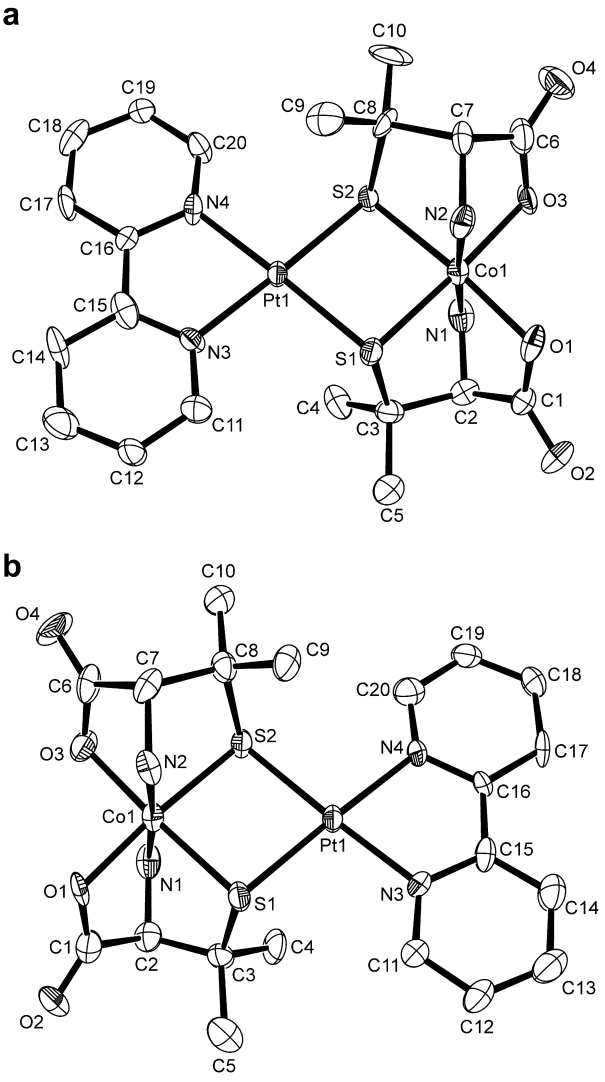


Fig. 1. Perspective views of complex cations in (a) $\mathbf{1}ClO_4 \cdot H_2O$ and (b) $\mathbf{2}ClO_4 \cdot H_2O$ with the atomic labelling schemes (50% probability ellipsoids).

Table 2
Selected bond distances (Å) and angles (°) of $\mathbf{1}(ClO_4)_3 \cdot H_2O$, $\mathbf{2}(ClO_4)_3 \cdot H_2O$, and $\mathbf{3}(ClO_4)_3 \cdot 2H_2O$

	$\mathbf{1}ClO_4 \cdot H_2O$	$\mathbf{2}ClO_4 \cdot H_2O$	$\mathbf{3}ClO_4 \cdot 2H_2O$
Pt(1)–S(1)	2.293(4)	2.295(4)	2.300(3)
Pt(1)–S(2)	2.286(4)	2.289(4)	2.299(2)
Pt(1)–N(3)	2.03(1)	2.05(1)	2.047(7)
Pt(1)–N(4)	2.06(1)	2.07(1)	2.054(9)
Co(1)–S(1)	2.227(4)	2.221(4)	2.216(2)
Co(1)–S(2)	2.230(4)	2.231(4)	2.222(3)
Co(1)–O(1)	1.936(9)	1.92(1)	1.922(9)
Co(1)–O(3)	1.926(9)	1.91(1)	1.948(7)
Co(1)–N(1)	1.93(2)	1.93(1)	1.940(9)
Co(1)–N(2)	1.93(2)	1.93(1)	1.94(1)
Pt(1)–S(1)–Co(1)	95.2(1)	95.1(2)	95.32(9)
S(2)–Pt(1)–S(1)	83.3(1)	83.3(2)	82.91(9)
N(3)–Pt(1)–S(1)	98.4(3)	98.8(4)	98.2(3)
N(4)–Pt(1)–S(1)	178.0(3)	178.0(4)	177.0(3)
Pt(1)–S(2)–Co(1)	95.3(1)	95.0(2)	95.15(9)
N(3)–Pt(1)–S(2)	178.2(3)	177.6(4)	177.8(3)
N(4)–Pt(1)–S(2)	98.7(3)	98.7(3)	99.3(2)
N(4)–Pt(1)–N(3)	79.6(4)	79.2(5)	79.6(3)
S(2)–Co(1)–S(1)	86.1(2)	86.4(2)	86.6(1)
N(1)–Co(1)–S(1)	87.9(4)	88.3(4)	87.9(2)
N(2)–Co(1)–S(1)	95.5(3)	95.3(4)	94.1(2)
O(1)–Co(1)–S(1)	89.7(3)	89.0(3)	90.7(2)
O(3)–Co(1)–S(1)	176.6(3)	176.7(4)	175.7(2)
N(1)–Co(1)–S(2)	95.1(4)	96.0(4)	95.2(3)
N(2)–Co(1)–S(2)	87.9(3)	87.3(4)	87.3(3)
O(1)–Co(1)–S(2)	175.1(3)	175.1(4)	176.1(3)
O(3)–Co(1)–S(2)	91.1(3)	91.0(3)	91.0(3)
N(1)–Co(1)–O(1)	82.2(5)	82.2(5)	81.9(4)
N(2)–Co(1)–O(1)	95.0(5)	94.7(5)	95.7(4)
O(3)–Co(1)–O(1)	93.2(4)	93.7(5)	91.8(4)
N(1)–Co(1)–O(3)	94.3(5)	93.9(5)	95.9(3)
N(2)–Co(1)–O(3)	82.4(5)	82.7(5)	82.1(3)
N(2)–Co(1)–N(1)	175.7(5)	175.3(5)	176.9(4)

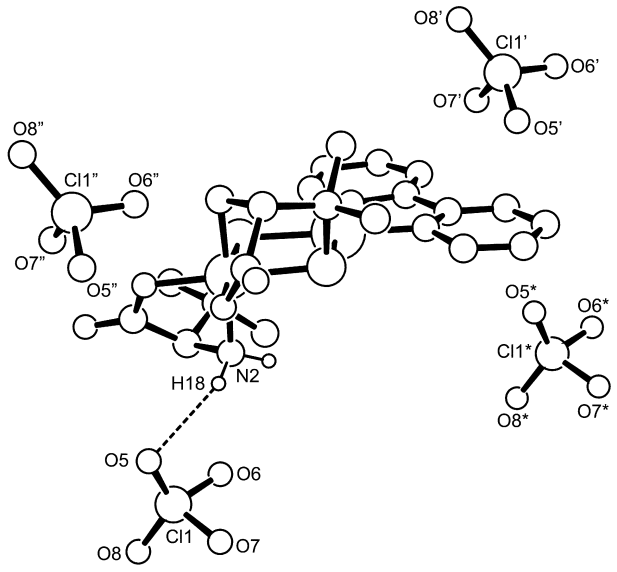


Fig. 2. Neighboring perchlorate anions around complex cation in $\mathbf{1}ClO_4 \cdot H_2O$. Symmetry codes for atoms with asterisks: x, y, $-1+z$; primes: $-x+y$, $-x$, $-2/3+z$; double primes: $-x+y$, $-x$, $1/3+z$.

ure of the counter anions [3]. On the other hand, each complex cation in $\mathbf{2}ClO_4 \cdot H_2O$, $\mathbf{2}Br \cdot 2H_2O$ and $\mathbf{2}I \cdot 2H_2O$ possesses the same structural features as those in $\mathbf{1}ClO_4 \cdot H_2O$, $\mathbf{1}Br \cdot 2H_2O$ and $\mathbf{1}I \cdot 2H_2O$, except for absolute configurations of the asymmetric carbons in the coordinated pen ligands, namely *S* and *R* configurations of the asymmetric carbon atoms in the D- and L-pen ligands, respectively (Fig. 1b). The two chiral S atoms in the complex cation of $\mathbf{2}ClO_4 \cdot H_2O$, $\mathbf{2}Br \cdot 2H_2O$, or $\mathbf{2}I \cdot 2H_2O$ are stereoselectively unified to the *R* configuration, in contrast to those with *S* configurations in $\mathbf{1}ClO_4 \cdot H_2O$, $\mathbf{1}Br \cdot 2H_2O$, or $\mathbf{1}I \cdot 2H_2O$.

In each crystal of $\mathbf{1}ClO_4 \cdot H_2O$, $\mathbf{1}Br \cdot 2H_2O$, $\mathbf{1}I \cdot 2H_2O$, $\mathbf{2}ClO_4 \cdot H_2O$, $\mathbf{2}Br \cdot 2H_2O$, and $\mathbf{2}I \cdot 2H_2O$, one of the counter anions is located in the vicinity of one coordinated amino group of the complex cation. As shown in Fig. 2 and Table 3, for instance, the N2 atom in the ocatahedral Co(III) unit is placed close to the O5 atom of the perchlorate anion in the crystal of $\mathbf{1}ClO_4 \cdot H_2O$. The distance between the two atoms is 3.10(3) Å and the angle of N(2)–H(18)···O(5) is 134(1)°, suggesting hydrogen bond formation. Similar hydrogen bond formations are also observed for $\mathbf{1}Br \cdot 2H_2O$, $\mathbf{1}I \cdot 2H_2O$, $\mathbf{2}ClO_4 \cdot H_2O$, $\mathbf{2}Br \cdot 2H_2O$, and $\mathbf{2}I \cdot 2H_2O$ (Table 3). In each crystal of $\mathbf{1}ClO_4 \cdot H_2O$, $\mathbf{1}Br \cdot 2H_2O$, $\mathbf{1}I \cdot 2H_2O$, $\mathbf{2}ClO_4 \cdot H_2O$, $\mathbf{2}Br \cdot 2H_2O$, and $\mathbf{2}I \cdot 2H_2O$, furthermore, one complex cation is surrounded by a total of four counter anions. In the case of $\mathbf{1}ClO_4 \cdot H_2O$, for example, four perchlorate anions are accessible to the complex cation **1** (Fig. 2). As a result, the complex cations are spaced out, whilst interfering with π–π stacking contacts between the bpy frameworks. Such trends are just as valid for $\mathbf{1}Br \cdot 2H_2O$, $\mathbf{1}I \cdot 2H_2O$, $\mathbf{2}ClO_4 \cdot H_2O$, $\mathbf{2}Br \cdot 2H_2O$, and $\mathbf{2}I \cdot 2H_2O$, and all of the optically active complexes show no intermolecular π–π stacking interactions.

The mixture of equimolar amounts of $\mathbf{1}ClO_4 \cdot H_2O$ and $\mathbf{2}ClO_4 \cdot H_2O$ in H_2O crystallizes as $\mathbf{3}ClO_4 \cdot 2H_2O$ in the centric space group of $P\bar{1}$, which is a remarkably contrast to the acentric space group of $P3_2$ for $\mathbf{1}ClO_4 \cdot H_2O$ and $P3_1$ for $\mathbf{2}ClO_4 \cdot H_2O$ (Table 1). In $\mathbf{3}ClO_4 \cdot 2H_2O$, a pair of enantiomeric complex cations, $[Pt(bpy)\{Co(D\text{-}pen)_2\}]^+$ (***D***) and $[Pt(bpy)\{Co(L\text{-}pen)_2\}]^+$ (***L***), forms a dimeric unit through a π–π stacking of the bpy frameworks, and the interplane distance between two π frameworks is 3.45 Å (Fig. 3). In both $\mathbf{3}NO_3 \cdot 3H_2O$ and $\mathbf{3}I \cdot 5.5H_2O$, dimeric units are also established by a pair of enantiomeric complex cations ***D*** and ***L***, accompanied by interplane distances of 3.61 Å for $\mathbf{3}NO_3 \cdot 3H_2O$ and 3.40 Å for $\mathbf{3}I \cdot 5.5H_2O$. The differences in interplane distances imply that such dimeric structures are influenced by the nature of the counter anions. Although the enantiomeric complex cations ***D*** and ***L*** also form a counterpart in $\mathbf{3}Br \cdot 2H_2O$, pairs of enantiomers develop a higher dimensional structure. As shown in Fig. 4, the enantiomeric complex cations ***D*** and ***L*** are arranged alternately whilst containing overlapping bpy planes along the *c* axis. All the bpy frameworks are placed evenly spaced apart by an interplane angle of 3.65 Å, in

Table 3
Hydrogen bonds between complex cations and counter anions (Å and °)[a]

Complex	Interaction	*d*(D–H)	*d*(H···A)	*d*(D···A)	∠(DHA)
1$ClO_4 \cdot H_2O$	N(2)–H(18)···O(5)	0.95(2)	2.37(3)	3.10(3)	134(1)
1$Br \cdot 2H_2O$	N(1)–H(9)···Br(1)	0.95(2)	3.15(1)	3.66(2)	115(1)
	$N(1a^1)$–$H(9a^1)$···$Br(1a^1)$	0.95(2)	3.15(1)	3.66(2)	115(1)
1$I \cdot 2H_2O$	N(1)–H(9)···I(1)	0.95(1)	3.22(1)	3.74(2)	116(1)
	$N(1b^1)$–$H(9b^1)$···$I(1b^1)$	0.95(1)	3.22(1)	3.74(2)	116(1)
2$ClO_4 \cdot H_2O$	N(2)–H(17)···O(5)	0.95(1)	2.34(3)	3.08(2)	135(1)
2$Br \cdot 2H_2O$	N(1)–H(8)···Br(1)	0.95(2)	3.12(2)	3.65(2)	116(1)
	$N(1c^1)$–$H(8c^1)$···$Br(1c^1)$	0.95(2)	3.12(2)	3.65(2)	116(1)
2$I \cdot 2H_2O$	N(1)–H(8)···I(1)	0.95(1)	3.24(1)	3.76(1)	116(1)
	$N(1d^1)$–$H(8d^1)$···$I(1d^1)$	0.95(1)	3.24(1)	3.76(1)	116(1)
3$NO_3 \cdot 3H_2O$	N(1)–H(8)···O(7)	0.95(1)	2.18(2)	3.02(2)	146(1)
	$N(1e^1)$–$H(8e^1)$···$O(7e^1)$	0.95(1)	2.18(2)	3.02(2)	146(1)
3$ClO_4 \cdot 2H_2O$	N(2)–H(18)···O(5)	0.95(1)	2.49(2)	3.11(2)	123(1)
	$N(2f^1)$–$H(18f^1)$···$O(5f^1)$	0.95(1)	2.49(2)	3.11(2)	123(1)
3$Br \cdot 2H_2O$	N(1)–H(9)···Br(1)	0.950(8)	2.590(5)	3.502(5)	161.0(5)
	$N(1g^1)$–$H(9g^1)$···Br(1)	0.950(8)	2.590(5)	3.502(5)	161.0(5)
	$N(1g^2)$–$H(9g^2)$···$Br(1g^3)$	0.950(8)	2.590(5)	3.502(5)	161.0(5)
3$I \cdot 5.5H_2O$	N(2)–H(18)···I(1)	0.95(1)	2.929(5)	3.801(5)	153.2(7)
	$N(2h^1)$–$H(18h^1)$···$I(1h^1)$	0.95(1)	2.929(5)	3.801(5)	153.2(7)

[a] Symmetry codes: $a^1 = 1-x,\ 1-y,\ z$; $b^1 = y,-x+y,\ -1/3+z$; $c^1 = 1-x,\ -y,\ z$; $d^1 = 1-x,\ -y,\ z$; $e^1 = -x,\ -y,\ 1-z$; $f^1 = 1-x,\ -y,\ -z$; $g^1 = 1-x,\ y,\ 5/2-z$; $g^2 = 1-x,\ y,\ 3/2-z$; $g^3 = x,\ y,\ -1+z$; $h^1 = 1-x,\ -y,\ 1-z$.

contrast to **3**$Cl \cdot 7H_2O$, in which two interaction modes with different interplane distances (3.46 and 3.55 Å) result in the formation of a polymeric π–π stacked chain [4]. It seems therefore that the nature of the counter anions also impinges on such one dimensional chain structures.

In either dimer (**3**$NO_3 \cdot 3H_2O$, **3**$ClO_4 \cdot 2H_2O$, or **3**$I \cdot 5.5H_2O$) or one dimensional chain (**3**$Br \cdot 2H_2O$), it is obvious that the fundamental unit is absolutely a pair of enantiomeric complex cations ***D*** and ***L***. Similarly to the cases of monomeric **1**$ClO_4 \cdot H_2O$, **1**$Br \cdot 2H_2O$, **1**$I \cdot 2H_2O$, **2**$ClO_4 \cdot H_2O$, **2**$Br \cdot 2H_2O$, and **2**$I \cdot 2H_2O$, one of the counter anions is located in the vicinity of one coordinated amino group of each complex cation in **3**$NO_3 \cdot 3H_2O$, **3**$ClO_4 \cdot 2H_2O$, **3**$Br \cdot 2H_2O$, and **3**$I \cdot 5.5H_2O$ (Table 3). As shown in Fig. 3, for instance, the N2 atom in the ocatahedral Co(III) unit is placed close to the O5 atom of the perchlorate anion in the crystal of **3**$ClO_4 \cdot H_2O$, accompanied by N(2)–H(18)···O(5) hydrogen bond formation. It should

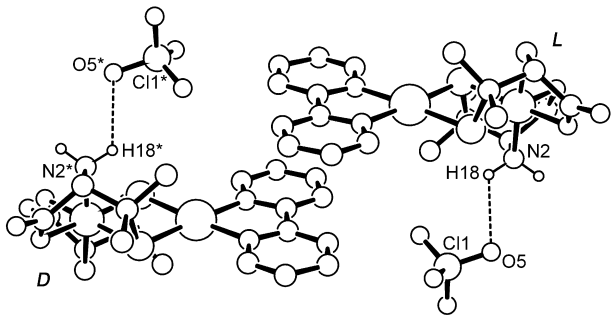


Fig. 3. Dimeric structure comprised of enantiomeric complex cations, $[Pt(bpy)\{Co(D\text{-pen})_2\}]^+$ (***D***) and $[Pt(bpy)\{Co(L\text{-pen})_2\}]^+$ (***L***), in **3**$ClO_4 \cdot 2H_2O$, together with hydrogen bonding perchlorate anions. Symmetry codes for atoms with asterisks: $1-x,-y,-z$.

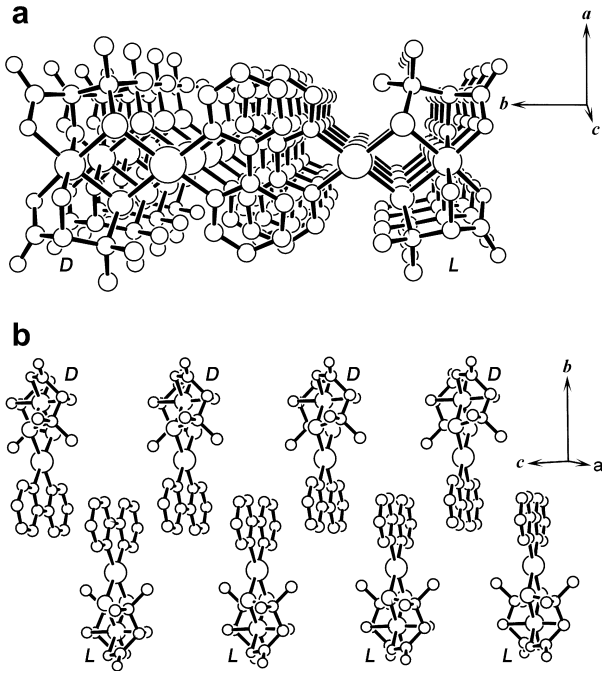


Fig. 4. Linear-chain structure comprised of enantiomeric complex cations, $[Pt(bpy)\{Co(D\text{-pen})_2\}]^+$ (***D***) and $[Pt(bpy)\{Co(L\text{-pen})_2\}]^+$ (***L***), in **3**$Br \cdot 2H_2O$ with respect to (a) *c* and (b) *a* axes.

be noted at this point that the hydrogen bonding amino group is on the opposite site of the π–π stacking phase. In addition, the extension of the hydrogen bonding counter anion depends on the nature of the counter anion itself. By comparison of the space-filling representation for each dimeric unit, the hydrogen bonding counter anion is, in fact, overhung to such an extent that further π–π stacking contacts with the bpy frameworks in the complex cations are blocked off (Fig. 5). Although inhibition by the hydrogen bonding counter anions in $\mathbf{3}NO_3 \cdot 3H_2O$ is far less than that in $\mathbf{3}ClO_4 \cdot 2H_2O$, and $\mathbf{3}I \cdot 5.5H_2O$, another two anions are located on the vacant sites of the bpy frameworks and interfere with any stacking (Fig. 5a). As a result, higher dimensional structures are impossible for $\mathbf{3}NO_3 \cdot 3H_2O$, $\mathbf{3}ClO_4 \cdot 2H_2O$, and $\mathbf{3}I \cdot 5.5H_2O$. With regard to the monoatomic counter anion, such as I^-, on the other hand, expansion of the hydrogen bonded bromide anion in $\mathbf{3}Br \cdot 2H_2O$ is much less than that in $\mathbf{3}I \cdot 5.5H_2O$ (Fig. 6). This results in the retention of sufficient space for further π–π stacking contacts to form a linear-chain structure for $\mathbf{3}Br \cdot 2H_2O$. However, the interplane distance between the stacking bpy frameworks in $\mathbf{3}Br \cdot 2H_2O$ is much more elongated than that in $\mathbf{3}Cl \cdot 7H_2O$ due to the increment of the ionic radii [4]. It can be concluded that the crystal structures of these complexes are considerably determined by the nature of the counter anions.

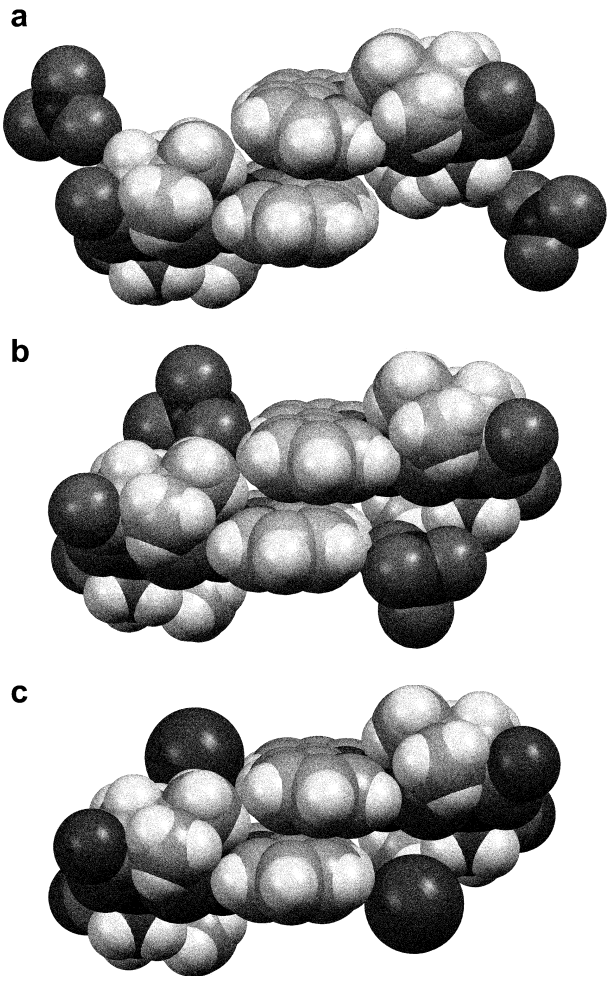


Fig. 5. Space-filling models for dimeric units of (a) $\mathbf{3}ClO_4 \cdot 2H_2O$, (b) $\mathbf{3}NO_3 \cdot 3H_2O$ and (c) $\mathbf{3}I \cdot 2H_2O$, together with the neighboring counter anions.

3.2. Characterization

In D_2O or a 1:1 mixed solvent of CD_3CN and D_2O, each of $\mathbf{1}NO_3 \cdot 6H_2O$, $\mathbf{1}ClO_4 \cdot H_2O$, $\mathbf{1}Br \cdot 2H_2O$, and $\mathbf{1}I \cdot 2H_2O$ exhibits five ^{13}C NMR signals due to D-pen ligands and five signals characteristic for the bpy ligand [1–5,20]. In D_2O, for instance, $\mathbf{1}NO_3 \cdot 6H_2O$ shows signals due to D-pen at δ 31.02, 34.56, 54.90, 75.85, and 183.58 ppm, and those characteristic for bpy at 127.07, 131.19, 144.87, 150.16, and 159.44 ppm. Among the five signals for D-pen, two signals at δ 31.02 and 34.56 ppm are assigned to the carbon atoms of $-CH_3$ groups [3,4,21,22]. The remaining three signals at δ 54.90, 75.85 and 183.58 ppm are ascribed to the carbon atoms of $-C(CH_3)_2S$, $-CH(COO)N$, and $-COO$ groups, respectively. Similarly, the ^{13}C NMR spectra of $\mathbf{2}NO_3 \cdot 6H_2O$, $\mathbf{2}ClO_4 \cdot H_2O$, $\mathbf{2}Br \cdot 2H_2O$, or $\mathbf{2}I \cdot 2H_2O$, which are enantiomers of $\mathbf{1}NO_3 \cdot 6H_2O$, $\mathbf{1}ClO_4 \cdot H_2O$, $\mathbf{1}Br \cdot 2H_2O$, or $\mathbf{1}I \cdot 2H_2O$, respectively, consists of ten signals based on L-pen and bpy ligands. Although two kinds of complex cation, $[Pt(bpy)\{Co(D\text{-}pen)_2\}]^+$ (***D***) and $[Pt(bpy)\{Co(L\text{-}pen)_2\}]^+$ (***L***), exist in $\mathbf{3}NO_3 \cdot 3H_2O$, $\mathbf{3}ClO_4 \cdot 2H_2O$, $\mathbf{3}Br \cdot 2H_2O$, and $\mathbf{3}I \cdot 5.5H_2O$, the ^{13}C NMR spectra exhibits two sets of five signals due to pen and bpy ligands. Independent of counter anion, furthermore, the spectral pattern of **3** is quite similar to those of **1** and **2**. A similar trend is also observed for the hydrogen atoms of the bpy framework in the ^1H NMR spectra of **1**, **2**, and **3** [3,4]. These facts indicate that there are no intermolecular interactions under the present conditions, namely, concentrations of 10^{-2} mol dm^{-3}.

Electronic absorption and CD spectra of $\mathbf{1}ClO_4 \cdot H_2O$ are shown in Fig. 7, together with the CD spectra of $\mathbf{2}ClO_4 \cdot H_2O$ and $\mathbf{3}ClO_4 \cdot 2H_2O$ in H_2O. The first absorption band of $\mathbf{1}ClO_4 \cdot H_2O$ consists of three components at

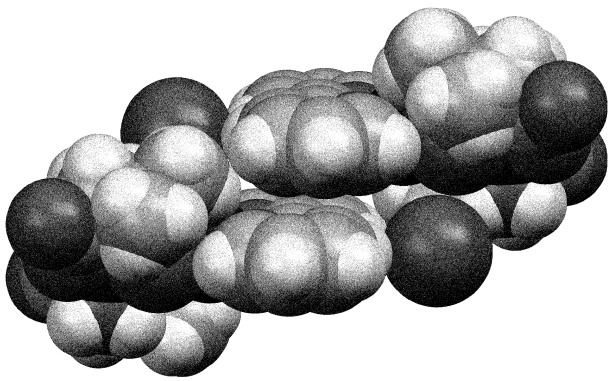


Fig. 6. Space-filling model for the clipping dimeric unit of $\mathbf{3}Br \cdot 2H_2O$.

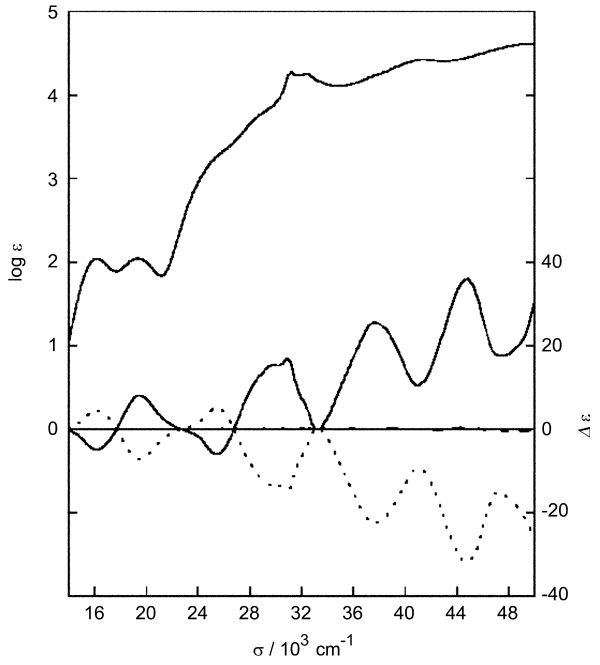


Fig. 7. Electronic absorption and CD spectra of $\mathbf{1}ClO_4 \cdot H_2O$ (solid line), together with CD spectra of $\mathbf{2}ClO_4 \cdot H_2O$ (dotted line) and $\mathbf{3}ClO_4 \cdot 2H_2O$ (broken line) in H_2O.

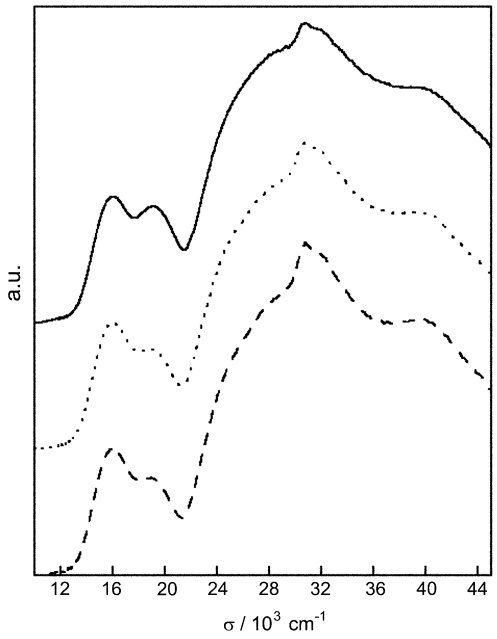


Fig. 8. Diffuse reflectance spectra of $\mathbf{1}ClO_4 \cdot H_2O$ (broken line), $\mathbf{2}ClO_4 \cdot H_2O$ (dotted line) and $\mathbf{3}ClO_4 \cdot 2H_2O$ (solid line).

16.16, 19.38, and 25.3×10^3 cm^{-1} [3,4]. The second d–d and sulfur-to-metal charge-transfer bands appear at 28.5 and 37.2×10^3 cm^{-1}, respectively. The characteristic electronic bands localized on the bpy framework are observed at 31.25 and 32.47×10^3 cm^{-1}. Reflecting the enantiomeric relationship, $\mathbf{2}ClO_4 \cdot H_2O$ shows the same absorption spectral behavior as $\mathbf{1}ClO_4 \cdot H_2O$. Although $\mathbf{3}ClO_4 \cdot 2H_2O$ involves two complex cation components, the spectral pattern is quite similar to that of $\mathbf{1}ClO_4 \cdot H_2O$ or $\mathbf{2}ClO_4 \cdot H_2O$. This result also supports that there is no significant interaction between the π electronic systems of $\mathbf{3}ClO_4 \cdot 2H_2O$. In the CD spectrum, $\mathbf{1}ClO_4 \cdot H_2O$ shows six positive signals at 19.46, 22.5, 29.4, 30.86, 37.74, and 44.84×10^3 cm^{-1}, and two negative signals at 16.21 and 25.51×10^3 cm^{-1}. While the absolute values of strengths and positions for CD bands in $\mathbf{2}ClO_4 \cdot H_2O$ correspond well with those in $\mathbf{1}ClO_4 \cdot H_2O$, each sign of the former is quite the opposite to the corresponding sign of the latter on the basis of the enantiomeric relationship. In contrast to the optically active $\mathbf{1}ClO_4 \cdot H_2O$ and $\mathbf{2}ClO_4 \cdot H_2O$, $\mathbf{3}ClO_4 \cdot 2H_2O$ shows no CD signals over the whole region in H_2O. Furthermore, similar trends in absorption and CD spectra are also observed for $\mathbf{1}NO_3 \cdot 6H_2O$, $\mathbf{1}Br \cdot 2H_2O$, $\mathbf{1}I \cdot 2H_2O$, $\mathbf{2}NO_3 \cdot 6H_2O$, $\mathbf{2}Br \cdot 2H_2O$, $\mathbf{2}I \cdot 2H_2O$, $\mathbf{3}NO_3 \cdot 3H_2O$, $\mathbf{3}Br \cdot 2H_2O$, and $\mathbf{3}I \cdot 5.5H_2O$. It can be concluded therefore that the crystal of $\mathbf{3}NO_3 \cdot 3H_2O$, $\mathbf{3}ClO_4 \cdot 2H_2O$, $\mathbf{3}Br \cdot 2H_2O$, and $\mathbf{3}I \cdot 5.5H_2O$ involve accurately equimolecular amounts of two enantiomers.

The reflectance spectrum of $\mathbf{1}ClO_4 \cdot H_2O$ consists of three peaks at 16.02, 18.92, and 30.82×10^3 cm^{-1}, and four shoulders at 25.2, 28.3, 32.0, and 40.0×10^3 cm^{-1} (Fig. 8). It is obvious that the 16.02, 18.92, 25.2, 28.3, 30.82, 32.0, and 40.0×10^3 cm^{-1} reflectance bands correspond to the 16.16, 19.38, 25.3, 28.5, 31.25, 32.47, and 41.32×10^3 cm^{-1} absorption bands in H_2O, respectively. Although all the bands are slightly shifted toward the lower-energy side than the corresponding absorption bands, an essential distinction is not found between both spectra. This implies that each cation in the solid state is comparatively put in a free environment, as well as in solution. While $\mathbf{2}ClO_4 \cdot H_2O$ shows the same reflectance spectral behavior as $\mathbf{1}ClO_4 \cdot H_2O$, some significant differences can be seen between the reflectance and absorption spectra of $\mathbf{3}ClO_4 \cdot 2H_2O$. It seems therefore that each complex cation in $\mathbf{3}ClO_4 \cdot 2H_2O$ is put under different surroundings in the two states. Furthermore, the reflectance spectral features for $\mathbf{3}ClO_4 \cdot 2H_2O$ are somewhat different from those for $\mathbf{1}ClO_4 \cdot H_2O$ or $\mathbf{2}ClO_4 \cdot H_2O$. In the $25–29 \times 10^3$ cm^{-1} region, for example, $\mathbf{1}ClO_4 \cdot H_2O$ and $\mathbf{2}ClO_4 \cdot H_2O$ show two well-resolved shoulders, while $\mathbf{3}ClO_4 \cdot 2H_2O$ has one broad shoulder at 26.9×10^3 cm^{-1}. Furthermore, the corresponding bands for the 30.82×10^3 cm^{-1} peak and 32.0×10^3 cm^{-1} shoulder in $\mathbf{1}ClO_4 \cdot H_2O$ or $\mathbf{2}ClO_4 \cdot H_2O$, which are assigned as localized electronic transitions on the bpy frameworks, shift slightly toward the lower-energy side in $\mathbf{3}ClO_4 \cdot 2H_2O$. These seem to reflect some distinction in the electronic natures between dimeric $\mathbf{3}ClO_4 \cdot 2H_2O$ and monomeric $\mathbf{1}ClO_4 \cdot H_2O$ or $\mathbf{2}ClO_4 \cdot H_2O$.

Responding to the dimeric structure in the crystalline state, as well as $\mathbf{3}ClO_4 \cdot 2H_2O$, each of $\mathbf{3}NO_3 \cdot 3H_2O$ and $\mathbf{3}I \cdot 5.5H_2O$ exhibits one broad shoulder in the $25–29 \times 10^3$ cm^{-1} region (Fig. 9). However, the band profiles and positions are considerably distinct from each other.

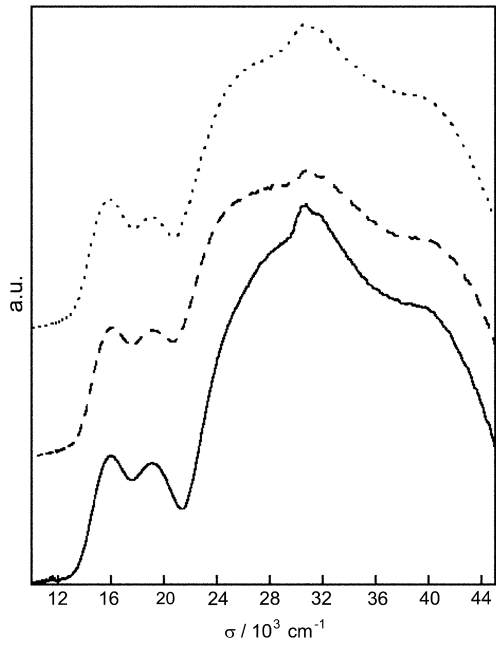


Fig. 9. Diffuse reflectance spectra of $\mathbf{3}NO_3 \cdot 3H_2O$ (solid line), $\mathbf{3}I \cdot 2H_2O$ (broken line) and $\mathbf{3}Br \cdot 2H_2O$ (dotted line).

The corresponding band for the $26.9 \times 10^3\ cm^{-1}$ band in $\mathbf{3}ClO_4 \cdot 2H_2O$ shifts toward the higher-energy side and appears at $27.3 \times 10^3\ cm^{-1}$ in $\mathbf{3}NO_3 \cdot 3H_2O$. In contrasted to $\mathbf{3}NO_3 \cdot 3H_2O$, the corresponding reflectance band of $\mathbf{3}I \cdot 5.5H_2O$ overhangs to the lower-energy side and is located at $25.4 \times 10^3\ cm^{-1}$. These indicate that the electronic natures of $\mathbf{3}NO_3 \cdot 3H_2O$, $\mathbf{3}ClO_4 \cdot 2H_2O$, and $\mathbf{3}I \cdot 5.5H_2O$ differ considerably from each other regardless of similar dimeric structures. In each crystal of $\mathbf{3}NO_3 \cdot 3H_2O$, $\mathbf{3}ClO_4 \cdot 2H_2O$, and $\mathbf{3}I \cdot 5.5H_2O$, as shown in Fig. 5, the dimeric unit is established by a pair of enantiomeric complex cations ***D*** and ***L***. In addition, the interplane distances between the bpy frameworks of $\mathbf{3}NO_3 \cdot 3H_2O$, $\mathbf{3}ClO_4 \cdot 2H_2O$, and $\mathbf{3}I \cdot 5.5H_2O$ are 3.61, 3.45, and 3.40 Å, respectively, depending on the nature of the counter anion. It should be noted that the interplane distances correlate with the band positions of the above broad shoulders. The broad shoulder shifts toward the lower-energy side as the interplane distance shortens, namely, the interaction between the π electronic systems intensifies. Therefore, the broad shoulder in the $25–29 \times 10^3\ cm^{-1}$ region can be regarded as characteristic for the dimeric structure composed of a pair of enantiomeric complex cations ***D*** and ***L***. In the $25–29 \times 10^3\ cm^{-1}$ region, the reflectance spectrum of $\mathbf{3}Br \cdot 2H_2O$ does not show two well-resolved shoulders but a single broad band around $27.0 \times 10^3\ cm^{-1}$ (Fig. 9). Although the interplane distance between two π electronic systems in $\mathbf{3}Br \cdot 2H_2O$ (3.65 Å) is slightly longer than that in $\mathbf{3}NO_3 \cdot 3H_2O$, the broad shoulder of the former appears at the lower-energy side in comparison with the latter. This seems to reflect the dimensional distinctions in π–π stackings between linear-chains and dimers. Considering these facts, it can be concluded that fluctuations by counter anions are brought not only to crystal structures but to electronic natures as well.

4. Supplementary material

CCDC 627218, 627219, 627220, 627221, 627222, 627223, 627224, 627225, 627226 and 627227 contain the supplementary crystallographic data for $\mathbf{1}ClO_4 \cdot H_2O$, $\mathbf{1}Br \cdot 2H_2O$, $\mathbf{1}I \cdot 2H_2O$, $\mathbf{2}ClO_4 \cdot H_2O$, $\mathbf{2}Br \cdot 2H_2O$, $\mathbf{2}I \cdot 2H_2O$, $\mathbf{3}NO_3 \cdot 3H_2O$, $\mathbf{3}ClO_4 \cdot 2H_2O$, $\mathbf{3}Br \cdot 2H_2O$ and $\mathbf{3}I \cdot 5.5H_2O$. These data can be obtained free of charge via http://www.ccdc.cam.ac.uk/conts/retrieving.html, or from the Cambridge Crystallographic Data Centre, 12 Union Road, Cambridge CB2 1EZ, UK; fax: (+44) 1223-336-033; or e-mail: deposit@ccdc.cam.ac.uk.

Acknowledgement

This work was partly supported by Grants-in-Aid for Scientific Research from the Ministry of Education, Culture, Sports, Science and Technology.

References

[1] Y. Yamada, M. Uchida, Y. Miyashita, K. Fujisawa, T. Konno, K. Okamoto, Bull. Chem. Soc. Jpn. 73 (2000) 913.
[2] Y. Yamada, Y. Maeda, T. Konno, K. Fujisawa, K. Okamoto, Bull. Chem. Soc. Jpn. 73 (2000) 1831.
[3] Y. Yamada, M. Uchida, M. Fujita, Y. Miyashita, K. Okamoto, Polyhedron 22 (2003) 1507.
[4] Y. Yamada, K. Okamoto, Inorg. Chim. Acta 359 (2006) 3963.
[5] Y. Yamada, M. Noda, M. Inoue, Y. Miyashita, K. Okamoto, M. Koikawa, T. Tokii, J. Coord. Chem., in press.
[6] Y. Yamada, K. Fujisawa, K. Okamoto, Bull. Chem. Soc. Jpn. 73 (2000) 2297.
[7] K. Okamoto, K. Wakayama, H. Einaga, S. Yamada, J. Hidaka, Bull. Chem. Soc. Jpn. 56 (1983) 165.
[8] N. Baidya, D. Ndreu, M. Olmstead, K. Mascharak, Inorg. Chem. 30 (1991) 2448.
[9] R.H. Herber, M. Croft, M.J. Coyer, B. Bilash, A. Sahiner, Inorg. Chem. 33 (1994) 2422.
[10] A.C. Larson, in: F.R. Ahmed (Ed.), Crystallographic Computing, Munksgaard, Copenhagen, 1970, pp. 291–294 (Eq. (22), with V replaced by the cell volume).
[11] SIR92: A. Altomare, G. Cascarano, C. Giacovazzo, A. Guagliardi, M. Burla, G. Polidori, M. Camalli, J. Appl. Crystallogr. 27 (1994) 435.
[12] DIRDIF99: P.T. Beurskens, G. Admiraal, G. Beurskens, W.P. Bosman, R. de Gelder, R. Israel, J.M.M. Smits, The DIRDIF-99 program system, Technical Report of the Crystallography Laboratory, University of Nijmegen, The Netherlands, 1999.
[13] PATTY: P.T. Beurskens, G. Admiraal, G. Beurskens, W.P. Bosman, S. Garcia-Granda, R.O. Gould, J.M.M. Smits, C. Smykalla, The DIRDIF program system, Technical Report of the Crystallography Laboratory, University of Nijmegen, The Netherlands, 1992.
[14] D.T. Cromer, J.T. Waber (Eds.), International Tables for X-ray Crystallography, vol. IV, The Kynoch Press, Birmingham, England, 1974, Table 2.2 A.
[15] J.A. Ibers, W.C. Hamilton, Acta Crystallogr. 17 (1964) 781.
[16] D.C. Creagh, W.J. McAuley, in: A.J.C. Wilson (Ed.), International Tables for Crystallography, vol. 1, Kluwer Academic Publishers, Boston, 1992, pp. 219–222.

[17] D.C. Creagh, J.H. Hubbell, in: A.J.C. Wilson (Ed.), International Tables for Crystallography, vol. C, Kluwer Academic Publishers, Boston, 1992, pp. 200–206.
[18] H.D. Flack, Acta Crystallogr. A39 (1983) 876.
[19] CrystalStructure 3.6.0: Crystal Structure Analysis Package, Rigaku and Rigaku/MSC, 9009 New Trails Dr. The Woodlands, TX 77381, USA, 2004.
[20] Y. Yamada, K. Fujisawa, K. Okamoto, Bull. Chem. Soc. Jpn. 73 (2000) 2067.
[21] Y. Yamada, M. Tsumita, A. Hirano, Y. Miyashita, K. Fujisawa, K. Okamoto, Inorg. Chim. Acta 332 (2002) 108.
[22] Y. Yamada, A. Hirano, M. Fujita, N. Amir, Y. Miyashita, K. Okamoto, Inorg. Chim. Acta 358 (2005) 667.

Available online at www.sciencedirect.com
ScienceDirect
Polyhedron 26 (2007) 2761–2766
POLYHEDRON
www.elsevier.com/locate/poly

The first bis(orotato–*N*,*O*) complex: Synthesis, crystal structure, spectroscopic and thermal characterization of $(chaH)_2[Cu(HOr–N,O)_2(cha)]\cdot 2H_2O$ (cha = cyclohexylamine and HOr = orotate(2−))

Okan Zafer Yeşilel [a,*], Hümeyra Paşaoğlu [b], Kamber Akdağ [b], Orhan Büyükgüngör [b]

[a] *Department of Chemistry, Faculty of Arts and Sciences, Eskişehir Osmangazi University, 26480 Eskişehir, Turkey*
[b] *Department of Physics, Faculty of Arts and Sciences, Ondokuz Mayıs University, 55139 Kurupelit, Samsun, Turkey*

Received 9 December 2006; accepted 16 January 2007
Available online 12 February 2007

Abstract

The novel bis(cyclohexylaminium) cyclohexylaminebis(orotate–*N*,*O*)cuprate(II) dihydrate, $(C_6H_{15}N)_2[Cu(C_5H_2N_2O_4)_2(C_6H_{14}N)]\cdot 2H_2O$, has been prepared and characterized by elemental analysis, magnetic measurements, FT-IR and UV–Vis spectroscopy, thermal analysis and X-ray diffraction. The Cu(II) complex crystallizes in the monoclinic space group $P2_1/c$. The copper atom in the five-coordinated $(chaH)_2[Cu(HOr–N,O)_2(cha)]\cdot 2H_2O$ is chelated by a deprotonated pyrimidine nitrogen atom and carboxylate oxygen atom as a bis(bidentate) ligand and the cyclohexylamine ligand completes the square-pyramidal coordination. The thermal decomposition of the complex has been predicted by the help of thermal analysis (TG, DTG and DTA).
© 2007 Elsevier Ltd. All rights reserved.

Keywords: Orotate complex; Cyclohexylamine complex; Copper(II) complex; Thermal decomposition

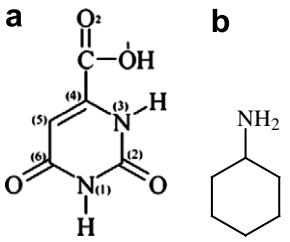
1. Introduction

Metal complexes of orotic acid (1,2,3,6-tetrahydro-2,6-dioxo-4-pyrimidine carboxylic acid, vitamin B13, H_3Or, Scheme 1a) and its substituted derivatives continue to attract attention because of its multidentate functionality and pivotal role in bioinorganic chemistry [1,2]. It is a precursor in the biosynthesis of pyrimidine bases and nucleic acids in living organisms [1,2]. It has been widely exploited in medicine [2,3]. It also exhibits bacteriostatic and cytostatic properties. The coordination chemistry of orotic acid was found to be very interesting. Its anions also are interesting multidentate ligands as they can coordinate through the pyrimidine nitrogen atoms, the carbonyl oxygen and the carboxyl oxygen. The incorporation of metals into supramolecular systems attracts much attention and some orotate complexes [4,5] have shown that the orotate ligand may be a good building block for the construction of supramolecular systems. The literature lists many reports on the coordinating presences of the orotate moiety in metal complexes. Although the most common coordination mode of H_3Or is ligation through the deprotonated carboxyl group and its adjacent nitrogen atom [4–15], no bis(orotate–*N*,*O*) metal complex is known. The first copper(II)–orotate complex, $[Cu(HOr)(NH_3)_2]$, was reported by Mutikainen and Lumme [6] in 1980. X-ray structures of other Cu(II)–orotate complexes, $[Cu(HOr)(H_2O)_2]_n$ [7], $[Cu(HOr)(phen)]$ [8], $[Cu(HOr)(H_2O)(en)]\cdot H_2O$ [9], $[Cu(HOr)(tea)]\cdot H_2O$ [10] and $[Cu(HOr)(bipy)(H_2O)]\cdot H_2O$ [11] (phen = 1.10-phenanthroline, en = ethylenediamine, tea = triethanolamine, bipy = 2,2′-bipyridine), have been studied.

In the present paper, we describe the synthesis, spectroscopic, thermal studies and crystal structure of the first *bis*(orotato–*N*,*O*) copper(II) complex with orotic acid and

* Corresponding author. Tel.: +90 02222393750/2867.
E-mail address: yesilel@ogu.edu.tr (O.Z. Yeşilel).

0277-5387/$ - see front matter © 2007 Elsevier Ltd. All rights reserved.
doi:10.1016/j.poly.2007.01.050



Scheme 1. Structures of the ligands: (a) orotic acid, (b) cyclohexylamine.

cyclohexylamine (cha, Scheme 1b), $(chaH)_2[Cu(HOr\text{-}N,O)_2(cha)]\cdot 2H_2O$ (**1**).

2. Experimental

2.1. Preparation of the complex

The cha ligand (1.00 g, 10 mmol) was added dropwise to a solution of $CuCl_2\cdot 2H_2O$ (0.43 g, 2.5 mmol) and $H_3Or\cdot H_2O$ (0.87 g, 5 mmol) dissolved in water (30 ml), and stirred for 10 h at 60 °C. The reaction mixture was then cooled to room temperature. Green crystals were filtered off and then washed with 10 ml of water and dried in air. *Anal.* Calc. for $C_{28}H_{49}N_7O_{10}Cu$: C, 47.55; H, 6.98; N, 13.86. Found: C, 47.58; H, 7.02; N, 13.84%.

2.2. Materials and measurements

All the chemicals used were analytical reagent and were commercially purchased. IR spectra were obtained with a Bruker Tensor 27 FT-IR spectrometer using KBr pellets in the 4000–400 cm^{-1} range. Elemental analysis for C, H and N were performed using a Carlo Erba 1106 microanalyser. Magnetic susceptibility measurement at room temperature was performed using a Sherwood Scientific MXI model Gouy magnetic balance. The UV–Vis spectrum was obtained for an aqueous solution of the complex (10^{-3} M) with a Unicam UV2 spectrometer in the range 900–190 nm. A Perkin Elmer Diamond TG/DTA thermal analyzer was used to record simultaneous TG, DTG and DTA curves in static air atmosphere at a heating rate of 10 K min^{-1} in the temperature range 20–600 °C using platinum crucibles.

2.3. Crystallographic analysis

Diffraction experiments were carried out at 293 K on a Stoe IPDS diffractometer. The structure was solved by direct methods using the program SHELXS97 [16]. All non-hydrogen atoms were refined anisotropically by full-matrix least-squares methods [16]. All hydrogen atoms except H1, H1w, H2w, H3w, H4w, H46 and H47 were located geometrically. The relevant crystal data and experimental conditions along with the final parameters are summarized in Table 1. Data collection: X-Area, cell refinement: X-Area, data reduction on: X-RED [17]; program(s) used to refine structure: SHELXL97 [16]; molecular graphics: ORTEP-3 for Windows [18]; software used to prepare material for publication: WINGX [19].

Table 1
Crystal data and structure refinement parameters for **1**

Empirical formula	$C_{28}H_{49}N_7O_{10}Cu_1$
Formula weight	707.28
Temperature (K)	293 (2)
Wavelength (Å)	0.71069 Mo Kα
Crystal system	monoclinic
Space group	$P2_1/c$
Unit cell dimensions	
a (Å)	16.352 (5)
b (Å)	11.533 (5)
c (Å)	18.553 (5)
β (°)	101.771 (5)
V (Å^3)	3425 (2)
Z	4
Absorption coefficient (mm^{-1})	0.699
D_{calc} (Mg m^{-3})	1.332
Crystal size (mm)	$0.520\times 0.417\times 0.260$
θ Range for data collection (°)	1.86–27.17
Measured reflections	51857
Independent reflections	7465
Absorption correction	integration Stoe X-RED (Stoe and Cie, 2001)
Refinement method	full-matrix least-squares on F^2
Final R indices [$F^2 > 2\,\sigma(F^2)$]	$R_1 = 0.0630$, $wR_2 = 0.1822$, R_1(all data) = 0.1150
Goodness-of-fit on F^2	0.960
Largest difference peak and hole (e Å^{-3})	0.473 and −0.865

3. Results and discussion

3.1. UV–Vis spectrum and magnetic susceptibility

The UV–Vis spectrum of **1** in H_2O displays a broad absorption band at 766 nm ($\varepsilon = 70$ L $mol^{-1}cm^{-1}$). These values were assigned to an $a_1 \rightarrow b_1$ transition. The complex exhibits a magnetic moment value of 1.72 BM which corresponds to one unpaired electron.

3.2. IR spectrum

Selected IR bands of the copper(II) complex are listed in Table 2. A comparison between the IR spectrum of orotic acid and the copper(II) complex may provide important evidence for the coordination of the orotate ligand to the copper(II) ion. The infrared spectrum of the Cu(II) complex shows a strong band at 3487 cm^{-1} due to the O–H stretching vibrations of water molecules. The intense bands at 3271–3397 cm^{-1} are attributed to the ν(NH) vibration of both cyclohexylamine and the protonated NH_2 group of a cha molecule in the IR spectrum of **1**. The relatively weak bands between 2862 and 2995 cm^{-1} can be assigned to the CH and CH_2 stretching vibrations of the HOr ligand and cha molecules. The position of the characteristic stretching modes of the carbonyl and N–H of the orotate moiety can be used to characterize the coordination mode

Table 2
Selected IR spectral data

Assignment	H_3Or	cha[a]	**1**
$\nu(OH)_{water}$			3487 s
$\nu(NH_2)$		3353 s, 3320 m	3422 m
$\nu(NH_3)$			3271, 3253 m
$\nu(N_{(3)}H)$	3154 m		
$\nu(N_{(1)}H)$	3137 m		3095 m
$\nu(CH)$ or $\nu(CH_2)$	3099 s	2926 w, 2897 m, sh	2995, 2935, 2862 m
$\nu(OH)_{acid}$	2500 m, b		
$\nu(C{=}O_{acid} + C_{(2)}{=}O)$	1729 vs, 1719 vs		1655 vs
$\nu(C_{(6)}{=}O + ring)$	1700 vs		1605 vs
$\nu(C{=}C)$	1653 vs		
$\nu(C–N)$, $\delta(N_{(1)}H)$	1435 s, b	1173 w	1466 m, 1162 w
M–N, M–O			450, 593 w

Abbreviations: w – weak; m – medium; s – strong; vs – very strong, b – broad.
[a] See [23].

of this ligand to metal ions. The carbonyl stretching band of orotic acid and ammonium orotate observed at 1729; 1719 and 1690 cm^{-1} of $[\nu_{C=O(acid)} + \nu_{C(2)=O}]$ and 1700; 1653 and 1650 cm^{-1} of $[\nu_{C(6)=O} + \nu_{ring} + \nu_{C=C}]$, respectively [20] were shifted to 1701 and 1639 cm^{-1} for the mono-deprotonated orotate ligand, $[Co(H_2Or)_2(H_2O)_4]\cdot 2H_2O$ [21], while the bis-deprotonated orotate ligand, $[Co(HOr)(H_2O)_4]\cdot H_2O$ [9], give a single and strong broad absorption band at 1632 cm^{-1} due to overlapping of the two bands. In the IR spectrum of $(chaH)_2[Cu(HOr–N,O)_2(cha)]\cdot 2H_2O$, two equally strong $\nu_{C=O}$ bands at 1654 and 1605 cm^{-1} correspond to the stretching of the carbonyl group in the bis-deprotonated orotate ligands. The band splitting of the stretching vibrations of the carbonyl group was attributed to the non-equivalence of the environment of these groups in the ring. The weak bands in the 450 and 593 cm^{-1} regions are due to Cu(II)–N and Cu(II)–O stretching vibrations, respectively [22]. From the IR spectrum, it can be assumed that in the copper(II) complex the orotate residues HOr are coordinated as bidentate ligands to the Cu(II) ion through the carboxylic oxygen and nitrogen (N_3) atoms from the pyrimidine ring.

3.3. Thermal analysis

The thermal decomposition behavior of **1** was followed up to 600 °C in static air atmosphere. The thermal analysis curves show that the complex exhibits a four stage mass loss process. The first stage is related to endothermic removal of two moles of crystal water molecules in the 87–141 °C temperature range (DTG_{max} = 138 °C). The experimental mass loss of 5.34% agrees well with the calculated mass loss of 5.09%. The second stage corresponds to the loss of one mole of cyclohexylamine molecule in the 142–237 °C temperature range (found 13.94, calcd. 14.16%), giving an exothermic effect (DTG_{max} = 211 °C). In the following endothermic stage between 228 and 443 °C, both cyclohexylamine and cyclohexylamine ligand were released and the orotate dianions decomposed, simultaneously. In the last stage, the strong exothermic mass loss process occurs in a single step. During this stage, the remaining organic part is abruptly burnt (DTG_{max} = 507 °C). The final decomposition product, namely CuO was identified by IR spectroscopy with corresponding spectra obtained under the same conditions as the pure oxide. The overall mass loss 88.16% (calcd. 88.75%) agrees with the proposed structure well.

3.4. Crystal structure of the complex

Details of the crystal structure are given in Table 1. The crystallographic analysis revealed that the complex, $(chaH)_2[Cu(HOr)_2(cha)]\cdot 2H_2O$, consists of a discrete $[Cu(HOr)_2(cha)]^{2-}$ anion, two protonated chaH cations and two crystal water molecules (Fig. 1). One of the interesting features of the structure is that the chaH molecules exhibit chemically different functions. While in one form they coordinate to the copper atom, in the other form they act as counter-ions. In addition, there are bis(deprotonated) HOr ligands coordinated to the Cu(II) ion. To the best of our knowledge, this has not been reported before, although there are many metal complexes of orotic acid. The Cu(II) ion has a distorted square-pyramidal coordination. The basal coordination plane is formed by atoms N3, N4, N7 and O4. The coordination is completed by atom O5 located at the pyramid apex. There are slight differences in Cu1–O5, Cu1–O4 bond distances and N3–Cu1–O5, N4–Cu1–O4 angles. This may be caused by the N(1)–H(1A)···O(4) hydrogen bond. The Cu–N_{HOr} bond distances are shorter than the Cu–N_{cha} bond distance. The Cu1–N3/N4 bond distances are in agreement with the

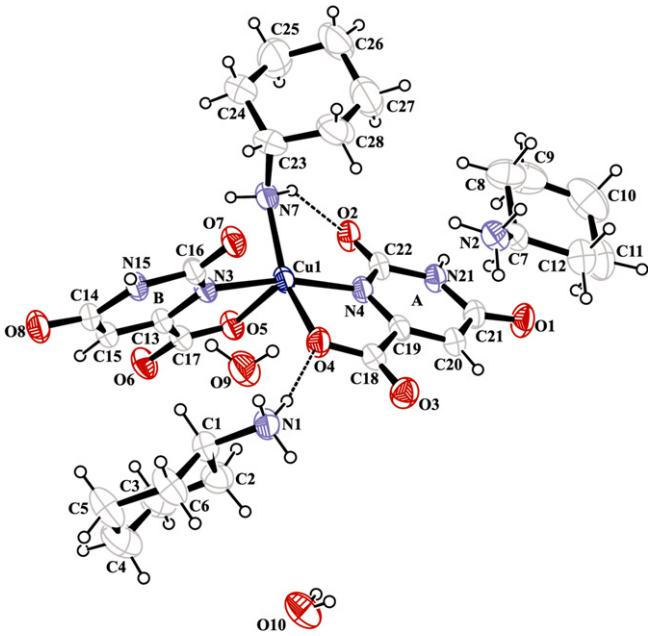


Fig. 1. Molecular structure of **1**.

corresponding values in related structures, while the Cu–O_{HOr} bonds are longer than previously reported values [8,9]. Although the bond distances of the coordinated cha and chaH ion are similar, the corresponding angles are different from each other [24,25,29]. The bond distances and angles of chaH ions are in agreement with the corresponding values in related structures [24,25]. Comparison of values of the M–O_{HOr}, M–N_{HOr}, M–N_{cha} distances, and of the O_{HOr}–M–N_{HOr} angle for similar orotate and cyclohexylamine metal complexes can be found in Table 3. The dihedral angle between the orotato ligands are 68.17(6)°. The angles of N3–Cu1–O5 [78.73(12)°] and N4–Cu1–O4 [81.16(13)°] are nearly equal. The orotato ligands are almost planar (the r.m.s deviations are 0.0218 and 0.0257 Å). The details of the hydrogen bonding geometry are given in Table 4. The nitrogen groups of the orotato ligands are involved in inter-molecular hydrogen bonding with the carbonyl oxygen of the orotate ligand. The cha ligands are involved in intra- and inter-molecular hydrogen bonding with the carbonyl oxygen and hydroxyl oxygen. The intra-molecular N(1)–H(1A)···O(4) and O(9)–H(4W)···O(3) bonds have H···O distances of 1.94 and 2.06(9) Å, respectively. The inter-molecular N21–H21···$O1^{ii}$, O10–H1W···$O6^{vi}$ and N1–H1C···$O9^{i}$ bonds have the H···O distances of 1.99, 1.72(8) and 1.92 Å, respectively. Some of these interactions are illustrated in Fig. 2.

4. Conclusion

We have successfully synthesized the first bis(orotate–*N*,*O*) complex, $(chaH)_2[Cu(HOr)_2(cha)]\cdot 2H_2O$, and have characterized it by elemental analysis, magnetic measurements, FT-IR and UV–Vis spectroscopy, thermal analysis and X-ray diffraction. The structure of $(chaH)_2[Cu(HOr)_2(cha)]\cdot 2H_2O$ displays several interesting features. Previous studies showed that all the aqua and mixed-ligand complexes of HOr with first-row divalent transition metal

Table 3
Comparison of the bond distances and angles of the HOr or cha complexes

Complexes		Orotate mode	M–$O1_{HOr}$/M–$N3_{HOr}$ (Å)	C–$O1_{acid}$/C–$O2_{acid}$ (Å)	M–N_{cha} (Å)	C–N_{cha}/C–N_{chaH}(Å)	O_1–Cu–N_3 (°)
$(chaH)_2[Cu(HOr-N,O)_2(cha)]\cdot 2H_2O$	**A**	bis(bidentate-(*N*3,*O*1))	2.013(3)/1.980(3)	1.277(5)/1.239(5)	2.031 (4)	1.483 (7)/1.511 (5),	78.73(12)
	B		2.208(3)/1.982(3)	1.262(5)/1.256(4)		1.484 (6)	81.16(13)
$[Cu(HOr)(en)(H_2O)]\cdot H_2O$ [9]		bidentate-(*N*3,*O*1)	1.990(2)/1.986(3)	1.270(4)/1.240(4)			81.9(1)
$[Cu(HOr)(H_2O)_2]_n$ [7]		bidentate-(*N*3,*O*1)	1.948(2)/1.975(2)	1.278(2)/1.232(2)			83.57(6)
$[Cu(HOr)(NH_3)_2]$ [6]		bidentate-(*N*3,*O*1)	1.962(3)/2.005(3)	1.285(4)/1.227(4)			82.5(1)
$[Co(HOr)(H_2O)_4]\cdot H_2O$ [9]		bidentate-(*N*3,*O*1)	2.057(2)/2.094(2)	1.256(3)/1.245(3)			78.9(1)
$[UO_2(H_2Or)_2(H_2O)_3]\cdot 2H_2O$ [26]		monodentate-(*O*1)	2.360(3)/–	1.275(5)/1.221(6)			
$[Li(H_2Or)(H_2O)]$ [27]		μ^3-tridentate-(O1, O3, O4)	1.881(3)/–	1.250(2)/1.252(2)			
$[Co(H_2O)_2(phen)_2](H_2Or)_2\cdot 2.25H_2O$ [28]		counter ion		1.242(2)/1.234(2)			
[Ni(cha)(tpimp)$_2$] [29]					1.948(5)	1.527, 1.472/–	
$(chaH)_2[CrO_4]$ [24]						1.475(4); 1.488(4)	

en = Ethylenediamine, phen = 1,10-phenanthroline, tpimp = 2-[(2-thiophenyl)iminomethyl]phenolate.

Table 4
Hydrogen bonding interactions in **1**

D–H···A	*d*(D–H) (Å)	*d*(H···A) (Å)	*d*(D···A) (Å)	∠(DHA) (°)
N2–H2A···$O10^{i}$	0.89	1.96	2.761 (5)	148
N2–H2B···$O2^{ii}$	0.89	2.00	2.884 (5)	173
N2–H2C···$O8^{iii}$	0.89	1.97	2.849 (5)	168
N1–H1B···$O7^{iii}$	0.89	1.99	2.838 (5)	159
N7–H23B···$O8^{iv}$	0.90	2.14	3.026 (4)	169
O10–H2W···$O6^{v}$	1.07 (8)	1.74 (9)	2.792 (6)	168 (7)
O10–H2W···$O5^{v}$	1.07 (8)	2.60 (8)	3.248 (5)	118 (5)
O10–H1W···$O7^{iii}$	0.65 (8)	2.36 (9)	2.847 (4)	133 (10)
O9–H4W···$O3^{i}$	0.86 (8)	2.08 (8)	2.880 (6)	155 (8)
O9–H3W···$O6^{ii}$	0.70 (8)	2.06 (9)	2.739 (4)	167 (10)
N15–H20···$O3^{i}$	0.80 (8)	2.17 (8)	2.943 (5)	164 (8)
N21–H19···$O1^{vi}$	0.84 (8)	2.01 (8)	2.828 (5)	164 (8)
N1–H1A···O4	0.89	1.93	2.816 (5)	170
N1–H1C···O9	0.89	1.92	2.788 (6)	166
N7–H23A···O2	0.90	2.20	2.956 (5)	142

Symmetry codes: (i) $-x+1, y-1/2, -z+1/2$; (ii) $x, -y+1/2, z+1/2$; (iii) $-x+1, y+1/2, -z+1/2$; (iv) $-x+1, -y, -z$; (v) $-x+1, -y+1, -z$; (vi) $-x, -y+1, -z$.

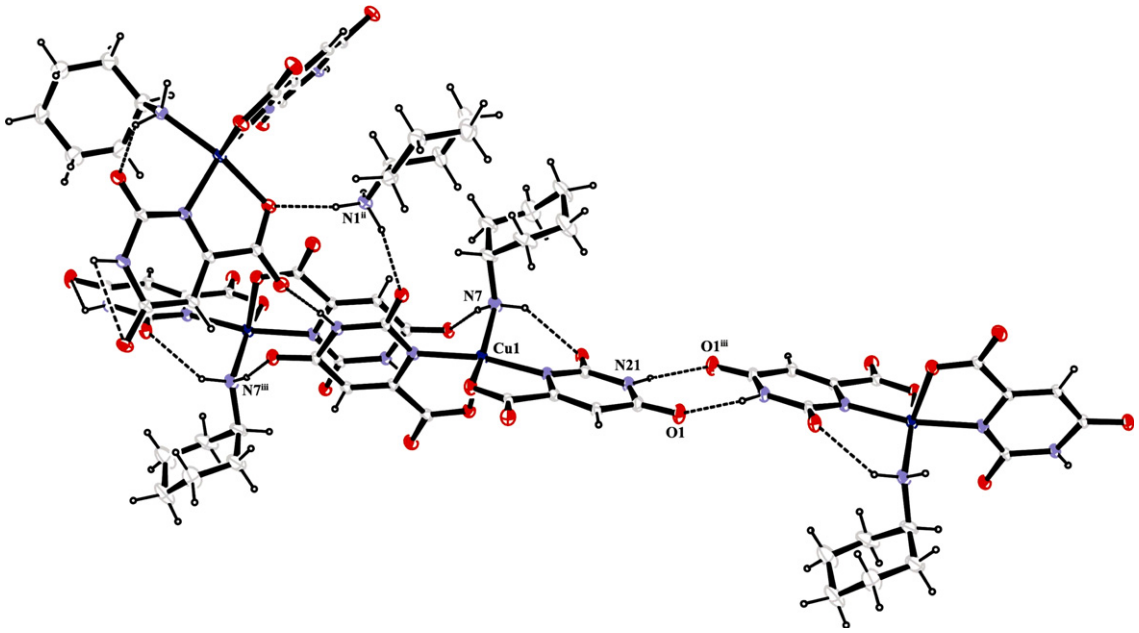


Fig. 2. The hydrogen bonding geometry of 1 ((i) $-x+1$, $y-1/2$, $z+1/2$, (ii) $-x+1$, $y+1/2$, $-z+1/2$, (iii) $-x$, $-y+1$, $-z$).

ions consist of neutral complexes, containing only one coordinated HOr ligand within the coordination sphere, hence the presence of two HOr ligands in the primary coordination sphere, as seen in $(chaH)_2[Cu(HOr)_2(cha)]\cdot 2H_2O$, is unusual. Therefore, the most interesting aspect of this complex is the coordination of two HOr ligands around the copper(II) ion and this complex is the first example exhibiting two coordinated HOr ligands in the same coordination sphere of a mononuclear unit. Additionally, the chaH molecules exhibit chemically different functions – in one form they coordinate to the copper atom, in the other form they act as counterions. In previous studies the orotato complexes are neutral, whereas the title complex consists of two chaH cations and one $[Cu(HOr)_2(cha)]^{2-}$ anion. It can be said that the stabilization of the $[Cu(HOr)_2(cha)]$ anion in the solid state may be due to the presence of the chaH cations which have a relatively large ionic radius.

Acknowledgment

This work was supported by the Eskişehir Osmangazi University by project No 200619013.

Appendix A. Supplementary material

CCDC 629229 contains the supplementary crystallographic data for this paper. These data can be obtained free of charge via http://www.ccdc.cam.ac.uk/conts/retrieving.html, or from the Cambridge Crystallographic Data Centre, 12 Union Road, Cambridge CB2 1EZ, UK; fax: (+44) 1223-336-033; or e-mail: deposit@ccdc.cam.ac.uk. Supplementary data associated with this article can be found, in the online version, at doi:10.1016/j.poly.2007.01.050.

References

[1] A. Lehninger, Biochemistry, Worth Publishhers Inc., New York, 1970, p. 661.
[2] J. Leberman, A. Kornberg, E.S. Simms, J. Biol. Chem. 215 (1955) 403.
[3] P. Castan, E. Colacio-Rodriguez, A.L. Beauchamp, S. Cros, S. Wimmer, J. Inorg. Biochem. 38 (1990) 225.
[4] D.J. Darenbourg, D.L. Larkins, J.H. Reibenspies, Inorg. Chem. 37 (1998) 6125.
[5] S.T. James, D.M.P. Mingos, X. Xu, A.J.P. White, D.J. Williams, J. Chem. Soc., Dalton Trans. (1998) 1335.
[6] I. Mutikainen, P. Lumme, Acta Crystallogr., Sect. B 36 (1980) 2233.
[7] T.T.B. Ha, A.M. Larsonneur-Galibert, P. Castan, J. Jaud, J. Chem. Crystallogr. 29 (1999) 565.
[8] X. Li, R. Cao, W. Bi, D. Sun, M. Hong, Acta Crystallogr., Sect. E 59 (2003) m228.
[9] H. İçbudak, H. Ölmez, O.Z. Yeşilel, F. Arslan, P. Naumov, G. Jovanovski, A.R. Ibrahim, A. Usman, H.K. Fun, S. Chantrapromma, S.W. Ng, J. Mol. Struct. 657 (2003) 255.
[10] H. Olmez, H. Icbudak, O.Z. Yeşilel, C. Arici, D. Ulku, Z. Kristallogr. 219 (2004) 300.
[11] O.Z. Yeşilel, H. Olmez, H. Icbudak, O. Büyükgüngör, Z. Naturforsch., Teil b 60 (2005) 1138.
[12] M.J. Plater, M.R.J. Foreman, J.M.S. Skakle, R.A. Howie, Inorg. Chim. Acta 332 (2002) 135.
[13] O.Z. Yeşilel, F. Tezcan, H. Ölmez, H. Paşaoğlu, O. Büyükgüngör, Z. Anorg. Allg. Chem. 631 (2005) 2497.
[14] O.Z. Yeşilel, H. Ölmez, I. Ucar, A. Bulut, C. Kazak, Z. Anorg. Allg. Chem. 631 (2005) 3100.
[15] G. Maistralis, A. Koutsodimou, N. Katsaros, Transition Met. Chem. 25 (2000) 166.
[16] G.M. Sheldrick, SHELXL-97, University of Göttingen, Germany, 1997.
[17] Data reduction: Stoe X-RED. The structure was solved by direct-methods using SIR97.
[18] M.N. Burnett, C.K. Johnson, OrtepIII. Report ORNL-6895, OAK Ridge National Laboratory, Tennessee, USA, 1996.
[19] L.J. Farrugia, J. Appl. Crystallogr. 32 (1999) 837.
[20] A. Hernanz, F. Billes, I. Bratu, R. Navarro, Biopolymers 57 (2000) 187.

[21] D.A. Kose, B. Zümreoğlu-Karan, O. Şahin, O. Büyükgüngör, J. Mol. Struct. 789 (2006) 147.
[22] K. Nakamoto, Infrared and Raman Spectra of Inorganic and Coordination Compounds, Wiley, New York, 1978.
[23] G.K. Kürkçüoğlu, Z. Kantarcı, R. Coşkun, M. Şenyel, J. Inclusion Phenomena Macrocyclic Chem. 45 (2003) 129.
[24] S.S. Yun, H.S. Moon, C.H. Kim, S.G. Lee, J. Coord. Chem. 57 (2004) 17.
[25] H.S. Moon, C.H. Kim, S.G. Lee, J. Coord. Chem. 57 (2004) 1425.
[26] D. Mentzafos, N. Katsaros, A. Terzis, Acta Crystallogr., Sect. C 43 (1987) 1905.
[27] M. Lutz, Acta Crystallogr., Sect. E 57 (2001) m103.
[28] A. Bulut, H. İçbudak, O.Z. Yeşilel, H. Ölmez, O. Büyükgüngör, Acta Crystallogr., Sect. E 59 (2003) m736.
[29] M.N. Tahir, D. Ülkü, O. Atakol, A. Kenar, Acta Crystallogr., Sect. C 52 (1996) 2178.

Available online at www.sciencedirect.com
ScienceDirect
Polyhedron 26 (2007) 2767–2776
POLYHEDRON
www.elsevier.com/locate/poly

Synthesis and solvent effects on the electronic absorption and fluorescence spectral properties of substituted zinc phthalocyanines

Mahmut Durmuş [a,b], Tebello Nyokong [b,*]

[a] Gebze Institute of Technology, Department of Chemistry, P.O. Box 141, Gebze 41400, Turkey
[b] Department of Chemistry, Rhodes University, Grahamstown 6140, South Africa

Received 13 October 2006; accepted 17 January 2007
Available online 26 January 2007

Abstract

The synthesis and spectroscopic properties of the following tetra- and octa-substituted aryloxy zinc(II) phthalocyanines are reported for the first time: 1,(4)-(tetrabenzyloxyphenoxyphthalocyaninato) zinc(II) (**7**); 2,(3)-(tetrabenzyloxyphenoxyphthalocyaninato) zinc(II) (**8**); 2,3-(octabenzyloxyphenoxyphthalocyaninato) zinc(II) (**9**). The new compounds have been characterized by elemental analysis, IR, ^{1}H NMR spectroscopy and electronic spectroscopy. Spectroscopic properties of these compounds were investigated in different solvents. Protonation of non-peripherally substituted complex **7** resulted in the splitting and red-shifting of the Q-band. The peripherally substituted derivatives **8** and **9**, did not show the split in the Q-band. Fluorescence spectra of the derivatives show Stokes shifts typical of MPc complexes.
© 2007 Elsevier Ltd. All rights reserved.

Keywords: Phthalocyanine; Zinc; Fluorescence; Aggregation; Solvent effect

1. Introduction

Phthalocyanines and metallophthalocyanines have been investigated in detail for many years because of their wide applications in many fields, including use and investigation in chemical sensors, liquid crystals, Langmuir–Blodgett films, nonlinear optics, optical data storage and as carrier generation materials in near-IR devices [1,2]. Substituted derivatives can also be used for photodynamic cancer therapy and other processes driven by visible light [1,2]. A decisive disadvantage of phthalocyanine and metal phthalocyanines is their low solubility in organic solvents or water. The solubility can be increased, however, by introducing alkyl or alkoxy groups into the peripheral and non-peripheral positions of the phthalocyanine framework [3]. Because of their lower degree of order in solid state, tetra-substituted phthalocyanines are more soluble than the corresponding octa-substituted ones. In contrast to octa-substituted systems, tetra-substituted phthalocyanines are obtained as a mixture of constitutional isomers by statistical synthesis starting from mono-substituted phthalonitriles or corresponding diiminoisoindolines. Depending on their substituent positions two types (non-peripherally and peripherally substituted) of tetra-substituted macrocycles which show significant differences in their chemical and physical behaviour can be obtained.

Recently, phthalocyanine complexes have found applications as photosensitisers in PDT since diamagnetic central metals, such as Zn or Mg enhance phototoxicity of phthalocyanines [4–7]. Zinc phthalocyanine complexes have attracted much interest because of their appreciably long triplet lifetimes [8–10]. Such long lifetimes constitute a great advantage since the number of diffusional encounters between the triplet excited state and ground state molecular oxygen increases with the lifetime of the excited

* Corresponding author. Address: Department of Chemistry, Rhodes University, Grahamstown 6140, South Africa. Tel.: +27 46 603 8260; fax: +27 46 622 5109.
E-mail address: t.nyokong@ru.ac.za (T. Nyokong).

0277-5387/$ - see front matter © 2007 Elsevier Ltd. All rights reserved.
doi:10.1016/j.poly.2007.01.018

state. The introduction of peripheral and non-peripheral substituents onto the MPc ring is expected to affect both the triplet quantum yield and lifetime, hence it is desirable to carry out studies on the effects of substituents on these parameters.

Addition of groups to the peripheral positions of MPc complexes is known to influence the properties of the MPc to a large degree [11–15]. For instance, the peripheral substituents increase the distance between the planar macrocycle rings carrying the π-electrons thereby making solvation easier. Solvents affect aggregation in phthalocyanine complexes. Organic solvents are known to reduce aggregation whereas aqueous medium results in highly aggregated complexes. However, many phthalocyanine complexes remain aggregated even in non-aqueous solutions [16–18]. Aromatic solvents such as benzene or toluene are known to give narrow Q-bands for phthalocyanines whereas broadening is observed in non-aromatic solvents [19].

In this work, we have synthesized tetra- and octa-substituted new zinc phthalocyanine compounds. We report on the effects of tetra (peripheral and non-peripheral) and octa ring substituents on the spectroscopic and aggregation properties of zinc phthalocyanine derivatives in different solvents (toluene, dichloromethane, chloroform, THF, and DMSO). Fluorescence properties of these compounds were also investigated in these solvents.

2. Experimental

2.1. Materials

Dimethylsulphoxide (DMSO), methanol, hexane, chloroform ($CHCl_3$), dichloromethane (DCM), tetrahydrofuran (THF), toluene, acetone, ethanol dimethylformamide (DMF) and *n*-pentanol were dried as described in Perrin and Armarego [20] before use. Zinc acetate, K_2CO_3, deuterated $CDCl_3$, 4-benzyloxyphenol, 1,8-diazabicyclo-[5.4.0]-undec-7-ene (DBU) were purchased from Aldrich. Column chromatography was performed on silica gel 60 (0.04–0.063 mm) and preparative thin layer chromatography was performed on silica gel 60 P F_{254}. 3-Nitrophthalonitrile (**1**) [21], 4-nitrophthalonitrile (**2**) [22] and 4,5-dichlorophthalonitrile [23] were synthesised and purified according to literature procedure.

2.2. Equipment

UV–Vis spectra were recorded on a Cary 500 UV–Vis/NIR spectrophotometer. Fluorescence excitation and emission spectra, were recorded on a Varian Eclipse spectrofluoremeter using 1 cm pathlength cuvettes at room temperature. IR spectra (KBr pellets) were recorded on a Perkin–Elmer spectrum 2000 FTIR spectrometer. ^1H NMR spectra were recorded in $CDCl_3$ solutions using a Bruker EMX 400 MHz NMR spectrometer. Elemental Analyses were performed at the University of Cape Town.

2.3. Synthesis

2.3.1. 3-(4-Benzyloxyphenoxy)phthalonitrile (4)

In a stream of nitrogen, 4-benzyloxyphenol (3.50 g, 17.5 mmol) and 3-nitrophthalonitrile (**1**) (3.00 g, 17.5 mmol) were dissolved in DMF (30 ml) and the mixture stirred at room temperature for 15 min. Thereafter, finely ground K_2CO_3 (7.50 g, 0.052 mol) was added potion-wise over a period of 2 h and the reaction mixture left to stir for a further 12 h at room temperature. The mixture was added to water (100 ml) and stirred for 30 min. The resulting precipitate was filtered off, thoroughly washed with water, dried and recrystallised from ethanol. Yield: 4.39 g (77%). IR [(KBr) ν_{max}/cm^{-1}]: 3092 (Ar–CH), 3079 (Ar–CH), 3029 (Ar–CH), 2900–2864 (CH_2), 2229 (C≡N), 1574 (C=C), 1193 (C–O–C). ^1H NMR ($CDCl_3$): δ, ppm 7.53 (1H, t, Ar–H), 7.31–7.47 (7H, m, Ar–H), 6.95–7.10 (4H, m, Ar–H), 5.08 (2H, s, CH_2).

2.3.2. 4-(4-Benzyloxyphenoxy)phthalonitrile (5)

Synthesis and purification was as outlined for **4** except 4-nitrophthalonitrile (**2**) instead of **1** was employed. The amounts of the reagents employed were: 4-benzyloxyphenol (3.50 g, 17.5 mmol), 4-nitrophthalonitrile (**2**) (3.00 g, 17.5 mmol) in DMF (30 ml). Yield: 4.63 g (82%). IR [(KBr) ν_{max}/cm^{-1}]: 3093 (Ar–CH), 3075 (Ar–CH), 3037 (Ar–CH), 2938-2876 (CH_2), 2230 (C≡N), 1588 (C=C), 1198 (C–O–C). ^1H NMR ($CDCl_3$): δ, ppm 7.69 (1H, d, Ar–H), 7.32–7.46 (5H, m, Ar–H), 7.17–7.25 (2H, m, Ar–H), 6.97–7.06 (4H, m, Ar–H), 5.08 (2H, s, CH_2).

2.3.3. 4,5-Bis-(4-benzyloxyphenoxy)phthalonitrile (6)

Synthesis and purification was as outlined for **4** except 4,5-dichlorophthalonitrile (**3**) instead of **1** was employed. The amounts of the reagents employed were: 4-benzyloxyphenol (6.70 g, 30.4 mmol), 4,5-dichlorophthalonitrile (**3**) (3.00 g, 15.2 mmol) in DMF (50 ml). Yield: 5.34 g (67%). IR [(KBr) ν_{max}/cm^{-1}]: 3092 (Ar–CH), 3064 (Ar–CH), 3035 (Ar–CH), 2940-2868 (CH_2), 2235 (C≡N), 1585 (C=C), 1197 (C–O–C). ^1H NMR ($CDCl_3$): δ, ppm 7.82 (2H, s, Ar–H), 7.33–7.47 (10H, m, Ar–H), 6.96–7.07 (8H, m, Ar–H), 5.09 (4H, CH_2).

2.3.4. 1,(4)-Tetrakis(4-benzyloxyphenoxyphthalocyaninato) zinc(II) (7)

A mixture of anhydrous zinc(II) acetate (2.25 g, 12.2 mmol), 3-(4-benzyloxyphenoxyphthalonitrile) (**4**) (2.00 g, 6.1 mmol) and dried *n*-pentanol (5 ml) was refluxed at 140 °C for 18 h under nitrogen atmosphere. After cooling, the solution was dropped in ethanol. The green solid product was precipitated and collected by filtration and washed with ethanol. The crude product was dissolved in CH_2Cl_2 and then filtered. After filtering and concentrating, the dark green waxy product was purified by passing through a silica gel column, using THF as the eluting solvent. Furthermore this product was purified with preparative thin layer chromatography (silica gel) using $CHCl_3$ as a solvent system. Yield:

0.79 g (37%). UV–Vis (DMSO): λ_{max} nm (log ε) 340 (4.58), 629 (4.50), 699 (5.24). IR [(KBr) ν_{max}/cm^{-1}]: 3055(Ar–CH), 3027(Ar–CH), 2949-2856(CH_2), 1583(C=C), 1194(C–O–C). ^1H NMR ($CDCl_3$): δ, ppm 8.11–8.94 (4H, m, Pc–H), 6.72–7.83 (44H, m, Pc–H, Phenyl–H), 4.96 (8H, s, CH_2). *Anal.* Calc. for $C_{84}H_{56}N_8O_8Zn$: C, 73.60; H, 4.12; N, 8.17. Found: C, 73.84; H, 4.15; N, 8.05%.

2.3.5. 2,(3)-Tetrakis(4-benzyloxyphenoxyphthalocyaninato) zinc(II) (8)

Synthesis and purification was as outlined for **7** except 4-(4-benzyloxyphenoxyphthalonitrile) (**5**) instead of 3-(4-benzyloxyphenoxyphthalonitrile) (**4**) was employed. The amounts of the reagents employed were: **5** (2.00 g, 6.1 mmol), anhydrous zinc(II) acetate (2.25 g, 12.2 mmol) in *n*-pentanol (5 ml). Yield: 0.93 g (44%). UV–Vis (DMSO): λ_{max} nm (log ε) 355 (4.81), 612 (4.52), 681 (5.23). IR [(KBr) ν_{max}/cm^{-1}]: 3056 (Ar–CH), 3027 (Ar–CH), 2949–2856 (CH_2), 1617 (C=C), 1193 (C–O–C). ^1H NMR ($CDCl_3$): δ, ppm 7.19–7.46 (24H, m, Pc–H, Phenyl–H), 6.36–7.13 (24H, m, Pc–H, Phenyl–H), 4.75 (8H, s, CH_2). *Anal.* Calc. for $C_{84}H_{56}N_8O_8Zn$: C, 73.60; H, 4.12; N, 8.17. Found: C, 72.08; H, 3.96; N, 7.82%.

2.3.6. 2,3-Octakis(4-benzyloxyphenoxyphthalocyaninato) zinc(II) (9)

Synthesis and purification was as outlined for **7** except 4,5-bis(4-benzyloxyphenoxyphthalonitrile) (**6**) instead of 3-(4-benzyloxyphenoxyphthalonitrile) (**4**) was employed. The amounts of the reagents employed were: **6** (2.00 g, 3.8 mmol), anhydrous zinc(II) acetate (1.40 g, 7.6 mmol) in *n*-pentanol (5 ml). Yield: 0.67 g (32%). UV–Vis (DMSO): λ_{max} nm (log ε) 350 (5.03), 629 (4.90), 680 (5.18). IR [(KBr) ν_{max}/cm^{-1}]: 3058 (Ar–CH), 3027 (Ar–CH), 2948–2855 (CH_2), 1603 (C=C), 1190 (C–O–C). ^1H NMR ($CDCl_3$): δ, ppm 7.18–7.81 (40H, br, Pc–H, Phenyl–H), 6.41–7.08 (40H, br, Phenyl–H), 4.81 (16H, s, CH_2). *Anal.* Calc. for $C_{136}H_{96}N_8O_{16}Zn$: C, 75.50; H, 4.47; N, 5.18. Found: C, 75.08; H, 4.26; N, 5.62%.

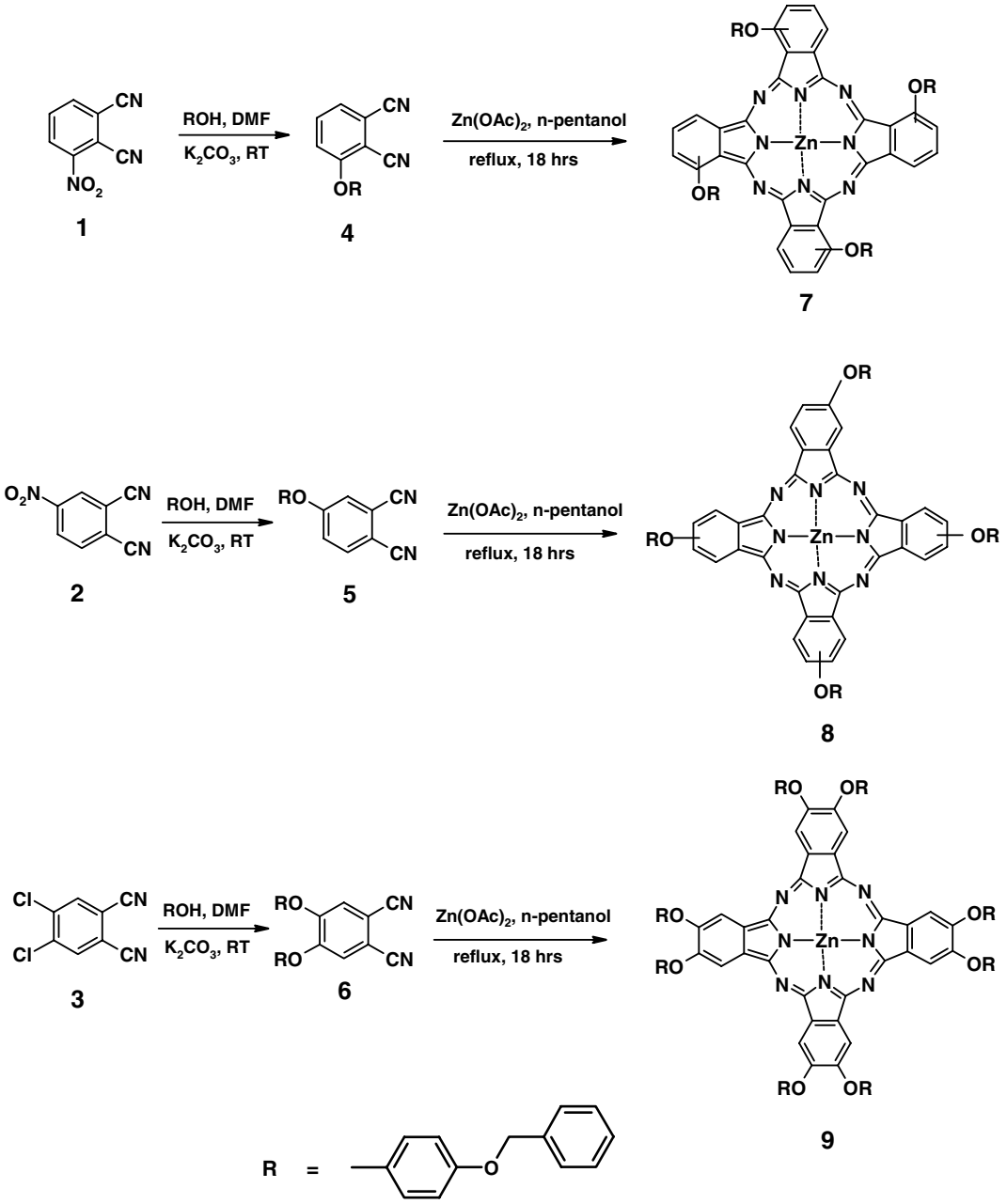
3. Results and discussion

Generally, substituted phthalocyanines are prepared by cyclotetramerization of substituted phthalonitriles or 1,3-diimino-1H-isoindoles. 2(3),9(10),16(17),23(24)-tetra-substituted phthalocyanines can be synthesized from 4-substituted phthalonitriles while 1(4),8(11),15(18),22(25)-tetra-substituted phthalocyanines are obtained from 3-substituted analogues [24]. Octa-substituted phthalocyanines can be synthesized from 4,5-dichlorophthalonitriles [23]. In both cases a mixture of four possible structural isomers are obtained for tetra-substituted phthalocyanines. The four probable isomers can be designed by their molecular symmetry as C_{4h}, C_{2v}, C_s and D_{2h}. The 2(3)-substituted compounds always occur in the expected statistical mixture of 12.5% C_{4h}, 25% C_{2v}-, 50% C_s- and 12.5% D_{2h}-isomer. But for the 1(4)-substituted complexes the composition depends on the central metal ion and the structure of the peripheral substituent [25]. In this study, synthesized tetra-substituted phthalocyanine compounds are obtained as mixtures of isomers as expected. No attempt was made to separate the isomers of **7** and **8**. 3-Nitrophthalonitrile (**1**), 4-nitrophthalonitrile (**2**) and 4,5-dichlorophthalonitrile (**3**) were used recently to prepare 3-monosubstituted, 4-monosubstituted and 4,5-disubstituted phthalonitrile derivatives, respectively, through base catalysed nucleophilic aromatic displacement [26–31]. The same route was applied to prepare 3-(4-benzyloxyphenoxyphthalonitrile) (**4**), 4-(4-benzyloxyphenoxyphthalonitrile) (**5**) and 4,5-bis(4-benzyloxyphenoxyphthalonitrile) (**6**) from 4-benzyloxyphenol and 3-nitrophthalonitrile (**1**), 4-nitrophthalonitrile (**2**), 4,5-dichlorophthalonitrile (**3**), respectively (Scheme 1). The reactions were carried out in dimethylformamide at room temperature and gave yields 77% for **4**, 82% for **5** and 67% for **6**.

The preparation of phthalocyanine derivatives from the aromatic nitriles occur under different reaction conditions. The syntheses of metallophthalocyanine complexes (**7**, **8** and **9**) were achieved by treatment of phthalonitriles **4**, **5** and **6** with zinc acetate in dried *n*-pentanol (Scheme 1). Complex **7** is non-peripherally (α) tetra-substituted, complex **8** is peripherally (β) tetra-substituted and complex **9** is octa-substituted. Column and preparative thin layer chromatography with silica gel was employed to obtain the pure products from the reaction mixtures.

Generally, phthalocyanine complexes are insoluble in most organic solvents; however introduction of substituents on the ring increases the solubility. All complexes (**7**, **8** and **9**) exhibited excellent solubility in organic solvents such as dichloromethane, chloroform, THF, toluene, acetone, DMSO. For comparative purposes, the 4-benzyloxyphenoxy group was tetra-substituted at the α and β positions and octa-substituted to the ring. The new compounds were characterized by UV–Vis, IR and NMR spectroscopies, elemental analysis and the analyses were consistent with the predicted structures as shown in the experimental section. The sharp peak for the C≡N vibrations of phthalonitriles **4**, **5** and **6** at ~2230 cm^{-1} disappeared after conversion into zinc phthalocyanines, indicative of metallophthalocyanine formation. The characteristic vibrations corresponding to ether groups (C–O–C) at ca. 1190–1198 cm^{-1}, aromatic CH stretching at ca. 3093–3027 cm^{-1} and aliphatic CH stretching at ca. 2949–2855 cm^{-1}.

^1H NMR investigations of phthalonitrile compounds **4**, **5** and **6** provide the characteristic chemical shifts for the structures as expected. In the ^1H NMR analysis of all these compounds in deuterated chloroform, methyl protons appear as a singlet at ca. 5.08 ppm. The aromatic protons appear as multiplets because the compounds contain different aromatic groups. The ^1H NMR spectra of phthalonitrile compound **4** shows as a triplet at 7.53 ppm, a multiplet at between 7.31 and 7.47 ppm and a multiplet at between 6.95 and 7.10 ppm, compound **5** shows as a



Scheme 1. Synthesis of 4-benzyloxyphenoxy tetra- and octa-substituted zinc phthalocyanine complexes.

doublet at 7.69 ppm, a multiplet at between 7.32 and 7.46 ppm, a multiplet at between 7.17 and 7.25 ppm and a multiplet at between 6.97 and 7.06 ppm for the aromatic hydrogens. On the other hand, the ^{1}H NMR spectrum of the other phthalonitrile compound **6** shows a singlet at 7.82 ppm, a multiplet at between 7.33 and 7.47 ppm and a multiplet at between 6.96 and 7.07 ppm for the aromatic hydrogens.

The ^{1}H NMR spectra of tetra-substituted phthalocyanine derivatives (**7** and **8**) show complex patterns owing to the mixed isomer character of these compounds and they have different aromatic protons. Octasubstituted derivative (**9**) also show complex patterns due to the different aromatic protons. The complexes were found to be pure by ^{1}H NMR with all the substituents and ring protons observed in their respective regions. The resonances belonging to aromatic protons were observed between 8.11–8.94 and 6.72–7.83 ppm as multiplets for non-peripherally tetra-substituted complex integrating for a total of 48 protons expected for aromatic protons. For the peripherally tetra-substituted complex (**8**) the resonances belonging to aromatic protons were observed between 7.19–7.46 and 6.36–7.13 ppm as multiplets integrating for a total of 48 protons expected for aromatic protons. For the octa-substituted complex (**9**) the resonances belonging to aromatic protons were observed between 7.18–7.81 and 6.41–7.08 ppm as broad peaks integrating for 40 protons each, making a total of 80 protons expected for aromatic

protons. The methyl protons were observed at 4.96 ppm for **7**, 4.75 ppm for **8** and 4.81 ppm for **9**; integrating for 8 protons for **7** and **8** and 16 protons for **9**. Although the presence of isomers for tetra-substituted complexes as well as phthalocyanine aggregation at the concentrations used for the NMR measurements may lead to broadening of the aromatic signals [32], the observed spectra of all the complexes were relatively well-resolved.

The electronic spectra of the complexes showed characteristic absorption in the Q-band region at 699 nm for **7**, 681 nm for **8** and 680 nm for **9** in DMSO, Table 1. The B band region was observed around 340–355 nm in DMSO (Fig. 1). The spectra showed monomeric behaviour evidenced by a single (narrow) Q-band, typical of metallated phthalocyanine complexes for **7** and **8** in DMSO [33]. Complex **9** showed a little bit aggregation in DMSO (Fig. 1). The Q-band of the non-peripheral tetra-substituted complex (**7**) is red-shifted 18 nm when compared to the corresponding peripherally tetra-substituted complex (**8**) and 19 nm when compared to the octa-substituted complex (**9**) in DMSO (Table 1). The observed red spectral shift is typical of phthalocyanines with substituents at the non-peripheral positions and has been explained [34,35] to be due to linear combinations of the atomic orbitals (LCAO) coefficients at the non-peripheral positions of the HOMO being greater than those at the peripheral positions. As a result, the HOMO level is destabilized more at the non-peripheral position that it is at the peripheral position. Essentially, the energy gap (ΔE) between the HOMO and LUMO becomes smaller, resulting in a ~20 nm bathochromic shift. The B-bands are broad due to the superimposition of the B_1 and B_2 bands in the 340–355 nm region.

Table 1
UV–Vis spectral data of complexes **7**, **8** and **9** in Toluene, DCM, THF, $CHCl_3$ and DMSO

Solvent	Q-band (nm)	B-band (nm)	N-band (nm)
7			
Toluene	698	349	
DCM	700,744	332	
THF	694	332	
$CHCl_3$	702,747	330	270
DMSO	699	340	
8			
Toluene	681	349	
DCM	681	342	286
THF	675	347	
$CHCl_3$	681	346	284
DMSO	681	355	
9			
Toluene	681	352	
DCM	623,681	343	290
THF	675	351	
$CHCl_3$	681	352	289
DMSO	626,680	350	

Aggregation is usually depicted as a coplanar association of rings progressing from monomer to dimer and higher order complexes. It is dependent on the concentration, nature of the solvent, nature of the substituents, complexed metal ions and temperature [36]. In the aggregated state the electronic structure of the complexed phthalocyanine rings are perturbed resulting in alternation of the ground and excited state electronic structures [37]. In this study, the aggregation behaviour of the phthalocyanine complexes (**7**, **8** and **9**) are investigated at different solvents (toluene, dichloromethane, chloroform, THF, DMSO) (Fig. 2 for complex **7** and Fig. 3 for complex **9**). While complex **7** showed a single peak in DMSO and THF, it showed a new peak at 747 nm in toluene, DCM and chloroform (Fig. 2).

Generally in MPc complexes, the peak due to aggregation is blue shifted with respect to the monomer. However, a less common type of aggregation in solution (called the *J* aggregation) results in a red-shifted peak [38]. In order to investigate the possibility that the extra peak at 747 nm is due to *J* aggregates, we diluted the solution of complex **7** in chloroform. This complex showed faster decrease of the peak at 702 nm compared to the peak at 747 nm, also the peak at 702 nm showed 11 nm red-shift as the concentration decreased (Fig. 4). Thus, the fact that the peak at 747 nm did not increase with dilutions confirms that it is

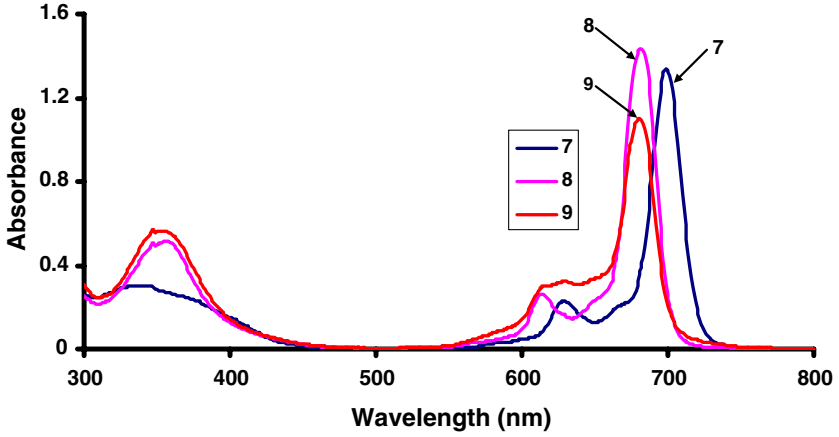


Fig. 1. Absorption spectra of the compound **7**, **8** and **9** in DMSO. Concentration = 4×10^{-6} mol dm^{-3}.

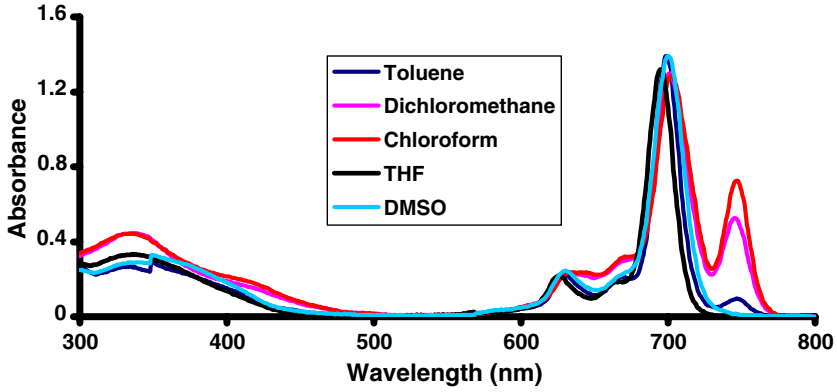


Fig. 2. Absorption spectra of the compound **7** in different solvents. Concentration = 4×10^{-6} mol dm^{-3}.

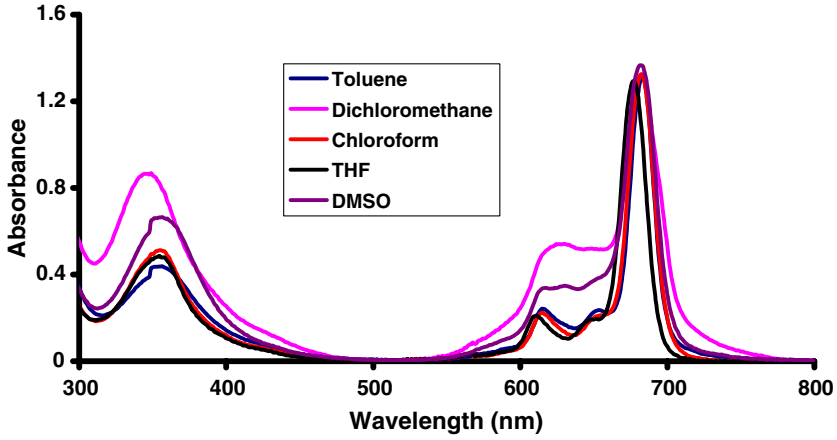


Fig. 3. Absorption spectra of the compound **9** in different solvents. Concentration = 4×10^{-6} mol dm^{-3}.

not due to aggregation. We suggest that this peak is a result of the splitting in the Q-band due to lowering in symmetry observed [39] due to protonation. Unprotonated Pcs are of D_{4h} symmetry. Monoprotonation of the nitrogen atoms leads to lowering of symmetry for the mono-, di- and triprotonated forms, resulting in splitting and a bathochro-

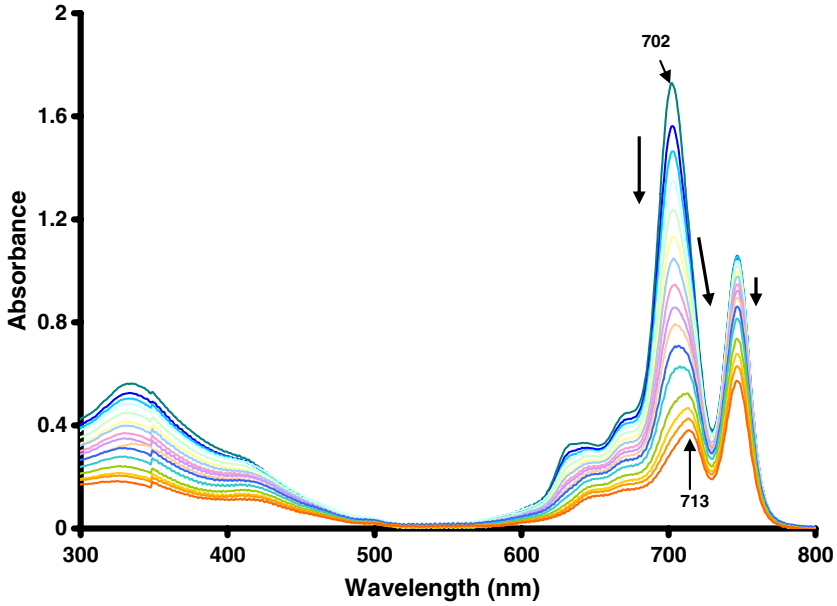


Fig. 4. Absorption spectra of **7** in chloroform at different concentrations. Concentrations from 1×10^{-5} to 2×10^{-6} mol dm^{-3}.

mic shift of the Q-band [8,39,40]. The tetra-protonated species then revert back to D_{4h} symmetry. In solvents which contain small amounts of acid such as DCM and chloroform (which contain some HCl), protonation of the inner nitrogen atoms may occur forming protonated MPc derivatives which are of lower symmetry than the parent MPc molecule, hence the Q-band is split. The fact that a small red shifted peak in addition to the Q-band is observed in toluene suggests this solvent also contains some limited amount of acid, hence complex **7** is also protonated (to a smaller degree compared to DCM and chloroform) in toluene. The spectral changes shown in Fig. 4 are similar to those observed on monoprotonation of MPc derivatives [40] and similar to spectral changes observed on addition of protonating agents such as: trifluoroacetic acid or using sulphuric acid. On dilution of the solution containing protonated derivatives in Fig. 4, the spectral changes show the prominence of the protonated derivatives relative to non-protonated MPc since with increase in solvents, there is increase of the protonating acid. In addition to protonation, a closer look at Fig. 2 shows an increase in absorption around 650 nm for complex **7** in chloroform and DCM, this is typical of aggregation in MPc complexes. Thus apart from the loss of symmetry due to protonation, there is also aggregation in DCM and chloroform. Complex **8** showed narrow Q-bands and there were no new peaks in all solvents. No formation of protonated derivatives was observed for both **8** and **9**, yet they were observed for **7**. Complex **7** contains electron donating groups at the alpha potion, hence close to the nitrogen atoms, making the latter more basic than for **8** and **9**, hence protonation occurs in **7** but not in **8** and **9**. Also complex **8** did not show aggregation in all solvents. This is surprising since complex **8**, which is peripherally substitute should show more aggregation than the non-peripherally substituted complex **7**. The latter are known to show less aggregation than the former [41]. The more pronounced aggregation of non-peripherally substituted complexes compared to peripherally substituted has been observed before [42].

Complex **9**, did not show aggregation in chloroform, THF and toluene but it showed broad band around 620 nm due to the aggregation in DMSO, Fig. 3. DMSO is known to prevent aggregation since it is strong coordinating solvent. However, it has been observed [42] before that aggregation occurs in DMSO and not in less coordinating solvents for some MPc complexes.

The aggregation behaviour of the phthalocyanine complexes (**7**, **8** and **9**) were also investigated at different concentrations in toluene (Fig. 5 for complex **9**). In toluene, as the concentration was increased, the intensity of absorption of the Q-band also increased and there were no new bands (normally blue shifted) due to the aggregated species for the all complexes (**7**, **8** and **9**) (Fig. 5 for complex **9**). The phthalocyanine derivatives (**7**, **8** and **9**) did not show aggregation in toluene at different concentrations. Beer–Lambert law was obeyed for all of these compounds in the concentrations ranging from 1.4×10^{-5} to 4×10^{-6} mol dm^{-3}.

All the complexes (**7**, **8** and **9**) showed similar fluorescence behaviour in DMSO. Fig. 6 shows the fluorescence emission spectra for complexes (**7**, **8** and **9**). In DMSO, emission peaks were observed at: 709 nm (**7**), 693 nm (**8**) and 691 nm (**9**) (Table 2). The excitation spectra were similar to absorption spectra and both were mirror images of the fluorescent spectra in DMSO (Fig. 7 for complex **8**). The proximity of the wavelength of each component of the Q-band absorption to the Q-band maxima of the excitation spectra for all complexes suggest that the nuclear configurations of the ground and excited states are similar and not affected by excitation in DMSO. The observed Stokes shift (Table 2) were typical of MPc complexes in DMSO. Fig. 8 shows the fluorescence emission spectra for complex **7** in different solvents (toluene, dichloromethane, chloroform, THF, DMSO). The spectra showed one peak in THF at 710 nm, in toluene at 711 nm and in DMSO at 718 nm. However, two peaks were evident in dichloromethane at 716 and 754 nm and in chloroform at 718 and 754 nm since it is the protonated derivative which

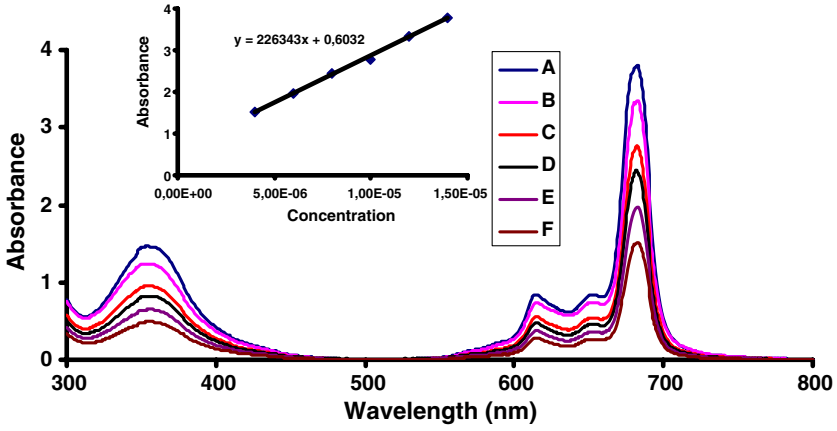


Fig. 5. Absorption spectra of **9** in toluene at different concentrations: 14×10^{-6} M (A), 12×10^{-6} (B), 10×10^{-6} (C), 8×10^{-6} (D), 6×10^{-6} (E), 4×10^{-6} (F) mol dm^{-3}.

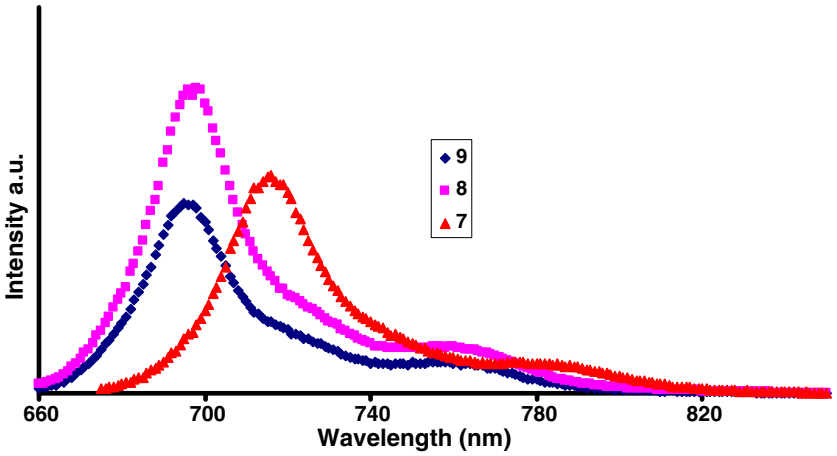


Fig. 6. Emission spectra of the compound **7**, **8** and **9** in DMSO. Concentration = 4×10^{-6} mol dm^{-3}. Excitation wavelength = 665 nm for **7**, 650 nm for **8** and **9**.

Table 2
Absorption, excitation and emission spectral data for tetra- and octa-substituted zinc phthalocyanine complexes (**7**, **8** and **9**) in DMSO

Compound	Q-band, λ_{max} (nm)	(log ε)	Excitation, λ_{Ex} (nm)	Emission, λ_{Em} (nm)	Stokes shift, Δ_{Stokes} (nm)
7	699	5.24	698	709	10
8	681	5.23	682	693	12
9	680	5.18	682	691	11

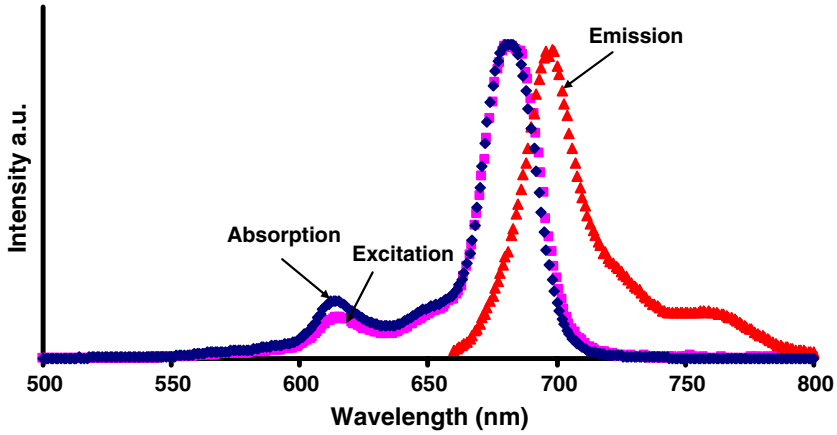


Fig. 7. Absorption, excitation and emission spectra of the compound **8** in DMSO. Excitation wavelength = 650 nm.

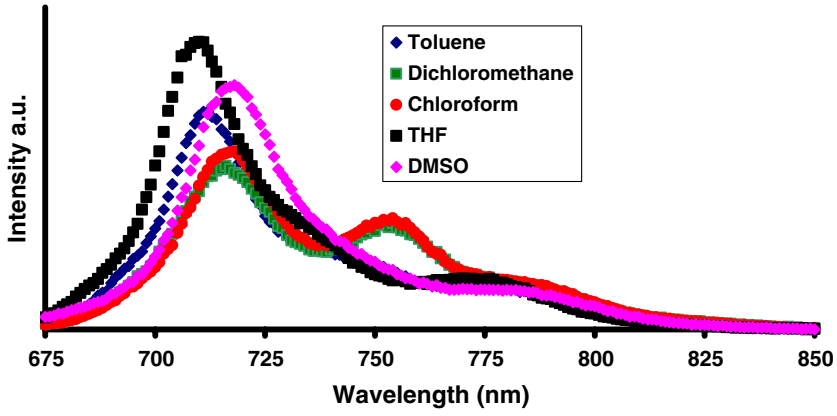


Fig. 8. Emission spectra of the compound **7** in different solvents. Concentration = 4×10^{-6} mol dm^{-3}. Excitation wavelength = 665 nm.

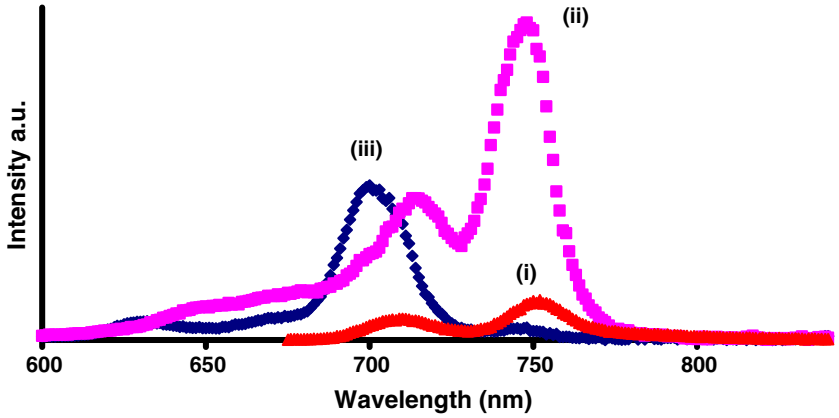


Fig. 9. Emission and excitation spectra of the compound **7** in chloroform: (i) emission spectrum; excitation at 665 nm; (ii) excitation spectrum for emission at 712 nm; (iii) excitation spectrum for emission at 751 nm.

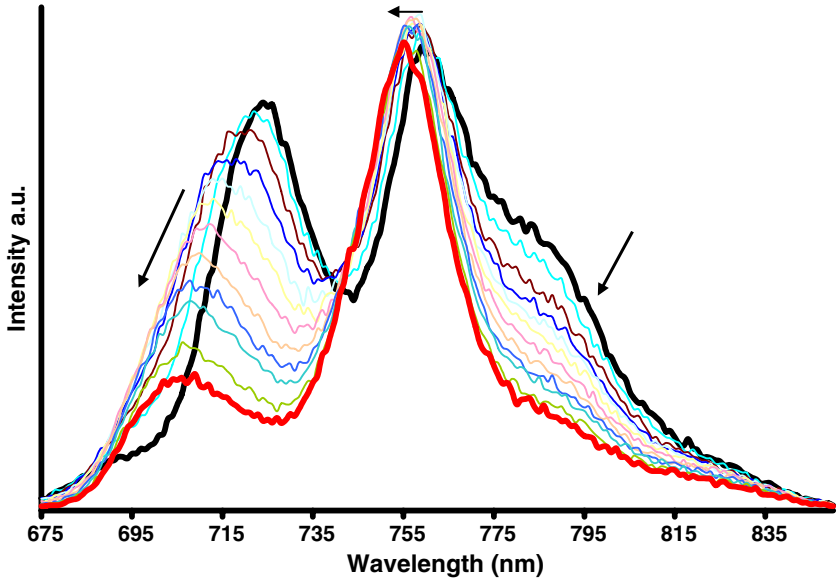


Fig. 10. Fluorescence spectra of **7** in chloroform at different concentrations. Excitation wavelength = 665 nm. Concentrations from 1×10^{-5} to 2×10^{-6}.

fluoresces. Fig. 9 shows the fluorescence excitation spectra using different emission wavelengths (712 and 751 nm) for complex **7**. The figure shows that the excitation spectra of protonated derivatives depends on the emission wavelength. We also studied the fluorescence of complex **7** at different concentrations in chloroform (Fig. 10). At the highest concentrations, complex **7** showed two peaks at 725 and 758 nm in chloroform. When the concentration is decreased, the peak at 725 nm marginal decreased and showed 19 nm blue-shift. Another peak at 758 nm showed a decrease in intensity a blue-shifted by 3 nm. These observations suggest different degree of protonation depending on the concentration of the MPc complex, each concentration will have a different amount of free acid.

4. Conclusion

In this study, we synthesized and characterized new non-peripheral and peripheral tetra-substituted and octa-substituted zinc phthalocyanine complexes. This work has also presented a comprehensive investigation of the effects of solvents on the aggregation and fluorescence properties of tetra- and octa-substituted zinc phthalocyanine complexes. We studied aggregation and fluorescence properties of these complexes in toluene, dichloromethane, chloroform, THF and DMSO. We studied the effect of the concentration on the aggregation and fluorescence properties in these solvents as well. All complexes did not show aggregation in toluene and THF. Complex **7** did not show aggregation in DMSO as well. It showed aggregation in chloroform and dichloromethane. Complex **7** showed split Q-band in the UV–Vis spectra. These split Q-band in the emission and excitation spectra of **7** was observed in chloroform and this is explained in terms of the lowering of symmetry by protonation in solvents containing some acid. Complex **8** did not show aggregation in all of these solvents and it showed similar fluorescence behaviour as typical MPc

complexes. Complex **9** showed aggregation in DMSO and interestingly in DCM.

Acknowledgement

This work was supported by the National Research Foundation of South Africa (NRF GUN # 2053657) as well as Rhodes University.

References

[1] C.C. Leznoff, A.B. P Lever (Eds.), Phthalocyanines, Properties and Applications, vols. 1–4, VCH, New York, 1989, 1993, 1996.
[2] M. Hanack, M. Lang, Adv. Mater. 6 (1994) 819.
[3] A. Beck, K-M. Mangold, M. Hanack, Chem. Ber. 124 (1991) 2315.
[4] J.E. van Lier, in: D. Kessel (Ed.), Photodynamic Therapy of Neoplastic Diseases, vol. 1, CRC Press, Boca Raton, FL, 1990.
[5] M.I. Rosenthal, Photochem. Photobiol. 53 (1991) 859.
[6] M.I. Rosenthal, in: C.C. Leznoff, A.B.P. Lever (Eds.), Phthalocyanines: Properties and Applications, vol. 4, VCH, New York, 1996, p. 481.
[7] M. Hu, N. Brasseur, S.Z. Yıldız, J.E. van Lier, C.C. Leznoff, J. Med. Chem. 41 (1998) 1789.
[8] A. Beeby, S. FitzGerald, C.F. Stanley, J. Chem. Soc., Perkin Trans. 2 (2001) 1978.
[9] X. Zhang, H. Wu, J. Chem. Soc., Faraday Trans. 89 (1993) 3347.
[10] S.M. Bishop, A. Beeby, A.W. Parker, M.S.C. Foley, D. Phillips, J. Photochem. Photobiol., A. Chem. 90 (1995) 39.
[11] A. Louati, M.E.I. Meray, J.J. Andre, J. Simon, K.M. Kadish, M. Gross, A. Girardeau, Inorg. Chem. 24 (1985) 1175.
[12] D. Wöhrle, V. Schmidt, J. Chem. Soc., Dalton Trans. (1988) 549.
[13] P.D. Hale, W.J. Pietro, M.A. Ratner, D.E. Ellis, T.J. Marks, J. Am. Chem. Soc. 109 (1987) 5943.
[14] D. Schlettwein, N.R. Armstrong, J. Phys. Chem. 98 (1994) 11771.
[15] H. Meeier, W. Albrecht, D. Wöhrle, A. Hahn, J. Phys. Chem. 90 (1986) 6349.
[16] S. Maree, T. Nyokong, J. Porphyr. Phthalocya. 5 (2001) 782.
[17] W.-F. Law, R.C.W. Liu, J. Jiang, D.K.P. Ng, Inorg. Chim. Acta 256 (1997) 147.
[18] M.P. Somashekarappa, J. Keshavayya, Synth. React. Inorg. Met.-Org. Chem. 31 (2001) 811.
[19] A. Ferencz, D. Neher, M. Schulze, G. Wegner, L. Viaene, F.C. Schryver, Chem. Phys. Lett. 245 (1995) 23.
[20] D.D. Perrin, W.L.F. Armarego, Purification of Laboratory Chemicals, 2nd ed., Pergamon Press, Oxford, 1989.
[21] R.D. George, A.W. Snow, J. Heterocyclic Chem. 32 (1995) 495.
[22] J.G. Young, W. Onyebuagu, J. Org. Chem. 55 (1990) 2155.
[23] D. Wöhrle, M. Eskes, K. Shigehara, A. Yamada, Synthesis (1993) 194.
[24] C.C. Leznoff, in: C.C. Leznoff, A.B.P. Lever (Eds.), Phthalocyanines: Properties and Applications, vol. 1, VCH Publishers, New York, 1989 (Chapter 1).
[25] M. Durmuş, S. Yeşilot, V. Ahsen, New J. Chem. 30 (2006) 675.
[26] N.B. McKeown, J. Painter, J. Mater. Chem. 4 (1994) 1153.
[27] K.E. Treacher, G.J. Clarkson, N.B. McKeown, Liq. Cryst. 19 (1995) 887.
[28] E.A. Corsellis, H.J. Coles, N.B. McKeown, P. Weber, D. Guillon, A. Skoulios, Liq. Cryst. 23 (1997) 475.
[29] M. Brewis, G.J. Clarkson, A.M. Holder, N.B. McKeown, Chem. Commun. (1998) 969.
[30] G.J. Clarkson, B.M. Hassan, D.R. Maloney, N.B. McKeown, Macromolecules 29 (1996) 1854.
[31] A.W. Snow, J.S. Shirk, R.G.S. Pong, J. Porphyr. Phthalocya. 4 (2000) 518.
[32] S. Gaspard, P. Maillard, Tetrahedron 43 (1987) 1083.
[33] M.J. Stillman, T. Nyokong, in: C.C. Leznoff, A.B.P. Lever (Eds.), Phthalocyanines: Properties and Applications, vol. 1, VCH Publishers, New York, 1989 (Chapter 3).
[34] A.B. Anderson, T.L. Gorden, M.E. Kenney, J. Am. Chem. Soc. 107 (1985) 192.
[35] M. Konami, M. Hatano, A. Tajiri, Chem. Phys. Lett. 166 (1990) 605.
[36] H. Enkelkamp, R.J.M. Nolte, J. Porphyr. Phthalocya. 4 (2000) 454.
[37] D.D. Dominguez, A.W. Snow, J.S. Shirk, R.G.S. Pong, J. Porphyr. Phthalocya. 5 (2001) 582.
[38] K. Adachi, H. Watarai, J. Mater. Chem. 15 (2005) 4701.
[39] P.A. Stuzhin, O.G. Khelevina, S. Angeoni, B.D. Berezin, in: C.C. Leznoff, A.B.P. Lever (Eds.), Phthalocyanines: Properties and Applications, vol. 4, VCH Publishers, New York, 1996.
[40] A. Ogunsipe, T. Nyokong, J. Mol. Struct. 689 (2004) 89.
[41] T. Nyokong, H. Isago, J. Porphyr. Phthalocya. 8 (2004) 1083.
[42] P. Tau, T. Nyokong, Dalton Trans. (2006) 4482.

Available online at www.sciencedirect.com
ScienceDirect
Polyhedron 26 (2007) 2777–2785
POLYHEDRON
www.elsevier.com/locate/poly

Synthesis and structures of cadmium(II) complexes of a series of multinucleating N/S donor ligands

Tanya K. Ronson [a], Harry Adams [a], Lindsay P. Harding [b], Ross W. Harrington [c], William Clegg [c,d], Michael D. Ward [a,*]

[a] *Department of Chemistry, University of Sheffield, Sheffield S3 7HF, UK*
[b] *Department of Chemistry and Biological Sciences, University of Huddersfield, Huddersfield, HD1 3DH, UK*
[c] *School of Natural Sciences (Chemistry), Newcastle University, Newcastle upon Tyne, NE1 7RU, UK*
[d] *CCLRC Daresbury Laboratory, Warrington WA4 4AD, UK*

Received 2 January 2007; accepted 16 January 2007
Available online 21 January 2007

Abstract

The coordination chemistry of a series of bis-bidentate ligands with cadmium(II) ions has been investigated. The ligands, containing two N,S-donor chelating (pyrazolyl/thioether) fragments, have afforded complexes of a variety of structural types (dinuclear M_2L_2 'mesocate' complexes, a one-dimensional chain coordination polymer and a simple mononuclear complex) according to whether the bis-bidentate ligands act as bridges spanning two metal ions, or a tetradentate chelate to a single metal ion. The *p*-phenylene and *m*-biphenyl spaced ligands L^1 and L^3 form dinuclear M_2L_2 complexes where the ligands are arranged in a 'side-by-side' fashion. In contrast the *m*-phenylene spaced ligand L^2 forms a one-dimensional coordination polymer where the ligands adopt a highly folded conformation. The 1,8-naphthalene spaced ligand L^4 adopts a tetradendate chelating mode and affords a simple mononuclear complex.
© 2007 Elsevier Ltd. All rights reserved.

Keywords: Cadmium; Coordination chemistry; Crystal structure; Mesocate; Coordination polymer

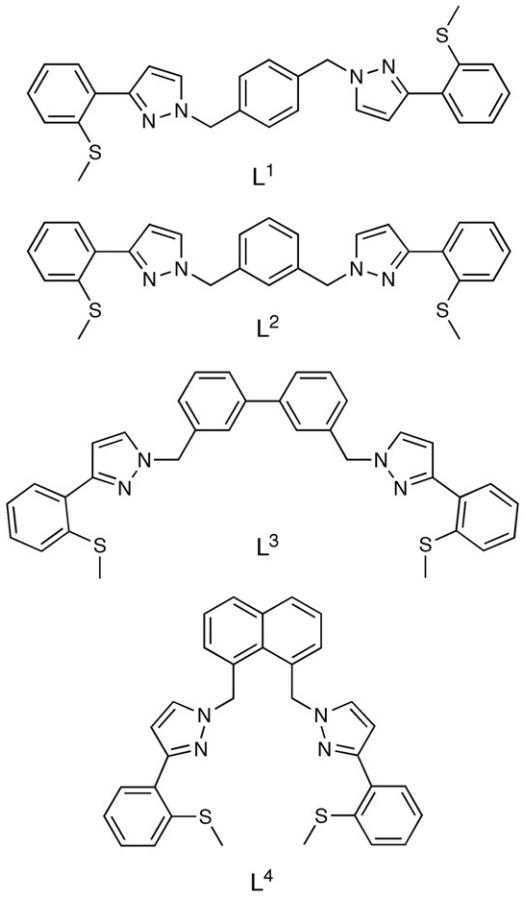
1. Introduction

The self-assembly of elaborate metallosupramolecular assemblies from relatively simple bridging ligands and labile metal ions continues to be an intensely popular area of study, partly because of the insight that these systems offer into control of self-assembly processes, and partly because the resulting assemblies can have a range of useful properties in materials and host-guest chemistry [1]. With regard to the ligands, a minimum condition is that the binding sites must be arranged so that they bridge two or more metal ions, otherwise simple mononuclear complexes may result. If a ligand is flexible, the competition between bridging and chelating coordination modes is an important factor in determining the course of a self-assembly reaction [2].

As part of our continuing studies into the coordination chemistry of flexible ligands containing bidentate chelating groups, we have recently reported the synthesis of a series of new ligands with potentially N,S-chelating arms derived from 3-[2-(methylsulfanyl)phenyl]pyrazole linked to central aromatic spacers by methylene units [3]. The reaction of these ligands with Ag(I) and Cu(I) ions resulted in a series of complexes with 1:1 metal:ligand stochiometry, in which each four-coordinate metal centre is bound by two coordinating arms to give one of three general structural types depending on the structure of the ligand and the nature of the spacer unit separating the two N,S-donor termini. These structural types are (i) dinuclear M_2L_2 complexes – either helicates, in which the ligands are twisted around one another, or mesocates, in which the ligands adopt a 'side-by-side' arrangement; (ii) infinite one-dimensional

* Corresponding author. Tel.: +44 0114 2229484; fax: +44 0114 2229346.
E-mail address: m.d.ward@sheffield.ac.uk (M.D. Ward).

0277-5387/$ - see front matter © 2007 Elsevier Ltd. All rights reserved.
doi:10.1016/j.poly.2007.01.012



Scheme 1.

coordination chains $[ML]_n$ which contain an alternating sequence M-(μ-L)-M-(μ-L)... along the chain, which may also have a chiral helicate structure; (iii) mononuclear complexes ML in which the ligand is flexible enough to coordinate both N,S-donor units to the same metal centre in a tetradentate chelating mode [3].

In this paper we describe the synthesis and structural characterisation of complexes of the potentially bis-bidentate ligands L^1–L^4 (see Scheme 1) with Cd(II). This metal ion commonly adopts a six-coordinate environment, so we may see either complexes with a M_2L_3 stoichiometry (or some higher multiple), or the involvement of additional ligands in the coordination sphere to complete the octahedral coordination environment. We note that bridging ligands based on two or more N,S-donor chelating units have recently been studied by several groups because of their propensity to form coordination networks and chains when coordinated to 'soft' metal ions [4].

2. Results and discussion

The ligands L^1–L^4 were prepared according to the previously described method, by reaction of 3-[2-(methylsulfanyl)phenyl]pyrazole with an appropriate bromomethylated aromatic compound (the spacer unit) in the presence of hydroxide ion under phase transfer conditions [3]. The crystal structures of L^1, L^2 and L^4 were reported previously [3]. The crystal structure of L^3 is shown in Fig. 1. The individual bond distances and angles within the molecule are unremarkable. The molecule lies across a centre of symmetry, such that the two halves are crystallographically equivalent. The (methylsulfanyl)phenyl/pyrazole units adopt a *cisoid* configuration with the methyl group pointing away from the lone pairs of the pyrazole nitrogen atoms resulting in an intramolecular N···S interaction. This is consistent with the known tendency of divalent S (and Se) atoms to interact with nucleophilic atoms [in this case the pyrazolyl N(2) nitrogen atom] giving short non-bonded contacts [5]. The non-bonded N(2)···S(1) distance of 2.878(2) Å is similar to that observed for L^1 [3] and the N(2)–S(1)–C(17) angle of 167.1(1)° shows a small deviation from linearity.

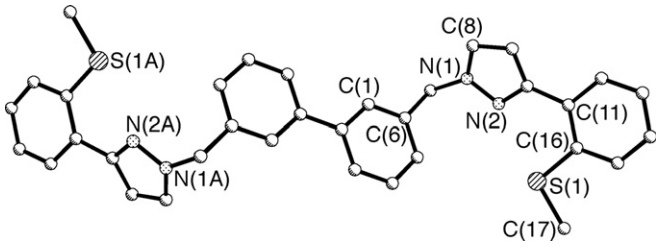


Fig. 1. Molecular structure of L^3. Symmetry operation to generate equivalent atoms: $(-x, -y, -z+1)$.

The reaction of tetradentate ligands L^1–L^4 with a metal ion that commonly displays six-fold coordination would be expected, in the absence of any coordinating anions or solvent molecules, to afford a complex with a 2:3 metal/ligand ratio. The reaction of the *p*-phenylene spaced ligand L^1 with $Cd(ClO_4)_2 \cdot H_2O$ in nitromethane gave a colourless solution; diisopropyl ether diffusion into this solution afforded crystals which analysed with a 1:1 metal/ligand ratio, independently of the starting M:L ratio used in the synthesis (2:3 or 1:1). The ES mass spectrum showed peaks at *m*/*z* 1489.0, 695.0 and 430.4 corresponding to the dinuclear species $[Cd_2(L^1)_2(ClO_4)_{4-x}]^{x+}$ ($x = 1, 2, 3$) showing sequential loss of ClO_4^- anions. An *m*/*z* value of 695.0 may also correspond to the mononuclear species $[CdL^1(ClO_4)]^+$, but the other two peaks are unambiguous. There are also peaks for fragmentation products at *m*/*z* 1177.2 and 1006.8 corresponding to $[Cd(L^1)_2(ClO_4)]^+$ and $[Cd_2(L^1)(ClO_4)_3]^+$, respectively.

The X-ray crystal structure shows that the crystalline material is the dinuclear complex $[Cd_2(L^1)_2(ClO_4)_2(H_2O)_2](ClO_4)_2$ (Fig. 2, Table 1). The complex is achiral with both bridging ligands spanning both metal centres in a 'side-by-side' arrangement commonly called a 'mesocate' [6]. This discrete dinuclear complex is in contrast to the polymeric coordination chains obtained from reaction of Cu(I) and Ag(I) with the same ligand [3]. The asymmetric unit contains one complete $[Cd_2(L^1)_2(ClO_4)_2(H_2O)_2]^{2+}$ cation [containing Cd(1) and Cd(2)], and another half-cation [containing Cd(3)] from which the second similar but crystallographically independent cation is generated by a two-

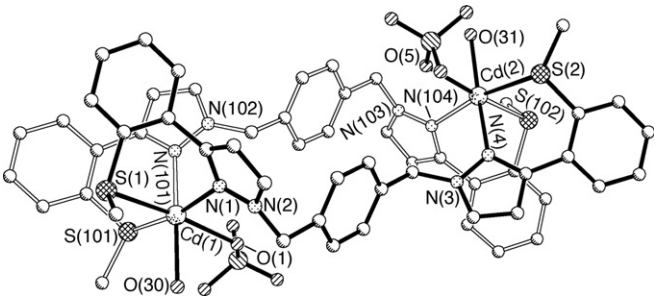


Fig. 2. Structure of the metal complex unit of $[Cd_2(L^1)_2(ClO_4)_2(H_2O)_2](ClO_4)_2 \cdot 4MeNO_2$. Only one of the two similar independent molecules is shown.

Table 1
Selected bond lengths (Å) and angles (°) for $[Cd_2(L^1)_2(ClO_4)(H_2O)](ClO_4)$

Cd(1)–O(30)	2.308(3)	O(30)–Cd(1)–N(1)	92.18(13)
Cd(1)–N(1)	2.321(4)	O(30)–Cd(1)–O(1)	78.93(13)
Cd(1)–O(1)	2.349(3)	N(1)–Cd(1)–O(1)	92.37(13)
Cd(1)–N(101)	2.355(4)	O(30)–Cd(1)–N(101)	170.96(13)
Cd(1)–S(101)	2.6642(12)	N(1)–Cd(1)–N(101)	95.44(13)
Cd(1)–S(1)	2.6803(12)	O(1)–Cd(1)–N(101)	95.87(13)
Cd(2)–O(31)	2.285(4)	O(30)–Cd(1)–S(101)	98.02(9)
Cd(2)–N(104)	2.321(4)	N(1)–Cd(1)–S(101)	169.66(10)
Cd(2)–N(4)	2.340(4)	O(1)–Cd(1)–S(101)	91.25(9)
Cd(2)–O(5)	2.362(4)	N(101)–Cd(1)–S(101)	74.55(10)
Cd(2)–S(2)	2.6723(14)	O(30)–Cd(1)–S(1)	91.83(9)
Cd(2)–S(102)	2.6933(14)	N(1)–Cd(1)–S(1)	82.30(10)
Cd(3)–O(32)	2.296(4)	O(1)–Cd(1)–S(1)	169.18(9)
Cd(3)–O(9)	2.328(4)	N(101)–Cd(1)–S(1)	94.00(10)
Cd(3)–N(202)	2.329(4)	S(101)–Cd(1)–S(1)	95.63(4)
Cd(3)–N(204)	2.358(4)	O(31)–Cd(2)–N(104)	92.46(15)
Cd(3)–S(202)	2.6872(13)	O(31)–Cd(2)–N(4)	169.88(15)
Cd(3)–S(201)	2.6979(13)	N(104)–Cd(2)–N(4)	95.74(14)
		O(31)–Cd(2)–O(5)	78.99(15)
O(32)–Cd(3)–O(9)	83.64(16)	N(104)–Cd(2)–O(5)	93.13(14)
O(32)–Cd(3)–N(202)	91.86(15)	N(4)–Cd(2)–O(5)	94.61(15)
O(9)–Cd(3)–N(202)	89.86(14)	O(31)–Cd(2)–S(2)	97.65(11)
O(32)–Cd(3)–N(204)	168.61(15)	N(104)–Cd(2)–S(2)	169.44(11)
O(9)–Cd(3)–N(204)	95.68(15)	N(4)–Cd(2)–S(2)	74.55(10)
N(202)–Cd(3)–N(204)	99.51(14)	O(5)–Cd(2)–S(2)	91.81(10)
O(32)–Cd(3)–S(202)	94.78(11)	O(31)–Cd(2)–S(102)	91.53(11)
O(9)–Cd(3)–S(202)	92.47(10)	N(104)–Cd(2)–S(102)	81.79(11)
N(202)–Cd(3)–S(202)	173.17(10)	N(4)–Cd(2)–S(102)	95.50(10)
N(204)–Cd(3)–S(202)	73.87(10)	O(5)–Cd(2)–S(102)	169.09(11)
O(32)–Cd(3)–S(201)	90.57(13)	S(2)–Cd(2)–S(102)	94.83(4)
O(9)–Cd(3)–S(201)	169.39(11)		
N(202)–Cd(3)–S(201)	81.42(10)		
N(204)–Cd(3)–S(201)	91.73(10)		
S(202)–Cd(3)–S(201)	96.88(4)		

fold rotation. The six-coordinate Cd(II) ions are coordinated by one N,S-chelating arm from each ligand, with a water molecule and a ClO_4^- anion completing the distorted octahedral coordination. The Cd···Cd separations within the dinuclear complex cations of 10.8 Å [between Cd(1) and Cd(2)] and 10.4 Å [between Cd(3) and its symmetry equivalent] are longer than those observed in the polymeric complexes of L^1 with Cu(I) (9.8 Å) and Ag(I) (7.6 Å). The Cd–S (average 2.68 Å) bonds are longer than the Cd–N (average 2.34 Å), $Cd–O_{perchlorate}$ (average 2.30 Å) and $Cd–O_{water}$ bonds (average 2.35 Å). The bidentate (methylsulfanyl)phenyl/pyrazole units show large deviations from planarity with torsion angles between the rings in the range 32–53°. The central phenylene spacers of the ligands are inclined parallel to each other [angle of approx. 1° between the rings for the molecule with Cd(1) and Cd(2) and exactly parallel by symmetry for the molecule with Cd(3)] and show a π–π stacking interaction. The distance between these stacked rings is 3.5–3.6 Å for the molecule containing Cd(1) and Cd(2) and 3.2 Å for the molecule containing Cd(3).

The ^1H NMR spectrum of the redissolved crystals of $[Cd_2(L^1)_2(ClO_4)_2(H_2O)_2](ClO_4)_2$ shows a two-fold-symmetric environment for L^1 in solution. The pyrazole H^5 signal is shifted downfield by *ca.* 0.3 ppm compared to the free ligand but there is little shift in the other signals.

The reaction of the *m*-phenylene spaced ligand L^2 with $Cd(ClO_4)_2 \cdot H_2O$ in acetonitrile resulted in a colourless solution. Diethylether diffusion into the reaction mixture gave colourless crystals whose elemental analysis indicated a 1:1 metal/ligand ratio. The FAB mass spectrum showed peaks at *m/z* 596 for $\{CdL^2\}^+$ and 695 $\{CdL^2(ClO_4)\}^+$. The X-ray crystal structure shows that the crystalline material is the infinite one-dimensional coordination polymer $\{[CdL^2(CH_3CN)_2](ClO_4)_2\}_\infty$ (Figs. 3 and 4, Table 2). Each Cd(II) ion is coordinated by an N,S-chelating arm from each of two separate ligands. Two *cis*-coordinated acetontrile molecules make up the distorted octahedral coordination. The Cd–S and Cd–N bond lengths are similar to those of $[Cd_2(L^1)_2(ClO_4)(H_2O)](ClO_4)$. The Cd···Cd separation between metals linked by the same bridging ligand is 7.33 Å, slightly longer than in the copper complex $\{[CuL^2](BF_4)\}_\infty$ (6.17 Å) [3]. The ligands are folded such that the pyrazole rings are almost perpendicular to the central phenyl spacer (angles of 94° and 96° between the mean planes of the rings). This folding brings the Cd(II) ions closer together than in the complex with L^1 [the average Cd···Cd separation in $[Cd_2(L^1)_2(ClO_4)_2(H_2O)_2](ClO_4)_2$ is

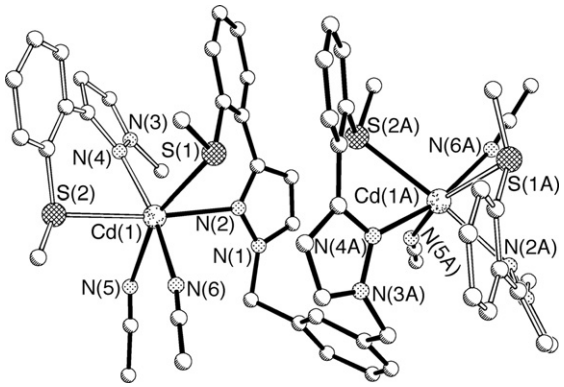


Fig. 3. Structure of the metal complex unit of $\{[CdL^2(CH_3CN)_2](ClO_4)_2\}_\infty$ showing the coordination geometry around the Cd(II) centres.



Fig. 4. Structure of the one-dimensional polymeric chain of $\{[CdL^2(CH_3CN)_2](ClO_4)_2\}_\infty$, with alternate ligands shaded differently for clarity. Only the N atoms of the coordinated MeCN ligands are shown.

10.6 Å] in which the ligand adopted a more extended conformation. The twist angles between the rings within each bidentate (methylsulfanyl)phenyl/pyrazole unit are *ca.* 34 and 28°. There is an angle of 24° between the planes of the pyrazole ring containging N(3) and a (methylsulfanyl)phenyl from the next ligand, for which the inter-ring separation covers the range 3.2–4.3 Å, possibly indicative of a weak π–π stacking interaction. The ^{1}H NMR spectrum of $\{[CdL^2(CH_3CN)_2](ClO_4)_2\}_\infty$ shows a two-fold-symmetric environment for L^2 in solution. The fact that the crystals dissolve in acetonitrile is indicative of the coordination polymer breaking up to form solvated $\{CdL^2\}^{2+}$ units.

The reaction of the *m*-biphenyl spaced ligand L^3 with one equivalent of $Cd(ClO_4)_2 \cdot H_2O$ in dry acetonitrile under an N_2 atmosphere followed by evaporation gave the crude complex as an oil. Recrystallisation by diethylether vapour diffusion into an acetonitrile/nitromethane (1:1) solution gave a crystalline material which was found to be the discrete dinuclear complex $[Cd_2(L^3)_2(MeCN)_2(H_2O)_2](ClO_4)_4$ (Fig. 5, Table 3), in contrast to the coordination polymers obtained from the reaction of the same ligand with Cu(I) and Ag(I) [3]. The complex lies astride a centre of symmetry such that the asymmetric unit contains one Cd(II) ion and one complete ligand; clearly therefore it is achiral and not a helicate. Both ligands bridge both metal centres with a Cd···Cd distance of 10.8 Å, almost identical to that

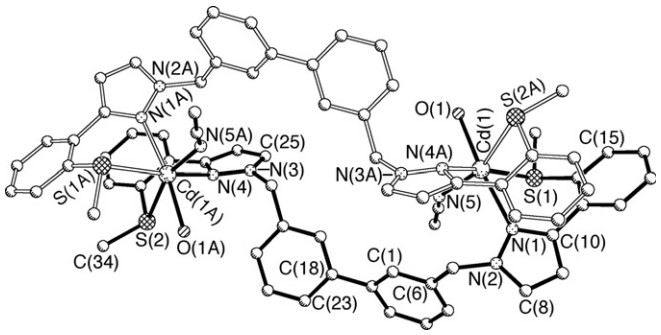


Fig. 5. Structure of the metal complex unit of $[Cd_2(L^3)_2(MeCN)_2(H_2O)_2](ClO_4)$.

Table 2
Selected bond lengths (Å) and angles (°) for $\{[CdL^2(CH_3CN)_2](ClO_4)_2\}_\infty$

Cd(1)–N(4)	2.300(13)
Cd(1)–N(2)	2.376(11)
Cd(1)–N(5)	2.389(11)
Cd(1)–N(6)	2.389(14)
Cd(1)–S(2)	2.636(4)
Cd(1)–S(1)	2.699(4)
N(4)–Cd(1)–N(2)	96.8(4)
N(4)–Cd(1)–N(5)	100.7(4)
N(2)–Cd(1)–N(5)	97.5(4)
N(4)–Cd(1)–N(6)	166.5(4)
N(5)–Cd(1)–S(2)	85.3(3)
N(6)–Cd(1)–S(2)	91.7(3)
N(4)–Cd(1)–S(1)	96.0(2)
N(2)–Cd(1)–S(1)	70.0(3)
N(2)–Cd(1)–N(6)	95.7(4)
N(5)–Cd(1)–N(6)	82.7(4)
N(4)–Cd(1)–S(2)	75.6(3)
N(2)–Cd(1)–S(2)	172.3(3)
N(5)–Cd(1)–S(1)	160.3(3)
N(6)–Cd(1)–S(1)	83.4(3)
S(2)–Cd(1)–S(1)	109.15(11)

Table 3
Selected bond lengths (Å) and angles (°) for $[Cd_2(L^3)_2(MeCN)_2(H_2O)_2](ClO_4)_4$

Cd(1)–N(5)	2.297(5)
Cd(1)–O(1)	2.307(3)
Cd(1)–N(4A)	2.314(4)
Cd(1)–N(1)	2.347(4)
Cd(1)–S(1)	2.6263(15)
Cd(1)–S(2A)	2.7678(15)
N(5)–Cd(1)–O(1)	82.06(15)
N(5)–Cd(1)–N(4A)	102.06(17)
O(1)–Cd(1)–N(4A)	99.39(13)
N(5)–Cd(1)–N(1)	95.43(15)
O(1)–Cd(1)–N(1)	168.43(13)
N(4A)–Cd(1)–N(1)	92.18(13)
N(5)–Cd(1)–S(1)	86.87(14)
O(1)–Cd(1)–S(1)	92.34(10)
N(4A)–Cd(1)–S(1)	166.08(10)
N(1)–Cd(1)–S(1)	76.21(10)
N(5)–Cd(1)–S(2A)	162.55(13)
O(1)–Cd(1)–S(2A)	84.16(10)
N(4A)–Cd(1)–S(2A)	69.71(10)
N(1)–Cd(1)–S(2A)	100.15(10)
S(1)–Cd(1)–S(2A)	104.37(4)

Symmetry transformations used to generate equivalent atoms: $(-x+1, -y+1, -z+1)$.

in $[Cd_2(L^1)_2(ClO_4)_2(H_2O)_2](ClO_4)_2$ despite the longer spacer in L^3. The Cd(II) ions are in a distorted octahedral geometry with one acetonitrile and one water molecule completing the coordination. The acetonitrile molecules are attached at an angle with the Cd–N–C angles being 142.8(5)°. The bond lengths to Cd(II) are typical of complexes in this series. The twist angles within the biphenyl spacers are 41.8° and the twist angles within each bidentate (methylsulfanyl)phenyl/pyrazole units are 34.2 and 28.8°. There is a π–π stacking interaction between the pyrazole ring containing N(1) and the (methylsulfanyl)phenyl ring of the other ligand (angle of 20.6° between the mean planes of the two rings, distance of 3.2–4.1 Å between the rings). The biphenyl spacers are not involved in any π–π stacking interactions.

The electrospray mass spectrum of the crystals shows peaks at *m/z* 1641.1, 771.1 and 480.7 corresponding to the dinuclear species $[Cd_2(L^3)_2(ClO_4)_{4-x}]^{x+}$ ($x = 1$, 2, 3) with sequential loss of perchlorate anions. The *m/z* value of 771.1 may also correspond to the mononuclear species $\{Cd(L^3)ClO_4\}^+$ but the other peaks are unambiguous. There are also peaks for Cd_2L^3 and $Cd(L^3)_2$ fragments. The ^1H NMR spectrum of $[Cd_2(L^3)_2(MeCN)_2(H_2O)_2](ClO_4)_4$ is broad, indicative of a dynamic process in solution.

The reaction of L^4 with one equivalent of $Cd(ClO_4)_2 \cdot H_2O$ in dry acetonitrile under an N_2 atmosphere resulted in a colourless solution. Diethylether diffusion into the reaction mixture gave colourless crystals whose elemental analysis was consistent with the formulation $[CdL^4(H_2O)_2](ClO_4)_4$. The electrospray mass spectrum showed peaks at *m/z* 744 $[\{CdL^4(ClO_4)\}^+]$ and 343 $[\{CdL^4(MeCN)\}^{2+}]$, consistent with formation of a mononuclear complex.

The X-ray crystal structure confirms that the crystalline material $[CdL^4(MeCN)_2](ClO_4)_2$ is a mononuclear complex (Fig. 6, Table 4) in contrast to the dinuclear structures obtained with L^1 and L^3 and the polymeric structure obtained with L^2. The complex has two-fold rotation symmetry such that the asymmetric unit contains half of a Cd(II) ion and half of a ligand. The Cd(II) ion is in a distorted octahedral N_4S_2 environment with L^4 acting as a tetradentate chelate. The donor atoms of L^4 form an approximate equatorial plane with an angle of 10.9° between the two Cd(NS) planes. The coordination environment is completed by two axially coordinated acetonitrile molecules. It is likely, on the basis of the elemental analysis, that these weakly bound solvent molecules are removed upon drying under vacuum and replaced by water from the atmosphere. The N,S-donor bidentate arms are not individually coplanar, with a substantial dihedral twist of 40.1° between the pyrazolyl and (methylsulfanyl)phenyl rings. The ^1H NMR spectrum $[CdL^4(MeCN)_2](ClO_4)_2$ shows two-fold symmetry in solution. The signals are shifted downfield from those of the free ligand and are consistent with complexation being retained in solution.

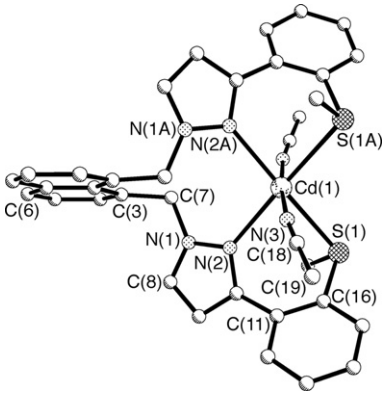


Fig. 6. Molecular structure of the metal complex unit of $[CdL^4(MeCN)_2](ClO_4)_2$. Symmetry transformations used to generate equivalent atoms: (y, x, $-z$).

Table 4
Selected bond lengths (Å) and angles (°) for $[Cd_2(L^1)_2(ClO_4)(H_2O)](ClO_4)$

Cd(1)–N(3)	2.329(4)
Cd(1)–N(2)	2.344(4)
Cd(1)–S(1)	2.7013(14)
N(3)–Cd(1)–N(3A)	175.1(2)
N(3)–Cd(1)–N(2)	87.49(14)
N(3A)–Cd(1)–N(2)	95.60(14)
N(3)–Cd(1)–N(2A)	95.60(14)
N(3A)–Cd(1)–N(2A)	87.49(14)
N(2)–Cd(1)–N(2A)	101.8(2)
N(3)–Cd(1)–S(1A)	85.64(11)
N(3A)–Cd(1)–S(1A)	91.29(11)
N(2)–Cd(1)–S(1A)	173.12(9)
N(2A)–Cd(1)–S(1A)	78.38(11)
N(3)–Cd(1)–S(1)	91.29(11)
N(3A)–Cd(1)–S(1)	85.64(11)
N(2)–Cd(1)–S(1)	78.38(11)
N(2A)–Cd(1)–S(1)	173.12(9)
S(1A)–Cd(1)–S(1)	102.30(7)

Symmetry transformations used to generate equivalent atoms: (y, x, $-z$).

In conclusion this set of ligands has afforded an interesting range of structural types in the complexes with Cd(II) ions. Depending on the separation between the N,S-donor units they can either bind to separate metal ions giving dinuclear complexes or one-dimensional chains, or chelate to a single Cd(II) centre giving a simple mononuclear complex. In all cases the Cd(II) centres are six-coordinate, bound by two N,S-donor units and two additional ligands (water, acetonitrile or perchlorate).

3. Experimental

3.1. General details

The ligands L^1–L^4 were prepared as previously described [3]. All other organic reagents and metal salts were purchased from Aldrich or Avocado and used as received. ^1H NMR spectra were recorded on Bruker AC-250, AMX-400 or DRX-500 spectrometers. Mass spectra (FAB and EI) were recorded on a VG AutoSpec magnetic sector instrument. Electrospray mass spectra were measured

at the University of Huddersfield on a Bruker MicroTOF instrument in positive ion mode, with capillary exit and first skimmer voltages of 30 V and 60 V, respectively. Samples were prepared at a concentration of *ca.* 2 mg/ml in MeCN or $MeNO_2$ and analysed by direct infusion using a Cole Parmer syringe pump at a flow rate of 3 μl/min. Spectra were acquired over an *m/z* range of 50–3000; several scans were averaged to provide the final spectrum. IR spectra were recorded on a Perkin–Elmer Spectrum One instrument. Samples for elemental analysis were vacuum-dried.

3.2. Preparation of $[Cd_2(L^1)_2(ClO_4)_2(H_2O)_2](ClO_4)_2$

A solution of $Cd(ClO_4)_2 \cdot H_2O$ (58 mg, 0.19 mmol) in $MeNO_2$ (2 cm^3) was added to a solution of L^1 (90 mg, 0.19 mmol) in $MeNO_2$ (2 cm^3). The colourless solution was stirred for 4 h. Diisopropyl ether diffusion into the solution gave colourless crystals of $[Cd_2(L^1)_2(ClO_4)_2(H_2O)_2](ClO_4)_2$ which were suitable for X-ray crystallography (Yield: 103 mg, 68%). *Anal.* Calc. for $C_{56}H_{52}Cd_2Cl_4N_8O_{16}S_4(H_2O)_2$ (1623.98): C, 41.42; H, 3.48; N, 6.90. Found: C, 41.39; H, 3.44; N, 6.82%. ES MS: *m/z* 1489.0 $\{Cd_2(L^1)_2(ClO_4)_3\}^+$, 1177.2 $\{Cd(L^1)_2(ClO_4)\}^+$, 1006.84 $\{Cd_2L^1(ClO_4)_3\}^+$, 695.0 $\{Cd_2(L^1)_2(ClO_4)_2\}^{2+}$ and/or $\{CdL^1ClO_4\}^+$, 430.4 $\{Cd_2(L^1)_2ClO_4\}^{3+}$. ^1H NMR (500 MHz, $MeNO_2$): δ (ppm) 7.65 (2H, d; pyrazolyl H^5), 7.48 (2H, m; methylthiophenyl H^3), 7.31–7.37 (4H, m; methylthiophenyl H^5, H^6), 7.25 (4H, s; phenyl), 7.20 (2H, ddd; methylthiophenyl H^4), 6.59 (2H, d; pyrazolyl H^4), 5.34 (4H, s; CH_2), 2.40 (6H, s; SMe). IR (KBr disk): *ν* (cm^{-1}) 3143 (w), 3054 (w), 2932 (w), 1627 (m), 1591 (w), 1519 (m), 1501 (m), 1465 (w), 1433 (s), 1407 (m), 1347 (m), 1331 (m), 1291 (w), 1278 (w), 1262 (w), 1222 (w), 1171 (m), 1121 (s), 1066 (s), 1039 (s), 1027 (s), 978 (m), 949 (w), 915 (m), 854 (w), 832 (w), 792 (m), 760 (s), 747 (m), 727 (w), 622 (s), 496 (w).

3.3. Preparation of $\{[CdL^2(CH_3CN)_2](ClO_4)_2\}_\infty$

$Cd(ClO_4)_2 \cdot H_2O$ (64 mg, 0.21 mmol) was added to a solution of L^2 (99 mg, 0.21 mmol) in dry MeCN (20 cm^3) under N_2. The colourless solution was stirred overnight and the volume reduced to ~10 cm^3. Diethylether diffusion into the solution gave off-white crystals of $\{[CdL^2(CH_3CN)_2](ClO_4)_2\}_\infty$ which were suitable for X-ray crystallography (Yield: 124 mg, 74%). *Anal.* Calc. for $C_{28}H_{26}CdCl_2N_4O_8S_2 \cdot (H_2O)$ (811.99): C, 41.42; H, 3.48; N, 6.90. Found: C, 41.49; H, 3.34; N, 7.21%. FAB MS: *m/z* 596 $\{CdL^2\}$, 695 $\{CdL^2(ClO)_4\}$. ^1H NMR (500 MHz, CD_3CN): δ (ppm) 7.64 (2H, d, pyrazolyl H^5), 7.47 (2H, ddd, methylthiophenyl H^3), 7.31–7.37 (5H, m, methylthiophenyl H^5, H^6, phenyl), 7.16–7.23 (5H, m, methylthiophenyl H^4, phenyl), 6.58 (2H, d, pyrazolyl H^4), 5.34 (4H, s, CH_2), 2.39 (6H, s, SMe).IR (KBr disk): *ν* (cm^{-1}) 3143 (w), 2932 (w), 1627 (m), 1614 (m), 1592 (w), 1517 (m), 1504 (m), 1433 (s), 1406 (m), 1350 (m), 1328 (m), 1278 (w), 1221 (m), 1113 (s), 949 (w), 917 (m), 787 (w), 758 (s), 740 (w), 727 (w), 624 (s).

3.4. Preparation of $[Cd_2(L^3)_2(MeCN)_2(H_2O)_2](ClO_4)_4$

$Cd(ClO_4)_2 \cdot H_2O$ (40 mg, 0.13 mmol) was added to a solution of L^3 (72 mg, 0.13 mmol) in dry MeCN (15 cm^3). The colourless solution was stirred overnight under N_2 and the solvent removed *in vacuo*. The crude product was recrystallised by diethylether diffusion into an acetonitrile/nitromethane (1:1) solution to give colourless crystals of $[Cd_2(L^3)_2(MeCN)_2(H_2O)_2](ClO_4)_4$ which were suitable for X-ray crystallography (yield: 90 mg, 75%). *Anal.* Calc. for $C_{72}H_{70}Cd_2Cl_4N_{10}O_{18}S_4(H_2O)_3$ (1912.33): C, 45.22; H, 4.01; N, 7.32. Found: C, 45.27; H, 3.73; N, 7.14%. ES MS: *m/z* 1641.1 $\{Cd_2(L^3)_2(ClO_4)_3\}^+$, 1329.3 $\{Cd(L^3)_2(ClO_4)\}^+$, 1080.9 $\{Cd_2L^3(ClO_4)_3\}^+$, 771.1 $\{Cd_2(L^3)_2(ClO_4)_2\}^{2+}$ and/or $\{CdL^3ClO_4\}^+$, 480.7 $\{Cd_2(L^3)_2ClO_4\}^{3+}$. ^1H NMR (500 MHz, CD_3CN): δ (ppm) 7.67 (2H, br s; pyrazolyl H^5), 7.43–7.56 (10H, br m), 7.36 (2H, br s), 7.29 (2H, br d), 7.01 (2H, br d), 6.61 (2H, br s; pyrazolyl H^4), 5.48 (4H, br s; CH_2), 2.41 (6H, br s; SCH_3). IR (KBr disk): *ν* (cm^{-1}) 3397 (s, br), 3141 (w), 3124 (w), 3014 (w), 2925 (w), 1676 (w), 1633 (w), 1605 (w), 1590 (w), 1517 (m), 1503 (m), 1463 (w), 1438 (m), 1404 (m), 1350 (m), 1343 (w), 1322 (w), 1223 (m), 1119 (s), 1104 (s), 1075 (s), 1016 (w), 931 (w), 882 (w), 789 (m), 770 (w), 754 (s), 727 (w), 695 (w), 623 (s).

3.5. Preparation of $[CdL^4(MeCN)_2](ClO_4)_4$

$Cd(ClO_4)_2 \cdot H_2O$ (47 mg, 0.15 mmol) was added to a solution of L^4 (80 mg, 0.15 mmol) in dry MeCN (20 cm^3) under N_2. The colourless solution was stirred overnight and the volume reduced to ~10 cm^3. Diethylether diffusion into the solution gave off-white crystals of $[CdL^4(MeCN)_2](ClO_4)_2$ which were suitable for X-ray crystallography. The crystals were dried *in vacuo* to yield, after exposure to air, $[CdL^4](ClO_4)_2 \cdot 2H_2O$ as a white powder (yield: 89 mg, 67%). *Anal.* Calc. for $CdC_{32}H_{28}N_4S_2Cl_2O_8 \cdot (H_2O)_2$ (880.07): C, 43.67; H, 3.66; N, 6.37%. Found: C, 44.09; H, 3.42; N, 6.44%. ES MS: 744 $\{CdL^4ClO_4\}^+$, 343 $\{CdL^4(CH_3CN)\}^{2+}$. ^1H NMR (500 MHz, $CDCl_3$): δ (ppm) 8.17 (2H, dd), 7.77 (2H, d), 7.67 (2H, dd), 7.61 (2H, dd), 7.60 (2H, dd), 7.54 (2H, td), 7.47 (2H, td), 7.43 (2H, d; pyrazolyl H^5), 6.66 (2H, d, pyrazolyl H^4), 5.78 (4H, s, CH_2), 2.63 (6H, s, SMe). IR (KBr disk): *ν* (cm^{-1}) 3146 (w), 3063 (w), 2932 (w), 1621 (w), 1600 (w), 1519 (m), 1505 (m), 1487 (m), 1460 (w), 1433 (s), 1406 (w), 1370 (m), 1328 (s), 1214 (m), 1101 (s), 961 (w), 950 (w), 849 (w), 823 (w), 785 (s), 769 (s), 729 (m), 681 (w), 623 (s).

3.6. X-ray crystallography

X-ray crystallographic data are summarised in Table 5. For each compound a suitable crystal was coated with hydrocarbon oil and attached to the tip of a glass fibre

Table 5
Crystallographic data for the five crystal structures[a]

Compound	L^3	$[Cd_2(L^1)_2(H_2O)_2(ClO_4)_2](ClO_4)_2 \cdot 4MeNO_2$	$\{[CdL^2(MeCN)_2](ClO_4)_2\}_\infty$	$[Cd_2(L^3)_2(H_2O)_2(MeCN)_2](ClO_4)_4$[a]	$[Cd(L^4)(MeCN)_2](ClO_4)_2$
Formula	$C_{34}H_{30}N_4S_2$	$C_{60}H_{68}Cd_2Cl_4N_{12}O_{26}S_4$	$C_{34}H_{35}CdCl_2N_7O_8S_2$	$C_{72}H_{66}Cd_2Cl_4N_{10}O_{18}S_4$	$C_{36}H_{34}CdC_{12}N_6O_8S_2$
Formula weight	558.74	1868.10	917.11	1854.19	926.11
T (K)	100(2)	100(2)	150(2)	120(2)	150(2)
Crystal system	orthorhombic	monoclinic	monoclinic	triclinic	tetragonal
Space group	*Pbca*	*C*2/*c*	*Cc*	$P\bar{1}$	*P*4(3)2(1)2
a (Å)	9.4207(8)	75.521(4)	21.489(13)	11.874(3)	11.1155(9)
b (Å)	8.8218(8)	18.1666(9)	12.675(7)	12.599(3)	11.1155(9)
c (Å)	33.408(3)	17.5515(9)	14.589(9)	14.684(4)	32.624(4)
α (°)	90	90	90	74.058(2)	90
β (°)	90	91.682(2)	90.855(10)	89.679(2)	90
γ (°)	90	90	90	63.440(2)	90
V (Å^3)	2776.4(4)	24069(2)	3973(4)	1871.7(8)	4030.9(7)
Z	4	12	4	1	4
D_{calc} (Mg/m^3)	1.337	1.547	1.533	1.645	1.526
μ (mm^{-1})	0.224	0.848	0.847	0.900	0.835
Crystal size (mm)	$0.22 \times 0.09 \times 0.04$	$0.32 \times 0.22 \times 0.12$	$0.24 \times 0.20 \times 0.10$	$0.10 \times 0.02 \times 0.02$	$0.40 \times 0.32 \times 0.18$
Reflections collected	39 267	362 445	17 606	19 014	46 277
Independent reflections [R_{int}]	3180 [0.0794]	21 186 [0.0483]	6962 [0.1173]	9907 [0.0459]	4657 [0.0599]
Data/restraints/parameters	3180/0/182	21186/62/1467	6962/34/486	9907/22/518	4657/0/252
Final R indices[b]	$R_1 = 0.0377$, $wR_2 = 0.1138$	$R_1 = 0.0551$, $wR_2 = 0.1377$	$R_1 = 0.0861$, $wR_2 = 0.2297$	$R_1 = 0.0670$, $wR_2 = 0.1880$	$R_1 = 0.0499$, $wR_2 = 0.1368$
Largest difference in peak and hole (e Å^{-3})	0.228 and −0.233	1.686 and −1.205	1.642 and −2.160	2.874 and −1.288	0.828 and −0.617

[a] The X-ray wavelength was 0.71073 Å (Mo Kα) in all cases except for $[Cd_2(L^3)_2(H_2O)_2(MeCN)_2](ClO_4)_4$ where it was 0.6709 Å.
[b] The value of R_1 is based on selected data with $I > 2\sigma(I)$; the value of wR_2 is based on all data.

and transferred to a Bruker-SMART 1000 or APEX-2 CCD diffractometer (graphite- monochromated Mo Kα radiation, $\lambda = 0.71073$ Å) under a stream of cold N_2. The data for $[Cd_2(L^3)_2(MeCN)_2(H_2O)_2](ClO_4)_4$were collected at the Daresbury Synchrotron Radiation Source (station 9.8) using a Bruker SMART-APEX2 diffractometer and Si(1 1 1)-monochromated synchrotron radiation with a wavelength close to the Zr absorption edge. In all cases the data were corrected for Lorentz and polarisation effects and for absorption by semi-empirical methods (SADABS) [7] based on symmetry-equivalent and repeated reflections. The structures were solved by direct methods or heavy atom Patterson methods and refined by full-matrix least-squares methods on F^2. Hydrogen atoms were placed geometrically and refined with a riding model and with U_{iso} constrained to be 1.2 (1.5 for methyl groups) times U_{eq} of the carrier atom. Structures were solved and refined using the SHELX suite of programs [8]. Significant bond distances and angles for the structures of the metal complexes are in Tables 1–4. Specific special features or problems associated with the structure determinations are as follows.

$[Cd_2(L^1)_2(ClO_4)(H_2O)](ClO_4) \cdot 4CH_3NO_2$: the asymmetric unit consists of one complete complex molecule, one half of another complex molecule, three non-coordinated anions and six nitromethane molecules. One of the ClO_4^- anions is disordered over two sites and was heavily restrained to ensure stable refinement. The SQUEEZE option of PLATON was used to account for severely disordered solvent molecules which could not be satisfactorily modelled. Diffraction was weak and only data with $2\theta \leqslant 50°$ were used in the final refinement.

$\{[CdL^2(CH_3CN)_2](ClO_4)_2 \cdot MeCN\}_\infty$: the asymmetric unit contains one Cd(II) ion, two half-ligands, two coordinated acetonitrile molecules, one acetonitrile solvent and two disordered ClO_4^- anions. Both anions were modelled with two parts and heavily restrained to ensure a stable refinement. Diffraction was weak and only data with $2\theta \leqslant 50°$ were used in the final refinement.

$[Cd_2(L^3)_2(MeCN)_2(H_2O)_2](ClO_4)_4$. The asymmetric unit contains one Cd(II) ion (with a coordinated MeCN and H_2O), one complete ligand and two ClO_4^- anions. One ClO_4^- anion is disordered over two parts and has been restrained accordingly. The hydrogen atoms on the coordinated H_2O molecule have not been located.

Acknowledgements

We thank the New Zealand Tertiary Education Commission for a Top Achiever Doctoral scholarship to T.K.R., EPSRC (UK) for funding of the UK National Crystallography Service, and CCLRC (UK) for access to synchrotron facilities.

Appendix A. Supplementary material

CCDC 631343, 631344, 631345, 631346 and 631347 contain the supplementary crystallographic data for this paper. These data can be obtained free of charge via http://www.ccdc.cam.ac.uk/conts/retrieving.html, or from the Cambridge Crystallographic Data Centre, 12 Union Road, Cambridge CB2 1EZ, UK; fax: (+44) 1223-336-033; or e-mail: deposit@ccdc.cam.ac.uk. Supplementary data associated with this article can be found, in the online version, at doi:10.1016/j.poly.2007.01.012.

References

[1] (a) J.-C.G. Bünzli, C. Piguet, Chem. Rev. 102 (2002) 1897;
(b) G.F. Swiegers, T.J. Malefetse, Coord. Chem. Rev. 225 (2002) 91;
(c) F.A. Cotton, C. Lin, C.A. Murillo, Account Chem. Res. 34 (2001) 759;
(d) C.H.M. Amijs, G.P.M. van Klink, G. van Koten, Dalton Trans. (2006) 308;
(e) D. Fiedler, D.H. Leung, R.G. Bergman, K.N. Raymond, Account Chem. Res. 38 (2005) 349;
(f) M. Fujita, M. Tominaga, A. Hori, B. Therrien, Account Chem. Res. 38 (2005) 369;
(g) S.R. Seidel, P.J. Stang, Account Chem. Res. 35 (2002) 972;
(h) N.W. Ockwig, O. Delgado-Friedrichs, M. O'Keeffe, O.M. Yaghi, Account Chem. Res. 38 (2005) 176;
(i) M. Eddaoudi, D.B. Moler, H.L. Li, B.L. Chen, T.M. Reineke, M. O'Keeffe, O.M. Yaghi, Account Chem. Res. 34 (2001) 176;
(j) O. Mamula, A. Zelewsky, Coord. Chem. Rev. 242 (2003) 87;
(k) J.-M. Lehn, Science 295 (2002) 2400.
[2] E.C. Constable, Polynuclear transition metal helicates, in: J.-P. Sauvage (Ed.), Comprehensive Supramolecular Chemistry, vol. 9, Elsevier, Oxford, 1996, p. 213.
[3] T.K. Ronson, H. Adams, M.D. Ward, Eur. J. Inorg. Chem. (2005) 4533.
[4] (a) M.C. Hong, W.P. Su, R. Cao, M. Fujita, J.X. Lu, Chem. Eur. J. 6 (2000) 427;
(b) C.Y. Su, S. Liao, H.L. Zhu, B.S. Kang, X.M. Chen, H.Q. Liu, J. Chem. Soc., Dalton Trans. (2000) 1985;
(c) S. Liao, C.Y. Su, H.X. Zhang, J.L. Shi, Z.Y. Zhou, H.Q. Liu, A.S.C. Chan, B.S. Kang, Inorg. Chim. Acta 336 (2002) 151;
(d) S. Tavacoli, T.A. Miller, R.L. Paul, J.C. Jeffery, M.D. Ward, Polyhedron 22 (2003) 507;
(e) Y. Zheng, M. Du, J.-R. Li, R.-H. Zhang, X.-H. Bu, Dalton Trans. (2003) 1509;
(f) M. Oh, C.L. Stern, C.A. Mirkin, Chem. Commun. (2004) 2684;
(g) Y.-B. Xie, C. Zhang, J.-R. Li, X.-H. Bu, Dalton Trans. (2004) 562;
(h) D.A. McMorran, C.M. Hartshorn, P.J. Steel, Polyhedron 23 (2004) 1055.
[5] (a) A.M.W. Cargill Thompson, D.A. Bardwell, J.C. Jeffery, L.H. Rees, M.D. Ward, J. Chem. Soc., Dalton Trans. (1997) 721;
(b) R.E. Rosenfeld Jr., R. Parthasarathy, J.D. Dunitz, J. Am. Chem. Soc. 99 (1977) 4860;
(c) F.T. Burling, B.M. Goldstein, J. Am. Chem. Soc. 114 (1992) 2313;
(d) F.T. Burling, B.M. Goldstein, Acta Crystallogr. B49 (1993) 738;
(e) G.R. Desiraju, V. Nalini, J. Mater. Chem. 1 (1991) 201;
(f) D. Britton, J.D. Dunitz, Helv. Chim. Acta 63 (1980) 1068;
(g) M. Iwaoka, S. Tomoda, J. Am. Chem. Soc. 118 (1996) 8077;
(h) M. Iwaoka, S. Takemoto, M. Okada, S. Tomoda, Bull. Chem. Soc. Jpn. 75 (2002) 1611;
(i) I. Vargas-Baca, T. Chivers, Phosphorus, Sulfur, Silicon Related Elements 164 (2000) 207;
(j) R.M. Minyaev, V.I. Minkin, Can. J. Chem. 76 (1998) 776.
[6] (a) A.M. Garcia-Deibe, J.S. Metalobos, M. Fondo, M. Vazquez, M.R. Bermejo, Inorg. Chim. Acta 357 (2004) 2561;
(b) X. Sun, D.W. Johnson, K.N. Raymond, E.H. Wong, Inorg. Chem. 40 (2001) 4504;
(c) Y.P. Cai, C.Y. Su, C.L. Chen, Y.M. Li, B.S. Kang, A.S.C. Chan, W. Kaim, Inorg. Chem. 42 (2003) 163;

(d) W. Schuh, H. Kopacka, K. Wurst, P. Peringer, Eur. J. Inorg. Chem. (2002) 2202;
(e) M. Albrecht, I. Janser, H. Houjou, R. Frohlich, Chem. Eur. J. 10 (2004) 2839;
(f) M. Albrecht, Chem. Eur. J. 3 (1997) 1466;
(g) T.K. Ronson, H. Adams, T. Riis-Johannessen, J.C. Jeffery, M.D. Ward, New J. Chem. 30 (2006) 26.
[7] G.M. Sheldrick, SADABS version 2.10, University of Göttingen, 2003.
[8] G.M. Sheldrick, SHELXS-97 and SHELXL-97, University of Göttingen, 1997.

Available online at www.sciencedirect.com
ScienceDirect
Polyhedron 26 (2007) 2786–2794
POLYHEDRON
www.elsevier.com/locate/poly

Reinvestigation of zinc(II) complexation by 2-thiophenecarboxylic hydrazide: X-ray structure of tris(2-thiophenecarboxyhydrazide)zinc(II) tetrachlorozincate(II) di(ethanol) and vibrational spectroscopy of its decomposition product

Anna Hołtra [a,b], Piotr Drożdżewski [b,*], Maria Kubiak [c]

[a] Faculty of Environmental Engineering, Wrocław University of Technology, Pl. Grunwaldzki 9, 50-370 Wrocław, Poland
[b] Faculty of Chemistry, Wrocław University of Technology, Wybrzeże St., Wyspiańskiego 27, 50-370 Wrocław, Poland
[c] Faculty of Chemistry, University of Wrocław, F. Joliot-Curie 14, 50-383 Wrocław, Poland

Received 21 December 2006; accepted 17 January 2007
Available online 30 January 2007

Abstract

Reaction of $ZnCl_2$ and 2-thiophenecarboxylic hydrazide (tch), in ethanol resulted in the crystalline product $[Zn(tch)_3][ZnCl_4] \cdot 2EtOH$, which slowly decomposes losing solvent molecules. The structure of the first compound has been determined by the single crystal X-ray method. Analysing the IR spectra of both compounds it has been found that the complex $[Zn(tch)_3]^{2+}$ cation and $[ZnCl_4]^{2-}$ anion are preserved after crystal decomposition. Vibrational spectra of the obtained substances were interpreted with the assistance of DFT calculations and metal isotope as well as deuterium replacement.
© 2007 Elsevier Ltd. All rights reserved.

Keywords: 2-Thiophenecarboxylic hydrazide; 2-Theonylhydrazine; Zinc complex; Crystal structure; Vibrational spectra; Metal isotope effect

1. Introduction

The biological activity of the 2-thiophene moiety has been widely recognized and practically applied in several drugs [1–3], herbicides [4] and fungicides [5,6]. Among them, there are also thiophenecarboxylic hydrazides which have been tested for antituberculous activity [7,8]. The metal coordination abilities of the mentioned hydrazides and the enhancement of biological activity observed for similar substances upon their metal coordination [9] have stimulated the search for new complexes, frequently with metal ions of high biological importance. The solid state complexes of the title ligand, 2-thiophenecarboxylic hydrazide (tch) and some d-electron metal ions were first reported by Singh et al. [10]. Employing elemental analyses, magnetic, spectroscopic measurements and selectively X-ray powder diffraction studies, these authors proposed the structures of seventeen compounds including a zinc(II) complex of $[ZnCl_2(tch)]$ composition and with a $ZnCl_2NO$ coordination sphere. Based on the preparation procedure described in this article, we have repeated the Zn(II) – tch synthesis and found that unstable monocrystals were obtained at the first step. Thus, we attempted to obtain the full X-ray structure of these monocrystals and propose the structure of its decomposition product, applying elemental analysis and IR spectroscopy. The interpretation of vibrational spectra was enhanced by isotope substitution and DFT calculations.

* Corresponding author. Tel./fax: +48 71 22 4330.
E-mail address: piotr.drozdzewski@pwr.wroc.pl (P. Drożdżewski).

0277-5387/$ - see front matter © 2007 Elsevier Ltd. All rights reserved.
doi:10.1016/j.poly.2007.01.027

2. Experimental

2.1. Preparation of the $[Zn(tch)_3][ZnCl_4]\cdot 2EtOH$ and $[Zn(tch)_3][ZnCl_4]$ complexes

The tch ligand (2-thiophenecarboxylic hydrazide) was purchased from Sigma Aldrich Chemical Co. The metal salt and solvent used were of analytical grade.

The complex synthesis was carried out according to the procedure described by Singh et al. [10], but a different product was obtained. An ethanolic solution of the ligand (0.05 mmol/2 cm^3) was mixed with 0.05 mmol $ZnCl_2$ dissolved in 1.5 cm^3 of the same solvent. The mixture was stored for two days at about 5 °C in a capped vial. Microscope observation of the obtained colourless monocrystals of $[Zn(tch)_3][ZnCl_4]\cdot 2EtOH$ revealed their partial decomposition in air, monitored by loss of transparency. Elemental analysis (given below) of the decomposition product suggested the escape of the solvent for the above process, leading to $[Zn(tch)_3][ZnCl_4]$.

Anal. Calc. for $C_{15}H_{18}N_6O_3S_3Cl_4Zn_2$: C, 25.77; H, 2.60; N, 12.02; S, 13.76. Found: C, 25.18; H, 2.49; N, 11.65; S, 13.84%. M.p. 197–202 °C.

The same complexes were also obtained for 2:3 metal:tch stoichiometry.

2.2. Preparation of isotopically substituted complexes

The ^{64}Zn–^{68}Zn labelled analogues were prepared according to the procedure for $[Zn(tch)_3][ZnCl_4]$ complexes of natural abundance, presented above.

The deuterated $[Zn(tch)_3][ZnCl_4]$ complex was synthesised using EtOD solutions of deuterated tch-ligand and anhydrous $ZnCl_2$. The ligand was previously deuterated by threefold recrystallization from D_2O.

2.3. Spectral measurements

Samples as Nujol mulls sandwiched between polyethylene plates were measured on a Perkin-Elmer FTIR 2000 spectrometer with 0.5 resolution and 200 scans applied for far-IR data acquisition. Middle-IR spectra were measured with 2 cm^{-1} resolution on a Perkin–Elmer FTIR 1600 instrument with the sample as a KBr pellet for $[Zn(tch)_3][ZnCl_4]$ powder and as Nujol or hexachlorobutadiene suspensions of $[Zn(tch)_3][ZnCl_4]\cdot 2EtOH$.

The Raman scattering was collected on a T64000 Jobin-Yvon instrument (0.5 cm^{-1} resolution) applying a 514.5 nm excitation of power below 100 mW, provided by an Ar–Kr laser. For better signal-to-noise ratio 300 scans were collected and averaged.

2.4. X-ray structure determination of $[Zn(tch)_3][ZnCl_4]\cdot 2EtOH$

The X-ray data were collected on a KUMA KM4CCD diffractometer system with Mo Kα radiation ($\lambda =$ 0.71073 Å). The structure was solved by the direct method option using the SHELXS 97 program [11] and developed using least-squares refinement and Fourier difference synthesis applying the SHELXL 97 software [12]. The thiophene rings in two crystallographically different ligand forms were disordered and modelled using two sets of positions. For this procedure, the ring distances and angles were restrained to constant values and the occupancy of two alternate orientations was constrained to unity. The refined occupancy was 0.762(6) and 0.238(6) for the ligand with the S1 atom and 0.882(7) and 0.118(7) for the ligand with the S2 atom. The hydrogen atoms were placed in geometrically calculated positions. Crystallographic parameters and structure refinement are summarized in Table 1. Selected crystal parameters were calculated employing the PARST 97 program [13], whereas all crystal structures were drawn with help of ORTEP 3 [14].

Table 1
Crystal data and structure refinement for $[Zn(tch)_3][ZnCl_4]\cdot 2EtOH$

Empirical formula	$C_{19}H_{30}Cl_4N_6O_5S_3Zn_2$
Formula weight	791.21
Temperature (K)	100(2)
Wavelength (Å)	0.71073
Crystal system	monoclinic
Space group	$P2(1)/n$
Unit cell dimensions	
a (Å)	15.110(4)
b (Å)	9.902(3)
c (Å)	20.768(5)
β (°)	90.50(3)
Volume (Å^3)	3107.2(15)
Z	4
D_{calc} (Mg/m^3)	1.691
Absorption coefficient (mm^{-1})	2.130
$F(000)$	1608
Crystal size (mm)	$0.5\times 0.04\times 0.03$
Θ Range for data collection (°)	3.25–28.53
Index ranges	$-19\leqslant h\leqslant 19$, $-13\leqslant k\leqslant 12$, $-24\leqslant l\leqslant 26$
Reflections collected/unique [R_{int}]	18 583/7247 [0.1135]
Refinement method	full-matrix least-squares on F^2
Data/restrains/parameters	7247/62/415
Goodness-of-fit on F^2	0.887
Final R indices [$I>2\sigma(I)$]	$R_1 = 0.0687$, $wR_2 = 0.0697$
R indices (all data)	$R_1 = 0.1792$, $wR_2 = 0.0964$
Largest difference in peak and hole (e Å^{-3})	0.547 and −0.482

3. Results and discussion

3.1. Description of the complex ions

In the investigated ionic compound (Fig. 1), both the cation and anion are complex ions, of quasi-octahedral and quasi-tetrahedral structure respectively.

The $[Zn(tch)_3]^{2+}$ cation is build up of a metal ion and three ligand molecules coordinating via amine nitrogen and carbonyl oxygen atoms. The arrangement of the

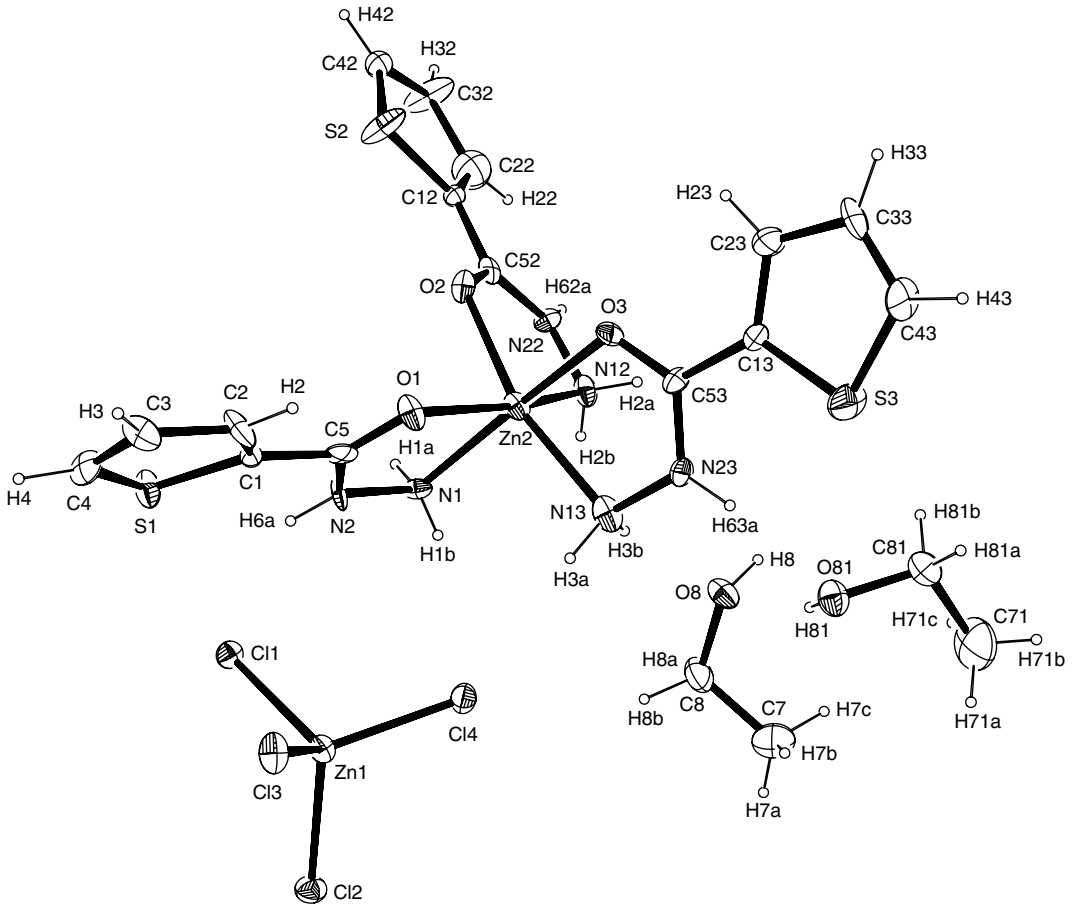


Fig. 1. Molecular structure of $[Zn(tch)_3][ZnCl_4] \cdot 2EtOH$. For better clarity, the thiophene rings of minor occupancy were omitted. Thermal ellipsoids are shown at 50% probability.

ligands around the central atom results in a fac-configuration of the $[ZnN_3O_3]$ centre. The distortion of the metal environment from an ideal octahedron is observed for coordination bond lengths as well as for the angles between them. As could be calculated from the structural data presented in Table 2, the average Zn–O distance (2.097(4) Å) is 0.075 Å shorter than that obtained for Zn–N bonds (2.172(6) Å). However, these distances vary from 2.069(4) Å (Zn2–O3) to 2.200(6) Å (Zn–N12).

The O–Zn–N angles located inside the chelate rings are about 77°, which is far from the right angle expected for an ideal octahedron and it is definitely due to the internal ring strain. In contrast, all angles between bonds belonging to different rings are above 90°, from 91.2(2)° to 101.2(2)°. Such an arrangement of the coordination bonds precludes any symmetry elements for the metal coordination sphere.

The chelate rings are close to planar. The most deviated atoms are the nitrogen atoms of the amine groups. These atoms are from 0.109(6) (N1 atom) to 0.142(6) Å (N12 atom) displaced from the respective best planes calculated for remaining chelate ring skeletal atoms, which are displaced by less than 0.025 Å. The orientations of the thiophene rings are more complicated. In ligands 1 and 2 (those with O1 and O2 atoms) the discussed units are structurally disordered with higher occupancies equal to 0.762(6) and 0.882(7), respectively. These positions will be discussed first. The thiophene rings are oriented almost parallel to the discussed chelate rings. The dihedral angles between the mentioned best planes of the chelate rings and thiophene rings are 14.2(2)°, 2.9(2)° and 7.6(2)° for ligands with O1, O2 and O3 atoms, respectively. Two thiophene rings of minor occupancy form dihedral angles of 5.2(1.3)° and 17.6(9)° with the corresponding major occupancy rings.

It is surprising that the S1 and S3 atoms are *trans*-oriented with respect to the O1 and O3 atoms, which is not typical for used ligand, where an attractive force between S1 and O1 atoms, together with repulsion of O1 and π electrons of the C1═C2 bond results mostly in a *cis*-configuration [15]. Such a configuration appears for the S2 and O2 atoms and also for the minor occupancy thiophene ring in ligand 1. In contrast, the minor occupancy thiophene ring in ligand 2 is *trans*-oriented. An explanation of the above problem will be proposed latter.

The structure of complex $[ZnCl_4]^{2-}$ ion is very close to tetrahedral. The observed Zn–Cl bond lengths differ less

Table 2
Selected bond lengths (Å) and angles (°) for $[Zn(tch)_3][ZnCl_4]\cdot 2EtOH$

Bonds	(Å)	Angles	(°)
Zn2 environment			
Zn2–N1	2.159(6)	N1–Zn2–O1	77.1(2)
Zn2–O1	2.115(4)	N12–Zn2–O2	76.9(2)
Zn2–N12	2.200(6)	N13–Zn2–O3	78.1(2)
Zn2–O2	2.108(4)	N1–Zn2–O3	170.7(2)
Zn2–N13	2.158(6)	N12–Zn2–O1	162.5(2)
Zn2–O3	2.069(4)	N13–Zn2–O2	164.6(2)
Ligand 1			
N1–N2	1.413(7)	Zn2–N1–N2	108.5(4)
N2–C5	1.350(7)	Zn2–O1–C5	114.8(4)
O1–C5	1.238(7)	N1–N2–C5	117.9(5)
C5–C1	1.499(10)	O1–C5–N2	121.3(6)
C1–C2[a]	1.363(9)	O1–C5–C1	122.4(6)
C2–C3[a]	1.416(9)	C5–C1–S1	124.1(6)
C3–C4[a]	1.347(8)	C1–S1–C4[a]	91.2(4)
C1–S1[a]	1.703(8)	S1–C1–C2[a]	111.4(6)
C4–S1[a]	1.704(8)	S1–C4–C3[a]	113.3(6)
		C1–C2–C3[a]	113.1(7)
		C2–C3–C4[a]	110.9(7)
Ligand 2			
N12–N22	1.400(7)	Zn2–N12–N22	107.3(4)
N22–C52	1.330(7)	Zn2–O2–C52	114.4(4)
O2–C52	1.258(7)	N12–N22–C52	119.1(5)
C52–C12	1.476(9)	O2–C52–N22	121.7(6)
		O2–C52–C12	120.3(6)
		C52–C12–S2	118.2(5)
Ligand 3			
N13–N23	1.428(7)	Zn2–N13–N23	107.1(4)
N23–C53	1.338(7)	Zn2–O3–C53	114.8(4)
O3–C53	1.236(7)	N13–N23–C53	117.4(5)
C53–C13	1.468(8)	O3–C53–N23	122.3(6)
C13–C23	1.368(8)	O3–C53–C13	121.5(6)
C23–C33	1.410(9)	C53–C13–S3	123.4(5)
C33–C43	1.340(9)	C43–S3–C13	91.2(3)
C13–S3	1.725(6)	S3–C13–C23	110.3(5)
C43–S3	1.691(7)	S3–C43–C33	113.7(5)
		C13–C23–C33	113.3(7)
		C23–C33–C43	111.4(7)
Zn1 environment			
Zn1–Cl1	2.3107(17)	Cl1–Zn1–Cl3	107.6(1)
Zn1–Cl2	2.2809(18)	Cl3–Zn1–Cl4	116.2(1)
Zn1–Cl3	2.2422(18)	Cl1–Zn1–Cl4	106.5(1)
Zn1–Cl4	2.2667(18)		
EtOH			
C7–C8	1.515(11)	O8–C8–C7	108.6(6)
C8–O8	1.452(7)	O81–C81–C71	110.7(6)
C71–C81	1.505(11)		
C81–O81	1.434(7)		

[a] The corresponding bond lengths and angles of the thiophene ring belonging to ligand 2 are similar (within theirs e.s.d.) to that of ligand 1.

than 2%, the Cl–Zn–Cl angles are in the 106.5(1)–116.2 (1)° range.

3.2. Crystal packing

All structural units, namely both complex ions and ethanol molecules, are arranged in stacks parallel to the [0 1 0] direction. In the perpendicular direction, these units are organized into layers parallel to the (1 0 1) plane. Each layer built of $[ZnCl_4]^{2-}$ anions and accompanied ethanol molecules is surrounded by two parallel layers of $[Zn(tch)_3]^{2+}$ cations. The external parts of such a sandwich-like layer are occupied exclusively by thiophene rings. However, the structure projection normal to these rings shows that there is no ''face-to-face'' or ''offset'' π-stacking [16]. The shortest S–S distance is 3.59 Å, which excludes any attractive interactions between thiophene rings. More probable are weak repulsive forces between sulfur atoms carrying small positive charges. Thus, the interactions between the mentioned sandwich layers are mainly of van der Waals nature.

The most important feature for the above structural arrangement are hydrogen bonds between hydrazine groups and tetrachlorozincate ions. Each $[ZnCl_4]^{2-}$ ion interacts with three $[Zn(tch)_3]^{2+}$ ions and two ethanol molecules, as has been presented in Fig. 2. Complex cations are attracted to chlorine atoms only via N–H···Cl systems which provide at least two contacts between the $[ZnCl_4]^{2-}$ anion and one of the three ligands present in each complex cation. In one case (of three $[Zn(tch)_3]^{2+}$ ions interacting with a $[ZnCl_4]^{2-}$ ion), a third hydrogen bond has been found between H1a and Cl2 atoms. Among two ethanol molecules found in the vicinity of $[ZnCl_4]^{2-}$, one is bonded via two interactions between its O–H group and two chlorine (Cl2, Cl3) atoms. The second EtOH molecule is oriented such that one hydrogen atom of the methyl group points to the Cl4 atom at a distance of 2.841(2) Å, which is in the range of C–H···Cl hydrogen bonds [17].

The complete set of strong hydrogen contacts formed by each $[Zn(tch)_3]^{2+}$ ion has been presented in Fig. 3. This figure shows that ligands 1 and 2 (those with O1 and O2 atoms) interact only with Cl acceptors, whereas ligand 3 forms two hydrogen bonds with two ethanol oxygen acceptors. The carbonyl groups of tch ligands do not form hydrogen bonds with N–H groups of neighbour cations. This is due to competition between possible acceptors. The negatively charged $[ZnCl_4]^{2-}$ ions are much stronger acceptors than carbonyl groups whose electron density have been lowered by metal coordination. In the resultant crystal arrangement, the carbonyl groups are neighbours of thiophene rings and ethanol methyl groups only. Weak hydrogen interactions between these subunits and carbonyl oxygen atoms may be taken into account, as has been done in Table 3, presenting structural details of hydrogen bonds.

Close inspection of the crystal structure and possible interactions may explain the mentioned problem of *trans* orientation of thiophene sulfur atoms with respect to carbonyl groups. In ligands 2 and 3, the internal S2···O2 and S3···N23 distances are comparable, being 2.945(5) and 3.025(5) Å, respectively, which suggests that respective interactions will be of comparable strength. However, the position of the S3 atom is additionally stabilized by two intermolecular interactions, namely S3···O81 (3.462(5) Å) and S3···Cl4^{v} (3.335(3) Å). A similar *trans* position of the S1 atom is analogously stabilized by S1···Cl1 = 3.913(3) Å and S1··· N22 = 3.513(6) Å interactions (N22 at x, $y-1$,

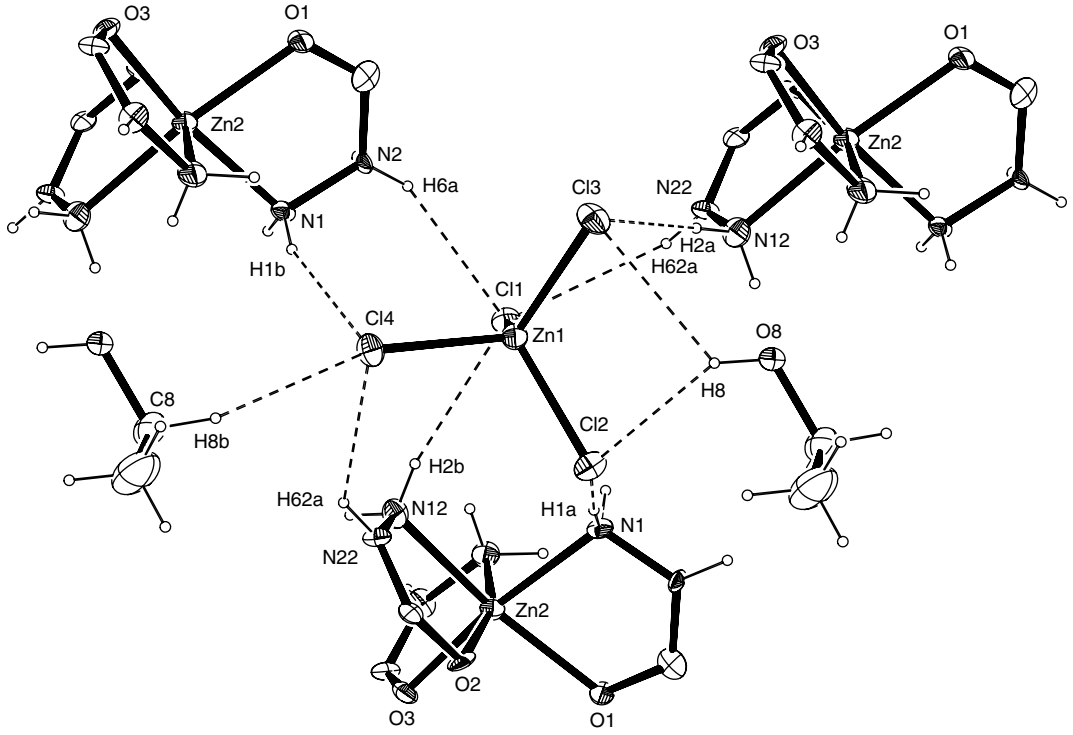


Fig. 2. Hydrogen bonding system around the $[ZnCl_4]^{2-}$ ion. The thiophene rings were omitted.

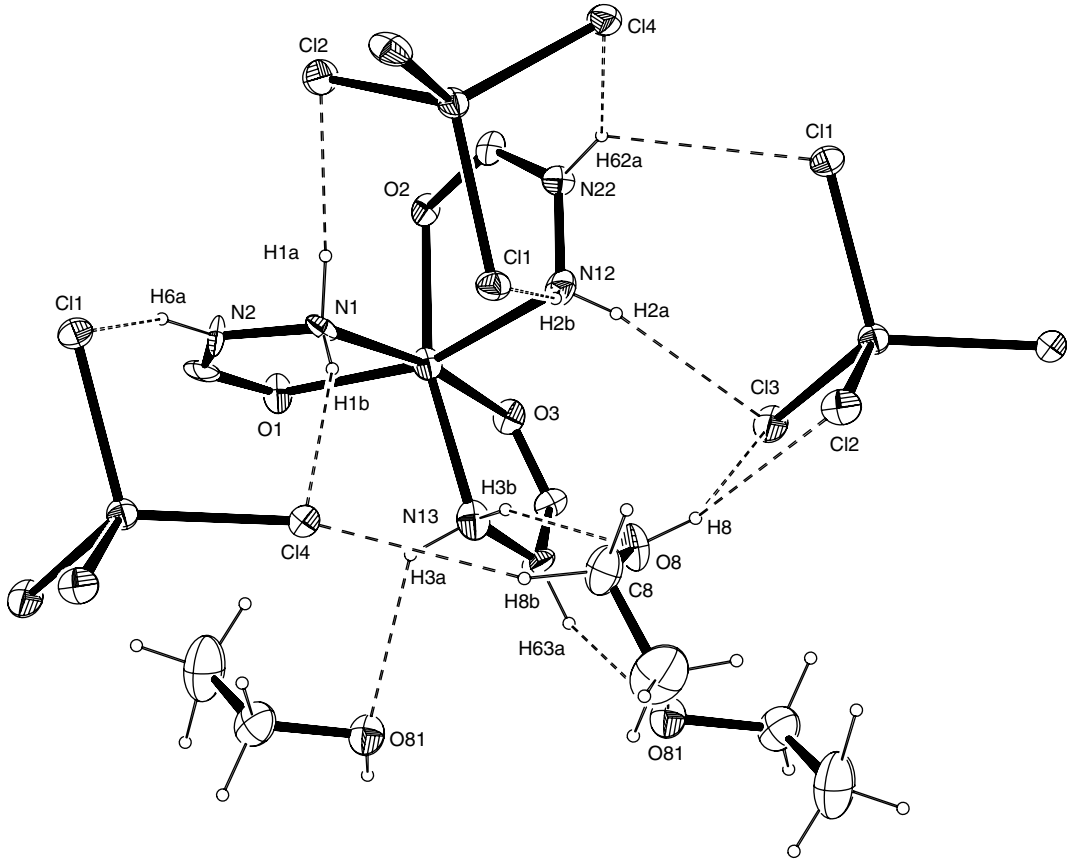


Fig. 3. Hydrogen bonding system around the $[Zn(tch)_3]^{2+}$ ion. The thiophene rings were omitted.

Table 3
Short N/O/C–H···Cl/O contacts (Å, °) with e.s.d.'s in parentheses

Bond	D–H	D···A	H···A	D–H···A
[Zn(tch)$_3$]$^{2+}$···[ZnCl$_4$]$^{2-}$				
N1–H1a···Cl2^{i}	0.95(6)	3.290(6)	2.34(6)	176(4)
N1–H1b···Cl4	0.77(6)	3.219(6)	2.48(6)	161(6)
N2–H6a···Cl1	0.88(1)	3.291(5)	2.52(0)	146(0)
N12–H2a···Cl3^{iii}	0.81(6)	3.284(6)	2.48(6)	169(6)
N12–H2b···Cl1^{i}	0.82(6)	3.370(6)	2.58(6)	162(6)
N22–H62a···Cl4^{i}	0.88(1)	3.436(5)	2.75(0)	136(0)
N22–H62a···Cl1^{iii}	0.88(1)	3.508(5)	2.90(0)	128(0)
[Zn(tch)$_3$]$^{2+}$···EtOH				
N13–H3a···O81^{v}	0.94(6)	3.035(7)	2.35(6)	129(5)
N13–H3b···O8	0.76(6)	2.913(7)	2.22(6)	154(6)
N23–H63a···O81	0.88(0)	2.870(7)	2.11(0)	145(0)
EtOH···ZnCl$_4$				
O8–H8···Cl2^{iii}	0.86(1)	3.278(5)	2.55(5)	143(5)
O8–H8···Cl3^{iii}	0.86(1)	3.428(5)	2.84(5)	127(5)
C8–H8b···Cl4	0.99(1)	3.772(7)	2.84(0)	157(0)
EtOH···EtOH				
O81–H81···O8	0.87(4)	2.857(6)	2.04(5)	158(3)
Thiophene/CH$_3$···C=O				
C3–H3···O1^{ii}	0.95(1)	3.520(15)	2.60(0)	163(1)
C33–H33···O2^{iv}	0.95(1)	3.703(9)	2.80(0)	159(0)
C42–H42···Cl4^{vi}	0.95(1)	3.565(8)	2.88(0)	130(1)
C43–H43···Cl2^{v}	0.95(1)	3.848(8)	2.98(0)	152(1)
C71–H71a···O1^{v}	1.00(8)	3.661(11)	2.73(8)	156(6)

Equivalent positions: (i) $-x+1/2+1, y+1/2, -z+1/2+1$; (ii) $-x+1/2, y-1/2, -z+1/2+1$; (iii) $x, y+1, z$; (iv) $-x+1/2, y+1/2, -z+1/2+1$; (v) $-x+1, -y+1, -z+2$.

z). For the atom S2, being at a *cis* position, only one weaker interaction with the Cl2 atom at $(x+1/2, -y+1/2, z+1/2)$ has been found at a distance less than 4.0 Å (S2···Cl2 = 3.816(3) Å). Thus, the *cis* configuration is forced here by the S1···O2 = 2.945(5) Å interaction.

The [Zn(tch)$_3$][ZnCl$_4$] · 2EtOH crystals are not stable in air, gradually losing the solvent molecules. Beside the intermolecular forces, this property is also due to the location of the ethanol molecules in less densely packed $[ZnCl_4]^{2-}$ layers, which allows for EtOH migration without destroying the main crystal frame.

3.3. Quantum calculations

The geometry optimization of $[Zn(tch)_3]^{2+}$ and $[ZnCl_4]^{2-}$ ions and subsequent computation of their normal vibrations were performed at the DFT level, employing the B3LYP functional [18] and LANL2DZ [19] basis set with d-polarization functions added to C, N, O, S and Cl atoms.

The optimized structures of both complex ions are close to those found by the X-ray method. The calculated Zn–Cl bonds lengths are about 0.1 Å longer than those observed. Similar differences are found between calculated and observed coordination bond lengths in the $[Zn(tch)_3]^{2+}$ cation. Calculated Zn–N bonds are longer than those observed, whereas the Zn–O bonds are shorter. The remain-

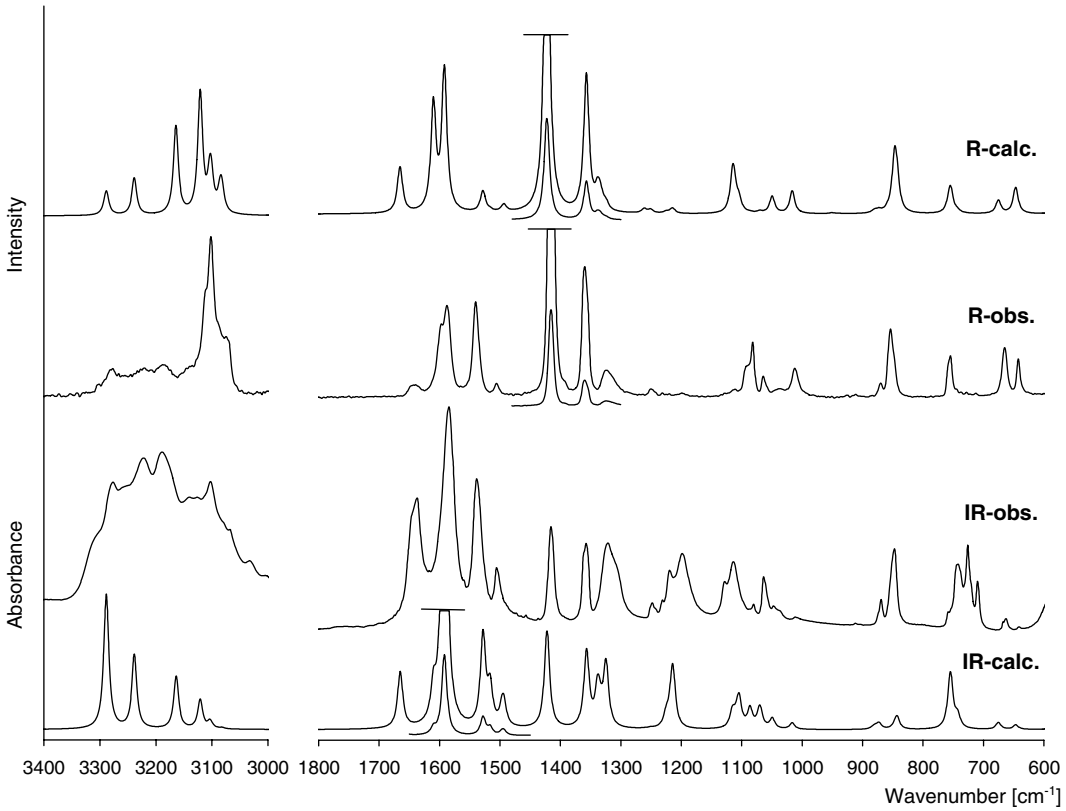


Fig. 4. Observed and DFT predicted vibrational spectra of [Zn(tch)$_3$][ZnCl$_4$]. Partially scaled frequencies (listed in Table 4) were used for the preparation of the theoretical spectra.

ing calculated skeletal bonds are mostly elongated, but their lengths deviate less than 0.05 Å from the observed values. Normal vibrations were computed applying the harmonic oscillator approximation. All computations were made using the GAUSSIAN 03 program [20]. The computation of theoretical spectra (with 5 cm^{-1} half-band-width) and animation of normal vibrations used for their description were performed by the CHEMCRAFT program [21]. For selected parts of the computed $[Zn(tch)_3]^{2+}$ spectra, the frequency scaling factors were applied as follows: 0.915 for stretching vibrations of NH and NH_2 groups, 0.955 for stretching C–H vibrations and 0.98 for normal vibrations of frequencies calculated between 1750 and 1350 cm^{-1}. For the scaled vibrations, the root-mean-square (RMS) of calculated–observed frequency correlation equals 15 cm^{-1}. Vibrations resulting from out-of-plane motions of NH_2 and NH groups were individually scaled to fit the observed positions of bands located unambiguously by deuterium substitution. The remaining vibrations were left unscaled, because they show a RMS of 13 cm^{-1}, which is within the range given in the literature for B3LYP theory level [22].

3.4. Vibrational spectroscopy

The structural resemblance of $[Zn(tch)_3][ZnCl_4] \cdot 2EtOH$ and its spontaneous decomposition product, $[Zn(tch)_3][ZnCl_4]$, is very well documented by their respective IR spectra, being practically the same in the far-IR region and exhibiting for the former compound only two additional mid-IR bands at 3490 and 1038 cm^{-1}, resulting from ethanol O–H and C–O stretching vibrations. This experiment confirms that both complex ions are preserved during decomposition. Since the latter compound is much more stable, its Raman and IR spectra were measured and will be further discussed.

The $[ZnCl_4]^{2-}$ anion vibrations were located at 296, 279 cm^{-1} (Raman) and 297, 145 cm^{-1} (IR) and well correspond to A_1 and T_2 species listed in the literature at 288, 298 and 130 cm^{-1} [23]. The attribution of the 297 cm^{-1} band was additionally confirmed by its 2.0 cm^{-1} metal isotope shift. For the second T_2 vibration, such a shift was not observed. Preliminary DFT calculations made for $[ZnCl_4]^{2-}$ revealed that this shift should be about four times smaller than the mentioned one, thus its detection may be difficult. The Raman active E mode, expected between 120 and 80 cm^{-1}, was not observed due to Rayleigh scattering.

The bands remaining after identification of $[ZnCl_4]^{2-}$ modes are generated by $[Zn(tch)_3]^{2+}$ vibrations. If an idealized C_{3v} symmetry is applied to the quasi-octahedral cation of *fac* configuration, the corresponding vibrations are classified into $A_1 + E$ irreducible representations. As results from the crystallographic data of $[Zn(tch)_3][ZnCl_4] \cdot 2EtOH$, $[Zn(tch)_3]^{2+}$ shows distortion from ideal C_{3v} symmetry. This distortion may cause the splitting of the degenerated E type vibrations, but it is difficult to evaluate how large this splitting is. In order to answer this question and to get some recognition about the vibrational behavior of the ZnN_3O_3 center and tch ligands, the DFT calculations were carried out for the $[Zn(tch)_3]^{2+}$ cation. Based on computed normal modes, the theoretical IR and Raman spectra were simulated and presented in Figs. 4 and 5, together with the observed ones. It should be emphasized that the observed spectra in Fig. 5 are the superposition of $[Zn(tch)_3]^{2+}$ and $[ZnCl_4]^{2-}$ absorptions, whereas the computed spectra are exclusively for the $[Zn(tch)_3]^{2+}$ cation. For this reason, the observed $[ZnCl_4]^{2-}$ bands were marked with asterisks and the corresponding $[Zn(tch)_3]^{2+}$ bands were joined with broken lines. Respective band wavenumbers are listed in Table 4, together with mode descriptions based on animation of computed normal vibrations. The calculations revealed that the mentioned splitting of the E modes is small and does not exceeds 5 cm^{-1}, which produces single peaks in the computed spectra. The wavenumbers of accompanying A_1 modes are also frequently close to the E ones. Thus, in Table 4, the one average frequency is listed if the discussed differences are below 10 cm^{-1}, otherwise two frequencies are typed, corresponding to A_1 and E modes, seen in the simulated spectra as two maxima.

Of most interest are the $[ZnN_3O_3]$ core vibrations. The calculations predict a predominant contribution of coordination bond stretching vibrations in normal modes at 527

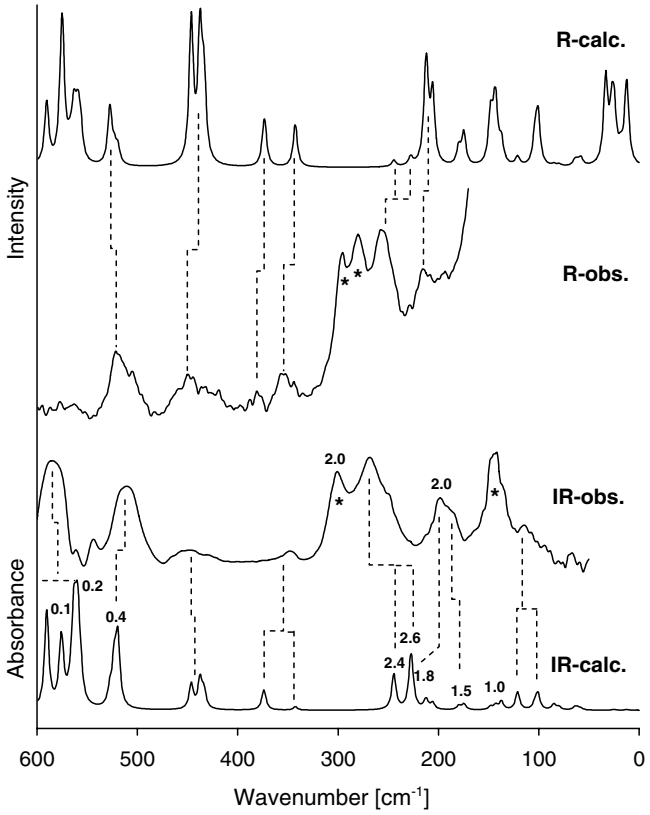


Fig. 5. Observed vibrational spectra of $[Zn(tch)_3][ZnCl_4]$ in the far-IR region, compared with calculated (scaled) spectra of the $[Zn(tch)_3]^{2+}$ cation. Observed bands attributed to $[ZnCl_4]^{2-}$ vibrations are marked with asterisks. The downshifts upon ^{64}Zn–^{68}Zn substitution are listed by the respective band maxima.

Table 4
A selection of observed wavenumbers and DFT computed normal vibrations of the $[Zn(tch)_3]^{2+}$ cation

No.	Band positions (cm^{-1}) of $[Zn(tch)_3][ZnCl_4]$		Normal vibrations of $[Zn(tch)_3]^{2+}$		
			Frequencies (cm^{-1})		Assignment[a]
	IR	R	Calculated	Scaled[b]	
1	3277	3277	3585	3287	ν(NH)
2	3222	3220	3531	3238	$\nu_a(NH_2)$
3	3189	3185	3449	3163	$\nu_s(NH_2)$
4		3110	3268	3121	ν(C–H)
5	3102	3102	3248	3102	ν(C–H)
6		3075	3228	3083	ν(C–H)
7	1637	1639	1708	1665	$\delta(NH_2)$
8	1585	1597, 1587	1651, 1633	1610, 1592	ν(C=O), ν(C1–C5)
9	1539	1540	1567, 1555	1528, 1516	ν_a(C1=C2, C3=C4), ν(C–N), ν(C=O)
10	1506	1505	1533	1495	δ(NH), ν(C–N),
11	1416	1416	1458	1422	ν(C2–C3)
12	1357	1360	1391	1356	ν_s(C1=C2, C3=C4), ν(C1–C5)
13	1321	1324	1339, 1324	1339, 1324	$\rho_t(NH_2)$
14	1310_{sh}	1310_{sh}	1334	1334	ν(C1–C5), δ(NH)
15	1248	1250	1254	1254	δ(C–H)
16	1198	1199	1217	1217	$\rho_w(NH_2)$, ν(N–N)
17	1128, 1114	1128, 1111	1114, 1105	1114, 1105	δ(C–H), $\rho_w(NH_2)$
18	1080, 1064	1081, 1064	1086, 1070	1086, 1070	ν(C2–C3), δ(C–H), $\rho_w(NH_2)$
19	1047, 1035	1038	1050, 1016	1050, 1016	ν(N–N), ν(C–N), ν(C1–S)
20	912	914	947	947	π(C–H)
21	n.o.	n.o.	883, 859	883, 859	π(C–H)
22	869	870	875	875	ν(C4–S), δ_2(T)
23	847	854	844	844	ν_s(C–S–C), δ_2(R)
24	742	754	755	755	ν_a(C–S–C), δ_2(T)
25	n.o.	n.o.	753	753	π(C–H)
26	710	710	743	743	π(C5)
27	663, 641	665, 643	675, 646	675, 646	δ_1(T), ν_s(C–S–C)
28	583	n.o.	476, 463	590, 574	$\rho_r(NH_2)$, π(NH), τ_2(T)
29	583	n.o.	574 (0.1), 558	574 (0.1), 558	τ_2(T), $\rho_r(NH_2)$
30	554	n.o.	397 (0.2), 386	562 (0.2), 546	π(NH), δ_1(R)
31	512	521	527	527	ν_s(Zn–O), δ_1(T), $\rho_r(NH_2)$
32	512	521	521 (0.4)	521 (0.4)	ν_a(Zn–O), δ_1(T)
33	n.o.	n.o.	476, 463_{sh}	476, 463_{sh}	τ_1(T), π(NH)
34	~450	447	446, 435	446, 435	δ_1(R), π(NH)
35	n.o. 346	380. 350	375, 342	375, 342	δ_2(R), δ(S–C–C–O)
36	270	256	244 (2.4), 228 (2.6)	244 (2.4), 228 (2.6)	ν_a(Zn–N)
37	195 (2.0)	192	226 (1.8)	226 (1.8)	ν_s(Zn–N)
38	n.o.	214	209	209	τ_1(R), lib(T)
39	180_{sh}	n.o.	176 (1.5)	176 (1.5)	δ(R–T), ν(Zn–N)
40	n.o.	n.o.	148, 138 (1.0)	148, 138 (1.0)	τ_2(R)
41	117	n.o.	102, 121	102, 121	τ(T–R)
42	n.o.	n.o.	85	85	δ(C–C–S), lib(T)
43	n.o.	n.o.	62	62	lib(T–R)
44	n.o.	n.o.	32, 26	32, 26	lib(L)
45	n.o.	n.o.	13	13	τ(L–L)

Abbreviations: ν, stretching; δ, in-plane bending; τ, torsion; π, out-of-plane bending; ρ_w, wagging; ρ_t, twisting; ρ_r, rocking; lib, librations; T, thiophene ring; R, chelate ring; L, ligand molecule; n.o., not observed; s, symmetric; a, asymmetric with respect to approximate local symmetry. Wavenumber shifts due to ^{64}Zn–^{168}Zn replacement are given in parentheses.

[a] Atomic numbering, given in Fig. 1, was used only when necessary.

[b] Scaling factors applied: 0.915 (vibrations nos. 1–3), 0.955 (4–6), 0.98 (7–12).

(A_1) and 521 cm^{-1} (E) for Zn–O bonds, and at 244, 228 (E) and 226 cm^{-1} (A_1) for Zn–N linkages. In the latter modes, the central atom is significantly displaced, which causes 1.8–2.6 cm^{-1} metal isotope shifts to be predicted for the corresponding theoretical bands. A similar shift was observed for the 195 cm^{-1} IR band, attributed to the ν_s(Zn–N) vibration. The ν_a(Zn–N) vibrations were assigned to the 270 cm^{-1} band of high intensity, enhanced probably by some lattice vibrations. However, this band shows a 12 cm^{-1} downshift upon NH and NH_2 group deuteration, which is typical for $\nu(Zn–NH_2)$ vibrations [24]. All ν(Zn–O) modes were assigned to a broad absorption with a maximum at 512 cm^{-1} and to a Raman transition at 521 cm^{-1}. The 512 cm^{-1} band shifts to 503 cm^{-1} upon H/D replacement, which is due to a small contribution of a $\rho_r(NH_2)$ vibration in this absorption. A metal isotope

shift was not observed for this band, which is probably caused by its small value, predicted as 0.4 cm^{-1}. Among four deformation modes expected for each five-membered chelate ring, only three were assigned to bands, at about 450, 380–350 and 214 cm^{-1} (Raman). The first δ_1(R) "in-plane" motion may roughly be described as C5–N2 bond displacement toward the zinc atom. In the second δ_2(R) mode, the same bond is moving parallel to its direction. The "out-of-plane" bending along the N2, O1 line characterizes the τ_1(R) mode, whereas similar bending along the N1, O1 direction is observed for the τ_2(R) vibration, overlapped in the IR spectrum by the $[ZnCl_4]^{2-}$ absorption.

Bands observed above 600 cm^{-1} result from the so-called "ligand vibrations", further presented for one example ligand with the lowest atom numbers. The stretching vibrations of C5–O1, C5–N2, N1–N2 bonds, being members of the chelate ring, contribute mainly in 1585, 1506 and 1047, 1035 cm^{-1} absorptions. The vibration of the C1–C5 bond, linking the chelate and thiophene rings, were computed at 1334 cm^{-1} and correlated with a 1310 cm^{-1} shoulder. The vibrations of the thiophene moiety may be compared with those of free thiophene [25], despite the fact, that in the present compound the thiophene ring is attached to the rest of the ligand at the C1 atom. The most visible difference concerns the splitting of the asymmetric (local symmetry) C–S bond vibrations, probably due to the mentioned ring attachment. In addition to typical ν_a(C–S–C) modes (coupled with ring deformation) calculated at about 755 cm^{-1}, the separate stretching vibrations of particular C–S bonds were predicted at 1016 cm^{-1} (C1–S) and 875 cm^{-1} (C4–S). The ligands also exhibit several normal modes, where thiophene rings librate (lib(T)), or whole ligands move (lib(L)), but these modes are of very low frequencies, being mostly below the observation limit.

Supplementary material

CCDC 627178 contains the supplementary crystallographic data for this paper. These data can be obtained free of charge via http://www.ccdc.cam.ac.uk/conts/retrieving.html, or from the Cambridge Crystallographic Data Centre, 12 Union Road, Cambridge CB2 1EZ, UK; fax: (+44) 1223-336-033; or e-mail: deposit@ccdc.cam.ac.uk.

Acknowledgements

The authors are grateful to the Poznań Supercomputing Center for computational conveniences.

References

[1] F. Leonard, U.V. Solmssen, J. Am. Chem. Soc. 70 (6) (1948) 2064.
[2] H. Staehelin, Eur. J. Cancer 6 (4) (1970) 303.
[3] V.S. Fang, C. Minkin, P. Goldhaber, Science 172 (3979) (1971) 163.
[4] L.F. Friesen, A.G. Nelson, R.C. Van Acker, Agron. J. 95 (5) (2003) 1342.
[5] R. Fischer, N. Lui, S. Dutzmann, G. Haenssler, Ger. Offen. Pat. 19649093 (1998) (CA 129, P24482).
[6] P. Plath, K. Eicken, W. Rohr, B. Zeeh, E.H. Pommer, Ger. Offen. Pat. 2 854 598 (1980) (CA 94 P15740f).
[7] R.I. Eltzer, A.D. Lewis, F.H. McMillan, J.D. Genzer, F. Leonord, J.A. King, J. Am. Pharm. Assoc. 42 (1953) 594.
[8] H.L. Yale, K. Losse, J. Martins, M. Holsing, F.M. Perry, J. Bernstein, J. Am. Chem. Soc. 75 (8) (1953) 1933.
[9] Z. Chohan, S.K.A. Sherazi, M. Praveen, Met.-Based Drugs 5 (6) (1998) 355.
[10] B. Singh, R.N. Singh, R.C. Aggarwal, Synth. React. Inorg. Met.-Org. Chem. 15 (7) (1985) 853.
[11] G.M. Sheldrick, SHELXS 97, Program for Solution of Crystal Structures, University of Göttingen, Göttingen, Germany, 1977.
[12] G.M. Sheldrick, SHELXL 97, Program for Crystal Structures Refinement, University of Göttingen, Göttingen, Germany, 1977.
[13] M. Nardelli, J. Appl. Cryst. 28 (1995) 659.
[14] L.J. Farrugia, J. Appl. Cryst. 30 (1997) 565.
[15] M.C. Fournié-Zaluski, B. Roques, Tetrahedron Lett. 56 (1970) 4909.
[16] C. Janiak, J. Chem. Soc., Dalton Trans. (2000) 3885.
[17] C. Janiak, T.G. Scharmann, Polyhedron 22 (8) (2003) 1123.
[18] A.D. Becke, J. Chem. Phys. 104 (1996) 1040.
[19] A.D. Hay, W.R. Wadt, J. Chem. Phys. 82 (1985) 270.
[20] M.J. Frisch, G.W. Trucks, H.B. Schlegel, G.E. Scuseria, M.A. Robb, J.R. Cheeseman, J.A. Montgomery Jr., T. Vreven, K.N. Kudin, J.C. Burant, J.M. Millam, S.S. Iyengar, J. Tomasi, V. Barone, B. Mennucci, M. Cossi, G. Scalmani, N. Rega, G.A. Petersson, H. Nakatsuji, M. Hada, M. Ehara, K. Toyota, R. Fukuda, J. Hasegawa, M. Ishida, T. Nakajima, Y. Honda, O. Kitao, H. Nakai, M. Klene, X. Li, J.E. Knox, H.P. Hratchian, J.B. Cross, C. Adamo, J. Jaramillo, R. Gomperts, R.E. Stratmann, O. Yazyev, A.J. Austin, R. Cammi, C. Pomelli, J.W. Ochterski, P.Y. Ayala, K. Morokuma, G.A. Voth, P. Salvador, J.J. Dannenberg, V.G. Zakrzewski, S. Dapprich, A.D. Daniels, M.C. Strain, O. Farkas, D.K. Malick, A.D. Rabuck, K. Raghavachari, J.B. Foresman, J.V. Ortiz, Q. Cui, A.G. Baboul, S. Clifford, J. Cioslowski, B.B. Stefanov, G. Liu, A. Liashenko, P. Piskorz, I. Komaromi, R.L. Martin, D.J. Fox, T. Keith, M.A. Al-Laham, C.Y. Peng, A. Nanayakkara, M. Challacombe, P.M.W. Gill, B. Johnson, W. Chen, M.W. Wong, C. Gonzalez, J.A. Pople, GAUSSIAN 03, Revision C.02, Gaussian, Inc., Wallingford, CT, 2004.
[21] G.A. Zhurko, D.A. Zhurko, http://www.chemcraftprog.com.
[22] X. Zhou, Ch.J.M. Wheeless, R. Liu, Vibr. Spectrosc. 12 (1996) 53.
[23] J.S. Avery, C.D. Burbridge, D.M.L. Goodgame, Spectrochim. Acta A 24 (1968) 1721.
[24] J.B. Kincaid, K. Nakamoto, Spectrochim. Acta A 32 (1967) 277.
[25] J.S. Kwiatkowski, J. Leszczyński, I. Teca, J. Mol. Struct. 436–437 (1997) 451.

Available online at www.sciencedirect.com
ScienceDirect
Polyhedron 26 (2007) 2795–2802
POLYHEDRON
www.elsevier.com/locate/poly

Synthesis and characterization of new macrocyclic Schiff base derived from 2,6-diaminopyridine and 1,7-bis(2-formylphenyl)-1,4,7-trioxaheptane and its Cu(II), Ni(II), Pb(II), Co(III) and La(III) complexes

Salih Ilhan [a], Hamdi Temel [a,*], Ismail Yilmaz [b], Memet Şekerci [c]

[a] *Dicle University, Faculty of Education, Department of Chemistry, 21280 Diyarbakır, Turkey*
[b] *İstanbul Technical University, Faculty of Arts and Sciences, Department of Chemistry, 23169İstanbul, Turkey*
[c] *Fırat University, Faculty of Arts and Sciences, Department of Chemistry, 23169 Elaziğ, Turkey*

Received 12 December 2006; accepted 18 January 2007
Available online 25 January 2007

Abstract

A new macrocyclic ligand, 1,3,5-triaza-2,4:7,8:16,17-tribenzo-9,12,15-trioxacyclooktadeca-1,5-dien (L) was synthesized by reaction of 2,6-diaminopyridine and 1,7-bis(2-formylphenyl)-1,4,7-trioxaheptane. Then, its Cu(II), Ni(II), Pb(II), Co(III) and La(III) complexes were synthesized by template effect by reaction of 2,6-diaminopyridine and 1,7-bis(2-formylphenyl)-1,4,7-trioxaheptane and $Cu(NO_3)_2 \cdot 3H_2O$, $Ni(NO_3)_2 \cdot 6H_2O$, $Pb(NO_3)_2$, $Co(NO_3)_2 \cdot 6H_2O$, $La(NO_3)_3 \cdot 6H_2O$, respectively. The ligand and its metal complexes have been characterized by elemental analysis, IR, ^1H and ^{13}C NMR, UV–Vis spectra, magnetic susceptibility, thermal gravimetric analysis, conductivity measurements, mass spectra and cyclic voltammetry. All complexes are diamagnetic and Cu(II) complex is binuclear. The Co(II) was oxidized to Co(III). The comparative electrochemical studies show that the nickel complex exhibited a quasi-reversible one-electron reduction process while copper and cobalt complexes gave irreversible reduction processes in DMSO solution.
© 2007 Elsevier Ltd. All rights reserved.

Keywords: Macrocyclic Schiff base; Macrocyclic Schiff base complexes; 2,6-Diaminopyridine and 1,7-bis(2-formylphenyl)-1,4,7-trioxaheptane

1. Introduction

The field of the macrocyclic chemistry of metals is developing very rapidly because of its applications [1,2] and importance in the area of coordination chemistry [3]. Studies on complexes of Schiff-base macrocyclic ligands with different size, and number and donor atoms for coordination with a variety of metal centers have been published [4,5]. Many transition metal ions in living systems work as enzymes or carriers in a macrocyclic ligand environment; meaningful research in this direction might generate simple models for biologically occurring metaloenzymes [6,7], and thus help in further understanding biological systems. The development of the field of bioinorganic chemistry has been another important factor in spurring the growth in interest in macrocyclic compounds [8]. The formation of macrocyclic complexes depends significantly on the dimension of internal cavity, on the rigidity of macrocycles, on the nature of its donor atoms and on the complexing properties of the anion involved in the coordination [9]. The interest in such species stems from the application of these complexes ranging from modelling the active sites of many metaloenzymes, to hosting and carrying small molecules or catalysis [10]. The development of the field of bioinorganic chemistry has been another important factor in spurring the growth in interest in macrocyclic compounds [11]. An effective way to use the molecular recognition capability of macrocycles for metal ion separation is to incorporate such ligands into solvent extraction and liquid membrane

* Corresponding author.
E-mail address: htemel@dicle.edu.tr (H. Temel).

0277-5387/$ - see front matter © 2007 Elsevier Ltd. All rights reserved.
doi:10.1016/j.poly.2007.01.015

systems [12]. During the past years, the separation of heavy metals and organic substances has become more important in water purification applications owing to the drastic strengthening of environmental protection laws. In this field, various separation techniques, precipitation, extraction, distillation and electrodialysis have all been employed. Membrane processes such as liquid-membrane transport systems are potentially quite important in this area [13]. In practical applications, three main types of liquid membranes containing a mobile carrier have been studied: liquid surfactant, supported liquid a dissolvent polymeric membranes [14–18].

In the present work, we have synthesized a new macrocyclic Schiff base by reaction of 2,6-diaminopyridine and 1,7-bis(2-formylphenyl)-1,4,7-trioxaheptane. Then, its Cu(II), Ni(II), Pb(II), Co(III) and La(III) complexes were synthesized by template effect by reaction of 2,6-diaminopyridine and 1,7-bis(2-formylphenyl)-1,4,7-trioxaheptane and $Cu(NO_3)_2 \cdot 3H_2O$, $Ni(NO_3)_2 \cdot 6H_2O$, $Pb(NO_3)_2$, $Co(NO_3)_2 \cdot 6H_2O$, $La(NO_3)_3 \cdot 6H_2O$, respectively. Then the spectral, magnetic, electrochemical properties of all compounds were studied in detail.

2. Experimental

2.1. Physical measurements

Elemental analysis was carried out on a LECO CHNS model 932 elemental analyzer. ^{1}H NMR and ^{13}C NMR spectra were recorded using a model BRUKER AVANCE DPX-400 NMR spectrometer. IR spectra were recorded on a PERKIN ELMER SPECTRUM RX1 FTIR spectrometer on KBr discs in the wave number range of 4000–400 cm^{-1}. Electronic spectral studies were conducted on a SHIMADZU model 160 UV Visible spectrophotometer in the wavelength 200–600 nm. Molar conductivity was measured with a WTW LF model 330 conductivity meter, using prepared solution of the complex in DMF–DMSO (1:1). Thermal gravimetric analysis was carried out on a TGA SHIMADZU model 50 thermal gravimetric analyzer. LC/MS-API-ES mass spectra were recorded using a AGILENT model 1100 MSD mass spectrophotometer. An EcoChemie Autolab-12 potentiostat with the electrochemical software package GPES 4.9 (Utrecht, The Netherlands) was used for voltammetric measurements. A three electrode system was used: a platinum wire counter electrode, an Ag/AgCl reference electrode, and a 2 mm sized platinum disc electrode as working electrode. The working electrode was polished with 0.05 μm alumina prior to each experiment. Throughout the experiment, oxygen-free nitrogen was bubbled through the solution for 10 min. Voltammetric experiments were performed at room temperature. Electrochemical grade tetraethylammonium perchlorate (TEAP) (0.1 mol dm^{-3}) was employed as the supporting electrolyte.

2.2. Materials

1,7-Bis(2-formylphenyl)-1,4,7-trioxaheptane was prepared by the literature method [19,20]. All the other chemicals and solvents were of analytical grade and used as received.

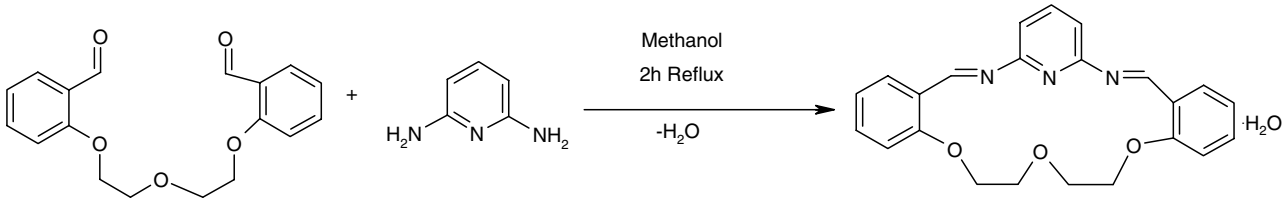
2.3. Preparation of 1,3,5-triaza-2,4:7,8:15,16-tribenzo-9, 15-dioxacycloheptadeca-1,5-diene (L)

The macrocyclic ligand (L) was prepared by the dropwise addition of a solution of the 2,6-diaminopyridine (0.22 g 2 mmol) in methanol (40 mL) to a stirred solution of 1,7-bis(2-formylphenyl)-1,4,7-trioxaheptane (0.63 g 2 mmol) in methanol (60 mL). After the addition was completed, the stirring was continued for 2 h. A yellow coloured compound was filtered. Then, CH_2Cl_2 was added to filtered compound and solved. Then, the solution was filtered and *n*-hexane was added to filtered solution. A yellow compound was obtained and filtered (Scheme 1). Yield: 0.47 g(%57). *Anal*. Calc. for $C_{23}H_{21}N_3O_3 \cdot H_2O$: C, 68.15; H, 5.68; N, 10.37. Found: C, 68.67; H, 5.74; N, 10.67%. ^{13}C NMR (DMSO-d_6, δ ppm): OCH_2: 68.9, CH_2OPh: 69.4, HC=N: 162.0, Aromatic C's: 114.4, 121.4, 124.9, 128.0, 136.9, 158.0, 189.6. ^{1}H NMR (DMSO-d_6, δ ppm): $\delta = 3.5$ (H_2O), $\delta = 3.92$ (t, $J = 4.43$ Hz) (OCH_2), $\delta = 4.30$ (t, $J = 4.42$ Hz) (CH_2OPh), $\delta = 7.00$–8.10 (Ar–H), $\delta = 10.39$ (HC=N). Selected IR data (KBr, ν cm^{-1}): 3382 $\nu(H_2O)$, 3069 ν(Ar–CH), 2938 ν(Alph. –CH), 1683 ν(C=N), 1598 ν[(C=N)(pyridine)], 1487, 1455 ν(Ar–C=C), 1286, 1241 ν(Ar–O), 1161 ν(R–O), 755 ν(Substitute benzene). UV–Vis (λ_{max}, nm) (DMF–DMSO (1:1)): 264, 322, 376. Mass spectra: m/z: 385.1 $[L-2H]^{+2}$.

2.4. Preparation of complexes

2.4.1. Preparation of the $[Cu_2(L)(NO_3)_2][NO_3]_2 \cdot H_2O$

To a stirred solution of 1,7-bis(2-formylphenyl)-1,4,7-trioxaheptane (0.63 g, 2 mmol) and $Cu(NO_3)_2 \cdot 3H_2O$ (0.96 g, 4 mmol) dissolved in methanol (60 mL) and then



Scheme 1.

added dropwise 2,6-diaminopyridine (0.22 g 2 mmol) in methanol (40 mL). After the addition was completed, the stirring was continued for 2 h. A brown coloured precipitation was filtered and washed with ethanol, $CHCl_3$ and diethylether, respectively. Then dried in air. Yield: 0.70 g (45%). *Anal*. Calc. for $Cu_2C_{23}H_{21}N_7O_{15}\cdot H_2O$: C, 35.38; H, 2.95; N, 12.56. Found: C, 35.75; H, 3.12; N, 12.24%. ^{1}H NMR (DMSO-d_6, δ ppm): $\delta = 3.5$ (H_2O), $\delta = 3.90$ (OCH_2), $\delta = 4.30$ (CH_2OPh), $\delta = 7.02$–8.10 (Ar–H), $\delta = 10.39$ (HC=N). Selected IR data (KBr, ν cm^{-1}): 3351 ν(H_2O), 3068 ν(Ar–CH), 2939, 2873 ν(Alph. –CH), 1615 ν(C=N), 1598 ν[(C=N)(pyridine)], 1488, 1455 ν(Ar–C=C), 1384 ν NO_3^-, 1287, 1242 ν(Ar–O), 1162, 1051 ν(R–O), 757 ν(Substitute benzene). $\Lambda_M = 161\ \Omega^{-1}\ mol^{-1}\ cm^2$. UV–Vis ($\lambda_{max}$, nm) (DMF–DMSO (1:1)): 272, 320. Mass spectra: m/z: 452 $[[Cu(L)] + H]^+$.

2.4.2. Preparation of the $[Ni(L)(NO_3)_2]\cdot 3H_2O$

To a stirred solution of 1,7-bis(2-formylphenyl)-1,4,7-trioxaheptane (0.63 g, 2 mmol) and $Ni(NO_3)_2\cdot 6H_2O$ (0.58 g, 2 mmol) dissolved in methanol (60 mL) and then added dropwise 2,6-diaminopyridine (0.22 g, 2 mmol) in methanol (40 mL). After the addition was completed, the stirring was continued for 2 h. A yellow coloured precipitation was filtered and washed with ethanol, $CHCl_3$ and diethylether, respectively. Then dried in air. Yield: 0.55 g (47%). *Anal*. Calc. for $NiC_{23}H_{21}N_5O_9\cdot 3H_2O$: C, 44.30; H, 4.65; N, 11.24. Found: C, 44.35; H, 4.67; N, 11.22%. ^{1}H NMR (DMSO-d_6, δ ppm): $\delta = 3.5$ (H_2O), $\delta = 3.92$ (OCH_2), $\delta = 4.30$ (CH_2OPh), $\delta = 7.07$–7.67 (Ar–H), $\delta = 10.38$ (HC=N). Selected IR data (KBr, ν cm^{-1}): 3358 ν (H_2O), 3065 ν (Ar–CH), 2938, 2872 ν (Alph. –CH), 1642 ν(C=N)1598 ν [(C=N)(pyridine)], 1487, 1450 ν (Ar–C=C), 1289, 1243 ν (Ar–O), 1160, 1125, 1050 ν (R–O), 754 ν (Sübstitue benzene). $\Lambda_M = 48\ \Omega^{-1}\ mol^{-1}\ cm^2$. UV–Vis ($\lambda_{max}$, nm) (DMF–DMSO (1:1)): 275, 323, 378. Mass spectra: m/z: 571 $[Ni(L)(NO_3)_2 + H]^+$.

2.4.3. Preparation of the $Pb(L)(NO_3)][NO_3]\cdot H_2O$

To a stirred solution of 1,7-bis(2-formylphenyl)-1,4,7-trioxaheptane (0.63 g, 2 mmol) and $Pb(NO_3)_2$ (0.66 g, 2 mmol) dissolved in methanol (60 mL) and then added dropwise 2,6-diaminopyridine (0.22 g 2 mmol) in methanol (40 mL). After the addition was completed, the stirring was continued for 2 h. A yellow coloured precipitation was filtered and washed with ethanol, $CHCl_3$ and diethylether respectively. Then dried in air. Yield: 0.81 g (55%). *Anal*. Calc. for $PbC_{23}H_{21}N_5O_9\cdot H_2O$: C, 37.50; H, 3.12; N, 9.51. Found: C, 37.56; H, 3.18; N, 9.60%. ^{1}H NMR could not be taken because of its insolubility. Selected IR data (KBr, ν cm^{-1}): 3355 ν(H_2O), 3068 ν(Ar–CH), 2931, 2873 ν(Alph. –CH), 1650 ν(C=N), 1598 ν[(C=N)(pyridine)], 1487, 1450 ν(Ar–C=C), 1384 νNO_3^-, 1289, 1243 ν(Ar–O), 1161, 1052 ν(R–O), 753 ν(Substitute benzene). $\Lambda_M = 89\ \Omega^{-1}\ mol^{-1}\ cm^2$. UV–Vis ($\lambda_{max}$, nm) (DMF–DMSO (1:1)): 276, 323, 378. Mass spectra: 627 $[Pb(L)-(NO_3)-(OCH_2)+H]^{+2}$.

2.4.4. Preparation of the $[Co(L)(NO_3)_2(OH)(H_2O)]\cdot H_2O$

To a stirred solution of 1,7-bis(2-formylphenyl)-1,4,7-trioxaheptane (0.63 g, 2 mmol) and $Co(NO_3)_2\cdot 6H_2O$ (0.58 g, 2 mmol) dissolved in methanol (60 mL) and then added dropwise 2,6-diaminopyridine (0.22 g 2 mmol) in methanol (40 mL). After the addition was completed, the stirring was continued for 2 h. A yellow coloured precipitation was filtered and washed with ethanol, $CHCl_3$ and diethylether, respectively. Then dried in air. Yield: 0.57 g (46%). *Anal*. Calc. for $CoC_{23}H_{24}N_5O_{11}\cdot H_2O$: C, 44.30; H, 4.17; N, 11.24. Found: C, 44.48; H, 4.32; N, 11.30%. ^{1}H NMR (DMSO-d_6, δ ppm): $\delta = 3.43$ (H_2O), $\delta = 3.94$ (OCH_2), $\delta = 4.31$ (CH_2OPh), $\delta = 7.03$–7.72 (Ar–H), $\delta = 10.39$ (HC=N). Selected IR data (KBr, ν cm^{-1}): 3381 ν(H_2O), 3066 ν(Ar–CH), 2934, 2879 ν(Alph. –CH), 1646 ν(C=N) 1598 ν[(C=N)(pyridine)], 1488, 1455 ν(Ar–C=C), 1286, 1238 ν(Ar–O), 1161, 1053 ν(R–O), 754 ν(Substitute benzene). $\Lambda_M = 36\ \Omega^{-1}\ mol^{-1}\ cm^2$. UV–Vis ($\lambda_{max}$, nm) (DMF–DMSO (1:1)): 275, 322, 376. Mass spectra: m/z: 571 $[Co(L)(NO_3)_2]^+$.

2.5. Preparation of the $[La(L)(NO_3)_3(H_2O)]\cdot H_2O$

To a stirred solution of 1,7-bis(2-formylphenyl)-1,4,7-trioxaheptane (0.63 g, 2 mmol) and $La(NO_3)_3\cdot 6H_2O$ (0.87 g, 2 mmol) dissolved in methanol (60 mL) and then added dropwise 2,6-diaminopyridine (0.22 g 2 mmol) in methanol (40 mL). After the addition was completed, the stirring was continued for 2 h. A yellow coloured precipitation was filtered and washed with ethanol, $CHCl_3$ and diethylether, respectively. Then dried in air. Yield: 0.69 g (46%). *Anal*. Calc. for $LaC_{23}H_{24}N_6O_{13}\cdot H_2O$: C, 37.00; H, 3.34; N, 11.26. Found: C, 37.05; H, 3.38; N, 11.29%. ^{1}H NMR (DMSO-d_6, δ ppm): 3.5 (H_2O), $\delta = 3.92$ (OCH_2), $\delta = 4.30$ (CH_2OPh), $\delta = 3.65$ (H_2O), $\delta = 6.95$–7.69 ppm (Ar–H), $\delta = 10.39$ ppm (CH=N). Selected IR data (KBr, ν cm^{-1}): 3371 ν(H_2O), 3065 ν(Ar–CH), 2927, 2872 ν(Alph. –CH), 1684 ν(C=N), 1598 ν[(C=N)(pyridine)], 1487, 1450 ν(Ar–C=C), 1286, 1243 ν(Ar–O), 1161, 1052 ν(R–O), 754 ν(Sübstitüe benzene). $\Lambda_M = 36\ \Omega^{-1}\ mol^{-1}\ cm^2$. UV–Vis ($\lambda_{max}$, nm) (DMF–DMSO (1:1)): 273, 323, 379. Mass spectra: m/z: 649 $[La(L)(NO_3)_2-H]^+$.

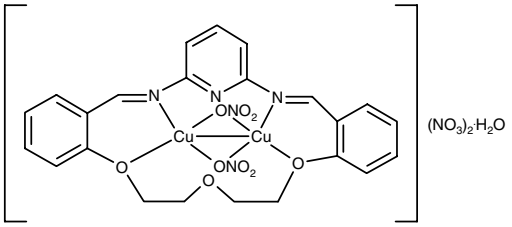
3. Result and discussion

3.1. Spectral studies

The ligand and complexes have been synthesized (Schemes 1 and 2) and characterized. The ligand and its complexes were identified by elemental analysis, IR, ^{1}H and ^{13}C NMR data, electronic spectra, magnetic susceptibility measurements, molar conductivity, mass spectra, thermogravimetric analyses and cyclic voltammeter (see Table 1 and Table 2). As the crystals were unsuitable for single-crystal X-ray structure determination and are

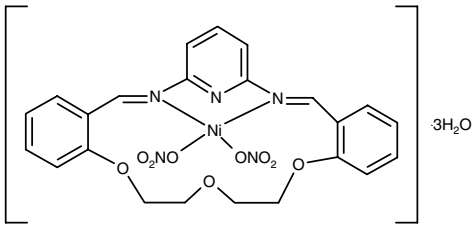
1,7-Bis(2-formylphenyl)-1,4,7-trioxaheptane + 2Cu(NO$_3$)$_2$.3H$_2$O + 2,6-diaminopyridine

[Cu$_2$(L)(NO$_3$)$_2$][NO$_3$]$_2$.H$_2$O + 7H$_2$O



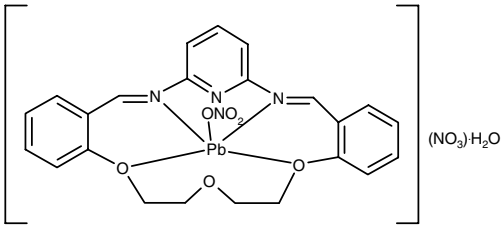
1,7-Bis(2-formylphenyl)-1,4,7-trioxaheptane + Ni(NO$_3$)$_2$.6H$_2$O + 2,6-diaminopyridine

[Ni(L)(NO$_3$)$_2$].3H$_2$O + 5H$_2$O

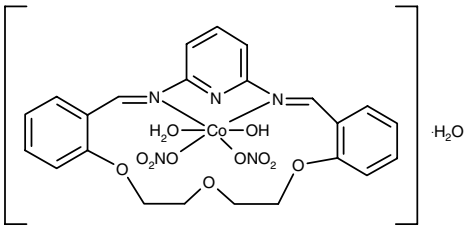


1,7-Bis(2-formylphenyl)-1,4,7-trioxaheptane + Pb(NO$_3$)$_2$ + 2,6-diaminopyridine

[Pb(L)(NO$_3$)][NO$_3$].H$_2$O + H$_2$O

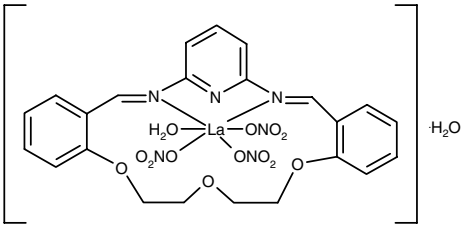


2.[1,7-Bis(2-formylphenyl)-1,4,7-trioxaheptane] +2[Co(NO$_3$)$_2$.6H$_2$O] + 2[2,6-diaminopyridine] + 1/2O$_2$ 2[Co(L)(NO$_3$)$_2$(OH)(H$_2$O)].H$_2$O + 11H$_2$O



1,7-Bis(2-formylphenyl)-1,4,7-trioxaheptane + La(NO$_3$)$_3$.6H$_2$O + 2,6-diaminopyridine

[La(L)(NO$_3$)$_3$(H$_2$O)].H$_2$O + 6H$_2$O



Scheme 2.

Table 1
Physical characterization, analytical, molar conductance, mass spectra and magnetic susceptibility data of the complexes

Compound	(Calc.) Found			λ_M (Ω^1 mol^{-1} cm^2)	Formula weight	MS/EI	Assignment	μ_{eff} (BM)
	%C	%H	%N					
$C_{23}H_{21}N_3O_3 \cdot H_2O$	(68.15) 68.67	(5.68) 5.74	(10.37) 10.67		405	385	$[L-2H]^{+2}$	
$[Cu_2(L)(NO_3)_2][NO_3]_2 \cdot H_2O$	(35.38) 35.75	(2.95) 3.12	(12.56) 12.24	161	780	452	$[Cu(L)+H]^+$	Dia
$[Ni(L)(NO_3)_2] \cdot 3H_2O$	(44.30) 44.35	(4.65) 4.67	(11.24) 11.22	48	623	571	$[Ni(L)(NO_3)_2+H]^+$	Dia
$[Pb(L)(NO_3)][NO_3] \cdot H_2O$	(37.56) 37.50	(3.12) 3.18	(9.51) 9.60	89	736	627	$[Pb(L)(NO_3)-(OCH_2)+H]^{+2}$	Dia
$[Co(L)(NO_3)_2(OH)(H_2O)] \cdot H_2O$	(44.30) 44.48	(4.17) 4.32	(11.24) 11.30	36	623	571	$[Co(L)(NO_3)_2]^+$	Dia
$[La(L)(NO_3)_3(H_2O)] \cdot H_2O$	(37.00) 37.05	(3.34) 3.38	(11.26) 11.26	36	748	649	$[La(L)(NO_3)_2-H]^+$	Dia

Table 2
IR (cm^{-1}) spectral data for the complexes

Compound	ν(C=N)	ν(C=N) pyridine	$\nu(H_2O)$	Ionic ν NO_3^-
$C_{23}H_{21}N_3O_3 \cdot H_2O$	1683	1598	3382	
$[Cu_2(L)(NO_3)_2][NO_3]_2 \cdot H_2O$	1635	1598	3351	1384
$[Ni(L)(NO_3)_2] \cdot 3H_2O$	1642	1598	3358	
$[Pb(L)(NO_3)][NO_3] \cdot H_2O$	1650	1598	3355	1384
$[Co(L)(NO_3)_2(OH)(H_2O)] \cdot H_2O$	1646	1598	3381	
$[La(L)(NO_3)_3(H_2O)] \cdot H_2O$	1684	1598	3371	

insoluble in most common solvents, including water, ethanol, ethyl acetate, and acetonitrile.

The IR spectrum of the ligand (L) shows a ν(C=N) peak at 1685 cm^{-1} and the absence of a ν(C=O) peak at around 1700 cm^{-1} is indicative of Schiff's base condensation. The IR spectra of all complexes show ν(C=N) bands at 1615–1684 cm^{-1} [3,5,21–23] and it is found that the ν(C=N)bands in the complexes are shifted by about 70–2 cm^{-1} to lower energy regions compared to that of the free ligand (L). This phenomenon appears to be due to the coordinated of azomethine nitrogen to the metal ion [5,24,25]. Also, a weak $\nu(H_2O)$ band of free ligand at about 3380 cm^{-1} is observed because of water molecule and the IR spectra of the Co(III) complex is characterized by the appearance of a broad band in the region at 3364 cm^{-1} due to OH groups [26–28]. The absorptions of the nitrate counterions, at ca. 1460–1452 (ν_5), 1300 (ν_1) and 1040 (ν_2) cm^{-1}, suggest the presence of bidentate nitrate groups: a intense band at ca. 1384 cm^{-1} attributable to ionic nitrate, is also present [4,7,29]. The IR spectra of the complexes clearly demonstrated that the COC and CCO stretching vibrations are altered compared to ligands due to conformational changes. The C–O–C absorption is shifted to lower wave numbers in complexes providing another evidence of complexing [30,31].

^{1}H NMR and ^{13}C NMR of the complexes in DMSO-d_6 solution show that they are NMR active. The ^{1}H NMR spectrum of the free ligand shows a multiplet in the range 7.1–8.0 ppm due to aromatic protons, 10.4 ppm due to imine protons and 3.4 ppm due to H_2O protons. ^{13}C NMR spectrum of the free ligand shows 161.3 ppm in the range due to imine carbon, 65.6 ppm due to OCH_2 carbon and 189.8 ppm due to pyridine carbon. The ^{1}H NMR spectra of the complexes exhibit almost the same values [32–34].

3.2. Electronic absorption spectroscopy

The electronic spectrum of the ligand (L) in DMSO–DMF (1:1) shows absorption bands at 276, 321, 376 nm. The bands are indicative of benzene and other chromophore moieties present in the ligand. The absorption bands of the complexes are shift to longer wave numbers compared to that of ligand [35]. No d–d transitions for the complexes were observed due to having low solubility of complexes. A moderately intensive band observed in the range of 320–380 nm is due to existence of a ligand-to-metal charge transfer transition, and the strong band observed in the range of 270–280 nm is due to an intraligand charge transition [32] for these complexes.

3.3. Magnetic and conductivity studies

The observed room-temperature magnetic moment value for the binuclear Cu(II) and the mononuclear other complexes are found to be diamagnetic. The diamagnetic behaviour of the binuclear complex may be explained by a very strong anti-ferromagnetic interaction in the Cu–Cu pair [36]. Co(II) complex was oxidised to Co(III) complex by O_2 in air [37]

$$2Co^{+2}+ \rightarrow 2Co^{+3} + 2e^-$$

$$1/2O_2 + 2e^- \rightarrow O^{-2}$$

$$O^{-2} + H_2O \rightarrow 2OH^-$$

Conductivity measurements of the lead(II) complex in DMF–D MSO resulted in Λ_M value 89 Ω^{-1} mol^{-1} cm^2, which indicate that it is of the 1:1 electrolyte type, and the binuclear copper(II) complex show Λ_M value in the range of 161 Ω^{-1} mol^{-1} cm^2 indicating that it is of 2:1 electrolyte type [4,8,23]. The other complexes are nonelectrolyte (Table 1).

It is seen that the complex formation reaction between ligand and relatively large Pb(II) and La(III) metal ions result in the $[Pb(L)(NO_3)][NO_3] \cdot H_2O$ and $[La(L)(NO_3)_3$-

$(H_2O)] \cdot H_2O$ complexes. The binding mode of the ligand for the $[Pb(L)(NO_3)][NO_3] \cdot H_2O$ complex is different than that of the $[La(L)(NO_3)_3(H_2O)] \cdot H_2O$ complexes. In the first case, the ligand behaves as a tetradentate ligand with the lone electron pairs of azomethine nitrogen atoms and the lone electron pairs of two oxygen in ether groups. In the second case, the ligand behaves as a bidentate ligand with the lone electron pairs of azomethine nitrogen atoms. The long distance binding process can be favoured for too large Pb(II) metal ion but not La(III) metal ion due to having smaller ion size than Pb(II) metal ion. So its coordination is satisfied with three NO_3^- and one H_2O in the second case. Similar binding mode was observed in literature for Pb(II) metal ions [9,30,36,38]. The absorptions of the coordinated nitrate ions, at ca. 1460–1452 (ν_5), 1300 (ν_1) and 1040 (ν_2) cm^{-1}, suggest the presence of the coordinated nitrate groups while a intense band at ca. 1384 cm^{-1} can be attributed to the ionic nitrate conterions [4,7,29]. Also, the conductivity measurements of the lead(II) complex in DMF–DMSO resulted in Λ_M value 89 Ω^{-1} mol^{-1} cm^2, which indicate that it is of the 1:1 electrolyte type. These results are clearly verify different binding mode of ligand in the case of the Pb(II) metal ion. As expected, in the case of the relatively small (Ni(II) and Co(III)) metal ions, the ligand behaves as a bidentate ligand with the lone electron pairs of azomethine nitrogen atoms and the inner coordination sphere is donated with NO_3^-, H_2O, and OH^- ligands. The conductivity measurements showed that these complexes are nonelectrolyte. On the other hand, the diamagnetic behaviour of the binuclear complex can be explained by a very strong anti-ferromagnetic interaction in the Cu–Cu pair [36]. Also, the structure was supported with the others spectroscopic data. Furthermore, the controlled potential coulometric (CPC) study indicated that the number of electrons transferred for the electrochemical reaction of the complex was two for the reduction process based on the copper metal as seen from the electrochemical study. Some Co(II), Ni(II), Ag(II), Zn(II) or Pb(II) complexes prepared with similar ligands have been known from literature.

3.4. Electrochemistry

The electrochemical behaviors of the nickel(II), copper(II), and cobalt(III) complexes were studied using cyclic voltammetric (CV) technique in DMSO solution containing 0.1 M TEAP. All CVs and their data are presented in Fig. 1 and Table 3. Fig. 1a shows the CV of the nickel complex which exhibited a quasi-reversible one-electron reduction in DMSO containing Ag/AgCl electrode system at 0.100 V s^{-1} scan rate with a corresponding anodic wave. This reduction wave is referred to the Ni(II)/Ni(I) couples. The quasi-reversibility of the reduction process are confirmed with the corresponding the peak separation value between cathodic peak potential and anodic peak potential ($\Delta E_p = 0.120$ V) and almost the unity of the ratio of the anodic peak current-to-cathodic peak current. The half-wave potential of the nickel complex was located at $E_{1/2} = -1.37$ V versus Ag/AgCl.

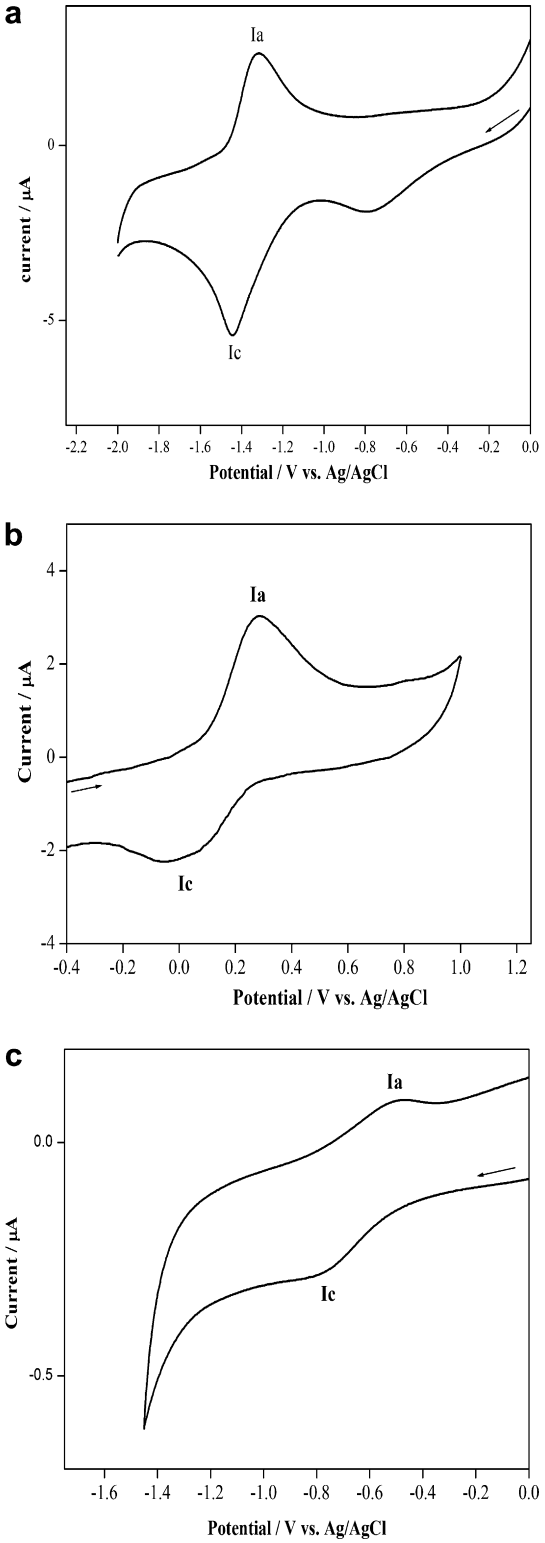


Fig. 1. Cyclic voltamograms of complexes, (a) nickel(II), (b) copper(II), and (c) cobalt(III), complexes in DMSO/0.1 M TEAP at 0.100 V s^{-1} scan rate.

Fig. 1b shows the CV of the copper complex which exhibited one irreversible reduction peak as a result of a

Table 3
Voltammetric data for the complexes in DMSO-TEAP

Complexes	$M^{3+}/M^{2+}E^{a}_{1/2}$ (V)	ΔE_p[b](V)	$M^{2+}/M^{+}E^{a}_{1/2}$ (V)	ΔE_p[c]
$[Ni(L)(NO_3)_2]\cdot 3H_2O$	−1.37	0.120		
$[Cu_2(L)(NO_3)_2][NO_3]_2\cdot H_2O$			−0.015[b]	0.300
$[Co(L)(NO_3)_2(OH)(H_2O)]\cdot H_2O$			−0.739[b]	0.223

[a] $E_{1/2}$ (V) = $E_{pa} + E_{pc}/2$.
[b] Cathodic peak potentials for irreversible processes.
[c] $\Delta E_p = E_{pc} - E_{pa}$ at 0.100 V s^{-1} scan rate.

Table 4
TGA data of the complexes

Compounds	Weight loss %, Calc. (Found) Decomposition group		
	First step (°C)	Second step (°C)	Third step (°C)
$[CoL(NO_3)_2(OH)(H_2O)]\cdot H_2O$	95.0–320.0 11.68 (11.70) H_2O and NO_3		
$[NiL(NO_3)_2]\cdot 3H_2O$	48.0–330.0		
$[Cu_2L(NO_3)_2][(NO_3)_2]\cdot H_2O$	60.0–215.0 2.31 (2.50) H_2O		
$[PbL(NO_3)][NO_3]\cdot H_2O$	34.0–67.0 2.83 (2.50) H_2O	67.0–154.0 9.76 (10.83) NO_3	154.0–308.0 9.76 (8.33) NO_3
$[LaL(NO_3)_3(H_2O)]\cdot H_2O$	59.0–310.0 4.82 (5.00) $2H_2O$		

large peak separation value ($\Delta E_p = 0.300$ V) at 0.100 V s^{-1} scan rate. This reduction wave is assigned to the Cu(II)/Cu(I) couples. The cathodic electrode potential are displayed at $E_{pc} = -0.015$ V. The controlled potential coulometric (CPC) study indicated that the number of electrons transferred for the electrochemical reaction of the complex was two for the reduction process based on the copper metal [39–43].

Fig. 1c shows the CV of the cobalt complex, which displayed irreversible one-electron reduction in DMSO containing Ag/AgCl electrode system with a peak separation value ($\Delta E_p = 0.223$ V). The reduction wave could be assigned to metal-based Co(III)/Co(II) couples in the complex. The cathodic peak potential of complex is located at $E_{pc} = -0.739$ V versus Ag/AgCl [39–43].

3.5. Thermal studies

The thermal stability of the complexes were investigated using TGA. The thermogravimetric analysis (TGA) were carried out (Table 4) at a heating rate of 10 °C/min in a nitrogen atmosphere over a temperature range of 20–900 °C.

The decomposition and weight losses of Co(III), Cu(II) and La(III) complexes were occured at the temperature ranges of 95.0–320.0 °C, 60.0–215.0 °C and 59.0–310.0 °C, respectively. The calculated and found weight loses indicated the departure group to be H_2O mainly. Thermal decomposition of all complexes are seen to be irreversible. The weight loses of Ni(II) complex was not observed clearly.

The H_2O and NO_3 groups departured from Pb(II) complex at the temperature range of 34.0–308.0 °C. The amount of H_2O and NO_3 groups stoichometrically corresponding to the weight losses are given in the proposal chemical formulas of complexes (Table 4).

3.6. Mass spectra

The mass spectra of the ligand and its metal complexes peaks attributable to the molecular ions. *m/z*: 385.1 $[L-2H]^+$, *m/z*: 452 $[[Cu(L)]+H]^+$, *m/z*: 571 $[Ni(L)(NO_3)_2+H]^+$, *m/z*: 571 $[Co(L)(NO_3)_2]^+$, *m/z*: 649 [La(L)-

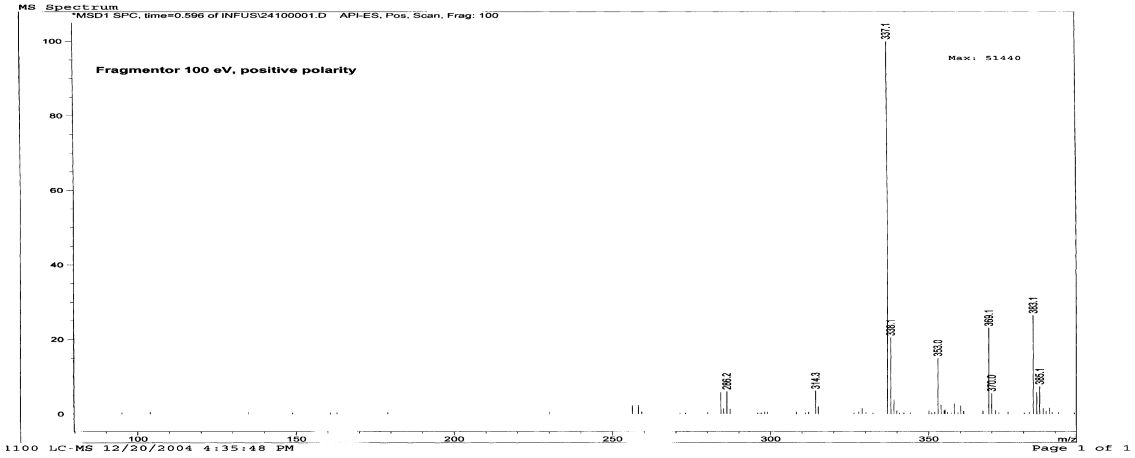


Fig. 2. The mass spectra of the ligand.

$(NO_3)_2-H]^+$. The spectrum of the ligand was shown in Fig. 2.

Acknowledgements

We are grateful to Dicle University Research Found (DUAPK-03-EF-24) for the support of this research.

References

[1] A. Chaudhary, N. Bansal, A. Gajraj, R.V. Singh, J. Inorg. Biochem. 93 (2003) 393.
[2] M.R. Malachowski, B.T. Dorsey, M.J. Parker, M.E. Adams, R.S. Kelly, Polyhedron 17 (8) (1998) 1289.
[3] S. Chandra, K. Gupta, Trans. Metal Chem. 27 (2002) 196.
[4] E. Bertolo, R. Bastida, A.D. Blas, D.E. Fenton, C. Loderio, A. Macias, A. Rodriguez, T. Rodriguez-Blas, J. Inclusion Phenom. Macrocyclic Chem. 35 (1999) 191.
[5] S. Chandra, K. Gupta, Trans. Metal Chem. 27 (2002) 329.
[6] A.A. Saleh, J. Coord. Chem. 58 (3) (2005) 255.
[7] D.S. Kumar, V. Alexander, Polyhedron 18 (1999) 1561.
[8] L. Valencia, H. Adams, R. Bastida, D.E. Fenton, A. Macias, Inorg. Chim. Acta 317 (2001) 45.
[9] C. Lodeiro, R. Bastida, E. Bertolo, A. Macias, A. Rodriguez, Inorg. Chim. Acta 343 (2003) 133.
[10] Adel A.A., Emara, Azza A.A., Abou-Hussen, Spectrochim. Acta Part A 64 (2006) 1010.
[11] G.A. Melson, Coordination Chemistry of Macrocyclic Compounds, Plenum Press, New York, 1979.
[12] M.J. Draxler, R. Marr, Sep. Sci. Technol. 23 (1988) 1659; S.V. Grigoriev, P. Muhl, J. Memb. Sci. 12 (1982) 133.
[13] R.W. Baker, M.E. Tuttle, D.J. Kelly, H.K. Lonsdale, J. Memb. Sci. 2 (1977) 213.
[14] P.R. Danesi, Sep. Sci. Technol. 20 (1985) 857.
[15] M.J. Sugiura, Coll. Interf. Sci. 81 (1981) 385.
[16] A. Nezhadali, J. Inclusion Phenom. Macrocyclic Chem. 54 (2006) 307.
[17] F. Benetollo, G. Bombieri, L. De Cola, A. Polo, D.L. Smailes, L.M. Vallarino, Inorg. Chem. 28 (18) (1989) 3447.
[18] D. Das, C.P. Cheng, J. Chem. Soc., Dalton Trans. 1081 (2000).
[19] K.R. Adam, A.J. Leong, L.F. Lindoy, H.C. Lip, B.W. Skelton, A.H. White, J. Am. Chem. Soc. 105 (1983) 4645.
[20] L.F. Lindy, L.G. Armstrong, Inorg. Chem. 14 (6) (1975) 1322.
[21] S.M. Nelson, C.V. Knox, M. McCann, J. Chem. Soc., Dalton Trans. 1669 (1981).
[22] C. Bianchini, G. Mantovani, A. Meli, F. Migliacci, F. Zanobini, F. Laschi, A. Sommazzi, Eur. J. Inorg. Chem. 1620 (2003).
[23] H. Adams, N.A. Bailey, Matthew J.S. Dwyer, D.E. Fenton, J. Chem. Soc., Dalton Trans. 1207 (1993).
[24] N.A. Bailey, D.E. Fenton, S.J. Kitchen, T.H. Lilley, M.G. Williams, P.A. Tasker, A.J. Leonng, L.F. Lindoy, J. Chem. Soc., Dalton Trans. 2989 (1991).
[25] N.A. Bailey, D.E. Fenton, R. Moody, C. Barbarin, I.N. Cciambarella, J.M. Latour, D. Limosin, V. Mckee, J. Chem. Soc., Dalton Trans. 2519 (1987).
[26] S.K. Mandal, K. Nag, J. Chem. Soc., Dalton Trans. 2141 (1984).
[27] N.A. Bailey, D.E. Fenton, M.G. Williams, D.J. Winter, J. Chem. Soc., Dalton Trans. 1727 (1989).
[28] H. Temel, B. Ziyadanogullari, H. Alp, I. Aydin, F. Aydin, S. Ilhan, Russ. J. Coord. Chemistry 32 (4) (2006) 282.
[29] S.Y. Uçan, B. Mercimek, Synthesis Reactivity Inorg., Metal-Organic Nano-Metal Chem. 35 (2005) 197.
[30] C. Lodeiro, R. Bastida, E. Bertolo, A. Rodriguez, Can. J. Chem. 82 (2004) 437.
[31] H. Temel, H. Hoşgören, M. Boybay, Spectrosc. Lett. 34 (5) (2001) 1.
[32] A.K. Varshney, S. Varshney, H.L. Singh, Synth. React. Inorg. Met.-Org. Chem. 29 (2) (1999) 245.
[33] L. Valencia, R. Bastida, A.D. Blas, D.E. Fenton, A. Macias, A. Rodriguez, T. Rodriguez-Blas, A. Castineiras, Inorg. Chim. Acta 282 (1998) 42.
[34] L. Valencia, H. Adams, R. Bastida, D.E. Fenton, A. Macias, Inorg. Chim. Acta 317 (2001) 45.
[35] K.R. Krishnapriya, M. Kandaswamy, Polyhedron 24 (2005) 113.
[36] V. Yilmaz, S. Hamamci, O. Andac, C. Thöne, W. Harrison, Trans. Metal Chem. 28 (2003) 676.
[37] H. Temel, S. Ilhan, M. Sekerci, R. Ziyadanogullari, Spectrosc. Lett. 35 (2) (2002) 219.
[38] A. Bashall, M. McPartlin, B.P. Murphy, D.E. Fenton, S.J. Kitchen, J. Chem. Soc., Dalton Trans. 505 (1990).
[39] M. Kandaz, S.Z. Coruhlu, I. Yilmaz, A.R. Ozkaya, Transit. Metal. Chem. 27 (2002) 877.
[40] I. Yilmaz, M. Kandaz, A.R. Özkaya, A. Koca, Monatshefte für Chemie 133 (2002) 609.
[41] T. Nakanishi, I. Yilmaz, N. Nakashima, K.M. Kadish, J. Phys. Chem. B 107 (2003) 12789.
[42] I. Yilmaz, M. Kocak, Polyhedron 23 (2004) 1279.
[43] I. Yilmaz, A.G. Gurek, V. Ahsen, Polyhedron 24 (2005) 791.

Available online at www.sciencedirect.com
ScienceDirect
Polyhedron 26 (2007) 2803–2809
POLYHEDRON
www.elsevier.com/locate/poly

Structural studies of two-coordinate complexes of tris(2-methoxylphenyl)phosphine and tris(4-methoxyphenyl)phosphine with gold(I) halides

Raymond C. Bott, Peter C. Healy, Graham Smith *

School of Science, Griffith University, Brisbane, Qld 4111, Australia

Received 19 December 2006; accepted 18 January 2007
Available online 25 January 2007

Abstract

A series of five gold(I) halide complexes with the two isomeric methoxy-substituted triarylphosphines, tris(2-methoxyphenyl)phosphine [P(oanis)$_3$], [AuP(oanis)$_3$X] [for X = Cl, (**1**); X = Br, (**2**) and X = I, (**3**)] and tris(4-methoxyphenyl)phosphine [P(panis)$_3$], [AuP(panis)$_3$X] [for X = Br (**4**) and X = I (**5**)] have been synthesized and characterized by single crystal X-ray diffraction and solution $^{31}P\{^1H\}$ NMR spectroscopy. The structure determinations confirm the expected presence of linear two-coordination about the gold centres in all five complexes with bond distance and angle data typical of this type of compound [Au–P, 2.239(2)–2.259(3) Å; Au–Cl, 2.294(2) Å; Au–Br, 2.385(2)–2.402(2) Å; Au–I, 2.546(1)–2.554(1) Å; P–Au–X; 175.3(1)–180°]. All analogues except the iodo complex **5** crystallize with one complex molecule in the crystallographic asymmetric unit. The bromo and iodo complexes **2** and **3** constitute a trigonal isomorphous set while the bromo complex **4** is also isomorphous with the previously determined chloro complex [AuP(panis)$_3$Cl]. The 2-methoxy analogues are stabilized by significant methoxy-O···Au interactions.
© 2007 Elsevier Ltd. All rights reserved.

Keywords: Gold(I) phosphine halides; Crystal structures; Metal complexes

1. Introduction

The linear two-coordinate complexes of the gold(I) halides with the tertiary-substituted arylphosphines of the type [AuP(Ar)$_3$X] (where X = Cl, Br, I) have received considerable attention with respect to the steric influence of substituent groups on the aryl groups of the phosphine and the variable electron donor properties of the chloride, bromide and iodide anions. To date a large number of crystal structures of this type of compound have been published, for example [1–20]. It has been observed that steric factors exert the most important influence on the packing environment about the Au centres, with possible Au···Au interactions only being reasonable in gold(I) halide complexes with small alkyl substituted phosphines, e.g. [P(Me)$_3$] and [P(Et)$_3$]. Thus among the total set of gold complexes of this type, only the isomorphous pair [AuP(Me)$_3$Cl] [17–19] and [AuP(Me)$_3$Br] [17–19] and [AuP(Et)$_3$Cl] [20] have short Au···Au interactions, varying from 3.27–3.98 Å. It was therefore very unusual to encounter in our previous series of compounds [6] a sterically encumbered ring-substituted triarylphosphinegold(I) complex, that with tris(4-methylphenyl)phosphine, [AuP(ptol)$_3$Cl] which had similar Au···Au interactions [3.375(1) Å], considering that the corresponding unsubstituted phosphine complex [AuP(Ph)$_3$Cl] [1–3] had none. Furthermore, a feature of that entire series of compounds was the common occurrence of isomorphous crystal sets among the halide complexes particularly with the bromide and iodide members, although isomorphous series which include all three halide homologues are known, e.g. with [P(Ph)$_3$] [1,2,19] and [P(otol)$_3$] [otol = tris(2-methylphenyl)phosphine] [6]. In addition, there is a high incidence of examples in which

* Corresponding author. Address: School of Physical and Chemical Sciences, Queensland University of Technology, Brisbane, Qld 4001, Australia. Tel.: +61 7 38642293; fax: +61 7 38641804.
E-mail address: g.smith@qut.edu.au (G. Smith).

0277-5387/$ - see front matter © 2007 Elsevier Ltd. All rights reserved.
doi:10.1016/j.poly.2007.01.014

there are two complex molecules in the crystallographic asymmetric unit, a phenomenon which appears to be a consequence of the conformational variability possible particularly in the aryl substituents on the phosphine ligand. This factor may be controlled to some extent by energetics, e.g. method of synthesis together with the conditions and solvents employed both in the synthesis and in recrystallization, e.g. $[AuP(otol)_3Cl]$ gives a monoclinic modification (the α-polymorph) from ethanol [5] while the orthorhombic β-polymorph [6] is obtained from dimethylformamide, and a similar dimorphism is observed with the isomeric $[AuP(p\text{-}tol)_3Cl]$ set [6,7].

It has also been noted that the methoxy oxygen atoms in tris(2,4,6-trimethoxylphenyl)phosphine $[P(tmp)_3]$ affect both the basicity of the ligand and the gold environment in the $[AuP(tmp)_3X]$ complexes [3,12]. Previously, it was also observed that the presence of *ortho*-methyl substituents in the $[P(otol)_3]$ complexes gave Au···H(methyl) interactions, resulting in regularity in the disposition of the phosphine phenyl rings [6]. We therefore were interested in determining the effect of a single methoxy substituent on both the intramolecular interactions (2-methoxy-O···Au) as well as upon intermolecular associations and crystal packing. With the unsymmetrically substituted complexes chloro(2-hydroxyphenyl)diphenylphosphinegold(I) [13], and iodo(2-aminophenyl)diphenylphosphinegold(I) [14], both the hydroxy oxygen and the amino proton give significant short Au···O [3.160(7) Å] and Au···N [3.61(3) Å] interactions. This effect is not present in the analogous but sterically demanding *ortho*-substituted phosphine complex, chloro[(2-trimethylsiloxyphenyl)diphenylphosphine]gold(I) [13] where no substituent group interaction is found. Similar steric effects are seen with the 2-iodo-substituted analogues iodo(2-iodophenyl)diphenylphosphinegold(I) [15] and iodo(2-iodo-3-methylphenyl)diphenylphosphinegold(I) [16].

We therefore set out to look at the structural effects of both *ortho*- and *para*-methoxy phosphine substitution on a series of gold(I) complexes. Reported here is the synthesis, the X-ray structures and solution $^{31}P\{^1H\}$ NMR spectra of the series of five halo-gold(I) complexes with the *ortho*- and *para*-anisyl-substituted phosphines, tris(2-methoxyphenyl)phosphine $[P(oanis)_3]$, $[AuP(oanis)_3X]$ [Series A: compounds **1**–**3**] and tris(4-methoxyphenyl)phosphine $[P(panis)_3]$, $[AuP(panis)_3X]$ [Series B: compounds **4**, **5**] (X = Br, I). The structure of the Series B chloro analogue $[AuP(panis)_3Cl]$ has been previously reported [11].

2. Experimental

2.1. Preparation of compounds

The complexes $[AuP(oanis)_3X]$ [Series A: for X = Cl (**1**); X = Br (**2**); X = I (**3**)] and $[AuP(panis)_3X]$ [Series B: for X = Br (**4**); X = I (**5**)] were synthesized using a previously described procedure [6] by the interaction of equimolar quantities of $[Bu_4N][AuX_2]$ (0.50 mmol; Cl, 0.255 g; Br, 0.300 g; I, 0.346 g) and the appropriate phosphine (0.50 mmol, 0.152 g) dissolved in 5 mL of dimethylformamide at ca. 50 °C. The resultant solutions were cooled to room temperature and allowed to stand for several days to yield well-formed colourless crystals of the expected complexes. Yields were 96%, 93%, 96%, 95% and 88% for **1**–**5**, respectively. Melting points and ν(Au–X) stretching frequencies obtained from FT raman data for **1**–**5** are listed in Table 1. No chemical analyses were completed.

Just as for the analogous Au(I) complex series with the isomeric *ortho*- and *para*-tolylphosphines [6,24], the chloride and bromide complexes **1**, **2** and **4** but not the iodide complexes **3** and **5** may be synthesized using either potentiostatic methods or galvanostatic methods.

2.2. Spectroscopy

Solution $^{31}P\{^1H\}$ NMR spectra were recorded in $CDCl_3$ solution on a Varian Gemini-2000 spectrometer at 80.86 MHz with 256 transients collected. Spectra were referenced internally to 85% H_3PO_4.

2.3. X-ray structure determinations

X-ray crystal data indicated that the Series A bromide and iodide complexes with $[P(oanis)_3]$ (**2** and **3**) appeared to comprise a trigonal isomorphous set. Similarly, in the Series B set the bromo complex with $[P(panis)_3]$ (**4**) had cell parameters and space group which indicated that it was isomorphous with the previously reported chloro analogue [11]. Both of these isomorphous series were confirmed in the structure analyses. With the iodo complex of $[P(panis)_3]$ (**5**), although having four molecules in a centrosymmetric triclinic cell could not be transformed into a higher symmetry cell, and this was subsequently justified in the analysis with the presence of two conformationally dissimilar molecules in the asymmetric unit.

Unique data sets for all compounds were measured at 297(2) K within the specified $2\theta_{max}$ limit using a Rigaku AFC 7R four-circle diffractometer [θ–2θ scan mode, monochromatized Mo Kα radiation ($\lambda = 0.71073$ Å), from a 12 kW rotating anode source] yielding N independent reflections, N_0 with $I > 3.0\sigma(I)$ (compounds **1**, **4** and **5**) or $I > 2.0\sigma(I)$ (compounds **2** and **3**) being considered 'observed' and used in the expression of the conventional refinement residual R. Crystal decay was negligible in most cases [1.5% maximum in **5**] and in the worst cases was allowed for by using a linear correction. The structures were solved by direct methods and refined by full-matrix least-squares refinement {on F for **1**, **4** and **5** or on F^2 for **2** and **3** (the latter using SHELX-97) [25]} after semi-empirical absorption corrections based on ψ-scans. Anisotropic thermal parameters were refined for all non-hydrogen atoms while $(x, y, z, U_{iso})_H$ were included and constrained at estimated values. Neutral atom complex scattering factors were employed while computation used the TeXsan

Table 1
Crystal and physical data for compounds **1**–**5**

	1	**2**	**3**	**4**	**5**
Compound identity	[AuP(oanis)$_3$Cl]	[AuP(oanis)$_3$Br]	[AuP(oanis)$_3$I]	[AuP(panis)$_3$Br]	[AuP(panis)$_3$I]
Formula	$C_{21}H_{21}AuClO_3P$	$C_{21}H_{21}AuBrO_3P$	$C_{21}H_{21}AuIO_3P$	$C_{21}H_{21}AuBrO_3P$	$C_{21}H_{21}AuIO_3P$
FW	584.79	629.24	676.24	629.24	676.24
Melting point (°C)	239–241	242–245	242	200–203	194–196
ν(Au–X) (cm^{-1})	330	231	149	231	150
CCDC reference	211 590	211 591	211 592	211 593	211 594
Temperature (K)	297(2)	297(2)	297(2)	297(2)	297(2)
λ (Å)	0.71073	0.71073	0.71073	0.71073	0.71073
Crystal system	triclinic	trigonal	trigonal	monoclinic	triclinic
Space group	$P\bar{1}$	$R\bar{3}$	$R\bar{3}$	$C2/c$	$P\bar{1}$
a (Å)	10.384(2)	13.509(3)	13.6159(6)	14.337(5)	10.778(2)
b (Å)	12.309(3)	13.509(3)	13.6159(6)	14.770(7)	20.163(2)
c (Å)	8.599(2)	20.027(7)	20.367(2)	20.511(5)	10.623(2)
α (°)	92.14(2)	90	90	90	95.45(1)
β (°)	101.29(1)	90	90	101.72(2)	95.60(1)
γ (°)	96.46(2)	120	120	90	101.600(9)
V (Å^3)	1069.0(4)	3165.0(9)	3270.0(4)	4253(3)	2235.0(6)
Z	2	6	6	8	4
D_x (Mg m^{-3})	1.817	1.981	2.060	1.965	2.010
μ (Mo Kα) (mm^{-1})	7.12	8.99	8.26	8.89	8.08
Crystal size (mm^3)	0.25 × 0.25 × 0.10	0.25 × 0.20 × 0.20	0.27 × 0.20 × 0.06	0.25 × 0.20 × 0.15	0.30 × 0.25 × 0.15
Crystal decay (%)	0.06	0.18	0.96	0.43	1.53
N (total)	4011	1416	1416	10 336	8323
N (unique)	3781	1285	1291	4904	7865
N_0 [$I > n(I)$]	3180 ($n = 3.0$)	1245 ($n = 2.0$)	1018 ($n = 2.0$)	2505 ($n = 3.0$)	3865 ($n = 3.0$)
$2\theta_{max}$ (°)	50	50	50	55	50
R[a]	0.050	0.032	0.026	0.037	0.034
R_w[b], wR_2[c]	0.078[b]	0.084[c]	0.074[c]	0.041[b]	0.032[b]

[a] $R = (\sum|F_o| - |F_c|)/\sum|F_o|$.
[b] $R_w = \{\sum w(F_o - F_c)^2/\sum w(F_o)^2\}^{1/2}$, $\{w^* = [\sigma^2(F_o)]^{-1}\}$.
[c] $wR_2 = \{\sum w[(F_o^2 - F_c^2)]^2 / \sum[w(F_o^2)^2]\}^{1/2}$, $\{w = [\sigma^2(F_o^2) + (AP)^2 + BP]^{-1}$ {where $P = [(\max F_o^2, 0) + 2(F_c^2)]/3\}$.

crystallographic software package of Molecular Structure Corporation [26].

3. Results and discussion

3.1. Structural chemistry

The series of five substituted triarylphosphine gold(I) halide complexes of the type [AuP(Ar)$_3$X] with isomeric tris(2-methoxyphenyl)phosphine [P(oanis)$_3$] and tris(4-methoxyphenyl)phosphine [P(panis)$_3$] have been characterized by X-ray diffraction and $^{31}P\{^1H\}$ NMR spectroscopy. Selected interatomic bond lengths and interbond angles for [AuP(oanis)$_3$X] (for X = Cl, Br and I) (Series A: compounds **1**–**3**) and [AuP(panis)$_3$X] (for X = Cl, Br and I) (Series B: compounds **4** and **5**) together with comparative data for the analogous [AuP(Ph)$_3$X] [1–3] and some mono-*ortho*-substituted phenyl phosphine complexes of the type [AuP(YPh)(Ph)$_2$X] (where Y = an interactive substituent, e.g. –OH, –NH$_2$), –OSi(Me)$_3$ [13,14], are given in Table 2.

All complexes have the expected linear two-coordination about the gold centres (see Figs. 1, 3, 5 and 6) with the mean P–Au–X bond angle [177.8°]. The largest deviation from linearity in the overall series of complexes of this type occurs with those members where packing allows short intermolecular Au···Au interactions, e.g. with the rare tris(4-methyltolyl)phosphine complex [AuP(ptol)$_3$Cl] [6] [Au···Au, 3.375(1) Å; P–Au–Cl, 173.2(2)°]. No examples of this type are found in the present Series A or B complexes. The mean Au–P and Au–X bond lengths are 2.25(1) Å (Au–P), 2.292(5) Å (Au–Cl), 2.394(5) Å (Au–Br) and 2.552(5) Å (Au–I) comparing with the series mean of 2.29(2), 2.29(2), 2.41(1) and 2.56(1) Å, respectively. With the Series A complexes (**1**–**3**), the *ortho*-substituted methoxy groups influence the conformational features of the substituted phosphine ligand. The triclinic chloro complex **1** [AuP(oanis)$_3$Cl] (Figs. 1 and 2), having one molecule in the asymmetric unit is significantly different from the bromo and iodo analogues (**2** and **3**) which constitute a trigonal isomorphous set, and have molecular C_3 symmetry coincident with crystallographic symmetry (Figs. 3 and 4), with the P–Au–X moiety lying on the three-fold axis and with the three methoxy groups in general positions. This implies that all methoxy groups adopt identical conformations in a perfect propeller conformation. It should be noted that although complexes **2** and **3** are isomorphous, the individual complex molecules in each have subtle conformational differences, one being right handed the other left [Fig. 1a and b]. This results from a simple rotation of the phenyl ring about the P1–C1 bond vector and is not a chiral relationship. In addition, the methoxy

Table 2
Important geometrical features [bond distances (Å) and angles (°)] for $[AuP(anis)_3X]$ complexes (**1**–**5**), compared with $[AuPPh_3X]$, $[AuP(tmpp)_3X]$ (X = Cl, Br, I) and unsymmetrically substituted examples of the type $[AuP(YPh)(Ph)_2I]$ (Y = interactive substituent group)

Compound	Au–P	Au–X	P–Au–X	τ_1[a]	τ_2	τ_3	Reference
$[AuP(Ph)_3Cl]$	2.235(3)	2.279(3)	179.6(1)	39(1)	58(1)	30(1)	[1]
$[AuP(Ph)_3Br]$	2.252(6)	2.407(6)	179.4(1)	44(2)	55(2)	33(2)	[2]
$[AuP(Ph)_3I]$	2.2499(2)	2.553(1)	175.65(9)	41(1)	58(1)	32(1)	[19]
$[AuP(tmpp)_3Cl]$	2.253(5)	2.303(6)	176.0(2)	−46(1)	−55(1)	−12(1)	[3]
$[AuP(tmpp)_3Br]$	2.255(5)	2.413(2)	175.9(1)	−48(1)	−55(1)	−16(1)	[3]
$[AuP(tmpp)_3I]$	2.239(7)	2.586(2)	177.7(2)	51(2)	54(2)	18(3)	[3]
$[AuP(2\text{-}OHPh)(Ph)_2Cl]$[b]	2.226(2)	2.285(2)	176.8(1)	−42(1)	−56(1)	−41(1)	[13]
$[AuP(2\text{-}OSiMe_3Ph)(Ph)_2Cl]$[c]	2.2295(8)	2.285(1)	177.3(1)	54.8(3)	43.3(3)	45.7(3)	[13]
$[AuP(2\text{-}NH_2Ph)(Ph)_2I]$[d]	2.235(3)	2.553(1)	178.5(1)	41(1)	41(1)	41(1)	[14]
$[AuP(oanis)_3Cl]$ (**1α**)	2.250(4)	2.294(5)	176.6(2)	56.3(15)	55.0(18)	−1.4(16)	this work
$[AuP(oanis)_3Br]$ (**2β**)	2.244(3)	2.402(2)	180.0(6)	−46.3(8)	−46.3(8)	−46.3(8)	this work
$[AuP(oanis)_3I]$ (**3β**)	2.259(3)	2.558(1)	180.0(1)	46.9(6)	46.9(6)	46.9(6)	this work
$[AuP(panis)_3Cl]\cdots$ (**α**)	2.235(2)	2.289(2)	176.1(1)	−29(1)	−62(1)	−3(1)	[11]
$[AuP(panis)_3Br]$ (**4α**)	2.239(2)	2.385(2)	175.3(1)	−29.9(8)	−62.7(8)	−3.1(7)	this work
$[AuP(panis)_3I]$ (**5β**$_1$)	2.259(3)	2.553(1)	176.9(1)	−4(1)	18(1)	80(1)	this work
$[AuP(panis)_3I]$ (**5β**$_2$)	2.254(3)	2.546(1)	177.1(1)	−38(1)	−21(1)	−43(1)	

τ_m is defined by the torsion angle Au–P–C(m1)–C(m2).
[a] **β**$_1$ and **β**$_2$ represent the two independent molecules in the crystallographic repeating unit.
[b] $[P(2\text{-}OHPh)(Ph)_2]$ = (2-hydroxyphenyl)diphenylphosphine.
[c] $[P(2\text{-}OSiMe3Ph)(Ph)_2Cl]$ = (2-trimethylsiloxyphenyl)diphenylphosphine.
[d] $[P(2\text{-}NH_2Ph)(Ph)_2]$ = (2-aminophenyl)diphenylphosphine.

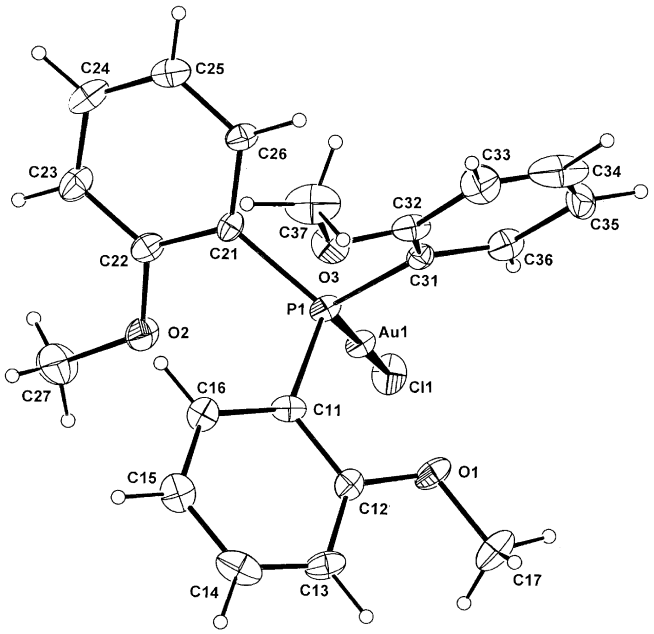


Fig. 1. Molecular configuration and atom numbering scheme for $[AuP(oanis)_3Cl]$ (**1**) with non-hydrogen atoms shown as 30% probability ellipsoids [27].

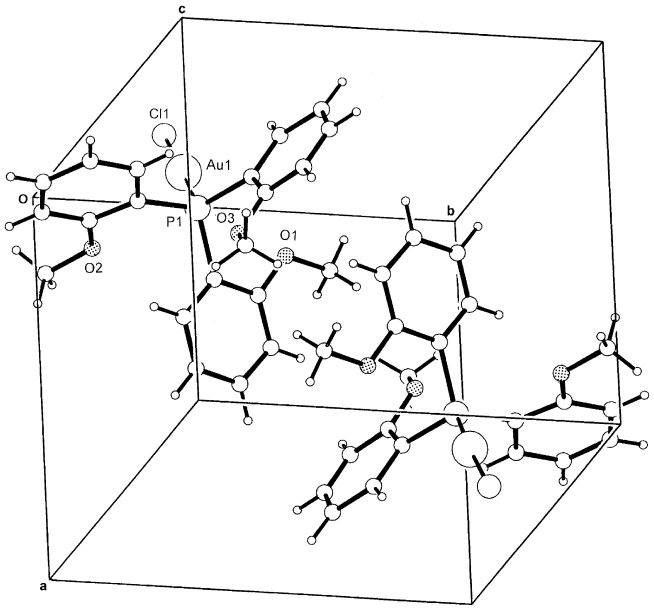


Fig. 2. Perspective view of the packing of **1** in the unit cell viewed down the approximate c-axial direction.

groups are essentially coplanar with the phenyl rings [torsion angle C1–C2–O2–C7, 178.1(8)° (**2**) and −177.2(7)° (**3**)] and have all three oxygen atoms directed towards the gold centre [Au···O, 3.250(6) Å (**2**) and 3.239(7) Å (**3**)]. In contrast, complex **1** has two methoxy groups directed towards and one away from the gold centre [torsion angles ($\tau_1 - \tau_3$), 56°, 55°, 178(1)°]. The Au···O distances for these *cis*-related methoxy groups are 3.27(1) and 3.36(1) Å indicating moderate interaction. Stronger interaction is certainly found with the (2-hydroxyphenyl)diphenylphosphinegold(I) chloride complex [13] where the single hydroxy group interacts with Au [Au···O, 3.160(7) Å] and has the hydroxy-H directed away from Au. The more sterically demanding (2-trimethylsiloxyphenyl)diphenylphosphine ligand in the gold(I) chloride complex [13] has a somewhat longer but still significant Au···O contact [3.353(2) Å]. With the corresponding tris(2,4,6-trimethoxy)phosphine analogues (Cl, Br, I) [3,12], one *o*-methoxy-O of each ring has an interactive Au···O contact [2.92–3.14(1) Å (Cl); 2.96–3.13(1) Å (Br); 3.01–3.10(1) Å

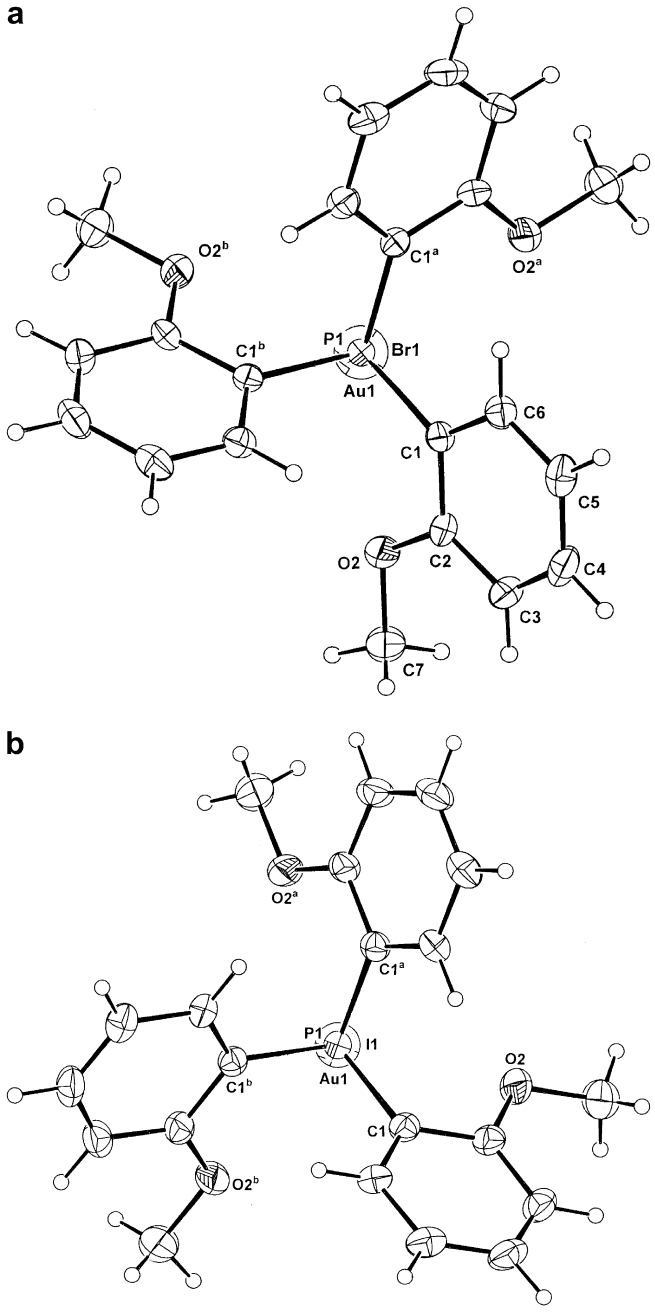


Fig. 3. Molecular configuration for the molecules of the isomorphous complexes (a) $[AuP(oanis)_3Br]$ (**2**), and (b) $[AuP(oanis)_3I]$ (**3**) viewed down molecular the C_3 axis of each, showing the subtle conformational difference between the two.

(I)]. The tris(*o*-tolyl)phosphine examples [6] in which the methyl-H···Au interactions are important in influencing conformation, have a mean Au···C distance of 3.44(1) Å. The effect of this conformational control can be gauged by inspecting the comparative torsion angles ($\tau_1 - \tau_3$) [corresponding to the angle Au–P–C(*m*1)–C(*m*2)] (Table 2). In examples having interaction, the angles are more regular, e.g. a 41–59° range for the $[AuP(otol)_3X]$ (X = Cl, Br and I) series cf. 17–57° for the $[AuP(ptol)_3X]$ (X = Cl, Br and I series) [6]. With the previous series the values were usually ordered small–large–small as is the case with the parent

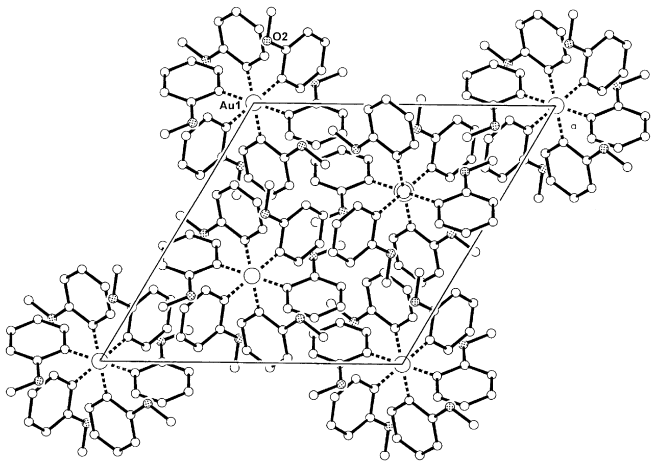


Fig. 4. Packing of the molecules of **2** in the unit cell viewed down the *c*-axial direction.

$[P(Ph)_3]$ [39°, 58°, 30° (X = Cl); 44°, 55°, 33° (X = Br); 41°, 58°, 32° (X = I) [1,2,19]. With the series (**1**–**5**) considered here, the same trend is observed, with values of 56.3(15)°, 55.0(18)°, −1.4(16)° for **1**, where only two methoxy groups are interactive [Au···O1, 3.356(12) Å and Au1···O2, 3.271(12) Å], compared to the constant values for the trigonal examples **2** [−46.3(8)°; Au···O1, 3.250(6) Å] and **3** [47.4(7)°; Au···O1, 3.239(7) Å]. In none of these three examples does the packing in the unit cell result in dimer formation through the back-to-back sextuple phenyl embrace (SPE) [6,21–23].

With the $[AuP(panis)_3X]$ examples in the Series B set, the bromo analogue $[AuP(panis)_3Br]$ (**4**) (Fig. 5) is found to be isomorphous with the previously reported first member of the series, $[AuP(panis)_3Cl]$ [11]. Both crystallize in *C*-centred monoclinic cells {comparative cell data for the chloro analogue [11]: $a = 14.2875(4)$, $b = 14.5396(4)$,

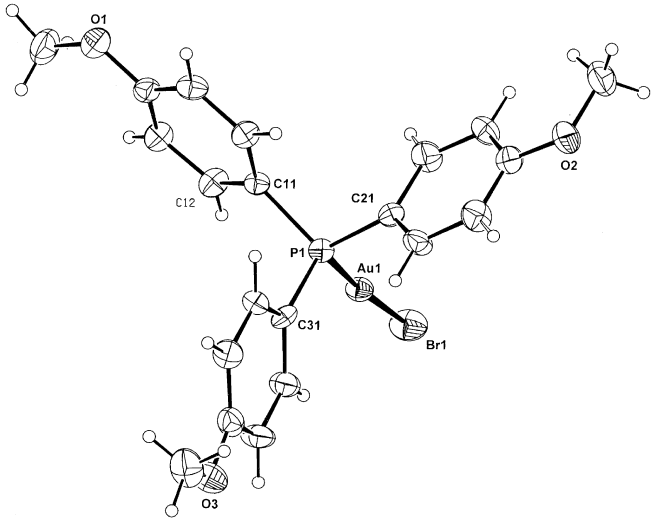


Fig. 5. Molecular configuration and naming scheme for the $[AuP(panis)_3Br]$ (**4**). Non-hydrogen atoms are drawn as 30% probability displacement ellipsoids.

$c = 20.2212(6)$ Å, $\beta = 101.504(1)°$, $Z = 8$; space group, $C2/c$} with one molecule in the asymmetric unit. This contrasts with the iodo analogue [AuP(panis)$_3$I] (**5**) which has two conformationally different molecules in the asymmetric unit, as indicated by the variation in the $\tau_1 - \tau_3$ values [−4°, 18°, 80(1)° (molecule 1) (Fig. 6a) and −38°, −21°, −43(1)° (molecule 2)] (Fig. 6b). These values compare with −29°, −62°, −3° for the Series B chloro complex [5] and −29.9(8)°, −62.7(8)° and −3.1(7)° for **4**. This variation is possible with the greater conformational freedom afforded by the absence of Au···O(*o*-methoxy) interactions cf. the *ortho*-anisyl-substituted phosphines.

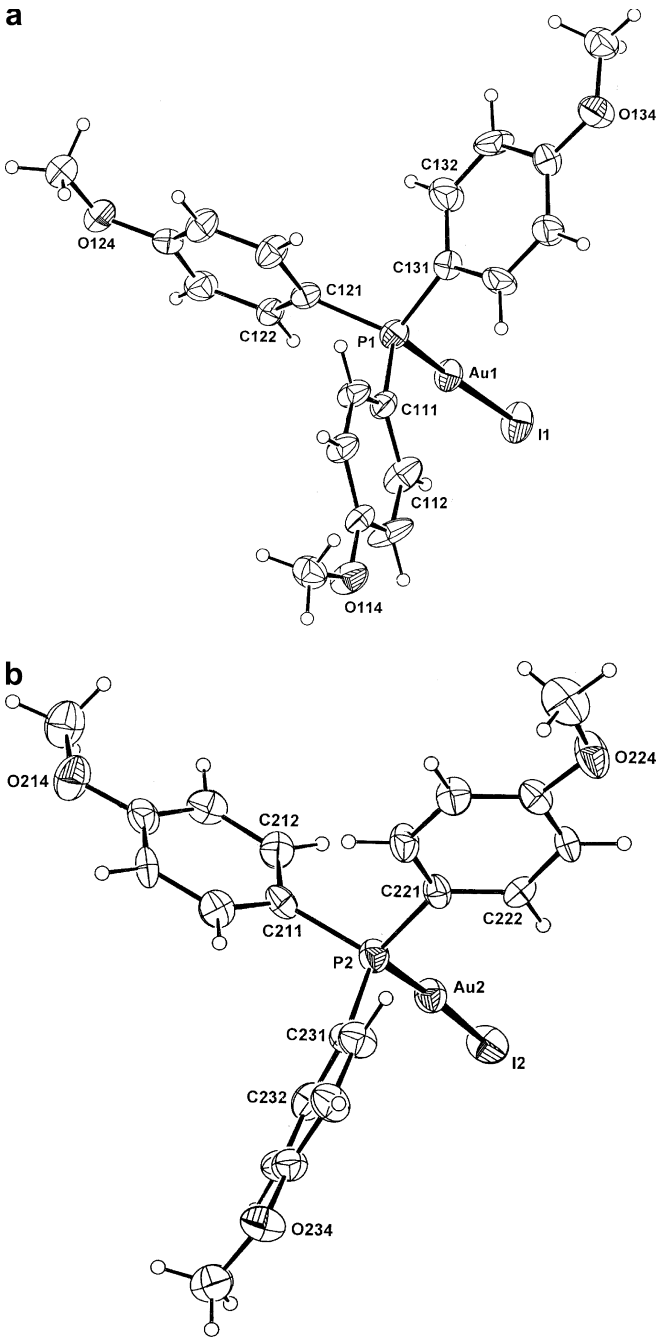


Fig. 6. The two conformationally different molecules of [AuP(panis)$_3$I] in the crystallographic asymmetric unit in **5**. (a) Molecule 1; (b) Molecule 2.

3.2. Solution NMR results

The solution $^{31}P\{^1H\}$ NMR spectra in $CDCl_3$ showed singlet peaks at 9.1, 12.6,19.1 ppm (Series A) and 32.2, 34.4, 38.9 ppm (Series B), respectively, which compare with 33.8, 34.6 and 38.4 ppm for the [P(Ph)$_3$] series of complexes (for X = Cl, Br, I, respectively) [1–3,6,17–19]. The corresponding coordination chemical shifts ($\Delta\delta = \delta$ complex $- \delta$ ligand), with the exception of that for **3** [38.1, 41.6, 48.1 ppm (Series A) and 39.4, 41.6, 45.7 ppm (Series B)] are similar to the [P(Ph)$_3$] complexes (38.5, 40.5, 43.1 ppm), respectively.

3.3. Conclusions

The presence of methoxy substituent groups in the triphenylphosphine molecule appears to have little influence on the nature of the gold(I) complex formed, but the presence of the *ortho*-methoxy substituent significantly affects the conformation of the phenyl rings, due to intramolecular methoxy-O···Au interactions. This is best seen with the isomorphous [AuP(oanis)$_3$Br] and [AuP(oanis)$_3$I] complexes where the rings adopt perfect C_3 symmetry. In addition the methoxy group appears to have less effect than the analogous methyl substituent group in triaryl phosphines upon the formation of crystals containing more than one independent complex molecule in the asymmetric unit. No short Au···Au interactions of the type found in [AuP(ptol)$_3$Cl] were expected or found in this series.

Acknowledgements

The authors acknowledge support of this work by Griffith University and a grant from the Australian Research Grants Scheme.

Appendix A. Supplementary material

CCDC 211590, 211591, 211592, 211593 and 211594 contain the supplementary crystallographic data for **1**, **2**, **3**, **4** and **5**. The data can be obtained free of charge via http://www.ccdc.cam.ac.uk/conts/retrieving.html, or from the Cambridge Crystallographic Data Centre, 12 Union Road, Cambridge CB2 1EZ, UK; fax: (+44) 1223-336-033; or e-mail: deposit@ccdc.cam.ac.uk. Supplementary data associated with this article can be found, in the online version, at doi:10.1016/j.poly.2007.01.014.

References

[1] N.C. Baenzinger, W.E. Bennett, D.M. Soboroff, Acta Crystallogr. B32 (1976) 962, {[AuP(Ph)$_3$Cl]}.
[2] P.F. Barron, L.H. Engelhardt, P.C. Healy, J. Oddy, A.H. White, Aust. J. Chem. 40 (1987) 1545, {[AuP(Ph)$_3$X], X=Br, I}.

[3] L.-J. Baker, R.C. Bott, G.A. Bowmaker, P.C. Healy, B.W. Skelton, P. Schwerdtfeger, A.H. White, J. Chem. Soc., Dalton Trans. (1995) 1341, {[Au(tmpp)$_3$X], X = Cl, Br, I}.
[4] H.W. Chen, E.R.T. Tiekink, Acta Crystallogr. E59 (2003) m50, {[AuP(pfPh)$_3$Cl]}.
[5] C.S.W. Harker, E.R.T. Tiekink, Acta Crystallogr. C46 (1990) 1546, {α-[AuP(otol)$_3$Cl]}.
[6] R.C. Bott, P.C. Healy, G. Smith, Aust. J. Chem. 57 (2004) 213, {β-[AuP(otol)$_3$X] and [AuP(ptol)$_3$X] (X = Cl, Br, I)}.
[7] P.D. Cookson, E.R.T. Tiekink, Acta Crystallogr. C 50 (1994) 1896, {β-[AuP(ptol)$_3$Cl]}.
[8] C.S.W. Harker, E.R.T. Tiekink, Acta Crystallogr. C47 (1991) 878, {[AuP(mtol)$_3$Cl]}.
[9] E.C. Alyea, G. Ferguson, J.F. Gallagher, J. Malito, Acta Crystallogr. C49 (1993) 1473 [AuP(mes)$_3$Cl] (mes = 2,4,6-trimethylphenyl)].
[10] R.C. Bott, G.A. Bowmaker, R.W. Buckley, P.C. Healy, M.C. Senake Parera, Aust. J. Chem. 53 (2000) 175, {[AuP(mes)$_3$X] (X = Cl, Br, I); [AuP(mes)$_3$Cl] · 0.5DMF}.
[11] S.Y. Ho, E.R.T. Tiekink, Acta Crystallogr. E57 (2001) m549, {[AuP(panis)$_3$Cl]}.
[12] E.C. Alyea, G. Ferguson, S. Kannon, Polyhedron 19 (2000) 2211, {[AuP(tmp)$_3$X] (X = Cl, Br, I; tmp = 2,4,6-trimethoxyphenyl)}.
[13] C. Hollatz, A. Schier, H. Schmidbaur, Z. Naturforsch, Teil B 54 (1999) 30, {[AuP(2-OH · Ph)(Ph)$_2$Cl] and [AuP(2-OSiMe$_3$ · Ph)(Ph)$_2$Cl]}.
[14] P. Papathanasiou, G. Salem, P. Waring, A.C. Willis, J. Chem. Soc., Dalton Trans. (1997) 3435.
[15] M.A. Bennett, S.K. Bhargava, D.C.R. Hockless, A.C. Willis, J. Am. Chem. Soc. 118 (1996) 10469.
[16] S.K. Bhargava, F. Mohr, M.A. Bennett, L.L. Welling, A.C. Willis, Organometallics 19 (2000) 5628.
[17] K. Angermaier, G.A. Bowmaker, E.N. de Silva, P.C. Healy, B.E. Jones, H. Schmidbaur, J. Chem. Soc., Dalton Trans. (1996) 3121, {[AuP(Me)$_3$Cl]}.
[18] K. Angermaier, E. Zeller, H. Schmidbaur, J. Organometal. Chem. 472 (1994) 371, {[AuP(Me)$_3$Br]}.
[19] S. Ahrland, K. Dreisch, B. Noren, A. Oskarsson, Acta Chem. Scand., Ser. A41 (1987) 173 [AuP(Me)$_3$I], [AuP(Ph)$_3$I]}.
[20] E.R.T. Tiekink, Acta Crystallogr. C45 (1989) 1233, {[AuP(Et)$_3$Cl]}.
[21] I. Dance, M. Scudder, J. Chem. Soc., Chem. Commun. (1995) 1039.
[22] I. Dance, M. Scudder, J. Chem. Soc., Dalton Trans. (1996) 3755.
[23] M. Scudder, I. Dance, J. Chem. Soc., Dalton Trans. (1998) 3167.
[24] R.C. Bott. PhD Thesis, Griffith University, Brisbane, 1998.
[25] SHELX-97, Program for Crystal Structure Determination, University of Göttingen, Germany, 1997.
[26] TeXsan, Crystal Structure Analysis Package, Molecular Structure Corporation, New Plains Drive, The Woodlands, TX 77381, USA, 1999.
[27] PLATON, A Multipurpose Crystallographic Tool, University of Utrecht, The Netherlands, 2007.

Available online at www.sciencedirect.com
ScienceDirect
Polyhedron 26 (2007) 2810–2816
POLYHEDRON
www.elsevier.com/locate/poly

Synthesis and characterization of near-infrared absorption tin octabutoxy naphthalocyanines

Cheolbeom Bae [a], Gwanghoon Kwag [a,*], Malcolm E. Kenney [b]

[a] R & BD Center, Korea Kumho Petrochemical Co., Ltd., P.O. Box 64, Yuseong, Taejeon 305-600, Republic of Korea
[b] Department of Chemistry, Case Western Reserve University, Cleveland, OH 44106, USA

Received 11 December 2006; accepted 22 January 2007
Available online 7 February 2007

Abstract

Synthesis and characterization of a series of tin octabutoxy naphthalocyanines are presented, which show near infrared absorptions (900–930 nm) with high extinction coefficients (*ca.* 1×10^5 M^{-1} cm^{-1}). The position of the Q-band is more red-shifted with the heavier halogen, which corresponds to the HOMO–LUMO gaps calculated with density functional theory (0.932, 0.911, 0.905, 0.893 eV). The interaction with $SnNc(OBu)_8Br_2$ and C_{60} moves the Q-band further to the infrared region (928 nm). In ^{119}Sn NMR, the upfield shift (−120 ppm) of $SnNc(OBu)_8I_2$ represents a relatively electron-rich environment at the tin nucleus, and the ^{119}Sn-resonance (237 ppm) of $SnNc(OBu)_8F_2$ is different from the other halides, where ^{119}Sn–^{19}F coupling, a triplet splitting (1:2:1), was observed with 1820 Hz coupling constant. In the optimized structures obtained with BLYP, the distortion angles vary from F to I (N–Sn–N angles 178.8°, 173.1°). The tin naphthalocyanine with the heavy halide ligand becomes more concave, and the Sn–X bond is located at a longer distance out of ring. The difference of the two axial bonds varies significantly from 0.003 to 0.104 Å with the change of the axial ligands from F to I. The distorted shape is larger in the order I > Br > Cl > F with increase of the atomic size (1.33, 1.15, 0.99, 0.71 Å, respectively) and decrease of electronegativity (2.21, 2.74, 2.83, 4.10, respectively). $SnNc(OMe)_8X_2$ has an electric dipole moment perpendicular to the naphthalocyanine plane, and the magnitudes are, 0.81, 0.50, 0.35 and 0.01 for F, Cl, Br and I, respectively. The transition dipole moment lies in the naphthalocyanine plane along the *x*- or *y*-axis perpendicular to the permanent dipole moment in the *z*-axis, which indicates a $\pi \rightarrow \pi^*$ ligand–ligand transition. The energies of the molecular orbitals which are mainly contributed to by the naphthalocyanine ring, including the HOMO and LUMO, are slightly changed as the axial ligands change from F to I.
© 2007 Elsevier Ltd. All rights reserved.

Keywords: Tin octabutoxy naphthalocyanine; Near infrared absorption; Q-band; Molecular orbitals

1. Introduction

Naphthalocyanines, extended conjugated macrocycles with high chemical and thermal stabilities, have been studied in many application areas for molecular electronics, non-linear optics, optical data storage, sensors, electrochromic devices, solar cells, electrocatalytic systems and photodynamic therapy [1–4]. As near infrared absorption (NIR) materials, napthalocyanine has chromophoric and low-band-gap properties, and the electronic structure of napthalocyanine can be tuned by the peripheral substitution of the ring, and the kind of central metal and axial ligands [5,6].

Our aim is to prepare a series of tin naphthalocyanine halides showing near infrared absorption and to understand their electronic and molecular structures.

2. Experimental

2.1. Materials

The tin halides (SnF_2, $SnCl_2 \cdot 2H_2O$, $SnBr_2$, SnI_2) and 1,4-dibutoxy-2,3-naphthalenedicarbonitrile were purchased

* Corresponding author. Tel.: +82 42 865 8698; fax: +82 42 862 5651.
E-mail address: gkwag@kkpc.com (G. Kwag).

0277-5387/$ - see front matter © 2007 Elsevier Ltd. All rights reserved.
doi:10.1016/j.poly.2007.01.045

from Aldrich Chemical. Polystyrene beads used in gel permeation column chromatography were obtained from Bio-Rad Laboratories.

2.2. Spectroscopies

The electronic spectra were obtained with a UV–Vis–NIR spectrophotometer (JASCO). ^{1}H, ^{19}F, ^{119}Sn NMR spectra were recorded with Varian XL-200, Gemini 300 and Bruker MSL-400 spectrometers. The low- and high-resolution fast-atom-bombardment (LR FAB and HR FAB) mass spectra were obtained from either the Midwest Center for Mass Spectrometry (University of Nebraska-Lincoln, NE) or Washington University Resource for Biomedical and Bio-organic Mass Spectrometry. The elemental analyses were carried out by a commercial laboratory (Galbraith Laboratories, Knoxville, TN).

2.3. Calculation

Geometry optimizations of $SnNc(OMe)_8X_2$ (X = F, Cl, Br and I) were carried out without any symmetry constraints. We introduced a methoxy group instead of the butoxy group for relatively insignificant rotational conformations of the butoxy group. Our calculations were based on the density functional theory at the generalized gradient approximation level, BLYP functional [7]. Energy-adjusted relativistic effective core potentials were used for Br, I and the central Sn atom [8]. Double numerical plus polarization basis sets were used for the C, N, O, H, F, Cl atoms and the valence electrons for Br, I and Sn [9]. All calculations were performed using the DMOL^3 program [10]. In order to aid the interpretation of the absorption spectrum, spectroscopic calculations were performed at the BLYP-optimized geometries within the ZINDO approximation implemented in the VAMP program [11,12].

2.4. Synthesis

$H_2Nc(OBu)_8$. $H_2Nc(OBu)_8$ was prepared according to the literature [13].

$SnNc(OBu)_8F_2$. Under N_2, a mixture of $H_2Nc(OBu)_8$ (40 mg, 0.031 mmol), SnF_2 (220 mg, 1.40 mmol) and dry 2-ethylpyridine (5 mL) was refluxed for 100 min, cooled and evaporated to dryness with a rotary evaporator (~30 °C, ~1 Torr). The solid was chromatographed (Bio-Beads S-X4, 1.7 × 30 cm; toluene), dried (~60 Torr, ~60 °C) and weighed (12 mg, 0.0083 mmol, 27%). IR (Nujol): 558 (Sn–F) cm^{-1}. ^{1}H NMR (300 MHz, C_6D_6): δ 9.17 (m, 1,4-Nc H), 7.67 (m, 2,3-Nc H), 5.25 (t, α-CH_2), 2.30 (m, β-CH_2), 1.66 (m, γ-CH_2), 1.05 (t, CH_3). ^{13}C NMR (75 MHz, C_6D_6): δ 152.1 (s), 149.4 (s), 131.8 (s), 128 (s), 125.0 (s), 77.8 (s), 33.4 (s), 19.9 (s), 14.5 (s). ^{119}Sn NMR (75 MHz, C_6D_6): δ 237 J^1(Sn–F) = 1820.2 Hz (24.4 ppm). ^{19}F NMR (376 MHz, C_6D_6): δ −126. MS-FD, *m*/*z*: calc. for $C_{80}H_{88}N_8O_8F_2Sn$ $(M)^+$, 1446; found 1446. MS-HRFAB exact mass, *m*/*z*: calc. for $C_{80}H_{88}N_8O_8F_2Sn^{116}$ $(M)^+$, 1442.5711; found 1442.5713, 1442.5663. UV–Vis (λ_{max} (nm), ε ($M^{-1}\,cm^{-1}$)) (CH_2Cl_2): 906, 1.1×10^5. The compound is dark brown. It is soluble in CH_2Cl_2, toluene, and slightly soluble in hexane. It is insoluble in CH_3OH and H_2O.

$SnNc(OBu)_8Cl_2$. Under N_2, a mixture of $H_2Nc(OBu)_8$ (58 mg, 0.045 mmol) and $SnCl_2 \cdot 2H_2O$ (300 mg, 1.33 mmol) was refluxed in dry dimethylformamide (5 mL) for 4 h, cooled and evaporated to dryness with a rotary evaporator (~30 °C, ~1 Torr). The solid was extracted with toluene (5 mL), and the extract was evaporated to dryness with a rotary evaporator (~30 °C, ~1 Torr). The solid thus obtained was chromatographed (Bio-Beads S-X4, 1.5 × 20 cm; toluene), dried (~60 °C, ~60 Torr) and weighed (20 mg, 0.014 mmol, 31%). ^{1}H NMR (300 MHz, C_6D_6): δ 9.14 (m, 1,4-Nc H), 7.67 (m, 2,3-Nc H), 5.25 (t, α-CH_2), 2.24 (m, β-CH_2), 1.62 (m, γ-CH_2), 1.01 (t, CH_3). ^{13}C NMR (75 MHz, C_6D_6): δ 152.4 (s), 148.8 (s), 132.0 (s), 128 (s), 125.0 (s), 122.9 (s), 77.9 (s), 33.3 (s), 19.8 (s), 14.6 (s). ^{119}Sn NMR (75 MHz, C_6D_6): δ 266. MS-FD, *m*/*z*: calc. for $C_{80}H_{88}N_8O_8Cl_2Sn$ $(M)^+$, 1479; found 1478. MS-HRFAB exact mass, *m*/*z*: calc. for $C_{80}H_{88}N_8O_8Cl_2Sn^{116}$ $(M)^+$, 1474.5119; found 1474.5064, 1474.5087. UV–Vis (λ_{max} (nm), ε ($M^{-1}\,cm^{-1}$)) (CH_2Cl_2): 923, 1.0×10^5. The compound is dark brown. It is soluble in CH_2Cl_2, toluene, benzene, and slightly soluble in hexane. It is insoluble in CH_3OH and H_2O.

$SnNc(OBu)_8Br_2$. Under N_2, a mixture of $H_2Nc(OBu)_8$ (45 mg, 0.035 mmol), $SnBr_2$ (190 mg, 0.682 mmol), dry 2-ethylpyridine (0.3 mL) and dry xylenes (3 mL) was refluxed for 3 h, and evaporated to dryness with a rotary evaporator (~30 °C, ~1 Torr). The solid was extracted with toluene (5 mL), and the extract was evaporated to dryness with a rotary evaporator (~30 °C, ~1 Torr). The resulting solid was chromatographed (Bio-Beads S-X4, 1.5 × 20 cm; toluene), dried (~60 Torr, ~60 °C) and weighed (19 mg, 0.012 mmol, 34%). ^{1}H NMR (300 MHz, C_6D_6): δ 9.13 (m, 1,4-Nc H), 7.67 (m, 2,3-Nc H), 5.25 (t, α-CH_2), 2.21 (m, β-CH_2), 1.60 (m, γ-CH_2), 0.99 (t, CH_3). ^{13}C NMR (75 MHz, C_6D_6): δ 152.5 (s), 148.7 (s), 132.1 (s), 128 (s), 125.0 (s), 122.7 (s), 77.92 (s), 33.27 (s), 19.84 (s), 14.40 (s). ^{119}Sn NMR (75 MHz, C_6D_6): δ 142. MS-FD, *m*/*z*: calc. for $C_{80}H_{88}N_8O_8Br_2Sn$ $(M)^+$, 1568; found, 1568. MS-HRFAB exact mass, *m*/*z*: calc. for $C_{80}H_{88}N_8O_8Sn^{120}$ $(M-2Br)^+$, 1408.5747; found, 1408.5730, 1408.5748. UV–Vis (λ_{max} (nm), ε ($M^{-1}\,cm^{-1}$)) (CH_2Cl_2): 924, 1.2×10^5. The compound is dark brown. It is soluble in CH_2Cl_2, toluene, and slightly soluble in hexane. It is insoluble in CH_3OH and H_2O.

$SnNc(OBu)_8I_2$. Under N_2, a mixture composed of $H_2Nc(OBu)_8$ (50 mg, 0.039 mmol), SnI_2 (99.9%, 280 mg, 0.752 mmol), dry 2-ethylpyridine (0.3 mL) and xylenes (3 mL) was refluxed for 4 h, cooled and evaporated to dryness with a rotary evaporator (~30 °C, ~1 Torr). The solid was extracted with toluene (5 mL) and the extracted was evaporated to dryness with a rotary evaporator (~30 °C, ~1 Torr). The solid thus obtained was chromatographed

(Bio-Beads S-X4, 1.5 × 20 cm; toluene), dried (~60 °C, ~60 Torr) and weighed (36 mg, 0.022, 56%). ^{1}H NMR (300 MHz, C_6D_6): δ 9.12 (m, 1,4-Nc H), 7.67 (m, 2,3-Nc H), 5.27 (t, α-CH_2), 2.18 (m, β-CH_2), 1.56 (m, γ-CH_2), 0.96 (t, CH_3). ^{13}C NMR (75 MHz, C_6D_6): δ 52.6 (s), 148.7 (s), 131.2 (s), 128 (s), 125.1 (s), 122.5 (s), 78.2 (s), 33.2 (s), 19.8 (s), 14.4 (s). ^{119}Sn NMR (75 MHz, C_6D_6): δ-120. *Anal.* Calc. for $C_{80}H_{88}N_8O_8I_2Sn$: C, 57.80; H, 5.34; I, 15.27. Found: C, 57.43; H, 5.47; I, 15.37%. MS-FD, *m*/*z*: calc. for $C_{80}H_{88}N_8O_8I_2Sn$ $(M)^+$, 1662; found 1662. UV–Vis (λ_{max} (nm), ε (M^{-1} cm^{-1})) (CH_2Cl_2): 926, 1.0×10^5. The compound is dark brown. It is soluble in toluene, CH_2Cl_2, and slightly soluble in hexane. It is insoluble in CH_3OH and H_2O.

SnNc(OBu)$_8$(OSi(n-C$_6$H$_{13}$)$_3$)$_2$. Under N_2, a mixture composed of $SnNc(OBu)_8Br_2$ (30 mg, 0.019 mmol) and a mixture of $HOSi(n\text{-}C_6H_{13})_3$ (100 μL, 0.26 mmol), $NaOCH_3$ (10 mg, 0.19 mmol) and dry toluene (5 mL), which had previously been refluxed for 1 h, was refluxed for 2 h and evaporated to dryness with a rotary evaporator (~40 °C, ~1 Torr). The solid was washed with ethanol (50 mL), dried (~25 °C, ~60 Torr), chromatographed (Bio-Beads S-X4, 1.7 × 25 cm; toluene), dried (~60 °C, ~60 Torr) and weighed (22 mg, 0.011 mmol, 58%). M.p.: 156–8 °C. ^{1}H NMR (300 MHz, C_6D_6): δ 9.20 (m, 1,4-Nc H), 7.67 (m, 2,3-Nc H), 5.60 (t, C_4H_9 α-CH_2), 2.45 (m, C_4H_9 β-CH_2), 1.78 (m, C_4H_9 γ-CH_2), 1.11 (t, C_4H_9 CH_3), 0.67 (m, C_6H_{13} ε-CH_2), 0.41 (t, C_6H_{13} CH_3), 0.39 (m, C_6H_{13}γ- and δ-CH_2), −0.14 (m, C_6H_{13} β-CH_2), −1.11 (m, C_6H_{13}α-CH_2). The compound is dark brown. It is soluble in CH_2Cl_2, toluene and hexane. It is insoluble in CH_3OH and H_2O.

3. Results and discussion

3.1. Synthesis

The synthetic routes for the preparation of $SnNc(OBu)_8X_2$ (X = F, Cl, Br, I) were a template cyclization and a metal insertion. Lithium butoxide catalyzed and templated cyclization of 1,4-dibutoxy-2,3-napthalenedicarbonitrile, and the lithiated naphthalocyanine was converted to the metal-free naphthalocyanine in an acidic work-up step. The halo tin naphthalocyanines were obtained by reactions with the metal-free octabutoxy naphthalocyanine and the corresponding metal halides. Here, octabutoxy groups render good solubility in organic solvents such as toluene or dichloromethane. It is interesting that both SnX_2 and SnX_4 reacted well for tin insertion except SnF_4, and SnX_2 showed higher reactivity than SnX_4. The halide ligands can be exchanged by the highly soluble trihexylsiloxy. $SnNc(OBu)_8(OSiHx_3)_2$ was made by the ligand exchange reaction of $SnNc(OBu)_8Br_2$ and $NaOSiHx_3$ in toluene. The trihexylsiloxy ligands provide good solubility in non-polar solvents such as *n*-hexane, which is important in high concentration applications for recording disks.

3.2. NMR spectra

In the proton NMR resonances of $SnNc(OBu)_8X_2$ (X = F, Cl, Br, I, $OSi(n\text{-}C_6H_{13})_3$), the α- and β-methylene resonances of the butoxy groups are in the ranges δ 5.2–5.3 and 2.2–2.3 ppm, respectively, for the halides and δ 5.60 and 2.45 ppm for $OSi(n\text{-}C_6H_{13})_3$, as shown in Table 1. This suggests that the shieldings of α- and β-protons of the tin halo naphthalocyanines arising from ring-current effects are similar to one another, but are different from those of the trihexylsiloxy naphthalocyanine. ^{119}Sn NMR spectra, a very sensitive technique for determination of the coordination environment of the tin atom, are useful to study the structures of tin octabutoxy naphthalocyanine halides [14]. Of the 10 naturally occurring isotopes of tin, only ^{119}Sn (I = 1/2, 8.6% abundance) is a practical choice due to its slightly higher abundance and its greater sensitivity to NMR detection. ^{119}Sn NMR resonances of $SnNc(OBu)_8X_2$ are seen in Fig. 1. The trend in chemical shifts is not linear with respect to the electronegativity of the ligands. A downfield shift appears from F to Cl and then a linear upfield shift occurs from Cl to I. Simply explained, the ^{119}Sn chemical shifts would depend on the properties of the axial ligands and directly reflect the electron density at the tin nucleus. The upfield shifts of $SnNc(OBu)_8I_2$ represent a relative electron-rich environment at the tin nucleus. $SnNc(OBu)_8F_2$ exhibits a NMR spectrum different from the other halides. For the first-row element F the σ-bonding effect dominates, but for the other halides the π-bonding effect should be considered as well. These halides possess weak participation of Sn–X p_π–p_π bonding. The observed Sn–F coupling for $SnNc(OBu)_8F_2$, a triplet splitting (1:2:1), is 1820 Hz, which results from the ^{119}Sn–^{19}F *J* coupling. The ^{19}F NMR was taken to study the structure of $SnNc(OBu)_8F_2$, and $CFCl_3$ is used as the chemical shift reference [15]. A strong intense peak with two pairs of coupling peaks at −126 ppm was found. The two doublets correspond to ^{117}Sn and ^{119}Sn spin couplings to axial fluorines.

3.3. UV–Vis–NIR spectra

The tin octabutoxy naphthalocyanine halides have very strong bands in the near infrared region (>900 nm), as shown in Fig. 2. These bands are considerably red shifted as compared to the spectra of a simple naphthalocyanine

Table 1
^{1}H NMR resonances of octabutoxy tin naphthalocyanines ($SnNc(OBu)_8X_2$) in C_6D_6

X	F	Cl	Br	I	$OSi(n\text{-}C_6H_{13})_3$
α-CH_2	5.25	5.25	5.25	5.27	5.60
β-CH_2	2.30	2.24	2.21	2.18	2.45
γ-CH_2	1.66	1.62	1.60	1.56	1.78
δ-CH_2	1.05	1.01	0.99	0.96	1.11
2,3-Nc H	7.67	7.67	7.67	7.67	7.67
1,4-Nc H	9.17	9.14	9.13	9.12	9.20

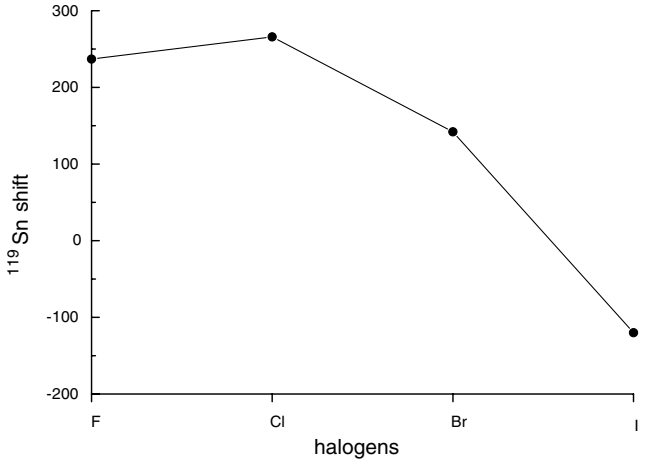


Fig. 1. Plot of the ^{119}Sn chemical shift of $SnNc(OBu)_8X_2$ vs. halogen.

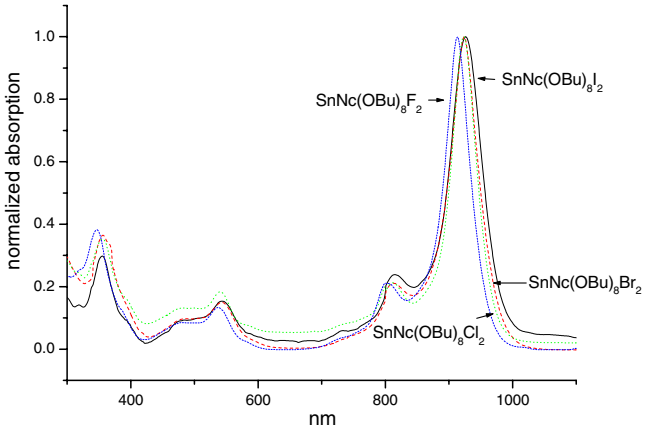


Fig. 2. UV–Vis spectra of $SnNc(OBu)_8X_2$ (X = F, Cl, Br, I).

(780 nm), octabutoxy naphthalocyanine (862 nm) or $PdNc(OBu)_8$ (892 nm). This result shows tin and halides (F, Cl, Br and I) can significantly influence the red shift of the Q-bands. The position of the Q-band in the series $SnNc(OBu)_8F_2$ (906 nm) to $SnNc(OBu)_8I_2$ (926 nm) is more shifted the heavier the halogen. The UV–Vis absorption data of a mixture of $SnNc(OBu)_8Br_2$ and C_{60} was obtained in CH_2Cl_2, as shown in Fig. 3. The extended aromatic surface of the naphthalocyanine will interact with C_{60} by π–π interactions. The Q band of $SnNc(OBu)_8Br_2$ was a little red-shifted to 928 nm (*ca.* 4 nm), and a peak at 330 nm appeared, partly attributed to C_{60}. The small red-shift would be the result of complexation of $SnNc(OBu)_8Br_2$ and C_{60}, lowering the π–π^* transition energy of the tin naphthalocyanine [16].

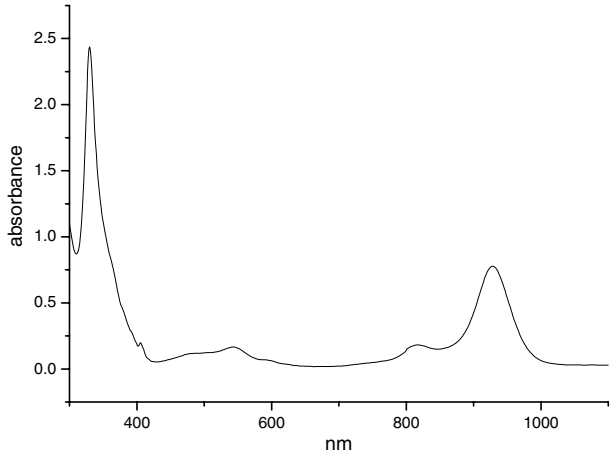


Fig. 3. UV–Vis absorption change of $SnNc(OBu)_8Br_2$ resulting from binding C_{60}.

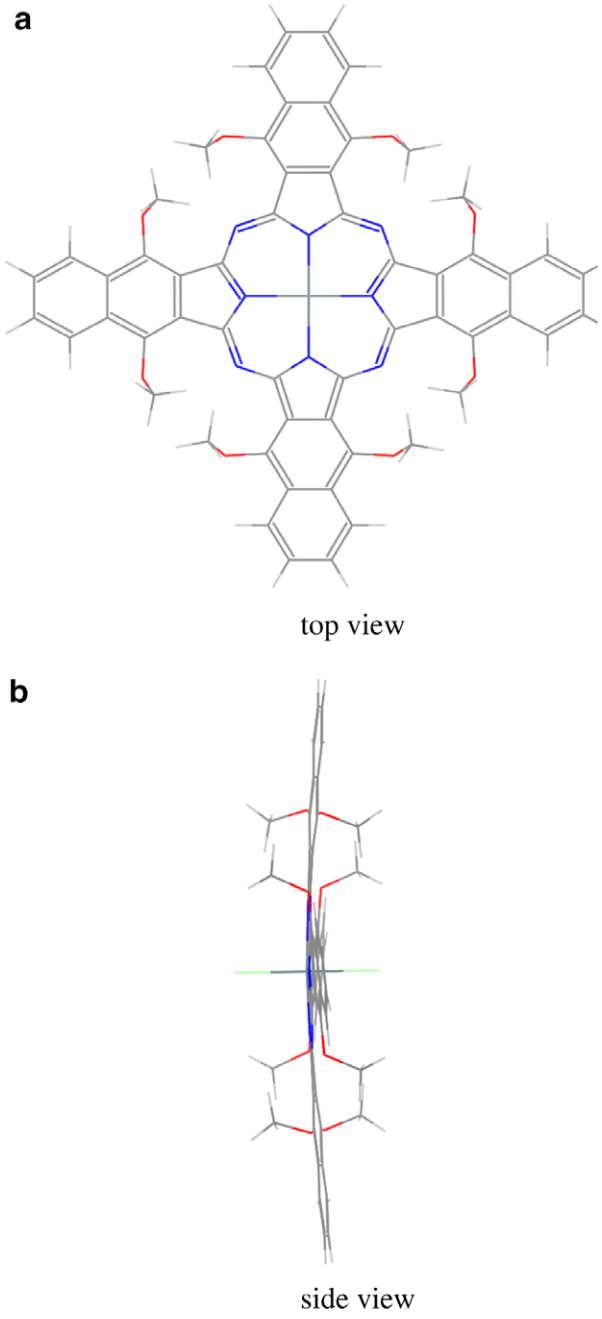


Fig. 4. The optimized molecular structure of $SnNc(OMe)_8X_2$, and the optimized bond lengths, distances and angles defined in the figure are compiled in Table 2. (a) Top view (b) side view.

Table 2
The optimized geometric parameters in the optimized structure of Fig. 4

X	Sn–X (Å)	Sn–X′ (Å)	Δ (Å)	Sn–N (Å)	h (Å)	N–Sn–N (°)	C_2–Sn–C_{20} (°)	C_3–Sn–C_{21} (°)
F	2.014	2.017	0.003	2.101	0.022	178.8	172.8	174.4
Cl	2.486	2.530	0.044	2.107	0.075	175.9	172.0	173.7
Br	2.667	2.728	0.061	2.108	0.092	175.0	171.7	173.4
I	2.900	3.004	0.104	2.110	0.127	173.1	170.4	172.2

Table 3
Experimental and calculated absorption wavelengths at the ZINDO using the BLYP-optimized geometries

X	λ_{max}^{EXP} (nm)	λ_{max}^{ZINDO} (nm)	Δ(LUMO–HOMO)^{BLYP} (nm (eV))
F	906	827.6	1330(0.932)
Cl	923	833.6	1361(0.911)
Br	924	836.4	1370(0.905)
I	926	841.0	1388(0.893)

3.4. Theoretical calculation

For a better understanding the spectroscopic results, a theoretical calculation was carried out using density functional theory at the generalized gradient approximation level, BLYP functional. Geometry optimizations of $SnNc(OMe)_8X_2$ (X = F, Cl, Br and I) were carried out without any symmetry constraints. We introduced a methoxy group instead of the butoxy group for relatively insignificant rotational conformations of OC_4H_9. The direction of methoxy on naphthalocyanine changes the planarity of naphthalocyanine, and results in several isomers. In the most stable isomer, two adjacent methoxy groups are locate in opposite directions to each other to reduce steric repulsion. In the case where all eight methoxy groups are located on the same upside or downside of the naphthalocyanine plane, the isomers have higher energies than the most stable isomers by *ca.* 20 kcal/mol. The optimized structure of the most stable $SnNc(OMe)_8X_2$ is shown in Fig. 4, and the optimized bond lengths, distances and angles defined in the figure are compiled in Table 2. As two methoxy groups on an isobenzoindole moiety are located on the upside and downside of the naphthalocyanine plane, the four isobenzoindole moieties of naphthalocyanine spread outwards in a propeller-shaped distortion. The increase of steric repulsion between the oxygen lone pairs of the facing alkoxy ligands is thought to lead to the distortion. Two C_2–Sn–C_{20} and C_3–Sn–C_{21} angles represent the degree of both naphthalocyanine planarity and distortion of isobenzoindole.[1] From F to I, the distortion of isobenzoindole increases with a slight increase of the difference between the C_2–Sn–C_{20} and C_3–Sn–C_{21} angles, and the naphthalocyanine plane becomes more concave. The deformation of the naphthalocyanine plane is accompanied by a displacement of the Sn atom out of the plane. The side view in Fig. 4b shows that the Sn atom lies above the naphthalocyanine plane. The distance, h, is defined as the out-of-plane distance of the Sn atom from the center of the naphthalocyanine plane. As the axial ligands change from F to I, the distance h varies from 0.022 to 0.127 Å. The angle N–Sn–N defined as the average bond angle between the Sn and the N atoms, also indicates the out-of-plane nature of the Sn atom. As the N–Sn–N angles decrease from F to I, the naphthalocyanine ring becomes a deep saucer-shape. The distorted shape (Sn–N angle 178.8°, 175.9°, 175.0°, 173.1°) is larger in the order of I > Br > Cl > F, with increase of the atomic size (1.33, 1.15, 0.99, 0.71 Å, respectively) and decrease of electronegativity (2.21, 2.74, 2.83, 4.10, respectively).[2] The non-planarity of the naphthalocyanine generates the two different axial-bond lengths. The axial Sn–X bond located inside of the concave, elongates more than the other axial Sn–X bond. The difference of the two axial bonds varies significantly from 0.003 to 0.104 Å with the change of the axial ligands from F to I. $SnNc(OMe)_8X_2$ has an electric dipole moment perpendicular to the naphthalocyanine plane. The electric dipole moment of $SnNc(OMe)_8X_2$ points from the halide located on the inside of the concave to the central Sn atom along the z-axis, and the magnitudes are, 0.81, 0.50, 0.35 and 0.01 for F, Cl, Br and I, respectively. A strong electronegative halide shows a high magnitude of dipole moment and presents a permanent dipole moment along the z-axis which could be advantageously used to achieve molecular orientation and poling. In order to aid the interpretation of the absorption spectra, spectroscopic calculations were performed at the BLYP-optimized geometries within the ZINDO approximation implemented in the VAMP program [11,12]. The calculated absorption λ_{max} values are also listed in Table 3. The calculations have not taken the solution environment into account, which may affect the electronic transitions and geometry. Compared with the experimental data, the calculated λ_{max} values are red-shifted by about 85 nm under the average error of 9%. In spite of the λ_{max} difference, good qualitative agreement is found between the calculations and experiments. The HOMO and LUMO gap decreases from F to I. The HOMO and LUMO at the BLYP level of theory are depicted in Fig. 5. The HOMO, filled π-type orbital, has a highly symmetric flowerlike structure with a big hole at the Sn atom, and presents nodes at every nitrogen atom of the naphthalocyanine. The LUMO, an empty π^*-type orbital, was doubly degenerate with a twofold spatial

[1] See supporting information Figure S1.

[2] http://periodic.lanl.govurlhttp://periodic.lanl.gov/default.htm.

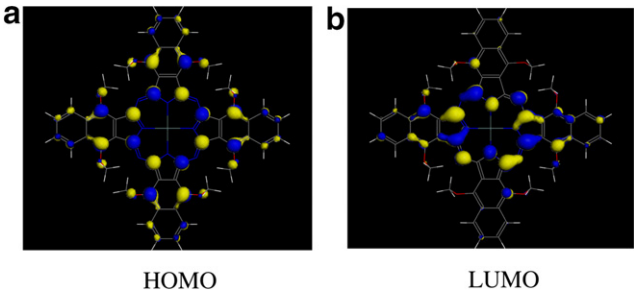


Fig. 5. The HOMO–LUMO at the BLYP level of theory (a) HOMO (b) LUMO.

symmetry. The LUMO + 1 has the same spatial structure but is rotated by 90° from the LUMO. The LUMO or LUMO + 1 consists mainly of π-orbitals, delocalized over the isobenzoindole moieties along the *x*- or *y*-axis. Disregarding the asymmetry introduced by the methoxy ligands, distortion and non-planarity, the symmetry of the HOMO and LUMO/LUMO + 1 are a_{2u} and e_g, respectively. The calculated absorption λ_{max} corresponds to the excitation from the HOMO(a_{1u}) to the LUMO or LUMO + 1(e_g). The transition dipole moment lies in the naphthalocyanine plane along the *x*- or *y*-axis, perpendicular to the permanent dipole moment in the *z*-axis, which also indicates λ_{max} results from a ligand–ligand transition ($\pi \rightarrow \pi^*$). The correlation diagram shows the molecular orbitals of $SnNc(OMe)_8X_2$ (X = F, Cl, Br and I) and their orbital energies in Fig. 6. The 4d subshell orbital of Sn is expected to be filled and is deep enough to form almost pure molecular orbitals. The overlap between the valence orbitals of Sn and the halogen ligands play a significant role in bonding, and the molecular orbitals mainly composed of the valence p orbitals of axial ligands are located under the HOMO. Moving down a column of the periodic table, valence s and p orbitals of halogen ligands are more extended with higher energy. The orbital energies of molecular orbitals mainly contributed from the valence p orbitals of axial ligands rise sharply as the axial ligands change from F to I. In the case of $SnNc(OMe)_8I_2$, the molecular orbitals mainly composed of p_x or p_y orbitals of the axial ligands are underneath the HOMO. The atomic charges on the axial ligands are expected to be distributed into the molecular orbital which is mainly composed of valence

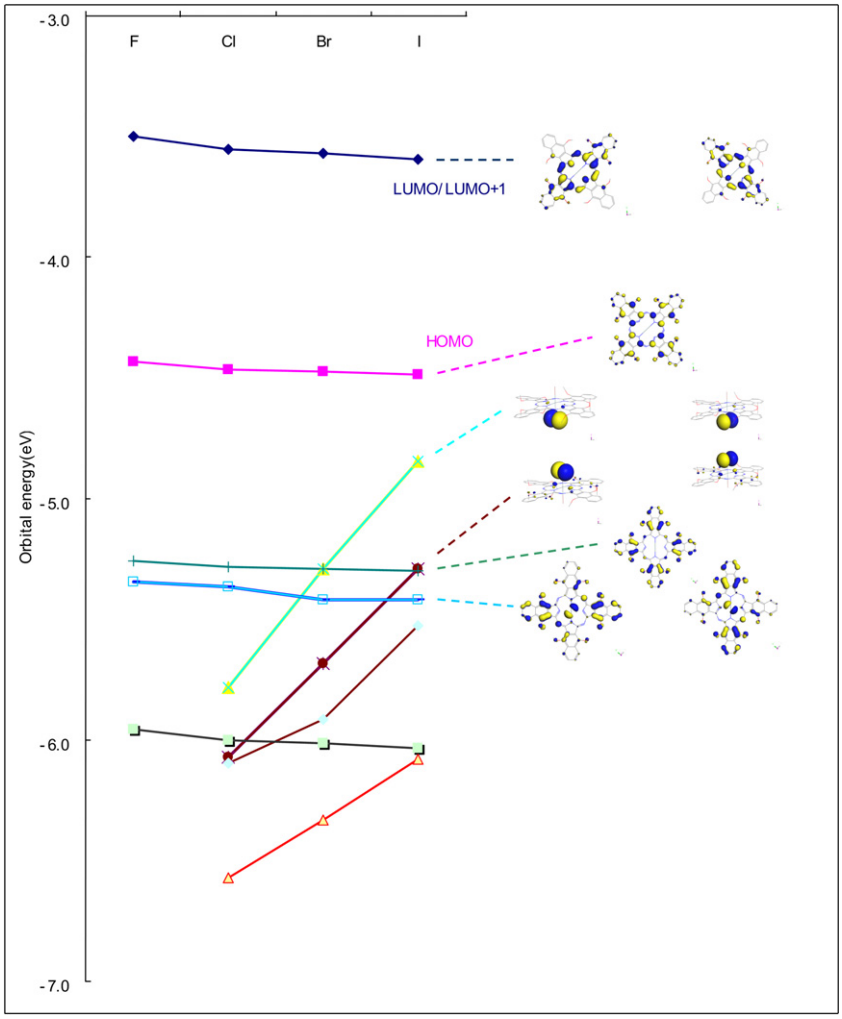


Fig. 6. The correlation diagram of the frontier molecular orbitals and their level ordering orbital energies for $SnNc(OBu)_8X_2$.

p_x and p_y orbitals. The bonding between Sn and the axial halogen ligands is described by the molecular orbitals whose main contribution is from the valence p_z orbitals of axial ligands and the Sn atom. As shown in Fig. 6, the energies of the molecular orbitals which are mainly contributed to by the naphthalocyanine ring, including the HOMO and LUMO, are slightly changed as the axial ligands change from F to I. As a result, the bonding between the Sn atom and the axial halogen ligands affects the structure of the naphthalocyanine ring and the shift of the Q-bands.

4. Conclusions

We have prepared and characterized a series of tin octabutoxy naphthalocyanines, which show near infrared absorption with a high extinction coefficient in the region 900–930 nm. The position of the Q-band in the series $SnNc(OBu)_8F_2$ (906 nm) to $SnNc(OBu)_8I_2$ (926 nm) is more red-shifted the heavier the halogen ligand. The tin naphthalocyanine with a heavy halide ligand becomes more concave, and the Sn–X bond is located at a longer distance out of the ring. The difference of the two axial bond lengths varies dramatically from 0.003 to 0.104 Å with the change of the axial ligands from F to I. The degree of the concave distortion is larger in the order $I > Br > Cl > F$, with the increase of atomic size and decrease of electronegativity. The transition dipole moment lies in the naphthalocyanine plane perpendicular to the permanent dipole moment in the tin–halide bond, which is related to the electronegativity of the axial halide. The energies of the molecular orbitals which are mainly contributed to by the naphthalocyanine ring, including the HOMO and LUMO, are slightly changed as the axial ligands change from F to I. As a result, the bonding between the Sn atom and the axial halogen ligands affects the structure of the naphthalocyanine ring and the shift of the Q-bands. The near-infrared absorption is further shifted to the infrared by the interaction with C_{60}. These tin halo naphthalocyanines could be a molecular engineering tool for spectral tuning in near infrared applications.

Appendix A. Supplementary material

Supplementary data associated with this article can be found, in the online version, at doi:10.1016/j.poly.2007.01.045.

References

[1] (a) A.B.P. Lever, Chemtech (1987) 506;
(b) R.O. Loutfy, A.M. Hor, G. DiPaola-Baranyi, C.K. Hsiao, J. Imaging Sci. 29 (1985) 116;
(c) N.J. Long, Angew. Chem., Int. Ed. Engl. 34 (1995) 21;
(d) M. Emmelius, G. Pawlowski, H.W. Vollmann, Angew. Chem., Int. Ed. Engl. 28 (1989) 1445;
(e) J. Fabian, H. Nakazumi, M. Matsuoka, Chem. Rev. (1992) 1197;
(f) J.W. Gregory, J.P. Sullivan, S.S. Wanis, N.M. Komerath, J. Acoust. Soc. Am. 119 (2006) 251.
[2] (a) M. Adachi, Y. Nagao, Chem. Mater. 11 (8) (1999) 2107;
(b) J. Fabian, H. Nakazumi, M. Matsuoka, Chem. Rev. 92 (1992) 1197;
(c) K.-Y. Law, Chem. Rev. 93 (1993) 449;
(d) S. Comby, D. Imbert, A.-S. Chauvin, J.-C. G. Bunzli, Inorg. Chem. 45 (2006) 732;
(e) K. McEwan, K. Lewis, G. Yang, L. Chng, Y. Lee, W. Lau, K. Lai, Adv. Funct. Mater. 13 (2003) 863;
(f) N.G. Pschirer, C. Kohl, F. Nolde, J. Qu, K. Mullen, Angew. Chem., Int. Ed. 45 (2006) 1401.
[3] (a) X. Huang, I.H. El-Sayed, W. Qian, M.A. El-Sayed, J. Am. Chem. Soc. 128 (2006) 2115;
(b) B. Xing, A. Khanamiryan, J. Rao, J. Am. Chem. Soc. 127 (2005) 4158.
[4] (a) R. Weissleder, C.H. Tung, U. Mahmood, A. Bogdanov, Nat. Biotech. 17 (1999) 375;
(b) A. Becker, C. Hessenius, K. Licha, B. Ebert, U. Sukowski, W. Semmler, B. Wiedenmann, C. Grotzinger, Nat. Biotech. 19 (2001) 327;
(c) S. Kim, Y.T. Lim, E.G. Soltesz, A.M. De Grand, J. Lee, A. Nakayama, J.A. Parker, T. Mihaljevic, R.G. Laurence, D.M. Dor, L.H. Cohn, M.G. Bawendi, J.V. Frangioni, Nat. Biotech. 22 (2004) 93;
(d) R. Weissleder, V. Ntziachristos, Nat. Med. 9 (2003) 123.
[5] (a) T.J. Dougherty, Photochem. Photobiol. 58 (1993) 895;
(b) T.J. Dougherty, Proc. SPIE IS 6 (1990) 1;
(c) J.C. Maziere, P. Morliere, R. Santus, J. Photochem. Photobiol. B: Biol. 8 (1991) 351;
(d) D. Phillips, Pure & Appl. Chem. 67 (1995) 117;
(e) S.I. Zaidi, R. Agarwal, G. Eichler, B.D. Rither, M.E. Kenney, H. Mukhtar, Photochem. Photobiol. 58 (1993) 204;
(f) M.W. Berns, Sci. Am. 1 (June) (1991) 84.
[6] (a) K. Mansour, J. Daniel Alvarez, K.J. Perry, I. Choong, S.R. Marder, J.W. Perry, Proc. SPIE 1853 (1993) 132;
(b) J.W. Perry, K. Mansour, S.R. Marder, C.-T. Chen, P. Miles, M.E. Kenney, G. Kwag, Mater. Res. Soc. Symp. Proc. 374 (1995) 257.
[7] (a) A.D. Becke, Phys. Rev. A88 (1988) 3098;
(b) C. Lee, W. Yang, R.G. Parr, Phys. Rev. B37 (1988) 785.
[8] M. Dolg, U. Wedig, H. Stoll, H. Preuss, J. Chem. Phys. 86 (1987) 866.
[9] (a) B. Delley, J. Chem. Phys. 92 (1990) 508;
(b) B. Delley, J. Chem. Phys. 113 (2000) 7756.
[10] Material Studio DMOL^3 User Guide, Accelrys Inc., San Diego, 2002.
[11] J. Ridley, M. Zerner, Theor. Chem. Acta 42 (1987) 347.
[12] T. Clark, A. Alex, B. Beck, F. Burkhardt, J. Chandrasekhar, P. Gedeck, A. Horn, M. Hutter, B. Martin, G. Rauhut, W. Sauer, T. Schindler, T. Steinke, VAMP, Version 8.0, Universitaẗ Erlangen, Erlangen, Germany, 2003, This version is provided as part of Materials Studio 4.0 by Accelrys Inc.
[13] B.D. Rihter, M.E. Kenney, W.E. Ford, M.A.J. Rodgers, J. Am. Chem. Soc. 115 (1993) 8146.
[14] (a) B.E. Mann, in: R.K. Harris, B.E. Mann (Eds.), Group IV-Silicon, Germanium, Tin and Lead, Academic, New York, 1978 (Chapter 4);
(b) D.P. Arnold, J.P. Bartly, Inorg. Chem. 33 (1994) 1486.
[15] R.K. Harris, J.D. Kennedy, W. McFarlane, in: R.K. Harris, B.E. Mann (Eds.), Group IV-Silicon, Germanium, Tin and Lead, Academic, New York, 1978 (Chapter 10).
[16] (a) P.D. Boyd, C.A. Reed, Acc. Chem. Res. 38 (2005) 235;
(b) D.M. Guldi, A. Gouloumis, P. Vazquez, T. Torres, V. Georgakilas, M. Prato, J. Am. Chem. Soc. 127 (2005) 5811;
(c) F. D'Souza, R. Chitta, S. Gadde, M.E. Zandler, A.L. McCarty, A.S.D. Sandanayaka, Y. Araki, O. Ito, J. Phys. Chem. A 110 (2006) 4338.

Available online at www.sciencedirect.com
ScienceDirect
Polyhedron 26 (2007) 2817–2828
POLYHEDRON
www.elsevier.com/locate/poly

Structural diversity of copper complexes with angular and linear dipyridyl ligands

Salomé Delgado [a,*], Agustín Molina-Ontoria [a], Manuela E. Medina [b], Cesar J. Pastor [b], Reyes Jiménez-Aparicio [c], José L. Priego [c]

[a] Departamento de Química Inorgánica de la Universidad Autónoma de Madrid, 28049 Madrid, Spain
[b] Servicio Interdepartamental de Investigación, Laboratory of Single Crystal X-ray Diffraction, Universidad Autónoma de Madrid, Spain
[c] Departamento de Química Inorgánica, Facultad de Ciencias Químicas, Universidad Complutense de Madrid, Ciudad Universitaria, 28040 Madrid, Spain

Received 11 December 2006; accepted 19 January 2007
Available online 27 January 2007

Abstract

The versatile coordination properties of the 2,2′ and 4,4′-long conjugated bidentate ligands 2,5-bis(2-pyridylethynyl)thiophene ($\mathbf{L_1}$), 2,2′-dipyridyldisulfide ($\mathbf{L_2}$) and 4,4′-dipyridyldisulfide ($\mathbf{L_3}$) with copper acetate has been investigated. Reactions with 2,5-bis(2-pyridylethynyl)thiophene ($\mathbf{L_1}$) and 4,4′-dipyridyldisulfide ($\mathbf{L_3}$) leads to two types of complexes. So, when methanol solutions of $Cu(OAc)_2 \cdot H_2O$ were allowed to diffuse into a solution of $\mathbf{L_1}$ or $\mathbf{L_3}$ (ratio 1:1), green crystals of the molecular 1:2 adduct $Cu_2(\mu\text{-}OAc)_4(L_1)_2$ (**1**) and the infinite coordination polymer $[Cu_2(\mu\text{-}OAc)_4(L_3)]_n$ (**2**) were obtained. The reaction with $\mathbf{L_2}$, under reflux in MeOH, affords the copper(I) cluster $Cu_6(SC_5H_4N)_6$ (**3**) and the dimer $[Cu(\mu\text{-}S)(L_2)]_2$ (**4**). Compound **3** was already known by reaction of the copper(I) salt $[Cu(NC\text{-}Me)_4]PF_6$ with SC_5H_4NH in acetone. The structures were determined by X-ray crystallography and their magnetic properties examined.
© 2007 Elsevier Ltd. All rights reserved.

Keywords: Acetate copper(II); Coordination polymers; N-ligands

1. Introduction

Networks propagated through metal–ligand coordination bonds, known as coordination polymers or metal–organic frameworks (MOFs), comprise a large and diverse area of activity within inorganic crystal engineering [1]. In recent years, it has become an important area of research due to the growing need for novel solid-state architectures with potential applications in fields such as magnetism [2], catalysis and separation [3], non-linear optics [4] and molecular sensing [5].

The structures and properties of coordination polymers can be controlled by choosing appropriate bridging ligands and metal ions. In particular, much research has been concentrated on the use of bridging 4,4′-bipyridine based rodlike ligands [6] and bent ligands are relatively less used as building blocks due to the difficulty in predicting structure.

Previously, we have studied how the effect of the 2,2′-positional orientation of the nitrogen atoms in bis-pyridine-type ligands such as 1,2-bis(2-pyridyl)butadiyne, 2,5-bis(2-pyridylethynyl)thiophene (rigid ligands) and 2,2′-dipyridyldisulfide (flexible ligand) with $Cu(hfac)_2$ and $Cu(OAc)_2 \cdot H_2O$, influences on the coordination framework and to affects the polymeric architectures of the crystalline materials. Moreover, the reaction between $Cu(hfac)_2$ and 2,2′-dipyridyldisulfide showed new interesting transformations due to the reactivity and cleavage of S–S bond and formation of S–C bonds [7].

As a continuation of our research concerning the use of these kind of ligands in the synthesis of coordination polymers and to investigate the effect of the counterion upon these reactions, herein we report the synthesis, crystal

* Corresponding author.
E-mail address: salome.delgado@uam.es (S. Delgado).

0277-5387/$ - see front matter © 2007 Elsevier Ltd. All rights reserved.
doi:10.1016/j.poly.2007.01.021

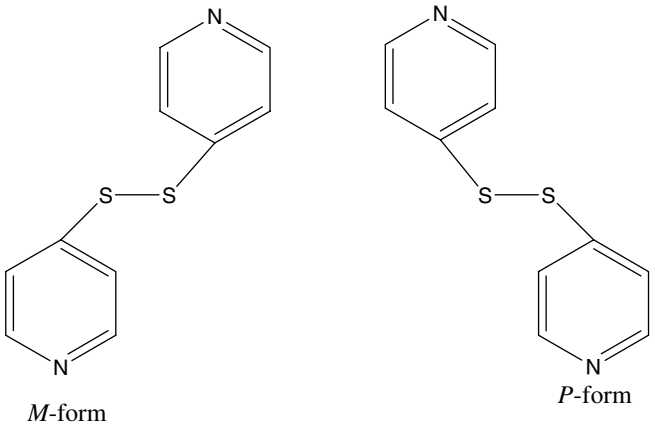


Fig. 1. Enantiomers forms of 4,4′-dipyridyldisulfide ($\mathbf{L_3}$).

structures and magnetic properties of new Cu(II)-compounds prepared by reactions between $Cu(OAc)_2 \cdot H_2O$ and 2,5-bis(2-pyridylethynyl)thiophene ($\mathbf{L_1}$) and 2,2′-dipyridyldisulfide ($\mathbf{L_2}$). Further, in order to compare how affects the position of the nitrogen atoms in the pyridine rings upon complexation, we choose the 4,4′-dipyridyldisulfide ligand ($\mathbf{L_3}$), which has a twisted conformation similar to $\mathbf{L_2}$ because of the flexible –S–S– group, with its two C–S–S–C torsion angles of approximately 90°, and with axial chirality generating *M*- and *P*-enantiomers as shown in Fig. 1. A recent review of the structural diversity derived from 4,4′-dipyridyldisulfide ligand has been published [8].

2. Results and discussion

In our previous work, we found that the reaction between $Cu(OAc)_2 \cdot H_2O$ and 2,2′-dipyridyldisulfide in methanol at room temperature, in a 1:1 molar ratio, afford the molecular 1:2 adduct $[Cu_2(\mu\text{-}OAc)_4(L_2)_2]$ instead of the polymeric compound $[Cu_2(\mu\text{-}OAc)_4(L_2)]_n$ [7]. To investigate how the nature of the ligand could affects to assembly processes, we evaluated the dependence of the orientation of the ligands on the structures. Because of it, we choose a rigid ligand as 2,5-bis(2-pyridylethynyl)thiophene ($\mathbf{L_1}$), with the same orientation than 2,2′-dipyridyldisulfide ($\mathbf{L_2}$), and a flexible ligand, 4,4′-dipyridyldisulfide ($\mathbf{L_3}$), similar to $\mathbf{L_2}$ but with a different orientation.

So, when methanol solutions of $Cu(OAc)_2 \cdot H_2O$ were allowed to diffuse, at room temperature, into a solution of $\mathbf{L_1}$ in CH_2Cl_2 or $\mathbf{L_3}$ in MeOH (ratio 1:1), green crystals of the molecular 1:2 adduct $Cu_2(\mu\text{-}OAc)_4(L_1)_2$ (**1**) and the infinite coordination polymer $[Cu_2(\mu\text{-}OAc)_4(L_3)]_n$ (**2**) were obtained within 9 and 6 days, respectively. These results shown as the orientation of the ligands influences on the

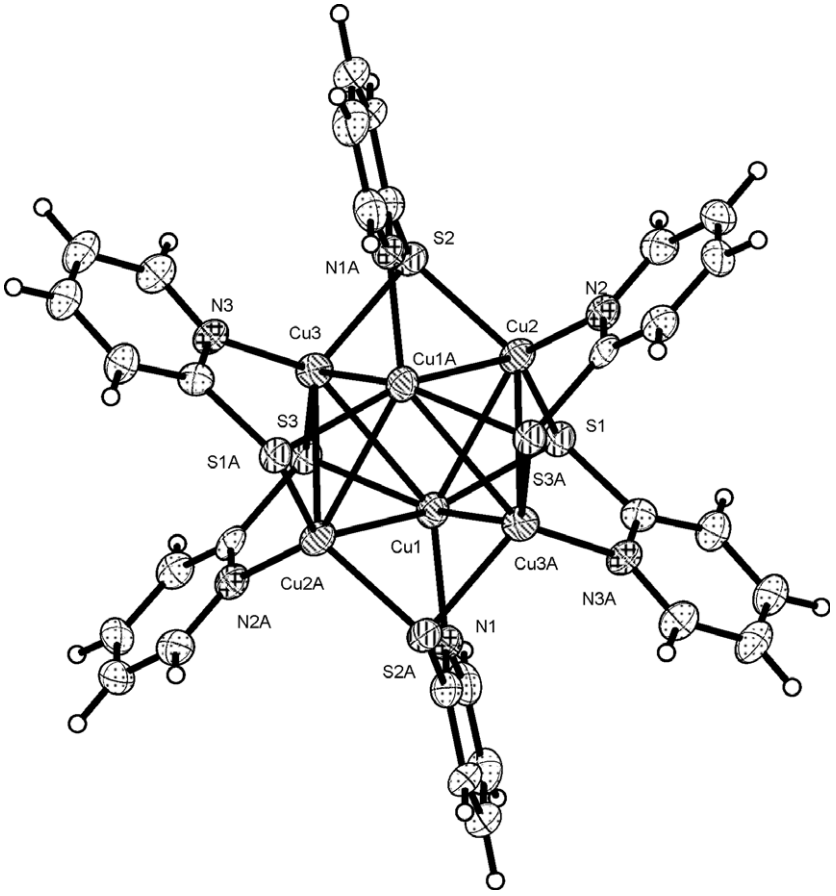


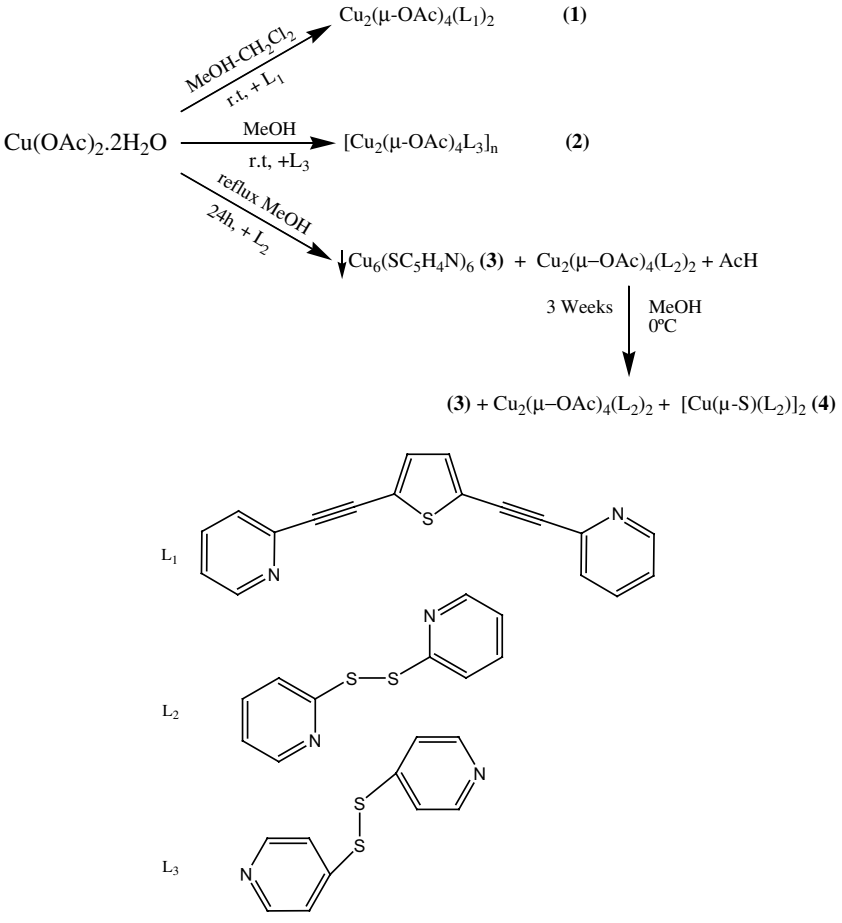
Fig. 2. ORTEP projection of the $Cu_6(SC_5H_4N)_6$ cluster, C and H atoms have no been labelled for clarity and displacement ellipsoids are shown at the 50% probability level.

self-assembly process. The dimeric compounds $[Cu_2(\mu\text{-}OAc)_4(L)_2]$ are obtained for $\mathbf{L_1}$ and $\mathbf{L_2}$, with 2,2′-orientation, probably due to steric factors, while the polymer $[Cu_2(\mu\text{-}OAc)_4(L_3)]_n$, is isolated for $\mathbf{L_3}$, with 4,4′-positions. While we were carrying out this study, a similar reaction between $Cu(OAc)_2 \cdot H_2O$ and $\mathbf{L_3}$, using also MeOH as solvent, was published. However, the product was recrystallized from DMF/diethyl ether giving $[Cu_4(OAc)_6(\mu_3\text{-}OH)_2(L_2)_2]_n$, with a ruffled ribbon topology [9]. These results demonstrate that not only the orientation of dipyridyl ligands but even also the recrystallizing solvent play important roles in the self-assembly processes.

On the other hand, we had previously observed in the reaction between 2,2′-dipyridyldisulfide and $Cu(hfac)_2$, under reflux in MeOH, the cleavage of the S–S bond in $\mathbf{L_2}$, giving new interesting transformations with formation of a zwitterionic organic compound and a mononuclear compound with Cu–C bond [7]. Likewise, the reaction with $Cu(NO_3)_2 \cdot 3H_2O$ in the same conditions, leads to an unexpected sulfinate–sulfonate mixed coordination polymer $[\{Cu(2\text{-}pySO_2)_2\}_n]$–$[\{Cu(2\text{-}pySO_3)_2\}_n]$ [10]. These observations led us to study in more detail the influence that the counteranions have on the cleavage of the S–S bond in $\mathbf{L_2}$.

When $Cu(OAc)_2 \cdot H_2O$ and $\mathbf{L_2}$ were allowed to react together under reflux in MeOH for one day, an orange solid readily precipitated and was isolated and characterized by X-ray diffraction as the copper(I) cluster $Cu_6(SC_5H_4N)_6$ (**3**) (Fig. 2). The structure of this compound was originally obtained by Kitagawa et al. [11], who prepared it by reaction of the copper(I) salt $[Cu(NCMe)_4]PF_6$ with SC_5H_4NH in acetone. In our reaction the green solution is slightly acid and has the characteristic odour of acetic acid. The IR spectrum shows a band at 1624 cm^{-1} attributable to ν(CO) of acetic acid. If the green solution is rapidly extracted to vacuum, only the dimer $[Cu_2(\mu\text{-}OAc)_4(L_2)_2]$ is isolated, but by standing of the solution at 0 °C for at least 3 weeks, the red compound $[Cu(\mu\text{-}S)(L_2)]_2$ (**4**) is isolated in a very low yield (4%) together with $Cu_6(SC_5H_4N)_6$ (**3**) and $[Cu_2(\mu\text{-}OAc)_4(L_2)_2]$ (Scheme 1).

One possible mechanism that could explain the formation of **3** and **4** involves the cleavage of the S–S bond in the $\mathbf{L_2}$ ligand, probably promoted by the Cu^{II} ion. It is known how the disulfide bond in R–S–S–R systems is broken by metal ions [12]. The nucleophilic attack by water gives pyridine-2-thiol, in tautomeric equilibrium with pyridine-2(1*H*)-thione [12,13], which produces the in situ reduction of copper(II) to copper(I) yielding the highly insoluble S,N-coordinated hexamer **3**, very stable termodynamically. The reaction of SC_5H_4NH with $Cu(OAc)_2 \cdot H_2O$



Scheme 1.

gives the same compound [14]. In order to test whether acetic acid plays a role in the formation of **3**, we have repeated the reaction in the same conditions, in the presence of acetic acid. We observe that the decomposition progress to **3** is retarded, due to the fact that in acidic conditions the nitrogen atom of the SC_5H_4NH ligand is protonated, preventing the involvement of the nitrogen atom in coordination.

The formation of **4** could be explained by carbon–sulfur bond cleavage of some thiolates; this processes constitute a classical route to obtain metal sulfides [15–18] and re-forming some disulfide as results of oxidation of pyridine-2-thiol.

All compounds have been characterized by analytical and IR spectroscopy data. Details are given in Section 5.

3. Description of the crystal structures

3.1. $[Cu_2(\mu\text{-}OAc)_4(L_1)_2]$ (**1**)

Fig. 3a shows the ORTEP drawing of the asymmetric unit of **1**, with the numbering scheme. Table 1 sums up its most important crystallographic data, and selected bond lengths and angles are summarized in Table 2. The structure consists of the molecular 1:2 adduct $Cu_2(\mu\text{-}OAc)_4(L_1)_2$ where the copper(II) ion is pentacoordinate to four oxygen atoms from four different acetate anions and one nitrogen atom from the pyridine ring of $\mathbf{L_1}$, in a square-based pyramidal fashion. The Cu(II) center deviates from the mean equatorial plane, defined by four coordinated oxygen atoms, towards the apical nitrogen atom by 0.207 Å, which is slightly longer than the same deviation of 0.1536 Å in the $[Cu_2(\mu\text{-}OAc)_4(L)_2]$ (L = 2,2′-dipyridyldisulfide) compound [7]. The Cu–O distances [1.9683(17)–1.9854(16) Å] are similar to those found in its analogous compounds [7,19,20] and the Cu–N distance [2.207(2) Å] is longer than the same distance for the polymer $[Cu(hfac)_2L_1]_n$ [2.0379(16) Å] and similar to the one for the dimer $[Cu_2(\mu\text{-}OAc)_4(L_2)_2]$ [2.252(3) Å] [7]. Four acetate anions bridge two Cu(II) center in *syn–syn* fashion to form a $[Cu_2(OAc)_4]$ binuclear building unit (Fig. 3b) with a Cu–Cu distance of 2.6528(6) Å, which is linked

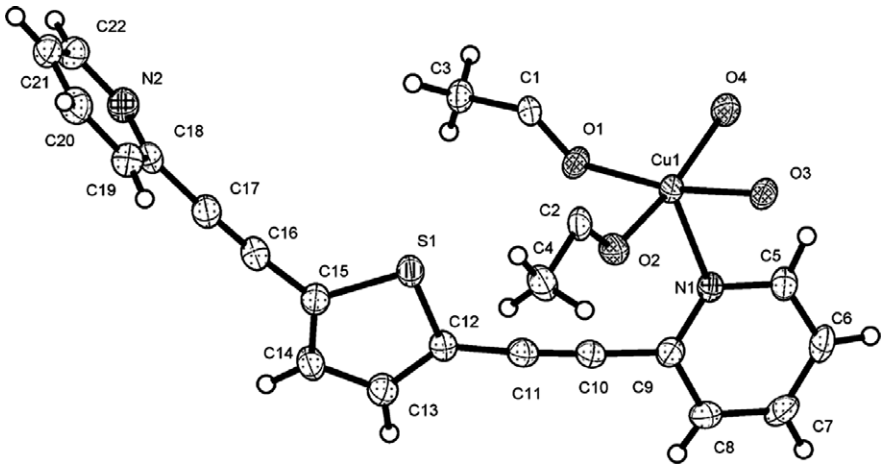


Fig. 3a. An ORTEP projection of the asymmetric unit of $[Cu_2(\mu\text{-}OAc)_4(L_1)_2]$ with displacement ellipsoids shown at the 50% probability level and H atoms no labelled for clarity.

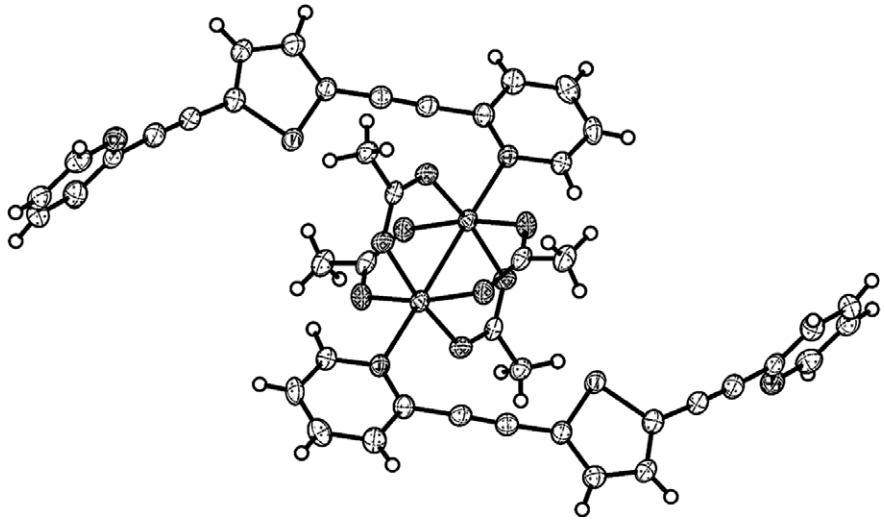


Fig. 3b. $[Cu_2(OAc)_4]$ binuclear building unit of compound **1**.

Table 1
Crystallographic data for **1**, **2** and **4** compounds

Compound	**1**	**2**	**4**
Empirical formula	$C_{44}H_{32}CU_2N_4O_8S_2$	$C_9H_{10}CuNO_4S$	$C_{20}H_{16}Cu_2N_4S_6$
Formula weight	935.94	291.78	631.81
Temperature (K)	100(2)	298(2)	100(2)
Wavelength (Å)	1.54178	1.54178	1.541 78
Crystal system	triclinic	orthorhombic	triclinic
Space group	$P\bar{1}$	*Pccn*	$P\bar{1}$
Unit cell dimensions			
a (Å)	10.0016(9)	12.7919(19)	8.05660(10)
b (Å)	10.2539(9)	24.158(4)	8.93560(10)
c (Å)	11.1815(10)	8.7705(13)	9.33060(10)
α (°)	64.206(3)	90	80.3980(10)
β (°)	81.412(3)	90	72.2400(10)
γ (°)	73.199(3)	90	65.4860(10)
Volume (Å^3)	988.03(15)	2710.3(7)	581.412(12)
Z	1	8	1
D_{calc} (Mg/m^3)	1.573	1.430	1.804
Absorption coefficient (mm^{-1})	2.832	3.732	7.441
F(000)	478	1184	318
Crystal size (mm)	$0.20 \times 0.08 \times 0.04$	$0.10 \times 0.08 \times 0.02$	$0.25 \times 0.14 \times 0.04$
θ Range for data collection (°)	4.39–67.02	3.91–71.83	4.98–71.23
Index ranges	$-11 < h < 10$, $-12 < k < 12$, $-11 < l < 13$	$-15 < h < 15$, $-28 < k < 29$, $-10 < l < 9$	$-9 < h < 9$, $-10 < k < 10$, $-11 < l < 11$
Reflections collected	7613	16 352	6312
Independent reflections (R_{int})	3286 (0.0290)	2591 (0.1384)	2133 (0.0335)
Completeness to theta = 70.57°/62.63°/70.63° (%)	93.2	97.4	94.6
Absorption correction	SADABS v. 2.03	SADABS v. 2.03	SADABS v. 2.03
Refinement method	full-matrix least-squares on F^2	full-matrix least-squares on F^2	full-matrix least-squares on F^2
Data/restraints/parameters	3286/0/335	2591/0/149	2133/293/145
Goodness-of-fit on F^2	1.057	0.917	1.054
Final *R* indices [$I > 2\sigma(I)$]	$R_1 = 0.0378$, $wR_2 = 0.0975$	$R_1 = 0.0527$, $wR_2 = 0.1143$	$R_1 = 0.00324$, $wR_2 = 0.0874$
R indices (all data)	$R_1 = 0.0435$, $wR_2 = 0.1012$	$R_1 = 0.0913$, $wR_2 = 0.1267$	$R_1 = 0.0337$, $wR_2 = 0.0888$
Largest difference in peak and hole (e A^{-3})	0.656 and −0.391	0.447 and −0.384 e A$^{\circ -3}$	0.850 and −0.532

Table 2
Selected bond lengths (Å) and angles (°) for compound **1**

Selected bond lengths (Å)		Selected angles (°)			
Cu(1)–O(2)	1.9683(17)	O(2)–Cu(1)–O(1)	91.72(7)	O(3)–Cu(1)–N(1)	92.76(7)
Cu(1)–O(1)	1.9731(16)	O(2)–Cu(1)–O(4)	167.85(7)	O(2)–Cu(1)–Cu(1)#1	80.93(5)
Cu(1)–O(4)	1.9821(16)	O(1)–Cu(1)–O(4)	88.42(7)	O(1)–Cu(1)–Cu(1)#1	83.81(5)
Cu(1)–O(3)	1.9854(16)	O(2)–Cu(1)–O(3)	89.27(7)	O(4)–Cu(1)–Cu(1)#1	87.01(5)
Cu(1)–N(1)	2.207(2)	O(1)–Cu(1)–O(3)	167.81(6)	O(3)–Cu(1)–Cu(1)#1	84.35(5)
Cu(1)–Cu(1)#1	2.6528(6)	O(4)–Cu(1)–O(3)	88.08(7)	N(1)–Cu(1)–Cu(1)#1	176.61(5)
		O(2)–Cu(1)–N(1)	97.29(7)	C(5)–N(1)–Cu(1)	114.62(15)
		O(1)–Cu(1)–N(1)	99.16(7)	C(9)–N(1)–Cu(1)	127.11(16)
		O(4)–Cu(1)–N(1)	94.68(7)		

by two $\mathbf{L_1}$ ligands in a *trans* disposition. The pyridyl groups of the $\mathbf{L_1}$ are not coplanar through the diyne portion and forming an angle of 79.35°. Two pyridyl rings within each $\mathbf{L_1}$ ligand are in a *cisoid* arrangement. This orientation leads to steric factors that could explain why the molecular compound $[Cu_2(\mu\text{-}OAc)_4(L_1)_2]$ (**1**) is formed instead of the polymeric complex $[Cu_2(\mu\text{-}OAc)_4(L_1)]_n$.

3.2. $[Cu_2(\mu\text{-}OAc)_4(L_3)]_n$ (**2**)

Fig. 4a shows an ORTEP drawing of the asymmetric unit of compound **2**. Apposed to **1**, compound **2** adopts a zig-zag chain structure, as it is shown in Fig. 4b. The crystallographic data are given in Table 1, while selected bond lengths and angles are listed in Table 3. As in **1**, for compound **2** the copper atom has a square-pyramid geometry with Cu–O bond

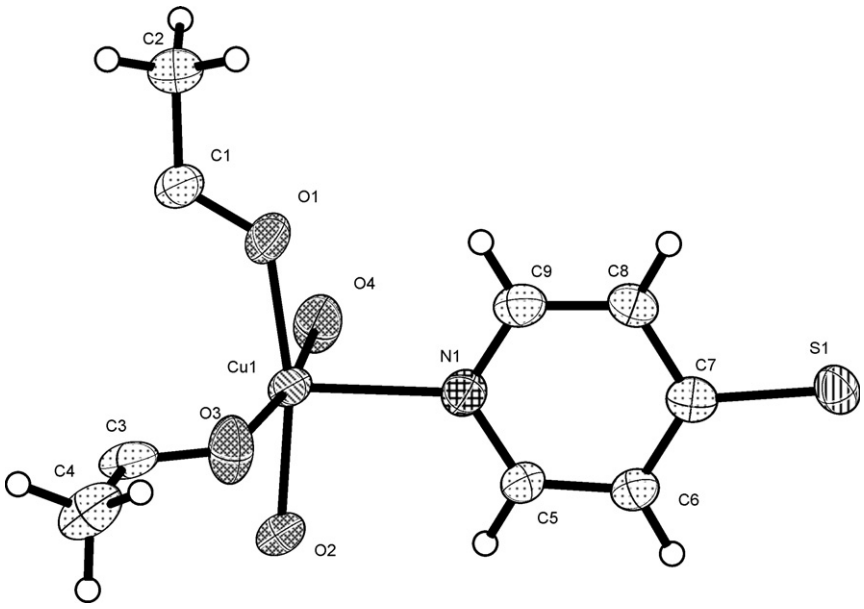


Fig. 4a. An ORTEP projection of the asymmetric unit of compound $[Cu_2(\mu\text{-}OAc)(L_3)]_n$ with displacement ellipsoids shown at the 50% probability level.

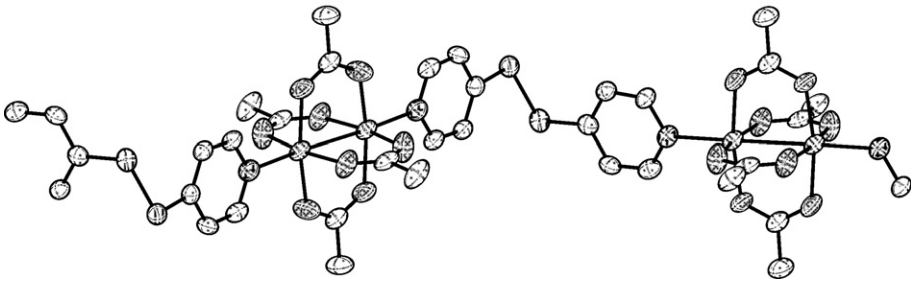


Fig. 4b. One of the zig-zag chains of compound **2**.

lengths very close to those found in compound **1** and Cu–N and Cu–Cu distances [2.162(4), 2.6088(14) Å] shorter than their equivalents found in **1** [2.207(2), 2.6528(6) Å], respectively. The $\mathbf{L_3}$ ligand supports its characteristic twisted conformation. The S–S distance [2.024(3) Å] and C–S–S–C torsion angles (89.59°) are comparable to those found in $[M(hfac)_2(\mathbf{L_3})]_n$(M = Cu,Mn,Co,Ni)and$[\{Cu(\mathbf{L_2})(H_2O)\} \cdot 2NO_3 \cdot 3H_2O]_n$ [21,22], and the angle between the two pyridine rings in each $\mathbf{L_3}$ ligand is 79.25°. Compared to the analogous structure which contains the 2,2′-dipyridyldisulfide ligand, the Cu–N distances [2.161(5) Å] is shorter than the same distance for $[Cu_2(\mu\text{-}OAc)_4(2,2'\text{-}dpds)_2]$ [2.252(3) Å] [7]. The polymer contains racemic components of $\mathbf{L_3}$ and chiral crystals of the coordination polymer have not been isolated.

3.3. *[Cu(μ-S)(L2)]2 (4)*

The crystallographic data for this compound are given in Table 1. Selected bond lengths and angles are listed in Table 4. Fig. 5a shows an ORTEP drawing of the asymetric unit of **4**. This is a molecular compound built up from two units $Cu(L_2)$ that are linked together by two μ-S atoms. In this case the copper center has a quasi-tetrahedral environment. Two positions of this tetrahedron are occupied by two nitrogen atoms from two pyridyl rings of $\mathbf{L_2}$ and at the other two positions two μ-S atoms are located. The first interactions result in the formation of a seven-membered chelate ring. The Cu–N distance [2.0170(2) and 1.9840(2) Å] are shorter than the same distances found for the polymer $[Cu(hfac)_2L_1]_n$ [2.0379(16) Å] and for the dimer $[Cu_2(\mu\text{-}OAc)_4(L_2)_2]$ [2.2520(3) Å] [7]. This binuclear building unit is shown in Fig. 5b, with a Cu–Cu distance of 3.1660(3) Å. The pyridyl groups of the $\mathbf{L_1}$ are not coplanar through the S–S bond, and form an angle of 138.8°. The S–S distance [2.0491(5) Å] is comparable to those found in $[M(hfac)_2(\mathbf{L_3})]_n$ (M = Cu, Mn,Co,Ni) and $[\{Cu(\mathbf{L_2})(H_2O)\} \cdot 2NO_3 \cdot 3H_2O]_n$ [21,22] whereas the C–S–S–C torsion angle (102.5°) is bigger than the others found for those compounds and shorter than the same angle for $[CuBr_2(L_2)]$ (108.9°) [23].

In Table 5 are summarized significant structural data for **2**, **4** and analogous Cu(II) complexes. From the values observed we can see that both $\mathbf{L_2}$ as $\mathbf{L_3}$ ligands support their characteristic twisted conformation and despite the rigidity of the S–S– bridging groups in $\mathbf{L_2}$ and $\mathbf{L_3}$, its compounds show various structures when assembled. The (S–S) bond lengths in all compounds present values very close to the typical values found in aromatic disulfides [24],

Table 3
Selected bond lengths (Å) and angles (°) for compound **2**

Selected bond lengths (Å)		Selected angles (°)			
Cu(1)–O(4)	1.961(4)	O(4)–Cu(1)–O(3)	168.34(16)	O(3)–Cu(1)–Cu(1)#1	85.98(11)
Cu(1)–O(3)	1.962(4)	O(4)–Cu(1)–O(1)	90.02(18)	O(1)–Cu(1)–Cu(1)#1	84.35(11)
Cu(1)–O(1)	1.963(4)	O(3)–Cu(1)–O(1)	89.61(18)	O(2)–Cu(1)–Cu(1)#1	84.20(11)
Cu(1)–O(2)	1.965(4)	O(4)–Cu(1)–O(2)	89.48(17)	N(1)–Cu(1)–Cu(1)#1	174.63(11)
Cu(1)–N(1)	2.162(4)	O(3)–Cu(1)–O(2)	88.58(17)	C(9)–N(1)–Cu(1)	122.9(3)
Cu(1)–Cu(1)#1	2.6088(14)	O(1)–Cu(1)–O(2)	168.51(15)	C(5)–N(1)–Cu(1)	119.5(3)
		O(4)–Cu(1)–N(1)	92.31(16)	C(1)–O(1)–Cu(1)	123.0(3)
		O(3)–Cu(1)–N(1)	99.33(15)	C(1)#1–O(2)–Cu(1)	123.2(3)
		O(1)–Cu(1)–N(1)	94.87(15)	C(3)–O(3)–Cu(1)	121.2(4)
		O(2)–Cu(1)–N(1)	96.63(15)	C(3)#1–O(4)–Cu(1)	125.8(3)
		O(4)–Cu(1)–Cu(1)#1	82.39(12)		

Table 4
Selected bond lengths (Å) and angles (°) for compound **4**

Selected bond lengths (Å)		Selected angles (°)			
		S(3)–Cu(1)–S(3)#1	97.80(2)	C(5)–N(1)–C(1)	117.6(2)
Cu(1)–N(1)	1.984(2)	N(1)–Cu(1)–N(2)	122.58(8)	C(5)–N(1)–Cu(1)	119.98(16)
Cu(1)–N(2)	2.017(2)	N(1)–Cu(1)–S(3)	117.74(6)	C(1)–N(1)–Cu(1)	122.34(17)
Cu(1)–S(3)	2.3467(6)	N(2)–Cu(1)–S(3)	108.71(6)	C(10)–N(2)–Cu(1)	128.73(16)
Cu(1)–S(3)#1	2.4679(6)	N(1)–Cu(1)–S(3)#1	102.56(6)	C(6)–N(2)–Cu(1)	114.20(16)
S(3)–Cu(1)#1	2.4679(6)	N(2)–Cu(1)–S(3)#1	102.61(6)	Cu(1)–S(3)–Cu(1)#1	82.20(2)

regardless of the metal species, coordination environment and counter anion, with exception of $[CuBr_2L_2]$ and $[Cu(\mu\text{-}S)(L_2)]_2$ (**4**), with longer distances and in which the 2,2′-dipyridyldisulfide ligand forms a seven-membered chelate ring. The same effect is observed if we compare the C–S–S–C torsion angle, maintaining a near 90° angle. However, $[CuBr_2L_2]$ and $[Cu(\mu\text{-}S)(L_2)]_2$ (**4**) are exhibiting angles significantly larger than 90°.

3.4. Magnetic properties

For complexes **1** and **2** the magnetic susceptibility curves show broad maximum from 330 to 125 K in both cases indicating a very strong antiferromagnetic interactions between the Cu(II) atoms of each dimetallic unit. At very low temperature, there is a very sharp increase of the magnetic susceptibility values indicating the presence of a paramagnetic impurity. Similar paramagnetic impurities are usually present in complexes with strong antiferromagnetic coupling. The temperature dependence of the magnetic moment towards temperature is also indicative of this antiferromagnetic coupling. Thus, the magnetic moment of **1** and **2** at room temperature are 1.65 and 1.82 μ_B, respectively. These magnetic moments are smaller than that expected for two magnetically isolated spin $S = 1/2$ centers per dicopper unit. The shape of the magnetic moment

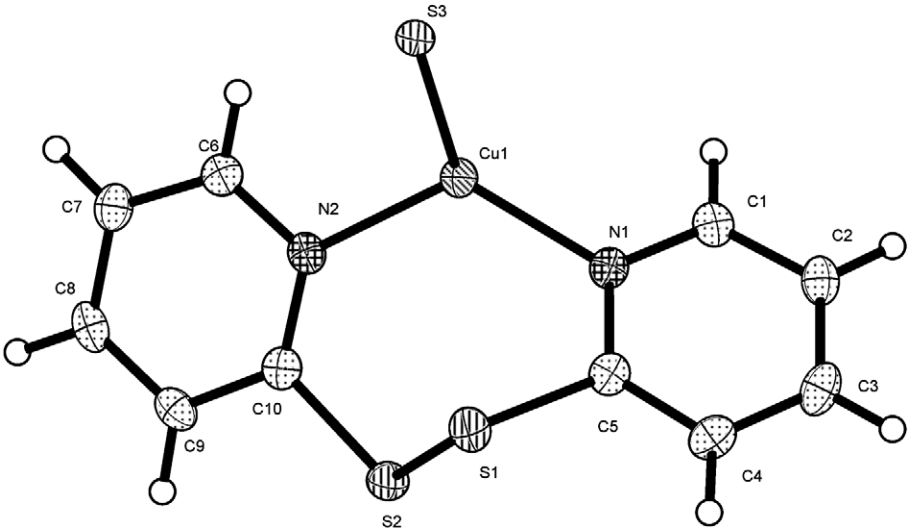


Fig. 5a. An ORTEP projection of the asymmetric unit of compound $[Cu(\mu\text{-}S)(L_2)]_2$. The displacement ellipsoids are shown at the 50% probability level.

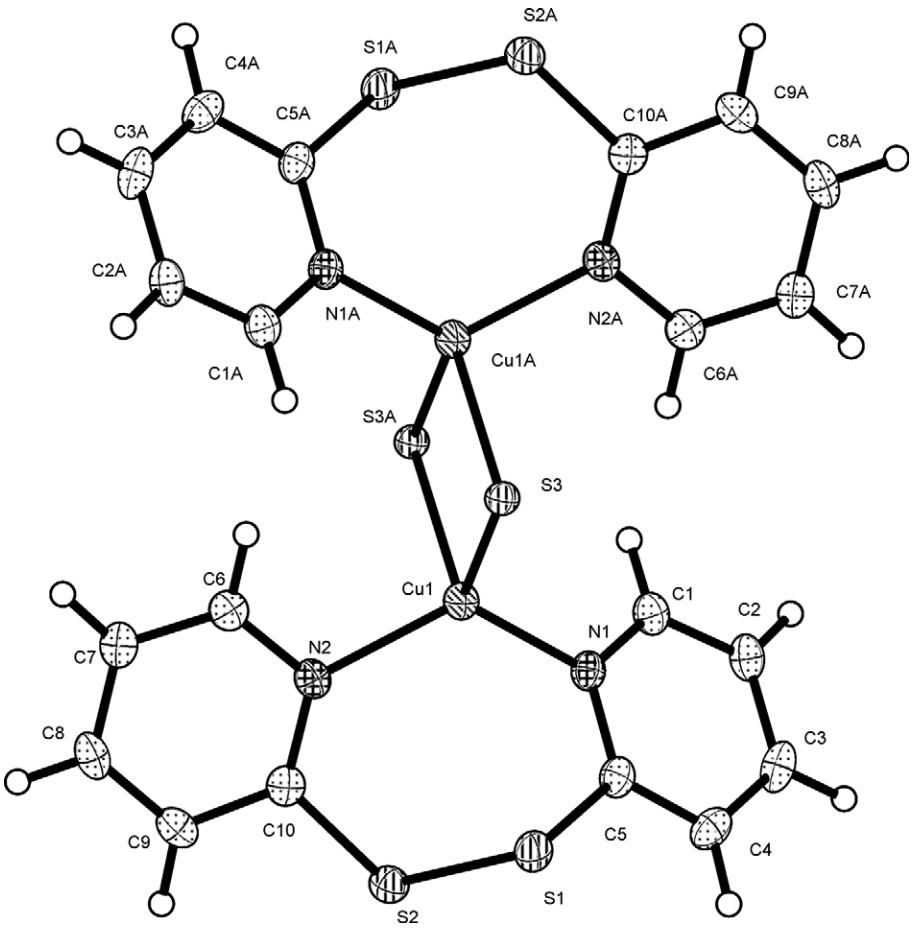


Fig. 5b. A view of this molecular compound, built up from two units $Cu(L_2)$. linked by two μ-S atoms.

Table 5
S–S bond lengths (Å), C–S–S–C torsion angles (°), the dihedral angles of the two pyridyl rings (°) in **2**, **4** and analogous Cu(II) complexes

Complexes	Topology	S–S distance (Å)	C–S–S–C torsion angle (°)	Dihedral angles of the two pyridyl rings (°)	Reference
$[Cu_2(\mu\text{-}OAc)_4(L_3)]_n$ (**2**)	zig-zag chain	2.024	89.6	79.2	this work
$[\{Cu(L_3)_2(H_2O)\} \cdot 2NO_3 \cdot 3H_2O]_n$	repeated rhomboid	2.027	89.8	98.6	[22]
$[\{Cu(L_3)_2(SO_4)\} \cdot 5H_2O \cdot CH_3OH]_n$	repeated rhomboid	2.033	88.4	83.5	[22]
$[Cu(hfac)_2(L_3)]_n$	helical chain	2.029	88.2	109.5	[21b]
$[Cu_2(\mu\text{-}OAc)_4(L_2)]_2$	dimer	2.035	89.4	107.2	[7]
$[Cu(hfac)_2(L_2)]_n$	zig-zag chain	2.037	79.8	79.8	[7]
$[CuBr_2L_2]$	molecular	2.059	108.9	64.8	[23]
$[CuCl_2(\mu\text{-}L_2)]_n$	helical chain	2.031	98.4	84.3	[23]
$[Cu(\mu\text{–}S)(\mu\text{-}L_2)]_2$ (**4**)	dimer	2.049	102.5	138.8	this work

L_2 = 2,2′-dipyridyldisulfide; L_3 = 4,4′-dipyridyldisulfide.

curves shows a pronounced decrease until 100 K and drops more slowly to 0.5 μ_B at 2 K in both complexes. The magnetic data of these compounds have been analysed [25] by a Bleaney–Bowers expression derived from the isotropic spin Hamiltonian of Eq. (1) with $S_1 = S_2 = 1/2$:

$$H = -JS_1S_2. \tag{1}$$

Terms corresponding to a paramagnetic impurity (P) and temperature independent paramagnetism (TIP) have been added [Eq. (2)]. N, g, β, k, and T have the usual meaning and P is the molar fraction of the non-coupled paramagnetic impurity. In this expression it is assumed that the paramagnetic impurity follows the Curie law and has the same molecular weight and the same g value as the respective complex:

$$\chi_M = \{2Ng^2\beta^2/kT[3 + \exp(-J/kT)] + \mathrm{TIP}\}(1 - P) + (Ng^2\beta^2/2kT)P. \tag{2}$$

A very good agreement between the experimental and calculated curves of the magnetic moment and the molar susceptibility for both complexes was observed with this model. The parameters obtained in these fits are collected in Table 6. Although in complex **1** the g value is slightly low (the value in Cu(II) complexes is usually greater than 2) and the TIP parameter is also low ($<10^{-5}$), the J value is consistent with those observed in analogous complexes and with the shape of the magnetic susceptibility curve. The large J value of -376 and $-363\ cm^{-1}$ for **1** and **2**, respectively, indicates very strong antiferromagnetic coupling between the Cu(II) centers of each dicopper unit. These coupling constants are in good agreement with those observed in other tetracarboxylatodicopper(II) complexes [7,25–28]. This interaction is probably produced through the carboxylate groups due to the large Cu–Cu distance as has been pointed out [28] in similar compounds. The other magnetic parameters are also analogous to described previously in others dicopper(II) compounds. Fig. 6 shows the experimental and calculated curves for complex **2**. Similar curves have been obtained for complex **1**.

3.5. Thermal properties

The thermal properties of compounds were examined by thermal gravimetric analysis (TGA/DTA) and differential scanning calorimetry (DSC). Compounds **1**–**4** were heated to 600 °C in a nitrogen atmosphere. TGA data suggest that the framework of **1** is stable up to 120 °C and shows a weight loss of 6.45% (calculated 6.30%) from 120 to 178 °C corresponding to the loss of one acetate ligand *per* formula unit. In the range 178–325 °C undergoes one weight loss step corresponding to remaining three acetate ligands (obsd. 18.6%, calcd. 18.9%) and in the range 325–500 °C the lost of one 2,5-bis(2-pyridylethynyl)thiophene ligand, $\mathbf{L_1}$ is observed (obsd. 30.36%, calcd. 30.66%). Above 500 °C, the weight loss observed is assigned to CuO (obsd. 8.82%, calcd. 8.50%). This behaviour is very similar that observed for 1D dimensional polymer [Cu(hfac)$_2$L$_1$]$_n$ [7].

The TG curve of **2** shows it is stable up to 195 °C; in the range 195–248 °C a sharp weight loss attributed to 4,4′-dipyridyldisulfide ($\mathbf{L_3}$) is observed (obsd. 38.20%, calcd. 37.75%) and between 248 and 310 °C, the weight loss is believed to be due to the loss of two acetate ligands (obsd. 21.70%, calcd. 20.22%).

Compound **3** is stable up to 385 °C. Above this temperature, weight loss attributed to six SC_5H_4N units is observed (obsd. 64.3%, calcd. 63.33%).

Compound **4** is stable up to 185 °C, in the 185–385 °C range, loss two 2,2′-dipyridyldisulfide ($\mathbf{L_2}$) ligands is observed (obsd. 67.98.3%, calcd. 69.74%). Above 400 °C, weight loss is also observed (9.4%) and is attributed to CuO (calcd. 9.52%). DSC analysis of hermetically sealed samples display sharp endothermic peaks at 137.0 °C which corresponds to the melting point.

Table 6
Magnetic parameters for complexes **1** and **2** obtained in the fits to the magnetic moment as a function of temperature

Compound	g	J (cm^{-1})	TIP (mL/mol)	P (%)	σ^{2a}
1	2.00	−376	3.5×10^{-9}	5.9	3.4×10^{-4}
2	2.07	−363	1.4×10^{-4}	1.99	1.12×10^{-4}

[a] $\sigma^2 = \sum(\mu_{\text{eff.calc.}} - \mu_{\text{eff. exp.}})^2 / \sum \mu^2_{\text{eff. exp.}}$.

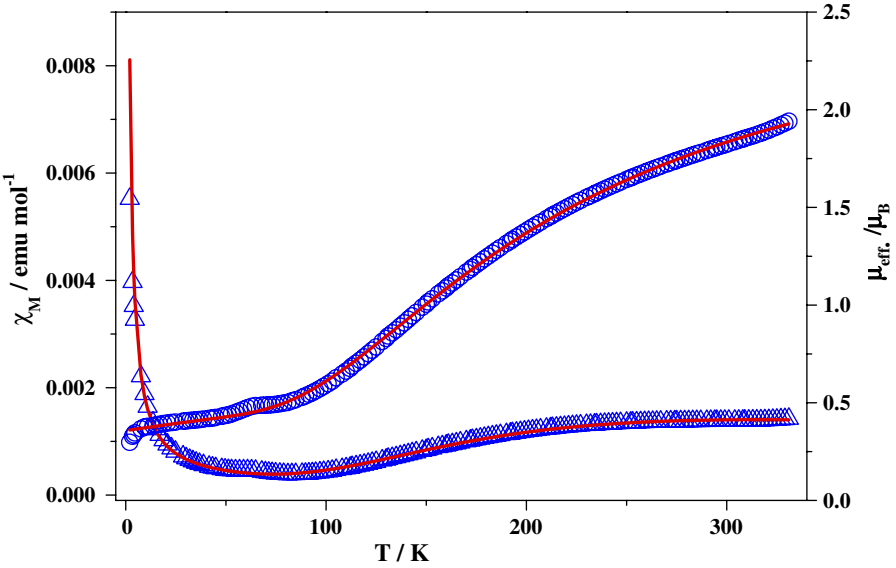


Fig. 6. Temperature dependence of the molar magnetic susceptibility χ_M (△) and μ_{eff} (○) for **2**. Solid lines result from least-squares fits using the model described in the text.

4. Conclusions

We have carried out a systematic study of chemistry of copper(II) salts with angular and linear dipyridyl ligands. The reactions with 2,5-bis(2-pyridylethynyl)thiophene (**L_1**) and 2,2′-dipyridyldisulfide (**L_2**) and copper acetate give the dimers $[Cu_2(\mu\text{-}OAc)_4(L)_2]$ whereas we had previously observed that the same reactions using $Cu(hfac)_2$ gave the one-dimensional polymers $[Cu(hfac)_2L]_n$. Likewise, the reaction with 4,4′-dipyridyldisulfide (**L_3**) gives the one-dimensional ziz-zag polymer $[Cu_2(\mu\text{-}OAc)_4(L_3)]_n$ (**2**) instead the one-dimensional helical chain structure obtained with $Cu(hfac)_2$. It is worth emphasizing that in the case of **2**, the **L_3** ligand chirality is independent of supramolecular topology, because both chiral and achiral combinations of the ligand can produce similar supramolecular structure.

Finally, the reactivity with the 2,2′-dipyridyldisulfide ligand shows varied and interesting coordination chemistry as consequence of cleavage of S–S and C–S bonds, giving the Cu(I) known cluster $Cu_6(SC_5H_4N)_6$ (**3**) and the dimer $[Cu(\mu\text{-}S)(L_2)]_2$ (**4**).

5. Experimental

5.1. General

All the solvents were of reagent grade quality and were used as received. 2,5-dibromothiophene (Aldrich), 2-ethynylpyridine (Aldrich), $PdCl_2$ (Aldrich), CuI (Aldrich) and $Cu(OAc)_2 \cdot H_2O$ (Aldrich), 2,2′-dipyridyldisulfide (**L_2**) and 4,4′-dipyridyldisulfide (**L_3**) (Lancaster) were used as received. Et_3N (Fluka) was distilled from KOH immediately before use. $Pd(PPh_3)_4$ [29] and **L_1** ligand [7] were prepared according to the literature procedure. Infrared spectra were measured on a Perkin–Elmer 1650 infrared spectrometer. Elemental analysis were performed by the Microanalytical of the University Autónoma of Madrid on a Perkin-Elemer 240 B microanalyzer. Single-crystal X-ray diffraction experiments were performed with samples mounted on a glass fiber and transferred to a Bruker SMART 6K CCD area-detector three-circle diffractometer with a Rigaku Rotating Anode (Cu Kα radiation, $\lambda = 1.54178$ Å) generator equipped with Goebel mirrors at settings of 50 kV and 100 mA. X-ray data were collected at 100 K, with a combination of six runs at different φ and 2θ angles, 3600 frames. The data were collected using 0.3° wide ω scans with a crystal-to-detector distance of 4.0 cm.

The substantial redundancy in data allows empirical absorption corrections (SADABS) to be applied using multiple measurements of symmetry-equivalent reflections [30].

The raw intensity data frames were integrated with the SAINT program, which also applied corrections for Lorentz and polarization effects [31].

The software package SHELXTL version 6.10 was used for space group determination, structure solution and refinement [32]. The space group determination was based on a check of the Laue symmetry and systematic absences and was confirmed using the structure solution. The structures were solved by direct methods (SHELXS-97), completed with difference Fourier syntheses, and refined with full-matrix least-squares using SHELXL-97 minimizing $w(F_o^2 - F_c^2)^2$. Weighted R factors (R_w) and all goodness of fit S are based on F^2; conventional R factors (R) are based on F. All scattering factors and anomalous dispersions factors are contained in the SHELXTL-6.10 program library. Table 1 contains crystal data for complexes **1**, **2** and **4**.

The variable-temperature magnetic susceptibilities were measured on polycrystalline samples with a Quantum Design MPMSXL SQUID (Superconducting Quantum Interference Device) susceptometer over a temperature range of 2–330 K at the constant field of 1 T (Complutense University of Madrid). All data were corrected for the diamagnetic contribution of both the sample holder and the compound to the susceptibility. The molar diamagnetic corrections for the complexes were calculated based on Pascal's constants.

5.2. Synthesis of $[Cu_2(\mu\text{-}OAc)_4(L_1)_2]$ (1)

A solution of $Cu(OAc)_2 \cdot H_2O$ (35 mg, 0.17 mmol) in MeOH (12 mL) was added to a solution of **L_1** (50 mg, 0.17 mmol) in CH_2Cl_2 (6 mL). The solution was left nine days at room temperature and green solid appeared. After recrystallization in CH_2Cl_2:MeOH (2:1) green crystals were isolated in a yield of 85% (153.3 mg). Mp: 240 °C. IR (KBr, cm^{-1}): 3053 (w), 2211 (s), 1617 (vs), 1590 (vs), 1559 (s), 1530 (m), 1482 (m), 1464 (vs), 1426 (vs), 1343 (w), 1286 (w), 1150 (w), 1046 (s), 1005 (s), 807 (s), 769 (vs), 736 (s), 678 (vs), 624 (s). *Anal.* Calc. for $C_{44}H_{32}Cu_2N_4O_8S_2$ (935.94 g/mol): C, 56.4; H, 3.4; N, 6.0, S, 6.8. Found: C, 56,3; H, 3,5; N, 6,1; S, 6,9%.

5.3. Synthesis of $[Cu_2(\mu\text{-}OAc)_4(L_3)]_n$ (2)

A solution of $Cu(OAc)_2 \cdot H_2O$ (45.4 mg, 0.23 mmol) in MeOH (16 mL) was layered onto a solution of 4,4′-dpds (50 mg, 0.23 mmol) in the same solvent (10 mL). Pale-green crystals were isolated when the solution was allowed to stand at room temperature for 2 days (65.6 mg, 90% yield). Mp: 225 °C (d). IR (KBr, cm^{-1}): 3055 (w), 1623 (vs), 1584 (vs), 1545 (m), 1482 (m), 1430 (vs), 1348 (w), 1221(w), 1064 (m), 1015 (m), 818 (m), 708 (s), 683 (vs), 629 (m), 501 (m). *Anal.* Calc. for $C_9H_{10}CuNO_4S$ (291.78 g/mol): C, 37.0; H, 3.4; N, 4.8; S, 11.0. Found: C, 37.2; H, 3.5; N, 4.7; S, 10.9%.

5.4. Synthesis of $[Cu(NC_5H_4N)]_6$ (3) and $[Cu(\mu\text{-}S)(L_2)]_2$ (4)

A solution of $Cu(OAc)_2 \cdot H_2O$ (272.3 mg, 1.36 mmol) in MeOH (30 mL) was added to a solution of L_2 (300 mg, 1.36 mmol) in the same solvent (15 mL). The resulting solution was heated to boiling and an orange solid was obtained. After 24 h, the green solution was filtered off,

the orange solid was isolated and characterized as the already known $[Cu(NC_5H_4N)]_6$ (**3**) (400 mg, 25% yield) and the solution was allowed to stand at 0 °C for 3 weeks. Red crystals were isolated in low yield (34.40 mg, 4%) and were identified as $[Cu(\mu\text{-}S)(L_2)]_2$ (**4**) together with $Cu_6(SC_5H_4N)_6$ (**3**) (240 mg, 15% yield) and the dimeric compound $[Cu_2(\mu\text{-}OAc)_4(L_2)_2]$ (129 mg, 15%). This last compound had previously been isolated and characterized as the only product when the reaction had been carried out at room temperature [7].

Compound **4**: IR (KBr, cm^{-1}): 3052 (w), 1575 (s), 1555 (s), 1455 (s), 1446 (vs), 1419 (vs), 1113 (m), 1087 (w), 1047 (m), 1007 (w), 785 (w), 762 (vs), 714 (w). *Anal*. Calc. for $C_{20}H_{16}Cu_2N_4S_6$ (631.81 g/mol): C, 38.0; H, 2.5; N, 8.9; S, 30.4. Found: C, 38.1; H, 2.6; N, 9.0; S, 30.3%.

Acknowledgements

We express our great appreciation to the Vicerrectorado de Investigación de la Universidad Autónoma de Madrid and to Dirección General de Investigación Científica y Tecnológica (Grant Nos. CTQ 2005-00397 and S-0505/MAT/0303).

Appendix A. Supplementary material

CCDC 629269, 629270 and 287411 contain the supplementary crystallographic data for **1**, **2** and **4**. These data can be obtained free of charge via http://www.ccdc.cam.ac.uk/conts/retrieving.html, or from the Cambridge Crystallographic Data Centre, 12 Union Road, Cambridge CB2 1EZ, UK; fax: (+44) 1223-336-033; or e-mail: deposit@ccdc.cam.ac.uk. Supplementary data associated with this article can be found, in the online version, at doi:10.1016/j.poly.2007.01.021.

References

[1] (a) C. Janiak, J. Chem. Soc., Dalton Trans. (2003) 2781;
(b) D. Braga, L. Brammer, N.R. Champness, CrystEngComm 7 (2005) 1;
(c) N.R. Champness, J. Chem. Soc., Dalton Trans. (2006) 877.
[2] (a) S. Kitagawa, S. Noro, Compr. Coord. Chem. 7 (2004) 231;
(b) L. Brammer, Chem. Soc. Rev. 8 (2004) 476;
(c) T. Yuen, C.L. Lin, T.W. Mihalisin, M.A. Lawandy, J. Li, J. Appl. Phys. 87 (2000) 6001;
(d) J.L. Manson, A.M. Arif, C.D. Incarvito, L.M. Liable-Sands, A.L. Reinghold, J.S. Miller, J. Solid State Chem. 145 (1999) 369;
(e) F. Lloret, G. De Munno, M. Julve, J. Cano, R. Ruiz, A. Caneschi, Angew. Chem., Int. Ed. Engl. 37 (1998) 135.
[3] (a) M.E. Kosal, J.-H. Chou, S.R. Wilson, K.S. Suslick, Nat. Mater. 1 (2002) 118;
(b) S. Kitagawa, R. Kitaura, S. Noro, Angew. Chem., Int. Ed. 43 (2004) 2334;
(c) M. Kondo, T. Okubo, A. Asami, S. Noro, T. Yoshimoti, S. Kitagawa, T. Ishii, H. Matzusaka, K. Seki, Angew. Chem., Int. Ed. Engl. 38 (1999) 140.
[4] (a) H. Hou, X. Meng, Y. Song, Y. Fan, Y. Zhu, H. Lu, C. Du, W. Shao, Inorg. Chem. 41 (2002) 4068;
(b) W. Lin, Z. Wang, L. Ma, J. Am. Chem. Soc. 121 (1999) 11249;
(c) C. Chen, K.S. Suslick, Coord. Chem. Rev. 128 (1993) 293.
[5] (a) M. Albrecht, M. Lutz, A.L. Spek, G. van Koten, Nature 406 (2000) 970;
(b) L.G. Beauvais, M.P. Sores, J.R. Long, J. Am. Chem. Soc. 122 (2000) 2763.
[6] (a) N.G. Pischirer, D.M. Ciurtin, M.D. Smith, U.H.F. Bunz, H.C. zur Loye, Ang. Chem. Int. Ed 114 (2002) 603;
(b) K. Biradha, Y. Hongo, M. Fujita, Ang. Chem. Int. Ed. 39 (2000) 3843;
(c) D. Hargman, R.P. Hammond, R. Haushalter, J. Zubieta, Chem. Mater. 10 (1998) 2091;
(d) M. Fujita, Y.J. Kwon, S. Washizu, K. Ogura, J. Am. Chem. Soc. 116 (1994) 1151;
(e) B. Moulton, M.J. Zaworotko, Chem. Rev. 101 (2001) 1629.
[7] S. Delgado, A. Barrilero, A. Molina-Ontoria, M.E. Medina, C.J. Pastor, R. Jiménez-Aparicio, J.L. Priego, Eur. J. Inorg. Chem. 14 (2006) 2746.
[8] R. Horikoshi, T. Mochida, Coord. Chem. Rev. 250 (2006) 2595.
[9] R. Horikoshi, M. Mikuriya, Bull. Chem. Soc. Jpn. 78 (2005) 827.
[10] S. Delgado, A. Molina-Ontoria, M.E. Medina, C.J. Pastor, R. Jiménez-Aparicio, J.L. Priego, Inorg. Chem. Commun. 9 (2006) 1289.
[11] S. Kitagawa, M. Munakata, H. Shimono, S. Matsuyama, H. Masuda, J. Chem. Soc., Dalton Trans. (1990) 2105.
[12] L.S. Higashi, M. Lundeen, E. Hilti, K. Seff, Inorg. Chem. 16 (1977) 310.
[13] A. Albert, G.B. Barlin, J. Chem. Soc. (1959) 2384.
[14] S. Stoyanov, I. Petkov, L. Antonov, T. Stoyanova, P. Karagiannidis, P. Aslanidis, Can. J. Chem. 68 (1990) 1482.
[15] S.C. Davies, M.C. Durrant, D.L. Hughes, K. Leidenberger, C. Stapper, R.L. Richards, J. Chem. Soc., Dalton Trans. (1997) 2409.
[16] W.E. Piers, L. Koch, D.S. Ridge, L.R. MacGillivray, M. Zaworotko, Organometallics 11 (1992) 3148.
[17] A.V. Firth, E. Witt, D.W. Stephan, Organometallics 17 (1998) 3716.
[18] H. Kawaguchi, K. Tstsumi, Organometallics 16 (1997) 307.
[19] D. Coucouvanis, A. Hadjikyriacou, M.G. Kanatzdis, J. Chem. Soc. (1985) 1224.
[20] (a) M. Du, Z. Huang, S.-T. Chen, Y.-M. Guo, Inorg. Chem. 42 (2003) 552;
(b) Z. Huang, H.-B. Song, M. Du, S.-T. Chen, X.-H. Bu, Inorg. Chem. 43 (2004) 931;
(c) P. Díaz, J. Benet-Buchholz, R. Villar, A.J. White, Inorg. Chem. 45 (2006) 1617.
[21] (a) R. Horikoshi, T. Mochida, N. Maki, S. Yamada, H. Moriyama, J. Chem. Soc., Dalton Trans. (2002) 28;
(b) R. Horikoshi, T. Mochida, H. Moriyama, Inorg. Chem. 40 (2001) 2430;
(c) R. Horikoshi, T. Mochida, M. Kurihara, M. Mikuriya, Cryst. Growth Des. 5 (2005) 243.
[22] J. Luo, M. Hong, R. Wang, D. Yuan, R. Cao, L. Han, Y. Xu, Z. Lin, Eur. J. Inorg. Chem. 19 (2003) 3623.
[23] I. Kinoshita, L.J. Wrigth, S. Kubo, K. Kimura, A. Sakata, T. Yano, R. Miyamoto, T. Nishioka, K. Isobe, J. Chem. Soc., Dalton Trans. (2003) 1993.
[24] L.S. Higashi, M. Lundeen, K. Seff, J. Am. Chem. Soc. 100 (1978) 8101.
[25] O. Kahn, Molecular Magnetism, VCH, New York, 1993, p. 107.
[26] J. Mrozinski, Coord. Chem. Rev. 249 (2005) 2534.
[27] (a) For example, see: Z. Huang, H.-B. Song, M. Du, S.-T. Chen, X.-H. Bu, J. Ribas, Inorg. Chem. 43 (2004) 931;

(b) P. Stachová, D. Valigura, M. Koman, M. Melník, M. Korabik, J. Mrozinski, T. Glowiak, Polyhedron 23 (2004) 1303;
(c) M. Du, X.-H. Bu, Z. Huang, S.-T. Chen, Y.-M. Guo, C. Díaz, J. Ribas, Inorg. Chem. 42 (2003) 552.
[28] M. Rusjan, Z. Chaia, O.E. Piro, D. Guillond, F.D. Cukiernik, Acta Crystallogr., Sect. B 56 (2000) 666.
[29] D.R. Coulson, Inorg. Synth. 28 (1990) 107.
[30] G.M. Sheldrick, SADABS version 2.03: A Program for Empirical Absorption Correction, Universität Göttingen, Göttingen, Germany, 1997–2001.
[31] SAINT + NT ver. 6.04. SAX Area-Detector Integration Program, Bruker AXS, Madison, WI, 1997–2001.
[32] Bruker AXS SHELXTL version 6.10. Structure Determination Package, Bruker AXS, Madison, WI, 2000.

Available online at www.sciencedirect.com
ScienceDirect
Polyhedron 26 (2007) 2829–2836
POLYHEDRON
www.elsevier.com/locate/poly

From discrete entity to three-dimensional architecture: Syntheses, crystal structures and optical properties of a series of transition metal complexes constructed from 4-carboxymethylbenzoic acid and 4,4′-bipyidine

Zheng-Fang Tian, Yang Su, Jian-Guo Lin, Qing-Jin Meng *

Coordination Chemistry Institute, State Key Laboratory of Coordination Chemistry, School of Chemistry and Chemical Engineering, Nanjing University, Nanjing 210093, PR China

Received 27 November 2006; accepted 21 January 2007
Available online 30 January 2007

Abstract

Five new interesting transition metal coordination polymers $[MnL_2(bpy)_2(H_2O)_2]_n$ (**1**) (H_2L = 4-carboxymethylbenzoic acid) (bpy = 4,4′-bipyidine), $[CoL(bpy)(H_2O)_3 \cdot H_2O]_n$ (**2**), $[CdL(bpy)(H_2O)_3 \cdot H_2O]_n$ (**3**), $[Cu_2L(bpy)_2 \cdot 3H_2O]_n$ (**4**) and $[Zn_2L_2(bpy) \cdot H_2O]_n$ (**5**) have been synthesized under solvothermal conditions and structurally characterized. This series of complexes has shown an intriguing variety of architectures, which firstly form zero- to two-dimensional frameworks by metal–ligand interactions, and secondly form three-dimensional supramolecular frameworks by intermolecular interactions such as hydrogen bonds. Compound **3** shows strong blue fluorescent emissions in the solid state upon photo-excitation at 359 nm at room temperature and may be an excellent candidate for blue-fluorescent materials. Compound **4** appears to be a good candidate for new hybrid inorganic–organic NLO materials.
© 2007 Elsevier Ltd. All rights reserved.

Keywords: 4-Carboxymethylbenzoic acid; X-ray structure; Optical properties

1. Introduction

Recently, the area of coordination polymers has become one of intense research activity not only because of the enormous variety of interesting structural topologies [1–4], but also because of the potential applications as functional materials, for example, in electrical, conductivity, magnetism, host–guest chemistry, ion exchange, catalysis, nanotechnology, fluorescence and non-linear optics [5–11]. By utilizing polyatomic organic ligands as linkers and the well-defined coordination geometries of metal centers as nodes, a series of architectures are produced [12–14]. Metal–ligand interactions and intermolecular interactions such as hydrogen bonds, π–π stacking interactions are the two main strategies in the crystal engineering. Various flexible carboxylate ligands can often be employed due to their versatile coordination modes and high structural stability [15]. In particular, multibenzenecarboxylate ligands have been shown to be good building blocks in the design of metal-organic materials [16–20]. For example, 1,4-benzenedicarboxylic acid has been widely researched because it has a H-bonding site, aromatic π cloud and metal coordination site [21–24]. However, the unsymmetrical benzenedicarboxylate has seldom been investigated. Only 2-carboxymethylbenzoic acid and 3-carboxymethylbenzoic acid have been researched in the literature [25,26]. 4-Carboxymethylbenzoic acid, compared with 1,4-benzenedicarboxylic acid, has 'CH_2' added and its flexibility has been modified. Coordination polymers constructed from 4-carboxymethylbenzoic acid have been not reported until

* Corresponding author. Tel.: +86 25 83597266; fax: +86 25 83314502.
E-mail address: mengqj@nju.edu.cn (Z.-F. Tian).

0277-5387/$ - see front matter © 2007 Elsevier Ltd. All rights reserved.
doi:10.1016/j.poly.2007.01.026

now. So now we elaborate on some new coordination polymers constructed from 4-carboxymethylbenzoic acid, transition-metals and 4,4′-bpy. In this paper, we report five interesting coordination polymeric complexes $[MnL_2(bpy)_2(H_2O)_2]_n$ (**1**) (H_2L = 4-carboxymethylbenzoic acid) (bpy = 4,4′-bipyidine), $[CoL(bpy)(H_2O)_3 \cdot H_2O]_n$ (**2**), $[CdL(bpy)(H_2O)_3 \cdot H_2O]_n$ (**3**), $[Cu_2L(bpy)_2 \cdot 3H_2O]_n$ (**4**) and $[Zn_2L_2(bpy) \cdot H_2O]_n$ (**5**). This series of complexes shows an intriguing variety of architectures, which firstly form zero to two-dimensional frameworks by metal–ligand interactions, and secondly form three-dimensional supramolecular frameworks by intermolecular interactions such as hydrogen bonds. The spectroscopic, thermal, fluorescence and nonlinear optical properties of complexes **1**–**5** are investigated.

2. Experimental

2.1. General materials and techniques

The reagents and solvents employed were commercially available and used as received without further purification. H_2L was prepared according to a procedure described in the literature [27,28].

The C, H and N microanalyses were carried out with a Perkin–Elmer 240 elemental analyzer. The IR spectra were recorded in KBr disks on a Bruker Vector 22 spectrophotometer in the 4000–400 cm^{-1} region. Luminescence spectra for the solid samples were recorded with a Hitachi 850 fluorescence spectrophotometer. Thermogravimetric analyses were performed on a simultaneous SDT 2960 thermal analyzer under N_2 with a heating rate of 10 °C/min between ambient temperature and 750 °C. A pulsed Q-switched Nd:YAG laser at a wavelength of 1064 nm was used to generate an SHG signal from the samples. The backward scattered SHG light was collected using a spherical concave mirror and passed through a filter which transmits only 532 nm radiation.

2.2. Syntheses of the compounds

2.2.1. $[MnL_2(bpy)_2(H_2O)_2]_n$ (1)

A mixture of $Mn(Ac)_2 \cdot 4H_2O$ (0.1 mmol), H_2L (0.1 mmol), 4,4′-bpy (0.1 mmol), triethylamine (one half drop), CH_3CN (1 cm^3) and H_2O (9 cm^3) was placed in a Parr Teflon-lined stainless steel vessel (25 cm^3), and then the vessel was sealed and heated at 120 °C for 3 days. After the mixture was slowly cooled to room temperature, colorless crystals of **1** were obtained (yield: 67% based on Mn). *Anal*. Calc. for $C_{38}H_{34}N_4O_{10}Mn$: C, 59.92; H, 4.50; N, 7.36. Found: C, 60.00; H, 4.55; N, 7.30%. IR spectrum (cm^{-1}): 3416 (vs), 2928 (w), 1603 (vs), 1536 (s), 1381(vs), 1313 (m), 1225 (w), 1062 (w), 803 (m), 750 (s), 627 (m).

2.2.2. $[CoL(bpy)(H_2O)_3 \cdot H_2O]_n$ (2)

The synthesis was similar to that described for **1** except using $Co(NO_3)_2 \cdot 6H_2O$ instead of $Mn(Ac)_2 \cdot 4H_2O$ and red crystals of **2** were obtained (yield: 84% based on Co). *Anal*. Calc. for $C_{19}H_{21}N_2O_8Co$: C, 49.15; H, 4.56; N, 6.32. Found: C, 49.18; H, 4.60; N, 6.35%. IR spectrum (cm^{-1}): 3260 (s), 1608 (s), 1586 (s), 1560 (s), 1535 (s), 1380 (vs), 1228 (m), 1063 (w), 808 (m), 752 (m), 673 (m), 630 (m).

2.2.3. $[CdL(bpy)(H_2O)_3 \cdot H_2O]_n$ (3)

The synthesis was similar to that described for **1** except using $Cd(NO_3)_2 \cdot 4H_2O$ instead of $Mn(Ac)_2 \cdot 4H_2O$ and colorless crystals of **3** were obtained (yield: 54% based on Cd) *Anal*. Calc. for $C_{19}H_{22}N_2O_8Cd$: C, 43.99; H, 4.27; N, 5.40. Found: C, 44.05; H, 4.32; N, 5.36%. IR spectrum (cm^{-1}): 3386 (s), 1603 (vs), 1542 (s), 1491 (s), 1374 (vs), 1290 (m), 1221 (m), 807 (s), 748 (m), 629 (m).

2.2.4. $[Cu_2L(bpy)_2 \cdot 3H_2O]_n$ (4)

The synthesis was similar to that described for **1** except using $Cu(NO_3)_2 \cdot 3H_2O$ instead of $Mn(Ac)_2 \cdot 4H_2O$ and the reaction was carried out at 160 °C and orange crystals of **4** were obtained (yield: 89% based on Cu). *Anal*. Calc. for $C_{29}H_{28}N_4O_7Cu_2$: C, 51.86; H, 4.20; N, 8.34. Found: C, 51.90; H, 4.25; N, 8.40%. IR spectrum (cm^{-1}): 3423 (s), 3043 (m), 1601 (vs), 1550 (s), 1482 (s), 1383 (vs), 1215 (m), 818 (m), 799 (s), 724 (m), 633 (m).

2.2.5. $[Zn_2L_2(bpy) \cdot H_2O]_n$ (5)

The synthesis was similar to that described for **1** except using $Zn(NO_3)_2 \cdot 6H_2O$ instead $Mn(Ac)_2 \cdot 4H_2O$ and colorless crystals of **5** were obtained (yield: 32% based on Zn). *Anal*. Calc. for $C_{28}H_{22}N_2O_9Zn_2$: C, 50.86; H, 3.35; N, 4.24. Found: C, 50.90; H, 3.40; N, 4.20%. IR spectrum (cm^{-1}): 3423 (w), 3058 (m), 1637 (vs), 1492 (s), 1393 (vs), 1315 (m), 1223 (s), 1023 (m), 814w (m), 747 (s), 644 (m).

2.3. X-ray crystal structural determinations

Data for all of the complexes **1**–**5** were collected on a Siemens SMART-CCD diffractometer with graphite monochromatic Mo Kα radiation ($\lambda = 0.71073$ Å) using the SMART and SAINT programs [29]. The structures were solved by direct methods and refined on F^2 using full matrix least-squares methods with SHELXTL version 5.1 [30]. Anisotropic thermal parameters were refined for the non-hydrogen atoms. Hydrogen atoms attached to carbon and nitrogen were positioned geometrically (C–H = 0.93 Å, N–H = 0.86 Å), and included in the refinement in a riding model approximation with an isotropicthermal displacement parameter fixed at 1.2 times U_{eq} of the atom to which they are attached. Crystallographic data and other pertinent information for all of the compounds are summarized in Table 1. Selected bond lengths and bond angles with their estimated standard deviations are listed in Table 2. Selected hydrogen-bonded bond lengths and bond angles for compounds **1**–**4** are listed in Table 3.

Table 1
Crystal data and structure refinement information for compounds **1**–**5**

Parameter	**1**	**2**	**3**	**4**	**5**
Empirical formula	$C_{38}H_{34}N_4O_{10}Mn$	$C_{19}H_{21}N_2O_8Co$	$C_{19}H_{22}N_2O_8Cd$	$C_{29}H_{28}N_4O_7Cu_2$	$C_{28}H_{22}N_2O_9Zn_2$
M_r	761.63	464.31	518.80	671.63	661.22
T (K)	298(2)	298(2)	298(2)	298(2)	298(2)
λ (Å)	0.71073	0.71073	0.71073	0.71073	0.71073
Crystal size (mm)	$0.30\times0.25\times0.24$	$0.32\times0.26\times0.24$	$0.30\times0.10\times0.10$	$0.32\times0.26\times0.24$	$0.30\times0.26\times0.24$
Crystal system	triclinic	monoclinic	triclinic	monoclinic	monoclinic
Space group	$P\bar{1}$	$P2_1$	$P\bar{1}$	Cc	$P2/c$
a (Å)	6.2082(15)	6.2541(12)	6.1257(14)	7.3589(13)	9.998(3)
b (Å)	7.4752(18)	13.851(3)	12.567(3)	17.951(3)	14.024(4)
c (Å)	19.331(5)	11.311(2)	14.045(3)	20.398(3)	10.921(3)
α (°)	85.919(5)	90	113.872(4)	90	90
β (°)	84.464(4)	105.202(4)	98.562(4)	90.705(3)	113.683(4)
γ (°)	66.770(4)	90	96.402(4)	90	90
U (Å^3)	820.0(4)	945.6(3)	959.9(4)	2694.2(8)	1402.4(6)
Z	1	2	2	4	2
d_{calcd} (g cm^{-1})	1.542	1.631	1.795	1.656	1.566
μ (mm^{-1})	0.473	0.960	1.189	1.636	1.767
θ_{max} (°)	25.00	25.99	25.00	25.99	26.00
Reflections collected	2833	3290	3322	4179	2748
Independent reflections	2336	2479	3035	3384	1921
R_{int}	0.0489	0.0327	0.0490	0.0375	0.0422
Number of parameters, restraints	241, 0	271, 1	271, 0	379, 2	198, 0
Final R_1[a], wR_2[b] $[I>2\sigma(I)]$	0.0435, 0.0900	0.0643, 0.1273	0.0308, 0.0749	0.0525, 0.1114	0.0599, 0.1209
R_1[a], wR_2[b] (all data)	0.0538, 0.0933	0.0856, 0.1326	0.0342, 0.0762	0.0679, 0.1158	0.0880, 0.1273

[a] $R_1 = \sum\|F_o| - |F_c\|/\sum|F_o|$.
[b] $wR_2 = \{\sum[w(F_o^2 - F_c^2)^2]/\sum[w(F_o^2)^2]\}^{1/2}$ where $w = 1/[\sigma^2(F_o^2) + (0.0474P)^2]$ where $P = (F_o^2 + 2F_c^2)/3$.

3. Results and discussion

3.1. Crystal structures of the compounds

3.1.1. $[MnL_2(bpy)_2(H_2O)_2]_n$ (**1**)

Compound **1** crystallizes in the space group $P\bar{1}$ and the coordination geometry around the Mn(II) center is a distorted octahedron, the equatorial plane of which is comprised of four oxygen atoms from two monocoordinated carboxymethyl groups of H_2L and two coordinated water molecules, the remaining apical coordination sites of which are occupied by two N atoms from 4,4′-bpy (Fig. 1a). One molecular unit contains one six coordinated Mn(II) ion, two L ligands and two bpy ligands. These molecular (0D) units are interlinked by a hydrogen bond O3–H3···N2 $(2-x, 1-y, 1-z)$ along the c-axis (Fig. 1b). In the a–b plane the units are connected into a layered structure by hydrogen-bonds which are in a quadrangle (Fig. 1c). The quadrangle comprises of O9 from the coordinated water and O2 from the uncoordinated carboxymethyl group of H_2L. In the a–b plane, the layers can be classified topologically as a $(6^4\times10^2)$ $(6^2\times4)_4$ network. By the hydrogen-bond interactions, **1** produces a 3-D network.

3.1.2. $[CoL(bpy)(H_2O)_3\cdot H_2O]_n$ (**2**)

A single-crystal XRD study has revealed that **2** crystallizes in the monoclinic system, $P2_1$ space group. The coordination geometry around the Co(II) center is a distorted octahedron, the equatorial plane of which is comprised of four oxygen atoms from one monocoordinated carboxymethyl group of H_2L and three coordinated water molecules, the apical coordination sites of which are occupied by two N atoms from 4,4′-bpy (Fig. 2a). It is worthy of note that the O7–H7C···O2 hydrogen bond is very strong and the distance between O7 from the free water and O2 from the carboxymethyl group is 1.93 Å (Fig. 2b) [31]. By 4,4-bpy, the units are linked into a 1-D chain along [1 0 1]. In 3-D space, three such chains are connected by hydrogen-bonded tetrahedra formed by O8 and O1, O3, O4 and O6, respectively (Fig. 2c). O1 and O4 come from the carboxymethyl group and the carboxyl group of H_2L of the first chain respectively, O3 comes from the carboxyl of H_2L of the second chain, and O6 comes from the coordinated water of the third chain. O1, O4, O3 and O6 lie at the four vertices of a distorted tetrahedron centered at the free water O8. In addition, an inter-chain hydrogen bond O5–H5B···O4 $(2-x, y-1/2, 1-z)$ enhances the chain interactions. In this way, the 1-D chains produce a 3-D framework.

3.1.3. $[CdL(bpy)(H_2O)_3\cdot H_2O]_n$ (**3**)

A single-crystal XRD study has revealed that **3** crystalizes in the monoclinic system, $P\bar{1}$ space group. The coordination geometry around Cd(II) center is same of the Co(II) of complex **2** (Fig. 3a). In the same, the units are linked to 1-D chain by 4,4′-bpy along [1 1 −1]. Perpendicular to the chain, the units are connected by hydrogen-bonds of which some are in quadrangles and the others

Table 2
Selected bond lengths (Å) and bond angles (°) for compounds **1**–**5**

Complex **1**[a]					
Mn(1)–O(1)	2.156(2)	Mn(1)–O(1)^{i}	2.156(2)	Mn(1)–O(9)	2.179(2)
Mn(1)–O(9)^{i}	2.179(2)	Mn(1)–N(1)	2.277(2)	Mn(1)–N(1)^{i}	2.277(2)
O(1)–Mn(1)–O(1)^{i}	180.0(1)	O(1)–Mn(1)–O(9)	94.6(1)	O(1)^{i}–Mn(1)–O(9)	85.4(1)
O(1)–Mn(1)–O(9)^{i}	85.4(1)	O(1)^{i}–Mn(1)–O(9)^{i}	94.6(1)	O(9)–Mn(1)–O(9)^{i}	180.0(1)
O(1)–Mn(1)–N(1)^{i}	90.4(1)	O(1)^{i}–Mn(1)–N(1)^{i}	89.6 (1)	O(9)–Mn(1)–N(1)^{i}	84.3(1)
O(9)^{i}–Mn(1)–N(1)^{i}	95.7(1)	O(1)–Mn(1)–N(1)	89.6(1)	O(1)^{i}–Mn(1)–N(1)	90.4(1)
O(9)–Mn(1)–N(1)	95.7(1)	O(9)^{i}–Mn(1)–N(1)	84.3(1)	N(1)–Mn(1)–N(1)^{i}	180.0(1)
Complex **2**[b]					
Co(1)–O(5)	2.039(5)	Co(1)–O(7)	2.059(5)	Co(1)–N(1)	2.184(5)
Co(1)–O(6)	2.026(6)	Co(1)–O(1)	2.162(6)	Co(1)–N(2)^{i}	2.172(5)
O(6)–Co(1)–O(5)	89.8(3)	O(6)–Co(1)–O(7)	89.7(2)	O(5)–Co(1)–O(7)	179.3(3)
O(6)–Co(1)–O(1)	175.4(3)	O(5)–Co(1)–O(1)	94.4(2)	O(7)–Co(1)–O(1)	86.2(2)
O(6)–Co(1)–N(2)^{i}	85.7(2)	O(5)–Co(1)–N(2)^{i}	93.0(3)	O(7)–Co(1)–N(2)^{i}	86.5(3)
O(1)–Co(1)–N(2)^{i}	92.2(2)	O(6)–Co(1)–N(1)	96.1(3)	O(5)–Co(1)–N(1)	90.3(3)
O(7)–Co(1)–N(1)	90.2(3)	O(1)–Co(1)–N(1)	85.7(3)	N(1)–Co(1)–N(2)^{i}	176.2(4)
Complex **3**					
Cd(1)–O(3)	2.279(3)	Cd(1)–N(1)	2.297(3)	Cd(1)–N(2)	2.314(3)
Cd(1)–O(5)	2.360(2)	Cd(1)–O(6)	2.352(2)	Cd(1)–O(7)	2.347(2)
O(3)–Cd(1)–N(1)	91.6(1)	O(3)–Cd(1)–N(2)	96.2(1)	N(1)–Cd(1)–N(2)	172.2(1)
O(3)–Cd(1)–O(7)	115.5(1)	N(1)–Cd(1)–O(7)	89.0(1)	N(2)–Cd(1)–O(7)	87.5(1)
O(3)–Cd(1)–O(6)	165.6(1)	N(1)–Cd(1)–O(6)	86.1(1)	N(1)–Cd(1)–O(6)	86.4(1)
O(7)–Cd(1)–O(6)	78.7(1)	O(3)–Cd(1)–O(5)	81.8(1)	N(1)–Cd(1)–O(5)	87.7(1)
N(2)–Cd(1)–O(5)	93.6(1)	O(7)–Cd(1)–O(5)	162.5(1)	O(6)–Cd(1)–O(5)	83.9(1)
Complex **4**[c]					
Cu(1)–N(1)	1.898(6)	Cu(1)–N(2)^{i}	1.911(5)	Cu(1)–O(1)	2.211(5)
Cu(2)–N(4)^{ii}	1.918(7)	Cu(2)–N(3)	1.955(6)	Cu(2)–O(2)	2.116(5)
N(1)–Cu(1)–N(2)^{i}	159.8(2)	N(1)–Cu(1)–O(1)	100.0(2)	N(2)^{i}–Cu(1)–O(1)	99.3(2)
N(4)^{ii}–Cu(2)–N(3)	156.0(2)	N(4)^{ii}–Cu(2)–O(2)	156.0(2)	N(3)–Cu(2)–O(2)	100.4(2)
Complex **5**[d]					
Zn(1)–N(1)	2.031(6)	Zn(1)–O(1)	2.011(4)	Zn(1)–O(1)^{iii}	2.011(4)
Zn(1)–O(3)^{i}	2.047(3)	Zn(1)–O(3)^{iv}	2.047(3)	Zn(1)–Zn(2)	2.927(2)
Zn(2)–N(2)^{ii}	1.981(7)	Zn(2)–O(2)	2.030(4)	Zn(2)–O(2)^{iii}	2.030(4)
Zn(2)–O(4)^{i}	2.052(3)	Zn(2)–O(4)^{iv}	2.052(3)		
O(1)–Zn(1)–O(1)^{iii}	158.4(2)	O(1)–Zn(1)–N(1)	100.8(1)	O(1)^{iii}–Zn(1)–N(1)	100.8(1)
O(1)–Zn(1)–O(3)^{i}	86.6(2)	O(1)–Zn(1)–O(3)^{iv}	90.4(2)	N(1)–Zn(1)–O(3)^{i}	98.1(1)
O(1)^{iii}–Zn(1)–O(3)^{i}	90.4(2)	O(1)^{iii}–Zn(1)–O(3)^{iv}	86.6(2)	N(1)–Zn(1)–O(3)^{iv}	98.1(1)
O(3)^{i}–Zn(1)–O(3)^{iv}	163.9(2)	O(1)–Zn(1)–Zn(2)	79.2(1)	O(1)^{iii}–Zn(1)–Zn(2)	79.2(1)
N(1)–Zn(1)–Zn(2)	180.0(1)	O(3)^{i}–Zn(1)–Zn(2)	81.9(1)	O(3)^{iv}–Zn(1)–Zn(2)	81.9(1)
O(2)–Zn(2)–O(2)^{iii}	160.4(2)	O(2)–Zn(2)–N(2)	99.8(1)	O(2)^{iii}–Zn(2)–N(2)	99.8(1)
N(2)–Zn(1)–O(4)^{i}	102.3(1)	O(2)–Zn(2)–O(4)^{i}	86.6(2)	O(2)^{iii}–Zn(2)–O(4)^{i}	89.2(1)
N(2)–Zn(1)–O(4)^{iv}	102.3(1)	O(2)–Zn(2)–O(4)^{iv}	89.2(1)	O(2)^{iii}–Zn(2)–O(4)^{iv}	86.6(2)
O(4)^{i}–Zn(1)–O(4)^{iv}	155.4(2)	N(2)–Zn(2)–Zn(1)	180.0(1)	O(2)–Zn(2)–Zn(1)	80.2(1)
O(2)^{iii}–Zn(2)–Zn(1)	80.2(1)	O(4)^{i}–Zn(2)–Zn(1)	77.7(1)	O(4)^{iv}–Zn(2)–Zn(1)	77.7(1)

[a] Symmetry code: (i) $1-x, 1-y, 1-z$.
[b] Symmetry code: (i) $1+x, 1y, 1+z$.
[c] Symmetry code: (i) $x+1/2, -y+1/2, z+1/2$; (ii) $x-1/2, -y+1/2, z-1/2$.
[d] Symmetry code: (i) $-1+x, y, z$; (ii) $x, 1+y, z$; (iii) $1-x, y, 3/2-z$; (iv) $2-x, y, 3/2-z$.

are in six-membered rings (Fig. 3b) [32,33]. O8, O2 and O6 form one six-membered ring, and O8, O1 and O5 form the other one. The two types of six-membered rings are comprised of a ribbon by sharing O8 (Fig. 3c). O8 comes from the free water, O1 and O2 come from carboxyl of H_2L, and O5 and O6 come from the coordinated water. The quadrangle is comprised of O7 from the coordinated water and O4 from the uncoordinated carboxymethyl group of H_2L (Fig. 3d). In whole, the chains are further arranged into 3-D networks by these hydrogen-bonded networks.

3.1.4. $[Cu_2L(bpy)_2 \cdot 3H_2O]_n$ (**4**)

Compound **4** crystallizes in a non-centrosymmetric space group *Cc*. The Cu(I) ions have a slightly distorted trigonal coordination geometry, coordinated by one oxygen atom from the carboxymethyl group of H_2L and two nitrogen atoms from the 4,4′-bpy ligand (Fig. 4a). The coordination mode to Cu(I) is less-common. The carboxymethyl group of H_2L bridges two Cu(I) ions, while it is monocoordinated in compounds **1**–**3**. The distance between the two Cu(I) ions is 3.214 Å. Along the [1 0 1] direction the asymmetric units are linked into a 1-D ladder-like chain. O1

Table 3
Selected hydrogen-bonded bond lengths (Å) and bond angles (°) for compounds **1**–**4**

D–H···A	D–H (Å)	H···A (Å)	D–H···A (Å)	Angle (°)
Complex **1**[a]				
O(9)–H(9A)···O(2)^{i}	0.84	1.90	2.702(2)	158.6
O(9)–H(9B)···O(2)^{ii}	0.84	1.96	2.776(2)	164.0
O(3)–H(3)···N(2)^{iii}	0.79	1.84	2.630(3)	179.3
Complex **2**[b]				
O(8)–H(8B)···O(3)^{i}	0.85	2.33	2.740(7)	110.1
O(8)–H(8B)···O(4)	0.85	2.51	2.928(7)	111.4
O(8)–H(8C)···O(1)^{iii}	0.85	2.31	2.986(8)	136.2
O(5)–H(5B)···O(4)^{ii}	0.85	2.45	2.869(8)	111.4
Complex **3**[c]				
O(5)–H(5A)···O(1)^{i}	0.85	1.87	2.717(3)	171.8
O(5)–H(5B)···O(8)^{ii}	0.85	1.95	2.783(3)	165.3
O(6)–H(6A)···O(2)^{iii}	0.85	2.02	2.781(4)	148.8
O(6)–H(6B)···O(8)^{iv}	0.85	1.97	2.816(3)	179.5
O(7)–H(7B)···O(4)^{v}	0.85	2.06	2.836(4)	151.3
O(8)–H(8C)···O(2)^{iii}	0.85	1.96	2.809(4)	178.0
O(8)–H(8D)···O(1)^{vi}	0.85	1.87	2.704(4)	168.8
Complex **4**[d]				
O(5)–H(5B)···O(1)^{i}	0.85	2.16	2.834(7)	136.0
O(5)–H(5B)···O(6)	0.85	2.32	2.813(6)	117.4
O(6)–H(6B)···O(4)^{ii}	0.85	2.19	2.954(7)	149.0
O(5)–H(5A)···O(4)	0.85	1.87	2.632(7)	149.1

[a] Symmetry code: (i) $1+x, y, 1-z$; (ii) $1-x, -y, 2-z$; (iii) $2-x, 1-y, 1-z$.
[b] Symmetry code: (i) $-1+x, y, z$; (ii) $2-x, y-1/2, 1-z$; (iii) $-1+x, y, -1+z$.
[c] Symmetry code: (i) $2-x, -y, 1-z$; (ii) $1+x, y, z$; (iii) $x, 1+y, z$; (iv) $1-x, 1-y, 1-z$; (v) $1-x, -y, -z$; (vi) $-1+x, 1+y, z$.
[d] Symmetry code: (i) $x, -y, z+1/2$; (ii) $-1+x, y, z$.

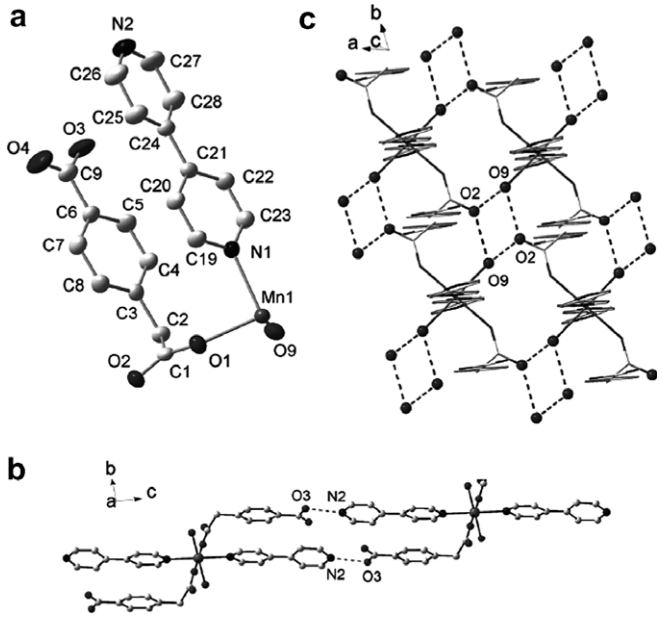


Fig. 1. (a) ORTEP view of compound **1**. Thermal ellipsoids are drawn at the 50% probability level. (b) 1-D chain of **1** along the *c*-axis. (c) Hydrogen-bonded networks in the *a*–*b* plane. Hydrogen atoms have been omitted for clarity.

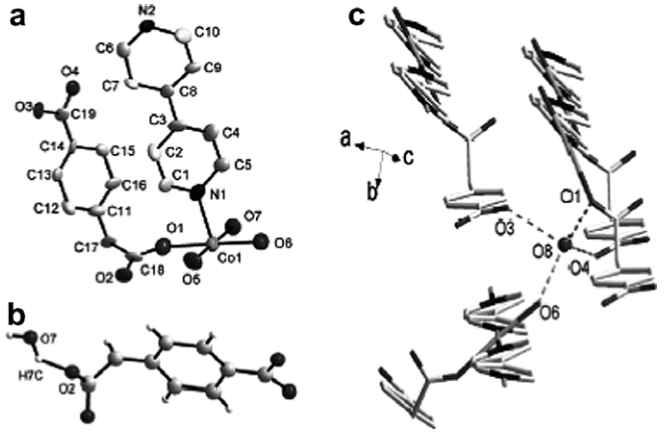


Fig. 2. (a) ORTEP view of compound **2**. Thermal ellipsoids are drawn at the 50% probability level. (b) O7–H7C···O2 hydrogen-bond in compound **2**. (c) Hydrogen-bonded tetrahedron in the three chains. Hydrogen atoms have been omitted for clarity.

from the carboxymethyl group of one chain and O4 from the carboxyl group of the other chain are linked to a short hydrogen-bonded chain by the free water O5. These short chains are linked into an infinite hydrogen-bonded chain by O5–H5B···O6 and O6–H6B···O4 $(-1+x, y, z)$ (Fig. 4b). Thus these ladder-like chains are further arranged to a 3-D supramolecular network by hydrogen-bonded chains composed of O1, O4, O5 and O6 (Fig. 4c).

3.1.5. $[Zn_2L_2(bpy)\cdot H_2O]_n$ (**5**)

Compound **5** crystallizes in the space group $P2/c$ and the coordination geometry around the Zn(II) center is a slightly distorted octahedron. Two oxygen atoms from the carboxymethyl group of H_2L and two oxygen atoms

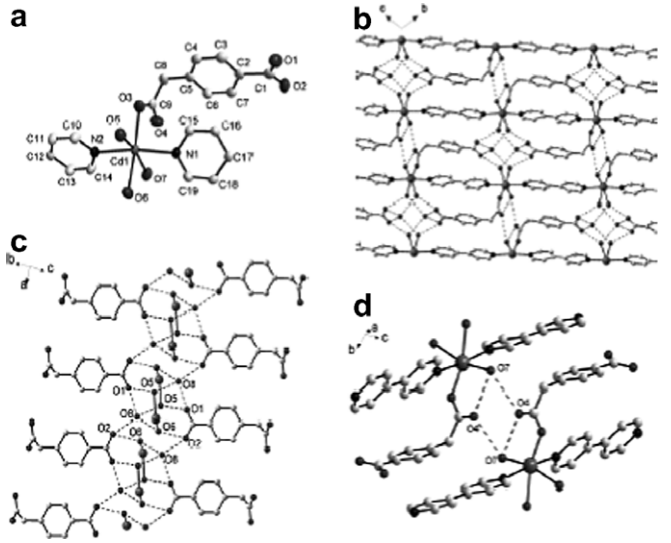


Fig. 3. (a) ORTEP view of compound **3**. Thermal ellipsoids are drawn at the 50% probability level. (b) 3-D hydrogen-bonded network of compound **3**. (c) A ribbon comprised of hydrogen-bonded six-membered rings in compound **3**. (d) Hydrogen-bonded quadrangle in compound **3**. Hydrogen atoms have been omitted for clarity.

from the carboxyl group of H_2L occupy the equatorial plane, and one nitrogen atom from the 4,4′-bpy and the other Zn atom occupy the axial positions (Fig. 5a). The two Zn(II) ions are bridged by two carboxymethyl groups and two carboxyl groups of H_2L to give binuclear clusters. The distance between the two Cu(I) ions is 2.927 Å. These clusters are interlinked by the ligands to form 1-D cluster chains. These chains are linked into 2-D sheets by 4,4′-bpy (Fig. 5b). The grid size is 4.8×8.3 Å^2. In whole, **5** is further arranged into a 3-D supramolecular network by hydrogen-bonding interactions. The free volume of **5** is estimated from the crystal structure to be 14%.

3.2. Thermal properties

Results of the thermogravimetric analysis (TGA) for frameworks **1**–**5** measured under a N_2 atmosphere are shown in Fig. 6. The TG curves indicate that compounds **1**–**4** lose all their water molecules below 130, 160, 147 and 177 °C. After the loss of the water molecules, the 3-D framework of compounds **1**–**4** begin to collapse. Compound **5** lost its free water molecules below 185 °C and then it began to decompose with a continuous weight loss up to 460 °C.

3.3. Photoluminescence properties

Coordination polymers containing cadmium and zinc usually exhibit photoluminescent properties [34,35], so we investigated the photoluminescent properties of **3** and **5** (Fig. 7). In the solid state, complex **3** exhibits strong fluorescent emission bands at ca. 421 and 393 nm upon excitation at ca. 359 nm. In addition, complex **5** displays intense blue fluorescent emission bands at ca. 411 nm upon excitation at ca. 362 nm. Because the Zn(II) or Cd(II) ions are difficult

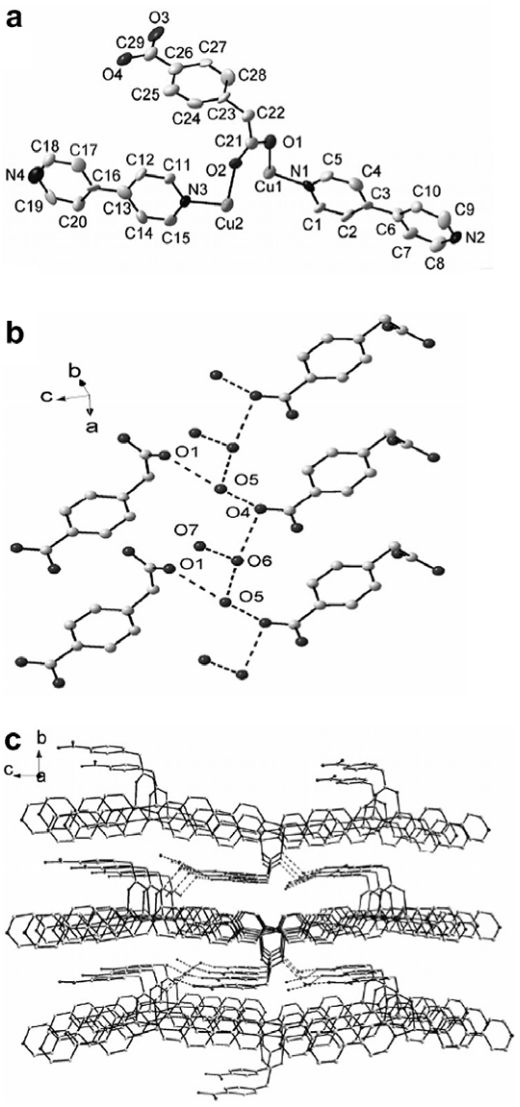


Fig. 4. (a) ORTEP view of compound **4**. Thermal ellipsoids are drawn at the 50% probability level. (b) Hydrogen-bonded chain in compound **4**. (c) 3-D hydrogen-bonded network of compound **4**. Hydrogen atoms have been omitted for clarity.

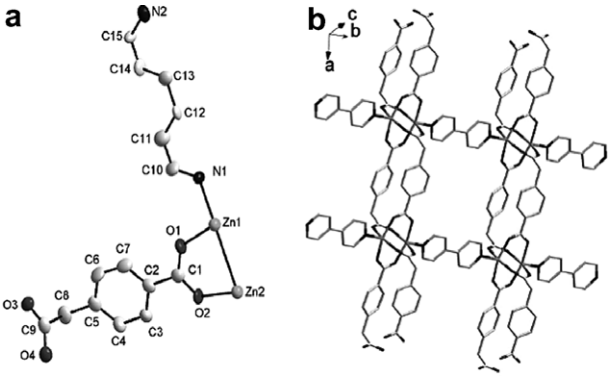


Fig. 5. (a) ORTEP view of compound **5**. Thermal ellipsoids are drawn at the 50% probability level. (b) 2-D network of compound **5**. Hydrogen atoms have been omitted for clarity.

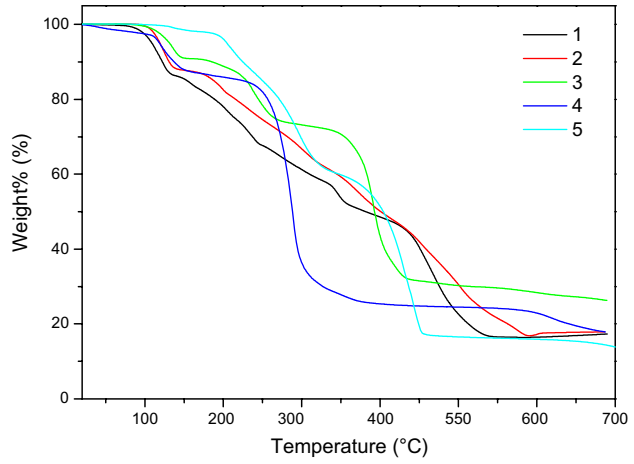


Fig. 6. TG curves for **1** (black), **2** (red), **3** (green), **4** (blue), **5** (cyan). (For interpretation of the references to colors in this figure legend, the reader is referred to the web version of this paper.)

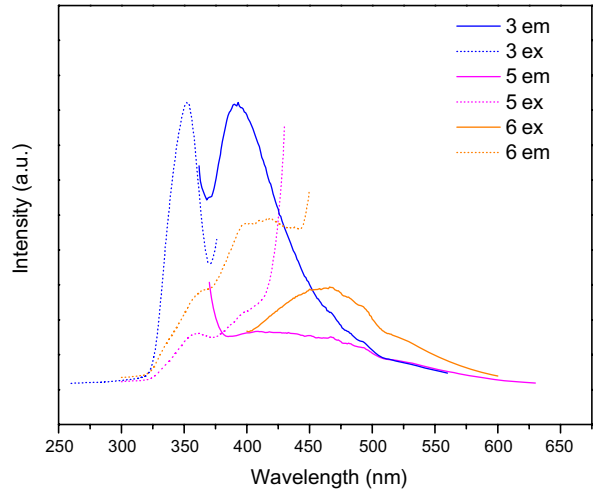


Fig. 7. The excitation (dotted line) and emission (solid line) spectra of **3** (blue), **5** (magenta), **6** (orange). (For interpretation of the references to colors in this figure legend, the reader is referred to the web version of this paper.)

to oxidize or to reduce due to their d^{10} configuration, these emissions can probably be assigned to intraligand (π–π^*) fluorescent emissions. At the same time, free H_2L (compound **6**) exhibits weak fluorescent emission bands at ca. 466 nm upon excitation at ca. 368 nm, which further supports this interpretation. It is clear that a hypsochromic shift of the emission occurs in **3** compared to other compounds, which is probably due to the differences of the ligands and the coordination environment around the central metal ions, because photoluminescence behavior is closely associated with the local environment around the metal ion. It appears to be a good candidate for novel hybrid inorganic–organic photoactive materials.

3.4. SHG measurement

Given that compound **4** crystallizes in a non-centrosymmetric space group (*Cc*) which has a polar point group (C_2), an investigation of its optical properties were undertaken. The SHG responses of the H_2L ligand and compound **4** were estimated by measuring a powder sample (ca. 80–120 μm in diameter, Kurtz powder test [36]), relative to urea. A pulsed Q-switched Nd:YAG laser at a wavelength of 1064 nm was used to generate the SHG signal. The backward scattered SHG light was collected using a spherical concave mirror and passed through a filter that transmits only 532 nm radiation. The SHG efficiency of H_2L and **4** is estimated to be approximately 0.5 and 0.6 times of that of urea. It indicates that H_2L may crystallize in a non-centrosymmetric space group [37].

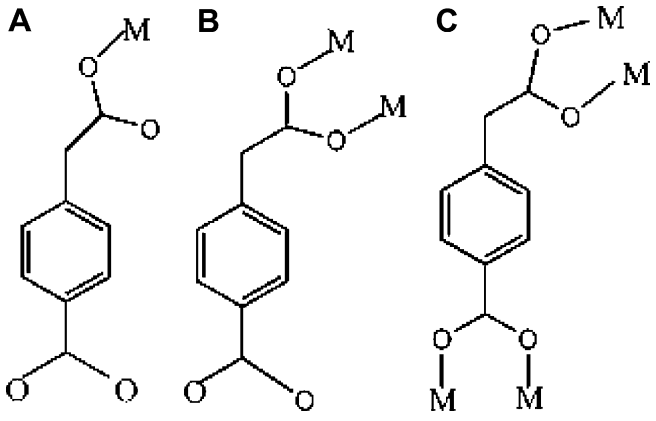
3.5. Discussion

As is well-known, the final structures of coordination polymers are influenced by the coordination modes, capabilities, size and shape of ligands and the coordination sphere of the metal centers. Although compounds **1**–**5** have been prepared with a molar ratio of 1:1:1 for metal salts/bpy/aromatic polycarboxylate, to our surprise, the final compounds all have different stoichiometries.

According to the above structural descriptions of our example compounds, the H_2L ligand exhibits three distinct kinds of coordination modes as shown in Scheme 1.

In compounds **1**–**3**, the L^- ligand monocoordinates the metal ions (A). In compound **4**, the L^{2-} ligand bridges two Cu(I) ions through two oxygen atoms of the carboxymethyl group (B). In compound **5**, the two carboxyl groups of the L^{2-} ligand both bridge two Zn(II) ions (C).

Aromatic polycarboxylate has good solubility in a mixture of water and CH_3CN, therefore, the superfluous reactant may remain in water under hydrothermal reactions. In most cases, water is not only a solvent but also acts as a competing ligand in these hydrothermal reactions. An interesting phenomenon can be observed whereby many coordination polymers constructed from polycarboxylate ligands usually contain water molecules as terminal or bridging ligands in the coordination sphere of the metal, thus increasing the variety of the assembled structural topologies of the polymers [38]. In compounds **1**–**5**, the



Scheme 1.

hydrogen-bonded frameworks exhibit different networks, for example, hydrogen-bonded quadrangle, hydrogen-bonded chain, hydrogen-bonded tetrahedron and hydrogen-bonded six-membered ring [39–41].

Compared with the complexes comprised of 1,4-benzenedicarboxylic acid, 4,4′-bipyidine and transition metals, the dimension of this series of complexes comprised of H_2L is lower, which may be a consequence of the more flexible configuration of H_2L.

4. Conclusion

In summary, five new polymers with different architectures, $[MnL_2(bpy)_2(H_2O)_2]_n$ (**1**), $[CoL(bpy)(H_2O)_3 \cdot H_2O]_n$ (**2**), $[CdL(bpy)(H_2O)_3 \cdot H_2O]_n$ (**3**), $[Cu_2L(bpy)_2 \cdot 3H_2O]_n$ (**4**) and $[Zn_2L_2(bpy) \cdot H_2O]_n$ (**5**), were constructed from the H_2L ligand and 4,4′-bpy, used as spacers, under mild hydrothermal conditions. For the first time, the H_2L ligand has been introduced into a trans-metal coordination polymer system. This study not only demonstrates that the nature of the ligand and the geometric needs of the metal atoms play an important role in the crystal packing of MOFs but also illustrates that hydrogen bonds affect the formation of supramolecular architectures. In addition, complex **3** may be an excellent candidate for blue-fluorescent materials and **4** appears to be a good candidate for novel hybrid inorganic–organic NLO materials.

Acknowledgments

Special thanks are offered to the reviewers for their constructive suggestions. We thank the National Nature Science Foundation of China (Grant No. 20490218), Jiangsu Science and Technology Department, and the Center of Analysis and Determining of Nanjing University for financial support.

Appendix A. Supplementary material

CCDC 615790, 612875, 612877, 612876 and 614096 contain the supplementary crystallographic data for **1**, **2**, **3**, **4** and **5**. The data can be obtained free of charge via http://www.ccdc.cam.ac.uk/conts/retrieving.html, or from the Cambridge Crystallographic Data Centre, 12 Union Road, Cambridge CB2 1EZ, UK; fax: (+44) 1223-336-033; or e-mail: deposit@ccdc.cam.ac.uk. Supplementary data associated with this article can be found, in the online version, at doi:10.1016/j.poly.2007.01.026.

References

[1] B.H. Ye, M.L. Tong, X.M. Chen, Coord. Chem. Rev. 249 (2005) 545.
[2] A.N. Khlobystov, A.J. Blake, N.R. Champness, D.A. Lemenovskii, A.G. Majouga, N.V. Zyk, M. Schroder, Coord. Chem. Rev. 222 (2001) 155.
[3] K. Inoue, H. Imai, P.S. Ghalsasi, K. Kikuchi, M. Ohba, H. Okawa, J.V. Yakhmi, Angew. Chem., Int. Ed. 40 (2001) 4242.
[4] J.J. Perry, G.J. McManus, M.J. Zaworotko, Chem. Commun. (2004) 2534.
[5] R. Matsuda, R. Kitaura, S. Kitagawa, Y. Kubota, R.V. Belosludov, T.C. Kobayashi, H. Sakamoto, T. Chiba, M. Takata, Y. Kawazoe, Y. Mita, Nature. 436 (2005) 238.
[6] R. Matsuda, R. Kitaura, S. Kitagawa, Y. Kubota, T.C. Kobayashi, S. Horike, M. Takata, J. Am. Chem. Soc. 126 (2004) 14063.
[7] S. Kitagawa, R. Kitaura, S. Noro, Angew. Chem., Int. Ed. 43 (2004) 2334.
[8] O.M. Yaghi, M. O'Keeffe, N.W. Ockwing, H.K. Chae, M. Eddaoudi, J. Kim, Nature 423 (2003) 705.
[9] C. Janiak, J. Chem. Soc., Dalton Trans. (2003) 2781.
[10] O.R. Evans, W. Lin, Acc. Chem. Res. 35 (2002) 511.
[11] M. Eddaoudi, D.B. Moler, H. Li, B. Chen, T. Reineke, M. O'Keeffe, O.M. Yaghi, Acc. Chem. Res. 34 (2001) 319.
[12] J.Y. Sun, L.H. Weng, Y.M. Zhou, J.X. Chen, Z.X. Chen, Z.C. Liu, D.Y. Zhao, Angew. Chem., Int. Ed. 41 (2002) 4471.
[13] X. Shi, G.S. Zhu, S.L. Qiu, K.L. Huang, J.H. Yu, R.R. Xu, Angew. Chem., Int. Ed. 43 (2004) 6482.
[14] Q.R. Fang, G.S. Zhu, M. Xue, Q.L. Zhang, J.Y. Sun, X.D. Guo, S.L. Qiu, S.T. Xu, P. Wang, D.J. Wang, Y. Wei, Chem. Eur. J. 12 (2006) 3754.
[15] N.L. Rosi, J. Kim, M. Eddaoudi, B.L. Chen, M. O'Keeffe, O.M. Yaghi, J. Am. Chem. Soc. 127 (2005) 1504.
[16] H.K. Chae, D.Y. Siberio-Pérez, J. Kim, Y.B. Go, M. Eddaoudi, A.J. Matzger, M. O'Keeffe, O.M. Yaghi, Nature. 427 (2004) 523.
[17] S.Q. Zang, Y. Su, Y. Song, Y.Z. Li, Z.P. Ni, H.Z. Zhu, Q.J. Meng, Cryst. Growth Des. 6 (2006) 2369.
[18] S.Q. Zang, Y. Su, Y.Z. Li, Z.P. Ni, Q.J. Meng, Inorg. Chem. 45 (2006) 174.
[19] S.Q. Zang, Y. Su, Y.Z. Li, H.Z. Zhu, Q.J. Meng, Inorg. Chem. 45 (2006) 2972.
[20] S.Q. Zang, Y. Su, Y.Z. Li, Z.P. Ni, H.Z. Zhu, Q.J. Meng, Inorg. Chem. 45 (2006) 3855.
[21] B.Q. Ma, K.L. Mulfort, J.T. Hupp, Inorg. Chem. 44 (2005) 4912.
[22] S.M.-F. Lo, S.S.-Y. Chui, L.-Y. Shek, Z. Lin, X.X. Zhang, G.-h. Wen, I.D. Williams, J. Am. Chem. Soc. 122 (2000) 6293.
[23] H. Chun, D.N. Dybtsev, H. Kim, K. Kim, Chem. Eur. J. 11 (2005) 3521.
[24] S.C. Manna, S. Konar, E. Zangrando, K. Okamoto, J. Ribas, N.R. Chaudhuri, Eur. J. Inorg. Chem. (2005) 4646.
[25] A.D. Burrows, R.W. Harrington, M.F. Mahon, S.J. Teat, Eur. J. Inorg. Chem. (2003) 766.
[26] F.A. Cotton, C. Lin, C.A. Murillo, Inorg. Chem. 40 (2001) 472.
[27] C.S. Marvel, E.A. Kraiman, J. Org. Chem. 18 (1953) 707.
[28] J.F. Codingtonz, E. Mosettig, J. Org. Chem. 17 (1952) 1035.
[29] SMART and SAINT, Area Detector Control and Integration Software, Siemens Analytical X-ray Systems, Inc., Madison, WI, 1996.
[30] G.M. Sheldrick, SHELXTL V5.1, Software Reference Manual, Bruker AXS, Inc., Madison, WI, 1997.
[31] S.P. Lewis, L.D. Henderson, B.D. Chandler, M. Parvez, W.E. Piers, S. Collins, J. Am. Chem. Soc. 127 (2005) 46.
[32] S.K. Ghosh, P.K. Bharadwaj, Inorg. Chim. Acta 359 (2006) 1685.
[33] J.C. Jiang, Y.S. Wang, H.C. Chang, S.H. Lin, Y.T. Lee, G. Niedner-Schatteburg, H.C. Chang, J. Am. Chem. Soc. 122 (2000) 1398.
[34] Z.Y. Fu, X.T. Wu, J.C. Dai, S.M. Hu, W.X. Du, H.H. Zhang, R.Q. Sun, Eur. J. Inorg. Chem. (2002) 2730.
[35] J. Tao, M.L. Tong, J.X. Shi, X.M. Chen, S.W. Ng, Chem. Commun. (2000) 2043.
[36] S.K. Kurtz, T.T. Perry, J. Appl. Phys. 39 (1968) 3798.
[37] X.F. Huang, Y.H. Li, Q. Wu, Q. Ye, R.G. Xiong, Inorg. Chim. Acta 358 (2005) 2097.
[38] J.C. Dai, X.T. Wu, S.M. Hu, Z.Y. Fu, J.J. Zhang, W.X. Du, H.H. Zhang, R.Q. Sun, Eur. J. Inorg. Chem. (2004) 2096.
[39] Y.F. Liu, J.C. Su, W.H. Li, J.G. Wu, Inorg. Chem. 44 (2005) 3890.
[40] N.S. Oxtoby, A.J. Blake, N.R. Champness, C. Wilson, Chem. Eur. J. 11 (2005) 4643.
[41] S.K. Ghosh, J. Ribas, P.K. Bharadwaj, Cryst. Growth Des. 5 (2005) 623.

Available online at www.sciencedirect.com
ScienceDirect
Polyhedron 26 (2007) 2837–2844
POLYHEDRON
www.elsevier.com/locate/poly

Oxorhenium complexes with the 8-quinolinolato ligand. X-ray structure and DFT calculations for $[ReOX_2(hqn)(AsPh_3)]$ and $[ReOX_2(hqn)(PPh_3)]$ complexes

B. Machura [a,*], S. Michalik [a], R. Kruszynski [b], J. Kusz [c]

[a] Department of Inorganic and Coordination Chemistry, Institute of Chemistry, University of Silesia, 9th Szkolna St., 40-006 Katowice, Poland
[b] Department of X-ray Crystallography and Crystal Chemistry, Institute of General and Ecological Chemistry, Lodz University of Technology, 116 Żeromski St., 90-924 Łódź, Poland
[c] Institute of Physics, University of Silesia, 4th Uniwersytecka St., 40-006 Katowice, Poland

Received 5 January 2007; accepted 23 January 2007
Available online 16 February 2007

Abstract

The reactions of $[ReOX_3(AsPh_3)_2]$ and $[ReOX_3(PPh_3)_2]$ with 8-hydroxyquinoline (Hhqn) have been examined and the complexes $[ReOX_2(hqn)(AsPh_3)]$ and $[ReOX_2(hqn)(PPh_3)]$ (X = Cl, Br) have been obtained, respectively. The crystal and molecular structures of $[ReOCl_2(hqn)(AsPh_3)]$ (**1**) and $[ReOBr_2(hqn)(PPh_3)]$ (**4**) have been determined. The electronic structure of **1** has been calculated with the density functional theory (DFT) method. The spin-allowed electronic transitions of **1** have been calculated with the time-dependent DFT method, and the UV–Vis spectrum of $[ReOCl_2(hqn)(AsPh_3)]$ has been discussed on this basis.
© 2007 Elsevier Ltd. All rights reserved.

Keywords: Rhenium oxo complexes; 8-Hydroxyquinoline; X-ray and electronic structure; DFT calculations; NBO analysis

1. Introduction

There is considerable interest in the chemistry of inorganic compounds containing an oxygen atom that is multiply bonded to a transition metal in a high oxidation state. These compounds can transfer an oxygen atom to reductants such as phosphines, sulfides and alkenes. For many years they have been in the centre of interest to those scientists engaged in basic research and to those trying to employ these complexes in catalytic processes. Oxygen atom transfer chemistry has been implicated in various reactions of industrial and biological importance, including olefin epoxidation and catalysis by cytochrome P-450 [1–3].

The chemistry of oxo rhenium complexes arouses particular interest among these compounds. It results from the favourable nuclear properties of ^{186}Re and ^{188}Re nuclides, which make the radioisotopes useful for diagnostic nuclear medicine and applications in radioimmunotheraphy [4,5]. In this context, the design, synthesis and reactivity of novel rhenium oxocomplexes has become the aim of several laboratories, including ours.

Previously, we investigated the reactivity of oxorhenium(V) species – $[ReO(OEt)X_2(PPh_3)_2]$, $[ReOX_3(PPh_3)_2]$ and $[ReOX_3(AsPh_3)(OAsPh_3)]$ (X = Cl or Br) – towards pyrazole, 3,5-dimethylopyrazole and benzotriazole [6]. In this report we focus on the examination of the reactions of $[ReOX_3(AsPh_3)_2]$ and $[ReOX_3(PPh_3)_2]$ with 8-hydroxyquinoline (Hhqn) and present the synthesis and the spectroscopic data for the complexes $[ReOCl_2(hqn)(AsPh_3)]$ (**1**), $[ReOBr_2(hqn)(AsPh_3)]$ (**2**), $[ReOCl_2(hqn)(PPh_3)]$ (**3**) and $[ReOBr_2(hqn)(PPh_3)]$ (**4**). X-ray studies have been performed for **1** and **4**.

Recently, several oxocomplexes of the general formula $[ReOCl_2(O–N)(PPh_3)]$, including compounds with 2-, 5- and/or 7-substituted 8-quinolinolato ligands, have been structurally and spectroscopically characterized [7–

* Corresponding author.
E-mail addresses: basia@ich.us.edu.pl (B. Machura), rafal.kruszynski@p.lodz.pl (R. Kruszynski).

0277-5387/$ - see front matter © 2007 Elsevier Ltd. All rights reserved.
doi:10.1016/j.poly.2007.01.054

10]. The oxorhenium(V) chelates $[ReOCl_2(O–N)(PPh_3)]$ with pyridinecarboxylate ligands have also been examined as catalysts for the carboxylation of ethane by CO in the presence of potassium peroxodisulfate $K_2S_2O_8$ [10].

In addition, this paper includes DFT (density functional theory) and TD-DFT (time-dependent DFT) calculations for complex **1**. Currently, density functional theory (DFT) is commonly used to examine the electronic structure of transition metal complexes. It meets with the requirements of being accurate, easy to use and fast enough to allow the study of relatively large molecules of transition metal complexes [11]. Recent calculations with the TD-DFT method for open- and closed-shell 5d-metal complexes (including rhenium complexes) have also supported the TD-DFT method to be applicable for such systems, giving good assignment of experimental spectra [12–14].

2. Experimental

2.1. General procedure

All reagents used for the synthesis were commercially available and were used without further purification. The $[ReOX_3(AsPh_3)_2]$ and $[ReOX_3(PPh_3)_2]$ complexes were prepared according to the literature methods [15].

IR spectra were recorded on a Nicolet Magna 560 spectrophotometer in the spectral range 4000–400 cm^{-1} with the samples in form of KBr pellets. Electronic spectra were measured on a spectrophotometer Lab Alliance UV–Vis 8500 in the range 1000–200 nm in chloroform solution. Elemental analyses (C H N) were performed on a Perkin–Elmer CHN-2400 analyzer.

2.2. Preparation of [$ReOCl_2$(hqn)($AsPh_3$)] (**1**)

A mixture of $[ReOCl_3(AsPh_3)_2]$ (0.5 g, 0.54 mmol), Hhqn (0.09, 0.62 mmol) and acetone (70 ml) was stirred for 12 h. Acetone (50 ml) was distilled off and 100 ml of diethyl ether was added. $[ReOCl_2(hqn)(AsPh_3)]$ was filtered off, washed with ethanol, diethyl ether and dried. Yield 85%. The crystals of **1** for X-ray investigation were obtained by recrystallization from acetonitrile.

IR (KBr; ν/cm^{-1}): 1609 (w), 1598 (m), 1577 (s), 1499 (s) ν_{CN} and $\nu_{C=C}$; 975(s) $\nu_{Re=O}$.

UV–Vis ($CHCl_3$; $\lambda_{max}(\varepsilon)$): 862.8 (100), 692.2 (300), 401.6 (8.15×10^3), 254.4 (2.62×10^4), 233.6 (2.99×10^4).

Anal. Calc. for $C_{27}H_{21}AsCl_2NO_2Re$: C, 44.82; H, 2.93; N, 1.94. Found: C, 44.72; H, 2.95; N, 1.85%.

2.3. Preparation of [$ReOBr_2$(hqn)($AsPh_3$)] (**2**)

A procedure similar to that for $[ReOCl_2(hqn)(AsPh_3)]$ was used with $[ReOBr_3(AsPh_3)_2]$ (0.5 g, 0.47 mmol) and Hhqn (0.08 g, 0.55 mmol). A crystalline precipitate of $[ReOBr_2(hqn)(AsPh_3)]$ was collected in 90% yield.

Table 1
Crystal data and structure refinement for complexes **1** and **4**

	1	**4**
Empirical formula	$C_{27}H_{21}AsCl_2NO_2Re$	$C_{27}H_{21}PBr_2NO_2Re$
Formula weight	723.47	768.44
Temperature (K)	293(2)	293(2)
Wavelength (Å)	0.71073	0.71073
Crystal system	triclinic	triclinic
Space group	$P\bar{1}$	$P\bar{1}$
Unit cell dimensions		
a (Å)	7.7162(4)	7.8186(5)
α (°)	95.297(3)	95.252(5)
b (Å)	8.1402(3)	8.1755(5)
β (°)	90.778(4)	99.999(5)
c (Å)	19.9622(8)	20.2571(13)
γ (°)	93.802(3)	95.163(5)
Volume ($Å^3$)	1245.51(9)	1262.41(14)
Z	2	2
D_{calc} (Mg/m^3)	1.929	2.022
Absorption coefficient (mm^{-1})	6.437	8.067
$F(000)$	696	732
Crystal size (mm)	$0.05\times0.08\times0.48$	$0.03\times0.08\times0.24$
θ Range for data collection (°)	2.86–32.80	3.02–25.00
Index ranges	$-11\leqslant h\leqslant 7$, $-11\leqslant k\leqslant 11$, $-29\leqslant l\leqslant 28$	$-5\leqslant h\leqslant 11$, $-11\leqslant k\leqslant 11$, $-29\leqslant l\leqslant 29$
Reflections collected	12 555	8006
Independent reflections (R_{int})	7885 (0.0283)	4315 (0.0229)
Completeness to $2\theta = 50°$ (%)	99.8	99.7
Minimum and maximum transmission	0.541 and 0.973	0.451 and 0.929
Data/restraints/parameters	7885/0/307	4315/0/307
Goodness-of-fit on F^2	0.941	0.928
Final R indices [$I>2\sigma(I)$]	$R_1 = 0.0326$, $wR_2 = 0.0688$	$R_1 = 0.021$, $wR_2 = 0.0437$
R indices (all data)	$R_1 = 0.0544$, $wR_2 = 0.0709$	$R_1 = 0.0299$, $wR_2 = 0.0446$
Largest difference in peak and hole (e $Å^{-3}$)	1.165 and −1.122	0.749 and −0.567

IR (KBr): 1606 (w), 1593 (m), 1572 (s), 1501 (s) ν_{CN} and $\nu_{C=C}$; 968 (s) $\nu_{Re=O}$.

UV–Vis ($CHCl_3$; $\lambda_{max}(\varepsilon)$): 783.4 (150), 630.6 (360), 405.6 (8.45×10^3), 253.4 (2.82×10^4), 233.6 (3.10×10^4).

Anal. Calc. for $C_{27}H_{21}AsBr_2NO_2Re$: C, 39.92; H, 2.61; N, 1.72. Found: C, 39.80; H, 2.65; N, 1.80%.

2.4. Preparation of [$ReOCl_2$(hqn)(PPh_3)] (**3**)

A procedure similar to that for $[ReOCl_2(hqn)(AsPh_3)]$ was used with $[ReOCl_3(PPh_3)_2]$ (0.5 g, 0.6 mmol) and Hhqn (0.1 g, 0.7 mmol). A crystalline precipitate of $[ReOCl_2(hqn)(PPh_3)]$ was collected in 85% yield.

IR (KBr): 1608 (w), 1594 (m), 1573 (s), 1500 (s) ν_{CN} and $\nu_{C=C}$; 975 (s) $\nu_{Re=O}$.

UV–Vis ($CHCl_3$; $\lambda_{max}(\varepsilon)$): 879.0 (200), 690.4 (310), 404.0 (8.5×10^3), 254.6 (3.6×10^4), 232.4 (3.9×10^4).

Anal. Calc. for $C_{27}H_{21}PCl_2NO_2Re$: C, 47.72; H, 3.11; N, 2.06. Found: C, 47.60; H, 3.20; N, 2.10%.

2.5. Preparation of $[ReOBr_2(hqn)(PPh_3)]$ (4)

A procedure similar to that for $[ReOCl_2(hqn)(AsPh_3)]$ was used with $[ReOBr_3(PPh_3)_2]$ (0.5 g, 0.52 mmol) and Hhqn (0.09 g, 0.62 mmol). A crystalline precipitate of $[ReOBr_2(hqn)(PPh_3)]$ was collected in 90% yield.

IR (KBr): 1606 (sh), 1593 (m), 1574 (m), 1551 (s), 1500 ν_{CN} and $\nu_{C=C}$; 970 (s) $\nu_{Re=O}$.

UV–Vis ($CHCl_3$; $\lambda_{max}(\varepsilon)$): 847.6 (140), 704.6 (270), 394.8 (6.25×10^3), 244.4 (3.4×10^4), 227.8 (4.1×10^4).

Anal. Calc. for $C_{27}H_{21}PBr_2NO_2Re$: C, 42.20; H, 2.75; N, 1.82. Found: C, 42.35; H, 2.65; N, 1.70%.

2.6. Crystal structure determination and refinement

The X-ray intensity data of **1** and **4** were collected on a KM-4-CCD automatic diffractometer equipped with a CCD detector and graphite monochromated Mo Kα radiation ($\lambda = 0.71073$ Å) at a temperature of 295(2) K. Details concerning crystal data and refinement are given in Table 1. Lorentz, polarization and empirical absorption correction using spherical harmonics implemented in the SCALE3 ABSPACK scaling algorithm [16] were applied. The structures were solved by the Patterson method and subsequently completed by difference Fourier recycling. All the non-hydrogen atoms were refined anisotropically using the full-matrix, least-squares technique. The hydrogen atoms were treated as "riding" on their parent carbon atoms and assigned isotropic temperature factors equal to 1.2 times the value of the equivalent temperature factor of the parent atom. SHELXS97 [17], SHELXL97 [18] and SHELXTL [19] programs were used for all the calculations. Atomic scattering factors were those incorporated in the computer programs.

3. Computational details

The GAUSSIAN03 program [20] was used in the calculations. The geometry optimisation of **1** was carried out with the DFT method with the use of the B3LYP functional [21,22]. The electronic spectrum of **1** was calculated with the TD-DFT method [23]. The calculations were performed by using the ECP basis set on the rhenium atom, the standard 6-31+G** basis for chlorine, oxygen, arsine and nitrogen, 6-31G* for carbon and 6-31G for hydrogen atoms. The Xe core electrons of Re were replaced by an effective core potential and a DZ quality Hay and Wadt Los Alamos ECP basis set (LANL2DZ) [24] was used for the valence electrons. An additional *d* function with exponent $\alpha = 0.3811$ and *f* function with exponent $\alpha = 2.033$ on the rhenium atom were added.

Natural bond orbital (NBO) calculations were performed with the NBO code [25,26] included in GAUSSIAN03.

4. Results and discussion

4.1. Preparation and infrared data

The $[ReOX_2(hqn)(EPh_3)]$ (X = Cl, Br; E = As, P) complexes were prepared in good yields by ligand exchange reactions starting from $[ReOX_3(EPh_3)_2]$ complexes and 8-hydroxyquinoline in acetone:

$$[ReOX_3(EPh_3)_2] + Hhqn \rightarrow [ReOX_2(hqn)(EPh_3)] + HX + EPh_3 \quad X = Cl, Br;\ E = As, P$$

They were isolated as greenish-brown microcrystalline solids, soluble in common organic solvents.

The strong ν(Re=O) stretching bands at 968–975 cm^{-1} are in the higher end of the range observed for $\{ReO\}^{3+}$ core complexes. This suggests that the Re–hydroxy bond *trans* to the oxo ligand does not compete effectively for the Re_d orbitals and the bond is relatively weak. Moreover, the narrow range in which the ν(Re=O) bands appear is very similar to those observed for Re(V)-oxo complexes with a monoanionic oxygen (RO^- and $R–COO^-$,) *trans* to the oxo group [27].

4.2. Crystal structures

Both complexes are isostructural and they crystallise in the triclinic space group $P\bar{1}$, and their structures consist of discrete and well-separated monomers. Intermolecular interactions with enough strength to govern crystal packing or molecule conformation were not found in the structures of **1** and **4**. Only intra- and intermolecular short contacts, which can be considered as weak C–H···O hydrogen bonds [28,29] were detected (Table 2).

The molecular structures of **1** and **4** are presented in Figs. 1 and 2, respectively, and selected bond distances and angles are collected in Tables 3 and 4, respectively. Both complexes show an octahedral geometry about the central rhenium atom defined by the terminal oxo-group, two halide ions in a *cis* arrangement, the phosphorus or arsine of the EPh_3 molecule, and the bidentate N,O donors of the hqn ligand. The oxygen atom of hqn is coordinated

Table 2
Hydrogen bonds for **1** and **4**

D	A	HA···A (Å)	D···A	D–H···A (°)
Compound ***1***				
C(19)	O(2)	2.53	2.957(6)	107.9
C(9)	$O(1)^{\#1}$	2.58	3.365(5)	142.5
Compound ***4***				
C(19)	O(2)	2.53	2.942(5)	107.3
C(9)	$O(1)^{\#2}$	2.58	3.380(5)	144.9
C(2)	O(1)	2.37	3.086(5)	133.2

$^{\#1}$: $x, -y+1, z$; $^{\#2}$: $x, 1+y, z$.

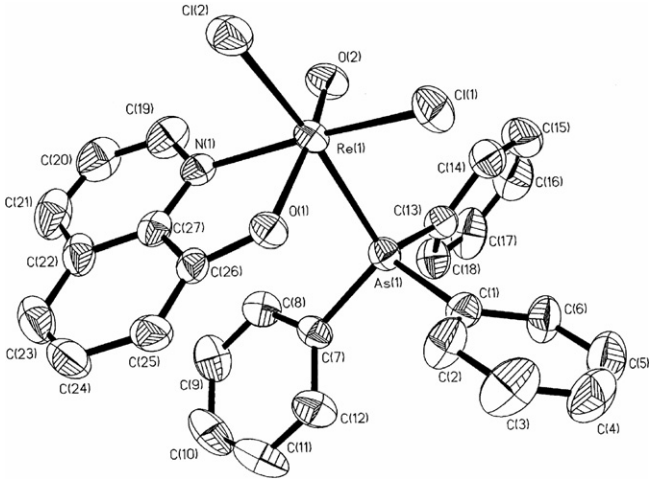


Fig. 1. The molecular structure of **1**. Displacement ellipsoids are drawn at 50% probability.

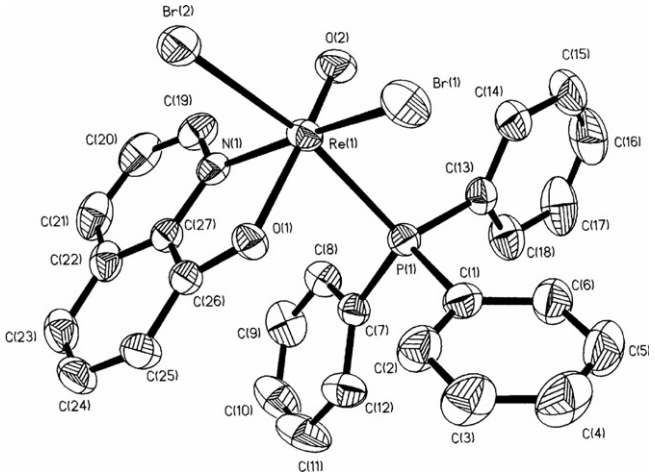


Fig. 2. The molecular structure of **4**. Displacement ellipsoids are drawn at 50% probability.

in a *trans* position to the terminal oxo ligand. The multiple bonding ligand (terminal oxo) and narrow bite angle of the chelating ligand contribute to clear distortions of the pseudooctahedral environment of the Re center in the $[ReOX_2(hqn)(EPh_3)]$ complexes. The high concentration of electronic density along the Re–O axis strongly influences the positions of the adjacent halogen atoms, which are pushed away.

A similar coordination geometry is observed for the other $[ReOCl_2(O–N)(PPh_3)]$ complexes with quinolinolato derivatives [7–9]. Accordingly, the 2-, 5- and/or 7-substituent of the 8-quinolinolato ligand does not affect the complexation.

Another geometry about the central atom can be noticed in the dibromooxo(*N*-phenylsalicylideneaminato)(triphenylphosphine)–rhenium(V) complex [30]. Similar to the $[ReOCl_2(O–N)(PPh_3)]$ complexes with 8-quinolinolato ligands, the oxygen atom of the *N*-phenylsalicylideneaminato ion occupies a *trans* position to the terminal oxo ligand, but the bromide ions are in a *trans* arrangement and the PPh_3 molecule is opposite the nitrogen atom of the *N*-phenylsalicylideneaminato ligand. It seems that electrostatic (not steric) factors are responsible for the changed geometry about the central atom in dibromooxo(*N*-phenylsalicylideneaminato)(triphenylphosphine)–rhenium(V) in comparison with the discussed 8-quinolinolato oxocomplexes. The pyridine ring of the 8-quinolinolato ligand is a good π acceptor, whereas the nitrogen atom of the *N*-phenylsalicylideneaminato ion is pure donor.

Table 3
The experimental and optimized bond lengths (Å) and angles (°) for **1**

Bond lengths	Experimental	Optimized
Re(1)–O(1)	1.995(2)	2.030
Re(1)–O(2)	1.681(3)	1.681
Re(1)–N(1)	2.147(3)	2.170
Re(1)–Cl(1)	2.3321(11)	2.406
Re(1)–Cl(2)	2.3889(12)	2.433
Re(1)–As(1)	2.5443(5)	2.618
O(2)–Re(1)–O(1)	160.94(13)	159.08
O(2)–Re(1)–N(1)	87.47(14)	87.03
O(1)–Re(1)–N(1)	75.95(12)	75.07
O(2)–Re(1)–Cl(1)	103.73(11)	105.13
O(1)–Re(1)–Cl(1)	93.40(8)	93.41
N(1)–Re(1)–Cl(1)	168.47(9)	167.59
O(2)–Re(1)–Cl(2)	100.06(11)	100.88
O(1)–Re(1)–Cl(2)	88.21(8)	88.65
N(1)–Re(1)–Cl(2)	85.84(9)	85.58
Cl(1)–Re(1)–Cl(2)	89.49(5)	89.61
O(2)–Re(1)–As(1)	92.08(11)	89.39
O(1)–Re(1)–As(1)	79.91(8)	81.83
N(1)–Re(1)–As(1)	93.78(9)	95.65
Cl(1)–Re(1)–As(1)	88.57(3)	87.10
Cl(2)–Re(1)–As(1)	167.82(3)	169.72

Table 4
The experimental bond lengths (Å) and angles (°) for **4**

Bond lengths	Experimental
Re(1)–O(1)	1.992(2)
Re(1)–O(2)	1.675(2)
Re(1)–N(1)	2.158(3)
Re(1)–Br (1)	2.4791(5)
Re(1)–Br(2)	2.5545(5)
Re(1)–P(1)	2.4542(10)
O(2)–Re(1)–O(1)	160.61(12)
O(2)–Re(1)–N(1)	86.37(13)
O(1)–Re(1)–N(1)	75.92(11)
O(2)–Re(1)–Br(1)	103.12(10)
O(1)–Re(1)–Br(1)	95.13(7)
N(1)–Re(1)–Br(1)	169.81(8)
O(2)–Re(1)–Br(2)	99.34(10)
O(1)–Re(1)–Br(2)	87.11(7)
N(1)–Re(1)–Br(2)	85.10(8)
Br(1)–Re(1)–Br(2)	89.634(17)
O(2)–Re(1)–P(1)	93.58(10)
O(1)–Re(1)–P(1)	80.16(8)
N(1)–Re(1)–P(1)	94.28(8)
Br(1)–Re(1)–P(1)	88.89(3)
Br(2)–Re(1)–P(1)	166.99(2)

Table 5
Atomic charges from the natural population analysis (NPA) for **1**

Atom	Charge
Re(1)	1.029
O(1)	−0.686
O(2)	−0.452
N(1)	−0.465
Cl(1)	−0.380
Cl(2)	−0.417
As(1)	1.394

The Re–O_t bond lengths of **1** and **4** fall in the range 1.639–1.76 Å, typical of mononuclear complexes of rhenium(V) having a $[ReO]^{3+}$ core, and indicate the presence of a triple Re≡O bond [31]. The interatomic distances between the rhenium atom and the oxygen atom of the hqn ligand are longer Re–O_{alkoxy} in the $[ReO(OR)X_2(PPh_3)_2]$ complexes [32], and only somewhat shorter than an ideal single Re–O bond length. The last bond length, predicted by the use of Pauling's covalent radius for oxygen and Cotton and Lippard's value for the octahedral covalent radius of rhenium(V), should be *ca.* 2.04 Å [33]. On the other hand, some differences of the Re–$O_{quinolinolato}$ bond

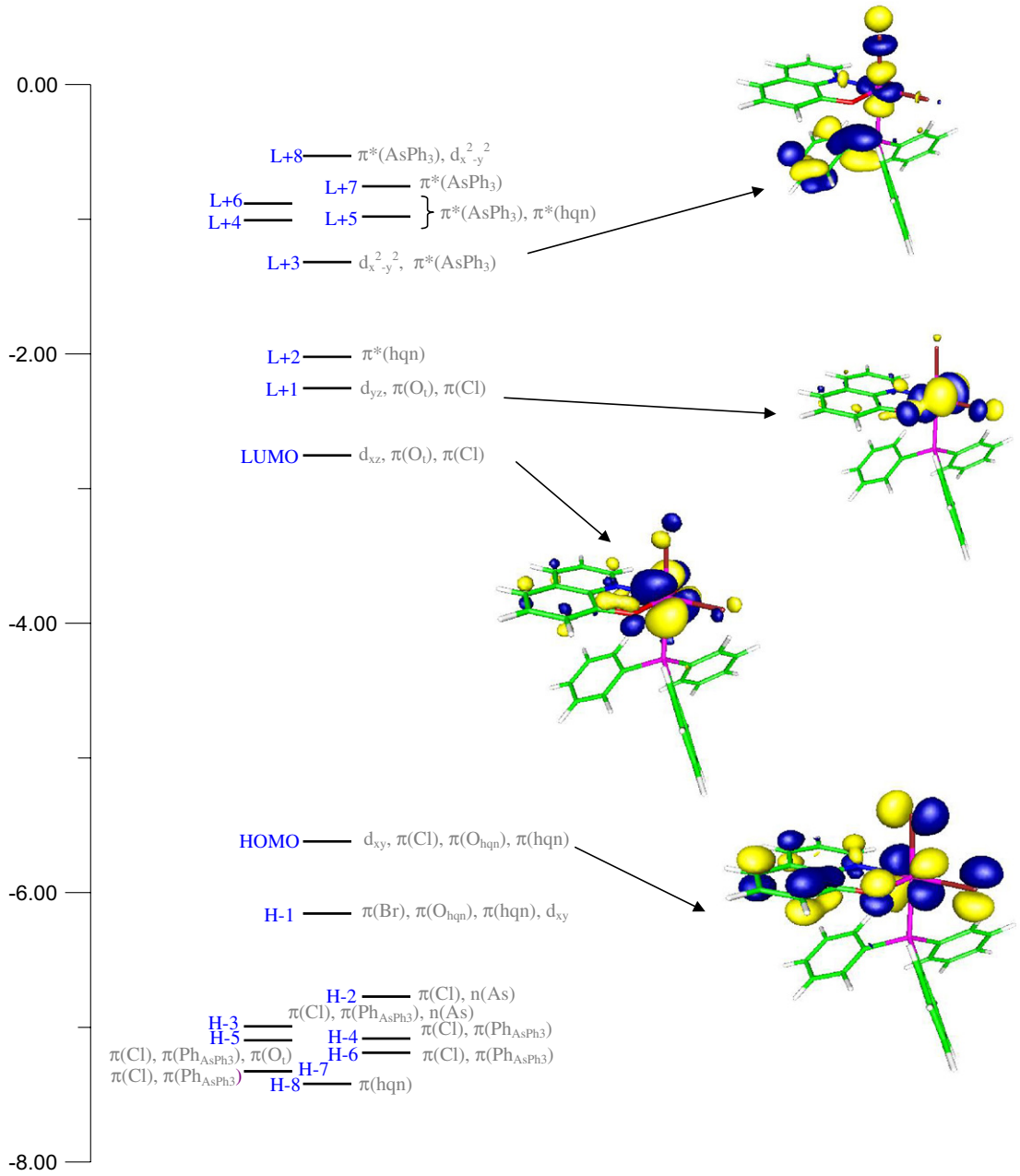


Fig. 3. The energy (eV), character and some contours of the molecular orbitals of **1**. Positive values of the orbital contour are represented in yellow (0.04 au) and negative values – in blue (−0.04 au). (For interpretation of the references in colour in this figure legend, the reader is referred to the web version of this article.)

are observed between [$ReOCl_2$(hqn)(PPh_3)], [$ReOCl_2$-(2-Me-hqn)(PPh_3)] and [$ReOCl_2$(5-Y-7-hqn)(PPh_3)]. The $Re–O_{quinolinolato}$ distances in complexes with 5- and 7-substituted 8-quinolinolato ligands are longer than those observed in [$ReOCl_2$(hqn)(PPh_3)] and [$ReOCl_2$(2-Me-hqn)(PPh_3)] [7,8].

The Re1–X(2) distances *trans* to the phosphorus or arsine atom of the EPh_3 molecule are slightly longer than the Re1–X(1) bonds *trans* to the quinoline nitrogen. It indicates a *structural trans* effect of the EPh_3 ligands. A similar trend is observed in all the oxorhenium(V) chelates [$ReOCl_2$(O–N)(PPh_3)] with 2-, 5- and/or 7-substituted 8-quinolinolato ligands [7,8].

4.3. Geometry optimisation, charge distribution, electronic structure and NBO analysis

The geometry of **1** was optimised in a singlet state by the DFT method with the B3LYP functional. The optimized geometric parameters of **1** are gathered in Table 3. In general, the predicted bond lengths and angles are in agreement with the values based upon the X-ray crystal structure data, and the general trends observed in the experimental data are well reproduced in the calculations.

Table 5 presents the atomic charges from the Natural Population Analysis (NPA) for **1**. The calculated charge on the rhenium atom in **1** is considerable lower than the formal charge of +5, and the populations of the d_{xy}, d_{xz}, d_{yz}, $d_{x^2-y^2}$ and d_{z^2} rhenium orbitals are as follows: 1.027, 0.925, 0.934, 1.722 and 0.855. It confirms significant charge donation from the ligands. The As atom is positively charged and the charges on the terminal oxo, chloride and oxygen atom of hqn^- are significantly smaller than −2, −1 and −1, respectively. The terminal oxo ion is less negative in comparison with the oxygen atom of the hqn ligand. It indicates higher electron density delocalization from the terminal ligands towards the rhenium centers and corresponds to the differences in the Re–O(2) and Re–O(1) bonds lengths.

Complex **1** is a closed-shell structure. Its molecular orbital diagram with several highest occupied MO and lowest unoccupied MO contours is presented in Fig. 3. The HOMO–LUMO gap equals 2.87 eV. The highest occupied MO of **1** is of d_{xy} type with some contributions from p_π chloride and hqn^- orbitals. The remaining four d-type orbitals of rhenium are found among the unoccuppied MOs. It confirms the d^2 configuration of the rhenium atom.

The rhenium–oxygen interaction in **1** is described as a triple bond. Assuming that rhenium uses its six valence orbitals, $5d_{x^2-y^2}$, $5d_{z^2}$, 6s, $6p_x$, $6p_y$ and $6p_z$ to form σ-bonds with the six ligands, empty $5d_{xz}$ and $5d_{yz}$ orbitals are available to overlap with $2p_x$ and $2p_y$ orbitals on the terminal oxygen to form an effective triple bond. The LUMO and LUMO + 1 (Fig. 3) are ascribed as π-antibonding rhenium–oxygen molecular orbitals.

Additional information about the nature of the rhenium–terminal oxygen bonding has been obtained by NBO analysis. The occupancy and composition of the calculated $Re–O_t$ natural bond orbitals (NBOs) are given in Table 6.

Each natural bond orbital (NBO) σ_{AB} can be written in terms of two directed valence hybrids (NHOs) h_A i h_B on atoms A and B:

$$\sigma_{AB} = c_A h_A + c_B h_B$$

where c_A and c_B are polarization coefficients. Each valence bonding NBO must in turn be paired with a corresponding valence *anti*-bonding NBO:

$$\sigma^*_{AB} = c_B h_A - c_A h_B$$

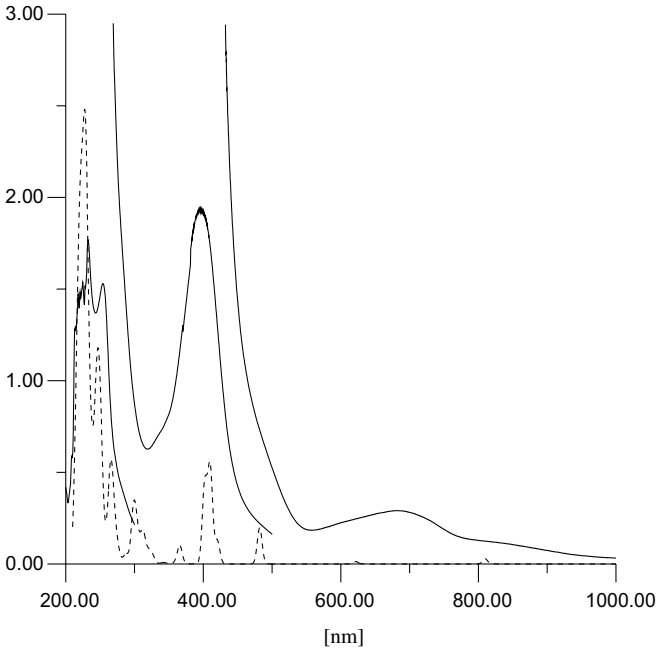


Fig. 4. The experimental (——) and calculated (----) electronic absorption spectra of **1**.

Table 6
The occupancy of the calculated natural bond orbitals (NBOs) between rhenium and the oxo ligand for **1**

BD	Occupancy	BD	BD[a]	Occupancy
$Re–O_t$	1.989	$0.562(d)_{Re} + 0.828(p)_O$	$0.828(d)_{Re} - 0.562(p)_O$	0.276
$Re–O_t$	1.993	$0.577(d)_{Re} + 0.817(p)_O$	$0.\ 817(d)_{Re} - 0.577(p)_O$	0.270

BD denotes 2-center bond.
[a] Denotes antibond NBO.

to complete the span of the valence space. The Lewis-type (donor) NBOs are thereby complemented by the non-Lewis-type (acceptor) NBOs that are formally empty in an idealized Lewis picture. The interactions between 'filled' Lewis-type NBOs and 'empty' non-Lewis NBOs lead to loss of occupancy from the localized NBOs of the idealized Lewis structure into the empty non-Lewis orbitals, and they are referred to as 'delocalization' corrections to the zeroth-order natural Lewis structure [34].

Although only two natural Re–O_t bond orbitals were detected for complex **1**, the rhenium–oxygen interaction can be described as a triple bond. Both the detected natural Re–O_t bond orbitals are orbitals of π character – the p_x and p_y oxygen orbitals and d_{xz} and d_{yz} rhenium orbitals are involved in their formation. The non-detected σ_{Re-O_t} bond has character of predominantly coulomb-type interactions between the central ion and ligands [35].

4.4. Electronic spectrum

The experimental and calculated electronic spectra of **1** are presented in Fig. 4. Each calculated transition is represented by a gaussian function $y = ce^{-bx^2}$ with the height (c) equal to the oscillator strength and b equal to 0.04 nm^{-2}.

Table 7
The energy and molar absorption coefficients of experimental absorption bands and the electronic transitions calculated with the TD-DFT method for **1**

The most important orbital excitations	Character	λ (nm)	E (eV)	f	Experimental Λ (nm) (E (eV)) ε
H → L	d → d	809.8	1.53	0.0036	862.8 (1.44) 100
H → L + 1	d → d	621.9	1.99	0.0016	692.2 (1.79) 300
H − 1 → L	π(Cl)/π(hqn)/d → d	481.9	2.57	0.0246	401.6 (3.09) 8150
H − 1 → L + 1	π(Cl)/π(hqn)/d → d	420.5	2.95	0.0157	
H → L + 2	d → π*(hqn)				
H − 1 → L + 1	π(Cl)/π(hqn)/d → d	410.1	3.02	0.0644	
H → L + 3	d → d/π*($AsPh_3$)	407.1	3.05	0.0010	
H − 2 → L	π (Cl)/n (As) → d	402.0	3.08	0.0532	
H − 3 → L	π (Cl)/n(As)π($AsPh_3$) → d	365.9	3.39	0.0122	
H → L + 6	d → π*($AsPh_3$)/π*(hqn)	311.8	3.98	0.0166	
H → L + 3	d → d/π*($AsPh_3$)				
H − 2 → L + 2	π (Cl)/n (As) → π*(hqn)	300.3	4.13	0.0107	254.4 (4.87) 26200
H − 1 → L + 3	π(Cl)/π(hqn)/d → d/π*($AsPh_3$)	298.2	4.16	0.0261	
H − 1 → L + 6	π(Cl)/π(hqn)/d → π*($AsPh_3$)/π*(hqn)	266.5	4.65	0.0207	
H − 2 → L + 3	π (Cl)/n(As) → d/π*($AsPh_3$)	265.2	4.68	0.0330	
H − 1 → L + 8	π(Cl)/π(hqn)/d → d/π*($AsPh_3$)	251.1	4.94	0.0343	
H → L + 12	d → d/π*($AsPh_3$)				
H − 5 → L + 3	π(Cl)/π($AsPh_3$)/π(O_t) → d/π*($AsPh_3$)	250.7	4.95	0.0297	
H − 3 → L + 3	π(Cl)/n(As)/π($AsPh_3$) → d/π*($AsPh_3$)				
H − 1 → L + 8	π(Cl)/π(hqn)/d → d/π*($AsPh_3$)	248.0	5.00	0.0200	
H − 1 → L + 8	π(Cl)/π(hqn)/d → d/π*($AsPh_3$)	246.2	5.04	0.0534	
H − 8 → L + 2	π (hqn) → π*(hqn)				
H − 3 → L + 3	π(Cl)/n(As)/π($AsPh_3$) → d/π*($AsPh_3$)	244.2	5.08	0.0389	
H − 12 → L + 2	π(Cl)/n (As)/π ($AsPh_3$) → π*(hqn)	237.0	5.23	0.0204	233.6 (5.31) 29890
H − 1 → L + 10	π(Cl)/π(hqn)/d → π*($AsPh_3$)	232.1	5.34	0.0204	
H − 7 → L + 3	π (Cl)/π($AsPh_3$) → d/π*($AsPh_3$)	230.4	5.38	0.0241	
H − 7 → L + 3	π(Cl)/π($AsPh_3$) → d/π*($AsPh_3$)	230.2	5.39	0.0257	
H − 3 → L + 4	π(Cl)/n(As)/π($AsPh_3$) → π *(hqn)/π*($AsPh_3$)	229.6	5.40	0.0614	
H − 3 → L + 5	π(Cl)/n(As)/π($AsPh_3$) → π*(hqn)/π*($AsPh_3$)	228.4	5.43	0.0388	
H − 3 → L + 4	π(Cl)/n(As)/π($AsPh_3$) → π*(hqn)/π*($AsPh_3$)	227.6	5.44	0.0759	
H − 10 → L + 3	π(Cl)/π($AsPh_3$) → d/π*($AsPh_3$)	225.7	5.49	0.0352	
H − 11 → L + 3	π(Cl)/π(O_t) → d/π*($AsPh_3$)				
H − 4 → L + 4	π(Cl)/π($AsPh_3$) → π*(hqn)/π*($AsPh_3$)	222.6	5.57	0.0170	
H − 2 → L + 7	π (Cl)/n(As) → π*($AsPh_3$)	222.2	5.58	0.0201	
H − 4 → L + 4	π(Cl)/π($AsPh_3$) → π*(hqn)/π*($AsPh_3$)				
H − 2 → L + 7	π (Cl)/n(As) → π*($AsPh_3$)	221.2	5.60	0.0173	
H − 5 → L + 4	π(Cl)/π(O_t)π($AsPh_3$) → π*(hqn)/π*($AsPh_3$)	220.6	5.62	0.0387	
H − 2 → L + 8	π (Cl)/n(As) → d/π*($AsPh_3$)	220.0	5.63	0.0307	
H − 4 → L + 5	π(Cl)/π($AsPh_3$) → π*(hqn)/π*($AsPh_3$)	218.1	5.69	0.0218	
H − 18 → L	σ (Cl) → d	216.0	5.74	0.0265	
H − 9 → L + 4	π($AsPh_3$) → π*(hqn)/π*($AsPh_3$)	214.0	5.79	0.0171	
H − 6 → L + 6	π(Cl)/π($AsPh_3$) → π*(hqn)/π*($AsPh_3$)				

ε – Molar absorption coefficient ($dm^3\ mol^{-1}\ cm^{-1}$).
f – Oscillator strength.
H – highest occupied molecular orbital.
L – lowest unoccupied molecular orbital.

The positions of the absorption bands for the other $[ReOX_2(hqn)(EPh_3)]$ complexes are given in Section 2.

The spin-allowed singlet–singlet electronic transitions calculated with the TD-DFT method for **1** are gathered in Table 7. For the high energy part of the spectrum, only transitions with oscillator strengths larger than 0.015 are listed in Table 7.

The two longest wavelength experimental bands of **1** at 862.8 and 692.2 nm are attributed to the transitions of d → d character, with small oscillator strengths calculated at 809.8 and 621.9 nm, respectively.

The broad and intense absorption band with a maximum at 401.6 nm is assigned to the metal–ligand charge transfer (occurring from the rhenium ion to the π-antibonding orbitals of the hqn and $AsPh_3$ ligands) and ligand–metal charge transfer ($\pi_{hqn}/n_{As}/\pi_{Cl}/\pi_O \rightarrow d$) transitions.

The experimental bands at 253.8 and 233.6 nm result mainly from ligand–ligand charge transfer and interligand (IL) transitions.

5. Supplementary material

CCDC 632496 and 632497 contain the supplementary crystallographic data for **1** and **4**. These data can be obtained free of charge via http://www.ccdc.cam.ac.uk/conts/retrieving.html, or from the Cambridge Crystallographic Data Centre, 12 Union Road, Cambridge CB2 1EZ, UK; fax: (+44) 1223-336-033; or e-mail: deposit@ccdc.cam.ac.uk.

Acknowledgement

The GAUSSIAN03 calculations were carried out in the Wrocław Centre for Networking and Supercomputing, WCSS, Wrocław, Poland.

References

[1] R.H. Holm, Chem. Rev. 87 (1987) 1401.
[2] C.C. Romão, F.E. Kühn, W.A. Hermann, Chem. Rev. 97 (1997) 3197.
[3] S.B. Seymore, S.N. Brown, Inorg. Chem. 39 (2000) 325.
[4] W. Volkert, W.F. Goeckeler, G.J. Ehrhardt, A.R. Ketring, J. Nucl. Med. 32 (1991) 174.
[5] E.A. Deutsch, K. Libson, J.L. Vanderheyden, Technetium and Rhenium in Chemistry and Nuclear Medicine, Raven Press, New York, 1990.
[6] B. Machura, Coord. Chem. Rev. 249 (2005) 591.
[7] X. Chen, F.J. Femia, J.W. Babich, J. Zubieta, Inorg. Chim. Acta 308 (2000) 80.
[8] Y. Miyashita, T. Ohashi, A. Imai, N. Amir, K. Fujisawa, K. Okamoto, Sci. Technol. Adv. Mater. 6 (2005) 660.
[9] O. Sigouin, A.L. Beauchamp, Can. J. Chem. 83 (2005) 460.
[10] A.M. Kirillov, M. Haukka, M.V. Kirillova, A.J.L. Pombeiro, Adv. Synth. Catal. 347 (2005) 1435.
[11] H. Chermette, Coord. Chem. Rev. 178–180 (1998) 699.
[12] M.C. Aragoni, M. Arca, T. Cassano, C. Denotti, F.A. Devillanova, F. Isaia, V. Lippolis, D. Natali, L. Niti, M. Sampietro, R. Tommasi, G. Verani, Inorg. Chem. Commun. 5 (2002) 869.
[13] P. Romaniello, F. Lelj, Chem. Phys. Lett. 372 (2003) 51.
[14] P. Norman, P. Cronstrand, J. Ericsson. Chem. Phys. 285 (2002) 207.
[15] G. Rouschias, G. Wilkinson, J. Chem. Soc. A (1966) 465.
[16] CrysAlis RED, Oxford Diffraction Ltd., Version 1.171.29.2.
[17] G.M. Sheldrick, Acta Crystallogr., Sect. A 46 (1990) 467.
[18] G.M. Sheldrick, SHELXL97. Program for the Refinement of Crystal Structures, University of Göottingen, Germany, 1997.
[19] G.M. Sheldrick, shelxtl: Release 4.1 for Siemens Crystallographic Research Systems, 1990.
[20] M.J. Frisch, G.W. Trucks, H.B. Schlegel, G.E. Scuseria, M.A. Robb, J.R. Cheeseman, J.A. Montgomery Jr., T. Vreven, K.N. Kudin, J.C. Burant, J.M. Millam, S.S. Iyengar, J. Tomasi, V. Barone, B. Mennucci, M. Cossi, G. Scalmani, N. Rega, G.A. Petersson, H. Nakatsuji, M. Hada, M. Ehara, K. Toyota, R. Fukuda, J. Hasegawa, M. Ishida, T. Nakajima, Y. Honda, O. Kitao, H. Nakai, M. Klene, X. Li, J.E. Knox, H.P. Hratchian, J.B. Cross, C. Adamo, J. Jaramillo, R. Gomperts, R.E. Stratmann, O. Yazyev, A.J. Austin, R. Cammi, C. Pomelli, J.W. Ochterski, P.Y. Ayala, K. Morokuma, G.A. Voth, P. Salvador, J.J. Dannenberg, V.G. Zakrzewski, S. Dapprich, A.D. Daniels, M.C. Strain, O. Farkas, D.K. Malick, A.D. Rabuck, K. Raghavachari, J.B. Foresman, J.V. Ortiz, Q. Cui, A.G. Baboul, S. Clifford, J. Cioslowski, B.B. Stefanov, G. Liu, A. Liashenko, P. Piskorz, I. Komaromi, R.L. Martin, D.J. Fox, T. Keith, M.A. Al-Laham, C.Y. Peng, A. Nanayakkara, M. Challacombe, P.M.W. Gill, B. Johnson, W. Chen, M.W. Wong, C. Gonzalez, J.A. Pople, GAUSSIAN 03, Revision B.03, Gaussian, Inc., Pittsburgh PA, 2003.
[21] A.D. Becke, J. Chem. Phys. 98 (1993) 5648.
[22] C. Lee, W. Yang, R.G. Parr, Phys. Rev. B 37 (1988) 785.
[23] M.E. Casida, in: J.M. Seminario (Ed.), Recent developments and applications in modern density functional theory, Theoretical and Computational Chemistry, vol. 4, Elsevier, Amsterdam, 1996.
[24] P.J. Hay, W.R. Wadt, J. Chem. Phys. 82 (1985) 299.
[25] E.D. Glendening, A.E. Reed, J.E. Carpenter, F. Weinhold, NBO (version 3.1).
[26] J.E. Carpenter, F. Weinhold, J. Mol. Struct. (Theochem) 169 (1988) 41.
[27] L. Wei, J. Babich, J. Zubieta, Inorg. Chim. Acta 358 (2005) 2413.
[28] G.A. Jeffrey, W. Saenger, Hydrogen Bonding in Biological Structures, Springer-Verlag, 1994.
[29] G.R. Desiraju, T. Steiner, The Weak Hydrogen Bond in Structural Chemistry and Biology, Oxford University Press, 1999.
[30] M. Sacerdoti, V. Bertolasi, G. Gilli, Acta Crystallograllogr., Sect. C 40 (1984) 968.
[31] J.M. Mayer, Inorg. Chem. 27 (1988) 3899.
[32] F.H. Allen, Acta Crystallograllogr., Sect. B 58 (2002) 380.
[33] S.R. Flechter, A.C. Skapski, J. Chem. Soc., Dalton Trans. (1972) 1073.
[34] A.E. Reed, L.A. Curtiss, F. Weinhold, Chem. Rev. 88 (1988) 899.
[35] M.L. Kuznestov, A.J.L. Pombeiro, J. Chem. Soc., Dalton Trans. (2003) 738.

Available online at www.sciencedirect.com
ScienceDirect
Polyhedron 26 (2007) 2845–2850
POLYHEDRON
www.elsevier.com/locate/poly

Synthesis, spectroscopic and X-ray structural studies of mercury(II) halide complexes of 4-methoxybenzoylmethylenetriphenylphosphorane

Seyyed Javad Sabounchei [a,*], Vida Jodaian [a], Hamid Reza Khavasi [b]

[a] *Faculty of Chemistry, Bu-Ali Sina University, Hamadan, Iran*
[b] *Department of Chemistry, Shahid Beheshti University, Evin, Tehran, 19839-63113, Iran*

Received 24 December 2006; accepted 23 January 2007
Available online 16 February 2007

Abstract

The reactions of the title ylide $\{(C_6H_5)_3PCHCOC_6H_4OCH_3)\}$ (MBPPY) with mercury(II) chloride and mercury(II) bromide in equimolar ratios using methanol as the solvent produces crystals of $[(MBPPY)\cdot HgCl_2]_2$ (**1**) and $[(MBPPY)\cdot HgBr_2]_2$ (**2**), respectively. Single crystal X-ray analyses reveal the presence of centrosymmetric dimeric structures containing the ylide and HgX_2 (X = Cl or Br) in both cases. The IR and NMR data of the product $[(MBPPY)\cdot HgI_2]_2$ (**3**), formed by the reaction of mercury(II) iodide with the same ylide, are similar to those of **1** and **2**. Analytical data indicate a 1:1 stoichiometry between the ylide and Hg(II) halide in each of the three products.
© 2007 Elsevier Ltd. All rights reserved.

Keywords: Phosphorus ylide; Mercury(II) halide complexes; X-ray Crystal structure; Triphenylphosphine

1. Introduction

The organometallic chemistry of phosphorous ylides $R_3P=C(R')(R'')$ (R, R′, R″ = alkyl or aryl groups) has undergone a great growth in the last few years, mainly due to their interesting application as reactants in organometallic and metal-mediated organic synthesis [1–4]. On the whole, the α-keto-stabilized phosphorous ylides $R_3P=C(R')COR''$ show interesting properties such as high stability (which allows them to be easily handled in air) and ambidentate character as ligands (*C*- versus *O*-coordination). This ambidentate character can be rationalized in terms of the resonance forms **A**–**C**, together with the isomeric form **D** (Scheme 1). Form **B** would account for *C*-coordination to a metal (M = metal) (which is presented as **G**) while isomers **C** and **D** would explain *O*-coordination (which are presented as *cisoid*, form **F**, and *transoid*, form **E**, respectively).

In the compounds reported to date, the chemical behavior of the α-keto phosphorous ylides has been clearly dominated by the *C*-coordinated form [5–8], and very few examples of *O*-coordinated ylides are known [9–13]. Some of these examples contain the ylide *O*-coordinated to a hard, very oxophilic metal center, as Sn(IV) [9,10] or group 4 metals with a high oxidation number [11]. Only W(0) complexes of the type $W(CO)_5L$ (L = ylide) [12] and Pd(II) complexes of the stoichiometry $[Pd(C_6F_5)L_2)(APPY)](ClO_4)$ [13] [APPY = Ph_3CCOMe; L = PPh_3, PBu_3; L_2 = bipy] contain stable ylides *O*-linked to a soft metal center. Other attempts to obtain this kind of *O*-coordination to "classical" soft metals such as Pd(II), Pt(II) or Hg(II) [6,14,15] invariably gave *C*-coordination. In this study, we describe the preparation, spectroscopic characterization (IR and NMR) of complexes of mercury(II) with the title ylide. By a comparison of the data collected and single crystal X-ray diffraction of **1** and **2**, it demonstrates *C*-coordination of the ylide to the metal.

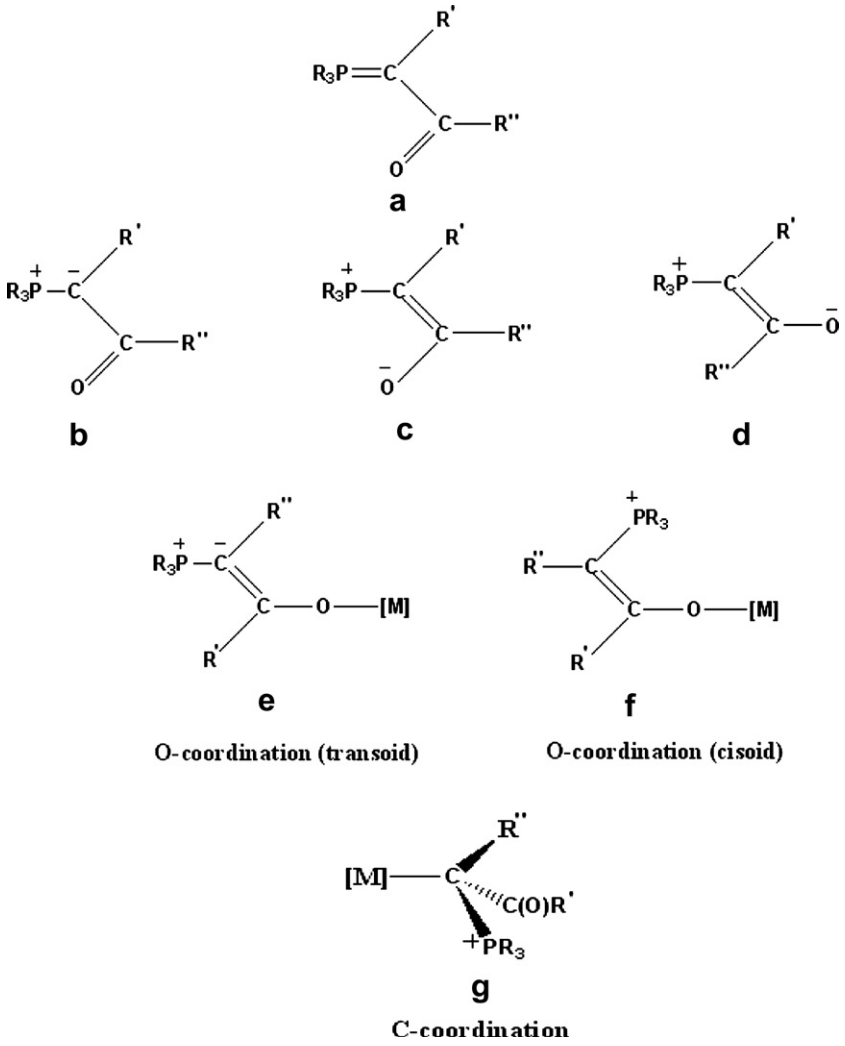
2. Experimental

2.1. Materials

Mercury halides, 4-methoxyacetophenone and triphenylphosphine were purchased from Merck. The ligand

* Corresponding author. Fax: +98 811 8257407.
E-mail address: jsabounchei@yahoo.co.uk (S.J. Sabounchei).

0277-5387/$ - see front matter © 2007 Elsevier Ltd. All rights reserved.
doi:10.1016/j.poly.2007.01.053



Scheme 1.

was synthesised by the reaction of triphenylphosphine with a chloroform solution of 2-bromo-4′-methoxyacetophenone and dehydrogenated by NaOH [16]. All solvents were dried by the reported methods [17].

2.2. Physical measurements

Melting points were measured on a SMPI apparatus. Elemental analysis for C, H and N were performed using a Perkin–Elmer 2400 series analyzer. Fourier transform IR spectra were recorded on a Shimadzu 435-U-04 spectrophotometer and samples were prepared as KBr pellets. ^{1}H, ^{13}C and ^{31}P spectra were recorded on a 200 MHz Bruker spectrometer in DMSO-d_6 or $CDCl_3$ solution at 25 °C.

The single crystal X-ray diffraction analysis was performed on a STOE IPDS-II two circle diffractometer at 298 K, using graphite monochromated Mo Kα radiation ($\lambda = 0.7107$ nm). A suitable crystal, grown from a methanol-diethylether solution, was mounted on a glass fiber. The data collection was performed at room temperature using the ω-scan technique and using the STOE X-AREA software package [18]. The crystal structure was solved by direct methods and refined by full-matrix least-squares on F^2 by SHELX [19] and using the X-STEP32[11] crystallographic software package [20]. All non-hydrogen atoms were refined anisotropically using reflections $I > 2\sigma(I)$. Hydrogen atoms were inserted at calculated positions using a riding mode with fixed thermal parameters. Data collection and refinement parameters are given in Table 1. ORTEP views of the X-ray crystal structures of the two complexes are shown in Figs. 1 and 2. Selected bond lengths (Å) and bond angles (°) for complexes **1** and **2** are given in Table 2.

2.3. Synthesis of MBPPY

To a chloroform solution (25 ml) of triphenylphosphine (0.131 g, 0.5 mmol) was added 2-bromo-4′-methoxyacetophenone (0.114 g, 0.5 mmol) and the resulting mixture was stirred for 12 h. The solution was filtered off, the precipitate washed with diethelyether and dried. Further treatment with aqueous NaOH solution (0.5 M) led to elimination of HBr, giving the free ligand MBPPY. M.p: 153–158 °C. *Anal*. Calc. for $C_{27}H_{23}O_2P$: C, 67.24; H, 4.84. Found: C, 66.05; H, 4.88%.

Table 1
Crystal data and refinement details for $[MBPPY \cdot HgCl_2]_2$ (**1**) and $[MBPPY \cdot HgBr_2]_2 \cdot 2(C_2H_5)_2O$ (**2**)

Compound	**1**	**2**
Empirical formula	$C_{54}H_{46}Cl_4Hg_2O_4P_2$	$C_{62}H_{66}Br_4Hg_2O_6P_2$
Formula weight	363.83	1689.87
Crystal system	triclinic	triclinic
Space group	$P\bar{1}$	$P\bar{1}$
Crystal size (mm)	$0.2 \times 0.13 \times 0.08$	$0.2 \times 0.15 \times 0.05$
a (Å)	10.3360(12)	11.181(6)
b (Å)	13.7444(16)	13.095(8)
c (Å)	19.657(2)	13.124(8)
α (°)	101.406(9)	115.88(4)
β (°)	91.117(9)	110.37(5)
γ (°)	108.725(9)	91.13(5)
V (Å^3)	2582.2(5)	186.8(16)
Temperature (K)	293(2)	293(2)
Z	2	1
Calculated density (Mg/m^3)	1.754	1.768
F (000)	1320	816
Reflections collected	23521	16157
θ_{max} (°)	1.6–26.80	1.77–28.22
Final R indices [$I > 2\sigma(I)$]		
R_1	0.0335	0.0832
wR_2	0.0559	0.1915
R indices (all data)		
R_1	0.0460	0.1105
wR_2	0.0593	0.2092
Goodness-of-fit on F^2	1.134	1.235

$R_1 = \sum \| F_o | - | F_c \| / \sum | F_o |$ for reflections with $I > 2\sigma I$.
$wR_2 = [\sum w(|F_o^2| - |F_c^2|)^2 / \sum |F_o^2|^2]^{1/2}$.

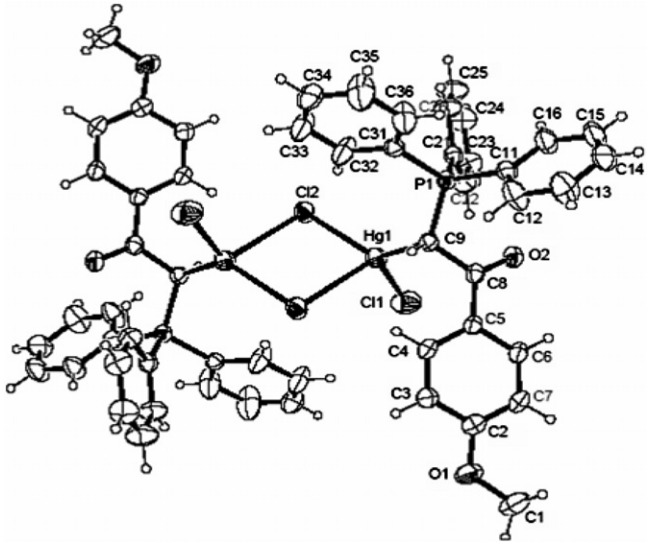


Fig. 1. ORTEP view of the X-ray crystal structure of $[MBPPY \cdot HgCl_2]_2$.

2.4. Synthesis of the complexes

2.4.1. $[MBPPY \cdot HgCl_2]_2$ (1)

To a methanolic solution (5 ml) of MBPPY (0.102 g, 0.25 mmol) was added mercury(II) chloride (0.067 g, 0.25 mmol). The mixture was stirred for 4 h. The white solid product was separated by filtration and washed with dietyl ether. Yield: 92.0%, m.p. 256–259 °C. *Anal.* Calc. for

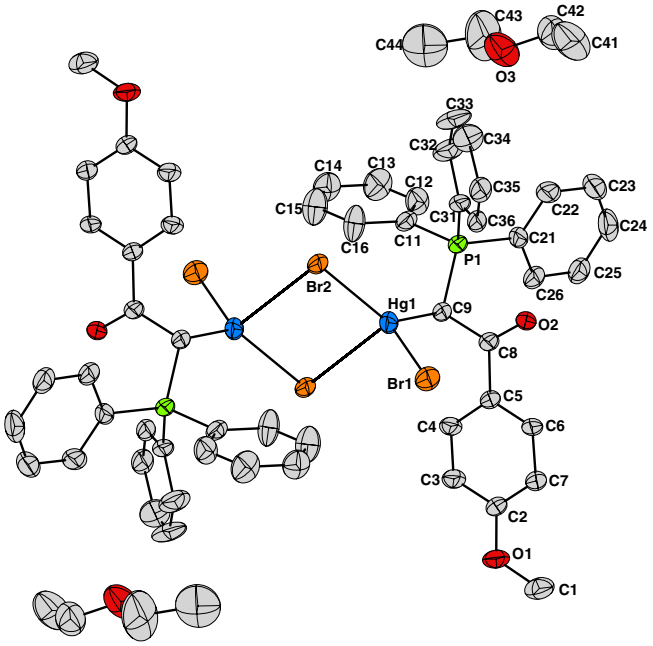


Fig. 2. ORTEP view of the X-ray crystal structure of $[MBPPY \cdot HgBr_2]_2 \cdot 2(C_2H_5)_2O$.

Table 2
Selected bond lengths (Å) and angles (°) for the structures of **1** and **2**

	1	**2**
Bond distances		
Hg (1)–C(9)	2.215(4)	2.218(11)
Hg(1)–Cl(1)	2.418(14)	2.559(2)
Hg(1)–Cl(2)	2.504(11)	2.603(3)
Hg(1)–Cl(2)#1	2.884(12)	3.022(2)
C(8)–O(2)	1.219(5)	1.251(13)
C(8)–C(9)	1.498(5)	1.470(16)
C(11)–P(1)	1.789(4)	1.796(13)
C(21)–P(1)	1.806(4)	1.806(11)
C(31)–P(1)	1.801(4)	1.800(12)
C(5)–C(8)	1.486(6)	1.528(14)
C(9)–P(1)	1.785(4)	1.827(11)
Bond angles		
Hg(1)–Cl(2)–Hg(1)#1	96.10(4)	90.16(7)
C(9)–Hg(1)–Cl(1)	119.34(10)	113.2(3)
C(9)–Hg(1)–Cl(2)	129.16(10)	132.9(3)
Cl(1)–Hg(1)–Cl(2)	106.59(5)	107.67(7)
C(9)–Hg(1)–Cl(2)#1	98.17(11)	99.8(3)
Cl(1)–Hg(1)–Cl(2)	110.86(5)	106.36(7)
Cl(2)–Hg(1)–Cl(2)#1	83.90(4)	89.84(7)
C(8)–C(9)–Hg(1)	104.9(2)	104.8(7)
P(1)–C(9)–Hg(1)	113.00(19)	114.3(5)
C(8)–C(9)–P(1)	112.4(3)	111.2(7)
C(9)–C(8)–C(5)	119.5(3)	118.8(9)
O(2)–C(8)–C(5)	121.3(3)	119.9(10)
C(11)–P(1)–C(9)	110.80(19)	105.5(5)
C(31)–P(1)–C(9)	107.86(1)	113.8(6)
C(21)–P(1)–C(9)	113.00(18)	112.4(5)
C(11)–P(1)–C(31)	107.62(19)	107.7(6)
C(11)–P(1)–C(21)	109.33(19)	108.6(6)
C(31)–P(1)–C(21)	108.05(18)	108.6(6)
O(2)–C(8)–C(9)	119.2(4)	121.2(10)

$C_{54}H_{46}O_4P_2Hg_2Cl_4$: C, 47.3; H, 3.6. Found: C, 48.80; H, 3.41%.

2.4.2. $[MBPPY \cdot HgBr_2]_2$ (2)

To a methanolic solution (5 ml) of MBPPY (0.102 g, 0.25 mmol) was added mercury(II) bromide (0.091 g, 0.25 mmol). The mixture was stirred for 4 h. The solvent was then removed in vacuo. The white product obtained was washed with ice-cold methanol and dried in vacuum. Yield: 87.2%, m.p. 203–205 °C. *Anal.* Calc. for $C_{54}H_{46}O_4P_2Hg_2Br_4$: C, 40.66; H, 3.11. Found: C, 40.73; H, 2.88%.

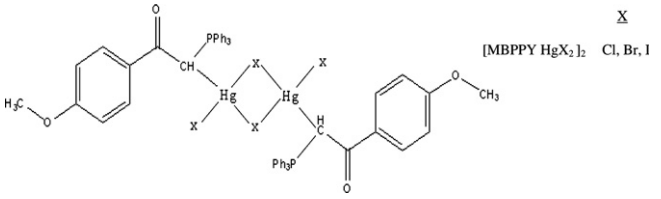
2.4.3. $[MBPPY \cdot HgI_2]_2$ (3)

To a methanolic solution (5 ml) of MBPPY (0.102 g, 0.25 mmol) was added mercury(II) iodide (0.113 g, 0.25 mmol). The mixture was stirred for 12 h. On concentration by removing the solvent by vacuum, a pale yellow precipitate was obtained. The products were washed with benzene and dried in vacuo. Yield: 81%, m.p. 242–245 °C. *Anal.* Calc. for $C_{54}H_{46}O_4P_2Hg_2I_4$: C, 37.49; H, 2.67. Found: C, 36.80; H, 2.64%.

3. Results and discussion

3.1. Synthesis

The ligand was synthesised by treating 2-bromo-4′-methoxyacetophenone (prepared by reacting 4-methoxyacetophenone with bromide in glacial acetic acid) with triphenylphosphine and removal of the proton from the phosphonium salt. Reactions of HgX_2 with the ylide in a 1:1 stoichiometry afforded the *C*-coordinated complexes with a halo-bridged dimeric structure:



3.2. Infra-red spectra

The ν(CO) band, which is sensitive to complexation, occurs at 1601 cm^{-1} in the parent ylide, as in the case of other resonance stabilized ylides [21]. Coordination of the ylide through *C*-coordination causes an increase in ν(CO) while for *O*-coordination a lowering of ν(CO) is expected. The IR absorption bands observed for the three complexes at 1630, 1626 and 1620 cm^{-1} indicate coordination of the ylide thorough carbon. The $\nu(P^+–C^-)$ which is also diagnostic of the coordination occurs at 837 cm^{-1} in $(C_6H_5)_3P^+–C–H_2$ and at 878 cm^{-1} in $(C_6H_5)_3PCHCOC_6H_5$ [22]. These assignments were confirmed by comparing the IR spectra of the corresponding ^{13}C substituted ylides. In the present study, the $\nu(P^+–C^-)$ values for all three complexes were shifted to lower frequencies and were observed at 825, 820 and 812 cm^{-1} for **1**, **2** and **3**, respectively, suggesting some removal of electron density from the P–C bond.

3.3. NMR spectral data

3.3.1. ^1H NMR spectra

The chemical shifts corresponding to the protons of the ligand and the complexes are listed in Table 3. The signals due to methine protons, when recorded in $CDCl_3$, were either broad or unobserved probably due to the very low solubility of all the complexes in $CDCl_3$. Similar behaviour was observed earlier in the case of ylide complexes of platinium(II) chloride [23]. However, a sharp doublet for the above proton was obtained in DMSO-d_6 for each of the three complexes in the same region. This indicates that the complexes do not react with DMSO-d_6. The appearance of a sharp doublet signal and expected downfield shift for the CH proton show the coordination of carbon through the methine group.

3.3.2. ^{31}P NMR spectra

The proton decoupled ^{31}P NMR spectra show only one sharp singlet between δ 22.65–24.58 ppm for the complexes (Table 3). Chemical shift values for the complexes appear to be downfield by about δ 8–10 ppm with respect to the parent ylide (δ 14.061 ppm), indicating coordination of the ylide has occurred. The appearance of single signals for the PCH group in each of the ^{31}P and ^1H NMR spectra indicates the presence of only one isomer for all the three complexes, as expected for *C*-coordination. It must be noted that *O*-coordination of the ylide generally leads to the formation of *cis* and *trans* isomers, giving rise to two different signals in ^{31}P and ^1H NMR spectra [24].

3.3.3. ^{13}CNMR

The ^{13}CNMR data of the complexes and the title ylide are listed in Table 3, along with possible assignments. The most interesting aspect of the ^{13}CNMR spectra of the complexes is the upfield shift of the signals due to the ylidic carbon. Such an upfield shift observed in $PdCl(\eta^3–2\text{-}XC_3H_4)$ $(C_6H_5)_3PCHCOR$ ($X = H$, CH_3; $R = CH_3$, C_6H_5) was attributed to the change in hybridization of the ylidic carbon [25]. Similar upfield shifts of 2–3 ppm with reference to the parent ylide were also observed in the case of $[(C_6H_5)_3PC_5H_4HgI_2]_2$ [23]. The ^{13}C shifts of the CO group in the complexes are around 189 ppm, relative to 184.265 ppm noted for the same carbon in the parent ylide, indicating much lower shielding of the carbon of the CO group in these complexes. No coupling to Hg was observed at room temperature in the ^1H, ^{13}C and ^{31}P NMR spectra for all these complexes. Failure to observe satellites in the above spectra was previously noted in the ylide complexes of Hg(II) [26] and Ag(I) [27], which had been explained by fast exchange of the ylide with the metal.

Table 3
^{1}H, ^{13}C and ^{31}P NMR data of MBPPY and its complexes with mercury (II) halides

Compound	^{1}H chemical shifts (δ ppm)	^{13}C chemical shifts (δ ppm)	^{31}P chemical shifts (δ ppm)
MBPPY	3.79 (3H, OCH_3) 4.25 (1H, d ($J = 15.68$ Hz), CH) 6.80–8.21 (19H, m, C_6H_5)	55.08 (s, OCH_3) 49.21 (d, ($J = 119.24$ Hz), CH) 126.77 (d, ($J = 74.8$ Hz), $PPh_3(i)$) 128.70 (d, ($J = 12.4$ Hz), $PPh_3(m)$) 131.89 (s, PPh_3(p)) 133.98 (d, ($J = 10.2$ Hz), $PPh_3(o)$) 160.65 (s, CO. Ph (*i*)) 184.26 (s, CO)	14.06 (s)
MBPPY · $HgCl_2$	3.83 (3H, OCH_3) 5.43 (1H, d, CH) 6.81–8.20 (19H, m, C_6H_5)	123.46 (d, ($J = 88.58$ Hz), $PPh_3(i)$) 129.32 (d, ($J = 12.61$ Hz), $PPh_3(m)$) 131.89 (s, PPh_3 (p)) 133.29 (d, ($J = 8.22$ Hz), $PPh_3(o)$) 162.58 (s, CO. Ph (*i*)) 189.76 (s, CO)	24.58 (s)
MBPPY · $HgBr_2$	3.81 (3H, OCH_3) 5.45 (1H, d, CH) 6.90–8.30 (19H, m, C_6H_5)	123.51 (d, ($J = 89.12$ Hz), $PPh_3(i)$) 129.37 (d, ($J = 12.7$ Hz), PPh_3 (*m*)) 130.41 (s, PPh_3(p)) 133.34 (d, ($J = 9.57$ Hz), $PPh_3(o)$) 162.58 (s, CO. Ph (*i*)) 190.56 (s, CO)	23.58 (s)
MBPPY · HgI_2	3.82 (3H, OCH_3) 22.67 (s) 5.25 (1H, d ($J = 6.98$ Hz), CH) 6.85–8.20 (19H, m, C_6H_5)	123.76 (d, ($J = 90.22$ Hz), $PPh_3(i)$) 129.45 (d, ($J = 12.79$ Hz), $PPh_3(m)$) 130.21 (s, PPh_3 (p)) 133.31 (d, ($J = 9.68$ Hz), $PPh_3(o)$) 162.43 (s, CO. Ph (*i*)) 188.71 (s, CO)	22.65 (s)

s = singlet, d = double, m = multiplet, *o* = *ortho*, *m* = *meta*, *p* = *para*, *i* = *ipso*.

3.4. Crystal structure

The solid state structures of complexes **1** and **2** have been established by single crystal X-ray analysis, which revealed triclinic units. The molecular structures are shown in Figs. 1 and 2, and selected interatomic parameters are collected in Table 2.

The dimeric structure adopted by complexes **1**, **2** and **3** is in contrast to the *O*-coordinated trinuclear mercury(II) complex of the phosphorus ylide $Ph_3PCHCOPh$ [28], but is similar to the structure of *trans*-di-μ-iododiiodobis(triphenylphosphoniumcyclopentadienylide) dimercury(II) reported by Baenziger et al. [29] and the *C*-coordinated dinuclear mercury(II) halide complexes of $Ph_3CHCOPh$ (BPPY) [30]. The *C*-coordination of MBPPY is in stark contrast to the *O*-coordination of the phosphorus ylide, $Ph_3PC(COMe)(COPh)$ (ABPPY), to a Hg(II) centre [31]. The difference in coordination mode between ABPPY and MBPPY to Hg(II) can be rationalized in terms of the electronic properties and steric requirements of the ylides. The nucleophilicity of the carbanion in ABPPY is less than for MBPPY; this is due to the additional delocalization of the ylide electron density in ABPPY which is facilitated by the second carbonyl group. This will reduce the ability of ABPPY to bind via the ylidic carbon. Belluco et al. have studied steric influences on the coordination modes of ylide molecules to Pt(II) systems [32]. These authors concluded that the preferred coordination mode is via the ylidic carbon, but that steric hindrance around the metal centre or the ylidic carbon will necessitate *O*-coordination. Indeed, this trend is reflected here, both BPPY and MBPPY are slightly less sterically demanding than ABPPY, and both are *C*-coordinated to Hg(II).

The Hg(II) centre forms four close contacts with sp^3 hybridization and has a 4-coordinate environment with one short Hg–X bond, one Hg–C bond and two asymmetric bridging Hg–X bonds at distances of 2.504(11) and 2.884(12) Å in **1** and 2.603(3) and 3.022(2) Å in **2**.

The significant shortening of the Hg–C bond length, 2.215(4) Å **1** and 2.218(11) Å **2** compared to analogous distances in $[(C_6H_5)_3PCHCOC_6H_5HgI_2]_2$ [30] and in $[(C_5H_4P(C_6H_5)_3HgI_2]_2$ [33] (2.312(13) and 2.292(8) Å, respectively) must be attributed to the use of mercury orbitals with high s character for bonding to the ylidic carbon. The use of non-equivalent hybrid orbitals with high s character to bond to low electronegative atoms was proposed by Bent in the concept of isovalent hybridization to account for the variation in bond lengths and bond angles around a central atom [34].

The terminal Hg–Cl bond length, 2.418(14) Å **1** is comparable to 2.400 Å observed in the case of $Hg_2Cl_5N_2C_{11}H_{12}$, which has a tetrahedral coordination environment around mercury with a bridging structure [35]. The two bridged Hg–Cl bonds fall within the range 2.620–3.080 Å reported for other structures [36] containing chloro bridged mercury.

The angles around mercury vary from 83.90(4)° to 129.16(10)° for the chloride and 89.84(7)° to 132.9(3)° for the bromide, a very distorted tetrahedral environment. This distortion must be due to the higher s character of the sp^3 hybrid mercury orbitals involved in the above bonds and the formation of a strong halogen bridge between the Hg atoms which requires the internal XHgX angle to be considerably smaller.

The stabilized resonance structure for the title ylide is destroyed by the complexes formation. Thus, the C(8)–C(9) bond length (1.498(5) Å, **1** and 1.470(16) Å, **2**) is significantly longer than the corresponding bond found in a similar uncomplexed phosphorane (1.407(8) Å) [37]. On the other hand, the bond length of P(1)–C(9) in the similar ylide is 1.706 Å [24] which shows that the above bond is considerably elongated to 1.785(4) Å and 1.827(11) Å in complexes **1** and **2**, respectively. The plane defined by the two mercury atoms and the two bridging halogens is perfectly planar in both structures. The internuclear distances between mercury atoms were found to be 3.901(7) Å and 3.994(8) Å in structures **1** and **2**, respectively. These distances are much longer than the sum of Van der Waals radii (1.5 Å) of the two mercury atoms [38] indicating the absence of significant bonding interactions between the mercury atoms in the molecular structures. The adaptation of dimeric structures in Hg(II) ylide complexes may be explained by both the preference of Hg(II) to four coordination and the stability of the 18 electron configuration around Hg(II).

4. Conclusions

The present study describes the synthesis and characterization of a series of mercury ylide complexes. On the basis of the physico-chemical and spectroscopic data we propose that MBPPY herein exhibits monodentate *C*-coordination to the metal center, which is further confirmed by the X-ray crystal structures of the complexes.

5. Supplementary material

CCDC 622081 and 620129 contains the supplementary crystallographic data for this paper. These data can be obtained free of charge via http://www.ccdc.ac.uk/conts/retrieving.html, or from the Cambridge Crystallographic Data Centre, 12 Union Road, Cambridge CB2 1EZ, UK; fax: (+44) 1223-336-033; or e-mail: deposit@ccdc.cam.ac.uk.

Acknowledgements

We are grateful to the Bu-Ali Sina for a Grant and Mr. Zebarjadian for recording the NMR spectra.

References

[1] Y. Shen, Acc. Chem. Res. 31 (1998) 584.
[2] C. Puke, G. Erker, N.C. Aust, E.U. Wurthweine, R. Frohich, J. Am. Chem. Soc. 120 (1998) 4863.
[3] O.I. Kolodiazhnyi, Russ. Chem. Rev. 66 (1997) 225.
[4] D.E.C. Cobridge, Phosphorus an Outline of Chemistry, Biochemistry and Uses, 5th ed., Elsevier, Amsterdam, 1995.
[5] H. Nishiyama, K. Itoh, Y. Ishii, J. Organomet. Chem. 87 (1975) 129.
[6] J. Vicent, M.T. Chicote, J. Fernandez-Baeza, J. Organomet. Chem. 364 (1989) 407.
[7] M. Onishi, Y. Ohama, K. Hiraki, H. Shintani, Polyhedron 1 (1982) 539.
[8] J. Vicent, M.T. Chicote, M.C. Lagunas, P.G. Jones, J. Chem. Soc., Dalton Trans. (1991) 2579.
[9] J. Buckle, P.G. Harrison, T.J. King, J.A. Richards, J. Chem. Soc., Chem. Commun. (1972) 1104.
[10] J. Buckle, P.G. Harrison, J. Organomet. Chem. 49 (1973) C17.
[11] J.A. Albanese, D.A. Staley, A.L. Rheingold, J.L. Burmeister, Inorg. Chem. 29 (1990) 2209.
[12] I. Kawafune, G. Matsubayashi, Inorg. Chim. Acta 70 (1983) 1.
[13] R. Uson, J. Fornies, R. Navarro, P. Espinet, C.J. Mendivil, Organomet. Chem. 290 (1985) 125.
[14] J.L. Burmeister, J.L. Silver, E.T. Weleski, E.E. Schweizer, C.M. Kopay, Synth. Inorg. Met. Org. Chem. 3 (1973) 339.
[15] M.L. Illingsworth, J.A. Teagle, J.L. Burmeister, W.C. Fultz, A.I. Rheingold, Organometallics 2 (1983) 1364.
[16] F. Ramirez, S. Dershowitz, J. Org. Chem. 22 (1957) 41.
[17] A.J. Gordon, R.A. Ford, The Chemist's Companion – A Handbook of Practical Data, Techniques and References, Wiley-Interscience, New York, 1972, p. 438.
[18] Stoe & Cie, X-AREA, version 1.30: Program for the Acquisition and Analysis of Data, Stoe & Cie GmbH, Darmatadt, Germany, 2005.
[19] G.M. Sheldrick, SHELX97. Program for Crystal Structure Solution and Refinement, University of Göttingen, Germany, 1997.
[20] Stoe & Cie, X-STEP32, Version 1.07b: Crystallographic Package, Stoe & Cie GmbH, Darmatadt, Germany, 2005.
[21] J. Vicente, M.T. Chicoto, M.C. Lagunas, P.G. Jones, J. Chem. Soc., Dalton Trans. (1991) 2579.
[22] W. Luttke, K. Wilhelm, Angew. Chem., Int. Ed. Engl. 4 (1965) 875.
[23] J.A. Teagle, J.L. Burmieister, Inorg. Chim. Acta 118 (1986) 65.
[24] R. Uson, J. Fornies, R. Navarro, P. Espinet, C. Mendivil, J. Organomet. Chem. 290 (1985) 125.
[25] G. Facchin, R. Bertani, M. Calligaris, G. Nardin, M. Mari, J. Chem. Soc., Dalton Trans. (1987) 1381.
[26] N.I. Holy, N.C. Baenziger, R.M. Flynn, D.C. Swenson, J. Am. Chem. Soc. 98 (1976) 7823.
[27] J. Vicente, M.T. Chicote, J. Fernandez-Baeza, J. Martin, I. Saura-Hamas, J. Iurpin, P.G. Jones, J. Organomet. Chem. 331 (1987) 409.
[28] M. Kalyanasundari, K. Panchanatheswaram, W.T. Robinson, Bull. Chem. Soc. Jpn. 72 (1999) 33.
[29] N.C. Baenziger, R.M. Flyuu, D.C. Swenson, Acta Crystallogr., Sect. B 34 (1978) 2300.
[30] M. Kalyanasundari, K. Panchanatheswaran, W.T. Robinson, H. Wen, J. Organomet. Chem. 491 (1995) 103.
[31] P. Laavanya, U. Venkatasubramanian, K. Panchanatheswaran, J.A. Krause Baure, Chem. Commun. (2001) 1660.
[32] U. Belluco, R.A. Michelin, R. Bertini, G. Facchin, G. Pace, L. Zanotto, M. Mozzon, M. Furlan, E. Zangrando, Inorg. Chim. Acta (1996) 355.
[33] N.I. Holy, N.C. Baenziger, R.M. Flynn, D.C. Swenson, J. Am. Chem. Soc. 98 (1976) 7823.
[34] H.A. Bent, Chem. Rev. 61 (1961) 75.
[35] A. Albinati, S.V. Meille, F. Cariati, G. Marcotrigiano, L. Menabue, G.C. Pellacani, Inorg. Chim. Acta 38 (1984) 221.
[36] N.A. Bell, S.J. Coles, M.B. Hursthouse, M.E. Light, K.A. Malik, R. Mansor, Polyhedron 19 (2000) 1719.
[37] M. Kalyanasundari, K. Panchanatheswaran, V. Parthasarathi, W.T. Robinson, H. Wen, Acta Crystallogr. 50 (1994) 1738.
[38] J.E. Huheey, Inorganic Chemistry Principles of Structure and Reactivity, 2nd ed., Harper Int. Ed., New York, 1978, p. 233.

Available online at www.sciencedirect.com
ScienceDirect
Polyhedron 26 (2007) 2851–2858
POLYHEDRON
www.elsevier.com/locate/poly

Hydrolysis products of water treatment chemical aluminium sulfate octadecahydrate by electrospray ionization mass spectrometry

Arja Sarpola [a,*], Heikki Hellman [b], Vesa Hietapelto [c], Jorma Jalonen [b], Jukka Jokela [c], Jaakko Rämö [a], Jaakko Saukkoriipi [b]

[a] *Water Resources and Environmental Engineering Laboratory, University of Oulu, Linnanmaa, P.O. Box 4000, 90014 University of Oulu, Finland*
[b] *Department of Chemistry, University of Oulu, Linnanmaa, P.O. Box 3000, 90014 University of Oulu, Finland*
[c] *Kemira Inc., P.O. Box 171, 90101 Oulu, Finland*

Received 2 October 2006; accepted 23 January 2007
Available online 3 February 2007

Abstract

Hydrolysis and speciation of aluminium sulfate octadecahydrate $Al_2(SO_4)_3 \cdot 18H_2O$ was studied by electrospray time of flight mass spectrometry (ESI TOF MS). Several novel polymeric species were determined. Highly charged polymers, characterized by other methods, such as the Keggin cation $[Al_{13}O_4(OH)_{24}(H_2O)_{12}]^{7+}$ and the octameric aluminium hydroxide cluster $[Al_8(OH)_{14}(H_2O)_{18}](SO_4)_5\ 16H_2O$, were found using ESI-MS as the anions $[Al_{13}O_4(OH)_{25}(SO_4)_4]^{2-}$ and $[Al_8O(OH)_{14}(SO_4)_5(H_2O)_4]^{2-}$. All the main species identified contained sulfate or hydrogen sulfate. The compositions of the determined ions mimicked those of several stable mineral forms.
© 2007 Elsevier Ltd. All rights reserved.

Keywords: Aluminium; Sulfate; Speciation; Mass spectrometry; Electrospray; Cluster ions

1. Introduction

Purified water is arguably the most precious chemical for mankind by far. In the industrialized world, its consumption per person per day can be several hundreds of litres. Meanwhile, billions of people have considerably insufficient drinking water, which in turn is a major reason, for example, for high infant death rates. In this light, there is astonishingly little research that focuses on the aqueous behavior of water treatment chemicals.

The present investigation is focused on the by far most used coagulation chemical, aluminium sulfate or alum. The major aim is to figure out complex species emerging when alum is dissolved in water. The current process optimization of coagulating flocculating units is based predominantly on single experiments, not on detailed speciation studies. Variations in composition of raw water cause problems, which can be managed if the most efficiently functioning species and particles are known. Improved the understanding of the impact of process parameters on purification results will provide a key to enhancing the material efficiency of processes. This can be achieved with an increased understanding of the chemistry behind the process.

On the other hand, many solid species are crystallized in aqueous aluminium sulfate environments [1–6]. Our secondary aim was to clarify to what extent the emerging aqueous species resemble elementary units of typical crystal aluminium minerals.

We have earlier [7–10] used electrospray mass spectrometry in order to investigate speciation of aqueous aluminium chloride solutions. The studies have offered new information on the hydrolysis chemistry of aluminium, because the speciation found by MS differs from that observed using conventional solution phase analyses [11,12].

* Corresponding author. Tel.: +358 8 553 4498; fax: +358 8 553 4507.
E-mail address: Arja.Sarpola@oulu.fi (A. Sarpola).

0277-5387/$ - see front matter © 2007 Elsevier Ltd. All rights reserved.
doi:10.1016/j.poly.2007.01.035

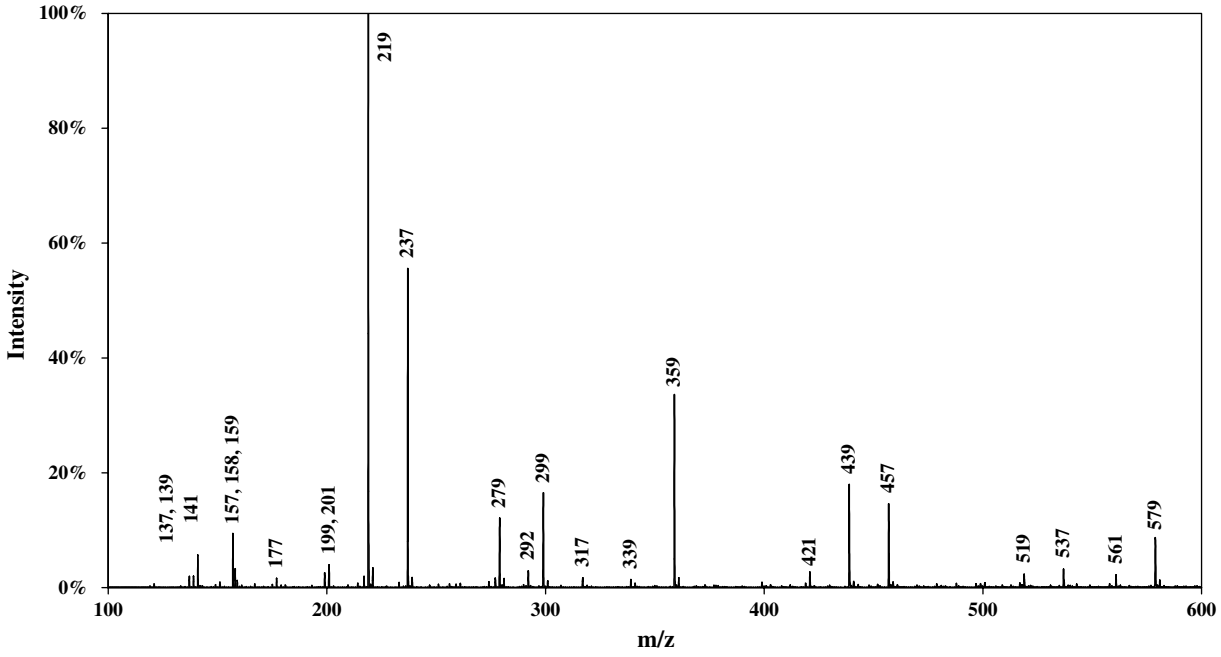


Fig. 1. The cationic spectrum of aluminium sulfate octadecahydrate $Al_2(SO_4)_3 \cdot 18H_2O$, 5 mM at pH 3.76.

2. Experimental

Aluminium sulfate octadecahydrate $Al_2(SO_4)_3 \cdot 18H_2O$ (Merck, purum) 0.3 g exposed to an open atmosphere was dissolved in 100 mL of deionized, distilled water (10 mM Al^{3+}). The solution was divided into two parts. The first part of the solution was left at its initial pH of 3.76 and the other part of the solution was adjusted to pH 3.95, by a drop-wise addition of concentrated tetramethyl ammonium hydroxide pentahydrate, $(CH_3)_4NOH \cdot 5H_2O$, (TMA, Fluka, reinst). TMA was found to be the only useful base, since alkali metals formed several intense chloride aggregate signals that interfere with the interpretation of the spectra. The pH was determined with a Mettler Toledo MP 220 pH meter using a Mettler Toledo InLab 410 Ag/AgCl-electrode calibrated with FF-Chemicals' buffer solutions pH 4.00 and 7.00. The samples were allowed to equilibrate prior to recording for 3 h. We note that more than one day may be needed for aluminium solutions to reach their complete equilibria [11,12], but in our previous studies [7,9] there was little difference between spectra of fresh and 2-week-aged 100 mM $AlCl_3$ solutions.

The ESI TOF mass spectra were recorded by a Micromass LCT mass spectrometer equipped with a Z-spray electrospray interface. The solutions were introduced into the spectrometer by a Harvard Apparatus Model 11 syringe pump at flow-rates of 10 μL/min. The operating conditions (Table 1) used were tested by an experimental design calculated by MODDE 3.0 software. Signals from both pH values were recorded for 2 min and combined to a sum spectrum. All the ESI mass spectral data in the positive and negative ion modes were acquired using Masslynx NT software (version 3.4).

Table 1
Operating conditions of a Micromass LCT mass spectrometer for the aluminium sulfate octadecahydrate $Al_2(SO_4)_3 \cdot 18H_2O$, 5 mM

Capillary	waters 70000341
Ionization	Z-spray electrospray
Ionization mode	ES− and ES+
Function type	TOF MS
Mass range	75–1000
Resolution	5000
Duration	1.0 min
Scan duration	1.10 s
Capillary potential voltage	4000 V
Sample cone voltage	40.0 V
RF lens	200.0 V
Extraction cone voltage	4.0 V
Desolvation gas and capillary temperature	150.0 °C
Source temperature	120.0 °C
Cone gas flow (N_2)	300 L/h
Desolvation gas flow	750 L/h

The interpretation of the spectra was done with the aid of compositions and structures of aluminium sulfate minerals [13] equilibrium calculations [14,15] and computational chemistry [16]. The most probable assignments have been chosen in Table 2 and written as structural formulas. When the structure has no calculated confirmation, the formulas were written according to the protonation order: first oxo, followed by sulfate ligands. Thus, the protonation of the sulfate group could be different than the one suggested: e.g. $[Al_2(OH)_3(SO_4)]^+$ could be $[Al_2O(OH)_2(HSO_4)]^+$. The calculation details are presented in our earlier study [17].

According to normal mass spectrometric practice sodium and potassium impurities were utilized in the interpretation. Sodium originates from the glass equipment used, whereas potassium is a major impurity in reagents.

Table 2
Cationic and anionic main signals (>2%) and assignments of the sum spectra of aluminium sulfate octadecahydrate $Al_2(SO_4)_3 \cdot 18H_2O$, 5 mM at pH 3.76

m/z	Cationic species	*m/z*	Anionic species
141	$[Al(OH)(HSO_4)]^+$	**139**	$\mathbf{[AlO(SO_4)]^-}$
159	$[Al(OH)(HSO_4)(H_2O)]^+$	157	$[Al(OH)_2(SO_4)]^-$
177	$[Al(OH)(HSO_4)(H_2O)_2]^+$	193	$[Al(OH)_3(HSO_4)(H_2O)]^-$
139	$[Al_2(OH)_5]^+$	172	$[Al(OH)_3(HSO_4)_2(H_2O)_4]^{2-}$
157	$[Al_2(OH)_5(H_2O)]^+$	**219**	$\mathbf{[Al(SO_4)_2]^-}$
201	$[Al_2(OH)_3(SO_4)]^+$	139	$[Al_2O_2(SO_4)_2]^{2-}$
219	$\mathbf{[Al_2(OH)_4(HSO_4)]^+}$	279	$[Al_2O(OH)(SO_4)_2]^-$
237	$[Al_2(OH)_4(HSO_4)(H_2O)]^+$	297	$[Al_2(OH)_3(SO_4)_2]^-$
299	$[Al_2(OH)_3(HSO_4)_2]^+$	179	$[Al_2O(SO_4)_3]^{2-}$
317	$[Al_2(OH)_3(HSO_4)_2(H_2O)]^+$	**270**	$\mathbf{[Al_4O_3(SO_4)_4]^{2-}}$
199	$[Al_3O(OH)_6]^+$	310	$[Al_4O_2(SO_4)_5]^{2-}$
279	$[Al_3(OH)_6(SO_4)]^+$	441	$[Al_5O_5(OH)_2(SO_4)_2]^-$
158	$[Al_3(OH)_6(HSO_4)(H_2O)_2]^{2+}$	340	$[Al_5O_3(OH)(SO_4)_5]^{2-}$
359	$\mathbf{[Al_3O(OH)_4(HSO_4)_2]^+}$	380	$[Al_5O_2(OH)(SO_4)_6]^{2-}$
421	$\mathbf{[Al_3O(OH)(HSO_4)(SO_4)_2(H_2O)]^+}$	420	$[Al_5O(OH)(SO_4)_7]^{2-}$
439	$[Al_3(OH)_4(HSO_4)_2(SO_4)]^+$	359	$[Al_6O_7(OH)_5]^-$
457	$[Al_3(OH)_5(HSO_4)_3]^+$	401	$[Al_6O_4(SO_4)_6]^{2-}$
519	$[Al_3(OH)_3(HSO_4)_3(SO_4)]^+$	441	$[Al_6O_3(SO_4)_7]^{2-}$
537	$[Al_3(OH)_4(HSO_4)_4]^+$	287	$[Al_7O_6(SO_4)_6]^{3-}$
339	$[Al_4O(OH)_7(SO_4)]^+$	314	$[Al_7O_5(SO_4)_7]^{3-}$
561	$[Al_4(OH)_4(HSO_4)(SO_4)_3]^+$	431	$[Al_7O_5(OH)_2(SO_4)_6]^{2-}$
579	$[Al_4(OH)_5(HSO_4)_2(SO_4)_2]^+$	471	$[Al_7O_4(OH)(SO_4)_7]^{2-}$
		511	$[Al_8(OH)_{16}(SO_4)_5(H_2O)_3]^{2-}$
m/z	non-aluminium containing species	428	$[Al_9O_5(SO_4)_{10}]^{3-}$
137	$[H_2K(SO_4)]^+$	481	$[Al_{10}O_9(OH)_4(SO_4)_5]^{2-}$
292	cationic impurity from the equipment	421	$[Al_{10}O_7(OH)(SO_4)_9]^{3-}$
97	$[HSO_4]^-$	448	$[Al_{10}O_6(OH)(SO_4)_{10}]^{3-}$
249	$[H_3(SO_4)_2(H_2O)_3]^-$	501	$[Al_{10}O_4(OH)(SO_4)_{12}]^{3-}$
209	$[H_4(SO_4)_3(H_2O)_6]^{2-}$	542	$[Al_{11}O_5(SO_4)_{13}]^{3-}$
249	$[H_6(SO_4)_4(H_2O)_6]^{2-}$	562	$[Al_{12}O_6(OH)(SO_4)_{13}]^{3-}$
171	$[K(SO_4)(H_2O)_2]^-$	532	$[Al_{13}O_6(OH)_{25}(SO_4)_2]^{2-}$
512[a]	$[TMA_3(HSO_4)_2(SO_4)]^-$	572	$[Al_{13}O_5(OH)_{25}(SO_4)_3]^{2-}$
212	anionic impurity from the equipment	612	$[Al_{13}O_4(OH)_{25}(SO_4)_4]^{2-}$

The calculated structures are in bold.
[a] Only in raised pH.

Especially the potassium proved to be very informative. Despite many investigations of sulfuric acid [18–23], $[SO_4]^{2-}/[SO_3]^{2-}$ redox reactions have not been observed in mass spectrometric studies and therefore have been ignored.

Isotopic patterns and ratios appeared to be the most informative aspect in this study. Aluminium and sodium are monoisotopes (^{27}Al and ^{23}Na) and give only single signals to mass spectra. Potassium, oxygen and sulfur have one minor isotope, in addition to the major isotopes. Hence they show duplets with characteristic relative intensities in mass spectra. All the following isotopes were considered in this study: ^{39}K and ^{41}K (6.73%), ^{16}O and ^{18}O (0.21%), and ^{32}S and ^{34}S (4.29%). Considering, e.g. the sulfate ion, for instance, the first isotopic signal, 5.11%, was thus a sum signal assigned to both $[^{34}S^{16}O_4]^{2-}$ (98u) and $[^{32}S^{16}O_3{}^{18}O]^{2-}$ (98u), 4.29% and $4 \times 0.21\%$, respectively, from the main signal $[^{32}S^{16}O_4]^{2-}$ (96u).

The charges were determined by examining the differences between isotopic signals. Differences of 2u, 1u and 0.66u in an isotopic pattern refer to singly-, doubly- and triply-charged complexes, respectively. The relative intensities of signal pairs helped to confirm the amount of sulfate ions in the complex. For example signals *m/z* 400.9 (10.7%) and 401.9 (3.1%, 29% of the *m/z* 400.9) were assigned to a double charged complex with a mass of 801.8 containing six sulfate ligands as $[Al_6O_4(SO_4)_6]^{2-}$, in agreement with theoretical abundance calculations.

As an example of assignation we will give here a detailed pathway for identification of the pentameric complex $[Al_5O_3(OH)(SO_4)_5]^{2-}$: first, we know all the elements injected in the instrument. The major part of the elements is bound as water, the secondary part as aluminium species and sulfate. Additionally, there are trace quantities of potassium and sodium impurities. The duplet signal at *m/z* values 340 and 341 (Fig. 3) had an intensity of over 20%, therefore it should be a rational mixture of the major elements Al, O and H as well as $SO_4{}^{2-}$.

The first isotopic *m/z* value 340 is even. The mass values of aluminium oxo-hydoxides, -sulfates and -chlorides are also always even (AlO(OH) 60u, $Al_2(SO_4)_3$ 342u, for instance). If the charge of the complex is even so is the *m/z* value. Since non-charged species cannot be detected by the mass spectrometer, the charge of this complex must be even.

There was a second signal of m/z 341 with relative intensity of 27.9% from the major signal of m/z 340. The 1u difference between the signals reveals that the charge of the complex is −2 and the ratio of the signals is near 25% which reveals that there are five sulfate groups (relative intensity of 5.11%). Hence, the assignation so far is $[Al_xO_y(OH)_z(SO_4)_5]^{2-}$ and the mass of the complex is $2 \times 340 = 680$u.

Since the charge of this preliminary complex is −2, detracting one sulfate from it we have an uncharged species $[Al_xO_y(OH)_z(SO_4)_4]^0$ with a mass of 584u. Thus the easiest way to figure out the rest of the complex is to divide it to calculatory pieces. We point out, that these pieces are relevant only in terms of matching the mass, they therefore have nothing to do with the structure or protonation order of the final assignation. We therefore next attempt to subtract the sulfates as neutral compounds: $Al_2(SO_4)_3$ 342u and $Al_2O_2(SO_4)$ 182u. The remaining mass is 582u – 342u – 182u = 60u, and the last piece should not contain anything besides aluminium, oxygen or hydroxide and possibly sodium. The neutral species AlO(OH) fulfills this requirement. After finding matching pieces they are combined to one species = $Al_2(SO_4)_3$ 342u + $Al_2O_2(SO_4)$ 182u + AlO(OH) 60u + SO_4^{2-} 96u = $[Al_5O_3(OH)(SO_4)_5]^{2-}$ m/z 340.

Now the simulated intensity of isotopic peak is $4 \times 0.21 + 5 \times 5.11 = 26.4$ which is close enough to the measured 27.9 and there are two signals with distances of 40u and 80u revealing a change of one oxygen to one sulfate and two oxygens to two sulfates. Their isotopic peaks also suit the pattern and therefore confirm the assignation.

3. Results and discussion

Aluminium salts precipitate in the neutral pH range [3]. The sulfate systems now studied showed transient opacity beginning at pH 3.95. The turbidity vanished quite rapidly and after 3 h the solution was clear again. Since at this pH value the chloride solution has earlier been perceived to be clear, consisting principally of dimeric and trimeric oxido and hydroxido variants [7,9], the now observed opacity originated probably from TMA sulfate interactions and not from precipitating aluminium hydroxide.

The differences in the mass spectra between pHs 3.76 and 3.95 were not significant. No new major signals were observed and no existing signals vanished in the spectra when the pH was raised. In the cationic spectra only minor signals, with intensities less than 1%, increased slightly in the m/z range 600–1000, corresponding to larger complexes, perhaps colloidal TMA-SO_4 adducts. In the anionic spectra, the effect of pH was more versatile. The number of minor signals was considerably higher in the whole spectral range, probably due to the exchange of neutral aqua ligands with counter anions during the spraying/nebulation process. The intensity of these signals decreased when the pH was raised from 3.76 to 3.95, indicating that the free sulfate forms diminished. Also, several minor signals in the m/z range 400–600 vanished, and instead new signals appeared in the m/z range 600–1000. The cationic and anionic spectra at the initial pH are illustrated in Figs. 1 and 3, respectively.

In contrast to the chloride systems, few signals assigned to TMA were observed and with very low intensities: the highest intensity, 6%, was m/z 512 $[H_2TMA_3(SO_4)_3]^-$. This refers to colloidal or uncharged TMA – sulfate compositions. Thus sulfate may play an unexpectedly active role in water purification processes if it is forming colloids with amine containing impurities such as biological decomposition products. This observation could also confirm that the coagulation principle of polyaluminium chlorides is different to that of alum, due to the remarkable role of the sulfate anion. There is also evidence from NMR-studies concerning the alteration of the pathway of aluminium polymerization to form polymeric and solid materials in the presence of sulfate ions [24]. The fact that all the main species identified in this study contained sulfate or hydrogen sulfate, as revealed in Table 2, also refers to this.

Only the monomers $[Al(H_2O)_6]^{3+}$, $[Al(SO_4)]^+$, $[Al(SO_4)_2]^-$, $[AlOH]^{2+}$, $[Al(OH)_2]^+$, $Al(OH)_3(aq)$, $[Al(OH)_4]^-$, and precipitating minerals are generally considered in equilibrium calculations, because knowledge of thermodynamic stability constants and heats of formation for polymeric aluminium species are not completely available. Due to this fact, these calculations [14,15] have limited relevance to our investigations: at the studied pH values, 3.76 and 3.95, according to the calculations the solution would be supersaturated towards precipitating minerals such as amorphous $Al(OH)_3$, *diaspore* (AlO(OH)) and *jurbanite* ($AlOHSO_4$) and the most stable aqueous species would be monomeric the Al^{3+} hexa aqua ion. Hence, the equilibrium approach was of limited benefit in the case of studying oligomeric aluminium chemistry, due to the absence of the suggested solid phases, (e.g. jurbanite has never been identified in soils and therefore remains a hypothetical equilibrium phase [25]), the slow kinetics of the suggested solid phases, polynuclear ions, as well as the high variability of apparent solubility constants [26–28].

An additional major difference to the chloride system [7–9] was the lack of a series of ions corresponding to the attachment of water to aluminium cores. In chloride systems the Gaussian distribution of signals, with a difference of 18u, suggests how many aqua ligands are attached to one species and helps to confirm the charge of the species [7–9]. Because in sulfate systems those distribution patterns are missing, rapid movement of aqua and hydroxide ligands in outer spheres takes place to a minor extent as compared to the chloride systems.

Most of the cationic assignments were of the form $[Al_n(OH)_x(HSO_4)_y]^+$ where $n = 1$–4 and $(x + y) = (n/3 - 1)$. With the ESI technique multiply charged ions can be obtained depending on the chemical structure of the analyte. Furthermore, the high polarity of water (dielectric constant ε_r 80.4152) stabilizes high charges in the solution [29]. However, there is the possibility of charge

reduction, which can take place during the evaporation due to protonation or deprotonation [30–32]. The other possible charge reduction process is ion pairing of the aluminium oxo hydroxide species with a counter anion during the evaporation [33–35]. The latter phenomenon explains quite well our findings, where almost all species found contained sulfate. Also the fact that in dilute solutions, where the amount of free counter anions is diminished, more pure oxo hydroxo species were found than in more concentrated solutions [9]. All the phenomena in the ESI process are still under intensive investigations [36,37].

The only cationic monomer with aqua ligands was $[Al(OH)(HSO_4)]^+$. The unhydrolyzed octahedral cation $[Al(OH_2)_6]^{3+}$ (m/z 45) was not observed due to the low m/z value, outside the measuring range of the instrument used. The trimeric cations were the most abundant species with the largest versatility. In the cations the number of hydroxo groups was on a regular basis equal or higher than that of aluminium ($x \geqslant n$). On the contrary, in the same core the number of aluminium atoms was equal or greater than the number of sulfates ($y \leqslant n$), except in two cases: with low intensity signals: m/z 519 and 537 assigned to $[Al_3(OH)_3(HSO_4)_3(SO_4)]^+$ and $[Al_3(OH)_4(HSO_4)_4]^+$, respectively (Table 2). *This could indicate that aluminium formes oxo hydroxo cores with sulfate terminal ligands*. Also, presence of the hydroxide in all the cationic assignments refers to this. Small size cationic complexes in which sulfates exist as a bridging ligands have been identified by Raman spectroscopy [38]. However, due to their low m/z-ratio, these species were beyond of the scope of this investigation.

Due to the lack of complete isotopic distribution for any single species, the signals with m/z values 157, 158 and 159 were probably combinations of three overlapping signals. In addition to the dimeric species $[Al_2(OH)_5(H_2O)]^+$ (Table 2) there could exist a pentameric complex $[Al_5(OH)_{11}(HSO_4)_2(H_2O)_6]^{2+}$, but probably at most to a minor extent because of the six aqua ligands. The number of those was two or less in other sulfate containing cations. $[Al\text{-}(HSO_4)(H_2SO_4)_4(H_2O)_6]^{2+}$ was also a possible assignation, but likely also to be minor because in our aluminium studies these kind of large cluster ions with no aluminium oxo hydroxide core structure have not been observed earlier and they could hardly survive in ESI with these measuring parameters.

The main cationic signal m/z 219 was assigned to the dimeric $[Al_2H_5O_4(SO_4)]^+$, because there is a clear 4% isotope peak with a difference of 2u at m/z 221. Writing the formula otherwise, $[Al_2(OH)_4(HSO_4)]^+$, the composition resembles *aluminite* [39], $Al_2(SO_4)(OH)_4 \cdot 7H_2O$. The only differences in the observed species as compared to aluminite are a proton in the sulfate and the lack of aqua ligands. Those are only ambiguously defined in solution and may evaporate easily during the measurement.

The second highest signal m/z 237 could be assigned to the same complex, but now with one aqua ligand $[Al_2(OH)_4(HSO_4)(H_2O)]^+$. We used computational ab initio methods [16] to investigate the minimum energy structure for this aluminite analogue ion to confirm the protonation of the sulfate group. The calculated structure of $[Al_2(OH)_4(HSO_4)]^+$ is illustrated in Fig. 2. The aluminium atoms are connected mainly by two hydroxide bridges associated with one bridging sulfate group.

Nine major signals were assigned to trimers and the most intensive one, m/z 359, was assigned to $[Al_3O(OH)_4(HSO_4)_2]^+$. This structure could be the precursor of precipitating minerals like *alunites* $MAl_3(SO_4)_2(OH)_6$, where M is an ammonium, oxonium or alkali metal cation [40–43]. The trimeric species are also considered precursors of the Keggin structure [44].

The monomeric aluminium hydroxo sulfate is known as a mineral; *jurbanite*, $AlSO_4(OH) \cdot 5H_2O$. An analogous composition was found in this study as the protonated cation m/z 159 $[Al(OH)(HSO_4)(H_2O)_{0-2}]^+$ and the deprotonated anion m/z 139 $[AlO(SO_4)]^-$, again missing the aqua ligands [45].

The main anionic signal m/z 219 with 7% isotope signal m/z 221 could be assigned to $[Al(SO_4)_2]^-$ as a precursor in solution to $MAl(SO_4)_2 \cdot 12H_2O$, where M is an ammonium or alkali metal cation [46–48], which also is called *alum* in geological literature. Also *mendozite*, $NaAl(SO_4)2 \cdot 11H_2O$ and *tamarugite*, $NaAl(SO_4)_2 \cdot 6H_2O$ have similar formulas, differing only in the number of water molecules in the crystal structure [49–51].

There was also a minor 2% signal at m/z 220, indicating that the main signal m/z 219 could be a sum signal of mono charged $[Al(SO_4)_2]^-$ and some double charged sulfate containing complex. The best assignation was $[Al_2(SO_4)_4]^{2-}$

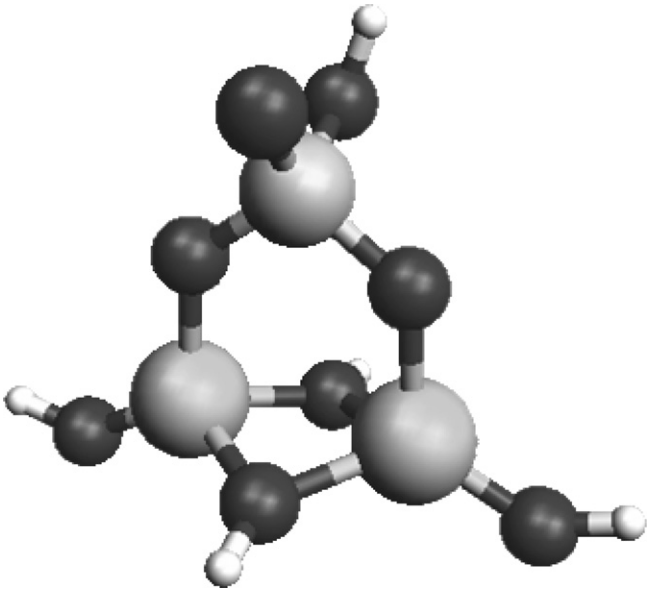


Fig. 2. The structure of the *aluminite* analogue $[Al_2(OH)_4(HSO_4)]^+$ calculated in the gas phase using the BP86 density functional with the polarized valence triple ζ (TZVP) basis set (Turbomole 5.6 program suite). The two aluminium atoms (light grey) are linked together with two hydroxo bridges (O dark grey and H white) and with one bridging protonated sulfate group (S grey). Both aluminium atoms have hydroxo groups as terminal ligands.

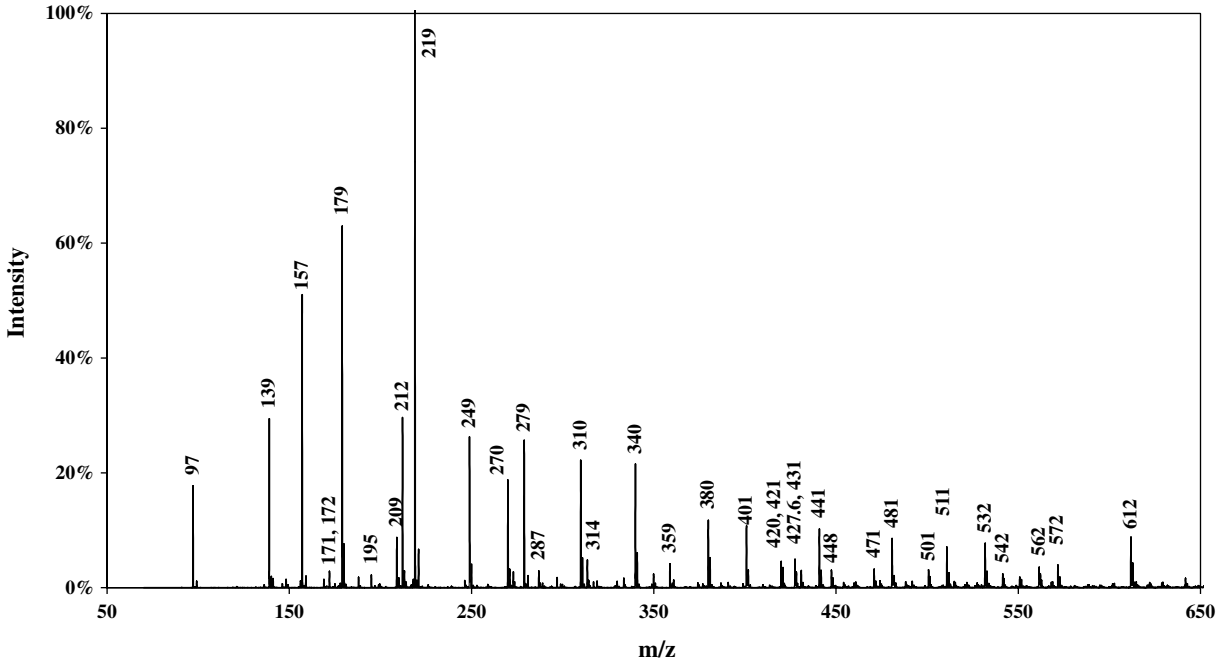


Fig. 3. The anionic spectrum of aluminium sulfate octadecahydrate $Al_2(SO_4)_3 \cdot 18H_2O$, 5 mM at pH 3.76.

since this dimeric four sulfate containing compound had the same composition as, for example, *dietrichite*, $ZnAl_2(SO_4)_4 \cdot 22H_2O$, and *apjohnite*, $MnAl_2(SO_4)_4 \cdot 22H_2O$ [52,53]. The now observed dimeric ion could be the precursor of these minerals.

In the anionic spectrum *m*/*z* 279 (20%) had a possible isotope peak at *m*/*z* 281, with a relative intensity of 12%, indicating mono charged species with one potassium (7%) and one sulfate (4%) or three sulfates. However, no sum formula for those assignations were found and these signals were considered individual signals. They were assigned to $[Al_2O(OH)(SO_4)_2]^-$ (Table 2) and $[Al_5O_7(OH)_2]^-$, respectively.

The trimeric species were absent in the anionic assignment. Instead, there were several polymeric aluminium complexes with a rising series of sulfate ligands and with only a few oxo or hydroxo ligands. Those anionic complexes had to contain bridging sulfate ligands because the number of oxo bridges was now not adequate to hold the structure together. The origin of these complexes is ambigious. It is possible, that they are cluster anions born during the evaporation due to the competition of aqua ligands and sulfate groups in free coordination places, or on the other hand they could be undissociated alum.

In Fig. 4 the structure of the double charged *m*/*z* 270 $[Al_4O_3(SO_4)_4]^{2-}$ is illustrated. Three of the aluminium atoms (I, II and III) are linked together with unhydrolyzed oxo bridges (A, B and C) forming a stable six-membered ring with one terminal unprotonated sulfate group (a) attached bidentally to aluminium (I). The fourth aluminium atom (IV) is connected to the trimer core via a common oxo bridge (B) and two bridging sulfate groups (b and c). These form two six-membered ring structures (Al_{II}–O_B–Al_{IV}–$O_{b'}$–S_b–$O_{b''}$ and Al_{III}–O_B–Al_{IV}–$O_{c'}$–S_c–$O_{c''}$). The fourth sulfate group (d) bridges tridentally the trimeric group and the fourth aluminium forming one six (Al_{II}–O_B–Al_{III}–$O_{d'}$–S_d–$O_{d''}$) and two eight-membered rings (Al_{II}–$O_{d''}$–S_d–$O_{d'''}$–Al_{IV}–$O_{b'}$–S_b–$O_{b''}$ and Al_{III}–$O_{d'}$–S_d–$O_{d'''}$–Al_{IV}–$O_{c'}$–S_c–$O_{c''}$). The six-membered rings are almost in the same plane and the fourth sulfate is above the plane. This two layered structure resembles lausenite [54].

Among the most interesting findings were highly charged polymers, which have been synthesized before from aqueous solution as sulfate salts and characterized by X-ray crystallography and ^{27}Al NMR spectroscopy: the Keggin cation [1,2] $[Al_{13}O_4(OH)_{24}(H_2O)_{12}]^{7+}$ now found as the anion $[Al_{13}O_4(OH)_{25}(SO_4)_4]^{2-}$ and the recently found octameric cluster [55] $[Al_8(OH)_{14}(H_2O)_{18}](SO_4)_5 \cdot 16H_2O$, now found as the anion $[Al_8O(OH)_{14}(SO_4)_5(H_2O)_4]^{2-}$. When the counter sulfate anions are attached to the aluminium oxo-hydroxo cores in the gas phase during the measurement, they reduce the high positive charges (in the forms of $[Al_{13}O_4(OH)_{25}]^{6+}$ and $[Al_8O(OH)_{14}]^{8+}$) and the cationic species in solution are observed as anions. If this reaction occurs already in bulk solution, the coagulating ability of these species diminish and the active agent of alum could be some other species.

In our previous studies concerning exclusively chloride environments [7–9], very stable Al_{13} structures were clearly observed, but always with an Al/unhydrolyzed oxo ratio 0.8–1.9, which is 3.25 in the solid Keggin system (see above) and 2.2–3.25 in the Al_{13} species found in this study. Also the Al_{14} which was always found in pure chloride systems [1] with Al_{13}, is now missing. This could indicate that sulfate forces aluminium to form more organized, compressed, solid like species even in an aqueous environment,

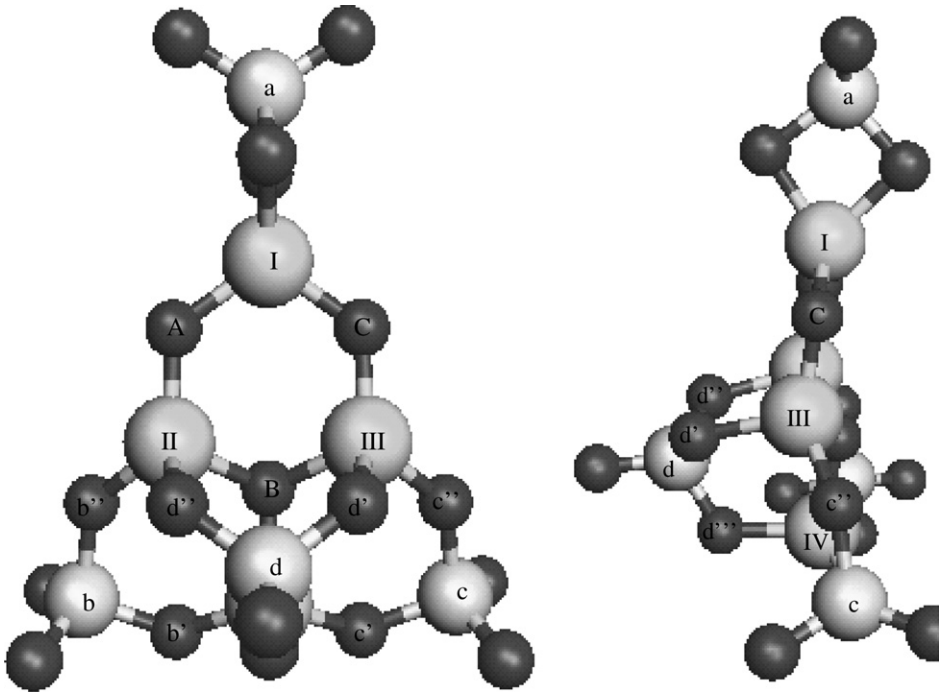


Fig. 4. The structure of the double charged, four aluminium and four sulfate group containing anion, m/z 270$Al_4O_3(SO_4)_4]^{2-}$, calculated in the gas phase using the BP86 density functional with the polarized valence triple ζ (TZVP) basis set (Turbomole 5.6 program suite). The aluminium atoms (light grey, I–IV) are linked together with unhydrolyzed oxo bridges (dark grey, A, B, C) and bridging sulfate groups (S, grey, a–d). Left, the front view, rights the side view.

whereas the chloride systems prefer more flexible speciation where hydroxo and chlorido ligands compete for free coordination places [56].

4. Conclusions

The variety of aqueous species is rich, and many new species were introduced and the presence of sulfate in those was evident. The various polymeric species may play a remarkable role while evaluating functional mechanisms involved in water treatment processes. The polyions may also have biological effects like abilities to increase cell membrane rigidities and cross link biomolecules. In general, resemblance between the observed aqueous polyions and the elementary units of typical natural aluminium compounds proved to be astonishingly high. In addition to water treatment applications this observation may play a role in geochemistry, for evaluating the formation of minerals, for instance.

The high ratio of unhydrolyzed oxygen ligands and aluminium and the lack of an Al_{14} complex in this study could indicate that sulfate forces aluminium to form more organized, compressed, solid like species even in an aqueous environment, whereas the chloride systems prefer more flexible speciation where hydroxo and chlorido ligands competite for free coordination places [56].

Also the lack of TMA-sulfate adducts indicates that sulfate may play an unexpectedly active role in water purification processes if it forms colloids with amine contain impurities like biological decomposition products. This observation could also indicate that the coagulation principle of polyaluminium chlorides is different than that of alum due to the remarkable role of the sulfate anion.

Acknowledgements

We are indebted to Päivi Joensuu for practical advice in using the MS-apparatus. Financial support from Kemira Oyj and Kemira Foundation, Ministry of Education (Graduate School of Inorganic Material Chemistry), Maj and Tor Nessling Foundation, Pharmaceutical Fund of Universisty of Oulu and Orion Research Foundation, is gratefully acknowledged.

References

[1] G. Johansson, Acta Chem. Scand. 16 (1962) 403, DOI not available.
[2] G. Johansson, Arkiv. Kemi. 20 (1963) 321, DOI not available.
[3] S. Von Schönherr, H. Görz, Z. Anorg. Allg. Chem. 503 (1983) 37, doi:10.1002/zaac.19835030805.
[4] A.C. Kunwar, A. Thompson, H.S. Gutowsky, E. Oldfield, J. Magn. Reson. 60 (1984) 467, doi:10.1016/0022-2364(84)90058-1.
[5] S.M. Bradley, R.A. Kydd, R. Yamdagni, Magn. Reson. Chem. 28 (1990) 746, doi:10.1002/mrc.1260280903.
[6] A.P. Lee, B.L. Phillips, M.M. Olmstead, W.H. Casey, Inorg. Chem. 40 (2001) 4485, doi:10.1021/ic010146e.
[7] A. Sarpola, V. Hietapelto, J. Jalonen, J. Jokela, R.S. Laitinen, J. Mass Spectrom. 39 (2004) 423, doi:10.1002/jms.607.
[8] A. Sarpola, V. Hietapelto, J. Jalonen, J. Jokela, R.S. Laitinen, J. Rämö, J. Mass Spectrom. 39 (2004) 1209, doi:10.1002/jms.722.
[9] A. Sarpola, V. Hietapelto, J. Jalonen, J. Jokela, J. Rämö, J. Environ. Anal. Chem. 86 (2006) 1007, doi:10.1080/03067310600687583.

[10] A. Sarpola, J. Saukkoriipi, V. Hietapelto, J. Jalonen, J. Jokela, P. Joensuu, K. Laasonen, J. Rämö, Phys. Chem. Chem. Phys. (2007), doi:10.1039/b614814j.
[11] C.F. Baes, R.E. Mesmer, The Hydrolysis of Cations, John Wiley and Sons, New York, 1976, p. 112.
[12] W. Stumm, J.J. Morgan, Aquatic Chemistry: Chemical Equilibria and Rates in Natural Waters, third ed., John Wiley and Sons, New York, 1996, p. 274.
[13] http://database.iem.ac.ru/mincryst/index.php.
[14] Environmental Research Software Hallowell ME, USA. MINEQL+, 2003.
[15] OLI Systems Inc., OLI Analyzers, 2005.
[16] Quantum Chemistry Group, University of Karlsruhe, Turbomole User's manual, Program Package for ab initio Electronic Structure Calculations, 2002, version 5.
[17] J. Saukkoriipi, A. Sillanpää, K. Laasonen, Phys. Chem. Chem. Phys. 7 (2005) 3785, doi:10.1039/b506949a.
[18] A. Wakisaka, H. Kobara, J. Mol. Liquids 88 (2000) 121, doi:10.1016/S0167-7322(00)00148-3.
[19] K.D. Froyd, E.R. Lovejoy, J. Phys. Chem. A 107 (2003) 9800, doi:10.1021/jp027803o.
[20] R.L. Wong, E.R. Williams, J. Phys. Chem. A 107 (2003) 10976, doi:10.1021/jp036583r.
[21] J.J. Singh, A.C. Smith, G.K. Yue, J. Aerosol Sci. 13 (1982) 285, doi:10.1016/0021-8502(82)90031-3.
[22] T.R. Sharp, J.H. Futrell, Int. J. Mass Spectrom. Ion Process. 90 (1989) 39, doi:10.1016/0168-1176(89)83052-6.
[23] H. Kobara, A. Wakisaka, K. Takeuchi, T. Ibusuki, J. Phys. Chem. A 106 (2002) 4779, doi:10.1021/jp0146216.
[24] C.C. Perry, K.L. Shafran, J. Inorg. Biochem. 87 (2001) 115, doi:10.1016/S0162-0134(01)00326-9.
[25] C.A.J. Appelo, D. Postma, in: Geochemistry, Groundwater and Pollution, third ed., A.A. Balkema, Rotterdam, 1996.
[26] M. Alveteg, H. Sverdrup, P. Warfvinge, Water Air Soil Pollut. 79 (1995) 377, doi:10.1007/BF01100448.
[27] P.R. Bloom, J. Soil Sci. Soc. Am. 47 (1983) 164, DOI not available.
[28] P.R. Bloom, M.S. Erich, J. Soil Sci. Soc. Am. 51 (1987) 1131, DOI not available.
[29] R.G. Bates, in: J.F. Coetzee, C.D. Ritchie (Eds.), Solute–Solvent Interactions, Dekker, New York, 1969, pp. 46–93.
[30] A.T. Blades, P. Jayaweera, M.G. Ikonomou, P. Kebarle, J. Chem. Phys. 92 (1990) 5900, doi:10.1063/1.458360.
[31] A.T. Blades, P. Jayaweera, M.G. Ikonomou, P. Kebarle, Int. J. Mass Spectrom. Ion Process. 102 (1990) 251.
[32] P. Jayaweera, A.T. Blades, M.G. Ikonomou, P. Kebarle, J. Am. Chem. Soc. 112 (1990) 2452.
[33] D.M. Tomazela, F.C. Gozzo, I. Mayer, F.M. Engelmann, K. Araki, H.E. Toma, M.N. Eberlin, J. Mass Spectrom. 39 (2004) 1161, doi:10.1002/jms.699.
[34] G.A. Lawrance, M. Maede, Y.-M. Neuhold, K. Szaciowski, A. Barbieri, Z. Stasicka, J. Chem. Soc., Dalton Trans. (2002) 3649, doi:10.1039/b205536h.
[35] K. Schug, H.M. McNair, J. Chromatogr. A 985 (2003) 531.
[36] K. Cottingham, Anal. Chem. 78 (2006) 5239.
[37] K. Mori, D. Asakawa, J. Sunner, K. Hiraoka, Rapid Commun. Mass Spectrom. 20 (2006) 2596.
[38] W.W. Rudolph, R. Mason, J. Solut. Chem. 30 (2001) 527, doi:10.1023/A:1010334818580.
[39] C. Sabelli, R.T. Ferroni, Acta Crystallogr., Sect. B: Struct. Crystallogr. Cryst. Chem. B34 (1978) 2407, doi:10.1107/S0567740878008341.
[40] R. Wang, W.F. Bradley, H. Steinfink, Acta Crystallogr. 18 (1965) 249, doi:10.1107/S0365110X65000555.
[41] M. Goreaud, B. Raveau, Am. Mineral. 65 (1980) 953, DOI not available.
[42] K. Okada, J. Hirabayashi, J. Ossaka, Neues Jahrb. Mineral., Monat. 12 (1982) 634, DOI not available.
[43] A.A. Moss, Mineral. Mag. 31 (1958) 884, DOI not available.
[44] M. Henry, J.P. Jolivet, J. Livage, Struct. Bond. 77 (1992) 153, doi:10.1007/BFb0036968.
[45] C. Sabelli, Z. Kristallogr. 173 (1985) 33, DOI not available.
[46] D.T. Cromer, M.I. Kay, A.C. Larson, Acta Crystallogr. 21 (1966) 383, doi:10.1107/S0365110X66002950.
[47] D.T. Cromer, M.I. Kay, A.C. Larson, Acta Crystallogr. 22 (1967) 182, doi:10.1107/S0365110X67000313.
[48] A.C. Larson, D.T. Cromer, Acta Crystallogr. 22 (1967) 793, doi:10.1107/S0365110X67001586.
[49] J.H. Fang, P.D. Robinson, Am. Mineral. 57 (1972) 1081, DOI not available.
[50] D.K. Nordstrom, P.D. Robinson, J.H. Fang, Z. Kristallogr. 129 (1969) 458, DOI not available.
[51] P.D. Robinson, Y.H. Fang, Am. Mineral. 54 (1969) 19, DOI not available.
[52] P. Ballirano, F. Bellatreccia, O. Grubessi, Eur. J. Mineral. 15 (2003) 1043, doi:10.1127/0935-1221/2003/0015-1043.
[53] S. Menchetti, C. Sabelli, Mineral. Mag. 40 (1976) 599, DOI not available.
[54] J. Majzlan, C. Bottez, P.W. Stephens, Am. Mineral. 90 (2005) 411, doi:10.2138/am.2005.1701.
[55] W.H. Casey, M.M. Olmstead, B.L. Phillips, Inorg. Chem. 44 (2005) 4888, doi:10.1021/ic050426k.
[56] B.Y. Gao, Q.Y. Yue, Chemosphere 61 (2005) 579, doi:10.1016/j.chemosphere.2005.03.013.

Available online at www.sciencedirect.com
ScienceDirect
Polyhedron 26 (2007) 2859–2863
POLYHEDRON
www.elsevier.com/locate/poly

Crystal structure and magnetic properties of $[\{Cu(cyclam)\}_3\{Fe(CN)_6\}_2]\cdot 6H_2O$, a cyano-bridged assembly with a rope-ladder chain structure

Antonio Rodríguez-Diéguez, Enrique Colacio *

Departamento de Química Inorgánica, Facultad de Ciencias, Universidad de Granada, 18071 Granada, Spain

Received 4 January 2007; accepted 23 January 2007
Available online 7 February 2007

Abstract

The synthesis, crystal structure and magnetic properties of the cyano-bridged complex $[\{Cu(cyclam)\}_3\{Fe(CN)_6\}_2]\cdot 6H_2O$ are reported. Its structure is made up of centrosymmetric S-shaped pentanuclear $[\{Cu(cyclam\}_3\{Fe(CN)_6)\}_2]$ units, in which three $[Cu(cyclam)]^{2+}$ units are alternatively bridged by two *trans*-CN groups of $[Fe(CN)_6]^{3-}$ anions and water molecules. The pentanuclear Fe_2Cu_3 units are held together by two complementary and very weak Fe–CN···Cu1 bonds, forming a rope-ladder chain along the *c* axis. The compound exhibits a ferromagnetic interaction between the Cu(II) and Fe(III) ions as a consequence of the orthogonality of their magnetic orbitals of σ and π nature, respectively. The magnetic data were fitted to the calculated magnetic susceptibility equation for a pentanuclear model, leading to the following magnetic parameters: $J_1 = 9.0(3)\ cm^{-1}$, $J_2 = 3.8(4)\ cm^{-1}$, $g = 2.2$, $\theta = -1.2$ K. These results show that the interactions through the long Cu–N axial bonds are not so weak as is usually assumed.
© 2007 Elsevier Ltd. All rights reserved.

Keywords: Cyano-bridged; Copper; Rope-ladder chain; Cu(II) complexes; Ferromagnetic; X-ray structure

1. Introduction

In the last two decades, the synthesis and characterization of multidimensional cyano-bridged metal complexes has attracted much interest [1]. The most common and controlled strategy to prepare this kind of system consists of the self-assembly of specifically designed precursors, typically a cyanometallate complex that acts as a ligand and a transition metal complex with free or available coordination sites for the nitrogen atoms of the cyanide groups. Following this route, a great variety of cyano-bridged bimetallic compounds have been prepared, which are playing an important role in areas such as high-Tc magnetic materials [2], SMM (single-molecule magnets) [3], SCM (single-chain magnets) [4], photo-induced magnetism [5], spin-crossover (SCO) materials [6], host-guest chemistry [7], vapochromic materials [8], magnetochirality [9], etc. The dimensionality and topology of these assemblies strongly depends on the nature of ML_x (number and disposition of empty or available coordination positions on M, coordination geometry, volume of the ligands, etc.) and the connectivity of the cyanometallate building block (number and arrangement of ML_x units around M′). As a continuation of our studies in this field [10], we have decided to use hexacyanoferrate(III) units to connect the highly thermodynamically stable $[Cu(cyclam)]^{2+}$ complex, which adopts the *trans*-configuration. In this paper, we are reporting the magneto-structural results for the complex $[\{Cu(cyclam)\}_3\{Fe(CN)_6\}_2]\cdot 6H_2O$ (**1**). These results are compared to those of the isostructural complex $[\{Cu(cyclam)\}_3\{Cr(CN)_6\}_2]\cdot 5H_2O$, which was recently reported by Sallah et al. [11]. This complex exhibits a J_{CrCu} value of $4.33\ cm^{-1}$, which is much higher than those usually observed for cyano-bridged complexes with similar Cu–NC–Cr pathways and long $Cu–N_{axial}$ bond distances.

* Corresponding author. Tel.: +34 958243236.
E-mail address: ecolacio@ugr.es (E. Colacio).

0277-5387/$ - see front matter © 2007 Elsevier Ltd. All rights reserved.
doi:10.1016/j.poly.2007.01.046

2. Experimental

2.1. Materials

[Cu(cyclam)](ClO$_4$)$_2$ was prepared according to experimental methods already described [12–14]. All other reagents were purchased from commercial sources and were used as received.

2.2. Synthesis of *1*

A solution of tetraethylamonium ferricyanide (0.055 g, 0.18 mmol) in a water–methanol–acetonitrile mixture (2:1:1, 20 ml) was added with continuous stirring to a solution of [Cu(cyclam)](ClO$_4$)$_2$ (0.042 g, 0.09 mmol) in the same mixture of solvents. The resulting mixture was stirred for 20 min and then filtered. The solution was left standing at room temperature for two days and then crystals of **1** formed, which were filtered off and air dried. Yield: 73%. IR (KBr pellets): $\nu_{CN} = 2153, 2143, 2110\ cm^{-1}$. *Anal.* Calc. for $C_{42}H_{82}N_{24}Cu_3Fe_2O_5$: C, 38.64; H, 6.33; N, 25.75. Found: C, 38.45; H, 6.23; N, 25.68%.

2.3. Physical characterisation

Elemental analyses were carried out at the Instrumentation Scientific Centre of the University of Granada on a Fisons-Carlo Erba analyser model EA 1108. The analysis of metals was performed by SEM on a LEO, mod. GEMINI-1530 microscope at the Instrumentation Scientific Centre of the University of Granada. IR spectra were recorded on powdered samples with a ThermoNicolet IR200FTIR by using KBr pellets. Magnetisation and variable-temperature (1.9–300 K) magnetic susceptibility measurements were carried out on polycrystalline samples with a Quantum Design SQUID operating at different magnetic fields. Magnetization versus applied field measurements were carried out at 2.0 K in the field range 0–5 T. Alternating current susceptibility measurements were performed in the frequency range 10–100 Hz and under an oscillating magnetic field of 1 Oe. The experimental susceptibilities were corrected for diamagnetism of the constituent atoms by using Pascal's tables [15].

2.4. X-ray crystallography

X-ray data were collected on a Bruker Smart Apex CCD diffractometer, using graphite monochromatized Mo Kα radiation. All data sets were corrected for Lorentz and polarization effects. A summary of the crystallographic data and structure refinements is given in Table 1. The structure was solved by direct methods and refined on F^2 by the SHELXL97 program [16] or SHELXTL [17]. The asymmetric unit contains 1.5{[Cu(cyclam)]$^{2+}$ cations, one [Fe(CN)$_6$)]$^{3-}$ anion and 2.5 disordered crystal water molecules. Non-hydrogen atoms were refined with anisotropic thermal displacement parameters. The hydrogen atoms of the macrocyclic ligands were treated as riding atoms using the SHELX97 default parameters. Hydrogen atoms of the water molecules could not be reliably positioned.

Table 1
Crystallographic structure refinement data

Formula	$C_{42}H_{82}N_{24}O_5Fe_2Cu_3$
M_r	1305.64
Crystal system	monoclinic
Space group	$P2_1/n$ (no. 14)
a (Å)	8.7784(8)
b (Å)	33.112(3)
c (Å)	9.7326(9)
α (°)	90
β (°)	96.357(2)
γ (°)	90
V (Å^3)	2811.6(5)
Z	4
T (K)	173(2)
λ (Å)	0.71073
ρ (g cm^{-3})	1.542
μ (cm^{-1})	16.84
Goodness-of-fit	1.036
R_1[a] $[I > 2\sigma(I)]$	0.0461
wR_2[b] $[I > 2\sigma(I)]$	0.1136

[a] $R_1 = \sum||F_o| - |F_c||/\sum|F_o|$.
[b] $wR_2 = \{\sum[w(F_o^2 - F_c^2)^2]/\sum[w(F_o^2)^2]\}^{1/2}$.

3. Results and discussion

The reaction of (NEt$_4$)$_3$[Fe(CN)$_6$] with [Cu(cyclam)](ClO$_4$)$_2$ in a water–methanol–acetonitrile mixture (2:1:1) afforded brown crystals of the compound [{Cu(cyclam)}$_3$-{Fe(CN)$_6$}$_2$]·6H$_2$O. The IR spectrum of this complex exhibits υ(CN) bands at 2110, 2143 and 2153 cm^{-1}. The lower frequency band, which is only slightly shifted as compared to the corresponding υ(CN) = 2100 cm^{-1} band of the [Fe(CN)$_6$]$^{3-}$ anion, is, therefore, reasonably assigned to the terminal cyanides. The higher energy bands, which appear 40–50 cm^{-1} higher than υ(CN) for the [Fe(CN)$_6$]$^{3-}$ anion, are assigned to the cyanide bridging ligands. This increase is due to the mechanical constraint of the motion of the CN group, originating from the presence of the Cu(II) metal centre (kinematic effect).

The structure of **1** is made up of centrosymmetric S-shaped pentanuclear [{Cu(cyclam}$_3${Fe(CN)$_6$)}$_2$] units, in which three [Cu(cyclam)]$^{2+}$ units are alternatively bridged by two *trans*-CN groups of [Fe(CN)$_6$]$^{3-}$ anions and water molecules (Fig. 1). The Cu2 ion, which is located on an inversion centre, and the Cu1 ion, both exhibit elongated tetragonal geometries, with the four nitrogen atoms of the macrocycle occupying the equatorial positions and the nitrogen atoms of the cyanide bridging ligands at the axial positions. In the bridging regions, the Cu1–N and Cu2–N bond distances are 2.573(3) and 2.451(3) Å, respectively, whereas the Fe···Cu1 and Fe···Cu2 distances are 5.322(1) and 5.037(1) Å, respectively. The Cu1–N–C and Cu2–N–C bond angles deviate significantly from linearity with values of 141.2(2)° and 134.5(2)°, respectively. The pentanuclear Fe$_2$Cu$_3$ units are held together by two com-

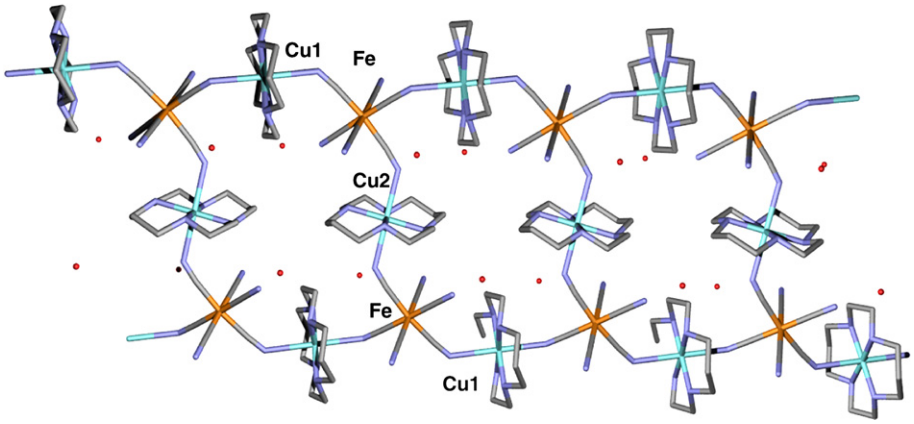


Fig. 1. Perspective view of the rope-ladder structure of **1**. Labelled metal atoms are those of the pentanuclear S unit.

plementary and very weak Fe–CN···Cu1 bonds (Cu1–N distance of 2.620(3) Å and Cu1–N–C angle of 133.2(2) Å and Fe···Cu1 distance of 5.175(1) Å) to form a rope-ladder chain along the *c* axis. In this description, each $[Fe(CN)_6]^{3-}$ is linked to three $[Cu(cyclam)]^{2+}$ units, in which the cyanide-bridging groups adopt a *mer* configuration.

The water molecules are located in between the chains and are involved in hydrogen bond interactions with the terminal cyanide groups and some NH macrocyclic groups.

This structure is similar to those observed for the compounds $[Ni(en)_2]_3[M(CN)_6]_2 \cdot 2H_2O$ (where en = ethylenediamine and M^{III} = Fe, Co, Mn, Cr) [18] and $[Cu(cyclam)]_3[Mo(CN)_8]_2 \cdot 5H_2O$ [19] and is isostructural to that of the compound $[Cu(cyclam)]_3[Fe(CN)_6)]_2] \cdot 6H_2O$ [11].

4. Magnetic properties

The magnetic properties of **1** in the form of a $\chi_M T$ versus T plot (χ_M is the susceptibility per Fe_2Cu_3 unit at a magnetic field of 1 T) is given in Fig. 2. The $\chi_M T$ product at room temperature (2.79 $cm^3\ mol^{-1}$ K) is higher than that calculated for magnetically non-interacting Fe^{III} and Cu^{II} ions (3.87 $cm^3\ mol^{-1}$ K with an average $g = 2$), thus indicating a significant orbital contribution from the octahedral low-spin Fe^{III} atoms. Upon cooling down, the $\chi_M T$ value decreases to reach a minimum at around 36 K, which is due to the spin–orbit coupling effects of the low-spin octahedral Fe^{III} atoms with a $^2T_{2g}$ ground term. In fact, when the $\chi_M T$ product between 40 K and room temperature for the compound $(rac\text{-}CTH_3)_3[Fe(CN)_6]_2 \cdot 8H_2O$ [20] (whose magnetic properties are essentially due to isolated Fe^{III} ions of the $[Fe(CN)_6]^{3-}$ units) is subtracted from the $\chi_M T$ versus T curve for **1**, the resulting $\chi_M T$ values remain almost constant in this temperature range with a value of 1.366 $cm^3\ mol^{-1}$ K, as expected for three isolated Cu(II) ions with $g = 2.2$. This result confirms that the magnetic behaviour of **1** in the high temperature range is due to spin–orbit coupling effects. Below 36 K, $\chi_M T$ increases to reach a maximum at 3 K (3.1 $cm^3\ mol^{-1}$ K), thus indicating a ferromagnetic exchange interaction between the Fe(III) and Cu(II) ions. Below 3 K, $\chi_M T$ decreases sharply to 2.88 $cm^3\ mol^{-1}$ K at 2 K, because of the intermolecular interactions and/or ZFS of the ground state.

In order to analyze the experimental $\chi_M T$ data in a suitable way, we removed the contribution of the spin–orbit coupling effects of the three Fe^{III} ions. For this we subtracted from the experimental $\chi_M T$ data of **1** those of the

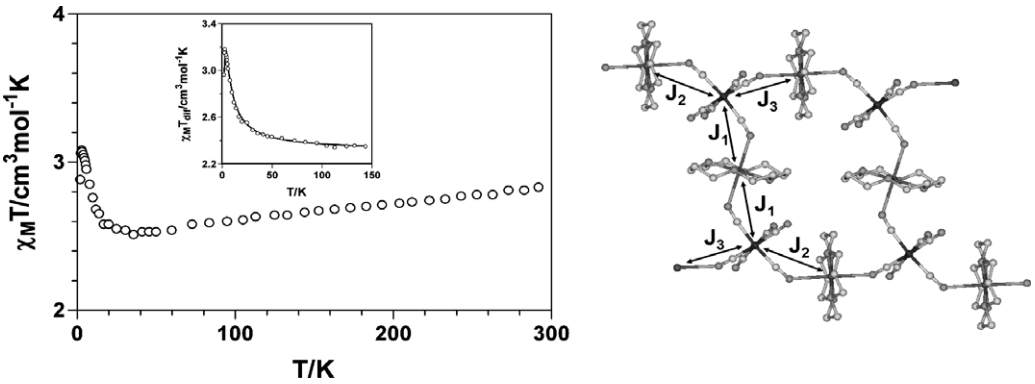


Fig. 2. Temperature dependence of the $\chi_M T$ product of **1** (left). The inset is the temperature dependence of the corrected $\chi_M T$ product of **1**. The solid line is the best-fit curve to the theoretical equation for a Fe_2Cu_3 linear system with $J_3 = 0$. Scheme showing the magnetic exchange pathways in **1** (right).

compound (*rac*-CTH–H_2)$_3$[Fe(CN)$_6$]$_2$ · 8H_2O and then the contribution of two isolated metal ions with $S = 1/2$ and $g = 2$ was added,

$$\chi_M T = \chi_M T\{[Cu(rac\text{-}CTH)]_3[Fe(CN)_6]_2\} - \chi_M T(CTH_3)_3[Fe(CN)_6]_2 \cdot 8H_2O\} + 2\frac{Ng^2\beta^2}{4k}$$

As can be observed in the corrected plot (Fig. 2, inset), upon cooling down $\chi_M T$ increases continuously from room temperature until reaching the maximum at 7 K, as expected for a weak ferromagnetic interaction between the paramagnetic centres. The Cu1 and Cu2 ions, with elongated octahedral geometries, have a $d_{x^2-y^2}$ magnetic orbital (directed toward the nitrogen atoms of the macrocycle) of σ symmetry. The t_{2g} (d_{xy}, d_{xz} and d_{yz}) magnetic orbitals of the low spin Fe^{III} ion are of π symmetry. Therefore, the interaction between orthogonal σ and π magnetic orbitals leads to the observed ferromagnetic interaction.

In keeping with the structural data for this compound, in principle, the magnetic properties should be interpreted through a model with three J parameters (see scheme Fig. 2). However, because the Cu1–$N_{cyanide}$ axial bond and Cu1–N–C angle involving the J_3 exchange pathway are, respectively, longer and sharper than those involving the J_1 and J_2 exchange pathways, the interaction between pentanuclear neighbouring units (J_3) must be much weaker than the intrapentanuclear interactions J_1 and J_2. In view of this and to simplify the model we have considered that $J_3 = 0$. On the basis of this approximation, the magnetic data were fitted to the calculated magnetic susceptibility equation for the pentanuclear unit using the MAGMUM program[1] with the spin Hamiltonian:

$$H = -J_1(FeCu_1 + Fe_ACu_{1A}) - J_2(Fe_ACu_2 + FeCu_2) + g\beta H(SCu_1 + SCu_{1A} + SCu_2 + SFe + SFe_A)$$

To assess the interpentanuclear magnetic interactions, a θ value was included into the magnetic model. The best least-squares fit, gives $J_1 = 9.0(3)$ cm^{-1}, $J_2 = 3.8(4)$ cm^{-1}, $g = 2.2$, $\theta = -1.2$ K. The calculated J_1 value appears to be too high, taking into account that: (i) the Cu_2–N bond distance is rather long (2.451 Å) and the Cu_2–N–C is relatively small (141.15°) and (ii) the nitrogen atom of the cyanide-bridging group is linked in an axial position. Also, the literature values for exchange coupling constants through similar Cu–N–C–Fe pathways (with long Cu–N_{axial} bond distances) are, in general, much smaller. It should be noted, however, that for the isostructural complex [Cu(cyclam)]$_3$[Cr(CN)$_6$]$_2$ · 5H_2O [11], with Cu–N_{axial} bond lengths in the range 2.474(9)–2.638(8) Å, a J value of 4.33 cm^{-1} was reported. Taking into account that in isostructural compounds J_{CrCu} values are smaller than J_{FeCu} values, the J_1 value for **1** might be considered as normal. Nevertheless, the obtained J values must be taken with some caution because of the adopted approximations: (i) the correction of the experimental data to eliminate the spin–orbit coupling effects and (ii) the J_3 exchange pathway was neglected.

In conclusion, the above magnetic results confirm that, in some cases, the magnetic exchange interactions through long Cu–N axial bonds are not so weak as is usually assumed and consequently caution should be exercised when this type of interaction is forced to be zero in the fitting procedure.

[1] MAGMUN4.0/OW0L is available as a combined package free of charge from the authors at http://www.ucs.mun.ca/~lthomp/. MAGMUN has been developed by Dr. Zhiqiang Xu and Laurence K. Thompson (Memorial University), and OW01.exe by Dr. O. Waldmann (University of Bern). The software calculates the total spin state values (S') and their associated energies (E') using the Kambe approach [21] and then substitutes the S' and E' values into the van Vleck equation to generate the variable temperature susceptibility profile (degenerate states are accounted for).

Acknowledgements

This work was supported by the Spanish Ministerio de Ciencia y Tecnología through projects BQU2001/3221 and Junta de Andalucía. A.R. thanks the Ministerio de Ciencia y Tecnología for a predoctoral fellowship.

Appendix A. Supplementary material

CCDC 606669 contains the supplementary crystallographic data for this paper. These data can be obtained free of charge via http://www.ccdc.cam.ac.uk/conts/retrieving.html, or from the Cambridge Crystallographic Data Centre, 12 Union Road, Cambridge CB2 1EZ, UK; fax: (+44) 1223-336-033; or e-mail: deposit@ccdc.cam.ac.uk. Supplementary data associated with this article can be found, in the online version, at doi:10.1016/j.poly.2007.01.046.

References

[1] (a) Some reviews: K.R. Dunbar, R.A. Heintz, Prog. Inorg. Chem. 45 (1997) 283;
(b) M. Verdaguer, Science 272 (1996) 698;
(c) M. Verdaguer, A. Bleuzen, V. Marvaud, J. Vaissermann, M. Seuleiman, C. Desplanches, A. Scuiller, C. Train, R. Garde, G. Gelly, C. Lomenech, I. Rosenman, P. Veillet, C. Cartier, F. Villain, Coord. Chem. Rev. 190 (1999) 1023;
(d) W.P. Fehlhammer, M. Fritz, Chem. Rev. 93 (1993) 1243;
(e) M. Ohba, K. Okawa, Coord. Chem. Rev. 198 (2000) 313;
(f) J. Černák, M. Orendáč, I. Potočňák, J. Chomič, A. Orendáčová, J. Skoršepa, A. Feher, Coord. Chem. Rev. 224 (2002) 51, and references therein;
(g) D.J. Chesnut, D. Hagrman, P.J. Zapf, R.P. Hammond, R. LaDuca, R.C. Haushalter, J. Zubieta, Coord. Chem. Rev. 190 (1999) 737, and references therein;
(h) J.S. Miller, J.L. Manson, Acc. Chem. Res. 34 (2001) 563;
(i) G. Rogez, E. Rivière, T. Mallah, C.R. Chimie 6 (2003) 283;
(j) M. Pilkington, S. Decurtins, in: J.A. MacCleverty, T.J. Meyer (Eds.), Comprehensive Coordination Chemistry II. From Biology to Nanotechnology, vol. 7, Elsevier, Amsterdam, 2004, p. 177;
(k) M. Pilkington, S. Decurtins, Perspect. Supramol. Chem. 7 (2003) 275;
(l) L.M. Beltran, J.R. Long, Acc. Chem. Res. 38 (2005) 325;
(m) M. Verdaguer, G. Girolami, in: J.S. Miller, M. Drillon (Eds.),

Magnetism: Molecules to Materials, vol. 5, Wiley-VCH, Weinheim, p. 283, and references therein.

[2] (a) H. Kou, S. Gao, J. Zhang, G.-H. Su, R.K. Zheng, X.X. Zhang, J. Am. Chem. Soc. 123 (2001) 11809;
(b) M. Ohba, N. Usuki, N. Fukita, H. Okawa, Angew. Chem. 111 (1999) 1911;
Angew. Chem., Int. Ed. 38 (1999) 1795;
(c) S. Tanase, F. Tuna, P. Guionneau, T. Maris, G. Rombaut, C. Mathionière, M. Andruh, O. Khan, J.P. Sutter, Inorg. Chem. 42 (2003) 1625.

[3] (a) S. Wang, J.L. Zuo, H.C. Zhou, H.J. Choi, Y. Ke, J.R. Long, X.Z. You, Angew. Chem., Int. Ed. 43 (2004) 5940;
(b) D. Li, S. Parkin, G. Wang, G.T. Yee, A.V. Prosvirin, S.M. Holmes, Inorg. Chem. 44 (2005) 4903;
(c) D. Li, R. Clérac, S. Parkin, G. Wang, G.T. Yee, S.M. Holmes, Inorg. Chem. 45 (2006) 5251;
(d) C.P. Berlinguette, D. Vaughn, C. Cañada-Vilalta, J.R. Galán-Mascarós, K.R. Dunbar, Angew. Chem., Int. Ed. 42 (2003) 1523;
(e) J.J. Sokol, A.G. Hee, J.R. Long, J. Am. Chem. Soc. 124 (2002) 7656;
(f) Z.-H. Ni, H.-Z. Kou, L.-F. Zhang, C. Ge, A.-L. Cui, R.-J. Wang, Y. Li, O. Sato, Angew. Chem., Int. Ed. 44 (2005) 7742;
(g) H. Misayaka, H. Takahashi, T. Madanbashi, K. Sugiura, R. Clérac, H. Nojori, Inorg. Chem. 44 (2005) 5969.

[4] (a) R. Lescouëzec, J. Vaissermann, C. Ruiz-Pérez, F. Lloret, R. Carrasco, M. Julve, M. Verdaguer, Y. Dromzée, D. Gatteschi, W. Wernsdorfer, Angew. Chem., Int. Ed. 42 (2003) 1483;
(b) M.L. Toma, R. Lescouëzec, F. Lloret, M. Julve, J. Vaissermann, M. Verdaguer, Chem. Commun. 15 (2003) 1850;
(c) M. Ferbinteanu, H. Miyasaka, W. Wernsdorfer, K. Nakata, K. Sugiura, M. Yamashita, C. Coulton, R. Clérac, J. Am. Chem. Soc. 127 (2005) 3090;
(d) S. Wang, J.-L. Zuo, S. Gao, Y. Song, H.-C. Zhou, Y.-Z. Zhang, X.-Z. You, J. Am. Chem. Soc. 126 (2004) 8900.

[5] (a) G. Rombaut, S. Golhen, L. Ouahab, C. Mathoniere, O. Kahn, J. Chem. Soc., Dalton Trans. 20 (2000) 3609;
(b) Y. Arimoto, S.I. Ohkoshi, Z.J. Zhong, H. Seino, Y. Mizobe, K. Hashimoto, J. Am. Chem. Soc. 125 (2003) 9240;
(c) C. Mathoniere, R. Podgajny, P. Guionneau, C. Labrugere, B. Sieklucka, Chem. Mater. 17 (2005) 442;
(d) J.M. Herrera, V. Marvaud, M. Verdaguer, J. Marrot, M. Kalisz, C. Mathoniere, Angew. Chem. 116 (2004) 5584;
(e) Angew. Chem., Int. Ed. 43 (2004) 5468.

[6] (a) J.A. Real, A.B. Gaspar, V. Niel, M.C. Muñoz, Coord. Chem. Rev. 236 (2003) 121;
(b) A. Galet, V. Niel, M.C. Muñoz, J.A. Real, J. Am. Chem. Soc. 125 (2003) 14224;
(c) Y. García, V. Niel, M.C. Muñoz, J.A. Real, Top. Curr. Chem. 233 (2004) 229;
(d) V. Niel, A.L. Thompson, A.E. Goeta, C. Enachescu, A. Hauser, A. Galet, M.C. Munoz, J.A. Real, Chemistry 11 (2005) 2047;
(e) C.P. Berlinguette, A. Dragulescu-Andrasi, A. Sieber, J.R. Galán-Mascarós, H.-U. Güdel, C. Achim, K.R. Dunbar, J. Am. Chem. Soc. 126 (2004) 6222.

[7] T. Iwamoto, J. Inc. Phenom. Mol. Recog. Chem. 24 (1996) 61.

[8] J. Lefebvre Julie, R.J. Batchelor, D.B. Leznoff, J. Am. Chem. Soc. 126 (2004) 16117.

[9] (a) K. Inoue, S. Ohkoshi, H. Imai, in: J.S. Miller, M. Drillon (Eds.), Magnetism: Molecules to Materials, vol. 5, Wiley-VCH, Weinheim, 2005, p. 41, and references therein;
(b) E. Coronado, C. Giménez-Saiz, J.M. Martínez-Agudo, A. Nuez, F.M. Romero, H. Stoeckli-Evans, Polyhedron 22 (2003) 2435;
(c) H. Imai, K. Inoue, K. Kikuchi, Y. Yoshida, M. Ito, T. Sunahara, S. Onaka, Angew. Chem., Int. Ed. 43 (2004) 5618.

[10] A. Rodríguez-Diéguez, R. Kivekäs, R. Sillanpää, J. Cano, F. Lloret, V. McKee, H. Stoeckli-Evans, E. Colacio, Inorg. Chem. 45 (2006) 10537, and references therein.

[11] M.S. El Fallah, J. Ribas, X. Solans, M. Font-Bardia, New J. Chem. 7 (2003) 895.

[12] E.J. Billo, Inorg. Chem. 23 (1984) 2223.

[13] J.-H. Choy, D.-K. Kim, J.-C. Park, S.-N. Choi, Y.-J. Kim, Inorg. Chem. 36 (1997) 189.

[14] L.Y. Martin, C.R. Sperati, D.H. Busch, J. Am. Chem. Soc. 99 (1977) 2969.

[15] O. Khan, Molecular Magnetism, VCH publisher, Inc., 1993.

[16] G.M. Sheldrick, SHELX97, University of Göttingen, Germany, 1997.

[17] G.M. Sheldrick, SHELXTL Version 6.12, Bruker AXS, Madison, WI, 2001.

[18] E. Colacio, M. Ghazi, H. Stoeckli-Evans, F. Lloret, J.M. Moreno, C. Pérez, Inorg. Chem. 40 (2001) 4876.

[19] S.Y. Young, D. Kim, Y. Do, SJ. Oh, C.S. Hong, Inorg. Chem. 43 (2004) 6899.

[20] A. Rodríguez-Diéguez, R. Kivekäs, R. Sillanpää, J. Cano, F. Lloret, V. McKee, H. Stoeckli-Evans, E. Colacio, Inorg. Chem. 45 (2006) 10537.

[21] K. Kambe, J. Phys. Soc. Jpn. 5 (1950) 48.

Available online at www.sciencedirect.com
ScienceDirect
Polyhedron 26 (2007) 2864–2870
POLYHEDRON
www.elsevier.com/locate/poly

Reduction-induced *o*-C–H bond activation of pyridine with decamethylzirconocene dichloride

Dmitrii P. Krut'ko [a,*], Roman S. Kirsanov [a], Sergey A. Belov [a], Maxim V. Borzov [a,b], Andrei V. Churakov [c], Judith A.K. Howard [d]

[a] *Department of Chemistry, M.V. Lomonosov Moscow State University, GSP-2, Leninskie Gory 1, Building 3, Moscow 119992, Russia*
[b] *Department of Chemistry, The North–West University, 229 North Taibai Avenue, Xi'an 710069, Shaanxi Prov., PR China*
[c] *N.S. Kurnakov Institute of General and Inorganic Chemistry, Russian Academy of Sciences, Leninskii Prosp. 31, Moscow 119991, Russia*
[d] *Department of Chemistry, University of Durham, South Road, Durham DH1 3LE, UK*

Received 12 January 2007; accepted 23 January 2007
Available online 4 February 2007

Abstract

Treatment of decamethylzirconocene dichloride $(\eta^5\text{-Cp}^*)_2ZrCl_2$ with amalgamated magnesium in pyridine results in formation of the *o*-C–H bond activation product $[\eta^5\text{-}C_5Me_5]_2ZrH[\eta^2\text{-}\kappa C,N\text{-}C_5H_4N]$ (**1**). X-ray diffraction analysis (solid state) and NMR spectroscopy data (solutions) reveal the lateral positioning of the nitrogen atom in **1**. At elevated temperatures, complex **1** smoothly rearranges into its isomer **2** with medial positioning of the N-atom. The parameters of equilibrium between **1** and **2** were measured at different temperatures. A reaction of **1** or a mixture of **1** and **2** (*ca.* 1:10) with $CDCl_3$ smoothly and under mild conditions leads to one and the same η^2-pyridyl chloride complex $[\eta^5\text{-}C_5Me_5]_2ZrCl[\eta^2\text{-}\kappa C,N\text{-}C_5H_4N]$ (**3**) with medial positioning of the N-atom. The thermodynamic and mechanistic concepts of the paper are discussed with application of the DFT computational data.
© 2007 Elsevier Ltd. All rights reserved.

Keywords: Zirconium; Titanium; Cyclopentadienyl ligands; Oxidative addition; Reduction; N ligands

1. Introduction

The reduction reactions of decamethylzirconocene dichloride, $Cp^*_2ZrCl_2$, as well as of its parent counterpart Cp_2ZrCl_2, were rather broadly studied under a variety of conditions. As it was clarified previously, in presence of ligands that exhibit not only *n*-donor, but, at least, weak π-acid properties, formation of true Zr(II) compounds of general type $Cp^*_2ZrL_2$ occurs. The most illustrative example is the reduction of $Cp^*_2ZrCl_2$ with sodium amalgam in presence of 1 atm. of molecular dinitrogen, yielding an dinuclear complex (N_2)–$(\eta^5\text{-Cp}^*)_2$Zr–N ≡ N–$(\eta^5\text{-Cp}^*)_2$-Zr–(N_2) [1–3]. Alternatively, reduction of $Cp^*_2ZrCl_2$ without the "support" of any π-acidic compounds processes ambiguously, with the fulvene-hydride type products of the oxidative addition of one of the C–H bonds from methyl groups, $(\eta^5\text{-Cp}^*)(\eta^5{:}\eta^1\text{-}\kappa C\text{-}C_5Me_4\text{–}CH_2\text{–})ZrH$, postulated as the dominating components of reaction mixtures [1,3].

While cationic Zr(IV) biscyclopentadienyl complexes are known to provide intermolecular CH-activation of pyridine type systems at the 2-position [4–8], by now there are not very many examples of the selective reduction-induced intermolecular activations of C–H or other inert (e.g., C–F) bonds in organic substrates with *in situ* generated low-valent zirconocenes (or titanocenes) [9–15]. In this paper, we report the unambiguously proceeding stochiometric *ortho*-activation of the C–H bond in pyridine with $Cp^*_2ZrCl_2$ and amalgamated magnesium.

* Corresponding author. Tel.: +7 095 9391234; fax: +7 095 9328846.
E-mail address: kdp@org.chem.msu.rurg.chem.msu.ru (D.P. Krut'ko).

0277-5387/$ - see front matter © 2007 Elsevier Ltd. All rights reserved.
doi:10.1016/j.poly.2007.01.036

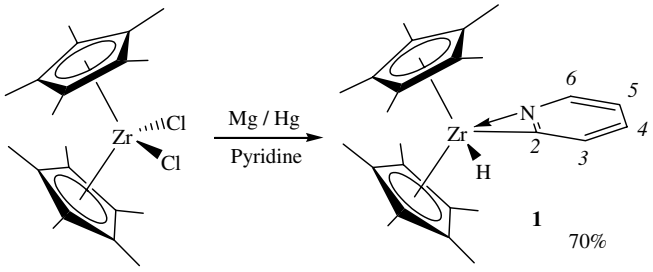
2. Results and discussion

2.1. Reduction-induced *o*-C–H bond activation in pyridine

Treatment of $Cp^*_2ZrCl_2$ with amalgamated magnesium in pyridine at 20 °C smoothly produces the *o*-C–H pyridine bond activation product **1** (see Scheme 1).

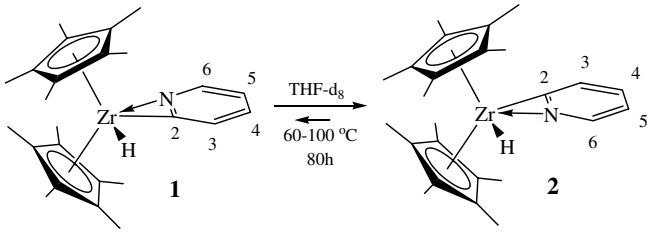
The product **1** was isolated in pure state from hexane in a good yield as colorless crystals. In ^{1}H NMR spectrum, the assignment of the signals is unambiguous due to the fact that, in pyridines, the H(2 or 6) peak always appears at the lowest field, with ^3J(H(6)–H(5)) being considerably smaller than ^3J(H(5)–H(4)) (~5 Hz versus 7–8 Hz, respectively). Coordination of the nitrogen atom and its lateral positioning was unambiguously established both in solutions (NMR data: irradiation of Zr–H proton reveals NOE enhancement of H(3) [$\eta_{H(3)}$(ZrH) = 1.1%], but not H(6), proton in the pyridine ring; the numbering is given in Scheme 1) and in crystalline state (X-ray diffraction analysis for an adduct of **1** with one-half molecule of pyridine, *vide infra*).

The lateral position of the N-atom in the initially formed **1** is somewhat untypical. For instance, analogous CH-bond activations in [η^5-$C_5(CH_3)_4CH_2CH_2N(CH_3)_2$]-[$\eta^5$-$C_5(CH_3)_5$]$ZrCl_2$ [16] and in [η^5-1,3-$(Me_3Si)_2$Indenyl]$_2ZrCl_2$ in presence of 4-*N*,*N*-dimethylaminopyridine [17] give only the η^2-κC,*N*-products with medially located N-atom. Thus, the question persisted if the rearrangement of **1** into its isomer with medially located N-atom is possible or not.



Scheme 1.

At room temperature, complex **1** in a THF-d_8 solution exhibits no tendency to any changes within months. However, if heated (60–100 °C), rearrangement of **1** into its isomer **2** with medially located N-atom takes place (see Scheme 2). The structure of isomer **2** in solution was proved by NMR data. Unlike in **1**, irradiation of Zr–H proton reveals NOE enhancement of H(6) [$\eta_{H(6)}$(Zr–H) = 1.4%], but not H(3) proton in the pyridine ring. The numbering is given in Scheme 2.



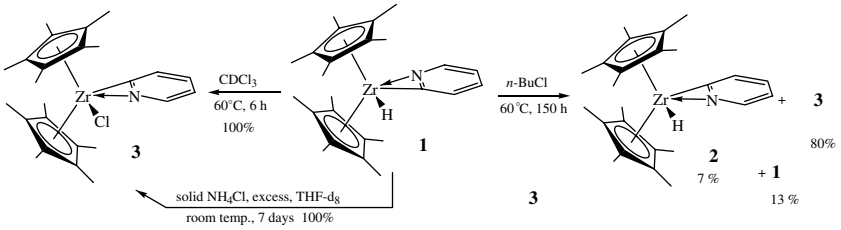
Scheme 2.

At elevated temperatures, complexes **1** and **2** are in equilibrium, with isomer **2** dominating in the mixture. However, this equilibrium is achieved rather slowly (80 h at 100 °C). The estimated equilibrium constant of the process little depends upon temperature (10, 9.8 and 8.7 at 66 °C, 80 °C and 100 °C, respectively), with ΔG lying within 6.5–6.8 kJ/mol range (for the details see Section 3). Noteworthy, no other reactions for both **1** and **2** were observed in this case.

The similar interconversion of the lateral/medial heteroatom isomers was reported earlier for formally related η^2-acetyl and η^2-iminoacyl complexes (η^5-$C_5H_5)_2$Zr[η^2-C(=X)R]R′ as a kinetically fast process [18]. The significantly lower rate for **1** ↔ **2** isomerization, evidently, is due to the sterical effect of the methyl groups at the Cp^*-rings.

Treatment of complex **1** with chloroform-*d* or with solid NH_4Cl in THF-d_8 quantitatively yields the corresponding chloride complex **3** as the only product (the only isomer) (see Scheme 3). Moreover, treatment of the equilibrium mixture of **1** and **2** (*ca.* 1:9) with $CDCl_3$ gives exclusively the same complex **3** as the only one of two possible isomers. η^2-Pyridyl–chloride complex **3** exhibits considerable resistance to oxidation and hydrolysis in the presence of air. This fact underlines the 18-electron nature of coordinatively saturated metal center.

The analogous process takes place if *n*-BuCl (3.5 equiv. in THF-d_8; concentration of **1** is taken approximately the same) is applied as a chlorinating agent. In this case the process is slow and even after 150 h at 60 °C the reaction is still rather far from completeness, with 13% of initial **1**



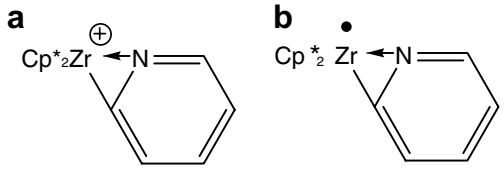
Scheme 3.

along with 7% of **2** (the product of the parallel **1** ↔ **2** interconversion) persisting in the mixture. However, comparison of $CDCl_3$ (pure solvent) and *n*-BuCl concentrations suggests that the rate constants in both of these cases are of the same order.

The molecular structure of complex **3** was established by NMR spectroscopy (in solutions) and X-ray diffraction analysis (*vide infra*). Independent on the preparation method, in complex **3** the N-atom occupies the medial position.

As far as it is difficult to imagine that **1** is unreactive towards chloroform itself and that intermediate conversion of it into **2** is required, the explanation should be given on the basis of some adequate mechanistic hypothesis. With evidence, the general mechanism is a multistep and complicated one. However, two possible alternatives should be considered. The first one involves formation of cationic particles (a), while the second one assumes formation of Zr(III) intermediates (b), as depicted in Scheme 4.

Quantum-chemical estimates provided us the optimized geometries for model $\{[\eta^5\text{-}C_5H_5]_2Zr[\eta^2\text{-}\kappa C,N\text{-}2\text{-pyridyl}]\}^+$ and $[\eta^5\text{-}C_5H_5]_2Zr[\eta^2\text{-}\kappa C,N\text{-}2\text{-pyridyl}]$ species (see Fig. 1).



Scheme 4.

The values of the principle geometrical parameters for these computed structures are compared in Table 1.

As it is clear from Fig. 1 and Table 1, the spatial organization of cationic and trivalent Zr species is markedly different. In the cation, the N-atom is positioned nearly exactly in the $Cp_{cent}(1)$–Zr–$Cp_{cent}(2)$ plane (deviation 0.131 Å), with the whole bond C–N situated on one side in respect to this plane. Thorough examination revealed that it is also the only stationary point for this cation (i.e., a structure where C- and N-atoms are changed in places is not realized). Contrarily, the Zr(III) hypothetical intermediate is rather "symmetrical" and in this case the $Cp_{cent}(1)$–Zr–$Cp_{cent}(2)$ plane intersects the C–N bond at its middle (deviation of the Cent(CN) 0.087 Å). In the $\{[\eta^5\text{-}C_5H_5]_2Zr[\eta^2\text{-}\kappa C,N\text{-}2\text{-pyridyl}]\}^+$ cation, the access to the Zr-center is provided only from the "N-side", whereas in the Zr(III) structure an approach of a reagent may happen from both C- and N-sides. Thus, taking into account both the experimental and computational data, participation of cationic particles **a**, at least as components of contact ion pairs, should be considered.

The hypothesis on the heterolytic mechanism finds arguments in literature data. Thus, cationic complex $\{[\eta^5\text{-}C_5H_5]_2Zr[\eta^2\text{-}\kappa C,N\text{-}2\text{-(6-methylpyridyl)}](THF)\}^+$ in CH_2Cl_2 was reported to degrade slowly to a mixture of two isomeric chlorides $[\eta^5\text{-}C_5H_5]_2Zr[\eta^2\text{-}\kappa C,N\text{-}2\text{-(6-methylpyridyl)Cl}$ and $[\eta^5\text{-}C_5H_5]_2ZrCl_2$ [8]. Meanwhile, when in presence of $[Me_3NCH_2Ph]Cl$ (provision of the chloride anion source), the only isomer of $[\eta^5\text{-}C_5H_5]_2Zr[\eta^2\text{-}\kappa C,N\text{-}2\text{-(6-methylpyridyl)Cl}$ was formed rapidly.

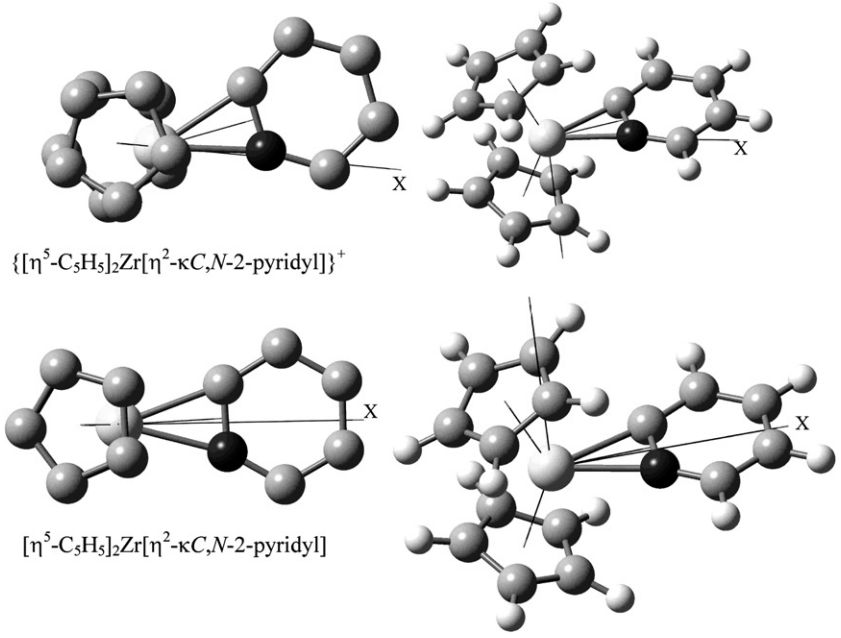


Fig. 1. Comparison of the DFT optimized structures for $\{[\eta^5\text{-}C_5H_5]_2Zr[\eta^2\text{-}\kappa C,N\text{-}2\text{-pyridyl}]\}^+$ and $[\eta^5\text{-}C_5H_5]_2Zr[\eta^2\text{-}\kappa C,N\text{-}2\text{-pyridyl}]$ (restricted and unrestricted B3LYP methods, basis set 3-21G**). The projections to the left are given along the $Cp_{cent}(1)$–$Cp_{cent}(2)$ axes, with all hydrogen atoms not depicted for clarity. Line Zr–X is the intersection of the $Cp_{cent}(1)$–Zr–$Cp_{cent}(2)$ plane and the mean plane of the pyridyl ring.

Table 1
Comparison of the structural parameters for DFT optimized geometries of $\{[\eta^5\text{-}C_5H_5]_2Zr[\eta^2\text{-}\kappa C,N\text{-}2\text{-pyridyl}]\}^+$ and $[\eta^5\text{-}C_5H_5]_2Zr[\eta^2\text{-}\kappa C,N\text{-}2\text{-pyridyl}]$

	$[Cp_2Zr(C_5H_4N)]^+$	$[Cp_2Zr(C_5H_4N)]$
$Zr–Cp_{cent}1$ (Å)	2.217	2.233
Zr–PL1 (Å)	2.217	2.232
$Zr–Cp_{cent}2$ (Å)	2.219	2.233
Zr–PL2 (Å)	2.219	2.232
Zr–C (Å)	2.204	2.273
Zr–N (Å)	2.215	2.215
Zr–Cent(CN) (Å)	2.102	2.168
$PL(Cp_{cent}1–Zr–Cp_{cent}2)–N$ (Å)	0.131	0.597
$PL(Cp_{cent}1–Zr–Cp_{cent}2)–C$ (Å)	1.392	0.770
$PL(Cp_{cent}1–Zr–Cp_{cent}2)$–Cent(CN) (Å)	0.761	0.087
PL(1)–PL(2)[a] (°)	136.27	135.90
X–Zr–N (°)	3.379	15.22
X–Zr–Cent(CN) (°)	21.23	2.29
C–Zr–N (°)	35.80	35.03
PL(Pyr)–Zr (Å)	0.009	0.000

[a] PL1 and PL2 are the mean planes of the first and the second Cp rings, respectively.

2.2. X-ray structural investigation of complexes *1* (adduct with pyridine) and *3*

Molecular structure of complex **1** is presented in Fig. 2. The selected bond lengths and angles are listed in Table 2. The molecule of **1** presents a bent-metallocene sandwich, with the angle $Cp^*_{cent}(1)–Zr–Cp^*_{cent}(2)$ [$Cp^*_{cent}(1)$ and $Cp^*_{cent}(2)$ mean the centroids of the C(11)–C(15) and C(21)–C(25) rings, respectively] equal to 141.9° that is within the range observed previously for Cp^*_2Zr fragments (129.4–145.1°, average value 137.5°; Cambridge Structural Database (release: August 2006) [19], 148 entries, 169 fragments). The distances Zr–PL(1) and Zr–PL(2) [PL(1) and PL(2) are the mean planes of the C(11)–C(15) and C(21)–C(25) rings, respectively] consist 2.2390(15) and 2.2400(14) Å that also matches the range typical for Cp^*_2Zr-moieties (2.171–2.420 Å, CSD [19]).

Table 2
Selected bond lengths (Å) and angles (°) for **1** and **3**

	1	**3a**	**3b**
Zr–N(1)	2.244(3)	2.222(3)	2.204(3)
Zr–C(1)	2.258(3)	2.233(4)	2.235(4)
$Zr–Cp^*_{cent}$	2.239, 2.240	2.258, 2.268	2.259, 2.265
C(1)–N(1)	1.344(4)	1.336(5)	1.323(5)
Zr–H	1.77(5)		
Zr–Cl		2.556(1)	2.549(1)
$Cp^*_{cent}–Zr–Cp^*_{cent}$	141.9	137.0	137.1
N(1)–Zr–C(1)	34.7(1)	34.9(1)	34.7(1)
N(1)–C(1)–Zr	72.1(2)	72.1(2)	71.4(2)
C(1)–N(1)–Zr	73.2(2)	73.0(2)	74.0(2)
C(1)–Zr–H	82(2)		
N(1)–Zr–Cl		82.16(8)	80.62(9)

Both C_5 rings are planar within 0.020(2) Å. As expected, all ten methyl group carbons are deviated 0.058(7)–0.292(7) Å in respect to the corresponding mean C_5-planes outwards from the Zr atom, with the greatest deviation values observed for the rare-positioned atoms C(20) and C(30).

The pyridyl ligand exhibits η^2-coordination mode towards the central atom, with the Zr–N(1) and Zr–C(1) distances equal to 2.244(3) and 2.258(3) Å, respectively. This agrees well with the same distances for similar complex $[(\eta^5\text{-Cp})_2Zr(PMe_3)(\eta^2\text{-}\kappa N,C\text{-}C_5H_3N\ (6\text{-}CH_3)]^+BPh_4^-$ 2.21(1) and 2.29(2) Å, respectively) [8]. All three atoms H, C(1), and N(1) lay in the bisector plane of the zirconocene, with the hydride atom H and N(1) atom occupying the lateral positions. The fragment {Zr,C(1)–C(5),N(1)} is planar within 0.012(3) Å, with the angles between its mean

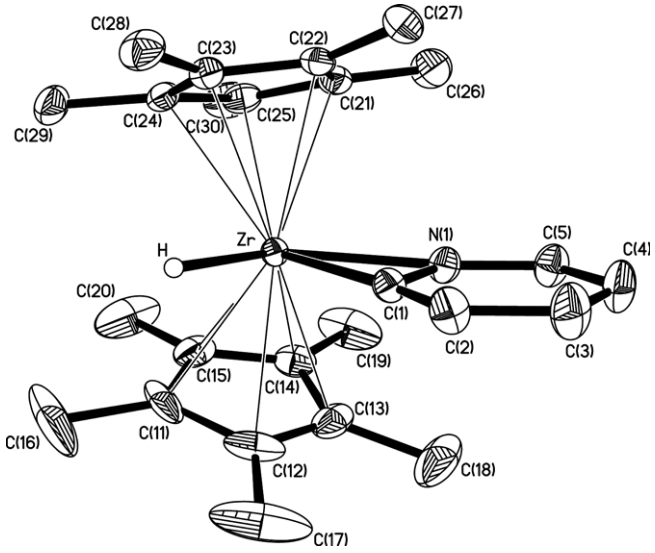


Fig. 2. Molecular structure of **1**. Displacement ellipsoids are shown at 50% probability level. All hydrogen atoms (except hydride) are omitted for clarity.

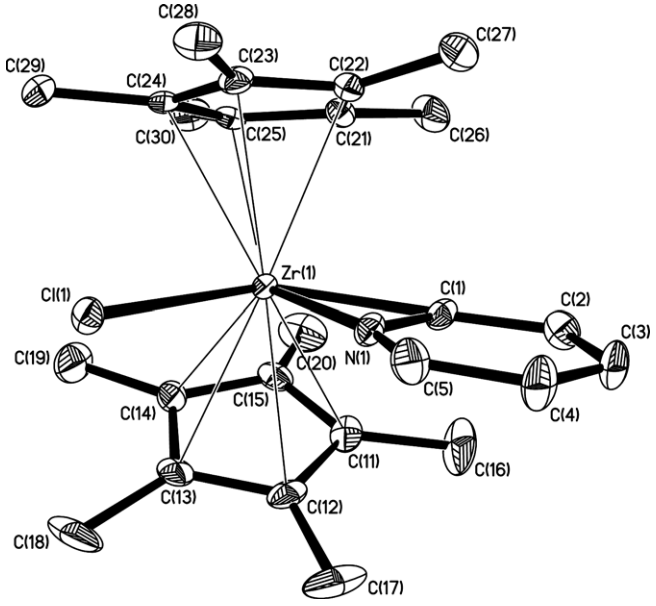


Fig. 3. Molecular structure of **3** (one independent molecule). Displacement ellipsoids are shown at 50% probability level. All hydrogen atoms are omitted for clarity.

Table 3
Crystal and structure refinement data for **1** and **3**

	1	**3**
Empirical formula	$C_{27.5}H_{37.5}N_{1.5}Zr_1$	$C_{25}H_{34}Cl_1N_1Zr_1$
Formula weight	480.31	475.20
Colour, habit	light-yellow block	colourless block
Crystal size (mm)	$0.20 \times 0.15 \times 0.15$	$0.20 \times 0.15 \times 0.10$
Crystal system	triclinic	monoclinic
Space group	$P\bar{1}$	$P2_1/c$
Cell dimensions		
a (Å)	10.5204(7)	15.7498(19)
b (Å)	10.8868(8)	16.748(2)
c (Å)	11.1028(8)	17.323(2)
α (°)	80.248(2)	90
β (°)	77.115(1)	88.188(3)
γ (°)	85.356(1)	90
V (Å^3)	1220.47(15)	4657.3(10)
Z	2	8
D_{calc} (g cm^{-3})	1.307	1.382
μ (mm^{-1})	0.465	0.609
$F(000)$	506	1984
θ range (°)	2.69–27.99	1.398–28.00
Index ranges	$-13 \leqslant h \leqslant 13$, $-14 \leqslant k \leqslant 14$, $-13 \leqslant l \leqslant 14$	$-20 \leqslant h \leqslant 20$, $-21 \leqslant k \leqslant 22$, $-16 \leqslant l \leqslant 22$
Reflections collected	8236	30 169
Independent reflections [R_{int}]	5512 [0.0193]	10 989 [0.0713]
Data/restraints/parameters	5512/0/285	10 989/0/525
Goodness-of-fit on F^2	1.193	1.038
R indices [$I > 2\sigma(I)$]	$R_1 = 0.0433$, $wR_2 = 0.1182$	$R_1 = 0.0602$, $wR_2 = 0.1046$
R indices (all data)	$R_1 = 0.0456$, $wR_2 = 0.1192$	$R_1 = 0.0084$, $wR_2 = 0.1128$
Largest differences in peak/hole (e Å^{-3})	1.335/ − 0.510	0.891/ − 1.365

plane and the planes PL(1) and PL(2) being nearly equal (19.3(2) and 19.1(2)°, respectively). The distance Zr–H is 1.77(5) Å and is close to observed previously for terminal Cp_2Zr–H bonds (1.68(8) Å [20] and 1.78(2) Å [21]).

In the crystal of **1**, the disordered solvent pyridine molecule is sited on crystallographic inversion center.

Molecular structure of complex **3** is shown in Fig. 3. In **3**, the asymmetric unit contains two independent molecules **3a** and **3b**. The geometry of both **3a** and **3b** are similar to that of **1** (see Table 2). However, in contrast to **1**, nitrogen atoms occupy medial sites. The Zr–Cl distances (2.549(1) and 2.556(1) Å) are in a good agreement with the one in $[\eta^5{:}\eta^2\text{-}\kappa C,N\text{-}C_5Me_4CH_2CH_2N(CH_3)CH_2](\eta^5\text{-}C_5Me_5)ZrCl$ [16] (see Table 3).

3. Experimental

3.1. General remarks

All procedures were performed in sealed-off evacuated glass vessels. The employed solvents (and their perdeuterated analogues) were dried with and distilled from conventional agents (namely: diethyl ether and THF – with sodium benzophenone ketyl; hydrocarbons – with Na–K alloy; pyridine and chlorinated hydrocarbons – with CaH_2). When performing procedures in evacuated vessels, the degassed solvents were stored in evacuated reservoirs over corresponding drying agent and transferred on a high vacuum line directly into reaction vessels by trapping them with liq. N_2. ^{1}H and ^{13}C NMR spectra were recorded on "Varian VXR-400" and "Bruker Avance-400" spectrometers at 400 and 100 MHz, respectively. For ^{1}H and ^{13}C spectra, the solvent resonances [$\delta_H = 7.24$ and $\delta_C = 77.0$ ($CDCl_3$), $\delta_H = 7.15$ and $\delta_C = 128.0$ (C_6D_6), $\delta_H = 1.73$ and $\delta_C = 25.3$ (THF-d_8)] were used as internal reference standards. Mass spectra were measured on "Bruker Autoflex II" spectrometer (N_2 lazer, 337 nm). The elemental analyses were performed on the Carlo-Erba automated analyser.

3.2. $[\eta^5\text{-}C_5Me_5]_2ZrH[\eta^2\text{-}\kappa C,N\text{-}C_5H_4N]$ (**1**)

A solution of decamethylzirconocene dichloride (306 mg, 0.707 mmol) in pyridine (20 mL) along with amalgamated magnesium powder (340 mg, 14.0 mmol) was stirred at room temperature for 10 days. Pyridine was removed by trapping with liq. N_2 and finally – on the high vacuum line. The residue was taken with hexane (20 mL), the extract was concentrated until crystallization started and left to stay at −15 °C. Crystalline **1** was flushed with minimal portion of cold hexane and dried on the high-vacuum line. Colorless crystals. Yield 240 mg (77%). ^{1}H NMR (30°C, THF-d_8): $\delta = 1.66$ [s, 30H, $C_5(CH_3)_5$], 3.96 (s, 1H, ZrH), 7.15 (dd, 1H, $^3J_{HH} = 7.3$ Hz, $^3J_{HH} = 5.2$ Hz, H^5), 7.50 (t, 1H, $^3J_{HH} = 7.3$ Hz, H^4), 7.81 (d, 1H, $^3J_{HH} = 7.3$ Hz, H^3), 8.60 (d, 1H, $^3J_{HH} = 5.2$ Hz, H^6). NOE data: $\eta_{H3}(ZrH) = 1.1\%$. $^{13}C\{^1H\}$ NMR (30 °C, THF-d_8): $\delta = 11.64$ [$C_5(CH_3)_5$], 113.87 [$C_5(CH_3)_5$],

123.16, 133.53, 136.09, 144.15 (CH in py), 203.60 (C^2). ^{1}H NMR (30 °C, C_6D_6): $\delta = 1.76$ [s, 30H, $C_5(CH_3)_5$], 4.43 (s, 1H, ZrH), 6.60 (ddd, 1H, $^3J_{HH} = 7.3$ Hz, $^3J_{HH} = 5.0$ Hz, $^4J_{HH} = 1.3$ Hz, H^5), 7.02 (td, 1H, $^3J_{HH} = 7.3$ Hz, $^4J_{HH} = 1.3$ Hz, H^4), 7.88 (dt, 1H, $^3J_{HH} = 7.3$ Hz, $^4J_{HH} = {}^5J_{HH} = 1.3$ Hz, H^3), 8.10 (dt, 1H, $^3J_{HH} = 5.0$ Hz, $^4J_{HH} = {}^5J_{HH} = 1.3$ Hz, H^6). $^{13}C\{^1H\}$ NMR (30°C, C_6D_6): $\delta = 11.61$ [$C_5(CH_3)_5$], 113.61 [$C_5(CH_3)_5$], 122.10, 133.20, 135.17, 143.11 (CH in py), 203.63 (C^2). *Anal.* Calc. for $C_{25}H_{35}NZr$ (440.77): C, 68.12; H, 8.00; N, 3.18. Found: C, 68.05; H, 8.10; N, 3.08%.

3.3. Isomerization of 1 (complex 2)

A solution of **1** (80 mg) in THF-d_8 (0.7 mL) was heated in a sealed-off NMR tube at 100 °C. Periodically, the sample was removed from the bath, and the ^{1}H NMR spectrum at 27 °C was measured. After 80 h (total heating time) there were no changes in the spectra. The relative molar ratio of **2** in respect to **1** was 8.7 (integration of the signals in ^{1}H NMR spectra). The same sample was used to measure the relative content of isomers **1** and **2** at 80 °C (total heating time 36 h, molar ratio **2** in respect to **1** 9.8) and 60 °C (total heating time 36 h, molar ratio **2** in respect to **1** 10.0). ^{1}H NMR (27°C, THF-d_8): $\delta = 1.67$ [s, 30H, $C_5(CH_3)_5$], 4.08 (s, 1H, ZrH), 7.10 (dd, 1H, $^3J_{HH} = 7.3$ Hz, $^3J_{HH} = 5.0$ Hz, H^5), 7.55 (t, 1H, $^3J_{HH} = 7.3$ Hz, H^4), 7.96 (d, 1H, $^3J_{HH} = 7.3$ Hz, H^3), 8.30 (d, 1H, $^3J_{HH} = 5.0$ Hz, H^6). NOE data: η_{H6}(ZrH) = 1.4%. $^{13}C\{^1H\}$ NMR (27°C, THF-d_8): $\delta = 11.74$ [C5(*C*H3)5], 113.70 [*C*5(CH3)5], 123.29, 130.35, 136.03, 147.04 (CH B py), 203.62 (C2).

3.4. Reactions of 1 and 2 with chlorinating agents (compound 3)

(A) Compound **1** (50 mg) was dissolved in $CDCl_3$ (0.7 mL), transferred into an NMR tube, sealed off and kept at room temperature. Content of **3** (molar %): 20 h – 85%, 7 days – reaction complete (^{1}H NMR monitoring data).

(B) A mixture of **1** and **2** (total amount 80 mg, molar ratio *ca.* 1:10) was dissolved in $CDCl_3$ (0.7 mL), transferred into an NMR tube, sealed off heated at 60 °C for 5 h. Reaction complete (^{1}H NMR monitoring data).

(C) Compound **1** (50 mg) was dissolved in THF-d_8 (0.7 mL) and excess of solid powdered NH_4Cl was added. The slurry was stirred for 7 days and the solution was transferred into an NMR tube by decantation. The reaction is complete (NMR spectroscopy data).

(D) Complex **1** (100 mg) was dissolved in $CHCl_3$ (5 mL) and heated at 60 °C for 5 h. The volatiles were removed by trapping with liq. N_2 and the product was dried on the high-vacuum line. Yield 110 mg (quantitatively). ^{1}H NMR (30°C, THF-d_8): $\delta = 1.63$ [s, 30H, $C_5(CH_3)_5$], 7.19 (ddd, 1H, $^3J_{HH} = 7.3$ Hz, $^3J_{HH} = 5.0$ Hz, $^4J_{HH} = 1.3$ Hz, H^5), 7.60 (td, 1H, $^3J_{HH} = 7.3$ Hz, $^4J_{HH} = 1.3$ Hz, H^4), 7.95 (dt, 1H, $^3J_{HH} = 7.3$ Hz, $^4J_{HH} = {}^5J_{HH} = 1.3$ Hz, H^3), 8.39 (dt, 1H, $^3J_{HH} = 5.0$ Hz, $^4J_{HH} = {}^5J_{HH} = 1.3$ Hz, H^6). $^{13}C\{^1H\}$ NMR (30°C, THF-d_8): $\delta = 11.61$ [$C_5(CH_3)_5$], 117.64 [$C_5(CH_3)_5$], 124.12, 129.26, 135.89, 142.89 (CH in py), 206.65 (C^2). ^{1}H NMR (30°C, $CDCl_3$): $\delta = 1.66$ [s, 30H, $C_5(CH_3)_5$], 7.16 (ddd, 1H, $^3J_{HH} = 7.3$ Hz, $^3J_{HH} = 5.1$ Hz, $^4J_{HH} = 1.0$ Hz, H^5), 7.58 (td, 1H, $^3J_{HH} = 7.3$ Hz, $^4J_{HH} = 1.3$ Hz, H^4), 7.91 (dt, 1H, $^3J_{HH} = 7.3$ Hz, $^4J_{HH} = {}^5J_{HH} = 1.2$ Hz, H^3), 8.46 (dt, 1H, $^3J_{HH} = 5.1$ Hz, $^4J_{HH} = {}^5J_{HH} = 1.3$ Hz, H^6). $^{13}C\{^1H\}$ NMR (30°C, $CDCl_3$): $\delta = 11.32$ [$C_5(CH_3)_5$], 117.32 [$C_5(CH_3)_5$], 123.30, 128.29, 135.12, 142.21 (CH in py), 205.53(C^2). MS (MALDI) (N_2 laser, 337 nm) *m/z* (%):473 (44.5) $[M]^+$, 458 (99.3) $[M - CH_3]^+$, 438 (100) $[M - Cl]^+$, 394 (58.8) $[M - C_5H_5N]^+$, 360 (5.3) $[(C_5Me_5)_2Zr]^+$, 338 (40.1) $[M - C_5Me_5]^+$. *Anal.* Calc. for $C_{25}H_{34}ClNZr$ (475.22): C, 63.19; H, 7.21; N, 2.95. Found: C, 63.29; H, 7.28; N, 2.71%.

3.5. X-ray crystallographic study

Experimental intensities for both **1** (an adduct with 0.5 molecule of pyridine, from hexane) and **3** (from hexane) were measured on a Bruker SMART CCD diffractometer (graphite monochromatized Mo Kα radiation, $\lambda = 0.71073$ Å) at 120 K. Semi-empirical absorption corrections based on the measurements of equivalent reflections were applied. The structures were solved by direct methods [22] and refined by full matrix least-squares on F^2 [23] with anisotropic thermal parameters for all non-hydrogen atoms. All hydrogen atoms (except hydride in the structure of **1**) were placed in calculated positions and refined using a riding model. Hydride atom was located from difference Fourier map and refined isotropically. The positions of N(1) and C(1) atoms were undoubtedly assigned by analysis of isotropic displacement parameters and confirmed by the best obtained final *R*-values. The possibility of partial positional disorder of N(1) and C(1) was also checked; no evidence of such disorder was found.

4. Computational details

The DFT calculations were performed using the GAUSSIAN-G03W program package [24].

5. Supplementary material

CCDC 619986 and 619987 contain the supplementary crystallographic data for this paper. These data can be obtained free of charge via http://www.ccdc.cam.ac.uk/conts/retrieving.html, or from the Cambridge Crystallographic Data Centre, 12 Union Road, Cambridge CB2 1EZ, UK; fax: (+44) 1223-336-033; or e-mail: deposit@ccdc.cam.ac.uk.

Acknowledgements

A.V.C. is grateful to the Russian Science Support Foundation. The financial support of the Russian Foundation for Base Research (Grant RFBR 04-03-32288-a) is gratefully acknowledged. Authors are thankful to Dr. P.I. Dem'yanov for his kind help with performing DFT calculations.

References

[1] J.M. Manriquez, J.E. Bercaw, J. Am. Chem. Soc. 96 (1974) 6229.
[2] R.D. Sanner, J.M. Manriquez, R.D. Marsh, J.E. Bercaw, J. Am. Chem. Soc. 98 (1976) 8351.
[3] J.M. Manriquez, D.R. McAlister, E. Rozenberg, A.M. Shiller, K.L. Williamson, S.I. Chan, J.E. Bercaw, J. Am. Chem. Soc. 100 (1978) 3078.
[4] S. Dagorne, S. Rodewald, R.F. Jordan, Organometallics 16 (1997) 5541.
[5] A.S. Guram, R.F. Jordan, Organometallics 10 (1991) 3470.
[6] S. Rodewald, R.F. Jordan, J. Am. Chem. Soc. 116 (1994) 4491.
[7] R.F. Jordan, D.F. Taylor, J. Am. Chem. Soc. 111 (1989) 778.
[8] R.F. Jordan, D.F. Taylor, N.C. Baenziger, Organometallics 9 (1990) 1546.
[9] I.M. Piglosiewicz, S. Kraft, R. Beckhaus, D. Haase, W. Saak, Eur. J. Inorg. Chem. (2005) 938.
[10] J.L. Kiplinger, T.G. Richmond, J. Am. Chem. Soc. 118 (1996) 1805.
[11] B.L. Edelbach, A.K.F. Raman, R.J. Lachicotte, W.D. Jones, Organometallics 18 (1999) 3170.
[12] M. Fujiwara, J. Ichikawa, T. Okauchi, T. Minami, Tetrahedron Lett. 40 (1999) 7261.
[13] K.I. Gell, J. Schwartz, J. Chem. Soc., Chem. Commun. (1979) 244.
[14] K.I. Gell, J. Schwartz, J. Am. Chem. Soc. 103 (1981) 2687.
[15] G. Erker, J. Organometal. Chem. 134 (1977) 189.
[16] D.P. Krut'ko, M.V. Borzov, R.S. Kirsanov, A.V. Churakov, L.G. Kuz'mina, J. Organometal. Chem. 690 (2005) 3243.
[17] C.A. Bradley, E. Lobkovsky, P.J. Chirik, J. Am. Chem. Soc. 125 (2003) 8110.
[18] M.F. Lappert, N.T. Luong-Thi, C.G.C. Milne, J. Organometal. Chem. 174 (1979) C35.
[19] F.H. Allen, Acta Crystallogr. Sect. B B58 (2002) 380.
[20] S.B. Jones, J.L. Petersen, Inorg. Chem. 20 (1981) 2889.
[21] F. Liu, B. Du, J. Liu, E.A. Meyers, S.G. Shore, Inorg. Chem. 38 (1999) 3228.
[22] G.M. Sheldrick, Acta Crystallogr. Sect. A A46 (1990) 467.
[23] G.M. Sheldrick, SHELXL-97, University of Gottingen, Germany, 1997.
[24] M.J. Frisch, G.W. Trucks, H.B. Schlegel, G.E. Scuseria, M.A. Robb, J.R. Cheeseman, J.A. Montgomery, Jr., T. Vreven, K.N. Kudin, J.C. Burant, J.M. Millam, S.S. Iyengar, J. Tomasi, V. Barone, B. Mennucci, M. Cossi, G. Scalmani, R.N., P.G.A., H. Nakatsuji, M. Hada, M. Ehara, K. Toyota, R. Fukuda, J. Hasegawa, M. Ishida, T. Nakajima, Y. Honda, O. Kitao, H. Nakai, M. Klene, X. Li, J.E. Knox, H.P. Hratchian, J.B. Cross, C. Adamo, J. Jaramillo, R. Gomperts, R.E. Stratmann, O. Yazyev, A.J. Austin, R. Cammi, C. Pomelli, J.W. Ochterski, P.Y. Ayala, K. Morokuma, G.A. Voth, P. Salvador, J.J. Dannenberg, V.G. Zakrzewski, S. Dapprich, A.D. Daniels, M.C. Strain, O. Farkas, D.K. Malick, A.D. Rabuck, K. Raghavachari, J.B. Foresman, J.V. Ortiz, Q. Cui, A.G. Baboul, S. Clifford, J. Cioslowski, B.B. Stefanov, G. Liu, A. Liashenko, P. Piskorz, I. Komaromi, R.L. Martin, D.J. Fox, T. Keith, M.A. Al-Laham, C.Y. Peng, A. Nanayakkara, M. Challacombe, P.M.W. Gill, B. Johnson, W. Chen, M.W. Wong, C. Gonzalez, J.A. Pople, GAUSSIAN 03, Revision B.04; Gaussian, Inc.: Pittsburgh PA, 2003.

Available online at www.sciencedirect.com
ScienceDirect
Polyhedron 26 (2007) 2871–2879
POLYHEDRON
www.elsevier.com/locate/poly

Synthesis, characterization, crystal structure and antiproliferative activity of platinum(II) complexes with 2-acetylpyridine-4-cyclohexyl-thiosemicarbazone

Dimitra Kovala-Demertzi *, Anastasia Galani, Nikolaos Kourkoumelis *, John R. Miller, Mavroudis A. Demertzis *

Department of Chemistry, University of Ioannina, 45110 Ioannina, Greece

Received 20 December 2006; accepted 23 January 2007
Available online 4 February 2007

Abstract

New platinum complexes have been synthesized by the reaction of Na_2PtCl_4 with 2-acetylpyridine-4-cyclohexyl-thiosemicarbazone, HAc4CyclHexyl (**1**). The new complexes [Pt(Ac4CyclHexyl)Cl] (**2**) and [Pt(Ac4CyclHexyl)$_2$] (**3**) have been characterized by elemental analyses and spectroscopic studies. The crystal structure of the complex [Pt(Ac4CyclHexyl)Cl] · DMF has been solved by single-crystal X-ray diffraction. The anion of Ac4CyclHexyl coordinates in a planar conformation to the central platinum(II) through the pyridyl N, azomethine N and thiolato S atoms. The crystal packing is determined by double intermolecular hydrogen interactions, π–π, Pt–C and Pt–π contacts. The cytotoxic activities of **1**–**3** have been evaluated for antiproliferative activity in vitro against the cells of three human cancer cell lines: MCF-7 (human breast cancer cell line), T24 (bladder cancer cell line), A-549 (non-small cell lung carcinoma) and a mouse L-929 (a fibroblast-like cell line cloned from strain L). The compounds **1**–**3** display IC_{50} values in a μM range better than that of the antitumor drug cisplatin and are considered as agents with potential antitumor activity candidates for further stages of screening in vitro and/or in vivo.
© 2007 Elsevier Ltd. All rights reserved.

Keywords: Platinum(II) complexes; Thiosemicarbazonato complexes; Crystal structure; Spectroscopic studies; Antineoplastic activity

1. Introduction

The chemistry of transition metal complexes of thiosemicarbazone, Tsc's, has been receiving considerable attention largely because their broad profile of pharmacological activity affords a diverse variety of compounds with different activities [1]. Tsc's are among the most potent inhibitors of ribonucleotide reductase, RR, activity. RR catalyses the synthesis of deoxyribonucleotides from their ribonucleotide precursors and as such is responsible for maintaining a balanced supply of the deoxyribonucleotides required for DNA synthesis and repair. Strong positive correlation has been established between RR activity and the rate of replication of cancer cells [2].

The combination of Tsc's with agents like platinum(II) or palladium(II) that damage DNA produces synergistic inhibition of tumour growth and may lead to improvements in the effectiveness of cancer chemotherapy regimens [3–8]. *cis*-Diamminadichloroplatinum(II) (cisplatin) has for a long time been of major significance in cancer therapy. In addition, several derivatives of this parent drug, such as iproplatin and carboplatin [9], have been tested clinically. The goal of reducing toxic side effects while maintaining therapeutical efficacy can be accomplished by improving the solubility of the complexes, by slowing down degradation processes through shielding of the platinum with bulky ligands, and by increasing membrane permeability with more lipophilic ligands.

* Corresponding authors. Tel.: +30 2651098425; fax: +30 2651044831.
E-mail addresses: dkovala@cc.uoi.gr (D. Kovala-Demertzi), nkourkou@cc.uoi.gr (N. Kourkoumelis), mdemert@cc.uoi.gr (M.A. Demertzis).

0277-5387/$ - see front matter © 2007 Elsevier Ltd. All rights reserved.
doi:10.1016/j.poly.2007.01.039

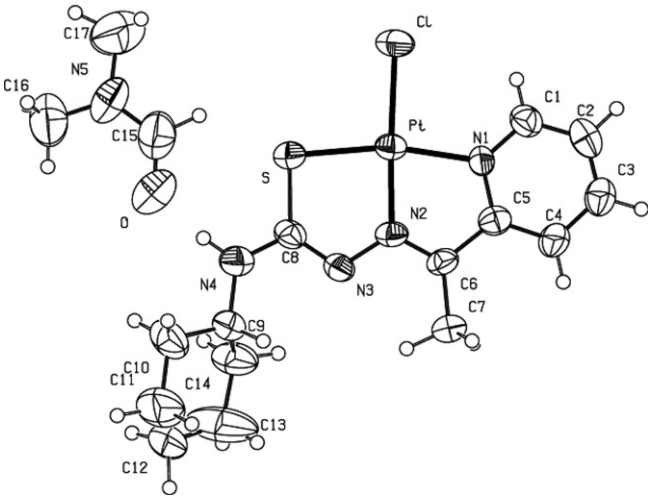


Fig. 1. ORTEP diagram for the complex [PtCl(Ac4CyclHexyl)] · DMF.

The present work is an extension of previously studied platinum(II) and palladium(II) complexes of 2-acetylpyridine-thiosemicarbazones with potentially interesting biological activities [5–8]. The present paper includes synthesis and spectral characterization of the newly prepared platinum(II) complexes with 2-acetylpyridine-4-cyclohexyl-thiosemicarbazone, HAc4CyclHexyl (**1**) (see Fig. 1) and the Pt(II) complexes [Pt(Ac4CyclHexyl)Cl] (**2**) and [Pt(Ac4CyclHexyl)$_2$] (**3**) and the crystal structure of the complex [Pt(Ac4CyclHexyl)Cl] · DMF. The cytotoxic activities of **1**–**3** have been evaluated for antiproliferative activity in vitro against the cells of three human cancer cell lines: MCF-7 (human breast cancer cell line), T24 (bladder cancer cell line), A-549 (non-small cell lung carcinoma) and a mouse L-929 (a fibroblast-like cell line cloned from strain L).

2. Experimental

2.1. General and instrumental

Solvents were purified and dried according to standard procedures. For the platinum(II) compounds a stock 0.02 M $[PtCl_4]^{2-}$ solution was prepared by dissolving $PtCl_2$ (2.66 g, 10 mmol) in concentrated HCl under reflux, filtering to remove a turbidity of undissolved material, neutralizing with Na_2CO_3 and diluting with distilled water up to 500 ml (pH 6.0–6.5). Infrared and far-infrared spectra were recorded on a Nicolet 55XC Fourier transform spectrophotometer using KBr pellets (4000–400 cm^{-1}) and nujol mulls dispersed between polyethylene disks (400–40 cm^{-1}). UV spectra were acquired with a JASCO V-570 UV/Vis/NIR spectrophotometer. The ^{1}H (250.13 MHz) spectra were obtained on a Bruker AMX-400 spectrometer at room temperature with the signal of free DMSO (at 2.49 ppm) as reference. Elemental analyses, C, H, N and S were performed on a Carlo Erba EA (model 1108).

2.2. Preparation of the ligand and platinum complexes

2.2.1. Preparation of the ligand HAc4CyclHexyl (*1*)

The ligand was prepared according to the method described in the literature [8], m.p. 160 °C. Compound **1**: IR (cm^{-1}): 3244s, 3139s, ν(NH); 2910, 2852s, ν(CH$_2$); 1561s, 1535mw, ν(C=N); 1110ms, ν(NN); 854s, ν(C=S); 588ms, δ(py); ^{1}H NMR: δ (ppm) = 10.18 (s, 1H, N(3)H); 8.56 (d, 1H, C(1)H); 8.05 (t, 1H, C(2)H); 8.21 (t, 1H, C(3)H); 7.75 (d, 1H, C(4)H); 3.26 (s, 3H, C(7)H$_3$); 7.33 (b, 1H, N(4)H); 4.02 (s, 1H, C(9)H); 2.46 (d, 2H, C(10)H, C(14)H); 2.33 (s, 2H, C(10)H, C(14)H); 1.65 (br, 2H, C(11)H, C(13)H); 1.61 (br, 2H, C(11)H, C(13)H); 1.22 (m, H, C(12)H); 1.17 (m, 1H, C(12)H); UV–Vis for **1** ($CHCl_3$) λ/nm (ε) 330 sh (30 000); 314 (45 000).

2.2.2. Preparation of the complexes

[PtCl(Ac4CyclHexyl)] (2): To a solution of HAc4CyclHexyl (0.55 mmol) in methanol (10 ml) was added the stock solution of $[PtCl_4]^{2-}$(30 ml, 0.6 mmol). The reaction mixture was stirred for 3 days at 24 °C and then left at 3–4 °C for 1 day. The red powder was filtered off, washed with cold methanol and ether, dried in vacuo over silica gel, and re-dried at 70 °C in vacuo over P_4O_{10}. Yield: 70%. D.p.256 °C. IR (cm^{-1}): 3315s, ν(NH); 2985, 2927s, ν(CH$_2$); 1556w, 1518vs, ν(C=N); 1159ms, ν(NN); 757s, ν(C=S); 627ms, δ(py); 427ms, ν(Pt–N); 388mw, ν(Pt–S) 338s, ν(Pt–Cl); 223ms, ν(Pt–N$_{py}$); ^{1}H NMR: δ (ppm) = 8.73 (d, 1H, C(1)H); 7.62 (t, 1H, C(2)H); 8.11 (t, 1H, C(3)H); 7.69 (d, 1H, C(4)H); 3.39 (s, 3H, C(7)H$_3$); 8.6 (b, 1H, N(4)H); 3.63 (s, 1H, C(9)H); 2.46 (t, 2H, C(10)H, C(14)H); 2.25 (br, 2H, C(10)H, C(14)H); 1.85 (br, 2H, C(11)H, C(13)H); 1.86 (br, 2H, C(11)H, C(13)H); 1.50 (m, H, C(12)H); 1.20 (m, 1H, C(12)H); UV–Vis for **2** ($CHCl_3$) λ/nm (ε) 500 (1100); 388 (17 000); 326 (21 300). Elemental *Anal*. Calc. for $C_{14}H_{19}N_4SPtCl$ (**2**): C, 33.2; H, 3.8; N, 11.1; S, 6.4. Found: C, 33.0; H, 3.8; N, 11.0; S, 6.3%. Slow evaporation of a dimethylformamide solution of **2** provided orange crystals of [PtCl(Ac4CyclHexyl)] · DMF suitable for X-ray crystallography.

[Pt(Ac4CyclHexyl)$_2$] (3): To a solution of HAc4CyclHexyl (0.62 mmol) in methanol (10 ml) was added the stock solution of $[PtCl_4]^{2-}$(15 ml, 0.3 mmol). The pH of the solution was adjusted to 9.0–10.0 by the addition of drops of Et_3N and the reaction mixture was stirred for 3 days 24 °C and then left at 3–4 °C for 1 day. The orange powder was filtered off, washed with cold methanol and ether, dried in vacuo over silica gel, and re-dried at 70 °C in vacuo over P_4O_{10}. Yield: 60%. dp 152 °C. Elemental analyses were consistent with the stoichiometry $C_{28}H_{38}N_8S_2Pt$: C, 45.1; H, 5.1; N, 15.0; S, 8.6. Found:C, 45.5; H, 5.7; N, 15.8; S, 8.8. IR (cm^{-1}): 3329s, 3221s, ν(NH); 2932vs, 2851s, ν(CH$_2$); 1580ms, 1565vw, 1523vs, ν(C=N); 1159ms, 1112ms, ν(NN); 779s, 761mw, ν(C=S); 657ms, 583s, δ(py); 442m, ν(Pt–N); 423m, 408m, ν(Pt–S); 246ms, ν(Pt–N$_{py}$). ^{1}H NMR: δ (ppm) = 10.24s (s, 1H, N(3)H); 8.54 (d, 1H, C(1)H); 7.82 (t, 1H, C(2)H); 8.13

(t, 1H, C(3)H); 8.23 (t, 1H, C(3)H); 7.38 (d, 1H, C(4)H); 3.32 (s, 3H, C(7)H_3); 8.70 (b, 1H, N(4)H); 4.16 (s, 1H, C(9)H); 2.49 (s, 2H, C(10)H, C(14)H); 2.33 (s, 2H, C(10)H, C(14)H); 2.33 (br, 2H, C(10)H, C(14)H); 1.81 (br, 2H, C(11)H, C(13)H); 1.85 (br, 2H, C(11)H, C(13)H); 1.54 (m, H, C(12)H); 1.32 (m, 1H, C(12)H); 1.454 (m, H, C(12)H); 1.22 (m, 1H, C(12)H); UV–Vis for **3**: ($CHCl_3$) λ/nm (ε) 497 (2000); 380sh (41 000); 316 (55 000).

2.3. X-ray crystallography

A summary of the crystal data, experimental details and refinement results are listed in Table 1. The crystals were not of excellent quality and even the best showed indications of splintering. A crystal of dimensions $0.60 \times 0.25 \times 0.08$ mm. was glued to a glass fibre and mounted on the head of an Enraf-Nonius CAD4 diffractometer. Graphite-monochromated Mo Kα ($\lambda = 0.71073$ Å) radiation was used. The unit cell was found to be triclinic from analysis of 25 centred reflections in the range of $21.5° < \theta < 23.6°$ ($a = 6.9856(19)$ Å, $b = 9.517(2)$ Å, $c = 17.777(3)$ Å, $\alpha = 86.895(17)°$, $\beta = 80.111(18)°$, $\gamma = 70.75(2)°$), $V = 1062.5(5)$ Å^3, $Z = 2$. Space group $P\bar{1}$ (No. 2) was assigned, with μ(Mo Kα) 6.91 mm^{-1}, d_{calc} 1.70 g cm^{-3}, temperature 291(1) K. 4560 reflections were collected ($h = 0$–8, $k = -10$–11, $l = -20$–21) in ω–2θ mode in the range $2° < \theta < 26°$. 3 standard reflections were collected every 2 h. Decay of ca. 51% was observed and corrected during processing [10,11]. Lorentz and polarization effects were corrected. An empirical absorption correction was made using ψ-scans of 9 reflections ($T_{max} = 0.999$, $T_{min} = 0.504$) [12]. 4181 unique reflections were measured ($R_{int} = 0.034$), with 3247 observed ($I_o > 2.0\sigma(I_o)$). The structure was solved by the Patterson heavy atom method and successive cycles of full-matrix refinement and Fourier difference syntheses [12–14]. All non-hydrogen atoms were refined anisotropically on F^2 by full-matrix least-squares. Hydrogen atoms were placed in calculated positions and used in structure factor calculations but not refined. Refinement converged to $R_1 = 0.058$, $wR = 0.14$, $S = 1.18$, $(\Delta/\sigma)_{max} < 0.001$. The final Fourier difference synthesis showed maximum and minimum peaks at 3.66 and -2.95 e Å^{-3}, respectively. The data did not show evidence for extinction. There were 4 strong difference peaks at the corners of a rhombus in the molecular plane approximately 1.0 Å from the Pt atom and two others at approximately 2.3 Å on either side of the plane. They could not be reasonably assigned to atoms and it is thought that they are errors due to series termination and to the inherently poor quality of the crystal. Molecular graphics were performed from PLATON [15].

Table 1
Crystal data and structure refinement for **2**

Empirical formula	$C_{17}H_{26}ClN_5OPtS$
Formula weight	579.03
Temperature (K)	291
Wavelength (Å)	0.71073
Crystal system	triclinic
Space group	$P\bar{1}$
Unit cell dimensions	
a (Å)	6.9856(19)
b (Å)	9.517(2)
c (Å)	17.177(3)
α (°)	86.895(17)
β (°)	80.111(18)
γ (°)	70.75(2)
Volume (Å^3)	1062.2(4)
Z	2
D_{calc} (Mg/m^3)	1.700
μ(Mo Kα) (mm^{-1})	6.91
F(000)	564
Crystal size (mm)	$0.08 \times 0.25 \times 0.60$
θ Range for data collection (°)	2.27–26.0
Index ranges	$0 \leqslant h \leqslant 8$, $-10 \leqslant k \leqslant 11$, $-20 \leqslant l \leqslant 21$
Reflections collected	4560
Independent reflections (R_{int})	4181 (0.034)
Refinement method	full-matrix least-squares on F^2
Data/restraints/parameters	3247/0/235
Goodness-of-fit on F^2	1.169
Final R indices [$I > 2\sigma(I)$]	$R_1 = 0.058$, $wR^2 = 0.146$
Largest difference peak and hole (e Å^{-3})	3.66 and -2.95

2.4. Calculations

All calculations were carried out using GAUSSIAN-03W [16] software package and the results were obtained by employing density functional methods (DFT). The initial geometry was fully optimized with the B3LYP [17,18] level of theory using the LANL2DZ [19] effective core potential basis set. Applying planarity restraints to molecule did not alter the results while attempts to use mixed basis sets LANL2DZ/6-31G** and LANL2DZ/6-311G** for S and Cl in order to increase the accuracy, were not succeeded to converge. To characterize the nature of the stationary points, harmonic vibrational frequencies are calculated with the method mentioned above and no imaginary frequencies were computed. TDDFT calculations [20a] were performed to study electronic excitation energies and oscillator strengths using the energy-adjusted relativistic pseudo-potentials proposed by Andrae et al. [21] for describing the Pt atom. Its valence basis set was extended with a set of diffuse functions $\alpha_s = 0.0075$, $\alpha_p = 0.013$, and $\alpha_d = 0.025$, and with optimized polarization functions $\alpha_f = 0.98$ [22]. For TDDFT calculations the fully optimized geometries of **1** and **2** were used. The solvent effect was simulated using the polarizable continuum model (PCM), in which the solvent cavity is seen as a union of interlocking atomic spheres [23]. All the calculations described here were carried out with the GAUSSIAN-03W package.

2.5. Antiproliferative assay in vitro

Compounds: Test solutions of the compounds tested (1 mg/ml) were prepared by dissolving the substance in 100 μl of DMSO completed with 900 μl of tissue culture

medium. Afterwards, the tested compounds were diluted in culture medium to reach the final concentrations of 100, 10, 1, and 0.1 μg/ml. The solvent (DMSO) in the highest concentration used in test did not reveal any cytotoxic activity.

Cells: The established in vitro human cancer cell line MCF-7 (human breast cancer cell line), T24 (bladder cancer cell line), A-549 (non-small cell lung carcinoma) and a mouse L-929 (a fibroblast-like cell line cloned from strain L) were applied: The cell lines are maintained in the Cell Culture Collection of the University of Ioannina. Twenty-four hours before addition of the tested agents, the cells were plated in 96-well plates at a density of 10^4 cells per well. The T-24 and MCF-7 cells were cultured in the DMEM (Dulbeco's modified Eagle's medium) medium supplemented with 1% antibiotic and 10% fetal calf serum. L-929 cells were grown in Hepes-buffered RPMI 1640 medium supplemented with 10% fetal calf serum, penicillin (50 U/ml) and streptomycin (50 mg/ml). A-549 cells were grown in F-12K Ham's medium supplemented with 1% glutamine, 1% antibiotic/antimycotic, 2% $NaHCO_3$ and 10% fetal calf serum. The cell cultures were maintained at 37 °C in a humid atmosphere saturated with 5% CO_2. Cell number was counted by the Trypan blue dye exclusion method. MCF-7, L-929 and A-549 cells were determined by the sulforhodamine B assay [24], and T24 cells by the 3-(4,5-dimethylthiazol-2-yl)-2,5-diphenyl tetrazolium bromide (MTT) assay [25].

SRB assay: The details of this technique were described by Skekhan et al. [24]. The cytotoxicity assay was performed after 72-h exposure of the cultured cells to varying concentrations (from 0.1 to 100 μg/ml) of the tested agents. The cells attached to the plastic were fixed by gently layering cold 50% trichloroacetic acid (TCA) on the top of the culture medium in each well. The plates were incubated at 4 °C for 1 h and then washed five times with tap water. The background optical density was measured in the wells filled with culture medium, without the cells. The cellular material fixed with TCA was stained for 30 min with 0.4% sulforhodamine B dissolved in 1% acetic acid. Unbound dye was removed by rinsing with 1% acetic acid. The protein-bound dye was extracted with 10 mM unbuffered Tris base for determination of optical density (at 540 nm) in a computer-interfaced, 96-well microtiter plate.

MTT: This technique was applied for cytotoxicity screening against T-24 cells growing in suspension culture. An assay was performed after 72 h exposure to varying concentrations (from 0.1 to 100 mg/ml) of the tested agents. For the last 3–4 h of incubation 20 μl of MTT solution was added to each well [MTT: 3-(4,5-dimethylthiazol-2-yl)-2,5-diphenyl tetrazolium bromide (Sigma); stock solution: 5 mg/ml]. The mitochondria of viable cells reduce a pale yellow MTT to a navy blue formazan, so if more viable cells are present in the well, more MTT will be reduced to formazan. When the incubation time was completed, 80 μl of the lysing mixture was added to each well (lysing mixture: 225 ml dimethylformamide, 67.5 g sodium dodecylsulfate (both from Sigma) and 275 ml of distilled water). After 24 h, when formazan crystals had dissolved, the optical densities of the samples were read on an Eliza spectra max 190 photometer at 570 nm wavelength. Each compound at a given concentration was tested in triplicate in each experiment, which was repeated three times.

3. Results and discussion

3.1. Description of structure

Interatomic distances, bond angles and hydrogen bonds for [PtCl(Ac4CyclHexyl)] · DMF are compiled in Table 2. Fig. 1 shows an ORTEP diagram of the molecular structure and the atom labelling scheme. The anionic Ac4CyclHexyl acts as a tridentate ligand which coordinates to platinum(II) through the pyridyl nitrogen, N(1), the azomethine nitrogen, N(2) and the thiolato sulfur atom. The tridentate ligand shows a *Z*,*E*,*Z* configuration for the donor centres nitrogen, nitrogen and sulfur, respectively. The stronger coordination of the metal to the azomethine nitrogen compared to the pyridyl notrogen is attributed to the higher basicity of N(2). The S–C bond distances are consistent with increased single-bond character while both thioamide C–N distances indicate increased double bond character. The negative charge of the deprotonated ligand is delocalized over the thiosemicarbazonato moiety. This delocalization reduces any basic properties which N(4) may otherwise possess, and allows N(4) to act as a hydrogen donor to the oxygen atom of the DMF solvent of crystallization.

The dihedral angles between the planes of the two five-membered chelate rings PtSC(8)N(3)N(2) and PtN(2)C(6)-C(5)N(1) and the five-membered ring PtSC(8)N(3)N(2) and the pyridyl ring are 1.4(4)° and 2.6(5)°, respectively. The dihedral angle between the PtSC(8)N(3)N(2) and DMF molecule is 3.1(12)°, while of PtSC(8)N(3)N(2) and

Table 2
Experimental and calculated bond distances (Å)and angles (°) for **2**

Vector	Experimental	Computed
Pt–Cl	2.311(3)	2.4097
Pt–S	2.250(3)	2.3982
Pt–N1	2.032(9)	2.0508
Pt–N2	1.946(8)	1.9975
S–C8	1.76(1)	1.8306
N1–C1	1.34(1)	1.3532
N1–C5	1.34(1)	1.3859
N2–N3	1.38(1)	1.3813
N2–C6	1.29(1)	1.3326
N3–C8	1.32(2)	1.3478
N4–C8	1.33(2)	1.3567
N4–C9	1.46(2)	1.481
Cl–Pt–S	97.1(1)	97.85
Cl–Pt–N1	96.8(3)	96.18
Cl–Pt–N2	177.1(3)	
S–Pt–N1	166.1(2)	165.98
S–Pt–N2	85.8(3)	85.12
N1–Pt–N2	80.4(4)	80.86

cyclohexyl ring is 56.1(9)°. The cyclohexyl ring is bonded equatorially to N(4) and adopts the usual chair conformation. Ring puckering analysis and least square planes calculations show that the cyclohexyl ring adopts a chair conformation.

There is an intermolecular hydrogen bond between the amido hydrogen, H(4N), of the tridentate ligand and the oxygen atom of DMF. The DMF molecules are connected by double intermolecular bonds of the type C–H···O The monomers of DMF form hydrogen bonded dimers linked by two O···H–C hydrogen bonds involving the methyl C(16)H(16B) hydrogen atom and the adjacent oxygen atom and vice versa of centrosymetrically related pairs of molecules. The observed pattern is of the DA = AD type, Fig. 2. The crystal packing is determined by π–π, Pt–π and Pt–C interactions. The monomers of [Pt(Ac4CyclHexyl)Cl] are linked in dimers in a head to tail fashion by double strong π–π interactions. The most significant $\pi \rightarrow \pi$ interaction is that between the pair of rings Pt–N(2)–C(6)–C(5)–N(1), Cg(2) and N(1)–C(1)–C(2)–C(3)–C(4)–C(5), Cg(3) and between the rings Pt–N(2)–C(6)–C(5)–N(1) {Cg(2)–Cg(3); symmetry operation; $1-x$, $1-y$, $1-z$; and $Cg(2) \rightarrow Cg(2)$ symmetry operation; $2-x$, $1-y$, $1-z$} at a centre to centre separation of 3.571(7) and 3.500(6) Å, respectively, Table 3, Fig. 3.

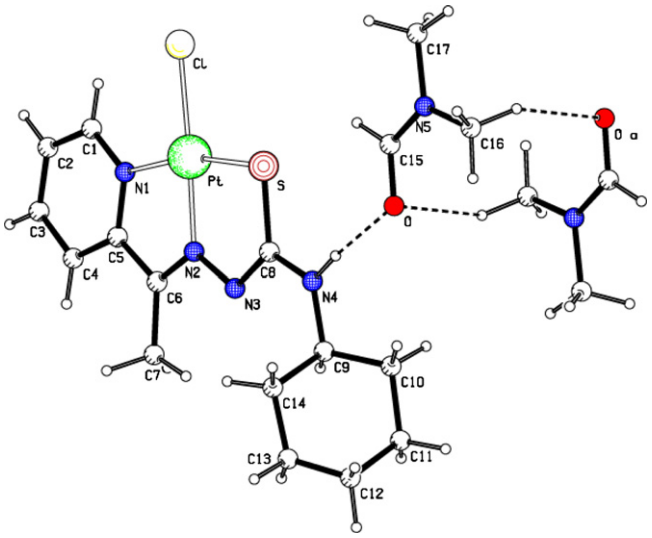


Fig. 2. Arrangement of the intermolecular hydrogen bonds in [PtCl(Ac4CyclHexyl)] · DMF.

The calculations were carried out on isolated molecules through the GAUSSIAN-03W [16] software package and the results were obtained by employing density functional methods (DFT). The optimized geometry is in good agreement with the experimental one, the largest differences are found for the Pt–Cl and Pt–S bond distances. The computed bond distances for Pt–Cl and Pt–S are 2.409 and 2.398 Å, respectively and are longer than the corresponding experimental values 2.311(3) and 2.250 (3) Å, respectively. The significant elongation of the calculated Pt–Cl (0.098 Å) and Pt–S (0.148 Å) bond length in comparison with the experimental ones, could be explained in part by contributions of Cl to a C(1)–H···Cl hydrogen bond and of S to a C(15)–H···S hydrogen bond. The formation of these hydrogen bonds causes local deficiency of electron density on the chloro and thiolato atoms and consequently these atoms are closer to the central metal ion in the experimental structure. The elongation of the M–chlorine bond lengths (up to 0.25 Å) in the B3LYP with different basis sets has been found in other rhenium–chlorine and

Table 3
Inter- and intra-molecular hydrogen bonds and π–π stacking interactions for **2**

Cg(I)–Cg(J)[a]	Cg–Cg (Å)[b]	β (°)[c]	Cg(I)–Perp (Å)[d]	Cg(J)–Perp (Å)[e]
$Cg(1) \rightarrow Cg(3)^{i}$	3.770(7)	23.62	3.432	3.455
$Cg(1) \rightarrow Cg(3)^{ii}$	3.582(7)	17.56	3.458	3.415
$Cg(2) \rightarrow Cg(2)^{i}$	3.727(6)	22.67	3.439	3.439
$Cg(2) \rightarrow Cg(2)^{ii}$	3.500(6)	9.56	3.452	3.452
$Cg(2) \rightarrow Cg(3)^{i}$	3.571(7)	15.67	3.431	3.438
$Cg(3) \rightarrow Cg(1)^{i}$	3.771(7)	24.44	3.455	3.433
$Cg(3) \rightarrow Cg(1)^{ii}$	3.582(7)	15.12	3.415	3.458
$Cg(3) \rightarrow Cg(2)^{i}$	3.571(7)	16.08	3.438	3.431

D	H	A[f]	D···A (Å)	H···A (Å)	∠D–H···A (°)
N(4)	H(4N)	O	2.07	2.93(2)	176
C(1)	H(1)	Cl	2.83	3.39(1)	120
C(7)	H(7A)	N(3)	2.34	2.79(2)	105
C(15)	H(15)	S	2.90	3.63(2)	137
C(16)	H(16A)	O	2.44	2.82(3)	104
$C(16)^{iii}$	H(16B)	O	2.70	3.47(3)	138

Symmetry transformations: (i) $1-x$, $1-y$, $1-z$; (ii) $2-x$, $1-y$, $1-z$; (iii) $2-x$, $1-y$, $2-z$.

[a] Cg(1), Cg(2) and Cg(3) refer to the centroids of rings Pt–S–C8–N3–N2, Pt–N2–C6–C5–N1 and, N1–C1–C2–C3–C4–C5, respectively.

[b] Cg–Cg is the distance between ring centroids or ring centroid and Pt(1).

[c] β is the angle between the Cg(I)–Cg(J) or Cg(I)–Pt vector and the normal to plane I.

[d] Cg(I)–Perp is the perpendicular distance of Cg(I) to ring J and Cg(J)–Perp is the perpendicular distance of Cg(J) or Pt to ring I.

[e] Cg(I)–Perp is the perpendicular distance of Cg(I) to ring J and Cg(J)–Perp is the perpendicular distance of Cg(J) or Pt to ring I.

[f] Where D is donor and A is acceptor.

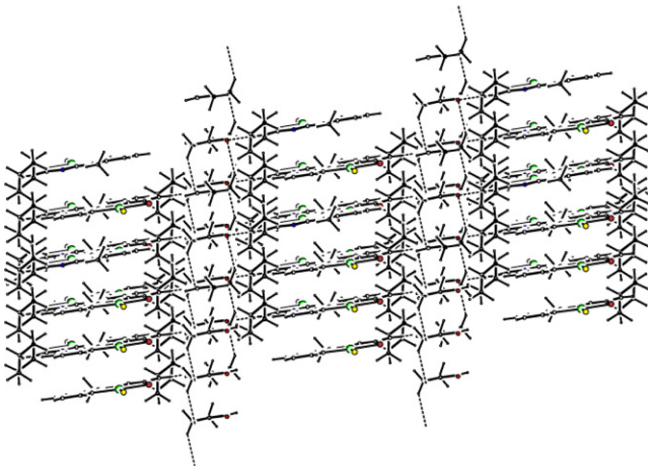


Fig. 3. A view of the extended network of [PtCl(Ac4CyclHexyl)] · DMF along the *b*-axis.

platinum–chloride complexes [20b,20c]. The computed bond distances for Pt–N(1) and Pt–N(2) are 2.050 and 1.997 Å and are in excellent agreement with the experimental values 2.032(9) and 1.946(8) Å.

3.2. Spectroscopy

Infrared spectroscopy: The significant IR bands of Pt(II) complexes are close in energy to those found in other compounds with tridentate coordination [3–8,26]. The bands assigned in the spectrum of HAc4Hexyl shift in the spectra of Pt(II) complexes. Coordination of the azomethine nitrogen to Pt(II) is reflected by the shift of the ν(C=N) band to lower frequencies along with the increase of the ν(N–N) band to higher frequency in the IR spectra of the complexes compared to those in the protonated ligand. The breathing motion of the pyridine ring is shifted to a higher frequency upon complexation and is consistent with pyridine nitrogen coordination. The thioamide band, which contains considerable ν(CS) character, is less intense in complexes and is found at a lower frequency, consistent with coordination of the metal through sulfur. Coordination of the imine nitrogen is also consistent with the presence of bands at 427 and 442 cm^{-1}, assignable to ν(Pt–N) for **2** and **3**, respectively. Bands at 388 cm^{-1} for **2** and at 423, 408 cm^{-1} for **3** are assigned to ν(Pt–S) while bands at 223 and 246 cm^{-1} to $\nu(Pt–N_{pyr})$ for **2** and **3**, respectively. In **3** the bands ν(C=N), ν(N–N), and the breathing motion of the pyridine ring are consistent with both complexed and uncomplexed azomethine and pyridine nitrogen coordination, suggesting tridentate and monodentate behaviour for the two deprotonated ligands [8].

UV/Vis absorption spectra: The two complexes are distinctly coloured, orange and red. Broad but relatively weak bands in the visible region are responsible for the colour. Table 4 shows the spin-allowed singlet–singlet electronic transitions calculated with the TDDFT method for **1** and **2** and the absorption data in chloroform solution; studies in dimethylformamide (DMF) showed essentially similar absorption features within experimental uncertainty (±3 nm) of λ_{max}.

Table 4
Selected calculated TDDFT singlet excitation energies for **1** and **2** in $CHCl_3$ solution, together with experimentally observed values

Compound	Experimental λ/nm (ε/M^{-1} cm^{-1})	Calculated[a] λ (nm)	Oscillator strength, *f*	Composition[b]
1	330 (30000)	333.36	0.1591	H-1 → L (+93%)
	314 (45000)	290.45	0.5921	H-2 → L (+79%) H-3 → L (+7%)
2	500 (1100)	551.9	0.0172	H → L (+90%)
		443.0	0.0022	H-2 → L (+95%)
	388 (17000)	406.3	0.1315	H-1 → L (+46%) H-3 → L (34%) H → L + 1 (10%)
	388 (17000)	380.5	0.3374	H-3 → L (+55%) H-1 → L (+30%)
	326 (21300)			

[a] G03W/B3LYP (PCM).
[b] H = HOMO, L = LUMO. Percentage contributions to wavefunctions of excited states are given in parenthesis.

Considering that the solution spectrum of **1** exhibits intense absorption bands in the 330–310 nm range some additional intraligand transitions are expected at higher energies in the calculation. The assignment of the calculated transitions to the experimental bands is based on the criterion of the energy and oscillator strength of the calculated transitions. The results are presented in Table 4, where selected transitions, with significant oscillator strengths, are listed. Due to the complex character of the MOs of **1** and **2**, only the main contributions were taken into consideration for the discussion of the electronic transitions.

The computed spectrum of **1** has major peaks at 333 and 290 nm (oscillator strengths 0.159 and 0.592, respectively) comparing well with the experimental shoulder at 330 and the band 314 nm (in $CHCl_3$). The shoulder at 330 nm is due to the HOMO − 1 → LUMO transition while the peak at 290 nm is due to the HOMO − 2 → LUMO transition. These bands correspond to intraligand charge transfer from sulfur to pyridyl ring.

The experimental band of **2** at 500 nm is assigned to the calculated transition at 552 nm (oscillator strength 0.0172). The lowest-energy absorption band at 500 nm is assigned to the spin-allowed HOMO → LUMO transition, which can be characterized as a d(Pt)/p(Cl/p(S)p(N2)/pN(3) → π^* (pyr) transition and thus as MLCT mixed with LLCT

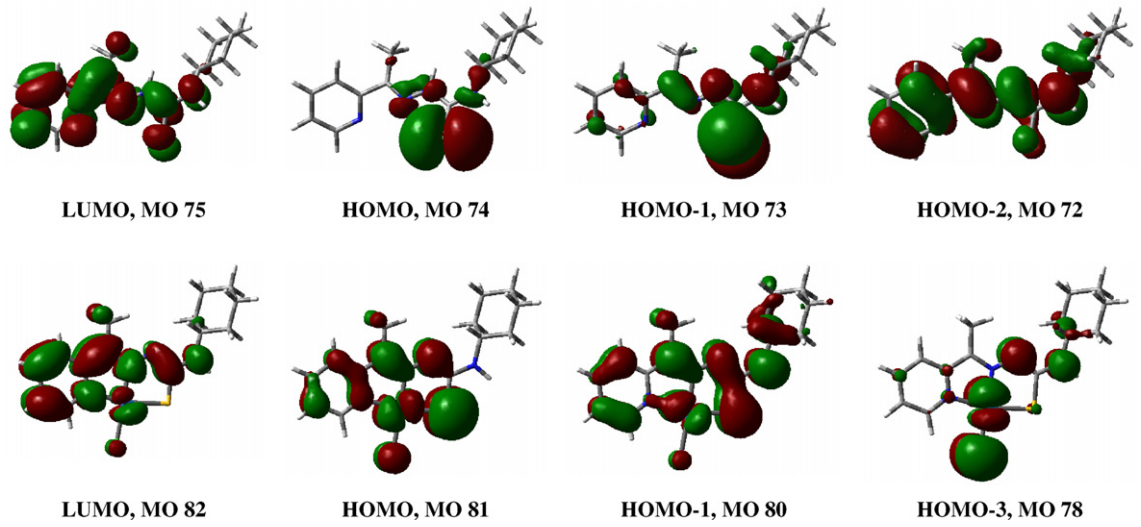


Fig. 4. Plots of relevant molecular orbitals involving in the electronic transitions of **1** and **2**.

(LLCT/MLCT) and a small contribution of d–d electronic transitions. The experimental band of **2** at 388 nm is assigned to the calculated transitions at 406 and 380 nm (oscillator strengths 0.135 and 0.337, respectively). The band at 388 nm is assigned to the spin-allowed HOMO − 3 → LUMO and HOMO − 1 → LUMO transitions. The HOMO − 3 MO has contributions from d(Pt)/p(Cl)/p(N4) and the HOMO − 1 from d(Pt)/p(S) and the function CNNCN, respectively. The transition at 388 nm is thus assigned as MLCT mixed with LLCT (LLCT/MLCT) and a contribution of d–d electronic transitions, Fig. 4. The shortest wavelength experimental band of 326 nm cannot be assigned completely to the calculated transitions.

3.3. Pharmacology: antiproliferative activity in vitro

Pd(II) and Pt(II) complexes of HFoTsc were found active in vivo against leukemia P388 cells and Pt(II) complexes of *N*-4-ethyl-2-formyl and 2-acetylpyridine thiosemicarbazones showed cytotoxicity and were found to be able to overcome the cisplatin resistance of A2780/Cp8 cells [6–8]. Also, Zn(II) complexes of HFoTsc and HAcTsc were found active against the MCF-7 (human breast cancer cell line), T24 (bladder cancer cell line) and a mouse L-929 (a fibroblast-like cell line cloned from strain L) [27].

The results of cytotoxic activity in vitro are expressed as ID_{50} – the concentration of compound (in M) that inhibits a proliferation rate of the tumor cells by 50% as compared to control untreated cells, Table 5. The compounds **1**–**3** were tested for their antiproliferative activity in vitro against the cells of three human cancer cell lines: MCF-7 (human breast cancer cell line), T24 (bladder cancer cell line), A-549 (non-small cell lung carcinoma) and a mouse fibroblast L-929 cell line and the results are compared with zinc(II) complexes of 2-acetylpyridine Thiosemicarbazone, HAcTsc [27].

The thiosemicarbazone and the two Pt(II) metal complexes exhibited cytotoxic activity against the MCF-7 cell line in a μM range better than that of cisplatin. It was found that [Pt(Ac4CyclHexyl)$_2$] in a concentration of 0.134 μM inhibits the proliferation rate of the MCF-7 cancer cells by 65% as compared to control untreated cells. The IC_{50} value for HAc4CyclHexyl against the MCF-7 cell line is 0.36 μM and for **2** is 0.63 μM. The IC_{50} value for HAc4CyclHexyl against the A-549 cell line is 11.1 μM and for **2** and **3** is 6.87 and 1.17 μM, respectively.

In the case of T-24 cell line the ligand and [PtCl(Ac4CyclHexyl)] are in the same μM range compared to cisplatin while the complex **3** is more cytotoxic. The IC_{50} value for HAc4CyclHexyl against the T-24 cell line is

Table 5
The antiproliferative activity in vitro of HAc4CyclHexyl, its Pt(II) and related Zn(II) complexes [27] (expressed as ID_{50} (M) against MCF-7, T-24, A-549 and L-929 cancer cell lines

Compounds	MCF-7	T-24	A-549	L-929
HAc4CyclHexyl	0.36×10^{-6}	10.10×10^{-6}	11.10×10^{-6}	3.31×10^{-6}
HAcTsc	3.29×10^{-6}	2.16×10^{-6}		2.06×10^{-6}
[PtCl(Ac4CyclHexyl)]	0.63×10^{-6}	9.17×10^{-6}	6.87×10^{-6}	6.06×10^{-6}
[Pt(Ac4CyclHexyl)]$_2$	$<0.13\times10^{-6}$	0.37×10^{-6}	1.17×10^{-6}	0.21×10^{-6}
[ZnCl$_2$(HAcTsc)]	1.36×10^{-6}	1.57×10^{-6}		1.06×10^{-6}
[Zn(AcTsc)$_2$]	0.88×10^{-6}	1.18×10^{-6}		4.65×10^{-6}
Cisplatin	8.00×10^{-6}	41.7×10^{-6}	1.53×10^{-6}	0.70×10^{-6}

10.10 μM and for the Pt(II) complexes of **2** and **3** is 9.17 and 0.13 μM, respectively. The IC_{50} value for HAc4CyclHexyl against the L-929 cell line is 3.31 μM and for the Pt(II) complexes of **2** and **3** is 6.06 and 0.21 μM, respectively. These values are in the same μM range compared to cisplatin.

The two zinc(II) complexes compared to the Pt(II) complexes are less active against these three cell lines, while the HAcTsc is more cytotoxic than HAc4CyclHexyl.

The compounds **1**–**3** display IC_{50} values in a μM range better than that of the antitumor drug cisplatin. Complex **3** was found to be 10, 16, and 30 times more cytotoxic than the parent Tsc against the A-549, L-929 and T24 cancer cell lines. All the zinc(II) and Pt(II) complexes are very active against MCF-7 cell line and the most cytotoxic of all was found to be the complex **3**. The best results were found against the MCF-7 and T-24 cell lines and the platinum complex **3**. Thus, compounds **1**–**3** are considered as agents with potential antitumor activity, and can therefore be candidates for further stages of screening in vitro and/or in vivo.

Appendix A. Supplementary material

CCDC 293435 contains the supplementary crystallographic data for **2**. These data can be obtained free of charge via http://www.ccdc.cam.ac.uk/conts/retrieving.html, or from the Cambridge Crystallographic Data Centre, 12 Union Road, Cambridge CB2 1EZ, UK; fax: (+44) 1223-336-033; or e-mail: deposit@ccdc.cam.ac.uk. Supplementary data associated with this article can be found, in the online version, at doi:10.1016/j.poly.2007.01.039.

References

[1] (a) S. Padhye, R.C. Chikate, P.B. Sonawane, A. Kumbhar, R. Yerande, D.X. West, A. Liberta, Coord. Chem. Rev. 123 (1993) 49;
(b) A.E. Liberta, D.X. West, Biometals 5 (1992) 121;
(c) J.G. Cory, A.H. Cory, G. Rappa, A. Lorico, M.C. Liu, T.-S. Lin, A.C. Sartorelli, Biochem. Pharmacol. 48 (1994) 335;
(d) F.A. French, J.E. Blanz, J. Med. Chem. 17 (1974) 17, and references cited therein.

[2] (a) R.A. Finch, M.-C. Liu, S.P. Grill, W.C. Rose, R. Loomis, K.M. Vasquez, Y.-C. Cheng, A.C. Sartorelli, Biochem. Pharmacol. 59 (2000) 983, and references cited therein;
(b) D.R. Richardson, Crit. Rev. Oncol./Hemat. 42 (2002) 267, and references cited therein.

[3] (a) H. Beraldo, D. Gambino, Mini Rev. Med. Chem. 4 (2004) 159;
(b) Z. Afrasiabi, E. Sinn, J. Chen, Y. Ma, A.L. Rheingold, L.N. Zakharov, N. Rath, S. Padhye, Inorg. Chim. Acta 357 (2004) 271;
(c) Z. Afrasiabi, E. Sinn, J. Chen, Y. Ma, S. Padhye, Toxicol. Appl. Pharmacol. 197 (2004) 40.

[4] (a) A. Gomez Quiroga, C. Navarro Ranninger, Coord. Chem. Rev. 248 (2004) 119;
(b) A.G. Quiroga, J.M. Pérez, I. López-Solera, J.R. Masaquer, A. Luque, P. Román, A. Edwards, C. Alonso, C. Navarro-Ranninger, J. Med. Chem. 41 (1998) 1399.

[5] (a) D. Kovala-Demertzi, M.A. Demertzis, E. Filiou, A.A. Pantazaki, P.N. Yadav, J.R. Miller, Y. Zheng, D.A. Kyriakidis, Biometals 16 (2003) 411;
(b) Z. Iakovidou, E. Mioglou, D. Mourelatos, A. Kotsis, M.A. Demertzis, A. Papagoorgiou, P.N. Yadav, D. Kovala-Demertzi, Anticancer Drugs 12 (2001) 65;
(c) D. Kovala-Demertzi, M.A. Demertzis, V. Varagi, A. Papageorgiou, D. Mourelatos, E. Mioglou, Z. Iakovidou, A. Kotsis, Chemotherapy 44 (1998) 421.

[6] (a) D. Kovala-Demertzi, P. Nath Yadav, M.A. Demertzis, M. Coluccia, J. Inorg. Biochem. 78/4 (2000) 347;
(b) A. Papageorgiou, Z. Iakovidou, D. Mourelatos, E. Mioglou, L. Boutis, A. Kotsis, D. Kovala-Demertzi, A. Domopoulou, D.X. West, M.A. Demertzis, Anticancer Res. 17 (1997) 247;
(c) D. Kovala-Demertzi, A. Domopoulou, M.A. Demertzis, G. Valle, A. Papageorgiou, J. Inorg. Biochem. 68 (1997) 147.

[7] (a) D. Kovala-Demertzi, M.A. Demertzis, J.R. Miller, C. Papadopoulou, C. Dodorou, G. Filousis, J. Inorg. Biochem. 86 (2001) 555;
(b) D. Kovala-Demertzi, J.R. Miller, N. Kourkoumelis, S.K. Hadjikakou, M.A. Demertzis, Polyhedron 18 (1999) 1005;
(c) D. Kovala-Demertzi, A. Domopoulou, M.A. Demertzis, A. Papageorgiou, D.X. West, Polyhedron 16 (20) (1997) 3625.

[8] (a) P. Nath Yadav, M.A. Demertzis, D. Kovala-Demertzi, S. Skoulika, D.X. West, Inorg. Chim. Acta 349 (2003) 30;
(b) M.A. Demertzis, P. Nath Yadav, D. Kovala-Demertzi, Helv. Chim. Acta 89 (9) (2006) 1959;
(c) D. Kovala-Demertzi, N. Kourkoumelis, M.A. Demertzis, J.R. Miller, C.S. Frampton, J.K. Swearingen, D.X. West, Eur. J. Inorg. Chem. (2000) 727.

[9] A. Pasini, F. Zunino, Angew. Chem., Int. Ed. Engl. 26 (1987) 615.

[10] CAD-4 Software. Version 5.0, Enraf-Nonius, Delft, The Netherlands, 1989.

[11] C.K. Fair, MolEN: An Interactive Intelligent, System for Crystal Structure Analysis, User Manual, Enraf-Nonius, Delft, The Netherlands, 1990.

[12] L.J. Farrugia, J. Appl. Crystallogr. 32 (1999) 837.

[13] G.M. Sheldrick, SHELXS86, Acta Cryst., 1990, A46, 467–473.

[14] G.M. Sheldrick, SHELXL-97: Program for Crystal Structure Refinement, University of Göttingen, Göttingen, Germany, 1997.

[15] A.L. Spek, PLATON: A Multipurpose Crystallographic Tool. A Program for the Automated Generation of a Variety of Geometrical Entities, Utrecht University, Utrecht, The Netherlands, 2001.

[16] M.J. Frisch, G.W. Trucks, H.B. Schlegel, G.E. Scuseria, M.A. Robb, J.R. Cheeseman, J.A. Montgomery Jr., T. Vreven, K.N. Kudin, J.C. Burant, J.M. Millam, S.S. Iyengar, J. Tomasi, V. Barone, B. Mennucci, M. Cossi, G. Scalmani, N. Rega, G.A. Petersson, H. Nakatsuji, M. Hada, M. Ehara, K. Toyota, R. Fukuda, J. Hasegawa, M. Ishida, T. Nakajima, Y. Honda, O. Kitao, H. Nakai, M. Klene, X. Li, J.E. Knox, H.P. Hratchian, J.B. Cross, V. Bakken, C. Adamo, J. Jaramillo, R. Gomperts, R.E. Stratmann, O. Yazyev, A.J. Austin, R. Cammi, C. Pomelli, J.W. Ochterski, P.Y. Ayala, K. Morokuma, G.A. Voth, P. Salvador, J.J. Dannenberg, V.G. Zakrzewski, S. Dapprich, A.D. Daniels, M.C. Strain, O. Farkas, D.K. Malick, A.D. Rabuck, K. Raghavachari, J.B. Foresman, J.V. Ortiz, Q. Cui, A.G. Baboul, S. Clifford, J. Cioslowski, B.B. Stefanov, G. Liu, A. Liashenko, P. Piskorz, I. Komaromi, R.L. Martin, D.J. Fox, T. Keith, M.A. Al-Laham, C.Y. Peng, A. Nanayakkara, M. Challacombe, P.M.W. Gill, B. Johnson, W. Chen, M.W. Wong, C. Gonzalez, J.A. Pople, GAUSSIAN-03, Revision C.02, Gaussian, Inc., Wallingford, CT, 2004.

[17] A.D. Becke, J. Chem. Phys. 98 (1993) 5648.

[18] C. Lee, W. Yang, R.G. Parr, Phys. Rev. B 37 (1988) 785.

[19] P.J. Hay, W.R. Wadt, J. Chem. Phys. 82 (1985) 299.

[20] (a) E. Runge, E.K.U. Gross, Phys. Rev. Lett. 52 (1984) 997;
(b) P.N. Kapoor, R. Kakkar, J. Mol. Struct. (Theochem.) 679 (2004) 149;
(c) B. Machura, M. Jaworska, R. Kruszynski, Polyhedron 23 (2004) 2005.

[21] D. Andrae, U. Haussermann, M. Dolg, H. Stoll, H. Preuss, Theor. Chim. Acta 77 (1990) 123.

[22] J.V. Burda, M. Zeizinger, J. Sponer, J.J. Leszczynski, Chem. Phys. 113 (2000) 2224.
[23] C. Amovilli, V. Barone, R. Cammi, E. Cances, M. Cossi, B. Mennucci, C.S. Pomelli, J. Tomasi, Adv. Quantum Chem. 32 (1999) 227.
[24] P. Skehan, R. Storeng, D. Scudiero, A. Monks, J. Mcmahon, D. Vistica, J.T. Warren, H. Bokesch, S. Kenney, M.R. Boyol, J. Natl. Cancer Inst. 82 (1990) 1107.
[25] (a) M. Ohno, T. Abe, J. Immunol. Meth. 145 (1991) 199;
(b) T.J. Sabo, V.M. Dinovic, G.N. Kaluderovic, T.P. Stanojkovic, G.A. Bogdanovic, Z.D. Juranic, Inorg. Chim. Acta 358 (2005) 2239;
(c) T. Mosman, J. Immunol. Methods 65 (1983) 55.
[26] J. Marthakutty, V. Suni, C.R. Nayar, R. Maliyeckal, P. Kurup, H.-K. Fun, J. Mol. Struct. 705 (2004) 63.
[27] D. Kovala-Demertzi, P. Nath Yadav, J. Wiecek, S. Skoulika, T. Varadinova, M.A. Demertzis, J. Inorg. Biochem. 100 (9) (2006) 1558.

Available online at www.sciencedirect.com
ScienceDirect
Polyhedron 26 (2007) 2880–2884
POLYHEDRON
www.elsevier.com/locate/poly

Covalently bonded infinite zigzag chain structure in a novel Zn(II) complex of 2,5-dihydroxy-1,6-benzenedicarboxylic acid

Nour Eddine Ghermani [a,c], Georges Morgant [b,*], Jean d'Angelo [b,*], Didier Desmaële [b], Bernard Fraisse [c], François Bonhomme [a], Emma Dichi [d], Mehrez Sgahier [d]

[a] Laboratoire PPB, UMR CNRS 8612, Faculté de Pharmacie, IFR 141, Université Paris-Sud, 5 rue J.-B. Clément, 92296 Châtenay-Malabry, France
[b] Laboratoire Biocis, UMR CNRS 8076, Faculté de Pharmacie, IFR 141, Université Paris-Sud XI, 5 rue J.-B. Clément, 92296 Châtenay-Malabry, France
[c] Laboratoire SPMS, UMR CNRS 8580, Ecole Centrale Paris, Grande Voie des Vignes, 92295 Châtenay-Malabry, France
[d] Equipe Matériaux et Santé, EA 401, Faculté de Pharmacie, Université Paris-Sud, 5 rue J.-B. Clément, 92296 Châtenay-Malabry, France

Received 14 December 2006; accepted 23 January 2007
Available online 30 January 2007

Abstract

Reaction of the disodium salt of 2,5-dihydroxy-1,6-benzenedicarboxylic acid (DHBDC) and zinc sulfate in aqueous solution at room temperature yields complex $[Zn(H_2O)_2(DHBDC)]_n$. The coordination tetrahedron around Zn center exhibits a highly irregular geometry, two carboxylato oxygen atom and two water–ligand oxygen atoms occupying the coordination sites. Structural analyses of this complex reveal that the individual zero-dimensional units (0D) are covalently linked through their metal ends, forming infinite 1D zigzag chains. These chains, in turn, are engaged in 2D hydrogen bonding, resulting in a 3D supramolecular architecture.
© 2007 Elsevier Ltd. All rights reserved.

Keywords: Crystal structure; Zn(II) complex; 2,5-Dihydroxy-1,6-benzenedicarboxylic acid ligand; Infinite zigzag chain structure; Hydrogen-bonded 3D supramolecular architecture

1. Introduction

Zinc salicylate and homologues are of considerable interest, due to their wide potential applications. For example, they have been selected for use as anti-oxidants and stabilizers for polymers. They have also been employed in the coatings on paper used in carbonless copying paper [1]. In other respects, the anti-inflammatory and anti-convulsant activities of zinc salicylates were found to be more effective than their parent ligands in animal models of inflammation and epilepsy [2]. As part of a systematic program devoted to the study of structure–activity relationships of (salicylato)metal complexes [3], we were recently interested in the preparation of metal complexes of 2,5-dihydroxy-1,6-benzenedicarboxylic acid (DHBDC, **1**). Because of the presence of two salicylate sites, the latter ligand can accommodate two metallic centers, thereby possibly generating various molecular architectures.

Recently, a Zn(II) complex of ligand **1** has been synthesized via the solvothermal method (heating at 105 °C in a sealed tube a mixture of **1** and zinc nitrate in DMF/2-propanol/water). The individual units of this complex $[Zn_2(DHBDC)(DMF)_2 \cdot (H_2O)_2]$ self-assemble via covalent bonds, resulting in helical rods consisting of edge-sharing ZnO_6 octahedra alternately opposite and next-neighbor to form either a 3_1 or a 3_2 helix [4]. In the present paper, we show that a new type of Zn(II) complex of DHBDC was formed by mixing aqueous solutions of the disodium salt of **1** and of zinc sulfate at room temperature. The individual units of this complex $[Zn(H_2O)_2(DHBDC)]$ are covalently linked, forming infinite zigzag chains, the ZnO_4 tetrahedra being at the vertices of the zigzag. These

* Corresponding authors. Tel.: +33 146835648 (G. Morgant)/+33 146835699 (J. d'Angelo).
E-mail addresses: georges.morgant@u-psud.fr (G. Morgant), jean.dangelo@u-psud.fr (J. d'Angelo).

0277-5387/$ - see front matter © 2007 Elsevier Ltd. All rights reserved.
doi:10.1016/j.poly.2007.01.025

chains, in turn, are further engaged in two-dimensional hydrogen bonding, yielding a 3D supramolecular architecture.

2. Experimental

2.1. Materials

High purity 2,5-dihydroxy-1,6-benzenedicarboxylic acid (2,5-dihydroxyterephthalic acid) and zinc sulfate heptahydrate were purchased from Aldrich (USA) and used without further purification.

2.2. Physical measurement

Elemental analyses (C, H, and N) were performed on a Perkin–Elmer 2400 analyzer. The IR spectra were recorded with Bruker Vector 22 spectrometer. Thermogravimetric analysis (TGA) and magnetization study were carried out on a TA Instruments TGA Q500 apparatus. Calibration was performed at different temperatures using Curie magnetic transitions for the recommended materials: alumel (163 °C), nickel (354 °C); calibration (mass) was carried out using a standard mass of 100 mg, calibration of the furnace was made between 100 and 900 °C to verify thermocouple operation. All the experiments were performed under dry nitrogen, with a flow rate of 6×10^{-2} l min^{-1}. Analysis of compounds out of nitrogen purging was conducted at heating rate of 20 °C min^{-1}, in order to determine the percentage of mass loss with the best precision. Differential scanning calorimetry (DSC) experiment has been carried out with a TA Instruments Universal V4.2E apparatus under nitrogen flow. Samples are introduced in aluminum pans and covered with holed caps in view to avoid uncontrolled variation of pressure. Calibration of temperature has been performed with indium (156.6 °C) and tin (231.9 °C) of quality 5 N at heating rate of 10 °C min^{-1}.

2.3. Preparation of the complex $[Zn(H_2O)_2(C_8H_4O_6)]$ (2)

The disodium salt of 2,5-dihydroxy-1,6-benzenedicarboxylic acid was prepared by neutralizing the acid (0.400 g, 2 mmol) with 4 ml of 1 M NaOH (4 mmol). A solution of $ZnSO_4 \cdot 7H_2O$ (0.575 g, 2.1 mmol) in water (3 ml) was added, resulting in the immediate precipitation of transparency ivory crystals. These were filtered off, successively washed with acetic acid and water, and dried at room temperature under vacuo (20 Torr) over anhydrous magnesium sulfate. Yield: 0.545 g (90%). The product is stable in air and insoluble in water and common organic solvents such as ethanol, acetonitrile, acetone, chloroform, DMF, DMSO, pyridine, and acetic acid. *Anal.* Calc. for $C_8H_8O_8Zn$ (**2**): C, 32.30; H, 2.69. Found: C, 31.65; H, 2.64% . IR (neat, cm^{-1}): 3267 (m), 1580 (m), 1444 (s), 1334 (s), 1232 (s), 1119 (s), 914 (m), 879 (m), 799 (s).

Table 1
Crystal data and structure refinement parameters for $C_8H_8O_8Zn$ (**2**)

Empirical formula	$C_8H_8O_8Zn$
Molecular weight	297.52
Color	ivory
Crystal system	monoclinic
Space group	$C2/c$
a (Å)	15.493(5)
b (Å)	5.252(5)
c (Å)	12.214(5)
α (°)	90
β (°)	111.418(5)
γ (°)	90
V (Å^3)	925.2(10)
Z	8
D_{calc} (g cm^{-3})	2.136
Absorption coefficient (mm^{-1})	2.688
$F(000)$	600
Crystal size (mm)	$0.17 \times 0.22 \times 0.27$
θ Ranges (°)	3.58–29.60
$h/k/l$	−21 to 20/0 to 7/0 to 16
T (K)	100
Number of reflections collected	3018
Number of independent reflections	1180
Number of reflections used $\geqslant 2\sigma(I)$	1017
Parameters	78
R [F^2]	0.0214
wR [F^2]	0.0237
Goodness-of-fit on F	1.1071
Residual density (e Å^{-3})	−0.26; 0.46
Refine ls shift/su.max	0.0004

2.4. X-ray diffraction study

Diffraction data were collected on a Bruker SMART three axis diffractometer equipped with a SMART 1000 CCD area detector using graphite monochromated Mo Kα X-radiation (wavelength $\lambda = 0.71073$ Å) at 100.0(1) K. The low temperature was reached by an evaporated liquid nitrogen stream over the crystal, provided by the Oxford Cryosystem device. Data collection and processing were carried out using Bruker SMART programs [5] and empirical absorption correction was applied using SADABS computer program [5]. The structure was solved by direct methods SIR97 [6], and refined by full-matrix least-squares based on F^2 using CRYSTALS software [7]. All non-hydrogen atoms were anisotropically refined. The hydrogen atoms were located in difference Fourier maps. H atoms were refined isotropically with $U_{iso} = 1.20 U_{eq}$ where U_{eq} is the equivalent isotropic atomic displacement parameter of the attached atom. The crystal parameters, data collection and the refinement details of compound **2** reported in Table 1.

3. Results and discussion

3.1. Description of the crystal structure

The structure determination show that this complex crystallizes in $C2/c$ monoclinic space group. The asymmet-

ric unit contains one half of the formula unit, that can be represented by $[Zn(H_2O)_2(C_8H_4O_6)]$ (**2**). The canonical drawing and the CAMERON [8] molecular structure are represented in Figs. 1 and 2, respectively, with the atom numbering system used in Table 2, which lists the most relevant bond distances and angles. The coordination tetrahedron around Zn center is depicted in Fig. 3. In **2**, Zn^{II} is covalently bonded to one 2,5-dihydroxy-1,6-benzenedicarboxylate ligand and harnessed to two water molecules. Compound **2** is a monomeric complex in which the coordination tetrahedron around Zn^{II} exhibits a highly irregular geometry, two carboxylato oxygen atoms [O(1) and $O(1^i)$] and two water–ligand oxygen atoms [O(4) and $O(4^i)$] occupying the coordination sites. Zn–O(1) and Zn–O(4) bond distances are equal to 2.001(2) and 1.986(2) Å, respectively, values significantly different with respect to the estimated standard deviations. Since Zn–O(1) and Zn–O(2) distances are highly different [2.000(2) and 2.575(2) Å, respectively] it is clear that the 2,5-dihydroxy-1,6-benzenedicarboxylate anion acts as a monodendate ligand. Regarding angles around Zn(II) center, O(1)–Zn–$O(4^i)$ and $O(1^i)$–Zn–O(1) are significantly different (127.47° and 124.63°, respectively) while $O(4^i)$–Zn–O(1) and O(4)–Zn–$O(1^i)$ are identical (89.98°). The crystal packing is mainly governed by intermolecular hydrogen bonds implying each hydrogen atom of the water molecules [H(41) and H(42)] and the carboxylato and the phenoxo oxygen atoms of neighbor ligand molecules [$O(3^i)$ and $O(2^{ii})$; symmetry codes: (i) $x+1/2$, $y-1/2$, z; (ii) x, $y-1$, z], and one intramolecular hydrogen bond implying H(3) and O(1) (Fig. 4 and Table 3).

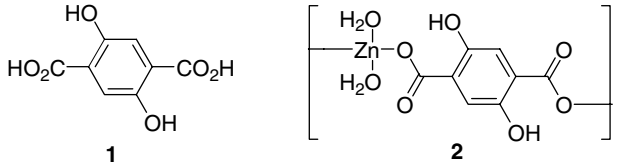


Fig. 1. Canonical representations of 2,5-dihydroxy-1,6-benzenedicarboxylic acid (**1**) and $[Zn(H_2O)_2(C_8H_4O_6)]$ (**2**).

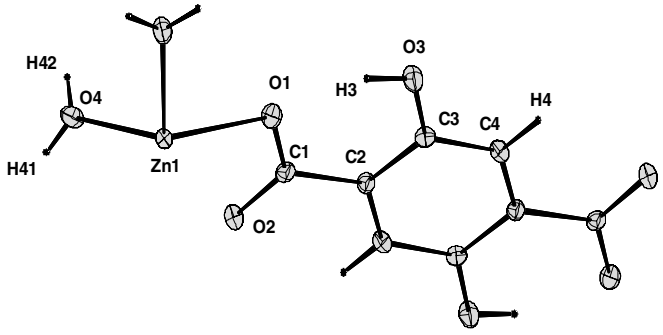


Fig. 2. Labeled CAMERON diagram of $[Zn(H_2O)_2(C_8H_4O_6)]$ (**2**). Ellipsoids are drawn at 50% probability level.

Table 2
Selected bond distances (Å) and bond angles (°) for $[Zn(H_2O)_2(C_8H_4O_6)]$ (**2**)

Bond lengths		*Bond angles*	
Zn–O(1)	2.001(2)	O(1)–Zn–O(4)	127.47(6)
Zn–O(2)	2.575(2)	$O(1^i)$–Zn–O(1)	124.63(6)
Zn–O(4)	1.986(2)	$O(4^i)$–Zn–O(1)	89.98(7)
Zn–C(1)	2.628(2)	Zn–O(1)–C(1)	103.89(9)
O(1)–C(1)	1.290(2)	O(1)–C(1)–O(2)	121.05(9)
O(2)–C(1)	1.243(2)	O(1)–C(1)–C(2)	117.05(9)
O(3)–C(3)	1.369(2)	O(2)–C(1)–C(2)	121.39(9)
C(1)–C(2)	1.497(2)	C(1)–C(2)–C(3)	121.56(9)
C(2)–C(3)	1.407(2)	C(2)–C(3)–O(3)	122.44(9)
C(3)–C(4)	1.392(2)	C(2)–C(3)–C(4)	119.66(9)
		O(3)–C(3)–C(4)	117.87(9)

Symmetry code: (i) $-x+2$, y, $-z+\frac{1}{2}$.

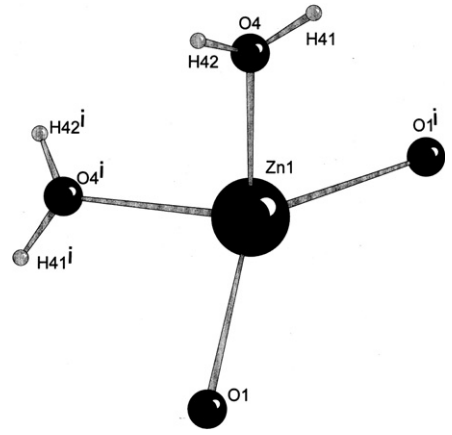


Fig. 3. Coordination tetrahedron around Zn center in $[Zn(H_2O)_2(C_8H_4O_6)]$ (**2**).

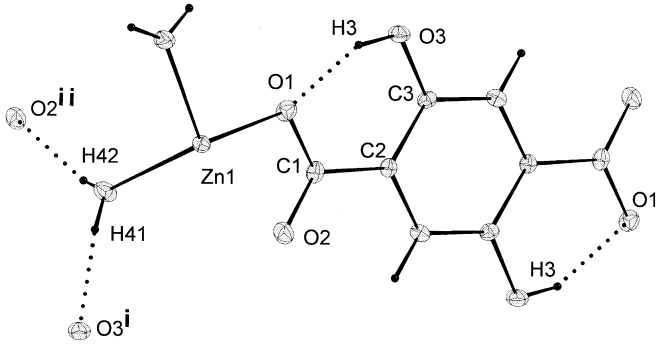


Fig. 4. Diagram of $[Zn(H_2O)_2(C_8H_4O_6)]$ (**2**) showing the H-bonded network (dashed lines). Symmetry codes: (i) $x+\frac{1}{2}, y-\frac{1}{2}, z$; (ii) $x, y-1, z$.

Table 3
H-bond donor/acceptor scheme (Å, °) for $[Zn(H_2O)_2(C_8H_4O_6)]$ (**2**)

D–H···A	*d*(D–H)	*D*(H···A)	∠(DHA)
O(3)–H(3)···O(1)	0.818(2)	1.817(2)	153.41(9)
O(4)–H(41)···$O(3)^i$	0.743(2)	2.011(2)	172.70(9)
O(4)–H(42)···$O(2)^{ii}$	0.763(2)	1.988(2)	155.58(9)

Symmetry codes: (i) $x+\frac{1}{2}, y-\frac{1}{2}, z$; (ii) $x, y-1, z$.

The individual zero-dimensional units (0D) are linked together in a covalent fashion through their metal ends, forming infinite 1D zigzag chains (Fig. 5). It is noteworthy that the cohesion of these chains is strengthened by the presence of internal hydrogen bonds. The intrachain separation of Zn centers is 10.93 Å, the metal atoms being at the vertices of the zigzag, with a Zn–Zn–Zn angle of 92.09°. The parallel chains are further engaged in hydrogen bonding implying H(42) with an interchain separation of 8.18 Å, resulting in 2D corrugated sheets (Fig. 6). These, in turn, self-assemble via hydrogen bonds implying H(41) with an interplanar separation of 6.12 Å, yielding a 3D

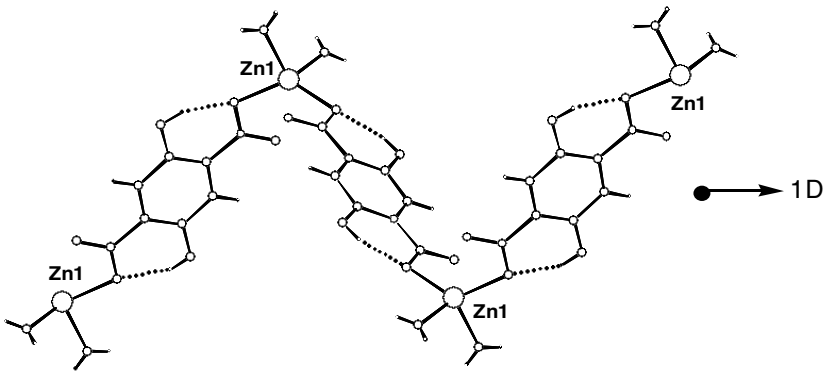


Fig. 5. Structure of part of $[Zn(H_2O)_2(C_8H_4O_6)]_n$ (**2**)$_n$, indicating the 1D zigzag chain structure with intrachain hydrogen bonds (dashed lines).

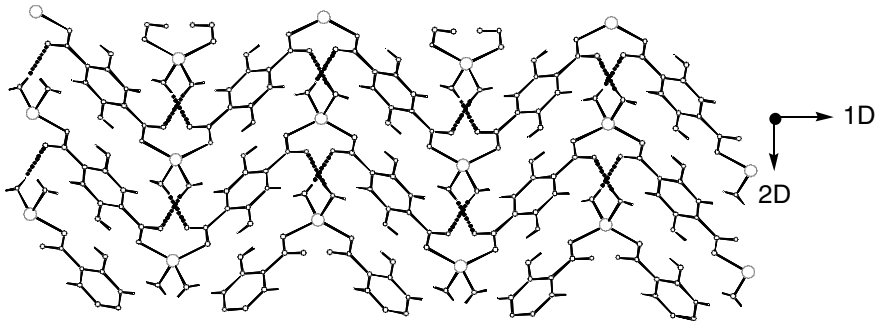


Fig. 6. 2D perspective diagram of packing of $[Zn(H_2O)_2(C_8H_4O_6)]_n$ (**2**)$_n$, showing the interchain H-bonded network (broken lines). Zn centers are symbolized by large circles.

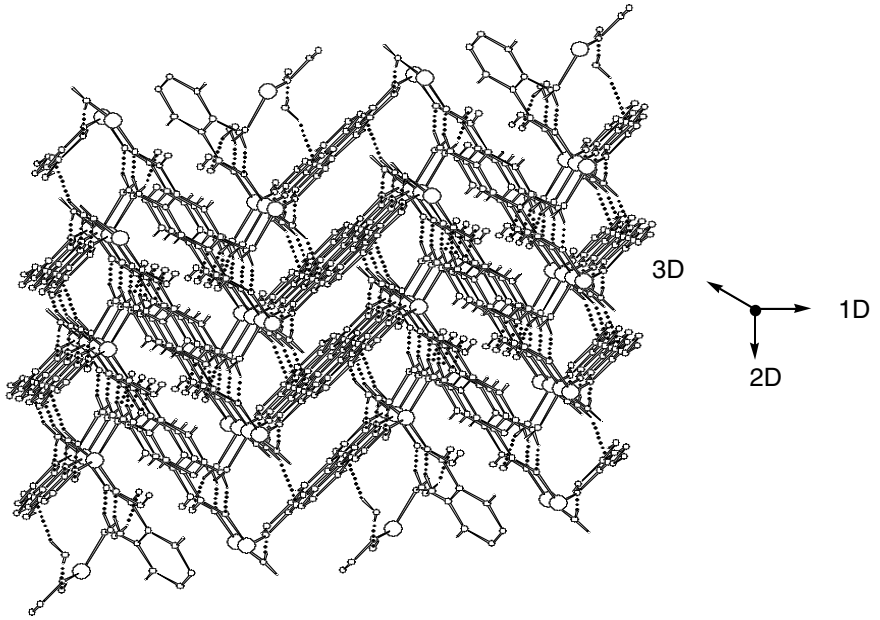


Fig. 7. 3D perspective diagram of packing of $[Zn(H_2O)_2(C_8H_4O_6)]_n$ (**2**)$_n$. Zn centers are symbolized by large circles.

supramolecular architecture (Fig. 7). The marked compactness of this architecture was reflected by the exceptionally high calculated density of compound **2** (2.14 g cm^{-3}, Table 1). In contrast, previously reported Zn(II) salicylates exhibited much lower densities, in the range of 1.26–1.76 g cm^{-3} [1,2a,2b,2c,3]. Note, however, that a density of 1.92 g cm^{-3} was reported for the above-mentioned Zn(II) complex of ligand **1**, elaborated according to the solvothermal method [4].

3.2. Thermal analysis

3.2.1. Thermolysis

Compound **2**, placed in a "vacuum sublimation apparatus", was heated gently until 320 °C (Woods metal bath) under reduced pressure (20 Torr). A white solid collected on the "cold finger" of the apparatus, consisting of pure hydroquinone (1,4-dihydroxybenzene). This was unambiguously identified by comparison with an authentic sample (melting point, R_f in TLC and ^{1}H NMR spectrum).

3.2.2. TGA, DSC, and magnetization studies

TGA analysis of **2** reveals a weight loss of 73.5% at 50–500 °C, with a rapid decrease between 260 and 280 °C, corresponding to loss of one molecule of water, two molecules of CO_2, and one molecule of hydroquinone (Calc. 72.6%). The non-volatile residue (26.5% of the starting material) corresponds to one molecule of ZnO (Calc. 27.4%). The DSC study of **2** reveals, as the main event, a narrow exotherm centered at 279 °C. Magnetization study of **2** reveals a rapid decrease between 270 and 288 °C. It is noteworthy that the TGA, DSC, and magnetization data match the thermal decomposition pattern of starting complex **2** (Section 3.2.1.).

4. Conclusion

We have shown that a new Zn(II) complex (**2**) of 2,5-dihydroxy-1,6-benzenedicarboxylic acid was formed by mixing aqueous solutions of the disodium salt of this acid and of zinc sulfate at room temperature. The individual units of this complex self-assemble in a covalent fashion, forming infinite zigzag chains which are further engaged in hydrogen bonding, leading to a 3D supramolecular architecture. There existed, as prior art, several compelling examples of salicylato(metal) complexes forming one-dimensional polymeric chains, particularly copper(II) [9], manganese(II, III) [10], and manganese(II) [11] derivatives. This work is being continued. The original metallo-organic framework of the present complex might be of peculiar interest in the design of functional materials. In particular, the close metal–metal distances observed in **2** (shortest separations: 6.12 and 8.18 Å) could be exploited for the elaboration of molecular conductors and/or magnetic materials.

5. Supplementary material

CCDC 630833 contains the supplementary crystallographic data for **2**. These data can be obtained free of charge via http://www.ccdc.cam.ac.uk/conts/retrieving.html or from the Cambridge Crystallographic Data Centre, 12 Union Road, Cambridge CB2 1EZ, UK; fax: (+44) 1223-336-033; or e-mail: deposit@ccdc.cam.ac.uk.

Acknowledgments

This paper is dedicated to Professor Dung Nguyen-Huy (Faculté de Pharmacie, Université Paris XI, France). Financial support of Université Paris XI, CNRS and Ecole Centrale Paris is gratefully acknowledged. The authors thank Mrs. S. Mairesse-Lebrun for performing elemental analyses.

References

[1] N.J. Brownless, D.A. Edwards, M.F. Mahon, Inorg. Chim. Acta 287 (1999) 89.
[2] (a) G. Morgant, B. Viossat, J.-C. Daran, M. Roch-Arveiller, J.-P. Giroud, D. Nguyen-Huy, J.R.J. Sorenson, J. Inorg. Biochem. 70 (1998) 137;
(b) A. Spasojevic-de Biré, N. Bouhmaida, A. Kremenovic, G. Morgant, N.E. Ghermani, J. Phys. Chem. A 106 (2002) 12170;
(c) P. Lemoine, B. Viossat, D. Nguyen-Huy, A. Tomas, G. Morgant, F.T. Greenaway, J.R.J. Sorenson, J. Inorg. Biochem. 98 (2004) 1734.
[3] G. Morgant, N. Bouhmaida, L. Balde, N.E. Ghermani, J. d'Angelo, Polyhedron 25 (2006) 2229.
[4] N.L. Rosi, J. Kim, M. Eddaoui, B. Chen, M. O'Keeffe, O.M. Yaghi, J. Am. Chem. Soc. 127 (2005) 1504.
[5] ASTRO (5.00), SAINT (5.007) and SADABS (5.007). Data Collection and Processing Software for the SMART System (5.054). Siemens (BRUKER-AXS) Analytical X-ray Instruments Inc., Madison, WI, 1998.
[6] A. Altomare, M.C. Burla, M. Camalli, G.L. Cascarano, G. Giacovazzo, A. Guagliardi, A. Grazia, G. Moliterni, G. Polidori, R. Spagna, SIR97 – a program for automatic solution of crystal structures by direct methods, J. Appl. Crystallogr. 32 (1999) 115.
[7] D.J. Watkin, C. K Prout, J.R. Carruthers, P.W. Betteridge, R.I. Prout, CRYSTALS Issue 11, Chemical Crystallography Laboratory, University of Oxford, UK, 2001.
[8] D.J. Watkin, C.K. Prout, L.J. Pearce, CAMERON, Chemical Crystallography Laboratory, University of Oxford, UK, 1996.
[9] H. Muhonen, Acta Crystallogr., Sect. B 38 (1982) 2041.
[10] X.S. Tan, J. Chen, Z.N. Chen, P.J. Zheng, W.X. Tang, Inorg. Chim. Acta 234 (1995) 27.
[11] M. Dereveux, M. Curran, M. McCann, R.M.T. Casey, V. McKee, Polyhedron 15 (1996) 2029.

Available online at www.sciencedirect.com
ScienceDirect
Polyhedron 26 (2007) 2885–2893
POLYHEDRON
www.elsevier.com/locate/poly

Mercury thiocyanate coordination polymers generated from rigid or flexible organic nitrogen donor-based ligands

Ghodrat Mahmoudi [a], Ali Morsali [a,*], Long-Guan Zhu [b]

[a] Department of Chemistry, Faculty of Sciences, Tarbiat Modares University, P.O. Box 14115-175, Tehran, Islamic Republic of Iran
[b] Department of Chemistry, Zhejiang University, Hangzhou 310027, PR China

Received 9 January 2007; accepted 23 January 2007
Available online 9 February 2007

Abstract

Four mercury(II) thiocyanate–organic polymeric complexes, $[Hg(\mu\text{-}4,4\text{-bipy})(SCN)_2]_n$ (**1**), $[Hg(\mu\text{-bpa})(SCN)_2]_n$ (**2**), $[Hg(\mu\text{-bpe})(SCN)_2]_n$ (**3**), $[Hg(\mu\text{-bpp})(SCN)_2]_n$ (**4**) {4,4-bipy = 4,4′-bipyridine, bpa = 1,2-bis(4-pyridyl)ethane, bpe = 1,2-bis(4-pyridyl)ethene and bpp = 1,3-di(4-pyridyl)propane} were prepared from reactions of mercury(II) thiocyanate with four rigid and flexible organic nitrogen donor-based ligands under thermal gradient conditions, brunched tube method. All these compounds were structurally determined by X-ray single-crystal diffraction. The thermal stabilities of compounds **1**–**4** were studied by thermal gravimetric (TG) and differential thermal analyses (DTA). Solid state luminescent spectra of compounds **1** and **3** indicate intense fluorescent emissions at 430 and 468 nm, respectively.
© 2007 Elsevier Ltd. All rights reserved.

Keywords: Mercury(II); 4,4′-Bipyridine; 1,2-Bis(4-pyridyl)ethane; 1,2-Bis(4-pyridyl)ethane; 1,3-Di(4-pyridyl)propane; Coordination polymer

1. Introduction

The metal coordination polymers have been studied widely due to an important interface between synthetic chemistry and materials science. Synthesis of metal coordination polymers is attracting interest in understanding how molecules can be organized and how functions can be achieved. Up to now, many attempts have been made to synthesize a variety of transitional metal complexes using the different oxobidentate ligands, and their structures and properties have been physically and chemically determined [1,2]. In contrast to coordination polymers of transition metal ions, the formation of polymers with heavy metal ions such as mercury(II) is unreasonably sparse when compared with that of some other metals. Mercury(II) compounds also offer attractive properties in terms of their potential applications as paper industry, paints, cosmetics, preservatives, thermometers, manometers, fluorescent lamps and mercury batteries [3]. Typically, the Hg(II) complexes with the rigid or flexible organic nitrogen donor-based ligands rarely reported until recently [4–7]. A search in the Cambridge Structural Database shows only 123 mercury(II) thiocyanate complexes [8] and the most of these mercury thiocyanate compounds are monomeric structures and coordination polymers type are rare. Continuing with our previous work on mercury(II) thiocyanate coordination polymers [9–17], in this paper, we report four new 1D coordination polymers of mercury(II) thiocyanate with organic nitrogen donor-based ligands, 4,4′-bipyridine (4,4-bipy), 1,2-bis(4-pyridyl)ethane (bpa), 1,2-bis(4-pyridyl)ethane (bpe) and 1,3-di(4-pyridyl)propane (bpp) (Fig. 1).

In this series of compounds four nitrogen donor-based ligands have been used. These ligands can be bridged and formed polymeric structures. In other hand, the SCN^- anions has been used as a counter-ion in these Hg(II) coordination polymers. This anion is a highly versatile ambidentate ligand with two donor atoms. It can coordi-

* Corresponding author. Tel.: +98 9122420568; fax: +98 2188006652.
E-mail address: morsali_a@yahoo.com (A. Morsali).

0277-5387/$ - see front matter © 2007 Elsevier Ltd. All rights reserved.
doi:10.1016/j.poly.2007.01.047

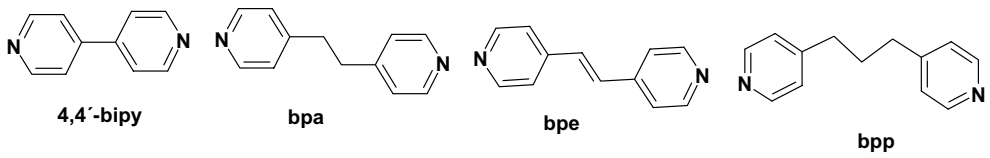


Fig. 1. Rigid and flexible organic nitrogen donor-based ligands used in the construction of mercury thiocyanate coordination polymer frameworks.

nate through either the N or the S atom, or both, giving rise to linkage isomers or polymers. The presence of thiocyanate anions as a bridging ligand and other different bridging ligands in one coordination system can form 1D, 2D or 3D coordination polymers either through thiocyanate-, or nitrogen donor-based ligand-bridging and or through both thiocyanate- and nitrogen donor-based ligand-bridging. Thus, in this context, it is still a great challenge to obtain the predicted products at these compounds. However, the rational construction of new structurally defined metal–organic frameworks using the thiocyanate- and nitrogen donor-based ligand-bridging strategy seems to be an excellent success.

2. Experimental

2.1. Materials and physical techniques

All reagents and solvents for the synthesis and analysis were commercially available and used as received. IR spectra were recorded using Perkin–Elmer 597 and Nicolet 510P spectrophotometers. Microanalyses were carried out using a Heraeus CHN-O-Rapid analyzer. Melting points were measured on an Electrothermal 9100 apparatus and are uncorrected. The thermal behavior was measured with PL-STA 1500 apparatus. ^{1}H and ^{13}C NMR spectra were measured with a BRUKER DRX-500 AVANCE spec-

Table 1
Crystal data and structure refinement for compounds **2**–**4**

Identification code	$[Hg(\mu\text{-bpa})(SCN)_2]_n$	$[Hg(\mu\text{-bpe})(SCN)_2]_n$	$[Hg(\mu\text{-bpp})(SCN)_2]_n$
Empirical formula	$C_{14}H_{12}HgN_4S_2$	$C_{14}H_{10}HgN_4S_2$	$C_{15}H_{14}HgN_4S_2$
Formula weight	500.99	498.97	515.01
Temperature	295(2)	295(2)	297(2)
Wavelength	0.71073	0.71073	0.71073
Crystal system	monoclinic	orthorhombic	monoclinic
Space group	$P2_1/c$	$Pbnn$	$P2_1/c$
Unit cell dimensions			
a (Å)	9.2952(7)	8.126(3)	10.0861(15)
b (Å)	6.1245(5)	13.037(3)	18.493(3)
c (Å)	14.5597(11)	15.075(3)	9.9968(14)
α (°)	90.00	90.00	90.00
β (°)	95.379(1)	90.00	105.348(5)
γ (°)	90.00	90.00	90.00
Volume (Å^3)	825.21(11)	1597.2(7)	1798.1(5)
Z	2	4	4
Density (calculated) (g cm^{-3})	2.016	2.075	1.902
Absorption coefficient (mm^{-1})	9.576	9.895	8.792
$F(000)$	472	936	976
Crystal size (mm^3)	$0.32 \times 0.28 \times 0.24$	$0.31 \times 0.24 \times 0.18$	$0.40 \times 0.20 \times 0.20$
Theta range for data collection (°)	2.2–27.8	3.1–27.5	2.09–28.00
Index ranges	$-11 \leqslant h \leqslant 11$, $-7 \leqslant k \leqslant 7$, $-17 \leqslant l \leqslant 17$	$-10 \leqslant h \leqslant 10$, $-16 \leqslant k \leqslant 16$, $-19 \leqslant l \leqslant 19$	$-11 \leqslant h \leqslant 13$, $-13 \leqslant k \leqslant 24$, $-13 \leqslant l \leqslant 10$
Reflections collected	1473	1833	4342
Independent reflections	1419	1287	2833
Absorption correction	multi-scan	multi-scan	multi-scan
Maximum and minimum transmission	0.2071 and 0.1496	0.1494 and 0.2689	0.165 and 0.034
Refinement method	full-matrix least-squares on F^2	full-matrix least-squares on F^2	full-matrix least-squares on F^2
Data/restraints/parameters	1473/0/97	1833/0/96	4342/12/210
Goodness-of-fit on F^2	1.011	1.021	1.014
Final R indices $[I > 2\sigma(I)]$	$R_1 = 0.0267$ $wR_2 = 0.0659$	$R_1 = 0.0249$ $wR_2 = 0.0551$	$R_1 = 0.0410$ $wR_2 = 0.1052$
R Indices (all data)	$R_1 = 0.0277$ $wR_2 = 0.0663$	$R_1 = 0.0417$ $wR_2 = 0.0608$	$R_1 = 0.0641$ $wR_2 = 0.1126$
Largest difference in peak and hole (e/Å^{-3})	2.087/−1.592.	−0.702/0.592	1.487/−1.609

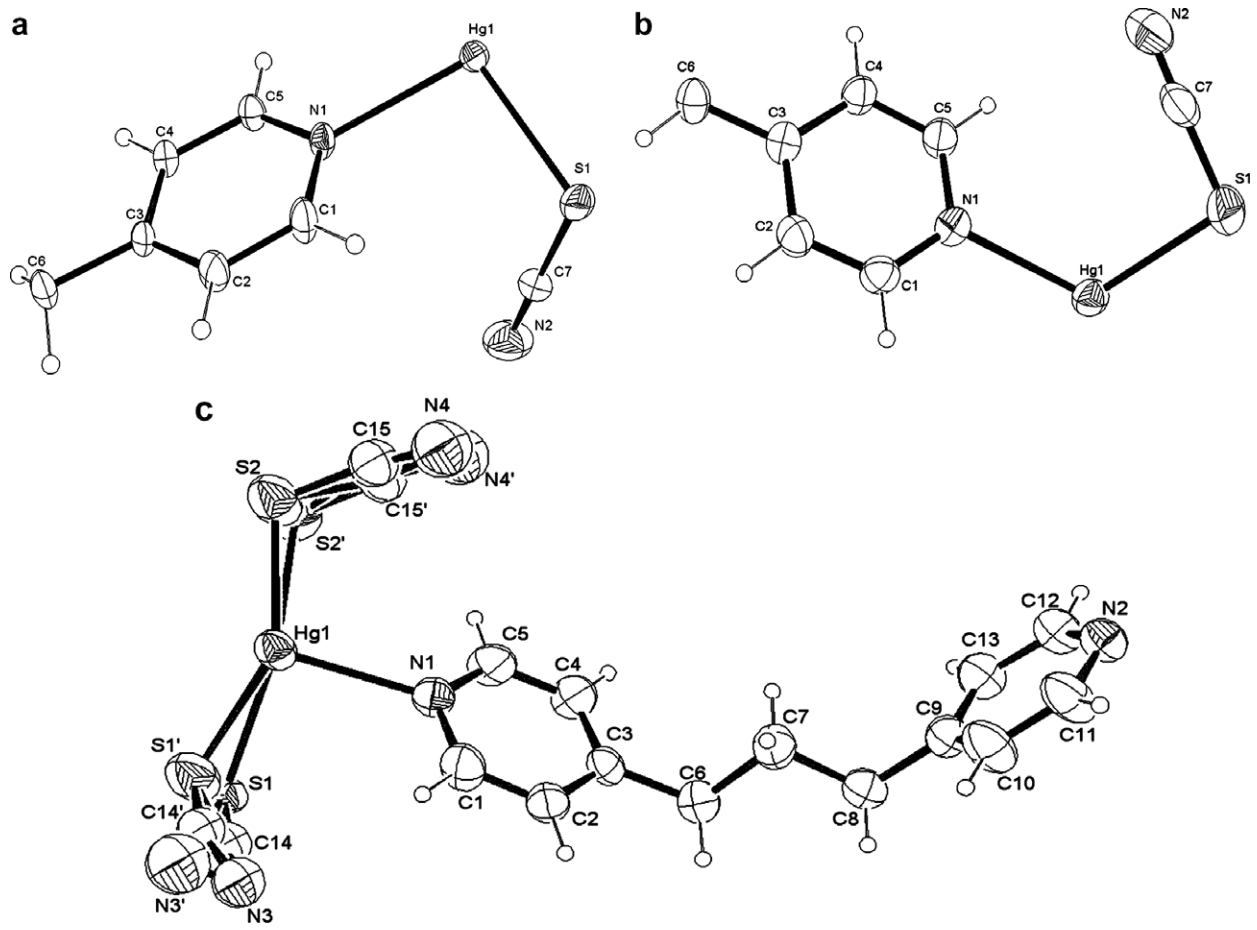


Fig. 2. The ORTEP and repeating units of the (a) $[Hg(\mu\text{-bpa})(SCN)_2]_n$, (b) $[Hg(\mu\text{-bpe})(SCN)_2]_n$ and (c) $[Hg(\mu\text{-bpp})(SCN)_2]_n$. Ellipsoids 30% probability.

trometer at 500 MHz and all chemical shifts are reported in δ units downfield from Me_4Si. The luminescent properties were measured with spectrofluorophotometer Shimadzu RF-5000.

Crystallographic measurements were made using a Bruker CCDC area detector system. The intensity data were collected using graphite monochromataed Mo Kα radiation ($\lambda = 0.71073$ Å). Accurate unit cell parameters and an orientation matrix for data collection were obtained from least-squares refinement. The structures were solved by direct methods and refined by full-matrix least-squares techniques on F^2. The structures were solved and refined with the program system SHELXTL [18]. The molecular structure plots were prepared by using the ORTEP III [19] and Mercury [20]. Crystallographic data and details of the data collection and structure refinements are listed in Table 1. Anisotropy thermal parameters, observed and calculated structure factors, full lists of bond distances, bond angles and torsion angles are given in the supplementary material. ORTEP diagrams and perspective view of the packing are shown in Figs. 2–4.

2.2. Syntheses of the compounds *1–4*

The different synthetic approaches have been offered for preparation of coordination polymers that some of them are (1) slow diffusion of the reactants into a polymeric matrix, (2) diffusion from the gas phase, (3) evaporation of the solvent at ambient or reduced temperatures, (4) precipitation or recrystallisation from a mixture of solvents, (5) temperature controlled cooling and (6) hydrothermal synthesis. I this paper, we use another simple method for construction of multi-dimensional heavy metal ion coordination polymers, brunched tube method [13,21]. The brunched tube method was employed for synthesis and preparation of suitable single crystals. This method is a straight forward, chip and trouble-free and can be used for preparation of all of this type coordination polymer, $HgL(SCN)_2$.

2.2.1. General procedure

The ligand (0.5 mmol) and mercury(II) thiocyanate (0.5 mmol) were placed in the bottom of main of a brunched tube. Methanol was carefully added to fill both arms, the tube sealed and the main arm immersed in oil bath at 60 °C while the brunched arm was at ambient temperature. After 2–7 days, very suitable single crystals had deposited in the cooler arm which was filtered off, washed with acetone and air dried.

Compound 1. [Reactant materials: 4,4′-bipy, mercury(II) thiocyanate].

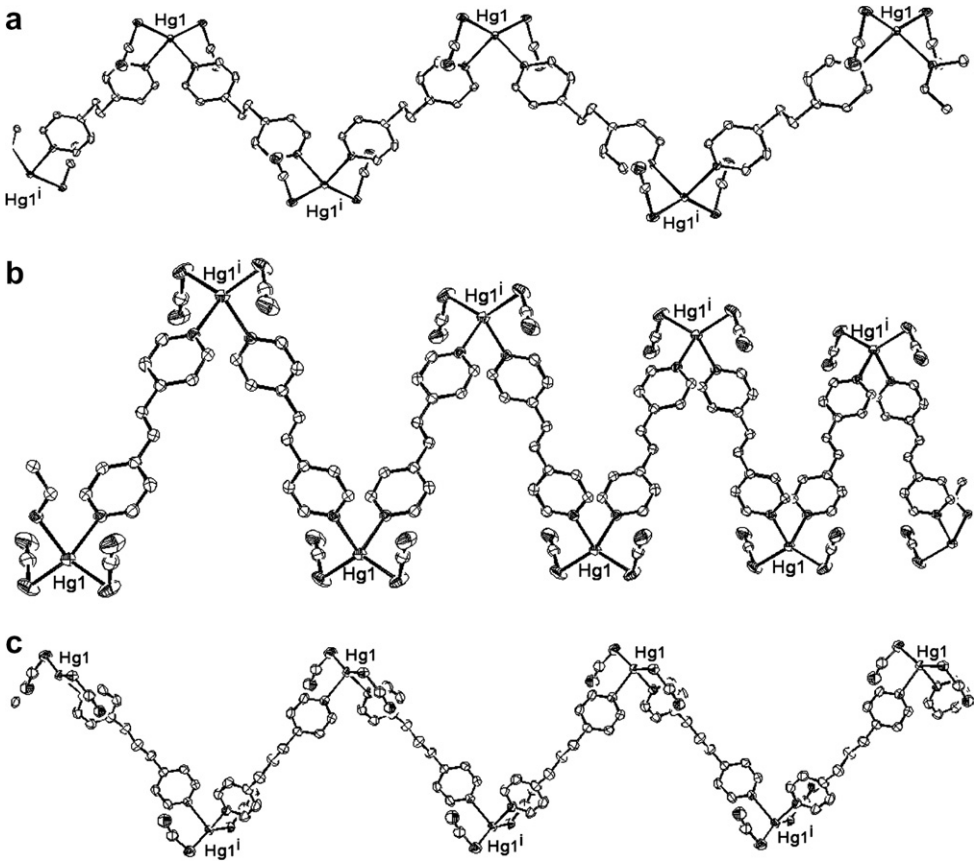


Fig. 3. 1D zigzag network of the (a) $[Hg(\mu\text{-bpa})(SCN)_2]_n$, (b) $[Hg(\mu\text{-bpe})(SCN)_2]_n$ and (c) $[Hg(\mu\text{-bpp})(SCN)_2]_n$. (i) $-x, -y, -z$ for compounds **2** and **3**, (i) $-x, y+1/2, -z+1/2$ for compounds **4**.

Product: Colorless crystals, m.p. 187.5 °C. Yield: 0.095 g, 40%. *Anal.* Calc. for $C_{12}H_8HgN_4S_2$: C, 30.47; H, 1.69; N, 11.84. Found: C, 30.10; H, 1.20; N, 11.70%.

IR (cm^{-1}) selected bands: 622(s); 804(s); 1212(m); 1390(s); 1588(vs); 2095(vs); 3050(w). ^1H NMR (DMSO): 8.10–8.20(q, 1H) and 8.90–9.00(q, 1H) ppm. ^{13}C–{^1H} NMR (DMSO): 123.5; 146.6 and 151.5 ppm.

Compound ***2***. [Reactant materials: (bpa, mercury(II) thiocyanate)].

Product: Colorless crystals, m.p. 149 °C. Yield: 0.130 g, 52%. *Anal.* Calc. for $C_{14}H_{12}HgN_4S_2$: C, 33.53; H, 2.40; N, 11.17. Found: C, 33.20; H, 2.45; N, 11.30%.

IR (cm^{-1}) selected bound: 533(s), 820(s), 1006(m), 1066(w), 1415(s), 1596(vs), 2070(vs), 2960(w), 3055(w). ^1H NMR (DMSO, δ): 3.00(s, 1H), 7.40(q, 1H) and 8.50(q, 1H) ppm. ^{13}C–{^1H} NMR (DMSO, δ): 34.4, 124.7, 149.9 and 151.3 ppm.

Compound ***3***. [Reactant materials: (bpe, mercury(II) thiocyanate)].

Product: Colorless crystals, m.p. 227 °C. Yield: 0.139 g, 56%. *Anal.* Calc. for $C_{14}H_{10}HgN_4S_2$: C, 33.67; H, 2.00; N, 11.22. Found: C, 33.80; H, 2.25; N, 11.50%.

IR (cm^{-1}) selected bound: 544(s), 820(s), 1005(w), 1062(w), 11413(w), 1592(vs), 2055(s) and 3045(w). ^1H NMR (DMSO, δ): 7.50(s, 1H), 7.60(m, 2H) and 8.6 0(m, 3H) ppm. ^{13}C–{^1H} NMR (DMSO, δ): 121.7, 144.1, 150.7 and 178.4 ppm.

Compound ***4***. [Reactant materials: (bpp, mercury(II) thiocyanate)].

Product: Colorless crystals, m.p. 137.5 °C. Yield: 0.108 g, 42%. *Anal.* Calc. for $C_{15}H_{14}HgN_4S_2$: C, 34.95; H, 2.72; N, 10.87. Found: C, 35.20; H, 2.50; N, 10.55%.

IR (cm^{-1}) selected bound: 507(m), 808(m), 1008(w), 1065(w), 1210(w), 1416(m), 1600(s), 2080(vs) and 3025(w). ^1H NMR (DMSO, δ): 2.10(m, 1H), 2.80(t, 2H), 7.50(q, 2H) and 8.54(q, 2H) ppm. ^{13}C–{^1H} NMR (DMSO, δ): 29.76, 33.74, 124.81, 149.94 and 152.46 pp.

3. Results and discussion

3.1. Synthesis and spectroscopy

Reaction between mercury(II) thiocyanate and four rigid or flexible organic nitrogen donor-based ligands under thermal gradient conditions, brunched tube method, provided crystalline materials analyzing as $[Hg(\mu\text{-}4,4\text{-bipy})(SCN)_2]_n$ (**1**), $[Hg(\mu\text{-bpa})(SCN)_2]_n$ (**2**), $[Hg(\mu\text{-bpe})(SCN)_2]_n$ (**3**) and $[Hg(\mu\text{-bpp})(SCN)_2]_n$ (**4**). The relatively weak absorption bands around 3025–3055 cm^{-1} in IR spectra is due to the C–H modes involving the aro-

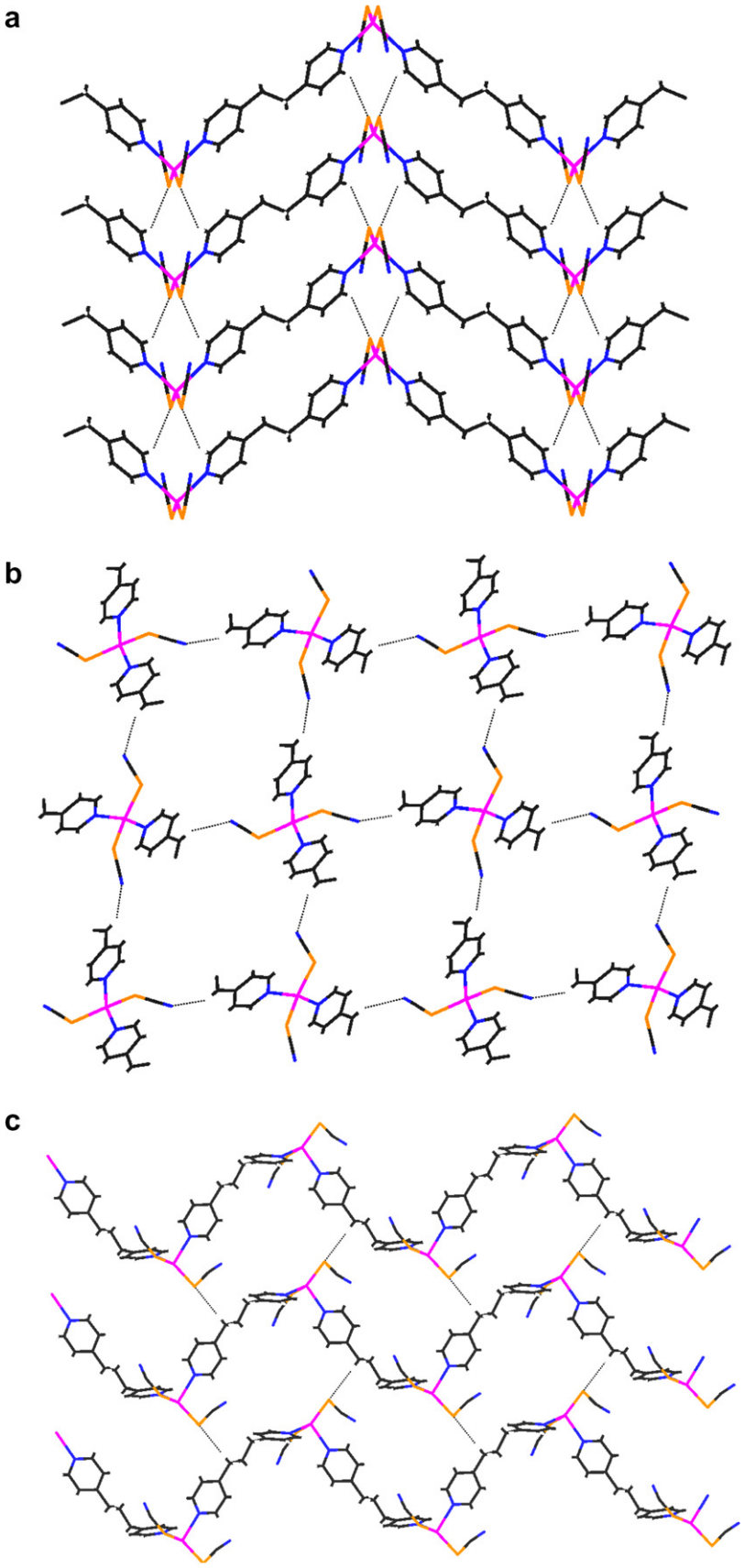


Fig. 4. Showing crystal packing of (a) S···HC interactions in the $[Hg(\mu\text{-bpa})(SCN)_2]_n$ (**2**) and (b) N···HC interactions in the $[Hg(\mu\text{-bpe})(SCN)_2]_n$ (**3**) (c) S···HC interactions in the $[Hg(\mu\text{-bpp})(SCN)_2]_n$ (**4**).

matic ring hydrogen atoms.The absorption bands with variable intensity in the frequency range 1404–1600 cm^{-1} correspond to vibrations of the pyridyl rings of ligands. The strong sharp singles stretching at 2095, 2070, 2055 and 2080 cm^{-1} are due to $\nu(SCN^-)$ in the infrared spectra of compounds **1**–**4**, respectively. These bands confirm the thiocyanato-S coordination with the mercury atom [22]. The SCN^- anion is a highly versatile ambient ligand with two donor atoms. It can coordinate through either the nitrogen or the sulfur atom, or both, giving rise to linkage isomers or polymers. The modes of mercury(II) coordination of thiocyanate anion is the best understood in terms of the hard and soft acid–base concept developed by Pearson, Basolo, and Burmeister. In accordance with the hard-soft acid–base concept, the S atom of the SCN^- ligand, being a soft base, preferentially coordinates to the soft acid whereas the N atom, being a hard base, preferentially coordinates to the hard acid. In the Zn–Cd–Hg triad, the Zn(II) complexes tend to be N-bonded, while the Hg(II) complexes are almost always S-bonded. Our findings together with the results concerning SCN^- in **1**–**4** suggest that the thiocyanate ligand has a strong tendency to coordinate mercury(II) ions through its sulfur atoms. The FT–IR results are consistent with the crystallographic study. The ^1H NMR spectrum of the DMSO solution of the compounds **1**–**4** displays two distinct resonance signals assigned to two different protons of ''py'' groups of the ligands 4,4-bipy, bpa, bpe and bpp. The ^1H NMR spectrum of the compounds **2** and **3** displays one other signals at 3.00 and 7.50 ppm assigned to protons of —CH=CH— and —CH_2—CH_2— group of ligands bpa and bpe molecules, respectively. The ^1H NMR spectrum of the compound **4** displays two other signals at 2.10 and 2.80 ppm assigned to protons of —CH_2—CH_2—CH_2— of ligand bpp. The ^{13}C NMR spectrum of the DMSO solution of the compounds **1**–**4** displays three distinct resonance signals assigned to the aromatic carbons of ''py'' groups of the ligands 4,4-bipy, bpa, bpe and bpp. The ^{13}C NMR spectrum of the **2** and **3** displays one other signals at 34.4 and 121.7 ppm assigned to carbons of —CH=CH— and —CH_2—CH_2— group of ligands bpa and bpe, respectively. The ^{13}C NMR spectrum of the compound **4** displays two other signals at 29.76 and 33.74 ppm assigned to carbons of —CH_2—CH_2—CH_2— of ligand bpp. However, the NMR data of the compounds **1**–**4** are not significantly different from free ligands, 4,4-bipy, bpa, bpe and bpp. This point shows that the compounds break up in DMSO solution and polymeric structures may retain in the DMSO solution and we use from NMR data only for characterization of new compounds.

3.2. Structural analysis of compounds *1*–*4*

Crystal data and structure refinements for compounds **2**–**4** are given in Table 1. Selected bond distances and angles for compounds **2**–**4** are listed in Table 2. Single X-ray crystal analysis reveals that $[Hg(\mu\text{-bpa})(SCN)_2]_n$ (**2**) and $[Hg(\mu\text{-bpp})(SCN)_2]_n$ (**4**) crystallize in monoclinic with space groups of $P2_1/c$ whereas the $[Hg(\mu\text{-bpe})(SCN)_2]_n$ (**3**) crystallize in orthorhombic with space groups *Pbnn*. The crystal structure **2**, **3** and **4** consists of one-dimensional zigzag chain type (Figs. 2 and 3). The ligands bpa, bpe and bpp as well as two thiocyanate anions in compounds **2**, **3** and **4** generate angular nodes of metal moieties. The nitrogen atoms of ligands ''bpa'', ''bpe'' and ''bpp'' are linked to two different mercury atoms and the thiocyanate atoms are coordinated to mercury *via* S atoms but are not bridged to two mercury atoms. The coordination number of Hg atoms is four (two of ''bpa'', ''bpe'' and ''bpp'' and two of sulfur atoms) and the environment is a distorted tetrahedral. The Hg–N and Hg–S bond lengths in the compounds **2**, **3** and **4** are nearly comparable whereas N–Hg–N and S–Hg–S bond angles in the compounds **2**, **3** and **4** are diverse, the N–Hg–N and S–Hg–S are 94.3(2)° and 137.46(8)° in the compound **2**, respectively, the N–Hg–N and S–Hg–S are 85.08(15)° and 123.27(9)° in the compound **3**, and the N–Hg–N and S–Hg–S are 92.55(19)° and 149.65(17)° in the compound **4**, respectively. This may be consistent with the assumption that bpa and bpp are the more flexible than bpe and may impose a better positioning of the donor atoms for forming one-dimensional zigzag chain and reduce the strict effect.

To find the packing controller factors a search was generally made for weak interactions of compounds **2** and **3**. The interesting feature compounds **2** and **3** is that, there are the weak hydrogen bonding of $C–H_{py}\cdots S_{thiocyanate}$

Table 2
Selected bond lengths (Å) and angles (°) for compounds **2**–**4**

$[Hg(\mu\text{-bpa})(SCN)_2]_n$		$[Hg(\mu\text{-bpe})(SCN)_2]_n$		$[Hg(\mu\text{-bpp})(SCN)_2]_n$	
Hg(1)–N(1)	2.362(4)	Hg(1)N(1)	2.349(3)	Hg(1)–S(1)	2.486(5)
Hg(1)–S(1)	2.4279(15)	Hg(1)–S(1)	2.4221(16)	Hg(1)–S(2)	2.415(9)
N(1)–Hg(1)– N(1)	94.3(2)	N(1)–Hg(1)–N(1)	85.08(15)	Hg(1)–N(1)	2.426(5)
N(1)–Hg(1)–S(1)	110.61(12)	N(1)–Hg(1)–S(1)	103.62(10)	Hg(1)–N(2)	2.340(6)
N(1)–Hg(1)–S(1)	98.12(12)	N(1)–Hg(1)–S(1)	117.69(9)	Hg(1)–N(3)	3.023(7)
S(1)–Hg(1)–S(1)	137.46(8)	S(1)–Hg(1)–S(1)	123.27(9)	N(2)–Hg(1)–S(2)	98.0(2)
				N(2)–Hg(1)–N(1)	92.55(19)
				S(2)–Hg(1)–N(1)	107.80(18)
				N(2)–Hg(1)–S(1)	106.28(17)
				S(2)–Hg(1)–S(1)	148.65(17)

and $C–H_{py}\cdots N_{thiocyanate}$ interactions in the compound **3** and **4**, respectively, as shown in Fig. 4. In compound **2** (Fig. 4a), there are C–H···S interactions between sulfur atoms of thiocyanate anions and hydrogen atoms of pyridyl with the distances of S···HC(py) = 2.698 Å, {HC(py)···S = 3.604 Å and ∠S···H–C = 133.75°}. In compound **3** (Fig. 4b), there are C–H···N interactions between nitrogen atoms of thiocyanate anions and hydrogen atoms of $–CH_2–$ with the distances of N···HC = 2.682 Å, {HC···N = 3.435 Å and ∠N···H–C = 138.49°}. In compound **4** (Fig. 4c), there are C–H···S interactions between sulfur atoms of thiocyanate anions and hydrogen atoms of $–CH_2–$ with the distances of S···HC = 2.989 Å, {HC···S = 3.754 Å and ∠S···H–C = 147.33°}.

In compounds **2**, **3** and **4** the C–H···S and C–H···N distances suggest strong interactions within this class of weak non-covalent contacts [23]. Consequently, C–H···S and C–H···N interactions, grow the 1D structures compounds **2**–**4** into a hybrid two- and three-dimensional networks, respectively. The thiocyanate anion in the compound **4** is disordered.

Meanwhile the other analogue of compounds **2**, **3** and **4** with ligand 4,4-bipyridine (4,4-bipy), $[Hg(\mu\text{-}4,4\text{-bipy})(SCN)_2]_n$ (**1**), has been synthesized by this method too and has been structurally characterized [13]. The structural of $[Hg(\mu\text{-}4,4\text{-bipy})(SCN)_2]_n$ (**1**) complex is also 1D Zigzag chain type, similar to compounds **2**, **3** and **4**. The thermal and fluorescence studies of compound **1** in this paper are reported.

3.3. Thermogravimetric analysis

In order to examine the thermal stability of the four compounds, thermal gravimetric (TG) and differential thermal analyses (DTA) were carried out for compounds **1**–**4** between 30 and 700 °C in the static atmosphere of air. Compound **1** is stable up to 197 °C at which temperature it begins to decompose. The TG curve of compound **1** indicates the release of 4,4-bipy molecule take place at 197–260 °C with one exothermic effect at 200 °C (Fig. 5). Decomposition of the thiocyanate anions seems to take place at 274 °C with one exothermic effect at 380 °C. The solid residue formed at around 400 °C is suggested to be HgO that under higher temperature is evaporated. The thermal decomposition behavior of compounds **2**–**4** is fairly similar with compound **1** and in the all compounds first the ligand release at 197–260 °C. The solid residue formed at around 265 °C suggested to be ligand-free $Hg(SCN)_2$ which is stable up to 390 °C and under higher temperature with one exothermic effect is decomposed (Figures S1–S3). In summary, the thermogravimetric analysis shows that all four frameworks have a remarkably thermal stability and only decompose above temperature of ca. 200 °C.

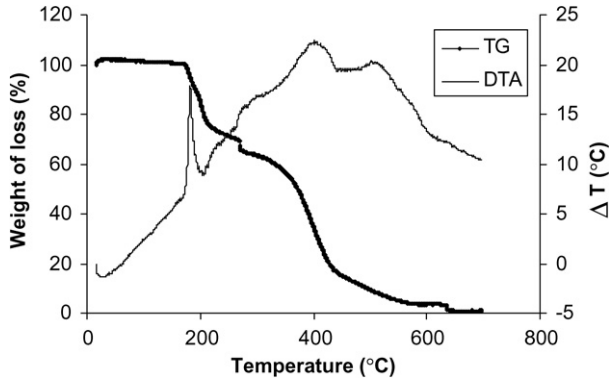


Fig. 5. Thermal behaviour of $[Hg(\mu\text{-}4,4'\text{-bipy})(SCN)_2]_n$ (**1**).

3.4. Luminescent properties

The fluorescence spectra of compounds **1**–**4** have been studied in the solid state. From the four compounds reported here only the compounds **1** and **3** have shown luminescent properties in solid (Figures S4 and S5) and however the UV/Vis and fluorescence spectra of the compounds **1** and **3** were studied. The UV/Vis spectra of compounds **1** and **3** in methanol display intense absorption bands with $\lambda_{max} = 265$ and $\lambda_{max} = 239$ nm (Figures S4 and S5), respectively, indicating that electronic transitions are mostly π–π^*, originating from the pyridyl groups of ligands 4,4′-bipy and bpe. The compounds **1** and **3** show broad emission bands with the maximum intensities at 430 and 468 nm upon excitation at 300 nm, respectively (Figures S4 and S5). These fluorescent emissions can be tentatively assigned to the intraligand fluorescence emission as similar emissions at 430 and 470 nm upon the same excitation at 300 nm (Figures S4 and S5) can also be observed for the free ligands 4,4′-bipy and bpe, respectively.

4. Conclusions

Four mercury(II) coordination polymers with the ligands 4,4-bipy, bpa, bpe and bpp, $[Hg(\mu\text{-}4,4\text{-bipy})(SCN)_2]_n$ (**1**), $[Hg(\mu\text{-bpa})(SCN)_2]_n$ (**2**), $[Hg(\mu\text{-bpe})(SCN)_2]_n$ (**3**), $[Hg(\mu\text{-bpp})(SCN)_2]_n$ (**4**), have been synthesized and characterized. The compounds are structurally similar showing one-dimensional zigzag motifs. In all four compounds the thiocyanate ions are coordinated as unidentate ligand via only sulfur atom. It is found that these 1D coordination polymers further extends into 2D and 3D networks via non-classical hydrogen bonding and extensive weak non-covalent interactions seem to play an important role in the crystal packing of the non-covalent frameworks. It seems that, in contrast to other previously reported $M(SCN)_2$ coordination polymers of the different ligands [24–29] that the thiocyanate anions are bridged and contain two- or three-dimensional polymers. In other word, the Hg^{II} coordination polymers with other counter-ions such as I^- and CN^- have been reported and showed that these anions were bridged and could increase structural dimensionality [30–32]. The

$Hg(SCN)_2$ coordination polymers with these ligands reported here result in the formation of only one-dimensional polymers, and thiocyanate thus seems to be the counter-ion of choice when one wants to prepare one-dimensional of rarely reported Hg^{II} coordination polymers. However this research not only shows the significant influences of the coordination modes and flexibilities of the ligands 4,4-bipy, bpa, bpe and bpp on the structural topology but also illustrates the effect of the counter-ions, here thiocyanate ions, on the polymeric components, which provides valuable instructions for the rational design of coordination polymers with desired molecular architectures. Also this study demonstrates the mercury(II) thiocyanate tend to form compounds with coordination number of four and consequently act in same form of coordination polymers with bridging bidentate ligands.

Acknowledgement

This work was supported by the Iran National Science Foundation (Project Number 84118).

Appendix A. Supplementary material

CCDC 632616, 632617 and 632618 contain the supplementary crystallographic data for **2**, **3** and **4**. These data can be obtained free of charge via http://www.ccdc.cam.ac.uk/conts/retrieving.html, or from the Cambridge Crystallographic Data Centre, 12 Union Road, Cambridge CB2 1EZ, UK; fax: (+44) 1223-336-033; or e-mail: deposit@ccdc.cam.ac.uk. Supplementary data associated with this article can be found, in the online version, at doi:10.1016/j.poly.2007.01.047.

References

[1] (a) H.K. Chae, D.Y. Siberio-Perez, J. Kim, Y. Go, M. Eddaoudi, A.J. Matzger, M. O'Keeffe, O.M. Yaghi, Nature 427 (2004) 523;
(b) Y. Kim, M. Suh, D.Y. Jung, Inorg. Chem. 43 (2004) 245;
(c) Z. Huang, H.-B. Song, M. Du, S.-T. Chen, X.-H. Bu, J. Ribas, Inorg. Chem. 43 (2004) 931;
(d) A.P. Carvalho, C. Castanheira, B. Cardoso, J. Pires, A.R. Silva, C. Freire, B. de Castro, M.B. de Carvalho, J. Mater. Chem. 14 (2004) 374;
(e) J.Y. Lu, A.M. Babb, Chem. Commun. (2003) 1346;
(f) Y.-G. Li, N. Hao, Y. Lu, E.-B. Wang, Z.-H. Kang, C.-W. Hu, Inorg. Chem. 42 (2003) 3119;
(g) R. Kitaura, S. Kitagawa, Y. Kubota, T.C. Kobayashi, K. Kindo, Y. Mita, A. Matsuo, M. Kobayashi, H.-C. Chang, T.C. Ozawa, M. Suzuki, M. Sakata, M. Takata, Science 298 (2002) 2358;
(h) B. Moulton, M.J. Zaworotko, Chem. Rev. 101 (2001) 1629;
(i) C. Janiak, J. Chem. Soc., Dalton Trans. (2003) 2781;
(j) S.L. James, Chem. Soc. Rev. 32 (2003) 276;
(k) S.-L. Zheng, X.-M. Chen, Aust. J. Chem. 57 (2004) 703;
(l) D. Maspoch, D. Ruiz-Molina, J. Veciana, J. Mater. Chem. 14 (2004) 2713;
(m) S.R. Batten, K.S. Murray, Coord. Chem. Rev. 246 (2003) 103;
(n) Y. Zhou, M. Hong, X. Wu, Chem. Commun. (2006) 135;
(o) S. Kitagawa, R. Kitaura, S. Noro, Angew. Chem., Int. Ed. 116 (2004) 2388;
(p) P.J. Hagrman, D. Hagrman, J. Zubieta, Angew. Chem., Int. Ed. 38 (1999) 2638;
(q) M. Eddaoudi, J. Kim, D. Vodak, A. Sudik, J. Wachter, M. O'Keeffe, O.M. Yaghi, PNAS 99 (2002) 4900;
(r) L. Carlucci, G. Ciani, D. Proserpio, Coord. Chem. Rev. 246 (2003) 247;
(s) M.J. Plater, M.R.St.J. Foreman, T. Gelbrich, S.J. Coles, M.B. Hursthouse, J. Chem. Soc., Dalton Trans. (2000) 3065;
(t) A.Y. Robin, K.M. Fromm, Coord. Chem. Rev. 250 (2006) 2127.
[2] (a) Y.H. Liu, Y.L. Liu, H.C. Wu, J.C. Wang, K.L. Lu, Inorg. Chem. 413 (2002) 2592;
(b) S.M. Kuznicki, V.A. Bell, S. Nair, H.W. Hillhouse, R.M. Jacubinas, C.M. Braunbarth, B.H. Toby, M. Tsapatsis, Nature 412 (2001) 720;
(c) S.A. Bourne, J. Lu, A. Mondal, B. Moulton, M.J. Zaworotko, Angew. Chem., Int. Ed. 40 (2001) 2111;
(d) J. Lu, A. Mondal, B. Moulton, M.J. Zaworotko, Angew. Chem., Int. Ed. 40 (2001) 2113;
(e) M. Aoyagi, K. Biradha, M. Fujita, J. Am. Chem. Soc. 121 (1999) 7457;
(f) C.V.K. Sharma, S.T. Griffin, R.D. Rogers, Chem. Commun. (1998) 215;
(g) S.R. Batten, B.F. Hoskins, R. Robson, J. Am. Chem. Soc. 117 (1995) 5385;
(h) J.Y. Lu, Coord. Chem. Rev. 248 (2004) 1159;
(i) S. Kitagawa, S. Masaoka, Coord. Chem. Rev. 246 (2003) 73;
(j) S.R. Batten, K.S. Murray, Coord. Chem. Rev. 246 (2003) 103;
(k) Sarah A. Barnett, Neil R. Champness, Coord. Chem. Rev. 246 (2003) 168;
(l) A. Erxleben, Coord. Chem. Rev. 246 (2003) 303;
(m) A.N. Khlobystov, A.J. Blake, N.R. Champness, D.A. Lemenovskii, A.G. Majouga, N.V. Zyk, M. Schröder, Coord. Chem. Rev. 222 (2001) 155;
(n) R.J. Puddephatt, Coord. Chem. Rev. 246 (2003) 313;
(o) A.Y. Robin, K.M. Fromm, Coord. Chem. Rev. 250 (2003) 2127.
[3] A. Lezzi, S. Cobianco, A. Roggero, J. Polym. Sci. A32 (1994) 1877.
[4] F.-F. Jian, H.i-L. Xiao, F.Q. Liu, J. Solid State Chem. 179 (2006) 3695.
[5] Y. Niu, Y. Song, H. Hou, Y. Zhu, Inorg. Chim. Acta 355 (2003) 151.
[6] J. Dai, X. Wang, G.-Q. Bian, J.-S. Zhang, L. Guo, M. Munakata, J. Mol. Struct. 690 (2004) 115.
[7] Y.-Y. Niu, Y.-L. Song, J. Wu, H. Hou, Y. Zhu, X. Wang, Inorg. Chem. Commun. 7 (2004) 471.
[8] Cambridge Structural Database, August 2006 Version, Cambridge Crystallographic Data Centre, 12 Union Road, Cambridge, UK, 2006.
[9] A. Morsali, A. Ramazani, A.R. Mahjoub, A.A. Soudi, Z. Anorg. Allg. Chem. 629 (2003) 2058.
[10] A.R. Mahjoub, A. Ramazani, A. Morsali, Z. Kristallogr. NCS. 218 (2003) 435.
[11] A. Morsali, M. Payheghader, M.R. Poorheravi, F. Jamali, Z. Anorg. Allg. Chem. 629 (2003) 1627.
[12] A. Morsali, A.R. Mahjoub, A. Ramazani, J. Coord. Chem. 57 (2004) 347.
[13] A. Ramazani, A. Morsali, A. Haji-Abolfath, Z. Kristallogr, NCS. 219 (2004) 245.
[14] A. Mahjoub, A. Morsali, J. Coord. Chem. 56 (2003) 779.
[15] A.R. Mahjoub, A. Morsali, R.E. Nejad, Z. Naturforsch 59b (2004) 1109.
[16] A. Morsali, V.T. Yilmaz, C. Kazak, Z. Anorg. Allg. Chem. 631 (2005) 1577.
[17] A. Morsali, L.G. Zhu, Helv. Chim. Acta 89 (2006) 81.
[18] Bruker Advanced X-ray Solutions SHELXTL (Version 6.14), Bruker AXS Inc., Madison, WI, USA, 2003.
[19] L.J. Farrugia, J. Appl. Crystallogr. 30 (1997) 565.
[20] Mercury 1.4.1, Copyright Cambridge Crystallographic Data Centre, 12 Union Road, Cambridge, CB2 1EZ, UK, 2001–2005.
[21] J.M. Harrowfield, H. Miyamae, B.W. Skelton, A.A. Soudi, A.H. White, Aust. J. Chem. 49 (1996) 1165.

[22] C. Balarew, R.J. Duhlew, Solid State Chem. 55 (1984) 1.
[23] (a) D.L. Reger, R.F. Semeniuc, V. Rassolov, M.D. Smith, Inorg. Chem. 43 (2004) 537;
(b) K. Reichenbacher, H.I. Suss, J. Hulliger, Chem. Soc. Rev. 34 (2005) 22.
[24] G.A. van Albada, R.A.G. De Graaff, J.G. Haasnoot, J. Reedijk, Inorg. Chem. 23 (1984) 1404.
[25] H. Zhang, X. Wang, K. Zhang, B.K. Teo, Coord. Chem. Rev. 183 (1999) 157.
[26] A.A. Newman (Ed.), Chemistry and Biochemistry of Thiocyanic Acid and its Derivatives, Academic Press, New York, 1975.
[27] A.M. Golub, H. Kohler, V. Skopenko (Eds.), Chemistry of Pseudohalides, Elsevier, Amsterdam, 1986.
[28] Q. Zhao, H. Li, Z. Chen, R. Fang, Inorg. Chim. Acta 336 (2002) 142.
[29] L. Yi, B. Ding, B. Zhao, P. Cheng, D.-Z. Liao, S.-P. Yan, Z.-H. Jiang, Inorg. Chem. 43 (2004) 33.
[30] B.F. Abrahams, M.J. Hardie, B.F. Hoskins, R. Robson, E.E. Sutherland, J. Chem. Soc., Chem. Commun. (1994) 1049.
[31] M. Fujita, Y.J. Kwon, M. Miyazawa, K. Ogura, J. Chem. Soc., Chem. Commun. (1994) 1977.
[32] D.P. Graddon, Rev. Inorg. Chem. 4 (1982) 211.

Available online at www.sciencedirect.com
ScienceDirect
Polyhedron 26 (2007) 2894–2900
POLYHEDRON
www.elsevier.com/locate/poly

Stereoselective synthesis of cobalt(III) anionic complexes with chiral pyruvylaminoacid oximes and metal–ligand interactions in aqueous solution

Aleksander Kufelnicki [a,*], Igor O. Fritsky [b], Tatiana Yu. Sliva [b], Inna F. Golovaneva [c], Rostislav D. Lampeka [b]

[a] *Laboratory of Physical and Biocoordination Chemistry, Faculty of Pharmacy, Medical University of Łódź, 1 Muszynski Str., 90-151 Łódź, Poland*
[b] *Department of Chemistry, Kiev National Taras Shevchenko University, 64, Vladimirska Str., 01033 Kiev, Ukraine*
[c] *N.S. Kurnakov Institute of General and Inorganic Chemistry of Russian Academy of Sciences, Leninskii pr. 31, 119991 Moscow, Russia*

Received 12 December 2006; accepted 23 January 2007
Available online 30 January 2007

Abstract

A series of cobalt(III) anionic complexes with hydroxyimino analogs of dipeptides – oximes of pyruvylglycine, pyruvyl-L-alanine, pyruvyl-L-methionine and pyruvyl-L-phenylalanine (H_2pamaco, amac = amino acid) of composition $Cat_3[Co(H_{-1}pamaco)_2]\cdot nH_2O$ (Cat – a monovalent metal cation) has been synthesized and investigated by UV–Vis, CD and ^{1}H NMR spectroscopy. It was established that for the two latter ligands, non-racemic mixtures of two diastereomeric complexes were formed as a result of synthesis. In comparison with the complex containing pyruvyl-L-alanine, in which the relative content of R (C_2) and S (C_2) isomers is approximately equal, the presence of bulky substituents in the molecules of Met- and Phe-containing ligands results in a significant discrimination in formation of the S (C_2) isomer. This conclusion was drawn upon analysis of the CD and NMR spectral data as well as from molecular modeling. The relative content of the diastereomers was evaluated on the basis of NMR data. The protonation constants of the ligands have been determined in aqueous solution by glass electrode potentiometry, whereas their interactions with Co(II) were studied both under argon and oxygen atmosphere.
© 2007 Elsevier Ltd. All rights reserved.

Keywords: Chiral pyruvylaminoacid oximes; Cobalt(III); Synthesis; Cobalt(II); Aqueous solution; Equilibria

1. Introduction

Pyruvylamino acid oximes represent a perspective class of polyfunctional ligands which can be regarded as hydroxyimino analogs of dipeptides. Both "free" ligands and their Co(III) complexes were shown to exhibit marked hypotensive effect, significantly exceeding this of the reference theobromine [1].

Earlier we have reported about the synthesis, study of molecular structure and spectral investigations of cobalt (III) anionic complexes with pyruvylaminoacid oximes of composition $Cat_3[Co(H_{-1}L)_2]\cdot nH_2O$ (Cat – a monovalent metal cation) [2,3]. These compounds contain triply deprotonated residues of the ligands, tridentately coordinated to the metal ion *via* the nitrogen atoms of the oxime and amide groups and the oxygen atom of the carboxyl group. We have also shown that upon formation of the anionic complexes in aqueous solution ionization of the oxime and amide groups proceeds cooperatively and is promoted by cobalt ions [1].

Herein, in continuation of research of pyruvylaminoacid oximes, we report a study of peculiarities of formation of diastereomeric cobalt(III) anionic complexes with chiral pyruvylaminoacid oximes by means of electronic, CD

* Corresponding author. Tel.: +48 42 6779204, fax: +48 42 678 83 98.
E-mail addresses: akuf@ich.pharm.am.lodz.pl (A. Kufelnicki), ifritsky@univ.kiev.ua (I.O. Fritsky).

0277-5387/$ - see front matter © 2007 Elsevier Ltd. All rights reserved.
doi:10.1016/j.poly.2007.01.023

and NMR spectroscopy. Moreover, we describe the complex formation of H_2pamaco with Co(II) inorganic salts in alkali aqueous solution under oxygen-free conditions and also in presence of dioxygen.

2. Experimental

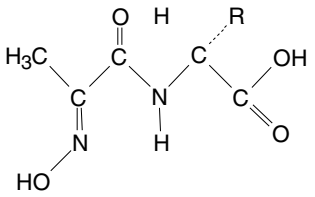
2.1. Additional abbreviations

H_2pgo – Pyruvylglycine oxime –CH_3–C(=NOH)–C(O)NH–CH_2–COOH; R=H.

H_2pao – Pyruvyl-L-alanine oxime – CH_3–C(=NOH)–C(O)NH–CH(CH_3)–COOH; R=CH_3.

H_2pmo – Pyruvyl-L-methionine oxime – CH_3–C(=NOH)–C(O)NH–CH($CH_2CH_2SCH_3$)–COOH; R=CH_2-CH_2SCH_3.

H_2ppo – Pyruvyl-L-phenylalanine oxime – CH_3–C(=NOH)–C(O)NH–CH(C_6H_5)–COOH; R=C_6H_5.



2.2. Measurement procedures

Preparation of cobalt(III) anionic complexes: $Na_3[Co(H_{-1}pgo)_2]\cdot 10H_2O$ (**1**), $K_3[Co(H_{-1}pao)_2]\cdot 5H_2O$ (**2**), $Na_3[Co(H_{-1}pmo)_2]\cdot 5H_2O$ (**3**) and $Tl_3[Co(H_{-1}ppo)_2]\cdot H_2O$ (**4**) was reported in [1,2]. UV–Vis absorption spectra of the prepared complexes in aqueous solution were recorded here on a Specord UV–Vis M 40 (Carl Zeiss, Jena) device in the range 50 000–11 000 cm^{-1}. ^1H and ^{13}C NMR spectra (solutions in D_2O and DMSO-d_6) were registered on a Bruker 300 MHz spectrometer using TMS as an internal standard.

CD spectra of the synthesized anionic complexes in aqueous solutions (1×10^{-3} M) were recorded on a MARK III Jobin Yvon dichrograph in the range 200–790 nm in cuvettes of different thickness (1, 0.1, 0.01 cm). In order to avoid trapping of aerial oxygen during the spectra recording, a steam of extra pure nitrogen was blown through the optical system. The obtained spectra were processed by calculation of $\Delta\varepsilon$ using formula: $\Delta\varepsilon = n\cdot A/c\cdot\alpha$ where $\Delta\varepsilon$ – the difference between extinction coefficients of left- and right-handed circular polarized light, n – distance from the top of maximum of Cotton effect to the base line (mm), A – sensitivity, c – concentration (mol dm^{-3}), α – thickness of the cuvette (cm).

The potentiometric equilibria studies were carried out by a precision PHM 85 pH-meter Radiometer (Copenhagen) with a combined electrode GK 241 C. The constant temperature 0.5 °C and ionic strength 0.1 (KNO_3) were in conformity with the conditions of dioxygen uptake. The protonation and formation constants were determined by pH-metric titration of 30.0 cm^3 samples. The glass electrode was calibrated in the $-\log[H^+]$ scale by titration of 0.005 M HNO_3 with 0.1 M NaOH, temp. 25 °C. Then concentration overall protonation constants $\beta_{lh} = [L_lH_h]/[L]^l[H]^h$ were calculated by SUPERQUAD [11]. The total concentration of the ligand in each sample ranged within $0.5–1.0\times10^{-2}$ mol dm^{-3}. The metal–ligand interaction was studied at ligand in excess and total metal concentration within $3.3–6.6\times10^{-3}$ mol dm^{-3}. $Co(NO_3)_2$ pa of POCh Gliwice was used. The standard solution was titrated with disodium salt of EDTA in presence of murexide.

Volumetric and simultaneously pH-metric measurements in presence of dioxygen were carried out by means of an isobaric laboratory set at 0.5 °C, $I = 0.1$ (KNO_3). The absorption spectra under O_2 atmosphere were recorded on a Specord UV–Vis M 40 spectrophotometer.

3. Results and discussion

Structure of the cobalt(III) anionic complex with $H_{-1}pgo^{3-}$ was determined earlier by single crystal X-ray analysis [3] as shown in Fig. 1.

C_2 point symmetry of the complex anion suggests its existence in two enantiometric forms (Fig. 2).

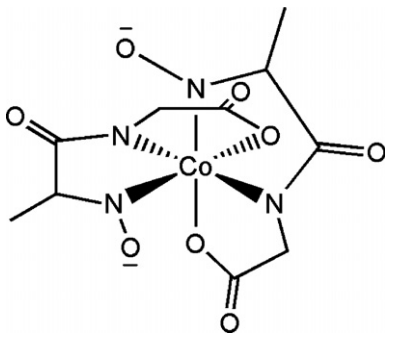


Fig. 1. View of the molecular structure of complex anion $[Co(H_{-1}pgo)_2]^{3-}$.

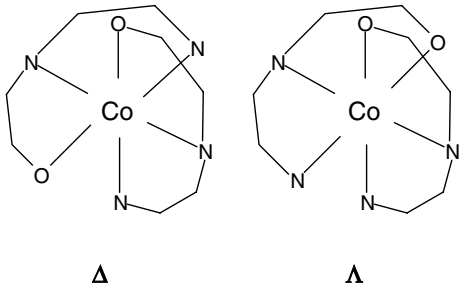


Fig. 2. Conformational isomers of cobalt(III) anionic complexes with pyruvylamino acid oximes.

In the centrosymmetric unit cell of the crystals **1** (space group $P\bar{1}$) the anions of both forms are to be found, so that the aqueous solution of the complex does not exhibit any optical activity as it contains a racemic mixture.

3.1. CD and UV–Vis spectra

The presence of an additional chiral center in the optically active ligands in $[Co(H_{-1}pao)_2]^{3-}$, $[Co(H_{-1}pmo)_2]^{3-}$ and $[Co(H_{-1}ppo)_2]^{3-}$ results in the fact that in the regarded complexes the configurational isomers become diastereomers. This allows making some *a priori* conclusions about their expected CD spectra. Taking into account the fact that contribution of the configurational and vicinal effects in total optical activity is regarded to be additive [4], one can conclude that the configurational effects of both isomers should be opposite, and an equal quantitative ratio of the isomers should result in quenching the optical activity.

Vicinal activity of both diastereomers in general case should be equal and the observed optical activity of their equimolar mixture should be equal to the double vicinal effect. Taking into account the planar conformation of rigid five-membered rings in $[Co(H_{-1}pgo)_2]^{3-}$ one should not expect any noticeable contribution of conformational effects in optical activity.

UV–Vis and CD spectra of aqueous solutions of **2** and **3** are presented in Fig. 3.

In the CD spectrum of **2** a negative Cotton effect with a minimum at 17200 cm^{-1} is registered in the region of $^1T_{1g} \leftarrow {}^1A_{1g}$ transition of Co(III). A more weak positive effect with a maximum at 18900 cm^{-1} is registered along with a strong negative band spreading over the region of $^1T_{1g} \leftarrow {}^1A_{1g}$ transition (with a minimum at 21700 cm^{-1}). Judging from the shape and the position of minimum of dichroism and $\Delta\varepsilon$ value, the latter represents an overlap of the third component of the *d-d* transition and charge transfer, the both bands being of negative sign. The $\Delta\varepsilon$ value in the CT region is significantly larger than in the case of the first two bands, so that the third component appears to be completely obscured. The intensities of the bands are in agreement with those expected for d–d transitions. It is worth to note, that the negative Cotton effect dominates in all the considered region. The $\Delta\varepsilon$ values and the character of alternation of two bands $(-+-)$ can be regarded as an expected situation for vicinal optical activity induced by the dipetide-like ligand containing L-amino acid residue in the C-terminal moiety [5]. The views of the spectrum and $\Delta\varepsilon$ values are close to those reported for the dipetide complexes possessing only vicinal activity [6]. The total negative rotatory strength of the $^1T_{1g} \leftarrow {}^1A_{1g}$ transition is characteristic for L-amino acid C-terminal residues [4,7].

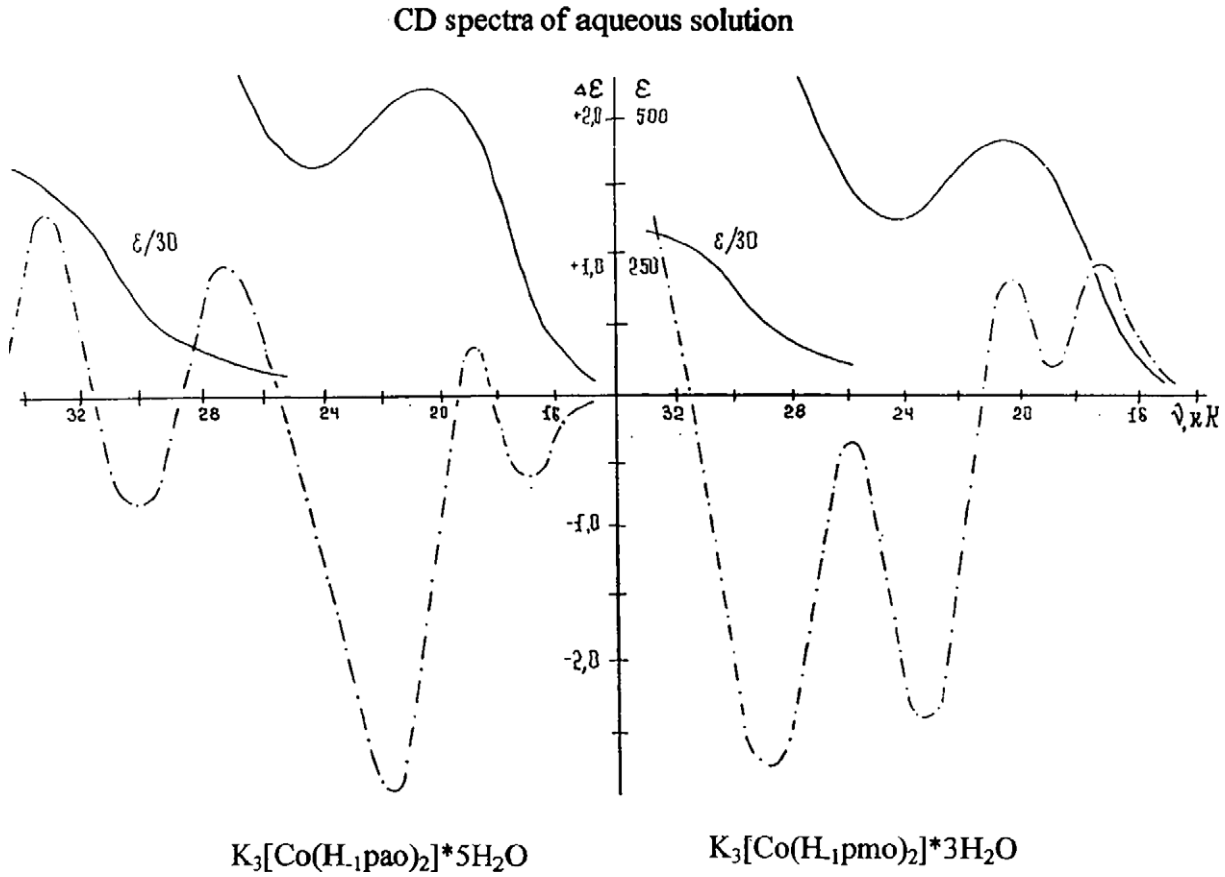


Fig. 3. UV–Vis (–––) and CD (–·–·–) spectra of aqueous solutions of: **2** and **3**.

In the considered spectrum the two low energy bands can be ascribed to the components of transition on ^1E; the $^1T_{2g} \leftarrow {}^1A_{1g}$ transition, as mentioned above, is obscured by the CT band. In the region of intraligand transitions and CT the Cotton effects of alternating signs are registered; their total rotatory strength is negative.

The CD spectrum of **3** is significantly different. First of all, this regards to the d–d transition region. In the spectrum a positive Cotton effect at 17 700 cm^{-1}, a band of positive dichroism with minimum at 19 100 cm^{-1} and another one, following the latter, positive band at 20 600 cm^{-1} are registered. At higher wave numbers a strong negative Cotton effect caused by charge-transfer is observed, the position of the corresponding maximum and $\Delta\varepsilon$ value is close to that in the spectrum of **2**. It is evident that the observed effects in the spectrum of **3** cannot be conditioned only by vicinal contribution. The registered spectrum is a result of overlapping of several Cotton effects of the opposite signs. Note, that within the whole considered region the negative dichroism predominates. Taking into account the total negative contribution of vicinal effect of L-isomer in the observed rotatory strength, one can make a conclusion about the existence of strong configurational contribution which in the present case can be caused only by configurational chirality. This is confirmed by noticeably higher $\Delta\varepsilon$ values in comparison with **2**.

Thus, it may be concluded that in **3** one of the possible configurational isomers is more abundant, so that enantioselectivity takes place rather on formation of complex **2** [8]. Contrariwise, during formation of **2** the diastereomers are indeed formed in approximately equal amounts [1].

3.2. ^1H NMR investigations

The last conclusion of CD studies is confirmed by ^1H NMR spectral investigations. Thus, the spectrum of **2** (Fig. 4) is characterized by the presence of two sets of signals, expected for the protons of the methyl and methane groups of the ligand.

In the spectrum of **2** one can register two singlets of the methyl {CH_3–C(NO)} protons (1.63 and 1.67 ppm), two doublets of the methyl protons of the side chain {CH_3–CH} {1.45 and 1.55 ppm, $^3J = 6.8$ Hz} and two quartets of the methine protons {4.06 and 4.22 ppm}. Comparison of integral intensity of the signals makes it possible to estimate quantitatively the content of the configurational isomers. As one can see from Fig. 4, the intensities of the corresponding signals in both sets are in fact equal (ratio of the integral intensities is 1:1.11). This corresponds to the relative content of the diastereomers in ratio of 52.6–47.4% which suggests their approximately equal quantities. In the ^{13}C NMR spectrum of **2** also two sets of signals are registered: 12.55 (12.64) ppm, {CH_3–C(NO)}, 19.52 (19.64) ppm {CH_3–CH}, 55.13 (55.90) ppm {CH}, 152.60 (153.25) ppm {C(N=O)}, 172.18 (173.05) ppm {C=O}, 186.40 (186.86) ppm {COO}.

^1H NMR spectra of complexes **3** and **4** are characterized by the presence of a relatively large number of signals in the region of the expected resonances of the methane and methylene groups, which complicates significantly their interpretation. Judging by view of the spectra in the region of singlets of the methyl {CH_3–C(NO)} groups, the spectra contain more than two sets of signals. The ratio of the corresponding integral intensities suggests noticeable domination of one of the isomers. It seems that in the regarded

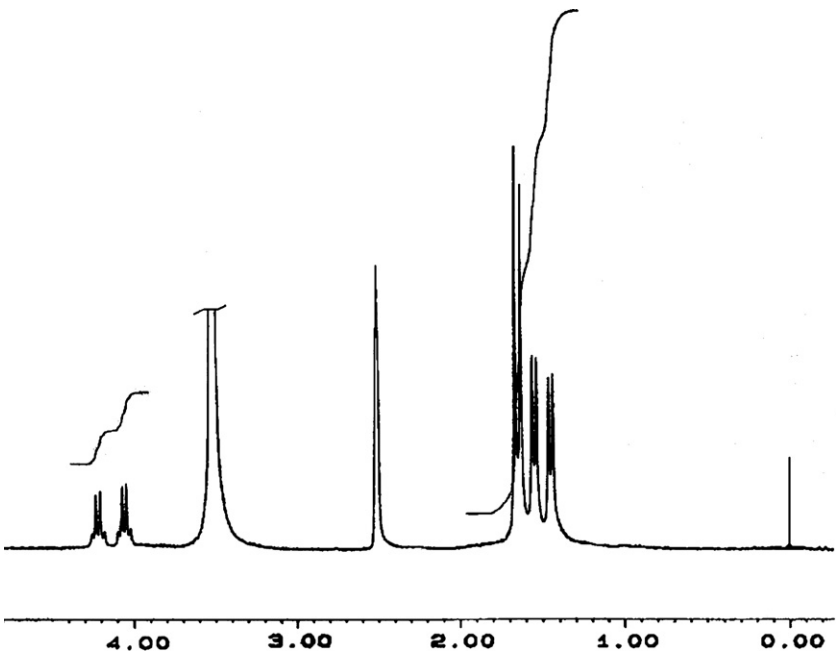


Fig. 4. ^1H NMR spectrum of **2** (solution in DMSO-d_6).

systems some additional effects take place, which results in non-equivalence of protons of the corresponding groups of two different ligands within the same coordination polyhedron. Such phenomena can be determined by peculiarities of solvatation of the complex anions in solutions and also by realization of non-equal conformations of the side chains of the ligands in bis(ligand) complexes. By their nature the mentioned effects are close to those observed in non-racemic mixtures of enantiomers, where no signals splitting is expected *a priori* [9]. This additional non-equivalence results in further splitting which contributes to further complication of the spectra. This conclusion is confirmed by the ^{13}C NMR spectra of **3** and **4**, in which in the region of the expected signals of each carbon atom 3–5 resonances are registered.

Note, that the intensity of the most intensive signal in each set is more than sum of intensities of more weak signals. The total positive rotary force of $^1T_{1g} \leftarrow {}^1A_{1g}$ transition under condition of negative contribution of the vicinal effect in the CD-spectrum of **2** makes it possible to assume, according to known empirical rules, a predominant formation of the configuration isomer possessing right screw chirality along the C_2 axis (i.e., R(C_2) isomer). Analysis of molecular models revealed that in the case of the S(C_2)-isomer the side chains appear to be situated in significantly more close proximity than in the case of R(C_2) isomer, which can result in intramolecular interligand interactions limiting conformational flexibility of the chains. Note, that a similar stereospecificity was noticed before for configurationally chiral Co(III) complexes [10]. Earlier, a preferential formation of R(C_2)-isomers it was also established in the Co(III)-dipeptide systems with an amino acid residue possessing L-configuration [5]. The mentioned interligand interactions are the reason of chiral discrimination in reactions of anionic complex formation in the systems containing ligands with bulky substituents in the side chain (i.e. derivatives of L-methionine and L-phenylalanine). At the same time in the complex with L-alanine derivative, the side chains (methyl groups) are quite compact and in the case of both R(C_2) and S(C_2) isomers significantly separated from each other, which thus results in prevention of noticeable interligand interactions between them. As a result, formation of Co(III) anionic complexes with this ligand is not accompanied by discrimination of one of the formed configurational isomers.

3.3. Equilibrium studies under inert atmosphere

The protonation constants of the oxime groups $\log K_{2H} = \log \beta_{011}$ (Table 1) are of two orders of magnitude higher than the constants characterizing the corresponding amino groups in dipeptides. E.g., for GlyGly under the same conditions: $\log \beta_{011}$ (–NH_2) = 8.31 [12]. On contrary, the stepwise protonation constants of the carboxyl functions (resulting from the total formation constants, $\log K_{2H} = \log \beta_{012} - \log \beta_{011}$) are similar – for GlyGly: $\log K_{2H} = 3.14$ [12]. Moreover, the deprotonation of the amide group has not been found within pH < 12, just like it is the case for dipeptides.

Table 1
Protonation and formation constants $\log \beta_{MLH}$ in Co(II)–H_2PyruvylAmacOxime (H_2pamaco) systems under inert atmosphere

Species[a,b]	H_2pgo	H_2ppo	H_2pmo
LH	10.55(3)	10.86(1)	10.72(1)
LH_2	13.83(4)	14.03(2)	13.91(3)
ML	5.38(5)	4.19(2)	4.20(3)
ML_2	8.90(8)	8.22(2)	–
MLH_{-1}	–	–	−4.47(1)
$ML(LH_{-1})$	−1.45(10)	−3.75(6)	−1.87(3)
$M(LH_{-1})_2$	–	−14.85(3)	–

Solv. H_2O. $I = 0.1$ (KNO_3), temp. 0.5 °C. Standard deviations in parentheses.
[a] L = pamaco – the carboxyl and oxime deprotonated ligand.
[b] $LH_{-1} = H_{-1}$pamaco – fully deprotonated ligand (also amide deprotonation).

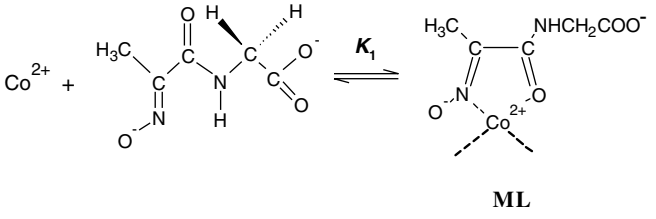
A higher basicity of the nitrogen containing oxime group leads to enhanced values of ML stability constants (Table 1). A comparison of $\log K_1$ with GlyGly ($\log K_1 = \log \beta_{110} = 3.41$) confirms this observation [12] (see Scheme 1).

In the presence of the Co^{2+} central ion a metal promoted amide deprotonation becomes possible already at pH > 8 (see Scheme 2).

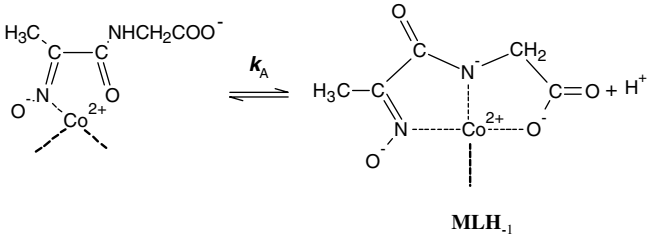
The symbol k_A denotes the amide deprotonation constant:

$$pk_A = -\log k_A = \log \beta_{110} - \log \beta_{11-1}$$

However, the MLH_{-1} species has been confirmed only for H_2pmo (Table 1). Other deprotonated complexes of composition M:L = 1:2 (i.e. $ML(LH_{-1})$ and $M(LH_{-1})_2$) may be formed via coordination of the second ligand molecule in a plane perpendicular to the first chelation plane. Indeed, the refinements confirmed the amide deprotonated complex $ML(LH_{-1})$ for all the ligands studied (cf. Table 1).



Scheme 1.



Scheme 2.

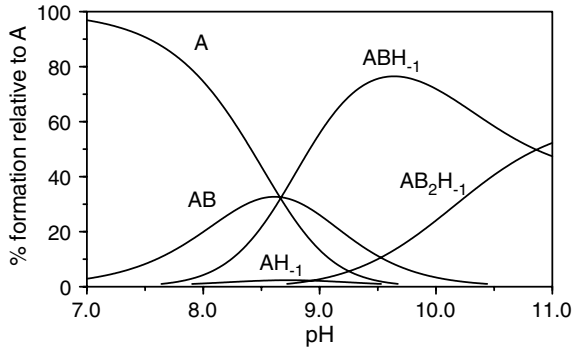


Fig. 5. Complex species distribution as a function of pH in the Co(II)–H_2pmo system in aqueous solution. $C_{Co} = 3.33 \times 10^{-3}$, $C_L = 1.0 \times 10^{-2}$ mol dm^{-3}. A = Metal, B = ligand = pmo.

The doubly deprotonated $M(LH_{-1})_2$ species was accepted only for H_2ppo but low contents in solution could not be excluded also for the other pyruvylaminoacid oximes at higher pH. The hydrolysis of the uncomplexed metal aquo-ion has been regarded by equilibrium:

$M \rightleftharpoons MH_{-1} + H$, where $\beta_{10-1} = [MH_{-1}][H][M]^{-1}$. The value of the hydrolysis constant under corresponding conditions $\log\beta_{10-1} = -9.80$ was taken from [13].

An exemplary distribution of complexes versus pH is presented in Fig. 5.

3.4. Reactions under O_2 atmosphere

The presence of at least three nitrogen donors in the inner coordination sphere makes it possible, in accordance to Fallabs 3N rule, to foresee an uptake of dioxygen by $ML(LH_{-1})$ or $M(LH_{-1})_2$ [14].

The titration curves in presence of molecular oxygen displayed a buffer zone within pH 6–8. This buffer zone corresponds to the straight line segment of the mmol $O_2 = f(V_{NaOH})$ dependence (Fig. 6a).

The mean slope $\Delta OH/\Delta O_2$ of five titrations amounted to $8.02 \approx 8$, thus indicating 8 protons being neutralized in the summary reaction. At the same time the number of mmoles of bound dioxygen attains a maximum: 0.42 per 1 mmol of cobalt at L:M = 2.0 (Fig. 6b). The value 0.42 is close to 0.5

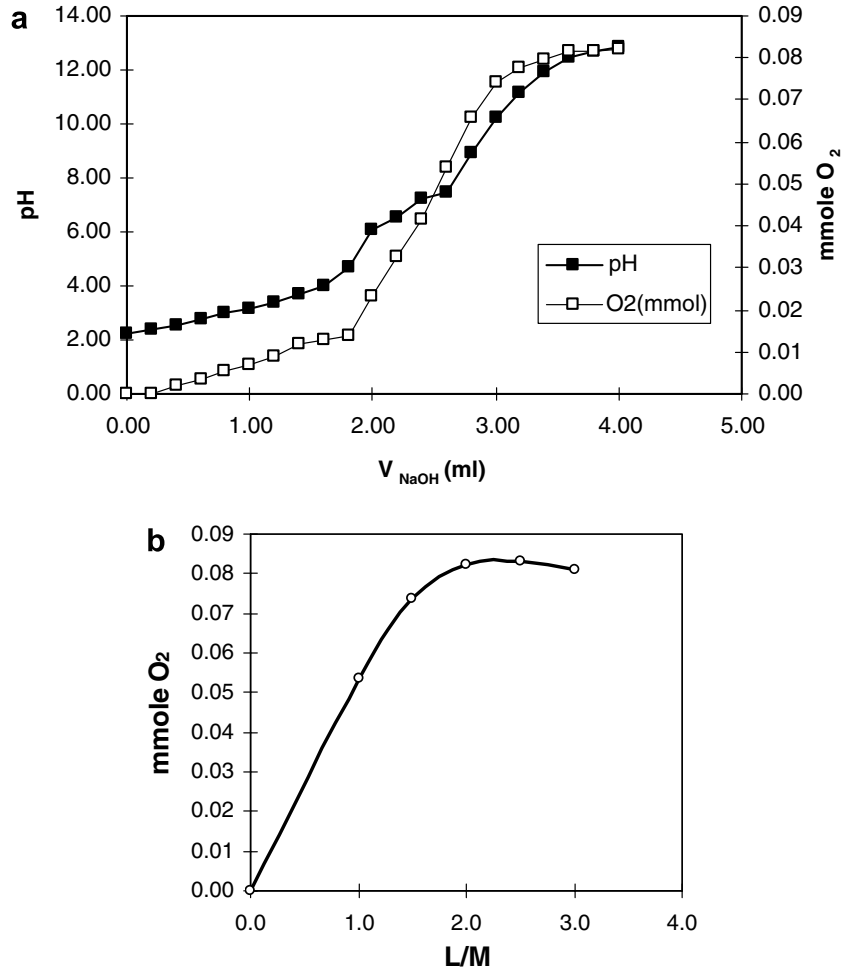


Fig. 6. (a) pH-metric and volumetric titration in the Co(II)–H_2pgo-O_2 system. Initial volume 40 cm^3. $C_{NaOH} = 0.4037$ M. The sample contained 0.2 mmol of $Co(NO_3)_2$ and 0.4 mmol of H_2pgo, (b) total amount of bound oxygen vs. ligand to metal concentration ratio.

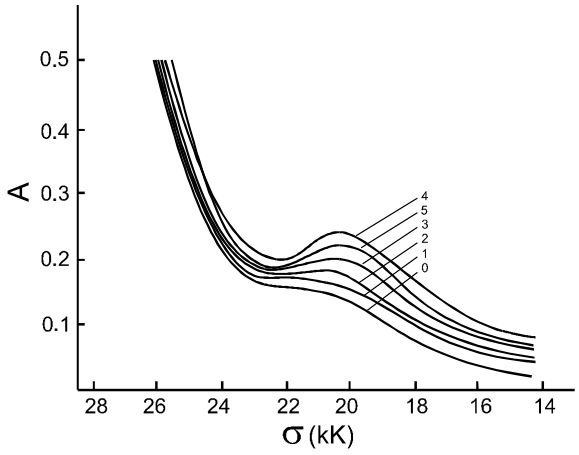


Fig. 7. UV–Vis absorption in aqueous solution after oxygenation of a sample containing Co(II) and pgo. Path length 1 cm. Temp. 0.5 °C. $C_{Co} = 5.0 \times 10^{-3}$, $C_L = 1.0 \times 10^{-2}$ mol dm^{-3}. Curves after: 0–3 min, 1–10 min, 2–20 min, 3–65 min, 4–72 h, 5–7 days since initiation of reaction.

expected for dimer formation. Hence the following summary reaction may be proposed for L = pamaco:

$$4H_2L + 8OH^- + 2Co^{2+} + O_2 = (LH_{-1})_2CoO_2Co(LH_{-1})_2^{4-} + 8H_2O$$

Although it may be concluded that $Co(LH_{-1})_2$ is the "active" complex able to take up dioxygen, also the $CoL(LH_{-1})$ complex should be taken into account. Hence two of the neutralized 8 protons may stem from the deprotonation:

$$2CoL(LH_{-1})^{2-} + O_2 = Co_2(LH_{-1})_4O_2^{4-} + 2H^+$$

Unlike the reactions of the corresponding dipeptides, the reaction of oxygen uptake studied herein was almost in 90% irreversible. The autooxidation of Co(II) to Co(III), concomitant to oxygen uptake, yields irreversibly inert Co(III) complexes. The peroxo dioxygen bridge is transformed to hydrogen peroxide:

$$(LH_{-1})_2Co^{III}O_2^{2-}Co^{III}(LH_{-1})_2^{4-} + 2H^+ \rightarrow 2Co^{III}(LH_{-1})_2^- + H_2O_2$$

and then dioxygen is re-emitted in a relatively slower reaction:

$$H_2O_2 \rightarrow H_2O + 1/2O_2$$

As a result it can be seen in Fig. 6b that the amount of bound dioxygen is less than 0.5 mmol per 1 mmol of cobalt, particularly when L/M is higher (then the duration time of titrations under oxygen is longer).

Spectrophotometric measurements in presence of O_2 also indicated the formation of a final violet solution in alkali medium which may be attributed to Co(III) species with the $^1T_{1g} \leftarrow {}^1A_{1g}$ band at $\sigma \approx 21 \times 10^3$ cm^{-1} – Fig. 7. The higher energetic spin allowed d^6 band $^1T_{2g} \leftarrow {}^1A_{1g}$ predicted by the crystal field theory is obscured by an intensive LMCT transition from the auxiliary ligand – pamaco.

Acknowledgement

Financial support of this work by the Medical University of Łódź (A. Kufelnicki – project 503-3014-2) is acknowledged.

References

[1] I.O. Fritsky, R.D. Lampeka, T.Yu. Sliva, Bioactivity of 3d- and s-metal complexes based on hydroxyimino analogues of amino acids and dipeptides, in: ESF Workshop on Impact of Non-Platinum Metal Ions on Drugs, Chemotherapeutics and Related Compounds, Karpacz, Poland, 1993, Book of Abstracts, pp. 83–84.
[2] V.V. Skopenko, I.O. Fritsky, R.D. Lampeka, Zhurn. Neorg. Khimii 39 (1994) 1478.
[3] I.O. Fritsky, R.D. Lampeka, V.V. Skopenko, Yu.A. Simonov, A.A. Dvorkin, T.I. Malnowsky, Z. Naturforsch. 48b (1993) 270.
[4] C. Hawkins, Absolute Metal Complexes Configuration, Mir, Moscow, 1974, p. 430.
[5] L.V. Boas, C.A. Evans, R.D. Gillard, P.R. Mitchell, D.A. Phipps, J. Chem. Soc., Dalton Trans. (1979) 582.
[6] I.G. Browning, R.D. Gillard, J.R. Lyons, P.R. Mitchell, D.A. Phipps, J. Chem. Soc., Dalton Trans. (1972) 1815.
[7] T. Yasui, H. Kawaguchi, T. Ama, Bull. Chem. Soc. Jpn. 54 (1981) 2918.
[8] V.A. Davankov, A.A. Kurganov, S.V. Rogozhin, Usp. Khimii 43 (1974) 1610.
[9] M.I. Kabachnik, T.A. Mastryukova, E.I. Fedin, et al., Usp. Khimii 47 (1978) 1541.
[10] L.G. Stadtherr, R.B. Martin, Inorg. Chem. 12 (1973) 1810.
[11] P. Gans, A. Sabatini, A. Vacca, J. Chem. Soc., Dalton Trans. (1985) 1195.
[12] A. Kufelnicki, Polish J. Chem. 65 (1991) 17.
[13] C.F. Baes Jr., R.E. Mesmer, The Hydrolysis of Cations, Krieger Publishing Co, Malabar, FL, 1986, p. 238.
[14] S. Fallab, Angew. Chem. 79 (1967) 500.

Available online at www.sciencedirect.com
ScienceDirect
Polyhedron 26 (2007) 2901–2905
POLYHEDRON
www.elsevier.com/locate/poly

Bimolecular homolytic reactions of alkylcobalt complexes

Shaoyung Lee *, Tsung Yao Ku

Department of Chemical Engineering, I-Shou University, Kaohsiung County 84008, Taiwan, ROC

Received 10 August 2006; accepted 24 January 2007
Available online 3 February 2007

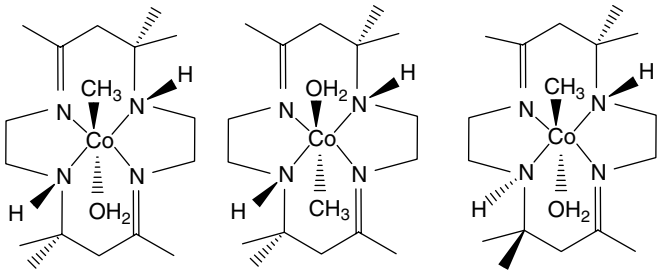
Abstract

The reactions of $RCoL^1(H_2O)^{2+}$ (R = CH_3, C_2H_5 and *n*-C_3H_7; L^1 = 5,7,7,12,14,14-hexamethyl-1,4,8,11-tetraazacyclotetradeca-4,11-diene) and $CH_3CoL^2(H_2O)^{2+}$ (L^2 = 1,4,8,11-tetraazacyclotetradecane) with Cr^{2+} in aqueous solution were studied. The reaction products were $CoL^1(H_2O)_2^{2+}$ (or $CoL^2(H_2O)_2^{2+}$) and RCr^{2+}, following which the related alkanes were obtained via acidolysis. The reaction mechanism appears to consist of an S_H2 displacement at the saturated carbon. The reactivity is clearly dependent on the size of the alkyl group, the ligand and the configuration of the complex. The kinetics for this reaction were also studied at various temperatures. The reaction of $RCoL^1(H_2O)^{2+}$ with V^{2+} was investigated as well in this study.
© 2007 Elsevier Ltd. All rights reserved.

Keywords: Kinetics; Bimolecular homolysis; Alkylcobalt complexes

1. Introduction

Coenzyme B_{12}(cobalamin) has attracted attention since the structure determination of a cobalt–carbon bond in the early 1960s [1,2]. Transition metal-alkyl bond dissociation energies are of importance in the context of a variety of organometallic and catalytic systems [3]. It is known that the steric hindrance around the metal center affects this metal–carbon bond [4–7]. Among the various alkylcobalt macrocyclic complexes prepared recently [8,9], the complex $CH_3CoL^1(H_2O)^{2+}$ (L^1 = 5,7,7,12,14,14-hexamethyl-1,4,8,11-tetraazacyclotetradeca-4,11-diene) had three configurational isomers, as shown in the following diagrams [10,11]. These complexes provide a good opportunity to examine the dependence of configurationally steric hindrance on their reactivity. The isomerization of these isomers reveals that *pri,rac-* is the most stable configuration and the isomerization rate is truly dependent on the alkyl group at the cobalt centre [12]. The substitution of SCN^- with H_2O for these three isomers of $CH_3CoL^1(H_2O)^{2+}$ also shows a remarkable steric effect with the following reactivity order: *sec,rac-* ≫ *meso-* ∼*pri,rac-* [13].



Although the dissociation energy of the cobalt–carbon bond was well determined through a kinetic study of the unimolecular homolysis of *meso*-$RCoL^1(H_2O)^{2+}$ (R = C_2H_5, *n*-C_3H_7), there is no information about the bond dissociation energy of the other configurational isomers of $RCoL^1(H_2O)^{2+}$. Both unimolecular and bimolecular homolysis were observed in the reaction of *meso*-$RCoL^1(H_2O)^{2+}$ with Cr^{2+} (R = C_2H_5, *n*-C_3H_7) [8]. The

* Corresponding author.
E-mail address: sylee@isu.edu.tw (S. Lee).

0277-5387/$ - see front matter © 2007 Elsevier Ltd. All rights reserved.
doi:10.1016/j.poly.2007.01.032

bimolecular homolytic reaction is interesting since homolytic metal–carbon bond cleavage and atom transfer is involved. In the present study, the reactions of alkylcobalt complexes with different ligands and various configurations with the metal ions Cr^{2+} and V^{2+} were investigated. The kinetics and the activation parameters for the reaction of *sec*,*rac*-$CH_3CoL^1(H_2O)^{2+}$, *pri*,*rac*-$RCoL^1(H_2O)^{2+}$ (R = CH_3, C_2H_5 and *n*-C_3H_7) and $CH_3CoL^2(H_2O)^{2+}$ (L^2 = 1,4,8,11-tetraazacyclotetradecane) with Cr^{2+} in aqueous solution are reported.

2. Experimental

2.1. Reagents

The macrocycle Me_6[14]4,11-dieneN_4 (L^1) was prepared by the condensation of 1,2-diaminoethane and acetone [14]. [14]aneN_4 (L^2) was purchased from Aldrich and used directly. *meso*-$CoL^1(H_2O)_2(ClO_4)_2$, *sec*,*rac*-$CH_3CoL^1(H_2O)(ClO_4)_2$, *meso*-$RCoL^1(H_2O)(ClO_4)_2$, *pri*,*rac*-$RCoL^1(H_2O)(ClO_4)_2$ (R = CH_3, C_2H_5, *n*-C_3H_7) and an aqueous solution of $CH_3CoL^2(H_2O)^{2+}$ were prepared according to a published procedure [6,8,12,15]. (*Caution*: Perchlorate salts of metal complexes with organic ligands are potentially explosive.) The products of the alkylcobalt macrocycles were characterized by UV–Vis and ^1H NMR spectra [13,16]. *t*-Butyl hydroperoxide was commercially available and used directly. The other alkyl hydroperoxides were prepared from the appropriate alcohol and hydrogen peroxide [17,18]. The concentration of the V^{2+} solution was determined from the absorbance at a wavelength (λ) of 850 nm [19]. All the other chemicals purchased were of reagent grade and were used directly. Water was purified using a Millipore Milli-Q SP system and was used for all the kinetic measurements.

2.2. Spectroscopy and kinetics

The UV–Vis spectra and single-wavelength absorbance versus time data were acquired by using the Hitachi 3000 or HP 8453 spectrophotometer. Temperature control of ±0.5 °C was maintained by circulating water from a constant-temperature bath through the jacket of a cell holder. All the kinetic measurements were made using sodium perchlorate and perchloric acid adjusted to $\mu = 0.5$ M in most cases. The ^1H NMR spectra were studied using a Varian GEMINI-200 spectrometer. The NMR experiments were carried out in D_2O with HOD as the reference. The gas products of the hydrolysis of the organochromium complexes were determined by GC (Perkin–Elmer) and a column of GS-GASPRO.

3. Results and discussion

The typical visible spectral changes observed on mixing *pri*,*rac*-$C_2H_5CoL^1(H_2O)^{2+}$ with Cr^{2+} are shown in Fig. 1. The increase in absorption at λ 330 and 390 nm corresponds to the formation of $CoL^1(H_2O)_2^{2+}$ and $C_2H_5Cr^{2+}$, respectively. However, the subsequent decrease in absorption at λ 390 nm is caused by the slow acidolysis of $C_2H_5Cr^{2+}$ [20,21]. The related alkanes were obtained as the gas products for the eventual reactions of Cr^{2+} with various $RCoL^1(H_2O)^{2+}$ complexes. The reactions involved are shown in:

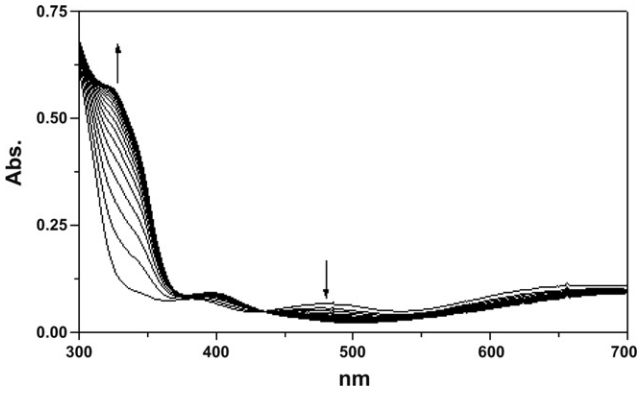


Fig. 1. Visible spectrum for the reaction of *pri*,*rac*-$C_2H_5CoL^1(H_2O)^{2+}$ with Cr^{2+}. The time interval is 60 s. [*pri*,*rac*-$C_2H_5CoL^1(H_2O)^{2+}$] = 2.5×10^{-4} M, [Cr^{2+}] = 0.02 M ($\mu = 0.5$ M, $T = 25$ °C).

$$RCoL^1(H_2O)^{2+} + Cr^{2+} \rightarrow RCr^{2+} + CoL^1(H_2O)_2^{2+} \quad (1)$$

$$RCr^{2+} + H^+ \rightarrow RH + Cr^{3+} \quad (2)$$

The kinetics of these reactions were studied under pseudo-first-order conditions with Cr^{2+} in excess and monitored by measuring the increase in absorption at $\lambda = 330$ nm as a function of time. The plots of $\ln(A_\infty - A_t)$ versus time showed a good linear behavior for at least three to four half-lives to establish the first order dependence on [$RCoL^1(H_2O)^{2+}$]. The observed rate constants depend linearly on the concentration of the excess chromous ions, as shown in Figs. 2 and 3. The plots for the reaction of *meso*-$C_2H_5CoL^1(H_2O)^{2+}$ and *meso*-$C_3H_7CoL^1(H_2O)^{2+}$ are

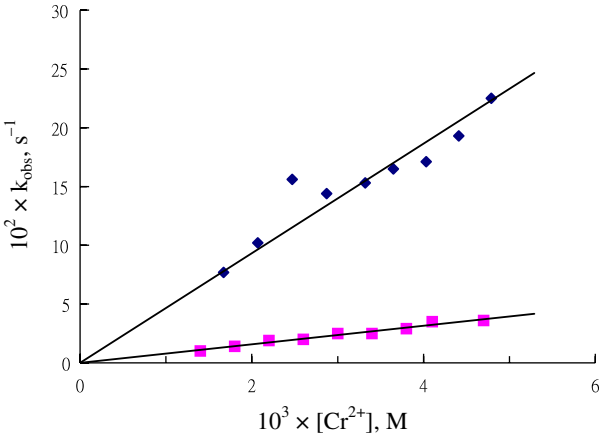


Fig. 2. Dependence of k_{obs} on [Cr^{2+}] for the reaction of $CH_3CoL^1(H_2O)^{2+}$ with Cr^{2+} at 25 °C and $\mu = 0.5$ M. ◆, *pri*,*rac*-$CH_3CoL^1(H_2O)^{2+}$; ■, *sec*,*rac*-$CH_3CoL^1(H_2O)^{2+}$.

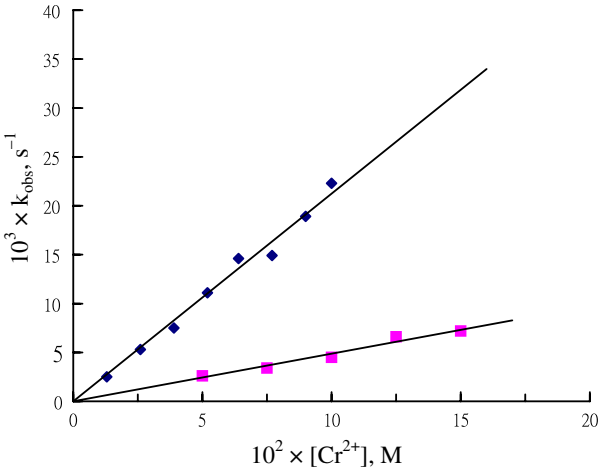


Fig. 3. Dependence of k_{obs} on $[Cr^{2+}]$ for the reaction of *pri,rac*-$RCoL^1(H_2O)^{2+}$ with Cr^{2+} at 25 °C. ◆, R = C_2H_5 ($\mu = 0.5$ M); ■, R = *n*-C_3H_7 ($\mu = 1.0$ M).

linear but with a significant intercept that corresponds to unimolecular homolysis, as shown in Eq. (3). The value of the unimolecular homolysis rate constant k_h for

$$\textit{meso}\text{-}RCoL^1(H_2O)^{2+} \rightarrow {}^{\cdot}R + CoL^1(H_2O)_2^{2+} \quad (R = C_2H_5 \text{ or } n\text{-}C_3H_7) \tag{3}$$

meso-$C_2H_5CoL^1(H_2O)^{2+}$ calculated in this study (9.1×10^{-4} s^{-1}, $\mu = 1.0$ M) is consistent with the value obtained in a previous report (3.5×10^4 s^{-1}, $\mu = 0.14$ M) [8]. These results suggest a general rate law for the reactions of Cr^{2+} with these alkylcobalt complexes:

$$-d[RCoL^1(H_2O)^{2+}]/dt = (k_h + k[Cr^{2+}])[RCoL^1(H_2O)^{2+}]$$

$$k_{obs} = k_h + k[Cr^{2+}]$$

The unimolecular homolysis rate constant k_h does not exist for these alkylcobalt complexes, except for *meso*-$C_2H_5CoL^1(H_2O)^{2+}$ and *meso*-$C_3H_7CoL^1(H_2O)^{2+}$. These results suggest that the configuration of the complex affects the bond energy of the cobalt–carbon bond in these alkyl cobalt complexes. *sec,rac*-$C_2H_5CoL^1(H_2O)^{2+}$ could not be prepared successfully probably due to the unstable cobalt–carbon bond. The values of the second-order rate constants k measured at 25 °C are listed in Table 1. The reactivity of *pri,rac*-$RCoL^1(H_2O)^{2+}$ with Cr^{2+} is clearly dependent on the size of the alkyl group R with the order $CH_3 > C_2H_5 > n\text{-}C_3H_7$. A larger alkyl group would prevent the attack by Cr^{2+}. This is consistent with the reactivity of $RCo(dmgBF_2)_2$ with Cr^{2+} [22]. Among the three different configurational isomers of $CH_3CoL^1(H_2O)^{2+}$, the *pri,rac*-form has the least steric hindrance and shows the highest reactivity with Cr^{2+}. However, the difference between the rate constants of *meso*- and *sec,rac*- is small. The larger hindrance of the *sec,rac*-configuration would certainly prevent the attack by Cr^{2+} and reduce the reaction rate. On the other hand, it would also decrease the cobalt–carbon bond energy and accelerate the reaction. The experimental results show a combination of these two factors and therefore the difference is not large. The kinetics of the reactions of $CH_3CoL^1(H_2O)^{2+}$ with Cr^{2+} were studied at different temperatures. The second-order rate constants are listed in Table 2. The data were fit to the Eyring equation with plots of $\ln(k/T)$ against $1/T$. The values of $\Delta H^{\ddagger}$ and $\Delta S^{\ddagger}$ are listed in Table 3.

The reaction of $CH_3CoL^2(H_2O)^{2+}$ with Cr^{2+} was also studied under pseudo-first-order kinetic conditions with Cr^{2+} in excess. Since the absorption of $CoL^2(H_2O)_2^{2+}$ in the visible region is small, the reaction was monitored at λ 390 nm, which was the maximum absorption of CH_3Cr^{2+}. A typical biphase kinetic trace was observed; the increase in absorption was followed by a decrease due to acidolysis (Eq. (2)). The slow acidolysis was caused by the first-order dependence on $[H^+]$, and it gave a second-order rate constant of 5×10^{-3} M^{-1} s^{-1}, which was in good agreement with the literature value of 4.94×10^{-3} M^{-1} s^{-1} [21]. The consecutive reaction analysis of the fast increase absorption established a first-order dependence on $[CH_3CoL^2(H_2O)^{2+}]$. The plot of k_{obs} versus $[Cr^{2+}]$ was linear with a slope equal to 0.268 ± 0.005 M^{-1} s^{-1}, as shown in Fig. 4. This reactivity is much slower than that of $CH_3CoL^1(H_2O)^{2+}$. This reactivity results from the stronger cobalt–carbon bond in $RCoL^2(H_2O)^{2+}$ [6,8]. No attempt to study the kinetic rate of the reaction of Cr^{2+} with

Table 1
Kinetic data for the reaction of $RCoL^1(H_2O)^{2+}$ with Cr^{2+}[a]

R	k (M^{-1} s^{-1})		
	meso-	*pri,rac*-	*sec,rac*-
CH_3	7.0 ± 0.1	46 ± 2	7.86 ± 0.01
C_2H_5	$(3.4 \pm 0.7) \times 10^{-2}$	$(2.12 \pm 0.04) \times 10^{-1}$	
n-C_3H_7	$(1.1 \pm 0.1) \times 10^{-3}$[b]	$(4.8 \pm 0.1) \times 10^{-3}$[b]	

[a] $T = 25$ °C, $\mu = 0.5$ M, $\lambda = 330$ nm; unless otherwise noted.
[b] $T = 25$ °C, $\mu = 1.0$ M, $\lambda = 330$ nm.

Table 2
Dependence of temperature for the reaction of $CH_3CoL^1(H_2O)^{2+}$ with Cr^{2+}[a]

Temperature (°C)	k (M^{-1} s^{-1})		
	meso-	*pri,rac*-	*sec,rac*-
15	3.7 ± 0.2	26.0 ± 0.8	5.0 ± 0.1
20	4.3 ± 0.1	39.8 ± 0.4	7.5 ± 0.1
25	7.0 ± 0.1	46 ± 2	7.86 ± 0.01
30	9.5 ± 0.2	59 ± 2	10.1 ± 0.2
35	11.6 ± 0.5	87 ± 2	12.5 ± 0.1

[a] $T = 25$ °C, $\mu = 0.5$ M, $\lambda = 330$ nm.

Table 3
Thermodynamic activation parameters for the reaction of $CH_3CoL^1(H_2O)^{2+}$ with Cr^{2+}

Configuration	$\Delta H^{\ddagger}$ (kJ/mol)	$\Delta S^{\ddagger}$ (J/K mol)
meso-	43 ± 4	-85 ± 10
pri,rac-	39 ± 4	-82 ± 9
sec,rac-	29 ± 4	-130 ± 25

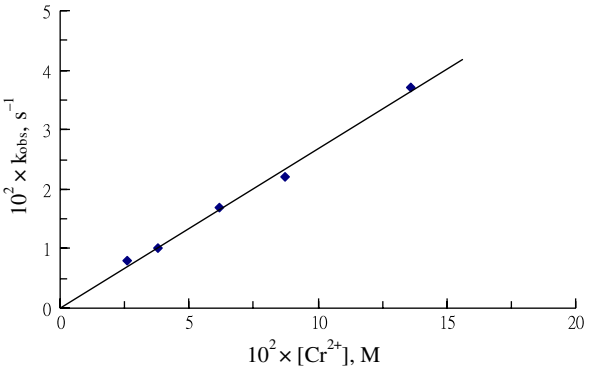


Fig. 4. Dependence of k_{obs} on $[Cr^{2+}]$ for the reaction of $CH_3CoL^2(H_2O)^{2+}$ with Cr^{2+} at 25 °C and $\mu = 1.0$ M.

Table 4
The second-order rate constants for the bimolecular reaction of $CH_3CoL(H_2O)^{2+}$ with Cr^{2+}

L	k ($M^{-1}\,s^{-1}$)
[14]aneN$_4$	0.27[a]
meso-Me$_6$[14]4, 11-dieneN$_4$	7[a]
pri,*rac*-Me$_6$[14]4, 11-dieneN$_4$	46[a]
sec,*rac*-Me$_6$[14]4, 11-dieneN$_4$	7.86[a]
Me$_6$[14]aneN$_4$	1.64[b]
(dmgBF$_2$)$_2$	50.8[c]

[a] This study.
[b] Ref. [8].
[c] Ref. [22].

$C_2H_5CoL^2(H_2O)^{2+}$ was made since the reaction was expected to be even slower.

The present kinetic studies clearly indicate that there is a bimolecular reaction between $RCoL(H_2O)^{2+}$ and Cr^{2+}. The reaction mechanism appears to consist of an S_H2 displacement at the saturated carbon [23]. The second-order rate constants for the methyl cobalt macrocyclic complexes with Cr^{2+} are summarized in Table 4. The reactivity shows a clear dependence on the structure of the ligand. It is noteworthy that the rate constant for the diene ligand (L^1) is higher than that for the saturated macrocycle Me$_6$[14]aneN$_4$(5,7,7,12,14,14-hexamethyl-1,4,8,11-tetraazatetradecane). This probably indicates that the former is less sterically crowded owing to the double bonds that cause the ring configuration to become more planar.

The reaction of $RCoL^1(H_2O)^{2+}$ with V^{2+} was also studied under pseudo-first-order kinetic conditions with V^{2+} in excess. A significant absorption change was observed only for the reactions with *meso*-$C_2H_5CoL^1(H_2O)^{2+}$ and *meso*-$C_3H_7CoL^1(H_2O)^{2+}$. The first-order kinetic plots of $\ln\Delta A$ versus time were linear for the reactions with both *meso*-$C_2H_5CoL^1(H_2O)^{2+}$ and *meso*-$C_3H_7CoL^1(H_2O)^{2+}$. However, the maximum value of the pseudo-first-order rate constants measured in these reactions ($[V^{2+}] = 5.5$–27.4 mM) were not even close to the values of the unimolecular homolysis rate constant, k_h, for these two complexes. The major gas products in the reaction with *meso*-$C_2H_5CoL^1(H_2O)^{2+}$ were ethylene and ethane. This shows that the reaction of ethyl radicals with *meso*-$C_2H_5CoL^1(H_2O)^{2+}$ was still effective under these conditions. This is due to V^{2+} which is not an effective scavenger for ethyl radicals. The slow rate of exchange with solvent results in the lower reactivity of $V(H_2O)_6^{2+}$ in electron transfer reactions [19]. The reactions involved were probably the following:

$$\textit{meso}\text{-}C_2H_5CoL^1(H_2O)^{2+} \rightarrow {}^{\cdot}C_2H_5 + CoL^1(H_2O)_2^{2+} \quad (4)$$

$$\textit{meso}\text{-}C_2H_5CoL^1(H_2O)^{2+} + {}^{\cdot}C_2H_5 \rightarrow C_2H_6 + C_2H_4 + CoL^1(H_2O)_2^{2+} \quad (5)$$

$$V^{2+} + {}^{\cdot}C_2H_5 + H^+ \rightarrow C_2H_6 + V^{3+} \quad (6)$$

The kinetics study was therefore repeated with a high concentration of V^{2+} ($[V^{2+}] = 0.08$–0.31 M). In this case, C_2H_6 was the sole gas product. The plot of k_{obs} versus $[V^{2+}]$ is linear with an intercept of $4.37 \times 10^{-4}\,M^{-1}\,s^{-1}$, which is consistent with the value of the homolysis rate constant of *meso*-$C_2H_5CoL^1(H_2O)^{2+}$. The slope of the line is $4.04 \times 10^{-4}\,M^{-1}\,s^{-1}$. Due to the poor linearity and small value of the slope for the plot of k_{obs} versus $[V^{2+}]$ and no change in absorption of the reaction of $CH_3CoL^1(H_2O)^{2+}$ with V^{2+} under similar conditions, a direct reaction between *meso*-$C_2H_5CoL^1(H_2O)^{2+}$ and V^{2+} was probably non-existent.

4. Conclusion

The kinetic studies clearly show that there is a bimolecular reaction between $RCoL^1(H_2O)^{2+}$ and Cr^{2+}. The reaction rates show a strong dependence on steric effects of the alkyl group, consistent with an S_H2 mechanism. The reactivity is also clearly dependent on the configuration of the complex. However, the difference between the rate constants of *meso*- and *sec*,*rac*- is small.

Acknowledgements

We thank the ISU for supporting this work through Grant ISU-94-02-13. A part of this work was supported through Grant NSC-90-2113-M-214-002.

References

[1] H. Barker, H. Weissbach, R.D. Smyth, Proc. Natl. Acad. Sci. USA (1958) 1093.
[2] P.G. Lenhert, Proc. R. Soc. London, Ser. 45 (1968) 303.
[3] J. Halpern, Acc. Chem. Res. 15 (1982) 238.
[4] F.T.T. Ng, G.L. Rempel, J. Halpern, J. Am. Chem. Soc. 104 (1982) 621.
[5] T.-T. Tsou, M. Loots, J. Halpern, J. Am. Chem. Soc. 104 (1982) 623.
[6] A. Bakac, J.H. Espenson, Inorg. Chem. 26 (1986) 4353.
[7] M.K. Geno, J. Halpern, J. Am. Chem. Soc. 109 (1987) 1238.
[8] S. Lee, J.H. Espenson, A. Bakac, Inorg. Chem. 29 (1990) 3442.
[9] B.S. Jaynes, T. Ren, A. Masschelein, S.J. Lippard, J. Am. Chem. Soc. 115 (1993) 5589.
[10] D.J. Szalda, C.L. Schwarz, C. Creutz, Inorg. Chem. 30 (1991) 586.
[11] C. Creutz, H.A. Schwarz, J.F. Wishart, E. Fujita, N. Sutin, J. Am. Chem. Soc. 113 (1991) 3361.

[12] S. Lee, H.C. Shih, T.H. Su, K.C. He, K.N. Chen, Inorg. Chim. Acta 357 (2004) 485.
[13] J.F. Endicott, K. Kumar, C.L. Schwarz, M.W. Perkovic, W.K. Lin, J. Am. Chem. Soc. 111 (1989) 7411.
[14] R.W. Hay, G.A. Lawrance, N.F. Curtis, J. Chem. Soc., Perkin. Trans. 1 (1975) 591.
[15] D.P. Rilema, J.F. Endicott, E. Papaconstantinou, Inorg. Chem. 10 (1971) 1739.
[16] D.T. Szalda, C.L. Schwarz, J.F. Endicott, E. Fujita, C. Creutz, Inorg. Chem. 28 (1989) 3214.
[17] N.A. Milas, D.M. Sugenor, J. Am. Chem. Soc. 68 (1946) 205.
[18] J.P. Leslie, J.H. Espenson, J. Am Chem. Soc. 98 (1976) 4839.
[19] J.H. Espenson, A. Bakac, J.H. Kim, Inorg. Chem. 30 (1991) 4830.
[20] W. Schmidt, J.H. Swinehart, H. Taube, J. Am. Chem. Soc. 93 (1971) 1117.
[21] M.R. Hyde, J.H. Espenson, J. Am. Chem. Soc. 98 (1976) 4463.
[22] A. Bakac, J.H. Espenson, J. Am. Chem. Soc. 106 (1984) 5197.
[23] J.H. Espenson, J.S. Shveima, J. Am. Chem. Soc. 95 (1973) 4468.

Available online at www.sciencedirect.com
ScienceDirect
Polyhedron 26 (2007) 2906–2910
POLYHEDRON
www.elsevier.com/locate/poly

Re(I)(tricarbonyl)(carboxylate) complexes with the [*N*,*N*′-*bis*(2,4,6-trimethylbenzene)-1,4-diazabutadiene] (2,4,6-Me_3G) and [*N*,*N*′-*bis*(2,4-dimethylbenzene)-2,3-dimethyl-1,4-diazabutadiene] (2,4-Me_2D) ligands – Syntheses and spectroscopic studies. The crystal structure of $[Re(CO)_3(2,4,6\text{-}Me_3G)(OCOCF_3)]$

Reza Kia [a], Valiollah Mirkhani [a,*], Alajos Kálmán [b], Andrea Deák [b,*]

[a] *Department of Chemistry, University of Isfahan, Isfahan 81746-73441, Iran*
[b] *Institute of Structural Chemistry, Chemical Research Center of the Hungarian Academy of Sciences, H-1525 Budapest, P.O. Box 17, Hungary*

Received 6 January 2007; accepted 27 January 2007
Available online 7 February 2007

Abstract

Two new carboxylato complexes, $[Re(CO)_3(DAB)(OCOCF_3)]$ (DAB = substituted aromatic diazabutadiene ligands), were prepared by the reaction of $[Re(CO)_5Cl]$ with the DAB ligands, and the subsequent reaction with $AgOCOCF_3$ gave the related carboxylate complexes. These new complexes were characterized by FTIR, NMR, UV–Vis spectra and elemental analysis. In both complexes, the Re atom has a distorted octahedral configuration and is coordinated by two carbonyl groups and the diimine group of the organic ligand in the equatorial plane. Octahedral coordination is completed at the axial positions by another carbonyl ligand and a carboxyl O atom of the trifluoroacetate anion. Electrochemical behaviour of the investigated complexes has been studied by cyclic voltammetry.
© 2007 Elsevier Ltd. All rights reserved.

Keywords: Rhenium(I) complexes; Diazabutadiene ligand; X-ray crystal structure

1. Introduction

The d^6 transition metal Re(I), Ru(II), Os(II) or Rh(III) complexes with α-diimine ligands have been the subject of intense investigations [1–4]. Complexes of the type $[Re(CO)_3(\alpha\text{-diimine})(X)]^{0/+}$, in which X is a halide, bridging ligand, organic donor/acceptor, nitrogen donor or some other monodentate ligand, have been the subject of a large number of studies. Furthermore, this permanently growing interest stems from the ability of these complexes and their reduced form to act as efficient sensitizers for energy and electron transfer processes [5], and as catalysts in the selective reduction of CO_2 [6], a process of interest in the conversion and storage of solar energy, and serve as models for natural photosynthesis [7,8]. Control of the excited state resulting from metal-to-ligand charge transfer (MLCT) and the redox properties of these complexes, through structural and electronic modifications in the α-diimine chelate and/or axial ligands, has been proposed as a way to improve the photo- and electrocatalytic properties of these compounds. Therefore, knowledge of the molecular and crystal structure of such complexes is essential for understanding and explaining their properties. Significant research has focused on common chelating ligands such as bipyridine (bpy) and phenanthroline (phen), but the chemistry of the *fac*-$[Re(CO)_3(X)]$ complexes with other bidentate α-diimine ligands remains largely unexplored. Bearing in mind all the above mentioned facts, we decided to pursue studies on the *fac*-$[Re(CO)_3(DAB)(OCOCF_3)]$

* Corresponding authors. Tel.: +98 311 7932713; fax: +98 311 6689732 (V. Mirkhani); tel.: +36 1 325 7547; fax: +36 1 438 4141/327 (A. Deák).
E-mail addresses: mirkhani@sci.ui.ac.ir (V. Mirkhani), deak@chemres.hu (A. Deák).

0277-5387/$ - see front matter © 2007 Elsevier Ltd. All rights reserved.
doi:10.1016/j.poly.2007.01.043

complexes in which DAB = [*N*,*N*-bis(2,4,6-trimethylbenzene)-1,4-diazabutadiene] (2,4,6-Me_3G), and [*N*,*N*-bis(2,4-dimethylbenzene)-2,3-dimethyl-1,4-diazabutadiene] (2,4-Me_2D). To the best of our knowledge, these complexes are the first reported Re(I)(tricarbonyl) carboxylate complexes with aromatic diazabutadiene ligands which were characterized by X-ray diffraction analysis, and the complex [$Re(CO)_3$(2,4-Me_2D)($OCOCF_3$)] is the first metal complex containing the *N*,*N*-*bis*(2,4-dimethylbenzene)-2,3-dimethyl-1,4-diazabutadiene ligand. The crystal structure of [$Re(CO)_3$(2,4-Me_2D)($OCOCF_3$)] has been reported elsewhere [9].

2. Experimental

2.1. General

All chemicals used were reagent grade and were used as received. Solvents used for the reactions were purified by literature methods [10]. The diazabutadiene ligands were prepared according to a modified literature procedure [11]. NMR spectra were obtained on a Bruker Avance DRX500 (500 MHz) spectrometer. The chemical shifts (δ) are reported in part per million (ppm) relative to an internal standard of Me_4Si. The UV–Vis spectra were recorded on a Shimadzu UV-160 spectrophotometer with quartz cells (1 cm path length). Elemental analyses were performed using a Heraeus elemental analyzer. IR spectra were recorded as KBr pellets on a Nicolet Impact 400D spectrophotometer. Electrochemical data were obtained by cyclic voltammetry (CV) with a three-electrode cell containing an Ag/AgCl reference electrode, a Pt wire counter electrode and a Pt working electrode. A Metrohm multipurpose instrument model 757 was used. CV measurements were performed in CH_2Cl_2 with 25 mM of Bu_4NClO_4 (TBAP) as a supporting electrolyte. In all electrochemical experiments, the solutions were purged with Ar gas for at least 5 min.

2.2. X-ray crystallography

Suitable single crystals of [Re(2,4,6-Me_3G)$(CO)_3$($OCOCF_3$)] (**1**) were obtained by diffusion of *n*-hexane vapour into a CH_2Cl_2 solution at −18 °C. Crystal data and refinement parameters for complex **1** are summarized in Table 1. Intensity data for complex **1** were collected on a Rigaku R-AXIS RAPID image plate diffractometer (λ(Mo Kα radiation) = 0.71070 Å) at 295 ± 2 K. Several scans in the ϕ and ω directions were made to increase the number of redundant reflections, which were averaged over the refinement cycles. An empirical (multi-scan) absorption correction was applied (ABSCOR) [12]. The structure was solved by the direct method (SIR92) [13] and refined by full-matrix least-squares (SHELXL-97) [14]. All calculations were carried out using the WINGX package of the crystallographic programs [15]. The benzene rings were restrained to be flat within a standard deviation of 0.1 Å (FLAT 0.10 instruction of SHELXL). The carbon atoms of the benzene rings were refined with distance restraints (SADI 0.002 instruction of SHELXL). All non-hydrogen atoms were refined anisotropically in the F^2 mode. Hydrogen atoms were constrained to idealized geometries and refined isotropically. The riding model was applied for the hydrogen atoms. In addition, the riding methyl hydrogen atoms were allowed to rotate freely during refinement.

Table 1
Crystal data and structure refinement parameters for complex **1**

Complex	**1**
Empirical formula	$C_{25}H_{24}F_3N_2O_5Re$
Formula mass	675.66
Crystal size (mm)	0.51 × 0.52 × 0.62
Colour	dark-red
Crystal system	monoclinic
Space group	$P2_1/c$
θ Range for data collection (°)	$3.0 \leqslant \theta \leqslant 27.5$
a (Å)	8.162(3)
b (Å)	13.581(4)
c (Å)	24.456(9)
β (°)	105.07(2)
V (Å^3)	2617.7(16)
Z	4
D_{calc} (Mg/m^3)	1.714
μ (mm^{-1})	4.700
F(000)	1320
Index ranges	$-10 \leqslant h \leqslant 10$, $-16 \leqslant k \leqslant 17$, $-31 \leqslant l \leqslant 31$
Number of collected reflections	20168
Number of independent reflections/R_{int}	5627/0.045
Number of observed reflections $I > 2\sigma(I)$	4644
Number of parameters	331
Goodness-of-fit (GOF)	1.06
R_1 (observed data)	0.0322
wR_2 (all data)[a]	0.0710

[a] $w = 1/[\sigma^2(F_o)^2 + (0.0094P)^2 + 8.4642P]$ where $P = (F_o^2 + 2F_c^2)/3$.

2.3. Synthesis

2.3.1. [*N*,*N*-bis(2,4,6-trimethylbenzene)-1,4-diazabutadiene] (2,4,6-Me_3G)

To a 500 ml round-bottom flask equipped with a magnetic stir bar was added 250 ml of ethanol and (15.115 g, 111.8 mmol) of 2,4,6-Me_3PhNH_2. Glyoxal (8.406 g, 40 wt% solution, 55.86 mmol) was added to the clear, faint yellow solution, and the resulting yellow solution was stirred at room temperature for 14 h. The solution was filtered and the bright yellow solid thus obtained was washed with cold ethanol and dried in vacuo. IR (KBr, cm^{-1}): υ_{max} 1617, 1479 (sym, asym C=N). ^{1}H NMR (500 MHz, $CDCl_3$): 2.21 (s, 12H, 2,6-(CH_3)$_2$); 2.34 (s, 6H, 4-(CH_3)); 6.94 (s, 4H, aromatic hydrogens); 8.15 (s, 2H, iminic hydrogens). ^{13}C{^{1}H} NMR (500 MHz, $CDCl_3$): 18.68; 21.23; 127.00; 129.42; 134.72; 147.85; 163.94 (^{13}C=N). UV–Vis: λ_{max}, ε (nm, M^{-1} cm^{-1}): 248 (12444); 370 (4445).

2.3.2. [N,N-bis(2,4-dimethylbenzene)-2,3-dimethyl-1,4-diazabutadiene] (2,4-Me_2D)

This ligand was prepared by a procedure similar to 2,4,6-Me_3G using (14.4 g, 118.8 mmol) of 2,4-Me_2PhNH_2 and (4.80 g, 55.80 mmol) of diacetyl. The bright yellow solid was washed with cold ethanol and dried in vacuo. IR (KBr, cm^{-1}): υ_{max} 1633, 1488 (sym, asym C=N). ^1H NMR (500 MHz, $CDCl_3$): 2.14 (s, 6H, 2-(CH_3)); 2.17 (s, 6H, 2-(CH_3)); 2.37 (s, 6H, iminic methyls); 6.58–6.60 (d, 2H, aromatic hydrogens); 7.04–7.05 (d, 2H, aromatic hydrogens); 7.09 (s, 2H, aromatic hydrogens). UV–Vis: λ_{max}, ε (nm, $M^{-1}\,cm^{-1}$): 243 (11 360); 345 (3973).

2.3.3. [Re(CO)$_3$(2,4,6-Me_3G)(OCOCF$_3$)] (1)

A mixture of $Re(CO)_5Cl$ (0.5 mmol, 111 mg) and 2,4,6-Me_3G (0.5 mmol, 146 mg) in 20 ml CH_2Cl_2 and 30 ml of absolute ethanol was heated at reflux for 3 h to give a red-brown solution. The solution was concentrated to half volume and a solution of $AgOCOCF_3$ (0.5 mmol, 110 mg) in THF was added. The mixture was refluxed for 4 h in the dark. After cooling, the AgCl precipitate was removed by filtration and the crude material was recrystallized from CH_2Cl_2/hexane to give the carboxylate complex **1** as pure dark-red crystals.

Anal. Calc. for $C_{24}H_{24}F_3N_2O_5Re$: C, 44.44; H, 3.58; N, 4.15. Found; C, 44.45; H, 3.56; N, 4.20%. IR (KBr, cm^{-1}): υ_{max} 2031, 1931, 1921 (CO). ^1H NMR (500 MHz, $CDCl_3$): 2.24 (s, 6H, CH_3); 2.29 (s, 6H, CH_3); 2.38 (s, 6H, CH_3); 7.03 (s, 4H, aromatic hydrogens); 8.79 (s, 2H, iminic hydrogens). UV–Vis: λ_{max}, ε (nm, $M^{-1}\,cm^{-1}$): 239 (13 720); 480 (8773).

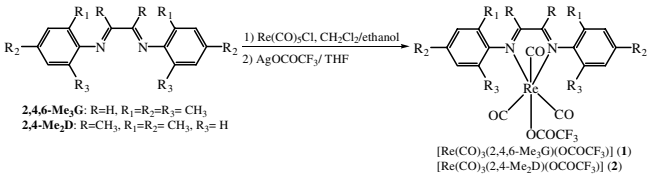
2.3.4. [Re(CO)$_3$(2,4-Me_2D)(OCOCF$_3$)] (2)

This complex was prepared by a procedure similar to **1**using 146 mg (0.5 mmol) of 2,4-Me_2D. The crude material was recrystallized from CH_2Cl_2/hexane to give [Re(CO)$_3$(2,4-Me_2D)(OCOCF$_3$)] as pure dark-red crystals. *Anal.* Calc. for $C_{25}H_{24}F_3N_2O_5Re$: C, 44.44; H, 3.58; N, 4.15. Found; C, 44.46; H, 3.60; N, 4.15%. IR (KBr, cm^{-1}): υ_{max} 2023, 1929 (CO). ^1H NMR (500 MHz, $CDCl_3$): 2.07–2.40 (s, 18H, 6CH_3); 6.7–7.2 (6H, aromatic hydrogens). $^{13}C\{^1H\}$ NMR (500 MHz, $CDCl_3$): 16.76, 17.25, 17.53, 20.16–20.18, 20.30, 20.90–20.94, 119.95–120.04, 120.55, 126.06, 126.62, 127.76, 127.96, 128.35–128.40, 131.90, 131.97, 132.26, 137.61–137.66, 145.73–145.78, 146.12, 176.59–176.80, 195.48. UV–Vis: λ_{max}, ε (nm, $M^{-1}\,cm^{-1}$): 239 (14 386); 430 (9573).

3. Results and discussion

3.1. General characterization

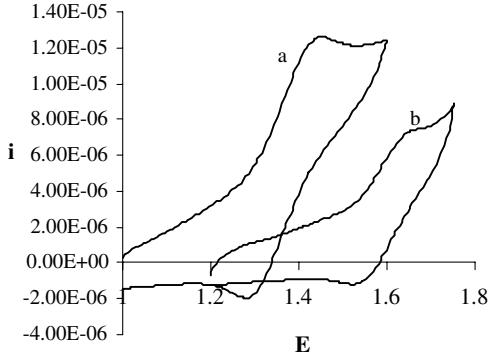
The new *fac*-[Re(CO)$_3$(DAB)(OCOCF$_3$)] (DAB = substituted aromatic diazabutadiene ligands) complexes were obtained via substitution reactions, as outlined in Scheme 1. The trifluoroacetateo complexes were synthesized by allowing the in situ reaction of the halide carbonyl with 1 equivalent of $AgOCOCF_3$ in a mixture of ethanol and THF in the dark. After cooling, the AgCl that formed during the reaction was removed by filtration. The partial removal of the solvent and addition of *n*-hexane resulted in the formation of the corresponding complexes **1** and **2** in good yield. These new complexes are stable in the solid state and in solution at room temperature and they were characterized by the usual spectroscopic techniques. The IR spectra of the free ligands exhibit the characteristic bands of the symmetrical and asymmetrical stretching of the imine group at 1617 and 1479 cm^{-1} for 2,4,6-Me_3G and 1633 and 1488 cm^{-1} for 2,4-Me_2D. The IR spectra of complexes exhibit the characteristic bands in the carbonyl stretching region as a sharp intense band at 2031 and 2023 cm^{-1} for complexes **1** and **2**, respectively, and two lower-energy bands closely spaced at 1936 and 1921 cm^{-1} for complex **1** and 1929 cm^{-1} for complex **2**, typical of Re(I) α-diimine tricarbonyl complexes [16,17]. The nature of the axial ligand in the [Re(CO)$_3$(NN)(X)] complexes influences, to some extent, the position and the shape of the absorption band in the IR spectra. The π-donor character of the oxygen atom in the trifluoroacetate group increases the Re → CO back-bonding, which decreases the energy of υ(CO) [18]. The NMR spectra and peak assignments of the ligands and their complexes are presented in Section 2. For complexes **1** and **2**, the signal due to the methyl groups in the *ortho* and *para* positions of the phenyl ring appears at about 2.24–2.38 and 2.07–2.40 ppm, respectively. The signal due to the iminic methyl in complex **2** appears at about 2.36 ppm. For complex **1**, the signal due to the iminic hydrogen appears at about 8.79 ppm. The signal due to the aromatic hydrogens appears at about 7.03 and 7.30 ppm for complex **1** and at about 6.72–7.25 ppm for complex **2**. All the signals due to the different hydrogens in the ^1H NMR spectra of complexes **1** and **2** are shifted to the low-field region with respect to the free ligands as a result of ligand coordination. The UV–Vis spectral data of the ligands and their complexes are presented in Table 2. The UV–Vis bands of the ligands are assigned to ligand-centered π → π* and n → π* transitions [11]. The absorption spectra of the complexes can be interpreted by comparison with other Re(I) complexes with ligands structurally related to those used in this work [19–21]. The higher energy bands observed in the spectra have been considered as intraligand π → π* transitions, and these are also present for the free ligands in the same spectral regions. The longer wavelength absorption bands show a maximum in the range 400–500 nm. These bands have been assigned partly to metal-to-ligand charge-transfer (MLCT)



Scheme 1.

Table 2
UV–Vis spectral data of the DAB ligands, and complexes **1** and **2**

Compound	Concentration (M)	Solvent	UV–Vis λ_{max} (nm) [ε] ($M^{-1}\,cm^{-1}$)
2,4,6Me_3G	9×10^{-5}	CH_2Cl_2	248 [12444], 370 [4445]
2,4Me_2D	1.5×10^{-3}	CH_2Cl_2	243 [11360], 345 [3973]
Complex **1**	7.5×10^{-5}	CH_2Cl_2	239 [13720], 480 [8773]
Complex **2**	7.5×10^{-5}	CH_2Cl_2	239 [14386], 430 [9573]



(a) Complex (**1**) and (b) Complex (**2**)

Fig. 1. Cyclic voltammograms of **1** (a) and **2** (b) in CH_2Cl_2 at 293 K (scan rate, 100 mV/s, $C = 2.5\times10^{-4}$ M).

transitions, mixed with a $\pi \rightarrow \pi^*$ transition of the Re(DAB) chelate. The electrochemical behaviour of complexes **1** and **2** was examined by means of cyclic voltammetry (CV) in CH_2Cl_2 (Fig. 1). Anodic scans reveal a single reversible oxidation at 1.44 and 1.66 V versus Ag/AgCl for the complexes **1** and **2**, respectively. This is assigned to the Re(II)/Re(I) redox couple, which is similar to the anodic peak potential reported for similar systems [22]. Complexes **1** and **2** show quasireversible redox couples with $E_{1/2}$ values of 1.36 and 1.59 V, respectively. The cyclic voltammetry peak-to-peak separations (ΔE_p) of 160 and 130 mV were observed at a scan rate (υ) of 100 mV^{-1} for complexes **1** and **2**, respectively.

*3.2. X-ray structure of [Re(CO)$_3$(2,4,6-Me$_3$G)(OCOCF$_3$)] (**1**)*

The molecular structure of **1** is shown in Fig. 2, selected bond lengths and angles are listed in Table 3. The Re atom has a distorted octahedral configuration and is coordinated by two carbonyl groups and the diimine group of the 2,4,6-Me_3G ligand in the equatorial plane. Octahedral coordination is completed at the axial positions by another carbonyl ligand and a carboxyl O atom of the trifluoroacetate anion. The equatorial Re–C distances are 1.909(6) and 1.923(5) Å, respectively. The equatorially disposed *N*,*N*′-bidentate chelating 2,4,6-Me_3G ligand forms a ReN_2C_2 five-membered chelate ring and the mean deviation of these atoms from the least-square plane is only 0.0274 Å. In this five-membered chelate ring the

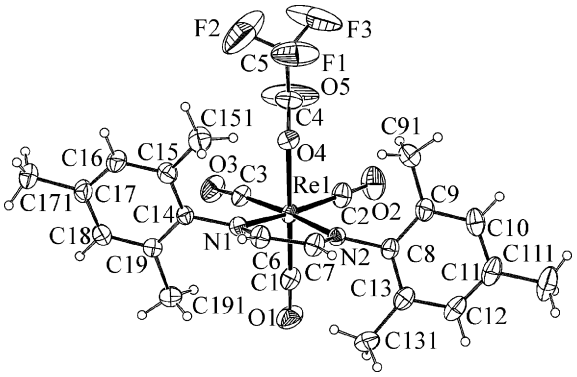


Fig. 2. ORTEP drawing for complex **1**. Non-hydrogen atoms are shown as 30% probability ellipsoids.

Table 3
Selected bond distances (Å) and angles (°) for complex **1**

Complex **1**			
Re(1)–N(1)	2.186(4)	C(1)–Re(1)–O(4)	179.7(2)
Re(1)–N(2)	2.160(4)	C(2)–Re(1)–C(3)	88.3(2)
Re(1)–O(4)	2.153(3)	C(3)–Re(1)–N(1)	99.4(2)
Re(1)–C(1)	1.896(6)	N(1)–Re(1)–N(2)	74.1(2)
Re(1)–C(2)	1.909(6)	N(2)–Re(1)–C(2)	98.3(2)
Re(1)–C(3)	1.923(5)		

Table 4
Parameters of hydrogen bonding interactions in complex **1**

Complex **1**	D–H···A	H···A (Å)	D···A (Å)	D–H···A (°)
	C(151)–H(15B)···O(4)	2.44	3.308(8)	150
	C(6)–H(6)···O(5)^{i}	2.13	2.940(8)	145
	C(131)–H(13A)···F(1)^{ii}	2.48	3.399(10)	159

Symmetry codes: (i) $1+x, y, z$; (ii) $1-x, -1/2+y, 1/2-z$.

N(1)–Re(1)–N(2) bite angle is 74.1(2)° and Re–N (N1, N2) bond lengths are 2.186(4) and 2.160(4) Å, respectively. Owing to the steric requirements of the *N*,*N*′-bidentate chelating 2,4,6-Me_3G ligand the equatorial bond angles range from 74.1(2)° to 99.4(2)°. The axial C(1)–Re(1)–O(4) bond angle is 179.7(2)°. Due to the π-donor character of the trifluoroacetate ligand, the axial Re–C bond length of 1.896(6) Å is slightly shorter than the corresponding equatorial Re–C distances. The CF_3 group has high thermal motion consistent with some unresolved rotational disorder, as is often found in other trifluoroacetate compounds [9,23,24]. The overall structural similarity of **1** with the previously reported [Re(CO)$_3$(2,4-Me_2D)(OCOCF$_3$)] complex [9] reflects the strong tendency of substituted diazabutadiene ligands to enforce a distorted-octahedral geometry at Re. In addition, there are weak intra- and intermolecular C–H···O, as well as intermolecular C–H···F interactions (Table 4) in the crystal lattice of **1**.

4. Conclusion

The *fac*-[$Re(CO)_3$(DAB)($OCOCF_3$)] (DAB = 2,4,6-Me_3G, 2,4Me_2D) rhenium(I) complexes have been prepared and characterized by IR, UV–Vis, NMR, electrochemical and X-ray diffraction techniques. Variations in the electronic properties related to rhenium(I), the carbonyl and X ligands, such as electronic transitions, CO stretching and some crystallographic parameters of the complexes, were interpreted on the basis of the DAB and X ligands. It is clear from the data that, by varying the nature of the DAB ligands attached to rhenium, the electronic properties of the *fac*-[$Re(CO)_3$(DAB)($OCOCF_3$)] complexes could be tuned.

Acknowledgements

R.K. and V.M. thank the University of Isfahan for partial support of this research. Mr. A. Siroueinezhad is acknowledged for the CV recordings.

Appendix A. Supplementary material

CCDC 630420 contains the supplementary crystallographic data for **1**. These data can be obtained free of charge via http://www.ccdc.cam.ac.uk/conts/retrieving.html, or from the Cambridge Crystallographic Data Centre, 12 Union Road, Cambridge CB2 1EZ, UK; fax: (+44) 1223-336-033; or e-mail: deposit@ccdc.cam.ac.uk. Supplementary data associated with this article can be found, in the online version, at doi:10.1016/j.poly.2007.01.043.

References

[1] A. Vlcek Jr., J. Heyrovsky, in: V. Balzani (Ed.), Electron Transfer in Chemistry, Part 2, vol. 2, Wiley-VCH Verlag GmbH, Weinheim, 2001, p. 804.
[2] A.J. Lees, Chem. Rev. 87 (1987) 711.
[3] A.I. Baba, J.R. Shaw, J.A. Simon, R.P. Thummel, R.H. Schmehl, Coord. Chem. Rev. 171 (1988) 43.
[4] D.J. Stufkens, A. Vlcek, Coord. Chem. Rev. 171 (1988) 127.
[5] D.J. Stufkens, Comments Inorg. Chem. 13 (1992) 359.
[6] (a) J. Hawecker, J.M. Lehn, R. Ziessel, J. Chem. Soc., Chem. Commun (1983) 536;
(b) B.P. Sullivan, T.J. Meyer, J. Chem. Soc., Chem. Commun. (1984) 1244;
(c) G. Calzaferri, K. Hadener, J. Li, J. Photochem. Photobiol. A 64 (1992) 259.
[7] C. Kutal, A.J. Corbin, G. Ferraudi, Organometallics 6 (1987) 553.
[8] B.P. Sullivan, T.J. Meyer, J. Chem. Soc., Chem. Commun. (1984) 1414, and references therein.
[9] R. Kia, V. Mirkhani, A. Deák, A. Kálmán, Acta Crystallogr., Sect. E 61 (2005) m566.
[10] D.D. Perrin, W.L. Armarego, D.R. Perrin, Purification of Laboratory Chemicals, second ed., Pergamon, New York, 1990.
[11] H. tom Dieck, I.W. Renk, Chem. Ber. 104 (1971) 92.
[12] T. Higashi, ABSCOR, Rigaku Corporation, Tokyo, Japan, 1995.
[13] A. Altomare, G. Cascarano, C. Giacovazzo, A. Guagliardi, M.C. Burla, G. Polidori, M. Camalli, J. Appl. Cryst. 27 (1994) 435.
[14] G.M. Sheldrick, SHELXL97-Program for the Refinement of Crystal Structures, University of Göttingen, Germany, 1997.
[15] L.J. Farrugia, J. Appl. Cryst. 32 (1999) 837.
[16] W. Kaim, H.E.A. Kramer, C. Vogler, J. Rieker, J. Organomet. Chem. 367 (1989) 107.
[17] E. Wolcan, G. Trochia, J. Tocho, O.E. Piro, P. Juliarena, G. Ruiz, M.R. Feliz, J. Chem. Soc., Dalton Trans. (2002) 2194.
[18] A. Klein, C. Vogler, W. Kaim, Organometallics 15 (1996) 236.
[19] C.H. Staal, A. Oskam, K. Vrieze, J. Organomet. Chem. 170 (1979) 235.
[20] R.W. Balk, D.J. Stufkens, A. Oskam, J. Chem. Soc., Dalton Trans. (1981) 1124.
[21] G.J. Stor, D.J. Stufkens, A. Oskam, Inorg. Chem. 31 (1992) 1318.
[22] R.N. Dominey, B. Hauser, J. Hubbard, J. Dunham, Inorg. Chem. 30 (1991) 4754.
[23] V.H. Rodrigues, J.A. Paixao, M.M.R.R. Costa, A. Beja Matos, Acta. Crystallogr., Sect. C 56 (2000) 1053.
[24] V.H. Rodrigues, J.A. Paixao, M.M.R.R. Costa, A. Beja Matos, Acta. Crystallogr., Sect. C 57 (2001) 417.

Available online at www.sciencedirect.com
ScienceDirect
Polyhedron 26 (2007) 2911–2918
POLYHEDRON
www.elsevier.com/locate/poly

Synthesis, crystal structure and spectroscopic characterization of new neutral and cationic (η^6-*p*-cymene)–ruthenium(II) complexes with phosphine–amide ligands

Gregorio Sánchez [a], Joaquín García [a], Juan J. Ayllón [a], José L. Serrano [b,*], Luis García [b], José Pérez [b], Gregorio López [a]

[a] *Departamento de Química Inorgánica, Universidad de Murcia, 30071 Murcia, Spain*
[b] *Departamento de Ingeniería Minera, Geológica y Cartográfica, Área de Química Inorgánica, 30203 Cartagena, Spain*

Received 10 January 2007; accepted 26 January 2007
Available online 3 February 2007

Abstract

The dimeric starting material [Ru(η^6-*p*-cymene)(μ-Cl)Cl]$_2$ reacts with the phosphino-amides *o*-Ph_2P–C_6H_4CO–NH–R [R = ^{i}Pr (**a**), Ph (**b**), 4-MeC_6H_4 (**c**), 4-FC_6H_4 (**d**)] to give the mononuclear compounds **1a**–**d** [RuCl(η^6-*p*-cymene)(*o*-Ph_2P–C_6H_4–CO–NH–R)]Cl. The subsequent reaction of these complexes with KPF_6 produced the cationic species **2a**–**d** [RuCl(η^6-*p*-cymene)(*o*-Ph_2P–C_6H_4–CO–NH–R)][PF_6] in which phosphino-amides also act as rigid *P*,*O*-chelating ligands. The molecular structures of **2b**–**d** were determined crystallographically. Amide deprotonation is achieved when complexes **2a**–**d** were made react with 1 M aqueous solution of KOH, affording the corresponding neutral species **3a**–**d** [RuCl(η^6-*p*-cymene)(*o*-Ph_2P–C_6H_4–CO–N–R)] in which a P,N-coordination mode is suggested.
© 2007 Elsevier Ltd. All rights reserved.

Keywords: Phosphino-amides; Hemilabile ligands; Coordination modes; (η^6-*p*-cymene) complexes; Crystal structures; Ruthenium

1. Introduction

Hybrid ligands that contain distinct chemical functions [1–5], such as soft phosphine and hard (e.g., N or O) donor atoms, have attracted continuous interest during last years as a result of their versatile coordination behaviour [6,7] and its potential hemilability [3–5]. These properties have been exploited in several ways, as the ''weak-link approach'' for the synthesis of supramolecular structures [8] or the use of some ligands and its complexes in chemical sensing [9–11] and catalytic processes. It is in this last field that phosphine–amide ligands have received growing attention: the asymmetric 1,4-addition reaction of arylboronic acids with cycloalkenones is catalysed by an amidophosphine rhodium(I) complex [12], amide derived phosphines possessing various *N*,*N*-dialkyl aromatic amide scaffolds have shown to be highly effective in Suzuki cross-coupling reactions [13,14], and 2-diphenylphosphinobenzamido nickel complexes have found application in ethylene polymerization, showing that slight variations in the ligand frame produce drastic changes in the catalytic behaviour [15].

On the other hand, half-sandwich ruthenium(II) complexes bearing hemilabile ligands have been studied as efficient catalyst in hydrogen transfer reactions [16–21], and the hemilabile properties of several P,N- or P,O-donor ligands have been investigated synthesizing complexes in which these ligands adopt different coordination modes to the ruthenium atom [22–26]. No analogous studies concerning the phosphino-amides *o*-Ph_2P–C_6H_4–CO–NH–R have been reported and, as far as we are aware, the ligand 1,2-bis-N[2′-(diphenylphosphinobenzoyl)]diaminonaphthalene and its dimeric *p*-cymene ruthenium complex is the closest precedent described to date [26].

* Corresponding author.
E-mail address: jose.serrano@upct.es (J.L. Serrano).

0277-5387/$ - see front matter © 2007 Elsevier Ltd. All rights reserved.
doi:10.1016/j.poly.2007.01.033

We have recently studied the coordination properties of these mixed-donor bidentate ligands in their first described palladium(II) complexes, containing cyclometallated [27] or pentafluorophenyl co-ligands [28]. As a extension of our work on *o*-Ph_2P–C_6H_4–CO–NH–R ligands in this paper we present the preparation and characterization of new neutral and cationic (η^6-*p*-cymene)–ruthenium(II) complexes.

2. Experimental

2.1. Methods and materials

C, H, and N analyses were carried out with a Carlo Erba instrument. IR spectra were recorded on a Perkin–Elmer spectrophotometer 16F PC FT-IR, using Nujol mulls between polyethylene sheets. NMR data (^1H, ^{31}P) were recorded on Bruker Avance 200 and 300 spectrometers. Mass spectrometric analyses were performed on a Fisons VG Autospec double-focusing spectrometer, operated in positive mode. Ions were produced by fast atom bombardment (FAB) with a beam of 25 keV Cs atoms. The mass spectrometer was operated with an accelerating voltage of 8 kV and a resolution of at least 1000. All the solvents were dried by conventional methods.

The diphenylphosphinobenzamides *o*-Ph_2P–C_6H_4–CO–NH–R (R = ^{i}Pr (**a**), Ph (**b**), 4-MeC_6H_4 (**c**), 4-FC_6H_4 (**d**)) were prepared by a reported procedure [28]. The starting dinuclear dichloro complex [Ru(η^6-*p*-cymene)(μ-Cl)Cl]$_2$ was prepared according to a published method [29].

2.2. Synthesis

2.2.1. Preparation of complexes [RuCl(η^6-p-cymene)-(o-Ph_2P–C_6H_4–CO–NH–R)]Cl (R = ^{i}Pr (**1a**); R = Ph (**1b**); R = 4-MeC_6H_4 (**1c**); R = 4-FC_6H_4 (**1d**))

The new complexes were obtained by treating [Ru(η^6-*p*-cymene)(μ-Cl)Cl]$_2$ with previously prepared 2-diphenylphosphine benzamides in molar ratio 1:2, using CH_2Cl_2 as solvent and according to the following general method. To a dichloromethane solution (15 mL) of the precursor (250 mg; 0.40 mmol) was added solid 2-diphenylphosphinebenzamide (0.80 mmol). The resulting solution was stirred for 60 min. at room temperature and then concentrated to half volume under reduced pressure. Addition of diethyl ether caused precipitation of the new complexes, which were filtered off, air dried and recrystallized from dicholoromethane–ether.

[RuCl(η^6-*p*-cymene)(*o*-Ph_2P–C_6H_4–CO–NH–^{i}Pr)]Cl (**1a**): (70% yield). *Anal.* Calc. for $C_{32}Cl_2H_{36}NOPRu$: C, 58.8; H, 5.5; N, 2.1. Found: C, 59.0; H, 5.7; N, 1.9%. FT-IR (Nujol mull cm^{-1}): *v*(NH) 3325(s); *v*(CO) 1608(vs). ^1H NMR (300 MHz, $CDCl_3$): δ (ppm): 10.88 (s, 1H, NH), 8.52 (m, 1H, P–C_6H_4–CO–), 7.88–7.44 (m, 11H, 10H, PPh_2 + 1H P–C_6H_4–CO–), 7.24 (m, 1H, P–C_6H_4–CO–), 6.51 (m, 1H, P–C_6H_4–CO–), 5.85 (d, J_{HH} = 6.0 Hz, 1H, Cy), 5.74 (d, J_{HH} = 6.0 Hz, 1H, Cy), 5.39 (m, 1H, Cy), 5.19 (d, J_{HH} = 6.0 Hz, 1H, Cy), 4.15 (m, 1H, CH, N–^{i}Pr), 2.38 (m, 1H, CH, ^{i}Pr–Cy), 1.88 (s, 3H, Me–Cy), 1.46 (d, J_{HH} = 6.4 Hz, 3H, Me, N–^{i}Pr), 1.21 (d, J_{HH} = 6.4 Hz, 3H, Me, N–^{i}Pr), 1.15 (d, J_{HH} = 6.6 Hz, 3H, Me, ^{i}Pr–Cy), 0.54 (d, J_{HH} = 6.4 Hz, 3H, Me, ^{i}Pr–Cy). ^{31}P NMR (300 MHz, $CDCl_3$): δ (ppm): 33.8 (s). FAB-MS (positive mode) *m*/*z*: 618 (M^+ − Cl), 583 (M^+ − 2Cl).

[RuCl(η^6-*p*-cymene)(*o*-Ph_2P–C_6H_4–CO–NH–Ph)]Cl (**1b**): (71% yield). *Anal.* Calc. for $C_{35}Cl_2H_{34}NOPRu$: C, 61.1; H, 5.0; N, 2.0. Found: C, 60.9; H, 5.2; N, 2.0%. FT-IR (Nujol mull cm^{-1}): *v*(NH) 3405(s); *v*(CO) 1600(vs). ^1H NMR (300 MHz, $CDCl_3$): δ (ppm): 12.99 (s, 1H, NH), 8.61 (m, 1H, P–C_6H_4–CO–), 7.92–7.31 (m, 15H, 10H PPh_2 + 5H N–Ph), 7.65 (m, 1H, P–C_6H_4–CO–), 7.21 (m, 1H, P–C_6H_4–CO–), 6.69 (m, 1H, P–C_6H_4–CO–), 5.86 (d, J_{HH} = 6.6 Hz, 1H, Cy), 5.79 (d, J_{HH} = 6.6 Hz, 1H, Cy), 5.28 (m, 1H, Cy), 4.89 (d, J_{HH} = 4.8 Hz, 1H, Cy), 1.89 (s, 3H, Me–Cy), 1.63 (m, 1H, CH, ^{i}Pr–Cy), 0.81 (d, J_{HH} = 6.0 Hz, 3H, Me, ^{i}Pr–Cy), −0.07 (d, J_{HH} = 6.9 Hz, 3H, Me,^{i}Pr–Cy). ^{31}P NMR (300 MHz, $CDCl_3$): δ (ppm): 33.4 (s). FAB-MS (positive mode) *m*/*z*: 652 (M^+−Cl), 617 (M^+−2Cl).

[RuCl(η^6-*p*-cymene)(*o*-Ph_2P–C_6H_4–CO–NH–C_6H_4– CH_3)]-Cl (**1c**): (81% yield). *Anal.* Calc. for $C_{36}Cl_2H_{36}NOPRu$: C, 61.6; H, 5.2; N, 2.1. Found: C, 61.8; H, 5.3; N, 2.1%. FT-IR (Nujol mull cm^{-1}): *v*(NH) 3402(s); *v*(CO) 1586(vs). ^1H NMR (300 MHz, $CDCl_3$): δ (ppm): 12.99 (s, 1H, NH), 8.63 (m, 1H, P–C_6H_4–CO–), 7.90 (m, 2H, N–C_6H_4–CH_3), 7.65 (m, 1H, P–C_6H_4–CO–), 7.52–7.39 (m, 10H PPh_2), 7.33 (m, 1H, P–C_6H_4–CO–), 7.14 (m, 2H, N–C_6H_4–CH_3), 6.68 (m, 1H, P–C_6H_4–CO–), 5.85 (d, J_{HH} = 6.6 Hz, 1H, Cy), 5.79 (d, J_{HH} = 6.6 Hz, 1H, Cy), 5.28 (m, 1H, Cy), 4.89 (d, J_{HH} = 5.1 Hz, 1H, Cy), 2.32 (s, 3H, Me, N–C_6H_4–CH_3), 1.87 (s, 3H, Me–Cy), 1.66 (m, 1H, CH, ^{i}Pr–Cy), 0.83 (d, J_{HH} = 6.9 Hz, 3H, Me, ^{i}Pr–Cy), −0.05 (d, J_{HH} = 6.6 Hz, 3H, Me, ^{i}Pr–Cy). ^{31}P NMR (300 MHz, $CDCl_3$): δ (ppm): 33.4 (s). FAB-MS (positive mode) *m*/*z*: 666 (M^+−Cl), 631 (M^+−2Cl).

[RuCl(η^6-*p*-cymene)(*o*-Ph_2P–C_6H_4–CO–NH–C_6H_4–F)]-Cl (**1d**): (62% yield). *Anal.* Calc. for $C_{35}Cl_2FH_{33}NOPRu$: C, 59.6; H, 4.7; N, 2.0. Found: C, 59.4; H, 4.5; N, 2.3%. FT-IR (Nujol mull cm^{-1}): *v*(NH) 3372(s); *v*(CO) 1586(vs). ^1H NMR (300 MHz, $CDCl_3$): δ (ppm): 13.25 (s, 1H, NH), 8.69 (m, 1H, P–C_6H_4–CO–), 7.90 (m, 2H, N–C_6H_4–F), 7.67–7.48 (m, 11H, 10H PPh_2 + 1H P–C_6H_4–CO–), 7.35 (m, 1H, P–C_6H_4–CO–), 7.06 (m, 2H, N–C_6H_4–F), 6.69 (m, 1H, P–C_6H_4–CO–), 5.87 (d, J_{HH} = 6.9 Hz, 1H, Cy), 5.79 (d, J_{HH} = 6.6 Hz, 1H, Cy), 5.27 (m, 1H, Cy), 4.92 (d, J_{HH} = 5.4 Hz, 1H, Cy), 1.87 (s, 3H, Me–Cy), 1.67 (m, 1H, CH, ^{i}Pr–Cy), 0.87 (d, J_{HH} = 6.9 Hz, 3H, Me, ^{i}Pr- -Cy), 0.01 (d, J_{HH} = 6.6 Hz, 3H, Me, ^{i}Pr–Cy). ^{31}P NMR (300 MHz, $CDCl_3$): δ (ppm): 33.3 (s). ^{19}F NMR (200 MHz, $CDCl_3$): δ (ppm): −114.9 (s). FAB-MS (positive mode) *m*/*z*: 670 (M^+−Cl), 635 (M^+−2Cl).

*2.2.2. Preparation of complexes [RuCl(η⁶-p-cymene)-(o-Ph₂P–C₆H₄–CO–NH–R)][PF₆] (R = ⁱPr (**2a**); R = Ph (**2b**); R = 4-MeC₆H₄ (**2c**); R = 4-FC₆H₄ (**2d**))*

The new complexes were obtained by treating 0.145 mmol of the corresponding complexes [RuCl(η⁶-*p*-cymene)(*o*-Ph_2P–C_6H_4–CO–NH–R)]Cl (R = ⁱPr (**1a**); R = Ph (**1b**); R = 4-MeC_6H_4 (**1c**); R = 4-FC_6H_4 (**1d**)) in acetone (20 ml) with stoichiometric KPF_6 (0.145 mmol). After 1/2 h stirring at room temperature, the mixture was filtered to remove KCl, and the resulting orange solution then concentrated to half volume under reduced pressure. Addition of diethyl ether caused precipitation of the new complexes, which were filtered off, air dried and recrystallized from acetone–ether.

[RuCl(η⁶-*p*-cymene)(*o*-Ph_2P–C_6H_4–CO–NH–ⁱPr)][PF_6] (**2a**): (85% yield). *Anal.* Calc. for $C_{32}ClF_6H_{36}NOP_2Ru$: C, 50.4; H, 4.8; N, 1.8. Found: C, 50.2; H, 5.0; N, 1.9%. FT-IR (Nujol mull cm^{-1}): *ν*(NH) 3378(s); *ν*(CO) 1596(vs); *ν*(PF_6) 844(s). FAB-MS (positive mode) *m*/*z*: 618 ($M^+ - PF_6$), 583 ($M^+ - PF_6 - Cl$).

[RuCl(η⁶-*p*-cymene)(*o*-Ph_2P–C_6H_4–CO–NH–Ph)][PF_6] (**2b**): (80% yield). *Anal.* Calc. for $C_{35}ClF_6H_{34}NOP_2Ru$: C, 52.7; H, 4.3; N, 1.8. Found: C, 52.9; H, 4.5; N, 1.9%. FT-IR (Nujol mull cm^{-1}): *ν*(NH) 3352(s); *ν*(CO) 1592(vs); *ν*(PF_6) 846(s). FAB-MS (positive mode) *m*/*z*: 652 ($M^+ - PF_6$), 617 ($M^+ - PF_6 - Cl$).

[RuCl(η⁶-*p*-cymene)(*o*-Ph_2P–C_6H_4–CO–NH–C_6H_4–CH_3)]-[PF_6] (**2c**): (69% yield). *Anal.* Calc. for $C_{36}ClF_6H_{36}NOP_2Ru$: C, 53.3; H, 4.5; N, 1.7. Found: C, 53.6; H, 4.7; N, 2.0%. FT-IR (Nujol mull cm^{-1}): *ν*(NH) 3354(s); *ν*(CO) 1594(vs); *ν*(PF_6) 847(s). FAB-MS (positive mode) *m*/*z*: 666 ($M^+ - PF_6$), 631 ($M^+ - PF_6 - Cl$).

[RuCl(η⁶-*p*-cymene)(*o*-Ph_2P–C_6H_4–CO–NH–C_6H_4–F)]-[PF_6] (**2d**): (67% yield). *Anal.* Calc. for $C_{35}ClF_7H_{33}NOP_2Ru$: C, 51.6; H, 4.1; N, 1.7. Found: C, 51.7; H, 4.3; N, 2.0%. FT-IR (Nujol mull cm^{-1}): *ν*(NH) 3354(s); *ν*(CO) 1592(vs); *ν*(PF_6) 845(s). FAB-MS (positive mode) *m*/*z*: 670 ($M^+ - PF_6$), 635 ($M^+ - PF_6 - Cl$).

*2.2.3. Preparation of complexes [RuCl(η⁶-p-cymene)-(o-Ph₂P–C₆H₄–CO–N–R)] (R = ⁱPr (**3a**); R = Ph (**3b**); R = 4-MeC₆H₄ (**3c**); R = 4-FC₆H₄ (**3d**))*

The new complexes were obtained by treating 0.145 mmol of the corresponding complexes [RuCl(η⁶-*p*-cymene)(*o*-Ph_2P–C_6H_4–CO–NH–R)][PF_6] (R = ⁱPr (**2a**); R = Ph (**2b**); R = 4-MeC_6H_4 (**2c**); R = 4-FC_6H_4 (**2d**)) in acetone (30 ml) with stoichiometric amount of 1 M KOH aqueous solution. After 1 h stirring at room temperature, the mixture was concentrated to half volume under reduced pressure. Addition of diethyl ether caused precipitation of the new complexes, which were filtered off, washed with water, air dried and recrystallized from acetone–ether.

[RuCl(η⁶-*p*-cymene)(*o*-Ph_2P–C_6H_4–CO–N–ⁱPr)] (**3a**): (78% yield). *Anal.* Calc. for $C_{32}ClH_{35}NOPRu$: C, 62.4; H, 5.6; N, 2.3. Found: C, 62.5; H, 5.8; N, 2.5%. FT-IR (Nujol mull cm^{-1}): *ν*(CO) 1586(vs). ^1H NMR (300 MHz, $CDCl_3$): *δ* (ppm): 8.36 (m, 1H, P–C_6H_4–CO–), 7.97 (m, 1H, P–C_6H_4–CO–), 7.60–7.27 (m, 10H, PPh_2), 7.04 (m, 1H, P–C_6H_4–CO–), 6.55 (m, 1H, P–C_6H_4–CO–), 5.68 (d, $J_{HH} = 6.2$ Hz, 1H, Cy), 5.46 (d, $J_{HH} = 6.2$ Hz, 1H, Cy), 5.35 (m, 1H, Cy), 4.99 (d, $J_{HH} = 5.6$ Hz, 1H, Cy), 4.10 (m, 1H, CH, N–ⁱPr), 2.48 (m, 1H, CH, ⁱPr–Cy), 1.89 (s, 3H, Me–Cy), 1.26 (d, $J_{HH} = 6.4$ Hz, 3H, Me, N–ⁱPr), 1.12 (d, $J_{HH} = 6.4$ Hz, 3H, Me, N–ⁱPr), 1.03 (d, $J_{HH} = 7.0$ Hz, 3H, Me,ⁱPr–Cy), (d, $J_{HH} = 7.0$ Hz, 3H, Me, ⁱPr–Cy). ^{31}P NMR (300 MHz, $CDCl_3$): *δ* (ppm): 30.2 (s). FAB-MS (positive mode) *m*/*z*: 617 (M^+), 580 ($M^+ - Cl$).

[RuCl(η⁶-*p*-cymene)(*o*-Ph_2P–C_6H_4–CO–N–Ph)] (**3b**): (52% yield). *Anal.* Calc. for $C_{35}ClH_{33}NOPRu$: C, 64.6; H, 5.1; N, 2.1. Found: C, 64.9; H, 5.3; N, 2.2%. FT-IR (Nujol mull cm^{-1}): *ν*(CO) 1596(vs). ^1H NMR (300 MHz, $CDCl_3$): *δ* (ppm): 8.46 (m, 1H, P–C_6H_4–CO–), 8.01-7.36 (m, 11H, 10H PPh_2 + 1H P–C_6H_4–CO), 7.24 (m, 2H, N–Ph), 7.08 (m, 3H, N–Ph), 6.92 (m, 1H, P–C_6H_4–CO–), 6.66 (m, 1H, P–C_6H_4–CO–), 5.35 (m, 2H, Cy), 5.16 (m, $1H_B$, Cy), 4.66 (d, $J_{HH} = 5.7$ Hz, 1H, Cy), 1.66 (s, 3H, Me–Cy), 1.60 (m, 1H, CH, ⁱPr–Cy), 0.77 (d, $J_{HH} = 6.9$ Hz, 3H, Me, ⁱPr–Cy), 0.23 (d, $J_{HH} = 6.9$ Hz, 3H, Me, ⁱPr–Cy). ^{31}P NMR (300 MHz, $CDCl_3$): *δ* (ppm): 28.9 (s). FAB-MS (positive mode) *m*/*z*: 651 (M^+), 61 ($M^+ - Cl$).

[RuCl(η⁶-*p*-cymene)(*o*-Ph_2P–C_6H_4–CO–N–C_6H_4–CH_3)] (**3c**): (61% yield). *Anal.* Calc. for $C_{36}ClH_{35}NOPRu$: C, 65.0; H, 5.3; N, 2.1. Found: C, 64.8; H, 5.5; N, 2.3%. FT-IR (Nujol mull cm^{-1}): *ν*(CO) 1572(vs). ^1H NMR (300 MHz, $CDCl_3$): *δ* (ppm): 8.47 (m, 1H, P–C_6H_4–CO–), 8.00 (m, 2H, P–C_6H_4–CO–), 7.57–7.37 (m, 10H PPh_2), 7.02 (m, 4H, N–C_6H_4–CH_3), 6.66 (m, 1H, P–C_6H_4–CO–), 5.41 (m, 2H, Cy), 5.20 (m, 1H, Cy), 4.64 (d, $J_{HH} = 5.6$ Hz, 1H, Cy), 2.31 (s, 3H, Me N–C_6H_4–CH_3), 2.17 (s, 3H, Me–Cy), 1.60 (m, 1H, CH, ⁱPr–Cy), 0.79 (d, $J_{HH} = 7.2$ Hz, 3H, Me, ⁱPr–Cy), 0.21 (d, $J_{HH} = 6.8$ Hz, 3H, Me, ⁱPr–Cy). ^{31}P NMR (300 MHz, $CDCl_3$): *δ* (ppm): 29.1 (s). FAB-MS (positive mode) *m*/*z*: 666 (M^+), 631 ($M^+ - Cl$).

[RuCl(η⁶-*p*-cymene)(*o*-Ph_2P–C_6H_4–CO–N–C_6H_4–F)] (**3d**): (54% yield). *Anal.* Calc. for $C_{35}ClFH_{32}NOPRu$: C, 62.8; H, 4.8; N, 2.1. Found: C, 62.9; H, 4.9; N, 2.2%. FT-IR (Nujol mull cm^{-1}): ν(CO) 1586(vs). ^1H NMR (300 MHz, $CDCl_3$): *δ* (ppm): 8.47 (m, 1H, P–C_6H_4–CO–), 8.00 (m, 2H, P–C_6H_4–CO–), 7.60–7.34 (m, 10H, PPh_2), 7.14–6.91 (m, 4H, N–C_6H_4–F), 6.68 (m, 1H, P–C_6H_4–CO–), 5.38 (m, 2H, Cy), 5.20 (m, 1H, Cy), 4.71 (d, $J_{HH} = 5.8$ Hz, 1H, Cy), 1.71 (m, 1H, CH, ⁱPr–Cy), 1.24 (s, 3H, Me–Cy), 0.83 (d, $J_{HH} = 7.2$ Hz, 3H, Me, ⁱPr–Cy), 0.29 (d, $J_{HH} = 7.2$ Hz, 3H, Me, ⁱPr–Cy). ^{31}P NMR (200 MHz, $CDCl_3$): *δ* (ppm): 29.1 (s). ^{19}F NMR (300 MHz, $CDCl_3$): *δ* (ppm): −124.1 (s). FAB-MS (positive mode): *m*/*z*: 670 (M^+), 635 ($M^+ - Cl$).

*2.3. Crystal structure determination of **2b–2d***

Crystals suitable for a diffraction study were prepared by slow diffusion of hexane into their dichloromethane solutions. Data collection was performed at −173 °C on

Table 1
Crystal data and structure refinement for compounds **2b–d**

	2b	**2c** · $1/2CH_2Cl_2$	**2d**
Empirical formula	$C_{35}H_{34}ClF_6NOP_2Ru$	$C_{36.5}H_{37}Cl_2F_6NOPRu$	$C_{35}H_{33}ClF_7NOPRu$
Formula weight	797.09	853.58	784.11
Temperature (K)	100(2)	100(2)	100(2)
Wavelength (Å)	0.71073	0.71073	0.71073
Crystal system	monoclinic	monoclinic	monoclinic
Space group	*P*21/*n*	*P*21/*n*	*P*21/*n*
Unit cell dimensions			
a (Å)	9.6313(4)	9.5651(4)	9.6494(7)
b (Å)	24.0527(10)	24.4322(9)	24.0892(18)
c (Å)	15.6647(6)	15.7079(6)	15.6671(12)
β (°)	93.0390(10)	92.8620(10)	93.0320(10)
V (Å^3)	3623.8(3)	3666.3(2)	3636.7(5)
Z	4	4	4
D_{calc} (Mg m^{-3})	1.461	1.546	1.432
Absorption coefficient (mm^{-1})	0.654	0.722	0.612
F(000)	1616	1732	1588
Crystal size (mm)	0.29 0.17 × 0.10	0.24 × 0.10 × 0.09	0.32 × 0.22 × 0.14
θ Range for data collection (°)	1.55–28.23	1.67–28.23	1.55–28.07
Index ranges	$-12 \leqslant h \leqslant 12$, $-31 \leqslant k \leqslant 30$, $-20 \leqslant l \leqslant 20$	$-12 \leqslant h \leqslant 12$, $-32 \leqslant k \leqslant 31$, $-20 \leqslant l \leqslant 20$	$-12 \leqslant h \leqslant 12$, $-31 \leqslant k \leqslant 30$, $-20 \leqslant l \leqslant 20$
Reflections collected	42063	42722	41122
Independent reflections [R_{int}]	8456 [0.0285]	8586 [0.0460]	8395 [0.0282]
Refinement method	full-matrix least-squares on F^2	full-matrix least-squares on F^2	full-matrix least-squares on F^2
Data/parameters	8456/424	8586/443	8395/433
R^a, Rw^b [I>2σ(I)]	$R_1 = 0.0500$, $wR_2 = 0.1625$	$R_1 = 0.0496$, $wR_2 = 0.1097$	$R_1 = 0.0791$, $wR_2 = 0.2310$
R^a, Rw^b [all data]	$R_1 = 0.0555$, $wR_2 = 0.1675$	$R_1 = 0.0603$, $wR_2 = 0.1146$	$R_1 = 0.0827$, $wR_2 = 0.2335$
S^c	1.738	1.117	1.141
Maximum, minimum Δ*ρ* (e Å^{-3})	4.849, −0.603	1.321, −0.726	6.095, −1.009

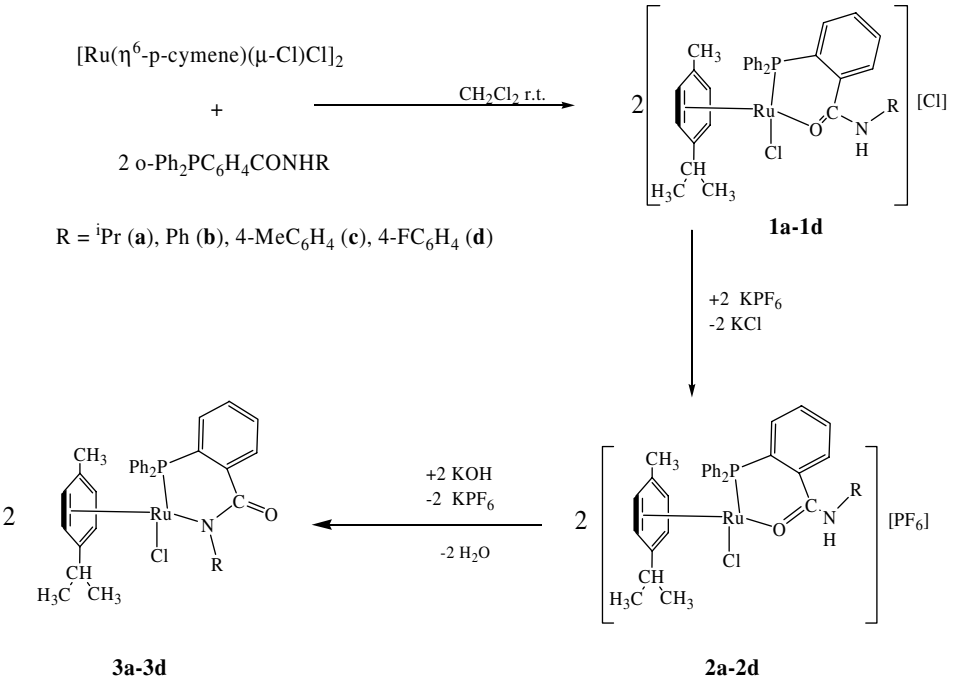
[a] $R = \sum |F_0| - |F_C| / \sum |F_0|$.
[b] $Rw = \{\sum [w(F_0^2 - F_c^2)^2] / \sum [w(F_0^2)^2]\}^{1/2}; w = 1/\sigma^2(|F_0^2|)$.
[c] $S = \left[\sum [w(F_0^2 - F_c^2)^2] / (N_{obs} - N_{param})\right]^{1/2}$.

a Bruker Smart CCD diffractometer with a nominal crystal to detector distance of 6.2 cm. Diffraction data were collected based on a ω scan run. A total of 2524 frames were collected at 0.3° intervals and 10 s per frame. The diffraction frames were integrated using the SAINT package [30] and corrected for absorption with SADABS [31].

The structures were solved by direct methods [32] and refined by full-matrix least-squares techniques using anisotropic thermal parameters for non-H atoms [32] (Table 1). Hydrogen atoms were introduced in calculated positions and refined during the last stages of the refinement.

3. Results and discussion

In dichloromethane, the precursor [Ru(η^6-*p*-cymene)(μ-Cl)Cl]$_2$ reacts at room temperature with *o*-Ph_2P–C_6H_4–CO–NH–R: (R = ^{i}Pr (**a**); R = Ph (**b**); R = 4-MeC_6H_4 (**c**); R = 4-FC_6H_4 (**d**)) (see Section 2 for details) yielding the orange compounds of general formula [RuCl(η^6-*p*-cymene)(*o*-Ph_2P–C_6H_4–CO–NH–R)]Cl (R = ^{i}Pr (**1a**); R = Ph (**1b**); R = 4-MeC_6H_4 (**1c**); R = 4-FC_6H_4 (**1d**)) in which an κ^2-*P*,*O* coordination mode for diphenylphosphine–benzamide ligands is observed. The characterizing spectroscopic and analytical data are in agreement with the proposed structures presented in Scheme 1. The appearance of the *ν*(CO) absorptions lowered by approximately 30 cm^{-1} with respect to those of the free ligands gives a first support to the formation of a P^O chelate around the Ru centre [27,28]. A medium *ν*(NH) vibration, shifted towards higher wavenumbers than free ligands, is the other remarkable aspect found in the IR spectra. The FAB mass spectrometry displays fragments corresponding to ($M^+ - Cl$) and ($M^+ - 2Cl$). The presence of diphenylphosphine–benzamide ligands is also confirmed by $^{31}P\{^1H\}$ NMR spectroscopy, the spectra consisting of singlets around 33 ppm. This range of chemical shift is typical of a P^O coordination of these ligands to palladium [27] (P-monodentate around 40 ppm) and is coincidental with the one shown later for **2a–d** ruthenium complexes. Further evidence of the proposed coordination comes from the ^1H NMR spectroscopy. It has been reported that heterobidentate P^X chelates produce chiral metal centers when bound to arene–ruthenium complexes, and such chirality in *p*-cymene complexes produces diasterotopic methyls in the isopropyl fragment, which serve as detector of the chirality at the metal [17,33]. Also four different aromatic CH



Scheme 1. Preparation of phosphino-amide derivatives.

groups are usually seen when P^X chelates are present, whereas only two CH's and one isopropylic methyl resonance are observed if the ligand acts as P-monodentate. In our case, the ^{1}H NMR spectra of complexes **1a**–**d** display two doublets attributed to diasterotopic methyl groups in the isopropyl of *p*-cymene, as well as four CH aromatic resonances.

It is worth it to mention that no evidence of equilibrium between coordination isomers [RuCl(η^6-*p*-cymene)(*o*-Ph_2P–C_6H_4–CO–NH–R)]Cl and [$RuCl_2$(η^6-*p*-cymene)(*o*-Ph_2P–C_6H_4–CO–NH–R)] was observed. The strong chelating ability of diphenylphosphine–benzamide ligands towards ruthenium is emphasized by the fact that our attempts to open the chelate ring with pyridine or bipyridine produced mixtures of compounds in which the arene had been removed.

This result is in contrast to our previous studies on the behaviour of these ligands coordinating palladium(II) [27], since κ^1-*P* binding mode was adopted when chloride ion was in competition for a position around the metal center. Only forcing the chloride exit with a silver salt that provided an appropriate counteranion the chelating coordination was achieved. Regarding ruthenium(II) arene complexes with potentially N̂P or ÔP hemilabile ligands, most of the studies reported lately starting from [Ru(η^6-*p*-cymene)(μ-Cl)Cl]$_2$ show that direct reaction with this precursor yields neutral complexes where the ligand is κ^1*P*-coordinated to the metal [16–25]. Once again the subsequent treatment with halide abstractors such silver or sodium salts (mostly BF_4^-, BPh_4^-, $CF_3SO_3^-$, PF_6^- or SbF_6^-) preferably in polar solvents provided a route to the chelating cationic compounds. Strong dependence with the solvent has been reported in the preparation of complexes [Ru(η^6-arene)(κ^1-*P*-N*)Cl_2]/[Ru(η^6-arene)(κ^2-*P*-*N**)Cl]Cl [34]. Thus, neutral complexes were obtained in dichloromethane while same reactions in methanol afforded the corresponding chelate complexes, that also were prepared by adding small amounts of methanol to solutions of [Ru(η^6-arene)(κ^1-*P*-N*)Cl_2] in chloroform. A mixture of neutral and cationic complexes has been reported when the P^N ligand was 2-(diphenylphosphinomethyl)pyridine [35]. In complexes **1a**–**d** even working in dichloromethane the chelating mode of diphenylphosphine–benzamides is preferred. Such behaviour has been previously found for chiral ruthenium complexes of bidentate bisphosphine monoxide ligands [Ru(η^6-arene)(κ^1-Ph_2PC(R)P(O)Ph_2)Cl_2]/[Ru(η^6-arene)(κ^2-Ph_2PC(R)P(*O*)Ph_2)Cl]Cl [33], for which an equilibrium in dichloromethane between the κ^1-*P* complexes and their respective κ^2-*P*,*O* coordination isomers is reported. The steric bulk in the ligands backbones seems to drive the chelation, and cationic κ^2-complexes were obtained with bulkier ligands, the κ^1-*P* complex with the lighter and mixtures of two coordination isomers for middle sized. In this previous study, as happens for complexes **1a**–**d**, conversion of the chloride salts to those with another counteranion allowed the preparation of crystals suitable for X-ray diffraction.

The reaction in acetone of compounds **1a**–**d** with stoichiometric KPF_6 under the mild conditions described in the experimental section yielded complexes [RuCl(η^6-*p*-cymene)(*o*-Ph_2P–C_6H_4–CO–NH–R)][PF_6] (R = ^{i}Pr (**2a**); R = Ph (**2b**); R = 4-MeC_6H_4 (**2c**); R = 4-FC_6H_4 (**2d**)) (Scheme 1). The presence of a P,O-chelate is supported by the appearance of the *ν*(CO) vibration in the same range

mentioned above for complexes **1a**–**d**. Other features of IR spectra are a sharp NH absorption around 3355 cm^{-1} and a single band at ca. 845 cm^{-1} that indicates the presence of PF_6^- also detected by ^{19}F and ^{31}P NMR. The rest of NMR data confirm the proposed formulae and, as expected, are quite similar to those of precursor complexes in chemical shift, number and multiplicity of signals and therefore have not been included in experimental section. Thus, again the asymmetry of the MLL′L″ three-legged fragment and consequent chirality at Ru centre raised diasterotopic isopropylic methyl groups and differentiated aromatic CH resonances.

As mentioned above, changing chloride by PF_6^- made possible to grow X-ray quality crystals that after diffraction study have confirmed the structures of **2b**–**d**. Each of them consisted of a cationic complex [RuCl(η^6-*p*-cymene)-(*o*-Ph_2P–C_6H_4–CO–NH–R)]$^+$ (Figs. 1–3, respectively) and an anion $[PF_6]^-$. While **2c** crystallizes with 1/2 molecule of dichoromethane, **2b** and **2d** also contain some unrefined solvent that causes high values of maximum $\Delta\rho$. As can be inferred from data in Table 1 the three complexes are isomorphous. Selected bond lengths and angles listed in Table 2 are very similar. Moreover, molecular conformation in the three compounds are similar, the phenyl ring bonded to the iminic group is oriented towards the isopropyl group from the η^6-arene, with distances from the centroid to the (Me)$_2$C–*H* hydrogen atom of 3.081, 2.948 and 3.010 Å for complexes **2b**, **2c**, and **2d**, respectively. The molecules displayed a pseudooctahedral three-legged piano-stool geometry around the ruthenium atom with the arene, the corresponding diphenylphosphine–benzamide ligand and the chloride completing the coordination. The distortion of the octahedral geometry is shown by the values of the O(1)–Ru(1)–P(1), O(1)–Ru(1)–Cl(1), and P(1)–Ru(1)–Cl(1) angles, in the range 82.49(8)–88.02(5)° (see Table 2).

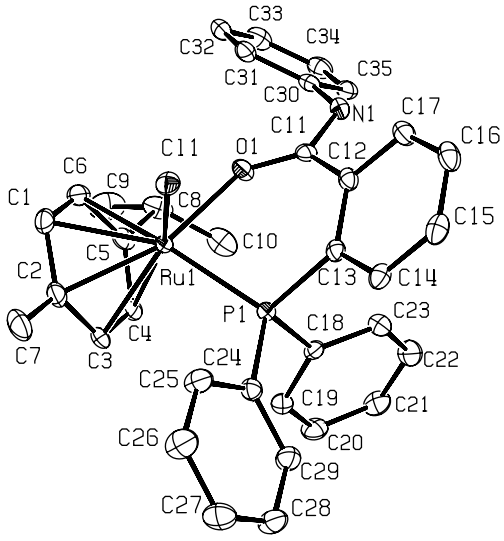


Fig. 1. ORTEP diagram of cation complex **2b** with the atom numbering scheme; thermal ellipsoids are drawn at the 50% probability level.

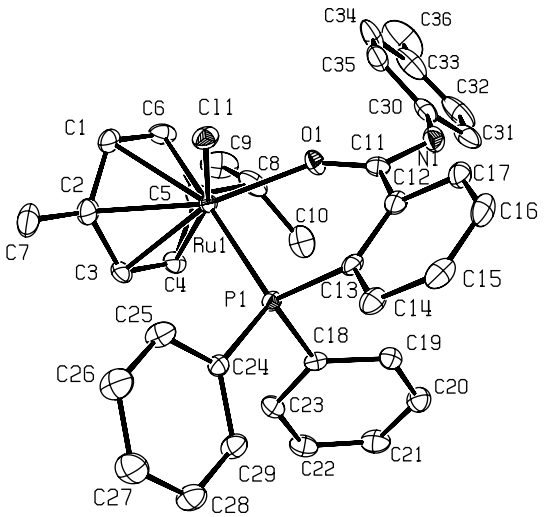


Fig. 2. ORTEP diagram of cation complex **2c**; thermal ellipsoids are drawn at the 50% probability level.

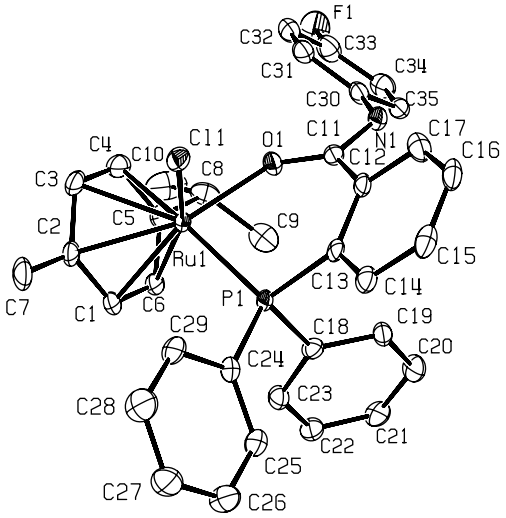


Fig. 3. ORTEP diagram of cation complex **2d**. Thermal ellipsoids are drawn at 50% probability.

The angles between the centroid of the arene ring, Ru, O, P, and Cl atoms are in the 125–133° range. The Ru–Cl bond distances fall within the range of reported values [16,24]. The average Ru–C bond distance is around 2.209 Å, whereas the distance between the ruthenium atom and the centroid of the ring is 1.693 Å for the three compounds. As has been previously reported [17 and references therein] a heterogeneous distribution of the Ru–C(*p*-cymene) bond distances was observed in the sense that distances *trans* to the more strongly donating phosphine group are longer that those *trans* to the chlorine atoms.

The diphenylphosphine–benzamide ligands are κ^2-*P*,*O* bonded to ruthenium forming a six-membered metallacycle that in the three compounds display a 10° distorted *screw–boat* conformation, according to the classification of Allen and Taylor [36].

Table 2
Selected distances (Å) and angles (°) of the new complexes

	2b	2c	2d
Ru(1)–O(1)	2.114(3)	2.114(2)	2.109(4)
Ru(1)–P(1)	2.3191(10)	2.3167(8)	2.3194(15)
Ru(1)–Cl(1)	2.3930(9)	2.3926(8)	2.3936(15)
Ru(1)–C(1)	2.237(4)	2.235(3)	2.166(6)
Ru(1)–C(2)	2.195(4)	2.189(3)	2.199(6)
Ru(1)–C(3)	2.169(4)	2.171(3)	2.232(6)
Ru(1)–C(4)	2.201(4)	2.205(3)	2.243(6)
Ru(1)–C(5)	2.209(4)	2.207(3)	2.205(6)
Ru(1)–C(6)	2.243(4)	2.240(6)	2.206(6)
Ru(1)–$C_{(average)}$	2.209	2.208	2.209
Ru(1)–$Cent_{(p-cimeno)}$	1.693	1.693	1.693
O(1)–C(11)	1.256(5)	1.250(4)	1.258(7)
O(1)–Ru(1)–P(1)	82.49(8)	82.56(7)	82.73(12)
O(1)–Ru(1)–Cl(1)	87.09(8)	87.41(7)	86.96(12)
P(1)–Ru(1)–Cl(1)	87.85(3)	87.75(3)	88.02(5)
O(1)–Ru(1)–Centr	125.73	125.30	125.62
P(1)–Ru(1)–Centr	132.29	132.34	132.04
Cl(1)–Ru(1)–Centr	126.32	126.49	126.46

The most significant difference between the solid state conformation of the free ligand **b** and the coordinated ligand in **2b** is the angle between planes O(1)–C(11)–C(12) and C(12)–C(13)–P(1) (53.11(13)° and 30.9(4)°, respectively). Similar values are found for complexes **2c** 30.6(3)° and **2d** 30.0(6)°. This value also diminishes slightly once the ligand is complexed to Ni or Pd: 38.4(2)°, 33.3(2)° and 41.3(2)° [28]. The relative position of the phenyl rings bonded to the N–CO-moiety stays without major variation upon coordination. In the free ligand both rings are nearly perpendicular (81.7°) and so happens in **2b** (79.8°), **2c** (81.8°) and **2d** (81.3°) while in the reported Ni complex the phenyl bonded to N rotated, becoming both rings parallels (10.2°) [28].

The new complexes exhibit intermolecular hydrogen bonding between F from PF_6^- and N(1) atoms (distance N(1)···F ranges 2.912–2.916 Å and angle N(1)–H···F ranges 152.37–155.01°).

In order to induce amide deprotonation in the ligands, and a likely κ^2-*P*,*N* coordination mode according to our previous studies with other metals, compounds **2a**–**d** were treated with KOH(aq) in acetone, as explained in the experimental section, to yield neutral complexes [RuCl(η^6-*p*-cymene)(*o*-Ph_2P–C_6H_4–CO–N–R)] (R = ^{i}Pr (**3a**); R = Ph (**3b**); R = 4-MeC_6H_4 (**3c**); R = 4-FC_6H_4 (**3d**)) (Scheme 1). The loss of both *ν*(NH) and *ν*(PF) bands in their IR spectra with regards to precursor compounds confirmed that the proposed reactions took place. The characterization in solid state was completed with the FAB mass spectrometry, that shows fragments at [M^+] and [$M^+ - Cl$]. A singlet shifted at ca. 7 ppm highfield compared to P^O-chelated compounds characterizes the $^{31}P\{^1H\}$ NMR spectra, and the expected pattern is observed in the ^1H NMR with significant absence of amidic proton resonance at low field. The solutions of new complexes turned black after 48 h thus preventing the obtention of crystals suitable for a diffraction analysis and a conclusive assertion about the coordination mode. Absence of arene was observed in the subsequent decomposition products.

4. Conclusion

Twelve new (η^6-*p*-cymene)–ruthenium(II) complexes with diphenylphosphine–benzamide ligands exhibiting different coordination modes have been prepared and characterized by spectroscopic techniques and single crystal X-ray diffraction analysis. Stronger κ^2-*P*,*O* chelating ability towards ruthenium can be attributed to these ligands in comparison with our previous results dealing with nickel and palladium. Also if compared with other potentially hemilabile P,O- or P,N-ligands in its reaction with the precursor [Ru(η^6-*p*-cymene)(μ-Cl)Cl]$_2$, that usually yields P- monodentate compounds.

Acknowledgements

Financial support of this work by Dirección General de Investigación (Project CTQ2005-09231-C02-01/02) and Fundación Séneca de la Región de Murcia (Projects 00484/PI/04 and 03010/PI/05) is gratefully acknowledged.

Appendix A. Supplementary material

CCDC 631104, 631105 and 631106 contain the supplementary crystallographic data for **2b**, **2c** and **2d**. These data can be obtained free of charge via http://www.ccdc.cam.ac.uk/conts/retrieving.html, or from the Cambridge Crystallographic Data Centre, 12 Union Road, Cambridge CB2 1EZ, UK; fax: +(44) 1223-336-033; or e-mail: deposit@ccdc.cam.ac.uk.

References

[1] A. Bader, E. Lindner, Coord. Chem. Rev. 108 (1991) 27.
[2] G.R. Newkome, Chem. Rev. 93 (1993) 2067.
[3] C.S. Slone, D.A. Weinberger, C.A. Mirkin, Prog. Inorg. Chem. 48 (1999) 233.
[4] P. Braustein, F. Naud, Angew. Chem., Int. Ed. 40 (2001) 680, and references cited therein.
[5] P. Braustein, J. Organomet. Chem. 689 (2004) 3953, and references cited therein.
[6] G.M. Kapteijn, M.P.R. Spee, D.M. Grove, H. Kooijman, A.L. Spek, G. van Koten, Organometallics 15 (1996) 1405.
[7] P. Braunstein, C. Frison, X. Morise, R.A. Adams, J. Chem. Soc., Dalton Trans. (2000) 2205.
[8] M.S. Khoshbin, M.V. Ovchinnikov, C.A. Mirkin, L.N. Zakharov, A.L. Rheingold, Inorg. Chem. 44 (2005) 496, and references cited therein.
[9] C.W. Rogers, Y. Zhang, B.O. Patrick, W.E. Jones Jr., M.O. Wolf, Inorg. Chem. 41 (2002) 1162.
[10] C.W. Rogers, M.O. Wolf, Coord. Chem. Rev. 233–234 (2002) 341.
[11] C.W. Rogers, M.O. Wolf, Angew. Chem., Int. Ed. 41 (2002) 1898.
[12] M. Kuriyama, K. Nagai, K. Yamada, Y. Miwa, T. Taga, K. Tomioka, J. Am. Chem. Soc. 124 (2002) 8932.
[13] F.Y. Kwong, W.H. Lam, C.H. Yeung, K.S. Chan, A.S.C. Chan, Chem. Commun. (2004) 1922.
[14] W-M. Dai, Y. Zhang, Tetrahedron Lett. 46 (2005) 1377.

[15] H.Y. Kwon, s.Y. Lee, B.Y. Lee, D.M. Shin, Y.K. Chung, J. Chem. Soc., Dalton Trans. (2004) 921.
[16] R. Tribó, S. Muñoz, J . Pons, R. Yáñez, A. Álvarez-Larena, J.F. Piniella, J. Ros, J. Organomet. Chem. 690 (2005) 4072.
[17] A. Caballero, F.A. Jalón, B.R. Manzano, G. Espino, M. Pérez-Manrique, A. Mucientes, F.J. Poblete, M. Maestro, Organometallics 23 (2004) 5694.
[18] V. Cadierno, P. Crochet, J. Diez, J. Garcia-Alvarez, SE. Garcia-Garrido, J. Gimeno, S. Garcia-Granda, M.A. Rodriguez, Inorg. Chem. 42 (2003) 3293.
[19] V. Cadierno, P. Crochet, J. García-Álvarez, S.E. García-Garrido, J. Gimeno, J. Organomet. Chem. 663 (2002) 32.
[20] C. Stanfest-Hauser, C. Slugovc, K. Mereiter, R. Schimd, K. Kirchner, L. Xiao, W. Weissensteiner, J. Chem. Soc., Dalton Trans. (2001) 2989.
[21] I. Moldes, E. de la Encarnación, J. Ros, A. Álvarez-Larena, J.F. Piniella, J. Organomet. Chem. 566 (1998) 165.
[22] V. Cadierno, J. Díez, S.E. García-Garrido, S. García-Granda, J. Gimeno, J. Chem. Soc., Dalton Trans. (2002) 1465.
[23] G. Henig, M. Schulz, B. Windmüller, H. Werner, J. Chem. Soc., Dalton Trans. (2003) 441.
[24] P. Govindaswamy, Y.A. Mozharivskyj, M.R. Kollipara, Polyhedron 23 (2004) 3115.
[25] P. Bhattacharyya, T.Q. Ly, A.M.Z. Slawin, J.D. Woollins, Polyhedron 20 (2001) 1803.
[26] S. Burger, B. Therrien, G. Süss-Fink, Inorg. Chim. Acta 357 (2004) 1213.
[27] G. Sánchez, J. García, D. Meseguer, J.L. Serrano, L. García, J. Pérez, G. López, J. Chem. Soc., Dalton Trans. (2003) 4709.
[28] G. Sánchez, J. García, D. Meseguer, J.L. Serrano, L. García, J. Pérez, G. López, Inorg. Chim. Acta 359 (2006) 1650.
[29] M.A. Bennett, T.-N. Huang, T.W. Matheson, A.K. Smith, Inorg. Synth. 21 (1982) 74.
[30] SAINT, Version 6.22, Bruker AXS Inc.
[31] G.M. Sheldrick, SADABS, University of Gottingen, 1996.
[32] G.M. Sheldrick, SHELX-97. Programs for Crystal Structure Analysis (Release 97-2), University of Göttingen, Germany, 1998.
[33] J.F. Faller, B.P. Patel, M.A. Albrizzio, M. Curtis, Organometallics 18 (1999) 3096.
[34] C.G. Arena, S. Calamia, F. Faraone, C. Graiff, A. Tiripicchio, J. Chem. Soc., Dalton Trans. (2000) 3149.
[35] H. Yang, N. Lugan, R. Mathieu, Ann. Quim. Int. Ed. 93 (1997) 28.
[36] F.H. Allen, R. Taylor, Acta Crystallogr. B47 (1991) 404.

Available online at www.sciencedirect.com
ScienceDirect
Polyhedron 26 (2007) 2919
POLYHEDRON
www.elsevier.com/locate/poly

Erratum

Erratum to: "Lanthanide complexes of 2 + 2 meso-type macrocycle derive from *trans*-1,2-diaminocyclohexane and 2,6-diformylpyridine: X-ray crystal structures of La(III) and Sm(III) complexes" [Polyhedron 25 (2006) 2745–2754]

Janusz Gregoliński, Andrzej Kochel, Jerzy Lisowski *

Department of Chemistry, University of Wrocław, 14 F. Joliot-Curie, 50-383 Wrocław, Poland

Available online 2 February 2007

The authors would like to add the following two sentences to their article at the end of the second paragraph (starting with: "The results...") on page 2752.

The conclusion that the good linear correlations obtained for the whole series of Ln(III) ions with some pairs of nuclei may be misleading, is strengthened by the fact that Eq. (6) is valid only for axial systems (we thank Prof. Claude Piguet for drawing our attention to the problem of applicability of Eq. (6) to non-axial systems), while in the present case considerable rhombic contribution is observed (vide infra). The analysis based on the crystal-field independent three-nuclei method developed by Prof. Claude Piguet's group for rhombic systems, confirms the conclusions above regarding the isostructurality of the discussed complexes. (See Supplementary material for details.)

Appendix A. Supplementary material

Supplementary data associated with this article can be found, in the online version, at doi:10.1016/j.poly.2007.01.029.

DOI of original article: 10.1016/j.poly.2006.04.001.
* Corresponding author. Tel.: + 48 71 3757 252; fax: +48 71 3282 348.
E-mail address: jurekl@wchuwr.chem.uni.wroc.pl (J. Lisowski).

0277-5387/$ - see front matter © 2007 Elsevier Ltd. All rights reserved.
doi:10.1016/j.poly.2007.01.029

Available online at www.sciencedirect.com
ScienceDirect
Polyhedron 26 (2007) 2921–2928
POLYHEDRON
www.elsevier.com/locate/poly

Preparation, NMR studies and crystal structure of mononuclear and dinuclear Pd(II) and Pt(II) complexes that contain 1,2-bis[3-(3,5-dimethyl-1-pyrazolyl)-2-thiapropyl]benzene

Antonio de León [a], Josefina Pons [a,*], Jordi García-Antón [a], Xavier Solans [b], Mercè Font-Bardia [b], Josep Ros [a,*]

[a] *Departament de Química, Unitat de Química Inorgànica, Universitat Autònoma de Barcelona, 08193 Bellaterra, Barcelona, Spain*
[b] *Cristal.lografia, Mineralogia i Dipòsits Minerals, Universitat de Barcelona, Martí i, Franquès s/n, 08028 Barcelona, Spain*

Received 13 January 2007; accepted 25 January 2007
Available online 12 February 2007

Abstract

The reaction between 1,2-bis[3-(3,5-dimethyl-1-pyrazolyl)-2-thiapropyl]benzene (**bddf**) and $[MCl_2(CH_3CN)_2]$ (M = Pd(II), Pt(II)) in a 1:1 M/L ratio in CH_2Cl_2 or acetonitrile solution, respectively, gave the complexes *trans*-$[MCl_2(bddf)]$ (M = Pd(II) (**1**), Pt(II) (**4**)), and in a 2:1 M/L ratio led to $[M_2Cl_4(bddf)]$ (M = Pd(II) (**2**), Pt(II) (**5**)). Treatment of **1** and **4** with $AgBF_4$ and $NaBPh_4$, respectively, gave the compounds $[Pd(bddf)](BF_4)_2$ (**3**) and $[Pt(bddf)](BPh_4)_2$ (**6**). When complexes **3** and **6** were heated under reflux in a solution of Et_4NBr in CH_2Cl_2/CH_3OH (1:1) for 24 h, analogous complexes to **1** and **4** with bromides instead of chlorides bonded to the metallic centre were obtained. These complexes were characterised by elemental analyses, conductivity measurements, infrared, ^1H, $^1H\{^{195}Pt\}$, $^{13}C\{^1H\}$, $^{195}Pt\{^1H\}$ NMR, HSQC and NOESY spectroscopies. The X-ray crystal structure of the complex $[Pd(bddf)](BF_4)_2 \cdot H_2O$ has been determined. The metal atom is tetracoordinated by the two azine nitrogen atoms of the pyrazole rings and two thioether groups.
© 2007 Elsevier Ltd. All rights reserved.

Keywords: Palladium(II); Platinum(II); Hybrid ligands; N ligands; S ligands; Pyrazole complexes; Crystal structures

1. Introduction

Ligands that contain significantly different chemical functions, such as hard and soft donors (hybrid ligands) find increasing use in chemistry because of the selectivity introduced in the metal–ligand interactions and their possible dynamic behaviour [1]. Pyrazole containing molecules are attractive potential hybrid ligands since they are relatively easy to prepare. Moreover, their steric and electronic properties can be tuned in a straightforward manner [2].

The use of flexible ligands to form supramolecular arrays has been circumspect, due to the less predictable nature of such systems. Taking into account the choice of organic ligands, researchers have shown thioether ligands containing a flexible backbone to be among the most important types of organic ligands, because their flexibility and conformational freedom allow for greater structural diversity. Thioether ligands bearing S- and N-coordinating sites may incline to coordinate metals with different modes, forming a great variety of molecular structures. The use of thioether–pyridine moieties in the preparation of new extended-reach ligands has been investigated for the construction of metallosupramolecular arrays [3].

We have focused our interests on the synthesis and characterisation of pyrazolic ligands with two donor groups, among others S- and N-, (1,8-bis(3,5-dimethyl-1-pyrazolyl)-3,6-dithiaoctane (bddo), 1,9-bis(3,5-dimethyl-1-pyrazolyl)-3,7-dithianonane (bddn), 1,6-bis(3,5-dimethyl-1-pyrazolyl)-2,5-dithiahexane (bddh), 1,7-bis(3,5-dimethyl-1-pyrazolyl)-

* Corresponding authors.
E-mail address: josefina.pons@uab.es (J. Pons).

0277-5387/$ - see front matter © 2007 Elsevier Ltd. All rights reserved.
doi:10.1016/j.poly.2007.01.051

2,6-dithiaheptane (bddhp) and 1,5-bis(3,5-dimethyl-1-pyrazolyl)-3,7-thiapentane (bdtp)), and the study of their reactivity with Pd(II) [4], Pt(II) [4] and Rh(I) [5].

We have recently reported the synthesis and coordinating properties of a new mixed pyrazole-thioether ligand, incorporating benzene in the thioether chain sub-unit, with Rh(I) [5]. In particular, the tetradentate ligand 1,2-bis[3-(3,5-dimethyl-1-pyrazolyl)-2-thiapropyl]benzene (**bddf**) has chelating properties strictly dependent on the conformational constraints imposed by the benzene unit on the S-donor thioether linker of the ring [5]. We report herein the results of our investigation on its coordination to platinum group metals, in particular Pd(II) and Pt(II).

2. Results and discussion

2.1. Synthesis and spectroscopic properties

Reaction of 1,2-bis[3-(3,5-dimethyl-1-pyrazolyl)-2-thiapropyl]benzene (**bddf**) with $[PdCl_2(CH_3CN)_2]$ in a 1:1 M/L ratio in CH_2Cl_2 solution led to $[PdCl_2(bddf)]$ (**1**). The complex $[Pd_2Cl_4(bddf)]$ (**2**) was obtained by the use of a 2:1 M/L ratio in CH_2Cl_2 solution. Treatment of **1** with $AgBF_4$ in CH_2Cl_2/CH_3OH (1:1) solution, gave compound $[Pd(bddf)](BF_4)_2$ (**3**).

Reaction of **bddf** with $[PtCl_2(CH_3CN)_2]$ in a 1:1 M/L ratio in acetonitrile solution led to $[PtCl_2(bddf)]$ (**4**). The complex $[Pt_2Cl_4(bddf)]$ (**5**) was obtained by the use of a 2:1 M/L ratio in acetonitrile solution. Treatment of **4** with $NaBPh_4$ in acetonitrile/CH_3OH (1:1) solution, gave compound $[Pt(bddf)](BPh_4)_2$ (**6**). When complexes **3** and **6** were heated under reflux in the presence of Et_4NBr in CH_2Cl_2/CH_3OH (1:1) for 24 h, analogous complexes to **1** and **4** with bromides instead of chlorides bonded to the metallic centre were obtained. This behaviour indicates that this ligand is hemilabile towards Pd(II) and Pt(II) [1a,1b].

Compounds **1**–**6** were characterised by elemental analyses, conductivity measurements, IR, ^1H, $^{13}C\{^1H\}$ NMR spectroscopies, and for compounds **4**–**6** $^1H\{^{195}Pt\}$ and $^{195}Pt\{^1H\}$ NMR spectroscopy, and mass spectrometry. All six compounds gave satisfactory C, H, N and S elemental analyses.

Conductivity data in acetonitrile are in agreement with a non-electrolytic nature for compounds **1**, **2**, **4** and **5** (9–37 Ω^{-1} cm^2 mol^{-1}), and 2:1 electrolytes for compounds **3** and **6** (280 Ω^{-1} cm^2 mol^{-1} and 250 Ω^{-1} cm^2 mol^{-1}, respectively). The reported values for 10^{-3} M solutions of non-electrolytic compounds are lower than 120 Ω^{-1} cm^2 mol^{-1} and between 220 and 300 Ω^{-1} cm^2 mol^{-1} for 10^{-3} M solutions of 2:1 electrolytic compounds in acetonitrile [6].

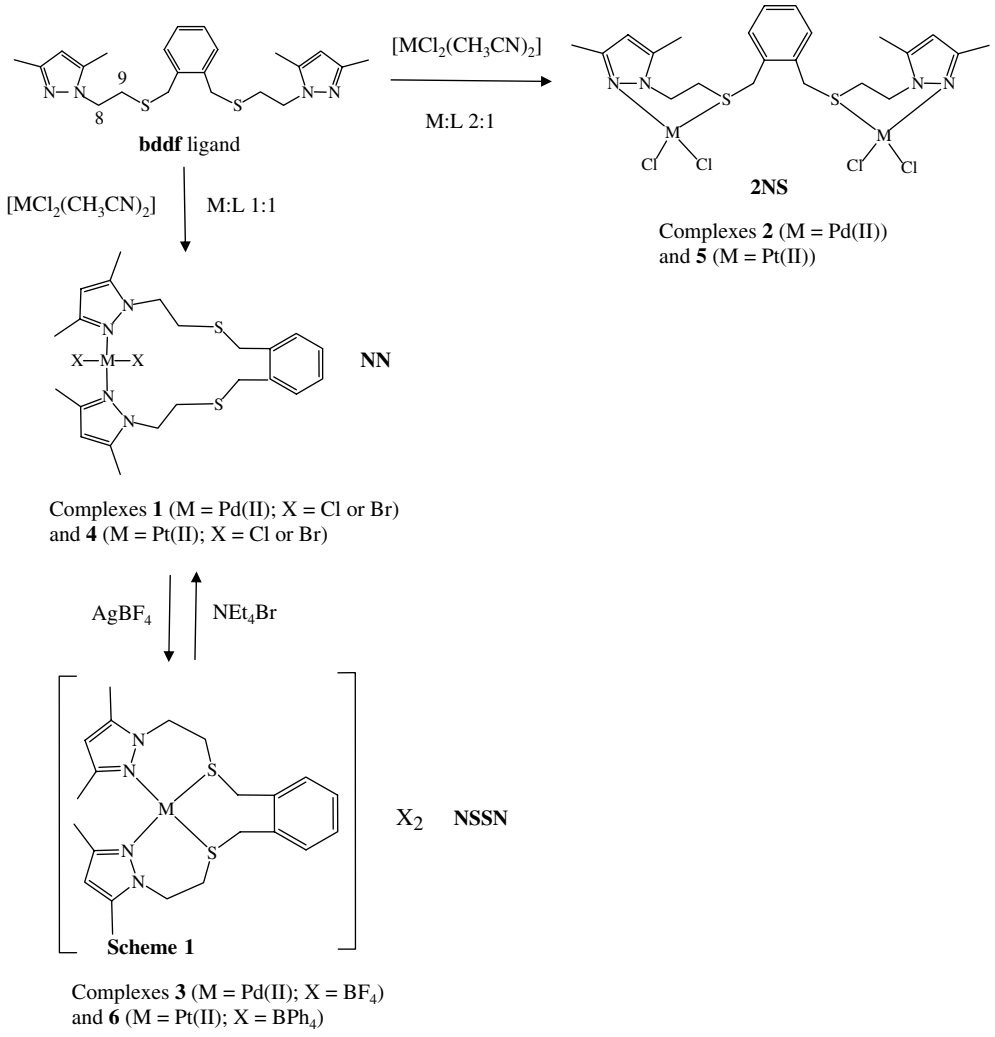
The positive ionisation spectrum of **1** gave a peak with a *m*/*z* value of 557 (100%; $[PdCl(bddf)]^+$). For **2**, three peaks at 793 (40%; $[Pd_2Cl_4(bddf)+Na]^+$), 735 (48%; $[Pd_2Cl_3(bddf)]^+$) and 557 (100%; $[PdCl(bddf)]^+$) are obtained. For **3**, a peak at 557 (100%; $[PdCl(bddf)]^+$) is obtained. The mass spectrum of **4** gives a peak at 645 (100%; $[PtCl(bddf)]^+$) and for **5**, a peak at 969 (100%; $[Pt_2Cl_4(bddf)+Na]^+$) is observed. Finally, the mass spectrum of compound **6** displays a peak at 645 (100%; $[PtCl(bddf)]^+$). The molecular peaks of the cations are observed with the same isotopic distribution as the theoretical ones.

The IR spectra of complexes **1**–**6** in the range 4000–400 cm^{-1} show that the **bddf** ligand is coordinated to Pd(II) or Pt(II). The ν(C=C), ν(C=N) and $\delta(C–H)_{oop}$ bands of the pyrazolic ligands increase their frequency when they are part of the complexes [5,7]. The IR spectrum of complex **3** presents a band that was assigned to ν(B–F) at 1054 cm^{-1}, and the IR spectrum of complex **6** presents a band that was assigned to ν(B–C) at 612 cm^{-1} [7]. The IR spectra of complexes **1**–**6** in the region 600–100 cm^{-1} were also studied. The presence of bands between 489 and 454 cm^{-1} assigned to ν(M–N) (M = Pd(II), Pt(II)) confirms the coordination of N_{pz} of the ligand to the metallic atom. The complexes **1** and **4** display one ν(M–Cl) band at 337 cm^{-1} (**1**) and 319 cm^{-1} (**4**). These bands indicate that the chlorine atoms are coordinated to Pd(II) or Pt(II) in a *trans* disposition. Complexes **2** and **5** display two well-defined ν(M–Cl) (M = Pd(II), Pt(II)) bands at 342, 323 cm^{-1} (**2**) and 319, 310 cm^{-1} (**5**). These bands clearly indicate that the chlorine atoms are coordinated to Pd(II) or Pt(II) in a *cis* disposition [8]. For complexes **2** and **3** the band ν(Pd–S) appears at 358 cm^{-1} (**2**) and 353 cm^{-1} (**3**), and for complexes **5** and **6** at 371 cm^{-1} (**5**) and 374 cm^{-1} (**6**). These bands confirm the coordination of the S atoms of the ligand to the metallic centre [8].

The ^1H NMR, $^{13}C\{^1H\}$NMR, HSQC, COSY and NOESY spectra were recorded in $CDCl_3$ for **1** and **4**, and acetonitrile for **2**, **3**, **5** and **6**, and show the signals of the ligand **bddf**. It is remarkable to note that Pt(II) complexes are less soluble than Pd(II) ones. NMR spectroscopic data are shown in Section 4. No significant differences between $^{13}C\{^1H\}$ NMR spectra of the free and coordinated ligands were observed. HSQC spectra of **1**–**3** were used to assign 8-H, 9-H and 10-H (Scheme 1). Coupling constants for complexes **2**, **3**, **5** and **6** could not be obtained due to the broadness of the bands. The ^1H NMR spectra of complexes **2**–**6** at 298 K show only sharp resonances for the CH and CH_3 groups of the pyrazolyl cycles.

For compound **1**, at room temperature, the methylene protons of the SCH_2ph chain appear as a singlet ($\delta = 4.10$ ppm) and the methylene protons of the $N_{pz}CH_2CH_2S$ chain appear as two triplets ($\delta = 3.50$ ppm, 4.95 ppm, $^3J = 8.2$ Hz). This behaviour is similar to that found for the free ligand.

The ^1H NMR spectrum of complex **4** shows broad bands at 4.98 and 3.50 ppm, attributable to methylene protons of the $N_{pz}CH_2CH_2S$ chain. The presence of broad bands is due to the coupling between Pt(II) and the hydrogens of the ethylenic chains. To corroborate this, we have registered the $^1H\{^{195}Pt\}$ NMR spectrum of **4** and we can observe that the methylene protons of the $N_{pz}CH_2CH_2S$ appear as two triplets ($\delta = 3.44$ ppm, 4.92 ppm, $^3J = 8.0$ Hz).



Scheme 1.

The room temperature ^{1}H NMR spectra of complexes **2** and **5** are little informative since, except for the sharp resonances of the pyrazolyl cycles, only broad resonances are observed. Lowering of the temperature to 233 K did not improve the shape of the signals.

For compound **3**, at 298 K the methylene protons of the $N_{pz}CH_2CH_2S$ chain appear as four poorly defined broad bands and the methylene protons of the SCH_2ph chain appear as two poorly defined broad bands. This led us to record variable-temperature ^{1}H NMR spectra in acetonitrile. At the higher temperature (333 K), only one signal can be observed for each CH_2 of the $N_{pz}CH_2CH_2S$ and SCH_2ph chains, whereas lowering of the temperature (233 K) provokes that the two NCH_2CH_2S and the two SCH_2ph chains become non-equivalents. Moreover, we observed the splitting of each CH_2 of each chain into two signals (four signals for each NCH_2CH_2S chain and two signals for each SCH_2ph chain). This suggests that at 333 K there is a fluxional process in which, with ring-flipping, the two hydrogens of each CH_2 are interconverted and only one signal can be observed (at this temperature both NCH_2CH_2S and both SCH_2ph chains are also equivalent). This process would take place with a $\Delta G^{\ddagger}$ value of ca. 57 kJ mol^{-1}, as deduced from the coalescence behaviour of the methylene resonances ($T_c = 273$ K) [9]. This behaviour is also observed in acetone solution ($T_c = 273$ K, $\Delta G^{\ddagger} = 58$ kJ mol^{-1}). These energy values could also be consistent with a mechanism that implies an inversion of the sulfur atom configuration [10] (Fig. 1).

Additional ^{195}Pt{^{1}H} NMR experiments for complexes **4**–**6** at 298 K revealed only one band for each complex ($\delta = -2247$ ppm for **4**, -2857 ppm for **5**, and -3884 ppm for **6**), confirming the presence of a single complex in solution and illustrating how the platinum chemical shifts are sensitive to the average ligand environment. The chemical shifts for a PtN_2Cl_2 core are expected between -1998 and -2279 ppm [11], a $PtNSCl_2$ core between -2868 and -3083 ppm [4b,12], and a PtN_2S_2 core between -3261 and -3884 ppm [4a,12c,13].

2.2. Crystal structure of $[Pd(bddf)](BF_4)_2 \cdot H_2O$ (**3**)

The structure of **3** (Fig. 2) consists of cationic units of $[Pd(bddf)]^{2+}$, BF_4^- anions and solvent molecules (H_2O).

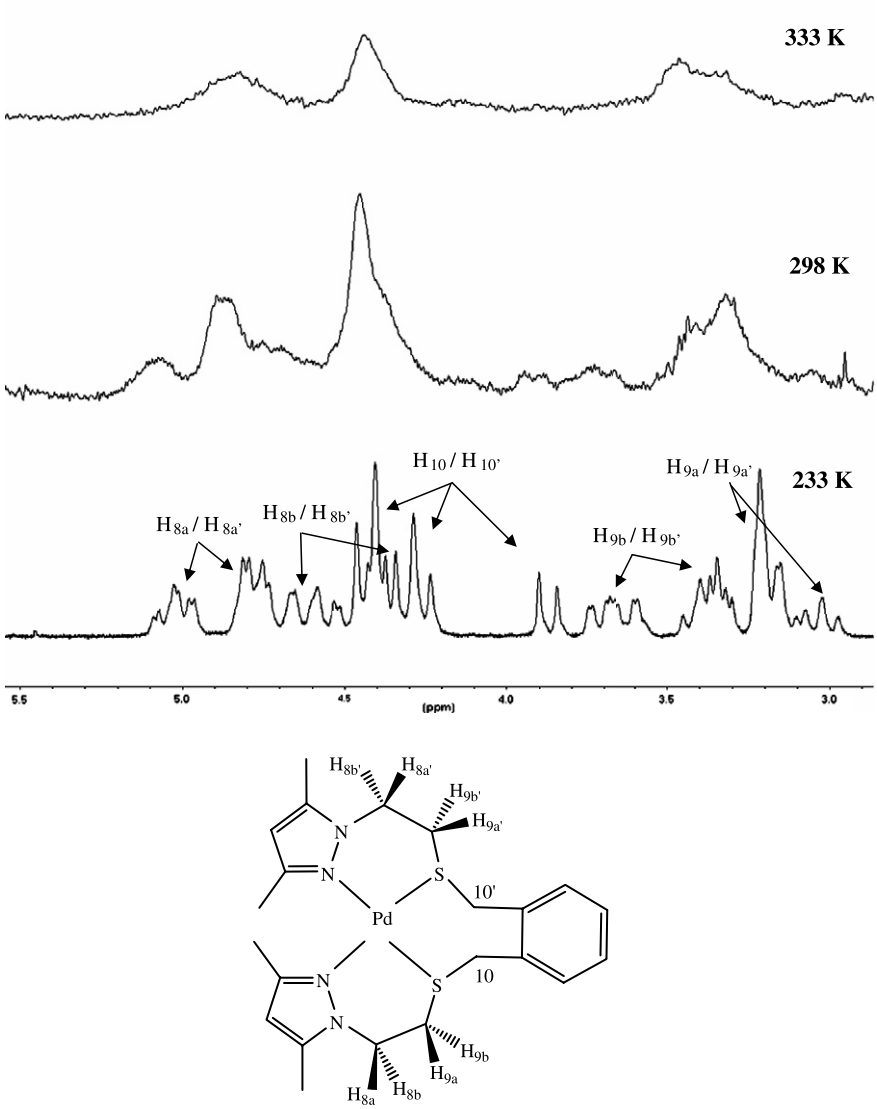


Fig. 1. ^{1}H NMR spectra (250 MHz) of complex **3** in acetonitrile at variable temperatures (233–333 K).

The BF_4^- anions are disordered. Two nitrogen atoms of the pyrazolyl groups and two thioether groups coordinate the palladium atom in a slightly distorted square-planar geometry. The pyrazolyl groups are *cis* to each other. The tetrahedral distortion of the square-planar geometry can be observed in the mean separation of the atoms linked to Pd from the mean plane, which is 0.014(14) Å. The dihedral angle between the two planes N1–Pd–N3 and S1–Pd–S2 is 25.28(8)°. Some selected bond lengths and bond angles for this complex are listed in Table 1.

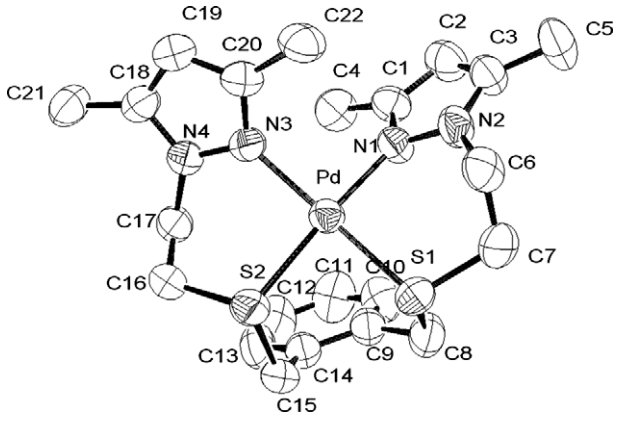


Fig. 2. ORTEP drawing of the cationic $[Pd(bddf)]^{2+}$ part of **3**, showing all non-hydrogen atoms and the atom numbering scheme; 50% probability amplitude displacement ellipsoids are shown.

The PdN_2S_2 core (N aromatic and S thioether) is found in 10 complexes in the literature [4d,4f,14]. The Pd–N (2.026(2) Å, 2.043(2) Å) and Pd–S (2.2803(10) Å, 2.3071(10) Å) distances are of the same order as those found in the literature for this kind of complex. The Pd–N_{pz} bond lengths are 1.990–2.086 Å [4d–f,14], and the Pd–S bond lengths are 2.257–2.897 Å [4d–f,14].

The **bddf** ligand acts as tetradentate chelate and forms two PdNNCCS six-membered rings and one PdSCCCCS seven-membered ring. The Pd–S2–C16–C17–N4–N3 six-membered ring has a boat conformation and the Pd–S1–C7–C6–N2–N1 six-membered ring has a twist-boat conformation. Bite angles are 91.55(8)° and 92.54(8)° for

Table 1
Selected bond lengths (Å) and bond angles (°) for $[Pd(bddf)](BF_4)_2 \cdot H_2O$ (**3**)

Pd–N(1)	2.026(2)	Pd–S(1)	2.2803(10)
Pd–N(3)	2.043(2)	Pt(1)–S(2)	2.3071(10)
N(1)–Pd–N(3)	90.92(11)	N(1)–Pd–S(1)	91.55 (8)
S(1)–Pd–S(2)	85.71(4)	N(3)–Pd–S(1)	172.52(8)
N(3)–Pd–S(2)	92.54(8)	N(1)–Pd–S(2)	173.50 (8)

N(1)–Pd–S(1) and N(3)–Pd–S(2), respectively. These bite angles are higher than those reported for $[Pd(bddo)](BF_4)_2 \cdot H_2O$, 88.2(2)° and 86.1(1)° (bddo = 1,8-bis(3,5-dimethyl-1-pyrazolyl)-3,6-dithiaoctane) [4f], and $[Pd(bddn)](BF_4)_2$, 86.81(12)° and 85.81(11)° (bddn = 1,9-bis(3,5-dimethyl-1-pyrazolyl)-3,7-dithianonane) [4d]. The S(1)–Pd–S(2) bite angle is 85.71(4)° and it is of the same order as that reported for $[PdCl_2L]$ 85.231° (L = 4-benzyloxy-2-(2′-pyridyl) phenoxydiphenylphosphinite) [15] and smaller than the bite angle found for the complex $[PdCl_2L']$ 90.03(9)° (L′ = 2-(3,5-dimethyl-1*H*-pyrazole-1-yl)ethyldiphenylphosphinite) [16].

3. Conclusion

The results presented here reveal that the ligand 1,2-bis[3-(3,5-dimethyl-1-pyrazolyl)-2-thiapropyl]benzene (**bddf**) shows similar behaviour towards Pd(II) and Pt(II). We have obtained complexes with the formula $[MCl_2(bddf)]$, $[M_2Cl_4(bddf)]$ and $[M(bddf)]X$ (M = Pd(II), X = BF_4; Pt(II), X = BPh_4). In complexes **1**–**6**, this ligand shows didentate coordination (*NN*) (**1**, **4**), or tetradentate coordination (*2NS*) (**2**, **5**) or (*NSSN*) (**3**, **6**). The reactivity of the ligand **bddf** with Pd(II) shows the same behaviour as the ligands bddo, and bddn, whereas the reactivity of the ligand **bddf** with Pt(II) is different, as mixtures of isomers were obtained with the aforementioned ligands and Pt(II). The presence of the benzene unit on the S-donor thioether chain produces pure products. Furthermore, we have demonstrated the hemilabile properties of this ligand when coordinated to Pd(II) and Pt(II).

4. Experimental

4.1. General details

The reactions were carried out under nitrogen atmosphere using vacuum line and Schlenk techniques. Solvents were dried and distilled according to standard procedures and stored under nitrogen. Elemental analyses (C, H, N, S) were carried out by the staff of the Chemical Analyses Service of the Universitat Autònoma de Barcelona on a Carlo Erba CHNS EA-1108 instrument. Conductivity measurements were performed at room temperature in 10^{-3} M acetonitrile solutions, employing a CyberScan CON 500 (Euthech instrument) conductimeter. Infrared spectra were run on a Perkin–Elmer FT spectrophotometer, series 2000 cm^{-1} as KBr pellets or polyethylene films in the range 4000–100 cm^{-1}. ^1H NMR, $^{13}C\{^1H\}$ NMR, HSQC, COSY and NOESY spectra were recorded on NMR-FT Bruker AC-250 MHz and DPX-360 Bruker spectrometers in $CDCl_3$ and acetonitrile solution at variable temperature. $^{195}Pt\{^1H\}$ NMR spectra were recorded at 298 °C and 77.42 MHz on a DPX-360 Bruker spectrometer in acetonitrile using aqueous solutions of $[PtCl_6]^{2-}$ (0 ppm) as an external reference and a delay time of 0.01 s. All chemical shifts values (δ) are given in ppm. Mass spectra were obtained with an Esquire 3000 ion-trap mass spectrometer from Bruker Daltonics. Samples of $[MCl_2(CH_3CN)_2]$ (M = Pd(II) [17], Pt(II) [18]) were prepared as described in the literature. 1,2-Bis[3-(3,5-dimethyl-1-pyrazolyl)-2-thiapropyl]benzene (**bddf**) was prepared according to the published methods [5] (Scheme 1).

4.2. Synthesis of the complexes

4.2.1. Synthesis of the complex [$PdCl_2$(bddf)] (*1*)

0.20 mmol (0.083 g) of the ligand **bddf**, dissolved in 15 ml of dry CH_2Cl_2, were added to a solution of 0.20 mmol (0.052 g) of $[PdCl_2(CH_3CN)_2]$ in 15 ml of dry CH_2Cl_2. The solution was stirred at room temperature for 12 h. When the volume of the resultant solution had been reduced to roughly 5 ml, diethyl ether (5 ml) was added to induce precipitation. The resulting precipitate was filtered and washed with 5 ml of diethyl ether, and dried in vacuum.

Yield: 0.085 g (75%). *Anal*. Calc. for $C_{22}H_{30}Cl_2N_4PdS_2$: C, 44.64; H, 5.11; N, 9.46; S, 10.83. Found: C, 44.19; H, 5.06; N, 9.19; S, 10.75%. MS(ESI): *m*/*z* (%) = 557 (100) $[PdCl(bddf)]^+$. Conductivity (Ω^{-1} cm^2 mol^{-1}, 1.13×10^{-3} M in acetonitrile): 16. IR (KBr, cm^{-1}): 3115 ν(C–H)$_{ar}$, 2978, 2924 ν(C–H)$_{al}$, 1554 (ν(C=C), ν(C=N))$_{ar}$, 1467, 1421 (δ(C=C), δ(C=N))$_{ar}$, 1040, 1014 δ(C–H)$_{ip}$, 758 δ(C–H)$_{oop}$. (Polyethylene, cm^{-1}): 459 ν(Pd–N), 337 ν(Pd–Cl). ^1H NMR ($CDCl_3$ solution, 250 Hz, 298 K) δ: 7.36 [4H, m, ph], 5.94 [2H, s, C*H*(pz)], 4.95 [4H, t, ^3J = 8.2 Hz, $N_{pz}CH_2CH_2S$], 4.10 [4H, s, SCH_2ph], 3.50 [4H, t, ^3J = 8.2 Hz, $N_{pz}CH_2CH_2S$], 2.92 [6H, s, CH_3(pz)], 2.31 [6H, s, CH_3(pz)] ppm. $^{13}C\{^1H\}$ NMR ($CDCl_3$ solution, 63 MHz, 298 K) δ: 150.3 (pz-*C*), 142.7 (pz-*C*), 135.7–127.6 (ph-*C*), 107.7 (*C*H(pz)), 49.2 ($N_{pz}CH_2CH_2S$), 33.9 (SCH_2ph), 31.6 ($N_{pz}CH_2CH_2S$), 14.8 (CH_3(pz)), 11.7 (CH_3(pz)) ppm.

4.2.2. Synthesis of the complex [Pd_2Cl_4(bddf)] (*2*)

0.20 mmol (0.083 g) of the ligand **bddf** dissolved in 15 ml of dry CH_2Cl_2 were added to a solution of 0.40 mmol (0.104 g) of $[PdCl_2(CH_3CN)_2]$ in 15 ml of dry CH_2Cl_2. The solution was stirred at room temperature for 12 h. When the volume of the resultant solution had been reduced to roughly 5 ml, diethyl ether (5 ml) was added to induce precipitation. The resulting precipitate was then filtered and washed with 5 ml of diethyl ether, and dried in vacuum.

Yield: 0.089 g (63%). *Anal*. Calc. for $C_{22}H_{30}Cl_4N_4Pd_2S_2$: C, 34.35; H, 3.93; N, 7.28; S, 8.34. Found: C, 34.35; H, 3.88; N, 7.54; S, 8.21%. MS(ESI): m/z (%) = 793 (40) $[Pd_2Cl_4(bddf)+Na]^+$, 735 (48) $[Pd_2Cl_3(bddf)]^+$, 557 (100) $[PdCl(bddf)]^+$. Conductivity ($\Omega^{-1}\,cm^2\,mol^{-1}$, 9.98×10^{-4} M in acetonitrile): 35. IR (KBr, cm^{-1}): 3115 ν(C–H)$_{ar}$, 2978, 2925 ν(C–H)$_{al}$, 1552 (ν(C=C), ν(C=N))$_{ar}$, 1467, 1420 (δ(C=C), δ(C=N))$_{ar}$, 1045, 1038 δ(C–H)$_{ip}$, 798 δ(C–H)$_{oop}$. (Polyethylene, cm^{-1}): 457 ν(Pd–N), 358 ν(Pd–S), 342, 323 ν(Pd–Cl). ^{1}H NMR (acetonitrile solution, 250 Hz, 298 K) δ: 7.51 [4H, br, ph], 6.09 [2H, s, C*H*(pz)], 4.80 [4H, s, SCH_2ph], 4.73 [2H, br, N$_{pz}$CH_2CH$_2$S], 3.95 [2H, br, N$_{pz}$CH_2CH$_2$S], 3.15 [2H, br, N$_{pz}$ CH$_2$CH_2S], 2.77 [2H, br, N$_{pz}$CH$_2$CH_2S], 2.57 [6H, s, CH_3(pz)], 2.35 [6H, s, CH_3(pz)] ppm. ^{13}C{^{1}H} NMR (acetonitrile solution, 63 MHz, 298 K) δ: 154.0 (pz-*C*), 145.4 (pz-*C*), 132.8–130.5 (ph-*C*), 109.4 (*C*H(pz)), 49.5 (S*C*H$_2$ph), 42.5 (N$_{pz}$*C*H$_2$CH$_2$S), 34.8 (N$_{pz}$CH$_2$*C*H$_2$S), 15.8 (*C*H$_3$(pz)), 12.2 (*C*H$_3$(pz)) ppm.

4.2.3. Synthesis of the complex [Pd(bddf)](BF$_4$)$_2\cdot H_2O$ (3)

A solution of 0.25 mmol (0.050 g) of $AgBF_4$ in 10 ml of CH_2Cl_2/CH_3OH (1:1) was added with vigorous stirring to a solution of $[PdCl_2(bddf)]$ (0.12 mmol, 0.080 g) in 10 ml of CH_2Cl_2/CH_3OH (1:1). The reaction was carried out in the dark to prevent reduction of Ag(I) to Ag(0). After 5 min, stirring was stopped and AgCl was filtered off. When the volume of the resultant solution had been reduced to roughly 5 ml, diethyl ether (5 ml) was added to induce precipitation. The resulting precipitate was then filtered and washed with 5 ml diethyl ether.

Yield: 0.098 g (60%). *Anal*. Calc. for $C_{22}H_{32}B_2F_8N_4OPdS_2$: C, 37.07; H, 4.52; N, 7.86; S, 8.99. Found: C, 37.09; H, 4.59; N, 7.75; S, 8.94%. MS(ESI): m/z (%) = 557 (100) $[PdCl(bddf)]^+$. Conductivity ($\Omega^{-1}\,cm^2\,mol^{-1}$, 1.08×10^{-3} M in acetonitrile): 280. IR (KBr, cm^{-1}): 3137 ν(C–H)$_{ar}$, 2996, 2926 ν(C–H)$_{al}$, 1550 (ν(C=C), ν(C=N))$_{ar}$, 1470, 1421 (δ(C=C), δ(C=N))$_{ar}$, 1054 ν(B–F), 801 δ(C–H)$_{oop}$. (Polyethylene, cm^{-1}): 454 ν(Pd–N), 353 ν(Pd–S). ^{1}H NMR (acetonitrile solution, 250 Hz, 333 K) δ: 7.70–7.36 [4H, m, ph], 6.07 [2H, s, C*H*(pz)], 4.85 [4H, br, N$_{pz}$CH_2CH$_2$S], 4.41 [4H, br, SCH_2ph], 3.20 [4H, br, N$_{pz}$CH$_2$CH_2S], 2.36 [6H, s, CH_3(pz)], 1.71 [6H, s, CH_3(pz)] ppm. ^{1}H NMR (acetonitrile solution, 250 Hz, 298 K) δ: 7.69–7.35 [4H, m, ph], 6.07 [2H, s, C*H*(pz)], 5.02 [2H, br, N$_{pz}$CH_2CH$_2$S], 4.69 [2H, br, N$_{pz}$ CH_2CH$_2$S], 4.41 [4H, br, SCH_2ph], 3.69 [2H, br, N$_{pz}$CH$_2$CH_2S], 3.27 [2H, br, N$_{pz}$CH$_2$CH_2S], 2.38 [6H, s, CH_3(pz)], 1.70 [6H, s, CH_3(pz)] ppm. ^{1}H NMR (acetonitrile solution, 250 Hz, 233 K) δ: 7.72–7.32 [4H, m, ph], 6.08 [1H, s, C*H*(pz)], 6.06 [1H, s, C*H*(pz)], 5.01 [1H, br, N$_{pz}$CH_2CH$_2$S], 4.82 [1H, br, N$_{pz}$CH_2CH$_2$S], 4.68 [1H, br, N$_{pz}$ CH_2CH$_2$S], 4.37 [1H, br, N$_{pz}$CH_2CH$_2$S], 4.41 [2H, d, ^2J = 14.0 Hz, SCH_2ph], 4.28 [1H, d, ^2J = 14.0 Hz, SCH_2ph], 3.88 [1H, d, ^2J = 14.0 Hz, SCH_2ph], 3.71 [1H, br, N$_{pz}$CH$_2$CH_2S], 3.40 [1H, br, N$_{pz}$CH$_2$CH_2S], 3.24 [1H, br, N$_{pz}$CH$_2$CH_2S], 3.04 [1H, br, N$_{pz}$CH$_2$CH_2S], 2.39 [6H, s, CH_3(pz)], 1.70 [6H, s, CH_3(pz)] ppm. ^{13}C{^{1}H} NMR (acetonitrile solution, 63 MHz, 298 K) δ: 152.0 (pz-*C*), 146.6 (pz-*C*), 133.2–130.6 (ph-*C*), 109.2 (*C*H(pz)), 49.0 (N$_{pz}$*C*H$_2$CH$_2$S), 41.6 (S*C*H$_2$ph), 35.8 (N$_{pz}$CH$_2$*C*H$_2$S), 12.7 (*C*H$_3$(pz)), 11.3 (*C*H$_3$(pz)) ppm.

4.2.4. Synthesis of the complex [PtCl$_2$(bddf)] (4)

0.20 mmol (0.083 g) of the ligand **bddf** dissolved in 15 ml of dry acetonitrile were added to a solution of 0.20 mmol (0.070 g) of $[PtCl_2(CH_3CN)_2]$ dissolved in 15 ml of dry acetonitrile. The mixture was refluxed for 24 h. The solvent was evaporated to dryness yielding a yellow solid. The resulting solid was washed with 10 ml of CH_2Cl_2/diethyl ether (1:1) and dried in vacuum. The product was recrystallised with a dichloromethane/*n*-pentane (1:1) mixture, and yellow crystals were obtained.

Yield: 0.058 g (50%). *Anal*. Calc. for $C_{22}H_{30}Cl_2N_4PtS_2$: C, 38.82; H, 4.44; N, 8.23; S, 9.42. Found: C, 38.53; H, 4.58; N, 8.46; S, 9.65%. MS(ESI): m/z (%) = 645 (100) $[PtCl(bddf)]^+$. Conductivity ($\Omega^{-1}\,cm^2\,mol^{-1}$, 9.73×10^{-4} M in acetonitrile): 37. IR (KBr, cm^{-1}): 3120 ν(C–H)$_{ar}$, 2957, 2922 ν(C–H)$_{al}$, 1555 (ν(C=C), ν(C=N))$_{ar}$, 1468, 1420 (δ(C=C), δ(C=N))$_{ar}$, 1084, 1035 δ(C–H)$_{ip}$, 794 δ(C–H)$_{oop}$. (Polyethylene, cm^{-1}): 485 ν(Pt–N), 319 ν(Pt–Cl). ^{1}H NMR ($CDCl_3$ solution, 250 Hz, 298 K) δ: 7.34 [4H, m, ph], 5.96 [2H, s, C*H*(pz)], 4.98 [4H, m, NpzCH_2CH$_2$S], 4.09 [4H, s, SCH_2ph], 3.50 [4H, m, N$_{pz}$CH$_2$CH_2S], 2.86 [6H, s, CH_3(pz)], 2.39 [6H, s, CH_3(pz)] ppm. ^{1}H{^{195}Pt} NMR ($CDCl_3$ solution, 360 Hz, 298 K) δ: 7.27 [4H, m, ph], 5.91 [2H, s, C*H*(pz)], 4.92 [4H, t, ^3J = 8.0 Hz, N$_{pz}$CH_2CH$_2$S], 4.04 [4H, s, SCH_2ph], 3.44 [4H, t, ^3J = 8.0 Hz, N$_{pz}$CH$_2$CH_2S], 2.81 [6H, s, CH_3(pz)], 2.35 [6H, s, CH_3(pz)] ppm. ^{13}C{^{1}H} NMR ($CDCl_3$ solution, 63 MHz, 298 K) δ: 152.0 (pz-*C*), 141.0 (pz-*C*), 131.3–129.1 (ph-*C*), 107.4 (*C*H(pz)), 50.7 (N$_{pz}$*C*H$_2$CH$_2$S), 34.3 (S*C*H$_2$ph), 31.9 (N$_{pz}$CH$_2$*C*H$_2$S), 14.9 (*C*H$_3$(pz)), 11.9 (*C*H$_3$(pz)) ppm. ^{195}Pt{^{1}H} NMR (acetonitrile solution, 77.42 MHz, 298 K) δ = singlet at −2447 ppm.

4.2.5. Synthesis of the complex [Pt$_2$Cl$_4$(bddf)] (5)

0.20 mmol (0.083 g) of the ligand **bddf** dissolved in 15 ml of dry acetonitrile were added to a solution of 0.40 mmol (0.140 g) of $[PtCl_2(CH_3CN)_2]$ dissolved in 15 ml of dry acetonitrile. The mixture was refluxed for 24 h. The solvent was evaporated to dryness leaving a yellow solid. The resulting solid was washed with 10 ml of CH_2Cl_2/diethyl ether (1:1) and dried in vacuum.

Yield: 0.078 g (60%). *Anal*. Calc. for $C_{22}H_{30}Cl_4N_4Pt_2S_2$: C, 27.91; H, 3.19; N, 5.92; S, 6.77. Found: C, 27.80; H, 3.16; N, 6.02; S, 6.74%. MS(ESI): m/z (%) = 969 (100) $[Pt_2Cl_4(bddf)+Na]^+$. Conductivity ($\Omega^{-1}\,cm^2\,mol^{-1}$, 9.92×10^{-4} M in acetonitrile): 9. IR (KBr, cm^{-1}): 3121 ν(C–H)$_{ar}$, 2974, 2922 ν(C–H)$_{al}$, 1555 (ν(C=C), ν(C=N))$_{ar}$, 1469, 1420 (δ(C=C), δ(C=N))$_{ar}$, 1037 δ(C–H)$_{ip}$, 791 δ(C–H)$_{oop}$. (Polyethylene, cm^{-1}): 472 ν(Pt–N), 371 ν(Pt–S), 319, 310 ν(Pt–Cl). ^{1}H NMR (acetonitrile solution,

250 Hz, 298 K) δ: 7.43 [4H, s, ph], 6.12 [2H, s, C*H*(pz)], 4.72 [6H, br, SCH_2ph, $N_{pz}CH_2CH_2S$], 3.99 [2H, br, $N_{pz}CH_2CH_2S$], 2.80 [4H, br, $N_{pz}CH_2CH_2S$], 2.57 [6H, s, CH_3(pz)], 2.36 [6H, s, CH_3(pz)] ppm. $^{13}C\{^1H\}$ NMR (acetonitrile solution, 63 MHz, 298 K) δ: 153.8 (pz-*C*), 144.2 (pz-*C*), 132.7–130.0 (ph-*C*), 108.6 (*C*H(pz)), 48.7 (S*C*H$_2$ph), 42.0 ($N_{pz}CH_2CH_2S$), 34.8 ($N_{pz}CH_2CH_2S$), 15.4 (*C*H$_3$(pz)), 12.2 (*C*H$_3$(pz)) ppm. $^{195}Pt\{^1H\}$ NMR (acetonitrile solution, 77.42 MHz, 298 K) δ = singlet at −2857 ppm.

4.2.6. Synthesis of the complex [Pt(bddf)](BPh$_4$)$_2$ (6)

A solution of NaBPh$_4$ (0.20 mmol, 0.070 g) in 10 ml acetonitrile/methanol (1:1) was added dropwise with vigorous stirring to a solution of [PtCl$_2$(bddf)] (0.11 mmol, 0.077 g) in 10 ml of acetonitrile/methanol (1:1). The solution was stirred at room temperature for 12 h. The yellowish solution was filtered to separate NaCl. When the volume of the resultant solution had been reduced to roughly 5 ml, diethyl ether (5 ml) was added to induce precipitation. The resulting precipitate was then filtered and washed with 5 ml diethyl ether.

Yield: 0.080 g (57%). *Anal.* Calc. for $C_{70}H_{70}B_2N_4PtS_2$: C, 67.36; H, 5.65; N, 4.49; S, 5.14. Found: C, 67.29; H, 5.64; N, 4.49; S, 5.13%. MS(ESI): m/z (%) = 645 (100) [PtCl(bddf)]$^+$. Conductivity (Ω^{-1} cm^2 mol^{-1}, 1.05×10^{-3} M in acetonitrile): 250. IR (KBr, cm^{-1}): 3054 ν(C–H)$_{ar}$, 2978, 2922 ν(C–H)$_{al}$, 1574, 1553 (ν(C=C), ν(C=N))$_{ar}$, 1474, 1425 (δ(C=C), δ(C=N))$_{ar}$, 801 δ(C–H)$_{oop(pz)}$, 736, 707 δ(C–H)$_{oop(ph)}$, 612 ν(B–C). (Polyethylene, cm^{-1}): 464 ν(Pt–N), 374 ν(Pt–S). $^1H\{^{195}Pt\}$ NMR (acetonitrile solution, 360 Hz, 298 K) δ: 7.76, 7.64 [1H/1H, d, ^3J = 7.2 Hz, ph(L)], 7.46, 7.36 [1H/1H, t, ^3J = 7.2 Hz, ph(L)], 7.31–6.78 [40H, br, ph(BPh$_4$)], 6.07 [1H, s, C*H*(pz)], 4.63 [7H, br, $N_{pz}CH_2CH_2S$, SCH_2ph], 3.86 [1H, d, ^2J = 14.0 Hz, SCH_2ph], 3.57 [1H, br, $N_{pz}CH_2CH_2S$], 3.32 [1H, br, $N_{pz}CH_2CH_2S$], 2.95 [1H, br, $N_{pz}CH_2CH_2S$], 2.71 [1H, br, $N_{pz}CH_2CH_2S$], 2.35 [6H, s, CH_3(pz)], 2.10 [6H, s, CH_3(pz)] ppm. $^{13}C\{^1H\}$ NMR (acetonitrile solution, 63 MHz, 298 K) δ: 165.9–123.0 (Ph), 150.0 (pz-*C*), 141.8 (pz-*C*), 134.9–128.8 (ph-*C*), 108.7 (*C*H(pz)), 48.3 ($N_{pz}CH_2CH_2S$), 42.3 (S*C*H$_2$ph), 36.2 ($N_{pz}CH_2CH_2S$), 12.0 (*C*H$_3$(pz)) ppm. $^{195}Pt\{^1H\}$ NMR (acetonitrile solution, 77.42 MHz, 298 K) δ = singlet at −3884 ppm.

4.3. X-ray crystal structure for compound [Pd(bddf)](BF$_4$)$_2$ · H$_2$O (3)

Suitable crystals for X-ray diffraction of the compound [Pd(bddf)](BF$_4$)$_2$ · H$_2$O (**3**) were obtained through crystallisation from acetonitrile solution. A prismatic crystal was selected and mounted on a MAR345 diffractometer with an image plate detector. Unit-cell parameters were determined from 681 reflections ($3° < \theta < 31°$) and refined by least-squares method. Intensities were collected with graphite-monochromatised Mo Kα radiation. 27417 reflections were measured in the range $1.73° \leqslant \theta \leqslant 30.00°$, 8088 of which were non-equivalent by symmetry (R_{int} (on I) = 0.038). 7271 reflections were assumed as observed applying the condition $I > 2\sigma(I)$. Lorentz-polarisation but no absorption corrections were made.

Table 2
Crystallographic data for [Pd(bddf)](BF$_4$)$_2$ · H$_2$O (**3**)

Empirical formula	$C_{22}H_{32}B_2F_8N_4OPdS_2$
Formula weight	712.66
Temperature (K)	293(2)
Crystal System	monoclinic
Space group	$P2_1/c$
Unit cell dimensions	
a (Å)	10.460(4)
b (Å)	18.064(6)
c (Å)	15.950(5)
α (°)	90
β (°)	103.07(2)
γ (°)	90
V (Å^3)	2935.7(17)
Z	4
D_{calc} (g cm^{-3})	1.612
μ (mm^{-1})	0.849
F(000)	1440
Crystal size (mm)	0.2 × 0.1 × 0.1
θ Range (°)	1.73–30.00
Index range	$-13 \leqslant h \leqslant 13$, $0 \leqslant k \leqslant 25$, $0 \leqslant l \leqslant 22$
Reflections collected/unique (R_{int})	27417/8088 (0.0383)
Completeness to θ_{max} (%)	94.4
Absorption correction	none
Data/restraints/parameters	8088/3/340
Goodness-of-fit on F^2	1.037
Final R_1, wR_2	0.0541, 0.1621
R_1 (all data), wR_2	0.0583, 0.1669
Maximum and minimum residual electron density (e Å^{-3})	0.707 and −0.814

The structure was solved by direct methods, using the SHELXS-97 computer program [19], and refined by full-matrix least-squares method with SHELX-97 computer programs [20] using 27417 reflections (very negative intensities were not assumed). The function minimised was $\sum w(|F_o|^2 - |F_c|^2)^2$ where $w = [\sigma^2(I) + (0.1115P)^2 + 1.2853P]^{-1}$, and $P = (F_o^2 + 2F_c^2)/3$. All H atoms were computed and refined, using a riding model, with an isotropic temperature factor equal to 1.2 times the equivalent temperature factor of the atom to which they are linked. The final $R(F)$ factor and $R_w(F^2)$ values as well as the number of parameters and other details concerning the refinement of the crystal structure are gathered in Table 2.

5. Supplementary material

CCDC 631793 contains the supplementary crystallographic data for this paper. These data can be obtained free of charge via http://www.ccdc.cam.ac.uk/conts/retrieving.html, or from the Cambridge Crystallographic Data Centre, 12 Union Road, Cambridge CB2 1EZ, UK; fax: (+44) 1223-336-033; or e-mail: deposit@ccdc.cam.ac.uk.

Acknowledgement

Support by the Spanish Ministerio de Educación y Cultura (Project BQU2003-03582) is gratefully acknowledged.

References

[1] (a) P. Braunstein, J. Organomet. Chem. 689 (2004) 3953;
(b) P. Braunstein, F. Naud, Angew. Chem., Int. Ed. 40 (2001) 680;
(c) C.S. Slone, D.A. Weinberger, C.A. Mirkin, Prog. Inorg. Chem. 48 (1999) 233;
(d) A. Bader, E. Lindner, Coord. Chem. Rev. 108 (1991) 27.

[2] (a) R. Mukherjee, Coord. Chem. Rev. 203 (2000) 151;
(b) G. La Monica, G.A. Ardizzoia, Prog. Inorg. Chem. 46 (1997) 151;
(c) S. Trofimenko, Scorpionates: The Coordination Chemistry of Polypyrazolylborate Ligands, Imperial College Press, London, 1999;
(d) S. Trofimenko, Chem. Rev. 93 (1993) 943;
(e) S. Trofimenko, Prog. Inorg. Chem. 34 (1986) 115;
(f) S. Trofimenko, Chem. Rev. 72 (1972) 497;
(g) P.K. Byers, A.J. Canty, R.T. Honeyman, Adv. Organomet. Chem. 34 (1992) 1.

[3] (a) R. Peng, D. Li, T. Wu, X.P. Zhou, S.W. Ng, Inorg. Chem. 45 (2006) 4035;
(b) D.B. Cordes, L.R. Hanton, Inorg. Chem. Commun. 8 (2005) 967;
(c) J.J.M. Amoore, C.A. Black, L.R. Hanton, M.D. Spicer, Crystal Growth Design 5 (2005) 1255;
(d) D.B. Cordes, A.S. Balley, P.L. Caradoc-Davies, D.H. Gregory, L.R. Hanton, K. Lee, M.D. Spicer, Inorg. Chem. 44 (2005) 2544;
(e) P.L. Caradoc-Davies, L.R. Hanton, J.M. Hodgkiss, M.D. Spicer, J. Chem. Soc., Dalton Trans. (2002) 1581;
(f) P.L. Caradoc-Davies, D.H. Gregory, L.R. Hanton, J.M. Turnbull, J. Chem. Soc., Dalton Trans. (2002) 1574;
(g) P.L. Caradoc-Davies, L.R. Hanton, Chem. Commun. (2001) 1098;
(h) P.L. Caradoc-Davies, L.R. Hanton, W. Henderson, J. Chem. Soc., Dalton Trans. (2001) 2749;
(i) L.R. Hanton, K. Lee, J. Chem. Soc., Dalton Trans. (2000) 1161;
(j) L.R. Hanton, K. Lee, Inorg. Chem. 38 (1999) 1634;
(k) Y. Suenaga, T. Kuroda-Sowa, M. Maekawa, M. Munakata, J. Chem. Soc., Dalton Trans. (1999) 2737;
(l) Z. Atherton, D.M.L. Goodgame, S. Menzer, D.J. Williams, Polyhedron 18 (1998) 237;
(m) C.M. Hartshorn, P.J. Steel, J. Chem. Soc., Dalton Trans. (1998) 3935;
(n) M.J. Hannon, C.L. Painting, W. Errington, Chem. Commun. (1997) 1805.

[4] (a) A. de León, J. Pons, J. García-Antón, X. Solans, M. Font-Bardía, J. Ros, Inorg. Chim. Acta (in press);
(b) A. de León, J. Pons, J. García-Antón, X. Solans, M. Font-Bardía, J. Ros. Polyhedron (in press);
(c) A. Rimola, M. Sodupe, J. Ros, J. Pons, Eur. J. Inorg. Chem. (2006) 447;
(d) J. García-Antón, J. Pons, J. Ros, X. Solans, M. Font-Bardía, Acta Crystallogr., Sect. E 60 (2004) m1087;
(e) J. García-Antón, J. Pons, X. Solans, M. Font-Bardía, J. Ros, Eur. J. Inorg. Chem. (2003) 3952;
(f) J. García-Antón, J. Pons, X. Solans, M. Font-Bardía, J. Ros, Eur. J. Inorg. Chem. (2002) 3319.

[5] J. García-Antón, R. Mathieu, N. Lugan, J. Pons, J. Ros, J. Organomet. Chem. (2004) 1599.

[6] W.J. Geary, Coord. Chem. Rev. 7 (1971) 81.

[7] D.H. Williams, I. Fleming, Spectroscopic Methods in Organic Chemistry, McGraw-Hill, London, 1995.

[8] K. Nakamoto, Infrared and Raman spectra of Inorganic and Coordination Compounds, Wiley, New York, 1986.

[9] (a) H. Friebolin, Basic One- and Two-Dimensional NMR Spectroscopy, Wiley–VCH/Verlag GmbH, Weinheim, 1998;
(b) A. Pañella, J. Pons, J. García-Antón, X. Solans, M. Font-Bardía, J. Ros, Eur. J. Inorg. Chem. (2006) 1678.

[10] E.W. Abel, S.K. Bhargava, K. Orell, Prog. Inorg. Chem. 32 (1994) 1.

[11] (a) L. Szucová, Z. Trávnicek, M. Zatloukal, I. Popa, Bioorg. Med. Chem. 14 (2006) 479;
(b) I. Lakomska, E. Szlyk, J. Sitkowski, L. Kozerski, J. Wietrzyk, M. Pelczynska, A. Nasulewicz, A. Opolski, J. Inorg. Biochem. 98 (2004) 167;
(c) Z. Trávnicek, M. Maloň, M. Zatloukal, K. Dolezal, K. Strnad, J. Marek, J. Inorg. Biochem. 94 (2003) 307;
(d) P. Tsiveriotis, N. Hadjiliadis, G. Slauropoules, Inorg. Chim. Acta 261 (1997) 83;
(e) Ch. Tessier, F.D. Rochon, Inorg. Chim. Acta 295 (1999) 25;
(f) P.S. Pregosin, Coord. Chem. Rev. 33 (1982) 247.

[12] (a) J. García-Antón, J. Pons, X. Solans, M. Font-Bardía, J. Ros, Eur. J. Inorg. Chem. (2003) 2992;
(b) X. Riera, V. Moreno, M. Font-Bardía, X. Solans, Polyhedron 18 (1999) 65;
(c) U. Bierbach, N. Farell, JBIC 3 (1998) 570.

[13] (a) G.J. Grant, M.L. Patel, L.F. Helm, Polyhedron 23 (2004) 1361;
(b) K.A. Mitchell, C.M. Jensen, Inorg. Chem. 34 (1995) 4441.

[14] (a) A.J. Blake, Y.V. Roberts, M. Schroder, J. Chem. Soc., Dalton Trans. (1996) 1885;
(b) H. Nikol, H.B. Burgi, K.I. Hardcastle, H.B. Gray, Inorg. Chem. 34 (1995) 6319;
(c) S.V. Kolotilov, E.A. Goreshnik, V.V. Pavlischuk, K.B. Yatsimirskii, Zh. Neorg. Khim. 45 (2000) 967;
(d) A.J. Blake, N.R. Champness, W.-S. Li, M. Schroder, Acta Crystallogr., Sect. C 54 (1998) IUC9800071;
(e) F. Contu, F. Demartin, F.A. Devillanova, A. Garau, F. Isaia, V. Lippolis, A. Salis, G. Verani, J. Chem. Soc., Dalton Trans. (1997) 4401;
(f) M. Arca, A.J. Blake, J. Casabó, F. Demartin, F.A. Devillanova, A. Garau, F. Isaia, V. Lippolis, R. Kivekas, V. Muñiz, M. Shorder, G. Verani, J. Chem. Soc., Dalton Trans. (2001) 1180.

[15] R. Kranich, K. Eis, O. Geis, S. Mühle, J.W. Bats, H.G. Schmalz, Chem. Eur. J. 6 (2000) 2874.

[16] S. Muñoz, J. Pons, X. Solans, M. Font-Bardía, J. Ros (in preparation).

[17] S. Komiya, Synthesis of Organometallic Compounds: A Practice Guide, Ed. Board, New York, 1997.

[18] F.P. Fanizzi, F.P. Intini, L. Maresca, G. Natile, J. Chem. Soc., Dalton Trans. (1990) 199.

[19] G.M. Sheldrick, SHELXS-97: Program for Crystal Structure Determination, University of Göttingen, Göttingen, Germany, 1997.

[20] G.M. Sheldrick, SHELXL-97: Program for Crystal Structure Refinement, University of Göttingen, Göttingen, Germany, 1997.

Available online at www.sciencedirect.com
ScienceDirect
Polyhedron 26 (2007) 2929–2934
POLYHEDRON
www.elsevier.com/locate/poly

Pentacoordination at antimony in dibenzostibocines via D–Sb transannular interactions (D = O, S): A structural study

José G. Alvarado-Rodríguez *, Simplicio González-Montiel, Noemí Andrade-López, Liliana B. López-Feliciano

Centro de Investigaciones Químicas, Universidad Autónoma del Estado de Hidalgo, Km. 4,5 Carretera Pachuca-Tulancingo, Pachuca, Hidalgo, C.P. 42076, Mexico

Received 5 January 2007; accepted 20 March 2007
Available online 31 March 2007

Abstract

Addition of $M_2SCN(CH_2R)_2$ to $D(C_6H_4S)_2SbCl$ in methylene chloride solution leaded to the formation of the stable compounds $D(C_6H_4S)_2SbS_2CN(CH_2R)_2$ (D = O, R = Me, **1**; D = S, R = Me, **2**; R = Ph, **3**). The new dibenzostibocines derivatives containing two different types of dithioligands were characterized by elemental analysis and spectroscopic studies (IR, ^1H and ^{13}C NMR). Single crystal X-ray diffraction determinations of complexes **1**–**3** revealed that the antimony atom acts as an acceptor atom exhibiting an intramolecular transannular interaction with the donor D atom, expanding its coordination from three to five and displaying a skew trapezoidal local geometry.
© 2007 Elsevier Ltd. All rights reserved.

Keywords: Antimony complexes; Hypervalent compounds; Dithiocarbamate derivatives; Structure elucidation

1. Introduction

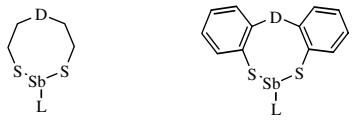
The preparative and structural chemistry of 1,1-dithioligands has been widely explored [1,2]. With regard to the structural studies, these ligands often display unsymmetrical bidentate coordination patterns toward heavier 15 group elements; the difference between the two metal–sulfur bond lengths diminishes as the metallic character increases in the order As, Sb, Bi. It has been surveyed that dithiocarbamate ligands mainly lead to the formation of discrete monomeric aggregates with lighter 15 elements (P, As) when they are surrounded by organic groups, and to polymeric associations in the case of heavier elements (Sb and Bi) [3].

On the other hand, the structural study of the antimony(III) complexes in sulfur rich environments has been dominated by the synthesis of tris–chelate complexes [4–13]. In order to study the influence of the usually strong coordination of the 1,1-dithioligands to the central acidic Sb atom in several intra- and intermolecular structural features, some antimony(III) compounds in a fully chalcogenate coordination sphere have been synthesized by means of potentially tridentate ligands containing chalcogen donors like oxygen or sulfur. One of these structural features is the transannular interaction between a chalcogen donor atom (D) and an acceptor atom in compounds of the types I and II (Scheme 1). In the case of type I complexes, several studies comprising exocyclic monoanionic 1,1-dithioligands $S_2PR_2^-$ attached to Sb have shown a weakening in the D–Sb transannular interaction when these complexes are compared with the halogen derivatives [14–16].

In contrast, to our knowledge there are not examples of complexes of the type II containing 1,1-dithioligands. We have studied by means of X-ray diffraction studies and theoretical calculations the nature of the transannular interaction D → Sb (D = O, S) in monohalogenated dibenzostibocines and have shown the existence of a strong transannular

* Corresponding author. Tel.: +52 771 7172000.
E-mail address: jgar@uaeh.edu.mx (J.G. Alvarado-Rodríguez).

0277-5387/$ - see front matter © 2007 Elsevier Ltd. All rights reserved.
doi:10.1016/j.poly.2007.03.038



I II

Scheme 1.

interaction, revealing that the antimony atom is in a distorted ψ-bipyramidal tetracoordinate geometry [17]. These results prompt us to analyze the influence of a potentially bidentate ligand linked to the antimony atom in that interaction. Here we report the synthesis and structural study of type II complexes with antimony(III) as acceptor atom in a chalcogen rich environment. After the description of the synthesis of the dithiocarbamatedibenzoestibocines, NMR and X-ray crystallographic data are presented and discussed.

2. Experimental

2.1. Reagents and general procedures

Unless noted otherwise, all reactions and operations were carried out under argon or dinitrogen at room temperature with use of standard Schlenk techniques. Solvents were dried and distilled before use. $NaS_2CNEt_2 \cdot 3H_2O$ was obtained commercially (Aldrich) and used as received. $KS_2CN(CH_2Ph)_2$ was prepared from the reaction of carbon disulfide, dibenzylamine and KOH in methylene chloride by modified procedures [18]. $D(C_6H_4S)_2SbCl$ (D = O, S) compounds were prepared as reported [17]. Melting points were determined on a Melt-Temp II instrument and are uncorrected. Elemental analyses were performed on a Perkin–Elmer Series II CHNS/O Analyzer. The IR spectra were recorded in the 4000–400 cm^{-1} range on a Perkin–Elmer System 2000 FT-IR spectrometer, as KBr pellets. The ^1H and ^{13}C NMR spectra were recorded on a Jeol Eclipse 400 spectrometer; with the residual protio-solvent signal used as referenced for ^1H NMR spectra. $^{13}C\{1H\}$ NMR spectra were referred through the solvent peaks. Chemical shifts are quoted on the δ scale (downfield shifts are positive) relative to tetramethylsilane (^1H, $^{13}C\{1H\}$). Spectra were recorded at 25 °C. ^1H; 399.78 MHz, $^{13}C\{1H\}$; 100.53 MHz. Suitable single crystals of the complexes **1**– **3** were grown by slow evaporation from a methylene chloride solution and were analyzed by single crystal X-ray diffraction. The data were collected at room temperature on a CCD Smart 6000 diffractometer through the use of Mo Kα radiation ($\lambda = 0.71073$ Å, graphite monochromator). Data were integrated, scaled, sorted, and averaged using the SMART software package. The structure of **1** was solved by heavy atom method and the structures of **2** and **3** were solved by direct methods using SHELXTL NT Version 5.10 and refined by full-matrix least squares against F^2 [19]. An empirical absorption correction based on the multiple measurement of equivalent reflections was applied by using the program SADABS [20]. The displacement parameters of non-hydrogen atoms were refined anisotropically. The positions of the hydrogen atoms were kept fixed with a common isotropic displacement parameter.

2.2. Synthesis of the dithiocarbamatedibenzostibocine derivatives

2.2.1. Synthesis of $O(C_6H_4S)_2SbS_2CN(CH_2CH_3)_2$ (1)

$NaS_2CNEt_2 \cdot 3H_2O$ (130 mg, 0.58 mmol) was added to a solution containing $O(C_6H_4S)_2SbCl$ (200 mg, 0.51 mmol) in methylene chloride (25 mL) at 25 °C. The yellow suspension was refluxed for 5 h, and then the resultant heterogeneous reaction mixture was allowed to cool to room temperature. The NaCl was removed by means of a column of Celite and Na_2SO_4. The solution was left under a dynamic dinitrogen flow to provide yellow crystals of **1**, which were washed with *i*PrOH (20 mL) and filtered by suction. Yield: 180 mg (70%). M.p. 198–201 °C. *Anal.* Calc. for $O(C_6H_5S)_2SbS_2CN(CH_2CH_3)_2$: C, 40.64; H, 3.61. Found: C, 41.27; H, 3.58%. IR (KBr, cm^{-1}): $\upsilon = 3058$, 2971, 2924, 2866, 1568, 1500, 1454, 1427, 1351, 1270, 1246, 1196, 1196, 1147, 1060, 986, 864, 800, 748, 730.

2.2.2. Synthesis of $S(C_6H_4S)_2SbS_2CN(CH_2CH_3)_2$ (2)

2 was prepared in a similar procedure. $NaS_2CNEt_2 \cdot 3H_2O$ (120 mg, 0.53 mmol) was added to a solution containing $S(C_6H_4S)_2SbCl \cdot 0.5C_6H_6$ (200 mg, 0.45 mmol) in methylene chloride (25 mL). Yield: 165 mg (71%). M.p. 174–176 °C. *Anal.* Calc. for $S(C_6H_5S)_2SbS_2CN(CH_2CH_3)_2$: C, 39.39; H, 3.50. Found: C, 39.49; H, 3.41%. IR (KBr, cm^{-1}): $\upsilon = 3046$, 2979, 2929, 2851, 1559, 1500, 1439, 1427, 1353, 1268, 1243, 1197, 1145,1073, 1037, 982, 907, 835, 755, 744.

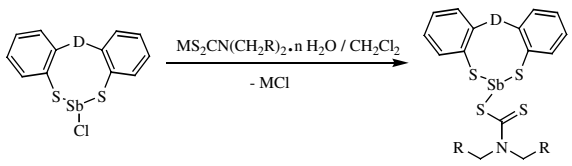
2.2.3. Synthesis of $S(C_6H_4S)_2SbS_2CN(CH_2C_6H_5)_2$

3 was prepared in a similar procedure. $KS_2CN(CH_2Ph)_2$ (130 mg, 0.42 mmol) was added to a solution containing $S(C_6H_4S)_2SbCl \cdot 0.5C_6H_6$ (150 mg, 0.34 mmol) in methylene chloride (25 mL). Yield: 115 mg (66%). M.p. 188–194 °C. *Anal.* Calc. for $S(C_6H_5S)_2SbS_2CN(CH_2CH_3)_2$: C, 50.47; H, 3.45. Found: C, 50.38; H, 3.52%. IR (KBr, cm^{-1}): $\upsilon = 3054$, 3042, 3028, 2921, 1492, 1467, 1452, 1438, 1418, 1350, 1245, 1212, 1079, 1028, 964, 803, 751, 697, 627.

3. Results and discussion

3.1. Synthesis of $D(C_6H_4S)_2SbS_2CN(CH_2R)_2$ (D = O, R = Me; D = S, R = Me, Ph)

The $D(C_6H_4S)_2SbCl$ (D = O, S) starting materials were prepared following the reported method [17]. Treatment of $O(C_6H_4S)_2SbCl$ or benzene solvate $S(C_6H_4S)_2SbCl \cdot 0.5C_6H_6$ with the corresponding dithiocarbamate salt in CH_2Cl_2 yielded $O(C_6H_4S)_2SbS_2CN(CH_2CH_3)_2$ (**1**), $S(C_6H_4S)_2SbS_2CN(CH_2CH_3)_2$ (**2**) and $S(C_6H_4S)_2SbS_2$-



	D	M	n	R
1	O	Na	3	Me
2	S	Na	3	Me
3	S	K	0	Ph

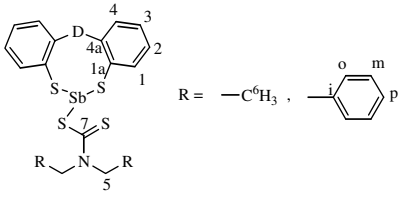
Scheme 2.

$CN(CH_2C_6H_5)_2$ (**3**), respectively, as yellow crystals (see Scheme 2 and Section 2 for details). All complexes are air-stable, soluble in methylene chloride, benzene and chloroform, and insoluble in pentane, hexane and 2-propanol.

3.2. NMR spectra of $D(C_6H_4S)_2SbS_2CN(CH_2R)_2$ (D = O, R = Me; D = S, R = Me, Ph)

The NMR spectra of the three complexes were recorded in $CDCl_3$ solutions at 25 °C and the chemical shifts are relative to TMS. The assignments of these complexes were carried out by heteronuclear and homonuclear correlation two dimension experiments (HETCOR, COLOC and COSY) and are shown in the Table 1. In solution the two DC_6H_4SSb halves are equivalent. In all compounds the two ethyl or benzyl groups in the dithiocarbamate moiety are also equivalent,

Table 1
^1H and ^{13}C NMR spectral data of dithiocarbamatedibenzostibocine derivatives



	Compound	^1H Chemical shift (ppm)	^{13}C Chemical shift (ppm)
1	$O(C_6H_4S)_2SbS_2CN(CH_2CH_3)_2$	7.50 (2H, m, H^1) 7.13 (2H, m, H^2) 7.08 (2H, m, H^3) 7.03 (2H, m, H^4) 3.80 (2H, q, $^3J = 7.3$, H^6) 1.33 (3H, t, $^3J = 7.3$, H^5)	195.0 (C^7) 155.8 (C^{4a}) 134.0 (C^1) 129.7 (C^{1a}) 126.8 (C^3) 125.1 (C^2) 120.7 (C^4) 49.8 (C^5) 12.2 (C^6)
2	$S(C_6H_4S)_2SbS_2CN(CH_2CH_3)_2$	7.52 (2H, dd, $^3J = 7.88$, $^4J = 1.28$, H^4) 7.43 (2H, dd, $^3J = 7.68$, $^4J = 1.48$, H^1) 7.18 (2H, ddd, $^3J = 7.68$, $^4J = 1.28$, H^2) 7.08 (2H, ddd, $^3J = 7.88$, 7.68, $^4J = 1.48$, H^3) 3.83 (2H, q, $^3J = 7.0$, H^6) 1.32 (3H, q, $^3J = 7.0$, H^5)	196.3(C^7) 142.7 (C^{1a}) 135.5 (C^{4a}) 134.5 (C^1) 133.5 (C^4) 129.0 (C^2) 126.5 (C^3) 49.3 (C^5) 12.3 (C^6)
3	$S(C_6H_4S)_2SbS_2CN(CH_2Ph)_2$	7.55 (2H, d, $^3J = 7.72$, H^4) 7.45 (2H, d, $^3J = 7.68$, H^1) 7.36 (6H, m, $H^{meta,para}$) 7.30 (4H, d, $^3J = 6.96$, H^{ortho}) 7.20 (2H, dd, $^3J = 7.72$, 7.68, H^3) 7.10 (2H, dd, $^3J = s7.72$, 7.68, H^2) 2.36 (2H, s, H^5)	200.7 (C^7) 142.7 (C^{1a}) 135.3 (C^{4a}) 134.5 (C^1) 134.4 (C^{ipso}) 133.5 (C^4) 129.1 (C^2) 129.0 (C^{meta}) 128.4 (C^{para}) 128.1 (C^{ortho}) 126.6 (C^3) 55.8 (C^5)

indicating a free rotation around the carbon–nitrogen bond at 25 °C.

3.3. Crystal and molecular structures of $D(C_6H_4S)_2SbS_2CN(CH_2R)_2$ (D = O, R = Me; D = S, R = Me, Ph)

The structures in the crystalline solid state of complexes **1**–**3** were determined by single-crystal X-ray diffraction analyses. Selected crystallographic data are given in Table 2 and selected bond lengths, angles and torsion angles are given in Table 3.

3.3.1. Molecular structures of complexes 1–3

The ORTEP drawings of the $D(C_6H_4S)_2SbS_2CN(CH_2R)_2$ (D = O, R = Me, **1**; D = S, R = Me, **2**; R = Ph, **3**) complexes are depicted in the Fig. 1.

Table 2
Crystal data and refinement details for $D(C_6H_4S)_2SbS_2CN(CH_2R)_2$ (D = O, R = Me, **1**; D = S, R = Me, **2**; R = Ph, **3**)

Compound	1	2	3
Empirical formula	$C_{17}H_{18}NOS_4Sb$	$C_{17}H_{18}NS_5Sb$	$C_{27}H_{22}NS_5Sb$
Mr (g/mol)	502.31	518.37	642.51
Crystal size (mm)	0.40 × 0.38 × 0.06	0.36 × 0.35 × 0.18	0.22 × 0.21 × 0.20
Crystal system	monoclinic	triclinic	triclinic
Space group	$P2(1)/c$	$P\bar{1}$	$P\bar{1}$
ρ_{calc} (Mg m^{-3})	1.668	1.703	1.616
Z	4	2	2
a (Å)	10.7274(6)	8.7266(6)	10.633(1)
b (Å)	12.2299(7)	10.4524(6)	10.702(1)
c (Å)	15.520(1)	12.7388(8)	12.846(2)
α (°)	90	105.833(1)	107.516(2)
β (°)	100.734(2)	95.676(1)	107.702(3)
γ (°)	90	111.877(1)	90.162(3)
V (Å^3)	2000.5(2)	1010.9(1)	1320.8(3)
μ (mm^{-1})	1.801	1.881	1.457
$F(000)$	1000	516	644
Temperature (K)	292	295	293
θ Range (°)	1.93–26.02	1.71–26.00	1.75–26.06
Goodness-of-fit	0.992	1.108	1.080
Absorption correction	SADABS	SADABS	SADABS
T_{min}, T_{max}	0.237, 0.692	0.551, 0.728	0.733, 0.747
Reflections collected	13383	6665	8872
Unique reflections	3925	3937	5201
R_{int}	0.0611	0.0173	0.0353
Solution method	heavy atom	direct	direct
R_1, wR_2 [$I > 2\sigma(I)$]	0.0355, 0.0817	0.0313, 0.1081	0.0330, 0.0811
R_1, wR_2 (all data)	0.0521, 0.0894	0.0359, 0.1169	0.0467, 0.0955
Large residuals (e Å^{-3})	0.487, −0.935	0.554, −1.027	0.512, −0.502

Table 3
Selected bond lengths (Å) and angles and torsion angles (°) for $D(C_6H_4S)_2SbS_2CN(CH_2R)_2$ (D = O, R = Me, **1**; D = S, R = Me, **2**; R = Ph, **3**)

Compound	1	2	3
D	O	S	S
D → Sb1	2.816(3)	3.019(1)	3.008(1)
Sb1–S1	2.448(1)	2.450(1)	2.457(1)
Sb1–S2	2.525(1)	2.523(1)	2.510(1)
Sb1–S3	2.475(1)	2.505(1)	2.509(1)
Sb1–S4	2.872(1)	2.849(1)	2.891(1)
N1–C13	1.305(5)	1.322(6)	1.337(5)
N1–C14	1.482(5)	1.468(8)	1.470(5)
N1–C16	1.475(6)	1.466(7)	
N1–C21			1.481(5)
S3–C13	1.759(4)	1.754(5)	1.750(4)
S4–C13	1.708(4)	1.703(5)	1.689(4)
C6–D	1.401(5)	1.770(5)	1.785(4)
D–C7	1.409(4)	1.767(4)	1.777(4)
C6–D–C7	114.9(3)	103.4(2)	102.1(2)
D → Sb1–S1	69.98(6)	73.19(3)	73.22(3)
D → Sb1–S2	68.58(6)	72.99(3)	73.72(3)
D → Sb1–S3	147.78(6)	150.76(4)	153.67(3)
D → Sb1–S4	135.48(6)	135.53(4)	133.03(3)
S1–Sb1–S2	96.74(4)	96.70(4)	94.88(4)
S1–Sb1–S3	98.93(4)	98.35(4)	97.77(4)
S1–Sb1–S4	79.39(4)	79.67(4)	79.17(4)
S2–Sb1–S4	148.72(4)	145.90(4)	146.87(3)
S2–Sb1–S3	83.48(4)	80.52(4)	82.69(3)
S3–Sb1–S4	66.76(3)	66.71(4)	66.15(3)
S3–C13–S4	117.3(2)	117.6(3)	119.0(2)
C13–N1–C14	122.0(4)	121.5(5)	122.4(3)
C13–N1–C16	122.3(4)	122.5(5)	
C13–N1–C21			123.7(3)
C14–N1–C16	115.7(4)	116.0(4)	
C14–N1–C21			113.9(3)
C7–D–C6–C1	136.5(4)	126.4(4)	122.9(3)
C6–D–C7–C12	−78.0(4)	−67.1(4)	−60.7(4)
S2–Sb1–S1–C1	−36.6(2)	−33.8(2)	−31.7(2)
S1–Sb1–S2–C12	105.0(1)	110.6(2)	112.5(1)

In order to describe the local geometry of the Sb central atom is convenient to discuss several structural features observed in the title compounds. Firstly, can be envisaged two different sets of antimony-sulfur distances. The first set comprises two Sb–S thiolate-like and one Sb–S dithiocarbamate-like distances that are close to the covalent radii sum [$\sum r_{cov}$(Sb,S) = 2.42 Å] [21], and, in spite of the similar Sb–S bond lengths, their bond angles are quite different, being the S2–Sb1–S3 angle the smallest [the bond angles range from 80.52(4)° to 83.48(4)°]. The other set of Sb–S distances comprises the second sulfur atom of the dithiocarbamate moiety and they are only 18–20% longer than the covalent radii sum. Secondly, in addition to these two types of Sb–S distances in each complex, there is a transannular intramolecular Sb···D interaction that is 32%, 25% and 24% longer than the Sb–D covalent radii sum for **1** (D = O), **2** and **3** (D = S) respectively, but significantly shorter than the van der Waals radii sum [$\sum_{vdW}$(Sb,O) = 3.64 Å [23]; $\sum_{vdW}$(Sb,S) = 3.92 Å [22]] and can be described as a secondary interaction [23]. Considering the three covalent bonds and the two secondary interactions, the Sb atom in all complexes is penta-coordi-

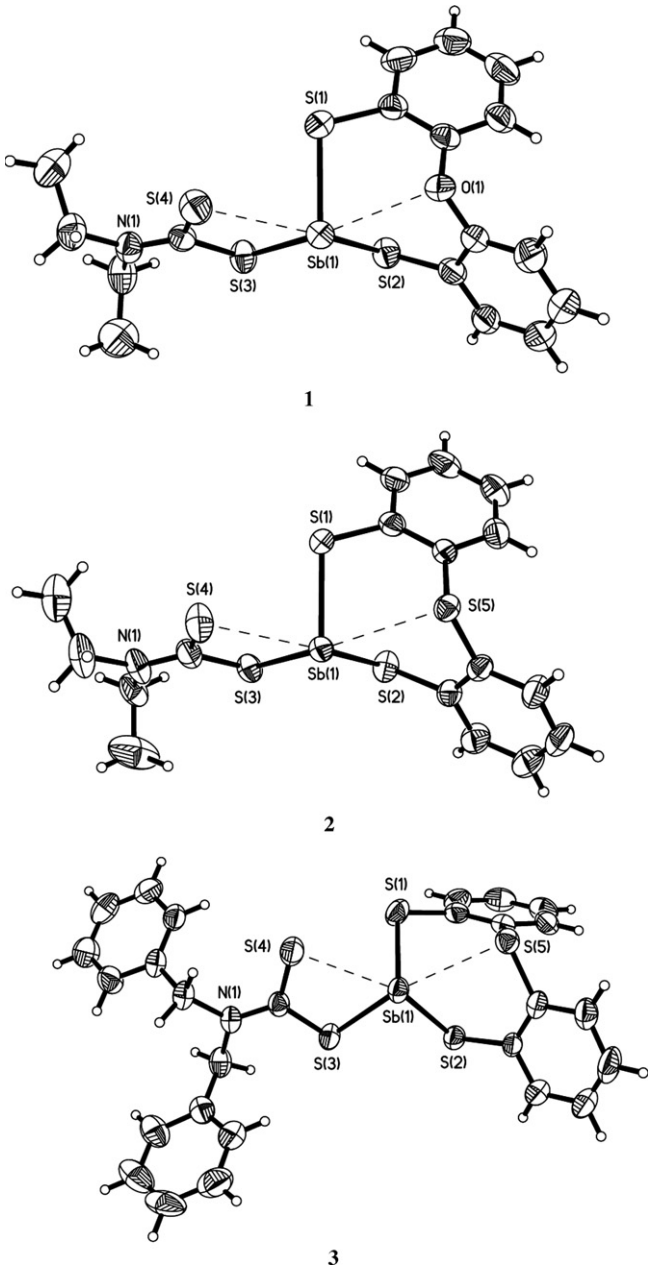


Fig. 1. ORTEP diagrams of $D(C_6H_4S)_2SbS_2CN(CH_2R)_2$ (D = O, R = Me, **1**; D = S, R = Me, **2**; R = Ph, **3**; 50% probability ellipsoids).

nate and its local geometry can be described as pyramidal with a skew-trapezoidal basis. Moreover, in terms of the VSEPR model, the local geometry of the penta-coordinate antimony atom in all complexes can be described as pyramidal pentagonal with a stereochemically active lone pair in a basal position.

In order to compare the magnitude of the transannular interaction in the complexes **1**–**3** we have calculated the Pauling-type bond order (BO) [24–26]. The bond order was calculated according to $BO = 10^{-[1.41(d_{exp}-\sum r_{cov})]}$ where d_{exp} is the D–Sb transannular distance. The BO are 0.1078, 0.1430 and 0.1482 for **1**, **2** and **3**, respectively, indicating that sulfur is a better donor than the oxygen atom towards antimony. Nevertheless these BO are even smaller than those calculated for the $D(C_6H_4S)_2SbCl$ starting materials (0.2195 for D = O and 0.2738 for D = S) [17]. These data indicate that the $D(C_6H_4S)_2^{2-}$ and the $(RCH_2)_2CNS_2^-$ ligands compete for the central antimony atom.

In relation to the coordination mode of the dithiocarbamate ligand, beside to the different Sb–S distances, the two C(13)–S bond lengths are significantly different. These data are consistent with an unsymmetrical bidentate mode.

On the other hand, the conformation of the eight-membered central ring in the dibenzostibocine system is highly distorted, as can be observed from the torsion angles listed in the Table 2, denoting the great flexibility of the potentially tridentate ligand $D(C_6H_4S)_2^{2-}$ to adopt several arrangements.

3.3.2. Crystal structures of complexes *1*, *2* and *3*

In order to analyze the intermolecular interactions we have adopted a similar conservative criterion as the proposed by Tiekink[3] with respect to the Sb···S distances operating in the crystal structures of group 15 dithiolates. Thus, those intermolecular distances lesser than 4.0 Å have been evaluated.

The solid state structures revealed polymeric associations in all cases which are shown in the Figs. 2–4.

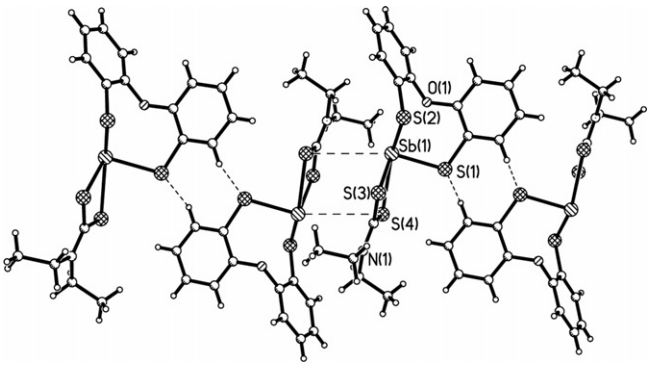


Fig. 2. Molecular associations of $O(C_6H_4S)_2SbS_2CN(CH_2CH_3)_2$ (**1**).

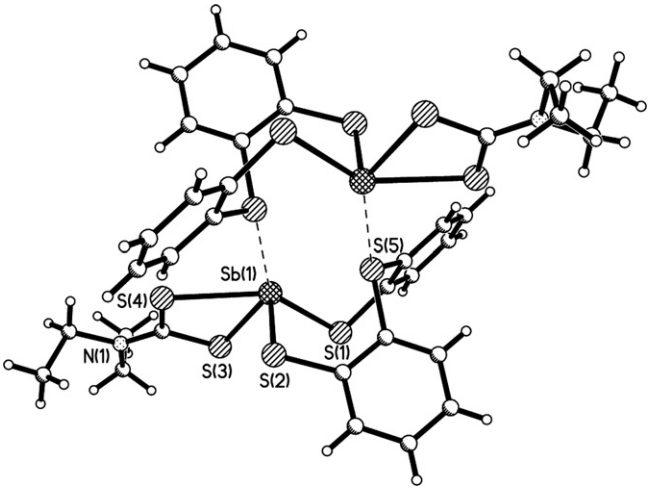


Fig. 3. Molecular associations of $S(C_6H_4S)_2SbS_2CN(CH_2CH_3)_2$ (**2**).

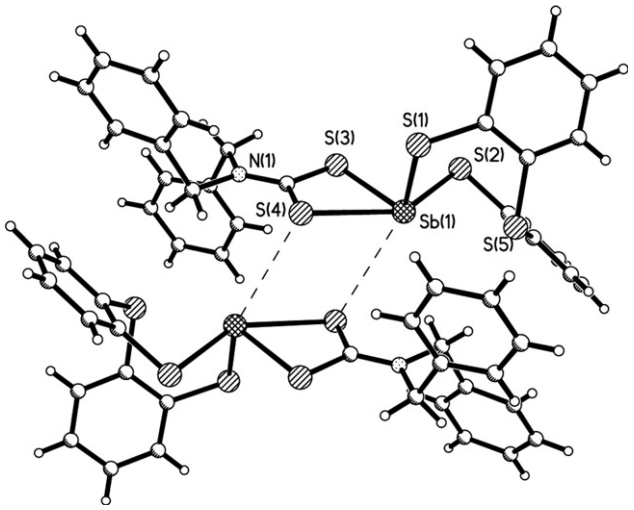


Fig. 4. Molecular associations of $S(C_6H_4S)_2SbS_2CN(CH_2C_6H_5)_2$ (**3**).

As shown in the Figs. 2–4 centrosymetric pairs of $D(C_6H_4S)_2SbS_2CN(CH_2R)_2$ associate via Sb···S interactions of 3.712(1), 3.639(1) and 3.897(1) Å for **1**, **2** and **3** respectively, which are shorter than the corresponding van der Waals radii sum ($\sum r_{vdW}$(Sb,S) = 3.92 Å). In compounds **1** and **3** the centrosymetric association is formed by the interaction of the antimony atom and a sulfur from the CS_2 fragment. On the other hand, in **2** the dimer is formed by the antimony atom and the sulfur thioether-like present in the $S(C_6H_4S)_2^{2-}$ ligand. In all cases the donor ability of the oxygen D atom towards antimony to establish intermolecular associations in **1** is overwhelmed by the sulfur ability donor, according to their hard and soft basic properties.

We also observed some weak C–H···S interactions spanning from 2.94 to 3.18 Å, which are shown in the Fig. 2.

Acknowledgements

J.G.A.R. fully acknowledges to the CONACyT (Project 44009) the financial support for this research. S.G.M. and L.B.L.P. fully acknowledge to CONACyT the scholarship for supporting their studies.

Appendix A. Supplementary material

CCDC 632313, 632315 and 632314 contain the supplementary crystallographic data for **1**, **2** and **3**. These data can be obtained free of charge via http://www.ccdc.cam.ac.uk/conts/retrieving.html, or from the Cambridge Crystallographic Data Centre, 12 Union Road, Cambridge CB2 1EZ, UK; fax: (+44) 1223-336-033; or e-mail: deposit@ccdc.cam.ac.uk. Supplementary data associated with this article can be found, in the online version, at doi:10.1016/j.poly.2007.03.038.

References

[1] For an outline see: I. Haiduc 1,1-dihiolate ligands, in: J.A. McLaverty, T.J. Meyer (Eds.), Comprehensive Coordination Chemistry II, vol. 349, 2002.
[2] S.S. Garje, V.K. Jain, Coord. Chem. Rev. 236 (2003) 35.
[3] E. Tiekink, Cryst. Eng. Commun. 8 (2006) 104.
[4] C.A. Kavounis, S.C. Kokkou, P.J. Rentzeperis, P. Karagiannidis, Acta Crystallogr., Sect. B 38 (1982) 2686.
[5] C.L. Raston, A.H. White, J. Chem. Soc., Dalton Trans. (1976) 791.
[6] Yu Liu, E.R.T. Tiekink, Cryst. Eng. Commun. 7 (2005) 20.
[7] I. Baba, B.W. Skelton, A.H. White, Aust. J. Chem. 56 (2003) 27.
[8] C. A Kavounis, S.C. Kokkou, P.J. Rentzeperis, P. Karagiannidis, Acta Crystallogr., Sect. B 36 (1980) 2954.
[9] V. Venkatachalam, K. Ramalingam, U. Casellato, R. Graziani, Polyhedron 16 (1997) 1211.
[10] V. Venkatachalam, K. Ramalingam, G. Bocelli, A. Cantón, Inorg. Chim. Acta 261 (1997) 23.
[11] R. Egle, W. Klinkhammer, A. Schmidt, Z. Anorg. Allg. Chem. 617 (1992) 72.
[12] I. Baba, S. Ibrahim, Y. Farina, A.H. Othman, I.A. Razak, H.K. Fun, S.W . Ng, Acta Crystallogr., Sect. E (Online) 57 (2001) m39.
[13] K.Y. Low, I. Baba, Y. Farina, A.H. Othman, A.R. Ibrahim, H.K. Fun, S.W. Ng, Main Group Met. Chem. 24 (2001) 451.
[14] R. Cea-Olivares, M.A. Muñoz-Hernández, S. Hernández-Ortega, C. Silvestre, Inorg. Chim. Acta 236 (1995) 31.
[15] M.A. Muñoz-Hernández, R. Cea-Olivares, S. Hernández-Ortega, Z. Anorg. Allg. Chem. 622 (1996) 1392.
[16] M.A. Muñoz-Hernández, R. Cea-Olivares, R.A. Toscano, S. Hernández-Ortega, Z. Anorg. Allg. Chem. 623 (1997) 642.
[17] J.G. Alvarado-Rodríguez, N. Andrade-López, S. González Montiel, G. Merino, A. Vela, Eur. J. Inorg. Chem. (2003) 3554.
[18] K. Gleu, R. Schwab, Angew. Chem. 62 (1950) 320.
[19] SHEXTL 5.10 Bruker AXS Inc., Madison, WI, USA, 1998.
[20] SADABS: Area-Detector Absorption Correction, Siemens Industrial Automation Inc., Madison, WI, 1996.
[21] r_{cov}(Sb) = 1.40, r_{cov}(O) = 0.73, r_{cov}(S) = 1.02, r_{vdW}(O) = 1.52, r_{vdw}(S) = 1.80 Å, from W.W. Porterfield, Inorganic Chemistry: A Unified Approach, 2nd ed., Academic Press Inc., USA, 1993, p. 214.
[22] r_{vdW}(Sb) = 2.12 Å, in A. Bondi, J. Phys. Chem. 68 (1964) 441.
[23] N.W. Alcock, Adv. Inorg. Chem. Radiochem. 15 (1972) 1.
[24] L. Pauling, The Nature of the Chemical Bond, 3rd ed., Cornell University Press, Ithaca, NY, 1960.
[25] U. Kolb, M. Beuter, M. Gerner, M. Draeger, Organometallics 13 (1994) 4413.
[26] D. Britton, J.D. Dunitz, J. Am. Chem. Soc. 103 (1981) 2971.

Available online at www.sciencedirect.com
ScienceDirect
Polyhedron 26 (2007) 2935–2941
POLYHEDRON
www.elsevier.com/locate/poly

Synthesis and spectroscopic investigations of Rh(III) and Pd(II) complex compounds with *N*-(pyridine-2-yl)morpholine-4-carbothioamide

Vladimir V. Bon [a,*], Svetlana I. Orysyk [a], Vasilii I. Pekhnyo [a], Viktor V. Orysyk [b], Sergei V. Volkov [a]

[a] *V.I. Vernadskii Institute of General and Inorganic Chemistry, Ukrainian NAS, Kyiv, Ukraine*
[b] *Institute of Organic Chemistry, Ukrainian NAS, Kyiv, Ukraine*

Received 27 November 2006; accepted 27 January 2007
Available online 7 February 2007

Abstract

The present paper describes the synthesis and spectral properties of Rh(III) and Pd(II) coordination compounds with *N*-(pyridine-2-yl)morpholine-4-carbothioamide (PMCTA). The compounds have the general composition $[RhL_2Cl_2]Cl \cdot C_2H_5OH$ (**1**), $[PdL_2]Cl_2$ (**2**), $[PdL_2](ClO_4)_2 \cdot 2C_3H_6O$ (**2a**), $[PdLCl_2] \cdot 2H_2O$ (**3**). All complexes were characterized by elemental analysis, IR, ^1H NMR, ^{13}C NMR, XPS and UV–Vis spectra. It has been shown that PMCTA behaves as a bidentate (N,S)-ligand, forming six membered metallocycles and coordinating to the metal ion through the carbothioamide sulfur atom and the pyridine nitrogen atom. The UV–Vis spectra suggest that the Pd(II) complexes are square planar, while the Rh(III) complex has an octahedral geometry. The molecular structure of the Pd(II) complex with PMCTA (M:L = 1:2) was determined by single-crystal X-ray diffraction.
© 2007 Elsevier Ltd. All rights reserved.

Keywords: Rhodium(III); Palladium(II); Morpholine; Carbothioamide; X-ray crystal structure

1. Introduction

The carbothioamide derivatives, especially thiosemicarbazones and thioureas, and their metal complexes are of considerable current interest because of their potentially beneficial pharmacological properties and wide variation in their modes of bonding and stereochemistry [1–5]. Some thiourea derivatives are selective analytical reagents, especially for the determination of transition metals [6,7]. The biological activity of some thiourea complexes have been successfully screened for various biological actions. In addition, the coordination chemistry of heterocycles containing thiones –N(H)–C(=S) ↔ –N=C–SH– is of immense interest because such compounds mimic cysteine sulfur coordination in metalloenzymes; show electronic and structural properties of the active sites in copper blue proteins involving S,N-coordination and comprise purine and pyrimidine bases. Similarly, thiourea derivatives containing this group are important ligands due to their coordination ability to form different kinds of complex compounds with a wide variety of donor atoms and their numerous biochemical properties [8].

In addition, the number of platinum complexes that show antitumor activity is still rapidly growing because of attempts to find complexes with greater potency and less toxicity than the existing clinical drugs. As a consequence, attention has turned to other platinum metals, like ruthenium, rhodium and palladium. Some platinum(II) and palladium(II) complexes with thiosemicarbazone derivatives have a wide spectrum of medicinal properties, including activity against tuberculosis, leprosy, different bacterial and viral infections [5,9,10]. A careful literature survey showed that there are only a few reports about platinum

* Corresponding author. Tel.: +380 638525383; fax: +380 444243070.
E-mail address: vlbony@ukr.net (V.V. Bon).

0277-5387/$ - see front matter © 2007 Elsevier Ltd. All rights reserved.
doi:10.1016/j.poly.2007.01.042

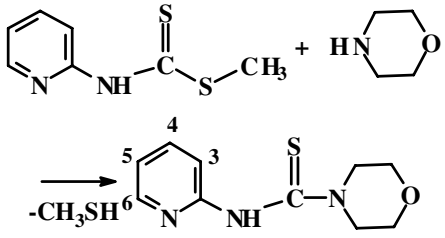
metal complexes with thiourea morpholine derivatives [11,12].

The present paper describes the synthesis and spectral characteristics of PMCTA complexes with Rh(III) and Pd(II). The X-ray crystal structure of a palladium(II) complex (M:L = 1:2) is reported.

2. Experimental

2.1. Preparation of N-(pyridine-2-yl)morpholine-4-carbothioamide

The ligand was prepared by refluxing a solution containing 1.84 g (0.01 mol) *S*-methyl-*N*-(2-pyridyl)dithiocarbamate and 0.96 ml (0.011 mol) morpholine in 5 ml ethanol for 2 h. The white precipitate thus formed, after the solution was cooled to room temperature, was filtered out and washed with small amounts of icy ethanol and pentane. The obtained powder was recrystallized from ethanol and dried in a desiccator with $CaCl_2$. Yield: 85% (1.89 g):



S-Methyl-*N*-(2-pyridyl)dithiocarbamate was obtained from 2-aminopyridine, carbon disulfide and methyl iodide by a known method [13]. Melting point 79 °C. *Anal.* Calc. for $C_{10}H_{13}N_3SO$: C, 53.81; H, 5.83; S, 14.35; N, 21.52. Found: C, 53.46; H, 6.04; S, 14.52; N, 21.67%. UV–Vis (DMSO) λ_{max}, nm: 260, 282, 357. IR KBr (cm^{-1}): ν(N–H) 3225; [δ(C–H) + δ(N–H) + ν(C–C) + ν(C–N)] 1595, 1535; [ν(C=S) + ν(C–N) + δ(C–H)] 1240; δ(N–C–S) 1128; ν(C=S) 780. ^{1}H NMR (DMSO-d_6): 3.65 (4H, t, $J = 4.8$ Hz, CH_2–N–CH_2); 3.89 (4H, t, $J = 4.8$ Hz, CH_2–O–CH_2); 7.06 (1H, dd, $J = 4.0$, 7.6 Hz, H_5); 7.61 (1H, d, $J = 8.1$ Hz, H_3); 7.71 (1H, dd, $J_1 = 2.0$, 7.9 Hz, H_4); 8.29 (1H, d, $J = 4.0$ Hz, H_6); 9.88 (1H, br, s, NH).

2.2. Preparation of the metal complexes

2.2.1. $[RhL_2Cl_2]Cl \cdot C_2H_5OH$ (**1**)

The complex was prepared by dissolving $RhCl_3 \cdot 4H_2O$ (1 mmol, 0.143 g) in 25 cm^3 of ethanol with heating and then adding an ethanol solution (25 cm^3) of the ligand (2 mmol, 0.223 g) in the molar ratio M:L = 1:2. The reaction mixture was heated under reflux for about 35 min with constant stirring. After the complex precipitated the brown product was filtered and washed several times with small portions of ethanol, Et_2O and dried in vacuum over $CaCl_2$. Melting point 303 °C. Yield: 69% (0.245 g). *Anal.* Calc. for $C_{22}H_{32}N_6S_2O_3Cl_3Rh$: Rh, 14.68; C, 37.63; H, 4.56; Cl, 15.18; S, 9.12; N, 11.97. Found: Rh, 14.21; C, 37.08; H, 4.85; Cl, 15.02; S, 9.56; N, 12.09%. UV–Vis (DMSO) λ_{max}, nm: 270, 365, 431, 476. IR KBr (cm^{-1}): ν(N–H) 3450; [δ(C–H) + δ(N–H) + ν(C–C) + ν(C–N)] 1615, 1550; [ν(C=S) + ν(C–N) + δ(C–H)] 1250; δ(N–C–S) 1120; ν(C=S) 760; ν(Rh–N) 460; ν(Rh–S) 360. ^{1}H NMR (DMSO-d_6): 3.53 (4H, t, $J = 4.2$ Hz, CH_2–N–CH_2); 3.75 (4H, t, $J = 4.2$ Hz, CH_2–O–CH_2); 7.47 (2H, m, H_3 and H_5); 8.08 (1H, m, H_4); 9.43 (1H, d, $J = 4.5$ Hz, H_6); 12.28 (1H, br, s, NH).

2.2.2. $[PdL_2]Cl_2$ (**2**)

The salt $PdCl_2$ (1 mmol, 0.097 g) was dissolved in 0.1 cm^3 of 6 N HCl by heating at 60 °C and then diluted to 25 cm^3. Twenty five millilitres of the ligand in ethanol solution (2 mmol, 0.223 g) was added dropwise to the Pd(II) solution. The reaction mixture was stirred and heated at 80 °C for about 30 min. Right away a yellow precipitate was isolated. The product was then filtered and washed with small portions of ethanol, Et_2O and dried in vacuo over $CaCl_2$. Melting point 212 °C. Yield: 54% (0.171g). *Anal.* Calc. for $C_{20}H_{26}N_6S_2O_2Cl_2Pd$: Pd, 17.01; C, 38.52; H, 4.17; Cl, 11.40; S, 10.27; N, 13.48. Found: Pd, 16.24; C, 37.85; H, 4.39; Cl, 11.28; S, 10.42; N, 13.61%. UV–Vis (DMSO) λ_{max}, nm: 284, 338, 400. IR KBr (cm^{-1}): ν(N–H) 3450; [δ(C–H) + δ(N–H) + ν(C–C) + ν(C–N)] 1615, 1550; [ν(C=S) + ν(C–N) + δ(C–H)] 1245; δ(N–C–S) 1125; ν(C=S) 770; ν(Pd–N) 440; ν(Pd–S) 380. ^{1}H NMR (DMSO-d_6): 3.77 (4H, t, $J = 4.7$ Hz, CH_2–N–CH_2); 4.03 (4H, t, $J = 4.7$ Hz, CH_2–O–CH_2); 7.43 (1H, dd, $J = 3.9$, 7.6 Hz, H_5); 7.52 (1H, d, $J = 8.2$ Hz, H_3); 8.10 (1H, dd, $J = 2.2$, 8.0 Hz, H_4); 8.97 (1H, d, $J = 4.2$ Hz, H_6); 11.46 (1H, br, s, NH).

2.2.3. $[PdL_2](ClO_4)_2 \cdot 2C_3H_6O$ (**2a**)

The salt $PdCl_2$ (1 mmol, 0.097 g) was dissolved in 0.1 cm^3 of 6 N HCl by heating at 60 °C and then diluted with acetone up to 25 cm^3. Twenty five millilitres of the ligand in acetone solution (2 mmol, 0.223 g) was added dropwise to the Pd(II) solution. After that, $NaClO_4$ (0.2 g) was added to the obtained mixture. The reaction mixture was stirred and heated at 55 °C for about 30 min, and then it was put to a desiccator with diethyl ether. After a few days of standing, yellow crystals were grown. Melting point 207 °C Yield: 36% (0.123 g). *Anal.* Calc. for $C_{26}H_{38}N_6S_2O_{12}Cl_2Pd$: Pd, 12.23; C, 35.99; H, 4.38; Cl, 8.19; S, 7.38; N, 9.69. Found: Pd, 11.85; C, 35.24; H, 5.03; Cl, 8.04; S, 7.44; N, 9.81%. UV–Vis (DMSO) λ_{max}, nm: 284, 338, 400. IR KBr (cm^{-1}): ν(N–H) 3480; [δ(C–H) + δ(N–H) + ν(C–C) + ν(C–N)] 1616, 1555; [ν(C=S) + ν(C–N) + δ(C–H)] 1245; $\nu(ClO_4^-)$ 1100; ν(C=S) 765; ν(Pd–N) 440; ν(Pd–S) 380. ^{1}H NMR (DMSO-d_6): 3.75 (4H, t, $J = 4.9$ Hz, CH_2–N–CH_2); 4.00 (4H, t, $J = 4.8$ Hz, CH_2–O–CH_2); 7.41 (1H, dd, $J = 3.8$, 7.5 Hz, H_5); 7.51 (1H, d, $J = 8.2$ Hz, H_3); 8.09 (1H, dd, $J = 2.1$, 7.8 Hz, H_4); 8.98 (1H, d, $J = 3.9$ Hz, H_6); 11.48 (1 H, br, s, NH).

2.2.4. $[PdLCl_2]\cdot 2H_2O$ (**3**)

The salt $PdCl_2$ (2 mmol, 0.194 g) was dissolved in 0.5 cm^3 of 6 N HCl by heating at 60 °C and then diluted to 25 cm^3. Twenty five millilitres of the ligand in ethanol solution (2 mmol, 0.223 g) was added dropwise to the Pd(II) solution in the molar ratio M:L = 1:1. The reaction mixture was stirred and heated at 80 °C for about 30 min. Right away a bright yellow precipitate was isolated. The product was then filtered and washed with small portions of ethanol, Et_2O and dried in vacuo over $CaCl_2$. Melting point 236 °C. Yield: 65% (0.271g). *Anal.* Calc. for $C_{10}H_{17}N_3SO_3Cl_2Pd$: Pd, 24.31; C, 27.52; H, 3.90; Cl, 16.28; S, 7.34; N, 9.63. Found: Pd, 23.78; C, 27.34; H, 4.32; Cl, 16.13; S, 7.47; N, 9.95%. UV–Vis (DMSO) λ_{max}, nm: 284, 338, 400. IR KBr (cm^{-1}): ν(N–H) 3510; [δ(C–H) + δ(N–H) + ν(C–C) + ν(C–N)] 1616, 1555; [ν(C=S) + ν(C–N) + δ(C–H)] 1240; δ(N–C–S) 1120; ν(C=S) 765; ν(Pd–N) 440; ν(Pd–S) 380; ν(Pd–Cl) 320–310. ^{1}H NMR (DMSO-d_6): 3.65 (4H, t, J = 4.8 Hz, CH_2–N–CH_2); 3.92 (4H, t, J = 4.7 Hz, CH_2–O–CH_2); 7.48 (1H, dd, J = 3.6, 7.7 Hz, H_5); 7.61 (1H, d, J = 8.1 Hz, H_3); 8.12 (1H, dd, J = 2.1, 7.9 Hz, H_4); 8.91 (1H, d, J = 4.1 Hz, H_6); 11.36 (1H, br, s, NH).

2.3. Physical measurements

Chemical analyses for carbon, hydrogen, nitrogen, sulfur and chlorine were performed by an analytical procedure [14]. ^{1}H NMR and ^{13}C NMR spectra were measured on Varian-VXR 300 MHz and Bruker AVANCE 400 spectrometers, respectively, using DMSO-d_6 as a solvent with Me_4Si as an internal standard. The IR spectra were recorded on a Specord M80 in the range 4000–200 cm^{-1} from KBr in pellets. Electronic spectra of DMSO solutions of PMCTA and its complexes (10^{-3} mol L^{-1}) were recorded on a Specord M40 spectrophotometer in the range 200–900 nm (50 000–11 000 cm^{-1}) using a 1 mm quartz cell. X-ray photolectron spectra (XPS) were measured on an ES-2402 device using Mo Kα radiation. Samples were prepared as thin films from an acetone suspension on a 10 × 10 mm aluminum base plate.

2.4. Crystal structure determination

The X-ray structure data of **2a** were collected at room temperature on a SMART APEX II diffractometer. Cell parameters were obtained from least-squares treatment of 2734 reflections. Intensity data were collected within the range $1.50 \leqslant \theta \leqslant 31.53°$ using Mo Kα radiation (λ = 0.71073 Å). The intensities of 9817 reflections have been collected (5291 unique reflections, R_{merg} = 0.0306). Data were corrected for Lorenz and polarisation effects. The structure was solved by direct methods and refined by the full-matrix least-squares technique in an anisotropic approximation for non-hydrogen atoms using SHELXS97 and SHELXS97 programs [15,16]. Relevant crystal data are given in Table 1. Data were corrected for absorption effects using the multiscan technique (SADABS) [17]. The ratio of minimum to maximum apparent transmission was 0.597137.

Table 1
Crystal data and structure refinement for **2a**

Molecular formula	$C_{26}H_{38}Cl_2N_6O_{12}PdS_2$
Formula weight	868.04
Temperature (K)	273(2)
Wavelength (Å)	0.71073
Crystal system	triclinic
Space group	$P\bar{1}$
a (Å)	8.1700(3)
b (Å)	8.7285(4)
c (Å)	14.2222(6)
α (°)	73.316(3)
β (°)	85.694(3)
γ (°)	63.887(3)
Volume (Å^3)	870.80(6)
Z	1
D_{calc} (Mg m^{-3})	1.655
μ (mm^{-1})	0.874
F(000)	444
Crystal size (mm)	0.35 × 0.15 × 0.06
θ_{min}, θ_{max} (°)	1.50, 31.53
Limiting indices	$-11 \leqslant h \leqslant 11$, $-12 \leqslant k \leqslant 11$, $-20 \leqslant l \leqslant 20$
Reflections collected	9817
Total unique reflections [R_{int}]	5291 (0.0306)
Completeness to θ = 31.53 (%)	91.3
Refinement method	full-matrix least-squares on F^2
Data/restraints/parameters	5291/0/227
Goodness-of-fit on F^2	1.002
Final R indices [$I > 2\sigma(I)$]	R_1 = 0.0454, wR_2 = 0.0980
R indices (all data)	R_1 = 0.0780, wR_2 = 0.1147
Largest difference in peak and hole (e Å^{-3})	0.581 and −0.597

3. Results and discussion

PMCTA is a thiourea morpholine derivative containing nucleophilic nitrogen and sulfur atoms at the stoichiometric advantageous positions. Thus, it can coordinate to metal ions as a bidentate ligand by forming metallochelates. Changing the reaction conditions (pH, temperature, heating time, molar ratio and concentrations of the parent compounds) affects only the number of coordinated molecules of PMCTA and chlorine anions. The melting points of all the synthesized complexes are above 200 °C, and melting occurs with the decomposition of the compound. All the complexes are soluble in DMSO and DMF, whereas the palladium complexes **2** and **2a** are also soluble in water and alcohols.

3.1. IR spectra

In order to study the binding mode in the complexes, their IR spectra were investigated in comparison with the IR spectrum of PMCTA. The IR spectrum of the ligand shows bonds in the regions 3225, 3070–2900, 1595–1535,

1240, 1128 and 780 cm^{-1}, which are assigned to ν(N–H), ν(C–H), [δ(C–H) + δ(N–H) + ν(C–C) + ν(C–N)], [ν(C=S) + ν(C–N) + δ(C–H)], δ(N–C–S) and ν(C=S) of PMCTA, respectively [3,4,18].

Depending on synthesis conditions, the ligand can exist in thione, thiol, or in both tautomeric forms at the same time due to the presence of the –NH–C=S functional group. The IR spectrum recorded for PMCTA in the solid state does not show a ν(S–H) band but exhibits a medium ν(N–H) band at 3225 cm^{-1}. This shows that in the solid state the ligand remains only in the thione form. However, the IR spectra of all the obtained complexes contain no ν(S–H) bands, which can be accounted for by the presence of only the thione tautomeric form of the ligand [4]. The considerable shift of absorption band (15–25 cm^{-1}) occurring at 1616, 1555 and 760 cm^{-1} indicates that the pyridine ring and the thiocarbamide group participate in coordination to the metal ion. The long-wave IR spectral region (1000–200 cm^{-1}) is practically the same both in ligand and in the complexes, except that some new medium-to-weak intensity bands appear in the spectra of the complexes at 460–440, 380–360 and 320–310 cm^{-1}, assigned to ν(M–N), ν(M–S) and ν(M–Cl) vibrations, which are in good agreement with references [3,4]. The appearance of only one ν(Rh–Cl) vibration in the Rh(III) complex (**1**) indicates that the chlorine anions are located at opposite positions to each other in the Rh(III) octahedral environment. On the other hand, the presence of two absorption bands at 320–310 cm^{-1} confirms the *cis*-configuration of the Pd(II) complex (**3**).

3.2. Electronic spectra

The UV–Vis spectrum of the Rh(III) complex (**1**) shows faint absorption bands at 431 (23 200 cm^{-1}) and 476 nm (21 000 cm^{-1}), which appear to be the split components of the transitions $^1A_{1g} \rightarrow {}^1T_{1g}$ and $^1A_{1g} \rightarrow {}^1A_{2g}$, expected for octahedral complexes [19]. This may be due to the lowering of the symmetry from O_h to D_{4h}, which is expected with the set of N, S and Cl donor atoms [19,20]. A third band at 373 nm (26 800 cm^{-1}) may be attributed to the transition $^1A_{1g} \rightarrow {}^1T_{2g}$, which is similar to related Co(III) complexes (d^6 system). However, there is a broad band in this region at 355–373 nm (28 170–26 800 cm^{-1}), which can be assigned to $\pi \rightarrow \pi^*$ (C=S) transitions of the ligands [19,21]. Therefore there is an overlap between the band which corresponds to an electron transition of the metal ion and other bands which are assigned to a charge-transfer of ligand functional groups. In addition, the ligand shows bands at ca. 260–280 nm (38 460–35 710 cm^{-1}), which are assigned to $n \rightarrow \pi^*$ transitions, associated with NH and Py groups. The splitting of the $^1A_{1g} \rightarrow {}^1T_{1g}$ band suggests that this complex has a trans structure, which is also supported by the IR spectrum. These bands are also observed in the UV–Vis spectra of all the complexes.

The electronic spectra of the Pd(II) complexes show bands in the regions 400 nm (25 000 cm^{-1}), 337–340 nm (29 670–29 400 cm^{-1}) and 282–287 nm (35 460–34 840 cm^{-1}). The first two bands are assigned to a combination of $^1A_{1g} \rightarrow {}^1A_{2g}$ and $^1A_{1g} \rightarrow {}^1E_g$ transitions by assuming a difference in the energies of $b_{2y}(xy)$ and $e_g(xz, yz)$ levels, which is very small [4]. The other spin-allowed bands for these Pd^{2+} complexes (**2** and **2a**) were assigned to the $^1A_{1g} \rightarrow {}^1B_{1g}$ transition. The absorption bands occuring at 357 nm (28 000 cm^{-1}) and 256–282 nm (39 060–35 460 cm^{-1}), are attributable to $\pi \rightarrow \pi^*$ (C=S) and $\pi \rightarrow \pi^*$ ($n \rightarrow \pi^*$) transitions in the ligand. The UV–Vis spectra of these complexes are comparable to other platinum complexes involving similar donor atoms [4,19]. The electronic spectra of PMCTA and its palladium complex (**2**) are shown in Fig. 1.

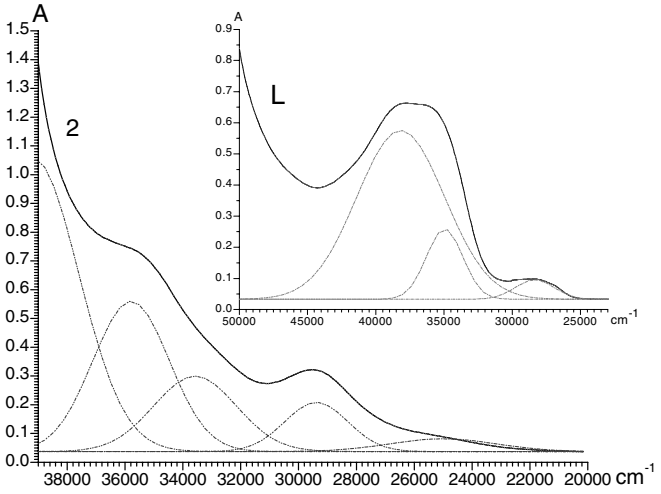


Fig. 1. Electronic spectra of PMCTA (L) and its Pd(II) (**2**) complex.

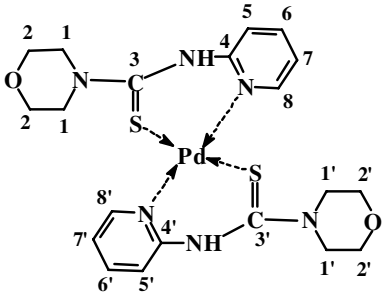
3.3. ^1H NMR and ^{13}C NMR spectra

The ^1H NMR spectrum of the ligand show signals at 7.06, 7.61, 7.71 and 8.29 ppm which are due to pyridine ring protons. A broad singlet corresponding to one proton at 9.88 ppm is assigned to the NH group. The morpholine ring protons give two triplets at 3.65 and 3.89 ppm, which correspond to –N–CH_2 and –O–CH_2 groups, respectively.

In the spectra of the complexes, the multiplets of the pyridine ring are observed at 7.41–7.61 ppm (H3 and H5) and 8.10–8.97 ppm (H4 and H6). This is due to involvement of the pyridine nitrogen in coordination to the metal ion. The NH group is included in the six membered metallocycle and the NH proton occupies an extended state in the S=C–NH system of the ligand. As a consequence, the peak observed at 9.88 ppm in the spectrum of the ligand is shifted downfield in the complexes and suggest, taking a belied view of the weak intensity, the involvement of the carbothioamide group in coordination to the metal. The morpholine proton signals are observed at 3.75 ppm (–N–CH_2) and 4.12 ppm (–O–CH_2).

The ^{13}C NMR spectrum of PMCTA shows the expected carbon structure of the compound (Table 2). The morphol-

Table 2
^{13}C NMR spectral data of PMCTA and **2**



Assignment	Values (ppm) PMCTA (**2**)
C_1, C_1'	48.35/50.03
C_2, C_2'	65.14/64.54
C_3, C_3'	180.67/170.15
C_4, C_4'	146.74/148.69
C_5, C_5'	136.22/139.89
C_6, C_6'	117.22/117.97
C_7, C_7'	118.74/121.21
C_8, C_8'	153.36/151.63

ine carbons of the ligand show peaks at 48.35 ppm (C_1, C_1') and 65.14 ppm (C_2, C_2'). Values of 117.22, 118.74, 136.22, 146.74 and 153.36 ppm can be assigned to the carbons of the pyridine ring – C_6, C_7, C_5, C_4 and C_8, respectively. The singlet corresponding to one carbon at 180.67 ppm is assigned to carbothioamide group (C_3) of the ligand, appreciable shifting of which in the spectrum of **2** to 170.15 ppm ($\Delta C_3 = 9.48$ ppm) confirms the coordination of the ligand through the sulfur atom of the carbothioamide group. Signals of the morpholine and pyridine carbons in the spectra of **2** are only slightly shifted [11,21].

3.4. XPS spectra

Table 3 shows the electron binding energies (eV) of the ligand and its complexes **1** and **2**. The position of the spectrum line of the element to be determined allows one to distinguish not only the valency of the element, but also the coordination manner and its location in the complex [22,23]. This is proved by the N1s, S2p and M3$d_{5/2}$ signals in the spectra of the compounds under investigation. The electron binding energies of N1s of the ligand show a doublet signal at 400.0 and 400.5 eV and a shoulder at 401.5 eV, which is assigned to three types of nitrogen atom in the ligand molecule: (NH), N_{morph} and N_{Py}. We have found three components at 399.0, 400.2 and 400.9 eV after the decomposition of the N1s line, which is assigned to three states of nitrogen. The shift of the N1s signals in the spectra of complexes **1** and **2** indicates that the pyridine and carbothioamide nitrogen of the ligand are involved in donor–acceptor interactions with metal ions.

The increase in the S2$p_{3/2}$ electron binding energy in the spectra of complexes **1** and **2** is in agreement with [22] and is accounted for by coordination of the carbothioamide sulfur atom to the metal ions. This means that the sulfur atom of the thiourea group binds to the central atom through (C=S) → M bond formation.

The positions of Rh3$d_{5/2}$ and Pd3$d_{5/2}$ signals at 311.1 eV and 339.0 eV are assigned to tri- and bi-valent states of the metal ions, respectively. There are three components assigned to different bonds (states) of Rh^{3+} and Pd^{2+} surrounded by non-equivalent nitrogen and sulfur atoms of the ligand (see Table 2).

3.5. X-ray structure determination

The molecular structure of compound **2a** was determined by single-crystal X-ray diffraction. A perspective view of molecule **2a** with the atom numbering is shown in Fig. 2.

One molecule of complex **2a** per unit cell is observed, and the atom Pd1 occupies a special position at the centre of inversion. The palladium atom is bound by two S and two N atoms with bond angles N1a–Pd1–N1 180.0°, S1a–Pd1–S1 180.0°, N1a–Pd1–S1a 85.74(7)° and N1a–Pd1–S1 94.26(7)° in a square-planar coordination geometry. The Pd1–Sl and Pd1–N1 bond distances are 2.315(8) and 2.029(2) Å, respectively. The bonding parameters agree with the coordinate patterns in [7,24,25]. The atoms N2 and N3 have planar configurations (the sum of bond angles is 360°) and C6–N2 and C6–N3 bond lengths are shorter than standard single C–N bond because of conjugation

Table 3
Binding energies of the ligand (PMCTA) and its complexes (**1**, **2**)

Compounds	N1s (eV)		S2$p_{3/2}$ (eV)		Rh3$d_{5/2}$ (eV)		Pd3$d_{5/2}$ (eV)	
	a	b	a	b	a	b	a	b
PMCTA	400.0	399.0	163.6					
	400.5	400.2						
	401.5	400.9						
1	400.3	399.2	164.5	163.5	311.1	310.6		
		400.1	165.7	164.4		311.1		
		400.6		165.4		311.3		
2	399.8	399.3	164.3	163.3			339.0	338.7
		400.6	165.4	164.2				339.1
		401.3		165.4				339.4

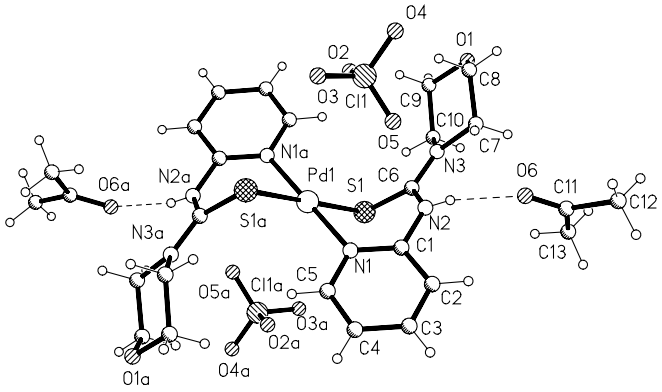


Fig. 2. Perspective view and atom labelling scheme of **2a**.

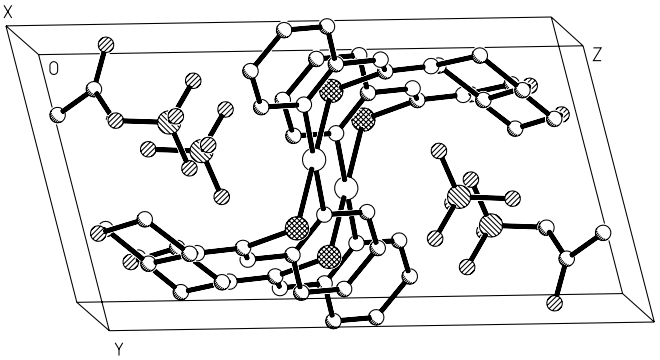


Fig. 3. Packing diagram of **2a**.

of the lone pair electrons of the nitrogen atoms N2 and N3 with the double 1.731(3) Å C(6)═S(1) bond. The pyridine ring is planar: the mean deviation from the least-square plane does not exceed 0.011 Å. The bond angles Pd(1)–S(1)–C(6) 92.98(10)°, S(1)–C(6)–N(2) 120.1(2)°, C(6)–N(2)–C(1) 127.4(3)°, N(2)–C(1)–N(1) 120.2(3)°, C(1)–N(1)–Pd(1) 123.13(18)°, N(1)–Pd(1)–S(1) 85.74(7)° of the six member chelate ring is similar to the respective angles in [24] and illustrate that the metallocycle is significantly distorted and has a bath form. The symmetric cycle Pd(1)S(1a)C(6a)N(2a)C(1a)N(1a) is analogous. The asymmetric unit also contains a solvate molecule of acetone, which is bonded to the complex by the N2–H2N···O6 hydrogen bond, with the following parameters: N2–H2N, 0.73(3); H2N···O6, 2.15(3); N2···O6, 2.864(4) Å; N2 H2N O6 166(3)°.Two perchlorate anions occupy the free space around the palladium atom, and the shortest Pd1–O2 distance of the perchlorate anion is 3.747 Å. The packing diagram of **2a** is shown in Fig. 3. Selected bond distances and angles are presented in Table 4.

Table 4
Selected bond distances (Å) and angles (°) for **2a**

Distances		Angles	
Pd1–N1	2.029(2)	N1–Pd1–N1a	180.00(14)
Pd1–S1	2.3151(8)	S1–Pd1–S1a	180.00
Pd1–N1a	2.029(2)	N1–Pd1–S1a	94.26(7)
Pd1–S1a	2.3151(8)	N1a–Pd1–S1a	85.74(7)
C1–N1	1.335(4)	N1–Pd1–S1	85.74(7)
C1–N2	1.400(4)	N1a–Pd1–S1	94.26(7)
C6–N2	1.349(4)	C6–S1–Pd1	92.98(10)
C6–S1	1.731(3)	N2–C6–S1	120.10(2)
C6–N3	1.315(4)	C6–N2–C1	127.4(3)
C1–C2	1.388(4)	N1–C1–N2	120.2(3)
C5–N1	1.350(4)	C1–N1–Pd1	123.13(18)
C7–N3	1.474(4)	C5–N1–Pd1	118.9(2)
C10–N3	1.475(4)	C1–N1–C5	117.8(3)
C11–O6	1.196(4)	N1–C1–C2	121.7(3)
C11–C13	1.474(6)	C2–C1–N2	118.1(3)
C11–C12	1.487(5)	N3–C6–N2	118.7(3)
		N3–C6–S1	121.2(2)
		C6–N3–C10	123.2(2)
		C6–N3–C7	124.1(3)

4. Conclusion

Allocation of the carbothioamide group to the α-position of the pyridine ring of *N*-(pyridine-2-yl)morpholine-4-carbothioamide enables the ligand to coordinate through the pyridine nitrogen atom and the sulfur atom of the thioamide group, forming six member metallocycles. Variation of the syntheses conditions (pH = 2–4, temperature, heating time) effects only a number of the coordinated ligand molecules. In all the newly synthesized complexes the ligand coordinates in the thione tautomeric form. Therefore, generally cationic complexes (**1**, **2** and **2a**) are formed. They are soluble in water, which enables the investigation of their biological activity.

Acknowledgements

Special thanks to Prof. A.N. Chernega and Dr. E.B. Rusanov (Institute of Organic Chemistry, Ukrainian NAS) for the single-crystal X-ray structure determination.

Appendix A. Supplementary material

CCDC 622366 contains the supplementary crystallographic data for **2a**. These data can be obtained free of charge via http://www.ccdc.cam.ac.uk/conts/retrieving.html, or from the Cambridge Crystallographic Data Centre, 12 Union Road, Cambridge CB2 1EZ, UK; fax: (+44) 1223-336-033; or e-mail: deposit@ccdc.cam.ac.uk. Supplementary data associated with this article can be found, in the online version, at doi:10.1016/j.poly.2007.01.042.

References

[1] A. Castineiras, R. Carballo, T. Perez, Polyhedron 20 (2001) 441.
[2] J.S. Casas, M.S. Garcia-Tasende, J. Sordo, Coord. Chem. Rev. 209 (2000) 197.
[3] O.P. Pandey, S.K. Sengupta, M.K. Mishra, C.M. Tripathi, Bioinorg. Chem. Appl. 1 (2003) 35.
[4] R.K. Agarwal, S. Prasad, Turk. J. Chem. 29 (2005) 289.
[5] R.V. Singh, N. Fahmi, M.K. Biyala, J. Iranian Chem. Soc. 2 (2005) 40.
[6] M. Schuster, J. Anal. Chem. 342 (1992) 791.
[7] G. Avsar, H. Arsland, Turk. J. Chem. 27 (2003) 281.
[8] T.S. Lobana, Proc. Indian Acad. Sci. 112 (2000) 323.
[9] B.T. Khan, K. Venkatasubramanian, K. Najmuddin, S. Shamsuddin, S.M. Zakeeruddin, Inorg. Chim. Acta 179 (1993) 117.
[10] S. Lady, G. Parameswaran, Asian J. Chem. 3 (1993) 712.
[11] N. Raman, S. Esthar, C. Thangaraja, J. Chem. Sci. 116 (2004) 209.
[12] E. Rodriguez-Fernandez, E. Garcia, M.R. Hermosa, A. Jimenez-Sanchez, M. Mar Sanchez, E. Monte, J.J. Criado, J. Inorg. Biochem. 75 (1999) 181.
[13] E.B. Knott, J. Chem. Soc. 6 (1956) 1644.
[14] V.A. Klimova, The main micromethods of organic compounds analysis, Moscow, Chemistry, 1967.
[15] G.M. Sheldrick, SHELXL97, Universitat Göttingen, Göttingen, Germany, 1999.
[16] G.M. Sheldrick, Acta Crystallogr., Sect. A 46 (1990) 467.
[17] G.M. Sheldrick, SADABS, Bruker AXS Inc., Madison, Wisconsin, USA, 2004.

[18] O. Algul, B. Ozcelik, U. Abbasoglu, F. Gumus, Turk. J. Chem. 29 (2005) 607.
[19] S.K. Sahni, P.C. Jain, V.B. Rana, Indian J. Chem. 18 (1979) 161.
[20] A.A. Abou-Hussen, N.M. El-Metwally, E.M. Saad, A.A. El-Asmy, J. Coord. Chem. 58 (2005) 1735.
[21] F.J. Barros-Garcia, F. Luna-Giles, M.A. Maldonado-Rogado, E. Vinuelas-Zahinos, Polyhedron 25 (2006) 43.
[22] W. Hernandes, E. Spodine, R. Richter, K.-H. Hallmeier, U. Schroder, L. Beyer, Z. Anorg. Allg. Chem. 629 (2003) 2559.
[23] V.I. Nefedov, X-ray electronic spectroscopy of the chemical compounds, Moscow, Chemistry, 1984.
[24] U. Schroder, R. Richter, L. Beyer, J. Angulo-Cornejo, M. Lino-Pacheco, A. Guillen, Anorg. Allg. Chem. 629 (2003) 1051.
[25] M. Joseph, M. Kuriakose, M.R. Prathapachandra Kurup, E. Suresh, A. Kishore, S.G. Bhat, Polyhedron 25 (2006) 61.

Available online at www.sciencedirect.com
ScienceDirect
Polyhedron 26 (2007) 2942–2948
POLYHEDRON
www.elsevier.com/locate/poly

Periodic trends in metal–metal bonding in edge-shared $[M_2Cl_{10}]^{4-}$ systems

Germán Cavigliasso, Chung-Yen Yu, Robert Stranger *

Department of Chemistry, Faculty of Science, Australian National University, Canberra, ACT 0200, Australia

Received 4 January 2007; accepted 29 January 2007
Available online 3 February 2007

Abstract

Periodic trends in metal–metal interactions in edge-shared $[M_2Cl_{10}]^{4-}$ systems, involving the transition metals from groups 4 through 8 and electronic configurations ranging from d^1d^1 through d^5d^5, have been investigated by calculating metal–metal bonding and spin-polarization (exchange) effects using density functional theory. The trends found in this study are compared with those for the analogous face-shared $[M_2Cl_9]^{3-}$ systems reported in earlier work. Strong linear correlations between the metal–metal bonding and spin-polarization terms have been obtained for all groups considered. In general, spin polarization and electron localization are predominant in 3d–3d species whereas electron delocalization and metal–metal bonding are favoured in 5d–5d species, with more variable results observed for 4d–4d systems. As previously found for face-shared $[M_2Cl_9]^{3-}$ systems, the strong correlations between the metal–metal bonding and spin polarization energy terms can be related to the fact that both properties appear to be similarly affected by the changes in the metal orbital properties and electron density occurring within the d^nd^n groups. A significant difference between the face-shared and edge-shared systems is that while the 4d metals in the former show a strong tendency for delocalized metal–metal bonded structures, the edge-shared counterparts display much greater variation with both metal–metal bonded and weakly coupled complexes observed. The tendency for weaker metal–metal interactions can be traced to the inability of the edge-shared bridging structure to accommodate the smaller metal–metal distances required for strong metal–metal bonding.
Crown Copyright © 2007 Published by Elsevier Ltd. All rights reserved.

Keywords: Metal–metal bonding; Edge-shared dimers; Density functional theory

1. Introduction

Dinuclear and polynuclear transition metal complexes exhibit great diversity in metal–metal interactions, ranging from weak magnetic coupling through to multiple metal–metal bonding [1]. Such interactions are intrinsically interesting for fundamental reasons, but are also important due to their potential applications in a variety of fields spanning metal surfaces, electronic and magnetic devices, catalysis, and bioinorganic chemistry [2–4].

The extent of the interaction between the metal centres is clearly dependent on the electronic properties of the constituent metals but the nature of the bridging ligand framework, if present, can also play a significant role. Among the species displaying metal–metal interactions, the dinuclear compounds represented by the face-shared $[M_2X_9]^{z-}$ and edge-shared $[M_2X_{10}]^{z-}$ (dimer) species are particularly noteworthy as they are formed by many transition metals and exhibit considerable variation in structural, electronic, and magnetic properties due to the competing effects of the metal–metal and metal–bridge interactions.

Although from a computational perspective, dinuclear face-shared $[M_2X_9]^{z-}$ and edge-shared $[M_2X_{10}]^{z-}$ systems are amenable to reasonably high-level calculations due to their relatively small size and high symmetry, the large range of metal–metal interactions makes the theoretical treatment of these complexes particularly challenging. Nevertheless, we have shown in our previous work that density

* Corresponding author.
E-mail addresses: german.cavigliasso@anu.edu.au (G. Cavigliasso), rob.stranger@anu.edu.au (R. Stranger).

0277-5387/$ - see front matter Crown Copyright © 2007 Published by Elsevier Ltd. All rights reserved.
doi:10.1016/j.poly.2007.01.034

functional theory in combination with the broken-symmetry approach of Noodleman and coworkers [5,6] can accurately describe the entire range of metal–metal interactions, from weak antiferromagnetic coupling through to multiple metal–metal bonds, as well as encompassing both high-spin and low-spin metal configurations. The success of this procedure can be exemplified by noting that our broken-symmetry density functional calculations have accurately reproduced experimentally observed properties in a large number of $[M_2X_9]^{z-}$ dimers with electronic configurations ranging from d^1d^1 through to d^5d^5 [7–14] as well as mixed-valence d^1d^2, d^2d^3, d^3d^4 and d^4d^5 configurations [15,16]. We have also used this methodology to successfully investigate metal–metal interactions in a variety of other dimer systems, including edge-shared $[M_2X_{10}]^{z-}$ and phosphine-bridged $[M_2X_6(P–P)_4]^{z-}$ systems [17,18], indicating that this theoretical approach is broadly applicable across many dinuclear transition metal complexes.

We have recently completed a detailed investigation of periodic trends in metal–metal interactions across an extensive series of $[M_2Cl_9]^{z-}$ species [19]. In this study, the periodic trends were investigated by means of density functional calculations on a large number of even-electron (same-valence) $[M_2Cl_9]^{3-}$ and $[M'M''Cl_9]^{3-}$ and odd-electron (mixed-valence) $[M_2Cl_9]^{2-}$ dimers involving the transition metals of groups 4 through 8. The degree of metal–metal bonding in these systems is determined by the relative magnitudes of two opposing terms, namely the spin polarization (exchange stabilization) energy which favours localization of the metal-based electrons and weak magnetic coupling, and the metal–metal bonding energy which favours delocalization of the metal-based electrons and thus (strong) metal–metal bonding. Remarkable linear correlations between the metal–metal bonding and spin polarization energy terms were obtained for all group and period series considered, and were rationalized on the basis that both properties appear to be similarly affected by changes in the metal orbital properties and electron density occurring within groups and across periods.

In the present work, the investigations of periodic trends in metal–metal interactions, using the concepts of metal–metal bonding energy and spin polarization energy, are extended to edge-shared $[M_2Cl_{10}]^{4-}$ systems. Computational studies of $[M_2L_{10}]^{z-}$ species have been reported previously, and include the work by Cotton and Feng [20] on Mo complexes ($[Mo_2Cl_6(PH_3)_4]$, $[Mo_2Cl_6(PH_2CH_2PH_2)_2]$, $[Mo_2Cl_6(CHO_2)_2(PH_3)_2]$, $[Mo_2Cl_6(NHCHNH)_2(PH_3)_2]$) using configuration interaction techniques, and our density functional investigations of Cr, Mo, and W complexes ($[M_2Cl_{10}]^{4-}$, $[M_2Cl_6(PH_3)_4]$, $[M_2Cl_6(PH_2CH_2PH_2)_2]$) [17,18]. However, all of these studies have focused on species with a formal d^3d^3 metal-based configuration, whereas in this work we consider $[M_2Cl_{10}]^{4-}$ systems involving all transition metals from group 4 through 8 and electronic configurations ranging from d^1d^1 through d^5d^5. Although both edge-shared and face-shared systems can in principle accommodate metal–metal bonds, the different bridging architectures give rise to fundamentally different orbital interactions. In the edge-shared system σ, π and δ bonds are possible, whereas in the face-shared complexes only σ and δ_π ($2/3\delta + 1/3\pi$) interactions are feasible. Due to the inherent differences in metal–metal interactions compared to the previously investigated face-shared complexes, the present study involving an extensive series of edge-shared dimers, provides an additional and useful check on the applicability of our approach to the analysis of periodic trends in metal–metal bonding across various classes of dinuclear systems.

2. Calculation details

All density-functional calculations reported in this article were carried out with the Amsterdam Density Functional (2004) package [21–23]. Functionals based on the Volko–Wilk–Nusair (VWN) form [24] of the local density approximation (LDA) [25] were utilized, and no gradient corrections or relativistic effects were included, as previous work has shown that these normally result in poorer agreement with experimental structural data [8,26]. Basis sets of triple-zeta quality and one polarization function (TZP or type IV), incorporating frozen cores (Cl.2p, and M.2p, M.3d, M.4f for the first, second, and third transition series, respectively), were employed [21–23].

3. Results and discussion

The molecular structure of edge-shared $[M_2Cl_{10}]^{4-}$ systems (shown in Fig. 1) is characterized by D_{2h} symmetry, with the metal sites lying in a distorted octahedral environment corresponding to C_{2v} local symmetry. This distorted environment implies that the metal-based octahedral t_{2g} d-type orbitals relevant to metal–metal bonding possess a_1, b_2, and a_2 (C_{2v}) symmetry and generate, respectively, bonding [σ, π, δ] and antibonding [σ*, π*, δ*] molecular orbitals that transform as the a_g, b_{2u}, b_{3g}, b_{3u}, b_{1g}, and a_u irreducible representations in the full D_{2h} symmetry of the $[M_2Cl_{10}]^{4-}$ systems. The correlation between the C_{2v}

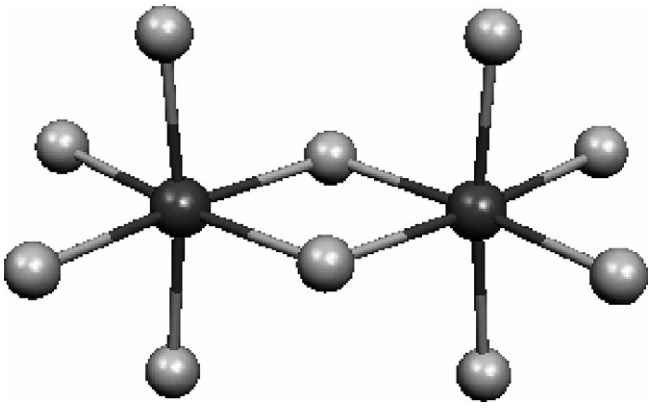


Fig. 1. Molecular structure of edge-shared $[M_2Cl_{10}]^{4-}$ dimers.

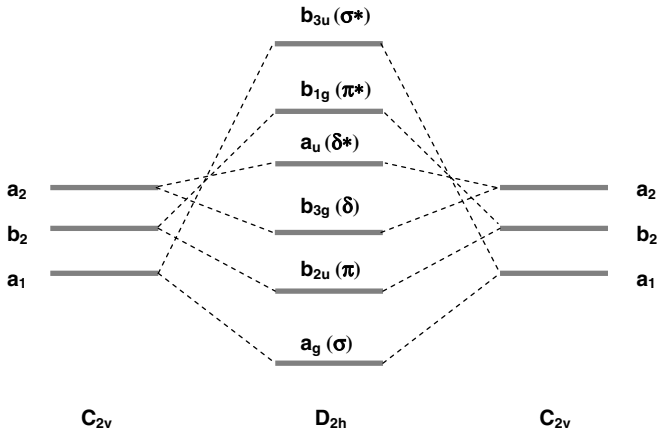


Fig. 2. Correlation between the metal-based molecular orbitals in C_{2v} and D_{2h} descriptions of edge-shared $[M_2Cl_{10}]^{4-}$ dimers.

and D_{2h} orbital descriptions is shown in Fig. 2 and plots of the metal–metal bonding and antibonding molecular orbitals obtained from calculations on (d^3d^3) $[W_2Cl_{10}]^{4-}$ are given in Fig. 3.

3.1. General results

In previous studies [19], periodic trends in metal–metal interactions have been described and analyzed in terms of two factors, namely, the metal–metal bonding (ΔE_{mbe}) energy and the spin-polarization (ΔE_{spe}) energy.

The metal–metal bonding term can be defined as the stabilization energy arising from bond formation between opposite metal centres, whereas the spin-polarization term represents the exchange stabilization energy associated with the presence of unpaired electron density on the metal centres. Significant bonding interaction between the metal atoms favours electron delocalization over both metal sites, whereas the spin-polarization effects favour electron localization on the opposite metal centres. The difference between the two terms (denoted $\Delta E_{spe} - \Delta E_{mbe}$) measures the tendency of the metal-based electrons to delocalize and thus determines the degree of metal–metal bonding.

Three separate calculations are required to determine the metal–metal bonding and spin-polarization terms (Fig. 4). These correspond to the $S = 0$ state, where complete delocalization of the metal-based electrons in metal–metal bonds occurs, the $S = S_{max}$ state, in which all metal-based electrons are unpaired and therefore weakly coupled, and the reference state (RS), which is defined so that the contributions from metal–metal bonding and spin polarization cancel. The energy of the reference state can be obtained from a spin-restricted calculation on an electronic configuration where the metal–metal bonding and antibonding orbitals are evenly occupied.

The metal–metal bonding energy and the spin-polarization energy are defined in terms of these three states as follows

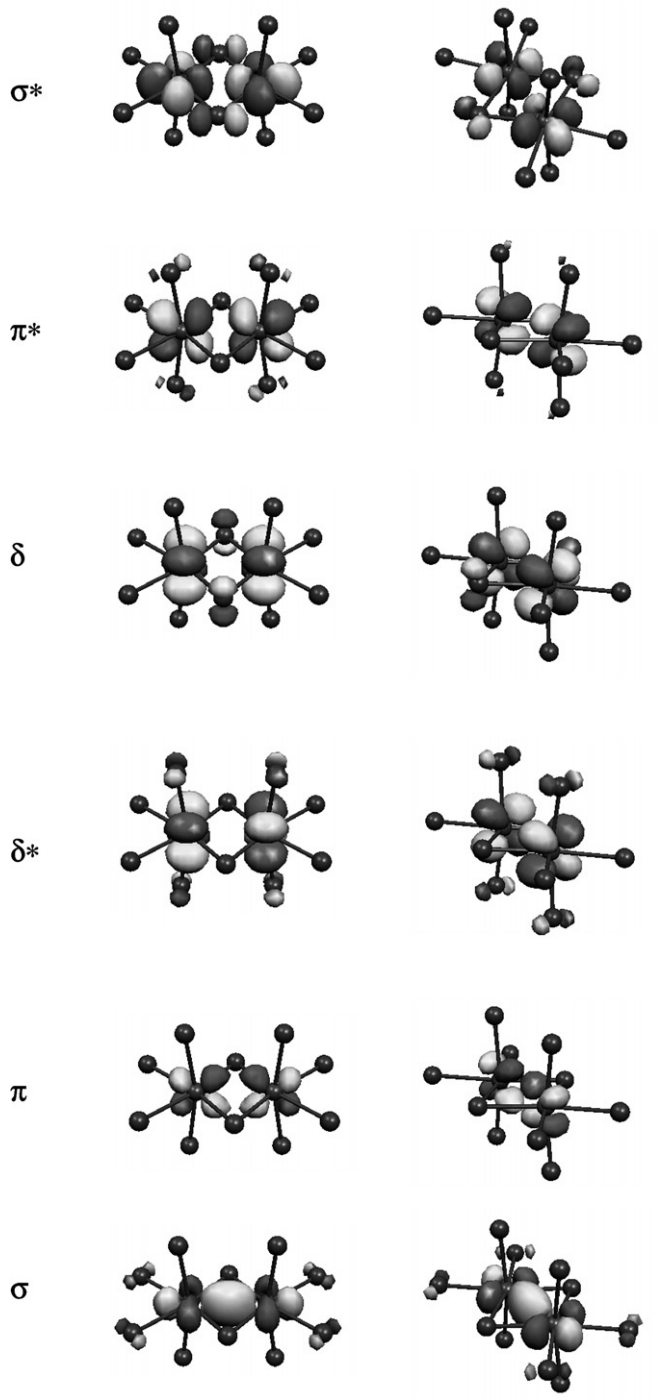


Fig. 3. Plots of the molecular orbitals representing the metal–metal interactions in $[W_2Cl_{10}]^{4-}$.

$$\Delta E_{mbe} = E(S = 0) - E(RS) \quad (1)$$

$$\Delta E_{spe} = E(S = S_{max}) - E(RS) \quad (2)$$

The occupancy of the metal-based orbitals in the metal–metal bonded $S = 0$ state for the five d^nd^n configurations can be schematically described as follows

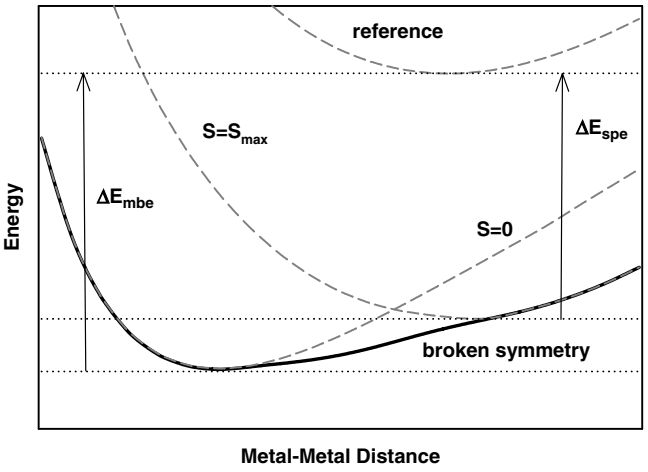


Fig. 4. Schematic definition of the metal–metal bonding (ΔE_{mbe}) energy and spin polarization (ΔE_{spe}) energy in relation to the $S = 0$, $S = S_{max}$, and reference states of $d^n d^n$ systems.

$d^1d^1 \quad (\sigma)^2(\pi)^0(\delta)^0(\delta^*)^0(\pi^*)^0(\sigma^*)^0$

$d^2d^2 \quad (\sigma)^2(\pi)^2(\delta)^0(\delta^*)^0(\pi^*)^0(\sigma^*)^0$

$d^3d^3 \quad (\sigma)^2(\pi)^2(\delta^*)^2(\delta)^0(\pi^*)^0(\sigma^*)^0$

$d^4d^4 \quad (\sigma)^2(\pi)^2(\delta)^2(\delta^*)^2(\pi^*)^0(\sigma^*)^0$

$d^5d^5 \quad (\sigma)^2(\pi)^2(\delta)^2(\delta^*)^2(\pi^*)^2(\sigma^*)^0$

where it should be noted that, for d^3d^3 systems, the most favourable occupation corresponds to an inversion of the δ and δ* orbitals [17,18].

For the "completely localized" $S = S_{max}$ states, the occupancy of the metal-based orbitals corresponds to the configurations

$d^1d^1 \quad (\sigma)^1(\pi)^0(\delta)^0(\delta^*)^0(\pi^*)^0(\sigma^*)^1 \quad (S = 1)$

$d^2d^2 \quad (\sigma)^1(\pi)^1(\delta)^0(\delta^*)^0(\pi^*)^1(\sigma^*)^1 \quad (S = 2)$

$d^3d^3 \quad (\sigma)^1(\pi)^1(\delta)^1(\delta^*)^1(\pi^*)^1(\sigma^*)^1 \quad (S = 3)$

$d^4d^4 \quad (\sigma)^1(\pi)^1(\delta)^2(\delta^*)^2(\pi^*)^1(\sigma^*)^1 \quad (S = 2)$

$d^5d^5 \quad (\sigma)^1(\pi)^2(\delta)^2(\delta^*)^2(\pi^*)^2(\sigma^*)^1 \quad (S = 1)$

The electronic configurations for the reference states are obtained by evenly distributing the metal-based electrons over the six relevant orbitals, as follows:

$d^1d^1 \quad (\sigma)^{1/3}(\pi)^{1/3}(\delta)^{1/3}(\delta^*)^{1/3}(\pi^*)^{1/3}(\sigma^*)^{1/3}$

$d^2d^2 \quad (\sigma)^{2/3}(\pi)^{2/3}(\delta)^{2/3}(\delta^*)^{2/3}(\pi^*)^{2/3}(\sigma^*)^{2/3}$

$d^3d^3 \quad (\sigma)^1(\pi)^1(\delta)^1(\delta^*)^1(\pi^*)^1(\sigma^*)^1$

$d^4d^4 \quad (\sigma)^{4/3}(\pi)^{4/3}(\delta)^{4/3}(\delta^*)^{4/3}(\pi^*)^{4/3}(\sigma^*)^{4/3}$

$d^5d^5 \quad (\sigma)^{5/3}(\pi)^{5/3}(\delta)^{5/3}(\delta^*)^{5/3}(\pi^*)^{5/3}(\sigma^*)^{5/3}$

Geometrical parameters for the reference, $S = 0$, and $S = S_{max}$ states, and the calculated values of the ΔE_{mbe}, ΔE_{spe}, and $\Delta E_{spe} - \Delta E_{mbe}$ terms for all species studied in the present work are given in Tables 1 and 2, respectively.

Table 1
Optimized metal–metal bond distance (Å) for the reference (RS), $S = 0$, and $S = S_{max}$ states of $d^n d^n$ $[M_2Cl_{10}]^{4-}$ systems

configuration	molecule	RS	$S = 0$	$S = S_{max}$
d^1d^1	$[Ti_2Cl_{10}]^{4-}$	3.976	3.214	3.926
	$[Zr_2Cl_{10}]^{4-}$	4.263	3.295	4.261
	$[Hf_2Cl_{10}]^{4-}$	4.271	3.296	4.271
d^2d^2	$[V_2Cl_{10}]^{4-}$	3.846	2.897	3.844
	$[Nb_2Cl_{10}]^{4-}$	4.084	2.801	4.097
	$[Ta_2Cl_{10}]^{4-}$	4.096	2.801	4.098
d^3d^3	$[Cr_2Cl_{10}]^{4-}$	3.755	2.791	3.762
	$[Mo_2Cl_{10}]^{4-}$	3.941	2.798	3.956
	$[W_2Cl_{10}]^{4-}$	4.000	2.800	4.000
d^4d^4	$[Mn_2Cl_{10}]^{4-}$	3.651	2.820	3.698
	$[Tc_2Cl_{10}]^{4-}$	3.842	2.711	3.894
	$[Re_2Cl_{10}]^{4-}$	3.885	2.767	3.931
d^5d^5	$[Fe_2Cl_{10}]^{4-}$	3.580	3.435	3.695
	$[Ru_2Cl_{10}]^{4-}$	3.753	3.035	3.815
	$[Os_2Cl_{10}]^{4-}$	3.824	3.106	3.898

Table 2
Metal–metal bonding (ΔE_{mbe}) energy (eV) and spin-polarization (ΔE_{spe}) energy (eV) for $d^n d^n$ $[M_2Cl_{10}]^{4-}$ systems

Configuration	Molecule	ΔE_{mbe}	ΔE_{spe}	$\Delta E_{spe} - \Delta E_{mbe}$
d^1d^1	$[Ti_2Cl_{10}]^{4-}$	0.25	0.54	+0.29
	$[Zr_2Cl_{10}]^{4-}$	1.01	0.49	−0.52
	$[Hf_2Cl_{10}]^{4-}$	1.11	0.48	−0.63
d^2d^2	$[V_2Cl_{10}]^{4-}$	0.37	1.63	+1.26
	$[Nb_2Cl_{10}]^{4-}$	1.79	1.08	−0.71
	$[Ta_2Cl_{10}]^{4-}$	2.05	1.00	−1.05
d^3d^3	$[Cr_2Cl_{10}]^{4-}$	0.57	3.62	+3.05
	$[Mo_2Cl_{10}]^{4-}$	1.84	2.21	+0.37
	$[W_2Cl_{10}]^{4-}$	2.15	1.98	−0.17
d^4d^4	$[Mn_2Cl_{10}]^{4-}$	−0.34	1.44	+1.78
	$[Tc_2Cl_{10}]^{4-}$	0.73	0.69	−0.04
	$[Re_2Cl_{10}]^{4-}$	1.05	0.56	−0.49
d^5d^5	$[Fe_2Cl_{10}]^{4-}$	−0.87	0.00	+0.87
	$[Ru_2Cl_{10}]^{4-}$	−0.51	−0.29	+0.22
	$[Os_2Cl_{10}]^{4-}$	−0.35	−0.36	−0.01

3.2. Periodic trends

Periodic trends in the metal–metal bonding (ΔE_{mbe}) and spin polarization (ΔE_{spe}) energy terms in all $[M_2Cl_{10}]^{4-}$ systems studied are schematically represented in the plots shown in Fig. 5.

For all five transition metal groups investigated, qualitatively similar trends in the variation of the metal–metal bonding and spin-polarization terms are observed. On descending each group, the calculated values of the metal–metal bonding energy increase while those of the spin polarization energy decrease, with the most significant differences found between 3d–3d and 4d–4d species.

An explanation for these qualitative trends can be given in terms of how the changes in the metal properties affect the two energetic factors [19]. As a group is descended,

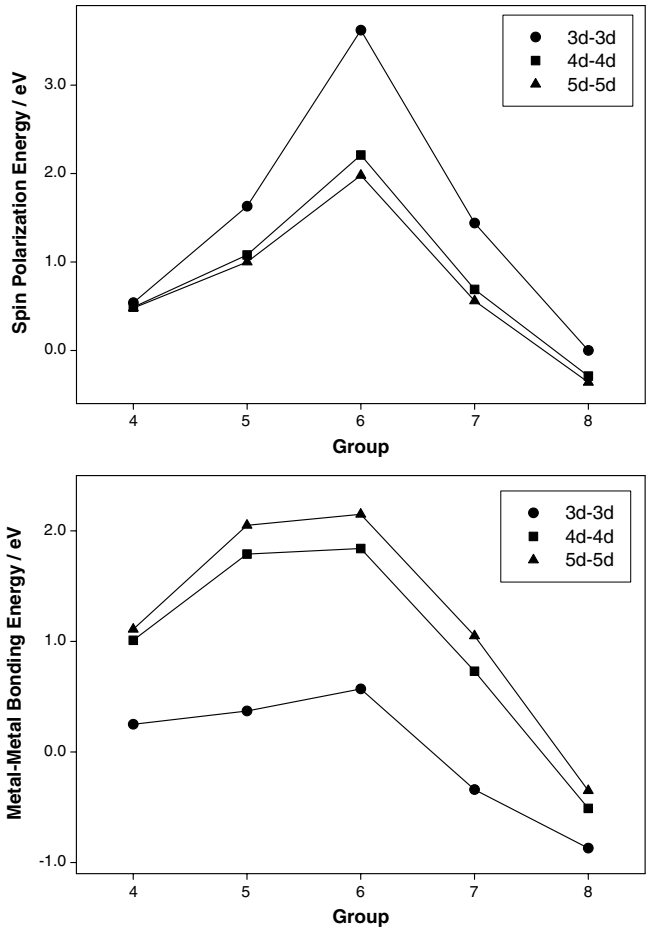


Fig. 5. Periodic variation of the spin-polarization and metal–metal bonding energy terms.

the greater size of the metal atoms and the more diffuse nature of the metal orbitals lead to an enhancement of the metal–metal bonding interactions, but to a reduction in spin polarization as a consequence of the increased average interelectronic separation.

Across a period, the changes in the spin-polarization energy reflect its dependence on the number of like-spin electrons, the calculated values increasing from d^1d^1 through to d^3d^3 configurations, and subsequently decreasing from d^3d^3 through to d^5d^5 configurations. For $[M_2Cl_9]^{3-}$ systems, the variation of the spin-polarization energy across a period is mirrored around the values for group 6, and an explanation for this result has been proposed [19] in terms of the electron–hole equivalence of the d^1d^1–d^5d^5 and d^2d^2–d^4d^4 configurations, and the relationship between the spin-polarization energy and the number (n) of like-spin electrons, represented by the expression

$$\Delta E_{spe} \propto (n!/2) \tag{3}$$

Unlike the $[M_2Cl_9]^{3-}$ systems, the variation in the spin-polarization energy is not symmetrical across the $[M_2Cl_{10}]^{4-}$ series. Although the results are similar for (d^2d^2) $[V_2Cl_{10}]^{4-}$ and (d^4d^4) $[Mn_2Cl_{10}]^{4-}$, in general, the values for d^4d^4 and d^5d^5 species are significantly smaller than those for d^2d^2 and d^1d^1 systems, respectively. A comparison of the structural data in Table 1 for the reference and $S = S_{max}$ states reveals structural differences between the $[M_2Cl_9]^{3-}$ and $[M_2Cl_{10}]^{4-}$ dimers that may account for the different trends observed in the spin-polarization energy results. In the former, the optimized metal–metal distances in the reference and $S = S_{max}$ states are almost identical, whereas in the latter, this pattern generally holds for d^1d^1 and d^2d^2 dimers, but not for d^4d^4 and d^5d^5 dimers, which exhibit shorter metal–metal bond lengths in the reference state than in the $S = S_{max}$ state.

In the case of the metal–metal bonding energy, the greater values obtained for d^2d^2 and d^4d^4 species relative to d^1d^1 and d^5d^5 systems, respectively, correlate with the increase in formal metal–metal bond order from 1.0 to 2.0. For d^3d^3 dimers, the δ–δ* orbital inversion implies that there is no formal triple bond despite the presence of six metal-based electrons, and the metal–metal interaction is more appropriately described as a formal double bond [20]. Accordingly, a comparative examination of the results for d^2d^2 and d^3d^3 species, in both the 4d–4d and 5d–5d series, reveals that the metal–metal bonding energy and the optimized bond lengths in the $S = 0$ state are largely similar. The metal–metal interaction appears somewhat stronger in $[Cr_2Cl_{10}]^{4-}$ than $[V_2Cl_{10}]^{4-}$, but a more significant change in the metal–metal distances is observed in this case. Analogous to the $[M_2Cl_9]^{3-}$ systems, the values of the metal–metal bonding energy for d^4d^4 and d^5d^5 dimers are smaller than those obtained for d^2d^2 and d^1d^1 dimers, respectively, and this result can be attributed to the influence of factors such as the occupation of antibonding orbitals and the expected contraction of the metal-based orbitals across a period.

Plots showing the variation of the metal–metal bonding energy as a function of the spin-polarization energy are shown in Fig. 6. Strong linear correlations have been obtained for all groups considered, as previously observed for face-shared $[M_2X_9]^{z-}$ series involving a variety of metals and ligands [19,27]. The dashed line corresponds to

$$\Delta E_{mbe} = \Delta E_{spe} \tag{4}$$

and thus separates the systems exhibiting a preference for electron delocalization and metal–metal bonding ($\Delta E_{mbe} > \Delta E_{spe}$) from those where electron localization and weak magnetic coupling is more favourable ($\Delta E_{mbe} < \Delta E_{spe}$). In general, delocalization and metal–metal bonding preferably occur in 5d–5d species whereas localization and weaker coupling between the metal atoms are favoured in 3d–3d species, with the results being more variable across 4d–4d systems. Although the general trends for the 3d–3d and 5d–5d series are similar to those described previously for $[M_2Cl_9]^{3-}$ systems [19], the behaviour of the 4d–4d dimers is rather different, as evidenced by the fact that metal–metal bonding is clearly preferred by all 4d–4d face-shared $[M_2Cl_9]^{3-}$ species whereas only the $[Zr_2Cl_{10}]^{4-}$ and $[Nb_2Cl_{10}]^{4-}$ edge-shared systems exhibit a definitive tendency

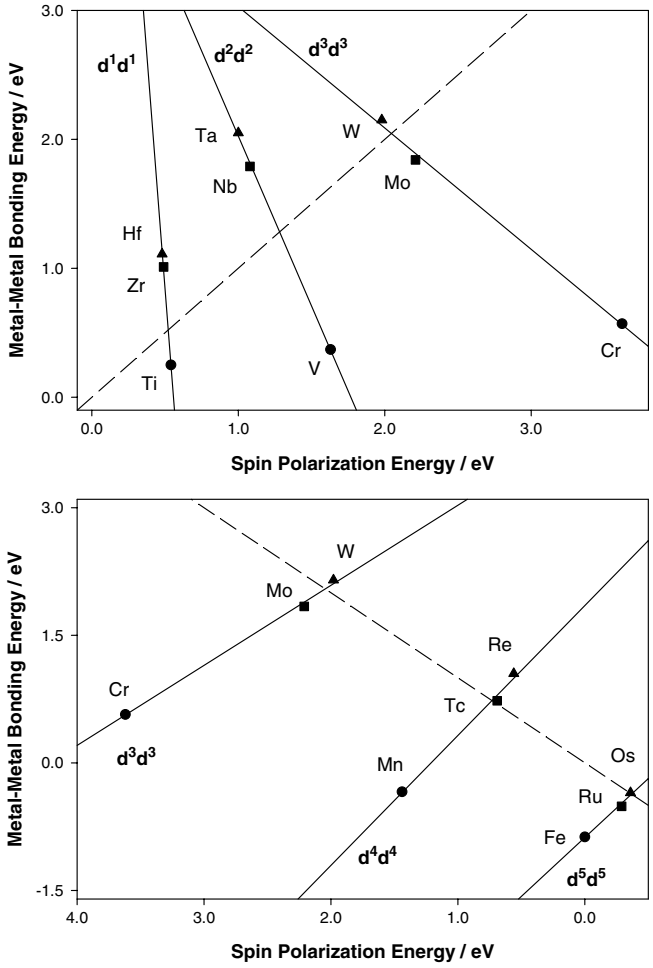


Fig. 6. Variation of the metal–metal bonding energy as a function of the spin-polarization energy.

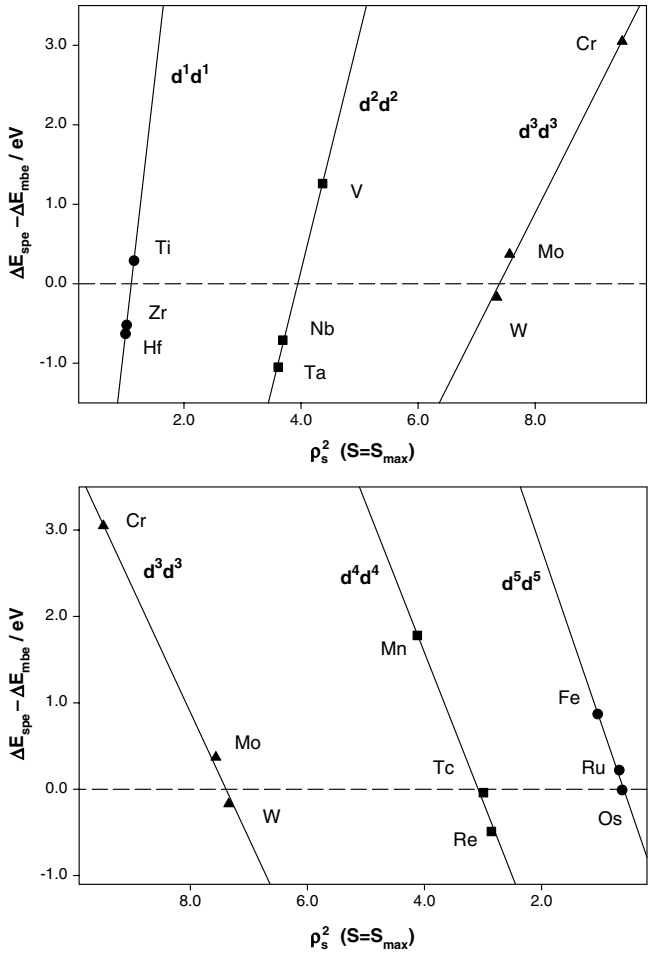


Fig. 7. Representation of the difference ($\Delta E_{spe} - \Delta E_{mbe}$) between the spin polarization and metal–metal bonding terms as a function of the square of the spin density (ρ_s^2) in the $S = S_{max}$ state.

towards electron delocalization and metal–metal bond formation. As previously noted [17], this result is related to the apparent inability of the edge-shared bridging structure to support the short metal–metal separations required for strong metal–metal bonding.

The strong correlation between the metal–metal bonding and spin polarization energy terms has been previously [19] rationalized on the basis that both properties appear to be similarly affected by changes in the metal orbital properties and electron density within each group. As found for the $[M_2Cl_9]^{3-}$ systems, a connection between the two energy terms and the electron density is also observed for the $[M_2Cl_{10}]^{4-}$ species, as revealed by the strong linear correlations between the $\Delta E_{spe} - \Delta E_{mbe}$ values and the square of the metal spin density (ρ_s^2) obtained from a Mulliken population analysis for the $S = S_{max}$ state (Fig. 7).

For all d^nd^n groups, the importance of metal–metal bonding relative to spin polarization is found to increase as the spin density decreases. Thus, the tendency towards metal–metal bond formation becomes stronger upon descending a given group, as indicated by the diminishing values of the $\Delta E_{spe} - \Delta E_{mbe}$ term, and can be correlated with the decrease in the spin density on the metal centres in the $S = S_{max}$ state.

Across the 3d–3d series, spin polarization effects become increasingly important as the number of unpaired electrons in the $S = S_{max}$ state and, consequently, the spin density on the metal centres, increases from d^1d^1 (Ti) and d^5d^5 (Fe), through d^2d^2 (V) and d^4d^4 (Mn), to d^3d^3 (Cr) systems. As observed in Fig. 5, the spin polarization and metal–metal bonding energy terms exhibit similar trends across the 3d–3d series, but the steeper variation displayed by the former leads to its increasingly dominant role across the [d^1d^1, d^2d^2, d^3d^3] and [d^5d^5, d^4d^4, d^3d^3] sets of systems within this period.

More variable results are observed across the 4d–4d and 5d–5d series but, in all cases, the smallest values of the $\Delta E_{spe} - \Delta E_{mbe}$ term, and therefore the most delocalized structures, have been obtained for the species with d^2d^2 and d^4d^4 configurations. Within their respective [d^1d^1, d^2d^2, d^3d^3] series, the d^3d^3 $[Mo_2Cl_{10}]^{4-}$ and $[W_2Cl_{10}]^{4-}$ dimers exhibit the largest $\Delta E_{spe} - \Delta E_{mbe}$ values, in accord with the observation that these systems have the highest number of unpaired electrons and metal spin density values

in the $S = S_{max}$ state, and the fact that their capacity for metal–metal bonding seems to be somewhat unfavourably affected by the δ–δ* orbital inversion. The Zr, Hf, Nb, and Ta dimers all show a preference for metal–metal bonding over electron localization, but a greater tendency towards delocalization is predicted for the d^2d^2 species ($[Nb_2Cl_{10}]^{4-}$ and $[Ta_2Cl_{10}]^{4-}$) than the d^1d^1 species ($[Zr_2Cl_{10}]^{4-}$ and $[Hf_2Cl_{10}]^{4-}$), respectively, due to fact that the greater strength of the metal–metal bonds in the former appears to dominate over the increased spin polarization resulting from a higher number of unpaired electrons and metal spin density in the $S = S_{max}$ state. These observations also apply to the 4d–4d species within the [d^5d^5, d^4d^4, d^3d^3] series, with the d^3d^3 dimer ($[Mo_2Cl_{10}]^{4-}$) displaying the greatest preference for electron localization while metal–metal bonding is more favourable in the d^4d^4 dimer ($[Tc_2Cl_{10}]^{4-}$) than the d^5d^5 dimer ($[Ru_2Cl_{10}]^{4-}$). In the case of the 5d–5d analogues, the greatest tendency towards delocalization and metal–metal bond formation is also predicted for the d^4d^4 dimer ($[Re_2Cl_{10}]^{4-}$), but in contrast with the trends for the 3d–3d and 4d–4d species, the d^5d^5 dimer ($[Os_2Cl_{10}]^{4-}$) is calculated to be the most localized system, rather than the d^3d^3 dimer ($[W_2Cl_{10}]^{4-}$).

4. Conclusion

Periodic trends in metal–metal interactions have been investigated by means of density functional calculations on a large number of edge-shared $[M_2Cl_{10}]^{4-}$ dimer systems, involving the transition metals from groups 4 through 8 and electronic configurations ranging from d^1d^1 through d^5d^5.

The tendency for metal–metal bond formation or electron localization has been analyzed in terms of periodic trends in metal–metal bonding and spin polarization effects. As found in a previous study of face-shared $[M_2Cl_9]^{z-}$ systems, remarkably strong linear correlations between these two energy terms have been obtained for all d^nd^n groups considered, and can be traced to a similar dependence of both factors on the radial dilation of the metal d orbitals and electron density within a given group.

Strong linear correlations are also observed, within all groups, between the square of the spin density on the metal centres (obtained from calculations on the $S = S_{max}$ state) and both the metal–metal bonding and spin polarization terms . However, unlike the $[M_2Cl_9]^{3-}$ systems, across the nd-nd series, the relationship between the two terms, and the dependence of both terms on the electron density, are, in general, not characterized by (similarly strong) linear correlations, possibly due to the influence of the δ–δ* orbital inversion in the $[M_2Cl_{10}]^{4-}$ dimers.

Not unexpectedly, the relative magnitudes of the metal–metal bonding and spin polarization terms indicate that delocalization and metal–metal bond formation are most favourable in the 5d–5d species whereas localization and weaker coupling between the metal atoms are preferred in the 3d–3d species. The results are more variable across the 4d–4d systems with the Zr and Nb dimers showing a tendency towards metal–metal bonding, but electron localization being favoured in the Ru and Mo dimers. This contrasts with the analogous face-shared systems where all 4d–4d dimers are predicted to be delocalized.

Overall, the $[M_2Cl_{10}]^{4-}$ dimers exhibit less delocalized structures than their face-shared $[M_2Cl_9]^{3-}$ counterparts, and this tendency can be attributed to the more inflexible nature of the edge-shared bridging structure, which is less able to accommodate the shorter metal–metal separations required for strong metal–metal bonding.

Acknowledgements

The authors gratefully acknowledge the Australian Research Council for financial support in the form of a Discovery Project Grant to RS. The Australian National University is also acknowledged for access to the APAC (Australian Partnership for Advanced Computing) facilities.

References

[1] F.A. Cotton, R.A. Walton, Multiple Bonds between Metal Atoms, 2nd ed., Oxford University Press, New York, 1993.
[2] O.S. Alexeev, B.C. Gates, Ind. Eng. Chem. Res. 42 (2003) 1571.
[3] R.D. Adams, F.A. Cotton (Eds.), Catalysis by Di and Poly Nuclear Metal Cluster Complexes, Wiley VCH, New York, 1999.
[4] R.H. Holm, P. Kennepohl, E.I. Solomon, Chem. Rev. 96 (1996) 2239.
[5] L. Noodleman, J.G. Norman, J. Chem. Phys. 70 (1979) 4903.
[6] L. Noodleman, J. Chem. Phys. 74 (1981) 5737.
[7] T. Lovell, J.E. McGrady, R. Stranger, S.A. Macgregor, Inorg. Chem. 35 (1996) 3079.
[8] J.E. McGrady, R. Stranger, T. Lovell, J. Phys. Chem. A 101 (1997) 6265.
[9] R. Stranger, J.E. McGrady, T. Lovell, Inorg. Chem. 37 (1998) 6795.
[10] T. Lovell, R. Stranger, J.E. McGrady, Inorg. Chem. 40 (2001) 39.
[11] R. Stranger, A. Turner, C.D. Delfs, Inorg. Chem. 40 (2001) 4093.
[12] S. Petrie, R. Stranger, Polyhedron 21 (2002) 1163.
[13] R. Stranger, T. Lovell, J.E. McGrady, Polyhedron 21 (2002) 1969.
[14] G. Cavigliasso, R. Stranger, Inorg. Chem. 43 (2004) 2368.
[15] G. Cavigliasso, P. Comba, R. Stranger, Inorg. Chem. 43 (2004) 6734.
[16] G. Cavigliasso, R. Stranger, Inorg. Chem. 44 (2005) 5081.
[17] J.E. McGrady, R. Stranger, T. Lovell, Inorg. Chem. 37 (1998) 3802.
[18] R. Stranger, T. Lovell, J.E. McGrady, Inorg. Chem. 38 (1999) 5510.
[19] G. Cavigliasso, T. Lovell, R. Stranger, J. Chem. Soc., Dalton Trans. (2006) 2017.
[20] F.A. Cotton, X. Feng, Int. J. Quantum Chem. 58 (1996) 671.
[21] ADF, SCM, Theoretical Chemistry, Vrije Universiteit, Amsterdam, The Netherlands (http://www.scm.com).
[22] C. Fonseca Guerra, J.G. Snijders, G. te Velde, E.J. Baerends, Theor. Chem. Acc. 99 (1998) 391.
[23] G. te Velde, F.M. Bickelhaupt, S.J.A. van Gisbergen, C. Fonseca Guerra, E.J. Baerends, J.G. Snijders, T. Ziegler, J. Comput. Chem. 22 (2001) 931.
[24] S.H. Vosko, L. Wilk, M. Nusair, Can. J. Phys. 58 (1980) 1200.
[25] W. Kohn, L.J. Sham, Phys. Rev. 140 (1965) A1133.
[26] S. Petrie, R. Stranger, Inorg. Chem. 43 (2004) 2597.
[27] G. Cavigliasso, R. Stranger, Inorg. Chem. 42 (2003) 5252.

Available online at www.sciencedirect.com
ScienceDirect
Polyhedron 26 (2007) 2949–2956
POLYHEDRON
www.elsevier.com/locate/poly

Synthesis, structure and physical properties of trinuclear $M_3tdt_3(PEt_3)_3$ ($M = Fe^{II}$, Co^{II}) clusters containing metal–metal bonds

Mihyang Kim, Jaehong Han *

Metalloenzyme Research Group, BET Research Institute and Department of Biotechnology, Chung-Ang University, Anseong 456-756, Republic of Korea

Received 15 January 2007; accepted 29 January 2007
Available online 11 February 2007

Abstract

Trinuclear $M_3tdt_3(PEt_3)_3$ ($M = Fe^{II}$ for **I**, Co^{II} for **II**) clusters have been synthesized from the reaction between $M(PEt_3)_2Cl_2$ and Na_2tdt (tdt = toluene-3,4-dithiolate) in MeCN. Both complexes have been characterized by elemental analyses, FT-IR, UV–Vis, FAB-MS, ^1H NMR and cyclic voltammetry. Structures of $Fe_3tdt_3(PEt_3)_3$ (**I**) and $Co_3tdt_3(PEt_3)_3$ (**II**) were determined by single crystal X-ray crystallography. The Fe_3 triangular core of the 48-electron complex **I**, with an isosceles triangular geometry, showed very short Fe–Fe distances of 2.4014(13) and 2.4750(12) Å, which are comparable to the extensive M–M frameworks found in the FeMo-cofactor in nitrogenase. The isostructural $Co_3tdt_3(PEt_3)_3$ (**II**), with an analogous Co_3 coordination geometry, showed short Co–Co distances of 2.4442(9) and 2.5551(10) Å. The slightly longer M–M distances in complex **II** were explained by a total valence electron counting argument. Cyclic voltammetry of $Fe_3tdt_3(PEt_3)_3$ (**I**) showed robust reduction waves compared to $Co_3tdt_3(PEt_3)_3$ (**II**). Temperature-dependent effective magnetic moment measurements of **I** and **II** showed both clusters behave similarly and the magnetic property of the M_3 equilateral triangle core with extensive metal–metal interactions was characterized as degenerate frustration.
© 2007 Elsevier Ltd. All rights reserved.

Keywords: Nitrogenase; Synthesis; Structure; Magnetic property; Metal–metal bonds; FeMo-cofactor

1. Introduction

The FeMo-cofactor in the MoFe protein of nitrogenase is a key complex for biological N_2 reduction [1]. The chemical formula of (*R*-homocitrate)$MoFe_7S_9X$ (X = unknown element) is unprecedented in biological or synthetic systems (Fig. 1). The identity of the unknown μ_6-atom was suggested as C, N or O by protein X-ray crystallography [2]. Although a nitrogen atom was favored by theoretical calculations [3], ENDOR and ESEEM spectroscopic studies did not find any evidences of a nitrogen atom [4]. One of the structural characteristics of the FeMo-cofactor is an extensive metal–metal (M–M) bonded framework. The Mo–Fe distances are found to be between 2.67 and 2.73 Å [2]. Especially, the trigonal prism of six Fe atoms shows very short Fe–Fe distances in a range between 2.58 and 2.67 Å. By comparison, most Fe/S clusters show Fe–Fe distances longer than 2.75 Å. The Fe–Fe bond lengths in the H-cluster of all-Fe hydrogenases are found between 2.57 and 2.62 Å, probably due to the π-acceptor CO and CN^- ligands [5–8]. The short M–M bonds in the FeMo-cofactor are unusual among biological inorganic clusters and the possible biological function of the M–M bonds in nitrogenase has been discussed [9]. Although it is controversial, synthetic Mo/Fe/S or Fe/S clusters with short M–M bonds may be of interest in understanding the mechanism of N_2 fixation in nitrogenase.

A plethora of metal-chalcogenide organometallic clusters have been reported, but inorganic clusters with a short Fe–Fe distance are rare. Recently, reactions under reducing conditions have been reported to produce $(Cl_4\text{-cat})_2Mo_2Fe_6S_8(PR_3)_6$ (R = Et, ^{n}Pr and ^{n}Bu) [10] and $(Cl_4\text{- cat})_2Mo_2Fe_3S_5(PEt_3)_5$ [11] compounds with short Mo–Fe and Fe–Fe bonds. These compounds were reported to show interesting chemical reactivity and physical properties.

* Corresponding author. Tel.: +82 31 670 4830.
E-mail address: jaehongh@cau.ac.kr (J. Han).

0277-5387/$ - see front matter © 2007 Elsevier Ltd. All rights reserved.
doi:10.1016/j.poly.2007.01.052

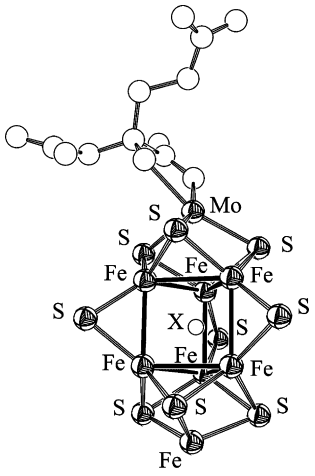


Fig. 1. Structure of FeMo-cofactor. The unknown atom is shown within the Fe_6 prismane frame (shown in solid bonds). The picture was generated by ORTEP-3 for Windows [35] after processing PDB data (1M1N) using Swiss-PdbViewer [36].

To understand the physical properties of clusters with short M–M bonds, we have prepared $M_3tdt_3(PEt_3)_3$ (**I** for M = Fe, **II** for M = Co) complexes from the reaction between $M(PEt_3)_2Cl_2$ and the bidentate thiolate ligand, Na_2tdt (where tdt = toluene-3,4-dithiolate). Although closely related complexes of $M_3tdt_3(P^nBu_3)_3$ (M = Fe or Co) and $Fe_3bdt_3(PEt_3)_3$ have been synthesized [13,14],[1] the synthetic method adopted here is different. Besides, due to the instability of the P^nBu_3 derivatives, these trinuclear Fe and Co clusters have never been completely characterized. The $M_3tdt_3(PEt_3)_3$ (**I** for M = Fe, **II** for M = Co) complexes were characterized structurally and physically by various methods. Complexes **I** and **II** are isostructural but have a different number of total valence electrons, so that shows different formal bond orders of the M–M bonds. These trinuclear $M_3tdt_3(PEt_3)_3$ complexes also are found to show interesting temperature-dependent magnetic properties.

2. Experimental

2.1. General

All experiments and reactions were carried out under a dinitrogen atmosphere using standard Schlenk line techniques or in an inert atmosphere glove box. All solvents were distilled under dinitrogen and nitrogen gas was bubbled through the solvents before each use in a glove box. $FeCl_2$, PEt_3 and toluene-3,4-dithiol were purchased from Aldrich and were used without further purification. Na_2tdt was prepared from the reaction between Na and toluene-3,4-dithiol in MeOH. The 2:1 molar ratio reaction resulted in a quantitative yield. $Fe(PEt_3)_2Cl_2$ was prepared from a 1:2 molar ratio of $FeCl_2$ and PEt_3 in THF. Anhydrous $CoCl_2$ was prepared by drying the hydrate form of $CoCl_2$ in a vacuum oven. A MeCN solution of $Co(PEt_3)_2Cl_2$ was prepared *in situ* from a 1:2 ratio of $CoCl_2$ and PEt_3.

^1H NMR spectra were recorded in $CDCl_3$ with a Bruker 400 MHz NMR spectrometer using non-deuteriated solvent as the internal standard. FT-IR spectra were collected on a Nicolet DX V. 4.56 FT-IR spectrometer in KBr pellets and the spectra were corrected for background effects. UV–Vis spectra were obtained on a Shimadzu UV-1601 UV–VIS spectrometer in the range 200–1000 nm. Elemental analyses were performed in the Microanalytical Laboratory at the University of Michigan. The data were corrected using acetanilide as a standard. FAB-Mass spectra were obtained with a 3-nitrobenzoyl alcohol matrix. Cyclic voltammetry was performed on a BAS-voltammograph. Three electrodes consisting of a glassy carbon working electrode, Pt auxiliary electrodes and a saturated calomel electrode (SCE) as a reference electrode were used for the measurements. $Fe_3tdt_3(PEt_3)_3$ (**I**) and $Co_3tdt_3(PEt_3)_3$ (**II**) were dissolved in 1,2-dichloroethane together with 0.1 M tetrabutylammonium hexafluorophosphate as a supporting electrolyte, and the scanning rate was 100 mV/s. Under the same conditions, 0.1 M of ferrocene in MeCN showed an oxidation wave at 480 mV. Magnetic susceptibilities of $Fe_3tdt_3(PEt_3)_3$ (**I**) and $Co_3tdt_3(PEt_3)_3$ (**II**) were measured in the temperature range of 4–300 K with a Quantum Design MPMS SQUID. The magnetic field of the measurements was 5000 G for the temperature-dependent experiments. The crystalline sample was put into a cellophane capsule under a dinitrogen atmosphere. The magnetic susceptibility of the holder was determined separately and diamagnetic corrections were estimated from Pascal's constants [15]. Magnetic moments per trinuclear cluster of **I** and **II** were reported.

2.2. $Fe_3tdt_3(PEt_3)_3$ (*I*)

$Fe(PEt_3)_2Cl_2$ (726 mg, 2.0 mmol) was dissolved in MeCN (30 mL) and Na_2tdt (400 mg, 2.0 mmol) was added into the solution. The reaction mixture turned immediately dark black and was stirred for 2 h, whereupon it turned reddish black. After overnight reaction, a reddish black precipitate was isolated by filtration. The product was extracted with diethyl ether (10 mL × 4) and the extract was dried under N_2. The black crystalline product was isolated in a 76.5% yield (500 mg, 0.51 mmol). ^1H NMR (CD_2Cl_2): $\delta = 32.5$ (br s, 9H, PCH_2CH_3), 14.6 (br s, 6H, PCH_2), 9.2 (br s), 8.2 (br d), 6.4 (br d), 1.6 (br d), 0.6 (br s), 0.08 (br s, 3H, tdt-CH_3), −0.1 (br s), −0.64 (br s), −11.2 (br s, 12H, PCH_2), −14.5 (br t, 18H, PCH_2CH_3). ($CDCl_3$): $\delta = 44.3$ (br s), 43.4 (br s), 14.75 (br s, 12H, PCH_2), 11.0 (t, 9H, PCH_2CH_3), 6.9 (br s), 6.6 (br s), 5.16 (br s, 9H, PCH_2CH_3), 2.24 (br s), 1.98 (br s), 0.58 (br s), 0.05 (br s, 9H, tdt-CH_3), −2.46 (br s, 9H, PCH_2CH_3), −4.94 (br s, 6H, PCH_2), −17 (br s), −43 (br s). FT-IR (KBr, cm^{-1}, relative intensity) 3032(m), 2956(m), 2929(s), 2897(m), 2873(s), 1450(s), 1031(vs) 761(s). Far-IR (KBr, cm^{-1}, relative intensity) 408(s), 356(s), 333(s). FAB^+-MS

[1] bdt = 1,2-benzenedithiolate.

(NBA, *m/z*) 984.1 ($[Fe_3tdt_3(PEt_3)_3]^+$), 868.1 ($[Fe_3tdt_3(PEt_3)_2]^+$), 748.0 ($[Fe_3tdt_3(PEt_3)]^+$), 629.9 ($[Fe_3tdt_3]^+$). *Anal.* Calc. for $C_{41}H_{68}Fe_3O_{0.5}P_3S_6$ (**I**, MW1021.83): C, 48.19; H, 6.71. Found: C, 47.48; H, 6.75%. UV–Vis (nm ($M^{-1}\,cm^{-1}$), purple in Et_2O): λ_{max} (ε) = 258 (7900), 275 (sh, 6200), 326 (sh, 2900), 650 (750). Cyclic voltammetry[2] (1,2-dichloroethane, 0.1 M of Et_4NPF_6) 0.74 (irr), 0.42 (irr), 0.08 (irr), −0.30 (rev), −0.52 (rev), −0.76 (rev).

2.3. $Co_3tdt_3(PEt_3)_3$ (**II**)

Anhydrous $CoCl_2$ (650 mg, 5.0 mmol) was dissolved in 15 mL of MeCN and stirred for 30 min to dissolve the $CoCl_2$. To this sky blue solution, PEt_3 (1.5 mL, 10.0 mmol) was added and the color of the solution changed to dark blue. The reaction mixture was filtered through a glass filter after 5 min. To the *in situ* prepared $Co(PEt_3)_2Cl_2$ MeCN solution was added Na_2tdt (1.0 g, 5 mmol) and the reaction mixture changed color immediately to yellowish black. After about 2 h, the reaction mixture turned greenish black. After stirring overnight, the reaction was stopped by filtration and a black precipitate was isolated. The precipitate was extracted with diethyl ether (20 mL × 4). The diethyl ether solvent was removed under N_2 and a golden black crystalline product was isolated in a 72.6% yield (1.2 g, 1.21 mmol). ^1H NMR (CD_2Cl_2): δ = 92.2 (br s), 8.0 (br s), 6.9 (br s), 6.6 (br s), 6.4 (br s), 4.1 (br s), 3.75 (br s), 3.44 (br s, 6H, PCH_2), 2.1(m), 1.83(m), 1.64(m), 1.27 (br s), 1.11 (t, 18H, PCH_2CH_3), 0.053 (br s, 9H, tdt-CH_3), −0.37 (br s, 9H, PCH_2CH_3), −1.16 (br s, 6H, PCH_2), −1.84 (br s, 6H, PCH_2), −2.44 (br s). FT-IR (KBr, cm^{-1}, relative intensity) 3030(m), ν(C–H of PEt_3); 2956(m), 2929(s), 2899(m), 2874(s), 1447(s), 1030(vs) 762(s). Far-IR (KBr, cm^{-1}, relative intensity) 414(s), 345(s), 333(s). FAB^+-MS (NBA, *m/z*) 993.2 ($[Co_3tdt_3(PEt_3)_3]^+$), 875.1 ($[Co_3tdt_3(PEt_3)_2]^+$), 756.9 ($[Co_3tdt_3(PEt_3)]^+$), 638.8 ($[Co_3tdt_3]^+$). *Anal.* Calc. for $C_{41}H_{68}Co_3O_{0.5}P_3S_6$ (**II**, MW 1031.10): C, 47.76; H, 6.65. Found: C, 47.34; H, 6.42%. UV–Vis (nm ($M^{-1}\,cm^{-1}$), green in Et_2O): λ_{max} (ε) = 263 (6000), 275 (sh, 5200), 328 (sh, 2400), 391 (2060). Cyclic voltammetry (1,2-dichloroethane, 0.1 M of Et_4NPF_6) 0.72 (irr), 0.5 (irr), −0.37 (rev), −0.51 (rev).

2.4. X-ray crystallography

Black rhombic-shaped crystals of $Fe_3tdt_3(PEt_3)_3$ (**I**) and $Co_3tdt_3(PEt_3)_3$ (**II**) were obtained from the ether extract of the reaction precipitate. The diffraction data were collected at 158(2) and 123(2) K for **I** and **II**, respectively, using a Bruker SMART area diffractometer. The crystal data and structural parameters are shown in Tables 1 and 2. The structures for compounds **I** and **II** were solved by direct methods to locate heavy atoms, and the non-hydrogen atoms were located through subsequent difference Fourier syntheses. Structural refinement was carried out by full-matrix least squares on F^2. All non-hydrogen atoms were refined with anisotropic thermal parameters. Hydrogen atoms were placed in calculated positions, allowed to ride on their corresponding atoms and refined isotropically except those on disordered carbon atoms. The carbon atoms of diethyl ether solvent molecules in **I** and **II** were severely disordered and the geometry restraints did not improve the refinement. All calculations were performed using SHELXTL-NT V. 5.1 software.

Table 1
Crystal data and structure refinement for $Fe_3tdt_3(PEt_3)_3$ (**I**) and $Co_3tdt_3(PEt_3)_3$ (**II**)

	$Fe_3tdt_3(PEt_3)_3$ (**I**)	$Co_3tdt_3(PEt_3)_3$ (**II**)
Empirical formula	$C_{82}H_{136}Fe_6OP_6S_{12}$	$C_{82}H_{136}Co_6OP_6S_{12}$
Formula weight	2043.55	2062.03
Temperature (K)	158(2)	123(2)
Wavelength (Å)	0.71073	0.71073
Crystal system	triclinic	triclinic
Space group	$P\bar{1}$	$P\bar{1}$
Unit cell dimensions		
a (Å)	11.3437(13)	11.301(4)
b (Å)	12.8765(15)	12.812(4)
c (Å)	33.108(4)	32.950(10)
α (°)	83.171(2)	83.326(5)
β (°)	85.415(2)	85.110(5)
γ (°)	89.195(2)	89.081(5)
Volume (Å^3)	4786.3(9)	4721.3(3)
Z	2	2
D_{calc} (Mg/m^3)	1.418	1.450
Absorption coefficient (mm^{-1})	1.289	1.439
F(000)	2148	2160
Crystal size (mm^3)	0.24 × 0.12 × 0.1	0.36 × 0.12 × 0.09
Θ Range for data collection (°)	1.59–24.76	1.78–26.51
Index ranges	$-13 \leqslant h \leqslant 13$, $-15 \leqslant k \leqslant 15$, $-38 \leqslant l \leqslant 39$	$-14 \leqslant h \leqslant 14$, $-16 \leqslant k \leqslant 16$, $-41 \leqslant l \leqslant 41$
Reflections collected	39215	86387
Independent reflections	16283	19418
R_{int}	0.0696	0.0821
Completeness to theta	24.76°, 99.2%	26.51°, 99.1%
Refinement method	full-matrix least-squares	full-matrix least-squares
Data/restraints/parameters	on F^2	on F^2
Goodness-of-fit on F^2	16283/0/964	19418/0/964
Final *R* indices [$I > 2\sigma(I)$]	0.899	1.018
R indices (all data)	$R_1 = 0.0561$, $wR_2 = 0.1194$	$R_1 = 0.0484$, $wR_2 = 0.0980$
	$R_1 = 0.1226$, $wR_2 = 0.1327$	$R_1 = 0.1000$, $wR_2 = 0.1142$

3. Results and discussion

3.1. Synthesis

Many Mo/Fe/S clusters as a model system of the FeMo-cofactor in the nitrogenase MoFe protein have been

[2] The redox potentials were reported versus SCE. rev = reversible, qr = quasi-reversible.

Table 2
Selected bond lengths (Å) and angles (°) for $Fe_3tdt_3(PEt_3)_3$ (**I**) and $Co_3tdt_3(PEt_3)_3$ (**II**)

$Fe_3tdt_3(PEt_3)_3$ (**I**)		$Co_3tdt_3(PEt_3)_3$ (**II**)	
Fe(1)–Fe(2)	2.4635(12)	Co(1)–Co(2)	2.5353(10)
Fe(1)–Fe(3)	2.4750(12)	Co(1)–Co(3)	2.5421(10)
Fe(2)–Fe(3)	2.4016(13)	Co(2)–Co(3)	2.4442(9)
Fe(4)–Fe(5)	2.4747(13)	Co(4)–Co(5)	2.5551(10)
Fe(4)–Fe(6)	2.4737(12)	Co(4)–Co(6)	2.5308(10)
Fe(5)–Fe(6)	2.4014(13)	Co(5)–Co(6)	2.4470(11)
Fe(1)–S(1)	2.2247(18)	Co(1)–S(1)	2.2250(14)
Fe(1)–S(2)	2.2226(19)	Co(1)–S(2)	2.2172(13)
Fe(1)–S(3)	2.2320(19)	Co(1)–S(3)	2.2170(14)
Fe(1)–S(4)	2.2271(18)	Co(1)–S(4)	2.2190(14)
Fe(2)–S(1)	2.2936(17)	Co(2)–S(1)	2.3047(13)
Fe(2)–S(3)	2.2896(18)	Co(2)–S(3)	2.3049(13)
Fe(2)–S(5)	2.2795(19)	Co(2)–S(5)	2.2872(14)
Fe(2)–S(6)	2.2641(18)	Co(2)–S(6)	2.2630(13)
Fe(3)–S(2)	2.2955(17)	Co(3)–S(2)	2.3081(13)
Fe(3)–S(4)	2.2947(18)	Co(3)–S(4)	2.3113(14)
Fe(3)–S(5)	2.2658(18)	Co(3)–S(5)	2.2696(14)
Fe(3)–S(6)	2.2809(18)	Co(3)–S(6)	2.2870(14)
Fe(4)–S(7)	2.225(2)	Co(4)–S(7)	2.2160(15)
Fe(4)–S(8)	2.2268(18)	Co(4)–S(8)	2.2165(14)
Fe(4)–S(9)	2.2251(17)	Co(4)–S(9)	2.2168(14)
Fe(4)–S(10)	2.223(2)	Co(4)–S(10)	2.2201(14)
Fe(5)–S(7)	2.2910(18)	Co(5)–S(7)	2.2983(15)
Fe(5)–S(9)	2.2862(18)	Co(5)–S(9)	2.2932(13)
Fe(5)–S(11)	2.2591(19)	Co(5)–S(11)	2.2499(14)
Fe(5)–S(12)	2.267(2)	Co(5)–S(12)	2.2676(14)
Fe(6)–S(8)	2.2987(18)	Co(6)–S(8)	2.3091(15)
Fe(6)–S(10)	2.306(2)	Co(6)–S(10)	2.3295(15)
Fe(6)–S(11)	2.302(2)	Co(6)–S(11)	2.3100(16)
Fe(6)–S(12)	2.2894(19)	Co(6)–S(12)	2.2942(14)
Fe(1)–P(1)	2.2752(18)	Co(1)–P(1)	2.1891(13)
Fe(2)–P(2)	2.265(2)	Co(2)–P(2)	2.1857(13)
Fe(3)–P(3)	2.268(2)	Co(3)–P(3)	2.1873(14)
Fe(4)–P(4)	2.2744(19)	Co(4)–P(4)	2.1920(14)
Fe(5)–P(5)	2.269(2)	Co(5)–P(5)	2.1877(15)
Fe(6)–P(6)	2.283(2)	Co(6)–P(6)	2.1931(14)
Fe(2)–Fe(1)–Fe(3)	58.20(3)	Co(2)–Co(1)–Co(3)	57.55(2)
Fe(1)–Fe(2)–Fe(3)	61.14(4)	Co(1)–Co(2)–Co(3)	61.36(2)
Fe(2)–Fe(3)–Fe(1)	60.66(4)	Co(2)–Co(3)–Co(1)	61.09(3)
Fe(5)–Fe(4)–Fe(6)	58.06(4)	Co(5)–Co(4)–Co(6)	57.52(3)
Fe(4)–Fe(5)–Fe(6)	60.95(4)	Co(4)–Co(5)–Co(6)	60.74(3)
Fe(4)–Fe(6)–Fe(5)	60.99(4)	Co(4)–Co(6)–Co(5)	61.74(2)
S(1)–Fe(1)–S(4)	156.64(7)	S(1)–Co(1)–S(4)	154.51(5)
S(2)–Fe(1)–S(3)	155.97(7)	S(2)–Co(1)–S(3)	154.98(5)
S(5)–Fe(2)–S(3)	156.11(7)	S(5)–Co(2)–S(1)	154.58(5)
S(6)–Fe(2)–S(1)	157.13(7)	S(6)–Co(2)–S(3)	155.80(5)
S(5)–Fe(3)–S(4)	156.39(7)	S(5)–Co(3)–S(2)	155.02(5)
S(6)–Fe(3)–S(2)	155.81(7)	S(6)–Co(3)–S(4)	154.51(5)
S(7)–Fe(4)–S(10)	156.18(8)	S(7)–Co(4)–S(10)	154.78(5)
S(8)–Fe(4)–S(9)	156.07(7)	S(8)–Co(4)–S(9)	154.41(5)
S(11)–Fe(5)–S(9)	157.16(8)	S(11)–Co(5)–S(9)	155.38(5)
S(12)–Fe(5)–S(7)	156.73(8)	S(12)–Co(5)–S(7)	154.84(5)
S(12)–Fe(6)–S(8)	156.25(7)	S(12)–Co(6)–S(8)	155.23(5)
S(11)–Fe(6)–S(10)	155.44(8)	S(11)–Co(6)–S(10)	154.14(5)

synthesized. These complexes were mainly achieved through self-assembly, exploiting the thermodynamic stability of the products [16,17], or rational assembly of simple building blocks under reducing conditions [11,18–20]. The complexes from the reducing conditions usually possess a reduced core with short M–M bonds. Although trigonal M_3 (M = Fe, Co) complexes with bidentate thiolate bridging ligands and trialkylphosphine terminal ligands have been reported [12–14], the synthesis of $M_3tdt_3(PEt_3)_3$ (M = Fe, Co) has never been published. The complex $Fe_3tdt_3(P^nBu_3)_3$ prepared from EtOH was reported to be unstable, but its PEt_3 analog, **I**, was stable enough for various physical characterizations. Although it was suggested that the electron-donating methyl group on the phenyl ring would destabilize the complex [14], the effect of methyl substitution seems to be negligible because it stays too remote from the metal ions. Rather, the relative electron-donating property of P^nBu_3 would be a more significant contributor to the stability of the complex [21]. Since PEt_3 is a comparatively stronger electron-withdrawing ligand than P^nBu_3, when we introduced PEt_3 to stabilize the M_3 core, the product $Fe_3tdt_3(PEt_3)_3$ (**I**) could be isolated even at room temperature. The Co analog, $Co_3tdt_3(PEt_3)_3$ (**II**), was also successfully prepared using anhydrous $CoCl_2$ under the same reaction conditions. The product **II** from the reaction was very soluble in MeCN. Diethyl ether extraction of the reaction precipitate was an efficient method to purify complex **II**. It should be pointed out that a minimum amount of MeCN is necessary to produce enough precipitate for the isolation of **II**. Both products were very soluble in most organic solvents.

The reaction conditions of using a 1:2 ratio of $FeCl_2$ and PEt_3 is reminiscent of $Fe(PEt_3)_2Cl_2$ in Mo/Fe/S and Fe/S chemistry. The reaction of $[(Cl_4\text{-cat})Mo(MeCN)Fe_3S_4Cl_3]^{2-}$ with $Fe(PEt_3)_2Cl_2$ produces the $(Cl_4\text{-cat})_2Mo_2Fe_6S_8(PEt_3)_6$ cluster and the reaction between $[Fe_4S_4Cl_4]^{2-}$ and $Fe(PEt_3)_2Cl_2$ produces the $Fe_6S_6(PEt_3)_4Cl_2$ cluster [11].

3.2. Structure

The single crystal X-ray structures of $Fe_3tdt_3(PEt_3)_3$ (**I**) and $Co_3tdt_3(PEt_3)_3$ (**II**) are shown in Figs. 2 and 3, respectively. The crystal data and structure refinement details, and selected bond lengths (Å) and angles (°) for complexes **I** and **II** are shown in Tables 1 and 2, respectively. Both structures are isostructural and crystallized in the same unit cell system with the same space group. Even the diethyl ether solvent molecules are found in the same positions for both X-ray structures.

Due to the asymmetric methyl position of the bridging tdt ligands, two different structural isomers of **I** were found in the triclinic unit cell (Fig. 2). The first molecule (**IA**) has a *cis*-arrangement of two methyl groups of tdt ligands on the Fe(1) center, while the second molecule (**IB**) shows a *trans*-arrangement of tdt ligands around the Fe(4) center. The same type of isomerism is found in the solid structure of $Co_3tdt_3(PEt_3)_3$ (**II**). The structure of the $Fe_3tdt_3(PEt_3)_3$ (**I**) cluster can be described as an isosceles triangle Fe_3 metal cluster with two long Fe–Fe bonds and one short Fe–Fe bond. The formation of the Fe_3 isosceles triangle geometry, instead of an equilateral triangle geometry, can be explained by different bridging modes of the tdt ligands (see Fig. 3). The Fe centers in **I** show coordination geome-

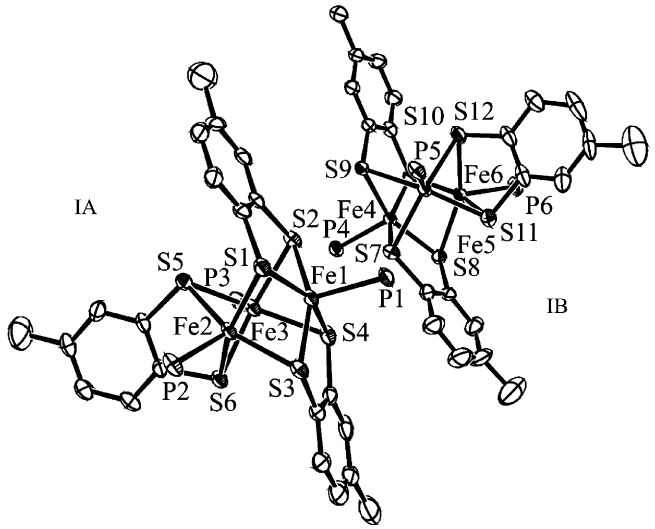


Fig. 2. Single-crystal X-ray structure of $Fe_3tdt_3(PEt_3)_3$ (**I**). Fe–Fe bonds, hydrogen atoms and ethyl groups of PEt_3 were omitted for clarity. Two unique molecules generated by different positions of the toluene methyl groups are shown.

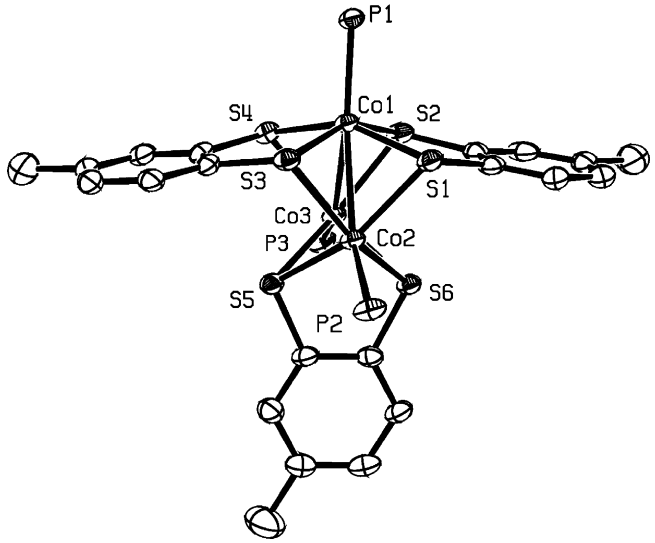


Fig. 3. Single-crystal X-ray structure of $Co_3tdt_3(PEt_3)_3$ (**II**). Hydrogen atoms and ethyl groups of PEt_3 were omitted for clarity.

tries of distorted square pyramids with a phosphorus axial ligand and four sulfur equatorial ligands. The toluene-3, 4-dithiolate ligand, with two bridging thiolates, is a eight-electron donor and the triethylphosphine terminal ligand is a two-electron donor [22]. The total number of valence electrons of 48 in **I** is six electrons fewer than the number expected for three-metal clusters based on the Wade–Mingos–Lauher rule [23]. Therefore, the Fe–Fe bonds in the $Fe_3tdt_3(PEt_3)_3$ (**I**) cluster are expected to have three formal metal–metal single bonds. Likewise, the total number of valence electrons in **II** is 51 and the complex is expected to have three Co–Co bonds with a formal bond order of 0.5. Such formal M–M bond order arguments can explain the differences of the bond distances between **I** and **II**.

The short Fe–Fe bond distances in **I** are 2.4016(13) and 2.4014(13) Å, which is longer than the value of 2.380(2) Å found for the $Fe_3tdt_3(P^nBu)_3$ complex [14]. The other long Fe–Fe distances are found to be in the range 2.4635(12)–2.4750(12) Å, and those of $Fe_3tdt_3(P^nBu)_3$ are 2.493(2) and 2.499(2) Å. The Fe–Fe bonds in the $Fe_3tdt_3(PEt_3)_3$ (**I**) cluster are even shorter than those found in the FeMo-cofactor of nitrogenase. Fe–Fe bonds distances in the FeMo-cofactor are found in the range between 2.58 and 2.67 Å. Two different ranges of Fe–S distances are found in complex **I**. The dithiolate ligands on the Fe(1) and Fe(4) centers have short Fe–S distances with an average value of 2.2258(10) Å.[3] The thiolate ligands on the other Fe centers show an average Fe–S distance of 2.285(4) Å. The difference of 0.06 Å is significant and implies a multiple Fe–S bond order between Fe(1)/Fe(4) and thiolate S [24]. Therefore, all three Fe–Fe bonds in the $Fe_3tdt_3(PEt_3)_3$ (**I**) cluster do not seem to have equally single-bond character and, instead, some Fe–S bonds also have multiple bond character. It could be another reason why the Fe_3 core has an isosceles triangular geometry.

Two unique molecules of the $Co_3tdt_3(PEt_3)_3$ (**II**) cluster in the unit cell do not exhibit significant differences from those of **I** and isosceles triangles of three cobalt ions are found. The Co_3 geometry is slightly different from the Fe_3 geometry, and the average vertex angle of the Co_3 and Fe_3 cores are found to be 57.54(3)° and 58.13(7)°, respectively. The Co–Co distances of **II** are significantly different, and are compared to **I** in Table 2. While the Fe–Fe distances of the legs of the isosceles Fe_3 core in **I** are in the range 2.4635(12)–2.4750(12) Å, the corresponding Co–Co distances of the isosceles Co_3 core in **II** are in the range 2.5308(10)–2.5551(10) Å. The base of the isosceles Co_3 core in **II** has an average Co–Co distance of 2.4456(14) Å , which is much longer than 2.4015(13) Å, the average distance of the isosceles base of the Fe_3 core in **I**. The average distance of the long Co–Co bonds is 2.541(5) Å and the average distance of the long Fe–Fe bonds is 2.472(3) Å. Average M–M distances of $Fe_3tdt_3(PEt_3)_3$ (**I**) and $Co_3tdt_3(PEt_3)_3$ (**II**) are 2.472(3) and 2.541(5) Å, respectively. Like complex **I**, two types of Co–S bonds are found in **II**. Co–S bonds around Co(1) and Co(4) atoms have an average distance of 2.2185(14) Å, which is shorter than the average distance of the other Co–S bonds (2.294(5) Å), and even shorter than the short Fe(1)/Fe(4)–S bond (average 2.2258(10) Å). It seems the Co(1)/Co(4)–S bonds of the $Co_3tdt_3(PEt_3)_3$ (**II**) cluster have more multiple bond character than **I** due to the non-integer bond order among the Co–Co bonds; three Co–Co bonds have a formal bond order of 0.5. It should be pointed out that each Co atom in

[3] The number in parenthesis represents the larger of the individual standard deviations or the standard deviation from the mean, $\sigma = [\sum_{i=1}^{n}(x_i - x)^2/n(n-1)]^{1/2}$, where x_i is an individual standard deviation, x is the average of individual standard deviations, and n is the number of individual standard deviations.

complex **II** has one more valence electron than each of the Fe atoms in complex **I**. Because both complexes are exactly same except for the metal ions, complex **II** may need less Co–Co bonding.

In organometallic clusters [25], the Fe–Fe distances of compounds with Fe–Fe double bonds are found in the range 2.215–2.326(4) Å. For the dinuclear organometallic clusters $Fe_2(NO)_2(\eta\text{-}C_5H_5)_2$ and $Co_2(NO)_2(\eta\text{-}C_5H_5)_2$, M–M distances of 2.326 and 2.372 Å are found for formal bond orders of 2 and 1.5, respectively [22,26]. The Fe_4S_4 cluster of the all-ferrous Fe protein, formally a 56-electron complex with two Fe–Fe double bonds and two Fe–Fe single bonds, shows two Fe–Fe distances at 2.52 Å and one Fe–Fe distance at 2.77 Å [27]. FeMo-cofactor with a $[Mo^{4+}4Fe^{2+}3Fe^{3+}(\mu\text{-}S)_3(\mu_3\text{-}S)_6(\mu_6\text{-}X)_6]$ core is supposed to have multiple M–S and M–M bonds and shows Fe–Fe distances between 2.58 and 2.67 Å [9,28]. The Fe–Fe bonds with distances of 2.4683(9) and 2.4721(9) Å found in $(Cl_4\text{-}cat)_2Mo_2Fe_3S_5(PEt_3)_5$ were suggested as intermediate of single and double bonds [11]. The average M–M distances of **I** and **II** are 2.448(15) and 2.509(20) Å, respectively. For comparison, the $Ni_3(S_2C_{10}Cl_6)_3(PPh_3)_3$ complex prepared from Ni(0) was reported to have a similar isosceles Ni_3 core as complexes of **I** and **II** do [29]. The Ni–Ni distance in this 54-electron complex was to be 2.641(4) Å.

3.3. Physical properties

^{1}H NMR spectra of $Fe_3tdt_3(PEt_3)_3$ (**I**) and $Co_3tdt_3(PEt_3)_3$ (**II**) in CD_2Cl_2 showed a broad distribution of the peaks. The chemical shifts of protons in complex **I** were found between 33 and −15 ppm, and those in complex **II** were found between 93 and −3 ppm. The wide range of chemical shifts can be attributed to paramagnetism and the high spin configuration of the complexes. Peaks from tdt were almost unassignable and only verified the asymmetric chemical environments of the protons. The dark red KBr pellet of **I** showed aromatic C–H stretching at 3032 cm^{-1} and the characteristic C–H stretching of PEt_3 at 2956, 2929, 2897 and 2873 cm^{-1}. The IR spectra of **I** and **II** are almost identical in both mid- and far-IR ranges. The chemical compositions of **I** and **II** were confirmed by CHN analysis and FAB^+-MS, and the isotope distributions of the molecular ion peaks of **I** and **II** were well matched to those of theoretical expectation.

UV–Vis spectra were measured in diethyl ether (Fig. 4). The purple solution of $Fe_3tdt_3(PEt_3)_3$ (**I**) showed absorptions at 258, 275, 326 and 650 nm and the green solution of $Co_3tdt_3(PEt_3)_3$ (**II**) showed similar absorptions at 263, 275, 328 and 391 nm. The absorption at 391 nm in **II** was found in place of the 650 nm absorption in **I**. Whilst the spectrum of **II** did not change, **I** in diethyl ether changed on exposure to air. The purple diethyl ether solution of **I** turned to dark blue upon air-oxidation and showed absorptions at 216, 252, 320, 370 and 522 nm (Fig. 5), which is reminiscent of the air-oxidation of the FeMo-cofactor. The dark green solution of the FeMo-cofactor was reported to show an absorption band at around 510 nm upon air-oxidation [30].

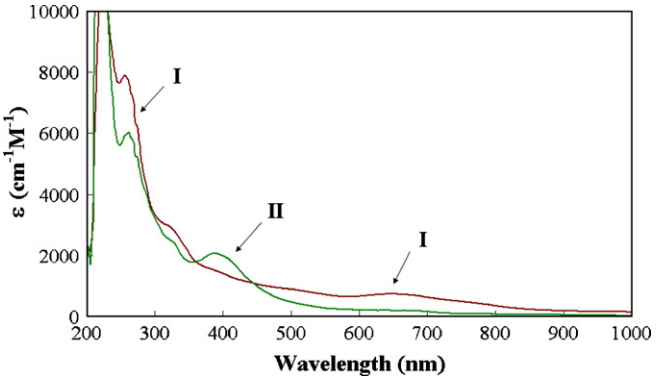


Fig. 4. UV–Vis spectra of $Fe_3tdt_3(PEt_3)_3$ (**I**) and $Co_3tdt_3(PEt_3)_3$ (**II**) in diethyl ether.

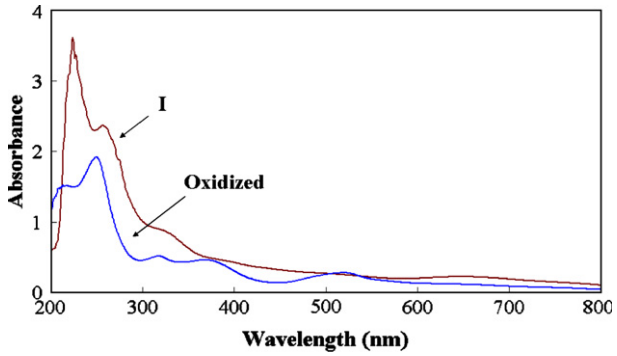


Fig. 5. UV–Vis spectrum change of $Fe_3tdt_3(PEt_3)_3$ (**I**) upon air-oxidation in diethyl ether.

3.4. Electrochemistry

The cyclic voltammetry of the complex $Fe_3tdt_3(PEt_3)_3$ (**I**) showed multiredox waves (Fig. 6). In CH_2ClCH_2Cl, **I** showed three reversible reduction waves at −0.30, −0.52 and −0.76 V and three irreversible oxidation waves at 0.74, 0.42 and 0.08 V. The three reversible reductions are very close, within a 460 mV potential spread, and corre-

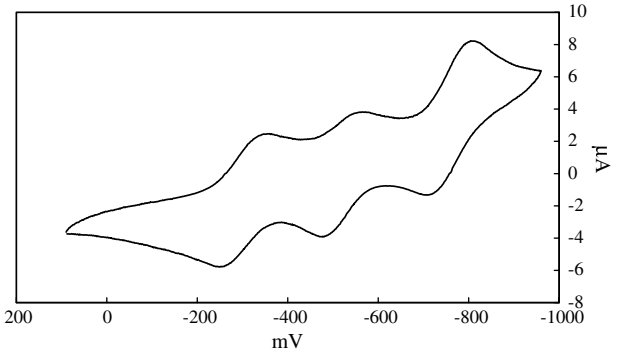


Fig. 6. Cyclic voltammetric responses of $Fe_3tdt_3(PEt_3)_3$ (**I**) in CH_2ClCH_2Cl.

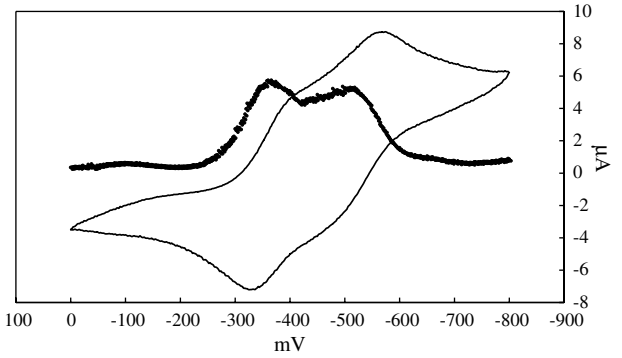


Fig. 7. Cyclic voltammetric responses of $Co_3tdt_3(PEt_3)_3$ (**II**) in CH_2ClCH_2Cl. The overlaid plot shows differential pulse voltammetry at the same potential.

spond to $\mathbf{I}^{0/-1}$, $\mathbf{I}^{-1/-2}$ and $\mathbf{I}^{-2/-3}$ reductions, respectively. Reduction of Fe(II) centers to Fe(I) ions is not physically feasible and only a two-electron reduction process is possible.[4] The observed three reversible reductions of **I** may be explained by the fact that the three M–M single bonds can accept multi-electrons. Such an exploitation of a M–M bond for electron transfer is very important for the catalytic mechanism of nitrogenase FeMo-cofactor and the direct possibility has been suggested before [9]. The complex $Co_3tdt_3(PEt_3)_3$ (**II**) showed a smaller number of redox waves than **I** (Fig. 7). The reduction waves of **II** are found at −0.37 and −0.51 V, and are only 0.14 V apart. Two independent reductions were confirmed by differential pulse voltammetry. Two irreversible oxidations at 0.72 and 0.5 V also were observed. Complex **I** showed much more versatile redox waves compared to complex **II**, which can be explained by the fact that $Fe_3tdt_3(PEt_3)_3$ (**I**) is more coordinatively unsaturated by total valence electron count arguments. It seems that the M–M bonds in the clusters are able to act as an electron reservoir and accept multi-electrons within a short range of potentials. This may be the reason why the FeMo-cofactor shows an extensive M–M bonding framework, so that multi-electron reduction of N_2 is possible.

3.5. Magnetic study

The magnetic susceptibilities of $Fe_3tdt_3(PEt_3)_3$ (**I**) and $Co_3tdt_3(PEt_3)_3$ (**II**) were measured over various temperatures at 5000 G, and field dependency experiments showed almost linear responses. $Fe_3tdt_3(PEt_3)_3$ (**I**) with three Fe(II) ions in an isosceles triangular geometry showed $\mu_{eff} = 2.60$ BM at 310 K, and the value is close to that for a $S_T = 1$ spin-state. The paramagnetic property of **I** is evident by ^{1}H NMR measurement at room temperature, which shows broad proton resonances between −43 and 45 ppm in $CDCl_3$. The mononuclear $Fe(bdt)_2(PMe_3)$ complex with a square pyramidal geometry was reported to show a low-spin/high-spin equilibrium [24]. Although it has a Fe(IV) center, this report suggests a possible spin-transition of the dithiolate phosphine Fe complex. The magnetic moment of **I** decreased to 0.31 μ_B when the temperature was lowered to 100 K (Fig. 8), which shows a strong antiferromagnetic coupling of the spin system. Below 100 K, the magnetic moment increases to 0.66 μ_B (15 K) and decreases again slightly to 0.60 μ_B (up to 4.2 K). The exchange coupling constants from the magnetic susceptibility data could not be obtained with the isotropic Heisenberg model [15].

Complex **II** showed temperature-dependent magnetic susceptibility similar to complex **I**, but with small exchange couplings (Fig. 8). This may be because complex **II** ia a three $S = 3/2$ system while complex **I** is a three $S = 2$ system. The magnetic moments of **I** and **II** at room temperature happen to be similar to each other. The magnetic moment of **II** (2.52 μ_B at 300 K) decreases to 1.76 μ_B at 80 K, probably due to the antiferromagnetic couplings. Below 80 K, the magnetic moment increases slowly to 1.84 μ_B (10 K) and decreases again slightly to 1.83 μ_B (up to 4 K). The complex $Co_3(bdt)_3(P^nBu_3)_3$ was reported to show an effective magnetic moment μ_{eff} of 2.6 μ_B at room temperature. Although it was suggested to have three low-spin Co^{II} (d^7, $S = 1/2$) atoms [14], our measurements, including ^{1}H NMR, suggest that complex **II** has three antiferromagnetically coupled high-spin Co^{II} centers. Similar temperature-dependent magnetic susceptibility was observed from the $(Cl_4\text{-cat})_2Mo_2Fe_3S_5(PEt_3)_5$ complex, which also has strong M–M interactions with a very short Fe–Fe distance. The complex has three Fe(II) centers with the same coordination environments as complexes **I** and **II**. The magnetic moment of the $(Cl_4\text{-cat})_2Mo_2Fe_3S_5(PEt_3)_5$ complex increased from 9.10 μ_B at 325 K to 10.96 μ_B at 95 K, and then decreased steeply to 3.08 μ_B at 4 K [11].

This type of temperature-dependent magnetic susceptibility change is unusual, and the observed spin-state

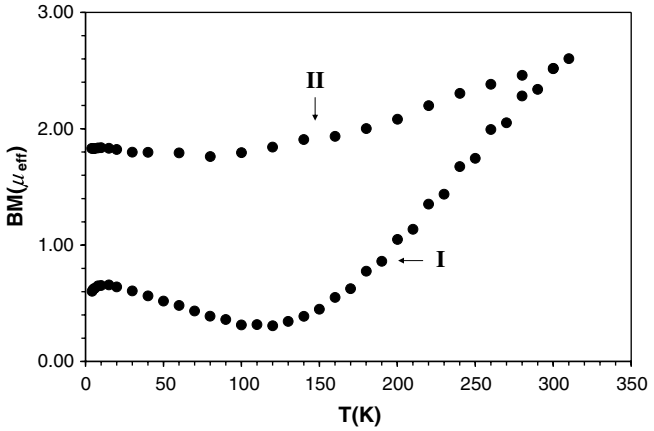


Fig. 8. Molar magnetic susceptibility of $Fe_3tdt_3(PEt_3)_3$ (**I**) and $Co_3tdt_3(PEt_3)_3$ (**II**), plotted μ_{eff} (per trinuclear cluster) versus temperature.

[4] Standard reduction potentials for Fe(III)/Fe(II) and Fe(II)/Fe(0) are 0.77 and −0.44 V, respectively.

transition has three possible explanations, namely spin crossover [31], spin-frustration [32] and degenerate frustration [33]. Thermal spin crossover for the magnetic properties of **I** and **II** can be excluded due to the complicated temperature-dependent magnetic susceptibility changes. Usual thermal spin crossover shows a directional magnetic moment change at a certain temperature. Spin-frustration is a status where geometric constraints of the molecule prevent neighboring spins from adopting a configuration of minimized magnetic energy [34]. But the strict meaning of spin-frustration is a state where the system cannot remain in a single ground state, which does not seem to be the case of the M_3 equilateral triangle complex [33]. Kahn also pointed out that this type of magnetic phenomena occurs whenever the symmetry of the system forces the magnetic ground state to be degenerate and not correspond to any defined spin coupling scheme. Therefore, the more precise terminology for the magnetism would be degenerate frustration. Although some of the clusters with short M–M distances, $(Cl_4\text{-cat})_2Mo_2Fe_3S_5(PEt_3)_5$ and complexes **I** and **II**, have shown the interesting magnetic property of degenerate frustration, there is no physical evidence that such a property is related to the metal–metal bonds.

In summary, we have successfully synthesized and characterized trinuclear $M_3tdt_3(PEt_3)_3$ ($M = Fe^{II}$, Co^{II}) clusters. These clusters show short M–M bonds and the M–M distance differences between **I** and **II** were explained by total valence electron counting arguments. Versatile redox behavior of the $M_3tdt_3(PEt_3)_3$ ($M = Fe^{II}$, Co^{II}) clusters is probably due to the valence unsaturation characteristics of the complexes, which may be relevant to the catalytic mechanism of nitrogenase FeMo-cofactor. The temperature-dependent magnetic susceptibility of these trinuclear clusters were also characterized as a degenerate frustration system, but the strong M–M interactions do not seem to be related to the unusual magnetic properties.

Acknowledgment

This work was supported by the Korean Research Foundation Grant (KRF-2006-331-F00015) funded by the Korean Government (MOEHRD).

Appendix A. Supplementary material

CCDC 629017 and 629018 contain the supplementary crystallographic data for $Fe_3tdt_3(PEt_3)_3$ (**I**) and $Co_3tdt_3(PEt_3)_3$ (**II**), respectively. These data can be obtained free of charge via http://www.ccdc.cam.ac.uk/conts/retrieving.html, or from the Cambridge Crystallographic Data Centre, 12 Union Road, Cambridge CB2 1EZ, UK; fax: (+44) 1223-336-033; or e-mail: deposit@ccdc.cam.ac.uk. Supplementary data associated with this article can be found, in the online version, at doi:10.1016/j.poly.2007.01.052.

References

[1] Y.-U. Kim, J. Han, J. Kor. Soc. Appl. Biol. Chem. 48 (2005) 189.
[2] O. Einsle, F.A. Tezcan, S.L.A. Andrade, B. Schmid, M. Yoshida, J.B. Howard, D.C. Rees, Science 297 (2002) 1696.
[3] (a) U. Huniar, R. Ahlrichs, D. Coucouvanis, J. Am. Chem. Soc. 126 (2004) 2588;
(b) I. Dance, Chem. Commun. (2003) 324;
(c) T. Lovell, T. Liu, D.A. Case, L. Noodleman, J. Am. Chem. Soc. 125 (2003) 8377.
[4] T.-C. Yang, N.K. Maeser, M. Laryukhin, H.-I. Lee, D.R. Dean, L.C. Seefeldt, B.M. Hoffman, J. Am. Chem. Soc. 127 (2005) 12804.
[5] J. Han, D. Coucouvanis, J. Chem. Soc., Dalton Trans. (2005) 1234.
[6] J.W. Peters, W.N. Lanzilotta, B.J. Lemon, L.C. Seefeldt, Science 282 (1998) 1853.
[7] B.J. Lemon, J.W. Peters, Biochemistry 38 (1999) 12969.
[8] Y. Nicolet, C. Piras, P. Legrand, C.E. Hatchikian, J.C. Fontecilla-Camps, Structure 7 (1999) 13.
[9] D. Coucouvanis, J. Han, N. Moon, J. Am. Chem. Soc. 124 (2002) 216.
[10] J. Han, K. Beck, N. Ockwig, D. Coucouvanis, J. Am. Chem. Soc. 121 (1999) 10448.
[11] J. Han, M. Koutmos, S. Al Ahmad, D. Coucouvanis, Inorg. Chem. 40 (2001) 5985.
[12] F. Jiang, X. Xie, M. Hong, B. Kang, R. Cao, D. Wu, H. Liu, J. Chem. Soc., Dalton Trans. (1995) 1447.
[13] H.-R. Gao, T.C.W. Mak, B.-S. Kang, B.-M. Wu, Y.-J. Xu, Y.-X. Tong, X.-L. Yu, J. Chem. Res. S. (1996) 186.
[14] B. Kang, J. Peng, M. Hong, D. Wu, X. Chen, L. Weng, X. Lei, H. Liu, J. Chem. Soc., Dalton Trans. (1991) 2897.
[15] L.N. Mulay, E.A. Boudreaux (Eds.), Theory and Applications of Molecular Paramagnetism, Wiley-Interscience, New York, 1976.
[16] C. Goh, B.M. Segal, J. Huang, J.R. Long, R.H. Holm, J. Am. Chem. Soc. 118 (1996) 11844.
[17] S.C. Lee, R.H. Holm, Chem. Rev. 104 (2004) 1135.
[18] J. Han, D. Coucouvanis, J. Am. Chem. Soc. 123 (2001) 11304.
[19] J. Han, M. Huang, D. Coucouvanis, Polyhedron 21 (2002) 2523.
[20] M. Koutmos, H. Kalyvas, Y. Sanakis, A. Simopoulos, D. Coucouvanis, J. Am. Chem. Soc. 127 (2005) 3706.
[21] J. Chatt, L.A. Duncanson, L.M. Venanzi, J. Chem. Soc. (1955) 4461.
[22] D. Michael, P. Mingos, A.S. May, Structure and bonding aspects of metal cluster chemistry, in: D.F. Shriver, H.D. Kaesz, R.D. Adams (Eds.), Chemistry of Metal Cluster Complexes, VCH, New York, 1990, pp. 11–119 (Chapter 2).
[23] J.W. Lauher, J. Am. Chem. Soc. 100 (1978) 5305.
[24] D. Sellmann, M. Geck, F. Knoch, G. Ritter, J. Dengler, J. Am. Chem. Soc. 113 (1991) 3819.
[25] F.A. Cotton, Chem. Soc. Rev. 4 (1975) 27.
[26] A.R. Pinhas, R. Hoffmann, Inorg. Chem. 18 (1979) 654.
[27] K.B. Musgrave, H.C. Angove, B.K. Burgess, B. Hedman, K.O. Hodgson, J. Am. Chem. Soc. 120 (1998) 5325.
[28] V. Vrajmasu, E. Munck, E.L. Bominaar, Inorg. Chem. 42 (2003) 5974.
[29] W.P. Bosman, H.G.M. Van der Linden, J. Chem. Soc., Chem. Commun. (1977) 714.
[30] (a) V.K. Shah, W.J. Brill, Proc. Natl. Acad. Sci. USA 74 (1977) 3249;
(b) S.-S. Yang, W.-H. Pan, G.D. Friesen, B.K. Burgess, J.L. Corbin, E.I. Stiefel, W.E. Newton, J. Biol. Chem. 257 (1982) 8042.
[31] G. Philipp, H.A. Goodwin (Eds.), Spin Crossover in Transition Metal Compounds II, Springer, Berlin, Heidelberg, 2004.
[32] J. Vannimenous, G. Toulouse, J. Phys. C 10 (1977) L537.
[33] O. Kahn, Chem. Phys. Lett. 265 (1997) 109.
[34] O. Cador, D. Gatteschi, R. Sessoli, A.-L. Barra, G.A. Timco, R.E.P. Winpenny, J. Magn. Magn. Mater. 290–291 (2005) 55.
[35] L.J. Farrugia, J. Appl. Cryst. 30 (1997) 565.
[36] <http://www.expasy.org/spdbv/>.

Available online at www.sciencedirect.com
ScienceDirect
Polyhedron 26 (2007) 2957–2963
POLYHEDRON
www.elsevier.com/locate/poly

New oxorhenium complexes with the 8-quinolinolato ligand: X-ray structure and DFT calculations for $[ReOBr(hqn)_2]$

B. Machura [a,*], R. Kruszynski [b]

[a] Department of Inorganic and Radiation Chemistry, Institute of Chemistry, University of Silesia, 9th Szkolna Street, 40-006 Katowice, Poland
[b] Department of X-ray Crystallography and Crystal Chemistry, Institute of General and Ecological Chemistry, Lodz University of Technology, 116 Żeromski Street, 90-924 Łódź, Poland

Received 19 December 2006; accepted 30 January 2007
Available online 16 February 2007

Abstract

The reactions of $[ReO(OEt)X_2(PPh_3)_2]$ (X = Cl or Br) with 8-hydroxyquinoline (Hhqn) have been examined and the $[ReOX(hqn)_2]$ complexes have been obtained. The crystal and molecular structures of $[ReOBr(hqn)_2]$ have been determined. The electronic structure of $[ReOBr(hqn)_2]$ has been calculated with the density functional theory (DFT) method, and additional information about binding in the ReO^{3+} unit has been obtained by NBO analysis. The spin-allowed electronic transitions of $[ReOBr(hqn)_2]$ have been calculated with the time-dependent DFT method, and the UV–Vis spectra of the $[ReOX(hqn)_2]$ compounds have been discussed on this basis.
© 2007 Elsevier Ltd. All rights reserved.

Keywords: Rhenium oxo complexes; 8-Hydroxyquinoline; X-ray and electronic structure; DFT calculations; NBO analysis

1. Introduction

There is considerable interest in the chemistry of inorganic compounds containing an oxygen atom that is multiply bonded to a transition metal in a high oxidation state. These compounds can transfer an oxygen atom to reductants such as phosphines, sulfides and alkenes. For many years they have been in the centre of interest to those scientists engaged in basic research and to those trying to employ these complexes in catalytic processes. Oxygen atom transfer chemistry has been implicated in various reactions of industrial and biological importance, including olefin epoxidation and catalysis by cytochrome P-450 [1–3].

The chemistry of oxo rhenium complexes arouses particular interest amongst these compounds. It results from the favourable nuclear properties of ^{186}Re and ^{188}Re nuclides, which make the radioisotopes useful for diagnostic nuclear medicine and applications in radioimmunotherapy [4,5].

In this context, the design, synthesis and reactivity of rhenium oxocomplexes has become the aim of several laboratories, including ours.

This work forms part of a program on the synthesis and characterization of new families of oxorhenium compounds with N–donor ligands [6]. Studies on rhenium oxocomplexes incorporating 8-hydroxyquinoline have been relatively rare and this provided us the initial lead for starting an examination of the reactions of $[ReO(OEt)X_2(PPh_3)_2]$ with 8-hydroxyquinoline (Hhqn). Additionally, we were encouraged by recent reports concerning investigations on the reactivity of $[(n\text{-}Bu)_4N][ReOX_4]$ towards 2-(2′-hydroxyphenyl)-2-oxazoline, 2-(2′-hydroxyphenyl)-2-thiazoline and 2-(2′-hydroxyphenyl)-2-benzoxazoline [7].

Here we present the synthesis and spectroscopic data for $[ReOX(hqn)_2]$ complexes (X = Cl or Br). X-ray studies have been performed for $[ReOBr(hqn)_2]$, and the electronic structure of the bromo oxocomplex has been calculated with the density functional theory (DFT) method. The spin-allowed singlet–singlet electronic transitions of $[ReOBr(hqn)_2]$ have been calculated with the time-dependent DFT method (TDDFT method), and the UV–Vis

* Corresponding author.
E-mail addresses: bmachura@poczta.onet.pl (B. Machura), rafal.kruszynski@p.lodz.pl (R. Kruszynski).

0277-5387/$ - see front matter © 2007 Elsevier Ltd. All rights reserved.
doi:10.1016/j.poly.2007.01.055

spectra of the $[ReOX(hqn)_2]$ compounds have been discussed on this basis.

Currently density functional theory (DFT) is commonly used to examine the electronic structure of transition metal complexes. It meets with the requirements of being accurate, easy to use and fast enough to allow the study of relatively large molecules of transition metal complexes [8]. Recent calculations with the TD-DFT method for open- and closed-shell complexes have also supported the TD-DFT method to be applicable for such systems, giving good assignment of experimental spectra [9–11].

Some theoretical investigations have been carried out on rhenium compounds. The electronic structures of nitrido, oxo, carbonyl, nitrosyl and nitrile rhenium complexes, as well as their spectroscopic properties, bonding and reactivity have been theoretically studied at the HF, MP2, EHT and DFT levels of theory using various basis sets [12–21]. Gancheff and co-workers [14] have performed extended tests on the ability of the B3LYP method in LANL2DZ basis set for geometry optimization and the calculation of spectral properties of rhenium compounds. Although this is not a very extended basis set, its use with DFT has shown to be sufficient for the geometry optimization and calculation of spectral properties. It gives good agreement with the experimental data and its use is justified in the case of large molecules.

2. Experimental

2.1. General procedure

All the reagents used in the synthesis were commercially available and were used without further purification. The $[ReO(OEt)X_2(PPh_3)_2]$ complexes were prepared according to the literature methods [22].

IR spectra were recorded on a Nicolet Magna 560 spectrophotometer in the spectral range 4000–400 cm^{-1} with the samples in the form of KBr pellets. Electronic spectra were measured on a spectrophotometer Lab Alliance UV–VIS 8500 in the range 1000–200 nm in dichloromethane solution. Elemental analyses (C H N) were performed on a Perkin–Elmer CHN-2400 analyzer.

2.2. Preparation of $[ReOCl(hqn)_2]$

$[ReO(OEt)Cl_2(PPh_3)_2]$ (0.5 g, 0.57 mmol) was added to 8-hydroxyquinoline (Hhqn) (0.30 g, 2.1 mmol) in ethanol (100 ml) and the reaction mixture was refluxed for 6 h. Sixty milliliters of ethanol was distilled off and 100 ml of diethyl ether was added. This produced a green crystalline precipitate of $[ReOCl(hqn)_2]$ that was collected by filtration. Yield 85%.

IR (KBr): 1608(m), 1594(w), 1573(m) and 1500(s) ν_{CN} and $\nu_{C=C}$; 975(vs) $\nu_{Re=O}$. *Anal.* Calc. for $C_{18}H_{12}ClN_2O_3Re$: C, 41.11; H, 2.30; N, 5.33. Found: C, 41.25; H, 2.28; N, 5.43%.

2.3. Preparation of $[ReOBr(hqn)_2]$

A procedure similar to that for $[ReOCl(hqn)_2]$ was used with $[ReO(OEt)Br_2(PPh_3)_2]$ (0.5 g, 0.5 mmol) and Hhqn (0.30 g, 2.1 mmol). A green crystalline precipitate of $[ReOBr(hqn)_2]$ was collected in 90% yield. Crystals suitable for X-ray structure determination were obtained by slow evaporation from an acetonitrile solution of $[ReOBr(hqn)_2]$.

IR (KBr): 1608(m), 1593(m), 1572(s) and 1500(vs) ν_{CN} and $\nu_{C=C}$; 970(vs) $\nu_{Re=O}$. *Anal.* Calc. for $C_{18}H_{12}BrN_2O_3Re$: C, 37.90; H, 2.12; N, 4.91. Found: C, 37.88; H, 2.25; N, 4.80%.

2.4. Crystal structure determination and refinement

The X-ray intensity data $[ReOBr(hqn)_2]$ were collected on a KM-4-CCD automatic diffractometer equipped with a CCD detector. Twenty-six seconds exposure time was used and all reflections inside the Ewald sphere were collected up to $\theta = 25.1°$. The unit cell parameters were determined from least-squares refinement of the setting angles of 4766 strongest reflections. Details concerning crystal data and refinement are given in Table 1. Lorentz, polarization and numerical absorption corrections [23] were applied. The structure was solved by the Patterson method and subsequently completed by difference Fourier recycling. All the non-hydrogen atoms were refined anisotropically using the

Table 1
Crystal data and structure refinement for the $[ReOBr(hqn)_2]$ complex

Empirical formula	$C_{18}H_{12}BrN_2O_3Re$
Formula weight	570.41
Temperature (K)	291.0(3)
Wavelength (Å)	0.71073
Crystal system	monoclinic
Space group	$P2_1/c$
Unit cell dimensions	
a (Å)	14.7977(13)
b (Å)	11.0046(14)
c (Å)	10.7377(13)
β (°)	106.009(9)
Volume (Å^3)	1680.7(3)
Z	4
Density (calculated) (Mg/m^3)	2.254
Absorption coefficient (mm^{-1})	9.627
$F(000)$	1072
Crystal size (mm)	$0.50 \times 0.38 \times 0.30$
θ Range for data collection (°)	3.31–25.13
Index ranges	$-17 \leqslant h \leqslant 17$, $-12 \leqslant k \leqslant 13$, $-12 \leqslant l \leqslant 12$
Reflections collected	16933
Independent reflections [R_{int}]	2993 [0.0781]
Completeness to 2θ (%)	99.5
Maximum and minimum transmission	0.193 and 0.054
Data/restraints/parameters	2993/0/226
Goodness-of-fit on F^2	1.223
Final R indices [$I > 2\sigma(I)$]	$R_1 = 0.0539$, $wR_2 = 0.1157$
R indices (all data)	$R_1 = 0.0594$, $wR_2 = 0.1185$
Largest difference in peak and hole (e Å^{-3})	1.869 and −2.402

full-matrix, least-squares technique. The hydrogen atoms were treated as "riding" on their parent carbon atoms and assigned isotropic temperature factors equal to 1.2 times the value of the equivalent temperature factor of the parent atom. SHELXS97 [24], SHELXL97 [25] and SHELXTL [26] programs were used for all the calculations. Atomic scattering factors were those incorporated in the computer programs.

3. Computational details

The GAUSSIAN03 program [27] was used in the calculations. The geometry optimisation of the neutral [ReOBr-(hqn)$_2$] complex in a singlet state was carried out with the DFT method with the use of the B3LYP functional [28,29]. The electronic spectrum of [ReOBr(hqn)$_2$] was calculated with the TDDFT method [30]. The calculations were performed using the ECP basis set on the rhenium atom, and the standard 6-31G basis set for other atoms. For bromine, oxygen, nitrogen and carbon atoms, diffuse and polarization functions were added [31,32]. The Xe core electrons of Re were replaced by an effective core potential and a DZ quality Hay and Wadt Los Alamos ECP basis set (LANL2DZ) [33] was used for the valence electrons. An additional *d* function with exponent $\alpha = 0.3811$ and *f* function with exponent $\alpha = 2.033$ on the rhenium atom were added [34].

Natural bond orbital (NBO) calculations were performed with the NBO code [35,36] included in GAUSSIAN03.

4. Results and discussion

4.1. Preparation and infrared data

The [ReOX(hqn)$_2$] complexes were prepared by refluxing [ReO(OEt)X$_2$(PPh$_3$)$_2$] with a large excess of 8-hydroxyquinoline in ethanol. They were isolated as air-stable, microcrystalline solids, soluble in common organic solvents.

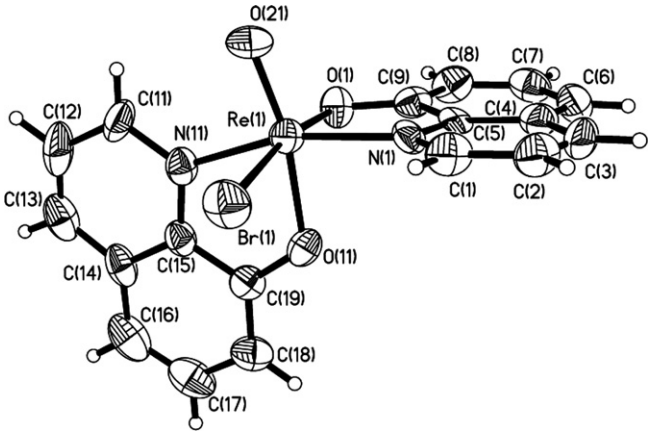


Fig. 1. The molecular structure of [ReOBr(hqn)$_2$].

The strong ν(Re=O) stretching bands at 970–975 cm^{-1} are in the higher end of the range observed for $\{ReO\}^{3+}$ core complexes. This suggests that the Re–hydroxy bond *trans* to the oxo ligand does not compete effectively for the d_{Re} orbitals and the bond is relatively weak. Moreover, the range in which the ν(Re=O) bands appear is very similar to those observed for [ReOXL$_2$] complexes with 2-(2′-hydroxyphenyl)-2-oxazoline, 2-(2′-hydroxyphenyl)-2-thiazoline and 2-(2′-hydroxyphenyl)-2-benzoxazoline [7].

4.2. Crystal structure

The crystallographic data for [ReOBr(hqn)$_2$] are given in Table 1, and the molecular structure of the complex is presented in Fig. 1. The complex crystallizes in a distorted octahedral configuration with two bidentate ligands, one halide ion and a terminal oxo (O$_t$) ligand about the metal center. The rhenium atom is displaced 0.259(4) Å from the equatorial plane formed by the two nitrogens, one oxygen and one bromide atom (plane A) and 0.079(3) and 0.0404(4) Å from the axial planes formed respectively by the three oxygen, one bromide atom (plane B) and two nitrogens and two oxygen atoms (plane C). The least

Table 2
The experimental and optimized bond lengths (Å) and angles (°) for [ReOBr(hqn)$_2$]

Bond lengths	Experimental	Optimized	Bond angles	Experimental	Optimized
Re(1)–O(1)	2.029(7)	2.037	O(21)–Re(1)–O(11)	167.5(3)	163.79
Re(1)–O(11)	2.014(7)	2.027	O(21)–Re(1)–O(1)	98.3(3)	98.04
Re(1)–O(21)	1.700(7)	1.682	O(11)–Re(1)–O(1)	84.8(3)	83.36
Re(1)–N(1)	2.078(8)	2.113	O(21)–Re(1)–N(1)	106.0(4)	105.56
Re(1)–N(11)	2.120(8)	2.160	O(11)–Re(1)–N(1)	86.4(3)	90.60
Re(1)–Br(1)	2.5643(12)	2.626	O(1)–Re(1)–N(1)	80.1(3)	79.47
			O(21)–Re(1)–N(11)	91.8(4)	88.40
			O(11)–Re(1)–N(11)	75.9(3)	75.39
			O(1)–Re(1)–N(11)	91.8(3)	93.51
			N(1)–Re(1)–N(11)	161.2(3)	165.04
			O(21)–Re(1)–Br(1)	91.9(3)	94.54
			O(11)–Re(1)–Br(1)	85.5(2)	85.19
			O(1)–Re(1)–Br(1)	169.8(2)	167.21
			N(1)–Re(1)–Br(1)	96.0(2)	94.99
			N(11)–Re(1)–Br(1)	89.1(2)	89.09

Table 3
Atomic charges from the natural population analysis (NPA) for $[ReOBr(hqn)_2]$

Atom	Charge
Re(1)	1.479
O(1)	−0.688
O(11)	−0.686
O(21)	−0.465
N(1)	−0.502
N(11)	−0.469
Br1(1)	−0.592

squares plane A is inclined at 89.77(19)° to plane B and at 88.47(18)° to plane C. The planes B and C are inclined at 85.60(17)°. The oxyquinoline ring systems can be considered as planar (maximum deviating atoms C(8) and C(13) are displaced 0.044(7) and 0.036(9) Å from their respective least squares planes) and are inclined at 85.24(17)°. The two bound nitrogens are coordinated *trans* to one another, while the bromide is *trans* to the equatorial coordinated oxygen. Clear distortions of the pseudooctahedral environment of the Re center in $[ReOBr(hqn)_2]$ is induced by the multiple bonding ligand (oxo) and narrow bite angle of the chelating ligands. Selected bond lengths and angles of $[ReOBr(hqn)_2]$ are given in Table 2. The Re–O_t bond length falls in the range 1.639–1.76Å, which is typical of mononuclear complexes of rhenium(V) having a $[ReO]^{3+}$ core, and indicates the presence of a triple Re≡O bond [37]. The interatomic distance between the rhenium atom

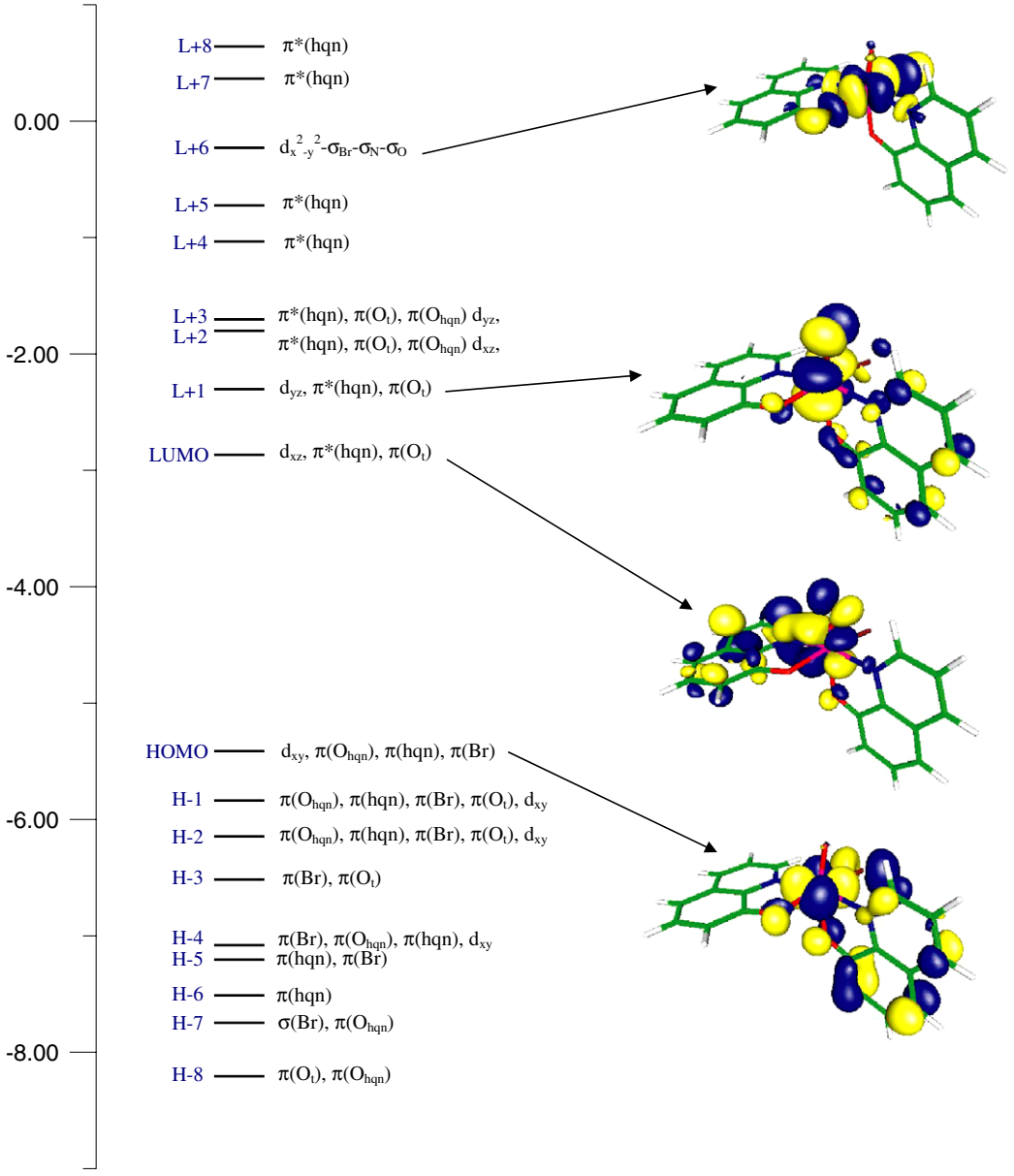


Fig. 2. The energy (eV), character and some contours of the occupied molecular orbitals of $[ReOBr(hqn)_2]$. Positive values of the orbital contours are represented in yellow (0.04 a.u.) and negative values – in blue (−0.04 a.u.). (For interpretation of the references to colour in this figure legend, the reader is referred to the web version of this article.)

and the oxygen atom of hqn in the *trans* position to the terminal oxo ion, is somewhat longer than the Re(1)–O(1) bond length. It indicates a small delocalization in the O(21)–Re(1)–O(1) moiety, and a similar trend is observed for many Re(V)–oxo complexes with a monoanionic oxygen *trans* to the oxo group [7].

4.3. Geometry optimisation, charge distribution, electronic structure and NBO analysis

The geometry of $[ReOBr(hqn)_2]$ was optimised in a singlet state by the DFT method with the B3LYP functional. The optimized geometric parameters of $[ReOBr(hqn)_2]$ are gathered in Table 2. In general, the predicted bond lengths and angles are in agreement with the values based upon the X-ray crystal structure data, and the general trends observed in the experimental data are well reproduced in the calculations. Plane A is inclined at 89.79° to plane B and at 89.32° to plane C, and planes B and C are inclined at 85.63°. The oxyquinoline ring systems are planar and they are inclined at 85.44°.

Table 3 presents the atomic charges from the natural population analysis (NPA) for $[ReOBr(hqn)_2]$. The calculated charge on the rhenium atom in $[ReOBr(hqn)_2]$ is considerable lower than the formal charge of +5. It indicates significant charge donation from the ligands. The charges on the terminal oxo, oxo atoms of hqn^- and the bromide are significantly smaller than −2, −1 and −1, respectively.

The $[ReOBr(hqn)_2]$ complex is a closed-shell structure. Its molecular orbital diagram with several highest HOMO and lowest LUMO contours is presented in Fig. 2. The HOMO–LUMO gap equals 2.55 eV. The highest occupied MO of $[ReOBr(hqn)_2]$ is of d_{xy} type with some contributions from p_π bromide and hqn^- orbitals. The remaining four d-type orbitals of rhenium are found among unoccuppied MOs. It confirms the d^2 configuration of the rhenium atom.

The rhenium atom uses its six valence orbitals, $5d_{x^2-y^2}$, $5d_z^2$, 6s, $6p_x$, $6p_y$ and $6p_z$ to form σ-bonds with the six ligands, empty $5d_{xz}$ and $5d_{yz}$ orbitals are available to overlap with $2p_x$ and $2p_y$ orbitals on the terminal oxygen to form an effective triple bond. The participation of the π^*_{Re-O} interaction is visible in the LUMO, LUMO + 1, LUMO + 2 and LUMO + 3 orbitals.

The presence of a triple rhenium-terminal oxygen bond confirms the NBO analysis. The occupancy and composition of the calculated $Re–O_t$ natural bond orbitals (NBOs) are given in Table 4. The detected natural $Re–O_t$ bond orbitals of $[ReOBr(hqn)_2]$ are orbitals of π character – the p_x and p_y oxygen orbitals and d_{xz} and d_{yz} rhenium orbitals are involved in their formation. The not detected σ_{Re-O_t} bond has character of predominantly Coulomb-type interaction between the central ion and ligand [38]. Similarly, the Re–O(11), Re–O(21), Re–N(1), Re–N(11) and Re–Br(1) bonds have predominant ionic character, they all were not detected in the NBO analysis.

4.4. Electronic spectra

The experimental and calculated electronic spectra of $[ReOBr(hqn)_2]$ are presented in Fig. 3. Each calculated transition is represented by a gaussian function $y = ce^{-bx^2}$ with the height (c) equal to the oscillator strength and b equal to 0.04 nm^{-2}. The shape of the UV–Vis spectrum of $[ReOCl(hqn)_2]$ is the same as for the bromo analogue; the absorption bands of the chloro complex were recorded at 870.8, 724.0, 406.2 and 255.0 nm.

The spin-allowed singlet–singlet electronic transitions calculated with the TDDFT method for $[ReOBr(hqn)_2]$ are gathered in Table 5. For the high energy part of the spectrum, only transitions with oscillator strengths larger than 0.020 are listed in Table 5.

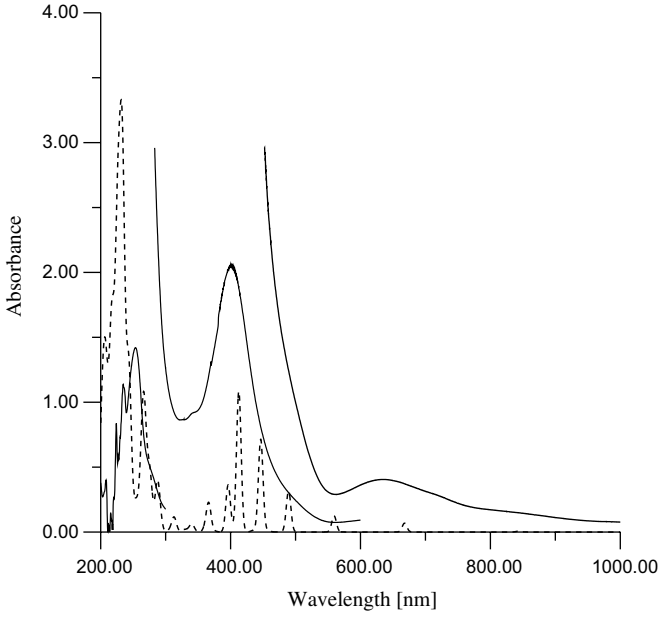


Fig. 3. The experimental electronic absorption spectrum of $[ReOBr(hqn)_2]$.

Table 4
The occupancies and composition of the calculated natural bond orbitals (NBOs) between the rhenium and the oxo ligands for $[ReOBr(hqn)_2]$

BD	Occupancy	BD	BD[a]	Occupancy
$Re–O_t$	1.995	$0.557(d)_{Re} + 0.831(p)_O$	$0.831(d)_{Re} - 0.557(p)_O$	0.317
$Re–O_t$	1.991	$0.571(d)_{Re} + 0.821(p)_O$	$0.821(d)_{Re} - 0.571(p)_O$	0.203

BD denotes 2-center bond.
[a] Denotes antibond NBO.

Table 5
The energy and molar absorption coefficients of experimental absorption bands and the electronic transitions calculated with the TDDFT method for [ReOBr(hqn)$_2$]

The most important orbital excitations	Character	λ (nm)	E (eV)	f	Experimental Λ (nm) (E (eV))ε
H → L	d → d	843.4	1.47	*0.0006*	865.4 (1.43) 70
H → L + 1	d → d	668.0	1.86	*0.0068*	639.0 (1.94) 220
H − 1 → L	π(hqn)/π(Br)/d → d	559.5	2.22	*0.0124*	
H − 2 → L	π(hqn)/π(Br)/π(O)/d → d	489.2	2.53	*0.0317*	
H − 1 → L + 1	π(hqn)/π(Br)/d → d	446.4	2.78	*0.0714*	414.4 (2.99) 5050
H → L + 2	d → π*(hqn)	412.6	3.00	*0.1084*	
H − 2 → L + 1	π(hqn)/π(Br)/π(O)/d → d	396.2	3.13	*0.0363*	
H − 3 → L + 1	π(Br)/π(O) → d	366.2	3.39	*0.0215*	
H − 1 → L + 4	π(hqn)/π(Br)/d → π*(hqn)	287.0	4.32	*0.0333*	
H − 4 → L + 2	π(Br)/π(hqn)/d → π*(hqn)	267.8	4.63	*0.0552*	
H − 4 → L + 3					
H − 6 → L + 1	π(hqn) → d	264.7	4.68	*0.0492*	
H − 2 → L + 4	π(hqn)/π(Br)/π(O)/d → π*(hqn)				
H → L + 7	d → π*(hqn)	243.9	5.08	*0.0265*	
H − 3 → L + 5	π(Br)/π(O) → π*(hqn)	243.3	5.10	*0.0765*	
H − 6 → L + 2	π(hqn) → π*(hqn)	235.1	5.27	*0.0371*	
H − 3 → L + 6	π(Br)/π(O) → d	234.5	5.29	*0.0236*	
H − 6 → L + 3	π(hqn) → π*(hqn)	233.5	5.31	*0.0602*	
H − 9 → L + 1	π(hqn)/π(Br)/π(O)/d → d	232.0	5.34	*0.1281*	
H − 6 → L + 3	π(hqn) → π*(hqn)				
H − 12 → L	n(hqn) → d	228.9	5.42	*0.0383*	253.6 (4.89) 28100
H − 12 → L	n(hqn) → d	226.1	5.48	*0.1118*	
H → L + 8	d → π*(hqn)				
H − 10 → L + 1	π(hqn)/π(O) → d	224.4	5.52	*0.0656*	
H − 1 → L + 7	π(hqn)/π(Br)/d → π*(hqn)	219.3	5.65	*0.0395*	
H − 4 → L + 6	π(Br)/π(hqn)/d → π*(hqn)	216.8	5.72	*0.0271*	
H − 5 → L + 4	π(hqn)/π(Br) → π*(hqn)	216.2	5.73	*0.0515*	
H − 5 → L + 4	π(hqn)/π(Br) → π*(hqn)	215.9	5.74	*0.0215*	
H − 13 → L	π(hqn)/π(Br) → d	207.4	5.98	*0.0412*	

ε, molar absorption coefficient (dm^3 mol^{-1} cm^{-1}]; f, oscillator strength; H, highest occupied molecular orbital; L, lowest unoccupied molecular orbital.

The two longest wavelength experimental bands of [ReOBr(hqn)$_2$] at 843.4 and 668.0 nm are attributed to the transitions of d → d character with small oscillator strengths calculated at 865.4 and 639.0 nm, respectively. In comparison with the bromo analogue, the ligand field (LF) absorption bands of [ReOCl(hqn)$_2$] are red shifted. This can indicate a slight decrease of the HOMO–LUMO energy gap for the chloro complex.

The broad and intense absorption band with a maximum at 414.4 nm is assigned to the *metal–ligand charge transfer* (occurring from the rhenium ion to the π-antibonding orbitals of the hqn ligands) and *ligand–metal charge transfer* ($\pi_{hqn}/\pi_{Br}/\pi_O \rightarrow$ d) transitions. For the chloro analogue, the band is slightly shifted to the higher energy range.

The experimental band at 253.6 nm results from *ligand-metal charge transfer* ($\pi_{hqn}/\pi_{Br}/\pi_O \rightarrow$ d), *ligand–ligand charge transfer* and interligand (IL) transitions. For the chloro complex, the band is observed at 255.0 nm.

5. Supplementary material

CCDC 631275 contains the supplementary crystallographic data for $C_{18}H_{12}BrN_2O_3Re$. These data can be obtained free of charge via http://www.ccdc.cam.ac.uk/conts/retrieving.html, or from the Cambridge Crystallographic Data Centre, 12 Union Road, Cambridge CB2 1EZ, UK; fax: (+44) 1223-336-033; or e-mail: deposit@ccdc.cam.ac.uk.

Acknowledgements

The GAUSSIAN03 calculations were carried out in the Wrocław Centre for Networking and Supercomputing, WCSS, Wrocław, Poland.

The crystallographic part was financed by funds allocated by the Ministry Science and Higher Education to the Institute of General and Ecological Chemistry, Technical University of Łódź.

References

[1] R.H. Holm, Chem. Rev. 87 (1987) 1401.
[2] C.C. Romão, F.E. Kühn, W.A. Hermann, Chem. Rev. 97 (1997) 3197.
[3] S.B. Seymore, S.N. Brown, Inorg. Chem. 39 (2000) 325.
[4] W. Volkert, W.F. Goeckeler, G.J. Ehrhardt, A.R. Ketring, J. Nucl. Med. 32 (1991) 174.
[5] E.A. Deutsch, K. Libson, J.L. Vanderheyden, Technetium and Rhenium in Chemistry and Nuclear Medicine, Raven Press, New York, 1990.
[6] B. Machura, Coord. Chem. Rev. 249 (2005) 591.

[7] E. Shuter, H.R. Hoveyda, V. Karunaratne, S.J. Retting, C. Orvig, Inorg. Chem. 35 (1996) 368.
[8] H. Chermette, Coord. Chem. Rev. 178–180 (1998) 699.
[9] M.C. Aragoni, M. Arca, T. Cassano, C. Denotti, F.A. Devillanova, F. Isaia, V. Lippolis, D. Natali, L. Niti, M. Sampietro, R. Tommasi, G. Verani, Inorg. Chem. Commun. 5 (2002) 869.
[10] P. Romaniello, F. Lelj, Chem. Phys. Lett. 372 (2003) 51.
[11] P. Norman, P. Cronstrand, J. Ericsson. Chem. Phys. 285 (2002) 207.
[12] A. Voigt, U. Abram, R. Böttcher, U. Richter, J. Reinhold, R. Kirmse, Chem. Phys. 253 (2000) 171.
[13] M. Lipowska, L. Hansen, R. Cini, X. Xu, H. Choi, A.T. Taylor, L.G. Marzilli, Inorg. Chim. Acta 339 (2002) 327.
[14] J. Gancheff, C. Kremer, E. Kremer, O.N. Ventura, J. Mol. Struct. (Theochem) 580 (2002) 107.
[15] M.L. Kuznestov, E.A. Klestova-Nadeeva, A.I. Dement'ev, J. Mol. Struct. (Theochem) 671 (2004) 229.
[16] N. Psaroudakis, K. Mertis, D.G. Liakos, E.D. Simandiras, Chem. Phys. Lett. 369 (2003) 490.
[17] X.-Y. Liu, S. Bouherour, H. Jacobsen, H.W. Schmalle, H. Berke, Inorg. Chim. Acta 330 (2002) 250.
[18] É. Bencze, J. Mink, I. Pápai, I.S. Butler, D. Lafleur, D.F.R. Gilson, J. Organomet. Chem. 616 (2000) 1.
[19] W.-Y. Wong, S.-H. Cheung, X. Huang, Z. Lin, J. Organomet. Chem. 655 (2002) 39.
[20] B. Machura, R. Kruszynski, M. Jaworska, Polyhedron 25 (2006) 1111.
[21] B. Machura, R. Kruszynski, Polyhedron 25 (2006) 1985.
[22] G. Rouschias, G. Wilkinson, J. Chem. Soc. A (1966) 465.
[23] STOE & Cie, X-RED. Version 1.18. STOE & Cie GmbH, Darmstadt, Germany, 1999.
[24] G.M. Sheldrick, Acta Crystallogr., Sect. A 46 (1990) 467.
[25] G.M. Sheldrick, SHELXL97, Program for the Solution and Refinement of Crystal Structures, University of Göttingen, Germany, 1997.
[26] G.M. Sheldrick, SHELXTL: Release 4.1 for Siemens Crystallographic Research Systems, 1990.
[27] M.J. Frisch, G.W. Trucks, H.B. Schlegel, G.E. Scuseria, M.A. Robb, J.R. Cheeseman, J.A. Montgomery Jr., T. Vreven, K.N. Kudin, J.C. Burant, J.M. Millam, S.S. Iyengar, J. Tomasi, V. Barone, B. Mennucci, M. Cossi, G. Scalmani, N. Rega, G.A. Petersson, H. Nakatsuji, M. Hada, M. Ehara, K. Toyota, R. Fukuda, J. Hasegawa, M. Ishida, T. Nakajima, Y. Honda, O. Kitao, H. Nakai, M. Klene, X. Li, J.E. Knox, H.P. Hratchian, J.B. Cross, C. Adamo, J. Jaramillo, R. Gomperts, R.E. Stratmann, O. Yazyev, A.J. Austin, R. Cammi, C. Pomelli, J.W. Ochterski, P.Y. Ayala, K. Morokuma, G.A. Voth, P. Salvador, J.J. Dannenberg, V.G. Zakrzewski, S. Dapprich, A.D. Daniels, M.C. Strain, O. Farkas, D.K. Malick, A.D. Rabuck, K. Raghavachari, J.B. Foresman, J.V. Ortiz, Q. Cui, A.G. Baboul, S. Clifford, J. Cioslowski, B.B. Stefanov, G. Liu, A. Liashenko, P. Piskorz, I. Komaromi, R.L. Martin, D.J. Fox, T. Keith, M.A. Al-Laham, C.Y. Peng, A. Nanayakkara, M. Challacombe, P.M.W. Gill, B. Johnson, W. Chen, M.W. Wong, C. Gonzalez, J.A. Pople, Gaussian 03 Revision B.03, Gaussian, Inc., Pittsburgh PA, 2003.
[28] A.D. Becke, J. Chem. Phys. 98 (1993) 5648.
[29] C. Lee, W. Yang, R.G. Parr, Phys. Rev. B 37 (1988) 785.
[30] M.E. Casida, in: J.M. Seminario (Ed.), Recent Developments and Applications in Modern Density Functional Theory, Theoretical and Computational Chemistry, vol. 4, Elsevier, Amsterdam, 1996.
[31] P.C. Hariharan, J.A. Pople, Theo. Chim. Acta 28 (1973) 213.
[32] V.A. Rassolov, M.A. Ratner, J.A. Pople, P.C. Redfern, L.A. Curtiss, J. Comp. Chem. 22 (2001) 976.
[33] P.J. Hay, W.R. Wadt, J. Chem. Phys. 82 (1985) 299.
[34] K. Eichkorn, F. Weigend, O. Treutler, R. Ahlrichs, Theor. Chem. Acc. 97 (1997) 119.
[35] E.D. Glendening, A.E. Reed, J.E. Carpenter, F. Weinhold, NBO (Version 3.1).
[36] A.E. Reed, L.A. Curtiss, F. Weinhold, Chem. Rev. 88 (1988) 899.
[37] J.M. Mayer, Inorg. Chem. 27 (1988) 3899.
[38] M.L. Kuznetsov, A.J.L. Pombeiro, J. Chem. Soc., Dalton Trans. (2003) 738.

Available online at www.sciencedirect.com
ScienceDirect
Polyhedron 26 (2007) 2964–2970
POLYHEDRON
www.elsevier.com/locate/poly

The structure of mimetite, arsenian pyromorphite and hedyphane – A Raman spectroscopic study

Ray L. Frost *, Jocelyne M. Bouzaid, Sara Palmer

Inorganic Materials Research Program, School of Physical and Chemical Sciences, Queensland University of Technology, GPO Box 2434, Brisbane, Qld 4001, Australia

Received 4 January 2007; accepted 31 January 2007
Available online 4 February 2007

Abstract

The minerals mimetite $Pb_5(AsO_4)_3Cl$, arsenian pyromorphite $Pb_5(PO_4,AsO_4)_3Cl$ and hedyphane $Pb_3Ca_2(AsO_4)_3Cl$ have been studied by Raman spectroscopy complimented with infrared spectroscopy. Mimetite is characterised by a band at 812–3 cm^{-1} attributed to the A_g mode. For the arsenian pyromorphite this band is observed at 818 cm^{-1} and for hedyphane at 819 cm^{-1}. For mimetite and hedyphane bands at 788 and 765 cm^{-1} are attributed to A_u and E_{1u} vibrational modes and are both Raman and infrared active. For the arsenian pyromorphite, Raman bands at 917–1014 cm^{-1} are attributed to phosphate stretching vibrations. Raman spectroscopy clearly identifies bands attributable to isomorphous substitution of arsenate by phosphate. The observation of low intensity bands in the 3200–3550 cm^{-1} region are assigned to adsorbed water and OH units, thus indicating some replacement of chloride ions with hydroxyl ions.
© 2007 Elsevier Ltd. All rights reserved.

Keywords: Arsenate; Mimetite; Hedyphane; Arsenian pyromorphite; Phosphate; Isomorphous substitution; Raman spectroscopy

1. Introduction

Mimetite lead chloroarsenate $Pb_5(AsO_4)_3Cl$ was named in 1835 from the Greek *mimethes*, meaning "imitator" because of its resemblance to pyromorphite $Pb_5(PO_4)_3Cl$. Mimetite is a secondary mineral of lead formed through mineralisation of the ore bodies. It is formed by the oxidation of galena and arsenopyrite. The mineral consists of small hexagonal crystals with colours ranging from pale yellow to yellowish-brown to orangish-yellow to orangish-red, white and colourless. Studies of the mimetite–pyromorphite series have been undertaken for nearly 100 years [1–3]. Mimetite has an apatite structure and forms solid solutions with pyromorphite and vanadinite [4–6]. Most crystals of mimetite–pyromorphite system are chemically zoned. Recently, the chemical variability in hedyphane was also reported in the journal American Mineralogist [7]. Although the crystal system of mimetite is known as a hexagonal (space group $P63/m$), mimetite has a dimorphic relationship with clinomimetite [8], which is a monoclinic system (space group $P2_1/m$). The phase transition between hexagonal system and monoclinic system shifts O(3) atom position in the crystal structure of mimetite [9,10].

Early investigations of the vibrational spectra of apatites including vanadinite were limited to mid-IR studies. Some early Raman studies of calcium apatites led to some questionable interpretations. Much work has been undertaken on the apatite-type minerals including mimetite, pyromorphite and vanadinite, containing the V group elements, namely As, P and V. In the apatite structure, isomorphous substitution can occur with replacement of F^- by Cl^- and also by OH groups, as in the case for selected mimetites and pyromorphites. The As(V) is replaceable by P(V) or V(V) and the Pb(II) is replaceable by for example Ca(II). Ross reported the infrared and Raman spectra of the free AsO_4^{3-} ion [11]. The v_1 band was observed at 810 cm^{-1}; v_2 at 342 cm^{-1}; v_3 at 810 cm^{-1} and v_4 at 398 cm^{-1}. Ross also reported the v_3 modes of vanadinites at 800 and

* Corresponding author. Tel.: +61 7 3864 2407; fax: +61 7 3864 1804.
E-mail address: r.frost@qut.edu.au (R.L. Frost).

0277-5387/$ - see front matter © 2007 Elsevier Ltd. All rights reserved.
doi:10.1016/j.poly.2007.01.038

Table 1
Table of the minerals, their origin and formula

Code	Mineral	Formula	Origin
Mime 1	Mimetite	$Pb_5(AsO_4)_3Cl$	Tsumeb, Namibia
Mime 2	Mimetite	$Pb_5(AsO_4)_3Cl$	Geronimo Mine, Yuma Co., Arizona, USA
Mime 3	Mimetite	$Pb_5(AsO_4)_3Cl$	Mount Bonnie Mine, NT
Pyro 8	Arsenian pyromorphite	$Pb_5(PO_4,AsO_4)_3Cl$	Bunker Hill Mine, Kellogg, Idaho, USA
Hedy 1	Hedyphane	$Pb_3Ca_2(AsO_4)_3Cl$	Puttapa Mine, Beltana, SA

736 cm^{-1} and the v_4 modes around 419, 380 and 322 cm^{-1}. In the work mentioned by Ross the position of the v_1 and v_2 vibrations were not reported. Gadsdsen also reported the infrared spectrum of the mimetite [12]. The v_3 mode is reported as lying between 700 to 900 cm^{-1} and the v_4 mode between 300 and 410 cm^{-1}. The v_1 mode, which was not observed in the infrared spectrum as the vibration is inactive, was suggested to be at around 870 cm^{-1}. Griffith reported the Raman spectra of mimetite [13]. Levitt and Condrate reported the infrared and Raman spectra of lead apatite powdered minerals [6]. They reported the v_2 bands for mimetites at 341 and 314 cm^{-1} [6,14–16]. Single crystal Raman spectra of a mimetite at 298 K have been reported [17]. Some arsenates as for sulphates have their symmetry reduced through acting as monodentate and bidentate ligands. In the case of bidentate behaviour both bridging and chelating ligands are known. This reduction in symmetry is observed by the splitting of the v_3 and v_4 in infrared spectra into two components under C_{3v} symmetry and into three components under C_{2v} symmetry. Single crystal spectra of mimetite were reported [18]. In this paper, the v_1 band for mimetite was observed at 816 cm^{-1}, the v_3 at 809 and 787 cm^{-1}, the v_2 at 414, 390 and 335 cm^{-1} and v_4 at 424, 373 and 314 cm^{-1}.

In this work we have obtained Raman and infrared spectra of selected mimetites, arsenian pyromorphite and hedyphane and related the spectra to the structure of the minerals.

2. Experimental

2.1. Minerals

The minerals used in this work, their formula and origin are listed in Table 1. The composition of the minerals was checked by X-ray diffraction and the chemical composition by EDX measurements.

Table 2
EDX analyses of the mimetites

Sample	Spectrum	O*	Al	S	Cl	As	Pb	Mo
Mimetite Pb5(AsO4)3.Cl	*Predicted from formula*	*12.90*			*2.38*	*15.10*	*69.61*	
Wulfenite Pb(MoO4)	*Predicted from formula*	*17.43*					*56.44*	*26.13*
Lead oxide (PbO)	*Predicted from formula*	*7.17*					*92.83*	
Sample 1	Mimetite1	15.36	1.36	0.00	2.32	14.64	66.32	
	Mimetite1b	13.77	0.63	0.00	2.61	14.84	68.14	
	Mimetite1c	12.12	0.96	0.00	2.85	12.78	71.29	
	Average	13.75	0.98	0.00	2.59	14.09	68.58	
	Conversion to At%	0.86	0.04	0.00	0.07	0.19	0.33	
	Divided by At% of Pb	2.60	0.11	0.00	0.22	0.57	1.00	
	Multiply by 5 → Atomic ratios relative to Pb	**12.98**	**0.55**	**0.00**	**1.11**	**2.84**	**5.00**	
Sample 2	Mimetite2	8.74	0.68	1.84	0.00	0.20	67.18	21.36
	Mimetite2b	12.55	0.57	1.16	0.00	0.20	63.81	21.71
	Mimetite2c	12.66	0.56	0.18	0.00	0.48	62.69	23.44
	Average	11.32	0.60	1.06	0.00	0.29	64.56	22.17
	Conversion to At%	0.71	0.02	0.03	0.00	0.004	0.31	0.23
	Divided by At% of Pb	2.27	0.07	0.11	0.00	0.01	1.00	0.74
	Multiply by 5 → Atomic ratios relative to Pb	**11.35**	**0.36**	**0.53**	**0.00**	**0.06**	**5.00**	**3.71**
Sample 3	Mimetite3	6.12	0.68	0.00	2.30	15.20	75.70	0.00
	Mimetite3b	6.27	0.86	0.00	2.53	10.63	79.71	0.00
	Mimetite3black	7.48	10.94	0.00	2.05	10.91	68.62	0.00
	Average	6.62	4.16	0.00	2.29	12.25	74.68	0.00
	Conversion to At%	0.41	0.15	0.00	0.06	0.16	0.36	0.00
	Divided by At% of Pb	1.15	0.43	0.00	0.18	0.45	1.00	0.00
	Multiply by 5 → Atomic ratios relative to Pb	**5.74**	**2.14**	**0.00**	**0.90**	**2.27**	**5.00**	**0.00**

Sample 2 appears to contain some wulfenite and possibly some oxide, very low in mimetite (Arsenic low).
Sample 3 especially mimetite3b may be a mixture of mimetite and oxide (Again arsenic low, and lead higher).
Sample called mimetite3black is unusually high in Al.

2.2. Raman spectroscopy

The crystals of mimetite were placed and oriented on the stage of an Olympus BHSM microscope, equipped with 10× and 50× objectives and part of a Renishaw 1000 Raman microscope system, which also includes a monochromator, a filter system and a Charge Coupled Device (CCD). Raman spectra were excited by a HeNe laser (633 nm) at a resolution of 2 cm^{-1} in the range between 100 and 4000 cm^{-1}. Repeated acquisition using the highest magnification was accumulated to improve the signal to noise ratio. Spectra were calibrated using the 520.5 cm^{-1} line of a silicon wafer. In order to ensure that the correct spectra are obtained, the incident excitation radiation was scrambled. Raman spectra of mimetite and related arsenate minerals have been collected using a very low powered HeNe laser as the excitation radiation. The beam was slightly defocused to prevent the destruction of the samples due to self-absorption of the incident beam and consequential damage to the mineral.

Previous studies by the authors provide more details of the experimental technique. Spectra at liquid nitrogen temperature were obtained using a Linkam thermal stage (Scientific Instruments Ltd., Waterfield, Surrey, England). Details of the technique have been published by the authors [19–22].

2.3. Mid-IR spectroscopy

Infrared spectra were obtained using a Nicolet Nexus 870 FTIR spectrometer with a smart endurance single bounce diamond ATR cell. Spectra over the 4000–525 cm^{-1} range were obtained by the co-addition of 64 scans with a resolution of 4 cm^{-1} and a mirror velocity of 0.6329 cm/s. Spectra were co-added to improve the signal to noise ratio.

Spectral manipulation such as baseline adjustment, smoothing and normalisation were performed using the Spectracalc software package GRAMS (Galactic Industries Corporation, NH, USA). Band component analysis was undertaken using the Jandel 'Peakfit' software package which enabled the type of fitting function to be selected and allows specific parameters to be fixed or varied accordingly. Band fitting was done using a Lorentz–Gauss cross-product function with the minimum number of component bands used for the fitting process. The Gauss–Lorentz ratio was maintained at values greater than 0.7 and fitting was undertaken until reproducible results were obtained with squared correlations of r^2 greater than 0.995.

3. Results and discussion

3.1. EDX analyses

The predicted molecular masses of mimetite, wulfenite and lead oxide are given in Table 2. A comparison of the average of three measurements is shown. Sample 1 seems to have an analysis close to mimetite. Sample 2 is not pure and may contain some wulfenite. Sample 3 is apparently a mixture of mimetite and lead oxide.

The XRD patterns of the mimetite show that the mimetite is hexagonal, and as the phosphate increased the structure changed to monoclinic. Most crystals in the mimetite, pyromorphite series are dimorphic and the crystals show zoning.

4. Raman spectroscopy

4.1. High wavenumber region

The Raman spectra of selected mimetites and hedyphane in the 700–1050 cm^{-1} region are shown in Fig. 1. The results of the band component analysis of the Raman spectra are reported in Table 3. The Raman spectra of mimetites 1 and 3 show a strong band at 812–3 cm^{-1}. The band is attributed to the A_g mode of mimetite. For the arsenian pyromorphite the band is observed at 818 cm^{-1} and for hedyphane at 819 cm^{-1}. The mode was assigned by Adams and Gardner to both the A_g and E_{2g} modes [17]. The spectrum of mimetite 2 is not that of mimetite but a mixture of minerals. It is probably related

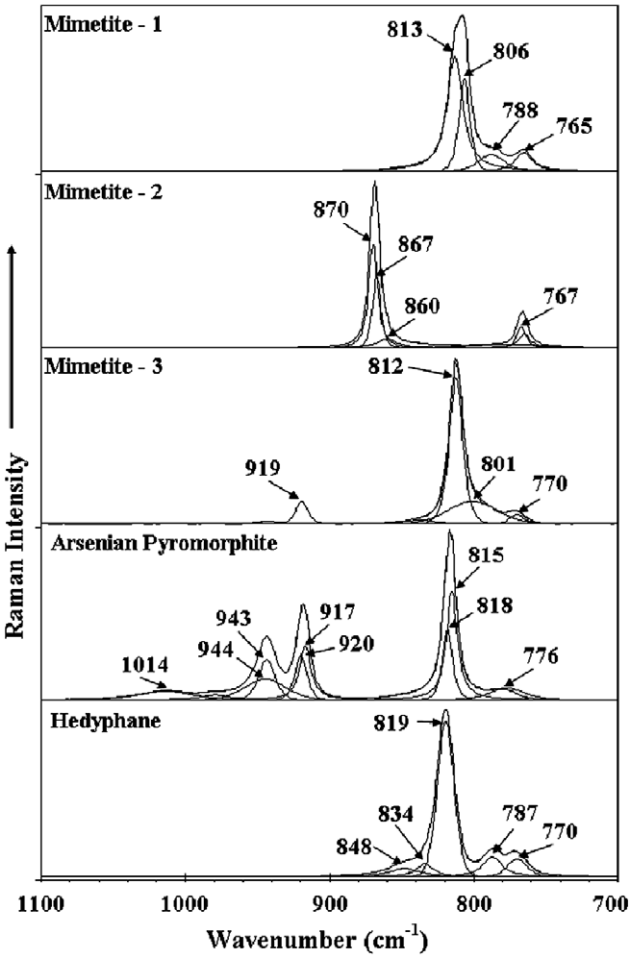


Fig. 1. Raman spectra of mimetite, arsenian pyromorphite and hedyphane in the high wavenumber region.

to the dimorphic nature of the mimetite–pyromorphite series. A second band is resolved at 806 cm^{-1} for mimetite 1 sample and 801 cm^{-1} for mimetite 3. Adams and Gardner reported a band at 808 cm^{-1} for a mimetite from Wheal Alfred Cornwall, England. For hedyphane other bands are observed on the higher wavenumber side at 834 and 848 cm^{-1}. In the Raman spectra a low intensity band is observed at around 765 cm^{-1} which Adams and Gardner also assigned to the AsO_4 stretching vibration. For mimetite 1 sample two bands are observed at 788 and 765 cm^{-1}. Similarly for hedyphane two bands are found at 787 and 770 cm^{-1}. Bands in these positions are intense in the infrared spectra and are ascribed to A_u and E_{1u} vibrational modes.

The Raman spectrum of mimetite 3 sample shows a low intensity band at 919 cm^{-1} which is ascribed to the PO symmetric stretching mode of phosphate anions in the mimetite structure. For the arsenian pyromorphite, a series of bands in the 917–1014 cm^{-1} are attributed to phosphate stretching vibrations. The bands at 917 and 920 cm^{-1} of the arsenian pyromorphite are attributed to the phosphate PO v_1 stretching vibrations. Adams and Gardner observed bands for pyromorphite at 920 and 919 cm^{-1} and assigned these bands to A_g and E_{2g} vibrational modes. These authors also stated that bands in these positions could be attributable to both v_1 and v_3 modes.

The infrared spectra of the mimetites, arsenian pyromorphite and hedyphane are shown in Fig. 2. All three

Table 3
Results of the Raman spectral analysis of mimetite, arsenian pyromorphite and hedyphane

Mimetite 1			Mimetite 2			Mimetite 3			Hedyphane			Arsenian pyromorphite		
Centre	FWHM	%	Centre	FWHM	%	Centre	FWHM	%	Centre	FWHM	%	Centre	FWHM	%
3716	102.3	0.37							3659	136.0	1.03			
3548	171.9	1.51							3563	139.6	1.73			
									3458	122.8	3.78	3444	123.7	1.93
3420	69.0	2.44							3409	62.7	2.26			
3381	44.0	1.46							3389	44.8	1.67	3378	68.7	3.71
3344	51.4	0.91							3352	51.6	1.52	3325	56.0	2.62
3301	25.2	0.25							3304	65.3	2.55	3291	16.9	0.09
3266	113.5	2.14							3258	7.0	0.07	3256	71.6	0.84
									3235	60.8	0.52			
												1014	42.8	5.09
												979	23.9	2.04
												944	33.4	8.34
						943	16.3	0.99				943	13.2	6.55
						919	9.9	5.44				920	9.8	5.47
			870	7.1	29.03							917	9.3	8.59
			867	6.8	16.54							825	44.4	5.15
			860	15.3	5.02									
			854	66.3	8.73				848	23.3	3.75			
						837	24.5	2.29	834	13.3	3.53			
813	12.8	40.29				812	10.6	40.59	819	13.6	34.19	818	8.1	7.53
806	8.6	16.85				801	39.9	21.03	811	81.4	10.98	815	8.9	15.98
788	21.1	6.85	776	52.4	5.42	770	11.0	2.36	787	15.2	6.28	776	27.7	4.25
			767	7.7	5.53				770	15.7	4.46	768	24.8	−2.53
765	13.7	5.92	765	8.7	4.94									
												573	12.6	0.45
												549	18.4	0.56
									452	17.8	2.14			
422	21.4	2.05				425	14.2	0.78	432	26.4	1.67	433	22.6	0.60
						411	20.3	2.08				414	17.1	2.14
408	14.7	1.24										409	13.1	1.94
									394	26.0	0.76	391	13.1	2.20
385	27.6	1.21				388	21.4	2.78	394	11.9	0.66	388	14.1	0.50
371	11.7	1.12				371	12.5	1.23	372	25.5	2.48	377	23.9	1.15
359	15.1	0.64	348	6.8	2.00				349	20.6	3.93	344	34.3	1.13
340	21.3	4.91				339	25.4	6.78	334	15.6	0.73	339	26.2	1.94
313	18.0	6.10	316	10.5	19.5	313	17.2	2.68	319	17.3	5.85	318	22.2	1.99
									201	24.4	0.68	206	39.8	1.21
						194	44.8	1.98	192	12.9	0.16	186	23.7	1.30
176	37.0	3.34				175	32.4	2.18	177	21.7	0.89	177	24.3	2.91
			167	14.3	3.3				162	20.8	0.77			
						150	21.1	1.90	151	18.5	0.64	152	29.5	3.17
145	15.3	0.38							141	13.1	0.33			
												111	11.7	0.60
						105	9.5	2.08				105	7.1	0.57
						98	0.0	2.81						

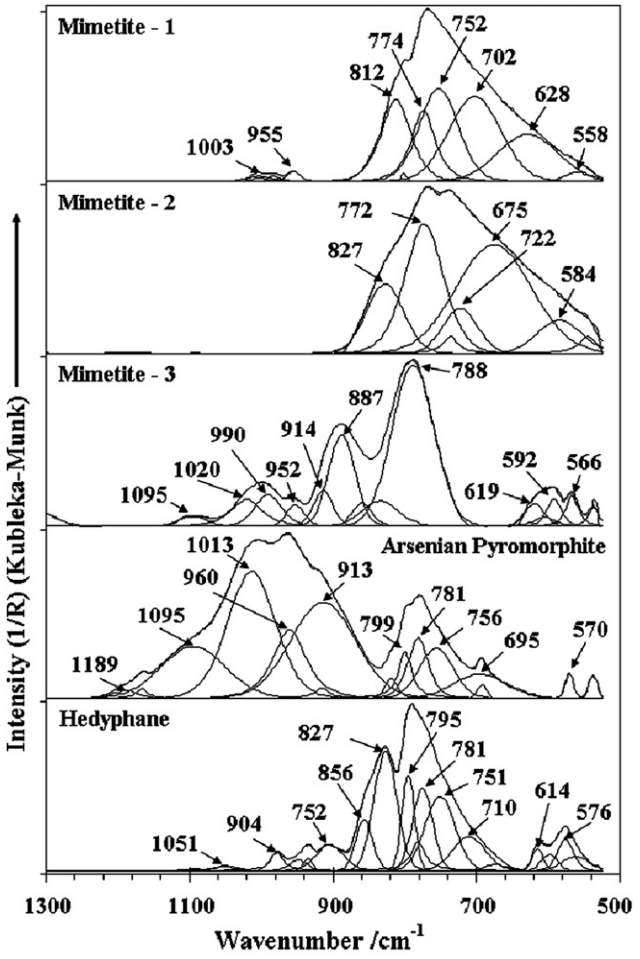


Fig. 2. Infrared spectra of mimetite, arsenian pyromorphite and hedyphane in high wavenumber region.

mimetites show a broad spectral profile in the 500–850 cm^{-1} region. Infrared bands for the mimetite 1 and 2 samples are observed at around 812, 774 and 752 cm^{-1} and are attributed to $(AsO_4)^{3-}$ stretching vibrations. Farmer published the results of the infrared spectra for mimetite at 810 and 875 cm^{-1} which are in good agreement with these results [23]. The infrared spectrum of mimetite-3 shows a series of infrared bands in the 900–1095 cm^{-1} region. These bands are attributed to $(PO_4)^{3-}$ stretching vibrations. This mimetite has substitution of the phosphate anion for arsenate. The spectrum of this mimetite closely resembles that of the arsenian pyromorphite. The infrared spectrum of this mineral shows bands at 799 and 781 cm^{-1} which are assigned to the $(AsO_4)^{3-}$ stretching vibrations. Farmer published the results of the infrared spectrum of pyromorphite [23] and stated that the ν_1 band occurred at 920 cm^{-1} and the ν_3 bands at 970 and 1030 cm^{-1}. The infrared spectrum of hedyphane shows intense bands at 827 and 795 cm^{-1} attributed to $(AsO_4)^{3-}$ stretching vibrations. Some low intensity bands at 904 and 1051 cm^{-1} are observed and these bands may be ascribed to $(PO_4)^{3-}$ stretching vibrations. Thus this is evidence for the replacement of the arsenate anion by phosphate in this mineral.

4.2. Low wavenumber region

The Raman spectra of the low wavenumber region are shown in Fig. 3. The spectra of the mimetite minerals are complex and many bands are observed. One way of addressing this complexity is to divide the spectra into sections (a) 400–450 cm^{-1} (b) 300–400 cm^{-1} and (c) less than 300 cm^{-1}. Regions (a) and (b) may be assigned to $(AsO_4)^{3-}$ bending modes; region (c) is best described as lattice vibrations. Four bands at 422, 408, 385 and 371 cm^{-1} are observed for mimetite sample 1. For mimetite sample 3 four bands are found at 425, 411, 388 and 371 cm^{-1}. These four bands are assigned to arsenate ν_4 bending modes. For the arsenian pyromorphite four bands are observed at 433, 414, 409 and 391 cm^{-1}. These bands may be ascribed to both $(AsO_4)^{3-}$ and $(PO_4)^{3-}$ bending modes. For the mineral hedyphane four bands are observed at 452, 432, 394 and 372 cm^{-1}. The effect of isomorphic substitution of Pb by Ca shifted the band positions by approximately 30 cm^{-1} when compared with mimetite. This effect could be due to zoning of the hedyphane in which the structure of the hedyphane alters from hexagonal to monoclinic. Further the effect of shielding of the arsenate anions by Ca instead of Pb results in a shift of 15–20 cm^{-1} for the arsenate bands.

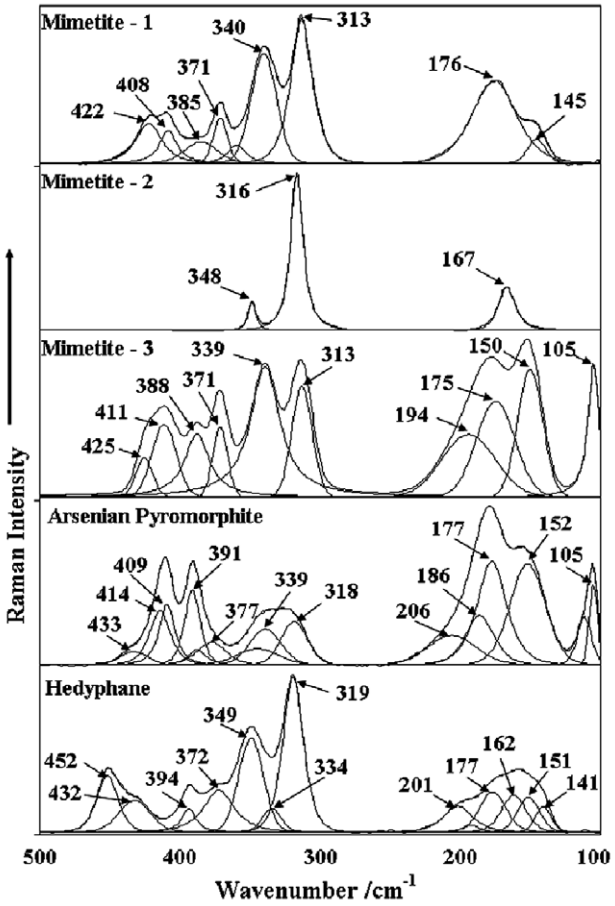


Fig. 3. Raman spectra of mimetite, arsenian pyromorphite and hedyphane in the low wavenumber region.

For mimetite sample 1 two bands are observed at 340 and 313 cm^{-1}; for mimetite sample 3 339 and 313 cm^{-1}; for arsenian pyromorphite 339 and 318 cm^{-1}; and for hedyphane 349 and 319 cm^{-1}. These bands are attributed to the v_2 bending modes. The two bands at 348 and 316 cm^{-1} for mimetite 2 are also assignable to this mode. Adams and Gardner observed Raman bands for mimetite at 335 and 314 cm^{-1} and assigned these bands to O–As–O bending modes [17].

4.3. OH stretching region

The Raman spectra of mimetite, arsenian pyromorphite and hedyphane are shown in Fig. 4. The results of the Raman spectra are reported in Table 2. The Raman spectra of mimetite shows a series of overlapping bands which are partially resolved into bands at 3716, 3548, 3420 3381 3344 and 3266 cm^{-1}. The observation of hydroxyl stretching bands is interesting in itself as according to the formula of mimetite $Pb_5(AsO_4)_3Cl$ there should be no OH bands observed at all. The observation of OH bands means that there is some isomorphic replacement of the Cl with OH units. Another explanation is that the lower wavenumber bands are ascribed to adsorbed water. The Raman spectrum in the OH stretching region of the arsenian pyromorphite also shows Raman bands at 3378, 3325 and 3256 cm^{-1}. The Raman spectrum in the OH stretching region of hedyphane $Pb_3Ca_2(AsO_4)_3Cl$ shows a band at around 3400 cm^{-1} superimposed upon a broad background. This suggests that there is some isomorphic replacement of the Cl units for OH units.

Studies have shown a strong correlation between OH stretching frequencies and both O···O bond distances and H···O hydrogen bond distances [24–27]. Libowitsky (1999) showed that a regression function can be employed relating the above correlations with regression coefficients better than 0.96 [28]. The function is $v_1 = 3592–304 \times 10^9 \exp(-d(O–O)/0.1321)$ cm^{-1}. What this means is that the variation in the water hydroxyl stretching frequency is a measure of the hydrogen bond strength between the OH unit of the water and the arsenate or phosphate anion. If the band positions of the OH stretching vibrations are used in the calculations then estimates of the hydrogen bond distances can be made. For the band at 3400 cm^{-1} for hedyphane a hydrogen bond distance of 2.80 Å is calculated, for arsenian pyromorphite the bands at 3256, 3325 and 3378 cm^{-1} give hydrogen bond distances of 2.72, 2.75 and 2.78 Å; for mimetite hydrogen bond distances of 2.72 Å (3266 cm^{-1}), 2.76 Å (3304 cm^{-1}), 2.78 Å (3381 cm^{-1}) and 2.99 Å (3548 cm^{-1}). The hydrogen bond distances are of the same order of magnitude for each of the mimetites and vary between 2.72 and 2.99 Å. It is possible that some substitution of OH units for Cl in the mimetite structure is required for stability.

Infrared bands are observed at around 628 cm^{-1} for mimetite 1, 675 for mimetite 2, in the 590–619 cm^{-1} region for mimetite 3. These bands are attributed to OH librational modes and although not of a high intensity confirm the presence of OH units in the mimetite structure and thus confirms the replacement of Cl by OH units.

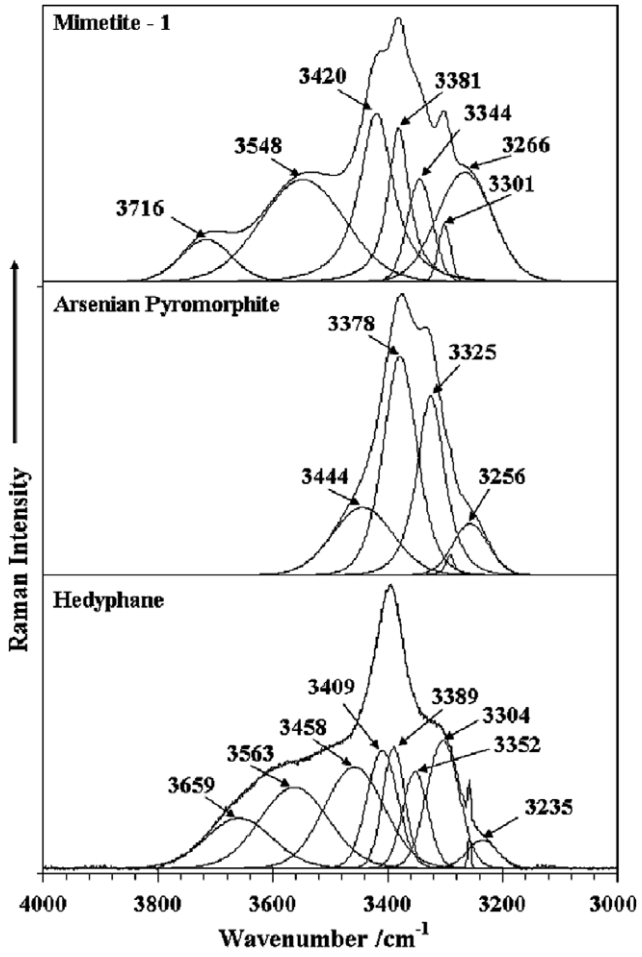


Fig. 4. Raman spectra of mimetite, arsenian pyromorphite and hedyphane in the OH stretching region.

5. Conclusions

A comparison of Raman spectra of mimetites with published infrared and Raman data of similar minerals has been made. Crystals of the mimetite–pyromorphite series are chemically zoned, resulting in changes in the crystal structure with the isomorphic replacement of arsenate by phosphate with the consequential change in crystal structure from hexagonal to monoclinic. Such dimorphic relationships are exemplified by the shift in the Raman spectral band positions of arsenate with increasing phosphate substitution.

This work clearly demonstrates the power of Raman spectroscopy as compared to infrared spectroscopy in determining the vibrational spectrum of these arsenates with an apatite structure. Isomorphous substitution of arsenate by phosphate in the case of mimetite and the substitution of phosphate by arsenate in the case of the arsenian pyromorphite are clearly identified. Further the replacement of Cl with OH units is also observed in the Oh stretching region

of the Raman spectra and the librational region of the infrared spectra. The application of Raman microscopy to the study of closely related mineral phases has enabled their molecular characterisation using their Raman spectrum thus enabling the rapid identification of phases in complex mixtures of secondary lead containing arsenates from the oxidised zones of base metal ore bodies.

Acknowledgements

The financial and infra-structure support of the Queensland University of Technology, Inorganic Materials Research Program is gratefully acknowledged. The Australian Research Council (ARC) is thanked for funding the instrumentation.

References

[1] O.C. Farrington, E.W. Tillotson Jr., Field Columbian Mus. Pub., Geol. Series 3 (1909).
[2] M. Amadori, E. Viterbi, Journal of Chemical Society, Abstracts 108 (1914) 358.
[3] C.C. Mcdonnell, C.M. Smith, American Journal of Science 42 (1916) 139.
[4] J. Lietz, Zeitschrift fuer Kristallographie, Kristallgeometrie, Kristallphysik, Kristallchemie 77 (1931) 437.
[5] T. Ishimori, H. Waki, K. Muta, Kobutsugaku Zasshi 2 (1955) 172.
[6] S.R. Levitt, R.A. Condrate, American Mineralogist 55 (1970) 1562.
[7] A.R. Kampf, I.M. Steele, R.A. Jenkins, American Mineralogist 91 (2006) 1909.
[8] J.W. Anthony, R.A. Bideaux, K.W. Bladh, M.C. Nichols, Handbook of Mineralogy, Volume IV. Arsenates, Phosphates, Vanadates, Mineral Data Publishing, Tuscon, AZ, 2000.
[9] Y. Dai, J.M. Hughes, P.B. Moore, Canadian Mineralogist 29 (1991) 369.
[10] Y. Dai, Mineralogical Record 24 (1993) 307.
[11] S.D. Ross, Inorganic Infrared and Raman Spectra, McGraw-Hill Book Company Ltd., London, 1972.
[12] J. Gadsden, Infrared Spectra of Minerals and Related Inorganic Compounds, Butterworth & Co. (Publishers) Ltd., London, England, 1975.
[13] W.P. Griffith, Journal of the Chemical Society [Section] A: Inorganic, Physical, Theoretical (1970) 286.
[14] S.R. Levitt, K.C. Blakeslee, R.A. Condrate, Memoires de la Societe Royale des Sciences de Liege, Collection in 8 Deg 20 (1970) 121.
[15] S.R. Levitt, R.A. Condrate, American Mineralogist 55 (1970) 522.
[16] S.R. Levitt, R.A. Condrate, Journal of Physics and Chemistry of Solids 34 (1973) 1109.
[17] D.M. Adams, I.R. Gardner, Journal of the Chemical Society, Dalton Transactions: Inorganic Chemistry 1972–1999 (1974) 1505.
[18] G. Bartholomai, W.E. Klee, Spectrochimica Acta, Part A: Molecular and Biomolecular Spectroscopy 34A (1978) 831.
[19] R.L. Frost, D.A. Henry, K. Erickson, Journal of Raman Spectroscopy 35 (2004) 255.
[20] R.L. Frost, Spectrochimica Acta, Part A: Molecular and Biomolecular Spectroscopy 60A (2004) 1469.
[21] R.L. Frost, O. Carmody, K.L. Erickson, M.L. Weier, J. Cejka, Journal of Molecular Structure 703 (2004) 47.
[22] R.L. Frost, O. Carmody, K.L. Erickson, M.L. Weier, D.O. Henry, J. Cejka, Journal of Molecular Structure 733 (2004) 203.
[23] V.C. Farmer, Mineralogical Society Monograph 4: The Infrared Spectra of Minerals, 1974.
[24] J. Emsley, Chemical Society Reviews 9 (1980) 91.
[25] H. Lutz, Structure and Bonding 82 (1995) 85.
[26] W. Mikenda, Journal of Molecular Structure 147 (1986) 1.
[27] A. Novak, Structure and Bonding 18 (1974) 177.
[28] E. Libowitsky, Monatschefte fÜr chemie 130 (1999) 1047.

Available online at www.sciencedirect.com
ScienceDirect
Polyhedron 26 (2007) 2971–2978
POLYHEDRON
www.elsevier.com/locate/poly

Transition metal complexes with thiosemicarbazide-based ligand – Part LV: Synthesis and X-ray structural study of novel Ni(II) complexes with pyridoxal semicarbazone and pyridoxal thiosemicarbazone

Vukadin M. Leovac [a], Ljiljana S. Jovanović [a,*], Violeta S. Jevtović [a], Giorgio Pelosi [b], Franco Bisceglie [b]

[a] Department of Chemistry, Faculty of Sciences, 21000 Novi Sad, Trg D. Obradovića 3, Serbia and Montenegro
[b] Dipartimento di Chimica Generale ed Inorganica, Chimica Analitica, Chimica Fisica, Università di Parma, 43100 Parma, Parco Area delle Scienze 17A, Italy

Received 13 December 2006; accepted 31 January 2007
Available online 7 February 2007

Abstract

Reaction of aqueous solutions of $Ni(NO_3)_2$ and pyridoxal semicarbazone (PLSC) in the presence of NaN_3 afforded two complexes, viz. green, paramagnetic binuclear octahedral $[Ni_2(PLSC)_2(\mu_{1,1}\text{-}N_3)_2(N_3)_2]\cdot 2H_2O$ (**1**) and, as admixture, red, octahedral $[Ni(PLSC–H)_2]\cdot 2H_2O$ (**2**) complex. Under the same reaction conditions, pyridoxal thiosemicarbazone (PLTSC) gave only one diamagnetic square-planar, red complex $[Ni(PLTSC–H)N_3]\cdot H_2O$ (**3**). In the absence of NaN_3, the reaction of PLTSC and $Ni(NO_3)_2$ yielded brown paramagnetic octahedral complex $[Ni(PLTSC)_2](NO_3)_2\cdot H_2O$ (**4**).

The complexes were characterized by elemental analysis, conductometric and magnetochemical measurements, IR and UV–Vis spectra, and the octahedral complexes **1**, **2** and **4** also by X-ray monocrystal diffraction method.
© 2007 Elsevier Ltd. All rights reserved.

Keywords: Nickel(II) complexes; Pyridoxal semi- and thiosemicarbazone; Synthesis; Physico-chemical characterization; Structural analysis

1. Introduction

Because of their simple preparation, excellent complexation of not only transition but also non-transition p-elements, interesting structural characteristics of their complexes, along with the possibility of their analytical application, semi- and thiosemicarbazones have become a subject of intense research interest of coordination chemists. This has resulted in a large number of papers and several reviews [1–4] that summarized various aspects of the chemistry of these compounds, such as methods of their synthesis, spectral, magnetic, stereochemical, structural, and other characteristics. An enhanced interest in these compounds has undoubtedly aroused the discovery of their biological activity. This is especially related to thiosemicarbazones and their complexes, which show a wider spectrum of biological activity than semicarbazones. Namely, it has been shown that many thiosemicarbazones and their complexes are active against viruses, bacteria, cancer, fungi, and malaria, which has been summarized in the reviews of West et al. [5,6] and Beraldo and Gambino [7]. Some thiosemicarbazones and their metal complexes such as marboran or triapine, are already used in medical practice [8].

One of thiosemicarbazone ligands that have been attracting attention of coordination and structural chemists for more than 20 years, and more recently of pharmacologists too, is the tridentate ONS, unsubstituted and substituted PLTSC (pyridoxal thiosemicarbazone). Namely, this ligand appeared to be a good complexing agent for various metals, and some of its derivatives showed a certain biological activity [8]. In contrast to this ligand, the interest in the coordination and structural

* Corresponding author. Tel.: +381 21 4852752.
E-mail addresses: vule@ih.ns.ac.yu (V.M. Leovac), lilij@ih.ns.ac.yu (L.S. Jovanović), giorgio.pelosi@unipr.it (G. Pelosi).

0277-5387/$ - see front matter © 2007 Elsevier Ltd. All rights reserved.
doi:10.1016/j.poly.2007.01.041

chemistry of its oxygen analogue, i.e. tridentate ONO pyridoxal semicarbazone (PLSC), is of a much recent date, so that the number of its investigated complexes is significantly smaller and limited to the complexes of Cu, Fe and Pt.

The most important results gained in studying metal complexes of these two ligands, including also complexes with pyridoxal isothiosemicarbazone, have been reviewed by Leovac et al. [9].

In our most recent work [10] we described the syntheses and some physical and structural characteristics of first mono(ligand) complexes of Ni(II) with PLSC, of the general formula $Ni(PLSC)X_2 \cdot nH_2O$ (X = Cl, NO_3, NCS), as well as two new complexes with PLTSC, [Ni(PLTSC–H)py]NO_3 and [Ni(PLTSC–H)NCS]. In this work we report the syntheses and structures of the first bis(ligand) complexes of Ni(II) with the mentioned Schiff bases, as well as of two mono(ligand) complexes.

2. Experimental

All commercially obtained reagent-grade chemicals were used without further purification, except for the ligands, which were prepared according to the previously described procedures [11].

Elemental (C, H, N) analysis of air-dried samples was carried out by standard micromethods in the Center for Instrumental Analysis, Faculty of Chemistry, Belgrade.

2.1. Synthesis of complexes

2.1.1. $[Ni_2(PLSC)_2(\mu_{1,1}\text{-}N_3)_2(N_3)_2] \cdot 2H_2O$ (**1**) and $[Ni(PLSC–H)_2] \cdot 2H_2O$ (**2**)

A mixture of 0.26 g (1 mmol) of $PLSC \cdot 2H_2O$ and 0.29 g (1 mmol) of $Ni(NO_3)_2 \cdot 6H_2O$ was dissolved by heating in 10 cm^3 of H_2O and 0.16 g (2.5 mmol) NaN_3 added to the warm solution. After 5 h, the green-reddish solution afforded dark-green crystals of complex **1** and a small amount of red crystals of compound **2**. The crystals were filtered off and washed with H_2O. Yield: 0.26 g (67%).

Complex **1** – *Anal.* Calc. for $Ni_2C_{18}H_{28}N_{20}O_8$: C, 28.07; H, 3.64; N, 36.39. Found: C, 27.67; H, 4.01; N, 35.68%. Λ_M (DMSO): 30.5 S cm^2 mol^{-1}. $\mu_{eff} = 2.80$ BM. λ_{max}/nm ($\varepsilon \times 10^{-3}$/$mol^{-1}$ dm^3 cm^{-1}) (DMF): 288 (28.5); 401 (16.2); 420 (5.0); 635 (0.063); 965 (0.030).

Complex **2** – *Anal.* Calc. for $NiC_{18}H_{26}N_8O_8$: C, 39.96; H, 4.84; N, 20.71. Found: C, 39.63; H, 4.92; N, 20.95%. Λ_M (DMF): 7.2 S cm^2 mol^{-1}. λ_{max}/nm ($\varepsilon \times 10^{-3}$/$mol^{-1}$ dm^3 cm^{-1}) (DMF): 286 (21); 404 (14); 421 (2.5); 636 (0.033); 949 (0.028).

2.1.2. $[Ni(PLTSC–H)N_3] \cdot H_2O$ (**3**)

A mixture of 0.15 g (0.5 mmol) of $PLTSC \cdot 2H_2O$ and 0.15 g (0.5 mmol) of $Ni(NO_3)_2$ was dissolved by heating in 10 cm^3 of H_2O and the warm solution of 0.07 g (1 mmol) of NaN_3 in 5 cm^3 of H_2O added to it. Red microcrystals that appeared already from the warm solution were filtered after 3 h and washed with H_2O and MeOH. Yield: 0.07 g (70%).

Anal. Calc. for $NiC_9H_{13}N_7O_3S$: C, 30.19; H, 3.66; N, 27.39. Found: C, 30.32; H, 3.61; N, 26.98%. Λ_M (DMF): 7.5 S cm^2 mol^{-1}. $\mu_{eff} = 0$ BM (diamagnetic). λ_{max}/nm ($\varepsilon \times 10^{-3}$/$mol^{-1}$ dm^3 cm^{-1}) (DMF): 296 (11.1); 328 (8.9); 400 (17.1); 474sh (1.7) (sh – shoulder).

2.1.3. $[Ni(PLTSC)_2](NO_3)_2 \cdot H_2O$ (**4**)

The mixture of 0.20 g (0.7 mmol) of $Ni(NO_3)_2$ and 0.15 g (0.5 mmol) of $PLTSC \cdot 3H_2O$ was poured over with 5 cm^3 H_2O and dissolved by heating. After 24 h, the obtained brown crystals were filtered and washed with H_2O and EtOH. Yield: 0.15 g (43%).

Anal. Calc. for $NiC_{18}H_{26}N_{10}O_{11}S_2$: C, 31.18; H, 3.92; N, 20.37. Found: C, 31.52; H, 3.81; N, 20.19%. Λ_M (H_2O): 202 S cm^2 mol^{-1}. $\mu_{eff} = 3.01$ BM. λ_{max}/nm ($\varepsilon \times 10^{-3}$/$mol^{-1}$ dm^3 cm^{-1}) (DMF): 336bp (12); 357 (1.4); 409 (7.0); 425(1.5); 472sh (1.0); ~836 (0.016); 977 (0.012); 1060 (0.008); 1200 (0.044) (bp – broad peak).

2.2. Physical measurements

Magnetic susceptibilities were measured at room temperature using a magnetic susceptibility balance MSB-MKL (Sherwood Scientific Ltd. Cambridge, England).

Molar conductivities of the freshly prepared 1×10^{-3} M solutions were measured on a Jenway 4010 conductivity meter.

IR spectra (KBr disk) were recorded on a Thermo Nicolet (NEXUS 670 FT-IR) instrument.

Electronic spectra of DMF solutions of complexes were recorded on a Secomam (Anthelie 2, Advanced, for the spectral range of 270–900 nm) spectrophotometer and on a Thermo Nicolet instrument (NEXUS 670 FT-IR, for the range 900–1400 nm).

2.3. Crystal structure determination

A single crystal, of the dimensions $0.2 \times 0.2 \times 0.1$ mm, $0.3 \times 0.3 \times 0.2$ mm, and $0.3 \times 0.2 \times 0.2$ mm, of complexes **1**, **2** and **4**, respectively, was mounted on a SMART (complex **1** and **2**) and Philips diffractometer (complex **4**) with Mo Kα radiation [$\lambda = 0.7107$ Å]. The structure was solved by direct methods using SIR97 [12] and refined using SHELXL97 [13] on F_2 by full matrix least squares with anisotropic displacement parameters for all atoms but the hydrogen atoms. All hydrogen atoms were found on a difference map. Final refinement converged to an $R_1 = 0.0256$ and a $wR_2 = 0.0699$ (complex **1**), $R_1 = 0.0283$ and a $wR_2 = 0.0817$ (complex **2**), and $R_1 = 0.0505$ and a $wR_2 = 0.1068$ (complex **4**). Experimental details for the X-ray data collection are reported in Table 1. The refinement procedure was carried out using the WINGX package [14] with the program PARST [15] for the geometrical description of the structures and ORTEP [16] and PLUTO [17] for the structure drawings.

Table 1
Crystal data for complex $[Ni_2(PLSC)_2(\mu_{1,1}\text{-}N_3)_2(N_3)_2]\cdot 2H_2O$ (**1**), $[Ni(PLSC\text{–}H)_2]\cdot 2H_2O$ (**2**) and $[Ni(PLTSC)_2](NO_3)_2\cdot H_2O$ (**4**)

	1	**2**	**4**
Empirical formula	$C_{18}H_{28}Ni_2N_{20}O_8$	$C_{18}H_{26}NiN_8O_8$	$C_{18}H_{26}NiN_{10}O_{11}S_2$
Molecular mass	769.97	541.16	681.30
Crystal system	triclinic	monoclinic	triclinic
Space group	$P\bar{1}$	$C2/c$	$P\bar{1}$
a (Å)	8.515(1)	16.306(3)	10.945(6)
b (Å)	8.715(1)	13.552(3)	16.678(7)
c (Å)	11.031(2)	12.487(3)	8.101(5)
α (°)	68.42(1)	90.0	99.00(5)
β (°)	81.84(1)	125.11(2)	105.89(3)
γ (°)	66.00(1)	90.0	101.64(6)
V (Å^3)	695.3(2)	2257(1)	1357(1)
Z	1	4	2
$F(000)$	396	1216	704
D_{calc} (Mg m^{-3})	1.839	1.705	1.667
μ (Mo Kα) (mm^{-1})	1.44	1.101	0.945
Crystal size (mm)	$0.2\times0.2\times0.1$	$0.5\times0.3\times0.2$	$0.3\times0.2\times0.2$
T (K)	298	298	298
Number of reflections measured	6650	12071	7940
θ Range (°)	$1.5<2\theta<50$	$2.00<2\theta<55.03$	$2.00<2\theta<60.01$
hkl Ranges	−10, 10; −10, 10; −13, 13	−20, 21; −17, 17; −16, 15	−15, 14; −23, 23; 0, 11
Number of unique reflections	2468	2538	7940
Number of reflections observed $I>2\sigma(I)$	2210	2100	3981
Number of parameters	273	175	387
R_1[a]	0.0256	0.0283	0.0505
Weight	$1/\sigma^2(F_o^2)+(0.0442\times P)^2+0.11\times P]$[b]	$1/\sigma^2(F_o^2)+(0.0458\times P)^2+1.08*P]$[b]	$1/\sigma^2(F_o^2)+(0.0348\times P)^2]$[b]
wR_2[c]	0.0699	0.0817	0.1068
Maximum Fourier difference (e/Å^3)	−0.39, 0.31	−0.24, 0.33	−0.61, 0.50

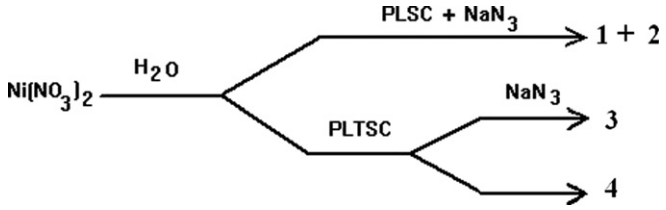
[a] $R_1=\sum\|F_o|-|F_c\|/\sum|F_o|$.
[b] $P=(\mathrm{Max}(F_o^2,0)+2\times F_c^2)/3$.
[c] $wR_2=\{\sum[w(F_o^2-F_c^2)^2/\sum[w(F_o^2)^2]\}^{1/2}$.

3. Results and discussion

3.1. Syntheses and physical characteristics of complexes

As can be seen from the coordination formula of the newly prepared Ni(II) complexes with PLSC and PLTSC, we are concerned with two mono- and two bis(ligand) complexes, of which complex **1**, thanks to the bridging role of the two azide ligands, represents the first authentic binuclear Ni(II) complex involving PLSC ligand.

Also, the first, but bis(PLSC/PLTSC) complexes of Ni(II) represent the compounds **2** and **4**. All complexes, including bis(ligand) complexes, were obtained from aqueous solutions, by the reaction of Ni(II) and Schiff base in a mole ratio 1:1 (Scheme 1) except for **4** where $Ni(NO_3)_2$ is in a 40% excess. It should be noticed that both PLSC complexes were obtained from the same reaction mixture, that is warm aqueous solutions of $Ni(NO_3)_2\cdot 6H_2O$, PLSC and NaN_3, whereby binuclear complex **1** was obtained as the main product and complex **2** as admixture. In the absence of azide, PLSC and $Ni(NO_3)_2$ would produce a complex of the formula $[Ni(PLSC)(H_2O)_3](NO_3)_2$ [10].



Scheme 1.

In contrast to PLSC, under the same reaction conditions, the reaction of PLTSC and $Ni(NO_3)_2$ in the presence of NaN_3 gave only one complex, viz. **3**. In the absence of NaN_3, the reaction of PLTSC and $Ni(NO_3)_2$ gave the brown bis(PLTSC) complex **4**. All complexes are stable in air. In contrast to complex **4**, which is well soluble in H_2O, DMF and DMSO and less soluble in alcohols, the other complexes are much less soluble. This is especially characteristic of complex **1**, which is in agreement with its dimeric structure. Molar conductivities correspond to the coordination formulas of the complexes. With the exception of complex **3**, which is diamagnetic, complexes **1** and **4** are paramagnetic, with the μ_{eff} values corresponding to octahedral Ni(II) complexes. The poor yield of complex **2**, whose crystals for the purpose of the analyses had to be separated mechanically from **1**, was the reason why it could not be characterized by magnetic measurements.

The presence of one or more bands in the IR spectra of complexes about 2850 cm^{-1} has been ascribed [18,19] to the $\nu(NH^+)$ vibrations, i.e. to the dipolar nature of the PL moiety, with a certain contribution of the ν(OH) of the hydroxyl group. In view of the fact that in the IR

spectrum of complex **2** there exist a medium-intensity band at 2876 cm^{-1} it can be concluded that it belongs to the ν(OH) of the CH_2OH group. It should be pointed out that the ν(C=O) band, which in the spectrum of free ligand occurs at 1680 cm^{-1}, is in the spectra of both PLSC complexes shifted due to coordination to lower energies by 15 cm^{-1} (complex **1**) and 39 cm^{-1} (complex **2**).

In the IR spectra of both azide complexes there is one $\nu_a(N_3)$ band, recognizable by its strong intensity, occurring at 2049 cm^{-1} (complex **1**) and 2064 cm^{-1} (complex **3**). It is interesting to note that this band in complex **1**, which contains differently coordinated azide ligands, two monodentate and two $\mu_{1,1}{}^{-}N_3$, is not split as in the case of the spectrum of the similar dimeric complex $[Ni_2(L)_2(\mu_{1,1}\text{-}N_3)_2(N_3)_2]$ (L = tridentate NNN ligand) [20].

3.2. Electronic spectra

The spectra of the complexes in DMF (in the range of 270–1200 nm) display several electronic transitions.

The spectrum of the diamagnetic azide complex **3** in DMF (as well in DMSO, not presented because of negligible difference) is the simplest. The bands at $\lambda < 360$ nm belong to intraligand transitions ($\pi \rightarrow \pi^*$, $n \rightarrow \pi^*$). Two bands at 400–474 nm may originate from LMCT and d–d electron transfer, respectively. Since no other d–d bands were observed up to 1200 nm, the simplicity of the spectra and the corresponding band intensities suggest the square-planar rather than tetrahedral configuration of the complex in solution [21].

The spectra of the other three complexes have certain similarities arising from their close geometric configuration. The spectrum of $[Ni(PLTSC)_2](NO_3)_2$ (**4**) in UV range is rather unresolved, consisting of two complex bands which are due to intraligand and LMCT transitions, respectively. On the other hand, the d–d spectral data (the bands at $\lambda_{max} > 470$ nm) for this complex in solution seem to support its distorted octahedral geometry.

The semicarbazone complexes **1** and **2** are slightly soluble in DMF, forming yellow solution. The spectra of both complexes are very similar in the whole range: the intraligand transitions (up to about 300 nm), those of CT (about 400 nm) and d–d transitions with three main bands corresponding to a distorted octahedral structure: at about 420, 635, and 940 nm. The first band, which is complex, is partly due to LMCT transition as was recorded for the mono(ligand) semicarbazone complexes [10].

3.3. Description of the structure of $[Ni_2(PLSC)_2\text{-}(\mu_{1,1}N_3)_2(N_3)_2]\cdot 2H_2O$ (1)

Experimental details are given in Table 1 and bonds and angles in Table 2. The analysis of the crystal structure of **1** shows its dimeric nature. The asymmetric unit consists of a tridentate ONO neutral ligand chelating the nickel atom together with three azides, two of which end-on (EO) bridging. The two halves of the dimer are related by a crystallographic inversion center, which lies at the center of the four-membered ring formed by the two Ni atoms and the coordinating atoms of the two bridging azide anions. An ORTEP view of the complex is shown in Fig. 1.

Table 2
Selected bond distances (Å) and angles (°) for complex **1**

Ni1–Ni1′	3.227(1)	Ni1′–Ni1–O1	97.65(4)
Ni1–O1	2.082(2)	Ni1′–Ni1–O2	90.12(4)
Ni1–O2	1.989(1)	Ni1′–Ni1–N3	136.09(5)
Ni1–N3	2.029(2)	Ni1′–Ni1–N5	41.46(5)
Ni1–N5	2.078(2)	Ni1′–Ni1–N8	136.78(5)
Ni1–N8	2.132(2)	O1–Ni1–O2	167.48(7)
Ni1A–N5	2.164(2)	O1–Ni1–N3	78.98(7)
		O1–Ni1–N5	100.67(7)
		O1–Ni1–N8	88.08(7)
		O2–Ni1–N3	88.61(7)
		O2–Ni1–N5	91.66(7)
		O2–Ni1–N8	92.97(7)
		N3–Ni1–N5	177.52(8)
		N3–Ni1–N8	87.11(7)
		N5–Ni1–N8	95.34(8)
		Ni1–Ni1′–N5	39.49(5)

′ = −x + 1, −y + 1, −z + 2.

The nickel atom presents a distorted octahedral geometry, where the N3–Ni–N5 and N8–Ni–N5′ are 177.52(7)° and 176.02(7)° respectively, very close to the theoretical 180°, but the O1–Ni–O2 is 167.48(6)°, due to the chelation rings strain.

In this compound the C–N–C angle of the pyridoxal ring is 124.4(2)°, revealing thus the protonation of the nitrogen (deprotonation of the phenolic oxygen), which is in agreement with the presence of two azides for each Ni(II) ion, to balance the metal positive charges. For the protonated pyridoxal nitrogen, angles reported in the literature are larger than 120° [9,22].

The whole ligand molecule, due to the extended system of conjugated double bonds, is almost planar, whereby the angle between the average planes of the hydrazone moiety and that of the pyridoxal ring is 11.40(8)°. The five-membered chelation ring has a $q_2 = 0.102(2)$ Å and a $\varphi_2 = -18(1)°$, corresponding to a twist ($^1T_5$) conformation, while the six-membered ring has a $\varphi_2 = 109.1(8)°$ and a

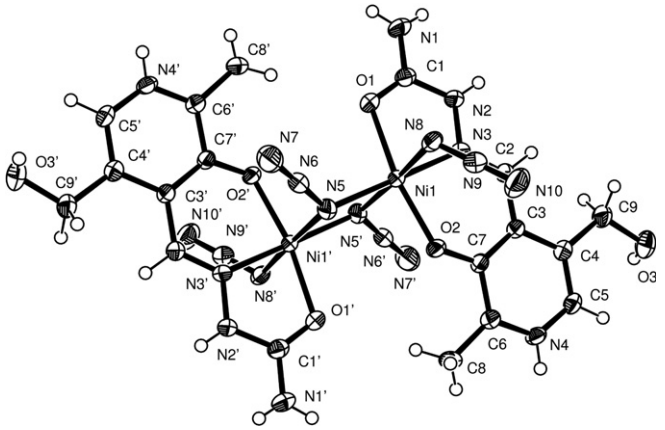


Fig. 1. ORTEP view of complex **1**.

total puckering amplitude of 0.141(2) Å [$\Theta_2 = 102.9(9)°$], corresponding to a boat (^{3,6}B) conformation.

The Ni···Ni′ separation is 3.227(1) Å, that is too long for a metal–metal bond [23] and in perfect agreement with the average value of 3.22(1) Å found for the Ni···Ni′ distances in the CSD (Cambridge Structural Database) [24] for azido-bridged Ni dimers. Ni(II) complexes with EO bridge(s) are ferromagnetically coupled, with the Ni–N–Ni angle(s) close to 103° or in any case in the range from 100° to 105° [25]. In this case, it is interesting to note that the Ni–N5–Ni° angle is 99.05(8)°.

The packing (Fig. 2) is determined by an extended network of hydrogen bondings as can be seen from Table 3.

3.4. Description of the structure of $[Ni(PLSC–H)_2]\cdot 2H_2O$ (2)

The analysis of the crystal structure of **2** has been carried out and the experimental details are presented in Table 1, whereas its geometrical features (bond distances and angles) are given in Table 4. The asymmetric unit consists of a tridentate monodeprotonated ligand molecule chelating the nickel atom, which lies in a special position on a binary axis, and a water molecule (see Fig. 3).

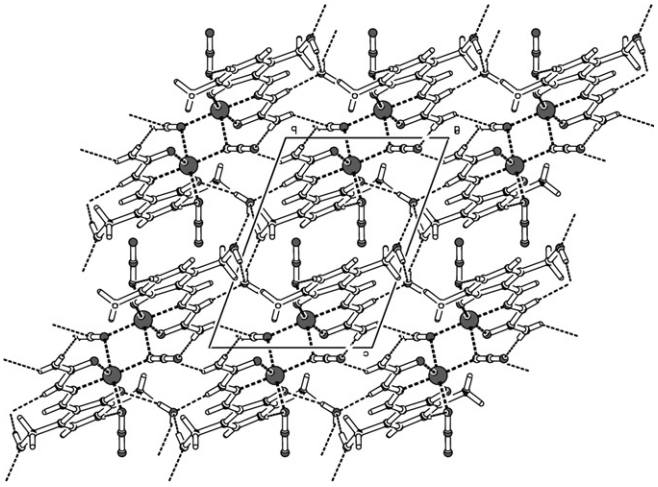


Fig. 2. Crystal structure of complex **1**, view in the *yz* plane.

Table 3
Hydrogen bonds for compound **1**

Donor···acceptor	donor–H···acceptor
O1W···O2(0)	O1W–H2W···O2(0)
2.779(3)	166(4)
N4···N8(1)	N4–H6···N8(1)
2.850(4)	171(3)
O1W···O3(2)	O1W–H1W···O3(2)
3.025(3)	162(6)
O3···O1W(3)	O3–H11···O1W(3)
2.864(3)	157(4)
N2···O1W(4)	N2–H3···O1W(4)
2.870(4)	164(3)

Equivalent positions: (0) x, y, z; (1) $x+1$, $+y$, $+z$; (2) $-x+2$, $-y+1$, $-z+1$; (3) $x+1$, $+y-1$, $+z$; (4) x, $+y-1$, $+z$.

Table 4
Selected bond distances (Å) and angles (°) for complex **2**

Ni1–O1	2.109(2)	O1–Ni1–O1^{I}	87.4(1)
Ni1—O2	1.976(2)	O1–Ni1–O2	166.9(1)
Ni1–N3	2.002(2)	O1–Ni1–O2^{I}	90.4(1)
		O1–Ni1–N3	78.5(1)
		O1–Ni1–N3^{I}	97.3(1)
		O2–Ni1–O2^{I}	94.6(1)
		O2–Ni1–N3	88.9(1)
		O2–Ni1–N3^{I}	94.9(1)
		N3–Ni1–N3^{I}	174.3(1)

$' = -x, y, -z + 1/2$.

The nickel atom presents a distorted octahedral geometry: in fact, the N3–Ni–N3′ angle [174.32(8)°] is very close to the theoretical 180°, but the other two, symmetry-related, O1–Ni–O2′ and O2–Ni–O1′ are 166.86(5)°, due to the chelation rings strain. In the ligand, the pyridoxal nitrogen is deprotonated and this is confirmed by the narrow angle C5–N4–C6 of 118.4(2)° (in protonated pyridoxal moieties, as said before, the reported angles are larger than 120° [9,22]). The whole ligand molecule, which possesses an extended system of conjugated double bonds and should be planar, is on the contrary significantly distorted, and the angle between the average planes of the hydrazone moiety and that of the pyridoxal ring is 26.07(8)°. The strain due to the coordination accounts for the larger distortion observed for the five-membered compared to the six-membered chelation ring. The five-membered ring has a $q_2 = 0.132(2)$ Å and a $\varphi_2 = 22.2(9)°$, corresponding to a twist (^{1}T$_2$) conformation while the six-membered ring has a $\varphi_2 = -30.4(4)°$ and a total puckering amplitude of 0.359(2) Å [$\varphi_2 = 62.2(3)°$] that corresponds to a skew

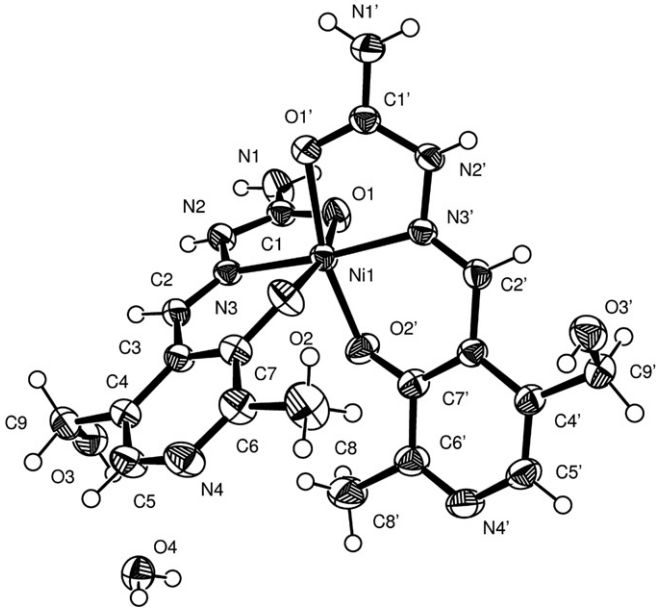


Fig. 3. ORTEP view of complex **2**.

(1S2) conformation. The packing (Fig. 4) is determined by an extended network of hydrogen bondings, as can be seen from Table 5.

3.5. Description of the structure of $[Ni(PLTSC)_2](NO_3)_2 \cdot H_2O$ (4)

The crystal structure of this complex was also determined and the corresponding experimental details are given in Table 1, while the bonds and angles are presented in Table 6. The asymmetric unit consists of a tridentate neutral ligand chelating the nickel atom, two nitrate ions, and one water molecule (see Fig. 5).

In this complex, the angles between the mean plane of the pyridoxal ring and that of the thiosemicarbazide moiety in the two ligands are 33.10(9)° and 31.65(8)°, and this is larger than reported for the hydrazone ligands, probably because of the larger strain due to a bulkier sulfur atom in the five-membered chelation ring. In this compound, the C5–N4–C6 angles of the pyridoxal rings are larger than 120° [124.7(3)° and 125.2(3)°], suggesting the protonation of the nitrogen, which is in agreement with the presence of two nitrates that balance the nickel positive charges.

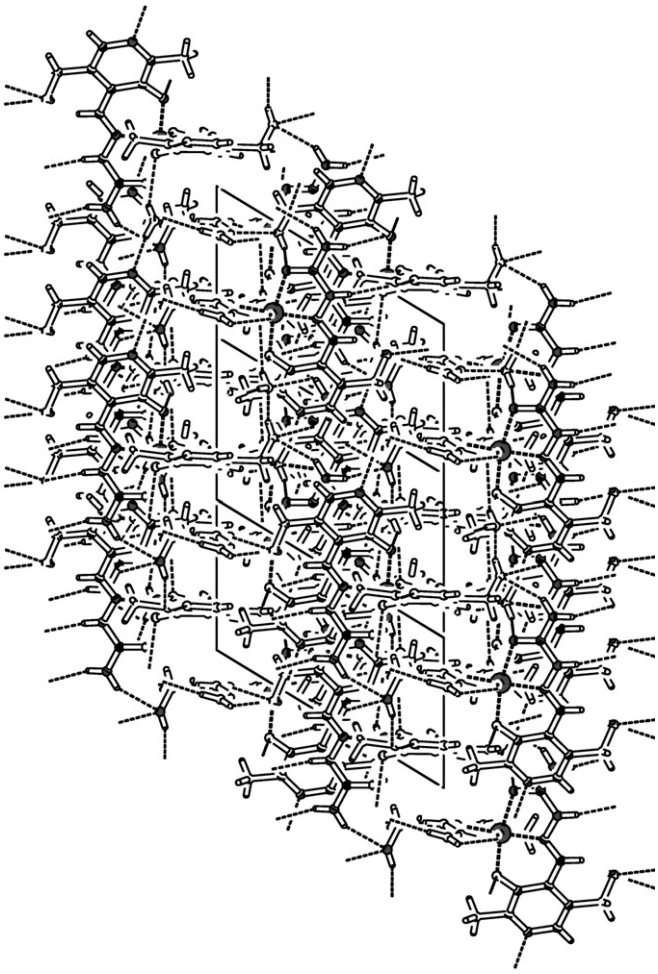


Fig. 4. Crystal structure of complex **2**, view in the *xz* plane.

Table 5
Hydrogen bonds for compound **2**

D···A (Å)	D–H·····A (°)
O3···O4(0)	O3–H11···O4(0)
2.727(3)	160(3)
N2···O4(1)	N2–H3···O4(1)
2.829(2)	171(2)
N1···O3(1)	N1–H2···O3(1)
3.058(2)	161.2(1)
O4···N4(2)	O4–H13···N4(2)
2.807(2)	172(3)
O4···O1(3)	O4–H12···O1(3)
3.018(3)	141(4)
O4···O2(4)	O4–H12···O2(4)
3.025(3)	135(3)

Equivalent positions: (0) x, y, z; (1) $-x-1/2, +y-1/2, -z-1/2$; (2) $-x, -y+1, -z$; (3) $-x-1/2, -y+1/2, -z$; (4) $x-1/2, -y+1/2, +z-1/2$.

Table 6
Selected bond distances (Å) and angles (°) for complex **4**

Ni1–S1	2.426(2)	S1–Ni1–S2	92.47(5)
Ni1–S2	2.410(2)	S1–Ni1–O1	168.40(6)
Ni1–O1	2.052(2)	S1–Ni1–O3	88.78(8)
Ni1–O3	2.039(3)	S1–Ni1–N3	82.09(9)
Ni1–N3	2.040(3)	S1–Ni1–N7	102.84(9)
Ni1–N7	2.057(3)	S2–Ni1–O1	88.50(8)
		S2–Ni1–O3	168.03(7)
		S2–Ni1–N3	103.84(9)
		S2–Ni1–N7	82.46(9)
		O1–Ni1–O3	92.68(10)
		O1–Ni1–N3	86.45(10)
		O1–Ni1–N7	88.74(10)
		O3–Ni1–N3	88.13(11)
		O3–Ni1–N7	85.65(11)
		N3–Ni1–N7	171.95(10)

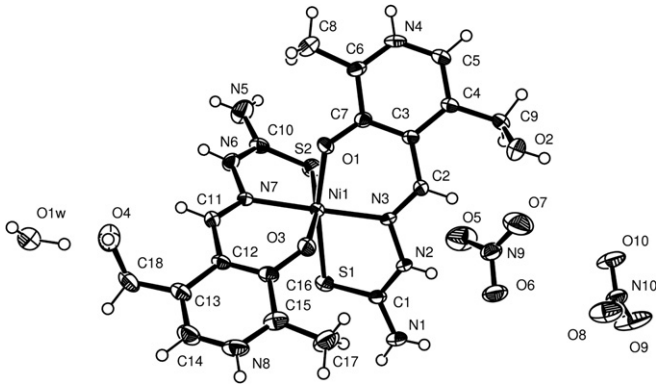


Fig. 5. ORTEP view of complex **4**.

The conformations of the coordination rings are almost identical in the two ligands (for the five-membered chelation rings) $q_2 = 0.316(3)$ Å, $\varphi_2 = 179.2(6)°$ for **1** and $q_2 = 0.322(3)$ Å, $\varphi_2 = -177.9(5)°$ for **2**, which corresponds to an envelope (^{1}E) and for the six-membered rings $\varphi_2 = -36.4(5)°$, QT = 0.406(3) Å and $\theta_2 = 67.8(5)°$ for **1** and $\varphi_2 = -39.3(4)$, QT = 0.415(2) Å and $\theta_2 = 67.4(4)°$ for **2**, which corresponds to a $^1S_6$ screw-boat conformation.

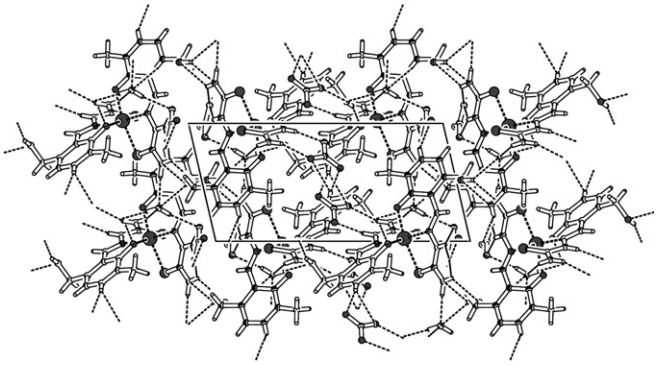


Fig. 6. Crystal structure of **4**, view in the *yz* plane.

Table 7
Hydrogen bonds for compound **4**

D···A (Å)	D–H···A (°)
O11···O4 (0)	O11–H25···O4(0)
2.798(4)	149(5)
N1···O11(1)	N1–H2···O11(1)
2.863(4)	159.0(2)
N5···O11(2)	N5–H14···O11(2)
2.896(4)	151.2(3)
N5···O8(3)	N5–H13···O8(3)
2.913(5)	151.9(2)
N6···O10(3)	N6–H15···O10(3)
2.811(.004)	157.4(2)
O11···O6(4)	O11–H26···O6(4)
2.886(.005)	159(5)
N8···O9(5)	N8–H18···O9(5)
2.837(.004)	154.2(2)
O4···O3(6)	O4–H24···O3(6)
2.663(.004)	156.1(2)

Equivalent positions: (0) x, y, z; (1) $-x+1, -y+1, -z+1$; (2) $-x, -y+1, -z$; (3) $-x, -y, -z$; (4) $x, +y+1, +z$; (5) $-x+1, -y, -z+1$; (6) $-x+1, -y+1, -z$.

The packing (Fig. 6) of this compound is determined by a large network of hydrogen bonds, a few of which are bifurcated among the complex molecules, the nitrate ions and the water molecule, the corresponding values being given in Table 7.

4. Conclusion

On the basis of the previous [9] and present X-ray structures it can be concluded that both ligands are coordinated via the ONX (X = O, PLSC; X = S, PLTSC) set of donor atoms, that is oxygen atom of the phenolic hydroxyl, hydrazine nitrogen, and oxygen or sulfur atom of the semi-/thiosemicarbazide moiety, forming thus one five- and one six-membered metallocycle. Also, it was found that both ligands can coordinate not only in neutral and monoanionic but also in their dianionic forms. The monoanionic form appears as a result of deprotonation of the enol/thiol form of the semi-/thiosemicarbazide moiety, while the dianionic form results from the additional deprotonation of the zwitterion PL moiety. Isolation of complex **2**, which contains monoanionic form of both PLSC molecules with deprotonated pyridine nitrogen atom, and not the enol form of the SC-residue, which has been proved by X-ray analysis, is in contrast to the above sequence of PLSC deprotonation. It should be noted that the order of PLTSC deprotonation is not questionable, since it has been confirmed by the X-ray analysis of several complexes [9].

Acknowledgements

This work was partly supported by the Ministry of Science and Environmental Protection of the Republic of Serbia (Grant No. 142028) and by the Provincial Secretariat for Science and Technological Development of AP Vojvodina.

Appendix A. Supplementary material

CCDC 615727, 615728 and 615729 contain the supplementary crystallographic data for **1**, **2** and **4**. These data can be obtained free of charge via http://www.ccdc.cam.ac.uk/conts/retrieving.html, or from the Cambridge Crystallographic Data Centre, 12 Union Road, Cambridge CB2 1EZ, UK; fax: (+44) 1223-336-033; or e-mail: deposit@ccdc.cam.ac.uk. Supplementary data associated with this article can be found, in the online version, at doi:10.1016/j.poly.2007.01.041.

References

[1] M.J.M. Campbell, Coord. Chem. Rev. 15 (1975) 279.
[2] S. Padhye, G.B. Kauffman, Coord. Chem. Rev. 63 (1985) 127.
[3] J.S. Casas, M.S. Garcia-Tasende, J. Sordo, Coord. Chem. Rev. 209 (2000) 197.
[4] R.B. Singh, B.S. Garg, R.P. Singh, Talanta 25 (1978) 619.
[5] D.X. West, A.E. Liberta, S.B. Padhye, R.C. Chikate, P.B. Sonawane, A.S. Kumbhar, R.G. Yerande, Coord. Chem. Rev. 123 (1993) 49.
[6] D.X. West, S.B. Padhye, P.B. Sonawane, Struct. Bond. 76 (1991) 1.
[7] H. Beraldo, D. Gambino, Mini.-Rev. Med. Chem. 4 (2004) 159.
[8] M. Belicchi Ferrari, F. Bisceglie, C. Casoli, S. Durot, I. Morgenstern-Badarau, G. Pelosi, E. Pilotti, P. Tarasconi, J. Med. Chem. 48 (2005) 1671, and refs. therein.
[9] V.M. Leovac, V.S. Jevtović, Lj.S. Jovanović, G.A. Bogdanović, J. Serb. Chem. Soc. 70 (2005) 393.
[10] V.M. Leovac, Lj.S. Jovanović, V. Divjaković, A. Pevec, I. Leban, T. Armstrong, Polyhedron 26 (2007) 49.
[11] V.S. Jevtović, Lj.S. Jovanović, V.M. Leovac, L.J. Bjelica, J. Serb. Chem. Soc. 68 (2003) 29.
[12] A. Altomare, M.C. Burla, M. Camalli, G.L. Cascarano, C. Giacovazzo, A. Guagliardi, A.G.G. Moliterni, G. Polidori, R. Spagna, J. Appl. Cryst. 32 (1999) 115.
[13] G.M. Sheldrick, SHELXL 97, A Program for Structure Refinement, University of Göttingen, Germany, 1997.
[14] L.J. Farrugia, J. Appl. Cryst. 32 (1999) 837.
[15] M. Nardelli, J. Appl. Cryst. 28 (1995) 659.
[16] C.K. Johnson, M.N. Burnett, ORTEP III. Report ORNL-6895, Oak Ridge National Laboratory, Tennessee, USA, 1996.
[17] A.L. Spek, PLATON. A Multipurpose Crystallographic Tool, Utrecht University, Utrecht, The Netherlands, 1999.
[18] M. Ferrari Belicchi, G. Fava Gasparri, E. Leporati, C. Pelizzi, P. Tarasconi, G. Tosi, J. Chem. Soc. Dalton Trans (1986) 2455.

[19] M. Mohan, P.H. Madhuranath, A. Kumar, M. Kumar, N.K. Jha, Inorg. Chem. 28 (1989) 96.
[20] S. Sarkar, A. Mondal, M.S. El Fallah, J. Ribas, D. Chopra, H. Stoeckil-Evans, K.K. Rajak, Polyhedron 25 (2006) 25.
[21] A.B.P. Lever, Inorganic Electronic Spectroscopy, Mir, Moskva, 1987, p. 2, Russian translation.
[22] C. Singh, Acta Cryst. 19 (1965) 861.
[23] H. Vahrenkamp, Angew. Chem. Int. Ed. Engl 17 (1978) 379.
[24] F.H. Allen, Acta Crystallogr., Sect. B 58 (2002) 380–388.
[25] J. Ribas, M. Monfort, B.K. Ghosh, X. Solans, Angew. Chem. Int. Ed. Engl. 33 (1994) 2087.

Available online at www.sciencedirect.com
ScienceDirect
Polyhedron 26 (2007) 2979–2986
POLYHEDRON
www.elsevier.com/locate/poly

Assembly of two novel three-dimensional networks driven by Alkali metals with an irreversible structural conversion

Jian Lü [a,b], Feng Li [a,b], Da-Qiang Yuan [a,b], Rong Cao [a,*]

[a] State Key Laboratory of Structural Chemistry, Fujian Institute of Research on the Structure of Matter, Chinese Academy of Sciences, Fujian, Fuzhou 350002, PR China
[b] Graduate School, Chinese Academy of Sciences, Beijing 100039, PR China

Received 20 December 2006; accepted 29 January 2007
Available online 20 February 2007

Abstract

Two novel three-dimensional (3-D) heterometallic frameworks containing dinuclear p-block metal–oxygen clusters, formulated as $[Na_2(H_2O)_3Cu_2(H_2O)_6(sip)_2]\cdot H_2O$ **1** and $[K_2(H_2O)_2Cu_2(H_2O)_5(sip)_2]\cdot H_2O$ **2** (sip^{3-} = 5-sulfoisophthalic anion), have been synthesized at room temperature. Single-crystal X-ray diffraction revealed that similar structural motifs (one-dimensional zigzag chain built by copper atoms and sip^{3-} ligands, and dinuclear p-block metal–oxygen clusters) can be found within their crystal structures. Compound **1** shows an interesting 3-D structure constructed from copper-sip chains interconnected by two kinds of dinuclear sodium–oxygen clusters adopting 4- and 6-connected fashions. Compound **2** displays a 3-D framework formed by cross-linking copper-sip chains via 6-connected dinuclear potassium–oxygen clusters. Interestingly, an irreversible structural conversion from **1** to **2** was observed.
© 2007 Elsevier Ltd. All rights reserved.

Keywords: Copper; Alkali metal; Metal-organic framework; Heterometallic; Three-dimensional

1. Introduction

Crystal engineering of metal-organic frameworks (MOFs) is realizable by the choice of metals and the numerous choice and design of ligands [1–5], which bears the weight of prospective applications in new chemical separation, molecular selection, ion exchange, gas adsorption and storage [6–9]. Recently, research targets have been focused upon the chemical design of heterometallic MOFs (denoted HMOFs hereafter) with intriguing topologies and fascinating properties. An increasing number of HMOFs containing d- and f-block metals, especially 3d–4f ones, have been successfully isolated and well investigated [10–14].

At the same time, alkali cations have captured more and more research attention from chemists and materials scientists owing to their low polarizability and various coordination modes to construct polymer materials featuring robust structures and predominant properties. Integration of p-block alkali metals into HMOFs may result in new materials with potential applications in magnetic ordering, catalytic and biological recognition [15]. However, HMOFs based on p-block metals have not been well exploited until now, and the successful preparation of p–d HMOFs still remains a synthetic challenge not only because of the difficulties in controlling the synergistic interactions between two kinds of distinct metal cations, but also in exploring organic ligands or co-ligands as suitable linkers.

In this work, a bifunctional (carboxylate and sulfonate) ligand, the 5-sulfoisophthalic anion (sip^{3-}), has been chosen to build HMOFs owing to the following two considerations: (a) it is well known that mixed ligands or a multifunctional ligand is required to realize the combination of metals with distinct electric configurations in HMOFs. However, the introduction of mixed ligands may lead to the occurrence of coordination competition

* Corresponding author. Tel./fax: +86 591 83796710.
E-mail address: rcao@fjirsm.ac.cn (R. Cao).

0277-5387/$ - see front matter © 2007 Elsevier Ltd. All rights reserved.
doi:10.1016/j.poly.2007.01.057

between different kinds of ligands, and a simple MOF built of a metal and organic ligand with a coordination preference is more likely to be obtained. In this regard, employment of a multifunctional ligand is a reasonable choice to achieve a HMOF by means of its distinctive functional groups; and (b) carboxyl ligands have been demonstrated to be a predominant structural linkage to construct MOFs with transition metals [1–5,10–14], and organic sulfonates prefer to coordinate to main group metals, especially alkaline metals and alkaline earth metals [16–18]. Very recently, Kitagawa and co-workers have reported a p–d HMOF prepared by using mixed carboxylate and sulfonate group ligand and proved that the alkali metal acts as an affinity site on the pore surface for guests and their adsorption [19]. On examination of the literature, it is found that the sip ligand adopts complicated coordination modes in transition metal-organic polymers because of its various coordination fashions and high coordination numbers that made it difficult to predict the final framework structures on the basis of rational design [20–23]. However, what captured our attention is that the sulfonate groups of sip ligands often remain uncoordinated, and thus the sip ligands exhibit relatively simple coordination modes similar to isophthalato ligands, when it coordinates to copper atoms. Furthermore, these resulting low-dimensional (0- or 1-D) copper-organic frameworks, partly a consequence of the chelating coordination fashion of the sip ligand, possess uncoordinated sulfonate groups pointing outward a cluster [24] or throwing out a chain like a fish-bone [25]. Such kind of arrangement of free sulfonate groups can offer effective coordination positions and a considerable spatial void for secondary p-block metals, favoring the formation of p–d HMOFs.

Inspired by our early research experience of the sip ligand and other sulfonate containing ligands [21–23,25,26], we isolated successfully two novel HMOFs by trial and error, formulated as $[Na_2(H_2O)_3Cu_2(H_2O)_6(sip)_2]\cdot H_2O$ **1** and $[K_2(H_2O)_2Cu_2(H_2O)_5(sip)_2]\cdot H_2O$ **2** (sip^{3-} = 5-sulfoisophthalic anion). Structural analyses indicate that **1** and **2** feature similar 3-D frameworks comprising dinuclear p-block metal–oxygen clusters. **1** possesses an interesting framework constructed from copper-sip chains interconnected by two kinds of dinuclear sodium–oxygen clusters adopting 4- and 6-connected fashions. **2** displays a 3-D framework formed by cross-linking similar 1-D copper-sip chains via 6-connected potassium–oxygen clusters. Interestingly, an irreversible structural conversion from **1** to **2** was observed.

2. Experimental

2.1. General

All chemicals were commercially purchased and were used without purification. Elemental analyses were carried out on an Elementar Vario EL III analyzer. Infrared (IR) spectra were recorded with Perkin–Elmer Spectrum One as KBr pellets in the range 400–4000 cm^{-1}. Thermogravimetric analysis was recorded with a NETZSCH STA 449C unit at a heating rate of 10 °C min^{-1} under nitrogen. Variable-temperature (2.0–300.0 K) magnetic susceptibility measurements were carried out on a Quantum Design PPMS60000 in a magnetic field of 10 kOe, and the diamagnetic corrections were evaluated using Pascal's constants. Single crystal X-ray diffraction was carried out using Rigaku Mercury CCD/AFC and Bruker SMART 1K diffractometers.

2.2. Syntheses of the complexes

2.2.1. $[Na_2(H_2O)_3Cu_2(H_2O)_6(sip)_2]\cdot H_2O$ (1)

A mixture of $Cu(NO_3)_2\cdot 3H_2O$ (0.049 g, 0.2 mmol) and NaCl (0.03 g, 0.5 mmol) was added to 10 ml water, and the pH value of the solution was adjusted to about 5.0 using dilute NaOH. After several minutes of stirring, the clear solution was transferred to a test tube. Another portion of NaH_2sip (0.054 g, 0.2 mmol) in 10 ml methanol was placed carefully on the surface, and allowed to diffuse. Blue block crystals of **1** suitable for single crystal X-ray diffraction analysis formed 2 weeks later, yielding 26 mg (31% based on Cu). *Anal.* Calc for $C_{16}H_{26}Cu_2Na_2O_{24}S_2$: C, 22.89; H, 3.12; Na, 5.48; Cu, 15.14. Found: C, 24.21; H, 3.16; Na, 5.42; Cu, 14.35%. IR characteristics (KBr, cm^{-1}): 3500m, 3198m, 1616s, 1461s, 1357s, 1251w, 1105s, 1026w, 890w, 871w, 834m, 786m, 609w, 655m, 554w, 507w.

2.2.2. $[K_2(H_2O)_2Cu_2(H_2O)_5(sip)_2]\cdot H_2O$ (2)

Compound **2** was prepared from a reaction procedure similar to **1**. KCl (0.035 g, 0.5 mmol) was used instead of NaCl, and the pH value of the reaction mixture was adjusted to about 5.0 using dilute KOH. Blue prism crystals of **2** suitable for single crystal X-ray diffraction analysis formed after several weeks, yielding 32 mg (38% based on Cu). *Anal.* Calc for $C_{16}H_{22}Cu_2K_2O_{22}S_2$ (%): C, 23.00; H, 2.65; K, 9.36; Cu, 15.21. Found (%): C, 23.54; H, 2.28; K, 9.66; Cu, 14.04%. IR characteristics (KBr, cm^{-1}): 3454m, 3172m, 1655s, 1556s, 1425s, 1373m, 1219w, 1039s, 1001m, 874m, 816w, 791m, 675m, 586w, 501w.

2.2.3. Structural conversion process

0.01 g (10 mg) crystals of **1** were dissolved in saturated KCl aqueous solution with stirring, and the pH value was kept at about 5.0. Blue crystals of **2** formed after a week (yielding 0.0047 g, 4.7 mg) and were characterized by single-crystal X-ray diffraction. However, no successful trials were observed when crystals of **2** were treated to obtain crystalline **1** by the same process.

2.3. X-ray structure determination

Diffraction intensities for **1** and **2** were collected on Rigaku Mercury CCD/AFC and Bruker SMART 1000 CCD

Table 1
Crystal data and structure refinement for compounds **1** and **2**

Empirical formula	$C_{16}H_{26}Cu_2Na_2O_{24}S_2$	$C_{16}H_{22}Cu_2K_2O_{22}S_2$
Formula weight	839.55	835.61
Temperature (K)	293(2)	293(2)
Wavelength (Å)	0.71073	0.71073
Crystal system	monoclinic	monoclinic
Space group	$P2_1/n$	$P2_1/n$
a (Å)	12.2979(19)	12.1899(2)
b (Å)	17.502(3)	17.5678(2)
c (Å)	13.986(2)	13.4748(2)
β (°)	109.830(2)	112.6530(2)
Volume (Å^3)	2831.8(8)	2663.01(7)
Z	4	4
Goodness-of-fit on F^2	1.092	1.052
Final R indices [$I > 2\sigma(I)$]	R_1[a] = 0.0381, wR_2[b] = 0.1146	R_1[a] = 0.0473, wR_2[b] = 0.1825
Indices (all data)	R_1[a] = 0.0427, wR_2[b] = 0.1209	R_1[a] = 0.0494, wR_2[b] = 0.1883

[a] $R_1 = \sum||F_o| - |F_c||/\sum|F_o|$.
[b] $wR_2 = \{\sum[w(F_o^2 - F_c^2)^2]/\sum[w(F_o^2)^2]\}^{1/2}$.

Table 2
Selected bond lengths for compounds **1** and **2**

1			
Cu(1)–O(1)	1.921(2)	Cu(2)–O(5)	1.952(2)
Cu(1)–O(7)#1	1.934 (2)	Cu(2)–O(3)	1.952(2)
Cu(1)–O(5W)	2.022(2)	Cu(2)–O(4W)	1.963(2)
Cu(1)–O(1W)	2.046(2)	Cu(2)–O(3W)	2.005(2)
Cu(1)–O(2W)	2.291(2)	Cu(2)–O(7W)	2.435(2)
Na(1)–O(13)	2.302(2)	Na(2)–O(6W)	2.289(4)
Na(1)–O(10W)#5	2.388(3)	Na(2)–O(6W)#8	2.416(4)
Na(1)–O(9W)#5	2.432(3)	Na(2)–O(11)#9	2.446(5)
Na(1)–O(10W)#6	2.443(3)	Na(2)–O(12)	2.454(4)
Na(1)–O(3W)#5	2.474(3)	Na(2)–O(2W)#2	2.465(4)
Na(2′)–O(12)	2.305(4)	Na(2′)–O(6W)	2.351(4)
Na(2′)–O(2W)#2	2.316(4)	Na(2′)–O(6W)#8	2.352(4)
Cu(1)–O(1)	1.921(2)	Cu(2)–O(5)	1.952(2)
Cu(1)–O(7)#1	1.934 (2)	Cu(2)–O(3)	1.952(2)
Cu(1)–O(5W)	2.022(2)	Cu(2)–O(4W)	1.963(2)
2			
Cu(1)–O(7)#1	1.939(2)	Cu(2)–O(5W)	1.965(2)
Cu(1)–O(1)	1.949(2)	Cu(2)–O(3)	1.972(2)
Cu(1)–O(2W)	2.012(3)	Cu(2)–O(4W)	1.973(2)
Cu(1)–O(3W)	2.043(2)	Cu(2)–O(5)	2.000(2)
Cu(1)–O(1W)	2.155(3)	K(2)–O(14)#8	2.662(3)
K(1)–O(10)#4	2.648(3)	K(2)–O(2)#9	2.725(3)
K(1)–O(13)	2.747(3)	K(2)–O(11)#10	2.806(3)
K(1)–O(5W)#2	2.793(3)	K(2)–O(7W)#11	2.853(3)
K(1)–O(6W)#2	2.835(3)	K(2)–O(14)	2.886(3)
K(1)–O(2W)#5	2.965(3)	K(2)–O(12)	3.067(3)
K(1)–O(10)#6	3.039(3)	K(2)–O(4W)#11	3.155(3)
K(1)–O(5)#2	3.259(3)	K(2)–O(8W)	3.429(3)
K(1)–O(1W)#5	3.316(4)		

Symmetry transformations used to generate equivalent atoms:
For **1** #1 $x, y-1, z$; #2 $-x, -y+1, -z$; #5 $x-1/2, -y+3/2, z-1/2$; #6 $-x-1/2, y+1/2, -z-1/2$; #8 $-x-1, -y+2, -z$; #9 $-x+1/2, y+1/2, -z+1/2$.
For **2** #1 $x, y-1, z$; #2 $-x, -y+2, -z$; #4 $-x+1/2, y+1/2, -z+1/2$; #5 $x-1, y+1, z$; #6 $x-3/2, -y+3/2, z-1/2$; #8 $-x-1, -y+2, -z-1$; #9 $x-1/2, -y+3/2, z-1/2$; #10 $-x+1/2, y+1/2, -z-1/2$; #11 $-x-1/2, y+1/2, -z-1/2$.

diffractometers, respectively, equipped with graphite-monochromated Mo Kα radiation with a radiation wavelength of 0.71073 Å by using the ω-scan technique. Absorption corrections were performed using CrystalClear and SADABS [27], respectively. Structures were solved by direct methods and refined on F^2 by full-matrix least-squares using the SHELXTL-97 program package [28]. All non-hydrogen atoms were refined anisotropically. The organic hydrogen atoms were positioned geometrically and the hydrogen atoms bonded to water oxygen atoms were not located. The crystallographic data for complexes **1** and **2** are listed in Table 1, and selected bonds are in Table 2.

3. Results and discussion

3.1. Crystal structure of $[Na_2(H_2O)_3Cu_2(H_2O)_6(sip)_2]\cdot H_2O$ (**1**)

X-ray crystallography reveals that the structure of **1** is constructed from individual one-dimensional (1-D) $\{Cu_2(H_2O)_6(sip)_2\}_n$ chains interconnected by two types of dinuclear sodium–oxygen clusters into a 3-D heterometallic framework. The basic building block of compound **1** is shown in Fig. 1a. There are two crystallographically independent copper sites and two unique sodium positions in the asymmetric unit. The Cu(1) atom links to two carboxyl oxygen atoms from two sip^{3-} ligands and three aqua ligands with Cu(1)–O distances in the range 1.921–2.291 Å. The O–Cu(1)–O bond angles are in the range 83.99–103.07°, which demonstrates that the basic plane of the $\{Cu(1)O_5\}$ square pyramid is a little distorted. The Cu(2) atom, possessing a similar coordination geometry to Cu(1), coordinates to two carboxyl oxygen atoms belonging to two sip^{3-} ligands and three aqua ligands with Cu(2)–O distances in the range 1.952–2.435 Å and O–Cu(2)–O bond angles in the range 86.51–99.23°, giving birth to a $\{Cu(2)O_5\}$ square pyramid. There is a weak interaction between Cu(2) and Ow7 (2.608 Å), if it is considered, the Cu(2) center may also be regarded as residing in an elongated octahedral environment on account of a considerable Jahn–Teller effect. The Na(1) atom, residing in a roughly distorted square pyramid, connects to one sulfonate O donor and four coordination water molecules. The other Na site is occupied by two disordered $\{NaO_5\}$ square pyramids with two Na atoms with 50% probability for each, sharing four O atoms located in the basic plane, and the separation between the two Na positions is 0.905 Å. Thus, the overall Na(2) site can be regarded as a $\{NaO_6\}$ octahedra with Na–O bonds varying from 2.302 Å to 2.474 Å. There are also two crystallographically independent sip^{3-} ligands and a non-coordinated water molecule.

In the structure of compound **1**, three types of individual building blocks, namely 1-D copper-organic chain, type I and type II dinuclear sodium–oxygen clusters, can be observed. Two $\{Na(1)O_5\}$ square pyramids connect to each

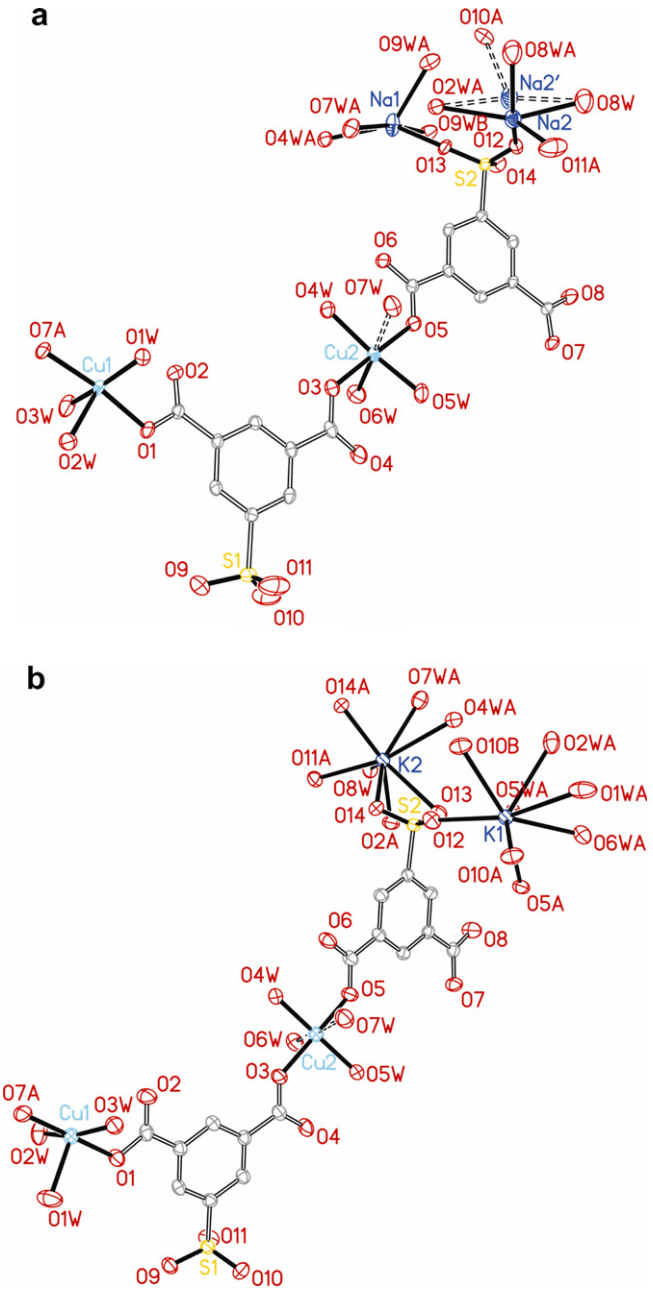


Fig. 1. ORTEP drawing of the basic building block in (a) **1** and (b) **2** showing the coordination environment around the metal centers with thermal ellipsoids at 50% probability. For the sake of clarity, only atoms coordinated to metal centers are labelled. Hydrogen atoms and non-coordinated water molecules are omitted.

other by sharing an edge to form the type I $\{Na_2O_8\}$ cluster. Similarly, two $\{Na(2)O_6\}$ octahedra link together in an edge-sharing mode to give the type II $\{Na_2O_{10}\}$ cluster. Adjacent Cu atoms are jointed together by the carboxyl groups of sip^{3-} ligands adopting a bis-monodented manner to generate a 1-D zigzag copper-organic chain running along the b axis. The individual 1-D chain built by copper atoms and sip^{3-} ligands assembles with uncoordinated sulfonate groups pointing outside as expected, very similar to the chains observed in our previous work [22]. The copper atoms in the zigzag chain are located nearly in line and the shortest copper-copper intra-chain separation is 9.335 Å. Such a pair of chains is held together via type I 4-connected $\{Na_2O_8\}$ clusters to give a double chain (Fig. 2a), and the double chains pack in layers with neighboring pairs of chains sharing their $\{Na_2O_8\}$ clusters (Fig. 2c). Alternatively, each $\{Na_2O_8\}$ cluster acts as a tetradented ligand bonding to four individual zigzag chains (Fig. S1a) generating a 2-D network (Fig. 2b). These four 1-D chains connect by a $\{Na_2O_8\}$ cluster are not orientated in planar positions due to the stereo geometry of the clusters, and therefore the layer is best described as a pleat net with mean planes of double chains inclined to the plane of the layer (Fig. 2c). It is also notable that strong intra-layer π–π interactions exist between neighboring double chains because of their sine–cosine arrangements (Fig. 2b), which may help to stabilize the structure, and the nearest distance

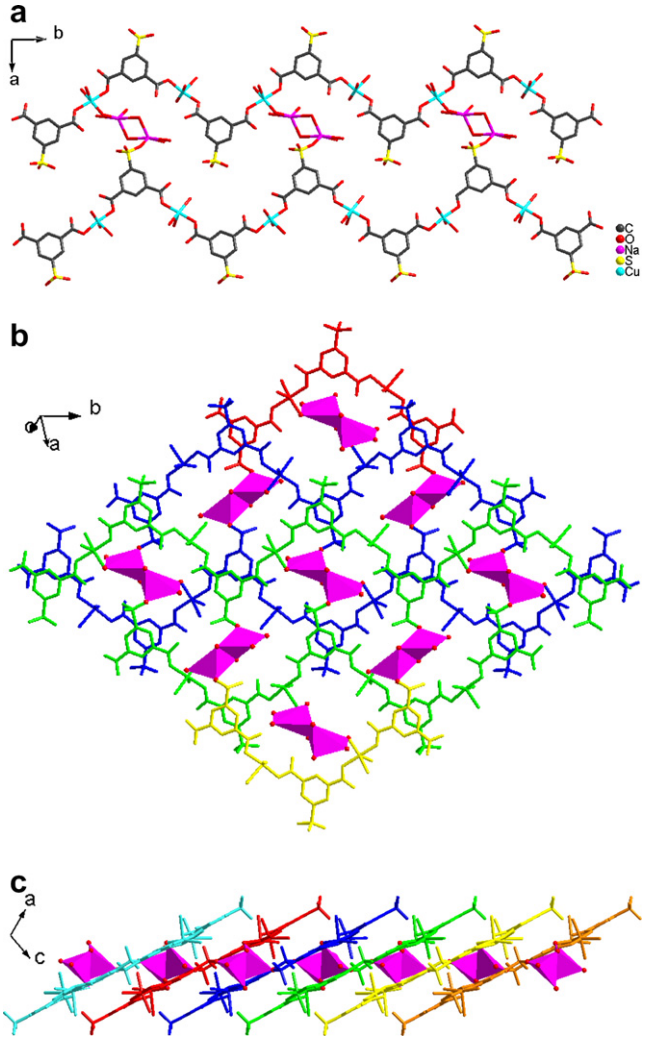


Fig. 2. (a) The double chain ribbon in **1** containing 4-connected type I dinuclear sodium–oxygen clusters. (b) The 2-D net built by double chain ribbons extended via type I cluster nodes. (c) A side view of the 2-D net with double chain ribbons distinguished by different colors. (For interpretation of the references to color in this figure legend, the reader is referred to the web version of this article.)

of parallel benzene rings is 3.460 Å. These 2-D layers are further connected into a 3-D framework via type II 6-connected $\{Na_2O_{10}\}$ clusters. Each $\{Na_2O_{10}\}$ cluster joints two adjacent layers by coordinating to six 1-D zigzag chains with three in one layer and three in the other, giving rise to a pillar-layered 3-D pattern, as shown in Fig. 3.

3.2. Crystal structure of $[K_2(H_2O)_2Cu_2(H_2O)_5(sip)_2]\cdot H_2O$ (2)

The structure of **2** features a 3-D heterometallic framework similar to **1**. There are two crystallographically independent copper sites and two potassium atoms in the asymmetric unit of **2** (Fig. 1b). The Cu(1) atom connects two carboxyl oxygen atoms from two sip^{3-} ligands and three aqua ligands with Cu(1)–O distances in the range 1.938–2.153 Å, to finish its square pyramidal geometry. The Cu(2) atom, adopting a square planar coordination mode, coordinates to two carboxyl oxygen atoms belonging to two sip^{3-} ligands and two aqua ligands with Cu(2)–O distances in the range 1.967–2.0 Å. There are weak interactions between Cu(2) and Ow6 (2.480 Å) and between Cu(2) and Ow7 (2.489 Å), and if they are taken into consideration, the Cu(2) center may also be regarded as residing in an elongated octahedral environment on account of a considerable Jahn–Teller effect, similar to the Cu(2) center in **1**. The K(5) atom, displaying a bi-capped triprismatic geometry, bonds to one carboxyl O atom, three sulfonate O atoms and four coordination water molecules. The K(6) atom links one carboxyl O donor, four sulfonate O atoms and three aqua ligands, showing a distorted bi-capped triprismatic coordination fashion (Fig. S3). The K–O bonds vary from 2.648 Å to 3.316 Å. There are also two crystallographically independent sip^{3-} ligands and a lattice water molecule.

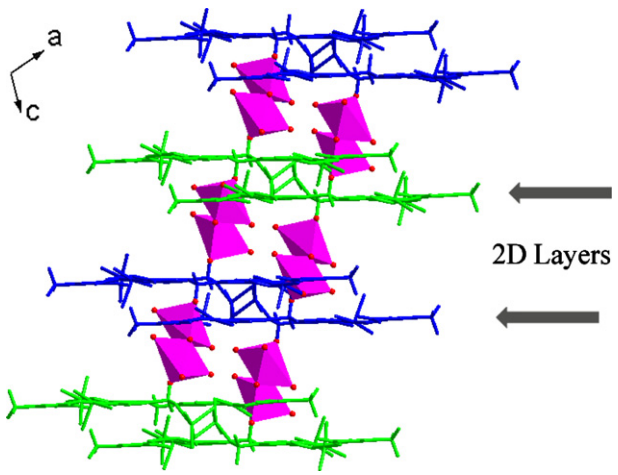


Fig. 3. A view of the 3-D framework of **1** along the *b* axis, showing the 6-connected type II sodium–oxygen clusters anchoring to the pleat 2-D nets. For the sake of clarity, each 2-D sheet is represented by one double chain ribbon.

In the structure of **2**, only two types of building blocks are observed, that is a 1-D copper-sip zigzag chain and a 6-connected dinuclear potassium–oxygen clusters. Similarly, Cu atoms are jointed together by the carboxyl groups of sip^{3-} ligands, giving birth to a 1-D zigzag copper-organic chain with uncoordinated sulfonate groups running along the *b* axis. Such a pair of chains is held together via 6-connected $\{K_2O_{14}\}$ clusters to give a double chain (Fig. 4a). The double chains pack in layers with neighboring pairs sharing their $\{K_2O_{14}\}$ clusters to form a 2-D net (Fig. 4b). There are also strong intra-layer π–π interactions between neighboring double chains because of their sine–cosine arrangements (Fig. 4b), with the nearest distance of parallel benzene rings being 3.467 Å. The 2-D nets extend into a 3-D framework by means of the connection of free sulfonate groups and $\{K_2O_{14}\}$ clusters belonging to adjacent layers (Fig. 4c). As a consequence, each $\{K_2O_{14}\}$ cluster links six individual 1-D copper-sip chains with four in a layer and other two from two adjacent layers, respectively.

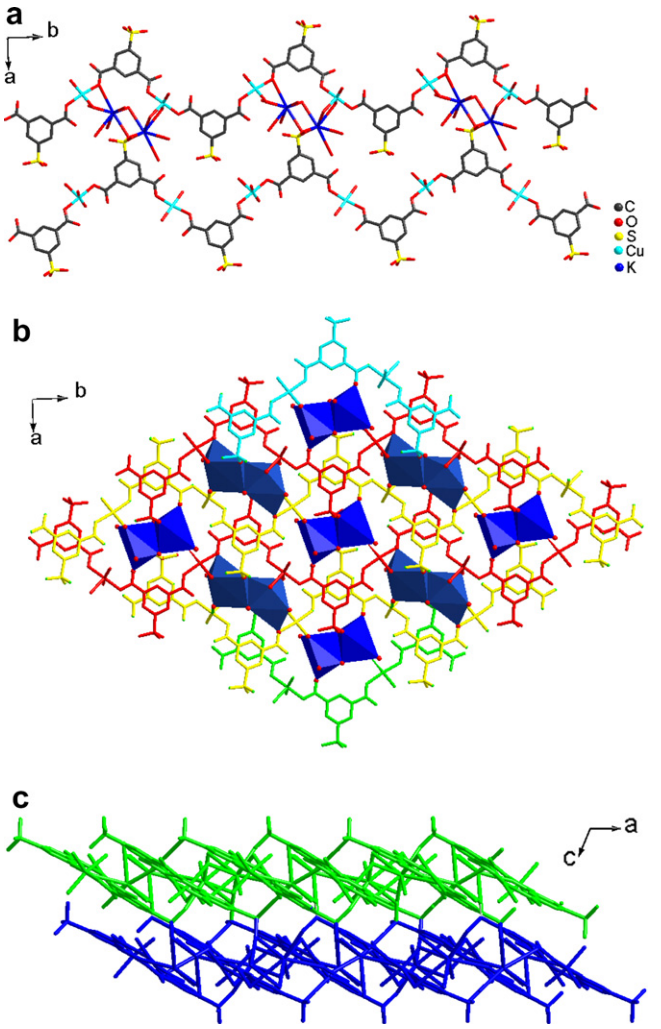


Fig. 4. A view of (a) the double chain ribbon in **2** containing dinuclear potassium–oxygen clusters; (b) the 2-D net in **2**, and (c) the 3-D framework of **2**.

3.3. Discussion

In the crystal structure of **1**, the type II $\{Na_2O_{10}\}$ cluster is a more commonly found dinuclear sodium–oxygen unit than the type I $\{Na_2O_8\}$ cluster [29–37]. Although, these two clusters have been observed as discrete cluster units in previously reported crystal structures [29,31] and known to be optional linkers of organometallic fragments, high-dimensional (2-D and 3-D) frameworks constructed by the linkages of dinuclear sodium–oxygen clusters are still rare. To our knowledge, the co-existence of the two sodium–oxygen clusters in a single structure has not been documented in the literature to date. In the structure of **2**, only one kind of dinuclear $\{K_2O_{14}\}$ cluster is observed. Although all the $\{K_2O_{14}\}$ clusters in **2** are 6-connected to zigzag chains, the $\{K_2O_{14}\}$ clusters display two kinds of linking manner, acting as hexa- and octa-dented ligands (Fig. S2a and S2b, respectively).

The basic 1-D copper-sip chains in both **1** and **2** have similar structures to those found in supramolecular polymers stabilized by organic amine molecules involving hydrogen bonds [22], previously observed by our group, in which the protonated sulfonate groups do not participate in the coordination. However, the sulfonate groups coordinate to p-block alkaline metals as expected in the current instance. We tried to isolate the individual copper-sip chain structure under similar reaction conditions but lacking the secondary organic ligands or alkaline metals, but all attempts failed. It is therefore believed the extra covalent or supramolecular contacts, or a combination of the two, may play crucial roles in the stabilization of the formation of the 1-D polymer structures.

1 and **2** were originally prepared from similar reactions, and an irreversible structural conversion from **1** to **2** controlled by p-block alkali metals was observed when a crystalline sample of **1** was treated with saturated KCl solution. Although the individual 1-D copper-sip chain has not been isolated, the successful structural conversion from **1** to **2** demonstrates that the 1-D copper-sip chain is controllable with the existence of alkali metals. Moreover, the possible reason for an irreversible structural conversion is ascribed to the formation of p-block metal–oxygen clusters as according to the structures the $\{K_2O_{14}\}$ cluster is larger than either a $\{Na_2O_8\}$ or $\{Na_2O_{10}\}$ cluster with more surface O donors, offering more coordination sites and displaying complicated coordination fashions, also it possesses stronger coordination ability and affinity to the host framework, resulting in an irreversible transformation process [38]. Another possible reason for the irreversible structural conversion may be the low solubility of **2** compared to **1**.

3.4. Thermal gravimetric analyses

The thermal gravimetric (TG) curve for compound **1** (Fig. 5a) exhibits a continuous mass loss in the temperature range from 30 °C to 800 °C. The first two steps, with a weight loss of 19.59% and a slight distinction between 50 °C and 250 °C, correspond to the dehydration of the non-coordinated and coordinated water molecules (calc. 21.46%). Other steps with a mass loss of 49.62% arise from the decomposition of organic ligands and further decomposition of the sample (calc. 50.30%). The total weight loss of 69.21% is in accordance with the calculated value 71.76%. The TG curve for **2** (Fig. 5b) exhibits a continuous mass loss in the temperature range from 30 °C to 800 °C. The first two steps, with a weight loss of 16.98% and a slight distinction between 60 °C and 280 °C, correspond to the dehydration of the non-coordinated and coordinated water molecules (calc. 17.23%). The mass loss of 51.44% in the temperature range from 280 to 750 is assigned to the decomposition of organic ligands and further decomposition of the sample (calc. 50.58%). The total weight loss of 68.42% is in accordance with the calculated value 67.81%.

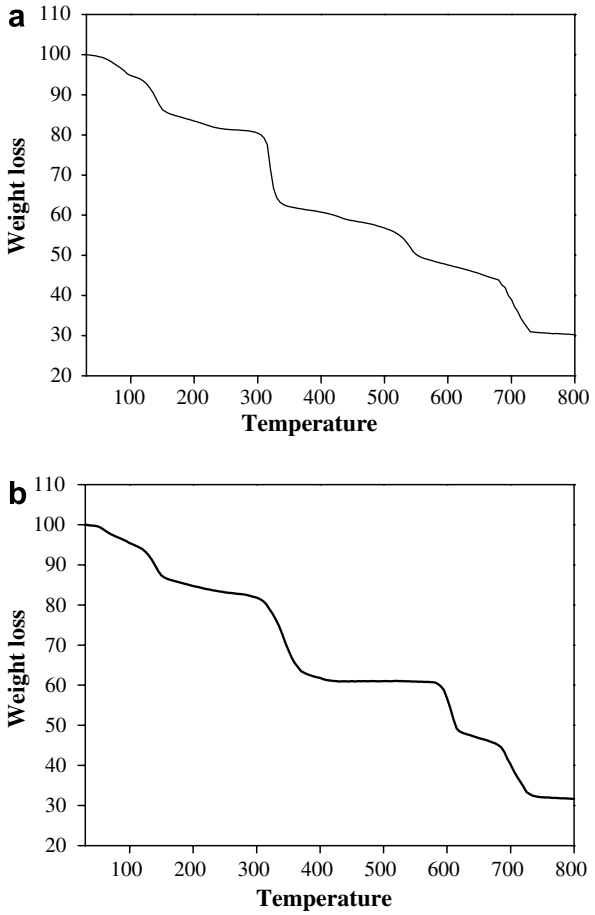


Fig. 5. TG curves for (a) **1**, and (b) **2**.

3.5. Magnetic properties of compound *1*

Considering the similar coordination environment around the copper centers and the Cu...Cu separations in **1** and **2**, only the magnetic properties of **1** were studied. The temperature dependence of the magnetic susceptibility of **1** is plotted in Fig. 6. A non-linear fit $\chi_M = C/$

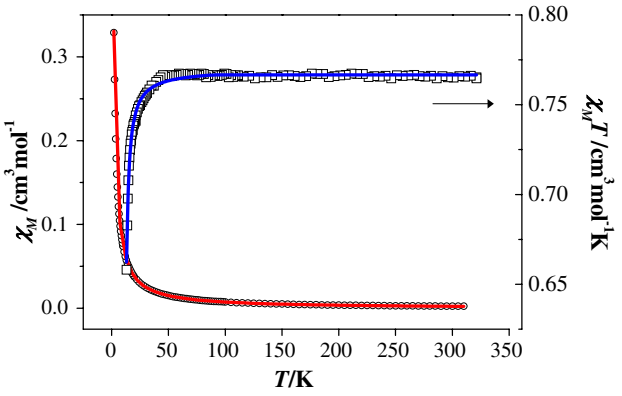


Fig. 6. Temperature dependence of χ_M and $\chi_M T$ for **1** with the solid line showing the best fit obtained through χ_M (red) and $\chi_M T$ (blue) values. (For interpretation of the references to color in this figure legend, the reader is referred to the web version of this article.)

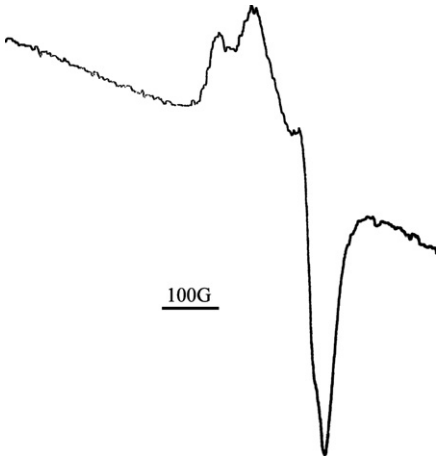


Fig. 7. EPR spectrum for **1**.

$(T-\theta)+\chi_0$ in the temperature range from 2 to 300 K reveals a Curie–Weiss behavior with a Curie constant $C = 0.77(7)\ \mathrm{cm^3\ mol^{-1}\ K}$ and Weiss constant $\theta = -0.3(3)$ K (background susceptibility $\chi_0 = -2.6\times10^{-4}\ \mathrm{cm^3\ mol^{-1}}$). The room-temperature $\chi_M T$ value of $0.766\ \mathrm{cm^3\ mol^{-1}\ K}$ is in good accordance with the value of $0.75\ \mathrm{cm^3\ mol^{-1}\ K}$ expected for two spin-only Cu(II) ions per formula unit. Upon cooling the system, $\chi_M T$ decreases smoothly until approximately 40 K and then it decreases at a faster rate, reaching a value of $0.658\ \mathrm{cm^3\ mol^{-1}\ K}$ at 2 K, showing a paramagnetic behavior for **1**. The EPR spectrum of **1** at 77 K shows a Cu^{2+} signal with $g_{\|} = 2.185$ and $g_{\perp} = 2.116$ (Fig. 7), which further confirms the structural analysis of five-coordinated Cu(II) centers. A fitting result by a mononuclear Cu(II) model gives a g factor of 2.126, which is in accordance with the EPR results.

4. Conclusion

In short, we report here two new HMOFs containing p- and d-block metals by the introduction of a multifunctional organic ligand. **1** shows an interesting 3-D structure constructed from copper-sip chains interconnected by two kinds of dinuclear sodium–oxygen clusters adopting 4- and 6-connected fashions. **2** displays a 3-D framework formed by cross-linking similar 1-D zigzag chains via 6-connected potassium–oxygen clusters. Furthermore, the structures exhibit an irreversible structural conversion from **1** to **2** via ion exchange. The successful preparation of compounds **1** and **2** indicate that use of organic ligands with multifunctional groups in constructing HMOFs is both promising and attractive.

Acknowledgements

This work was financially supported by 973 program (2006CB932900), NSFC (90206040, 20325106, 20521101, 20333070), NSF of Fujian Province (2005HZ01-1), Fujian Key Laboratory of Nanomaterials (2006L2005) and CAS. J.L. thanks Dr. Stuart R. Batten for helpful discussion on the structures.

Appendix A. Supplementary material

CCDC 606994 and 611175 contain the supplementary crystallographic data for **1** and **2**. These data can be obtained free of charge via http://www.ccdc.cam.ac.uk/conts/retrieving.html, or from the Cambridge Crystallographic Data Centre, 12 Union Road, Cambridge CB2 1EZ, UK; fax: (+44) 1223-336-033; or e-mail: deposit@ccdc.cam.ac.uk. Supplementary data associated with this article can be found, in the online version, at doi:10.1016/j.poly.2007.01.057.

References

[1] H. Li, M. Eddaoudi, M. O'Keeffe, O.M. Yaghi, Nature 402 (1999) 276.
[2] S.S-Y. Chui, S.M.-F. Lo, J.P.H. Charmant, A.G. Orpen, I.D. Williams, Science 283 (1999) 1148.
[3] B. Chen, M. Eddaoudi, S.T. Hyde, M. O'Keeffe, O.M. Yaghi, Science 291 (2001) 1021.
[4] M. Eddaoudi, J. Kim, N. Rosi, D. Vodak, D.V. Wachter, M. O'Keeffe, O.M. Yaghi, Science 295 (2002) 469.
[5] N.L. Rosi, J. Eckert, M. Eddaoudi, D.T. Vodak, J. Kim, M. O'Keeffe, O.M. Yaghi, Science 300 (2003) 1127.
[6] S.L. James, Chem. Soc. Rev. 32 (2003) 276.
[7] M. Kondo, T. Okubo, A. Asami, S.I. Noro, T. Yoshitomi, S. Kitagawa, T. Ishii, H. Matsuzaka, K. Seki, Angew. Chem., Int. Ed. 38 (1999) 140.
[8] D. Braga, Chem. Commun. (2003) 2751.
[9] R.H. Wang, M.C. Hong, J.H. Luo, R. Cao, J.B. Weng, Chem. Commun. (2003) 1018.
[10] R.E.P. Winpenny, Chem. Soc. Rev. 27 (1998) 447.
[11] B. Zhao, P. Cheng, Y. Dai, C. Cheng, D.Z. Liao, S.P. Yan, Z.H. Jiang, G.L. Wang, Angew. Chem., Int. Ed. 42 (2003) 934.
[12] B. Zhao, P. Cheng, X. Chen, C. Cheng, W. Shi, D. Liao, S. Yan, Z. Jiang, J. Am. Chem. Soc. 126 (2004) 3012.
[13] S. Tanase, M. Andruh, A. Muller, M. Schmidtmann, C. Mathoniere, G. Rombaut, Chem. Commun. (2001) 1084.
[14] Q. Yue, J. Yang, G.H. Li, G.D. Li, W. Xu, J.S. Chen, S.N. Wang, Inorg. Chem. 44 (2005) 5241.

[15] J. He, J. Yu, Y. Zhang, Q. Pan, R. Xu, Inorg. Chem. 44 (2005) 9279.
[16] A.P. Côté, G.K.H. Shimizu, Chem. Eur. J. 9 (2003) 5361.
[17] G. Mezei, R.G. Raptis, New J. Chem. 27 (2003) 1399.
[18] S.A. Dalrymple, G.K.H. Shimizu, Chem. Eur. J. 8 (2002) 3010.
[19] This reference appeared during the course of the preparation of this paper S. Horike, R. Matsuda, D. Tanaka, M. Mizuno, K. Endo, S. Kitagawa, J. Am. Chem. Soc. 128 (2006) 4222.
[20] J. Tao, X. Yin, Z.-B. Wei, R.-B. Huang, L.-S. Zheng, Eur. J. Inorg. Chem. (2004) 125.
[21] D. Sun, R. Cao, Y. Sun, W. Bi, X. Li, Y. Wang, Q. Shi, X. Li, Inorg. Chem. 42 (2003) 7512.
[22] D. Sun, R. Cao, Y. Sun, X. Li, W. Bi, M. Hong, Y. Zhao, Eur. J. Inorg. Chem. (2003) 94.
[23] X. Li, R. Cao, W. Bi, D. Yuan, D. Sun, Eur. J. Inorg. Chem. (2004) 2228.
[24] G.J. McManus, Z. Wang, M.Z. Zaworotko, J. Cryst. Growth Des. 4 (2004) 11.
[25] X. Li, R. Cao, D. Sun, W. Bi, D. Yuan, Eur. J. Inorg. Chem. (2005) 3156.
[26] D. Sun, R. Cao, Y. Sun, W. Bi, D. Yuan, Q. Shi, X. Li, Chem. Commun. (2003) 1528.
[27] Molecular Structure Corporation & Rigaku, 2000. CrystalClear, Version 1.36. MSC, 9009 New Trails Drive, The Woodlands, TX 77381-5209, USA, and Rigaku Corporation, 3-9-12 Akishima, Tokyo, Japan; and G.M. Sheldrick, SADABS, Program for Empirical Absorption Correction of Area Detector Data, University of Göttingen, 1996.
[28] G.M. Sheldrick, SHELXS-97, Program for Crystal Structure Solution and Refinement, University of Göttingen, 1997.
[29] S. Laborda, R. Clérac, C.E. Anson, A.K. Powell, Inorg. Chem. 43 (2004) 5931.
[30] G.K. Fukin, S.V. Lindeman, J.K. Kochi, J. Am. Chem. Soc. 124 (2002) 8329.
[31] M. Oh, G.B. Carpenter, D.A. Sweigart, Organometallics 21 (2002) 1290.
[32] S. Bruce, D.E. Hibbs, C. Jones, J.W. Steed, R.C. Thomas, T.C. Williams, New J. Chem. 27 (2003) 466.
[33] P. King, R. Clérac, C.E. Anson, A.K. Powell, J. Chem Soc., Dalton Trans. (2004) 852.
[34] T. Kajiwara, T. Ito, Angew. Chem., Int. Ed. 39 (2000) 230.
[35] C.-F. Wang, E.-Q. Gao, Z. He, C.-H. Yan, Chem. Commun. (2004) 720.
[36] C.-X. Yin, R.G. Finke, J. Am. Chem. Soc. 127 (2005) 9003.
[37] D.S. Kim, P.M. Forster, R.L. Toquin, A.K. Cheetham, Chem. Commun. (2004) 2148.
[38] A.J. Celestian, J.B. Parise, C. Goodell, A. Tripathi, J. Hanson, Chem. Mater 16 (2004) 2244.

Available online at www.sciencedirect.com
ScienceDirect
Polyhedron 26 (2007) 2987–2996
POLYHEDRON
www.elsevier.com/locate/poly

Preparation and characterization of cobalt-containing alcohols and diols

Jian-Cheng Lee, Yu-Chang Chang, Yi-Jung Ho, Kang-Ming Chu, Hsueh-Liang Chen, Fung-E Hong *

Department of Chemistry, National Chung Hsing University, Taichung 40227, Taiwan

Received 10 November 2006; accepted 31 January 2007
Available online 4 February 2007

Abstract

A series of cobalt-containing alcohols and diols were prepared and characterized. Intramolecular hydrogen-bonding was observed for the cobalt-containing diols $[Co_2(CO)_6(\mu\text{-}\eta\text{-}(HO)R_1R_2CC{\equiv}CCR_1R_2(OH)]$ (**1**: $R_1 = CH_3$, $R_2 = C_2H_5$; **2**: $R_1 = CH_3$, $R_2 = C_3H_7$), $[Co_2(CO)_6(\mu\text{-}\eta\text{-}(HO)Ph_2CC{\equiv}CCPh_2(OH)]$ (**3**) and $[(\mu\text{-}PPh_2CH_2PPh_2)Co_2(CO)_4(\mu\text{-}\eta\text{-}(HO)Ph_2CC{\equiv}CCPh_2(OH)]$ (**4**). Potentially all the four compounds could serve as chelating O,O-ligands. In principle, it is possible for compounds $[(\mu\text{-}PPh_2NHPPh_2)Co_2(CO)_4(\mu\text{-}\eta\text{-}HC{\equiv}CCPh_2OH)]$ (**5b**), $[Co_2(CO)_6(\mu\text{-}\eta\text{-}HC{\equiv}CC_2H_4OH]$ (**6**) and $[Co_2(CO)_6(\mu\text{-}\eta\text{-}HC{\equiv}CC_3H_6OH)]$ (**7**) in their *syn*-conformations to behave as chelating O,N-ligands. To the best of our knowledge, compounds **5b**, **6** and **7** are the first reported examples of PPh_2NHPPh_2-bridged dicobalt complexes.
© 2007 Elsevier Ltd. All rights reserved.

Keywords: Cobalt-containing diols; Cobalt-containing alcohols; Alkyne-bridged dicobalt complex; Dppm; PPh_2NHPPh_2

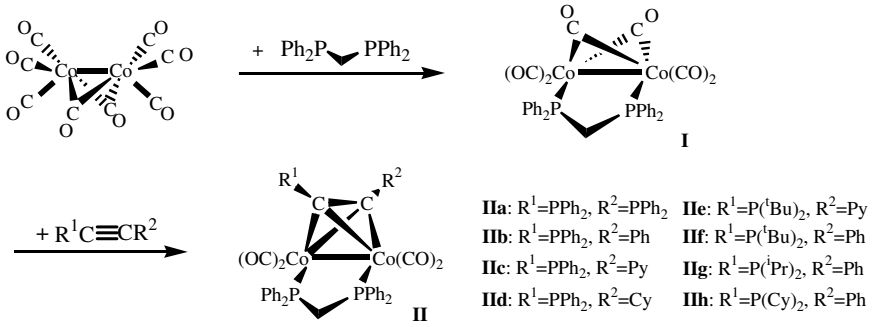
1. Introduction

Alkynes are highly reactive building blocks in organic synthesis. The fact that alkyne-bridged dicobalt system has been studied extensively is in part due to its indisputable role played in the Pauson–Khand reaction [1]. Complexes of this class are usually obtained from the direct reaction of dicobalt octacarbonyl ($Co_2(CO)_8$) with alkynes [2]. The bridging alkyne makes use of both sets of filled π- and unfilled π^*-orbitals in bonding to the dicobalt framework. The former set is responsible for donation of the electron-density to the metal center; meanwhile, the latter one accepts the electron-density from the metal through back-bonding [3]. This synergetic effect enhances the rigidity of the Co_2C_2 core. The character and reactivity of the bridging alkyne is significantly changed after the coordination to the metal moiety. A general methods of preparation of cobalt-containing mono- or bidentate phosphine ligands has been established in our previous studies (Scheme 1) [4]. It has also been revealed that ligands of this type can be characterized as authentic phosphine ligands with bulky, and, in some cases, electron-rich, character [4b]. Moreover, some of the palladium complexes with type II ligands have been demonstrated to perform as effective catalysts in the renowned Suzuki reactions [5].

Alcohols or diols are readily accessible precursors of alkoxides. The alkoxy ligands have been long known to stabilize metals in high oxidation states [6]. Metal alkoxides are also of great interest due to their current and potential uses in catalysis. For example, $Al(O^iPr)_3$ has been widely used as a catalyst in organic synthesis as well as in the ring-opening polymerization of aliphatic cyclic esters [7]. Numerous organic alkoxides as well as their metal-containing counterparts were prepared. Their chemical reactivities toward metals were thoroughly examined. Much rich chemistry of the letter were demonstrated [8]. Herein, we

* Corresponding author.
E-mail address: fehong@dragon.nchu.edu.tw (F.-E. Hong).

0277-5387/$ - see front matter © 2007 Elsevier Ltd. All rights reserved.
doi:10.1016/j.poly.2007.01.037



Scheme 1.

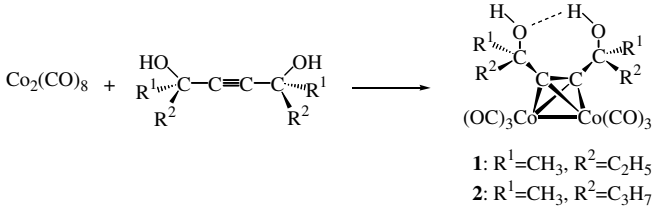
report the preparation and characterization of a series of cobalt-containing alcohols and diols using a methodology similar to the one shown in Scheme 1.

2. Results and discussion

2.1. Preparation of cobalt-containing diols

The room temperature reaction of $(HO)R_1R_2CC{\equiv}CCR_1R_2(OH)$ with $Co_2(CO)_8$ in toluene furnished $[Co_2(CO)_6(\mu\text{-}\eta\text{-}(HO)R_1R_2CC{\equiv}CCR_1R_2(OH)]$ (**1**: $R_1 = CH_3$, $R_2 = C_2H_5$; **2**: $R_1 = CH_3$, $R_2 = C_3H_7$) in good yields in 4 h (Scheme 2). Compounds **1** and **2** were characterized by spectroscopic means as well as by single-crystal X-ray diffraction. The molecular structures of both compounds revealed a pseudo-tetrahedral Co_2C_2 core typical for an alkyne-bridged dicobalt complex (Table 1, Figs. 1 and 2). Both substituents of the alkyne are bent away from the dicobalt moiety, as predicted by Dewar–Chatt–Duncanson's model, and reside on the same side [9]. In this regard, **1** and **2** can be considered as potentially chelating metal-containing diols.

All carbonyl ligands of compound **1** and other cobalt-containing alcohols and diols mentioned below are in terminal positions. The C(1)–C(2)–C(3) and C(2)–C(1)–C(7) angles are 138.6(4)° and 139.6(3)°, respectively, deviated from the 180° angle characteristic of their free states as predicted. The C–C bond distance of the bridging alkyne is 1.341(5) Å, which is within the regular double bond range. The Co–Co bond distance is 2.472 Å, which is comparable to alkyne-bridging dicobalt complex reported earlier (Table 1, Fig. 1). In general, the cluster core "$-Co_2(-C{\equiv}C-)$" of a common dicobalt complex of this type is a tetrahedron where the alkyne unit is almost perpendicular to the metal-metal bond. The structure also shows that the acetylenic ligands fold in upon coordination to the cluster core. The distance between the oxygen and hydrogen atoms of two hydroxyl groups are 2.052 Å for **1**, which is well within the intramolecular hydrogen-bonding range [10]. The ^1H and ^{13}C NMR spectra of **1** are trivial. In contrast with the observed two non-equivalent hydroxyl protons in solid state, two hydroxyl protons are equivalent on the NMR timescale giving rise to a broad signal at 2.99 ppm in ^1H NMR in $CDCl_3$. In the structure of **2**, the C(2)–C(1)–C(3) and C(1)–C(2)–C(8) angles are 137.5(2)° and 136.9(2)°, respectively. The C–C bond distance of the bridged alkyne is 1.324(3) Å. The Co–Co bond distance is 2.4639(5) Å. The distance between oxygen atoms of the two hydroxyl groups are 2.637 Å for **2** (Table 1, Fig. 2). Again, in solution two hydroxyl protons are equivalent and give rise to a broad signal at 2.98 ppm in ^1H NMR in $CDCl_3$.



Scheme 2.

As seen above, the two hydroxyl groups of the coordinated alkyne come closer in a well-defined rigid geometry in these alkyne dinuclear clusters. This observable fact suggests that any charged functional groups at these positions will be disposed in a clamp-like fashion and are potentially capable of binding ions of the opposite charge [11]. Unfortunately, attempts to isolate the expected aluminum complexes were not successful (Scheme 3). The reactions of both **1** and **2** with trimethyl aluminum always led to precipitation of compounds of unknown composition. Besides, the complex would undergo an elimination reaction in acidic medium and produce the related olefinic compounds [12].

Subsequently, the heating $Co_2(CO)_8$ with $(HO)Ph_2CC{\equiv}CCPh_2(OH)$ in toluene at 60 °C for 3 h produced $[Co_2(CO)_6(\mu\text{-}\eta\text{-}(HO)Ph_2CC{\equiv}CCPh_2(OH)]$ (**3**). Further reaction of **3** with $PPh_2CH_2PPh_2$ (dppm) in toluene at 100 °C for 16 h yielded $[(\mu\text{-}PPh_2CH_2PPh_2)Co_2(CO)_4(\mu\text{-}\eta\text{-}(HO)Ph_2CC{\equiv}CCPh_2(OH)]$ (**4**) (Scheme 4). In several occasions, the bridging dppm is a necessity, especially when the reaction is conducted at elevated temperatures. Without the protection provided by the bridging dppm, intermolecular attacks among $Co_2(CO)_6(\mu\text{-}\eta\text{-}RC{\equiv}CR)$

Table 1
Crystal data of **1**, **2**, **3**, **5a**, **5b**, **6**, and **7**

Compound	**1**	**2**	**3**	**5a**	**5b**	**6**	**7**
Formula	$C_{32}H_{36}Co_4O_{16}$	$C_{18}H_{22}Co_2O_8$	$C_{68}H_{44}Co_4O_{16}$	$C_{21}H_{12}Co_2O_7$	$C_{43}H_{33}Co_2NO_5P_2$	$C_{62}H_{50}Co_4N_2O_{10}P_4$	$C_{64}H_{54}Co_4N_2O_{10}P_4$
Formula weight	912.36	484.22	1352.75	494.17	823.50	1342.64	1370.69
Crystal system	monoclinic	monoclinic	monoclinic	triclinic	monoclinic	triclinic	orthorhombic
Space group	$P2(1)/c$	$P2(1)/c$	$P2(1)/c$	$P\bar{1}$	$P2(1)/c$	$P\bar{1}$	*Pbca*
a (Å)	9.7269(7)	8.9360(9)	15.3065(13)	6.6972(8)	10.9974(7)	11.1751(10)	17.6826(12)
b (Å)	32.247(2)	11.0808(11)	20.3771(17)	10.8070(13)	17.5744(12)	16.5038(15)	20.3498(13)
c (Å)	12.6768(9)	22.386(2)	20.1655(17)	14.9215(17)	20.1312(14)	18.1966(17)	34.949(3)
α (°)				104.299(2)		100.689(2)	
β (°)	91.1600(10)	90.850(2)	101.572(2)	98.911(2)	102.9600(10)	105.976(2)	
γ (°)						98.860(2)	
V (Å^3)	3975.5(5)	2216.4(4)	6161.8(9)	1008.7(2)	3094.8(5)	12576.0(15)	
Z	4	4	4	2	4	2	8
D_c (Mg/m^3)	1.585	1.451	1.458	1.627	1.443	1.441	1.448
λ (Mo Kα) (Å)	0.71073	0.71073	0.71073	0.71073	0.71073	0.71073	0.71073
μ (mm^{-1})	3.416	1.534	1.128	1.685	1.006	1.214	1.197
θ Range (°)	2.04–25.99	1.82–26.02	1.44–26.01	1.99–25.99	1.56–26.04	1.53–26.03	1.63–25.99
Observed reflections ($F > 4\sigma(F)$)	7787	4353	12080	3918	7465	11979	12344
Number of refined parameters	469	253	809	271	478	747	757
[a]R_1 for significant reflections	0.0459	0.0411	0.0393	0.0437	0.0408	0.0502	0.0461
[b]wR_2 for significant reflections	0.1139	0.0993	0.0872	0.1071	0.0791	0.1306	0.0827
[c]Goodness-of-fit	0.995	1.019	0.927	0.949	0.901	0.981	0.808

[a] $R_1 = |\sum(|F_o| - |F_c|)/|\sum F_o||$.

[b] $wR_2 = \{\sum[w(F_o^2 - F_c^2)]^2/\sum[w(F_o^2)^2]\}^{1/2}$; $w = 0.0668$, 0.0622, 0.0540, 0.0704, 0.0405, 0.0919, and 0.0386 for **1**, **2**, **3**, **5a**, **5b**, **6**, and **7**, respectively.

[c] Goodness-of-fit $= [\sum[w(F_o^2 - F_c^2)^2/(N_{rflns} - N_{params})]^{1/2}$.

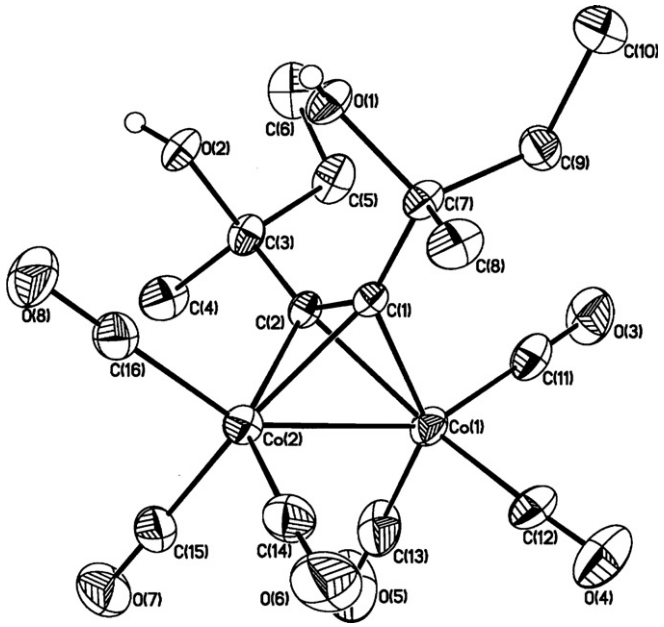


Fig. 1. ORTEP drawing of **1**. Hydrogen atoms are omitted for clarity. Selected bond lengths (Å) and bond angles (°): Co(1)–C(2) 1.965(4); Co(1)–C(1) 1.965(4); Co(1)–Co(2) 2.4720(8); Co(2)–C(1) 1.968(4); Co(2)–C(2) 1.969(4); O(1)–C(7) 1.444(4); O(2)–C(3) 1.438(5); C(1)–C(2) 1.341(5); C(1)–C(7) 1.497(5); C(2)–C(3) 1.508(5); C(3)–C(5) 1.531(6); C(3)–C(4) 1.538(6); C(7)–C(8) 1.532(6); C(7)–C(9) 1.538(6); C(2)–Co(1)–C(1) 39.89(15); C(1)–Co(2)–C(2) 39.81(15); C(2)–C(1)–C(7) 139.6(3); Co(1)–C(1)–Co(2) 77.87(14); Co(1)–C(2)–Co(2) 77.87(14); C(1)–C(2)–C(3) 138.6(4); O(2)–C(3)–C(2) 106.5(3); O(1)–C(7)–C(1) 105.7(3); C(1)–C(7)–C(8) 112.7(3); C(1)–C(7)–C(9) 110.0(3).

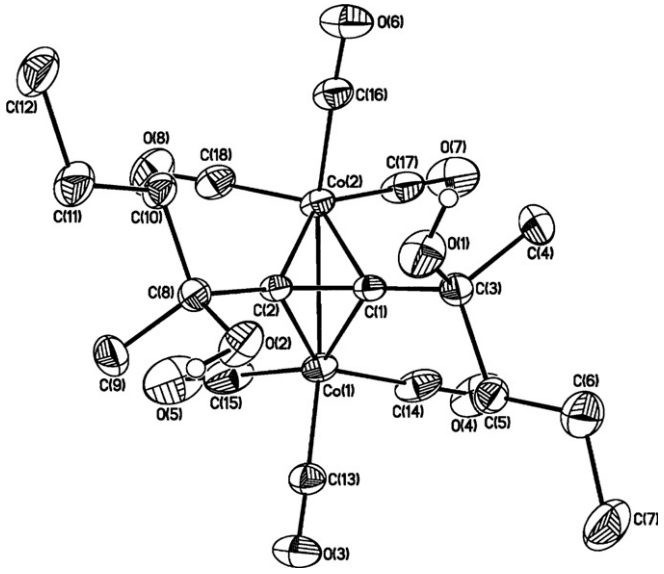
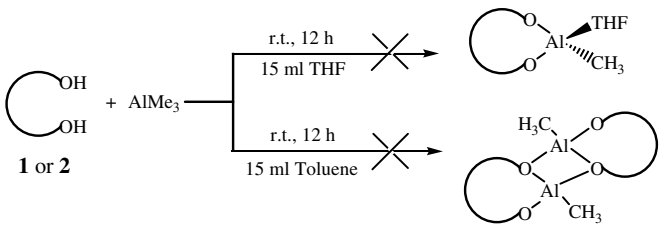
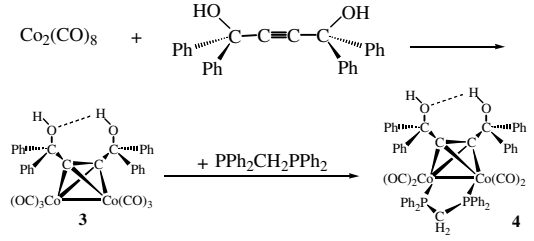


Fig. 2. ORTEP drawing of **2**. Hydrogen atoms are omitted for clarity. Selected bond lengths (Å) and bond angles (°): Co(1)–Co(2) 2.4639(5); C(1)–C(2) 1.324(3); Co(1)–C(1) 1.965(2); Co(1)–C(2) 1.971(2); Co(2)–C(2) 1.951(3); Co(2)–C(1) 1.972(2); C(1)–C(3) 1.522(4); C(2)–C(8) 1.526(4); O(1)–C(3) 1.445(3); O(2)–C(8) 1.434(3); C(2)–C(1)–C(3) 137.5(2); C(1)–C(2)–C(8) 136.9(2); O(1)–C(3)–C(1) 106.4(2); O(2)–C(8)–C(2) 103.4(2); C(1)–Co(1)–C(2) 39.30(10); C(2)–Co(2)–C(1) 39.44(10); Co(1)–C(1)–Co(2) 77.49(9); Co(2)–C(2)–Co(1) 77.86(9).



Scheme 3.



Scheme 4.

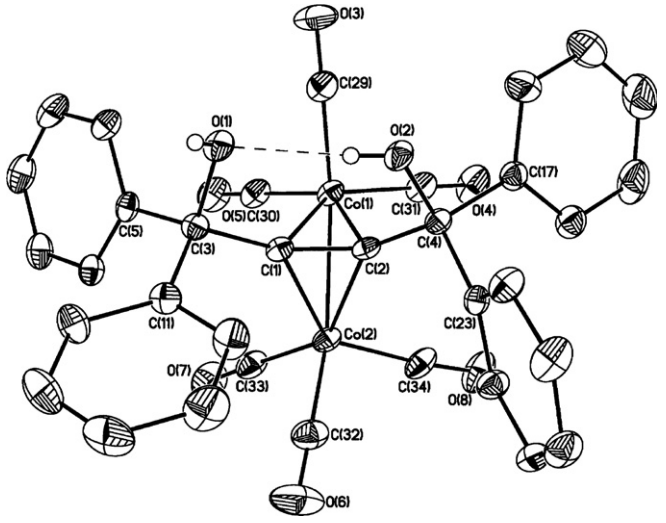


Fig. 3. ORTEP drawing of **3**. Hydrogen atoms are omitted for clarity. Selected bond lengths (Å) and bond angles (°): Co(1)–C(1) 1.972(3); Co(1)–C(2) 1.978(3); Co(1)–Co(2) 2.4472(6); Co(2)–C(1) 1.952(3); Co(2)–C(2) 1.985(3); O(1)–C(3) 1.445(4); O(2)–C(4) 1.435(3); C(1)–C(2) 1.346(4); C(1)–C(3) 1.521(4); C(2)–C(4) 1.536(4); C(1)–Co(1)–C(2) 39.84(11); C(1)–Co(2)–C(2) 39.98(11); Co(2)–C(1)–Co(1) 77.15(10); Co(1)–C(2)–Co(2) 76.28(10); C(2)–C(1)–C(3) 140.4(3); C(1)–C(2)–C(4) 138.2(3); O(1)–C(3)–C(1) 102.8(2); O(2)–C(4)–C(2) 106.9(2).

molecules do occur and the self-aggregation process always lead to a great amount of precipitation. The sequence of reactions shown in Scheme 1 is reversed in the synthesis of **4**. Firstly, the alkynyl alcohol is allowed to bridge to the dicobalt fragment. As predicted by the Dewar–Chatt–Duncanson's model, bulky substituents of the alkyne bend away from the dicobalt center. Then, the dppm is added to the alkyne bridged dicobalt fragment. The dppm-alkynyl alcohol sequence will not lead to **4**

due to the bulkiness of the latter. Compounds **3** and **4** were characterized by spectroscopic means. In addition, the molecular structure of **3** was determined by a single-crystal X-ray diffraction method. As revealed from the crystal structure, there is an intramolecular hydrogen-bonding between the oxygen atom of one and the hydrogen atom of another hydroxyl group. The H···O distance is 1.934 Å for **3**. Two hydroxyl protons of **3** and **4** are equivalent resulting in broad signals at 4.31 ppm and 2.51 ppm, respectively, in their ^{1}H NMR spectra in $CDCl_3$. A triplet signal at 3.69 ppm ($J_{P\text{-}H} = 10.5$ Hz) observed in the ^{1}H NMR spectra of **4** is assigned to the methylene protons (Figs. 3 and 4).

2.2. Preparation of cobalt-containing alcohols

Several cobalt-containing alcohols were prepared using a procedure similar to the one for synthesis of diols. The reaction of $Co_2(CO)_8$ with $HCC{\equiv}CCPh_2OH$ in toluene at 60 °C for 2 h furnished $[Co_2(CO)_6(\mu\text{-}\eta\text{-}HC{\equiv}CCPh_2OH]$ (**5a**). Further reaction of **5a** with PPh_2NHPPh_2 in toluene at 80 °C for 16 h produced $[(\mu\text{-}PPh_2NHPPh_2)Co_2(CO)_4(\mu\text{-}\eta\text{-}HC{\equiv}CCPh_2OH)]$ (**5b**) (Scheme 5). The alkynyl alcohol was first allowed to bridge to the dicobalt fragment. Then, PPh_2NHPPh_2 was added to alkyne-bridged dicobalt fragment. Again, reversing the sequence did not lead to the formation of **5b**. Here PPh_2NHPPh_2 was chosen

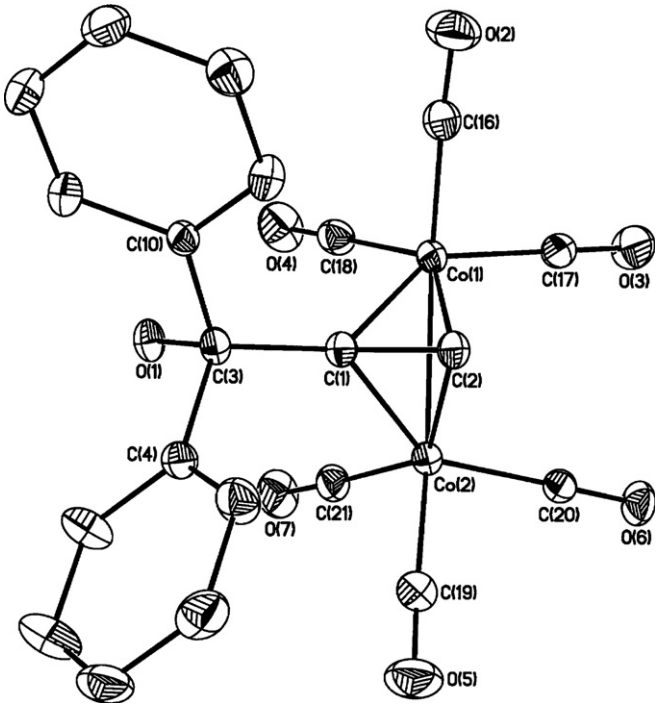


Fig. 4. ORTEP drawing of **5a**. Hydrogen atoms are omitted for clarity. Selected bond lengths (Å) and bond angles (°): Co(1)–C(2) 1.969(4); Co(1)–C(1) 1.986(4); Co(1)–Co(2) 2.4729(8); Co(2)–C(2) 1.951(4); Co(2)–C(1) 1.977(4); O(1)–C(3) 1.436(4); C(1)–C(2) 1.340(5); C(1)–C(3) 1.499(5); C(2)–Co(1)–C(1) 39.60(15); C(2)–Co(2)–C(1) 39.88(15); C(2)–C(1)–C(3) 146.5(4); Co(2)–C(2)–Co(1) 78.21(15); Co(2)–C(1)–Co(1) 77.22(13); O(1)–C(3)–C(1) 109.3(3).

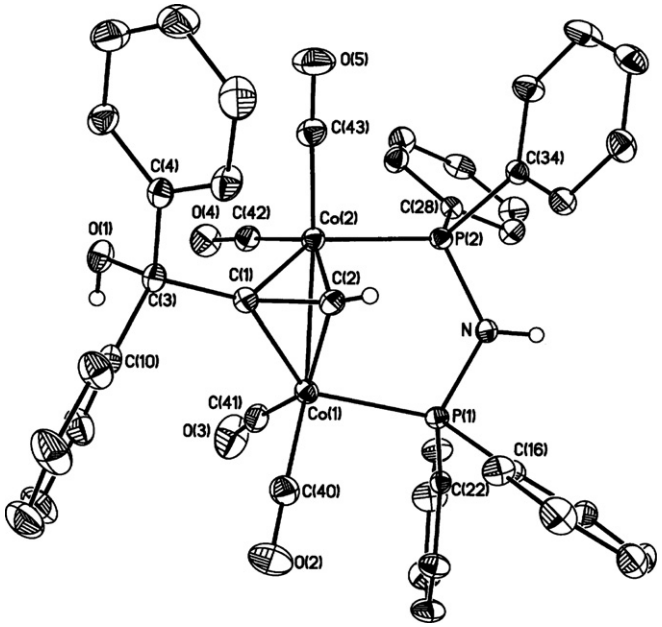
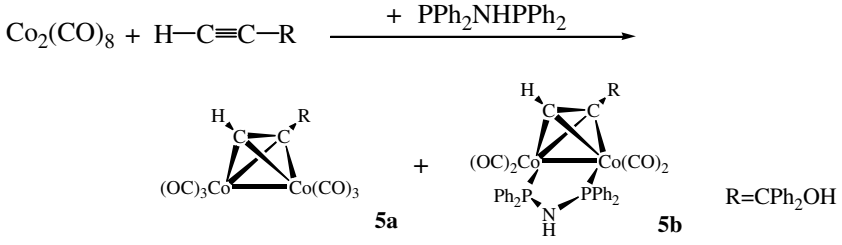


Fig. 5. ORTEP drawing of **5b**. Hydrogen atoms are omitted for clarity. Selected bond lengths (Å) and bond angles (°): Co(1)–Co(2) 2.4467(6); Co(1)–C(2) 1.932(3); Co(1)–C(1) 1.973(3); Co(1)–P(1) 2.2028(10); Co(2)–C(2) 1.956(3); Co(2)–C(1) 1.957(3); Co(2)–P(2) 2.1997(10); P(1)–N 1.687(3); P(2)–N 1.679(3); O(1)–C(3) 1.451(4); C(1)–C(2) 1.339(4); C(1)–C(3) 1.523(4); C(2)–Co(1)–C(1) 40.09(13); C(2)–Co(2)–C(1) 40.01(13); N–P(1)–Co(1) 111.64(10); N–P(2)–Co(2) 112.53(10); P(2)–N–P(1) 122.53(16); C(2)–C(1)–C(3) 141.8(3); Co(2)–C(1)–Co(1) 77.01(12); Co(1)–C(2)–Co(2) 77.99(13); O(1)–C(3)–C(1) 107.4(3).



Scheme 5.

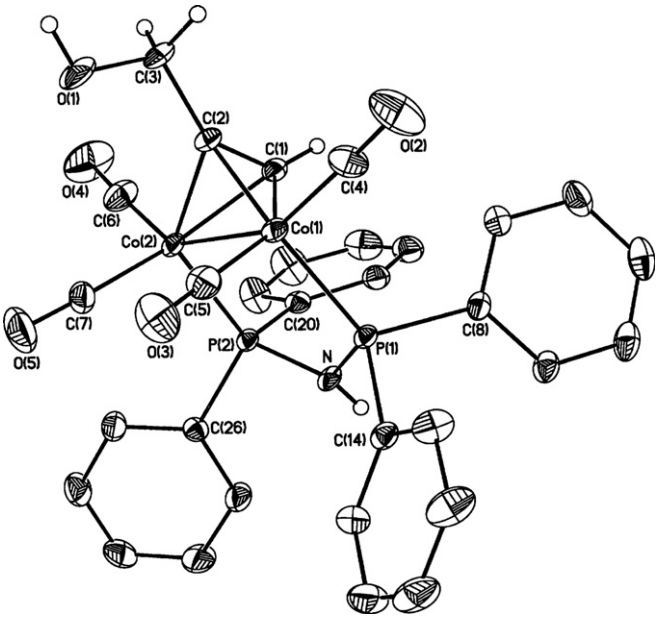
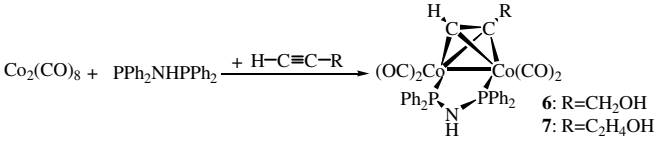


Fig. 6. ORTEP drawing of **6**. Hydrogen atoms are omitted for clarity. Selected bond lengths (Å) and bond angles (°): Co(1)–Co(2) 2.4675(7); Co(1)–C(2) 1.950(4); Co(1)–C(1) 1.960(4); Co(1)–P(1) 2.2018(9); Co(2)–C(2) 1.957(4); Co(2)–C(1) 1.966(4); Co(2)–P(2) 2.2045(9); P(1)–N 1.683(3); P(2)–N 1.687(3); O(1)–C(3) 1.411(5); C(1)–C(2) 1.341(5); C(2)–C(3) 1.489(4); C(2)–Co(1)–C(1) 40.10(14); C(2)–Co(2)–C(1) 39.96(14); N–P(1)–Co(1) 111.46(10); N–P(2)–Co(2) 111.76(10); P(1)–N–P(2) 123.19(17); Co(1)–C(1)–Co(2) 77.86(13); C(1)–C(2)–C(3) 141.8(4); Co(1)–C(2)–Co(2) 78.32(13); O(1)–C(3)–C(2) 110.0(3).



Scheme 6.

as a bridging ligand to stabilize the dicobalt complex as the dppm did in the case of compound **4**. This choice is due to the PPh_2NHPPh_2 ability to function as an amine-like ligand, which dppm does not have. In addition to the characterization by spectroscopic means the molecular structures of **5a** and **5b** were determined by the single-crystal X-ray diffraction method. The structure of **5b** revealed that the –OH and -NH groups point at different directions. In $CDCl_3$, a hydroxyl proton is observed at 2.60 and 3.00 ppm for **5a** and **5b**, respectively, in ^1H NMR. A broad signal at 3.62 ppm and a triplet signal at 5.75 ppm ($J_{PH} = 9.0$ Hz) are assigned to the acetylenic proton and NH proton, respectively, of **5b** (see Figs. 5 and 6).

The reaction of $Co_2(CO)_8$ with PPh_2NHPPh_2 in toluene at 65 °C produced $[Co_2(CO)_6(\mu\text{-}\eta\text{-}PPh_2NHPPh_2]$ in 12 h. Further reaction of the latter compound with HC≡CR (R = CH_2OH or C_2H_4OH) in toluene at 65 °C furnished $[Co_2(CO)_6(\mu\text{-}\eta\text{-}HC{\equiv}CR]$ (**6**: R = CH_2OH; **7**: R=C_2H_4-OH) in 12 h (Scheme 6). Compounds **6** and **7** were characterized by spectroscopic means. Their molecular structures were determined by the single-crystal X-ray diffraction method. To the best of our knowledge, compounds **5b**, **6** and **7** are the first reported examples of PPh_2NHPPh_2-bridged dicobalt complexes. The crystal structures of **6** and **7** show that the –OH and –NH groups point at different directions as those in **5b** does (see Fig. 7).

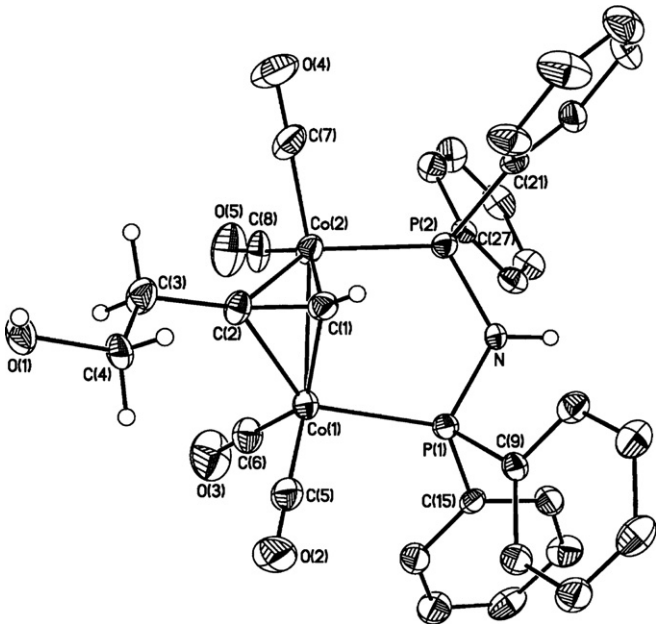


Fig. 7. ORTEP drawing of **7**. Hydrogen atoms are omitted for clarity. Selected bond lengths (Å) and bond angles (°): Co(1)–Co(2) 2.4701(10); Co(1)–C(1) 1.925(6); Co(1)–C(2) 1.965(6); Co(1)–P(1) 2.2017(15); Co(2)–C(2) 1.944(6); Co(2)–C(1) 1.947(6); Co(2)–P(2) 2.2023(16); O(1)–C(4) 1.445(5); P(1)–N 1.669(4); P(2)–N 1.687(4); C(1)–C(2) 1.313(7); C(2)–C(3) 1.505(7); C(3)–C(4) 1.458(7); C(2)–Co(2)–C(1) 39.5(2); C(1)–Co(1)–C(2) 39.4(2); N–P(1)–Co(1) 112.24(15); N–P(2)–Co(2) 110.88(15); P(1)–N–P(2) 123.3(2); Co(1)–C(1)–Co(2) 79.3(2); C(1)–C(2)–C(3) 140.1(6); Co(2)–C(2)–Co(1) 78.4(2); C(4)–C(3)–C(2) 113.1(5); O(1)–C(4)–C(3) 111.4(5).

Signals observed at 1.69 and 2.01 ppm in the ^1H NMR spectra of **6** and **7**, respectively, in $CDCl_3$ are assigned to the corresponding hydroxyl protons. Broad signals appearing at 3.60 ppm for **6** and 3.52 ppm for **7** are assigned to terminal acetylene protons. The triplet signals at 5.34 ppm for **6** and 5.30 ppm for **7** are assigned to the NH protons of the bridging PPh_2NHPPh_2.

2.3. Structural comparison of cobalt-containing diols and alcohols

Selected structural parameters of **1**, **2**, **3**, **5a**, **5b**, **6**, and **7** are given in Table 2 for the purpose of comparison. The atom numbering scheme of the framework of all these compounds is the same. As shown in Table 2, these frameworks are not very different. Again, it shows that the alkyne-bridging dicobalt framework (Co_2C_2) is a rigid structure (Diagram 1).

Table 2
Comparison of selected structural parameters of **1**, **2**, **3**, **5a**, **5b**, **6**, and **7**

	1	2	3	5a	5b	6	7
Bond length (Å)							
Co(1)–Co(2)	2.4720(8)	2.4639(5)	2.4472(6)	2.4729(8)	2.4467(6)	2.4675(7)	2.4701(10)
C(1)–C(2)	1.341(5)	1.324(3)	1.346(4)	1.340(5)	1.339(4)	1.341(5)	1.313(7)
C(1)–Co(1)	1.965(4)	1.965(2)	1.972(3)	1.986(4)	1.973(3)	1.960(4)	1.925(6)
C(1)–Co(2)	1.968(4)	1.972(2)	1.952(3)	1.977(4)	1.957(3)	1.966(4)	1.947(6)
C(2)–Co(1)	1.965(4)	1.971(2)	1.978(3)	1.969(4)	1.932(3)	1.950(4)	1.965(6)
C(2)–Co(2)	1.969(4)	1.951(3)	1.985(3)	1.951(4)	1.956(3)	1.957(4)	1.944(6)
C(1)–C(A)	1.497(5)	1.522(4)	1.521(4)	1.499(5)	1.523(4)		
C(2)–C(B)	1.508(5)	1.526(4)	1.536(4)			1.489(4)	
C(A)–O(1)	1.444(5)	1.445(3)	1.445(4)	1.436(4)	1.451(4)	1.411(5)	
C(B)–O(2)	1.438(5)	1.434(3)	1.435(3)				
Co(1)–P(1)					2.2028(10)	2.2018(9)	2.2017(15)
Co(2)–P(2)					2.1997(10)	2.2045(9)	2.2023(16)
P(1)–X					1.687(3)	1.683(3)	1.669(4)
P(2)–X					1.679(3)	1.687(3)	1.687(4)
Distance (Å)							
O(2)–H(1)	2.052	3.303	1.934				
O(1)–O(2)	2.847	2.637	2.709				
Angle (°)							
C(A)–C(1)–C(2)	139.6(3)	137.5(2)	140.4(3)	146.5(4)	141.8(3)		140.1(6)
C(B)–C(2)–C(1)	138.6(4)	136.9(2)	138.2(3)			141.8(4)	
Co(1)–C(1)–Co(2)	77.87(14)	77.49(9)	77.15(10)	77.22(13)	77.01(12)	77.86(13)	79.3(2)
Co(1)–C(2)–Co(2)	77.87(14)	77.86(9)	76.28(10)	78.21(15)	77.99(13)	78.32(13)	78.4(2)
C(1)–Co(1)–C(2)	39.89(15)	39.30(10)	39.84(11)	39.60(15)	40.09(13)	40.10(14)	39.4(2)
C(1)–Co(2)–C(2)	39.81(15)	39.44(10)	39.98(11)	39.88(15)	40.01(13)	39.96(14)	39.5(2)
P(1)–X–P(2)					122.53(16)	123.19(17)	123.3(2)
Co(1)–P(1)–X					111.64(10)	111.46(10)	112.24(15)
Co(2)–P(2)–X					112.53(10)	111.76(10)	110.88(15)
C(1)–C(A)–O(1)	105.7(3)	106.4(2)	102.8(2)	109.3(3)	107.4(3)		
C(2)–C(B)–O(2)	106.5(3)	103.4(2)	106.9(2)			110.0(3)	

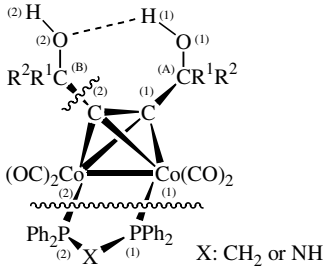


Diagram 1. A generalized structure for **1**, **2**, **3**, **5a**, **5b**, **6**, and **7**.

2.4. Summary

Several cobalt-containing alcohols and diols were prepared and characterized by NMR spectroscopic and single-crystal X-ray diffraction. Their molecular structures were compared. Unfortunately, reactions of the metal-containing diol ligands with aluminum complexes such as $AlEt_3$ or $AlMe_3$ resulted in a number of unidentified products.

3. Experimental

General information: All manipulations were carried out under a dry nitrogen atmosphere. Solvents including deuterated solvents were purified before use. Most of separations were performed by Centrifugal Thin Layer Chromatography (CTLC, Chromatotron, Harrison model 8924). The ^1H and ^{31}P NMR spectra were recorded on a Varian-400 spectrometer at 400.44 and 162.10 MHz, respectively; ^{13}C NMR spectra were recorded on a Varian VXR-300 S spectrometer at 75.43 MHz. Chemical shifts are reported in ppm relative to the residual proton signals of deuterated $CHCl_3$ or CH_2Cl_2. Mass spectra were recorded on a JOEL JMS-SX/SX 102A GC/MS/MS spectrometer. Elemental analyses were obtained on a Heraeus CHN-O-S-Rapid instrument.

3.1. Synthesis of *1* and *2*

$Co_2(CO)_8$ (0.342 g, 1.000 mmol), 3,6-dimethyl-4-octyn-3,6-diol (0.170 g, 1.000 mmol) and 10 mL of THF were placed in a 100 mL round-bottomed flask charged with a magnetic stirrer. The solution was stirred at 25 °C for 4 h. Then the solvent was removed under reduced pressure, and the resulted dark-red residue was separated by CTLC. A red band was eluted out using a mixed solvent system (CH_2Cl_2/EA = 1:1). The product was identified as **1** (0.437 g, 0.96 mmol, 96%). A similar procedure was used for the preparation of **2**. $Co_2(CO)_8$ (0.342 g, 1.000 mmol), 4,7-dimethyl-5-decyn-4,7-diol (0.198 g, 1.000 mmol) and

10 mL of THF were placed in 100 mL round-bottomed flask charged with a magnetic stirrer. The solution was stirred at 25 °C for 4 h followed by workup. A dark-red band was eluted out using a mixed solvent system (EA:CH_2Cl_2 = 1:1). The product was identified as **2** (0.460 g, 0.95 mmol, 95%).

1: ^{1}H NMR ($CDCl_3$, δ/ppm): 1.09(br., 6H, C–CH_2–CH_3), 1.54(br., 6H, C–CH_3), 1.83(br., 4H, C–CH_2), 2.99(br., 2H, OH); ^{13}C NMR ($CDCl_3$, δ/ppm): 8.76(s, C–CH_2–CH_3), 28.79(s, C–CH_2), 37.90(s, C–CH_3), 75.15(s, C≡C), 106.89(s, C–OH), 199.83(s, CO); *Anal*. Calc. for **1**: C, 42.13; H, 3.98. Found: C: 41.17, H: 3.84%. IR(KBr/cm^{-1}): 2017.7(s), 2052.5(s), 2093.0(s), 3332.0(br.); color: red (solid state).

2: ^{1}H NMR ($CDCl_3$, δ/ppm): 0.99(br., 6H, C–CH_2–CH_3), 1.56(br., 10 H, C–CH_2, C–CH_3), 1.77(br., 4H, C–CH_2), 2.98(br., 2H, OH); ^{13}C NMR ($CDCl_3$, δ/ppm): 14.40(s, C–CH_2–CH_2-CH_3), 17.70(s, C–CH_2–CH_3), 29.48, 29.66(d, C–CH_2), 47.77(s, C–CH_3), 75.13(s, C≡C), 106.96(s, C–OH), 199.8(s, CO); *Anal*. Calc. for **2**: C, 44.65; H, 4.58. Found: C: 44.48, H: 4.70%; IR(KBr/cm^{-1}): 2022.6(s), 2053.5(s), 2091.7(s), 3257.9(br.); color: red (solid state).

3.2. Synthesis of *3*

A 100 cm^3 flask was charged with dicobalt octacarbonyl, $Co_2(CO)_8$ (0.171 g, 0.500 mmol) and 1,1,4,4-tetraphenyl-2-butyn-1,4-diol (0.195 g, 0.500 mmol) in 5 ml of THF. The mixture was stirred at 60 °C for 3 h resulting in a red solution. The solvent was removed under reduced pressure, and the resulting residue was chromatography by CTLC. A red band was eluted out using a mixed solvent system (CH_2Cl_2/hexane = 1:1). The product was identified as **3** (0.316 g, 0.467 mmol, 93.4%).

3: ^{1}H NMR ($CDCl_3$, δ/ppm): 4.31(s, 2H, OH), 7.28 (br., 12H, Ph), 7.61(br., 8H, Ph); ^{13}C NMR ($CDCl_3$, δ/ppm): 80.62(s, C≡C), 108.23(s, C–(OH)Ph_2), 126.93(s, arene), 127.67(s, arene), 128.03(s, Ph), 146.12(s, *ipso* of arene), 198.46(br., COs); *Anal.* Calc. for **3**: C, 60.37, H, 3.28. Found: C, 59.60; H, 3.62%; color: red (solid state).

3.3. Synthesis of *4*

A 100 cm^3 flask was charged with complex **3** (0.344 g, 0.509 mmol) and dppm (0.196 g, 0.509 mmol) in 5 ml of toluene. The mixture was stirred at 100 °C for 16 h yielding a dark-brown solution. The solvent was removed under reduced pressure, and the resulting residue was chromatography by CTLC. The first band was eluted out using a mixed solvent system (CH_2Cl_2/hexane = 2:1). The product was identified as the title compound **4** (0.501 g, 0.499 mmol, 97.9%).

4: ^{1}H NMR ($CDCl_3$, δ/ppm): 2.51(s, 2H, OH), 3.69(t, J_{PH} = 10.5 Hz, 2H, CH_2), 7.15–7.46(br. 40 H, arene); ^{13}C NMR ($CDCl_3$, δ/ppm): 36.28(t, J_{PC} = 82.5 Hz, CH_2), 81.09(s, C≡C), 109.81(s, C–(OH)Ph_2), 126.95–131.52(br., arene), 146.72(s, *ipso* of arene), 204.68(br., COs); ^{31}P NMR ($CDCl_3$, δ/ppm): 35.8(s, dppm); *Anal.* Calc. for **4**: C, 68.14; H, 4.14. Found: C, 64.64; H, 4.55%; IR(KBr/cm^{-1}): 1966.5(s), 1992.7(s), 2022.8(s); MS (*m*/*z*): 977(M^+−CO). color: brown (solid state).

3.4. Synthesis of *5a* and *5b*

$Co_2(CO)_8$ (0.171 g, 0.500 mmol), 1,1-diphenyl-2-propyn-1-ol (0.104 g, 0.500 mmol) and 5 ml of toluene were placed in a 100 mL round-bottomed flask charged with a magnetic stirrer. The red colored solution was stirred at 60 °C for 2 h. To the mixture was then added *N*,*N*-bis(diphenylphosphino)amine (0.192 g, 0.500 mmol) with 5 cm^3 of toluene followed by stirring at 80 °C for additional 16 h. The solvent was removed under reduced pressure, and the resulting residue was chromatography by CTLC. Complex **5a** was obtained from the first red band eluted by hexane, while complex **5b** from the second red-pink band by CH_2Cl_2/hexane (1/1) solution. The yields for **5a** and **5b** were 33.9% (0.084 g, 0.170 mmol) and 39.1% (0.161 g, 0.196 mmol), respectively.

5a: ^{1}H NMR ($CDCl_3$, δ/ppm): 2.60(s, 1H, OH), 6.52(s, 1H, CH), 7.23–7.25(br., 2H, arene), 7.30–7.32(br., 4H, arene), 7.69–7.71(br., 4H, arene); ^{13}C NMR ($CDCl_3$, δ/ppm): 73.06, 80.08(s, C≡C), 105.80(s, C–(OH)Ph_2), 125.71(s, arene), 127.48(s, arene), 128.26(s, Ph), 146.71(s, *ipso* of arene), 198.88(br., COs); Anal. Calc. for **5a**: C, 51.04; H, 2.45. Found: C, 50.07; H, 2.99%; IR(KBr/cm^{-1}): 1977.7(w), 2002.7(s), 2027.8(s), 2051.8(s), 2093.9(m); MS (*m*/*z*): 466 (M^+−CO); color: red (solid state).

5b: ^{1}H NMR ($CDCl_3$, δ/ppm): 3.00(s, 1H, OH), 3.61(br. 2 H, CH_2 or NH), 5.75(t, J_{PH} = 9.0 Hz, 1H, CH), 7.15–7.78(br., 30 H, arene); ^{13}C NMR ($CDCl_3$, δ/ppm): 73.12(s, C≡CH), 80.61(s, C≡C(OH)Ph_2), 126.31–130.90(br., arene), 147.92(s, *ipso* of arene), 201.20(br., COs), 206.24(br., COs); ^{31}P NMR($CDCl_3$, δ/ppm): 98.6(s, 2 P, dppm); *Anal*. Calc. for **5b**: N, 1.70; C, 62.71; H, 4.04. Found: N, 2.89; C, 61.85; H, 4.21%; IR(KBr/cm^{-1}): 1977.0(s), 2003.0(s), 2027.7(s); MS (*m*/*z*): 823 (M^+); color: red (solid state).

3.5. Synthesis of *6* and *7*

A 100 cm^3 round flask was charged with $Co_2(CO)_8$ (0.342 g, 1.000 mmol) and *N*,*N*-bis(diphenylphosphino)amine (0.385 g, 1.000 mmol) with 15 cm^3 of THF. The mixture was warmed up to 65 °C and stirred for 12 h. Then, one molar equivalent of 2-propyn-1-ol (0.056 g, 1.000 mmol) was added. The mixture was stirred at 65 °C for another 12 h. The resulting green solution was purified by centrifugal thin-layer chromatography (CTLC). The second red-colored band was eluted out with CH_2Cl_2. The solvent was removed in vacuo, and the resulting solid was identified as **6** (0.618 g, 0.920 mmol, 92% yield). A similar procedure was used for the preparation

of **7**. $Co_2(CO)_8$ (0.342 g, 1.000 mmol), *N*,*N*-bis(diphenylphosphino)amine (0.385 g, 1.000 mmol) and 15 mL of THF were placed in a 100 mL round-bottomed flask equiped with a magnetic stirrer. The solution was stirred at 65 °C for 12 h. Then, one molar equivalent of 3-butyn-1-ol (0.070 g, 1.000 mmol) was added. The solution was stirred at 65 °C for another 12 h. The resulting green solution was purified by centrifugal thin-layer chromatography (CTLC). The second red-colored band was eluted out with CH_2Cl_2. The solvent was removed in vacuo, and the residual solid was identified as **7** (0.589 g, 0.86 mmol, 86% yield).

6: ^{1}H NMR ($CDCl_3$, δ/ppm): 1.69(s, 1H, OH), 3.60(s, 1 H, NH), 4.76(d, $J_{H-H} = 6.0$ Hz, 2H, CH_2), 5.34(t, 1H, ≡CH), 7.38–7.46(br., 10H, arene); ^{13}C NMR ($CDCl_3$, δ/ppm): 65.10(s, CH_2–OH), 71.10(s, C–CH_2–OH), 101.84(s, ≡CH), 128.47–130.41(arene), 140.10(d, $J_{p-c} = 36.6$ Hz, *ipso*-arene), 202.6 (br, COs), 206.3 (br, COs); ^{31}P NMR ($CDCl_3$, δ/ppm): 33.7(s, PNP); *Anal.* Calc. for **6**: C, 55.46, H, 3.75, N, 2.09%. Found: C, 54.54, H, 3.90, N, 2.71%; M.S.(FAB): 643(M^+−CO); color: red (solid state).

7: ^{1}H NMR ($CDCl_3$, δ/ppm): 2.01(s, 1H, OH), 3.12(d, $J_{H-H} = 6.0$ Hz, 2H, CH_2–OH), 3.52(s, 1H, NH), 3.98(d, $J_{H-H} = 6.0$ Hz, 2H, CH_2–CH_2), 5.30(t, 1 H, ≡CH), 7.37–7.44(br., 10H, arene); ^{13}C NMR ($CDCl_3$, δ/ppm): 38.32(s, CH_2–CH_2–OH), 64.44(s, CH_2–OH), 71.10(s, C–CH_2–CH_2–OH), 98.61(s, ≡CH), 128.65–130.87(arene), 140.64(d, $J_{p-c} = 73.9$ Hz, *ipso*-arene), 203.4(s, CO), 206.7 (s, CO); ^{31}P NMR ($CDCl_3$, δ/ppm): 33.8(s, PNP); *Anal.* Calc. for **7**: C, 56.08; H, 3.97; N, 2.04%; Found: C, 56.36; H, 4.12; N, 2.25%; M.S.(FAB): 685(M^++1); color: red (solid state).

3.6. X-ray crystallographic studies

Suitable crystals of **1**, **2**, **4**, **5a**, **5b**, **6**, and **7** were sealed in thin-walled glass capillaries under nitrogen atmosphere and mounted on a Bruker AXS SMART 1000 diffractometer. Intensity data were collected in 1350 frames with increasing ω (width of 0.3° per frame). The absorption correction was based on the symmetry equivalent reflections using SADABS program. The space group determination was based on a check of the Laue symmetry and systematic absences, and was confirmed using the structure solution. The structure was solved by direct methods using a SHELXTL package [13]. All non-H atoms were located from successive Fourier maps and hydrogen atoms were refined using a riding model. Anisotropic thermal parameters were used for all non-H atoms, and fixed isotropic parameters were used for H atoms[1]. Crystallographic data for compounds **1**, **2**, **3**, **5a**, **5b**, **6**, and **7** are summarized in Table 1.

[1] The hydrogen atoms were ride on carbons or oxygens in their idealized positions and held fixed with the C–H distances of 0.96 Å.

Acknowledgement

We thank the National Science Council of the R.O.C. (Grant NSC-94-2113-M-005-011) for the financial support.

Appendix A. Supplementary material

CCDC 616907, 616908, 616909, 616910, 616911, 616912 and 616913 contain the supplementary crystallographic data for compounds **1**, **2**, **3**, **5a**, **5b**, **6**, and **7**. These data can be obtained free of charge via http://www.ccdc.cam.ac.uk/conts/retrieving.html, or from the Cambridge Crystallographic Data Centre, 12 Union Road, Cambridge CB2 1EZ, UK; fax: (+44) 1223-336-033; or e-mail: deposit@ccdc.cam.ac.uk. Supplementary data associated with this article can be found, in the online version, at doi:10.1016/j.poly.2007.01.037.

References

[1] (a) For Pauson-Khand reaction see I.U. Khand, G.R. Knox, P.L. Pauson, W.E. Watts, J. Chem. Soc., Chem. Commun. (1971) 36;
(b) I.U. Khand, G.R. Knox, P.L. Pauson, W.E. Watts, J. Chem. Soc., Perkin I. (1973) 975;
(c) I.U. Khand, G.R. Knox, P.L. Pauson, W.E. Watts, M.I. Foreman, J. Chem. Soc., Perkin I. (1973) 977;
(d) For alkyne-bridged dimetallic complexes, see S.G. Davies, Organotransition Metal Chemistry Applications to Organic Synthesis, vol. 2, Pergamon Press, 1982, pp. 32 and references therein;
(e) G.W. Parshall, S.D. Ittel, Homogeneous Catalysis, second ed., Wiley, 1992, Chapter 8;
(f) K.P.C. Vollhardt, Acc. Chem. Res. 10 (1977) 1;
(g) B. Cornils, W.A. Herrmann (Eds.), Applied Homogeneous Catalysis with Organometallic Compounds, vols. 1 & 2, VCH, New York, 1996.

[2] (a) A.J.M. Caffyn, K.M. Nicholas, in: E.W. Abel, F.G.A. Stone, G. Wilkinson (Eds.), Comprehensive Organometallic Chemistry II, vol. 12, Elsevier Science Inc., New York, USA, 1995, p. 685;
(b) N.E. Schore, in: E.W. Abel, F.G.A. Stone, G. Wilkinson (Eds.), Comprehensive Organometallic Chemistry II, vol. 12, Elsevier Science Inc., New York, USA, 1995, p. 703;
(c) J.L. Templeton, in: F.G.A. Stone, R. West (Eds.), Advances in Organometallic Chemistry, vol. 29, siam, New York, 1989, p. 1;
(d) C.M. Lukehart, Fundamental Transition Metal Organometallic Chemistry, Brools/Cole Publishing Company, Monterey, CA, 1985;
(e) M.J. Chetcuti, in: E.W. Abel, F.G.A. Stone, G. Wilkinson (Eds.), Comprehensive Organometallic Chemistry II, vol. 10, Elsevier Science Inc., New York, USA, 1995, p. 23.

[3] (a) For Dewar-Chatt-Duncanson's model, see M.J.S. Dewar, Bull. Soc. Chim. Fr. 18 (1951) C71;
(b) J. Chatt, L.A. Duncanson, J. Chem. Soc. (1953) 2939.

[4] (a) F.-E. Hong, Y.-C. Chang, R.-E. Chang, S.-C. Chen, B.-T. Ko, Organometallics 21 (2002) 961;
(b) F.-E. Hong, Y.-C. Chang, C.-P. Chang, Y.-L. Huang, Dalton Trans. (2004) 157.

[5] (a) C.-P. Chang, Y.-L. Huang, F.-E. Hong, Tetrahedron 61 (2005) 3835;
(b) F.-E. Hong, Y.-J. Ho, Y.-C. Chang, Y.-L. Huang, J. Organomet. Chem. 690 (2005) 1249;
(c) F.-E. Hong, Y.-J. Ho, Y.-C. Chang, Y.-C. Lai, Tetrahedron 60 (2004) 2639.

[6] D.C. Bradly, R.C. Mehrotra, D.P. Gaur, Metal Alkoxides, Academic Press, New York, San Francisco, 1978.

[7] (a) J.-M. Vion, R. Jerome, P. Teyssie, M. Aubin, R.E. Prudhomme, Macromolecules 19 (1986) 1828;
(b) H.R. Kricheldorf, M. Beri, M. Scharnagi, Macromolecules 27 (1988) 286;
(c) N. Ropson, Ph. Dubois, R. Jerome, P. Teyssie, Macromolecules 26 (1993) 6378;
(d) A. Löfgren, A.-C. Albertsson, Ph. Dubois, R. Jerome, P. Teyssie, Macromolecules 27 (1994) 5556;
(e) A. Duda, S. Penczek, Macromolecules 28 (1995) 5981, and references therein.

[8] (a) D. Bradley, R.C. Mehrotra, I. Rothwell, A. Singh, Alkoxo and aryloxo derivatives of metals, Academic Press, San Diego, 2001;
(b) M. Veith, Chem. Rev. 90 (1990) 3;
(c) M. Veith, S. Hill, V. Huch, Eur. J. Inorg. Chem. 8 (1999) 1343;
(d) M. Veith, M. Ehses, V. Huch, New J. Chem. 29 (2005) 154.

[9] (a) M.J.S. Dewar, Bull. Soc. Chim. Fr. 18 (1951) C71;
(b) J. Chatt, L.A. Duncanson, J. Chem. Soc. (1953) 2939.

[10] The commonly observed hydrogen-bonding ranges from 2.05 Å to 2.40 Å R. Taylor, O. Kennard, J. Am. Chem. Soc. 104 (1982) 5063.

[11] (a) A. Gelling, J.C. Jeffery, D.C. Powey, M.J. Went, J. Chem. Soc., Chem. Commun. (1991) 341;
(b) H.-L. Chen, B.-T. Ko, B.-H. Huang, C.-C. Lin, Organometallics 20 (2001) 5076;
(c) M.-L. Hsueh, B.-H. Huang, C.-C. Lin, Macromolecules 35 (2001) 5763.

[12] M. Gruselle, B. Malezieux, J. Vaissermann, Organometallics 17 (1998) 2337.

[13] G.M. Sheldrick, SHELXTL PLUS User's Manual. Revision 4.1 Nicolet XRD Corporation, Madison, Wisconsin, USA, 1991.

Available online at www.sciencedirect.com
ScienceDirect
Polyhedron 26 (2007) 2997–3002
POLYHEDRON
www.elsevier.com/locate/poly

Synthesis, thermal stability and structural characterisation of iron(II) phthalocyanine complex with 4-cyanopyridine

Jan Janczak *, Ryszard Kubiak

Institute of Low Temperature and Structure Research, Polish Academy of Sciences, Okólna 2 str., P.O. Box 1410, 50-950 Wrocław, Poland

Received 22 November 2006; accepted 31 January 2007
Available online 7 February 2007

Abstract

A new complex of bis-axially coordinated iron(II) phthalocyanine by 4-cyanopyridine (4-CNpy) has been obtained in crystalline form as an adduct with two 4-CNpy molecules. The $[FePc(4\text{-}CNpy)_2]\cdot 2(4\text{-}CNpy)$ crystallises in the monoclinic system, space group $P2_1/c$ with two molecules in the unit cell. The iron(II) coordinates four isoindole nitrogen atoms of the almost planar phthalocyaninato(2−) macroring and axially two nitrogen atoms of 4-CNpy molecules. The coordination polyhedron around the Fe(II) atom approximates to a tetragonal by-pyramid. Four equatorial Fe–N bonds are shorter (1.936(2) Å) than two axial Fe–N bonds (2.027(2) Å). The centrosymmetric $FePc(4\text{-}CNpy)_2$ molecules form alternating sheets parallel to the *bc* crystallographic plane and solvated 4-CNpy molecules that are anti-parallel oriented by their polar cyano groups are located between the sheets of $FePc(4\text{-}CNpy)_2$ molecules. Ligation of the intermediate-spin iron(II) phthalocyanine by 4-CNpy molecules leads to the low spin Fe(II) complex. The importance of the $d(\pi) \rightarrow \pi^*(Pc)$ back donation is manifested in the difference between the values of C–N isoindole and C–N azamethine bond lengths of the Pc macrocycle. The thermal analysis of the crystals of $[FePc(4\text{-}CN)_2]\cdot 2(4\text{-}CNpy)$ shows two steps responsible for a loss of solvated (∼170 °C) and coordinated (∼235 °C) 4-CNpy molecules.
© 2007 Elsevier Ltd. All rights reserved.

Keywords: Iron phthalocyaninie; Low-spin complex; Bis-axially coordination; Crystal structure

1. Introduction

Iron phthalocyanine and its additive complexes are still of wide interest because of its close analogy to the iron porhyrin and blood hemine [1]. We are especially interested in this study, trying to explore how the ligand bis-axially bonded to the phthalocyanine metal influences the feature and stability of the complex formed. A few years ago, we have synthesised and characterised the metal(II) phthalocyanine complexes with bis-axially coordinated pyridine molecules: $MgPc(py)_2$ [2], $FePc(py)_2$ and $CoPc(py)_2$ [3] and $MnPc(py)_2$ [4]. These all dipyridinated M(II)Pc complexes are structurally isomorphic and crystallise in the monoclinic system.

Previously, the iron and cobalt phthalocyanine crystalline complexes with 4-methylpyridine (4-Mepy) with the formula of $[MPc(4\text{-}Mepy)_2]\cdot 2(4\text{-}Mepy)$ (where M = Fe(II) or Co(II)) have been studied by Cariati et al. [5]. These compounds are also structurally isomorphic, but orthorhombic. Several crystal structures of bis-axially coordinated iron phthalocyanine derivatives have been reported [6–14] but they contain iron(III) or iron(IV) in the center of phthalocyaniniato ligand. Besides above-mentioned bis-axially ligated iron(II) phthalocyanines, the crystal structure of a low-spin iron(II) phthalocyanine complex ligated by 4-methylpiperidine (4-Mepip) with the composition of $[FePc(4\text{-}Mepip)_2]\cdot 2(4\text{-}Mepip)$ has been described [15].

In this paper, we describe the synthesis, thermal stability, crystal structure and magnetic properties of bis-axially coordinated iron(II) phthalocyanine complex by another pyridine derivative, i.e. 4-cyanopyridine (4-CNpy).

* Corresponding author. Tel.: +48 71 343 5021; fax: +48 71 441029.
E-mail address: j.janczak@int.pan.wroc.pl (J. Janczak).

0277-5387/$ - see front matter © 2007 Elsevier Ltd. All rights reserved.
doi:10.1016/j.poly.2007.01.040

2. Experimental

2.1. Synthesis of the [FePc(4-CNpy)$_2$].2(4-CNpy) complex in the crystalline form

Iron phthalocyanine (FePc) and 4-cyanopyridine (4-CNpy) compounds were mixed in the molar proportion of 1:5, respectively. Next the mixture was pressed into pellets of 2 g in mass. The pellet was inserted into a glass ampoule, ca. 10 cm in length, which next was degassed and sealed off. The sample in the ampoule was thermally processed by about one weak. At first the temperature was increased to 120 °C. After as apparently uniform suspension was formed, the temperature was increased again to 180 °C and held constant by one day and next lowered to 150 °C by a second day. As only the well developed iron phthalocyaninato complex crystals were seen (up to 1 mm in edge), the ampoule was firstly cooled to room temperature and next placed into temperature gradient, with 50 °C at the hot zone. After several days the excessive 4-CNpy migrates to the cold zone. At such state the ampoule was opened and the crystals of iron phthalocyanine complex were selected for further experiments. Elemental analysis of the crystalline iron phthalocyanine complex has been performed on an energy dispersive spectrometer. *Anal.* Calc. for $C_{56}H_{32}N_{16}Fe$: Fe, 5.67; C, 68.30; N, 22.75; H, 3.28. Found: Fe, 5.72; C, 68.41; N, 22.68, H, 3.19%. We want to add that another pellets with the various excesses of 4-cyanopyridine were processed at lower and at higher temperatures as well, however, these attempts were not satisfactory, regarding the [FePc(4-CNpy)$_2$].2(4-CNpy) complex formation.

2.2. Thermal measurements

Thermal analysis was carried out on a Lineis L81 thermobalance apparatus with Pt crucibles. The powdered Al_2O_3 has been used as a standard reference. The measurements were performed on samples of 15–20 mg under static air atmosphere on heating from room temperature to 300 °C with the heating rate of 5 °C min^{-1}.

2.3. X-ray single crystal measurement

Data collection was carried out on a KUMA KM-4 diffractometer with a two-dimensional area CCD detector. The graphite-monochromatised Mo Kα radiation ($\lambda = 0.71073$ Å) and ω-scan technique with $\Delta\omega = 0.75°$ for one image were used for data collection. The 960 images for six different runs covering over 99% of the Ewald sphere were performed. One image as a standard was used for monitoring the stability of the intensities after every 40 images. Integration of the intensities, corrections for Lorenz and polarisation effects were made using a KUMA KM-4 CCD program package [16]. The face-indexed analytical absorption was calculated using the SHELXTL program [17]; maximum and minimum transmission factors being 0.941 and 0.910. 5975 independent reflections (a total of 30 225 reflections were integrated, $R_{int} = 0.0579$) were used for crystal structure solution and refinement. The structure was solved by direct methods. The hydrogen atoms of the phenyl rings were located from the $\Delta\rho$ maps, but in the final refinement their positions were constrained using HFIX 43 with the isotropic thermal parameters of $1.2U_{eq}$ of the carbon atoms linked directly to the H atoms. The structure was refined with anisotropic thermal parameters for all non-hydrogen atoms by full-matrix least-squares methods using SHELXL-97 program [18]. The final difference map calculation showed no peaks of chemical significance; the largest were +0.294 and −0.215 e Å^{-3}. More details of the data collection parameters and the final agreement factors are collected in Table 1. Selected bond lengths and angles are listed in Table 2.

2.4. Magnetic susceptibility measurements

The temperature dependence of the magnetic susceptibility of [FePc(4-Mepy)$_2$] · 2(4-Mepy) was recorded from 300 to 1.8 K on Quantum Design SQUID magnetometer (San Diego, CA) on the sample of 85 mg. The magnetisation on magnetic field dependence was recorded from 0 to 5 T at 1.9 K.

3. Results and discussion

3.1. Characterisation of the FePc recrystallisation process in the 4-cyanopyridine

According to our observations during several days of thermal processing of the iron phthalocyanine with 4-cyanopyridine (in excess), roughly three characteristic temperature ranges could be distinguished. In the range above the melting point of the 4-cyanopyridine (∼80 °C) and to ca. 150 °C, the suspension is formed, which again completely separates, as soon as the temperature falls below the 4-cyanopyridine solidification point. At the temperature range 150–180 °C the most characteristic products registered are the parallelepipedal violet crystals of the additive complex of the iron phthalocyanine, [FePc(4-CNpy)$_2$].2(4-CNpy) and individual colourless crystals of 2,4,6-tris-(4′-pyridyl)-triazine molecules that are formed by the cyclotrimerisation of 4-cyanopyridine molecules. The 2,4,6-tris-(4′-pyridyl)-triazine crystallises in *C*2/*c* space group of the monoclinic system and the structure was earlier described [19]. When the mixture containing the violet and colourless crystals is quickly cooled from the above-mentioned temperature (150–180 °C) to the room temperature, the crystals of iron phthalocyanine complex with 4-cyanopyridine are preserved and can be separated for the X-ray analysis. Otherwise, i.e. if the temperature of the sample is slowly lowered (during a few days), the crystals of iron phthalocyanine complex with 4-cyanopyridine vanish and again non-coordinated iron phthalocyanine (FePc), in the form of fine crystalline needles, is present in the sample.

Table 1
Crystal data and structure refinement for $[FePc(4\text{-}CNpy)_2].2(4\text{-}CNpy)$

Chemical formula	$C_{56}H_{32}N_{16}Fe$
Formula weight	984.83
Temperature (K)	295(2)
Wavelength (Å)	0.71073
Crystal system	monoclinic
Space group	$P2_1/c$
Unit cell dimensions	
a (Å)	13.719(3)
b (Å)	15.923(3)
c (Å)	11.446(2)
β (°)	108.86(3)
Volume (Å^3)	2366.1(9)
Z	2
D_{calc} and $D_{measure}$ (Mg/m^3)	1.382 and 1.38
Absorption coefficient (mm^{-1})	0.378
Crystal size (mm)	$0.28 \times 0.22 \times 0.14$
θ_{max} for data collection (°)	28.49
Limiting indices	$-18 \leqslant h \leqslant 18$, $-21 \leqslant k \leqslant 20$, $-15 \leqslant l \leqslant 15$
Reflections collected/unique/observed with $[F^2 > 2\sigma(F^2)]$ (R_{int})	30225/5975/3727 (0.0579)
Refinement method	full-matrix least-squares on F^2
Data/restraints/parameters	5975/0/331
Goodness-of-fit on F^2	1.038
Final R[a] indices $[I > 2\sigma(I)]$	0.0595
wR[b] indices (all data)	0.1483
Largest peak and hole on Δ map (e Å^{-3})	+0.294 and −0.215

[a] $R = \sum\|F_o| - |F_c\|/\sum F_o$.
[b] $wR = \{\sum[w(F_o^2 - F_c^2)^2]/\sum wF_o^4\}^{1/2}$; $w^{-1} = [\sigma^2(F_o^2) + (0.0628P)^2 + 0.7299P]$ where $P = (F_o^2 + 2F_c^2)/3$.

Table 2
Selected bond lengths (Å) and angles (°) for $[FePc(4\text{-}CNpy)_2] \cdot 2(4\text{-}CNpy)$

Fe1–N2	1.938(2)		
Fe1–N4	1.934(2)		
Fe1–N21	2.027(2)		
N2–Fe1–N4	90.27(9)		
N2^i–Fe1–N4	89.73(9)		
N2–Fe1–N21	89.64(8)		
N4–Fe1–N21	90.28(8)		
C–N(pyrrole)		C–N(azamethine)	
C1–N2	1.377(3)	C1–N1	1.327(3)
C8–N2	1.370(3)	C8–N3	1.331(3)
C9–N4	1.371(3)	C9–N3	1.330(3)
C16–N4	1.376(3)	C16–N1^i	1.331(3)
C–CN		C≡N	
C23–C26	1.446(4)	C26–N22	1.137(4) (coordinated 4-CNpy)
C33–C36	1.420(7)	C36–N32	1.140(6) (solvated 4-CNpy)

Symmetry code: (i) $-x$, $-y$, $-z$.

At temperature 200 °C and above, the processing firstly leads to the 2,4,6-tris-(4′-pyridyl)-triazine crystals growth, which is the catalytic effect of the FePc presence in the sample (similar catalytic effect is observed in presence of MgPc and has been registered by us [19]). However, progressively with the time the thermal processing leads markedly to the demetallation of iron phthalocyanine and destructive decomposition (the violet phthalocyanine colour vanishes). If the processing is interrupted at a proper moment, the evolved nano-dispersed iron particles cause that the sample moves under a solid magnet (the effect does not vanish even after several months). Prolonged heating, however, causes further, destructive transformation of the sample, leading to the oxidation of the iron particles, and in the result the sample does not show magnetic behaviour.

3.2. Thermal analysis of $[FePc(4\text{-}CNpy)_2].2(4\text{-}CNpy)$ complex

The first marked step on TG (see Fig. 1), registered in the range of 165–175 °C, is ascribed to the loss of two lattice held 4-cyanopyridine molecules from the complex, $[FePc(4\text{-}CNpy)_2](4\text{-}CNpy)_2 \rightarrow [FePc(4\text{-}CNpy)_2] + 2(4\text{-}CNpy)$. The further mass loss is observed at about 230 °C. Above this temperature two axial equivalent Fe–N(4-CNpy) bonds break simultaneously giving FePc in a powder form. Both processes are endothermic and characteristic of the loss of the 4-CNpy molecules as a lattice solvent (first step) or the loss of coordinated 4-CNpy molecules. Further increase of the temperature leads to oxidative destruction of the sample, since above 275 °C the mass loss of the sample is observed.

3.3. Description of the structure

The molecular structure of $[FePc(4\text{-}CNpy)_2] \cdot 2(4\text{-}CNpy)$ complex is illustrated in Fig. 2. The central iron cation lies at the inversion center, thus the $[FePc(4\text{-}CNpy)_2]$ molecule is centrosymmetric. The coordination polyhedron around Fe(II) approximates to a tetragonal bypyramid. The central iron atom and the four isoindole nitrogen

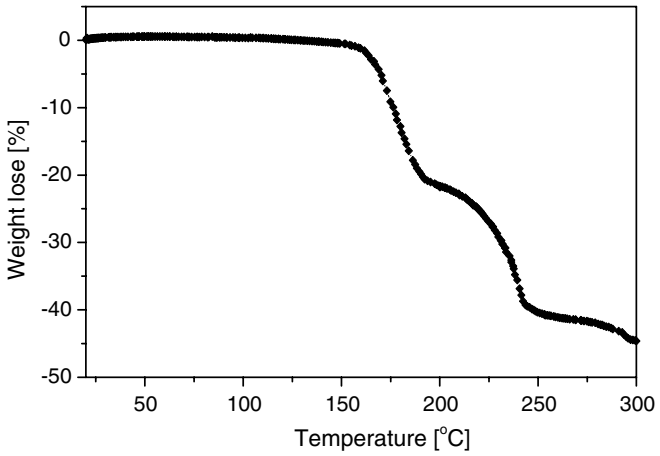


Fig. 1.

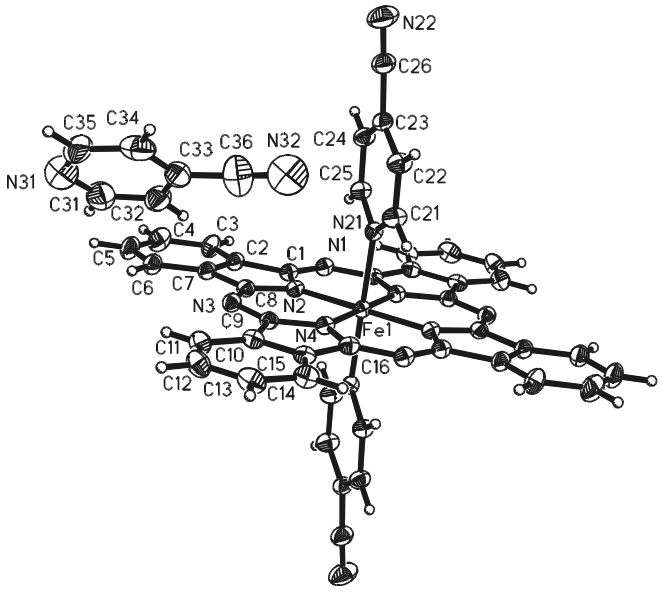


Fig. 2.

atoms of the phthalocyaninato(2−) macrocycle lie on a plane. As shown in Fig. 2, the two axial 4-CNpy molecules are coordinated by their lone-electron pair at the ring nitrogen atoms to the central Fe(II) atom. The dihedral angle between the N_4-isoindole plane of phthalocyaninato(2−) macrocycle and that containing the axially coordinated 4-CNpy molecules is close but markedly different from 90°, i.e. 85.2(1)°. For comparison the respective value of the deviation is not greater than 1°, when the 4-Mepy or py molecules are ligated [3,5]. The orientation of the axial 4-CNpy ligands relative to the phthalocyaninato(2−) macroring is well described by the torsion angle of N4–Fe1–N21–C21. The rotation of 4-CNpy ligand around the Fe1–N21 axis would reduce the steric hindrance, i.e. the non-bonding distances between the hydrogen atoms of the axial 4-CNpy ligand in *ortho* positions and the atoms of phthalocyaninato(2−) macrocycle. In particular, if the rotation angle is equal 0, the 4-CNpy molecule is parallel to the Fe1–N4 bond or at equivalent position rotated by 90°, the 4-CNpy molecule is parallel to the Fe1–N2 bond, making the non-bonding C···H distances greater than 2.6 Å. The second orientation, with the rotation angle of 45°, makes the axial 4-CNpy ligand plane parallel to the Fe1···N(azamethine) axis and reduce the non-bonding distances between the hydrogen atoms of 4-CNpy (H in *ortho* positions) and the azamethine nitrogen atoms of phthalocyaninato(2−) macrocycle. This conformation is the most stable, and is preferable in the solution, due to the strongest interaction between the *ortho*-H atoms of 4-CNpy molecules and the *N*-azamethine atoms of phthalocyaninato(2−) macroring. This conformation is also present in the crystal, however, due to the intermolecular interactions and crystal packing forces this angle is slightly different from 45° (see Table 3). This angle is comparable to that observed in the crystal of $[FePc(4\text{-}Mepy)_2]\cdot 2(4\text{-}Mepy)$ [5] but significantly different from those in the crystal of $FePc(py)_2$ [3]. The differences between the rotation angle of the axially coordinated 4-CNpy (or 4-Mepy) and pyridine molecules, are likely due to the interaction with the solvated 4-CNpy (or 4-Mepy) molecules present in the structure.

The axial Fe1–N21 bond distance is longer by ~0.1 Å than equatorial four Fe–N bonds [average 1.936 Å]. A similar pattern of the Fe–N bonds is observed in the other axially coordinated iron phthalocyanine derivatives (see Table 3). The values of the axial Fe–N bond lengths in axially coordinated FePc derivatives point to their strength and correlate well with their thermal stability. For example, in this complex, the Fe–N(4-CNpy) bond length is shorter than Fe–N(py) in $FePc(py)_2$ and correlate with the thermal breaks of the axial Fe–N bond (~235 °C and ~225 °C for $[FePc(4\text{-}CNpy)_2]\cdot 2(4\text{-}CNpy)$ and $FePc(py)_2$, respectively). In the crystal of $[FePc(4\text{-}Mepip)_2]\cdot 2(4\text{-}Mepip)$ complex the elongation of the axial Fe–N bond (2.119(3) Å) can be explain by a steric effect of the 4-methylpiperidine ligand rather than the electronic structure.

The C–C and C–N bond lengths of the phthalocyaninato(2−) macrocycle in the $[FePc(4\text{-}CNpy)_2]\cdot 2(4\text{-}CNpy)$ are normal in the sense that their values are not very different from the corresponding values found in various metallophthalocyanines [20]. However, it should be noted that small differences between the values of C–N(isoindole) and C–N(azamehtine) bond lengths are observed (see Table 2). These differences indicate an accumulation of the charge density on the outer carbon atoms of pyrrole rings as well as on the bridging azamethine N atoms and can, therefore, be explained by an important electron back donation from the metal d(π) orbitals to the ligand $\pi^*(e_g)$ antibonding orbital, since the maximum charge density is mainly located at those atoms. The accumulation of the charge density on the outer carbon atoms of pyrrole rings and on the bridging azamethine nitrogen atoms of phthalocyaninato(2−) macroring has also been evidenced in the

Table 3
Comparison of the bis-axially ligated iron(II) phthalocyanine complexes and FePc

Compound	Fe–N_{iso} (Å)	Fe–N_{axial} (Å)	Rotation angle (°)	C–N_{iso} (Å)	C–N_{aza} (Å)	Thermal stability (°C)	Reference
$[FePc(4\text{-}CNpy)_2]\cdot 2(4\text{-}CNpy)$	1.936(2)	2.027(2)	47.1(2)	1.374(3)	1.330(3)	~170–235	this work
$[FePc(4\text{-}Mepy)_2]\cdot 2(4\text{-}Mepy)$	1.935(3)	2.040(3)	42.6(4)	1.373(7)	1.328(4)		[5]
$FePc(py)_2$	1.938(2)	2.039(2)	36.1(2)	1.377(3)	1.331(3)	~225	[3]
$[FePc(4\text{-}Mepip)]\cdot 2(4\text{-}Mepip)$	1.931(3)	2.119(2)		1.376(3)	1.324(3)		[15]
FePc	1.926(2)			1.378(3)	1.322(3)		[24]

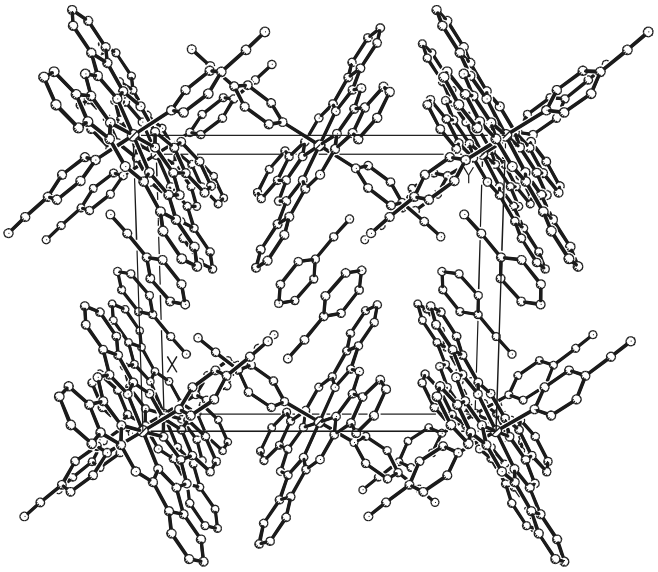


Fig. 3.

experimental density maps derived from the low temperature high resolution X-ray experiment [21–23].

The arrangement of the $[FePc(4\text{-}CNpy)_2]\cdot 2(4\text{-}CNpy)$ molecules in the unit cell is illustrated in Fig. 3. The crystal is built up from isolated $FePc(4\text{-}CNpy)_2$ molecules that are related by screw axis and glide plane, which form alternating sheets parallel to the *bc* crystallographic plane, and solvated 4-CNpy molecules (Fig. 3). The rings of solvated 4-CNpy molecules related by an inversion center are parallel to each other, but oriented anti-parallel by their polar cyano groups. This orientation of solvated 4-CNpy molecules reduces the repulsive forces between the dipoles of 4-CNpy molecules. The dihedral angle between the plane of solvated 4-CNpy molecule and phthalocyaninato(2−) macroring of 42.9(2)° and the plane of the ligated 4-CNpy molecule of 73.8(2)° as well as the intermolecular nonbonding distances that are greater than the sum of the commonly accepted van der Waals radii indicate that there are no π–π interactions in the structure. The geometry of ligated and solvated 4-CNpy molecules are comparable, however, the both N–C lengths in the ring of coordinated 4-CNpy molecule are longer than in solvated one.

3.4. Magnetic properties

The magnetic susceptibility measurement on the sample of $[FePc(4\text{-}CNpy)_2]\cdot 2(4\text{-}CNpy)$ shows its diamagnetic character. This experiment clearly evidenced that ligation of the iron phthalocyanine with the intermediate state $(d_{xz}, d_{yz})^3$-$(d_{xy})^2(d_{z^2})^1$ with two unpaired electrons [24–28] leads to the change of the ground-state from $S = 1$ (for $FePc, e_g^3 b_{2g}^2 a_{1g}^1$) to $S = 0$ (for $[FePc(4\text{-}CNpy)_2]\cdot 2(4\text{-}CNpy), e_g^4 b_{2g}^2$). Thus the $[FePc(4\text{-}CNpy)_2]\cdot 2(4\text{-}CNpy)$ complex is a low-spin complex, according to the molecular orbital diagram of Fe(II) in a strong-field tetragonal environment [29].

4. Conclusion

The formation of the Fe–N(4-CNpy) bond, between the central iron ion of FePc and the ring nitrogen of the 4-CNpy, in the early stages of dissolution the iron phthalocyanine grains is relatively easy reversible, i.e. as long as the bonding is not complete and not stabilised by an intermolecular order of the units in the assembly. It is so, because both FePc, as well as the ligated 4-CNpy molecules, characterise a distinct planarity and strong rigidity. Moreover, the axially coordinated 4-CNpy molecules preserve, in spite of their marked extension in relation to that of Pc edge value, a strong propensity for close to perpendicular orientation to the Pc plane. For such extended units as building blocks, there are only limited opportunities to arrange themselves into a tightly packed configuration. Therefore, the newly formed molecules composing the building block may go again apart, and for that moment they are in the excited state. In a consequence of it, when FePc is thermally processed (recrystallised) in 4-CNpy, both components show highly time and temperature dependent behaviour. Here we want to add, that according to Hanack et al. [30] one could expect also that the freshly formed 2,4,6-tris-(4′-pyridyl)-triazine molecules, if it is the cause, as -tridenadate ligand will form very stable complexes with the FePc present in the system. However, we have not observed the 2,4,6-tris-(4′-pyridyl)-triazine splitting at 342 °C or at higher temperature as mentioned in [30].

Appendix A. Supplementary material

Details on data collection and refinement, fractional atomic coordinates, anisotropic displacement parameters and full list of bond lengths and angles in CIF format have been deposited at the Cambridge Crystallographic Data Centre. CCDC 628342 contains the supplementary crystallographic data for this paper. These data can be obtained free of charge via http://www.ccdc.cam.ac.uk/conts/retrieving.html, or from the Cambridge Crystallographic Data Centre, 12 Union Road, Cambridge CB2 1EZ, UK; fax: (+44) 1223-336-033; or e-mail: deposit@ccdc.cam.ac.uk. Supplementary data associated with this article can be found, in the online version, at doi:10.1016/j.poly.2007.01.040.

References

[1] F.A. Walker, U. Simonis, in: L.J. Berliner, J. Reuben (Eds.), Encyclopedia of Inorganic Chemistry, Plenum Press, New York, 1993, pp. 133–274.
[2] J. Janczak, R. Kubiak, Polyhedron 21 (2002) 265.
[3] J. Janczak, R. Kubiak, Inorg. Chim. Acta 342 (2003) 64.
[4] J. Janczak, R. Kubiak, M. Śledź, H. Borrmann, Y. Grin, Polyhedron 22 (2003) 2689.
[5] F. Cariati, F. Morazzoni, M. Zocchi, J. Chem. Soc., Dalton Trans. (1978) 1018.
[6] L.A. Yatsunyk, M.D. Carducci, F.A. Walker, J. Am. Chem. Soc. 125 (2003) 15986.

[7] H. Kuppers, W. Kalz, H. Homborg, Acta Crystallogr., Sect. C 41 (1985) 1420.
[8] M. Matsuda, T. Asari, T. Naito, T. Inabe, N. Hanasaki, Bull. Chem. Soc. Jpn. 76 (2003) 1935.
[9] B. Moubaraki, M. Ley, D. Benlian, J.P. Sorbier, Acta Crystallogr., Sect. C 46 (1990) 379.
[10] R. Potz, H. Hückstädt, H. Homborg, Z. Anorg. Allg. Chem. 624 (1998) 173.
[11] M. Matsuda, T. Naito, T. Inabe, N. Hanasaki, H. Tijama, J. Mater. Chem. 11 (2001) 2493.
[12] L. Galich, A. Kienast, H. Hückstädt, H. Homborg, Z. Anorg. Allg. Chem. 624 (1998) 1235.
[13] F. Calderazzo, G. Pampaloni, D. Vitali, G. Pelizzi, I. Collamali, S. Frediani, A.M. Serra, J. Organomet. Chem. 191 (1980) 217.
[14] A. Geiss, H. Vahrenkamp, Inorg. Chem. 39 (2000) 4028.
[15] V.N. Nemykin, N. Kobayashi, V.Y. Chernii, V.K. Belsky, Eur. J. Inorg. Chem. (2001) 733.
[16] KUMA Diffraction, KUMA KM-4 CCD program package, Ver. 173.12., 2004, Wrocław, Poland.
[17] G.M. Sheldrick, SHELXTL Program, Siemens Analytical X-ray Instrument Inc., Madison, WI, 1991.
[18] G.M. Sheldrick, SHELXL-97: Program for the Solution and Refinement of Crystal Structures, University of Göttingen, Göttingen, Germany, 1997.
[19] J. Janczak, M. Śledź, R. Kubiak, J. Mol. Strut. 659 (2003) 71.
[20] F.H. Allen, Acta Crystallogr., Sect. B 58 (2002) 380.
[21] P. Coppens, L. Liand, N.J. Zhu, J. Am. Chem. Soc. 105 (1983) 6173.
[22] A. Holiday, P. Leung, P. Coppens, Acta Crystallogr., Sect. A 39 (1983) 377.
[23] N. Li, Z. Su, P. Coppens, J. Landrum, J. Am. Chem. Soc. 112 (1990) 7294.
[24] J.F. Kirner, W. Down, W.R. Scheidt, Inorg. Chem. 15 (1976) 1685.
[25] A.B.P. Lever, J. Chem. Soc. (London) (1965) 1821.
[26] B.N. Figgs, R.S. Nyholm, J. Chem. Soc. (1959) 338.
[27] B.W. Dale, R.J.P. Williams, C.E. Johnson, T.L. Thorp, J. Chem. Phys. 49 (1968) 3441.
[28] B.W. Dale, R.J.P. Williams, R.P. Edwards, C.E. Johnson, J. Chem. Phys. 49 (1968) 3445.
[29] B.W. Dale, R.J.P. Williams, R.P. Edwards, C.E. Johnson, Trans. Faraday Soc. 64 (1968) 620.
[30] M. Hanack, M. Fiedler, L.R. Subramanian, Synth. Met. 100 (1999) 123.

Available online at www.sciencedirect.com
ScienceDirect
Polyhedron 26 (2007) 3003–3007
POLYHEDRON
www.elsevier.com/locate/poly

The structure of *N-meso*-(6,8,8,14,16,16-hexamethyl-1,5,9,13-tetraazacyclohexadeca-5,13-diene)nickel(II) chloro(isothiocyanato)zincate(II)

Neil F. Curtis [a,*], Rebekah Pawley [b], Ward T. Robinson [b]

[a] *School of Chemical and Physical Sciences, Victoria University of Wellington, Box 600, Wellington, New Zealand*
[b] *Chemistry Department, University of Canterbury, Christchurch, New Zealand*

Received 26 October 2006; accepted 2 February 2007
Available online 13 February 2007

Abstract

A yellow compound which was crystallised from a solution of (6,8,8,14,16,16-hexamethyl-1,5,9,13-tetraazacyclohexadeca-5,13-diene)bis(isothiocyanato)nickel(II) in aqueous zinc(II) chloride has cations with singlet ground state nickel(II) in square-planar coordination by the nitrogen atoms of the macrocycle. The asymmetric unit has two similar cations. The N_4 group of one cation is near coplanar (r.m.s. displacements ±0.009(1) Å, with Ni displaced by 0.048(1) Å from this plane) while the other cation has significant tetrahedral twisting of the N_4 group (r.m.s. displacements of N atoms ±0.126(2) Å, with Ni displaced by 0.027(2) Å from this plane). The mean Ni–N distances are $Ni–N_{amine} = 1.950(6)$ and $Ni–N_{imine} = 1.897(6)$ Å. Both cations have *N-meso* configurations with saddle conformations, with the substituted chelate rings in boat conformations tilted to one side of the NiN_4 'plane' and the unsubstituted chelate rings tilted to the other side, one in a boat conformation and the other with the central methylene group disordered, the components forming boat {s.o.f. 0.70(1) and 0.74(1) for the two cations} and chair conformation chelate rings. The counter-ions have tetrahedrally coordinated zinc(II) ions, one as $[ZnCl_2(NCS)_2]^{2-}$ ions and the other with one ligand site with disordered Cl^- {s.o.f. 0.78(1)} and NCS^- ligands, i.e. with disordered $[ZnCl_2(NCS)_2]^{2-}$ and $[ZnCl(NCS)_3]^{2-}$ ions, with an overall composition of [Ni(*trans*-Me_6[16]diene)]-$[ZnCl_{1.9}(NCS)_{2.1}]$.
© 2007 Elsevier Ltd. All rights reserved.

Keywords: Nickel(II); Coordination; Azamacrocycle; Tetraazacyclohexadecadiene; Cyclic imine; Cyclic amine; Dichloro-bis(thiocyanato)zinc(II); Crystal structure

1. Introduction

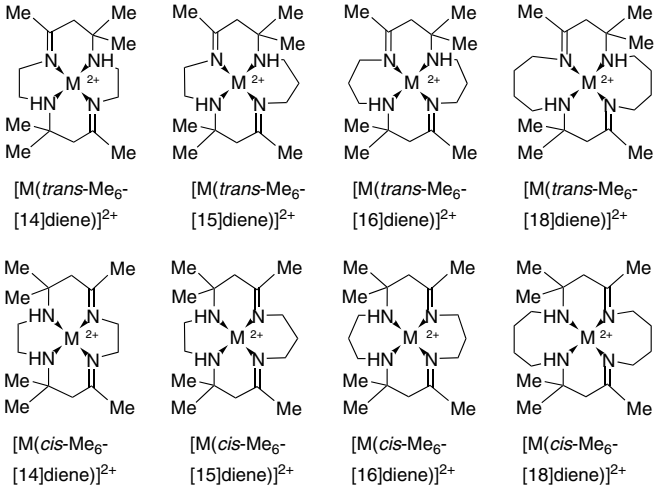
The preparations of compounds of nickel(II) and copper(II) with hexamethyl-substituted diimine–diamine tetraaza-macrocycles with 14- to 18-ring members, by reactions of diamine compounds of the cations with acetone, have been reported [1].

For both metal ions the reactions of ethane-1,2-diamine compounds with acetone yield a mixture of isomeric tetraaza-cyclotetradecadiene macrocyclic cations with 4,14(1)-diimine functions, [M(*cis*-Me_6[14]diene)]$^{2+}$, and with 4,11-diimine functions, [M(*trans*-Me_6[14]diene)]$^{2+}$ [2,3], see Scheme 1. Structures have been reported for numerous compounds of both isomeric cations for both metal ions (below).

Reactions of copper(II) compounds of butane-1,4-diamine with acetone form both 6,18(1)-diimine, [Cu(*cis*-Me_6[18]diene)]$^{2+}$, and 6,15-diimine, [Cu(*trans*-Me_6[18]-diene)]$^{2+}$, tetraaza-cyclooctadecadiene macrocyclic ligand cations [4]. Structures of the isomeric copper(II) cations, as perchlorate salts, were reported [5]. With nickel(II) only the 6,15-diimine cation, [Ni(*trans*-Me_6[18]diene)]$^{2+}$, was isolated [4].

* Corresponding author. Tel.: +64 4463 6514; fax: +64 4 463 5237.
E-mail address: neil.curtis@vuw.ac.nz (N.F. Curtis).

0277-5387/$ - see front matter © 2007 Elsevier Ltd. All rights reserved.
doi:10.1016/j.poly.2007.02.002



Scheme 1. 14–18-membered tetraaza-cyclo-diene cations formed by reaction of copper(II) and nickel(II) diamine compounds with acetone.

Reactions with acetone of compounds of the cations with propane-1,3-diamine form compounds of homologous tetraaza-cyclohexadecadiene macrocycles [6,7]. For nickel(II) the *trans*-structure of the product was supported by a structural study of the disordered perchlorate salt [8] and by proton magnetic resonance studies for the cyclic tetraiimine oxidation product [9]. The imine functions of the nickel(II) cation were reduced by hydrogenation [10] and by $NaBH_4$ [11] to yield the cyclic tetraamine ligand cation. This was demetallated, by reaction with hydrochloric acid, to give the cyclic amine hydrochloride, from which compounds with cobalt(II) and copper(II) were prepared [11]. Structures of compounds of the cyclic tetraamine with cobalt(II), nickel(II) and copper(II) were reported [11].

A structural study of the perchlorate salt of the copper(II) tetraaza-cyclohexadecadiene cation shows a disordered structure with both *cis*- and *trans*-diimine cations present, indicating that the preparation yields a mixture of the isomeric cations [12]. The structure of N-*rac*-[Cu(*cis*-Me_6[16]diene)][$ZnCl_4$], prepared from the mixed perchlorate salt, unambiguously confirms the presence of the *cis*-diimine isomer [12].

2. Results

When a soluble thiocyanate salt is added to an aqueous solution of [Ni(*trans*-Me_6[16]diene)](ClO_4)$_2$ the sparingly water-soluble blue–violet dithiocyanato compound *trans*-[Ni(*trans*-Me_6[16]diene)(NCS)$_2$] precipitates. This dissolves in aqueous solutions of zinc(II) salts to form yellow solutions, apparently by reduction of the thiocyanate ion concentration by complexation with the zinc(II) ions. When zinc(II) chloride is used, sparingly water-soluble, yellow crystals can be isolated and these have been characterised by the structural study below. When other, non-halide, zinc(II) salts, e.g. zinc(II) nitrate or acetate, are substituted for the chloride the *trans*-Ni(*trans*-Me_6[16]diene)(NCS)$_2$] dissolves to form yellow solutions, but crystalline products are generally not formed. When additional thiocyanate is added then a sparingly soluble yellow crystalline product forms, of probable composition [Ni(*trans*-Me_6[16]diene)]-[$Zn(NCS)_4$].

3. Structural study

The structure of the yellow crystalline product obtained from the reaction of [Ni(*trans*-Me_6[16]diene)-(NCS)$_2$] with zinc chloride, and recrystallised from water, was determined by X-ray diffractometry (see Section 4.1 for details) to establish the configuration of the macrocycle, and to permit comparison of the structural parameters of homologous azamacrocycle cations with varying ring size.

The asymmetric unit of the compound contains two independent singlet ground state square-planar (tetraazacyclohexadecadiene)nickel(II) cations. Cation 1, with configuration 1*R*,9*S*, includes atom Ni1 and ring atoms N1–C16. Cation 2, with configuration 21*R*,29*S*, includes atom Ni2 and ring atoms N21–N36. Two independent tetrahedral chloro-(thiocyanato)zincate anions are present. Anion 2 includes zinc atom Zn5, two thiocyanate ions (N51, C51, S51) and (N52, C52, S52) with two chloride ions Cl51 and Cl52. Anion 1, with zinc atom Zn4, is disordered, see below, with two full occupancy thiocyanate ions with atoms (N41, C41 and S41) and (N42, C42 and S42) and chloride ion Cl41. Partial occupancy thiocyanate ion with atoms (N43, C43, and S43) and chloride ion Cl42 occupy one coordination site, with complementary s.o.f., see Fig. 1.

Both cations have 5,13-diimine (*trans*) structures, with the *N-meso* configuration (with the secondary amine

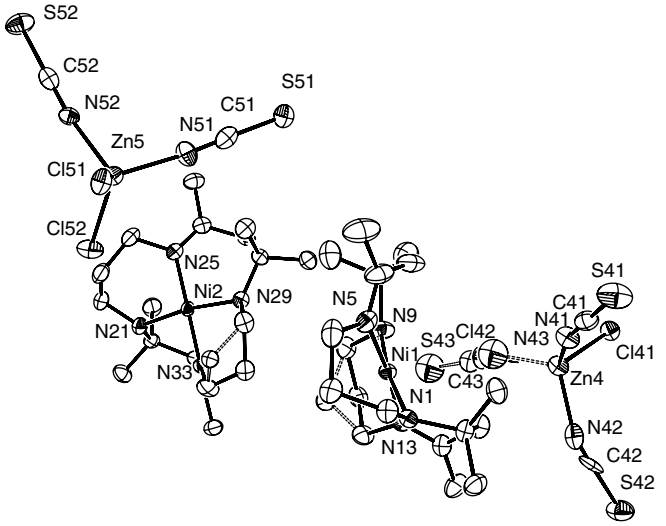


Fig. 1. Asymmetric unit, drawn with displacement ellipsoids at 50% confidence level. Hydrogen atoms are omitted for clarity. Site C11 has s.o.f. of 0.70(1), C31 of 0.74(1) and Cl42 of 0.779(4), with complementary s.o.f. for C11a, C31a and (N43, C43 and S43).

hydrogen atoms H1 and H9 on opposite sides of the Ni1, N1, N5, N9, N13 'plane'), and with the axially oriented methyl groups C82 and C162 both oriented to the same side of this plane as H9, see Fig. 2. which shows cation 1. Cation 2 is similar with N29, C262 and C282 oriented to the same side of the Ni2N21, N25, N29, N33 'plane' as H29.

The N_4 donor atom group of cation 1 is appreciably tetrahedrally twisted (r.m.s. displacements of N atoms ±0.126(2) Å, with atom Ni1 displaced by 0.027(2) Å from this plane). The N_4 donor atom group of the cation 2 is near coplanar (r.m.s. displacements ±0.009(1) Å, with atom Ni2 displaced by 0.048(1) Å from this plane).

The short bond lengths N5–C6, N1–C16, N25–C26 and N21–C36 and the near trigonal bond angles about these atoms (Table 1) confirm the locations of the imine functions. There is no indication of the orientational disorder in the location of the imine functions and axially oriented methyl substituents observed for [Cu(*cis*-Me_6[16]diene)]-[Cu(*trans*-Me_6[16]diene)]$(ClO_4)_4$ [12] and related compounds [13].

The Ni–N distances (Table 1) are only marginally longer than those observed for singlet ground state compounds of homologous [Ni(*trans*-Me_6[14]diene)]$^{2+}$ and [Ni(*trans*-Me_6[15]diene)]$^{2+}$ cations (Table 2), with Ni–N shorter for the imine than secondary amine nitrogen atoms, as is usual. While the calculated minimal strain "hole size" of amine–imine tetraaza-macrocycles for planar N_4 conformations increases significantly with ring size, the observed Ni–N distances for coordinated 14- to 16-membered rings increase only marginally, with the resulting strain accommodated by tetrahedral twisting of the N_4 group and/or increased buckling of the macrocycle, the latter being most significant for the [Ni(*trans*-Me_6[16]diene)]$^{2+}$ cations. The mean displacements of the ring atoms from the least-squares best plane for all ring atoms, is 1.06 Å for both cations, indicative of similar levels of ring puckering. The tetrahedral twisting of the NiN_4 group for cation 1 is appreciable and for the cation 2 is small, indicative of the flexibility of these macrocycles. There are no significant axial interactions with the nickel ions, the only atom closer than 4 Å is partial occupancy S43 (x, $-y+1/2$, $z+1/2$) at 3.66 Å from Ni1.

Table 1
Geometric parameters (Å, °)

Ni1–N1	1.933(3)	Ni2–N21	1.948(3)
Ni1–N5	1.905(3)	Ni2–N25	1.898(3)
Ni1–N9	1.967(3)	Ni2–N29	1.950(3)
Ni1–N13	1.888(3)	Ni2–N33	1.900(3)
N5–C6	1.318(5)	N25–C26	1.274(4)
Zn4–N41	1.988(3)	Zn5–N51	2.004(3)
Zn4–N42	2.027(4)	Zn5–N52	2.015(3)
Zn4–Cl41	2.261(1)	Zn5–Cl51	2.259(1)
Zn4–Cl42	2.288(2)	Zn5–Cl52	2.252(1)
N41–C41	1.148(4)	C51–N51	1.135(4)
C41–S41	1.621(4)	C51–S51	1.648(4)
N42–C42	1.019(5)	C52–N52	1.130(4)
C42–S42	1.693(5)	C52–S52	1.642(4)
Zn4–N43	1.92(2)		
N43–C43	1.14(2)		
C43–S43	1.61(2)		
N1–Ni1–N5	93.1(1)	N21–Ni2–N25	94.0(1)
N1–Ni1–N9	167.4(1)	N21–Ni2–N29	170.6(1)
N1–Ni1–N13	85.6(1)	N21–Ni2–N33	84.2(1)
N5–Ni1–N13	173.7(1)	N25–Ni2–N29	94.7(1)
N5–Ni1–N9	95.7(2)	N25–Ni2–N33	177.0(1)
N9–Ni1–N13	86.9(1)	N29–Ni2–N33	87.0(1)
C4–N5–C6	118.1(3)	C24–N25–C26	119.1(3)
N5–C6–C61	123.1(4)	N25–C26–C261	125.6(3)
N5–C6–C7	117.4(3)	N25–C26–C27	118.1(3)
C61–C6–C7	119.4(4)	C261–C26–C27	116.2(3)
N41–Zn4–N42	109.7(1)	N51–Zn5–N52	104.0(1)
N41–Zn4–Cl41	107.7(1)	N51–Zn5–Cl52	113.7(1)
N42–Zn4–Cl41	107.6(1)	N52–Zn5–Cl52	109.5(1)
N41–Zn4–Cl42	110.4(1)	N51–Zn5–Cl51	109.9(1)
N42–Zn4–Cl42	108.3(1)	N52–Zn5–Cl51	108.0(1)
Cl41–Zn4–Cl42	113.07(4)	Cl52–Zn5–Cl51	111.33(5)
C41–N41–Zn4	161.7(3)	C51–N51–Zn5	174.6(3)
N41–C41–S41	179.3(4)	N51–C51–S51	177.8(3)
N42–C42–S42	178.3(4)	N52–C52–S52	179.4(3)
C42–N42–Zn4	150.0(3)	C52–N52–Zn5	169.7(3)
N43–C43–S43	167(2)		
C43–N43–Zn4	136(2)		

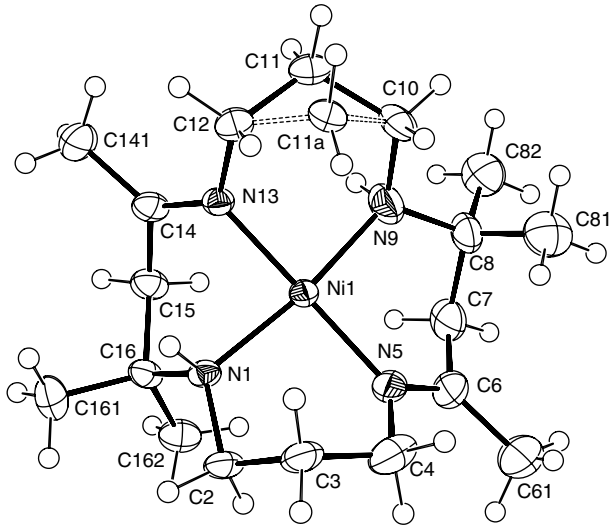


Fig. 2. Cation 1, drawn as for Fig. 1 but with hydrogen atoms shown as circles of arbitrary radii. Site C11 has s.o.f. of 0.70(1), C11a of 0.30(1). The cation 2 is similar.

Both cations have the macrocycle in 'saddle' conformations, with the substituted (hexamethyl-1,3-amine–imine) and the unsubstituted (1,3-diamine) chelate rings tilted to opposite sides of the NiN_4 'plane'. The amine–imine chelate rings all have asymmetrical boat conformations. The 1,3-diamine chelate rings Ni1, N1, N5 and Ni2, N21, N25 have boat conformations, while the opposing chelate rings (Ni1, N9, N13 and Ni2, N29, N33) have the central methylene group disordered. The major components C11 {s.o.f. = 0.65(1)} for the Ni1, N9, N13 chelate ring and C31 {s.o.f. = 0.73(1)}

Table 2
Structural parameters for related compounds (mean values, Å)

Compound	Distance, Ni–N_{amine}	Distance, Ni–N_{imine}	r.m.s. Tetrahedral displacement of N_4 group	Reference
rac-[Ni(*trans*-Me_6[14]diene)]$(ClO_4)_2$	1.915(4)	1.884(5)	0.06	[17]
meso-[Ni(*trans*-Me_6[14]diene)]$(ClO_4)_2$	1.938(2)	1.907(2)	0	[17]
rac-[Ni(*cis*-Me_6[14]diene)]$(ClO_4)_2$	1.89	1.93	0.007	[18]
rac-[Ni(*trans*-Me_6[15]diene)]$(ClO_4)_2$	1.919(6)	1.893(6)	0.20	[19]
rac-[Ni(*cis*-Me_6[15]diene)]$(ClO_4)_2$	1.922(3)	1.922(3)	0.26	[20]
rac-[Ni(*trans*-Me_7[15]ene)]$(ClO_4)_2$	1.925(5)	1.907(5)	0.23	[21]
meso-[Ni(*trans*-Me_6[16]diene)][$ZnCl_2(NCS)_2$]; cation 1	1.950(4)	1.897(4)	0.130(2)	this work
meso-[Ni(*trans*-Me_6[16]diene)][$ZnCl_2(NCS)_2$]; cation 2	1.947(4)	1.899(4)	0.009(1)	this work

Table 3
Parameters for specified hydrogen bonds (Å, °), D–H = 0.91 Å

Atoms	H···A	D···A	D–H···A	Symmetry operators
N1–H1···Cl41	2.41	3.270(3)	158	$x+1, y+1/2, -z+1/2$
N9–H9···Cl42	2.56	3.464(4)	173	
N21–H21···S51	2.68	3.583(3)	169	$x+1, y, z$
N29–H29···Cl51	2.44	3.354(3)	177	$x+1, y+1/2, -z+3/2$

for the Ni2, N29, N33 chelate ring form a chair conformation chelate ring, while the minor components {C11A and C31A, respectively} complete a boat conformation chelate ring.

The anion 2 has Zn5 in approximately tetrahedral coordination by two chloride and two *iso*-thiocyanate ligands, with the Zn–N–C groups appreciably bent (see Table 1). When the anion 1 was modeled as a similar $[ZnCl_2(NCS)_2]^{2-}$ ion then persistent residual electron density peaks were associated with the Cl42 site. This ion was modeled with partial substitution of chloride Cl42 by a thiocyanate ion N43–C43–S43, with complementary s.o.f. {s.o.f. = 0.78(1) for Cl42, 0.22(1) for N43, C43 and S43}. The s.o.f. for the atoms of the other chloride and thiocyanate ions around Zn4 are normal, excluding possible structures with rotational disorder of a stiochiometric $[ZnCl_2(NCS)_2]^{2-}$ ion. The structure is considered to have disordered $[ZnCl_2(NCS)_2]^{2-}$ and $[ZnCl(NCS)_3]^{2-}$ ions, with overall stiochiometry $[ZnCl_{1.89}(NCS)_{2.11}]^{2-}$. Alternatively, the major residual electron density peak was less satisfactorily modeled as a fractional (s.o.f. 0.33) water molecule. The Zn···O distance was approximately the same as the Zn···S distances for a coordinated thiocyanato group, but the Cl42···O distance at 2.3 Å was unreasonably short and no associated hydrogen atoms could be located. The partial occupancy site S43 lies between the partial occupancy sites C11 and C31A on the two cations (S43···C11 = 3.00; S43···C31A = 3.18 Å), so the disorder at the three sites is probably correlated. Significant hydrogen bonding interactions are shown in Table 3.

Compounds with mixed chloro-thiocyanato-zincate anions have been reported [14–16], including the structure of a compound with a $[ZnCl(NCS)_3]^{2-}$ anion [16].

4. Experimental

4.1. (6,8,8,14,16,16-Hexamethyl-1,5,9,13-tetraazacyclothexadeca-5,13-diene)nickel(II)perchlorate, [Ni(Me_6[16]diene)]$(ClO_4)_2$

The compound was prepared by reaction of Tris-(propane1,3-diamine)nickel(II) perchlorate with acetone [6,7].

4.2. (6,8,8,14,16,16-Hexamethyl-1,5,9,13-tetraazacyclothexadeca-5,13-diene)(dithiocyanato)-nickel(II), [trans-Ni(Me_6[16]diene)$(NCS)_2$]

Sodium thiocyanate was added to a hot aqueous solution of [Ni(Me_6[16]diene)]$(ClO_4)_2$ when the sparingly water-soluble blue–violet product precipitated. This was filtered off, washed with cold water and recrystallised from dichloromethane/propan-2-ol.

4.3. N-meso-(trans-6,8,8,14,16,16-Hexamethyl-1,5,9,13-tetraazacyclothexadeca-5,13-diene)nickel(II)chloro-(isothiocyanato)zinc(II), N-meso-[Ni(trans-Me_6[16]diene)][$ZnCl_{1.91}(NCS)_{2.08}$]

A hot aqueous solution of zinc chloride was added to a hot aqueous solution/suspension of [Ni(*trans*-Me_6[16]-diene)$(NCS)_2$] when it dissolved to form a yellow solution from which yellow crystals separated upon cooling. The sparingly water-soluble yellow solid was filtered from the cold solution, washed with a little cold water then ethanol. The product recrystallised from hot water was usually contaminated with [Ni(*trans*-Me_6[16]diene)-$(NCS)_2$]. Alternatively it could be recrystallised from DMF/propan-2-ol. The crystal used in the structural study was obtained by slow evaporation of an aqueous solution. IR spectrum: ν(NH) 3132; ν(C≡N) 2078 vs ν(C=N) 1637 cm^{-1}. Analytical results for different batches varied, but were consistent with formation of a range of products with varying proportions of chloride and thiocyanate ions.

5. Structure determination

5.1. Crystal data

$[(C_{18}H_{36}N_4)Ni][(CNS)_{1.9}Cl_{2.1}Zn]$	$Z = 8$
$M_r = 621.97$	$D_x = 1.507$ Mg m^{-3}
Monoclinic, $P2_1/c$	Mo Kα radiation
$a = 18.80(1)$ Å	Cell parameters from 3215 reflections
$b = 15.368(8)$ Å	$\theta = 2.5$–$28.6°$
$c = 19.02(1)$ Å	$\mu = 1.93$ mm^{-1}
$\beta = 92.39(1)°$	$T = 273(2)$ K
$V = 5488(5)$ Å^3	Block, orange, $0.27 \times 0.17 \times 0.16$ mm

5.2. Data collection

Bruker CCD diffractomer	8954 reflections with $I > 2\sigma(I)$
phi and omega scans	$R_{int} = 0.070$
Absorption correction: multi-scan (based on symmetry-related measurements) [23]	$\theta_{max} = 30.2°$
$T_{min} = 0.525$, $T_{max} = 0.735$	$h = -26 \rightarrow 26$
77 334 measured reflections	$k = -21 \rightarrow 20$
16 135 independent reflections	$l = -26 \rightarrow 26$

5.3. Ref. [16]

Refinement on F^2	H atoms constrained to parent site
$R[F^2 > 2\sigma(F^2)] = 0.045$	Calculated weights $w = 1/[\sigma^2(F_o^2) + (0.0585P)^2]$ where $P = (F_o^2 + 2F_c^2)/3$
$wR(F^2) = 0.096$	$S = 0.86$
16 135 reflections	612 parameters

Hydrogen atoms are in calculated positions and riding on their parent atom. Atoms C11 and C11A, C31 and C31A, and Cl42 and (N43, C43 and S43) were refined with complementary s.o.f., N43, C11A, C31A, C43 and S43 were refined with isotropic parameters. Distance restraints (DFIX with default parameters) were applied to C10–C11A, C12–C11A, C30–C31A and C32–C31A (1.54 Å), Zn4–Cl142 (2.26 Å), Zn4–N43 (2.00 Å), N43–C43 (1.13 Å) and C43–S43 (1.64 Å).

5.4. Computer programs

Data collection: Bruker SMART. Cell refinement: Bruker SAINT. Data reduction: Bruker SAINT [22]. Program(s) used to solve structure: SHELXS-97 (Sheldrick, 1990) [24]. Program(s) used to refine structure: SHELTXL-97 (Sheldrick, 1997) [24]. Molecular graphics: ORTEP 3.2 (Farrugia, 1997) [25].

Appendix A. Supplementary material

CCDC 624119 contains the supplementary crystallographic data for this paper. These data can be obtained free of charge via http://www.ccdc.cam.ac.uk/conts/retrieving.html, or from the Cambridge Crystallographic Data Centre, 12 Union Road, Cambridge CB2 1EZ, UK; fax: (+44) 1223-336-033; or e-mail: deposit@ccdc.cam.ac.uk. Supplementary data associated with this article can be found, in the online version, at doi:10.1016/j.poly.2007.02.002.

References

[1] N.F. Curtis, Coord. Chem. Rev. 3 (1968) 3.
[2] N.F. Curtis, Y.M. Curtis, H.K.J. Powell, J. Chem. Soc., Sect. A. (1966) 1015.
[3] N.F. Curtis, J. Chem. Soc., Dalton Trans. (1972) 1357.
[4] J.W.L. Martin, J.H. Timmons, A.E. Martell, C.J. Willis, Inorg. Chem. 19 (1980) 2328.
[5] J.H. Timmons, P. Rudolf, A.E. Martell, J.W.L. Martin, A. Clearfield. Inorg. Chem. 19 (1980) 2331.
[6] D.A. House, N.F. Curtis, J. Am. Chem. Soc. 86 (1964) 223.
[7] D.F. Cook, N.F. Curtis, J. Chem. Soc., Dalton Trans. (1973) 1076.
[8] G.J. Gainsford, D. Rae, Personal Communication.
[9] D.H. Busch, E.K. Barefield, Inorg. Chem. 10 (1971) 108.
[10] D.H. Busch, E.K. Barefield, Inorg. Chem. 10 (1971) 1216.
[11] N.F. Curtis, O.P. Gladkikh, Aust. J. Chem. 53 (2000) 727.
[12] N.F. Curtis, K. Flood, C.E.F. Rickard, W.T. Robinson, J.M. Waters, Unpublished observations.
[13] N.F. Curtis, K. Flood, W.T. Robinson, Polyhedron 25 (2006) 1313.
[14] G.V. Tsintsadze, Tr. Gruz, Politekh. Inst. 3 (1970) 81.
[15] A. Shvelashvili, M. Churadze, L. Metreveli, Bull. Georgian Acad. Sci. 153 (1996) 232.
[16] M. Alexiou, E. Katsoulakou, C. Dendrinou-Samara, C.P. Raptopoulou, V. Psycharis, E. Manessi-Zoupa, S.P. Perlepes, D.P. Kessissoglou, Eur. J. Inorg. Chem. (2005) 1964.
[17] D.J. Szalda, E. Fujita, Acta Cryst., Sect. C. 48 (1992) 1767.
[18] M.F. Bailey, I.E. Maxwell, J. Chem. Soc., Dalton Trans. (1972) 938.
[19] N.F. Curtis, G.J. Gainsford, Aust. J. Chem. 39 (1986) 1509.
[20] N.F. Curtis, J.M. Waters, C.E. Rickard, Acta Cryst., Sect. E. 57 (2001) m48.
[21] N.F. Curtis, C.E.F. Rickard, J.M. Waters, Aust. J. Chem. 53 (2000) 945.
[22] Bruker SMART (Version 5.054), SADABS (Version 2.03) and SAINT (Version 6.02A), Bruker AXS Inc., Madison, WI, USA, 1997.
[23] R.H. Blessing, Acta Crystallogr., Sect. A 51 (1995) 33.
[24] G.M. Sheldrick, SHELXTL (Version 5.10, 1997). Programs for the solution and refinement of crystal structures.
[25] J. Farrugia, ORTEP-32, J. Appl. Crystallogr. 30 (1997) 565.

Available online at www.sciencedirect.com
ScienceDirect
Polyhedron 26 (2007) 3008–3016
POLYHEDRON
www.elsevier.com/locate/poly

Copper(II) complexes of N_4 tetradentate ligands with flexible alkyl spacers: Crystal structure, DNA binding and cleavage studies

Varadarajan Uma [a], Alfonso Castineiras [b], Balachandran Unni Nair [a,*]

[a] Chemical Laboratory, Central Leather Research Institute, Adyar, Chennai 600 020, Tamil Nadu, India
[b] Universidad de Santiago de Compostela, Departamento de Química Inorgánica, Campus Universitario Sur, E-15782 Santiago de Compostela, Spain

Received 5 January 2007; accepted 6 February 2007
Available online 28 February 2007

Abstract

Mononuclear copper(II) complexes, [Cu L1] $(ClO_4)_2$ (**1**), [Cu L2] $(ClO_4)_2$ (**2**) and [Cu L3] $(ClO_4)_2$ (**3**) with quadridentate Schiff base ligands L1 (*N*,*N*′-bis-pyridin-2-ylmethyl-butane-1,4-diimine), L2 (*N*,*N*′-bis-pyridin-2-ylmethyl-pentane-1,5-diimine) and L3 (*N*,*N*′-bis-pyridin-2-ylmethyl-hexane-1,6-diimine) have been synthesized and characterized. The crystal structure data of **1** reveals the existence of the complex in two different geometries, namely a square pyramid and a distorted octahedron, which eventually leads to the packing of the molecule into helical and anti-parallel structures respectively. Absorption titration studies with calf thymus DNA for all three complexes are suggestive of groove binding with binding constant values for **1**, **2** and **3** being $2.6 \pm 0.2 \times 10^4$ M^{-1}, $11.5 \pm 0.2 \times 10^4$ M^{-1} and $1.83 \pm 0.2 \times 10^4$ M^{-1} respectively. Control cleavage experiments using pBR 322 plasmid DNA and distamycin suggest minor groove binding for these complexes. In the presence of ascorbic acid, the complexes show efficient DNA cleavage, the order of efficiency being **1** > **2** ≅ **3**.
© 2007 Elsevier Ltd. All rights reserved.

Keywords: Copper(II) complex; Tetradentate ligand; Crystal structure; DNA binding; Nuclease activity

1. Introduction

Studies on the interaction of small molecules with DNA continue to attract considerable attention due to their importance in cancer therapy and molecular biology [1–3]. In this respect, transition metal complexes have attracted special attention due to their unique spectroscopic and electrochemical signatures [4–6]. The interest in the DNA recognition by transition metal complexes has been substantially aided by the DNA cleaving ability of some of these metal complexes [7–15]. Artificial metallonucleases have proven to be efficient tools for the footprinting and sequence-specific targeting of nucleic acids [16–18]. They are composed of a transition or lanthanide metal ion and a ligand which plays two major roles – it modulates the reactivity of the metal ion and, by interacting with the nucleic acid, it delivers the reactive metal ion species to the vicinity of the sensitive functionalities of the biopolymer.

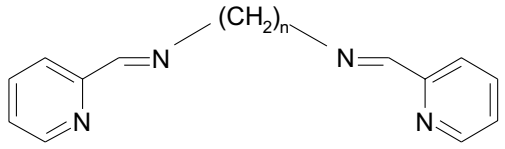
Copper is a bioessential element with relevant oxidation states +1 and +2. Coordination compounds of copper, in both its oxidation states, have been extensively used in metal mediated DNA cleavage through the generation of hydrogen abstracting activated oxygen species [19–25]. Copper(II) complexes under certain ligand environments have also been shown to bring about photocleavage of DNA as well as RNA and DNA scission via phosphodiester transesterification [26–32]. Among the various copper complexes so far investigated, those of phenanthroline

Abbreviations: CT DNA, calf thymus DNA; Tris, tris(hydroxymethyl)methylamine; DMSO, dimethyl sulphoxide; TBE, tris-boric acid-EDTA; DPPH, diphenylpicrylhydrazyl.

* Corresponding author. Tel.: +91 (0)44 2441 1630; fax: +91 (0)44 2491 1589.
E-mail address: bunair@clri.info (B.U. Nair).

0277-5387/$ - see front matter © 2007 Elsevier Ltd. All rights reserved.
doi:10.1016/j.poly.2007.02.020

and its derivatives have attracted much attention for their various functions. Copper(II) complexes of 1,10-phenanthroline have been shown to inhibit DNA and RNA polymerase activities and induce strand scission of DNA in the presence of H_2O_2 or thiol [33–36]. The substitution of the phenanthroline has been shown to influence the reactivity of the complexes with DNA [37]. Because of the fact that copper(II) is a substitutionally labile metal ion, multidentate ligands are believed to be better than bidentate ligands in keeping the copper(II) ion chelated in solution. We have been investigating the metallonuclease property of copper(II) complexes of N_3 tridentate ligands [38–40]. In this communication we describe the synthesis and DNA cleaving abilities of a homologous series of copper(II) complexes of N_4 tetradentate ligands L1, L2 and L3.



n = 4, L1

n = 5, L2

n = 6, L3

2. Materials and methods

2.1. Chemicals

2-Pyridine carboxaldehyde, 1,4-diaminobutane, 1,5-diaminopentane and 1,6-diaminohexane were obtained from Sigma Aldrich, USA and were used as received. Tris (hydroxymethyl) methylamine (Tris) and Calf Thymus DNA (CT DNA) were obtained from SRL chemicals, Mumbai. All chemicals and reagents used were of analytical grade and were received from Ranbaxy, Mumbai. A stock solution of DNA was prepared by stirring a sample dissolved in 10 mM Tris buffer (pH 7.5) at 4 °C. The solution was dialyzed exhaustively against Tris buffer for 48 h. and filtered using a membrane filter obtained from Sartorius (0.45 μm). The filtered DNA solution in the buffer gave a UV absorbance ratio (A_{260}/A_{280}) of about 1.9, indicating that the DNA was sufficiently free from protein [41]. The concentration of DNA was determined using an extinction coefficient of 6600 M^{-1} cm^{-1} at 260 nm [42].

2.2. Syntheses

2.2.1. [Cu L1](ClO4)2 (1)

1,4 Diaminobutane (0.88 g, 10 mmol) was added to 2-pyridine carboxaldehyde (2.14 g, 20 mmol) and refluxed in methanolic medium for 15 min. To this solution copper(II) perchlorate (3.70 g, 10 mmol) dissolved in methanol was added and refluxing was continued for another half an hour. The bluish-green solid that separated out on cooling, was filtered and washed with diethyl ether and dried in vacuo over $CaCl_2$. Slow evaporation of an acetonitrile solution of the complex yielded single crystals suitable for X-ray diffraction. *Anal. Calc.* for $[C_{16}H_{18}CuN_4](ClO_4)_2$: C, 36.29; H, 3.40; N, 10.58; Cu, 12.00; Found: C, 36.21; H, 3.33; N, 10.68; Cu, 12.05%. IR spectra [KBr disc, cm^{-1}]: 2933 (w), 1600 (s), 1088 (br), 781 (s), 622 (s); (s-strong, br-broad, w-weak). FAB MS, base peak at *m/z*: 329 $(ML1-H)^+$. The complex is freely soluble in water and acetonitrile.

2.2.2. [Cu L2](ClO4)2 (2)

This complex was prepared by a similar procedure to that of complex **1** by taking 1,5 diaminopentane (1.02 g, 10 mmol), 2-pyridine carboxaldehyde (2.14 g, 20 mmol) and copper(II) perchlorate (3.7 g, 10 mmol) in the molar ratio 1:2:1. The complex separates out as a dark brown solid from the methanolic medium. Our attempts to grow single crystals of the complex have not been successful so far. *Anal. Calc.* for $[C_{17}H_{20}CuN_4](ClO_4)_2$: C, 37.56; H, 3.68; N, 10.31; Cu, 11.69; Found: C, 37.50; H, 3.72; N, 10.26; Cu, 11.63%. IR spectra [KBr disc, cm^{-1}]: 2939 (w), 1598 (s), 1093 (br), 775 (s), 623 (s). FAB MS, base peak at *m/z*: 343 $(ML2\text{-}H)^+$. The complex is partially soluble in water and freely soluble in acetonitrile and DMSO.

2.2.3. [Cu L3](ClO4)2 (3)

This complex was prepared by a similar procedure to that of complex **1** by taking 1,6 diaminopentane (1.16 g, 10 mmol), 2-pyridine carboxaldehyde (2.14 g, 20 mmol) and copper(II) perchlorate (3.7 g, 10 mmol) in the molar ratio 1:2:1. The complex separates out as brown solid from the reaction medium. *Anal. Calc.* for $[C_{18}H_{22}CuN_4](ClO_4)_2$: C, 38.78; H, 3.95; N, 10.05; Cu, 11.39; Found: C, 38.59; H, 3.85; N, 10.09; Cu, 11.30%. IR spectra [KBr disc, cm^{-1}]: 2937 (w), 1598 (s), 1100 (br), 776 (s), 623 (s). FAB MS, base peak at *m/z*: 357 $(ML3\text{-}H)^+$. The complex is partially water soluble and completely soluble in acetonitrile and DMSO.

2.2.4. Instrumentation

UV–visible spectra of the complex and DNA binding studies were recorded on a Perkin–Elmer Lambda 35 double beam spectrophotometer at 25 °C. The infrared spectra of the complexes were recorded on a Perkin–Elmer FTIR spectrometer. The FAB mass spectra were recorded on a JEOL SX 102/DA-6000 mass spectrometer using argon (6 kV, 10 mA) as the FAB gas. m-Nitrobenzyl alcohol was used as the matrix. Elemental analyses were performed using a Heraeus CHN–O– rapid analyzer. Cyclic voltammetry was performed on CH-Instruments, electrochemical analyzer, CH-620 B. X-band electron paramagnetic resonance (EPR) spectra at room temperature and liquid-nitrogen temperatures were recorded on a Bruker EMX 6/1 spectrometer and the g calibration was done using

diphenylpicrylhydrazyl (DPPH). Circular dichroic spectra were recorded using a J-715 spectropolarimeter (Jasco) at 25 ° C with a 0.1 cm pathlength cuvette.

2.2.5. X-ray crystallography of [Cu L1](ClO$_4$)$_2$

A green crystal of an approximate size of $0.71 \times 0.27 \times 0.18$ mm was mounted on a glass fiber and used for data collection. Cell constants and an orientation matrix for data collection were obtained by least-squares refinement of the diffraction data from 23 reflections in the range of $1.5 < \theta < 27.99°$ on an Enraf Nonius MACH3 automatic diffractometer. Data were collected at 293 K using Cu Kα radiation ($\lambda = 1.54184$ Å) and the $\omega/2\theta$-scan technique, and corrected for Lorentz and polarization effects. A semi-empirical absorption correction (Psi-scans) was made. The structure was solved by the Patterson method and subsequent difference Fourier maps and refined on F^2 by a full-matrix least-squares procedure using anisotropic displacement parameters [43]. All hydrogen atoms were included in geometrically idealized positions employing appropriate riding models with isotropic displacement parameters constrained to 1.2U ~ (eq) of their carrier atoms. Criteria of a satisfactory complete analysis were the ratios of rms shifts to standard deviations of less than 0.001 and no significant features in the final difference maps. Atomic scattering factors were from the ''International Tables for Crystallography'', molecular graphics from PLATON and SCHAKAL. A summary of the crystal data is given in Table 1.

2.2.6. DNA-binding and cleavage experiments

The electronic spectra of complexes **1** and **2** were monitored both in the absence and presence of DNA at around 281 and 275 nm, respectively. Absorption titration experiments were performed by maintaining a constant metal complex concentration (20 μM) and varying the nucleic acid concentration (0–200 μM). The same DNA concentration was maintained in the reference cell so as to nullify the absorbance due to DNA at the measured wavelength. From the absorption titration data, the binding constant was determined using:

$$[\mathrm{DNA}]/(\varepsilon_a - \varepsilon_f) = [\mathrm{DNA}]/(\varepsilon_b - \varepsilon_f) + 1/K_b(\varepsilon_b - \varepsilon_f), \quad [44]$$

where ε_a, ε_f and ε_b correspond to A_{obsd}/[Cu], the extinction coefficient for the free copper complex and the extinction coefficient for the copper complex in the fully bound form, respectively. A plot of [DNA]/($\varepsilon_a - \varepsilon_f$) versus [DNA] gives $K_b$as the ratio of the slope to the intercept.

Voltammetric experiments were carried out using a standard three electrode system comprising of a glassy carbon working electrode, platinum auxillary electrode and saturated calomel reference electrode (SCE). The samples were prepared in DMSO and the solutions were deoxygenated by purging nitrogen gas for 10 min. prior to measurement. Cyclic and differential pulse voltammetric investigations on complexes **1**–**3** have been carried out with a complex concentration of 0.2×10^{-3} M using 1 mM Tris buffer, 100 mM NaCl (pH 7.5) as a supporting electrolyte. The formal potentials, E^0 (or voltammetric $E_{1/2}$) values were determined from the DPV peak potential, E_p, using the relation $E_{1/2} = E_p + \Delta E/2$, where $E_{1/2}$ is the equivalent of the average of E_{pc} and E_{pa} in CV experiments and ΔE is the pulse amplitude (50 mV).

The cleavage of plasmid DNA was monitored using agarose gel electrophoresis. Supercoiled pBR322 DNA (0.25 μg) in (Tris) buffer (50 mM, pH 7.5) with 50 mM NaCl was treated with the copper(II) complexes (80 μM) and ascorbic acid (300 μM). The samples were incubated for 90 min at 37 °C. In the inhibition reactions, additives like distamycin or DMSO were added to the supercoiled DNA and the incubation carried out for 15 min. at 37 °C prior to the addition of the complex and ascorbic acid. A loading buffer containing 0.25% bromophenol blue, 40% (w/v) sucrose and 0.5 M EDTA was added and the electrophoresis of the DNA cleavage products was performed on 0.8% agarose gel containing 0.5 μg/mL ethidium bromide. The gels were run at 50 V for 3 h in Tris-boric acid-ethylenediamine tetraacetic acid (TBE) buffer and the bands were photographed by a gel documentation system. The relative amounts of plasmid DNA were quantified using the Bio Rad Quantity one package.

Table 1
Crystal Structure data for [CuL1](ClO$_4$)$_2$ (**1**)

Empirical formula	$C_{32}H_{36}C_{14}Cu_2N_8O_{16}$
Formula weight	1057.57
Temperature (K)	293(2)
Wavelength (Å)	0.71073
Crystal system, space group	monoclinic, *P*2(1)/*n* (no. 14)
Unit cell dimensions	
a (Å)	20.117(2)
b (Å)	7.4288(8)
c (Å)	28.642(3)
α (°)	90
β (°)	109.346(2)
γ (°)	90
Volume (°)	4038.6(8)
Z, Calculated density (Mg/m^3)	4, 1.739
Absorption coefficient (mm^{-1})	1.400
F(000)	2152
Crystal size (mm)	$0.71 \times 0.27 \times 0.18$
θ Range for data collection (°)	1.50–27.99
Completeness to theta = 27.99 (%)	93.6%
Data/restraints/parameters	9130/0/559
Goodness-of-fit on F^2	1.016
Final *R* indices [$I > 2\sigma(I)$]	$R_1 = 0.0723$, $wR_2 = 0.1934$
R indices (all data)	$R_1 = 0.1152$, $wR_2 = 0.2149$

3. Results and discussion

3.1. Synthesis

The complexes **1**–**3** could be prepared through template condensation of the corresponding diamine and aldehyde in a 1:2 mole ratio in the presence of copper(II) perchlorate.

The authenticity of the compounds prepared was ascertained from mass spectral data and could be formulated as $[CuL](ClO_4)_2$, and was confirmed by the single crystal X-ray structure determination of complex **1**. In the present series of complexes, there is a systematic increase in the chain length of the alkyl backbone of the ligand and this is expected to influence the structure, electronic and redox properties of the complexes. Hence they are expected to show variations in their DNA binding affinity and cleavage activity.

3.2. Crystal structure of complex *1*

Complex **1** crystallizes as monoclinic crystals with the space group $P2_1/n$. The unit cell contains four asymmetrically independent molecules with two different geometries. The molecular structure of the two different molecules A and B are shown in Fig. 1. The copper(II) ion in molecule A is five coordinate with a square pyramidal geometry. The four nitrogen atoms of the Schiff base form the basal plane and the oxygen of the perchlorate ion occupies the apical position. The four Cu–N bond lengths vary in the range 1.980(4)–1.996(4) Å. The perchlorate oxygen occupies the apical position with an elongated Cu–O bond length of 2.457(4) Å. The N–Cu–N bond angles vary from 82.1(18)° to 166(2)°. The bridging tetramethylene group of the Schiff base is found to exhibit a boat conformation and induces steric hinderance for the adjacent packing of the molecules. As a result, the molecule takes a helical shape with the assistance of the perchlorate ion as shown in Fig. 2a.

In the case of molecule B, the copper atom is six coordinate with four nitrogens of the Schiff base and two perchlorate oxygens forming a distorted octahedral geometry. The Cu–N bonds in molecule B has been found to vary from 1.962(4) to 2.010(4) Å and the two Cu–O bond lengths are 2.602(5) and 2.612(5) Å. In this molecule, three of the four Cu–N bond distances are much shorter than the fourth one. This is due to the fact that the bridged tetramethylene group in molecule B exhibits a chair conformation. The perchlorate anion assists the packing of molecule B in anti-parallel sheets in contrast to the helical shape of molecule A (Fig. 2b). The perchlorate anion not only assists the packing of the complex in two different geometries, but also it participates in bridging of molecules A and B. The important bond lengths and bond angles for complex **1** are given in Table 2. It is of importance to note that the capability of the bridging tetramethylene group to exist in chair as well as boat conformations is one of the reasons for the crystallization of complex **1** with two different structural parameters. The perchlorate ion subsequently brings about the assembly of the two types of molecules into helical as well as sheet structures.

3.3. Electronic and EPR spectra

The electronic spectra of all the three complexes exhibit intra-ligand transitions in almost the same spectral region (275–280 nm) but their ligand field transitions appear at different regions (Table 3). While complex **1** shows only one broad band in the visible region, **2** and **3** show one broad and one sharp band indicating that the increase in the number of methylene groups in the backbone of the ligand results in a change in the geometry around the metal ion. This fact is further supported by EPR spectral studies. The X-band EPR spectrum of complex **1** (Fig. 3a) taken at 77 K, examined as a frozen DMSO solution, reveals the presence of axial symmetry out of a distorted tetragonal copper(II) site in the complex. The spectrum shows four $g_{\|}$ components and a broad $g_{\perp}$ component. The 77 K EPR spectra of complexes **2** and **3** in DMSO exhibit almost similar spectral features, but they are qualitatively different from that of complex **1.** Fig. 3b shows the EPR spectrum of complex **2**. The simulation fits the experimental spectrum

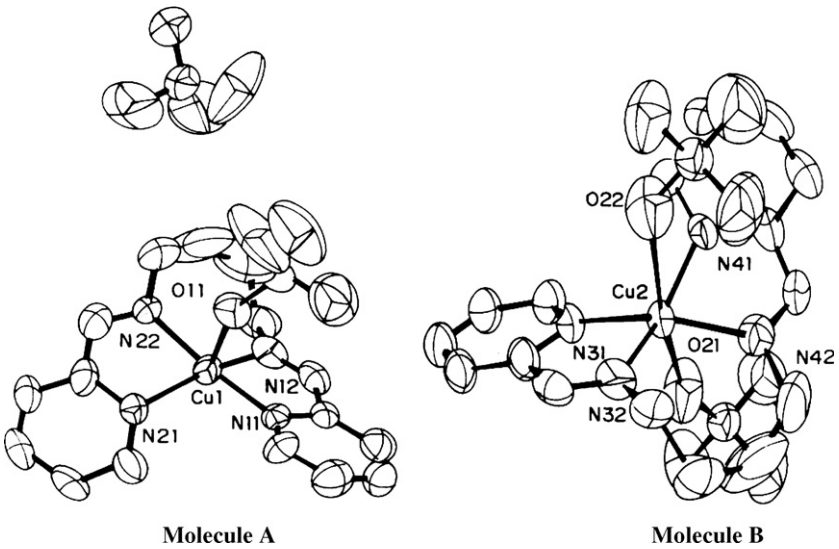


Fig. 1. ORTEP diagram of complex **1**.

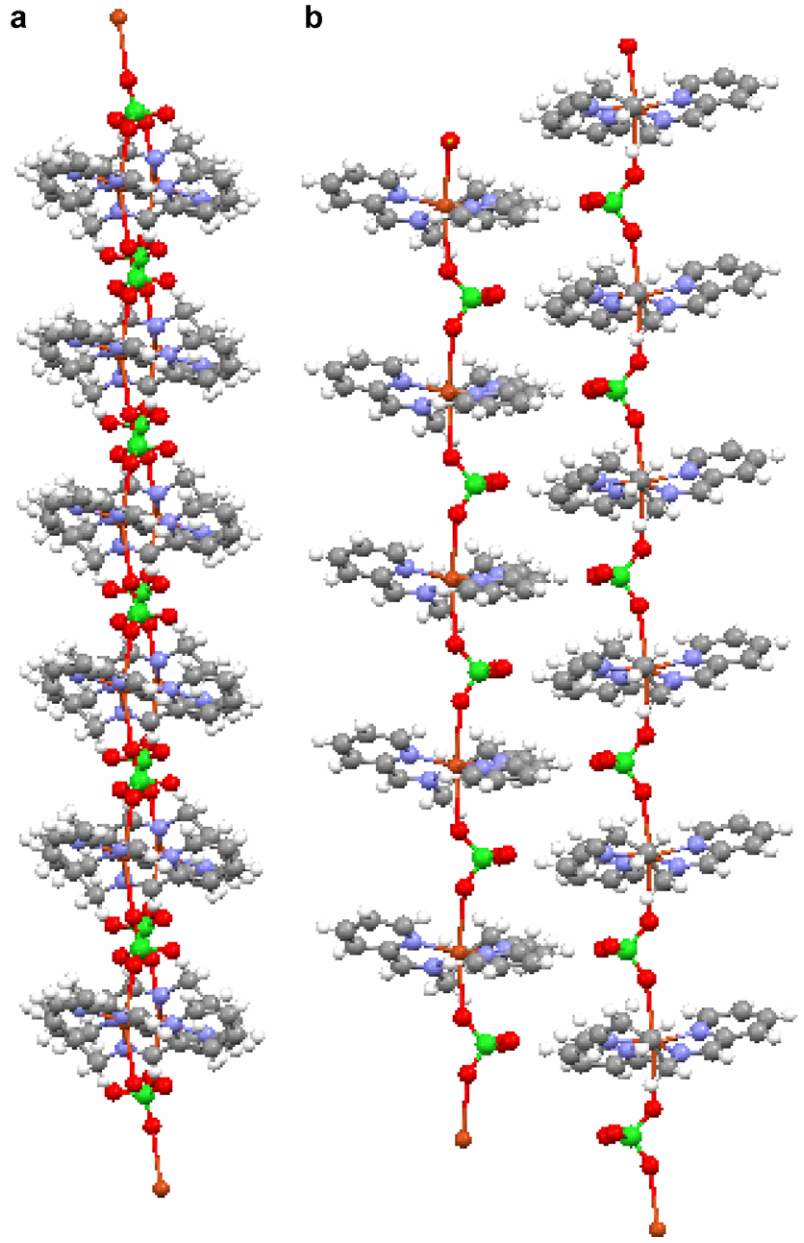


Fig. 2. Packing of complex **1** in two different geometries: (a) helical assembly and (b) anti-parallel sheet.

best assuming rhombic character. The EPR spectral parameters for all three complexes are listed in Table 3. The rhombic character of complexes **2** and **3** suggests considerable deviation from the square planar geometry as compared to **1**. Also, on comparing the A_Z values of **2** and **3**, we find that **3** has a lower A_Z value which is indicative of an increase in the degree of distortion as we move from **2** to **3**.

3.4. DNA binding studies

Even though in its crystalline form the perchlorate ion is coordinated to copper(II) in complex **1**, in aqueous

Table 2
Selected bond lengths (Å) and bond angles (°) for [Cu L1]$(ClO_4)_2$ (**1**)

Cu(1)–N(12)	1.980(4)	Cu(2)–N(32)	1.962(4)
Cu(1)–N(11)	1.981(4)	Cu(2)–N(41)	1.970(4)
Cu(1)–N(22)	1.989(4)	Cu(2)–N(42)	1.989(4)
Cu(1)–N(21)	1.996(4)	Cu(2)–N(31)	2.010(4)
Cu(1)–O(11)	2.457(4)	Cu(2)–O(22)#2	2.602(5)
Cu(1)–O(12)#1	2.790(7)	Cu(2)–O(21)	2.612(5)
N(12)–Cu(1)–N(11)	82.10(18)	N(32)–Cu(2)–N(41)	160.34(17)
N(12)–Cu(1)–N(22)	100.6(2)	N(32)–Cu(2)–N(42)	99.20(18)
N(11)–Cu(1)–N(22)	166.0(2)	N(41)–Cu(2)–N(42)	82.53(17)
N(12)–Cu(1)–N(21)	153.20(19)	N(32)–Cu(2)–N(31)	81.91(17)
N(11)–Cu(1)–N(21)	101.97(16)	N(41)–Cu(2)–N(31)	102.22(16)
N(22)–Cu(1)–N(21)	81.83(18)	N(42)–Cu(2)–N(31)	162.9(2)

Table 3
Electronic and EPR (taken at 77 K) spectral parameters for complexes **1**–**3**

Complex	Electronic spectra[a] λ, nm (ε, M^{-1} cm^{-1})		g values	A values, cm^{-1}
Complex **1**	280 (21,165)	700 br (159)	$g_{\parallel} = 2.255$	$A_{\parallel} = 175.5 \times 10^{-4}$
			$g_{\perp} = 2.0785$	$A_{\perp} = 10.0 \times 10^{-4}$
Complex **2**	275 (21, 895)	580 br (183)	$g_x = 2.0755$	$A_x = 5.5 \times 10^{-4}$
		440 sh (434)	$g_y = 2.0575$	$A_y = 6.5 \times 10^{-4}$
			$g_z = 2.2407$	$A_z = 195.5 \times 10^{-4}$
Complex **3**	278 (26,120)	646 br (104)	$g_x = 2.075$	$A_x = 12.6 \times 10^{-4}$
		465 sh (598)	$g_y = 2.025$	$A_y = 12.6 \times 10^{-4}$
			$g_z = 2.250$	$A_z = 182 \times 10^{-4}$

[a] br – broad, sh – shoulder.

solution the perchlorate will be replaced by water. The complexes will therefore exist as $[CuL(H_2O)_2]^{2+}$. DNA binding capabilities of the complexes were investigated by monitoring their intraligand spectral band as a function of DNA concentration. Binding of the complexes leads to perturbation of their ligand centered band. Spectral bands of complexes **1**–**3** show hyperchromism with increasing concentrations of DNA, as depicted in Fig. 4. Such spectral behaviour clearly rules out intercalative binding of the complexes to DNA, since intercalation leads to hypochromism in the spectral band of the intercalating molecule [45–48]. No detectable changes in the energy of ligand field bands of these complexes were observed in the presence of DNA, ruling out binding of these complexes to DNA bases. The spectral changes observed in the presence of DNA can be rationalized in terms of groove binding [49]. However since all the three complexes contain aromatic rings in their ligand structure, partial intercalation of these molecules cannot be fully ruled out. Analysis of the spectral data in the presence of DNA gave binding constants, K_b, of $2.6 \pm 0.2 \times 10^4$ M^{-1}, $11.5 \pm 0.2 \times 10^4$ M^{-1} and $1.83 \pm 0.2 \times 10^4$ M^{-1} for complexes **1**, **2** and **3** respectively. From the binding constant values, it is clear that the complexes are moderate binders and complex **2** shows the highest binding affinity amongst them.

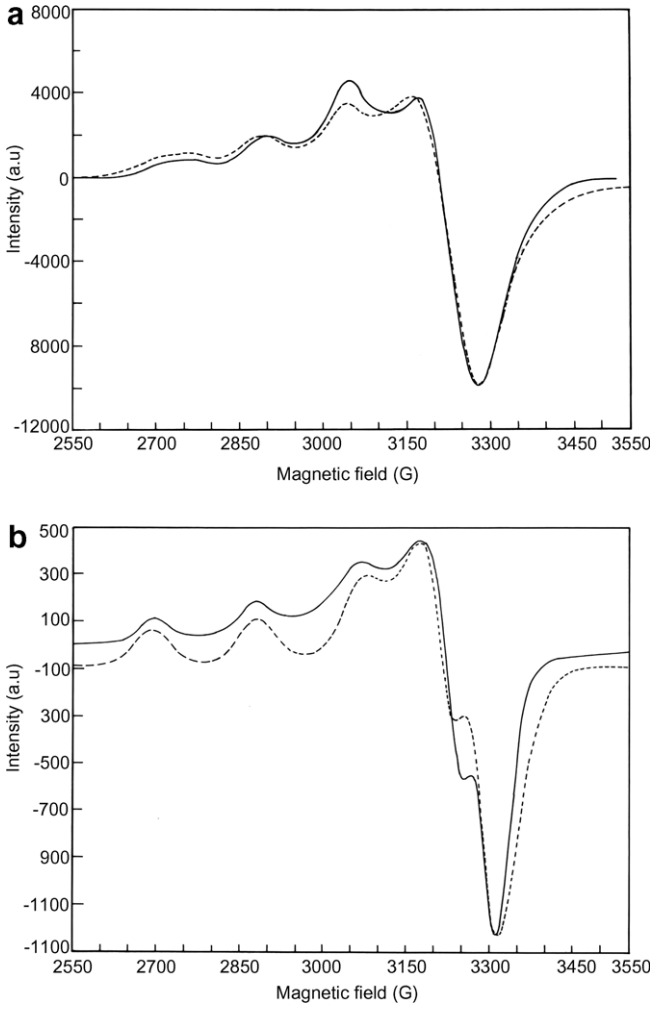


Fig. 3. (a) EPR spectra of a frozen solution of complex **1** and (b) complex **2** at 77 K (Microwave frequency = 9.23 GHz, power = 1 mW, modulation frequency = 100 kHz, modulation amplitude = 3 G). Solid line represents experimental spectrum and dotted line, simulated spectrum.

3.5. Electrochemical studies

Cyclic and differential pulse voltammetric techniques have been employed to study the interaction of the redox

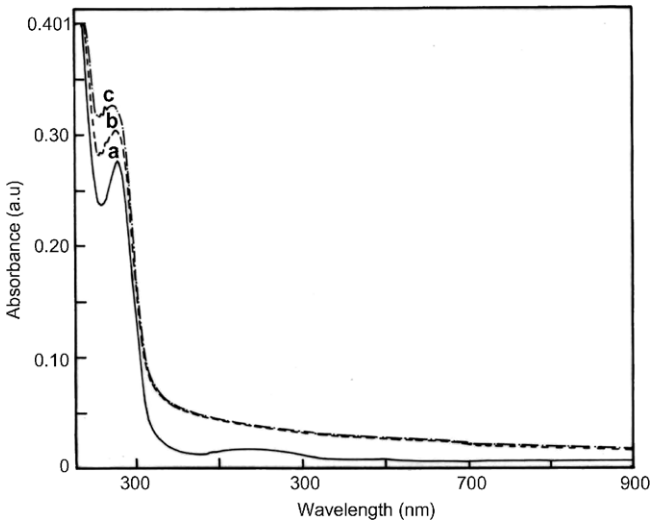


Fig. 4. Absorption spectra of complex **2** (20 μM) in the absence (a) and presence (b and c) of increasing concentrations of CT DNA (40 and 80 μM).

Table 4
Electrochemical behaviour of complexes **1**–**3** in the absence and presence of CT DNA

Complexes	R[a]	$E_{1/2}$(V)		ΔE_p (mV)	i_{pc}/i_{pa}	K_+/K_{2+}[b]
		CV	DPV			
1	0	−0.139	−0.128	103	0.60	
	5	−0.130	−0.120	94	0.71	1.36
2	0	−0.034	−0.016	75	0.68	
	5	−0.024	−0.009	89	0.58	1.31
3	0	+0.047	+0.056	72	0.75	
	5	+0.056	+0.061	73	0.69	1.21

[a] R = [DNA]/[Complex].
[b] Based on the $E_{1/2}$ values of DPV.

active copper(II) complexes with DNA to further explore the DNA binding modes. Electrochemical studies carried out for all three complexes is summarised in Table 4. The cyclic voltammograms of the complexes in the absence of DNA reveal a non-Nernstian but a fairly reversible/quasi-reversible one electron redox process involving the Cu(II)/Cu(I) couple, as judged from the peak potential separation of 72–103 mV (59 mV for a one electron transfer process). It is seen that the reduction potential of the Cu(II)/Cu(I) couple becomes more positive on moving from complex **1** to **3** and also becomes more reversible as can be seen from the ΔE_p values. This clearly shows that the tetragonal distortion increases as one goes from complex **1** to **3**. Hence as we move from complex **1** to **3**, the nuclear reorganization energy for Cu(II) to Cu(I) conversion decreases. A reduction in the diffusion current is also seen as we move from **1** to **3** for a fixed concentration of the complex. This again reflects the fact that the bulky nature of the ligand increases from **1** to **3**.

In the presence of DNA ([DNA]/[Cu] = 5), there is a decrease in the reduction peak current indicating that the complexes are bound to the macromolecule. The $E_{1/2}$ values of the DNA-bound complexes follow the same order as the free complexes (Table 4).

The DPV for all three complexes in the absence and presence of DNA is shown in Fig. 5. The observed shifts in the $E_{1/2}$ values to more positive potentials on binding to DNA suggests that the complex displays better binding affinity in the Cu(I) state compared to the Cu(II) state. This is illustrated by the ratio of the equilibrium constants (K_{+1}/K_{+2}) for the binding of Cu(I) and Cu(II) species to DNA. These values (Table 4) have been estimated from the net shift in $E_{1/2}$ (DPV) on the addition of DNA, assuming reversible electron transfer, using the following equation: $E_b^0 - E_f^0 = 0.0591 \log(K_{+1}/K_{+2})$ where E_b^0 and E_f^0 are the formal potentials of the redox couple in the DNA bound and free form respectively [50] and K_+ and K_{2+} are the corresponding binding constants for the binding of the 1+ and 2+ species to DNA, respectively. The values of K_{+1}/K_{+2} for all the complexes have been found to be greater than unity, suggesting preferential stabilization of the Cu(I) form over the Cu(II) form on binding to DNA.

3.6. CD spectral studies

Circular dichroic spectral techniques give us useful information on how the conformation of DNA is influenced by the binding of the metal complex to DNA. The observed CD spectrum of calf thymus DNA consists of a positive band at 277 nm due to base stacking and a negative band at 245 nm due to helicity, which is characteristic of DNA in the right-handed B form. While groove binding and electrostatic interaction of small molecules with DNA show little or no perturbations on the base stacking and helicity bands, intercalation enhances the intensities of both the bands, stabilizing the right-handed B conformation of CT DNA. The CD spectra of DNA taken after incubation of the complexes with CT DNA are shown in Fig. 6. In all three cases, there is a decrease in the intensity of the positive band while the negative band is relatively less perturbed. These changes are indicative of a non-intercalative mode

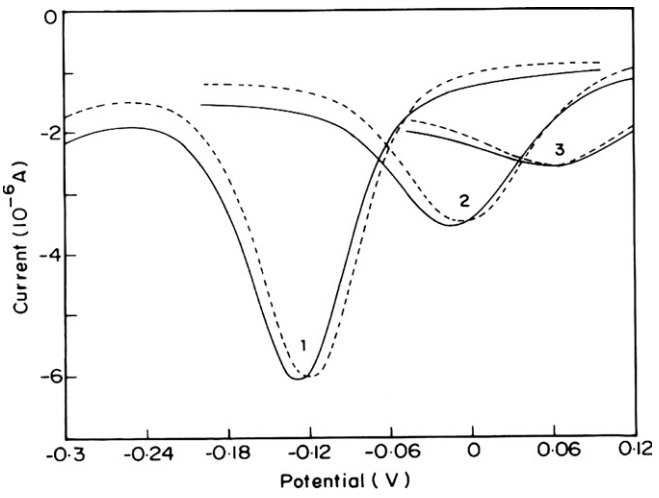


Fig. 5. Differential pulse voltammogram of complexes **1**, **2** and **3** (0.2 mM) in the absence (———) and presence of 1 mM of CT DNA (— — —); Supporting electrolyte, 1 mM Tris/ 100 mM NaCl buffer (pH 7.5).

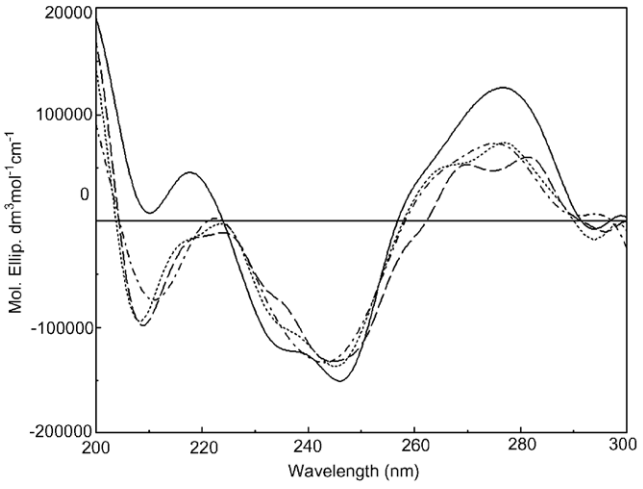


Fig. 6. CD spectra of CT DNA (200 μM) in the absence (——) and presence of 50 μM of **1** (. . . . . .), **2** (-·-·-·-·-·-) and **3** (– – – –).

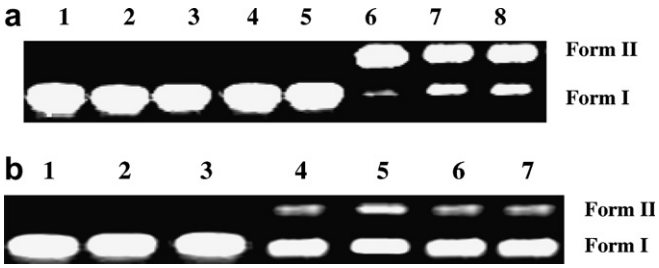


Fig. 7. (a) Cleavage of pBR322 DNA by complexes **1**–**3** in the presence of ascorbic acid. DNA (0.25 μg) was incubated with the complexes for 60 min. in Tris buffer (pH 7.5). Lane 1, DNA control; lane 2, DNA + **1** (80 μM) alone; lane 3, DNA + complex **2** (80 μM) alone; lane 4, DNA + **3** (80 μM) alone; lane 5, DNA + ascorbic acid (300 μM); lane 6, DNA + **1** (80 μM) + ascorbic acid (300 μM); lane 7, DNA + **2** (80 μM) + ascorbic acid (300 μM); lane 8, DNA + **3** (80 μM) + ascorbic acid (300 μM) and (b) Cleavage of pBR322 DNA by complexes in the presence of minor groove binder distamycin. DNA (0.25 μg) was incubated with 100 μM distamycin for 15 min. in Tris buffer (7.5). Lane 1, DNA control; lane 2, DNA + DMSO (2 μL) alone; lane 3, DNA + distamycin (100 μM) alone; lane 4, DNA + **1** (80 μM) + ascorbic acid (300 μM) + DMSO (2 μL); lane 5, DNA + **1** (80 μM) + ascorbic acid (300 μM) + distamycin (100 μM); lane 6, DNA + **2** (80 μM) + ascorbic acid (300 μM) + distamycin (100 μM); lane 7, DNA + **3** (80 μM) + ascorbic acid (300 μM) + distamycin (100 μM).

of binding of these complexes and offer support to their groove binding nature [51].

3.7. DNA cleavage studies

The oxidative cleavage of DNA in the presence of a reducing agent (ascorbic acid 300 μM) has been studied with supercoiled pBR322 DNA (SC DNA) and the extent of cleavage monitored by agarose gel electrophoresis. Fig. 7a shows the results of a gel electrophoresis experiment carried out with SC DNA in the absence and presence of complexes **1**–**3**. Lane 1 in the figure shows the control DNA without any additives. Incubation of DNA with ascorbic acid or with a complex alone does not bring about any apparent cleavage of DNA, as seen in lanes 2–5. Hence it is clear that these copper(II) complexes are not capable of bringing about any hydrolytic cleavage of DNA. This is not surprising since hydrolytic cleavage requires coordinative binding of the copper(II) complex to the phosphate moiety of the nucleic acid [52]. Since these complexes do not interact coordinatively with either DNA bases or phosphate, one cannot expect them to promote hydrolytic cleavage. Lanes 6–8 represent the cleavage brought about by complexes **1**–**3** at a concentration of 80 μM in the presence of 300 μM of ascorbic acid, wherein the conversion of SC DNA to the open circular form is clearly seen by the disappearance of form I and the appearance of form II. We have investigated the mechanistic aspects of the DNA cleavage reactions using inhibiting reagents like hydroxyl radical scavenger DMSO and minor groove binder distamycin. The gel electrophoresis results are given in Fig. 7b. Control experiments performed with SC DNA in the presence of DMSO and distamycin show the absence

Table 5
Extent of DNA cleavage by complexes **1**–**3**

Complexes	Without distamycin		Pretreated with distamycin	
	% SC[a]	% NC[a]	% SC	% NC
1	30	70	70	30
2	39	61	74	26
3	40	60	73	27

[a] SC – supercoiled, NC – nicked circular.

of any significant cleavage (lanes 2 and 3). In the presence of DMSO, the DNA cleavage brought about by the complexes is inhibited to a large extent, as observed in lanes 4 and 5. This observation validates the involvement of hydroxyl radical in DNA cleavage promoted by these complexes. The mechanistic pathway is summed up in the scheme shown below and is similar to that proposed by Sigman and coworkers for the nuclease activity of bis(phen) copper species [53].

$$[\text{Copper(II)complex}] \xrightarrow{\text{Reducingagent}} [\text{Copper(I)complex}] \xrightarrow{O_2} [OH^{\cdot}]$$

$$[OH^{\cdot}] \xrightarrow{\text{SCDNA}} \text{Nicked DNA}$$

The percentage of cleavage for all three complexes is given in Table 5. It is seen that the cleavage efficiency of **1** is marginally greater than that of **2** and **3**, both of which exhibit almost equal efficiency. Considering the fact that the cleavage mechanism goes through a Cu(I) intermediate for the generation of a hydroxyl radical, the decrease in the efficiency of DNA damage among the complexes could be thus explained. The reduced Cu(I) complex could be partly oxidized by O_2 solvated in the solution before it binds to DNA causing considerable reduction in the DNA damage, and this process is more feasible in complexes **2** and **3** as compared to **1** because of their greater electrochemical reversibility. Treatment of SC DNA with distamycin prior to the addition of the complexes inhibited the DNA cleaving ability of these complexes to a large extent (lanes 5–7). These results clearly show that the complexes prefer minor groove binding and binding of the complexes to DNA is a prerequisite for their DNA cleaving ability.

4. Conclusion

In summary, the present work describes the synthesis, characterization and DNA binding studies of copper(II) complexes **1**, **2** and **3** with N_4 Schiff base ligands containing a flexible alkyl spacer. The crystal structure of complex **1** shows that the compound exists in two different geometries, namely a square pyramid and a distorted octahedron, in its unit cell and this leads to the packing of the molecule in helical and anti-parallel structures respectively. As the number of $-CH_2-$ groups in the backbone increases along the series, the geometry of the copper complex is found to acquire more rhombic nature. Even though the change in spacer length does not affect the mode of DNA binding of these complexes, it does affect the binding constant

value. The complexes prefer binding at the minor groove of DNA. They exhibit efficient nuclease activity in presence of ascorbic acid and the cleavage efficiency is dictated mainly by the reversibility of the Cu(II)/Cu(I) couple.

Acknowledgements

Thanks are due to RSIC, Lucknow for providing mass spectral data. VU thanks the University Grants Commission for a teacher fellowship. The help and support provided by V.G. Vaidyanathan during the course of the work is gratefully acknowledged.

Appendix A. Supplementary material

CCDC 232473 contains the supplementary crystallographic data for **1**. These data can be obtained free of charge via http://www.ccdc.cam.ac.uk/conts/retrieving.html, or from the Cambridge Crystallographic Data Centre, 12 Union Road, Cambridge CB2 1EZ, UK; fax: (+44) 1223-336-033; or e-mail: deposit@ccdc.cam.ac.uk. Supplementary data associated with this article can be found, in the online version, at doi:10.1016/j.poly.2007.02.020.

References

[1] E.L. Hegg, J.N. Burstyn, Coord. Chem. Rev. 173 (1998) 133.
[2] C.J. Burrows, J.G. Muller, Chem. Rev. 98 (1998) 1109.
[3] C.J. Burrows, S.E. Rokita, Acc. Chem. Res. 27 (1994) 295.
[4] C. Metcalfe, C. Rajput, J.A. Thomas, J. Inorg. Biochem. 100 (2006) 1314.
[5] X.-Y. Wang, J. Zhang, K. Li, N. Jiang, S.-Y. Chen, H.-H. Lin, Y. huang, L.-J. Ma, X.-Q. Yu, Bioorg. Med. Chem. 14 (2006) 6745.
[6] P. Nagababu, S. Satyanarayana, Polyhedron (2007), doi:10.1016/j.poly.2006.12.027.
[7] M.E. Branum, L. Que Jr., J. Biol. Inorg. Chem. 4 (1999) 593.
[8] R. Hettich, H.-J. Schneider, J. Am. Chem. Soc. 19 (1997) 5638.
[9] V.G. Vaidyanathan, B.U. Nair, J. Chem. Soc., Dalton Trans. (2005) 2842.
[10] P.R. Reddy, K.S. Rao, B. Satyanarayana, Tetrahedron Lett. 47 (2006) 7311.
[11] C.H. Ng, H.K.A. Ong, C.W. Kong, K.W. Tan, R.N.Z.R.A. Rahman, B.M. Yamin, S.W. Ng, Polyhedron 25 (2006) 3118.
[12] Y. An, S.-D. Liu, S.-Y. Deng, L.-N. Ji, Z.-W. Mao, J. Inorg. Biochem. 100 (2006) 1586.
[13] C. Liu, S. Yu, D. Li, Z. Liao, X. Sun, H. Xu, Inorg. Chem. 41 (2002) 9132.
[14] M.S. Surendra Babu, K. Hussain Reddy, P.G. Krishna, Polyhedron 26 (2007) 572.
[15] V.G. Vaidyanathan, B.U. Nair, Eur. J. Inorg. Chem. (2003) 3633.
[16] D.S. Sigman, Acc. Chem. Res. 19 (1986) 180.
[17] G. Pratviel, J. Bernadou, B. Meunier, Angew. Chem., Int. Ed. Engl. 34 (1995) 746.
[18] W.K. Pogozelski, T.D. Tullius, D.S. Sigman, Chem. Rev. 98 (1998) 1089.
[19] X.L. Wang, H. Chao, H. Li, X.-L. Hong, L.-N. Ji, X.-Y. Li, J. Inorg. Biochem. 98 (2004) 423.
[20] Y.-L. Wang, Y.-C. Liu, Z.-S. Yang, G.-C. Zhao, Bioelectrochem. 65 (2004) 77.
[21] C. Liu, J. Zhou, Q. Li, L. Wang, Z. Liao, H. Xu, J. Inorg. Biochem. 75 (1999) 233.
[22] M. Pitie, C.J. Burrows, B. Meunier, Nucleic Acids. Res. 28 (2000) 4856.
[23] C. Tu, Y. Shao, N. Gan, Q. Xu, Z. Guo, Inorg. Chem. 43 (2004) 4761.
[24] B. Selvakumar, V. Rajendiran, P. Uma Maheswari, H.S. Evans, M. Palaniandavar, J. Inorg. Biochem. 100 (2006) 316.
[25] S. Ferrer, R. Ballesteros, A. Sambartolomé, M. González, G. Alzuet, J. Borrás, M. Liu, J. Inorg. Biochem. 93 (2004) 1436.
[26] H.J. Eppley, S.M. Lato, A.D. Ellington, J.M. Zaleski, Chem. Commun. (1999) 2405.
[27] S. Dhar, M. Nethaji, A.R. Chakravarty, J. Inorg. Biochem. 99 (2005) 805.
[28] G.N. De Iuliis, G.A. Lawrence, S.F. Makaroff, Inorg. Chem. Commun. 3 (2000) 307.
[29] A. Bencini, E. Berni, A. Bianchi, C. Giorgi, B. Valtancoli, D.K. Chand, H.–J. Schneider, J. Chem. Soc., Dalton Trans. (2003) 793.
[30] M. Scarpellini, A. Nevis, R. Horner, A.J. Bortoluzzi, B. Szpoganics, C. Zucco, R.A. Nome Silva, V. Drago, A.S. Mangrich, W.A. Ortiz, W.A.C. Passos, M.C.B. de Oliveira, H. Terenzi, Inorg. Chem. 42 (2003) 8353.
[31] S. Dhar, A.R. Chakravarty, Inorg. Chem. 42 (2003) 2483.
[32] T. Gajda, R. Kramer, A. Jancso, Eur. J. Inorg. Chem. (2000) 1635.
[33] D.S. Sigman, D.R. Graham, V. D'Aurora, A.M. Stern, J. Biol. Chem. 254 (1979) 12269.
[34] K.M. Dowrey, B.G. Que, A.G. So, Biochem. Biophys. Res. Commun. 93 (1980) 264.
[35] D.S. Sigman, A. Mazumder, D.M. Perrin, Chem. Rev. 93 (1993) 2295.
[36] M. Chikira, Y. Tomizawa, D. Fukita, T. Sugizaki, N. Sugawara, T. Yamazaki, A. Sasano, H. Shindo, M. Palaniandavar, W.E. Antholine, J. Inorg. Biochem. 89 (2002) 163.
[37] S. Mahadevan, M. Palaniandavar, Inorg. Chem. 37 (1998) 3927.
[38] V.G. Vaidyanathan, B.U. Nair, J. Inorg. Biochem. 93 (2003) 271.
[39] V. Uma, V.G. Vaidyanathan, B.U. Nair, Bull. Chem. Soc. Jpn. 78 (2005) 845.
[40] V. Uma, M. Kanthimathi, T. Weyhermuller, B.U. Nair, J. Inorg. Biochem. 99 (2005) 2299.
[41] J. Marmur, J. Mol. Biol. 3 (1961) 208.
[42] R.E. Reichmann, S.A. Rice, C.A. Thomas, P.J. Doty, J. Am. Chem. Soc. 76 (1954) 3047.
[43] (a) G.M. Sheldrick, Acta Cryst. A 46 (1990) 467;
(b) G.M. Sheldrick, SHELXL-97. Program for the Refinement of Crystal structures, University of Göttingen, Germany, 1997.
[44] A.M. Pyle, J.P. Rehmann, R. Meshoyrer, C.V. Kumar, N.J. Turro, J.K. Barton, J. Am. Chem. Soc. 111 (1989) 3051.
[45] G.Y. Bai, B. Dong, Y.–Y. Lu, K.–Z. Wang, L.–P. Jin, L.–H. Gao, J. Inorg. Biochem. 98 (2004) 2011.
[46] J.K. Barton, A.T. Danishefsky, J.M. Goldberg, J. Am. Chem. Soc. 106 (1984) 2172.
[47] X.-L. Wang, H. Chao, H. Li, X.-L. Hong, Y.-J. Liu, L.-F. Tan, L.-N. Ji, J. Inorg. Biochem. 98 (2004) 1143.
[48] S.A. Tysoe, R.J. Morgan, A.D. Baker, T.C. Strekas, J. Phys. Chem. 97 (1993) 1707.
[49] R. Vijayalakshmi, M. Kanthimathi, V. Subramanian, B.U. Nair, Biochem. Biophys. Acta 1475 (2000) 157.
[50] M.T. Carter, M. Rodriguez, A.J. Bard, J. Am. Chem. Soc. 111 (1989) 8901.
[51] P. Uma Maheswari, M. Palaniandavar, J. Inorg. Biochem. 98 (2004) 219.
[52] V. Uma, M. Kanthimathi, J. Subramanian, B.U. Nair, Biochim. Biophys. Acta 1760 (2006) 814.
[53] D.S. Sigman, A. Mazumder, D.M. Perrin, Chem. Rev. 93 (1993) 2295.

Available online at www.sciencedirect.com
ScienceDirect
Polyhedron 26 (2007) 3017–3022
POLYHEDRON
www.elsevier.com/locate/poly

New 3D two-fold interpenetrating polyoxometallate compounds built up of dititanium-substituted Keggin polyoxotungstates and transition metals

Chun-Ling Wang, Shu-Xia Liu *, Lin-Hua Xie, Yuan-Hang Ren, Da-Dong Liang, Chun-Yan Sun, Hai-Yan Cheng

Key Laboratory of Polyoxometallates Science of Ministry of Education, College of Chemistry, Northeast Normal University, Changchun 130024, PR China

Received 2 December 2006; accepted 2 February 2007
Available online 20 February 2007

Abstract

The unprecedented transition metals (TMs) bridged 1,4-dititanium(IV)-substituted Keggin-type polyoxotungstates $K_3\{M(H_2O)_4\}_2PTi_2W_{10}O_{40}\cdot 8H_2O$ (M = Co^{II} (**1**), Ni^{II} (**2**), Mn^{II} (**3**)) have been synthesized and characterized by FT-IR, UV, element analyses, X-ray powder diffraction analyses, ^{183}W NMR spectroscopy, cyclic voltammetry, TG and X-ray single-crystal analyses. It is the first time that Ti-containing polyoxotungstate $[\alpha\text{-}PTi_2W_{10}O_{40}]^{7-}$ fragments are linked by TMs based on novel Ti–O–M bonds, and it is the first example of a three-dimensional (3D) two-fold interpenetrating pure inorganic framework structure based on Keggin polyoxometallates and TMs.
© 2007 Elsevier Ltd. All rights reserved.

Keywords: Polyoxometallates; Ti-substituted; Transition metals bridged; Entangled network

1. Introduction

Entangled network structures have rapidly attracted current attention, not only for their intriguing variety of topologies and entanglement motifs, but also for their potential applications in porous materials, gas storage, non-linear optics and catalysis [1]. Up until now, most of the reported entangled structures are based on metal-organic frameworks (MOFs) and have been extensively discussed in comprehensive reviews by Batten and Robson [2]. In contrast to the interpenetrating networks based on MOFs, those constructed from polyoxometallates (POMs) are much more attractive, whilst relatively rare. POMs, known as metal–oxygen clusters, are of current interest due to the enormous structural variety combined with interesting properties. They can be viewed as multi-dentate anionic ligands [3], and have capabilities similar to those of organic ligands in linking metal centers to construct molecular structures with cavities encapsulating guest molecules or ions. Such structures can be regarded as zeolite-related nets, which have important applications as molecular sieves and heterogeneous catalysts. Recently, our group and others have determined *n*-fold interpenetrating networks containing POMs connected through a bridging metal organic subunit [4]. However, it is difficult to construct a 3D pure inorganic entangled network incorporating POMs without organic ligands. The main reason is probably that the large molecular size essentially baffles the steric extension. To the best of our knowledge, there is only one example of $\{V_{18}O_{42}\}$ cages linked by a $M(H_2O)_4$ (M = Fe, Co) group into two interpenetrating 3D inorganic networks [5]. Therefore, constructing pure inorganic interpenetrating frameworks containing POMs remains a challenge.

Among the wide varieties of POMs, the Keggin series, represented by the general formula $[XM_{12}O_{40}]^{n-}$ (X =

* Corresponding author. Fax: + 86 431 85099328.
E-mail address: liusx@nenu.edu.cn (S.-X. Liu).

0277-5387/$ - see front matter © 2007 Elsevier Ltd. All rights reserved.
doi:10.1016/j.poly.2007.02.005

P^{5+}, Si^{4+}; M = W^{6+}, Mo^{6+}), have been studied most [6]. Although connections through either rare-earth cations or TM ions have been widely presented in the vacancies of POMs [7], the intact Keggin units are difficult to link by additional pure inorganic lanthanides or TM cations. However, substituted Keggin anions containing peripheral heteroatoms with an oxidation state less than 6 have more surface negative charge than integer Keggin anions and exhibit enhanced coordinating active sites [8]. Ti substituted POM complexes have been the subject of much interest, and are especially valuable for studies in medicine and catalysis [9]. The known examples include substituted Ti derivative POMs, $[(C_2H_5)_2NH_2]_4Na[H_2PTi_2W_{10}O_{40}]\cdot H_2O$ [9c], $K_4H_{2.2}PTi_{1.60}W_{10.40}O_{40}\cdot 13H_2O$ [9f], α-[(η^5-C_5H_5)Ti($PW_{11}O_{39}$)]$^{4-}$ [11], [(η^5-C_5H_5)Ti($P_2W_{18}O_{61}$)]$^{7-}$ [12], $K_5H_2[FeW_{11}TiO_{40}]\cdot 17H_2O$ [13], $K_5H_2[CrW_{11}TiO_{40}]\cdot 17H_2O$ [13], dimeric forms of POMs [α-1,2-$PW_{10}Ti_2O_{39}$]$_2^{10-}$ [10], $Ti_6Si_2W_{18}O_{77}^{14-}$ [14], $Ti_6Ge_2W_{18}O_{77}^{14-}$ [15], $K_{10}H_2[P_2W_{18}Ti_6O_{77}]\cdot 17H_2O$ [16], [($TiP_2W_{15}O_{55}OH$)$_2$]$^{14-}$ [19], [{γ-$SiTi_2W_{10}O_{36}(OH)_2$}$_2$(μ-O)$_2$]$^{8-}$ [21], tetrameric forms of [($P_2W_{15}Ti_3O_{60.5}$)$_4$]$^{36-}$ [17], [(α-1,2,3-$P_2W_{15}Ti_3O_{62}$)$_4${$Ti(OH)_3$}$_4$Cl]$^{45-}$ [18], [{$Ti_3P_2W_{15}O_{57.5}$ $(OH)_3$}$_4$]$^{24-}$ [19], [{β-$Ti_2SiW_{10}O_{39}$}$_4$]$^{24-}$ [20]. Interestingly most of the species mentioned above are reported as being polymeric with Ti–O–Ti bridged anhydride formation. Indeed the titanium atoms incorporated into the polyoxoanions with reactive sites have a strong tendency to form polymers through Ti–O–Ti bonds as shown above. However, observing Ti-containing POMs without Ti···Ti polymerization in aqueous solution is a challenge in POM synthetic chemistry. In this paper we have isolated a new kind of Ti-containing POM, which contains a Ti–O–M bond without Ti···Ti converging. It was originally reported that [α-$PTi_2W_{10}O_{40}$]$^{7-}$ reacts with divalent manganese, iron, cobalt, nickel, copper and zinc to form isolable complexes $MTi_2PW_{10}O_{40}^{5-}$ on the basis of visible spectra and element analyses [9b]. We have now succeeded in isolating three complexes with 3D two-fold interpenetrating network structures constructed from [α-$PTi_2W_{10}O_{40}$]$^{7-}$ and TMs. It is the first time that a Ti–O–M bond coordination fashion for POMs has been reported, and also it is the first report on higher dimensional *n*-fold interpenetrating network compounds incorporating titanium substituted POMs and TMs.

2. Experimental

2.1. Materials and physical methods

All reagents were used as purchased commercially without further purification. The starting sample of $K_4H_{2.2}PTi_{1.60}W_{10.40}O_{40}\cdot 13H_2O$ was prepared according to a recently reported method and the purity was confirmed by IR [9f]. Elemental analyses of K, P, W, Ti, Co, Ni and Mn were determined by a Leaman inductively coupled plasma (ICP) spectrometer. IR spectra were obtained on a Nicolet 205 FT/IR spectrometer with KBr pellets in the 400–4000 cm^{-1} region. UV spectra were recorded on a 756 CRT UV–Vis spectrophotometer. ^{183}W NMR spectra were recorded on a Bruker Am-500 spectrometer and were referenced to an external standard of saturated Na_2WO_4–D_2O solution. TG analyses were performed on a Perkin–Elmer TGA7 instrument in flowing N_2 with a heating rate of 10 °C/min^{-1}. Powder X-ray diffraction measurements were performed on a Rigaku D/MAX-3 instrument with Cu Kα radiation in the angular range $2\theta = 3$–90° at 293 K. Cyclic voltammetry measurements were carried out on a CHI 660 electrochemical workstation using a conventional three-electrode single compartment cell at room temperature. The working electrode was a glassy carbon disc electrode. The surface of the glass carbon electrode was polished with 0.3 μm alumina and washed with distilled water before each experiment. Platinum gauze was used as counter electrode and an Ag/AgCl was used as a reference electrode. The solutions were degassed with pure nitrogen for 15 min before use and blanketed with nitrogen gas during the voltammetric scans. All experiments were performed at room temperature.

2.1.1. Synthesis of K_3{$Co(H_2O)_4$}$_2PTi_2W_{10}O_{40}\cdot 8H_2O$ (1)

A sample of $K_4H_{2.2}PTi_{1.60}W_{10.40}O_{40}\cdot 13H_2O$ (3 g, 1 mmol) (synthesized according to ref [9f]) was dissolved in 20 mL aqua solution, and then $CoCl_2$ (0.260 g, 2 mmol) was added. To this solution, 3 M HCl was dropped in slowly with vigorous stirring until the pH was adjusted to 5. The solution was heated at 80 °C for 2 h and after cooling to room temperature it was filtered. The filtrate was allowed to evaporate at room temperature. After 7 days a pink crystalline product started to appear. (Yield: 60%, based on Co). *Anal.* Calc. for $K_3H_{32}Co_2PTi_2W_{10}O_{56}$ (3128.49): K, 3.75; P, 0.99; W, 58.76; Co, 3.76; Ti, 3.06. Found: K, 3.73; P, 0.95; W, 58.74; Co, 3.72; Ti, 3.03%. IR (KBr): $\tilde{\nu} = 958$ (s), 879 (s), 813 (s), 685 (w), 526 (m), 456 (s) cm^{-1}.

2.1.2. Synthesis of K_3{$Ni(H_2O)_4$}$_2PTi_2W_{10}O_{40}\cdot 8H_2O$ (2)

This compound was prepared similarly to **1**, with 0.259 g (2 mmol) $NiCl_2$ solid instead of $CoCl_2$. Green crystals were formed after four days (Yield: 65%, based on Ni). *Anal.* Calc. for $K_3H_{32}Ni_2PTi_2W_{10}O_{56}$ (3128.01): K, 3.75; P, 0.99; W, 58.77; Ni, 3.75; Ti, 3.06. Found: K, 3.74; P, 0.97; W, 58.71; Ni, 3.73; Ti, 3.04%. IR (KBr): $\tilde{\nu} = 943$ (s), 816 (m), 689 (m), 526 (s), 473 (s), 457 (s), 419 (w) cm^{-1}.

2.1.3. Synthesis of K_3{$Mn(H_2O)_4$}$_2PTi_2W_{10}O_{40}\cdot 8H_2O$ (3)

This compound was also prepared similarly to **1**, with 0.306 g (2 mmol) $MnSO_4$ solid instead of $CoCl_2$. Yellow crystals were formed after 7 days (Yield: 70%, based on Mn). *Anal.* Calc. for $K_3H_{32}Mn_2PTi_2W_{10}O_{56}$ (3120.50): K, 3.76; P, 0.99; W, 58.91; Mn, 3.52; Ti, 3.07. Found: K, 3.73; P, 0.98; W, 58.87; Mn, 3.50; Ti, 3.04%. IR (KBr): $\tilde{\nu} = 934$ (s), 815 (s), 699 (s), 473 (m), 419 (w) cm^{-1}.

Table 1
Crystal data and details of the data collection and refinement for complexes **1**–**3**

	1	**2**	**3**
Empirical formula	$K_3Co_2PTi_2W_{10}O_{56}H_{32}$	$K_3Ni_2PTi_2W_{10}O_{56}H_{32}$	$K_3Mn_2PTi_2W_{10}O_{56}H_{32}$
Formula weight	3135.53	3167.35	3127.55
Space group	*P4/mnc*	*P4/mnc*	*P4/mnc*
a (Å)	14.1680(5)	14.098(2)	14.2530(10)
b (Å)	14.1680(5)	14.098(2)	14.2530(10)
c (Å)	12.4936(6)	12.508(3)	12.4854(12)
Volume (Å^3)	2507.87(17)	2486.0(7)	2536.4(4)
Z	2	2	2
Temperature (K)	293(2)	293(2)	293(2)
Wavelength (Å)	0.71073	0.71073	0.71073
D_{calc} (Mg m^{-3})	2.148	2.527	2.656
Absorption coefficient (mm^{-1})	2.942	3.409	3.345
R [$I > 2\sigma(I)$][a]	0.0568	0.0602	0.0559
wR_2 [$I > 2\sigma(I)$][b]	0.0496	0.0572	0.0440
R_1 (all data)[a]	0.1219	0.1295	0.1229
R_w (all data)[b]	0.1189	0.1284	0.1176

[a] $R_1 = \sum ||F_o| - |F_c|| / \sum |F_o|$.
[b] $R_w = \left[\sum w(F_o^2 - F_c^2)^2 / \sum w(F_o^2)^2\right]^{1/2}$.

2.2. X-ray crystallography

The reflection intensity of **2** was collected on a Rigaku R-AXIS RAPID IP diffractometer with graphite monochromatic Mo Kα radiation at 293 K. The reflection intensities of **1** and **3** were collected on a SMART CCD diffractometer equipped with graphite monochromatic Mo Kα radiation at 293 K, and empirical absorption corrections by SADABS were applied to the intensity data. All the structures were solved by direct methods and refined using the full-matrix least-squares method on F^2 with the SHELXTL crystallographic software package. Anisotropic thermal parameters were refined for all non-hydrogen atoms, except for the water oxygen atoms. No attempt was made to locate the hydrogen atoms of water. A summary of the crystallographic data and structure refinements for compounds **1**–**3** are given in Table 1.

3. Results and discussion

In contrast to the entangled hybrid POMs, which are synthesized by hydrothermal methods, we have made use of classical open-air techniques to isolate compounds **1**–**3**. Although in most cases the exact reaction mechanisms in one pot methods remain elusive, the pH value, starting materials, reaction time and concentrations can directly influence the final product. Our interest is to obtain new inorganic materials utilizing POMs. Choosing a suitable POM cluster as a building block is crucial for obtaining the extended structure. We select a Ti-substituted Keggin POM that has enhanced surface reaction activity which could make it possible to construct a high dimensional structure.

Single-crystal X-ray diffraction revealed that **1**–**3** are isomorphic with only slight differences in bond lengths and angles, **1** is described as an example below. The crystal structure of **1** consists of a $[\alpha\text{-}PTi_2W_{10}O_{40}]^{7-}$ cluster, two Co^{II} cations, three potassium cations and eight guest water molecules, as shown in Fig. 1. The $[\alpha\text{-}PTi_2W_{10}O_{40}]^{7-}$ anion shows crystallographic disorder as found in many crystal structures with Keggin anions [8]. The central atom P is surrounded by a cube of eight oxygen atoms, with each oxygen site half-occupied, and the W atoms situated at the corners of a regular cubic octahedron. The P–O bonds are all 1.551 Å, which are in the usual P–O range. The two Ti atoms in the Keggin unit are disordered over four positions, with the occupancy factors all being 50% for W/Ti. Thus, two of the 12 octahedrally coordinated W atoms are substituted by Ti atoms statistically. The two-substituted Keggin anion has five possible isomers with C_s, C_2, C_{2v}, and C_1 symmetry (As shown in Fig. S1). The ^{183}W NMR spectrum of **1** shows five lines with an intensity ratio of 2:2:2:2:2, which is similar to that of $[\alpha\text{–}PTi_2W_{10}O_{40}]^{7-}$ and can be ascribed to C_2 symmetry formed by 1,4-substitution

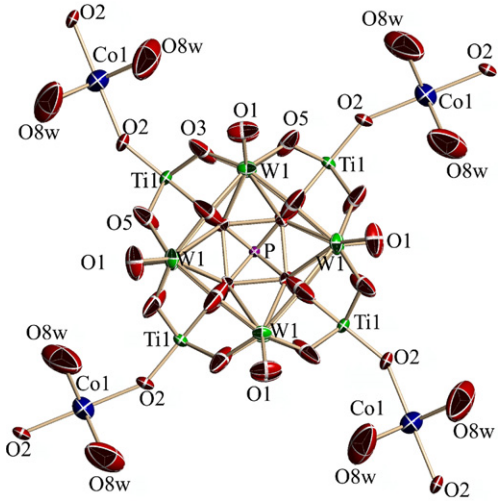


Fig. 1. Crystal structure of compound **1**. Only some of the atoms are labelled. All H atoms are omitted for clarity.

[9]. For **1**, all tungsten sites exhibit a +6 oxidation state, which is confirmed by bond valence sum calculations. The Ti/W–O bond lengths are found in the 1.695–1.706 Å range, which is a little shorter than the normal Ti–O bond lengths [10,16,18]. This result may be due to the influence of the outer coordination environment in compound **1**. As shown in Fig. 1, the corresponding terminal oxygen atom of W/Ti is coordinated by the divalent TM cation, Co^{II}. The Co–O distances are in the range 1.966–2.078 Å, which are comparable to those observed for metal oxygen bond lengths. The Ti–O–Co angles are in the 150.811–153.420° range, comparable with those in the recently reported Ti–O–Ti 136.4–176.4° [10,18]. As described above, the TM in complex **1**, as $\{CoO_6\}$ units, bridges $[\alpha\text{-}PTi_2W_{10}O_{40}]^{7-}$, leading to the formation of a two-dimensional anionic $[Co_2PTi_2W_{10}O_{40}]^{3-}$ layer running parallel to the *ab*-plane of the unit cell (Fig. 2), which is just like a beautiful of hound's-tooth formation. Potassium cations link the layers to form a three-dimensional structure (Fig. S2). In other words, this structure can also be described as a series of two-dimensional layers, and the neighboring layers are held together by potassium cations, forming a 3D framework. X-ray powder diffraction (XRPD) patterns of compounds **1**–**3** have been recorded, and their diagrams are presented in Fig. S3. The computer-simulated patterns, obtained using the single crystal X-ray data for **1**–**3**, match very well with the respective experimentally observed patterns, which confirm the homogeneity and the purity of the bulk samples of **1**, **2** and **3**.

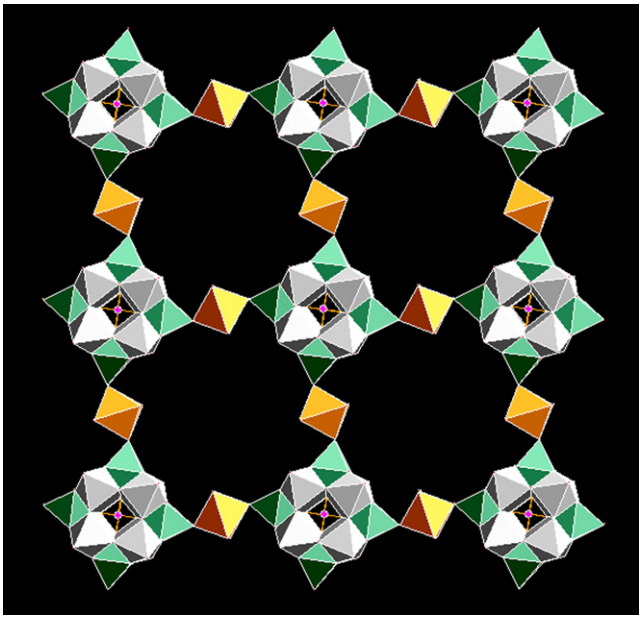


Fig. 2. Polyhedral 2D view of compound **1** along the *c* axis.

The most fascinating feature of **1** is that it exhibits two sets of structures, as described above, penetrating each other to form a two-fold interpenetrating network (Fig. 3). The molecular squares with a Co···Co separation of 14.1680(5) Å contain large cube like boxes of approximate dimensions $7.3 \times 7.3 \times 7.5$ Å^3. These cavity spaces are large enough to hold the other set of $[\alpha\text{-}PTi_2W_{10}O_{40}]^{7-}$ globes. This kind of entanglement is quite uncommon in POM chemistry. Therefore, compound **1** provides a remarkable new structural motif, and represents the first example of a 3D array of a Keggin series in an interpenetrating manner. It is also a rare example having both POM and TM characteristics and could equally well be considered as being formed by interconnected interpenetrating factions. The overall structure can be seen as a porous framework containing channels that approximate constitute 13.5% of the crystal volume (calculated by PLATON), which are filled by guest water molecules. In order to examine the stability of these frameworks, thermal gravimetric (TG) analyses were carried out for **1**–**3** between 20 and 600 °C (Fig. S4). The TG curves show a weight loss step (20–300 °C) corresponding to the release of the guest H_2O molecules and coordinated H_2O molecules (found: (**1**) 9.96% (**2**) 9.47% (**3**) 9.33%; calculated: (**1**) 9.21% (**2**) 9.21% (**3**) 9.23%). The total weight losses are in good accordance with the calculated values. The curves also prove that the frameworks of **1**–**3** are stable in the range 300 to 600 °C. To further investigate the porosity of **1**, the as-synthesized crystalline sample was placed in a vacuum oven at

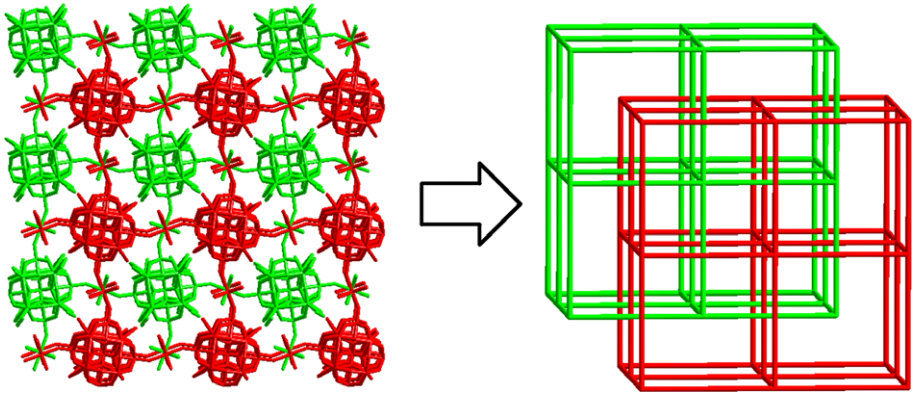


Fig. 3. Simplified schematic representation of the 3D twofold interpenetrating network of **1**.

120 °C for 6 h to release the guest water molecules (with a 9.69% weight loss) and to get the evacuated solid. In the XRPD pattern of the evacuated solid, the main sharp diffraction peaks are consistent with those of the as-synthesized solid (Fig. S5). This fact may be used to confirmed that the framework is still stable and retains high periodicity.

The infrared spectrum of $K_4H_{2.2}PTi_{1.6}W_{10.4}O_{40}\cdot 13H_2O$ (Fig. 4a) in the range 400–1200 cm^{-1} measured as a KBr disk shows the characteristic asymmetric stretching vibrational peaks of the Keggin anion as $\{PW_{12}\}$. The most notable difference between $[\alpha\text{-}PTi_2W_{10}O_{40}]^{7-}$ and $\{PW_{12}\}$ is that the asymmetric phosphate stretch is split into three peaks for $\upsilon_{as}(P\text{–}O_a)$, which can be explained by some W atoms being replaced by Ti atoms to depress the symmetry $T_d \rightarrow C_2$. FT-IR spectra of **1**–**3** (Fig. 4b–d) are closely related to that of the parent compound $[\alpha\text{-}PTi_2W_{10}O_{40}]^{7-}$, with the exception of a 10 cm^{-1} shift to lower wave numbers of the strong $\upsilon_{as}(P\text{–}O_a)$ bands. This effect is a common feature already observed for metal-bridged POM derivatives by comparison with their parent analogues, and has been assigned to the framework cohesion through metals, leading to a decrease of the stretching force constants.

The UV spectra of the compounds **1**–**3** checked in aqueous solution in the 200–350 nm region are similar to that of $K_4H_{2.2}PTi_{1.6}W_{10.4}O_{40}\cdot 13H_2O$ (Fig. S6). All of the spectra display two intense absorption bands, appearing at 262 and 216 nm (224 nm for $K_4H_{2.2}PTi_{1.6}W_{10.4}O_{40}\cdot 13H_2O$). The weaker absorption bands at 262 nm (Fig. S6 a–d) are attributed to a charge-transfer absorption $O_{b(c)} \rightarrow W$, whereas the stronger absorption peaks are assigned to a charge-transfer absorption of $O_t \rightarrow W$ in the polyoxoanions. It is noteworthy that the stronger absorption bands at about 216 nm of compounds **1**–**3** are blue-shifted by 8 nm relative to the absorption peak at 224 nm for that of the parent compound $K_4H_{2.2}PTi_{1.6}W_{10.4}O_{40}\cdot 13H_2O$. This may be due to the affect of the incorporated TMs.

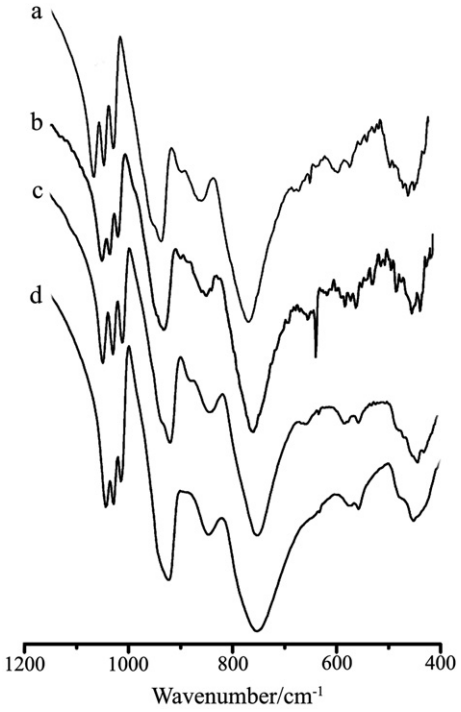


Fig. 4. FT-IR spectra of the di-Ti-substituted Keggin polyoxoanion in the region 400–1200 cm^{-1}, measured as KBr disks, of: (a) $K_4H_{2.2}PTi_{1.6}W_{10.4}O_{40}\cdot 13H_2O$, (b) $K_3\{Co(H_2O)_4\}_2PTi_2W_{10}O_{40}\cdot 8H_2O$ (**1**), (c) $K_3\{Ni(H_2O)_4\}_2PTi_2W_{10}O_{40}\cdot 8H_2O$ (**2**) and (d) $K_3\{Mn(H_2O)_4\}_2PTi_2W_{10}O_{40}\cdot 8H_2O$ (**3**).

The electrochemical behaviors were investigated by cyclic voltammetry in 1 M (CH_3COONa/CH_3COOH) pH 4.8 buffer under a nitrogen atmosphere at the scan rate of 20 mV s^{-1} (Fig. S7). In the potential range 0 to −1000 mV, the parent compound $[\alpha\text{-}PTi_2W_{10}O_{40}]^{7-}$ exhibits one quasi-reversible redox wave and the mean peak potential $E_{1/2} = (E_{pa} + E_{pc})/2$ is −805 mV. The reduction wave can be attributed to the reduction of W^{VI} to W^{V}, however, stepwise reduction of the W centers is not observed in contrast to the saturated Keggin structure PW_{12} (the electrochemistry behavior of $\{PW_{12}\}$ has been described previously [22]). The cyclic voltammetric run of **1**–**3** under the same experimental conditions reveals the analogical redox activities but no electrochemical activity was detected for the transition metals. **1**–**3**, upon reduction of the W centers, parallels the behavior of $[\alpha\text{-}PTi_2W_{10}O_{40}]^{7-}$, which also indicates that the transition metals have no obvious effect on the electrochemical behavior of the W centers.

4. Conclusion

In summary, compounds **1**–**3** provide unprecedented 3D two-fold interconnecting frameworks formed by di-Ti-subsitituted Keggin polyoxotungstates and transition metals, Co^{II}, Ni^{II} and Mn^{II}. The successful syntheses of **1**–**3** not only confirm the formation of a Ti–O–M bond faction without Ti···Ti polymerization in aqueous solutions, but also provide examples of multidimensional pure inorganic frameworks incorporating POMs with a highly symmetric structure, which were synthesized by open-air techniques. In view of the rapidly expanding pool of well-characterized metal oxide clusters, this work has provided access for the further synthesis of POM-based purely inorganic porous framework materials.

Acknowledgement

This research was supported by the National Science Foundation of China (Grant No. 20571014) and the Scientific Research Foundation for Returned Overseas Chinese Scholars, the Ministry of Education.

Appendix A. Supplementary material

CCDC **1**, **2** and **3** contain the supplementary crystallographic data for 417092, 417093 and 417094. These data can be obtained free of charge via http://www.ccdc.cam.

ac.uk/conts/retrieving.html, or from the Cambridge Crystallographic Data Centre, 12 Union Road, Cambridge CB2 1EZ, UK; fax: (+44) 1223-336-033; or e-mail: deposit @ccdc.cam.ac.uk. Supplementary data associated with this article can be found, in the online version, at doi:10.1016/j.poly.2007.02.005.

References

[1] (a) D.M. Proserpio, R. Hoffman, P. Preuss, J. Am. Chem. Soc. 116 (1994) 9634;
(b) J.P. Sauvage, Acc. Chem. Res. 31 (1998) 611;
(c) B. Moulton, M.J. Zaworotko, Chem. Rev. 101 (2001) 1629;
(d) L. Carlucci, G. Ciani, M. Moret, D.M. Proserpio, S. Rizzato, Angew. Chem. Int. Ed. 39 (2000) 1506;
(e) S.A. Bourne, J. Lu, B. Moulton, M.J. Zaworotko, Chem. Commun. (2001) 861;
(f) O.R. Evans, W. Lin, Acc. Chem. Res. 35 (2002) 511;
(g) R. Kitaura, K. Seki, G. Akiyama, S. Kitagawa, Angew. Chem. Int. Ed. 42 (2003) 428;
(h) N.W. Ockwig, O. Delgado-Friedrichs, M. O'Keeffe, O.M. Yaghi, Acc. Chem. Res. 38 (2005) 176;
(i) C.N.R. Rao, S. Natarajan, R. Vaidhyanathan, Angew. Chem. Int. Ed. 43 (2004) 1466;
(j) X.L. Wang, C. Qin, E.B. Wang, Y.G. Li, Z.M. Su, L. Xu, L. Carlucci, Angew. Chem. Int. Ed. 44 (2005) 5974.

[2] (a) S.R. Batten, R. Robson, Angew. Chem. Int. Ed. 37 (1998) 1460;
(b) S.R. Batten, CrystEngComm 3 (2001) 67.

[3] (a) M.T. Pope, Heteropoly and Isopoly Oxometallates, Springer, Berlin, 1983;
(b) M.T. Pope, A. Müller, Angew. Chem. Int. Ed. 30 (1991) 34;
(c) Special issue on Polyoxometallates (Guest Ed.: C.L. Hill): Chem. Rev. 98 (1998) 1;
(d) M.T. Pope, A. Müller (Eds.), Polyoxometallate Chemistry: From Topology via Self-Assembly to Applications, Kluwer, Dordrecht, 2001.

[4] (a) Z.Y. Shi, X.J. Gu, J. Pen, X. Yu, E.B. Wang, Eur. J. Inorg. Chem. (2006) 385;
(b) C.D. Zhang, S.X. Liu, L.H. Xie, B. Gao, C.Y. Sun, D.H. Li, J. Mol. Struct. 753 (2005) 40;
(c) S.X. Liu, L.H. Xie, B. Gao, C.D. Zhang, C.Y. Sun, D.H. Li, Z.M. Su, Chem. Commun. (2005) 5023;
(d) C.D. Zhang, S.X. Liu, B. Gao, C.Y. Sun, L.H. Xie, M. Yu, J. Peng, Polyhedron (in press).

[5] M.I. Khan, E. Yohannes, R.J. Doedens, Angew. Chem. Int. Ed. 38 (1999) 1292.

[6] (a) S. Reinoso, P. Vitoria, L. Lezama, A. Luque, J.M. Gutierrz-Zorrilla, Inorg. Chem. 42 (2003) 3709;
(b) A.M. Khenkin, R. Neumann, J. Am. Chem. Soc. 124 (2002) 4198;
(c) X. Lopez, J.M. Maestre, C. Bo, J.M. Poblet, J. Am. Chem. Soc. 123 (2001) 9571;
(d) Z. Xin, J. Peng, T. Wang, B. Xue, Y. Kong, L. Li, E. Wang, Inorg. Chem. 45 (2006) 8856;
(e) S. Uchida, R. Kawamoto, N. Mizuno, Inorg. Chem. 45 (2006) 5136.

[7] (a) U. Kortz, S. Nellutla, A.C. Stowe, N.S. Dalal, J. van Tol, B.S. Bassil, Inorg. Chem. 43 (2004) 144;
(b) B. Keita, I.M. Mbomekalle, L. Nadjo, T.M. Anderson, C.L. Hill, Inorg. Chem. 43 (2004) 3257;
(c) M.D. Ritorto, T.M. Anderson, W.A. Neiwert, C.L. Hill, Inorg. Chem. 43 (2004) 44;
(d) L.H. Fan, L. Xu, G.G. Gao, F.Y. Li, Z.K. Li, Y.F. Qiu, Inorg. Chem. Commun. 9 (2006) 1308.

[8] (a) S. Reinoso, P. Vitora, L. Lezama, A. Luque, J.M. Gutierrez-Zorrilla, Inorg. Chem. 42 (2003) 3709;
(b) L.S. Felices, P. Vitoria, J.M. Gutierrez-Zorrilla, S. Reinoso, J. Etxebarria, L. Lezama, Chem. Eur. J. 10 (2004) 5138;
(c) H. Weiner, H.J. Lunk, R. Friese, H. Hartl, Inorg. Chem. 44 (2005) 7751;
(d) S. Reinoso, P. Vitoria, L.S. Felices, L. Lezama, J.M. Gutiérrez-Zorrilla, Chem. Eur. J. 11 (2005) 1538;
(e) S. Reinoso, P. Vitoria, L.S. Felices, L. Lezama, J.M. Gutiérrez-Zorrilla, Inorg. Chem. 45 (2006) 108;
(f) L.S. Felices, P. Vitoria, J.M. Gutiérrez-Zorrilla, L. Lezama, S. Reinoso Inorg. Chem. 45 (2006) 7748.

[9] (a) W.H. Knoth, P.J. Domaille, D.C. Roe, Inorg. Chem. 22 (1983) 198;
(b) P.J. Domaille, W.H. Knoth, Inorg. Chem. 22 (1983) 818;
(c) T. Ozeki, T. Yamase, Acta Crystallogr. Sect. C 47 (1991) 693;
(d) T. Yamase, T. Ozeki, S. Motomuba, Bull. Chem. Soc. Jpn. 65 (1992) 1453;
(e) K. Nomiya, M. Takahashi, J.A. Widegren, T. Aizawa, Y. Sakai, N.C. Kasuga, J. Chem. Soc., Dalton Trans. (2002) 3679;
(f) H.J. Zhai, S.X. Liu, Y.X. Li, E.B. Wang, N.H. Hu, Wuji Huaxue Xuebao 21 (2005) 1798, Synthesis of $K_4H_{2.2}PTi_{1.60}W_{10.40}O_{40} \cdot 13H_2O$: A 10 g (30.3 mmol) sample of $Na_2WO_4 \cdot 2H_2O$ was dissolved in a 33 mL of H_2O, and then NaH_2PO_4 (2 g 13.3 mmol) was added with vigorous stirring. 0.6 mL $TiCl_4$ was dropped into the mixture very slowly. The solution was refluxed for 20 min and filtered after it cooled. To the filtrate 3.3 g KCl was added, followed by adjustment of the solution to pH 6 with 1.0 M aqueous HCl. Stirring was continued for 20 min, then a white precipitate was isolated. The white precipitate was redissolved in hot aqua solution (60 °C, 30 mL). Slow evaporation at room temperature led to the crystalline solid, suitable for X-ray diffraction, after 10 days.

[10] J.H. He, X.H. Wang, Y.G. Chen, J.F. Liu, N.H. Hu, H.Q. Jia, Inorg. Chem. Commun. 5 (2002) 796.

[11] R.K.C. Ho, W.G. Klemperer, J. Am. Chem. Soc. 100 (1978) 6772.

[12] J.F.W. Keana, M.D. Ogan, J. Am. Chem. Soc. 108 (1986) 7951.

[13] Y.G. Chen, J.F. Liu, Polyhedron 15 (1996) 3433.

[14] Y. Lin, T.J.R. Weakley, R. Rapko, R.G. Finke, Inorg. Chem. 32 (1993) 5095.

[15] T. Yamase, T. Ozeki, H. Sakamoto, S. Nishiya, A. Yamamoto, Bull. Chem. Soc. Jpn. 66 (1993) 103.

[16] K. Nomiya, M. Takahashi, K. Ohsawa, J.A. Widegren, J. Chem. Soc., Dalton Trans. (2001) 2872.

[17] K. Nomiya, Y. Arai, Y. Shimizu, M. Takahashi, T. Takayama, H. Weiner, T. Nagata, J.A. Widegren, R.G. Finke, Inorg. Chim. Acta 300–302 (2000) 285.

[18] Y. Sakai, K. Yoza, C.N. Kato, K. Nomiya, Chem. Eur. J. 9 (2003) 4077.

[19] U. Kortz, S.S. Hamzeh, N.A. Nasser, Chem. Eur. J. 9 (2003) 2945.

[20] F. Hussain, B.S. Bassil, L.H. Bi, M. Reicke, U. Kortz, Angew. Chem. Int. Ed. 43 (2004) 3485.

[21] Y. Goto, K. Kamata, K. Yamaguchi, K. Uehara, S. Hikichi, N. Mizuno, Inorg. Chem. 45 (2006) 2347.

[22] M.T. Pope, G.M. Varga Jr., Inorg. Chem. 5 (1966) 1249.

Available online at www.sciencedirect.com
ScienceDirect
Polyhedron 26 (2007) 3023–3028
POLYHEDRON
www.elsevier.com/locate/poly

Synthesis, structure and magnetic properties of a novel Tb_4 spin cluster and synthesis of a Tb chain

Roland Bircher [a], Brendan F. Abrahams [b], Hans U. Güdel [a,*], Colette Boskovic [b,*]

[a] *Department of Chemistry and Biochemistry, University of Bern, Freiestrasse 3, CH-3000 Bern 9, Switzerland*
[b] *School of Chemistry, University of Melbourne, Vic. 3010, Australia*

Received 14 December 2006; accepted 2 February 2007
Available online 13 February 2007

Abstract

The syntheses of two new polynuclear Tb^{III} compounds are reported. A tetranuclear complex $[Tb_4(H_2L)_2(H_4L)_2(OAc)_8]$ (**1**), with H_4L = 2-((2-hydroxy-benzylidene)-amino)-2-hydroxy-methyl-propane-1,3-diol, has a butterfly-type structure, while $[Tb(OAc)_3MeOH]_\infty$ (**2**) is a linear chain. A novel binding mode for H_2L^{2-} is observed in **1**, with two alkoxides each bridging three Tb^{III} ions. The magnetic properties of **1** are determined by the superposition of the ligand field split $^7F_6$ states of Tb^{III} single-ions located on two crystallographically distinct sites. Weak antiferromagnetic exchange interactions possibly contribute to the lowering of the magnetic moment at the lowest temperatures.
© 2007 Elsevier Ltd. All rights reserved.

Keywords: Lanthanide; Rare earth metal; Spin cluster; Magnetic measurements; Magnetic anisotropy

1. Introduction

The discovery in the early 1990s of the first single-molecule magnet (SMM), a dodecanuclear Mn complex (Mn_{12} acetate), has prompted considerable research in this area [1]. SMMs are isolated high spin molecules that exhibit magnetization hysteresis at low temperatures, which is otherwise a property of bulk magnets. Large spin ground states combined with predominantly uniaxial anisotropy are responsible for this behavior. The quantum nature of SMMs is manifested by quantum tunneling of the magnetization. In the last 15 years more than a hundred new examples of SMMs have been prepared by synthetic chemists, many of them containing Mn and belonging to the same structural family as Mn_{12} acetate [2,3], or to a family of Mn_4 SMMs [4]. SMM synthesis has also been extended to other transition metal ions such as Fe, Ni, V and Co [5,6]. Below the so-called blocking temperature, SMMs display slow relaxation of the magnetization. However, despite the large number of new molecules, no significant increase has been achieved in the blocking-temperature. Very recently, the first SMMs containing rare earth ions were reported [7,8]. Rare earth ions can provide up to seven unpaired electrons and introduce a large magnetic anisotropy. The most striking examples among this new class of SMMs have been described by Ishikawa et al. [8]. Tb, Dy or Ho ions sandwiched between two phthalocyanine molecules were the first mononuclear SMMs, and slow relaxation of the magnetization was observed at significantly higher temperatures than for conventional transition metal SMMs. These findings have triggered the exploration of new molecular clusters containing rare earth ions.

We have turned our attention to the Schiff base proligand 2-((2-hydroxy-benzylidene)-amino)-2-hydroxymethyl-propane-1,3-diol (H_4L, Chart 1). It has a potentially pentadentate $\{O_4N\}$ donor set and possesses both chelating and bridging capacities. The large number of potential binding sites is suitable for rare earth ions, which often have coordination numbers of eight or nine. H_4L is a member of a family of Schiff base ligands that we have successfully employed in the synthesis of new transition metal spin

* Corresponding authors. Tel.: +61 383444971; fax: +61 393475180.
E-mail address: c.boskovic@unimelb.edu.au (C. Boskovic).

0277-5387/$ - see front matter © 2007 Elsevier Ltd. All rights reserved.
doi:10.1016/j.poly.2007.02.003

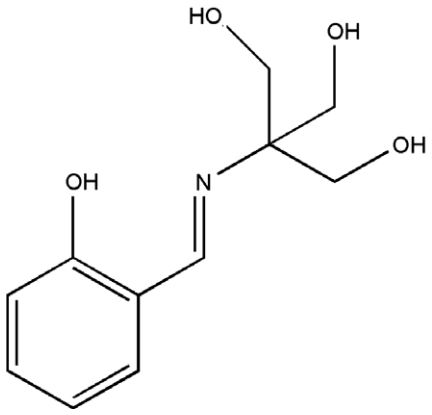


Chart 1. Proligand H_4L.

clusters [9]. Several clusters incorporating derivatives of H_4L and Mn, Ni and Cu have been reported in the literature [10]. Although the ability of H_4L to coordinate rare earth ions has not previously been explored, it would appear to be an excellent candidate as O and N are good donor atoms for rare earth ions.

2. Experimental

2.1. Syntheses

All manipulations were performed under aerobic conditions, using materials as received. 2-((2-hydroxy-benzylidene)-amino)-2-hydroxymethyl-propane-1,3-diol (H_4L) was prepared as described [11].

2.1.1. $[Tb_4(H_2L)_2(H_4L)_2(OAc)_8]$ (1)

$Tb(OAc)_3 \cdot H_2O$ (0.68 g, 2.0 mmol) and H_4L (0.46 g, 2.0 mmol) were dissolved in MeOH (50 cm^3), and the resulting mixture was stirred overnight. The white precipitate was removed by filtration and the filtrate was evaporated to dryness and redissolved in a minimum amount of MeOH. After two days, a mixture of crystals of **1** and **2** was filtered off and the remaining yellow solution was layered with Et_2O. After a further three days, pale yellow plate shaped crystals of $\mathbf{1} \cdot 2Et_2O$ formed. The crystals were isolated and washed with minimum MeOH and Et_2O; 25% yield. A sample for crystallography was maintained in contact with mother liquor to prevent the loss of interstitial solvent. *Anal.* Calc. for $[Tb_4(H_2L)_2(H_4L)_2(OAc)_8] \cdot Et_2O$, $C_{64}H_{90}N_4O_{33}Tb_4$: C, 36.97; H, 4.36; N, 2.69. Found: C, 37.20; H, 4.28; N, 2.36%. Selected IR data (cm^{-1}): 3401 (s), 2931 (w), 2874 (w), 1642 (s), 1631 (s), 1558 (s), 1493 (m), 1453 (m), 1345 (w), 1311 (w), 1242 (w), 1199 (w), 1154 (w), 1057 (m), 1019 (m), 946 (w), 763 (w), 668 (m), 615 (w), 574 (m), 473 (w).

2.1.2. $[Tb(OAc)_3MeOH]_\infty$ (2)

Under the same reaction conditions as for **1**, needle shaped crystals of **2** could be manually isolated from the mixture of crystals formed from a concentrated methanolic solution. A pure sample of **2** could not be obtained for physical measurements, as the crystallization conditions enhanced the simultaneous formation of $\mathbf{1} \cdot 2H_2O$. A sample for crystallography was maintained in contact with mother liquor to prevent loss of interstitial solvent.

2.2. Physical measurements

2.2.1. X-ray crystallography

The intensity data of compounds $\mathbf{1} \cdot 2Et_2O$ and **2** were collected on a Bruker CCD diffractometer using graphite monochromated Mo Kα radiation ($\lambda = 0.71073$ Å). Crystals were transferred directly from the mother liquor to a protective oil, which was used to prevent solvent loss. The structures were solved using direct methods and refined using a full-matrix least squares procedure based on F^2 using all data [12]. Crystallographic data for $\mathbf{1} \cdot 2Et_2O$ and **2** are given in Table 1.

2.2.2. Magnetic measurements

Variable temperature magnetic measurements were performed on a Quantum Design MPMS-XL SQUID magnetometer equipped with a 5 T magnet. Data were collected on a randomly oriented polycrystalline sample of $\mathbf{1} \cdot Et_2O$ restrained in eicosane to prevent torquing. Diamagnetic corrections were made using Pascal's constants and a value of $\mu_{Dia} = -1.3 \times 10^{-8}$ emu/g for the sample and eicosane, respectively. DC susceptibility measurements were performed with measuring fields of 0.01, 0.1 and 3 T. AC susceptibility data were collected with an alternating field of 3×10^{-4} T and frequencies ranging between 10 and 10^3 Hz. Isothermal magnetization measurements were performed at 2, 3, 4, 5, 10 and 20 K in a field range of 0–5 T.

Table 1
Crystallographic data for $\mathbf{1} \cdot 2Et_2O$ and **2**

	$\mathbf{1} \cdot 2Et_2O$	**2**
Formula[a]	$C_{68}H_{100}N_4O_{34}Tb_4$	$C_7H_{13}O_7Tb$
Fw (g mol^{-1})	2153.2	369.09
Space group	$P\bar{1}$ (2)	$P2_1/c$(14)
a (Å)	10.5188(5)	11.9785(10)
b (Å)	13.3615(6)	11.9409(10)
c (Å)	15.4902(7)	7.6080(6)
α (°)	91.273(1)	90
β (°)	109.422(1)	90.424(2)
γ (°)	96.181(1)	90
V (Å^3)	2037.36(16)	1088.17(16)
Z	1	4
T (K)	130(1)	130(1)
ρ_{calc} (g cm^{-3})	1.755	2.247
μ (mm^{-1})	3.516	6.512
Reflections measured	12826	6713
Unique reflections	8893	2464
Observed data [$I > 2\sigma(I)$]	8210	2223
R_1[b]	0.0263	0.0272
wR_2[c]	0.0729	0.0517

[a] Including solvent molecules.
[b] $I > 2\sigma(I)$.
[c] F^2, all data.

2.2.3. Other measurements

Infrared spectra (KBr disk) were recorded on a Perkin–Elmer Spectrum One FTIR spectrometer. Elemental analyses were performed at the Ecole d'ingénieurs et architectes de Fribourg, Switzerland.

3. Results and discussion

3.1. Syntheses

The overnight treatment of $Tb(OAc)_3 \cdot nH_2O$ with a methanolic solution of 1–2 equiv. of H_4L affords a yellow solution and a white precipitate. Filtration followed by evaporation of the solvent produces a yellow oil, re-dissolution of the residue in a minimum amount of MeOH yields a mix of crystals of $\mathbf{1} \cdot 2Et_2O$ and **2** after two days. Subsequent filtration and layering of the filtrate with Et_2O affords plate shaped crystals of $\mathbf{1} \cdot 2Et_2O$ after three days in 25% yield. The reactions may be written as

$$4Tb(OAc)_3 \cdot nH_2O + 4H_4L \rightarrow [Tb_4(H_2L)_2(H_4L)_2(OAc)_8] + 4HOAc + 4nH_2O \quad (1)$$

$$Tb(OAc)_3 \cdot nH_2O + MeOH \rightarrow [Tb(OAc)_3MeOH] + nH_2O \quad (2)$$

The formation of **1** involves the protonation of acetate ligands in conjunction with double deprotonation and coordination of the H_4L ligand. This is commonly observed during the synthesis of polynuclear complexes. A likely driving force is the chelate effect attributed to the multidenticity of the ligand. The formation of **2** involves the substitution of H_2O ligands with MeOH as well as the change of the binding modes of the acetate ligands. The ligand H_4L is not incorporated in the structure.

3.2. Structure descriptions

Compound $\mathbf{1} \cdot 2Et_2O$ crystallizes in the triclinic space group $P\bar{1}$ with one molecule per unit cell, together with disordered solvent. The molecule has C_i point symmetry. A summary of interatomic distances and angles is given in Table 2. A complete list can be obtained from the authors. The structure of **1** in $\mathbf{1} \cdot 2Et_2O$ is shown in Fig. 1a.

Bond valence sum calculations [13] are in good agreement with the expected oxidation state of 3+ for the Tb ions in the cluster. The Tb centers are arranged in a planar rhomb (Fig. 1b), linked by four μ_3 alkoxide bridges from two Schiff-base ligands and four μ_2-O atoms from acetate ligands. The coordination sphere is completed by N-atoms from the central Schiff-base ligands, acetates and two additional Schiff-base ligands. The structure comprises two crystallographically distinct Tb^{III} sites, both with C_1 point symmetry. Two different binding modes can be observed for H_4L and H_2L^{2-} (Fig. 2). The central doubly deprotonated ligands bind in a $\eta^1{:}\eta^1{:}\eta^2{:}\eta^4{:}\mu_4$-fashion with four out of five potential binding sites complexing Tb. The peripheral H_4L ligands bind to Tb only via the phenol

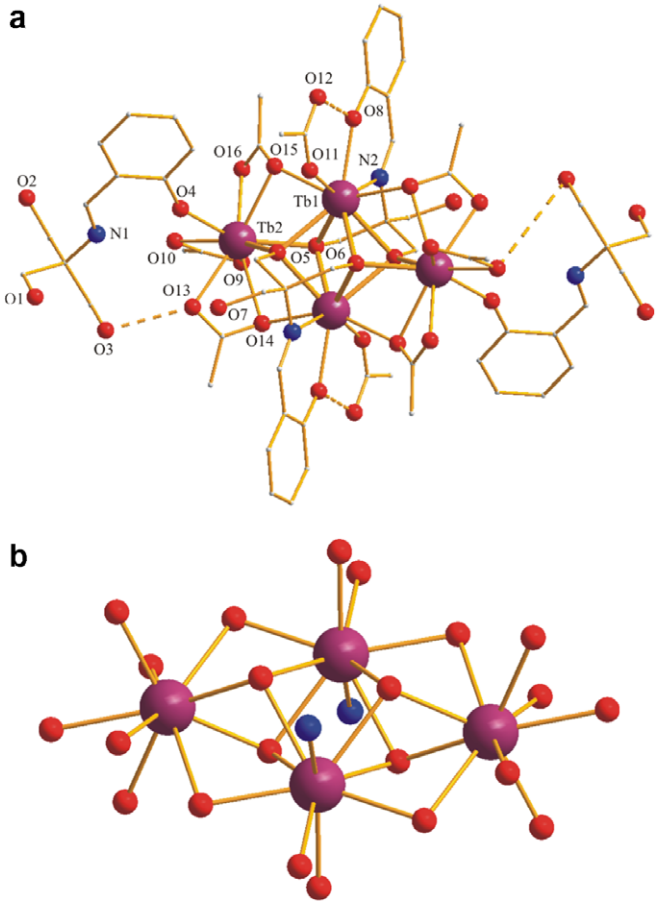


Fig. 1. (a) Ball and stick representation of complex **1** in $\mathbf{1} \cdot 2Et_2O$. Hydrogen atoms are omitted for clarity. (b) Coordination spheres of the Tb^{III} ions in $\mathbf{1} \cdot 2Et_2O$. Tb purple; O, red; N, blue; C, gray. (For interpretation of the references to color in this figure legend, the reader is referred to the web version of this article.)

Table 2
Selected bond distances (Å) and angles (deg) for $\mathbf{1} \cdot 2Et_2O$ and **2**

Parameter	$\mathbf{1} \cdot 2Et_2O$	**2**
Tb–Tb	3.3640(3)–3.7190(3)	4.0128(4)
Tb–O[a]	2.335(2)–2.590(2)	2.367(2)–2.480(2)
Tb1–O–Tb1	85.79(7)–86.95(7)	109.97(9)–113.30(9)
Tb1–O–Tb2	96.32(8)–102.24(8)	
O···O[b]	2.466(3)–2.709(4)	

[a] μ_3-O and μ_2-O atoms.
[b] Intramolecular hydrogen bonds.

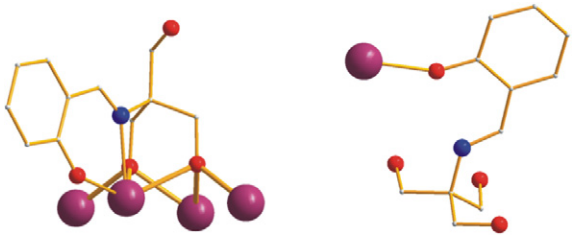


Fig. 2. Binding modes of H_2L^{2-} and H_4L in **1**: $\eta^1{:}\eta^1{:}\eta^2{:}\eta^4{:}\mu_4$ and η^1.

alcohol group. Two of the alcohol arms are linked by an intramolecular hydrogen bond and bind to an acetate group via a further intramolecular hydrogen bond (Table 2). Four of the acetates act as bridges between Tb ions in a $\eta^1{:}\eta^2{:}\mu_2$-fashion, two acetates act as η^2 chelates and two of the acetates bind as terminal ligands in *syn* η^1-fashion (Chart 2). An intramolecular hydrogen bond is formed between the latter and the phenol alcohol of a H_2L^{2-} ligand.

The Tb_4 plane of **1** lies perpendicular to the crystallographic *a*-axis. Adjacent clusters in the *a*-direction are linked by intermolecular hydrogen bonds between the remaining alcohol arm of H_2L^{2-} (O7) and one of the acetates (O16). In addition, one of the alcohol arms of H_4L (O2) is involved in hydrogen bonding with disordered solvent.

Several tetranuclear terbium complexes are reported in the literature [14], but the core structure of **1** is unique. Similar core topologies have been described for transition metal complexes, especially the so-called butterfly structures with a $[M_4O_2]$ core [6,15]. The rhombic arrangement of transition metal ions comprises only two μ_3 alkoxide bridges, as the metal ions are six-coordinate. Owing to the higher coordination number of rare earth ions (all Tb^{III} ions in **1** are nine-coordinate) additional bridging atoms are necessary to obtain the same butterfly type arrangement of the magnetic centers.

Compound **2** crystallizes in the monoclinic space group $P2_1/c$. It comprises Tb^{III} ions linked by acetate groups to form chains (Fig. 3). The ligand H_4L is not incorporated in the structure of **2** [13]. Bond valence sum calculations are consistent with the standard oxidation state of 3+ for Tb. The structure contains only one crystallographic Tb^{III} site with C_1 point symmetry. The asymmetric unit contains two chain fragments, each consisting of two Tb^{III} ions. The Tb^{III} centers are linked by three acetates, two bridging in

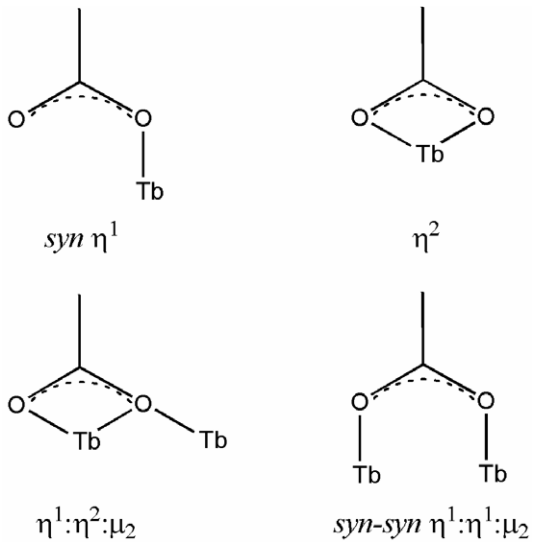


Chart 2. Binding modes of the acetate groups in complexes **1** and **2**.

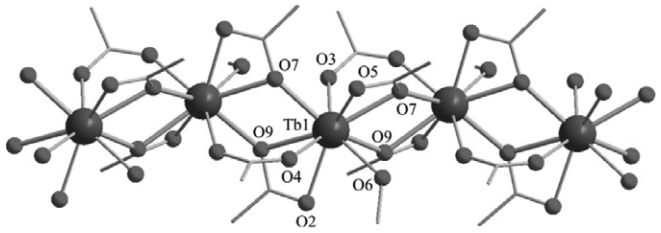


Fig. 3. Section of the chain structure of **2**, showing the coordination sphere of the Tb^{III} ions. Hydrogen atoms are omitted for clarity. Tb, purple; O, red; C, gray. (For interpretation of the references to color in this figure legend, the reader is referred to the web version of this article.)

$\eta^1{:}\eta^1{:}\mu_2$ fashion and one in a *syn–syn* $\eta^1{:}\eta^1{:}\mu_2$-arrangement. The remaining peripheral ligation is completed with a MeOH molecule. A summary of interatomic distances and angles is given in Table 2. It is worthwhile to compare the structure of **2** with the crystal structure of the starting material $Tb(OAc)_3 \cdot nH_2O$ [16], in which Tb^{III} dimers are linked by two acetates in $\eta^1{:}\eta^2{:}\mu_2$-fashion, while the other four acetates chelate a single Tb. The four remaining positions are occupied by H_2O. In **2**, the water molecules are replaced by two MeOH ligands, the free coordination sites are occupied by two $\eta^1{:}\eta^2{:}\mu_2$ bridges and there are two acetate links with a *syn–syn* $\eta^1{:}\eta^1{:}\mu_2$-mode instead of four chelating acetates.

The chains in **2** are parallel to the crystallographic *c*-axis of the monoclinic structure. They are well isolated from each other, no hydrogen bonding pathway can be observed. The shortest distance between Tb^{III} ions of different chains is 8.2 Å. A Tb chain similar to **2** has been reported in the literature, namely $[Tb(O_2CPh)_3(MeOH)_2(H_2O)]_\infty$ [17]. Interestingly, it was also obtained as a co-crystallized product from a reaction mixture containing other ligands. This complex incorporates benzoate, with binding modes different to those observed for acetate in **2**. The chains form hydrogen-bonded sheets. The fact that the chains in **2** are well isolated makes the structure unique.

3.3. Magnetic study of $1 \cdot Et_2O$

Variable temperature AC and DC susceptibility measurements were performed on a sample of randomly oriented crystals of $1 \cdot Et_2O$. The DC data measured at 0.1 T are plotted as χT versus T and χ versus T in Fig. 4. Between 300 and 100 K, χT stays nearly constant at the room temperature value of 44.4 emu mol^{-1} K. Upon further cooling, χT decreases first gradually and then steeply below 5 K. Isothermal magnetization data collected at six temperatures between 2 and 20 K are plotted in Fig. 5 as M versus H/T. The isotherms do not superimpose and the magnetization at 2 K does not completely saturate at the high-field limit of our instrument; it reaches a value $M = 19.3\ N\mu_B$ at 5 T.

Tb^{III} has a $4f^8$ electron configuration, and the ^7F ground term is split by spin–orbit coupling, leading to seven ^7F_J

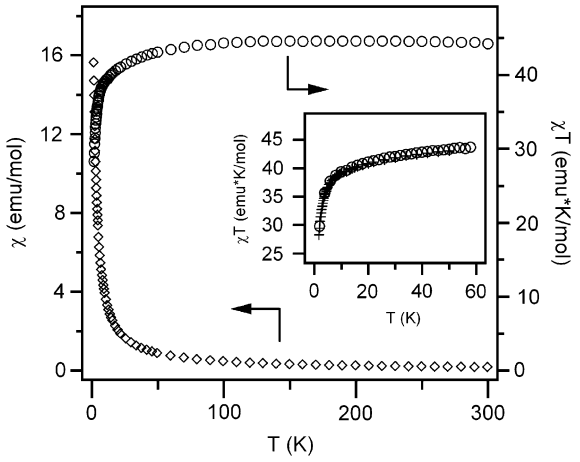


Fig. 4. χT vs. T and χ vs. T for $\mathbf{1}\cdot Et_2O$, measured in an applied field of 0.1 T. The inset shows the low temperature regime of χT vs. T for $\mathbf{1}\cdot Et_2O$. Plus signs correspond to DC measurements with a measuring fields of 0.1 T, circles denote data from an AC measurement with a field of 3×10^{-4} T oscillating with a frequency of 60 Hz.

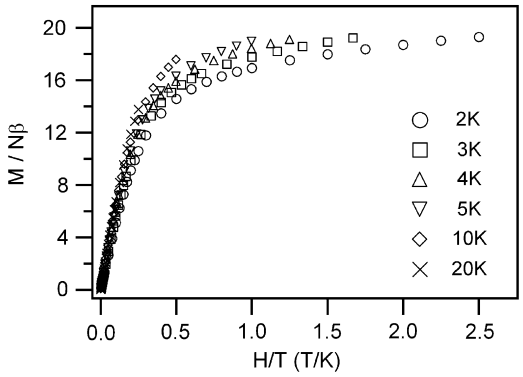


Fig. 5. Isothermal magnetization measurements on a sample of randomly oriented crystals of $\mathbf{1}\cdot Et_2O$, measured in a field range of 0–5 T at six temperatures between 2 and 20 K.

states. The ground state is $^7F_6$, which is separated by approximately 2000 cm^{-1} from the first excited $^7F_5$ state. $^7F_6$ is further split into a maximum of 13 sublevels by the low symmetry ligand field. The total splitting is expected to be of the order of 300–600 cm^{-1} [18]. A superposition of the splittings of the two crystallographically distinct Tb^{III} ions determines the magnetic properties of $\mathbf{1}\cdot Et_2O$. We restrict ourselves to a mainly qualitative discussion, as a more quantitative approach would be pointless in the absence of suitable information on the anisotropy of the magnetic properties of $\mathbf{1}\cdot Et_2O$.

The room temperature value of $\chi T = 44.4$ emu mol^{-1} K is lower than $\chi T = 47.3$ emu mol^{-1} K calculated for four uncoupled Tb^{III} ions in a free-ion approximation with an isolated and degenerate $^7F_6$ ground state and a Landé-factor $g_J = 3/2$ [19]. An almost identical room temperature value $\chi T = 44.3$ emu mol^{-1} K was measured for a Tb_4 cube [14a], as well as for a mononuclear Tb^{III} complex ($\chi T =$ 11.1 emu mol^{-1} K for one Tb^{III}) [20], both containing eight-coordinate Tb^{III} in a low symmetry ligand field. The reduction from the free-ion value indicates that all the crystal-field levels of $^7F_6$ are not equally populated at 300 K. Upon cooling below 100 K, higher crystal field levels are depopulated, leading to the observed decrease in χT. The same behavior was found in the above mentioned mononuclear and tetranuclear Tb^{III} compounds [14a,20]. The superposition of the χT versus T curves measured with $H = 0.1$ T and in AC mode with no applied DC field (inset of Fig. 4) indicates that the low temperature decrease in χT is not due to the effect of the applied field. In addition to the dominant ligand field effects, a contribution of antiferromagnetic exchange interactions to the magnetic susceptibility at the lowest temperatures cannot be excluded. These interactions are generally very small between rare earth ions, for example. $J = -0.040$ cm^{-1} was determined for a Tb^{III} dinuclear complex by inelastic neutron scattering [21]. The divergence of the isothermal magnetization curves in the M versus H/T plot (Fig. 5) indicates that more than one of the sublevels of $^7F_6$ are populated in the temperature range 2–20 K. The magnetization is not saturated at 5 T, but the absolute value $M = 19.3\ N\mu_B$ at 2 K and 5 T is much lower than the maximum value $M = 36\ N\mu_B$ for $^7F_6$ [19]. This suggests that the wavefunctions of the lowest energy substates are predominantly built up from basis functions with small M_J values. A further interpretation is difficult, especially because the measured properties are a superposition of the properties of the two distinguishable Tb^{III} ions in the cluster. Site selective low-temperature luminescence spectroscopy might be a way to disentangle the two contributions and determine the individual energy splittings.

Sensitized by the phthalocyanine rare earth sandwich SMMs [8], we performed AC magnetic measurements to look for slow relaxation of the magnetization in $\mathbf{1}\cdot Et_2O$. No out-of-phase signal was detected in the full temperature range down to 1.8 K. In the Tb^{III} sandwich complex reported by Ishikawa et al. the ligand field of the two phthalocyanines generates a fortunate situation with the two lowest substates separated by an energy gap of more than 400 cm^{-1} from the next excited substates [8]. In the exceptional case of the sandwich compound SMM behavior can be attributed to the quasi-axial symmetry of the ligand field. A considerable mixing of basis functions with different M_J values and a more complex energy level scheme are expected for Tb^{III} ions with C_1 point symmetry.

4. Conclusions

Complex **1** was successfully prepared by incorporating the proligand H_4L in two different binding modes in its neutral and double deprotonated state. The displayed chelating and bridging properties of this ligand make it an ideal candidate for the synthesis of spin clusters. In addition to **1**, compound **2** was also isolated from the reaction mixture, exhibiting a novel Tb-chain structure. Cluster **1** did not show SMM behavior. This is mainly attributed to

the low symmetry of the ligand field, as compared to the quasi-axial symmetry of the ligand field in the Tb^{III} sandwich complex [8]. In order to impose axial-type coordination of the rare earth centers it seems necessary to use more rigid ligands than H_4L.

Acknowledgement

This work was supported by the Swiss National Science Foundation and the Australian Research Council.

Appendix A. Supplementary material

CCDC 630776 and 630777 contain the supplementary crystallographic data for this paper. These data can be obtained free of charge via http://www.ccdc.cam.ac.uk/conts/retrieving.html, or from the Cambridge Crystallographic Data Centre, 12 Union Road, Cambridge CB2 1EZ, UK; fax: (+44) 1223-336-033; or e-mail: deposit@ccdc.cam.ac.uk. Supplementary data associated with this article can be found, in the online version, at doi:10.1016/j.poly.2007.02.003.

References

[1] (a) R. Sessoli, D. Gatteschi, A. Caneschi, M.A. Novak, Nature 365 (1993) 141;
(b) R. Sessoli, H.L. Tsai, A.R. Schake, S. Wang, J.B. Vincent, K. Folting, D. Gatteschi, G. Christou, D.N. Hendrickson, J. Am. Chem. Soc. 115 (1993) 1804;
(c) A. Caneschi, D. Gatteschi, R. Sessoli, A.L. Barra, L.C. Brunel, M. Guillot, J. Am. Chem. Soc. 113 (1991) 5873.

[2] K. Petukhov, S. Hill, N.E. Chakov, K.A. Abboud, G. Christou, Phys. Rev. B 70 (2004) 054426.

[3] T. Lis, Acta Cryst. B36 (1980) 2042.

[4] S.M.J. Aubin, N.R. Dilley, M.W. Wemple, M.B. Maple, G. Christou, D.N. Hendrickson, J. Am. Chem. Soc. 120 (1998) 839.

[5] (a) S.T. Ochsenbein, M. Murrie, E. Rusanov, H. Stoeckli-Evans, C. Sekine, H.U. Güdel, Inorg. Chem. 41 (2002) 5133;
(b) M. Murrie, S.J. Teat, H. Stoeckli-Evans, H.U. Güdel, Angew. Chem., Int. Ed. 42 (2003) 4653;
(c) E.-C. Yang, D.N. Hendrickson, W. Wernsdorfer, M. Nakano, L.N. Zakharov, R.D. Sommer, A.L. Rheingold, M. Ledezma-Gairaud, G. Christou, J. Appl. Phys. 91 (2002) 7382;
(d) J.C. Goodwin, R. Sessoli, D. Gatteschi, W. Wernsdorfer, A.K. Powell, S.L. Heath, Dalton Trans. (2000) 1835;
(e) A.L. Barra, P. Debrunner, D. Gatteschi, C.E. Schulz, R. Sessoli, Europhys. Lett. 35 (1996) 133;
(f) A.L. Barra, A. Caneschi, A. Cornia, F.F. de Biani, D. Gatteschi, C. Sangregorio, R. Sessoli, L. Sorace, J. Am. Chem. Soc. 121 (1999) 5302.

[6] S.L. Castro, Z. Sun, C.M. Grant, J.C. Bollinger, D.N. Hendrickson, G. Christou, J. Am. Chem. Soc. 120 (1998) 2365.

[7] (a) S. Osa, T. Kido, N. Matsumoto, N. Re, A. Pochaba, J. Mrozinski, J. Am. Chem. Soc. 126 (2004) 420;
(b) A. Mishra, W. Wernsdorfer, A. Abboud Khalil, G. Christou, J. Am. Chem. Soc. 126 (2004);
(c) C.M. Zaleski, E.C. Depperman, J.W. Kampf, M.L. Kirk, V.L. Pecoraro, Angew. Chem., Int. Ed. 43 (2004) 3912.

[8] (a) N. Ishikawa, M. Sugita, T. Ishikawa, S.-Y. Koshihara, Y. Kaizu, J. Am. Chem. Soc. 125 (2003) 8694;
(b) N. Ishikawa, M. Sugita, T. Ishikawa, S. Koshihara, Y. Kaizu, J. Phys. Chem. B 108 (2004) 11265;
(c) N. Ishikawa, M. Sugita, W. Wernsdorfer, Angew. Chem., Int. Ed. 44 (2005) 2931.

[9] (a) C. Boskovic, E. Rusanov, H. Stoeckli-Evans, H.U. Güdel, Inorg. Chem. Commun. 5 (2002) 881;
(b) C. Boskovic, R. Bircher, P.L.W. Tregenna-Piggott, H.U. Güdel, C. Paulsen, W. Wernsdorfer, A.-L. Barra, E. Khatsko, A. Neels, H. Stoeckli-Evans, J. Am. Chem. Soc. 125 (2003) 14046;
(c) C. Boskovic, A. Sieber, G. Chaboussant, H.U. Güdel, J. Ensling, W. Wernsdorfer, A. Neels, G. Labat, H. Stoeckli-Evans, S. Janssen, Inorg. Chem. 43 (2004) 5053;
(d) A. Sieber, C. Boskovic, R. Bircher, O. Waldmann, S.T. Ochsenbein, H.U. Güdel, N. Kirchner, J. van Slageren, W. Wernsdorfer, A. Neels, H. Stoeckli-Evans, S. Janssen, F. Juranyi, H. Mutka, Inorg. Chem. 44 (2005) 4315.

[10] (a) D.P. Kessissoglou, C.P. Raptopoulou, E.G. Bakalbassis, A. Terzis, J. Mrozinski, Inorg. Chem. 31 (1992) 4339;
(b) D.P. Kessissoglou, M.L. Kirk, M.S. Lah, X. Li, C. Raptopoulou, W.E. Hatfield, V.L. Pecoraro, Inorg. Chem. 31 (1992) 5424;
(c) M. Dey, C.P. Rao, P.K. Saarenketo, K. Rissanen, Inorg. Chem. Commun. 5 (2002) 924;
(d) M. Dey, C.P. Rao, P.K. Saarenketo, K. Rissanen, Inorg. Chem. Commun. 5 (2002) 380.

[11] M. Dey, C.P. Rao, P.K. Saarenketo, K. Rissanen, E. Kolehmainen, P. Guionneau, Polyhedron 22 (2003) 3515.

[12] G.M. Sheldrick, SHELX97 Programs for Crystal Structure Analysis. Institut für Anorganische Chemie der Universität Göttingen, Tammanstrasse 4, D-3400 Göttingen, Germany, 1998.

[13] A. Trzesowska, R. Kruszynski, T.J. Bartczak, Acta Cryst. B60 (2004) 174.

[14] (a) X.-M. Chen, Y.-L. Wu, Y.-X. Tong, Z. Sun, D.N. Hendrickson, Polyhedron 16 (1997) 4265;
(b) P. Thomas, J.C. Trombe, J. Chem. Cryst. 30 (2001) 633;
(c) A.W.H. Lam, W.T. Wong, G. Wen, X.X. Zhang, S. Gao, New J. Chem. 25 (2001) 531;
(d) U.P. Singh, S. Tyagi, C.L. Sharma, H. Goerner, T. Weyhermueller, Dalton Trans. 23 (2002) 4464.

[15] (a) J. Yoo, E.K. Brechin, A. Yamaguchi, M. Nakano, J.C. Huffman, A.L. Maniero, L.C. Brunel, K. Awaga, H. Ishimoto, G. Christou, D.N. Hendrickson, Inorg. Chem. 39 (2000) 3615;
(b) J.K. McCusker, J.B. Vincent, E.A. Schmitt, M.L. Mino, K. Shin, D.K. Coggin, P.M. Hagen, J.C. Huffman, G. Christou, D.N. Hendrickson, J. Am. Chem. Soc. 113 (1991) 3012.

[16] B. Barja, R. Baggio, M.T. Garland, P.F. Aramendia, O. Pena, M. Perec, Inorg. Chim. Acta 346 (2003) 187.

[17] C. Seward, N.-X. Hu, S. Wang, Dalton Trans. (2001) 134.

[18] (a) J.B. Gruber, B. Zandi, H.J. Lozykowski, W.M. Jadwisienczak, J. Appl. Phys. 92 (2002) 5127;
(b) T.R. Faulkner, J.P. Morley, F.S. Richardson, R.W. Schwartz, Mol. Phys. 40 (1980) 1481.

[19] O. Kahn, Molecular Magnetism, VCH Publishers., New York, 1993.

[20] A. Caneschi, A. Dei, D. Gatteschi, S. Poussereau, L. Sorace, Dalton Trans. (2004) 1048.

[21] A. Furrer, H.U. Güdel, H. Blank, A. Heidemann, Phys. Rev. Lett. 62 (1989) 210.

Available online at www.sciencedirect.com
ScienceDirect
Polyhedron 26 (2007) 3029–3036
POLYHEDRON
www.elsevier.com/locate/poly

Synthesis, characterization, DNA-binding and DNA-photocleavage studies of $[Ru(bpy)_2(BPIP)]^{2+}$ and $[Ru(phen)_2(BPIP)]^{2+}$ (BPIP = 2-(4′-biphenyl)imidazo[4,5-*f*][1,10]phenanthroline)

Li-Feng Tan [a,*], Hui Chao [b], Yang-Fan Zhou [a], Liang-Nian Ji [b,c]

[a] *College of Chemistry, Xiangtan University, Xiangtan 411105, PR China*
[b] *Department of Chemistry, Sun Yat-Sen University, Guangzhou 510275, PR China*
[c] *Department of Chemistry, Tongji University, Shanghai 200092, PR China*

Received 14 November 2006; accepted 4 February 2007
Available online 12 February 2007

Abstract

New ligand 2-(4′-biphenyl)imidazo[4,5-*f*][1,10]phenanthroline (BPIP) and its complexes $[Ru(bpy)_2(BPIP)]^{2+}$ (**1**) (bpy = 2,2′-bipyridine) and $[Ru(phen)_2(BPIP)]^{2+}$ (**2**) (phen = 1,10-phenanthroline) have been synthesized and characterized by mass spectroscopy, ^1H NMR and cyclic voltammetry. The interaction of two Ru(II) complexes with calf thymus DNA (CT-DNA) was investigated by spectroscopic and viscosity measurements. Results indicate that both complexes bind to DNA via an intercalative mode and the DNA-binding affinity of complex **2** is much greater than that of complex **1**. Furthermore, when irradiated at 365 nm, both complexes have also been found to promote the photocleavage of plasmid pBR 322 DNA.
© 2007 Elsevier Ltd. All rights reserved.

Keywords: Ruthenium(II) complex; Polypyridyl ligand; DNA-binding; Photocleavage

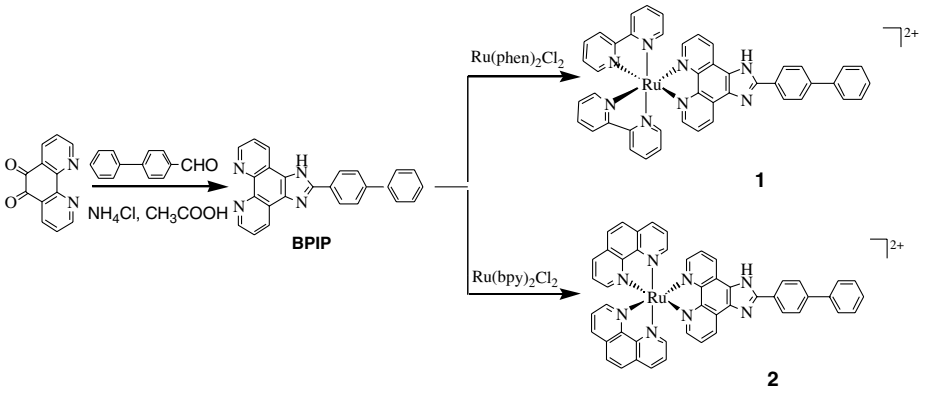
1. Introduction

During the past decades, metal complexes have been the subjects of tremendous research interest owing to the interactions of complexes with nucleic acids [1–3]. In particular, ruthenium(II) complexes with polypyridine ligands, due to a combination of easily constructed rigid chiral structures spanning all three spatial dimensions and a rich photophysical repertoire, have attracted considerable attention [1,4–10]. However, it is noticed that the investigations of intercalative ligand size has been very limited [11–18]. In fact, molecular shape contributes to stabilizing the metal complex on the DNA helix is one of the most significant factors [19]. Some of these complexes also exhibit interesting properties upon binding to DNA [20,21]. Varying substitutive group or substituent position in the intercalative ligand can create some interesting differences in the space configuration and the electron density distribution of Ru(II) polypyridyl complexes, which will result in some differences in spectral properties and the DNA-binding behaviors of the complexes, and will be helpful to more clearly understand the binding mechanism of Ru(II) polypyridyl complexes to DNA. Therefore, further studies using different structural ligands to evaluate and understand the factors that determine the DNA-binding mode are necessary.

We recently reported $[Ru(phen)_2(NMIP)]^{2+}$ (NMIP = 2′-(2″-nitro-3″,4″-methylene-dioxyphenyl)imidazo[4′,5′-*f*]-[1,10]-phenanthroline) [20] bind to DNA via partial intercalative mode. Furthermore, irradiation at 456 nm, complex $[Ru(phen)_2(NMIP)]^{2+}$ is efficient photocleavers of the plasmid pBR 322 DNA. Based on this, a novel ligand 2-(4′-bphenyl)imidazo[4,5-*f*][1,10]phenanthroline (BPIP, Scheme 1) has been prepared by condensation of 1,10-phenanthroline-5,6-dione and 4-biphenylcarbaldehyde to spread the planarity of phenanthroline. In this paper, we report the synthesis and characterization for the two

* Corresponding author. Fax: +86 732 8293997.
E-mail address: lfwyxh@yahoo.com.cn (L.-F. Tan).

0277-5387/$ - see front matter © 2007 Elsevier Ltd. All rights reserved.
doi:10.1016/j.poly.2007.02.001



Scheme 1. Synthetic routes for the preparation of the BPIP ligand and Ru(II) complexes **1** and **2**.

ruthenium(II) complexes $[Ru(bpy)_2(BPIP)]^{2+}$ (bpy = 2,2′-bipyridine) (**1**) and $[Ru(phen)_2(BPIP)]^{2+}$ (phen = 1,10-phenanthroline) (**2**), and also explore the interactions of the complexes with DNA and DNA cleavage assay.

2. Experimental

2.1. Materials

All the experiments involving interaction of the complex with DNA were conducted in twice distilled buffer containing tris(hydroxymethyl)-aminomethane (Tris, 5 mM) and NaCl (50 mM) and adjusted to pH 7.2 with hydrochloric acid. A solution of calf thymus DNA in the buffer gave a ratio of UV absorbance at 260 and 280 nm of about 1.8–1.9:1, indicating that the DNA was sufficiently free of protein [22]. The DNA concentration per nucleotide was determined by absorption spectroscopy using the molar absorption coefficient (6600 $M^{-1}\,cm^{-1}$) at 260 nm [23].

2.2. Synthesis

The compounds 1,10-phenanthroline-5,6-dione [24], *cis*-$[Ru(bpy)_2Cl_2]\cdot 2H_2O$ [25] and *cis*-$[Ru(phen)_2Cl_2]\cdot 2H_2O$ [25] were synthesized according to the literature methods.

2.2.1. 2-(4′-biphenyl)imidazo[4,5-f][1,10]phenanthroline (BPIP)

A mixture of 4-biphenylcarbaldehyde (0.275 g, 1.5 mmol), 1,10-phenanthroline-5,6-dione (0.105 g, 1.5 mmol), ammoniumacetate (2.31 g, 30 mmol) and glacial acetic acid (15 mL) was refluxed with stirring at 130 °C for 2 hours. The cooled solution was filtered, diluted with water (ca, 20 mL) and neutralized with concentrated aqueous ammonia. The orange precipitate was collected and purified by column chromatography on alumina with ethanol-toluene (14:1 v/v) as eluent to give the title compound as amorphous yellow solid. Yield, 0.46 g, 87%. *Anal.* Calc. for $C_{20}H_{14}N_4O_3$: C, 73.88; H, 4.46; N, 13.78. Found: C, 73.67; H, 4.54; N, 13.69%. FAB-MS: *m/z* 373.4 [M+1].

2.2.2. $[Ru(bpy)_2(BPIP)](ClO_4)_2\cdot 2H_2O$ (1)

A mixture of *cis*-$[Ru(bpy)_2Cl_2]\cdot 2H_2O$ (0.13 g, 0.25 mmol, BPIP (0.093 g, 0.25 mmol) and ethylene glycol (15 mL) was thoroughly deoxygenated. The purple mixture was heated for 8 h at 120 °C under argon. When the solution finally turned brown, it was cooled to room temperature and equal volume of saturated aqueous sodium perchlorate solution was added under vigorous stirring. The brownish solid was collected and washed with small amounts of water, ethanol and diethyl ether, then dried in 50 °C. Purification by chromatography on a neutral alumina column was performed with a mixture of acetonitrile and methylbenze (v/v, 1:1) as eluent. Yield: 0.21 g, 81%. *Anal.* Calc. for $C_{45}H_{35}Cl_2N_8O_{10}Ru$: C, 53.00; H, 3.46; N, 10.99. Found: C, 52.84; H, 3.61; N, 10.83%. UV λ_{max}/nm ($\varepsilon/M^{-1}\,cm^{-1}$, CH_3CN): 458 (20215), 289 (77540), 240 (36410). ^1H NMR (400 MHz, ppm, d_6-DMSO): δ 9.00 (d, 2H, $J = 8.5$), 8.86 (d, 2H, $J = 8.5$), 8.82 (d, 2H, $J = 8$), 8.65 (d, 2H, $J = 2$), 8.20 (t, 2H), 8.09 (t, 2H), 7.87 (t, 4H), 7.85–7.52(m, 8H), 7.59 (dd, 2H, $J_1 = 6.5$, $J_2 = 6$), 7.50 (t, 4H), 7.33 (s, 1H), 7.35–7.41 (m, 1H). ES–MS (CH_3CN): *m/z* 886.0 ($[M-ClO_4]^+$), 785.3 ($[M-2ClO_4-H^+]^+$), 393.3 ($[M-2ClO_4]^{2+}$).

2.2.3. $[Ru(phen)_2(BPIP)](ClO_4)_2\cdot 2H_2O$ (2)

This red complex was synthesized in a manner identical to that described for complex **1**, with *cis*-$[Ru(phen)_2Cl_2]\cdot 2H_2O$ (0.15 g, 0.25 mmol) in place of *cis*-$[Ru(bpy)_2Cl_2]\cdot 2H_2O$. Yield: 0.22 g, 87%. *Anal.* Calc. for $C_{49}H_{35}Cl_2N_8O_{10}Ru$: C, 55.11; H, 3.30; N, 10.49. Found: C, 54.97; H, 3.48; N, 10.32%. UV λ_{max}/nm ($\varepsilon/M^{-1}\,cm^{-1}$, CH_3CN): 456 (23145), 290 (60925), 263 (68375). ^1H NMR (400 MHz, ppm, d_6-DMSO): δ 9.08 (d, 2H, $J = 8$), 8.77 (d, 4H, $J = 8$), 8.44 (d, 2H, $J = 6$), 8.39 (s, 4H,), 8.13 (d, 2H, $J = 6.5$), 8.09 (d, 2H, $J = 6$), 7.95 (dd, 2H, $J_1 = 4.5$, $J_2 = 8.5$), 7.81–7.76 (m, 7H), 7.82 (d, 1H, $J = 1.5$), 7.75 (dd, 2H), 7.58 (t, 4H), 7.53 (t, 4H), 7.43 (t, 1H). ES–MS (CH_3CN): *m/z* 933.00 ($[M-ClO_4]^+$), 833.33 ($[M-2ClO_4-H+]^+$), 417.40 ($[M-2ClO_4]^{2+}$).

2.3. Physical measurements

Microanalyses (C, H and N) were carried out on a Perkin–Elmer 240Q elemental analyzer. UV–Vis (UV–visible) spectra were recorded on a Perkin–Elmer Lambda-25 spectrophotometer and emission spectra were recorded on a Perkin–Elmer LS-55 luminescence spectrometer at room temperature. Fast atom bombardment (FAB) mass spectra were recorded on a VG ZAB-HS spectrometer in a 3-nitrobenzyl alcohol matrix. Electrospray mass spectra (ES–MS) were recorded on a LQC system (Finngan MAT, USA) using CH_3CN as mobile phase. ^1H NMR spectra were recorded on a Avance-400 spectrometer with d_6-DMSO (dimethyl sulfoxide) as solvent at room temperature and TMS (tetramethylsilane) as the internal standard. Circular dichroism (CD) spectra were measured on a JASCO-J810 spectropolarimeter. Cyclic voltammetric measurements were performed on a CHI 660A Electrochemical Workstation. All samples were purged with nitrogen prior to measurements. A standard three-electrode system comprising of platinum microcylinder working electrode, platinum-wire auxiliary electrode and a saturated calomel reference electrode (SCE) was used.

2.4. DNA-binding and cleavage experiments

Viscosity experiments were carried out using an Ubbelodhe viscometer maintained at a constant temperature at 30.0 ± 0.1 °C in a thermostatic water-bath. Calf thymus DNA samples approximately 200 base pairs in average length were prepared by sonicating in order to minimize complexities arising from DNA flexibility [26]. Flow time was measured with a digital stopwatch, and each sample was measured three times, and an average flow time was calculated. Data were presented as $(\eta/\eta_0)^{1/3}$ versus binding ratio [27], where η is the viscosity of CT DNA in the presence of complex, and η_0 is the viscosity of CT DNA alone.

Equilibrium dialyses were conducted at ambient temperature with 10 cm^3 of CT-DNA (1.0 mM) sealed in a dialysis bag and 10 cm^3 of the complex (50 μM) outside the bag with the solution stirring for 38 h. The dialysis membrane was purchased from Union Carbide Co. and treated by means of the general procedure before use.

For the gel electrophoresis experiments, supercoiled pBR 322 DNA (0.1 μg) was treated with Ru(II) complexes in 50 mM Tris–acetate, 18 mM NaCl buffer, pH = 7.2, and the solutions were incubated for 1 h in the dark, then irradiated at room temperature with a UV lamp (365 nm, 10 W). The samples were analyzed by electrophoresis for 30 min at 75 V in Tris–acetate buffer containing 1% agarose gel. The gel was stained with 1 $\mu g/mL^{-1}$ ethidium bromid and then photographed under UV light.

3. Results and discussion

3.1. Synthesis and characterization

An outline of the synthesis of the ligand and Ru(II) complexes is presented in Scheme 1. The ligand BPIP was synthesized on the basis of the method for imidazole ring preparation established by Steck et al. [28]. Ru(II) complexes were prepared by direct reaction of the ligand BPIP with the appropriate mole ratios of the precursor complexes *cis*-$Ru(bpy)_2Cl_2$or *cis*-$Ru(phen)_2Cl_2$ in ethylene glycol in relative high yield, respectively. The yields were good to moderate in each case. The desired ruthenium(II) complexes were isolated as the perchlorates and purified by column chromatography. In the ES–MS spectra for the complex, the signals $[M–ClO_4^-]^+$, $[M–2ClO_4^-–H^+]^+$ and $[M–2ClO_4^-]^{2+}$ were observed. The measured molecular weights were consistent with expected values.

The Ru(II) complexes **1** and **2** give well-defined ^1H NMR spectra (Fig. 1), which permit unambiguous identification and assessment of purity. The proton chemical shifts are assigned with the aid of ^1H–^1H COSY experiments and comparison with those of similar compounds [16,20]. Due to the shielding influences of the adjacent BPIP and bpy (or phen), the bpy (or phen) protons of complexes exhibit two distinct sets of signals. In addition, the proton resonance on the nitrogen atom of the BPIP imidazole ring was not observed, because the proton is active and exchanges quickly between the two nitrogens of the imidazole ring. A similar example has been reported previously [16].

The absorption spectra of the complexes are shown in Table 1 and characterized by intense π–π* ligand transitions in the UV and metal-to-ligand charge transfer (MLCT) transition in the visible region. The broad MLCT absorption bands appear at 458 and 456 nm for complexes **1** and **2**, respectively. These bands are bathochromically shifted by comparison with that of $[Ru(bpy)_3]^{2+}$ (452 nm) [29], in accord with the extension of the corresponding π framework. The peak below 320 nm is assigned to the internal π–π* transition of the ligands.

The electrochemical behaviors of the two complexes have been determined in acetonitrile. Each complex exhibits one oxidation and three reduction waves in the sweep range from −2.0 to +2.0 V (Table 1). The electrochemical behavior of the Ru(Π) polypyridyl complex has been rationalized in terms of a metal-based oxidation and a series of reductions which are ligand-based occurring in a stepwise manner for each π* system [30]. As expected, the oxidation potentials of complexes **1** and **2** are more positive than that of $[Ru(bpy)_3]^{2+}$ in according with the extension of the corresponding π framework. With reference to previous studies on similar systems [16,20,31–33], the first reduction, which is usually controlled by the ligand having the most lowest unoccupied molecular orbital (LUMO), is assigned to a reduction centered on

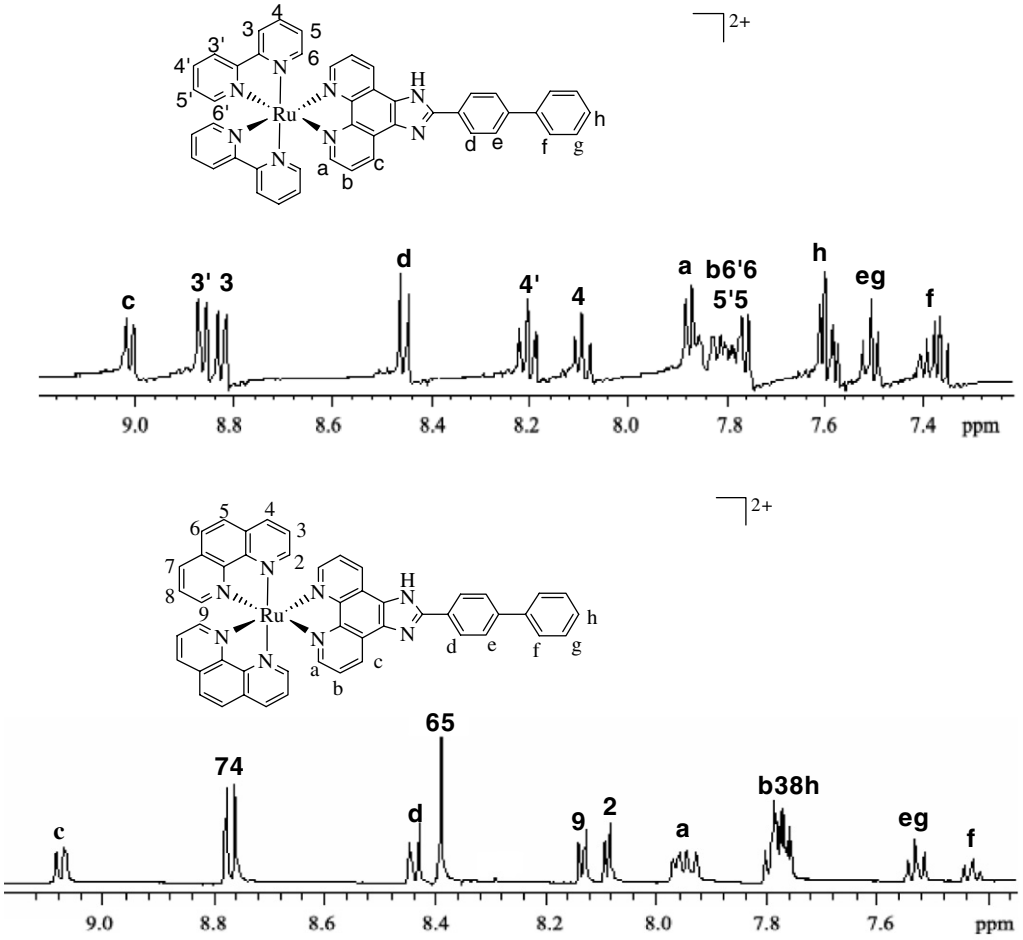


Fig. 1. ^{1}H NMR aromatic region of complex **1** (top) and complex **2** (bottom) in $(CD_3)SO$ (400 MHz).

Table 1
Electrochemical and absorption data of the ruthenium(II) complexes

Complex	$E_{1/2}$/V vs SCE[a]				λ_{max}/nm[b] (ε/dm^3 mol^{-1} cm^{-1})
	$Ru^{II/III}$	Ligand reduction			
1	1.32	−0.91	−1.42	−1.59	459 (12200), 288 (57700)
2	1.33	−0.85	−1.43	−1.60	462 (16700), 287 (76200)

[a] All complexes were measured in 0.1 M NBu_4ClO_4–CH_3CN, error in potentials was ±0.02 V; $T = 23 \pm 1$ °C; scan rate = 100 mV S^{-1}.
[b] In CH_3CN.

BPIP and the last reductions are characteristic of the co-ligand (bpy or phen).

3.2. Electronic absorption titration

The application of electronic absorption spectroscopy in DNA-binding studies is one of the most useful techniques [34]. Complex binding with DNA through intercalation usually result in hypochromism and bathchromism, due to the intercalative mode involving a strong stacking interaction between an aromatic chrommphore and the base pairs of DNA. The extent of the hypochromism commonly parallels the intercalative binding strength. The absorption spectra of complexes **1** and **2** in the absence and presence of CT-DNA (at a constant concentration of complexes, [Ru] = 20 μM) are given in Fig. 2. As the concentration of DNA is increased, for complex **1**, the hypochromism in the MLCT band reaches as high as 39.4% at 467 nm with a red shift of 7 nm at a ratio of [DNA]/[Ru] of 32.4. For complex **2**, upon addition of DNA, the MLCT band at 465 nm exhibits hypochromism of about 30.6% with a 6 nm red shift at a ratio of [DNA]/[Ru] of 24.3. These spectral characteristics suggest that there are some interactions between the complexes and DNA.

In order to compare quantitatively the binding strength of the two complexes, the intrinsic binding constants K_b of the two complexes with DNA were obtained by monitoring the changes in absorbance at 467 nm for complex **1** and

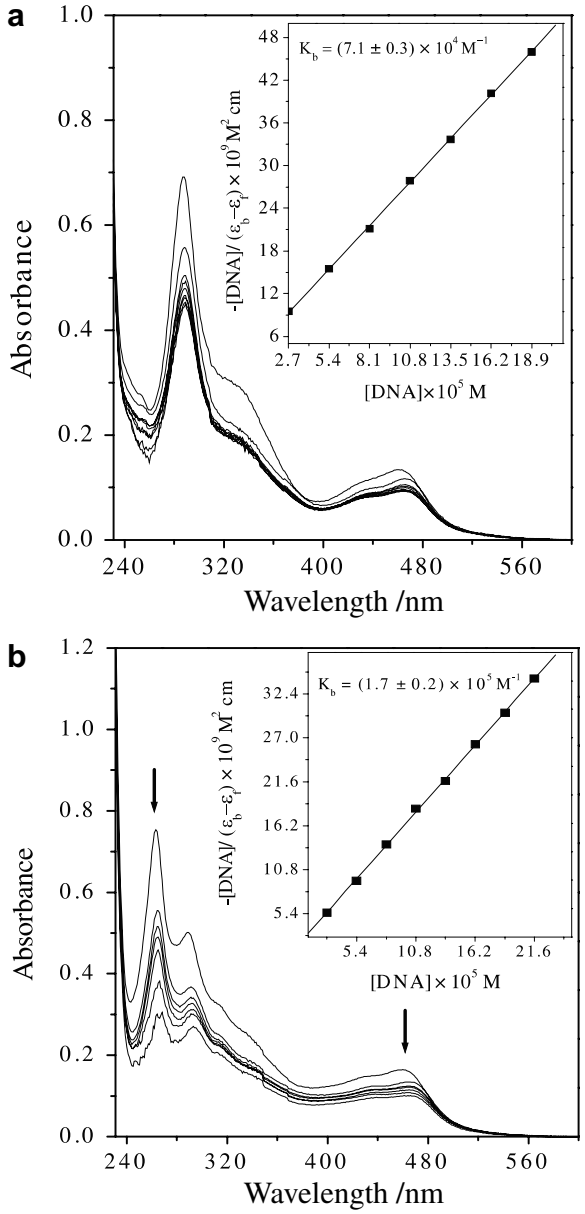


Fig. 2. Absorption spectra of complex **1** (a) and **2** (b) in Tris–HCl buffer upon addition of CT DNA. [Ru] = 20 μM, [DNA] = 0-216 μM. Arrow shows the absorbance changing upon the increase of DNA concentration. Plots of [DNA]/($\varepsilon_a - \varepsilon_b$) vs. [DNA] for the titration of DNA with Ru(II) complexes.

465 nm for complex **2** with increasing concentration of DNA using the following equation [35]:

$$[DNA]/(\varepsilon_a - \varepsilon_f) = [DNA]/(\varepsilon_b - \varepsilon_f) + 1/[K_b(\varepsilon_b - \varepsilon_f)]$$

where [DNA] is the concentration of DNA in base pairs, the apparent absorption coefficient ε_a, ε_f and ε_b correspond to A_{obsd}/ [Ru], the extinction coefficient for the free ruthenium complex and the extinction coefficient for the ruthenium complex in the fully bound form, respectively. In plots of [DNA]/(ε_a–ε_f) versus [DNA], K_b is given by the ratio of slope to the intercept. The intrinsic binding constants K_b of complexes **1** and **2** were $(1.70 \pm 0.2) \times 10^5\ M^{-1}$ and $(7.03 \pm 0.3) \times 10^4\ M^{-1}$, respectively. The values are bigger than that of those so-called DNA-intercalative Ru(II) complexes (1.1×10^4–$4.8 \times 10^4\ M^{-1}$) [21,36], but smaller than that observed for $[Ru(bpy)_2(dppz)]^{2+}$ (>10^6) [8]. The different DNA-binding properties of complexes **1** and **2** are due to the ancillary ligand. On going from bpy to phen, the plane area and hydrophobicity increase, leading to a greater DNA-binding affinity for complex **2**.

3.3. Steady-state emission studies

In the absence of DNA, complexes **1** and **2** can emit luminescence in Tris buffer at ambient temperature, with a maximum appearing at 599 and 591 nm, respectively. Upon addition of CT DNA, the emission intensities of complexes **1** and **2** increase to around 1.97 and 2.59 times larger than the original, respectively (Fig. 3). This implies

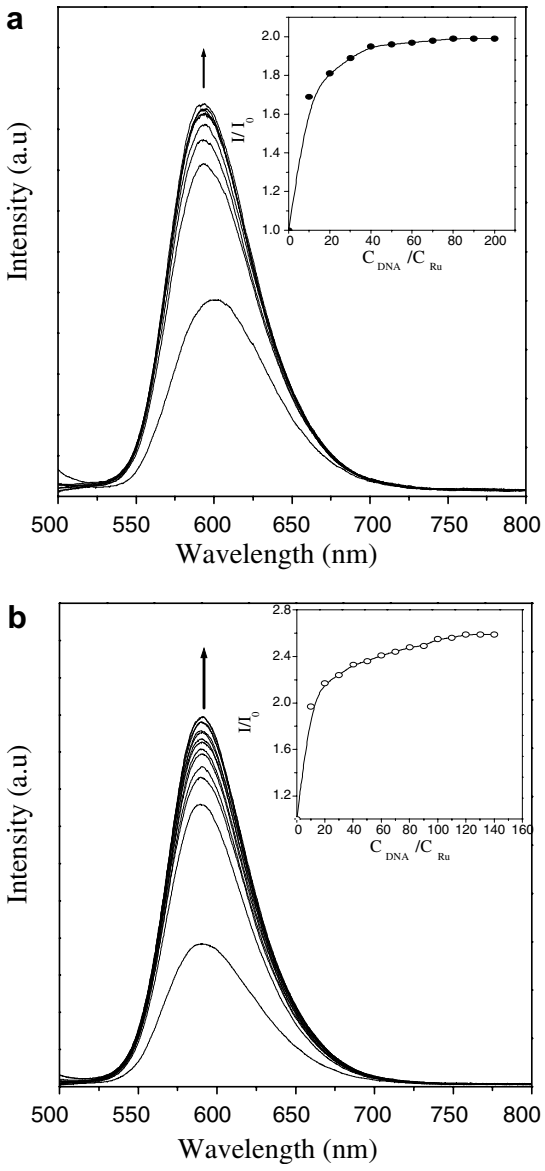


Fig. 3. Emission spectra of complex **1** (a) and **2** (b) in Tris–HCl buffer in the absence and presence of CT DNA. Arrow shows the intensity change upon increasing DNA concentrations.

that both complexes can interact with DNA and be protected by DNA. Compared **1** with **2**, complex **2** can be protected by DNA more effectively, which due to the stronger binding affinity of it with DNA.

Steady-state emission quenching experiments using $[Fe(CN)_6]^{4-}$ as quencher may provide further information about the binding of complexes with DNA. As illustrated in Fig. 4, in the absence of DNA, the emission of complexes **1** and **2** was efficiently quenched by $[Fe(CN)_6]^{4-}$ and the plots are not linear which imply that the quenching process is both dynamic and static [37]. However, in the presence of DNA, the Stern–Volmer plots are changed drastically (slopes 0.37 and 0.30, respectively), and the emission intensity was hardly affected by the addition of anionic quencher. This may be explained by repulsion of the highly negative $[Fe(CN)_6]^{4-}$ from the DNA polyanion backbone which hinders access of $[Fe(CN)_6]^{4-}$ to the DNA-bound complexes [38]. The plots for the DNA-bound complexes become linear, indicative of only dynamic quenching, which is consistent with the strong DNA-binding affinity of complexes **1** and **2** hence the complex is difficult to form between the two ruthenium(II) complexes and ferrocyanide. The curvature reflects different degrees of protection or relative accessibility of bound cations, a larger slope for the Stern–Volmer curve parallels poorer protection and low binding. From the results, complex **2** binds to DNA more strongly than does complex **1.**

3.4. Viscosity measurements

To further clarify the nature of the interaction between the complexes and DNA, viscosity measurements were carried out. Optical photophysical probes provide necessary, but not sufficient, evidence to support the binding model of Ru(II) complexes with DNA. Hydrodynamic measurements that are sensitive to length change (i.e. viscosity and sedimentation) are regarded as the least ambiguous and the most critical tests of a binding model in solution in the absence of crystallographic structural data [39,40]. A classical intercalation model demands that the DNA helix must lengthen as base pairs are separate [39,40]. The effects of complexes **1** and **2**, together with $[Ru(bpy)_3]^{3+}$ and ethidium bromide (EB) on the viscosity of rod-like DNA were shown in Fig. 5. As expected, EB

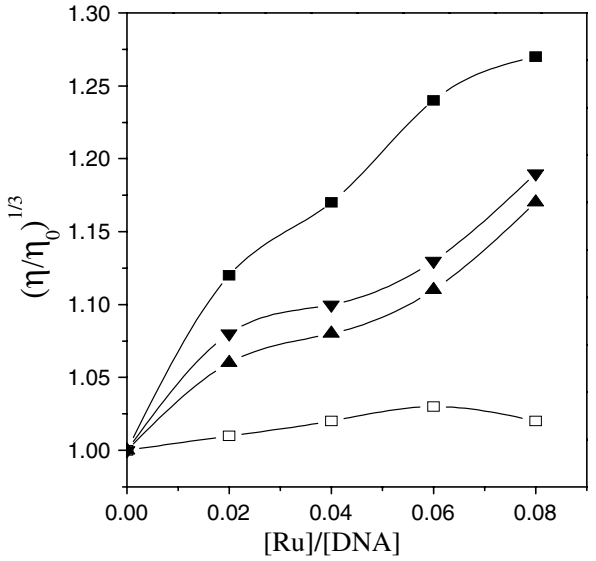


Fig. 5. Effect of increasing amounts of ethidium bromide (■), $[Ru(bpy)_3]^{2+}$ (□), complex **1** (▲) and complex **2** (▼) on the relative viscosity of calf thymus DNA at 30 (±0.1) °C. The total concentration of DNA is 0.5 mM.

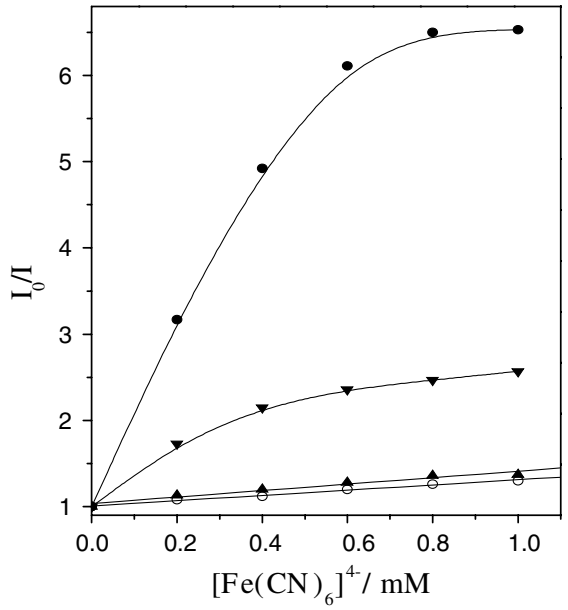


Fig. 4. Emission quenching with $[Fe(CN)_6]^{4-}$ for free (▼) or DNA-bound (▲) complex **1** and free (●) or DNA-bound (○) complex **2** ([Ru] = 2 μmol dm^{-3}, [DNA]/[Ru] = 40).

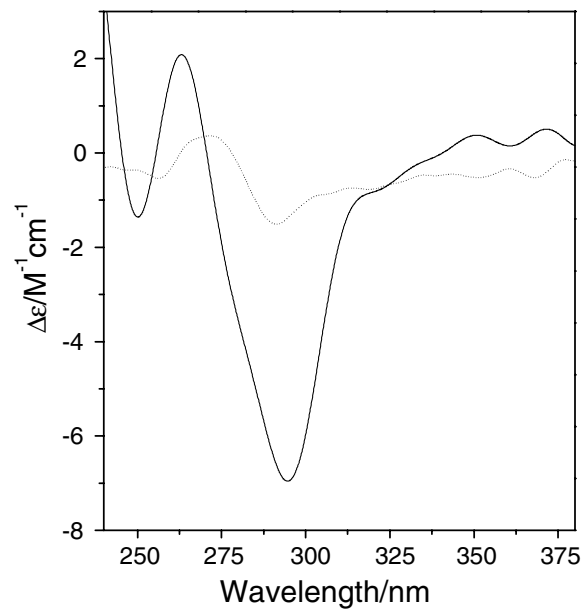


Fig. 6. Circular dichroism spectra of the dialyzate of complex **1** (dash line) and **2** (solid line) after 38 h dialysis against CT DNA with the solution stirred.

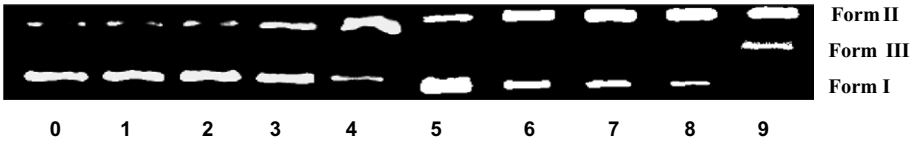


Fig. 7. Photoactivated cleavage of pBR 322 DNA in the presence of Ru(II) complexes, light after 60 min irradiation at 365 nm. Lane 0 and Lane 5, DNA alone; Lanes 1–4, in the different concentrations of complex **1**: (1) 20; (2) 40; (3) 60; (4) 80 μM; Lanes 6–9, in the different concentrations of complex **2**: (6) 20; (7) 40; (8) 60; (9) 80 μM.

increase the relative specific viscosity for the lengthening of the DNA double helix resulting from intercalation. While for complex $[Ru(bpy)_3]^{2+}$, which has been known to bind with DNA in electrostatic mode, it exerts essentially no effect on DNA viscosity. On increasing the amounts of **1** and **2**, the relative viscosity of DNA increasing steadily, which is similar to the behavior of the ethidium bromide. The results suggest that complex **1** and **2** intercalates between the base pair of DNA, which are consistent with our foregoing hypothesis.

3.5. Enantioselective binding

Equilibrium dialysis experiments may offer the opportunity to examine the enantioselectivity of complexes binding to DNA. According to the proposed binding model [41,42], the Δ enantiomer of the complex, a right-handed propeller-like structure, will display a greater affinity than the *Λ* enantiomer with the right-handed calf thymus DNA helix, due to the appropriate steric matching. The CD spectra in the UV region of complexes **1** and **2** after their racemic solution have been dialyzed against CT DNA are shown in Fig. 6. The dialysate for complexes **1** and **2** show two CD signals with a positive peak at 271 and 263 nm, and a negative peak at 291 and 295 nm, respectively. Although both complexes have not been resolved into their pure enantiomers, and we cannot determine which enantiomer binds DNA enantioselectively for both complexes, it is certain that complexes **1** and **2** interact with CT DNA enantioselectively. The stronger CD signals of complex **2** suggest the large difference between interactions of its two isomers with DNA.

3.6. Photoactivated cleavage of pBR 322 DNA by Ru(II) complexes

There is substantial and continuing interest in DNA endonucleolytic cleavage reactions that are activated by metal ions [43,44]. The cleavage reaction on plasmid DNA can be monitored by agarose gel electrophoresis. When circular plasmid DNA is subject to electrophoresis, relatively fast migration will be observed for the intact supercoil form (Form I). If scission occurs on one strand (nicking), the supercoil will relax to generate a slower-moving open circular form (Form II). If both strands are cleaved, a linear form (Form III) that migrates between Form I and Form II will be generated [45]. Fig. 7 shows gel electrophoresis separation of pBR 322 DNA after incubation with two Ru(II) complexes and irradiation at 365 nm. No DNA cleavage was observed for controls in which complex was absent (lane 0, 5). With increasing concentration of the Ru(II) complexes (lanes 1–4, 6–9), the amount of Form I of pBR322 DNA diminish gradually, whereas Form II increases and Form III is also produced (lane 9). Under comparable experimental conditions, complex **2** exhibits more effective DNA cleavage activity than complex **1**. This may be related to the molecular structure of these complexes, which has been testified in other cases [14,18]. Although DNA photocleavage by $[Ru(phen)_3]Cl_2$ has been reported to involve an $^1O_2$-based mechanism [43,46], the nature of reactive intermediates involved in the efficient DNA photocleavage by complexes **1** and **2** observed here is not clear. Further studies in detail are currently underway to clarify the cleavage mechanism.

4. Conclusions

Two new ruthenium(II) complexes of $[Ru(bpy)_2BPIP]^{2+}$ and $[Ru(phen)_2BPIP]^{2+}$ have been synthesized and characterized. Their DNA-binding and photocleavage properties were also investigated. Spectroscopic studies and viscosity experiments supported that the two complexes can intercalate into DNA base pairs via BPIP ligand. When irradiated at 365 nm, two Ru(II) complexes are efficient photocleavers of the plasmid pBR 322 DNA.

Acknowledgements

The authors thank the Provincial Natural Science Found of Hunan (06JJ5023), the Scientific Research Found of Hunan Provincial Education Department (06C828) and the Doctoral Foundation of Xiangtan University (05QDZ11) for their support of this research.

References

[1] A. Sigel, H. Sigel (Eds.), Metal Ions in Biological Systems, vol. 33, Marcel Dekker, New York, 1996.
[2] A.M. Pyle, J.K. Barton, in: S.J. Lippard (Ed.), Progress in Inorganic Chemistry, vol. 38, New York, 1990.
[3] D.S. Sigman, A. Mazumder, D.M. Perrin, Chem. Rev. 93 (1993) 2295.
[4] P.J. Dandliker, R.E. Holmlin, J.K. Barton, Science 275 (1997) 1465.
[5] W.J. Mei, J. Liu, K.C. Zheng, L.J. Lin, H. Chao, A.X. Li, F.C. Yun, L.N. Ji, J. Chem. Soc., Dalton Trans. (2003) 352.
[6] I. Ortmans, C. Moucheron, A. Kirsch-De Mesmaeker, Coord. Chem. Rev. 168 (1998) 233.

[7] Y. Xiong, L.-N. Ji, Coord. Chem. Rev. 185–186 (1999) 711.
[8] A.E. Friedman, J.C. Chambron, J.P. Sauvage, N.J. Turro, J.K. Barton, J. Am. Chem. Soc. 112 (1990) 4960.
[9] D. Lawrence, V.G. Vaidyanathan, B.U. Nair, J. Inorg. Bioche. 100 (2006) 1244.
[10] J.G. Collins, A.D. Sleeman, J.R. Aldrich-Wright, I.D. Greguric, T.W. Hambley, Inorg. Chem. 37 (1998) 133.
[11] M. Narra, P. Elliott, S. Swavey, Inorg. Chim. Acta. 359 (2006) 2256.
[12] S. Shi, J. Liu, J. Li, K.C. Zheng, X.M. Huang, C.P. Tan, L.M. Chen, L.N. Ji, J. Inorg. Biochem. 100 (2006) 385.
[13] B. Önfelt, P. Lincoln, B. Nordén, J. Am. Chem. Soc. 121 (1999) 10846.
[14] X.W. Liu, J. Li, H. Li, K.C. Zheng, H. Chao, L.N. Ji, J. Inorg. Biochem. 100 (2006) 385.
[15] A. Ambroise, B.G. Maiya, Inorg. Chem. 39 (2000) 4264.
[16] J.Z. Wu, B.H. Ye, L. Wang, L.N. Ji, J.Y. Zhou, R.H. Li, Z.Y. Zhou, J. Chem. Soc., Dalton Trans. (1997) 395.
[17] P.U. Maheswari, V. Rajendiran, M. Palaniandavar, R. Parthasarathi, V. Subramanian, J. Inorg. Biochem. 100 (2006) 3.
[18] H. Chao, W.J. Mei, Q.W. Huang, L.N. Ji, J. Inorg. Biochem. 92 (2002) 165.
[19] A.M. Pyle, J.P. Rehmann, R. Meshoyrer, C.V. Kumar, N.J. Turro, J.K. Barton, J. Am. Chem. Soc. 111 (1989) 3051.
[20] L.F. Tan, H. Chao, Y.J. Liu, H. Li, B. Sun, L.N. Ji, Inorg. Chim. Acta. 358 (2005) 2191.
[21] J.L. Morgan, D.P. Buck, A.G. Turley, J.G. Collins, F.R. Keene, Inorg. Chim. Acta. 359 (2006) 888.
[22] J. Marmur, J. Mol. Biol. 3 (1961) 208.
[23] M.E. Reichmann, S.A. Rice, C.A. Thomas, P. Doty, J. Am. Chem. Soc. 76 (1954) 3047.
[24] M. Yamada, Y. Tanaka, Y. Yoshimato, S. Kuroda, I. Shimao, Bull. Chem. Soc. Jpn. 65 (1992) 1006.
[25] B.P. Sullivan, D.J. Salmon, T.J. Meyer, Inorg. Chem. 17 (1978) 3334.
[26] J.B. Chaires, N. Dattagupta, D.M. Crothers, Biochemistry 21 (1982) 3933.
[27] G. Cohen, H. Eisenberg, Biopolymers 8 (1969) 45.
[28] E.A. Steck, A.R. Day, J. Am. Chem. Soc. 65 (1943) 452.
[29] G.M. Bryant, J.E. Fergusson, H.K.J. Powell, Aust. J. Chem. 24 (1971) 257.
[30] S. Zails, V. Drchal, Chem. Phys. 118 (1987) 313.
[31] B.K. Ghosh, A. Chakra-Vorty, Coord. Chem. Rev. 95 (1989) 239.
[32] J.E. B Johnson, R.R. Ruminski, Inorg. Chim. Acta. 208 (1993) 231.
[33] A. Juris, V. Balzani, F. Barigelletti, S. Campagna, P. Belser, A. Von Zelewsky, Coord. Chem. Rev. 84 (1988) 85.
[34] J.K. Barton, J.J. Dannenberg, A.L. Raphael, J. Am. Chem. Soc. 106 (1984) 2172.
[35] A. Wolf, G.H. Shimer Jr., T. Meehan, Biochemistry 26 (1987) 6392.
[36] A.M. Pyle, J.P. Rehmann, R. Meshoyrer, C.V. Kumar, N.J. Turro, J.K. Barton, J. Am. Chem. Soc. 111 (1989) 3051.
[37] J.R. Lakowicz, Principles of Fluorescence Spectroscopy, Plenum Press, New York, 1983.
[38] C.V. Kumar, N.J. Turro, J.K. Barton, J. Am. Chem. Soc. 107 (1985) 5518.
[39] S. Satyanarayana, J.C. Dabroniak, J.B. Chaires, Biochemistry 31 (1992) 9319.
[40] S. Satyanaryana, J.C. Daborusak, J.B. Chaires, Biochemistry 32 (1993) 2573.
[41] J.K. Barton, J.J. Dannenberg, A.L. Raphael, J. Am. Chem. Soc. 106 (1984) 2172.
[42] J.K. Barton, Science 233 (1986) 727.
[43] D.S. Sigman, Acc. Chem. Res. 19 (1986) 180.
[44] S. Sitlani, E.C. Long, A.M. Pyle, J.K. Barton, J. Am. Chem. Soc. 114 (1992) 2303.
[45] J.K. Barton, A.L. Raphael, J. Am. Chem. Soc. 106 (1984) 2466.
[46] H.Y. Mei, J.K. Barton, Proc. Natl. Acad. Sci. USA 85 (1988) 339.

Available online at www.sciencedirect.com
ScienceDirect
Polyhedron 26 (2007) 3037–3044
POLYHEDRON
www.elsevier.com/locate/poly

Insulin-like model complexes: Synthesis, spectra characterization and crystal structure of two novel oxovanadium complexes with poly(pyrazolyl)borate ligands $VO(HB(pz)_3)(H_2B(pz)_2)$ and $VO(B(pz)_4)_2$

Yong-Heng Xing [a,*], Bao-Li Zhang [a], Yuan-Hong Zhang [a], Hou-Qun Yuan [a], Zheng Sun [b], Mao-Fa Ge [b]

[a] *Bioinorganic Laboratory, Liaoning Normal University, Dalian 116029, PR China*
[b] *Institute of Chemistry, The Chinese Academy of Sciences, Beijing 100080, PR China*

Received 13 December 2006; accepted 6 February 2007
Available online 17 May 2007

Abstract

Two new oxovanadium (IV) complexes $VO(HB(pz)_3)(H_2B(pz)_2)$ (**1**) and $VO(B(pz)_4)_2$ (**2**) have been obtained by the reaction of oxovanadium sulfate with the corresponding ligands $KHB(pz)_3$, $KH_2B(pz)_2$ and $KB(pz)_4$, respectively. The two complexes were characterized by elemental analyses, IR, UV–Vis and X-ray diffraction. Complex **1** crystallizes in the orthorhombic space group, $Pca2_1$. Complex **2** crystallizes in the orthorhombic space group, $Pna2_1$. In both complexes, five nitrogen atoms and one oxygen atom coordinate to the vanadium atom, forming a distorted octahedral geometry (VON_5). In addition, related spectra characterization, hydrogen-binding properties, structural configuration and quantum chemistry calculations are also discussed.
© 2007 Elsevier Ltd. All rights reserved.

Keywords: Oxovanadium (IV) complexes; Poly(pyrazolyl)borate; Crystal structure; Quantum chemistry calculation

1. Introduction

Vanadium is a bioessential element that is found in abiotic and biotic systems [1]. Since two classes of vanadium enzymes, vanadium-nitrogenases which are used to fix nitrogen and vanadium-haloperoxidases which can catalyze the oxidation of bromide to hypobromite [2], are found in nature, vanadium biochemistry and its potential biological roles have received more and more attention. In recent years, the study of vanadium's antidiaetic action has been widely developed. The antidiaetic action of vanadium may be due to the inhibition of several enzymes involved in carbohydrate and fat metabolism such as phosphodiesterase and tyrosine phosphatases [3,4]. Vanadium compounds have long been known to lower diabetic hyperlipidemia in rats with STZ-induced diabetes [5]. Vanadium complexes with organic ligands are often less toxic and can have improved aqueous solubility and lipophilicity [3]. Also chelated vanadium complexes have the property of increasing permeation into tissues by passive diffusion and correspondingly increased insulin mimetic efficacy. Some vanadium complexes with several kinds of organic ligands have been proposed for clinical use for humans. For example, bis(maltolato)oxovanadium (IV) [3,6], which is under clinical trials, is three times more effective in vivo as an insulin mimetic agent than $VOSO_4$.

Poly(pyrazolyl)borate ligands $[H_xB(pz)_{4-x}]$, introduced by Trofimenko [7], are utilized extensively in organometallic and coordination chemistry for their outstanding chelating power and unusual structural features. Because of the close similarity between the imidazole moiety of the amino acid histidine and pyrazole, the poly(pyrazolyl)borate complexes

* Corresponding author.
E-mail address: yhxing2000@yahoo.com (Y.-H. Xing).

0277-5387/$ - see front matter © 2007 Elsevier Ltd. All rights reserved.
doi:10.1016/j.poly.2007.02.031

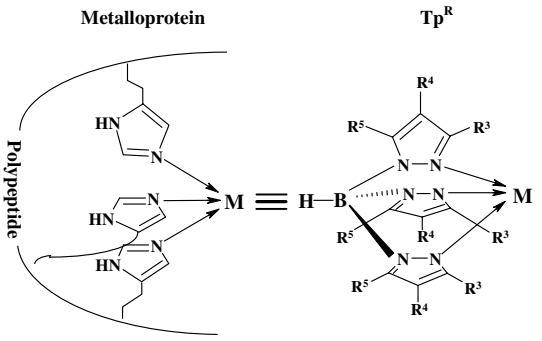


Fig. 1. Concept of the application of Tp^R to biological inorganic chemistry.

can be considered as model complexes of metalloenzymes [8] (Fig. 1). Concerning its biomimetic chemistry, many complexes with the mono-tris(pyrazolyl)borate ligand were synthesized as can be considered as complexes of metalloenzymes such as carbonic anhydrase (CA), nitrite reductases (NiR), hemocyanin (Hc) and blue copper proteins [9].

In the course of our ongoing studies on vanadium complexes containing the tris(pyrazolyl)borate ligand, we are exploring bis(pyrazolyl)borate-vanadium and tetra(pyrazolyl)borate-vanadium. To our knowledge, no vanadium complexes with bis(pyrazolyl)borate or tetra(pyrazolyl)borate as ligands have been reported. Complex **1** contains mixed poly(pyrazolyl)borate ligands, and the coordination environment of the complexes can be considered full-sandwich-like complexes. Many vanadium complexes containing poly(pyrazolyl)borate ligands have been reported [10], but it is worth noting that these reported vanadium complexes contain only one tris(pyrazolyl)-borate or one tris(3,5-dimethylpyrazolyl)borate ligand, forming a half-sandwich structure, except $[(Tp')_2V]BPh_4$, a sandwich vanadium (III) complex reported by Carrano and co-workers [10b]. Due to the steric effects of the poly(pyrazolyl)borate ligands, it is difficult to synthesize oxo-vanadium complexes with a full-sandwich structure.

As a part of the coordination chemistry and bioactivity of our research series on oxo-vanadium complexes, we report in this paper the syntheses, structures, luminescence properties, quantum chemistry and thermal stability of original oxovanadium (IV), '3+2' mixed-ligand complexes carrying both a common N3 tridentate and N2 bidentate ligand, namely, $VO(HB(pz)_3)(H_2B(pz)_2)$ (**1**) and $VO(B(pz)_4)_2$ (**2**).

2. Experimental

2.1. Methods and materials

The reactions were carried out at room temperature. Solvents were dried by molecular sieves (4 Å). All other reactants were used as purchased. The infrared spectra were recorded on a FT/IR-480 PLUS Fourier Transform spectrometer with pressed KBr pellets in the range 4000–200 cm^{-1}. The UV–Vis spectra were recorded on JASCO V-570 spectrometer (200–1100 nm, CH_2Cl_2 solution). Luminescence spectra were recorded on Spectrofluorometer JASCO FP-6500 (1100–200 cm^{-1}) with solid samples. Elemental analyses was performed on a PE 240C automatic analyzer. The thermal curves were recorded on a Perkin–Elmer Diamond TG/DTA. $KHB(pz)_3$, $KHB(3,5\text{-}Me_2pz)_3$ and $KB(pz)_4$ were prepared according to the literature methods [11].

2.2. Syntheses of complexes *1* and *2*

2.2.1. Synthesis of complex *1*

$VOSO_4 \cdot nH_2O$ (0.23 g, 1 mmol, based on 70% $VOSO_4$), potassium tris(pyrazolyl)borate (0.26 g, 1 mmol) and potassium bis(pyrazolyl)borate (0.20 g, 1 mmol) were dissolved in MeOH (15 mL). The mixture was stirred for 4 h at room temperature to obtain a dark-green suspended mixture. Then the precipitate was filtered and dissolved in CH_2Cl_2/MeOH solution. The solution was stood at room temperature overnight, after which blue crystals suitable for X-ray diffraction were obtained. Yield: 0.26 g, 62% (based on V). *Anal.* Calc. for $C_{15}H_{18}B_2N_{10}OV$ (FW 426.95): C, 42.16; H, 4.22; N, 32.79. Found: C, 41.56; H, 4.01; N, 32.17%. IR (KBr, ν, cm^{-1}): 3144, 2510, 2408, 2288, 1504, 1406, 1308, 1213, 1190, 1152, 1118, 1059, 988, 973, 922, 884, 764, 717, 667, 635, 395, 361, 311.

2.2.2. Synthesis of complex *2*

$VOSO_4 \cdot nH_2O$ (0.23 g, 1 mmol, based on 70% $VOSO_4$) and potassium tetra(pyrazolyl)borate (0.33 g, 1 mmol) were dissolved in MeOH, and the resulting mixture was stirred for 7 h at room temperature, forming a blue suspended mixture. The resultant solution was filtered, and the blue filtrate was stood at room temperature. From the mother liquid, blue crystals suitable for X-ray diffraction were discovered after 4 days. Yield: 0.36 g, 58% (based on V). *Anal.* Calc. for $C_{24}H_{27}B_2N_{16}OV$ (FW 628.18): C, 45.85; H, 4.30; N, 35.66. Found: C, 45.56; H, 4.11; N, 35.23%. IR (KBr, ν, cm^{-1}): 3430, 3137, 1505, 1435, 1408, 1389, 1297, 1212, 1197, 1108, 1070, 982, 921, 889, 855, 837, 823, 788, 759, 751, 678, 655, 617, 407, 378, 352, 307.

2.3. Crystal structure determination and refinement of the structure

The crystals of **1** and **2** were mounted on glass fibres for X-ray measurement. Reflection data were collected at room temperature on an APEX II CCD diffractometer with graphite-monochromated Mo Kα radiation ($\lambda = 0.7107$ Å) and the ω scan mode. All the measured independent reflections were used in the structural analyses, and semi-empirical absorption corrections were applied using the SADABS program. The crystal data and refinement details are summarized in Table 1.

The structures were solved by the direct method using SHELXS-86 and refined using SHELXL-97. All the non-hydrogen atoms were refined anisotropically and the contributions

Table 1
A summary of the fundamental crystal and refinement data of complexes **1** and **2**

Complex	**1**	**2**
Empirical formula	$C_{30}H_{36}B_4N_{20}O_2V_2$	$C_{24}H_{27}B_2N_{16}OV$
Formula weight (g mol^{-1})	853.91	628.18
Color	blue	blue
Size (mm)	$0.10 \times 0.45 \times 0.50$	$0.20 \times 0.25 \times 0.40$
Crystal system	orthorhombic	orthorhombic
Space group	$Pca2_1$	$Pna2_1$
a (Å)	15.677(3)	18.000(4)
b (Å)	8.6120(15)	13.255(3)
c (Å)	29.583(5)	12.117(2)
α (°)	90	90
β (°)	90	90
γ (°)	90	90
V (Å^3)	3994.2(12)	2891.0(10)
Z	4	4
D_{calc} g cm^{-3}	1.420	1.443
λ(Mo Kα) (Å)	0.71073	0.71073
F(000)	1752	1296
μ(Mo Kα) (cm^{-1})	0.526	0.395
θ Range (°)	2.36–24.99	3.07–27.44
Reflections collected	6708	6574
Independent reflections $[I > 2\sigma(I)]$	6399	4656
Parameters	523	397
$\Delta\rho$ (e Å^{-3})	0.221 and −0.160	0.354 and −0.336
Goodness-of-fit	1.045	0.985
R^a	0.0324 (0.0342)[b]	0.0509 (0.0798)[b]
wR_2^a	0.0814 (0.824)[b]	0.1238 (0.1376)[b]

[a] $R = \sum\|F_o| - |F_c\|/\sum|F_o|$, $wR_2 = [\sum w(F_o^2 - F_c^2)^2/\sum(w(F_o^2)^2)]^{1/2}$; $[F_o > 4\sigma(F_o)]$.
[b] Based on all data.

of the hydrogen atoms were included in calculated positions, constrained to ride on their carbon atoms with group U_{iso} values assigned. Atomic scattering factors and anomalous dispersion terms were as in SHELXL-97. The drawings were made with DIAMOND 2.1c, and all calculations were performed on a pentium4 computer.

2.4. Thermal analysis

Thermogravimetric analyses (TGA) experiments were carried out on a Perkin–Elmer Diamond TG/DTA instrument. The samples were initially heated for 1 h at 50 °C. During the simple ramping experiment, weight changes were recorded as a function of temperature for a 10 °C/min temperature ramp between 50 and 750 °C in a nitrogen environment. The mass weight was 1.839 mg for complex **1** and 5.880 mg for complex **2**.

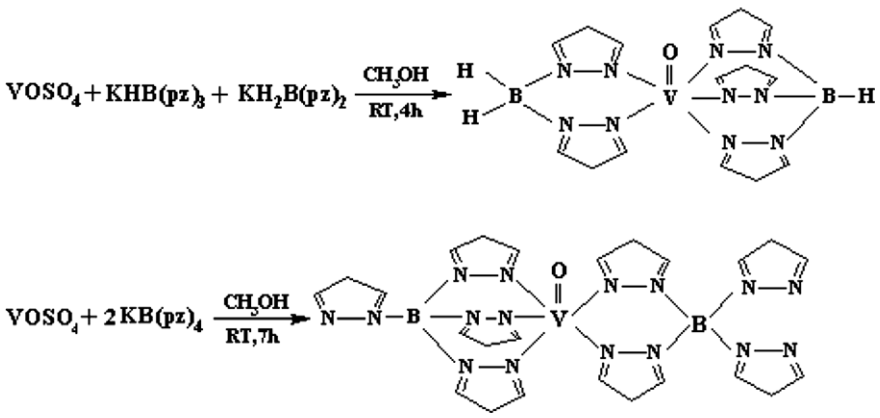
3. Results and discussion

3.1. Syntheses

In this work, the tridentate ligand of potassium tris(pyrazolyl)borate ($KHB(pz)_3$), bidentate ligand of potassium bis(pyrazolyl)borate ($KH_2B(pz)_2$) and tetradentate ligand of potassium tetra(pyrazolyl)borate ($KB(pz)_4$) were used. They were prepared by the sublimation reaction of pyrazole and KBH_4 with stoichiometric ratios of 3:1, 2:1 and 4:1, respectively. The complexes **1** and **2** were obtained from the mixture of $VOSO_4$ and the corresponding ligands in a MeOH solution at room temperature. Metal:ligand molar ratios of 1:1:1 for **1** and 1:2 for **2** were used for the syntheses of the complexes. The synthetic process of both complexes can be simplified as in Scheme 1.

For complex **1**, crystals for X-ray analysis can be obtained by the slow evaporation of a CH_2Cl_2/MeOH solution of the complex. Some other solvents, MeOH, CH_2Cl_2, CH_3CN, etc., were also used for recrystallization, but no suitable crystals for X-ray diffraction were separated. So we can conclude that the solvents play an important role in the crystallization for complex **1**.

In addition, using V_2O_5 as a starting material to react with the $KHB(pz)_3$ and $KH_2B(pz)_2$ or $KB(pz)_4$ ligands, respectively, both title complexes were also obtained (proved by the IR data). In the reaction process, an oxidation–reduction process occurs, the oxidation state of vanadium changes from V to IV. Complexes **1** and **2** are stable in air at room temperature and are readily soluble in CH_3Cl, CH_2Cl_2, CH_3CN, THF and CH_3COCH_3, slightly soluble in MeOH and EtOH, and insoluble in water, ether and hexane.



Scheme 1. Reaction process of complexes **1** and **2**.

3.2. IR spectra

The IR spectrum of complex **1** (Fig. S1) can be assigned as follows: the signal at 3144 cm^{-1} is assigned to the vibration of C–H from pyrazole rings, the characteristic bands of B–H vibrations are found at 2510, 2408 and 2288 cm^{-1} [12], the bands at 1059–1504 cm^{-1} are assigned to C=N and C=C vibrations from the pyrazole rings. The band at 988 cm^{-1} is the characteristic vibration of V=Ot [10b,g,h], and the bands at 311–395 cm^{-1} are assigned to the vibrations of V–N [13].

For the IR spectrum of complex **2** (Fig. S2), the signal at 3430 cm^{-1} can be attributed to the N–H vibration, the signal at 3137 cm^{-1} is assigned to the C–H vibration from pyrazole rings, The C=N and C=C vibrations from the pyrazole rings appear at 1070–1505 cm^{-1}. The characteristic band of V=Ot is found at 982 cm^{-1} [10b,g,h], and the bands at 307–407 cm^{-1} are assigned to the V–N vibrations [13].

3.3. UV spectra

The UV spectra (Figs. S1 and S4) for both complexes are recorded in CH_2Cl_2. The strong and broad absorption signals at 240 nm are assigned to the π–π^* transitions of the ligands (LLCT). However, no absorption bands could be observed in the region of 310–400 nm, suggesting that all LMCT (or MLCT) transitions in complexes **1** and **2** are probably hidden in the UV region of the strong intraligand π–π^* transitions. Two weak and broad split peaks at 496 and 668 nm for complex **1**, 500 and 652 nm for complex **2** are attributed to the $d \rightarrow d^*$ transition of the centre vanadium (MMCT). The characterization of the UV spectra for complexes **1** and **2** is similar to that of the complexes $VO(HB(pz)_3)(pzH)(SCN)$ and $VO(HB(3,5\text{-}Me_2pz)_3)(3,5\text{-}Me_2pz)(SCN)(SCNH)_2$ [13].

3.4. Emission spectra

The fluorescence (Figs. S5 and S6) of both complexes were also tested with excitation at 260 nm, and luminescence bands at 302, 398–469, 743 nm and 302, 416–469, 742 nm for **1** and **2**, respectively, were present. The spectra exhibit three distinct regions. The first region presents a sharp band at 302 nm; in the second and the third regions there are some broad bands (398–469 and 743 nm for **1**; 416–469, 742 nm for **2**) at longer wavelengths. On comparison of the corresponding absorption and emission spectra, the emission peaks of complexes **1** and **2** can be assigned as follows: two emission bands in the UV region (302, 398–469 nm for **1**; 302, 416–469 nm for **2**) come from the π–π^* transitions of the ligands (LLCT); the weak and broad emission bands at 743 nm for **1** and 742 nm for **2** should be attributed to the $d \rightarrow d^*$ transition of the central vanadium (MMCT). On comparing the luminescence bands of complexes **1** and **2** with the complexes $VO(HB(pz)_3)(pzH)(SCN)$ and $VO(HB(3,5\text{-}Me_2pz)_3)(3,5\text{-}Me_2pz)(SCN)(SCNH)_2$ [13], it is found that the emission band in the high energy region (302 nm) has a blue shift of about 53 nm, and those in the low energy region (742, 743 nm) have a red shift of about 43 nm.

3.5. Crystal structures of $VO(HB(pz)_3)(H_2B(pz)_2)$ (1) and $VO(B(pz)_4)_2$ (2)

The overall view and labelling of the atoms for complex **1** in two independent molecules (designated as molecule 1 and molecule 2) are displayed in Fig. 2. Each vanadium atom has a six-coordinated structure with three nitrogen atoms provided by one tridentately ligating $HB(pz)_3^-$, two nitrogen atoms from one bidentately ligating $H_2B(pz)_2^-$ and an oxo oxygen atom. Around the mental center, a distorted octahedral geometry is formed. Two nitrogen atoms from the tridentate $HB(pz)_3^-$ ligand with the other two nitrogen atoms from the bidentate $H_2B(pz)_2^-$ ligand form an equatorial plane (N4, N6, N8, N10 and N14, N16, N18, N20 for molecules 1 and 2, respectively). The axial positions are occupied by the remaining one nitrogen (N2 and N12 for molecules 1 and 2, respectively) from the tridentate $HB(pz)_3^-$ ligand and a terminal oxygen atom (O1 and O2 for molecules 1 and 2, respectively). As for complex **2**, the coordination environment is similar to that of complex **1**. The structure and atomic labelling scheme for complex **2** are presented in Fig. 3.

For complex **1**, the deviations from the least-squares plane containing the N4, N6, N8 and N10 atoms are −0.026(1), 0.026(1), 0.025(1) and −0.026(1) Å, respectively, showing that these atoms are almost on one plane. The atoms V1, O1 and N2 lie 0.319(2), 1.911(2) and −1.981(3) Å out of this plane, respectively, indicating that V1 lies towards the apical oxo atom O1, *trans* to N2. The deviations from the least-square plane containing the N14, N16, N18 and N20 atoms are −0.012(1), 0.012(1), 0.012(1) and −0.012(1) Å, respectively, showing that these atoms are also almost on a plane. The atoms of V2, O2 and N12 lie 0.297(2), 1.884(2) and −1.999(2) Å out of this plane, respectively, indicating that V2 lies towards the apical oxo atom O2, *trans* to N12. For complex **2**, the deviations from the least-squares plane containing the N4, N6,

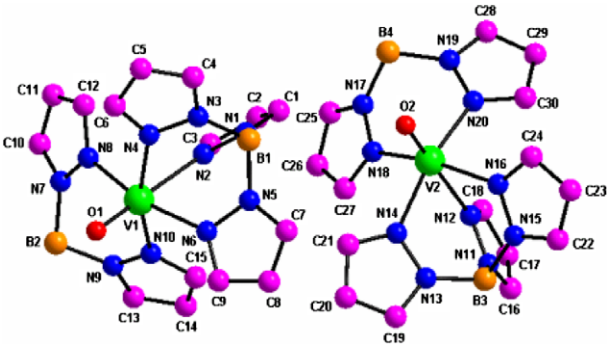


Fig. 2. A view of the molecular structure of complex **1**.

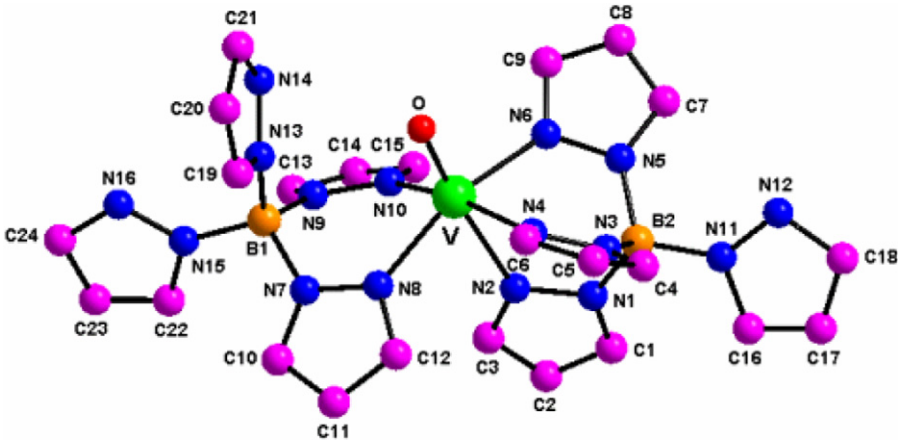


Fig. 3. A view of the molecular structure of complex **2**.

N8 and N10 atoms are −0.023(2), 0.023(2), 0.023(2) and −0.023(2) Å, respectively, showing that these atoms are almost on a plane. The atoms of V, O and N2 lie −0.297(2), −1.880(3) and 1.975(4) Å out of this plane, respectively, indicating that V lies towards the apical oxo atom O, *trans* to N2.

Some selected bond distances and angles for complexes **1** and **2** are listed in Table 2. For complex **1**, the V–O distances in complex **1** are 1.592(2) Å (for molecule 1) and 1.590(2) Å (for molecule 2), which are close to those reported previously [10h,14]. The average V–N_{cis} bond distance is 2.105(2) Å for molecules 1 and 2; and the V–N_{trans} bond distance is 2.298(2) Å for molecules 1 and 2. For complex **2**, the V–O distance is 1.588(3) Å. The average V–N_{cis} bond distance is 2.100(3) Å and the V–N_{trans} distance is 2.274(3) Å. There is no difference between the V–N_{cis} distance of the two complexes, while the V–O and V–N_{trans} distances of complex **1** are slightly longer than the corresponding bond distances of complex **2**. This may be attributed to the fact that the donor electron ability of tetra(pyrazolyl)borate is stronger than that of tris(pyrazolyl)borate or bis(pyrazolyl)borate.

The O–V–N_{trans} angle (177.0(1)°) for molecule 1 (in complex **1**) is bigger than that of complex **2** (173.2(1)°),

Table 2
Some selected bond distances (Å) and angles (°) for complexes **1** and **2**

Complex **1**				Complex **2**	
V(1)–O(1)	1.592(2)	V(2)–O(2)	1.590(2)	V–O	1.588(3)
V(1)–N(2)	2.298(2)	V(2)–N(12)	2.298(2)	V–N(2)	2.274(3)
V(1)–N(4)	2.098(2)	V(2)–N(14)	2.104(2)	V–N(4)	2.094(3)
V(1)–N(6)	2.119(2)	V(2)–N(16)	2.118(2)	V–N(6)	2.099(3)
V(1)–N(8)	2.095(2)	V(2)–N(18)	2.097(2)	V–N(8)	2.110(3)
V(1)–N(10)	2.106(2)	V(2)–N(20)	2.102(2)	V–N(10)	2.095(3)
O(1)–V(1)–N(2)	177.0(1)	O(2)–V(2)–N(12)	174.4(1)	O–V–N(2)	173.2(1)
O(1)–V(1)–N(4)	97.5(1)	O(2)–V(2)–N(14)	96.6(1)	O–V–N(4)	94.9(2)
O(1)–V(1)–N(6)	96.3(1)	O(2)–V(2)–N(16)	95.4(1)	O–V–N(6)	95.0(1)
O(1)–V(1)–N(8)	99.7(1)	O(2)–V(2)–N(18)	101.5(1)	O–V–N(8)	100.0(1)
O(1)–V(1)–N(10)	101.3(1)	O(2)–V(2)–N(20)	98.9(1)	O–V–N(10)	102.6(1)
N(4)–V(1)–N(2)	80.4(1)	N(14)–V(2)–N(12)	81.4(1)	N(4)–V–N(2)	80.9(1)
N(6)–V(1)–N(2)	81.4(1)	N(16)–V(2)–N(12)	79.3(1)	N(6)–V–N(2)	79.3(1)
N(8)–V(1)–N(2)	82.6(1)	N(18)–V(2)–N(12)	83.8(1)	N(8)–V–N(2)	84.1(1)
N(10)–V(1)–N(2)	80.7(1)	N(20)–V(2)–N(12)	83.0(1)	N(10)–V–N(2)	83.1(1)
N(4)–V(1)–N(6)	85.0(1)	N(14)–V(2)–N(16)	86.0(1)	N(4)–V–N(6)	84.7(1)
N(8)–V(1)–N(4)	93.0(1)	N(18)–V(2)–N(14)	91.4(1)	N(4)–V–N(10)	92.8(1)
N(4)–V(1)–N(10)	160.9(1)	N(20)–V(2)–N(14)	164.4(1)	N(4)–V–N(8)	165.0(1)
N(8)–V(1)–N(6)	164.0(1)	N(18)–V(2)–N(16)	163.2(1)	N(8)–V–N(6)	162.4(1)
N(10)–V(1)–N(6)	89.6(1)	N(20)–V(2)–N(16)	91.4(1)	N(6)–V–N(10)	92.6(1)
N(8)–V(1)–N(10)	87.3(1)	N(18)–V(2)–N(20)	86.6(1)	N(10)–V–N(8)	85.4(11)
N(1)–N(2)–V(1)	120.5(2)	N(11)–N(12)–V(2)	120.3(2)	N(1)–N(2)–V	123.1(2)
N(3)–N(4)–V(1)	121.7(2)	N(13)–N(14)–V(2)	122.2(2)	N(3)–N(4)–V	122.1(2)
N(5)–N(6)–V(1)	121.8(2)	N(15)–N(16)–V(2)	121.6(2)	N(5)–N(6)–V	125.0(2)
N(7)–N(8)–V(1)	122.7(2)	N(17)–N(18)–V(2)	123.0(2)	N(9)–N(10)–V	125.0(2)
N(9)–N(10)–V(1)	123.1(2)	N(19)–N(20)–V(2)	122.5(2)	N(7)–N(8)–V	125.8(2)

while the O–V–N_{trans} angle (174.4(1)°) for molecule 2 (in complex **1**) is close to that of complex **2**. The average O–V–N_{cis} angle of complex **1** (97.9(1)° for molecule 1, 98.4(1)° for molecule 2) is close to that of complex **2**(98.1(1)°).

It is worthy noting that each of two pyrazoles from a poly(pyrazolyl)borate can provide four nitrogen atoms forming a plane, and both V and B atoms lie above or below of the plane, showing that the $V(N–N)_2B$ rings are arranged in shallow boat configurations (Fig. S7). The V1···B1, V1···B2, V2···B3 and V2···B4 distances are 3.302(3), 3.363(3), 3.304(3) and 3.345(3) Å, respectively, somewhat similar to the coordination environment of the complex $M(H_2B(pz)_2)_2$ (M = Cu, Ni), which we have reported previously [15]. Similarly for complex **2**, the $V(N–N)_2B$ rings are arranged in shallow boat configurations (Fig. S8), and the V1···B1, V1···B2 distances are 3.416(4) and 3.327(4) Å, respectively.

As shown in Fig. 4, two kinds of weak interactions between adjacent molecules were observed in complex **1**, C–H···O hydrogen bonds and C–H···B hydrogen bonds. The C19A–H19A···O2 (H19A: $-0.5 + x$, $3 - y$, z) and C1B–H1B···O2 (H1B: x, $1 + y$, z) distances are 2.646 and 2.545 Å, respectively, and the C–H···B hydrogen bond distances are 2.902 Å (C29A–H29A···B2) (H29A: $0.5 - x$, $1 + y$, $0.5 + z$) and 3.129 Å (C17A–H17A···B2) (H17A: $1 - x$, $2 - y$, $0.5 + z$). It is obvious that the C–H···O hydrogen bonds are stronger than the C–H···B hydrogen bonds.

For complex **2**, C–H···O hydrogen bonding is also observed between the molecules (Fig. 5). The C–H···O hydrogen bond distance is 2.585 Å (C23A–H23A···O, H23A: $0.5 - x$, $0.5 + y$, $0.5 + z$). Adjacent molecules are connected by C–H···O hydrogen bonds, forming a one-dimension chain structure. No C–H···B hydrogen bonds were observed.

3.6. Thermal decomposition process

As shown in Fig. 6, the thermal decomposition of complex **1** exhibits a two-step process. In the range 296–325 °C, there is a 10.58% weight loss, which is attributed to the release of one pyrazole moiety (10.67% theoretical weight loss). This step is followed by a weight loss of 41.18%, which can be attributed to the release of four pyrazole moieties (42.68% theoretical weight loss) in the range 325–439 °C.

The thermal decomposition of complex **2** (Fig. S9) also exhibits a two-step process. In the range 245–288 °C, there is a 23.53% weight loss, which is attributed to the release of one pyrazole moiety (23.54% theoretical weight loss). This step is followed by weight loss of 31.42%, which can be attributed to the release of two pyrazole moieties (31.38% theoretical weight loss) in the range 290–441 °C.

On comparison of the starting decomposition temperature of both complexes, 296 °C for complex **1** and 245 °C for complex **2**, we can see that complex **1** is more stable than complex **2**.

3.7. Quantum chemistry calculations of the complexes

According to molecular orbital theory, the frontier orbitals and nearby molecular orbitals are the most important factors to the stability. The larger the difference between the frontier orbitals, the more stable the molecular structure is. The energy values of ΔE ($\Delta E = E_{LUMO} - E_{HOMO}$)

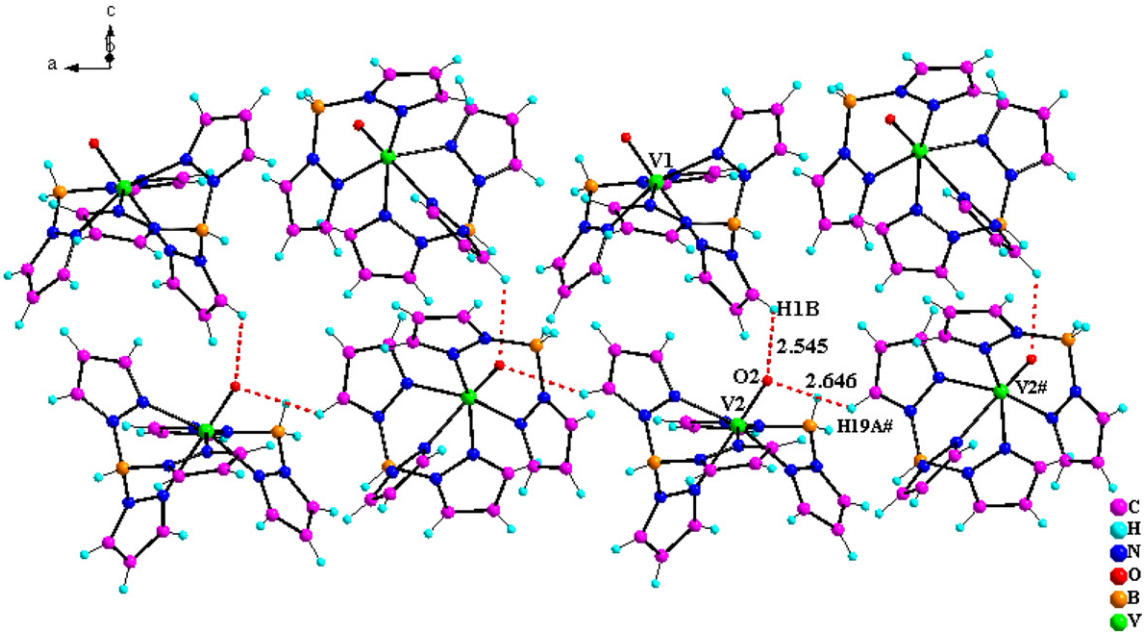


Fig. 4. A view of the hydrogen-bonding in complex **1**.

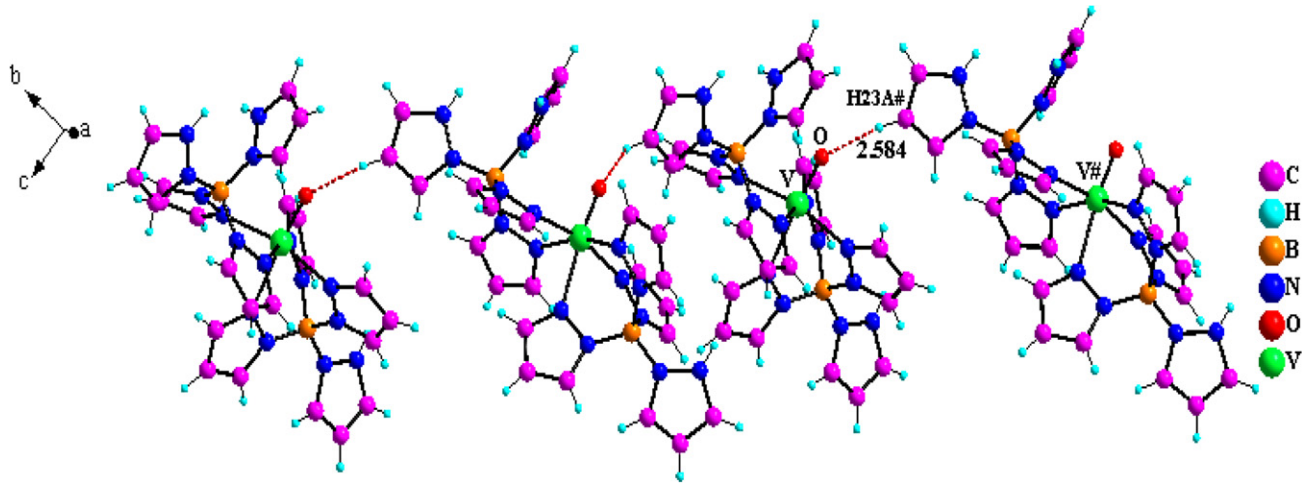


Fig. 5. A view of the hydrogen-bonding in complex **2**.

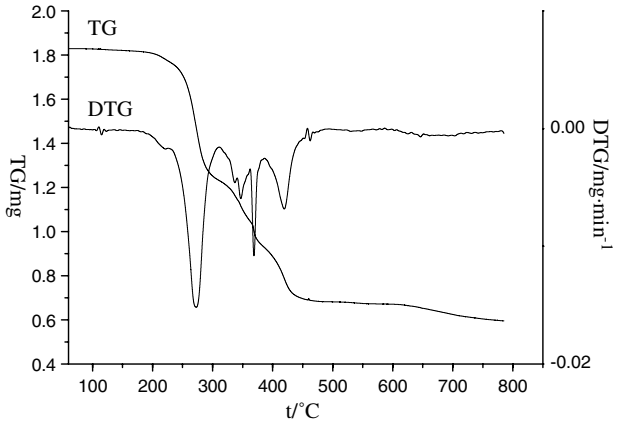


Fig. 6. The TG/DTG curve of complex **1**.

Table 3
The atomic net charge for complexes **1** and **2** calculated with NBO analysis

Atom	Complex **1**	Complex **2**
V1(V)	2.38744	1.8881
O1(O)	−0.87793	−1.09264
N2	−0.47855	−0.44354
N4	−0.51023	−0.43566
N6	−0.51023	−0.43392
N8	−0.53253	−0.40766
N10	−0.53253	−0.41272
N12		−0.49439
N14		−0.24644
N16		−0.37501
B1	0.83565	1.27705
B2	0.40870	1.28075

are 0.2332 and 0.01273, respectively, for complex **1** and **2** (Table S1), which show that the order of stability of the complexes is **1** > **2**. This result corresponds to the results of the thermal decomposition.

The atomic net charges for the complexes calculated in the NBO analysis are listed in Table 3. The charge of the central V metal for complex **1** is 2.38744. The net change of the terminal oxygen (O1) is −0.87793. The net charge of the coordinated N atoms (N2, N4, N6, N8, N10) range from −0.47855 to −0.53253, and N4/N6, N8/N10 share the same net charges, respectively. The charge of the central V metal for complex **2** is 1.8881. The net charge of the terminal oxygen (O) is −1.09264. The net charges of the coordinated N atoms (N2, N4, N6, N8, N10) range from −0.40766 to −0.44354, the net charges of the uncoordinated N atoms (N12, N14, N16) range from −0.24644 to −0.49439. Comparing both complexes, the net charges of the central V metal are less than +4, showing that the V atom has been coordinated by the ligand and its charge transfers to the ligand, and the net charge of complex **1** is more positive than that of complex **2**. The net charges of the coordinated N atoms for complex **1** are more negative than those of complex **2**. The net charges of the B atoms for complex **1** are less positive than those of complex **2**. From the data above we can see the net charges of the V atom for complexes **1** and **2** are different, attributed to the fact that the donor electron ability of tetra(pyrazolyl)-borate is stronger than that of tris(pyrazolyl)borate or bi(pyrazolyl)borate.

The NBO bond order (Table 4) between V and O is greater than that between V and N (N2, N4, N6, N8, N10), showing V–O possesses double bond character, while the V–N bonds (N2, N4, N6, N8, N10) have single bond character.

Table 4
Selected NBO bond order for complexes **1** and **2**

Bond	Complex **1**	Complex **2**
V1–O1(V–O)	0.7129	0.6908
V1–N2	0.1204	0.0947
V1–N4	0.1808	0.1560
V1–N6	0.1808	0.1541
V1–N8	0.1934	0.1509
V1–N10	0.1934	0.1491

Acknowledgements

We express our sincere thanks to the National Natural Science Foundation of China (No. 20571036), Education Foundation of Liaoning Province (No. 05L212) and SRF for ROCS, SEM for financial assistance.

Appendix A. Supplementary material

CCDC 610430 and 610429 contain the supplementary crystallographic data (tables of atomic coordinates, anisotropic thermal parameters and complete bond distances and angles) for **1** and **2**. These data can be obtained free of charge via http://www.ccdc.cam.ac.uk/conts/retrieving.html, or from the Cambridge Crystallographic Data Centre, 12 Union Road, Cambridge CB2 1EZ, UK; fax: (+44) 1223-336-033; or e-mail: deposit@ccdc.cam.ac.uk. Supplementary data associated with this article can be found, in the online version, at doi:10.1016/j.poly.2007.02.031.

References

[1] (a) J.C. Pessoa, I. Tomaz, R.T. Henriques, Inorg. Chim. Acta 356 (2003) 121;
(b) A. Pohlmann, S. Nica, T.K.K. Luong, W. Plass, Inorg. Chem. Commun. 8 (2005) 289.
[2] M. Kaliva, C.P. Raptopoulou, A. Terzis, A. Salifoglou, Inorg. Chem. 43 (2004) 2895.
[3] S. Ahmad, A.A. Isab, S. Ali, A.R. Al-Arfaj, Polyhedron 24 (2005) 1.
[4] (a) D. Rehder, Inorg. Chem. Commun. 6 (2003) 604;
(b) K. Kanamori, K. Nishida, N. Miyata, T. Shimoyama, K. Hata, C. Mihara, K. Okamoto, Y. Abe, S. Hayakawa, S. Matsugo, Inorg. Chem. 43 (2004) 7127.
[5] (a) D.C. Crans, M. Mahroof-Tahir, M.D. Johnson, P.C. Wilkins, L.Q. Yang, K. Robbins, A. Johnson, J.A. Alfano, M.E. Godzala III, L.T. Austin, G.R. Willsky, Inorg. Chim. Acta 356 (2003) 365;
(b) Y. Sechter, I. Foldwaser, M. Mironchik, M. Fridkin, D. Gefel, Coor. Chem. Rev. 237 (2003) 3.
[6] (a) R. Shukla, V. Barve, S. Padhyeb, R. Bhondea, Bioorg. Med. Chem. Lett. 14 (2004) 4961;
(b) B.D. Liboiron, K.H. Thompson, G.R. Hanson, E. Lam, N. Aebischer, C. Orvig, J. Am. Chem. Soc. 127 (2005) 5104.
[7] (a) S. Trofimenko, J. Am. Chem. Soc. 88 (1966) 1842;
(b) J.P. Jesson, S. Trofimenko, D.R. Eaton, J. Am. Chem. Soc. 89 (1967) 3148;
(c) S. Trofimenko, J. Am. Chem. Soc. 89 (1967) 3904;
(d) S. Trofimenko, J. Am. Chem. Soc. 89 (1967) 3170.
[8] Y.J. Sun, L.Z. Zhang, P. Cheng, H.K. Lin, S.P. Yan, W. Sun, D.Z. Liao, Z.H. Jiang, P.W. Shen, Inorg. Chem. 42 (2003) 508.
[9] Y.J. Sun, L. Yi, X. Yang, Y. Liu, P. Cheng, D.Z. Liao, S.P. Yan, Z.H. Jiang, Inorg. Chim. Acta 358 (2005) 396.
[10] (a) E. Kime-Hunt, K. Spartalian, M. DeRusha, C.M. Nunn, C.J. Carrano, Inorg. Chem. 28 (1989) 4392;
(b) M. Mohan, S.M. Holmes, R.J. Butcher, J.P. Jasinski, C.J. Carrano, Inorg. Chem. 31 (1992) 2029;
(c) S. Holmes, C.J. Carrano, Inorg. Chem. 30 (1991) 1231;
(d) L.M. Mokry, J. Thompson, M.R. Bond, T. Otieno, M. Mohan, C.J. Carrano, Inorg. Chem. 33 (1994) 2705;
(e) N.S. Dean, L.M. Mokry, M.R. Bond, C.J. O'Connor, C.J. Carrano, Inorg. Chem. 35 (1996) 2818;
(f) N.S. Dean, L.M. Mokry, M.R. Bond, M. Mohan, T. Otieno, C.J. O'Connor, K. Spartalian, C.J. Carrano, Inorg. Chem. 36 (1997) 1424;
(g) R.L. Beddoes, D. Collison, F.E. Mabbs, M.A. Passand, Polyhedron 9 (1990) 2483;
(h) M. Herberhold, G. Frohmader, T. Hofmann, W. Milius, J. Darkwa, Inorg. Chim. Acta 267 (1998) 19.
[11] (a) J. Reglinski, M. Garner, I.D. Cassidy, P.A. Slavin, M.D. Spicer, D.R. Armstrong, J. Chem. Soc., Dalton Trans. 13 (1999) 2119;
(b) S. Trofimenko, J. Am. Chem. Soc. 89 (1967) 6288.
[12] M. Onishi, M. Yamaguchi, S. Kumagae, H. Kawano, Y. Arikawa, Inorg. Chim. Acta 359 (2006) 2826.
[13] Y.H. Xing, Z. Sun, H.Q. Yuan, M.F. Ge, S.Y. Niu, F.Y. Bai, Chin. Sci. Bull. 51 (2006) 661.
[14] (a) P. Plitt, H. Prizkow, R. Krämer, J. Chem. Soc., Dalton Trans. 15 (2004) 2314;
(b) D. Collison, F.E. Mabbs, S.S. Truner, A.K. Powell, E.J.L. Mclnnes, L.J. Yellowlees, J. Chem. Soc., Dalton Trans. 7 (1997) 1201.
[15] Y.H. Xing, H.Q. Yuan, B.L. Zhang, Y.H. Zhang, S.Y. Niu, F.Y. Bai, J. Coord. Chem. 60 (2007) 163.

Available online at www.sciencedirect.com
ScienceDirect
Polyhedron 26 (2007) 3045–3053
POLYHEDRON
www.elsevier.com/locate/poly

Synthesis, structure and reactivity of novel palladiumdichloride-2,2′-bipyridine with 4,4′-bis(fluorous-ponytail)

Norman Lu [a,*], Yan-Chou Lin [a], Jeng-Yung Chen [a], Tsung-Chi Chen [a], Shih-Chieh Chen [a], Yuh-Sheng Wen [b], Ling-Kang Liu [b,*]

[a] *Institute of Organic and Polymeric Materials, National Taipei University of Technology, Taipei 106, Taiwan*
[b] *Institute of Chemistry, Academia Sinica, Taipei 115, Taiwan*

Received 4 November 2006; accepted 6 February 2007
Available online 21 February 2007

Dedicated to the memory of Professor Tong-In Ho who passed away at his prime time.

Abstract

With the readily available fluorous alkanols R_fCH_2OH, a series of novel fluorous-ponytailed bpy ligands, 4,4′-bis($R_fCH_2OCH_2$)-2,2′-bpy (**1a**–**e**), were prepared and treated with $[PdCl_2(CH_3CN)_2]$ to result in the corresponding novel Pd complexes [$PdCl_2$(4,4′-bis-($R_fCH_2OCH_2$)-2,2′-bpy)] (**2a**–**e**) where $R_f = n\text{-}C_3F_7$ (**a**), $HCF_2(CF_2)_3$ (**b**), $HCF_2(CF_2)_7$ (**c**), $n\text{-}C_8F_{17}$ (**d**), $n\text{-}C_{10}F_{21}$ (**e**). The new ligands and Pd complexes were spectroscopically characterized by multi-nuclei NMR (^1H, ^{19}F and ^{13}C), FTIR and high resolution mass (FAB). The structure for the Pd complex **2b**, the first with fluorinated ponytails on bpy and not on phosphine, was also established by a single crystal X-ray diffraction study. The TGA data of both ligands and Pd complexes indicated that the Pd-complexes were resistant to higher temperatures than the corresponding ligands. The Pd catalysts derived from **2a**–**c** showed an almost quantitative conversion and could be reused for eight runs with Heck reactions, in that the products and unspent reactants were directly removed by distillation. With the highest fluorine content in the series, Pd complex **2e** was successfully applied in the Heck reaction using the fluorous biphasic catalysis strategy.
© 2007 Elsevier Ltd. All rights reserved.

Keywords: Fluorinated palladium complexes; Bis(fluorous ponytailed)bipyridine; X-ray structure analysis; Heck reaction; Catalyst recycling; Fluorous biphasic catalysis

1. Introduction

The concept of fluorous biphasic catalysis (FBC) was first introduced by Horvath and Rabai in 1994 [1]. In the past decade, this field has evolved rapidly [2] and fluorous biphasic catalysis [3,4] has become nowadays one of the important strategies in the design and reuse of homogeneous metal catalysts.

As a common bidentate ligand, 2,2′-bipyridine (2,2′-bpy) upon coordination to a metal center is known to maintain its bonding geometry at the metal center even when the metal center is oxidized or reduced. It is also known that modification of a molecule with fluorous segments alters the physical properties of the original molecule. Furthermore, Pd complexes are amongst the most popular transition metal compounds as catalysts in organometallics [5]. Thus, the combination of a Pd metal center with fluorous-ponytailed 2,2′-bpy ligands should result in a rich chemistry [6,7].

In this study, a series of fluorous-ponytailed 2,2′-bpy ligands have been prepared, whose partitions between organic and fluorous solvents were measured, and the

* Corresponding authors. Tel.: +886 2 2771 2171x2417; fax: +886 2 2731 7174 (N. Lu); tel.: +886 2 2789 8532; fax: +886 2 2783 1237 (L.-K. Liu).
E-mail addresses: normanlu@ntut.edu.tw (N. Lu), liuu@chem.sinica.edu.tw (L.-K. Liu).

0277-5387/$ - see front matter © 2007 Elsevier Ltd. All rights reserved.
doi:10.1016/j.poly.2007.02.009

catalytic properties of the resultant metal complexes with light fluorine content ligands and those of metal complexes with high fluorine content ligands were studied. The ligands with high fluorine content and the associated metal complexes are expected to be only soluble in perfluorinated solvents and insoluble in common organic solvents, a property applicable to the abovementioned fluorous biphasic catalysis.

Previously reported single crystal X-ray structures carrying fluorous segments are mainly based on phosphine ligands [8–11], none being based on fluorous-ponytailed 2,2′-bpy ligands [12,13]. Along with our recycling studies of the fluorous-ponytailed 2,2′-bpy Pd catalysts using the Heck reaction as the test reaction, an X-ray diffraction study on one of the Pd complexes prepared was carried out.

2. Experimental

2.1. General

Gas chromatographic/mass spectrometric data were obtained using an Agilent 6890 Series gas chromatograph with a series 5973 mass selective detector. The GC monitoring employed a HP 6890 GC using a 30 m × 0.250 mm HP-1 capillary column with a 0.25 μm stationary phase film thickness. Infrared spectra were obtained on a Perkin–Elmer RX I FT-IR Spectrometer. NMR spectra were recorded on Bruker AM 500 and Joel AM 200 using 5 mm sample tubes. The residual peaks of CD_3OD, CD_2Cl_2, $CDCl_3$ and deuterated Me_2SO were used as the reference peaks for both ^1H and ^{13}C NMR spectra; Freon® 11 ($CFCl_3$) for ^{19}F NMR spectra. Thermogravimetric analyses (TGA) were obtained on a TA Instruments TGA51.

2.2. Starting materials

Chemicals, reagents and solvents employed were commercially available and were used as received. $HCF_2(CF_2)_3CH_2OH$ and $HCF_2(CF_2)_7CH_2OH$ were obtained from Daikin, Taiwan. $C_3F_7CH_2OH$, $C_8F_{17}CH_2OH$ and $C_{10}F_{21}CH_2OH$ were purchased from Aldrich and SynQuest.

2.3. Preparation of 4,4′-bis($R_fCH_2OCH_2$)-2,2′-bpy **1a–e**, where R_f = n-C_3F_7 (**a**), $HCF_2(CF_2)_3$ (**b**), $HCF_2(CF_2)_7$ (**c**), n-C_8F_{17} (**d**), n-$C_{10}F_{21}$ (**e**)

2.3.1. General procedure

Thirty percent of CH_3ONa/CH_3OH (1.1 g) and R_fCH_2OH (6.0 mmol) were charged into a round-bottomed flask, then continuously stirred at 65 °C under N_2 atmosphere for 4 h before CH_3OH was vacuum removed to drive the reaction to the fluorinated alkoxide side. The resultant fluorinated alkoxide (6.0 mmol) was then dissolved in 20 mL of dry CH_3CN (or HFE 7100), and 4,4′-bis($BrCH_2$)-2,2′-bpy (5.8 mmol) added. The mixture was brought to reflux for 4 h, and the completeness of the reaction was checked by sampling the reaction mixtures and analyzing the aliquots with GC/MS. The product was purified by vacuum sublimation to obtain a white solid.

2.3.2. Analytical data of **1a**

Yield 86.2%; ^1H NMR (500 MHz, *d*-Me_2SO) δ 8.67 (2H, d, $^3J_{HH} = 4.5$ Hz, H_6), 8.37 (2H, s, H_3), 7.38 (2H, d, $^3J_{HH} = 4.5$ Hz, H_5), 4.84 (4H, s, bpy-CH_2), 4.34 (4H, t, $^3J_{HF} = 14.5$ Hz, CF_2CH_2); ^{19}F NMR (470.5 MHz, *d*-Me_2SO) δ −80.4 (t, $^3J_{HF} = 9$ Hz, CF_3), −119.7 (m, $CF_3CF_2CF_2$), −126.8 (s, $CF_3CF_2CF_2$); ^{13}C NMR (113 MHz, *d*-Me_2SO) δ 71.9 (bpy-CH_2), 66.5 (CH_2CF_2), 118.6, 122.2, 147.5, 149.6, 155.2 (bpy), 113.0–117.0 ($CF_2CF_2CF_3$); GC/MS (EI): 580 (M^+), 382 ($M^+-OCHC_3F_7$), 183 ($C_5H_3NCH_2C_5H_3NCH_3^+$), 91 ($C_5H_3NCH_2^+$); FT-IR (cm^{-1}): 1596, 1558 (*ν*bpy, m), 1225, 1120 (*ν*CF_2, vs); m.p.: 68–70 °C.

2.3.3. Analytical data of **1b**

Yield 71.1%; ^1H NMR (500 MHz, *d*-Me_2SO) δ 8.67 (2H, d, $^3J_{HH} = 4.5$ Hz, H_6), 8.37 (2H, s, H_3), 7.39 (2H, d, $^3J_{HH} = 4.5$ Hz, H_5), 7.06 (2H, tt, $^2J_{HF} = 51.9$ Hz, $J_{HF} = 5.5$ Hz, CF_2CF_2H), 4.84 (4H, s, bpy-CH_2), 4.29 (4H, t, $^3J_{HF} = 13.7$ Hz, CF_2CH_2); ^{19}F NMR (470.5 MHz, *d*-Me_2SO) δ −119.5 (2F, t, $^3J_{HF} = 14$ Hz, CH_2CF_2), −125.3 (2F, s, $CH_2CF_2CF_2$), −130.1 (2F, t, $^3J_{HF} = 5.5$ Hz, HCF_2CF_2), −137.2 (2F, d, $^2J_{HF} = 52$ Hz, HCF_2); ^{13}C NMR (113 MHz, *d*-Me_2SO) δ 73.0 (bpy-CH_2), 67.6 (CH_2CF_2), 119.4, 121.9, 147.1, 149.4, 155.7 (bpy), 105.0–116.0 (CF_2)$_4$; GC/MS (*m*/*z*; EI): 644 (M^+), 414 ($M^+-OCH_2C_4F_8$), 183 ($C_5H_3NCH_2C_5H_3NCH_3^+$), 91 ($C_5H_3NCH_2^+$); FT-IR (cm^{-1}): 1599, 1463 (*ν*bpy, m), 1208, 1144 (*ν*CF_2, vs); m.p.: 42 °C.

2.3.4. Analytical data of **1c**

Yield 85%; ^1H NMR (500 MHz, $CDCl_3$) δ 8.69 (2H, d, $^3J_{HH} = 4.5$ Hz, H_6), 8.33 (2H, s, H_3), 7.36 (2H, d, $^3J_{HH} = 4.5$ Hz, H_5), 6.03 (1H, tt, $^2J_{HF} = 51.9$ Hz, $^3J_{HF} = 5.5$ Hz CF_2H), 4.78 (4H, s, bpy-CH_2), 4.04 (4H, t, $^3J_{HF} = 13.7$ Hz, CF_2CH_2); ^{19}F NMR (470.5 MHz, $CDCl_3$) δ −119.1 (s, 2F, –CH_2CF_2), −121.9 (s, 6F), −123.0 (s, 4F), −128.9 (s, 2F, HCF_2CF_2–), −138.5 (d, 2F, $^2J_{HF} = 52$ Hz, HCF_2–); ^{13}C NMR (113 MHz, $CDCl_3$) δ 72.4 (bpy-CH_2), 67.1 (CH_2CF_2), 118.9, 122.7, 146.9, 149.6, 156.1 (bpy), 108.0–116.3 (CF_2)$_8$; GC/MS (*m*/*z*; EI): 614 ($M^+-OCH_2C_8F_{16}$), 198 ($C_5H_3NCH_2C_5H_3NCH_2O^+$), 183 ($C_5H_3NCH_2C_5H_3NCH_3^+$), 91 ($C_5H_3NCH_2^+$); FT-IR ($cm^{-1}$): 1596, 1558 (*ν*bpy, m), 1208, 1140 (*ν*CF_2, vs); m.p.: 86–88 °C.

2.3.5. Analytical data of **1d**

Yield 80%; ^1H NMR (500 MHz, $CDCl_3$) δ 8.67 (2H, d, $^3J_{HH} = 4.9$ Hz, H_6), 8.40 (2H, s, H_3), 7.34 (2 H, d, $^3J_{HH} = 4.9$ Hz, H_5), 4.77 (4H, s, bpy-CH_2), 4.04 (4H, t, $^3J_{HF} = 13.5$ Hz, CF_2CH_2); ^{19}F NMR (470.5 MHz, $CDCl_3$) δ −80.8 (3F), −119.3 (2F), −121.9 (6F), −122.7 (2F), −123.2 (2F), −126.1 (2F); ^{13}C NMR (113 MHz, $CDCl_3$) δ 73.0 (bpy-CH_2), 67.7 (CH_2CF_2), 119.2, 121.9, 146.9,

149.6, 156.1 (bpy), 108.0–119.0 (C_8F_{17}); GC/MS (*m*/*z*; EI): 632 ($M^+-OCHC_8F_{17}$), 198 ($C_5H_3NCH_2C_5H_3NCH_2O^+$), 183 ($C_5H_3NCH_2C_5H_3NCH_3^+$), 91 ($C_5H_3NCH_2^+$); FT-IR ($cm^{-1}$): 1602, 1560, 1465 (*v*bpy, m), 1204, 1145 (*v*CF_2, vs); m.p.: 113–115 °C.

2.3.6. Analytical data of **1e**

Yield 65%; ^1H NMR (500 MHz, $CDCl_3$) δ 8.69 (2H, d, $^3J_{HH} = 5.1$ Hz, H_6), 8.40 (2H, s, H_3), 7.38 (2H, d, $^3J_{HH} = 4.2$ Hz, H_5), 4.80 (4H, s, bpy-CH_2), 4.06 (4H, t, $^3J_{HF} = 13.3$ Hz, CF_2CH_2); ^{19}F NMR (470.5 MHz, $CDCl_3$) δ −80.7 (3F), −119.3 (2F), −121.7 (6F), −121.8 (4F), −122.6 (2F), −123.1 (2F), −126.0 (2F); ^{13}C NMR (113 MHz, $CDCl_3$) δ 73.1 (bpy-CH_2), 68.1 (CH_2CF_2), 119.8, 122.2, 144.7, 149.4, 154.1 (bpy), 105.5–116.2 ($C_{10}F_{21}$); GC/MS (*m*/*z*; EI): 732 ($M^+-OCHC_{10}F_{21}$), 198 ($C_5H_3NCH_2C_5H_3NCH_2O^+$), 183 ($C_5H_3NCH_2C_5H_3NCH_3^+$), 91 ($C_5H_3NCH_2^+$); FT-IR ($cm^{-1}$): 1602, 1562 (*v*bpy, m), 1215, 1151 (*v*CF_2, vs); m.p.: 140–142 °C.

2.4. Preparation of Pd complexes **2a**–**e** where $R_f = n\text{-}C_3F_7$ (**a**), $HCF_2(CF_2)_3$ (**b**), $HCF_2(CF_2)_7$ (**c**), $n\text{-}C_8F_{17}$ (**d**), $n\text{-}C_{10}F_{21}$ (**e**)

Equal molar amounts of $[PdCl_2(CH_3CN)_2]$ (134.9 mg, 0.52 mmol) and the respective ligands **1a**–**e** (0.52 mmol) for the different reactions were charged into a round bottomed flask, and CH_2Cl_2 (3 mL) added as a solvent. The color of solution changed from red to yellow after mixing for several minutes. The solution was further stirred at room temperature for 24 h before the solvents and volatiles were removed under vacuum. The resulting yellow solids were collected as spectroscopically pure products.

2.4.1. Analytical data of **2a**

Yield 98%; ^1H NMR (500 MHz, *d*-Me_2SO) δ 9.08 (2H, d, $^3J_{HH} = 5.9$ Hz, H_6), 8.37 (2H, s, H_3), 7.74 (2H, d, $^3J_{HH} = 5.9$ Hz, H_5), 4.96 (4H, s, bpy-CH_2), 4.42 (4H, t, $^3J_{HF} = 14.6$ Hz, CF_2CH_2); ^{19}F NMR (470.5 MHz, *d*-Me_2SO) δ −119.8 (2 F, CH_2CF_2), −127.1 (2F, s, $CH_2CF_2CF_2$), −80.4 (3F, t, $^3J_{HF} = 9.2$ Hz, CF_3); ^{13}C NMR (113 MHz, *d*-Me_2SO) δ 70.4 (bpy-CH_2), 65.5 (CH_2CF_2), 121.0, 124.7, 149.6, 152.1, 156.1 (bpy), 115.0–119.0 ($CF_2CF_2CF_3$); FT-IR (cm^{-1}): 1623, 1560 (*v*bpy, m), 1232, 1197 (*v*CF_2, vs); HR-MS (FAB): (M^+; *m*/*z*=) $C_{20}N_2H_{14}F_{14}O_2Pd^{35}Cl_2$ Calc. 755.9244. found 755.9266. $C_{20}N_2H_{14}F_{16}O_2Pd^{35}Cl^{37}Cl$ Calc. 757.9190; found 757.9199. $C_{20}N_2H_{14}F_{16}O_2Pd^{37}Cl_2$ Calc. 759.9185, found 757.9192.

2.4.2. Analytical data of **2b**

Yield 98%; ^1H NMR (500 MHz, *d*-Me_2SO) δ 9.05 (2H, d, $^3J_{HH} = 6.0$ Hz, H_6), 8.40 (2H, s, H_3), 7.72 (2H, d, $^3J_{HH} = 6.0$ Hz, H_5), 7.04 (2H, tt, $^2J_{HF} = 50.3$ Hz, $^3J_{HF} = 5.5$ Hz, HCF_2), 4.95 (4H, s, bpy-CH_2), 4.36 (4H, t, $^3J_{HF} = 14.7$ Hz, CF_2CH_2); ^{19}F NMR (470.5 MHz, *d*-Me_2SO) δ −119.3 (2F, t, $^3J_{HF} = 14$ Hz, CH_2CF_2), −124.8 (2F, s, $CH_2CF_2CF_2$), −129.7 (2F, t, $^3J_{HF} = 5.5$ Hz, HCF_2CF_2), −138.4 (d, 2F, $^2J_{HF} = 52$ Hz, HCF_2); ^{13}C NMR (113 MHz, $CDCl_3$) δ 71.7 (bpy-CH_2), 67.3 (bpy-CH_2OCH_2), 105.0–116.2 (CF_2)$_4$, 116.2, 121.7, 150.1, 152.7, 156.5 (bpy); FT-IR: 162, 1560 (*v*bpy, m), 1173, 1147 (*v*CF_2, vs) cm^{-1}; HR-MS (FAB): (M^+; *m*/*z*=) $C_{22}N_2H_{16}F_{16}O_2Pd^{35}Cl_2$ Calc. 819.9368, found 819.9363; $C_{22}N_2H_{16}F_{16}O_2Pd^{35}Cl^{37}Cl$ Calc. 821.9339, found 821.9348; $C_{22}N_2H_{16}F_{16}O_2Pd^{37}Cl_2$ Calc. 823.9343, found 823.9343.

2.4.3. Analytical data of **2c**

Yield 96%; ^1H NMR (500 MHz, *d*-Me_2SO) δ 9.08 (2H, d, $^3J_{HH} = 5.8$ Hz, H_6), 8.34 (2H, s, H_3), 7.73 (2H, dd, $^3J_{HH} = 5.8$ Hz, H_5), 7.19 (2H, tt, $^2J_{HF} = 50.3$ Hz, $^3J_{HF} = 5.3$ Hz, CF_2H), 4.96 (4H, s, bpy-CH_2), 4.41 (4H, t, $^3J_{HF} = 14.6$ Hz, CF_2CH_2); ^{19}F NMR (470.5 MHz, *d*-Me_2SO) δ −119.1 (s, 2F, CH_2CF_2), −121.9 (s, 6F), −122.9 (s, 4F), −128.7 (s, 2F, HCF_2CF_2), −138.5 (d, 2F, $^2J_{HF} = 52$ Hz, HCF_2); ^{13}C NMR (113 MHz, *d*-Me_2SO) δ 71.0 (bpy-CH_2), 66.8 (CH_2CF_2), 120.6, 124.3, 149.3, 151.6, 155.6 (bpy), 106.5–118.2 (CF_2)$_8$; FT-IR (cm^{-1}): 1654, 1560 (*v*bpy, m), 1210, 1147 (*v*CF_2, vs); HR-MS (FAB): (M^+; *m*/*z*=) $C_{30}N_2H_{16}F_{32}O_2Pd^{35}Cl_2$ Calc. 1219.9113, found 1219.9169; $C_{30}N_2H_{16}F_{32}O_2Pd^{35}Cl^{37}Cl$ Calc. 1221.9041, found 1221.9041; $C_{30}N_2H_{16}F_{32}O_2Pd^{37}Cl_2$ Calc. 1223.9054, found 1223.9009.

2.4.4. Analytical data of **2d**

(NMR data collected in *d*-DMF at 90 °C because of solubility): Yield 96%; ^1H NMR (500 MHz, *d*-DMF) δ 9.29 (2H, d, $^3J_{HH} = 5.9$ Hz, H_6), 8.48 (2H, s, H_3), 7.82 (2H, d, $^3J_{HH} = 5.9$ Hz, H_5), 5.08 (4H, s, bpy-CH_2), 4.47 (4H, t, $^3J_{HF} = 14.3$ Hz, C_8F_{17}–CH_2); ^{19}F NMR (470.5 MHz, *d*-DMF) δ −80.9 (3F), −119.1 (2F), −121.3 (6F), −122.1 (2F), −122.7 (2F), −125.5 (2F); ^{13}C NMR (113 MHz, *d*-DMF) δ 72.4 (bpy-CH_2), 68.3 (CH_2CF_2), 121.7, 125.3, 151.6, 153.1, 157.2 (bpy), 105.0–120.0 (C_8F_{17}); FT-IR (cm^{-1}): 1623, 1559, 1437 (*v*bpy, m), 1204, 1148 (*v*CF_2, vs); HR-MS (FAB): (M^+; *m*/*z*=) $C_{30}N_2H_{14}F_{34}O_2Pd^{35}Cl_2$ Calc. 1255.8924, found 1255.8920; $C_{30}N_2H_{14}F_{34}O_2Pd^{35}Cl^{37}Cl$ Calc. 1257.8928, found 1257.8954; $C_{30}N_2H_{14}F_{34}O_2Pd^{37}Cl_2$ Calc. 1259.8899, found 1259.8844.

2.4.5. Analytical data of **2e**

(NMR data collected in *d*-DMF at 90 °C because of solubility): yield 96%; ^1H NMR (500 MHz, *d*-DMF) δ 9.29 (2H, d, $^3J_{HH} = 5.8$ Hz, H_6), 8.47 (2H, s, H_3), 7.81 (2H, d, $^3J_{HH} = 5.8$ Hz, H_5), 5.08 (4H, s, bpy-CH_2), 4.47 (4H, t, $^3J_{HF} = 14.6$ Hz, $C_{10}F_{21}$–CH_2); ^{19}F NMR (470.5 MHz, *d*-DMF) δ −80.9 (3F), −119.1 (2F), −121.0 (10F), −122.1 (2F), −122.7 (2F), −125.5 (2F); ^{13}C NMR (113 MHz, *d*-DMF) δ 74.2 (bpy-CH_2), 68.2 (CH_2CF_2), 120.3, 124.5, 140.9, 151.8, 157.3 (bpy), 105.0–116.0 ($C_{10}F_{21}$); FT-IR (cm^{-1}): 1623, 1558 (*v*bpy, m), 1208, 1151 (*v*CF_2, vs); HR-MS (FAB): (M^+; *m*/*z*=) $C_{34}N_2H_{14}F_{42}O_2Pd^{35}Cl_2$ Calc. 1455.8869, found 1455.8842; $C_{34}N_2H_{14}F_{42}O_2Pd^{35}Cl^{37}Cl$

Calc. 1457.8767, found 1457.8741; $C_{34}N_2H_{14}F_{42}O_2Pd^{37}Cl_2$ Calc. 1459.8737, found 1459.8734.

2.5. Heck reaction experiments

2.5.1. Complexes **2a–c** as the catalyst precursors

In a typical run, the reaction vessel was charged with C_6H_5I (102.0 mg, 0.50 mmol), $H_2C{=}CHCO_2Me$ (64.5 mg, 0.75 mmol), NEt_3 (50.6 mg, 0.50 mmol) and the respective Pd-catalysts **2a–c** (0.5 mol%) or the recovered Pd-catalyst after distillation. Then the reaction mixture was set to reflux in DMF (4 mL), at 140 °C for 3 h before GC analysis then work-up. The DMF solvent, products and unspent reactants were vacuum removed initially at 100 °C and later between 150 and 200 °C. The Pd catalysts stayed in the reaction vessel for reuse in the next run.

2.5.2. Complex **2e** as the catalyst precursor

Under the fluorous biphasic system, the vessel was charged with DMF (3 mL), FC77 (3 mL), C_6H_5I (102 mg, 0.50 mmol), $H_2C{=}CHCO_2Me$ (64.5 mg, 0.75 mmol), NEt_3 (50.6 mg, 0.50 mmol) and the Pd-catalyst **2e** (0.5 mol%; 3.64 mg). Then the reaction mixture was set to reflux at 140 °C for 6 h before the reaction was stopped and the two layers separated using a separating funnel at 0 °C. The FC77 fraction was retained for recycling experiments.

2.5.3. Partition ratio determination [14]

A 10 mL vial was charged with the fluorinated ligand (0.0160 mmol), FC77 (2.000 mL), and organic solvent (2.000 mL), fitted with a min-inert valve, and vigorously shaken (2 min). After 12 h (24 °C), a 0.400 mL aliquot of each layer was added to a hexane solution of eicosane

Table 1
Crystal data and structure refinement details for **2b**

Empirical formula	$C_{22}H_{16}Cl_2F_{16}N_2O_2Pd$
Formula weight	821.67
Temperature (K)	100.0(1)
Wavelength (Å)	0.71073
Crystal system	triclinic
Space group	$P\bar{1}$
Unit cell dimensions	
a (Å)	7.1302(8)
b (Å)	11.5033(15)
c (Å)	16.419(2)
α (°)	80.095(7)
β (°)	86.552(7)
γ (°)	82.868(7)
Volume (Å^3)	1315.3(3)
Z	2
D_{calc} (Mg/m^3)	2.075
Absorption coefficient (mm^{-1})	1.050
$F(000)$	804
Crystal size (mm)	$0.16 \times 0.06 \times 0.04$
θ Range for data collection (°)	1.26 to 25.03
Index ranges	$-8 \leqslant h \leqslant 8$, $-13 \leqslant k \leqslant 13$, $-19 \leqslant l \leqslant 19$
Reflections collected	9646
Independent reflections (R_{int})	4623 (0.0631)
Completeness to $\theta = 25.03°$	99.5%
Absorption correction	semi-empirical from equivalents
Maximum and minimum transmission	0.9947 and 0.8386
Refinement method	full-matrix least-squares on F^2
Data/restraints/parameters	4623/0/401
Goodness-of-fit on F^2	0.610
Final R indices [$I > 2\sigma(I)$]	$R_1 = 0.0365$, $wR_2 = 0.0465$
R indices (all data)	$R_1 = 0.0775$, $wR_2 = 0.0511$
Largest difference in peak and hole (e Å^{-3})	0.548 and −0.658

Table 2
Fractional atomic coordinates ($\times 10^4$) and equivalent isotropic displacement parameters (Å$^2 \times 10^3$) for **2b**

	x	y	z	U (equiv)[a]
Pd	2775(1)	−1300(1)	4233(1)	14(1)
Cl(1)	3942(2)	−1551(1)	2947(1)	21(1)
Cl(2)	1958(2)	−3182(1)	4469(1)	21(1)
F(1)	8575(3)	6632(2)	3160(2)	27(1)
F(2)	9393(3)	4762(2)	3624(2)	28(1)
F(3)	7596(3)	6101(3)	1735(2)	35(1)
F(4)	8311(3)	4219(2)	2167(2)	34(1)
F(5)	10853(3)	5237(2)	1129(2)	32(1)
F(6)	11853(3)	4444(2)	2353(2)	33(1)
F(7)	10670(4)	7423(2)	1548(2)	38(1)
F(8)	13423(3)	6366(2)	1648(2)	40(1)
F(9)	−714(3)	−2310(3)	9712(2)	34(1)
F(10)	−2689(3)	−984(3)	10207(2)	38(1)
F(11)	−2912(3)	−2432(2)	8529(2)	26(1)
F(12)	−4677(3)	−811(2)	8710(2)	31(1)
F(13)	−3938(3)	−3271(2)	10249(2)	34(1)
F(14)	−6140(3)	−1774(2)	10089(2)	34(1)
F(15)	−5168(4)	−4145(3)	9035(2)	43(1)
F(16)	−6980(3)	−2523(3)	8624(2)	39(1)
O(8)	5750(4)	4265(3)	3469(2)	21(1)
O(28)	−425(4)	−745(3)	8230(2)	22(1)
N(1)	3299(4)	398(3)	4109(2)	10(1)
N(21)	1957(4)	−954(3)	5371(2)	13(1)
C(2)	2871(5)	926(4)	4772(3)	12(1)
C(3)	3150(5)	2085(4)	4765(3)	14(1)
C(4)	3863(5)	2752(4)	4050(3)	13(1)
C(5)	4256(5)	2217(4)	3360(3)	12(1)
C(6)	3939(5)	1055(4)	3398(3)	13(1)
C(7)	4230(6)	4007(4)	4051(3)	18(1)
C(9)	6178(5)	5428(4)	3434(3)	23(1)
C(10)	8190(6)	5515(4)	3123(3)	21(1)
C(11)	8688(6)	5310(4)	2244(3)	18(1)
C(12)	10773(6)	5380(4)	1933(3)	22(1)
C(13)	11659(6)	6470(4)	2003(3)	26(1)
C(22)	2174(5)	147(4)	5500(3)	10(1)
C(23)	1739(5)	494(4)	6252(3)	13(1)
C(24)	1083(5)	−301(4)	6911(3)	15(1)
C(25)	858(5)	−1414(4)	6767(3)	14(1)
C(26)	1339(5)	−1724(4)	6006(3)	14(1)
C(27)	592(6)	104(4)	7722(3)	20(1)
C(29)	−1076(6)	−366(4)	8972(3)	31(2)
C(30)	−1995(7)	−1358(5)	9500(3)	26(1)
C(31)	−3642(6)	−1774(4)	9104(3)	20(1)
C(32)	−4964(6)	−2522(4)	9692(3)	20(1)
C(33)	−6213(6)	−3222(5)	9291(3)	28(1)

[a] U (equiv) is defined as one third of the trace of the orthogonalized U_{ij} tensor.

(2.000 mL, 0.0273 M). Then GC analysis was used to determine the partition ratios.

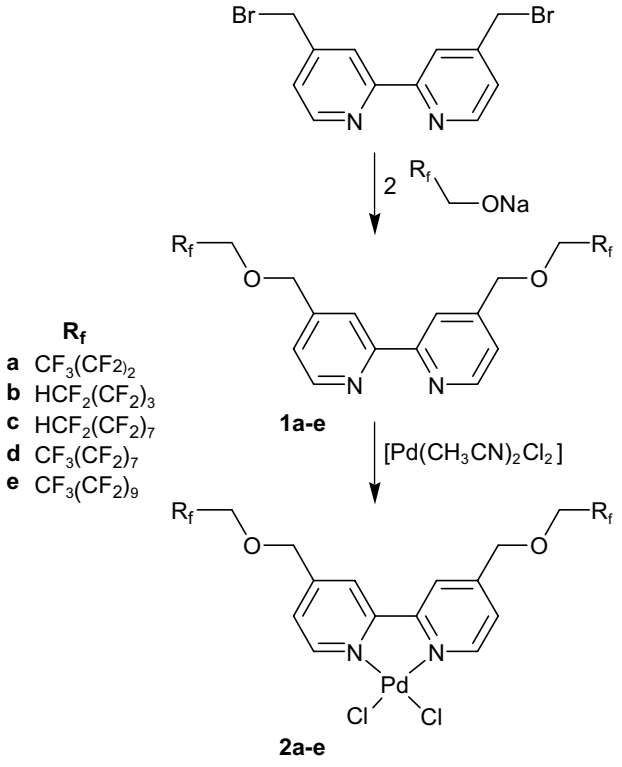
2.6. X-ray crystallography of Pd complex **2b**

Single crystals of Pd complex **2b** were obtained as yellow needles after 10 days at room temperature when the pure yellow powder of **2b** was dissolved in Me_2SO and then CH_3OH layered on top. The resultant yellow needles, with the residual Me_2SO solvent washed away using a large quantity of CH_3OH, were collected for single crystal structure determination. The crystal data and structure refinement for the Pd complex **2b** are listed in Table 1 and final fractional coordinates are in Table 2.

3. Results and discussion

3.1. Synthesis and spectroscopic characterization

The preparation of fluorous-ponytailed 2,2′-bpy ligands started from deprotonation of readily available fluorous alkanols R_fCH_2OH, where $R_f = n\text{-}C_3F_7$ (**a**), $HCF_2(CF_2)_3$ (**b**), $HCF_2(CF_2)_7$ (**c**), $n\text{-}C_8F_{17}$ (**d**), $n\text{-}C_{10}F_{21}$ (**e**). Fluorous alkanols R_fCH_2OH were treated with 30% CH_3ONa/CH_3OH to give the corresponding alkoxides. The alkoxides were then reacted with 4,4′-bis($BrCH_2$)-2,2′-bpy [15–17] to result in [(4,4′-bis($R_fCH_2OCH_2$)-2,2′-bpy)] (**1a**–**e**). An early preparation by Pozzi and co-workers [12] resulted in mixtures of mono-and bis-substituted bpy, presumably in their preparations the alkoxides were generated in situ without isolation. As shown in Scheme 1, equal molar amounts of [$PdCl_2(CH_3CN)_2$] and the fluorous bpy ligands **1a**–**e** were stirred in CH_2Cl_2 for 24 h at room temperature to yield the Pd complexes [$PdCl_2$(4,4′-bis($R_fCH_2OCH_2$)-2,2′-bpy)] (**2a**–**e**), which were all pale yellow solids, air and moisture stable. Both [$PdCl_2(CH_3CN)_2$] and ligands **1a**–**e** are more soluble in CH_2Cl_2 than the corresponding complexes **2a**–**e**.



Scheme 1.

The new Pd complexes **2a**–**e** have been characterized by multi-nuclei NMR, IR and high resolution FAB, with the data listed in Section 2. The ^1H NMR spectra are also used in monitoring the progress of the reaction. There are three kinds of bpy protons in the fluorous bpy ligands and Pd complexes, the assignments being the low field most signal for *H6*, the second low field signal for *H3* and the third for *H5*. As one example, shown in Fig. 1, the top and bottom spectra are the expanded ^1H NMR spectra for **1b** and **2b**, respectively, in the region ranging δ 9.2–3.8. The signals at *ca* δ 7.1 (triplet of triplets) are assigned to the ω-proton of the $-CF_2H$ group. The singlets at *ca* δ 4.9 are assigned to the bpy-CH_2 and the triplets at *ca* δ 4.3 to CF_2CH_2. Upon complex formation, the signals of H6 and H5 are downfield shifted by *ca* 0.3 δ-units and the signals of H3 stay almost at the same chemical shift.

3.2. Structure of **2b**

The structure of **2b** was established by single crystal X-ray diffraction. Fig. 2 reveals a molecular plot of **2b**, which is believed to be the first structure of a (2,2′-bpy)$PdCl_2$ type molecule carrying a fluorous ponytailed bipyridine skeleton. In **2b** the structural parameters around the square planar Pd coordination sphere conform to those found in the common (2,2′-bpy)$PdCl_2$, without noticeable differences [18].

A search of the Cambridge Structural Database reveals that there are many reported (2,2′-bpy)$PdCl_2$ structures, among those the ones with 4,4′- or 5,5′-substitutions were compared, but not the ones with 6,6′-substitutions that are structurally more distorted because of more steric interactions. Scheme 2 shows the reported (2,2′-bpy)$PdCl_2$ structures. In addition to the parent compound (**4**) [19,20], there are structures with varying ponytails including alkyls (**5**–**6**) [21–23], amides (**7**) [24], esters (**8**–**9**) [25,26] and ethers (**10**) [27]. The Pd–N lengths in **4**–**10** range from 2.002 to 2.041 Å, and the Pd–Cl lengths in **4**–**10** range from 2.271 to 2.319 Å. Both Pd–N and Pd–Cl bond distances in **2b** are at the low end of the range, partly because the temperature was experimentally maintained at 100 K when the diffraction data of **2b** was collected. The N–Pd–N angle in **2b** is 79.8(2)°, whereas it ranges from 79.6° to 81.6° in **4**–**10**.

There are two different crystal structures of parent **4** reported. One structure shows CH_2Cl_2-solvate separated (2,2′-bpy)$PdCl_2$ molecules in the solid state without any noted supramolecular π–π interactions. The other, without solvate in the crystalline state, exhibits a supramolecular π–π interaction between the (2,2′-bpy)$PdCl_2$ molecules at a distance of *ca* 3.42 Å. The structures **5**–**10** exhibit similar

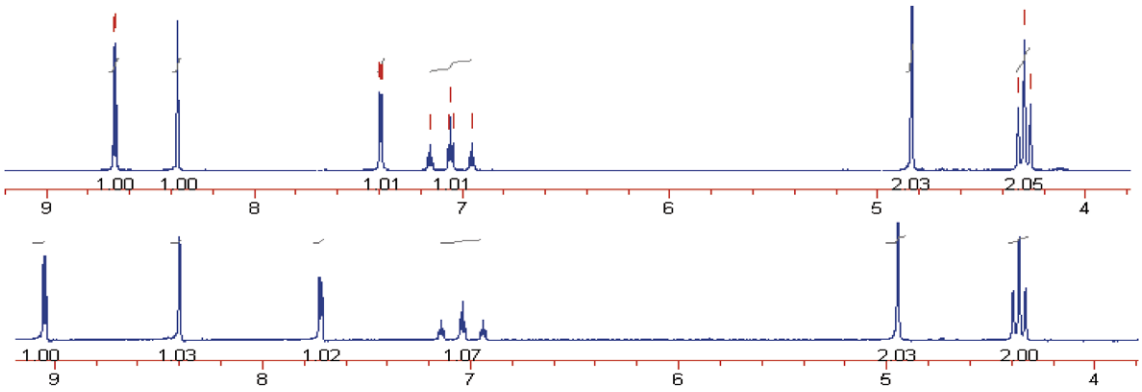


Fig. 1. ^{1}H NMR spectra of ligand **1b** (top) and Pd complex **2b** (bottom).

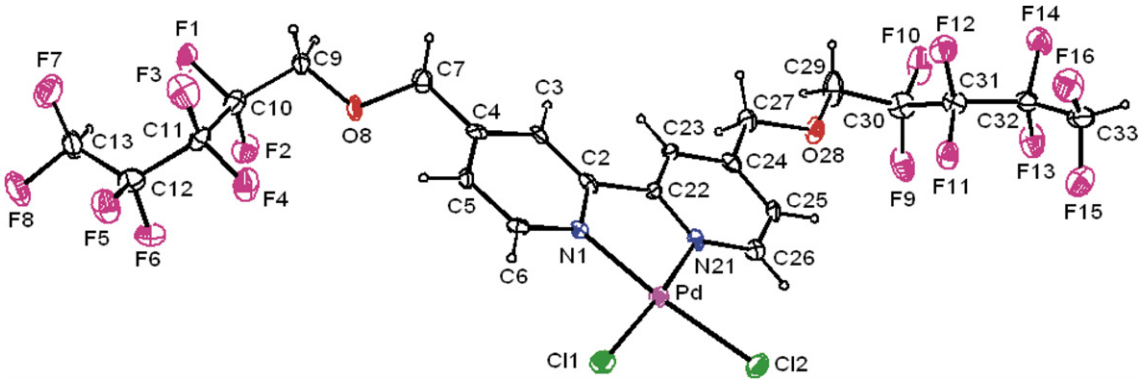


Fig. 2. Molecular plot of **2b.** Selected bond lengths (Å) and angles (°): Pd–N(1) 2.008(3), Pd–N(21) 2.014(3), Pd–Cl(1) 2.274(1), Pd–Cl(2) 2.274(1); N(1)–Pd–N(21) 79.8(2), N(1)–Pd–Cl(1) 94.9(1), N(1)–Pd–Cl(2) 174.4(1), N(21)–Pd–Cl(1) 173.7(1), N(21)–Pd–Cl(2) 95.2(1), Cl(1)–Pd–Cl(2) 90.2(1).

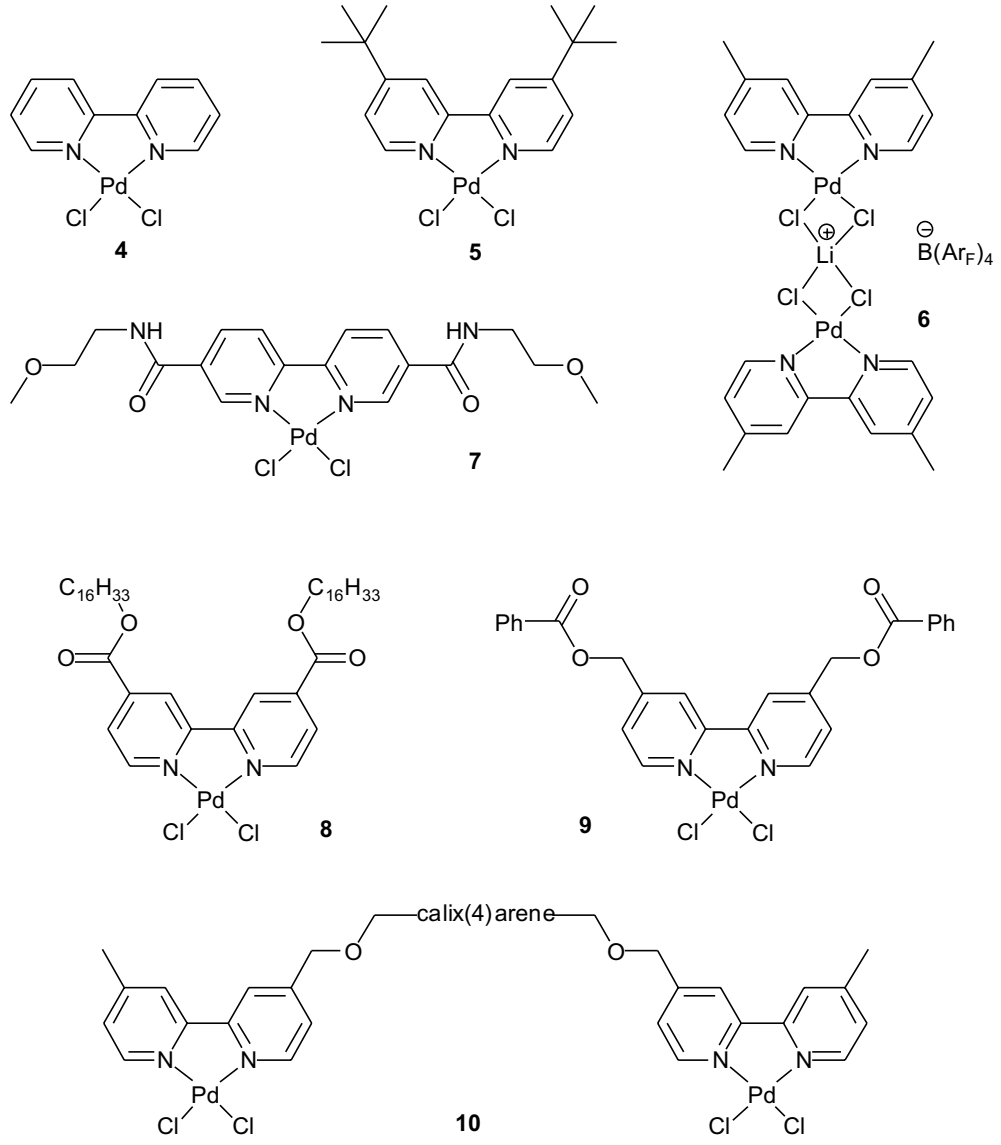
supramolecular π–π interactions in the solid state. In the structure of **5**, the separation is *ca* 3.54 Å between the (2,2′-bpy)$PdCl_2$ molecules; in **7**, *ca* 3.46 Å; in **8**, *ca* 3.44 Å; in **9**, *ca* 3.46 Å; in **10**, *ca* 3.42 Å. In **6**, the supramolecular π–π interactions exhibit a distance of *ca* 3.43 Å between the dimeric (2,2′-bpy)$PdCl_2$ and the $B(Ar_f)_4^-$ anion. In the crystal structure of **2b**, a supramolecular π–π interaction could be evidenced with a separation of *ca* 3.26 Å between the (2,2′-bpy)$PdCl_2$ molecules. The shorter distance in **2b** results from the low temperature on data collection at 100 K.

According to Bennett et al. [7], the fluorous modification of an aromatic ligand coordinated to a transition metal center may be accomplished without impacting the electronic character by replacement of an aromatic –H with a fluorinated substituent $–(CH_2)_3R_f$, $R_f = CF_3$, C_6F_{13}, etc. In **2b**, the $–CH_2OCH_2–$ spacer has been introduced between the fluorous ponytail and the bpy skeleton. In Fig. 2, the fluorous regions in **2b** are seen to be distal to the Pd center.

3.3. Fluorine content of the ligands

When a fluorous ponytail is introduced into the bpy skeleton, a spacer, such as the $–CH_2OCH_2–$ linkage, in between is needed in order to minimize the electron-withdrawing effect of the fluorinated segment on bpy, and hence on the donor N atom [7]. Indeed, the $–CH_2OCH_2–$ spacer does, to some extent, isolate the electronic effect of the fluorous ponytail, as reflected by the fact that the catalytic activity of the Pd complexes **2a**–**e** does not change very much in the Heck reactions [28].

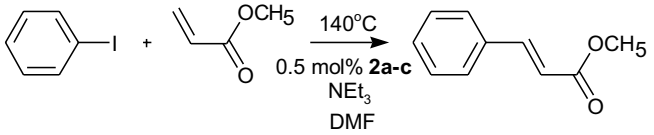
In this study, there are five different numbers of F-atoms on the fluorous ponytail, namely, 7, 8, 16, 17 or 21 F-atoms. Table 3 lists the fluorine percentage of ligands **1a**–**e**. According to their fluorine content, they could be divided into two subgroups, those below 50% [29,30] and those above [31]. Correspondingly, the Pd complexes **2a**–**b** are light in ligand fluorine content [29,30] and the Pd complexes **2c**–**e** high in ligand fluorine content [31]. It is well known that Pd complexes with light fluorine content ligands are still soluble in organic solvents in general. Alternatively, when the fluorine content of ligand is greater than 50%, the resultant Pd complex is then more soluble in perfluorinated solvents. For instance, Pd complex **2e** has been found to be soluble in perfluorinated solvents, but insoluble in organic solvents. With a high ligand fluorine content, Pd complex **2c**, however, has also the presence of the ω-CF_2H group. This terminally polar $–CF_2H$ group makes ligand **1c** only soluble in organic solvents and not in perfluorinated solvents, for instance FC77 (mainly C_8F_{18} in



Scheme 2.

Table 3
The fluorine percentage of ligands **1a**–**e**

Ligand	Fluorine content (%)
1a	45.9
1b	47.2
1c	58.3
1d	59.8
1e	62.3



Scheme 3.

composition). Thus the solubility properties of ligand **1c** are different from those of ligands **1d**–**e**.

3.4. Pd complexes *2a*–*c* as recyclable catalysts in Heck reactions

The Pd complexes **2a**–**b**, with light ligand fluorine contents, are soluble in organic solvents. The Pd complex **2c**, containing the polar ω-CF_2H group, is also soluble in organic solvents. Apparently, Pd complexes **2a**–**c** are not suitable homogeneous catalysts to be recovered with the fluorous biphasic strategy. Nonetheless, Pd complexes **2a**–**c** have been tested as catalyst precursors in the recycling Heck reaction of C_6H_5I and $H_2C{=}CHCO_2CH_3$, as shown in Scheme 3.

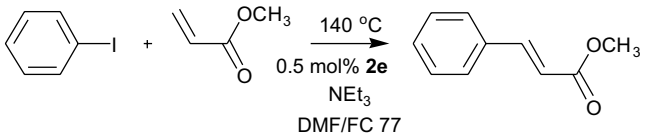
The high T_{90} points (*vide infra*) suggested that Pd-complexes **2a**–**c** should allow their isolation when everything else in the reaction mixture is distilled away. Accordingly,

at the end of reaction, the condenser was adjusted towards distillation instead of reflux. The more volatile materials were vacuum removed and the Pd catalysts stayed in the reaction vessel. Without further treatment, the reaction vessel was charged with a new batch of substrates, base and DMF, for the new run of the Heck reaction.

Table 4 shows the results from the above recycling usage of Pd-catalysts derived from **2a–c** in the Heck reaction, with the yields being based on GC analysis (with NMP as the internal standard). The product was 100% *trans*-PhCH=CHCO$_2$Me selectively. We noticed that for eight consecutive runs in all cases studied, the yields after 3 h were constantly greater than 99%. The simple recovery procedure kept, in the reaction vessel, Pd-containing materials that still maintain the catalytic activity.

3.5. Heck reaction under the fluorous biphasic system using Pd complex 2e

The ligands **1d–e** have a high fluorine content and are insoluble in organic solvents. The ligand **1d** is not very soluble in FC77 at room temperature in a partition experiment for measuring the coefficients under CH_2Cl_2/FC77 and DMF/FC77 conditions. The Pd complex **2d** was sparingly soluble in FC 77. When Pd complex **2d** was used as the catalyst precursor for the Heck reaction under the DMF/FC 77 biphasic condition, a very low yield resulted in the second run, which was attributed to the fact that the Pd catalyst derived from **2d** was more soluble in DMF. In comparison, the ligand **1e** shows a good solubility in FC77, giving reasonable partition ratios in the binary systems of CH_2Cl_2/FC77 (=1/42) and DMF/FC77 (=~0.1/100). Derived from ligand **1e**, the Pd complex **2e** was judged to be the choice for use as the catalyst precursor in Heck reactions under the fluorous biphasic system [6]. Thus, the reaction shown in Scheme 4 was performed for the Pd catalyst recycling experiments under the fluorous biphasic system, in order to see to what extent the Pd catalyst stays in the fluorous layer. The results are shown in Table 5, indicating that the Pd catalyst derived from **2e** could be recycled up to 8 times with an average yield of 93% before a drop in reactivity [32].



Scheme 4.

As the purpose of this study was to investigate the recyclability of the catalysts, no detailed study on the nature of the active Pd catalysts was made. It was assumed that the Pd catalysts derived from **2a–c** and **2e** are homogeneous molecules. However, it could not be ruled out that the true catalysts are nanoparticles as indicated by Gladysz and coworkers [14,33] or Pd colloids reported by de Vries et al. [34,35].

3.6. Thermal properties

The thermal stabilities of ligands **1a–e** and their corresponding Pd metal complexes **2a–e** were measured. The TGA weight loss curves of ligands **1a–e** exhibited the stability of general hydrocarbons despite the fact that they have fluorinated segments. The T_{90} points in weight loss for all five ligands were observed between 225 and 275 °C, the T_{90} points increasing with increasing molecular weights.

The weight loss curves of Pd complexes **2a–e** revealed that upon coordination, the Pd complexes have greater T_{90} points than the corresponding ligands. As one example shown in Fig. 3, the ligand **1b** started to lose weight at 250 °C and the complex **2b** at 330 °C, i.e., the Pd complex **2b** is about 80 °C more heat resistant than the corresponding ligand **1b**. The TGA data of **2b** suggested that **2b** loses its fluorous chain at 330 °C, followed by its bipyridine skeleton, resulting in Pd-oxychlorides with 18% of the original weight in the sample holder. The reason for the increase of

Table 4
Recycling results of the Heck reaction of C_6H_5I and H_2C=$CHCO_2CH_3$, using **2a–c**, as catalyst precursors

Run#[a]	Yields[b]		
	2a	**2b**	**2c**
1	>99	100	100
2	>99	100	100
3	>99	100	100
4	100	100	100
5	100	100	100
6	>99	100	100
7	>99	100	100
8	>99	100	100

[a] *Reaction conditions*: 140 °C; 3 h; DMF (4 mL); iodobenzene (102.0 mg, 0.50 mmol), methyl acrylate (64.5 mg, 0.75 mmol), NEt_3 (50.6 mg, 0.50 mmol), 0.5 mol% Pd complex (**2a** 1.9 mg, **2b** 2.0 mg, **2c** 3.0 mg,); At the end of each run, the DMF solvent, the products and any unreacted reactants were vacuum removed at 200 °C, and the remaining Pd containing materials were used for the next run.

[b] Based on GC analysis. (NMP as the internal standard).

Table 5
Recycling results of Pd complex **2e** as a catalyst in the Heck reaction under the DMF/FC77 biphasic system

Run#[a]	Yield%[b]	Run#[a]	Yield%[b]
1	96.8	5	92.0
2	98.5	6	98.5
3	95.3	7	88.2
4	100	8	77.4

[a] *Reaction conditions*: 100 °C; 6 h; DMF (3 mL); FC 77 (3 mL); iodobenzene (102 mg, 0.5 mmol), methyl acrylate (64.5 mg, 0.75 mmol), NEt_3 (50.6 mg, 0.5 mmol), 0.5 mol% Pd complex **2e** (3.64 mg); the two layers were separated at 0 °C using a separatory funnel after each run. The fluorous layer containing Pd metal complex **2e** was washed with 2 mL DMF (or CH_2Cl_2) before proceeding to the next run.

[b] Based on GC analysis. (NMP as the internal standard).

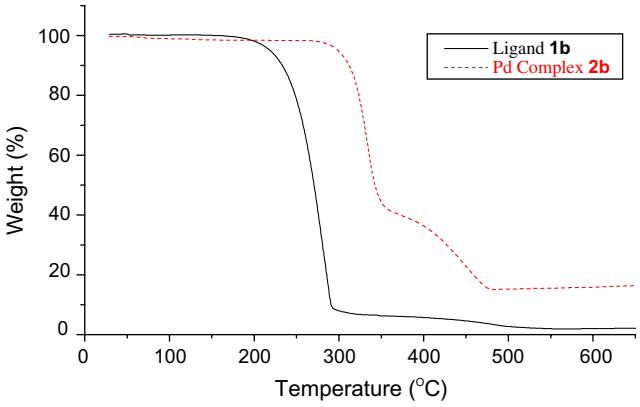


Fig. 3. The weight loss curves of ligand **1b** and Pd complex **2b**.

thermal stability upon bpy coordination to a Pd metal center is likely the requirement of *N*,*N*′-*cis* bpy for bonding to the Pd metal center and the supramolecular π–π interactions in the solid state Pd complexes.

4. Conclusions

The fluorous bpy ligands **1a**–**e** and Pd complexes **2a**–**e** were prepared and characterized by spectroscopic methods and the single crystal X-ray structure of **2b** was determined. The novel Pd complexes show nice catalytic activity in the Heck reaction and are recyclable. A part of the properties arises from the fact that the Pd complexes are thermally more stable than the corresponding ligands.

Acknowledgement

The authors thank the National Research Council in Taiwan for the financial support.

Appendix A. Supplementary material

CCDC 613935 contains the supplementary crystallographic data for **2b**. These data can be obtained free of charge via http://www.ccdc.cam.ac.uk/conts/retrieving.html, or from the Cambridge Crystallographic Data Centre, 12 Union Road, Cambridge CB2 1EZ, UK; fax: (+44) 1223-336-033; or e-mail: deposit@ccdc.cam.ac.uk. Supplementary data associated with this article can be found in the online version, at doi:10.1016/j.poly.2007.02.009.

References

[1] I.T. Horváth, J. Rabai, Science 266 (1994) 72.
[2] J.A. Gladysz, D.P. Curran, I.T. Horváth, Handbook of Fluorous Chemistry, Wiley–VCH, Weinheim, 2004.
[3] E.G. Hope, A.M. Stuart, J. Fluorine Chem. 100 (1999) 75.
[4] I.T. Horvath, Acc. Chem. Res. 31 (1998) 641.
[5] J.K. Cho, R. Najman, T.W. Dean, O. Ichihara, C. Muller, M. Bradley, J. Am. Chem. Soc. 128 (2006) 6276.
[6] J. Moineau, G. Pozzi, S. Quici, D. Sinou, Tetrahedron Lett. 40 (1999) 7683.
[7] B.L. Bennett, K.A. Robins, R. Tennant, K. Elwell, F. Ferri, I. Bashta, G. Aguinaldo, J. Fluorine Chem. 127 (2006) 140.
[8] D.J. Adams, D. Gudmunsen, J. Fawcett, E.G. Hope, A.M. Stuart, Tetrahedron 58 (2002) 3827.
[9] J. Fawcett, E.G. Hope, D.R. Russell, A.M. Stuart, D.R.W. Wood, Polyhedron 20 (2001) 321.
[10] P. Bhattacharyya, B. Croxtall, J. Fawcett, J. Fawcett, D. Gudmunsen, E.G. Hope, R.D.W. Kemmitt, D.R. Pagie, D.R. Rusell, A.M. Stuart, D.R.W. Wood, J. Fluorine Chem. 101 (2000) 247.
[11] E.G. Hope, R.D.W. Kemmitt, D.R. Paige, A.M. Stuart, D.R.W. Wood, Polyhedron 18 (1999) 2913.
[12] S. Quici, M. Cavazzini, S. Ceragioli, F. Montanari, G. Pozzi, Tetrahedron Lett. 40 (1999) 3647.
[13] N. Lu, J.Y. Chen, C.W. Fan, Y.C. Lin, in: Proceedings of the 18th International Symposium on Fluorine Chemistry, Meeting Abstract No. 193, Bremen, Germany, 2006.
[14] C. Rocaboy, J.A. Gladysz, New J. Chem. 27 (2003) 39.
[15] L.D. Ciana, W.J. Dressick, J. Heterocyclic Chem. 27 (1990) 163.
[16] A.R. Oki, R.J. Morgan, Synth. Commun. 25 (1995) 4093.
[17] G. Will, G. Boschloo, S.N. Rao, D. Fitzmaurice, J. Phys. Chem. B 103 (1999) 8067.
[18] A.G. Orpen, L. Brammer, F.H. Allen, O. Kennard, D.G. Watson, R. Taylor, J. Chem. Soc., Dalton Trans. (1989) S1.
[19] M. Maekawa, M. Munakata, S. Kitagawa, M. Nakamura, Anal. Sci. 7 (1991) 521.
[20] A.J. Canty, B.W. Skelton, P.R. Traill, A.H. White, Aust. J. Chem. 45 (1992) 417.
[21] Z. Qin, M.C. Jennings, R.J. Puddephatt, Inorg. Chem. 41 (2002) 3967.
[22] E.J. MacLean, R.I. Robinson, S.J. Teat, C. Wilson, S. Woodward, J. Chem. Soc., Dalton Trans. 18 (2002) 3518.
[23] H. Shen, I.M. Steele, R.F. Jordan, Acta Crystallogr. (C) 59 (2003) m405.
[24] P.D. Beer, N.C. Fletcher, M.G.B. Drew, T.J. Wear, Polyhedron 16 (1997) 815.
[25] D. Pucci, G. Barberio, A. Crispini, O. Francescangeli, M. Ghedini, M. La Deda, Eur. J. Inorg. Chem. 19 (2003) 3649.
[26] G. Barberio, A. Bellusci, A. Crispini, M. Ghedini, A. Golemme, P. Prus, D. Pucci, Eur. J. Inorg. Chem. 1 (2005) 181.
[27] R. Dorta, L.J.W. Shimon, H. Rozenberg, Y. Ben-David, D. Milstein, Inorg. Chem. 42 (2003) 3160.
[28] F.Y. Tsai, C.L. Wu, C.Y. Mou, M.C. Chao, H.P. Lin, S.T. Liu, Tetrahedron Lett. 45 (2004) 7503.
[29] D.P. Curran, Z. Luo, J. Am. Chem. Soc. 121 (1999) 9069.
[30] A. Studer, P. Jeger, P. Wipf, D.P. Curran, J. Org. Chem. 62 (1997) 2917.
[31] Q. Yao, Y. Zhang, J. Am. Chem. Soc. 126 (2004) 74.
[32] N. Lu, Y.C. Lin, J.Y. Chen, C.W. Fan, L.K. Liu, Tetrahedron 63 (2007) 2019.
[33] C. Rocaboy, J.A. Gladysz, Org. Lett. 4 (2002) 1993.
[34] J.G. de Vries, J. Chem. Soc., Dalton Trans. 3 (2006) 421.
[35] M.T. Reetz, J.G. de Vries, Chem. Commun. 10 (2004) 1559.

Available online at www.sciencedirect.com
ScienceDirect
Polyhedron 26 (2007) 3054–3062
POLYHEDRON
www.elsevier.com/locate/poly

Reactivity of $[ReOX_3(PPh_3)_2]$ complexes towards pyridazine. X-ray structures of $[\{ReOCl_2\}_2(\mu\text{-}O)(\mu\text{-}pyd)_2]\cdot C_6H_6$ and $[\{ReOBr_2\}_2(\mu\text{-}O)(\mu\text{-}pyd)_2]\cdot CH_3CN$, and DFT calculations for $[\{ReOCl_2\}_2(\mu\text{-}O)(\mu\text{-}pyd)_2]$

B. Machura [a,*], R. Kruszynski [b], J. Kusz [c]

[a] Department of Crystallography, Institute of Chemistry, University of Silesia, 9th Szkolna Street, 40-006 Katowice, Poland
[b] Department of X-ray Crystallography and Crystal Chemistry, Institute of General and Ecological Chemistry, Lodz University of Technology, 116 Żeromski Street, 90-924 Łódź, Poland
[c] Institute of Physics, University of Silesia, 4th Uniwersytecka Street, 40-006 Katowice, Poland

Received 19 January 2007; accepted 7 February 2007
Available online 27 February 2007

Abstract

The reactions of the $[ReOX_3(PPh_3)_2]$ (X = Cl, Br) complexes with pyridazine (pyd) have been examined and $[\{ReOX_2\}_2(\mu\text{-}O)(\mu\text{-}pyd)_2]$ dinuclear oxocomplexes with a bent $Re_2O_3^{4+}$ core have been obtained. The X-ray structures of $[\{ReOCl_2\}_2(\mu\text{-}O)(\mu\text{-}pyd)_2]\cdot C_6H_6$ (**1** · C_6H_6) and $[\{ReOBr_2\}_2(\mu\text{-}O)(\mu\text{-}pyd)_2]\cdot CH_3CN$ (**2** · CH_3CN) have been determined. The electronic structure of **1** has been calculated with the density functional theory (DFT) method, and additional information about binding in the $Re_2O_3^{4+}$ unit has been obtained by NBO analysis. The spin-allowed electronic transitions of **1** have been calculated with the time-dependent DFT method, and the UV–Vis spectrum of $[\{ReOCl_2\}_2(\mu\text{-}O)(\mu\text{-}pyd)_2]$ has been discussed on this basis.
© 2007 Elsevier Ltd. All rights reserved.

Keywords: Rhenium oxo complexes; Pyridazine; X-ray structure; DFT calculations

1. Introduction

During the last decade the preparation, structures and properties of dinuclear rhenium complexes with a $(ReO)_2(\mu\text{-}O)$ core have attracted much attention since these species can produce specific structures, properties and reactivities, not found for mononuclear complexes. Generally, these compounds can be divided into two groups: (i) complexes with a linear Re–O–Re core, and (ii) species with a bent Re–O–Re bridge. The preparation, structures and properties of the dinuclear rhenium complexes with the $(ReO)_2(\mu\text{-}O)$ core have been discussed in detail in paper [1].

Most diaza ligands can coordinate in a monodentate way or act as bridging ligands [2]. Treatment of $[ReOX_3(PPh_3)_2]$ with 3,5-Me_2pzH in acetone at room temperature leads to the isolation of the symmetrically substituted dinuclear rhenium complexes of the $[\{Re(O)\text{-}X(PPh_3)\}_2(\mu\text{-}O)(\mu\text{-}3,5\text{-}Me_2pz)_2]$ composition, whereas refluxing of $[ReO(OEt)X_2(PPh_3)_2]$ with 3,5-Me_2pzH in ethanol gives the unsymmetrically substituted dinuclear rhenium $[\{Re(O)X(PPh_3)\}(\mu\text{-}O)(\mu\text{-}3,5\text{-}Me_2pz)_2\{Re(O)X(3,5\text{-}Me_2pzH)\}]$ complexes. Both $[\{Re(O)X(PPh_3)\}_2(\mu\text{-}O)(\mu\text{-}3,5\text{-}Me_2pz)_2]$ and $[\{Re(O)X(PPh_3)\}(\mu\text{-}O)(\mu\text{-}3,5\text{-}Me_2pz)_2\{Re(O)X(3,5\text{-}Me_2pzH)\}]$ contain the bent $Re_2O_3^{4+}$ unit. Treatment of the $[ReOX_3(AsPh_3)(OAsPh_3)]$ complexes (X = Cl or Br) with 3,5-Me_2pzH in acetone at room temperature leads to replacement of $AsPh_3$ and $OAsPh_3$ ligands and formation of $[\{Re(O)X_2(3,5\text{-}Me_2pzH)_2\}_2(\mu\text{-}O)]$ with the nearly linear O═Re–O–Re═O moiety [3]. For benzotriazole, only the

* Corresponding author.
E-mail addresses: basia@ich.us.edu.pl (B. Machura), rafal.kruszynski@p.lodz.pl (R. Kruszynski).

0277-5387/$ - see front matter © 2007 Elsevier Ltd. All rights reserved.
doi:10.1016/j.poly.2007.02.019

symmetrically substituted dinuclear rhenium [{Re(O)X-(PPh$_3$)}$_2$(μ-O)(μ-C$_6$H$_4$N$_3$)$_2$] complexes with the bent Re–O–Re bridge have been isolated [4]. Refluxing [ReOX$_3$(PPh$_3$)$_2$] with pyrazole in ethanol leads to [{Re(O)X(PPh$_3$)}$_2$(μ-O)(μ-N$_2$C$_3$H$_3$)$_2$], but treatment of [ReOX$_3$(PPh$_3$)$_2$] with pzH in acetone at room temperature gives the mononuclear rhenium(V) complexes – [Re(O)-X$_2$(PPh$_3$)(η^2-N$_2$C$_6$H$_9$O-N,O)]. In the second case, pyrazole firstly adds to acetone yielding the C$_3$H$_3$N$_2$C(CH$_3$)$_2$OH adduct, which reacts with the starting oxo complex [5]. Treatment of the [ReOBr$_3$(AsPh$_3$)(OAsPh$_3$)] complex with pyrazine (pyz) in acetone at ambient temperature leads to the [{ReOBr$_2$(pyz)$_2$}$_2$(μ-O)] complex, with a nearly linear O═Re–O–Re═O moiety, whereas the reaction of [ReOBr$_3$(AsPh$_3$)(OAsPh$_3$)] with pyridazine (pyd) affords [{ReOBr$_2$}$_2$(μ-O)(μ-pyd)$_2$] with a bent Re$_2$O$_3^{4+}$ unit [6].

The studies show dependence of these reactions on the starting material, ring size and positions of the nitrogen atoms in the rings of the N-donor ligands, solvent and temperature. The [ReOX$_3$(AsPh$_3$)(OAsPh$_3$)] compounds generally form dinuclear oxorhenium complexes with a linear O═Re–O–Re═O moiety, whereas dinuclear oxorhenium compounds with a bent Re$_2$O$_3^{4+}$ unit are usually formed in the reactions with [ReOX$_3$(PPh$_3$)$_2$]. However, treatment of the [ReOBr$_3$(AsPh$_3$)(OAsPh$_3$)] complex with pyridazine leads to [{ReOBr$_2$(pyd)$_2$}$_2$(μ-O)] with a bent Re–O–Re bridge.

In this report we focus on the examination of the reactions of [ReOX$_3$(PPh$_3$)$_2$] with pyridazine and present the synthesis and spectroscopic data for [{ReOX$_2$(pyd)$_2$}$_2$-(μ-O)] complexes. For pyridazine, the course of the reaction does not depend on the starting material – both [ReOX$_3$(AsPh$_3$)(OAsPh$_3$)] and [ReOX$_3$(PPh$_3$)$_2$] react with pyridazine to give dinuclear [{ReOX$_2$(pyd)$_2$}$_2$(μ-O)] complexes with the bent Re$_2$O$_3^{4+}$ unit. X-ray studies have been performed for [{ReOCl$_2$}$_2$(μ-O)(μ-pyd)$_2$]·C$_6$H$_6$ (**1**·C$_6$H$_6$) and [{ReOBr$_2$}$_2$(μ-O)(μ-pyd)$_2$]·CH$_3$CN (**2**·CH$_3$CN). The first one is a novel compound, whereas **2**·CH$_3$CN is another solvate of [{ReOBr$_2$}$_2$(μ-O)(μ-pyd)$_2$]. The [{ReOBr$_2$}$_2$(μ-O)(μ-pyd)$_2$]·CH$_3$COCH$_3$ complex has been isolated in the reaction of [ReOBr$_3$(AsPh$_3$)(OAsPh$_3$)] with pyridazine in acetone at ambient temperature. The electronic structure of [{ReOCl$_2$}$_2$(μ-O)(μ-pyd)$_2$] has been calculated with the density functional theory (DFT) method. Currently density functional theory (DFT) is commonly used to examine the electronic structure of transition metal complexes. It meets with the requirements of being accurate, easy to use and fast enough to allow the study of relatively large molecules of transition metal complexes [7]. The singlet–singlet electronic transitions of [{ReOCl$_2$}$_2$(μ-O)(μ-pyd)$_2$] have been calculated with the time-dependent DFT method (TD-DFT method), and the UV–Vis spectrum of **1** has been discussed on this basis. Recent calculations with the TD-DFT method for open- and closed-shell 5d-metal complexes have supported the TD-DFT method to be applicable for such systems giving good assignment of experimental spectra [8,9].

2. Experimental

2.1. General procedure

All manipulations and reactions were carried out open to the atmosphere. All solvents were of reagent grade and

Table 1
Crystal data and structure refinement for complexes **1**·C$_6$H$_6$ and **2**·CH$_3$CN

	1·C$_6$H$_6$	**2**·CH$_3$CN
Empirical formula	C$_{14}$H$_{14}$Cl$_4$N$_4$O$_3$Re$_2$	C$_{10}$H$_{11}$Br$_4$N$_5$O$_3$Re$_2$
Formula weight	800.49	941.28
Crystal system	orthorhombic	orthorhombic
Space group	*Pnma*	*Pnma*
Unit cell dimensions		
a (Å)	14.0702(5)	14.1074(8)
b (Å)	13.6190(3)	13.7416(8)
c (Å)	10.3985(4)	10.8326(5)
Volume (Å^3)	1992.58(11)	2100.0(2)
Z	4	4
D_{calc} (Mg/m^3)	2.668	2.977
θ Range for data collection (°)	2.86–25.00	3.25–25.11
Index ranges	$-13 \leqslant h \leqslant 16$, $-16 \leqslant k \leqslant 16$, $-12 \leqslant l \leqslant 12$	$-13 \leqslant h \leqslant 16$, $-16 \leqslant k \leqslant 16$, $-12 \leqslant l \leqslant 12$
Reflections collected	11 816	21 366
Independent reflections (R_{int})	1835 (0.0287)	1951 (0.0984)
Completeness to $2\theta = 50$ (%)	98.3	99.6
Data/restraints/parameters	1835/0/111	1951/0/116
Goodness-of-fit on F^2	1.008	1.291
Final *R* indices [$I > 2\sigma(I)$]	$R_1 = 0.0196$, $wR_2 = 0.0454$	$R_1 = 0.0427$, $wR_2 = 0.0970$
R indices (all data)	$R_1 = 0.0317$, $wR_2 = 0.0471$	$R_1 = 0.0456$, $wR_2 = 0.0988$
Largest difference in peak and hole (e Å^{-3})	0.985 and −0.626	1.683 and −1.743

Table 2
Hydrogen bonds for $\mathbf{1}\cdot C_6H_6$ and $\mathbf{2}\cdot CH_3CN$

D	A	H···A (Å)	D···A (Å)	D–H···A (°)
1 $\cdot C_6H_6$				
C(1)	O(2)	2.57	2.943(6)	104.6
C(3)	O(2)	2.58	2.956(6)	104.5
C(1)	O(2)$^{\#1}$	2.48	3.174(6)	131.7
C(3)	Cl(2)$^{\#2}$	2.75	3.510(5)	139.4
C(99)	N(1)$^{\#3}$	2.32	3.218(14)	161.9
C(99)	N(1)$^{\#4}$	2.32	3.218(14)	161.9
2 $\cdot CH_3CN$				
C(3)	O(2)	2.58	2.958(10)	105.0
C(1)	O(2)$^{\#1}$	2.36	3.110(10)	137.2
C(3)	Br(2)$^{\#2}$	2.92	3.621(8)	133.0

$^{\#1}$ $-x, -y, -z$; $^{\#2}$ $-x+1/2, -y, z-1/2$; $^{\#3}$ $x, y, z+1$; $^{\#4}$ $x, -y+1/2, z+1$.

were used as received. Ammonium perrhenate, triphenylphosphine and pyridazine were purchased from Aldrich and were used as received. The $[ReOX_3(PPh_3)_2]$ complexes were prepared according to the literature method [10].

Infrared spectra were recorded on a Nicolet Magna 560 spectrophotometer in the spectral range 4000–400 cm^{-1} with the samples in the form of potassium bromide pellets. The electronic spectrum of **1** was measured on a spectrophotometer Lab Alliance UV–VIS 8500 in the range 1000–200 nm in CH_3CN solution. Elemental analyses (C H N) were performed on a Perkin–Elmer CHN-2400 analyzer.

2.2. Preparation of $[\{ReOCl_2(pyd)_2\}_2(\mu\text{-}O)]\cdot C_6H_6$ ($\mathbf{1}\cdot C_6H_6$)

$[ReOCl_3(PPh_3)_2]$ (0.83 g, 1 mmol) was suspended in a solution of pyridazine (0.2 g, 2.5 mmol) in acetone (50 ml) and the reaction mixture was stirred for 24 h. Diethyl ether (100 ml) was added and the black precipitate thus obtained was filtered. Good quality crystals for X-ray investigation were obtained by recrystallization from benzene. Yield 85%.

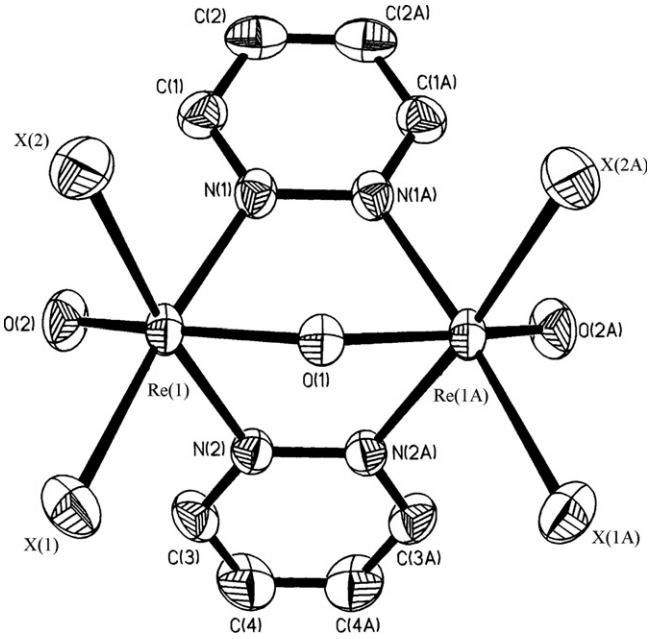


Fig. 1. The molecular structures of **1** and **2** (X = Cl or Br). Displacement ellipsoids are drawn at 50% probability.

IR (KBr, cm^{-1}): 1698(m), 1594(w), 1566 ν(CN) and ν(C=C); 958(s) ν(Re=O); 692 ν_{as}(Re–O–Re).

Anal. Calc. for $C_{14}H_{14}Cl_4N_4O_3Re_2$: C, 21.01; H, 1.76; N, 7.00. Found: C, 20.90; H, 1.85; N, 7.12%.

2.3. Preparation of $[\{ReOBr_2\}_2(\mu\text{-}O)(\mu\text{-}pyd)_2]\cdot CH_3CN$ ($\mathbf{2}\cdot CH_3CN$)

A procedure similar to that for **1** was used with $[ReOBr_3(PPh_3)_2]$ (0.97 g, 1 mmol) and pyridazine (0.2 g, 1.5 mmol). Good quality crystals for X-ray structure inves-

Table 3
The experimental and optimized bond lengths (Å) and angles (°) for $\mathbf{1}\cdot C_6H_6$

Bond lengths			Bond angles		
	Experimental	Optimized		Experimental	Optimized
Re(1)–O(1)	1.8995(19)	1.911	O(2)–Re(1)–O(1)	160.45(17)	154.61
Re(1)–O(2)	1.686(3)	1.699	O(2)–Re(1)–N(2)	87.56(16)	85.35
Re(1)–N(1)	2.164(4)	2.206	O(1)–Re(1)–N(2)	78.40(16)	77.24
Re(1)–N(2)	2.160(4)	2.206	O(2)–Re(1)–N(1)	86.93(15)	85.35
Re(1)–Cl(1)	2.3415(12)	2.360	O(1)–Re(1)–N(1)	79.47(15)	77.24
Re(1)–Cl(2)	2.3362(13)	2.360	N(2)–Re(1)–N(1)	89.41(14)	92.62
			O(2)–Re(1)–Cl(2)	101.61(13)	101.09
			O(1)–Re(1)–Cl(2)	92.04(13)	96.47
			N(2)–Re(1)–Cl(2)	170.43(11)	173.53
			N(1)–Re(1)–Cl(2)	88.34(10)	87.38
			O(2)–Re(1)–Cl(1)	99.45(12)	101.09
			O(1)–Re(1)–Cl(1)	94.20(13)	96.48
			N(2)–Re(1)–Cl(1)	90.27(10)	87.38
			N(1)–Re(1)–Cl(1)	173.59(10)	173.54
			Cl(2)–Re(1)–Cl(1)	90.92(5)	91.90
			Re(1)–O(1)–Re(1)#1	127.5(2)	129.14

Symmetry transformations used to generate equivalent atoms: $^{\#1}$ $x, -y+1/2, z$.

Table 4
The experimental and optimized bond lengths (Å) and angles (°) for $2 \cdot CH_3CN$

Bond lengths	Experimental	Bond angles	Experimental
Re(1)–O(1)	1.913(3)	O(2)–Re(1)–O(1)	160.0(3)
Re(1)–O(2)	1.705(5)	O(2)–Re(1)–N(2)	86.5(2)
Re(1)–N(1)	2.165(6)	O(1)–Re(1)–N(2)	78.6(2)
Re(1)–N(2)	2.180(5)	O(2)–Re(1)–N(1)	87.3(2)
Re(1)–Br(1)	2.4951(9)	O(1)–Re(1)–N(1)	79.3(3)
Re(1)–Br(2)	2.4902(8)	N(2)–Re(1)–N(1)	89.3(2)
		O(2)–Re(1)–Br(2)	101.34(18)
		O(1)–Re(1)–Br(2)	93.06(17)
		N(2)–Re(1)–Br(2)	171.65(15)
		N(1)–Re(1)–Br(2)	88.21(15)
		O(2)–Re(1)–Br(1)	99.48(19)
		O(1)–Re(1)–Br(1)	93.8(2)
		N(2)–Re(1)–Br(1)	89.58(15)
		N(1)–Re(1)–Br(1)	173.07(16)
		Br(2)–Re(1)–Br(1)	91.90(3)
		Re(1)–O(1)–Re(1)#1	127.3(3)

Table 5
Atomic charges from the natural population analysis (NPA) for **1**

Atom	Charge
Re(1)	1.254
O(1)	−0.755
O(2)	−0.525
Cl(1)	−0.341
Cl(2)	−0.341
N(1)	−0.242
N(2)	−0.242

tigation were obtained by recrystallization from acetonitrile.

IR (KBr, cm^{-1}): 1698(w), 1585(w), 1565 ν(CN) and ν(C=C); 956(s) ν(Re=O); 680 ν_{as}(Re–O–Re).

Anal. Calc. for $C_{10}H_{11}Br_4N_5O_3Re_2$: C, 12.76; H, 1.18; N, 7.44. Found: C, 12.89; H, 1.24; N, 7.55%.

2.4. Crystal structure determination and refinement

The X-ray intensity data $1 \cdot C_6H_6$ and $2 \cdot CH_3CN$ were collected on a KM-4-CCD automatic diffractometer equipped with a CCD detector. 20 and 60 s exposure times were used respectively and reflections were collected up to $\theta = 25°$. The unit cell parameters were determined from the least-squares refinement of the setting angles of 8946 and 6685 strongest reflections respectively for **1** and **2**. Details concerning crystal data and refinement are given in Table 1. Lorentz, polarization and numerical absorption corrections [11] were applied. The structures were solved by the partial structure expansion method and subsequently completed by difference Fourier recycling. All the non-hydrogen atoms were refined anisotropically using the full-matrix least-squares technique. The hydrogen atoms bonded to the aromatic atoms were treated as "riding" on their parent carbon atoms and assigned isotropic temperature factors equal to 1.2 times the value of equivalent temperature factor of the parent atom. The methyl groups were allowed to rotate about their local threefold axis. SHELXS97 [12], SHELXL97 [13] and SHELXTL [14] programs were used for all the calculations. Atomic scattering factors were those incorporated in the computer programs.

3. Computational details

The GAUSSIAN03 program [15] was used in the calculations. The geometry optimization of **1** was carried out with the DFT method with the use of the B3LYP functional [16,17]. The electronic spectrum of **1** was calculated with the TD-DFT method [18]. The calculations were performed by using the ECP basis set on the rhenium atom, the standard 6-31+G** basis for chlorine, oxygen and nitrogen, 6-31G* for carbon and 6-31G for hydrogen atoms. The Xe core electrons of Re were replaced by an effective core potential and a DZ quality Hay and Wadt Los Alamos ECP basis set (LANL2DZ) [19] was used for the valence electrons. An additional d function with exponent $\alpha = 0.3811$ and f function with exponent $\alpha = 2.033$ on the rhenium atom were added.

Natural bond orbital (NBO) calculations were performed with the NBO code [20] included in GAUSSIAN03.

4. Results and discussion

4.1. Preparation

The $[ReOX_3(PPh_3)_2]$ complexes react with pyridazine (pyd) in acetone at ambient temperature to give $[\{ReOX_2\}_2(\mu\text{-}O)(\mu\text{-}pyd)_2]$. The formation of the dinuclear compounds doubtlessly involves water and intermediate

Table 6
The occupancy and hybridization of the calculated natural bond orbitals (NBOs) between the rhenium and the oxo ligands for **1**

BD	Occupancy	BD	BD[a]	Occupancy
Re(1)–O(2)	1.932	$0.531(d)_{Re} + 0.847(p)_O$	$0.847(d)_{Re} - 0.531(p)_O$	0.262
Re(1)–O(2)	1.983	$0.569(d)_{Re} + 0.822(p)_O$	$0.822(d)_{Re} - 0.569(p)_O$	0.334
Re(1)–O(1)	1.783	$0.395(sd^{3.62})_{Re} + 0.919(sp^{3.16})_O$	$0.919(sd^{3.62})_{Re} - 0.394(sp^{3.16})_O$	0.489
Re(1A)–O(2A)	1.993	$0.559(d)_{Re} + 0.829(p)_O$	$0.829(d)_{Re} - 0.559(p)_O$	0.293
Re(1A)–O(2A)	1.983	$0.569(d)_{Re} + 0.822(p)_O$	$0.822(d)_{Re} - 0.569(p)_O$	0.334

BD denotes 2-center bond.
[a] Denotes antibond NBO.

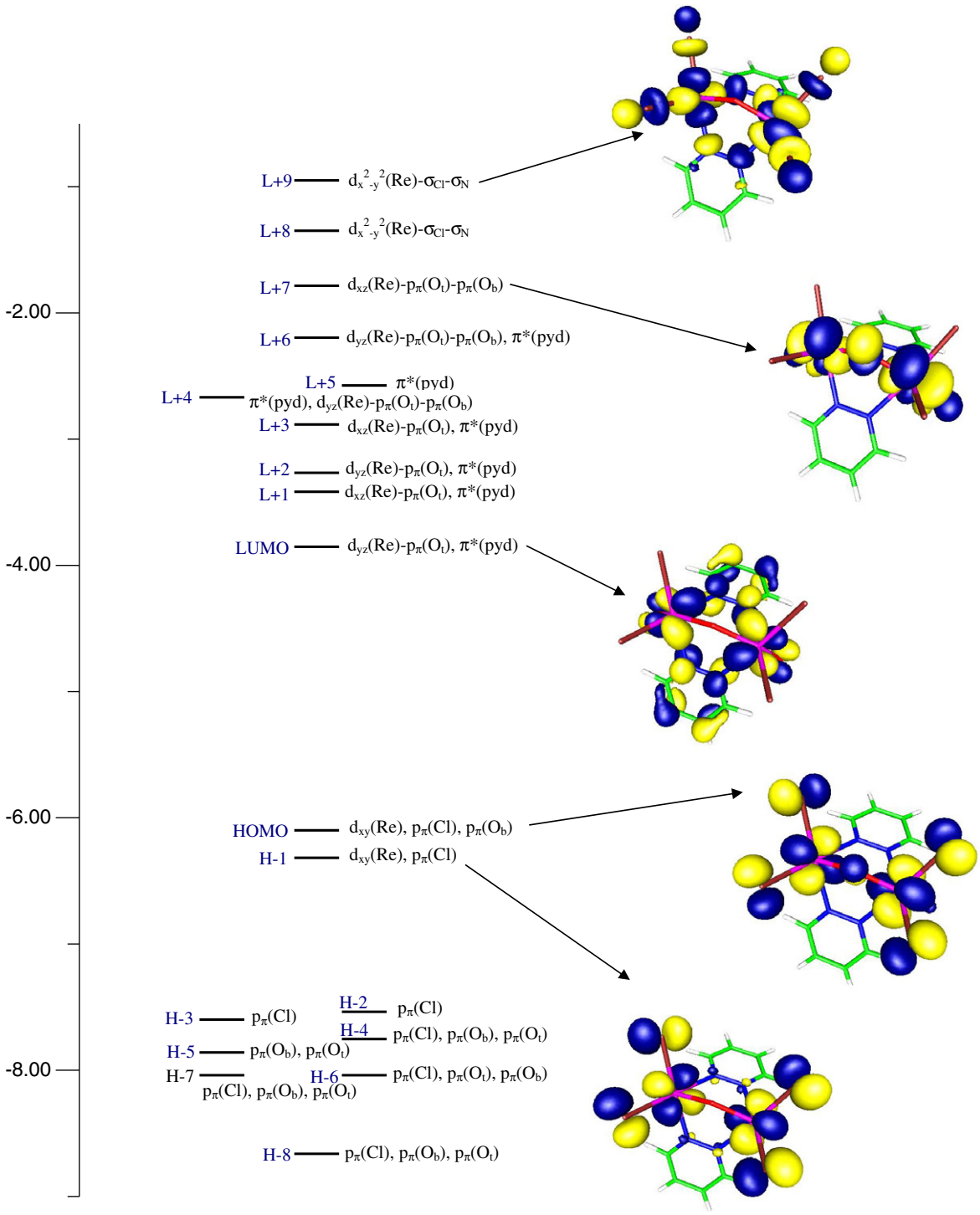


Fig. 2. The energy (eV), character and contour of the occupied and unoccupied molecular orbitals of **1** with the largest contributions of the d rhenium orbitals.

hydroxo-species. A water elimination reaction between two hydroxo complexes affording the oxygen bridged dinuclear species has been proposed and accepted and probably represents an alternative route to the direct deprotonation of an hydroxo intermediate affording the O=Re=O unit. Factors determining the formation and stabilization of μ-oxo dinuclear complexes as well as the conversion of the dinuclear complex to the mononuclear complex have not yet been investigated systematically and are dependent on reaction conditions [1].

4.2. Infrared data

The IR spectra of **1** and **2** show sharp bands at 958 and 956 cm^{-1} assignable to the symmetric Re=O stretch. The strong bands at 692 cm^{-1} for **1** and 680 cm^{-1} for **2** result

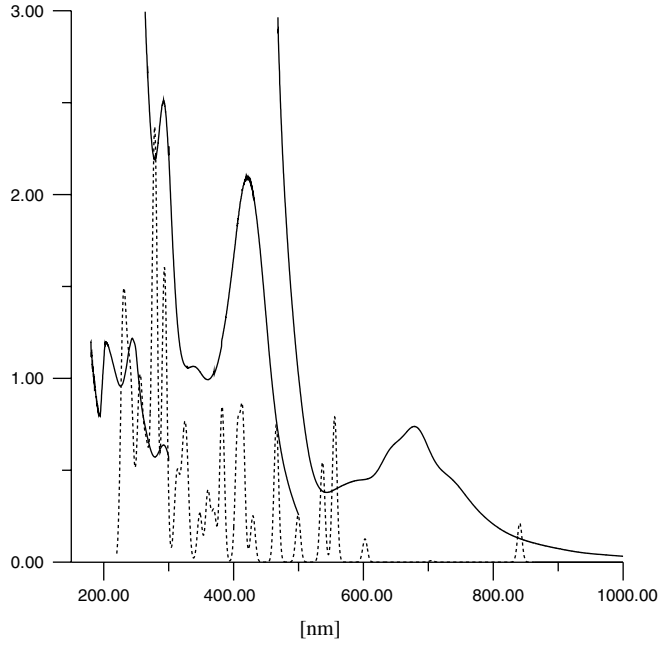


Fig. 3. The experimental (—) and calculated (----) electronic absorption spectra of **1**.

from overlapping of the antisymmetric Re–O–Re stretching modes with the aromatic ring out-of-plane deformation vibrations. In comparison with the $[(ReCl_5)_2(\mu\text{-}O)]^{4-}$ complex with an antisymmetric ν_{as}(Re–O–Re) stretching mode in the range 850–855 cm^{-1} [21], a significant reduction in the frequency of ν_{as}(Re–O–Re) is observed for compounds **1** and **2**. It is a consequence of the electron-withdrawing effect of the terminal Re=O groups causing a relative weakening of the bridging Re–O bonds.

4.3. Crystal structure

Both complexes are isostructural and isomorphic despite the fact that they crystallize as different solvates, $\mathbf{1}\cdot C_6H_6$ and $\mathbf{2}\cdot CH_3CN$. The molecules have an internal crystallographic mirror plane going through the bridging oxygen atom (special position c with site symmetry *m* of the orthorhombic space group *Pnma*) and mid-points of the pyridazine N–N bonds. Additionally, solvents molecules in both cases also have an internal crystallographic mirror plane. The benzene solvate molecule in **1** shows the symptoms of disorder which is exhibited in relatively large values of some orthogonalized displacement parameters (larger than 0.10) and a slight shortening of C–C distances. Because of the perpendicular mirror plane going through the benzene ring, it was difficult to unambiguously determine the reason of the disorder. Solving the structure in a lower symmetry space group leads to an insignificant decrease of the displacement parameters, but a shortening of C–C distances was not observed. Additionally, in the refined structure the benzene ring diagonal was inclined at 1.2° to the higher symmetry space group mirror plane direction. In both cases of refinement, introducing two or a multipositional disorder model did not improve the quality of the displacement parameters, thus it can be supposed that the disorder is mainly dynamical in character and the symmetry plane insignificantly influences the quality of solvate refinement, and thus the higher symmetry space group was chosen as a correct one. To prevent the distances from abnormal shortening, the benzene C–C bonds were restrained to 1.395(1) Å.

The accurate cell parameters and crystal data for $\mathbf{1}\cdot C_6H_6$ and $\mathbf{2}\cdot CH_3CN$ are given in Table 1. The solvent molecules from crystallization are not bonded to any other atom, with the exception of some rather weak hydrogen bonds. The weak intra- and intermolecular hydrogen bonds [22,23] of $\mathbf{1}\cdot C_6H_6$ and $\mathbf{2}\cdot CH_3CN$ are presented in Table 2. The synthesis, crystal and molecular structure of the monoclinic acetone solvate of $[\{ReOBr_2\}_2(\mu\text{-}O)(\mu\text{-}pyd)_2]$ has been presented in a previous paper [6]. In both polymorphs (orthorhombic and monoclinic), the complex molecules are isomorphic and have an internal symmetry plane, but the existence of solvent dimethylketone molecules in the monoclinic form prevents the existence of higher crystallographic symmetry. Slight differences in the unit cell volume and density of both forms result from differences in molecular mass and molecular volumes of the solvent molecules.

The structures of **1** and **2** reveal the presence of two rhenium(V) centers linked through two bridging pyridazine molecues and an oxo group (Fig. 1). Each rhenium atom is in a pseudooctahedral environment of two pyridazine molecules and two halide ions in the equatorial plane, and the terminal and bridging oxo ligands in axial positions. The considerable distortions from ideal octahedron in **1** and **2** result from both electronic repulsion of the short Re=O bond and steric interactions of bridging N–N ligands.

The most important bond lengths and angles for compounds **1** and **2** are reported in Tables 3 and 4, respectively. The Re–N, Re–O_t and Re–O_b bond lengths in **1** and **2** agree well with comparable values found in rhenium compounds with the O=Re–O–Re=O framework [1]. The Re–O_t bond lengths fall in the range 1.639–1.76 Å, typical of mononuclear complexes of rhenium(V) having a $[ReO]^{3+}$ core, and indicate the presence of a triple Re≡O_t bond [24]. The Re–O_b bond distances of 1.8995(19) and 1.913(3) Å for **1** and **2** suggest that a small amount of overlap also occurs between the d_{xz} and d_{yz} rhenium orbitals and the suitable p orbitals of the bridging oxygen. An ideal single Re–O bond length, predicted by the use of Pauling's covalent radius for oxygen and Cotton and Lippard's value for the octahedral covalent radius of rhenium(V), should be *ca.* 2.04 Å [25].

4.4. Geometry optimization

The optimized geometric parameters of **1** are gathered in Table 3. In general, the predicted bond lengths and angles are in agreement with the values based upon the X-ray

crystal structure data, and the general trends observed in the experimental data are well reproduced in the calculations.

4.5. Charge distribution and NBO analysis

Table 5 presents the atomic charges from the natural population analysis (NPA) for **1**. The calculated charges on the rhenium atoms are considerable lower than the formal charge of +5. The populations of the d_{xy}, d_{xz}, d_{yz}, $d_{x^2-y^2}$ and d_{z^2} orbitals of the central atoms in **1** are as follows: 0.864, 1.122, 0.929, 1.374 and 1.054. This is a result of significant charge donation from the oxo ligands and chloride ions. The charges on the oxo ligands and chloride ions are significantly smaller than −2 and −1, respectively. Considerable differences in values of charges are observed for the terminal and bridging oxo ligands – the terminal oxo ligands are less negative. It indicates higher electron density delocalization from the terminal ligands towards the rhenium centers and corresponds to differences in the Re–O_t and Re–O_b bonds lengths.

Table 6 presents the occupancy and hybridization of the calculated natural bond orbitals (NBOs) between the rhenium and the oxo ligands for **1**.

For each Re atom of **1**, two natural Re–O_t bond orbitals were detected. They are polarized towards the oxygen atom, and the p oxygen orbitals and d rhenium orbitals are involved in the Re–O_t bond formation. The atomic orbital compositions of the detected Re–O_t bond orbitals indicate their π character. The non-detected σ_{Re-Ot} bonds have character of predominant Coulomb-type interactions between the central ion and ligands [26]. Each terminal oxo

Table 7
The energy and molar absorption coefficients of experimental absorption bands and the electronic transitions calculated with the TD-DFT method for **1**

The most important orbital excitations	Character	λ (nm)	*E* (eV)	*f*	Experimental Λ (nm) (*E* (eV)) ε
H − 1 → L	d → d/π*(pyd)	840.8	1.47	0.0106	748.2 (1.66) 290
H → L + 1	d → d/π*(pyd)	703.8	1.76	0.0004	679.0 (1.83) 530
H − 1 → L + 1	d → d/π*(pyd)	602.5	2.06	0.0063	591.0 (2.10) 320
H − 1 → L + 2	d → d/π*(pyd)	555.7	2.23	0.0395	
H → L + 3	d → d/π*(pyd)	537.1	2.31	0.0272	
H − 1 → L + 1	d → d/π*(pyd)	499.4	2.48	0.0128	428.8 (2.89) 7360
H − 2 → L + 3	π(Cl) → d/π*(pyd)				
H → L + 4	d → π*(pyd)/d	465.8	2.66	0.0374	
H → L + 5	d → π*(pyd)	429.7	2.89	0.0126	
H − 2 → L	π(Cl) → d/π*(pyd)				
H − 2 → L	π(Cl) → d/π*(pyd)	413.9	3.00	0.0364	
H → L + 6	d → d/π*(pyd)	406.3	3.05	0.0325	
H − 4 → L	π(Cl)/π(O_b)/π(O_t) → d/π*(pyd)	382.3	3.24	0.0407	
H → L + 8	d → d	380.5	3.26	0.0018	
H → L + 7	d → d	371.2	3.34	0.0014	
H − 4 → L	π(Cl)/π(O_b)/π(O_t) → d/π*(pyd)	369.9	3.35	0.0114	
H − 2 → L + 1	π(Cl) → d/π*(pyd)	360.1	3.44	0.0180	
H − 1 → L + 7	d → d	350.1	3.54	0.0020	338.4 (3.66) 3850
H − 2 → L + 2	π(Cl) → d/π*(pyd)	347.7	3.57	0.0113	
H − 4 → L + 2	π(Cl)/π(O_b)/π(O_t) → d/π*(pyd)	326.5	3.80	0.0233	
H − 2 → L + 3	π(Cl) → d/π*(pyd)	322.1	3.85	0.0185	
H − 7 → L + 1	π(Cl)/π(O_b)/π(O_t) → d/π*(pyd)	313.4	3.96	0.0160	
H − 9 → L	π(Cl)/π(pyd) → d/π*(pyd)	294.6	4.21	0.0468	292.2 (4.24) 9050
H − 5 → L + 3	π(Cl)/π(O_t) → d/π*(pyd)	292.2	4.24	0.0273	
H − 7 → L + 3	π(Cl)/π(O_b)/π(O_t) → d/π*(pyd)	280.5	4.42	0.0383	
H − 8 → L + 1	π(Cl)/π(O_b)/π(O_t) → d/π*(pyd)	278.3	4.46	0.0375	
H − 1 → L + 9	d → d	277.7	4.46	0.0050	
H − 6 → L + 3	π(Cl)/π(O_b)/π(O_t) → d/π*(pyd)	277.0	4.48	0.0393	
H − 4 → L + 4	π(Cl)/π(O_b)/π(O_t) → π*(pyd)/d				
H − 5 → L + 4	π(Cl)/π(O_t) → π*(pyd)/d	273.1	4.54	0.0101	
H − 9 → L + 1	π (Cl)/π(pyd) → d/π*(pyd)	262.0	4.73	0.0114	
H − 9 → L + 2	π (Cl)/π(pyd) → d/π*(pyd)	256.5	4.83	0.0357	
H − 10 → L + 2	π(Cl)/π(O_b)/π(O_t)/n(N) → d/π*(pyd)	252.4	4.91	0.0176	244.0 (5.08) 22050
H − 8 → L + 3	π(Cl)/π(O_b)/π(O_t) → d/π*(pyd)				
H − 12 → L + 1	π (Cl)/n(N) → d	240.0	5.17	0.0123	206.6 (6.00) 21360
H − 2 → L + 8	π (Cl) → d	235.6	5.26	0.0161	
H − 13 → L + 1	π(Cl)/π(O_b) → d/π*(pyd)	230.1	5.39	0.0391	
H − 8 → L	π(pyd) → d/π*(pyd)	228.0	5.44	0.0215	

ligand of **1** has two lone pairs, and the electron density from one of them is strongly delocalized into the non-Lewis rhenium orbitals. The bridging oxygen ligand has three lone pairs (LP) and one Re–O_b bond orbital was detected. The detected Re(1)–O(1) bond is strongly polarized towards the bridging oxygen atom, and the s and p oxygen orbitals and s and d rhenium orbitals take part in the bond formation. The non-detected Re(1A)–O(1) bond has predominantly ionic character.

4.6. Electronic structure

The energy and character of the selected unoccupied and occupied MOs for **1** are presented in Fig. 2. The local symmetry of the rhenium centers has been considered in the discussion. The z axis goes along the O_t–Re–O_b linkage, x and y axes – through the Cl–Re–N bonds. The HOMO–LUMO gap equals 2.25 eV. The two highest MOs of **1** are of d_{xy} type with an antibonding contribution from p_π chlorine and oxygen orbitals. The remaining eight d-type orbitals of rhenium are found among the unoccuppied MOs. It confirms the d^2 configuration of the rhenium atoms. The d_{xz} and d_{yz} rhenium orbitals are dispersed amongst a large number of molecular orbitals. Significant participation of the d_{xz} and d_{yz} orbitals is visible in the LUMO, LUMO + 1, LUMO + 2, LUMO + 3, LUMO + 6 and LUMO + 7 orbitals. The d_{xz} and d_{yz} orbitals bear antibonding character towards the oxygen atoms, and some participation of π-antibonding orbitals of the pyridazine rings is visible in these molecular orbitals. The LUMO + 8 and LUMO + 9 are of $d_{x^2-y^2}$-σ_{Cl}–σ_N character. As can be seen from Fig. 3, each molecular orbital is a plus or minus combination of the symmetry equivalent d orbitals of the two rhenium atoms.

4.7. Electronic spectrum

The experimental and calculated electronic spectra of **1** are presented in Fig. 3. Each calculated transition is represented by a gaussian function $y = ce^{-bx^2}$ with the height (c) equal to the oscillator strength and b equal to 0.04 nm^{-2}.

Table 7 shows the singlet-singlet electronic transitions calculated with the TDDFT method for **1**. For the high energy part of the spectrum, only transitions with oscillator strenghts larger than 0.010 are listed in Table 7. The investigated complex is of a large size, the number of basis functions is equal to 430. A hundred electron transitions calculated with the TD-DFT method do not comprise all the experimental absorption bands. The UV–Vis spectrum of **1** was calculated to ~228 nm, so the shortest wavelength experimental band is not assigned to the calculated transitions. Some additional intraligand and interligand transitions are expected to be found at higher energies in the calculations for this complex.

The longest wavelength experimental bands at 748.2, 679.0 and 591.0 nm correspond to the transitions from the HOMO and HOMO − 1 to LUMO, LUMO + 1 and LUMO + 3 orbitals. Due to significant participation of π^* orbitals of the pyridazine ligands in the unoccupied molecular orbitals, the character of these electronic transitions is ascribed as d → d/π^*(pyd).

The absorption band at 428.8 nm is assigned to the electronic transitions calculated in the range 500–360 nm. These transitions are of π(Cl)/π(O) → d/π^*(pyd), π(Cl) → d/π^*(pyd), d → π^*(pyd) and d → d origin.

The experimental bands at 338.4, 292.2 and 244.0 nm correspond mainly to the transitions of LMCT (π(Cl)/π(O) → d) and LLCT (π(Cl)/π(O) → π^*(pyd)) character.

5. Supplementary material

CCDC 634230 and 634231 contain the supplementary crystallographic data for $C_{14}H_{14}Cl_4N_4O_3Re_2$ and $C_{10}H_{11}Br_4N_5O_3Re_2$. These data can be obtained free of charge via http://www.ccdc.cam.ac.uk/conts/retrieving.html, or from the Cambridge Crystallographic Data Centre, 12 Union Road, Cambridge CB2 1EZ, UK; fax: (+44) 1223-336-033; or e-mail: deposit@ccdc.cam.ac.uk.

Acknowledgement

The GAUSSIAN03 calculations were carried out in the Wrocław Centre for Networking and Supercomputing, WCSS, Wrocław, Poland under Calculational Grant No. 51/96.

References

[1] B. Machura, Coord. Chem. Rev. 249 (2005) 591.
[2] S. Trofimenko, Inorg. Chem. 34 (1986) 115.
[3] B. Machura, J.O. Dzięgielewski, R. Kruszynski, T.J. Bartczak, J. Kusz, Inorg. Chim. Acta 357 (2004) 1011.
[4] B. Machura, J.O. Dzięgielewski, R. Kruszynski, T.J. Bartczak, Polyhedron 22 (2003) 2869.
[5] B. Machura, J.O. Dzięgielewski, S. Michalik, R. Kruszynski, T.J. Bartczak, J. Kusz, Transition Met. Chem. 28 (2003) 939.
[6] B. Machura, R. Kruszynski, M. Jaworska, P. Lodowski, Polyhedron 24 (2005) 1893.
[7] H. Chermette, Coord. Chem. Rev. 178–180 (1998) 699.
[8] M.C. Aragoni, M. Arca, T. Cassano, C. Denotti, F.A. Devillanova, F. Isaia, V. Lippolis, D. Natali, L. Niti, M. Sampietro, R. Tommasi, G. Verani, Inorg. Chem. Commun. 5 (2002) 869.
[9] P. Romaniello, F. Lelj, Chem. Phys. Lett. 372 (2003) 51.
[10] G. Rouschias, G. Wilkinson, J. Chem. Soc. A (1966) 465.
[11] (a) STOE & Cie, X-RED. Version 1.18. STOE & Cie GmbH, Darmstadt, Germany, 1999;
(b) CrysAlis RED, Oxford Diffraction Ltd., Version 1.171.29.2.
[12] G.M. Sheldrick, Acta Crystallogr., Sect. A 46 (1990) 467.
[13] G.M. Sheldrick, SHELXL97. Program for the Solution and Refinement of Crystal Structures, University of Göottingen, Germany, 1997.
[14] G.M. Sheldrick, SHELXTL: Release 4.1 for Siemens Crystallographic Research Systems, 1990.
[15] M.J. Frisch, G.W. Trucks, H.B. Schlegel, G.E. Scuseria, M.A. Robb, J.R. Cheeseman, J.A. Montgomery Jr., T. Vreven, K.N. Kudin, J.C. Burant, J.M. Millam, S.S. Iyengar, J. Tomasi, V. Barone, B. Mennucci, M. Cossi, G. Scalmani, N. Rega, G.A. Petersson, H. Nakatsuji, M. Hada, M. Ehara, K. Toyota, R. Fukuda, J. Hasegawa, M. Ishida, T. Nakajima, Y. Honda, O. Kitao, H. Nakai, M. Klene, X. Li, J.E. Knox, H.P. Hratchian, J.B. Cross, C. Adamo, J. Jaramillo,

Gomperts, R.E. Stratmann, O. Yazyev, A.J. Austin, R. Cammi, C. Pomelli, J.W. Ochterski, P.Y. Ayala, K. Morokuma, G.A. Voth, P. Salvador, J.J. Dannenberg, V.G. Zakrzewski, S. Dapprich, A.D. Daniels, M.C. Strain, O. Farkas, D.K. Malick, A.D. Rabuck, K. Raghavachari, J.B. Foresman, J.V. Ortiz, Q. Cui, A.G. Baboul, S. Clifford, J. Cioslowski, B.B. Stefanov, G. Liu, A. Liashenko, P. Piskorz, I. Komaromi, R.L. Martin, D.J. Fox, T. Keith, M.A. Al-Laham, C.Y. Peng, A. Nanayakkara, M. Challacombe, P.M.W. Gill, B. Johnson, W. Chen, M.W. Wong, C. Gonzalez, J.A. Pople, GAUSSIAN 03, Revision B.03, Gaussian, Inc., Pittsburgh PA, 2003.

[16] A.D. Becke, J. Chem. Phys. 98 (1993) 5648.

[17] C. Lee, W. Yang, R.G. Parr, Phys. Rev. B 37 (1988) 785.

[18] M.E. Casida, in: J.M. Seminario (Ed.), Recent Developments and Applications in Modern Density Functional Theory, Theoretical and Computational Chemistry, vol. 4, Elsevier, Amsterdam, 1996.

[19] P.J. Hay, W.R. Wadt, J. Chem. Phys. 82 (1985) 299.

[20] E.D. Glendening, A.E. Reed, J.E. Carpenter, F. Weinhold, NBO (version 3.1).

[21] W.P. Griffith, T.D. Wickins, J. Chem. Soc. A (1967) 675.

[22] G.A. Jeffrey, W. Saenger, Hydrogen Bonding in Biological Structures, Springer-Verlag, 1994.

[23] G.R. Desiraju, T. Steiner, The Weak Hydrogen Bond in Structural Chemistry and Biology, Oxford University Press, 1999.

[24] J.M. Mayer, Inorg. Chem. 27 (1988) 3899.

[25] S.R. Fletcher, A.C. Skapski, J. Chem. Soc., Dalton Trans. (1972) 1073.

[26] M.L. Kuznestov, A.J.L. Pombeiro, J. Chem. Soc., Dalton Trans. (2003) 738.

Available online at www.sciencedirect.com
ScienceDirect
Polyhedron 26 (2007) 3063–3068
POLYHEDRON
www.elsevier.com/locate/poly

Synthesis, structures and catalytic properties of stable oxo-bridged half-sandwich titanium complexes

Qiao-Lin Wu [a], Guang-Hua Li [b], Ling Ye [a], Wei Gao [a], Ying Mu [a,*]

[a] Key Laboratory for Supramolecular Structure and Materials of Ministry of Education, School of Chemistry, Jilin University, 2699 Qianjin Street, Changchun 130012, People's Republic of China

[b] State Key Laboratory of Inorganic Synthesis and Preparative Chemistry, School of Chemistry, Jilin University, 2699 Qianjin Street, Changchun 130012, People's Republic of China

Received 29 October 2006; accepted 7 February 2007
Available online 20 February 2007

Abstract

Hydrolysis of 1,2-diphenyl-4-R-cyclopentadienyl titanium trichloride (R = Me (**1**), *n*-Bu (**2**)) affords the corresponding oxo-bridged monocyclopentadienyl titanium compounds (1,2-Ph_2-4-R-$CpTiCl_2)_2(\mu$-O) (R = Me (**3**), *n*-Bu (**4**)), new dinuclear species. The molecular structures of complexes **3** and **4** have been confirmed by single-crystal X-ray diffraction. Both complexes have been characterized by elemental analysis, ^{1}H and ^{13}C NMR spectroscopy. When activated with $Al(^iBu)_3$ and $Ph_3C^+B(C_6F_5)_4^-$, complexes **3** and **4** show reasonable catalytic activity for ethylene polymerization, producing polyethylenes with moderate molecular weights, and upon activation with methylaluminoxane (MAO), complexes **3** and **4** exhibit high catalytic activity and syndiospecificity for the polymerization of styrene.
© 2007 Elsevier Ltd. All rights reserved.

Keywords: Metallocene; Olefin polymerization; Polyethylene; Syndiotactic polystyrene; Titanium

1. Introduction

Group 4 metallocene catalysts have attracted extensive interest due to their applications in the fields of organometallic chemistry, catalysis and polymer science [1–3]. In particular titanium catalysts based on the cyclopentadienyl ligand have been widely studied as active catalysts employed in industry and academic institutions [4–15]. It is well known that even minor modification of the ligands can result in remarkable changes in catalytic activity, as well as polymer properties, such as molecular weight, comonomer incorporation and stereoregularity [16–20]. Thus, it is of great significance to develop new homogeneous catalysts producing a number of high performance polyolefins. Recently we have reported a series of diphenyl substituted cyclopentadienyl titanium trichloride complexes as precatalysts for styrene polymerization [21]. Further study on these titanium systems found that these complexes could be readily hydrolyzed to produce corresponding dimeric compounds in solution. In previous instances, dinuclear complexes bearing a cyclopentadienyl ligand play a significant role in some catalytic processes, because a cooperative effect of two close reactive metal centers is generated to accomplish unusual coordination modes [22]. Herein we report the synthesis and structural characterization of the oxo-bridged binuclear complexes, as well as their catalytic performance in ethylene and styrene polymerization.

2. Experimental

2.1. General comments

All manipulations involving air and moisture sensitive compounds were carried out under a nitrogen atmosphere (ultra-high purity) using either standard Schlenk techniques or glovebox techniques. Et_2O and toluene were

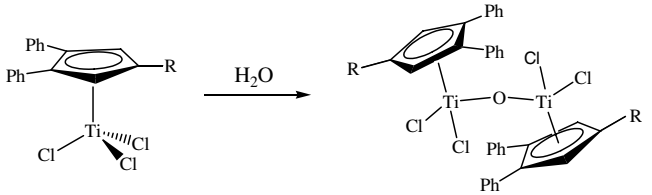
* Corresponding author. Tel.: +86 431 5168472; fax: +86 431 5193421.
E-mail address: YMu@jlu.edu.cn (Y. Mu).

0277-5387/$ - see front matter © 2007 Elsevier Ltd. All rights reserved.
doi:10.1016/j.poly.2007.02.007

dried over sodium/benzophenone under nitrogen and were freshly distilled prior to use. CH_2Cl_2 and *n*-hexane were refluxed under nitrogen over calcium hydride and distilled before use. Methylaluminoxane (MAO, 10 wt.% solution in toluene, $M = 800\ g\ mol^{-1}$, Al = 5.3 wt.%) was purchased from Wtico. Al(^{i}Bu)$_3$, methyl lithium, *n*-butyl lithium and titanium tetrachloride were purchased from Aldrich. 1,2-Diphenyl-4-methyl-cyclopentadienyl titanium trichloride (**1**), 1,2-diphenyl-4-*n*-butyl-cyclopentadienyl titanium trichloride (**2**) [21] and $Ph_3C^+B(C_6F_5)^-$ [23–25] were prepared according to the literature procedures. The crystal structure was determined with a CCD diffraction apparatus. NMR spectra were measured using a Varian Mercury-300 NMR spectrometer. Elemental analyses were performed on a Perkin–Elmer 240c element analyzer. Viscosity-average molecular weights of the polyethylenes were determined in decahydronaphthalene at 135 °C using a Schott Gerate Mod. AVS/T2 Ubbelohde viscosimeter. Viscosity-average molecular weights of the polystyrenes were determined in *o*-dichlorobenzene at 135 °C using a Schott Gerate Mod. AVS/T2 Ubbelohde viscosimeter. Melting transition temperatures (T_m) of the polyethylenes and polystyrenes were determined by DSC (Du Pont 910 differential scanning calorimeter) at a heating rate of 10 °C min^{-1}.

2.2. Synthesis of (1,2-Ph$_2$-4-Me-CpTiCl$_2$)$_2$(μ-O) (3)

A mixture of Et_2O (20 mL) and distilled H_2O (9.0 μL, 0.50 mmol) was slowly added at −15 °C to solid complex **1** (385.5 mg, 1.00 mmol), and the obtained solution was warmed to room temperature and stirred for 48 h (Scheme 1). The solvent was removed *in vacuo*, and the resulting residue was extracted with a mixed solvent of CH_2Cl_2/*n*-hexane (1:3, 15 × 2 mL). The solution was concentrated to give a red solid (317.3 mg, 88.6%). Red crystals of the complex suitable for X-ray diffraction were obtained by recrystallization from a mixture of CH_2Cl_2/*n*-hexane (1:5) at room temperature. *Anal.* Calc. for $C_{36}H_{30}Cl_4OTi_2$ (716.20): C, 60.37; H, 4.22. Found: C, 60.31; H, 4.18%. ^{1}H NMR ($CDCl_3$, 300 MHz, 298 K): δ 2.40 (s, 6H, CH_3), 6.87 (s, 4H, C_5H_2), 7.28–7.50 (m, 20H, C_6H_5). ^{13}C NMR ($CDCl_3$, 75 MHz, 298 K): δ 17.2 (CH_3), 128.9, 133.4, 137.9 (C_5H_2), 123.2, 128.4, 129.7, 136.3 (C_6H_5).



1 R = **Me**
2 R = *n*-Bu

3 R = **Me**
4 R = *n*-Bu

Scheme 1. Synthetic procedure of complexes **3**–**4**.

2.3. Synthesis of (1,2-Ph$_2$-4-*n*-Bu-CpTiCl$_2$)$_2$(μ-O) (4)

Compound **4** was prepared in the same manner as described above for the synthesis of **3** (Scheme 1), and isolated in 89.2% as a red crystalline solid. *Anal.* Calc. for $C_{42}H_{42}Cl_4OTi_2$ (800.36): C, 63.03; H, 5.29. Found: C, 63.05; H, 5.21%. ^{1}H NMR ($CDCl_3$, 300 MHz, 298 K): δ 0.91 (t, $^3J_{HH} = 7.7$ Hz, 6H, CH_3), 1.35 (m, $^3J_{HH} = 7.5$ Hz, 4H, CH_2), 1.60 (m, $^3J_{HH} = 7.6$ Hz, 4H, CH_2), 2.73 (t, $^3J_{HH} = 7.8$ Hz, 4H, CH_2), 6.88 (s, 4H, C_5H_2), 7.27–7.50 (m, 20H, C_6H_5). ^{13}C NMR ($CDCl_3$, 75 MHz, 298 K): δ 14.1, 22.6, 31.4, 32.7 (C_4H_9), 128.9, 133.4, 143.3 (C_5H_2), 122.3, 128.4, 129.8, 136.1 (C_6H_5).

2.4. X-ray structure determination of 3 and 4

Crystals of **3** and **4** suitable for X-ray structure determination were obtained from a saturated solution of CH_2Cl_2/*n*-hexane (1:5, v/v) at room temperature. Diffraction data were collected at 293 K on a Bruker SMART-CCD diffractometer using Mo Kα radiation. The structures were solved using direct methods and refined by full-matrix least-squares procedures [26]. All non-hydrogen atoms were refined anisotropically and the hydrogen atoms were included in ideal positions. All calculations were performed using the SHELXTL crystallographic software packages [27]. Relevant crystallographic data are summarized in Table 1.

2.5. Polymerization of ethylene

The ethylene polymerizations (runs 1–8) were carried out according to the following procedure: A dry 250 mL steel autoclave with a magnetic stirrer was charged with 70 mL of toluene, thermostated at the desired temperature and saturated with ethylene (1.5 bar). The polymerization reaction was initiated by addition of a mixture solution of precatalyst and Al(^{i}Bu)$_3$ in toluene (5 mL) and a solution of $Ph_3C^+B(C_6F_5)_4^-$ in toluene (5 mL) at the same time. The gaseous ethylene was then admitted into the reactor vessel through a gas purification column. The gas pressure was maintained at 6 bar throughout the polymerization period by means of a pressure manometer. After 15 min, the polymerization was quenched by addition of 120 mL of 1:1 (v/v) methanol and HCl solution. The white polymer was collected by filtration, washed several times with water, methanol, and dried to a constant weight under vacuum.

2.6. Polymerization of styrene

The styrene polymerizations (runs 1–10) with complexes **3** and **4** were carried out according to the following procedure: A 250 mL Schlenk flask with a magnetic stirrer was attached to high vacuum line and then sealed under a nitrogen atmosphere. Fifty milliliters of toluene, 5 mL of freshly distilled styrene and an appropriate amount of MAO were added to the flask which was placed in an oil bath at the

Table 1
Crystal data and structural refinements details for **3** and **4**

	3	**4**
Empirical formula	$C_{36}H_{30}Cl_4OTi_2$	$C_{42}H_{42}Cl_4OTi_2$
Formula weight	716.20	800.36
Crystal system	monoclinic	monoclinic
Temperature (K)	293(2)	293(2)
Wavelength (Å)	0.71073	0.71073
Space group	*C*2/*c*	*C*2/c
a (Å)	25.099(2)	26.3294(10)
b (Å)	10.5871(8)	9.7594(4)
c (Å)	17.1279(11)	16.8576(8)
β (°)	132.224(3)	116.657(2)
Volume (Å^3)	3370.4(4)	3871.3(3)
Z	4	4
D_{calc} (g cm^{-3})	1.411	1.373
F(000)	1464	1656
Absorption coefficient (mm^{-1})	0.819	0.721
Scan type	*ω*–2*θ*	*ω*–2*θ*
2*θ* Range (°)	$4.38 \leqslant 2\theta \leqslant 50.00$	$3.46 \leqslant 2\theta \leqslant 46.62$
Reflections collected	9058	9136
Reflections unique [R_{int}]	2960 [0.0570]	2800 [0.0328]
Refinement method	full-matrix least-squares on F^2	full-matrix least-squares on F^2
Data/restraints/parameters	2960/0/204	2800/0/222
Goodness-of-fit on F^2	0.921	1.028
Final *R* indices [$I > 2\sigma(I)$]	$R_1 = 0.0403$, $wR_2 = 0.0889$	$R_1 = 0.0319$, $wR_2 = 0.0861$
R indices (all data)	$R_1 = 0.0807$, $wR_2 = 0.1046$	$R_1 = 0.0449$, $wR_2 = 0.0921$
Largest difference peak and hole (e Å^{-3})	0.349 and −0.271	0.322 and −0.323

desired temperature, and the mixture was stirred for 10 min. The titanium catalyst (2.5 μmol) in toluene was injected into the flask and the polymerization was performed at 25 °C, 50 °C or 75 °C for the desired reaction times. The polymerization was terminated by addition of 10% HCl in methanol. The precipitated polymer was washed three times with methanol and dried at 80 °C *in vacuo* to a constant weight. The polymer was extracted with refluxing 2-butanone for 24 h in a Soxhlet extractor to remove any atactic polymer and dried again at 80 °C for 24 h.

3. Results and discussion

3.1. Synthesis and analysis of complexes 3 and 4

Complexes **3** and **4** were synthesized readily via the hydrolysis reaction of complexes **1** and **2** in solution, and obtained after recrystallization in good yields as red crystalline solids. These titanium complexes are quite soluble in most organic solvents, such as Et_2O, CH_2Cl_2 and toluene. Both complexes can be stored at room temperature, under an inert nitrogen atmosphere, without obvious change, either in the solid state or solution. It is noteworthy that they also exhibit good thermostability and can be heated to about 90 °C in toluene without decomposition. The stability of titanium complexes to water-induced metathesis has been reported previously [28–30]. Complexes **3** and **4** have been confirmed by X-ray diffraction, elemental analysis, ^{1}H and ^{13}C NMR spectroscopy.

The ^{1}H and ^{13}C NMR spectra indicate higher symmetry in solution than in the solid state, and complexes **3** and **4** have similar resonance signals, with just slight shifts to higher field, compared to those of **1** and **2**. The ^{1}H NMR spectra show only one single signal for the protons of the Cp groups (6.87 ppm for **3**, 6.88 ppm for **4**), since they are equivalent in solution for C_{2c} symmetric complexes, and the ^{13}C NMR signals for the Cp groups of complexes **3** and **4** shift 0.5–2.6 ppm to higher field compared to the signals of the Cp groups of complexes **1** and **2** [21].

3.2. Crystal structures of 3 and 4

The molecular structures of complexes **3** and **4** were confirmed by single-crystal X-ray diffraction analysis. The ORTEP drawing of the molecular structure is shown in Fig. 1 and Fig. 2. Selected bond lengths and angles are summarized in Table 2. The molecular structure shows a dimetallic moiety with two (1,2-Ph_2-4-R-$CpTiCl_2$)$_2$(μ-O) (R = Me (**3**), *n*-Bu (**4**)) units linked by Ti–O bonding. The coordination geometry around the titanium atom can be described as pseudo-tetrahedral, formed by a substituted cyclopentadienyl ring, two chloride atoms and an oxygen atom (oxo-bridge). The Ti1–C distances for **3** and **4** are in the range of 2.336(3)–2.430(2) Å, which are similar to the corresponding values of **1** and **2** [21]. The average

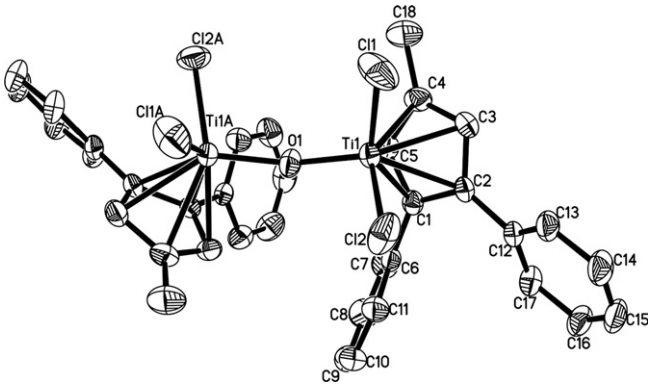


Fig. 1. Structure of complex **3** (thermal ellipsoids are drawn at the 30% probability level).

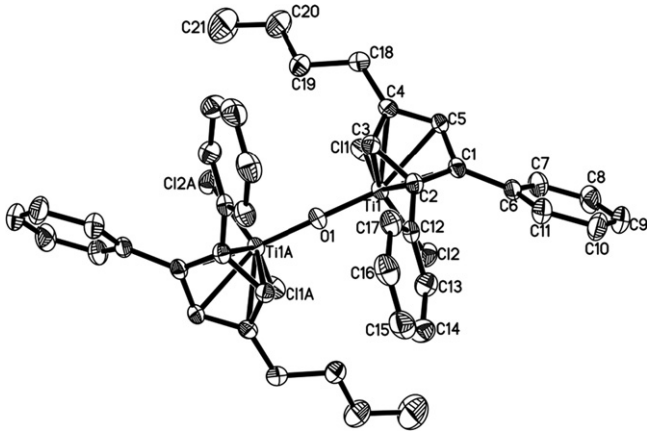


Fig. 2. Structure of complex **4** (thermal ellipsoids are drawn at the 30% probability level).

Ti–Cl distance of 2.219 (1) Å in **3** is shorter than that of 2.247(1) Å in **4**, which could be attributed to the difference in the crowded environment on the titanium atoms. The Ti–O bond lengths (1.786(1) Å for **3** and 1.800(1) Å for **4**) are slightly shorter than the average Ti–O distance in other known complexes [31–34]. For this reason, we suggest that there is relatively higher electron density at the metal atoms of **3** and **4**, which is responsible for the high stability of **3** and **4**. The Ti–O–Ti angles of complexes **3** and **4** (157.0(2)°, 159.6 (2)° respectively) fall within the range of observed values (154–180°) in similar structures, which indicates that there exists different π back-bonding affected by intramolecular steric effects [35,36] (Fig. 2).

Table 2
Selected bond lengths and angles for complexes **3** and **4**

Complex **3**			
Ti(1)–O(1)	1.786(1)	Ti(1)–C(5)	2.339(3)
Ti(1)–C(1)	2.386(3)	Ti(1)–Cl(1)	2.197(2)
Ti(1)–C(2)	2.417(3)	Ti(1)–Cl(2)	2.242(1)
Ti(1)–C(3)	2.369(3)	Ti(1)–Cp(cent)	2.041(3)
Ti(1)–C(4)	2.345(3)		
O(1)–Ti(1)–Cl(1)	108.2(3)	O(1)–Ti(1)–C(4)	107.3(1)
O(1)–Ti(1)–Cl(2)	103.7(1)	O(1)–Ti(1)–C(5)	84.4(1)
Cl(1)–Ti(1)–Cl(2)	95.4(3)	Cp(cent)–Ti(1)–O(1)	114.5(2)
O(1)–Ti(1)–C(1)	97.5(1)	Cp(cent)–Ti(1)–Cl(1)	114.6(3)
O(1)–Ti(1)–C(2)	132.2(1)	Cp(cent)–Ti(1)–Cl(2)	118.3(3)
O(1)–Ti(1)–C(3)	140.7(1)	Ti(1)–O(1)–Ti(2)	157.0(2)
Complex **4**			
Ti(1)–O(1)	1.800(1)	Ti(1)–C(5)	2.378(2)
Ti(1)–C(1)	2.430(2)	Ti(1)–Cl(1)	2.251(1)
Ti(1)–C(2)	2.370(3)	Ti(1)–Cl(2)	2.242(1)
Ti(1)–C(3)	2.336(3)	Ti(1)–Cp(cent)	2.048(2)
Ti(1)–C(4)	2.363(3)		
O(1)–Ti(1)–Cl(1)	102.2(1)	O(1)–Ti(1)–C(4)	109.4(1)
O(1)–Ti(1)–Cl(2)	104.6(4)	O(1)–Ti(1)–C(5)	142.2(1)
Cl(1)–Ti(1)–Cl(2)	101.1(4)	Cp(cent)–Ti(1)–O(1)	115.7(3)
O(1)–Ti(1)–C(1)	132.1(1)	Cp(cent)–Ti(1)–Cl(1)	115.3(5)
O(1)–Ti(1)–C(2)	97.6(1)	Cp(cent)–Ti(1)–Cl(2)	115.9(1)
O(1)–Ti(1)–C(3)	85.9(1)	Ti(1)–O(1)–Ti(2)	159.6(2)

3.3. Ethylene polymerization studies

Ethylene polymerizations were carried out in toluene using complexes **3** and **4** as precatalysts under different conditions, and the results of the polymerization catalyzed by complexes **3** and **4** are summarized in Table 3. When activated with $Al(^iBu)_3$ and $Ph_3C^+B(C_6F_5)_4^-$, complexes **3** and **4** both show good catalytic activity for ethylene polymerization, producing moderate molecular weight polyethylene

Table 3
Summary of ethylene polymerization catalyzed by complexes **3** and **4** activated with $Al(^iBu)_3$ and $Ph_3C^+[B(C_6F_5)_4]^-$ [a]

Run	Catalyst	Al:Ti	T_p (°C)	Yield (g)	A [b] ($\times 10^{-5}$)	M_η [c] ($\times 10^{-4}$)	T_m [d] (°C)
1	**3**	50	80	0.47	1.56	5.3	124.3
2	**3**	100	80	1.08	3.60	4.6	135.0
3	**3**	200	80	1.59	5.31	4.2	126.4
4	**3**	300	80	1.12	3.73	3.5	124.0
5	**4**	50	80	0.66	2.20	5.0	126.7
6	**4**	100	80	1.25	4.17.	4.7	130.1
7	**4**	200	80	1.87	6.23	3.9	127.2
8	**4**	300	80	1.02	3.40	3.6	123.6

[a] Polymerization conditions: [Ti] 2 μM, B/Ti ratio 1.2, reaction time 15 min, polymerization temperature 80 °C, ethylene pressure 6 bar.
[b] Activity = g PE (mol Ti)$^{-1}$ bar^{-1} h^{-1}.
[c] Measured in decahydronaphthalene at 135 °C.
[d] Determined by DSC at a heating rate of 10 °C min^{-1}.

with melting temperatures in the range 123–135°. As seen in Table 3, the catalytic activity increases in the order **3** < **4**, which indicates that the activity is influenced by the nature of the substituents on the cyclopentadiene ring. It is well known that the electron-donating effect and steric effect of the *n*-Bu group would stabilize the active species and hence increase the catalytic activity of complex **4**. For both **3** and **4**, the catalytic activity is affected by the Al/Ti molar ratio and the highest catalytic activity is reached at an Al/Ti ratio of about 200. A further increase in the Al/Ti ratio results in a decrease in the catalytic activity. During the polymerization, the molecular weight of the polymer gradually decreases with an increase in the Al/Ti molar ratio, which points out that a high Al/Ti molar ratio results in premature chain termination of the polymer, influenced by the relative rates of the two competing processes: β-hydride elimination and chain propagation.

3.4. Styrene polymerization studies

Styrene polymerizations were carried out in toluene using complexes **3** and **4** as precatalysts under different conditions, and the results of the styrene polymerization with complexes **3** and **4** are summarized in Table 4. The **3** or **4**/MAO systems show good catalytic performance for styrene polymerization in terms of catalytic activity and polymer properties, such as syndiotacticity, melting temperature and molecular weight of the produced polystyrene. In comparison with the **1** or **2**/MAO systems [21], the title catalyst systems were found to be active for syndiotactic polymerization of styrene at a low Al/Ti ratio of 2000, thus reducing the costs of the catalysts. The findings could be attributed to the important factor of the cooperative effect caused by the two adjacent metal centers in this type of catalyst. One catalytically active site can construct a crowded environment around the other site in the catalyst systems, which effectively protects the active species, resulting in a reduction in the amount of MAO in regard to the reactivation of the dormant catalyst species.

The catalytic activity of the title type catalyst is dependent on the polymerization temperature. The catalytic activity of complexes **3** and **4** increases with an increase in polymerization temperature, and the highest activity observed is about 1.35×10^7 g PS (mol Ti)$^{-1}$ (mol styrene)$^{-1}$ h^{-1} at 50 °C. The catalytic activity then decreases at higher polymerization temperatures. These findings are similar to the polymerization behavior of the mother titanium catalyst [21]. The catalytic performance of the title type catalyst is dependent on the polymerization time too. For complexes **3** and **4**, better catalytic behavior was observed for 10 min polymerization experiments, which indicates the partial decomposition of the syndiospecific active species and/or increased viscosity during the polymerization. Furthermore, the results in Table 4 are also consistent with the fact that the catalytic activity and polymer properties depend greatly on the electronic and steric effects of the substituted cyclopentadiene ligands in half-sandwich titanocenes as homogeneous catalysts. The catalytic activity is in the order **3** < **4**, which indicates that both the electronic and steric factors of the substituted cyclopentadiene group play a remarkable role in the styrene polymerizing process.

4. Conclusion

Two new oxo-bridged dinuclear titanium complexes **3** and **4** have been synthesized by hydrolysis of the corresponding monocyclopentadienyl titanium compounds **1** and **2**. The structures of **3** and **4** have been confirmed by ^{1}H and ^{13}C NMR spectra and X-ray crystallography. Upon activation with Al(^{i}Bu)$_3$ and $Ph_3C^+B(C_6F_5)_4^-$, complexes **3** and **4** exhibit reasonable catalytic activity for ethylene polymerization, producing moderate molecular weight polyethylene with melting temperatures in the range 123–135°. The **3** or **4**/MAO systems show good catalytic performance for styrene polymerization in terms of catalytic activity, syndiotacticity, melting temperature and molecular weight of the produced polystyrene.

Table 4
Summary of styrene polymerization catalyzed by complexes **3** and **4** activated with MAO[a]

Run	Catalyst	Time (min)	T_p (°C)	A[b] (×10^{-7})	SY[c] (%)	T_m[d] (°C)	M_η[e] (×10^{-5})
1	**3**	10	25	0.78	92.7	272.3	1.26
2	**3**	10	50	1.21	95.2	269.8	0.94
3	**3**	10	75	0.93	94.0	270.6	1.13
4	**3**	15	50	1.12	92.6	271.5	0.92
5	**3**	30	50	0.90	91.8	271.2	1.17
6	**4**	10	25	0.82	92.6	272.8	1.19
7	**4**	10	50	1.35	95.7	270.4	0.92
8	**4**	10	75	0.91	95.1	272.3	1.06
9	**4**	15	50	1.16	94.3	271.9	0.95
10	**4**	30	50	1.03	93.5	271.0	1.10

[a] Polymerization conditions: [Ti] 50 μM; [Al]/[Ti] 2000; reaction time 10 min, 15 min, or 30 min; [styrene] 0.87 M.
[b] A (activity) = (g bulk polymer)/(mol Ti)(mol monomer)(h).
[c] Percentage s-PS = [(g of 2-butanone insoluble polymer)/(g of butanone polymer)] × 100.
[d] T_m, melting temperature of s-PS, determined with DSC at a heating rate of 10 °C min^{-1}.
[e] M_η, Measured in *o*-dichlorobenzene at 135 °C.

5. Supplementary material

CCDC 601715 and 601716 contain the supplementary crystallographic data for **3** and **4**. These data can be obtained free of charge via http://www.ccdc.ac.uk/conts/retrieving.html, or from the Cambridge Crystallographic Data Centre, 12 Union Road, Cambridge CB2 1EZ, UK; fax: (+44) 1223-336-033; or e-mail: deposit@ccdc.cam.ac.uk.

Acknowledgement

This work was supported by the National Natural Science Foundation of China (No. 20374023).

References

[1] H.H. Brintzinger, D. Fischer, R. Mülhaupt, B. Rieger, R.M. Waymouth, Angew. Chem., Int. Ed. Engl. 34 (1995) 1143.
[2] A.L. McKnight, R.M. Waymouth, Chem. Rev. 98 (1998) 2587.
[3] M. Bochmann, J. Chem. Soc., Dalton Trans. (1996) 255.
[4] J.A.M. Canich, U.S. Patent 5,079,205, 1992.
[5] Dow Chemical Co. Eur. Pat. Appl. 0416815.
[6] Exxon Chemical Co. U.S. Patent 5,026,798, 1991. U.S. Patent 5,055,438, 1991.
[7] J.C. Flores, J.C.W. Chien, M.D. Rausch, Organometallics 13 (1994) 4140.
[8] M. Enders, R. Rudolph, H. Pritzkow, Chem. Ber. 129 (1996) 459.
[9] A.A.H. van der Zeijden, C. Mattheis, R. Fröhlich, Organometallics 16 (1997) 2651.
[10] A.M. Cardoso, R.J.H. Clark, S. Moorhouse, J. Chem. Soc., Dalton Trans. (1980) 1156.
[11] Y. Qian, G. Li, W. Chen, B. Li, X. Jin, J. Organomet. Chem. 373 (1989) 185.
[12] H. Sinn, W. Kaminsky, Adv. Org. Chem 18 (1990) 99.
[13] P. Foster, J.C.W. Chien, M.D. Rausch, Organometallics 15 (1996) 2404.
[14] R. Fandos, A. Meetsma, J.H. Teuben, Organometallics 10 (1991) 59.
[15] J. Okuda, K.E. du Plooy, P.J. Toscanno, J. Organomet. Chem. 495 (1995) 195.
[16] P. Jutzi, M.D. Kristen, J. Dahlhaus, B. Newmann, H.-G. Stammler, Organometallics 12 (1993) 2906.
[17] F.G. Sernetz, R. Mülhaupt, S. Fokken, J. Okuda, Macromolecules 30 (1997) 1562.
[18] W. Kaminsky, F. Freidanck, Macromol. Symp. 183 (2002) 89.
[19] D. Ruchatz, G. Fink, Macromolecules 31 (1998) 4669.
[20] W. Spaleck, M. Antberg, J. Rohrmann, A. Winter, B. Bachmann, P. Kiprof, J. Behm, W.A. Herrmann, Angew. Chem., Int. Ed. Engl. 31 (1992) 1347.
[21] Q.-L. Wu, Q. Su, G.-H. Li, W. Gao, Y. Mu, S.-H. Feng, Polyhedron 25 (2006) 2565.
[22] (a) E. Royo, P. Royo, T. Cuenca, M. Galakhov, Organometallics 19 (2000) 5559;
(b) T. Cuenca, M. Galakhov, G. Jimézez, E. Royo, P. Royo, M. Bochmann, J. Organomet. Chem. 543 (1997) 209;
(c) G. Jimézez, P. Royo, T. Cuenca, M. Galakhov, Organometallics 20 (2001) 5237.
[23] J.C.W. Chien, W.M. Tsai, M.D. Rasch, J. Am. Chem. Soc. 113 (1991) 8570.
[24] A.G. Massey, A.J. Park, J. Organomet. Chem. 5 (1966) 218.
[25] A.G. Massey, A.J. Park, J. Org. Chem. 2 (1962) 245.
[26] SHELXTL, PC Siemens Analytical X-ray Instruments, Madison WI, 1993.
[27] G.M. Sheldrick, SHELXTL Structure Determination Programs, Version 5.0; PC Siemens Analytical Systems, Madison, WI, 1994.
[28] J.C. Flores, J.S. Wood, J.C.W. Chien, M.D. Rausch, Organometallics 15 (1996) 4944.
[29] L.M. Bobcock, V.W. Day, W.G. Klemperer, J. Chem. Soc., Chem. Commun. (1987) 858.
[30] M. Björgvinssson, S. Halldorssson, I. Amason, J. Magull, D. Fenske, J. Organomet. Chem. 544 (1997) 207.
[31] S.P. Varkey, M. Schormann, T. Pape, H.W. Roesky, et al., Inorg. Chem. 40 (2001) 2427.
[32] J.L. Pearson, Inorg. Chem. 19 (1980) 181.
[33] S.G. Blanco, M.P. Gómez-Sal, S.M. Carreras, M. Mena, et al., J. Chem. Soc., Chem. Commun. (1986) 1572.
[34] S.L. Troyanov, V.B. Rybakov, V. Varga, P. Sedmera, K. Max, Metalloorg. Khim. 4 (1991) 1004.
[35] U. Thewalt, D. Schomburg, J. Organomet. Chem. 127 (1977) 169.
[36] P. Gowik, T. Klapötke, J. Pickardt, J. Organomet. Chem. 393 (1990) 343.

Available online at www.sciencedirect.com
ScienceDirect
Polyhedron 26 (2007) 3069–3073
POLYHEDRON
www.elsevier.com/locate/poly

Kinetics of oxidation of cysteine and captopril via $Cs_3[Mo(CN)_8]$ and $Cs_3[W(CN)_8]$

Rana N. Zahdeh, Ribhi A. Zaru, Hamdallah A. Hodali *

Department of Chemistry, University of Jordan, Amman 11942, Jordan

Received 21 December 2006; accepted 9 February 2007
Available online 13 February 2007

Abstract

The kinetics of the oxidation of cysteine and captopril via octacyanomolybdate(V) and octacyanotungstate(V) in a buffered acidic media (pH range 2.20–4.80) have been studied spectrophotometrically. The rate law for the oxidation is: Rate $= k$ [RSH] [Ox] $[H^+]^{-1}$, where RSH is cysteine or captopril and Ox is $Cs_3[Mo(CN)_8]$ or $Cs_3[W(CN)_8]$. The activation parameters (E_a, $\Delta H^{\#}$, $\Delta G^{\#}$, $\Delta S^{\#}$) for the oxidation of cysteine and captopril via $Cs_3[Mo(CN)_8]$ or $Cs_3[W(CN)_8]$ have been determined. The results indicate that $Cs_3[Mo(CN)_8]$ is more reactive than $Cs_3[W(CN)_8]$ as an oxidizing agent. Effects of pH, ionic strength, temperature, dielectric constant of the reaction medium and copper(II) ions on the oxidation rate have been studied. Mechanisms for the oxidation of cysteine to cystine and captopril to the corresponding disulfide have been proposed.
© 2007 Elsevier Ltd. All rights reserved.

Keywords: Cysteine; Captopril; Octacyanomolybdate(V) ion; Octacyanotungstate(V) ion; Copper catalysis; Copper inhibition

1. Introduction

Thiol-containing compounds are effective antioxidants and act as scavengers for reactive oxygen species [1]. In biological systems, cysteine (an amino acid with a thiol group) plays an important role as an antioxidant and thus helps in the protection of cells from the destructive effect of free radicals [2]. Additional interest has been focused on cysteine in biological systems due to the effect of its oxidation on cell immune function [3]. Kinetic studies of the oxidation of cysteine *in vitro* are expected to shed light on its oxidation in biological systems. A large variety of oxidizing agents, such as cobalt(III) complexes [4–6], iron(III) complexes [6,7], vanadium(V) complexes [8], per-manganate ion [9], copper(II) complexes [10], sodium *N*-chlorotoluenesulphonamide [11], penta-cyanonitrosyl ferrate(III) ion [12], and manganese(III) ion [13], have been employed in the study of the kinetics of oxidation of cysteine. Oxidizing agents involving molybdenum have been used [14–16] in an attempt to mimic enzymatic oxidation of cysteine in biological systems. The catalytic role of trace amounts of copper(II) ions in the oxidation of cysteine has been reported by many researchers [17–19].

Herein, we report on the oxidation of cysteine and captopril [20] in acidic media (pH 2.20–4.80). Captopril is a thiol compound (1-[(2*S*)-3-mercapto-2-methyl-1-oxopropyl]-L-proline) widely used as antihypertensive drug [21–25].

2. Experimental

2.1. Materials

The cyano complexes, $K_4[Mo(CN)_8]\cdot 2H_2O$ [26], $K_4[W(CN)_8]\cdot 2H_2O$ [27], $Cs_3[Mo(CN)_8]\cdot 2H_2O$ and $Cs_3[W(CN)_8]\cdot 2H_2O$ [28,29], were prepared following the literature procedures. The above cesium salts were recrystallized from water and were used without further purification.

* Corresponding author. Tel.: +962 6 5355000/2329; fax: +962 65348932.
E-mail address: h-hodali@ju.edu.jo (H.A. Hodali).

0277-5387/$ - see front matter © 2007 Elsevier Ltd. All rights reserved.
doi:10.1016/j.poly.2007.02.004

Analytical grade reagents and distilled water were used. The aqueous solutions of cysteine, captopril and oxidizing agents were freshly prepared. The desired buffer solutions for varying the pH of the reaction medium were prepared by mixing suitable volumes of 0.10 M HCl and 0.10 M potassium hydrogen phthalate to give pH values in the range (2.20–3.80), while for the pH range (4.20–4.80) suitable volumes of 0.10 M NaOH and 0.10 M potassium hydrogen phthalate were mixed. The pH was measured with a WTM 3000 pH meter.

2.2. Kinetic measurements

Reactions were carried out in buffered acidic media using thermostatted bath (HAAK, MD-BRUE/PU) to regulate the temperature to ±0.2 °C. Kinetic measurements were carried out in aqueous solutions unless otherwise specified. The pH was measured with a WTM 3000 pH meter. The pH meter was calibrated using standard pH solutions. The measured pHs were corrected for 50% v/v aqueous/methanol using the relationship [30,31]: $PH_{corr.} = PH_{meas.} + 0.08$. The ionic strength was adjusted to a constant value of 0.0800 M or 0.100 M by the addition of $NaClO_4$. The progress of the reaction was followed by measuring the absorbance (A_t) of the unconsumed $[Mo(CN)_8]^{3-}$ or $[W(CN)_8]^{3-}$ at 390 and 356 nm, respectively. The absorption measurements were carried out with use of a thermostatted Jasco V530 UV/Vis spectrophotometer. Solutions of cysteine, captopril and the cyano complexes were protected from light. By maintaining stoichiometric amounts of (1:1) of the thiol (RSH = cysteine, captopril) and the oxidizing agent ($Cs_3[Mo(CN)_8]$, $Cs_3[W(CN)_8]$) and performing spectrophotometric measurements at the proper wavelength. The following stoichiometric equation was found to hold for the two oxidants:

$$2RSH + 2[M(CN)_8]^{3-} = RSSR + 2[M(CN)_8]^{4-} + 2H^+$$

where M = Mo or W; RSSR = cystine or the corresponding disulfide of captopril. The disulfide compounds, cystine (m.p. = >250 °C) and the corresponding disulfide of captopril (m.p. = 220–224 °C) precipitated from reacted solutions were identified by their melting points. Formation of $[Mo(CN)_8]^{4-}$ and $[W(CN)_8]^{4-}$ in the oxidation reactions was evidenced in the oxidation reaction by the gradual increase of the absorption bands at $\lambda = 410$ and 428 nm, respectively.

3. Results and discussion

3.1. Effect of thiol concentration

The oxidation of cysteine and captopril were investigated at a constant pH and ionic strength. The concentration of the oxidants, $[Mo(CN)_8]^{3-}$ or $[W(CN)_8]^{3-}$, was kept constant at 1.00×10^{-3} M, while the concentration of cysteine or captopril was varied to study the effect of thiol concentration on reaction rate. For each run a plot of ln A versus time gave a good straight line, and the corresponding observed first-order rate constant (k) was obtained. The results for the oxidation of cysteine via the two oxidants are shown in Table 1. The effect of cysteine concentration on the reaction rate indicates a first-order kinetics with respect to cysteine.

However, when the reaction was carried out at stoichiometric amounts of the reactants (thiol-to-$[M(CN)_8]^{3-}$ = 1:1, where thiol = cysteine or captopril; M = Mo, W), absorption measurements for about 70% completion indicated second-order kinetics as shown in Fig. 1.

3.2. Effect of H^+ concentration

With other variables constant, the rate constant for the oxidation of cysteine has been found to decrease with increasing acidity (Table 2).

Plotting the second-order rate constant (k') versus $1/[H^+]$ for the oxidation of cysteine by $[Mo(CN)_8]^{3-}$, in the pH range 2.20–2.80, gave a straight line indicating first-order kinetics with respect to $1/[H^+]$ (Fig. 2). Similar behavior was observed for the oxidation of captopril by both oxidants.

3.3. Effect of ionic strength

The variation of the rate constant with ionic strength was investigated in the presence of $NaClO_4$ over a range of ionic strength $I = 0.100$–0.250 M. The results are shown in Table 3. A Plot of log k versus $\sqrt{I}$ gave a straight line in both cases. From the slope of such plots, values of $Z_A Z_B$

Table 1
Observed first-order rate constants for the oxidation of cysteine via $[Mo(CN)_8]^{3-}$ and $[W(CN)_8]^{3-}$[a]

103 [cys]	$[Mo(CN)_8]^{3-}$ 10^3 k (s^{-1})	$[W(CN)_8]^{3-}$ 10^3 k (s^{-1})
4.00	16.9	4.42
5.00	21.4	5.50
6.00	25.6	6.63
7.00	30.0	7.70

[a] $[Mo(CN)_8]^{3-} = [W(CN)_8]^{3-} = 1.00 \times 10^{-3}$ M, $T = 15.0$ °C, $I = 0.0800$ M, pH 2.20.

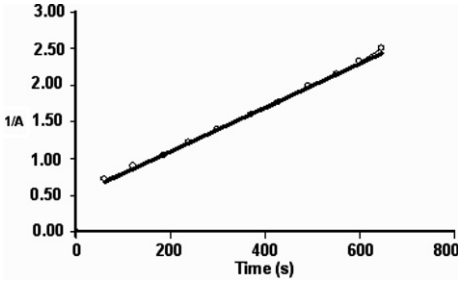


Fig. 1. A plot of $1/A$ vs. t for the oxidation of cysteine: $[Mo(CN)_8]^{3-} = [Mo(CN)_8]^{3-} = [cys] = 1.00 \times 10^{-3}$ M, pH 2.20, $I = 0.100$ M, $T = 15.0$ °C.

Table 2
Acid dependence of the kinetics of oxidation of cysteine using $[Mo(CN)_8]^{3-}$ and $W(CN)_8]^{3-}$[a]

pH	$[Mo(CN)_8]^{3-}$ k' (M^{-1} s^{-1})[b]	$[W(CN)_8]^{3-}$ k' (M^{-1} s^{-1})[b]
2.20	1.70	0.604
2.40	3.39	1.00
2.60	6.40	1.70
2.80	10.3	3.09

[a] $[Mo(CN)_8]^{3-} = [W(CN)_8]^{3-} = [cys] = 1.00 \times 10^{-3}$ M, $T = 15.0$ °C, $I = 0.0800$ M, 50% aqueous methanol.
[b] k' = second-order rate constant from plot of $1/A$ vs. time at different pH values.

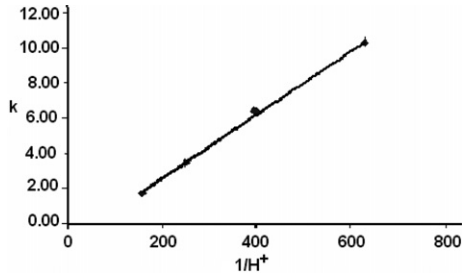


Fig. 2. A plot of k vs. $1/[H^+]$ for the oxidation of cysteine by $[Mo(CN)_8]^{3-}$ in 50% aqueous methanol. $[Mo(CN)_8]^{3-} = [cys] = 1.00 \times 10^{-3}$ M, $I = 0.0800$ M, $T = 15.0$ °C.

Table 3
Ionic strength dependence of the kinetics of oxidation of cysteine via $[Mo(CN)_8]^{3-}$ and $[W(CN)_8]^{3-}$

I (M)	$[Mo(CN)_8]^{3-}$[a] 10^3 k (s^{-1})	$[W(CN)_8]^{3-}$[b] 10^3 k (s^{-1})
0.100	22.3	5.50
0.150	25.0	6.54
0.200	27.5	7.44
0.250	30.5	8.54

[a] $[Mo(CN)_8]^{3-} = 1.00 \times 10^{-3}$ M, $[cys] = 5.00 \times 10^{-3}$ M, $T = 15.0$ °C, pH 2.20.
[b] $[W(CN)_8]^{3-} = 1.00 \times 10^{-3}$ M, $[cys] = 5.00 \times 10^{-3}$ M, $T = 15.0$ °C, pH 2.20.

for the reacting species at the rate determining step were obtained. These values are: +1.61 (cystein/$[Mo(CN)_8]^{3-}$), +1.00 (cystein/$[W(CN)_8]^{3-}$) and +0.570 (captopril/$[W(CN)_8]^{3-}$). This is an indication of a positive salt effect which implies that the reacting species at the rate determining step are RS- and the ion-pairing of the form $Na_n[M(CN)_8]^{n-3}$, where M = Mo or W. Values of n in the range 1.4–2.4 were experimentally obtained. Attempts to study the effect of ionic strength on the oxidation of captopril by $[Mo(CN)_8]^{3-}$ were unsuccessful due to precipitation problems.

3.4. Effect of dielectric constant

The influence of the solvent dielectric constant has been studied by varying the dielectric constant using aqueous methanol solutions with different compositions. The results show no significant effect on the reaction rate with the dielectric constant of the reaction medium.

3.5. Evaluation of E_a, $\Delta H^{\#}$, $\Delta G^{\#}$ and $\Delta S^{\#}$

Reactions were investigated at 10.0, 15.0, 20.0 and 25.0 °C for the oxidation of captopril by $[Mo(CN)_8]^{3-}$ at stoichiometric amounts of reactants, constant pH (4.80) and constant ionic strength (0.100 M). Values of $\Delta H^{\#}$ and E_a (Table 4) were evaluated from plots of $\ln k$ versus $1/T$, where k is the second-order rate constant (Fig. 3). Applying Eyring equation at $T = 25.0$ ° C values of $\Delta G^{\#}$ and $\Delta S^{\#}$ were calculated.

The higher reactivity of $[Mo(CN)_8]^{3-}$ as an oxidizing agent in comparison with $[W(CN)_8]^{3-}$ is shown clearly from the values of the rate constants for the oxidation of cysteine via both oxidizing agents. The rate constant for the former is about four times greater than that for the latter under the same conditions (Table 1). This is consistent with the higher reduction potential [32] of $[Mo(CN)_8]^{3-}$ and lower activation energy for the oxidation process (Table 4).

3.6. Effect of trace metal ions

Trace elements, that are usually present in the reagents or buffers used in the kinetic studies, seem to play a catalytic role in the oxidation process of cysteine and related thiols [17–19]. Reports about the catalytic role of copper ions in the oxidation of cysteine and the low values of activation energies for the oxidation of cysteine determined in this study, encouraged us to study the catalytic

Table 4
Activation parameters for the kinetics of oxidation of cysteine and captopril via $[Mo(CN)_8]^{3-}$ and $[W(CN)_8]^{3-}$

Activation parameters	Cysteine[a]		Captopril[c]	
	$[Mo(CN)_8]^{3-}$[b]	$[W(CN)_8]^{3-}$	$[Mo(CN)_8]^{3-}$	$[W(CN)_8]^{3-}$
E_a (kJ mol^{-1})	30.1	38.8	6.43	9.59
$\Delta S^{\#}$ (J mol^{-1} K^{-1})	−144	−162	−212	−204
$\Delta G^{\#}$ (kJ mol^{-1})	43.0	84.8	67.2	67.9
$\Delta H^{\#}$ (kJ mol^{-1})	27.6	36.4	3.95	7.11

[a] $[Mo(CN)_8]^{3-} = [W(CN)_8]^{3-} = 1.00 \times 10^{-3}$ M, $[cys] = 5.00 \times 10^{-3}$ M, pH 2.20, $I = 0.0800$ M.
[b] 50% aqueous methanol.
[c] $[Mo(CN)_8]^{3-} = [W(CN)_8]^{3-} = [captopril] = 1.00 \times 10^{-3}$M, pH 4.80, $I = 0.100$ M.

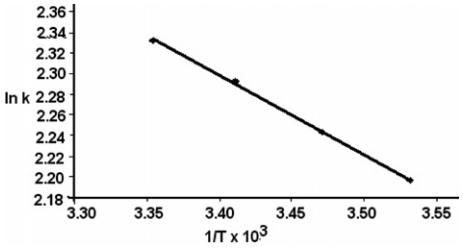


Fig. 3. A plot of $\ln k$ vs. $1/T$ for the oxidation of captopril by $[Mo(CN)_8]^{3-}$. $[Mo(CN)_8]^{3-} = [\text{captopril}] = 1.00 \times 10^{-3}$ M, pH 4.80, $I = 0.100$ M.

Table 5
Effect of $[Cu^{2+}]$ on the oxidation rate of captopril by $[Mo(CN)_8]^{3-}$

$[Cu^{2+}]$ (ppm)	k' ($M^{-1}\,s^{-1}$)
0.00	1.34
10.0	2.51
20.0	3.09
40.0	3.7

$[Mo(CN)_8]^{3-} = [\text{captopril}] = 1.00 \times 10^{-3}$ M, $T = 15.0$°C, pH 2.80, $I = 0.100$ M.

effect of $[Cu^{2+}]$. Table 5 shows how the rate constant for the oxidation of captopril by $[Mo(CN)_8]^{3-}$ increases with increasing Cu^{2+} ions concentration. Same effects have been observed for the oxidation of captopril by $[W(CN)_8]^{3-}$ and for the oxidation of cysteine by the two oxidants.

3.7. Effect of dipicolinic acid on the oxidation rate

Dipicolinic acid (a dibasic acid with $pK_{a_1} = 2.07$ and $pK_{a_2} = 4.66$) is known for its strong binding with Cu^{2+} and thus acts as an inhibitor for the Cu^{2+} catalytic role [17,18,33,34]. In this study it is observed that $t_{1/2}$ is 310 s for the oxidation of cysteine (1.00×10^3 M) via $[Mo(CN)_8]^{3-}$ (1.00×10^3 M) at pH 2.20 and 15.0 °C. Under these conditions, $t_{1/2}$ is increased up to 405 s upon using a 1.00×10^3 M concentration of dipicolinic acid.

Increasing the concentration of dipicolinic acid to 2.00×10^3 M indicates no further inhibition to the oxidation rate. It seems that a concentration of 1.00×10^3 M of dipicolinic acid is sufficient to mask the catalytic effect due to the impurity levels of Cu^{2+} ions.

In view of the above results the following mechanism is proposed:

$$RSH \underset{k_{-1}}{\overset{k_1}{\leftrightarrows}} RS^- + H^+$$

$$Cu^{2+} + RS^- \overset{k_2}{\rightarrow} Cu^+ + RS^{\cdot}$$

$$Cu^+ + [M(CN)_8]^{3-} \underset{k_{-3}}{\overset{k_3}{\leftrightarrows}} Cu^{2+} + [M(CN)_8]^{4-}$$

$$RS^- + [M(CN)_8]^{3-} \underset{\text{(slow)}}{\overset{k_4}{\leftrightarrows}} RS^{\cdot} + [M(CN)_8]^{4-}$$

$$2RS^{\cdot} \overset{k_5}{\rightarrow} RSSR$$

Assuming that the fourth step is the rate determining step and applying the steady state assumption for the thiolate anion (RS^-), the rate law can be derived as follows:

$$-\frac{d[M(CN)_8]^{3-}}{dt} = k_4[RS^-][M(CN)_8]^{3-}$$

$$k_1[RSH] = k_{-1}[RS^-][H^+] + k_2[Cu^{2+}][RS^-] + k_4[M(CN)_8]^{3-}[RS^-]$$

$$[RS^-] = \frac{k_1[RSH]}{k_2[Cu^{2+}] + k_{-1}[H^+] + k_4[M(CN)_8]^{3-}}$$

$k_{-1}[H^+] \gg k_2[Cu^{2+}] + k_4[M(CN)_8]^{3-}$, the $[H^+]$ is sufficiently high.

$$-\frac{d[M(CN)_8]^{3-}}{dt} = k_4k_1/k_{-1}[RSH][M(CN)_8]^{3-}[H^+]^{-1},$$

$$-\frac{d[M(CN)_8]^{3-}}{dt} = k_{obs}[RSH][M(CN)_8]^{3-}[H^+]^{-1}$$

where $k_{obs} = k_4k_1/k_{-1}$.

References

[1] M.J. Akers, J. Parenteral Sci. Tech. 36 (1989) 222.
[2] G.I. Giles, C. Jacob, Biol. Chem. 383 (2002) 375.
[3] S.E. Moriarty, J.H. Shah, M. Lynn, S. Jiang, K. Openo, D.P. Jones, P. Sternberg, Free Radical Biol. Med. 35 (2003) 1582.
[4] D.A. Dixon, T.P. Dasgupta, N.P. Sadler, Inorg. Reaction Mechanisms 1 (1998) 41.
[5] H.M. Abdel-Halim, Int. J. Chem. 11 (2001) 131.
[6] H.M. Abdel-Halim, A.S. Abu-Surrah, H.M. Baker, Z. Naturforsch B Chem. Sci. 61 (2006) 1346.
[7] R.F. Jameson, W. Linert, A. Tschinkowitz, J. Chem. Soc., Dalton Trans. (1988) 2109.
[8] F.P. Ballistreri, E.G. Barbuzzi, G.A. Tomaselli, R.M. Toscano, J. Inorg. Biochem. 80 (2000) 173.
[9] H.M. Abdel-Halim, Y.M. Ailawatia, Asian J. Chem. 6 (1994) 655.
[10] R.C. Smith, V.D. Reed, W.E. Hill, Phosphorus, Sulfur Silicon Related Elements 90 (1994) 147.
[11] R. Saldanha, S. Ananda, B. Venkatesha, M. Jagadeesha, Indian Oxidation Comm. 22 (1999) 464.
[12] P.J. Morando, E.B. Broghi, L.M. De Schteingart, M.A. Blesa, J. Chem. Soc., Dalton Trans. (1981) 435.
[13] C. Salamon, R. Jameson, W. Linert, Inorg. Chim. Acta 357 (2004) 41.
[14] J. Martin, J. Spence, J. Phys. Chem. 74 (1970) 2863.
[15] J. Martin, J. Spence, J. Phys. Chem. 74 (1970) 3589.
[16] A. Kay, P. Mitchell, Nature 219 (1968) 267.
[17] M. Hung, D.M. Stanbury, Inorg. Chem. 44 (2005) 3541.
[18] M. Olatunji, R. Okechukwu, Inorg. Chim. Acta 131 (1987) 89–94.
[19] G. Bridgart, M. Fuller, I. Wilson, J. Chem. Soc., Dalton Trans. (1973) 1274.
[20] T.Y. Lee, R.E. Nortari, Pharm. Res. 4 (1987) 98.
[21] D. Rabenstein, Y. Theriault, Can. J. Chem. 63 (1985) 33.
[22] S. El-Ashry, F. Ibrahim, Anal. Lett. 25 (1992) 1657.
[23] S. Sypniewski, E. Bald, J. Chromatogr. A 729 (1996) 335.
[24] Y. Pramar, G.V. Das, C. Bethea, J. Clin. Pharm. Therapeut. 17 (1992) 185.
[25] M.B. Clearfield, N. Lee, L. Armstrong, P. Defazio, B.J. Kudchodkar, A.J. Lacko, Pharmacol. Toxicol. 75 (1994) 218.
[26] J.G. Leipoldt, L.D.C. Bok, P.J. Cilliers, Z. Anorg. Allg. Chem. 409 (1974) 343.
[27] P.J. Cilliers, J.G. Leipoldt, L.D.C. Bok, Z. Anorg. Allg. Chem. 407 (1974) 350.
[28] L.D. Bok, J.G. Leipoldt, S.S. Basson, Z. Anorg. Allg. Chem. 415 (1975) 81.

[29] C.R. Dennis, A.J.V. Wyk, S.S. Basson, J.G. Leipoldt, Trans. Met. Chem. 17 (1992) 471.
[30] R.G. Bates, R.A. Robinson, in: B.C. Conway (Ed.), Chemical Physics of Ionic Solutions, Wiley, New York, 1964 (Chapter 12).
[31] E. Kozakova, B. Csefalvayova, Chem. Zvesti 34 (1980) 610.
[32] R.A. El-Zaru, H.A. Hodali, Polyhedron 9 (1990).
[33] R. Munday, C.M. Munday, C.C. Winterbourn, Free Radical Biol. Med. 36 (2004) 757.
[34] B. Saha, M. Hung, D.M. Stanbury, Inorg. Chem. 41 (2002) 5538.

Available online at www.sciencedirect.com
ScienceDirect
Polyhedron 26 (2007) 3074–3084
POLYHEDRON
www.elsevier.com/locate/poly

Synthesis and characterization of Cu(II), Co(II) and Ni(II) coordination polymers containing bis(imidazolyl) ligands

Shou-Wen Jin, Wan-Zhi Chen *

Department of Chemistry, Zhejiang University, Xixi Campus, Hangzhou 310028, PR China

Received 19 January 2007; accepted 9 February 2007
Available online 12 March 2007

Abstract

Two structurally related flexible imidazolyl ligands, bis(*N*-imidazolyl)methane (L_1) and 1,4-bis(*N*-imidazolyl)butane (L_2), were reacted with Cu(II), Co(II) and Ni(II) salts of aliphatic/aromatic dicarboxylic acids resulting in the formation of a number of novel metal–organic coordination architectures, $[CuB_2(ox)_2(L_1)_2(H_2O)_2]\cdot 4H_2O$ (**1**) (ox = oxalate), $[Cu(pdc)(L_2)_{1.5}]\cdot 4H_2O$ (**2**, pdc = pyridine-2, 6-dicarboxylate), $[Co(L)_2(H_2O)_2](tp)\cdot 4H_2O$ (**3**, tp = terephthalate), $[Ni(L_1)_2(H_2O)_2](ip)\cdot 5H_2O$ (**4**, ip = isophthalate), $[Cu_2(L_1)_4(H_2O)_4](tp)_2\cdot 7H_2O$ (**5**), $[Co(mal)(L_1)(H_2O)]\cdot 0.5MeOH$ (**6**, mal = malonate), $[Co(pdc)(L_1)(H_2O)]$ (**7**). All the complexes have been structurally characterized by X-ray diffraction analysis. The different coordination modes of the dicarboxylate anions, due to their chain length, rigidity and diimidazolyl functionality, lead to a wide range of different coordination structures. The coordination polymers exhibit 1D single chain, ladder, 2D sheet and 2D network structures. The aliphatic and aromatic dicarboxylates can adopt chelating μ_2 and chelating-bridging μ_3 coordination modes, or act as uncoordinated counter anions. The central metal ions are coordinated in N_2O_4, N_4O_2, N_2O_3 and N_3O_3 fashions, depending on the ancillary ligands. The topology of **1** gives rise to macrocycles which are connected through hydrogen bonds to form 1D chains, whereas compound **2** exhibits a 1D polymeric ladder in which the carboxylate acts as a pincer ligand. Compounds **3**–**5** show doubly bridged 1D chains, and the dicarboxylate groups are not coordinated but form 2D corrugated sheets with water molecules intercalated between the cationic layers. Compound **6** has a 2D network sheet structure in which each metal ion links three neighboring Co atoms by the bis(*N*-imidazolyl)methane ligand. The cobalt compound **7**, with a 2D polymeric double sheet structure, is built from pincer carboxylate (pdc) and 1,4-bis(*N*-imidazolyl)methane ligands.
© 2007 Elsevier Ltd. All rights reserved.

Keywords: Dicarboxylic acid; Cu(II); Co(II); Ni(II); Mixed ligands; Coordination polymers

1. Introduction

The design and synthesis of metal–organic framework structures have received enormous attention [1] in recent years due to their potential applications in diverse areas such as electrical conductivity [2], magnetism [3], host–guest chemistry [4], molecular separation [5], gas storage [6], sensors [7] and catalysis [8]. The framework structure of the coordination polymers is primarily dependent upon the coordination preferences of the central metal ions and the functionality of the ligands. Aside from the coordination bonding interactions, the hydrogen bonding and π–π stacking interactions, the solvent molecules, counterions and the ratio of metal salt to organic ligand also influence the formation of the ultimate architectures.

It is well known that carboxylate ligands play an important role in coordination chemistry and can adopt various binding modes such as terminal monodentate, chelating to one metal center, bridging bidentate in a *syn–syn*, *syn–anti* and *anti–anti* configuration to two metal centers, and bridging tridentate to two metal centers [9]. The rigid rod-like spacer molecules 4,4′-bipyridine (bipy) and pyrazine (pz) have been widely used as building blocks for the construction of metal–organic coordination frameworks [10]. The use of organic spacers, particularly flexible

* Corresponding author. Tel./fax: +86 571 8827 3314.
E-mail address: chenwzz@zju.edu.cn (W.-Z. Chen).

0277-5387/$ - see front matter © 2007 Elsevier Ltd. All rights reserved.
doi:10.1016/j.poly.2007.02.029

dicarboxylates ($R(COO)_2^{2-}$ anion) bridging ligands and rigid planar bidentate diimines (bipy or pyz) as building blocks to construct various metal assemblies is of growing interest in the field of molecular materials [11]. Recently, great success has been achieved by the combination of flexible aliphatic dicarboxylates and bipy as chelating bridging ligands, which resulted in compounds having 1–3D frameworks and unique physicochemical properties [12–20]. A large number of novel architectures assembled through this combination, such as extended networks having grid [21], honeycomb [22], brick wall [23] and other geometries [24], have been reported in recent years. In contrast to rigid spacers, flexible ligands, which can adopt various conformations, may induce coordination polymers with novel topologies. However, flexible ligands containing imidazolyl groups and polycarboxylate ligands have not been well studied to date [25–30]. 1,1′-bis(*N*-imidazolyl)methane (L_1) and 1,4-bis(*N*-imidazolyl)butane (L_2) can be used as flexible divergent ligands to construct coordination polymer materials. The remarkable coordination abilities of dicarboxylic acid ligands and flexible bidentate diimines have prompted us to design and synthesize new coordination polymeric compounds containing both ligands.

To examine the influence of the chain length and the rigidity of the ligands, here we report the preparation of a few novel metal–organic coordination polymers by reacting transition metal salts of dicarboxylates with flexible bidentate ligands. Their structures are fully characterized by IR and X-ray diffraction.

2. Experimental

2.1. Materials and methods

All reagents and solvents were purchased from commercial sources and were used as received. L_1 and L_2 were prepared according to the reported procedure [31]. Elemental analyses were determined with a Carlo Erba 1110 instrument. IR spectra were measured as KBr discs using a Bruker Vector 22 spectrophotometer. Thermogravimetric analyses (TGA) were studied by a Delta Series TA-SDT Q600 in a N_2 atmosphere in the temperature range from room temperature to 800 °C (heating rate = 10 °C min^{-1}) using Al crucibles.

2.2. Synthesis

2.2.1. $[Cu_2(ox)_2(L_1)_2(H_2O)_2]\cdot 4H_2O$ (**1**)

A mixture of $CuCl_2\cdot 2H_2O$ (17.1 mg, 0.1 mmol), NaOH (8 mg, 0.2 mmol), and oxalic acid (12.7 mg, 0.1 mmol) in water was stirred for 10 min at 60 °C, then L_1 (15 mg, 0.1 mmol) was added to the mixture. After stirring for 30 min, a blue precipitate was collected and dissolved in a minimum amount of ammonia. Blue single crystals of **1** were obtained by slow evaporation of the ammonia solution at ambient temperature. Yield: 30 mg, 42.4%. *Anal.* Calc. for $C_{18}H_{28}Cu_2N_8O_{14}$: C, 30.56; H, 3.99; N, 15.84. Found: C, 30.50; H, 3.91; N, 15.75%. IR data (KBr, cm^{-1}): 3451s, 3117s, 1673s, 1513s, 1401s, 1288s, 1238s, 1099s, 1035w, 952m, 856m, 785s, 713s, 657m, 615m, 545m, 478m.

2.2.2. $[Cu(pdc)(L_2)_{1.5}]\cdot 4H_2O$ (**2**)

Compound **2** was prepared similarly using $CuCl_2\cdot 2H_2O$ (17.1 mg, 0.1 mmol), NaOH (8 mg, 0.2 mmol), and pyridine-2,6-dicarboxylic acid (16.7 mg, 0.1 mmol), L_2 (19 mg, 0.1 mmol). The resulting blue precipitate was collected and dissolved in a minimum amount of ammonia. Blue single crystals of **2** were obtained by slow evaporation of the ammonia solution at ambient temperature. Yield: 40 mg, 68.3%. *Anal.* Calc. for $C_{22}H_{32}CuN_7O_8$: C, 45.08; H, 5.50; N, 16.73. Found: C, 45.04; H, 5.46; N, 16.72%. IR data (KBr, cm^{-1}): 3419s, 3106m, 2941w, 1649s, 1586m, 1523m, 1453w, 1420w, 1375m, 1351m, 1276, 1240w, 1184w, 1104m, 1034m, 946w, 903w, 855w, 789w, 766w, 750w, 726w, 698w, 663m, 629w.

2.2.3. $[Co(L_1)_2(H_2O)_2](tp)\cdot 4H_2O$ (**3**)

An aqueous solution of terephthalic acid (16.7 mg, 0.1 mmol) and NaOH (8 mg, 0.2 mmol) were treated with $Co(NO_3)_2\cdot 6H_2O$ (29.1 mg, 0.1 mmol). After the mixture was stirred for a few minutes, L_1 (14.8 mg, 0.1 mmol) was added to give a violet solution. Slow evaporation of the resulting solution yielded violet crystals after a few days, which were collected and washed with water and ethanol. Yield: 40 mg, 63.7%. *Anal.* Calc. for $C_{22}H_{32}CoN_8O_{10}$: C, 42.11; H, 5.14; N, 17.86. Found: C, 42.07; H, 5.10; N, 17.72%. IR data (KBr, cm^{-1}): 3214s, 3114w, 1636w, 1567s, 1527w, 1503w, 1393m, 1284m, 1234m, 1091m, 935w, 829w, 747m, 713w, 660m, 508w.

2.2.4. $[Ni(L_1)_2(H_2O)_2](ip)\cdot 5H_2O$ (**4**)

This compound was prepared similarly as for **3** from isophthalic acid (16.7 mg, 0.1 mmol), NaOH (8 mg, 0.2 mmol), $NiCl_2\cdot 6H_2O$ (24 mg, 0.1 mmol) and L_1 (14.8 mg, 0.1 mmol). Light blue crystals were isolated after slow evaporation of its solution. Yield: 45 mg, 69.7%. *Anal.* Calc. for $C_{22}H_{34}N_8NiO_{11}$: C, 40.95; H, 5.31; N, 17.37. Found: C, 40.88; H, 5.23; N, 17.29%. IR data (KBr pellet, cm^{-1}): 3382s, 3128w, 1602m, 1551s, 1422w, 1365s, 1286m, 1232m, 1089m, 1032w, 939m, 751m, 713w, 659m, 612w.

2.2.5. $[Cu_2(L_1)_4(H_2O)_4](tp)_2\cdot 7H_2O$ (**5**)

This compound was prepared by the same procedure as for compound **1** from $CuCl_2\cdot 2H_2O$ (17.1 mg, 0.1 mmol), NaOH (8 mg, 0.2 mmol), terephthalic acid (16.7 mg, 0.1 mmol) and L_1 (15 mg, 0.1 mmol). The resulting blue precipitate was collected and dissolved in a minimum amount of ammonia. Blue single crystals of **5** were obtained by slow evaporation of the ammonia solution at ambient temperature. Yield: 40 mg, 32%. *Anal.* Calc. for $C_{44}H_{62}Cu_2N_{16}O_{19}$: C, 42.40; H, 5.01; N, 17.98. Found: C, 42.34; H, 4.95; N, 17.92%. IR data (KBr, cm^{-1}): 3415s, 3115s, 1646m, 1573s, 1530s, 1508s, 1373s, 1290s, 1229s, 1096s, 1025w, 1012w, 948m, 885w, 824m, 754s, 713m, 655m, 614m, 499m.

2.2.6. [Co(mal)(L_1)(H_2O)] · 0.5MeOH (6)

Compound **6** was prepared in the same manner as for **3** from malonic acid (10.4 mg, 0.1 mmol), NaOH (8 mg, 0.2 mmol), $CoCl_2 \cdot 6H_2O$ (24 mg, 1 mmol) and L_1 (14.8 mg, 0.1 mmol). The compound was isolated as violet block crystals. Yield: 23 mg, 67%. Elemental analysis performed on crystals exposed to the atmosphere: *Anal*. Calc. for $C_{10.5}H_{14}CoN_4O_{5.5}$: C, 36.75; H, 4.11; N, 16.33. Found: C, 36.70; H, 4.06; N, 16.27%. IR data (KBr pellet, cm^{-1}): 3277br, 3127w, 1642w, 1566s, 1437m, 1394w, 1348m, 1288w, 1235m, 1161m, 1100m, 1035m, 940m, 848m, 760m, 715m, 659m, 618w, 575m.

2.2.7. [Co(pdc)(L_1)(H_2O)] (7)

Compound **7** was prepared similarly as for **3** using pyridine-2,6-dicarboxylic acid (16.7 mg, 0.1 mmol), NaOH (8 mg, 0.2 mmol), $CoCl_2 \cdot 6H_2O$ (24 mg, 0.1 mmol) and L_1 (14.8 mg, 0.1 mmol). Violet crystals were obtained by slow evaporation of the aqueous solution. Yield: 28 mg, 72%. *Anal*. Calc. for $C_{14}H_{13}CoN_5O_5$: C, 43.09; H, 3.36; N, 17.95. Found: C, 43.01; H, 3.29; N, 17.88%. IR (KBr pellet, cm^{-1}): 3118m, 2363w, 1632s, 1502m, 1417m, 1359m, 1280m, 1228m, 1176m, 1088m, 1038m, 936w, 911w, 846w, 817w, 766m, 721m, 690w, 666w, 619w.

2.3. X-ray crystallography

Single-crystal X-ray diffraction data for complexes **1**–**7** were collected at 298(2) K on a Siemens Smart/CCD area-detector diffractometer with Mo Kα radiation ($\lambda = 0.71073$ Å) by using an ω scan mode. Data collection and reduction were performed using the SMART and SAINT software [32]. The structures were solved by direct methods and the non-hydrogen atoms were subjected to anisotropic refinement by full-matrix least-squares on F_2 using the SHELXTXL package [33]. Hydrogen atom positions for all of the structures were calculated and allowed to ride on their respective C atoms with C–H distances of 0.93–0.97 Å and $U_{iso}(H) = -1.2U_{eq}(C)$. Hydrogen atoms bound to water molecules were located in the Fourier difference map and their distances were fixed. Further details of the structural analysis are summarized in Table 1. Selected bond lengths and angles for complexes **1**–**7** are listed in Table 2.

3. Results and discussion

3.1. Synthesis and general characterization

Complexes **1**–**7** were prepared in water, and they are insoluble in water and common organic solvents. Crystals

Table 1
Summary of X-ray crystallographic data for complexes **1**–**7**

Compound	**1**	**2**	**3**	**4**	**5**	**6**	**7**
Formula	$C_{18}H_{28}Cu_2N_8O_{14}$	$C_{22}H_{32}CuN_7O_8$	$C_{22}H_{32}CoN_8O_{10}$	$C_{22}H_{34}N_8NiO_{11}$	$C_{44}H_{62}Cu_2N_{16}O_{19}$	$C_{10.5}H_{14}CoN_4O_{5.5}$	$C_{14}H_{13}CoN_5O_5$
Formula weight	707.56	586.09	627.49	645.28	1246.18	343.19	390.22
Crystal system	triclinic	triclinic	monoclinic	monoclinic	orthorhombic	monoclinic	monoclinic
Space group	$P\bar{1}$	$P\bar{1}$	$P2_1/c$	$P2_1/c$	$Ccca$	$P2_1/c$	$C2/c$
a (Å)	8.910(3)	7.983(6)	10.192(6)	10.917(2)	22.742(3)	8.384(2)	10.502(6)
b (Å)	9.288(3)	10.067(7)	16.815(9)	16.610(3)	25.715(3)	22.108(6)	22.614(13)
c (Å)	9.795(3)	16.564(12)	16.996(10)	16.723(3)	19.322(3)	8.337(2)	7.794(5)
α (°)	66.315(3)	84.801(8)					
β (°)	75.740(3)	87.554(9)	102.488(9)	104.498(2)		116.420(3)	123.870(6)
γ (°)	83.426(3)	88.938(9)					
V (Å^3)	719.3(4)	1324.4(16)	2844(3)	2935.8(9)	1130.0(2)	1383.9(7)	1536.9(16)
Z	1	2	4	4	8	4	4
D_{calc} (Mg/m^3)	1.633	1.470	1.466	1.460	1.465	1.647	1.686
Absorption coefficient (mm^{-1})	1.556	0.883	0.670	0.730	0.838	1.271	1.155
F(000)	362	612	1308	1352	5184	704	796
Crystal size (mm)	0.42 × 0.34 × 0.27	0.26 × 0.23 × 0.15	0.21 × 0.14 × 0.11	0.22 × 0.17 × 0.15	0.56 × 0.54 × 0.15	0.28 × 0.22 × 0.16	0.20 × 0.17 × 0.15
θ Range (°)	2.33–25.00	2.03–25.01	1.72–25.01	1.76–25.01	1.58–25.01	1.84–25.01	1.80–25.00
Limiting indices	$-9 \leqslant h \leqslant 10$, $-11 \leqslant k \leqslant 8$, $-10 \leqslant l \leqslant 11$	$-5 \leqslant h \leqslant 9$, $-11 \leqslant k \leqslant 11$, $-19 \leqslant l \leqslant 19$	$-11 \leqslant h \leqslant 12$, $-16 \leqslant k \leqslant 20$, $-16 \leqslant l \leqslant 20$	$-12 \leqslant h \leqslant 11$, $-19 \leqslant k \leqslant 18$, $-11 \leqslant l \leqslant 19$	$-14 \leqslant h \leqslant 27$, $-30 \leqslant k \leqslant 30$, $-22 \leqslant l \leqslant 22$	$-5 \leqslant h \leqslant 9$, $-25 \leqslant k \leqslant 26$, $-9 \leqslant l \leqslant 9$	$-9 \leqslant h \leqslant 12$, $-26 \leqslant k \leqslant 26$, $-9 \leqslant l \leqslant 6$
Reflections collected	3720	6860	14496	14873	28223	7121	3943
Reflections independent (R_{int})	2496 (0.0178)	4583 (0.0421)	5002 (0.0365)	5168 (0.0991)	4993 (0.0563)	2424 (0.0416)	1360 (0.0360)
Goodness-of-fit on F^2	1.071	0.984	1.016	1.000	1.064	1.039	1.036
R indices [$I > 2\sigma I$]	$R_1 = 0.0301$, $wR_2 = 0.0797$	$R_1 = 0.0649$, $wR_2 = 0.1576$	$R_1 = 0.0361$, $wR_2 = 0.0904$	$R_1 = 0.0520$, $wR_2 = 0.1040$	$R_1 = 0.0379$, $wR_2 = 0.0810$	$R_1 = 0.0421$, $wR_2 = 0.0987$	$R_1 = 0.0351$, $wR_2 = 0.0807$
R indices (all data)	$R_1 = 0.0338$, $wR_2 = 0.0831$	$R_1 = 0.1014$, $wR_2 = 0.1830$	$R_1 = 0.0560$, $wR_2 = 0.1035$	$R_1 = 0.1537$, $wR_2 = 0.1454$	$R_1 = 0.0799$, $wR_2 = 0.1073$	$R_1 = 0.0662$, $wR_2 = 0.1143$	$R_1 = 0.0514$, $wR_2 = 0.0891$

Table 2
Selected bond lengths (Å) and angles (°) for **1**–**7**

Compound ***1***			
Cu(1)–O(1)	1.970(2)	Cu(1)–O(3)	1.971(2)
Cu(1)–N(4)	1.978(2)	Cu(1)–N(2)	1.999(2)
Cu(1)–O(5)	2.356(2)	O(1)–Cu(1)–O(3)	83.1(1)
O(1)–Cu(1)–N(4)	175.9 (1)	O(3)–Cu(1)–N(4)	93.9(1)
O(1)–Cu(1)–N(2)	90.2(1)	O(3)–Cu(1)–N(2)	163.2(1)
N(4)–Cu(1)–N(2)	93.3(1)	O(1)–Cu(1)–O(5)	90.4(1)
O(3)–Cu(1)–O(5)	99.3(1)	N(4)–Cu(1)–O(5)	87.4(1)
N(2)–Cu(1)–O(5)	96.2(1)		
Compound ***2***			
Cu(1)–N(7)	1.991(4)	Cu(1)–N(1)	2.006(4)
Cu(1)–N(3)	2.057(4)	Cu(1)–N(5)	2.061(4)
Cu(1)–O(3)	2.312(4)	Cu(1)–O(1)	2.418(4)
N(7)–Cu(1)–N(1)	178.4(2)	N(7)–Cu(1)–N(3)	91.9(2)
N(1)–Cu(1)–N(3)	88.6(2)	N(7)–Cu(1)–N(5)	88.5(2)
N(1)–Cu(1)–N(5)	90.9(2)	N(3)–Cu(1)–N(5)	175.2(2)
N(7)–Cu(1)–O(3)	105.3(2)	N(1)–Cu(1)–O(3)	76.2(2)
N(3)–Cu(1)–O(3)	93.3(2)	N(5)–Cu(1)–O(3)	91.2(2)
N(7)–Cu(1)–O(1)	103.5(2)	N(1)–Cu(1)–O(1)	75.0(2)
N(3)–Cu(1)–O(1)	87.5(2)	N(5)–Cu(1)–O(1)	87.7(2)
O(3)–Cu(1)–O(1)	151.2(2)		
Compound ***3***			
Co(1)–O(5)	2.128(2)	Co(1)–O(6)	2.134(2)
Co(1)–N(4)	2.137(2)	Co(1)–N(6)	2.137(2)
Co(1)–N(2)	2.140(2)	Co(1)–N(7)	2.143(2)
O(5)–Co(1)–O(6)	179.8(1)	O(5)–Co(1)–N(4)	89.4(1)
O(6)–Co(1)–N(4)	90.6(1)	O(5)–Co(1)–N(6)	89.2(1)
O(6)–Co(1)–N(6)	90.8(1)	O(5)–Co(1)–N(2)	90.8(1)
O(6)–Co(1)–N(2)	89.4(1)	N(4)–Co(1)–N(2)	90.9(1)
N(6)–Co(1)–N(2)	90.1(1)	O(5)–Co(1)–N(7)	91.9(1)
O(6)–Co(1)–N(7)	87.9(1)	N(4)–Co(1)–N(7)	88.8(1)
N(6)–Co(1)–N(7)	90.3(1)	N(2)–Co(1)–N(7)	177.3(1)
Compound ***4***			
Ni(1)–O(6)	2.082(3)	Ni(1)–N(6)	2.090(4)
Ni(1)–N(8)	2.090(4)	Ni(1)–N(4)	2.092(5)
Ni(1)–N(2)	2.108(4)	Ni(1)–O(5)	2.114(3)
O(6)–Ni(1)–N(6)	90.7(2)	O(6)–Ni(1)–N(8)	89.4(2)
N(6)–Ni(1)–N(8)	90.8(2)	O(6)–Ni(1)–N(4)	92.7(2)
N(6)–Ni(1)–N(4)	174.9(2)	N(8)–Ni(1)–N(4)	93.1(2)
O(6)–Ni(1)–N(2)	87.3(2)	N(6)–Ni(1)–N(2)	86.6(2)
N(8)–Ni(1)–N(2)	175.8(2)	N(4)–Ni(1)–N(2)	89.7(2)
O(6)–Ni(1)–O(5)	177.5(2)	N(6)–Ni(1)–O(5)	88.2(2)
N(8)–Ni(1)–O(5)	88.4 (2)	N(4)–Ni(1)–O(5)	88.7(2)
N(2)–Ni(1)–O(5)	94.9(2)		
Compound ***5***			
Cu(1)–N(6)	2.010(3)	Cu(1)–N(2)	2.010(3)
Cu(1)–O(5)	2.427(2)	Cu(2)–N(8)	1.993(3)
Cu(2)–N(4)	1.997(3)	Cu(2)–O(6)	2.509(3)
N(6)#1–Cu(1)–N(6)	89.3(2)	N(6)#1–Cu(1)–N(2)	90.5(1)
N(6)–Cu(1)–N(2)	178.2(1)	N(2)–Cu(1)–N(2)#1	89.8(2)
N(6)–Cu(1)–O(5)	89.6(1)	N(2)–Cu(1)–O(5)	88.6(1)
N(2)#1–Cu(1)–O(5)	89.5(1)	O(5)–Cu(1)–O(5)#1	177.3(1)
N(8)#2–Cu(2)–N(8)	89.0(1)	N(8)–Cu(2)–N(4)#2	91.8(1)
N(8)–Cu(2)–N(4)	177.4(1)	N(4)#2–Cu(2)–N(4)	87.5(1)
N(8)#2–Cu(2)–O(6)	87.7(1)	N(8)–Cu(2)–O(6)	92.4(1)
N(4)#2–Cu(2)–O(6)	89.8(1)	N(4)–Cu(2)–O(6)	90.1(1)

Table 2 (*continued*)

Compound ***6***			
Co(1)–O(1)	2.092(3)	Co(1)–O(5)	2.093(3)
Co(1)–N(2)	2.118(4)	Co(1)–O(3)	2.125(3)
Co(1)–N(4)	2.131(3)	Co(1)#2–O(4)	2.141(3)
O(1)–Co(1)–O(5)	175.2(1)	O(1)–Co(1)–N(2)	92.2(1)
O(5)–Co(1)–N(2)	92.5(1)	O(1)–Co(1)–O(3)	85.4(1)
O(5)–Co(1)–O(3)	93.8(1)	N(2)–Co(1)–O(3)	87.7(1)
O(1)–Co(1)–N(4)	89.1(1)	O(5)–Co(1)–N(4)	91.9(1)
N(2)–Co(1)–N(4)	89.3(1)	O(3)–Co(1)–N(4)	173.6(1)
O(1)–Co(1)–O(4)#1	88.2(1)	O(5)–Co(1)–O(4)#1	87.1(1)
N(2)–Co(1)–O(4)#1	178.6(1)	O(3)–Co(1)–O(4)#1	91.0(1)
N(4)–Co(1)–O(4)#1	92.0(1)		
Compound 7			
Co(1)–O(3)	2.014(3)	Co(1)–N(1)	2.060(3)
Co(1)–N(3)	2.146(3)	Co(1)–O(1)	2.170(2)
O(3)–Co(1)–N(1)	180.0	O(3)–Co(1)–N(3)	91.0(1)
N(1)–Co(1)–N(3)	89.0(1)	N(3)–Co(1)–N(3)#1	178.0(1)
O(3)–Co(1)–O(1)	104.6(1)	N(1)–Co(1)–O(1)	75.4(1)
N(3)–Co(1)–O(1)	90.0(1)	N(3)#1–Co(1)–O(1)	89.5(1)
O(1)–Co(1)–O(1)#1	150.9(1)		

Symmetry code for **5**: #1 $-x+1$, $-y+1/2$, z; #2 $-x+3/2$, $-y+1$, z. Symmetry codes for **6**: #1 x, $-y+1/2$, $z+1/2$; #2 $-x$, $-y$, $-z$. Symmetry code for **7**: #1 $-x$, y, $-z+1/2$.

of **3**, **4**, **6** and **7** suitable for X-ray diffraction analysis were obtained by standing their aqueous solutions at room temperature, but crystals of complexes **1**, **2** and **5** were obtained by slow evaporation of their ammonia solutions. The elemental analysis data for the compounds are in good agreement with their formula.

The infrared spectra of **1**–**7** are consistent with their chemical formula as determined by elemental analysis and further confirmed by X-ray diffraction analysis. The very strong and broad features at approximately 3400–3200 cm^{-1} in their vibration spectra arise from O–H stretching frequencies of either coordinated or uncoordinated water molecules. Aromatic and imidazolyl ring stretching and bending are attributed to the medium intensity bands in the regions 1500–1630 cm^{-1} and 600–750 cm^{-1}, respectively. The intense peaks at ca. 1640 cm^{-1} are derived from the existence of C=O stretches of the carboxylates, and the bands at 1285 cm^{-1} show the presence of the C–O stretches.

3.2. Structural description

Compound **1**, of the formula $[Cu_2(ox)_2(L_1)_2(H_2O)_2]\cdot 4H_2O$, was obtained by reacting Cu^{2+}, oxalic acid and bis(*N*-imidazolyl)methane (L_1) in basic aqueous solution and was isolated as blue crystals. Compound **1** belongs to the triclinic $P\bar{1}$ space group. X-ray diffraction analysis showed that **1** is a discrete dinuclear complex, and the asymmetric unit consists of one Cu ion, one oxalate and one bis(*N*-imidazolyl)methane molecule. The value of τ is 0.21 and the coordination environment of the copper atoms is between the idealized square-pyramidal and trigonal-bipyramidal extremes [34]. As shown in Fig. 1a, the Cu ion adopts

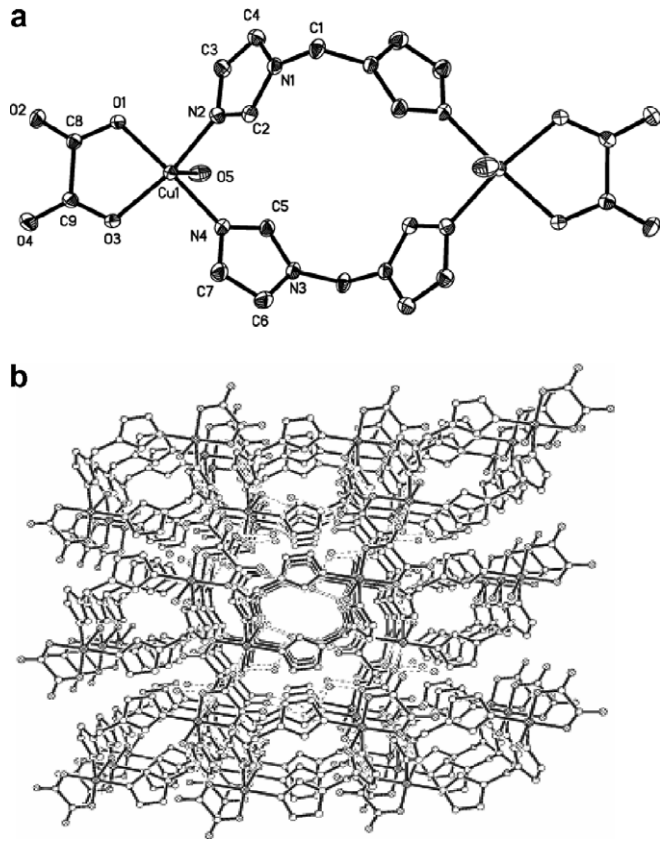


Fig. 1. (a) X-ray crystal structure of complex **1** with the atom numbering scheme. The thermal ellipsoids are drawn at 30% probability. (b) Three-dimensional network structure connected via hydrogen bonds.

a tetragonal pyramidal geometry and each copper atom is coordinated by two nitrogen atoms from two independent bis(*N*-imidazolyl)methane bridging ligands, two oxygen atoms from one oxalate anion in a chelating mode and one water molecule, completing its tetragonal pyramidal geometry with a N_2O_3 donor set. The Cu–O(water) bond distance, being 2.356(2) Å, is much longer than that of the Cu–O(carboxylate) bond distance (1.971(2) Å). The Cu–N distances of 1.999(2) and 1.978(2) Å are normal and are consistent with those of known Cu–imidazole complexes, which range from 1.876(13) to 2.049(8) Å [35]. The oxalate anion acts as a bis-unidentate ligand and forms a five-membered ring with the central metal ion, while two L_1 and two Cu atoms generate a 16-membered ring. The dimeric units are connected through strong multiple hydrogen bonds with water molecules, yielding a three-dimensional network structure, which is illustrated in Fig. 1b. The O–H···O distances range from 2.830 to 3.107 Å. The copper dimeric units are located in the channels built from the hydrogen bonding between the coordinated oxygen atoms and water molecules.

3.2.1. 1D polymeric ladder of $[Cu(pdc)(L_2)_{1.5}]\cdot 4H_2O$ (2)

Single crystals of **2** suitable for X-ray diffraction analysis were obtained by evaporating an ammonia solution of **2**. The central Cu(II) ion is hexacoordinated with a distorted octahedral geometry. Each Cu(II) ion is bonded equatorially to a pdc^{2-} (pdc^{2-} = pyridinedicarboxylate) and one nitrogen atom of a L_2 ligand (Fig. 2a). The pyridyl rings of pdc^{2-} and the imidazolyl ring are essentially co-planar. Two nitrogen atoms from two different 1,4-bis(*N*-imidazolyl)butane ligands fulfill the apical positions with Cu–N distances of 2.057(4) and 2.061(4) Å. The equatorial Cu–N bond does not show any significant difference to the axial Cu–N bonds, and the bond distances are similar to the values in the literature for other related Cu(II) complexes [36–38]. The two Cu–O bond distances,

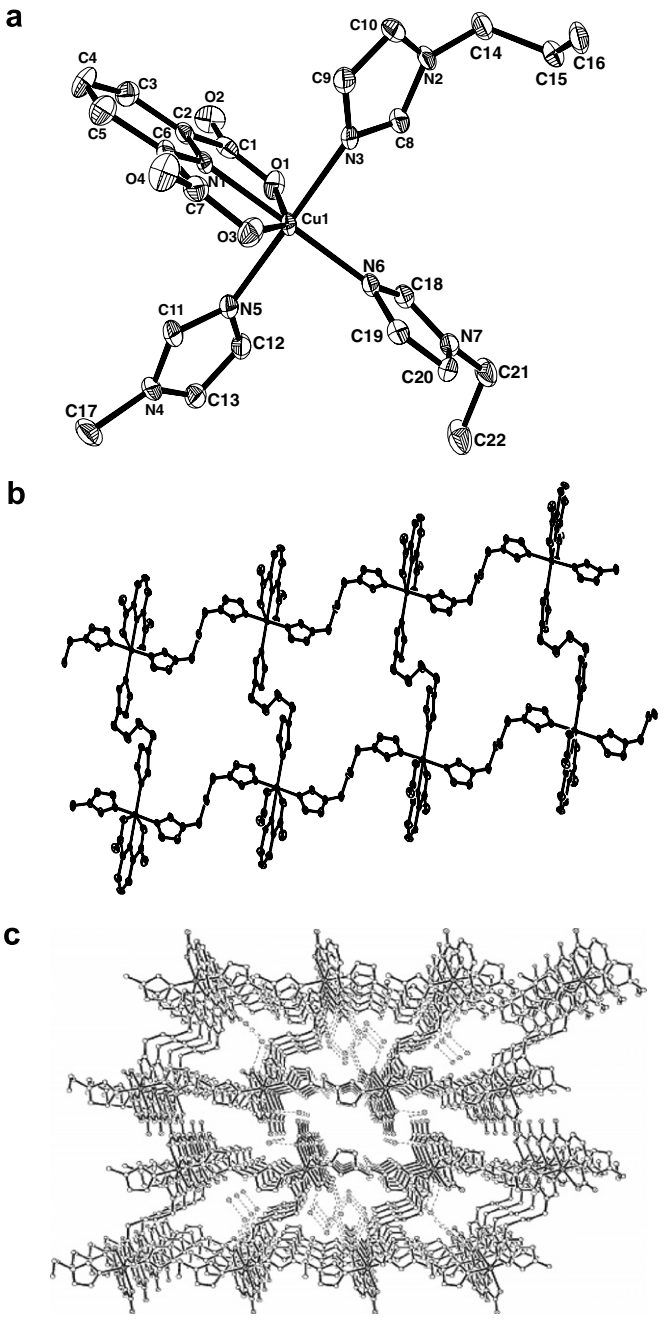


Fig. 2. (a) Local coordination environment of copper in polymer **2**. (b) Projection view of polymer **2** showing the one-dimensional ladder. (c) View of the 3D network structure based on the hydrogen bonds between the ladders and water molecules.

being 2.312(4) and 2.418(4) Å, are remarkably longer than normal Cu–O bonds for copper carboxylate complexes [25].

Each Cu ion is linked to three adjacent copper centers through three diimidazolyl ligands, extending into a one-dimensional ladder-like chain structure (Fig. 2b). Along the chains four L_2 ligands and four Cu cations form 36-membered square grids. The chains are built from repeated interconnection of the grids. Three lattice water molecules form pentagonal rings with two oxygen atoms of pdc^{2-} ligands via strong hydrogen bonds. The pentagonal rings are located in the channels constructed by the 36-membered rings. The water rings and the one-dimensional ladders are further connected by hydrogen bonds between water hydrogen atoms and the oxygen atoms of dicarboxylate groups with O–H···O distances ranging from 2.683(9) to 2.987(6) Å (Fig. 2c).

3.2.2. 1D polymeric hinged chains of $[M(L_1)_2(H_2O)_2]X\cdot nH_2O$ (3, M = Co, X = terephthalate; 4, M = Ni, X = isophthalate; 5, M = Cu, X = terephthalate)

The complexes of the general formula $[M(L_1)_2(H_2O)_2]X\cdot nH_2O$ (**3**, M = Co, X = terephthalate; **4**, M = Ni, X = isophthalate; **5**, M = Cu, X = terephthalate) were obtained by mixing the corresponding disodium dicarboxylate, metal salt and bis(*N*-imidazolyl)methane. The most common feature of the three compounds is that the dicarboxylate units are not coordinated to the central metals and act as counter anions. Although complexes **3**, **4** and **5** crystallize in different space groups, the structures of the cationic sections are essentially the same and thus only the structure of **3** is discussed in detail. The Co atom coordinates to four nitrogen atoms of four different bis(*N*-imidazolyl)methane molecules and two water molecules. The Co atom is in an octahedron environment (Fig. 3). Unlike compounds **1** and **2**, the terephthalate anion does not show any direct bonding interactions with the cobalt ion; it only acts as a counteranion. The Co–O_w distances, being 2.128(2) and 2.134(2) Å, are very close to those found for known cobalt complexes [39]. The Co–N distances (2.137(2), 2.140(2), and 2.143(2) Å) are not unusual and are well consistent with those observed for known compounds [39]. Adjacent Co ions are doubly bridged by two bis(*N*-imidazolyl)methane ligands and thus form infinite one-dimensional zigzag chains with a Co–Co separation of 8.960 Å.

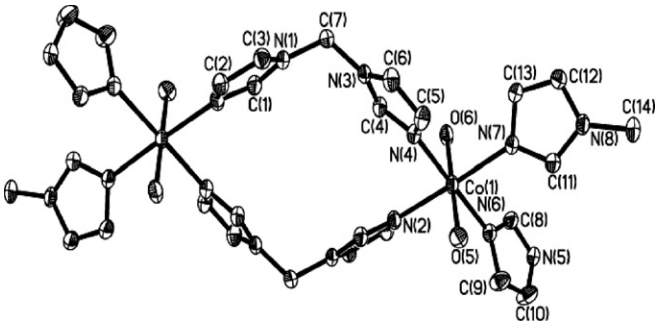


Fig. 3. X-ray crystal structure of the cationic section of complex **3** with the atomic numbering scheme. The uncoordinated anions and water molecules are omitted. The thermal ellipsoids are drawn at 30% probability.

The whole molecules are organized in a three-dimensional structure involving hydrogen bonds, both intercationic and between cations and terephthalate anions or water molecules. The O···O distances of the hydrogen bonding are observed to be in the range of 2.659(2)–2.775(3) Å for **3** and 2.644(2)–2.77(3) Å for **4**. The one-dimensional cationic chains arrange in a parallel way forming cationic layers, whereas the uncoordinated terephthalate anions and water molecules are connected into two-dimensional corrugated layers through strong hydrogen bonds. The two layers are alternatively stacked in an ABAB sequence and are intercalated with each other, as shown in Fig. 5a and b. Normally, aqueous hydrogen bonding to carboxylate oxygen atoms attracts water molecules causing a localized high density water clustering. It is interesting to note that in **3** and **4** free water molecules, coordinated water molecules and the anions form various polygonal oxygen rings, which link the coordinated water molecules and the chains through hydrogen bonds. The 2D sheets of dicarboxylate–water clusters consisting of p-$C_6H_4(CO_2^-)_2\cdot 4H_2O$ in **3** and m-$C_6H_4(CO_2^-)_2\cdot 5H_2O$ in **4** are depicted in Fig. 4a and b. Fig. 4a and b clearly shows that cyclic hexamer water clusters exist and display an ice-like chair conformation. These six-membered water rings hold the terephthalate or isophthalate ions together yielding supramolecular sheets in **3** and **4**. These hexamer water clusters have also been observed recently in a few inorganic and organic lattices [40]. Water clusters have been extensively studied both theoretically and experimentally [41]. A variety of water clusters $(H_2O)_n$ ($n = 2$–10) found in a number of crystal hosts, have been characterized and display different configurations. The hexamer water cluster is particularly interesting because this cluster can exhibit some of the properties of bulk water and may well provide an interesting model for the smallest piece of ice. How the size and symmetry of the anions influence the formation of water clusters in our cases have not been fully understood?

Although **5** consists of the same one-dimensional double chain structure as **3** and **4**, the chains extend in two directions (i.e. along the *a*- and *c*-axes), the chains in the *a*-axis direction are perpendicular to the chains in the *c*-axis direction, shown in Fig. 5c. The chains are connected to each other through multiple hydrogen bonds between tp anions and coordinated water molecules, resulting in a three-dimensional structure.

3.2.3. 2D network sheets of complexes $[Co(mal)(L_1)(H_2O)]\cdot 0.5MeOH$ (6)

The compound $[Co(mal)(L_1)(H_2O)]\cdot 0.5MeOH$ (**6**) was obtained from a basic aqueous solution of $CoCl_2$, malonic acid and bis(*N*-imidazolyl)methane. X-ray diffraction analysis revealed that the cobalt centers are interlocked

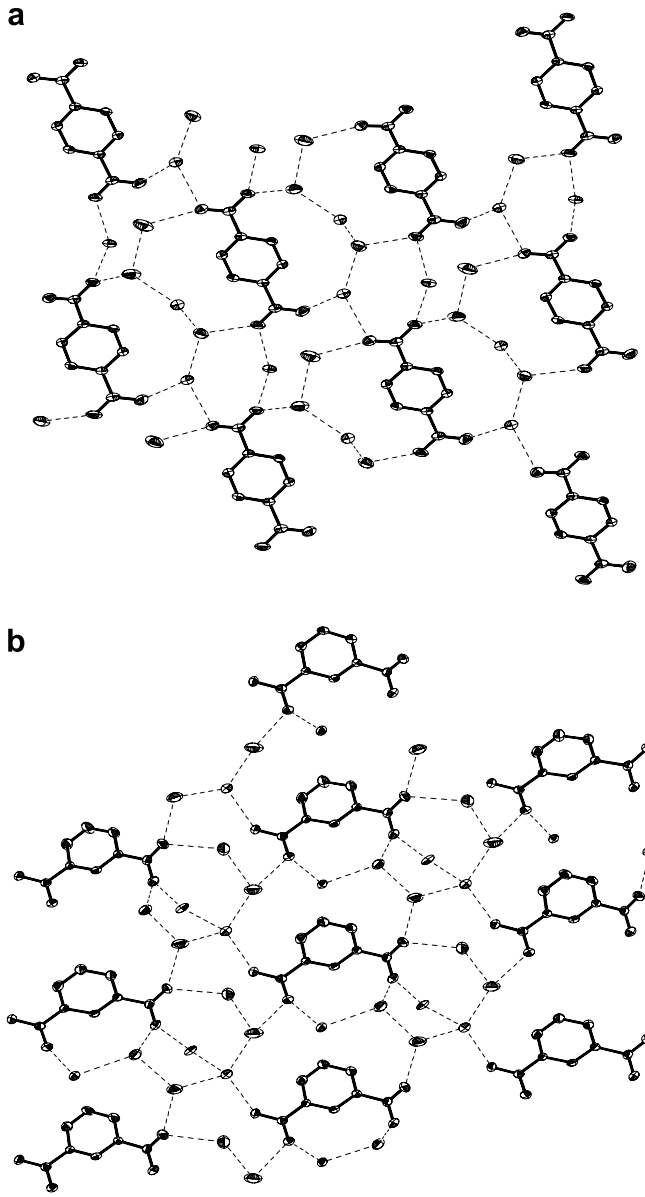


Fig. 4. Perspective view of the 2D corrugated sheets of hydrated dicarboxylates connected by hydrogen bonds. Metal ions and all carbon, nitrogen atoms other than the anions are omitted: (a) p-$C_6H_4(CO_2^-)_2 \cdot 4H_2O$ in **3**; (b) m-$C_6H_4(CO_2^-)_2 \cdot 5H_2O$ in **4**.

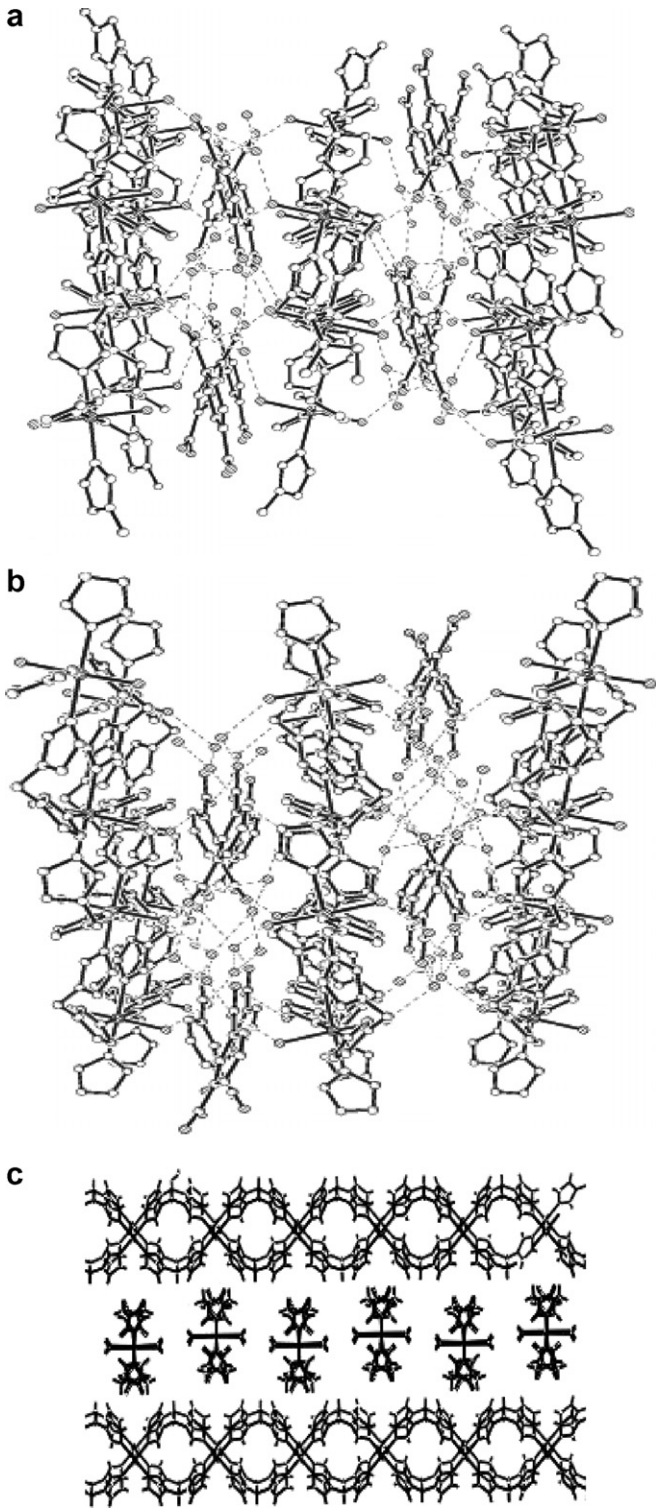


Fig. 5. (a) Space arrangement of intercalated cationic layers and anions layers in **3** (viewed along the c-axis). (b) Space arrangement of intercalated cationic layers and anions layers in **4** (viewed along the c-axis). (c) Chain arrangement of **5** (viewed along the a-axis).

by malonate ligands, giving an infinite two-dimensional network structure, as shown in Fig. 6b. The Co atom is six coordinated in a compressed octahedral environment. Two imidazolyl nitrogen donors coordinate to the center metal with Co–N distances of 2.118(4) and 2.131(3) Å. Another four sites are occupied by four oxygen atoms, one from a water molecule, others from carboxylate groups of two different malonate anions with Co–O distances ranging from 2.092(3) to 2.125(3) Å. The Co–O_w distance, being 2.093(3) Å, is slightly shorter. The malonate anion coordinates to one metal ion in a chelating form with two of the four oxygen atoms, and further bridges the second metal ion with one of the remaining two oxygen atoms (Fig. 6a). This coordinating mode has only been observed in a few examples [36]. Thus compound **6** may be viewed as an aggregate of the dimeric unit $[Co_2(mal)_2(L_1)_2]$ in which two Co centers are doubly bridged by two bis(N-imidazolyl)methane ligands. The dimeric units are

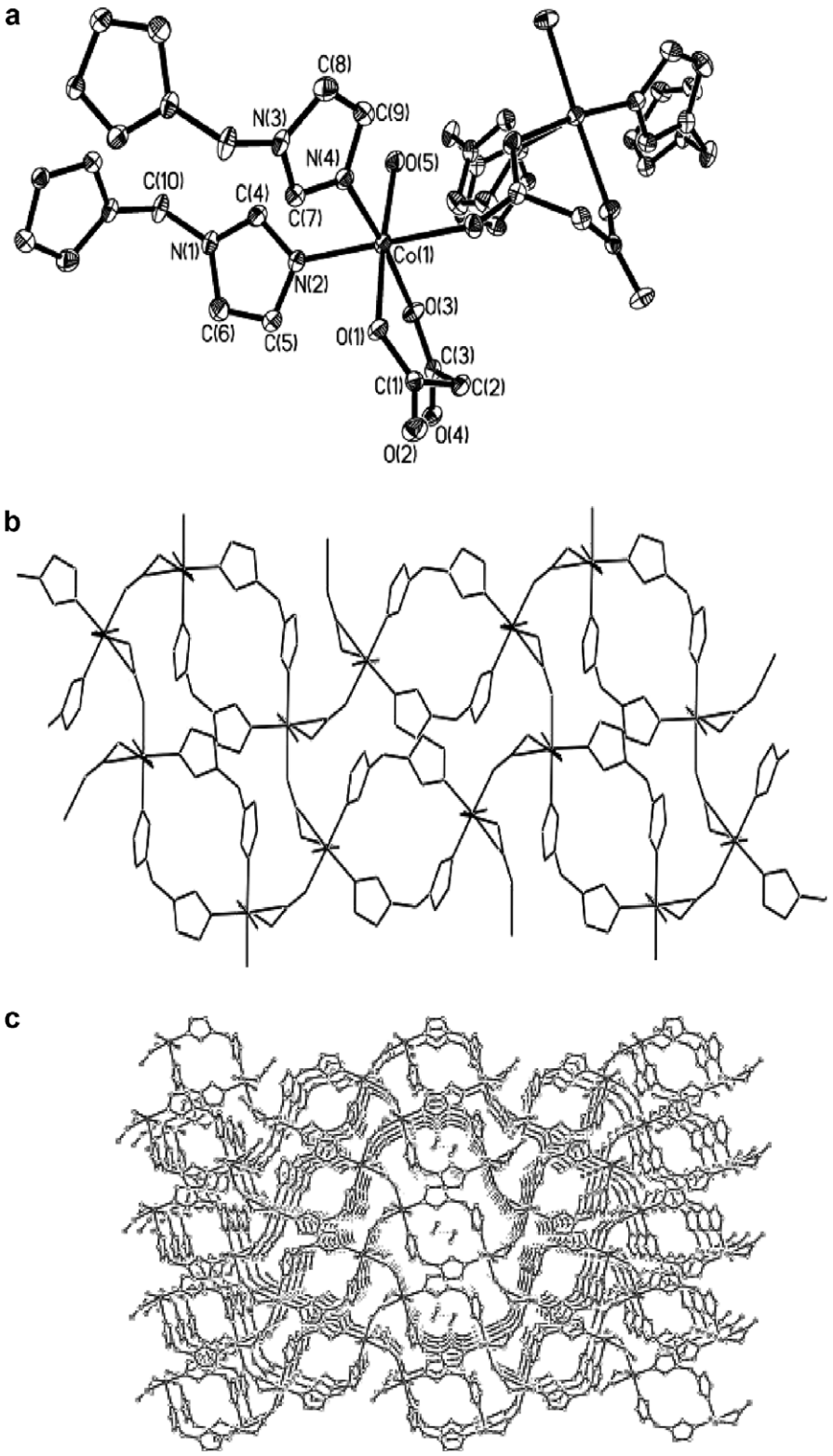


Fig. 6. (a) Structure of **6** showing the coordination environment of the metal atom with the atomic numbering scheme. (b) A segment of the 2D sheet. (c) Three-dimensional network structure showing the microchannels built by the parallel chains.

further held together via malonate anions in a μ_3 mode. This linkage leads to the construction of a two-dimensional sheet structure (Fig. 6b). Another oxygen atom O(2) forms a hydrogen bond with a crystal lattice water molecule with an O(2)···O(5w) distance of 2.712(4) Å.

The hydrogen atoms of the coordinated water and free water molecules are engaged in hydrogen bonding interactions with the oxygen atoms of the malonate anions, resulting in the formation of a three-dimensional channel structure, viewed down the *a*-axis as shown in Fig. 6c.

The short O···O contacts arising from hydrogen bonding are in the range 2.712(4)–2.985(8) Å.

3.2.4. 2D polymeric double sheet of [Co(pdc)(L_1)(H_2O)] (7)

The cobalt compound was prepared in the same manner as for the copper complex **2**. The structure of compound **7**, shown in Fig. 7a, is different from that observed for **6**. The structural analysis revealed that the coordination environment of the cobalt ion is a distorted octahedron surrounded by a 2,6-pyridinedicarboxylate and a water molecule in its equatorial positions, and the two axial positions are occupied by two imidazolyl rings. The Co–$N_{pyridyl}$ bond distance (2.060(3) Å) is shorter than that of Co–$N_{imidazolyl}$ (2.146(3) Å), and other bond distances are normal. The planar [Co(pdc)(H_2O)] units are linked to each other by bis(*N*-imidazolyl)methane, and this coordination mode generates a one-dimensional neutral polymeric chain structure.

The one-dimensional chains are arranged in a parallel fashion in the *ab*-plane. The adjacent chains interact with each other owing to the formation of hydrogen bonds between the coordinated waters. Such an arrangement generates an infinite two-dimensional double sheet structure in the *ab*-plane. These sheets stack into a layered structure as shown in Fig. 7b. The O3–H···$O3^i$ distance (symmetry

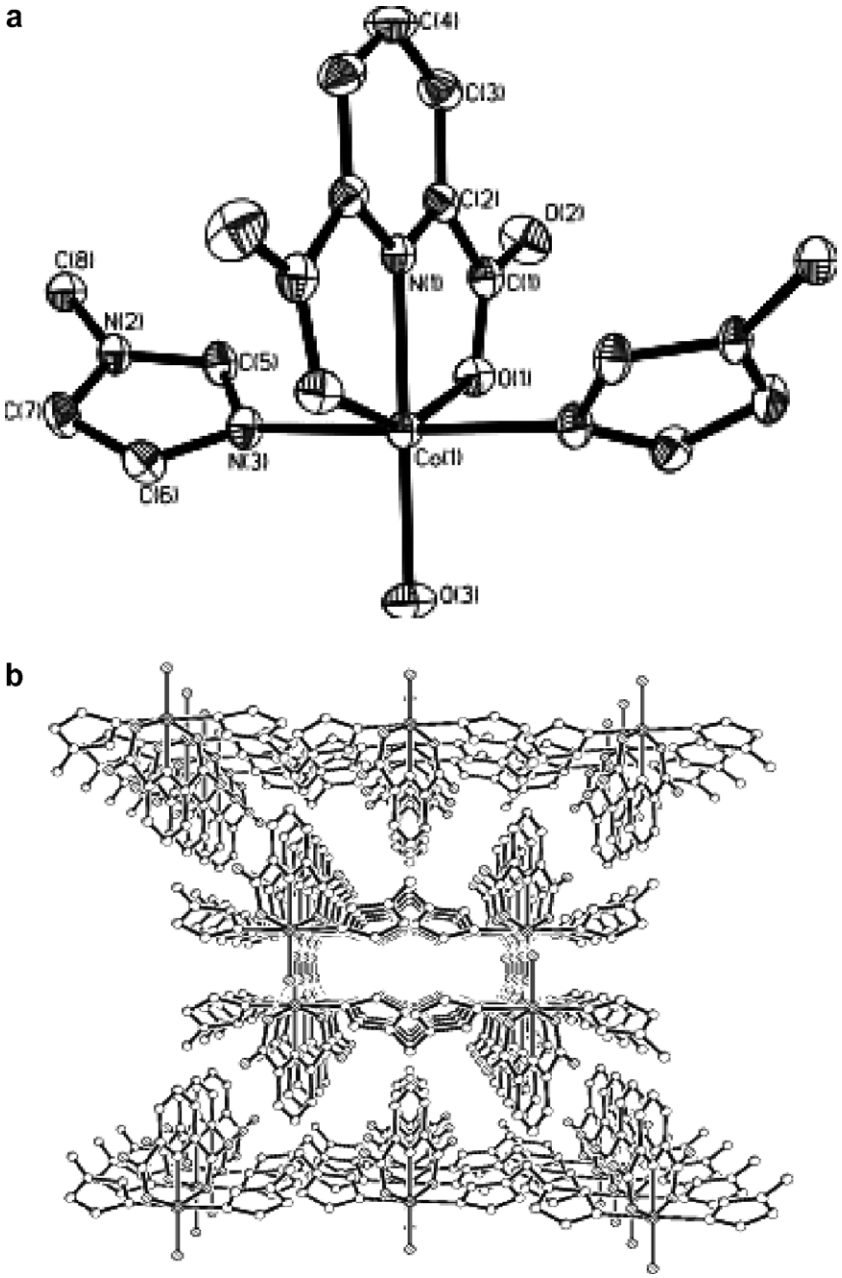


Fig. 7. (a) Local coordination environment of cobalt in polymer **7**. (b) The packing arrangement of the double sheet structure linked by hydrogen bonds between coordinated water molecules viewed down the *c*-axis.

code: i $x, -y+1, z+1/2$) is 2.723(3) Å with an almost linear geometry (169.5°). The intra-sheet Co···Co distance is 4.961 Å, illustrating that the chains are closely connected.

3.3. Thermal properties

The thermogravimetric analysis showed that the coordination polymers **2**–**5**, displaying a one-dimensional chain motif, and the dinuclear complex **1** normally begin to lose either their coordinated or uncoordinated water molecules at a relatively low temperature, ranging from 51 to 117 °C. Complex **1** is the least stable and decomposed at 179 °C, and the weight loss of 20.46% (calc. 20.92%) corresponds to the loss of one L_1 ligand in the temperature range of 179–192 °C. Higher temperature led to complete decomposition with the weight loss of 45.11% (calc. 45.79%) corresponding to one L_1 ligand and two oxalate anions in the range of 215–255 °C. The molecular structure of **2** began to collapse at 250 °C, and the weight loss of 48.56% in the range of 250–350 °C corresponds to the loss of L^2 (calc. 48.63%). Complex **3** begins its decomposition at 231 °C. The weight loss between 231 and 253 °C is attributed to the loss of one L_1ligand (obsd. 23.15%, calc. 23.59%), and finally at 350 °C it decomposed completely to yield metal oxide. Complex **4** began its decomposition at 303 °C, and the weight loss of 22.15% (calc. 22.94%) corresponds to the loss of one L_1 ligand in the range 303.9–309.9 °C. For complex **5**, the weight loss of 23.43% (calc. 23.75%) corresponds to the loss of two L_1 ligands in the range 202–235 °C, and another weight loss of 36.40% (calc. 36.91%) corresponds to the loss of two L_1 ligands and one tp anion in the range 287–295 °C.

In contrast to the one-dimensional chain compounds, complexes **6** and **7**, having two-dimensional layered structures, are much more stable. They began to lose their uncoordinated or coordinated water molecules at 162.1–196.5 °C for **6** and 209.1–243.2 °C for **7**. For **6**, the weight loss of 29.21% (calc. 29.72%) corresponds to the decomposition of one malonate ligand in the temperature range 242.3–295.5 °C, whereas **7** releases its L_1 ligand (obsd. 37.48%, calc. 37.93%) in the temperature range 310.3–380.7 °C. The above data clearly demonstrated that the 2D structures are more thermally stable.

4. Conclusion

A series of Cu(II), Ni(II) and Co(II) coordination polymers with different topologies have been synthesized and structurally characterized. The different coordination modes of the dicarboxylate anions, due to their different chain length, rigidity and diimidazolyl functionality, lead to a wide range of different coordination structures. The dicarboxylates can be coordinated or act as anions. The coordination polymers exhibit 1D single chain, ladder, 2D sheet and 3D network structures. The aliphatic and aromatic dicarboxylates can adopt chelating μ_2 bridging μ_2 and chelating-bridging μ_3 coordination modes, or act as uncoordinated counter anions. The central metal ions are coordinated in N_2O_4, N_4O_2, N_2O_3 and N_3O_3 fashions depending on the ancillary ligands. Both bis(*N*-imidazolyl)methane and 1,4-bis(*N*-imidazolyl)butane act as bidentate bridging ligands. The results illustrate that it is quite feasible to prepare various coordination polymers of diverse network structures by utilization of flexible dicarboxylates and diimidazolyl compounds as building blocks. The employment of flexible ligands does not inevitably yield 3D interpenetrated structures. The structural features observed within the seven polymers presented above tell that desirable functional materials of various structural motives can be achieved through the selection of suitable flexible ligands.

Acknowledgements

The authors thank the National Natural Science Foundation of China (No. 20572096) and Natural Science Foundation of Zhejiang Province (No. R405066) for financial support.

Appendix A. Supplementary material

CCDC 631795, 615384, 615386, 621796, 631796, 621795 and 621794 contain the supplementary crystallographic data for **1**, **2**, **3**, **4**, **5**, **6** and **7**. These data can be obtained free of charge via http://www.ccdc.cam.ac.uk/conts/retrieving.html, or from the Cambridge Crystallographic Data Centre, 12 Union Road, Cambridge CB2 1EZ, UK; fax: (+44) 1223-336-033; or e-mail: deposit@ccdc.cam.ac.uk. Supplementary data associated with this article can be found, in the online version, at doi:10.1016/j.poly.2007.02.029.

References

[1] J.M. Lehn, Supramolecular Chemistry: Concepts and Perspectives, VCH, Weinheim, 1995.
[2] O. Ermer, Adv. Mater. 3 (1991) 608, and references cited therein.
[3] K. Inoue, T. Hayamizu, H. Iwamura, D. Hashizume, Y. Ohashi, J. Am. Chem. Soc. 118 (1996) 1803.
[4] T. Kitazawa, S. Nishikiori, R. Kuroda, T. Iwamoto, J. Chem. Soc., Dalton Trans. (1994) 1029, and references cited therein.
[5] (a) K.S. Min, M.P. Suh, Chem. Eur. J. 7 (2001) 303;
(b) K. Uemura, S. Kitagawa, M. Kondo, K. Fukui, R. Kitaura, H.C. Chang, T. Mizutani, Chem. Eur. J. 8 (2002) 3587;
(c) D.N. Dybtsev, H. Chun, S.H. Yoon, D. Kim, K. Kim, J. Am. Chem. Soc. 126 (2004) 32.
[6] (a) S. Noro, S. Kitagawa, M. Kondo, K. Seki, Angew. Chem., Int. Ed. 39 (2000) 2081;
(b) M. Eddaoudi, J. Kim, N.L. Rosi, D.T. Vodak, J. Wachter, M. O'Keeffe, O.M. Yaghi, Science 295 (2002) 469;
(c) L. Pan, M.B. Sander, X.Y. Huang, J. Li, M. Smith, E. Bittner, B. Bochrath, J.K. Johnson, J. Am. Chem. Soc. 126 (2004) 1308.
[7] (a) M. Albrecht, M. Lutz, A.L. Spek, G. Koten, Nature 406 (2000) 970;
(b) G.L. Beauvais, M.P. Shores, J.R. Long, J. Am. Chem. Soc. 122 (2000) 2763.

[8] M. Fujita, Y.J. Kwon, S. Washizu, K. Ogura, J. Am. Chem. Soc. 116 (1994) 1151.
[9] (a) C. Policar, F. Lambert, M. Cesario, I. Morgenstern-Badarau, Eur. J. Inorg. Chem. (1999) 2201;
(b) P.R. Levstein, R. Calvo, Inorg. Chem. 29 (1990) 1581;
(c) E. Colacio, J.M. Dominguez-Vera, R. Kivekäs, J.M. Moreno, A. Romerosa, J. Ruiz, Inorg. Chim. Acta 212 (1993) 115;
(d) J.-M. Rueff, N. Masciocchi, P. Rabu, A. Sironi, A. Skoulios, Eur. J. Inorg. Chem. (2001) 2843.
[10] (a) R.W. Gable, B.F. Hoskins, R. Robson, J. Chem. Soc., Chem.Commun. (1990) 1677;
(b) L. Carlucci, G. Ciani, D.M. Proserpio, A. Sironi, Inorg. Chem. 34 (1995) 5698;
(c) S. Subramanian, M.J. Zaworotko, Angew. Chem., Int. Ed. 34 (1995) 2127;
(d) F. Lloret, G. De Munno, M. Julve, J. Cano, R. Ruiz, A. Caneschi, Angew. Chem., Int. Ed. 37 (1998) 135;
(e) A.J. Blake, N.R. Champness, M. Crew, L.R. Hanton, S. Parsons, M. Schröder, J. Chem. Soc., Dalton Trans. (1998) 1533;
(f) S. Kitagawa, M. Munakata, T. Tanimura, Inorg. Chem. 31 (1992) 1714;
(g) M.L. Tong, B.I. Ye, J.W. Cai, X.M. Chen, S.W. Ng, Inorg. Chem. 37 (1998) 2645;
(h) J. Lu, C. Yu, T. Niu, T. Paliwala, G. Crisci, F. Somosa, A.J. Jacobson, Inorg. Chem. 37 (1998) 4637;
(i) M.L. Tong, X.M. Chen, X.L. Yua, T.C.W. Mak, J. Chem. Soc., Dalton Trans. (1998) 5.
[11] (a) C.J. O'Connor, C.L. Lein, R.J. Ajeste, L.M. Fonas, Inorg. Chem. 21 (1982) 64;
(b) H. Oschio, U. Nagashima, Inorg. Chem. 29 (1990) 3321.
[12] J. Li, H. Zeng, J. Chen, Q. Wang, X. Wu, Chem. Commun. (1997) 1213.
[13] J.-M. Li, Y.-G. Zhang, J.-H. Chen, L. Rui, Q.-M. Wang, X.-T. Wu, Polyhedron 19 (2000) 1117.
[14] Y. Rodriguez-Martin, C. Ruiz-Perez, J. Sanchiz, F. Lloret, M. Julve, Inorg. Chim. Acta 318 (2001) 159.
[15] Y. Rodriguez-Martin, M. Hernandez-Molina, F.S. Delgado, J. Pasan, C. Ruiz-Perez, J. Sanchiz, F. Lloret, M. Julve, CrystEngComm 4 (2002) 440.
[16] P. Lightfoot, A. Snedden, J. Chem. Soc., Dalton Trans. (1999) 3549.
[17] T.K. Maji, S. Sain, G. Mostafa, T.-H. Lu, J. Ribas, M. Monfort, N.R. Chaudhuri, Inorg. Chem. 42 (2003) 709.
[18] B. Rather, M. Zaworotko, Chem. Commun. (2003) 830.
[19] X. Zhang, C. Lu, Q. Zhang, S. Lu, W. Yang, J. Liu, H. Zhuang, Eur. J. Inorg. Chem. (2003) 1181.
[20] T.-F. Liu, H.-L. Sun, S. Gao, S.-W. Zhang, T.-C. Lau, Inorg. Chem. 42 (2003) 4792.
[21] (a) M. Eddaoudi, D.B. Moler, H. Li, B. Chen, T.M. Reineke, M. O'Keeffe, O.M. Yaghi, Acc. Chem. Res. 34 (2001) 319;
(b) M.E. Braun, C.D. Steffek, J. Kim, P.G. Rasmussen, O.M. Yaghi, Chem. Commun. (2001) 2532;
(c) C. Ruiz-Pérez, P. Lorenzo-Luis, M. Hernández-Molina, M.M. Laz, F.S. Delgado, P. Gili, M. Julve, Eur. J. Inorg. Chem. (2004) 3873.
[22] (a) B.Q. Ma, P. Coppens, Chem. Commun. (2003) 2290;
(b) E. Coronado, J.R. Galán-Mascarós, C.J. Gómez-García, E. Martínez-Ferrero, S.V. Smaalen, Inorg. Chem. 43 (2004) 4808.
[23] (a) M. Oh, G.B. Carpenter, D.A. Sweigart, Angew. Chem., Int. Ed. 42 (2003) 2025;
(b) F.A.A. Paz, J. Klinowski, Inorg. Chem. 43 (2004) 3882.
[24] (a) J.F. Ma, J. Yang, G.L. Zheng, L. Li, J.F. Liu, Inorg. Chem. 42 (2003) 7531;
(b) D.N. Dybtsev, H. Chun, K. Kim, Angew. Chem., Int. Ed. 43 (2004) 503.
[25] J. Yang, J.F. Ma, Y.Y. Liu, S.L. Li, G.L. Zheng, Eur. J. Inorg. Chem. (2005) 2174.
[26] J.F. Ma, J. Yang, G.L. Zheng, L. Li, J.F. Liu, Inorg. Chem. 42 (2003) 7531.
[27] J.F. Ma, J. Yang, G.L. Zheng, L. Li, Y.M. Zhang, F.F. Li, J.F. Liu, Polyhedron 23 (2004) 553.
[28] L.L. Wen, D.B. Dang, C.Y. Duan, Y.Z. Li, Z.F. Tian, Q.J. Meng, Inorg. Chem. 20 (2005) 7161.
[29] L. Wen, Y.Z. Li, Z.D. Lu, J.G. Lin, C.Y. Duan, Q.J. Meng, Cryst. Growth Des. 6 (2006) 530.
[30] L.L. Wen, Z.D. Lu, J.G. Lin, Z.F. Tian, H.Z. Zhu, Q.J. Meng, Cryst. Growth Des. 7 (2007) 93.
[31] V.W. Schutze, H. Schubert, J. Prakt. Chem. 8 (1959) 307.
[32] G.M. Sheldrick, SADABS: Siemens Area Detector Absorption Correction, University of Göttingen, Göttingen, Germany, 1996.
[33] SHELXTL-PC, version 5.03, Siemens Analytical Instruments, Madison, WI.
[34] A.W. Addison, T.N. Rao, J. Reedijk, J. van Rijn, G.C. Verschoor, J. Chem. Soc., Dalton Trans. (1984) 1349.
[35] H.F. Zhu, J. Fan, T. Okamura, W.Y. Sun, N. Ueyama, Cryst. Growth Des. 5 (2005) 289.
[36] E.C. Alyea, S.A. Dias, G. Ferguson, M.A. Khan, P.J. Roberts, Inorg. Chem. 18 (1979) 2433.
[37] D. Sun, R. Cao, Y. Liang, Q. Shi, W. Su, M. Hong, J. Chem. Soc., Dalton Trans. (2001) 2335.
[38] J.Y. Lu, A.M. Babb, Inorg. Chem. 41 (2002) 1339.
[39] J.F. Ma, J.F. Liu, Y.C. Liu, Y. Xing, H.Q. Jia, Y.H. Lin, New J. Chem. 24 (2000) 759.
[40] (a) S.K. Ghosh, P.K. Bharadwaj, Inorg. Chem. 42 (2003) 8250;
(b) W. Zhu, Z. Wang, S. Gao, J. Chem. Soc., Dalton Trans. (2006) 765;
(c) I. Bernal, J.L. Bear, J. Chem. Crystallogr. 32 (2003) 485.
[41] (a) K. Liu, J.D. Cruzan, R.J. Saykally, Science 271 (1996) 929;
(b) J.M. Ugald, I. Alkorta, J. Elguero, Angew. Chem., Int. Ed. Engl. 39 (2000) 717;
(c) R. Ludwig, Angew. Chem., Int. Ed. Engl. 40 (2001) 1808;
(d) J. Yang, J.F. Ma, Y.Y. Liu, J.C. Ma, H.Q. Jia, N.H. Hu, Eur. J. Inorg. Chem. (2006) 1208.

Available online at www.sciencedirect.com
ScienceDirect
Polyhedron 26 (2007) 3085–3091
POLYHEDRON
www.elsevier.com/locate/poly

Structure and magnetic properties of a copper(II) compound with *syn–anti* carboxylato- and linear Cu–Cl–Cu chloro-bridges

Bogumiła Żurowska, Jerzy Mroziński *, Zbigniew Ciunik

Faculty of Chemistry, University of Wroclaw, 50383 Wroclaw, Poland

Received 26 October 2006; accepted 11 February 2007
Available online 22 February 2007

Abstract

The copper(II) polymer Cu(2-qic)Cl (2-qic = quinoline-2-carboxylate) was synthesized and then characterized by X-ray crystal structure determination, spectroscopic and magnetic studies. The crystal structure consists of copper(II) ions with two different chromophores: four-coordinated in a square-planar geometry and five-coordinated in an environment between square-pyramidal and trigonal-bipyramidal. The copper ions are bridged sequentially through the carboxylate groups in a *syn–anti* conformation, forming an infinite one-dimensional zigzag chain with two alternating non-equivalent copper(II) chromophores. The chloride atom acts as a single chloro-bridge link to adjacent chains, forming a ribbon type structure (1D). The variable-temperature (1.8–300 K) magnetic susceptibility data of the complex were interpreted with the dimer law using the molecular field approximation. The results obtained indicate a very weak ferromagnetic ($J_2 = 0.37\ cm^{-1}$) interchain interaction through the *syn–anti* carboxylate bridge. A relatively strong antiferromagnetic interaction, transmitted through the chloro-bridge with an exchange coupling of $J_1 = -57.0\ cm^{-1}$, dominates the magnetic properties of this complex. The magnitude and the nature of the exchange coupling are explained on the basis of the structural results.
© 2007 Elsevier Ltd. All rights reserved.

Keywords: Copper; Quinolinecarboxylate; Carboxylate bridge; Chloride bridge; Magnetism

1. Introduction

Structural and magnetic studies of binuclear and polynuclear complexes containing monoatomic and multidentate bridging ligands are of considerable interest from the standpoint of inorganic and bioinorganic chemistry [1–3]. Particularly interesting is the phenomenon of interaction between metal centers, which is important for the physics of magnetic materials. Much attention has been focused on the magneto-structural correlation and the exchange mechanism [4,5]. In particular, the coordination chemistry of copper(II) complexes containing carboxylates is interesting from structural and magnetic points of view. Copper(II) carboxylates are structurally a very diverse group of coordination compounds due to the various coordination modes of the carboxylate ligands. From a magnetic point of view, the range of magnetic behaviors as a function of different coordination modes was pointed out: from strongly coupled to moderate or weak antiferromagnetic compounds and even ferromagnetic ones [6]. It should be underlined that complexes containing *syn–anti* carboxylate bridges are still few and show unique magnetic properties [6–11].

Singly and doubly chloro-bridged copper(II) systems (singly chloro-bridged chains and doubly chloro-bridged dimers and chains) have become a very active subject of research in the last three decades. For such systems some theoretical analyses [12] and magneto-structural ideas have been presented [4,13,14]. However, no simple magneto-structural relationship has been established relating the value of the magnetic exchange constant J to the Cu–Cl–Cu bonding angle, Cu–Cl or Cu···Cu distances. This may be due to a large variation in structural features observed, together with the fact that chloride possesses both p and d orbitals which may participate in creating

* Corresponding author. Fax: +48 71 204420.
E-mail address: jmroz@wchuwr.chem.uni.wroc.pl (J. Mroziński).

0277-5387/$ - see front matter © 2007 Elsevier Ltd. All rights reserved.
doi:10.1016/j.poly.2007.02.013

an exchange pathway. In contrast to the above chloro-bridged Cu(II) compounds, dinuclear Cu(II) complexes involving only one chloride bridge are rare [15,16] and therefore are of special interest.

It is interesting to note that although some structural analyses of Cu(II) complexes with linear and near linear Cu–Cl–Cu bridging systems have been reported [15–17], only two such Cu(II) compounds, to the best of our knowledge, have been magnetically investigated and characterized so far [15,16].

In this work, we present a synthesis, the spectral and magnetic properties, and the X-ray single-crystal analysis of a new copper(II) compound with a quinoline-2-carboxylate ligand of the formula Cu(2-qic)Cl, where 2-qic = quinoline-2-carboxylate. This complex is an example of a polynuclear copper(II) compound based on *syn–anti* carboxylato-bridges and linear μ_2-chloro bridging motifs.

It is worth noting that recently we have determined the magnetic properties of a polynuclear copper(II) compound with pyridine-2-carboxylate, of the formula Cu(pyridine-2-carboxylate)Cl [6]. The crystal structure of the two-dimensional (2D) polymeric compound consists of a dinuclear $Cu_2(\mu\text{-}Cl)_2$ moiety interconnected with Cu_4 units containing single *syn–anti* carboxylate bridges. The copper ions within a given layer are coupled ferromagnetically.

From the synthetic and structural points of view, it is interesting that both these compounds (i.e. that with the picolinate [6] and the quinaldinate ligands) were obtained in an unusual oxidative P-dealkylation/dephosphorylation reaction. Unfortunately, in this reaction we have not succeeded in preparing crystals suitable for X-ray studies of Cu(quinoline-2-carboxylate)Cl. Therefore, here we describe the results of a structural and magnetic investigation of the Cu(2-qic)Cl compound obtained directly from quinaldinic acid. The results of the studies of the structural and magnetic properties are presented, and possible magneto-structural correlations are discussed.

2. Experimental

2.1. Reagents and physical measurements

Starting materials and solvents for the synthesis were obtained commercially and were used as received. The metal content was determined using a Carl-Zeiss-Jena atomic absorption spectrophotometer. Elemental analyses were carried out using a Perkin–Elmer elemental analyzer 2400CHN.

Infrared spectra (100–4000 cm^{-1}) were recorded on a Bruker IFS 113v spectrophotometer using KBr pellets, and solid-state electronic spectra (28 000–4000 cm^{-1}) were performed on a Cary 500 spectrophotometer.

Solid-state EPR spectra were recorded at room temperature and at 77 K on a Bruker ESP 300E spectrometer operating at X-band and equipped with a Bruker NMR gaussmeter ER 0.35 M and a Hewlett–Packard microwave frequency counter HP 5350B. The spectrum at 4.5 K was measured with an X-band radiopan SE/X 2543 spectrometer.

Magnetic measurements of a polycrystalline sample were carried out with a Quantum Design SQUID magnetometer (MPMSXL-5 type). The measurements were recorded at a magnetic field of 0.5 T over the temperature range 1.8–300 K. The correction for diamagnetism of the experimental susceptibility was based on subtracting the sample-holder signal and estimating the contribution χ_D from Pascal constants [18]. The effective magnetic moments were calculated from $\mu_{eff} = 2.83(\chi_M T)^{1/2}$, using a temperature-independent paramagnetism of 60×10^{-6} cm^3 mol^{-1} for Cu(II).

2.2. X-ray crystallography

Crystal data are given in Table 1, together with the refinement details. X-ray data were collected at low temperature using an Oxford Cryosystem device on an Xcalibur PX κ-axis diffractometer with graphite-monochromated Cu Kα radiation ($\lambda = 1.5418$ Å) and an Onyx CCD camera. The crystal was positioned at 85 mm from the CCD camera. Frames (1872) were measured at 1.0° intervals with a counting time of 60 s. Accurate cell parameters were determined and refined by a least-squares fit of 3600 strongest reflections. The data were corrected for Lorentz and polarization effects. An analytical absorption correction was also applied. Data reduction and analysis

Table 1
Crystal data and structure refinement for Cu(2-qic)Cl

Empirical formula	$C_{10}H_6NO_2ClCu$
Formula weight	271.15
T (K)	100(2)
Wavelength (Å)	1.54180
Crystal system	monoclinic
Space group	$C2/c$
a (Å)	15.973(3)
b (Å)	13.994(3)
c (Å)	9.078(2)
α (°)	90
β (°)	114.26(3)
γ (°)	90
V (Å^3)	1850.0(7)
Z	8
D_{calc} (Mg m^{-3})	1.947
μ (mm)$^{-1}$	5.792
$F(000)$	1080
Crystal size (mm)	$0.05 \times 0.03 \times 0.02$
Minimum/maximum absorption correction	0.7605/0.8930
Θ Range for data collection (°)	4.38–54.99
Ranges of h,k,l	$-14 \geqslant 16$, $-13 \geqslant 14$, $-9 \geqslant 5$
Reflections collected	3922
Independent reflections (R_{int})	1109 (0.0939)
Data/parameters	1109/138
Goodness-of-fit (F^2)	1.030
Final R_1/wR_2 indices ($I > 2\sigma I$)	0.0576/0.1462
Largest difference in peak/hole (e Å^{-3})	1.31/−0.604

were carried out with Oxford Diffraction (Poland) Sp. z o.o. programs. The structure was solved by direct methods (program SHELXS97 [19]) and refined by the full-matrix least-squares method on all F^2 data using the SHELXL97 [20] program. Non-hydrogen atoms were refined with anisotropic displacement parameters; hydrogen atoms were included from the geometry of molecules and $\Delta\rho$ maps. They were refined with isotropic displacement parameters as riding atoms.

2.3. Synthesis

$CuCl_2 \cdot 2H_2O$ (1.5 mmol) dissolved in ethanol (50 cm^3) was added to a solution of quinaldinic acid (1 mmol) in ethanol (50 cm^3). The resulting green solution was filtered and left to evaporate slowly at room temperature. Green monocrystals suitable for X-ray determination were collected after three weeks. This compound is insoluble in most common organic and inorganic solvents.

Anal. Calc. for $C_{10}H_6CuNO_2Cl$: C, 44.29; H, 2.23; N, 5.17; Cu, 23.43. Found: C, 44.32; H, 2.22; N, 5.45; Cu, 23.71%.

3. Results and discussion

3.1. Crystal structure

Crystallographic parameters are summarized in Table 1. Selected bond distances and angles are listed in Table 2.

A fragment of the structure of Cu(2-qic)Cl (2-qic = quinoline-2-carboxylate), showing the local coordination environment of the Cu(II) ions with the crystallographic numbering, is depicted in Fig. 1.

2-Qic acts as a didentate N,O-bonded chelate ligand, coordinating through the quinoline nitrogen and a carboxylate oxygen atom, forming a five-membered ring. The second carboxylate oxygen is involved in coordination to the copper ion of an adjacent molecule (Fig. 1). The crystal structure consists of copper(II) ions bridged sequentially through carboxylate groups in a *syn–anti* conformation, forming an infinite one-dimensional zigzag chain with

Table 2
Selected bond lengths (Å) and angles (°) for Cu(2-qic)Cl

Cu(1)–O(1)	1.983(6)	O(2C)–Cu(2)–N	97.0(3)
Cu(1)–Cl(1)	2.349(4)	O(2)–Cu(2)–N	82.4(3)
Cu(1)–Cl(2)	2.232(4)	N–Cu(2)–N(C)	178.2(4)
Cu(2)–O(2)	1.976(5)	O(2)–Cu(2)–Cl(1A)	110.17(18)
Cu(2)–N	2.028(7)	N–Cu(2)–Cl(1A)	90.90(19)
Cu(2A)–Cl(1)	2.513(4)	Cu(1)–Cl(1)–Cu(2A)	180.0
O(1)–C(1)	1.264(10)	C(1)–O(1)–Cu(1)	108.5(5)
O(2)–C(1)	1.252(10)	C(1)–O(2)–Cu(2)	113.2(5)
O(1)–Cu(1)–O(1B)	176.5(3)	O(2)–C(1)–O(1)	123.1(8)
O(1)–Cu(1)–Cl(2)	91.74(17)	O(2)–C(1)–C(2)	119.1(8)
O(1)–Cu(1)–Cl(1)	88.26(17)	O(1)–C(1)–C(2)	117.8(8)
Cl(2)–Cu(1)–Cl(1)	180.0	N–C(2)–C(3)	121.9(8)
O(2C)–Cu(2)–O(2)	139.7(4)	N–C(2)–C(1)	113.8(8)

Symmetry transformations used to generate equivalent atoms: $A = -x, -y+1, -z+1$; $B = -x, y, -z+1/2$; $C = -x, y, -z+3/2$.

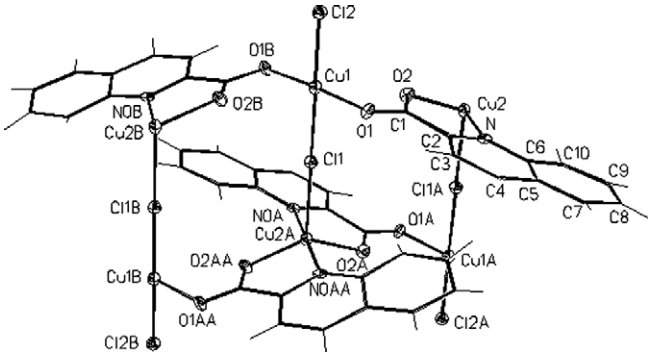


Fig. 1. Fragment of the structure of Cu(2-qic)Cl showing the local environment of the Cu(II) ions and the atomic numbering. Hydrogen atoms are omitted for clarity.

two alternating non-equivalent copper(II) chromophores. The Cu···Cu distance of 4.640(1) Å is in the near range of the reported values of ca. 5 Å observed for polyatomic bridges [21]. Chloride atoms link adjacent chains, forming a ribbon type structure (Fig. 2) extended along the *z*-axis (Cu···Cu distance of 4.860(3) Å). Parallel pyridine rings are stacked. The perpendicular distances between the parallel pyridine rings are 3.3 Å. The crystal packing is depicted in Fig. 3.

As mentioned above the copper(II) ions exhibit two different coordination polyhedra. The Cu(1) atom is in a nearly square-planar geometry, which is clearly demonstrated by the Cl(1)–Cu(1)–Cl(2) and O(1)–Cu(1)–O(1B) angles of 180° and 176.5(3)°, respectively. This geometry is formed by two chloride atoms, bridged Cl(1) and terminal Cl(2), and two carboxylate oxygens atoms, O(1) and O(1B), belonging to adjacent molecules (CuO_2Cl_2 chromophore). The Cu(1)–O(1) distance is 1.983(6) Å. The Cu(1)–Cl(1) and Cu(1)–Cl(2) distances of 2.349(4) and 2.232(4) Å, respectively, are different from each other. The Cu(1)–Cl(2) bond length is typical of a terminal Cu–Cl bond [22]. The geometry around Cu(2) involves a strongly distorted five-coordinate stereochemistry, intermediate between two ideal geometries: square-pyramidal and trigonal-bipyramidal (CuN_2O_2Cl chromophore). This is consistent with the calculation of the structural parameter $\tau = 0.64$ (τ is defined as $(\beta - \alpha)/60$, where β and α are the largest coordination angles). A regular trigonal-bipyramid (TBP) and square-based pyramid (SP) have τ values of 1 and 0, respectively [23]. In the trigonal-bipyramidal description of the environment around Cu(2), the basal plane is defined by the O(2), O(2C) and bridging Cl(1A) atoms, while the N and N(C) atoms occupy apical positions. The pseudotrigonal axis does not show too much distortion from linearity. The N–Cu(2)–N(C) angle is 178.2(4)°. However, the angles in the equatorial plane depart significantly from the theoretical 120° value, being 110.17(18)°, 110.17(18)° and 139.7(4)°. Therefore, the coordination geometry is best described as a distorted tetragonal-pyramid. In this model, the equatorial plane is composed of O(2), O(2C), N and N(C). The N–Cu(2)–N(C) and O(2)–Cu(2)–O(2C) angles

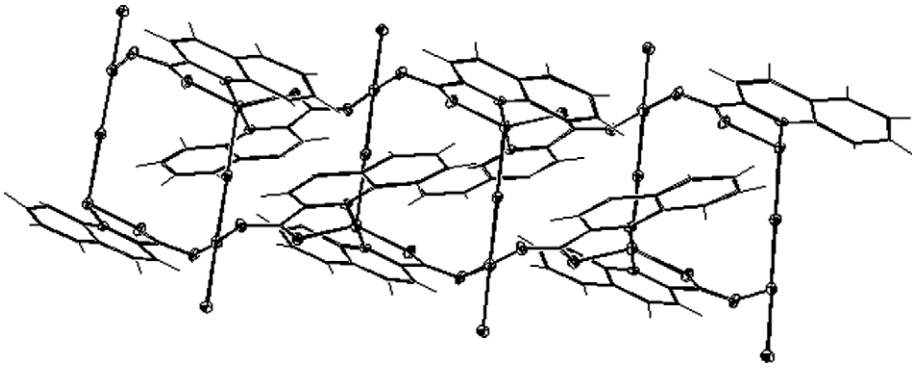


Fig. 2. View of the structure of Cu(2-qic)Cl along the crystallographic *z*-axis.

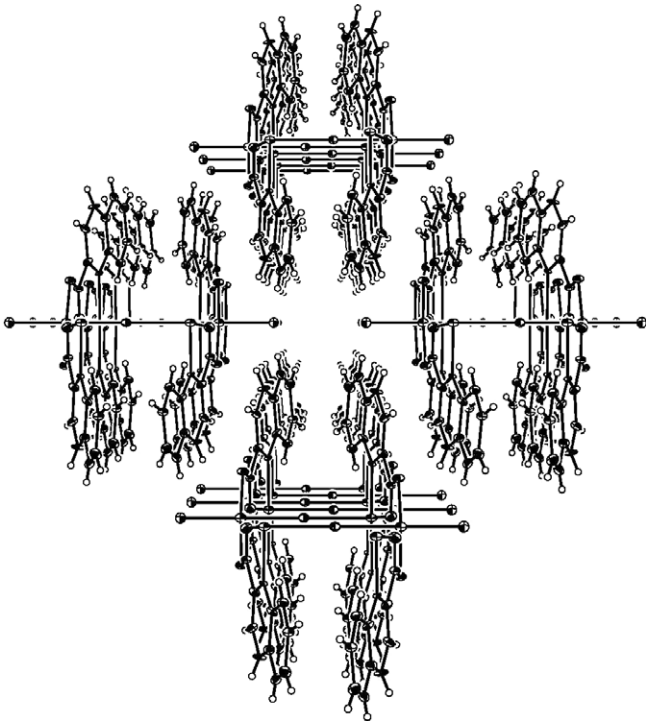


Fig. 3. Crystal packing of Cu(2-qic)Cl.

of the basal plane are 178.2(4)° and 139.7(4)°, respectively. Also, the observed bond distances are in better agreement with a tetragonal-pyramidal model involving long apical Cu(2)–Cl(1A) bonding of 2.513(4) Å. If the coordination of Cu(2A) is described in terms of a square-pyramidal geometry, the plane of Cu(1) is perpendicular to the equatorial plane of Cu(2A) (O_2N_2 set of donor atoms), i.e. the planes are approximately oriented at 90° to each other. This angle leads to a Cu(1)–Cl(1)–Cu(2A) bridging angle of 180°. The Cu(1)–Cl(1) bond distance [2.349(4) Å], is shorter than the Cu(2A)–Cl(1) bond length [2.513(4) Å], which is consistent with the lower coordination number for Cu(1). The Cu(2A)–Cl bond length [2.513(4) Å] is in the range observed for the few reported Cu(II) complexes with a linear μ_2-chloro-bridging motif [17].

Regarding the carboxylate group, the Cu–O–C–O–Cu′ bridges are planar. Furthermore, the two C–O distances [1.264(10) and 1.252(10) Å] and the related Cu–O distances [1.983(6) and 1.976(5) Å] are nearly identical.

3.2. Spectroscopic properties

This compound shows strong carboxylate stretching frequencies ν_{as}(COO) and ν_s(COO) at 1600 and 1413 cm^{-1}, respectively, in the range characteristic of copper(II) carboxylate compounds [24,25]. The observed $\Delta\nu$ separation value of 187 cm^{-1} is in the range expected for a bridging carboxylate group. According to Nakamoto, $\Delta\nu$ values of ca. 180 cm^{-1} are generally associated with classical carboxylate bridges Cu–O–C–O–Cu [26]. The very strong bands at 290 and 184 cm^{-1} are tentatively assigned to Cu–Cl vibrations, suggesting the presence of terminal and bridging chlorides [27,28].

The ligand field spectrum shows poorly resolved broad-band envelopes with a shoulder at ca. 14.0×10^3 cm^{-1} and a band at 11.8×10^3 cm^{-1}. This broad envelope may be the result of the presence of two different copper chromophores [29].

The polycrystalline EPR spectrum reveals a very broad isotropic signal with *g* equal to 2.12 at 293, 77 and 4.2 K. This broad unresolved signal can be due to a narrowing

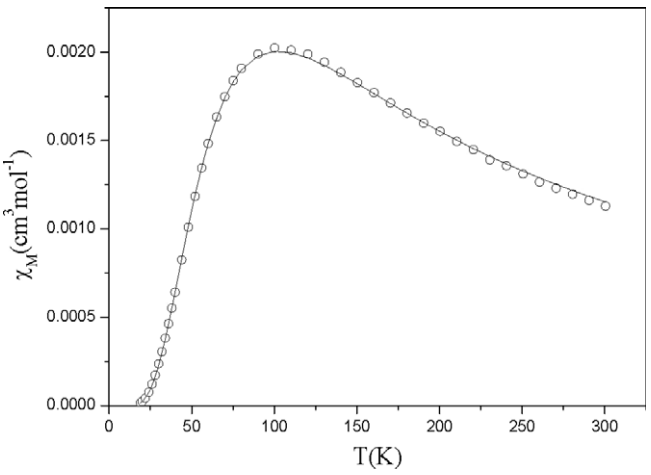


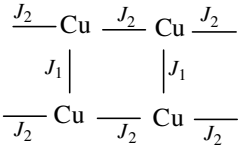
Fig. 4. Plot of the experimental χ_{Cu} (○) and calculated χ_{Cu} (—) *vs.* temperature for Cu(2-qic)Cl.

exchange, as well as to the fact that the compound contains two different copper sites. There are no signals concerning the $\Delta M_s = \pm 2$ transition.

3.3. Magnetic properties

The variable-temperature magnetic susceptibility data (1.8–300 K) illustrated in Fig. 4 show a broad maximum in χ_{Cu} near 90 K, which is consistent with strong antiferromagnetic coupling.

The crystal structure of Cu(2-qic)Cl suggests that two kinds of coupling parameters must be considered to interpret the magnetic properties, according to the scheme:



where J_1 and J_2 are the constants for exchange coupling via the mono-μ-chlorobridge in the dimeric unit and the carboxylate bridge in the chain, respectively. Experimental data from 300 down to 24 K have been fitted with the dimer law with a molecular field correction in order to account for interdimer interactions of the complex. Therefore, for two exchange coupled copper(II) ions the Bleaney–Bowers equation (1) was used with a molecular field correction (2) [30–32]:

$$\chi_{Cu} = \frac{Ng^2\beta^2}{3kT}[1 + 1/3\exp(-2J/kT)]^{-1} \quad (1)$$

$$\chi^{exp} = \frac{\chi_{Cu}}{1 - (2zJ'/Ng^2\mu_B^2)\chi_{Cu}} \quad (2)$$

where χ^{exp} is the measured magnetic susceptibility, $zJ' = z J_2$ is the interdimer exchange parameter, and z is the number of nearest neighbours. Within the frame of this approximation, with the interaction Hamiltonian $H = -J\widehat{S}_1 \cdot \widehat{S}_2$, the best-fit parameters obtained by least-squares fit through Eq. (2) are as follows: $J_1 = -57.0\ cm^{-1}$, $zJ_2 = 1.47\ cm^{-1}$ ($z = 4$), $g = 2.09$ with an R value of 1.61×10^{-6}, where R is the agreement factor defined as

$$R = \sqrt{\sum \frac{1}{(\chi_i^{exp})^2}(\chi_i^{exp} - \chi_i^{calc})^2 / \sum \frac{1}{(\chi_i^{exp})^2}}$$

A satisfactory match of the experimental data is obtained through this approach, as shown in Fig. 3. The fitted g value is lower than the g value of 2.12 obtained by EPR, but as the EPR spectrum gives a very broad unresolved signal, no accuracy can be given on that observed spectroscopic splitting factor value.

3.4. Magneto-structural correlations

Weak antiferromagnetic or ferromagnetic interactions are observed in these carboxylato bridged copper(II) complexes in which the carboxylate adopts the *syn–anti* conformation, as has been shown in the few well-characterized copper(II) complexes [6].

Examination of the magneto-structural data of well-characterized copper(II) complexes in which the carboxylate adopts the *syn–anti* conformation indicates that weak ferromagnetic or antiferromagnetic coupling depends on the structural features of the Cu–O–C–O–Cu′ bridge and the coordination geometry of the exchange-coupled copper ions. As indicated by the structural data, the geometry of the Cu(1) polyhedron is square-planar. In such a geometry, the ground state of the copper ion is adequately described by the $d(x^2 - y^2)$ orbital. Thus, the unpaired electron localized in the $d(x^2 - y^2)$ orbital is pointing along the Cu–O direction in the equatorial plane. However, the geometry of the Cu(2) polyhedron is intermediate between square-pyramidal and trigonal-bipyramidal. In this case, the orbital ground state of the copper ion should have a significant admixture of the $d(x^2 - y^2)$ and $d(z^2)$ orbitals. Because of low site symmetry of the Cu(2) ion between D_{3h} and C_{4v}, it is difficult to attribute the exchange interactions to a specific pathway. The low symmetry of the Cu(2) chromophore ($C_{4v} \leftrightarrow D_{3h}$) causes a weak delocalization of the magnetic orbital on the oxygen atom of the carboxylate bridge from the Cu(2) atom in contrast to the magnetic orbital on Cu(1) directly delocalized toward the 2p oxygen orbital of the COO bridge. For a *syn–anti* carboxylate bridged copper(II) ion with very low symmetries of the coordination environment of both copper ions ($\tau = 0.39$), a very weak ferromagnetic coupling ($J = 0.38\ cm^{-1}$) has been obtained by us before [6]. Finally, the weak ferromagnetic interaction through the *syn–anti* carboxylate bridge observed for our compounds is expected in the light of the above structural and electronic features.

In almost all mono-chloride bridged Cu(II) complexes reported so far, the copper coordination geometries observed are distorted square-pyramidal, and the cases in which the coordination environment of the Cu(II) ions is trigonal-bipyramidal or octahedral are quite rare [35]. The environment of the Cu(II) ions in the compound studied here shows different geometries, viz. one intermediate between square-pyramidal and trigonal-bipyramidal, and the other square-planar.

As mentioned earlier, Cu(II) complexes with a linear Cu–Cl–Cu bridging system are known, and in accordance with a qualitative explanation provided by the Goodenough–Kanamori rules [33] and the Anderson model [34] for the linear bridge, antiferromagnetic coupling is expected. Up until now, to the best our knowledge, only two Cu(II) compounds with a nearly (177.35°) [15] and a strictly [16] linear Cu–Cl–Cu bridge have been characterized structurally and magnetically. In these compounds, the Cu(II) ions have almost perfect square-pyramidal geometry (reflected by the τ parameter being <0.1), and the exchange pathway through the Cu–Cl–Cu chloride bridge involves a chloride ion in the axial position on both copper atoms. Because the magnetic orbital of the

copper(II) is mainly delocalized in the equatorial plane, a very weak spin density is expected on its axial position. In fact, very weak antiferromagnetic exchange couplings, with J values of $-1.30\ cm^{-1}$ [15] and $-0.86\ cm^{-1}$ [16], have been observed.

From a magnetic point of view, it is interesting that the antiferromagnetic exchange coupling in Cu(2-qic)Cl, transmitted by the bridging chloride ion with the value of $J = -52\ cm^{-1}$, is the strongest observed for chloro-bridged systems up to now. The exchange pathway in the linear Cu–Cl–Cu system in the studied compound involves an equatorial position on the Cu(1) (see structure). Because the magnetic orbital of the Cu(1) is located in the equatorial plane, in this case its spin density on the bridge is expected to be large. Owing to the fact that the Cu(1)–$Cl(1)_{eq}$ pathway in Cu(2-qic)Cl is more effective in allowing for spin delocalization than the Cu–Cl_{ax} pathway in the mono-chloro-bridged dimers of an axial(apical)–axial(apical) type cited above [15,16], an increase of the antiferromagnetic exchange transmitted through the bridging chloride ion in our compound is expected.

On the other hand, distortion from a square-pyramidal towards a trigonal-bipyramidal copper coordination geometry is expected to increase the spin density on the bridge, and calculation on a hypothetical mono-chloro-bridged copper(II) dimer have predicted an increase of the antiferromagnetic coupling as such a distortion proceeds [12]. Therefore, the distortion from the square-pyramidal to the trigonal-bipyramidal geometry (reflected by the τ parameter of 0.64) coordination environment of Cu(2) may play a significant role in the coupling. As a result of the distortion, an increase of the antiferromagnetic interaction in Cu(2-qic)Cl can be expected in comparison to the mono-chloro-bridged linear dimer with an almost perfect square-pyramidal geometry about the copper(II) cited above [16].

Finally, although more examples of complexes like Cu(2-qic)Cl with linear Cu–Cl–Cl bridges are needed for a meaningful magneto-structural correlation, on the basis of the observed influence of the parameter τ on the value of J for other chloro-bridged systems [13,14] we believe that the latter effect, i.e. the influence of the distortion towards trigonal-bipyramidal geometry on the value of the antiferromagnetic coupling in our compound, should be less important. In other words the τ parameter has a minor influence on the relatively superexchange interaction through the linear chloride bridge. However, mutual orientation of the equatorial planes of Cu(1) and Cu(2A) (see structure) causes that the Cu(1)–$Cl(1)_{eq}$ pathway in the linear Cu(1)–Cl(1)–Cu(2A) bridge is mainly responsible for the observed strength of the magnetic interaction.

One should also pay attention to the fact that the observed strength of the antiferromagnetic exchange through the linear chloro-bridge in our compound ($J = -57\ cm^{-1}$) is the strongest compared to those already published for chloro-bridged systems, in particular those with linear and close to linear chloro-bridges.

In summary, the electronic and structural features of the linear Cu–Cl–Cu bridge in Cu(2-qic)Cl mentioned above are favorable for the propagation of strong interactions, and hence a relatively strong antiferromagnetic coupling between the copper ions transmitted by the chloride bridging atom, despite the large Cu···Cu distance of 4.860(3) Å, is observed.

Acknowledgement

This work was supported by the Polish Ministry of Science and Higher Education Grant No. 1T09A 12430.

Appendix A. Supplementary material

CCDC 263353 contains the supplementary crystallographic data for this paper. These data can be obtained free of charge via http://www.ccdc.cam.ac.uk/conts/retrieving.html, or from the Cambridge Crystallographic Data Centre, 12 Union Road, Cambridge CB2 1EZ, UK; fax: (+44) 1223-336-033; or e-mail: deposit@ccdc.cam.ac.uk. Supplementary data associated with this article can be found, in the online version, at doi:10.1016/j.poly.2007.02.013.

References

[1] O. Kahn, Angew. Chem., Int. Ed. Engl. 24 (1985) 834.
[2] O. Kahn, Struct. Bond. (Berlin) 68 (1987) 89.
[3] D. Gatteschi, O. Kahn, J.S. Miller, F. Palacio (Eds.), Magnetic Molecular Materials, NATO ASI Series, vol. E198, Kluwer, Dordrecht, 1991.
[4] W.E. Hatfield, in: R.D. Willett, D. Gatteschi, O. Kahn (Eds.), Magneto-Structural Correlation's in Exchange Coupled Systems, D. Reidel, Dordrecht, 1985, p. 567, and references therein.
[5] D.J. Hodgson, Prog. Inorg. Chem. 19 (1975) 173.
[6] B. Żurowska, J. Mroziński, Inorg. Chim. Acta 342 (2003) 23, and references therein.
[7] P.K. Coughlin, S.J. Lippard, J. Am. Chem. Soc. 106 (1984) 2328.
[8] E. Colacio, J.M. Dominguez-Vera, J.P. Costes, R. Kivekäs, J.P. Laurent, J. Ruiz, M. Sundberg, Inorg. Chem. 31 (1992) 774.
[9] E. Colacio, J.M. Dominguez-Vera, R. Kivekäs, J. Ruiz, Inorg. Chim. Acta 218 (1994) 109.
[10] E. Colacio, J.P. Costes, R. Kivekäs, J.P. Laurent, J. Ruiz, Inorg. Chem. 29 (1990).
[11] E. Colacio, J.M. Dominguez-Vera, R. Kivekäs, J.M. Moreno, A. Romerosa, J. Ruiz, Inorg. Chim. Acta 212 (1993) 115.
[12] P.J. Hay, J.C. Thibeault, R. Hoffmann, J. Am. Chem. Soc. 97 (1977) 4884.
[13] M. Hernández-Molina, J. González-Platas, C. Ruiz-Pérez, F. Lloret, M. Julve, Inorg. Chim. Acta 284 (1999) 258, and references therein.
[14] M. Grove, J. Sletten, M. Julve, F. Lloret, J. Chem. Soc., Dalton Trans. 2487 (2001), and references therein.
[15] M. Du, Y.M. Guo, X.H. Bu, J. Ribas, M. Monfort, New J. Chem. 26 (2002) 939, and references therein.
[16] G. Seeber, B.M. Kariuki, L. Cronin, P. Kögerler, Polyhedron 24 (2005) 1651.
[17] (a) K.D. Karlin, J.W. McKown, J.C. Hayes, J.P. Hutchinson, J. Zubieda, Transition Met. Chem. 9 (1984) 405;
(b) O.P. Gladkikh, N.F. Curtis, Acta Crystallogr. Sect C: Cryst. Struct. Commun. 52 (1996) 1418;
(c) T. Lu, S. Chen, Z. Mao, A.E. Martell, L. Ji, Inorg. Chem. Commun. 6 (2003) 1068;

(d) L. Antolini, G. Marcotrigiano, L. Menabue, G.C. Pellacani, J. Am. Chem. Soc. 102 (1980) 5506;
(e) R. Crescenzi, E. Solari, C. Floriani, A. Chiesi-Villa, C. Rizzoli, J. Am. Chem. Soc. 121 (1999) 1695;
(f) M.H. Choi, B.J. Kim, I.C. Kim, S.H. Kim, Y. Kim, J.M. Harrowfield, M.K. Lee, M. Mocerino, E. Rukmini, B.W. Skelton, A.H. White, J. Chem. Soc., Dalton Trans. 707 (2001);
(g) M. Rossignoli, G.A. Lawrance, M. Maeder, D.C.R. Hockless, B.W. Skelton, A.H. White, Aust. J. Chem. 49 (1996) 1307;
(h) P.S. Donnelly, J.M. Harrowfield, B.W. Skelton, A.H. White, Inorg. Chem. 39 (2000) 5817;
(i) E.H. Alilou, M. Giorgi, M. Pierrot, M. Reglier, Acta Crystallogr. Sect. C: Cryst. Struct. Commun. 48 (1992) 1612;
(j) J. Pickard, I. Hoffmeister, Z. Naturforsch. B: Chem. Sci. 50 (1995) 828;
(k) C.W. Liu, M.D. Irwin, A.A. Mohamed, J.P. Fackler Junior, Inorg. Chim. Acta 357 (2004) 3950;
(l) G.F. Manbeck, A.J. Lipman, R.A. Stockland Junior, A.L. Freidl, A.F. Hasler, J.J. Stone, I.A. Guzei, J. Org. Chem. 70 (2005) 244.
[18] E. König, Magnetic Properties of Coordination and Organometallic Transition Metal Compounds, Springer, Berlin, 1966.
[19] G.M. Sheldrick, Acta Crystallogr. A46 (1990) 467.
[20] G.M. Sheldrick, SHELXL97, Program for Crystal Structure Refinement, University of Göttingen, 1997.
[21] E. Colacio, J.P. Costes, R. Kivekäs, J.P. Laurent, J. Ruiz, M. Sundberg, Inorg. Chem. (1991) 1475.
[22] J.A.G. van Ooijen, J. Reedijk, A.L. Spek, J. Chem. Soc., Dalton Trans. (1979) 1415.
[23] A.W. Addison, T.N. Rao, J. Reedijk, J. van Rijn, G.C. Verschoor, J. Chem. Soc., Dalton Trans. (1984) 1349.
[24] G.B. Deacon, R.J. Phillips, Coord. Chem. Rev. 33 (1980) 227.
[25] K. Nakamoto, Infrared in Raman Spectra of Inorganic and Coordination Compounds, 4th ed., Wiley, New York, 1986.
[26] K. Nakamoto, J. Fujita, S. Tanaka, M. Kobayashi, J. Am. Chem. Soc. 79 (1957) 4904.
[27] R.J.H. Clark, in: V. Guttman (Ed.), Halogen Chemistry, vol. 3, Academic Press, New York, 1967.
[28] J. Reedijk, A.R. Siedle, R.A. Velapoldi, J.A.M. Hest, Inorg. Chim. Acta 74 (1983) 109, and references therein.
[29] B.J. Hathaway, in: G. Wilkinson, R.D. Gill, J.A. McCleverty (Eds.), Comprehensive Coordination Chemistry, vol. 5, Pergamon, Oxford, 1987.
[30] B. Bleaney, K.D. Bowers, Proc. Roy. Soc. London, Ser. A 214 (1952) 451.
[31] J.W. Stout, R.C. Chisholm, J. Chem. Phys. 36 (1962) 979.
[32] D.K. Towle, S.K. Hoffmann, W.E. Hatfield, P. Singh, P. Chaudhuri, K. Weighardt, Inorg. Chem. 24 (1985) 4393.
[33] J.B. Goodenough, Magnetism and the Chemical Bond, Interscience, New York, 1963, pp. 165–184.
[34] P.W. Anderson, in: G.T. Rado, H. Suhl (Eds.), Magnetism, vol. 1, Academic Press, New York, 1963 (Chapter 2).

Available online at www.sciencedirect.com
ScienceDirect
Polyhedron 26 (2007) 3092–3096
POLYHEDRON
www.elsevier.com/locate/poly

Synthesis, spectral, and structural investigation of $[ML(NO_3)_2]$: M = Co, Ni, Cu; L = *N*-(2-pyridylethyl)pyridine-2-methylketimine

Sumanta Kumar Padhi, Vadivelu Manivannan *

Department of Chemistry, Indian Institute of Technology Guwahati, Guwahati 781 039, Assam, India

Received 11 January 2007; accepted 13 February 2007
Available online 21 February 2007

Abstract

Synthesis and structural characterization of distorted pentagonal bipyramidal Co(II), pseudo-octahedral Ni(II) and Cu(II) complexes of the type $[ML(NO_3)_2]$, {L = *N*-(2-pyridylethyl)pyridine-2-methylketimine} are reported. Characterization includes elemental analysis, spectral, magnetism, and X-ray crystallographic studies. In case of cobalt (**1**) both the nitrates coordinate in bidentate fashion resulting overall distorted pentagonal bipyramidal geometry. In nickel (**2**) and copper (**3**) complexes, bivalent metal ion is coordinated by the three nitrogen atoms of the tridentate **L** with two pyridine-N occupying *trans* positions and amongst the two nitrates one coordinates in a bidentate fashion while other adopts a monodentate fashion. All the complexes exhibit d–d transitions in the visible region. Complex **1** is high-spin in nature and the X-band EPR spectra of **1**, and **3** at room temperature and 77 K are reported.
© 2007 Elsevier Ltd. All rights reserved.

Keywords: Schiff base; Crystal structures; Optical properties; Magnetism; Electron paramagnetic resonance

1. Introduction

The coordination chemistry of Schiff base is vast since its first report [1–3]. The imine function in combination with other functions is useful for metal binding, as they can easily be derived from suitable carbonyl groups (aldehyde or ketone) and primary amines. Design and construction of molecular architectures and supramolecular macrocycles having imine as well as pyridyl groups are of considerable attention [4–13]. The coordination chemistry and tyrosinase activity of tridentate Schiff base ligand containing pyridine rings are reported [14–22]. Recently we have reported that one such a tridentate Schiff base containing pyridyl function, *N*-(2-pyridylmethyl)pyridine-2-methylketimine, readily converted to 4′-(2-pyridyl)-2,2′:6′,2″-terpyridine in the presence of $Cu(NO_3)_2 \cdot 3H_2O$ [13]. This prompted us to explore the metal chemistry of *N*-(2-pyridylethyl)pyridine-2-methylketimine. In this article, we report the synthesis, spectra, and structural studies of $[ML(NO_3)_2]$, where M = Co(II), Ni(II), Cu(II), and **L** = N-(2-pyridylethyl)pyridine-2-methylketimine.

2. Experimental

2.1. Instrumentation and methods

UV–Vis spectra were recorded in a Perkin–Elmer Lambda 25 spectrometer. A Perkin–Elmer Spectrum One spectrometer was used to record FT-IR spectrum in the range 4000–400 cm^{-1}. ^1H NMR spectrum was recorded on a Varian Mercury plus 400 MHz NMR Spectrometer. Elemental analysis was performed by a Perkin–Elmer Series II CHNS/O Analyzer 2400. The EPR spectra were recorded on a JEOL JES FA-200 X-band EPR spectrometer. $Co(NO_3)_2 \cdot 6H_2O$, $Ni(NO_3)_2 \cdot 6H_2O$, $Cu(NO_3)_2 \cdot 3H_2O$ were purchased from Merck India Ltd. and 2-acetylpyridine, 2-(2-aminoethyl)-pyridine from M/S Aldrich, USA.

* Corresponding author. Tel.: +91 361 258 2306; fax: +91 361 258 2349.
E-mail address: mani@iitg.ernet.in (V. Manivannan).

0277-5387/$ - see front matter © 2007 Elsevier Ltd. All rights reserved.
doi:10.1016/j.poly.2007.02.010

All the chemicals and solvents were of reagent grade and were used as received without further purifications.

2.1.1. X-ray crystallography

X-ray crystallographic data were collected using Bruker SMART APEX-CCD diffractometer with Mo Kα radiation ($\lambda = 0.71073$ Å). The intensity data were corrected for Lorentz and polarization effects and empirical absorption correction was applied using SAINT program [23,24]. All the structures were solved by direct methods using SHELXS-97 [25]. Non-hydrogen atoms located from the difference Fourier maps were refined anisotropically by full-matrix least squares on F^2, using SHELXL-97 [25]. The hydrogen atoms were included in the calculated positions and refined isotropically using a riding model.

2.2. Syntheses

*N-(2-Pyridylethyl)pyridine-2-methylketimine (**L**).* To anhydrous $MgSO_4$ (2.5 g) suspended in 30 mL of CH_2Cl_2, 2-(2-aminoethyl)-pyridine (283 mg, 2.31 mmol) and 2-acetylpyridine (281 mg, 2.31 mmol) were added and heated at reflux for 1.5 h. The solution was then stirred at ambient temperature for another 3 h, filtered, washed with 2×10 mL portions of CH_2Cl_2 and the volatile components in the combined solution were removed by evaporation in vacuum. The crude product was obtained as yellowish oil, which is pure enough as inferred from the ^{1}H NMR spectrum and was used without further purification. Yield: 385 mg (74%). ^{1}H NMR (δ (*J*, Hz), $CDCl_3$): 2.73 (3H, s), 2.92 (2H, t, 6.4), 3.11 (2H, t, 6.6), 7.10 (1H, t, 5.8), 7.15 (1H, d, 7.6), 7.45 (1H, t, 6.6), 7.58 (1H, t, 7.4), 7.81 (1H, t, 8.4), 8.02 (1H, d, 8.0), 8.51 (1H, d, 4.0) and 8.66 (1H, d, 4.8). IR (neat, cm^{-1}): 1639 ($C{=}N_{im}$), 1590 ($C{=}N_{py}$).

*[Co**L**(NO$_3$)$_2$] (**1**).* To $Co(NO_3)_2 \cdot 6H_2O$ (168 mg, 0.58 mmol) dissolved in 50 mL of methanol, **L** (130 mg 0.58 mmol) was added with stirring and after 4 h, the reaction mixture was left to crystallize. Orange block-like crystals deposited were collected and washed with ice-cold methanol. Yield: 0.19 g (80%). IR (KBr, cm^{-1}): 1650 ($C{=}N_{im}$), 1602 ($C{=}N_{py}$). *Anal.* Calc. for $C_{14}H_{15}N_5O_6Co$: C, 41.15; H, 3.67; N, 17.15. Found: C, 41.26; H, 3.69; N, 17.34%.

*[Ni**L**(NO$_3$)$_2$] (**2**)* and *[Cu**L**(NO$_3$)$_2$] (**3**)* were prepared using the same procedure as **1**, in similar yields. For compound **2**: IR (KBr, cm^{-1}): 1645 ($C{=}N_{im}$), 1600 ($C{=}N_{py}$). *Anal.* Calc. for $C_{14}H_{15}N_5O_6Ni$: C, 41.17; H, 3.67; N, 17.16. Found: C, 41.39; H, 3.74; N, 17.44%. For compound **3**: IR (KBr, cm^{-1}): 1650 ($C{=}N_{im}$), 1602 ($C{=}N_{py}$). *Anal.* Calc. for $C_{14}H_{15}N_5O_6Cu$: C, 40.69; H, 3.63; N, 16.96. Found: C, 40.35; H, 3.71; N, 17.14%.

3. Results and discussion

3.1. Electronic spectra

In acetonitrile, **1**, **2**, and **3** exhibit d–d transitions in the visible region. The λ_{max} and their molar extinction coefficient values were obtained after fitting to a Gaussian are listed in Table 1. The complex **1** shows characteristic d–d transitions at 497 and 407 nm. Both **2** and **3** have been established to have a pseudo octahedral geometry by structural studies (*vide infra*). The $^3A_{2g} \rightarrow {}^3T_{2g}$ and $^3A_{2g} \rightarrow {}^3T_{1g}(F)$ transitions in complex **2** appear near 920 and 568 nm, but $^3A_{2g} \rightarrow {}^3T_{1g}(P)$ is not observed, may be it is obscured by the intra-ligand transitions in the higher energy region. The characteristic feature of **3** is, two d–d transitions at 640 and 370 nm. Since the distortion from the perfect octahedral symmetry is present, these can be, respectively, due to $d_{x^2-y^2} \rightarrow d_{z^2}$ and $d_{x^2-y^2} \rightarrow d_{xy}$ transitions. In all the three cases intra-ligand transitions occur in the 315–260 nm region and the molar extinction coefficient of these bands is higher than that observed for the free ligand.

3.2. Magnetism and EPR spectra

The room temperature magnetic moments (Table 1) of **1**, **2**, and **3** is in agreement with the presence of 3 (high-spin Co(II)), 2 and 1 unpaired electrons, respectively. In all the three cases $\mu_{eff} > \mu_{so}$ is consistent with more than half-filled configuration and the trend, $\mu_{S+L} > \mu_{eff} > \mu_{so}$, shows the existence of spin–orbit coupling [26–28]. The X-band (9.44 GHz) EPR data of all the complexes is given in Table 1. In the frozen glass **1** shows a broad single-line spectrum but is not observable at room temperature. At room tem-

Table 1
Spectroscopic and magnetic data

Compound	UV–Vis spectra	μ_{eff}	EPR Spectra	
	λ_{max}, nm (ε, M^{-1} cm^{-1})[a]	(B.M.)	293 K	77 K
[Co**L**(NO$_3$)$_2$]	497(23), 407(110), 313(6,290), 285(16,470), 263(25,645)	3.967	not observed	$g_{iso} = 1.931$[c,d]
[Ni**L**(NO$_3$)$_2$]	920(112), 568(70), 290(18,200), 280(24,100), 270(26,575), 265(26,500)	3.886	very weak signal observed	very weak signal observed
[Cu**L**(NO$_3$)$_2$]	640(385), 370(520)[b], 295(15,100), 285(21,260), 270(24,625), 265(26,820)	2.072	$g = 2.136$,[a] $A = 70$ G	$g_1 = 2.252$,[c] $A_1 = 174$ G, $g_2 = 2.051$, $g_3 = 2.001$

[a] In acetonitrile.
[b] Shoulder.
[c] Acetonitrile–methanol (3:1) glass.
[d] Very broad.

perature, **3** in acetonitrile solution exhibits a four-line spectrum (A in Fig. 1), which is due to the presence of hyperfine splitting of the single-line spectrum. However at 77 K, an axial spectrum with splitting due to a slight rhombic symmetry (B in Fig. 1) is present and the trend $g_{zz} > g_{yy} > g_{xx}$ is observable. Hyperfine splitting of the g_{zz} signal is present. These features suggest that the unpaired electron is in the $d_{x^2-y^2}$ orbital [14,15,18,21].

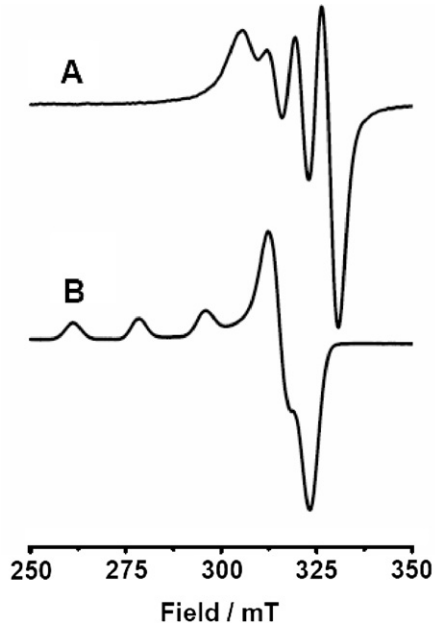


Fig. 1. EPR spectra of **3** in CH_3CN solution (A) at 293 K and in frozen glass (B).

3.3. Molecular structures

The molecular structures of **1**, **2**, and **3** were determined by X-ray crystallography. The crystallographic data and refinement parameters are summarized in Table 2 and selected bond parameters are listed in Table 3. A perspective view of **1** is shown in Fig. 2. The bivalent metal ion in each case, is coordinated by the three nitrogen atoms of the tridentate **L** with two pyridine-N spanning the *trans* positions. In **1** both the nitrates coordinate in a bidentate fashion and consequently the bivalent cobalt adopts distorted pentagonal bipyramidal geometry. The atoms O1, O2, O4, O5, N2 form the pentagonal plane and N1, N3 occupy the apical positions. In **2** and **3**, of the two nitrate ions, one binds in bidentate fashion and the other in a monodentate fashion, resulting in an overall pseudo-octahedral geometry at the metal center. The basal plane contains the O1, O2, O4, N2 and the apical positions are occupied by N1, N3.

The **L** binds the metal ion by a five-membered and a six-membered chelate ring. Five-membered chelate ring is nearly planar in **1**, **2** but deviate from planarity to have an envelope conformation in **3**. Six-membered ring is puckered in all the three complexes. The N1–M–N2 angle of the five-membered chelate ring is 78.2(2)°, 79.8(2)°, and 82.8(8)°, while N2–M–N3 of the six-membered ring is 93.1(2)°, 94.5(2)°, and 93.0(8)°, respectively, in **1**, **2**, and **3**. These angles are deviating significantly from the ideal value 90° due to the sizes of five-membered and the six-membered non-planer chelate rings. Average M–N lengths are shorter by 0.170(5) Å (**1**), 0.119(3) Å (**2**), 0.256(9) Å (**3**) than that of the M–O distances of the bidentate NO_3^-. Bidentate NO_3^- has a longer contact with Ni1 than when it

Table 2
Crystallographic data and refinement parameters

	1	**2**	**3**
Empirical formula	$C_{14}H_{15}N_5O_6Co$	$C_{14}H_{15}N_5O_6Ni$	$C_{14}H_{15}N_5O_6Cu$
CCDC number	630610	626663	626664
Formula weight	408.24	408.02	412.85
Temperature	296(2)	296(2)	296(2)
Wavelength (Å)	0.71073	0.71073	0.71073
Crystal system	monoclinic	monoclinic	monoclinic
Space group	*P*2(1)/*c*	*P*2(1)/*c*	*Cc*
a (Å)	8.6923(3)	8.4604(4)	8.6226(2)
b (Å)	15.5099(6)	19.9967(8)	15.6562(4)
c (Å)	14.2193(6)	9.9209(4)	12.2668(2)
β (°)	119.579(3)	95.610(3)	97.4760(10)
V (Å^3)	1667.17(11)	1670.38(12)	1641.91(6)
Z	4	4	4
D_{calc} (g cm^{-3})	1.628	1.622	1.670
μ (mm^{-1})	1.076	1.205	1.375
Goodness-of-fit on F^2[a]	1.077	1.045	1.062
R indices (all data)	$R_1 = 0.0692$,[b] $wR_2 = 0.2100$[c]	$R_1 = 0.0523$,[b] $wR_2 = 0.1296$[c]	$R_1 = 0.0600$,[b] $wR_2 = 0.1521$[c]
	$R_1 = 0.0769$,[b] $wR_2 = 0.2166$[c]	$R_1 = 0.1026$,[b] $wR_2 = 0.1603$[c]	$R_1 = 0.0919$,[b] $wR_2 = 0.1786$[c]

[a] GOF $= [\sum[w(F_o^2 - F_c^2)^2]/M - N]^{1/2}$ (M = number of reflections, N = number of parameters refined).
[b] $R_1 = \sum ||F_o| - |F_c|| / \sum |F_o|$.
[c] $wR_2 = [\sum[w(F_o^2 - F_c^2)^2] / \sum[w(F_o^2)^2]]$.

Table 3
Selected bond distances and angles

Bond distances (Å)				Bond angles (°)			
Bond	1	2	3	Angle	1	2	3
M–N1	2.089(4)	2.056(3)	2.037(9)	O1–M–O2	52.8(2)	58.9(2)	45.8(4)
M–N2	2.094(7)	2.023(3)	1.958(6)	O1–M–O4	128.4(2)	112.3(2)	72.2(3)
M–N3	2.115(4)	2.051(3)	1.928(13)	O2–M–O4	178.7(2)	171.2(2)	117.3(5)
M–O1	2.293(7)	2.198(4)	2.143(6)	O4–M–O5	55.3 (2)		
M–O2	2.272(5)	2.127(3)	2.317(15)	O1–M–N1	95.7(2)	93.4(2)	86.6(3)
M–O4	2.298(4)	2.062(3)	2.334(16)	O1–M–N2	142.6(2)	152.4(2)	142.3(5)
M–O5	2.214(5)			O1–M–N3	91.4(2)	91.5(2)	95.6(4)
N2–C6	1.400(8)	1.291(5)	1.644(31)	O2–M–N1	89.2(2)	90.7(2)	91.3(4)
N2–C7	1.301(12)	1.445(5)	1.329(18)	O2–M–N2	90.1(2)	94.2(2)	98.3(5)
C6–C14	1.360(12)	1.483(6)	1.190(23)	O2–M–N3	96.6(2)	89.4(2)	87.4(4)
C5–C6	1.439(7)	1.502(6)	1.522(24)	O4–M–N1	91.2(2)	90.1(2)	93.6(5)
C7–C8	1.335(12)	1.526(6)	1.334(14)	O4–M–N2	88.8(2)	94.6(2)	144.4(5)
C8–C9	1.489(9)	1.509(6)	1.490(17)	O4–M–N3	88.4(2)	90.6(2)	90.9(5)
N1–C5	1.344(6)	1.342(5)	1.374(15)	N1–M–N2	78.2(2)	79.8(2)	82.8(8)
N3–C9	1.314(6)	1.363(5)	1.318(15)	N2–M–N3	93.1(2)	94.5(2)	93.0(8)
				N1–M–N3	171.2(2)	174.3(2)	175.4(3)

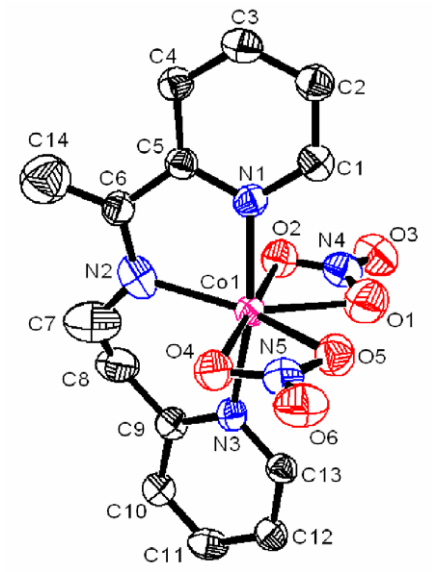


Fig. 2. ORTEP diagram of **1** (30% probability, hydrogens are omitted for clarity).

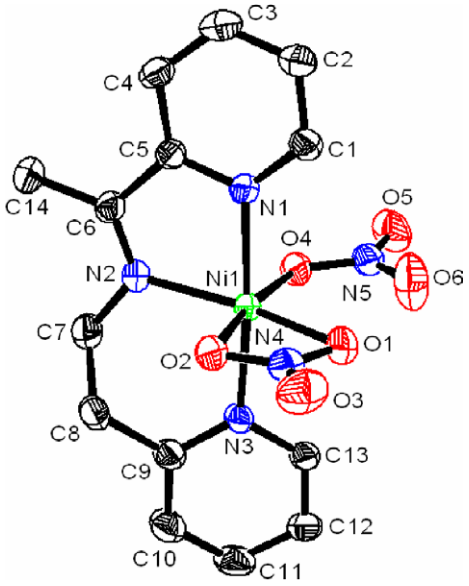


Fig. 3. ORTEP diagram of **2** (30% probability, hydrogens are omitted for clarity).

coordinates with one oxygen atom but it is shorter in case of **3**. In **1** the NO_3^- chelate bite angles are 52.8(2)° and 55.3(2)°, while in **2** and **3** it is 58.9(2)° and 45.8(4)°, respectively. A perspective view of **2** and **3** are shown in Figs. 3, and 4. In **3**, a long axial Cu1···O5 contact of 2.848(11) Å is present.

The M–N_{im} and M–N_{py} bond lengths follow the order Co > Ni > Cu and is consistent with the trend in the relative size of the bivalent ions. Notable is the parameters of the methylketimine function in complex **3**: N2–C6 and C6–C14 bonds in **3** are, respectively, longer and shorter than those observed in **1** and **2**. In **3**, the sum of the three angles subtended at N2 and C6 are, respectively, 355.7(16)° and 354.3(19)° and these values are very much closer to 360° in **1** and **2**.

A perspective view of molecular packing diagram of **1** shown in Fig. 5 indicates the presence of C3···O2, C3···O4, C11···O2, C11···O4, C13···O6, and C14···O5 donor-acceptor interactions. The molecular packing of **2** shows a transverse wave like pattern along the *b*-axis with a distance of around 18.91 Å between two crests. The intermolecular interactions C3···O4, C4···O4, C4···O5, and C12···O6, are present in this packing. In case of **3**, a layered sheet observed on viewing down the *b*-axis. Non-bonded intermolecular contacts C11···O5, C12···O6, C14···O4, C3···O5, C2···O3, C1···O3, and π–π interaction of 3.365(13) Å between C4···C10, are important factors responsible for layered stacking.

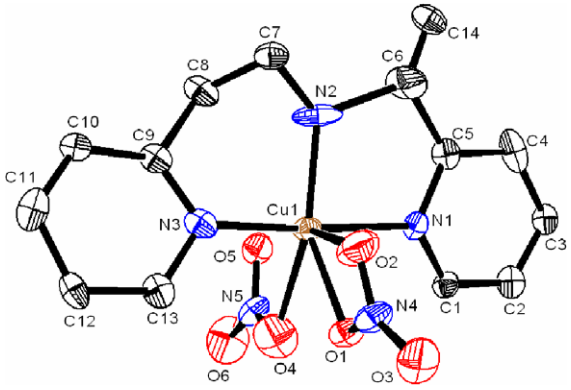


Fig. 4. ORTEP diagram of **3** (30% probability, hydrogens are omitted for clarity).

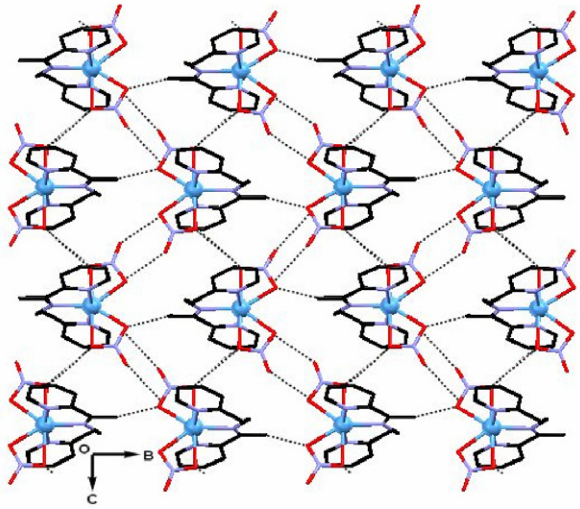


Fig. 5. Molecular packing of **1** viewing down the *a*-axis.

4. Conclusion

Cobalt (**1**) has overall distorted pentagonal bipyramidal geometry with N_3O_4 chromophore whereas nickel (**2**) and copper (**3**) complexes have pseudo-octahedral geometry with N_3O_3 chromophore. The $M–N_{im}$ and $M–N_{py}$ bond lengths follow the order Co > Ni > Cu. The X-band EPR spectra of **3** shows an isotropic spectrum splitted by hyperfine coupling at room temperature and an axial spectrum with splitting due to a slight rhombic symmetry at 77 K. The trend, $g_{zz} > g_{yy} > g_{xx}$ and hyperfine splitting of the g_{zz} signal are observed.

Acknowledgements

We are grateful to the Department of Science and Technology (DST) New Delhi for a financial grant (SR/S1/IC-01/2002) and for establishing single crystal X-ray diffractometer facility under FIST scheme. Authors are thankful to Babulal Das for X-ray data and Central Instruments Facility, IIT Guwahati for EPR and NMR facilities.

Appendix A. Supplementary material

CCDC 630610, 626663 and 626664 contain the supplementary crystallographic data for **1**, **2** and **3**. These data can be obtained free of charge via http://www.ccdc.cam.ac.uk/conts/retrieving.html, or from the Cambridge Crystallographic Data Centre, 12 Union Road, Cambridge CB2 1EZ, UK; fax: (+44) 1223-336-033; or e-mail: deposit@ccdc.cam.ac.uk. Supplementary data associated with this article can be found, in the online version, at doi:10.1016/j.poly.2007.02.010.

References

[1] H. Schiff, Ann. Chem. Suppl. 3 (1864) 343.
[2] H. Schiff, Ann. Chem. 150 (1869) 193.
[3] H. Schiff, Ann. Chem. 151 (1869) 186.
[4] J.-M. Lehn, Supramolecular Chemistry, VCH, Weinheim, 1995.
[5] S. Yamada, Coord. Chem. Rev. 190–192 (1999) 537.
[6] R. Ziessel, Coord. Chem. Rev. 216–217 (2001) 195.
[7] Y. Sunatsuki, Y. Motoda, N. Matsumoto, Coord. Chem. Rev. 226 (2002) 199.
[8] S.A. Barnett, N.R. Champness, Coord. Chem. Rev. 246 (2003) 145.
[9] P.A. Vigato, S. Tamburini, Coord. Chem. Rev. 248 (2004) 1717.
[10] W. Radecka-Paryzek, V. Patroniak, J. Lisowski, Coord. Chem. Rev. 249 (2005) 2156.
[11] J. Lewinski, J. Zachara, I. Justyniak, M. Dranka, Coord. Chem. Rev. 249 (2005) 1185.
[12] R.E. Rülke, J.M. Ernsting, A.L. Spek, C.J. Elsevier, Inorg. Chem. 32 (1993) 5769.
[13] S.K. Padhi, V. Manivannan, Inorg. Chem. 45 (2006) 7994.
[14] S.K. Padhi, V. Manivannan, Polyhedron (2007), doi:10.1016/j.poly.2006.11.046.
[15] R. Cortés, L. Lezama, J.I. Ruiz de Larramendi, G. Madariaga, J.L. Mesa, F.J. Zuñiga, T. Rojo, Inorg. Chem. 34 (1995) 778.
[16] Y. S-Yan, L. Q-Hui, X. X-You, S. M-Chang, H. L-Ren, Polyhedron 13 (1994) 1583.
[17] K. Ramesh, R.N. Mukherjee, Indian J. Chem. A 30 (1991) 1057.
[18] T. Rojo, R. Cortés, J.I. Ruiz de Larramendi, G. Madariaga, J. Chem. Soc., Dalton Trans. 13 (1992) 2125.
[19] G.J. Stor, M. van der Vis, D.J. Stufkens, A. Oskam, J. Fraanje, K. Goubitz, J. Organomet. Chem. 482 (1994) 15.
[20] R.E. Rülke, V.E. Kaasjager, D. Kliphuis, C.J. Elsevier, Piet W.N.M. van Leeuwen, K. Vrieze, K. Goubitz, Organometallics 15 (1996) 668.
[21] W.A. Alves, I.A. Bagatin, A.M. Da costa Ferreira, Inorg. Chim. Acta 321 (2001) 11.
[22] W.A. Alves, S.A. de A-Filho, M.V. de Almeida, A. P-Filho, C.C. Becerra, A.M. Da Costa Ferreira, J. Mol. Catal. A 198 (2003) 63.
[23] G.M. Sheldrick, SADABS, University of Göttingen, Göttingen, Germany, 1996.
[24] SMART and SAINT, Siemens Analytical X-ray Instruments Inc., Madison, WI, 1996.
[25] G.M. Sheldrick, SHELXS-97 and SHELXL-97, University of Göttingen, Göttingen, Germany, 1997.
[26] C.J. O'Connor, Prog. Inorg. Chem. 29 (1982) 203.
[27] O. Kahn, Molecular Magnetism, Wiley-VCH, 1993.
[28] D. Arcon, K. Prassides, π-Electron magnetism, in: J. Veciana (Ed.), Structure and Bonding, vol. 100, Springer, Berlin, 2001, p. 129.

Available online at www.sciencedirect.com
ScienceDirect
Polyhedron 26 (2007) 3097–3102
POLYHEDRON
www.elsevier.com/locate/poly

Structural and spectral investigations on some new Ni(II) complexes of di-2-pyridyl ketone *N*(4)-phenylthiosemicarbazone

V. Suni [a], Maliyeckal R. Prathapachandra Kurup [a,*], Munirathinam Nethaji [b]

[a] *Department of Applied Chemistry, Cochin University of Science and Technology, Kochi 682 022, Kerala, India*
[b] *Department of Inorganic and Physical Chemistry, Indian Institute of Science, Bangalore, 560 012, India*

Received 7 November 2005; accepted 11 February 2007
Available online 24 February 2007

Abstract

Ni(II) complexes (**1**–**5**) of di-2-pyridyl ketone *N*(4)-phenylthiosemicarbazone (HL) have been synthesized and spectrochemically characterized. Elemental analyses revealed a $NiL_2 \cdot 2H_2O$ stoichiometry for compound **1**. However, the single crystals isolated revealed a composition $NiL_2 \cdot 0.5(H_2O)0.5(DMF)$. The compound crystallizes into a monoclinic lattice with the space group $P2_1/n$. Complexes **2**, **3** and **4** are observed to show a 1:1:1 ratio of metal:thiosemicarbazone:gegenion, with the general formula $NiLX \cdot yH_2O$ [X = NCS, $y = 2$ for **2**; X = Cl, $y = 3$ for **3** and X = N_3, $y = 4.5$ for **4**]. Compound **5** is a dimer with a metal:thiosemicarbazone:gegenion ratio of 2:2:1, with the formula $[Ni_2L_2(SO_4)] \cdot 4H_2O$.
© 2007 Elsevier Ltd. All rights reserved.

Keywords: Di-2-pyridyl ketone; Thiosemicarbazone; Ni(II) complexes; Crystal structure

1. Introduction

Nickel species in various coordination environments are of interest to inorganic biochemists, for instance, some nickel complexes of thiosemicarbazone derivatives are observed to exhibit antitumour activity [1]. Some mono- and bis-chelated nickel complexes of di-2-pyridyl ketone derivatives of *S*-methyldithiocarbazate are observed to have antifungal and antibacterial properties [2]. Ni(II) complexes of substituted thiosemicarbazones [3,4] and their di-2-pyridyl ketone derivatives [5–7] have been previously reported. There are also reports on the magnetic behaviour of coordination complexes of nickel. For the past few years we have been under constant pursuit of the versatile coordination chemistry of di-2-pyridyl ketone thiosemicarbazones [7–10]. However, studies on the chemistry of nickel complexes of di-2-pyridyl ketone *N*(4)-substituted thiosemicarbazones are very rare, and here we report some new Ni(II) complexes of di-2-pyridyl ketone *N*(4)-phenylthiosemicarbazone.

2. Experimental

2.1. Materials

Di-2-pyridyl ketone (Fluka), $Ni(OAc)_2 \cdot H_2O$ (CDH), $NiClO_4$ (Fluka), $NiSO_4$ (Merck), $NiCl_2 \cdot 2H_2O$ (SD Fine), NaN_3(Reidel-De Haen) and KSCN (BDH) were used as received. The solvent used, ethyl alcohol was repeatedly distilled before use.

2.2. Physical measurements

Elemental analyses were carried out at the Sophisticated Analytical Instruments Facility, Kochi, India using a Vario-EL III CHNS. The magnetic susceptibility measurements were carried out in the polycrystalline state on a Vibrating Sample Magnetometer (VSM) at 5.0 kOe field strength at the Indian Institute of Technology, Roorkee, India. Infrared spectral measurements were done on an ABB Bomem

* Corresponding author. Tel.: +91 484 2575804; fax: +91 484 2577595.
E-mail addresses: mrp@cusat.ac.in, mrp_k@yahoo.com (Maliyeckal R. Prathapachandra Kurup).

0277-5387/$ - see front matter © 2007 Elsevier Ltd. All rights reserved.
doi:10.1016/j.poly.2007.02.015

FTIR instrument using KBr pellets for spectra in the region 4000–500 cm^{-1}. The far IR spectra were recorded using polyethylene pellets in the 500–100 cm^{-1} region on a Nicolet Magna 550 FTIR instrument at the Regional Sophisticated Instrumentation Facility, Indian Institute of Technology, Bombay. An Ocean Optics SD 2000 Fiber Optic spectrometer was used to measure solid-state reflectance spectra in the range 200–900 nm. NMR spectra were recorded using a Bruker AMX 400 FT-NMR spectrometer using TMS as the internal standard at the Sophisticated Instruments Facility, Indian Institute of Science, Bangalore.

2.3. X-ray crystallography

Single crystal X-ray diffraction measurements were carried out on a Bruker Smart Apex CCD diffractometer equipped with a fine-focused sealed tube. The unit cell parameters were determined and the data collections were performed using graphite-monochromated Mo Kα ($\lambda = 0.71073$ Å) radiation. The data collected were reduced using the SAINT program [11] and the empirical absorption corrections were carried out using the SADABS program [12]. The trial structure was obtained by direct methods [13] using SHELXS-97, which revealed the position of all non-hydrogen atoms, and was refined by full-matrix least squares on F^2 (SHELXL-97) [14] and the graphics tool used was DIAMOND version 3.0 [15]. All non-hydrogen atoms were refined anisotropically, while the hydrogen atoms were placed in calculated positions and refined as riding atoms.

2.4. Synthesis of the ligand

The ligand used is di-2-pyridyl ketone *N*(4)-phenylthiosemicarbazone, HL (Fig. 1). Preparation of the ligand was done as described previously [16].

2.5. Preparation of complexes

2.5.1. $NiL_2 \cdot 2H_2O$ (**1**)

A solution of $Ni(OAc)_2 \cdot H_2O$ (0.199 g, 1 mmol) in 10 ml of ethanol was added to an ethanolic solution of HL (0.333 g, 1 mmol) and refluxed for 4 h. The resulting brown product was washed with an ethanol–water mixture followed by ether and dried over P_4O_{10} *in vacuo*. Single crystals suitable for X-ray diffraction were grown at room temperature by slow evaporation of a 1:1:1 solution of the complex in methanol, chloroform and dimethylformamide. Colour: light brown, Yield: 0.36 g (67%), $\mu_{eff} = 2.98$ BM, Elemental *Anal.* Calc.: C, 56.04; H, 5.75; N, 18.15. Found: C, 55.83; H, 5.09; N, 17.71%.

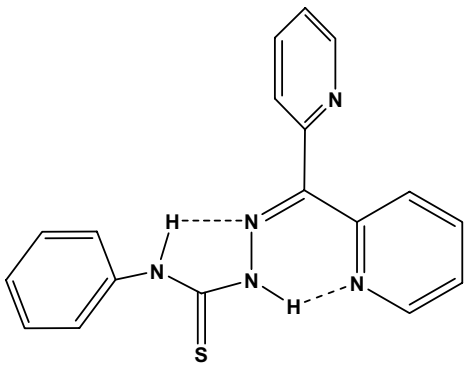


Fig. 1. Structure of compound HL.

2.5.2. $NiLNCS \cdot 2H_2O$ (**2**)

To an ethanolic solution of HL (0.333 g, 1 mmol), $Ni(OAc)_2 \cdot H_2O$ (0.199 g, 1 mmol) dissolved in ethanol (10 ml) was added, and the resulting mixture was refluxed for the preparation of compound **2**. After 15 min, an aqueous solution of KSCN (0.097 g, 1 mmol) was added to the solution followed by a further refluxing for three hours. The product that separated out was collected, washed with ether and dried *in vacuo*. Colour: dark brown, Yield: 0.49 g (77%), Elemental *Anal.* Calc.: C, 47.03; H, 3.74; N, 17.32. Found: C, 46.58; H, 3.79; N, 17.17%. ^{1}H NMR: δ (ppm) 8.70 (t, N5H); 8.05 (d, C1H); 7.65 (d, C11H); 7.25 (m, aromatic H).

2.5.3. $NiLCl \cdot 3H_2O$ (**3**)

A solution of $NiCl_2 \cdot 2H_2O$ (0.166 g, 1 mmol) in 10 ml of ethanol was added to an ethanolic solution of HL (0.333 g, 1 mmol), and the resulting mixture was refluxed for 4 h. The product that separated out was washed with ethanol followed by ether and dried over P_4O_{10} *in vacuo*. Colour: brown, Yield: 0.32 g (63%), Elemental *Anal.* Calc.: C, 44.98; H, 4.19; N, 14.57. Found: C, 44.85; H, 3.71; N, 13.92%. ^{1}H NMR: δ (ppm) 9.75 (s, N5H); 8.85 (d, C1H); 8.75 (d, C11H); 7.60 and 7.35 (m, aromatic H).

2.5.4. $NiLN_3 \cdot 4.5H_2O$ (**4**)

To an ethanolic solution of HL (0.333 g, 1 mmol), 1 mmol of $Ni(OAc)_2 \cdot H_2O$ (0.199 g) dissolved in ethanol (10 ml) was added and the resulting mixture was refluxed. An aqueous solution of NaN_3 (0.0651 g, 1 mmol) was then added to the solution followed by a further refluxing for three hours. The product that separated out was collected, washed with ether and dried *in vacuo*. Colour: light brown, Yield: 0.42 g (71%), $\mu_{eff} = 2.88$ BM, Elemental *Anal.* Calc.: C, 42.05; H, 4.51; N, 21.79. Found: C, 41.33; H, 3.60; N, 21.52%.

2.5.5. $[Ni_2L_2(SO_4)] \cdot 4H_2O$ (**5**)

HL (0.333 g, 1 mmol) was dissolved in ethanol (15 ml) and refluxed with a solution of $NiSO_4$ (0.223 g, 1 mmol) in 10 ml of water. A crystalline product separated out, which was filtered and washed with ether and dried over P_4O_{10} *in vacuo*. Colour: brown, Yield: 0.29 g (52%), $\mu_{eff} = 3.41$ BM, Elemental *Anal.* Calc.: C, 45.50; H, 3.82; N, 14.74. Found: C, 45.50; H, 3.77; N, 15.06%.

3. Results and discussion

3.1. Synthesis of the compounds

Single crystals suitable for X-ray diffraction of compound **1** were grown at room temperature by slow evaporation of a 1:1:1 solution of the complex in methanol, chloroform and dimethylformamide. The elemental analyses revealed a $NiL_2 \cdot 2H_2O$ stoichiometry for compound **1**. However, the single crystals prepared from the compound revealed a composition incorporating one molecule each of water and DMF additionally in the lattice. The molecular structure of NiL_2 with the atom labelling scheme is given in Fig. 2. The tentative structures of compounds **2**, **3**, **4**, **5** and the ^1H NMR labelling scheme are provided in Fig. 3. Complexes **2**, **3** and **4** were observed to show a 1:1:1 ratio of metal:thiosemicarbazone:gegenion, with the general formula $NiLX \cdot yH_2O$ [X = NCS, $y = 2$ for **2**; X = Cl, $y = 3$ for **3** and X = N_3, $y = 4.5$ for **4**]. Compound **5** was revealed to be a dimer with a metal:thiosemicarbazone:gegenion ratio of 2:2:1, with the formula $[Ni_2L_2(SO_4)] \cdot 4H_2O$. Recently, we have reported a tetranuclear copper complex with four and five coordinated copper centers bridged through sulfate linkages, the structure of which was confirmed by single crystal X-ray diffraction [17]. Magnetic studies reveal the compounds **1**, **4** and **5** to be paramagnetic while compounds **2** and **3** are diamagnetic.

3.2. Crystal structure of $NiL_2 \cdot 0.5(H_2O)0.5(DMF)$

There are two crystallographically independent molecules in the asymmetric unit of $NiL_2 \cdot 0.5(H_2O)0.5(DMF)$. The compound crystallizes into a monoclinic lattice with the space group $P2_1/n$. The structural refinement parameters are given in Table 1 and the selected bond distances and bond angles are given in Table 2. The bonding parameters in the crystallographically independent molecules in the asymmetric lattice bear almost identical features. In addition to the two NiL_2 moieties, there are two solvent molecules, i.e., one molecule each of water and DMF in the lattice.

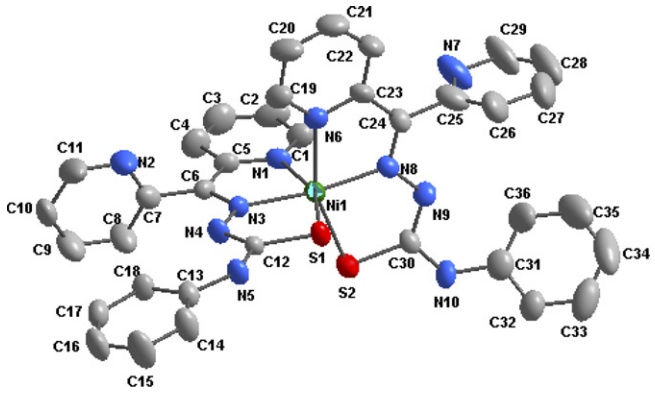
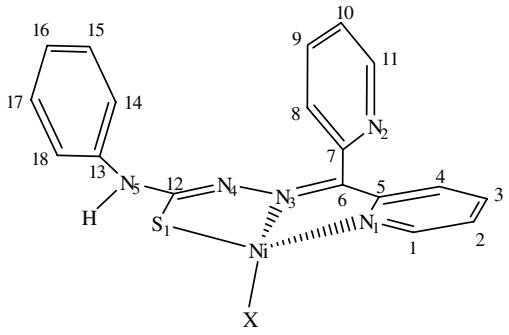
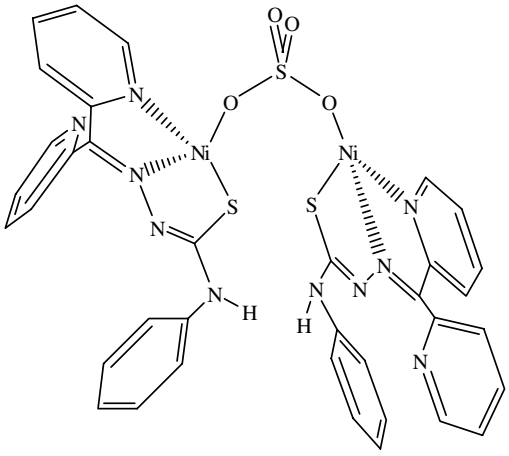


Fig. 2. Structure of NiL_2 showing the atom numbering scheme. The ellipsoids are shown with 50% probability and the hydrogen atoms, water and DMF are omitted for clarity.



(a) X = -NCS (Compound **2**)
-Cl (Compound **3**)
-N_3 (Compound **4**)



(b) Compound **5**

Fig. 3. (a) Structures of compounds **2**, **3** and **4** with the NMR labelling scheme and (b) structure of compound **5**.

The bond distances and angles from the single crystal X-ray diffraction studies reveal that the independent units of the molecules exist in a distorted octahedral geometry around the metal center. There are two deprotonated ligand moieties of HL around each metal center and they are bonded through the azomethine nitrogen, pyridyl nitrogen and thiolate sulfur of each of the thiosemicarbazone moieties, thus effecting a six-coordinate environment about the metal center. In the present Ni(II) complex, the thiosemicarbazone moiety reveals an *ZZ* conformation with *cis* configurations about both the C6–N3 and N4–C12 bonds, contrary to the *ZE* conformation in the free ligand. The S1–C12–N4–N3 torsion angle value is 2.9(7)°, which reveals a *cis* nature of the thiocarbonyl S1 atom with the hydrazinic N3 atom. The two ligand moieties in the present compound are aligned almost perpendicular to each other, as revealed from the dihedral angle of 85.55(1)° of the C6/N3/N4/C12/N5/S1 plane with that of the C24/N8/N9/C30/N10/S2 plane. The distortion from an ideal octahedral stereochemistry is suggested by the values for the orthogonal bite angles N1–Ni1–N3 (77.62(18)°); S1– Ni1–N3

Table 1
Crystal data and structure refinement for $NiL_2 \cdot 0.5(H_2O)0.5(DMF)$

Parameters	$NiL_2 \cdot 0.5(H_2O)0.5(DMF)$
Empirical formula	$C_{37.5}H_{30.5}N_{10.5}NiOS_2$
Formula weight (M)	765.5
Temperature (K)	293(2)
Wavelength (Mo Kα) (Å)	0.71073
Crystal system	monoclinic
Space group	$P2_1/n$
Lattice constants	
a (Å)	14.643(6)
b (Å)	29.365(11)
c (Å)	17.453(7)
α (°)	90.00
β (°)	104.476(8)
γ (°)	90.00
Volume V (Å^3)	7266(5)
Z	8
Calculated density (ρ) (Mg m^{-3})	1.406
Absorption coefficient (μ) (mm^{-1})	0.696
$F(000)$	3192
Crystal size (mm)	$0.35 \times 0.33 \times 0.31$
θ Range for data collection	1.59–24.04
Limiting indices	$-16 \leqslant h \leqslant 16$, $-33 \leqslant k \leqslant 33$, $-19 \leqslant l \leqslant 20$
Reflections collected	64276
Unique reflections	11443 [$R_{int} = 0.1088$]
Completeness to θ	24.04 (99.8%)
Absorption correction	multiscan
Maximum and minimum transmission	0.8131 and 0.7907
Data/restraints/parameters	11443/0/1149
Goodness-of-fit on F^2	1.059
Final R indices [$I > 2\sigma(I)$]	$R_1 = 0.0784$, $wR_2 = 0.1447$
R indices (all data)	$R_1 = 0.1476$, $wR_2 = 0.1709$
Largest difference peak and hole (e A^{-3})	0.674 and −0.343

Table 2
Comparison of selected bond lengths (Å) and bond angles (°) of HL and $NiL_2 \cdot 0.5(H_2O)0.5(DMF)$

	HL	$NiL_2 \cdot 0.5(H_2O)0.5(DMF)$
Ni1–N1		2.131(4)
Ni1–N3		2.030(4)
Ni1–S1		2.4365(18)
Ni1–N6		2.115(5)
Ni1–N8		2.030(4)
Ni1–S2		2.4294(18)
S1–C12	1.6763(12)	1.731(5)
N3–C6	1.2858(8)	1.306(6)
N4–N3	1.3573(10)	1.359(6)
N4–C12	1.3616(9)	1.320(6)
S2–C30		1.727(6)
N8–C24		1.294(7)
N9–N8		1.358(6)
N9–C30		1.330(7)
N1–Ni1–N3		77.62(17)
N1–Ni1–S1		157.50(12)
N1–Ni1–N6		90.08(17)
N3–Ni1–S1		79.99(12)
N6–Ni1–N8		77.69(18)
N6–Ni1–S1		90.09(12)
N6–Ni1–S2		157.98(13)
N6–Ni1–N3		96.17(18)
N8–Ni1–S2		80.29(13)
N8–Ni1–N1		97.01(17)
S2–Ni1–N1		93.00(12)

(79.99(13)°); N6–Ni1–N8 (77.65(18)°) and S2–Ni1–N8 (80.25(13)°). The maximum mean plane deviation of the equatorial plane consisting of N3, N6, N8, S2 and Ni1 is 0.0556(4) Å at N8 and the central Ni(II) atom is displaced out of this mean plane at a distance of −0.0423(4) Å. The two metal chelate rings in one of the thiosemicarbazone moieties, comprising of atoms Ni1, N1, C5, C6, N3, N4, C12 and S1, are found to be almost coplanar with rms values of 0.0196 (4) and 0.0203 (4) Å, respectively. It is interesting to note that the azomethine and thiolate bond distances are slightly increased in the complex, when compared to the corresponding values in the free ligand HL, and this supports coordination. A significant amount of metal-to-ligand π back bonding generates a delocalized conjugating effect along the metal–chelate rings which imparts partial single and double bond nature to the N4–C12 and N3–N4 hydrazinic bonds in the thiosemicarbazone moiety, owing to the extensive delocalization over the entire coordination framework.

Two independent molecules in the asymmetric unit constitute the repeating unit of the crystal packing in the unit cell. The sets of two molecules repeat one- dimensionally in the lattice. Intermolecular π–π interactions are observed at distances greater than 3.5 Å, and hence they contribute little towards the effective packing of the molecules in the lattice. However, some C–H···π interactions, which are rather short, appear significant. The list of intermolecular interactions is given in Table 3.

3.3. IR and electronic spectra

A broad band around 3500 cm^{-1} in the IR spectra of the complexes is assigned to the –OH stretching vibrations of lattice water. The azomethine stretching vibration is observed at 1592 cm^{-1} in the ligand HL. However, in the complex this band is shifted as the azomethine nitrogen is coordinated to the Ni(II) centre. In complex **3**, the coordinated azomethine band is observed as a strong combination band at 1641 cm^{-1}. In other complexes, it is shifted to the range 1562–1541 cm^{-1}. The stretching vibrations of the newly formed N4=C12 bond, due to coordination through deprotonation, appear as sharp bands in the region near 1585 cm^{-1}. The δ(CS) band observed at 806 cm^{-1} in the ligand is shifted to the region near 750 cm^{-1} in the complex due to the enolization of thiosemicarbazone moiety upon coordination. The IR spectrum of compound **2** shows a sharp band at 2095 cm^{-1} corresponding to the antisymmetric ν(NCS) vibrations. The δ(Ni–N_{NCS}) band at 498 cm^{-1} shows that the thiocyanate group is N-bonded to the nickel centre. Another band at 438 cm^{-1} is assigned to the ν(NiN) vibration and it supports the coordination of the imine nitrogen. A medium band at 384 cm^{-1} corresponds to the ν(NiS) vibration, con-

Table 3
H-bonding, π–π and CH···π interaction parameters of the compound $NiL_2 \cdot 0.5(H_2O)0.5(DMF)$

H-bonding[A]				
D···H···A	D–H (Å)	H···A (Å)	D···A (Å)	D–H···A (°)
C36–H36–N9	0.93	2.39	2.82	108.00
C4A–H4A–N2A	0.94	2.58	3.01	109.06
C36A–H36A–N9A	0.93	2.31	2.87	118.40
π–π interactions				
Cg(I)–Res(1)···Cg(J)	Cg–Cg (Å)	$\alpha°$	$\beta°$	
Cg(13) [2] → Cg(14)[a]	3.9393	10.71	25.04	
Cg(16) [1] → Cg(18)[b]	3.9144	22.86	17.10	
Equivalent position codes		Cg(13) = N6, C19, C20, C21, C22, C23		
$a = 1 + x, y, z$		Cg(14) = N6A, C19A, C20A, C21A, C22A, C23A		
$b = 1/2 + x, 1/2 - y, 1/2 + z$		Cg(16) = N7A, C25A, C26A, C27A, C28A, C29A		
		Cg(18) = C13A, C14A, C15A, C16A, C17A, C18A		
C–H···π interactions				
X–H(I)···Cg(J)	H...Cg (Å)	X–H···Cg (°)	X...Cg (°)	
C19–H19 [2] → Cg(1)[a]	2.9047	104.95	3.2711	
C19-H19 [2] → Cg(3)[a]	3.0758	98.54	3.3435	
C19A-H19A [1] → Cg(5)[a]	2.9075	100.68	3.2127	
C1A-H1A [1] → Cg(6)[a]	3.1175	101.36	3.4247	
Equivalent position code		Cg(1) = Ni1, S1, C12, N4, N3		
$a = x, y, z$		Cg(3) = Ni1, N1, C5, C6, N3		
		Cg(5) = Ni1A, S1A, C12A, N4A, N3A		
		Cg(6) = Ni1A, S2A, C30A, N9A, N8A		

[A] No classic hydrogen bonds found.

firming the coordination of the thiolate sulfur. Coordination of the pyridyl nitrogen results in the ν(NiN) band appearing as a strong band with two splits at 291 and 281 cm^{-1}. In compound **3**, a sharp band at 397 cm^{-1} reveals the presence of a terminal chlorine in the complex. The IR spectrum of **4** reveals a sharp band at 2066 cm^{-1} corresponding to the asymmetric stretching vibrations of the coordinated azido group. The ν(Ni–N_3) band is observed at 395 cm^{-1} and a band at 457 cm^{-1} is assigned to the ν(NiN) vibrations, supporting the coordination through the imine nitrogen. In the sulfato complex **5**, the ν_1 and ν_2 vibrations, observed as weak bands at 979 and at 455 cm^{-1}, suggest the bridged bidentate nature of the sulfato anion in the complex. The ν_3 vibration is observed at 1050 cm^{-1}, while the ν_4 vibrations are observed near 615 and 510 cm^{-1}, similar to the corresponding values of other complexes where the sulfate anion exists in the bridged bidentate form [18]. The Ni–$N_{azomethine}$ and Ni–$S_{thiolate}$ stretching vibrations are observed at 418 and 385 cm^{-1}. The solid state electronic spectra of the complexes reveal that the $\pi \rightarrow \pi^*$ and the $n \rightarrow \pi^*$ transitions appear in regions near 280 and 300 nm respectively. The ligand to metal charge transfer transitions are observed either as a shoulder or as a broad band near 400 nm. Weak shoulders near 500 nm correspond to the d–d transitions [19]. Selected electronic spectral data are given in Table 4.

Table 4
Electronic spectral data (nm) of the Ni(II) complexes

Compound	$\pi \rightarrow \pi^*$	$n \rightarrow \pi^*$	Charge transfer	d–d
HL	283	358		
$NiL_2 \cdot 2H_2O$ (**1**)	298	325	441 b	551 sh
				587 sh
			408	489
$NiLNCS \cdot 2H_2O$ (**2**)	353	379	423	578 b
			449	
$NiLCl \cdot 3H_2O$ (**3**)	270	314	434 b	512 sh
	284			558 sh
$NiLN_3 \cdot 4.5H_2O$ (**4**)	299	322	417 sh	
			446 b	585 sh
$[Ni_2L_2(SO_4)] \cdot 4H_2O$ (**5**)	279	298	402 s	570 sh
			462 b	637 sh

b = broad, s = strong, sh = shoulder.

3.4. Nuclear magnetic resonance studies

The numbering scheme used in the ^1H NMR spectra is shown in Fig. 3a. A sharp singlet at 14.55 ppm in the ^1H NMR spectrum of HL due to the proton on the N4 nitrogen is absent in the spectra of the complexes, which supports coordination of the thiosemicarbazone moiety in the thiolate form after enolization and deprotonation. The ^1H NMR spectrum of compound **2** reveals a triplet centred around 8.70 ppm, which does not reveal any coupling interactions in the ^1H–^1H COSY spectrum. Hence it can be assigned to the proton on the nitrogen atom N5 of the thiosemicarbazone moiety, the resonance due to which splits into a triplet by quadrupole splitting. It is interesting to note that the coordination through the pyridyl nitrogen is clearly evident in the NMR spectra. The resonances corresponding to the protons on carbons adjacent to the pyridyl nitrogen are observed at 8.05 and 7.65 ppm in the complex, which are shifted from the

corresponding values of 8.85 and 8.68 ppm in the ligand HL. Both resonances show correlation with the aromatic protons. A slight shift in the alpha proton resonance of the uncoordinated pyridyl nitrogen may be attributed to the absence of hydrogen bonding interactions in the complex, unlike in the ligand. The low intensity of the multiplets in the aromatic region may be attributed to the delocalization of electron density due to coordination in the complex. The ^{1}H NMR spectrum of compound **3** is also resolved in a similar fashion as that of compound **2**.

Acknowledgements

V. Suni is thankful to the Kerala State Council for Science, Technology and Environment for financial support in the form of a Junior Research Fellowship. M.R.P. Kurup acknowledges the Department of Science and Technology, Government of India for financial support (No. SR/SI/IC31/2002). Authors also acknowledge DST IRPHA for the data collection and Sophisticated Analytical Instruments Facility, Kochi, India for the elemental analysis.

Appendix A. Supplementary material

CCDC 288854 contains the supplementary crystallographic data for this paper. These data can be obtained free of charge via http://www.ccdc.cam.ac.uk/conts/retrieving.html, or from the Cambridge Crystallographic Data Centre, 12 Union Road, Cambridge CB2 1EZ, UK; fax: (+44) 1223-336-033; or e-mail: deposit@ccdc.cam.ac.uk. Supplementary data associated with this article can be found, in the online version, at doi:10.1016/j.poly.2007.02.015.

References

[1] M. Wang, L.-F. Wang, Y.-Z. Li, Q.-X. Li, Z.-D. Xu, D.-M. Qu, Transit. Met. Chem. 26 (2001) 307.
[2] M.A. Ali, A.H. Mirza, M. Nazimuddin, H. Rahman, R.J. Butcher, Transit. Met. Chem. 27 (2002) 268.
[3] D.X. West, A.A. Nassar, F.A. EL-Saied, M.I. Ayad, Transit. Met. Chem. 23 (1998) 423.
[4] H. Beraldo, W.F. Nacif, L.R. Teixeira, J.S. Reboucas, Transit. Met. Chem. 27 (2002) 85.
[5] J.K. Swearingen, D.X. West, Transit. Met. Chem. 26 (2001) 252.
[6] J.K. Swearingen, W. Kaminsky, D.X. West, Transit. Met. Chem. 27 (2002) 724.
[7] V. Philip, V. Suni, M.R.P. Kurup, M. Nethaji, Polyhedron 23 (2004) 1225.
[8] V. Philip, V. Suni, M.R.P. Kurup, M. Nethaji, Polyhedron 23 (2005) 1133.
[9] V. Philip, E. Manoj, M.R.P. Kurup, M. Nethaji, Acta Crystallogr. C 61 (2005) m488.
[10] V. Philip, V. Suni, M.R.P. Kurup, M. Nethaji, Spectrochim. Acta A 64 (2006) 174.
[11] SMART and SAINT, Area Detector Control and Integration Software, Siemens Analytical X-ray Instrunments Inc., Madison, Wisconsin, USA, 1996.
[12] G.M. Sheldrick, SADABS, Program for Empirical absorption correction of Area Detector Data, University of Göttingen, Göttingen, Germany, 1997.
[13] G.M. Sheldrick, Acta Crystallogr. A46 (1990) 467.
[14] G.M. Sheldrick, SHELXS-97 Program for the Solution of Crystal Structures, University of Göttingen, Göttingen, Germany, 1997.
[15] K. Brandenburg, H. Putz, DIAMOND Version 3.0, Crystal Impact, GbR, Postfach 1251, D-53002 Bonn, Germany, 2004.
[16] V. Suni, M. Nethaji, M.R.P. Kurup, Spectrochim. Acta 63 (2006) 174.
[17] V. Philip, V. Suni, M. Nethaji, M.R.P. Kurup, Polyhedron 25 (2006) 1931.
[18] K. Nakamoto, in: Infrared and Raman Spectra of Inorganic and Coordination Compounds, fourth ed., John Wiley & Sons, New York, 1986.
[19] A.B.P. Lever, Inorganic Electronic Spectroscopy, second ed., Elsevier Science Publishers, BV, The Netherlands, 1984.

Available online at www.sciencedirect.com
ScienceDirect
Polyhedron 26 (2007) 3103–3111
POLYHEDRON
www.elsevier.com/locate/poly

Syntheses, crystal structures and photoluminescence of three coordination polymers with 2,3-pyrazinedicarboxylic acid and N-donor ligands

Hua Yin [a], Shi-Xiong Liu [a,b,*]

[a] Department of Chemistry, Fuzhou University, Fuzhou 350002, PR China
[b] State Key Laboratory of Structural Chemistry, Fujian Institute of Research on the Structure of Matter, the Chinese Academy of Sciences, Fuzhou 350002, PR China

Received 23 October 2006; accepted 13 February 2007
Available online 22 February 2007

Abstract

The reactions between $Cd(OAc)_2$/$Cu(NO_3)_2$ and mixed ligands (2,3-pyrazinedicarboxylic acid (pzdc) and N-donor ligands) under different reaction conditions give the three title complexes **1**, **2** and **3**. There is a (4,8) net 2D network structure and a rectangular grid network structure in the cadmium complexes $[Cd(pzdc)(phen)]\cdot H_2O$ (**1**) and $Cd_2(pzdc)_2(4,4'\text{-bpy})(H_2O)_2$ (**2**), respectively. The complex $[Cu_4(pzdc)_4(phen)_2(H_2O)_4]\cdot 10H_2O$ (**3**) has a 1D zigzag chain structure. The influences of coordination modes of the pzdc ligand and N-donor ligands on the superstructural diversity have been discussed. Complexes **1** and **2** exhibit strong fluorescent emission bands in the solid state at room temperature. The EPR spectrum of **3** is typical for a square-pyramidal geometry of copper (II) ions.
© 2007 Elsevier Ltd. All rights reserved.

Keywords: Supermolecular chemistry; Cadmium; Copper; Pyrazinedicarboxylic acid; Mixed ligands

1. Introduction

The design and construction of coordination polymers are of great interest due to their intriguing structural topologies [1–3]. In particular, polycarboxylate ligands have been shown to be good building blocks in the design of metal-organic materials with desired topologies owing to their rich coordination modes. For example, some complexes with pyridine-2,3-dicarboylate [4], 2,3-pyrazinedicarboxylic acid (pzdc) [5–16], 2,3,5,6-pyrazinetetracarboxylic acid, imidazoldicarboxylic acid [17,18] and polybenzenecarboxylate ligand [19,20] have been reported. Susumu Kitagawa's group selected $\{Cd(pzdc)_n\}$ as a layer, and a pillar ligand as a second ligand to obtain novel porous frameworks [9–11]. The coordination polymers constructed by polycarboxylate ligands and N-bonding ligand are also of great interest [21,22]. In order to understand the role of N-donor ligands as a second ligand, we report the syntheses and structures of three complexes containing $\{Cd(pzdc)_n\}$ with 1D or 2D structures and a N-donor ligand. The three title complexes are $[Cd(pzdc)(phen)]\cdot H_2O$ (**1**), $Cd_2(pzdc)_2(4,4'\text{-bpy})(H_2O)_2$ (**2**) and $[Cu_4(pzdc)_4(phen)_2(H_2O)_4]\cdot 10H_2O$ (**3**). The influences of the coordination modes of pzdc and the mixed ligands on the number of possible superstructures (i.e. discrete structures or 1D, 2D or 3D networks) have been studied.

2. Experimental

2.1. Materials

All chemicals are commercially available and were used as received without further purification.

* Corresponding author. Address: Department of Chemistry, Fuzhou University, Fuzhou 350002, PR China. Tel./fax: +86 591 83729860.
E-mail address: shixiongliu@yahoo.com (S.-X. Liu).

0277-5387/$ - see front matter © 2007 Elsevier Ltd. All rights reserved.
doi:10.1016/j.poly.2007.02.011

2.2. Syntheses of the complexes

2.2.1. [Cd(pzdc)(phen)] · H_2O (1)

$Cd(OAC)_2$ (0.1 mmol), 2,3-pyrazinedicarboxylic acid (0.1 mmol), phen (0.1 mmol) and H_2O (16 ml) in a molar ratio of 1:1:1:8888 were loaded into a 23 cm^3 Teflon-lined stainless-steel vessel, which was then sealed and placed in a programmable furnace. The resulting mixture was heated at 160 °C for 4 days and then cooled to room temperature. The colorless crystals of **1** were obtained with a 36% yield based on Cd. *Anal*. Calc. for $Cd_1C_{18}H_{12}N_4O_5$: C, 45.31; H, 2.52; N, 11.75. Found: C, 45.23; H, 2.59; N, 11.86%. FT-IR (KBr pellet, 4000–400 cm^{-1}): 3415 s, 1627 s, 1568 s, 1460 m, 1436 w, 1392 s, 1361 m, 1201 m, 1169 m, 1123 m, 1069 s, 896 m, 843 m, 780 w, 751 w, 668 s, 602 s, 541 s, 441 m.

2.2.2. $Cd_2(pzdc)_2(4,4'\text{-bpy})(H_2O)_2$ (2)

An aqueous solution of $Cd(OAC)_2$ (0.1 mmol) was added to an aqueous solution of 2,3-pyrazinedicarboxylic acid (0.1 mmol) and 4,4′-bpy (0.05 mmol), and the resulting mixture was stirred for 2 min, filtered immediately and left in air. After several days, colorless crystals of the title compound were obtained. Yield: ca. 28% based on Cd. *Anal*. Calc. for $Cd_2C_{22}H_{16}N_6O_{10}$: C, 35.24; H, 2.14; N, 11.21. Found: C, 35.32; H, 2.19; N, 11.16%.

2.2.3. $[Cu_4(pzdc)_4(phen)_2(H_2O)_4] \cdot 10H_2O$ (3)

The synthetic procedure is similar to that for compound **2**, using $Cu(NO_3)_2$ and phen instead of $Cd(OAC)_2$ and 4,4′-bpy. Blue crystals of **3** were obtained in two days. Yield: ca. 45% based on Cu. *Anal*. Calc. for $Cu_4C_{48}H_{52}N_{12}O_{30}$: C, 37.62; H, 3.40; N, 10.97. Found: C, 37.93; H, 3.42; N, 10.89%.

2.3. Physical measurements

IR absorption spectra (KBr pellets) were recorded on a Perkin–Elmer spectrum 2000 spectrophotometer. Elemental analyses were carried out on a Vario EL III. Fluorescent data were collected on an Edinburgh FL-FS920 TCSPC system. Thermal gravimetric analysis (TGA) was tested under nitrogen with a heating rate of 10 °C min^{-1} using a Perkin–Elmer TGA-7 Thermal Analysis system. EPR spectra were recorded at room temperature at X-band frequency with a Bruker EMX 10/12 automatic spectrometer.

2.4. Crystal structure determination

Crystals of the three title compounds of a suitable size were mounted on glass fibers. Intensity data were collected on a Rigaku RAPID Weissengberg IP diffractometer with graphite-monochromated Mo Kα radiation ($\lambda = 0.71073$ Å) and the ω scan mode. The structures were solved by direct methods with SHELXS-97 [23] and refined by full-matrix least-squares calculations with SHELXL-97 [24]. All the non-hydrogen atoms in the three complexes were refined anisotropically, except for the oxygen atoms of crystal water molecules in **3** which were refined isotropically. Most of the hydrogen atoms in the three complexes were located in calculated positions or found from difference Fourier maps. Crystallographic data for **1**, **2** and **3** are listed in Table 1.

Table 1
Crystal data and structural refinement parameters for complexes **1**, **2** and **3**

Compound	1	2	3
Formula	$C_{18}H_{12}N_4O_5Cd_1$	$C_{22}H_{16}N_6O_{10}Cd_2$	$C_{48}H_{52}N_{12}O_{30}Cu_4$
Formula weight	476.72	749.21	1531.18
Crystal system	monoclinic	monoclinic	orthorhombic
Space group	$P2_1/c$	$P2_1/n$	$P2_12_12_1$
a (Å)	11.7975(11)	10.915(5)	13.715(3)
b (Å)	14.4706(12)	7.576(4)	16.334(3)
c (Å)	10.0012(8)	13.719(6)	26.250(4)
α (°)	90	90	90
β (°)	95.193(3)	92.976(19)	90
γ (°)	90	90	90
V (Å^3)	1700.4(3)	1132.9(9)	5881(2)
Z	4	4	4
D_{calc} (g cm^{-3})	1.862	2.196	1.729
T (K)	293(2)	293(2)	293(2)
Color	colourless	colourless	blue
Dimension (mm)	0.05 × 0.08 × 0.10	0.08 × 0.10 × 0.12	0.29 × 0.38 × 0.46
μ (mm^{-1})	1.326	1.953	1.531
F(000)	944	732	3120
θ_{min}, θ_{max} (°)	2.23, 27.48	3.07, 27.48	3.00, 27.48
$h_{min-max}$	−15 → 15	−14 → 13	−17 → 17
$k_{min-max}$	−18 → 0	−9 → 9	−21 → 21
$l_{min-max}$	0 → 12	−17 → 17	−34 → 32
R_{int}	0.0443	0.0492	0.0454
Number of unique data	3888	2591	13384
Number of observed	2980	2098	11475
Number of variables	255	183	839
R	0.0285	0.0348	0.0441
wR	0.0755	0.0712	0.1262
Goodness-of-fit	1.043	1.074	1.046
$(\Delta\rho)_{max,min}$ (e/Å^3)	0.501,−0.571	0.932, −1.005	0.770, −0.742
$(\Delta/\sigma)_{max}$, $(\Delta/\sigma)_{min}$	0.001, 0.000	0.000, 0.000	0.001, 0.000

$R = \sum\|F_o| - |F_c\|/\sum|F_o|$. $wR = [\sum w(F_o^2 - F_c^2)^2/\sum(F_o^2)^2]^{1/2}$.

3. Results and discussion

3.1. Crystal structures

3.1.1. [Cd(pzdc)(phen)] · H_2O (1)

As shown in Fig. 1, the Cd1 atom in complex **1** is coordinated by three carboxyl oxygen atoms (O1, O4A and O3B) and one nitrogen atom N1 from the three surround-

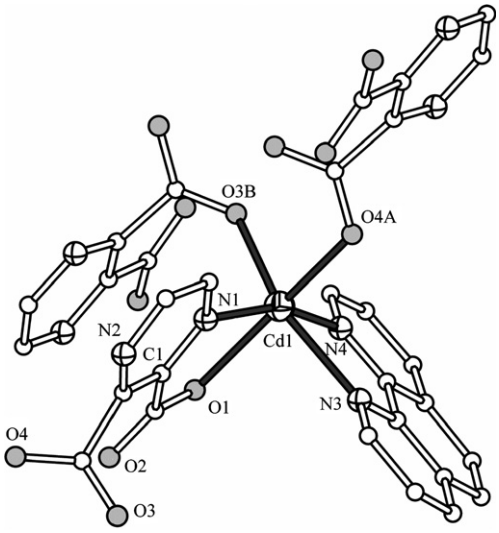


Fig. 1. The coordination environment of the cadmium atom in 1.

ing $pzdc^{2-}$ ligands (where symmetry codes A and B are $-x+1, y+1/2, -z+1/2$ and $x, -y+1/2, z-1/2$, respectively), and two nitrogen atoms (N3 and N4) from a terminal phen, forming a distorted octahedron. Each pzdc ligand in **1** is coordinated to three cadmium atoms through its three carboxyl oxygen donors and one nitrogen donor. The carboxyl group C5O1O2 coordinates to Cd through O1 atom in a monodentate fashion. Two oxygen atoms of the other carboxyl group C6O3O4 coordinate to other two Cd atoms.

Two Cd ions and four pzdc ligands form a basic binuclear unit $Cd_2(pzdc)_4(phen)_2$. The ring B of the binuclear unit $Cd_2(pzdc)_4(phen)_2$ is cyclic eight-membered $[Cd_2(-O_2C-)_2]$ ring with a Cd···Cd distance of 4.904(2) Å, and then four binuclear units are connected to each other by sharing the pzdc ligands to get a (4,8) net 2D network [25] along the *bc* plane, as shown in Fig. 2 and Scheme 1. There are two kinds of macrocyclic rings, the 16-member ring (ring A) and the 8-member ring (ring B), in the 2D network.

Selected bond lengths and angels are given in Table 2. The Cd–O(N) lengths range from 2.271 to 2.372 Å. The

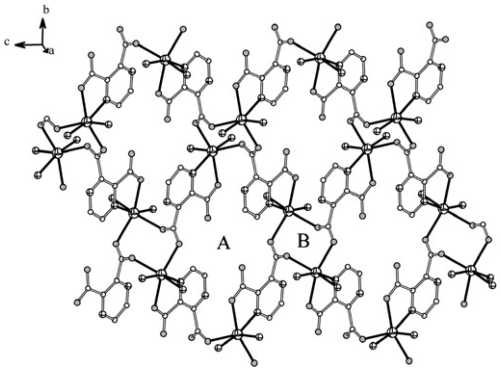
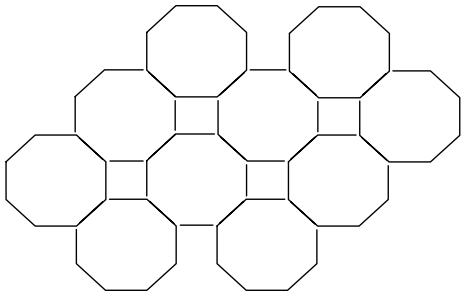


Fig. 2. (4,8) net 2D network in **1** with phen omitted for clarity.



Scheme 1. Schematic representation of the 2D 4.82 net.

Cd–O distances in the title complex are a little longer than the Cd–O bond distance in $[H_3O_2]_x[Cd(pzdc)_2]_x$ [6] (2.246) Å, and the Cd–N bond distances are almost the same as corresponding one in $[H_3O_2]_x[Cd(pzdc)_2]_x$ [6] (2.354 Å).

There are some intermolecular hydrogen bonds O(1W)–H(2WA)···O(2) and O(1W)–H(1WA)···O(4C) between the uncoordinated water molecules and the carboxyl oxygen atoms in the network. As illustrated in Fig. 3, these hydrogen bonds are in the hole of the network. The title complex **1** and the complex reported in [15] are allomorphic. The two complexes have the same chemical formula and the same molecular configuration, but they have different molecular packing. A comparison among the known complexes with the pzdc ligand and the three title complexes with the pzdc ligand is shown in Table 3.

3.1.2. $Cd_2(pzdc)_2(4,4'\text{-bpy})(H_2O)_2$ (**2**)

As shown in Fig. 4, the coordination geometry of the cadmium atom in complex **2** is a distorted octahedron with three carboxyl oxygen atoms (O1, O4A and O4B) and one nitrogen atom (N1) from three $pzdc^{2-}$ ligands (where symmetry codes A and B are $x, y+1, z$ and $-x, -y, -z$, respectively), one nitrogen atom (N3) from 4,4′-bpy and one oxygen atom (O1W) from a coordinated water molecule. Selected bond lengths and angels are listed in Table 4. The Cd–O and Cd–N bond lengths in **2** are in the range 2.293–2.378 Å and are similar to those in complex **1**.

Every pzdc ligand is coordinated to three cadmium atoms through two oxygen atoms from its two carboxylate groups and one nitrogen atom. The pzdc ligand adopts a chelate interaction to one cadmium atom and one μ_2-bridging oxygen atom to the other two cadmium atoms. The two Cd(II) ions are combined by the two μ_2-bridging oxygen atoms with a Cd···Cd interatomic distance of 3.76(3) Å, forming a basic binuclear structure unit $Cd_2(pzdc)_4$ with a Cd_2O_2 core. Two neighboring binuclear units are connected together through the bridging carboxylate groups to obtain a 1D double chain along the *b*-axis, as illustrated in Fig. 5.

The 1D chains are further connected by the bridging 4,4′-bpy to result in 2D networks (Fig. 6). There are intermolecular hydrogen bonds O(1W)–H(01B)···O(1C) and O(1W)–H(01B)···O(2C) between the O(1W)–H(01B) group in the coordinated water molecule and the carboxyl oxygen atom (see Table 4). As shown in Fig. 7 and Fig. S1,

Table 2
Selected interatomic lengths (Å) and angles (°) for complex **1**

Cd(1)–O(3B)	2.271(2)	Cd(1)–O(1)	2.306(2)	Cd(1)–O(4A)	2.310(2)
Cd(1)–N(1)	2.365(2)	Cd(1)–N(3)	2.369(3)	Cd(1)–N(4)	2.372(3)
O(1W)···O(4C)	2.903	O(1W)···O(2)	2.825		
O(3B)–Cd(1)–O(1)	101.12(9)		O(3B)–Cd(1)–O(4A)	91.68(8)	
O(1)–Cd(1)–O(4A)	157.93(8)		O(3B)–Cd(1)–N(1)	105.95(9)	
O(1)–Cd(1)–N(1)	70.44(8)		O(4A)–Cd(1)–N(1)	88.86(8)	
O(3B)–Cd(1)–N(3)	152.66(9)		O(1)–Cd(1)–N(3)	86.70(9)	
O(4A)–Cd(1)–N(3)	90.09(9)		N(1)–Cd(1)–N(3)	101.36(9)	
O(3B)–Cd(1)–N(4)	82.82(9)		O(1)–Cd(1)–N(4)	93.39(8)	
O(4A)–Cd(1)–N(4)	106.10(8)		N(1)–Cd(1)–N(4)	162.64(9)	
N(3)–Cd(1)–N(4)	70.50(9)		O(1W)–H(2WA)···O(2)	160.87	
O(1W)–H(1WA)···O(4C)	166.26				

Symmetry codes. A: $-x+1$, $y+1/2$, $-z+1/2$; B: x, $-y+1/2$, $z-1/2$; C: $-x+1$, $-y$, $-z$.

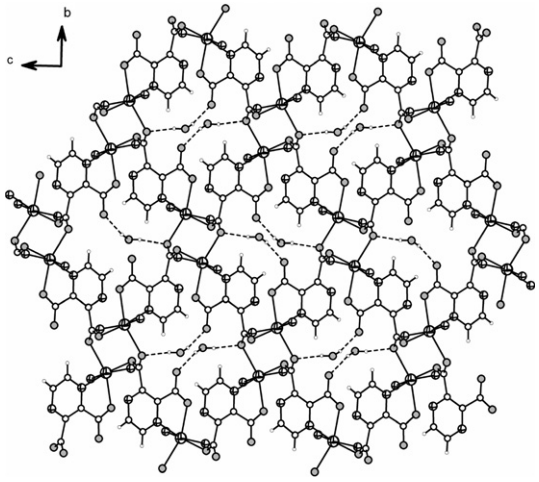


Fig. 3. Hydrogen bonds in the 2D network of complex **1**, with phen omitted for clarity.

the 2D sheet subunits are linked into a 3D coordination framework through these intermolecular hydrogen bonds. Kitagawa et al. reported the guest shape-responsive fitting

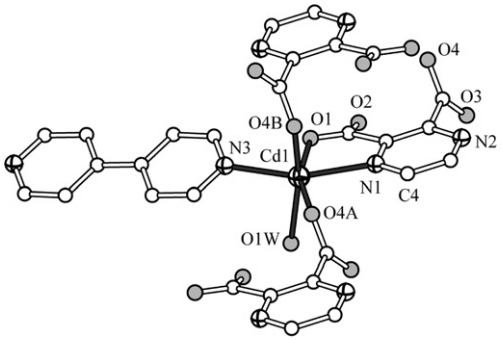


Fig. 4. Perspective view of the coordination environment of the cadmium atom in **2**.

Table 3
The types of crystal structure and the coordination models in 2,3-pzdc complexes

Complex	Coordination models[a]	Type of structure formed between 2,3-pzdc and metal atoms	Type of structure in crystal	References
$[H_3O]_{2x}[Cd(pzdc)_2]_x$	a	1D	1D	[6]
$Cu(pzdc)\cdot HCl$	b	1D	1D	[5]
$[Mn(pzdc)(H_2O)_2]_x\cdot 2xH_2O$	c	1D	1D	[6]
$[\{[Cu_2(pzdc)_2(pia)]\cdot xH_2O\}_n]$	c	2D	2D	[11]
$[Co(pzdc)(phen)]\cdot H_2O$	c	2D	3D	[15]
$[Cd(pzdc)(phen)]\cdot H_2O$	c	2D	2D	complex **1**
$\{Cu(pzdc)_2\cdot 3(H_2O)\cdot 2(idzc)\}_n$	d	1D	1D	[7]
$[Mn(pzdc)(H_2O)_2\cdot 2HO]_n$	d	1D	1D	[8]
$\{[Cu_2(pzdc)_2(bpy)]\cdot G\}_n$	d	2D	2D	[16]
$[Cu_4(pzdc)_4(phen)_2(H_2O)_4]\cdot 10H_2O$	d	1D	1D	complex **3**
$[\{[Cu_2(pzdc)_2(dpyg)]\cdot 8H_2O\}_n]$	e	2D	3D	[9]
$Cd_2(pzdc)_2(4,4'\text{-bpy})(H_2O)_2$	e	1D	2D	complex **2**
$\{[Cd(pzdc)(azpy)]\cdot 2H_2O\}_n$	f	3D	3D	[10]
$[Ag_2(pzdc)(H_2O)]$	g	3D	3D	[12]
$[Ag_2(pzdc)]$	h	3D	3D	[12]
$[NH_4][Ag(pzdc)]$	i	2D	2D	[13]
$[Ag_2(pzdc)(NH_3)]_{2n}$	j	2D	2D	[14]

[a] The coordination models are shown in Scheme 2.

Table 4
Selected interatomic lengths (Å) and angles (°) for complex **2**

Cd(1)–O(1)	2.293(3)	Cd(1)–O(1W)	2.303(3)	Cd(1)–O(4A)	2.312(3)
Cd(1)–O(4B)	2.339(3)	Cd(1)–N(3)	2.358(3)	Cd(1)–N(1)	2.378(3)
O(1W)···O(1C)	2.966(4)	O(1W)···O(2A)	2.916(5)	O(1W)···O(2C)	3.048(4)
O(1)–Cd(1)–O(4A)	161.5(1)		O(1)–Cd(1)–N(1)	70.6(1)	
O(1)–Cd(1)–O(4B)	107.8(1)		O(1)–Cd(1)–N(3)	82.3(1)	
O(1)–Cd(1)–O(1W)	94.9(1)		O(4A)–Cd(1)–N(1)	90.9(1)	
O(4A)–Cd(1)–O(4B)	72.3(1)		O(4A)–Cd(1)–N(3)	116.1(1)	
O(4A)–Cd(1)–O(1W)	88.3(1)		N(1)–Cd(1)–O(4B)	92.5(1)	
N(1)–Cd(1)–N(3)	152.6(1)		N(1)–Cd(1)–O(1W)	101.3(1)	
O(4B)–Cd(1)–N(3)	91.7(1)		O(4B)–Cd(1)–O(1W)	156.4(1)	
N(3)–Cd(1)–O(1W)	84.9(1)		O(1W)–H(01B)···O(1C)	138.42	
O(1W)–H(01A)···O(2A)	138.64		O(1W)–H(01B)···O(2C)	157.44	

Symmetry codes. A: x, $y+1$, z; B: $-x$, $-y$, $-z$; C: $-x+1/2$, $-z+1/2$.

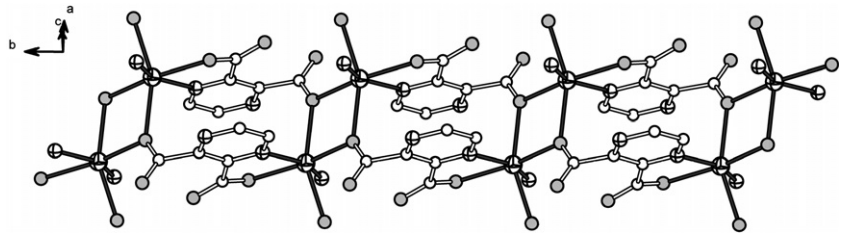


Fig. 5. View of the 1D double chain formed by Cd(II) ions and 2,3-pzdc ligands in complex **2**. All the H atoms are omitted for clarity.

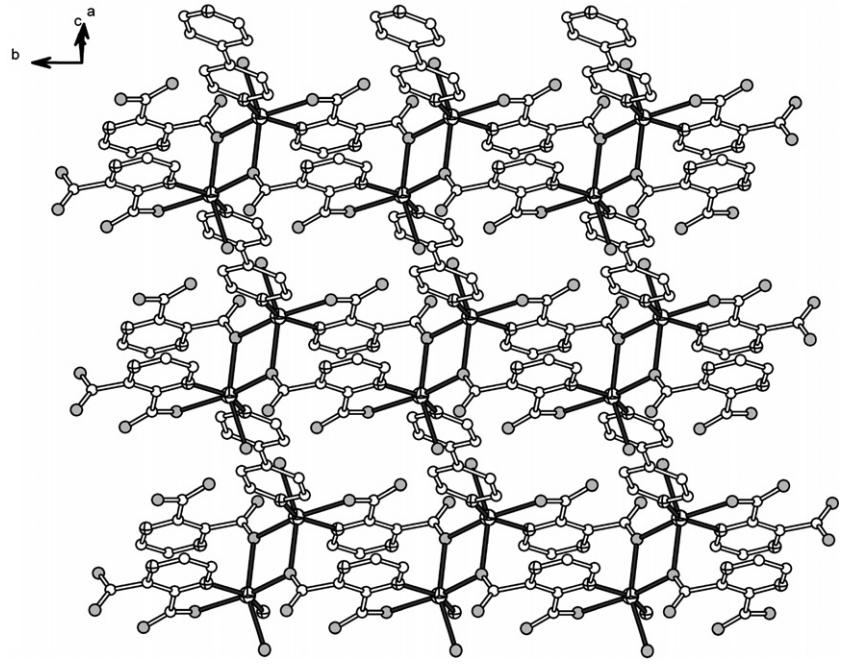


Fig. 6. The 2D covalent pleated sheet of complex **2** with hydrogen atoms omitted for clarity.

of porous coordination polymers $\{[Cu_2(pzdc)_2(bpy)]\cdot G\}$ (where G are H_2O and benzene) [16]. An important structural phenomenon for the two complexes is that there is the existence of a pore structure in $\{[Cu_2(pzdc)_2(bpy)]\cdot G\}$ and the non-existence of a pore structure in $Cd_2(pzdc)_2(4,4'\text{-bpy})(H_2O)_2$, although the two complexes have the same 4,4′-bpy ligand. One of the reasons of this important structural phenomenon is the following structural fact. The coordination configuration of the metal atom and the coordination mode of the pzdc ligand in $\{[Cu_2(pzdc)_2(bpy)]\cdot G\}$ are quite different from that in the title complex $Cd_2(pzdc)_2(4,4'\text{-bpy})(H_2O)_2$ (**2**).

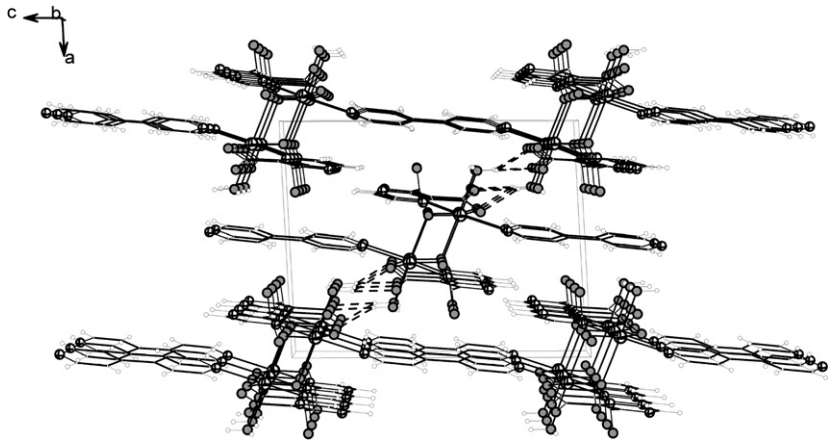


Fig. 7. The extended 3D network of complex **2** interconnected by hydrogen bonds between the layers.

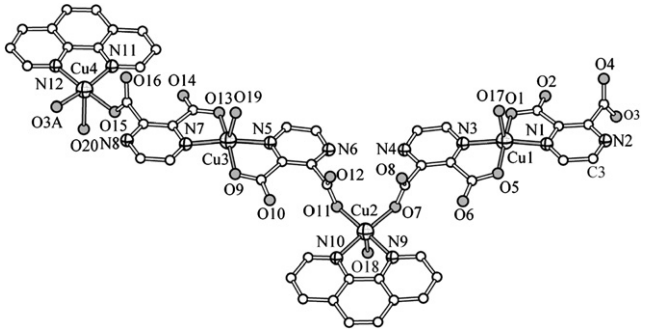


Fig. 8. Molecular structure of complex **3** with hydrogen atoms omitted for clarity.

3.1.3. $[Cu_4(pzdc)_4(phen)_2(H_2O)_4]\cdot 10H_2O$ (**3**)

As illustrated in Fig. 8 and Table 5, there are four crystallographically independent Cu centers in complex **3**. The four copper atoms in **3** have a distorted square-pyramidal geometry with CuN_2O_3 coordination, but all 1,10'-phen ligands are coordinated to Cu2 and Cu4 atoms only, not to Cu1 and Cu3 atoms. The Cu1 and Cu3 atoms are coordinated by two oxygen atoms and two nitrogen atoms from two pzdc ligands and one water oxygen atom. However, Cu2 and Cu4 atoms are coordinated by two oxygen atoms of two pzdc ligands, two nitrogen atoms of one terminal 1,10'-phen ligand and one water oxygen atom. The τ values

Table 5
Selected interatomic lengths (Å) and angles (°) for complex **3**

Cu(1)–O(5)	1.942(3)	Cu(1)–O(1)	1.947(3)	Cu(1)–N(3)	1.983(3)
Cu(1)–N(1)	1.983(3)	Cu(1)–O(17)	2.199(4)	Cu(2)–O(7)	1.937(3)
Cu(2)–O(11)	1.938(3)	Cu(2)–N(9)	1.995(3)	Cu(2)–N(10)	2.013(3)
Cu(2)–O(18)	2.300(3)	Cu(3)–O(13)	1.934(3)	Cu(3)–O(9)	1.938(3)
Cu(3)–N(7)	1.998(3)	Cu(3)–N(5)	2.006(3)	Cu(3)–O(19)	2.182(4)
Cu(4)–O(3A)	1.954(3)	Cu(4)–O(15)	1.975(3)	Cu(4)–N(12)	2.017(3)
Cu(4)–N(11)	2.033(3)	Cu(4)–O(20)	2.284(3)	O(19)···O(21)	2.684
O(5)–Cu(1)–O(1)	168.4(1)		O(5)–Cu(1)–N(3)	83.4(1)	
O(1)–Cu(1)–N(3)	94.6(1)		O(5)–Cu(1)–N(1)	96.5(1)	
O(1)–Cu(1)–N(1)	82.9(1)		N(3)–Cu(1)–N(1)	166.7(1)	
O(5)–Cu(1)–O(17)	92.0(1)		O(1)–Cu(1)–O(17)	99.5(1)	
N(3)–Cu(1)–O(17)	92.9(1)		N(1)–Cu(1)–O(17)	100.4(1)	
O(7)–Cu(2)–O(11)	90.0(1)		O(7)–Cu(2)–N(9)	93.7(1)	
O(11)–Cu(2)–N(9)	174.7(1)		O(7)–Cu(2)–N(10)	175.4(1)	
O(11)–Cu(2)–N(10)	94.1(1)		N(9)–Cu(2)–N(10)	82.1(1)	
O(7)–Cu(2)–O(18)	84.6(1)		O(11)–Cu(2)–O(18)	86.0(1)	
N(9)–Cu(2)–O(18)	98.1(1)		N(10)–Cu(2)–O(18)	97.9(1)	
O(13)–Cu(3)–O(9)	167.6(2)		O(13)–Cu(3)–N(7)	82.8(1)	
O(9)–Cu(3)–N(7)	94.2(1)		O(13)–Cu(3)–N(5)	97.8(1)	
O(9)–Cu(3)–N(5)	83.0(1)		N(7)–Cu(3)–N(5)	169.5(2)	
O(13)–Cu(3)–O(19)	101.0(2)		O(9)–Cu(3)–O(19)	91.3(1)	
N(7)–Cu(3)–O(19)	99.9(1)		N(5)–Cu(3)–O(19)	90.3(1)	
O(3A)–Cu(4)–O(15)	89.3(1)		O(3A)–Cu(4)–N(12)	94.7(1)	
O(15)–Cu(4)–N(12)	176.0(1)		O(3A)–Cu(4)–N(11)	171.3(1)	
O(15)–Cu(4)–N(11)	94.3(1)		N(12)–Cu(4)–N(11)	81.8(1)	
O(3A)–Cu(4)–O(20)	91.7(1)		O(15)–Cu(4)–O(20)	82.0(1)	
N(12)–Cu(4)–O(20)	98.1(1)		N(11)–Cu(4)–O(20)	96.6(1)	
O(19)–H(19A)···O(21)	161.04				

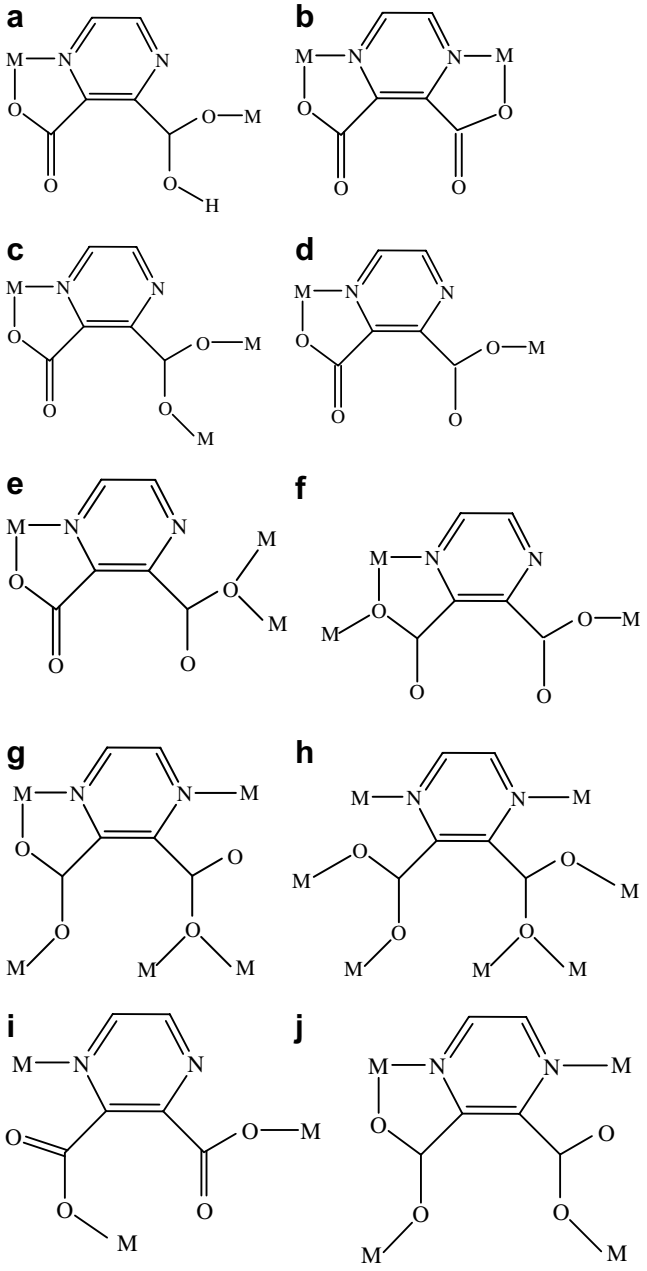
Symmetry codes. A: $x, y, z+1$.

of the pentacoordinated polyhedra are 0.03, 0.01, 0.03 and 0.08 for Cu1, Cu2, Cu3 and Cu4 atoms, respectively [26]. In the basal plane, the Cu–O and Cu–N bond distances are from 1.934(3) to 1.975(3) Å and from 1.983(3) to 2.033(3) Å, respectively. The Cu–O(water) bond distances in the axial position are in the range 2.182(4)–2.300(3) Å. These Cu–N and Cu–O bond distances are similar to the corresponding ones in known copper complexes [5].

Every pzdc ligand is coordinated to two neighboring copper atoms through its two carboxyl oxygen atoms and one nitrogen atom, i.e. the pzdc ligand adopts a chelate interaction to one copper atom and bonding through a single carboxylate oxygen to the other copper atom. Therefore, neighboring tetranuclear copper complex molecules are combined together by the bridging pzdc ligands to form a 1D covalently bonded chain along the *c*-axis (Fig. 9). The adjacent Cu–Cu distances are 7.936, 7.910, 7.990 and 7.943 Å.

3.1.4. The influence of the coordination modes of the pzdc ligand on the dimensions of the polymer

As shown in Scheme 2 and Table 3, there are 10 kinds of coordination modes of the six donor atoms of the pzdc ligand in known complexes and the three title complexes. The structures constructed between the pzdc ligands and the metal atoms for some coordination modes of the pzdc ligand are 1D and 2D. For example, supermolecular 1D and 2D structures are observed with coordination mode c. The type of the second ligand, such as 4,4′-bipy and dpyg, sometimes may increase the superstructural diversity. For example, the dimensions in the crystal structures increase from 1D to 2D and from 2D to 3D in the title complex **2** and the complex reported in reference [9], respectively. But for some other kinds of second ligand, its existence does not affect the dimensions of the crystal structure. Therefore, the selection of the second ligand plays an important role in the design of supermolecular structures.



Scheme 2. Coordination modes of 2,3-pyrazinedicarboxylic acid.

3.2. Elemental analysis and TGA measurement

The elemental analysis data for complexes **1**, **2** and **3** are consistent with the formulas $[Cd(pzdc)(phen)]\cdot H_2O$ (**1**), $Cd_2(pzdc)_2(4,4'\text{-bpy})(H_2O)_2$ (**2**) and $[Cu_4(pzdc)_4(phen)_2(H_2O)_4]\cdot 10H_2O$ (**3**). The TGA data of complex **1** indicate two obvious weight losses as shown in Fig. S2. The first weight loss starts at ca. 70–130 °C to give a total weight loss of 3.84%, corresponding to the loss of one guest H_2O molecule per formula unit. Then at ca. 300 °C

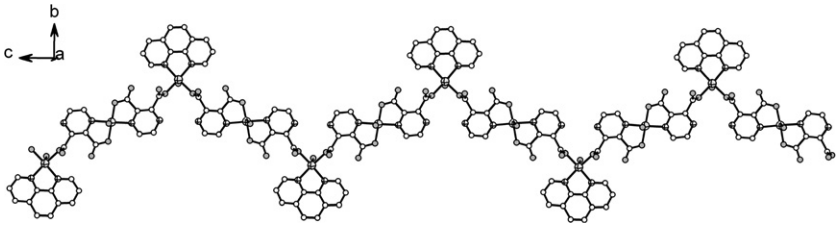


Fig. 9. 1D zigzag chain of complex **3** with hydrogen atoms omitted for clarity.

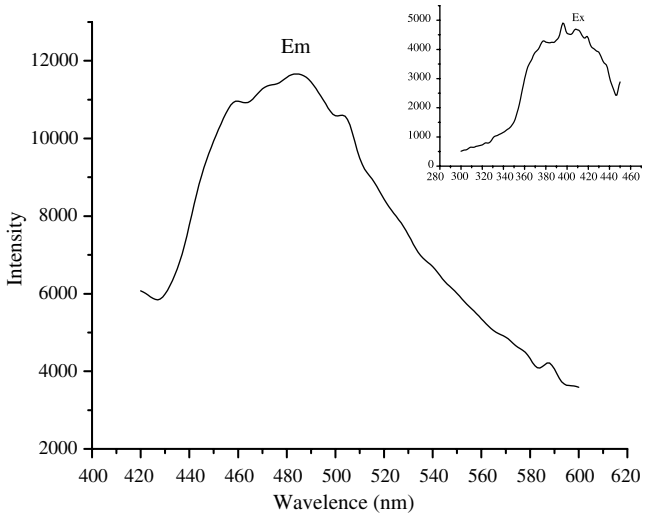


Fig. 10. Solid-state emission spectra of complex **1** at room temperature.

complex **1** undergoes degradation in essentially one step. Thermogravimetric analysis data of **3** shows three obvious weight losses (Fig. S3) starting at ca. 50–80 °C and 80–120 °C to give a total loss of 3.49% and 8.04%, corresponding to the loss of $10H_2O$ molecules per formula unit. At ca. 150 °C a total loss of 4.42% corresponds to the loss of $4H_2O$ molecules per formula unit, then at ca. 200 °C it undergoes degradation in essentially one step, which indicates that complex **3** is unstable. A similar behavior has been observed in several 2,3-pyrazinedicarboxylate complexes of the first transition series [6], which are all found to decompose into the corresponding metal oxides.

3.3. Spectroscopy and luminescent properties

The luminescent properties of the free ligand 2,3-pyrazinedicarboxylic acid, complex **1** and complex **2** were investigated in the solid state at room temperature. No luminescent properties were found for the free ligand, 2,3-pyrazinedicarboxylic acid. However, complex **1** gives an intense broad emission band from 440 nm to 550 nm with the maximum at 484 nm upon excitation at 396 nm, as shown in Fig. 10, and complex **2** gives an intense broad emission band from 470 nm to 650 nm with the maximum at 567 nm upon excitation at 400 nm, as shown in Fig. 11. The emission may be assigned to the ligand-to-metal-charge-transfer bands (LMCT).

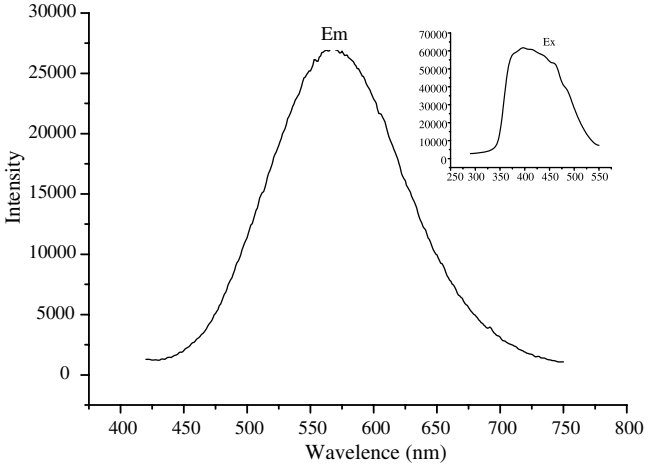


Fig. 11. Solid-state emission spectra of complex **2** at room temperature.

3.4. Magnetic study of complex 3

The EPR spectrum of complex **3** was measured at room temperature and is typical for a square-pyramidal geometry of the copper (II) ions, $g_{\parallel} = 2.43$ and $g_{\perp} = 2.10$ (average $g = 2.15$, in agreement to the value obtained by the susceptibility fit) according to the EPR measurements as shown in Fig. S4.

Acknowledgements

This Project was financially supported by the Natural Science Foundation of China (Nos. 20431010 and 20171012), the Natural Science Foundation of Fujian Province, China (E0110010), and the Spanish Government (Grant BQU2003/00539).

Appendix A. Supplementary material

CCDC 624413, 624414, 624415 contain the supplementary crystallographic data for **1**, **2** and **3**. These data can be obtained free of charge via http://www.ccdc.ac.uk/conts/retrieving.html, or from the Cambridge Crystallographic Data Centre, 12 Union Road, Cambridge CB2 1EZ, UK; fax: (+44) 1223-336-033; or e-mail: deposit@ccdc.cam.ac.uk. Supplementary data associated with this article can be found, in the online version, at doi:10.1016/j.poly.2007.02.011.

References

[1] O.M. Yaghi, H. Li, C. Davis, D. Richardson, T.L. Groy, Acc. Chem. Res. 31 (1998) 474.
[2] P.J. Hagrman, D. Hagrman, J. Zubieta, Angew. Chem., Int. Ed. 38 (1999) 2638.
[3] B. Moulton, M.J. Zaworotko, Chem. Rev. 101 (2001) 1629.
[4] B.O. Patrick, C.L. Stevens, A. Storr, R.C. Thompson, Polyhedron 22 (2003) 3025.
[5] C.J. O'connor, C.L. Klein, R.J. Majeste, L.M. Trefonas, Inorg. Chem. 21 (1982) 64.
[6] L. Mao, S.J. Rettig, R.C. Thompson, J. Trotter, S.-H. Xia, Can. J. Chem. 74 (1996) 2413.
[7] X.-H. Li, Q. Shi, M.-L. Hu, H.-P. Xiao, Inorg. Chem. Commun. 7 (2004) 912.
[8] J.-Z. Zou, Z. Xu, W. Chen, K.M. Lo, X.-Z. You, Polyhedron 18 (1999) 1507.
[9] R. Kitaura, K. Fujimoto, S.-i. Noro, M. Kondo, S. Kitagawa, Angew. Chem., Int. Ed. 41 (2002) 133.
[10] T.K. Maji, K. Uemura, H.-C. Chang, R. Matsuda, S. Kitagawa, Angew. Chem., Int. Ed. 43 (2004) 3269.
[11] M. Kondo, T. Okubo, A. Asami, S.-i. Noro, T. Yoshitomi, S. Kitagawa, T. Ishii, H. Matsuzaka, K. Seki, Angew. Chem., Int. Ed. 38 (1999) 140.

[12] J.-H. Yang, S.-L. Zheng, X.-L. Yu, X.-M. Chen, Cryst. Growth Design 4 (2004) 831.
[13] G. Smith, A.N. Reddy, K.A. Byriel, C.H.L. Kennard, J. Chem. Soc., Dalton Trans. (1995) 3565.
[14] F. Jaber, F. Charbonnier, R. Faure, J. Chem. Cryst. 24 (1994) 681.
[15] B.-S. Zhang, Chin. J. Struct. Chem. 24 (2005) 478.
[16] R. Matsuda, R. Kitaura, S. Kitagawa, Y. Kubota, T.C. Kobayashi, S. Horike, M. Takata, J. Am. Chem. Soc. 126 (2004) 14063.
[17] J.Y. Lu, Z.-H. Ge, Inorg. Chim. Acta 358 (2005) 828.
[18] C.-F. Wang, E.-Q. Gao, Z. He, C.-H. Yan, Chem. Commun. (2004) 720.
[19] R. Cao, Q. Shi, D.-F. Sun, M.-C. Hong, W.-H. Bi, Y.-J. Zhao, Inorg. Chem. 41 (2002) 6161.
[20] J.-X. Chen, S.-X. Liu, E.-Q. Gao, Polyhedron 23 (2004) 1877.
[21] R.-Q. Zou, X.-H. Bu, R.-H. Zhang, Inorg. Chem. 43 (2004) 5382.
[22] Y.-F. Zeng, F.-C. Liu, J.-P. Zhao, S. Cai, X.-H. Bu, J. Ribas, Chem. Commun. (2006) 2227.
[23] G.M. Sheldrick, SHELXS-97: Program for X-ray Crystal Structure Solution, University of Göttingen, Göttingen, Germany, 1997.
[24] G.M. Sheldrick, SHELXS-97: Program for X-ray Crystal Structure Refinement, University of Göttingen, Göttingen, Germany, 1997.
[25] D.-L. Long, A.J. Blake, N.R. Champness, M. Schröder, Chem. Commun. (2000) 1369.
[26] A.W. Addison, T.N. Rao, J. Reedjik, J. van Rijn, C.G. Verschoor, J. Chem. Soc., Dalton Trans. (1984) 1349.

Available online at www.sciencedirect.com
ScienceDirect
Polyhedron 26 (2007) 3112–3120
POLYHEDRON
www.elsevier.com/locate/poly

Nickel(II) and zinc(II) complexes with *N*-(5,6-dihydro-4H-1,3-thiazin-2-yl)-2-aminobenzimidazole (BzTz): Synthesis, spectral and structural characterization

M.A. Maldonado-Rogado, E. Viñuelas-Zahínos, F. Luna-Giles, A. Bernalte-García *

Departamento de Química Orgánica e Inorgánica, Facultad de Ciencias, Universidad de Extremadura, 06071 Badajoz, Spain

Received 19 January 2007; accepted 14 February 2007
Available online 24 February 2007

Abstract

The reaction of nickel and zinc chlorides and nitrates with the ligand *N*-(5,6-dihydro-4H-1,3-thiazin-2-yl)-2-aminobenzimidazole (BzTz) leads to the formation of the new complexes: $[NiCl_2(BzTz)_2]$ (**1**), $[Ni(NO_3)(BzTz)_2(H_2O)_3](NO_3)$ (**2**), $[ZnCl_2(BzTz)_2]$ (**3**) and $[Zn(NO_3)_2(BzTz)_2]$ (**4**). They have been characterized by spectroscopic methods (electronic, infrared and NMR) and magnetic susceptibility measurements. Additionally, the crystal structures of the complexes **1** and **3** have been determined by X-ray single-crystal diffraction. The ligand exhibits the *N*-benzimidazole coordination mode on interacting with the metal centers. The X-ray structure of the complexes **1** and **3** reveals a distorted tetrahedral coordination geometry around the metal center, with the metallic atoms coordinated to two chlorine atoms and two benzimidazole nitrogen atoms. These two complexes are isostructural, crystallizing in the monoclinic system and *Cc* space group. In complex **2** the geometry around the nickel atom could be described as a distorted octahedron whereas in case of complex **4** the zinc atom is in a distorted tetrahedral environment.
© 2007 Elsevier Ltd. All rights reserved.

Keywords: Nickel(II) complexes; Zinc(II) complexes; Crystal structures; Spectral characterization; Thiazine; 2-Aminobenzimidazole

1. Introduction

Transition metal complexes with N-donor ligands are studied not only because of their interesting magnetic and spectral properties but also for their use as corrosion inhibitors for metals and alloys and for applications in the pharmaceutical industry for their potential antibacterial, antiviral and antitumor effects [1–3]. Moreover, metal complexes of biologically important ligands are sometimes more effective than the free ligand [1].

In this way, *N*-(5,6-dihydro-4H-1,3-thiazin-2-yl)-2-aminobenzimidazole (BzTz) is an organic compound containing important biological heterocycles that possesses potentially four nitrogen and one sulfur donor atom that can be coordinated to the central atoms in different coordination modes.

Thus, the benzimidazole moiety is structurally related to purina bases and is found in a variety of naturally occurring compounds, such as vitamin B_{12}. Benzimidazole derivatives exhibit a wide variety of pharmacological properties including antitumor activity [4] and inhibition of nucleic acid synthesis [5]. Transition metal complexes with 2-substituted benzimidazole ligands act as cytotoxic [6,7], antiviral [7] and antiamoebic agents [8].

Likewise, thiazine derivatives have also been reported as well known useful therapeutic agents [9–12] and have shown anticancer, antihistaminic, antibacterial, antidiabetic, anti-inflammatory and analgesic activities [13–21].

With regard to the different coordination modes of the BzTz ligand, we have previously reported [22] the characterization of this ligand and its cobalt(II) and cadmium(II)

* Corresponding author.
E-mail address: alberga@unex.es (A. Bernalte-García).

0277-5387/$ - see front matter © 2007 Elsevier Ltd. All rights reserved.
doi:10.1016/j.poly.2007.02.016

complexes in which BzTz behaves as a monodentate ligand through the nitrogen atom of the benzimidazole ring. We now report the synthesis of four new nickel(II) and zinc(II) complexes with BzTz and their characterization by means of elemental and thermal analyses, IR, UV–Vis–NIR spectra, magnetic susceptibility measurements, proton and carbon nuclear magnetic resonance (^{1}H NMR and ^{13}C NMR) and moreover, in the cases of $[NiCl_2(BzTz)_2]$ (**1**) and $[ZnCl_2(BzTz)_2]$ (**3**) by X-ray diffraction. The evidence from these spectral and structural data suggests that in these new metal complexes, coordination through the *N*-benzimidazole is also observed.

2. Experimental

2.1. Preparation of *N*-(5,6-dihydro-4H-1,3-thiazin-2-yl)-2-aminobenzimidazole (BzTz)

The ligand was prepared by the reaction of 2-aminobenzimidazole and 3-chloropropylisothiocyanate in dry glyme following a previously described method [22,23]. ^{1}H NMR (DMSO): δ 7.48 (d, $J = 7.6$ Hz, 1H), 7.16 (d, $J = 7.6$ Hz, 1H), 7.02 (t, $J = 7.2$ Hz, 1H), 6.91 (t, $J = 7.6$ Hz, 1H), 6.80 (s, 2H), 3.88 (t, $J = 5.4$ Hz, 2H), 3.30 (t, $J = 6.0$ Hz, 2H), 1.92 (m, 2H); ^{13}C NMR (DMSO): δ 153.3, 145.8, 142.9, 131.8, 122.3, 118.9, 115.5, 110.8, 46.9, 26.9, 19.0. *Anal*. Calc. for $C_{11}H_{12}N_4S$: C, 56.87; H, 5.21; N, 24.12; S, 13.80. Found: C, 56.72; H, 5.24; N, 23.83; S, 14.05%. UV–Vis (EtOH): λ_{max}, nm; (ε, L mol^{-1} cm^{-1}) 208 (40210), 244 (22370), 279 (6755) [22].

2.2. Preparation of $[NiCl_2(BzTz)_2]$ (1)

$NiCl_2 \cdot 6H_2O$ (102 mg, 0.43 mmol) dissolved in methanol (1 mL) was added to a methanol solution (15 mL) of BzTz (100 mg, 0.43 mmol). The resulting dissolution was surrounded with ether using a liquid–vapour diffusion method to obtain blue crystals (80.7 mg, 31.6%). The crystals were filtrated, washed with cold ether and finally air-dried. *Anal*. Calc. for $C_{22}H_{24}Cl_2NiN_8S_2$: C, 44.51; H, 4.07; N, 18.88; S, 10.80. Found: C, 44.33; H, 4.32; N, 18.49; S, 10.51%.

2.3. Preparation of $[Ni(NO_3)(BzTz)_2(H_2O)_3](NO_3)$ (2)

This complex was prepared by reacting a methanol solution (1 mL) of $Ni(NO_3)_2 \cdot 6\,H_2O$ (125 mg, 0.43 mmol) with a methanol solution (15 mL) of BzTz (100 mg, 0.43 mmol). The blue precipitate (93.2 mg, 30.9%) that was obtained was filtered, washed with cold ether and air-dried several times. *Anal*. Calc. for $C_{22}H_{24}NiN_{10}O_6S_2 \cdot 3H_2O$: C, 37.78; H, 4.33; N, 20.02; S, 9.17. Found: C, 38.10; H, 4.12; N, 19.87; S, 9.07%.

2.4. Preparation of $[ZnCl_2(BzTz)_2]$ (3)

This complex was prepared by reacting a methanol solution (1 mL) of $ZnCl_2$ (59 mg, 0.43 mmol) with a methanol solution (15 mL) of BzTz (100 mg, 0.43 mmol), giving colourless crystals after slow evaporation of the solution at room temperature (87.0 mg, 67.3%). The crystals were filtrated and washed with cold ether and finally air-dried. ^{1}H NMR (DMSO): δ 7.51 (d, $J = 7.6$ Hz, 1H), 7.39 (s, 2H), 7.35 (d, $J = 7.6$ Hz, 1H), 7.09 (t, $J = 7.6$ Hz, 1H), 7.03 (t, $J = 7.8$ Hz, 1H), 3.91 (t, $J = 5.6$ Hz, 2H), 3.32 (t, $J = 5.8$ Hz, 2H), 1.94 (m, 2H); ^{13}C NMR (DMSO): δ 153.3, 144.8, 138.9, 130.7, 123.1, 120.8, 114.9, 111.0, 47.2, 27.0, 18.7. *Anal*. Calc. for $C_{22}H_{24}Cl_2ZnN_8S_2$: C, 43.97; H, 4.03; N, 18.65; S, 10.67. Found: C, 43.74; H, 4.18; N, 18.36; S, 10.29%. UV–Vis (EtOH): λ_{max}, nm; (ε, L mol^{-1} cm^{-1}) 208 (39618), 243 (22886), 280 (7387).

2.5. Preparation of $[Zn(NO_3)_2(BzTz)_2]$ (4)

$Zn(NO_3)_2 \cdot 6H_2O$ (128 mg, 0.43 mmol) was dissolved in methanol (1 mL) and added to a solution of BzTz (100 mg, 0.43 mmol) in methanol (15 mL). A colourless powder (106 mg, 36.2%) was obtained, which was filtered and washed with cold ether and air-dried several times. ^{1}H NMR (DMSO): δ 7.48 (d, $J = 8.0$ Hz, 1H), 7.21 (d, $J = 7.6$ Hz, 1H), 7.05 (t, $J = 7.6$ Hz, 1H), 6.94 (t, $J = 7.7$ Hz, 1H), 6.90 (s, 2H), 3.89 (t, $J = 5.6$ Hz, 2H), 3.30 (t, $J = 5.8$ Hz, 2H), 1.92 (m, 2H); ^{13}C NMR (DMSO): δ 153.3, 145.5, 141.7, 131.5, 122.5, 119.5, 115.7, 111.0, 47.0, 27.0, 18.9. *Anal*. Calc. for $C_{22}H_{25}ZnN_{10}O_6S_2 \cdot 1.5H_2O$: C, 38.80; H, 4.00; N, 20.56; S, 9.41. Found: C, 38.97; H, 3.67; N, 20.87; S, 9.28%. UV–Vis (EtOH): λ_{max}, nm; (ε, L mol^{-1} cm^{-1}) 207 (102005), 243 (43295), 281 (13831).

2.6. Instrumental procedures

The carbon, hydrogen, nitrogen and sulfur contents of the compounds were determined on a Leco CHNS-932 microanalyser. IR spectra were recorded on a Perkin–Elmer FT-IR 1720 spectrophotometer, from KBr pellets in the 4000–370 cm^{-1} range and on a Perkin–Elmer FT-IR 1700X spectrophotometer, from polyethylene pellets in the 500–150 cm^{-1} range. Solution electronic spectra of the ligand and the zinc complexes were measured on a Shimadzu UV-3101 PC using a 10 mm quartz cell. Solid state electronic spectra for the nickel complexes in the 200–1200 nm range were obtained from pellets of the samples, using a Shimadzu UV-3101 PC spectrophotometer and $BaSO_4$ as a reference. Magnetic susceptibility measurements were performed on polycrystalline samples using a magnetometer with a pendulum MANICS DSM8, equipped with a helium continuous-flow cryostat and an electromagnetometer DRUSCH EAF 16 UE. Data were corrected for temperature independent paramagnetism and diamagnetic contributions, which were estimated from the Pascal constants. ^{1}H (400 MHz) and ^{13}C NMR (100 MHz) spectra were recorded in DMSO on a Bruker AM 400 instrument using Me_4Si as a reference. A thermal study was carried out on a Mettler TA-3000 system, provided with a Mettler TG-50 thermobalance. The TG curve

Table 1
Crystal data, data collection and refinement details for **1** and **3**

	1	**3**
Crystal shape	prism	prism
Colour	blue	colourless
Size (mm)	$0.38 \times 0.36 \times 0.16$	$0.64 \times 0.46 \times 0.28$
Chemical formula	$C_{22}H_{24}Cl_2N_8NiS_2$	$C_{22}H_{24}Cl_2N_8ZnS_2$
Formula weight	594.2	600.9
Crystal system	monoclinic	monoclinic
Space group	*Cc*	*Cc*
Unit cell dimensions		
a (Å)	11.547(1)	11.595(2)
b (Å)	18.023(1)	18.119(2)
c (Å)	12.591(1)	12.644(1)
β (°)	103.968(4)	104.678(2)
Cell volume (Å^3)	2542.9(2)	2569.8(5)
Z	4	4
D_{calc} (g cm^{-3})	1.552	1.553
μ (mm^{-1})	4.807	4.995
$F(000)$	1224	1232
θ Range (°)	4.7–74.8	4.6–74.8
Index ranges	$-14 \leqslant h \leqslant 14$, $0 \leqslant k \leqslant 22$, $0 \leqslant l \leqslant 15$	$-12 \leqslant h \leqslant 14$, $-12 \leqslant k \leqslant 22$, $-15 \leqslant l \leqslant 15$
Independent reflections	2739	4428
Observed reflections $[F > 4.0\sigma(F)]$	2639	4390
Data completeness	0.998	0.992
Maximum/minimum transmission	0.203/0.462	0.105/0.248
Number of refined parameters	311	315
R $[F > 4.0\sigma(F)]$[a]	0.082	0.056
wR $[F > 4.0\ \sigma(F)]$[b]	0.209	0.152
GOF [c]	1.06	1.045
$\rho_{maximum}$, $\rho_{minimum}$ (e Å^{-3})	2.205/−0.945	1.825/−0.852

[a] $R = \sum \| F_o| - |F_c| \| / \sum — F_o|$.

[b] $R = \left\{ \sum \left[w\left(F_o^2 - F_c^2\right)^2 \right] / \sum \left[w\left(F_o^2\right)^2 \right] \right\}^{1/2}$.

[c] The goodness-of-fit (GOF) equals $\left\{ \sum \left[w\left(F_o^2 - F_c^2\right)^2 \right] / (N_{reflections} - N_{parameters}) \right\}^{1/2}$.

was obtained on heating a sample of the solid in a dynamic pure air atmosphere (200 mL min^{-1}) in the 30–200 °C temperature range with a heating rate of 10 °C min^{-1} and samples varying in weight from 9 to 15 mg.

2.7. Crystal structure determinations

The single crystals of **1** and **3** of suitable size were mounted in an Enraf Nonius CAD4 diffractometer equipped with graphite-monochromated Cu Kα radiation ($\lambda = 1.5418$ Å) and the intensity data were collected using the ω–2θ scan technique. Semiempirical absorption corrections were made based on psi-scan application using the WINGX [24] package. The structures were solved by direct methods and subsequent Fourier differences using the SHELXS-97 [25] program included in WINGX package [24] and refined by full-matrix least-squares on F^2 with the SHELXL-97 program [26]. All non-hydrogen atoms were refined with anisotropic displacement parameters, except atoms involved in disorder which were refined with isotropic displacement parameters. In the structure of the nickel complex, the two thiazine rings show a dynamic disorder affecting the C(2), C(2A), C(3), C(3A), N(1), N(1A), C(14) and C(14A) atoms. In the first ring, the value of the refined occupancies are 0.45(2) for C(2), C(3) and N(1), and 0.55(2) for C(2A), C(3A) and N(1A). Likewise, in the second one the occupancies are 0.52(2) for C(14) and 0.48(2) for C(14A). In the structure of the zinc complex, the two thiazine rings show a dynamic disorder affecting the C(3), C(3A), N(5), N(5A), C(13) and C(13A) atoms, the value of the refined occupancies being 0.58(3) for C(3), 0.42(3) for C(3A), 0.64(2) for N(5) and C(13), and 0.36(2) for N(5A) and C(13A). Hydrogen atoms attached to carbon and nitrogen atoms were positioned geometrically, with U_{iso} values derived from U_{eq} values of the corresponding carbon and nitrogen atoms. Details of the crystal parameters, data collection, structure determinations and refinement parameters for **1** and **3** are listed in Table 1.

3. Results and discussion

3.1. Thermal study

Since the elemental analyses of complexes **2** and **4** indicate that these compounds are hydrated, thermogravimetric dehydration studies has been performed in the 30–200 °C temperature range to determinate the nature of the water molecules involved in these complexes. TG–DTG curves for **2** and **4** are shown in Figs. 1 and 2, respectively.

The TG–DTG curve of **2** displays between 44 °C and 162 °C a first effect centered at 127 °C, that can be assigned to 2.7 waters molecules per mol of complex, with an associated mass loss of 6.87% of the initial sample ($-\Delta_{m\ exp} = 6.95\%$). This behaviour, in agreement with the IR data, suggests that this effect could be attributed to coordinated water molecules [27]. Nevertheless, in the TG–DTG curve of **4**, no effect is observed in the region 30–200 °C, therefore water molecules detected by chemical

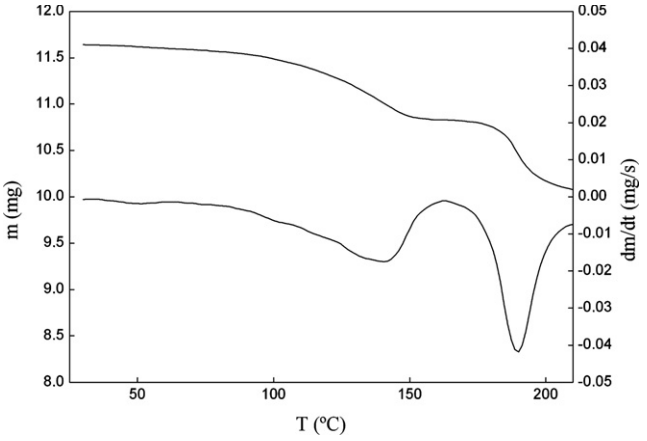


Fig. 1. TG–DTG curve for **2**.

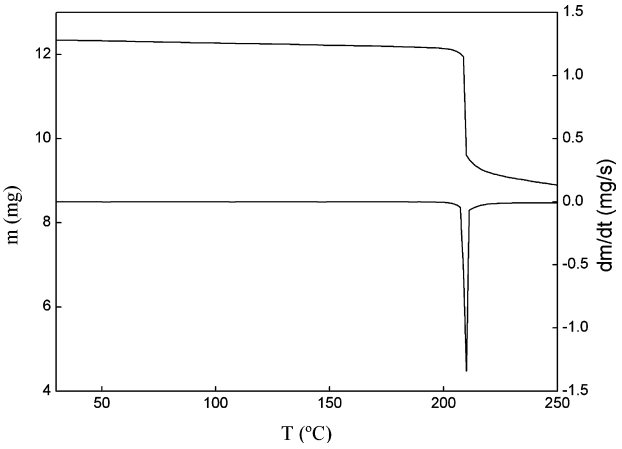


Fig. 2. TG–DTG curve for **4**.

analyses could be due to the humidity of sample, which do not form part of the compound.

3.2. Spectroscopic properties

The IR spectra of the complexes exhibit characteristic bands that emulate the features observed for the *N*-benzimidazole coordination mode in Co(II) and Cd(II) complexes with the BzTz ligand [22]. In general, for all complexes, the stretching vibrations of the benzimidazole ring are shifted to lower frequencies in relation to the free ligand, which is indicative of coordination through the benzimidazole nitrogen atom.

In addition, other bands due to nitrate ligands are registered at 727 and 700 cm^{-1} (ν_4), 1358 cm^{-1} (ν_3) and 1043 cm^{-1} (ν_1) for **2** and at 723, 713, 695 and 681 cm^{-1} (ν_4), 1385 cm^{-1} (ν_3), 820 cm^{-1} (ν_2) and 1021 and 1038 cm^{-1} (ν_1) for **4** [28]. It can be observed that there is splitting of the ν_4 band in both complexes, which suggests the presence of nitrate groups in some coordination mode. Likewise, the presence of bands at 1385, 1021 and 743 cm^{-1} for **2** indicates the existence of some nitrate groups.

Moreover, the IR spectra of complexes **2** and **4** were investigated to obtain evidence for ionic or coordinated nitrate groups, according to the method of Lever and coworkers [28–31]. The bands registered at 1770, 1749 and 1733 cm^{-1} for **2** are assigned to ($\nu_1 + \nu_4$) combination bands. The first one is assignable to combination band of an ionic nitrate group [28]. The splitting value ($\Delta = 16$ cm^{-1}) for the last two bands reveals the presence of one monodentate nitrate group, in agreement with Lever's criteria [28]. For **4**, the 1800–1700 cm^{-1} region only shows three bands at 1749 and 1733 cm^{-1} and at 1716 cm^{-1}, with a separation of 16 cm^{-1} for the first two bands and 17 cm^{-1} for the last two bands. These bands can be assigned to two monodentate nitrate groups [28].

These observations, together with those obtained by thermal and chemical analyses, have been further supported by the appearance of new bands at low frequencies, which can be assigned to M-ligand stretching vibration modes. Tentative assignments for the chloro complexes (**1**, **3**) and nitrate complexes (**2**, **4**) are listed in Table 2. The strong bands in the region 326–280 cm^{-1} are assigned to the ν(M–Cl) vibration [22,29,32–35] and the bands at 247–171 cm^{-1} can be tentatively attributed to ν(M–$N_{benzimidazole}$) vibrations [22,35,36]. In addition, the presence of a Ni–O_{water} bond in complex **3** is supported by the identification of a band due to ν(Ni–O_{water}) vibration at 300 cm^{-1} [37–39]. Finally, ν(M–ONO_2) vibrations [40–42] are registered in the spectra at 330–277 cm^{-1}.

Table 2
Far IR bands (cm^{-1}) with tentative assignments

Compound	ν(M–$N_{bencimidazole}$)	ν(M–Cl)	ν(M–O_{water})	ν(M–ONO_2)
1	247 m	326 s		
	226 m	280 s		
2	200 m		300 s	277 s
3	180 m	290 s		
	171 m	280 s		
4	203 m			330 m
	177 m			281 m

Abbreviations: (s) strong; (m) medium.

In the nickel(II) complex **1**, the electronic spectrum shows two intense bands at 380 nm (26 320 cm^{-1}) and 278 nm (35 970 cm^{-1}), which are assigned to a charge-transfer band and the $\pi \rightarrow \pi^*$ transitions of the organic ligand, respectively. Moreover, the spectrum exhibits an absorption band at 1008 nm (9920 cm^{-1}) with a shoulder at 822 nm (12 170 cm^{-1}) and an asymmetric band at 576 nm (17 360 cm^{-1}). These bands may be assigned to: $\nu_2[^3T_1(F) \rightarrow {}^3A_2(F)]$, $[^3T_1(F) \rightarrow {}^1E(G)]$ and $\nu_3[^3T_1(F) \rightarrow {}^3T_1(P)]$ transitions, respectively, in an idealized T_d symmetry. The position of the allowed d–d transitions permits the calculation of the ligand field parameters 10 Dq and *B*, using the following relationships [43]:

$$\nu_2[^3T_1(F) \rightarrow {}^3A_2(F)] = 1/2(30\ Dq - 15B) + 1/2[(10\ Dq + 15B)^2 - 12B \cdot 10\ Dq]^{1/2}$$

$$\nu_3[^3T_1(F) \rightarrow {}^3T_1(P)] = [(10\ Dq + 15B)^2 - 12B \cdot 10\ Dq]^{1/2}$$

The calculated values of the ligand field parameters 10 Dq = 5231 cm^{-1} and $B = 881$ cm^{-1} are consistent with those observed for several tetrahedral Ni(II) complexes [44].

The electronic spectrum of **2** shows a shape characteristic of octahedral complexes. The higher intensity band registered at 292 nm (34 250 cm^{-1}) can be assigned to the $\pi \rightarrow \pi^*$ transitions of the organic ligand. Also, the spectrum exhibits the presence of four absorption bands due to d–d transitions in an octahedral NiN_2O_4 crystal field [1020 nm (9800 cm^{-1}), 630 nm (15 870 cm^{-1}) with a shoulder at 802 nm (12 470 cm^{-1}) and a shoulder at 380 nm (26 320 cm^{-1})]. The four previous bands can be assigned to $\nu_1[^3A_{2g}(F) \rightarrow {}^3T_{2g}(F)]$, $[^3A_{2g}(F) \rightarrow {}^1E_g(D)]$, $\nu_2[^3A_{2g}(F) \rightarrow {}^3T_{1g}(F)]$ and $\nu_3[^3A_{2g}(F) \rightarrow {}^3T_{1g}(P)]$, respectively. We have calculated the value of 10 Dq and the Racah interelectronic repulsion parameters using the following relationships [43]:

$$\nu_1[^3A_{2g}(F)\rightarrow{}^3T_{2g}(F)] = 10\ Dq$$

$$\nu_2[^3A_{2g}(F)\rightarrow{}^3T_{1g}(F)] = (1/2)(15B + 30\ Dq) - (1/2)[(15B - 10\ Dq)^2 + 12B\cdot 10\ Dq]^{1/2}$$

$$\nu_3[^3A_{2g}(F)\rightarrow{}^3T_{1g}(P)] = (1/2)(15B + 30\ Dq) + 1/2[(15B - 10\ Dq)^2 + 12B\cdot 10\ Dq]^{1/2}$$

The calculated values of the ligand field parameters $10\ Dq = 9800\ cm^{-1}$ and $B = 853\ cm^{-1}$ are consistent with the presence of the chromophore group $[Ni^{II}N_2O_4]$ [44,45].

In the ^1H NMR spectrum of **3**, the downfield shift of H-7 (δ 7.16 ppm in BzTz; 7.35 in the complex) and NH_2 (δ 6.80 ppm in BzTz; 7.39 in the complex) suggests an $M–N_{benzimidazole}$ coordination [46]. The trends in the shifts in the carbon-13 spectrum are less straightforward. However, in the ^{13}C NMR spectrum of **3** the higher field shift of the C-5 signal (δ 142.9 ppm in BzTz; 138.9 in the complex) is likewise attributable to coordination through the benzimidazole nitrogen atom. This fact is supported by the X-ray diffraction structure of $[ZnCl_2(BzTz)_2]$. In the ^1H NMR and ^{13}C NMR spectra of **4**, the signals do not show the downfield shifts normally observed, which could suggest the total dissociation of the complex in dmso-d_6 [47].

3.3. Magnetic measurements

The molar magnetic susceptibility for complexes **1** and **2** were corrected for diamagnetism and temperature-independent paramagnetism to provide the fully corrected magnetic moment at room temperature ($\mu = 3.4$ BM for **1**; $\mu = 3.2$ BM for **2**). These results suggest a tetrahedral geometry for **1** and an octahedral geometry for **2** [45,48].

3.4. Crystal structures of the complexes *1* and *3*

The molecular structure of **1** is shown in Fig. 3 together with the atomic numbering scheme. Selected bond lengths, angels and hydrogen-bonds parameters are given in Table 3.

The structure of compound **1** consists of discrete neutral monomeric units in which the environment around the metallic atom may be described as a distorted tetrahedral geometry. This distorted tetrahedral geometry about the metal is completed by two chlorine atoms [Ni–Cl(1) = 2.245(2) Å; Ni–Cl(2) = 2.232(3) Å] and two benzimidazole nitrogen atoms from two BzTz ligands [Ni–N(3) = 1.998(6) Å; Ni–N(7) = 1.997(6) Å]. The Ni–Cl

Table 3
Selected bond lengths (Å), angles (°) and hydrogen-bond parameters for **1** and **3**

	1	**3**
M–Cl(1)	2.245(2)	2.234(2)
M–Cl(2)	2.232(3)	2.255(2)
M–N(3)	1.998(6)	2.039(4)
M–N(7)	1.997(6)	2.021(4)
N(3)–C(5)	1.313(10)	1.319(6)
N(7)–C(16)	1.323(9)	1.333(6)
N(3)–C(6)	1.390(10)	1.398(7)
N(7)–C(17)	1.414(8)	1.392(7)
Cl(1)–M–Cl(2)	120.7(1)	114.3(1)
Cl(1)–M–N(3)	110.1(2)	111.5(1)
Cl(1)–M–N(7)	107.3(2)	109.2(1)
Cl(2)–M–N(3)	107.9(2)	108.3(1)
Cl(2)–M–N(7)	109.7(2)	111.6(1)
N(3)–M–N(7)	99.0(2)	101.3(2)
C(5)–N(3)–C(6)	106.5(6)	106.3(4)
C(16)–N(7)–C(17)	106.6(5)	105.8(4)

D–H···A	D–H (Å)	H···D (Å)	D···A (Å)	D–H···A (°)
1				
N(4)–H(4B)···N(1)	0.860(8)	2.878(26)	2.310(26)	121.6(9)
N(4)–H(4B)···N(1A)	0.860(8)	2.485(21)	1.811(20)	134.3(9)
N(8)–H(8B)···N(5)	0.860(8)	2.782(12)	2.208(10)	123.9(6)
3				
N(4)–H(4B)···N(1)	0.860(7)	2.784(9)	2.211(8)	123.5(4)
N(8)–H(8B)···N(5)	0.860(7)	2.842(11)	2.301(12)	122.1(5)
N(8)–H(8B)···N(5A)	0.860(7)	2.49(11)	1.833(20)	133.4(6)

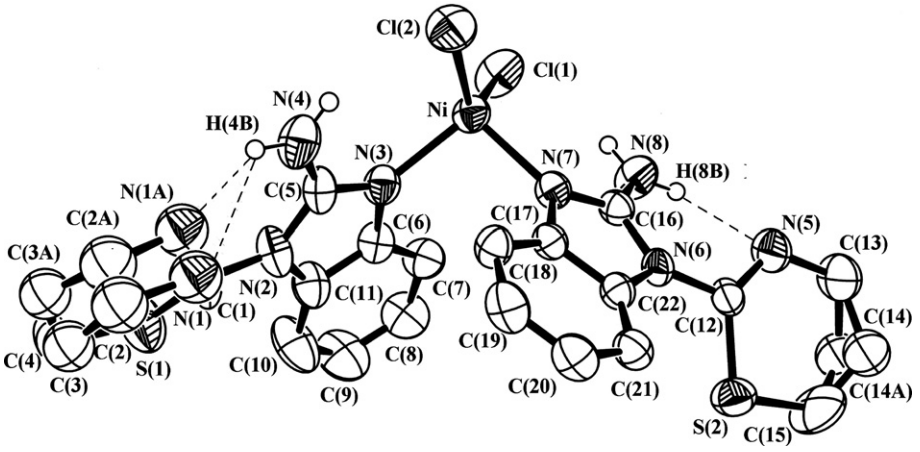


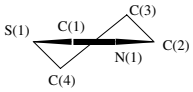
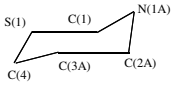
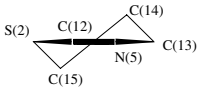
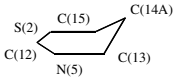
Fig. 3. Molecular structure of **1**, showing the atom-numbering scheme. The thermal ellipsoids are plotted at the 40% probability level. Figure includes a view of the hydrogen bonds.

bond lengths are similar and are comparable to the calculated average value [2.230(30) Å] for 19 tetrahedral nickel(II) complexes with a $NiCl_2N_2$ chromophore group, obtained from CONQUEST software [49] from the Cambridge Structural Database (CSD, Version v5.28, November 2006) [50]. Likewise, the Ni–$N_{benzimidazole}$ bond distances are similar and comparable to the mean value [1.995(40) Å] calculated for 23 tetrahedral nickel(II) complexes. The ligand–metal–ligand bite angles differ from the ideal value of 109.5°, varying between 99.0(2)° [N(3)–Ni–N(7)] and 120.7(1)° [Cl(1)–Ni–Cl(2)].

The conformations and the puckering parameters calculated according to Cremer and Pople [51] for the thiazine rings of **1** are shown in Table 4.

The crystal structure of this complex presents intramolecular hydrogen-bonds in which nitrogen atoms N(1),

Table 4
Types of conformation and puckering parameters of thiazine rings in **1**

Ring and conformation	Puckering parameters	Least square plane deviation for apex (Å)	Maximum least square plane deviation (Å)
 Half-chair	$Q = 0.218$ Å $\theta = 144.1°$ $\phi = 101.3°$	0.080 [C(3)] −0.246 [C(4)]	N(1) = 0.048
 Chair	$Q = 0.341$ Å $\theta = 10.3°$ $\phi = 134.5°$	−0.415 [N(1A)] 0.330 [C(4)]	C(2A) = 0.051
 Half-chair	$Q = 0.343$ Å $\theta = 51.0°$ $\phi = -102.3°$	−0.379 [C(14)] 0.120 [C(15)]	C(13) = 0.006
 Half-boat	Q = 0.332 Å $\theta = 124.8°$ $\phi = 49.8°$	0.470 [C(14A)]	C(15) = 0.079

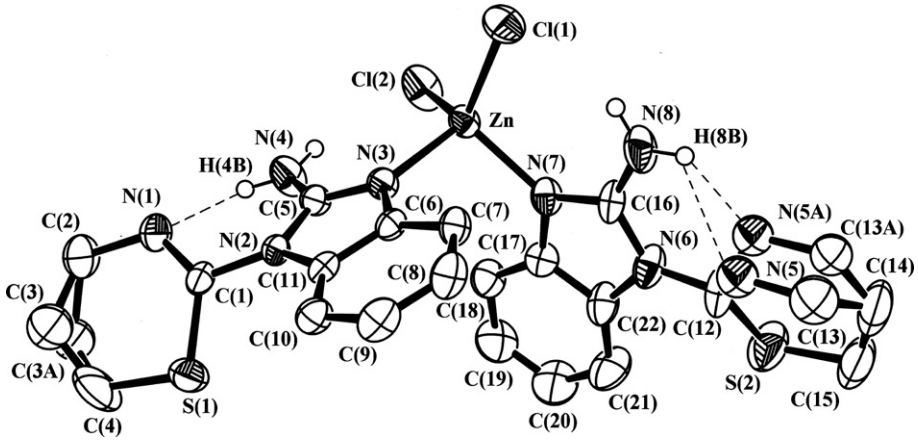
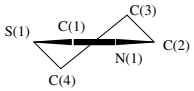
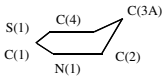
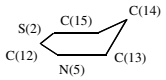
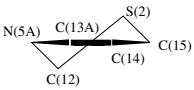


Fig. 4. Molecular structure of **3**, showing the atom-numbering scheme. The thermal ellipsoids are plotted at the 40% probability level. Figure includes a view of the hydrogen bonds.

Table 5
Types of conformation and puckering parameters of thiazine rings in **3**

Ring and conformation	Puckering parameters	Least square plane deviation for apex (Å)	Maximum least square plane deviation (Å)
 Half-chair	$Q = 0.342$ Å $\theta = 129.2°$ $\phi = 80.0°$	−0.363 [C(3)] 0.141 [C(4)]	N(1) = 0.006
 Half-boat	$Q = 0.348$ Å $\theta = 55.9°$ $\phi = -131.5°$	0.495 [C(3A)]	C(4) = 0.091
 Half-boat	$Q = 0.470$ Å $\theta = 120.0°$ $\phi = 56.6°$	−0.635 [C(14)]	C(15) = −0.077
 Half-chair	$Q = 0.291$ Å $\theta = 154.5°$ $\phi = -139.8°$	0.217 [C(12)] −0.208 [S(2)]	C(3A) = 0.112

N(1A) and N(5) act as acceptors of hydrogen, whereas nitrogen atoms of the amino groups N(4) and N(8) act as donors. A diagram showing these intramolecular hydrogen-bonds is given in Fig. 3.

Complex **3** is isostructural with **1** and with a Co(II) complex previously reported [22] (same crystal system, comparable cell dimensions, same space group and similar internal atomic coordinates). The formation of isomorphous and isostructural Co(II), Ni(II) and Zn(II) coordination compounds is common enough and occurs in particular with the coordination number 4, (pseudo)tetrahedral geometry [33,52–55] or with coordination number 6, (pseudo)octahedral geometry [53,56–62]. This phenomenon is favoured by the similarity of Zn(II), Ni(II) and high spin Co(II) ionic radii in these environments (0.74, 0.69 and 0.72 Å with coordination number 4; 0.88, 0.83 and 0.88 Å with coordination number 6, respectively) [63].

Fig. 4 shows the molecular structure of **3** and the atomic numbering system used. Selected bond lengths, angles and hydrogen-bond parameters are given in Table 3.

The tetrahedral environment of the zinc(II) ion is distorted, with the ligand–metal–ligand bite angles varying between 101.3(2)° [N(7)–Zn–N(3)] and 114.3(1)° [Cl(1)–Zn–Cl(2)]. This distortion is similar to that in **1** and $[CoCl_2(BzTz)_2]$ [22], this fact being indicated by the dihedral angles (88.4° for complex **1**, 87.8° for complex **3** and 87.2° for Co(II) complex).

The Zn–Cl and the Zn–N distances are comparable to the calculated average value [Zn–Cl = 2.222(25) Å; Zn–N = 2.051(34) Å] for 187 four-coordinated zinc(II) complexes with a $ZnCl_2N_2$ chromophore group in the CSD [49,50].

The conformations and the puckering parameters for the thiazine rings of **3** are shown in Table 5.

The crystal structure presents three intramolecular hydrogen-bonds as is shown in Fig. 4, in which the nitrogen atoms of the amino groups N(4) and N(8) act as donors of hydrogen, whereas nitrogen atoms N(1), N(5) and N(5A) act as acceptors.

4. Conclusion

In conclusion, four complexes bearing 2-aminobenzimidazole and thiazine have been synthesized. The coordination involved for the metal complexes is via *N*-benzimidazole. In the same way as that in the cadmium(II) and cobalt(II) complexes preliminary reported [22], it should be pointed out that BzTz acts as a monodentate ligand through the nitrogen atom of the benzimidazole ring probably due to the existence of an intramolecular hydrogen bond between the amine group and the thiazine nitrogen atom in the free ligand and the complexes. The formation of this metal–$N_{benzimidazole}$ bond results in an increase the N(3)–C(5) [or N(7)–C(16)] and N(3)–C(6) [or N(7)–C(17)] distances with respect to the structure of free BzTz.

The results of the present study clearly demonstrate the distorted tetrahedral coordination geometry for complexes **1** and **3**.

A study of all the characterization methods applied to compounds **2** and **4** suggests that these complexes could

be formulated as $[Ni(NO_3)(BzTz)_2(H_2O)_3](NO_3)$ and $[Zn(NO_3)_2(BzTz)_2]$, respectively. The geometry around the nickel atom could be described as a distorted octahedron whereas in case of the zinc atom as a distorted tetrahedron.

Acknowledgements

We thank the Junta de Extremadura (Consejería de Educación, Ciencia y Tecnología) and the FEDER [Project 2PR04A011] for financial support.

Appendix A. Supplementary material

CCDC 634051 and 634052 contain the supplementary crystallographic data for $[NiCl_2(BzTz)_2]$ and $[ZnCl_2(BzTz)_2]$. These data can be obtained free of charge via http://www.ccdc.cam.ac.uk/conts/retrieving.html, or from the Cambridge Crystallographic Data Centre, 12 Union Road, Cambridge CB2 1EZ, UK; fax: (+44) 1223-336-033; or e-mail: deposit@ccdc.cam.ac.uk. Supplementary data associated with this article can be found, in the online version, at doi:10.1016/j.poly.2007.02.016.

References

[1] S. Yurdakul, M. Kurt, J. Mol. Struct. 650 (2003) 181.
[2] F. Saczewski, E. Dziemidowicz-Borys, P.J. Bednarski, R. Grünert, M. Gdaniec, P. Tabin, J. Inorg. Biochem. 100 (2006) 1389.
[3] P. Kopel, J. Kamenícek, V. Petrícek, A. Kurecka, B. Kalinska, J. Mrozinski, Polyhedron 26 (2007) 535.
[4] A.A. Spasov, I.N. Yozhitsa, L.I. Bugaeva, V.A. Anisimova, Pharm. Chem. J. 33 (1999) 232.
[5] R.A. Bucknall, S.B. Carter, Nature (1967) 1099.
[6] F. Gumus, O. Algul, G. Eren, H. Eroglu, N. Diril, S. Gur, A. Ozkul, Eur. J. Med. Chem. 38 (2003) 473.
[7] M. Gocke, S. Utku, S. Gur, A. Rozkul, F. Gumus, Eur. J. Med. Chem. 40 (2005) 135.
[8] N. Bharti, M.T. Shailendra, Bioorg. Med. Chem. Lett. 12 (2002) 869.
[9] W. Reifscheider, B.B. Ershadi, J.E. Dripps, J.B. Barron, US Patent 5075293 (1991).
[10] W. Reifscheider, B.B. Ershadi, J.E. Dripps, J.B. Barron, Chem. Abstr. 116 (1992) 129294f.
[11] J. Goto, K. Sakane, Jpn. Kokai 121 (1989) 6997.
[12] J. Goto, K. Sakane, Chem. Abstr. 112 (1990) 2165541f.
[13] M. Koketsu, K. Tanaka, Y. Takenaka, C.D. Kwong, H. Ishihara, Eur. J. Pharm. Sci. 15 (2002) 307.
[14] B. Tozkoparan, G. Aktay, E. Yesilada, Il Farmaco 57 (2002) 145.
[15] J.D. Bourzat, C. Cotrel, C. Guyon, Ph. Pitchen, US Patent 4994569 (1991).
[16] R.F. Schinazi, R.A. Floyd, PCT Int. Appl. WO 90 13,296 (Cl. A61K31/54) (1991).
[17] R.F. Schinazi, R.A. Floyd, Chem. Abstr. 115 (1991) 105989.
[18] J.F. Gonzales, P.A. Todd, Drugs 34 (1987) 298.
[19] W. Nawrocka, Bull. Chim. Farm. 135 (1996) 18.
[20] N., Tomaji, M., Yoshiyuki, H., Ishikawa, PCT Int. Appl. WO 00 94, 22 (1996) 875.
[21] N. Tomaji, M. Yoshiyuki, H. Ishikawa, Chem. Abstr. 122 (1995) 214086u.
[22] F.J. Barros-García, A. Bernalte-García, F. Luna-Giles, M.A. Maldonado-Rogado, E. Viñuelas-Zahínos, Polyhedron 24 (2005) 1764.
[23] R.D. Haugwitz, B.V. Maures, A.J. Martínez, G.A. Jacobs, V.L. Narayanan, Synthesis (1976) 336.
[24] L.J. Farrugia, J. Appl. Cryst. 32 (1999) 837.
[25] M. Sheldrick, SHELXS-97, Program for Crystal Structures Solution, University of Göttingen, Germany, 1997.
[26] M. Sheldrick, SHELXL-97, Program for Crystal Structures Refinement, University of Göttingen, Germany, 1997.
[27] T. Hatakeyama, Z. Liu, Handbook of Thermal Analysis, John Wiley and Sons, Chichester, 1998.
[28] A.B.P. Lever, E. Mantovani, B.S. Ramaswamy, Can. J. Chem. 49 (1971) 1957.
[29] K. Nakamoto, in: Infrared and Raman Spectra of Inorganic and Coordination Compound, 5th ed., Wiley, New York, 1997.
[30] C.C. Addison, D. Sutton, Prog. Inorg. Chem. 8 (1967) 195.
[31] B.N. Gaterhouse, S.E. Livingstone, R.S. Nyholm, J. Chem. Soc. (1957) 4222.
[32] J.R. Ferraro, Low-Frequency Vibrations of Inorganic and Coordination Compounds, Plenum Press, New York, 1971.
[33] A. Bernalte-García, F.J. García-Barros, F.J. Higes-Rolando, F. Luna-Giles, Polyhedron 20 (2001) 3315.
[34] C. Pettinari, F. Marchetti, A. Cingolani, S.I. Troyanov, A. Drozdov, Polyhedron 17 (1998) 1677.
[35] R. López-Garzón, M.D. Gutiérrez-Valero, M.L. Rodino-Salido, A. Sánchez-Rodrigo, M. Nogueras-Montiel, J.M. Moreno, R. Odedra, K.H.A.M. El-Bayouki, Inorg. Chim. Acta 258 (1997) 33.
[36] M.J.M. Campbell, D.W. Card, R. Grzeskowiak, M. Goldstein, J. Chem. Soc., Dalton Trans. 15 (1972) 1687.
[37] A. Bernalte-García, F.J. García-Barros, F.J. Higes-Rolando, A.M. Pizarro-Galán, C. Valenzuela-Calahorro, Thermochim. Acta 339 (1999) 95.
[38] M.A. Ali-Beg, S. Ashfaq-Husain, Polyhedron 2 (1983) 881.
[39] F.J. Barros-García, A. Bernalte-García, F.J. Higes-Rolando, F. Luna-Giles, R. Pedrero-Marín, Polyhedron 23 (2004) 1453.
[40] C. Preti, G. Tosi, J. Chem. Soc., Dalton Trans. (1976) 685.
[41] E. López-Torres, M.A. Mendiola, J. Rodríguez-Procopio, M.T. Sevilla, E. Colacio, J.M. Moreno, I. Sobrados, Inorg. Chim. Acta 323 (2001) 130.
[42] H.A. Tajmir-Riahi, Polyhedron 2 (1983) 723.
[43] D.K. Rastogi, K.C. Sharma, S.K. Dua, M.P. Teotia, J. Inorg. Nucl. Chem. 37 (1975) 685.
[44] A.B.P. Lever, Inorganic Electronic Spectroscopy, Elsevier, Amsterdam, 1984.
[45] L. Sacconi, F. Mani, A. Bencini, in: G. Wilkinson (Ed.), Comprehensive Coordination Chemistry, vol. 5, Pergamon Press, New York, 1987.
[46] S. Wang, Y. Cui, R. Tan, Q. Luo, J. Shi, Q. Wu, Polyhedron 13 (1994) 1661.
[47] A. Amoedo-Portela, R. Carballo, J.S. Casas, E. García-Martínez, A. Sánchez-González, J. Sordo, E.M. Vázquez-López, Polyhedron 22 (2003) 1077.
[48] J. Reedijk, P.W.N.M. Van-Leeuwen, W.L. Groeneveld, Rec. Trav. Chim. Pays-Bas 87 (1968) 129.
[49] F.H. Allen, Acta Crystallogr., Sect. B 58 (2002) 380.
[50] I.J. Bruno, J.C. Cole, P.R. Edington, M. Kessler, C.F. Macrae, P. McCabe, J. Pearson, R. Taylor, Acta Crystallogr., Sect. B 58 (2002) 389.
[51] D. Cremer, J.A. Pople, J. Am. Chem. Soc. 97 (1975) 1354.
[52] D.A. Clemente, A. Marzotto, F. Benetollo, Polyhedron 21 (2002) 2161.
[53] S.G. Baca, I.G. Filippova, O.A. Gherco, M. Gdaniec, Y.A. Simonov, N.V. Gerbeleu, P. Franz, R. Basler, S. Decurtins, Inorg. Chim. Acta 357 (2004) 3419.
[54] I. G Fomina, A.A. Sidorov, G.G. Aleksandrov, T.B. Mikhailova, E.V. Pakhmutova, V.M. Novotortsev, V.N. Ikorskii, I.L. Eremenko, Russ. Chem. Bull. 53 (2004) 1477.
[55] N. Duran, W. Clegg, L. Cucurull-Sanchez, R.A. Coxal, H.R. Jimenez, J.-M. Moratal, F. lloret, P. Gonzales-Duarte, Inorg. Chem. 39 (2000) 4821.
[56] R.D. Pike, M.J. Lim, E.A.L. Willcox, T.A. Tronic, J. Chem. Crystallogr. 36 (2006) 781.

[57] J.E. Fiscus, N. Pschirer, R.E. Hipp, A.M. Goforth, C. Chapman, S. Shotwell, R.C. Layland, M.D. Smith, U.H.F. Bunz, H.-C. zur Loye, J. Chem. Crystallogr. 35 (2005) 125.
[58] S.A. Barnett, N.R. Champness, C. Wilson, Eur. J. Inorg. Chem. (2005) 1572.
[59] M. Barceló-Oliver, A. Terrón, A. García-Raso, J.J. Fiol, E. Molins, C. Miravitlles, J. Inorg. Biochem. 98 (2004) 1703.
[60] G. Wrzeszcz, L. Dobrzanska, A. Wojtczak, A. Grodzicki, J. Chem. Soc., Dalton Trans. (2002) 2862.
[61] S. Defazio, R. Cini, J. Chem. Soc., Dalton Trans. (2002) 1888.
[62] R.M. McCarrick, M.J. Eltzroth, P.J. Squattrito, Inorg. Chim. Acta 311 (2000) 95.
[63] G.E. Rodgers, in: Química Inorgánica, McGraw-Hill, Madrid, 1995.

Available online at www.sciencedirect.com
ScienceDirect
Polyhedron 26 (2007) 3121–3128
POLYHEDRON
www.elsevier.com/locate/poly

Structural variations in Ni(II) complexes of salen type di-Schiff base ligands

Pampa Mukherjee [a], Chaitali Biswas [a], Michael G.B. Drew [b], Ashutosh Ghosh [a,*]

[a] *Department of Chemistry, University College of Science, University of Calcutta, 92, A.P.C. Road, Kolkata 700 009, India*
[b] *School of Chemistry, The University of Reading, P.O. Box 224, Whiteknights, Reading RG6 6AD, UK*

Received 16 January 2007; accepted 13 February 2007
Available online 20 February 2007

Abstract

Three di-Schiff-base ligands, *N*,*N*′-bis(salicylidene)-1,3-propanediamine (H_2Salpn), *N*,*N*′-bis(salicylidene)-1,3-pentanediamine (H_2Salpen) and *N*,*N*′-bis(salicylidine)-ethylenediamine (H_2Salen) react with $Ni(SCN)_2 \cdot 4H_2O$ in 2:3 molar ratios to form the complexes; mononuclear $[Ni(HSalpn)(NCS)(H_2O)] \cdot H_2O$ (**1a**), trinuclear $[\{Ni(Salpen)\}_2Ni(NCS)_2]$ (**2b**) and trinuclear $[\{Ni(Salen)\}_2Ni(NCS)_2]$ (**3**) respectively. All the complexes have been characterized by elemental analyses, IR and UV–VIS spectra, and room temperature magnetic susceptibility measurements. The structures of **1a** and **2b** have been confirmed by X-ray single crystal analysis. In complex **1a,** the Ni(II) atom is coordinated equatorially by the tetradentate, mononegative Schiff-base, HSalpn. Axial coordination of isothiocyanate group and a water molecule completes its octahedral geometry. The hydrogen atom attached to one of the oxygen atoms of the Schiff base is involved in a very strong hydrogen bond with a neighboring unit to form a centrosymmetric dimer. In **2b,** two square planar [Ni(Salpen)] units act as bidentate oxygen donor ligands to a central Ni(II) which is also coordinated by two mutually cis N-bonded thiocyanate ligands to complete its distorted octahedral geometry. Complex **3** possesses a similar structure to that of **2b**. A dehydrated form of **1a** and a hydrated form of **2b** have been obtained and characterized. The importance of electronic and steric factors in the variation of the structures is discussed.
© 2007 Elsevier Ltd. All rights reserved.

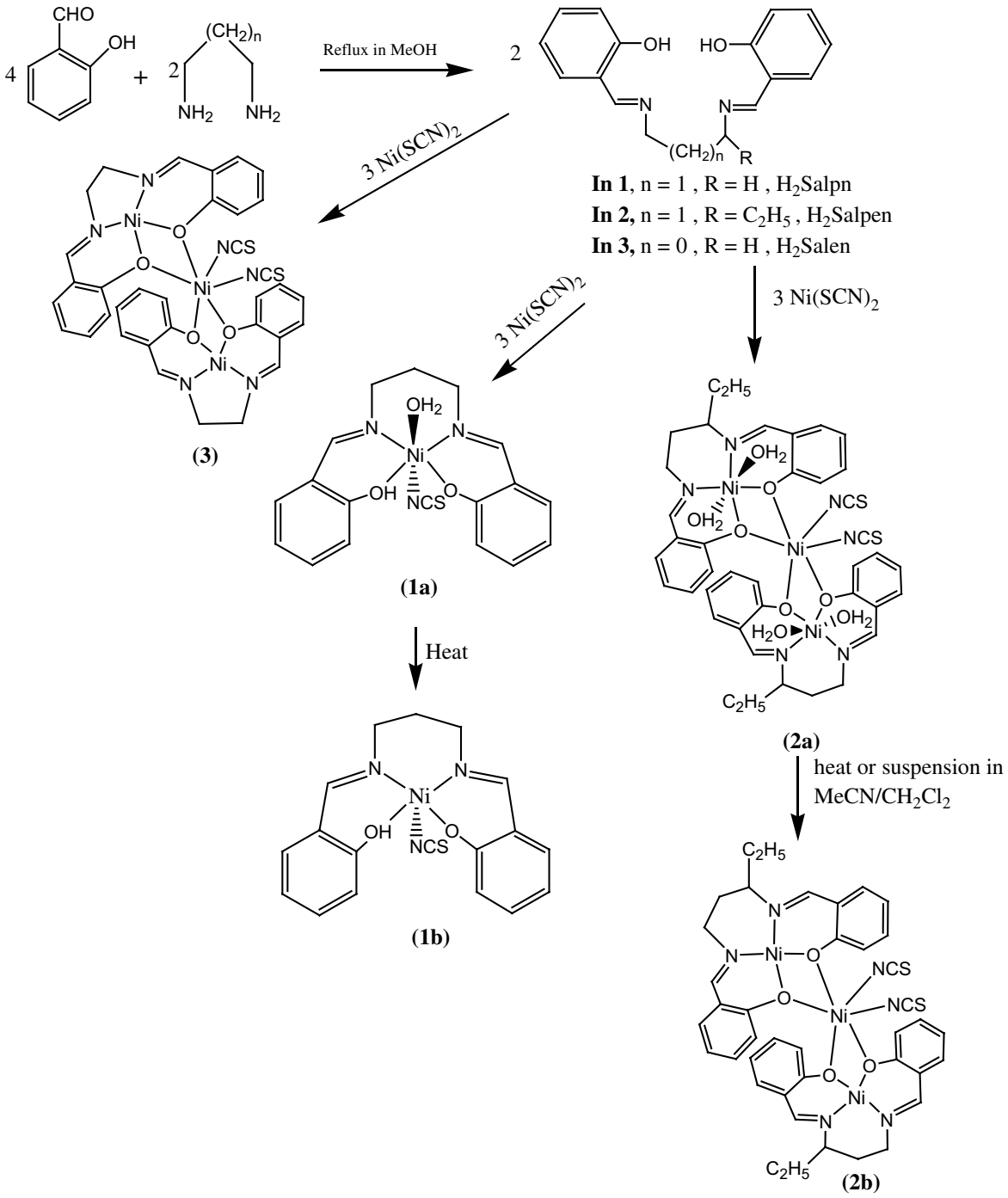
Keywords: Nickel(II); Schiff base; Thiocyanate; Crystal structures; H-bonding

1. Introduction

The salen type di-Schiff base complexes of transition metals are one of the most exhaustively studied topic in coordination chemistry [1]. Their interest stems from the ease with which they can be synthesized, their versatility and wide range of complexing ability. They not only have played an important role in the development of modern coordination chemistry [2], but they can also be found at key points in the development of inorganic biochemistry [3], catalysis [4,5], magnetism, medical imaging [6] etc. Since nickel compounds are present in the active sites of urease and are used extensively in the design and construction of new magnetic materials, the study of nickel compounds is of great interest in various aspects of chemistry [7–9]. In general, the reaction of H_2Salen or related ligands with Ni(II) yields complexes in which the deprotonated, di-negative Schiff base acts as a tetradentate chelating ligand [10–21]. However, in some cases it has been found that the oxygen atoms of the Schiff base can bridge another metal ion to form multinuclear (homo- or heteronuclear) complexes [22–35]. In all the reported homonuclear nickel complexes, the oxygen atoms of two mononuclear units bridge a third Ni(II) to form a trinuclear entity and in all but one case, an additional bridging anionic ligand (e.g. acetate, nitrite etc.) was required to provide the required stability for the polynuclear structure [22–25]. Interestingly, most of the trinuclear complexes reported so far are of Salpn (Scheme 1) and contain the additional anion bridge. The geometry of all three Ni(II)

* Corresponding author.
E-mail address: ghosh_59@yahoo.com (A. Ghosh).

0277-5387/$ - see front matter © 2007 Elsevier Ltd. All rights reserved.
doi:10.1016/j.poly.2007.02.006



Scheme 1.

ions in those complexes is octahedral in a linear structure. To our knowledge, only one trinuclear complex has been reported incorporating Salen as the ligand and that does not have the additional anion bridge [26]. The molecule is bent and the geometry of the three Ni(II) is square planar-octahedral-square planar. On the other hand, a more flexible Schiff base *N*,*N*′-bis(salicylidene)-1,4-butanediamine shows an interesting conformational isomerism and different anion bridging behavior in its trinuclear complexes [23]. However, to have a clear idea about the steric and electronic factors that determine the structure and connectivity of such complexes, it is necessary to synthesis some more complexes.

Herein, we report the structural variation in the complexes of three di-Schiff base ligands, H_2Salpn, H_2Salpen and H_2Salen (Scheme 1) with Ni(II) thiocyanate. It is

observed that small differences in the diamine fragment can cause remarkable change in the composition and geometry of the complexes. A probable explanation for such difference in structures has also been provided.

2. Experimental

2.1. Materials

All the chemicals were of reagent grade and used without further purification. The three double-condensed Schiff-base ligands, *N*,*N*′–bis(salicylidene)-1,3-propanediamine (H_2Salpn), *N*,*N*′-bis(salicylidine)-1,3-pentanediamine (H_2Salpen) and *N*,*N*′-bis(salicylidine)-ethylenediamine (H_2Salen) have been synthesized in our laboratory by the methods described below.

2.2. Synthesis of the Schiff-base ligands (H_2Salpn, H_2Salpen and H_2Salen)

The three Schiff bases were prepared by standard methods [23,36,37]. Briefly, 10 mmol of salicylaldehyde (1.05 cm^3) were mixed with 5 mmol of the required amine, 1,3-propanediamine (0.420 cm^3), 1,3-pentanediamine (0.596 cm^3) and 1,2-ethanediamine (0.308 cm^3) for the ligands H_2Salpn, H_2Salpen and H_2Salen, respectively in methanol (10 cm^3). The resulting mixture were refluxed for an hour, filtered when hot and allowed to cool. The desired yellow precipitates were filtered off, washed with methanol and dried in a vacuum desiccator containing anhydrous $CaCl_2$.

2.2.1. Synthesis of [Ni(HSalpn)(NCS)(H_2O)] · H_2O (**1a**)

A solution of $Ni(SCN)_2 \cdot 4H_2O$ (1.84 g, 7.5 mmol) in methanol–water (9:1 v/v) mixture (10 cm^3) was added to a solution of H_2Salpn (1.4 g, 5 mmol) in methanol (10 cm^3) with constant stirring. The mixture was stirred for 1 h at room temperature and then filtered. The filtrate was left to stand overnight in air, when green X-ray quality single crystals appeared at the bottom of the vessel on slow evaporation of the solvent. The crystals were isolated, washed with methanol and dried in vacuum desiccator containing anhydrous $CaCl_2$. Yield: 1.52 g (70%). *Anal.* Calc. for $C_{18}H_{21}NiN_3O_4S$: C, 49.80; H, 4.88; N, 9.68; Ni, 13.52. Found: C, 49.52; H, 4.36; N, 9.57; Ni, 13.14%. $\lambda_{Max/nm}$ (solid, reflectance) 594 and 1042 nm; IR: ν(C=N), 1634 cm^{-1}, ν(SCN), 2094 cm^{-1}, ν(H_2O), 3328 cm^{-1}, $\mu_{eff} = 3.3$ BM.

2.2.2. Synthesis of [Ni(HSalpen)(NCS)] (**1b**)

Complex **1b** was produced as a dirty green compound by heating the complex **1a** at 140 °C for 15 mins. *Anal.* Calc. for:$C_{18}H_{17}NiN_3O_2S$: C, 51.95; H, 4.60; N, 10.10; Ni, 14.10. Found: C, 51.64; H, 4.42; N, 10.17; Ni, 14.01%. $\lambda_{Max/nm}$ (solid, reflectance) 595 and 1148 nm; IR: ν(C=N), 1611 cm^{-1}, ν(SCN), 2086 cm^{-1}, $\mu_{eff} = 3.0$ BM.

2.2.3. Synthesis of [{Ni(Salpen)(H_2O)$_2$}$_2$Ni(NCS)$_2$] · 2H_2O (**2a**)

A methanol solution of $Ni(SCN)_2 \cdot 4H_2O$ (1.84 g, 7.5 mmol) in methanol–water (9:1 v/v) mixture (10 cm^3) was added to a solution of H_2Salpen (1.54 g, 5 mmol) in methanol (10 cm^3) with constant stirring. A green precipitate appeared immediately. The mixture was stirred for 1 h at room temperature. The precipitate was filtered, washed with methanol and dried in air. Yield: 1.8 g. (70%). *Anal.* Calc. for $C_{40}H_{52}Ni_3N_6O_{10}S_2$: C, 47.24; H, 5.15; N, 8.26; Ni, 17.31. Found: C, 47.02; H, 5.11; N, 8.12; Ni, 17.17%. $\lambda_{Max/nm}$ (solid, reflectance), 595, 908 and 1175 nm; IR: ν(C=N), 1626 cm^{-1}, ν(SCN), 2098 cm^{-1}, ν(H_2O), 3401 cm^{-1}, $\mu_{eff} = 5.1$ BM per trinuclear unit.

2.2.4. Synthesis of [{Ni(Salpen)}$_2$Ni(NCS)$_2$] (**2b**)

The green precipitate of complex **2a** was dissolved in hot MeCN solution. The color of the solution changes from green to yellow during dissolution. On keeping the filtrate overnight in air, red block-shaped crystals of **2b**, suitable for X-ray analysis were obtained. Yield: 1.36g (60%). *Anal.* Calc. for $C_{40}H_{40}Ni_3N_6O_4S_2$: C, 52.85; H, 4.44; N, 9.25; Ni, 19.37. Found: C, 52.32; H, 4.36; N, 9.12; Ni, 19.48%. $\lambda_{Max/nm}$ (solid, reflectance) 490, 1182 and 1389 nm; IR: ν(C=N), 1610 cm^{-1}, ν(SCN), 2090 cm^{-1}, $\mu_{eff} = 3.3$ BM per trinuclear unit.

2.2.5. Synthesis of [{Ni(Salen)}$_2$Ni(NCS)$_2$] (**3**)

A solution of $Ni(SCN)_2 \cdot 4H_2O$ (1.84 g, 7.5 mmol) in methanol–water (9:1 v/v) mixture (10 cm^3) was added to a solution of H_2Salen (1.40 g, 5 mmol) in methanol (10 cm^3) with constant stirring. An immediate red precipitate appeared. The mixture was stirred for 1 h at room temperature. The solid was collected by filtration, washed with methanol and allowed to dry in air. The complex was only sparingly soluble in hot methanol and in DMF. However, suitable single crystals for X-ray analysis could not be grown. Yield: 1.65 g (80%). *Anal.* Calc. for $C_{34}H_{28}Ni_3N_6O_4S_2$: C, 49.51; H, 3.42; N, 10.19; Ni, 21.35. Found: C, 49.32; H, 3.26; N, 10.12; Ni, 20.37%. $\lambda_{Max/nm}$ (solid, reflectance), 510 800 and 1252 nm; IR: ν(C=N), 1627 cm^{-1}, ν(SCN), 2077 cm^{-1}, $\mu_{eff} = 3.2$ BM per trinuclear unit.

2.3. Physical measurements

Elemental analyses (carbon, hydrogen and nitrogen) were performed using a Perkin–Elmer 240C elemental analyzer. The nickel content in all the complexes was estimated gravimetrically using DMG. IR spectra in KBr (4500–500 cm^{-1}) were recorded using a Perkin–Elmer RXI FT-IR spectrophotometer. Electronic spectra in acetonitrile (1500–350 nm) and in the solid state were recorded in a Hitachi U-3501spectrophotometer. The thermal analyses (TGA-DTA) were carried out on a Mettler Toledo TGA/DTA 851 thermal analyzer in a dynamic atmosphere of dinitrogen (flow rate: 30 $cm^3 min^{-1}$). The samples were heated in an alumina crucible at a rate of 10 °C min^{-1}.

The effective moments at room temperature were evaluated from magnetic susceptibility measurement with an EG and G PAR 155 vibrating-sample magnetometer.

2.4. Crystallographic studies

Intensity data were measured using the Oxford X-Calibur CCD System using Mo Kα radiation. The crystals were positioned at 50 mm from the CCD. 321 frames were measured with a counting time of 3 s. Data analyses were carried out with the CRYSALIS program [38] to give 5654, 11 524 independent reflections for **1a** and **2b** respectively. The structures were solved using direct methods with the SHELX97 program [39]. The non-hydrogen atoms were refined with anisotropic thermal parameters. The hydrogen atoms bonded to carbon were included in geometric positions and given thermal parameters equivalent to 1.2 times those of the atom to which they were attached. In **2b** a sulfur atom of a thiocyanate ligand was disordered over three positions each with occupancy of 0.333. Hydrogen atoms on water molecules and on O(11) were readily located in **1a** from a difference Fourier map. Absorption corrections were carried out using the ABSPACK program [40]. The structures were refined on F^2 using SHELX97 [39] to give wR 0.0569, 0.1253, wR_2 0.0825, 0.2445 for 3273, 4384 reflections with $I > 2\sigma(I)$. The relatively high R value of **2b** is due to the poor quality of the crystal. Despite our best efforts with a state-of-the-art CCD diffractometer we were unable to get a lower value. The data were collected (and refined) up to a theta angle of 60°; on refinement with a theta max of 50°, the R_1 is 0.0837 and wR_2 is 0.2225. We would like to use as much data as possible and so prefer to report the refinement using all data up to 60°. Details of crystallographic data and refinements of the complexes **1a** and **2b** are summarized in Table 1 while selected bond lengths and bond angles are presented in Tables 2 and 3 respectively. A list of H-bonds in the two complexes is given in Table 4.

Table 1
Crystal data and structure refinement of complexes **1a** and **2b**

	1a	**2b**
Formula	$C_{18}H_{21}N_3NiO_4S$	$C_{40}H_{40}N_6Ni_3O_4S_2$
M	434.15	908.02
Crystal system	monoclinic	monoclinic
Space group	$P2_1/c$	$P2_1/n$
a (Å)	10.724(1)	11.384(2)
b (Å)	12.710(1)	20.800(3)
c (Å)	14.875(1)	18.011(4)
β (°)	104.49(1)	103.74(2)
U (Å^3)	1963.0(2)	4142.7(14)
Z	4	4
D_c (g cm^{-3})	1.469	1.456
μ (Mo Kα) (mm^{-1})	1.123	1.497
R_{int}	0.069	0.108
Number of unique data	5654	11524
Number of data with $I > 2\sigma(I)$	3273	4384
R_1, wR_2	0.0569, 0.0939	0.1253, 0.3046

Table 2
Selected bond lengths (Å) and bond angles (°) for complex **1a**

Ni1–O31	2.025(2)	Ni1–N19	2.042(2)
Ni1–N23	2.036(2)	Ni1–N1	2.075(3)
Ni1–O11	2.039(2)	Ni–O100	2.132(2)
O11–Ni1–O31	85.47(8)	O100–Ni1–N1	178.40(9)
O11–Ni1–O100	89.46(8)	O100–Ni1–N19	89.95(9)
O11–Ni1–N1	91.96(9)	O100–Ni1–N23	88.01(9)
O11–Ni1–N19	88.44(9)	N1–Ni1–N19	90.83(9)
O11–Ni1–N23	174.23(2)	N1–Ni1–N23	90.52(10)
O31–Ni1–O100	86.10(8)	N19–Ni1–N23	96.73(9)
O31–Ni1–N1	93.27(9)		
O31–Ni1–N19	172.77(9)		
O31–Ni1– N23	89.19(8)		

Table 3
Selected bond lengths (Å) and bond angles (°) for complex **2b**

Ni1–O11	2.096(6)	Ni2–O31	1.860(6)
Ni1–O31	2.102(6)	Ni2–N19	1.868(8)
Ni1–O41	2.057(6)	Ni2–N23	1.883(9)
Ni1–O61	2.137(6)	Ni3–O41	1.876(7)
Ni1–N1	2.015(9)	Ni3–O61	1.878(6)
Ni1–N2	2.009(9)	Ni3–N53	1.909(9)
Ni2–O11	1.854(7)	Ni3–N49	1.914(9)
O11–Ni1–O31	70.7(2)	O11–Ni2–O31	81.7(3)
O11–Ni1–O41	156.8(3)	O11–Ni2–N19	92.8(3)
O11–Ni1–O61	93.5(3)	O11–Ni2–N23	172.8(3)
O11–Ni1–N1	101.7(3)	O31–Ni2–N19	172.8(4)
O11–Ni1–N2	94.7(3)	O31–Ni2–N23	91.5(3)
O41–Ni1–O61	70.7(3)	N19–Ni2–N23	94.2(4)
O41–Ni1–N1	95.9(3)		
O41–Ni1–N2	99.0(3)	O41–Ni3–O61	80.6(3)
O61–Ni1–N1	91.9(3)	O41–Ni3–N49	91.6(3)
O61–Ni1–N2	168.7(3)	O41–Ni3–N53	167.9(3)
N1–Ni1–N2	94.1(4)	O61–Ni3–N49	168.4(3)
		O61–Ni3–N53	93.4(3)
		N49–Ni3–N53	95.7(4)

Table 4
Hydrogen bonding distances (Å) and angles (°) for the complex **1a**

Compound	D–H···A	D–H	D···A	A···H	∠D–H···A
1a	O100–H1···O200	0.90(3)	1.84(3)	2.718(4)	164(3)
	O100–H2···S1^{j}	0.85(3)	2.54(4)	3.379(2)	170(3)
	O200–H4···N1^{k}	0.88(3)	2.44(3)	3.264(4)	156(3)
	O11–H11···O31^{l}	0.90(2)	1.54(2)	2.438(3)	175(2)

Symmetry elements: (j) $x, 1/2 - y, 1/2 + z$; (k) $1 - x, -y, 2 - z$; (l) $1 - x, -y, 2 - z$.

3. Results and discussion

3.1. Synthesis of the complexes

We have synthesized three di-Schiff base ligands, H_2Salen, H_2Salpn, and H_2Salpen (Scheme 1) and allowed them to react separately with Ni(II) thiocyanate in 2:3 molar ratios. Although the ligands are very similar, the

composition and structure of the products are considerably different as shown in Scheme 1. H_2Salpn results a mononuclear complex, $[Ni(HSalpn)(NCS)(H_2O)]\cdot H_2O$ (**1a**) where Ni(II) is chelated by the mono-negative HSalpn. H_2Salpen produces initially a trinuclear complex $[\{Ni(Salpen)(H_2O)_2\}_2Ni(NCS)_2]\cdot 2H_2O$ (**2a**) in which the geometry around all three Ni(II) atoms is octahedral. **2a** on heating or crystallization from acetonitrile or even in contact with organic solvents e.g. dichloromethane loses the water molecules and transforms into the square planar–octahedral–square planar trinuclear complex, $[\{Ni(Salpen)\}_2Ni(NCS)_2]$ (**2b**). H_2Salen, on the other hand, yields immediately the 'square planar-octahedral-square planar' trinuclear complex $[\{Ni(Salen)\}_2Ni(NCS)_2]$ (**3**). Complexes, **1a** and **2b** have been characterized by single crystal X-ray analysis. We failed to obtain suitable single crystals for the other complexes and characterized them by elemental analyses, thermal analysis, room temperature magnetic moment measurement, IR and UV–VIS spectra.

3.2. Description of structures of *1a* and *2b*

3.2.1. Complex *1a*

The structure of **1a**, shown in Fig. 1, contains the metal in a six-coordinate, distorted octahedral environment in which O(11), N(19), N(23) and O(31) of the mono-negative Schiff base constitute the equatorial plane. The deviations of the four basal donor atoms from their mean plane are within ±0.015 Å. The Ni atom deviates from the mean plane by −0.0567(4) Å. The two axial positions are occupied by N(1) of a thiocyanate group and O(100) of a water molecule. The six-membered ring comprising the nickel, imine N atoms and three propylene C atoms adopts a chair conformation. The complex contains another non-coordinated water molecule and there is a strong hydrogen bond between the coordinated and uncoordinated two water molecules as shown in Fig. 1. A weaker H-bond is also formed between one of the hydrogen atoms of this uncoordinated water molecule (H4) and the N(1) atom of the coordinated isothiocyanate (Table 4). One interesting feature of this complex is that one of the oxygen atoms (O11) of the Schiff base is protonated which allows the charge on the complex to be balanced. The presence of H on O(11) is substantiated by the longer Ni(1)–O(11) bond distance of 2.039(3) Å compare to Ni(1)–O(31) bond distance of 2.025(2) Å. However, it should also be noted that the difference in bond distances is not remarkable and the Ni(1)–O(31) bond is rather long compare to that found in octahedral Ni(Salpn) type complex (2.017(2) Å) [13]. This can be explained by the involvement of this hydrogen (H11) in a very strong hydrogen bond with O(31) of another unit to form a centrosymmetric dimer as shown in Fig. 2. The symmetry related dimers are linked by weaker O100–H(2)···S(1) intermolecular hydrogen bonds to form a two dimensional layer structure as shown in Fig. 3. It is interesting to note that the same ligand has previously been reacted with nickel(II) thiocyanate adopting a different procedure [41] to form the complex, $[Ni(HSalpn)(NCS)(CH_3OH)]$ which is analogous to **1a**. The only difference is that the axially coordinated water of **1a** is replaced by a MeOH molecule. The bond angles and distances of the two compounds are very similar. However, the difference (0.040 Å) between two Ni–O (Schiff base) bond distances (2.054 and 2.014 Å) of that complex is slightly higher than that (0.014 Å) in **1a** probably due to the weaker H-bond that is formed involving the hydrogen atom attached to the Schiff base of that compound.

3.2.2. Complex *2b*

The structure of **2b** is a trinuclear compound as shown in Fig. 4 containing three independent nickel atoms. Ni(1) is six-coordinate with a distorted octahedral environment, while Ni(2) and Ni(3) are four-coordinate with a square planar environment. Each of the two

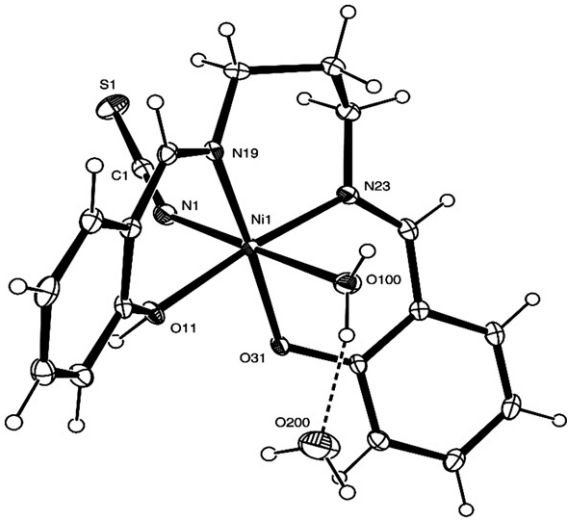


Fig. 1. Ortep-3 view of the complex **1a** with ellipsoids at 50% probability.

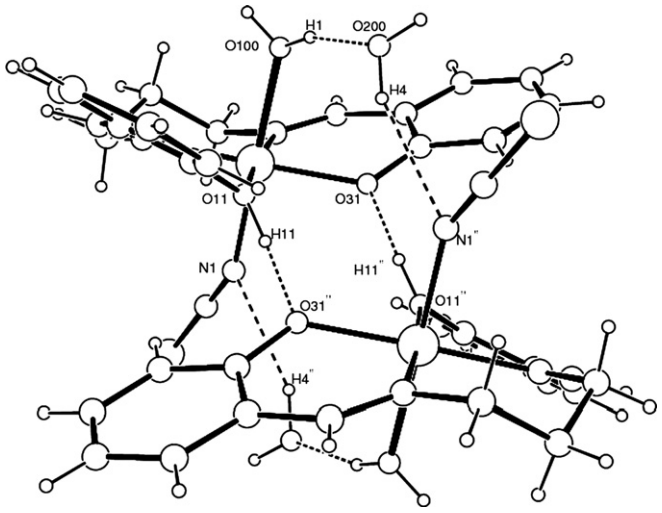


Fig. 2. Ortep-3 view of the dimeric unit c of **1a** with ellipsoids at 20% probability.

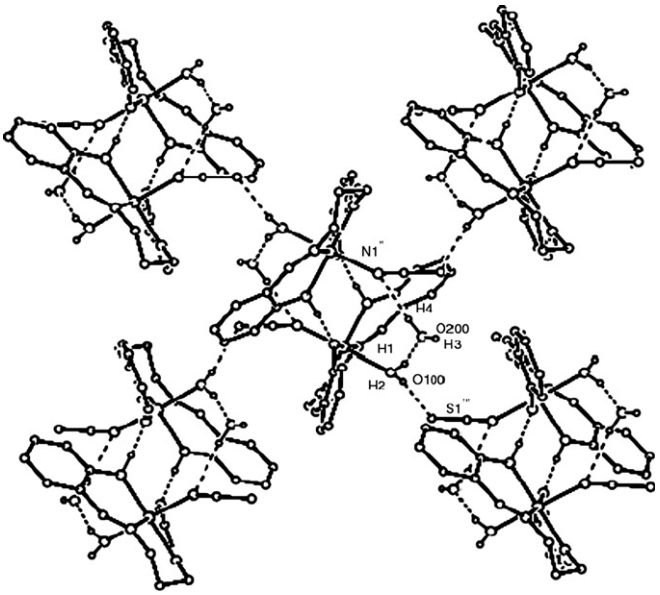


Fig. 3. Extended hydrogen-bonding network in complex **1a**.

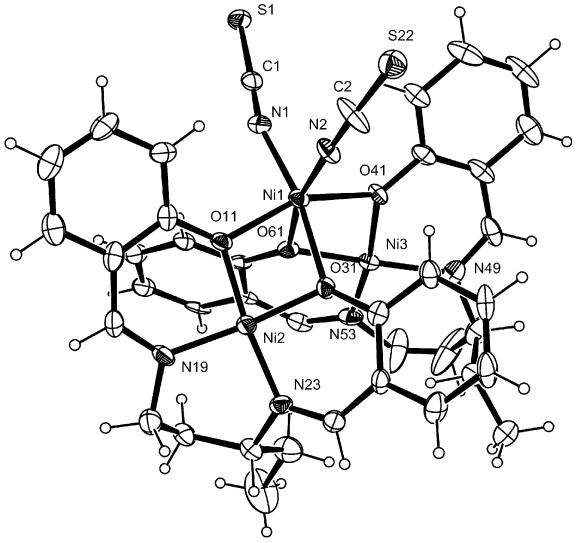


Fig. 4. ORTEP-3 view of the complex **2b** with ellipsoids at 25% probability.

terminal nickel atoms, Ni(2) and Ni(3) are coordinated by the two nitrogen atoms and two oxygen atoms of the deprotonated, chelating Schiff base ligand, H_2Salpen. The average trans angles are 172.8° and 168.2° for Ni(2) and Ni(3), respectively indicate that there is slight tetrahedral distortion from the ideal square planar geometry. The deviations of Ni(2) and Ni(3) from the respective mean planes passing through the coordinating atoms are 0.019(1) and −0.018(1) Å. The six-membered chelate rings containing the diamine fragment and nickel atom adopt boat and half-chair conformations for Ni(2) and Ni(3), respectively.

The four oxygen atoms of the two Ni(Salpen) moieties are also bonded to a third nickel atom Ni(1) forming the phenoxo bridged trinuclear complex. In addition Ni(1) is bonded to two mutually cis isothiocyanate ligands with Ni(1)–N(1) 2.016(9), Ni(1)–N(2) 2.009(9) Å to complete its distorted octahedral coordination. The small bite of Ni(Salpen) on coordinating to Ni(1) (average angle 70.8°) is the main cause of distortion from the ideal octahedron. The bond lengths, Ni(1)–O(11) 2.096(6), Ni(1)–O(31) 2.102(6) Å with the oxygen atoms bridging to Ni(2) and Ni(1)–O(41) 2.057(6) Å, Ni(1)–O(61) 2.137(6) Å with the oxygen atoms bridging to Ni(3) are significantly longer than Ni(2)–O and Ni(3)–O distances at 1.853(6), 1.859(6), 1.876(6), 1.878(6) Å. This difference is expected as in Ni(II) complexes, the bond distances in square planer geometry are usually less than that in octahedral geometry indicating that the axial coordination weakens the equatorial ligand field strength [12,13,15,41]. The Ni(2)–O and Ni(3)–O bonds are, however, slightly longer than those found in the mono-nuclear square planar Ni(Salpn) complex (1.845 Å) as a result of lower electron density of the oxygen upon bridging. A comparison of the structures of the similar complexes reveals an interesting feature – when trinuclear Ni(II) complexes are formed by both phenoxo- and anion bridges, the resulting complexes are linear in which the four phenoxo groups occupy a square plane (four meridional positions) of the central Ni(II) leaving its *trans* axial positions to be occupied by the bridging anions [22–25]. However in the case of complexes containing phenoxo bridges only (as is **2b**), the four oxygen atoms coordinate in facial manner to the central Ni(II) to result in a bent structure [26]. In **2b,** the Ni(2)–Ni(1)–Ni(3) angle is 87.88(5)° and the two Ni(Salpen) planes are disposed at a dihedral angle of 37.9°, compared to17.6° for the Ni(Salen) complex [26].

3.3. IR and UV–VIS spectra, thermal analysis and magnetic moment of the complexes

*3.3.1. Complexes **1a** and **1b***

The coordination mode of the thiocyanate anion to the transition metal is detected by the intense IR band due to (SCN) which occurs above 2000 cm^{-1}. The CN stretching frequency for N-bonded thiocyanate usually appears below 2100 cm^{-1} and that of S-bonded thiocyanate appears above 2100 cm^{-1} [42]. Complex **1a** shows a strong absorption band at 2094 cm^{-1} corroborating the presence of N-bonded thiocyanate group. It shows a strong and broad band, centering at 3328 cm^{-1} due to the presence of water molecule. Generally, stretching vibration for water appears above 3400 cm^{-1}. The shift of this band towards lower wave number and its broadness indicate the presence of strong hydrogen bonding as is substantiated by crystal structure. The band due to azomethine (C=N) appears at 1634 cm^{-1}. The magnetic moment ($\mu_{eff} = 3.3$ BM) and the appearance of two bands in the UV–VIS spectra of the complex corroborate its octahedral geometry. The highest energy d–d transition band is obscured by the CT band at that region.

The simultaneous TGA–DTA curves of complex **1a** reveal that upon heating it starts to lose water molecules at 90 °C and becomes dehydrated at ca. 150 °C in a single step. The observed weight loss (8.6%) corroborates the loss

of two water molecules (calc. 8.29%). Both the coordinated and crystallized water molecules are lost simultaneously as they are linked by strong hydrogen bonds. The dehydrated species (**1b**) is dirty-green in color and reabsorbs the two water molecules on keeping in open atmosphere for several days. It, however, does not absorb any organic solvent (e.g. methanol or acetonitrile) on keeping as suspension in these solvents. The magnetic moment of **1b** ($\mu_{eff} = 3.0$ BM) shows the presence of two unpaired electrons. Its electronic spectra indicate either penta-cordinated or hexa-coordinated geometry around Ni(II). The IR spectra of **1b** expectedly do not show any band due to water molecule. The (SCN) stretching vibration occurs nearly at the same wave number (2095 cm^{-1}) as in **1a** indicating no change of its coordination behavior on deaquation. Therefore, a penta-coordinated geometry around Ni(II) with an N-bonded thiocyanate is suggested for **1b**.

*3.3.2. Complexes **2a** and **2b***

The green compound **2a** is unstable and loses its water molecules on drying in a desiccator or in contact with organic solvents such as chloroform, dichloromethane etc. to transform into the red colored compound, **2b**. Therefore, an air dried sample of **2a** has been used for all physico-chemical studies. Complex **2a** shows a single absorption band at 2099 cm^{-1} due to the presence of coordinated isothiocyanate group. A strong and broad band around 3400 cm^{-1} indicates the presence of water molecules in it. The band due to azomethine appears at 1630 cm^{-1}. The magnetic moment ($\mu_{eff} = 5.1$ BM for trinuclear structure; 3.0 BM per Ni ion) and electronic spectra of the compound are typical of octahedral Ni(II) complexes. Therefore, a phenoxo bridged, trinuclear structure in which the two terminal Ni(II) have axially coordinated water molecules is suggested for it (Scheme 1). Upon heating, it starts to lose water molecules at ca. 40 °C and become anhydrous at ca. 110 °C. The observed weight loss (11.0%) corresponds to the presence of six molecules of water per trinuclear unit (calc.10.6%). The color of the species changes from green to red on dehydration. It does not reabsorb any water molecule on keeping in open atmosphere. The spectral and analytical results of the dehydratd species confirm that it is identical to compound **2b**.

The physico-chemical studies of **2b** corroborate its trinuclear structure as elucidated by X-ray analysis. The electronic spectra clearly show the presence of both octahedral and square planar Ni(II) in the compound. The magnetic moment ($\mu_{eff} = 3.3$ BM) corresponds to the presence of one paramagnetic octahedral Ni(II) per trinuclear unit. In IR spectra, stretching vibration band due to thiocyanate (SCN) and azomethine (C=N) appears at 2090 cm^{-1} and 1610 cm^{-1}, respectively and there is no band due to water around 3400 cm^{-1}.

*3.3.3. Complex **3***

The analytical, spectral and magnetic data of **3** indicate that it has similar composition and structure to that of **2b.** In IR spectra, no band due to water is found. The (SCN) and (C=N) bands appear at 2077 cm^{-1} and 1627 cm^{-1}, respectively. In the electronic spectra, peaks due to both square planar and octahedral Ni(II) appear and the magnetic moment indicates the presence of one paramagnetic Ni(II) with two unpaired electron per trinuclear unit.

3.4. Variation of structures with chain length and substitution in diamine fragment

The three Schiff bases that have been used here are very similar (Scheme 1). Salen forms a five membered chelate ring with the metal ion by the coordination of two nitrogen atoms. The diamine fragment in Salpn is 1,3-propanediamine and consequently a six membered ring is formed on chelation of the two nitrogen atoms of the Schiff base. Salpen forms a similar six-membered chelate ring but there is an ethyl substitution in one of the ring carbon atoms. On reaction with Ni(II) thiocyanate both Salen and Salpen form phenoxo bridged, square planar–octahedral–square planar trinuclear complexes (**3** and **2b**, respectively). The initial formation of trinuclear species with all three nickel atoms in octahedral environments (**2a**) with Salpen but not with Salen may be explained by their slight difference in ligand field strength. The steric hindrance due to the bulkier trimethylene group between the N atoms causes a weaker ligand field for the Schiff bases derived from 1,3-propanediamine and its derivative. As a result, water molecules can coordinate to Ni(II) axially as is found in **2a**. In fact, for this reason, all the Ni(II) complexes where Salen acts as a chelate are square planar [10–21] but complexes of Salpn type ligands can be square planar [12], penta- [15] or hexa-coordinate [13,41] species. It also explains the existence of several trinuclear Ni(II) complexes which are bridged both by phenoxo and an anionic ligand to form octahedral geometry around all three Ni(II) containing Salpn but not Salen as ligand [22–25].

The composition and structure of **1a**, on the other hand, is very different from the complexes that are usually formed by salen-type Schiff base ligands. The hydrogen atoms present in the –OH group of these types of Schiff bases are acidic in nature. Generally, when metal ion is added, the two oxygen atoms coordinate to the metal center and consequently their acidity is increased so much that these protons are lost readily and a complex with di-negative Schiff base is formed. Complex **1a** is an interesting exception in which the very uncommon mono-negative Schiff base is stabilized making the stoichiometry and structure of **1a** different from other related complexes. An explanation for the formation of this exceptional compound may be as follows:

The weak ligand field of Salpn as discussed above allows axial coordination of a thiocyanate and a water molecule (or methanol [41]). The proton bonded to one of the oxygen atoms is stabilized by the formation of a very strong H-bonded dimer (Fig. 2) The supramolecular two-dimensional H-bond structure involving the water molecules and thioyanate group (Fig. 3) also tilts the balance

in favor of the mononuclear complex containing the mononegative Schiff base over the trinuclear one. Salen does not allow the formation of such a complex as axial coordination to Ni(II) is unfavorable. The ethyl group present in the Salpen ligand probably prevents the formation of the H-bonding network and consequently the trinuclear complex is formed. The formation of phenoxo bridged trinuclear or H-bonded mononuclear compounds of Ni(II) is thus a delicate balance of electronic and steric effects of the Schiff base ligand as well as the capability of different donor and acceptor sites to form intermolecular hydrogen bonds to an adjacent coordinated ligand.

4. Conclusion

The present study shows that in Schiff base complexes of Ni(II), the environment at coordination center can be modified by changing the chain length or introducing substitution in carbon atom of the diamine. A minor difference in the subunit structure can bring about drastic change in molecular and crystal structure. The examples nicely illustrate the importance of steric and electronic properties for the fine tuning of composition and structure. Formation of **2a** demonstrates the importance of hydrogen bonding in the formation of unusual compounds.

Acknowledgements

P.M. and C.B. are thankful to CSIR, India and UGC, India respectively for research fellowships [Sanction no.09/028 (0663)/2006-EMR-I and UGC/29/Jr. Fellow (Sc.) 05-06]. We also thank EPSRC and the University of Reading for funds for the X-Calibur system.

Appendix A. Supplementary mateiral

CCDC 633271 and 633272 contain the supplementary crystallographic data for **1a** and **2b**. These data can be obtained free of charge via http://www.ccdc.cam.ac.uk/conts/retrieving.html, or from the Cambridge Crystallographic Data Centre, 12 Union Road, Cambridge CB2 1EZ, UK; fax: (+44) 1223-336-033; or e-mail: deposit@ccdc.cam.ac.uk. Supplementary data associated with this article can be found, in the online version, at doi:10.1016/j.poly.2007.02.006.

References

[1] S. Yamada, Coord. Chem. Rev. 192 (1999) 537.
[2] R.H. Holm, J. Am. Chem. Soc. 82 (1960) 5632.
[3] E.C. Niederhoffer, J.H. Timmons, A.E. Martell, Chem. Rev. 84 (1984) 137.
[4] K. Srinivasan, P. Michaud, J.K. Kochi, J. Am. Chem. Soc. 108 (1986) 2309.
[5] W. Zhang, J.L. Loebach, S.R. Wilson, E.N. Jacobsen, J. Am. Chem. Soc. 112 (1990) 2801.
[6] J. Tisato, F. Refosco, F. Bandoli, Coord. Chem. Rev. 135 (1994) 325.
[7] P.A. Karplus, M.A. Pearson, Acc. Chem. Res. 30 (1997) 330.
[8] H.L. Zhu, L.M. Zheng, J. Zhao, W.M. Bu, W.X. Tang, Trans. Met. Chem. 24 (1999) 131.
[9] H.L. Zhu, Y.X. Tong, X.M. Chen, C.X. Ren, Trans. Met. Chem. 26 (2001) 528.
[10] F. Akhtar, M.G.B. Drew, Acta Crystallogr., Sect. B: 38 (1982) 1149.
[11] H.J. Goodwin, K. Henrick, L.F. Lindoy, M. McPartlin, P.A. Tasker, Inorg. Chem. 21 (1982) 3261.
[12] M.G.B. Drew, R.N. Prasad, R.P. Sharma, Acta Crystallogr., Sect. C: 41 (1985) 1755.
[13] L. Gomes, C. Sousa, C. Freire, B.de. Castro, Acta Crystallogr., Sect. C: 56 (2000) 1201.
[14] A. Elmali, C.T. Zeyrek, Y. Elerman, Z. Naturforsch., B: Chem. Sci. 59 (2004) 228.
[15] Y. Elerman, M. Kabak, O. Atakol, Acta Crystallogr., Sect. C: 49 (1993) 1905.
[16] N. Clarke, D. Cunningham, T. Higgins, P. McArdle, J. McGinley, M. O' Gara, J. Organomet. Chem. 469 (1994) 33.
[17] C. Arici, F. Ercan, R. Kurtaran, O. Atakol, Acta Crystallogr., Sect. C: 57 (2001) 812.
[18] S.M.M. Sony, K. Saraboji, M.N. Ponnuswamy, J. Manonmani, M. Kandasamy, H.K. Fun, Cryst. Res. Technol. 39 (2004) 185.
[19] A. Elmali, C.T. Zeyrek, Y. Elerman, I. Svoboda, Acta Crystallogr., Sect. C: 56 (2000) 1302.
[20] A. Elmali, C.T. Zeyrek, Y. Elerman, T.N. Durlu, J. Chem. Cryst. 30 (2000) 167.
[21] Z.L. You, Acta Crystallogr., Sect. E: 61 (2005) m1637.
[22] A. Elmali, Y. Elerman, I. Svoboda, H. Fuess, K. Griesar, W. Haase, Z. Naturforsch., B: Chem. Sci. 51 (1996) 665.
[23] J. Reglinski, S. Morris, D.E. Stevenson, Polyhedron 21 (2002) 2167.
[24] D. Ulku, F. Ercan, O. Atakol, F.N. Dincer, Acta Crystallogr., Sect. C: 53 (1997) 1056.
[25] O. Atakol, C. Arici, M.N. Tahir, R. Kurtaran, D. Ulku, Anal. Sci. 15 (1999) 933.
[26] L. Carbonaro, M. Isola, P. La Pegna, L. Senatore, F. Marchetti, Inorg. Chem. 38 (1999) 5519.
[27] H. Ohta, K. Harada, K. Irie, S. Kashino, T. Kambe, G. Sakane, T. Shibahara, S. Takamizawa, W. Mori, M. Nonoyama, M. Hirotsu, M. Kojima, Chem. Lett. (2001) 842.
[28] T. Yamaguchi, Y. Sunatsuki, M. Kojima, H. Akashi, M. Tsuchimoto, N. Re, S. Osa, N. Matsumoto, Chem. Commun. (2004) 1048.
[29] O. Atakol, H. Nazir, C. Arici, I. Svoboda, H. Fuess, Main Group Metal Chemistry 24 (2001) 125.
[30] C. Arici, D. Ulku, O. Atakol, Anal. Sci. 18 (2002) 959.
[31] M.N. Tahir, C. Arici, D. Ulku, O. Atakol, Acta Crystallogr., Sect. E: 57 (2001) m283.
[32] H. Nazir, C. Arici, I. Svoboda, E. Duzgun, O. Atakol, H. Fuess, Main Group Metal Chemistry 24 (2001) 313.
[33] M.D. Ulku, O. Atakol, O. Cakirer, Acta Crystallogr., Sect. C: 54 (1998) 468.
[34] F. Ercan, O. Atakol, Acta Crystallogr., Sect. C: 54 (1998) 1268.
[35] D. Ulku, M.N. Tahir, O. Atakol, H. Nazir, Acta Crystallogr., Sect. C: 53 (1997) 872.
[36] P. Pfeiffer, E. Breith, E. Lubbe, T. Tsumaki, J. Liebigs, Ann. Chem. 503 (1939) 84.
[37] M. Sari, O. Atakol, I. Svoboda, X-ray Struct. Anal. 21 (2005) 205.
[38] Crysalis, Oxford Diffraction Ltd, Version 1 (2005).
[39] G.M. Sheldrick, SHELX97, Program for Crystal Structure Calculations, 1997, University of Gottingen.
[40] Abspack, Oxford Diffraction Ltd (2005).
[41] Z.L. You, H.L. Zhu, W.S. Liu, Acta Crystallogr., Sect. E: 60 (2004) m805.
[42] K. Nakamoto, Infrared and Raman Spectra of Inorganic and Coordination Compounds, Part B: Application in coordination, Organometalic, and Bioinorganic Chemistry, 5th ed., Wiley, New York, 1997, p.116.

Available online at www.sciencedirect.com
ScienceDirect
Polyhedron 26 (2007) 3129–3135
POLYHEDRON
www.elsevier.com/locate/poly

Synthesis, characterization and redox behavior of bis(*N*-1-adamantanyl- and *N*-2-adamantanyl-3,5-^{t}Bu$_2$-salicylaldiminato)copper(II) complexes

Veli T. Kasumov [a,*], Ali İ. Öztürk [a], Fevzi Köksal [b]

[a] *Department of Chemistry, Harran University, Osmanbey, 63300 Şanlıurfa, Turkey*
[b] *Department of Physics, Faculty of Arts and Sciences, Ondokuz Mayıs University, 55139 Kurupelit, Samsun, Turkey*

Received 5 December 2006; accepted 15 February 2007
Available online 23 February 2007

Abstract

Two new bulky ligands, *N*-(1-adamantyl)-3,5-^{t}Bu$_2$-salicylaldimine (**1**), and *N*-(2-adamantyl)-3,5-^{t}Bu$_2$-salicylaldimine (**2**), and their copper bis-chelate complexes, **3** and **4**, have been prepared and their analytical, spectroscopic and magnetic properties, chemical and electrochemical redox reactivity are described. EPR and UV/Vis results [higher $g_{\|}/A_{\|}$, lower energy λ (nm)] for **3** and **4** suggest a distorted square planar geometry with a higher degree of distortion for **3** than for **4**. Chemical oxidation of **1**–**4** by ACN, on the basis of their EPR and UV/Vis spectra results in the formation of the free $\mathbf{1}^{\cdot+}$, $\mathbf{2}^{\cdot+}$ phenoxyl and Cu(II)-phenoxyl radicals complexes [$g = 2.0065$ ($\mathbf{3}^{\cdot+}$), 2.0099 ($\mathbf{4}^{\cdot+}$) and λ_{max} at *ca.* 430 and 720 nm]. Electrochemical studies have shown that the complexes possess ligand- and copper(II)-centered quasi-reversible and irreversible responses and the more distorted complex **3**, having the bulkier 1-adamantyl on the imine nitrogen, was reduced at a more negative potential than the less distorted complex **4**.
© 2007 Elsevier Ltd. All rights reserved.

Keywords: Bis[*N*-(adamantyl)-3,5-^{t}Bu$_2$-salicylaldiminato]Cu(II) complexes; Spectroscopy; Electrochemistry; Chemical oxidation; Phenoxyl radical

1. Introduction

There has been considerable interest in copper (II) salicylaldimine (SA) complexes, for example they have been studied as model compounds for biological dioxygen carriers [1], metalloenzymes [1b], oxidative coupling reactions of phenol compounds [2] or used as catalysts in catalytic reactions [3]. The ability of copper-containing enzymes such as tyrosinases and catechol oxidases to reversibly bind and activate molecular oxygen plays a vital role in biological oxidation catalyses [3]. The discovery of the Cu^{II}-phenoxyl radical in the active site of copper(II)-containing enzymes (galactose and glyoxal oxidases) [4] has stimulated the development of structural and functional model transition metal complexes with coordinated phenolate or phenol ligands which are used for the direct generation of coordinated or uncoordinated M^{II,III}-phenoxyl radical complexes [4–6]. Model complexes of this kind are important because they allow the definitive establishment of spectroscopic features of *coordinated versus uncoordinated* phenoxyl radicals and to understand their chemical reactivity.

Nevertheless, in simple systems such as bis-bidentate SA complexes there are still some stereochemical and conformational questions. For instance, it has been reported that tetrahedral distortion is enhanced in bis(*N*-alkyl-SA)copper(II) complexes as the bulkiness of the alkyl group increases and in parallel to this the reduction potential shifts to more positive values as the distortion from planarity of those complexes is enhanced [7]. However, in the analogous bis(*N*-cycloalkyl-naphthaldiminato)copper(II) complexes, the above trend is inversed [8].

In continuation of our early studies [9,10] on the chemistry and reactivity of metal complexes with salicylaldimines bearing sterically protected 2,6- or

* Corresponding author. Tel.: +90 4143440020; fax: +90 4143440051.
E-mail address: vkasumov@harran.edu.tr (V.T. Kasumov).

0277-5387/$ - see front matter © 2007 Elsevier Ltd. All rights reserved.
doi:10.1016/j.poly.2007.02.012

3,5-^{t}Bu$_2$-substituted phenol arms, which enable them to produce stable phenoxyl radical complexes, we report herein the synthesis, spectroscopic characterization, as well as chemical oxidation and electrochemical behaviors of bis[*N*-(adamantly)-3,5-^{t}Bu$_2$-salicylaldiminato]Cu(II) complexes. The *N*-(1-adamantyl)-3,5-^{t}Bu$_2$-salicylaldimine (L_1H) and *N*-(2-adamantyl)-3,5-^{t}Bu$_2$-salicylaldimine (L_2H) ligands and their corresponding Cu(L_1)$_2$ and Cu(L_2)$_2$ bis(ligand) complexes are abbreviated as **X** (**X**=**1**, **2**, **3** and **4**, respectively).

2. Experimental

2.1. Measurements

The C, H, N elemental analyses were performed on a LECO CHNS-932 model analyzer by the microanalytical services of the Department of Chemistry at the University of Inonu. Electronic absorption spectra were recorded on a Shimadzu 1601 UV–Vis spectrophotometer in the range 1100–200 nm. IR spectra were recorded on a Perkin–Elmer FTIR spectrometer using KBr disks. ^{1}H NMR spectra were recorded on a Bruker Spectro spin Avance DPX-400 Ultra Shield Model NMR using TMS as an internal standard in $CDCl_3$. The room temperature (r.t.) magnetic susceptibility measurements were performed by using a Sherwood Scientific magnetic balance and the diamagnetic corrections were evaluated using Pascal's constants. ESR spectra were taken on a Varian E109 C X-band spectrometer. The field and frequency calibration were made using DPPH ($g = 2.0037$) powder.

Electrochemical measurements were recorded on a PC-controlled Eco Chemie-Autolab-12 potentiostat/galvanostat in nitrogen degassed solutions of *ca.* 10^{-3}–10^{-4} M of **X** containing 0.05 M Et_4NBF_4 as the supporting electrolyte. The potentiostat/galvanostat has an iR compensation option. Cyclic voltammetry were taken in a conventional three-electrode cell consisting of a Pt auxiliary electrode, an Ag/AgCl reference electrode and a 2 mm sized Pt disc working electrode. Prior to running the voltammograms, the solutions were purged with dry nitrogen for 3–4 min in order to remove dissolved oxygen. The potentials are referred to Ag/AgCl in the potential range +1.5 to −1.85 V.

2.2. Materials

All commercial chemicals and solvents were of spectroscopic and HPCL grade and were used without further purification. *N*,*N*-Dimethylformamide (DMF), dimethylsulfoxide (DMSO), acetonitrile (MeCN), chloroform, alcohols, 2,4-di-*tert*-butylphenol, $(NH_4)_2Ce(NO_3)_6$ (ACN), Et_4NBF_4, copper(II) acetate monohydrate, 1-adamantanamine, 2-adamantanamine hydrochloride were obtained from Aldrich Chemical Co, Inc. 3,5-^{t}Bu$_2$-salicylaldehyde was prepared as described in the literature [11]. The ligands and the copper(II) complexes were prepared by methods described elsewhere [10].

2.3. Preparation of the ligands and the complexes

N-(1-Adamantanyl)-3,5-^{t}Bu$_2$-salicylaldimine (**1**) and *N*-(2-adamantanyl)-3,5-^{t}Bu$_2$-salicylaldimine (**2**) were prepared using standard procedures involving the condensation of 3,5-^{t}Bu$_2$-salicylaldehyde with the appropriate 1-adamantanamine and 2-adamantanamine in refluxing ethanol in the presence of a catalytic amount of formic acid. The yellow products were recrystallized from methanol and air-dried. **1**: yield 65%, M.p. 140 °C. IR (KBr, pellet, cm^{-1}): 1631 (CH=N), 2902–2964 (C–H of ^{t}Bu), 2600 (H-bonding OH). ^{1}H NMR (400 MHz, $CDCl_3$): $\delta = 13.71$ (very br, s, 1H, O*H*), 8.35 (s, 1H, C*H*=N), 7.36 (d, 1H, $J = 1.0$ Hz, *meta*-coupled doublet in salicylic ring), 7.088 (d, 1H, $J = 1.2$ Hz, *meta*-coupled doublet in salicylic ring), 2.18 (s, 3H, C*H*), 1.86 (d, 6H, N–C–CH_2–, $J = 2.4$ Hz), 1.73 (qu. 6H, –CH_2–, $J = 4.8$ Hz), 1.437 (s, 9H, C(CH_3)$_3$), 1.298 (s, 9H, C(CH_3)$_3$). Elemental *Anal*. Calc. for $C_{25}H_{37}NO$: C, 81.69; H, 10.15; N, 3.81. Found: C, 81.06; H, 10.62; N, 3.57%. **2**: M.p. 119 °C. Yield 66.3%. IR (KBr, pellet, cm^{-1}): 1618 (CH=N), 2902–2964 (C–H ^{t}Bu), 2670 (H-bonding OH). ^{1}H NMR (400 MHz, $CDCl_3$): δ 14.11 (s, 1H, O*H*), 8.43 (s, 1H, C*H*=N), 7.38 (d, 1H, $J = 2.8$ Hz, *meta*-coupled doublet in salicylic ring), 7.11 (d, 1H, $J = 2.0$ Hz, *meta*-coupled doublet in salicylic ring.), 3.47 (s, 1H, N–C*H*–), 2.49 (d, 2H, C*H*, $J = 12.4$ Hz), 1.86 (mul., 10H, CH_2), 1.45 (d, 2H, –C*H*). *Anal.* Calc. for $C_{25}H_{37}NO$: C, 81.69; H, 10.15; N, 3.81. Found: C, 81.04; H, 10.44; N, 3.68%. The complexes **3** and **4** were prepared by refluxing methanolic solutions of Cu(ac)$_2$H$_2$O and L_xH in a 1:2 molar ratio for *ca.* 1.5 h. The volume of the resulting solution was reduced to 20 ml and left to stand under atmospheric conditions. The black precipitate **3** and brown crystals **4** were collected by filtration, washed with cold methanol and dried in vacuo to give **3** and **4** with yields of 75.3% and 73.4%, respectively. **3**: M.p. 240 °C. IR (KBr, cm^{-1}): 1608 (CH=N), 2864–2956 (C–H in ^{t}Bu). *Anal*. Calc. for $C_{50}H_{72}N_2O_2Cu$ (**3**): C, 75.38; H, 9.11; N, 3.52. Found: C, 75.42; H, 9.53; N, 3.10%. Magnetic moment $\mu_{eff}/\mu_B = 1.66$ at 300 K. **4**: M.p. > 260 °C, IR (KBr, cm^{-1}): 1620 (CH=N), 2864–2956 (C–H in ^{t}Bu). *Anal*. Calc. for $C_{50}H_{72}N_2O_2Cu$ (**4**): C, 75.38; H, 9.11; N, 3.52; Found: C, 74.29; H, 9.25; N, 3.12%. Magnetic moment $\mu_{eff}/\mu_B = 1.83$ at 300 K.

3. Results and discussion

All of the SA ligands and complexes studied were prepared in good yields as yellow (**1**,**2**) and brown (**3**,**4**) crystalline solid products. Satisfactory elemental analyses were obtained for all of the compounds. Spectroscopic (IR and ^{1}H NMR) data for the ligands are consistent with the formulations of **1** and **2**. The ligands are soluble in MeOH, EtOH, MeCN, CH_2Cl_2 and $CHCl_3$, but the complexes are less soluble in solvents such as alcohols, MeCN and benzene; in addition complex **4** is very poorly soluble even in MeCN and DMSO.

3.1. IR, ^{1}H NMR and electronic spectra

Important IR absorption frequencies of **1**–**4**, along with their assignments, are given in Section 2. The IR spectra of **1** and **2** exhibit a broad absorption band at *ca.* 2660 cm^{-1} due to ν(OH) involved in intramolecular (O–H···N) H-bonding that disappears upon complexation. The ν(C=N) vibration (~1632 cm^{-1}) of **1** and **2** undergoes shifts to lower frequencies in the spectra of **3** and **4** (1608 and 1620 cm^{-1}), indicating coordination of the iminic nitrogen [12a]. The ^{1}H NMR spectral results obtained for **1** and **2** in $CDCl_3$, with their assignments, are given in Section 2. The ^{1}H NMR signals were assigned on the basis of their integral intensity, spin–spin coupling pattern and chemical shift values.

The electronic spectra of **1**–**4** and their oxidized intermediates recorded in ethanol, MeCN and $CHCl_3$ are presented in Table 1. The intraligand absorptions <400 nm are assigned to $\pi \rightarrow \pi^*$ and $n \rightarrow \pi^*$ transitions in the enoliminic tautomer. The low intensity band at *ca.* 416 nm is assigned to a $n \rightarrow \pi^*$ transition in the dipolar zwitterionic or ketoamine tautomeric structures of **1** and **2** (Table 1) [12b,12c]. Within the visible region, **3** and **4** manifest absorptions at *ca.* 525 and 800(sh) nm and 480 and 680(sh) in $CHCl_3$ and MeCN, respectively (Table 1). In each case, the higher energy transition is assigned to a phenolate-to-Cu(II) charge transfer transition, on the basis of comparisons with the UV/Vis spectra of other Cu(II)-phenolate complexes [6b]. The bands observed around 700 and 800 nm are assigned to d–d transitions in the pesudotetrahedral geometry [7b,7c].

3.2. EPR and magnetic properties of the complexes

The X-band EPR spectra of polycrystalline samples of both complexes **3** and **4** have been recorded in the temperature range from 300 K to 113 K, which clearly exhibit three and five resolved lines in the $g_{\|}(g_{zz})$ region, respectively, and one unresolved asymmetric pattern in $g_{\perp}(g_{xx}/g_{yy})$ region (Figs. 1 and 2). These facts suggest the absence of dipolar broadening and that spin exchange between adjacent molecules is not fast enough to average the A-anisotropy [13a]. When the temperature was decreased from 298 to 133 K, with a slight change in the line widths and g-factors ($g_{\|} = 2.286$, $A_{\|} = 112$ G, $\Delta H_{\|} = 56$ G at 298 K and $g_{\|} = 2.276$, $A_{\|} = 124$ G, $\Delta H_{\|} = 62$ G at 113 K for **3**), increases of the signal intensities by factors of about 2.6 and 2.2 for **3** and **4**, respectively, were detected. These behaviors are indicative of ferromagnetic type exchange interactions [14]. An antiferromagnetic exchange interaction would decrease the ESR intensity with a decrease of temperature. The appearance of five non-equally separated lines, which were detected as a broad peaks and overlapped shoulders in the $g_{\|}$ region of the powder ESR spectrum of **4** is not typical for mononuclear or binuclear Cu(II) complexes. In addition, the $CHCl_3$ solution spectrum of this sample at 300 and 193 K is typical for mononuclear copper(II) species. The reason of this anomaly is not apparent. It is thought that one reason of this behavior may be anisotropic spin relaxation effects in the crystal state. It is interesting that the powder spectrum of **4** exhibits appreciable line broadening at lower temperature and as a result of this, along with disappearance of the fifth line around 2960 G, the other $g_{\|}$ components become ill-defined at 113 K. Spin-Hamiltonian parameters g_{iso}, A_{iso}, $A_{\|}$ and $g_{\|}$, extracted from experimental spectra of polycrystalline, frozen glass and solution samples, are collected in Table 2. The spectra of **3** exhibits three well resolved lines of the four g_{zz} components in the temperature range 293 to 113 K, which is typical of a Cu(II) complex possessing a $(d_{x^2-y^2})^1$ or $(d_{xy})^1$ ground state ($S = 1/2$), with $g_{\|} > g_{\perp} > g_e$ [13b]. The appearance of five non-equally spaced line components in the $g_{\|}$ region in the solid-state spectrum of **4** is unusual for $S = 1/2$ Cu(II) systems and suggests the existence of magnetically non-equivalent copper(II) ions in the unit cell, having different g- and A-tensors

Table 1
Electronic spectral data for **1**–**4** and their oxidized intermediates

Compound	Solvent	Electronic spectra, λ (nm), ($\log\varepsilon$, M^{-1} cm^{-1}); absorbance (A)
1	EtOH	215(4.4), 262(3.57), 280[a], 329(3.1), 414(2.3)
1	MeCN	262, 323, 411
1 + ACN	MeCN	263, 313, 399, 712(2.2); (A) lowered from 1.16 to 0.26 for 11 min
2	EtOH	223(4.5), 263(3.9), 330(3.5), 416(2.3)
2	MeCN	265(3.9), 324(3.8), 410(2.9)
2 + ACN	MeCN	722(1.8); (A) lowered from 0.59 to 0.31 for 10 min
3	$CHCl_3$	262(5.0), 280[a], 335(3.9), 445[a], 526(2.5), 800[a](2.2)
3 + CAN	$CHCl_3$	264, 289, 328, 410[a]; $\lambda_{max}(A)$ shifted from 660(0.27) to 710(0.81)
3	MeCN	263, 329(4.1), 382(3.9), 526(2.5), 800[a](2.3)
3 + ACN	MeCN	258, 312, 428, 716(2.3)
4	$CHCl_3$	268[a], 331(4.7), 372(4.6), 480[a](2.9), 680[a](2.3)
4 + CAN	$CHCl_3$	264, 330, 403[a], 430[a]; $\lambda_{max}(A)$ shifted from 686(0.99) to 722 (0.69)
4	MeCN	260[b], 330(4.2), 365(4.2), 500[a](2.7), 680[a](2.3)
4 + ACN	MeCN	257, 310, 430, 719(2.2)

[a] Shoulder.
[b] This data are obtained in MeCN/$CHCl_3$ = 8/1 (v/v ratio).

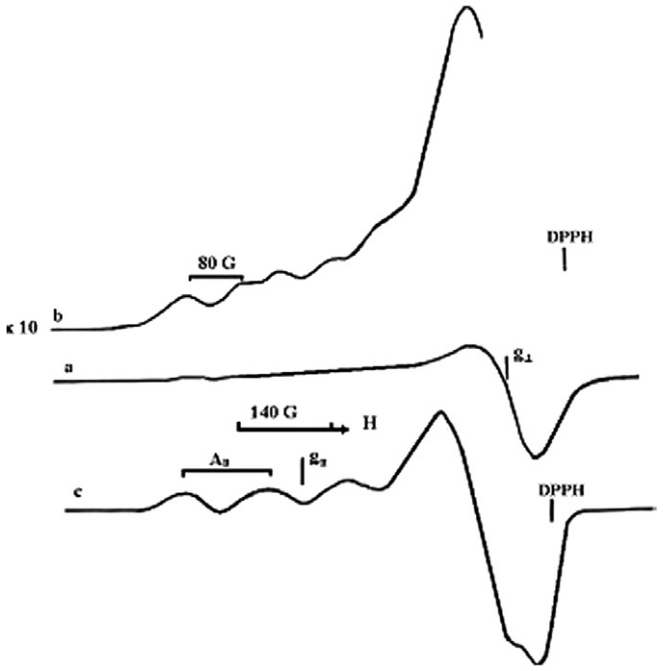


Fig. 1. The polycrystalline EPR spectra of **4** at 300 K (a and b) and **3** at 253 K.

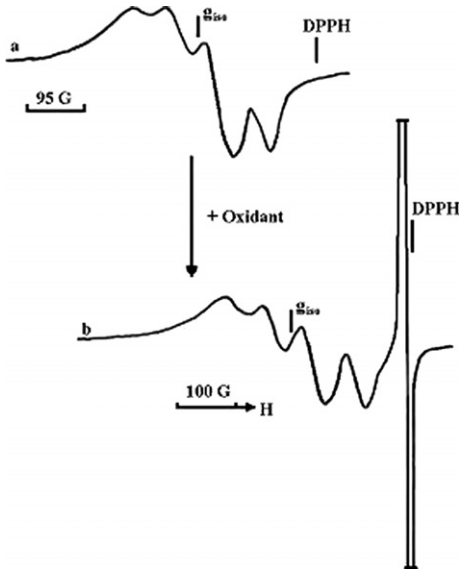


Fig. 2. (a) Solution EPR spectrum for **4** and (b) for the **4** + ACN system at 300 K in $CHCl_3$ solution.

($g_\parallel = 2.248$, $A_\parallel = 144$ G, $g_\parallel/A_\parallel = 166$ cm and $g_\parallel = 2.178$, $A_\parallel = 152$ G, $g_\parallel/A_\parallel = 154$ cm at 293 K). The $g_\parallel/A_\parallel$ ratio, which reflects the degree of the tetrahedral distortion from square-planar geometry in the Cu(II) complexes, for powder samples of **3** and **4** were found to be 208 cm and 162 cm (average) at 293 K, respectively, suggesting that the former complex is considerably more distorted than the latter in the solid state [15]. It should be noted that due to the overlapping of $g_\parallel$ components in the spectra of powder samples of **4** (Fig. 1b), a more accurate estimation of the $g_\parallel$ and $A_\parallel$ tensors is difficult. Thus the observed $g_\parallel > g_\perp > g_e$ and the $G = (g_\parallel - g_e)/(g_\perp - g_e)$ in the range 3–5 are consistent with a $(d_{x^2-y^2})$ or d_{xy} ground state having a small exchange coupling [13b]. Comparison of the $g_\parallel/A_\parallel$ values indicates that the degree of tetrahedral distortion in **3** is higher than that in **4**.

The X-band ESR spectra of **3** and **4** obtained in $CHCl_3$ solution at 300 and 173 K correspond to the common spectra for monomeric copper(II) complexes with the axial $g_\parallel > g_\perp > g_e$ trend, typical for copper(II) complexes with a $(d_{x^2-y^2})^1$ or $(d_{xy})^1$ ground state ($S = 1/2$), (Table 2). Their solution spectra do not display superhyperfine features from the nuclear spin of the coordinated nitrogen atoms (^{14}N; $I = 1$), not in the g_{xx}/g_{yy} region (173 K) or on the high field components of the r.t. spectra. According to the values of the $g_\parallel/A_\parallel$ ratio (Table 2), in $CHCl_3$ solution the tetrahedral distortion in **3** is significantly higher than that in **4**. The ratio of $g_\parallel/A_\parallel = 142$ cm, determined from the frozen glass spectrum of **4**, suggests that the CuN_2O_2 chromophore of this complex adopts a square-planar geometry in $CHCl_3$ solution. At the same time, the $g_\parallel/A_\parallel$ quotient for the solid state (220 cm) and solution (189 cm) spectra of **3** indicate that the tetrahedral geometry of this complex practically remains unchanged upon dissolution. It is necessary to note that for a four-coordinate copper(II) system, the $g_\parallel/A_\parallel$ ratio is a function not only of the tetrahedral distortion from the square-planar structure but also is dependent upon the nature and numbers of the atoms (for example, O_4, N_4, S_4, N_2O_2, N_2S_2, O_2S_2 and others) coordinated to copper(II) [14b,16].

The room temperature effective magnetic moments of **3** and **4** were found to be $1.66\mu_B$ and $1.83\mu_B$, respectively, which is reasonable compared to the theoretical spin-only value of $1.73\mu_B$ for $S = 1/2$ systems. Although the μ_B value of **4** is typical for square-planar or pseudo-tetrahedral mononuclear copper(II) complexes, the value for **3** is similar to those in magnetically dilute systems, in which the magnetic centers are separated by more than 8 Å [13b].

Table 2
ESR parameters for complexes **3** and **4**

Complex	Polycrystalline spectra				Solution ($CHCl_3$) spectra							
	$g_\parallel$	$g_\perp$	$A_\parallel$	G	g_{iso}	$g_\parallel$	$g_\perp$	A_{iso}	$A_\parallel$	$A_\perp$	$g_\parallel/A_\parallel$	G
3	2.286	2.084	118	3.47	2.127	2.275	2.054	66	130	23	186.9	5.27
4	2.248	2.062	140	4.11	2.117	2.237	2.077	68	168	18	142.4	3.14
	2.178	2.062	152	2.94								

3.3. Chemical oxidation of 1–4 with ACN

Our recent studies demonstrated that the chemical oxidation of bis[*N*-alkyl(aryl)-3,5-^{t}Bu$_2$-salicylaldiminato]copper(II) complexes by $(NH_4)_2[Ce(NO_3)_6]$ (ACN) in $CHCl_3$ was accompanied by a decrease of the intensity of their ESR spectra and the appearance of radical signals [9]. A similar EPR investigation of the oxidative behavior of **3** and **4** revealed that when they are treated with a 2–3 fold excess of ACN in $CHCl_3$ at r.t., along with a color change from dark brown to green, a decrease in intensity of their EPR spectra and appearance of new radical signals with $g = 2.0099$ and 2.0065, respectively, were observed (Fig. 2b). The observed g values are slightly greater than that observed for free phenoxyl radicals (~2.004–2.005) [17]. The decrease in the EPR signal intensity of the oxidized complexes probably results from magnetic coupling between a $S = 1/2$ Cu(II) center and a $S = 1/2$ coordinated radical ligand in Cu^{II}-·OPh radical species. Our suggestion, the generation of M-phenoxyl radical complexes, is supported by EPR, UV/Vis and X-ray evidences, which recently were reported for bis(*N*-aryl(alkyl)-3,5-^{t}Bu$_2$-salicylaldiminato)M(II) complexes where M = Cu(II), Co(II) and Pd(II), and other types of various metal complexes bearing di-*tert*-butyl protecting groups on the ligands [5,6,9].

The spectral changes for **X** + ACN systems were monitored by UV/Vis spectroscopy during the progress of the oxidation of **X** in $CHCl_3$. The oxidant is insoluble in $CHCl_3$ so the reaction system was heterogeneous and prior to each scanning, the solution of the sample was mixed with the oxidant by using a spatula for 5–6 s. Then the solution was transferred into a 1 cm quartz cuvette to measure the spectrum. When a 3–4 fold excess of ACN was added to the solutions of **3** and **4** in $CHCl_3$ at r.t., the dark brown solutions turned green with a decrease of the intensity of their original visible bands in the 480–800 nm region, and a new band at *ca.* 660–690 nm was detected (Fig. 3). After 2–3 scans, the initial bands

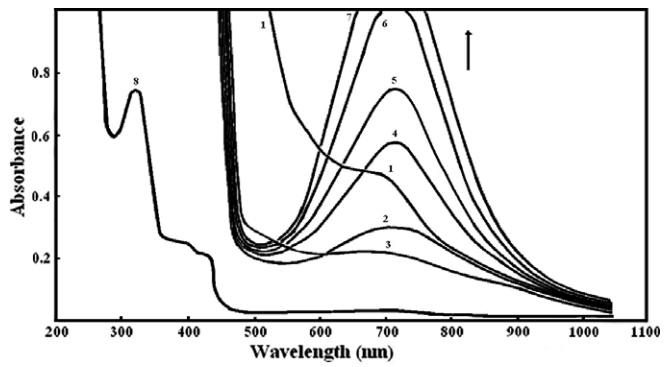


Fig. 3. The change in the absorbance of UV/Vis spectra of the **4** + ACN system in the time course (5 min) in $CHCl_3$ solution at r.t. and aerobic conditions. 1 – initial spectrum of **4** in $CHCl_3$; each spectrum from 2 to 7 is scanned after mixing the reaction mixture; 8 – is a scanned dilute solution of sample 7. The arrow indicates the direction of increasing absorbance.

in the region 480–800 nm completely disappeared and new maxima began to appear, whose intensities gradually increased after each mixing of the reaction system, and in parallel to this their λ_{max} value shifted to higher wavenumbers (Fig. 3 and Table 1). For example, as can be seen from Table 1, the λ_{max} (A) values of a new band for the **3** + ACN system after 10 repeated mixing and scanning, shifted from 660(0.27) to 710(0.81) nm, and then the spectrum reached a steady-state with no further change in position upon mixing. When the reaction mixtures are scanned without mixing over 30 min, a decrease in the absorbance of λ_{max} and a change in color from deep green to yellowish green were observed. Similar behavior also was observed for the **4**+ ACN system (Table 1).

It is interesting that the spectral features of the **X** + ACN systems in MeCN were different from those in $CHCl_3$. As soon as ACN and **X** were dissolved in MeCN, the oxidation of the ligands and their complexes was carried out with one and two equivalent molar amounts ACN. The results of these experiments show that on mixing equivalent molar amounts of the ligands and ACN in MeCN, the yellow color of the ligands simultaneously turns to deep green, and along with the disappearance of the original band at *ca.* 415 nm a new maximum peak appears at 712 and 721 nm for oxidized **1** and **2** (Table 1), respectively. Note that practically without any change in position, the intensity of both new bands decreased from 712 (1.1622) to 711 (0.2698) nm after 12 min and from 722 (0.5938) to 721 (0.3090) nm after 10 min, respectively, for the oxidized ligands **1** and **2** (Table 1). The green color of these oxidized systems after *ca.* 1 h gradually converted to brownish yellow, and then to light yellow after ~ 3 h. Similar behaviors also were observed in the oxidation of complexes **3** and **4**. For example, after addition of 1 or 2 equivalents of ACN to MeCN solutions **3** and **4**, a simultaneous change of the dark brown color to dark green with the disappearance of bands in the 480–800 nm region, and the appearance of a new maximum band at *ca.* 720 nm were observed (Table 1). On standing, the green color of this mixture gradually converts to brownish yellow. However, the rate of decrease in the peak absorbance for the oxidized complexes was significantly lower than that for the ligands. Note that the observed less intense band at *ca.* 720 nm and the strong absorption at *ca.* 430 nm detected in the spectra of the oxidized **X** compounds (Table 1) are characteristic for phenoxyl type radicals [6b,6d]. The absorption at *ca.* 430 nm is assigned to the $\pi \rightarrow \pi^*$ transition of the phenoxyl radical ligand, as ascribed in the UV/Vis spectra of several other Cu(II)- and Zn(II)-phenoxyl radical complexes. The detection of an identical band around 720 nm for the oxidized ligands and complexes confirm that the chemical oxidation occurs at the ligand centers of complexes **3** and **4**. These bands could arise from ligand based ($\pi \rightarrow \pi^*$ or $n \rightarrow \pi^*$) MLCT, LMCT or LLCT transitions [5c,5d,6d].

3.4. Electrochemistry

The electrochemical redox properties of **1**–**4** were investigated by cyclic voltammetry in potentials ranging from −1.5 to + 1.85 V vs. Ag/AgCl at 300 K under N_2 in MeCN, DMF and DMSO, containing Et_4NBF_4 (0.05 M) as the background electrolyte. Selected results are collected in Table 3. Typical cyclic voltammograms (CV) of the **1** and **2** ligands recorded in MeCN are presented in Fig. 4a and b. The i_{pc}/i_{pa} ratios are less than unity (0.4–0.7) and increase as the scan rate is increased. In the above potential range, the initial CV of **1** displays an oxidation peak at 1.12 V, with the reverse weak reduction curve at *ca.* 0.83 V and ill-defined cathodic shoulders at *ca.* −0.94 V (E_{pc}) and −0.31 V (E_{pa}). The initial CV of **2** in the same potential range exhibits quasi-reversible oxidation and reduction waves at $E_{1/2} + 1.02$ V and at $E_{1/2} - 0.69$ V, respectively. At the same time, CVs of the ligands recorded in the anodic potential range from 0.0 to 1.5 V exhibit very similar well defined quasi-reversible oxidation waves at $E^1_{1/2} + 1.02$ V for **1** and $E^2_{1/2} + 1.03$ V for **2** (Fig. 4a). In the case of the cathodic scan from 0.0 to −1.5 V for both **1** and **2** the identical quasi-reversible reduction waves at $E^1_{1/2} - 0.82$ V and $E^2_{1/2} - 0.78$ V, respectively, were detected (Fig. 4b). The observed quasi-reversible anodic oxidation waves were assigned to the phenolate/phenoxyl couple. The waves detected at a negative potential have been ascribed to the reduction of the imine group [18].

The CV of **3** recorded in the potential range from −1.5 to 1.5 V versus Ag/AgCl in DMSO solution shows two well defined oxidation processes, in the cathodic region at $E^1_{1/2} - 0.38$ V, which can be assigned to the Cu^I/Cu^{II} couple and a quasi-reversible anodic oxidation wave at $E^1_{1/2} + 0.26$ V assignable to a Cu(II)/Cu(III) or ligand centered one-electron oxidation. A poorly defined response at *ca.* $E_{1/2} + 1.03$ V is assigned to a ligand centered oxidation.

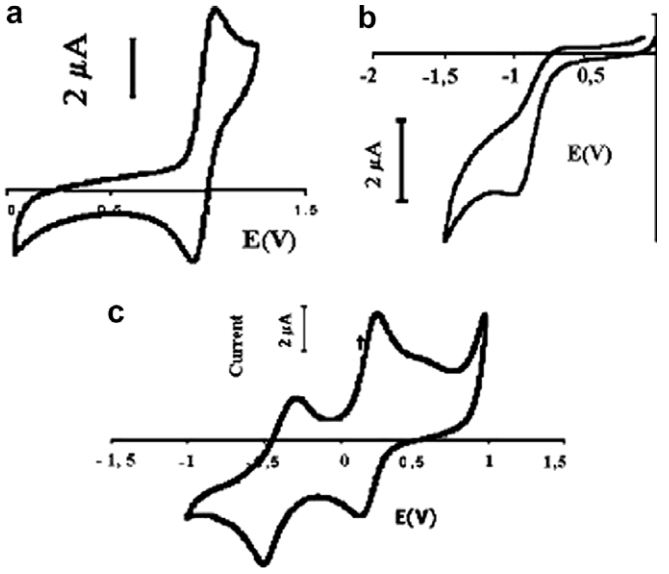


Fig. 4. Cyclic voltammograms of **1** (0.5 mM) in MeCN containing 0.05 M TEATFB at a scan rate of 0.1 V/s: (a) in the potential range 0.0 to + 1.25 V and (b) in the potential range −1.5 to 0.0 V; (c) CV of **3** (0.4 mM) in DMSO containing 0.1 M TETFB at a scan rate of 0.1 V/s. Working electrode Pt, counter electrode Pt wire, reference electrode Ag/AgCl were used in all experiments.

On the other hand, in MeCN solution for this complex only a quasi-reversible feature with $E_{pa}/E_{pc} = 1.43/1.36$ V was observed. A departure from the electrochemical reversibility is evident from the peak to peak separations, $\Delta E_p = E_{pa} - E_{pc}$ of 0.19 − 0.40 V, which are considerably greater than those expected for a reversible system (0.06 V), suggesting a quasi-reversible charge-transfer. In addition, the current relationship (i_{pa}/i_{pc}) is less than unity in each case. Similar ligand and metal centered redox responses with $E_{1/2}$ values of 0.24, 1.01, −0.88 V and an irreversible weak peak at $E_{pc} = -1.32$ V, were detected

Table 3
Cyclic voltammetric data for **1**–**4** compounds

Compound	Solvent	Scan range (V)	Cathodic scan			Anodic scan		
			E^1_{pa}/E^1_{pc}	E^2_{pc}	$E^1_{1/2}$	E^1_{pa}/E^1_{pc}	E^2_{pa}/E^2_{pc}	$E^1_{1/2}$
1	MeCN	−1.5 to 1.85	−0.31/−0.94		−0.63	1.12/0.83		0.98
		−1.5 to 0.0	−0.62/−1.04		−0.83			
		0.0 to 1.5				−1.06/0.97		1.02
2	MeCN	−1.5 to1.85	−0.46/−0.92		−0.69	1.11/0.92		0.99
		−1.5 to 0.0	−0.57/−0.98		−0.67			
		0.0 to 1.5				1.08/0.96		1.02
3	DMSO	−1.5 to 1.5	−0.20/−0.57		−0.39	0.32/0.08	1.19/0.87	0.20
		−1.0 to 1.0	−0.20/−0.57		0.38	0.31/0.08		0.19
	DMF	−1.5 to 1.5	−0.63/−1.12	−1.32[a]	−0.88	0.35/0.13	1.14/0.88	0.24
		−1.5 to 0.0	−0.68/−1.04		−0.86			
		0.0 to 1.5				1.14/0.76	0.15[a]	0.95
4	DMF	−1.5 to 1.5	−0.69/−1.03	−1.32[a]	−0.86	0.38/0.14		0.26
		−1.5 to 0.0	−0.69/−0.98	−1.33[a]	−0.84			
		0.0 to 1.5				1.16[a]		

[a] Irreversible shoulder.

for **3** in DMF (Table 3). The CV of **4** in the potential range from −1.5 to 1.5 V in DMF exhibits an anodic oxidation curve at *ca.* $E_{1/2} = 0.26$ V, $E_{pc} = -1.03$ V (with an associated broad anodic oxidation curve centered at the potential ~−0.71 V) and an irreversible weak peak at −1.31 V (Table 3). It is worth noting that the first reduction potential of the more distorted **3** ($E_{pc} = -1.12$ V) in DMF is more negative than that for the less distorted **4** ($E_{pc} = -1.03$ V), which is the inverse to the reported trend observed in a series of bis(*N*-alkyl-SA)copper(II) complexes, where it was found that the more distorted bis-chelate complexes are easier to reduce than their planar analogs [7a]. The CV of **4** in MeCN exhibits irreversible reductions at $E^1_{pc} = -1.35$ V and $E^2_{pc} = -0.73$ V and an oxidation curve at *ca.* 0.21 V. The wave at −1.35 V is assigned to the reduction of the free anionic ligand **2** [19]. On the other hand, on cathodic (from 0.0 to −1.5 V) and anodic (from 0.0 to 1.5 V) scans of **4** in MeCN no reduction and oxidation responses were detected.

Comparing the voltammetric data (E_{pc}) in DMF with those from the ESR ($A_{\|}$, $g_{\|}$), it is noticeable that for **3** and **4**, as the bulkiness of the adamantly group increases, the E_{pc} values become more negative. These observations are in good agreement with the results suggesting that the more negative the E_{pc} value, the more voluminous the alkyl substituent on the imine nitrogen, as reported by J.M. Fernandez-G and co-workers [8].

Acknowledgement

We thank the Harran University Grant Commission (HUBAK) for financial support.

References

[1] (a) R.H. Holm, G.W. Everett, A. Chakravorty, Prog. Inorg. Chem. 7 (1966) 83;
(b) C.G. Pierpont, C.W. Lnge, Prog. Inorg. Chem. 41 (1994) 331;
(c) N. Hoshno, Coord. Chem. Rev. 174 (1998) 77;
(d) S. Yamada, Coord. Chem. Rev. 190 (1999) 537.
[2] D. Chen, A.E. Martell, Y. Sun, Inorg. Chem. 28 (1989) 2647.
[3] (a) E.I. Solomon, U.M. Sandaram, T.E. Machonkin, Chem. Rev. 96 (1996) 2563;
(b) C. Eicken, F. Zippel, K. Büldt-Karentzopoulos, B. Krebs, FEBS. Lett. 436 (1998) 293.
[4] (a) N. Ito, S.E. Phillips, C. Stevens, Z.B. Ogel, M.J. McPherson, J.N. Keen, K.D.S. Yadav, P.F. Knowles, Nature 350 (1991) 87;
(b) A. Sokolowsky, J. Müller, R. Schenepf, T. Weyhermüller, P. Hildebrant, K. Hildenbrand, K. Bothe, K. Wieghardt, J. Am. Chem. Soc. 119 (1997) 8889.
[5] (a) P. Chaudhuri, M. Hess, U. Flörke, K. Wieghardt, Angew. Chem. Int. Ed. 37 (1998) 2217;
(b) P. Chaudhuri, M. Hess, T. Weyhermüller, K. Wieghardt, Angew. Chem. Int. Ed. 38 (1999) 1095;
(c) P. Chaudhuri, M. Hess, J. Müller, K. Hildebrand, E. Bill, T. Weyhermüller, K. Wieghardt, J. Am. Chem. Soc. 121 (1999) 9599;
(d) E. Bill, J. Müller, T. Weyhermüller, K. Wieghardt, Inorg. Chem. 38 (1999) 5795.
[6] (a) J.-L. Pierre, Chem. Soc. Rev. 29 (2000) 251;
(b) B.A. Jazdewski, W.B. Tolmen, Coord. Chem. Rev. 200–202 (2000) 833;
(c) F. Thomas, G. Gellon, I. Gautier-Luneau, E. Saint-Aman, J.-L. Pierre, Angew. Chem. Int. Ed. 41 (2002) 3047;
(d) L. Benisvy, A.J. Blake, D. Collison, G. Whittaker, C. Wilson, J. Chem. Soc., Dalton Trans. (2003) 1975.
[7] (a) G.S. Patterson, R.H. Holm, Bioinorg. Chem. 4 (1975) 257;
(b) H. Yokoi, A.W. Addison, Inorg. Chem. 16 (1977) 1341;
(c) J. Ferguson, J. Chem. Phys. 40 (1964) 3406.
[8] (a) J.M. Fernandez-G, S. Hernandez-Ortega, R. Cetina-Rosado, N. Macias-Ruvalcaba, M. Aguilar-Martinez, Polyhedron 17 (1998) 2425;
(b) M.A. Martinez, R.S. Augliar, N.M. Ruvalcaba, R.C. Rosado, A.N. Vazquez, V.G. Vidales, A.Z. Dehesa, J.M. Fernandez-G, S.J.M. Fernandez-G, J. Chem. Soc., Dalton Trans. (2001) 2346.
[9] (a) V.T. Kasumov, F. Köksal, A. Sezer, Polyhedron 24 (2005) 1203;
(b) T. Kasumov, E. Taş, F. Köksal, Ş.Ö. Yaman, Polyhedron 4 (2005) 319;
(c) V.T. Kasumov, A. Bulut, F. Köksal, M. Aslanoğlu, İ. Uçar, C. Kazak, Polyhedron 25 (2005) 1133;
(d) V.T. Kasumov, F. Köksal, Y. Zeren, Spectrochim. Acta, Part A 63 (2006) 330.
[10] (a) A.A. Medjidov, V.T. Kasumov, H.S. Mamedov, Koord. Khim. 7 (1981) 66;
(b) M.K. Guseyinova, A.A. Medjidov, V.T. Kasumov, J. Struct. Chem. 23 (1982) 114;
(c) V.T. Kasumov, A.A. Medjidov, Rus. J. Coord. Chem. 16 (1990) 1355;
(d) V.T. Kasumov, A.A. Medjidov, R.Z. Rzaev, I.A. Golubeva, Rus. J. Coord. Chem. 19 (1993) 933.
[11] J.F. Larrow, E.N. Jacobsen, Y. Gao, Y. Hong, X. Nie, C.M. Zeppe, J. Org. Chem. 59 (1994) 1939.
[12] (a) J.E. Kovacic, Spectrochim. Acta 23A (1967) 183;
(b) S.M. Crawford, Spectrochim. Acta 19 (1963) 255;
(c) P.W. Alexander, R.J. Sleet, Aust. J. Chem. 23 (1970) 1183.
[13] (a) V.H. Growford, W.H. Hatfield, Inorg. Chem. 16 (1977) 1336;
(b) B.J. Hathaway, D.E. Billing, Coord. Chem. Rev. 5 (1970).
[14] (a) B. Blaney, K.D. Bowers, Proc. R. Soc. Lond. Ser. A 214 (1952) 451;
(b) J.R. Pilbrow, Transition Ion Electron Paramagnetic Resonance, Clarendon Press, New York, 1990.
[15] (a) U. Sakaguchi, A.W. Addison, J. Chem. Soc., Dalton Trans. (1979) 600;
(b) V.V. Pavlischuk, Theor. Exp. Chem. 31 (1995) 1.
[16] J. Peisach, W.E. Blumberg, Arch. Biochem. Biophys. 1965 (1974) 691.
[17] (a) E.R. Altwicker, Chem. Rev. 67 (1967) 475;
(b) E.J. Land, G. Porter, E. Strachan, Trans. Faraday Soc. 57 (1961) 1885.
[18] M. Shivakumar, K. Pramanik, P. Ghosh, A. Chakravorty, Inorg. Chem. 37 (1998) 5968.
[19] M.J. Samide, D.G. Peters, J. Electroanal. Chem. 443 (1998) 95.

Available online at www.sciencedirect.com
ScienceDirect
Polyhedron 26 (2007) 3136–3142
POLYHEDRON
www.elsevier.com/locate/poly

Structural and spectroscopic studies of the complex $[BuMeIm]_2[UCl_6]$ in the solid state and in hydrophobic room temperature ionic liquid $[BuMeIm][Tf_2N]$

Sergey I. Nikitenko [a,*], Christoph Hennig [b], Mikhail S. Grigoriev [c], Claire Le Naour [d], Celine Cannes [d], Didier Trubert [d], Emilie Bossé [e], Claude Berthon [e], Philippe Moisy [e]

[a] CNAB, UMR 5084, Université de Bordeaux 1, CNRS, BP 120, Le Haut Vigneau, F-33175 Gradignan Cedex, France
[b] Forschungszentrum Rossendorf, Institute of Radiochemistry, P.O. Box 510119, 01314 Dresden, Germany
[c] A. N. Frumkin Institute of Physical Chemistry and Electrochemistry, RAS, Leninskii Prosp. 31, 119991 Moscow, Russia
[d] Université Paris-Sud, CNRS, UMR 8608, Institut de Physique Nucléaire, Orsay F-91406, France
[e] CEA, Valrhô/Marcoule, DEN, DRCP, SCPS, Bât. 399, BP 17171, 30207 Bagnols sur Cèze, France

Received 5 December 2006; accepted 15 February 2007
Available online 22 February 2007

Abstract

The complex $[BuMeIm]_2[UCl_6]$ was characterized in the solid state and in a solution of $[BuMeIm][Tf_2N]$ room temperature ionic liquid using single-crystal XRD, EXAFS, visible absorption spectroscopy and NMR techniques.The structure of solid $[BuMeIm]_2[UCl_6]$ contains two crystallographically independent formula units (U(1) and U(2)).The U–Cl distances in UCl_6^{2-} anions range from 2.576(6) to 2.638(4) Å, the average values being 2.621(6) and 2.601(8) Å for U(1) and U(2), respectively.The $BuMeIm^+$ cations have four different conformations of C_4H_9 chains.The shortest distances between the centres of the five-member rings of the $BuMeIm^+$ cations and U atoms of $[UCl_6]^{2-}$ anions are in the range 5.53–4.90 Å.Single-crystal XRD data reveal the existence of a hydrogen bond between the most acidic H atom of the imidazolium ring (C2) and the chloride anion of the UCl_6^{2-} octahedron, with the shortest distance Cl···H(C2) equal to 2.57 Å.Quantitative EXAFS measurements indicate that the octahedral complex UCl_6^{2-}($R_{U-Cl} = 2.632(2)$ Å) is the predominant chemical form of U(IV) in $[BuMeIm][Tf_2N]$ solution.Visible absorption spectroscopy and ^1H NMR spectroscopy confirm the existence of hydrogen bonding between theUCl_6^{2-} anion and the acidic proton of the $BuMeIm^+$ cation in RTIL solution, similar to that in the solid state.
© 2007 Elsevier Ltd. All rights reserved.

Keywords: Uranium; Hexachloride complexes; Room temperature ionic liquids; EXAFS; Single-crystal structure; UV/Vis spectroscopy; ^1H NMR

1. Introduction

The unique properties of water-stable room temperature ionic liquids (RTIL) create an opportunity to obtain fundamental data on actinide chemistry without interference from hydrolysis reactions [1,2]. These solvents also offer the possibility to develop new processes for the recovery and purification of actinides [2,3]. Most published studies on actinide behaviour in ionic liquids are focused on spectroscopic and electrochemical investigations of actinide(IV) hexachloro complexes, $AnCl_6^{2-}$ [4–6]. UV/VIS/NIR spectroscopic studies reveal that the complexes $AnCl_6^{2-}$, where An(IV) is U(IV), Np(IV) and Pu(IV), preserve their centrosymmetric octahedral environment in Tf_2N^- based hydrophobic ionic liquids, where Tf_2N^- is the bis(trifluoromethyl-sulfonyl)-imide anion. To obtain detailed information about the U(IV) coordination shell in RTIL solutions, EXAFS and ^1H NMR measurements of UCl_6^{2-} have been carried out for the first time in the hydrophobic ionic liquid [BuMeIm]-$[Tf_2N]$, where $BuMeIm^+$ is the 1-butyl-3-methyl-imidazo-

* Corresponding author. Tel.: +33 557120905; fax: +33 557120900.
E-mail address: nikitenk@cenbg.in2p3.fr (S.I. Nikitenko).

0277-5387/$ - see front matter © 2007 Elsevier Ltd. All rights reserved.
doi:10.1016/j.poly.2007.02.014

lium cation. The single-crystal structure of the complex $[BuMeIm]_2[UCl_6]$ is also reported.

2. Experimental

Complex $[BuMeIm]_2[UCl_6]$ was precipitated from U(IV) solution in concentrated HCl in the presence of a slight excess of [BuMeIm]Cl, as previously described [6a]. To obtain single crystals of $[BuMeIm]_2[UCl_6]$, the powder was recrystallized from a MeOH-MeCN (50/50) mixture under reduced pressure. It should be noted that the crystals available for single-crystal XRD study cannot be obtained from neat MeOH or MeCN. The solid complex $Cs_2[UCl_6]$, used in the EXAFS measurements as a reference, was precipitated by a well known procedure [4]. All U(IV) solids as well as their solutions were prepared and stored in an argon-filled dry box.

The ionic liquid was prepared by a metathesis reaction of [BuMeIm]Cl and HTf_2N in an aqueous medium. [BuMeIm]Cl was synthesized via quaternization of 1-methylimidazole by 1-chlorobutane and washed with ethyl acetate as recently described [1]. The initial chemicals (Aldrich, highest purity) were used in the synthesis without additional purification. To remove chloride ions and protonic impurities the as-prepared RTIL was washed with deionized water (18 MΩ cm) until a neutral pH was obtained. The control of chloride ions was performed by an $AgNO_3$ test. Organic impurities were removed from the RTIL with activated charcoal for 12 h, after which the mixture was passed through a column with small amounts of acidic alumina. ^{1}H NMR test revealed the absence (<1%) of residual reagents in the purified ionic liquid. The RTIL was dried overnight under reduced pressure (~5 mbar) at 70 °C. The water concentration in the dried RTIL was measured by coulometric Karl–Fisher titration and found to be equal to 0.008(2) M.

Single crystal ($0.3 \times 0.12 \times 0.04$ mm) X ray data were collected on a Nonius KappaCCD area detector diffractometer. The crystal was introduced into a Lindemann glass capillary. The lattice parameters were determined from ten images recorded with 1° ϕ-scans and later refined on all data. A hemisphere of the reciprocal space has been measured. The crystal-to-detector distance was fixed at 30 mm. The data were processed with the HKL package [7]. Absorption effects were empirically corrected with the program MULABS from PLATON [8]. The structure was solved by the heavy-atom method with SHELXS97 and subsequent difference Fourier-syntheses and refined by full-matrix least-squares on F^2 with SHELXL97 [9]. All non-hydrogen atoms were refined anisotropically. The hydrogen atoms were placed in idealized calculated positions and refined as riding atoms with displacement parameters equal to 1.2 (CH_2) or 1.5 (CH_3) times that of the attached carbon atom. Restrictions were imposed on the bond lengths and angles in all butyl groups. The structure was refined as a racemic twin with a Flack parameter between 0 and 1 [10]. It should be noted that refinement in the space group $P2_1$ is also appropriate. The molecular drawings were done with SHELXTL [11].

Uranium L_{III}-edge EXAFS spectra were collected at the Rossendorf Beamline at the ESRF (6.0 GeV, 200 mA) [12]. The measurements were carried out in transmission mode using argon-filled chambers at ambient temperature and pressure. The measurements were performed using a double crystal Si (1 1 1) monochromator. Data were collected in equidistant k-steps of 0.05 Å^{-1} across the EXAFS region. Six to ten scans were recorded for each sample and then averaged. A Y metal foil (first inflection point at 17038 eV) was used for energy calibration. The U L_{III} threshold energy, $E_{k=0}$, was defined as 17185 eV. EXAFS data were extracted from the raw absorption spectra by standard methods including a spline approximation for the atomic background using the program EXAFSPAK [13]. Theoretical phase and amplitude functions were calculated with FEFF 8.2 [14]. The scattering path and amplitude functions were calculated using the crystal structure of $[BuMeIm]_2[UCl_6]$ described here. The amplitude reduction factor, S_0^2, was defined as 1.0 in the FEFF calculation and fixed to that value in the data fits.

UV/Vis spectra were collected with a Shimadzu UV-3101 PC spectrophotometer using of 1 cm quartz cells sealed airtight by Teflon stoppers. The UV/Vis spectra of solids were obtained in NaCl pellets.

^{1}H NMR spectra were measured with Varian-INOVA 400 instrument in anhydrous CH_2Cl_2 solutions. The ^{1}H chemical shifts were externally referenced to d^6-benzene at 7.15 ppm.

3. Results and discussion

3.1. Single-crystal X-ray study

Crystal data for the structure of $[BuMeIm]_2[UCl_6]$ are given in Table 1. The structure of $[BuMeIm]_2[UCl_6]$ contains two crystallographically independent formula units,

Table 1
Crystallographic data of the $[BuMeIm]_2[UCl_6]$ complex

Chemical formula	$C_{16}H_{30}Cl_6N_4U$
Formula weight	729.17
Space group	$P2_1$ (No. 4)
a (Å)	10.2509(4)
b (Å)	9.5129(2)
c (Å)	27.4386(10)
β (°)	99.4712(14)
V (Å^3)	2639.22(15)
Z	4
D_{calc} (g cm^{-3})	1.835
T (°C)	−153(2)
λ (Å)	0.71073
μ (mm^{-1})	6.767
$R(F)$[a] ($I > 2\sigma(I)$)	0.0589
$wR(F^2)$[a] (all data)	0.1515

[a] $R(F) = \sum ||F_o| - |F_c|| / \sum |F_o|$; $wR(F^2) = \{\sum[w(F_o^2 - F_c^2)^2]/[\sum F_o^4]\}^{1/2}$.

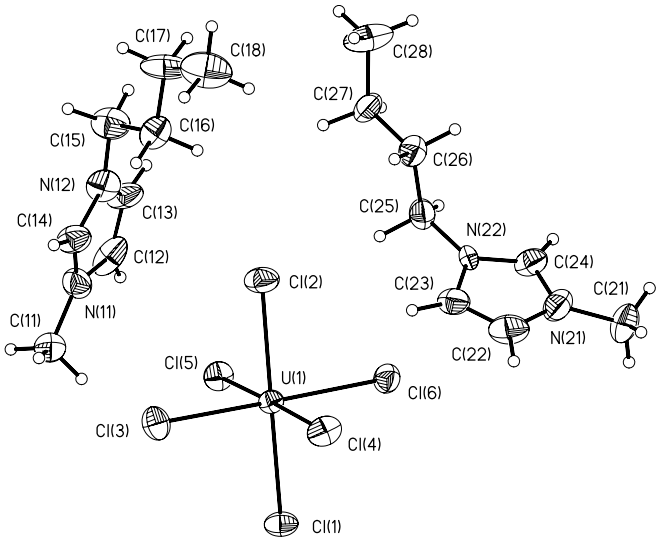


Fig. 1. A view of $[BuMeIm]_2[UCl_6]$, showing the atom-labelling scheme. Displacement ellipsoids are drawn at the 50% probability level and H atoms are represented by circles of arbitrary size. Only one crystallographically independent formula unit is shown.

Table 2
U–Cl bond lengths (Å) of the $[BuMeIm]_2[UCl_6]$ complex

U(1)–Cl(1)	2.625(4)
U(1)–Cl(2)	2.605(4)
U(1)–Cl(3)	2.620(4)
U(1)–Cl(4)	2.638(4)
U(1)–Cl(5)	2.606(3)
U(1)–Cl(6)	2.632(4)
U(2)–Cl(7)	2.620(5)
U(2)–Cl(8)	2.618(4)
U(2)–Cl(9)	2.603(5)
U(2)–Cl(10)	2.576(6)
U(2)–Cl(11)	2.587(5)
U(2)–Cl(12)	2.604(5)

one of them is shown in Fig. 1. Table 2 indicates that the U–Cl distances of the $[UCl_6]^{2-}$ anions range from 2.576(6) to 2.638(4) Å and the average values is 2.621(6) and 2.601(8) Å for U(1) and U(2), respectively. These values are close to each other and are in a good agreement with the average U–Cl distance for the Cs_2UCl_6 complex (2.62 Å) [15]. All bond lengths and torsion angles are presented in Supplementary material. Fig. 2 shows the packing of cations and anions in the unit cell.

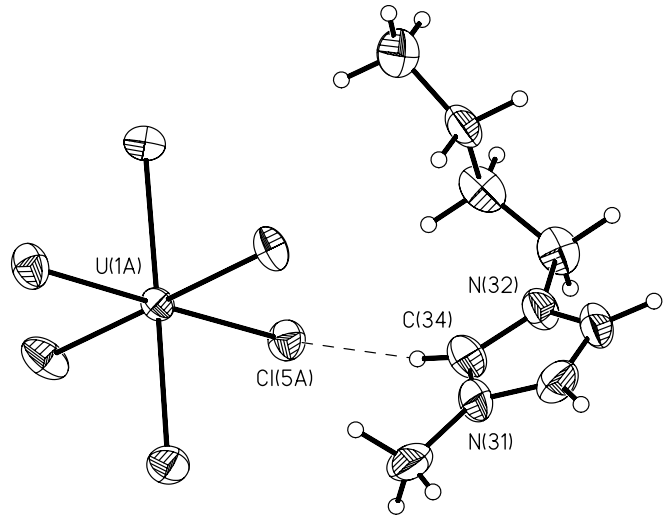


Fig. 3. A schematic view of the shortest H-bond in the $[BuMeIm]_2[UCl_6]$ structure.

The $BuMeIm^+$ cations have four different conformations of C_4H_9 chains and the shortest distances between the centres of the five-membered rings of $BuMeIm^+$ and the U atoms of $[UCl_6]^{2-}$ are 5.53, 5.39, 5.38 and 4.90 Å for the four crystallographically independent cations (see Supplementary material). For the shortest contact of 4.90 Å, the plane of the five-member ring of the cation is parallel to one face of UCl_6^{2-} octahedron. Single crystal XRD reveals the existence of a hydrogen bond between the most acidic H (C34) atom of the imidazolium ring and a chloride of UCl_6^{2-}, where the C34 atom of the structural nomenclature corresponds to the C2 atom between the nitrogen atoms of the imidazolium ring, as shown in Fig. 3. The Cl···H distance, equal to 2.57 Å, is close to the H-bond distance between Cl^- and H(C2) of [PrMeIm]Cl, where $PrMeIm^+$ is a propylmethylimidazolium cation [16]. It should be

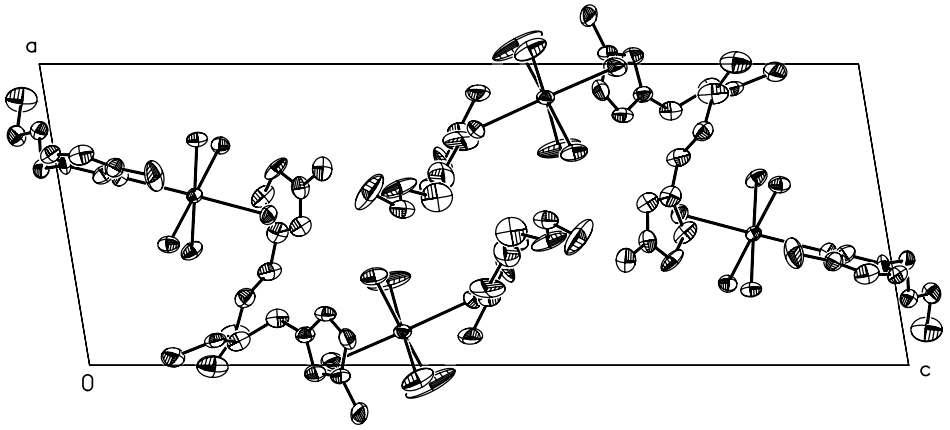


Fig. 2. Content of the unit cell of the $[BuMeIm]_2[UCl_6]$ structure.

Table 3
Geometry of some C–H···Cl bonds of $[BuMeIm]_2[UCl_6]$ and $[EtMeIm]_2[UCl_6]$ complexes in the crystalline state

Complex	C–H···Cl distances/Å	C–H···Cl angles/°
$[BuMeIm]_2[UCl_6]$ our data	C2–H···Cl : 2.57	C2–H···Cl : 128.57
$[EtMeIm]_2[UCl_6]$	C4–H···Cl : 2.74	C4–H···Cl : 132.83
Ref. [17]	C2–H···Cl : >2.96	No H-bonding

emphasized that only 3 Cl···H contacts from 10 with a distance less than 2.80 Å correspond to such a kind of interaction, and the mentioned contact of 2.57 Å is the shortest one. Very recently the existence of extremely weak hydrogen bonds was reported for the solid complex $[EtMeIm]_2[UCl_6]$, where $EtMeIm^+$ is 1-ethyl-3-methylimidazolium [17]. The geometries of some C–H···Cl contacts are shown in Table 3 for the complexes $[BuMeIm]_2[UCl_6]$ and $[EtMeIm]_2[UCl_6]$. The shortest distance for the low acidity hydrogen donor atom Cl···H(C4) (2.74 Å) of $[EtMeIm]_2[UCl_6]$ is significantly longer than the shortest distance Cl···H(C2) of $[BuMeIm]_2[UCl_6]$. Surprisingly, the most acidic hydrogen atom H(C2) is not involved in hydrogen bonding in the case of the $[EtMeIm]_2[UCl_6]$ complex, indicating that even a small modification in the structure of the 1,3-dialkylimidazolium cation may have a large effect on the hydrogen bonding in solids. The origin of such phenomenon could be related to differences in the packing of cations and anions in the unit cell for the studied complexes. However, additional study is needed to elucidate the effect of the side alkyl chain in 1,3-dialkylimidazolium rings on the hydrogen bonding with metal complexes in RTILs.

3.2. EXAFS study

EXAFS measurements were performed to investigate the coordination of U(IV) in a solution of [BuMeIm][Tf_2N]. Fig. 4a shows the U L_{III}-edge k^3 weighted EXAFS spectra and the corresponding Fourier transforms (Fig. 4b) for a solid powder of $[BuMeIm]_2[UCl_6]$ (IL-1), Cs_2UCl_6 (IL-2) and a 0.02 M solution of $[BuMeIm]_2[UCl_6]$ in [BuMeIm][Tf_2N] (IL-3). The structural parameters are presented in Table 4. The k^3-weighted EXAFS signal, $\chi(k)k^3$, shows a single sine-like oscillation without any beat node. This indicates clearly, that the first coordination shell consists only of a single type of backscatter. A quantitative analysis of sample IL-3 gives a Cl^- shell with a U–Cl bond distance very close to the reference samples and coordination numbers equal to 6, with a deviation in the typical range of 10–15%. Thus the EXAFS measurements confirm that the octahedral complex UCl_6^{2-} is the predominant chemical form of U(IV) in Tf_2N^- based hydrophobic ionic liquids.

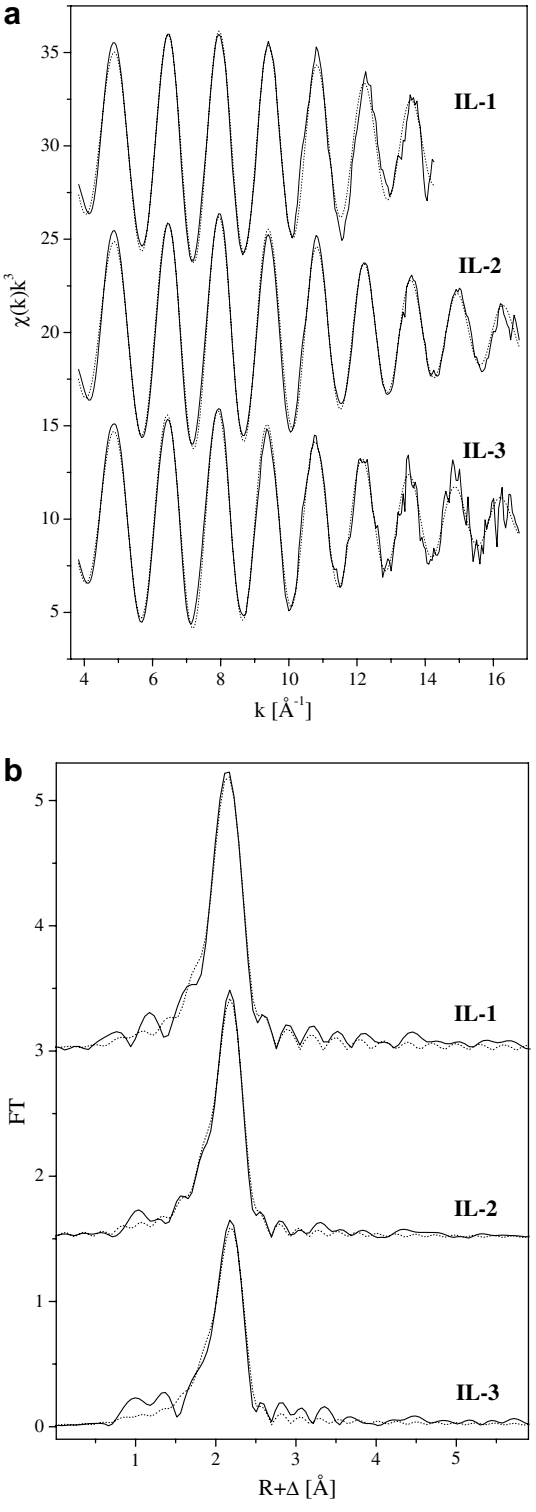


Fig. 4. U L_{III}-edge k^3 weighted EXAFS spectra (a) and the corresponding Fourier transforms (FT) (b) for a solid powder of $[BuMeIm]_2[UCl_6]$-(IL-1), Cs_2UCl_6, (IL-2) and 0.02 M solution of $[BuMeIm]_2[UCl_6]$ in [BuMeIm][Tf_2N] (IL-3).

3.3. Absorption spectroscopy

Fig. 5 shows the visible spectrum of $[BuMeIm]_2[UCl_6]$ in [BuMeIm][Tf_2N] solution and the spectra of solid $[BuMeIm]_2[UCl_6]$ and $Cs_2[UCl_6]$. Complex $Cs_2[UCl_6]$ exhibits two ro-vibronic bands at 593 and 601 nm. A third $f \rightarrow f$ electron transition band appears at 597 nm in the presence of the $BuMeIm^+$ cation in the solid state as well

Table 4
Structure parameters of $[BuMeIm]_2[UCl_6]$ obtained from EXAFS shell fit

Sample	Δk (Å^{-1})	N[a]	R[b] (Å)	σ^2 (Å^2)	ΔE (eV)	Fit error
IL-1	3.8–14.3	6.5	2.619(2)	0.0045	−1.1	0.35
IL-2	3.8–16.8	6.1	2.620(1)	0.0040	−1.2	0.17
IL-3	3.8–16.8	6.1	2.632(2)	0.0044	−0.3	0.28

[a] Errors in coordination numbers N are ±15%.
[b] Errors in distances R are ±0.01 Å standard deviations for R, as estimated by EXAFSPAK, are given in brackets, errors in coordination numbers N are ±15%, σ – Debye–Waller factor. Il-1: $[BuMeIm]_2[UCl_6]$ in the solid state; IL-2: Cs_2UCl_6 in the solid state; IL-3: $[BuMeIm]_2[UCl_6]$ 0.02 M in $[BuMeIm][Tf_2N]$.

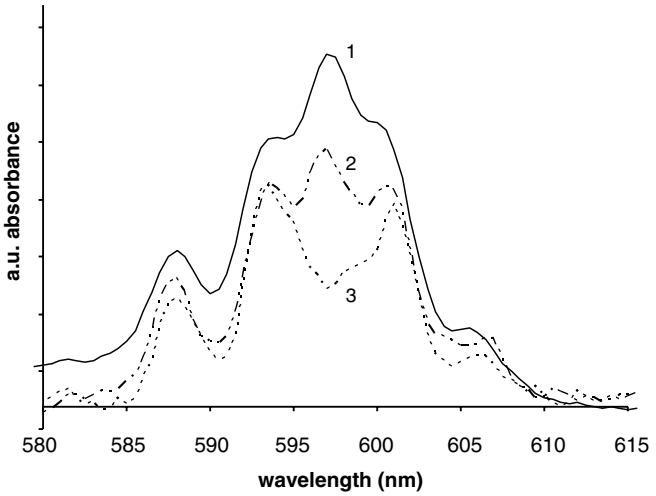


Fig. 5. Visible absorption spectra of $[BuMeIm]_2[UCl_6]$ in $[BuMeIm][Tf_2N]$ solution (1), solid $[BuMeIm]_2[UCl_6]$ (2) and solid $Cs_2[UCl_6]$ (3).

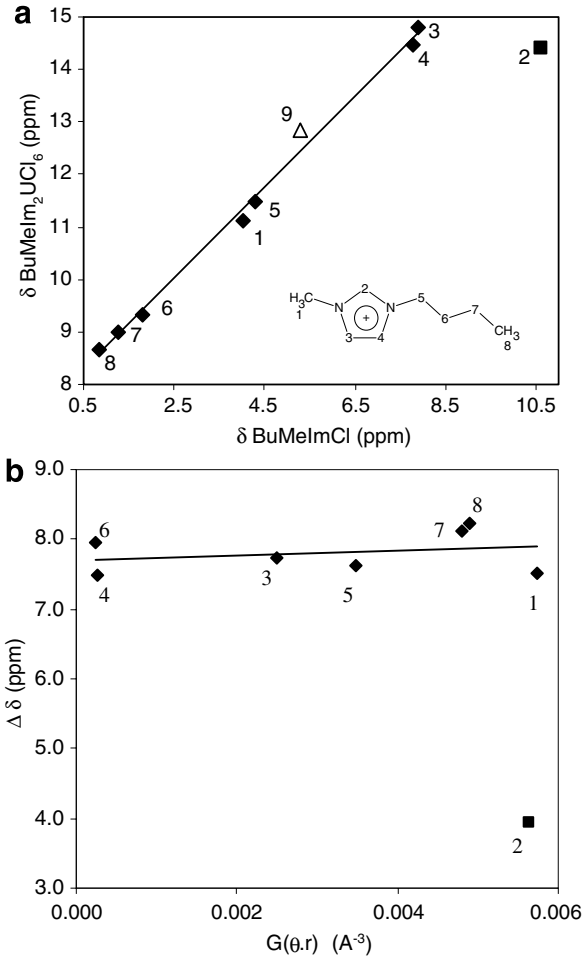


Fig. 6. (a) Relationship between the proton chemical shifts of $[BuMeIm]_2[UCl_6]$ and [BuMeIm]Cl in CH_2Cl_2, (Δ) CH_2Cl_2 protons. (b) Protons isotropic shifts, $\Delta\delta_I$, vs. the geometric factor $G(\theta_i, r_i)$ for $[BuMeIm]_2[UCl_6]$ in CH_2Cl_2.

as in RTIL solutions. It should be noted that only this difference can be clearly observed in the visible spectra of the studied complexes. Other ro-vibronic and $f \rightarrow f$ transitions are not sufficiently resolved to be correctly interpreted.

An absorption band at 597 nm was observed for UCl_6^{2-} in MeCN solutions in the presence of strong hydrogen-bond donors [18], indicating that the UCl_6^{2-} anion acts as a hydrogen bond acceptor. The slight distortion of the UCl_6^{2-} octahedral structure due to the hydrogen bonding causes the appearance of $f \rightarrow f$ electron transitions which are Lapport forbidden in the centrosymmetrical complexes. Thus the visible absorption spectra suggest the existence of hydrogen bonding in $[BuMeIm][Tf_2N]$ solutions of the UCl_6^{2-} complex.

3.4. NMR study

^{1}H NMR spectra were collected on [BuMeIm]Cl and $[BuMeIm]_2[UCl_6]$ in weakly solvating dichloromethane to avoid hydrogen bond dissociation. The observed isotropic shifts are widely displaced to low fields due to the uranium(IV) paramagnetism. Surprisingly, Fig. 6a reveals a linear relationship between the proton chemical shifts of [BuMeIm]Cl and $[BuMeIm]_2[UCl_6]$ for the overall protons, except for the acidic H(C2) proton. Obviously, the isotropic shifts essentially arise from a dipolar interaction between the UCl_6^{2-} anion and the $BuMeIm^+$ cation, and not from a covalent interaction. Even the proton chemical shift of the dichloromethane solvent lies on this linear relationship, which emphasizes that the paramagnetic shift mainly comes from a dipolar effect. Neglecting the contact shift and considering that the axial symmetry applies according to the $[BuMeIm]_2[UCl_6]$ single-crystal XRD results, the isotropic shift, $\Delta\delta_i$, can be expressed as [19]:

$$\Delta\delta_I = \delta_{U_i} - \delta_i = \frac{g^2\beta^2 S(S+1)}{3kT} \cdot \left(\frac{3\cos^2\theta_i - 1}{r_i^3}\right) = K \cdot G(\theta_i, r_i), \quad (1)$$

where δ_{U_i} and δ_i are the proton Hi chemical shift of the ionic liquid respectively with and without the UCl_6^{2-} complex. All the geometric parameters are collected in the $G(\theta_i, r_i)$ function whereas K is a fixed term for all nuclei in solution.

The EXAFS data indicate the strong similarity of the UCl_6^{2-} structure in solution and in the solid state.

Thus the geometric factors $G(\theta_i, r_i)$ for solutions can be computed from X-ray crystallographic data considering r_i, the distance in Å between the Hi proton and U(IV), and θ_i, the angle between r_i and the vector formed by the U and Cl atoms. The isotropic shifts versus $G(\theta_i, r_i)$ averaged for the overall protons of $[BuMeIm]_2[UCl_6]$ and [BuMeIm]Cl in $[BuMeIm][Tf_2N]$ are plotted in Fig. 6b. The K parameter is given by the 31.5 slope, indicating that a relationship exists between proton isotropic shifts and geometric factors, except for H(C2). Then short distance between H(C2) and U(IV) cannot explain this deviation and one can presume a contact contribution to the isotropic shift. Moreover, a large intercept value (roughly 7.7 ppm) for the overall protons (Fig. 6b) indicates that the relative shifts are induced by the complex formation. The diamagnetic contribution caused by the organization around the UCl_6^{2-} anion should be taken into account rather than the simple diamagnetic δ_I contribution of the free ionic liquid.

Assuming a 7.7 ppm diamagnetic shift and 0.177 ppm dipolar shift from the aforementioned calculations, one can estimate the contact interaction between the anion UCl_6^{2-} and the proton H(C2). Taking into account the $5f^2$ electronic configuration of U(IV), Eq. (1) gives the following expression of the contact shift:

$$\delta_C = \frac{A}{h}\langle S_z \rangle. \quad (2)$$

Eq. (2) yields a $\frac{A}{h}$ hyperfine coupling constant equal to 1.23 ppm. The average value of the component along the field of the electron spin magnetization of the uranium(IV), $\langle S_z \rangle$ is calculated using the published procedure [20] for the lanthanide Pr(III). The contact contribution found for the proton H(C2) of the $BuMeIm^+$ cation with UCl_6^{2-} species is small and of the same magnitude as those of CH_2 protons in the α position of the nitrogen in tetra *n*-alkylammonium cations [21]. It can be thus concluded that the anomalous H(C2) proton chemical shift in the $BuMeIm^+ \cdot UCl_6^{2-}$ ion pair is related to the hydrogen bonding. The proton chemical shifts demonstrate much higher sensitivity to hydrogen bonding that the electronic or EXAFS spectra.

4. Concluding remarks

In the solid state, the single-crystal XRD study of the $[BuMeIm]_2[UCl_6]$ complex shows the existence of two crystallographically independent formula units and four conformations of C_4H_9 chains in $BuMeIm^+$. The average U-Cl distances of the UCl_6^{2-} octahedral complex are equal to 2.621(6) and 2.601(8) Å for the units U(1) and U(2), respectively.

In $[BuMeIm][Tf_2N]$ solution, EXAFS quantitative measurements confirm that the octahedral complex UCl_6^{2-} is the predominant chemical form of U(IV). The average U–Cl distance in RTIL solution is equal to 2.632(2) Å, which is very close to that in the solid state.

Single-crystal XRD, visible absorption spectroscopy and ^1H NMR reveal the presence of H bonding between the chloride anion of UCl_6^{2-} and the most acidic proton H(C2) of the imidazolium ring, both in the solid state and in ionic liquid solution. In the solid state, the $Cl^{\cdots}H(C2)$ distance is 2.57 Å. An isotropic shift for the acidic H(C2) proton in the ^1H NMR spectrum of $[BuMeIm]_2[UCl_6]$ in CH_2Cl_2 solutions also clearly indicates hydrogen bonding.

Acknowledgements

This work was supported by European ACTINET network and GDR PARIS (French program).

Appendix A. Supplementary material

CCDC 635360 contains the supplementary crystallographic data for $[BuMeIm]_2[UCl_6]$. These data can be obtained free of charge via http://www.ccdc.cam.ac.uk/conts/retrieving.html, or from the Cambridge Crystallographic Data Centre, 12 Union Road, Cambridge CB2 1EZ, UK; fax: (+44) 1223-336-033; or e-mail: deposit @ccdc.cam.ac.uk. Supplementary data associated with this article can be found, in the online version, at doi:10.1016/j.poly.2007.02.014.

References

[1] P. Wasserscheid, T. Welton (Eds.), Ionic Liquids in Synthesis, Wiley, Weinheim Germany, 2003.
[2] (a) R.C. Thied, J.E. Hatter, K.R. Seddon, W.R. Pitner, D.W. Rooney, D. Hebditch, World Pat., WO01/13379A1, 18 August 1999; (b) W.J. Oldham, D.A. Costa, W.H. Smith, Development of room-temperature ionic liquids for applications in actinide chemistry, in: R.D. Rogers, K.R. Seddon, (Eds.), Ionic Liquids: Industrial Applications for Green Chemistry, ACS Symposium Series, 818, Washington, DC, chap. 15, 2002, p. 188.
[3] (a) A.E. Visser, R.D. Rogers, J. Solid State Chem. 109 (2003) 113 (and cited Ref.);
(b) S. Dai, Y.H. Ju, C.E. Barnes, J. Chem. Soc., Dalton Trans. (1999) 1201;
(c) M.L. Dietz, J.A. Dzielawa, Chem. Commun. (2001) 2124.
[4] (a) R. De Waele, L. Heerman, W. D'Olieslager, J. Electroanal. Chem. 142 (1982) 137;
(b) P.B. Hitchcock, T.J. Mohammed, K.R. Seddon, J.A. Zora, C.L. Hussey, E.H. Ward, Inorg. Chim. Acta 113 (1984) L25;
(c) C.J. Anderson, M.R. Deakin, G.R. Choppin, W. D'Olieslager, L. Heerman, D. Pruett, J. Inorg. Chem. 30 (1991) 4013.
[5] (a) S. Dai, Y.S. Shin, L.M. Toth, C.E. Barnes, Inorg. Chem. 36 (1997) 4900;
(b) C.J. Anderson, G.R. Choppin, D.J. Pruett, D. Costa, W. Smith, Radiochim. Acta 84 (1999) 31;
(c) T.A. Hopkins, J.M. Berg, D.A. Costa, H.S. Wayne, H.J. Dewey, Inorg. Chem. 40 (2001) 1820;
(d) D.A. Costa, W.H. Smith, H.J. Dewey, Electrochem. Soc. Proc. 99-41 (2000) 80.
[6] (a) S.I. Nikitenko, C. Cannes, C. Le Naour, P. Moisy, D. Trubert, Inorg. Chem. 44 (2005) 9497;
(b) S.I. Nikitenko, P. Moisy, Inorg. Chem. 45 (2006) 1235.
[7] Z. Otwinowski, W. Minor, in: C.W. Carter, R.M. Sweet (Eds.), Methods in Enzymology, Macromolecular Crystallography, Part A, vol. 276, Academic Press, New York, 1997, p. 307.

[8] A.L. Spek, PLATON – A Multipurpose Crystallographic Tool, Utrecht University, Utrecht, The Netherlands, 2003.
[9] G.M. Sheldrick, SHELXL97 and SHELXS97, University of Göttingen, Germany, 1997.
[10] H.D. Flack, Acta Crystallogr., Sect. A: Found. Crystallogr. 39 (1983) 876.
[11] G.M. Sheldrick, SHELXTL. Version 5.10, Bruker AXS Inc., Madison, Wisconsin, USA, 1997.
[12] W. Matz, N. Schell, G. Bernhard, F. Prokert, T. Reich, J. Claußner, W. Oehme, R. Schlenk, S. Dienel, H. Funke, F. Eichhorn, M. Betzl, D. Pröhl, U. Strauch, G. Hüttig, H. Krug, W. Neumann, V. Brendler, P. Reichel, M.A. Denecke, H. Nitsche, J. Synchrotron Rad. 6 (1999) 1076.
[13] G.N. George, I.J. Pickering, EXAFSPAK, A Suite of Computer Programs for Analysis of X-ray Absorption Spectra, Stanford Synchrotron Radiation Laboratory, Stanford Synchrotron Radiation Laboratory, Stanford, 2000.
[14] A.L. Ankudinov, B. Ravel, J.J. Rehr, S.D. Conradson, Phys. Rev. B58 (1998) 7565.
[15] T. Schleid, G. Meyer, L.R. Morss, J. Less-Common Met. 132 (1987) 69.
[16] J. Dupont, J. Braz. Chem. Soc. 15 (2004) 341.
[17] M. Deetlefs, C.L. Hussey, T.Y. Mohammed, K.R. Seddon, J.-A. Van den Berg, J.A. Zora, J. Chem. Soc., Dalton Trans. (2006) 2334.
[18] J.L. Ryan, Inorg. Chem. (1964) 211.
[19] F. Inagaki, T. Miyazawa, Progr. NMR Spectrosc. 14 (1981) 67.
[20] W.B. Lewis, J.A. Jackson, J.F. Lemons, H. Taube, J. Chem. Phys. 36 (1962) 694.
[21] I.M. Walker, L. Rosenthal, M.S. Quereshi, Inorg. Chem. 10 (1971) 2463.

Available online at www.sciencedirect.com
ScienceDirect
Polyhedron 26 (2007) 3143–3152
POLYHEDRON
www.elsevier.com/locate/poly

Synthesis, characterization and catalytic activity of halo-methyl-bis(salicylaldehyde)ethylenediamine cobalt(II) complexes

Aurel Pui [a,*], Jean-Pierre Mahy [b]

[a] *Al. I. Cuza University, Faculty of Chemistry, Bvd. Carol I, No. 11, 6600 Iasi, Romania*
[b] *Paris Sud (XI) University, Laboratory of Bioorganic and Bioinorganic Chemistry, Institute of Molecular Chemistry and Materials, Bât 420, 91405 Orsay Cedex, France*

Received 7 October 2006; accepted 14 February 2007
Available online 21 April 2007

Abstract

The synthesis, characterization and catalytic activity of a series of tetra-halo-dimethyl salen and di-halo-tetramethyl-salen ligands are reported in this paper: α,α′-dimethyl-Salen (dMeSalen) (**L**[1]); 3,3′,5,5′-tetrachloro-α,α′-dimethyl-Salen, (tCldMeSalen) (**L**[2]); 3,3′-dibromo-5,5′-dichloro-α,α′-dimethyl-Salen, (dCldBrdMeSalen) (**L**[3]); 3,3′,5,5′-tetrabromo-α,α′-dimethyl-Salen, (tBrdMeSalen) (**L**[4]); 3,3′,5,5′-tetraiodo-α,α′-dimethyl-salen, (tIdMeSalen) (**L**[5]); 3,3′-dichloro-5,5′,α,α′-tetramethyl-Salen (dCltMeSalen) (**L**[6]); 3,3′-dibromo-5,5′,α,α′-tetramethyl-Salen (dBrtMeSalen) (**L**[7]); and 3,3′-diiodo-5,5′,α,α′-tetramethyl-Salen (dItMeSalen) (**L**[8]) (Salen = bis(salicylaldehyde)ethylenediamine). Upon reaction with Co(II) ions, these ligands form complexes with square planar geometry that have been characterized by elemental analysis, cyclic voltammetry, UV–Vis, IR and EPR spectroscopies. In the presence of pyridine the obtained Co(II) complexes were found able to bind reversibly O_2, which was shown by EPR spectroscopy and cyclic voltammetry. They were also found able to catalyze the oxidation of 2,6-di-*tert*-butylphenol (DtBuP) (**9**) with formation of 2,6-di-*tert*-butyl-1,4-benzoquinone (DtBuQ) (**10**) and 2,6,2′,6′-tetra-*tert*-butyl-1,1′-diphenobenzoquinone (TtBuDQ) (**11**). These properties are first influenced by the coordination of pyridine in axial position of the Co(II) ion that causes an increase of the electronic density on the cobalt ion and as a consequence a decrease in the $E_{1/2}$ value and an increase of the reducing power of the Co(II) complex. It is noteworthy that, under those conditions the complexes also show a remarkable quasi-reversible behaviour. Second, complex properties are also influenced by the substituents (methyl and halogen) grafted on the aromatic ring and on the azomethynic groups. The donating methyl substituent on the azomethynic groups causes a decrease in the $E_{1/2}$ value, whereas the halogen substituents on the aromatic rings have two effects: a mesomeric donating effect that tends to lower the redox potential of the complex, and a steric effect that tends to decrease the conjugation of the ligand and then to increase the redox potential of the Co(II) complex. In pyridine, the steric effect predominates, which causes both an increase of the redox potential and a decrease of the selectivity of the oxidation of phenol **9**. As a result of all these effects, it then appears that the best catalysts to realize the selective oxidation of 2,6-di-*tert*-butyl-phenol (**9**) by O_2 are the Co complexes of ligands bearing CH_3 donating substituents, Co(dMeSalen) **1** ($2CH_3$ substituents), and Co-di-halo-tetra-methyl-salen complexes **6**, **7** and **8** ($4CH_3$ substituents), in the presence of pyridine.
© 2007 Elsevier Ltd. All rights reserved.

Keywords: Co(II)-halo-methyl-salen complexes; EPR; ESMS; Cyclic voltammetry; Catalytic activity

1. Introduction

Transition metal complexes of Schiff bases are of paramount scientific interest, due to their multiple uses as biomimetic systems of enzymes involved in the transport, storage and activation of dioxygen [1–5]. First, some of such complexes are able to bind reversibly dioxygen, and can be used as simplified models in the study of the reversible binding of dioxygen by its natural transporters. In particular, the Co(II) ions form coordinative compounds with Schiff bases, with a square planar geometry, capable of

* Corresponding author. Tel.: +40 232 201276; fax: +40 232 201313.
E-mail address: aurel@uaic.ro (A. Pui).

0277-5387/$ - see front matter © 2007 Elsevier Ltd. All rights reserved.
doi:10.1016/j.poly.2007.02.030

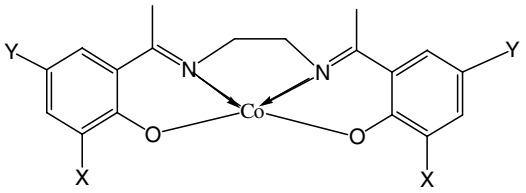


Fig. 1. General formula of the cobalt(II)–salen complexes (1–8) studied in this paper. 1, X = Y = H; 2, X = Y = Cl; 3, X = Br, Y = Cl; 4, X = Y = Br; 5, X = Y = I; 6, X = Cl, Y = CH_3; 7, X = Br, Y = CH_3; 8, X = I, Y = CH_3.

reversibly binding dioxygen [6–8]. Second, cobalt complexes can be used as catalysts in highly selective oxidation reactions using molecular oxygen as oxidant, and therefore can serve as models for oxygenases, peroxidases or mono- and dioxygenases. So, cobalt complexes of Schiff bases are able to catalyze the oxidation of phenols, alcohols, flavonoides, nitroalkanes, hydrazines or olefins [9–11]. Finally, more recently, Mn and Cr complexes of Schiff bases have been used as metal cofactors for the elaboration of artificial metalloenzymes used as new biocatalysts for selective oxidation reactions [1,12,13].

This study aims at obtaining new coordinative compounds with similar properties but with improved efficiency and selectivity. Therefore, the present paper describes the synthesis, characterization and catalytic activity of some tetra-halo-di-methyl-salen- [14] and some new di-halo-tetra-methyl-salen-cobalt complexes, which are presented in Fig. 1. The influence of halogens substituents (Cl, Br, I) grafted on the positions 3 and 5 of the aromatic rings and of the methyl substituent on the azomethyne bridge on the chemical properties was studied. The relationship between the electrochemical potential and the catalytic activity of these compounds was also studied.

2. Experimental

2.1. Materials and methods

Elemental analysis (C, H, N) was performed by the Service de Microanalyses at Gif-sur-Yvette, France. ^{1}H and ^{13}C NMR analysis were performed on a Bruker AM 250 or a Bruker AC 250 spectrometer, operating at 250 MHz. All spectra were obtained in $CDCl_3$ and chemical shifts calculated in ppm with respect to TMS ($\delta = 0$) or to the solvent residual peak ($\delta = 7.26$ for proton and 77.1 for carbon). UV–Vis spectra were recorded on DES device, operating with a SAFAS program. The FT-IR spectra were obtained on a Brucker IFS 66 apparatus in KBr pellets.

Cyclic voltammetry experiments were performed on a Digilab apparatus, in a glass cell incorporating a conventional three-electrode configuration using a vitreous carbon electrode ($A = 3.8$ mm^2) as working electrode, a saturated calomel electrode (SCE) as reference electrode and a platinum wire as auxiliary electrode. Cyclic voltammograms were recorded at 293 K, from 2 mM solutions of Co-complexes in DMF, under argon atmosphere, using lithium perchlorate as support electrolyte. Potentials are reported versus SCE, using the ferrocenium/ferrocene couple (Fc^+/Fc) as internal standard ($E_{Fc^+/Fc} = 0.466$ V, under these experimental conditions: scan rate = 0.1 V/s, concentration 2 mM).

EPR spectra were recorded in frozen DMF solution at 10 K, on a Brucker Elexis apparatus. To prepare the EPR samples, 1.2 mg of complex was dissolved in 2 mL of DMF previously degassed under argon, and 0.1 mL of pyridine (Py) was further added. Approximately, 0.3 mL of this solution was then transferred under argon via a syringe into the quartz EPR tube sealed with a septum. The tube was then frozen in liquid nitrogen, prior to analysis by EPR spectroscopy. Oxygenated samples of the Co complexes were obtained by bubbling dioxygen into the solution before freezing.

Magnetic susceptibility measurements were made on solid samples by a Quantum Desing model MPMS, SQUID. The measurements were calibrated using a recrystallized $HgCo(NCS)_4$ standard. The appropriate diamagnetic corrections were made.

ESMS (electrospray mass spectra) were recorded in a $MeOH/CH_2Cl_2$ (1/1, vol.) mixture on an Excalibrus device.

To assay the catalytic activity of the Co complexes, the oxidation of 2,6-di-*tert*-butyl-phenol (**9**) by dioxygen was realized in the presence of catalytic amounts of complex as previously described [14]. The reaction was performed at room temperature (21–22 °C) in a 100 mL round-bottomed flask sealed with a rubber septum. The flask was connected via a syringe needle to a gas burette. In a typical experiment, 2.5×10^{-2} mmol of complex (5% with respect to the substrate) were dissolved in 5 mL of dry DMF, degassed under argon. 2.5 mmol of pyridine and 103 mg (0.5 mmol) of **9** dissolved in 5 mL of DMF were subsequently added. Argon was then removed under vacuum, and the flask was refilled with dioxygen and connected to the burette. Stirring was started and dioxygen consumption was then monitored using the gas burette. After 24 h, the reaction was stopped and the products were separated by flash chromatography, using dichloromethane/heptane 1/1 (v/v) as eluent. After evaporation of the volatiles, the fractions were analyzed by ^{1}H NMR on a Bruker AM 250 and by gas-chromatography on a Fison 9000 GLC apparatus, respectively, which allowed determining the conversion and the yields of the products.

2.2. Preparation of the ligands and cobalt (II) complexes

2.2.1. Preparation of the halogeno derivatives of 2-hydroxyacetophenone

The 3,5-dichloro-2-hydroxyacetophenone and 2-hydroxy-5-methylacetophenone are commercially available. The bromo- and iodo-2-hydroxyacetophenone derivatives were obtained by bromination and iodination of 2-hydroxyacetophenone derivatives.

The 3-chloro-5-methyl-2-hydroxy-acetophenone was obtained by the Friedel–Crafts substitution of the corresponding 2-chloro-4-methylphenol with acetyl chloride [15]. CH_3COCl (1.25 g, 0.16 mol) was added, with stirring, to 2-chloro-4-methylphenol (2.19 g, 0.15 mol) at room temperature (r.t.). The mixture was heated (40 °C) until no gas evolved anymore and then $AlCl_3$ (2 g) was added slowly. The reaction mixture was heated at 180 °C for 30 min, cooled down at r.t. and then a mixture of HCl conc./H_2O (12 mL/50 mL) was added and the mixture was allowed to stand overnight. The resulting white crystals were filtered, washed with water and recrystallized from ethanol. The purity was checked by ^1H NMR and confirmed by elemental analysis. Melting point (M.p.) 88–89 °C; ^1H NMR ($CDCl_3$) δ (ppm): 11.70 (s, OH), 7.45 (s, 1 Har), 7.41 (s, Har), 2.65 (s, 3H, CH_3), 2.30 (s, 3H, CH_3).

2.2.2. Bromination [16]

2.2.2.1. 3,5-Dibromo-2-hydroxyacetophenone. A mixture of 2-hydroxyacetophenone (1.36 g, 0.01 mol) and pyridinium bromochromate (PBC) (5.16 g, 0.02mol) in glacial acetic acid (8–10 ml) was heated at 40 °C for 2 h. The reaction mixture turned green, and was heated until the reaction was completed (TLC). It was then poured into ice-cold water. The solid thus obtained was filtered, washed with water and recrystallized from aqueous ethanol. Its purity was checked by ^1H NMR and confirmed by elemental analysis. M.p. 105–107 °C; ^1H NMR ($CDCl_3$) δ (ppm): 2.66 (s, 3H, CH_3); 7.68–7.69 (d, 1H, ArCH); 7.73–7.74 (d, 1H, ArCH); 12.85 (s, 1H, OH).

2.2.2.2. 3-Bromo-5-chloro-2-hydroxyacetophenone. This was obtained by the same procedure from 5-chloro-2-hydroxyacetophenone and PBC. M.p. 112 °C, ^1H NMR ($CDCl_3$) δ (ppm): 2.66 (s, 3H, CH_3); 7.81–7.82 (d, 1H, ArCH); 7.85–7.86 (d, 1H, ArCH); 12.87 (s, 1H, OH).

2.2.2.3. 3-Bromo-5-methyl-2-hydroxy-acetophenone. This was obtained by bromination of 2-hydroxy-5-methylacetophenone. M.p. 86–88 °C, ^1H NMR ($CDCl_3$) δ (ppm): 12.75 (s, OH), 7.57 (s, 1 Har), 7.49 (s, 1 Har), 2.64 (s, 3H, CH_3), 2.31 (s, 3H, CH_3).

PBC (pyridinium bromochromate) was synthetized as follows. A solution of 20 g (0.2 mol) of chromium trioxide in water (25 ml) was cooled down to 0 °C. To this solution, 47% HBr (38 ml, 0.21 mol) was added slowly with constant stirring, the temperature being kept constant at 0 °C. Pyridine (16.3 ml, 0.2 mol) was then added over 15–20 min, to give a brown solid. The reaction mixture was chilled for 4–5 h. The dark brown crystals were then filtered and dried. The product was recrystallized from aqueous acetic acid (40:60 v/v) and its purity was checked by TLC and confirmed by elemental analysis and melting point 108 °C.

2.2.3. Iodination [17]

2.2.3.1. 3,5-Diiodo-2-hydroxyacetophenone. A suspension of 2-hydroxyacetophenone (1.36 g, 0.01 mol), excess HgO, (6.51 g, 0.03 mol) and excess iodine (7.63 g, 0.03 mol) in CH_2Cl_2 was stirred at r.t. for 20 h. The reaction was followed by TLC. The precipitate was removed by suction filtration. The filtrate was washed with 5% aq. $Na_2S_2O_3$ (20 ml) and water (30 ml), dried over $MgSO_4$, and evaporated to dryness. The residue was recrystallized from ethanol and its purity was checked by ^1H NMR and elemental analysis. Melting point 125–127 °C, ^1H NMR ($CDCl_3$) δ (ppm): 2.64 (s, 3H, CH_3); 7.98–7.99 (d, 1H, ArCH); 8.18–8.19 (d, 1H, ArCH); 13.09 (s, 1H, OH).

2.2.3.2. 3-Iodo-5-methyl-2-hydroxy-acetophenone. This was obtained by iodination 2-hydroxy-5-methyl acetophenone. Melting point (97–99 °C), ^1H NMR ($CDCl_3$) δ(ppm): 12.49 (s, OH), 7.72 (s,1 Har), 7.64 (s, 1 Har), 2.39 (s, 3H, CH_3), 1.92 (s, 3H, CH_3).

2.3. Preparation of the ligands

The ligands were obtained according to already described general methods, by the reaction between 3-X, 5-Y, 2-OH acetophenone (where X and Y are H, Cl, Br, I, CH_3), and ethylenediamine in a 2:1 molar ratio [18–20].

A solution of 2 equiv. 3-X, 5-Y, 2-OH acetophenone derivatives and 1 equiv. ethylenediamine, was stirred for 2–3 h in MeOH or EtOH at 40 °C. The ligands were recrystallized from MeOH or EtOH.

Bis(α-CH_3-salicylaldehyde)ethylenediimine ($\mathbf{L^1}$): To 2.72 g (0.02 mol) of 2-hydroxy acetophenone, dissolved in 30 mL MeOH at 40 °C, was added dropwise 0.6 g ethylenediimine dissolved in 8 ml MeOH. The reaction mixture was refluxed with stirring at 40 °C for 2 h and allowed to stand overnight at r.t. Then, the solid obtained was filtered, washed with water and MeOH, dried and recrystallized from methanol. A yellow solid was obtained, (91% yield). M.p. 202–203 °C, ^1H NMR ($CDCl_3$) δ (ppm): 2.84 (s, 6H, 2CH_3); 3.98 (s, 4H, 2CH_2); 6.76–7.54 (m, 8H, ArCH); 13.29 (s, 2H, OH). IR (cm^{-1}): 1610 ($\nu_{C=N}$), 1290 ($\delta_{Ar\text{-}OH}$), 1158 (ν_{C-N}), 1065 (ν_{C-O}). UV–Vis (λ [nm], logε[l/mol × cm]): 390 (2.96), 336 (3.10), 232 (2.47). Elemental *Anal.* Calc. for $C_{18}H_{20}N_2O_2$: Calc. C, 72.95; H, 6.80; N 9.45. Found: C, 72.78; H, 6.82; N, 9.39%.

The other ligands were prepared by same procedure.

$\mathbf{L^2}$: yellow solid (90% yield). M.p. 95–97 °C,^1H NMR ($CDCl_3$) δ (ppm): 2.42 (s, 6H, 2CH_3); 4.04 (s, 4H, 2CH_2); 7.26 (s, 2H, ArCH); 7.42 (s, 2H, ArCH); 12.89 (s, 2H, OH). IR (cm^{-1}): 1611 ($\nu_{C=N}$), 1268 ($\delta_{Ar\text{-}OH}$), 1185 (ν_{C-N}), 1058 (ν_{C-O}). UV–Vis (λ [nm], logε[l/mol × cm]): 418 (3.54), 340 (3.46), 258 (3.05). Elemental *Anal* Calc. for $C_{18}H_{16}Cl_4N_2O_2$: C, 49.80; H, 3.71; N, 6.45. Found: C, 49.78; H, 3.67; N, 6.39%.

$\mathbf{L^3}$: yellow solid (95% yield). M.p. 252–253 °C,^1H NMR ($CDCl_3$) δ (ppm): 2.42 (s, 6H, 2CH_3); 4.03 (s, 4H, 2CH_2); 7.46 (d, 2H, ArCH); 7.79–7.84 (d, 2H, ArCH); 12.84 (s, 2H, OH). IR (cm^{-1}): 1605 ($\nu_{C=N}$), 1251 ($\delta_{Ar\text{-}OH}$), 1174 (ν_{C-N}), 1078 (ν_{C-O}). UV–Vis (λ [nm], logε[l/mol × cm]): 416 (3.12), 342 (3.18), 236 (3.07). Elemental Anal. Calc.

for $C_{18}H_{16}Br_2Cl_2N_2O_2$: C, 41.33; H, 3.08; N, 5.36. Found: C, 41.28; H, 3.07; N, 5.39%.

L[4]: yellow solid (87% yield). M.p. 238–239 °C, ^{1}H NMR ($CDCl_3$) δ(ppm): 2.17 (s, 6H, $2CH_3$); 4.03 (s, 4H, $2CH_2$); 7.57–7.59 (d, 2H, ArCH); 7.70–7.71 (d, 2H, ArCH); 12.92 (s, 2H, OH). IR (cm^{-1}): 1604 ($\nu_{C=N}$), 1259 ($\delta_{Ar\text{-}OH}$), 1176 (ν_{C-N}), 1074 (ν_{C-O}). UV–Vis (λ [nm], log ε[l/mol × cm]): 416 (3.45), 340 (3.37), 242 (3.19). Elemental *Anal*. Calc. for $C_{18}H_{16}Br_4N_2O_2$: C, 35.33; H, 2.64; N, 4.58. Found: C, 35.28; H, 2.67; N, 4.59%.

L[5]: yellow solid (84% yield). M.p. 209–210 °C,^{1}H NMR ($CDCl_3$) δ (ppm): 2.17 (s, 6H, $2CH_3$); 4.02 (s, 4H, $2CH_2$); 7.15–7.16 (d, 2H, ArCH); 7.72–7.74 (d, 2H, ArCH); 12.98 (s, 2H, OH). IR (cm^{-1}): 1601 ($\nu_{C=N}$), 1256 ($\delta_{Ar\text{-}OH}$), 1165 (ν_{C-N}), 1050 (ν_{C-O}). UV–Vis (λ [nm], log ε[l/mol × cm]): 422 (3.78), 322 (3.42), 244 (3.48). Elemental Anal. Calc. for $C_{18}H_{16}I_4N_2O_2$: C, 27.03; H, 2.02; N, 3.50. Found: C, 26.98; H, 2.02; N, 3.43.

L[6]: yellow solid (87% yield). M.p. 225–226 °C, ^{1}H NMR δ (ppm): 11.96 (s, 2H, OH), 7.25 (d, 2H ar), 7.23 (d, 2H ar), 4.01 (s, $2CH_2$), 2.39 (s, $2CH_3$), 2.26 (s, $2CH_3$). IR (cm^{-1}): 1611 ($\nu_{C=N}$), 1258 ($\delta_{Ar\text{-}OH}$), 1213 (ν_{C-N}), 1067 (ν_{C-O}). UV–Vis (λ [nm], log ε[l/mol × cm]): 424 (3.19), 314 (3.02), 278 (3.18). Elemental *Anal*. Calc. for $C_{20}H_{22}Cl_2N_2O_2$: C, 61.08; H, 5.64; N, 7.12. Found: C, 60.98; H, 5.57; N, 7.09%.

L[7]: yellow solid (79% yield). M.p. 230–232 °C, ^{1}H NMR δ(ppm): 12.85 (s, 2H, OH), 7.44 (d, 2H ar), 7.23 (d, 2H ar), 4.00 (s, $2CH_2$), 2.41 (s, $2CH_3$), 2.27 (s, $2CH_3$). IR (cm^{-1}): 1608 ($\nu_{C=N}$), 1265 ($\delta_{Ar\text{-}OH}$), 1167 (ν_{C-N}), 1085 (ν_{C-O}). UV–Vis (λ [nm], log ε[l/mol × cm]): 432 (3.20), 304 (3.13), 278 (3.21). Elemental *Anal*. Calc. for $C_{20}H_{22}Br_2N_2O_2$: C, 49.82; H, 4.60; N, 5.81. Found: C, 49.79; H, 4.54; N, 5.79%.

L[8]: yellow solid (81% yield). M.p. 219–220 °C, ^{1}H NMR δ (ppm): 12.99 (s, 2H, OH), 7.67 (d, 2H ar), 7.29 (d, 2H ar), 3.99 (s, $2CH_2$), 2.39 (s, $2CH_3$), 2.25 (s, $2CH_3$). IR (cm^{-1}): 16108 ($\nu_{C=N}$), 12645 ($\delta_{Ar\text{-}OH}$), 1165 (ν_{C-N}), 1071 (ν_{C-O}). UV–Vis (λ [nm], log ε[l/mol × cm]): 432 (3.20), 304 (3.13), 278 (3.21). Elemental *Anal*. Calc. for $C_{20}H_{22}I_2N_2O_2$: C, 41.69; H, 3.85; N, 4.86%.

2.4. Preparation of the cobalt complexes

The cobalt complexes were prepared as described in literature [21–23]. One equivalent of $Co(OAc)_2 \cdot 4H_2O$, dissolved in 5 mL of water, was added dropwise to a solution of 1 equiv. of ligand, dissolved in 25 mL of EtOH or MeOH, at 40 °C under argon. In the case of the less soluble ligands, (in EtOH or MeOH) 2 equiv. of NaOH were added. The complexes immediately started to precipitate. The mixture was further stirred at 40 °C for 1 h. After cooling down at room temperature, the solid was filtered and washed successively with water, ethanol–water (1/1, v/v) and absolute ethanol. After drying in vacuum, the cobalt complexes were isolated and analyzed.

Compound **1**: Yield: 65%. *Anal*. Calc. for $C_{18}H_{18}N_2O_2Co$ (353.3): C, 61.20; H, 5.14; N, 7.93. Found: C, 60.89; H, 5.15; N, 7.83%. $m/z = 352.3$. IR (cm^{-1}): 1598 ($\nu_{C=N}$), 1176 (ν_{C-N}), 1078 (ν_{C-O}), 616 (ν_{M-N}), 452 (ν_{M-O}). UV–Vis (λ [nm], log ε[l/mol × cm]): 525 (2.51), 414 (3.25), 330 (3.22), 248 (2.94).

Compound **2**: Yield: 54%. *Anal*. Calc. for $C_{18}H_{14}Cl_4N_2O_2Co$ (491.1): C, 44.03; H, 2.87; N, 5.70. Found: C, 43.83; H, 2.87; N, 5.62%. $m/z = 490.7$. IR (cm^{-1}): 1603 ($\nu_{C=N}$), 1184 (ν_{C-N}), 1085 (ν_{C-O}), 657 (ν_{M-N}), 420 (ν_{M-O}). UV–Vis (λ [nm], log ε [l/mol × cm]): 516 (2.53), 438 (3.47), 330 (3.29), 268 (3.03).

Compound **3**: Yield: 57%. *Anal*. Calc. for $C_{18}H_{14}Br_2Cl_2N_2O_2Co$ (579.9): C, 37.28; H, 2.43; N, 4.83. Found: C, 37.01; H, 2.32; N, 4.71%. $m/z = 578.9$. IR (cm^{-1}): 1634 ($\nu_{C=N}$), 1185 (ν_{C-N}), 1091 (ν_{C-O}), 656 (ν_{M-N}), 411 (ν_{M-O}). UV–Vis (λ [nm], log ε [l/mol × cm]): 500 (2.49), 434 (3.58), 328 (3.78), 256 (2.94).

Compound **4**: Yield: 49%. *Anal*. Calc. for $C_{18}H_{14}Br_4N_2O_2Co$ (668.9): C, 32.32; H, 2.11; N, 4.19. Found: C, 32.11; H, 2.34; N, 4.12%. $m/z = 667.9$. IR (cm^{-1}): 1621 ($\nu_{C=N}$), 1192 (ν_{C-N}), 1082 ($\nu_{CndashO}$), 689 (ν_{M-N}), 414 (ν_{M-O}). UV–Vis (λ [nm], ε[l/mol × cm]): 560 (2.07), 398 (3.89), 300 (3.45), 232 (3.41).

Compound **5**: Yield: 53%. *Anal*. Calc. for $C_{18}H_{14}I_4N_2O_2Co$ (856.9): C, 25.23; H, 1.65; N, 3.27. Found: C, 25.02; H, 1.73; N, 3.31%. $m/z = 855.9$. IR (cm^{-1}): 1621 ($\nu_{C=N}$), 1184 (ν_{C-N}), 1068 (ν_{C-O}), 678 (ν_{M-N}), 407 (ν_{M-O}). UV–Vis (λ [nm], log ε [l/mol × cm]): 510 (2.59), 410 (3.31), 302 (3.19), 238 (3.20).

Compound **6**: Yield: 59%. *Anal*. Calc. for $C_{20}H_{20}Cl_2N_2O_2Co$ (450.2): C, 53.35; H, 4.48; N, 6.22. Found: C, 53.23; H, 4.41; N, 6.19%. $m/z = 449.1$. IR (cm^{-1}): 1558 ($\nu_{C=N}$), 1216 (ν_{C-N}), 1012 (ν_{C-O}), 554 (ν_{M-N}), 443 (ν_{M-O}). UV–Vis (λ [nm], ε[l/mol × cm]): 516 (2.19), 384 (3.00), 336 (3.08), 250 (3.25).

Compound **7**: Yield: 55%. *Anal*. Calc. for $C_{20}H_{20}Br_2N_2O_2Co \cdot 2H_2O$ (575.1): C, 41.76; H, 4.21; N, 4.87. Found: C, 41.53; H, 4.13; N, 4.79%. $m/z = 575.0$. IR (cm^{-1}): 1607 ($\nu_{C=N}$), 1237 (ν_{C-N}), 1021 (ν_{C-O}), 558 (ν_{M-N}), 441 (ν_{M-O}). UV–Vis (λ [nm], log ε [l/mol × cm]): 500 (2.60), 420 (3.22), 307 (3.05), 250 (3.27).

Compound **8**: Yield: 53%. *Anal*. Calc. for $C_{20}H_{20}I_2N_2O_2Co \cdot 0.5\ H_2O$ (642.1): C, 37.41; H, 3.30; N, 4.36. Found: C, 37.43; H, 3.21; N, 4.27%. $m/z = 632.9$. IR (cm^{-1}): 1600 ($\nu_{C=N}$), 1249 (ν_{C-N}), 1085(ν_{C-O}), 517 (ν_{M-N}), 448 (ν_{M-O}). UV–Vis (λ [nm], log ε[l/mol × cm]): 510 (2.59), 410 (3.31), 302 (3.19).

3. Results and discussion

The 3,5-dihalo derivatives of 2-hydroxyacetophenone were obtained as described in Section 2.1, using already reported procedures for introducing halogen atoms into the aromatic ring by bromination or iodination of 2-hydroxyacetophenone [15–17]. The ligands were obtained from the reaction between 3X-, 5Y, 2OH-, acetophenone (where X and Y are Cl, Br, I) and ethylenediamine in a 2:1 molar ratio [18–20]. The cobalt(II) complexes were obtained by a general method from an aqueous solution

of $Co(OAc)_2 \cdot 4H_2O$ and solutions of ligands in EtOH, under argon [21–23]. The elemental analysis of all complexes was in agreement with a 1:1 metal:ligand ratio, which was also confirmed by ESMS spectroscopy.

After coordination of cobalt (II) to the tetradentate Schiff bases which contain four donor atoms, O, N, N, O, highly thermodynamically stable three-rings planar chelates were obtained. The compounds were isolated as powders that were not suitable for X-ray diffraction analysis. Until now further attempts to obtain crystals were not successful.

The oxygenated species were not isolated; they were obtained and studied "in situ" only.

3.1. ESMS spectra

Although, the ESMS spectra for neutral complexes are not always very accurate for the determination of molecular weights, because of chemical ionisation of these complexes [24], the obtained results can be used for confirmation of the structure. Our Co(II)-salen complexes were all analyzed by ESMS spectroscopy and their spectra all exhibited a peak at a m/z value corresponding to their molecular weight. For example, for the complex **3** a maximum molecular peak was obtained at $m/z = 578.9$ (Fig. 2a). Around this value, some other peaks were present that could be assigned to the molecular weight of the compounds with the various isotopes of the Cl and Br atoms. The peak at $m/z = 601.9$ was assigned to **3-Na**, and the other peaks around it corresponded to molecular weight of the compounds with the various isotopes of Cl and Br [25]. In the ESMS simulated spectra (Fig. 2b) a maximum peak at 578.8 was observed. In addition, other peaks around this value were observed, that corresponded to the molecular weight of the compounds with various isotopes of the Cl and Br atoms (see Fig. 2).

3.2. Infrared spectra

The IR spectra of the ligands and complexes (Section 2) all showed major bands around of 1605 cm^{-1} that can be assigned to $\nu_{C=N}$, and around 1560 cm^{-1} and 1500 cm^{-1} that can be assigned to ring vibrations. The band around 1280 cm^{-1} was assigned to the deformation of the Ar-OH outside the plane of the ArOH moiety, δ_{OH}, and the bands around 1230 $cm^{-1}$and 1050 cm^{-1} were assigned to ν_{C-N}, and ν_{C-O}, respectively [26,27], (see Fig. 3).

In the spectra of the cobalt (II) complexes, the bands corresponding to $\nu_{C=N}$, ring vibrations and ν_{C-N} and ν_{C-O} appeared to be shifted when compared to the corresponding bands in the spectra of the free ligands. In addition, the band characteristic of the deformation of the Ar-OH outside the plane of the ArOH moiety, $\delta_{Ar\text{-}OH}$, in the spectra of the free ligands was absent in the spectra

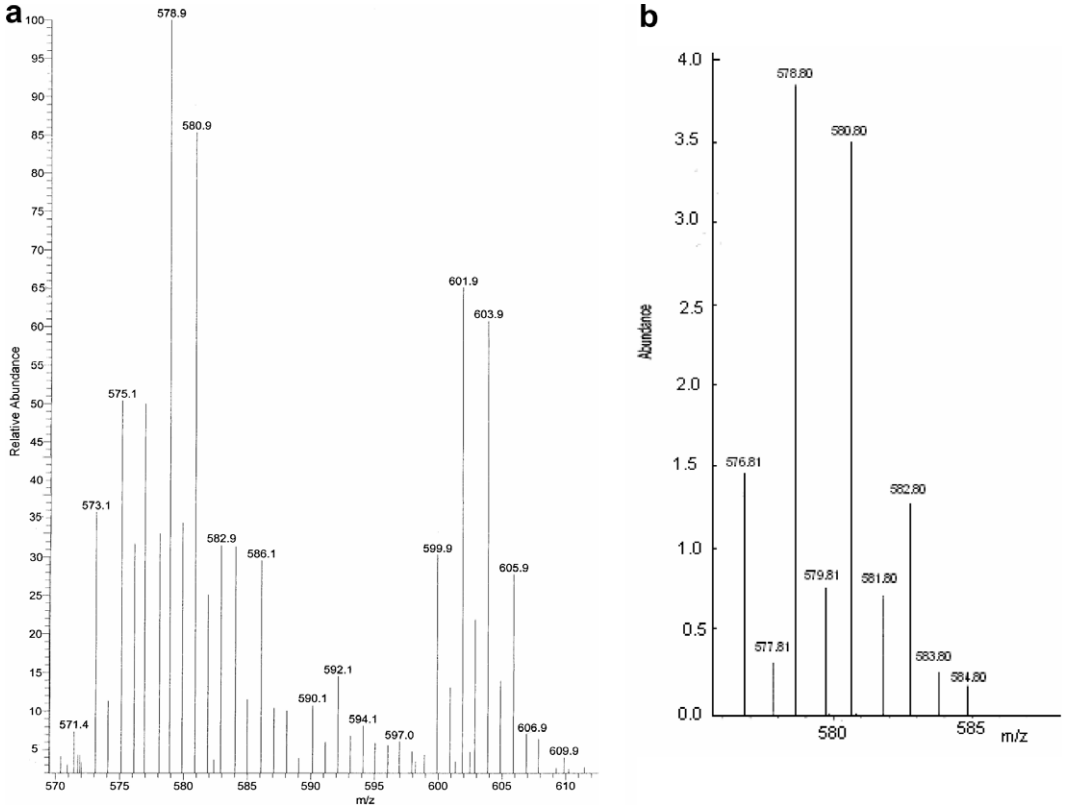


Fig. 2. ESMS spectrum of the complex **3**: (a) recorded; and (b) simulated.

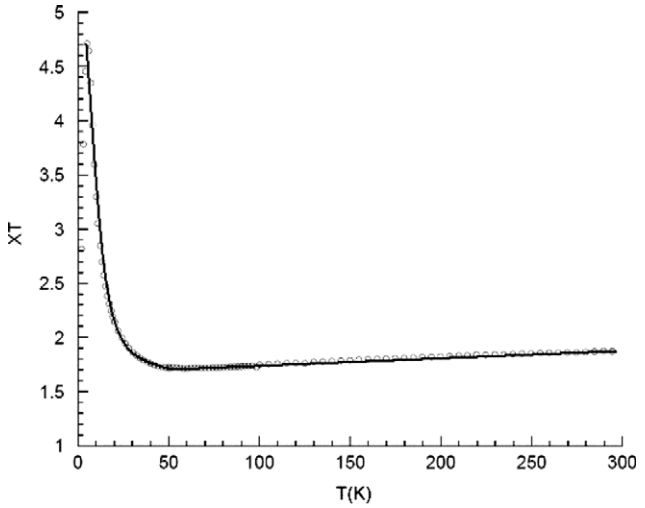


Fig. 3. Magnetic susceptibility of **7** collected at 1000 G plotted as χ_T vs. temperature (K).

of the Co(II) complexes, as a consequence of the involvement of the oxygen anion into a σ bond with the metal ion. The formation of cobalt–oxygen and cobalt–nitrogen σ bonds was proven by the appearance of some new absorption bands in the 400–690 cm^{-1} region of the spectra of the Co(II) complexes that could be assigned to ν_{Co-O} and ν_{Co-N} vibrations [28].

As a conclusion, the recorded IR spectra were in complete agreement with the formation of complexes by the coordination of Co(II) to the azomethyne nitrogen and to the phenolic oxygen atoms [28,29].

3.3. Electronic spectra

The electronic spectra of the free ligands in DMF showed two strong absorption bands in the UV–Vis region (316–432 nm) (Section 2), that could be attributed respectively to the π–π^* and n–π^* transitions. The free ligands also exhibited a UV band between 232 nm and 422 nm that attributed to the n–π^* and n–σ^* transitions [30,31]. In the spectra of the corresponding Co(II) complexes, the position and intensity of the bands characteristic of the ligand appeared to be modified with respect to those of the free ligand. In addition, these spectra also presented new bands (sometimes not well-defined) between 500 and 560 nm that were characteristic of the formed Co(II) complexes.

The bands located in the 404–438 nm region were attributed to the d–π^* charge-transfer transitions, which overlap with the π–π^* or n–π^* transitions of the ligands. The new band that appeared over 500 nm could be attributed to the d-d transitions of the divalent cobalt complexes [32,33]. These modifications in shifts and intensity for the absorption bands supported the coordination of the ligand to the central Co(II) ion.

A square planar geometry with four donor atoms (O, N, N, O) in the same plane was proposed for the complexes in the solid state. But, in solution, cobalt (II) complexes can coordinate 2 solvent molecules in axial positions, leading to a complex with an octahedral geometry. These solvent molecules can be replaced by coordinating amine bases such as pyridine, imidazole, etc. Accordingly, after addition of pyridine to DMF solutions of the Co(II) complexes, the [LCo(py)(DMF)] or [$LCo(Py)_2$] complexes were formation [34].

3.4. Magnetic measurement

The magnetic moment μ_{eff}, of the complex **7** was found to be 4.89 MB, at 295 K. This value is well within the reported range for high-spin octahedral cobalt (II) monomer complexes [31]. For the other complexes we appreciate similarly values. Variable-temperature magnetic susceptibility data (2–300 K) were collected for **7** in a 195 applied magnetic field of 1000 G (Fig. 4).

The susceptibility data turn over at 30 K, indicating the presence of a ferromagnetic exchange interaction.

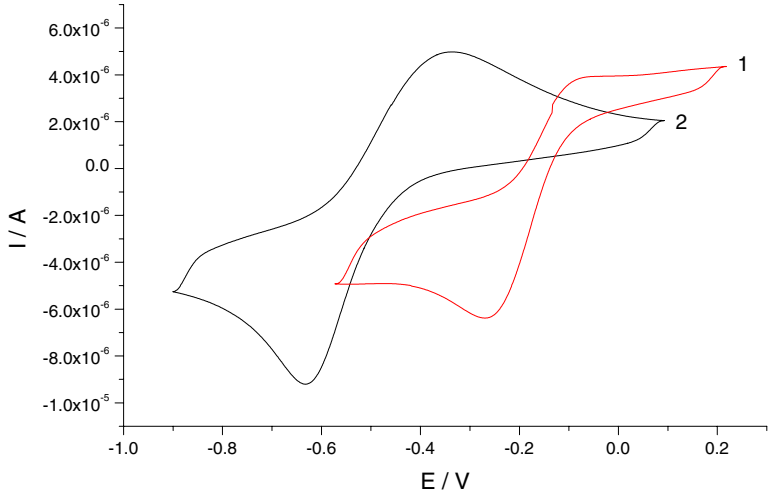


Fig. 4. Cyclic voltamogram for the complex **7**, $C_{CoL}=2\pm10^{-3}$ M, in DMF, scan rate = 0.1 V/s, vs. the saturated calomel electrode (SCE): (1) initial, under argon atmosphere, (2) after addition of pyridine, $c_{py}=0.2$ M.

3.5. Electrochemistry

The redox potential of the Co(II)/Co(III) couple is an important parameter for the catalytic activity of the Cobalt(II)-salen complexes in the oxidation of substrates by O_2. Its value is strongly influenced both by the nature of the axial ligand of the cobalt ion and by the structure of the ligand (Table 1).

All the cyclic voltammograms for the Co-salen complexes were recorded in the presence or not of 0.2 M pyridine. The corresponding anodic (E_{pa}), cathodic (E_{pc}) and half-wave ($E_{1/2}$) potentials, as well as the ΔE values measured for each Co(II) complex are reported in Table 1. In order to compare the half-wave ($E_{1/2}$) potentials values more easily to literature data, they are also reported to those of the ferrocenium/ferrocene (Fc^+/Fc) couple (i.e. $E'_{1/2}$) [35,36]. Examining the data showed in Table 1, one can observe that, in the absence of pyridine (lines 1–9) all the complexes have a non-reversible behavior, except the Co(salen) complex which presents a quasi-reversible behavior. The electrochemical data of the Co-complexes of substituted salens (lines 2–8) can be compared with those of the Co complex of non substituted salen (line 1). Substitution by a methyl group in the α-position of the ligand, in complex **1** causes a decrease of the $E_{1/2}$ value from –0.159 V for Co(salen) to −0.280 V (for complex **1**). This correlates with the donating effect of the methyl substituent which causes an increase of the reducing power of the Co-salen complexs. Surprisingly, substitution of the aromatic rings by halogen atoms leads to a further decrease of the $E_{1/2}$ value around 0.370 ± 0.010 V (lines 3–6) with almost no difference whatever the halogen substituent. Thus, these results cannot be explained by the electronegativity of the halogen substituents, which would have been expected to cause an increase in the $E_{1/2}$ value. It is then likely that, in this case, it is the donating mesomeric effect of the halogen atoms that is predominant and causes an increase in the reducing power of the Co-salen complexes.

Table 1
Electrochemical data for the cobalt(II)-salen complexes

Compounds	E_{pa} (V)	E_{pc} (V)	ΔE	$E_{1/2}$ (V)	$E'_{1/2}$ (V)
Co(Salen)	−0.106	−0.213	0.107	−0.159	0.307
1	−0.028	−0.532	0.501	−0.280	0.186
2	−0.067	−0.658	0.591	−0.362	0.104
3	−0.061	−0.701	0.640	−0.381	0.085
4	−0.059	−0.690	0.631	−0.374	0.092
5	0.023	−0.695	0.672	−0.359	0.107
6	−0.123	−0.268	0.145	−0.195	0.271
7	−0.003	−0.265	0.262	−0.134	0.332
8	0.009	−0.123	0.132	−0.057	0.409
Co(Salen), py	−0.320	−0.550	0.230	−0.430	0.040
1, py	−0.327	−0.645	0.318	−0.486	−0.020
2, py	−0.287	−0.473	0.186	−0.380	0.086
3, py	−0.325	−0.516	0.191	−0.420	−0.046
4, py	−0.209	−0.370	0.161	−0.283	0.183
5, py	−0.208	−0.405	0.197	−0.306	0.160
6, py	−0.244	−0.659	0.415	−0.552	−0.015
7, py	−0.340	−0.630	0.290	−0.485	−0.019
8, py	−0.312	−0.409	0.097	−0.361	0.106

$C_{CoL} = 2 \times 10^{-3}$ M; $c_{py} = 2 \times 10^{-1}$ M; scan rate 100 mV/s; E_{pa} and E_{pc} are the anodic and cathodic peak potentials, respectively. $\Delta E = E_{pa} - E_{pc}$ in 0.1 M $LiClO_4$ in DMF. $E_{1/2} = (E_{pa} + E_{pc})/2$. $E'_{1/2}$ is $E_{1/2}$ reported to the potential of the couple Fc^+/Fc, where Fc = ferrocene, $E_{Fc^+/Fc} = 0.466$ V.

As shown in Fig. 4 in the typical case of the complex **7**, addition of 0.2 M pyridine to the solution of Co-salen complex caused a large change in the shape of the cyclic voltammogram (Fig. 4, curve 2). In particular, it caused a severe decrease in the half-wave ($E_{1/2}$) potential from −0.134 V to −0.485 V (Table 1, compare line 8 and line 17).

Under those conditions, the decrease in ΔE was observed for all the complexes, leading to ΔE values between 0.161 V and 0.318 V (Table 1, lines 12–18) and their behaviour became quasi-reversible.

The decrease of the half-wave potential was due to the replacement of the axial solvent molecules by pyridine, which has a stronger basic character, enhancing electronic density on the Co(II) ion, and thus increasing its reducing power [37,38]. This effect, however, was not observed for all complexes, as in the case of the complexes **4** and **5** higher $E_{1/2}$ values were found in the presence of pyridine (resp. −0.283 V and −0.306 V, Table 1 lines 14 and 15) than without pyridine (resp. −0.374 V and −0.359 V, Table 1 lines 5 and 6). It is then likely that in these cases, in the presence of pyridine, steric hindrance, which diminishes the conjugation of the ligand ring, occurs.

EPR spectra of non-oxygenated and oxygenated cobalt(II) complexes were measured at 10 K as a frozen DMF solution, in the presence of excess pyridine. All the spectra were similar to those shown in Fig. 5 in the case of the complex **3.** In the absence of O_2, the spectrum of the complex **3** exhibits a signal centred around $g = 2$, characteristic of a low-spin Co(II) complex, with a rhombic distortion from ideal axial symmetry, with $g_1 = 2.08$, $g_2 \cong g_3 = 2.02$. The perpendicular component of the spectrum appears as a clearly identifiable 8 lines signal, corresponding to ^{59}Co ($I = 7/2$) hyperfine splitting (and $A = 9.4$ G) (Fig. 5a). In addition, in the presence of pyridine the eight-line signal corresponding to the parallel component g_3 is further split into three or five lines due to the coupling of the cobalt (II) centre with one or two axially coordinated pyridine nitrogen atoms [31,39].

In the presence of O_2, a new spectrum characteristic of **3**-$O_2$was obtained (Fig. 5b). It also exhibited a signal

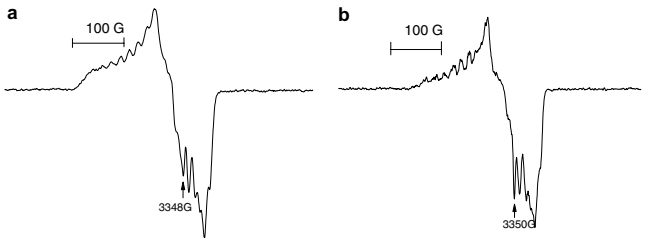


Fig. 5. EPR spectra of: (a) complex **3**, (b) adduct **3**-O_2, in DMF at 10 K, in the presence of excess pyridine.

centred around $g = 2$, characteristic of a Co(II) complex, with a rhombic distortion from ideal axial symmetry, with $g_1 = 2.03$, $g_2 \cong g_3 = 2.01$ The perpendicular component of the spectrum appeared as a clearly identifiable 8 lines signal (diminished as intensity, 3/1), corresponding to ^{59}Co ($I = 7/2$) hyperfine splitting ($A = 9.4$ G) (Fig. 5b). The formation of 1/1 complex **3**/O_2 adduct was thus EPR spectra confirmed [40].

3.6. Catalytic activity

2,6-Di-*tert*-butylphenol (**9**), can easily be oxidized by molecular oxygen in the presence of metal complexes as catalysts to give mainly two products: 2,6-di-*tert*-butyl-1,4-benzoquinone (**10**) and 2,6,2′,6′-tetra-*tert*-butyl-1,1′-diphenobenzoquinone (**11**), respectively (Scheme 1) [41,42]. Their formation depends on the nature of the metallic ion present in the complex, which may influence their relative proportions.

Table 2 shows the yields and relative proportions of these two products, determined by ^1H NMR and GC as described in Section 2.1, when phenol **9**, 0.1 M in dry DMF was oxidized by O_2 in the presence of 0.5 M pyridine and 0.5×10^{-2} M (5% molar with respect to the substrate) Co-salen complex as catalyst. Increasing the catalyst/substrate ratio did not lead to any significant increase in the yield (1–2% at the most).

The presence of pyridine was crucial for the reaction, as in the absence of the pyridine, much lower yields were obtained (below 50%) and the reaction proved to be not selective with the formation of up to 60% of quinone **10**. Finally, kinetic studies indicated a second order reaction, par rapport a metallic complex.

Table 2
Reaction products of catalytic oxidation of the phenol **9** with Cobalt (II) complexes[a]

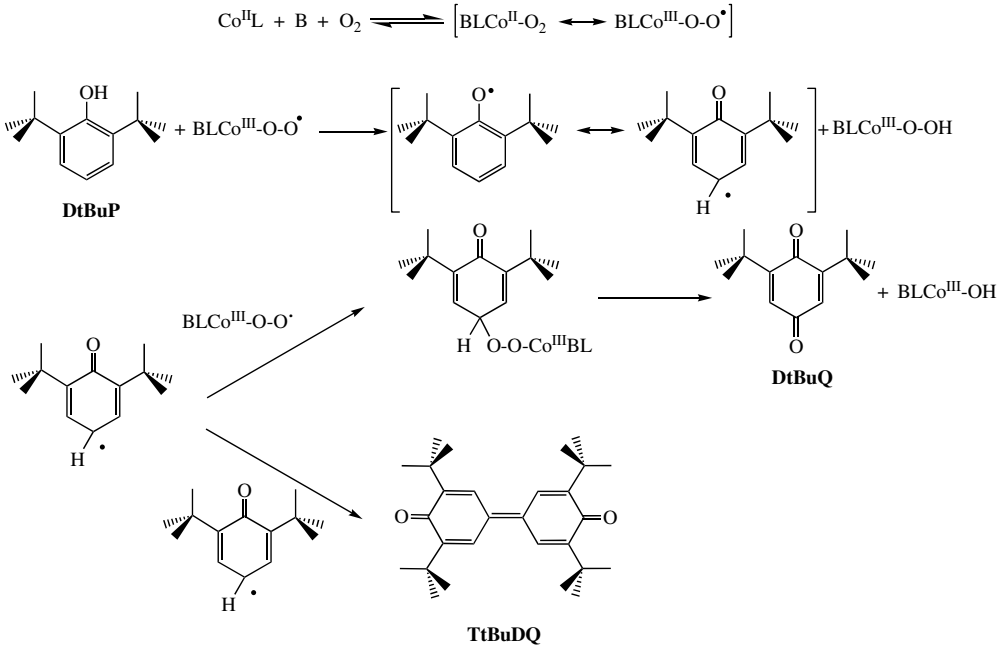
Compounds	Yield %[a]	**10** (%)	**11** (%)
1	97	98	2
2	95	91	9
3	94	87	13
4	89	64	36
5	90	71	29
6	100	94	6
7	100	96	4
8	100	97	0

[a] Error +/−0.5%.

From Table 2, it appears that the highest yield as well as the best selectivity in favor of the formation of **11** are obtained with the Co complexes of ligands bearing $2CH_3$ substituents, Co(dMeSalen) **1**, or 4 CH_3 substituents (Co-3,3′-dichloro-5,5′,α,α′-tetramethyl-Salen **6**; Co-3,3′-dibromo 5,5′,α,α′-tetramethyl-Salen **7**; and 3,3′-diiodo 5,5′,α,α′-tetramethyl-Salen **8**), as catalysts. Both the yield and mainly the selectivity decrease when the aryl rings of the salen ligand are substituted by halogen atoms, and in addition, a good correlation was found between the half-wave potential $E_{1/2}$ and both the yield of the reaction and the relative proportion of DtBuQ formed (Fig. 6).

From Fig. 5, it is clear that the lower was the value of the half-wave potential, the higher were the catalytic activity and the selectivity in favor of **10**.

To explain the formation of **10** or **11** it is necessary to consider the mechanism of the reaction, which has been thoroughly studied [43,44]. The main steps involved in this mechanism are described in Scheme 1.



Scheme 1. Reaction pathway for oxygenation of phenol **9** with molecular oxygen, in the presence of Co(II) complexes (B is axial base, this can be DMF or py molecule).

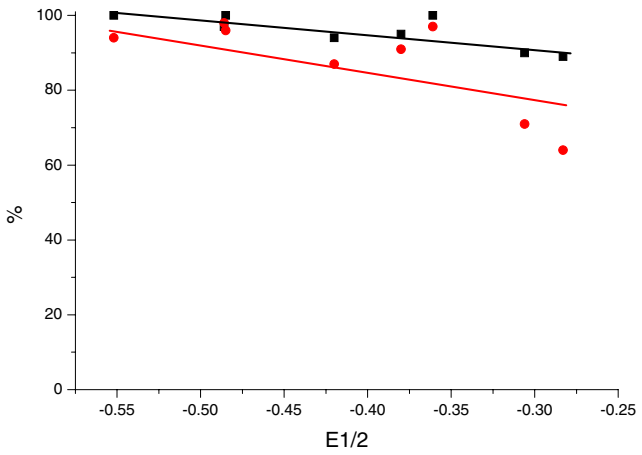


Fig. 6. Yield (%) and proportion of **10** formed as a function of the half wave potential.

In presence of pyridine, the first step of the mechanism involves the reversible formation of a Co–O_2 adduct. This was confirmed in our case not only by EPR spectroscopy, but also by cyclic voltammetry in the case of **7** (Fig. 7).

When molecular dioxygen is bubbled into a solution of the complex **7**, 2 mM in DMF, in the presence of pyridine (in excess, 10/1), its quasi-reversible voltammogram (Fig. 7(1)) is replaced by an irreversible one (Fig. 7(3)). Further, argon bubbling into the solution, led to the replacement of this voltammogram by a new quasi-reversible one (Fig. 7(2)), that was almost superimposible to that of the starting complex **7**. This was in agreement with the formation of a Co^{II}–O_2 adduct which could be reversed by bubbling argon into the solution.

This Co^{II}–O_2 is then able to perform the one electron-reduction of phenol **9** into a semi-quinone radical. The further, formation of the compounds **10** and **11** depends upon the evolution of this radical. Either it reacts with another Co^{II}–O_2 adduct to form a BLCo-O-O-DtBuP peroxo complex (**12**), that is then hydrolyzed to lead to the quinone **10**, or its dimerization, followed by an oxidation steep, lead to diphenoquinone **11** (Scheme 1) [40].

Since the kinetic studies have shown that the reaction was bimolecular, it is likely that the determining step of the process is the one electron reduction of phenol **9** into a semi-quinone radical by the Co(II)–O_2 adduct. It may then be expected that the best reactivity occur with the best reducing complex, i.e. the one that have the lowest half-wave potential. This is in agreement with our results, since the best yield (98%) was obtained with the Co-salen complexes having the lowest half-wave potential in the presence of pyridine (complex **1**), $E_{1/2} = -0.486$ V, (Table 1), and since a good correlation was observed between the yield of the reaction and $E_{1/2}$, the yield decreasing as $E_{1/2}$ increased (Fig. 6). In this case, the dimerization of this semi-quinone radical into **11** was the predominant reaction observed [45].

Concerning the selectivity of the reaction, the ratio between quinone **10** and diphenoquinone **11** is governed by the ability of semi-quinone radical to react with a Co^{II}–O_2 adduct to give the peroxo complex **12** which is further hydrolyzed into **10**. This reaction is disfavoured when the steric hindrance around the Co(II) ion is important. This is in agreement with our results, since the relative proportion of **10** formed decreases from 98% to about 65% when the aromatic rings of the dMeSalen ligands are substituted with bulky bromine and iodine atoms (Table 2). Since the ligands substituted by the more bulky atoms are also the ones that have the lowest reducing power, a good correlation is also observed between the $E_{1/2}$ value and the relative proportion of **10** formed (Fig. 6).

In the absence of pyridine, a lower yield was obtained because of the irreversible oxidation process of Co(II) to Co(III), which disfavoured the reaction of the semi-

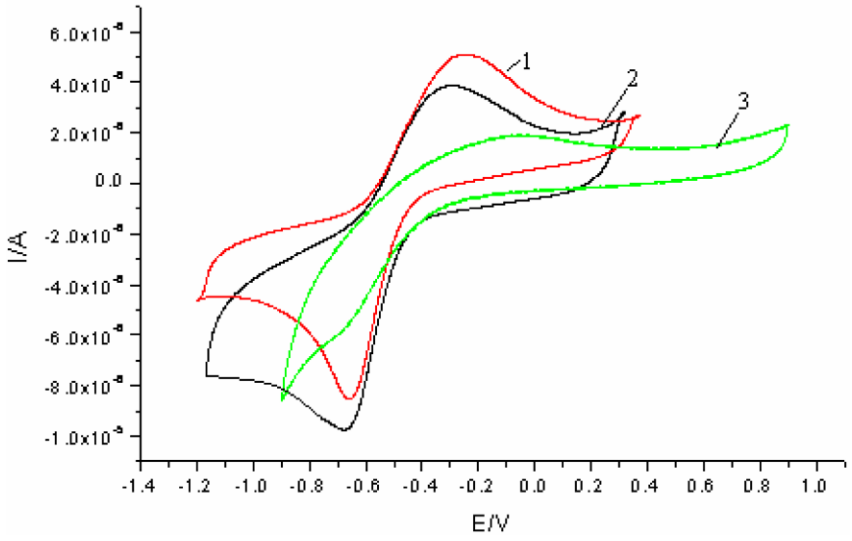


Fig. 7. Cyclic voltammograms for the complex **7**, $C_{CoL} = 2$ mM, in DMF; Scan rate = 100 mV/s: 1, initial, under Ar atmosphere; 2, after elimination of O_2 (Ar bubbling, under Ar atmosphere.); 3, in the presence of O_2.

quinone radical with Co^{II}–O_2 to lead to the peroxo complex **12** and then to quinone **10**.

4. Conclusion

Grafting of various halogen substituents on the aromatic ring and of a methyl substituent on the azomethynic group of Salen type ligands leads to the formation of some new ligands which form complexes with square planar geometry upon reaction with Co(II) ions. Such compounds are of interest for the reversible binding of dioxygen and for their catalytic activity in the oxidation reactions of substrates by O_2. These properties are first influenced the coordination of pyridine in axial position of the Co(II) ion causes an increase of the electronic density on the cobalt ion and as a consequence a decrease in the $E_{1/2}$ value and an increase of the reducing power of the Co(II) complex. It is noteworthy that, under those conditions the complexes also show a remarkable quasi-reversible behaviour. Second, complex properties are also influenced by the substituents (methyl and halogen) grafted on the aromatic ring and on the azomethynic group. The donating methyl substituent on the azomethynic group causes a decrease in the $E_{1/2}$ value, whereas the halogen substituents on the aromatic rings have two effects: a mesomeric donating effect that tends to lower the redox potential of the complex, and a steric effect that tends to decrease the conjugation of the ligand and then to increase the redox potential of the Co(II) complex. In pyridine, the steric effect predominates, which causes both an increase of the redox potential and a decrease of the selectivity of the oxidation of phenol **9**. As a result of all these effects, it then appears that the best complex to realize the selective oxidation of the phenol **9** by O_2, in the presence of pyridine, is complexes **6**, **7**, **8** and **1**.

Acknowledgement

A.P. wishes to thank to the AUF and CNCSIS (Grant. 1163/2006) for the financial support.

References

[1] T. Ueno, N. Yokoi, M. Unno, T. Matsui, Y. Tokita, M. Yamada, M. Ikeda-Saiti, H. Nakajima, Y. Watanabe, PNAS 103 (2006) 9416.
[2] K.P. Bryliakov, E.P. Talsi, Angew. Chem., Int. Ed. 43 (2004) 5282.
[3] L. Dyers Jr., S.Y. Que, D. VanDerveer, X.R. Bu, Inorg. Chim. Acta 359 (2006) 197.
[4] P.A. Vigato, S. Tamburinii, Coord. Chem. Rev. 248 (2004) 1717.
[5] J.P. Collman, L. Zeng, J.I. Brauman, Inorg. Chem. 43 (2004) 2672.
[6] L.I. Simàndi, Dioxygen Activation and Homogeneous Catalytic Oxydation, Elsevier, Amsterdam, 1991.
[7] M.-C. Cheng, M.C.-W. Chan, S.-M. Peng, K.-K. Cheung, C.-M. Che, J. Chem. Soc., Dalton Trans. (1997) 3479.
[8] S.M. Been-saber, A.A. Maihub, S.S. Hudere, M.M. El-Ajail, Microchem. J. 81 (2005) 191.
[9] E.C. Niederhoffer, J.H. Timmons, A.E. Martell, Chem. Rev. 84 (1984) 137.
[10] K. Ambroziak, R. Pelech, E. Michert, E. Dziembowska, T. Rozwadowski, Z.J. Mol. Catal. A: Chem. 211 (2004) 9.
[11] L. J Simándi, T.M. Simándi, Z. May, G. Besenyei, Coord. Chem. Rev. 245 (2003) 85.
[12] J.R. Carey, S.K. Ma, T.D. Pfister, D.K. Garner, H.K. Kim, J.A. Abramite, Z. Wang, Z. Guo, Y. Lu, J. Am. Chem. Soc. 126 (2004) 10812.
[13] T. Ueno, M. Ohashi, K. Kono, A. Suzuki, T. Yamane, Y. Watanabe, Inorg. Chem. 43 (2004) 2852.
[14] A. Pui, C. Policar and J.-P. Mahy, Inorg. Chim. Acta, in press.
[15] J.N. Kim, E.K. Ryu, Synth. Commun. (1996) 67.
[16] S.B. Patwari, M.A. Basser, B.Z. Vibhute, S.R. Bhusare, Tetrahedron Lett. 44 (2003) 4893.
[17] K. Orito, T. Hatakeyama, M. Takeo, H. Suginome, Synthesis (1995) 1273.
[18] Al. Cascaval and Gh. Z. Stoica, Patent $^{(19)}$Ro$^{(11)}$105122.
[19] N. Choudhary, D.L. Hughes, U. Kleinkens, L.F. Larkworthy, G.J. Leigh, M. Maiwald, C.J. Marmion, J.R. Sanders, G.W. Smith, C. Sudbrake, Polyhedron 16 (1997) 1517.
[20] R.H. Bailles, M. Calvin, J. Am. Chem. Soc. 69 (1947) 1886.
[21] D. Chen, A.E. Martel, Y. Sun, Inorg. Chem. 28 (1989) 2647.
[22] P.E. Riley, V.L. Pecoraro, C.J. Carramo, J.A. Bonaies, K.N. Raymond, Inorg. Chem. 25 (1986) 154.
[23] D. Chen, A.E. Martel, Inorg. Chem. 26 (1987) 1026.
[24] S.M. Schidcrout, S. SriHari, J. Masnovi, Inorg. Chem. 34 (1995) 4117.
[25] R. Droes, G. Nardin, L. Randaccio, P. Siega, G. Tauzher, V. Vrdojak, Inorg. Chim. Acta 348 (2003) 239.
[26] T. Joseph, S.B. Halligudi, C. Satyanarayan, D.P. Sawant, S. Gopinathan, J. Mol. Catal. A: Chem. 168 (2001) 87.
[27] K. Nakamoto, Infrared and Raman Spectra of Inorganic and Coordination Compounds, Part B, 5th ed., Wiley, 1997.
[28] A. Ramachandraiah, P.N. Rao, M. Ramaiah, Ind. J. Chem. 28A (1989) 309.
[29] X. Tai, X. Yin, Q. Chen, M. Tan, Molecules 8 (2003) 439.
[30] A.B.P. Lever, Inorganic Electronic Spectroscopy, 2nd ed., Elsevier, London, 1992.
[31] S. Djebar-Sid, O. Benali-Baitich, J.P. Deloume, J. Mol. Struct. 569 (2001) 121.
[32] B. Ortiz, S.M. Park, Bull. Korean Chem. Soc. 21 (2000) 405.
[33] M.J. Carter, D.P. Rillema, F. Basolo, J. Am. Chem. Soc. 96 (1974) 392.
[34] E. Eichhon, A. Reiker, B. Speiser, H. Stahl, Inorg. Chem. 36 (1997) 3307.
[35] G.A. Mabbott, J. Chem. Educ. 60 (1983) 697.
[36] S.J. Dzugan, D.H. Busch, Inorg. Chem. 29 (1990) 2528.
[37] A. Brőttcher, T. Takeuki, K.I. Hardcastle, T.J. Meade, H.B. Gray, D. Vwikel, M. Kapon, Z. Dori, Inorg. Chem. 36 (1997) 2498.
[38] R.R. Gagne, C.A. Koval, G.C. Lisensky, Inorg. Chem. 18 (1980) 2854.
[39] N. Venkatalakshmi, M.V. Rajasekharan, Proc. Indian Acad. Sci. (Chem. Sci.) 4 (1995) 327.
[40] M.D. Braydich, J.J. Fortman, S.C. Cummings, Inorg. Chem. 22 (1983) 484.
[41] M.F. Rio, D. Pujol, C.B. Chateron, M.P. Fauvet, A. Gaudmer, J. Chem. Soc., Perkin Trans. I (1984) 1971.
[42] K. Omura, J. Org. Chem. 61 (1996) 2006.
[43] T. Punniyamurthy, S. Velusamy, J. Iqbal, Chem. Rev. 105 (2005) 2329.
[44] Y. Deng, D.H. Busch, Inorg. Chem. 34 (1995) 6380.
[45] L.I. Simándi, T.M. Simándi, Z. May, G. Besenyei, Coord. Chem. Rev. 245 (2003) 85.

Available online at www.sciencedirect.com
ScienceDirect
Polyhedron 26 (2007) 3153–3160
POLYHEDRON
www.elsevier.com/locate/poly

Studies on the synthesis, characterization and reactivity of new ferrocenylacetylenylbiphenyl derivatives

Quan-Ling Suo [a,*], Yue-Guang Bai [a], Yi-Bing Wang [a], Li-Min Han [a], Lin-Hong Weng [b]

[a] *Chemical Engineering College, Inner Mongolia University of Technology, Hohhot 010051, PR China*
[b] *Department of Chemistry, Fudan University, Shanghai 200433, PR China*

Received 14 December 2006; accepted 15 February 2007
Available online 1 March 2007

Abstract

A series of ferrocenylacetylenylbiphenyl derivatives Fc-C≡C—R [R = C_6H_4—C_6H_5 (**1**), C_6H_4—C_6H_4—I (**2**), C_6H_4—C_6H_4—NO_2 (**3**), $C_6H_3(NO_2)$—C_6H_4I (**4**)] and Fc-C≡C—R′—C≡C—R″ [R″ = Fc, R′ = C_6H_4—C_6H_4 (**5**), $C_6H_3(NO_2)$—C_6H_4 (**6**); R″ = C_6H_5, R′ = C_6H_4—C_6H_4 (**7**)] were synthesized from FcC≡CH and biphenyl iodides by the Castro–Stephens and Sonogashira coupling reactions, in which compounds **1**, **2**, **3**, **4**, **6** and **7** are new. Seven new complexes [Fc-C≡C—R][$Co_2(CO)_6$] [R = C_6H_4—C_6H_5 (**8**), C_6H_4—C_6H_4—I (**9**), C_6H_4—C_6H_4—NO_2 (**10**), $C_6H_3(NO_2)$—C_6H_4I (**11**)] and [Fc-C≡C—R′—C≡C—R″] [$Co_2(CO)_6$]$_2$ [R″ = Fc, R′ = C_6H_4—C_6H_4 (**12**), $C_6H_3(NO_2)$—C_6H_4 (**13**); R″ = C_6H_5, R′ = C_6H_4—C_6H_4 (**14**)] were obtained by the reaction of the ligands Fc-C≡C—R and Fc-C≡C—R′—C≡C—R″ with $Co_2(CO)_8$, respectively. Compounds **1**–**7** and their complexes **8**–**14** have been characterized by element analysis and spectroscopy, as well as by X-ray diffraction for **1**, **4, 8, 9** and **11**. The electrochemical data of compounds **1–12** have been obtained by cyclic voltammetry.
© 2007 Elsevier Ltd. All rights reserved.

Keywords: Ethynylferrocene; Coupling reaction; Biphenyl derivative; Cobalt carbonyl complex

1. Introduction

In recent years, the design of materials for application in molecular wires has focused on how to arrange organometallic redox-active centers to enhance the capability of transferring electrons along a conjugated molecular axis [1–3]. The diyne $Co_2(CO)_6$ complexes are probably better candidates and have displayed some electronic communication and interactions between redox-active centers [4–6]. A variety of ferrocenyl π-conjugated derivatives have been designed and synthesized by Castro–Stephens, Sonogashira and other coupling reactions [7–13] because these compounds can be used as an approach to construct linear donor-π-conjugated spacer-accepter assemblies. π-Conjugated compounds with aryl groups have largely been reported [14–16], but ferrocenylacetylenylbiphenyl derivatives are rare [17]. Here we describe the preparation and structural characterization of seven ferrocenylacetylenylbiphenyl derivatives Fc-C≡C—R [R = C_6H_4—C_6H_5 (**1**), C_6H_4—C_6H_4—I (**2**), C_6H_4—C_6H_4—NO_2 (**3**), $C_6H_3(NO_2)$—C_6H_4I (**4**)] and Fc-C≡C—R′—C≡C—R″ [R″ = Fc, R′ = C_6H_4—C_6H_4 (**5**), $C_6H_3(NO_2)$—C_6H_4 (**6**); R″ = C_6H_5, R′ = C_6H_4—C_6H_4 (**7**)], in which **1**, **2**, **3**, **4**, **6** and **7** are new compounds. Compound **1** was synthesized by the Castro–Stephens coupling reaction of Fc-C≡C—Cu and I—C_6H_4—C_6H_5, and compounds **2**–**4** were obtained by the Sonogashira coupling reaction of ethynylferrocene with the relevant iodobiphenyl derivatives, and compounds **5**–**7** were prepared by a second Sonogashira coupling reaction of ethynylferrocene with compounds **2** and **4**, or ethynylbenzene with compound **2**, respectively. Seven new cobalt carbonyl complexes [Fc-C≡C—R][$Co_2(CO)_6$] [R = C_6H_4—C_6H_5 (**8**), C_6H_4—C_6H_4—I (**9**), C_6H_4—C_6H_4—NO_2 (**10**),

* Corresponding author.
E-mail address: szj@imut.edu.cn (Q.-L. Suo).

0277-5387/$ - see front matter © 2007 Elsevier Ltd. All rights reserved.
doi:10.1016/j.poly.2007.02.023

$C_6H_3(NO_2)$—C_6H_4I (**11**)] and [Fc-C≡C—R′—C≡C—R″]-$[Co_2(CO)_6]_2$ [R″ = Fc, R′ = C_6H_4—C_6H_4 (**12**), $C_6H_3(NO_2)$—C_6H_4 (**13**); R″ = C_6H_5, R′ = C_6H_4—C_6H_4 (**14**)] have successfully been synthesized by using the reactivity of the alkyne bonds of compounds **1**–**7** with $Co_2(CO)_8$. The molecular and crystal structures of compounds **1**, **4** and complexes **8**, **9** and **11** have been determined by X-ray single crystal analysis. The electrochemical properties of compounds **5**, **6** and **12** reveal that no significant electronic communication between the two ferrocenyl units was observed.

2. Experimental

Published procedures or extensions thereof were used to synthesize the initial intermediates Fc-C≡CH, Fc-C≡CCu [8], $C_6H_5C_6H_4I$, IC_6H_4—C_6H_4I, IC_6H_4—$C_6H_4NO_2$, $IC_6H_3(NO_2)$—C_6H_4I [18,19]. Other chemicals were purchased and used as received.

Unless stated otherwise, all reactions and manipulations were carried out using standard Schlenk techniques under an atmosphere of inert gases. Solvents were purified, dried and distilled under a nitrogen atmosphere prior to use. Reactions were monitored by TLC. Chromatographic separations and purifications were performed on 200–300 mesh silica gel or neutral alumina.

IR spectra were recorded on a Nicolet FTIR spectrometer as KBr discs. Elemental analyses were carried out on an Elementar var III-type analyzer. ^1H and ^{13}C NMR spectra in $CDCl_3$ were recorded on an Inova 500FT-MHz spectrometer. The mass spectra were determined using a Polaris Q MS and a Micromass Autospec ultima- TOF instrument. The electrochemical properties were determined with a BAS 100A-type analyzer. Melting points were recorded using XT-4 melting point apparatus.

2.1. Synthesis of 4-ferrocenylacetylenylbiphenyl (*1*)

Fc-C≡CCu (304 mg, 1.12 mmol) and $C_6H_5C_6H_4I$ (313 mg, 1.12 mmol) were dissolved in 15 ml pyridine. The mixture solution was stirred for 8 h under reflux. The solvent of the resulting brown mixture was removed in vacuum. The residue was dissolved in a minimal amount of CH_2Cl_2. The filtrate was concentrated and subjected to chromatographic separation on a neutral alumina column (2 × 30 cm). Elution with hexane–benzene (10:1, v/v) afforded an orange band **1**. The yellow solid **1** was obtained by crystallizing from hexane–benzene. Yield, 46%. m.p. 149–151 °C. *Anal.* Calc. for $C_{24}H_{18}Fe$: C, 79.58; H, 5.01. Found: C, 78.92; H, 4.98%. IR (KBr disk): ν(C≡C) 2218 (m) cm^{-1}. ^1H NMR ($DCCl_3$, δ): 7.26–7.62 (m, 9H, C_6H_4—C_6H_5), 4.28 (s, 5H, C_5H_5), 4.54 (s, 4H, C_5H_4). ^{13}C NMR ($DCCl_3$, δ): 122.88, 126.95, 127.50, 128.83, 131.78, 140.33, 140.47 (C_6H_4—C_6H_5), 85.63, 89.08 (C≡C), 65.41, 68.93, 70.07, 71.47 (Cp). MS (EI, *m*/*z*, relative abundance): 362 (M^+, 100%).

2.2. Syntheses of ferrocenylacetylenylbiphenyl derivatives *2* and *5*

Ethynylferrocene (375 mg, 1.79 mmol) and 4,4′- diiodobiphenyl (501 mg, 1.79 mmol) were stirred in diisopropylamine (20 ml) with $Pd(PPh_3)_2Cl_2$ (30 mg, 0.04 mmol) and $Cu(OAc)_2$ (4 mg, 0.02 mmol) for 20 h under reflux. The solvent of the resulting orange mixture was removed in vacuum. The residue was dissolved in a minimal amount of CH_2Cl_2. The filtrate was concentrated and subjected to chromatographic separation on a neutral alumina column (2 × 30 cm). Elution with hexane–dichloromethane (4:1 for **2**; 2:1 for **5**, v/v) afforded a yellow band **2** and an orange band **5**. Yellow crystalline **2** was obtained by re-crystallizing from hexane–dichloromethane at −20 °C. Yield, 11%. m.p. 191 °C. *Anal.* Calc. for $C_{24}H_{17}FeI$: C, 59.05; H, 3.51. Found: C, 59.43; H, 3.54%. IR (KBr disk): ν(C≡C) 2197 (m) cm^{-1}. ^1H NMR ($DCCl_3$, δ): 7.16–7.79 (m, 8H, C_6H_4—C_6H_4), 4.63 (s, 5H, C_5H_5), 4.95 (br s, 4H, C_5H_4). ^{13}C NMR ($DCCl_3$, δ): 93.28, 123.39, 126.67, 128.76, 131.89, 137.92, 139.09, 139.96 (C_6H_4—C_6H_4), 85.47, 89.51 (C≡C), 65.33, 69.05, 70.13, 71.53 (Cp). MS (EI, *m*/*z*, relative abundance): 488 (M^+, 13%). Orange crystalline **5** was obtained by re-crystallizing from THF at room temperature. Yield, 34%. m.p. 233 °C (dec.). *Anal.* Calc. for $C_{36}H_{26}Fe_2$: C, 75.82; H, 4.60. Found: C, 75.07; H, 4.49%. IR (KBr disk): ν(C≡C) 2208 (m) cm^{-1}. ^1H NMR ($DCCl_3$, δ): 7.48–7.70 (m, 8H, C_6H_4—C_6H_4), 4.42 (br s, 14H, C_5H_5, C_5H_4), 4.70 (br s, 4H, C_5H_4). ^{13}C NMR ($DCCl_3$, δ): 123.14, 126.73, 131.83, 139.51 (C_6H_4—C_6H_4), 85.59, 89.38 (C≡C), 68.99, 70.10, 71.50 (Cp). MS (EI, *m*/*z*, relative abundance): 570 (M^+, 9%).

2.3. Syntheses of new compounds *3*, *4*, *6* and *7*

For the syntheses of the new compounds **3**, **4**, **6** and **7** see Table 1, the separation method being similar to that of compounds **1**, **2** and **5**. The chemical and spectroscopic characterization are as follows:

Compound **3**: *Anal.* Calc. for $C_{24}H_{17}FeNO_2$: C, 70.78; H, 4.21; N, 3.44. Found: C, 70.62; H, 4.14; N, 3.46%. IR (KBr disk): ν(C≡C) 2203 (m), ν_{asNO_2}1507 (s), ν_{sNO_2} 1341 (vs) cm^{-1}. ^1H NMR ($DCCl_3$, δ): 7.26–8.32 (m, 8H, C_6H_4—C_6H_4), 4.40 (s, 5H, C_5H_5), 4.68 (br s, 4H, C_5H_4). ^{13}C NMR ($DCCl_3$, δ): 124.18, 124.81, 127.22, 127.58, 132.05, 137.61, 146.82, 147.13 (C_6H_4—C_6H_4), 85.20, 90.62 (C≡C), 65.01, 69.20, 70.17, 71.61 (Cp). MS (EI, *m*/*z*, relative abundance): 407 (M^+, 100%).

Compound **4**: *Anal.* Calc. for $C_{24}H_{16}FeINO_2$: C, 54.03; H, 3.19; N, 2.63. Found: C, 53.93; H, 3.00; N, 2.66%. IR (KBr disk): ν(C≡C) 2208 (m), ν_{asNO_2}1527 (vs), ν_{sNO_2}1358 (s) cm^{-1}. ^1H NMR ($DCCl_3$, δ): 7.04–7.92 (m, 7H, C_6H_3—C_6H_4), 4.33 (s, 5H, C_5H_5), 4.60 (br s, 4H, C_5H_4). ^{13}C NMR ($DCCl_3$, δ): 94.48, 125.04, 126.71, 129.59, 131.63, 133.86, 134.70, 136.54, 137.88, 148.84 (C_6H_3—C_6H_4), 83.24, 92.54 (C≡C), 63.93, 69.53, 70.25,

Table 1
Syntheses of new compounds **3**, **4**, **6** and **7**

Reactants[a]	Catalyst[b]	Time (h)	Product	Yield (%)	m.p. (°C)
Ethynylferrocene and 4-nitro-4′-iodo-biphenyl	A	20	**3**	51	216–217
Ethynylferrocene and 2-nitro-4,4′-diiodo-biphenyl	A	19	**4**	31	157–158
			6	15	179–180
Ethynylbenzene and 4-iodo-4′-ferrocenylethynyl-biphenyl	B	16	**7**	69	240 (dec.)

[a] Mol ratio = 1:1 (for **3**, **4**, **6**), 1:2 (for **7**); solvent: diethylamine (for **3**, **4**, **6**), THF/diisopropylamine (V:V = 3:1, for **7**); reaction temperature: reflux (for **3**, **4**, **6**), 60 °C (for **7**).
[b] A: $Pd(PPh_3)_2Cl_2$/CuI (1:1, 2.4 mol%), B: $Pd(PPh_3)_2Cl_2/Cu(OAc)_2$ (1:1, 6 mol%).

71.78 (Cp). MS (EI, *m*/*z*, relative abundance): 533 (M^+, 16%).

Compound **6**: *Anal.* Calc. for $C_{36}H_{25}Fe_2NO_2$: C, 70.24; H, 4.06, N, 2.28. Found: C, 69.66; H, 4.11, N, 2.39%. IR (KBr disk): ν(C≡C) 2208 (m), ν_{asNO_2}1537 (vs), ν_{sNO_2}1358 (s) cm^{-1}. ^1H NMR ($DCCl_3$, δ): 7.23–7.58 (m, 7H, C_6H_3—C_6H_4), 4.24 (s, 14H, C_5H_5, C_5H_4), 4.50 (s, 4H, C_5H_4). ^{13}C NMR ($DCCl_3$, δ): 122.44, 123.25, 123.31, 126.81, 128.31, 128.37, 131.62, 131.86, 132.09, 139.39, 140.16 (C_6H_3—C_6H_4), 85.56, 89.25, 89.48, 92.30 (C≡C), 65.19, 68.90, 69.99, 71.45 (Cp). MS (EI, *m*/*z*, relative abundance): 615 (M^+, 43%).

Compound **7**: *Anal.* Calc. for $C_{32}H_{22}Fe$: C, 83.12; H, 4.76. Found: C, 83.70; H, 4.89%. IR (KBr disk): ν(C≡C) 2203 (m) cm^{-1}. ^1H NMR ($DCCl_3$, δ): 7.26–7.96 (m, 13H, C_6H_4—C_6H_4, C_6H_5), 4.29 (br s, 5H, C_5H_5), 4.54 (br s, 4H, C_5H_4). ^{13}C NMR ($DCCl_3$, δ): 124.30, 124.77, 126.69, 127.80, 131.69, 134.41, 134.60, 136.04, 149.02 (C_6H_4—C_6H_4, C_6H_5), 83.36, 85.26, 89.97, 92.34 (C≡C), 64.95, 69.35, 70.09, 71.66 (Cp). MS (EI, *m*/*z*, relative abundance): 462 (M^+, 100%).

2.4. Synthesis of complex [Fc-C≡C—C_6H_4—C_6H_5][$Co_2(CO)_6$] (**8**)

A benzene solution of equimolar amounts of compounds Fc-C≡C—C_6H_4—C_6H_5 (**1**) and $Co_2(CO)_8$ was stirred for 4 h at 20 °C. The solvent of the resulting black mixture was removed in vacuum. The residue was dissolved in a minimal amount of benzene and subjected to chromatographic separation on a silica gel column (1.2 × 30 cm). Elution with hexane–benzene (10:1) afforded a black band. Crystals of the complex [Fc-C≡C—C_6H_4—C_6H_5][$Co_2(CO)_6$] (**8**) were obtained by recrystallizing the black solid from hexane–dichloromethane at −20 °C. Complex **8**: Yield, 61%. m.p. 119–120 °C. *Anal.* Calc. for $C_{30}H_{18}Co_2FeO_6$: C, 55.59; H, 2.80. Found: C, 55.83; H, 3.19%. IR (KBr disk) ν(CO) 2085 (s), 2049 (vs), 2008 (vs) cm^{-1}. ^1H NMR ($DCCl_3$, δ): 7.26–7.96 (m, 9H, C_6H_4—C_6H_5), 4.21 (s, 5H, C_5H_5), 4.44, 4.54 (2s, 4H, C_5H_4). ^{13}C NMR ($DCCl_3$, δ): 199.45 (CO), 92.36, 126.96, 127.46, 127.57, 128.90, 137.66, 140.46, 140.85 (C_6H_4—C_6H_5), 85.26, 91.16 (C≡C), 69.36, 69.66, 70.10 (Cp). MS (FAB, relative abundance): 648 (M^+, 4%), 592 (M^+−2CO, 41%), 564 (M^+−3CO, 100%), 508 (M^+−5CO, 53%), 480 (M^+−6CO, 58%).

2.5. Syntheses of new complexes **9**, **10**, **11**, **12**, **13** and **14**

The syntheses of new complexes **9, 10, 11, 12, 13** and **14**, see Table 2, and the separation method is similar to that of complex **8.** The chemical and spectroscopic characterizations are as follows:

Complex **9**: *Anal.* Calc. for $C_{30}H_{17}Co_2FeIO_6$: C, 46.55; H, 2.31. Found: C, 46.52; H, 2.37%. IR (KBr disk) ν(CO) 2080 (s), 2044 (vs), 2008 (vs) cm^{-1}. ^1H NMR ($DCCl_3$, δ): 7.17–7.88 (m, 8H, C_6H_4—C_6H_4), 4.12 (br s, 5H, C_5H_5), 4.37 (br s, 4H, C_5H_4). ^{13}C NMR ($DCCl_3$, δ): 199.38 (CO), 127.25, 130.24 (C_6H_4—C_6H_4), 85.20 (C≡C), 69.38, 69.66, 70.12 (Cp). MS (FAB, relative abundance): 718 (M^+−2CO, 9%), 690 (M^+−3CO, 58%), 662 (M^+−4CO, 24%), 634 (M^+−5CO, 14%), 606 (M^+−6CO, 18%).

Complex **10**: *Anal.* Calc. for $C_{30}H_{17}Co_2FeNO_8$: C, 51.96; H, 2.47; N, 2.02. Found: C, 52.06; H, 2.65; N, 2.16%. IR (KBr disk) ν(CO) 2077 (s), 2044 (vs), 2011 (vs) cm^{-1}. ^1H NMR ($DCCl_3$, δ): 7.24–8.33 (m, 8H, C_6H_4—C_6H_4), 4.19 (s, 5H, C_5H_5), 4.44, 4.50 (d, 4H, C_5H_4). ^{13}C NMR ($DCCl_3$, δ): 199.23 (CO), 124.28, 127.58, 127.82, 130.34, 137.92, 139.98, 146.83 (C_6H_4—C_6H_4), 85.02, 90.08 (C≡C), 69.50, 69.68, 70.12

Table 2
Syntheses of new complexes **9**, **10**, **11**, **12**, **13** and **14**

Reactants[a]	Temperature (°C)	Time (h)	Product	Yield (%)	m.p. (°C)
Fc-C≡C—C_6H_4—C_6H_4—I and $Co_2(CO)_8$	35	4	**9**	65	150 (dec.)
Fc-C≡C—C_6H_4—C_6H_4—NO_2 and $Co_2(CO)_8$	50	0.5	**10**	73	131 (dec.)
Fc-C≡C—$C_6H_3(NO_2)$—C_6H_4I and $Co_2(CO)_8$	20	0.5	**11**	90	121 (dec.)
Fc-C≡C—C_6H_4—C_6H_4—C≡C-Fc and $Co_2(CO)_8$	60	1	**12**	93	110 (dec.)
Fc-C≡C—$C_6H_3(NO_2)$—C_6H_4— C≡C-Fc and $Co_2(CO)_8$	40	1	**13**	74	134 (dec.)
Fc-C≡C—C_6H_4—C_6H_4—C≡C—C_6H_5 and $Co_2(CO)_8$	40	1	**14**	68	168 (dec.)

[a] Mol ratio = 1:1 (for **9**, **10**, **11**), 1:2 (for **12**, **13**, **14**); solvent: benzene.

(Cp). MS (FAB, relative abundance): 609 (M^+-3CO, 32%), 581 (M^+-4CO, 21%), 553 (M^+-5CO, 6%), 525 (M^+-6CO, 7%).

Complex **11**: *Anal.* Calc. for $C_{30}H_{16}Co_2FeINO_8$: C, 43.96; H, 1.95; N, 1.71. Found: C, 43.29; H, 2.18; N, 1.67%. IR (KBr disk) ν(CO) 2090 (s), 2049 (vs), 2013 (vs) cm^{-1}. ^1H NMR ($DCCl_3$, δ): 7.12–8.46 (m, 7H, C_6H_3—C_6H_4), 4.22 (br s, 5H, C_5H_5), 4.47 (br s, 4H, C_5H_4). ^{13}C NMR ($DCCl_3$, δ): 198.78 (CO), 92.31, 94.58, 123.79, 129.60, 132.57, 133.98, 136.62, 137.96, 140.72, 148.98 (C_6H_3—C_6H_4), 84.16, 86.52 (C≡C), 69.79, 69.97, 71.67 (Cp). MS (FAB, relative abundance): 763 (M^+-2CO, 16%), 735 (M^+-3CO, 100%), 707 (M^+-4CO, 62%), 651 (M^+-6CO, 47%).

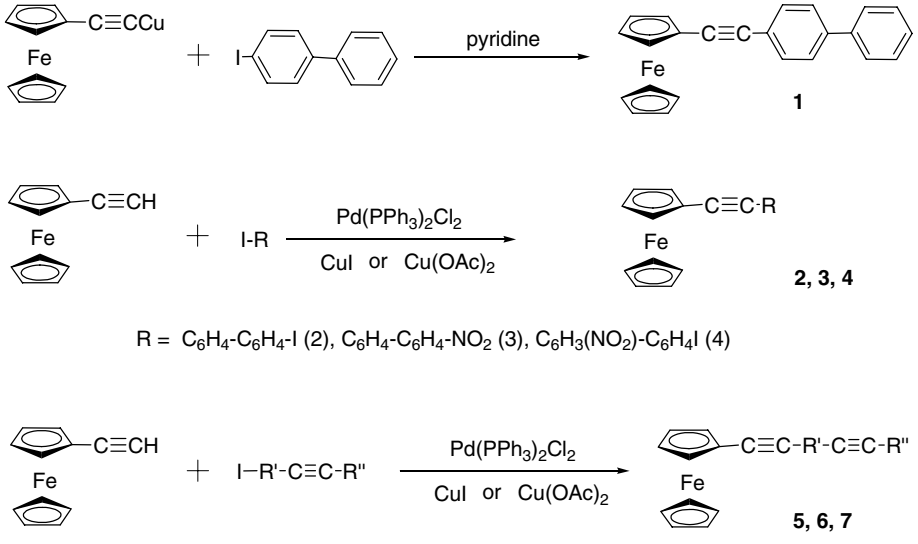
Complex **12**: *Anal.* Calc. for $C_{48}H_{26}Co_4Fe_2O_{12}$: C, 50.48; H, 2.29%. Found: C, 50.96; H, 3.20%. IR (KBr disk), ν(CO): 2085 (s), 2049 (vs), 2013 (vs) cm^{-1}. ^1H NMR ($DCCl_3$, δ): 7.26–7.95 (m, 8H, C_6H_4—C_6H_4), 4.20 (br s, 14H, C_5H_5, C_5H_4), 4.44, 4.52 (d, 4H, C_5H_4). ^{13}C NMR ($DCCl_3$, δ): 199.38 (CO), 127.25, 128.75, 130.20, 138.01, 138.29, 139.40, 139.97 (C_6H_4—C_6H_4), 85.18, 90.78, 92.36,93.37 (C≡C), 69.40, 69.68, 70.10 (Cp). MS (FAB, relative abundance): 1059 (M^+-3CO, 24%), 1031 (M^+-4CO, 8%), 1003 (M^+-5CO, 3%), 976 (M^+-6CO, 6%).

Complex **13**: *Anal.* Calc. for $C_{48}H_{25}Co_4Fe_2NO_{14}$: C, 48.53; H, 2.11; N, 1.18. Found: C, 48.05; H, 2.35; N, 1.23%. IR (KBr disk), ν(CO): 2080 (s), 2049 (vs), 2013 (vs) cm^{-1}. ^1H NMR ($DCCl_3$, δ): 7.26-8.48 (m, 7H, C_6H_3—C_6H_4), 4.19, 4.25 (2s, 14H, C_5H_5, C_5H_4), 4.45, 4.49, 4.52 (t, 4H, C_5H_4). ^{13}C NMR ($DCCl_3$, δ): 198.80, 199.29 (CO), 92.38, 92.72, 123.90, 128.34, 129.99, 132.69, 133.83, 134.73, 136.28, 139.36, 140.43, 149.18 (C_6H_3—C_6H_4), 84.23, 85.07, 86.75, 90.53 (C≡C), 69.42, 69.68, 69.80, 70.01, 70.15 (Cp). MS (FAB, relative abundance): 733 ($M^+-12CO-2Co$, 7%), 615 [$M^+-Co_4(CO)_{12}$, 12%].

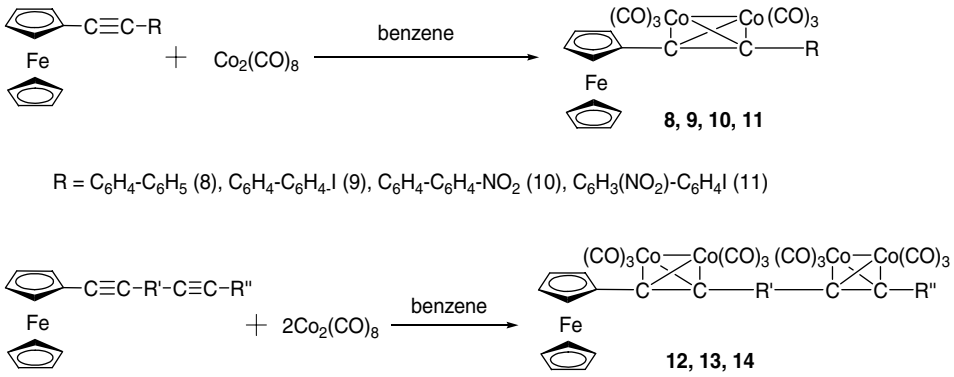
Complex **14**: *Anal.* Calc. for $C_{44}H_{22}Co_4FeO_{12}$: C, 51.06; H, 2.13. Found: C, 50.51; H, 1.97%. IR (KBr disk), ν(CO): 2085 (s), 2049 (vs), 2018 (vs) cm^{-1}. ^1H NMR ($DCCl_3$, δ): 7.21–7.96 (m, 8H, C_6H_4—C_6H_4, C_6H_5), 4.19, 4.21 (2s, 5H, C_5H_5), 4.26 (br s, 1H, C_5H_4), 4.44, 4.53 (2t, 3H, C_5H_4). ^{13}C NMR ($DCCl_3$, δ): 199.43, 199.23 (CO), 126.82, 127.26, 127.37, 127.45, 127.95, 128.40, 128.73, 129.03, 129.27, 129.81, 130.27, 131.64, 132.21, 137.81, 138.13, 138.32, 139.82, 139.92 (C_6H_4—C_6H_4, C_6H_5), 85.80, 90.06 (C≡C), 69.41, 69.70, 70.01, 70.17 (Cp). MS (FAB, relative abundance): 1034 (M^+, 8%), 978 (M^+-2CO, 18%), 866 (M^+-6CO, 37%), 810 (M^+-8CO, 39%), 754 (M^+-10CO, 10%), 698 (M^+-12CO, 4%), 580 ($M^+-12CO-2Co$, 7%), 462 ($M^+-12CO-4Co$, 7%).

2.6. X-ray crystallography of compounds *1*, *4*, *8*, *9* and *11*

Black crystals of compounds **1**, **4**, **8**, **9** and **11** were mounted on a glass fibres. All measurements were made on Bruker SMART APEX CCD diffractometers with graphite monochromated Mo Kα ($\lambda = 0.71073$ Å) radiation. All data were collected at 20 °C using the ϕ and ω scan techniques. All structures were solved by direct methods and expanded using a Fourier technique [20]. An absorption correction based on SADABS was applied [21]. All non–hydrogen atoms were refined by full matrix least-squares on F^2. Hydrogen atoms were located and refined by a geometry method. The cell refinement, data collection and reduction were done by Bruker SMART and SAINT programs [22]. The solution and refinement of the structures were performed by SHELXSL97 [23].



Scheme 1.



Scheme 2.

Table 3
Crystal data and relevant structural parameters of compounds **1**, **4**, **8**, **9** and **11**

Compounds	1	4	8	9	11
Empirical formula	$C_{24}H_{18}Fe$	$C_{24}H_{16}FeINO_2$	$C_{30}H_{18}Co_2FeO_6$	$C_{30}H_{17}Co_2FeIO_6$	$C_{30}H_{16}Co_2FeINO_8$
Crystal system	monoclinic	triclinic	triclinic	monoclinic	monoclinic
Space group	$P2(1)/c$	$P\bar{1}$	$P\bar{1}$	$P2(1)/n$	$P2(1)/c$
a (Å)	11.585(3)	9.198(4)	9.963(7)	10.240(4)	8.708(3)
b (Å)	7.3723(19)	11.899(5)	15.111(11)	22.047(8)	23.492(9)
c (Å)	20.928(6)	18.935(8)	19.554(14)	12.559(5)	14.813(5)
α (°)	90.00	83.676(6)	71.002(11)	90	90
β (°)	101.345(5)	89.663(6)	87.090(12)	98.728(4)	98.691(6)
γ (°)	90.00	82.237(7)	79.626(13)	90	90
Volume, Z	1752.5(8), 4	2040.8(14), 4	2738(3), 4	2802.6(18), 4	2995.4(19), 4
D_{calc} (g/cm^3)	1.373	1.735	1.572	1.835	1.816
μ (mm^{-1})	0.862	2.272	1.762	2.825	2.654
$F(000)$	752	1048	1304	1512	1600
θ Range (°)	1.79–25.01	3.127–25.24	1.10–25.01	1.85–26.01	1.64–25.01
Reflections collected	7020	8555	11600	12767	12454
Independent reflections	3088	7052	9507	5523	5259
Completeness to θ (%)	99.7	98.2	98.5	99.9	99.7
Maximum and minimum transmission	0.9342 and 0.8465	0.8047 and 0.6593	0.8719 and 0.7780	0.8056 and 0.6020	0.7772 and 0.5567
Data/restraints/parameters	3088/0/226	7052/0/523	9507/0/703	5523/0/361	5259/0/388
Goodness-of-fit	0.955	0.933	0.842	0.930	1.033
Final R indices [$I > 2\sigma(I)$]	R_1, 0.1081; wR_2, 0.1047	R_1, 0.0446; wR_2, 0.1059	R_1, 0.0551; wR_2, 0.1138	R_1, 0.0304; wR_2, 0.0665	R_1, 0.0688; wR_2, 0.1493
R-indices (all data)	R_1, 0.2561; wR_2, 0.1333	R_1, 0.0656; wR_2, 0.1132	R_1, 0.1207; wR_2, 0.1422	R_1, 0.0444, wR_2, 0.0708	R_1, 0.1046, wR_2, 0.1666
Largest difference in peak and hole (e Å^{-3})	0.331 and −0.313	0.627 and −1.015	0.713 and −0.384	0.642 and −0.562	1.599 and −0.958

3. Results and discussion

3.1. Syntheses and characterizations of the ferrocenylacetylenylbiphenyl derivatives and their complexes

The coupling reactions carried out in this work are summarized in Scheme 1. The addition reactions of the ligands Fc-C≡C—R and Fc-C≡C—R′—C≡C—R″ with $Co_2(CO)_8$ are summarized in Scheme 2. The complexes **8**, **9**, **10**, **11**, **12**, **13** and **14** were prepared by the addition reaction between the Co—Co bond of $Co_2(CO)_8$ and the C≡C triple bond of the ligands Fc-C≡C—R and Fc-C≡C—R′—C≡C—R″

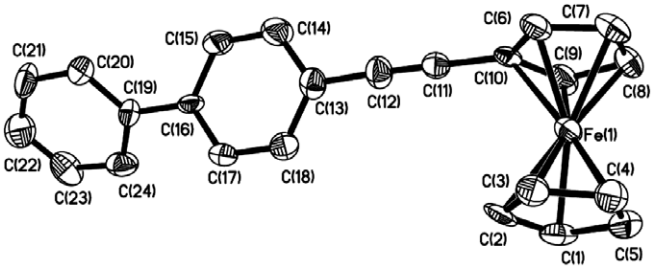


Fig. 1. Molecular structure of compound **1**.

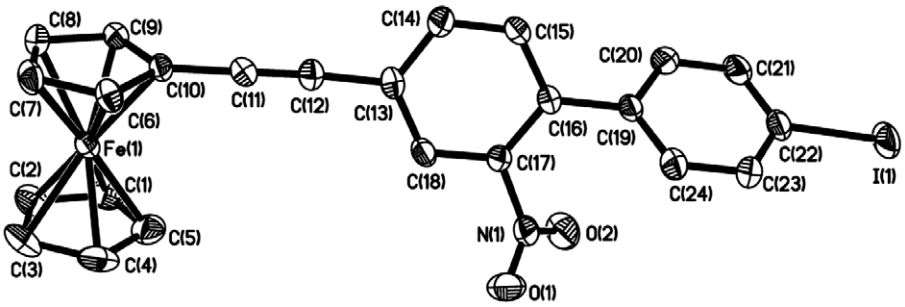


Fig. 2. Molecular structure of compound **4**.

with the mole ratios of $Co_2(CO)_8$ to ligand fixed at 1:1 and 1:2, respectively. The compounds are yellow for **1** and **2** and orange for **3**, **4**, **5**, **6** and **7**, and they are air-stable crystalline compounds which are slightly soluble in non-polar solvents such as hexane, and easily soluble in benzene and polar solvents such as dichloromethane. The complexes **8**–**14** are black crystals and their solubilities are similar to the corresponding ligands. The IR spectra (2077–2018 cm^{-1}) confirm that there are coordinated $Co_2(CO)_6$ species with C≡C triple bonds in complexes **8**–**14**. The compositions and structures of compounds **1**–**14** are further proved by the data of their element analyses, ^1H, ^{13}C NMR and MS.

3.2. Molecular structures of compounds *1, 4, 8, 9* and *11*

The molecular structures of compounds **1**, **4, 8, 9, 11** were determined by X-ray single crystal analysis. Crystal data and relevant structural parameters are enumerated in Table 3. The structures of compounds **1**, **4, 8, 9** and **11**, with the atom numbering scheme, are shown in Figs. 1–5, respectively, and selected bond lengths and angles are listed in Table 4.

The molecules of compounds **1**, **4**, **8**, **9** and **11** are constituted of a π-conjugated alkynyl system with terminal ferrocenyl and biphenyl or substituted biphenyl units, respectively. In **1** the bond distance C(11)–C(12) (1.183 Å) shows there is a carbon–carbon triple bond. The bond distances C(10)–C(11) (1.45 Å) and C(12)–C(13) (1.44 Å) are shorter than that of C(16)–C(19) (1.51 Å) as a result of stronger electron delocalization

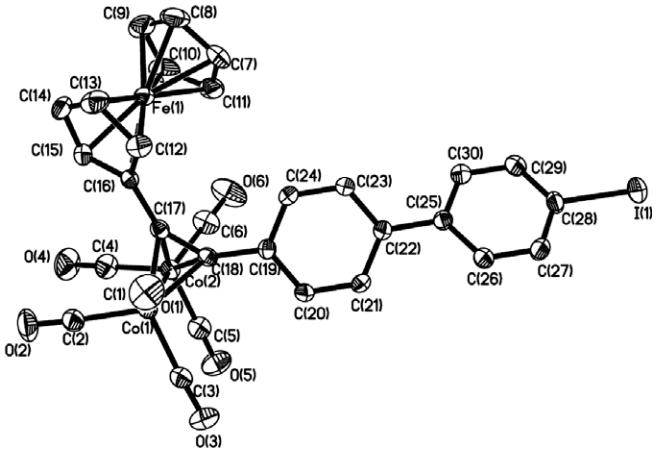


Fig. 4. Molecular structure of compound **9**.

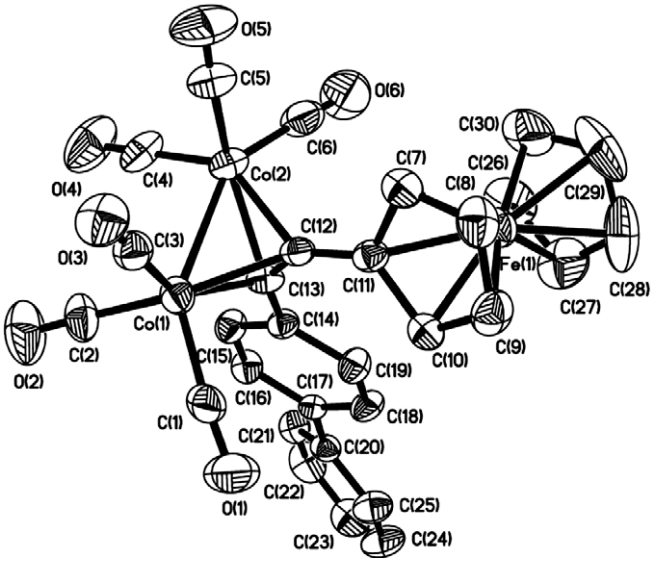


Fig. 3. Molecular structure of compound **8**.

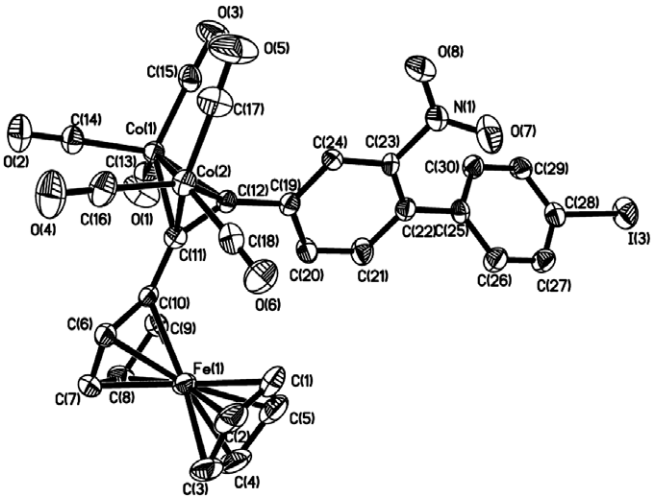


Fig. 5. Molecular structure of compound **11**.

between the C≡C bond (sp-C) and biphenyl (sp^2-C) or the C≡C bond (sp-C) and ferrocenyl group (sp^2-C) than that between two phenyl groups (two sp^2-C). The bond angle data in Table 2 demonstrate that the linear structure of compound **1** is altered to a non-linear structure in **8**, while the alkyne bond of **1** is coordinated to a $Co_2(CO)_6$ unit. The molecular structures of compounds **4** and **11** are similar to the structures of compounds **1** and **8**, respectively (see Figs. 2, 5 and 1, 3). The coordinated $Co_2(CO)_6$ units with the C≡C bond in complexes **8**, **9** and **11** are all approximately tetrahedral μ-alkyne dicobalt moieties. The alkyne bond adopts a typical μ_2–η^2 coordination fashion with the alkyne bond lying essentially perpendicular to the Co—Co bond in the C_2Co_2 unit. The average Co—Co bond distance (2.46 Å) is typical of classical alkyne dicobalt complexes. The average C—C bond length (1.34 Å) of the C_2Co_2 fragments shows a bond distance of the coordinated C≡C bond located in the scope of a C—C double bond. In complexes **8**, **9** and **11** the $Co_2(CO)_6$ units coordinated to the alkyne bond are in a trans configuration with the biphenyl and ferrocenyl groups, and the two terminal groups (biphenyl or substituted biphenyl and ferrocenyl groups) are orientated *cis* to each other (see Fig. 3–5).

In compounds **1**, **4**, **8**, **9** and **11**, the data of the dihedral angles (40.12° for **1**, 52.52° for **4**, 26.30° for **8**, 35.41° for **9** and 57.51° for **11**) between the two phenyl rings are different from each other, and have been affected by the substituted group on the biphenyl ring and the coordinated $Co_2(CO)_6$ unit with the alkyne. The dihedral angle between the two phenyl rings in **1** is smaller than that in **4** because of the effect of the substituted group (NO_2) on the phenyl ring. The data of the dihedral angles (1.97° for **1**, 0.88° for **4**, 4.01° for **8**, 5.58° for **9** and 2.97° for **11**) between the two Cp planes in compounds **1**, **4**, **8**, **9** and **11** reveal that the two Cp planes are nearly parallel in **4**, but are slightly deviated from parallel in **1**, **8**, **9** and **11**.

3.3. Electrochemical properties of compounds 1–12

The electrochemical properties of compounds **1**–**12** have been studied by cyclic voltammetry at 298 K in a standard three-electrode system with *n*-NBu_4ClO_4(TBAP) in CH_2Cl_2 solution as the supporting electrolyte. The results are given in Table 5.

For compounds **1**–**7** and complexes **8**, **10** and **12** the usual electrochemically quasi-reversible ferrocene (0/1+) peak couples and a one-electron redox process were observed (see Table 1), but for complexes **9** and **11** an irreversible redox process was observed. Only a pair of redox peaks appears, which reveals that there are no Fe–Fe interactions in the di-ferrocenyl compounds **5**, **6** and **12** through the conjugated biphenyl ethynyl bridges [17]. However, a redox behavior study of ethynyl-bridged ferrocenes, such as the Fc-$(C{\equiv}C)_2$-Fc ligand and its clusters, demonstrates two one-electron redox processes, which show there are Fe–Fe interactions [24]. The irreversible reduction peaks within range $E_{pc} = -0.55$ to -0.88 V in complexes **8**–**12** were regarded as the result of a reducing process on the $Co_2(CO)_6$ moieties. Although there are substituted electron-withdrawing groups on the biphenyl rings in compounds **2**, **3**, **4**, **6**, **9**, **10** and **11**, and the coordinated $Co_2(CO)_6$ units for complexes **8**–**12**, no significant variation of E^0 was observed.

Table 4
Selected bond lengths (Å) and angles (°) for **1**, **4**, **8**, **9** and **11**

Bond lengths				Bond angles			
1							
C(10)–C(11)	1.45(1)	C(12)–C(13)	1.44(1)	C(10)–C(11)–C(12)	179.2(1)	C(15)–C(16)–C(19)	120.3(8)
C(11)–C(12)	1.18(1)	C(16)–C(19)	1.51(1)	C(11)–C(12)–C(13)	177.6(1)	C(16)–C(19)–C(20)	120.8(1)
4							
C(10)–C(11)	1.44(6)	C(12)–C(13)	1.44(6)	C(10)–C(11)–C(12)	178.3(5)	C(17)–C(16)–C(19)	123.3(4)
C(11)–C(12)	1.18(6)	C(16)–C(19)	1.48(6)	C(11)–C(12)–C(13)	176.5(5)	C(16)–C(19)–C(24)	121.6(4)
8							
C(11)–C(12)	1.44(9)	Co(1)–C(12)	1.99(7)	C(11)–C(12)–C(13)	145.9(6)	Co(1)–C(12)–C(13)	68.6(4)
C(12)–C(13)	1.33(8)	Co(1)–C(13)	1.95(7)	C(12)–C(13)–C(14)	144.5(7)	Co(1)–C(13)–C(12)	71.9(4)
C(13)–C(14)	1.46(8)	Co(2)–C(12)	1.96(6)	C(13)–C(14)–C(15)	122.0(6)	Co(2)–C(12)–C(13)	70.5(4)
Co(1)–Co(2)	2.46(2)	Co(2)–C(13)	1.97(6)	C(18)–C(17)–C(20)	121.6(6)	Co(2)–C(13)–C(12)	69.7(4)
9							
C(16)–C(17)	1.45(4)	Co(1)–C(17)	2.00(3)	C(16)–C(17)–C(18)	144.2(3)	Co(1)–C(17)–C(18)	68.2(2)
C(17)–C(18)	1.33(4)	Co(1)–C(18)	1.94(3)	C(17)–C(18)–C(19)	141.9(3)	Co(1)–C(18)–C(17)	72.4(2)
C(18)–C(19)	1.46(4)	Co(2)–C(17)	1.95(3)	C(18)–C(19)–C(20)	122.2(3)	Co(2)–C(17)–C(18)	71.8(2)
Co(1)–Co(2)	2.46(8)	Co(2)–C(18)	1.99(3)	C(21)–C(22)–C(25)	120.9(3)	Co(2)–C(18)–C(17)	68.7(2)
11							
C(10)–C(11)	1.44(1)	Co(1)–C(11)	2.01(7)	C(10)–C(11)–C(12)	144.8(7)	Co(1)–C(11)–C(12)	68.6(4)
C(11)–C(12)	1.34(1)	Co(1)–C(12)	1.97(7)	C(11)–C(12)–C(19)	141.5(7)	Co(1)–C(12)–C(11)	72.1(4).
C(12)–C(19)	1.45(9)	Co(2)–C(11)	1.96(7)	C(12)–C(19)–C(20)	120.5(7)	Co(2)–C(11)–C(12)	70.6(4)
Co(1)–Co(2)	2.46(2)	Co(2)–C(12)	1.97(7)	C(22)–C(25)–C(26)	121.8(7)	Co(2)–C(12)–C(11)	69.5(4)

Table 5
Voltammetric data[a]

Compound	E_{pc}	E_{pa}	i_{pc}/i_{pa}	E^0 (0/1+)	Reduction of Co, E_{pc}
1	0.33	1.28	0.96	0.81	
2	0.36	1.19	1.01	0.78	
3	0.44	1.21	0.82	0.83	
4	0.42	1.19	0.93	0.81	
5	0.34	1.50	1.00	0.92	
6	0.35	1.40	1.00	0.88	
7	0.36	1.24	1.04	0.80	
8	0.34	1.40	0.99	0.87	−0.72
9	0.37	1.09	0.19	0.73	−0.58
10	0.37	1.21	0.92	0.79	−0.88
11	0.48	1.10	0.21	0.79	−0.55
12	0.26	1.37	0.89	0.82	−0.77

E_{pc} = cathodic peak potential (V); E_{pa} = anodic peak potential (V); i_{pc} = cathodic peak current (A); i_{pa} = anodic peak current (A); $E^0 = 1/2(E_{pc} + E_{pa})$ (V).

[a] Platinum electrode (Ag/Ag^+ standard) in a 0.001 M n-Bu_4NClO_4(TBAP) solution (CH_2Cl_2) at 20 °C with a 100 mV scan rate.

4. Conclusion

Ferrocenylacetylenylbiphenyl and bisferrocenylacetylenyl-biphenyl derivatives could be synthesized by Sonogashira coupling and a second Sonogashira coupling reaction, respectively, and their cobalt coordinated complexes could be obtained by the addition reaction of $Co_2(CO)_6$ units to the alkyne bond. The molecular structures of complexes **8**, **9** and **11** show the $Co_2(CO)_6$ units coordinated to the alkyne bond are in a trans configuration with the terminal biphenyl derivatives and ferrocenyl groups. The data of dihedral angles reveal two phenyl rings of biphenyl derivatives in compounds **1**, **4**, **8**, **9** and **11** are deviated from parallel.

Acknowledgements

We are grateful to the Specialized Research Fund for the Doctoral Program of Higher Education of China (20060128001) and the Natural Science Foundation of Inner Mongolia for financial support of this work.

Appendix A. Supplementary material

CCDC 625423, 625424, 625425, 625426 and 625427 contain the supplementary crystallographic data for **1**, **8**, **4**, **11** and for **9**. These data can be obtained free of charge via http://www.ccdc.cam.ac.uk/conts/retrieving.html, or from the Cambridge Crystallographic Data Centre, 12 Union Road, Cambridge CB2 1EZ, UK; fax: (+44) 1223-336-033; or e-mail: deposit@ccdc.cam.ac.uk. Supplementary data associated with this article can be found, in the online version, at doi:10.1016/j.poly.2007.02.023.

References

[1] W.Y. Wong, Coord. Chem. Rev. 249 (2005) 971.
[2] L.B. Gao, L.Y. Zhang, L.X. Shi, Z.N. Chen, Organometallics 24 (2005) 1678.
[3] T.Y. Dong, S.W. Chang, S.F. Lin, M.C. Lin, Y.S. Wen, L.S. Lee, Organometallics 25 (2006) 2018.
[4] N. Duffy, J. McAdam, C. Nervi, D. Osella, M. Ravera, B. Robinson, J. Simpson, Inorg. Chim. Acta 247 (1996) 99.
[5] D. Osella, L. Milone, C. Nervi, M. Ravera, Eur. J. Inorg. Chem. (1998) 1473.
[6] J. McAdam, J.J. Brunton, B.H. Robison, J. Simpson, J. Chem. Soc., Dalton Trans. (1999) 2487.
[7] R.D. Stephens, C.E. Castro, J. Org. Chem. 28 (1963) 3313.
[8] M. Rosenblum, N. Brawn, J. Papenmeier, M. Applebaum, J. Organomet. Chem. 6 (1966) 173.
[9] H. Nock, H. Schottenberger, J. Org. Chem. 58 (1993) 7045.
[10] R.P. Hsung, C.E.D. Chidsey, L.R. Sita, Organometallics 14 (1995) 4808.
[11] A. Arques, D. Aunon, P. Molina, Tetrahedron Lett. 45 (2004) 4337.
[12] P.F.H. Schwab, J.R. Smith, J. Michl, Chem. Rev. 105 (2005) 1197.
[13] H. Lang, R. Packheiser, B. Wolfort, Organometallics 25 (2006) 1836.
[14] I.P. Beletskaya, A.V. Tsvetkov, G.V. Latyshev, V.A. Tafeenko, N.V. Lukashev, J. Organomet. Chem. 637-639 (2001) 653.
[15] F. Alonso, I.P. Beleskaya, M. Yus, Chem. Rev. 104 (2004) 3079.
[16] E. Lindner, R. Zong, K. Eichele, M. Strobele, J. Organomet. Chem. 660 (2002) 78.
[17] N. Chawdhury, N.J. Long, M.F. Mahon, L.L. Ooi, P.R. Raithby, S. Rooke, A.J.P. White, D.J. Williams, M. Younus, J. Organomet. Chem. 689 (2004) 840.
[18] V.H.O. Wirth, O. Konigstein, W. Kern, J. Liebigs Ann. Chem. 634 (1960) 83.
[19] A.H. Hobukob, Zhurnal Obshchei Khimii 29 (1959) 58.
[20] G.M. Sheldrick, Acta Crystallogr. A 46 (1990) 467.
[21] G.M. Sheldrick, SADABS, Siemens Area Detector Absorption, Correction Software, University of Göttingen, Germany, 1997.
[22] Bruker, SMART and SAINT, Area Detector Control and Integration Software, Bruker Analytical X-ray Instruments Inc., Madison, WI, USA, 1998.
[23] G.M. Sheldrick, SHELXL-97, Program for Crystal Structure Analysis, University of Göttingen, Germany, 1997.
[24] R.D. Adams, B. Qu, M.D. Smith, T.A. Albright, Organometallics 21 (2002) 2970.

Available online at www.sciencedirect.com
ScienceDirect
Polyhedron 26 (2007) 3161–3167
POLYHEDRON
www.elsevier.com/locate/poly

'Electronic bending' of imido ligands and the effect on the coordination mode of a tridentate ancillary ligand

Vernon C. Gibson [a], Carl Redshaw [b,*], William Clegg [c], Mark R.J. Elsegood [d]

[a] Department of Chemistry, Imperial College, South Kensington, London SW7 2AY, UK
[b] School of Chemical Sciences and Pharmacy, University of East Anglia, Norwich NR4 7TJ, UK
[c] School of Natural Sciences, University of Newcastle, Newcastle upon Tyne NE1 7RU, UK
[d] Chemistry Department, Loughborough University, Loughborough LE11 3TU, UK

Received 4 January 2007; accepted 15 February 2007
Available online 20 February 2007

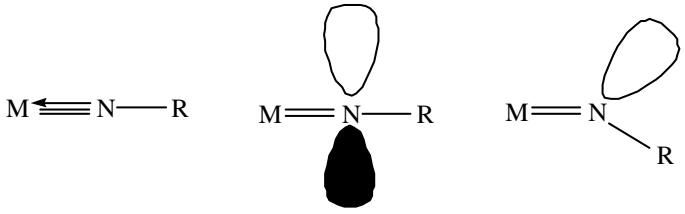
Abstract

The five-coordinate mixed-imido complex [Mo(N*t*-Bu)(NC_6F_5)(L)] (**1**) can be prepared in high yield via treatment of [Mo(N*t*-Bu)(NC_6F_5)(O*t*-Bu)$_2$] with LH_2, where LH_2 is 2,6-bis(2-hydroxy-2,2-diphenylethyl)pyridine. Contrastingly, the reaction of [Mo(N-Ad)(NC_6F_5)(O*t*-Bu)$_2$] (Ad = adamantyl, C_6H_{10}) with LH_2 gave [Mo(NAd)$_2$(L)] (**2**) via an imido-exchange reaction. Complex **2** can also be synthesised via treatment of in situ generated [Mo(NAd)$_2$(O*t*-Bu)$_2$] with LH_2; the latter method also results in trace amounts of the five-coordinate complex [MoCl(NAd)$_2$(L_{dehyd})] (**3**) (L_{dehyd} = 2-(2-hydroxy-2,2-diphenylethenyl)pyridine). The structures of **1**–**3** have been determined by X-ray crystallographic study. In each complex, the geometry at the metal is distorted trigonal bipyramidal with the pyridinediolate ligand adopting an 'aea' bonding arrangement in **1** and an 'eee' arrangement in **2**. The angle associated with the imido moiety also varies, with the greatest deviations found in **1** and **3**, indeed, the pentafluoroimido ligand in **1** has one of the largest deviations from linearity for an M–N–C angle recorded to-date [135.98(16)°]. This has been rationalised on the basis of an electronic effect rather than intramolecular steric interactions or crystal packing forces.
© 2007 Elsevier Ltd. All rights reserved.

Keywords: Molybdenum; Imido; Crystal structures

1. Introduction

The organoimido function has featured heavily in coordination chemistry over the last three decades [1]. Interest in bis(imido) complexes of group VI in-particular continues, primarily because of their use as precursors to useful catalytic systems [2]. The vast majority of terminal organoimido (NR, R = alkyl or aryl) groups in the literature are sp-hybridised at nitrogen and hence triple-bond in nature (four electron donors). The softness of the M–N–C angle has been noted previously with angles in the range 180–150° considered linear (**I**) [3]. An additional linear form (**II**) with a formal M = N double bond has also been noted [4]. Contrastingly, there are few examples of bent imido groups (**III**), although a number of chelate species are known where the restricted imido bond angle is a function of the bite angle of the ligand [5]. In the case of **III**, the lone pair resides on the sp^2-hybridised nitrogen atom and the metal imido group can be described as possessing double-bond character (2 electron donor).



I **II** **III**

* Corresponding author.
E-mail address: Carl.Redshaw@uea.ac.uk (C. Redshaw).

0277-5387/$ - see front matter © 2007 Elsevier Ltd. All rights reserved.
doi:10.1016/j.poly.2007.02.008

The earliest structurally characterised example [Mo(NPh)$_2$(S$_2$CNEt$_2$)$_2$], a 20 electron complex, was found to possess one bent [Mo–N–C = 139.4(4)°] and one linear [Mo–N–C = 169.4(4)°] imido group at −80 °C [6]; only slight differences were observed in a later room temperature study [7]. Interestingly, the related complexes [Mo(NAr)$_2$(S$_2$CNEt$_2$)$_2$] (Ar = 2-MeC$_6$H$_4$, 2,6-Me$_2$C$_6$H$_3$, 2,6-*i*-Pr$_2$C$_6$H$_3$ and 2,6-Cl$_2$C$_6$H$_3$) do not contain bent imido groups, leading to the conclusion that the bending of the imido ligand in this system is attributable to intramolecular steric interactions and/or crystal packing forces [7]. Examples of bent imido ligands for other metals (see Table 1) include the manganese complexes [Mn(N*t*-Bu)$_3$X] (X = Cl, OC(O)Me, OC$_6$F$_5$ and SC$_6$F$_5$) for which the Mn–N–C angles fall in the range 138.5(3)–144.6(3)° [8], and the rhenium(VII) complex {[Re(N*t*-Bu)$_2$(η^1-C$_5$H$_5$)]$_2$(μ- C$_5$H$_4$)(μ-O)} [9]. Recently, Odom et al. have carried out a statistical analysis of bis(imido) group VI complexes using data from the Cambridge Structural Data Base, and presented the data in terms of the sum of the imido angles [10]. The average sum of the imido angles was found to be 328° (standard deviation 8°), whilst it was also apparent that bending of the imido group was no more prevalent for 6-coordinate complexes than for 4- or 5-coordinate species.

In our previous studies on the 2,6-bis(2-hydroxy-2,2-diphenylethyl)pyridine (LH$_2$), **IV**, we have described the synthesis and X-ray crystal structure of the five-coordinate molybdenum (VI) compound [Mo(NAr)$_2$(L)], where Ar = N-2,6-*i*-Pr$_2$C$_6$H$_3$ [3]. In this case the pyridinediolate ligand adopts a *'facial'*, (eae) coordination mode[1] leaving one of the imido ligands to occupy an axial coordination site within the trigonal bipyramidal structure, the other imido group occupies an equatorial site. The structure of this complex revealed a severe bending of the equatorial imido ligand, [144.8(5)°] the axial imido group remaining essentially linear [164.7(4)°]. In order to help understand whether the bending was due to an electronic or steric effect, the related alkylidene complex was prepared and structurally characterised. Here, the alkylidene ligand was found to preferentially occupy the equatorial site and is of course necessarily bent due to the sp^2-hybridised alkylidene carbon centre. Indeed, it was thought likely that the alkylidene ligand would prefer the equatorial site since in that position there exists only one dπ metal orbital available for bonding to the π-ligand. Thus, the bending of the imido group in this environment may be attributed to an electronic explanation rather than due to steric effects or crystal packing forces. In extending this work, we wished to probe the effect of incorporating differing imido ligands, especially those with different electronic requirements, i.e. an electron-withdrawing substituent and an electron-releasing substituent within this 5-coordination geometry. Furthermore, would an imido ligand with a strong electron-withdrawing substituent show a preference for the equatorial site. We were also interested to compare the effect of *facial* (eae) coordination of the [O,N,O] ligand with *meridional* (eee) coordination, and the effect this might have on the imido ligand bonding.

Table 1
Bent imido groups

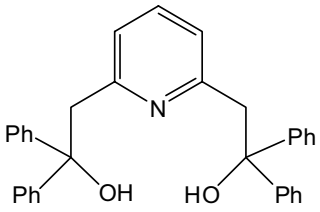
Compound	M–N–C angle (°)	Metal coordination number	Reference
[CrO(N*t*-Bu)(O(Ph$_2$SiO)$_2$)$_2$]	145.6(6) 146.4(6)	4	[11]
[Cr(NAr)(O)(N*i*–Pr$_2$)(Ar)]	146.2(3)	4	[12]
[Cr(O)(NSiMe$_3$)(py)]$_2$-(μ-OSiMe$_3$)	144.1(3)	5	[13]
[Mo(NPh)$_2$(S$_2$CNEt$_2$)$_2$]	139.4(4) [141.4(5)] 169.4(4) [170.9(6)]	6	[6,7]
[Mo(NAr)$_2$L]	144.8(5) 164.7(4)	5	[3]
[Mo(N*t*-Bu)(NC$_6$F$_5$)L]	135.98(16) 173.52(18)	5	this work
[Mo(NAd)$_2$Cl(LH$_{dehyd}$)]	148.6(3) 170.9(3)	5	this work
[Mn(N*t*-Bu)$_3$Cl]	138.5(3) 141.8(3) 140.6(3)	4	[8]
[Mn(N*t*-Bu)$_3$(OC(O)Me)]	144.6(3) 140.1(5) 142.2(5)	4	[8]
[Mn(N*t*-Bu)$_3$(OC$_6$F$_5$)]	141.9(2) 139.9(2) 140.7(2)	4	[8]
[Mn(N*t*-Bu)$_3$(NH$_2$*t*-Bu)](PF$_6$)[a]	141.0(6) 141.4(6) 146.5(6)	4	[8]
[Mn(N*t*-Bu)$_3$(NH$_2$*t*-Bu)](O$_3$SCF$_3$)[a]	135.8(6) 140.5(7) 136.2(4)	4	[8]
[Mn(N*t*-Bu)$_3$(SC$_6$F$_5$)]	143.1(2) 142.0(2) 142.2(2)	4	[8]
{[Re(N*t*-Bu)$_2$(η^1-C$_5$H$_5$)]$_2$-(μ-C$_5$H$_4$)(μ-O)}	146.1(10) 152.5(12) 173.4(11) 176.2(12)	5	[10]
[Re(N*t*-Bu)$_3$(mesityl)]	142.4(22)	4	[14]
[MoCl(N*t*-Bu)$_2$(O–O)][b]	148.37	5	[15]
[Re(N*t*-Bu)$_3$(NH$_2$*t*-Bu)]-(SO$_3$CF$_3$)	146.0(8) 139.8(7)[c]	4	[16]
[Re$_4$(N*t*-Bu)$_8$(μ-O)$_2$(μ$_3$-O)$_2$-(O$_3$SCF$_3$)$_4$]	143.9(6)	5	[17]
[Os(p-NC$_6$H$_4$NO$_2$)$_2$(TTP)][d]	144.74 141.91	6	[18]
[Os(p-NC$_6$H$_4$NO$_2$)$_2$-(4-Cl-TTP)][d]	143.8(6) 141.3(6)	6	[19]

[a] Severe disorder prevented an accurate structure determination.
[b] (O–O) = ring-opened biaryl lactone.
[c] Thought to be protonated.
[d] TTP = tetratolylporphyrin.

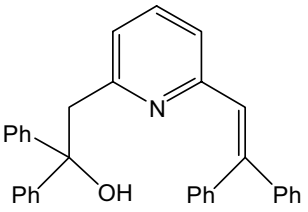
[1] We have opted not to use the terms *fac* and *mer* here, as IUPAC usually reserves such descriptions for hexa-coordinate centres.

In this paper, we report the successful synthesis and structural characterisation of two complexes [Mo(N*t*-Bu)(NC_6F_5)(L)] (**1**) and [Mo(NAd)$_2$(L)] (**2**), which possess the desired *facial* and *meridional* coordination geometries, respectively. The structure of the trace product [MoCl(-NAd)$_2$(L_{dehyd})] (**3**) is also reported.

Few other studies of the tridentate ligand L have been reported, examples include oxo, nitrido and imido complexes of osmium [20], the dioxo complexes of molybdenum reported by Holm [21], a titanium dichloride complex [$TiCl_2$L] [22] and the main-group complex [$SiMe_2$L] [23–25]. We have also recently reported the isodiazene complex [MoCl(O_3SCF_3)($NNPh_2$)L] which contains a *meridional* ligand [26].



LH_2 (IV)



LH_{dehyd} (V)

2. Results and discussion

Starting materials of the form [Mo(NR′)(NR″)Cl_2(dme)] (R′ = *t*-Bu, R″ = C_6F_5; R′ = Ad, R″ = C_6F_5) have been used previously for the synthesis of mixed-imido compounds [27]. The five-coordinate complex [Mo(N*t*-Bu)(NC_6F_5)(L)] (**1**) can be prepared in multigram quantities via treatment of [Mo(N*t*-Bu)(NC_6F_5)(O*t*-Bu)$_2$] (prepared in situ from [Mo(N*t*-Bu)(NC_6F_5)$_2Cl_2$(dme)] and LiO*t*-Bu) with LH_2.

Crystals of **1** suitable for an X-ray determination were grown from a saturated MeCN solution upon standing at room temperature. The molecular structure is shown in Fig. 1 and key bond lengths and angles are given in Table 2, crystal data are given in Table 3. The molecular structure is best described as a distorted trigonal pyramid with the pyridine of the diolate and the *tert*-butylimido groups occupying axial sites, i.e. an 'aea' set.

The 'aea' arrangement of the pyridinediolate (L) is similar to that observed in [Mo(NAr)$_2$L] (Ar = N-2,6-*i*-$Pr_2C_6H_3$)[2] and [OsNCl(L)] [20]. The structural parameters associated with the two imido groups in **1** reflect their differing electronic properties. The result is one linear *tert*-butylimido ligand [Mo(1)–N(1) = 1.7228(19) Å, Mo(1)–N(1)–C(1) = 173.52(18)°] and one bent pentafluorophenylimido group [Mo(1)–N(2) = 1.8074(19) Å, Mo(1)–N(2)–C(5) = 135.98(16)°]; a feature attributed to the more electron-releasing nature of the *tert*-butylimido ligand. In the bent ligand, there is also a diminished metal-nitrogen π contribution due to the presence of π-bonding between the nitrogen and the *ipso*-carbon of the phenyl ring as evidenced by the short C(5)–N(2) distance [1.379(3) Å cf. 1.449(3) Å for C(1)–N(1)]. Table 1 contains literature examples of 'bent' imido groups and reveals that for complex **1** the imido group has one of the greatest deviations from linearity observed to-date. The sum of the imido angles for **1** = ca. 309.5(°), which is very close to that observed for [Mo(NPh)$_2$(S_2CNEt_2)$_2$] [309°] – which is the lowest 'sum' in the literature.

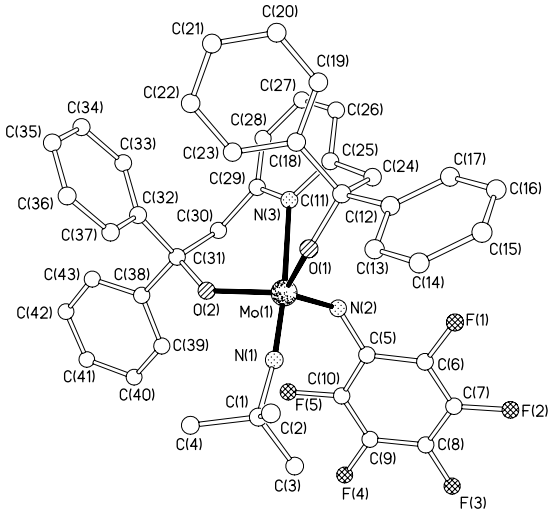


Fig. 1. The molecular structure of **1** with H-atoms omitted.

Table 2
Selected bond lengths (Å) and angles (°) for **1**

Mo(1)–N(1) 1.7228(19)	Mo(1)–N(2) 1.8074(19)
Mo(1)–O(1) 1.9173(15)	Mo(1)–O(2) 1.9274(15)
Mo(1)–N(3) 2.3914(18)	
N(1)–Mo(1)–N(2) 103.55(9)	N(1)–Mo(1)–O(1) 95.40(8)
N(2)–Mo(1)–O(1) 116.97(8)	N(1)–Mo(1)–O(2) 93.86(8)
N(2)–Mo(1)–O(2) 115.49(8)	O(1)–Mo(1)–O(2) 122.51(7)
Mo(1)–N(1)–C(1) 173.52(18)	Mo(1)–N(2)–C(5) 135.98(16)

The five-coordinate complex [Mo(NAd)$_2$(L)] (**2**) can be prepared via treatment of [Mo(NAd)(NC_6F_5)(O*t*-Bu)$_2$] (prepared in situ from [Mo(NAd)(NC_6F_5)Cl_2(dme)] and LiO*t*-Bu) with LH_2 in refluxing toluene. The production of complex **2** at elevated temperatures indicates that under these conditions imido-ligand exchange occurs. Similar imido ligand exchange has been observed for the four-coordinate complexes [MoX_2(O*t*-Bu)$_2$] (X = O or NR), the tetratungstate [W_4(N*t*-Bu)$_4O_4Cl_{10}$]$^{2-}$ and more recently for the *tert*-butylimido titanium complex [Ti(N*t*-Bu)Cl_2(py)$_2$] [28–30]. It is also noteworthy that the bis(imido) complexes [Mo(NR)$_2Cl_2$(dme)] (R = *t*-Bu, 2,6-C_6H_3-*i*-Pr_2) and [Mo(NAr)$_2$(O*t*-Bu)$_2$] undergo metathesis with the imines PhN = CH(*t*-Bu) or (*n*-Pr)N = CHPh [31]. Crystals of **2** · MeCN suitable for an X-ray determination were obtained from a saturated MeCN solution upon prolonged standing at ambient temperature. The molecular structure is shown in Fig. 2a and b; key bond lengths and angles

Table 3
Summary of crystal data and structure determination for compounds **1**, **2** · MeCN and **3**

Compound	**1**	**2** · MeCN	**3**
Formula	$C_{43}H_{36}F_5N_3O_2Mo$	$C_{53}H_{57}N_3O_2Mo \cdot C_2H_3N$	$C_{53}H_{56}ClN_3OMo$
M	817.69	905.01	882.40
Temperature (K)	160	160	160
Crystal size (mm)	$0.42 \times 0.17 \times 0.11$	$0.29 \times 0.23 \times 0.23$	$0.25 \times 0.18 \times 0.16$
Crystal colour, habit	yellow, block	yellow, block	yellow, block
Crystal system	monoclinic	monoclinic	monoclinic
Space group	$P2_1/c$	$P2_1/c$	$P2_1/c$
a (Å)	11.0769(5)	25.762(11)	12.4861(12)
b (Å)	33.8115(16)	8.671(4)	18.1988(17)
c (Å)	11.2651(5)	21.877(11)	19.0842(18)
β (°)	116.687(2)	111.99(2)	99.806(2)
V (Å^3)	3769.6(3)	4531(4)	4273.2(7)
Z	4	4	4
D_{calc} (g cm^{-3})	1.441	1.327	1.372
μ (mm^{-1})	0.414	2.726	0.413
θ Range (°)	2.06–28.40	3.70–60.09	1.56–25.85
Maximum indices: h	−14 to 8	−28 to 28	−15 to 12
k	−43 to 38	−9 to 5	−22 to 14
l	−14 to 14	−24 to 24	−21 to 22
Reflections measured	23182	6721	18725
Unique reflections {observed $F^2 > 2\sigma(F^2)$}	8566 {7205}	6721 {5814}	7387 {6108}
R_{int}	0.0297		0.0494
R [$F^2 > 2\sigma(F^2)$][a]	0.0383	0.0615	0.0530
wR_2 [all data][b]	0.0766	0.1345	0.1086
Number of refined parameters	491	560	533
Largest difference map features (e Å^{-3})	0.354, −0.590	1.631, −1.417	0.453, −0.693

[a] $R = \sum \|\|F_o| - |F_c\|| / \sum |F_o|$.
[b] $wR_2 = \{\sum[w(F_o^2 - F_c^2)^2] / \sum[w(F_o^2)^2]\}^{1/2}$.

are given in Table 4 and crystal data appear in Table 3. Each molecule of **2** crystallises with a molecule of MeCN. The molecular structure is best described as a distorted trigonal pyramid with the pyridine of the diolate and the two imido groups in equatorial positions, i.e. 'eee' ligated L.

The ^{1}H NMR spectrum of **1** reveals an *AB* quartet at 3.86 ppm for the ligand backbone methylene units consistent with the diastereotopic proton environments in the 'aea' coordinated ligand. Contrastingly the room temperature ^{1}H NMR spectrum of **2** reveals a broadened singlet consistent with the 'eee' coordination geometry.

Meridional arrangements for L have been observed previously in the 6-coordinate complexes $[Mo(O)_2(L)(Me_2SO)]$ and $[Os(O)_2(L)(H_2N\textit{t}\text{-Bu})]$ [20,21]. In **2**, a non-crystallographic 2-fold-axis bisects the N(1)–Mo–N(2) angle between the imido groups and passes along the Mo–N(3) bond of the pyridinediolate. The bond parameters associated with the equatorial imido ligands are of particular interest to us here. The Mo–N distances are similar, viz Mo–N(1) = 1.710(5), Mo–N(2) = 1.727(4) Å, whereas the angles at the imido nitrogens are quite different, 168.8(4)° and 159.6(4)° (sum of angles = 328.4°), however, both imido ligands are still considered to be 'linear'.

Reaction of $[Mo(NAd)_2(O\textit{t}\text{-Bu})_2]$ (prepared in situ from $[Mo(NAd)_2Cl_2(dme)]$ and Li*O*t-Bu) with LH_2 led to complex **2** together with trace amounts of yellow plate-like crystals, which were shown by X-ray diffraction to be the complex $[MoCl(NAd)_2(LH_{dehyd})]$ (**3**), where LH_{dehyd} is the partially dehydrated ligand **V**. The structure of **3** is shown in Fig. 3, with selected bond lengths and angles given in Table 5. There is approximate trigonal bipyramidal geometry at the metal centre, with the pyridine of the chelate and two imido ligands equatorial. As in **1**, the two imido ligands are quite different: Mo(1)–N(3) 1.724(3) Å/Mo(1)–N(3)–C(44) 170.9(3)° versus Mo(1)–N(2) 1.745(3) Å/Mo(1)–N(2)–C(34) 148.6(3)°; the latter is now in the range associated with bent imido groups (sum of angles = 319.5°). This bending could arise as a consequence of steric interactions with the pendant alkenyl arm of the chelate ligand. Pyridinediols have previously been found to act as HCl receptors, and the structure of the partially dehydrated ligand **V** · HCl (i.e., the HCl adduct of LH_{dehyd}) was shown to contain a Cl^- ion hydrogen-bonded to a protonated pyridine nitrogen atom. Interestingly, in order to achieve complete dehydration, neat H_3PO_4 had to be used at elevated temperatures [32].

3. Summary

We have described the synthesis and characterisation of two bis(imido)molybdenum complexes that differ in the coordination geometry of a tridentate [O,N,O] ligand: one of the complexes also has two electronically differing imido substituents. In this case the imido ligands with an electron-releasing tertiary-butyl substituent occupies the axial site within the trigonal bipyrimidal coordination

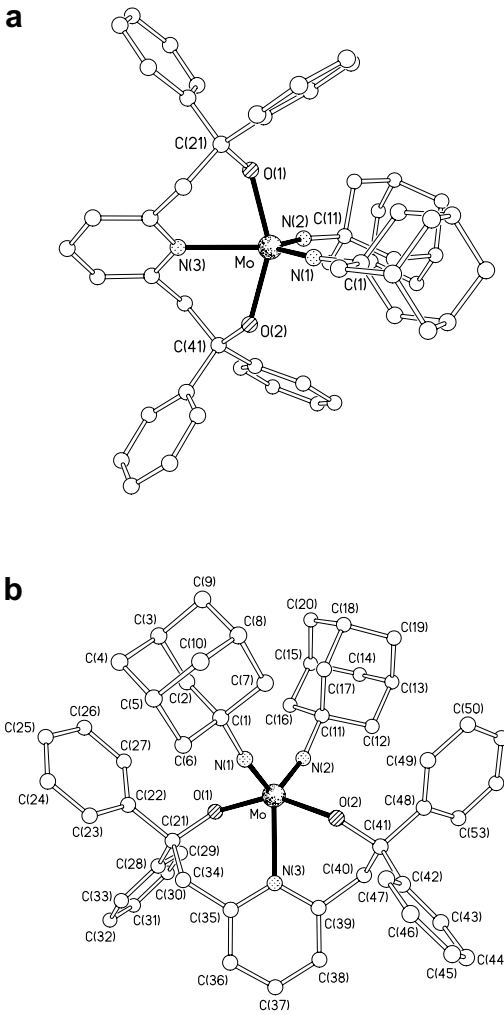


Fig. 2. (a,b) Two views of the molecular structure of **2** with H-atoms and MeCN of crystallisation omitted.

Table 4
Selected bond lengths (Å) and angles (°) for **2**

Mo–N(1) 1.710(5)	Mo–N(2) 1.727(4)
Mo–O(1) 1.995(3)	Mo–O(2) 2.020(4)
Mo–N(3) 2.299(4)	
N(1)–Mo–N(2) 111.8(2)	N(1)–Mo–O(1) 101.22(18)
N(2)–Mo–O(1) 95.99(18)	N(1)–Mo–O(2) 94.99(19)
N(2)–Mo–O(2) 100.05(18)	O(1)–Mo–O(2) 151.05(14)
Mo–N(1)–C(1) 168.8(4)	Mo–N(2)–C(11) 159.6(4)

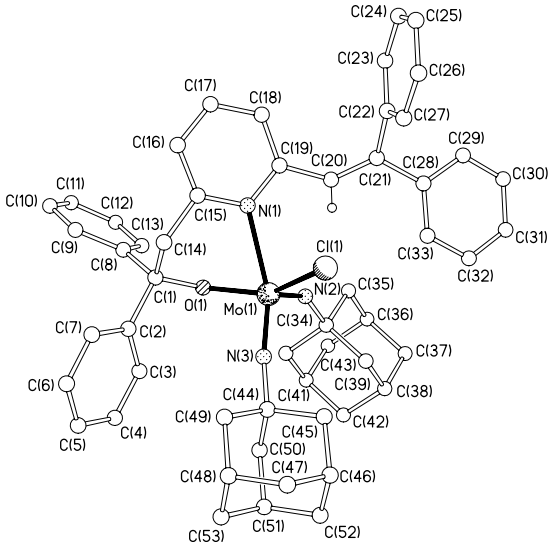


Fig. 3. The molecular structure of **3** with H-atoms omitted.

Table 5
Selected bond lengths (Å) and angles (°) for **3**

Mo(1)–N(1) 2.366(3)	Mo(1)–N(2) 1.745(3)
Mo(1)–O(1) 1.962(2)	Mo(1)–Cl(1) 2.4196(11)
Mo(1)–N(3) 1.724(3)	
N(1)–Mo(1)–N(2) 104.62(12)	N(1)–Mo(1)–O(1) 76.25(10)
N(2)–Mo(1)–O(1) 97.16(12)	N(1)–Mo(1)–N(3) 147.41(13)
N(3)–Mo(1)–O(1) 100.77(12)	N(3)–Mo(1)–N(2) 107.93(14)
N(3)–Mo(1)–Cl(1) 90.59(11)	N(2)–Mo(1)–Cl(1) 108.03(10)
Mo(1)–N(2)–C(34) 148.6(3)	Mo(1)–N(3)–C(44) 170.9(3)

geometry, the electron-withdrawing pentafluorophenyl imido group, the equatorial site. This would appear to be a favourable arrangement allowing the tertiary-butylimido group to maximise its π-donor group capacity through the formation of two π bonds. In the equatorial position, there is only a single dπ metal orbital available to overlap with the imido nitrogen π orbital thereby restricting the imido group to a single π-bond. A consequence of this is a formally sp^2-hybridised nitrogen and an accordingly bent imido ligand. The structure of **2** lends further support to the observation that for electronically similar imido groups in identical coordination environments, especially when placed in direct competition for the available metal dπ orbitals, an imido bend angle in the range 150–180° is anticipated. The M–N–C angle then appears to be dictated by intramolecular steric effects and crystal packing forces, a consequence of a relatively shallow potential energy well for M–N–C bending when the two imido groups are in chemically equivalent sites and therefore in direct competition for the available metal π-orbitals.

4. Experimental

4.1. General

All manipulations were carried out under an atmosphere of nitrogen using standard Schlenk and cannula techniques or in a conventional nitrogen-filled glove-box. Solvents were refluxed over an appropriate drying agent, and distilled and degassed prior to use. Elemental analyses were performed by the microanalytical services of the Department of Chemistry at Durham and of Imperial College. NMR spectra were recorded on a Varian VXR 400S spectrometer at 400.0 MHz (^{1}H), and 376.3 MHz (^{19}F) at 298 K; chemical shifts are referenced to the residual protio

impurity of the deuterated solvent; IR spectra (nujol mulls, CsI windows), Perkin–Elmer 577 and 457 grating spectrophotometers. [Mo(N*t*-Bu)(NC_6F_5)Cl_2(dme)], [Mo(NAd)(NC_6F_5)Cl_2(dme)], [Mo(NAd)$_2Cl_2$(dme)] and LH_2 were prepared by the literature methods [27,21]. All other chemicals were obtained commercially and used as received unless stated otherwise.

4.2. Preparation of [Mo(Nt-Bu)(NC_6F_5)L] (1)

To [Mo(N*t*-Bu)(NC_6F_5)(O*t*-Bu)$_2$] [prepared in situ from [Mo(N*t*-Bu)(NC_6F_5)Cl_2(dme)] (1.50 g, 2.98 mmol) and LiO*t*-Bu (0.48 g, 6.00 mmol)] in ca. 50 cm^3 diethyl ether was added LH_2 (1.37 g, 2.91 mmol). After stirring for 5–10 min, the volatiles were removed in vacuo. Toluene (ca. 40 cm^3) was added and the system was refluxed for 12 h. On cooling, volatiles were removed in vacuo and the residue was extracted with hot MeCN (40 cm^3). On standing at room temperature large yellow prisms of **1** formed. Yield: 1.90 g, 80%. *Anal.* Calc. for $MoF_5O_2N_3C_{43}H_{36}$ requires C, 63.2; H, 4.4; N, 5.1. Found: C, 63.4; H, 4.4; N, 5.0%. IR: 1600w, 1575w, 1494m, 1343m, 1312m, 1292m, 1261s, 1239m, 1211m, 1189m, 1093s, 1060s, 1023s, 977m, 960m, 947m, 916m, 892m, 875m, 801s, 770m, 753m, 733m, 724m, 701m, 658w, 638w, 619w, 607w, 600w, 592w, 565w, 512w, 497w, 484w, 452w, 427w, 417w, 404w. ^{1}H NMR ($CDCl_3$): δ 7.46–6.74 (several m, 23H, aryl*H*), 3.86 (ABq, 4H, CH_2), 1.12 (s, 9H, C(CH_3)$_3$). ^{19}F NMR ($CDCl_3$): δ −152.00 (m, 2F, *o*-F), −165.36 (tm,* 2F, $^3J_{FF}$ 18 Hz, $^4J_{FF}$ 3Hz, *m*-F), −167.44 (m, 1F, *p*-F). * triplet of multiplets.

4.3. Preparation of [Mo(NAd)$_2$L] (2)

As for **1**, using [Mo(NAd)(NC_6F_5)Cl_2(dme)] (2.00 g, 3.42 mmol) and LiO*t*-Bu (0.54 g, 6.75 mmol) and LH_2 (1.60 g, 3.39 mmol) affording **2** · MeCN as golden-yellow prisms. Yield: 1.37 g, 89%. *Anal.* Calc. for $MoO_2N_3C_{53}H_{55} \cdot CH_3CN$ (sample dried for 12 h in vacuo) requires C, 73.2; H, 6.5; N, 6.2. Found: C, 73.7; H, 6.5; N, 6.1%. IR: 2359m, 2342m, 1737w, 1705w, 1654w, 1602w, 1580w, 1560w, 1500s, 1308w, 1242m, 1182w, 1119w, 1096w, 1062m, 1044s, 1027s, 984w, 963w, 924w, 890w, 812w, 784m, 752w, 701s, 606s. ^{1}H NMR (Acetone-d_6) δ: 7.65–7.16 (several m, 23H, aryl*H*), 4.08 (bs, 4H, CH_2), 1.98 (m, 6H, C*H*ad), 1.57 (m, 12H, CH_2ad), 1.56 (m, 12H, CH_2ad).

4.4. Preparation of [MoCl(NAd)$_2$(L_{dehyd})] (3)

As for **1**, but using [Mo(NAd)$_2Cl_2$(dme)] (0.93 g, 1.69 mmol) and LiO*t*-Bu (0.26 g, 3.25 mmol) with LH_2 (0.80 g, 1.70 mmol) affording on recrystallisation from hot acetonitrile **2** (0.61 g, 80%) and **3** (0.11 g, 15% based on Mo). For **3**, *Anal.* Calc. for $MoClON_2C_{43}H_{40}$ requires C, 70.5; H, 5.5; N, 3.8. Found: C, 69.4; H, 5.7; N, 3.8%. IR: 2359m, 2325m, 1654w, 1603m, 1568w, 1491m, 1302w, 1267w, 1233m, 1181w, 1122m, 1095m, 1053s, 1027m, 950m, 907w, 821w, 779m, 735w, 701s, 666s, 598s. ^{1}H NMR (CD_3CN) δ: 7.83–7.01 (several m, 23H, aryl*H*), 6.50 (d, 1H, C*H*), 4.09 (bs, 2H, CH_2), 1.97 (m, 18H, Ad*H*), 1.65 (m, 12H, Ad*H*).

4.5. X-ray crystallography

Crystallographic data and details of the data collection procedures and structure refinement for structures **1**, **2** and **3** are presented in Table 3.

Data for **1** and **3** were collected on a Bruker AXS SMART 1K CCD area detector diffractometer using graphite monochromated Mo Kα radiation (λ = 0.71073 Å) and narrow frames (0.3° in ω). Corrections were applied for Lorentz-polarisation effects and semi-empirically for absorption based on symmetry equivalent and repeated data. Programs used were Bruker AXS SMART (machine control) and SAINT (frame integration) [33]. Data for **2** were collected on a Stoe-Siemens diffractometer with ω/θ scans and on-line profile fitting [34] with all machine-control calculations performed using Stoe DIF4 software and with graphite monochromated Cu Kα radiation (λ = 1.54184 Å). Corrections were applied for Lorentz-polarisation effects and semi-empirically for absorption using Ψ-scans. The structures were solved by direct methods for **1** and **3**, (Patterson synthesis for **2)** and refined by full-matrix least-squares on all data using F^2 values. All non-H atoms were refined anisotropically, H atoms, initially located in difference maps, were included using a riding model with U_{iso} equal to 1.2 times that of the carrier atom (1.5 times for methyl H). The program SHELXTL [35] was used for crystal structure solution and refinement and molecular graphics.

5. Supplementary material

CCDC 147054, 147055 and 147056 contain the supplementary crystallographic data for this paper. These data can be obtained free of charge via http://www.ccdc.cam.ac.uk/conts/retrieving.html, or from the Cambridge Crystallographic Data Centre, 12 Union Road, Cambridge CB2 1EZ, UK; fax: (+44) 1223-336-033; or e-mail: deposit@ccdc.cam.ac.uk.

Acknowledgements

The Engineering and Physical Sciences Research Council and The University of East Anglia are thanked for financial support.

References

[1] (a) W.A. Nugent, B.L. Haymore, Coord. Chem. Rev. 31 (1980) 123;
(b) W.A. Nugent, J.M. Mayer, Metal-Ligand Multiple Bonds, Wiley-Interscience, New York, 1988;
(c) D.E. Wigley, Prog. Inorg. Chem. 42 (1994) 239;

(d) P.R. Sharp, Comm. Inorg. Chem. 21 (1999) 85;
(e) P.R. Sharp, J. Chem. Soc., Dalton Trans. (2000) 2647;
(f) R.A. Eikey, M.M. Abu-Omar, Coord. Chem. Rev. 243 (2003) 83;
(g) W.-H. Leung, Eur. J. Inorg. Chem. (2003) 583;
(h) U. Radius, Z. Anorg. Allg. Chem. 630 (2004) 957.
[2] (a) See for example R.R. Schrock, J. Mol. Cat. A: Chem. 213 (2004) 21;
(b) V.R. Jensen, K.J. BØrve, Chem. Commun. (2002) 542.
[3] V.C. Gibson, E.L. Marshall, C. Redshaw, W. Clegg, M.R.J. Elsegood, J. Chem. Soc., Dalton Trans (1996) 4197.
[4] G. Parkin, A. van Asselt, D.J. Leahy, L.R. Whinnery, N.G. Hua, R.W. Quan, L.M. Henling, W.P. Schaefer, B.D. Santarsiero, J.E. Bercaw, Inorg. Chem. 31 (1992) 82.
[5] (a) O.D. Sloan, P. Thornton, Polyhedron 7 (1988) 329;
(b) M. Minelli, M.R. Carson, D.W. Whisenhunt Jr., W. Imhof, G. Huttner, Inorg. Chem. 29 (1990) 4801;
(c) W.A. Hermann, D.W. Marz, E. Herdtweck, Z. Naturforsch Teil B 46 (1991) 747;
(d) M. Minelli, R.L. Kuhlman, S.J. Schaffer, M.Y. Chiang, Inorg. Chem. 31 (1992) 3891;
(e) S.D. Gray, D.P. Smith, M.A. Bruck, D.E. Wigley, J. Am. Chem. Soc. 114 (1992) 5462;
(f) M.T. Ahmet, B. Coutinho, J.R. Dilworth, J.R. Miller, S.J. Parrott, Y. Zheng, M. Harman, M.B. Hursthouse, A. Malik, J. Chem. Soc., Dalton Trans. (1995) 3041;
(g) F. Refosco, F. Tisato, A. Moreesco, G. Bandoli, J. Chem. Soc., Dalton Trans. (1995) 3475;
(h) R.R. Schrock, S.W. Seidel, N.C. Moesch-Zanetti, D.A. Dobbs, K.-Y. Shih, W.M. Davis, Organometallics 16 (1997) 5195;
(i) T.I. Gountchev, T.D. Tilley, J. Am. Chem. Soc. 119 (1997) 12831;
(j) R.R. Schrock, S.W. Seidel, N.C. Mosch-Zanetti, D.A. Dobbs, K.Y. Shih, W.M. Davis, Organometallics 16 (1997) 5195;
(k) S. Cai, R.R. Schrock, R.R. Kempe, W.M. Davis, Polyhedron 17 (1998) 747;
(l) U. Siemeling, T. Türk, W.W. Schoeller, C. Redshaw, V.C. Gibson, Inorg. Chem. 37 (1998) 4738;
(m) V.C. Gibson, C. Redshaw, W. Clegg, M.R.J. Elsegood, Inorg. Chem. Comm. 4 (2001) 95.
[6] B.L. Haymore, E.A. Maatta, R.A.D. Wentworth, J. Am. Chem. Soc. 101 (1979) 2063.
[7] P. Barrie, T.A. Coffey, G.D. Forster, G. Hogarth, J. Chem. Soc., Dalton Trans. (1999) 4519.
[8] (a) A.A. Danopoulos, G. Wilkinson, T. Sweet, M.B. Hursthouse, Chem. Commun. (1993) 495;
(b) A.A. Danopoulos, G. Wilkinson, T. Sweet, M.B. Hursthouse, J. Chem. Soc., Dalton Trans. (1994) 1037.
[9] A.A. Danopoulos, G. Wilkinson, D.J. Williams, Chem. Commun. (1991) 181.
[10] J.T. Ciszewski, J.F. Harrison, A.L. Odom, Inorg. Chem. 43 (2004) 3605.
[11] L. King, M. Motevalli, A.C. Sullivan, J. Chem. Soc., Dalton Trans. (1999) 3225.
[12] E.W. Jandeiu, P. Legzdins, W.S. McNeil, B.O. Patrick, K.M. Smith, Chem. Commun. (2000) 1809.
[13] H.-W. Lam, G. Wilkinson, B. Hussain-Bates, M.B. Hursthouse, J. Chem. Soc., Dalton Trans. (1993) 1477.
[14] A. Gutierrez, G. Wilkinson, B. Hussain-Bates, M.B. Hursthouse, Polyhedron 9 (1990) 2081.
[15] J. Sundermeyer, K. Weber, H. Werner, N. Mahr, G. Bringmann, O. Schupp, J. Organomet. Chem. 444 (1993) C37.
[16] V. Saboonchian, A.A. Danopoulos, A. Gutierrez, G. Wilkinson, D.J. Williams, Polyhedron 10 (1991) 2241.
[17] H.-W. Lam, G. Wilkinson, D.J. Williams, Polyhedron 10 (1991) 2647.
[18] J.A. Smieja, K.M. Omberg, G.L. Breneman, Inorg. Chem. 33 (1994) 614.
[19] J.A. Smieja, K. Shirzad, M. Roy, K. Kittilstved, B. Twamley, Inorg. Chim. Acta 335 (2002) 141.
[20] Z-Y. Li, W-Y. Yu, C-M. Che, C-K. Poon, R-J. Wang, T.C.W. Mak, J. Chem. Soc., Dalton Trans (1996) 4197.
[21] J.M. Berg, R.H. Holm, J. Am. Chem. Soc. 107 (1985) 917.
[22] H. Mack, M.S. Eisen, J. Chem. Soc., Dalton Trans. (1998) 917.
[23] E. Gómez, V. Santes, V. de la Luz, N. Farfán, J. Organomet. Chem. 590 (1999) 237.
[24] T.K. Prakasha, A. Chandrasekaran, R.O. Day, R.R. Holmes, Inorg. Chem. 35 (1996) 4342.
[25] J.J.H. Edema, R. Libbers, A. Ridder, R.M. Kellogg, A.L. Spek, J. Organomet. Chem. 464 (1994) 127.
[26] J.R. Dilworth, V.C. Gibson, N. Davies, C. Redshaw, A.J.P. White, D.J. Williams, J. Chem. Soc., Dalton Trans. (1999) 2695.
[27] R.C.B. Copley, P.W. Dyer, V.C. Gibson, J.A.K. Howard, E.D. Marshall, W. Wang, B. Whittle, Polyhedron 15 (1996) 3001.
[28] M. Jolly, J.P. Mitchell, V.C. Gibson, J. Chem. Soc., Dalton Trans (1992) 1331.
[29] W. Clegg, R.J. Errington, C. Redshaw, D.C.R. Hockless, J. Chem. Soc., Dalton Trans (1993) 1965.
[30] A.J. Blake, P.E. Collier, S.C. Dunn, W.-S. Li, P. Mountford, O.V. Shishkin, J. Chem. Soc., Dalton Trans (1997) 1549.
[31] G.K. Cantrell, T.Y. Meyer, J. Chem. Soc., Chem. Commun. (1997) 1551.
[32] J.H. Edema, R.J. Libbers, A.M. Ridder, R.M. Kellog, F. van Bolhuis, H. Kooijman, A.L. Spek, J. Chem. Soc., Chem. Commun. (1993) 625.
[33] SMART and SAINT software for CCD diffractometers, Bruker AXS Inc. Madison, WI, 1994.
[34] W. Clegg, Acta. Crystallogr., Sect A 37 (1981) 22.
[35] G.M. Sheldrick, SHELXTL Manual, Version 5, Bruker AXS Inc., Madison, WI, USA, 1994.

Available online at www.sciencedirect.com
ScienceDirect
Polyhedron 26 (2007) 3168–3174
POLYHEDRON
www.elsevier.com/locate/poly

Synthesis and characterization of some dimethylsilicon(IV) complexes with internally functionalized oximes: Crystal and molecular structure of $[Me_2Si\{ON{=}C(H)C_4H_3O\text{-}2\}_2]$. Formation of mesoporous materials by the hydrolytic study of $[Me_2Si\{ON{=}C(CH_3)C_4H_3O\text{-}2\}_2]$ in the presence of $Al(OPr^i)_3$

Veena Dhayal [a], Nikita Sharma [a], Vinita Sharma [a], Rakesh Bohra [a,*], John E. Drake [b], Charles L.B. MacDonald [b]

[a] *Department of Chemistry, University of Rajasthan, Jaipur 302004, India*
[b] *Department of Chemistry and Biochemistry, University of Windsor, Windsor, Canada ONN9B 3P4*

Received 18 December 2006; accepted 16 February 2007
Available online 4 March 2007

Abstract

Reactions of Me_2SiCl_2 in a 1:2 molar ratio with internally functionalized oximes in the presence of Et_3N in anhydrous benzene afford compounds of the type $[Me_2Si\{ON{=}C(R)Ar\}_2]$ {where R = Me, Ar = 2-C_5H_4N (**1**), 2-C_4H_3O (**2**), 2-C_4H_3S (**3**); R = H, Ar = 2-C_5H_4N (**4**), 2-C_4H_3O (**5**), 2-C_4H_3S (**6**)}. Molecular weight measurements of all these derivatives in freezing benzene and the FAB mass spectral studies of **1** and **6** indicate that these complexes are monomeric. The ^1H and $^{13}C\{^1H\}$ NMR spectra suggest that the oximate moieties are monofunctional monodentate in solution. $^{29}Si\{^1H\}$ NMR signals appear in the region expected for tetra-coordinated dimethyl silicon atoms. Single crystal X-ray diffraction analysis of $[Me_2Si\{ON{=}C(H)C_4H_3O\text{-}2\}_2]$ (**5**) confirms the presence of a distorted tetrahedron as the immediate environment around silicon. Secondary weak β-donor bonding is also observed in the solid state, indicating that silicon is in the (4+2) coordination state. The TGA curve of $[Me_2Si\{ON{=}C(H)C_4H_3O\text{-}2\}_2]$ shows the high thermal stability and volatile nature of the complex. A comparison of hydrolytic studies of a mixture of $[Me_2Si\{ON{=}C(CH_3)C_4H_3O\text{-}2\}_2]$ and $Al(OPr^i)_3$ in a 1:2 molar ratio with those of pure $Al(OPr^i)_3$ under similar conditions by the sol–gel technique suggests the formation of a silicon embedded amorphous powder **7** and γ-alumina **8**, respectively. The variation in specific surface area, total pore volume and pore size indicate formation of mesoporous materials.
© 2007 Elsevier Ltd. All rights reserved.

Keywords: Functionalized oximes; β-Donor interactions; (4+2) Coordination; γ-Alumina

1. Introduction

Modified mesoporous silica materials are receiving special attention [1], because of their variety of applications in adsorption [2], separation [3], catalysis [4], environmental degradation processes [5], drug delivery [6] and electronic devices [7]. The syntheses of these materials require suitable tailor-made precursors, such as organosilicon complexes containing SiON units [8,9].

Recently, we have reported that the η^2 coordination mode, which is the interaction of a β-positioned donor atom with the central acceptor atom, is favored in complexes of transition metals containing functionalized oximes [10], as demonstrated by V–N = 1.980(4) Å in $[VOCl\{ON{=}C(CH_3)C_4H_3S\text{-}2\}_2]\cdot CH_3OH$ compared to V–ON = 1.925(4) Å [10i] and Zr–N = 2.239(2) Å in $(acac)_2Zr\{ON{=}C(CH_3)C_4H_3O\text{-}2\}_2$ compared to Zr–ON = 2.109(10) Å [10d].

* Corresponding author.
E-mail address: rkbohra@satyam.net.in (R. Bohra).

0277-5387/$ - see front matter © 2007 Elsevier Ltd. All rights reserved.
doi:10.1016/j.poly.2007.02.025

Table 1
Physical and analytical data of dimethylsilicon(IV) complexes with internally functionalized oximes

Complexes	State	% Analysis Found (calc.)				Molecular weight Found (calc.)
		C	H	N	Si	
$[Me_2Si\{ON{=}C(CH_3)C_5H_4N\text{-}2\}_2]$ (**1**)	Solid	58.76 (58.51)	5.98 (6.14)	16.87 (17.06)	8.53 (8.55)	327 (328.4)
$[Me_2Si\{ON{=}C(CH_3)C_4H_3O\text{-}2\}_2]$ (**2**)	Viscous	54.50 (54.88)	5.90 (5.92)	8.91 (9.14)	9.09 (9.17)	307 (306.4)
$[Me_2Si\{ON{=}C(CH_3)C_4H_3S\text{-}2\}_2]$ (**3**)	Solid	49.18 (49.67)	5.18 (5.36)	8.06 (8.27)	8.15 (8.30)	335 (338.5)
$[Me_2Si\{ON{=}C(H)C_5H_4N\text{-}2\}_2]$ (**4**)	Solid	55.26 (55.98)	5.25 (5.37)	18.32 (18.65)	9.34 (9.35)	298 (300.4)
$[Me_2Si\{ON{=}C(H)C_4H_3O\text{-}2\}_2]$ (**5**)	Solid	51.39 (51.78)	5.31 (5.07)	9.97 (10.06)	10.01 (10.09)	277 (278.3)
$[Me_2Si\{ON{=}C(H)C_4H_3S\text{-}2\}_2]$ (**6**)	Viscous	46.12 (46.42)	4.41 (4.55)	8.97 (9.02)	9.00 (9.05)	311 (310.5)

However, no such studies on the β-donor capability of functionalized oximes in their silicon derivatives have been undertaken. Therefore, we report herein the synthesis of some dimethylsilicon(IV) complexes with internally functionalized oximes along with the single crystal X-ray diffraction structure of $[Me_2Si\{ON{=}C(H)C_4H_3O\text{-}2\}_2]$, which demonstrates the existence of β-bonding with [4+2] coordination around silicon. Thermal analysis of the same derivative as well as formation of mesoporous materials by the hydrolytic study of $[Me_2Si\{ON{=}C(CH_3)C_4H_3O\text{-}2\}_2]$ in the presence of $Al(OPr^i)_3$ has also been reported.

2. Experimental

All manipulations (except hydrolysis) were carried out under strictly anhydrous conditions. The solvents and reagents were dried and purified prior to use by conventional methods [11]. Appropriate precautions were taken in handling hazardous chemicals and solvents such as benzene. Dichlorodimethylsilane was used as supplied (Merck). Oximes were prepared by conventional methods [10c,12]. Silicon was estimated gravimetrically as SiO_2 [11]. IR spectra (4000–400 cm^{-1}) were recorded as Nujol mulls between CsI plates or as dry KBr pellets on a Shimadzu FTIR 8400 spectrometer. NMR [^1H, $^{13}C\{^1H\}$ and $^{29}Si\{^1H\}$] data were collected on a JEOL FX 300 FT NMR spectrometer in $CDCl_3$ solutions at 300.4, 75.45 and 59.60 MHz frequencies for ^1H, $^{13}C\{^1H\}$ and $^{29}Si\{^1H\}$ NMR, respectively, using TMS as an internal standard. FAB mass spectra were obtained on a JEOL SX 102/DA-6000 mass spectrometer using *m*-nitrobenzyl-alcohol matrix. Molecular weight measurements were carried out by determining the depressions in freezing point of anhydrous benzene using a Beckmann's Thermometer [Einstellthermometer *n*-Bek] fitted in a glass assembly (supplied by JSGW, India). XRD patterns were obtained on a Phillips-1840 diffractometer using a Fe source at $\lambda = 1.937$ Å. Microanalyses were carried out on a Heracus Carlo Erba 1108 analyzer. Thermogravimetric analysis was performed on Mettler Toledo Star SW 701 with a heating rate of 25–650/10 °C.

2.1. Preparation of $[Me_2Si\{ON{=}C(CH_3)C_5H_4N\text{-}2\}_2]$ (*1*)

A benzene solution of 2-acetyl pyridyl oxime (2.24 g, 16.45 mmol) and triethyl amine (1.68 g, 16.60 mmol) was added dropwise to a stirred ice-cooled benzene solution of dichlorodimethylsilane (1.06 g, 8.21 mmol). The mixture was stirred for 1 h and then refluxed for 5 h. The triethylaminehydrochloride [2.24 g, 16.27 mmol] formed was filtered off and the filtrate was concentrated in vacuo to give a pink liquid [2.65 g, 98.5% yield], which solidified on standing for a few days.

All other dimethylsilicon(IV) derivatives were prepared by a similar route. Their physical and analytical data are summarized in Table 1.

2.2. X-ray diffraction analysis

A colorless block crystal of $[Me_2Si\{ON{=}C(H)C_4H_3O\text{-}2\}_2]$ (**5**) was covered in Paratone-N and placed rapidly into the cold N_2 stream of a Kryo-Flex low temperature device.

Table 2
Crystal data and structure refinement for $[Me_2Si\{ON{=}C(H)C_4H_3O\text{-}2\}_2]$

Empirical formula	$C_{12}H_{14}N_2O_4Si$
Formula weight	278.34
Temperature (K)	173(2)
Wavelength (Å)	0.71073
Crystal system	monoclinic
Space group	*C*2/*c*
a (Å)	20.082(3)
b (Å)	6.3951(9)
c (Å)	14.790(2)
β (°)	132.522(1)
Volume (Å^3)	1400.0(3)
Z	4
D_{calc} (g/cm^3)	1.321
Absorption coefficient (mm^{-1})	0.179
F(000)	584
Crystal size (mm)	$0.50 \times 0.40 \times 0.40$
θ Range for data collection (°)	2.75–28.28
Index ranges	$-26 \leqslant h \leqslant 26$, $-8 \leqslant k \leqslant 8$, $-18 \leqslant l \leqslant 19$
Reflections collected	7601
Independent reflections [R_{int}]	1654 [0.0265]
Maximum and minimum transmission	0.9319 and 0.9159
Refinement method	full-matrix least-squares on F^2
Data/restraints/parameters	1654/0/115
Goodness-of-fit on F^2	1.054
Final *R* indices [$F^2 > 4\sigma(F^2)$]	$R_1 = 0.0412$, $wR_2 = 0.1016$
R indices (all data)	$R_1 = 0.0495$, $wR_2 = 0.1070$
Largest difference in peak and hole (e Å^{-3})	0.287 and −0.208

Table 3
Fragmented molecular ion/*m*/*e* values in FAB mass spectra of dimethylsilicon(IV) complexes **1** and **6**

Complexes	Fragmented ions	*m*/*e* Values obs. (calc.)
$[Me_2Si\{ONC(CH_3)C_5H_4N\}_2]$ (**1**)	$[Me_2Si\{ONC(CH_3)C_5H_4N\}_2+1]^{(M+1)}$	329 (329.43)
	$[MeSi\{ONC(CH_3)C_5H_4N\}_2]^+$	313 (313.40)
	$[Si\{ONC(CH_3)(C_5H_4N)\}\{ONC(CH_3)(C_5H_3N)\}]^+$	297 (297.36)
	$[Si\{ONC(CH_3)(C_5H_4N)\}\{ONC(C_5H_2N)\}]^+$	281 (281.31)
	$[Si\{ONC(CH_3)(C_5H_4N)\}\{ONC(C_4N)\}]^+$	267 (267.29)
	$[Si\{ONC(CH_3)(C_5H_4N)\}\{C_4\}]^+$	211 (211.27)
	$[Si\{ONC(CH_3)(C_5H_4N)\}\{ON\}]^+$	193 (193.23)
	$[Si\{OC(CH_3)(C_5)\}\{C_4\}]^+$	179 (179.22)
	$[Si\{ONC(CH)(C_3N)\}]^+$	133 (133.16)
	$[Si\{OC(CH_3)(C_4)\}]^+$	119 (119.17)
	$[Si\{OHC_5\}]^+$	105 (105.14)
$[Me_2Si\{ON\text{-}C(H)C_4H_3S\}_2]$ (**6**)	$[Me_2Si\{ONC(H)C_4H_3S\}_2+1]^{(M+1)}$	311 (311.46)
	$[MeSi\{ONC(H)(C_4H_3S)\}_2]^+$	295 (295.42)
	$[HSi\{ONC(H)(C_4H_3S)\}_2]^+$	281 (281.40)
	$[MeSi\{ONC(H)(C_4H_3S)\}\{ONC(H)(CH_2S)\}]^+$	258 (258.39)
	$[HSi\{ONC(H)(C_4H_3S)\}\{ONC(H)(C_2H)\}]^+$	223 (223.29)
	$[HSi\{ONC(C_3S)\}\{ONC(H)(C_2H)\}]^+$	207 (207.25)
	$[HSi\{ONC(H)(CS)\}\{ONC(H)(C_2H)\}]^+$	184 (184.24)
	$[HSi\{NC_3\}\{ONC(H)(C_2H)\}]^+$	147 (147.18)
	$[Si\{NC_2\}\{ONC(H)(C_2)\}]^+$	133 (133.16)
	$[Si\{N\}\{ONC(H)(C_2H)\}]^+$	110 (110.15)
	$[Si\{N\}\{NOC_2H\}]^+$	97 (97.13)

Table 4
Selected IR spectral data (in cm^{-1}) of dimethylsilicon(IV) complexes with internally functionalized oximes

Complexes	ν(C=N)	ν(Si–O)	ν(N–O)
$[Me_2Si\{ON{=}C(CH_3)C_5H_4N\text{-}2\}_2]$ (**1**)	1578 (s)	812 (vs)	930 (vs)
$[Me_2Si\{ON{=}C(CH_3)C_4H_3O\text{-}2\}_2]$ (**2**)	1566 (m)	833 (vs)	950 (vs)
$[Me_2Si\{ON{=}C(CH_3)C_4H_3S\text{-}2\}_2]$ (**3**)	1592 (w)	850 (vs)	945 (vs)
$[Me_2Si\{ON{=}C(H)C_5H_4N\text{-}2\}_2]$ (**4**)	1580 (s)	841 (vs)	963 (vs)
$[Me_2Si\{ON{=}C(H)C_4H_3O\text{-}2\}_2]$ (**5**)	1607 (s)	823 (vs)	962 (vs)
$[Me_2Si\{ON{=}C(H)C_4H_3S\text{-}2\}_2]$ (**6**)	1613 (s)	805 (vs)	985 (vs)

The data were collected on a Bruker APEX CCD diffractometer using a graphite monochromator with Mo Kα radiation ($\lambda = 0.71073$ Å). A hemisphere of data was collected using a counting time of 20 s per frame. The data were collected at −100 °C. Details of crystal data, data collection and structure refinement are listed in Table 2. Data reduction were performed using the SAINT software [13] and the data were corrected for Lorentz, polarization and absorption effects using the SAINT and SADABS programs [14]. The structure was solved by direct methods using SIR 92 [15] and was refined using the WINGX version [16] of SHELX-97 [17]. All of the non-hydrogen atoms were treated anisotropically. Hydrogen atoms were located in the difference map and refined isotropically. The final cycle of full-matrix least squares refinement was based on 1654 observed reflections (1415 for $F^2 > 4\sigma(F^2)$) and 115 variable

Table 5
^1H, $^{13}C\{^1H\}$ and $^{29}Si\{^1H\}$ NMR data (in δ ppm) for dimethylsilicon(IV) complexes with internally functionalized oximes

Complexes	^1H NMR	$^{13}C\{^1H\}$ NMR	$^{29}Si\{^1H\}$ NMR
$[Me_2Si\{ON{=}C(CH_3)C_5H_4N\text{-}2\}_2]$ (**1**)	0.53 (s, 6H, Si–Me_2); 2.42 (s, 6H, oxime-Me); 7.24 (m, 2H, H-4), 7.63 (m, 2H, H-5); 7.97 (d, 2H, $J = 8.0$ Hz, H-3); 8.60 (d, 2H, $J = 4.8$ Hz, H-6)	−3.1 (Si–Me_2); 11.3 (oxime-Me); 120.9 (C-5); 123.7 (C-3); 136.1 (C-4); 148.6 (C-6); 154.4 (C-2); 161.4 (C=N)	13.3
$[Me_2Si\{ON{=}C(CH_3)C_4H_3O\text{-}2\}_2]$ (**2**)	0.42 (s, 6H, Si–Me_2); 2.16 (s, 6H, oxime-Me); 6.36 (m, 2H, H-4); 6.61 (d, 2H, $J = 3.8$ Hz, H-3); 7.39 (d, 2H, $J = 1.8$ Hz, H-5)	−3.7 (Si–Me_2); 11.1 (oxime-Me); 110.1 (C-4); 111.2 (C-3); 143.7 (C-5); 147.5 (C-2); 150.1 (C=N)	13.1
$[Me_2Si\{ON{=}C(CH_3)C_4H_3S\text{-}2\}_2]$ (**3**)	0.45 (s, 6H, Si–Me_2); 2.21 (s, 6H, oxime-Me); 6.90 (m, 2H, H-4); 7.13 (d, 2H, $J = 3.5$ Hz, H-3); 7.16 (d, 2H, $J = 4.6$ Hz, H-5)	−3.3 (Si–Me_2); 12.9 (oxime-Me); 126.3 (C-4); 126.7 (C-3); 127.1 (C-5); 140.3 (C-2); 151.7 (C=N)	13.1
$[Me_2Si\{ON{=}C(H)C_5H_4N\text{-}2\}_2]$ (**4**)	0.46 (s, 6H, Si–Me_2); 7.24 (m, 2H, H-4); 7.67 (m, 2H, H-5); 7.88 (d, 2H, $J = 8.1$ Hz, H-3); 8.34 (s, 2H, CH); 8.55 (d, 2H, $J = 4.9$ Hz, H-6)	−3.4 (Si–Me_2); 120.0 (C-5); 124.3 (C-3); 136.5 (C-4); 149.4 (C-6); 151.6 (C-2); 155.6 (C=N)	15.4
$[Me_2Si\{ON{=}C(H)C_4H_3O\text{-}2\}_2]$ (**5**)	0.46 (s, 6H, Si–Me_2); 6.45 (m, 2H, H-4); 7.31 (d, 2H, $J = 3.5$ Hz, H-3); 7.39 (d, 2H, $J = 1.4$ Hz, H-5); 7.63 (s, 2H, CH)	−3.7 (Si–Me_2); 112.2 (C-4); 118.5 (C-3); 143.3 (C-5); 145.2 (C-2); 158.0 (C=N)	14.9
$[Me_2Si\{ON{=}C(H)C_4H_3S\text{-}2\}_2]$ (**6**)	0.52 (s, 6H, Si–Me_2); 6.97 (m, 2H, H-4); 7.28 (d, 2H, $J = 3.8$ Hz, H-3); 7.44 (d, 2H, $J = 5.1$ Hz, H-5); 7.84 (s, 2H, CH)	−3.5 (Si–Me_2); 125.8 (C-4); 131.5 (C-3); 131.9 (C-5); 140.0(C-2); 149.1 (C=N)	14.0

parameters and converged (largest parameter shift was 0.001 times its esd).

2.3. Hydrolytic studies: preparation of mesoporous materials 7 and 8 by the hydrolysis of a mixture of $[Me_2Si\{ON{=}C(CH_3)C_4H_3O\text{-}2\}_2]$ and $Al(OPr^i)_3$ in a 1:2 molar ratio and of pure $Al(OPr^i)_3$ by the sol–gel technique

$[Me_2Si\{ON{=}C(CH_3)C_4H_3O\text{-}2\}_2]$ (1.08 g, 3.52 mmol) and $Al(OPr^i)_3$ (1.44 g, 7.05 mmol) were dissolved in toluene and refluxed for about 6 h. The clear solution was dried in vacuo to give a brownish viscous liquid [$^{29}Si\{^1H\}$ NMR in $CDCl_3$ {δ ppm}: 5.1 and −17.4]. This was re-dissolved in dry isopropanol. To this clear solution a drop of water was added and the mixture was stirred for 1 h. Gel formation occurred immediately. A few more drops of water were added and the mixture was stirred for about 24 h. The whole mixture was dried at 100 °C in a preheated oven, to give a brown powder, which was washed thoroughly with an acetone–hexane mixture. This powder was sintered at 900 °C for about 1 h to yield **7**.

Using a similar procedure on pure $Al(OPr^i)_3$ dissolved in dry isopropanol, sample **8** was obtained.

3. Results and discussion

3.1. Preparation

Metathetical reactions of Me_2SiCl_2 with internally functionalized oximes in a 1:2 stoichiometry in the presence of triethylamine afford compounds of the type $[Me_2Si\{ON{=}C(R)Ar\}_2]$ in quantitative yield as depicted below:

$$Me_2SiCl_2 + 2HON{=}C(R)Ar + 2Et_3N \xrightarrow{\text{benzene}} \underset{(\mathbf{1}-\mathbf{6})}{[Me_2Si\{ON{=}C(R)Ar\}_2]} + 2Et_3N.HCl\downarrow$$

where R = Me or H and Ar = 2-C_5H_4N, 2-C_4H_3O or 2-C_4H_3S.

With the exception of complex **1**, a pink liquid which slowly solidifies on standing, all other derivatives are brown yellow solids or liquids that are highly soluble in common organic solvents. Molecular weight measurements in freezing benzene, along with the FAB mass spectral studies of two of the derivatives **1** and **6**, indicate the monomeric nature of all these complexes (Table 3).

Elemental analysis correspond to the expected formulae (Table 1).

3.2. IR spectra

The IR spectra of all these derivatives were interpreted by comparison with the spectra of the free oximes and related derivatives [8i,10c]. Some important absorption bands are given in Table 4. The absence of vibrations attributable to the hydroxyl group of the oximes (in the region 3200–3400 cm^{-1}) in all these derivatives and the presence of a new strong intensity vibration in the region 805–850 cm^{-1} (assigned to νSi–O) indicate the deprotonation of the oxime and concomitant bond formation with silicon. Absorptions in the region 929–985 cm^{-1} and 710–750 cm^{-1} have been assigned to ν(N–O) and ν(Si–C), respectively. The ν(C=N) absorption appeared at slightly lower wave numbers (a shift of 14–38 cm^{-1}) in comparison to the free oximes.

Table 6
Selected bond lengths (Å) and angles (°) for $[Me_2Si\{O{=}NC(H)C_4H_3O\text{-}2\}_2]$ (**5**)[a]

Si(1)–O(1)	1.666(1)	Si(1)–O(1)=	1.666(1)
Si(1)–C(1)	1.834(2)	Si(1)–C(1)=	1.834(2)
O(1)–N(1)	1.420(2)	N(1)–C(2)	1.274(2)
C(2)–C(3)	1.437(2)	C(3)–O(2)	1.378(2)
O(2)–C(4)	1.361(2)	C(4)–C(5)	1.328(3)
C(5)–C(6)	1.414(2)	C(6)–C(3)	1.352(2)
Si(1)—N(1)	2.554(1)		
O(1)–Si(1)–O(1)=	108.80(9)	O(1)=Si(1)–O(1)	108.80(9)
O(1)–Si(1)–C(1)=	102.84(7)	O(1)=Si(1)–C(1)	102.84(7)
O(1)–Si(1)–C(1)	112.66(8)	O(1)=Si(1)–C(1)=	112.66(8)
C(1)–Si(1)–C(1)=	117.1(1)	C(1)=Si(1)–C(1)	117.1(1)
Si(1)–O(1)–N(1)	111.48(9)	O(1)–N(1)–C(2)	111.0(1)
N(1)–C(2)–C(3)	129.4(1)	C(2)–C(3)–O(2)	113.4(1)
C(3)–O(2)–C(4)	106.0(1)	O(2)–C(4)–C(5)	111.1(2)
C(4)–C(5)–C(6)	106.7(2)	C(5)–C(6)–C(3)	106.9(2)
C(6)–C(3)–O(2)	109.3(1)	C(6)–C(3)–C(2)	137.3(2)

[a] Symmetry equivalent position (−x, y, −z + 2) given by a prime.

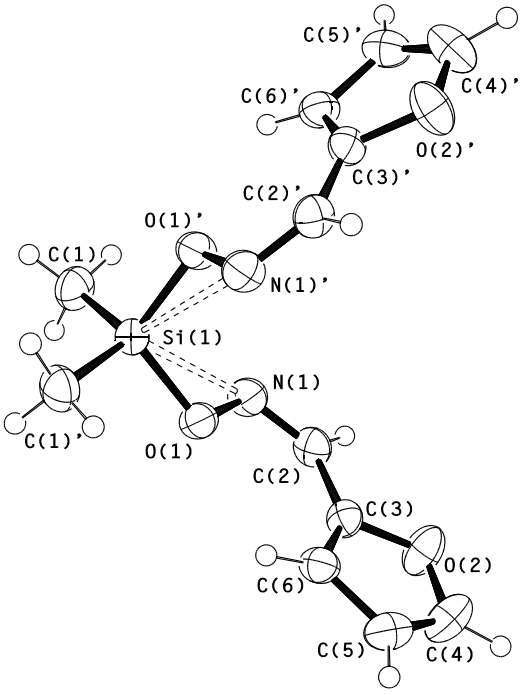


Fig. 1. ORTEP plot of $[Me_2Si\{ON{=}C(H)C_4H_3O\text{-}2\}_2]$. The non-hydrogen atoms are drawn with 50% probability ellipsoids.

3.3. NMR spectra

The ^{1}H and $^{13}C\{^{1}H\}$ NMR spectra of the complexes were interpreted by comparing them with those of the free oximes (Table 5) [10a,10c]. The hydroxyl proton resonances of the free oximes (δ 8.58–9.23 ppm) were absent in the ^{1}H NMR spectra of all these complexes indicating again the deprotonation of the oximes and their bond formation with silicon. There were no significant shifts in the hetero aryl ring proton/carbon resonances in the $^{1}H/^{13}C\{^{1}H\}$ NMR spectra, as is to be expected if the heteroatom of the ring is not taking part in coordination with the central silicon atom. The position of the C=N carbon resonance of the ligand moiety is almost unchanged in the $^{13}C\{^{1}H\}$ NMR spectra suggesting that the oximate moiety in these complexes in solution is probably monofunctional monodentate.

Only a single absorption signal is observed in the region δ 13.1–15.4 ppm in the $^{29}Si\{^{1}H\}$ NMR spectra of all these derivatives, which falls within the expected range for a tetra-coordinated dimethyl silicon atom [18].

3.4. X-ray diffraction analysis

The molecule $[Me_2Si\{ON{=}C(H)C_4H_3O\text{-}2\}_2]$ (**5**) crystallizes in the space group *C*2/*c*. Distances and bond angles are given in Table 6 and the molecule is displayed as an ORTEP diagram in Fig. 1. The immediate environment around silicon is distorted tetrahedral with the C(1)–Si(1)–C(1)′ angle of 117.1(1)° being considerably larger than that of O(1)–Si(1)–O(1)′ (108.80(9)°). Two of the O(1)–Si(1)–C(1) angles are considerably smaller (102.84(7)°) than the other two 112.66(8)°). This degree of distortion is relatively unusual for the Me_2SiO_2 moiety unless there are clear restraints.

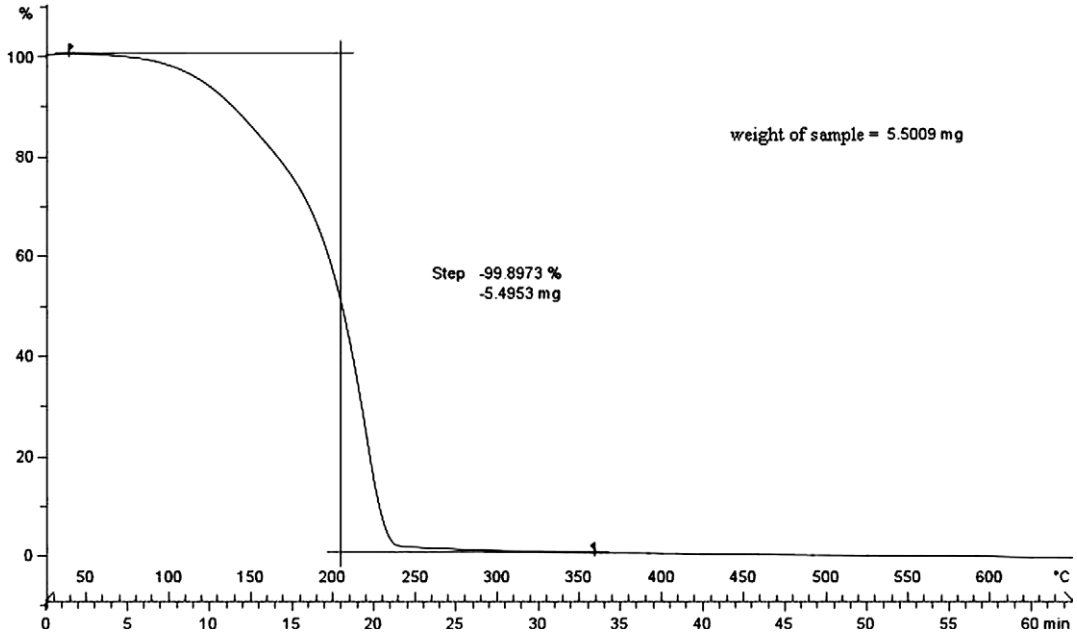


Fig. 2. TGA curve (weight % vs. temperature °C) of $[Me_2Si\{ON{=}C(H)C_4H_3O\text{-}2\}_2]$ (**5**).

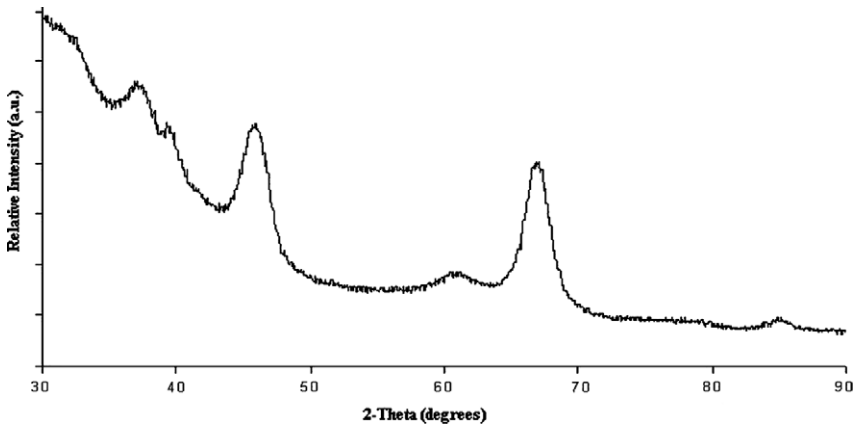


Fig. 3a. XRD of **8**.

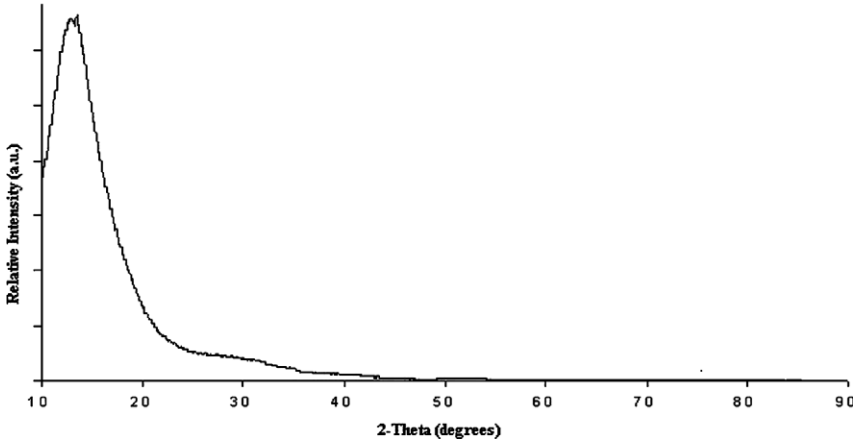


Fig. 3b. XRD of **7**.

The Si–O–N bond angle of 111.48(9)° and Si–N bond distance of 2.554(1) Å are of particular interest. It has been proposed that when the value of the Si–O–N bond angle is less than 116° it is reasonable to assume a degree of Si–N interaction in SiON compounds [8f]. Further, the bond distance of 2.554(1) Å is less than the sum of Bartell's one-angle radii of 2.69 Å for Si and N [8a]. Thus the description of this molecule as containing weak β-donor SiON bonds, resulting in (4 + 2) coordination [8g], is justified.

3.5. Thermogravimetric analysis

A thermogravimetric experiment was performed on complex **5** with the heating rate 25–650/10 °C. A great weight loss (~99.9%) step in the TGA curve (Fig. 2) reveals the thermal stability and volatility of the compound.

3.6. Crystallinity, surface area, pore volume and average pore size of mesoporous materials 7 and 8

The crystallinity of the materials was studied by X-ray diffraction, which exclusively showed the formation of γ-alumina for sample **8** (Fig. 3a). The XRD pattern of sample **7** indicated its amorphous nature (Fig. 3b). The nitrogen adsorption–desorption isotherms for samples **7** and **8** are shown in Fig. 4. The variations in specific surface area, total pore volume and average pore size samples are presented in Table 7. The isotherm of sample **8** shows a hysteresis loop, suggesting that the alumina under study is basically mesoporous with a pore size of 11.1 nm and a high surface area of 216.5 m^2/g. Similarly, sample **7** also has a relative high surface area of 192.3 m^2/g, but with a small pore volume of 0.13 cm^3/g. The TEM image of the mesoporous aluminum oxide is shown in Fig. 5. There is

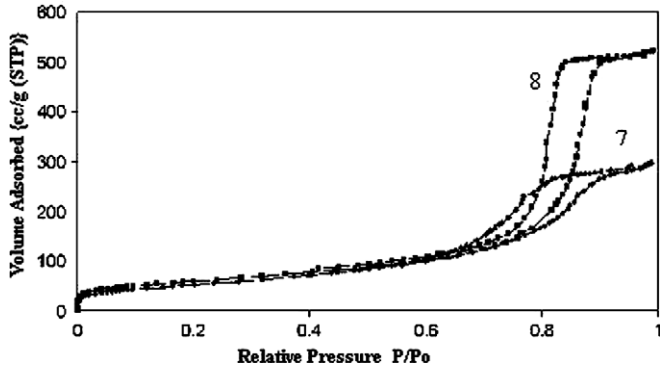


Fig. 4. Nitrogen adsorption–desorption isotherms of **7** and **8**.

Table 7
Properties of the studied samples **7** and **8**

Sample	Specific area BET (m^2/g)	Pore volume (cm^3/g)	Pore diameter (BJH) (nm)
7	192.3	0.13	8.5
8	216.5	0.63	11.1

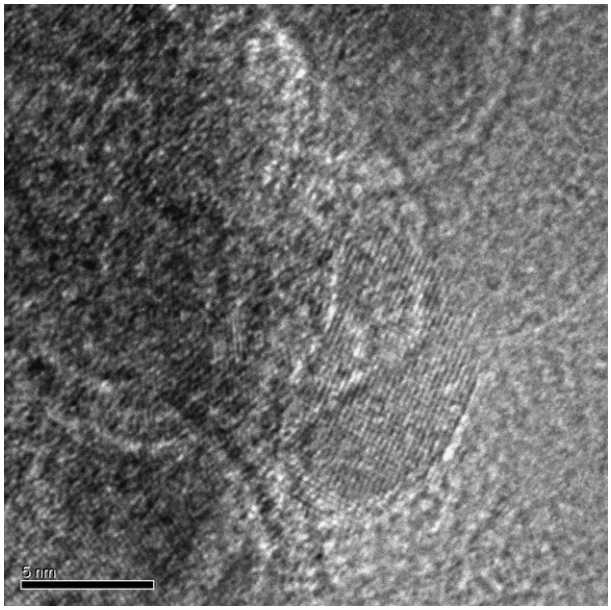


Fig. 5. A TEM image of **8**.

no long-range order in the pore structure. However, the pores are reasonably uniform in size.

4. Supplementary material

CCDC 625959 contains the supplementary crystallographic data for this paper. These data can be obtained free of charge via http://www.ccdc.cam.ac.uk/conts/retrieving.html, or from the Cambridge Crystallographic Data Centre, 12 Union Road, Cambridge CB2 1EZ, UK; fax: (+44) 1223-336-033; or e-mail: deposit@ccdc.cam.ac.uk.

Additional material comprises the final atomic coordinates for all the atoms, thermal parameters and a complete listing of bond distances and angles.

Acknowledgements

We are highly grateful to DST-, CSIR- and UGC-New Delhi for financial support. C.L.B.M. thanks the Natural Sciences and Engineering Research Council of Canada and J.E.D the University of Windsor for financial support. We are grateful to Prof. Paul O'Brien and Dr. M. Afzaal for carrying out Powder XRD, Nitrogen adsorption-desorption isotherms and TEM at the University of Manchester, Oxford.

References

[1] (a) B.J. Melde, B.T. Holland, C.F. Blanford, A. Stein, Chem. Mater. 11 (1999) 3302;
(b) J.R. Matos, M. Kruk, L.P. Mercuri, M. Jaroniec, T. Asefa, N. Coombs, G.A. Ozin, T. Kamiyama, O. Terasaki, Chem. Mater. 14 (2002) 1903;
(c) W. Wang, S. Xie, W. Zhou, A. Sayari, Chem. Mater. 16 (2004) 1756;
(d) R.M. Grudzien, B.E. Grabicka, S. Pikus, M. Jaroniec, Chem. Mater. 18 (2006) 1722;
(e) S.A. Alekseev, V.N. Zaitsev, Chem. Mater. 18 (2006) 1981.

[2] M.C. Burleigh, S. Dai, E.W. Hagaman, J.S. Lin, Chem. Mater. 13 (2001) 2537.

[3] G. Mohammad, D. Azadeh, H.-B. Leila, B. Alireza, S. Kamal, Z. Ghodsi, M. Abolghasem, Water Air Soil Pollut. 173 (2006) 71.

[4] (a) P.V.D. Voort, M. Baltes, E.F. Vansant, J. Phys. Chem. B. 103 (1999) 10102;
(b) A.P. Wight, M.E. Davis, Chem. Rev. 102 (2002) 3589.

[5] J.H. Zhu, S.-L. Zhou, Y. Xu, Y. Cao, Y.-L. Wei, Chem. Lett. 32 (2003) 338.

[6] M. Arruebo, M. Galán, N. Navascués, C. Téllez, C. Marquina, M.R. Ibarra, J. Santamaría, Chem. Mater. 18 (2006) 1911.

[7] R.G. Gordon, J. Becker, D. Hausmann, S. Suh, Chem. Mater. 13 (2001) 2463.

[8] (a) L.S. Bartell, J. Chem. Phys. 32 (1960) 827;
(b) N.W. Mitzel, A.J. Blake, D.W.H. Rankin, J. Am. Chem. Soc. 119 (1997) 4143;
(c) N.W. Mitzel, U. Losehand, J. Am. Chem. Soc. 120 (1998) 7320;
(d) U. Losehand, N.W. Mitzel, J. Chem. Soc., Dalton Trans. (1998) 2537;
(e) C. Yoshina-Ishii, T. Asefa, N. Coombs, M.J. MacLachlan, G.A. Ozin, Chem. Commun. (1999) 2539;
(f) N.W. Mitzel, U. Losehand, B. Bauer, Inorg. Chem. 39 (2000) 1998;
(g) U. Losehand, N.W. Mitzel, J. Chem. Soc., Dalton. Trans. (2000) 1049;
(h) S.-J. Kim, I.N. Jung, B.R. Yoo, S.H. Kim, J. Ko, D. Byun, S.O. Kang, Organometallics 20 (2001) 2136;
(i) M. Nath, S. Goyal, Phosphorous, Sulfur Silicon 177 (2002) 447;
(j) R. Pietschnig, K. Merz, Organometallics 23 (2004) 1373;
(k) N. Azizi, M.R. Saidi, Organometallics 23 (2004) 1457;
(l) Y. Xiao, D.Y. Son, Organometallics 23 (2004) 4438;
(m) R. Pietschnig, F. Belaj, J.J. Tirrée, Organometallics 23 (2004) 4897;
(n) M. Unno, Y. Kishimoto, H. Matsumoto, Organometallics 23 (2004) 6221.

[9] M.G. Voronkov, E.A. Maletina, V.K. Roman, Heterosiloxanes, Derivatives of Nitrogen and Phosphorous, vol. 2, Harwood Academic Publishers, Chur, 1991.

[10] (a) A. Gupta, R.K. Sharma, R. Bohra, V.K. Jain, J.E. Drake, M.B. Hursthouse, M.E. Light, Polyhedron 21 (2002) 2387;
(b) V. Sharma, R.K. Sharma, R. Bohra, V.K. Jain, J.E. Drake, M.B. Hursthouse, M.E. Light, J. Organomet. Chem. 66 (2002) 664;
(c) A. Gupta, R.K. Sharma, R. Bohra, V.K. Jain, J.E. Drake, M.B. Hursthouse, M.E. Light, J. Organomet. Chem. 667 (2003) 61;
(d) M. Pathak, R. Bohra, R.C. Mehrotra, I.P. Lorenz, H. Piotrowski, Z. Anorg. Allg. Chem. 14 (2003) 2493;
(e) N. Sharma, A.K. Jain, R.K. Sharma, R. Bohra, J.E. Drake, M.B. Hursthouse, M.E. Light, Polyhedron 22 (2003) 2943;
(f) V. Sharma, S. Agrawal, R. Bohra, V.K. Jain, J. Chem. Res. (2004) 1273;
(g) V. Sharma, S. Agrawal, R. Bohra, R. Ratnani, J.E. Drake, M.B. Hursthouse, M.E. Light, Inorg. Chim. Acta 359 (2006) 1404;
(h) S. Agrawal, V. Sharma, R. Bohra, J. Chem. Res. 426 (2006);
(i) Vineet Sharma, Vinita Sharma, R. Bohra, J.E. Drake, M.B. Hursthouse, M.E. Light, A.L. Bingham, Trans. Met. Chem. (in press).

[11] A.I. Vogel, Text Book of Quantitative Inorganic Analysis, 5th ed., 1989.

[12] (a) W. Huckel, M. Sachs, Ann. Chem. 498 (1932) 176;
(b) F. Nerdel, I. Huldschinsky, Chem. Ber. 86 (1953) 1005;
(c) R.C. Mehrotra, A.K. Rai, A. Singh, R. Bohra, Inorg. Chim. Acta. 13 (1975) 91.

[13] SAINT, Bruker AXS, Inc. Madison, WI, 2001.

[14] G.M. Sheldrick, SADABS V 2.10, 2003.

[15] A. Altomare, G. Cascarano, C. Giacovazzo, A. Gualardi, J. Appl. Cryst. 26 (1993) 343.

[16] L.J. Farrugia, J. Appl. Cryst. 32 (1999) 837.

[17] G.M. Sheldrick, SHELXL 97, University of Gottingen, Germany, 1997.

[18] (a) G. Tsantes, N. Auner, T. Müller, in: N. Auner, J. Weis (Eds.), Organosilicon Chemistry V, VCH, Weinheim, 2003, p. 334;
(b) M. Veith, J. Frères, V. Huch, M. Zimmer, Organometallics (2006) 1875.

Available online at www.sciencedirect.com
ScienceDirect
Polyhedron 26 (2007) 3175–3181
POLYHEDRON
www.elsevier.com/locate/poly

Magnetic interactions in a series of paramagnetic Ln(III) complexes with a chelated imino nitroxide radical

Toshiaki Tsukuda *, Takayoshi Suzuki, Sumio Kaizaki

Department of Chemistry, Graduate School of Science, Osaka University, Toyonaka 560-0043, Japan

Received 29 November 2006; accepted 17 February 2007
Available online 1 March 2007

Abstract

The magnetic interactions in a new series of isostructural imino nitroxide radical lanthanide(III) complexes, $[Ln(hfac)_3(IM2py)]$ (Ln = Gd–Yb: IM2py = 2-(2′-pyridyl)-4,5-dihydro-4,4,5,5-tetramethyl-1H-imidazoline-1-oxy; hfac = 1,1,1,5,5,5-hexafluoro-2,4-pentanedione), are examined by considering the intrinsic paramagnetic contribution of the Ln(III) ion from the corresponding $[Ln(hfac)_3(pybzim)]$ with a diamagnetic pybzim(2-(2-pyridyl)benzimidazole) ligand; the Ln(III)–IM2py interaction being antiferromagnetic for the $4f^7$ to $4f^{13}$ Ln(III) complexes and negligibly small for the other complexes. This series is the first example reverse to the previous cases for the series of Ln–Cu or Ln–aminoxyl(NIT) radical (4,5-dihydro-4,4,5,5-tetramethyl-1H-imidazoline-3-oxide-1-oxy) complexes, other than only a few examples of semiquinone Ln complexes. This reverse nature of the magnetic interaction, as compared with the NIT complexes, validates the empirical approach by O. Kahn et al. [Inorg. Chem. 38 (1999) 3692; J. Am. Chem. Soc. 122 (2000) 3413] in the spin-coupled systems for a series of Ln(III) complexes.
© 2007 Elsevier Ltd. All rights reserved.

Keywords: Imino nitroxide radical; Lanthanide complexes; Magnetic properties

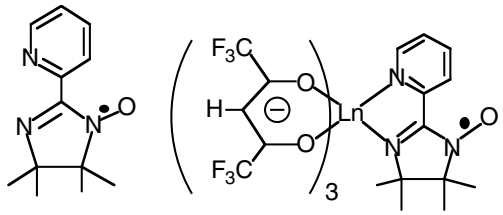
1. Introduction

Following a number of previous investigations of nitroxide radical complexes, aiming to construct molecular-based magnetic materials in terms of the so-called radical approach [1], we have recently studied the magneto-optical properties for lanthanide complexes with an imino nitroxide radical (IM2py = 2-(2′-pyridyl)-4,5-dihydro-4,4,5,5-tetramethyl-1H-imidazoline-1-oxy; Chart 1, left), $[Ln(hfac)_3(IM2py)]$ (Chart 1, right) [2], as well as those for transition metal complexes with nitronyl and imino nitroxide radical(s), in order to reveal the rational relationship of the optical properties with the magnetic interaction [3–6]. In our case [2a], the Gd(III) IM2py complex was found to give an antiferromagnetic interaction. This is one of a few recently described exceptions [7–9] for an antiferromagnetic interaction in nitronyl nitroxide radical (NIT2py = 2-(2′-pyridyl)-4,5-dihydro-4, 4,5,5-tetramethyl-1H -imidazoline-3-oxide-1-oxy) Gd(III) complexes, in contrast to the claim that the intramolecular Gd(III)–radical magnetic interaction was intrinsically ferromagnetic [10].

As for the nature of the magnetic interactions in Ln–radical complexes, except the isotropic Gd(III) complexes, there is little information partly, owing to the orbital contribution arising from the ground state splitting into Stark sublevels from the $^{2S+1}L_J$ spectroscopic energy terms due to the crystal field perturbation, or the violation of the Curie law corresponding to a depopulation of the sublevels. In order to overcome this difficulty for the Ln(III) ions, Kahn et al. have proposed an empirical approach to obtain greater insight into the nature of the magnetic interactions, where conclusive information on the ferro- or antiferromagnetic nature of the Ln–radical or Ln–Cu(II) interaction in the Ln–radical [10] or Ln–Cu(II) complexes [11] was given by comparing the magnetic characteristics with those of the corresponding Ln–non-radical or

* Corresponding author. Tel.: +81 422373759; fax: +81 422373871.
E-mail address: tsukuda@st.seikei.ac.jp (T. Tsukuda).

0277-5387/$ - see front matter © 2007 Elsevier Ltd. All rights reserved.
doi:10.1016/j.poly.2007.02.024



IM2py **[Ln(hfac)$_3$(IM2py)]**

Chart 1. IM2py and the lanthanide-radical complex, [Ln(hfac)$_3$(IM2py)].

Ln–Zn(II) complexes through isostructurality in a series of lanthanide complexes. This approach has been applied to another type of Ln–Cu(II) or Ni(II) [12] and Ln–Fe(III) complexes [13]. Recently, this was analytically confirmed for Dy and Ho NIT radical complexes by qualitative and quantitative approaches [14]. For the Kahn's case, however, there are intraligand magnetic interactions between two nitronyl nitroxide radical ligands in addition to the two intramolecular magnetic interactions between Ln and the nitronyl nitroxide in the Ln complexes. Moreover, the validity of this approach could be confirmed by applying it to the opposite antiferromagnetic case for the Gd complexes. A few years ago, semiquinone Gd(III) complexes were found to display antiferromagnetic interactions [15–17] and the Kahn's approach was testified [16]. One of the appropriate candidates for the nitroxide complexes could be our recently synthesized mono(IM2py)Gd complex, in which the magnetic interaction is antiferromagnetic, showing a reverse case to the nitronyl nitroxide radical Gd complexes [2a]. The magnetic study for a series of lanthanide imino nitroxide radical complexes other than the Gd complex is expected to gain more unambiguous information concerning the magnetic interaction in comparison with the semiquinone radical complexes [16]. Recently, these aspects concerning lanthanide ions in molecular exchange coupled systems were reviewed [17].

In this paper, the nature of the magnetic interaction in Ln–imino nitroxide radical complexes from Nd to Yb are examined by comparing the magnetic character of the Ln–radical complexes, [Ln(hfac)$_3$(IM2py)] with the corresponding Ln–non-radical 2-(2-pyridyl)benzimidazole(pybzim) complexes, [Ln(hfac)$_3$(pybzim)].

2. Experimental

2.1. Synthesis

The [Ln(hfac)$_3$(IM2py)] (Ln = Nd–Lu) complexes were obtained according to the procedures described [2a]. 2-(2-Pyridyl)benzimidazole(pybzim), which was purchased from Aldrich, was reagent grade and used without purification. [Ln(hfac)$_3$(pybzim)] complexes were prepared by a similar procedure with use of pybzim instead of IM2py. These complexes gave satisfactory elemental analyses (Table 1).

Table 1
Elemental analysis for [Ln(hfac)$_3$(pybzim)]

Ln	C%	H%	N%
	Found (calc.)	Found (calc.)	Found (calc.)
Nd	33.48 (33.76)	1.10 (1.26)	4.39 (4.37)
Sm	33.52 (33.54)	1.01 (1.25)	4.38 (4.35)
Eu	33.23 (33.49)	0.96 (1.25)	4.28 (4.34)
Gd	33.06 (33.31)	0.99 (1.24)	4.41 (4.32)
Tb	33.25 (33.25)	0.92 (1.24)	4.28 (4.31)
Dy	33.46 (33.13)	1.08 (1.24)	4.58 (4.29)
Ho	33.06 (33.05)	0.89 (1.23)	4.29 (4.28)
Er	32.77 (32.97)	0.96 (1.23)	4.61 (4.27)
Tm	33.13 (32.91)	0.83 (1.23)	4.69 (4.26)
Yb	32.59 (32.78)	1.02 (1.22)	3.98 (4.25)

Magnetic susceptibility data were collected at 2000 Oe between 2 and 300 K using a SQUID susceptometer (MPMS-5S, Quantum Design). Pascal's constants were used to determine the constituent atoms diamagnetism.

2.2. X-ray structural analysis

Colorless crystals of [Gd(hfac)$_3$(pybzim)] suitable for X-ray crystal analyses were obtained by slowly evaporating a solution of the complex in a mixture of dichloromethane and *n*-heptane. A crystal was mounted on a glass fibre. The X-ray intensities were measured at 23 °C with graphite-monochromated Mo Kα radiation ($\lambda = 0.71073$ Å) on a Rigaku AFC-5R or four-circle diffractometer using the ω–2θ scan technique. Final lattice constants were determined by least-squares refinements of the orientation angles of 25 centered reflections in the range $25° < 2\theta < 30°$. Three standard reflections were monitored every 150 reflections and showed no serious decomposition. ($|F_0|/(|F_0|)_{initial} > 99\%$). The intensities collected for $(-h, +k, \pm l)$ octants at $2\theta \leqslant 60°$ were corrected for Lorentz-polarization effects, and absorption corrections were made by the Gauss numerical integration method [18]. The structure could be solved reasonably by using the direct method (SHELXS-97 [19a]) and refined by the SHELXL-97 program [19b]. The positions of hydrogen atoms were fixed at calculated positions and only their isotropic displacement parameters were refined. All calculations were carried out by Crystal Structure software [20].

3. Results and discussion

3.1. Crystallographic studies of the non-radical complex [Gd(hfac)$_3$(pybzim)]

[Gd(hfac)$_3$(pybzim)] forms colorless crystals with the space group $P2_1/n$ by recrystallization from dichloromethane–*n*-heptane solution. The molecular structure of [Gd(hfac)$_3$(pybzim)] is illustrated in Fig. 1 and the crystallographic data are shown in Table 2. The Gd atom of [Gd(hfac)$_3$(pybzim)] is eight-coordinated with three didentate hfac ligands and one didentate pybzim ligand. Selected

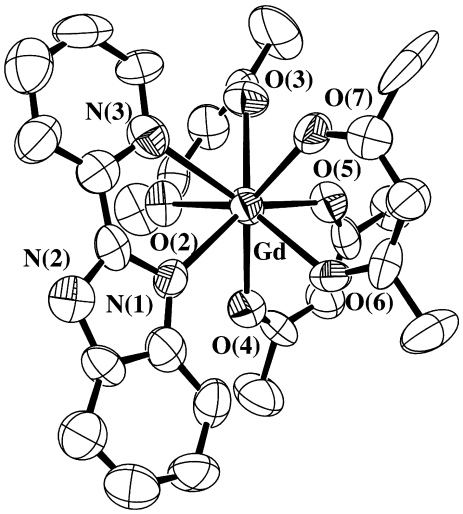


Fig. 1. Molecular structure of [Gd(hfac)$_3$(pybzim)] (F atoms are omitted).

Table 2
Crystallographic data for [Gd(hfac)$_3$(pybzim)]

	[Gd(hfac)$_3$(pybzim)]
Formula	$C_{27}H_{12}O_6N_3F_{18}Gd$
Formula weight	973.72
Crystal system	monoclinic
Space group	$P2_1/n$
a (Å)	14.192 (3)
b (Å)	13.220 (4)
c (Å)	19.188 (4)
β (°)	108.93 (2)
V (Å^3)	3405 (3)
Z	4
D_{calc} (g cm^{-3})	1.706
μ (Mo Kα) (cm^{-1})	17.54
R_1	0.064
wR_2	0.157

bond lengths and angles of [Gd(hfac)$_3$(pybzim)] are summarized in Table 3. The range of the Gd–O bond lengths, from 2.335 to 2.430 Å, is close to that (2.315–2.420 Å) for [Gd(hfac)$_3$(IM2py)] [2a]. The average bond length (2.547 Å) of Gd–N is similar to that (2.550 Å) of [Gd(hfac)$_3$-(IM2py)] [2a]. The interplane distance between the pybzim planes in the adjacent molecules is ca. 3.60 Å, indicating negligibly small intermolecular interactions.

An examination by the semi-quantitative method of polytopal analysis [21] suggests that the N_2O_6 eight coordinate geometry around the Gd atom in [Gd(hfac)$_3$(pybzim)] is intermediate between a square antiprism and a square-bicapped trigonal prism, being isostructural to [Gd(hfac)$_3$-(IM2py)].

In view of the similarity in geometrical structure between [Ln(hfac)$_3$(IM2py)] and [Ln(hfac)$_3$(pybzim)], the crystal field effects of these complexes are similar to each other.

Table 3
Selected bond distances (Å), bond angles (°) of [Gd(hfac)$_3$(pybzim)]

Bond lengths			
Gd–O(2)	2.430 (7)	Gd–O(3)	2.402 (7)
Gd–O(4)	2.382 (7)	Gd–O(5)	2.338 (7)
Gd–O(6)	2.346 (7)	Gd–O(7)	2.335 (7)
Gd–N(1)	2.474 (8)	Gd–N(3)	2.619 (9)
Bond angles			
O(2)–Gd–O(3)	70.5 (3)	O(2)–Gd–O(4)	71.3 (2)
O(2)–Gd–O(5)	90.1 (2)	O(2)–Gd–O(6)	144.6 (2)
O(2)–Gd–O(7)	142.6 (2)	O(2)–Gd–N(1)	91.5 (2)
O(2)–Gd–N(3)	80.7 (2)	O(3)–Gd–O(4)	125.7 (3)
O(3)–Gd–O(5)	70.6 (3)	O(3)–Gd–O(6)	135.9 (3)
O(3)–Gd–O(7)	74.8 (3)	O(3)–Gd–N(1)	139.4 (3)
O(3)–Gd–N(3)	76.0 (3)	O(4)–Gd–O(5)	72.4 (2)
O(4)–Gd–O(6)	73.4 (3)	O(4)–Gd–O(7)	143.7 (3)
O(4)–Gd–N(1)	77.8 (3)	O(4)–Gd–N(3)	132.4 (3)
O(5)–Gd–O(6)	81.4 (3)	O(5)–Gd–O(7)	91.2 (2)
O(5)–Gd–N(1)	147.9 (3)	O(5)–Gd–N(3)	146.5 (3)
O(6)–Gd–O(7)	72.3 (2)	O(6)–Gd–N(1)	78.8 (3)
O(6)–Gd–N(3)	123.4 (3)	O(7)–Gd–N(1)	106.4 (3)
O(7)–Gd–N(3)	77.9 (3)	N(1)–Gd–N(3)	65.0 (3)
Torsion angles			
N(1)–C(1)–C(2)–N(3)	1.6 (14)		

3.2. Magnetic properties

In order to manifest the unambiguous interaction, the contribution to $\chi_M{}^{Ln}T$(IM2py) for the Ln–IM2py complexes due to the thermally depopulated Stark sublevels of Ln(III) is deducted from $\chi_M{}^{Ln}T$(pybzim) for the Ln–pybzim complexes. The temperature dependence in direct conjunction with the local contribution of the crystal field in the Ln(III) ion can be given by the isostructural Ln(III) complexes with analogous diamagnetic ligands. The requirement for this approach is that there is the same crystal field in the non-radical complex as that in the radical complex. This may be fulfilled in view of the similar coordination geometry around the metal ion between the diamagnetic pybzim complexes and the radical IM2py ones.

Taking into consideration the isostructurality of the coordination geometry of [Ln(hfac)$_3$(IM2py)] for Sm, Gd, Dy, Er and Yb, as previously reported [2a], it is plausible that the corresponding Nd and Tb complexes may have the same crystal structure. Thus, the present series of Ln(III) complexes gives only the intramolecular magnetic interaction.

3.2.1. Gd ($4f^7$) compounds

According to the temperature dependence of the magnetic susceptibilities for [Gd(hfac)$_3$(IM2py)] [2a], the magnetic interaction between the Gd(III) ion and the IM2py radical is found to be antiferromagnetic ($J = -3.00$ cm^{-1}). This is confirmed for the analogous IMBzImH(2,3-bis(hydroxylamino)-2,3-dimethyl-butane-2-(2-benzyimdazolyl)-4,4,5,5-tetramethylimidazoline-1-oxide) complex, as well as the IM2py complex by Lescop et al. [9b].

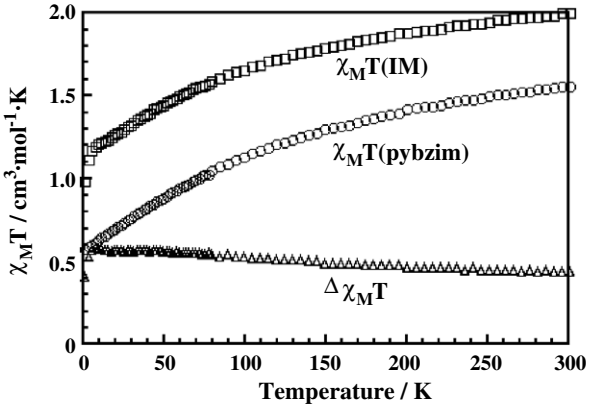


Fig. 2. Temperature dependence of $\chi_M T$(IM) (□), $\chi_M T$(pybzim) (○) and $\Delta\chi_M T$ (△) for Nd(III) complexes.

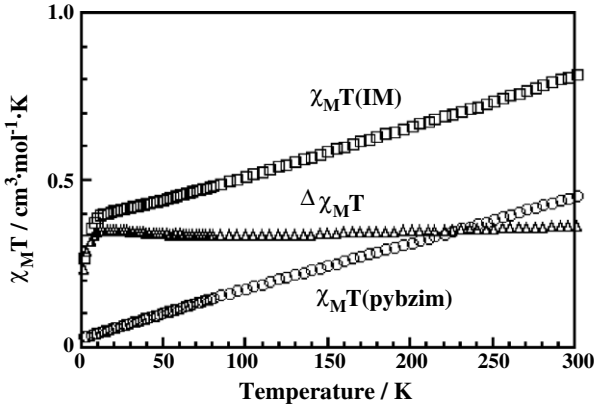


Fig. 3. Temperature dependence of $\chi_M T$(IM) (□), $\chi_M T$(pybzim) (○) and $\Delta\chi_M T$ (△) for Sm(III) complexes.

3.2.2. Nd ($4f^4$) and Sm ($4f^5$) compounds

The temperature dependence of the magnetic susceptibility of [Nd(hfac)$_3$(IM2py)] is shown as a product of the magnetic susceptibility and temperature, ${\chi_M}^{Nd}T$, versus the temperature T plot in Fig. 2. At 300 K, ${\chi_M}^{Nd}T$(IM) is equal to 2.00 cm^3 K mol^{-1}, close to the sum of the calculated values for the uncorrelated $\chi_M T$ of the Nd(III) ion and IM2py. On the other hand, the ${\chi_M}^{Nd}T$(pybzim) versus T plots of [Nd(hfac)$_3$(pybzim)] does not follow the Curie law (Fig. 2). Similarly as for the IM2py complex, the ${\chi_M}^{Nd}T$(pybzim) value decreases on lowering the temperature. Since the first $^4I_{11/2}$ excited state of the free Nd(III) ion is located at ca. 2000 cm^{-1} above the ground $^4I_{9/2}$ state, the excited $^4I_{11/2}$ state is expected to be completely depopulated at room temperature. The deviation of the magnetic behavior with respect to the Curie law results from the crystal field by which the $^4I_{9/2}$ free-ion ground state is split into five Kramers doublets (Stark sublevels). The Kramers doublets are almost equally populated at 300 K, but on lowering the temperature they are progressively depopulated until the lowest Kramers doublet is completely populated. This results in the decreases in $\chi_M T$. At 300 K, the difference value ($\Delta{\chi_M}^{Nd}T = {\chi_M}^{Nd}T$(IM) − ${\chi_M}^{Nd}T$(pybzim)) is 0.44 cm^3 K mol^{-1}, close to the expected value for an uncorrelated $S = 1/2$ spin for IM2py, as shown in Fig. 2. The $\Delta{\chi_M}^{Nd}T$ values gradually increase on lowering the temperature to 10 K. However, the variation of $\Delta{\chi_M}^{Nd}T$ values is too small to yield a conclusive result. Since our recent low temperature magnetic circular dichroism measurement of the 4f–4f transition at 4 K demonstrates little difference in the pattern between [Nd(hfac)$_3$(IM2py)] and [Nd(hfac)$_3$(bpy)](non-radical ligand bpy = 2,2′-bipyridine) [22], the small variation may be responsible for the difference of the ground state splitting by the crystal field between [Nd(hfac)$_3$(IM2py)] and [Nd(hfac)$_3$(pybzim)], but not for the small ferromagnetic interaction between the Nd(III) and IM2py radical ligand.

The situation for the Sm complex is more complex than that for the Nd complex, though their magnetic behavior is similar to each other. The temperature dependences of ${\chi_M}^{Sm}T$(IM), ${\chi_M}^{Sm}T$(pybzim) and $\Delta{\chi_M}^{Sm}T$ are shown in Fig. 3. Since the spin–orbit coupling parameter in the Sm(III) ion is of the order of 200 cm^{-1}, the first excited state $^6H_{7/2}$ can be populated at room temperature. Thus in the lower temperature range, the decrease of the $\chi_M T$ value results from both the multiplet splitting and Stark splitting. At 300 K, the ${\chi_M}^{Sm}T$(IM) and ${\chi_M}^{Sm}T$(pybzim) values are 0.82 and 0.45 cm^3 K mol^{-1}, respectively. These values are slightly larger than the expected values of ${\chi_M}^{Sm}T$(IM) and ${\chi_M}^{Sm}T$(pybzim). This deviation from the theoretical values may be responsible for the crystal field effect. The difference value $\Delta{\chi_M}^{Sm}T$ (0.37 cm^3 K mol^{-1}) is close to the expected value for an uncorrelated $S = 1/2$ spin for IM2py at 300 K, and is almost constant above 100 K. The profile with a gradual increase of $\Delta{\chi_M}^{Sm}T$ below 100 K results from the ground state splitting by the crystal field, but not necessarily from the ferromagnetic interaction.

3.2.3. Tb ($4f^8$) to Yb ($4f^{13}$) complexes

$\chi_M T$(IM) for a series of [Ln(hfac)$_3$(IM2py)] complexes (Ln = Tb–Yb) (Fig. S1) decreases on lowering the temperature. For the Yb complex, ${\chi_M}^{Yb}T$ (IM) (2.71 cm^3 K mol^{-1}) at 300 K is close to the sum of the expected $\chi_M T$ values for uncorrelated Yb(III) and IM2py spin, and decreases to attain 2.50 cm^3 K mol^{-1} at 2 K. The ${\chi_M}^{Yb}T$(pybzim) value for the pybzim complex also decreases on lowering the temperature (Fig. 4). Though the first excited $^2F_{5/2}$ state of Yb(III) ion can be fully depopulated, the contribution arising from the thermal depopulation of the Stark sublevels is relatively large. However, the decreasing slope of ${\chi_M}^{Yb}T$ (pybzim) is more gradual than that of [Yb(hfac)$_3$(IM2py)], and ${\chi_M}^{Yb}T$ (pybzim) is 1.41 cm^3 K mol^{-1} at 2 K, which is larger than ${\chi_M}^{Yb}T$ (IM). The difference value $\Delta{\chi_M}^{Yb}T$ gradually decreases on lowering the temperature. The profile of $\Delta{\chi_M}^{Yb}T$ also shows different behavior from that of the Nd(III) or Sm(III) complexes (Fig. 4). The variation of $\Delta{\chi_M}^{Yb}T$ is relatively large compared with that of the Nd

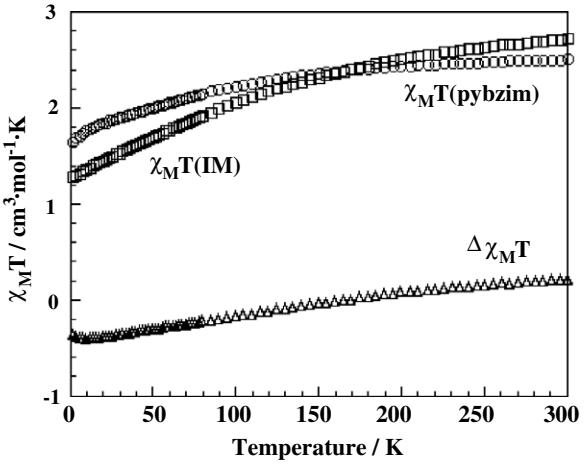


Fig. 4. Temperature dependence of χ_MT(IM) (□), χ_MT(pybzim) (○) and $\Delta\chi_M$T (△) for Yb(III) complexes.

or Sm complexes. Therefore, it is likely that the interaction between the Yb(III) ion and IM2py is antiferromagnetic.

The Tb(III) complexes give more remarkable behavior (Fig. 5). The $\chi_M{}^{Tb}T$(pybzim) value is 11.6 cm^3 K mol^{-1} at 300 K, which is close to the theoretical value of the Tb(III) free ion. At lower temperatures, the values gradually increase to attain 11.8 cm^3 K mol^{-1} at around 50 K. The larger $\chi_M{}^{Tb}T$(pybzim) value at lower temperature is attributed to the contribution of the thermal population in the ground $^7F_6$ state for Tb(III) in contrast to Eu(III) with the non-magnetic $^7F_0$ state (vide infra). On the other hand, the $\chi_M{}^{Tb}T$ (IM2py) value is 12.6 cm^3 K mol^{-1} at 300 K and then the gradual decreases are observed as the temperature is lowered. The temperature dependent $\Delta\chi_M{}^{Tb}T$ also tends to decrease at lower temperatures (Fig. 5). This apparently indicates that the magnetic interaction between the Tb(III) ion and IM2py is antiferromagnetic.

The Dy ($4f^9$), Ho ($4f^{10}$) and Er ($4f^{11}$) complexes exhibit higher $\chi_M{}^{Ln}T$ (pybzim) than $\chi_M{}^{Ln}T$ (IM2py) or a decrease of $\Delta\chi_M{}^{Ln}T$ (IM2py) at lower temperatures (Figs. S2–S4), but for the Tm complex, $\Delta\chi_M{}^{Tm}T$ (IM2py) increase on lowering the temperature (Fig. S5). Thus the magnetic interaction in the Ln–IM2py complexes with more than seven 4f electrons is antiferromagnetic, except for Tm whose magnetic properties could not be definitely determined.

3.2.4. Eu ($4f^6$) compound

As shown in Fig. 6, both $\chi_M{}^{Eu}T$(IM2py) and $\chi_M{}^{Eu}T$-(pybzim) decrease with a lowering of temperature, similar to the magnetic behaviors of the Tb–Yb complexes. The profile of $\Delta\chi_M{}^{Eu}T$ shows a decrease at lower temperatures, but the magnetic interaction between the Eu(III) ion and IM2py is not necessarily considered to be antiferromagnetic, as in the case of the other Ln–IM2py complexes, since the lowest level in the ground state of Eu(III) is non-magnetic ($^7F_0$). It is found that the $\chi_M{}^{Eu}T$(IM) value of [Eu(hfac)$_3$(IM2py)] is close to that of the isolated unpaired spin of IM2py at low temperature, as shown in Fig. 6. According to the theoretical model for the non-magnetic ground state, having no Stark sublevel in Eu(III) [23], the magnetic properties of [Eu(hfac)$_3$(IM2py)] can be estimated in terms of the temperature dependent magnetic behavior of [Eu(hfac)$_3$(pybzim)]. For the uncorrelated spin system of [Eu(hfac)$_3$(IM2py)], the $\chi_M{}^{Eu}T$(IM) value is expressed as $\chi_M{}^{Eu}T(\mathrm{IM}) = \chi_M{}^{Eu}T(\mathrm{pybzim}) + \chi_M T(\mathrm{IM2py})$. At 2 K, the observed $\chi_M T$ value is similar to the theoretical value of the $S = 1/2$ unpaired spin in IM2py. This confirms no intermolecular magnetic interaction as well as no intramolecular interaction in the Eu–IM2py complex. This is somewhat different from the magnetic behavior in [Eu(NO$_3$)$_3$(NITtrz)$_2$] at lower temperature, which is responsible for the intraligand (NIT–NIT) antiferromagnetic interaction [10a]. At higher temperatures, the $\chi_M{}^{Eu}T$ (IM) values are larger than the sum of the uncorrelated values for the system ($\chi_M{}^{Eu}T$(pybzim) + $\chi_M T$(IM2py)), or $\Delta\chi_M{}^{Eu}T$ increases with increasing temperature. This increase may be responsible for the difference in crystal

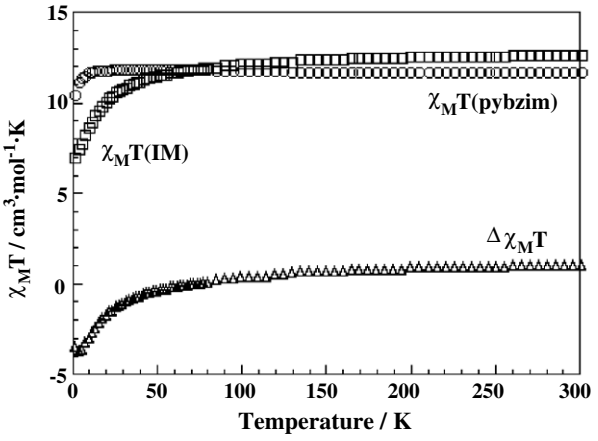


Fig. 5. Temperature dependence of χ_MT(IM) (□), χ_MT(pybzim) (○) and $\Delta\chi_M$T (△) for Tb(III) complexes.

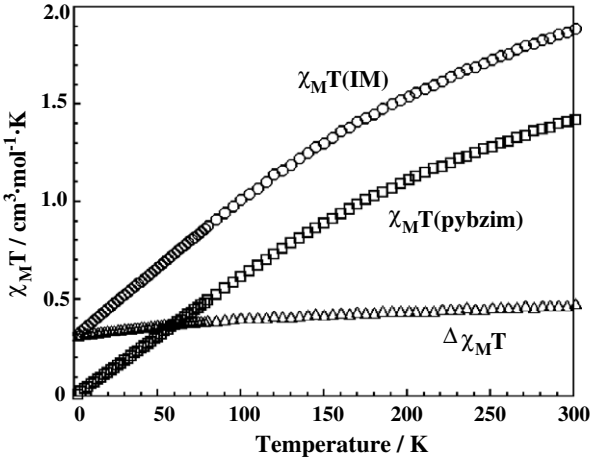


Fig. 6. Temperature dependence of χ_MT(IM) (□), χ_MT(pybzim) (○) and $\Delta\chi_M$T (△)for Eu(III) complexes.

Table 4
Nature of the magnetic interaction between Ln(III) ions and some radical ligands

Ln(III)	Nd	Sm	Eu	Gd	Tb	Dy	Ho	Er	Tm	Yb	Ref.
Aminoxyl	AF	AF	ND	F	F	F	F	ND	ND	ND	[10a]
Semiquinone	ND	ND	ND	AF	ND	ND	AF	ND	ND	F	[15c]
IM2py	ND	ND	ND	AF	AF	AF	AF	AF	ND	AF	this work

AF = antiferromagnetic; F = ferromagnetic; ND = not determined.

field between the IM2py and pybzim complexes, but not for the ferromagnetic interaction between an IM2py radical and the excited $^7F_1$ state in Eu which is populated at higher temperature at the expense of the depopulation of the non-magnetic ground $^7F_0$ state.

In summary, from the temperature dependence of $\Delta\chi_M{}^{Ln}T$ in a series of [Ln(hfac)$_3$(IM2py)] complexes, the Ln–IM2py interaction is antiferromagnetic for the Ln complexes with more than seven 4f electrons, from Tb to Yb, except Tm. This is exactly the reverse behavior to that found for the Ln–NIT complexes with more than seven 4f electrons [10] as summarized in Table 4. Thus, Kahn's approach is also applicable to the present Ln–IM2py complexes. However, for the Ln–IM2py complexes with less than seven 4f electrons (Ln = Nd, Sm and Eu), the magnetic interaction seems to be negligibly small as compared with the difference in crystal field between the pybzim and IM2py complexes.

4. Conclusion

The simpler two spin system of the mono(IM2py) Ln complexes rather than the three spin systems of the bis (NIT type) radical Ln complexes provides more reliable elucidation of the nature of the magnetic interaction in a series of paramagnetic Ln(III) complexes with a radical ligand, without involving interligand nitroxide radicals interactions which were estimated to be comparable to the intramolecular Ln–NIT interaction in the latter case [10a]. This is the first series for a reverse case to the nature of the magnetic interaction for the aminoxyl radical complexes with more than seven 4f electrons, whereas the semiquinone Ln complexes show only few examples for such a reverse case [15c], as shown in Table 4. It is noted that the chelate ring of IM2py in the IM2py complexes is planar, in common with that of the semiquinone ligands in the semiquinone Ln(III) complexes, and in contrast to the NIT2py complexes with non-planar rings. Such a difference in planarity of the chelate rings may result in the reverse magnetic behavior between the IM2py and NIT2py radical complexes, which were discussed for the IM2py and IM2imH Gd(III) complexes in relation to the orbital orthogonality between the 5d orbitals of Gd and SOMOπ^* orbital of the IM radical [2a,2c], in analogy to the case of IM2py and NIT2py Ni(II) complexes [4]. This notion may give some hint in revealing the nature of the magnetic interaction in radical lanthanide(III) complexes.

Appendix A. Supplementary material

CCDC 627506 contains the supplementary crystallographic data for [Gd(hfac)$_3$(pybzim)] in CIF format. These data can be obtained free of charge via http://www.ccdc.cam.ac.uk/conts/retrieving.html, or from the Cambridge Crystallographic Data Centre, 12 Union Road, Cambridge CB2 1EZ, UK; fax: (+44) 1223-336-033; or e-mail: deposit@ccdc.cam.ac.uk. The temperature dependence of the experimental χ_MT values of [Ln(hfac)$_3$(IM2py)] (Ln = Tb–Yb) (Fig. S1), χ_MT(IM), χ_MT(pybzim) and $\Delta\chi_M$T of Dy(III), Ho(III), Er(III) and Tm(III) complexes (Fig. S2-S5) are available free of charge via the Internet. Supplementary data associated with this article can be found, in the online version, at doi:10.1016/j.poly.2007.02.024.

References

[1] (a) J.S. Miller, A.J. Epstein, Angew. Chem. Int. Engl. 33 (1994) 385;
(b) J.S. Miller, Inorg. Chem. 19 (2000) 4392, and references therein;
(c) A. Caneschi, D. Gatteschi, R. Sessoli, P. Rey, Acc. Chem. Res. 22 (1989) 392;
(d) A. Caneschi, D. Gatteschi, P. Rey, Prog. Inorg. Chem. 39 (1991) 331, and references therein;
(e) K.E. Vostrikova, D. Luneau, W. Wernsdorfer, P. Rey, M. Verdaguer, J. Am. Chem. Soc. 122 (2000) 718.
[2] (a) T. Tsukuda, T. Suzuki, S. Kaizaki, J. Chem. Soc., Dalton Trans. (2002) 1721;
(b) T. Tsukuda, T. Suzuki, S. Kaizaki, Mol. Cryst. Liq. Cryst. 379 (2002) 159;
(c) T. Tsukuda, T. Suzuki, S. Kaizaki, Inorg. Chim. Acta 358 (2004) 1253;
(d) T. Tsukuda, M. Ogita, T. Suzuki, S. Kaizaki, Eur. J. Inorg. Chem. (2004) 4463.
[3] (a) S. Kaizaki, Bull. Chem. Soc. Jpn. 76 (2003) 673, and the references therein;
(b) S. Kaizaki, Coord. Chem. Rev. 250 (2006) 1804, and the references therein.
[4] (a) Y. Tsukahara, T. Kamatani, T. Suzuki, S. Kaizaki, Inorg. Chem. 41 (2002) 4363;
(b) Y. Tsukahara, T. Kamatani, T. Suzuki, S. Kaizaki, J. Chem. Soc., Dalton Trans. (2003) 1276.
[5] (a) M. Ogita, Y. Yamamoto, T. Suzuki, S. Kaizaki, Eur. J. Inorg. Chem. (2002) 886;
(b) A. Iino, T. Suzuki, S. Kaizaki, J. Chem. Soc., Dalton Trans. (2003) 4604.
[6] (a) Y. Yamamoto, T. Suzuki, S. Kaizaki, J. Chem. Soc., Dalton Trans. (2001) 1566;
(b) Y. Yamamoto, T. Suzuki, S. Kaizaki, J. Chem. Soc., Dalton Trans. (2001) 2943;
(c) H. Kanda, Y. Narumi, Y. Hosokoshi, T. Suzuki, S. Kawata, K. Kindo, K. Inoue, S. Kaizaki, Inorg. Chim. Acta 357 (2004) 3125.
[7] C. Benelli, D. Gatteschi, Chem. Rev. 102 (2002) 2369.

[8] C. Lescop, D. Luneau, E. Belorizky, P. Fries, M. Guillot, P. Rey, Inorg. Chem. 38 (1999) 5472.
[9] (a) C. Lescop, E. Belorizky, D. Luneau, P. Rey, Inorg. Chem. 41 (2002) 3375;
(b) C. Lescop, D. Luneau, P. Rey, G. Bussière, C. Reber, Inorg. Chem. 41 (2002) 5566.
[10] (a) M.L. Kahn, J.-P. Sutter, S. Golhen, P. Guionneau, L. Ouahab, O. Kahn, D. Chasseau, J. Am. Chem. Soc. 122 (2000) 3413;
(b) J.-P. Sutter, M.L. Kahn, O. Kahn, Adv. Mater. 11 (1999) 863.
[11] (a) M.L. Kahn, C. Mathonière, O. Kahn, Inorg. Chem. 38 (1999) 3692;
(b) M.L. Kahn, P. Lecante, M. Verelst, C. Mathoniere, O. Kahn, Chem. Mater. 12 (2000) 3073.
[12] A. Figuerola, C. Diaz, J. Ribas, V. Tangoulis, J. Granell, F. Lloret, J. Mathia, M. Maestro, Inorg. Chem. 42 (2003) 641.
[13] R. Koner, H.-H. Lin, H-H. Wei, S. Mohanta, Inorg. Chem. 44 (2005) 2524.
[14] (a) J.-P. Sutter, M.L. Kahn, K.P. Mortl, R. Ballou, P. Porcher, Polyhedron 20 (2001) 1593;
(b) M.L. Kahn, R. Ballou, P. Porcher, J.-P. Sutter, Chem. Eur. J. 8 (2002) 525.
[15] (a) A. Caneschi, A. Dei, D. Gatteschi, L. Sorace, K. Vostrikova, Angew. Chem. Int. Ed. 39 (2000) 246;
(b) A. Caneschi, A. Dei, D. Gatteschi, C.A. Massa, L.A. Pardi, S. Poussereau, L. Sorace, Chem. Phys. Lett. 371 (2003) 694;
(c) A. Caneschi, A. Dei, D. Gatteschi, S. Poussereau, L. Sorace, J. Chem. Soc., Dalton Trans. (2004) 1048.
[16] T. Nankawa, M. Watanabe, M. Murata, H. Nishihara, Chem. Lett. 32 (2003) 286.
[17] J.-P. Sutter, M.L. Kahn, in: J.S. Miller, M. Drillon (Eds.), Magnetism: Molecules to Materials, vol. 5, 2005, pp. 161–187.
[18] W.L. Busing, H.A. Levy, Acta Crystallogr. 10 (1957) 180.
[19] (a) G.M. Sheldrick, SHELXS97: Program for Crystal Structure Determination, University of Göttingen, 1997;
(b) G.M. Sheldrick, SHELXL-97: Program for the Refinement of Crystal Structures, University of Göttingen, 1997.
[20] Crystal Structure: Crystal Structure Analysis Package, Version 2.00, Rigaku and Molecular Structure Corporation, 2001.
[21] M.G.B. Drew, Coord. Chem. Rev. 24 (1977) 179.
[22] Y. Maruhashi, Master Thesis, Department of Chemistry, Graduate School of Science, Osaka University, 2005.
[23] M. Andruh, E. Bakalbassis, O. Kahn, J.P. Trombe, P. Porcher, Inorg. Chem. 32 (1993) 1616.

Available online at www.sciencedirect.com
ScienceDirect
Polyhedron 26 (2007) 3182–3188
POLYHEDRON
www.elsevier.com/locate/poly

Syntheses, structures, and optical properties of heteroselenometallic W–Se–Ag polymer compounds $\{[Et_4N][(\mu\text{-}WSe_4)Ag]\}_n$ and $\{[Ln(Me_2SO)_8][(\mu_3\text{-}WSe_4)_3Ag_3]\}_n$ (Ln = Pr, Er)

Ji-Xiang Dai [a], Qian-Feng Zhang [a,*], Yinglin Song [b], Wai-Yeung Wong [c], Alexander Rothenberger [d], Wa-Hung Leung [e]

[a] Department of Applied Chemistry, Anhui University of Technology, Ma'anshan, Anhui 243002, China
[b] Department of Physics, Harbin Institute of Technology, Harbin 150001, China
[c] Department of Chemistry, Hong Kong Baptist University, Waterloo Road, Kowloon Tang, Hong Kong, China
[d] Institut für Anorganische Chemie, Universität Karlsruhe (TH), 76128 Karlsruhe, Germany
[e] Department of Chemistry, The Hong Kong University of Science and Technology, Clear Water Bay, Kowloon, Hong Kong, China

Received 8 January 2007; accepted 1 March 2007
Available online 15 March 2007

Abstract

The one-dimensional linear polymer W–Se–Ag compound $\{[Et_4N][(\mu\text{-}WSe_4)Ag]\}_n$ (**1**) was obtained from the reaction of $[Et_4N]_2[WSe_4]$ and $AgNO_3$ in a mixed solvent, MeCN/DMF (1:10). Treatment of a solution of **1** in Me_2SO with $Ln(NO_3)_3 \cdot 6H_2O$ resulted in the formation of a helical chain polymer compound $\{[Ln(Me_2SO)_8][(\mu_3\text{-}WSe_4)_3Ag_3]\}_n$ (Ln = Pr **2**, Er **3**). The solid-state structures of the three polymer compounds **1**, **2**, and **3** have been established by X-ray crystallography. The third-order non-linear optical properties of the linear polymer compound **1** were determined by *z*-scan techniques with 7 ns pulses at 532 nm.
© 2007 Elsevier Ltd. All rights reserved.

Keywords: Heteroselenometallate; Silver compounds; Selenide compounds; Optical properties; Cluster compounds

1. Introduction

Selenometallates, such as tetraselenomolybdate and tetraselenotungstate, have been extensively used in the synthesis of transition metal selenides [1,2]. A number of coinage-metal/MSe_4 heteroselenometallic cluster compounds with various structural types including linear, butterfly, cubane, incomplete-cubane, co-planar T-frame, and open cross-frame, crown, cage, and pin-wheel shapes have been isolated from the interactions of $[MSe_4]^{2-}$ (M = Mo, W) anions with a series of coinage-metal species [3–9]. For the Mo(W)–Se–Ag system, a few discrete heteroselenometallic cluster compounds have been obtained to date, such as linear trinuclear $[(\mu\text{-}WSe_4)(AgPR_3)_2]$ (R = Ph or Cy, Cy = cyclohexyl) [4,10] and $[(\mu\text{-}WSe_4)(AgPPh_3)\{Ag(PPh_3)_2\}]$ [11], incomplete cubic $[(\mu\text{-}WSe_4)(AgPPh_3)_2(\mu\text{-}C_5H_5NS)]$ [5], cubane-like $[(\mu_3\text{-}MSe_4)(AgPR_3)_3\text{-}(\mu_3\text{-}X)]$ (M = Mo, W; R_3 = Ph_3, $PhMe_2$, Cy_3; X = Cl, Br, I) [4,12,13], open butterfly $[(\mu_3\text{-}WSe_4)Ag_3(\mu_3\text{-}I)(\mu\text{-}dppm)_2]$ [4], and hexanuclear $[(\mu_3\text{-}WSe_4)_2Ag_4(\mu\text{-}dppm)_3]$ [dppm = bis(diphenylphosphino)methane] [4], but polymer compounds of this kind are much fewer. The only one example is a one-dimensional helical polymer cluster compound $\{[La(Me_2SO)_8][(\mu_3\text{-}WSe_4)_3Ag_3]\}_n$ [14]. Wu and his coworkers have found that the assembling of $[WS_4]^{2-}$ and Ag^+ is flexible through non-bonding interactions with complementary small molecules (or cations) and the solvent, which can assemble into polymeric clusters with different configurations, such as single linear, zigzag and helical and double chains [15–20]. With this idea in mind, we are interested to extend the study of polymeric heterometallic

* Corresponding author. Tel.: +86 555 2312041; fax: +86 555 2311552.
E-mail address: zhangqf@ahut.edu.cn (Q.-F. Zhang).

0277-5387/$ - see front matter © 2007 Elsevier Ltd. All rights reserved.
doi:10.1016/j.poly.2007.03.013

compounds from sulfides to selenides within our long-term interest in heterometallic cluster compounds based on the $[MSe_4]^{2-}$ anions [2]. A reasonable speculation originates from the fact that selenium-containing compounds have important applications, such as precursors for low-band-gap semiconductors [21] and non-linear optics [22], and in part the reactivity of selenide compounds parallels that of their sulfur counterparts [23]. Herein, we report the syntheses, structures and optical properties of the polymer compounds $\{[Et_4N][(\mu\text{-}WSe_4)Ag]\}_n$ (**1**) and $\{[Ln(Me_2SO)_8][(\mu_3\text{-}WSe_4)_3Ag_3]\}_n$ (Ln = Pr **2**, Er **3**).

2. Results and discussion

2.1. Synthetic reaction

Reaction of $[Et_4N]_2[WSe_4]$ and $AgNO_3$ in a 1:1 molar ratio in a mixed MeCN/DMF (1:10) solution resulted in the formation of the linear polymer compound $\{[Et_4N][(\mu\text{-}WSe_4)Ag]\}_n$ (**1**) as dark red crystals in 77% yield. Treatment of **1** in Me_2SO with $Ln(NO_3)_3 \cdot 3H_2O$ gave a dark brown solution, from which black block crystals of the helical chain polymer compounds $\{[Ln(Me_2SO)_8][(\mu\text{-}WSe_4)_3Ag_3]\}_n$ (Ln = Pr **2**, Er **3**) were obtained in about 70% yield. In the present reaction, the oxygenphilic Ln^{3+} cations may coordinate the oxygen atoms of the Me_2SO solvent to form the larger complex trivalent cations $[Ln(Me_2SO)_8]^{3+}$ which can displace the relatively small organic univalent cation $[Et_4N]^+$, accordingly the original univalent cluster anion $[(\mu\text{-}WSe_4)Ag]^-$ self-assembles into the trivalent cluster anions $[(\mu\text{-}WSe_4)_3Ag_3]^{3-}$ with a large size so as to match the complex cations. From the results reported here and previously, it is clear that a trend of the dependence of the cluster anion geometric sphere, which may be of a novel structure, on the size of the counterion appears to emerge. Larger cations, such as bivalent $[Ca(Me_2SO)_6]^{2+}$ and trivalent $[Ln(Me_2SO)_8]^{3+}$, effect a polynuclear W/Se(S)/Ag cluster anion polymer (e.g. $\{[W_4S_{16}Ag_4]^{4-}\}_n$ zigzag chain [17] and $\{[W_3Se_{12}Ag_3]^{3-}\}_n$ helical chain [14]), while small ones, such as univalent $[Et_3NH]^+$ and $[Et_4N]^+$, favor a binuclear cluster anion polymer (e.g. $\{[WS_4Ag]^-\}_n$ [15,16], and $\{[WSe_4Ag]^-\}_n$ linear chains).

The W–Se stretching modes of the polymeric clusters **1**–**3** can be identified since they appear as strong and sharp bands in the low wavenumber region, below 400 cm^{-1} [3,4]. The terminal W–Se_t absorptions at 312 cm^{-1} for **2** and 314 cm^{-1} for **3** appear at relatively high wavenumbers compared to the ν(W–Se) absorption at 305 cm^{-1} in $[WSe_4]^{2-}$ [1]. However, the bridging W–μ_n-Se ($n = 2$–3) vibrations in the range 295–300 cm^{-1} are observed at relatively lower wavenumbers from that of $[WSe_4]^{2-}$ [1]. The IR spectra of **2** and **3** also show bands in the range 990–1010 cm^{-1} which can be assigned to ν(S=O) of the Me_2SO solvent ligands.

2.2. Crystal structures

The structure determination shows that the cluster **1** is composed of independent $[Et_4N]^+$ cations and polymeric linear chains of $[(\mu\text{-}WSe_4)Ag]^-$ anions. An ORTEP drawing of a portion of the linear chain structure is shown in Fig. 1, with the packing diagram of the unit cell shown in Fig. 2. Although a similar structure has been seen previously in heterothiometallic systems such as $[Ph_4P]_n[MoS_4Ag]_n$ [24], $[\alpha\text{-MepyH}]_n[MoS_4Ag]_n$ (py = pyridine) [25], $[WS_4Ag \cdot NH_4]_n$ [15] and $[WS_4Ag \cdot NH_3C(CH_2OH)_3 \cdot 2DMF]_n$ [16], the current arrangement appears to be the

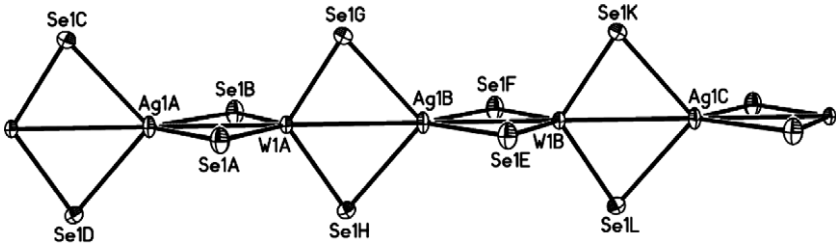


Fig. 1. ORTEP drawing of a portion of the $\{[(\mu\text{-}WSe_4)Ag]^-\}_n$ anion in **1**, thermal ellipsoids are drawn at the 50% probability level.

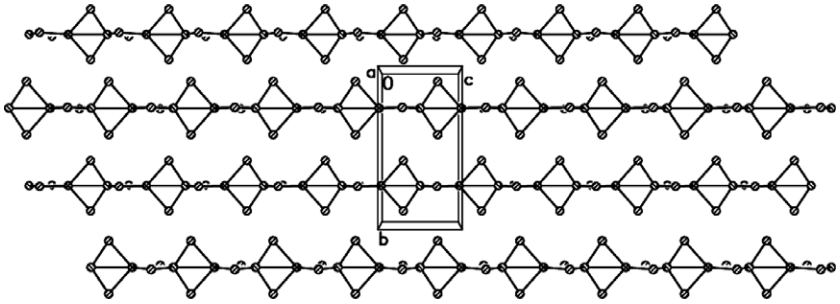


Fig. 2. Packing diagram of the linear chain polymeric $\{[(\mu\text{-}WSe_4)Ag]^-\}_n$ anion in **1**, $[Et_4N]^+$ cations are omitted for clarity.

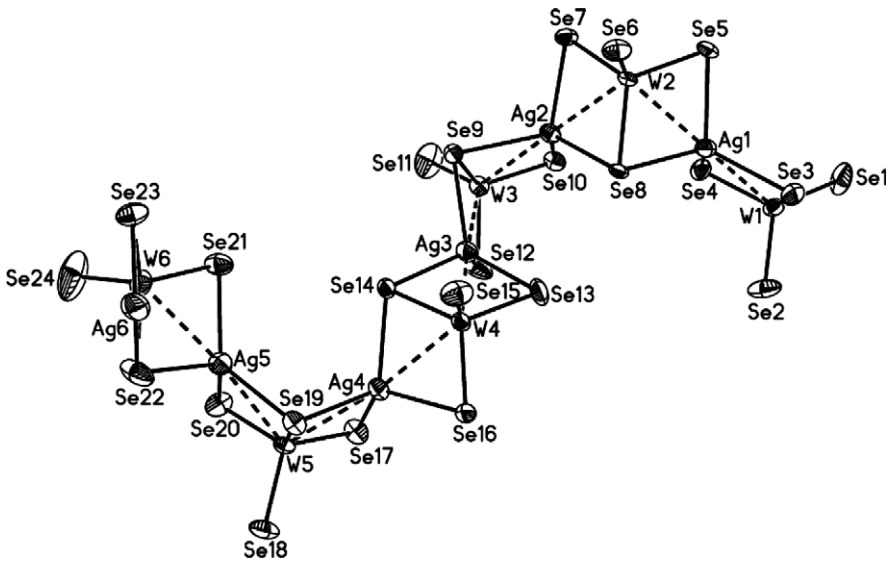


Fig. 3. ORTEP drawing of a portion of the $\{[(\mu\text{-}WSe_4)_3Ag_3]^{3-}\}_n$ anion in **2**, thermal ellipsoids are drawn at the 50% probability level.

first example of a heteroselenometallic compound with a polymeric linear chain. Both metal atoms display tetrahedron coordination in a selenium-rich environment, comparatively, the coordination geometry of the silver atoms [Se–Ag–Se: 97.00(4)–116.04(2)°] is more distorted than the tungsten atoms [Se–W–Se: 107.65(2)–113.18(5)°]. The chain has a straight linear configuration with a Ag–W–Ag angle of 180°. The W–μ-Se and Ag–μ-Se bond lengths are 2.3404(9) and 2.6085(9) Å, respectively. The $AgSe_2W$ units are co-planar, and neighboring ones are perpendicular to each other. The W–Ag distance of 3.0169(2) Å in **1** is comparable to those in $[(\mu\text{-}WSe_4)(AgPCy_3)_2]$ (av. 2.928(2) Å) [4] and $[(\mu\text{-}WSe_4)(AgPPh_3)\{Ag(PPh_3)_2\}]$ (av. 2.996(1) Å) [11].

Single-crystal X-ray diffraction analyses reveal that clusters **2** and **3**, with the same space group, have different units in the cells. Both are composed of non-interacting $\{[Ln(Me_2SO)_8]^{3+}\}_n$ (Ln = Pr **2**, Er **3**) cations and $\{[(\mu_3\text{-}WSe_4)_3Ag_3]^{3-}\}_n$ macroanions. A similar structure has been reported previously in $\{[Ln(Me_2SO)_8][(\mu_3\text{-}MS_4)_3Ag_3]\}_n$ (Ln = Nb, La; M = W, Mo) [18,19] and $\{[La(Me_2SO)_8][(\mu_3\text{-}WSe_4)_3Ag_3]\}_n$ [14]. The basic repeating unit is a butterfly-type $SeWSe_3Ag_2$ unit, containing a bridging WSe_4 group which is linked through interactions with the Ag atom of one fragment and a Ag atom of another to form an intriguing helical array of repeating $[(\mu_3\text{-}WSe_4)_3Ag_3]^{3-}$ cluster units. Fig. 3 shows a view of an individual helical chain in cluster **2**. Fig. 4 represents the packing of the $\{[(\mu_3\text{-}WSe_4)_3Ag_3]\}_n^{3n-}$ chain in the unit cell with the $[Er(Me_2SO)_8]^{3+}$ ions in cluster **3**. This chain is made up of two sets of helices which alternatively propagate along the chain. The tetrahedral tungsten atoms have Se–W–Se angles in the range 105.51(11)–114.23(9)° for **2** and 106.94(3)–113.80(3)° for **3**, and three types of W–Se bond lengths, W–Se_t (2.261(3) Å for **2** and 2.282(1) Å for **3**), W–μ-Se (2.324(3) Å for **2** and 2.336(1) Å for **3**) and W–μ_3-Se (2.377(3) Å for **2** and 2.375(1) Å for **3**). The geometry about the Ag atoms may be described as highly distorted tetrahedral, with angles in the range 95.47(8)–130.00(10)° for **2** and 96.08(3)–126.03(3)° for **3**. The average W–Ag distances [3.004(2) Å for **2** and 3.027(1) Å for **3**] are close to those observed in related heteroselenometallic W–Se–Ag clusters. The larger trivalent cations $[Ln(Me_2SO)_8]^{3+}$ are arrayed amongst the anionic helical chains and are well separated from each other and the anionic chains. Each Ln(III) atom is eight-coordinated by oxygen atoms of eight Me_2SO molecules. The average Pr–O bond length is 2.428(13) Å and the O–Pr–O angles range from 69.9(4)–146.8(4)° in **2**, while the average Er–O bond length is 2.344(4) Å and the O–Er–O angles range from 71.2(2)° to 143.7(2)° in **3**.

2.3. Optical properties

The non-linear optical (NLO) properties of **1** were investigated in DMF using a *z*-scan technique [26,27]. The open and closed *z*-scan data are given in Fig. 5. The observed curves clearly show the presence of both non-linear optical

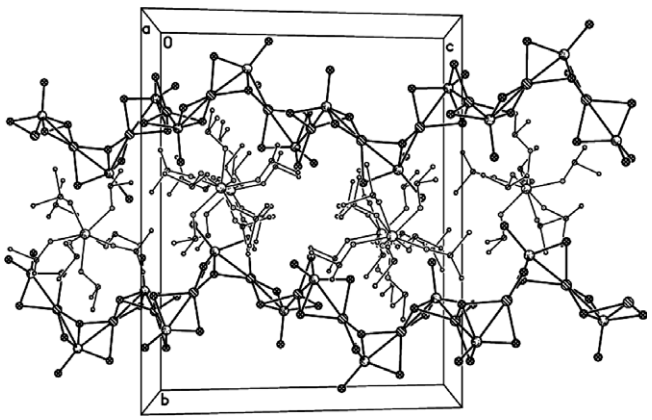


Fig. 4. Packing drawing of **3** down the *b*-axis.

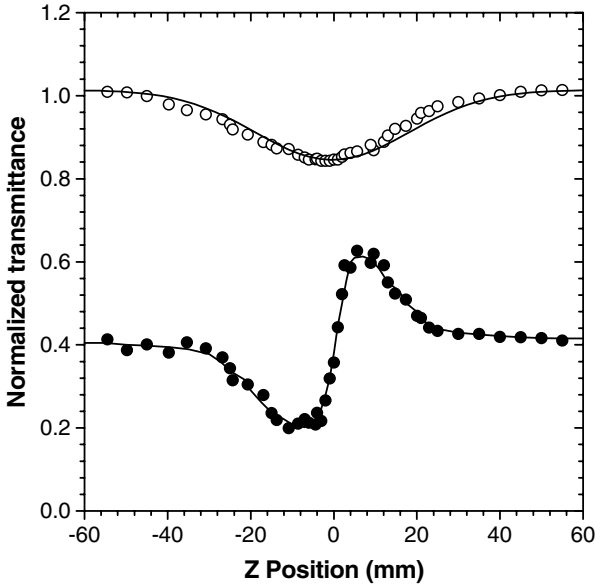


Fig. 5. z-Scan data of 1.78×10^{-4} M **1** at 532 nm with $I_0 = 1.65\times10^{-9}$ W/m^2. (a) The data shown by open circles are those collected under an open aperture configuration, and the solid curve is a theoretical fit based on $T(Z) = \frac{1}{\pi^{1/2}q(Z)}\int_{-\infty}^{\infty}\ln[1+q(z)]e^{-\tau^2}d\tau$ and $q(Z) = \alpha_2 I_i(Z)\frac{(1-e^{-\alpha_0 L})}{\alpha_0}$. (b) The data shown by filled circles were obtained by dividing the normalized z-scan data measured under a closed aperture configuration by the normalized z-scan data of (a).

absorption and non-linear optical refraction. The valley-peak pattern of the normalized transmittance curve obtained under a close aperture configuration shows characteristic self-focusing behavior of propagating light in the sample. The non-linear absorption component was evaluated under an open aperture configuration. The theoretical curve of transmittance against the z position was fitted to the observed z-scan data by varying the α_2 value, where the experimentally measured α_0, L and $I_i(z)$ values were adopted. The solid curve in Fig. 5 (top) was the theoretical curve calculated with $\alpha_2 = 1.2\times10^{-10}$ m W^{-1} for **1**. The non-linear refractive component of **1** was assessed by dividing the normalized z-scan data obtained under the closed aperture configuration with those obtained under the open aperture configuration. The theoretical curve in Fig. 5 (bottom) is superimposed for comparison, where the estimated n_2 value is 3.6×10^{-15} m^2 W^{-1}. The DMF solution of **1** caused self-focusing of the propagating light, while DMF solvent itself is known to show a negative dn/dT of -5.6×10^{-4} K^{-1} [28]. Therefore, the observed NLO properties are not due to a solvent thermal effect. By a comparison with the NLO properties of polymer compound $\{[La(Me_2SO)_8][(\mu\text{-}WSe_4)_3Ag_3]\}_n$ [14], both non-linear optical absorptive and refractive effects of linear polymer compound **1** are inferior to those found in the polynuclear polymer compound $\{[La(Me_2SO)_8][(\mu\text{-}WSe_4)_3Ag_3]\}_n$, which has a helical chain, suggesting that aggregation of metal atoms in heteroselenometallic clusters may possibly assist to improve the NLO properties of the clusters. Whether the structural variation from linear chain to helical chain might influence the NLO properties of the clusters will be further studied by way of the designed syntheses of this class of cluster with different structural types [22,29].

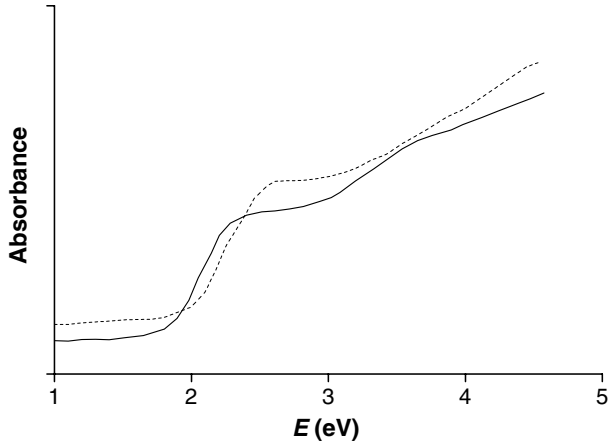


Fig. 6. Solid-state UV–Vis spectra of **1** (dashed line) and **2** (solid line), recorded as suspensions in Nujol.

To gain insight into the optoelectronic properties of **1** and **2**, we measured the UV–Vis solid-state absorption spectra of the polymeric clusters **1** and **2** (see Fig. 6). The absorption onsets of **1** and **2** were observed at $E = 1.92$ eV (647 nm) and 2.11 eV (590 nm), respectively, which may be tentatively assigned to the optical bandgap energy at the lowest electronic excitation in the solid state. On comparison to heteroselenometallic polymer compounds with ternary metal-selenide compounds [30], the differences in the optical bandgaps may probably be attributed to differences in the coordination environment as well as the nature of the organic and metal-complex cations of **1** and **2** [31].

In summary, we have synthesized and structurally characterized inorganic polymer complexes, one-dimensional linear $\{[Et_4N][(\mu\text{-}WSe_4)Ag]\}_n$ and helical $\{[Ln(Me_2SO)_8][(\mu_3\text{-}WSe_4)_3Ag_3]\}_n$ (Ln = Pr, Er). The present heteroselenometallic W–Se–Ag polymer compounds, without peripheral ligands, show middling non-linear optical absorption and refraction in solution and a normal optical bandgap energy at the lowest electronic excitation in the solid state. We are currently investigating more structural types of heteroselenometallic W–Se–Ag polymer complexes and clusters and are further studying their optical and electronic properties so that some desired optoelectronic functions with new inorganic cluster materials will be achieved.

3. Experimental

3.1. Materials and measurements

All syntheses were performed in oven-dried glassware under a purified nitrogen atmosphere using standard Schlenk techniques. The solvents were purified by conventional methods and degassed prior to use. $[Et_4N]_2[WSe_4]$ was prepared by a modification of the literature method

[32]. $AgNO_3$, $Pr(NO_3)_3 \cdot 6H_2O$, and $Er(NO_3)_3 \cdot 6H_2O$ were purchased from Strem Ltd. and were used without further purification. All elemental analyses were carried out using a Perkin–Elmer 2400 CHN analyzer. Infrared spectra were recorded on a Digilab FTS-40 spectrophotometer with the use of pressed KBr pellets. UV–Vis spectra were recorded on a Perkin–Elmer spectrometer Lambda 900, employing the double-beam technique. The samples were measured in Nujol, prepared by grinding single crystals in a drop of Nujol. The mixture was placed between two quartz plates and rapidly brought into the UV–Vis beam.

A DMF solution of cluster **1** was placed in a 1 mm quartz cuvette for non-linear optical measurements, which were performed with linearly polarized 7 ns pulses at 532 nm generated from a Q-switched frequency-doubled Nd:YAG laser. The cluster is stable toward air and laser light under the experimental conditions. The spatial profiles of the pulsed laser were focused on the sample cell with a 30 cm focal length mirror. The spot radius of the laser beam was measured to be 55 μm (half-width at $1/e^2$ maximum). The incident and transmitted pulse energies were measured simultaneously by two energy detectors (Laser Precision Rjp-735), which were linked to a computer by an IEEE interface [26,27]. The NLO properties of the samples were manifested by moving the samples along the axis of the incident laser irradiance beam (z-direction) with respect to the focal point and with the incident laser irradiance kept constant (z-scan methods). The closed-aperture curves are normalized to the open aperture curves. An aperture of 0.2 mm radius was placed in front of the detector to measure the transmitted energy when assessment of the laser beam distortion was needed. To eliminate scattering effects, a lens was mounted after the samples to collect the scattered light.

Table 1
Selected bond lengths (Å) and angles (°) for $\{[Et_4N][(\mu\text{-}WSe_4)Ag]\}_n$ (**1**)

W(1)–Se(1)	2.3404(9)	Ag(1)–Se(1)	2.6085(9)
W(1)–Ag(1)	3.0169(2)		
Se(1)#1–W(1)–Se(1)	107.65(2)	Se(1)–W(1)–Se(1)#3	107.65(2)
Se(1)–W(1)–Se(1)#2	113.18(5)	Ag(1)#4–W(1)–Ag(1)	180.0
Se(1)#2–Ag(1)–Se(1)	97.00(4)	Se(1)#5–Ag(1)–Se(1)	116.04(2)
W(1)–Se(1)–Ag(1)	74.91(3)		

Symmetry codes: #1 $y+\frac{1}{2}, -x+1, -z+1$; #2 $-x+\frac{3}{2}, -y+\frac{1}{2}, z$; #3 $-y+1, x-\frac{1}{2}, -z+1$; #4 $x, y, z+1$; #5 $-y+1, x-\frac{1}{2}, -z$.

Table 2
Selected bond lengths (Å) for $\{[Pr(Me_2SO)_8]_2[(\mu\text{-}WSe_4)_6Ag_6]\}_n$ (**2**)[a]

W(1)–Se(1)	2.324(3)	W(1)–Se(2)	2.271(3)
W(1)–Se(3)	2.333(3)	W(1)–Se(4)	2.375(2)
W(2)–Se(5)	2.324(2)	W(2)–Se(6)	2.281(2)
W(2)–Se(7)	2.323(2)	W(2)–Se(8)	2.383(2)
W(3)–Se(9)	2.369(2)	W(3)–Se(10)	2.316(2)
W(3)–Se(11)	2.251(3)	W(3)–Se(12)	2.313(3)
W(4)–Se(13)	2.316(2)	W(4)–Se(14)	2.386(2)
W(4)–Se(15)	2.265(3)	W(4)–Se(16)	2.319(2)
W(5)–Se(17)	2.329(2)	W(5)–Se(18)	2.265(3)
W(5)–Se(19)	2.369(2)	W(5)–Se(20)	2.323(3)
W(6)–Se(21)	2.337(3)	W(6)–Se(22)	2.381(4)
W(6)–Se(23)	2.332(3)	W(6)–Se(24)	2.232(4)
Ag(1)–Se(3)	2.602(3)	Ag(1)–Se(5)	2.610(3)
Ag(1)–Se(4)	2.651(3)	Ag(1)–Se(8)	2.627(2)
Ag(2)–Se(7)	2.624(2)	Ag(2)–Se(8)	2.652(2)
Ag(2)–Se(9)	2.654(2)	Ag(2)–Se(10)	2.635(3)
Ag(3)–Se(9)	2.648(3)	Ag(3)–Se(12)	2.612(3)
Ag(3)–Se(13)	2.618(3)	Ag(3)–Se(14)	2.618(2)
Ag(4)–Se(14)	2.634(3)	Ag(4)–Se(16)	2.608(2)
Ag(4)–Se(17)	2.605(3)	Ag(4)–Se(19)	2.645(3)
Ag(5)–Se(19)	2.600(3)	Ag(5)–Se(20)	2.634(3)
Ag(5)–Se(21)	2.595(3)	Ag(5)–Se(22)	2.593(3)
Ag(6)–Se(1)#2	2.644(4)	Ag(6)–Se(4)#2	2.688(3)
Ag(6)–Se(22)	2.632(4)	Ag(6)–Se(23)	2.576(4)
W(1)–Ag(6)#1	3.005(3)	W(1)–Ag(1)	3.006(2)
W(2)–Ag(1)	3.003(2)	W(2)–Ag(2)	3.023(2)
W(3)–Ag(3)	2.998(2)	W(3)–Ag(2)	3.035(2)
W(4)–Ag(3)	2.992(2)	W(4)–Ag(4)	3.012(2)
W(5)–Ag(5)	2.997(2)	W(5)–Ag(4)	3.021(2)
W(6)–Ag(5)	2.955(2)	W(6)–Ag(6)	2.968(3)

Symmetry codes: #1 $x-1, y, z$; #2 $x+1, y, z$.

[a] Selected bond angles are in the Supporting information in cif format.

Table 3
Selected bond lengths (Å) and angles (°) for $\{[Er(Me_2SO)_8][(\mu\text{-}WSe_4)_3\text{-}Ag_3]\}_n$ (**3**)

W(1)–Se(1)	2.336(1)	W(1)–Se(2)	2.277(1)
W(1)–Se(3)	2.347(1)	W(1)–Se(4)	2.376(1)
W(2)–Se(5)	2.326(1)	W(2)–Se(6)	2.284(1)
W(2)–Se(7)	2.375(1)	W(2)–Se(8)	2.339(1)
W(3)–Se(9)	2.375(1)	W(3)–Se(10)	2.331(1)
W(3)–Se(11)	2.338(1)	W(3)–Se(12)	2.285(1)
Ag(1)–Se(1)	2.640(1)	Ag(1)–Se(4)	2.666(1)
Ag(1)–Se(9)#2	2.648(1)	Ag(1)–Se(11)#2	2.635(1)
Ag(2)–Se(3)	2.587(1)	Ag(2)–Se(4)	2.637(1)
Ag(2)–Se(5)	2.751(1)	Ag(2)–Se(7)	2.695(1)
Ag(3)–Se(7)	2.656(1)	Ag(3)–Se(8)	2.609(1)
Ag(3)–Se(9)	2.662(1)	Ag(3)–Se(10)	2.585(1)
W(1)–Ag(1)	3.055(1)	W(1)–Ag(2)	3.024(1)
W(2)–Ag(2)	3.011(1)	W(2)–Ag(3)	2.996(1)
W(3)–Ag(1)#1	3.062(1)	W(3)–Ag(3)	3.012(1)
Se(2)–W(1)–Se(1)	106.95(3)	Se(2)–W(1)–Se(3)	106.94(3)
Se(1)–W(1)–Se(3)	107.97(3)	Se(2)–W(1)–Se(4)	108.11(3)
Se(1)–W(1)–Se(4)	113.80(3)	Se(3)–W(1)–Se(4)	112.70(3)
Se(6)–W(2)–Se(5)	108.95(3)	Se(6)–W(2)–Se(8)	108.13(3)
Se(5)–W(2)–Se(8)	108.46(3)	Se(6)–W(2)–Se(7)	107.83(3)
Se(5)–W(2)–Se(7)	109.65(3)	Se(8)–W(2)–Se(7)	113.72(3)
Se(12)–W(3)–Se(10)	106.56(3)	Se(12)–W(3)–Se(11)	107.97(3)
Se(10)–W(3)–Se(11)	108.15(3)	Se(12)–W(3)–Se(9)	107.77(4)
Se(10)–W(3)–Se(9)	113.17(3)	Se(11)–W(3)–Se(9)	112.90(3)
Se(11)#2–Ag(1)–Se(1)	112.04(3)	Se(11)#2–Ag(1)–Se(9)#2	96.08(3)
Se(1)–Ag(1)–Se(9)#2	124.02(3)	Se(11)#2–Ag(1)–Se(4)	127.92(3)
Se(1)–Ag(1)–Se(4)	96.13(3)	Se(9)#2–Ag(1)–Se(4)	103.20(3)
Se(3)–Ag(2)–Se(4)	97.64(3)	Se(3)–Ag(2)–Se(7)	110.43(3)
Se(4)–Ag(2)–Se(7)	126.40(3)	Se(3)–Ag(2)–Se(5)	126.03(3)
Se(4)–Ag(2)–Se(5)	109.58(3)	Se(7)–Ag(2)–Se(5)	89.78(3)
Se(10)–Ag(3)–Se(8)	114.92(4)	Se(10)–Ag(3)–Se(7)	120.68(3)
Se(8)–Ag(3)–Se(7)	97.14(3)	Se(10)–Ag(3)–Se(9)	96.94(3)
Se(8)–Ag(3)–Se(9)	116.25(3)	Se(7)–Ag(3)–Se(9)	112.22(3)
Ag(3)–W(2)–Ag(2)	81.11(2)	Ag(3)–W(3)–Ag(1)#1	86.17(2)
Ag(2)–W(1)–Ag(1)	90.32(2)	W(2)–Ag(2)–W(1)	160.84(2)
W(2)–Ag(3)–W(3)	168.83(3)	W(1)–Ag(1)–W(3)#2	176.62(2)

Symmetry codes: #1 $x+\frac{1}{2}, -y+\frac{1}{2}, z+\frac{1}{2}$; #2 $x-\frac{1}{2}, -y+\frac{1}{2}, z-\frac{1}{2}$.

3.2. Preparation of $\{[Et_4N][(\mu\text{-}WSe_4)Ag]\}_n$ (1)

A solution of $AgNO_3$ (42.5 mg, 0.25 mmol) in MeCN (1 mL) was added dropwise to a solution of $[Et_4N]_2[WSe_4]$ (190 mg, 0.25 mmol) in DMF (10 mL). The mixture was stirred for a while at room temperature, resulting in a purple-red solution with a small amount of black precipitate, and then filtered to afford a dark red filtrate. Dark-red prism crystals of **1** were obtained after allowing the filtrate to stand at room temperature for three days. Yield: 117 mg (77%). IR (KBr, cm^{-1}): ν(W–Se) 297 (m). *Anal.* Calc. for $C_8H_{20}NSe_4WAg$: C, 13.0; H, 2.71; N, 1.90. Found: C, 12.8; H, 2.66; N, 1.92% (Table 1).

3.3. Preparations of $\{[Ln(Me_2SO)_8][(\mu\text{-}WSe_4)_3Ag_3]\}_n$ (Ln = Pr 2, Er 3)

To a solution of **1** (111 mg, 0.15 mmol) in 10 mL Me_2SO was added a solution of $Pr(NO_3)_3 \cdot 6H_2O$ (62 mg, 0.20 mmol) or $Er(NO_3)_3 \cdot 6H_2O$ (68 mg, 0.20 mmol) in 5 mL of Me_2SO with slow stirring. A brown solution was gradually formed along with a little black precipitate. The clear filtrate was allowed to stand at room temperature for two days to afford black block crystals suitable for a single-crystal X-ray diffraction analysis, which were identified as **2** or **3**, respectively. For **2**: Yield: 94 mg (70%). IR (KBr, cm^{-1}): ν(S=O) 1003 (s), 997 (s); ν(W–Se), 297 (m). *Anal.* Calc. for $C_{16}H_{48}O_8S_8Se_{12}W_3Ag_3Pr$: C, 7.42; H, 1.85. Found: C, 7.38; H, 1.82%. For **3**: Yield: 90 mg (68%). IR (KBr, cm^{-1}): ν(S=O) 1001 (s), 992 (s); ν(W–Se), 296 (m). *Anal.* Calc. for $C_{16}H_{48}O_8S_8Se_{12}W_3Ag_3Er$: C, 7.34; H, 1.84. Found: C, 7.32; H, 1.85% (Tables 2 and 3).

3.4. X-ray crystallography

Well developed single-crystals of **1** ($0.25 \times 0.15 \times 0.10\ mm^3$), **2** ($0.16 \times 0.13 \times 0.10\ mm^3$), and **3** ($0.18 \times 0.16 \times 0.10\ mm^3$) were mounted in a random orientation on glass fibers. Diffraction data were collected on a Bruker APEX CCD area-detecting diffractometer equipped with graphite monochromated Mo Kα radiation ($\lambda = 0.71073$ Å) by using an ω-scan technique (for **1**, $1.53° < \theta < 28.20°$; for **2**, $1.53° < \theta < 25.00°$; for **3**, $1.37° < \theta < 25.00°$). The collected frames were processed with the software SAINT [33]. The data were corrected for absorption using the program SADABS [34]. Structures were solved by direct methods and refined by full-matrix least-squares on F^2 using the SHELXTL software package [35]. All non-hydrogen atoms were refined anisotropically. The positions of all hydrogen atoms were generated geometrically (C–H bond fixed at 0.96 Å), assigned isotropic thermal parameters and allowed to ride on their respective parent C atoms before the final cycle of least-squares refinement. For **2** and **3**, sulfur and carbon atoms in two of Me_2SO groups were clearly observed to be disordered. Their site occupancies were each initially set to 0.5, but they were then refined with the restriction that their sum should add up to unity, which resulted in site occupancy values (see Supporting information). The large peaks in the final difference maps had a height of 2.698 e Å^{-3} for **1** and 2.947 e Å^{-3} for **2**, and are in the vicinity of the W atoms. The final cycle of full-matrix least squares refinement converged to give R_1 and wR_2 values which along further details of the structure analyses are listed in Table 4.

Table 4
Crystallographic data and structure refinement parameters for $\{[Et_4N][(\mu\text{-}WSe_4)Ag]\}_n$ (**1**), $\{[Pr(Me_2SO)_8][(\mu\text{-}WSe_4)Ag]\}_n$ (**2**), and $\{[Er(Me_2SO)_8][(\mu\text{-}WSe_4)_3Ag_3]\}_n$ (**3**)

Compound	1	2	3
Empirical formula	$C_8H_{20}NSe_4WAg$	$C_{32}H_{96}O_{16}S_{16}Se_{24}W_6Ag_6Pr_2$	$C_{16}H_{48}O_8S_8Se_{12}W_3Ag_3Er$
Formula mass	737.81	5177.23	2614.96
Crystal system	tetragonal	monoclinic	monoclinic
Space group	*P*4/*nmm*	$P2_1/n$	$P2_1/n$
a (Å)	11.7119(4)	19.3391(12)	12.6976(6)
b (Å)		19.0051(12)	23.7494(12)
c (Å)	6.0339(4)	32.975(2)	19.420(1)
β (°)		105.425(1)	100.280(1)
V (Å^3)	827.66(7)	11683.1(13)	5762.3(5)
Z	4	2	4
D_{calc} (g cm^{-3})	5.921	2.943	3.014
T (K)	293(2)	293(2)	293(2)
μ (mm^{-1})	33.794	15.477	16.301
F(000)	1328	9328	4700
Reflections collected	4657	56278	28480
Independent reflections	587	20404	10120
R_{int}	0.0302	0.0712	0.0376
R_1,[a] wR_2[b] ($I \geqslant 2\sigma(I)$)	0.0322, 0.0975	0.0684, 0.1274	0.0271, 0.0597
*R*1, wR_2 (all data)	0.0384, 0.1039	0.0908, 0.2004	0.0396, 0.0641
Good-of-fit[c]	1.045	1.013	1.019

[a] $R_1 = \|F_o| - |F_c\|/|F_o|$.
[b] $wR_2 = [w(|F_o^2| - |F_c^2|)^2/w|F_o^2|^2]^{1/2}$.
[c] $GoF = [w(|F_o| - |F_c|)^2/(N_{obs} - N_{param})]^{1/2}$.

Acknowledgments

This project was supported by the Natural Science Foundation of China (project number: 90301005) and the Hong Kong Research Grants Council (project number: 601506). Q.-F.Z. thanks the Science and Technological Fund of Anhui Province for Outstanding Youth (06046100) and the Research Fund for the Returned Overseas Talents of Anhui Province (2006Z041).

Appendix A. Supplementary material

CCDC 628304, 628305 and 628306 contain the supplementary crystallographic data for this paper. These data can be obtained free of charge via http://www.ccdc.cam.ac.uk/conts/retrieving.html, or from the Cambridge Crystallographic Data Centre, 12 Union Road, Cambridge CB2 1EZ, UK; fax: (+44) 1223-336-033; or e-mail: deposit @ccdc.cam.ac.uk. Supplementary data associated with this article can be found, in the online version, at doi:10.1016/j.poly.2007.03.013.

References

[1] A. Müller, E. Diemann, R. Jostes, H. Bögge, Angew. Chem., Int. Ed. Engl. 20 (1981) 934.
[2] Q.F. Zhang, W.H. Leung, X.Q. Xin, Coord. Chem. Rev. 224 (2002) 35.
[3] C.C. Christuk, M.A. Ansari, J.A. Ibers, Inorg. Chem. 31 (1992) 4365.
[4] Q.F. Zhang, J. Ding, Z. Yu, Y. Song, A. Rothenberger, D. Fenske, W.H. Leung, Inorg. Chem. 45 (2006) 8638.
[5] Q.M. Wang, X.T. Wu, Q. Huang, T.L. Sheng, P. Lin, Polyhedron 16 (1997) 1439.
[6] M.C. Hong, M.H. Wu, X.Y. Huang, F.L. Jiang, R. Cao, H.Q. Liu, J.X. Lu, Inorg. Chim. Acta 260 (1997) 73.
[7] M.C. Hong, Q.F. Zhang, R. Cao, D.X. Wu, J.T. Chen, W.J. Zhang, H.Q. Liu, J.X. Lu, Inorg. Chem. 36 (1997) 6251.
[8] Q.F. Zhang, Z. Yu, J. Ding, Y. Song, A. Rothenberger, D. Fenske, W.H. Leung, Inorg. Chem. 45 (2006) 5187.
[9] C.C. Christuk, M.A. Ansari, J.A. Ibers, Angew. Chem., Int. Ed. Engl. 31 (1992) 1477.
[10] A. Müller, H. Bögge, J. Schimanski, M. Penk, K. Nieradzik, D. Dartmann, E. Krickemyer, J. Schimanski, C. Römer, M. Römer, H. Dornfeld, U. Wienböker, W. Hellmann, M. Zimmermann, Monatsch. Chem. 120 (1989) 367.
[11] Q.F. Zhang, W.H. Leung, Y.L. Song, M.C. Hong, C.L. Kennard, X.Q. Xin, New J. Chem. 25 (2001) 465.
[12] Q.F. Zhang, M.C. Hong, H.Q. Liu, Transition Met. Chem. 22 (1997) 156.
[13] W.R. Yao, Y.L. Song, X.Q. Xin, Q.F. Zhang, J. Mol. Struct. 655 (2003) 391.
[14] Q.F. Zhang, W.H. Leung, X.Q. Xin, H.K. Fun, Inorg. Chem. 39 (2000) 417.
[15] Q. Huang, X.T. Wu, Q.M. Wang, T.L. Sheng, J.X. Lu, Angew. Chem., Int. Ed. Engl. 35 (1996) 868.
[16] Q. Huang, X.T. Wu, T.L. Sheng, Q.M. Wang, Inorg. Chem. 34 (1995) 4391.
[17] Q. Huang, X.T. Wu, J.X. Lu, Inorg. Chem. 35 (1996) 7445.
[18] Q. Huang, X.T. Wu, J.X. Lu, Chem. Commun. (1997) 703.
[19] H. Yu, W.J. Zhang, X.T. Wu, T.L. Sheng, Q.M. Wang, P. Lin, Angew. Chem., Int. Ed. Engl. 37 (1998) 2520.
[20] L. Chen, X.T. Wu, X.C. Gao, W.J. Zhang, P. Lin, J. Chem. Soc., Dalton Trans. (1999) 4303.
[21] See any issue of The Bulletin of the Selenium–Tellurium Development Association, Grimbergen, Belgium, 1991.
[22] B.J. Coe, in: J.A. McCleverty, T.J. Meyer (Eds.), Comprehensive Coordination Chemistry II, Vol. 9, Elsevier Pergamon, Oxford, UK, 2004, p. 621.
[23] M.A. Ansari, C.-N. Chau, C.H. Mahler, J.A. Ibers, Inorg. Chem. 28 (1989) 650.
[24] A. Müller, W. Jaegrmann, W. Hellmann, J. Mol. Struct. 100 (1983) 559.
[25] J.P. Lang, J.G. Li, S.A. Bao, X.Q. Xin, Polyhedron 12 (1993) 801.
[26] M. Sheik-Bahae, A.A. Said, T.H. Wei, D.J. Hagan, E.W. van Stryland, IEEE J. Quantum Electron. 26 (1990) 760.
[27] M. Sheik-Bahae, A.A. Said, E.W. van Stryland, Opt. Lett. 44 (1989) 955.
[28] J.A. Riddick, W.B. Bunger, T.K. Sakano, Organic Solvents: Physical Properties and Method of Purification, 4th ed., John Wiley & Sons, New York, 1986.
[29] S. Shi, Non-linear Optical Properties of Inorganic Clusters, in: D.M. Roundhill, J.P. FacklerJr. (Eds.), Optoelectronic Properties of Inorganic Compounds, Plenum Press, 1999, p. 55.
[30] B. Tell, H.M. Kasper, J. Appl. Phys. 45 (1974) 5367.
[31] S. Dehnen, M.K. Brandmayer, J. Am. Chem. Soc. 125 (2003) 6618.
[32] S.C. O'Neal, J.W. Kolis, J. Am. Chem. Soc. 110 (1988) 1971.
[33] SMART and SAINT+ for Windows NT Version 6.02a. Bruker Analytical X-ray Instruments Inc., Madison, WI, USA, 1998.
[34] G.M. Sheldrick, SADABS, University of Göttingen, Germany, 1996.
[35] G.M. Sheldrick, SHELXTL Software Reference Manual. Version 5.1, Bruker AXS Inc., Madison, WI, USA, 1997.

Available online at www.sciencedirect.com
ScienceDirect
Polyhedron 26 (2007) 3189–3198
POLYHEDRON
www.elsevier.com/locate/poly

Hetero-metallic frameworks of $[Pd(CN)_4]^{2-}$ and Cu(II) with triamines: A rare example of a tetracyanometallate bridged 2D coordination polymer

Subal Chandra Manna [a], Joan Ribas [b], Ennio Zangrando [c,*], Nirmalendu Ray Chaudhuri [a,*]

[a] Department of Inorganic Chemistry, Indian Association for the Cultivation of Science, Kolkata 700 032, India
[b] Departament de Química Inorgànica, Universitat de Barcelona, Diagonal, 647, 08028 Barcelona, Spain
[c] Dipartimento di Scienze Chimiche, University of Trieste, 34127 Trieste, Italy

Received 17 December 2006; accepted 18 February 2007
Available online 2 March 2007

Abstract

Four cyano bridged Cu(II)–Pd(II) heterometallic complexes, $[Cu(dpt)Pd(CN)_4]_n$ (**1**), $\{[Cu_2(medpt)_2Pd(CN)_4](ClO_4)_2 \cdot 3H_2O\}_n$ (**2**), $\{[Cu_2(dien)_2Pd(CN)_4](ClO_4)_2 \cdot 2CH_3OH\}_n$ (**3**) and $\{[Cu_2(i\text{Prdien})_2Pd(CN)_4](ClO_4)_2 \cdot 2H_2O\}_n$ (**4**) [dpt = 3,3′-iminobispropylamine; medpt = 3,3′-diamino-*N*-methyldipropylamine; dien = diethylenetriamine and *i*prdien = *N*′-isopropyldiethylenetriamine] have been synthesized and characterized by single crystal X-ray diffraction analysis, magnetic measurement and thermal study. Complexes **1**, **2** and **3** are 1D coordination polymers, while **4** presents a 2D network. In **1**, the *cis*-directed cyanide ligands of $[Pd(CN)_4]^{2-}$ anions link two Cu(dpt) units to form a neutral coordination polymer, whereas in **2**, **3** and **4**, all the cyanide groups of $[Pd(CN)_4]^{2-}$ take part in bonding with four adjacent Cu(II) ions, resulting in cationic coordination polymers counterbalanced by perchlorate anions. The structures are compared with those of analogous $[Ni(CN)_4]^{2-}$ derivatives. The magnetic behavior shows antiferromagnetic interactions in all the complexes.
© 2007 Elsevier Ltd. All rights reserved.

Keywords: Cu(II); Tetracyanopalladate; Triamine; Crystal structure; Magnetic behavior

1. Introduction

Recently the design and synthesis of coordination polymers with specific properties have received significant attention in the field of material science [1]. The formation of polymeric structures depends on several factors [2] i.e.; (i) stereo electronic molecular information encoded in the ligand(s); (ii) reading of the information by metal ions having a set of coordination numbers and stereochemical preferences depending on their size, charge and electronic structure; and (iii) external conditions, e.g. solvent, counterions, which have a strong influence in the crystallization process as well as on the solid-state architecture.

Cyanometallate complexes have been intensively investigated in view of their potential application in the design of molecule-based magnets [3] or microporous inorganic materials mimicking zeolites [4]. It has been observed that when the second coordination center is a transition metal ion, $\sigma \rightarrow \pi$ back donation stabilizes the resulting complexes making them robust [5].

Cyanometallate anions may be either diamagnetic or paramagnetic, and the latter center generates unique multidimensional structures with useful magnetic properties, even magnetic ordering [3], when combined with suitable coordination metal centers. On the other hand, diamagnetic cyanometallate entities do not show noticeable magnetic properties, but due to the rigidity of the structure, these frameworks are potentially useful as analogues to zeolites [6]. Square planar tetracyanometallates, which are generally formed by d^8 metal ions, have received little

* Corresponding authors.
E-mail addresses: ezangrando@units.it (E. Zangrando), icnrc@iacs.res.in (N. Ray Chaudhuri).

0277-5387/$ - see front matter © 2007 Elsevier Ltd. All rights reserved.
doi:10.1016/j.poly.2007.02.028

attention for designing coordination polymers and a literature survey reveals that reports on coordination polymers using $[Pd(CN)_4]^{2-}$ or $[Pt(CN)_4]^{2-}$ as building blocks are scarce [7,8].

Recently our group reported [5] a novel porous framework, $\{[Cu_2(medpt)_2Ni(CN)_4](ClO_4)_2 \cdot 2.5H_2O\}_n$ [medpt = bis(3-aminopropyl)methylamine], where all the CN groups of $Ni(CN)_4^{2-}$ are involved in bridging, and this material retains crystallinity upon removal of water guest molecules. The dehydrated species shows novel zeolitic properties. Related heterometallic frameworks of Cu(II) with $Ni(CN)_4^{2-}$ along with their magneto structural correlations have also been reported by us [9]. Thus, as an extension of our work on these systems we report here the synthesis, crystal structure, thermal study and magnetic behavior of $[Cu(dpt)Pd(CN)_4]_n$ (**1**), $\{[Cu_2(medpt)_2Pd(CN)_4](ClO_4)_2 \cdot 3H_2O\}_n$ (**2**), $\{[Cu_2(dien)_2Pd(CN)_4](ClO_4)_2 \cdot 2CH_3OH\}_n$ (**3**) and $\{[Cu_2(i\text{prdien})_2Pd(CN)_4](ClO_4)_2 \cdot 2H_2O\}_n$ (**4**) [dpt = 3,3′-iminobispropylamine; medpt = 3,3′-diamino-*N*-methyldipropylamine; dien = diethylenetriamine and *i*prdien = *N*′-isopropyldiethylenetriamine]. Of these, complex **4** is a rare example of a 2D coordination polymer in tetracyanometallato-bridged systems.

2. Experimental

2.1. Materials

High purity 3,3′-iminobispropylamine (dpt); 3,3′-diamino-*N*-methyldipropylamine (medpt); diethylenetriamine (dien); *N*′-isopropyldiethylenetriamine (*i*prdien) and potassium tetracyanopalladate(II) trihydrate were purchased from the Aldrich Chemical Co. Inc. and were used as received. All other chemicals were of AR grade.

2.2. Physical measurements

Elemental analysis (carbon, hydrogen and nitrogen) was performed using a Perkin–Elmer 240C elemental analyzer. IR spectra were measured from KBr pellets on a Nicolet 520 FTIR spectrometer. Magnetic measurements were carried out in the "Servei de Magnetoquímica (Universitat de Barcelona)" on polycrystalline samples (30 mg) with a Quantum Design SQUID MPMS-XL magnetometer working in the 2–300 K range, the magnetic field was 0.1 T. The diamagnetic corrections were evaluated from Pascal's constants. Thermal analysis was done on a Perkin–Elmer Pyris Diamond system.

2.3. Synthesis

Suitable single crystals of complexes **1**–**4** were obtained from the filtrate derived after mixing the reactants and stirring for 30 min. Syntheses were conducted in water–methanol (2:1) and the chemical reactions are schematically given below:

$$2n\text{Cu}(\text{ClO}_4)_2 \cdot 6\text{H}_2\text{O} + 2n\text{dpt} + n\text{K}_2[\text{Pd}(\text{CN})_4] \rightarrow [\text{Cu}(\text{dpt})\text{Pd}(\text{CN})_4]_n \quad (1)$$

$$2n\text{Cu}(\text{ClO}_4)_2 \cdot 6\text{H}_2\text{O} + 2n\text{medpt} + n\text{K}_2[\text{Pd}(\text{CN})_4] \rightarrow \{[\text{Cu}_2(\text{medpt})_2\text{Pd}(\text{CN})_4](\text{ClO}_4)_2 \cdot 3\text{H}_2\text{O}\}_n \quad (2)$$

$$2n\text{Cu}(\text{ClO}_4)_2 \cdot 6\text{H}_2\text{O} + 2n\text{dien} + n\text{K}_2[\text{Pd}(\text{CN})_4] \rightarrow \{[\text{Cu}_2(\text{dien})_2\text{Pd}(\text{CN})_4](\text{ClO}_4)_2 \cdot 2\text{CH}_3\text{OH}\}_n \quad (3)$$

$$2n\text{Cu}(\text{ClO}_4)_2 \cdot 6\text{H}_2\text{O} + 2ni\text{prdien} + n\text{K}_2[\text{Pd}(\text{CN})_4] \rightarrow \{[\text{Cu}_2(i\text{prdien})_2\text{Pd}(\text{CN})_4](\text{ClO}_4)_2 \cdot 2\text{H}_2\text{O}\}_n \quad (4)$$

2.3.1. *[Cu(dpt)Pd(CN)$_4$] (1)*

A methanolic solution (10 ml) of 3,3′-iminobispropylamine (dpt) (2 mmol, 0.262 g) was added dropwise to an aqueous solution (10 ml) of $Cu(ClO_4)_2 \cdot 6H_2O$ (2 mmol, 0.740 g) with constant stirring over a few minutes. To the resulting deep blue solution, an aqueous solution (10 ml) of $K_2[Pd(CN)_4] \cdot 3H_2O$ (1 mmol, 0.342 g) was added slowly and the reaction mixture was stirred for 30 min and then filtered, and the filtrate was kept in a $CaCl_2$ desiccator. Shiny deep blue single crystals suitable for X-ray analysis were obtained after a few days. Yield: 80%. *Anal.* Calc. for $C_{10}H_{17}CuN_7Pd$ (405.25): C, 29.61; H, 4.19; N, 24.18. Found: C, 29.13; H, 4.03; N, 23.81%. The infrared spectra exhibited the following absorptions: 3304(vs), 3219(s), 3144(vs), 2932(vs), 2864(s), 2183(s), 2140(vs), 1594(s), 1434(w), 1275(w), 1151(s), 1028(w), 999(vw), 896(vw), 697(vw), 512(vw) cm^{-1}.

2.3.2. *[Cu$_2$(medpt)$_2$Pd(CN)$_4$](ClO$_4$)$_2$ · 3H$_2$O (2), [Cu$_2$(dien)$_2$Pd(CN)$_4$](ClO$_4$)$_2$ · 2CH$_3$OH (3) and [Cu$_2$(iPrdien)$_2$Pd(CN)$_4$](ClO$_4$)$_2$ · 2H$_2$O (4)*

The complexes were synthesized following the procedure adopted for complex **1** using 3,3′-diamino-*N*-methyldipropylamine (medpt) (2 mmol, 0.290 g), diethylenetriamine (dien) (2 mmol, 0.206 g) and *N*′-isopropyldiethylenetriamine (*i*prdien) (2 mmol, 0.284 g) for **2**, **3** and **4**, respectively instead of dpt. Suitable blue crystals of **2**, **3** and **4** for X-ray diffraction analysis were obtained from the filtrate kept in a $CaCl_2$ desiccator. The yields were 72%, 70 % and 74% for **2**, **3** and **4**, respectively.

Elemental analyses are in good agreement with the calculated values. *Anal.* Calc. for $C_{18}H_{44}Cl_2Cu_2N_{10}O_{11}Pd$ (**2**) (881.01): C, 24.51; H, 4.99; N, 15.89. Found: C, 24.82; H, 4.81; N, 16.12%. IR spectra: 3500–3030(sbr), 2975(vs), 1899(s), 2159(vs), 1600(s), 1457(s), 1275(w), 1219(vw), 1127(vs), 1114(vs), 1090(vs), 1021(w), 1004(vw), 932(w), 763(w), 691(w), 628(w), 533(w), 420(w) cm^{-1}. *Anal.* Calc. for $C_{14}H_{34}Cl_2Cu_2N_{10}O_{10}Pd$ (**3**) (806.89): C, 20.82; H, 4.21; N 17.35. Found: C, 21.09; H, 4.12; N, 17.73%. IR spectra: 3550–3320(sbr), 3314(s), 3239(vs), 3153(s), 2957(s), 2891(w), 2189(s), 2161(vs), 2141(s), 1632(s), 1602(vs), 1460(w), 1256(w), 1141(vs), 1130(vs), 1089(vs), 1025(s), 975(vw), 712(vw), 629(s), 527(w), 435(vw) cm^{-1}. *Anal.* Calc. for

$C_{18}H_{42}Cl_2Cu_2N_{10}O_{10}Pd$ (**4**) (863.00): C, 25.03; H, 4.86; N, 16.22. Found: C, 25.47; H, 4.67; N, 16.52%. IR spectra: 3550–3310(sbr), 3286(s), 3214(vs), 3171(s), 2969(vs), 2926(s), 2188(vs), 2166(w), 2137(vs), 1603(vs), 1449(w), 1383(w), 1160(w), 1124(vw), 1100(w), 1043(vw), 990(w), 676(w), 440(vw) cm^{-1}.

2.4. Crystallographic data collection and refinement

Diffraction data of complex **4** were collected at room temperature on a Brucker Kappa CCD imaging plate mounted on a Nonius FR591 rotating anode ($\lambda = 1.54178$ Å), those of **1**, **2** and **3** on a Nonius DIP-1030H system with Mo Kα radiation ($\lambda = 0.71073$ Å). Cell refinement, indexing and scaling of the data sets were carried out using programs DENZO [10] and SCALEPACK [10]. All the structures were solved by Patterson and Fourier analyses [11] and refined by the full-matrix least-squares method based on F^2 with all observed reflections [11]. The ΔF maps of **2** revealed some residuals interpreted as three water oxygens (0.5 occupancy each, H atoms not assigned), while a molecule of water (H atoms from Fourier map) and one of methanol was found in the crystal structures of **4** and of **3**, respectively. The hydrogen atoms were placed at geometrically calculated positions, except those of water molecules as indicated above. Crystallographic data and experimental details are reported in Table 1. All the calculations were performed using the WINGX System, Ver 1.70.01 [12].

3. Results and discussion

3.1. Description of the structures

The X-ray structure determinations of complexes **1**–**4** reveal coordination polymers built up by Cu(triamine) units connected through bridging tetracyanopalladate anions. In all of these structures the copper(II) atom exhibits a distorted square pyramidal coordination sphere accomplished by the tridentate amine ligand and a cyanide nitrogen in the basal plane, whereas the apex is occupied by another CN group from a symmetry related $[Pd(CN)_4]^{2-}$ anion. The coordination bond lengths and angles are reported in Table 2 together with other relevant geometrical data. These values compare well with those found in the analogous $[Ni(CN)_4]^{2-}$ complexes [9].

3.1.1. Complex *1*

Complex **1** is isomorphous and isostructural to the $[Ni(CN)_4]^{2-}$ derivative [13] and it consists of neutral $-[Cu(dpt)–Pd(CN)_4]_n-$ polymers having a zigzag arrangement developed along the *b*-axis, where $Pd(CN)_4^{2-}$ anions connect Cu(dpt) units in a *cis* fashion (Figs. 1 and 2). The Cu–N bond distances in the basal plane of the square pyramidal geometry (range 2.006(4)–2.039(3) Å) are significantly shorter than that observed for the apical Cu–N bond, 2.193(4) Å. The donor atoms in the base display a slight tetrahedral distortion (±0.084 Å) with the copper displaced by about 0.266(2) Å towards the vertex of the

Table 1
Crystal data and details of the structure determination for complexes **1**–**4**

Complex	**1**	**2**	**3**	**4**
Formula sum	$C_{10}H_{17}CuN_7Pd$	$C_{18}H_{44}Cl_2Cu_2N_{10}O_{11}Pd$	$C_{14}H_{34}Cl_2Cu_2N_{10}O_{10}Pd$	$C_{18}H_{42}Cl_2Cu_2N_{10}O_{10}Pd$
Formula weight	405.25	881.01	806.89	863.00
Wavelength (Å)	0.71073	0.71073	0.71073	1.54178
Crystal system	monoclinic	monoclinic	triclinic	monoclinic
Space group	$P2_1/n$	$P2_1/m$	$P\bar{1}$	$P2_1/c$
a (Å)	11.587(3)	7.787(3)	7.063(2)	14.313(4)
b (Å)	10.270(3)	14.857(5)	7.634(2)	9.065(3)
c (Å)	13.679(4)	15.257(3)	14.469(4)	14.563(5)
α (°)			92.804(10)	
β (°)	108.64(2)	96.73(2)	92.25(2)	111.45(2)
γ (°)			114.63(2)	
Cell volume (Å^3)	1542.4(8)	1752.9(10)	706.8(3)	1758.6(10)
Z	4	2	1	2
D_{calc} (g cm^{-3})	1.745	1.669	1.896	1.630
μ (mm^{-1})	2.542	1.924	2.374	7.396
F(000)	804	896	406	876
Reflections collected	15663	18241	7756	17211
Unique reflections	3593	4478	3191	2415
R_{int}	0.0455	0.0400	0.0290	0.0640
Reflections $I > 2\sigma(I)$	2776	3459	2393	1644
Parameters	173	242	180	202
Goodness-of-fit	0.953	0.979	0.957	1.039
R_1[a]	0.0368	0.0488	0.0399	0.0659
wR_2 ($I > 2\sigma(I)$)[a]	0.1019	0.1349	0.1073	0.1791
Residuals (e Å^{-3})	0.701, −0.557	1.021, −0.811	0.591, −0.504	0.688, −0.616

[a] $R_1 = \sum||F_o| - |F_c||/\sum|F_o|, wR_2 = [\sum w(F_o^2 - F_c^2)^2/\sum w(F_o^2)^2]^{1/2}$.

Table 2
Selected bond lengths (Å) and angles (°) of complexes **1**–**4**

	1	2	3	4
Pd–C(4)	1.999(4)	2.003(4)	1.996(4)	1.993(11)
Pd–C(5)	1.993(4)	1.998(4)	2.015(4)	1.993(12)
Pd–C(6)	1.988(5)			
Pd–C(7)	1.987(5)			
Cu–N(1)	2.023(3)	2.024(4)	2.016(4)	2.049(9)
Cu–N(2)	2.039(3)	2.077(3)	2.007(3)	2.007(8)
Cu–N(3)	2.003(4)	2.014(4)	2.030(4)	2.044(10)
Cu–N(4)	2.023(3)	2.030(4)	1.999(3)	1.974(8)
Cu–N(5′)	2.193(3)	2.191(4)	2.337(4)	2.166(11)
N(1)–Cu–N(2)	94.07(13)	94.60(17)	84.02(13)	84.6(4)
N(1)–Cu–N(3)	166.65(17)	166.10(18)	161.00(15)	154.6(5)
N(1)–Cu–N(4)	84.05(14)	83.27(18)	94.33(14)	89.8(4)
N(1)–Cu–N(5′)	93.36(13)	92.91(19)	98.51(15)	108.3(4)
N(2)–Cu–N(3)	92.71(15)	92.54(14)	83.96(13)	82.7(4)
N(2)–Cu–N(4)	159.99(14)	161.50(16)	169.59(13)	158.0(4)
N(2)–Cu–N(5′)	99.40(14)	98.12(14)	91.68(13)	99.1(4)
N(3)–Cu–N(4)	85.64(16)	86.17(16)	94.83(14)	93.9(4)
N(3)–Cu–N(5′)	96.87(18)	97.87(17)	96.50(15)	95.4(4)
N(4)–Cu–N(5′)	100.60(14)	100.34(17)	98.73(13)	102.9(3)
C(4)–N(4)–Cu	176.2(3)	176.6(4)	175.9(4)	168.1(9)
C(5′)–N(5′)–Cu	141.1(3)	154.6(4)	178.1(4)	172.2(8)
Pd–Pd[a]	6.813	7.597	7.952	8.471
Pd–Pd–Pd	97.83	155.80	180.0	64.70/115.30

Symmetry codes for primed atoms: $-x+3/2,\ y+1/2,\ -z+3/2$ (**1**); $-x+2,\ -y+1,\ -z+1$ (**2**); $-x+2,\ -y+1,\ -z$ (**3**); $-x+2,\ y-1/2,\ -z+1/2$ (**4**).

[a] Intra-chain distance in **1**–**3**, edge of the net in **4**.

pyramid. Correspondingly Pd–C bond distances are comparable within their e.s.d.'s [1.987(5)–1.999(4) Å]. The C–N–Cu coordination angles involving the cyano groups are significantly different, being 141.1(4)° and 176.1(4)° for the group located at the vertex and in the basal plane

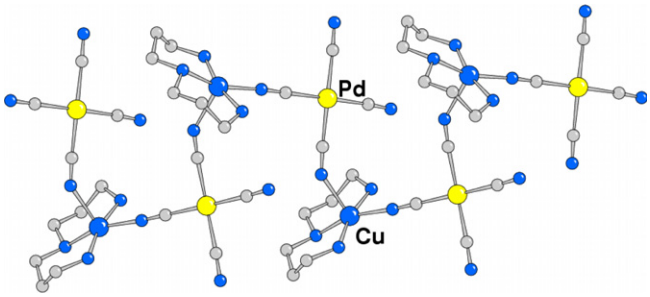


Fig. 1. Coordination polymer of complex **1**.

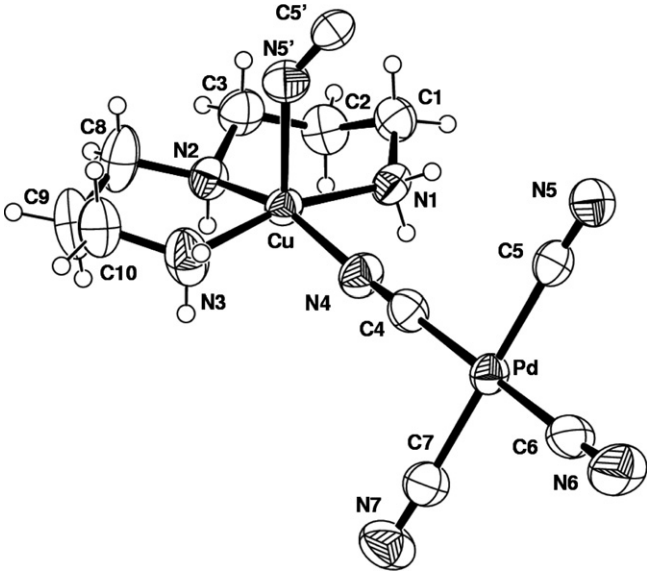


Fig. 2. ORTEP drawing (40% probability level) of the metal coordination spheres of complex **1**.

Table 3
H-bonding in complexes **1**–**4**

D–H···A	*d*(D–H)	*d*(H···A)	∠DHA	*d*(D···A)	Symmetry
Complex ***1***					
N1–H1b···N6	0.900	2.168	161.93	3.036	$[x-1/2, -y+3/2, z-1/2]$
N2–H2···N7	0.910	2.080	175.28	2.988	$[-x+1/2, y+1/2, -z+3/2]$
N3–H3b···N7	0.900	2.472	135.36	3.176	$[-x+1, -y+2, -z+2]$
Complex ***2***					
N1–H1a···O1w	0.900	2.140	170.25	3.031	$[x, -y+1/2, z]$
N1–H1b···O1w	0.900	2.142	145.76	2.930	$[-x+1, y+1/2, -z+1]$
N1–H1b···O4	0.900	2.367	171.94	3.260	$[-x+1, y+1/2, -z+1]$
N3–H3a···O3w	0.900	2.181	175.33	3.079	$[-x+1, -y+1, -z+1]$
Complex ***3***					
N1–H1a···O4	0.900	2.322	150.43	3.136	
N1–H1b···O5	0.900	2.053	172.46	2.948	$[-x+2, -y, -z]$
N2–H2···O2	0.910	2.068	168.82	2.966	$[x+1, y+1, z]$
N3–H3b···O5	0.900	2.341	149.84	3.151	$[-x+1, -y, -z]$
O5–H5···O2	0.820	2.212	152.12	2.961	$[-x+1, -y, -z]$
Complex ***4***					
N1–H1···O2	0.910	2.363	157.19	3.221	
N2–H2···O1w	0.910	2.149	149.82	2.971	$[x, -y+1/2, z-1/2]$
N3–H3b···O1w	0.900	2.204	150.08	3.018	
O1w–H1···O1	1.166	1.812	170.08	2.967	
O1w–H2···O3	1.163	2.054	129.73	2.937	$[-x+1, y-1/2, -z+1/2]$

of the square pyramid, respectively. It is obvious that the configuration of this and other polymers depend on the latter values and also on the orientation assumed by the $Pd(CN)_4$ plane with respect to the copper environment. The formation of weak H-bonding interactions (Table 3) between the $–NH_2$ groups and uncoordinated cyano nitrogen atoms of adjacent chains gives rise to a 3D supramolecular architecture.

3.1.2. Complexes 2 and 3

These structures appear very similar at a first glance, showing cationic 1D coordination polymeric chains, $–[Pd(CN)_4Cu_2(L)_2]_n–$ (L = medpt for **2** and dien for **3**), where the tetracyanopalladate groups have all μ-bridging CN ligands (Fig. 3). However the Pd atoms in the case of **2** have a zigzag arrangement (Pd···Pd···Pd angle 155.80°) separated by 7.597 Å, whilst in **3** they are collinear (Pd···Pd···Pd = 180.0°) at a distance of 7.952 Å (Table 2). The charge is counterbalanced by perchlorate anions.

The ORTEP drawings of the Cu(II) coordination sphere with the atom labeling scheme are shown in Figs. 4 and 5. In both complexes the square pyramidal coordination environment shows the basal Cu–N bond distances significantly shorter with respect to the apical ones, which are 2.191(4) and 2.337(4) Å in **2** and **3**, respectively, and the latter is the longest among those reported by us for CN–Cu bond lengths. The square planar basal plane displays almost coplanar nitrogen donors with the Cu ion slightly displaced by about 0.259(2) and 0.229(2) Å in **2** and **3**, respectively, towards the vertex of the pyramid. The palladium atom in the $Pd(CN)_4^{2-}$ anions is located on a crystallographic symmetry plane in **2** and on a inversion center in **3**. The Pd–C bond distances are comparable within 3σ, varying in the range 1.996(4)–2.015(4) Å. The cyanide groups reveal different coordination geometries, being almost linearly coordinated to copper (175.9(4)–178.1(4)°), with the exception of that located at the apical position of the square pyramidal sphere of copper in **2** (C(5)–N(5)–Cu 154.6(4)°). The polymers are involved in a H-bonding (Table 3), evolved through the amine groups, the perchlorate anions and the lattice water molecules in **2**, which enhances the dimensionality to 3D. The packing appears to be determined by the number of methylene units and the methyl groups at the ancillary medpt triamine

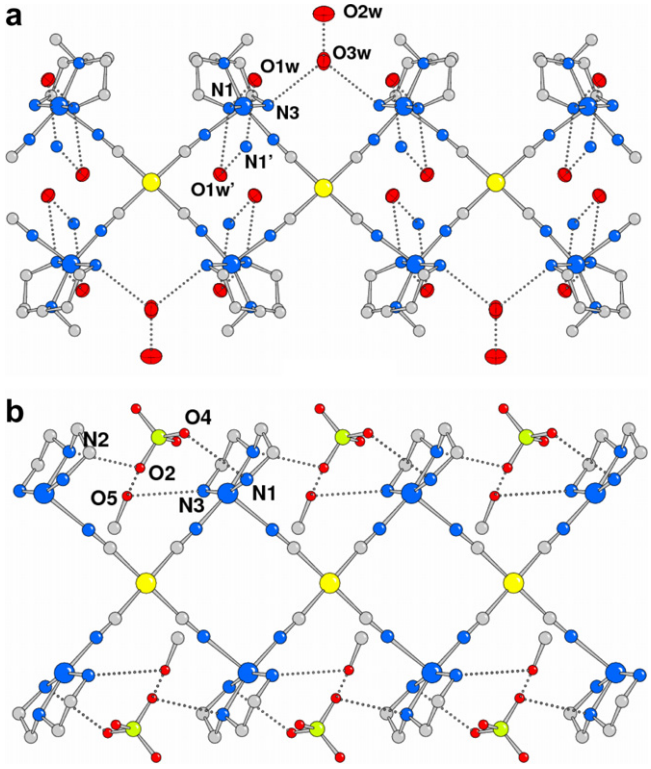


Fig. 3. Coordination polymer of complexes **2** and **3** with H-bonds (dotted lines) involving lattice amine groups with water molecules (a) and perchlorate and methanol molecules (b).

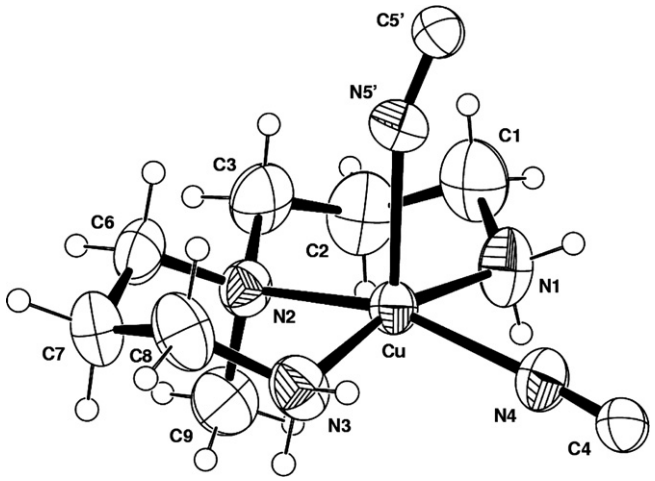


Fig. 4. ORTEP drawing (40% probability level) of the copper coordination sphere of complex **2**.

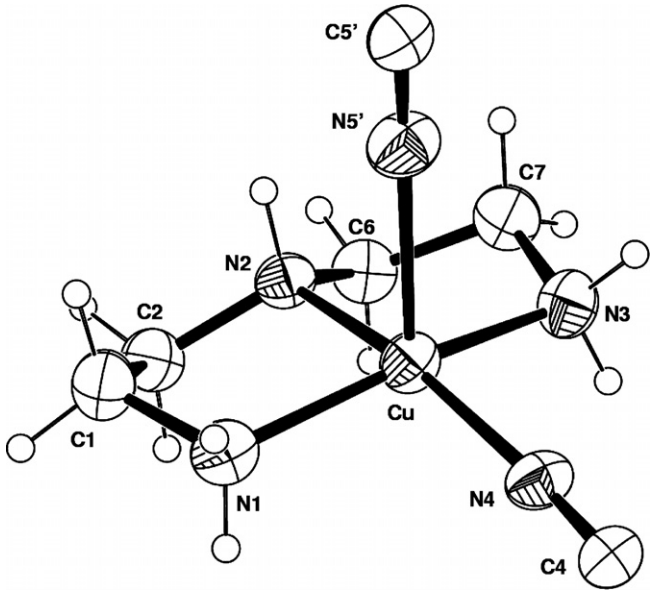


Fig. 5. ORTEP drawing (40% probability level) of the copper coordination sphere of complex **3**.

ligand, the void space (amongst the chains) being occupied by the counter anions and ultimately by solvent molecules.

Complex **2** is isomorphous and isostructural to the tetranickellate derivative [5], differing only by a small amount due to the disordered lattice water molecules. The water molecule O(3w) (which is appended to O(2w)) bridges through H-bonding to symmetry related N(3) atoms, while O(1w) enhances the dimensionality to 3D by connecting N(1) amines of adjacent chains (Fig. 3). On the other hand, it is worth noting that complex **3**, with dien ligands, crystallizes in a different space group than that detected with $Ni(CN)_4^{2-}$ anions [9]. This is due to the presence of a lattice methanol, used for crystallization, rather than a water molecule which also modifies the topological arrangement of the dien ligands along the chain. Beside the intra-chain H-bonds depicted in Fig. 3, the methanol –OH group acts also as a H acceptor towards N(1), connecting close packed polymers. Although these interactions appear rather weak (Table 3), they give rise to a 3D arrangement. The H-bonding interaction involving the amine groups with the guest methanol molecules and perchlorate anions results in a different orientation assumed by the CuL moieties and thus affects the crystal symmetry. We have provided a simple scheme to indicate the polymer topology through an oriented vector indicating the Cu–N(2) bond [9], as shown in Fig. 6.

3.1.3. Complex *4*

The crystal structure includes 2D rhomboid grid sheets extended in the *bc* plane, perchlorate anions and lattice water molecules. The Pd(II) ions, located on inversion centers, occupy the knots of the grid and are linked by the –CN–Cu(*i*prdien)–NC– units at a distance of 8.471(2) Å (Fig. 7). A side view (Fig. 7, down) indicates a pattern very similar to that of the 1D polymers **2** and **3**. In the distorted square pyramidal geometry of copper (Fig. 8), the central Cu–N(*i*prdien) bond distance, of 2.007(8) Å, is shorter than the others 2.049(9), 2.044(10) Å, and the Cu–N(nitrile) in

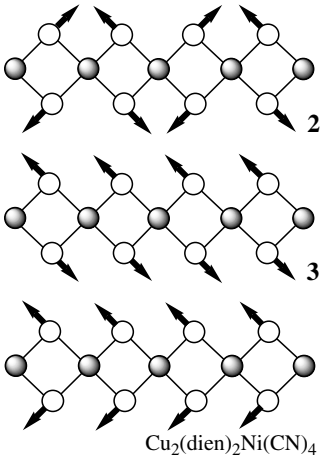


Fig. 6. Coordination polymer topologies of **2**, **3** and of $-[Cu_2(dien)_2Ni(CN)_4]_n^-$ [9].

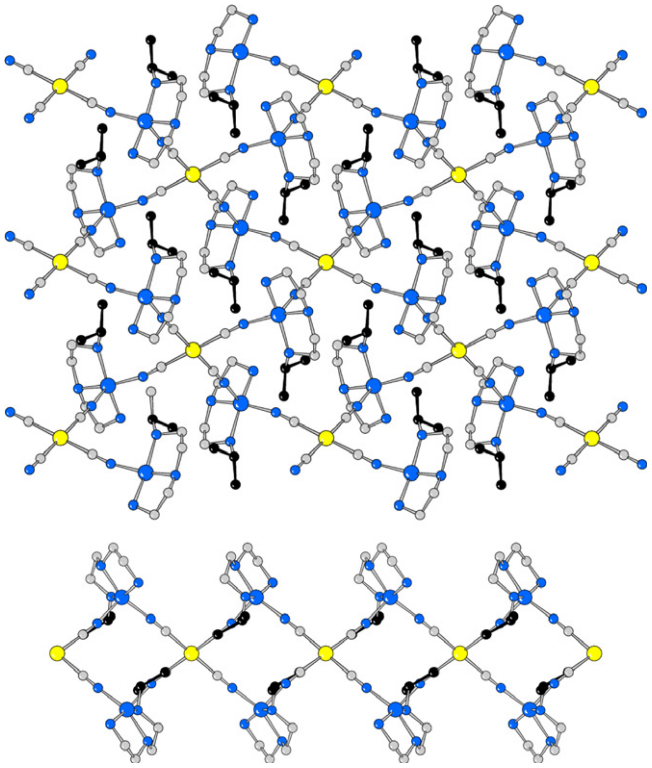


Fig. 7. 2D layered structure of **4** extended in the *bc* plane and side view down the *b* axis (*i*-propyl group of triamine ligand evidenced in black).

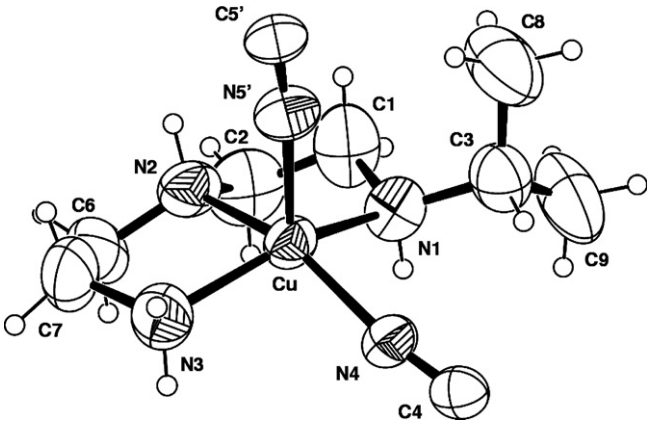


Fig. 8. ORTEP drawing (40% probability level) of the copper coordination sphere of complex **4**.

the pyramid base is considerably shorter (1.974(8) Å) with respect to the apical one (2.166(11) Å). The packing shows an H-bonding motive built by $-[H_2O-(ClO_4)]_n-$ chains running along the *b* axis, (Fig. 9), where each lattice water molecule plays a crucial role in giving rise to a 3D network arrangement, acting as a double H-bond donor towards ClO_4^- oxygens and double acceptor towards N(2) and N(3) amine groups (Table 3).

With regard to structures **2** and **3**, and to the strictly related 1D polymers built up by $[Ni(CN)_4]^{2-}$ anions, complex **4**, represents an unexpected outcome since it has the same molecular formula. It is difficult to rationalize how

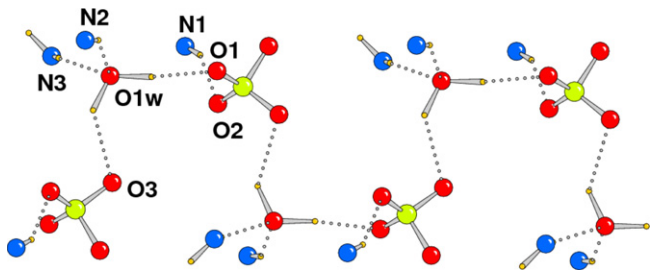


Fig. 9. The H-bonding motive involving water molecules, ClO_4^- anions and amine nitrogens from different layers.

the bulkiness of the ancillary ligand *i*prdien may affect the orientation of the $[Pd(CN)_4]^{2-}$ mean plane in the copper coordination and ultimately the crystal packing towards a 2D architecture. As a matter of fact the complex $[Ni_2(tren)_2Pt(CN)_4](ClO_4)_2$ (tren = tris(2-aminoethyl)amine) [8e], of the same formulation as **2**–**4**, still presents a 1D polymeric structural motif. A few examples of 2D layered structures containing tetracyano anions have been reported. Among them it is worth noting that the neutral structures reported by Gutierrez [7a], [Ni(dien)M(CN)$_4$] (M = Pd, Pt), were formed by hexacoordinated Ni(II) units that have more degrees of freedom in the network assembly with respect to pentacoordinated Cu(II).

3.2. Magnetic properties

The magnetic properties of complexes **1**–**4** as $\chi_M T$ vs T plots (χ_M is the molar magnetic susceptibility for one Cu(II) ion) and the reduced magnetization ($M/N\beta$ vs H) are shown in Figs. 10–13. The values of $\chi_M T$ at 300 K varies from 0.41 to 0.43 $cm^3\ mol^{-1}$ K for complexes **1**–**4** respectively, as expected for one magnetically quasi-isolated spin doublet ($g > 2.00$). Starting from room temperature, the $\chi_M T$ values are practically constant to 50 K and below this temperature they quickly decrease to 0.34–0.40 $cm^3 mol^{-1}$K at 2 K. This feature indicates a very weak antiferromagnetic interaction. The reduced molar magnetization at 2 K (Figs. 11–13 inset) clearly corroborates that the antiferromagnetic coupling is very small. The $M/N\beta$ value at 5 T is close to 1.0 $N\beta$ in all four cases and the curve follows the Brillouin function for a g value close to 2.10.

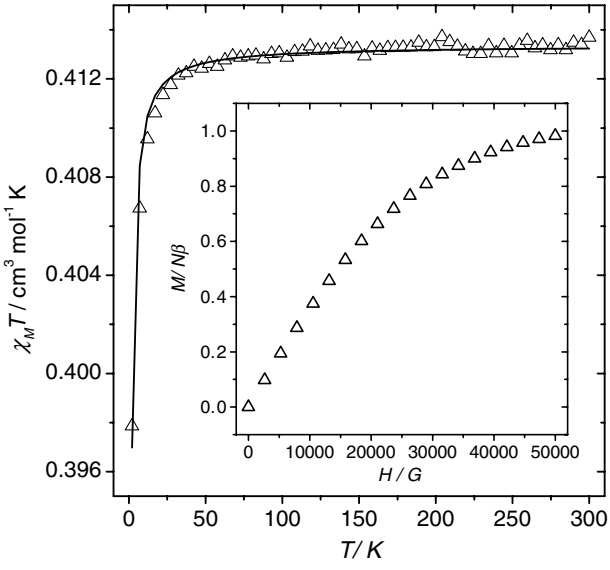


Fig. 10. Plot of $\chi_M T$ vs T for complex **1** (solid line indicates the best fit). Inset: plot of the reduced magnetization ($M/N\beta$) vs T at 2 K.

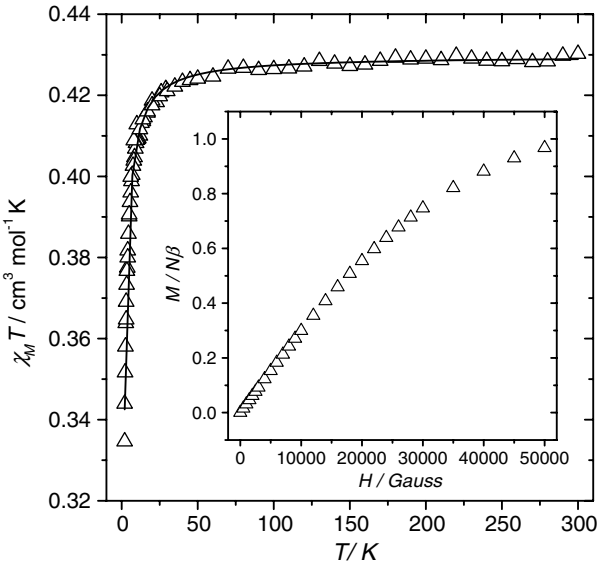


Fig. 11. Plot of $\chi_M T$ vs T for **2** (solid line indicates the best fit). Inset: plot of the reduced magnetization ($M/N\beta$) vs T at 2 K.

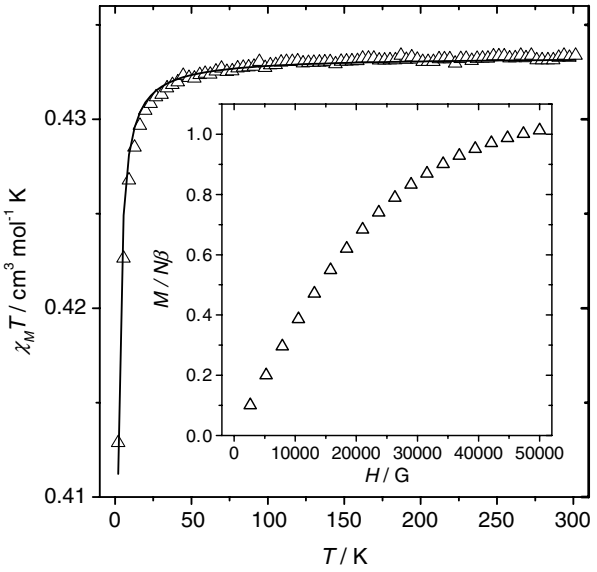


Fig. 12. Plot of $\chi_M T$ vs T for **3** (solid line indicates the best fit). Inset: plot of the reduced magnetization ($M/N\beta$) vs T at 2 K.

Complexes **1**–**4** are actually 1D and 2D copper(II) entities with $[Pd(CN)_4]^{2-}$ as bridging ligand, and all the copper(II) ions show a distorted square planar geometry. For **1**–**3** (1D systems) we have fitted the experimental data

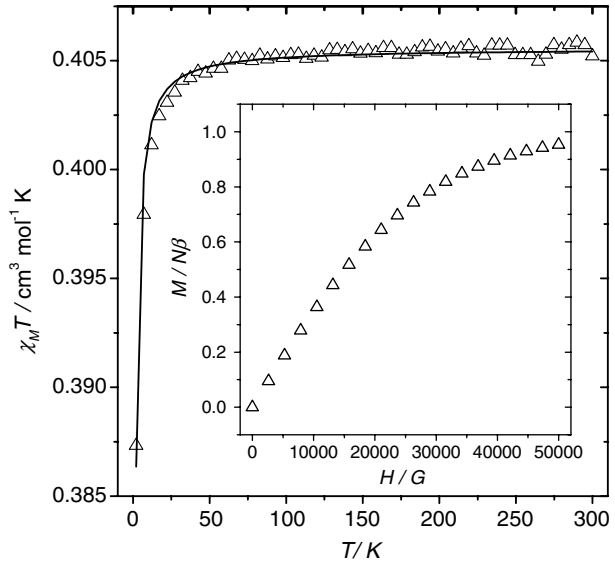


Fig. 13. Plot of $\chi_M T$ vs T for **4** (solid line indicates the best fit). Inset: plot of the reduced magnetization (M/Nβ) vs T at 2 K.

applying the formula for a uniform 1D copper(II) system, given by Bonner and Fisher [14]. The main structural data are indicated in Table 4 together with the best-fit parameters obtained. The 2D layer of complex **4** can be considered as a pseudo-quadratic net. Taking into account these structural features, we have fitted the susceptibility data by the expression given by Rushbrooke and Wood for a Heisenberg square planar system [15]. The calculated J and g values are given in Table 4. The small (almost negligible) J values for the four complexes can be interpreted as a consequence of the almost nil overlap between the copper(II) ions through the long diamagnetic $[Pd(CN)_4]^{2-}$ bridge. These too small J values do not allow any attempt to draw magneto-structural correlations, because in all cases the intermolecular interactions have not been taken into account in the formulae used. These interactions can have the same order of magnitude of the main J values. Looking at the literature, we note several copper(II) systems with diamagnetic $[M(CN)_4]^{2-}$ bridging ligands (M = Ni, Pd, Pt), but without magnetic studies [16b,16c,16d,16e]. The number of analogous complexes with magnetic studies is scarce, giving always very small antiferromagnetic coupling [7b,16a].

The magnetism of these four new Pd–Cu complexes is similar (but in general, smaller) to those previously reported for the analogous $[Ni(CN)_4]^{2-}$ derivatives. Considering the small J values in both series (Ni and Pd) it is impossible to draw any conclusion, because together with the intra-chain coupling, there are also inter-chains magnetic pathways that, due to the diamagnetic character of the cyanide bridge, can be of a similar order. Thus these diamagnetic ligands do not allow a strong (or medium) magnetic coupling, as expected.

3.3. Thermal studies

Complex **1** is stable up to 150 °C and it collapses beyond this temperature. The TG profile of complex **2** shows

Table 4
Structural and magnetic parameters of complexes **1**–**4**, and comparison with $[Ni(CN)_4]^{2-}$ analogues

Complex	Structure	τ	d[a] (Å)	Pathways	J (cm^{-1})	g
1	single chain	0.11	short = 2.022 long = 2.193	short–long	−0.20	2.10
2	double chain	0.08	short = 2.030 long = 2.191	long–long short–short short–long	−0.24	2.12
3	double chain	0.14	short = 1.999 long = 2.337	long–long short–short short–long	−0.22	2.15
4	2D	0.06	short = 1.974 long = 2.166	long–long short–short short–long	−0.19	2.08
Ni analogues (numbering corresponding to Ref. [9])						
4	single chain	0.115	short = 2.003 long = 2.171	short–short long–long	−1.96	2.20
1	double chain	0.105	short = 2.020 long = 2.186	short–short short–long long–long	−1.45	2.10
2	double chain	0.067	short = 2.008 long = 2.290	short–short short–long long–long	−0.56	2.12
3	double chain	0.110	short = 1.981 long = 2.297	short–short short–long	−1.39	2.20
		0.160	short = 1.967 long = 2.244	long–long		

[a] short = equatorial; long = apical.

(Fig. 1S) that the loss of lattice water molecules starts at 30 °C and the sample becomes completely deaquated at 40 °C. The deaquated species is stable up to 170 °C and shows decomposition upon further heating. Thermogravimetric analysis (Fig. 2S) of complex **3** reveals that it starts to lose solvent molecules at 65 °C and the process completes at 225 °C. The desolvated species collapses immediately upon further heating. The range of temperatures of desolvation and the collapse of the network immediately after desolvation corroborate the participation of lattice methanol in constructing the 3D supramolecular architecture. Complex **4** shows deaquation (Fig. 3S) in the temperature range 40–100 °C, and the corresponding dehydrated species is stable up to 150 °C, showing decomposition beyond this temperature.

4. Conclusion

We have demonstrated that square planar tetracyanometallates are proper building blocks for designing polynuclear cyano-bridged complexes in conjunction with suitable Cu(II)-triamine units, having the copper ion in a square pyramidal coordination geometry. The structure determinations reveal **1** and **2** are isomorphous to the corresponding $[Ni(CN)_4]^{2-}$ derivatives, but the presence of methanol used in the crystallization of **3** modifies the polymer topology. Finally, in **4** the use of *i*prdien as an ancillary ligand results in an unexpected 2D layered structure. The H-bonding interactions enhance the dimensionality to 3D and play a key role in designing the topology of the coordination polymers.

Acknowledgement

N. R. C. thanks the Council of Scientific and Industrial Research, New Delhi and J.R. thanks the Spanish Goverment (BQU2003/00539) for financial support.

Appendix A. Supplementary material

CCDC 617821, 617822, 617823 and 617824 contain the supplementary crystallographic data for **1**, **2**, **3** and **4**. These data can be obtained free of charge via http://www.ccdc.cam.ac.uk/conts/retrieving.html, or from the Cambridge Crystallographic Data Centre, 12 Union Road, Cambridge CB2 1EZ, UK; fax: (+44) 1223-336-033; or e-mail: deposit@ccdc.cam.ac.uk. Supplementary data associated with this article can be found, in the online version, at doi:10.1016/j.poly.2007.02.028.

References

[1] (a) M. Eddaoudi, J. Kim, N. Rosi, D. Vodak, J. Wachter, M. O'Keeffee, O.M. Yaghi, Science (Washington, D.C.) 295 (2002) 469;
(b) C. Boskovic, E.K. Brechin, W.E. Streib, K. Folting, J.C. Bollinger, D.N. Hendrickson, G. Christou, J. Am. Chem. Soc. 124 (2002) 3725;
(c) S.A. Bourne, J. Lu, A. Mondal, B. Moulton, M.J. Zaworotko, Angew. Chem., Int. Ed. 40 (2001) 2111;
(d) M.E. Davis, Nature (London) 417 (2002) 813;
(e) S.S.-Y. Chui, S.M.–F. Lo, J.P.H. Charmant, A.G. Orpen, I.D. Williams, Science (Washington, D.C.) 283 (1999) 1148;
(f) J.S. Seo, D. Whang, H. Lee, S.I. Jun, J. Oh, Y.J. Jeon, K. Kim, Nature (London) 404 (2000) 982.

[2] H.W. Roesky, M. Andruh, Coord. Chem. Rev. 236 (2003) 91.

[3] (a) A. Scuiller, T. Mallah, M. Verdaguer, A. Nivorozkhin, J.-L. Tholence, P. Veillet, New J. Chem. 20 (1996) 1;
(b) M. Ohba, N. Fukita, H. Okawa, Y. Hashimoto, J. Am. Chem. Soc. 119 (1997) 1011;
(c) R.J. Parker, L. Spiccia, K.J. Berry, G.D. Fallon, B. Moubaraki, K.S. Murray, Chem. Commun. (2001) 333;
(d) Z.J. Zhong, H. Seino, Y. Mizobe, M. Hidai, A. Fujishima, S. Ohkoshi, K. Hashimoto, J. Am. Chem. Soc. 122 (2000) 2952;
(e) J. Larionova, M. Gross, M. Pilkington, H. Andres, H. Stoeckli-Evans, H.U. Gudel, S. Decurtins, Angew. Chem., Int. Ed. 39 (2000) 1605;
(f) R. Podgajny, C. Desplanches, B. Sieklucka, R. Sessoli, V. Villar, C. Paulsen, W. Wernsdorfer, Y. Dromzee, M. Verdaguer, Inorg. Chem. 41 (2002) 1323;
(g) F. Thetiot, S. Triki, J.S. Pala, C.J. Gomez-Garcıa, S. Golhen, Chem. Commun. (2002) 1078;
(h) E. Coronado, C.J. Gomez-Garcia, A. Nuez, F.M. Romero, E. Rusanov, H. Stoeckli-Evans, Inorg. Chem. 41 (2002) 4615;
(i) H.-Z. Kou, S. Gao, C.-H. Li, D.-Z. Liao, B.C. Zhou, R.-J. Wang, Y.-D. Li, Inorg. Chem. 41 (2002) 4756;
(j) H.-Z. Kou, B.C. Zhou, S. Gao, D.-Z. Liao, R.-J. Wang, Inorg. Chem. 42 (2003) 5604.

[4] (a) H. Yuge, T. Iwamoto, J. Chem. Soc., Dalton Trans. (1994) 1237;
(b) A.J. Blake, N.R. Champness, P. Hubberstey, W.-S. Li, A. Withersby, M. Schroder, Coord. Chem. Rev. 183 (1999) 117;
(c) M. Eddaoudi, H. Li, O.M. Yaghi, J. Am. Chem. Soc. 122 (2000) 1391;
(d) C. Janiak, Angew. Chem., Int. Ed. 36 (1997) 1431;
(e) S. Willemin, J. Larionova, R. Clerac, B. Donnadieu, B. Henner, X.F. Le Goff, C. Guerin, Eur. J. Inorg. Chem. (2003) 1866.

[5] T.K. Maji, P.S. Mukherjee, G. Mostafa, E. Zangrando, N. Ray Chaudhuri, Chem. Commun. (2001) 1368.

[6] (a) T. Iwamoto, in: D.D. MacNicol, F. Toda, R. Bishop (Eds.), Comprehensive Supramolecular Chemistry, vol. 6, Pergamon Press, Oxford, 1996 (Chapter 19);
(b) I. Muga, J.M. Gutierrez-Zorrila, A. Luque, P. Roman, F. Lloret, Inorg. Chem. 36 (1997) 743.

[7] (a) I. Muga, J.M. Gutierrez-Zorrilla, P. Vitoria, P. Roma, Luis Lezama, J.I. Beitia, Eur. J. Inorg. Chem. (2004) 1886;
(b) J. Cernak, J. Skorsepa, K.A. Abboud, M.W. Meisel, M. Orendac, A. Orendacova, A. Feher, Inorg. Chim. Acta 326 (2001) 3;
(c) H. Zhang, J. Cai, X.-L. Feng, H.-Y. Sang, J.-Z. Liu, X.-Y. Li, L.-N. Ji, Polyhedron 21 (2002) 721;
(d) M. Ruegg, A. Ludi, Theor. Chim. Acta 20 (1971) 193;
(e) J. Cernak, J. Lipkowski, E. Cizmar, A. Orendacova, M. Orendac, A. Feher, M.W. Meisel, Solid State Sciences 5 (2003) 579;
(f) J. Kuchar, J. Cernak, K.A. Abboud, Acta Cryst. C60 (2004) m492;
(g) J. Liu, D.W. Knoeppel, S. Liu, E.A. Meyers, S.G. Shore, Inorg. Chem. 40 (2001) 2842;
(h) M. Morita, T. Miyoshi, T. Miyamoto, T. Iwamoto, Y. Sasaki, Bull. Chem. Soc. Jpn. 40 (1967) 1556.

[8] (a) I. Escorihuela, L.R. Falvello, M. Tomas, J. Cluster Sci. 15 (2004) 425;
(b) F. Bonadio, M.-C. Senna, J. Ensling, A. Sieber, A. Neels, H. Stoeckli-Evans, S. Decurtins, Inorg. Chem. 44 (2005) 969;
(c) R.W. Gable, B.F. Hoskins, R. Robson, Chem. Commun. (1990) 762;
(d) M. Munakata, J.C. Zhong, I. Ino, T. Kuroda-Sowa, M. Maekawa, Y. Suenaga, N. Oiji, Inorg. Chim. Acta 317 (2001) 268;
(e) M.-L. Flay, H. Vahrenkamp, Z. Anorg. Allg. Chem. 630 (2004) 2508.

[9] D. Ghoshal, A.K. Ghosh, T.K. Maji, J. Ribas, G. Mostafa, E. Zangrando, N. Ray Chaudhuri, Inorg. Chim. Acta 359 (2006) 593.
[10] Z. Otwinowski, W. Minor, Processing of X-ray Diffraction Data Collected in Oscillation Mode, in: C.W. CarterJr., R.M. Sweet (Eds.), Methods in Enzymology, Volume 276, Academic Press, New York, 1997, p. 307.
[11] SHELX97 Programs for Crystal Structure Analysis (Release 97-2). G.M. Sheldrick, University of Göttingen, Germany (1998).
[12] L.J. Farrugia, J. Appl. Crystallogr. 32 (1999) 837.
[13] Z. Smekal, I. Cisarova, J. Mrozinski, Polyhedron 20 (2001) 3301.
[14] J.C. Bonner, M.E. Fisher, Phys. Rev A 135 (1964) 640.
[15] G.S. Rushbrooke, P. Wood, Mol. Phys. 6 (1963) 409.
[16] (a) Z. Smekal, Z. Travnicek, J. Mrozinski, J. Marek, Inorg. Chem. Commun. 6 (2003) 1395;
(b) J. Cernaka, K.A. Abboud, Acta Cryst. C58 (2002) m167;
(c) N.F. Curtis, H. Puschmann, Acta Cryst. C60 (2004) m410;
(d) L.R. Falvello, M. Tomas, Chem. Commun. (1999) 273;
(e) M.-L. Flay, H. Vahrenkamp, Eur. J. Inorg. Chem. (2003) 1719.

Available online at www.sciencedirect.com
ScienceDirect
Polyhedron 26 (2007) 3205–3216
POLYHEDRON
www.elsevier.com/locate/poly

Coordination chemistry of 1,4-bis(carboxymethyl)-1,4,7-triazacyclononane: Synthesis and characterization of mononuclear and binuclear μ-oxo-bridged iron(III) complexes, and a 1D-helical copper(II) chain

Ute Kreher [a,b], Milton T.W. Hearn [b], Boujemaa Moubaraki [a], Keith S. Murray [a], Leone Spiccia [a,*]

[a] School of Chemistry, Monash University, Clayton, 3800 Victoria, Australia
[b] Centre for Green Chemistry, Monash University, Clayton, 3800 Victoria, Australia

Received 23 January 2007; accepted 21 February 2007
Available online 2 March 2007

Abstract

The syntheses of the pentadentate ligand 1,4-bis(carboxymethyl)-1,4,7-triazacyclononane ($\mathbf{LH_2}$) and its use in the preparation of $[LHCu]ClO_4$ (**1**), and a mononuclear iron(III) complex ([LFeCl] **(2)**) are reported. The hydrolysis of **2** in the presence of an excess of $NaClO_4$ resulted in the crystallization of a binuclear complex, $[Fe_2(\mu\text{-}O)L_2] \cdot (NaClO_4)_3 \cdot CH_3OH \cdot 3H_2O$ **(3)**. The crystal structures of **1**–**3** have been determined by single-crystal X-ray crystallography. In complex **1**, the Cu(II) centre is in square based pyramidal environment, with two nitrogen atoms from the tacn ring and two oxygen atoms from two different carboxylate groups lying in the basal plane and the third nitrogen atom occupying the apical position. One pendant acetic acid group is protonated and, instead of coordinating to the copper(II) centre, participates in hydrogen bonding interactions with the perchlorate counter-ion. The coordinated carboxylate group forms a bridge to the copper atom of an adjacent $[LHCu]^+$ molecule, thus generating 1D-helical chains. The compound exhibits weak ferromagnetic coupling probably due to weak interactions between $[LHCu]^+$ molecules. In complex **2**, the iron(III) centre is in a distorted octahedral geometry, with the *fac*-coordinated triamine ring, two carboxylate groups and one chloride ligand occupying the coordination sphere. In the binuclear complex **3**, two iron(III) centres are bridged by one oxygen atom to form a μ-oxo-diiron(III) complex with an Fe···Fe distance of 3.423(3) Å and a non-linear Fe–O–Fe angle of 144.4°. This binuclear complex features strong antiferromagnetic coupling between the two iron(III) centres.
Crown Copyright © 2007 Published by Elsevier Ltd. All rights reserved.

Keywords: Macrocyclic ligands; 1,4,7-triazacyclononane derivatives; Coordination chemistry; X-ray crystal structures; Oxo-bridged iron(III) dimer; Copper(II) complex

1. Introduction

Binuclear (and higher nuclearity) transition metal complexes featuring bridging groups between the metal centres have been widely studied over the past few decades. The drive for these studies derives from many quarters, with one major focus being complexes with novel molecular structures and magnetic behaviour [1–6]. Polynuclear complexes have also been actively pursued as models for multimetal centre units found at the active sites of important enzymes [7–10]. For example, oxo-bridged iron complexes have attracted considerable interest because diiron centres have been found at the active site of a variety of non-heme proteins (hemerythrin, purple acid phosphatase, ribonucleotide reductase, methane monooxygenase) [11–16].

Ligands based on 1,4,7-triazacyclononane, tacn, are particularly effective for forming binuclear (and higher nuclearity) complexes because they bind strongly to one

* Corresponding author. Fax: +61 3 99054597.
E-mail address: leone.spiccia@sci.monash.edu.au (L. Spiccia).

0277-5387/$ - see front matter. Crown Copyright © 2007 Published by Elsevier Ltd. All rights reserved.
doi:10.1016/j.poly.2007.02.027

face of the metal polyhedron while at the same time leaving one or more accessible coordination sites for the introduction of bridging ligands. The tacn macrocycle also lends itself readily to further structural elaboration through attachment of potentially coordinating pendant arms (e.g. pyridyl, carboxylate, phosphonate) or non-coordinating organic groups to one or more of the three secondary nitrogens of the tacn ring. Variation in the number and types of pendant groups incorporated into the ligand framework therefore offers a potential means of controlling metal complex stability, selectivity for particular metal ions, as well as the redox potential and stereochemistry of coordinated metal ions. In terms of the formation of multinuclear complexes, the number of pendant groups dictates the number of coordination sites left available for auxiliary ligands to bridge between the metal centres. In some cases, the pendant groups may themselves act as endogenous bridging groups.

Complexes featuring ligands with pendant carboxylate groups [1,2] are of interest because the carboxylate moiety is found in many metalloproteins where aspartate or glutamate side chains act as coordinating groups. In addition, the presence of carboxylate groups increases the probability of forming complexes with interesting magnetic properties because these groups can adopt a variety of coordination modes, ranging from terminal monodentate to several different bridging configurations (*syn–syn*, *syn–anti*, etc.) [17].

We, and others, recently described the synthesis and characterization of stable metal complexes of the ligand, 1,4,7-triazacyclononane-*N*-acetate, that include mononuclear complexes [1,18–20], binuclear complexes [1,20] and helical chains, in which copper(II) atoms are bridged by the carboxylate pendant arms [21]. We have now begun to investigate the coordination behaviour of another carboxylate-bearing tacn ligand, 1,4-bis(carboxymethyl)-1,4,7-triazacyclononane ($\mathbf{LH_2}$). Herein we report an efficient and high yielding synthetic route to $\mathbf{LH_2}$, together with the synthesis and properties of a Cu(II) complex, [(LH)Cu](ClO$_4$) (**1**) and two novel Fe(III) complexes, [LFeCl] (**2**) and [Fe$_2$(μ-O)L$_2$] · (NaClO$_4$)$_3$ · CH$_3$OH · 3H$_2$O (**3**) of this ligand.

2. Experimental

2.1. Materials

All chemicals were purchased from commercial suppliers and used without purification with the exception of 1,4,7-triazacyclononane trihydrochloride (tacn · 3HCl) [22] and 1,4,7-triazatricyclo[5.2.1.0^{4,10}]decane (tacn orthoamide) [23,24], which were prepared by literature methods.

2.2. Physical measurements

NMR spectra were obtained on a Bruker AV 200 or DPX 300 (CDCl$_3$) spectrometer, IR spectra were recorded using KBr pellets on a Perkin–Elmer 1600 FTIR spectrometer at a resolution of 8 cm^{-1}. Electronic spectra were recorded on a Cary 5G UV–Vis–NIR spectrophotometer in 1 cm quartz cells. Mass spectra were obtained using a Micromass platform mass spectrometer with an electrospray source. Microanalyses were performed by the Campbell Microanalytical Service, University of Otago, New Zealand. Magnetic susceptibilities were measured on powdered samples contained in calibrated gelatine capsules using a Quantum Design MPMS 5 Squid magnetometer operating in a field of 1 T. The instrument was calibrated against a standard Pd sample supplied by the company and against a chemical calibrant (CuSO$_4$ · 5H$_2$O).

2.3. Syntheses

Caution: Although no problems were encountered during this work, perchlorate salts of transition metal complexes are potentially explosive and should be handled with extreme care and be prepared only in small quantities.

2.3.1. 1-Ethylacetato-4-formyl-1,4,7-triazacyclononane (II)

A solution of bromoethylacetate (3.6 g, 22 mmol) in acetonitrile (40 mL) was added to a solution of tacn orthoamide (3 g, 22 mmol) in acetonitrile (40 mL). The mixture was stirred at room temperature overnight. The resulting white product **I** was collected by filtration, washed with diethyl ether (2 × 30 mL) and air dried. The solid was then dissolved in water (100 mL) and heated to reflux for 4 h. After removal of the solvent by rotary evaporation and drying at 90 °C for 2 h, a dark red-orange oil of **II** was obtained. Yield: 2.50 g, 93%. Selected IR bands (KBr, cm^{-1}): 3426 [ν(O–H)], 2935 [ν(C–H)], 1730 [ν(CO ester)], 1660 [ν(CO formyl)]. ^{1}H NMR spectrum (CDCl$_3$): δ (ppm) 1.28 and 1.29* (3H, t, C*H*$_3$–CH$_2$), 2.93–3.89 (12H, m, CH$_2$-ring), 3.55 and 3.7* (2H, s, N–C*H*$_2$–COOEt), 4.2 and 4.18* (2H, q, CH$_3$–C*H*$_2$), 8.38 and 8.18* (1H, s, CHO), 9.18 (1H, s, N–*H*). * splitting of signals due to two resonance forms of the formyl group.

2.3.2. 1,4-Bis(ethylacetato)-7-formyl-1,4,7-triazacyclononane (III)

Compound **II** (2.8 g, 10 mmol) was dissolved in acetonitrile (40 mL) and a solution of bromoethylacetate (2.02 g, 10 mmol) in acetonitrile (40 mL) slowly added. Sodium carbonate (7 g) was added and the mixture stirred overnight under reflux. The suspension was filtered to remove the insoluble inorganic salts and the solvent was removed from the filtrate under reduced pressure to yield a very viscous brown oil. This was placed under high vacuum to remove volatile impurities. Yield: 3.1 g, 89%. ^{1}H NMR spectrum (CDCl$_3$): δ (ppm) 1.26 and 1.27* (6H, t, C*H*$_3$–CH$_2$–O), 2.68, 2.76, 3.00, 3.21, 3.31, 3.51 (6 × 2H, 6m, ring-NC*H*$_2$), 3.4 (4H, s, N–C*H*$_2$–COOEt), 4.15 and 4.16* (4H, q, C*H*$_2$–CH$_3$), 8.06 (1H, s, N–C*H*O). ^{13}C NMR spectrum (CDCl$_3$): δ (ppm) 14.57 *C*H$_3$–CH$_2$–O, 47.33 and 50.44* ring-N*C*H$_2$ next to CHO, 54.4 and 58.11*, 55.03

and 58.30* ring-N*C*H$_2$, 55.3 and 58.46* N–*C*H$_2$–COOEt, 60.7 CH$_3$–*C*H$_2$–O, 164 *C*HO, 172 *C*OO. * splitting of signals due to two resonance forms of the formyl group.

2.3.3. 1,4- Bis(carboxymethyl)-1,4,7-triazacyclononane (*LH$_2$*)

Compound **III** (3.08 g, 8.01 mmol) was dissolved in 5 M HCl (80 mL) and the solution refluxed for 2 days. Removal of the solvent gave a light brown oil, which was dissolved in 50 mL of water and decolorized by heating with activated charcoal. The solution was filtered, reduced to dryness and re-dissolved in water (50 mL). The water was then removed on a rotary evaporator and the residue taken up in 33% hydrobromic acid (10 mL) and glacial acetic acid (5 mL). The white precipitate that formed immediately was filtered, washed with acetone (2 × 20 mL) and dried under nitrogen to yield the product as a white solid. Yield: 4.47 g, 86%. Selected IR bands (KBr, cm^{-1}): 3450 [ν(O–H)], 2951 [ν(C–H)], 1739vs, [ν_{as}(CO)], 1422vbr, [ν_s(CO)]. ^{1}H NMR spectrum (NaOD/D$_2$O): δ (ppm) 3.43 (4H, s, NC*H*$_2$), 3.58 (8H, m, NC*H*$_2$), 4.03 (4H, s, C*H*$_2$–COOH), ^{13}C NMR spectrum (CDCl$_3$): δ (ppm) 42.9 ring-N*C*H$_2$ next to CHO, 50.36, 50.98 ring-N*C*H$_2$, 56.46 N–*C*H$_2$–COOH, 172 *C*OO. Electrospray mass spectrum (*m*/*z* for **LH$_2$**): Calc.: 245. Found: 246 [M+H]$^+$. Microanalysis Calc. for C$_{10}$H$_{23}$N$_3$O$_4$Br$_4$ · 4H$_2$O: C, 18.7; H, 4.8; N, 6.6; Br, 49.8. Found: C, 18.7; H, 4.9; N, 6.7; Br, 48.6%.

2.3.4. [LHCu](ClO$_4$) (*1*)

The pH of a warm aqueous solution of **LH$_2$** (0.22 g, 0.34 mmol in 10 mL water) was adjusted to 7 with NaOH (0.5 M) and Cu(ClO$_4$)$_2$ · H$_2$O (0.33 g, 0.89 mmol) was added. The pH of the solution dropped to ~2 and after cooling to room temperature, thin blue crystals suitable for X-ray analysis formed. These were filtered, washed with ethanol and diethyl ether and air dried. Yield: 92 mg, 68%. Selected IR bands (KBr, cm^{-1}): 3300 [ν(N–H)], 1756, 1628 and 1575 [ν_{as}(CO)], 1442 and 1404 [ν_s(CO)], 1101 and 624 [ν(ClO$_4$)]. UV–Vis spectrum (H$_2$O) [λ_{max}, nm (ε_{max}, l mol^{-1} cm^{-1})]: 667 (106); 1032, (24); 267 (3340). Microanalysis Calc. for C$_{10}$H$_{17}$N$_3$O$_4$CuClO$_4$: C, 29.5; H, 4.2; N, 10.3. Found: C, 29.5; H, 4.5; N, 10.3%.

2.3.5. [LFeCl] (*2*)

To an aqueous solution of **LH$_2$** (0.62 g, 0.95 mmol) was added NaOH (0.5 M) to adjust the pH to 7. The solution was warmed to 50 °C and Fe(NO$_3$)$_3$ · 9H$_2$O (0.38 g, 0.95 mmol) was added, whereupon the color changed to deep orange and the pH dropped to ~2. Orange crystals suitable for X-ray analysis were obtained upon slow cooling overnight. These were filtered and washed with ethanol and diethyl ether. Yield: 0.24 g, 74%. Selected IR bands (KBr, cm^{-1}): 3213 [ν(N–H)], 1658 [ν_{as}(CO)], 1329 [ν_s(CO)]. UV–Vis spectrum (H$_2$O) [λ_{max}, nm (ε_{max}, l mol^{-1} cm^{-1})]: 235 (900); 272 (700); 308 (520). Microanalysis Calc. for C$_{10}$H$_{17}$N$_3$O$_4$FeCl: C, 35.9; H, 5.1; N, 12.6. Found: C, 36.0; H, 5.1; N, 12.6%.

2.3.6. [Fe$_2$(μ-O)L$_2$] · (NaClO$_4$)$_3$ · CH$_3$OH · 3H$_2$O (*3*)

Compound **2** (0.21 g, 0.6 mmol) was dissolved in water (5 mL) at 50 °C. An aqueous solution (10 mL) containing sodium acetate (0.50 g, 6.1 mmol) and sodium perchlorate

Table 1
Crystallographic data for complexes **1**–**3**

	1	**2**	**3**
Empirical formula	C$_{10}$H$_{18}$N$_3$O$_8$CuCl	C$_{10}$H$_{17}$N$_3$O$_4$ClFe	C$_{21}$H$_{32}$N$_6$O$_{25}$Cl$_3$Fe$_2$Na$_3$
M (g/mol)	407.26	334.57	1055.55
Crystal system	monoclinic	orthorhombic	monoclinic
Space group	*P*2(1)	*Pna*2$_1$	*P*2$_1$/*n*
a (Å)	8.3143(2)	15.1012(3)	18.5103(2)
b (Å)	8.6622(2)	7.38570(10)	9.23720(10)
c (Å)	10.4171(4)	11.6782(2)	24.2158(4)
α (°)	90	90	90
β (°)	91.9400(1)	90	107.59(9)
γ (°)	90	90	90
V (Å^3)	749.81(4)	1302.50(4)	3946.99(9)
Z	2	4	4
D_{calc} (g m^{-3})	1.804	1.706	1.776
μ (mm^{-1})	1.681	1.377	1.070
θ Range (°)	3.88–27.88	3.53–27.86	1.22–28.22
Reflections collected	9687	14237	47437
Independent reflections	3334	3073	9488
Goodness-of-fit on F^2	1.060	1.023	1.034
F(000)	418	692	2144
R_{int}	0.0449	0.0474	0.0609
R_1^a, wR_2^b [$I > 2\sigma(I)$]	0.0446, 0.0949	0.0295, 0.0686	0.0626, 0.1429
Largest residual peak (e Å^3)	1.52	0.39	1.45

[a] $R_1 = \sum\|F_o\| - |F_c\|/\sum|F_o|$.
[b] $wR_2 = [\sum w(F_o^2 - F_c^2)^2/\sum w(F_o^2)^2]^{1/2}$.

(0.50 g, 4.1 mmol) was added dropwise. A dark brown solution was obtained whose volume was reduced to 5 mL. Vapour diffusion of methanol produced a dark green crystalline product which was filtered, washed with ethanol and diethyl ether and air dried. Yield: 0.46 g, 66%. Selected IR bands (KBr, cm^{-1}): 3450 [ν(O–H)], 3370 [ν(N–H)], 1654 [ν_{as}(CO)], 1364 [ν_s(CO)], 1079 and 629 [ν(ClO_4)], 813 [ν Fe–O–Fe]. UV–Vis spectrum (H_2O): [λ_{max}, nm (ε_{max}, $l\,mol^{-1}\,cm^{-1}$)], 600 (131); 491 (436); 313 (13200); 273 (12100); 233 (14300). Microanalysis Calc. for $C_{20}H_{36}N_6O_9Fe_2Na_3 \cdot (ClO_4)_3 \cdot CH_3OH \cdot 3H_2O$: C, 21.5; H, 3.6; N, 7.2. Found: C, 21.5; H, 3.4; N, 7.2%.

2.4. Crystallography

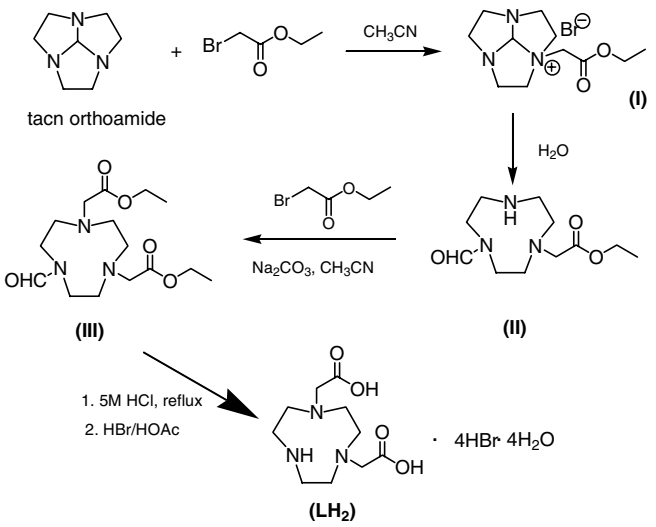
Single-crystals of **1**, **2** and **3** were mounted on thin glass fibres. X-ray crystallography data were obtained on an Enraf-Nonius CAD4 diffractometer with monochromated Mo Kα radiation. ($\lambda = 0.71073$ Å) at 123(2) K using phi and/or omega scans. Data were corrected for Lorentz and polarization effects. The structures were solved by direct method and all crystallographic calculations were performed with use of the programs SHELXS-97 [25] and SHELXL-97 [25], respectively. All non-hydrogen atoms were located on Fourier difference-maps and were refined anisotropically. For all complexes, the methylene hydrogen atoms were located on Fourier difference maps and restrained to idealized geometries with d(C–H) = 0.99 Å, as were the amine hydrogen atoms for complex **1** and **3** (d(N–H) = 0.93 Å). All solvent water protons were located on Fourier difference maps and restrained to idealized geometries. The program X-Seed [26] was used as an interface to the SHELX programs and to prepare the figures. In the ORTEP [27] plots thermal ellipsoids for non-hydrogen atoms have been drawn at the 30% probability level and hydrogen bonds are presented by dashed lines. Cell parameters and details of data collection and structure solution are given in Table 1. For complex **3**, three of the carbon atoms of the macrocycle ring (C(12), C(13), and C(15)) and oxygen atoms (O(6), O(7), O(8), O(11), O(12), O(10)) of the perchlorates (C(l2) and C(l3)) were disordered over two positions. Each disordered position is given half occupancy and the atoms involved were refined isotropically.

3. Results and discussion

3.1. Syntheses

3.1.1. Ligand

The ligand 1,4-bis(carboxymethyl)-1,4,7-triazacyclononane (**LH_2**) has been reported previously [28–31]. The published syntheses, however, can yield a mixture of di- and trisubstituted products [30,31]. We therefore developed a new synthetic route, which yielded the tetrahydrobromide salt of **LH_2**, that uses 1,4,7-triazatricyclo[5.2.1.$0^{4,10}$]decane (tacn orthoamide) [23,24], a synthon that has been used to prepare a variety of functionalized tacn derivatives [18].



Scheme 1. Synthetic pathway leading to 1,4-bis(carboxymethyl)-1,4,7-triazacyclononane.

Our approach, depicted in Scheme 1, involves four straight forward steps, which produce the various intermediates in high yield. In each case, the intermediates were sufficiently pure to proceed directly to the next step. The reaction of tacn orthoamide with ethyl bromoacetate in acetonitrile gave the insoluble monoamidinium bromide salt **I** [32], which was hydrolyzed to yield the formyl-monoester derivative **II**. The IR spectrum showed absorption bands at 1730 and 1660 cm^{-1} due to ν(C=O) stretches associated with the ester and formyl group, respectively. As indicated by Blake et al. [33], the formyl group can have two conformational isomers as a result of slow rotation about the C–N amide bond. These can be seen at 8.38 ppm and 8.18 ppm in the ^{1}H NMR spectrum of compound **II**.

The second pendant carboxylate group was attached in similar fashion to step 1, but in the presence of a base. Hydrolysis of **III** in 5 M HCl removed the formyl and ester groups and the final ligand, **LH_2** was isolated from a HBr/glacial acetic acid mixture. Microanalytical data were consistent with the composition for $LH_2 \cdot 4HBr \cdot 4H_2O$, which indicated that the three amines are protonated and that there was an extra molecule of HBr in the crystal lattice. The ESI mass spectrum showed a signal for the parent molecular ion $[M+H]^+$ at $m/z = 246$, and the spectroscopic data (^{1}H NMR and ^{13}C NMR spectrum) were as expected.

3.1.2. Metal complexes

The blue complex, [**LHCu**](**ClO_4**) (**1**), was obtained on addition of copper(II) perchlorate to a neutralized aqueous solution of the $LH_2 \cdot 4HBr$ salt. The formation of a dark blue solution and an instant pH change from pH 7 to 2 were observed, indicating the formation of a copper(II) complex. Slow evaporation of the dark blue solution gave blue thin crystals suitable for X-ray-crystallography.

In the IR spectrum of **1**, a band at 3300 cm^{-1} is attributable to the N–H stretches of the secondary amine in the

ligand and several bands in the range of 1400–1800 cm^{-1}, which are due to ($\nu_{as}C{=}O$) and ($\nu_{s}C{=}O$) stretches of the carboxylate groups. While some of these bands are quite weak and difficult to assign, strong asymmetric vibrations due to the protonated carboxylate and the relatively uncommon *syn*, *anti* bridging carboxylate conformation [34,35] can be found at 1756, 1628 and 1575 cm^{-1}. The UV–Vis spectrum of **1** displays absorption maxima at 667 nm ($\varepsilon = 106\ l\ mol^{-1}\ cm^{-1}$) and 1032 nm ($\varepsilon = 24\ l\ mol^{-1}\ cm^{-1}$), which indicates that in solution the copper(II) centres are in a square pyramidal ligand environment with a $(d_{x^2-y^2})^1$ electronic structure [1].

Complex **2**, [LFeCl], was prepared by reacting iron(III) nitrate with a neutralized aqueous solution of the $\mathbf{LH_2}$ salt (pH 7). An instant color change to dark yellow and decrease in pH to ~2 were indicative of immediate complex formation. Orange crystals of **2** precipitated overnight from this solution, which were suitable for single X-ray crystallography. In the IR spectrum, bands due to the asymmetric and symmetric stretching mode of the carboxylate groups were observed at 1658 cm^{-1} and 1329 cm^{-1}. The large separation between the bands ($\Delta\nu = 329\ cm^{-1}$) is indicative of monodentate coordination mode.

Dark green crystals of the oxo-bridged complex **3**, $[Fe_2(\mu\text{-}O)L_2]\cdot(NaClO_4)_3\cdot CH_3OH\cdot 3H_2O$, deposited slowly from a solution prepared by dissolving complex **2** in an aqueous solution of sodium perchlorate and sodium acetate. As expected for iron(III) and other μ-oxo-bridged complexes, which feature asymmetric ν_{as}(M–O–M) stretches in the 800–850 cm^{-1} region, complex **3** exhibited a strong absorption band at 813 cm^{-1} [36] The IR spectrum of **3** also showed a ν_{as}(COO)] stretch at 1654 cm^{-1} and a ν_{s}(COO)] stretch at 1364 cm^{-1}, which are indicative of monodentate carboxylate coordination [37,38].

The electronic absorption spectrum of **3**, recorded in acetonitrile, is shown in Fig. 1. The electronic transitions of μ-oxo-diiron complexes have been studied intensively and assigned from analyses of absorption and CD spectra [39], polarized single-crystal spectra [40,41] and Raman excitation profiles [42]. These studies have been reviewed in detail [7,8,36,43,44]. The electronic spectrum of **3**, recorded in acetonitrile is shown in Fig. 1. In the 200–400 nm, the transitions can be assigned as oxo → Fe^{3+} ligand to metal charge-transfer transitions (LMCT) [39]. The lower energy, lower intensity band found at 408 nm ($10\,560\ l\ mol^{-1}\ cm^{-1}$) can be assigned to exogenous ligand → metal charge-transfer transitions [39,42,45] and to forbidden oxo-Fe^{3+} charge-transfer transitions which enhance the intensity of the weaker ligand field transition. For **3**, these bands are less intense than those in spectra of (μ-oxo)bis(μ-X)diiron(III) complexes [1,10,46]. The sharp absorbance band at 491 nm ($436\ l\ mol^{-1}\ cm^{-1}$) has been assigned to transitions into higher energy levels, $^6A_1 \rightarrow {}^4A_1, {}^4E$, [47] and has also been observed in the spectrum of metHr [48]. A broad band at 600 nm ($131\ l\ mol^{-1}\ cm^{-1}$) was rather unexpected because for a high spin iron(III) d^5 configuration, d–d electronic transitions in an octahedral ligand field are spin forbidden. Since no d–d-transitions were present in the UV–Vis spectrum of the mononuclear Fe^{3+} complex, **2**, these observed transitions must be due to the unique structure of the dimeric unit [41,43].

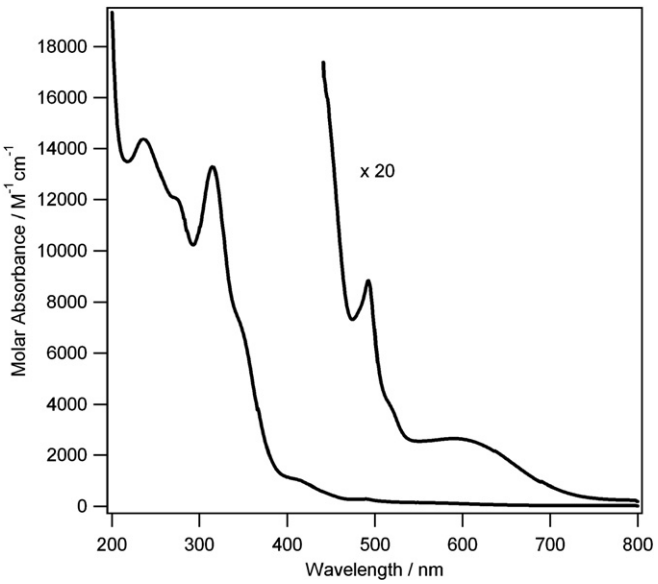


Fig. 1. Electronic spectrum of μ-oxo-diiron(III) complex.

3.2. Crystal structure determinations

The structures of **1**–**3** were determined by X-ray crystallography (see Section 2) and selected crystallographic data are found in Table 1.

3.2.1. [LHCu](ClO4) (1)

Fig. 2 shows the molecular structure of the complex cation of **1**, while Table 2 lists selected bond lengths and angles. The Cu(II) centre is in a distorted square-pyramidal geometry formed by the three nitrogen atoms from the macrocycle, one oxygen atom (O(2)) from the carboxylate group and a second O-atom (O*(1)) from the equivalent

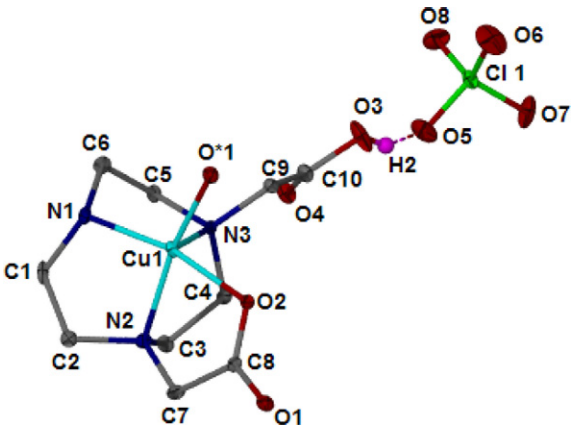


Fig. 2. Asymmetric unit of **1**. C–*H* and N–*H* atoms have been omitted for clarity.

Table 2
Selected bond lengths (Å) and angles (°) for complex **1**

Cu(1)–O(1)*	1.967(3)	O(1)–Cu(2)	1.972(3)
Cu(1)–O(2)	1.972(3)	O(2)–C(8)	1.269(5)
Cu(1)–N(1)	1.984(3)	O(1)–C(8)	1.253(5)
Cu(1)–N(2)	2.051(4)	O(3)–C(10)	1.342(5)
Cu(1)–N(3)	2.232(3)		
O(2)–Cu(1)–O(1)*	84.2(1)	O(1)*–Cu(1)–N(1)	106.1(1)
O(1)*–Cu(1)–N(3)	102.8(1)	N(2)–Cu(1)–N(3)	85.8(1)
N(1)–Cu(1)–N(2)	85.7(2)	C(8)–O(1)–Cu(1)	123.3(3)
O(2)–Cu(1)–N(2)	83.0(1)	C(1)–N(1)–Cu(1)	110.8(3)
N(1)–Cu(1)–N(3)	84.8(1)	C(6)–N(1)–Cu(1)	105.7(3)
O(2)–Cu(1)–O(1)*	84.2(1)	C(8)–O(2)–Cu(1)	113.5(3)
O(2)–Cu(1)–N(3)	101.2(1)	C(9)–N(3)–Cu(1)	110.3(2)
O(1)*–Cu(1)–N(2)	165.8(1)	C(4)–N(3)–Cu(1)	99.6(2)
O(2)–Cu(1)–N(1)	166.8(1)	C(5)–N(3)–Cu(1)	105.2(2)

carboxylate on an adjacent complex unit. Interestingly, the second pendant acetic acid arm of the ligand remains protonated and does not coordinate, but is instead bent away from the copper centre and participates in H-bonding interactions (see below). A similar structure has been observed in VO_2(LH) [30] where again only one pendant arm was coordinated to the V(V) centre.

As observed in copper(II) complexes of other tacn derivatives the two nitrogen atoms, N(1) and N(2), that are part of the base of the pyramid have shorter Cu–N bond length [1.984(3) Å and 2.051(4) Å, respectively] than the third apical nitrogen atom [Cu–N(3) = 2.232(3) Å]. The formation of the five-membered Cu–O–C–C–N ring may induce a shortening of the in-plane Cu–N bonds in order to reduce the strain within this chelate ring [30].

Each coordinated carboxylate group bridges between two Cu(II) centres in a *syn*, *anti*-fashion, thus forming 1D-helical chains [21] (Fig. 3). The bond lengths Cu–O*(1) and Cu–O(2) are identical [1.967(3) and 1.972(3) Å] (Table 2).

The oxygen atom (O(3)) from the uncoordinated carboxylate group is protonated and forms a hydrogen bond to the perchlorate oxygen atom O(5) [O(3)···O(5) 2.769(5) Å]. There is also a hydrogen bond between the protonated secondary macrocyclic amine N(1) and the oxygen atom O(2) from the coordinated acetate group of an adjacent complex [N(1)···O(2)# 2.819(5) Å]. Hydrogen bond interactions occur only within the chain and there are no such interactions between the strands. The intra-strand Cu···Cu distance is 4.9898(4) Å, whereas the shortest strand-to-strand Cu···Cu distance is 13.10 Å (Fig. 4).

3.2.2. *[LFeCl] (**2**)*

The crystal structure of the mononuclear complex **2** shows that the iron(III) centre is in a highly distorted octahedral coordination environment (Fig. 5). In the equatorial plane, there are two tacn ring nitrogens and two oxygens, one from each of the carboxylate groups. One axial position is occupied by the third nitrogen atom from the tacn ring, while a chloride ligand, lying in the opposite axial position, completes the octahedral coordination sphere.

The asymmetry of the iron(III) coordination sphere is highlighted by the fact that the three Fe–N and two Fe–O distances (Table 3) involving the ligand donor atoms are all different. In particular, the Fe(1)–N(1) bond is sig-

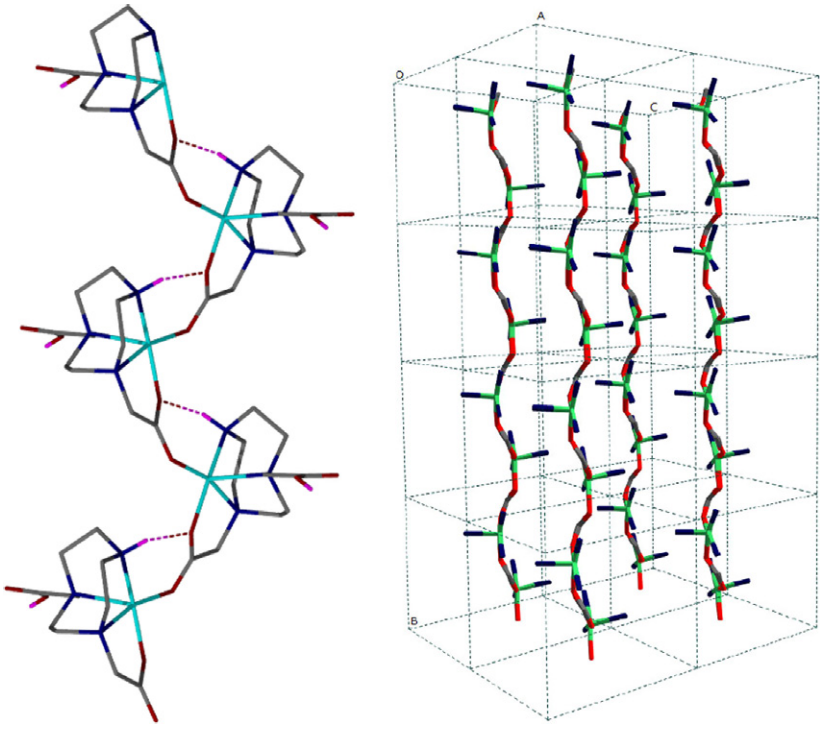


Fig. 3. Left: Segment of a 1D-chain formed by [LHCu] units in the crystal structure of **1**. Hydrogen atoms and perchlorate anions have been omitted for clarity. Right: Helical chains in unit cells (dashed lines). C, N and O atoms which are not part of the chains have been removed for clarity.

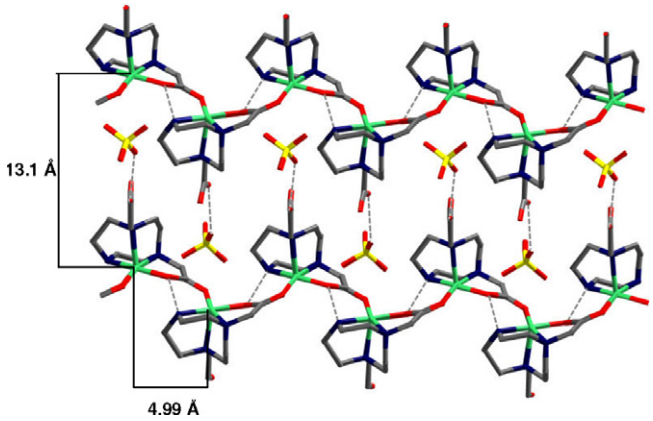


Fig. 4. Hydrogen bond interactions (dashed lines) in 1D-chains formed by [LHCu]·ClO_4 units. C–*H* and N–*H* atoms have been omitted for clarity.

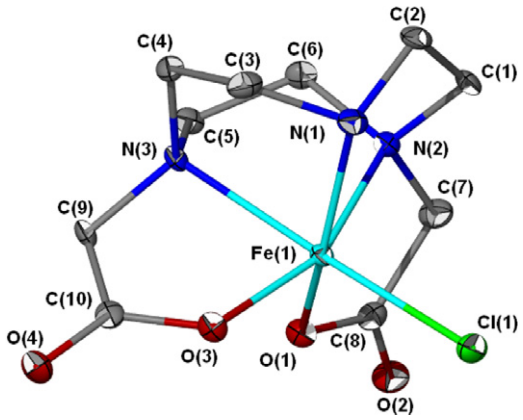


Fig. 5. Asymmetric unit in **2**. C–*H* and N–*H* atoms have been omitted for clarity.

nificantly shorter [2.137(2) Å] probably because this atom is less sterically hindered compared to the Fe(1)–N(2) [2.186(2) Å] and Fe(1)–N(3) [2.218(2) Å] bonds. The two Fe–O bond lengths are also different but only slightly so [1.9796(2) Å and 1.9493(2) Å]. The longer Fe(1)–N(3) distance, cf. Fe(1)–N(2), could be a reflection of the quite high affinity of the *trans* chloro ligand for Fe(III). The three N–Fe–N chelate ring angles are all well below 90°, as expected for a non-idealized octahedral structure. An interesting

Table 3
Selected bond length (Å) and angles (°) for complex **2**

Fe(1)–N(1)	2.137(2)	Fe(1)–O(1)	1.980(2)
Fe(1)–N(2)	2.186(2)	Fe(1)–O(3)	1.949(2)
Fe(1)–N(3)	2.218(2)	Fe(1)–Cl(1)	2.290(2)
N(1)–Fe(1)–N(2)	79.88(9)	O(3)–Fe(1)–N(3)	78.91(8)
N(1)–Fe(1)–N(3)	80.07(8)	O(3)–Fe(1)–O(1)	98.71(8)
N(2)–Fe(1)–N(3)	79.15(7)	O(3)–Fe(1)–N(1)	99.37(8)
O(1)–Fe(1)–N(1)	157.28(8)	O(3)–Fe(1)–Cl(1)	99.23(5)
O(1)–Fe(1)–N(2)	78.18(8)	N(1)–Fe(1)–Cl(1)	95.23(7)
O(1)–Fe(1)–N(3)	90.06(7)	N(2)–Fe(1)–Cl(1)	102.91(6)
O(1)–Fe(1)–Cl(1)	95.33(5)	N(3)–Fe(1)–Cl(1)	174.52(6)
O(3)–Fe(1)–N(2)	157.83(8)		

intermolecular hydrogen bonding network is created including the nitrogen atom N(1) to two oxygen atoms of carboxylate moieties of two adjacent [LFeCl] unit with distances of 3.104(3) Å [N(1)–H(3)···O(2)#1] and 3.141(3) Å [N(1)–H(3)···O(1)#1]. The network is supported by quite short C–H···O hydrogen bond interactions which range from 3.1 Å to 3.5 Å (see Table 4). Of note is the [C(4)–H(4B)···O(4)] interaction which links chains together and creating a 2D-network (Fig. 6).

3.2.3. $[Fe_2(\mu\text{-}O)L_2]\cdot(NaClO_4)_3\cdot CH_3OH\cdot 3H_2O$ (**3**)

The crystal structure determination of **3** verified that the compound has two Fe(III) centres linked *via* a single μ-oxo-bridge (see Fig. 7). Selected bond angles and bond distances are summarized in Table 5. The Fe···Fe distance of 3.422(3) Å and a non-linear Fe–O–Fe angle of 144.4° are quite similar to those observed for $[(salen)Fe]_2O$ and other related binuclear complexes (see Table 6). The comparison of the structural parameters of the Fe–O–Fe core for a selection of mono-oxo-bridged Fe(III) complexes (Table 6) reveals that the differences in the Fe···Fe distances in these compounds can be attributed exclusively to the variation in the Fe–O–Fe angles, as all Fe–O distances are virtually identical.

In the structure of complex **3**, the three nitrogen donors coordinate facially to each iron(III) centre, two further coordination sites are occupied by two carboxylate oxygens and the sixth (*trans* to the secondary amine) is taken up by a bridging oxygen atom. As in compound **2**, the geometry around the iron(III) centres is significantly distorted from octahedral. The iron(III) centre is located slightly out of the plane (0.356 Å) formed by two nitrogen atoms of the macrocyclic ring and two oxygen atom of the pendant carboxylate arms. The relatively short Fe–O_{oxo} bond 1.797(1) Å (average of both Fe–O_{oxo} bonds) indicates substantial double bond character. The μ-oxo group exerts a strong *trans* influence which results in elongation of the Fe(1)–N(3) [2.284(4) Å] and Fe(2)–N(6) [2.261(4) Å] bonds. The two in-plane Fe–N distances in each unit are much shorter [2.136(3)–2.184(3) Å] than the axial distance and the distance to the secondary nitrogen atoms, N(1) and N(4), is shorter than that to the tertiary nitrogen atoms N(2) and N(5), as was the case for complex **2**. It is interesting to note that, apart from the longer Fe–N bonds *trans* to the bridging oxo group all other distances are similar to those in complex **2**. However, the two Fe–N distances to the two secondary nitrogen atoms are clearly different [Fe(1)–N(1), 2.136(3) Å] than N(4) [Fe(2)–N(4), 2.168(4) Å]. This may be due to the involvement of the hydrogen atom on N(1) in hydrogen bonding with an oxygen atom of a perchlorate anion [N(1)–H(1)···O(12P)#1, 3.069(5) Å, 167°] (see Table 7).

Complex **3** crystallizes with one methanol and three water molecules of solvation as well as three sodium ions and three perchlorate ions, which are located between two $[Fe_2(\mu\text{-}O)L_2]$ units. The two water molecules O(2W) and O(3W) are hydrogen bonded to the oxygen atoms of

Table 4
Hydrogen bonds and close contacts in **2**

D–H···A	*d*(D–H) (Å)	*d*(H···A) (Å)	*d*(D···A) (Å)	∠(DHA) (°)
N(1)–H(3)···O(2)#1	0.81(3)	2.36(3)	3.104(3)	153(3)
N(1)–H(3)···O(1)#1	0.81(3)	2.54(3)	3.141(3)	132(3)
C(1)–H(1B)···O(2)#2	0.89(3)	2.49(3)	3.373(3)	177(3)
C(2)–H(2A)···O(1)#1	1.01(3)	2.46(2)	3.113(3)	122(2)
C(2)–H(2B)···O(4)#3	0.95(3)	2.45(3)	3.278(3)	146(2)
C(4)–H(4B)···O(4)#3	0.97(3)	2.59(3)	3.306(3)	131(2)
C(6)–H(6A)···O(3)#4	0.89(3)	2.58(3)	3.446(3)	167(3)

Symmetry transformations used to generate equivalent atoms: #1 $-x+2$, $-y$, $z-1/2$; #2 $-x+2$, $-y-1$, $z-1/2$; #3 $-x+3/2$, $y-1/2$, $z-1/2$ #4 x, $y-1$, z.

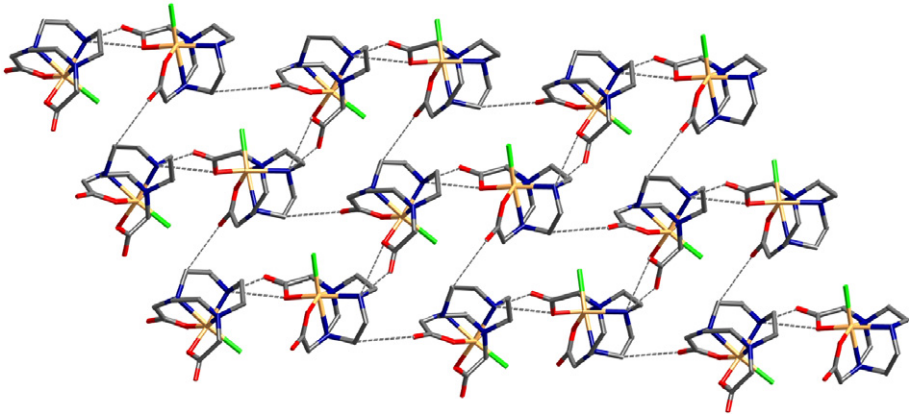


Fig. 6. Packing of [LFeCl] units showing N–H···O and C–H···O hydrogen bonding interactions. Carbon– and nitrogen–hydrogen atoms have been omitted for clarity.

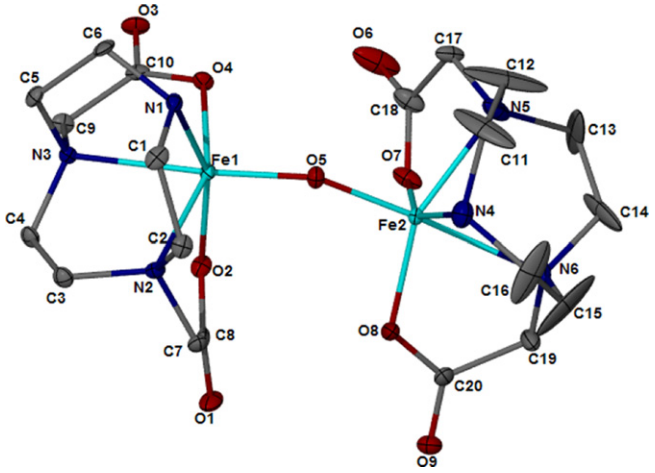


Fig. 7. Plot of the diiron unit of complex **3** with the atomic labelling scheme. C–*H* and N–*H* atoms perchlorate anions, sodium cations and lattice water molecules have been omitted for clarity.

the carboxylate groups of the macrocyclic ring and the methanol molecule is coordinated to sodium ion Na(3). Two sodium cations Na(1) and Na(2), are seven-coordinate, while the third, Na(3), is six-coordinate (Fig. 8). These sodium atoms are linked together by Na–O–Na bridges with Na–O distances in the range of 2.310(3) Å to 2.764(5) Å (see Table 5) for which the oxygen atoms are primarily provided by the carboxylate groups of two binuclear Fe(III) units (Fig. 8). Additional coordination sites are occupied by perchlorate oxygens, which act as counter-ions, as well as oxygens from water solvent molecules. These water molecules also participate in various H-bonding interactions (Table 7).

The geometry of Na(1) is defined by five carboxylate oxygens atoms, two of them, O(8) and O(1), are from one [Fe_2-(μ-O)L_2] unit, the other three oxygen atoms, O(3), O(4) and O(6) from another [Fe_2(μ-O)L_2] unit (Fig. 8). Consequently, this unique sodium atom not only links the two Fe(III) units of one binuclear μ-oxo complex via an O(1)–Na(1)–O(8) bridge, it also connects the [Fe_2(μ-O)L_2] complexes. In addition, Na(1) is the only sodium atom, which is chelated by the carboxylate oxygen atoms O(3)* and O(4)*. These interactions join two macrocyclic complexes together forming a chain, whereas the oxygen atom O(6PA) from the perchlorate anion provides a link to another chain, resulting in an one-dimensional ensemble, where clusters of composition [$Na_6(ClO_4)_4$] are flanked by [Fe_2(μ-O)L_2] units (Fig. 9). These 1D-chains are connected by only one hydrogen bond [O(10)–H(10)···O(5P)#, 3.053(5) Å, 167°] which is of particular interest as it is the only interaction holding the 1D-chains together.

Complex **3** exhibits a number of carboxylate coordination modes (Fig. 10), some of which were recently reported for the copper(II) complex of 1-propylamino-4-acetato-1,4,7-triazacyclononane [54]. In **3**, binding modes Ia to Ic

Table 5
Selected bond lengths (Å) and angles (°) for complex **3**

Fe(1)–O(5)	1.799(3)	Fe(2)–O(5)	1.795(3)
Fe(1)–O(4)	1.996(3)	Fe(2)–O(9)	1.967(3)
Fe(1)–O(2)	2.028(3)	Fe(2)–O(7)	2.084(3)
Fe(1)–N(1)	2.136(3)	Fe(2)–N(4)	2.168(4)
Fe(1)–N(2)	2.184(3)	Fe(2)–N(5)	2.172(4)
Fe(1)–N(3)	2.284(4)	Fe(2)–N(6)	2.261(4)
Na(1)–O(1)	2.310(3)	Na(2)–O(8PA)#3	2.612(1)
Na(1)–O(8)	2.315(4)	Na(2)–O(2W)#3	2.358(4)
Na(1)–O(3)#2	2.615(4)	Na(2)–O(3W)#3	2.313(4)
Na(1)–O(4)#2	2.477(3)	Na(2)–O(1W)	2.683(5)
Na(1)–O(6)#2	2.764(5)	Na(2)–O(8PA)#3	2.612(1)
Na(1)–O(9P)	2.634(4)	Na(3)–O(1)	2.327(3)
Na(1)–O(1W)	2.606(4)	Na(3)–O(10)	2.331(4)
Na(2)–O(8)	2.322(4)	Na(3)–O(3)#2	2.309(3)
Na(2)–O(6)#2	2.405(4)	Na(3)–O(4P)	2.367(4)
Na(2)–O(6PA)#3	2.768(8)	Na(3)–O(6PA)	2.426(8)
Fe(2)–O(5)–Fe(1)	144.4(2)	O(5)–Fe(2)–O(9)	101.6(1)
O(5)–Fe(1)–O(4)	104.0(1)	O(5)–Fe(2)–O(7)	95.4(1)
O(5)–Fe(1)–O(2)	100.5(1)	O(9)–Fe(2)–O(7)	94.4(1)
O(4)–Fe(1)–O(2)	97.8(1)	O(5)–Fe(2)–N(4)	92.6(1)
O(5)–Fe(1)–N(1)	93.3(1)	O(9)–Fe(2)–N(4)	106.0(1)
O(4)–Fe(1)–N(1)	97.4(1)	O(7)–Fe(2)–N(4)	155.8(1)
O(2)–Fe(1)–N(1)	156.1(1)	O(5)–Fe(2)–N(5)	104.9(1)
O(5)–Fe(1)–N(2)	101.0(1)	O(9)–Fe(2)–N(5)	152.3(1)
O(4)–Fe(1)–N(2)	154.9(1)	O(7)–Fe(2)–N(5)	75.8(1)
O(2)–Fe(1)–N(2)	77.9(1)	N(4)–Fe(2)–N(5)	80.1(1)
N(1)–Fe(1)–N(2)	80.4(1)	O(5)–Fe(2)–N(6)	169.2(1)
O(5)–Fe(1)–N(3)	171.9(1)	O(9)–Fe(2)–N(6)	77.3(1)
O(4)–Fe(1)–N(3)	77.2(1)	O(7)–Fe(2)–N(6)	95.3(1)
O(2)–Fe(1)–N(3)	87.1(1)	N(4)–Fe(2)–N(6)	77.4(1)
N(1)–Fe(1)–N(3)	78.5(1)	N(5)–Fe(2)–N(6)	77.8(1)
N(2)–Fe(1)–N(3)	77.8(1)		

are characterized by one oxygen atom of the carboxylate group coordinating to the iron(III) centre, whereas the second oxygen atom binds to two sodium atoms. However, these modes differ in the number of water molecules hydrogen bonded to one or both oxygen atoms of the carboxylate group. The type II mode is unique in that it features one sodium atom chelated by the same carboxylate group.

3.3. Magnetism

The temperature dependence of the magnetic susceptibility of diiron(III) complex **3** (Fig. 11) measured from 2 to 300 K, indicates that strong antiferromagnetic coupling exists between the two iron(III) centers. As a consequence of this strong coupling, the magnetic moment calculated at room temperature (298 K) is $1.99\mu_B$, decreasing to $0.4\mu_B$ at 4 K. The susceptibility data were fitted with an expression derived from the Heisenberg–Dirac–van Vleck spin exchange Hamiltonian [55]. $H = -2JS_1 \cdot S_2$, where $S_1 = S_2 = 5/2$. The agreement between the observed and calculated data was very good and the best fit values were $g = 2.06$, $J = -101\ cm^{-1}$, including a correction for a small amount (0.2%) of monomeric impurity. The J value ($-101\ cm^{-1}$) is in good agreement with literature values observed for other single μ-oxo-diiron(III) compounds, which have been found to be between -80 and $-105\ cm^{-1}$ (see for example, Refs. [2,8,36]). As may have been anticipated, the linking of the dinuclear molecules by $NaClO_4$ moieties does not affect the J values.

Table 7
Hydrogen bonds for complex **3**

D–H···A	*d*(D–H)	*d*(H···A)	*d*(D···A)	∠(DHA)
N(1)–H(1)···O(12P)#1	0.93	2.16	3.069(5)	167
O(10)–H(10)···O(5P)#2	0.83(2)	2.31(4)	3.053(5)	148(6)
O(1W)–H(1WB)···O(3W)	0.91(1)	2.04(1)	2.900(6)	157(1)
O(3W)–H(3WA)···O(7)	0.83(2)	2.03(2)	2.848(4)	173(6)
O(3W)–H(3WB)···O(2)	0.83(2)	2.01(2)	2.839(4)	172(8)
O(2W)–H(2WA)···O(3)	0.83(2)	2.21(3)	2.982(4)	154(6)
O(2W)–H(2WB)···O(6)	0.84(2)	2.09(3)	2.915(5)	169(9)

Symmetry transformations used to generate equivalent atoms: #1 x, $y+1$, z; #2 $-x$, $-y+1$, $-z+1$.

Fig. 12 shows the temperature dependence of the effective magnetic moment of the copper(II) complex **1**. At temperatures above 70 K, simple Curie behaviour (1.94 μ_B/Cu at room temperature), indicative of an uncoupled system with $S = 1/2$ is observed. Below 70 K the magnetic moment increases to a maximum of $2.6\mu_B$ at 3 K. Fitting of the data to a 1/2 Fisher chain model (solid line in Fig. 12) yielded parameters for $g = 2.19$, $J = 3.05\ cm^{-1}$ and $TIP = 60 \times 10^{-6}\ cm^3\ mol^{-1}$, indicative of weak ferromagnetic coupling. This coupling arises from the exchange route between the copper(II) centres, which occur *via* the acetate group where the carboxylate group connects the $d_{x^2-y^2}$

Table 6
Comparison of structural parameters for **3** with those of related mono-oxo-bridged diiron(III) complexes

Complex	α(Fe–O–Fe) (°)	Fe–oxo[a] (Å)	Fe···Fe (Å)	Ref.
3	144.4(1)	1.797(3)	3.423(3)	This work
$enH_2[(FeHEDTA)_2O] \cdot 6H_2O$	165(1)	1.79(1)	3.56(1)	[49]
[(salen)Fe]$_2$O[b,c]	144.6(6)	1.78(1)	3.39(1)	[50]
[(tsalen)Fe]$_2$O[d]	144.6(6)	1.78(1)	3.39(1)	[51]
$[Fe_2L^1_2(\mu\text{-}O)] \cdot H_2O$	155.3(3)	1.787(1)	3.491*	[52]
$[(H_2O)_5Fe\text{–}O\text{–}Fe(H_2O)_5](NO_3)_4$	170.2	1.781(11)	3.549(2)	[53]

* Calculated from Fe–O distances and Fe–O–Fe angle in Ref. [52].
[a] Average.
[b] H_2salen = *N*,*N*′-bis(salicylidene)ethylenediamine.
[c] Prepared by recrystallising [Fe salen(acetate)] from methanol.
[d] H_2tsalen = *N*,*N*′-ethylenebis(thiosalicylideneimine); L^1 = 4-(3-*tert*-butyl-2-hydroxybenzyl)-1,4,7-triazacyclononane-1-acetate.

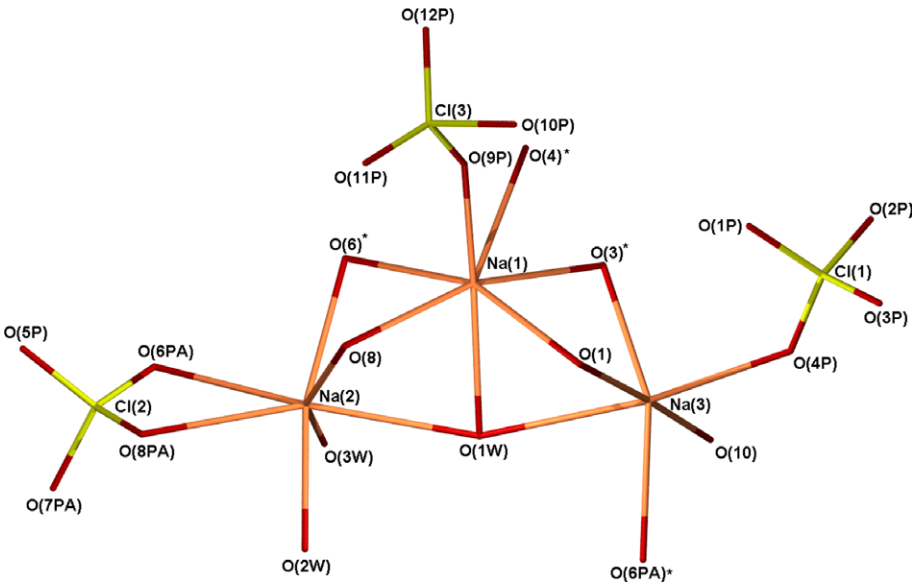


Fig. 8. Coordination environment of sodium atoms in complex **3**. $[Fe_2(\mu\text{–}O)L_2]$ units and O–*H* atoms have been omitted for clarity. (*) indicates symmetry-related atom.

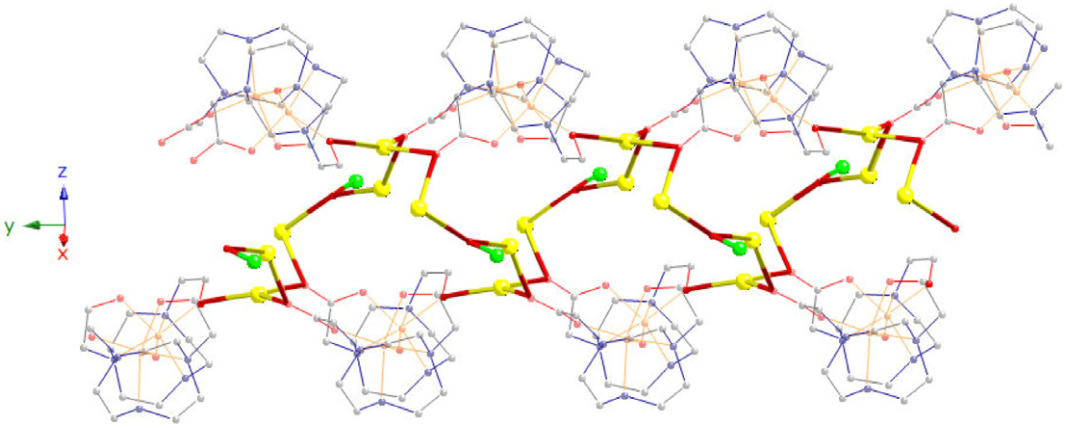


Fig. 9. 1D-Chains (along the *y*-axis) formed by sodium perchlorates flanked by $[Fe_2(\mu\text{-}O)L_2]$ moieties. C–*H* and N–*H* atoms as well as oxygen atoms and perchlorate which are not part of the chains have been omitted for clarity.

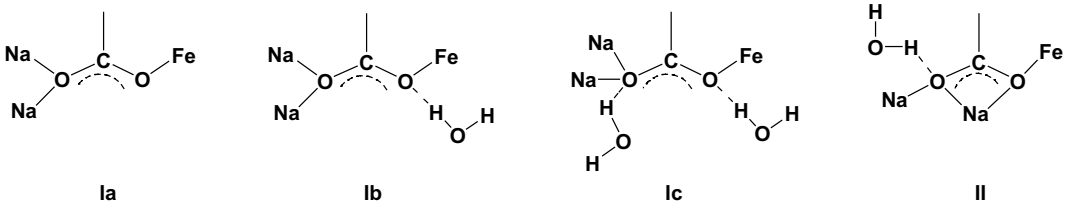


Fig. 10. Different coordination environments of carboxylate groups found in **3**.

orbitals in a *syn*, *anti*-fashion [19]. The magnetic properties of **1** are similar to those of the copper complex of 1,4,7-triazacyclononane-*N*-acetate, reported by Wieghardt [19] and co-workers ($J = 2.8(1)\ cm^{-1}$). This compound also features 1D-chains of complex units connected by carboxylate groups.

4. Supplementary material

CCDC 609193, 609194 and 609195 contain the supplementary crystallographic data for this paper. These data can be obtained free of charge via http://www.ccdc.cam.ac.uk/conts/retrieving.html, or from the Cambridge Crys-

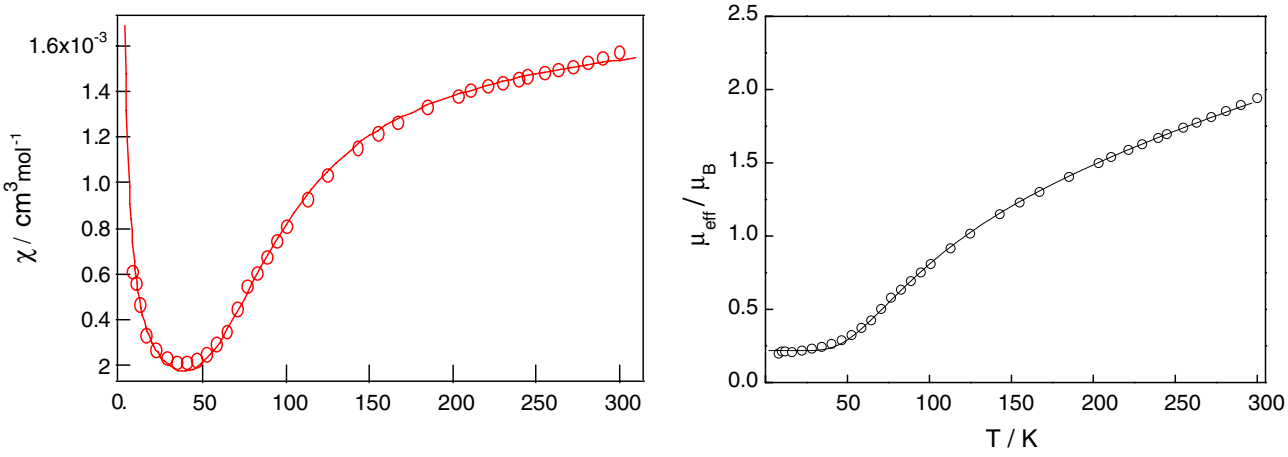


Fig. 11. Temperature dependence of magnetic susceptibility and magnetic moment for complex **3**. The solid lines correspond to the theoretical fits to the data (circles).

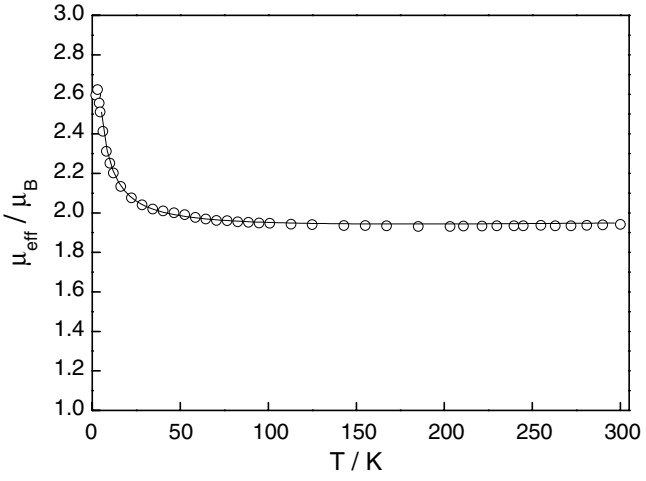


Fig. 12. Temperature dependence of the magnetic moment μ_{eff} per Cu(II), for complex **2**. The solid line corresponds to the theoretical fits to the data (circles).

tallographic Data Centre, 12 Union Road, Cambridge CB2 1EZ, UK; fax: (+44) 1223-336-033; or e-mail: deposit@ccdc.cam.ac.uk.

Acknowledgements

L.S., M.T.W.H. and K.S.M. acknowledge financial support from the Australian Research Council. UK was the recipient of a Postgraduate Research Scholarship from the Centre for Green Chemistry, Monash University.

References

[1] B. Graham, B. Moubaraki, K. Murray, L. Spiccia, J.D. Cashion, D.C.R. Hockless, J. Chem. Soc., Dalton Trans. (1997) 887.
[2] P.C. Junk, B.J. McCool, B. Moubaraki, K. Murray, L. Spiccia, J.D. Cashion, J.W. Steed, J. Chem. Soc., Dalton Trans. (2002) 1024.
[3] J.R. Hartman, R.L. Rardin, P. Chaudhuri, K. Pohl, K. Wieghard, B. Nuber, J. Weiss, G.C. Papaefthymiou, R.B. Frankel, S.J. Lippard, J. Am. Chem. Soc. 109 (1987) 7387.
[4] C. Fernandes, A. Neves, I. Vencato, A.J. Bortoluzzi, V. Drago, T. Weyermueller, E. Rentschler, Chem. Lett. (2000) 540.
[5] P. Ammala, J.D. Cashion, C.M. Kepert, B. Moubaraki, K. Murray, L. Spiccia, B.O. West, Angew. Chem., Int. Ed. 39 (2000) 1688.
[6] X. Wang, S. Wang, L. Li, E.B. Sundberg, G.P. Gacho, Inorg. Chem. 42 (2003) 7799.
[7] J. Sanders-Loehr, Iron Carriers and Iron Proteins, VCH, New York, 1989, p. 373.
[8] D.M. Kurtz Jr., Chem. Rev. 90 (1990) 585.
[9] R.H. Beer, W.B. Tolman, S.G. Bott, S.J. Lippard, Inorg. Chem. 30 (1991) 2082.
[10] R.E. Norman, S. Yan, L. Quen Jr., G. Backes, J. Ling, J. Sanders-Loehr, J.H. Zhang, C.J. O'Connor, J. Am. Chem. Soc. 112 (1990) 1554.
[11] E.I. Solomon, T.C. Brunold, M.I. Davis, J.N. Kemsley, S.K. Lee, N. Lehnert, F. Neese, A.J. Skulan, Y.S. Yang, J. Zhou, Chem. Rev. 100 (2000) 235.
[12] D.M. Kurtz Jr., J. Biol. Inorg. Chem. 2 (1997) 159.
[13] R.A. Friesner, M.H. Baik, B.F. Gherman, V. Guallar, M. Wirstam, R.B. Murphy, S.J. Lippard, Coord. Chem. Rev. 238–239 (2003) 267.
[14] A.L. Feig, S.J. Lippard, Chem. Rev. 94 (1994) 759.
[15] R.E. Stenkamp, Chem. Rev. 94 (1994) 715.
[16] P.C. Wilkins, R.G. Wilkins, Coord. Chem. Rev. 7 (1987) 195.
[17] R.C. Mehrotra, R. Bohra, Metal Carboxylates, Academic, New York, 1983.
[18] D. Schulz, T. Weyhermueller, K. Wieghardt, B. Nuber, Inorg. Chim. Acta 240 (1995) 217.
[19] D. Schulz, T. Weyhermueller, K. Wieghardt, C. Butzlaff, A.X. Trautwein, Inorg. Chim. Acta 246 (1996) 387.
[20] D. Odom, C.J. Gramer, V.G. Young Jr, S.A. Hilderbrand, S.E. Sherman, Inorg. Chim. Acta 297 (2000) 404.
[21] M. Studer, A. Riesen, T.A. Kaden, Helv. Chim. Acta 72 (1989) 307.
[22] J.E. Richman, T.J. Atkins, J. Am. Chem. Soc. 96 (1974) 2268.
[23] T.J. Atkins, J. Am. Chem. Soc. 102 (1980) 6346.
[24] G.R. Weisman, V. Johnson, R. Fiala, Tetrahedron Lett. 21 (1980) 3635.
[25] G.M. Sheldrick, SHELXS-97, University of Goettingen, Germany, 1997.
[26] L.J. Barbour, J. Supramol. Chem. 1 (2001) 189.
[27] C.K. Johnson, ORTEP II, Oak Ridge National Laboratory, TN, 1976.
[28] I. Lazar, R. Kiraly, Z. Takacs, J. Coord. Chem. 51 (2000) 293.
[29] Z. Kovacs, A.D.J. Sherry, J. Chem. Soc., Chem. Commun. (1995) 185.
[30] A. Neves, W. Walz, K. Wieghardt, B. Nuber, J. Weiss, Inorg. Chem. 27 (1988) 2484.

[31] J.M. Lyon, E. Gunther, J. Coord. Chem. 34 (1995) 13.
[32] G.R. Weisman, D.J. Vachon, V.B. Johnson, D.A. Gronbeck, J. Chem. Soc., Chem. Commun. (1987) 886.
[33] A. Blake, I.A. Fallis, S. Parsons, S.A. Ross, M. Schroeder, J. Chem. Soc., Dalton Trans. (1996) 525.
[34] R.L. Rardin, W.B. Tolman, S.J. Lippard, New J. Chem. 15 (1991) 417.
[35] G.B. Deacon, R.J. Phillips, Coord. Chem. Rev. (1980) 227.
[36] K.S. Murray, Coord. Chem. Rev. 12 (1974) 1.
[37] K. Nakamoto, Infrared and Raman Spectra of Inorganic and Coordination Compounds, fourth ed., Wiley, New York, 1986, pp. 231.
[38] G.B. Deacon, F. Huber, Inorg. Chim. Acta 104 (1985) 41.
[39] R.C. Reem, J.M. McCormick, D.E. Richardson, F.J. Devlin, P.J. Stephens, R.L. Musselman, E.I. Solomon, J. Am. Chem. Soc. 111 (1989) 4688.
[40] H.J. Schugar, G.R. Rossmann, C.G. Barraclough, H.B. Gray, J. Am. Chem. Soc. 94 (1972) 2683.
[41] C.A. Brown, G.J. Remar, R.L. Musselman, E.I. Solomon, Inorg. Chem. 34 (1995) 688.
[42] W.H. Armstrong, A. Spool, G.C. Papaefthymiou, R.B. Frankel, S.J. Lippard, J. Am. Chem. Soc. 106 (1984) 3653.
[43] E.I. Solomon, F. Tuczek, D.E. Root, C.A. Brown, Chem. Rev. 94 (1994) 827.
[44] L. Que Jr., R.C. Scarrow, Clusters in Proteins, American Chemical Society, Washington DC, 1988, p. 306.
[45] A. Spool, I. Williams, S.J. Lippard, Inorg. Chem. 24 (1984) 2156.
[46] J. Glerup, K. Michelsen, N. Arulsamy, D.J. Hodgson, Inorg. Chim. Acta 274 (1998) 155.
[47] J. Fergusen, Spectroscopy of 3d complexes, Progress in Inorganic Chemistry, vol. 12, Wiley-Interscience, 1979, pp. 159–294.
[48] J.S. Loehr, T.M. Loehr, A.G. Mauk, H.B. Gray, J. Am. Chem. Soc. 102 (1986) 6992.
[49] S.J. Lippard, H.J. Schugar, C. Walling, Inorg. Chem. 6 (1967) 1825.
[50] J.E. Davies, B.M. Gatehouse, Acta Crystallogr., Sect. B (1973) 1934.
[51] P.J. Marini, K.J. Berry, K.S. Murray, B.O. West, J. Chem. Soc., Dalton Trans. (1983) 879.
[52] C. Stockheim, L. Hoster, T. Weyermueller, K. Wieghard, B. Nuber, J. Chem. Soc., Dalton Trans. (1996) 4409.
[53] P.C. Junk, B.J. McCool, B. Moubaraki, K.S. Murray, L. Spiccia, Angew. Chem., Int. Ed. 38 (1999) 2224.
[54] A.C. Warden, L. Spiccia, M.T.W. Hearn, J.F. Boas, J.R. Pilbrow, J. Chem. Soc., Dalton Trans. (2005) 1804.
[55] C.J. O'Connor, Prog. Inorg. Chem. 29 (1982) 203.

Available online at www.sciencedirect.com
ScienceDirect
Polyhedron 26 (2007) 3217–3226
POLYHEDRON
www.elsevier.com/locate/poly

Mannich aminomethylation reactions of a series of bis(α-amino acidato)metal(II) complexes with formaldehyde and diethylmalonate: Crystal structure of (5,5-dicarboxyethyl-3,7-diazanonanedioato)copper(II) monohydrate

Subrahmanian Supriya [a], Aravamudhan Raghavan [a,*], V.R. Vijayaraghavan [b], Kandasamy Chinnakali [c], Hoong-Kun Fun [d], J. Subramanian [e]

[a] *Department of Polymer Science, University of Madras, Guindy Campus, Chennai 600 025, India*
[b] *Department of Physical Chemistry, University of Madras, Guindy Campus, Chennai 600025, India*
[c] *Department of Physics, Anna University, Chennai 600 025, India*
[d] *X-ray Crystallography Unit, School of Physics, Universiti Sains Malaysia 11800, Penang, Malaysia*
[e] *NMR Lab, CLRI, Adyar, Chennai 600 025, India*

Received 20 January 2007; accepted 21 February 2007
Available online 24 February 2007

Abstract

Mannich aminomethylation reactions involving $M(aa)_2$, where M = Cu, Ni and aa = glycine(gly), DL-alanine(DL-ala), L-alanine-(L-ala), with formaldehyde and diethylmalonate have been carried out, resulting in carboxylate appended systems in high yield. All the compounds have been characterized by UV-Vis spectroscopy, infrared spectroscopy and elemental analysis. One of the synthesized complexes, (5,5-dicarboxyethyl-3,7-diazanonanedioato)copper(II) monohydrate, has been characterized by single crystal XRD and has been used as catalyst in the hydrogen peroxide-induced degradation of pyrocatechol violet (PCV) dye. The variations in the rate of degradation of the dye with respect to change in concentration of hydrogen peroxide, dye, catalyst and pH have been studied. Effect of addition of NaCl has been studied and a suitable mechanism based on the formation of free radical species during the degradation process has been proposed.
© 2007 Elsevier Ltd. All rights reserved.

Keywords: Diethylmalonate; Metal complexes; Mannich aminomethylation; Pyrocatechol violet dye

1. Introduction

Mannich aminomethylation reactions involving chelated metal complexes, formaldehyde and a 'carbon acid' bridging group have been extensively studied during the past several years [1]. Nitroalkanes and malonic esters have been predominantly used as ring-closing agents leading to nitro- and carboxylate-appended macrocycles. Several other compounds such as primary amines [2], amides and sulfonamides [3] have also been used as nucleophiles. Chelated amino acid complexes undergo aldol condensation or Mannich aminomethylation reactions depending upon the pH and the nature of the α-alkyl substituents [4]. Mannich aminomethylation reaction of chelated amino acid complexes using diethylmalonate as the carbon acid is yet unreported in the literature. Hence, this paper reports Mannich aminomethylation reaction of a series of bis(α-amino acidato) metal(II), $M(aa)_2$, with formaldehyde and diethylmalonate as the carbon acid under both acidic and alkaline conditions which would further help in understanding the chemistry of the chelated amino acid complexes.

* Corresponding author.
E-mail address: doc_raghavan@rediffmail.com (A. Raghavan).

0277-5387/$ - see front matter © 2007 Elsevier Ltd. All rights reserved.
doi:10.1016/j.poly.2007.02.017

Study of the catalytic effect of metal complexes has been the subject of extensive research during the past several decades. Coordination complexes have been successfully used as catalysts in several organic reactions [5]. One of the important and useful areas of investigation is the recycling of textile wastewater by decolorization techniques for its subsequent use in dyeing processes [6]. There are several decolorization techniques such as adsorption, coagulation, electrochemical method, chlorination and ozonation, advanced oxidation using UV/TiO_2 and biological oxidation [7]. The need to reduce the amount of toxic wastes and byproducts arising from chemical processes requires increasing emphasis on the use of less toxic and environmentally compatible materials. In this aspect, our attempt to use one of the synthesized Mannich aminomethylation products as a catalyst in the hydrogen peroxide induced degradation of pyroctechol violet (PCV) dye appears to suggest a promising technique.

PCV, a phenolic organic compound, is used as a model in this study as it is a recommended reagent in spectrophotometric studies and has enhanced analytical potential towards metal ion extraction and determination [8]. H_2O_2 is the widely used oxidizing agent in the degradation processes [9]. Transition metal complexes are found to activate H_2O_2 by releasing highly active and nonspecific hydroxyl radicals that oxidize organic pollutants [10].

This paper reports the synthesis of products containing carboxylate bridging groups starting from amino acid complexes of Cu and Ni and one of the synthesized Mannich aminomethylation product, (5,5-dicarboxyethyl-3,7-diazanonanedioato)copper(II) monohydrate, has been tested for its catalytic activity in the H_2O_2 induced degradation of PCV.

2. Experimental

Glycine(gly), DL-alanine(DL-ala), L-alanine(L-ala) and 2-propanol were supplied by SRL laboratories, diethylmalonate and pyrocatechol violet {2-[(3,4-dihydroxyphenyl)-(3-hydroxy-4-oxocyclohexa-2,5-dien-1-ylidene)methyl] benzenesulphonic acid} (PCV) was obtained from Lancaster chemicals, 37% aqueous formaldehyde solution and AR grade hydrogen peroxide (30%) free of inhibitors were obtained from Merck. The initial concentration of H_2O_2 was determined iodometrically using a standard solution of sodium thiosulphate. $Cu(aa)_2$ and $Ni(aa)_2$ were prepared as reported in the literature [11].

2.1. Physical measurements

Electronic spectra of the complexes and the kinetic measurements were carried out on a Zhimadzu UV-160A spectrophotometer. The infrared spectra were recorded on a Themo Mattson Satellite FT-IR spectrophotometer from 4000 to 450 cm^{-1} as KBr discs. Elemental analyses were carried out with an Elementar Vario EL III Carlo Erba 1108 analyzer available at CDRI, Lucknow. ESR measurements were done using BRUKER X-Band EMX-EPR spectrometer available at CLRI, Chennai. About 3 mM solutions of the complexes in DMSO were used for measurements at 77 K.

2.2. Reactions and syntheses

All reactions of $M(aa)_2$, where M = Cu, Ni and aa = glycine, DL-alanine and L-alanine, with formaldehyde and diethylmalonate were carried out in the absence of base and in the pH range between 6.0 and 9.0. The pH of each reaction mixture was adjusted by the addition of aqueous Na_2CO_3 solution.

2.2.1. (5,5-Dicarboxyethyl-3,7-diazanonanedioato)-copper(II) (**1a**)

A reaction mixture consisting of $Cu(gly)_2 \cdot H_2O$ (1 g, 4.4 mmol), formaldehyde (6.6 ml, 0.08 mol) and diethylmalonate (1.3 ml, 8.8 mmol) in 100 ml of water:methanol mixture (3:1) was stirred thoroughly at room temperature for 2 days. The reaction mixture on concentration (~30 ml) using rotary evaporator and on standing at room temperature yielded deep blue crystalline product. The crystals were collected by filtration, washed with cold ethanol and diethyl ether and finally dried over $CaCl_2$ for 2 h. Yield: 1.23 g, 68%. Elemental *Anal.* Calc. for $C_{13}H_{20}N_2O_8Cu.H_2O$: C, 37.75; H, 5.31; N, 6.77. Found: C, 37.61; H, 5.30; N, 6.92%. $\lambda_{max}(H_2O)$/nm 248 (ε/$dm^3\ mol^{-1}\ cm^{-1}$ 447.5) and 615 (47.9). IR (cm^{-1}): 3612, 3433, 3249, 3184, 2980, 2935, 1733, 1655, 1586, 1455, 1382, 1345, 1276, 1239, 1195, 1146, 1080, 1027, 974, 942, 856, 775, 746, 644, 583, 510, 465. This complex could be synthesized between pH 4.0 and 7.0. Yield of the product decreases above pH 7 (<10%) and no product could be isolated above pH 8. Reactions carried out with different mole ratios of the reactants did not enhance the yield of the product.

2.2.2. (5,5-Dicarboxyethyl-2,8-dimethyl-3,7- diazanonanedioato)copper(II) (**1b**)

A reaction mixture consisting of $Cu(DL\text{-}ala)_2 \cdot H_2O$ (1 g, 3.8 mmol), formaldehyde (5.8 ml, 0.07 mol) and diethylmalonate (1.2 ml, 7.7 mmol) in 100 ml water:methanol mixture (3:1) was stirred thoroughly at room temperature for 5 days. On concentration by rotary evaporator (~30 ml) and on standing at room temperature, deep blue crystalline product was obtained. The crystals were collected by filtration, washed with cold ethanol and diethyl ether and finally dried over $CaCl_2$ for 2 h. Yield: 1.02 g, 61%. Elemental *Anal.* Calc. for $C_{15}H_{24}N_2O_8Cu.H_2O$: C, 40.79; H, 5.88; N, 6.34. Found: C, 40.62; H, 5.92; N, 6.29%. $\lambda_{max}(H_2O)$/nm 284 (ε/$dm^3\ mol^{-1}\ cm^{-1}$684.4) and 604 (99.3). IR (cm^{-1}): 3428, 3343, 3233, 3180, 2984, 2943, 1728, 1622, 1464, 1443, 1378, 1313, 1292, 1239, 1207, 1178, 1109, 1019, 913, 885, 856, 783, 669, 658, 607, 522, 453. This complex could be synthesized between pH 4.0 and 7.0. Yield of the product decreases above pH 7

(<10%) and no product could be isolated above pH 8. Reactions carried out with different mole ratios of the reactants did not enhance the yield of the product.

2.2.3. (5,5-Dicarboxyethyl-2,8-dimethyl-3,7-diazanonanedioato)copper(II) (**1c**)

A reaction mixture consisting of Cu(L-ala)$_2$ (0.5 g, 2.0 mmol), formaldehyde (0.8 ml, 0.01 mol) and diethylmalonate (0.3 ml, 2.0 mmol) in 100 ml water:methanol mixture (3:1) was stirred thoroughly at room temperature for 5 days. On concentration by rotary evaporator (~30 ml) and on standing at room temperature, a deep blue product was obtained. The product was collected by filtration, washed with cold ethanol and diethyl ether and finally dried over $CaCl_2$ for 2 h. Yield: 0.37 g, 42%. Elemental *Anal.* Calc. for $C_{15}H_{24}N_2O_8Cu$: C, 42.52; H, 5.66; N, 6.61. Found: C, 42.41; H, 5.61; N, 6.52%. $\lambda_{max}(H_2O)$/nm 282 (ε/dm^3 mol^{-1} cm^{-1} 665.0) and 607 (91.0). IR (cm^{-1}): 3233, 3182, 2987, 2919, 1733, 1623, 1451, 1437, 1382, 1315, 1292, 1239, 1203, 1182, 1105, 1019, 913, 890, 852, 791, 678, 606, 520, 460. Product yield is poor above pH 7.0 (~5%).

2.2.4. (5,5-Dicarboxyethyl-3,7-diazanonanedioato)-nickel(II) (**2a**)

A reaction mixture consisting of Ni(gly)$_2 \cdot 2H_2O$ (1 g, 4.1 mmol), formaldehyde (6.2 ml, 0.08 mol) and diethylmalonate (1.2 ml, 8.2 mmol) in 250 ml water:methanol mixture (4:1) was stirred thoroughly at 40 °C for 6 h. On concentration by rotary evaporator (~50 ml) and on standing at room temperature, a pale blue crystalline product was obtained which was collected by filtration, washed with cold ethanol and diethyl ether and finally dried over $CaCl_2$ for 2 h. Yield: 0.70 g, 40%. Elemental *Anal.* Calc. for $C_{13}H_{20}N_2O_8Ni.2H_2O$: C, 36.58; H, 5.62; N, 6.56. Found: C, 36.61; H, 5.73; N, 6.71%. $\lambda_{max}(H_2O)$/nm 288 (ε/dm^3 mol^{-1} cm^{-1} 7.7), 365 (9.8), 603 (6.0) and 742 (6.5). IR (cm^{-1}): 3408, 3286, 3241, 2976, 2935, 1729, 1610, 1451, 1394, 1370, 1341, 1309, 1284, 1252, 1227, 1199, 1150, 1060, 1027, 962, 930, 860, 742, 644, 616, 575, 510, 432. This complex could be synthesized between pH 4.0 and 6.0. No product could be isolated above pH 8.0.

2.2.5. (5,5-Dicarboxyethyl-2,8-dimethyl-3,7-diazanonanedioato)nickel(II) (**2b**)

The complex was prepared according to the synthetic method described for the analogous **2a**, using Ni(DL-ala)$_2 \cdot 3H_2O$ as starting material. Yield: 1.03 g, 63%. Elemental *Anal.* Calc. for $C_{15}H_{24}N_2O_8Ni.3H_2O$: C, 38.10; H, 6.34; N, 5.92. Found: C, 38.18; H, 6.26; N, 5.72%. $\lambda_{max}(H_2O)$/nm 289 (ε/dm^3 mol^{-1} cm^{-1}6.5), 349 (8.3), 602 (5.0) and 742 (8.2). IR (cm^{-1}): 3416, 3270, 3217, 2997, 2945, 1729, 1606, 1464, 1390, 1347, 1279, 1239, 1170, 1148, 1075, 1027, 969, 948, 860, 778, 743, 638, 592, 501, 461. Yield of the product is maximum in the pH range 4.0–7.0.

2.2.6. (5,5-Dicarboxyethyl-2,8-dimethyl-3,7-diazanonanedioato)nickel(II) (**2c**)

The complex was prepared according to the synthetic method described for the analogous **2a**, using Ni(L-ala)$_2 \cdot 3H_2O$ as starting material. Yield: 0.94 g, 58%. Elemental *Anal.* Calc. for $C_{15}H_{24}N_2O_8Ni \cdot 3H_2O$: C, 38.10; H, 6.34; N, 5.92. Found: C, 38.21; H, 6.24; N, 5.81%. $\lambda_{max}(H_2O)$/nm 289 (ε/dm^3 mol^{-1} cm^{-1}6.4), 351 (7.7), 605 (4.8) and 748 (7.4). IR (cm^{-1}): 3427, 3363, 3256, 3230, 2984, 2938, 1737, 1590, 1460, 1411, 1366, 1339, 1256, 1226, 1165, 1117, 1062, 1036, 931, 909, 860, 771, 733, 627, 543. Yield of the product is maximum at pH 7.0.

2.3. Degradation of PCV using **1a**

In each experiment, a conical flask of volume 100 cm^3 containing definite quantity of the catalyst together with 20 cm^3 of double distilled water was placed in water thermostat for 30 min. To the flask was added the required quantity of PCV/H_2O_2 mixture and zero time was noted at half the addition point. The reaction mixture was stirred continuously using a magnetic stirrer. At regular time intervals, an aliquot was withdrawn and the absorbance at $\lambda_{max} = 441$ nm ($\varepsilon = 15.766$ dm^3 mol^{-1} cm^{-1}) was recorded. The absorbance of PCV/H_2O_2 mixture remains constant for several hours in the absence of the catalyst.

2.4. Structure determination of **1a**

A blue crystal of size $0.44 \times 0.34 \times 0.04$ mm was used for intensity data collection on a Bruker SMART APEX2 CCD area-detector diffractometer with Mo Kα radiation ($\lambda = 0.71073$ Å) at 100 K. Empirical absorption correction was applied by using the SADABS program [12]. The structure was solved by direct methods and refined by full-matrix least-squares techniques on F^2 by using SHELXTL [13] with 3252 reflections ($2.51° \leqslant \theta \leqslant 26.00°$) and 236 parameters. All non-hydrogen atoms were refined anisotropically, and C and N-bound hydrogen atoms were positioned geometrically and refined using a riding model. The hydrogen atoms of the water molecules were located in a difference map and refined isotropically with distance restraints. The final cycle of the refinement converged with

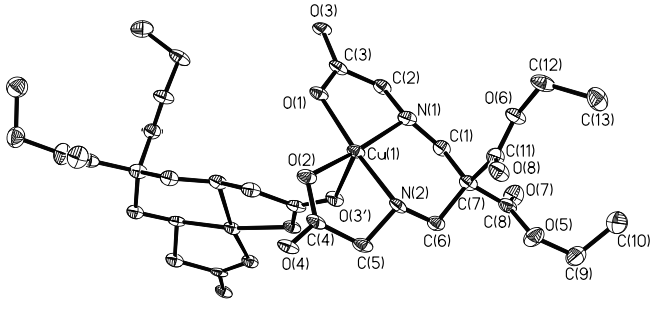


Fig. 1. An ORTEP plot of **1a** from the crystal structure analysis. The water molecule is not shown in the figure.

$R = 0.072$. The highest residual density peak (2.72 e/Å^3) and the deepest hole (−1.84 e/Å^3) are located 0.96 and 0.86 Å, respectively, from Cu(1) atom. The poor residuals may be as a result of the plate-like nature of the crystal. No disorder is found in the carboxyethyl groups or in the water molecule. The structure is illustrated as an ORTEP [14] plot in Fig. 1. Crystal data, selected bond lengths and angles are listed in Tables 1 and 2.

Table 1
Crystallographic data for **1a**

Formula	$C_{13}H_{20}CuN_2O_8 \cdot H_2O$
Formula weight	413.586
Crystal system	monoclinic
Space group	$C2/c$ (No. 15)
a (Å)	29.728(3)
b (Å)	8.4556(7)
c (Å)	13.6370(13)
α (°)	90
β (°)	104.919(6)
γ (°)	90
Volume (Å^3)	3312.4(5)
Z	8
D_{calc} (g/cm^{-3})	1.660
Absorption coefficient (mm^{-1})	1.371
$F(000)$	1720
Crystal size (mm)	$0.04 \times 0.34 \times 0.44$
Temperature (K)	100
Wavelength (Å)	0.71073
θ Range (°)	2.5–26.0
Index ranges	$-36 \leqslant h \leqslant 36$; $-10 \leqslant k \leqslant 10$; $-16 \leqslant l \leqslant 16$
Total number of data measured	12758
Number of unique observed data	3252
R_{int}	0.078
Observed data [$I > 2.0\ \sigma(I)$]	2384
No of reflections, no of parameters	3252, 236
R, wR_2, S	0.0719, 0.2233, 1.05
Maximum and average shift/error	0.00, 0.00
Minimum and maximum resdiual density [e/Å^3]	−1.84, 2.72

Weighting scheme: $w = 1/[\sigma^2(F_o^2) + (0.1454P)^2 + 8.2602P]$, where $P = (F_o^2 + 2F_c^2)/3$.

Table 2
Selected bond distances (Å) and bond angles (°) for **1a**

Cu(1)–O(1)	1.954(4)	Cu(1)–O(2)	1.954(4)
Cu(1)–N(1)	2.002(5)	Cu(1)–N(2)	1.992(4)
Cu(1)–O(3′)	2.288(4)	Cu(1)–O(2″)	2.754(4)
O(1)–Cu(1)–O(2)	93.38(16)	O(1)–Cu(1)–N(1)	84.06(17)
O(1)–Cu(1)–N(2)	169.44(17)	O(1)–Cu(1)–O(3′)	102.11(15)
O(1)–Cu(1)–O(2″)	85.12(14)	O(2)–Cu(1)–N(1)	169.04(17)
O(2)–Cu(1)–N(2)	84.27(18)	O(2)–Cu(1)–O(3′)	95.79(14)
O(2)–Cu(1)–O(2″)	89.75(13)	N(1)–Cu(1)–N(2)	96.30(19)
O(3′)–Cu(1)–N(1)	95.17(16)	O(2″)–Cu(1)–N(1)	79.42(15)
O(3′)–Cu(1)–N(2)	88.38(16)	O(2″)–Cu(1)–N(2)	84.58(15)
O(2″)–Cu(1)–O(3′)	170.57(13)		

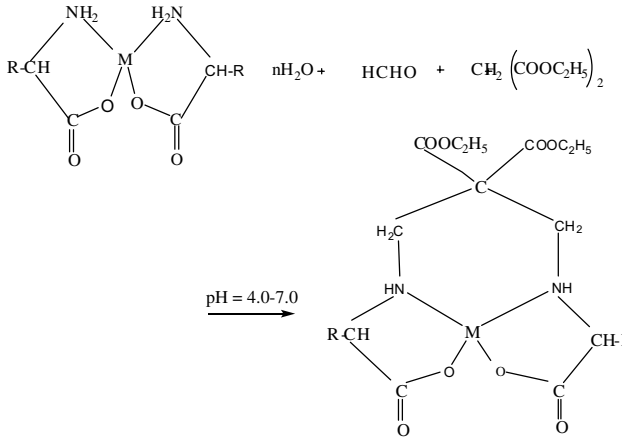
Symmetry transformations used to generate equivalent atoms: prime, $1/2 - x$, $-1/2 + y$, $1/2 - z$; double prime, $1/2 - x$, $3/2 - y$, $-z$.

3. Results and discussion

Chelated amino acid complexes undergo condensation reactions, via two different pathways such as aldol-type condensation reaction resulting in the formation of oxazolidine ring-containing compound [15] or Mannich aminomethylation in the presence of formaldehyde and a third compound containing labile protons [4].

In the present study, Mannich aminomethylation of glycine and alanine chelated to Cu and Ni with formaldehyde and diethylmalonate has been carried out. More than 60% yield of the Mannich aminomethylation products were obtained when Cu(gly)$_2$, Cu(DL-ala)$_2$ and Ni(DL-ala)$_2$ are used as the starting materials.

The products obtained from the reactions of Cu(aa)$_2$ and Ni(aa)$_2$ with formaldehyde and diethylmalonate are schematically shown below.



M(aa)$_2$

1a – 2c

1a, R = H, M = Cu
1b, R = CH_3, M = Cu
1c, R = CH_3, M = Cu
2a, R = H, M = Ni
2b, R = CH_3, M = Ni
2c, R = CH_3, M = Ni

Details of the reactions of copper(II) and nickel(II) complexes of glycine, DL and L forms of alanine with formaldehyde and diethylmalonate at different pH conditions are described in Section 2. The reactions of Cu(gly)$_2 \cdot H_2O$, Cu(DL-ala)$_2 \cdot H_2O$ and Ni(gly)$_2 \cdot 2H_2O$ with formaldehyde and diethylmalonate yielded crystalline products **1a**, **1b** and **2a**, respectively, and their structures are assigned based on their IR and elemental analysis data. The structure of the product **1a** is characterized by X-ray diffraction studies. The product, **1c**, obtained for Cu(L-ala)$_2$ with formaldehyde and diethylmalonate has been identified as (5,5-dicarboxyethyl-2,8-dimethyl-3,7-diazanonanedioato)copper(II) from the IR spectrum and elemental analysis data.

The reactions of Cu(L-ala)$_2$, Ni(DL-ala)$_2 \cdot 3H_2O$ and Ni(L-ala)$_2 \cdot 3H_2O$ with formaldehyde and diethylmalonate

yielded blue colored products. However, the crystals were not suitable for X-ray analysis and our best attempts to grow single crystals of the complexes were unsuccessful. The products **2a**, **2b** and **2c** were assigned structures similar to that of their analogous **1a**, **1b** and **1c** from their IR and elemental analysis data.

The IR spectra of all the complexes exhibit a sharp band at ~3250 cm^{-1}, indicating the presence of an N–H group. Hence, only one proton of the $–NH_2$ group of the chelated amino acids takes part in the Mannich aminomethylation reaction which is consistent with the results reported previously [1,16]. The ester carbonyl stretching is observed at ~1730 cm^{-1} for all the products. All the synthesized complexes **1a**, **1b**, **1c**, **2a**, **2b** and **2c** exhibit typical coordinated carboxylate asymmetric stretching and symmetric stretching frequencies at ~1600 cm^{-1} and ~1400 cm^{-1}, respectively. The absence of a triplet in the IR region 1200–1050 cm^{-1}, attributed to an oxazolidine ring system, shows that the α-carbon protons in the products are unaffected by the formaldehyde attack in the pH range 4.0 and 7.0. All the complexes, except **1c**, exhibit bands at ~3450 cm^{-1} indicating the presence of water molecules. Thus, it is clear from the IR data that the products are the result of the reactions of their corresponding chelated amino acids, $Cu(aa)_2$ or $Ni(aa)_2$, with formaldehyde and diethylmalonate. Furthermore, microanalytical data support the postulated formulae of these complexes.

The formation of the products in all the cases must necessarily involve the initial loss of amino protons of bis(amino acidato)M(II), a phenomenon which has been well documented [17]. This step leads to electrophilic attack on the nitrogen atom by formaldehyde molecules, followed by subsequent condensation with diethylmalonate resulting in the formation of a heterocyclic ring system. Diethylmalonate is weakly acidic ($pK_a \sim 13.3$), and is found to be reactive [18].

No role of chirality is observed in this work, as both DL and L-alaninato complexes of Cu(II) and Ni(II) were found to undergo Mannich aminomethylation to give the same product, in contrast to the earlier reports [19].

3.1. Description of the crystal structure of *1a*

In the coordination polymer (Fig. 1), each copper atom is five-coordinated by two carboxyl O atoms and two N atoms from two glycine units and one carboxyl O atom from a symmetry-related ligand; the local coordination environment around each copper atom can be best described as a distorted square-pyramidal geometry, with atoms O(1), O(2), N(1) and N(2) defining the basal plane, and the copper atom deviates by 0.184(2) Å from that plane, in the direction of the O(3′) atom which occupies the apical site, with a Cu(1)–O(3′) bond distance of 2.288(4) Å. This coordination results in the formation of a one-dimensional chain structure along the crystallographic *b* axis. In the chain, the shortest Cu···Cu distance is 5.910(1) Å. But there exists a long semi-coordinate Cu(1)–O(2″) bond of 2.754(4) Å between the adjacent symmetry related chain. If this longer coordination is considered to be significant, then the coordination around each copper atom may be alternatively explained as distorted octahedral and it results in the formation of two-dimensional coordination polymer (Fig. 2) extending along the crystallographic bc plane, with a short Cu(1)···Cu(1″) contact of 3.383(1) Å. The three *trans* angles at each copper centre lie in the range 169.04(17)°–170.57(13)°. All other angles subtended at each copper atom are ranging from 79.42(15)° to 102.11(15)°, which indicates a distorted octahedral geometry of atom Cu(1). N–H···O and O–H···O hydrogen bonds involving the carboxylate and solvate water O atoms are observed within the layer (range of N···O = 2.951(6)–3.128(6) Å and that of O···O = 2.856(7)–3.179(7) Å). No interaction is observed between the layers.

3.2. Solution spectroscopy of the copper(II) complexes

The ESR spectra of **1a** and **1b** have been recorded in DMSO solution at liquid nitrogen temperatures. The solution ESR spectrum of the complex **1a** (Fig. 3) looks very similar to that of an earlier report [4d] and is typical of a square planar CuN_2O_2 coordination geometry with weakly bound axial ligand. This is in agreement with the crystal structure of **1a**. Apparently, the sample contains both monomeric and dimeric Cu centers.

The ESR spectrum of **1b** (Fig. 3a) appears to be a typical triplet state spectrum arising from a dimer. A computer simulation of the ESR spectrum (Fig. 3b) was attempted using the approach of Pilbrow [20]. A computer program reported was used [21]. The interaction between the Cu

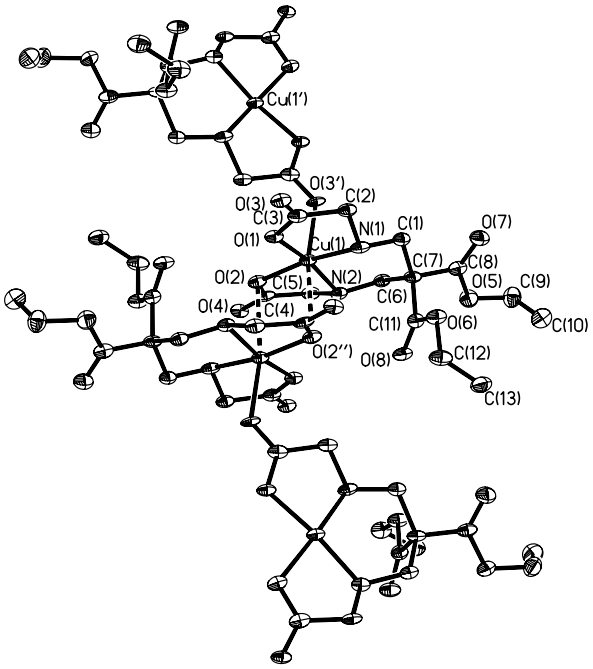


Fig. 2. Two-dimensional view of the coordination polymer.

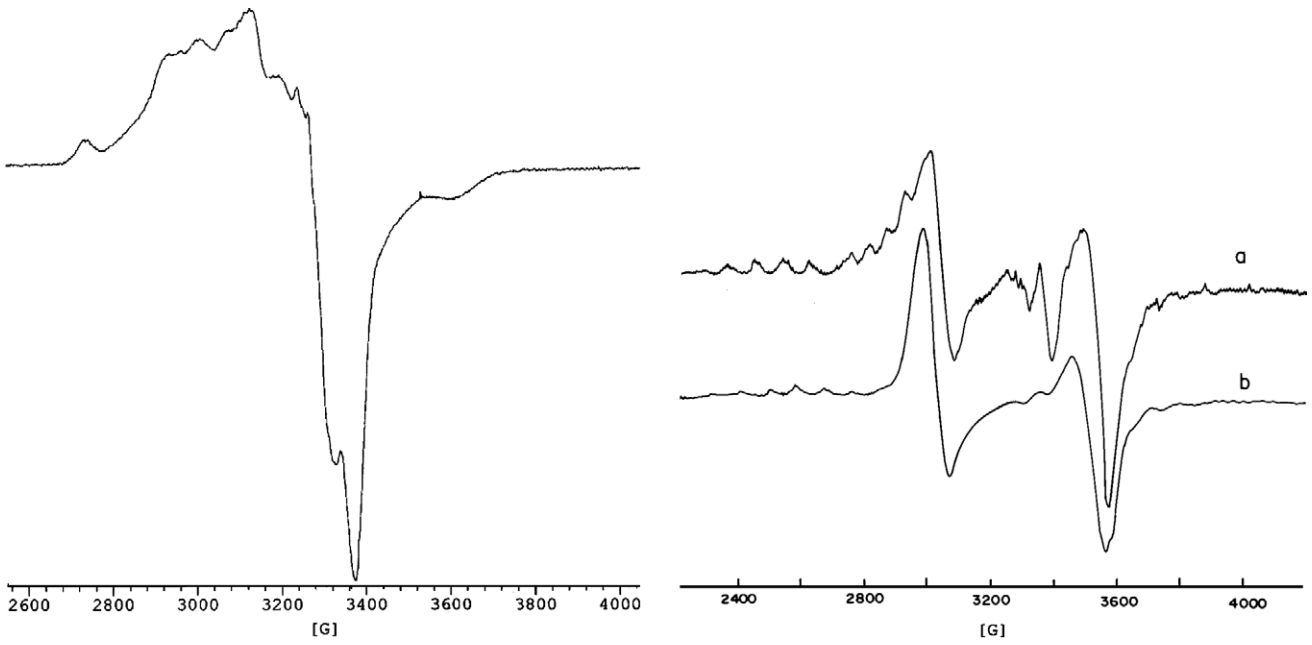


Fig. 3. ESR spectrum of **1a** at 77 K in DMSO at microwave frequency of 9.502 GHz and field modulation frequency of 100 kHz. (a) ESR spectrum of **1b** at 77 K in DMSO at microwave frequency of 9.502 GHz and field modulation frequency of 100 KHz. (b) Computer simulated ESR spectrum of **1b**.

centers is assumed to arise predominantly from dipolar interactions. An exchange coupling of about $-2\ cm^{-1}$(ferromagnetic) in the simulation was obtained. A distance of 3.9 Å between the two Cu centers gave a good agreement between the experimental and the computer simulated spectrum. The computer simulated spectrum of **1b** yielded the parameters $g_{11} = 2.220$, $g_{\perp} = 2.080$, $A_{11} = 191.0 \times 10^{-4}\ cm^{-1}$ and $A_{\perp} = 35.0 \times 10^{-4}\ cm^{-1}$.

3.3. Catalytic activity

Spectrophotometric measurements in phosphate buffer solutions revealed that no absorbance change was observed when H_2O_2 is mixed with PCV at concentrations used in this work. However on addition of the catalyst the absorbance at 441 nm was found to decrease at a much higher rate than the uncatalyzed reaction (Fig. 4).

The kinetic measurements were carried out under pseudo-first-order conditions with respect to [PCV]. The value of the rate constant, k, is obtained from the slope of the straight lines of the equation, $\ln A_t = \ln A_0 - kt$, where A_t is the absorbance at time t, A_0 is the absorbance at time = 0.

Experiments carried out at constant temperature and pH to determine the order of reaction with respect to PCV and H_2O_2 revealed that the reaction rate increases with a first order dependence on H_2O_2 (Fig. 5) in the range 0.009–0.12 M at 30 °C. Thus, activation of H_2O_2 by the catalyst leads to the formation of hydroxyl or perhydroxyl radicals which attack PCV and degrade it. The influence of [PCV] on the rate of reaction was studied by varying $[PCV]_0$ in the range $0.5–3.8 \times 10^{-4}$ M at 30 °C (Fig. 6) at constant $[H_2O_2]_0$ and pH value. The reaction obeyed a first order dependence on $[PCV]_0$ at lower concentrations.

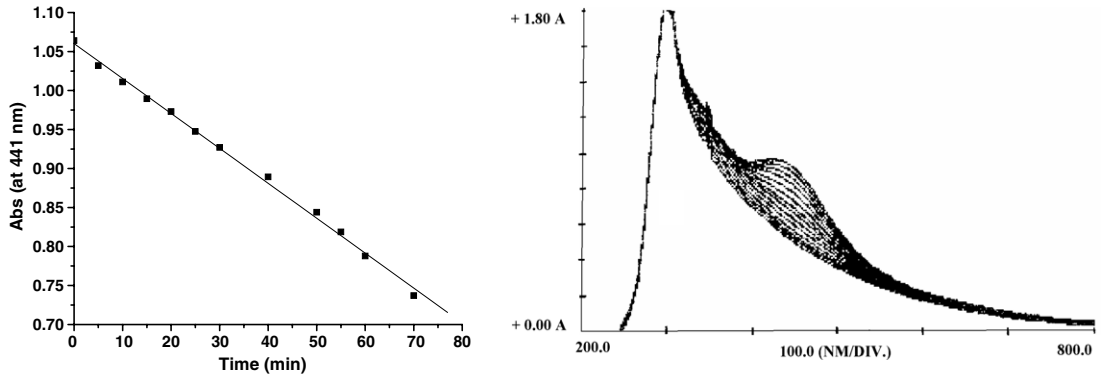


Fig. 4. The variation of absorbance for the reaction of 1.2×10^{-4} M $[PCV]_0$ with 0.01 M $[H_2O_2]_0$ in the presence of 0.01 g of the catalyst at 30 °C.

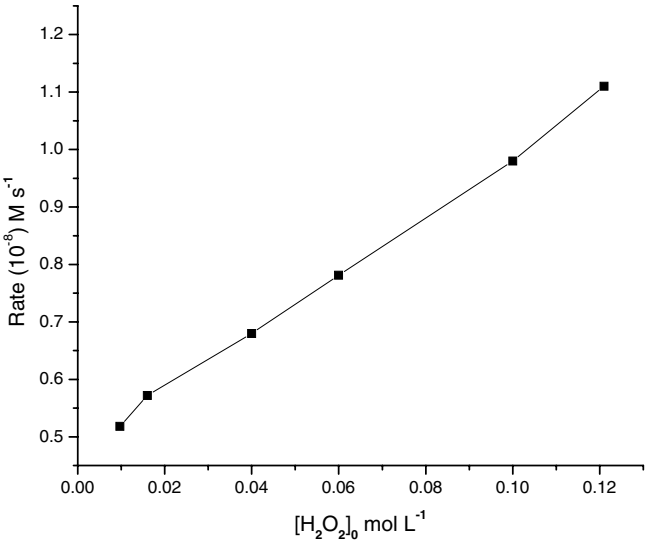


Fig. 5. Dependence of the initial rate on the $[H_2O_2]_0$ for the reaction of 1.2×10^{-4} M $[PCV]_0$ in the presence of 0.01 g of the catalyst at 30 °C.

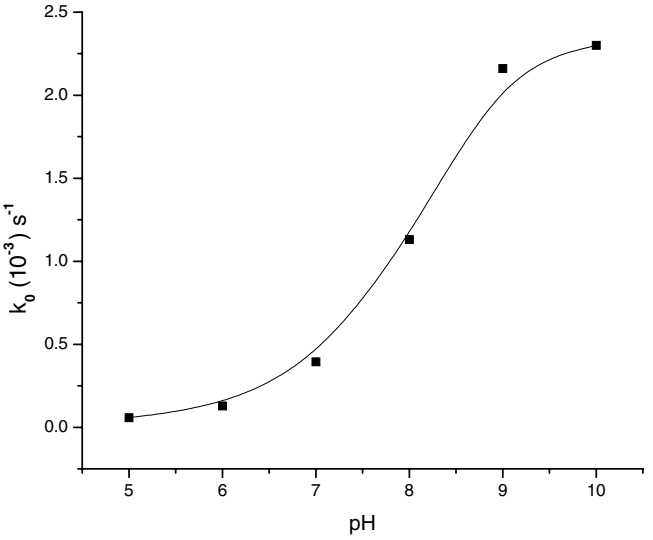


Fig. 7. Dependence of the rate constant on pH for the reaction of 1.2×10^{-4} M $[PCV]_0$ with 0.01 M $[H_2O_2]_0$in the presence of 0.01 g of the catalyst at 30 °C.

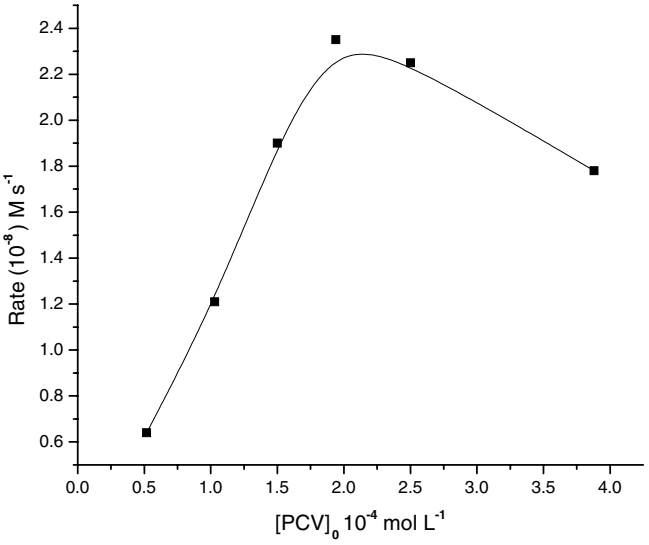


Fig. 6. Dependence of the initial rate on the $[PCV]_0$ for the reaction of 0.01 M $[H_2O_2]_0$ in the presence of 0.01 g of the catalyst at 30 °C.

However, the order reached almost zero at higher concentrations.

Rate of the reaction is found to increase with increase in concentration of the catalyst. The effect of increase in the concentration of the catalyst on the degradation of the dye was studied by fixing $[PCV]_0$ and $[H_2O_2]_0$ at constant values and taking 0.01, 0.02 and 0.03 g of the catalyst. The absorbance value is found to decrease with increase in the concentration of the catalyst, thereby increasing the rate of the reaction.

The effect of pH on the rate of reaction was studied using phosphate buffer in the range 5–9, and NaOH for pH > 9 at 30 °C. PCV, a tetraprotic acid (H_4L) exists in the form H_3L^- (yellow) under weakly acidic condition (pH 3–7) and shows maximum absorbance at $\lambda_{max} =$ 441 nm. Under alkaline conditions (pH > 7), PCV exists in the form H_2L^{2-} (violet) having maximum absorbance at 596 nm [8]. The value of the rate constant increases slowly at the beginning and then attains maximum value at pH 9.0, after which it levels off resulting in an S-shape curve (Fig. 7). This increase in the reaction rate could be attributed to the deprotonation of H_2O_2 which in turn favors the formation of the peroxo intermediate [22]. Thus, the generation of the active peroxo species brings about easy oxidation of PCV. The change in the electronic configuration of PCV under alkaline condition would have made it more susceptible for oxidation. However, at pH > 10, the solution turned turbid thereby making the experimental determination of the absorbance difficult.

The effect of chloride ions on the reaction rate was studied at fixed concentrations of $[PCV]_0$, $[H_2O_2]_0$ and the catalyst. The rate constant was found to increase with increasing [NaCl] (Fig. 8). This increase in rate may be attributed to the oxidation of chloride ions by H_2O_2 to produce other oxidizing agents such as OCl^- and Cl_2 that assist in the oxidation of PCV [23].

The formation and the role of the free radical species such as $OH^{\cdot}$ and $HO_2^{\cdot}$ by the decomposition of H_2O_2 by transition metal complexes has already been confirmed by spectroscopic methods [24]. Also, organic radical scavengers like 2-propanol and a chromogen 2,2′-azino-bis(3-ethylbenz-thiazoline)-6-sulphonate diammonium salt (ABTS) were used as a probe to confirm the generation of free radical species [25]. Our attempt to use 2-propanol as the radical scavenger also proved the formation of free radical species during the degradation process. Addition of 2-propanol to the reaction mixture resulted in a drastic decrease in the rate of the reaction. The rate of the reaction with the addition of 2-propanol was found to be approximately 10

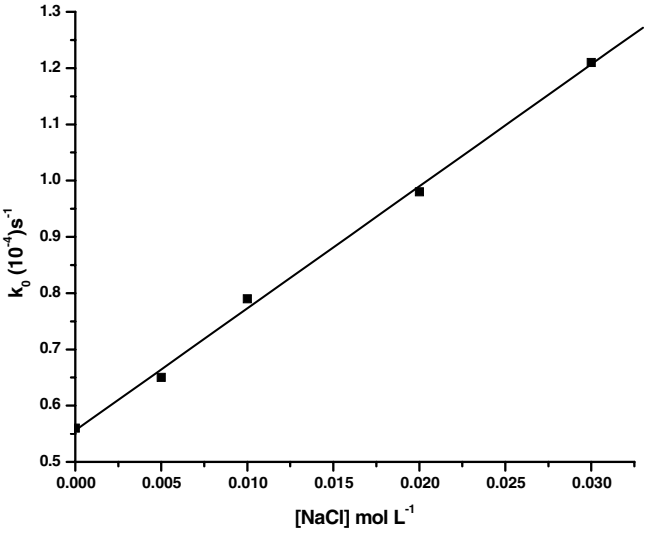


Fig. 8. Variation of rate constant with [NaCl] for the reaction of 1.2×10^{-4} M $[PCV]_0$ with 0.01 M $[H_2O_2]_0$ and 0.01 g of the catalyst at 30 °C.

times less than the rate of the reaction without the addition of 2-propanol (Fig. 9). This confirms the generation of radical species by the transition metal complex from H_2O_2. Based on the results and discussion given above, the reaction mechanism which involves the formation of the highly active hydroxyl radical, formed by the interaction of the catalyst with H_2O_2, has been proposed. The hydroxyl radical, which is an active oxidant, attacks PCV forming PCV-radical adduct which gets decomposed in the rate-determining steps resulting in the formation of the final oxidation products as given under:

$$[Cu^{II}L] + H_2O_2 \underset{k_{-1}}{\overset{k_1}{\leftrightarrows}} [Cu^{II}L(HO_2^-)] + H^+ \quad (1)$$

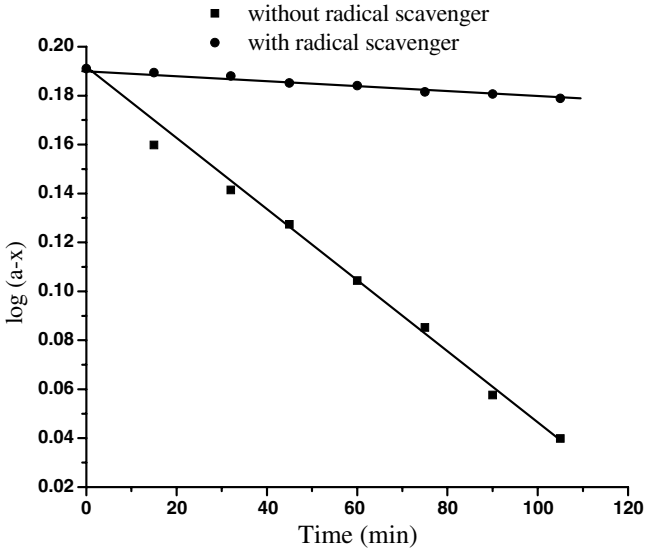


Fig. 9. Effect of the radical scavenger on the rate of the reaction.

$$[Cu^{II}L(HO_2^-)] \xrightarrow{k_2} [Cu^{I}L] + OH^{\cdot} + \frac{1}{2}O_2 \quad (2)$$

$$PCV + (HO^{\cdot})] \xrightarrow{k_3} \underset{\text{Dye-radical adduct}}{[PCV(HO^{\cdot})]} \quad (3)$$

$$[PCV(HO^{\cdot})] \underset{\text{slow}}{\xrightarrow{k_4}} \text{Oxidation products,} \quad (4)$$

$$[Cu^{I}L] + HO^{\cdot} \xrightarrow{k_5} [Cu^{II}L] + OH^- \quad (5)$$

$$OH^- + H^+ \rightarrow H_2O \quad (6)$$

From Eq. (1), the concentration of the peroxo complex is given by

$$[[Cu^{II}L(OH_2^-)]] = K_1[[Cu^{II}L]][H_2O_2]/[H^+] \quad (7)$$

where $K_1 = k_1/k_{-1}$.

Applying steady-state approximation for the determination of $[OH^{\cdot}]$ and $[PCV(HO)^{\cdot}]$

$$\frac{d[OH^{\cdot}]}{dt} = k_2[[Cu^{II}L(OH_2^-)]] - k_3[PCV][HO^{\cdot}] - k_5[[Cu^{I}L]][OH^{\cdot}] = 0 \quad (8)$$

$$\frac{d[PCV(OH^{\cdot})]}{dt} = k_3[PCV][HO^{\cdot}] - k_4[PCV(HO^{\cdot})] = 0. \quad (9)$$

Assuming, $[Cu^{II}L(HO_2^-)] = [Cu^{I}L]$ and substituting from Eq. (7) into Eq. (8) we get,

$$[HO^{\cdot}] = \frac{k_2K_1[[Cu^{II}L]][H_2O_2]}{k_3[PCV][H^+] + k_5K_1[[Cu^{II}L]][H_2O_2]}. \quad (10)$$

Substituting for $[HO^{\cdot}]$ from Eq. (10) in (9) we get,

$$[PCV(HO^{\cdot})] = \frac{k_2k_3K_1[PCV][[Cu^{II}L]][H_2O_2]}{k_3k_4[PCV][H^+] + k_4k_5K_1[[Cu^{II}L]][H_2O_2]}. \quad (11)$$

From Eq. (4),

$$\text{Rate} = k_4[PCV(HO^{\cdot})]. \quad (12)$$

Substituting for $[PCV(HO^{\cdot})]$ in Eq. (12) we get,

$$\text{Rate} = \frac{k_2k_3K_1[PCV][[Cu^{II}L]][H_2O_2]}{k_3[PCV][H^+] + k_5K_1[[Cu^{II}]][H_2O_2]}. \quad (13)$$

Expressing the initial concentration of both reactants, $[PCV]_0$ and $[H_2O_2]_0$

$$[H_2O_2]_0 = [H_2O_2] + [[Cu^{II}L(HO_2^-)]] + [OH^{\cdot}] \quad (14)$$

$$[PCV]_0 = [PCV] + [PCV(OH^{\cdot})]. \quad (15)$$

Substituting from Eqs. (7) and (10) assuming $k_3[PCV][H^+ \ll k_5K_1\ [[Cu^{II}L]][H_2O_2]$

$$[H_2O_2] = \frac{[H^+]\{k_5[H_2O_2]_0 - k_2\}}{k_5[H^+] + k_5K_1[[Cu^{II}L]]}. \quad (16)$$

Substituting from Eq. (11) in Eq. (15) and assuming $k_3k_4[PCV][H^+] \ll k_4k_5K_1[[Cu^{II}L]][H_2O_2]$

$$[PCV] = \frac{k_4k_5[PCV]_0}{k_4k_5 + k_2k_3}. \quad (17)$$

Substituting for $[H_2O_2]$ and [PCV] in Eq. (13), we get

$$\text{Rate}=\frac{k_2k_3k_4k_5K_1[\text{PCV}]_0[[\text{Cu}^{\text{II}}\text{L}]][\text{H}_2\text{O}_2]_0}{k_3k_4k_5[\text{PCV}]_0\{[\text{H}^+]+K_1[[\text{Cu}^{\text{II}}\text{L}]]\}+K_1k_5[[\text{Cu}^{\text{II}}\text{L}]][\text{H}_2\text{O}_2]_0\{K_1k_5k_4+k_2K_3\}}.$$

Assuming $k_4k_5K_1 \gg k_2k_3$

$$\text{Rate}=\frac{k_2k_3K_1[\text{PCV}]_0[[\text{Cu}^{\text{II}}\text{L}]][\text{H}_2\text{O}_2]_0}{k_3[\text{PCV}]_0\{[\text{H}^+]+K_1[[\text{Cu}^{\text{II}}\text{L}]]\}+K_1^2k_5[[\text{Cu}^{\text{II}}\text{L}]][\text{H}_2\text{O}_2]_0} \quad (18)$$

From Eq. (18) it is clear that the rate of the reaction is first-order with respect to $[PCV]_0$ and $[H_2O_2]_0$ at lower concentrations and attains a limiting value at higher concentrations which is also found to be the same from the results obtained from the kinetic studies. The rate of dye degradation also increases with increasing pH and attains maximum value at pH 9.0 (Fig. 7).

4. Conclusion

Straightforward syntheses of Mannich aminomethylation products using diethylmalonate as the carbon acid have been carried out. The experimental procedure reported here proves to be the suitable condition for the synthesis of Mannich aminomethylation products in high yield by minimizing side reactions such as hydrolysis and decarboxylation reactions that normally occur with this carbon acid as in earlier reports. Competing processes normally occur in the reactions of $M(aa)_2$ with formaldehyde and carbon acids yielding products resulting from Mannich aminomethylation or aldol-type condensation reactions. The nature of α-substituents and the pH of the reaction determine the preferred pathway. The experimental conditions used in this work result only in Mannich aminomethylation reaction and no aldol condensation take place at all. It may be noted here, that in the case of amino acid chelates used in this work, the proton under attack is sufficiently labile even under weakly acid or near neutral conditions and at room temperature, whereas, in the reports in the literature, alkaline conditions have been necessary, as also elevated temperatures with diethylmalonate as the carbon acid. The Mannich aminomethylation also works with Ni(II) complexes, hitherto unreported. No difference in reactivity is observed with DL-ala and L-ala in the course of the reaction.

One of the Mannich aminomethylation products have been successfully used as a catalyst in the color removal of the pyrocatechol violet dye. Hydrogen peroxide alone could not degrade PVC but in the presence of the catalyst immediate degradation and color removal is observed. The rate of degradation of the dye is correlated with the variation in the concentration of the dye, H_2O_2 and catalyst. Variation of rate with pH and [NaCl] is also given and the mechanism is proposed based on the formation of the highly active hydroxyl radical.

Acknowledgment

We thank Dr. K. Victor Babu, Scientist, CLRI for his help in ESR interpretation.

Appendix A. Supplementary material

CCDC 622034 contains the supplementary crystallographic data for this paper. These data can be obtained free of charge via http://www.ccdc.cam.ac.uk/conts/retrieving.html, or from the Cambridge Crystallographic Data Centre, 12 Union Road, Cambridge CB2 1EZ, UK; fax: (+44) 1223-336-033; or e-mail: deposit@ccdc.cam.ac.uk. Supplementary data associated with this article can be found, in the online version, at doi:10.1016/j.poly.2007.02.017.

References

[1] (a) M. Salavati-Niasari, Polyhedron 24 (2005) 1405;
(b) G.A. Lawrance, M. Maeder, M.A. O'leary, F. Woon, Polyhedron 9 (1990) 2227;
(c) G.A. Lawrance, T.M. Manning, M.A. O'leary, Polyhedron 7 (1988) 1263;
(d) M. Salavati-Niasari, A. Amiri, Transition Met. Chem. 30 (2005) 720.
[2] S.G. Kang, K. Ryu, M.P. Suh, J.H. Jeong, Inorg. Chem. 36 (1997) 2478.
[3] A. De Blas, G. De Santis, L. Fabbrizzi, M. Lichelli, A.M.M. Lanfretti, P. Morosini, P. Pallavicini, J. Ugozzoli, J. Chem. Soc., Dalton Trans. (1993) 1411.
[4] (a) C.H. Ng, Y.T. Lim, N. Moris, S.G. Teoh, Polyhedron 22 (2003) 521;
(b) C.H. Ng, C.M. Lin, T.M. Chang, S.G. Teoh, S.W. Yap, S.W. Ng, Polyhedron 25 (2006) 1287;
(c) C.R.K. Rao, N. Arulsamy, P.S. Zacharias, D.J. Hodgson, J. Chem. Soc., Dalton Trans. 23 (1993) 3581;
(d) P. Comba, T.W. Hambley, G.A. Lawrence, L.L. Martin, P. Renold, K. Varnagy, J. Chem. Soc., Dalton Trans. (1991) 277;
(e) C.H. Ng, T.S. Chong, S.G. Teoh, F. Adams, S.W. Ng, J. Chem. Soc., Dalton trans. (2002) 3361.
[5] (a) L.M. Sayre, D.V. Nadkarni, J. Am. Chem. Soc. 116 (1994) 3157;
(b) S. Velusamy, A. Srinivasan, T. Punniyamurthy, Tetrahedron Lett. 47 (2006) 923;
(c) M. Salavati-Niasari, M. Bazarganipour, Catal. Commun. 7 (2006) 336;
(d) G.J.P. Britovsek, S.P.D. Baugh, O. Hoarau, V.C. Gibson, D.F. Wass, A.J.P. White, D.J. Williams, Inorg. Chim. Acta 345 (2003) 279;
(e) G. Cerchiaro, G.A. Micke, M.F.M. Tavares, A.M.C. Ferreira, J. Mol. Catal. A 221 (2004) 29;
(f) S. Velusamy, T. Punniamurthy, Tetrahedron Lett. 44 (2003) 8955.
[6] U. Ayse, Color Technol. 117 (2001) 111.
[7] A.H. Gemeay, I.A. Mansour, R.G. El-Sharkawy, A.B. Zaki, J. Coll. Interface Sci. 263 (2003) 228, and references therein.
[8] A. Ricciu, F. Secco, M. Venturini, B. Garcia, J.M. Leal, J. Phys. Chem. A 104 (2000) 7036.
[9] (a) D. Drijvers, H.V. Langenhoue, M. Beckers, Water Res. 33 (1999) 1187;
(b) G. Centi, S.T. Perathoner, Torre, M.G. Verduna, Catal. Today 55 (2000) 61.
[10] (a) D. Georgiou, P. Melidis, A. Aivasidis, K. Gimouhopoulos, Dyes Pigments 52 (2002) 69;
(b) C. Galindo, A. Kalt, Dyes Pigments 42 (1999) 199.

[11] (a) D.N. Sen, S. Mizushima, C. Curran, J.V. Quagliano, J. Am. Chem. Soc. 77 (1955) 211;
(b) D. Segnini, C. Curran, J.V. Quagliano, Spectrosc. Chim. Acta 16 (1960) 540.
[12] BrukerAPEX2 (Version 1.27), SAINT (Version 7.21a) and SADABS (Version 2004/1), Bruker AXS Inc., Madison, WI, USA, 2005.
[13] G.M. Sheldrick, SHELXTL, Version 5.1, Bruker AXS Inc., Madison, WI, USA, 1998.
[14] L.J. Farrugia, J. Appl. Crystallogr. 30 (1997) 565.
[15] (a) J.R. Brush, R.J. Magee, M.J. O'Connor, S.B. Teo, R.J. Geue, M.R. Snow, J. Am. Chem. Soc. 95 (1973) 2034;
(b) J.P. Aune, P. Maldonado, G. Larcheres, M. Pierrot, J. Chem. Soc., Chem. Commun. (1970) 1351.
[16] P. Comba, N.F. Curtis, G.A. Lawrence, M.A. O'Leary, B.W. Skelton, A.H. White, J. Chem. Soc., Dalton Trans. (1988) 2145.
[17] (a) C.H. Ng, S.B. Teo, S.G. Teoh, J.P. Declercq, J. Coord. Chem. 55 (2002) 909;
(b) C.H. Ng, S.B. Teo, S.G. Teoh, J.P. Declercq, S.W. Ng, Aust. J. Chem. 54 (2001) 743;
(c) S.B. Teo, C.H. Ng, E. Horn, E.R.T. Tiekink, Inorg. Chim. Acta 183 (1991) 25.
[18] W.P. Jencks, J. Regenstein, in: H.A. Sobar (Ed.), Ionization Constants of Acids and Bases, second ed., Handbook of Biochemistry, Chemical Rubber, Cleveland, 1970.
[19] S.B. Teo, S.G. Teoh, M.R. Snow, Inorg. Chim. Acta 107 (1985) 211.
[20] T.D. Smith, J.R. Pilbrow, Coord. Chem. Rev. 13 (1974) 173.
[21] C. Mengersen, J. Subramanian, J.-H. Fuhrhop, Mol. Phys. 32 (1976) 893.
[22] (a) I.A. Salem, Monatsh Chem. 131 (2000) 1139;
(b) I.A. Salem, M. El-Maazawi, Chemosphere 41 (2000) 1173.
[23] I.A. Salem, Transition Met. Chem. 25 (2000) 599.
[24] T. Ozawa, A. Hanaki, J. Chem. Soc., Chem. Commun. (1991) 330.
[25] (a) A.H. Gemeay, M.A. Salem, I.A. Salem, Colloids Surf. A 116 (1996) 277;
(b) I.A. Salem, R.I. El-hag, K.M.S. Khalil, Transition Met. Chem. 25 (2000) 260;
(c) A.H. Gemeay, M.A. Salem, I.A. Salem, Colloids Surf. A 117 (1996) 245;
(d) M. Anbar, R.A. Munoz, P. Roma, J. Phys. Chem. 63 (1963) 2708.

Available online at www.sciencedirect.com
ScienceDirect
Polyhedron 26 (2007) 3227–3232
POLYHEDRON
www.elsevier.com/locate/poly

Evaluation of 1-methyl-3,4-hydroxypyridinecarboxylic acids as possible bidentate chelating agents for iron(III): Metal–ligand solution chemistry

Valerio B. Di Marco [a,*], Annalisa Dean [a], Robert A. Yokel [b], Haitao Li [b,1], G. Giorgio Bombi [a]

[a] Department of Chemical Sciences, University of Padova, via Marzolo 1, 35131 Padova, Italy
[b] College of Pharmacy, 511C Pharmacy Building, University of Kentucky Medical Center, Rose Street, Lexington, KY 40536-0082, USA

Received 22 January 2007; accepted 27 February 2007
Available online 1 March 2007

Abstract

The chemical interactions of 1-methyl-3-hydroxy-4-pyridinecarboxylic acid (1M3H4P) and 1-methyl-4-hydroxy-3-pyridinecarboxylic acid (1M4H3P) with Fe(III) were investigated in aqueous 0.6 m (Na)Cl at 25 °C by means of potentiometric titrations and UV–Vis spectrophotometry. A large number of complexes were formed in solution with stoichiometry FeL_xH_y, $x = 1, 2, 3$ and $y = 0, -1, -2$. In view of a possible application to Fe(III) chelation therapy, the efficiencies of the ligands to chelate the metal ion were evaluated *in vitro* at physiological pH. 1M3H4P and 1M4H3P show a lower complexation efficiency with Fe(III) than that of other available chelators, but higher than that of their non-methylated analogs 3H4P and 4H3P.
© 2007 Elsevier Ltd. All rights reserved.

Keywords: Iron; Carboxylate ligands; Chelation therapy; Potentiometry; UV–Vis; Solution chemistry

1. Introduction

The therapy for metal overload pathologies usually involves the administration of suitable chelating agents to selectively remove the metal from the body. Regarding Fe(III) and Al(III), there is a need for new, safe, inexpensive, efficient, and orally effective chelators [1–3], because the existing ones, *i.e.* desferrioxamine (DFO) and deferiprone (L1), have a number of drawbacks, including oral inefficacy and the high cost for the former [4–6], and several toxic side effects and controversial efficiency for the latter [5–8].

In previous work (*e.g.* [9–11]) we proposed hydroxypyridinecarboxylic acids as new possible orally active chelating agents for Fe(III) and Al(III). Our results showed that the unsubstituted derivatives 3-hydroxy-4-pyridinecarboxylic acid (3H4P) and 4-hydroxy-3-pyridinecarboxylic acid (4H3P) [9,10] cannot be regarded as possible alternatives to DFO and L1, because they do not adequately complex Fe(III) and Al(III) at physiological pH. As a strategy to improve the metal complexation ability, without affecting the beneficial properties, alkylation of the pyridinic ring was proposed [9], because the electron-donor properties of alkyl substituents can be expected to increase the basicity of chelating oxygens and therefore to increase the affinity towards hard metal ions, such as Fe(III) and Al(III).

Recently, we studied the complexation between Al(III) and either 1-methyl-3-hydroxy-4-pyridinecarboxylic acid (1M3H4P) or 1-methyl-4-hydroxy-3-pyridinecarboxylic acid (1M4H3P) (Fig. 1) [11]. A significant increase of complex stability was observed for 1M3H4P compared to 3H4P. In the present paper, the complexing ability of 1M3H4P and 1M4H3P towards Fe(III) has been assessed

* Corresponding author. Tel.: +39 0498275219; fax: +39 0498275175.
E-mail address: valerio.dimarco@unipd.it (V.B. Di Marco).
[1] Present address: Department of Pharmaceutics, Amgen, Inc., One Amgen Center Drive, Thousand Oaks, CA 91320, United States.

0277-5387/$ - see front matter © 2007 Elsevier Ltd. All rights reserved.
doi:10.1016/j.poly.2007.02.026

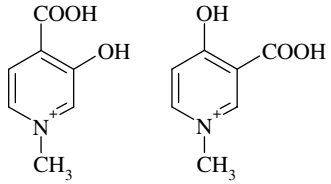


Fig. 1. 1-Methyl-3-hydroxy-4-pyridinecarboxylic acid (1M3H4P) and 1-methyl-4-hydroxy-3-pyridinecarboxylic acid (4H3P), shown in their protonated forms (H_2L^+).

in aqueous solution by means of potentiometric titrations. The speciation data obtained have been compared to the results of studies using UV–Vis. The efficiency of the ligands to chelate Fe(III) at physiological pH has been determined *in vitro* [10].

2. Experimental

2.1. Thermodynamic study

The experimental apparatus, reagents and measurement methods are summarized in the following. Details are reported only when different from those previously described [12].

2.1.1. Apparatus

All potentiometric measurements were performed with a Radiometer ABU93 Triburette apparatus. UV–Vis spectra were recorded with a Perkin–Elmer Lambda 40 instrument. Elemental analyses were performed with a Perkin–Elmer 903 atomic absorption spectrometer for Fe, and with a Perkin–Elmer Elemental Analyzer Model 240B for C, N and H.

2.1.2. Reagents

All concentrations for potentiometric and UV–Vis measurements are expressed in molality (mol/kg of water), and the ionic strength of all the solutions was adjusted to 0.6 m (≈0.594 M) (Na)Cl. Working solutions of HCl (0.2 m), NaOH (0.2 m), Fe(III) (0.05 m in 0.27 m HCl) and ligands 1M3H4P and 1M4H3P (0.015 m) were prepared and standardised as described [10–12].

2.1.3. Potentiometric measurements

Titrations were carried out at 25.0 ± 0.1 °C. Duplicate potentiometric measurements were obtained by using two different glass electrodes (Radiometer pHG201 and BDH 309/1015/02). The glass electrodes were standardised in the concentration scale. As the reference, a Ag/AgCl/0.6 m NaCl electrode with a J-shaped junction was used [13–15].

The HCl–NaOH titrations allowed the standardisation of the base and the evaluation of the autoprotolysis constant for water ($pK_w = 13.707 \pm 0.002$, means ± standard deviation of the mean). This value is in agreement with previous reports [9–12,15,16] at the same temperature and ionic strength conditions, thus confirming the reliability of the present experimental results.

Titrations of solutions containing one of the ligands and the metal ion with NaOH were executed at different ligand and metal concentrations: for 1M3H4P, $[L]_0 = 1.15–3.75 \times 10^{-3}$ m and $[M]_0 = 0.29–1.04 \times 10^{-3}$ m. For 1M4H3P, $[L]_0 = 1.26–4.09 \times 10^{-3}$ m and $[M]_0 = 0.41–1.12 \times 10^{-3}$ m. Metal-to-ligand ratios ranged from 1:1 to 1:8. The precipitation of the metal hydroxide was always observed at slightly basic pH values ($pH \leqslant 9$). All stability constants were calculated using the computer programme PITMAP [17]. The programme minimises the sum of the squares of the differences between experimental and calculated *e.m.f.* values. Optimization is performed using pitmapping [18] or simplex [19] as nonlinear least squares algorithms. Mass balance equations are solved, *i.e.* species concentration at equilibrium are obtained, by means of Newton–Raphson method [19].

2.1.4. UV–Vis measurements

Spectra were obtained at very acidic pH values (ranging from 0.22 to 1.48) for solutions containing known concentrations of ligand and metal ion. The pH of these solutions was computed directly from the stoichiometric concentration of added HCl [10]. Additional spectra at higher pH values (ranging from 1.60 to 6.71) were obtained for Fe/1M4H3P. Logβ values were computed as described [15]. Spectra of the ligands and of the metal alone, required for this method, have been obtained previously [11,15].

2.2. Solid state study

Solid A: 50 mL of a solution containing 0.1 m Fe(III), 0.3 m 1M4H3P, and *ca.* 10^{-2} m HCl were basified to pH 4.5 by adding NaOH 1 M. An orange powder-like precipitate was formed. It was washed three times with water and dried by lyophilization before being analyzed. Results: C = 45.32, N = 7.41, H = 3.50, Fe = 11.10%. The molar ratios Fe/C and Fe/N suggest a 1:3 metal-to-ligand stoichiometric ratio (Fe/C = 0.24 and Fe/N = 1.50; expected ratios for FeL_3: Fe/C = 0.22, Fe/N = 1.32).

Solid B: 50 mL of a solution containing 0.1 m Fe(III), 0.3 m 1M4H3 P, and *ca.* 10^{-2} m HCl were basified to pH 3.5 by adding NaOH 1 M. An orange powder-like precipitate was formed. It was washed three times with water and dried by lyophilization before being analyzed. Results: C = 40.54, N = 6.94, H = 3.82, Fe = 11.71%. The molar ratios Fe/C and Fe/N suggest a 1:2 metal-to-ligand stoichiometric ratio (Fe/C = 0.29 and Fe/N = 1.69; expected ratios for FeL_2: Fe/C = 0.33, Fe/N = 1.98).

2.3. In vitro study

The method employed to assess chelation efficiency in vitro is a modification of a similar method previously developed for aluminium [20].

An octanol/aqueous system containing 125 mM NaCl, 25 mM $NaHCO_3$, 4.5 mM KCl and 50 mM HEPES at pH 7.4 was used. Equal volumes (typically four milliliters) of the aqueous phase and 1-octanol (Sigma Scientific Co., St. Louis, MO) were placed in a screw-cap polypropylene tube. The octanol phase was saturated with the aqueous solution before use, to avoid a larger redistribution of hydrophilic compounds into the octanol phase: as the aqueous phase (containing test compound) saturates the octanol phase, a falsely elevated concentration of ligand in the octanol phase would be obtained. The opposite (*i.e.* the saturation of the aqueous phase with octanol) was not needed for these hydrophilic ligands.

For each experiment to assess a ligand, duplicate tubes were prepared to contain (1) only the octanol and the aqueous phase; (2) as (1) plus 1–2 mg of basic ferric acetate (Pfaltz & Bauer Inc., Waterbury, CT) to provide an excess of undissolved Fe, thus saturating the aqueous and octanol phases with Fe; (3) as (1) plus the ligand introduced into the aqueous phase at 1×10^{-3} M; (4) as (3) plus 1–2 mg of basic ferric acetate. The tubes were agitated overnight at room temperature to establish equilibrium.

The tubes were centrifuged (~3400*g*, 10 min), both phases were filtered together through a 5.0 μm hydrophilic nitrocellulose membrane and then analyzed by electrothermal atomic absorption spectroscopy, using a Perkin–Elmer 4100 ZL spectrophotometer, to determine Fe concentration.

The amount of Fe in each liquid phase of tubes with added Fe but no ligand minus the amount of Fe in tubes without added Fe or ligand represented Fe solubility from basic ferric acetate. The increase in Fe in each liquid phase in the presence of ligand over that seen in the absence of the ligand was taken as complexation of Fe by the ligand.

Chelator efficiency was calculated by

$$\frac{x[\text{sum of the M Fe concentration in each phase}]}{1 \times 10^{-3}\ \text{M}}$$

where x equals the ligand-to-iron ratio. For DFO, where at pH 7.4 a 1:1 ligand:iron complex was anticipated, $x = 1$. DFO was included in this study as a positive, internal control to confirm the reliability of this method, with the expectation that a value close to 100% chelator efficiency would be obtained when $x = 1$. For a bidentate ligand, that exists totally as a 3:1 ligand:Fe complex, $x = 3$. For a bidentate ligand for which 50% of the complexation species are 2:1 ligand:Fe complexes and 50% are 3:1 ligand:Fe complexes, $x = 2.5$.

3. Results and discussion

For both ligands, metal–ligand complexation was nearly quantitative at the starting pH value (*ca.* 2) of the potentiometric titrations. As potentiometric results below pH 2 are inherently inaccurate, very acidic solutions were investigated by means of UV–Vis spectrophotometry. Fig. 2a shows the spectra for Fe/1M3H4P. Spectra are very similar

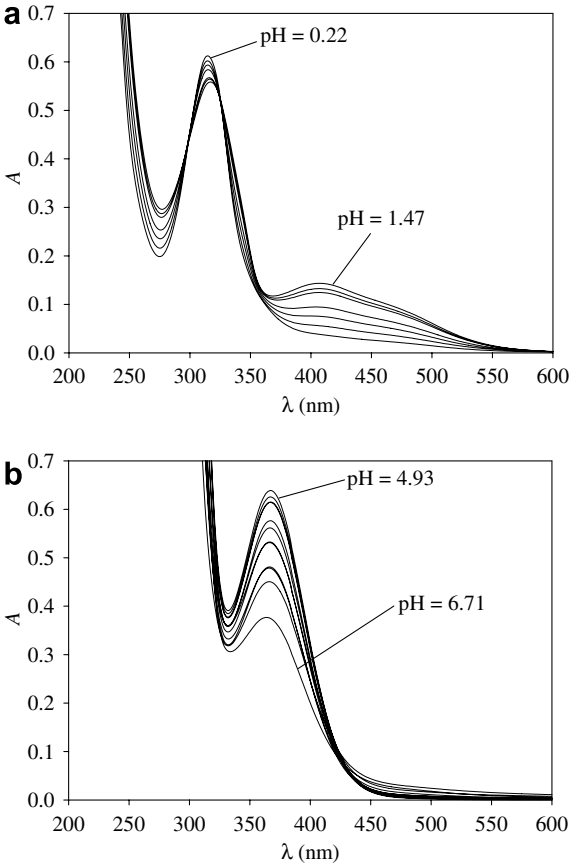


Fig. 2. (a) UV–Vis spectra for Fe/1M3H4P. $[M]_0 = [L]_0 = 1.00 \times 10^{-3}$ m (path cell 0.1 cm), pH: 0.22, 0.40, 0.59, 0.77, 1.16, 1.28, and 1.47. Calculations were performed at $\lambda = 273$, 312, 337, 404, 416 nm. (b) UV–Vis spectra for Fe/1M4H3P. $[M]_0 = 1.07 \times 10^{-4}$ m, $[L]_0 = 1.964 \times 10^{-3}$ m (path cell 0.1 cm), pH: 4.93, 5.26, 5.38, 5.56, 5.80, 5.96, 6.13, 6.24, 6.36, 6.40, 6.52, and 6.71. Calculations were performed at $\lambda = 367$ nm.

to those obtained for 3H4P and 4H3P [10]. For 1M3H4P, the main peak at 312 nm is due to pyridinic ring $\pi \rightarrow \pi^*$ transitions, and by increasing the pH a weak charge-transfer peak appears at 416 nm. For 1M4H3P, the same signals are observed at lower wavelengths. For both ligands, UV–Vis spectra allowed the detection of the species FeL^{2+} and the calculation of the corresponding stability constant $\beta_{1,1,0}$ (Table 1, first line). The value of $\beta_{1,1,0}$ was kept constant in the subsequent elaboration of potentiometric data.

Table 1
Stability constants for Fe–L complexes, at 25 °C in aqueous (Na)Cl 0.6 m (reactions: $m\text{Fe}^{3+} + a\text{L}^- + h\text{H}^+ \rightleftharpoons \text{Fe}_m\text{L}_a\text{H}_h^{3m-a+h}$)

m,a,h	$\log\beta$ Fe(III)/1M3H4P	$\log\beta$ Fe(III)/1M4H3P
1,1,0	9.225 ± 0.005 (UV)	8.94 ± 0.02 (UV)
1,1,−1	6.17 ± 0.05	5.64 ± 0.07
1,2,0	17.18 ± 0.03	16.29 ± 0.04
1,2,−1	13.5 ± 0.1	12.0 ± 0.2
1,2,−2	5.88 ± 0.08	
1,3,0	22.85 ± 0.06	22.17 ± 0.02
1,3,−1		16.0 ± 0.2

* The reported uncertainty is the standard deviation of the mean (for potentiometric titrations) or of the weighted mean (for UV–Vis spectra).

Potentiometric data were elaborated in a sequential manner, as described previously [9], to avoid the difficulties produced by the strong correlation between the parameters to be optimised in the presence of a large number of metal–ligand species. Each species is considered to be present if its inclusion in the speciation model improves fitting quality by at least 20–30%.

The metal–ligand $\log\beta$ results are reported in Table 1 (here and in the following, charges are omitted for simplicity). The acidic properties of the ligands have been determined previously [11]: for 1M3H4P $pK_{H2L} = 0.28 \pm 0.05$, $pK_{HL} = 6.6326 \pm 0.0008$; for 1M4H3P $pK_{H2L} = 0.12 \pm 0.02$, $pK_{HL} = 5.9578 \pm 0.0006$ (reported standard deviations measure the spread of experimental results, and they probably underestimate the typical uncertainty of potentiometric and UV–Vis experimental data, especially for very low pK_a values). The stability constants for Fe(III)/hydroxo complexes have been taken from the literature: $\log\beta_{FeOH} = -2.87$, $\log\beta_{Fe(OH)_2} = -6.16$ [15], $\log\beta_{Fe(OH)_3} = -12.16$, $\log\beta_{Fe(OH)_4} = -22.16$, $\log\beta_{Fe_2(OH)_2} = -2.9$, $\log\beta_{Fe_3(OH)_4} = -6.3$, $\log\beta_{Fe_{12}(OH)_{34}} = -48.9$ [21]. After data elaboration of metal–ligand titrations we found that Fe(III)/hydroxo species have always a negligible concentration, apart at the start of hydroxide precipitation (points discarded in the calculation).

For Fe/1M4H3P UV–Vis spectra at various pH values (some are reported in Fig. 2b) were obtained to verify the unexpected presence of the species FeL_3H_{-1} (see below). From spectroscopic data, the following stability constants could be computed: $\log\beta_{1,2,0}$ (16.07 ± 0.03), $\log\beta_{1,3,0}$ (21.8 ± 0.3), and $\log\beta_{1,3,-1}$ (15.7 ± 0.3) (other complexes could not be detected because they have a very low concentration at the conditions chosen for the UV–Vis measurements). These results compare well with the corresponding potentiometric values reported in Table 1. This agreement suggests the absence of systematic errors in the results.

Typical distribution diagrams for Fe/1M3H4P and for Fe/1M4H3P are shown in Fig. 3. The two speciations are very similar at acidic pH values, whereas significant differences are evident in slightly acidic and neutral solutions. In particular, FeL_2H_{-1} and FeL_2H_{-2} prevail for Fe/1M3H4P above pH 6. For Fe/1M4H3P these mixed hydroxo-species are much less important at all pH values (FeL_2H_{-2} could not even be detected), and at pH values between 3 and 6 the prevailing species is FeL_3. The latter deprotonates above pH 6 to form FeL_3H_{-1}.

Although potentiometric and UV–Vis data do not give any structural information, it is reasonable that in all complexes the ligands coordinate the metal ion with the hydroxyl and carboxyl oxygens (bidentate chelation), and that Fe(III) is hexa-coordinated, as it is generally the case [22]. The formation of hepta-coordinated Fe(III) complexes is not very rare (*e.g.* [23] and references therein). In the species FeL_3H_{-1} (found in Fe(III)/1M4H3P solutions by both potentiometric titrations and UV–Vis measurements), as no deprotonation can occur from the bound ligand, the presence of a coordinated water molecule must be assumed. Therefore, Fe(III) is probably hepta-coordinated. The alternative structural hypothesis, *i.e.* that Fe(III) is hexa-coordinated and a ligand is bound monodentately, is less probable, because it is not compatible with the high stability of FeL_3H_{-1} (it is the prevailing species above pH 6).

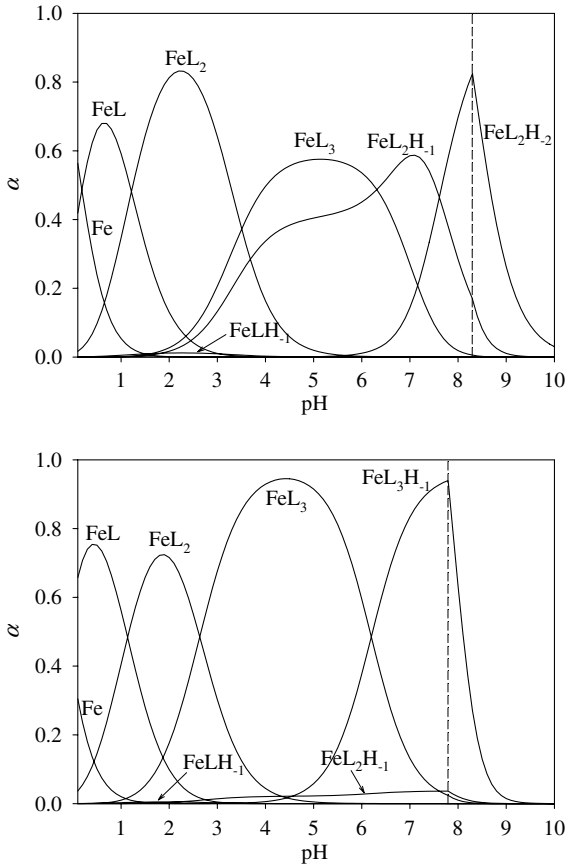


Fig. 3. Distribution diagrams of the most important iron species in the presence of 1M3H4P (above) and 1M4H3P (below) in aqueous (Na)Cl 0.6 m, $T = 25$ °C; $[Fe]_0 = 5 \times 10^{-4}$ m, $[L]_0 = 4 \times 10^{-3}$ m. Dashed lines show the theoretical starting pH for hydroxide precipitation.

The octanol/water distribution coefficients of 1M3H4P and 1M4H3P at pH 7.4 were 0.0054 ± 0.0042, and 0.0015 ± 0.0013, respectively [11]. For Fe(III)/ligand complexes lower $D_{o/a}$ values were obtained at physiological pH, *i.e.*, the complexes were even more hydrophilic than the free ligands.

The results obtained in the chelation efficiency studies are shown in Table 2. Results for 3H4P and 4H3P [10] are reported for comparison. The chelation efficiencies for 1M3H4P and 1M4H3P are lower than that of DFO, although higher than those observed for 3H4P and 4H3P.

The affinities of the various hydroxypyridinecarboxylic acids (3H4P, 4H3P, 1M3H4P and 1M4H3P) towards the metal can be compared by computing pFe ($=-\log[Fe^{3+}]$) *versus* pH at a given metal and ligand concentration: the stronger the complexes the higher the pFe. In Fig. 4, pFe plots are shown, together with that of L1 (data at 25 °C, KCl 0.1 M [25]). Among the hydroxypyridinecarboxylic

Table 2
Fe(III) chelation efficiencies of DFO, 3H4P [10], 4H3P [10], 1M3H4P, and 1M4H3P

Chelator	Chelator efficiency (%)[a]
DFO	82 ± 8
3H4P	6 ± 1
4H3P	11 ± 3
1M3H4P	21 ± 6
1M4H3P	19 ± 2

[a] Data are shown as the means of four experiments, each conducted in duplicate. For DFO, x in the chelator efficiency calculation was = 1, for 3H4P and 4H3P x was = 3 [10], and for 1M3H4P $x = 2.15$ and for 1M4H3P $x = 3$, based on potentiometric results.

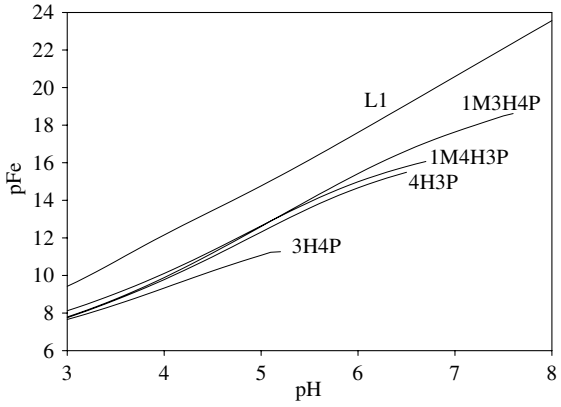


Fig. 4. pFe for several ligands (see text); $[Fe]_0 = 10^{-6}$ m, $[L]_0 = 5 \times 10^{-5}$ m [24].

acids, the complex stability increases in the order 3H4P < 4H3P < 1M4H3P < 1M3H4P. This result is in agreement with the chelation efficiency data, and it confirms our hypothesis, *i.e.*, that alkylation of the pyridinic ring can be a good strategy towards the synthesis of stronger Fe(III) chelators. If Al(III) results are also considered [11], it appears that for both metal ions the alkylation of 3H4P produced a larger increase of complexation strength than the alkylation of 4H3P. Other derivatives should be investigated to further test this beneficial effect of alkyl addition to 3-hydroxy-4-carboxylic and to 4-hydroxy-3-carboxylic pyridinic ring.

Both Fig. 4 and Table 2 show that the pFe and the chelation efficiencies of all hydroxypyridinecarboxylic acids are lower than those of DFO and L1. For 1M3H4P, and to a lesser extent also for 1M4H3P, the chelation strength difference is not very large, *e.g.*, its pFe is only about 2 orders of magnitude lower than that of L1.

4. Conclusions

Both 1M3H4P and 1M4H3P form strong complexes in solution with Fe(III). Potentiometric data allowed the determination of the stoichiometry and stability constants of the species. UV–Vis spectra studies gave the stability constants of FeL, and additional spectra for 1M4H3P confirmed the $\log\beta$ values of the major species obtained by potentiometry. The *in vitro* chelation efficiencies are significant, and they are in agreement with thermodynamic data (pFe values) at physiological pH.

The metal–ligand complexes are very hydrophilic at physiological pH. This should be regarded as a positive property. Although chelating agents having $D_{o/w}$ values around 0.2 were hypothesized to be most suitable as iron chelators [26], in our evaluation of a series of 3,4-hydroxypyridinones we found that very hydrophilic compounds can be the most orally bioavailable and effective chelators [27–29].

On the other hand, the iron complexes formed by 1M3H4P and 1M4H3P are weaker than those formed by DFO and L1 at all pH values. Therefore, 1M3H4P and 1M4H3P are probably not as effective iron chelators *in vivo* as DFO and L1.

The relative complexation strength of 1M3H4P and 1M4H3P in comparison with the unsubstituted derivatives 3H4P and 4H3P, especially as regards 3-hydroxy-4-carboxylic compounds, is significantly higher. The same results were obtained for Al(III) [11]. This suggests that further alkylation of the pyridinic ring can be a good strategy towards the synthesis of stronger Fe(III) chelators. To not significantly reduce the high hydrophilicity of the complexes, methyl derivatives seem to be promising. Towards this goal, the syntheses of 2-methyl and 1,2-dimethyl derivatives of 3H4P and 4H3P, and the thermodynamic and *in vitro* studies of the complexation with Fe(III), are in progress.

References

[1] C. Hershko (Guest Editor), Sem. Hematol. 42 (2, Suppl. 1) (2005).
[2] M.D. Cappellini, Best Pract. Res. Clin. Haemat. 18 (2005) 289.
[3] G.J. Kontoghiorghes, K. Pattichis, K. Neocleous, A. Kolnagou, Curr. Med. Chem. 11 (2004) 2161.
[4] G.J. Kontoghiorghes, Analyst 120 (1995) 845.
[5] G. Faa, G. Crisponi, Coord. Chem. Rev. 184 (1999) 291.
[6] R.A. Yokel, P. Ackrill, E. Burgess, J.P. Day, J.L. Domingo, T.P. Flaten, J. Savory, J. Toxicol. Environ. Health 48 (1996) 667.
[7] M.L. Albina, M. Belles, D.J. Sanchez, J.L. Domingo, Teratology 62 (2000) 86.
[8] N.F. Olivieri, G.M. Brittenham, C.E. McLaren, D.M. Templeton, R.G. Cameron, R.A. McClelland, A.D. Burt, K.A. Fleming, New Engl. J. Med. 339 (1998) 417.
[9] V.B. Di Marco, R.A. Yokel, M.G. Ferlin, A. Tapparo, G.G. Bombi, Eur. J. Inorg. Chem. (2002) 2648.
[10] V.B. Di Marco, R.A. Yokel, H. Li, A. Tapparo, G.G. Bombi, Inorg. Chim. Acta 357 (2004) 3753.
[11] V.B. Di Marco, A. Dean, M.G. Ferlin, R.A. Yokel, H. Li, A. Venzo, G.G. Bombi, Eur. J. Inorg. Chem. (2006) 1284.
[12] V.B. Di Marco, A. Tapparo, G.G. Bombi, Ann. Chim. (Rome) 89 (1999) 397.
[13] G.J. Janz, Silver–silver halide electrodes, in: D.J.G. Ives, G.J. Janz (Eds.), Reference Electrodes: Theory and Practice, Academic Press, New York, London, 1961.
[14] G. Biedermann, L.G. Sillén, Ark. Kemi 5 (1953) 425.
[15] V.B. Di Marco, A. Tapparo, G.G. Bombi, Ann. Chim. (Rome) 91 (2001) 595.
[16] L.O. Öhman, Inorg. Chem. 27 (1988) 2565.

[17] V.B. Di Marco, Ph.D. Thesis, University of Padova, 1998.
[18] L.G. Sillén, Acta Chem. Scand. 18 (1964) 1085.
[19] W.H. Press, B.P. Flannery, S.A. Teukolsky, W.T. Vetterling, Numerical Recipes: The Art of Scientific Computing, Cambridge University Press, Cambridge, 1986.
[20] R.A. Yokel, H.B. Kostenbauder, Toxicol. Appl. Pharmacol. 91 (1987) 281.
[21] C. M Flynn Jr., Chem. Rev. 84 (1984) 31.
[22] A.F. Cotton, G. Wilkinson, C.A. Murillo, M. Bochmann, Advanced Inorganic Chemistry, John Wiley & Sons, New York, 1999.
[23] R. Meier, S. Bedell, G. Henkel, Inorg. Chim. Acta 337 (2002) 337.
[24] T. Kiss, E. Farkas, Perspec. Bioinorg. Chem. 3 (1996) 199.
[25] E.T. Clarke, A.E. Martell, Inorg. Chim. Acta 191 (1992) 57.
[26] J.B. Porter, E.R. Huehns, R.C. Hider, Clin. Haematol. 2 (1989) 257.
[27] R.A. Yokel, A.M. Fredenburg, K.A. Meurer, T.L. Skinner, Drug Metab. Dispos. 23 (1995) 1178.
[28] R.A. Yokel, K.A. Meurer, T.L. Skinner, A.M. Fredenburg, Drug Metab. Dispos. 24 (1996) 105.
[29] R.A. Yokel, K.A. Meurer, C.B. Hong, K.M. Dickey, T.L. Skinner, A.M. Fredenburg, Drug Metab. Dispos. 25 (1997) 182.

Available online at www.sciencedirect.com
ScienceDirect
Polyhedron 26 (2007) 3233–3241
POLYHEDRON
www.elsevier.com/locate/poly

Synthesis, crystal structure, electrochemical, EPR and magnetic properties of dinuclear complexes with an Okawa-style unsymmetrical diphenolato Schiff base macrocyclic ligand

H. Zhou [a,b], Z.-H. Peng [b,*], Z.-Q. Pan [a,*], Y. Song [c], Q.-M. Huang [a], X.-L. Hu [a]

[a] *Hubei Key Laboratory of Chemical, Reactor and Green Chemical Technology, Wuhan Institute of Technology, Wuhan 430073, PR China*
[b] *College of Chemistry and Molecular Science, Wuhan University, Wuhan 430072, PR China*
[c] *Department of Chemistry, Hebai North University, ZhangJiakou 075131, PR China*

Received 2 December 2006; accepted 2 March 2007
Available online 21 March 2007

Abstract

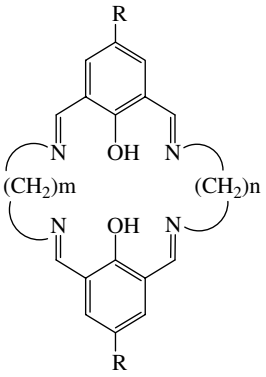
Three dimetallic complexes of the unsymmetrical macrocycle $(L)^{2-}$, $[M_1M_2L]^{2+}$ (M_1M_2 = NiNi, CuZn, CuCd), have been synthesized by cyclocondensation between *N*,*N*′-bis(3-formyl-4-*n*-butylsalicylidene)ethylenediimine and 1,3-diaminopropane in the presence of M_1^{2+} and M_2^{2+}.The crystal structure of the complex $[Ni_2L^4(H_2O)_2](ClO_4)_2 \cdot 0.5CH_3OH$ was determined by X-ray diffraction techniques.The asymmetric unit contains two complete macrocyclic complexes which are nevertheless quite similar to one another.The nickel–nickel separations, bridged by the two phenoxides, are 2.977 Å and 2.982 Å.In each molecule, the Ni(II) located in the ethylene chain linked site has a square planar geometry whereas the Ni(II) located in the propylene chain linked site has an octahedral environment.The results of ES-MS and cycle voltammograms confirm that Cu–Zn, Ni–Ni form stable complexes with the macrocyclic ligand L, however the complex composed of Cu–Cd was unstable, and easily lost Cd^{2+} from the complex in methanol solution.The cyclic voltammograms of the complexes show that each complex undergoes a stepwise reduction process, e.g.$[Ni_2L]^{2+}$ with $E^1_{1/2} = -0.862$ V and $E^2_{1/2} = -1.20$ V.Magnetic measurements in the 2–300 K range indicate weak antiferromagnetism for the dinuclear nickel(II) complex with the exchange constant$J = -0.90\ cm^{-1}$.
© 2007 Elsevier Ltd. All rights reserved.

Keywords: Crystal structure; Electrochemistry; Dinuclear macrocyclic complexes; Magnetism

The Okawa-style phenoxide Schiff base unsymmetrical macrocycles (Scheme 1) with ($R = CH_3$), synthesized by the condensation of 2,6-diformyl-4-methyl-phenol and alkylenediamine, have a powerful coordinating interaction with transition metal ions and are extensively used for synthesizing homo- and heterodinuclear complexes and mixed-valence complexes [1–3]. With short distances between the two metal ions in the complexes, they show special electrical and magnetic properties. Much attention has been paid to this kind of complexes to understand the relationship between structure and properties. Previous works showed that the electron density on ligands can be transmitted directly to the metal centers [4], and influence the magnetic exchange due to the fact that they adopt a flat structure and form a highly delocalized framework in most cases [5]. So changing the R group would cause a change of the electron-density in the macrocycle and subsequently affect the electron-density on metals, thereby alter the properties of the complexes. It is well known that the electron donating ability of the butyl group is greater than that of the methyl group, hence it is reasonable to believe that the electronic density around the metal ions in the complexes with R = butyl would be higher than that in the

* Corresponding authors. Fax: +86 27 8719-4465 (Z.-Q. Pan).
E-mail address: zhiqpan@163.com (Z.-Q. Pan).

0277-5387/$ - see front matter © 2007 Elsevier Ltd. All rights reserved.
doi:10.1016/j.poly.2007.03.016



Scheme 1. Chemical structures of H_2L ($m = 2$, 3, $n = 3$–5 and R = CH_3, here, $m = 2$, $n = 3$ and R = *n*-butyl).

complexes with R = CH_3. Therefore, the $E_{1/2}$ value of the former complexes should be more negative than the latter ones, and this was proved by our previous study [6]: the $E_{1/2}$ values of two dinuclear copper(II) complexes with similar macrocyclic ligands (H_2L: $m = 2$, $n = 2$, R = CH_3, R = *n*-butyl), in which the only difference was that they have different substitutes on the phenyl group, show a similar trend. Derived from the electron-density around the metal ions, the $E_{1/2}$ value of the complex with R = *n*-butyl is more negative than the related complex with R = CH_3. Furthermore, in the processes of synthesizing phenoxide Schiff base macrocyclic complexes, we have found that a base is required in the reaction systems to prevent the destruction of azomethine when R is *n*-butyl on the phenyl ring [7], whilst for the other analogous system, R = CH_3, it is not especially needed [8,9]. This is because when the phenolate groups are deprotonated and coordinate to the metal ions, the protons may attack the rich-electron C=N bond and destroy it, and the bigger the electron-density around C=N, the more likely it is to be attacked. Due to the fact that C=N in the macrocyclic ligand with R = *n*-butyl has richer electron-density than that with R = CH_3, a base must be added to protect the C=N bond from being attacked.

The magneto-structural relationships of phenoxide-bridged dinuclear nickel complexes have been extensively studied. The research showed that complexes with centrosymmetric structures have a linear dependence of J on the Ni–O–Ni bridge angle and Ni–Ni distance, and the magnetism of complexes with no centrosymmetric structure largely depends on their structures [10,11]. Although S. Mohanta reported the synthesis and the room temperature magnetic moment of an asymmetric dinickel macrocyclic complex with $m = 2$, $n = 3$ and R = CH_3 [12], its crystal structure and variable-temperature magnetism have not been reported. To understand the effect of the substituents of phenoxide macrocyclic ligands on the coordination environments, and the relationship between the magnetism and the structure of the complexes, we synthesized three unsymmetric macrocyclic complexes: $[M_1M_2L](ClO_4)_2$ (M_1M_2 = Ni Ni, Cu Zn, Cu Cd). ES-MS, spectroscopy, electrochemistry and magnetic properties of the complexes were investigated and the X-ray crystal structure of $[Ni_2L(H_2O)_2](ClO_4)_2 \cdot 0.5CH_3OH$ was also determined.

1. Experimental

1.1. Materials

All solvents and chemicals were of analytical grade and were used as received, except for methanol that was purified to absolute one by a general method. 2,6-Diformyl-4-*n*-butyl-phenol and *N*,*N*′-bis(3-formyl-5-*n*-butyl-salicylidene)ethylenediimine ($\mathbf{L}^1$) were prepared according to the literature methods [13].

1.2. Preparation of the complexes

$[Ni_2L(H_2O)_2](ClO_4)_2 \cdot 0.5CH_3OH$ (***1***). A suspension of $\mathbf{L}^1$ (0.218 g, 0.5 mmol) in 30 ml absolute methanol was added a methanol solution of $Ni(OAc)_2 \cdot 2H_2O$ (0.105 g, 0.5 mmol), and the mixture was stirred at ambient temperature for about 3 h, then triethylamine (5 ml) and a methanol solution (5 ml) containing $Ni(ClO_4)_2 \cdot 6H_2O$ (0.183 g, 0.5 mmol) were added, and the mixture was further stirred for about 10 h. A methanol solution (10 ml) containing 1,3-diaminopropane (0.037 g, 0.5 mmol) was added dropwise over 40 min, the mixture was refluxed for 1 h to give a red solution. Red needle crystals of $[Ni_2L(H_2O)_2](ClO_4)_2 \cdot 0.5CH_3OH$, suitable for X-ray diffraction, were obtained by slow diffusion of diethyl ether into the mother solution over one week (yield:12%). *Anal.* Calc. for $C_{29.5}H_{42}N_4O_{12.5}Cl_2Ni_2$: C, 42.13; H, 5.03; N, 6.66; Ni, 13.96. Found: C, 42.10; H, 5.08; N, 6.60; Ni, 13.52%. IR (KBr, ν/cm^{-1}), 3452 (O–H), 1643 (C=N), 1090 and 626 (ClO_4^-).

$[CuZnL](ClO_4)_2 \cdot 3H_2O$ (***2***). **2** was prepared by a similar procedure as described above, except that $Cu(OAc)_2 \cdot 2H_2O$ and $Zn(ClO_4)_2 \cdot 6H_2O$ were used instead of $Ni(OAc)_2 \cdot 2H_2O$ and $Ni(ClO_4)_2 \cdot 6H_2O$, respectively. Yield: 36%. *Anal.* Calc. for $C_{29}H_{42}N_4O_{13}Cl_2CuZn$: C, 40.76; H, 4.95; N, 6.56; Cu, 7.43; Zn, 7.65. Found: C, 40.37; H, 4.61; N, 6.72; Cu, 7.31; Zn, 7.42%. IR (KBr, ν/cm^{-1}): 3440 (O–H), 1644 (C=N), 1086.6 and 623.9 (ClO_4^-).

$[CuCdL](ClO_4)_2 \cdot 3H_2O$ (***3***). **3** was prepared by a similar procedure as described above, except that $Cu(OAc)_2 \cdot 2H_2O$ and $Cd(ClO_4)_2 \cdot 6H_2O$ were used instead of $Ni(OAc)_2 \cdot 2H_2O$ and $Ni(ClO_4)_2 \cdot 6H_2O$, respectively. Yield: 32%. *Anal.* Calc. for $C_{29}H_{42}N_4O_{13}Cl_2CuCd$: C, 38.64; H, 4.70; N, 6.21; Cu, 7.05; Cd, 12.47. Found: C, 38.23; H, 4.52; N, 5.96; Cu, 7.13; Cd, 12.47%. IR (KBr, ν/cm^{-1}): 3446.9 (O–H), 1645.06 (C=N), 1087.66 and 621.48 (ClO_4^-).

1.3. Physical measurements

IR spectra were recorded on a Vector 22 FI-IR spectrophotometer using KBr discs. Electronic spectra were

performed on an UV-2450 spectrophotometer. Elemental analyses were measured with a Perkin–Elmer 240 analyzer. The contents of metals in the complexes were determined by a general method in which samples were decomposed by dilute hydrogen nitrate, and then titrated with EDTA. Electrospray mass spectra (ES-MS) were determined on a Finnigan LCQ ES-MS mass spectrograph using methanol as the mobile phase with a concentration of approximate 1.0 mmol dm^{-3}. This diluted solution was electrosprayed at a flow rate of 5×10^{-6} dm^3 min^{-1} with a needle voltage of +4.5 kV. The temperature of the heated capillary in the interface was set at 200 °C and a fuse silica sprayer was used. Thermoanalyses of the complexes were performed on a SDT 2960 TA thermoanalyzer under an argon atmosphere at a rate of 10 °C min^{-1}.

Magnetic susceptibilities of a crystalline-powdered samples were measured on a SQUID-based sample magnetic meter in the temperature range 2.0–300 K, and diamagnetic corrections were made according to Pascal's constants. EPR spectra were recorded at room temperature and 110 K on a Bruker EMX-10/12 spectrometer operating at 9.4 GHz with DPPH as an external calibrant. Cyclic voltammograms were run on a CHI model 750 B electrochemical analyzer in a DMF solution containing tetra(*n*-butyl)ammonium perchlorate (TBAP) as the supporting electrolyte. A three-electrode cell was used, which was equipped with a glassy carbon-working electrode, a platinum wire as the counter electrode and a Ag/AgCl electrode as the reference electrode. Scanning rates were in the range 20–200 mV s^{-1}. The solution was deaerated for 15 min before measurements. The half-wave potentials were calculated approximately from $(E_{pa} + E_{pc})/2$, and the measured error was ±2 mV.

1.4. Crystal structure determination

Diffraction intensity data were collected on a SMART-CCD area-detector diffractometer at 293 K using graphite monochromatic Mo Kα radiation ($\lambda = 0.71073$ Å). Data reduction and cell refinement were performed by SMART and SAINT programs [14]. The structure was solved by direct methods (Bruker SHELXTL) and refined on F^2 by full-matrix least squares (Bruker SHELXTL) using all unique data [15]. The non-H atoms in the structure were treated as anisotropic. Hydrogen atoms were located geometrically and refined in a riding mode.

2. Results and discussion

2.1. Synthesis and characterization

Because of hydrolysis of the Schiff base in the macrocycle, there are two by-products in the systems, and the yields of the complexes are lower than other analogs [16]. In the IR spectra of the complexes, the strong band at 1680 cm^{-1} in $\mathbf{L}^1$ has disappeared [7], and sharp C=N stretching vibration bands corresponding to four imine groups of the macrocyclic framework are observed at 1643 cm^{-1} for **1**, 1644 cm^{-1} for **2** and 1645 cm^{-1} for **3**, indicating that macrocyclic complexes are formed. In addition, the very strong bands centered at 1090 and 621 cm^{-1}, 1087 and 623 cm^{-1}, and 1088 and 621.48 cm^{-1} can be ascribed to the vibration of ClO_4^- groups for **1**, **2** and **3**, respectively. The ν_3 vibration of the perchlorate ion appeared as a sharp band around 1090 cm^{-1} in complex **1**, implying that the anion is not coordinated to the nickel(II) ion, and the vibrations of ClO_4^- in complexes **2** and **3** exhibit broad bands centered at 1087 and 1088 cm^{-1}, respectively, implying that the ClO_4^- groups are coordinated to metal ions in the solid state [17].

The electronic spectra of the complexes are measured in acetonitrile solution. In complex **1**, the bands at ca 545 and 386 nm can be attributed to the octahedral nickel(II) center with $^3A_{2g} \rightarrow {}^3T_{1g}$ and $^3A_{2g} \rightarrow {}^3T_{1g}(P)$ transitions, respectively. The intensity of the absorption at 386 nm indicates that the $^3A_{2g} \rightarrow {}^3T_{1g}(P)$ transition must be admixed with the intraligand $\pi \rightarrow \pi^*$ transition and a charge transfer process [12,16]. The band at ca 315 nm was assigned to the charge transition from Ni(II) in a different coordination environment to azomethine. The band of the π–π* transition was observed at 253 nm. Comparing with analogs [8,12,16]] (Table 1), the absorption band at 900 nm in this complex is not observed because the measured range of the instrument used is 200–800 nm. The bands at 564 and 568 in complexes **2** and **3** are clearly due to the d–d transition of the copper(II) center because zinc and cadmium have no d–d transitions, having d^{10} electronic configurations. The bands at 360 and 384 nm were ascribed to the absorptions of Zn(II) and Cu(II) to azomethine in complex **2**, and the bands at 420 and 395 nm were ascribed to the Cd(II) and Cu(II) to azomethine in complex **3**, respectively, which indicate that the mixed metal complexes **2** and **3** are formed [12]. The additional band at 190–225 nm in acetonitrile solution may be the π–π* absorption peak of C≡N,

Table 1
UV–Vis, IR, magnetic and electrochemical data for the complexes and their analogs

Complex	UV–Vis λ (nm)	Electrochemical data $E_{1/2}$ (V)	μ_{eff}/μ_B	Ref.
$[Ni_2L^{2,4}(ClO_4)_2 \cdot H_2O \cdot i\text{PrOH}$	383, 525sh	−1.01, −1.23 (110) in DMSO	3.25 (298 k)	[8]
$[Ni_2L^{2,3}(H_2O)_2] \cdot (ClO_4)_2$	990, 525sh, 385	−0.95, −1.20 in CH_3CN	3.18 (298 k)	[12]
$[Ni_2(H_2L)(H_2O)_2Cl_2] \cdot 2H_2O$	590, 383, 267, 251		2.75, $J = -23$ cm^{-1}	[16]
$[Ni_2L(H_2O)_2](ClO_4)_2 \cdot 0.5CH_3OH$	545, 386, 315, 253	−0.864, −1.20 in DMF	3.17 (298 k) $J = -0.9$ cm^{-1}, $g = 2.24$	this work
$[CuZnL(H_2O)](ClO_4)_2 \cdot 2H_2O$	213, 251, 360, 494	−0.398, −0.858 in DMF		this work
$[CuCdL(H_2O)](ClO_4)_2 \cdot 2H_2O$	219, 262, 395, 568	−0.382, −0.810 in DMF		this work

implying that acetonitrile is coordinated to the metal ions in solution.

2.2. Electrospray mass spectra

The ES-MS spectrum of complex **1** in MeOH solution is shown in Fig. 1. It shows that the peak at m/z 294.5, corresponding to $[Ni_2L]^{2+}$, is dominant and can be ascribed to the molecule ionic peak of complex **1**, confirming the formation of the macrocyclic complex. The peak at m/z 701.1 is due to the new species $[NiL(H_3O)_2(ClO_4)MeOH]^+$, whose relative abundance is lower than 25%, indicating that there is little opportunity for the complex to lose one Ni^{2+} in MeOH solution. The other peaks in the ES-MS of complex **1** are not discussed for they have relatively low abundance (<5%). The ES-MS spectra of complexes **2** and **3** show that $[CuZnL]^{2+}$ is very stable in MeOH solution, and $[CuCdL]^{2+}$ is unstable in MeOH solution and easily to loses Cd^{2+} to give [CuLH] [13]. The results are consistence with UV–Vis and thermogravimetric analyses.

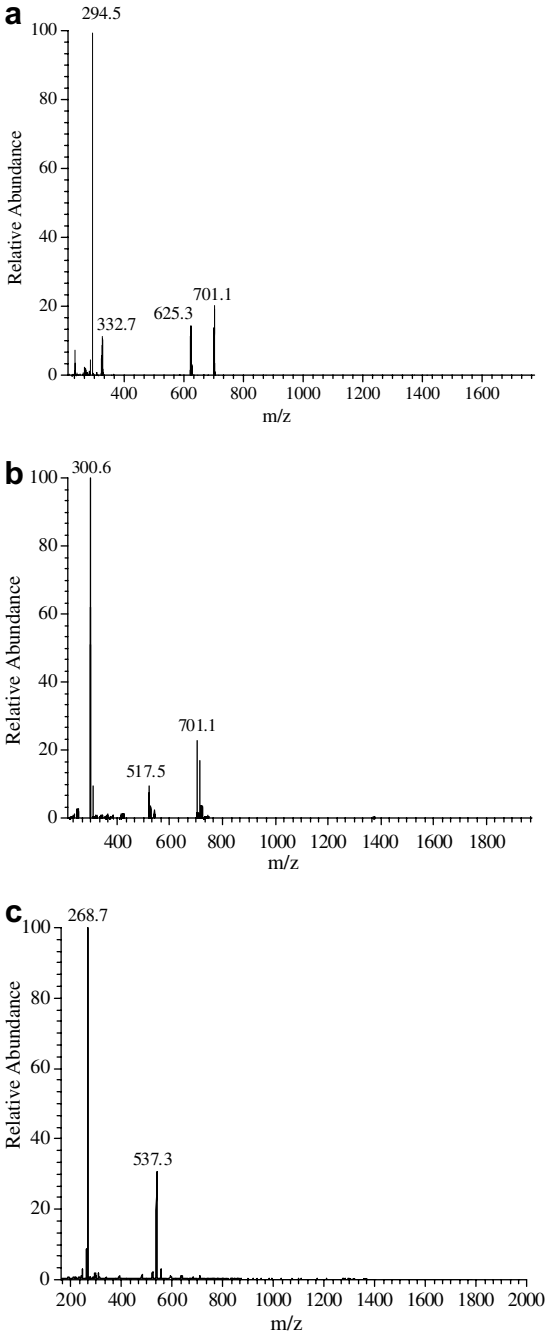


Fig. 1. (a) The ES-MS spectrum of complex **1** in MeOH solution. (b) The ES-MS spectrum of complex **2** in MeOH solution. (c) The ES-MS spectrum of complex **3** in MeOH solution.

Thermogravimetric analyses show the number of water molecules in the complexes. In the thermogram of complex **1**, there are two weight loss processes in the range 25–120 °C. Complex **1** begins to lose 2.0% and 4.4% of its weight at 80–90 °C and 100–115 °C, corresponding to the loss of 0.5 methanol molecules and two water molecules, respectively. The thermograms of complexes **2** and **3** are similar to complex **1**. The complexes begin to lose 6.2% and 6.0% of their weights at about 105–115 °C of their weights for **2** and **3**, respectively, corresponding to the loss of three water molecules. The results are consistent with the elemental analyses and ES-MS spectra of the complexes, which demonstrate that the unsymmetrical complexes were formed. All the complexes decomposed above 250 °C.

2.3. Crystal structure of $[Ni_2L(H_2O)_2](ClO_4)_2 \cdot 0.5CH_3OH$ (1)

The perspective view of $[Ni_2L(H_2O)_2](ClO_4)_2 \cdot 0.5CH_3OH$ (**1**) is given in Fig. 2, together with the atom numbering scheme. Crystallographic data and details about the data collection are presented in Table 2. The asymmetric unit contains two complete macrocyclic complexes which are quite similar to one another. Selected bond lengths and angles relevant to the nickel coordination spheres of the two molecules are listed in Table 3. Except for the *n*-butyl groups which are disordered, the macrocyclic molecules adopt essentially a flat structure. In molecule B, the nickel–nickel separation bridged by the two phenolic oxygens is 2.982 Å, and the coordination polyhedra of the two nickel(II) centres are different, where Ni(3) and Ni(4) are better described approximately as square planar and octahedral with Ni–O–Ni angles of 100.04° and 100.38°, respectively. The distances between nickel Ni(3) and the coordinated atoms near the ethylene chain fall in the range 1.778–1.877 Å and nickel Ni(3) departs by 0.0202 Å from the mean N_2O_2 basal plane, while the distances of nickel Ni(4) and coordinated atoms near the propylene chain fall in the range 1.985–2.015 Å and (Ni(4)) deviates 0.0085 Å from the mean N_2O_2 basal plane. This is consistent with the expectations for the low spin and high spin electronic configurations of square planar and octahedral Ni(II) sites, respectively. The coordination polyhedra around each Ni(II) in complex **1** are the same as the ones in the counterpart of the complex $[Ni_2L]^{2+}$ with $m = 2$, $n = 3$ and $R = CH_3$ [12]. Two water molecules occupy the apical positions in an arrangement with somewhat longer contacts,

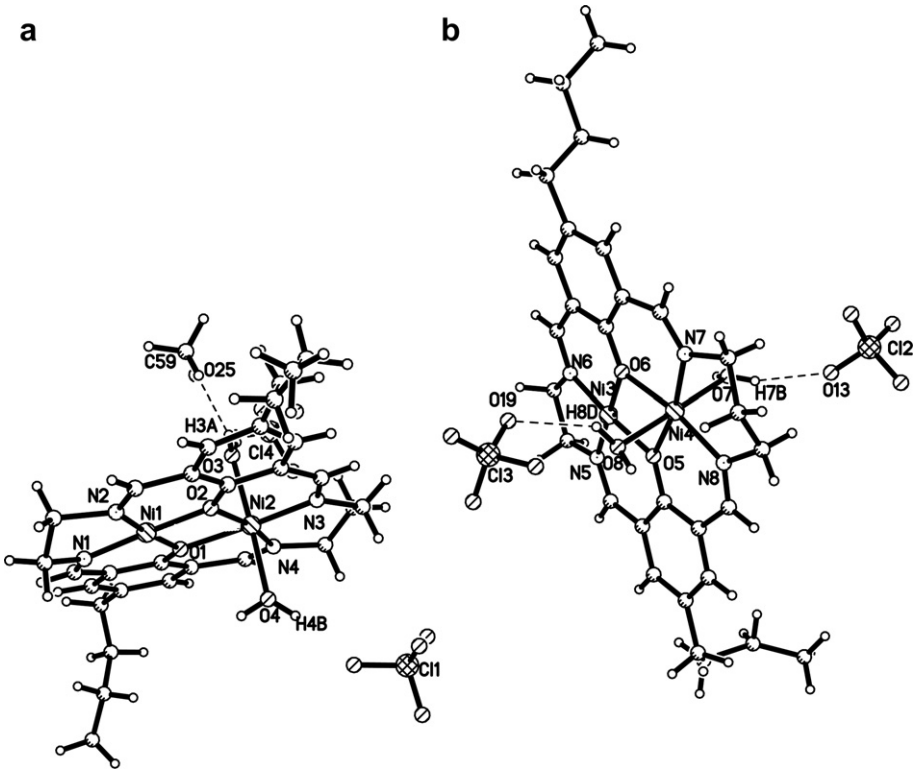


Fig. 2. Perspective view of the two independent molecules of complex **1** with atomic labeling.

Table 2
Crystal data and details of the structure determination for complex **1**

Formula	$Ni_4C_{59}H_{84}N_8O_{25}Cl_4$
Formula weight	1681.98
Z	8
Crystal system	monoclinic
D_c (g/cm^3)	1.507
Space group	$P2_1/c$ (No. 14)
T (K)	292
a (Å)	10.259(8)
b (Å)	23.296(18)
c (Å)	31.12(2)
μ(Mo Kα) (/mm)	1.224
α (°)	90
α (°)	94.473(2)
γ (°)	90
F(000)	3496
V (Å^3)	7415.3(9)
Number of reflections	14561
Number of parameters	946
θ Range (°)	1.1, 26.0
R, wR_2, S	0.0439, 0.1356, 1.04
Crystal size (mm)	$0.18 \times 0.22 \times 0.24$
Minimum and maximum residual density (e Å)	−1.51, 1.64

Table 3
Selected bond lengths (Å) and angles of the molecules A and B in complex **1**

Molecule A		Molecule B	
Bond	Distance (Å)	Bond	Distance (Å)
Ni1–O1	1.836(3)	Ni3–O5	1.877(3)
Ni1–O2	1.835(3)	Ni3–O6	1.865(2)
Ni1–N1	1.829(3)	Ni3–N5	1.788(3)
Ni1–N2	1.184(3)	Ni3–N6	1.817(3)
Ni2–O1	2.005(3)	Ni4–O5	2.014(3)
Ni2–O2	2.017(3)	Ni4–O6	2.015(2)
Ni2–O3	2.085(3)	Ni4–O7	2.145(3)
Ni2–O4	2.153(3)	Ni4–O8	2.142(3)
Ni2–N3	2.003(3)	Ni4–N7	1.991(3)
Ni2–N4	2.001(3)	Ni4–N8	1.985(3)
Bond	Angle (°)	Bond	Angle (°)
N1–Ni1–N2	89.2(1)	N5–Ni3–N6	87.7(1)
N1–Ni1–O1	95.1(1)	N5–Ni3–O5	94.3(1)
O1–Ni1–O2	83.0(1)	O5–Ni3–O6	83.3(1)
O2–Ni1–N2	92.8(1)	O6–Ni3–N6	95.0(1)
N3–Ni2–N4	101.5(1)	N7–Ni4–N8	102.2(1)
N3–Ni2–O2	92.3(1)	N8–Ni4–O5	90.5(1)
O2–Ni2–O1	74.4(1)	O5–Ni4–O6	76.2(1)
O1–Ni2–N4	91.9(1)	O6–Ni4–N7	91.2(1)
O3–Ni2–N3	93.3(1)	O7–Ni4–O8	177.8(1)

2.143 Å and 2.145 Å. It is interesting that the two water molecules in turn form hydrogen bonds with the oxygen atoms of the perchlorate anions with distances 2.310 Å (O(19)–H(8D)O(8)) and 2.069 Å (O(13)–H(7B)O(7)), on opposite sides of the macrocyclic plane.

Molecule A contains two nickel(II) ions which are coordinated by four and six atoms, with an intermetallic distance of 2.977 Å and Ni–O–Ni angles of 101.50° and 101.09°. The coordination polyhedra of Ni(1) and Ni(2) are almost the same as the relative ones of Ni(3) and Ni(4), in which the two coordinated waters also form hydrogen bonds with the oxygen atoms of the perchlorate

anions (O(10)···H(4B)O(4), 2.437 Å and O(24)···H(3B)O(3), 2.400 Å), the difference is that one of the water molecules makes a hydrogen bond with an oxygen atom from a methanol molecule (O(25)–H(3A) 1.918 Å). This is the reason why the formula of the complex contains 0.5 molecule of methanol, because only one methanol molecule exists in the two molecules of the unit. From the two molecular structures A and B, it is clearly observed that the torsion angles consisting of N(1), C(8), C(9), N(2) as well as N(5), C(37), C(38), N(6), close to the four coordinated Ni(II) in the molecules A and B, are different (−36.4° and −4.9°, respectively), and it may be a partial reason as to the difference of the bond distances and angles in the two molecules.

The spacial arrangement of the two molecules A and B is shown in Fig. 3. For distinction, the atoms marked Ni(1) and Ni(2) are in the same molecule, so are the atoms marked Ni(3) and Ni(4). The molecules containing Ni(3) and Ni(4) are parallel to each other and are connected by hydrogen bond interactions between the hydrogen atoms in coordinated water molecules and the oxygen atoms in perchlorate anions, which can be regarded as a bridging group (O(12)···H(7A)O(7), 2.020 Å and O(9)···H(8C)O(8), 2.060 Å), and weak coordination interactions between the oxygen atoms of the perchlorate anions and Ni(II)(O(12)–Ni(3), 3.044(3) Å) (Fig. 3a). The different molecules A and B are also linked by perchlorate anions (Fig. 3b) (O(24)···H(3B)O(3), 2.400 Å and O(23)···H(54)C(54),

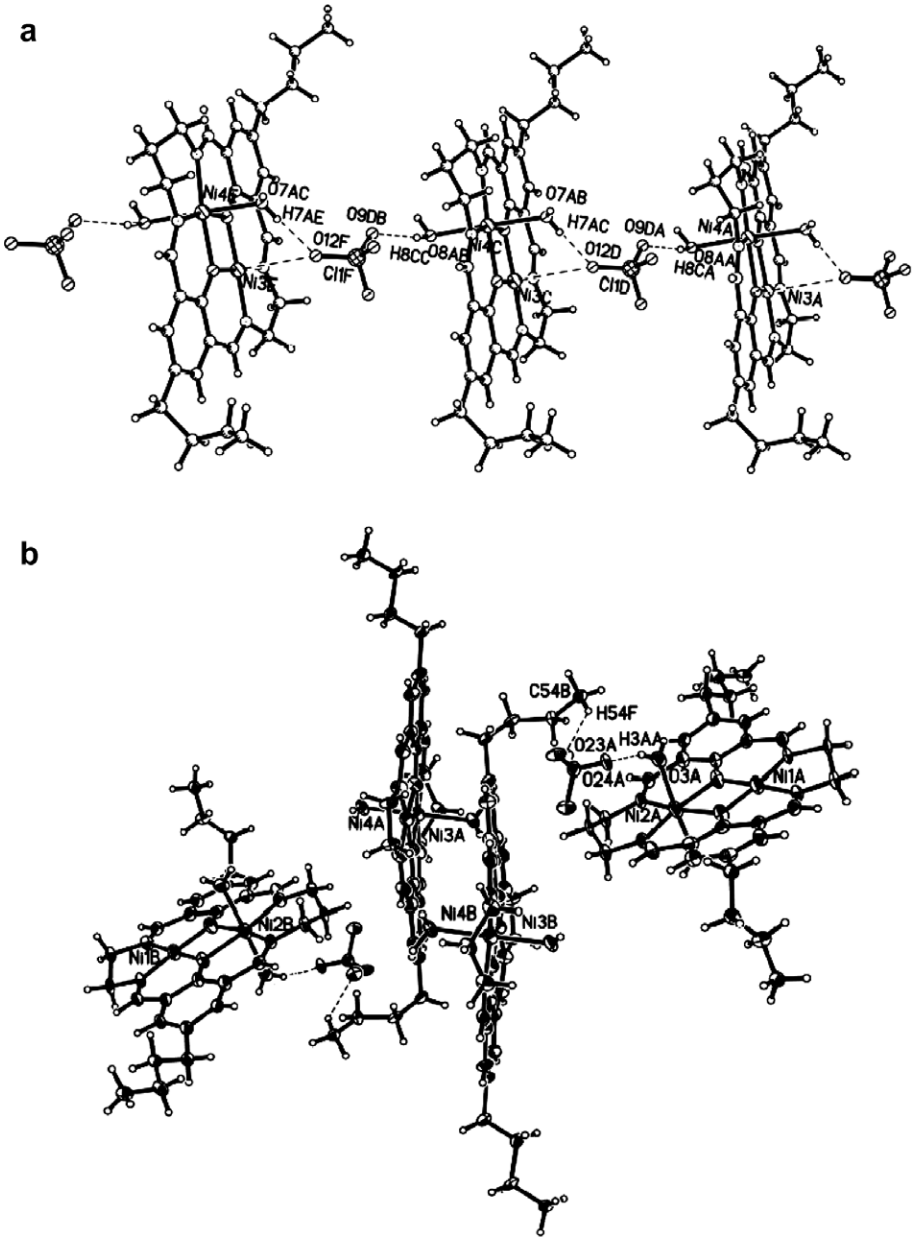


Fig. 3. The H-bonding patterns in complex **1**. (a) Viewed along the *b* axis, (b) viewed along the *a* axis.

2.523 Å), a similar hydrogen bond was found in Ref. [18]. The molecules containing Ni(1) and Ni(2) have a large intermolecular distance and no interactions between the molecules were found, but they are parallel to each other. Table 2 shows that the maximum and minimum residual electron density are both high despite nice R_1 and wR_2 values, the reason is that the residual electron density is located on the nearside of Ni(II), which can be ascribed to the cut-tail effect of nickel(II).

2.4. Electrochemical properties of the complexes

The electrochemical properties of **1**–**3** have been studied by the cyclic voltammetry technique in DMF solvent containing 0.1 M tetra(*n*-butyl)ammonium perchlorate. A typical cyclic voltammogram of complex **1** in DMF is given in Fig. 4 and the numerical data of complexes **2** and **3** are summarized in Table 1. For complex **1**, when scanning from 0 to −1.5 V, the cyclic voltammogram shows two pairs of anodic and cathodic peaks. The cathodic and anodic peak currents appearing at half-wave potentials ($E_{1/2}$) −0.862 V are almost equal. The value of $i_{pc}/v^{1/2}$ remained constant when the scan rate was varied between 50 and 150 mV s^{-1}, indicating that this process was controlled by diffusion, and was pseudo-reversible with $\Delta E = 111$ mV at $v = 50$ mV s^{-1}. The first electron transfer reaction in the complex can be ascribed to the square-planar nickel(II) site [11], because it is an easier site to be reduced than that of Ni(II) in an octahedral configuration. The second couple appearing at the half wave potential −1.201 V is also pseudo-reversible ($\Delta E = 108$ mV). With enhancement of the scan rates, the ratio of $i_{pc}/v^{1/2}$ increases and the value of E_{pc} becomes more negative, furthermore an augmentation in height of the anodic peak occurs to a greater extent relative to that of the cathodic peak. These facts reveal that the reduced Ni(I)Ni(I) species is weakly adsorbed on the electrode surface. The electrochemical properties are similar to the related analogs [8,12] in spite of the fact that they have a different substituent on the phenyl ring (see Table 1); this may be caused by the different solution used in the CV experiments. The redox processes may be tentatively considered as:

$$[\mathrm{Ni(II)Ni(II)L}] \underset{-e}{\overset{+e}{\rightleftharpoons}} [\mathrm{Ni(I)Ni(II)L}] \underset{-e}{\overset{+e}{\rightleftharpoons}} [\mathrm{Ni(I)Ni(I)L}]$$

The electrochemistry of the heterodinuclear complex **2** shows one pseudo-reversible redox couple, with an $E_{1/2}$ value of −0.398 V in the potential range 0.0 to −1.2 V, and an irreversible reduction peak. For complex **3**, a similar process was observed, with $E_{1/2} = -0.382$ and $E_{pc} = -0.810$ V, but two additional cathodic peaks also are displayed at −0.643 V and −1.062 V, which can be assigned to two reduction processes caused by the mononuclear copper(II) complex of the same ligand, which is consistence with the results of the ES-MS. The four redox processes may be described as follows:

$$[\mathrm{Cu(II)Cd(II)L}] \underset{-e}{\overset{+e}{\rightleftharpoons}} [\mathrm{Cu(I)Cd(II)L}] \overset{+e}{\rightarrow} [\mathrm{Cu(0)Cd(II)L}]$$

$$[\mathrm{Cu(II)L}] \overset{+e}{\rightarrow} [\mathrm{Cu(I)L}] \overset{+e}{\rightarrow} [\mathrm{Cu(0)L}]$$

The differences of the redox processes between complexes **1**, **2** and **3** are partially due to the stability of the complexes in solution. The ES-MS results of the complexes show that complexes **1** and **2** are relative stable but complex **3** easily loses Cd^{2+} to form a mononuclear copper(II) complex, so the cyclic voltammogram of complex **3** has two more cathodic peaks than those of complexes **1** and **2**.

2.5. Magnetic properties of complex *1*

The temperature dependence of the magnetic susceptibility of complex **1** from 300 to 2 K is shown in Fig. 5 in the form of a $\chi_M T$ versus T plot with non-linear least-square fitting of the theoretical Eq. (1) [19] to the experimental data. The magnetic parameters of complex **1** can be estimated as $g = 2.24, J = -0.90\ \mathrm{cm}^{-1}$ and $\rho = 0.061$, with $R = 1.1 \times 10^{-4}$

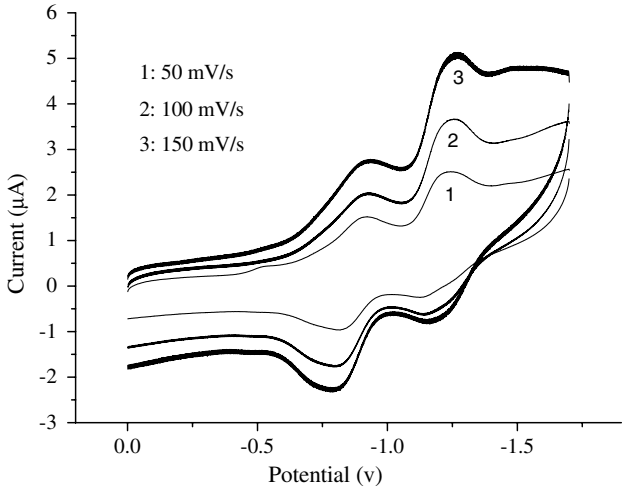


Fig. 4. Cyclic voltammogram of complex **1** in DMF solution at different scan rates.

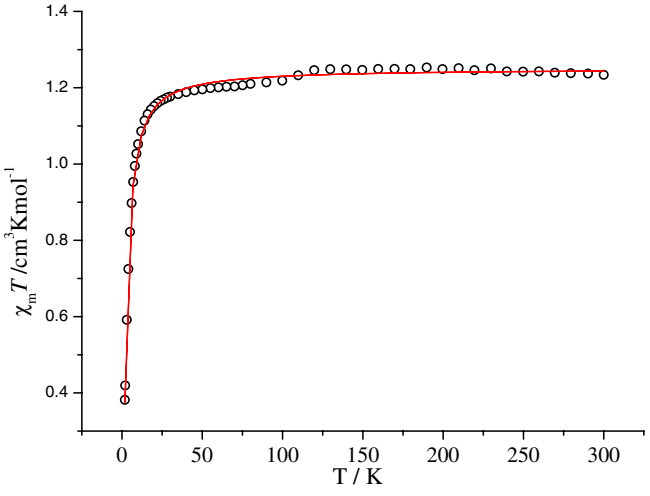


Fig. 5. Experimental and calculated plots of $\chi_M T$ vs. T. The solid line shows the fit with Eq. (1).

(R is an agreement factor defined as $R = \sum[(\chi_M T)_{calc} - (\chi_M T)_{obs}]^2 / \sum(\chi_M T)^2_{obs}$), and these values are indicative of a relatively weak antiferromagnetic coupling between the two nickel(II) ions in complex **1**

$$\chi = \frac{Ng^2\beta^2}{kT} \times \frac{[5 + \exp(-4J/kT)](1-\rho)}{5 + 3\exp(-4J/kT) + \exp(-6J/kT)} + \frac{(2Ng^2\beta^2)\rho}{3kT} \quad (1)$$

where χ and g have their usual meanings and ρ is the ratio of the paramagnetic impurity.

According to the effective magnetism quadrature formula $\mu_{eff} = 2.83(\chi_M T)^{1/2}$, the experimental effective magnetic moment of the complex equals 3.17 emu K mol^{-1} at room temperature, where $\chi_M T = 1.26$ emu K mol^{-1}, which is equal to the theoretic value of 3.17 emu K mol^{-1} calculated from $\mu_{eff} = g[S(S+1)]^{1/2}$ (when $g = 2.24$, $S = 1$) based on a NiNi unit without any interaction between the two nickel ions ($J < 1$ cm^{-1}). Alternatively it can be said that it is consistent with the value expected for a combination of a low-spin ($S = 0$) and a high-spin ($S = 1$) nickel(II) center and it agrees well with the crystal structure in which the two nickel(II) centres are in square planar and octahedral coordination polyhedra, respectively, and similar magnetic behavior was observed for the structurally characterized analogous dinickel(II) complexes [12]. The $\chi_M T$ value of 1.26 emu K mol^{-1} is practically constant in the range 300–20 K, and then rapid decreases to 0 emu K mol^{-1} due to zero field splitting. The magnetic parameters of complex **1** obey the rule reported by Thompson and Nag, as well as Okawa, where the Ni–O–Ni angle in a phenoxide-bridged molecule is larger than 97° [11,20]. It exhibits antiferromagnetic behavior, but the antiferromagnetic exchange interaction J of complex **1** is very small, which does not follow the trend [11] that for centrosymmetric complexes J increases with increasing Ni–O–Ni angles and Ni–Ni distance (Table 4). The magnetic parameters of complex **1** are somewhat like other complexes with no centrosymmetric structure (Table 4), in which the smaller J value in complex **1** is produced by the special coordination polyhedra around each Ni(II) centre.

2.6. EPR spectra

The X-band EPR spectrum for complex **1** is shown in Fig. 6. The complex exhibits a broad band centered at approximately $g = 2.23$, which is in agreement with the magnetic parameters, indicating that there is an unpaired electron in complex **1**.

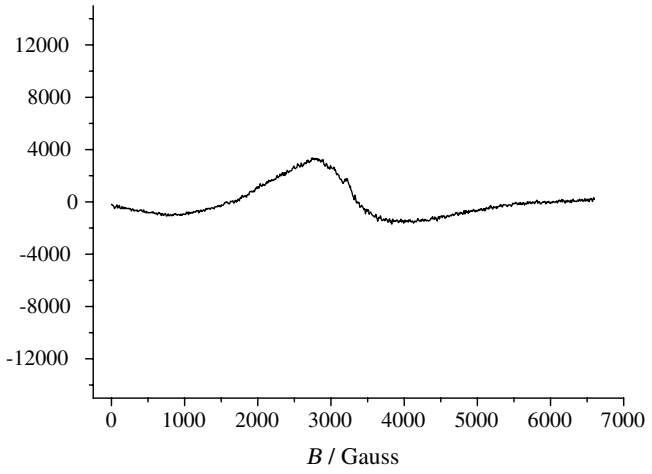


Fig. 6. EPR spectra of **1** determined at room temperature on a crystalline powder sample ($f = 9.4853$ GHz).

The X-band EPR spectra of the crystalline powder and ethanol solution of complex **2** were measured at room temperature and 110 K, as shown in Figs. 7 and 8. No detectable zero field splitting or half-filled signal were observed. Fig. 8 shows four lines with a nuclear hyperfine spin 3/2 due to hyperfine splitting. From the observed g and A values

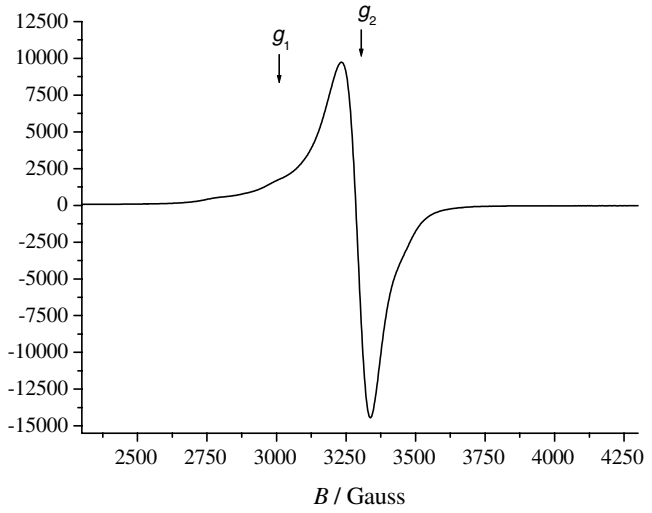


Fig. 7. EPR spectra of **2** determined at 110 K on a crystalline powder sample ($f = 9.4875$ GHz).

Table 4
Magneto-structural parameters for complex **1** and its analogs

Complex	Bond distance (Å)	Bond angle (°)	Coordination number	Magnetism data (J cm^{-1})
$[Ni_2L^{2,2}(CH_3COO)_2] \cdot 10H_2O$	3.005	95.6	six[a]	$J = 10.1$, $g = 2.15$ [19]
$[Ni_2L^{3,3}(\mu\text{-}O_2CCH_2NH_3)(H_2O)_2](ClO_4)_2 \cdot 2H_2O$	3.066	95.0, 92.6	six	$J = -1.1$, $g = 2.21$ [10]
$[Ni_2L(H_2O)_4](ClO_4)_2 4NH_2CONH_2$	3.100	99.5	six[a]	$J = -17.0$, $g = 2.15$ [10]
$[Ni_2(H_2L)(H_2O)_2Cl_2] \cdot 2H_2O$	3.10	101.5	six[a]	$J = -23$ [15]
$[Ni_2L(py)_2](ClO_4)_2$	3.206	105.7	five[a]	$J = -67.1$, $g = 2.24$ [10]
$[Ni_2L(H_2O)_2](ClO_4)_2 \cdot 0.5CH_3OH$	2.977	101.5, 101.1	four and six	$J = -0.9$, $g = 2.24$, this work

[a] Centrosymmetric.

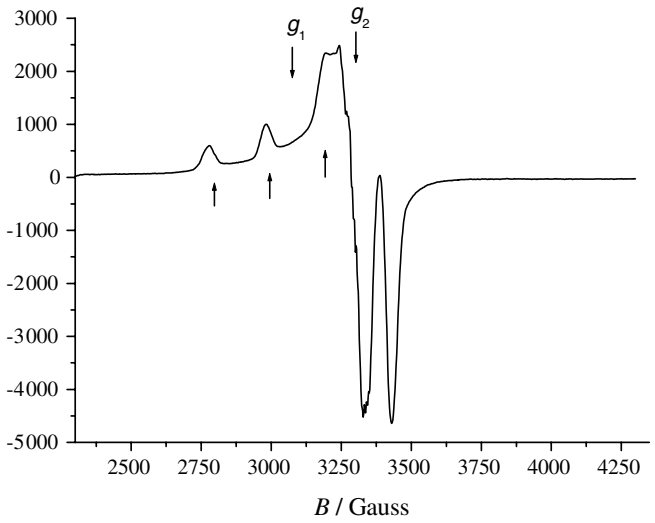


Fig. 8. EPR spectra of **2** determined at 110 K on an ethanol solution of the crystalline powder sample ($f = 9.4853$ GHz).

($g_{\parallel} = 2.20$, $g_{\perp} = 2.06$, $A_{\parallel} = 0.0188\ \mathrm{cm}^{-1}$ and $A_{\perp} = 0.0091$), it is evident that the unpaired electron predominantly occupies the $d_{x^2-y^2}$ orbital and the copper(II) ion is in a tetragonal pyramidal environment [21], which is in agreement with the crystal structure [13].

3. Conclusion

Three unsymmetrical macrocyclic complexes $[M_1M_2L]^{2+}$ (M_1M_2 = Ni Ni, Cu Zn, Cu Cd) have been obtained by adding triethylamine in the synthetic processes. Studies on the crystal structure and temperature-dependence of the magnetic susceptibility of complex **1** show that the two nickel(II) ions are located in square planar and octahedral centers with low spin and high spin electronic configurations, respectively. The results of ES-MS and cycle voltammograms show that the stability of the complexes decreases in the order CuZn > NiNi > CuCd. The R group is unlikely to change the coordination polyhedra for the dinuclear nickel(II) complex in the macrocyclic ligand (H_2L) described here.

Acknowledgement

This project was supported by National Nature Science Foundation of China [20271039].

Appendix A. Supplementary material

CCDC 606413 contains the supplementary crystallographic data for **1**. These data can be obtained free of charge via http://www.ccdc.cam.ac.uk/conts/retrieving.html, or from the Cambridge Crystallographic Data Centre, 12 Union Road, Cambridge CB2 1EZ, UK; fax: (+44) 1223-336-033; or e-mail: deposit@ccdc.cam.ac.uk. Supplementary data associated with this article can be found, in the online version, at doi:10.1016/j.poly.2007.03.016.

References

[1] H. Okawa, S. Kida, Bull. Chem. Soc. Jpn. 45 (1972) 1759.
[2] H. Okawa, J. Nishio, M. Ohba, M. Tadokoro, N. Matsumoto, M. Koikawa, S. Kida, D.E. Fenton, Inorg. Chem. 32 (1993) 2949.
[3] H. Okawa, H. Furutachi, D.E. Fenton, Coord. Chem. Rev. 174 (1998) 51.
[4] C.Y. Shen, M.F. Hu, Q.H. Luo, M.C. Shen, J. Inorg. Biochem. 68 (1997) 195.
[5] H. Actheimer, W. Haase, J. Chem. Phys. 85 (1986) 1427.
[6] B. Liu, H. Zhou, Z.Q. Pan, H.P. Zhang, J.D. Hu, X.L. Hu, Trans. Metal Chem. 30 (2005) 1020.
[7] H. Zhou, Z.H. Peng, Z.Q. Pan, D.C. Li, B. Liu, Z. Zhang, R.A. Chi, J. Mol. Struct. 743 (2005) 59.
[8] J. Nishio, H. Ōkawa, S.I. Ohtsuka, M. Tomono, Inorg. Chim. Acta 218 (1994) 27.
[9] M. Tadokoro, H. Ōkawa, N. Matsumoto, M. Koikawa, S. Kida, J. Chem. Soc., Dalton Trans. (1991) 1657.
[10] K.K. Nanda, R. Das, L.K. Thompson, K. Venkatsubramanian, P. Paul, K. Nag, Inorg. Chem. 33 (1994) 1188.
[11] K.K. Nanda, L.K. Thompson, J.N. Bridson, K. Nag, J. Chem. Soc., Chem. Commun. (1994) 1337.
[12] S. Mohanta, S. Baitalik, S.K. Dutta, B. Adhikary, Polyhedron 17 (1998) 2669.
[13] H. Zhou, Z.H. Peng, Z.Q. Pan, B. Liu, X.L. Hu, Y.Q. Liu, J. Coord. Chem. 58 (2005) 443.
[14] SMART and SAINT. Area Detector Control and Integration Software. Siemens Analytical X-ray Systems, Inc., Madison, WI, USA, 1996.
[15] G.M. Sheldrick, SHELXTL V5.1 Software Reference Manual, Bruker AXS Inc., Madison.
[16] A.J. Downard, V. Mckee, S.S. Tandon, Inorg. Chim. Acta 173 (1990) 181.
[17] C.R.K. Rao, P.S. Zacharias, Polyhedron 16 (1997) 1201.
[18] S.B. Wang, R.F. Li, G.M. Yang, D.Z. Liao, Z.H. Jiang, S.P. Yan, Inorg. Chim. Acta 358 (2005) 2595.
[19] Y. Hosokawa, H. Yamane, Y. Nakao, K. Matsumoto, Inorg. Chim. Acta 283 (1998) 118.
[20] Y. Aratake, M. Ohba, H. Sakiyama, M. Tadokoro, N. Matsumoto, H. Okawa, Inorg. Chim. Acta 212 (1993) 183.
[21] S. Chandra, L.K. Gupta, Spectrochim. Acta Part A 60 (2004) 1563.

Available online at www.sciencedirect.com
ScienceDirect
Polyhedron 26 (2007) 3242–3246
POLYHEDRON
www.elsevier.com/locate/poly

The reactions of phosphorus(III) halides with β-diketiminato ligands

Leslie A. Lesikar, William D. Woodul, Anne F. Richards *

Department of Chemistry, Texas Christian University, Fort Worth, TX 76129, United States

Received 20 December 2006; accepted 2 March 2007
Available online 12 March 2007

Abstract

Reactions of the lithium or sodium salt, $[HC(CMeNDipp)_2]M$ (Dipp = 2,6-diisopropylbenzene, M = Li or Na), with PBr_3 or PCl_3 affords a series of phosphenium cations that were characterized in the solid state by X-ray crystallography. Solid-state analysis reveals that for compounds **1** and **2**, C–H activation of the ligand occurs and the phosphorus is bound to a nitrogen and carbon atom of the ligand. Compound **3** exhibits the more traditional nitrogen chelation of the ligand to the phosphorus atom.
© 2007 Elsevier Ltd. All rights reserved.

Keywords: β-Diketiminato ligands; Phosphorus(III) halides; X-ray crystallography

1. Introduction

Research on β-diketiminato ligands (often abbreviated to nacnac = $[HC(CMeNDipp)_2]$ (Dipp = 2,6-diisopropylbenzene)) has increased dramatically over recent years [1]. The combination of these ligands with main group elements has afforded a series of low oxidation state compounds that often exhibit novel bonding arrangements [2].

Until recently, *NN′* chelation of the group 15 elements with β-diketiminato (nacnac) ligands remained uncharacterized. The research of Burford and Lappert [3] revealed that the preferred coordination mode of the phosphorous was at the γ-carbon (Fig. 1A).

Recently, Cowley et al. reported the first example of a phosphenium cation supported by *N*,*N′* chelation of a β-diketiminato ligand [4] (Fig. 1B) followed by a second report of a N–C bonded phosphenium cation [5] formed via C–H activation that shows structural similarity to our previous antimony studies [6] (Fig. 1C).

Herein we report the isolation of two N, C bonded phosphenium ions, compounds **1** and **2** and an *N*,*N′* coordinated phosphenium ion with an anionic arsenic counter-ion. Compounds **1** and **3** are prepared by a facile one pot synthesis that can be compared to the earlier more sophisticated methods [4,5]. Compound **2** is isolated in low yield but exhibits previously unobserved coordination of a rearranged β-diketiminato ligand with phosphorus(III) bromide.

2. Experimental

Solvents used were dried over sodium or potassium and degassed before use. All manipulations were performed under anaerobic conditions using standard Schlenk techniques. NacnacH and the corresponding lithium and sodium salts were prepared according to published procedures [7]. All other reagents were purchased from Aldrich and used as received.

3. Preparation of compound 1

A THF solution of nacnacNa (0.5 g, 1.13 mmol) was added dropwise at −78 °C to a stirred THF solution of PBr_3 (0.11 mL, 1.13 mmol). The resulting yellow solution was immediately removed from the dry-ice bath and allowed to warm to ambient temperature. Stirring was maintained overnight. Following the removal of THF in vacuo, the pale yellow solid was extracted in hexane and filtered. Concentration under reduced pressure of the hexane

* Corresponding author. Tel.: +1 817 257 6220; fax: +1 817 257 5851.
E-mail address: a.richards@tcu.edu (A.F. Richards).

0277-5387/$ - see front matter © 2007 Elsevier Ltd. All rights reserved.
doi:10.1016/j.poly.2007.03.004

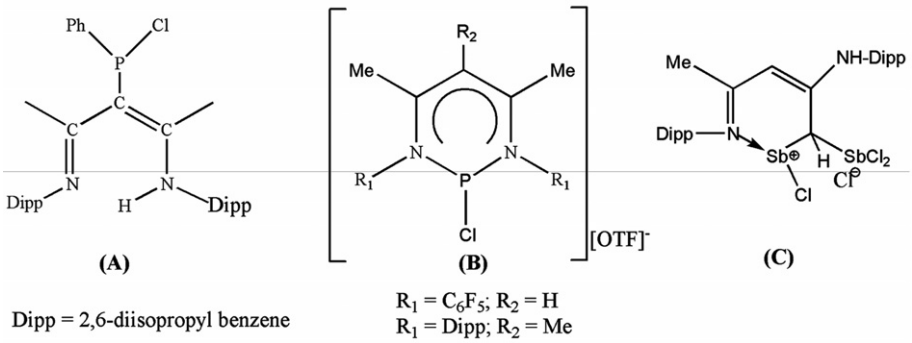
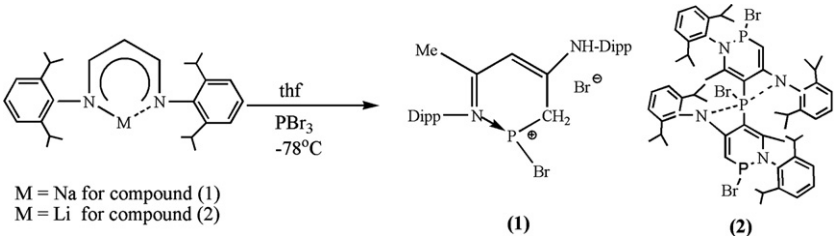


Fig. 1. Example of β-diketiminato ligand coordination to phosphorus and antimony.



Scheme 1.

solution and storage at 25 °C afforded (**1**) in moderate yield (51.79%). M.p. 135–137 °C. ^{1}H NMR (C_6D_6, 25 °C): δ (ppm) 0.651–1.275 (m, 24H, ^{i}Pr–CH_3), 1.647 (s, 3H, CH_3 backbone), 3.252–3.380 (septet, 2H, ^{i}Pr C–H), 3.480 (s, 2H, CH_2), 3.712–3.860 (septet, 2H, ^{i}Pr C–H), 4.695 (s, 1H, CH), 6.571–6.920 (m, 6H, H_{aryl}), 8.013 (s, 1H, N–H); ^{13}C NMR (C_6D_6, 25 °C): δ (ppm) 21.636, 22.197, 22.449, 22.976, 23.204, 23.323, 23.983, 24.769 (^{i}Pr–*Me*), 25.692 (*Me*–C_α), 27.177, 27.291, 27.780, 28.066 (^{i}Pr–*C*), 98.194 (C_β), 123.273, 124.024, 124.284, 124.745 (C_m), 128.451, 129.027 (C_p), 144.443, 145.299, 146.145, 146.530 (C_o), 147.710, 148.610 (C–N), 167.911 (C_α), 179.427 (C_β–*C*–

Table 1
Crystal data for compounds **1**–**3**

Compound name	**1**	**2**	**3**
Chemical formula	$C_{80}H_{104}Br_3N_4P_3$	$C_{29}H_{41}Br_2N_2P$	$C_{58}H_{82}As_4Br_{14}Cl_2N_4P_2$
Formula weight	1454.31	608.43	2386.54
Crystal system	monoclinic	orthorhombic	triclinic
Space group	*C*2/*c*	*Pbca*	$P\bar{1}$
T (K)	91(2)	91(2)	91(2)
a (Å)	34.726(5)	13.865(3)	13.9356(11)
b (Å)	10.1123(14)	20.166(4)	14.4167(11)
c (Å)	21.353(3)	21.969(4)	20.4743(17)
α (°)	90.00	90.00	93.362(2)
β (°)	91.226(2)	90.00	103.713(2)
γ (°)	90.00	90.00	91.409(2)
V (Å^3)	7496.6(18)	6143.5(19)	3986.1(5)
Z	4	8	2
Reflections collected	32481	49893	21454
Independent reflections	6785	5567	14255
Data/restraints/parameter ratio	6785/0/418	5567/0/307	14255/0/775
Unique data (R_{int})	0.0695	0.0392	0.0358
D_{calc} (Mg/m^3)	1.289	1.316	1.988
Absorption coefficent (mm^{-1})	1.723	2.710	8.823
F(000)	3048	2512	2288
Crystal size (mm)	0.20 × 0.14 × 0.13	0.03 × 0.02 × 0.01	0.17 × 0.14 × 0.11
θ Range for collection (°)	1.17–25.25	2.01–25.25	1.61–25.25
R indices (all data)	$R_1 = 0.0570$, $wR_2 = 0.0947$	$R_1 = 0.0464$, $wR_2 = 0.1243$	$R_1 = 0.1130$, $wR_2 = 0.2162$
Final *R* indices [$I > 2\sigma(I)$]	$R_1 = 0.0358$, $wR_2 = 0.0882$	$R_1 = 0.0330$, $wR_2 = 0.1087$	$R_1 = 0.0667$, $wR_2 = 0.1783$
Largest difference in peak and hole (e Å^{-3})	0.531 and −0.576	0.441 and −0.490	1.131 and −2.150

CH_2), 192.447 (CH_2–P); $^{31}P\{^1H\}$ NMR (C_6D_6, 25 °C): δ (ppm) 139. 306 (s); IR (υ cm^{-1}, Nujol mull): 3192.86 (shoulder, N–H stretch).

3.1. Preparation of compound 2

NacnacLi (0.5 g, 1.18 mmol) had 1.1 equiv. of PBr_3 (0.11 ml, 1.3 mmol) added neat in the dry-box. An immediate reaction was observed. The yellow colored solid was dissolved in toluene and stirred over night. The reaction mixture was filtered from the lithium bromide. Concentration to ~5 ml followed by storage at room temperature for 5 days, yielded large yellow crystals of **2**. M.p. 144–148 °C Due to the low yield, no further spectroscopic data were obtained.

3.2. Preparation of compound 3

NacnacLi (0.5 g, 1.18 mmol) had 1.1 equiv. of PCl_3 (0.11 ml, 1.3 mmol) added neat in the dry-box. An immediate reaction was observed. The yellow colored solid was dissolved in THF, and cooled to −78 °C. $AsBr_3$ (0.37 g, 1.18 mmol), dissolved in THF, was added drop-wise. There was no observable color change and the resulting yellow colored solution was brought to ambient temperature and stirred overnight. Following the removal of THF in vacuo, the yellow solid was extracted in toluene. Concentration of the solution and storage at −5 °C afforded compound **3** in moderate yield (67%, based on PCl_3). M.p. 96–99 °C. ^1H NMR (C_6D_6, 25 °C): δ (ppm) 0.725 (d, 12H, CHMe*Me*′), 0.776 (d, 12H, CH*Me*Me′), 1.057 (m, 4H, C*H*MeMe′), 1.489 (s, 6H, CH_3 backbone), 5.746 (s, 1H, CH backbone), 6.788 (6H, H $_{aryl}$); ^{13}C NMR (C_6D_6, 25 °C): δ (ppm) 21.709 (*Me*–C_α), 23.391 (CHMe*Me*′), 26.925 (CH*Me*Me′), 28.791 (*C*HMeMe′), 92.959 (C_β), 117.953 (C_m), 118.392 (C_p), 139.036 (C_o), 147.458 (C–N), 197.545 (C_α); $^{31}P\{^1H\}$ NMR (C_6D_6, 25 °C): δ (ppm) 130. 243 (s).

Table 2
Selected bond lengths (Å) and angles (°) for compound **1**

P(1)–N(1)	1.718(2)
P(1)–Br(1)	2.2629(9)
P(1)–C(17)	1.817(2)
N(1)–P(1)–C(17)	98.98(10)
N(1)–P(1)–Br(1)	103.35(7)

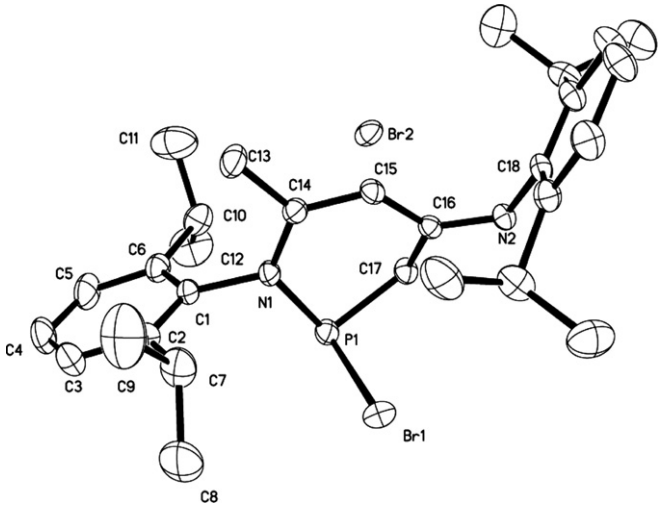


Fig. 2. ORTEP of compound **1**, thermal ellipsoids shown at 30% probability, hydrogen atoms are removed for clarity.

4. Results and discussion

To a −78 °C THF solution of PBr_3, a THF solution of nacnacNa was added drop-wise (Scheme 1).

Following work-up of the reaction mixture in hexanes, compound **1** was isolated as colorless needles. (Crystal data for compounds **1** to **3** is given in Table 1.)

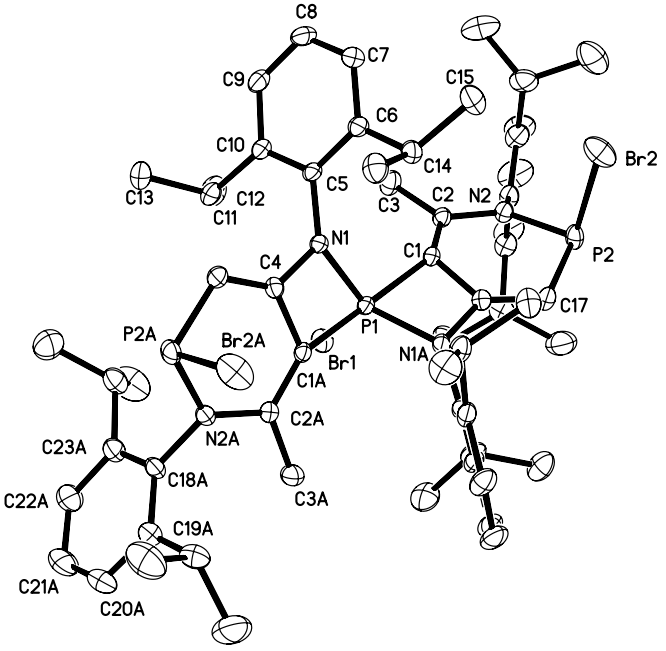


Fig. 3. ORTEP of compound **2**, the upper projection shows the asymmetric unit, and the lower, the full molecule. Thermal ellipsoids are shown at 30% probability; the two toluene molecules and hydrogen atoms are removed for clarity.

Table 3
Selected bond lengths (Å) and angles (°) for compound **2**

P(1)–C(1)	1.872(2)
P(1)–N(1)	1.7226(17)
P(1)–Br(1)	2.2972(9)
N(1)–C(4)	1.407(3)
C(1)–C(2)	1.339(3)
C(6)–C(7)	1.384(3)
P(2)–C(17)	1.764(2)
P(2)–N(2)	1.703(2)
P(2)–Br(2)	2.3477(8)
C(2)–N(2)	1.407(3)
N(1)–P(1)–C(1)	102.36(9)
Br(1)–P(1)–C(1)	94.22(7)
C(4)–N(1)–P(1)	96.95(13)
C(17)–P(2)–N(2)	100.97(10)
P(2)–N(2)–C(2)	126.57(15)

The unit cell parameters were determined and the data collected with a Bruker SMART diffractometer in $\theta/2\theta$ scan mode using graphite monochromatized molybdenum radiation ($\lambda = 0.7107$ Å). The data were corrected for absorption. The structure was solved by direct methods using the SHELXS-97 program [8] and refined [9] via full-matrix least squares. All non-hydrogen atoms were refined anisotropically. Hydrogen atoms were included in calculated positions and were assigned thermal parameters equal to those of the atom to which they were bonded (see Table 1).

Single crystal X-ray analysis revealed that the backbone of the nacnac ligand in compounds **1** and **2** had undergone intramolecular C–H activation (Figs. 2 and 3). This is not a new phenomenon for these ligands, however, is usually associated with more reactive species, for example the early transition elements [10] and the nacnac compounds of the alkaline earth metals [2a]. The intramolecular C–H activation is thought to be attributed to the presence of the reactive P–X (X = halide) [11] and the reaction conditions. Compound **1** is analogous to (B) [5] (Fig. 1), and has remarkably similar bond lengths and angles. The major difference is the bromide counter-ion that sits at a distance of 4.675 Å from the cation phosphorus center. The closest interaction is 3.935 Å with the isopropyl group, (Table 2).

In the course of experimental work leading to the formation of compound **1**, compound **2** was isolated in low yield (Fig. 3). Given the interesting structural features of this molecule, we feel it noteworthy to report, (see Table 3).

Compound **2** was isolated from the reaction of solid nacnacLi with 1 equiv. of neat PBr_3 (*l*) added in the drybox. An immediate reaction was observed. Toluene was added to the solid, resulting in a yellow colored solution that was stirred overnight. Following filtration and concentration of the reaction mixture, yellow crystals were obtained of compound **2** after storage at room temperature for 12 h. The solid-state analysis of **2** is exhibited in Fig. 3. The P–N, and P–C bond lengths are slightly longer than observed in **1**, but indicate single bonds around the phosphorus center. The P–Br bonds show no noteworthy discrepancies. The geometry around the P(III) center is distorted trigonal pyramidal. The bond lengths of 1.339(3) and 1.384(3) Å between C(1)–C(2) and C(6)–C(7), respectively, are indicative of double bond character.

The exact mechanism that leads to formation of compounds **1** and **2** is unclear. From the repeated isolation of compound **1** this is assumed the primary product.

In order to elucidate the mechanism for formation of compounds **1** and **2**, numerous experiments were performed under varied conditions. Following the isolation of compound **2**, we believed that C–H activation occurred

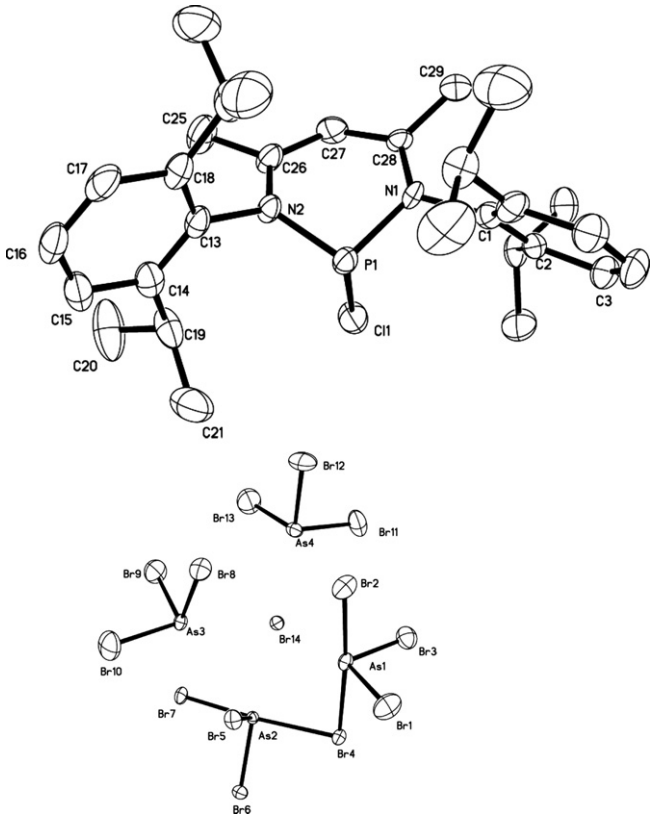
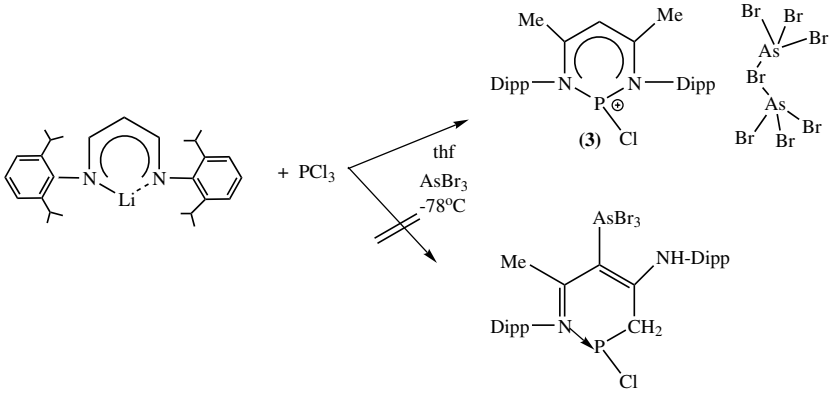


Fig. 4. ORTEP of compound **3**, thermal ellipsoids at 30% probability, hydrogen atoms are removed for clarity.



Scheme 2. Formation of compound **3** expected and obtained products.

Table 4
Selected bond lengths (Å) and angles (°) for compound **3**

P(1)–N(1)	1.742(9)
P(1)–N(2)	1.691(8)
P(1)–Cl(1)	2.072(4)
N(2)–P(1)–N(2)	98.9(4)
N(1)–P(1)–Cl(1)	97.6(3)
N(2)–P(1)–Cl(1)	101.2(3)

initially and then compound **2** resulted from subsequent activation of the γ carbon. To this end, the reaction of nacnacLi with PCl_3, was performed in a similar manner as described for compound **2**. Following addition of thf, the reaction mixture was cooled to −78 °C, and 1.2 equiv. of $AsBr_3$ were added drop-wise (Scheme 2).

It was anticipated that addition of $AsBr_3$, would lead to a product similar to that shown in Scheme 2. Instead, compound **3**, (Fig. 4) was isolated in moderate to high yield (68%), and could be obtained whether the initial reaction was performed in toluene or thf. It shows structural similarity to the *NN′*phosphenium cation discussed earlier reported by Cowley and co-workers [4]. Compound **3** crystallizes in the triclinic space group $P\bar{1}$, with two phosphenium cations present in the asymmetric unit. The charge is counterbalanced by the presence of an arsenic anion, $[As_2Br_7]^-$, and a free bromide ion, located between the anion and two neutral $AsBr_3$ molecules. The phosphorus atom sits in the pocket and is coordinated to two nitrogen atoms, the P–N bonds are very similar in length. Selected bond lengths and angles are given in Table 4.

5. Conclusion

Three phosphorus complexes derived from reactions with β-diketiminato ligands are described. Two of the reported structures compliment the existing published work of Cowley et al. Compound **2** reveals a novel arrangement of the C–H activated nacnac ligand. Further experimental efforts are underway to elucidate a more definitive mechanism.

Acknowledgements

We are grateful for the financial support provided by TCU-RCAF and the Robert A Welch Foundation.

Appendix A. Supplementary material

CCDC 631252, 631250 and 631251 contain the supplementary crystallographic data for **1**, **2** and **3**. These data can be obtained free of charge via http://www.ccdc.cam.ac.uk/conts/retrieving.html, or from the Cambridge Crystallographic Data Centre, 12 Union Road, Cambridge CB2 1EZ, UK; fax: (+44) 1223-336-033; or e-mail: deposit@ccdc.cam.ac.uk. Supplementary data associated with this article can be found, in the online version, at doi:10.1016/j.poly.2007.03.004.

References

[1] L. Bourget-Merle, M.F. Lappert, J.R. Severn, Chem. Rev. 102 (2002) 3031, and references therein.
[2] (a) S. Harder, Angew. Chem., Int. Ed. Engl. (2003) 3430;
(b) A.H. Cowley, Z. Lu, J.N. Jones, J.A. Moore, J. Organomet. Chem. 33 (2002) 648;
(c) J.E. Bercaw, D.L. Davies, P.T. Wolczanski, Organometallics 5 (1986) 443;
(d) Y. Ding, H.W. Roesky, M. Noltemeyer, H.G. Schmidt, P.P. Power, Organometallics 20 (2001) 1190;
(e) P.B. Hitchcock, S.A. Holmes, M.F. Lappert, S.J. Tian, J. Chem. Soc., Chem. Commun. (1994) 2691.
[3] (a) N. Burford, M. D'eon, P.J. Ragogna, R. Mcdonald, M.J. Ferguson, Inorg. Chem. 43 (2004) 734;
(b) P.J. Ragogna, N. Burford, M. D'eon, R. Mcdonald, Chem. Commun. (2003) 1052;
(c) P.B. Hitchcock, M.F. Lappert, J.E. Nycz, Chem. Commun. (2003) 1142.
[4] D. Vidovic, Z. Lu, G. Reeske, J.A. Moore, A.H. Cowley, Chem. Commun. 33 (2006) 3501.
[5] Z. Lu, G. Reeske, J.A. Moore, A.H. Cowley, Chem. Commun. 48 (2006) 5060.
[6] L.A. Lesikar, A.F. Richards, J. Organomet. Chem. 691 (2006) 4250.
[7] M. Stender, R.J. Wright, B.E. Eichler, J. Prust, M.M. Olmstead, H.W. Roesky, P.P. Power, J. Chem. Soc., Dalton Trans. 23 (2001) 3465.
[8] G.M. Sheldrick, SHELXS-97, Program for the Solution of Crystal Structures, University of Göttingen, Germany, 1997.
[9] G.M. Sheldrick, SHELXL-97, Program for the Refinement of Crystal Structures.
[10] (a) F. Basuli, B.C. Bailey, L.A. Watson, J. Tomaszewski, J.C. Huffmann, D.J. Mindiola, Organometallics 24 (2005) 5901;
(b) G. Bai, P. Wei, D.W. Stephan, Organometallics 25 (2006) 2649;
(c) A.R. Bulls, W.P. Schaefer, M. Serfas, J.E. Bercaw, Organometallics 6 (1987) 1219.
[11] (a) N. Burford, K.D. Conroy, J.C. Landry, P.J. Ragogna, M.J. Ferguson, R. McDonald, Inorg. Chem. 43 (2004) 8245;
(b) T. Chivers, M.C. Copset, C. Fedorchuk, A. Parvez, M. Stubbs, Organometallics 24 (2005) 1919.

Available online at www.sciencedirect.com
ScienceDirect
Polyhedron 26 (2007) 3247–3254
POLYHEDRON
www.elsevier.com/locate/poly

Electronic structure of dinuclear iron nitrosyl complexes with different ligands at two iron centers

Maria Jaworska *

Institute of Chemistry, University of Silesia, Szkolna 9, 40-006 Katowice, Poland

Received 13 December 2006; accepted 2 March 2007
Available online 27 March 2007

Abstract

The electronic structures of three dinuclear iron complexes were determined with the DFT method. The complexes contain a $\{Fe(NO)_2\}^9$ unit and thiolate, nitrosyl, carbonyl and amine ligands at the second iron atom. The two iron atoms are bridged by thiolate ligands. In the lowest energy states of these complexes, the iron atoms possess spin $S = 1$, 3/2 or 5/2, depending on the coordinated ligands and their mutual arrangement. Nitrosyl is coordinated as NO^- antiferromagnetically coupled to iron, and the two iron units are antiferromagnetically coupled to each other.
© 2007 Elsevier Ltd. All rights reserved.

Keywords: Iron; Carbonyl; Nitrosyl; DFT

1. Introduction

Iron nitrosyl complexes are studied as models for nitric oxide interaction with heme and non-heme enzymes [1–8]. Their potential use as NO delivery or absorbing agents in medicine is also widely investigated [9–13]. The electronic configuration of a metal–nitrosyl unit is described as $\{MNO\}^n$ in the Feltham–Enemark notation [14], where n stands for the number of d electrons on the metal center plus the one unpaired electron of the nitrosyl group. Because of the presence of an unpaired electron, nitric oxide can bind to a metal ion as a cationic, anionic or neutral ligand. The electronic structure of iron–nitrosyl complexes has also been studied by theoretical methods [15–19]. For many high-spin $\{FeNO\}^7$ complexes and iron enzyme centers, theoretical calculations and experimental data show antiferromagnetic coupling between the high-spin Fe(III) ion and NO^- ligand with spin $S = 1$ [15,16,18–21]. The electronic structure of nitrosyl–metal complexes is important from the point of view of their reactivity and photochemistry.

Sulfur ligands are low field ligands and they usually promote a high spin central atom in complexes. However, many five and six-coordinate both high-spin and low-spin iron–sulfur complexes are known [22–26]. This is also relevant for thiolate containing iron enzymes, which can occur in a low-spin (e.g. nitrile hydratase [27]) or high-spin (e.g. superoxide reductase [28]) electronic configuration. The low-spin state of a nitrile hydratase model complex was explained by the interaction of in-plane sulfur π orbitals with the iron d_{xy}, $d_{x_2-y_2}$ orbitals [23]. CO ligated iron centers show a strong preference for a low-spin configuration. This is pertinent to the low-spin and low oxidation states in iron hydrogenase enzyme, in which iron atoms are complexed by sulfur, carbonyl and cyanide ligands [29].

The aim of the present paper was to investigate the electronic structure of structurally similar dinuclear iron complexes with nitrosyl and carbonyl ligands with the use of the DFT method. We were interested in the character of Fe–NO and metal–metal bonding and at which metal center the unpaired electrons are placed in the case of non-singlet states. The influence of the ligand environment on the

* Tel.: +48 032 359 1507.
E-mail address: mj@ich.us.edu.pl

0277-5387/$ - see front matter © 2007 Elsevier Ltd. All rights reserved.
doi:10.1016/j.poly.2007.03.021

electronic structure of the investigated complexes was examined.

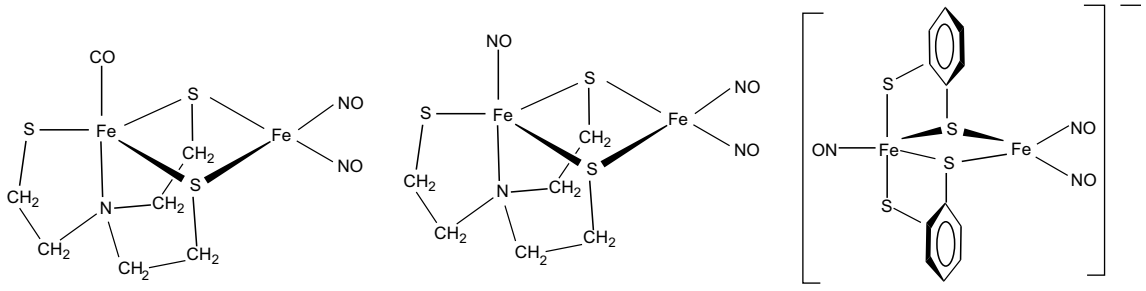
2. Calculational details

The calculations were carried out with the use of the GAUSSIAN03 program [30]. The geometry optimization was carried out with the DFT/BLYP method [31,32]. The 6-311G* basis set was employed in the calculations. The electronic structure of the investigated complexes was calculated with the unrestricted B3LYP method [33] (UB3LYP). In the case of singlet spin states the respective wave functions were obtained with the use of the STABLE keyword in the GAUSSIAN program.

3. Results and discussion

The investigated dinuclear complexes are models of the synthetic compounds $[Fe(NO)_2\{Fe(NS_3)(CO)\}$-S,S′], $[Fe(NO)_2\{Fe(NS_3)(NO)\}$-S,S′] [34] and $[(NO)Fe(S,S\text{-}C_6H_4)_2\text{–}Fe(NO)_2]^-$ [35], where NS_3 denotes the $N(CH_2CH^2S)_3^{3-}$ ligand (Scheme 1). The model complexes are presented in Fig. 1. In the models **1**–**3** the ethylene chains in NS_3 and the benzylidene group were replaced by hydrogen atoms at nitrogen and methyl groups at sulfur. All three complexes contain the $Fe(NO)_2$ unit. The second iron center is coordinated by carbonyl, nitrosyl, amine and thiolate ligands. It is interesting how a different ligand environment influences the electronic structure of such complexes. DFT calculations for the symmetric systems Roussin Red Salt ($Fe_2S_2(NO)_4^{2-}$) and Roussin Red Ester ($Fe_2SR_2(NO)_4$) showed that the two iron atoms are antiferromagnetically coupled to two NO^- ligands, and two such units are antiferromagnetically coupled to each other [18,19].

Complex **1** has an odd number of electrons and its effective magnetic moment is 2.91 μ_B at 293 K [34], which indicates that there is a spin equilibrium between the $S = 1/2$ and $S = 3/2$ states. **2** has a magnetic moment of 2.81 μ_B [34], indicating a triplet ground state, while **3** has a singlet ground state [36]. The geometries of all the complexes were optimized with the B3LYP and BLYP methods in the low-spin states (doublet for **1**, singlet for **2** and **3**). The BLYP optimized geometries for **1** and **3** are in good agreement with the experimental data, better than by the B3LYP method, and these geometries were used in the calculations of the electronic structure. The optimized geometrical parameters are gathered in Table 1. In the optimization, C_s symmetry was used for **1** and C_2 for **3**. As it can be seen from Table 1, the calculated geometrical parameters for **1** and **3** are in very good agreement with experimental data, although the Fe–S bond lengths are somewhat longer than the experimental ones. The geometry optimized for the singlet state of **2** was different from the experimental results, which is due to the fact that this is not the ground state. The optimization of the triplet state led to a much too long Fe–Fe distance (calculated 2.92 Å, versus experimental 2.766 Å), which did not agree with the crystal structure of **2**. Because of that, the experimental geometry was used for **2**. The same was found for the triplet state of **3**, where the optimization leads to a very long Fe–Fe distance of 3.357 Å, and for this reason the same geometry was used for the low-spin and high-spin states in the cal-



Scheme 1.

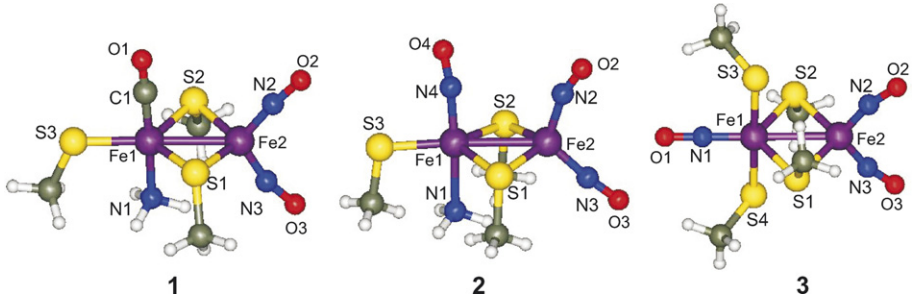


Fig. 1. Optimized geometries of the model complexes **1**–**3**.

Table 1
Calculated geometry parameters of **1**–**3**

1			**2**[b]		**3**		
	Calculated	Experimental		Experimental		Calculated	Experimental
Fe1–Fe2	2.668	2.679	Fe1–Fe2	2.766	Fe1–Fe2	2.689	2.669
Fe1–N1	2.058	2.052	Fe1–N1	2.231	Fe1–N1	1.626	1.632
Fe1–C1	1.763	1.770	Fe1–N4	1.738	Fe1–S1	2.273	2.240[a]
Fe1–S1	2.299	2.247[a]	Fe1–S1	2.331[a]	Fe1–S3	2.404	2.297[a]
Fe1–S3	2.259	2.195	Fe1–S3	2.230	Fe2–N2	1.652	1.660
Fe2–N2	1.655	1.665	Fe2–N2	1.672	Fe1–N1–O1	179.9	178.2
Fe2–N3	1.660	1.679	Fe2–N3	1.660	Fe2–N2–O2	165.7	169.2
Fe2–S1	2.294	2.283[a]	Fe2–S1	2.294[a]			
Fe1–C1–O1	179.3	178.7	Fe1–N4–O4	145.2			
Fe2–N2–O2	172.3	175.4	Fe2–N2–O2	161.6			
Fe2–N3–O3	163.4	168.5	Fe2–N3–O3	173.3			

Bond lengths in Å.
[a] Average.
[b] Calculations performed with the experimental geometry.

culations. Similarly, the same geometry was used for the low and high spin states of **2**. The problem of geometry optimization using the spin unrestricted DFT method was analyzed by Blasco et al. [37] for sulfur bridged dinuclear iron complexes. If there is a direct metal–metal bond in such a complex, the optimization leads to a much longer bond distance than the experimental one. This was explained by the fact that in the unrestricted spin wave function there is an admixture of a higher spin state which leads to bond elongation.

The electronic structures of **1**–**3** were calculated with the UB3LYP method. The B3LYP functional was used, since it was shown that it is able to reproduce correctly the ground spin states of iron sulfur complexes [38]. In Table 2 the energies, atomic charges and spin densities of the two lowest spin states of the investigated complexes are collected. One may note the large expectation values of the $\hat{S}^2$ operator and of atomic spin densities in Table 2. This is typical for the spin-unrestricted approach (broken-symmetry approach) where orbitals of different spin become localized on different parts of a molecule. This usually takes place in the case of weak metal–metal or metal–ligand bonds. In this way non-dynamical electron correlation is taken into account. In the broken-symmetry wave function spin densities different from zero are obtained, even for the singlet states. Spin densities of opposite sign on adjacent atoms indicate antiferromagnetic electron coupling. Such broken-symmetry calculations are used to study the electronic structure and magnetic properties of transition metal complexes [39–42].

From the UB3LYP wave functions the natural orbitals are generated for **1**–**3**. The natural orbitals are used, since they are more easy to analyze than the broken-symmetry molecular orbitals. Their occupation numbers are between 0 and 2. Selected natural orbitals are depicted in Figs. 2–4. The spin density plots from UB3LYP calculations for **1**–**3** are presented in Fig. 5, the relevant spin structures are depicted in Scheme 2.

3.1. Complex *1*

For **1**, the calculated doublet state has a lower energy than the quartet state of 10.2 kcal/mol (Table 2). The atomic charges on both iron atoms are positive in the doublet state, the Mulliken charge is more positive on Fe1, The NBO charge is smaller on Fe2. The charges on the nitrosyl ligands are negative. The spin densities on the iron atoms in the doublet state of **1** are of opposite sign, with a smaller absolute value on Fe1. There are large spin densities on the nitrosyls, of the opposite sign to the spin densities of the iron atom to which they are bound. The pictures of the natural orbitals of **1** in Fig. 2 show that the singly occupied orbital is d_{xy} of Fe1 (NO91). The d_{z_2} orbital of Fe1 is empty (NO99). The d_{yz} and d_{xz} orbitals of Fe1 (NO84, NO85) are doubly occupied as the result of donor–acceptor bonding with the carbonyl ligand. NO90 and NO92 are respective bonding and antibonding orbitals of the weak, antiferromagnetic metal–metal bond. The plots of spin densities and a schematic description of the electronic configurations are depicted in Fig. 5 and Scheme 2, respectively. Some negative spin density on CO can be noted from Table 2 and Fig. 5. Such spin densities on carbonyl ligands were also found in other iron complexes [43].

Complex **1** in the doublet state can be described as a $Fe^{2+}(S = 1)$ CO unit antiferromagnetically coupled to a $\{Fe(NO)_2\}^9(S = 1/2)$ unit. In $\{Fe(NO)_2\}^9$, the Fe^{3+} cation is antiferromagnetically coupled to two NO^- ligands, each with $S = 1$. The $\{Fe(NO)_2\}^9$ fragment has a similar electronic structure to Roussin Red Ester and Roussin Red Salt [18,19]. The mononuclear iron complex with NS_3 and CO ligands has a triplet spin state [35]. Calculations indicate that such a unit is antiferromagnetically bonded to the $\{Fe(NO)_2\}^9$ fragment in the dimeric complex.

The atomic charges and spin density values for the quartet state of **1** are similar but with one important difference, that is the spin densities on both irons are of the same sign, indicating ferromagnetic coupling of both units. It means

Table 2
Relative energy, spin densities and atomic charges of different spin states for **1**, **2** and **3**

1						
	$S = 1/2$			$S = 3/2$		
E (kcal/mol)	0.0			10.2		
$\langle \hat{s}^2 \rangle$	2.842			5.029		
	Mulliken charges	NBO charges	Spin densities	Mulliken charges	NBO charges	Spin densities
Fe1	1.019	0.857	1.771	1.036	0.896	1.920
S1	−0.315	−0.316	−0.026	−0.345	−0.358	0.170
S2	−0.315	−0.316	−0.026	−0.345	−0.358	0.170
S3	−0.324	−0.333	0.123	−0.322	−0.338	0.130
N1	−1.041	−1.018	−0.018	−1.042	−1.020	−0.022
C1	−0.013	0.371	−0.093	−0.014	0.364	−0.110
O1	−0.175	−0.436	−0.037	−0.176	−0.437	−0.050
Fe2	0.988	0.973	−2.651	1.006	1.016	2.709
N2	−0.122	−0.079	0.479	−0.109	−0.073	−0.453
O2	−0.182	−0.190	0.468	−0.175	−0.184	−0.460
N3	−0.199	−0.154	0.519	−0.189	−0.150	−0.503
O3	−0.198	−0.218	0.503	−0.192	−0.213	−0.499
2						
	$S = 1$			$S = 0$		
E (kcal/mol)	0.0			12.8		
$\langle \hat{s}^2 \rangle$	4.638			3.319		
Fe1	1.138	1.165	3.264	1.055	1.009	1.716
S1	−0.376	−0.376	0.036	−0.359	−0.354	−0.012
S2	−0.363	−0.361	0.027	−0.351	−0.342	0.004
S3	−0.358	−0.384	0.215	−0.327	−0.341	0.128
N1	−1.125	−1.051	0.028	−1.108	−1.025	−0.031
N4	−0.130	−0.069	−0.394	−0.112	−0.006	−0.598
O4	−0.111	−0.177	−0.414	−0.110	−0.182	−0.451
Fe2	1.005	0.961	−2.668	1.003	0.957	−2.655
N2	−0.118	−0.060	.459	−0.120	−0.061	0.459
O2	−0.142	−0.160	0.444	−0.143	−0.161	0.444
N3	−0.173	−0.129	0.521	−0.176	−0.132	0.527
O3	−0.193	−0.204	0.482	−0.196	−0.207	0.484
3						
	$S = 0$			$S = 1$		
E (kcal/mol)	0.0			11.2		
$\langle \hat{s}^2 \rangle$	2.598			4.764		
Fe1	0.963	0.887	1.807	1.106	1.165	3.256
S1	−0.365	−0.344	−0.071	−0.385	−0.374	0.007
S2	−0.365	−0.344	−0.071	−0.384	−0.374	0.007
S3	−0.419	−0.380	−0.107	−0.500	−0.491	0.167
S4	−0.419	−0.380	−0.107	−0.500	−0.491	0.167
N1	−0.086	−0.013	−0.429	−0.098	−0.073	−0.477
O1	−0.256	−0.282	−0.342	−0.232	−0.256	−0.426
Fe2	1.032	1.007	−2.680	1.037	1.017	−2.702
N2	−0.141	−0.094	0.536	−0.133	−0.088	0.525
O2	−0.239	−0.255	0.466	−0.233	−0.248	0.463
N3	−0.141	−0.095	0.537	−0.133	−0.088	0.525
O3	−0.239	−0.255	0.466	−0.233	−0.248	0.463

that in the quartet state, the two electrons engaged in the metal–metal bond are decoupled.

3.2. Complex *2*

For **2** the triplet state is lower in energy than the singlet state, in agreement with the experiment [34]. The calculated energy difference is 12.8 kcal/mol (Table 2). From the atomic spin density values and natural orbital plots presented in Fig. 3, the electronic structure of the triplet state can be described as a $Fe^{3+}(S = 5/2)NO^{-}(S = 1)$ unit with a spin state $S = 3/2$ antiferromagnetically coupled to a $\{Fe(NO)_2\}^9$ unit of spin 1/2 (see Scheme 2). The resulting spin state of the molecule is $S = 1$, two unpaired electrons

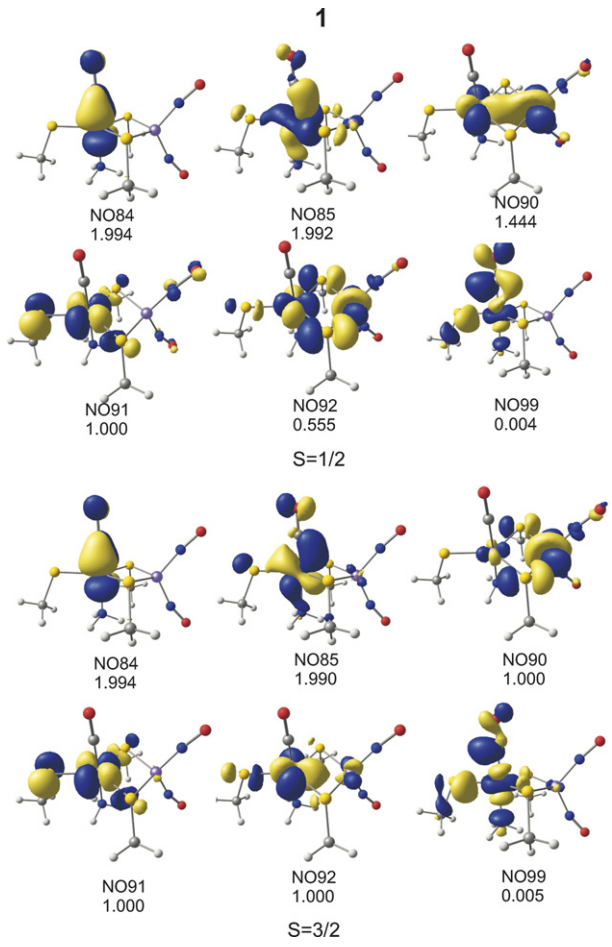


Fig. 2. Selected natural orbitals and their occupation numbers of **1**.

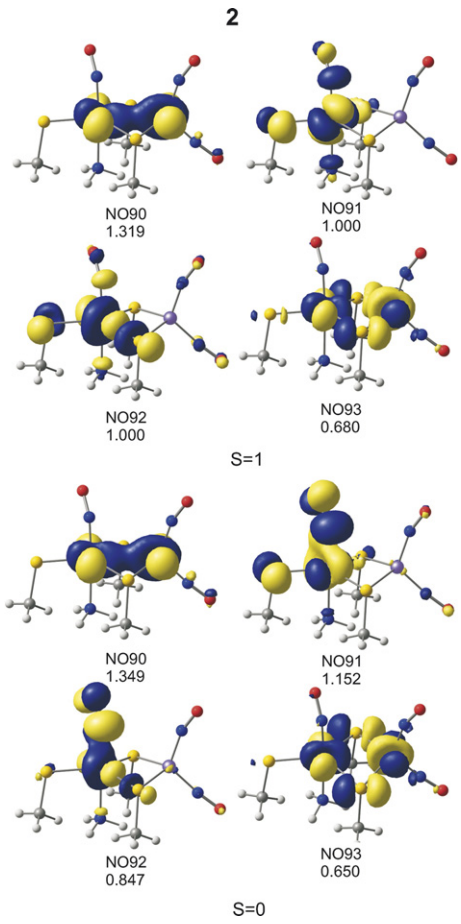


Fig. 3. Selected natural orbitals of **2**.

are placed in the d_{xy} and d_{z_2} orbitals of Fe1 (NO91 and NO92 in Fig. 3), which are rotated to avoid interaction with the electron density of axial ligands at Fe1. The absolute value of spin density on Fe1 is larger than that on Fe2 (Table 2), since the d_{xy}, d_{z_2} electrons are not engaged in forming any bonds. The mononuclear complex of iron with NO and NS_3 is also known [35], and it possesses three unpaired electrons. Antiferromagnetic coupling between Fe^{3+} and NO^- is suggested for this complex [35]. This agrees with the results of the present calculations, according to which the $Fe(NO)(NS_3)$ unit with $S = 3/2$ is antiferromagnetically coupled to the $\{Fe(NO)_2\}^9$ unit with $S = 1/2$.

The energetically higher singlet state of **2** may be described as possessing an intermediate $S = 3/2$ spin state Fe1 center, where two unpaired electrons on the d_{xy}, d_{z_2} (NO91, NO92) orbitals are coupled to the singlet state, as can be seen in Fig. 3. In addition these two natural orbitals contain a large admixture of nitrosyl orbitals.

3.3. Complex *3*

The calculated low energy state of **3** is a singlet, which is in accordance with the experimental data [36]. The triplet state is higher in energy by 11.2 kcal/mol (Table 2). In the singlet state, the d_{yz} orbital on Fe1 (NO90 in Fig. 4) is doubly occupied, and the d_{z_2} orbital is empty (NO107).The fact that the d_{z_2} orbital is unoccupied is a result of avoiding electrostatic repulsion with the electron density from the axial thiolate ligands on Fe1. In **2** there is an amine ligand in the axial position (modelled by ammonia) whose electron density is much more compact, which reduces the repulsing interaction. In the triplet state both these orbitals are singly occupied (NO99 and NO100). On the basis of the natural orbital occupancy and atomic spin densities and charges from Table 2, the electronic structure of **3** can be described as $Fe^{3+}(S = 3/2)NO^-(S = 1)$ with spin 1/2, antiferromagnetically coupled to $\{Fe(NO)_2\}^9$, which results in a total spin of the molecule of $S = 0$. The magnetic measurements also indicate that the two iron atoms are antiferromagnetically coupled [36].

The spin densities and charges in **3** show antiferromagnetic coupling of NO^- to Fe1, which is also visible in the spin density drawings in Fig. 5. This is atypical, as the NO1 ligand has a linear arrangement, which is often considered as an indication of NO cationic character, and the bent NO group as NO^- or $NO^{\cdot}$. However in the octahedral, high-spin $\{FeNO\}^7$ configuration the bending may result from avoiding repulsion between the electron on the d_{z_2} orbital of Fe and on π^* orbitals of NO. In complex **3** the

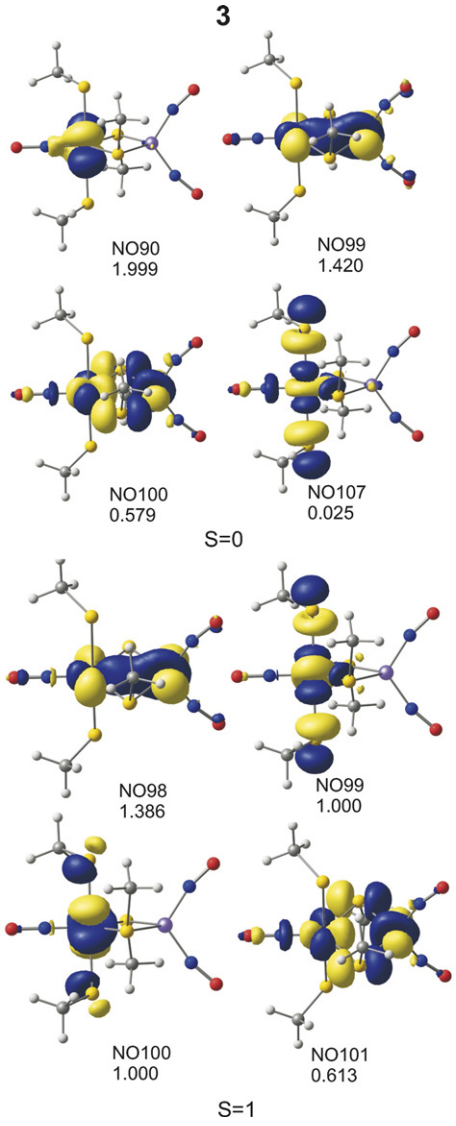


Fig. 4. Selected natural orbitals of **3**.

iron *d* orbital placed along the Fe1–NO1 axis, $d_{x_2-y_2}$, (NO99) has its maximum value directed towards Fe2, to form weak antiferromagnetic bonding with a similar orbital on Fe2. As a result, the interaction of this electron with electrons on NO1 is reduced. On the other hand, in may be noted that the negative charge and spin densities on NO1 are somewhat smaller than those on NO2 and NO3.

The triplet state of **3** is higher in energy (Table 2). Fig. 4 shows that the singly occupied orbitals are d_{z_2} and d_{yz} (NO99, NO100) on Fe1, hybridized to avoid a repulsive interaction with the electron density of sulfur atoms S3 and S4.

The low energy states are correctly determined by the B3LYP method for **1**, **2** and **3**. The three complexes **1**–**3** are examples of dinuclear iron compounds with nitric oxide and thiolate ligands. In each of them, two iron atoms are antiferromagnetically bonded. The electronic structure of the $\{Fe(NO)_2\}^9$ fragment is basically the same in all three complexes. In the low energy state the Fe1 cation exists in the $S = 1$ (**1**), $S = 5/2$ (**2**) or $S = 3/2$ (**3**) spin state. In **1** the CO ligand, which is a strong π-acceptor, causes the low-spin state of Fe1. The other ligands and the mutual position of the thiolate ligands also influence the spin state of Fe1 in **2** and **3**.

The interesting difference between **1** and **2**, **3** is that in the high-spin state the two iron atoms are ferromagnetically coupled in **1**, in contrast to **2** and **3** where antiferromagnetic coupling between the two iron atoms exists in the low and high-spin states, which means that in the two latter complexes the change in Fe1 configuration is energetically easier than in **1**. In **2** and **3** the low-spin–high-spin transition is related to one iron atom (Fe1). It shows that in polynuclear iron complexes, both one-center spin transitions and two-center antiferromagnetic–ferromagnetic transitions are possible, which one is more facile depends on the ligand environment of the iron atoms. Such flexibility in the electronic structure change as a result of the

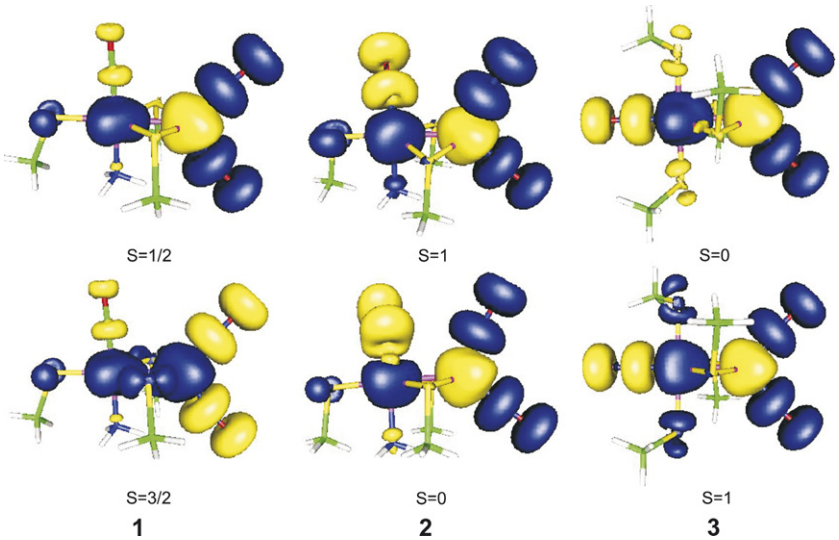
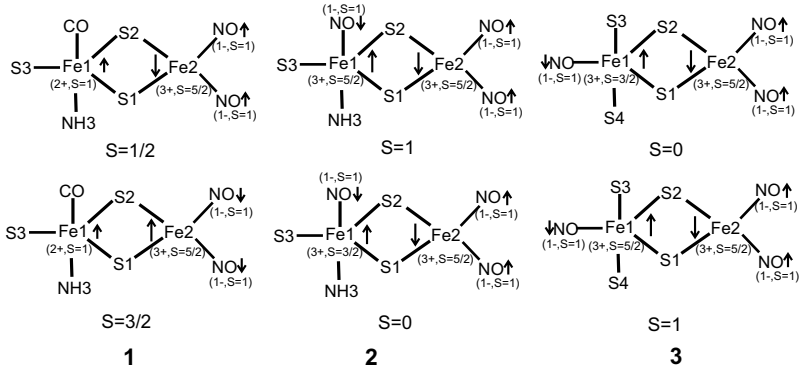


Fig. 5. Spin density plots for **1**–**3**.



Scheme 2.

dependence on the attached ligands is why iron can be used in many enzymes performing diverse biological functions.

4. Conclusions

The electronic structures of three dinuclear iron complexes containing the $\{Fe(NO)_2\}^9$ unit have been determined with the DFT method. The second iron atom is coordinated by carbonyl, nitrosyl, thiolate and amine ligands. The two iron atoms are bridged by thiolate ligands. According to the calculations the low-spin–high-spin transition in the carbonyl complex is related to an antiferromagnetic–ferromagnetic coupling change between the iron atoms, while in the nitrosyl complexes it is the low-spin–high-spin one iron center change. The total spin state of the investigated complexes depends on the coligands (amine, thiolate) and their mutual arrangement.

Acknowledgement

The GAUSSIAN03 calculations were carried out in the Wrocław Center for Supercomputing and Networking, WCSS, Wrocław, Poland under calculational Grant No. 51/96.

References

[1] P.C. Ford, L.E. Laverman, Coord. Chem. Rev. 249 (2005) 391.
[2] M. Hoshino, L. Laverman, P.C. Ford, Coord. Chem. Rev. 187 (1999) 75.
[3] J.-C. Chottard, D. Mansuy, I. Artaud, Inorg. Chim. Acta 336 (2002) 19.
[4] T.C. Harrop, M.M. Olmstead, P.K. Mascharak, Inorg. Chem. 44 (2005) 6918.
[5] C.A. Grapperhaus, A.K. Patra, M.S. Mashuta, Inorg. Chem. 41 (2002) 1039.
[6] C.-M. Lee, C.-H. Chen, H.-W. Chen, J.-L. Hsu, G.-H. Lee, W-F. Liaw, Inorg. Chem. 44 (2005) 6670.
[7] M.-L. Tsai, C.-C. Chen, I-J. Hsu, S.-C. Ke, C.-H. Hsieh, K.-A. Chiang, G.-H. Lee, Y. Wang, J.-M. Chen, J.-F. Lee, W.-F. Liaw, Inorg. Chem. 43 (2004) 5159.
[8] N.A. Sanina, S.M. Aldoshin, Russ. Chem. Bull., Int. Ed. 53 (2004) 2428.
[9] M.S. Ward, R.E. Shepherd, Inorg. Chim. Acta 286 (1999) 197.
[10] T.-N. Chen, F.-C. Lo, M.-L. Tsai, K.-N. Shih, M.-H. Chiang, G.-H. Lee, W.-F. Liaw, Inorg. Chim. Acta 359 (2006) 2525.
[11] R.K. Afshar, A.K. Patra, M.M. Olmstead, P.K. Mascharak, Inorg. Chem. 43 (2004) 5736.
[12] C.-Y. Chiang, M.Y. Darensbourg, J. Biol. Inorg. Chem. 11 (2006) 359.
[13] A.K. Patra, J.M. Rowland, D.S. Marlin, E. Bill, M.M. Olmstead, P.K. Mascharak, Inorg. Chem. 42 (2003) 6812.
[14] J.H. Enemark, R.D. Feltham, Coord. Chem. Rev. 13 (1974) 339.
[15] C.A. Brown, M.A. Pavlosky, T.E. Westre, Y. Zhang, B. Hedman, K.O. Hodgson, E.I. Solomon, J. Am. Chem. Soc. 117 (1995) 715.
[16] G. Schenk, M.Y.M. Pau, E.I. Solomon, J. Am. Chem. Soc. 126 (2004) 505.
[17] S.N. Greene, N.G.J. Richards, Inorg. Chem. 43 (2004) 7030.
[18] M. Jaworska, Z. Stasicka, J. Organomet. Chem. 689 (2004) 1702.
[19] M. Jaworska, Z. Stasicka, New J. Chem. 29 (2005) 604.
[20] E.C. Wasinger, M.I. Davis, M.Y. Pau, A.M. Orville, J.M. Zaleski, B. Hedman, J.D. Lipscomb, K.O. Hodgson, E.I. Solomon, Inorg. Chem. 42 (2003) 365.
[21] M.D. Clay, C.A. Cosper, F.E. Jenney Jr., M.W.W. Adams, M.K. Johnson, Proc. Nat. Acad. Sci. 100 (2003) 3796.
[22] J.C. Noveron, M.M. Olmstead, P.K. Mascharak, J. Am. Chem. Soc. 123 (2001) 3247.
[23] P. Kennepohl, F. Neese, D. Schweitzer, H.L. Jackson, J.A. Kovacs, E.I. Solomon, Inorg. Chem. 44 (2005) 1826.
[24] A.T. Fiedler, H.L. Halfen, J.A. Halfen, T.C. Brunold, J. Am. Chem. Soc. 127 (2005) 1675.
[25] G.D. Fallon, B.M. Gatehouse, P.J. Minari, K.S. Murray, B.O. West, J. Chem.Soc., Dalton Trans. (1984) 2733.
[26] D. Sellmann, H. Kunstmann, F. Knoch, M. Moll, Inorg. Chem. 27 (1988) 4183.
[27] A. Miyanaga, S. Fushinobu, K. Ito, H. Shoun, Eur. J. Biochem. 271 (2004) 429.
[28] A.P. Yeh, Y. Hu, F.E. Jenney Jr., M.W.W. Adams, D.C. Rees, Biochemistry 39 (2000) 2499.
[29] X. Liu, S.K. Ibrahim, C. Tard, C.J. Pickett, Coord. Chem. Rev. 249 (2005) 1641.
[30] Gaussian 03, Revision C.02, M.J. Frisch, G.W. Trucks, H.B. Schlegel, G.E. Scuseria, M.A. Robb, J.R. Cheeseman, J.A. Montgomery, Jr., T. Vreven, K.N. Kudin, J.C. Burant, J.M. Millam, S.S. Iyengar, J. Tomasi, V. Barone, B. Mennucci, M. Cossi, G. Scalmani, N. Rega, G.A. Petersson, H. Nakatsuji, M. Hada, M. Ehara, K. Toyota, R. Fukuda, J. Hasegawa, M. Ishida, T. Nakajima, Y. Honda, O. Kitao, H. Nakai, M. Klene, X. Li, J.E. Knox, H.P. Hratchian, J.B. Cross, C. Adamo, J. Jaramillo, R. Gomperts, R.E. Stratmann, O. Yazyev, A.J. Austin, R. Cammi, C. Pomelli, J.W. Ochterski, P.Y. Ayala, K. Morokuma, G.A. Voth, P. Salvador, J.J. Dannenberg, V.G. Zakrzewski, S. Dapprich, A.D. Daniels, M.C. Strain, O. Farkas, D.K. Malick, A.D. Rabuck, K. Raghavachari, J.B. Foresman, J.V. Ortiz, Q. Cui, A.G. Baboul, S. Clifford, J. Cioslowski, B.B. Stefanov,

G. Liu, A. Liashenko, P. Piskorz, I. Komaromi, R.L. Martin, D.J. Fox, T. Keith, M.A. Al-Laham, C.Y. Peng, A. Nanayakkara, M. Challacombe, P.M.W. Gill, B. Johnson, W. Chen, M.W. Wong, C. Gonzalez, J.A. Pople, Gaussian, Inc., Wallingford, CT, 2004.
[31] A.D. Becke, Phys. Rev. A 38 (1988) 3098.
[32] C. Lee, W. Yang, R.G. Parr, Phys. Rev. B 37 (1988) 785.
[33] A.D. Becke, J. Chem. Phys. 98 (1993) 5648.
[34] S.C. Davies, D.J. Evans, D.L. Hughes, M. Konkol, R.L. Richards, R. Sanders, P. Sobota, J. Chem. Soc., Dalton Trans. (2002) 2473.
[35] S.C. Davies, M.C. Durrant, D.L. Hughes, L.R. Richards, J.R. Sanders, J. Chem. Soc., Dalton Trans. (2000) 4694.
[36] H.-W. Chen, C.-W. Lin, C.-C. Chen, L.-B. Yang, M.-H. Chiang, W.-F. Liaw, Inorg. Chem. 44 (2005) 3226.
[37] S. Blasco, I. Demachy, Y. Jean, A. Lledos, Theochem 621 (2003) 113.
[38] M. Swat, A.R. Groenhof, A.W. Ehlers, K. Laamertsma, J. Phys. Chem. A 108 (2004) 5479.
[39] L. Noodleman, D.A. Case, A. Aizman, J. Am. Chem. Soc. 110 (1988) 1001.
[40] L. Noodleman, C.Y. Peng, D.A. Case, J.M. Mouesca, Coord. Chem. Rev. 144 (1995) 199.
[41] F.A. Walker, S. Licoccia, R. Paolesse, J. Inorg. Biochem. 100 (2006) 810.
[42] A. Chanda, D.-L. Popescu, F. Tiago de Oliveira, E.L. Bominaar, A.D. Ryabov, E. Münck, T.J. Collins, J. Inorg. Biochem. 100 (2006) 606.
[43] A. Ghosh, J. Biol. Inorg. Chem. 11 (2006) 712.

Available online at www.sciencedirect.com
ScienceDirect
Polyhedron 26 (2007) 3255–3262
POLYHEDRON
www.elsevier.com/locate/poly

DNA binding and antimicrobial studies of some polyethyleneimine-copper(II) complex samples containing 1,10-phenanthroline and L-theronine as co-ligands

R. Senthil Kumar, S. Arunachalam *

School of Chemistry, Bharathidasan University, Palkalaiperur, Tiruchirappalli 620 024, Tamil Nadu, India

Received 6 January 2007; accepted 2 March 2007
Available online 6 March 2007

Abstract

The polymer–copper(II) complex samples, $[Cu(phen)(L\text{-}Thr)(BPEI)]ClO_4 \cdot 2H_2O$ (L-Thr = L-theronine, phen = 1,10-phenanthroline and BPEI = branched polyethyleneimine), with varying degrees of copper(II) chelate content in the polymer chain, were prepared by ligand substitution method in water–ethanol medium and characterized by Infra-red, UV–Vis, EPR spectral and elemental analysis methods. The binding of these complex samples with calf thymus DNA (CT-DNA) has been investigated by absorption spectroscopy and emission spectroscopy and gel electrophoresis techniques. The experimental results indicate that the polymer–copper(II) complex is an avid DNA binder and the binding constant increased with the increase in amount of copper(II) chelate content in the polymer chain. Besides the electrostatic interaction between a negatively charged DNA molecule and a positively charged polymer–copper(II) complex molecule, other binding modes, such as van der Waals interaction, hydrogen bonding and partial intercalation binding modes may also exist in this system. A sample of polymer–copper(II) complex was tested for its antibacterial and antifungal activity and it was found to have good antibacterial and antifungal activities.
© 2007 Elsevier Ltd. All rights reserved.

Keywords: Polymer–copper(II) complexes; L-Theronine; 1,10-Phenanthroline; DNA binding

1. Introduction

The interaction of transition metal complexes with DNA has long been the subject of intense investigation in relation to the development of new reagents for biotechnology and medicine [1–3]. In these complexes, metal or ligands can be varied in an easily controlled way to facilitate the individual applications. There are several types of sites in the DNA molecule where binding of metal complexes can occur: (i) between two base pairs (intercalation), (ii) in the minor groove, (iii) in the major groove, and (iv) on the outside of the helix [4].

Copper(II) complexes have been found to be possible medical uses in the treatment of many diseases including cancer [5]. Among the various copper complexes so far investigated, those containing phenanthroline and its derivatives have attracted much attention for their various biological activities such as anticandida [6], antimycobacterial [7] and antimicrobial [8] activities. Amino acids are the basic structural units of proteins that recognize a specific base sequence of DNA. Metal complexes with amino acid ligands are involved in the exchange and transport mechanisms of trace metal ions in the human body [9]. Copper complexes containing amino acids have been studied as models for the behaviour of copper enzymes [10] and some copper complexes with amino acid ligands were reported to exhibit potent antitumor and artificial nuclease activities [11,12].

Significant developments have occurred in recent years in the field of biopolymers and biomaterials. Especially interesting are the investigations of

* Corresponding author.
E-mail address: arunasurf@yahoo.com (S. Arunachalam).

0277-5387/$ - see front matter © 2007 Elsevier Ltd. All rights reserved.
doi:10.1016/j.poly.2007.03.001

pharmacologically active compounds as drugs or carriers for normal pharmaceutical agents [13–15]. Drug–polymer conjugates are potential candidates for the selective delivery of anticancer agents to tumor tissues [16] and only a very few reports are available for the use of polymer–metal complexes as anticancer drugs [17]. Polyethyleneimine (PEI) is a cationic polymer exhibiting the highest positive charge density potential [18] and recently PEI has appeared as a possible alternative to viral and liposomal routes of gene delivery [19]. PEI possesses quite a number of advantages as polymer chelating agent, such as good water solubility, high content of functional groups and good physical and chemical stability and suitable molecular weights [20]. Recently we have reported some interesting results on the various interacting natures of some surfactant-metal and polymer-metal complexes with DNA [21,22].

In this paper, we have reported the synthesis of some novel water-soluble polymer (PEI)–copper(II) complex samples (containing both 1,10-phenanthroline and L-theronine ligands) with varying degrees of copper(II) complex content in the polymer chain. The binding properties of these complexes to calf thymus DNA have been carried out using different physico-chemical methods and the binding modes are discussed. The experimental results show that these polymer–copper(II) complex samples can be candidates for DNA-binding reagents, as well as laying the foundation for the rational design of new useful DNA probes. We have also reported the antimicrobial activities of a sample of polymer–copper(II) complex against Gram +ve and Gram −ve bacteria and fungus.

2. Experimental

2.1. Materials

Calf thymus DNA and branched polyethyleneimine (BPEI) (M_w ca. 25000) were obtained from Sigma-Aldrich, Germany, and were used as such. Copper(II) chloride dihydrate, 1,10-phenanthroline were purchased from Merck, India and L-threonine was obtained from Loba Chemie, India. The spectroscopic titrations were carried out in the buffer (50 mM NaCl–5 mM Tris–HCl, pH 7.1) at room temperature. A solution of calf thymus DNA in the buffer gave a ratio of UV absorbance at 260 and 280 nm of ~1.8–1.9:1, indicating that the DNA was sufficiently free of protein [23]). Plasmid pBR322 DNA was purchased from Genei, India. Milli-Q water was used to prepare the solutions. The complex, [Cu(phen)(L-Thr)(H_2O)]ClO_4, was prepared as reported earlier [24].

2.2. Physical measurements

The carbon, hydrogen and nitrogen contents of samples were determined at SAIF, Lucknow, India. Absorption spectra were recorded on a UV–Vis–NIR Cary300 Spectrophotomer using cuvettes of 1-cm path length, and emission spectra were recorded on a JASCO FP 770 spectrofluorimeter. FT-IR spectra were recorded on a FT-IR Perkin Elmer spectrophotometer with samples prepared as KBr pellets. EPR spectra were recorded on Varian E-112 EPR spectrometer at room temperature and at LNT (77 K), the field being calibrated with diphenylpicryl hydrazyl (DPPH, $g = 2.0037$) at SAIF, I.I.T., Chennai, India. Electrochemical measurements were made on a Princeton EG and G-PARC model potentiostat. A three-electrode system comprising a glassy carbon working electrode, a platinum wire auxillary electrode and a saturated calomel reference (SCE) electrode was used for voltammetric work. The buffer (5 mM Tris–HCl/50 mM NaCl, pH 7.2) solution was used as supporting electrolyte. The antimicrobial screening studies were carried out at Pharmaceutical laboratory, Periyar College of Pharmaceutical Sciences, Tiruchirappalli, India and the bacteria and fungus species were obtained from National Chemical Laboratory (NCL), Pune, India.

2.3. Synthesis of polymer–copper(II) complexes

To a solution of 0.15 g of BPEI dissolved in 15 mL of ethanol, 1.5 g of [Cu(phen)(L-Thr)(H_2O)]ClO_4 in 15 mL of water was added slowly with stirring. The mixture was heated between 50 and 60 °C for 6–12 h in a water bath. After being warmed enough, the dark blue coloured mixture was filtered and the filtrate was dialyzed against cold water for days together. Afterwards the solvent was evaporated by a rotary evaporator under reduced pressure at room temperature. A dark bluish filmy substance was obtained. This was pulverized and dried. Yield, 0.25 g. (*Anal*. Calc.: C, 39.94; H, 8.05; N, 18.23. Found: C, 39.94; H, 8.20; N, 18.59% and $x = 0.203$ (where x is the degree of coordination)). The other polymer–copper(II) complex samples with various degrees of coordination were synthesised with slight modifications, like changing the concentration of reagents, and the reaction time, in the experimental procedure.

2.4. DNA-binding experiments

The DNA-binding experiments were performed at 30.0 ± 0.2 °C. The DNA concentration per nucleotide was determined by electronic absorption spectroscopy using the known molar extinction coefficient value of 6600 M^{-1} cm^{-1} at 260 nm [25]. Absorption titration experiments of polymer–copper(II) complexes in buffer (50 mM NaCl–5 mM Tris–HCl, pH 7.1) were performed by using a fixed complex concentration to which increments of the DNA stock solutions were added. Polymer–copper(II) complex–DNA solutions were allowed to incubate for 10 min before the absorption spectra were recorded.

For fluorescence quenching experiments DNA was pretreated with ethidium bromide (EB) for 30 min. The polymer–copper(II) complexes were then added to this mixture and their effect on the emission intensity was measured.

Samples were excited at 450 nm and emission was observed between 500 and 700 nm.

For the gel electrophoresis experiments, supercoiled pBR322 DNA (0.1 μg) was treated with the polymer–copper(II) complex in 50 mM Tris–HCl, 18 mM NaCl buffer, pH 7.2. The samples were electrophoresed for 3 h at 50 V on a 0.8% agarose gel in Tris–acetic acid–EDTA buffer. The gel was stained with 0.5 μg/mL of ethidium bromide and photographed under UV light.

2.5. Microbial assay

The in vitro antimicrobial screening of the polymer–copper(II) complex ($x = 0.203$) was tested for its effect on certain human pathogenic bacteria and fungus by disc diffusion method. The complex was stored dry at room temperature and dissolved in DMSO. Both the Gram + (*Staphylococcus aureus*, *Bacillus subtilis*) and Gram – (*Escherichia coli*, *Pseudomonas aeruginosa*) bacteria were grown in nutrient agar medium and incubated at 37 °C for 48 h followed by frequent subculture to fresh medium and was used as test bacteria. The fungi *Candida albicans* grown in sabourad dextrose agar medium were incubated at 27 °C for 72 h followed by periodic subculturing in fresh medium and were used as test fungus. Then the petriplates were inoculated with a loop full of bacterial and fungal culture and spread throughout the petriplates uniformly with a sterile glass spreader. To each disc the test samples (10 ppm) and reference ciprofloxacin (1 μg/disc for bacteria) or clotrimazole (10 μg/disc for fungus) were added with a sterile micropipette. The plates were then incubated at 35 ± 2 °C for 24–48 h and 27 ± 1 °C for bacteria and fungus, respectively. Plates with disc containing respective solvents served as control. Inhibition was recorded by measuring the diameter of the inhibitory zone after the period of incubation. All the experiments were repeated thrice and the average values were presented.

3. Results and discussion

3.1. Degree of coordination

The structure of the polymer–copper(II) complex is shown in Fig. 1. In this figure 'x' represents degree of coordination. The degree of coordination, (x), means the number of moles of copper(II) chelate per mole of the repeating unit (amine group) of polymeric ligand. If all the repeating units (amine groups) in the polymer are coordinated to copper, then the value of x is 1. The degree of coordination, (x), of the copper chelate in the polymer–copper(II) complex was calculated either from the carbon content [26,27] or copper content [28]. The degree of coordination (x) thus obtained for the polymer–copper(II) complexes synthesised are 0.141, 0.169 and 0.203. Even if the copper chelate was added in large excess or the reaction mixture was warmed for more than 10 h, we could not obtain polymer–copper(II) complex sample with degree of coordination more than 0.203. This may be ascribed to the steric hindrance between metal complex units in the polymer chain which prevents further coordination [26].

3.2. Spectral and electrochemical characterization

In the IR region, the bands around 1518 cm^{-1} and 1425 cm^{-1} can be attributed to the ring stretching frequencies [ν(C=C) and ν(C=N)] of 1,10-phenanthroline [24]. The IR values, δ (C–H) 853 cm^{-1} and 737 cm^{-1} observed for phenanthroline are red shifted to 849 cm^{-1} and 725 cm^{-1}. These shifts can be explained by the fact that each of the two nitrogen atoms of phenanthroline ligands donate a pair of electrons to the central copper metal forming a coordinate covalent bond [29]. The bands around 2925 cm^{-1} can be assigned to C–C stretching vibration of aliphatic CH_2 of BPEI. The broad band observed around 3428 cm^{-1} is assigned to the N–H stretching of BPEI [20] and the band around 1091 cm^{-1} has been assigned to ν(Cl–O) of perchlorate anions [24].

In the UV–Vis region, the intense absorption bands appeared from 200 to 300 nm are attributed to intraligand transitions. Another band which appeared around 638 nm is assigned to ligand field transitions.

The solid state EPR spectra of the polymer–copper(II) complex ($x = 0.203$) was recorded in X-band frequencies at room temperature as well as in frozen solution (77 K) (Fig. 2). At room temperature the complex exhibits well defined single isotropic feature near $g = 2.053$. Such isotropic lines are usually the results of intermolecular spin exchange, which broaden the lines. This intermolecular

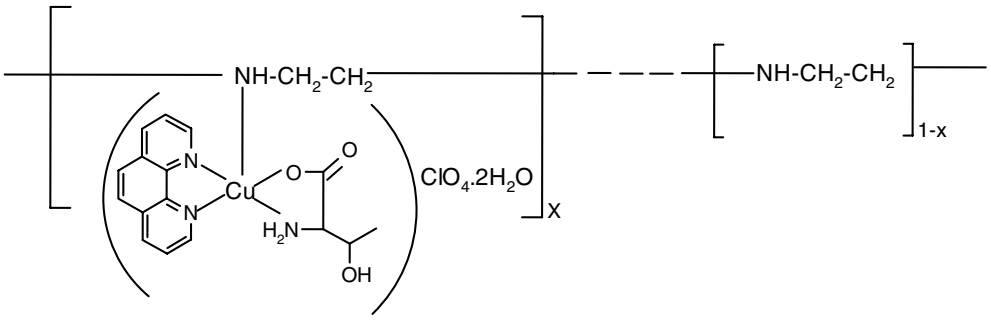


Fig. 1. Structure of [Cu(phen)(L-Thr)(BPEI)]$ClO_4 \cdot 2H_2O$ ($x = 0.203$, where x is the degree of coordination).

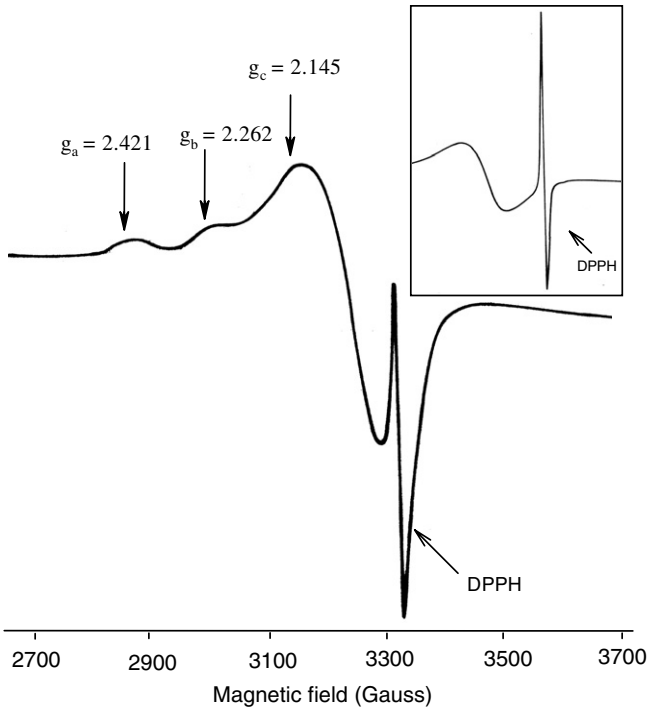


Fig. 2. EPR spectrum of [Cu(phen)(L-Thr)(BPEI)]$ClO_4 \cdot 2H_2O$ ($x = 0.203$) in DMSO at liquid nitrogen temperature (Inset: solid state EPR spectrum at room temperature).

type of spin exchange is caused by the strong spin coupling which occurs during a coupling of two paramagnetic species.

At 77 K we observed three peaks with the third being broad. This is because the copper complex units have been mounted on a polymer chain resulting in some spin–spin coupling between the copper complex units which leads to a small amount of broadening.

The cyclic voltammogram of the polymer–copper(II) complex ($x = 0.203$) in Tris–HCl buffer is shown in Fig. 3. The complex displays a quasireversible cyclic voltammetric response which can be assigned to the Cu(II)/Cu(I) couple. The cathodic peak potential (E_{pc}) and the anodic peak potential (E_{pa}) are −253.98 and −11.28 mV, respectively. The separation of the anodic and cathodic peak potentials (ΔE_p) is 242.7 mV. The formal peak potential, $E_{1/2}$, taken as the average of E_{pa} and E_{pc}, is −0.133 V.

3.3. DNA binding studies

3.3.1. Electronic spectral studies

Electronic absorption spectroscopy was an effective method to examine the binding mode of DNA with metal complexes [30–32]. In general, hypochromism and red-shift are associated with the binding of the complex to the helix by an intercalative mode involving strong stacking interaction of the aromatic chromophore of the complex between the DNA base pairs. Fig. 4 shows the UV absorption spectra of polymer–copper(II) complex ($x = 0.203$) in the absence and presence of DNA. In the ultraviolet region

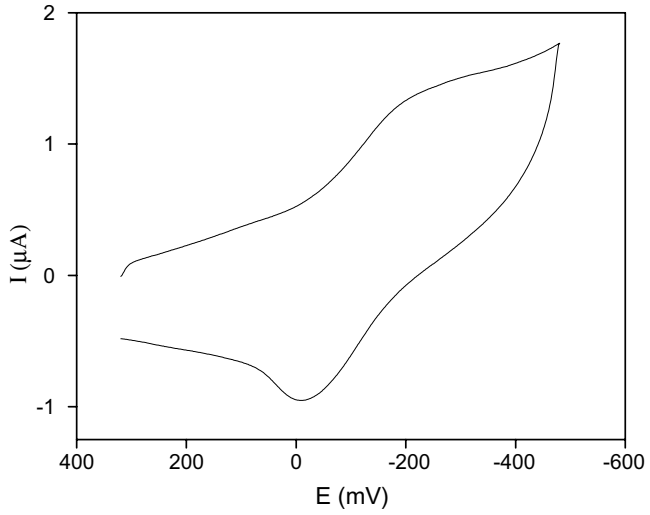


Fig. 3. Cyclic voltammogram of [Cu(phen)(L-Thr)(BPEI)]$ClO_4 \cdot 2H_2O$ ($x = 0.203$), 5 mM) in buffer containing 50 mM NaCl–5 mM Tris–HCl, pH 7.2. Scan rate: 100 mV s^{-1}.

from 200 to 300 nm, the complex had strong absorption peaks at 272 nm, besides a shoulder band around 294 nm. The absorption intensity of the polymer–copper(II) complex sample increased (hyperchromism) evidently after the addition of DNA, which indicated the interactions between DNA and the complex.

The polymer–copper(II) complex can bind to the double stranded DNA in different binding modes on the basis of their structure and charge and type of ligands. As DNA double helix possesses many hydrogen bonding sites which are accessible both in the minor and major grooves, it is likely that the amine groups of polyethyleneimine and –OH groups of L-theronine ligand in the copper(II) complex form hydrogen bonds with DNA, which may contribute to

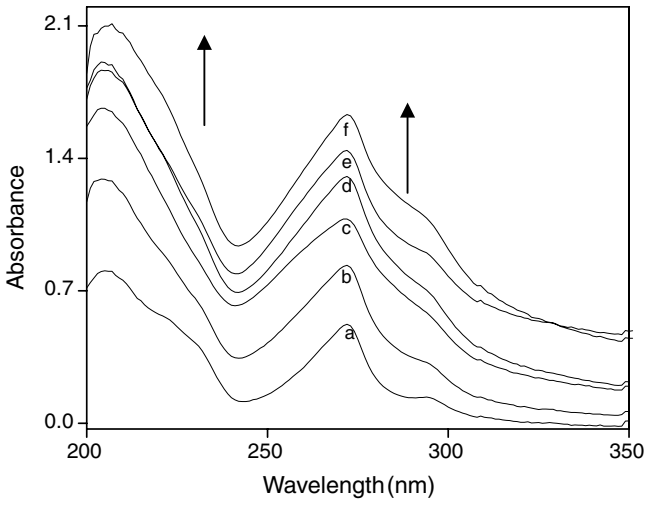


Fig. 4. Absorption spectra of [Cu(phen)(L-Thr)(BPEI)]$ClO_4 \cdot 2H_2O$ ($x = 0.203$) in the absence (a) and in the presence of increasing amounts of DNA (b–f), [Complex] = 12 μM, [DNA] = 0.2–1 μM. Arrow shows the absorbance changes upon increasing DNA concentrations.

the hyperchromism observed in the absorption spectra. On the other hand, our polymer–copper(II) complex, which possesses several methylene groups of the branched polyethyelene (BPEI) can bind to DNA by van der Waals interactions between the methylene groups and the thymine methyl groups [33] . The hyperchromic effect may also be due to the electrostatic interaction between positively charged polymer (BPEI) and the negatively charged phosphate backbone at the periphery of the double helix CT DNA [34]. In our complex, the copper(II) chelates are randomly coordinated to the branched polymer, hence complete intercalation of the phenanthroline ligand between a set of adjacent base pairs is sterically impossible, but some type of partial intercalation can be envisioned [35]. But this needs further clarification of the DNA binding mode of the complex by viscosity measurements. But as our copper complexes are polymeric and DNA being another polymer we were not able to use viscosity method, because changes in the structure of these polymer systems would change the viscosity. It is almost impossible to resolve the changes in the viscosity behaviour.

Determinations of intrinsic binding constants, K_b, based upon these absorption titrations may be made with the following equation [4]:

$$[\mathrm{DNA}]/(\varepsilon_a - \varepsilon_f) = [\mathrm{DNA}]/(\varepsilon_b - \varepsilon_f) + 1/K_b(\varepsilon_b - \varepsilon_f),$$

where [DNA] is the concentration of DNA in base pairs, ε_a, ε_f and ε_b correspond to A_{obsd}/[total copper complex units], the extinction coefficient of the free polymer–copper(II) complex and the extinction coefficient of the complex in the fully bound form, respectively. A plot of [DNA]/$(\varepsilon_a - \varepsilon_f)$ versus [DNA], gives K_b as the ratio of the slope to the intercept (Fig. 5). The K_b values of polymer–copper(II) complexes, thus obtained with different degrees of coordinated copper(II)-chelates are shown in Table 1. As reflected in the K_b values, the significant difference in DNA binding affinity of polymer–copper(II) complexes with different copper(II) complex chelates can be understood as a result of the fact that the polymer–copper(II) complex with higher degree of copper(II) chelate binds strongly with DNA. This may be due to the high positive charges and large number of copper(II) chelates present in the complex which cooperatively act to increase the overall binding ability of the polymer–copper(II) complex molecule to DNA. The K_b values obtained for our polymer–copper(II) complex samples are very much higher than those for any other known simple mononuclear or binuclear copper(II) complexes including complexes such as $[Cu_2phen_2Cl_4]$ (K_b, 4.75×10^4 M^{-1}) [36], $[Cu(phen)_2Cl_2]$ (K_b, 2.70×10^3 M^{-1}) [37] and $[Cu(phen)(L\text{-}Thr)(H_2O)]ClO_4$ (K_b, 6.35×10^3 M^{-1}) [24].

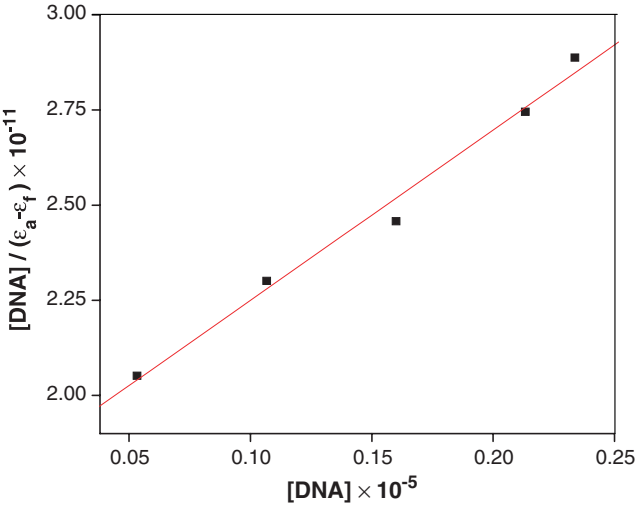


Fig. 5. Plot of [DNA]/$(\varepsilon_a - \varepsilon_f)$ vs. [DNA].

Table 1
The intrinsic binding constants (K_b) of $[Cu(phen)(L\text{-}Thr)(BPEI)]\text{-}ClO_4 \cdot 2H_2O$ with calf thymus DNA

Degree of coordination (x)	K_b (M^{-1})
0.141	1.32×10^5
0.169	1.78×10^5
0.203	2.48×10^5

3.3.2. Fluorescent spectral studies

No fluorescence was observed for the polymer–copper(II) complex samples either in aqueous solution or in the presence of calf thymus DNA. So the binding of polymer–copper(II) complex samples with DNA cannot be directly presented in the emission spectra. So the binding of polymer–copper(II) complex samples to CT-DNA have been studied by competitive ethidium bromide (EB) binding experiments. The molecular fluorophore, EB, is known to show intense fluorescence light when bound to DNA, due to its strong intercalation between the adjacent DNA base pairs [38]. In earlier literature, it was reported that the fluorescent light of EB–DNA system can be reduced by the addition of a second molecule [39], indicating the competition of second molecule with EB in binding to DNA. Recently Ni et al. [40] found that fluorescence reduction of fluorophore NR (neutral red dye) in the presence of DNA by $Cu(phen)^{2+}$ may be due to the replacement of the DNA intercalator, NR. This means that the complex interacts with the same site as NR does. Zhang et al. [36] also indicate that a binuclear copper(II) complex of 1,10-phenanthroline ligand competitively binds to the EB–DNA system by intercalation. On the other hand, Bronich et al. [41] have reported that the addition of a pure organic copolymer (i.e. polyethyleneglycol–polyethyleneimine (PEI)) to EB–DNA complex results in quenching of the fluorescence due to the displacement of EB by the copolymer. Xiao et al. [34] have studied the effect of polymeric schiff base–nickel complexes on the fluorescence of EB–DNA system and they suggested that a portion of the metal complex, possessing a planar aromatic moiety, intercalates to adjacent base pairs, which inhibits EB binding to calf thymus DNA competitively. In our studies the addition of the polymer–copper(II) complexes to DNA pretreated with EB causes appreciable reduction in the emission

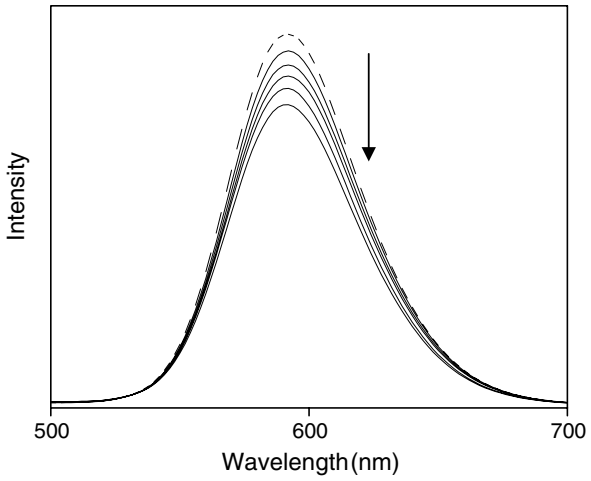


Fig. 6. Emission spectra of EB bound to DNA in the absence (---) and in the presence of [Cu(phen)(L-Thr)(BPEI)]$ClO_4 \cdot 2H_2O$ (—) ($x = 0.203$), [EB] = 4 μM, [DNA] = 4 μM, [Complex] = 0–4 μM.

intensity (Fig. 6), indicating that the replacement of the EB fluorophore by the polymer–copper(II) complex, results in a decrease in the emission intensity. The polymer–copper(II) complex with higher degree of coordination has lead toa large reduction in emission intensity in the presence of DNA. This may be due to the larger number of copper(II) chelates present in the polymer chain, which hinder intercalation of EB into DNA and thus decreasing the binding ability between EB and calf thymus DNA.

3.3.3. Gel electrophoresis studies

Preliminary results from the absorption and fluorescence spectral studies show that the polymer–copper(II) complex with high copper(II) chelate content binds strongly to DNA. Binding of this complex with DNA was also studied by gel electrophoresis using plasmid pBR 322 DNA. This DNA moves on agarose gel under the influence of electrical field. This movement is retarded when they are bound to other molecules.

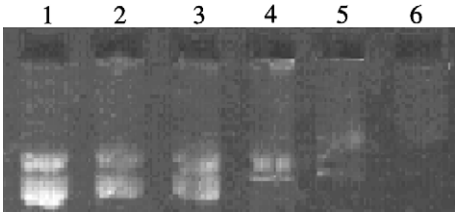


Fig. 7. Gel retardation behaviour of pBR322 DNA by [Cu(phen)(L-Thr)(BPEI)]$ClO_4 \cdot 2H_2O$ ($x = 0.203$). Lane 1: DNA alone, Lanes 2–6: DNA + polymer–copper(II) complex in the concentration of 20, 30, 40, 50 and 60 μM.

Many polycationic organic polymer molecules interact with DNA through electrostatic interactions between phosphate groups of the DNA and oppositely charged groups of polymer [42,43,18]. Forrest et al. [44] and Vinogradov et al. [45] have reported that the organic polymer, polyethyleneimine (PEI), retards the DNA migration in agarose gel electrophoresis and they have suggested that the binding between DNA and polyethyleneimine (PEI) have occurred mainly through electrostatic interactions among the participating species. Recently Annaraj et al. [46] observed that the phenanthroline containing mixed ligand copper(II) complexes retard the mobility of DNA due to the intercalation of the planar phenanthroline groups. Similar retardation in the DNA mobility is also observed due to the intercalation by ruthenium complexes [47]. In order to substantiate the binding of our polymer–copper(II) complexes to DNA, gel electrophoresis has been performed with a sample of the polymer–copper(II) complex ($x = 0.203$) (Fig. 7). Lane 1 is pure DNA not treated with complex. Lanes 2–6 represent the DNA treated with the polymer–copper(II) complex of various solution concentrations. As reported by previous workers on the interaction of DNA-polyethyleneimine alone, in our work also the migration of the DNA band is retarded as the concentration of polymer–copper(II) complex in the solution is increased. This clearly demonstrates that the cationic segments of the branched polyethyleneimine neutralize the negative charges of DNA, which could have facilitated further due to the increased planar phenanthroline groups of copper(II) complex moieties present in the polymer chain.

3.4. Antibacterial and antifungal screening

The polymer–copper(II) complex ($x = 0.203$) was screened in vitro for its microbial activity against certain pathogenic bacterial and fungal species using disc diffusion method. The complex was found to exhibit considerable

Table 2
Anti-microbial activities of [Cu(phen)(L-Thr)(BPEI)]$ClO_4 \cdot 2H_2O$ ($x = 0.203$)

Test organisms	Diameter of zone inhibition (mm)				
	Cu(phen)(L-Thr)$(H_2O)]ClO_4$	BPEI	Standard	Cu(phen)(L-Thr)(BPEI)]$ClO_4 \cdot 2H_2O$	Standard
Staphylococcus aureus	4	7	15	11	16
Bacillus subtilis	2	9	16	13	17
Escherichia coli	3	8	17	10	16
Pseudomonas auregenosa	4	7	17	12	17
Candida albicans	3	6	10	10	12

Standard – Ciprofloxacin for bacteria and Clotrimazole for fungus.
Solvent – DMSO (showed nil effect against the microorganisms under test).

activity against Gram +ve and Gram −ve bacteria and the fungus *C. albicans*. The test solutions were prepared in dimethyl sulphoxide and the results of the antimicrobial activities are summarized in Table 2.

Zoroddu et al. [48] have reported that neither phenanthroline ligand alone nor copper(II) chloride itself showed any significant activity against the Gram +ve and Gram −ve bacteria but the copper(II)–phenanthroline complex has exhibited considerable activity against Gram +ve *S. aureus* and Gram −ve *E. coli*, but inactive against Gram −ve *P. aeruginosa*. In our biological experiments, using polymer–copper(II) complex ($x = 0.203$), we have observed considerable antibacterial activity against Gram +ve bacteria *S. aureus* and *B. subtilis* and Gram −ve bacteria *E. coli* and *P. aeruginosa*. The polymer–copper(II) complex has shown a high activity against Gram +ve than Gram −ve bacteria. The polymer–copper(II) complex is also active against the fungus *C. albicans*. Also we carried out the tests with polymer (BPEI) and ordinary copper complex $[Cu(phen)(L\text{-}Thr)(H_2O)]ClO_4$ separately. Both showed some activity against all microorganisms but the effect is very small compared to polymer–copper complex. It may be concluded that our polymer–copper(II) chelate inhibits the growth of bacteria and fungi to a greater extent.

4. Conclusion

We described here the synthesis of some novel water-soluble polymer–copper(II) complex samples with varying amounts of copper(II) chelate content in the polymer chain. The characterization of complex sample was achieved through Infra-red, UV–Vis, EPR spectral and elemental analysis methods. Spectroscopic studies suggest that the presence of multiple copper(II) complex moieties and free NH groups, in a single big size polymer molecule, can enhance the various binding ability i.e. with CT-DNA. The polymer–copper(II) chelates could bind to DNA molecules mainly by electrostatic interaction. Besides this, ionic interaction, van der Waals interaction, hydrogen bonding and other partial intercalation binding modes may also exist in this system. The polymer–copper(II) complex sample showed good antimicrobial activity against Gram +ve and Gram −ve bacteria and fungi.

Acknowledgements

We are grateful to the UGC-SAP & COSIST and DST-FIST programmes and University Research Fellowship sanctioned to one of the authors, RSK, by the Bharathidasan University, Tiruchirappalli, India. We thank Dr. L. Uma and Dr. D. Prabhakaran, National Centre for Marine Cyanobacteria, for providing the Gel documentation facility. We also thank the CSIR for sanction of a research scheme (01(2075)/06/EMR-II) to one of the authors, S. Arunachalam.

References

[1] C. Tu, X. Wu, Q. Li, X. Wang, Q. Xu, Z. Guo, Inorg. Chim. Acta 357 (2004) 95.
[2] S.R. Chowdhary, K.K. Mukherjee, R. Bhattacharyya, Trans. Met. Chem. 30 (2005) 601.
[3] Y.-M. Song, X.-L. Lu, M.-L. Yang, X.-R. Zheng, Trans. Met. Chem. 30 (2005) 499.
[4] A.M. Pyle, J.P. Rehmann, R. Meshoyrer, C.V. Kumar, N.J. Turro, J.K. Barton, J. Am. Chem. Soc. 111 (1989) 3051.
[5] J.R.J. Sorenson, Chem. Br. 16 (1984) 1110.
[6] G. Majella, S. Vivienne, M. Malachy, D. Micheal, M. Vickie, Polyhedron 18 (1999) 2931.
[7] D.K. Saha, U. Sandbhor, K. Shirisha, S. Padhye, D. Deobagkar, C.E. Ansond, A.K. Powell, Bioorg. Med. Chem. Lett. 14 (2004) 3027.
[8] M. Tumer, H. Koksal, S. Serin, Trans. Met. Chem. 24 (1999) 13.
[9] S. Lau, B. Sarkar, Can. J. Chem. 53 (1975) 710.
[10] F.A. Cotton, G. Wilkinson, Advanced Inorganic Chemistry, Wiley, New York, 1972.
[11] R. Ren, P. Yang, W. Zhang, Z. Hua, Inorg. Chem. 39 (2000) 5454.
[12] A.K. Patra, S. Dhar, M. Nethaji, A.R. Chakravarty, Dalton Trans. (2005) 896.
[13] D. Putnam, J. Kopecek, Adv. Polym. Sci. 122 (1995) 55.
[14] H.J. Ringsdorf, J. Polym. Sci. 51 (1975) 135.
[15] J.G. Joseph, React. Funct. Polym. 39 (1999) 99.
[16] B.A. Howell, E.W. Walls, R. Rashidianfar, Makromol. Chem. Macromol. Symp. 19 (1988) 329.
[17] B. Schechter, R. Arnon, M. Wilchek, React. Polym. 25 (1995) 167.
[18] A.V. Harpe, H. Petersen, Y. Li, T. Kissel, J. Control. Release 69 (2000) 309.
[19] W.T. Godbey, K.K. Wu, A.G. Mikos, J. Control. Release 60 (1999) 149.
[20] K. Geckeler, G. Lange, H. Eberhardt, E. Bayer, Pure Appl. Chem. 52 (1980) 883.
[21] R.S. Kumar, S. Arunachalam, Polyhedron 25 (2006) 3113.
[22] N. Kumaraguru, S. Arunachalam, R.S. Kumar, V.S. Periasamy, C.P. Paul, M.A. Akbarsha, Polyhedron, in press.
[23] J. Marmur, J. Mol. Biol. 3 (1961) 208.
[24] S. Zhang, Y. Zhu, C. Tu, H. Wei, Z. Yang, L. Lin, J. Ding, J. Zhang, Z. Guo, J. Inorg. Biochem. 98 (2004) 2099.
[25] M.F. Reichmann, S.A. Rice, C.A. Thomas, P. Doty, J. Am. Chem. Soc. 76 (1954) 3047.
[26] E. Tsuchida, H. Nishide, T. Ohkawa, Bull. Sci. Res. Lab. 69 (1975) 31.
[27] Y. Kurimura, E. Tsuchida, M. Kaneko, J. Polym. Sci. Part A-1 9 (1971) 3511.
[28] J.W. Kolis, D.E. Hamilton, N.K. Kildahl, Inorg. Chem. 18 (1979) 1826.
[29] L. Jin, P. Yang, Polyhedron 16 (1997) 3395.
[30] J.K. Barton, A.L. Rapheal, J. Am. Chem. Soc. 106 (1984) 2172.
[31] T.M. Kelly, A.B. Tossi, D.J. McConnell, T.C. Strekas, Nucleic Acids Res. 13 (1985) 6017.
[32] S.A. Tysoe, R.J. Morgan, A.D. Baker, T.C. Strekas, J. Phys. Chem. 97 (1993) 1707.
[33] C.L. Liu, J.Y. Zhou, Q.X. Li, L.J. Wang, Z.R. Liao, H.B. Xu, J. Inorg. Biochem. 75 (1999) 233.
[34] Y.–N. Xiao, C.–X. Zhan, J. Appl. Polym. Sci. 84 (2002) 887.
[35] S. Satyanarayana, J.C. Cabrowiak, J.B. Chaires, Biochemistry 32 (1993) 2573.
[36] Q.–Q. Zhang, F. Zhang, W.–G. Wang, X.–L. Wang, J. Inorg. Biochem. 100 (2006) 1344.
[37] T. Gupta, S. Dhar, M. Nethaji, A.R. Chakravarty, Dalton Trans. (2004) 1896.
[38] J. Olmsted, D.R. Kearns, Biochemistry 16 (1977) 3647.
[39] B.C. Baguley, M. Lebret, Biochemistry 23 (1984) 937.
[40] Y. Ni, D. Lin, S. Kokot, Anal. Biochem. 352 (2006) 231.

[41] T.K. Bronich, H.K. Nguyen, A. Eisenberg, A.V. Kabanov, J. Am. Chem. Soc. 122 (2000) 8339.
[42] T.K. Bronich, A.V. Kabanov, L.A. Marky, J. Phys. Chem. B 105 (2001) 6042.
[43] M.X. Tang, F.C. Szoka, Gene Ther. 4 (1997) 823.
[44] M.L. Forrest, J.T. Koerber, D.W. Pack, Bioconjugate Chem. 14 (2003) 934.
[45] S.V. Vinogradov, T.K. Bronich, A.V. Kabonov, Bioconjugate Chem. 9 (1998) 805.
[46] J. Annaraj, S. Srinivasan, K.M. Ponvel, P.K. Athappan, J. Inorg. Biochem. 99 (2005) 669.
[47] E.C. Long, J.K. Barton, Acc. Chem. Res. 23 (1990) 271.
[48] M.A. Zoroddu, S. Zanetti, R. Pongi, R. Basosi, J. Inorg. Biochem. 63 (1996) 291.

Available online at www.sciencedirect.com
ScienceDirect
Polyhedron 26 (2007) 3263–3270
POLYHEDRON
www.elsevier.com/locate/poly

Coordination to copper(II) strongly enhances the *in vitro* antimicrobial activity of pyridine-derived *N*(4)-tolyl thiosemicarbazones

Isolda C. Mendes [a], Juliana P. Moreira [a], Antonio S. Mangrich [b], Solange P. Balena [b], Bernardo L. Rodrigues [c], Heloisa Beraldo [a,*]

[a] *Departamento de Química, Universidade Federal de Minas Gerais, 31270-901 Belo Horizonte, Brazil*
[b] *Departamento de Química, Universidade Federal do Paraná, 81531-970 Curitiba, Brazil*
[c] *Instituto de Física, Universidade de São Paulo, São Carlos, Brazil*

Received 12 January 2007; accepted 2 March 2007
Available online 12 March 2007

Abstract

Five copper(II) complexes with *N*(4)-*ortho*, *N*(4)-*meta* and *N*(4)-*para*-tolyl thiosemicarbazones derived from 2-formyl and 2-acetylpyridine were obtained and thoroughly characterized. The crystal structure of *N*(4)-*meta*-tolyl-2-acetylpyridine thiosemicarbazone (H2Ac4mT) was determined, as well as that of its copper(II) complex [Cu(2Ac4mT)Cl], which contains an anionic ligand and a chloride in the coordination sphere of the metal. The *in vitro* antimicrobial activities of all thiosemicarbazones and their copper(II) complexes were tested against *Salmonella typhimurium* and *Candida albicans*. Upon coordination a substantial decrease in the minimum inhibitory concentration, from 225 to 1478 μmol L^{-1} for the thiosemicarbazones to 5–30 μmol L^{-1} for the complexes was observe against the growth of *Salmonella typhimurium* and from 0.7–26 to 0.3–7 μmol L^{-1} against the growth of *C. albicans*, suggesting that complexation to copper(II) could be an interesting strategy of dose reduction.
© 2007 Elsevier Ltd. All rights reserved.

Keywords: Thiosemicarbazones; Copper(II) complexes; Crystal structures; Antimicrobial activity; *Salmonella typhimurium*; *Candida albicans*; Dose reduction

1. Introduction

Thiosemicarbazones present a wide range of pharmacological applications as anticancer, antiviral and antimicrobial agents [1–3]. The biological properties of thiosemicarbazones are often related to metal coordination. Firstly, lipophilicity, which controls the rate of entry into the cell, is modified by coordination. Also, the metal complex can be more active than the free ligand, or the metal complex can be a vehicle for activation of the ligand as the cytotoxic agent [1–3].

The antimicrobial action of thiosemicarbazones against a variety of bacteria and fungi has been investigated. The activity of 2-formyl and 2-acetylpyridine thiosemicarbazones has been demonstrated in clinical isolates of bacteria [1,4]. Significant activity has been found toward gram positive bacilli but poor antibacterial activity has been shown toward gram negative cultures [1,4,5]. In addition, the *in vitro* inhibitory activity of 2-acetylpyridine-derived thiosemicarbazones has been demonstrated against clinically significant bacterial cultures, including isolates with known antibiotic resistance [1,4,5]. A variety of metal complexes of these ligands has also shown to present potent antibacterial activity [1]. Less attention has been given to 2-benzoylpyridine-derived thiosemicarbazones.

Some 2-formyl and 3-formylpyridine thiosemicarbazones and their metal complexes were tested against *Candida albicans* and *Apergillus fumigatus*. In addition, *N*(4)-alkyl and *N*(4)-dialkyl-2-acetylpyridine thiosemicarbazones showed marked inhibitory activity of *A. niger* growth. Moreover, metallocene derivatives of titanium and zirconium with

* Corresponding author. Tel.: +55 31 3499 5740; fax: +55 31 3499 5700.
E-mail address: hberaldo@ufmg.br (H. Beraldo).

0277-5387/$ - see front matter © 2007 Elsevier Ltd. All rights reserved.
doi:10.1016/j.poly.2007.03.002

thiosemicarbazones derived from 2-acetylpyridine, 2-acetylfuran, 2-acetylthiophene and 2-acetylnaphtalene were tested against a number of pathogenic fungi and bacteria. All the complexes were more active against the studied organisms than the free thiosemicarbazones [1].

It has been demonstrated that the presence of a bulky group at *N*(4) strongly improves the biological activity of thiosemicarbazones [2,3], probably due to an increase in lipophilicity.

In previous works, we started an evaluation of the antimicrobial and cytotoxic activities of pyridine-derived thiosemicarbazones and their metal complexes. *N*(4)-alkyl- and *N*(4)-phenyl-substituted 2-benzoylpyridine thiosemicarbazones have been prepared, as well as their palladium(II), tin(IV) and iron(II) complexes [6–8].

Taking into consideration that copper(II) complexes have found possible medical uses in the treatment of many diseases including microbial infections [2,3,9] we recently prepared *N*(4)-tolyl thiosemicarbazones derived from 2-benzoylpyridine as well as their copper(II) complexes. Both ligands and complexes proved to be active against the growth of *C. albicans* with low values of minimum inhibitory concentration. The activity is improved upon coordination to copper [10].

Salmonella sp. is a *gram*-negative facultative rod-shaped bacterium which causes infections about 12–24 h following ingestion of contaminated food. Strains of *Salmonella* which are resistant to a range of antimicrobials, including first-choice agents for the treatment of humans have emerged, and are threatening to become a serious public health problem [11]. The same occurs with strains of fungi. Among the azole drugs used against infections caused by *C. albicans*, fluconazole and itraconazole exhibit satisfactory safety and efficacy. However, the emergence of clinical resistance during long-term therapy is well known [12].

Resistance results from the use of antimicrobials both in humans and animal husbandry. Multi-drug resistance to critically important antimicrobials is compounding the problems [13]. Therefore, preparation of new antimicrobials with activity in low doses is extremely important.

In the present work, we studied the activity of *N*(4)-*ortho*-, *N*(4)-*meta*- and *N*(4)-*para*-2-formyl (hereafter named H2Fo4oT, H2Fo4mT, H2Fo4pT), 2-acetyl (H2Ac4oT, H2Ac4mT, H2Ac4pT) and 2-benzoylpyridine thiosemicarbazones (H2Bz4oT, H2Bz4mT, H2Bz4pT) (see Fig. 1) and their copper(II) complexes against the growth of *Salmonella typhimurium* and *C. albicans*.

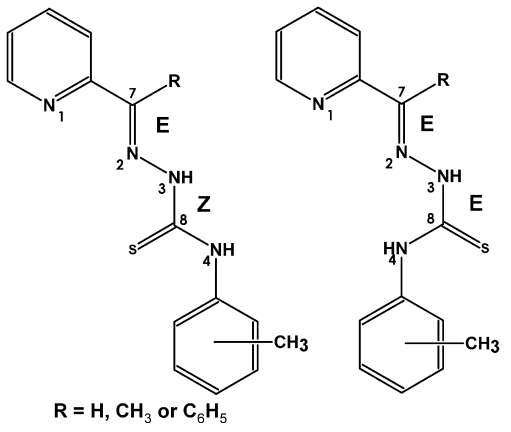


Fig. 1. General structure of *N*(4)-*ortho*-, *N*(4)-*meta*- and *N*(4)-*para*-tolyl 2-formyl 2-acetyl and 2-benzoylpyridine thiosemicarbazones, *E* and *Z* configurations.

2. Experimental

2.1. Apparatus

Partial elemental analyses were performed on a Perkin Elmer CHN 2400 analyzer. Infrared spectra were recorded on a Perkin Elmer FT-IR Spectrum GX spectrometer using CsI/nujol; an YSI model 31 conductivity bridge was employed for molar conductivity measurements. Magnetic susceptibility measurements were carried out on a Johnson Matthey MSB/AUTO balance. Electron paramagnetic resonance (EPR) spectra of samples in frozen DMF solution were obtained in quartz tubes of 3 mm of internal diameter at liquid N_2 temperature (77 K) on a Bruker ESP300E equipment with modulation frequency of 100 kHz operating at 9.5 GHz (X-band). Spectra simulations were performed using the WINSIMFONIA Bruker package. Crystal structures of H2Ac4mT and its copper complex [Cu(2Ac4mT)Cl] (see below) were investigated using single-crystal X-ray diffractometry. Data have been collected at room temperature in a Kappa CCD diffractometer, Mo Kα monochromated radiation, $\lambda = 0.71073$ Å. Crystal data, data collection procedure, structure determination methods and refinement results are summarized in Table 1. The structures were solved by direct methods and refined on F^2 by full-matrix least-squares using the SHELX 97 [14,15] program in a WINGX system [16,17]. Although some of the hydrogen atoms could be identified in a Fourier difference map, in the final model they were geometrically positioned and refined using a riding model. All non-H atoms were refined anisotropically.

2.2. Synthesis of the copper(II) complexes with 2-formyl- and 2-acetylpyridine N(4)-tolyl thiosemicarbazones

The thiosemicarbazones were prepared as described in the literature [18]. The copper(II) complexes were obtained by refluxing an ethanol solution (25 mL) of the desired thiosemicarbazone (3 mmol) with $CuCl_2 \cdot 2H_2O$ (Aldrich) in 1:1 ligand-to-metal molar ratio for 5 h. The resulting solids were filtered then washed with ethanol followed by diethyl ether, and dried *in vacuo*. Crystals of H2Ac4mT were grown by slow diffusion from ethanol solution and crystals of its copper(II) complex from a 1:9 DMSO/acetone solution.

The copper(II) complexes will be hereafter numbered as follows: [Cu(H2Fo4oT)Cl_2] (**1**), [Cu(2Fo4mT)Cl] (**2**),

Table 1
Crystal data and structure refinement for H2Ac4mT and [Cu(2Ac4mT)Cl] (**5**)

Empirical formula	$C_{15}H_{16}N_4S$	$C_{15}H_{15}N_4SCuCl$
Crystal size (mm)	$0.14 \times 0.10 \times 0.04$	$0.13 \times 0.09 \times 0.02$
Molecular weight (g mol^{-1})	284.38	382.36
Crystal system, space group	monoclinic, $P2_1/c$	triclinic, $P\bar{1}$
Lattice parameters		
a(Å)	10.3812(4)	7.8130(3)
b (Å)	5.7074(2)	8.1716(3)
c (Å)	24.606(1)	12.8239(5)
α (°)	90	100.925(3)
β (°)	100.059(2)	100.400(3)
γ (°)	90	97.327(2)
V (Å^3)	1435.5(1)	779.52(5)
Z	4	2
F(000)	600	390
D_{calc} (g cm^{-3})	1.316	1.629
Absorption coefficient (mm^{-1})	0.211	1.706
θ Range for data collection (°)	2.37–25.05	3.31–25.00
Limiting indices	$-12 \leqslant h \leqslant 12$, $-6 \leqslant k \leqslant 6$, $-29 \leqslant l \leqslant 29$	$-9 \leqslant h \geqslant 9$, $-9 \leqslant k \geqslant 9$, $-15 \leqslant l \geqslant 15$
Reflections collected	19929	11681
Reflections unique [R_{int}]	2536 [0.0874]	2750 [0.1036]
Completeness to θ (%)	99.7	99.8
Absorption correction	none	analytical
Parameters/restraints	182/0	199/0
Final R indices [$I > 2\sigma(I)$]	$R_1 = 0.0488$, $wR_2 = 0.1100$	$R_1 = 0.0441$, $wR_2 = 0.0946$
R indices (all data)	$R_1 = 0.0898$, $wR_2 = 0.1356$	$R_1 = 0.0809$, $wR_2 = 0.1108$
Goodness-of-fit on F^2	1.030	0.995
Largest difference in peak and hole (e Å^{-3})	0.231 and −0.247	0.376 and −0.433

[Cu(2Fo4pT)Cl] (**3**), [Cu(2Ac4oT)Cl] (**4**), [Cu(2Ac4mT)Cl] (**5**), [Cu(2Ac4pT)Cl] (**6**), [Cu(H2Bz4oT)Cl_2] (**7**), [[Cu(H2-Bz4mT)Cl_2] (**8**), [Cu(H2Bz4pT)Cl_2] (**9**) (see Section 3 for the discussion of the proposed formulations). Complex **1**, previously reported by other authors [18] and complexes **7**–**9**, recently prepared by us [10] are listed in the present work because this is the first investigation on their antibacterial activity.

Chloro(*N*(4)-*m*-tolyl-2-formylpyridine-thiosemicarbazonato)copper(II) [Cu(2Fo4mT)Cl] (**2**): Green solid; *Anal.* Calc. for $CuC_{14}H_{11}N_4SCl$: C, 45.65; H, 3.56; N, 15.20. Found: C, 45.60; H, 3.42; N, 14.94%; FW: 368.34 g mol^{-1}. $UV_{solution}$: λ_{max} (cm^{-1}): 30860 (sh), 27780 (sh), 24210 (4.40), 16304 (2.20). UV_{solid}: λ_{max} (cm^{-1}): 27770, 22568, 19305, 16703. IR (CsI/nujol, cm^{-1}): ν(NH) 3325 ν(C=N) + ν(C=C) 1607–1547, ν(C=S) 760, ρ(py) 624, ν(CuN) 456, ν(CuN_{py}) 343, ν(CuS) 333, ν(CuCl) 311. Molar conductivity (1×10^{-3} mol L^{-1}, dimethylformamide, DMF): 13 Ω^{-1} cm^2 mol^{-1}. Effective magnetic moment = 1.73 (BM). Yield: 84%.

Chloro(N(4)-*p*-tolyl-2-formylpyridine-thiosemicarbazonato)copper(II) [Cu(2Fo4pT)Cl] (**3**): Green solid; *Anal.* Calc. for $CuC_{14}H_{11}N_4SCl$: C, 45.65; H, 3.56; N, 15.20. Found: C, 45.58; H, 3.45; N, 14.99%; FW: 368.34 g mol^{-1}. $UV_{solution}$: λ_{max} (cm^{-1}): 30960 (sh), 27030 (4.40), 16520 (2.28). UV_{solid}: λ_{max} (cm^{-1}): 31230, 27160, 23652, 22543, 16920. IR (CsI/nujol, cm^{-1}): ν(NH) 3332 ν(C=N) + ν(C=C) 1607–1538, ν(C=S) 782, ρ(py) 601, ν(CuN) 416, ν (CuN_{py}) 360, ν(CuS) 330, ν(CuCl) 307. Molar conductivity (1×10^{-3} mol L^{-1} DMF): 15 Ω^{-1} cm^2 mol^{-1}. Effective magnetic moment = 1.76 BM. Yield: 88%.

Chloro(N(4)-*o*-tolyl-2-acetylpyridine-thiosemicarbazonato)copper(II)[Cu(2Ac4oT)Cl] (**4**): Green solid; *Anal.* Calc. for $CuC_{15}H_{13}N_4SCl$: C, 47.12; H, 3.95; N, 14.65. Found: C, 46.92; H, 3.94; N, 14.35%; FW: 382.37 g mol^{-1}. $UV_{solution}$: λ_{max} (cm^{-1}): 32467 (sh), 27624 (4.33), 24213 (4.43), 16393 (2.67). UV_{solid}: λ_{max} (cm^{-1}): 33512, 27770, 22868, 15818. IR (CsI/nujol, cm^{-1}): ν(NH) 3429 ν(C=N) + ν(C=C) 1602–1536, ν(C=S) 763, ρ(py) 604, ν(CuN) 460, ν(CuN_{py}) 346, ν(CuS) 329, ν(CuCl) 308. Molar conductivity (1×10^{-3} mol L^{-1} DMF): 56 Ω^{-1} cm^2 mol^{-1}. Effective magnetic moment = 1.96 BM. Yield: 90%.

Chloro(*N*(4)-*m*-tolyl-2-acetylpyridine-thiosemicarbazonato)copper(II)[Cu(2Ac4mT)Cl] (**5**): Green solid; *Anal.* Calc. for $CuC_{15}H_{13}N_4SCl$: C, 47.12; H, 3.95; N, 14.65. Found: C, 47.52; H, 3.90; N, 14.29%; FW: 382.37 g mol^{-1}. $UV_{solution}$: λ_{max} (cm^{-1}): 31150 (4.53), 27170 (sh), 24750 (4.41), 16530 (2.47). UV_{solid}: λ_{max} (cm^{-1}): 32062, 27330, 23277, 19810, 16958. IR (CsI/nujol, cm^{-1}): ν(NH) 3320 ν(C=N) + ν(C=C) 1604–1547, ν(C=S) 765, ρ(py) 610, ν(CuN) 449, ν(CuN_{py}) 374, ν(CuS) 337, ν(CuCl) 318. Molar conductivity (1×10^{-3} mol L^{-1} DMF): 55 Ω^{-1} cm^2 mol^{-1}. Effective magnetic moment = 1.85 BM. Yield: 82%.

Chloro(*N*(4)-*p*-tolyl-2-acetylpyridine-thiosemicarbazonato)copper(II)[Cu(2Ac4pT)Cl] (**6**): Green solid; *Anal.* Calc. for $CuC_{15}H_{13}N_4SCl$: C, 47.12; H, 3.95; N, 14.65. Found: C, 47.07; H, 3.97; N, 14.37%; FW: 382.37 g mol^{-1}. $UV_{solution}$: λ_{max} (cm^{-1}): 31250 (4.47), 26600 (sh), 24570 (4.40), 16650 (2.51). UV_{solid}: λ_{max} (cm^{-1}): 31450, 25710, 22830, 17240. IR (CsI/nujol, cm^{-1}): ν(NH) 3322 ν(C=N) + ν(C=C) 1604–1541, ν(C=S) 757, ρ(py) 608, ν(CuN) 446, ν(CuN_{py}) 360, ν(CuS) 341, ν(CuCl) 317. Molar conductivity (1×10^{-3} mol L^{-1}, DMF): 37 Ω^{-1} cm^2 mol^{-1}. Effective magnetic moment = 2.03 BM. Yield: 87%.

2.3. Antibacterial activity

Antibacterial activity was evaluated by minimum inhibitory concentration (MIC) using the macro dilution test [19–21]. *S. typhimurium* ATCC13311 stored in Brain Heart Infusion (BHI) broth was subcultured for testing in the same medium and grown at 37 °C. Then the bacterial cells were suspended, according to the McFarland protocol in saline solution [21], to produce a suspension of about 10^5 CFU mL^{-1} (colony-forming units per mL). Serial dilutions of the test compounds, previously dissolved in dimethyl sulfoxide (DMSO), were prepared in test tubes to final concentrations of 512, 256, 128, 64, 32, 16, 8, 4, 2, and 1 μg mL^{-1}; 100 μL of a 24-h-old-inoculum was added to each tube. The MIC, defined as the lowest concentration of the test compound, which inhibits the visible

growth after 20 h, was determined visually after incubation for 20 h at 37 °C. Tests using chloramphenicol as reference and DMSO as negative control were carried out in parallel. All tests were performed in triplicate with full agreement between results.

As previously, antifungal activity was evaluated by minimum inhibitory concentration (MIC) using the macro dilution test [19–21]. *C. albicans* (ATCC 18804) stored in Sabouraud broth, was subcultured for testing in the same medium and grown at 37 °C. Then the yeast cells were suspended, according to the McFarland protocol in saline solution [21], to produce a suspension of about 10^5 CFU mL^{-1}. Serial dilutions of the test compounds, previously dissolved in dimethyl sulfoxide (DMSO), were prepared in test tubes to final concentrations of 512, 256, 128, 64, 32, 16, 8, 4, 2, 1, 0.5, 0.3 and 0.1 μg mL^{-1}. 100 μL of a 24-h-old inoculum was added to each tube. The MIC was determined visually after incubation for 18 h at 37 °C and DMSO was used as negative control. All tests were performed in triplicate.

3. Results and discussion

Microanalyses suggest the formation of [CuLCl] for complexes **2**–**6**, in which the thiosemicarbazones coordinate as anionic ligands. The molar conductivity data reveal that the complexes are non-electrolytes [22], in accordance with the proposed formulations. The values of magnetic moments in the 1.73–2.03 BM range are close to the calculated value of 1.73 BM, characteristic of the presence of one unpaired electron as in copper(II) complexes.

Complexes **1** and **7**–**9** obtained previously [18,10] were formulated as $[Cu(HL)Cl_2]$, in which the thiosemicarbazones coordinate as neutral ligands. Once again the complexes are non-electrolytes, in agreement with the presence of two chlorides in the metal coordination sphere.

3.1. Structural characterization of H2Ac4mT and [Cu(2Ac4mT)Cl] (5)

The structure of H2Ac4mT was refined in the monoclinic system, $P2_1/c$ and that of [Cu(2Ac4mT)Cl] (**5**) in the triclinic system, $P\bar{1}$, both with one molecule in the asymmetric unit. Selected intra-molecular bond distances and angles are given in Table 2; hydrogen bond distances and angles are detailed in Table 3 and angles between planes in Table 4. The asymmetric units are shown in perspective in Figs. 2 and 3.

H2Ac4mT adopts the *EE* configuration in relation to the C7–N2 and C8–N3 bonds (see Fig. 1). In complex **5** the ligand adopts the *EZ*, configuration, to match the sterical requirements of coordination through the N_{py}–N–S chelating system. The C8–N3 bond distance goes from 1.359(3) Å in the free base to 1.311(5) Å in the complex, due to deprotonation at N3 and formation of new predominantly double bond. The C8–S bond changes from 1.671(3) Å in H2Ac4mT to 1.749(4) Å in complex **5** in agreement with deprotonation at N3 and formation of a thiolate bond. Significant modifications have also been observed in the bond angles upon coordination (see Table 2). For example, the N2–N3–C8 bond angle changes from 118.5(2)° in the free base to 111.6(3)° in the complex, and N3–C8–S goes from 120.3(2)° to 125.2(3)° (see Table 2).

The bond distances and angles in **5** are comparable to those related in the literature for copper(II) complexes containing anionic thiosemicarbazones [23].

In H2Ac4mT N3-H forms an intermolecular hydrogen bond with a sulfur of an adjacent molecule, N3–H···S1 ($-x$, $-y+1$, $-z+1$). In [Cu(2Ac4mT)Cl] (**5**) N4 is hydrogen bonded to a thiolate sulfur of a second adjacent molecule forming dimers (see Fig. 4); N4–H···S ($-x+1$, $-y+1$, $-z+2$), d(D–H) = 2.68 Å, ∠DHA = 173.4° and d(D···A) 3.539(3) Å (Table 3).

The C7–N2–N3–C8S1–N4 skeleton is approximately planar in the structures of both H2Ac4mT and complex **5**, with mean deviation from planarity of 0.0591 Å in the free thiosemicarbazone and 0.0132 Å in **5**.

The angle between the pyridine plane and the thiosemicarbazone moiety is 17.2° in H2Ac4mT and 2.6° in complex **5**. Similarly, the angle between the thiosemicarbazone chain and the tolyl ring is 65.4° in H2Ac4mT and 3.2° in **5**, due to the almost planar structure of the complex (see Table 4).

Table 2
Selected bond distances and angles for H2Ac4mT and [Cu(2Ac4mT)Cl] (**5**)

Atoms	H2Ac4mT (Å)	**5** (Å)	Atoms	H2Ac4mT (°)	**5** (°)
S1–C8	1.671(3)	1.749(4)	N2–N3–C8	118.5(2)	111.6(3)
N2–C7	1.289(3)	1.299(5)	N3–C8–S1	120.3(2)	125.2(3)
N2–N3	1.381(3)	1.380(4)	N4–C8–N3	114.8(2)	119.3(4)
N3–C8	1.359(3)	1.311(5)	N4–C8–S1	124.9(2)	115.3(3)
N4–C8	1.339(3)	1.353(5)	C7–N2–N3	119.0(2)	118.3 (3)
N4–C9	1.429(3)	1.419(5)	C8–N4–C9	125.7(2)	131.2(3)
Cu–N1		2.012(3)	N2–Cu–N1		80.5(1)
Cu–N2		1.960(3)	N2–Cu–S1		84.12(9)
Cu–S1		2.253(1)	N2–Cu–Cl1		175.2(1)
Cu–Cl1		2.211(1)	N1–Cu–Cl1		97.8(1)
			N1–Cu–S1		164.6(1)
			Cl1–Cu–S1		97.56(4)

Table 3
Hydrogen bonds parameters for H2Ac4mT and [Cu(2Ac4mT)Cl] (**5**)

Compound	D–H···A	*d* (D–H)	*d*(H···A)	DHA	*d*(D···A)
H2Ac4mT	N3–H···S1 [$-x, -y+1, -z+1$]	0.86	2.78	174.7	3.642(2)
[Cu(2Ac4mT)Cl]	N4–H···S1 [$-x+1, -y+1, -z+2$]	0.86	2.68	173.4	3.539(3)

Table 4
Angles between planes in the structures of H2Ac4mT and [Cu(2Ac4mT)Cl] (**5**)

Atoms defining the plane	Deviation from the plane (Å)		Angle between planes (°)	
	HAc4mT	**5**	H2Ac4mT	**5**
N1–C2–C3–C4–C5–C6	0.0021	0.0016	17.2(2)	2.6(2)
C7–N2–N3–C8–S1–N4	0.0591	0.0132		
C7–N2–N3–C8–S1–N4	0.0591	0.0132	65.39(8)	3.2(2)
C9–C10–C11–C12–C13–C14	0.0031	0.0068		

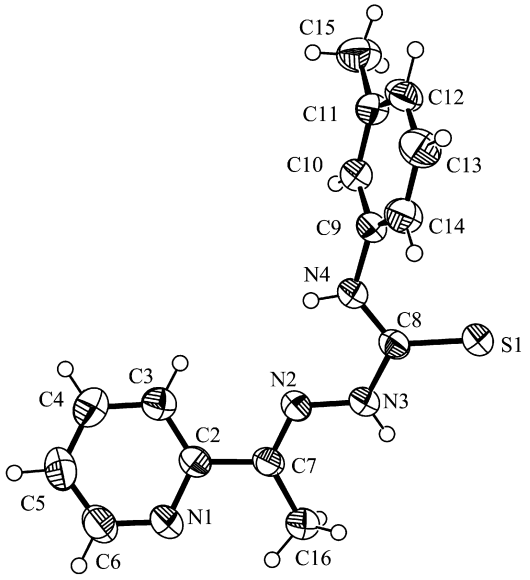


Fig. 2. Molecular plot of H2Ac4mT showing the labeling scheme of the non-H atoms with displacement ellipsoids at the 50% probability level.

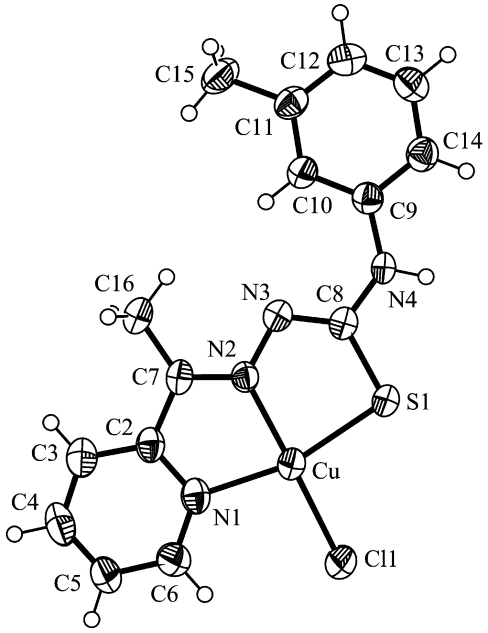


Fig. 3. Molecular plot of [Cu(2Ac4mT)Cl] (**5**) showing the labeling scheme of the non-H atoms with displacement ellipsoids at the 50% probability level.

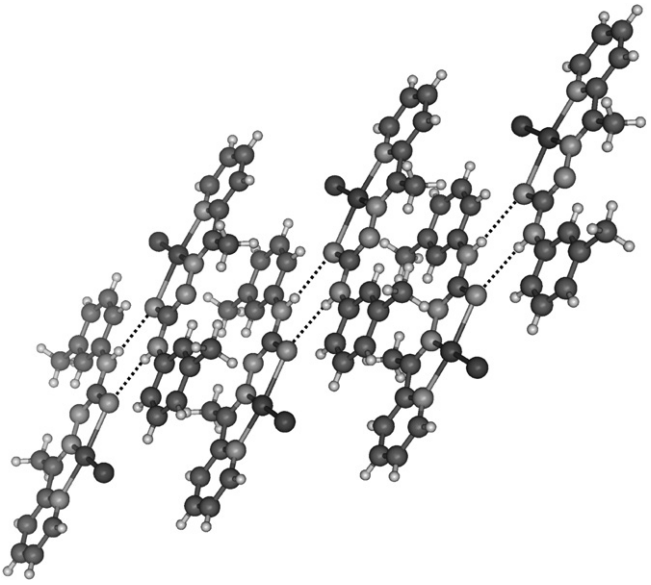


Fig. 4. Molecular packing of [Cu(2Ac4mT)Cl] (complex **5**) showing the presence of dimers.

3.2. Infrared spectra

The ν(C=C) + ν(C=N) composed mode observed in the 1608–1564 cm^{-1} in the spectra of the thiosemicarbazones shifts 1607–1538 cm^{-1} in the spectra of the complexes, indicating coordination of the azomethine nitrogen N2 [6–8,10].

The ν(C=S) absorption at 870–821 cm^{-1} in the spectra of the uncomplexed thiosemicarbazones is observed at 782–757 cm^{-1} in those of the complexes, in accordance with coordination through a thiolate sulfur. The 88–64 cm^{-1} shift observed upon complexation is compatible with coordination of an anionic thiosemicarbazone in all cases [6–9]. The pyridine in-plane deformation mode at 639–595 cm^{-1} in the spectra of the ligands shifts to 624–601 cm^{-1} in those of the complexes, suggesting coordination of the heteroaromatic nitrogen [6–8,10]. In addition, new absorptions at 460–416 cm^{-1} and 374–343 cm^{-1} have been attributed to ν(Cu–N) and ν(Cu–N_{py}), respectively,

and bands in the 341–329 cm^{-1} range have been assigned to ν(Cu–S). An absorption at 318–308 cm^{-1} has been attributed to ν(Cu–Cl) [23,24].

The infrared data for the complexes indicate coordination of the thiosemicarbazones through the N_{py}–N–S chelating system.

3.3. Electronic spectra

In the electronic spectra of the thiosemicarbazones (DMSO) the π–π* absorptions at ca. 37 000 cm^{-1} are not significantly modified upon complexation. The absorption at 31 153–30 395 cm^{-1} in the spectra of the free bases was attributed to n–π* transitions associated to the azomethine and thioamide [6–8,10] functions which overlap under the same envelope. In the spectra of complexes three absorptions were observed at 31 250–30 860 cm^{-1}, 27 780–26 600 cm^{-1} and 24 750–24 210 cm^{-1}. The first two were assigned to n–π* transitions of the azomethine and thioamide functions, and the latter to N–Cu^{II} and S–Cu^{II} ligand-to-metal charge transfer transitions [10,24]. Ligand field transitions were found at 16 650–16 304 cm^{-1} [10,24]. The electronic spectra of the solids are not significantly different, particularly in the d–d region.

3.4. ESR spectra

Fig. 5 shows the experimental EPR spectra in frozen DMF solution, liquid nitrogen (77 K), for the studied complexes. The Hamiltonian parameters obtained from the spectra, together with the d–d ligand field transitions, are resumed in Table 5.

The g values are in agreement with the relation $g_{\parallel} > g_{\perp} > 2$, indicating the presence of $d_{x^2-y^2}$ ground states. The $g_{\parallel}/A_{\parallel}$ ratio can be used as a convenient empirical index of distortion from square-planar structure. This value ranges from ca. 105 to 135 cm for square-planar structure, and this quotient increases on the introduction of tetrahedral distortion to the chromospheres [25]. The values of the $g_{\parallel}/A_{\parallel}$ ratio (Table 5) indicate nearly square-planar environments for complexes **2**–**6**, some with small distortions, which is in good agreement with the X-ray determined structure for complex **5**. The relatively low g values of the studied compounds are characteristic of an N enriched environment around the Cu(II) ions [26].

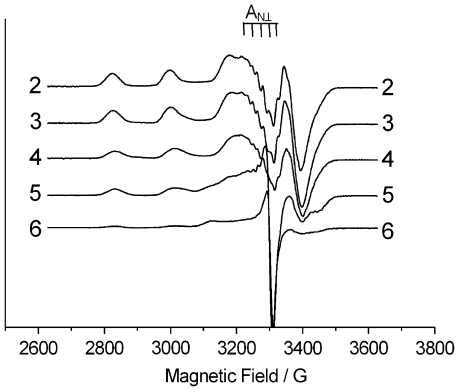


Fig. 5. X-band EPR spectra of [Cu(2Fo4mT)Cl] (**2**), [Cu(2Fo4pT)Cl] (**3**), [Cu(2Ac4oT)Cl] (**4**), [Cu(2Ac4mT)Cl] (**5**) and [Cu(2Ac4pT)Cl] (**6**) in DMF at 77 K (Inset: five perpendicular super-hyperfine interaction lines – $A_{N\perp} \approx 16 \times 10^{-4}$ cm^{-1} – of two ^{14}N ($I = 1$) atoms with the Cu(II) ions from each complex).

An interesting feature of the spectra is the appearance of nitrogen super-hyperfine lines (five lines) in the $g_{\perp}$ region, which generally mirror the number of nitrogen donors ($2nI + 1$, where $I = 1$ for nitrogen and n is the number of nitrogen atoms in the same chemical environment). The five lines correspond to two nitrogen donor atoms in the equatorial positions. The $A_{N\perp}$ values, around 16×10^{-4} cm^{-1} are in agreement with the imine/amine N coordination to the Cu(II) ions [27].

3.5. Antimicrobial activity

Table 6 lists the minimum inhibitory concentration (MIC) of the thiosemicarbazones and their copper(II) complexes against the growth of *S. typhimurium* and Table 7 lists the MIC against *C. albicans*. Included in this section are values previously obtained for 2-benzoylpyridine *N*(4)-tolyl thiosemicarbazones and their copper(II) complexes [10].

For the antibacterial action, MIC values in the 225–1478 μmol L^{-1} range were found for the thiosemicarbazones. Upon coordination, a substantial decrease in MIC was observed, with values in the 5–30 μmol L^{-1} range. Among the thiosemicarbazones, the lowest values of MIC were found for the 2-acetylpyridine derivatives, but in the complexes the lowest values were found for those with the 2-benzoylpyridine-derived thiosemicarbazones (**7**–**9**). The most significant decrease upon coordination occurred for these same complexes (Table 6). Interestingly, in the latter a neutral ligand is attached to the metal center, along with two chloride ions, forming species with coordination number five and with geometries which are different from that of complexes **2**–**6**.

To our knowledge this is one of the few cases of thiosemicarbazones' activity against *gram* negative bacilli, which indicates new possibilities of applications for this class of compounds.

Much lower values of MIC were obtained for the thiosemicarbazones against *C. albicans* (0.5–26 μmol L^{-1}) (Table 7), indicating selectivity. Upon coordination a decrease of the MIC values was observed as well, although not as significant as in the case of the antibacterial action, probably because the free thiosemicarbazones were already very active.

On complexation modifications of lipophilicity can occur [1,2]. Also, the rigid structure of the ligand in the complex could facilitate its interaction with the biological target, so that the metal complex may be a vehicle for activation of the ligand as the antimicrobial agent. Since the copper salt presents antimicrobial action as well, a syner-

Table 5
Ligand field transitions in the electronic spectrum of frozen DMF solution, at liquid N_2 temperature (77 K), parameters for the copper(II) complexes of *N*(4)-tolyl 2-formyl and *N*(4)-tolyl 2-acetylpyridine thiosemicarbazones

Compound	$g_{\parallel}$	$A_{\parallel}$[a]	$g_{\parallel}/A_{\parallel}$	$g_{\perp}$	$A_{\perp}$[a]	$A_{N\perp}$[a]	ΔE(d–d)[b]
[Cu(2Fo4mT)Cl] (**2**)	2.1850	177	123	2.0435	22	17	16703
[Cu(2Fo4pT)Cl] (**3**)	2.1830	177.5	122	2.0435	22	17	16920
[Cu(2Ac4oT)Cl] (**4**)	2.1745	182	119	2.0480	15	16	15818
[Cu(2Ac4mT)Cl] (**5**)	2.1740	162	134	2.0460	22	16	16958
[Cu(2Ac4pT)Cl] (**6**)	2.1745	184	118	2.0460	20	16	17240

[a] A values in 10^{-4} cm^{-1} units.
[b] ΔE(d–d) transitions, in cm^{-1} units, of the solid compounds.

Table 6
Minimum inhibitory concentration (MIC) against *Salmonella typhimurium* ATCC13311 for *N*(4)-tolyl 2-formyl, *N*(4)-tolyl 2-acetyl and *N*(4)-tolyl 2-benzoylpyridine thiosemicarbazones and their copper(II) complexes

Compounds	MIC (μmol L^{-1})	Complexes	MIC (μmol L^{-1})
H2Fo4oT	959	[Cu(HL1)Cl_2] (**1**)	30
H2Fo4mT	959	[Cu(2Fo4mT)Cl] (**2**)	24
H2Fo4pT	966	[Cu(2Fo4pT)Cl] (**3**)	20
H2Ac4oT	890	[Cu(2Ac4oT)Cl] (**4**)	21
H2Ac4mT	225	[Cu(2Ac4mT)Cl] (**5**)	15
H2Ac4pT	450	[Cu(2Ac4pT)Cl] (**6**)	13
H2Bz4oT	1478	[Cu(H2Bz4oT)Cl_2] (**7**)	12
H2Bz4mT	985	[Cu(H2Bz4mT)Cl_2] (**8**)	5
H2Bz4pT	985	[Cu(H2Bz4pT)Cl_2] (**9**)	8
Cloramphenicol	12	$CuCl_2 \cdot 2H_2O$	2663

Table 7
Minimum inhibitory concentration (MIC) against *Candida albicans* ATCC 18804 for *N*(4)-tolyl 2-formyl, *N*(4)-tolyl 2-acetyl and *N*(4)-tolyl 2-benzoylpyridine thiosemicarbazones and their copper(II) complexes

Compounds	MIC (μmol L^{-1})	Complexes	MIC (μmol L^{-1})
H2Fo4oT	3	[Cu(HL1)Cl_2] (**1**)	4
H2Fo4mT	3	[Cu(2Fo4mT)Cl] (**2**)	3
H2Fo4pT	3	[Cu(2Fo4pT)Cl] (**3**)	2
H2Ac4oT	14	[Cu(2Ac4oT)Cl] (**4**)	7
H2Ac4mT	5	[Cu(2Ac4mT)Cl] (**5**)	4
H2Ac4pT	26	[Cu(2Ac4pT)Cl] (**6**)	4
H2Bz4oT	6	[Cu(H2Bz4oT)Cl_2] (**7**)	2
H2Bz4mT	23	[Cu(H2Bz4mT)Cl_2] (**8**)	0.5
H2Bz4pT	0.7	[Cu(H2Bz4pT)Cl_2] (**9**)	0.3
Amphotericin B	4.4	$CuCl \cdot 2H_2O$	375

gistic effect of both ligand and metal acting together is also possible.

It is interesting to compare the values of MIC found for the studied complexes (5–30 μmol L^{-1} in the case of the antibacterial action and 0.3–7 μmol L^{-1} in the case of the antifungal action) with the values observed for the clinically used drugs chloramphenicol (12 μmol L^{-1}) and amphotericin (4.4 μmol L^{-1}). As already mentioned, resistance to used drugs has increased due to the increased and indiscriminate use of antibiotics and antifungal agents in the treatment of humans and animals [13].

These results suggest that coordination of the studied thiosemicarbazones with copper(II) could be an interesting strategy for preparing new antimicrobial agents which could be used against clinically significant bacteria and fungi cultures presenting resistance. In the case of the antifungal action, the free *N*(4)-tolyl thiosemicarbazones could be promising drug candidates, as well as their copper(II) complexes.

Structure–activity relationship analyses are presently underway in our laboratory as well as an investigation on the mechanisms of action of the studied compounds.

4. Supplementary material

CCDC 632461 and 632460 contain the supplementary crystallographic data for H2Ac4mT and [Cu(2Ac4mT)Cl] (**5**). These data can be obtained free of charge via http://www.ccdc.cam.ac.uk/conts/retrieving.html, or from the Cambridge Crystallographic Data Centre, 12 Union Road, Cambridge CB2 1EZ, UK; fax: (+44) 1223-336-033; or e-mail: deposit@ccdc.cam.ac.uk.

Acknowledgements

This work was supported by CNPq and Instituto do Milênio-Inovação e Desenvolvimento de Novos Fármacos e Medicamentos (IM-INOFAR, Proc. CNPq 420015/05-1).

References

[1] H. Beraldo, D. Gambino, Mini. Rev. Med. Chem. 4 (2004) 31 (and references therein).
[2] D.X. West, A. Liberta, S.B. Padhye, R.C. Chikate, P.B. Sonawane, A.S. Kumbhar, R.G. Yerande, Coord. Chem. Rev. 123 (1993) 49.
[3] D.X. West, S.B. Padhye, P.B. Sonawane, Struct. Bond. 76 (1991) 1.
[4] A.S. Dobek, D.L. Klayman, E.T. Dickson Jr., J.P. Scovill, E.C. Tramont, Antimicrob. Agents Chemother. 18 (1980) 27.
[5] A.S. Dobek, D.L. Klayman, J.P. Scovill, E.T. Dickson Jr., J. Chemother. 32 (1986) 25.
[6] A.P. Rebolledo, M. Vieites, D. Gambino, O.E. Piro, E.E. Castellano, C.L. Zani, E.M. Souza-Fagundes, L.R. Teixeira, A.A. Batista, H. Beraldo, J. Inorg. Biochem. 99 (2005) 698.

[7] A.P. Rebolledo, G.M. De Lima, L.N. Gambi, N.L. Speziali, D.F. Maia, C.B. Pinheiro, J.D. Ardisson, M.E. Cortés, H. Beraldo, Appl. Organometal. Chem. 17 (2003) 945.
[8] R.F.F. Costa, A.P. Rebolledo, T. Matencio, H.D.R. Calado, J.D. Ardisson, M.E. Cortès, B.L. Rodrigues, H. Beraldo, J. Coord. Chem. 58 (2005) 1307.
[9] B. Halova-Lajoie, V. Brumas, M.L. Fiallo, G. Berthon, J. Inorg. Biochem. 100 (2006) 362.
[10] I.C. Mendes, J.P. Moreira, L.N. Speziali, A.S. Mangrich, J.A. Takahashi, H. Beraldo, J. Braz. Chem. Soc. 17 (8) (2006) 1571.
[11] E.J. Threlfall, J.A. Frost, L.R. Ward, B. Rowe, Lancet 347 (1996) 1053.
[12] A. Valentin, R. Le Guennec, E. Rodriguez, J. Reynes, M. Mallie, J.M. Bastide, Antimicrob Agents Chemother. 40 (6) (1996) 1342.
[13] C.E. Briggs, P.M. Fratamico, Antimicrob. Agents Chemother. 43 (4) (1999) 846.
[14] G.M. Sheldrick, SHELXS-97; Program for the Solution of Crystal Structures, University of Göttingen, Germany, 1997.
[15] G.M. Sheldrick, SHELXL-97; Program for Crystal Structures Analysis, University of Göttingen, Germany, 1997.
[16] L.J. Farrugia, J. Appl. Cryst. 30 (1997) 565.
[17] L.J. Farrugia, J. Appl. Cryst. 32 (1999) 837.
[18] M.C. Miller, C.N. Stineman, J.R. Vance, D.X. West, I.H. Hall, Anticancer Res. 18 (1998) 4131 (and references therein).
[19] E.J.L. Lana, F. Carazza, J.A.J. Takahashi, Agric. Food Chem. 54 (2006) 2053.
[20] J.C.P. Resende, M.A. Resende, Mycoses 42 (1999) 641.
[21] National Committee for Clinical Laboratory Standards, Reference Method for Broth Dilution Antifungal Susceptibility Testing of Yeasts; Approved Standard-Second Edition. NCCLS document M27-A2 [ISBN 1-56238-469-4]. NCCLS, Pennsylvania, USA, 2002.
[22] W.J. Geary, Coord. Chem. Rev. 7 (1971) 81.
[23] D.X. West, J.S. Ives, J. Krejci, M. Salberg, T.L. Zumbahlen, G. Bain, A. Liberta, J.V. Martinez, S.H. Ortiz, R. Toscano, Polyhedron 14 (1995) 2189.
[24] M. Joseph, M. Kuriakose, P. Kurup, E. Suresh, A. Kishore, S.G. Bhat, Polyhedron 25 (2006) 61.
[25] S.M.M. Romanowski, F. Tormena, V.A. Santos, M.F. Hermann, A.S. Mangrich, J. Braz. Chem. Soc. 15 (6) (2004) 897.
[26] E. Guimarães, A.S. Mangrich, V.G. Machado, D.G. Traghetta, M.A. Lobo, J. Braz. Chem. Soc. 12 (2001) 734.
[27] E. Guimarães, A.S. Mangrich, V.G. Machado, D.G. Traghetta, M.A. Lobo, J. Braz. Chem. Soc. 12 (6) (2001) 734.

Available online at www.sciencedirect.com
ScienceDirect
Polyhedron 26 (2007) 3271–3276
POLYHEDRON
www.elsevier.com/locate/poly

Synthesis and spectral characterization of some complexes of platinum(II) containing η^2-methyleugenol

Tran Thi Da, Nguyen Thi Tuyet Minh, Nguyen Thi Thanh Chi, Nguyen Huu Dinh *

Department of Chemistry, Hanoi National Pedagogic University, Hanoi, Vietnam

Received 7 February 2007; accepted 3 March 2007
Available online 21 March 2007

Abstract

Several complexes of the formula *trans*-[Pt(Meug)(Am)Cl_2], Meug: methyleugenol (4-allyl-1,2-dimethoxybenzene), a η^2-coordinated olefin, and Am: ammine, methylamine, diethylamine, *o*-toluidine, *m*-toluidine, *p*-toluidine, *o*-anisidine, *m*-anisidine and *p*-anisidine have been prepared. UV, IR, Raman, ^{1}H NMR, ^{13}C NMR and 2D NMR spectra of the complexes were recorded and analyzed.
© 2007 Elsevier Ltd. All rights reserved.

Keywords: Platinum complexes; Olefin complexes; Methyleugenol; ^{1}H NMR; ^{13}C NMR

1. Introduction

Platinum–olefin complexes quite long ago attracted the attention of chemists [1,2]. Various olefin ligands have been used. Amongst the arylolefin ligands, phenylethylene (styrene) and substituted phenylethylenes were widely studied [3,4], but phenylpropylenes were rare. Today substituted phenylpropylenes, which are easily available from natural resources, have been used as valuable starting materials in various synthetic processes [5]. In many cases transition metals-olefin complexes are present as key intermediates.

Eugenol, izoeugenol and methyleugenol (4-allyl-1,2-dimethoxybenzene) represents interesting phenylpropylenes, extracted from essential clove oil, which can be transformed into coniferyl aldehyde, coniferyl alcohol, vanilin and vanillic acid, compounds commonly used in the flavour and fragrance industry [6]. In this paper we describe some platinum(II) complexes containing methyleugenol, which are prepared as follows:

$$K[Pt(C_2H_4)Cl_3] \xrightarrow{\text{Methyleugenol}} \underset{(\mathbf{1})}{K[Pt(Meug)Cl_3]} \xrightarrow{\text{Amine}} \underset{(\mathbf{2})\text{–}(\mathbf{10})}{\textit{trans}\text{-}[Pt(Meug)(Am)Cl_2]}$$

Meug: Methyleugenol (4-allyl-1,2-dimethoxybenzene, formula I).
Am: NH_3 (**2**), CH_3NH_2 (**3**), $(C_2H_5)_2NH$ (**4**), *o*-$CH_3C_6H_4NH_2$ (**5**), *m*-$CH_3C_6H_4NH_2$ (**6**), *p*-$CH_3C_6H_4NH_2$ (**7**), *o*-$CH_3OC_6H_4NH_2$ (**8**), *m*-$CH_3OC_6H_4NH_2$ (**9**), *p*-$CH_3OC_6H_4NH_2$ (**10**).

2. Results and discussion

The complexes [Pt(Meug)(Am)Cl_2] were prepared by replacement of a Cl ligand from K[Pt(Meug)Cl_3] (**1**) by an amine, Am. According to the *trans*-effect, the Cl ligand in the opposite position to Meug is replaced by the amine. For volatile amines such as methylamine, diethylamine and NH_3, the reaction was carried out at 10–15 °C, with 1.2 mmol of amine per 1 mmol of **1**. For toluidines and anisidines, the reaction was carried out at 25–30 °C, with 1.1 mmol of amine per 1 mmol of **1**. The neutral complexes [Pt(Meug)(Am)Cl_2] precipitate out and can be easily

* Corresponding author. Tel.: +84 4 8 346 632.
E-mail address: nguyenhuudinh1954@yahoo.com (N.H. Dinh).

0277-5387/$ - see front matter © 2007 Elsevier Ltd. All rights reserved.
doi:10.1016/j.poly.2007.03.017

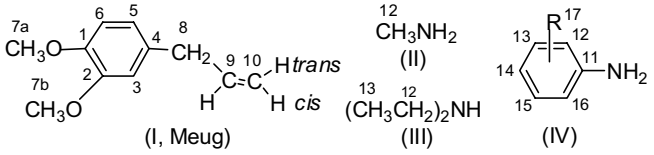
isolated, then purified by recrystallizing from aqueous EtOH solution.

The molar conductivity (μ) of 10^{-4} M K[Pt(Meug)Cl_3] solution is 95 Ω^{-1} cm^2 mol^{-1}. The molar conductivity (μ) of a $5.10^{-5} - 10^{-4}$ M solution of *trans*-[Pt(Meug)(Am)Cl_2] is in the range 15–22 Ω^{-1} cm^2 mol^{-1}, indicating its non-electrolytic nature (Table 1).

The electronic spectra of the synthesized complexes are given in Table 1. All the examined complexes are slight soluble. Their spectra were recorded at a concentration as small as 10^{-4} M in 96% by volume aqueous EtOH. Thus only charge-transfer and ligand spectra were obtained.

In Table 1, the *v*(Pt–N), *v*(Pt–Cl) values were taken from the Raman spectra. Because the intensity of *v*(NH) in the Raman spectra was too weak, the *v*(NH) value was taken from the IR spectra. These values are in general agreement with those in the literature [1,7].

The NMR data of the examined compounds are presented in Tables 2–4. The numeration of the examined compounds for the analysis of the NMR spectra is as follows:



The assignment of the NMR signals is based on their chemical shift, spin-spin splitting patterns, HMQC, HMBC and NOESY spectra. For example, the assignment of some ambiguous signals from the ^{13}C NMR spectrum of complex **8** and then the signals of H7a, H7b, H17 have been assigned as illustrated in Fig. 1.

In Fig. 1, the signals of all the protons, except H-7a, H-7b and H-17, have been unambiguously assigned, the signals of ring carbons are thus identified. Two cross peaks *a* and *b* of H-16 (7.29 ppm) show that two signals at 152.0 and 127.0 ppm belong to C-12 and C-14, respectively. Two cross peaks *c*, *d* of H-14 (7.15 ppm) show signals of C-12 (152.0), C-16 (124.1). Two cross peaks *e*, *f* of H-13 (6.98 ppm) show signals of C-11 (130.52), C-15 (121.81). Two cross peaks *g*, *h* of H-5 (6.96 ppm) show signals of C-1 (148.83), C-3 (113.88). Two cross peaks *i*, *k* of H-6 (6.86 ppm) show signals of C-2 (150.11), C-4 (132.3). Two cross peaks *l*, *m* of H-15 (6.88 ppm) show signals of C-11 (130.52), C-13 (112.88). The cross peaks of C-12, C-2 and C-1, in turn, allow one to distinguish the signals of H-17, H-7b and H-7a.

Upon coordination to Pt(II), the resonances of the ethylenic protons (H-9, H-10 *cis* and H-10 *trans*, Table 2) are upfield in comparison to those of non-coordinated methyleugenol (5.86, 4.96 and 4.98 ppm, respectively). The ^{195}Pt satellites in the signals from H-9 are broadened beyond detection, but two satellites in the signals from H-10 *cis* and H-10 *trans* are clear, with a $^2J_{PtH}$ value of 60–70 Hz (Table 2). The resonances of the ethylenic carbons (C-9, C-10) are upfield too (Table 4). These indicate that methyleugenol is present as an η^2-coordinated olefin.

For non-coordinatinated methyleugenol, two protons H-8 (formula I) give rise to a doublet at 3.22 ppm with $^3J = 6.5$ Hz, but in the spectra of the examined complexes we usually observed one doublet of doublets centered at 3.38–3.55 ppm for H-8a and another doublet of doublets centered at 3.01–3.21 ppm for H-8b. This is expected since upon coordination to Pt(II), atom C-9 becomes a chiral center, and H-8a and H-8b become diastereotopic.

It is interesting that in ^1H NMR and ^{13}C NMR spectra of *trans*-[Pt(Meug)(Et_2NH)Cl_2] (**4**), recorded in d_6-acetone, two CH_2 groups of diethylamine give rise to two complicated proton signals (one multiplet centered at 2.88 ppm and another at 3.17 ppm, H12a and H12b in Fig. 2) and two ^{13}C signals at 49.67 and 49.69 ppm; two CH_3 groups give rise to two triplets (one centered at 1.400 and another at 1.395 ppm) and the two ^{13}C signals are at 14.67 and 14.74 ppm. This anomaly also happens in the spectra of **4** recorded in CD_3CN. It is noted that we have just prepared *trans*-[Pt(Saf)(Et_2NH)Cl_2] (**4a**) and *trans*-[Pt(Saf)(Me_2-NH)Cl_2] (**4b**) (Saf: 4-allyl-1,2-methylendioxybenzene, Et: $-CH_2CH_3$, Me: CH_3). In the spectra of **4a** recorded in d_6-acetone, two CH_2 groups of diethylamine give rise to two complicated proton signals (one multiplet centered at

Table 1
Molar conductivity (μ), the main bands in UV-, IR- and Raman spectra of the synthesized complexes

Compound	μ, Ω^{-1} cm^2 mol^{-1}	λ_{max} (nm)/log ε	*v* (NH) (IR, cm^{-1})	*v* (Pt–N) (Raman cm^{-1})	*v* (Pt–Cl) (Raman cm^{-1})
1	95	231/4.25; 284/3.38; 341/3.37			330
2	22	240/3.98; 280/3.82	3274, 3191	525	335
3	21	230/3.78; 279/3.17	3270, 3221	525	336
4	20	231/4.03; 279/3.90	3224	492	334
5	15	232/4.16; 276/3.86	3225, 3203	485	333
6	18	232/4.06; 279/3.75	3302, 3225	470	332
7	16	230/4.27; 274/4.00	3282, 3220	489	340
8	19	233/4.25; 283/3.96	3248, 3213	489	331
9	17	230/3.78; 281/3.27	3283, 3233	485	338
10	18	225/4.43; 279/4.16	3293, 3229	502	340

Table 2
The resonances of protons H-3 to H-9 of the examined complexes, δ (ppm), J (Hz)

Compound (solvent)	H-3	H-5	H-6	H-7a	H-7b	H-8a	H-8b	H-9
1	7.36 d	6.93 dd	6.91 d	3.87 s	3.89 s	2.90 dd	3.49 dd	5.21 m
(CD_3OD)	^4J 1.5	^3J 8, ^4J 1.5	^3J 8	[a]	[a]	^2J 15, ^3J 6.5	^2J 15, ^3J 7	
2	6.87 s	6.89 dd	6.84 d	3.89 s	3.87 s	3.21 dd	3.55 dd	5.60 m
($CDCl_3$)		^3J 8, ^4J 1.5	^3J 8			^2J 15, ^3J 8	^2J 15, ^3J 6	
3	6.87 d	6.89 dd	6.84 d	3.89 s	3.87 s	3.21 dd	3.52 dd	5.59 m
($CDCl_3$)	^4J 1.5	^3J 8, ^4J 1.5	^3J 8			^2J 15, ^3J 7.5	^2J 15, ^3J 6.5	
4	7.02 d	6.92 dd	6.90 d	3.83 s	3.78 s	3.19 dd	3.43 dd	5.45 m
(CD_3COCD_3)	^4J 2	^3J 8, ^4J 2	^3J 8			^2J 15, ^3J 7.5	^2J 15, ^3J 6.5	
5	6.97 s	6.92 dd	6.88 d	3.78 s	3.76 s	3.09 dd	3.42 dd	5.53 m
(CD_3COCD_3)		^3J 8.5, ^4J 1.5	^3J 8.5			^2J 15, ^3J 6	^2J 15, ^3J 7.5	
6	6.99 d	6.95 dd	6.77 d	3.78 s	3.75 s	3.01 dd	3.39 dd	5.40 m
(CD_3CN)	^4J 2	^3J 8, ^4J 2	^3J 8			^2J 15, ^3J 6.5	^2J 15, ^3J 8	
7	6.97 s	6.94 dd	6.78 d	3.79 s	3.75 s	3.01 dd	3.38 dd	5.39 m
(CD_3COCD_3)	^4J 2	^3J 8, ^4J 2	^3J 8			^2J 15, ^3J 6	^2J 15, ^3J 8	
8	7.00 d	6.96 dd	6.86 d	3.80 s	3.76 s	3.03 dd	3.40 dd	5.44 m
(CD_3CN)	^4J 1.5	^3J 8, ^4J 1.5	^3J 8			^2J 15, ^3J 6	^2J 15, ^3J 7.5	
9	7.03 d	6.92 dd	6.81 d	3.79 s	3.78 s	3.08 dd	3.45 dd	5.42 m
(CD_3COCD_3)	^4J 2	^3J 8.5, ^4J 2	^3J 8.5			^2J 15, ^3J 6.5	^2J 15, ^3J 7.5	
10	7.01 d	6.95 dd	6.80 d	3.79 s	3.75 s	3.06 dd	3.41 dd	5.38 m
(CD_3COCD_3)	^4J 2	^3J 8, ^4J 2	^3J 8			^2J 15, ^3J 6.5	^2J 15, ^3J 7.5	

[a] Because of methanol.

Table 3
The resonances of protons H-10 to H-17 of the examined complexes, δ (ppm), J (Hz)

Compound[a]	H-10 *cis*	H-10 *trans*	H-12	H-13	H-14	H-15	H-16	Others
1	4.30 d	4.46 d						
(a)	^3J 7.5, J_{PtH} 70	^3J 7.5, J_{PtH} 70						
2	4.62 dd, ^2J 1,	4.69 dd, ^2J 1,						3.55 s: NH_3
(b)	^3J 8, J_{PtH} 65	^3J 14, J_{PtH}65						
3	4.56 dd,^2J 1,	4.69 dd,^2J 1,	2.66 t,					3.85 s: NH_2
(b)	^3J 7.5, J_{PtH} 70	^3J 14, J_{PtH} 70	^3J 6.5					
4	4.40 dd, ^2J 1.5,	4.53 dd, ^2J 1.5	3.17 m,	1.400 t,				5.28 s: NH
(c)	^3J 8, J_{PtH} 68	^3J 14, J_{PtH} 64	2.88 m	1.395 t				
5	4.44 d	4.54 d		7.13 dd	7.08 td	7.07 td	7.24 dd	
(c)	^3J 8, J_{PtH} 68	^3J 14, J_{PtH} 68		^3J 6.5, ^4J 2	^3J 7, ^4J 2	^3J 7, ^4J 2	^3J 7, ^4J 2	2.28 s: H-17
6	4.43 d	4.55 d	7.08 s		7.03 d	7.19 t	7.06 d	6.40 s: NH_2
(d)	^3J 7.5, J_{PtH} 68	^3J 14, J_{PtH} 68			^3J 7.5	^3J 7.5	^3J 8	2.31 s:H-17
7	4.42 d	4.53 d	7.15 d	7.11 d		7.11 d	7.15 d	6.39 s: NH_2
(c)	^3J 7.5, J_{PtH} 65	^3J 14, J_{PtH} 65	^3J 8.5	^3J 8.5		^3J 8.5	^3J 8.5	2.30 s: H-17
8	4.44 d	4.57 d		6.99 dd	7.15 td	6.87 td	7.29 dd	6.16 s: NH_2
(d)	^3J 7, J_{PtH} 65	^3J 15, J_{PtH} 65		^3J 8, ^4J 1.5	^3J 8, ^4J 1.5	^3J 8, ^4J 1.5	^3J 8, ^4J 1.5	3.83 s: H-17
9	4.41 dd, ^2J 1.5	4.54 dd, ^2J 1.5	7.07 t		6.88 dd	7.26 t	7.02 d	7.35 s: NH_2
(c)	^3J 7.5, J_{PtH} 65	^3J 14, J_{PtH} 65	^4J 2		^3J 8.5, ^4J 2	^{3}J8.5	^3J 8.5	3.80 s: H-17
10	4.37 dd, ^2J 1.5	4.49 dd, ^2J 1.5	7.34 d	6.87 d		6.87 d	7.34 d	7.25 s: NH_2
(c)	^3J 7.5, J_{PtH} 65	^3J 14, J_{PtH} 65	^3J 9	^3J 8		^3J 8	^3J 9	3.81 s: H-17

[a] Solvent, a: CD_3OD, b: $CDCl_3$, c: CD_3COCD_3, d: CD_3CN.

2.87 ppm and another at 3.18 ppm) and two ^{13}C signals at 49.67 and 49.71 ppm; two CH_3 group give rise to one proton signal (at 1.408 ppm) but two ^{13}C signals (at 14.64 and 14.74 ppm). In the spectra of **4b** recorded in d_6-acetone, two CH_3 groups of dimethylamine give rise to two proton signals (at 2.65 and 2.70 ppm) and two ^{13}C signals (at 40.09 and 41.99 ppm). The analogous appearance was still observed when d_6-acetone was replaced by CD_3CN or CD_3Cl. Whilst for *cis*-[Pt(Morpholine)(Et_2NH)Cl_2], the two CH_2 groups of ethylamine give rise to one proton signal, and the two CH_3 groups of ethylamine also give rise to one proton signal [7], for *trans*-[$PtCl_2(C_2H_4)(Et_2NH)$] the two CH_2 groups of ethylamine give rise to one carbon signal (at 48.979 ppm), and the two CH_3 groups of ethylamine also give rise one carbon signal (at 14.699 ppm) and one proton signal (at 1.573 ppm). This asks the question, what causes the two ethyl groups in *trans*-[Pt(Meug)(Et_2NH)Cl_2] to become non-equivalent?

To answer this, we recorded NOESY spectra of **4**, **4a**, **4b**, **7** and **8**. The signals of H-9, H-10 *cis and* H-10 *trans* of all the 10 complexes are shaped and resolved. The cross peaks *n* and *p* (Fig. 2) indicate that only group CH_2-a (H-12a) is adjacent

Table 4
^{13}C NMR signals of complexes **1**–**10**, δ (ppm) (For numeration of the C atoms see formula I–IV, for solvents see Table 2)

	1	2	3	4	5	6	7	8	9	10
C-1	148.97	149.08	147.81	149.21	149.06	148.80	148.89	148.83	148.10	148.79
C-2	150.38	150.41	149.03	150.52	150.39	150.08	150.17	150.11	150.40	150.08
C-3	114.29	113.87	112.24	114.07	113.11	112.74	112.90	113.88	111.70	112.74
C-4	133.74	132.56	131.03	132.24	132.08	132.26	132.39	132.30	130.68	132.30
C-5	122.10	121.62	120.84	121.81	121.83	121.84	121.89	121.47	121.83	121.85
C-6	113.21	113.08	111.49	113.28	113.85	113.79	113.93	112.85	113.07	113.83
C-7a	56.58	56.18	55.97	56.27	56.21	56.32	56.42	56.25	56.08	56.30
C-7b	56.54	56.08	55.97	56.12	56.08	56.28	56.34	56.27	55.76	56.27
C-8	39.87	40.14	40.10	40.13	39.70	39.80	39.82	39.89	40.01	39.77
C-9	92.11	98.01	99.71	99.21	101.44	100.48	100.45	99.64	101.08	100.62
C-10	65.20	69.26	69.35	69.19	70.08	69.21	69.20	68.45	70.04	69.19
C-11					146.39	140.82	138.52	130.52	132.29	133.30
C-12			32.22	49.71	132.12	127.18	130.67	152.00	116.48	124.30
				49.67						
C-13				14.74	121.87	140.31	122.66	112.88	161.23	115.29
				14.67						
C-14					127.46	120.10	135.99	126.98	113.63	158.55
C-15					128.05	123.38	122.66	121.81	113.92	115.29
C-16					131.59	130.05	130.67	124.11	131.00	124.30
C-17					19.13	21.41	20.94	56.83	56.21	56.21

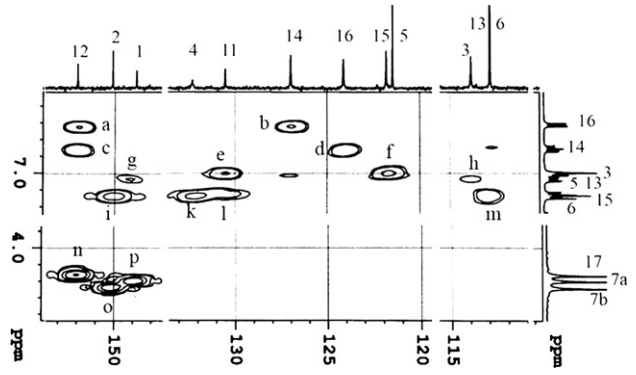


Fig. 1. A part of the HMBC spectrum of [Pt(Meug)(*o*-CH_3O-$C_6H_4NH_2$)Cl_2] (**8**).

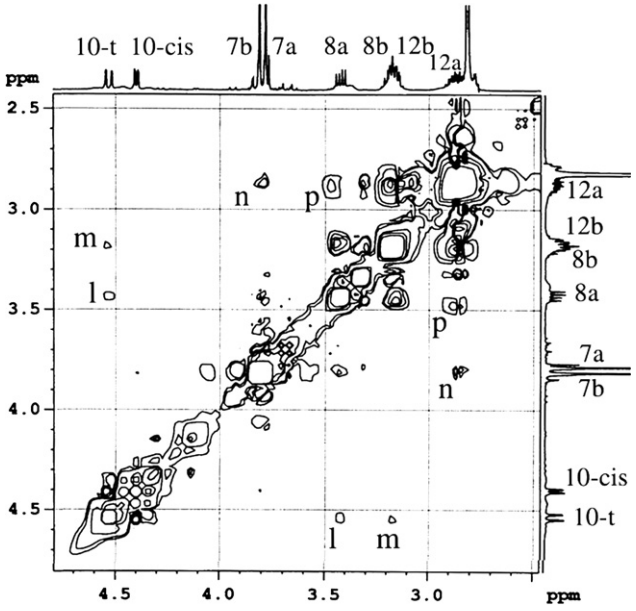


Fig. 2. A part of the NOESY spectrum of [Pt(Meug)(Et_2NH)Cl_2] (**4**).

to the protons H-7b and H-8a, while group CH_2-b (H-12b) is not. This demonstrates that a rotation around the coordination axes (Pt–olephin bond and Pt–N bond) does not occur on the NMR timescale at the recorded temperature. Thus the atom Pt becomes asymmetrical.

3. Experimental

Elemental analysis: Pt was analyzed according to the weight method [8], and C, H, N analyses were performed at the Ho Chi Minh City Center of Analytical Service. Experimentation used an automatic elemental analyzer. The molar conductivity was measured using a conductivity Meter HI 88119 N. The UV spectra were recorded on a GCB Instrument-2855 spectrophotometer. The Raman spectra were carried out on a Micro Raman LABRAM in the range 4000–100 cm^{-1}, using excited radiation at 632.8 nm from a heli-neon laser. The IR spectra were recorded on an IMPACK-410 NICOLET spectrometer in KBr discs in the range 400–4000 cm^{-1}. The NMR spectra were recorded on a Bruker AVANCE 500 MHz, all at 298–300 K, with TMS as the internal standard in a suitable solvent (Tables 2 and 3).

3.1. 4-Allyl-1,2-dimethoxybenzene (Methyleugenol, Meug)

Methyleugenol is prepared by reaction of eugenol (from *Ocimum Sanetum* L.) with dimethyl sulfate in alkaline medium, Bp. (15 mm Hg), 125–126 °C; (125–127 °C, according to [9]). ^1H NMR ($CDCl_3$, δ, ppm, J, Hz, formula I): 6.61, d, ^4J 1.8, 1H: H3; 6.62, dd, ^3J 8, ^4J 1.8, 1H: H5; 6.68, d, ^3J 8, 1H: H6; 3.73, s, 3H, 3.75, s, 3H: H7a, H7b; 3.22, d, ^3J 6.5, 2H: H8; 5.86, m, 1H: H9; 4.96, m, *J cis* 7, 1H: H10 *cis*; 4.98, m, *J trans* 12.5, 1H: H10 *trans*.

3.2. Potassium trichloro(methyleugenol)platinat(II), K[Pt(Meug)Cl$_3$] (**1**)

To a stirred solution of 3.68 g (10 mmol) of Zeise's salt in 80 ml of ethanol was slowly added a solution of 2.5 ml (16 mmol) of methyleugenol in 20 ml of ethanol. The reaction mixture was stirred at 40–45 °C for an hour. Then it was allowed to cool to room temperature. Yellow plate crystals were collected and washed with cool water, then cool ethanol, and were then dried in a vacuum at 50 °C for 2 h. The yield was 4.15 g (80%). For ^{1}H and ^{13}C NMR see Tables 2–4. *Anal.* Calc. for $KPtC_{11}H_{14}O_2Cl_3$: Pt + K_2SO_4, 54.39; C, 24.46; H, 2.70. Found: Pt + K_2SO_4, 54.75; C, 24.18; H, 2.54%.

3.3. trans-Dichloro(methyleugenol)(ammine)platinum(II), [Pt(Meug)(NH$_3$)Cl$_2$] (**2**)

K[Pt(Meug)Cl$_3$] (0.518 g, 1 mmol) was dissolved in 16 ml of 50% by volume aqueous EtOH. To this solution 8 ml of 1.5 M NH_3 solution was slowly added over 30 minutes and stirred at 10–15 °C for an additional 3 h. The resulting yellow precipitate was collected, washed with a solution of 0.1 N HCl, cool water, cool ethanol and recrystallized from 75% by volume aqueous EtOH. The light yellow crystals were dried in a vacuum at 50 °C for 2 h. The yield was 0.32 g (70%). *Anal.* Calc. for [$PtC_{11}H_{17}NO_2Cl_2$]: Pt, 42.30; C, 28.63; H, 3.69; N, 3.04. Found: Pt, 42.58; C, 28.40; H, 3.88; N, 2.82%.

3.4. trans-Dichloro(methyleugenol)(methylamine)-platinum(II), [Pt(Meug)(MeNH$_2$)Cl$_2$] (**3**)

This complex was prepared starting from 0.52 g (1 mmol) K[Pt(Meug)Cl$_3$] and 1.3 ml aqueous solution of 30% methylamine (1.2 mmol), according to the procedure for the preparation of **2**. The yield was 0.36 g (75%), light yellow crystals. *Anal.* Calc. for [$PtC_{12}H_{19}NO_2Cl_2$]: Pt, 41.05; C, 30.32; H, 4.00; N, 2.95. Found: Pt, 41.30; C, 29.98; H, 4.12; N, 2.76%.

3.5. trans-Dichloro(methyleugenol)(diethylamine)-platinum(II), [Pt(Meug)(Et$_2$NH)Cl$_2$] (**4**)

This complex was prepared starting from 0.52 g (1 mmol) K[Pt(Meug)Cl$_3$], 0.13 ml (1.2 mmol) diethylamine, according to the procedure for the preparation of **2**. The yield was 0.36 g (70%), light yellow crystals. *Anal.* Calc. for [$PtC_{15}H_{25}NO_2Cl_2$] (%): Pt, 37.72; C, 34.82; H, 4.83; N, 2.71. Found: Pt, 37.58; C, 34.98; H, 4.62; N, 2.89%.

3.6. trans-Dichloro(methyleugenol)(o-toluidine)platinum(II), [Pt(Meug)(o-$CH_3C_6H_4NH_2$)Cl$_2$] (**5**)

This complex was prepared starting from 0.52 g (1 mmol) K[Pt(Meug)Cl$_3$], 0.12 ml (1.1 mmol) *o*-toluidine, at 25–30 °C, according to the procedure for the preparation of **2**. The yield was 0.44 g (80%), light yellow crystals. *Anal.* Calc. for [$PtC_{18}H_{23}NO_2Cl_2$]: Pt, 35.39; C, 39.20; H, 4.17; N, 2.54. Found: Pt, 35.52; C, 39.48; H, 4.32; N, 2.32%.

3.7. trans-Dichloro(methyleugenol)(m-toluidine)-platinum(II), [Pt(Meug)(m-$CH_3C_6H_4NH_2$)Cl$_2$] (**6**)

This complex was prepared starting from 0.52 g (1 mmol) K[Pt(Meug)Cl$_3$], 0.118 g (1.1 mmol) *m*-toluidine, at 25–30 °C, according to the procedure for the preparation of **2**. The yield was 0.40 g (75%), light yellow crystals. *Anal.* Calc. for [$PtC_{18}H_{23}NO_2Cl_2$]: Pt, 35.39; C, 39.20; H, 4.17; N, 2.54. Found: Pt, 35.25; C, 39.37; H, 4.35; N, 2.65%.

3.8. trans-Dichloro(methyleugenol)(p-toluidine)-platinum(II), [Pt(Meug)(p-$CH_3C_6H_4NH_2$)Cl$_2$] (**7**)

This complex was prepared starting from 0.52 g (1 mmol) K[Pt(Meug)Cl$_3$], 0.118 g (1.1 mmol) *p*-toluidine, at 25–30 °C, according to the procedure for the preparation of **2**. The yield was 0.38 g (70%), light yellow crystals. *Anal.* Calc. for [$PtC_{18}H_{23}NO_2Cl_2$]: Pt, 35.39; C, 39.20; H, 4.17; N, 2.54. Found: Pt, 35.51; C, 39.38; H, 4.36; N, 2.72%.

3.9. trans-Dichloro(methyleugenol)(o-anisidine)-platinum(II), [Pt(Meug)(o-$CH_3OC_6H_4NH_2$)Cl$_2$] (**8**)

This complex was prepared starting from 0.52 g (1 mmol) K[Pt(Meug)Cl$_3$], 0.11 ml (1.1 mmol) *o*-anisidine, at 25–30 °C, according to the procedure for the preparation of **2**. The yield was 0.48 g (84%), light yellow crystals. *Anal.* Calc. for [$PtC_{18}H_{23}NO_3Cl_2$] (%): Pt, 34.39; C, 38.09; H, 4.06; N, 2.47. Found: Pt, 34.54; C, 38.22; H, 4.21; N, 2.33%.

3.10. trans-Dichloro(methyleugenol)(m-anisidine)-platinum(II), [Pt(Meug)(m-$CH_3OC_6H_4NH_2$)Cl$_2$] (**9**)

This complex was prepared starting from 0.52 g (1 mmol) K[Pt(Meug)Cl$_3$], 0.11 ml (1.1 mmol) *m*-anisidine, at 25–30 °C, according to the procedure for the preparation of **2**. The yield was 0.45 g (81%), light yellow crystals. *Anal.* Calc. for [$PtC_{18}H_{23}NO_3Cl_2$] (%): Pt, 34.39; C, 38.09; H, 4.06; N, 2.47. Found: Pt, 34.21; C, 38.25; H, 3.87; N, 2.62%.

3.11. trans-Dichloro(methyleugenol)(p-anisidine)-platinum(II), [Pt(Meug)(p-$CH_3OC_6H_4NH_2$] (**10**)

This complex was prepared starting from 0.52 g (1 mmol) K[Pt(Meug)Cl$_3$], 0.123 g (1.1 mmol) *p*-anisidine, at 25–30 °C, according to the procedure for the preparation of **2**. The yield was 0.46 g (82%), light yellow crystals. *Anal.* Calc. for [$PtC_{18}H_{23}NO_3Cl_2$] (%): Pt, 34.39; C, 38.09; H, 4.06; N, 2.47. Found: Pt, 34.26; C, 37.91; H, 4.26; N, 2.29%.

References

[1] Umberto Belluco, Organometallic and Coordination Chemistry of Platinum, Academic press, London and NewYork, 1974.
[2] M.R. Plutino, S. Otto, A. Roodt, L.I. Elding, Inorg. Chem. 38 (1999) 1233.
[3] T. Kinugasa, M. Nakamura, H. Yamada, A. Saika, Inorg. Chem. 7 (1968) 2649.
[4] S. Shinoda, Y. Yamaguchi, Y. Saito, Inorg. Chem. 18 (1979) 673.
[5] L. Colla'r, E. Farkas, J. B©tiv, J. Mol. Catal. A: Chem. 115 (1977) 283.
[6] E. Simo0ni, T. Baasov, U. Ravid, Y. Shoham, J. Biotechnol. 105 (2003) 61.
[7] Nguyen Huu Dinh, Tran Thi Da, J. Coord. Chem. 57 (2003) 485.
[8] A.D. Ghelman, E.F. Karandasova, L.N. Essen, Izv. Sectora Platinum, Inst. Obsch. Nheorg. Khim. AN SSSR 24 (1949) 68.
[9] J. Buckingham, Dictionary of Organic Compounds, Vol. 4, Chapman & Hall, New York – London – Toronto, 1982.

Available online at www.sciencedirect.com
ScienceDirect
Polyhedron 26 (2007) 3277–3285
POLYHEDRON
www.elsevier.com/locate/poly

X-ray structure and EPR behavior of a new dimeric copper(II) complex with 4-amino-*N*-(5-methoxy-2-pyrimidinyl)benzenesulfonamide

J. Ellena [a], E. Kremer [b], G. Facchin [b], E.J. Baran [c], O.R. Nascimento [d], A.J. Costa-Filho [d], M.H. Torre [b,*]

[a] *Laboratorio de Cristalografía, Instituto de Física de São Carlos, Universidade de São Paulo, C.P. 369, 13560 São Carlos (SP), Brazil*
[b] *Química Inorgánica, DEC, Facultad de Química, Universidad de la República, Gral. Flores 2124, CC1157 Montevideo, Uruguay*
[c] *Centro de Química Inorgánica (CEQUINOR/CONICET, UNLP), Facultad de Ciencias Exactas, Universidad Nacional de La Plata, 1900-La Plata, Argentina*
[d] *Grupo de Biofísica Sérgio Mascarenhas, Instituto de Física de São Carlos, Universidade de São Paulo, C.P. 369, 13560 São Carlos (SP), Brazil*

Received 26 October 2006; accepted 3 March 2007
Available online 12 March 2007

Abstract

A new complex, $[Cu_2(sulfameter)_4]_3 \cdot 2.5H_2O$ (sulfameter = 4-amino-*N*-(5-methoxy-2-pyrimidinyl)benzenesulfonamide), has been synthesized. Its structure has been determined by single-crystal X-ray diffraction and its spectroscopic properties (EPR, IR, Raman, UV–Vis) have been analyzed. The structure presented three different dimeric units in the unit cell and the EPR spectra, characteristic of antiferromagnetically coupled dimers, revealed two magnetically different dimeric environments.
© 2007 Elsevier Ltd. All rights reserved.

Keywords: Copper complexes; Sulfameter; Crystal structure; EPR

1. Introduction

There are many topics of considerable importance in sulfonamide coordination chemistry. In the analytical area, sulfonamides have been investigated as reagents for the separation, concentration, and selective determination of many of the first-row transition metal cations [1–3]. As a result, analytical tests using reactions with sulfonamides, have been included in modern pharmacopoeias (Ph.Eur, BP, USP). Moreover, some sulfonamide complexes have proved to be relevant catalysts in chemical reactions, such as Zn-sulfonamide complexes that catalyzes enantioselective cyclopropanations [4] and also as reagents for the cleavage of nucleic acids [5–7]. On the other hand, numerous sulfonamide complexes have been studied as simple models of metal–protein interactions [8–11].

In addition, some metal sulfonamides have drawn much attention due to the fact that they are used in medicine especially as antibacterial drugs. It is known that coordination with metals can modify the toxicological and pharmacological properties of free sulfonamides [12–17].

In all the above reported areas knowledge of the structure of the involucrate sulfonamide complexes is extremely useful for understanding their activity.

Due to their versatility, these ligands can act as monodentate, bidentate or polydentate coordinating groups, providing monomeric structures, dimeric, and polymeric arrangements [8,18–21]. Sulfameter (4-amino-*N*-(5-methoxy-2-pyrimidinyl)benzenesulfonamide), a well-known antibacterial sulfadrug, has several groups with donor atoms that can interact with metal ions, such as the ^{4}N from aryl amine, the ^{1}N and O from the sulfonamide group, and heterocyclic N (N_h) as shown in Fig. 1. In spite of the fact that a copper complex with sulfameter is reported [22] until now no single-crystal X-ray diffraction studies have been performed.

* Corresponding author. Tel.: +598 2 9249739; fax: +598 2 9241806.
E-mail address: mtorre@fq.edu.uy (M.H. Torre).

0277-5387/$ - see front matter © 2007 Elsevier Ltd. All rights reserved.
doi:10.1016/j.poly.2007.03.005

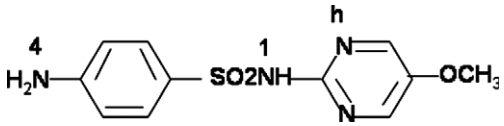


Fig. 1. Sulfameter (4-amino-*N*-(5-methoxy-2-pyrimidinyl)benzenesulfonamide) scheme.

As a part of our work on biologically interesting copper complexes [21,23–25] and with the aim to contribute with structural information useful for the general understanding of the microbiological behavior of metal–sulfonamide complexes, the synthesis and structural characterization of $[Cu_2(sulfameter)_4]_3 \cdot 2.5H_2O$ were reported. Its structure was analyzed and compared with spectroscopic results. Although there are different molecules with sulfonamides reported with similar dimeric Cu–Cu interactions [26–31], this structure presented three dimeric units in the unit cell and the EPR spectra revealed two magnetically different dimeric environments.

2. Experimental

2.1. Materials and methods

Sulfameter and $CuSO_4 \cdot 5H_2O$ were provided by SIGMA and Fluka, respectively, and all reagents were of analytical grade.

The decomposition point was measured with a Gallenkamp apparatus.

The elemental analysis was performed with a Carlo Erba EA1108 elemental analyzer. The copper content was determined by iodometric method.

X- (9.5 GHz) and Q-band (35 GHz) EPR measurements were carried out on polycrystalline samples using a Varian E109 spectrometer and cavities with 100 kHz field modulation. The measurements were performed at room temperature and a Cr(III) ($g = 1.9797$) sample was used for field calibration. The *g*-values and zero-field splitting (D and E terms) of the spin Hamiltonian were obtained from the simultaneous spectral simulation of the X- and Q-band spectra using the EasySpin program.

IR spectra, in the range between 4000 and 200 cm^{-1}, were recorded on a BOMEM M 102 FTIR spectrophotometer using the KBr pellet technique.

Raman spectra were scanned on a Brucker FRA 106 instrument mounted on an IFS 66 Fourier transform optical bench. A Nd/YAG laser (power = 100 mW) was used for excitation.

Electronic spectra were registered on a Beckman DU 70 spectrophotometer using a suspension in Nujol.

2.2. Synthesis of $[Cu_2(sulfameter)_4]_3 \cdot 2.5H_2O$

The complex was synthesized according to the procedure described by Bult et al. [32]. A solution of NaOH 1 M was added drop wise over a suspension of sulfameter (2.8 g, 10 mmol) in 100 mL of water until total dissolution (pH 9–10). To the resulting solution 50 mL of 0.5 M $CuSO_4 \cdot 5H_2O$ was added with stirring. After half an hour the brown precipitate formed was filtered, washed with water, dried at room temperature and protected from light. The complex was recrystallized from acetone. Yield (4.6 g, 73%). The decomposition point was 226 °C. The results of the elemental analysis were: *Anal*. Calc. for $[Cu_2(sulfameter)_4]_3 \cdot 2.5H_2O$ ($C_{132}H_{137}N_{48}O_{38.5}S_{12}Cu_6$): C, 41.97; N, 17.81; H, 3.63; S, 10.17; Cu, 10.10. Found: C, 41.86; N, 17.70; H, 3.70; S, 9.93; Cu, 10.22%.

2.3. Crystal structure determination

Low temperature X-ray diffraction data collection was performed at 150(2) K, on an Enraf-Nonius Kappa-CCD diffractometer equipped with an Oxford Cryosystem liquid N_2 device, using graphite-monochromated MoKα radiation (0.71073 Å). Data were collected up to 50.8° in 2θ, with a redundancy of 4 in the ϕ scans mode. The final unit cell parameters were based on all reflections. Data collections were made using the COLLECT program [33]. Integration and scaling of the reflections were performed with the HKL Denzo–Scalepack system of programs [34]. Multi-scan absorption correction was applied [35].

The structures were solved by direct methods with SHELXS-97 [36]. The models were refined by full-matrix least squares on F^2 with SHELXL-97 [37]. All the hydrogen atoms were stereochemically positioned and refined with the riding model [37]. Hydrogen atoms of the CH and CH_2 groups were set isotropic with a thermal parameter 20% greater than the equivalent isotropic displacement parameter of the atom to which each one was bonded. This percentage was set to 50% for the hydrogen atoms of the CH_3 groups and the water molecules. Data collections and experimental details for the complexes are summarized in Table 1. The programs SHELXL-97 and ORTEP-3 [38] were used within WinGX [39] to prepare materials for publication. Atomic coordinates, bond lengths and angles, and thermal parameters have been deposited at the Cambridge Crystallographic Data Centre.

3. Results and discussion

The synthesis of the complex was performed in an alkaline medium were the deprotonation of the amide group took place, additionally favored by the coordination through this group. Consequently, the copper complex was neutral.

The experimental elementary analysis values are in reasonable agreement with the calculated ones.

3.1. Crystal structure determination of $[Cu_2(sulfameter)_4]_3 \cdot 2.5H_2O$

The unit cell comprises three slightly different dimeric units. Fig. 2 presents an ORTEP diagram of one of these

Table 1
Crystal data and structure refinement of $[Cu_2(sulfameter)_4]_3 \cdot 2.5H_2O$

Empirical formula	$[C_{44}H_{44}N_{16}O_{12}S_4Cu_2]_3 \cdot 2.5H_2O$
Formula weight	3777.86
Crystal system	monoclinic
Space group	$P2_1/c$
Unit cell dimensions	
a (Å)	19.567(1)
b (Å)	43.197(2)
c (Å)	18.885(1)
β (°)	97.494(2)
Volume (Å^3)	15825.9(14)
Z	4
D_{calc} (Mg/m^3)	1.586
Absorption coefficient (mm^{-1})	1.043
$F(000)$	7756
Crystal size (mm)	$0.20 \times 0.12 \times 0.04$
θ Range for data collection (°)	2.92–25.40
Index ranges	$-23 \leqslant h \leqslant 23$, $-50 \leqslant k \leqslant 52$, $-22 \leqslant l \leqslant 22$
Reflections collected	55826
Independent reflections [R(int)]	28930 [0.2094]
Completeness to theta = 25.4°	99.5%
Absorption correction	semi-empirical from equivalents
Maximum and minimum transmission	0.9403 and 0.8022
Data/restraints/parameters	28930/1/2146
Goodness-of-fit on F^2	1.020
Final R indices [$I > 2\sigma(I)$]	$R_1 = 0.0793$, $wR_2 = 0.0949$
R indices (all data)	$R_1 = 0.2604$, $wR_2 = 0.1276$
Largest difference in peak and hole (e Å^{-3})	0.561 and −0.455

dimeric units, showing the atoms labeling and the 30% probability ellipsoids.

Each copper atom of the dinuclear unit is four-coordinated with a slightly distorted square planar environment. It is bonded to four sulfameter ligands through two N_h pyridazine atoms from two sulfameter molecules and two ^{1}N atoms from the other sulfameter ligands as scheme in Fig. 3 shows. In the coordination polyhedra both N_h atoms are in trans position and consequently the ^{1}N atoms show the same disposition.

In addition, each copper interacts with two sulfonamide O atoms, as Fig. 3 shows and as it can be inferred from the IR spectrum. This coordination environment is different from that previously suggested for a similar copper complex ($[Cu(sulfameter)_2] \cdot 3H_2O$) were the spectroscopic data indicated the coordination through the sulfonyl oxygen and sulfonamide nitrogen [22]. The two copper ions of each unit are bridged by four-triatomic ^{1}N–C–N_h chemical path (see Fig. 3).

Fig. 4 shows the disposition of the three slightly different dimeric units in the unit cell.

Selected bond distances and angles around the copper atoms for the three dimeric units are presented in Table 2. For the sake of clarity the N atoms are labeled with the nomenclature noted in Fig. 1 and not to the ORTEP diagram.

As shown in Table 2, in some copper centers the Cu–N_h bond distances are shorter than the Cu–N^1 ones, while in other centers the opposite behavior is observed. However, in all cases the Cu–N_h ($\Delta = 1.951$–2.025 Å) and the Cu–^{1}N ($\Delta = 1.993$–2.036 Å) bond lengths are in the range of those previously reported in similar copper complexes with sulfonamides [19,21,5]. The Cu–Cu distances in the unit 1 and 2 are similar to those of most of the structurally related complexes [19,28,40,41]. On the opposite, unit 3 presented a short Cu–Cu distance (2.535 Å) comparable with those of several complexes like $[Cu_2(CH_3COO)_4(H_2O)_2] \cdot 2dmf$ (2.541 Å) [42], $[Cu_2(N\text{-}p\text{-tolylsulfonyl pyridine})_4]$ (2.516 Å), and $[Cu_2(1,3\text{-di-phenyltriazenato})_4]$

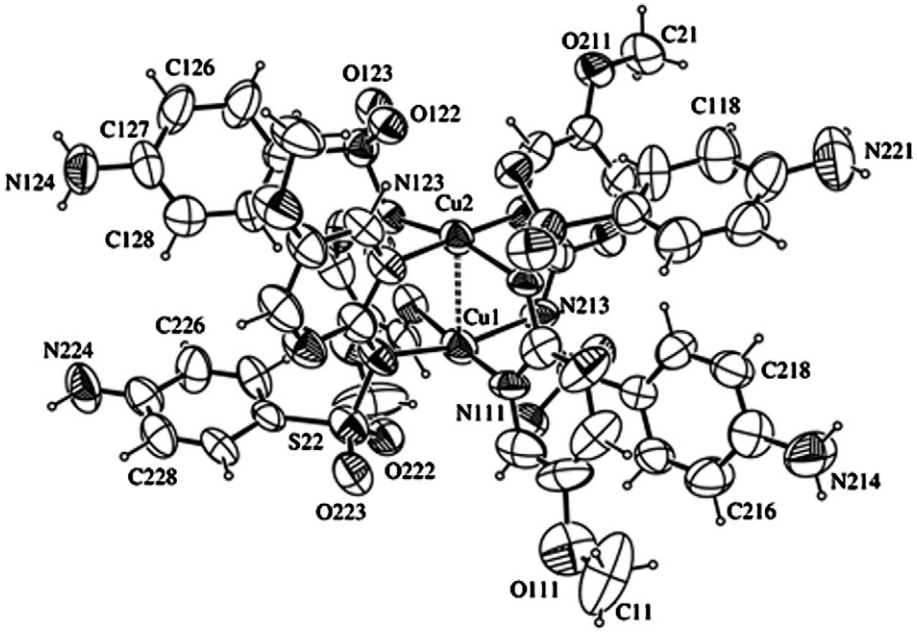


Fig. 2. ORTEP view of a dimeric unit of $[Cu_2(sulfameter)_4]_3 \cdot 2.5H_2O$, showing the atoms labeling and the 30% probability ellipsoids.

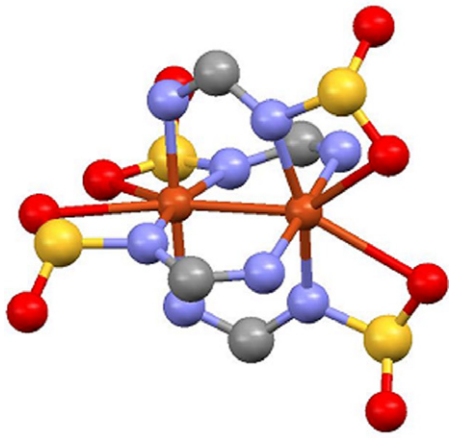


Fig. 3. Scheme of copper coordination environment.

(2.441 Å) [43]. This different Cu–Cu bond length in unit 3 seems to be related to an increment in two of the four Cu–O distances (see Table 2). It is interesting to observe that, in the three units, the sulfonamidic O atoms participate in a short interaction with the pyrimidinic N atoms, not bonded to the metal (ranging between 2.85(1) and 3.04(1) Å), forming a five member ring.

The square planar geometry of all copper ions presents distortions as it is shown in the Cu–N_4 plane distances in Table 2.

The bond angles of the Cu–N_4 square plane are close to 90°. The Cu–N_4 planes of each dimeric unit are almost coplanar and perpendicular to the Cu–Cu axes. Besides, the angles between the Cu–Cu axes for units 1 and 3 are almost parallel ($\alpha = 17.79(4)°$) while for unit 1 and 2 are almost perpendicular ($\alpha = 89.90(3)°$). The N1–C–Nh angles of the unit 3 bridge are slightly greater than those of the dimeric units 1 and 2.

Taking into account these results, it can be said that units 1 and 2 present little difference between each other, differing by the orientation of the cyclic groups and their substituents while unit 3 differs in several bond distances and angles, principally in the Cu–Cu distance.

The study of the crystal packing shows that the three-dimensional structure is stabilized by several networks of inter- and intra-molecular interactions (see Table 3). The structure shows four H-bond intra-unit between the Nh and the sulfonic O of the same sulfonamide. Besides, three H-bond inter-unit are formed: one of them between the sulfonic O of one unit and the ^{4}N of the second unit, the second one between the O from the –OCH_3 of one unit and the N_h of the other unit, and the third between two sulfonic oxygen of different units. The water molecules bond the dimeric units 2 and 3 through moderated hydrogen bonds [44] involving the O atoms from the –SO_2 groups, whereas unit 1 does not have any interaction with the water molecules. An interesting feature of this complex's crystal packing is that ligand arrangement gives rise to a hydrophilic region formed by the NH_2–Ar, the –SO_2N–, and the –OCH_3 groups placed to the external surface of a cylindrical area with a hydrophobic region in the inside. However, no stacking between the aromatic rings is observed.

3.2. Vibrational spectra

The IR and Raman spectra of the complex were compared with those of previously reported complexes

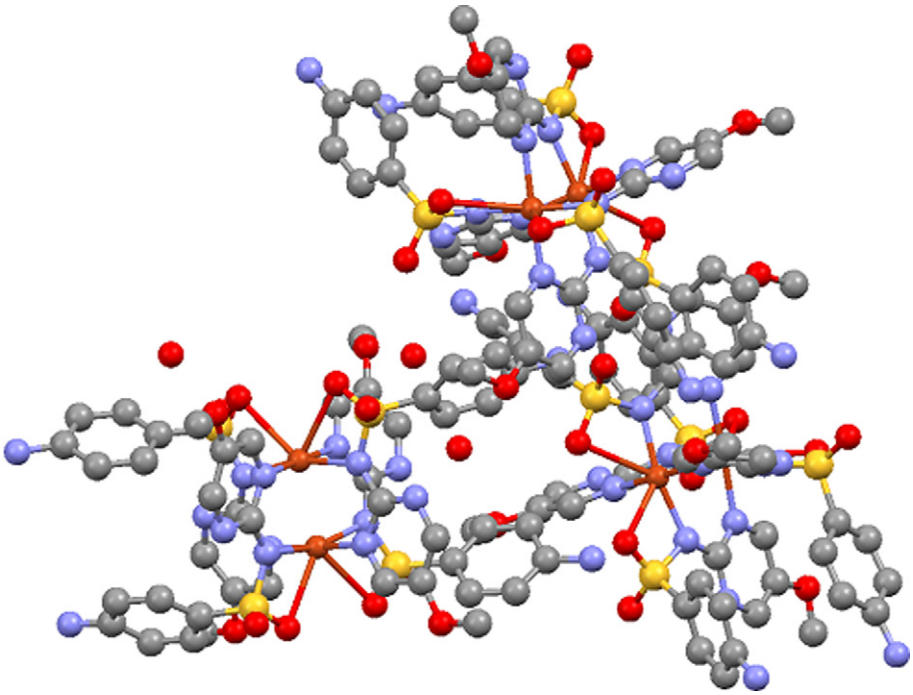


Fig. 4. ORTEP view of the asymmetric unit of $[Cu_2(sulfameter)_4]_3 \cdot 2.5H_2O$.

Table 2
Selected bond distances (Å) and angles (°) for the three dimeric units of $[Cu_2(sulfameter)_4]_3 \cdot 2.5H_2O$

Unit 1	Cu1–Nh	2.027(6)/1.956(7)	Cu2–Nh	2.017(6)/1.990(6)
	Cu1–N1	2.009(6)/2.008(6)	Cu2–N1	2.016(5)/2.012(6)
	Cu1–$O_{sulfonic}$	2.679(6)/2.566(6)	Cu2–$O_{sulfonic}$	2.725(6)/2.485(6)
	Cu1–N_4 plane	0.1919(9)	Cu2–N_4 plane	0.1731(9)
	Cu1–Cu2 2.557(1)			
	Nh–Cu1–N1	90.8(2)/88.3(2)/89.2(2)/90.8(2)	Nh–Cu2–N1	90.5(2)/89.5(2)/89.0(2)/90.5(2)
	N1–Cu1–N1	164.0(2)	N1–Cu2–N1	164.8(2)
	Nh–Cu1–Nh	176.9(3)	Nh–Cu2–Nh	177.5(3)
	Nh–Cu1–Cu2	91.3(2)/85.7(2)	Nh–Cu2–Cu1	92.0(2)/86.0(2)
	N1–Cu1–Cu2	79.90(18)/84.19(17)	N1–Cu2–Cu1	79.66(16)/85.16(17)
	^{1}N–C–N_h	113.9(9)/115.0(9)/115.8(9)/118.0(9)		
Unit 2	Cu3–Nh	1.990(6)/1.990(6)	Cu4–Nh	2.012(6)/2.005(6)
	Cu3–N1	2.034(5)/2.008(5)	Cu4–N1	2.022(6)/2.005(5)
	Cu3–$O_{sulfonic}$	2.626(6)/2.545(6)	Cu4–$O_{sulfonic}$	2.600(6)/2.552(6)
	Cu3–N_4 plane	0.1773(8)	Cu4–N_4 plane	0.1437(8)
	Cu3–Cu4 2.556(1)			
	Nh–Cu3–N1	90.7(2)/89.9(2)/89.8(2)/89.1(2)	Nh–Cu4–N1	90.0(2)/88.4(2)/90.0(2)/91.5(2)
	N1–Cu3–N1	164.1(3)	N1–Cu4–N1	165.0(2)
	Nh–Cu3–Nh	177.8(3)	Nh–Cu4–Nh	178.3(2)
	Nh–Cu3–Cu4	89.2(2)/88.7(2)	Nh–Cu4–Cu3	90.46(19)/88.9(2)
	N1–Cu3–Cu4	82.47(16)/81.67(16)	N1–Cu4–Cu3	81.88(17)/83.24(17)
	^{1}N–C–N_h	114.6(9)/116.6(9)/115.1(9)/115.3(9)		
Unit 3	Cu5–Nh	1.992(7)/1.990(6)	Cu6–Nh	2.018(6)/2.016(7)
	Cu5–N1	2.034(6)/1.978(6)	Cu6–N1	1.997(7)/1.992(6)
	Cu5–$O_{sulfonic}$	2.798(6)/2.509(6)	Cu6–$O_{sulfonic}$	2.749(6)/2.549(6)
	Cu5–N_4 plane	0.1647(9)	Cu6–N_4 plane	0.1519(9)
	Cu5–Cu6 2.535(1)			
	Nh–Cu5–N1	90.2(3)/88.0(2)/90.3(2)/90.3(2)	Nh–Cu6–N1	91.5(2)/90.1(3)/87.1(2)/90.5(2)
	N1–Cu5–N1	167.7(3)	N1–Cu6–N1	167.6(3)
	Nh–Cu5–Nh	174.6(4)	Nh–Cu6–Nh	175.5(3)
	Nh–Cu5–Cu6	86.6(2)/88.2(3)	Nh–Cu6–Cu5	89.5(2)/86.1(2)
	N1–Cu5–Cu6	85.74(18)/82.04(19)	N1–Cu6–Cu5	84.47(18)/83.3(2)
	^{1}N–C–N_h	116.7(9)/117.5(9)/119.0(9)/117.1(9)		

[14,18,20,45–53]. Table 4 summarizes the main bands and their proposed assignments.

In Table 4, the bands of the complex assigned to ν_a(NH) and ν_s(NH) appeared at similar frequencies to those obtained for the free sulfameter, which agree with the fact that the amino group did not participate in the coordination. The Raman spectrum of the complex did not show these bands in accordance with the bibliographic data [53]. Furthermore, δNH_2 bands are almost unchanged in the IR spectra and have exhibited no Raman signals.

The free ligand spectrum presented a strong broad band at 3230 cm^{-1} possibly involving the NH stretching of the sulfonamide group and other vibrational modes characteristic of ligand. In the complex spectrum this band changed to a medium-intensity signal at 3238 cm^{-1}. The change in this band is probably due to the disappearance of the ν(NH) of the sulfonamide group after deprotonation, remaining the other vibrational modes of the molecule. This behavior was previously reported in other copper complexes with sulfonamides [54].

The heteroaromatic ring motions cannot be interpreted as simple vibrational modes as most of them are of complex origin and involve different vibrational types. Some ring absorption bands can shift upon complexation to metal ions through the nitrogen atom, but most of them are not metal-dependent. As shown Table 5, only one band presented a significant shift ($\Delta = 21$ cm^{-1}) to lower frequencies, while in most bands no change was observed.

The asymmetric and symmetric $-SO_2$ group stretching vibrations shifted to lower frequencies in the copper complex ($\Delta = 40$ cm^{-1} and $\Delta = 27$ cm^{-1}, respectively). This behavior is in accordance with the fact that each copper interacts with two sulfonamide O atoms from two different sulfameter molecules as shown in Fig. 2.

Furthermore, complex spectrum showed a broad band at 3580 cm^{-1} assigned to the presence of a water molecule in the complex. Other bands corresponding to water molecule modes could not be assigned due to the fact that they were overlapped with other signals.

3.3. Electronic spectrum

The copper complex presented three wide bands at 358, 557, and 841 cm^{-1}. According to some authors, the band at

Table 3
Intra- and inter-molecular hydrogen bonds in the three dimeric units of $[Cu_2(sulfameter)_4]_3 \cdot 2.5H_2O$

D–H···A	D–H (Å)	D···A (Å)	H···A (Å)	D–H···A (°)
Intra-molecular interactions				
N324–H32B···O113	0.880	3.155(7)	2.642(4)	118.2(4)
N424–H42A···O123	0.880	3.002(8)	2.182(5)	154.8(4)
N424–H42B···O512	0.880	2.885(8)	2.016(5)	168.8(4)
O1W–H11W···O423	0.850	2.865(9)	2.200(4)	135.0(5)
O1W–H12W···O613	0.850	2.785(9)	1.936(5)	176.8(5)
O2W–H21W···O423	0.850	3.236(7)	2.648(5)	127.5(4)
O2W–H21W···N422	0.850	2.829(8)	2.544(6)	100.8(4)
O2W–H21W···O1W	0.850	3.015(9)	2.785(8)	97.4(4)
O2W–H22W···O511	0.850	2.955(8)	2.108(6)	174.2(4)
O2W–H22W···O1W	0.850	3.015(9)	2.682(8)	104.9(4)
O3W–H31W···O413	0.850	2.896(8)	2.106(5)	154.5(4)
Inter-molecular interactions				
N224–H22C···O123^{i}	0.880	3.011(8)	2.146(5)	167.7(4)
N224–H22D···O512^{i}	0.880	2.993(8)	2.131(5)	166.5(4)
N124–H12A···O523^{i}	0.880	2.979(8)	2.259(5)	139.0(4)
N214–H21A···O422^{ii}	0.880	3.089(8)	2.315(4)	146.7(4)
N214–H21B ···O321^{ii}	0.880	3.294(9)	2.536(6)	144.7(5)
N221–H22B ···O311^{ii}	0.880	2.875(9)	2.066(5)	152.5(5)
N624–H62A···O322^{iii}	0.880	3.092(7)	2.290(4)	151.5(4)
N324–H32A···O2W^{iii}	0.880	2.932(7)	2.084(5)	161.3(4)
N221–H22A···O311^{iii}	0.880	3.14(1)	2.678(6)	113.6(5)
N221–H22A···O423^{iii}	0.880	3.195(8)	2.733(4)	114.1(5)
N514–H51B···O313^{iii}	0.880	2.970(7)	2.105(4)	167.5(4)
N314–H31B···O112^{iv}	0.880	3.208(7)	2.372(4)	158.7(4)
N314–H31B ···N112^{iv}	0.880	3.20(1)	2.593(8)	127.2(4)
N314–H31A ···O521^{v}	0.880	3.327(9)	2.935(7)	109.0(4)
N414–H41B···O623^{v}	0.880	2.955(7)	2.120(4)	158.0(4)
N314–H31A···O3W^{vi}	0.880	2.985(9)	2.146(6)	159.2(4)
N414–H41A···N412^{vi}	0.880	3.105(9)	2.235(7)	169.7(4)
O3W–H32W···O622^{vii}	0.850	2.989(7)	2.299(5)	138.5(4)
O3W–H32W···O623^{vii}	0.850	3.234(7)	2.443(4)	155.0(4)
N614–H61B···O213^{viii}	0.880	3.282(8)	2.549(5)	141.3(4)
N614–H61B···N212^{viii}	0.880	3.126(9)	2.347(7)	147.6(4)
N524–H52A···O213^{viii}	0.880	3.04(1)	2.206(5)	157.4(6)
N514–H51A···O221^{ix}	0.880	2.907(8)	2.114(5)	149.5(4)
N624–H62B···O323^{ix}	0.880	2.918(8)	2.170(5)	142.4(4)
N614–H61A···O222^{x}	0.880	2.995(7)	2.202(4)	149.7(4)

Symmetry codes: i: $x, -y-1/2, +z+1/2$; ii: $x+1, +y, +z$; iii: $-x-1, -y, -z-1$; iv: $-x-1, -y, -z$; v: $-x-2, -y, -z-1$; vi: $-x-2, -y, -z$; vii: $x, +y, +z+1$; viii: $x-1, +y, +z$; ix: $x, +y, +z-1$; x: $x-1, -y-1/2, +z-1/2$.

Table 4
Characteristic IR and Raman (R) bands (cm^{-1}) of the spectra of sulfameter and $[Cu_2(sulfameter)_4]_3 \cdot 2.5H_2O$ complex

IR (Sulfameter)	IR $[Cu_2(sulfameter)_4]_3 \cdot 2.5H_2O$	R $[Cu_2(sulfameter)_4]_3 \cdot 2.5H_2O$	Assignment
–	3580 (m)	–	ν(OH)
3465 (s)	3467 (br, s)	–	$\nu_{as}(NH_2)$
3370 (s)	3369 (s)	–	$\nu_{s}(NH_2)$
3230 (s)	3238 (m)	–	ν(NH)sulf.
3072 (w)	3068 (w)	3065 (w)	ν(=CH)pyrimidine ring
1632 (s)	1630 (m)	–	$\delta(NH_2)$
1594 (s), 1502 (s)	1596 (s), 1503 (m)	1596 (s)	ν(C=C) aromatic
1569 (s),1464 (s), 1422 (s)	1548 (m), 1464 (s), 1422 sh	1500 (vw), 1455 (w), 1428 (w)	ν pyrimidinic ring
1320 (s, br)	1280 (s)	1285 (w)	$\nu_{as}(SO_2)$
1152 (s, br)	1125 (s)	1126 (s)	$\nu_{s}(SO_2)$
1090 (s)	1082 (s)	1086 (w)	δ(CH) aromatic

ν (stretching), ν_a (asymmetric stretching), ν_s (symmetric stretching), br (broad), s (strong), m (medium), w (weak), (–) no band.

358 cm^{-1} is related to a binuclear nature of copper complexes [32], while other authors assigned it as either metal–ligand [14,45] or ligand–metal [50] charge transfers. In this case, the first assignment is in accordance with the structure found for the complex. In spite of this, there are different copper-sulfonamide complexes which present

Table 5
EPR parameters obtained by spectral simulation using EASYSPIN Program for $S = 1$ paramagnetic system

Dimer species	g-Factor (± 0.001)	D (cm^{-1})	E (cm^{-1})	$A_{\parallel}$ (MHz)
1	$g_z = 2.240$	0.12	0.002	230
	$g_y = 2.039$			
	$g_x = 2.041$			
2	$g_z = 2.250$	0.18	0.005	275
	$g_y = 2.043$			
	$g_x = 2.043$			

The experimental spectra used in simulation were measured at X- and Q-band spectrometer at room temperature.

this band and do not bear dimeric structure [21]. The other two bands correspond to d–d transitions [51].

3.4. EPR measurements

The X-band EPR spectrum (Fig. 5A) of the title complex shows major lines centered at ~150, ~270, ~315, and ~380 mT. This set of resonances can be rationalized in terms of a coupled dimmer ($S = 1$) of Cu(II) ions. The copper coupling is antiferromagnetic as determined from the absence of EPR signal at 4 K, which indicates a $S = 0$ ground state for the spin system. The $g = 2$ (~315 mT) resonance in this case is most likely due to mononuclear impurities in the sample.

In the $S = 1$ case, the zero-field contribution gives rise to two allowed transitions per principal direction (x, y, z) [55], thus yielding a six-line pattern in the EPR spectrum [56]. The resonance fields for each of those transitions are denoted H_{x1}, H_{x2}, H_{y1}, H_{y2}, H_{z1}, H_{z2}, and expressions for them can be found elsewhere [57]. The two major lines observed in Fig. 5A result from the overlap at X-band of resonance corresponding to H_{x1} and H_{y1} (~270 mT) and H_{x2} and H_{y2} (~380 mT). The H_{z2} EPR signal is barely seen as a slight shoulder around ~420 mT. Another resonance is observed at ca. 150 mT (Fig. 5A) and is due to a collapse of the half-field transition ($\Delta M_s = \pm 2$), present in coupled systems, with the H_{z1} resonance. At Q-band (Fig. 5B), the otherwise overlapped signals corresponding to the half-field (~580 mT) and H_{z1} (~990 mT) transitions are clearly resolved. The other resonance in the $g \sim 2$ region can also be unambiguously assigned to the additional peaks observed in the spectrum ($H_{x1}, H_{y1} \sim 1150$ mT and $H_{x2}, H_{y2} \sim 1250$ mT). Moreover, the Q-band spectrum reveals extra peaks that indicate the existence of a second magnetically non-equivalent copper dimer (see calculated spectra for each component in Fig. 5B). This second less intense component presents the same pattern of resonance fields discussed above.

To further investigate the origin of the spectra at both frequencies, we firstly performed spectral simulation of the Q-band spectrum (Fig. 5B) using the EasySpin package [58]. This software has been recently made available to the EPR community and is designed to address several types of EPR simulations including solid-state spectra of both single crystals and disordered systems with any electronic spin S. In our case, the spin Hamiltonian includes the following interactions:

$$\mathscr{H} = \beta B \cdot g \cdot S + S \cdot D \cdot S + S \cdot A \cdot I$$

where B is the applied magnetic field, g is the gyromagnetic tensor, D is the *zero-field interaction* or spin–spin tensor and A is the hyperfine interaction. The experimental spectrum was simulated with two sets of g-values (Table 5), which yielded a very reasonable calculated spectrum (Fig. 5B), thus confirming our initial assumption of two non-equivalent types of dimers. The g, A, and D parameters determined from the Q-band simulation were then used to simulate the X-band spectrum and resulted in a very good agreement (Fig. 5A – short dotted line). Minor adjustments in the linewidth parameters were made to achieve the best simulated spectra. The g- and D-values obtained from our simulation are in agreement with values previously determined for other copper dimers [42,19,59].

In our EPR spectrum we can then distinguish two sets of dimers (species 1 and 2), whose differences in coupling mechanism could be related to difference in the Cu–Cu distance as observed from the X-ray data. As described by

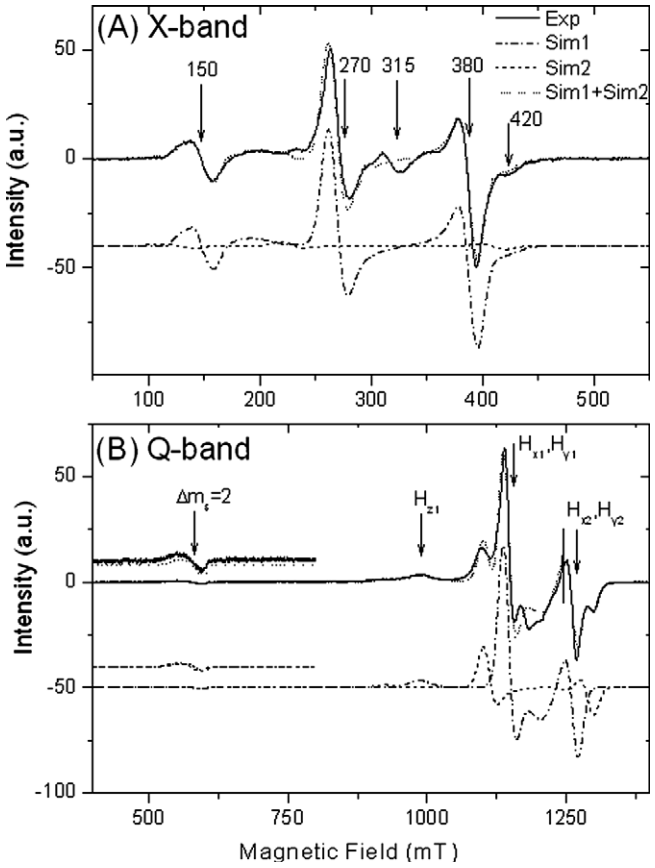


Fig. 5. (A) X- and (B) Q-band EPR spectra (solid lines) of polycrystalline sample of $[Cu_2(sulfameter)_4]_3 \cdot 2.5H_2O$ and their respective simulations (short dotted lines) obtained using the EasySpin software. The calculated spectra for each component (sim1 and sim2) are also shown in the figure. Arrows indicate the resonance fields discussed in the text.

Casanova et al. [40], in this kind of copper arrangement this distance plays an important role in the exchange coupling.

4. Conclusions

This work showed a new copper(II) complex with sulfameter as ligand. Its structure presented three dimeric units in the asymmetric unit. Two of them are similar whilst the other presented structural differences. The EPR spectra indicated the copper coupling is antiferromagnetic and showed the existence of two magnetically non-equivalent dimers. The IR spectra is in accordance with the coordination of copper(II) through the sulfonamidic N and the heterocyclic N and the electronic spectra agreed with the structure found.

Acknowledgements

The authors thank PEDECIBA-Química, CSIC (Uruguayan organizations), and PRONEX/FAPESP/CNPq (Grant No. 03/09859-2) in Brazil for financial support.

Appendix A. Supplementary material

CCDC 289562 contains the supplementary crystallographic data for this paper. These data can be obtained free of charge via http://www.ccdc.cam.ac.uk/conts/retrieving.html, or from the Cambridge Crystallographic Data Centre, 12 Union Road, Cambridge CB2 1EZ, UK; fax: (+44) 1223-336-033; or e-mail: deposit@ccdc.cam.ac.uk. Supplementary data associated with this article can be found, in the online version, at doi:10.1016/j.poly.2007.03.005.

References

[1] N. Hirayama, J. Taga, S. Oshima, T. Honjo, Anal. Chim. Acta 466 (2002) 295.
[2] A.C. Moffat (Ed.), Clarke's Isolation and Identification of Drugs, The Pharmaceutical Press, London, 1986.
[3] A. Bult, Metal Ions in Biological Systems, vol. 16, M. Dekker, N. York, 1983.
[4] S.E. Denmark, S.R.O. Connor, S.R. Wilson, Angew. Chem. 37 (1998) 1149.
[5] B. Macias, I. Garcia, M.V. Villa, J. Borras, M. Gonzalez-Alvarez, A. Castineiras, Inorg. Chim. Acta 353 (2003) 139.
[6] M. González-Álvarez, G. Alzuet, J. Borrás, M. Pitié, B. Meunier, J. Biol. Inorg. Chem. 8 (2003) 644.
[7] B. Macías, M.V. Villa, E. Fiz, I. García, A. Castiñeiras, M. González-Álvarez, J. Borrás, J. Inorg. Biochem. 88 (2002) 101.
[8] C.A. Otter, S.M. Couchman, J.C. Jeffery, K.L.V. Mann, E. Psillakis, M.D. Ward, Inorg. Chim. Acta 278 (1998) 178.
[9] A.B. Corradi, E. Gozzoli, L. Menabue, M. Saladini, L.P. Battaglia, P. Sgarabotto, J. Chem. Soc., Dalton Trans. 3 (1994) 273.
[10] L. Menabue, M. Saladini, Inorg. Chem. 30 (1991) 1651.
[11] L. Menabue, M. Saladini, M. Sola, Inorg. Chim. Acta 176 (1990) 95.
[12] J.R.J. Sorenson, Chem. Br. (1984) 1110.
[13] E.E. Chufán, J.C. Pedregosa, J. Borrás, Vib. Spectrosc. 15 (1997) 191.
[14] F. Blasco, L. Perelló, J. Latorre, J. Borrás, S. García-Granda, J. Inorg. Biochem. 61 (1996) 143.
[15] P. Ranganatham, S. Sankara, K. Subbannaya, Indian Drugs 17 (1979) 72.
[16] S.C. Chaturvedi, S.H. Mishra, K.L. Bhargava, Sci. Cult. 46 (1980) 401.
[17] S.C. Chaturvedi, S.H. Mishra, K.L. Bhargava, Indian Drugs 17 (1980) 357.
[18] E. Borrás, G. Alzuet, J. Borrás, J. Server-carrió, A. Castiñeiras, M. Liu-González, F. Sanz-Ruiz, Polyhedron 19 (2000) 1859.
[19] R. Cejudo-Marín, G. Alzuet, S. Ferrer, J. Borrás, A. Castiñeiras, E. Monzani, L. Casella, Inorg. Chem. 43 (2004) 6805.
[20] J. Casanova, G. Alzuet, J. Latorre, J. Borrás, Inorg. Chem. 36 (1997) 2052.
[21] M.H. Torre, G. Facchin, E. Kremer, E.E. Castellanos, O.E. Piro, E.J. Baran, J. Inorg. Biochem. 94 (2003) 200.
[22] L. Yang, X. Yang, L. Liu, Y. Li, Q. Lou, Q. Liu, J. Coord. Chem. 56 (2003) 1131.
[23] G. Facchin, M.H. Torre, E. Kremer, E.J. Baran, A. Mombrú, H. Pardo, M.P. Araujo, A.A. Batista, A.J. Costa-Filho, Inorg. Chim. Acta 355 (2003) 408.
[24] G. Facchin, M.H. Torre, I. Viera, E. Kremer, E.J. Baran, Met. Ions Biol. Med. 7 (2002) 1.
[25] G. Facchin, M.H. Torre, E. Kremer, O. Piro, E.E. Castellano, E.J. Baran, J. Inorg. Biochem. 89 (2002) 174.
[26] L.P. Battaglia, A.B. Corradi, L. Menabue, J. Chem. Soc., Dalton Trans. (1986) 1653.
[27] M.D. Mazus, A.L. Kovalenko, Y.A. Simonov, V.N. Polyakov, Russ. J. Inorg. Chem. 32 (1987) 2718.
[28] J. Jezierskaa, T. Gowiak, A. Ozarowski, Y.V. Yablokov, Z. Rzaczynska, Inorg. Chim. Acta 28 (1998) 275.
[29] R. Gupta, Z.H. Zhang, D. Powell, M.P. Hendrich, A.S. Borovik, Inorg. Chem. 41 (2002) 5100.
[30] H. Ackermann, G. Geiseler, K. Harms, R. Leo, W. Massa, F. Weller, K. Dehnicke, Z. Anorg. Allg. Chem. 625 (1999) 1500.
[31] P. Reiss, D. Fenske, Z. Anorg. Allg. Chem. 626 (2000) 1317.
[32] A. Bult, J.D. Uitterdijk, H.B. Klasen, Transit. Met. Chem. 4 (1979) 285.
[33] Enraf-Nonius COLLECT; Nonius BV: Delft, The Netherlands, 1997.
[34] Z. Otwinowski, W. Minor, in: C.W. Carter, R.M. Sweet (Eds.), HKL Denzo and Scalepack, vol. 276, Academic Press, New York, 1997, p. 307.
[35] R.H. Blessing, Acta Cryst. A51 (1995) 33.
[36] G.M. Sheldrick, SHELXS-97, Program for Crystal Structure Resolution; University of Gottingen, Gottingen, Germany, 1997.
[37] G.M. Sheldrick, SHELXL-97, Program for Crystal Structures Analysis; University of Göttingen, Göttingen, 1997.
[38] L.J. Farrugia, J. Appl. Cryst. 30 (1997) 565.
[39] L.J. Farrugia, WinGX. An Integrate System of Windows Programs for the Solution, Refinement and Analysis of Single Crystal X-ray Diffraction Data, Universsity of Glasgow, 1997.
[40] J. Casanova, G. Alzuet, J. Borrás, J.M. Amigó, T. Debaerdemaeker, Inorg. Chem. 36 (1997) 2052.
[41] F.A. Cotton, G. Wilkinson, C.A. Murillo, M. Bochman, Advanced Inorganic Chemistry, 6th ed., Wiley-Interscience, United States of America, 1999.
[42] L. Gutiérrez, G. Alzuet, J. Borrás, A. Castiñeiras, A. Rodríguez-Forte, E. Ruiz, Inorg. Chem. 40 (2001) 3089.
[43] H. Cheng, P. Cheng, C. Lee, S. Peng, Inorg. Chim. Acta 181 (1991) 145.
[44] G.A. Jeffrey, An Introduction to Hydrogen Bonding, Oxford University Press, Oxford, 1997.
[45] K.K. Narang, J.K. Gupta, Indian J. Chem. 13 (1975) 705.
[46] F. Blasco, R. Ortiz, L. Perelló, J. Borrás, J. Amigó, T. Debaerdemaeker, J. Inorg. Biochem. 53 (1994) 117.
[47] J. Casanova, G. Alzuet, S. Ferrer, J. Borrás, S. García-Granda, E.J. Pérez-Carreño, J. Inorg. Biochem. 51 (1993) 689.
[48] G. Casanova, G. Alzuet, J. Borrás, J. Timoneda, S. García-Granda, I. Cándano-González, J. Inorg. Biochem. 56 (1994) 65.

[49] J. Casanova, G. Alzuet, J. Borrás, J. Latorre, M. Sanaú, S. García-Granda, J. Inorg. Biochem. 60 (1995) 219.
[50] J.K. Gupta, N.K. Jha, Indian J. Chem. 60 (1987) 529.
[51] K.K. Narang, J.K. Gupta, Transition Met. Chem. 2 (1977) 83.
[52] B.C. Rudy, B.Z. Senkowski, K. Florey, Analytical Profiles of Drug Substances, New York, vol. 2, 1973.
[53] D. Lin-Vien, N.B. Colthup, W.G. Fateley, J.G. Grasselli, The Handbook of Infrared and Raman Characteristic Frequencies of Organic Molecules, Academic Press, INC, Boston, 1991.
[54] E. Kremer, G. Facchin, E. Estévez, P. Alborés, E.J. Baran, J. Ellena, M.H. Torre, J. Inorg. Biochem. 100 (2006) 1167.
[55] J.R. Wasson, C.-I. Shyr, C. Trapp, Inorg. Chem. 7 (1968) 469.
[56] B. Bleaney, K.D. Bowers, Proc. Roy. Soc. London Ser. A – Math. Phys. Sci. 214 (1952) 451.
[57] E. Wasserman, L.C. Snyder, W.A. Yager, J. Chem. Phys. 41 (1964) 1763.
[58] S. Stoll, A. Schweiger, J. Magn. Reson. 42 (2006) 178.
[59] R. Cejudo, G. Alzuet, M. Gonzalez-Alvarez, J.L. Garcia-Gimenu, J. Borras, M. Liu-Gonzalez, J. Inorg. Biochem. 100 (2006) 70.

Available online at www.sciencedirect.com
ScienceDirect
Polyhedron 26 (2007) 3286–3290
POLYHEDRON
www.elsevier.com/locate/poly

Synthesis and structural characterization of two five coordinate aluminum alkyl and bis(trimethylsilyl)amino complexes bearing acyclic tetradentate Schiff bases

C.R. Wade [a], B.J. Lamprecht [a], V.W. Day [b], J.A. Belot [a,*]

[a] Department of Chemistry and Center for Materials Research Analysis, University of Nebraska-Lincoln, Lincoln, NE 68588-0304, USA
[b] Department of Chemistry, University of Kansas, 1251 Wescoe Hall Drive, Lawrence, KS 66045, USA

Received 30 October 2006; accepted 3 March 2007
Available online 15 March 2007

Abstract

Two acyclic Schiff-base ligands, bis-5,5′-(1,3-propanediyldiimino)-2,2-dimethyl-4-hexene-3-one and bis-5,5′-(1,3-ethanediyldiimino)-2,2-dimethyl-4-hexene-3-one, were used to complex homoleptic triethylaluminum and tris[bis(trimethylsilyl)amino]aluminum, respectively. The acid–base reactions proceeded in excellent yields with elimination of ethane or bis(trimethylsilyl)amine during *in situ* deprotonation of the protio Schiff-base. The colorless aluminum complexes crystallized from *n*-pentane and were characterized by standard methods including single crystal X-ray diffraction. Polymerization of racemic lactide, with addition of alcohol, yielded PLA with narrow polydispersities but low molecular weights.
© 2007 Elsevier Ltd. All rights reserved.

Keywords: Aluminum; Schiff-base; X-ray; Catalysis; Polymerization

1. Introduction

Schiff-bases (SB) constitute one of the oldest chelator classes in inorganic chemistry and continue to receive considerable attention. One active research area is the binding of Group 13 elements to SBs affording 5-coordinate species where bonding occurs through classical N_2O_2 ligation [1]. Analogously, we have been interested in assessing the extent to which steric factors of the Schiff-base, as well as those of other ligands bound to the metal (typically monodentate monoanions) can influence catalysis [1]. Previously, our focus concentrated on modifying the frontal, ''saturated'' SB steric bulk, and now we sought to include direct comparisons of linker length (Fig. 1). Indeed, much of the resurgence associated with similar complexes is attributable to their activity in numerous catalytic cycles and relativity low envirotoxicity (for Al^{3+}) [2]. Particularly relevant is the use of aluminum centers with aromatic Salen-type ligands for the polymerization of biodegradable and biocompatible polymers, such as those derived from lactones, lactides, carbon dioxide and epoxides, and other renewable resources [3–7]. Recent reviews by Atwood [1] and Lewinski and Zachara [8] serve as testament to the burgeoning activity in this area. In our hands we, for the first time, wanted to evaluate ''saturated'' SB Al^{3+} complexes for the polymerization of racemic lactide. The advantages of these complexes would be the lack of aromaticity and tunable peripheral steric bulk, both precluding the possibility of oligomerization in the solution and solid-state species [9].

Our secondary interest in these Group 13 complexes stems from their utility as benchmarks to isoelectronic five-coordinate rare earth Schiff-base complexes [9]. The present study was also designed to compare Al^{3+} structural features and activities with those of these heavier congeners. To this end, we synthesized a new ligand (bis-5,5′-(1,3-ethanediyldiimino)-2,2-dimethyl-4-hexene-3-one, **(1)**

* Corresponding author. Tel.: +1 4024725666; fax: +1 4024729402.
E-mail address: jbelot2@unl.edu (J.A. Belot).

0277-5387/$ - see front matter © 2007 Elsevier Ltd. All rights reserved.
doi:10.1016/j.poly.2007.03.008

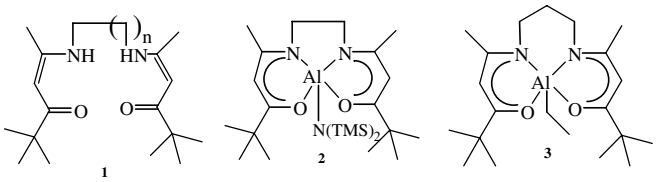


Fig. 1. "Saturated" Schiff-base ligand (**1**) and the two Al^{3+} complexes (**2** and **3**).

and two, five-coordinate metal complexes (**2** and **3**) exploiting *in situ* deprotonation reactions. Marked structural differences exist between **2** and **3** and amongst their square pyramidal rare earth counterparts. The Al^{3+} coordination polyhedron is rigorously trigonal bipyramidal in **3** and distorted trigonal pyramidal in **2**; this difference is due at least in part to the Schiff-base ethylene spacer in **2** that is less flexible than the propylene spacer in **3**.

2. Experimental

2.1. Materials and methods

Standard Schlenk techniques and a Vacuum Atmospheres N_2-filled glovebox were used throughout the isolation and handling of all aluminum complexes. 1,2-diaminoethane (Acros), absolute ethanol (EtOH, Pharmco), Et_3Al solution (Aldrich) and benzene (C_6H_6) were used as received whereas alkali earth bis(trimethylsilyl)amides (Gelest) and *rac*-lactide were first purified by double sublimation at $\sim 10^{-5}$ Torr. 2,2-Dimethyl-3,5-hexanedione [10] and bis-5,5′-(1,3-propanediyldiimino)-2,2-dimethyl-4-hexene-3-one [9] were synthesized using literature methods. Toluene (C_7H_8) and deuterated benzene (C_6D_6) with sodium metal and pentane (C_5H_{12}, CaH_2) were dried and distilled immediately before use. Polymerization reactions followed Nomura's procedure [6], and dry MeOH was added to activate the catalysts. ^1H and ^{13}C NMR were recorded on a GE 300 MHz (^1H) and processed using NUTS software. The solid-state molecular structures of **2** and **3** were determined by single crystal X-ray diffraction at Wake Forest University (Table 1) and elemental analyses were performed at Midwest Microlabs (Indianapolis, IN). Melting points were determined using a modified Mel-Temp II with digital thermocouple readouts and are uncorrected.

2.2. Synthesis of bis-5,5′-(1,3-ethanediyldiimino)-2,2-dimethyl-4-hexene-3-one (*1*)

Under ambient conditions, to a 250 mL 24/40 1-neck round bottom flask charged with 50 mL EtOH and 17.3 g (122 mmol) 2,2-dimethyl-3,5-hexanedione was added 3.7 g (61 mmol) 1,3-diaminoethane in 35 mL EtOH dropwise over 30 minutes. Following this, a condenser replaced the 125 mL addition funnel and the reaction heated at reflux overnight, after which time it was diluted with 100 mL *d*H_2O and extracted twice with 30 mL Et_2O. The organics were washed with 4×20 mL H_2O, dried over Na_2SO_4, filtered, and removed in vacuo yielding a dull-yellow wax. This crude product was subjected to a C_6H_6 azeotrope and recrystallized from C_7H_{16} affording colorless crystals of **1** in unoptimized yields between 60% and 80%; ^1H NMR (δ, $CDCl_3$): 1.21 (s, 18H), 1.92 (m, 6H), 3.40 (m, 4H), 5.15 (s, 2H), 11.1 (b, 2H); ^{13}C NMR (δ, $CDCl_3$): 19.3, 28.0, 41.5, 43.6, 91.5, 163.8, 204.7; *Anal.* Calc. for $C_{18}H_{32}N_2O_2$: C, 70.09; H, 10.46; N, 9.08. Found C, 69.85; H, 10.06; N, 9.03%.

2.3. Bis-5,5′-(1,3-ethanediyldiimino)-2,2-dimethyl-4-hexene-3-onato aluminum bis(trimethylsilyl)amino (*2*)

Forty milliliters of C_7H_{16} dissolved 0.316 g (1.02 mmol) anhydrous **1** and simultaneously, in a 100 mL, 1-neck round bottom flask 0.528 g (1.04 mmol) $Al[N(TMS)_2]_3$ [11] was dissolved in 10 mL C_7H_{16}. The ligand solution was then added to the flask containing $Al[N(TMS)_2]_3$ via syringe in one portion and the reaction stirred at reflux overnight, after which time the solvent was removed in vacuo. The white solids were then recrystallized from minimal C_5H_{12} in a −20 °C freezer for 2 days to afford colorless crystals. Yield 92%; m.p. 141–143 °C (dec.); ^1H NMR (C_6D_6): δ 0.39 (s, 9H); 1.29 (s, 9H); 1.35 (s, 3H); 2.66 (m, 1H); 3.28 (m, 1H); 5.21 (s, 1H); ^{13}C NMR (C_6D_6): δ 5.5; 21.2; 28.6; 39.1; 45.7; 95.4; 171.3; 188.8; *Anal.* Calc. for $C_{24}H_{48}N_3O_2Si_2Al$: C, 58.37; H, 9.80; N, 8.51. Found: C, 56.88; H, 9.23; N, 8.01%.

2.4. Bis-5,5′-(1,3-propanediyldiimino)-2,2-dimethyl-4-hexene-3-onato ethylaluminum (*3*)

4.75 mL of 1.0 M $AlEt_3$ (4.75 mmol) was slowly added, via a syringe, to a 100 mL Schlenk flask containing a solution of 1.54 g (4.77 mmol) **1** in 35 mL dry C_7H_8. Addition of $AlEt_3$ caused the reaction to become yellow and evolve ethane gas. After stirring (~5 min) the solution returned to colorless. The reaction was heated at reflux overnight and solvent removed in vacuo to afford an off-white solid. The product crystallized from C_5H_{12} to present large, clear, colorless plates. Yield 94%; m.p. 124–125 °C (dec.); ^1H NMR (C_6D_6): δ 0.48 (m, 1H); 1.25 (m, 1H); 1.34 (s, 9H); 1.58 (s, 3H); 1,64 (m, 3H) 2.29 (m, 1H); 2.75 (m, 1H); 3.01 (m, 1H); 5.22 (s, 1H). ^{13}C NMR (C_6D_6): δ 11.5; 21.7; 26.2; 28.6; 39.1; 49.4; 94.7; 172.0; 188.9 *Anal.* Calc. for $C_{21}H_{37}N_2O_2Al$: C, 66.99; H, 9.90; N, 7.44. Found: C, 66.56; H, 9.76; N, 7.39%.

2.5. Polymeriation of racemic lactide

Two 25 mL Schlenk flasks under N_2 were each charged with 720 mg (5.0 mmol) *rac*-lactide, 10 mL toluene, and a stir bar. To one, 0.2 mL of MeOH was added and both flasks heated to 70 °C until the *rac*-lactide dissolved. Following this 0.0188 g (0.05 mmol) of **3** was added to each

Table 1
Crystal data and structure refinement for **2** and **3**

	2	**3**
Empirical formula	$C_{24}H_{48}AlN_3O_2Si_2$	$C_{21}H_{37}AlN_2O_2$
Formula weight	493.81	376.51
Temperature (K)	193(2)	193(2)
Wavelength (Å)	0.71073	0.71073
Crystal system	triclinic	triclinic
Space group	$P\bar{1}$	$P\bar{1}$
Unit cell dimensions		
a (Å)	11.646(1)	9.581(1)
b (Å)	11.844(1)	10.029(1)
c (Å)	11.986(1)	12.629(2)
α (°)	71.476(2)	96.657(2)
β (°)	89.022(2)	95.382(2)
γ (°)	73.228(2)	110.849(2)
Volume (Å^3)	1495.9(3)	1114.4(2)
Z	2	2
D_{calc} (Mg/m^3)	1.096	1.122
Absorption coefficient (mm^{-1})	0.171	0.107
$F(000)$	540	412
Crystal size (mm)	$0.185 \times 0.17 \times 0.08$	$0.50 \times 0.25 \times 0.04$
θ Range for data collection (°)	3.95–27.50	4.13–27.50
Index ranges	$-15 \leqslant h \leqslant 15$, $-15 \leqslant k \leqslant 15$, $-15 \leqslant l \leqslant 15$	$-12 \leqslant h \leqslant 12$, $-13 \leqslant k \leqslant 12$, $-16 \leqslant l \leqslant 16$
Reflections collected	13383	9808
Independent reflections (R_{int})	6775 [0.056]	5049 [0.073]
Completeness to $\theta = 27.50°$ (%)	98.60	98.40
Absorption correction	empirical	empirical
Maximum and minimum transmission	1.000 and 0.898	1.000 and 0.794
Refinement method	full-matrix least-squares on f^2	full-matrix least-squares on f^2
Data/restraints/parameters	6775/0/303	5049/0/244
Goodness-of-fit on F_2	0.982	1.033
Final R indices [$I > 2\sigma(I)$]	$R_1 = 0.060$, $wR_2 = 0.143$	$R_1 = 0.077$, $wR_2 = 0.208$
R indices (all data)	$R_1 = 0.086$, $wR_2 = 0.155$	$R_1 = 0.097$, $wR_2 = 0.221$
Largest difference in peak and hole (e Å^{-3})	0.41 and −0.27	0.93 and −0.50

as a 0.05 M toluene solution. The reaction flasks remained immersed in an oil bath heated to 70 °C and polymerization progress monitored by ^{1}H NMR. Near completion (~90% conversion by disappearance of monomer) each flask containing polymer and catalyst were precipitated and quenched with MeOH, respectively and dried in vacuo.

3. Results and discussion

3.1. Ligands

Organic **1** originates from a non-commercial diketone and the large frontal ^{t}Bu groups afford only one of three possible structural isomers following the Schiff-base condensation. A noteworthy and requisite ketoiminate purification step is a benzene azeotrope to remove all spurious H_2O (the reaction byproduct), as anhydrous starting materials are essential or metallation will fail. Overall, ligand choice was predicated by our previous successes in isolating and structurally characterizing anhydrous, 5-coordinate Schiff-base lanthanide (III) complexes that all exhibited mononuclear, slightly distorted square pyramidal metal coordination geometry (vide supra). Since the metal coordination in $(C_2H_5)Al(sal_2en)$ was reported to also be distorted square-pyramidal [1], we (incorrectly) anticipated a distorted square-pyramidal coordination for the Al^{3+} ion in **2** and **3** [12]. With the ligand set in **2** being nearly identical to that in some of our earlier studies with lanthanide(III) complexes, a structural characterization of **2** would allow us to assess the effects of reducing metal size on coordination geometry. Structural comparisons of **2** with **3**, would also allow us to explore the extent to which changes in steric factors of the ligand set can effect metal coordination geometry: The SB in **3** has one more methylene group and the terminally-bonded ligand is considerably less bulky.

3.2. Complexes

Al^{3+} introduction occurs using commercial Et_3Al solution or $Al(N[TMS]_2)_3$ [13], the latter was synthesized and purified using literature preparations [11]. Addition of either to a heptane solution of the protio Schiff-base briefly causes a light-yellow color and then the reactions return to their transparent, colorless appearance. With Et_3Al, evolution of C_2H_6 is rapid and obvious (as evidenced by bubbling of the isolated the Schlenk N_2 bubbler), whereas for bulkier $Al(N[TMS]_2)_3$ steric factors slow the acid–base reaction. To assure completion, both reactions were heated

Table 2
Selected bond lengths (Å) and angles (°) for compounds **2** and **3**

2		**3**	
Al–O(1)	1.842(2)	Al–O(1)	1.868(2)
Al–O(2)	1.813(2)	Al–O(2)	1.802(2)
Al–N(1)	1.974(2)	Al–N(1)	1.954(2)
Al–N(2)	2.005(2)	Al–N(2)	2.060(2)
Al–N(3)	1.861(2)	Al–C(21)	1.984(3)
C(2)–C(3)	1.376(4)	C(2)–C(3)	1.377(4)
C(3)–C(4)	1.420(4)	C(3)–C(4)	1.413(4)
C(7)–C(8)	1.432(3)	C(8)–C(9)	1.432(4)
C(8)–C(9)	1.363(3)	C(9)–C(10)	1.363(3)
O(2)–Al–O(1)	87.90(7)	O(2)–Al–O(1)	87.78(8)
O(2)–Al–N(3)	122.44(8)	O(2)–Al–N(1)	113.21(9)
O(1)–Al–N(3)	99.28(8)	O(1)–Al–N(1)	88.10(9)
O(2)–Al–N(1)	123.71(8)	O(2)–Al–C(21)	119.88(13)
O(1)–Al–N(1)	89.30(8)	O(1)–Al–C(21)	93.22(10)
N(3)–Al–N(1)	113.48(8)	N(1)–Al–C(21)	126.90(13)
O(2)–Al–N(2)	87.74(7)	O(2)–Al–N(2)	88.48(9)
O(1)–Al–N(2)	162.42(8)	O(1)–Al–N(2)	173.63(8)
N(3)–Al–N(2)	97.44(8)	N(1)–Al–N(2)	88.65(9)
N(1)–Al–N(2)	79.03(8)	C(21)–Al–N(2)	93.11(10)

overnight at reflux. Once purified by recrystallization in C_5H_{12} the colorless compounds exhibit melting points proportional to increased monoanion molecular dissymmetry and molecular weight (i.e. m.p. **2** > **3**), and each decomposes before volatilizing at $<10^{-5}$ Torr. There is no spectroscopic (NMR) or structural evidence to support complex dimerization or oligomerization [1,2], and the lack of ligand aromaticity promotes the formation of mononuclear species in both solution and the solid-state [14–16], although fluxional behavior is suggested by the methylene proton splittings.

The X-ray diffraction-derived molecular structures of **2** and **3** are shown in Fig. 2. Both compounds contain a 5-coordinate Al^{3+} ion that is terminally-bonded to a monoanion and complexed to all four donor atoms of an N_2O_2 Schiff-base (Table 2). While the bis(trimethylsilyl)amino monoanion [16] in **2** is considerably bulkier than the ethyl monoanion in **3**, the ethylene bridged Schiff-base in **2** is slightly more compact and more restricted than the propylene-bridged N_2O_2 Schiff-base of **3**. The Al^{3+} coordination geometry in both complexes is best described as trigonal bipyramidal with a distorted polyhedron ($\tau = 0.65$) in **2** and a nearly ideal polyhedron ($\tau = 1.00$) in **3** [12]. Axial atoms O(1) and N(2) subtend angles of 162.4(1)° and 173.6(1)° in **2** and **3**, respectively. The less ideal trigonal bipyramidal coordination geometry in **2** probably results from the smaller "bite" angle and increased rigidity attributable to its ethylene spacer as well as the increased bulk of its terminally-bonded anion when compared to **3**. This anion Al–N(3) bond length of 1.86 Å is one of the shortest "apical" bond lengths amongst this class of compounds, and more closely resemble that of the hindered organometallic imido Cp*AlNSiPh$_3$ [1,17]. The wrapping pattern adopted by the Schiff-base in both complexes is the one expected: it spans 3 contiguous polyhedral edges that would ideally subtend a 90° angle at the metal. Furthermore, the SB Al–O and Al–N distances in **2** and **3** all exhibit the sterically-anticipated trigonal-bipyramidal trend of longer bonds to axial ligands than to equatorial ligands. Interestingly, these differences in SB Al–O and Al–N distances are considerably larger for the nearly ideal **3** (0.066–0.106 Å) than the more distorted **2** (0.029–0.031 Å). The C–C bond lengths within the ketoiminato rings [C(2)–C(3) < C(3)–C(4), C(8)–C(9) < C(7)–C(8) in **2** and C(2)–C(3) < C(3)–C(4), C(9)–C(10) < C(8)–C(9) in **3**] suggest more enolic character [3] with the primary resonance structure favoring the harder oxygen atoms upon chelation in both complexes. The remaining C–O, C–N and C–C bond lengths in **2** and **3** are unremarkable.

While complex **2** contains a terminally-bonded bis(trimethylsilyl)amido group and an ethylene-bridged Schiff-base, organometallic complex **3** has a terminally-bonded ethyl group and a propyl-bridged Schiff-base [1,16]. The equatorial plane has a slight deformation [12] with C(21) canted from an idealized N_2O_2 normal although equally centered between N(2) and O(1). It resides forward toward O(2)

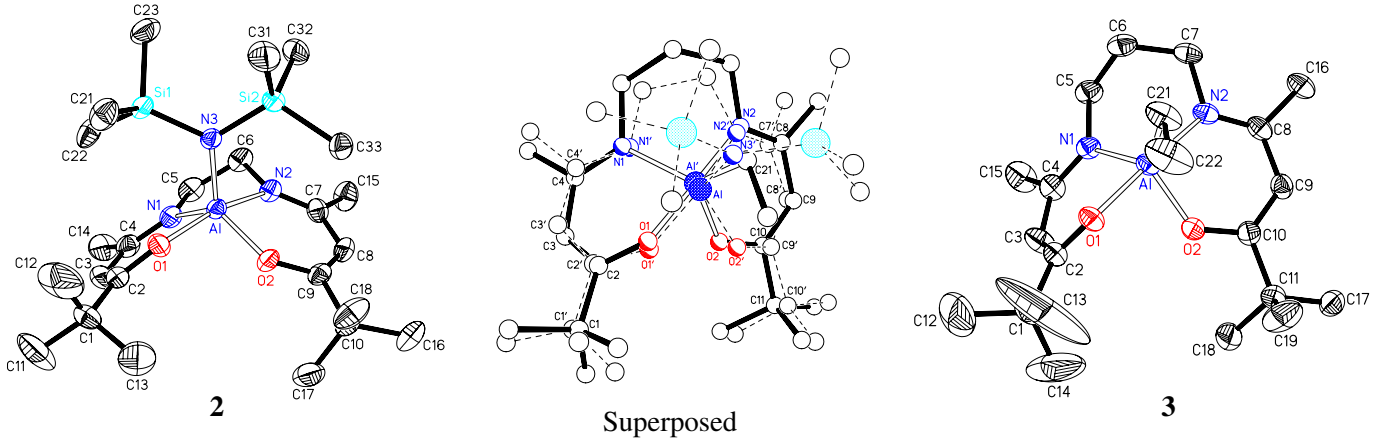


Fig. 2. X-ray diffraction-derived molecular structures of **2** and **3** and each coordination environment superposed. Relevant bond lengths and angles can be found in Table 2 and discussions throughout the text. Hydrogen atoms were removed for clarity and thermal ellipsoids are at 30% probability.

and the C(21)–Al–O(2) and C(21)–Al–N(1) angles are 119.9 ° and 126.9 °, respectively. This distortion is most likely due to the frontal steric constraints forming an unsymmetric pocket above one of the ^{t}Bu groups and removal of the eclipsed hydrogen conformation along the methylenes of the larger C_3 linker [1]. This C_3 backbone of the propyl bridge in **3** forms a six-membered chelate ring, Al–N(1)–C(6)–C(7)–C(8)–N(2), that adopts the boat conformation. Fig. 2 also shows a superposition of **2** and **3.** The labeled atoms from the ketoiminato halves, the coordinated atoms from the monodentate ligands, and the exocyclic carbons have an rms deviation of 0.283 Å and a maximum deviation of 0.482 Å. One of the Schiff-base ^{t}Bu groups in each molecule also superimposes quite closely. The regions where the two Schiff-bases in **2** and **3** do not superimpose are near the linker groups and the second ^{t}Bu group which is rotated about the C(1)–C(2) bond in **2** relative to **3**. Although the ligand set in **2** is virtually identical (with the exception of one less methylene group in the linker) to that for the earlier trivalent lanthanide complexes [9], the ionic radius of 5-coordinate Al^{3+} is smaller. The net result of replacing a trivalent lanthanide ion with the smaller Al^{3+} ion is therefore to ''pull'' all of the ligands radially toward the central metal ion. This produces shorter intraligand contacts unless the relative orientations of the ligands change. A minor reorientation (linked-ligand Berry pseudo-rotation) of the square-pyramidal lanthanide amido/Schiff-base ligand set would give distorted trigonal bipyramidal Al^{3+} coordination in **2** with shorter metal–ligand distances.

Lactide polymerizations to produce polylactic acid (pLA) are an intensely active area within green chemistry. Inspired by Nomura and others using Al Salen complexes [4–7] we began evaluating our ''saturated'' complexes as polymerization catalysts for this biocompatible material. Initially, **2** and **3** were used to initiate polymerization, however no activity was observed with **2** and only modest turnovers with **3**. Furthermore, polymers derived from **3** exhibited low molecular weights, broad polydispersities, and no stereocontrol. Following these efforts, and anticipating that the apical ligand and metal center were too encumbered with peripheral steric bulk to allow monomer insertion, we began activating the Al Schiff-base complexes with methanol and benzyl alcohol. Although our efforts are only beginning, using the aforementioned systems (with various loadings) we have recovered atactic pLA with molecular weight control (up to 20,000 Da) and monomodal polydispersities (<1.3). Currently, we are optimizing reaction conditions, performing more detailed mechanistic studies, and attempting to control tacticity [6].

4. Conclusions

This report presents our initial results on a new organic Schiff-base (**1**) and the molecular structures of two new Al^{3+} complexes bearing ''saturated'' Schiff-bases (**2** and **3**). Unlike the square pyramidal geometry of their isoelectronic rare earth congeners, both aluminum complexes adopt ideal and slightly distorted trigonal bipyramidal coordination environments. Initial polymerization results with either the terminal ethyl or bis(trimethylsilyl)amino ligand failed; however, activation with trace MeOH yielded biodegradable polymers with some control over both molecular weights and polydispersity.

Acknowledgements

This work was supported by the Nebraska Research Initiative. J.A.B. also thanks Steve A. Schuetz for early explorations into this project.

Appendix A. Supplementary material

CCDC 624040 and 624041 contain supplementary crystallographic data for **2** and **3**. These data can be obtained free of charge via http://www.ccdc.cam.ac.uk/conts/retrieving.html, or from the Cambridge Crystallographic Data Centre, 12 Union Road, Cambridge CB2 1EZ, UK; fax: (+44) 1223-336-033; or e-mail: deposit@ccdc.cam.ac.uk. Supplementary data associated with this article can be found, in the online version, at doi:10.1016/j.poly.2007.03.008.

References

[1] D.A. Atwood, M.J. Harvey, Chem. Rev. 101 (2001) 37.
[2] V.C. Gibson, S.K. Spitzmesser, Chem. Rev. 103 (2003) 283.
[3] H. Sugimoto, H. Ohtsuka, S. Inoue, J. Polym. Sci. Part A: Polym. Chem. 43 (2005) 4172.
[4] Z. Tang, X. Chen, X. Pang, Y. Yang, X. Zhang, X. Jing, Biomacromolecules 5 (2004) 965.
[5] Z. Tang, X. Chen, Y. Yang, X. Pang, J. Sun, X. Zhang, X. Jing, J. Polym. Sci. Part A: Polym. Chem. 42 (2004) 5974.
[6] N. Nomura, R. Ishii, M. Akakura, K. Aoi, J. Am. Chem. Soc. 124 (2002) 5938.
[7] D. Jhurry, A. Bhaw-Luximon, N. Spassky, Macromol. Symp. 175 (2001) 67.
[8] J. Lewinski, J. Zachara, I. Justyniak, M. Dranka, Coord. Chem. Rev. 249 (2005) 1185.
[9] S.A. Schuetz, C.M. Silvernail, C.D. Incarvito, A.L. Rheingold, J.L. Clark, V.W. Day, J.A. Belot, Inorg. Chem. 43 (2004) 6203, and references therein.
[10] J.T. Adams, C.R. Hauser, J. Am. Chem. Soc. 66 (1944) 1220.
[11] P.J. Brothers, R.J. Wehmschulte, M.M. Olmstead, K. Ruhlandt-Senge, S.R. Parkin, P.P. Power, Organometallics 13 (1994) 2792.
[12] A.W. Addison, T.N. Rao, J. Reedijk, J. van Rijn, G.C. Verschoor, J. Chem. Soc., Dalton Trans. (1984) 1349.
[13] A.K. Jain, A. Gupta, R. Bohra, I.-P. Lorenz, P. Mayer, Polyhedron 25 (2006) 654.
[14] Q. Liu, M. Ding, J. Organomet. Chem. 553 (1998) 179.
[15] Q. Liu, M. Ding, Y. Lin, Y. Xing, J. Organaomet. Chem. 548 (1997) 139.
[16] S.J. Dzugan, V.L. Goedken Inorg. Chem. 25 (1986) 2858.
[17] M.-A. Munoz-Hernandez, T.S. Keizer, P. Wei, S. Parkin, D.A. Atwood, Inorg. Chem. 40 (2001) 6782.

Available online at www.sciencedirect.com
ScienceDirect
Polyhedron 26 (2007) 3291–3300
POLYHEDRON
www.elsevier.com/locate/poly

Aurichalcite – An SEM and Raman spectroscopic study

Ray L. Frost *, Matt C. Hales, B. Jagannadha Reddy

Inorganic Materials Research Program, School of Physical and Chemical Sciences, Queensland University of Technology, GPO Box 2434, Brisbane, Queensland 4001, Australia

Received 27 November 2006; accepted 3 March 2007
Available online 7 March 2007

Abstract

Raman spectroscopy complimented with supplementary infrared spectroscopy has been used to characterise the vibrational spectrum of aurichalcite a zinc/copper hydroxy carbonate $(Zn,Cu^{2+})_5(CO_3)_2(OH)_6$. XRD patterns of all specimens show high orientation and indicate the presence of some impurities such as rosasite and hydrozincite. However, the diffraction patterns for all samples are well correlated to the standard reference patterns. SEM images show highly crystalline and ordered structures in the form of micron long fibres and plates. EDAX analyses indicate variations in chemical composition of Cu/Zn ratios ranging from 1/1.06 to 1/2.87. The symmetry of the carbonate anion in aurichalcite is C_s and is composition dependent. This symmetry reduction results in multiple bands in both the symmetric stretching and bending regions. The intense band at 1072 cm^{-1} is assigned to the $\nu_1(CO_3)^{2-}$ symmetric stretching mode. Three Raman bands assigned to the $\nu_3(CO_3)^{2-}$ antisymmetric stretching modes are observed for aurichalcite at 1506, 1485 and 1337 cm^{-1}. Multiple Raman bands are observed in 800–850 cm^{-1} and 720–750 cm^{-1} regions and are attributed to ν_2 and ν_4 bending modes confirming the reduction of the carbonate anion symmetry in the aurichalcite structure. An intense Raman band at 1060 cm^{-1} is attributed to the δ OH deformation mode.
© 2007 Elsevier Ltd. All rights reserved.

Keywords: Aurichalcite; Hydrozincite; Hydroxy carbonates; Infrared; Near-infrared and Raman spectroscopy

1. Introduction

The mineral aurichalcite $(Zn,Cu^{2+})_5(CO_3)_2(OH)_6$ is one of a large number of highly coloured copper bearing minerals [1–3]. Aurichalcite forms in the oxidation zones of zinc–copper deposits. Crystals are acicular and fibrous and often found in aggregates. The color is an attractive grass green to pale blue–green. Aurichalcite will often partially cover red limonite and be associated with such colorful minerals as rosasite, azurite, smithsonite and malachite. Aurichalcite may be confused with rosasite minerals because of their similar appearance. Rosasite minerals including glaukosphaerite; kolwezite; mcguinnessite are usually more massive and not lamellar. Other related hydroxy carbonates are nullaginite and pokrovskite. It appears that aurichalcite is similar to hydrozincite and both minerals are formed under the same conditions when copper is present in the solution [4]. Williams further states that up to one quarter of the cation sites are occupied by Cu^{2+}. Greater concentrations of copper give rise to other discrete phases such as malachite and rosasite. Interestingly the range of substitution of other transition metal ions in the aurichalcite lattice is very limited. The minerals in the hydroxy carbonate group have been synthesised because of their potential as catalysts [2]. Further studies of synthetic hydroxy carbonates incorporated Al^{3+} into the structures [5]. The mineral is monoclinic as are many of the other hydroxy carbonates such as malachite. Anthony et al. (2003) reports aurichalcite to be acicular to lath-like crystals with prominent crystal growth along the [0 1 0] axis, commonly straited parallel to [0 0 1] axis. The mineral is of point group $2/m$ and space group $P2_1/m$ [6]. The model for the structure of aurichalcite based upon the crystallographic studies of this mineral using

* Corresponding author. Tel.: +61 7 3864 2407; fax: +61 7 3864 1804.
E-mail address: r.frost@qut.edu.au (R.L. Frost).

0277-5387/$ - see front matter © 2007 Elsevier Ltd. All rights reserved.
doi:10.1016/j.poly.2007.03.003

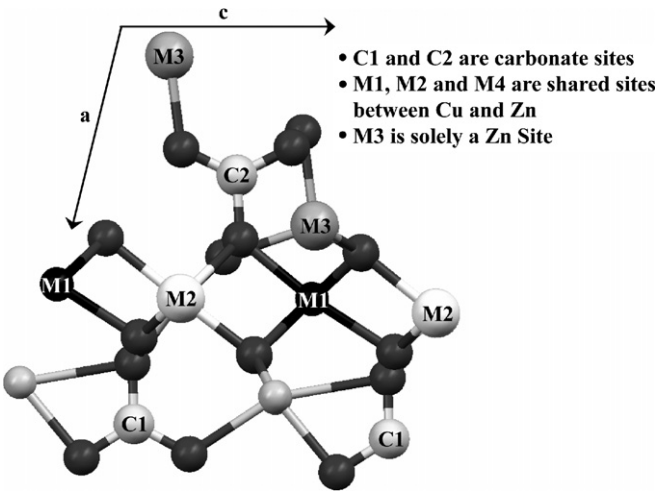


Fig. 1. Model of the structure of aurichalcite.

synchrotron radiation by Harding et al. [8] is shown in Fig. 1. Based on this structure the symmetry of the carbonate anion is C_s. The accurate X-ray crystallography of aurichalcite is difficult to obtain because of its very small interwoven needles which makes obtaining single crystal studies difficult [3,6–8]. Harding et al. showed the positions in the structure of aurichalcite are octahedrally coordinated. The atom positions occupied by zinc have tetrahedral coordination [8].

Spectroscopic studies of aurichalcites and related minerals have been sparse. Reports regarding the chemical analysis, ESR, electronic and some limited infrared spectroscopic studies have been published [9]. These workers reported optical spectra revealing the presence of copper in D_{4h} symmetry with crystal field (Dq) and tetragonal field (Ds and Dt). This research was further extended in a comparison of rosasite and aurichalcite [10]. Optical and EPR spectra of aurichalcite accounted for Cu^{2+} ion in the distorted octahedron site [10]. Stoilova et al. [29] reported the infrared spectra of a series of synthetic hydroxy carbonates containing Cu^{2+}.

Raman spectroscopy has proven very useful for the study of minerals [11–13]. Indeed Raman spectroscopy has proven most useful for the study of diagentically related minerals as often occurs with carbonate minerals [14–18]. Some previous studies have been undertaken by the authors using Raman spectroscopy to study complex secondary minerals formed by crystallisation from concentrated sulphate solutions [19]. The authors have undertaken some comprehensive studies of selected carbonate minerals [20–24]. The importance of this work rests with the application of Raman spectroscopy to the study of minerals and inorganic compounds which show no or limited symmetry. As part of our comprehensive research on the molecular structure of secondary minerals, we report the Raman spectroscopic study complemented by X-ray diffraction and electron microscopy of selected aurichalcites from different origins.

2. Experimental

2.1. Mineral samples

Selected minerals were obtained from the Mineralogical Research Company and other sources including Museum Victoria, Victoria, Australia. The samples were phase analysed by X-ray diffraction and for chemical composition by EDX measurements.

2.2. X-ray diffraction

X-ray diffraction patterns were collected using a Philips X'pert wide angle X-ray diffractometer, operating in step scan mode, with Cu Kα radiation (1.54052 Å). Patterns were collected in the range 5–90 ° 2θ with a step size of 0.02° and a rate of 41.75 s per step. Samples were prepared as powders and pressed into a depression quartz low background plate.

2.3. SEM and EDX

Mineral samples were coated with a thin layer of evaporated carbon and secondary electron images were obtained using a scanning electron microscope (FEI Quanta 200 SEM, FEI Company, Hillsboro, OR, USA). For X-ray microanalysis (EDX), three samples were embedded in Araldite resin and polished with diamond paste on Lamplan 450 polishing cloth using water as a lubricant. The samples were coated with a thin layer of evaporated carbon for conduction and examined in a JEOL 840A analytical SEM (JEOL Ltd., Tokyo, Japan) at 25 kV accelerating voltage. Preliminary analyses of the carbonate mineral samples were carried out on the FEI Quanta SEM using an EDAX X-ray microanalyser, and microanalyses of the clusters of fine crystals were carried out using a full standards quantitative procedure on the JEOL 840 SEM using a JEOL-2300 energy-dispersive X-ray microanalysis system (JEOL Ltd., Tokyo, Japan). Oxygen was not measured directly but was calculated using assumed stoichiometry to the other elements analysed.

2.4. Raman microprobe spectroscopy

The crystals of aurichalcite were placed and oriented on the stage of an Olympus BHSM microscope, equipped with 10× and 50× objectives and part of a Renishaw 1000 Raman microscope system, which also includes a monochromator, a filter system and a charge coupled device (CCD). Raman spectra were excited by a He–Ne laser (633 nm) at a resolution of 2 cm^{-1} in the range between 100 and 4000 cm^{-1}. Repeated acquisition using the highest magnification was accumulated to improve the signal to noise ratio. Spectra were calibrated using the 520.5 cm^{-1} line of a silicon wafer. In order to ensure that the correct spectra are obtained, the incident excitation radiation was scrambled. Details of the technique have been published by the authors.

2.5. Mid-IR spectroscopy

Infrared spectra were obtained using a Nicolet Nexus 870 FTIR spectrometer with a smart endurance single bounce diamond ATR cell. Spectra over the 4000–525 cm^{-1} range were obtained by the co-addition of 128 scans with a resolution of 4 cm^{-1} and a mirror velocity of 0.6329 cm/s. Spectra were co-added to improve the signal to noise ratio.

Spectral manipulation such as baseline adjustment, smoothing and normalisation were performed using the Spectracalc software package GRAMS (Galactic Industries Corporation, NH, USA). Band component analysis was undertaken using the Jandel Scientific 'Peakfit' software package which enabled the type of fitting function to be selected and allows specific parameters to be fixed or varied accordingly. Band fitting was done using a Lorentz–Gauss cross-product function with the minimum number of component bands used for the fitting process. The Gauss–Lorentz ratio was maintained at values greater than 0.7 and fitting was undertaken until reproducible results were obtained with squared correlations of r^2 greater than 0.995. The reason for using this type of mathematical function is that this function best fits vibrational spectroscopic data where the central peak is Lorentzian and the wings of the peak are Gaussian. It should be noted that where sharp bands are obtained in the Raman spectra fitting is unique. If one starts with different starting parameters, then the fit will converge to a unique result. When bands are broad the uniqueness of the fit is open to question. Band fitting offers a procedure to determine the exact position of bands.

3. Results and discussion

3.1. X-ray diffraction

The X-ray diffraction patterns of the three mineral samples together with likely impurities are shown in Fig. 2. The XRD patterns of the samples from Durango and Chihuahua are highly oriented (ref. Pattern 17-0743). The XRD patterns match that of the standard reference pattern The aurichalcite from Arizona does show some impurities of rosasite (ref. Pattern 36-1475). To make an XRD pattern all material on the surface of the host rock is scraped off for analysis, so it is not unexpected that the XRD patterns will show some impurity. In terms of both Raman spectroscopy and SEM analysis a group of crystals or even a single crystal may be collected for spectroscopic analysis.

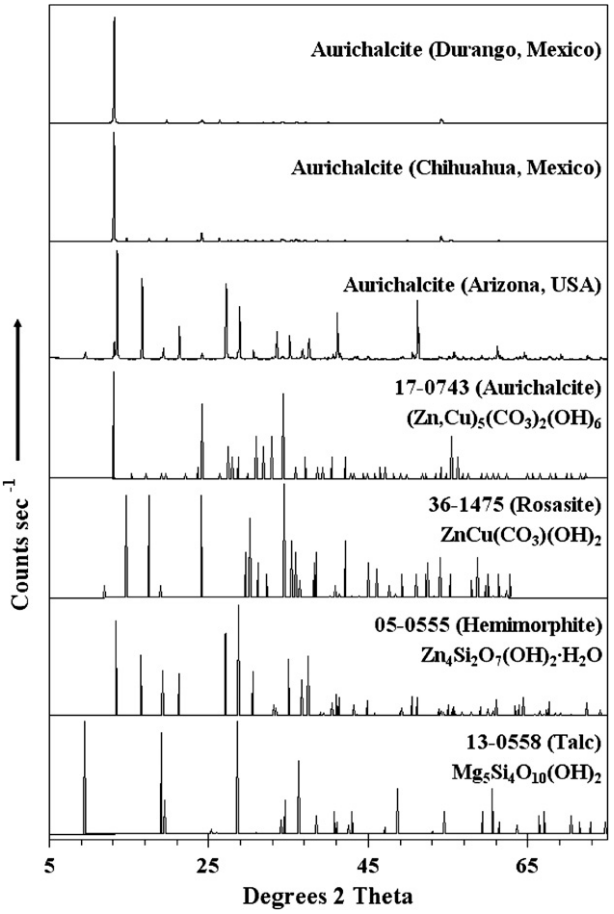


Fig. 2. X-ray diffraction patterns of aurichalcite minerals.

3.2. SEM and EDX

The SEM pictures of the three aurichalcite minerals studied in this work are shown in Fig. 3 (Durango), (b) (Chihuahua) and (c) (Arizona). The aurichalcite minerals appear to exist in two different forms (a) acicular as for Durango and (b) lath-like as is illustrated by the SEM images of the Chihuahua and Arizona samples. Often the acicular crystals appear to radiate from one centre. This suggests crystal growth from solution occurs from one nucleation point. The crystals are directed along [0 1 0] and appear often to have wedge like terminations. The crystals are quite large and may be several microns long. Crystals are acicular or fibrous and found in tufted aggregates. The crystal forms enable the mineral to be distinguished from other copper–zinc hydroxy carbonates such as malachite.

EDX measurements for the Durango aurichalcite show a Cu/Zn ratio of 1/1.06; for the Chihuahua sample the Cu/Zn ratio is 1/1.85; and for the Arizona sample is 1:/2.87. It is proposed that the morphology of the aurichalcite mineral is controlled by the Cu/Zn ratio. When the ratio is close to 1, the acicular morphology is obtained. If the Cu/Zn ratio is close to 2 or even 3, then the lath-like crystals are obtained.

3.3. Raman spectroscopy

Only a very limited number of Raman studies have been reported on the carbonate anion in hydrozincite type minerals [1,25,26]. When the carbonate species is present as a free ion not involved in any bonding it will exhibit a space

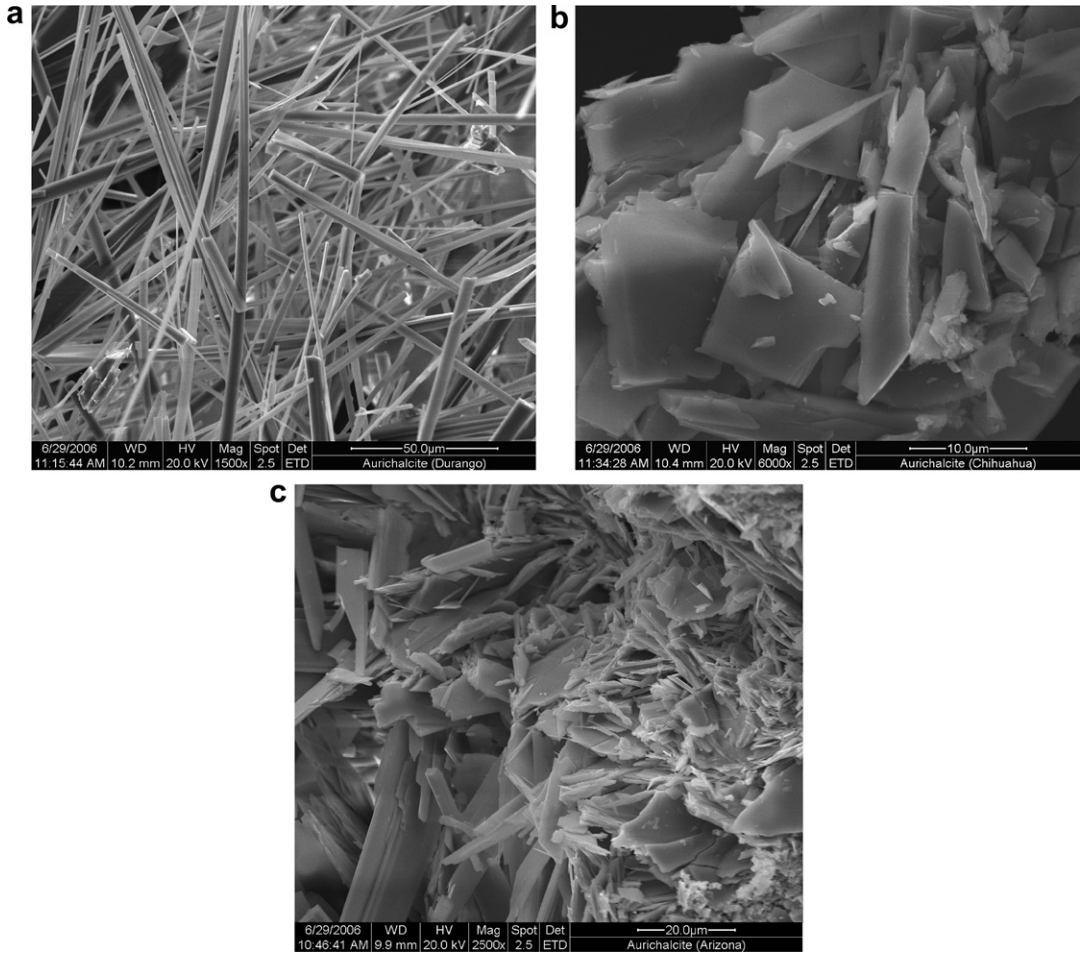


Fig. 3. SEM images of aurichalcite minerals: (a) Durango; (b) Chihuahua; (c) Arizona.

group of D_{3h}. In the Raman spectrum one will observe $v_1(A'1)$, $v_3(E')$ and $v_4(E')$. As a result three bands, the bending non-planar mode $v_2(A''2)$, the anti-symmetrical stretching mode $v_3(E')$ and the bending angular mode $v_4(E')$, will be observed in the infrared spectrum around 880, 1415 and 680 cm^{-1}, while the symmetric stretching mode $v_1(A'1)$ is infrared inactive. However, changes can be expected when the carbonate ion is bonded in a mineral structure as it will be affected by interactions with water molecules and OH-groups. In comparison with free CO_3^{2-} a shift towards lower wavenumbers is generally observed for the carbonate anion in minerals. Interaction between interlayer water molecules and the carbonate ion is reflected by the presence of bands in the OH-stretching region of the infrared spectrum around 3000–3100 cm^{-1}. The shift towards lower wavenumbers indicates a loss of freedom compared to free CO_3^{2-} and as a consequence a lowering of the carbonate symmetry from D_{3h} to probably C_{2v} or C_s.

3.4. Raman spectroscopy

The Raman spectra of aurichalcite in the 650–1700 cm^{-1} region are shown in Fig. 4. The results of the band component analysis of the Raman spectra are reported in Table 1. Two intense Raman bands are observed at 1072 and 1060 cm^{-1}. Some variation in the peak position is observed for different mineral samples especially for the second peak at around 1060 cm^{-1}. The first band at 1072 cm^{-1} is assigned to the v_1 symmetric stretching mode of the carbonate unit and the intense Raman band at ~1060 cm^{-1} is assigned to the Raman activated δ OH deformation mode. Little information on the Raman spectra of aurichalcite is available. Bouchard and Smith [45] published a Raman spectrum of an aurichalcite of unknown origin with an intense peak observed at 1074 cm^{-1}. An additional band is observed for the aurichalcite from Durango, Mexico. It is likely that this band is due variations in the chemical composition of the mineral . It is noted that the Cu/Zn ratio for the Durango aurichalcite is 1/1. In the infrared spectrum low intensity band is observed at around 1084 cm^{-1} (Fig. 6) as a shoulder on a infrared spectral profile which is dominated by bands at around 1032 cm^{-1} attributed to the δ OH deformation mode. Raman spectra of aurichalcite should be similar to that of the other hydroxy carbonates such as the rosasite mineral group [21]. For rosasite two intense Raman bands were observed at 1096 and 1056 cm^{-1}. In the infrared spectrum of Arizona aurichalcite two intense bands are observed at 1084

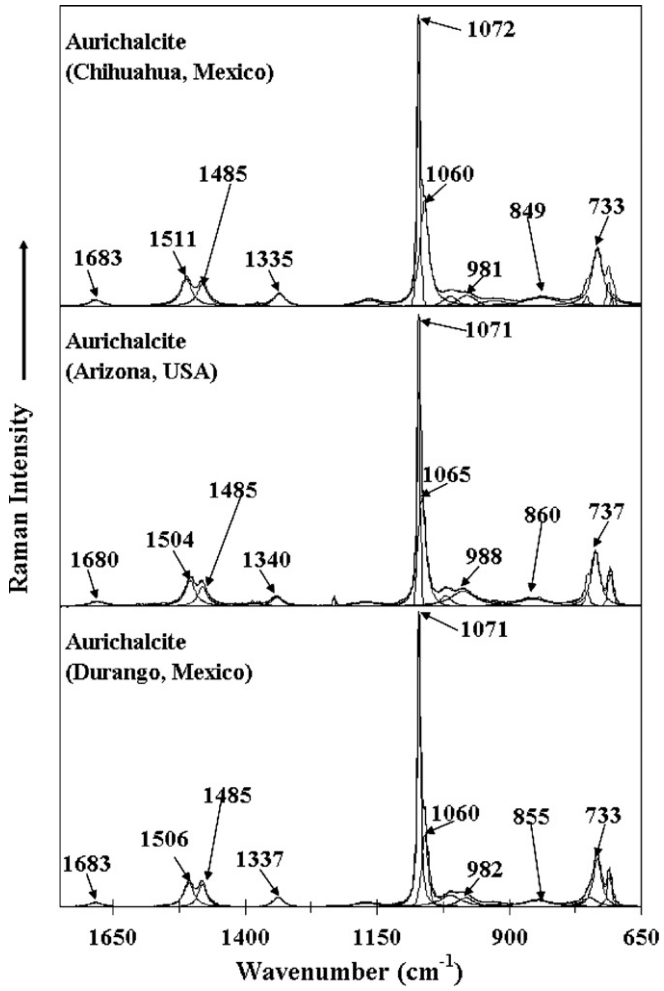


Fig. 4. Raman spectra of aurichalcite in the 650–1700 cm^{-1} region.

and 1029 cm^{-1} with an additional band at 924 cm^{-1} (Fig. 6). The first band at 1084 cm^{-1} is assigned to the v_1 symmetric stretching mode of the carbonate unit.

Bands have been observed in the infrared spectra of malachite at 1095 cm^{-1} and for azurite 1090 cm^{-1} [30,31]. The infrared spectrum of hydrocerrusite showed an intense band at 1090 cm^{-1} [32]. Interestingly the $(CO_3)^{2-}$ v_1 band of the aurichalcite mineral should not be infrared active. However because of symmetry reduction of the carbonate anion the band becomes activated. The intense Raman band observed at 1096 cm^{-1} for rosasite is assigned to the $v_1(CO_3)^{2-}$ symmetric stretching vibration. The intense Raman band at 1029 cm^{-1} is assigned to the δ OH deformation mode.

A number of low intensity bands are observed in the 1300–1500 cm^{-1} region (Fig. 4). These bands may be ascribed to the $v_3(CO_3)^{2-}$ antisymmetric stretching modes. Three bands are observed for the Durango aurichalcite at 1506, 1485 and 1337 cm^{-1}. Additional low intensity bands are observed at 1683, 1382 and 1170 cm^{-1}. Bands are observed at 1504, 1485 and 1340 cm^{-1} for the Arizona aurichalcite. For the Chihauhau aurichalcite bands in this region are observed at 1683, 1511, 1485, 1335 and 1165 cm^{-1}. The number of bands in this spectral region is attributed to the lack of symmetry of the carbonate anion in the aurichalcite structure. In the spectrum reported by Bouchard and Smith [45] two bands were reported at 1511 and 1479 cm^{-1}. Their spectra showed low signal to noise ratio and any low intensity bands would not be observed. Infrared spectra show multiple bands in the 1200–1600 cm^{-1} region (Fig. 5). For the Durango aurichalcite infrared bands are observed at 1563, 1503 1471, 1406 1353 and 1308 cm^{-1}. A similar pattern is observed for the Chihauhau aurichalcite with bands observed at 1567, 1503, 1477, 1406, 1343 and 1304 cm^{-1}. These bands are attributed to the infrared active $v_3(CO_3)^{2-}$ antisymmetric stretching vibrations.

The bands for the Arizona aurichalcite appear to be shifted to higher wavenumbers. The band at 1633 cm^{-1} is attributed to water bending modes. The band is not observed for the other aurichalcite minerals. The question arises as to whether water is bonded in the structure of the aurichalcite replacing some of the OH units. The infrared spectral patterns are similar for all three minerals. The complexity of the infrared spectra in this spectral region may be attributed to the combination of spectra from two different carbonate units. The 1557 cm^{-1} band may be associated with the 1412 cm^{-1} band. The second band at 1509 cm^{-1} is likely to be associated with bands at 1366 and 1361 cm^{-1}.

3.5. Comparison with the spectra of other hydroxy carbonates

A comparison may be made with the spectra of other hydroxy carbonate minerals. For rosasite $[(Cu,Zn)_2(CO_3)(OH)_2]$ [33–35] Raman bands for the 298 K spectrum are observed at 1516, 1493, 1458 and 1364 cm^{-1}. The Raman spectrum of malachite in this spectral region displays bands at 1516, 1493 and 1363 cm^{-1}. The band positions for rosasite and related minerals strongly resemble that of malachite. These results indicate two concepts: (a) the identification of more than one carbonate anion in the structure as implied from the symmetric stretching vibrations and (b) the crystal structure the reduction of symmetry of the carbonate anion [8]. These two factors combine to give multiple bands in this spectral region. Spectra may be compared with that of the other rosasite minerals: The Raman spectrum of kolwezite $[(Cu,Co)_2(CO_3)(OH)_2]$ [36] in $v_3(CO_3)^{2-}$ antisymmetric stretching region shows bands at 1515, 1495, 1456, 1426 and 1363 cm^{-1}. The Raman spectrum of glaukosphaerite $[(Cu,Ni)_2(CO_3)(OH)_2]$ [37–39] showed four bands at 1522, 1496, 1460 and 1367 cm^{-1}. For the mineral nullaginite $[(Ni)_2(CO_3)(OH)_2]$ [40–42], the Raman spectrum of the 1300–1500 cm^{-1} region showed an intense sharp band at 1426 cm^{-1} (with band width 15.0 cm^{-1}) with an additional higher wavenumber component at 1441 cm^{-1}. Although

Table 1
Table of the results of the Raman spectra of aurichalcite

Aurichalcite (Chihuahua, Mexico)			Aurichalcite (Arizona, USA)			Aurichalcite (Durango, Mexico)			Suggested assignment
Centre	FWHM	% Area	Centre	FWHM	% Area	Centre	FWHM	% Area	
3355	148.7	20.41	3348	139.5	16.33	3338	166.8	22.67	OH-stretching vibration
1683	26.1	0.63	1683	28.8	0.61	1680	36.5	0.62	
1511	24.0	2.97	1506	22.7	3.29	1506	23.9	3.21	$v_3(CO_3)^{2-}$
1485	22.0	2.27	1485	18.6	2.50	1485	21.2	2.15	
1377	12.8	0.15				1382	46.3	0.65	
1335	25.4	1.11	1337	22.8	1.10	1337	23.8	0.95	
						1231	4.6	0.15	
						1227	2.6	0.03	
1165	47.3	0.89	1171	42.9	1.18	1170	60.5	1.20	
1072	7.2	5.94	1071	6.6	13.24	1071	6.7	5.23	$v_1(CO_3)^{2-}$
1060	19.6	9.26	1065	13.9	5.31	1060	17.8	8.42	
						1020	23.8	1.36	
1012	31.3	0.94	1011	45.9	3.78				
981	38.8	1.28	982	33.4	1.73	988	54.7	4.40	
927	54.5	0.92	929	35.9	0.47				
849	78.6	2.94	860	57.9	2.57	855	66.8	2.61	$v_2(CO_3)^{2-}$
753	8.9	0.40	748	33.5	1.81	752	9.0	0.73	$v_4(CO_3)^{2-}$
733	24.6	6.30	733	18.0	5.34	737	19.4	4.95	
711	9.6	0.70	710	9.6	1.71	708	11.5	1.37	
703	7.3	0.29							
			533	32.0	0.48	540	15.5	0.27	
524	53.2	1.47							
						515	20.8	0.79	
498	32.8	2.72	499	27.0	2.35	499	26.7	2.68	v_1(CuO)
460	23.2	2.50	460	19.2	2.51	463	19.0	4.27	
430	27.8	1.73	428	25.9	0.87	432	19.5	1.79	
388	21.2	4.29	390	17.7	4.45	392	16.5	5.84	v_1(ZnO)
369	27.3	0.77	370	30.8	0.66	372	29.4	0.86	
351	12.9	0.49	352	15.1	0.84	353	14.2	1.08	
			328	19.3	2.38	328	18.7	1.91	
313	75.2	9.72	310	31.6	3.10	312	35.1	2.39	
278	19.2	0.50	283	36.1	2.70	282	36.0	1.82	
252	30.2	1.58							
232	20.7	1.98	238	25.4	1.12	240	28.0	1.82	
			229	13.8	0.82	227	13.2	0.98	
207	24.6	2.23	209	17.3	3.48	207	19.1	2.09	
185	14.2	1.39	185	18.3	1.34	189	12.1	0.69	
177	8.9	1.45	178	7.0	0.61	176	11.2	1.29	
166	13.6	5.39	167	10.7	6.18	166	12.3	3.68	
155	7.8	0.40	159	17.7	1.38	155	15.3	1.36	
142	13.5	3.44	141	9.1	3.27	139	9.7	2.74	v_2(CuO)/v_2(ZnO)
						128	8.8	0.18	
118	17.2	0.38	119	12.2	0.37	119	8.8	0.61	
108	7.3	0.15	108	8.7	0.12	108	7.6	0.15	

these bands are in different positions to that of rosasite the bands are attributed to the $v_3(CO_3)^{2-}$ antisymmetric stretching vibrations.

The bands for aurichalcite are shown in Fig. 4. The v_2 bending modes for carbonates vary from around 890 to 850 cm^{-1}. A single band is observed for the Durango aurichalcite at 855 cm^{-1} assigned to the v_2 bending mode. The band is observed at 860 cm^{-1} for the Arizona aurichalcite and 849 cm^{-1} for the Chihuahua aurichalcite. It is probable that more than one band is observed in this region; however the intensity of the band is so low, it makes band fitting difficult. In the Raman spectra of the rosasite group of minerals in the 850–800 cm^{-1} region only very low intensity bands are also observed. The observation of more than one v_2 mode suggests symmetry reduction of the carbonate anion in the structure. For the Durango spectrum two Raman bands may be resolved at 860 and 845 cm^{-1}. Multiple bands are observed for the carbonate v_4 in phase bending modes in the Raman spectrum of aurichalcite. For the Durango aurichalcite three bands are observed at 752, 733 and 708 cm^{-1}; for the Arizona aurichalcite 748, 737 and 710 cm^{-1}; and for the Chihuahua aurichalcite 753, 733 and 711 cm^{-1}. These bands are ascribed to the v_4 bending modes.

For azurite two bands are observed 834 and 765 cm^{-1} and are attributed to the v_2 out of phase and v_4 in phase

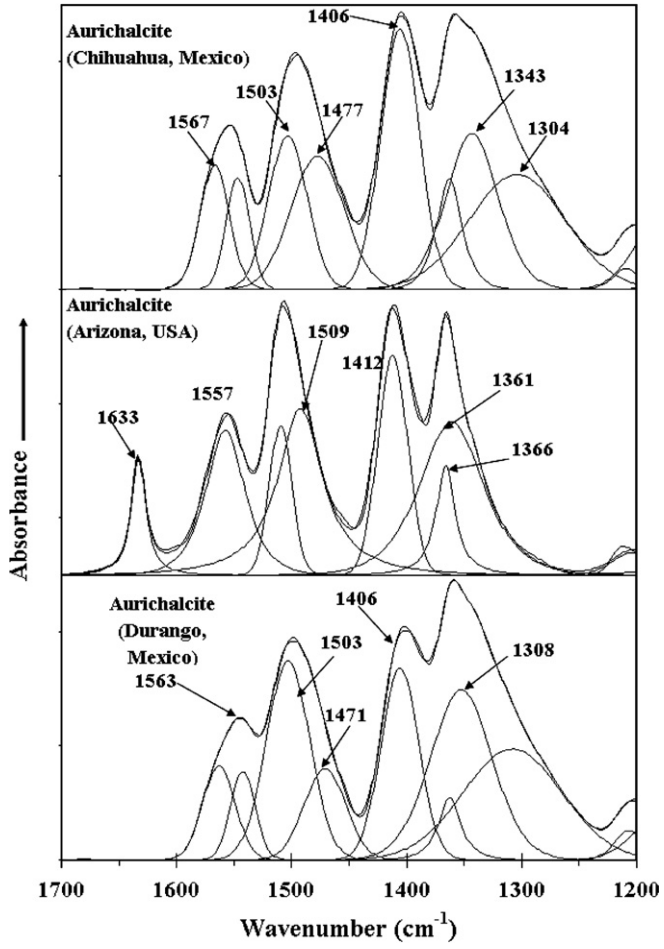


Fig. 5. Infrared spectra of aurichalcite in the 1200–1700 cm^{-1} region.

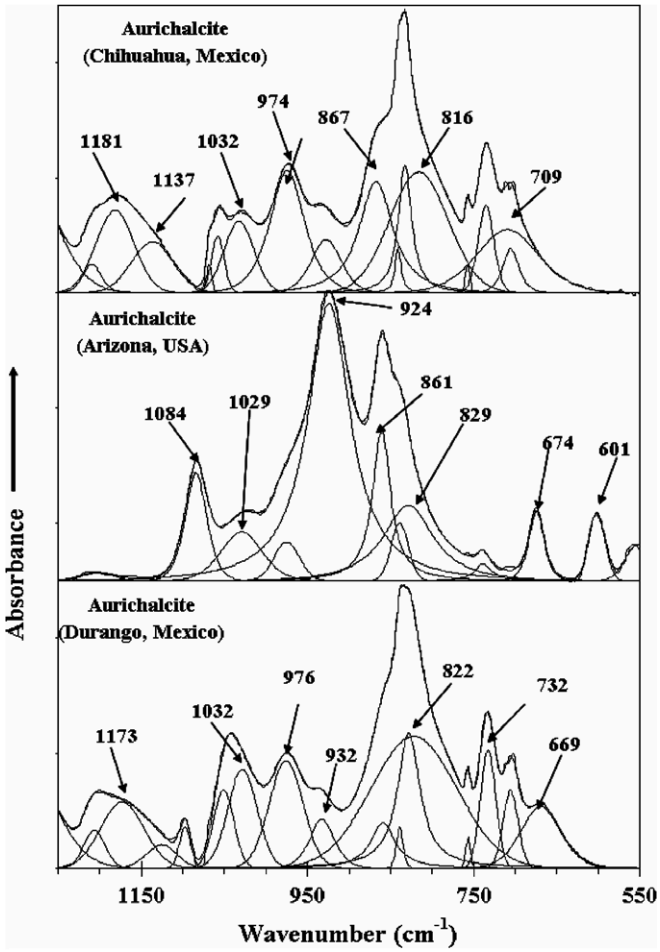


Fig. 6. Infrared spectra of aurichalcite in the 550–1150 cm^{-1} region.

bending modes of carbonate in azurite [30]. A component band is observed at 739 cm^{-1} and is also assigned to the v_4 mode. The number of bands observed in this spectral region may be attributed to the structural distortion of the mineral. Only a single band at 817 cm^{-1} is observed in this region for malachite. The FTIR spectrum of malachite showed two bands at 879 and 821 cm^{-1} [30]. This FTIR spectral region is more complex for azurite with bands observed at 872, 837, 815 and 796 cm^{-1}. This complexity is again ascribed to the loss of degeneracy. The equivalent Raman bands for malachite are observed at 752 and 717 cm^{-1}. In the infrared spectra bands are observed at 779, 754 and 701 cm^{-1} for azurite and at 780, 750 and 715 cm^{-1} for malachite [30].

The Raman spectra of the low wavenumber region are reported in Fig. 7. It is expected that bands in this region are associated with CuO and ZnO stretching and bending vibrations. Strong bands are observed at around 498, 460 and 390 cm^{-1}. In the structure as shown in Fig. 1, there are three structurally distinct MO stretching vibrations. The M3 site is a solely Zn site. The M1, M2 and M4 sites are shared randomly between Cu and Zn [43]. The above bands are associated with these CuO and ZnO stretching modes. Bouchard and Smith [45] reported Raman bands at 503, 463, and 389 cm^{-1} which are in agreement with the band positions reported here; however no assignments were offered. The number of bands observed in this spectral region may be attributed to the structural distortion of the mineral. Two intense bands are observed at around 166 and 142 cm^{-1}. These bands are assigned to the OCuO and OZnO bending vibrations.

3.6. Raman spectroscopy of the hydroxyl stretching region

The Raman spectra of the OH-stretching region of the three aurichalcite mineral samples are shown in Fig. 8. A single symmetric band is observed for the Durango aurichalcite at 3338 cm^{-1} which may be compared with the value of 3348 cm^{-1} for Arizona aurichalcite and 3355 cm^{-1} for the Chihuahua aurichalcite. A comparison can be made with rosasite where two distinct bands are observed at 3387 and 3319 cm^{-1}. The bands are assigned to the OH-stretching vibration. Bouchard and Smith [45] reported a noticeably broad band in the Raman spectrum of aurichalcite at 3331 cm^{-1}. This value is in good agreement with the results reported in this work. In the infrared spectra, more complexity is observed. Infrared bands for the Durango aurichalcite are observed at 3491, 3350,

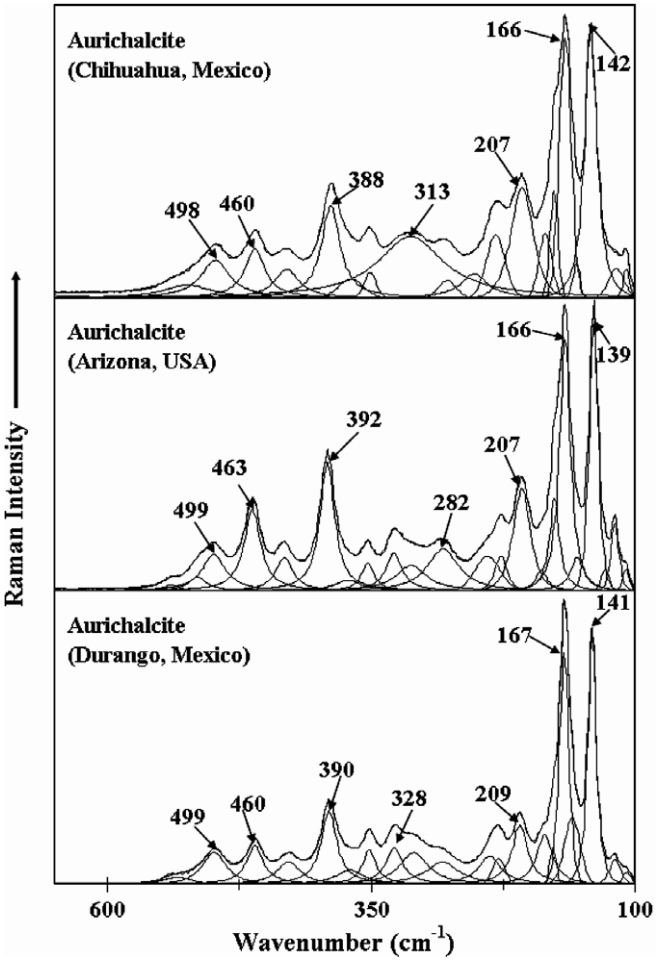


Fig. 7. Raman spectra of aurichalcite in the 100–600 cm^{-1} region.

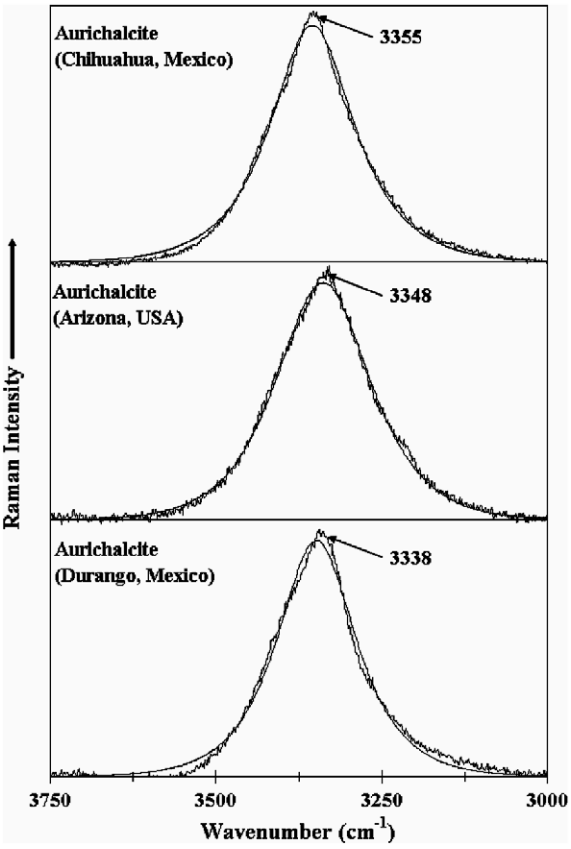


Fig. 8. Raman spectra of aurichalcite in the 3000–3750 cm^{-1} region.

3244 and a broad band at 3173 cm^{-1}. The infrared spectrum of the sample from Chihuahua gave bands at 3359, 3249 and 3106 cm^{-1}. The broad band at around 3163 cm^{-1} may be ascribed to adsorbed water. The first two bands are assigned to OH-stretching vibrations.

The question can be asked as to why the bands in the hydroxyl stretching region occurs in various positions for the different minerals. The reason is attributed to variation in hydrogen bond distances between the OH units and the oxygens of adjacent carbonate units. If a Libowitzky type formula [44] is employed an estimate of the hydrogen bond distances can be made. The two IR band positions for the Chihuahua aurichalcite gives H-bond distances of 2.77_3 and 2.72_1 Å. A comparison of hydrogen bond distances may be made with either hydroxy carbonates such as rosasite and malachite. Hydrogen bond distances vary for rosasite from 2.78_0 to 2.86_7 Å. These values are in harmony with the values for malachite which are 2.863_6 and 2.801_7 Å. Further the hydrogen bond distances for pokrovskite are significantly longer with values between 2.83 and 3.28_0 Å. It is concluded that the hydrogen bond distances for aurichalcite are shorter than for the other hydroxy carbonates.

3.7. A comparison with other minerals

The spectra are composition dependent and additional bands may be ascribed to divalent cation content. The generic formula for aurichalcite is $(Zn,Cu^{2+})_5(CO_3)_2(OH)_6$. The ratio of Zn to Cu may vary between samples and some Zn may be replaced by Ca and other cations. The composition of the aurichalcite from mapimi, Duarango, Mexico is 20.8% CuO, 53.2% ZnO, 16.1% CO_2, 9.9% H_2O [6]. This leads to a formula of $Zn_{3.6}Cu_{1.4}(CO_3)_2(OH)6$. Another analysis of aurichalcite from Salida, Chaffee Co., CO, USA gave a formula of $Zn_{3.75}Cu_{1.25}(CO_3)_2(OH)_6$. Variation in the ZnO content varies from 55.8% to 44.8% by weight whilst CuO varies from 18.2% to 14.5%. Further minor amounts of other cations may influence the spectra. Studies by Charnock et al. [46] have shown using EXAFS techniques that only divalent cations are in the crystal structure of aurichalcite and that the Cu may take up more than one position in that structure. The Cu:Zn ratio may vary between 1:3 and 1:1.5. Charnock et al. have shown using EXAFS that the copper atoms preferentially enter the Jahn–Teller elongated, octahedral (M2) and trigonal bipyramidal (M4) sites, with the zinc atoms entering the more regular octahedral (M1) and tetrahedral (M3) site. Furthermore, substantial solid solution towards the zinc rich region is

facilitated by the substitution of copper by zinc on the M2 and M4 sites [43].

4. Conclusions

Raman spectroscopy complimented with infrared data, X-ray diffraction, electron microscopy and EDAX have been used to characterise the structure and chemical composition of the mineral aurichalcite. The spectra are correlated with the structure of the mineral. Compositional variation for aurichalcite is observed for minerals of different origin. This compositional variation affects the Raman spectral profile. A similar cation substitution reliance is observed for the hydroxyl stretching vibrational modes. This is related to the hydrogen bond distances of the OH units and the adjacent carbonate units in the aurichalcite structure.

The XRD patterns of all three samples (but more so for the specimens from Durango and Chihuahua) indicate high orientation and contain some expected impurities such as rosasite and hydrozincite but never the less match the standard reference patterns. SEM analysis of the non-mechanochemically activated sample confirms the XRD orientation of the ground sample findings as images show highly crystalline and ordered structures in the form of micron long fibres and plates. EDAX analysis indicates vast differences in metal ion chemical composition (Cu/Zn ratios) ranging from 1/1.06 to 1:/2.87.

The question arises as to why there are similar Raman spectral patterns for aurichalcite as compared with other hydroxy carbonate minerals such as hydrozincite and members of the rosasite mineral group. The answer must infer that the minerals must have the same structure or at least related structures. Aurichalcite is monoclinic as is malachite with point group $2/m$. The rosasite mineral group has spectra similar to that of malcachite. Therefore it can be suggested that the structure of the rosasite group of minerals is monoclinic, although at this point in time remains unproven. This conclusion is in agreement with the assumptions of Anthony et al. (2003) who state that rosasite and related minerals have monoclinic structure by analogy with malachite.

Acknowledgement

The financial and infra-structure support of the Queensland University of Technology, Inorganic Materials Research Program is gratefully acknowledged. The Australian Research Council (ARC) is thanked for funding the instrumentation. Professor B. Jagannadha Reddy wishes to thank the Inorganic materials research program for a QUT visiting professorial fellowship.

References

[1] R.S. Braithwaite, G. Ryback, Mineral. Mag. 33 (1963) 441.
[2] R.G. Herman, C.E. Bogdan, P.L. Kumler, D.M. Nuszkowski, Mater. Chem. Phys. 35 (1993) 233.
[3] J.L. Jambor, Can. Mineral. 8 (1964) 92.
[4] P.A. Williams, Oxide Zone Geochemistry, Ellis Horwood Ltd., Chichester, West Sussex, England, 1990.
[5] G. Sengupta, R.K. Sharma, V.B. Sharma, K.K. Mishra, M.L. Kundu, R.M. Sanyal, S. Dutta, J. Solid State Chem. 115 (1995) 204.
[6] J.W. Anthony, R.A. Bideaux, K.W. Bladh, M.C. Nichols, Handbook of Mineralogy, vol. 5, Mineral Data Publishing, Tiscon, AZ, USA, 2003.
[7] J.L. Jambor, I.D. Macgregor, Paper – Geological Survey of Canada 74-1(Pt. B) (1974) 172.
[8] M.M. Harding, B.M. Kariuki, R. Cernik, G. Cressey, Acta Crystallogr., Sect. B: Struct. Sci. B50 (1994) 673.
[9] S. Vedanand, B.M. Sudhana, B.J. Reddy, P.S. Rao, Bull. Mater. Sci. 19 (1996) 1089.
[10] B.J. Reddy, F. Nieto, A.S. Navas, Neues Jahrbuch fuer Mineralogie Monatshefte (2004) 302.
[11] R.L. Frost, S.J. Palmer, J.M. Bouzaid, B.J. Reddy, J. Raman Spectrosc. 38 (2007) 68.
[12] R.L. Frost, D.A. Henry, M.L. Weier, W. Martens, J. Raman Spectrosc. 37 (2006) 722.
[13] R.L. Frost, A.W. Musumeci, J.T. Kloprogge, M.O. Adebajo, W.N. Martens, J. Raman Spectrosc. 37 (2006) 733.
[14] R.L. Frost, J. Cejka, M. Weier, W.N. Martens, J. Raman Spectrosc. 37 (2006) 879.
[15] R.L. Frost, M.L. Weier, J. Cejka, J.T. Kloprogge, J. Raman Spectrosc. 37 (2006) 585.
[16] R.L. Frost, J. Cejka, M.L. Weier, W. Martens, J. Raman Spectrosc. 37 (2006) 538.
[17] R.L. Frost, M.L. Weier, B.J. Reddy, J. Cejka, J. Raman Spectrosc. 37 (2006) 816.
[18] R.L. Frost, M.L. Weier, W.N. Martens, J.T. Kloprogge, J. Kristof, J. Raman Spectrosc. 36 (2005) 797.
[19] R.L. Frost, R.-A. Wills, M.L. Weier, W. Martens, J. Raman Spectrosc. 36 (2005) 435.
[20] R.L. Frost, D.L. Wain, W.N. Martens, B.J. Reddy, Polyhedron 26 (2007) 275.
[21] R.L. Frost, J. Raman Spectrosc. 37 (2006) 910.
[22] R.L. Frost, M.L. Weier, J. Cejka, G.A. Ayoko, Spectrochim. Acta, Part A 65 (2006) 529.
[23] R.L. Frost, K.L. Erickson, M.L. Weier, O. Carmody, J. Cejka, J. Mol. Struct. 737 (2005) 173.
[24] R.L. Frost, B.J. Reddy, D.L. Wain, M.C. Hales, J. Near Infrared Spectrosc. 14 (2006) 317.
[25] M. Bouchard, D.C. Smith, Asian Chem. Lett. 5 (2001) 157.
[26] J. Kasperek, M. Lenglet, Rev. Metall./Cahiers d'Informations Tech. 94 (1997) 713.
[29] D. Stoilova, V. Koleva, V. Vassileva, Spectrochim. Acta, Part A: Mol. Biomol. Spectrosc. 58A (2002) 2051.
[30] R.L. Frost, W.N. Martens, L. Rintoul, E. Mahmutagic, J.T. Kloprogge, J. Raman Spectrosc. 33 (2002) 252.
[31] R.L. Frost, Z. Ding, J.T. Kloprogge, W.N. Martens, Thermochim. Acta 390 (2002) 133.
[32] R.L. Frost, W. Martens, J.T. Kloprogge, Z. Ding, Spectrochim. Acta, Part A 59A (2003) 2705.
[33] D. Lovisato, Atti. Accad. Lincei 17 (2) (1910) 723.
[34] G.P. Bolgov, N.A. Rozybakieva, Sbornik Nauch. Trudov Kazakh. Gorno-Met. Inst. (1956) 34.
[35] C. Perrier, Am. Mineral. 6 (1921) 166.
[36] M. Deliens, P. Piret, Bull. Mineral. 103 (1980) 179.
[37] M.W. Pryce, J. Just, Mineral. Mag. 39 (1974) 737.
[38] L.B. Railsback, Carbonates Evaporites 14 (1999) 1.
[39] J.L. Jambor, Can. Mineral. 14 (Pt. 4) (1976) 574.
[40] E.H. Nickel, J.A. Hallbert, R. Halligan, J. Geol. Soc. Austr. 26 (1979) 61.
[41] E.H. Nickel, L.G. Berry, Can. Mineral. 19 (1981) 315.

[42] E.H. Nickel, J.F.M. Clout, B.J. Gartrell, Mineral. Record 25 (1994) 283.
[43] J.M. Charnock, P.F. Schofield, C.M.B. Henderson, G. Cressey, B.A. Cressey, Mineral. Mag. 60 (1996) 887.
[44] E. Libowitzky, Monatshefte fuer Chemie 130 (1999) 1047.
[45] M. Bouchard, D.C. Smith, Spectrochimica Acta, Part A: Mol. Biomol. Spectrosc. 59A (2003) 2247.
[46] J.M. Charnock, P.F. Schofield, C.M.B. Henderson, G. Cressey, B.A. Cressey, Mineral. Mag. 60 (1996) 887.

Available online at www.sciencedirect.com
ScienceDirect
Polyhedron 26 (2007) 3301–3309
POLYHEDRON
www.elsevier.com/locate/poly

Cu(II) and Pd(II) complexes of *N*-(2-hydroxybenzyl)aminopyridines

Bahattin Yalçın [a,*], Perizad A. Fatullayeva [b], Orhan Büyükgüngör [c], Başak Koşar [c], Sülin Taşcıoğlu [a], Akif I. Israfilov [b], Zaur D. Ibayev [b], Ajdar A. Medjidov [b], Adnan Aydın [a]

[a] *Marmara University, Faculty of Science and Letters, Department of Chemistry, Göztepe, Istanbul, Turkey*
[b] *Institute of Chemical Problems of Azerbaijan Academy of Sciences, Baku, Azerbaijan*
[c] *Ondokuzmayıs University, Faculty of Art and Science, Department of Physics, Samsun, Turkey*

Received 8 January 2007; accepted 3 March 2007
Available online 21 March 2007

Abstract

N-(2-Hydroxybenzyl)aminopyridines (L^i) react with Cu(II) and Pd(II) ions to form complexes in the compositions $Cu(L^i)_2(CH_3COO)_2 \cdot nH_2O$ ($n = 0, 2, 4$), $Pd(L^i)_2Cl_2 \cdot nC_2H_5OH$ ($n = 0, 2$) and $Pd(L^2)_2Cl_2 \cdot 2H_2O$. In the complexes, the ligands are neutral and monodentate which coordinate through pyridinic nitrogen. Crystal data of the complexes obtained from 2-amino pyridine derivative have pointed such a coordinating route and comparison of the spectral data suggests the validity of similar complexation modes of other analog ligands. Cu(II) complex of *N*-(2-hydroxybenzyl)-2-aminopyridine (L^1), $[Cu(L^1)_2(CH_3COO)_2]$ has slightly distorted square planar *cis*-mononuclear structure which is built by two oxygen atoms of two monodentate carboxylic groups disposed in *cis*-position and two nitrogen atoms of two pyridine rings. The remaining two oxygen atoms of two carboxylic groups form two Cu and H bridges containing cycles which joint at same four coordinated copper(II) ion. IR and electronic spectral data and the magnetic moments as well as the thermogravimetric analyses also specify on mononuclear octahedric structure of complexes $[Cu(L^2)_2(CH_3COO)_2 \cdot 2H_2O]$ and $[Cu(L^3)_2(CH_3COO)_2 \cdot 4H_2O]$ where L^2 and L^3 are *N*-(2-hydroxybenzyl)-2- or 3-aminopyridines, respectively.

X-ray analysis for $[Pd(L^1)_2Cl_2 \cdot 2C_2H_5OH]$ show square planar environment around Pd(II) ion formed by two chlorine atoms in *trans* position and two nitrogen atoms of pyridine rings. The spectral data indicate structural similarity in the complexes obtained via ligand exchange between $PdCl_2(PhCN)_2$ and 3-amino and 4-aminopyridine derivatives.
© 2007 Elsevier Ltd. All rights reserved.

Keywords: Aminopyridines; Mononuclear copper complexes; Mononuclear palladium complexes; Cu, H cycle

1. Introduction

Aminopyridines and their derivatives in most cases act as monodentate ligands which coordinate the metal ions through the nitrogen of the ring [1–4], though there are several works on 2-aminopyridine complexes in which the amino group also participates in coordination [5,6]. The 2-amino group was reported to participate in H-bond with phenol oxygen, which stabilizes the complex unit but no direct coordination to metal ion was observed [6].

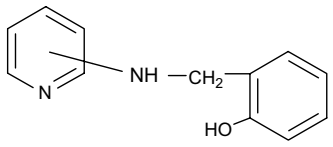
Many works on transition metal complexes with Schiff bases of aminopyridines have been reported [7–18]. In all of these compounds metal ion is coordinated via phenolic oxygen and azomethine nitrogen albeit endocyclic nitrogen atom usually does not participate in coordination. In the former reports, there are very few data on the complexes of "hydrogenated" analogues of the above-stated compounds [19,20]. The reduction of azomethine bond which interferes π conjugation between phenolic oxygen and azomethine nitrogen atoms should change the coordinating ability of such compounds.

We have investigated the coordinating behaviour of *N*-(2-hydroxybenzyl)aminopyridines which have been received by the reduction of corresponding Schiff's bases obtained from salicylaldehyde and aminopyridines. Very

* Corresponding author. Tel.: +90 216 348 77 59; fax: +90 216 349 25 81.
E-mail address: byalcin@marmara.edu.tr (B. Yalçın).

0277-5387/$ - see front matter © 2007 Elsevier Ltd. All rights reserved.
doi:10.1016/j.poly.2007.03.015

few complexes of *N*-(2-hydroxybenzyl)aminopyridines have been reported in the chemical literature [19,20]. The ligands have three electron donating atoms (NNO) and mono- and dianionic forms of the ligands present in the complexes. In our work, copper(II) acetate which is known to have binuclear structure which partially decomposes in the presence of water, is used to allow to keep the acetate as ligand in the complexes, since the preservation of acetate leads the formation of complexes with different coordination modes. Palladium(II) complexes of neutral ligands have been synthesized by the ligand exchange reactions of $PdCl_2(PhCN)_2$. The structures of complexes have been elucidated by spectral means, TGA and magnetic measurements. X-ray crystal data have also been obtained for the copper(II) and palladium(II) complexes of *N*-(2-hydroxybenzyl)-2-aminopyridine (L^1).



L^1 : 2-aminopyridine derivative

L^2 : 3-aminopyridine derivative

L^3 : 4-aminopyridine derivative

2. Experimental

2.1. Physical and chemical measurements

IR. IR spectra were recorded on a Specord-M80 (Charles Zeiss Jena) infrared spectrophotometer as KBr tablets in the range of 4000–400 cm^{-1}.

UV–Vis. The electronic spectra were recorded on spectrophotometers Specord-M40 and Shimadzu UV–Vis 240.

Magnetic susceptibility measurements were carried out at room temperature on Faraday magnetic balance with $Hg[Co(SCN)_4]$ as standard.

Thermogravimetric measurements were made on derivatograph MIM (Hungary).

Elemental analyses. The elemental analyses were performed in the analytical laboratory Tübitak, Ankara on LECO CHNS 932.

X-ray data have been obtained on a STOE IPDS 2 diffractometer with graphite monochromated Mo Kα radiation at 296 K.

2.2. Syntheses of ligands and complexes

2.2.1. Reagents

Aminopyridines, salicylaldehyde, sodium borohydride and the solvents used in the preparations were all Merck p.a. products.

Schiff bases have been synthesized by the reaction of aminopyridines with salicylaldehyde in ethanolic solutions The properties of the Schiff bases coincided with those of given in the literature [17,18].

2.2.2. Borohydride reduction of Schiff bases

N-(2-Hydroxybenzyl)aminopyridines have been obtained by the reduction of corresponding Schiff bases by sodium borohydride in ethanolic solutions. A typical procedure for the reduction is given below.

2.2.2.1. N-(2-Hydroxybenzyl)-2-aminopyridine (L^1). Into a solution of *N*-2-pyridylsalicylaldimine (25 mmol, 5 g) in 15 mL ethanol was added sodium borohydride in small portions until initial yellow-orange colour of the solution was discoloured. The mixture was poured into 60 mL water, mixed well and left to crystallize for 3 h. Fine needle crystals have been filtered, washed well with water up to neutral reaction against litmus. The crystals have been dried and recrystallized from ethanol to yield 3.2 g L^1 (65%). White powder. Mp: 104 °C. ^{1}H NMR (DMSO-d_6, δ): 10.55 (s, 1H, Ph–OH); 6.45–7.96 (m, 8H, arom.CH); 4.35 (s, 2H, CH_2), 3.50 (s, 1H, NH). *Anal.* Calc. for $C_{12}H_{12}N_2O$: C, 71.98; H, 6.04; N, 13.99. Found: C, 71.55; H, 5.68; N, 13.59%.

2.2.2.2. N-(2-Hydroxybenzyl)-3-aminopyridine (L^2). White powder. Mp: 196 °C. ^{1}H NMR (DMSO-d_6, δ): 9.65 (s, 1H, Ph–OH); 6.25–8.15 (m, 8H, arom.CH); 4.25 (s, 2H, CH_2); 3.4 (s, 1H, NH). *Anal.* Calc. for $C_{12}H_{12}N_2O$: C, 71.98; H, 6.04; N, 13.99. Found: C, 71.12; H, 5.95; N, 13.73%.

2.2.2.3. N-(2-Hydroxybenzyl)-4-aminopyridine (L^3). White powder. Mp: 177 °C. ^{1}H NMR (DMSO-d_6, δ): 8.05 (s, 1H, Ph–OH); 6.50–8.15 (m, 8H, arom.CH); 4.25 (s, 2H, CH_2); 3.2 (s, 1H, NH). *Anal*. Calc. for $C_{12}H_{12}N_2O$: C, 71.98; H, 6.04; N, 13.99. Found: C, 71.48; H, 5.45; N, 13.54%.

2.2.3. Copper(II) complexes of N-(2-hydroxybenzyl)-aminopyridines

A typical procedure for copper(II) complexes of *N*-(2-hydroxybenzyl)aminopyridines is given below.

2.2.3.1. Diacetato-bis(N-(2-hydroxybenzyl)-2-aminopyridine)-copper(II) [$Cu(L^1)_2(CH_3\ COO)_2$]. L^1 (1 mmol, 0.20 g) in 10 mL ethanol was mixed with copper acetate monohydrate (0.5 mmol, 0.10 g) solution in 5 mL water and the mixture was heated at 50–60 °C for 30 min. During cooling to room temperature, dark blue rhombic crystals were collected from dark green solution, washed with water and dried in vacuo (0.27 g, 90% yield). Mp: 170–175 °C (decomp.). $\mu_{eff} = 1.78$. TGA data (°C) (weight loss%) (Calc. weight loss%) [Endo. peak temp. °C]: (50–174 °C) (5.65) (5.15, calc. for −0.5AcOH); (174–244 °C) (18.05) (15.46, −1.5AcOH); (244–485 °C) (32.39); (485–735 °C) (28.05); [170; 244; 465 °C].

Anal. Calc. for $C_{28}H_{30}N_4O_6Cu$: C, 57.77; H, 5.19; N, 9.62; Cu, 10.91. Found: C, 57.86; H, 4.87; N, 9.77; Cu, 10.35%.

2.2.3.2. Diacetato-bis(N-(2-hydroxybenzyl)-3-aminopyridine)-copper(II)dihydrate [Cu(L^2)$_2$(CH_3COO)$_2$] · 2H_2O. Green powder. Mp: 160–165 °C (decomp.). $\mu_{eff} = 1.90$. TGA data (°C) (weight loss%) (Calc. weight loss%) [Endo. peak temp. °C]: (50–130 °C) (2.52) (2.91, calc. for –H_2O); (130–175 °C) (2.87) (2.91, –H_2O); (175– 251 °C) (43.3); (351–819 °C) (36.52); [170, 296; 422 °C]. *Anal.* Calc. for $C_{28}H_{34}N_4O_8Cu$: C, 54.39; H, 5.54; N, 9.06; Cu, 10.28. Found: C, 53.42; H, 5.62; N, 8.85; Cu, 10.20%.

2.2.3.3. Diacetato-bis(N-(2-hydroxybenzyl)-4-aminopyridine)copper(II)tetrahydrate[Cu(L^3)$_2$(CH_3COO)$_2$] · 4H_2O. Blue powder. Mp: 121–125 °C (decomp.). $\mu_{eff} = 1.81$. TGA data (°C) (weight loss%) (Calc. weight loss%) [Endo. peak temp. °C]: (50–130 °C) (3.24) (2.75, calc. for –H_2O); (130–198 °C) (6.82) (8.26, –3H_2O); (198–268 °C) (9.44) (9.17, –AcOH); (778 °C) (51.12); [130, 198, 268; 645 °C]. *Anal.* Calc. for $C_{28}H_{38}N_4O_{10}Cu$: C, 51.41; H, 5.85; N, 8.56; Cu, 9.71. Found: C, 51.17; H, 5.22; N, 8.11; Cu, 9.39%.

Refluxing the reaction mixture for 5 h yields Cu_2O as by-product. Oxidative dehydrogenations of the ligands to give *N*-(2-pyridyl)salicylaldimines were not observed.

2.2.4. Palladium(II) complexes of N-(2-hydroxybenzyl)-aminopyridines

A typical procedure for palladium(II) complexes of *N*-(2-hydroxybenzyl)aminopyridines is given below.

2.2.4.1. Dichloro-bis(N-(2-hydroxybenzyl)-2-aminopyridine)palladium(II)diethanol [Pd(L^1)$_2$Cl$_2$] · 2C_2H_5OH. L^1 (2 mmol, 0.40 g) in 10 mL ethanol was mixed with Pd(C_6H_5CN)$_2$Cl$_2$ (1 mmol, 0.383 g) solution in 15 mL ethanol. The mixture was heated at ~40 °C for 30 min, filtered hot and left for crystallization. Light yellow crystals were collected and dried in vacuo (0.44 g, 65% based on Pd). Yellow crystals. Mp: 127–130 °C (decomp.).

^{1}H NMR (DMSO-d_6, δ): 10.55 (b, 1H, Ph–OH); 9.75 (s, 1H, Ph–OH); 8.61 (d, 1H, arom.CH); 8.3 (d, 1H, arom.CH); 6.25–7.60 (m, 14H, arom.CH); 4.55 (s, 4H, CH_2–OH); 4.35 (s, 4H, CH_2); 3.40, 3.42 (s, 2H, NH) 1, 17 (s, 6H, CH_3).

Mass data (70 equiv) (*m*/*z*) (%): 623.95 (0.1, M*−EtOH); 577.9 (0.4, M*−2EtOH); 543 (25.9, PdL$_2$Cl+H); 542 (11.0, PdL$_2$Cl); 541 (25.4, PdL$_2$Cl–H); 540 (17.3, PdL$_2$Cl–2H); 203.15 (1.2); 202.1 (13.6, L+2H); 201.1 (100.0, L+H); 130.2 (4.7); 107.1 (14.4, Pd); 96.1 (4.3). TGA data (°C) (weight loss%) (Calc. weight loss%) [Endo. peak temp. °C]: (95–146 °C) (14.07) (13.75, calc. for –2C_2H_5OH); (146–345 °C) (33.11); (345–926 °C) (39.42); [146; 213; 345 °C]. *Anal.* Calc. for $C_{28}H_{36}N_4O_4Cl_2Pd$: C, 50.20; H, 5.42; N, 8.36; Pd, 15.89. Found: C, 50.02; H, 4.61; N, 8.66; Pd, 15.93%.

2.2.4.2. Dichloro-bis(N-(2-hydroxybenzyl)-3-aminopyridine)palladium(II)dihydrate [Pd(L^2)$_2$Cl$_2$] · 2H_2O. Yellow powder. Mp: 231–235 °C (decomp). ^{1}H NMR(DMSO-d_6, δ): 9.75 (s, 2H, Ph–OH); 8.20 (d, 1H, arom.CH); 7.85 (d, 1H, arom.CH); 6.7–7.4 (m, 14H, arom.CH); 4.20 (s, 4H, CH_2); 3.15, 3.18 (s, 2H, NH). TGA data (°C) (weight loss%) (Calc. weight loss%) [Endo. peak temp. °C]: (148–284 °C) (8.58) (8.87, calc. for –(HCl+H_2O)); (284–329 °C) (3.19) (2.94, –H_2O); (329–374 °C) (27.90); (374–638 °C) (40.60); [240; 273; 329; 638; 832 °C]. *Anal.* Calc. for $C_{24}H_{28}N_4O_4Cl_2Pd$: C, 46.96; H, 4.60; N, 9.13; Pd, 17.34. Found: C, 46.66; H, 3.11; N, 9.62; Pd, 18.25%.

2.2.4.3. Dichloro-bis(N-(2-hydroxybenzyl)-3-aminopyridine)-palladium(II) [Pd(L^3)$_2$Cl$_2$]. Yellow powder. Mp: 303–305 °C (decomp). ^{1}H NMR(DMSO-d_6, δ): 9.70 (s, 2H, Ph–OH); 6.2–8.2 (m, 16H, arom.CH); 4.22 (s, 4H, CH_2); 3.15, 3.18 (s, 2H, NH); TGA data (°C) (weight loss%) (Calc. weight loss%) [Endo. peak temp. °C]: (69–198 °C) (6.34) (6.31, calc. for –HCl); (198–290 °C) (7.31) (6.31, –HCl); (290–411) (22.93); (411–651 °C) (53.66); [242; 391; 476 °C]. *Anal.* Calc. for $C_{24}H_{24}N_4O_2Cl_2Pd$: C, 49.89; H, 4.18; N, 9.69; Pd, 18.42. Found: C, 49.84; H, 3.79; N, 9.15; Pd, 18.12%.

2.3. X-ray structural analyses of complexes

Blue plate [Cu(II) complex of L^1] and colorless prism [Pd(II) complex of L^1] single crystals suitable for data collection were mounted on a glass fiber and data collection processes were performed on a STOE IPDS 2 diffractometer with graphite monochromated Mo Kα radiation at 296 K. Details of crystal data, data collection and refinement results for the two crystals [21] are given in Table 1. The structures were solved by direct-methods using SHELXS-97 [22] and refined by full-matrix least-squares methods on F^2 using SHELXL-97 [20]. Molecular drawings were obtained using ORTEP-III [23] for Windows. Materials were prepared for publication using software WinGX [24].

2.3.1. Crystal structure of diacetato-bis(N-(2-hydroxybenzyl)-2-aminopyridine)copper(II) [Cu(L^1)$_2$(CH_3COO)$_2$]

The compound, namely diacetato-bis[*N*-(2-hydroxybenzyl)-2-aminopyridine]copper(II), crystallize in triclinic space group $P\bar{1}$ and molecular structure of this compound is shown in Fig. 1. Title compound has intramolecular and intermolecular hydrogen bonds; geometric parameters are given in Table 2. In three-dimensional networks, the molecules are linked by two intramolecular N–H···O and two intermolecular O–H···O hydrogen bonds. Fig. 2 shows the packing of molecules in unit cell. All hydrogen atoms except for H4A and H5A were refined using a riding model and H bond distances were set to 0.930 Å for CH, 0.960 Å for CH_2, 0.970 Å for CH_3 and 0.820 Å for OH (Table 3).

Crystal data and refinement results are listed in Table 1. Atomic coordinates and equivalent isotropic displacement parameters and the geometric parameters of molecule are available from the Cambridge Crystallographic Data Center, CCDC 605890.

Data collection: X-AREA; Cell refinement: X-AREA; Data reduction and absorption correction: X-RED32 [21].

Table 1
Crystal data of compounds and structure refinement results

	For Cu(II) complex	For Pd(II) complex
Moiety formula	$C_{28}H_{30}CuN_4O_6$	$C_{24}H_{24}C_{12}N_4O_2Pd$, $2(C_2H_5OH)$
Sum formula	$C_{28}H_{30}CuN_4O_6$	$C_{28}H_{36}C_{12}N_4O_4Pd$
Formula weight	582.10	669.91
Temperature (K)	296	296
Wavelength (Å)	0.71073	0.71073
Crystal system	triclinic	monoclinic
Space group	$P\bar{1}$	$P2_1/c$
Unit cell dimensions		
a (Å)	9.8146 (6)	10.3604 (7)
b (Å)	11.6563 (7)	7.7407 (4)
c (Å)	14.7944 (9)	19.9255 (14)
α (°)	66.760 (5)	90
β (°)	80.730 (5)	107.958 (5)
γ (°)	66.544 (5)	90
Volume (Å^3)	1426.65 (15)	1520.11 (17)
Z	2	2
Calculated density (Mg/m^3)	1.369	1.464
Absorption coefficient (mm^{-1})	0.812	0.825
$F(000)$	606	688
Crystal size (mm)	$0.69 \times 0.42 \times 0.14$	$0.57 \times 0.37 \times 0.18$
θ Range for data collection	1.50–26.11	2.01–27.24
Index ranges	$-12 < h < 12$, $-14 < k < 14$, $-18 < l < 18$	$-12 < h < 12$, $-9 < k < 9$, $-24 < l < 24$
Independent reflection	5466	2988
Measurement reflection	12214	18906
Absorption correction	integration	integration
Refinement method	full-matrix least-squares on F^2	full-matrix least-squares on F^2
Goodness-of-fit on F^2	1.164	1.068
Final R indices [$I > 2\sigma(I)$]	$R_1 = 0.0467$	$R_1 = 0.0258$
R indices (all data)	$R_1 = 0.0615$	$R_1 = 0.0697$
Largest difference peak and hole (e Å^{-3})	0.881 and −0.339	0.400 and −0.591

2.3.2. *Crystal structure of dichloro-bis(N-(2-hydroxybenzyl)-2-aminopyridine) palladium(II) diethanol* $Pd(L^1)_2Cl_2 \cdot 2C_2H_5OH$

Dichloro-bis[*N*-(2-hydroxybenzyl)-2-aminopyridine]palladium(II)diethanol, crystallize in monoclinic space group $P2_1/c$ and molecular structure of this compound is shown in Fig. 4. The asymmetric unit of the title compound contains two independent molecules. Title compound has an intramolecular and two intermolecular hydrogen bonds, geometric parameters are given in Table 2. In three-dimensional network, the molecules are linked by intramolecular O–H···O and intermolecular N–H···O and O–H···Cl hydrogen bonds. Fig. 5 shows the packing of molecules in unit cell. All non-hydrogen atoms were refined with

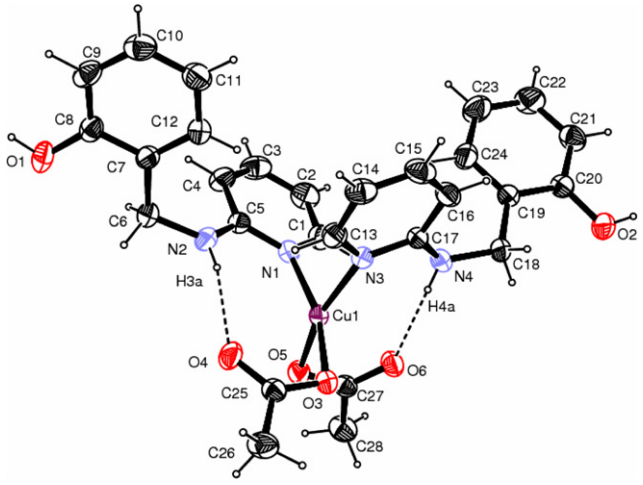


Fig. 1. An ORTEP3 view of $[Cu(L^1)_2(CH_3COO)_2]$, with the atom-numbering scheme and 30% probability displacement ellipsoids. H atoms are shown as small spheres of arbitrary radii.

Table 2
Hydrogen-bonding geometries of compounds (Å, °)

D–H···A	D–H	H···A	D···A	D–H···A
For Cu(II) complex				
O1–H1A···O4^{i}	0.82	1.91	2.630 (4)	146.2
O2–H2A···O6^{ii}	0.82	1.94	2.679 (4)	149.7
N2–H3A···O4	0.78 (4)	2.21 (4)	2.985 (5)	170 (4)
N4–H4A···O6	0.79 (4)	2.18 (4)	2.959 (5)	174 (4)
i = $-x$, $1-y$, $-z$; ii = $2-x$, $-y$, $1-z$				
For Pd(II) complex				
O2–H2B···O1	0.82	2.20	3.002 (3)	166.8
N2–H2A···O2^{i}	0.86	2.45	3.114 (3)	134.0
O1–H1A···Cl1^{i}	0.82	2.34	3.1342 (16)	162.2
i = $1-x$, $1/2+y$, $1/2-z$				

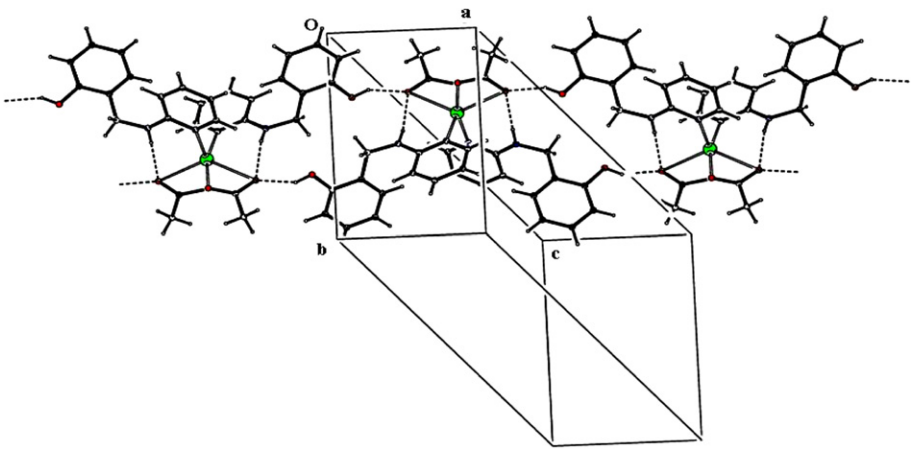


Fig. 2. A packed diagram of $[Cu(L^1)_2(CH_3COO)_2]$. Dashed lines show the intra- and intermolecular hydrogen bonds.

Table 3
Selected bond lengths and angles (Å, °) of compounds

For Cu(II) complex			
N1–Cu1	2.001 (3)	N3–Cu1	1.997 (3)
O3–Cu1	1.979 (2)	O5–Cu1	1.956 (3)
O5–Cu1–O3	89.53 (11)	O5–Cu1–N3	164.41 (11)
O3–Cu1–N3	91.77 (11)	O3–Cu1–N1	164.24 (11)
O5–Cu1–N1	90.88 (11)	N3–Cu1–N1	92.05 (11)
For Pd(II) complex			
N1–Pd1	2.0155 (16)	Cl1–Pd1	2.3052 (16)
N1–Pd1–N1^{ii}	180.00	N1–Pd1–Cl1^{ii}	89.67 (5)
N1–Pd1–Cl1	90.33 (5)	Cl1–Pd1–Cl1^{ii}	180.00

ii = $1 - x$, $1 - y$, $1 - z$

anisotropic parameters. All hydrogen atoms were refined using a riding model and H bond distances were set to 0.930 Å for CH, 0.960 Å for CH_2, 0.970 Å for CH_3, 0.820 Å for OH and 0.860 Å for NH.

The palladium ion is four coordinated by two Cl atoms and N atoms of two pyridine rings. In Pd(II) complex, the coordination environment of metal is very slightly distorted square planar. There is no significantly deviation from Pd1/Cl1/N1/Cl1^i/N1^i plane.

The N–Pd–N1 angle is 180° and N–Pd–Cl angles are 89.67° and 90.33°. Pd–N and Pd–Cl distances are 2.0155 Å and 2.3052 Å, respectively.

Crystal data and refinement results, selected bond lengths and angles are listed in Tables 1 and 3. Atomic coordinates and equivalent isotropic displacement parameters and the geometric parameters of molecule are available from the Cambridge Crystallographic Data Center, CCDC 605890.

3. Results and discussion

3.1. Infrared spectra of the ligands

The absorption bands of secondary amine N–H stretching vibrations appear at different frequencies depending on their positions in the pyridine ring, e.g., 3328 cm^{-1} for L^1; 3360 cm^{-1} for L^2 and 3355 cm^{-1} for L^3. Phenolic O–H stretching bands appear clearly at 3400 cm^{-1} only for L^3.

Prominent feature of *N*-(2-hydroxybenzyl)aminopyridines is the presence of two broad absorption bands in the region of 2500–1650 cm^{-1}, which notify the presence of intramolecular hydrogen bond between phenolic hydroxyl and secondary amino group. Although position of the band at around 2500 cm^{-1} do not change for all ligands, position of the low-frequency band shifts depending on the basicity of secondary amino group. Log *K* of amino group of aminopyridines depends on its position in the pyridine ring and has the values of 7, 6; 6.1 and 1.5 for 2-amino-; 4-amino- and 3-aminopyridine, respectively [25]. It can be inferred that similar sequence should be observed for secondary amino groups in 2-hydroxybenzyl derivatives of aminopyridines. L^1 with the least basic amino group shows maximum absorption at ~1780 cm^{-1}, L^3 at 1840 cm^{-1} and L^2 at 1860 cm^{-1}. These bands, apparently, may be attributed to the deformation vibrations of protonated secondary amino group NH_2^+.

O–H bending and C–O stretching absorptions of phenols appear at 1210–1270 cm^{-1} and 1330–1360 cm^{-1} range, respectively.

3.2. Characterization of the complexes

3.2.1. Cu(II) complexes of N-(2-hydroxybenzyl)-aminopyridines

In the IR spectra of Cu(II) complexes, displacements of absorption bands to lower frequencies were observed, by which broad peaks assigned for O–H and N–H stretching vibrations with maximum absorptions at ~3328, ~3260 and 3280 cm^{-1} appeared for $[Cu(L^1)_2(CH_3COO)_2]$, $[Cu(L^2)_2(CH_3COO)_2]\cdot 2H_2O$ and $[Cu(L^3)_2(CH_3COO)_2]\cdot 4H_2O$ complexes, respectively. 3420 and 3400 cm^{-1} bands in the spectra of L^2-Cu(II) and L^3-Cu(II) complexes assigned for the coordination water O–H stretching appear as weak and strong peaks, respectively.

The broad bands of the ligands around 2500 and 1850 cm^{-1} which are assigned for proton transfer or hydrogen bonding between phenolic OH and secondary amine NH disappear in the spectra of all complexes.

The carboxylic group stretching v_{as} in the copper complexes are obscured with ligand bands at 1624 and 1584 cm^{-1}. For complex $[Cu(L^1)_2(CH_3COO)_2]$, v_{sym} of COO^- is observed at 1448 cm^{-1}. $\Delta v = v_{as} - v_{sym} =$ 176 cm^{-1} and corresponds to bridge structure [26] which in the complex should be placed between Cu(II) ion and secondary amino group. v_{sym} of COO^- in complexes $[Cu(L^2)_2(CH_3COO)_2]\cdot 2H_2O$ and $[Cu(L^3)_2(CH_3COO)_2]\cdot 4H_2O$ are observed at 1392 cm^{-1} and 1420 cm^{-1} with $\Delta v = 192$ and 204 cm^{-1}, respectively, by which monodentate character of acetate and the absence of bridge structures in those complexes are noticed [27].

O–H bending and C–O stretching bands of phenol in 1220–1260 cm^{-1} range and at 1340, 1350 cm^{-1} frequencies, respectively, do not change their position in Cu(II) complexes to indicate the nonparticipation of phenolic O–Hs in complexation which was also clearly observed in X-ray studies of L^1-Cu(II) complex.

According to the data of elemental analyses and thermogravimetric measurements Fig. 3, ligands L^2 and L^3 form Cu(II) complexes in the composition of $[Cu(L^2)_2(CH_3COO)_2]\cdot 2H_2O$ and $[Cu(L^3)_2(CH_3COO)_2]\cdot 4H_2O$.

Electronic spectra of Cu(II) complexes in DMF solution contain three absorption bands around 400 (ε 18 $M^{-1}\,cm^{-1}$), 488 (sh) (ε 6 $M^{-1}\,cm^{-1}$) and 690 (ε 4 $M^{-1}\,cm^{-1}$) nm which accordingly can be attributed to charge transfer band and d–d transition. In the electronic spectra of $[Cu(L^2)_2(CH_3COO)_2]\cdot 2H_2O$ and $[Cu(L^3)_2(CH_3COO)_2]\cdot 4H_2O$ taken in DMF the absorption bands at 410 (ε 20 $M^{-1}\,cm^{-1}$), 488 (ε 7 $M^{-1}\,cm^{-1}$) and 699 (ε 5 $M^{-1}\,cm^{-1}$) nm and at 365 (ε 25 $M^{-1}\,cm^{-1}$), 488 (ε 6 $M^{-1}\,cm^{-1}$) and 730 (ε 4 $M^{-1}\,cm^{-1}$) nm are observed, respectively. The obtained data allow assuming that coordination routes with acetate and pyridine ligands in complexes are same. For L^2 and L^3 complexes of Cu(II), coordination of Cu(II) up to the extended octahedron is possible due to the water molecules.

Magnetic moments of the complexes are between 1.78–1.90 BM which correspond to bivalent copper complexes and specify the absence of antiferromagnetic interaction.

The X-ray study of $[Cu(L^1)_2(CH_3COO)_2]$ obtained from *N*-(2-hydroxybenzyl)-2-aminopyridine has shown that the coordination environment around Cu(II) is slightly distorted from square planar and is composed from two oxygen atoms of two monodendate carboxylic groups, disposed in *cis*-position and two nitrogen atom of two pyridine rings. In complex L^1-Cu(II), the remaining two oxygen atoms of two carboxylic groups form two 8-membered cycles both of which contain Cu and H bridges through hydrogen atoms of secondary amine groups. Earlier such cycles with Cu and H bridges have been reported for binuclear Cu(II) complexes of 2-aminopyridine such as $[Cu_2(CH_3COO)_4(NH_2C_6H_4N)_2]$ and $[Cu_2(CH_3COO)_4\cdot(NH_2C_6H_4N)_2\cdot C_4H_8O_2]$ [28] in which acetate ion acted as bidentate bridging ligand. However, mononuclear copper(II) complex $[Cu(L^1)_2(CH_3COO)_2]$ has two 8-membered cycles which are joint at the same four coordinated copper ion with square planar environment.

3.2.2. Pd(II) complexes of N-(2-hydroxybenzyl)-aminopyridines

The spectral data of the Pd(II) complexes have been supported by the XRD data. In the IR spectra of Pd(II) complexes, secondary amino group absorption of the ligand does not shift by complexation and appears at 3373 cm^{-1} for $[Pd(L^1)_2Cl_2]\cdot 2C_2H_5OH$ and 3352 cm^{-1} for $[Pd(L^2)_2Cl_2]\cdot 2H_2O$ and $Pd(L^1)_2Cl_2$, by which nonparticipation of amino group in coordination with palladium ion is notified.

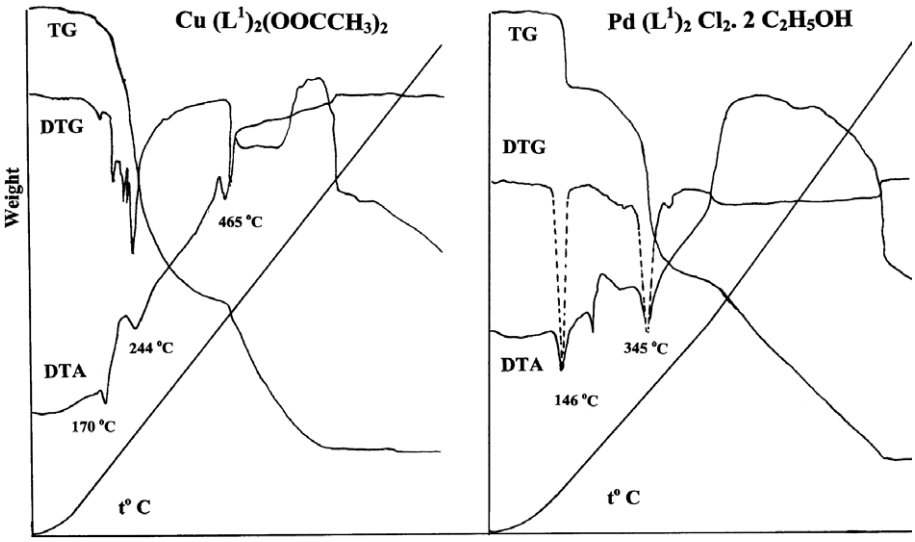


Fig. 3. TG, DTG and DTA diagrams of $[Cu(L^1)_2(CH_3COO)_2]$ and $[Pd(L^1)_2Cl_2]\cdot 2C_2H_5OH$.

Since the absorption bands of phenolic hydroxyl appear in 3350–3500 cm^{-1} range for stretching and 1210–1270 cm^{-1} range for bending modes in all Pd(II) complexes, ligand coordination should be built through endocyclic nitrogen atom which was also proved by XRD studies (Figs. 4 and 5).

Another indication for the participation of pyridine nitrogen in coordination has been shown earlier, the band groups in the region of 1600–1340 cm^{-1}, referring to pyridine ring absorption by complex formation displaces aside high frequencies in comparison with the same bands of free ligands [29,30]. However, in work [14], it has been shown that high frequency shift of IR absorption bands of pyridine ring not always can be a reliable indication on the participation of pyridine nitrogen in coordination. In [14] it was reported that in the Schiff bases of aminopyridine derivatives high-energy shift of pyridine ring bands was observed, however the X-ray data have shown the absence of coordination with endocyclic nitrogen. Regarding those band groups, our studies showed that the frequency shifts of the bands are not reliable in discussions about the contribution of pyridinic nitrogen into coordination. IR analysis of Pd complexes with *N*-(2-hydroxybenzyl)aminopyridines shows that stretching frequencies of pyridine rings decreased in $[Pd(L^1)_2Cl_2]\cdot 2C_2H_5OH$, while increased in $[Pd(L^3)_2Cl_2]$. For complex $[Pd(L^2)_2Cl_2]\cdot 2H_2O$ irregular band shifts were observed.

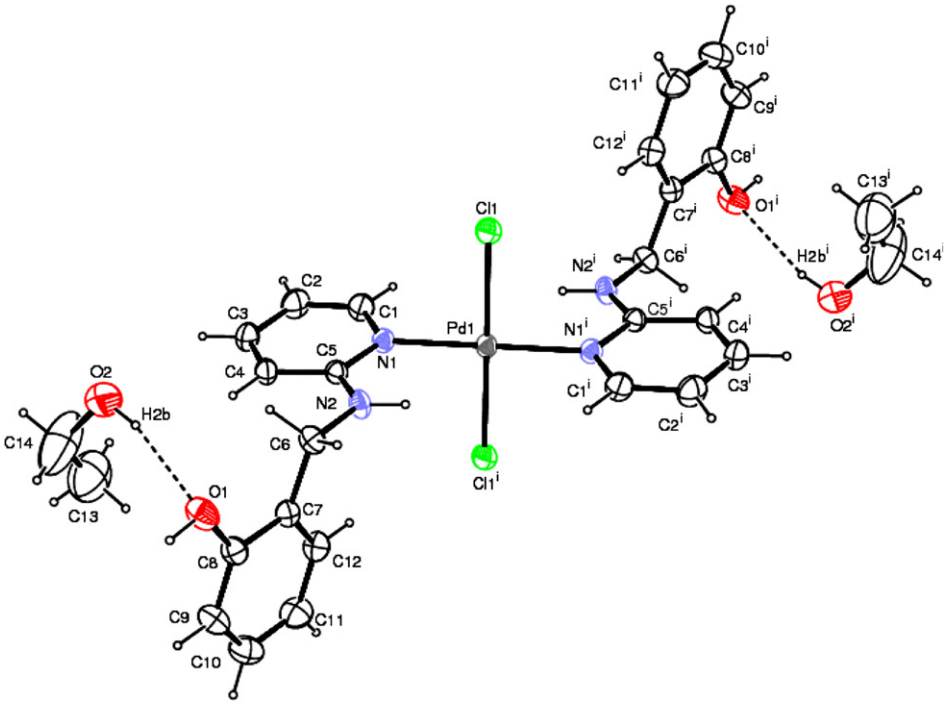


Fig. 4. An ORTEP3 view of $[Pd(L^1)_2Cl_2]\cdot 2C_2H_5OH$, with the atom-numbering scheme and 30% probability displacement ellipsoids. H atoms are shown as small spheres of arbitrary radii.

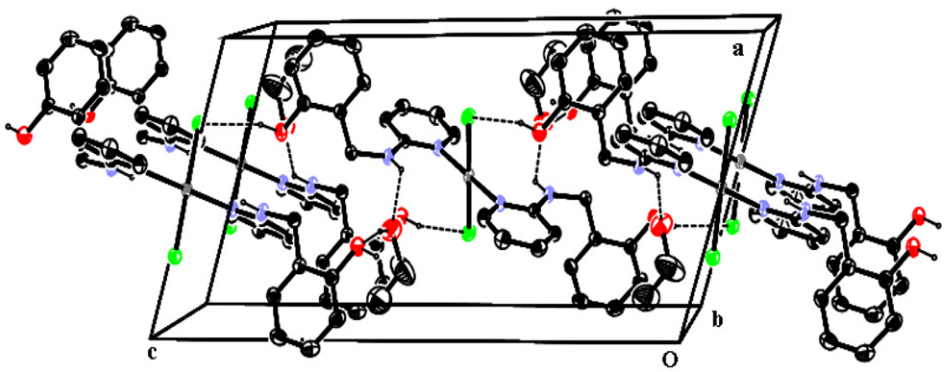


Fig. 5. A packed diagram of $[Pd(L^1)_2Cl_2]\cdot 2C_2H_5OH$. Dashed lines show the intra- and intermolecular hydrogen bonds. The hydrogen atoms which have no contribution in bonding were omitted for clarity.

Elemental analyses and TG data in Fig. 3 indicated the presence of two ethanol solvate molecules in complex $[Pd(L^1)_2Cl_2]\cdot 2C_2H_5OH$. In X-ray crystallography, the second ethanol on the outside of the unit cell was not observed. In the IR spectrum of L^1-Pd(II) complex, O–H stretching and methyl CH_2 bands of ethanol which is hydrogen bonded to phenolic oxygen and found in unit cell appear at 3311 and 1392 cm^{-1}, respectively. The free ethanol O–H stretching appears at 3544 cm^{-1} as a strong sharp peak. The C–O stretching of alcohol absorbs at 1060 cm^{-1}. ^1H NMR data also indicate the presence of two ethanol molecules in the complex.

In electronic spectra of Pd(II) complexes dissolved in DMF, two weak absorption bands at 425 and 500 nm were observed, which can be attributed to d–d transitions in square planar complexes of palladium [26].

3.3. Discussion

N-(2-Hydroxybenzyl)aminopyridines (L) (L^1: 2-amino; L^2: 3-amino; L^3: 4-amino derivative) react with Cu(II) acetate and $Pd(C_6H_5CN)_2Cl_2$ to give mononuclear complexes in which accompanying anions and neutral ligands coordinate the metal ions

$$Cu_2(CH_3COO)_4\cdot 2H_2O + 4L + (2n-2)H_2O \rightarrow 2([CuL_2(CH_3COO)_2]\cdot nH_2O) \quad (n=0,2,4)$$

$$Pd(C_6H_5CN)_2Cl_2 + 2L + nC_2H_5OH \rightarrow PdL_2Cl_2\cdot nC_2H_5OH + 2C_6H_5CN \quad (n=0,2)$$

$$Pd(C_6H_5CN)_2Cl_2 + 2L_2 + 2H_2O \rightarrow Pd(L_2)_2Cl_2\cdot 2H_2O + 2C_6H_5CN$$

However, distinctive feature of *N*-(2-hydroxybenzyl)aminopyridines is their low coordinating ability. We have attempted to obtain complexes with other metal ions such as Co(II), Ni(II), Mn(II), etc., but because of instability of these compounds, we could not succeed in their isolation in pure state.

N-(2-Hydroxybenzyl)aminopyridines have three electron donating atoms (NNO): pyridinic nitrogen, secondary amine nitrogen and phenolate oxygen. During complexation, aromatic hydroxyl and also secondary amine NH can be deprotonated to give mono and dianionic ligands. Pyridinic nitrogen can also participate in the coordination of metal. Thus, complexation behaviour of ligands depends on the reaction conditions as well as the kind of the metal.

In alkaline solutions, *N*-(2-hydroxybenzyl)-2-aminopyridine behave as tridentate ligand, as in the Ru-complex, in which secondary amino NH also deprotonates to make the ligand dianionic tridentate [19]. However, in acetone solution of the reactants, as in the formation of Re-complex, the secondary amino NH group has not been deprotonated, pyridinic nitrogen does not coordinate the metal and consequently the ligand acts as a monoanionic didentate chelate [20].

Contrary to above mentioned results, our work showed that, in both Pd(II) complexes and acetate containing complexes of Cu(II), *N*-(2-hydroxybenzyl)-2-aminopyridine as well as its 3-amino and 4-aminopyridine analogs behaved as monodentate ligand coordinating only through pyridinic nitrogen while the phenolic hydroxyl and secondary amino groups have not participated in coordination. The ligands form neutral ligand complexes. Neither secondary amine NH nor aromatic hydroxyl is deprotonated. These groups have been stabilized *via* intra- or intermolecular hydrogen bonding. This coordinating behaviour is the basic difference from corresponding Schiff bases which coordinate metal ions through phenolic oxygen and azomethine nitrogen while pyridine nitrogen has not any role in coordination. The crystal data of the complexes obtained from 2-aminopyridine derivative have supported these observations and comparison of the spectral data suggested the validity of similar complexation modes with other analog ligands.

The reactant copper(II) acetate $Cu_2(CH_3COO)_4\cdot 2H_2O$ is known to have binuclear structure which consists of four three atom bridges of carboxylate groups uniting two contiguous copper(II) ions [31]. Two water molecules occupy the terminal positions. Although its dimeric structure is destroyed in water to form monomeric hydrated Cu(II) acetate in ionic and molecular form, this destruction can be avoided in alcohol like organic solvents which have much weaker coordinating power than the water molecule [32]. The bonds between the carboxylate and Cu(II) ions should be strong enough in such solvent systems.

In our work, we have used ethanol/water (2:1) solvent mixture so that partial decomposition of dimeric structure of copper(II) acetate may take place and the acetate bridges are mainly cleaved by the attack of ligand's pyridinic nitrogen, without elimination of acetates from simultaneously formed mononuclear complex. In the working solution, interaction between the free acetate which is in the low concentration and Ar–OH would be at minimum level and consequently the bonding competition between acetate and phenolate might be negligible. Thus, the participation of deprotonated phenolic O–H in coordination is not favored. XRD data confirmed such kind of coordinating behaviour of the ligands in copper complexes.

In Cu(II) complex of L^1 (Fig. 1), hindering the Cu(II) ion from phenolate coordination via the formation of Cu, H eight membered two cycles through hydrogen bonding between acetate oxygen and secondary amine NH, may be an additional but minor reason. High yields (around 90%) of the acetatoCu(II) complexes of neutral ligands support this reaction pathway. The complexes $[Cu(L^2)_2(CH_3COO)_2]\cdot 2H_2O$ and $[Cu(L^3)_2(CH_3COO)_2]\cdot 4H_2O$ have similar structure with $[Cu(L^1)_2(CH_3COO)_2]$, but apparently without Me, H cycles.

In similar way, Pd(II) complexes are obtained in aqueous ethanol (90%) via the attack of pyridinic nitrogen to substitute benzonitrile ligand of $Pd(C_6H_5–CN)_2Cl_2$. *N*-(2-hydroxybenzyl)-aminopyridines yield light yellow

complexes in compositions of $[Pd(L^1)_2Cl_2]\cdot 2C_2H_5OH$, $[Pd(L^2)_2Cl_2]\cdot 2H_2O$ and $[Pd(L^3)_2Cl_2]$. XRD data of $[Pd(L^1)_2Cl_2]\cdot 2C_2H_5OH$ indicate coordination through pyridinic nitrogen. $[Pd(L^1)_2Cl_2]\cdot 2C_2H_5OH$ with slightly distorted square planar coordination of Pd(II) ion is realized by two nitrogen atoms of pyridine rings and two chlorine atoms in *trans*-position. Similar spectroscopic data have been obtained for the other complexes.

Appendix A. Supplementary material

CCDC 605889 and 605890 contain the supplementary crystallographic data for Pd(II) and Cu(II) complexes. These data can be obtained free of charge via http://www.ccdc.cam.ac.uk/conts/retrieving.html, or from the Cambridge Crystallographic Data Centre, 12 Union Road, Cambridge CB2 1EZ, UK; fax: (+44) 1223-336-033; or e-mail: deposit@ccdc.cam.ac.uk. Supplementary data associated with this article can be found, in the online version, at doi:10.1016/j.poly.2007.03.015.

References

[1] W.R. McWhinnie, J. Chem. Soc. (1964) 2959.
[2] E. Uhlig, M. Madler, Z. Anorg. Allgem. Chem. 338 (1965) 199.
[3] M.S. Novakovskij, V.N. Vojnova, A.A. Starodub, V.K. Soshko, Zh. Neorg. Chim. (Russia) 17 (1972) 2615.
[4] E.M. Ehairy, Egypt. J. Chem. 20 (1977) 33.
[5] R.K. Poddar, U. Agarwala, J. Inorg. Nucl. Chem. 35 (1973) 3769.
[6] A. Garcia-Raso, J.J. Fiol, A. Lopez-Zafra, A. Cabrero, I. Mata, E. Molins, Polyhedron 18 (1999) 871.
[7] D.A. Gavnovski, M.F.C. Guedes da Silva, M.N. Kopylovich, A.D. Gavnovski, J.J.R. Frausto da Silva, A.J.L. Pombeiro, Polyhedron 22 (2003) 1335.
[8] A.J. Deeming, R. Peters, M.B. Hursthouse, J.D. Baker-Dirks, J. Dalton Trans. (1982) 1205.
[9] K. Burgess, B.F.G. Johnson, J. Lewis, P.R. Raithby, J. Dalton Trans. (1983) 1661.
[10] O.A. Osipov, V.I. Minkin, D.Sh. Verkhovodova, M.L. Knyazhanski, Zh. Neorg. Khim. 12 (1967) 1549.
[11] S. Yamada, K. Yamanouchi, Bull. Chem. Soc. Jpn. 42 (1969) 2562.
[12] G.A. Kolawole, J. Coord. Chem. (1987) 67.
[13] R.K. Parashar, R.C. Sharma, A. Kumar, G. Mohan, Inorg. Chim. Acta 151 (1988) 201.
[14] A. Castineiras, J.A. Castro, M.L. Duran, J.A. Garcia-Vazquez, A. Macias, J. Romero, A. Sousa, Polyhedron 21 (1989) 2543.
[15] M.R. Mahmoud, M.T. El-Haty, J. Inorg. Nucl. Chem. 42 (1980) 349.
[16] M.I. Ayad, Sh.A. Sallam, H.E. Mabrouk, Thermochim. Acta 189 (1991) 65.
[17] T.A.K. Al-Allaf, A.Z.M. Sheet, Polyhedron 14 (1995) 239.
[18] Y.Z. Shen, H. Gu, Y. Pan, G. Dong, T. Wu, X.P. Jin, X.Y. Huang, H. Hu, J. Organomet. Chem. 605 (2000) 234.
[19] H. Miyasaka, T. Izawa, K.-I. Sugiura, M. Yamashita, Inorg. Chem. 42 (2003) 7683.
[20] A. Abrahams, G. Bandoli, S. Gatto, T.I.A. Gerber, J.G.H. Du Preez, J. Coord. Chem. 42 (1997) 303.
[21] Stoe & Cie, X-AREA (Version 1.18) and X-RED32 (Version 1.04), Stoe & Cie, Darmstadt, Germany, 2002.
[22] G.M. Sheldrick, SHELXL97 and SHELXS97, University of Göttingen, Germany, 1997.
[23] L.J. Farrugia, J. Appl. Crystallogr. 30 (1997) 565.
[24] L.J. Farrugia, WinGX, University of Glasgow, Scotland, 1999.
[25] S.J. Angyl, C.L. Angyal, J. Chem. Soc. (1952) 1461.
[26] A.B.P. Lever, Inorganic Electronic Spectroscopy, second ed., Elsevier, 1984.
[27] K. Nakamoto, Infrared and Raman Spectra of Inorganic and Coordination Compounds, Wiley and Sons, New York, 1986.
[28] A.S. Anzishkina, M.A. Porai-Koshiz, V.N. Ostrikova, D.A. Garnovski, A.P. Sadimenko, O.A. Osipov, Koordinazionnaya Khim. 13 (1987) 836.
[29] N.S. Gill, R.H. Nuttall, D.E. Scaife, D.W.A. Sharp, J. Inorg. Nucl. Chem. 18 (1961) 79.
[30] D.P. Madden, M.M. da Mota, S.M. Nelson, J. Chem. Soc. A (1970) 790.
[31] J.N. Van Niekerk, F.R.L. Schoening, Nature 171 (1953) 36;
J.N. Van Niekerk, F.R.L. Schoening, Acta Cryst. 6 (1953) 227.
[32] M. Kato, H.B. Jonassen, J.C. Fanning, Chem. Rev. 64 (1964) 99.

Available online at www.sciencedirect.com
ScienceDirect
Polyhedron 26 (2007) 3310–3322
POLYHEDRON
www.elsevier.com/locate/poly

Synthesis, vibrational spectra and thermal stability of Ag_3O_4 and related Ag_7O_8X salts ($X = NO_3^-, ClO_4^-, HSO_4^-$)

Geoffrey I.N. Waterhouse *, James B. Metson, Graham A. Bowmaker

Department of Chemistry, University of Auckland, Private Bag 90219, Auckland, New Zealand

Received 12 February 2007; accepted 6 March 2007
Available online 12 March 2007

Abstract

The titled compounds were synthesized in high purity and yield by passing an ozone/oxygen mixture (5 vol% O_3 in O_2) through aqueous solutions of different Ag(I) salts at 273–298 K. Ag_3O_4 is obtained by ozonolysis of neutral or mildly acidic solutions of AgF (0.05 M) or $AgBF_4$ (0.05 M) at 273 K. Ozonolysis of aqueous solutions of $AgNO_3$, $AgClO_4$, Ag_2SO_4 and CH_3COOAg at 273–298 K afforded $Ag_7O_8NO_3$, $Ag_7O_8ClO_4$, $Ag_7O_8HSO_4$ and Ag_2O_2, respectively. Products were characterized by XRD, SEM, XPS, FT-IR, Raman spectroscopy and DSC. The spectroscopic data show that Ag_3O_4 and the Ag_7O_8X salts behave as metals at room temperature, due to overlap between valence and conduction bands in their electronic structure. The correct valence formulations for these compounds are $(Ag^{2.67+})_3O_4$ and $(Ag^{2.67+})_6O_8 \cdot Ag^+X^-$, respectively. The thermal stability in air of the ozonolysis products was determined by DSC and also complementary XRD, FT-IR and Raman measurements. Ag_3O_4 was the least stable product, and thermally decomposed to $1.5Ag_2O_{2(s)} + 0.5O_{2(g)}$ within 20 h at 298 K. Thermal stabilities in air increased in the order $Ag_3O_4 < Ag_7O_8ClO_4$, $Ag_7O_8HSO_4 < Ag_7O_8NO_3 < Ag_2O_2$. This work resolves long-standing debate about the valence states of silver in Ag_3O_4 and Ag_7O_8X salts, and also provides valuable new spectroscopic information for these compounds. Attempts to prepare Ag_2O_3 by the ozonolysis route proved unsuccessful.
© 2007 Elsevier Ltd. All rights reserved.

Keywords: Silver oxides; Ozone; Ag_3O_4; $Ag_7O_8NO_3$; XPS; FT-IR; Raman

1. Introduction

The oxides of silver are a structurally diverse group of compounds that attract attention due to the widespread use of Ag_2O and Ag_2O_2 as cathode materials in Zn–silver oxide "button cell" batteries [1–3]. To date, five binary oxides have been isolated and structurally characterized in the silver–oxygen system [4–12]; Ag_6O_2, Ag_2O, Ag_2O_2, Ag_3O_4, and Ag_2O_3. It should be noted that Ag_2O_2 and Ag_3O_4 are both mixed-valence compounds (formally written as $Ag^+Ag^{3+}O_2$ and $Ag^{2+}(Ag^{3+})_2O_4$, respectively), and that Ag_2O_2 crystallizes in two different polymorphic forms [6–11]. The existence of other binary oxide phases, such as Ag_4O_3 and a hexagonal form of Ag_2O have been suggested [13,14], although supporting evidence for these phases is lacking.

Due to their technological importance, Ag_2O and Ag_2O_2 have been the subjects of numerous structural and spectroscopic investigations [5–9,14–23]. Accordingly, literature pertaining to these two compounds is extensive and generally reliable. By comparison, data for Ag_3O_4 and Ag_2O_3 is extremely limited [10–12,22,23], which stems largely from the thermal instability of these two compounds. Thermal stability decreases rapidly with increasing silver oxidation state (cf. Ag_2O, Ag_2O_2 and Ag_2O_3; $\Delta_f G^0 = -11.2$, 27.6 and 121.4 kJ mol^{-1}, respectively) [24]. Ag_2O_3 decomposes completely to Ag_2O_2 in less than 1 h at 298 K, whereas Ag_2O is stable indefinitely at this temperature. Crystalline specimens of Ag_3O_4 and Ag_2O_3 have been obtained by electrolytic deposition from aqueous solutions of different Ag(I) salts at 273 K [10–12], and their crystal structures solved. Ag_2O_3 crystallizes in the

* Corresponding author. Tel.: +64 9 3737599x85876; fax: +64 9 3737422.
E-mail address: g.waterhouse@auckland.ac.nz (G.I.N. Waterhouse).

0277-5387/$ - see front matter © 2007 Elsevier Ltd. All rights reserved.
doi:10.1016/j.poly.2007.03.006

orthorhombic system Fdd2 with $Z = 8$, and is isomorphous with Au_2O_3 [12]. The structure contains approximately square-planar AgO_4 groups linked together via common oxygen atoms in a three-dimensional network, with an average Ag–O bond length of 2.02 Å. Ag_3O_4 crystallizes in the monoclinic system $P2_1/c$ with $Z = 2$ [10,11], and has the formal valence electron configuration $Ag^{2+}(Ag^{3+})_2O_4$. The crystal structure comprises a three-dimensional network of distorted edge- and corner-sharing square-planar AgO_4 units. Silver cations occupy two crystallographically independent sites; Ag^{3+} cations are square-coordinated by four oxygens at an average distance of 2.07 Å, while Ag^{2+} cations have four nearest neighbours at 2.03 Å. This result is somewhat anomalous, since shorter Ag–O bond lengths are expected about the Ag^{3+} cations. Recently, van Wüllen et al. reported ^{109}Ag solid state magic angle spinning (MAS) NMR spectra for a number of binary and ternary silver oxides [23]. The ^{109}Ag MAS NMR spectrum for Ag_3O_4 showed only one broad isotropic signal at −795 ppm, which was tentatively assigned to Ag^{3+} centres (cf. Ag^{3+} centres in Ag_2O_2 and Ag_2O_3 showed chemical shifts of 1970 and 2015 ppm, respectively). No signal was observed for the Ag^{2+} cations in Ag_3O_4. Results of the X-ray crystallographic and ^{109}Ag MAS NMR investigations can be rationalized if an alternative valence configuration of $(Ag^{2.67+})_3O_4$ is considered for the compound. O'Keefe calculated Madelung potentials at Ag and O sites in a number of binary silver oxides [25]. Madelung potentials are approximately proportional to valence and may be used to determine valences in mixed-valence oxides. In the case of Ag_3O_4, no preferred valence configuration was found between $Ag^{2+}(Ag^{3+})_2O_4$ and $(Ag^{2.67+})_3O_4$, evidence of electron delocalization and metallic behaviour. Further work is necessary to clarify the electronic structure of Ag_3O_4. Also, important spectroscopic data for Ag_2O_3 and Ag_3O_4 has yet to be reported (such as FT-IR and Raman spectra), clearly justifying further work in this area.

Closely related to the binary silver oxides are the silver oxide clathrate salts of empirical formula Ag_7O_8X ($X = NO_3^-, ClO_4^-, HSO_4^-, HCO_3^-$ or HF_2^-) [26–36]. The formal valence configuration for these compounds is $(Ag^{2+})_2(Ag^{3+})_4O_8 \cdot Ag^+X^-$, although their physical properties and structural data suggest a $(Ag^{2.67+})_6O_8 \cdot Ag^+X^-$ formulation is more accurate [26–32]. At room temperature, all Ag_7O_8X salts have a *fcc* crystal structure (space group $Fm\bar{3}m$, $Z = 4$, $a = 9.82$–9.94 Å) based on face-sharing, 26-sided, cubo-octahedra [26–32]. Oxygen anions in the 'Ag_6O_8' structural unit are located at the 24 corners of the cubo-octahedra (each is common to three cubo-octahedral units). The six Ag cations in the 'Ag_6O_8' unit occupy structurally equivalent positions in the square faces common to two cubo-octahedra (each is square-planar coordinated by oxygen with Ag–O = 2.05 Å). As these cations are structurally indistinguishable, an intermediate valency of 2.67 is implied. Ag^+ ions in the Ag_7O_8X lattice occupy cubic sites between the cubo-octahedra, and are coordinated 8-fold by oxygen at an average Ag–O distance of 2.52 Å. Anions occupy sites at the centre of the cubo-octahedra. Fundamental interest in these compounds relates to their fascinating physical properties which include metallic conductivity ($\rho = 2.5 \times 10^{-3}$ Ω cm for $Ag_7O_8NO_3$ at 300 K) and low temperature superconductivity ($T_c = 1.04$ K for $Ag_7O_8NO_3$) [27,28]. The metallic properties of Ag_7O_8X salts are attributed to promotion of two electrons from the face-sharing 'Ag_6O_8' structural units into a conduction band that utilizes Ag 4d and O 2p orbitals. The Ag_7O_8X salts are two electron class III-B mixed-valence compounds under the classification system of Robin and Day [30], and as such are expected to show an absorption edge (typically in the infrared) and metallic reflectivity in the visible region. Accordingly, they should be very interesting materials to study by FT-IR and Raman spectroscopy. To date, no reliable vibrational spectroscopic data have been reported for these salts, and minimal experimental data exists examining their electronic structure (e.g. XPS, UPS or XANES) [35]. Further spectroscopic studies of the Ag_7O_8X compounds are needed to fill these gaps.

Traditionally, Ag_3O_4, Ag_2O_3 and Ag_7O_8X salts have been synthesized by electrochemical routes (e.g. by anodic polarization of a platinum electrode). The disadvantage of the electrochemical approach is the fact that crystal growth rates are slow and yields typically low (scale-up procedures are not practical due to the high cost of Pt electrodes). Chemical routes, rather than electrochemical, are thus more attractive for the large-scale synthesis of these compounds. O_3 is one of the strongest oxidants known ($O_2/O_3\varepsilon_0^{acid} = 2.075$ V) and capable of oxidising Ag^+ to Ag^{2+} ($Ag^+/Ag^{2+}\varepsilon_0^{acid} = 1.980$ V) and Ag^+ to Ag^{3+} ($Ag^+/AgO^+\varepsilon_0^{acid} = 2.00$ V) [24]. The application of ozonolysis to synthesize Ag_2O_2 from metallic Ag or Ag_2O has already been demonstrated [9,19,20,37,38]. The synthesis of Ag_2O_2, Ag_3O_4, Ag_2O_3 and Ag_7O_8X salts by ozone-oxidation of aqueous Ag^+ is also theoretically viable (Eqs. (1)–(4) below). Minimal reliable work has been reported in this area to date [39], clearly justifying further research effort.

$$2Ag^+_{(aq)} + O_{3(g)} + H_2O_{(l)} \rightarrow Ag_2O_{2(s)} + O_{2(g)} + 2H^+_{(aq)} \quad (1)$$

$$6Ag^+_{(aq)} + 5O_{3(g)} + 3H_2O_{(l)} \rightarrow 2Ag_3O_{4(s)} + 5O_{2(g)} + 6H^+_{(aq)} \quad (2)$$

$$2Ag^+_{(aq)} + 2O_{3(g)} + H_2O_{(l)} \rightarrow Ag_2O_{3(s)} + 2O_{2(g)} + 2H^+_{(aq)} \quad (3)$$

$$7Ag^+_{(aq)} + X^-_{(aq)} + 5O_{3(g)} + 3H_2O_{(l)} \rightarrow Ag_7O_8X_{(s)} + 5O_{2(g)} + 6H^+_{(aq)} \quad (4)$$

For the reasons outlined above, a comprehensive study of the aqueous Ag^+/O_3 system was undertaken. We aimed to synthesize Ag_2O_2, Ag_3O_4, Ag_2O_3 and Ag_7O_8X salts by the ozonolysis route (Eqs. (1)–(4)), then comprehensively characterize the reaction products using a variety of spectroscopic and thermo-analytical methods. Particular emphasis is placed on examination of the vibrational spectra and electronic structure of these compounds.

2. Experimental

2.1. General

Silver(I) salts were purchased from Aldrich and used without further purification. Ag_2O and Ag_2O_2 powders were prepared from $AgNO_3$ in accordance with established procedures [40,41], and used as reference materials.

2.2. Synthesis of the binary silver oxides and Ag_7O_8X salts

During preliminary studies, we determined that the product obtained during ozonolysis of aqueous solutions of Ag^+ at 298 K was highly dependent on the anion of the silver salt used to prepare the silver solution. Ozonolysis of aqueous solutions of $AgNO_3$, $AgClO_4$ and Ag_2SO_4 afforded $Ag_7O_8NO_3$, $Ag_7O_8ClO_4$ or $Ag_7O_8HSO_4$, respectively, whereas ozonolysis of 0.05 M aqueous solutions of AgF or $AgBF_4$ yielded Ag_3O_4. To prevent thermal decomposition of Ag_3O_4 during the synthesis, the ozonolysis of aqueous solutions of AgF or $AgBF_4$ was performed at 273 K. Monoclinic Ag_2O_2 was the product collected by ozonolysis of aqueous solutions of CH_3 COOAg at 273–298 K.

The general procedure used to prepare these compounds was as follows. Aqueous solutions of the silver salts were prepared using milli Q water. Ag^+ concentrations used in the ozonolysis experiments were determined by the respective solubilities of the different silver salts in H_2O at 273–298 K. The pH of the Ag^+ solution was measured, after which it was transferred to a 1 L. glass round-bottomed flask; fitted with a stirrer, a sintered glass frit bubbler for introducing gaseous O_3-O_2 mixtures and a gas outlet tube. The flask was then placed in a thermostated water bath and allowed to equilibrate for 1 h at a specified temperature in the range 273–298 K. An O_3–O_2 gas mixture (5 vol% O_3 in O_2, total flow rate $O_3 + O_2 = 200$ L h^{-1}), generated from dry O_2 using a commercial ozone generator (Fischer model 502), was then bubbled through the silver(I) solution for a specified time (0.5–15 h). After the specified time, ozonolysis was discontinued and the solid product collected by vacuum filtration on a pre-weighed sintered glass crucible (porosity 4). The filtrate was retained and its pH measured. The solid product was then washed repeatedly with ice-cold deionised water, then acetone. Ag_7O_8X salts ($X = NO_3^-$, ClO_4^-, HSO_4^-) were dried at 313 K under vacuum for 2 h. After drying, the sample and sintered glass crucible were reweighed, and the yield of product determined by difference. Ag_3O_4 powders were not vacuum dried, and instead were immediately transferred to a freezer at 255 K to prevent thermal decomposition before spectroscopic analysis.

2.3. Product characterization

2.3.1. XRD

Powder X-ray diffraction patterns were acquired using a Philips PW-1130 diffractometer, equipped with a Cu anode X-ray tube and curved graphite filter monochromator. XRD data was collected at room temperature, using monochromatized Cu K_α X-rays ($\lambda = 1.5418$ Å). Additional acquisition parameters were: 2θ range, 2–90°; step size, 0.02°; and scan rate, 2° min^{-1}. Diffraction patterns were referenced against the JCPDS database for sample identification [42–47].

2.3.2. SEM

Sample morphology was examined using a Philips XL-30 field emission gun scanning electron microscope (FEG-SEM). All micrographs were collected at an electron gun accelerating voltage of 5 kV. Specimens were mounted on black carbon tape for analysis.

2.3.3. XPS

XPS spectra were collected using a Kratos XSAM800 instrument equipped with an analytical chamber of base pressure $\sim 5 \times 10^{-10}$ Torr, a dual anode X-ray source (Mg/Al), and a hemispherical electron energy analyzer with multi-channel detector. For analysis, samples were lightly pressed to form a pellet then mounted on stainless steel stubs using carbon sticky dots. Spectra were excited using Mg Kα radiation ($h\nu = 1253.6$ eV). The hemispherical analyzer was operated in the fixed analyzer transmission (FAT) mode, and the analyzer axis was normal to the sample surface. Survey spectra were collected at an analyzer pass energy of 65 eV. Multiplet spectra were collected over narrow spectral regions at a pass energy of 38 eV. All XPS spectra were referenced against the Fermi edge. Elemental compositions were determined from the survey spectra by standard quantification procedures using peak areas and spectrometer-modified Scofield cross-sections. Estimated uncertainty in the percentage atomic concentration reported for each element is approximately 1–2%.

2.3.4. FT-IR

Far-infrared measurements were performed on a Digilab FTS-60 series spectrometer. Incorporated equipment included an FTS-60V vacuum optical bench with a 5 lines/mm wire mesh beam splitter, a mercury lamp source and a pyroelectric triglycine sulfate detector. Spectra were recorded at 2 cm^{-1} resolution over the range 50–700 cm^{-1} using 500 signal-averaged scans. Prior to data collection, the optical bench was evacuated to a pressure of $\sim 10^{-2}$ Torr. Mid-infrared studies were carried out using a Digilab FTS-60 series spectrometer employing a DTGS detector. Acquisition parameters were: range = 400–4000 cm^{-1}; resolution = 2 cm^{-1}; number of signal-averaged scans, = 500. Samples were analyzed using the polyethylene disk sampling method (solid state ion exchange reactions between the silver compounds and KBr precluded the use of the KBr disk technique). Fresh sample (5 mg) was mixed with polyethylene powder (20 mg) then compressed at a pressure of 5 ton per-square-inch for 5–10 min to form thin disks of diameter 13 mm. Pellets were

mounted in a stainless steel disc holder for the collection of infrared spectra.

2.3.5. Raman

Raman spectra were taken on a Renishaw RM-2 Raman microscope system, fitted with an Olympus 20× objective lens. Raman spectra were excited using either 785 nm radiation from a diode laser or 488 nm radiation from an argon ion laser, and scattered light was collected at an angle 180° to the incident beam direction (180° backscattering sampling geometry). The laser power at the sample for routine data collection was ~0.3 mW, although higher powers were also used to study the photosensitivity of selected samples. Spectra were collected over the range 200–2000 cm^{-1} and at a resolution of *ca.* 2 cm^{-1}. To improve the signal-to-noise ratio of the data reported 20 consecutive scans were added to produce a spectrum.

2.3.6. DSC

DSC data was obtained on a DSC-2 instrument (Rheometric Scientific Ltd.). Samples (10–15 mg) were weighed into open aluminium crucibles, and referenced against an empty aluminium crucible during calorimetric measurements. DSC traces were recorded at a heating rate of 10 K min^{-1}, under a dry air purge.

3. Results and discussion

3.1. Ozone-mediated synthesis of binary silver oxides and Ag_7O_8X salts

3.1.1. Effect of silver(I) salt

The first objective of this study was to identify of the product(s) formed by sparging ozone through aqueous solutions of different Ag(I) salts. Table 1 summarizes our key findings. Results are discussed in conjunction with Fig. 1, which shows XRD patterns for the various reaction products isolated. As mentioned in Section 2.2, the anion of the silver(I) salt had a strong influence on the ozonolysis product. Ozonolysis of neutral or mildly acidic solutions of $AgNO_3$, $AgClO_4$ or Ag_2SO_4 at 298 K afforded $Ag_7O_8NO_3$, $Ag_7O_8ClO_4$ and $Ag_7O_8HSO_4$, respectively. XRD patterns for these clathrate compounds were indistinguishable (Fig. 1a–c), in agreement with the fact that the crystallographic parameters for all Ag_7O_8X salts are similar (space group $Fm\bar{3}m$, $Z = 4$, $a = 9.82$–9.94 Å) [26–32]. For each synthesis, the molar yield ratio H^+/Ag_7O_8X ($X = NO_3^-, ClO_4^-, HSO_4^-$) was in the range 5.8–5.9, close to the theoretical ratio of 6 predicted by Eq. (4). The nature of the anion appears to be important for the stabilization of the Ag_7O_8X clathrate structure. Polyoxoanions appear to be ideal in this regard. Ozone treatment of aqueous solutions of AgF or $AgBF_4$ at 273 K yielded Ag_3O_4 in high purity (Fig. 1d and e). This is an exciting result and the first reported synthesis of Ag_3O_4 by non-electrochemical routes. The molar yield ratio H^+/Ag_3O_4 for both experiments was 2.9, in good accord with the theoretical value of 3 (Eq. (2)). Monoclinic Ag_2O_2 was the product obtained by ozonolysis of aqueous solution of silver acetate at 273–298 K (Fig. 1f). Acetate ions acted to buffer the solution, since the pH of the solution decreased only from 8.7 to 5.9 after 3 h ozonolysis. Ag_2O_2 may have formed directly as described by Eq. (1), or alternatively is a decomposition product of a higher silver oxide, possibly Ag_2O_3. The latter is very thermally unstable at 298 K [12]. Our attempts to prepare Ag_2O_3 by ozonolysis of aqueous solutions of $AgClO_4$ or $AgBF_4$ at low temperature, as has been achieved electrochemically [11,12], have proved unsuccessful to date.

To examine the effect of other experimental parameters on the ozone-mediated syntheses, the precipitation of $Ag_7O_8NO_3$ was examined in further detail.

Table 1
Products obtained by the ozonolysis of aqueous solutions of different Ag(I) salts

Silver salt	Conc. (M)	Vol. (L)	*I* (M)	Ozonolysis temp. (K)	Ozonolysis time (h)	Initial pH	Final pH	Product	% Yield
$AgNO_3$	0.1	0.75	0.1	298	0.5	5.5	2.9	$Ag_7O_8NO_3$	1.9
	0.1	0.75	0.1	298	2	5.5	2.2	$Ag_7O_8NO_3$	9.1
	0.1	0.75	0.1	298	5	5.5	1.7	$Ag_7O_8NO_3$	23.8
	0.1	0.75	0.1	298	10	5.5	1.5	$Ag_7O_8NO_3$	42.0
	0.1	0.75	0.1	298	15	5.5	1.4	$Ag_7O_8NO_3$	52.7
$AgNO_3$	0.1	0.75	1.1	298	5	0	2.1	$Ag_7O_8NO_3$	11.1
	0.1	0.75	1.1	298	5	2	1.8	$Ag_7O_8NO_3$	18.9
	0.1	0.75	1.1	298	5	5.5	1.7	$Ag_7O_8NO_3$	24.0
	0.1	0.75	1.1	298	5	10	1.7	$Ag_7O_8NO_3$	24.5
	0.1	0.75	1.1	298	10	14*		Ag_2O_2	99.8
$AgClO_4$	0.1	0.75	0.1	298	5	5.5	1.7	$Ag_7O_8ClO_4$	23.6
Ag_2SO_4	0.015	0.75	0.045	298	5	5.5	1.9	$Ag_7O_8HSO_4$	55.5
AgF	0.05	0.30	0.05	273	3	5.5	1.6	Ag_3O_4	46.1
$AgBF_4$	0.05	0.30	0.05	273	3	5.5	1.6	Ag_3O_4	44.7
CH_3COOAg	0.05	0.75	0.05	273	3	8.7	5.9	Ag_2O_2	30.1

* At pH 14, Ag(I) precipitates from solution as Ag_2O, which is oxidized by O_3 to monoclinic Ag_2O_2.

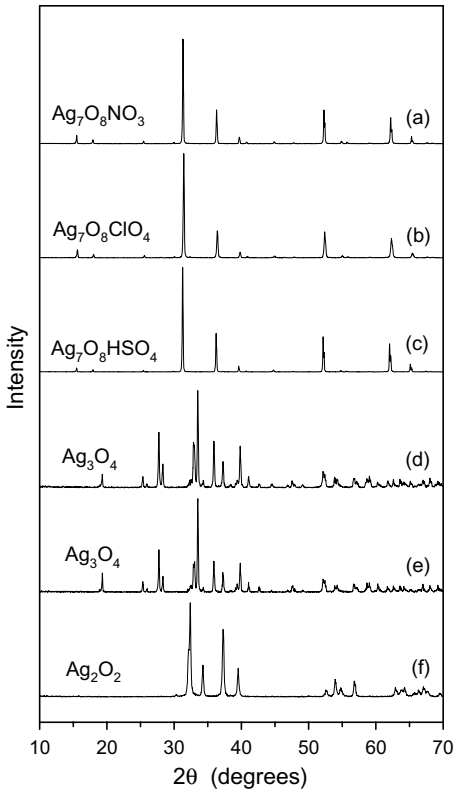


Fig. 1. Powder XRD patterns for the products obtained by ozonolysis of aqueous solutions of (a) $AgNO_3$ (0.1 M, 298 K, 5 h); (b) $AgClO_4$ (0.1 M, 298 K, 5 h); (c) Ag_2SO_4 (0.015 M, 298 K, 5 h); (d) AgF (0.05 M, 273 K, 3 h); (e) $AgBF_4$ (0.05 M, 273 K, 3 h) and (f) CH_3COOAg (0.05 M, 273 K, 3 h). Silver salt concentrations, reaction temperatures and ozonolysis times are given in parentheses. Products identified are listed next to the XRD patterns.

3.1.2. Effect of ozonolysis time

Ozonolysis of 0.1 M $AgNO_3$ (initial pH 5.5) at 298 K for 0.5–15 h yielded $Ag_7O_8NO_3$ as the only solid phase (Table 1). The yield of $Ag_7O_8NO_3$ increased almost linearly with time during the first 5 h of reaction, but tended towards an asymptotic limit of approximately 55% at longer reaction times. A yield of 52.7% was achieved after 15 h. The pH of the solution decreased sharply during the initial stages of the reaction, but maintained an almost constant value of ~1.4 after 15 h. The molar yield ratio $H^+/Ag_7O_8NO_3$ at all times was between 5.7 and 5.9, again close to the theoretical value of 6 predicted by Eq. (4).

Results suggest that the precipitation of $Ag_7O_8NO_3$ is likely affected by competing dissolution processes at low pH. To test whether competing precipitation-dissolution phenomena were a factor in our studies, we determined a dissolution curve for $Ag_7O_8NO_3$ powder in aqueous HNO_3 (not shown). The stability of $Ag_7O_8NO_3$ particles in HNO_3 solution decreased sharply in the pH range 1–2. This confirmed that competitive precipitation and dissolution of $Ag_7O_8NO_3$ particles was likely during ozonolysis at low pH values, and this limits the yield of product achievable.

3.1.3. Effect of initial pH

To investigate the effect of initial pH on the synthesis of $Ag_7O_8NO_3$, we prepared 0.1 M $AgNO_3$ solutions in either dilute HNO_3 (pH 0–4) or NaOH (pH 8–14) and used these in the ozonolysis experiments. $NaNO_3$ was also added to achieve a constant ionic strength (1.1 M).

The data in Table 1 shows that the initial pH had a strong influence on product composition and yields. For initial pH 0–10, ozonolysis yielded $Ag_7O_8NO_3$ exclusively. Product yields increased with initial pH in this range. For pH 10–13, the precipitation of Ag_2O and the oxidation by O_3 of Ag_2O to Ag_2O_2 compete with $Ag_7O_8NO_3$ formation. The proportions of Ag_2O and Ag_2O_2 in the product increased with increasing initial pH. At pH 13 and above, only Ag_2O and Ag_2O_2 formed. At pH 14, complete oxidation of the initially formed Ag_2O precipitate to Ag_2O_2 was achieved in 10 h.

3.2. SEM characterization of the ozonolysis products

The growth morphology of the products was examined by SEM. Fig. 2a–d shows the morphological evolution of $Ag_7O_8NO_3$ particles as a function of ozonolysis time. Particles formed after 30 min were predominantly of cubic shape (exposing 6 square {1 0 0} faces) and submicron size (Fig. 2a). With increasing ozonoloysis time, the particles became larger and developed an octahedral habit (exposing 8 triangular {1 1 1} faces) or forms derived from octahedra by truncation of corners and edges (Fig. 2b–d). After 15 h ozonolysis, the $Ag_7O_8NO_3$ particles were typically of truncated octahedral habit, twinned and of average size ~5 μm (Fig. 2d). Similar growth morphologies were observed for the $Ag_7O_8ClO_4$ and $Ag_7O_8HSO_4$ powders (SEM micrographs not shown).

Ag_3O_4 obtained by ozonolysis of aqueous solutions of AgF at 273 K displayed a rhombohedral prismatic habit (Fig. 2e). Monoclinic Ag_2O_2 resulting from the ozonolyis of aqueous silver acetate crystallized in the form of irregular platelets (Fig. 2f).

3.3. Electronic structure, vibrational spectra and thermal decomposition of Ag_7O_8X salts

As stated in the introduction, Ag_7O_8X salts are metals and the only known clathrates to exhibit low temperature superconductivity [28,29]. Minimal spectroscopic information is available for these compounds, motivating a detailed investigation here.

3.3.1. XPS characterization of $Ag_7O_8NO_3$ and $Ag_7O_8HSO_4$

Information about the electronic states of silver in these compounds can be deduced from the high-resolution XPS spectra shown in Fig. 3. The spectra are discussed in conjunction with Table 2, which provides XPS data summaries for the Ag_7O_8X salts and reference data collected for metallic silver and other relevant silver compounds. It is useful to note that the spectra presented in Fig. 3 are in

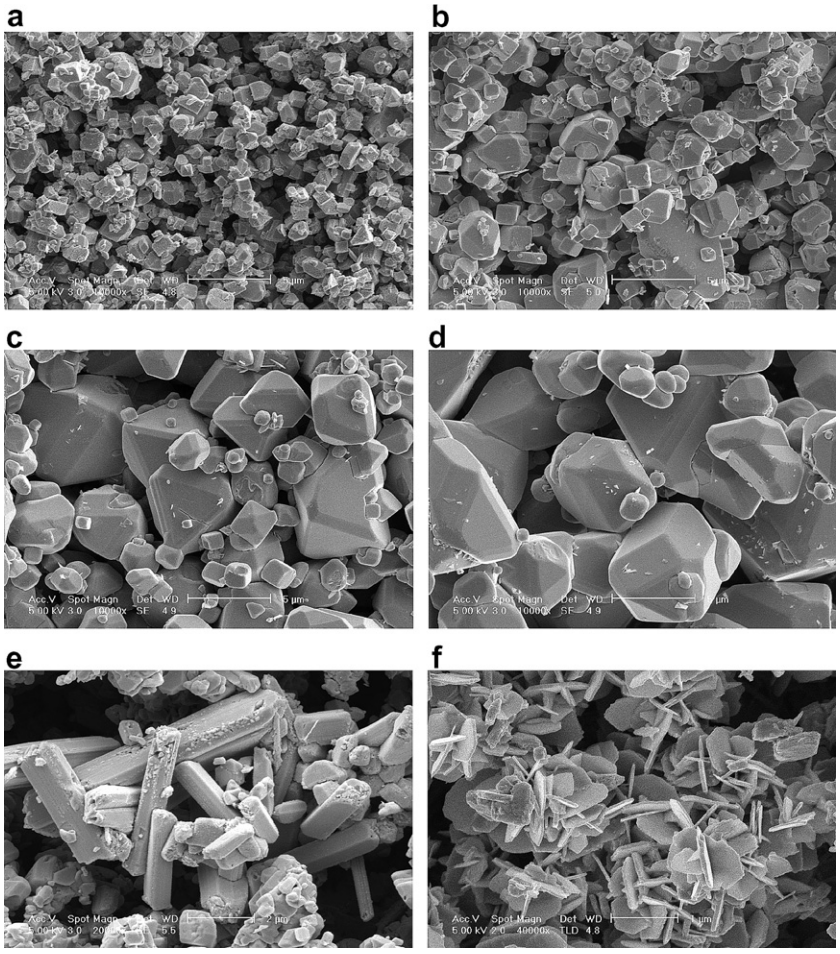


Fig. 2. SEM micrographs of $Ag_7O_8NO_3$ powders obtained by the ozonolysis of 0.1 M $AgNO_3$ at 298 K for (a) 0.5 h; (b) 2 h; (c) 5 h and (d) 15 h. Fig. 2e shows the Ag_3O_4 powder obtained by ozonolysis of 0.05 M AgF at 273 K for 3 h and Fig. 2f monoclinic Ag_2O_2 precipitated by ozonolysis of 0.05 M CH_3COOAg at 273 K for 3 h. Image magnifications are 10000, 10000, 10000, 10000, 20000 and 40000×, respectively.

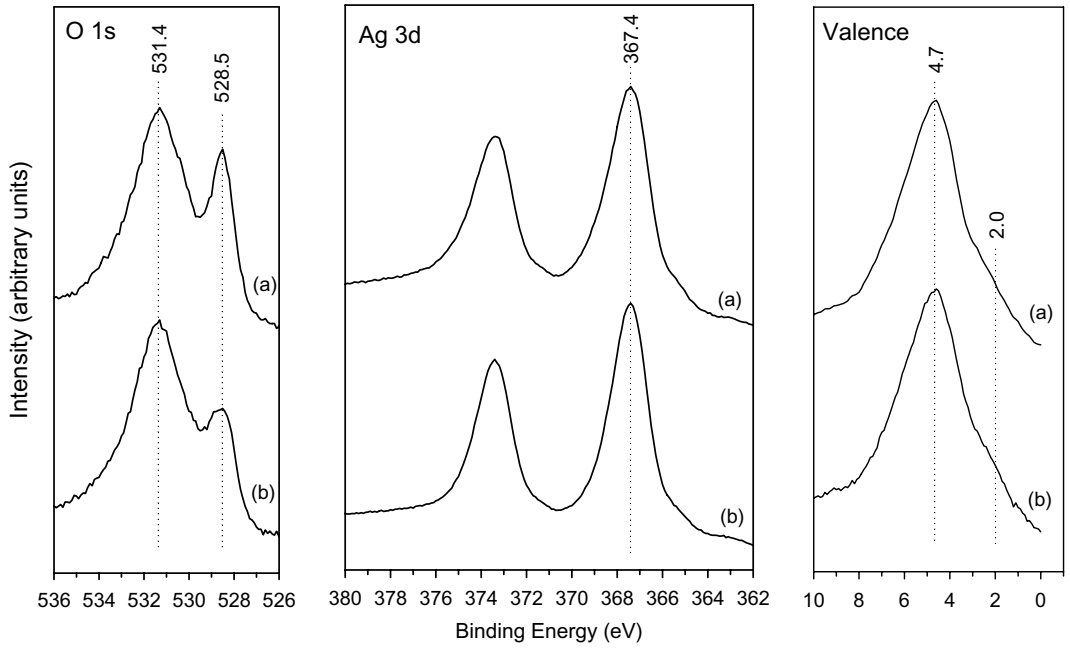


Fig. 3. XPS O 1s, Ag 3d and valence-band spectra for (a) $Ag_7O_8NO_3$ and (b) $Ag_7O_8HSO_4$. Spectra were referenced relative to the Fermi edge ($E_F = 0$ eV).

Table 2
Summarized XPS data for metallic silver and various silver compounds

Sample	Atomic composition (%)					O/Ag ratio		Binding energy (eV)			
	Ag	O	N	S	C	Theor.	Exp.	Ag $3d_{5/2}$	O 1s	N 1s	S $2p_{3/2}$
Ag	60.9	19.0			20.1	0	0.31	368.2	531.0		
Ag_2O	38.9	22.4			38.7	0.5	0.58	367.8	529.6		
$AgNO_3$	15.5	46.8	15.7		22.0	3.0	3.02	368.0	532.1	406.1	
Ag_2SO_4	24.6	48.9		12.2	14.3	2.0	1.99	367.9	531.7		168.0
Ag_2O_2	36.8	39.9			23.3	1.0	1.08	367.4	528.6		
$Ag_7O_8NO_3$	21.9	40.3	3.1		34.3	1.57	1.84	367.4	528.5	405.8	
$Ag_7O_8HSO_4$	21.4	41.8		3.2	33.6	1.71	1.95	367.4	528.5		167.6

excellent qualitative agreement with data reported by Bao et al. for electrochemically synthesized $Ag_7O_8NO_3$ [35].

XPS spectra collected for non-metallic samples typically need to be corrected for specimen charging during X-ray irradiation, unless precautions are taken to dissipate the build up of positive charge (such as flooding the specimen surface with low energy electrons during data acquisition). No such charging correction was necessary for spectra taken from the Ag_7O_8X salts, evidence of their metallic character.

The elemental composition determined by quantitative XPS analysis for $Ag_7O_8NO_3$ was Ag (21.9%), O (40.3%), N (3.1%) and C (34.3%) (Table 2). The carbon impurity results predominantly from the adsorption of residual hydrocarbons in the UHV chamber of the XPS instrument. The experimental Ag/N ratio was close to 7, consistent with the empirical formula of the compound. The O/Ag ratio of 1.84 exceeded the theoretical value of 1.57. Independent ICP-MS and thermogravimetric analyses of the compound revealed a composition very close to $Ag_7O_8NO_3$, indicating that the oxygen excess determined by XPS was likely localized at the specimen surface (XPS is surface-analytical technique). The cause of this oxygen excess is examined below. The elemental composition data for $Ag_7O_8HSO_4$ was similar (Table 2), in that the Ag/S ratio was approximately 7, but the O/Ag ratio of 1.95 slightly exceeded the theoretical value of 1.71.

The core-level Ag 3d spectra for $Ag_7O_8NO_3$ and $Ag_7O_8HSO_4$ show broad, asymmetric peaks at 373.4 eV and 367.4 eV (FWHM = 2.0 eV), which are readily assigned to core-level Ag $3d_{3/2}$ and Ag $3d_{5/2}$ photoemissions, respectively. The Ag 3d peaks are shifted by −0.8 eV relative to a those of Ag metal (Ag $3d_{5/2}$ = 368.2 eV), the magnitude and direction of the shift typical for highly oxidized states of silver [16–20,35]. Silver is unusual in that its core-levels photoemissions shift to lower binding energy with increasing oxidation state (cf. Table 2, Ag $3d_{5/2}$ binding energies for Ag, Ag_2O and Ag_2O_2 are 368.2, 367.8 and 367.4 eV, respectively). For most metals, positive binding energy shifts are observed when the metal is oxidized, on account of the extra coulombic attraction of core-level electrons towards the nucleus in the oxidized state. The negative binding energy shift observed for silver with increasing oxidation state is rationalized in terms of the large contribution of final state relaxation effects to the XPS chemical shift [16–18]. The Ag 3d peaks for $Ag_7O_8NO_3$ and $Ag_7O_8HSO_4$ were also broad compared to those measured for Ag and Ag_2O (FWHM = 1.25 eV and 1.47 eV, respectively), and of similar width to those of measured for Ag_2O_2 (FWHM = 1.9 eV), strong evidence that Ag_7O_8X compounds contain silver in several different oxidation states. The Ag 3d spectra for the Ag_7O_8X salts also show satellites on the low binding energy side of the Ag $3d_{3/2}$ and Ag $3d_{5/2}$ peaks, arising from final state relaxation effects.

The O 1s spectra contain two distinct peak maxima. The narrow peak at 528.5 eV (FWHM 1.4 eV) is typical for lattice oxygen (formally O^{2-}) in silver oxides [15–20], and in excellent agreement with XPS data reported here for bulk Ag_2O_2 (Table 2). We assign this feature to oxide ions of the face-sharing Ag_6O_8 structural units in $Ag_7O_8NO_3$ and $Ag_7O_8HSO_4$. The feature at ~531.4 eV in the O 1s spectra of both compounds is very broad (FWHM 2.8 eV), suggesting the presence of multiple oxygen species. The polyoxoanions of the Ag_7O_8X salts will contribute to this feature (cf. $AgNO_3$ O 1s = 532.1 eV; Ag_2SO_4 O 1s = 531.7 eV), as also will surface hydroxyl species (531.7 eV) and possibly chemisorbed H_2O (533.0 eV) since the compounds were prepared from aqueous solution [18–20]. For both compounds, spectroscopic evidence was found in the C 1s spectrum for a surface carbonate species (C 1s = 289.0 eV), which typically gives an O1s peak between 530.5 and 531 eV [19,20]. Carbonate formation results from the reaction between surface oxygen atoms and atmospheric CO_2, and is a characteristic common to all silver oxides (cf. Table 2, carbonate formation is responsible for the high O/Ag ratios observed experimentally for Ag_2O and Ag_2O_2). The presence of surface hydroxyl and carbonate species, and possibly chemisorbed H_2O, satisfactorily explain the high O/Ag ratios determined by quantitative XPS analysis for the Ag_7O_8X salts.

N 1s and S $2p_{3/2}$ binding energies measured for the NO_3^- and HSO_4^- ions in $Ag_7O_8NO_3$ and $Ag_7O_8HSO_4$, respectively, were in excellent agreement with those determined for the same anions in the $AgNO_3$ and Ag_2SO_4 (Table 2). S 2p binding energies are similar for metal salts containing HSO_4^- and SO_4^{2-} (both S^{6+}) [48].

Valence-band spectra for $Ag_7O_8NO_3$ and $Ag_7O_8HSO_4$ (Fig. 3) comprise an intense peak at 4.7 eV and a weaker feature at 2.0 eV. The 4.7 eV peak exhibits asymmetry on

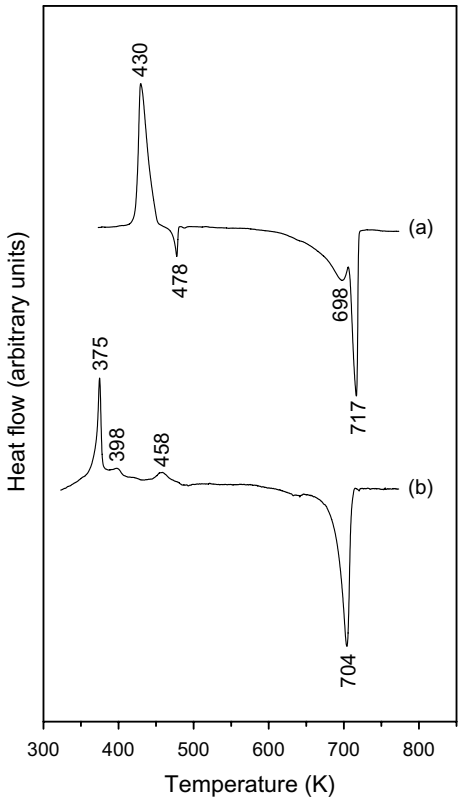


Fig. 4. DSC curves for (a) $Ag_7O_8NO_3$ and (b) Ag_3O_4. All data was collected at a heating rate of 10 K min^{-1} under a dry air purge.

the high binding energy side, consistent with presence of more than one component. By comparison with valence-band spectra reported for other silver compounds [15–20], we assign the 4.7 eV peak to orbitals of Ag 4d character. The broadness and asymmetry of the peak reflect the mixed-valence nature of the Ag_7O_8X compounds. The feature at about 2.0 eV originates from valence orbitals of mostly O 2p character. The metallic conductivity of Ag_7O_8X salts is attributed to promotion of two electrons from the face-sharing Ag_6O_8 structural units into a conduction band involving Ag 4d–O 2p orbitals (i.e. electron hopping between metal centres of the 'Ag_6O_8' units via bridging oxygen atoms). Consistent with this proposal, the valence-band spectra of the $Ag_7O_8NO_3$ and $Ag_7O_8HSO_4$ show overlap between valence and conduction bands at the Fermi edge ($E_F = 0$ eV). The XPS data thus strongly supports the mixed-valence formulation $(Ag^{2.67+})_6O_8 \cdot Ag^+X^-$ for these compounds.

3.3.2. Thermal decomposition of $Ag_7O_8NO_3$ in air under dynamic heating conditions

Detailed knowledge about the thermal stability of the Ag_7O_8X salts synthesized in this work is important as these compounds show commercial application potential in several areas; most notably in antibacterial coatings on account of the enormous oxidising power of Ag^{2+} and Ag^{3+} centres [36]. Here, we examined the thermal decomposition of $Ag_7O_8NO_3$ in air under both dynamic heating conditions (DSC) and stepwise isothermal heating conditions (XRD and FT-IR spectroscopy, Section 3.3.3. below).

The DSC trace for $Ag_7O_8NO_3$ (Fig. 4a) comprises a large exothermic peak at 430 K, two small endothermic peaks at 478 K and 698 K, and a large endothermic peak at 717 K. The trace is qualitatively similar to that reported for electrochemically synthesized $Ag_7O_8NO_3$ [33], and the peaks assigned accordingly. The large exothermic peak at 430 K is due predominantly to the thermal decomposition of $Ag_7O_8NO_3$ (Eq. (5)), but will also contains contributions from the thermal decomposition of Ag_2O_2 (Eq. (6)) and the orthorhombic → tetragonal phase transition of $AgNO_3$ [21,33].

$$Ag_7O_8NO_{3(s)} \rightarrow 3Ag_2O_{2(s)} + AgNO_{3(s)} + O_{2(g)} \quad (5)$$

$$3Ag_2O_{2(s)} \rightarrow 3Ag_2O_{(s)} + 1.5O_{2(g)} \quad (6)$$

The endothermic peaks at 478 K, 698 K and 717 K in Fig. 4a result from the melting of tetragonal $AgNO_3$, the thermal decomposition of $AgNO_3$ (Eq. (7)) and the thermal decomposition of Ag_2O (Eq. (8)), respectively.

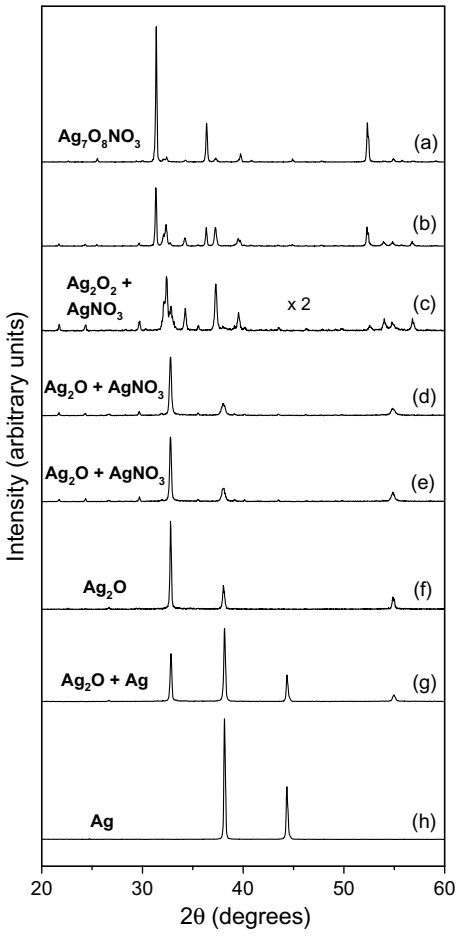


Fig. 5. XRD patterns for the thermal decomposition of $Ag_7O_8NO_3$ in air. Fresh samples were calcined 1 h at (a) 363 K; (b) 388 K; (c) 398 K; (d) 423 K; (e) 573 K; (f) 623 K; (g) 648 K and (h) 673 K. All data was collected at room temperature. The main phases identified are listed on the left side of the figure.

$$AgNO_{3(l)} \rightarrow 0.5Ag_2O_{(s)} + NO_{2(g)} + 0.25O_{2(g)} \quad (7)$$

$$3.5Ag_2O_{(s)} \rightarrow 7Ag_{(s)} + 1.75O_{2(g)} \quad (8)$$

The overall decomposition reaction for $Ag_7O_8NO_3$ in air is thus

$$Ag_7O_8NO_{3(s)} \rightarrow 7Ag_{(s)} + NO_{2(g)} + 4.5O_{2(g)} \quad (9)$$

DSC curves for $Ag_7O_8ClO_4$ and $Ag_7O_8HSO_4$ heated in air were also collected (not shown). The curves were similar in most respects to that presented in Fig. 4a for $Ag_7O_8NO_3$, although the onset temperature for the thermal decomposition of these compounds was *ca.* 5 K lower than that observed for $Ag_7O_8NO_3$, suggesting they have slightly lower thermal stability.

3.3.3. Vibrational spectra and thermal decomposition of $Ag_7O_8NO_3$ in air under isothermal heating conditions

Structural changes occurring during the thermal decomposition of $Ag_7O_8NO_3$ in air under isothermal conditions were followed by powder XRD (Fig. 5) and FT-IR spectroscopy (Fig. 6). Freshly prepared $Ag_7O_8NO_3$ powders were calcined for 1 h at selected temperatures in the range 323–773 K, then quickly cooled to room temperature and analyzed by the two techniques. Due to the nature of the heating program, onset temperatures for reactions 5–8 registered by XRD and FT-IR spectroscopy were considerably lower than those determined by DSC.

The XRD pattern obtained following calcination of $Ag_7O_8NO_3$ at 363 K (Fig. 5a) was identical to that collected for the freshly prepared salt (cf. Fig. 1a), indicating no decomposition occurred during this treatment. The corresponding mid-IR and far-IR spectra for the compound dispersed in a low-density polyethylene disk are shown in Fig. 6a The spectra contain no discernable peaks, and were identical to that of a pure polyethylene disk of the same thickness (not shown), except for the fact they showed significantly increased absorbance (i.e. relative to the spectrum of pure polyethylene, spectra for $Ag_7O_8NO_3$ in polyethylene were shifted up the absorbance axis by an amount proportional to the $Ag_7O_8NO_3$ loading). The fact that bands due to the component ions of $Ag_7O_8NO_3$ are not evident in Fig. 6a is indicative of metallic behaviour and lends further support for the valence formulation $(Ag^{2.67+})_6O_8 \cdot Ag^+NO_3^-$.

The thermal decomposition of $Ag_7O_8NO_3$ commenced around 373 K, in agreement with literature reports that $Ag_7O_8NO_3$ is transformed to $3Ag_2O_2 + AgNO_3 + O_2$ with prolonged immersion in boiling water [7]. Spectroscopic evidence to support this is found in Fig. 5a–c, where XRD peaks characteristic for $Ag_7O_8NO_3$ disappeared on increasing the calcination from 363 K to 398 K. Simultaneously, new peaks appeared and were indexed to monoclinic Ag_2O_2 [43], orthorhombic $AgNO_3$ [44] and Ag_2O [45]. The same changes manifest themselves in the FT-IR

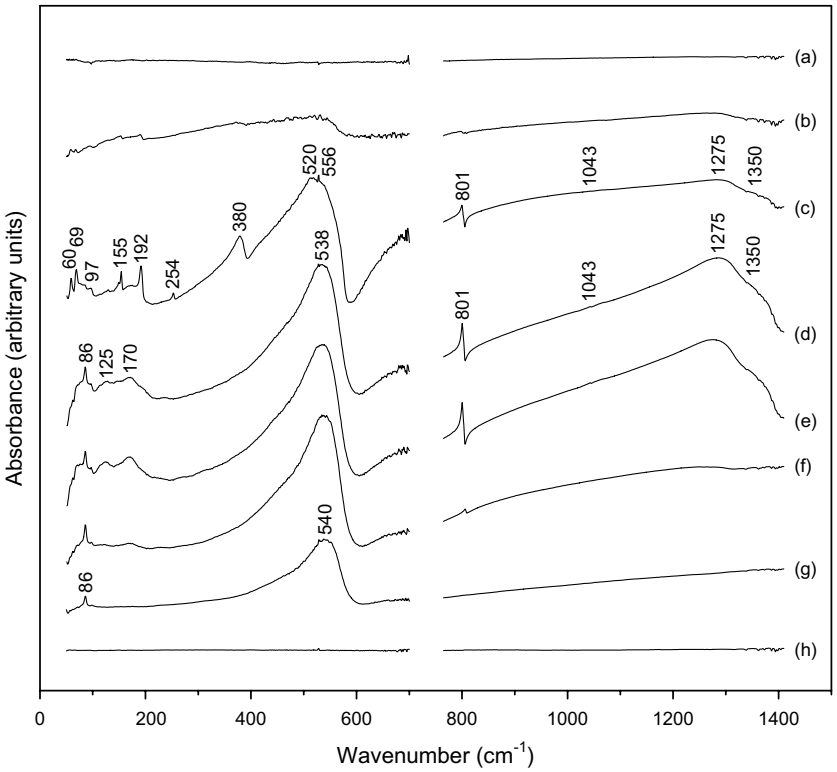


Fig. 6. FT-IR absorbance spectra for the thermal decomposition of $Ag_7O_8NO_3$ in air. Fresh samples were calcined 1 h at (a) 363 K; (b) 388 K; (c) 398 K; (d) 423 K; (e) 573 K; (f) 623 K; (g) 648 K and (h) 673 K. All data was collected at room temperature using the pressed polyethylene disk sampling method. The spectrum of the polyethylene disk was removed by subtraction.

spectra of Fig. 6a–c, where bands characteristic for monoclinic Ag_2O_2 (60, 69, 97, 155, 192, 254, 380, 520, 556 cm^{-1}) and orthorhombic $AgNO_3$ (80, 103, 125, 170, 801, 1043, 1275, 1350 cm^{-1}), then Ag_2O (86, ~540 cm^{-1}), develop with increasing calcination temperature up to 398 K. Assignments for these bands may be found in Refs [21,49,50]. The XRD and FT-IR data obtained following sample heating at 423 K (Figs. 5d and 6d, respectively) were those of Ag_2O and $AgNO_3$, indicating that complete thermal decomposition of the initially formed Ag_2O_2 was effected by this treatment.

Diffraction peaks and IR bands characteristic for $AgNO_3$ lost intensity with temperature between 573 K and 623 K (Figs. 5e–f and 6e–f), which is explained by the thermal decomposition of $AgNO_3$ (Eq. (7)) [51]. With increasing temperature above 623 K, spectral data typical of Ag_2O was progressively replaced by that of Ag metal (Figs. 5f–h and 6f–h), reflecting the thermal decomposition of Ag_2O to its component elements (Eq. (8)). Silver was the only phase identified by XRD after sample calcination at 673 K (Fig. 5h). Note the similarity between the FT-IR spectra of $Ag_7O_8NO_3$ (Fig. 6a) and silver metal (Fig. 6h).

3.3.4. Raman spectra for $Ag_7O_8NO_3$

Fig. 7a shows a Raman spectrum for $Ag_7O_8NO_3$ excited at 785 nm and low laser power (~0.3 mW at sample). The spectrum shows no discernable features, and was identical to a spectrum collected at the same laser power using 488 nm excitation (not shown). Results confirm the metallic reflectivity of $Ag_7O_8NO_3$ powders over the visible and near-infrared regions. Excitation at 785 nm and higher laser power (*ca.* 10 mW at sample) produced the spectrum shown in Fig. 7b, which contains bands at 219, 300, 376, 428, 467, 485, 525 (broad), 972 and 1043 cm^{-1}. By comparison with Raman spectra collected for monoclinic Ag_2O_2 (Fig. 7c), and orthorhombic $AgNO_3$ (Fig. 7d), it is clear that the use of a high laser power caused sample heating and the thermal decomposition of $Ag_7O_8NO_3$ to $3Ag_2O_2 + AgNO_3 + O_2$ (Eq. (5)). The broad band at 525 cm^{-1} is characteristic for Ag_2O [19–21], indicating partial decomposition of Ag_2O_2 also occurred (Eq. (6)). Fig. 7b is qualitatively similar to a spectrum reported by Pettinger et al. for electrochemically synthesized $Ag_7O_8NO_3$ [34], suggesting laser damage to the sample also occurred in that study (a laser power of 20 mW was used for data acquisition).

3.4. Electronic structure, vibrational spectra and thermal decomposition of Ag_3O_4

The synthesis of Ag_3O_4 in high purity is a key finding of the present study. In view of fact that the electronic structure of Ag_3O_4 is unclear and minimal spectroscopic information is available for the compound, we used DSC,

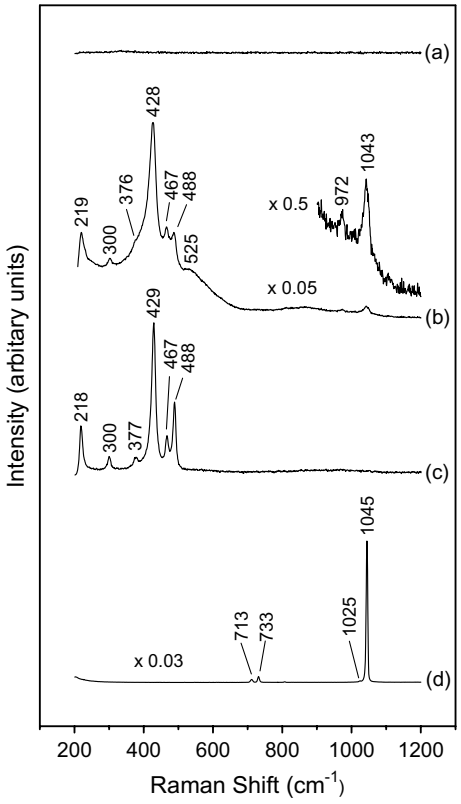


Fig. 7. Raman spectra excited at 785 nm for (a) $Ag_7O_8NO_3$, 0.3 mW; (b) $Ag_7O_8NO_3$, 10 mW; (c) monoclinic Ag_2O_2, 5 mW and (d) orthorhombic $AgNO_3$, 5 mW. Laser powers at the sample are also given.

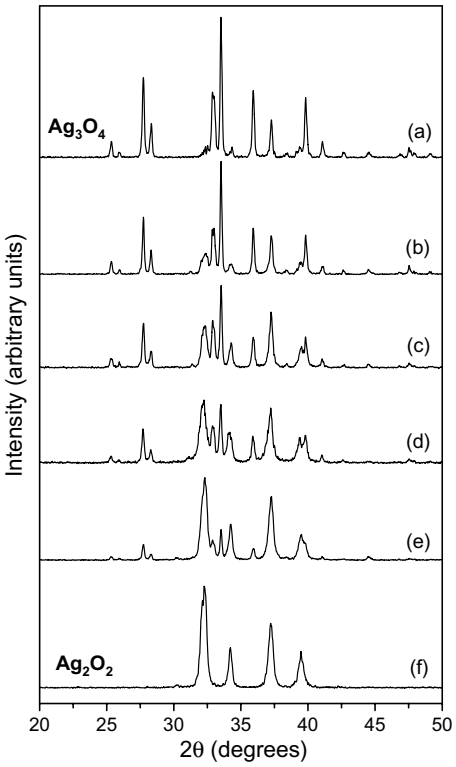


Fig. 8. XRD patterns for the thermal decomposition of Ag_3O_4 in air at 298 K. Time after preparation was (a) 0.5 h; (b) 4 h; (c) 8 h; (d) 12 h; (e) 16 h and (f) 20 h.

XRD, FT-IR and Raman spectroscopy to examine the thermal decomposition of Ag_3O_4 in air. From the vibrational spectra, we hoped to establish the correct valence structure for the compound. Attempts to collect XPS data for Ag_3O_4 proved unsuccessful due to the thermal instability of the compound.

3.5. Thermal decomposition of Ag_3O_4 in air under dynamic heating conditions

The DSC trace for Ag_3O_4 (Fig. 4b) shows a large exotherm at 375 K, several weak exotherms at 398 K and 458 K, and a large endotherm at 704 K. These peaks are assigned as follows. The endotherm at 375 K results from thermal decomposition of Ag_3O_4 (Eq. (10)); the weak endotherm at 398 K is due to crystallization of monoclinic Ag_2O_2; the endotherm at 458 K is due to thermal decomposition of Ag_2O_2 (Eq. (11)); and the strong exotherm at 704 K reflects thermal decomposition of Ag_2O to its elements (Eq. (12)).

$$Ag_3O_{4(s)} \rightarrow 1.5Ag_2O_{2(s)} + 0.5O_{2(g)} \quad (10)$$

$$1.5Ag_2O_{2(s)} \rightarrow 1.5Ag_2O_{(s)} + 0.75O_{2(g)} \quad (11)$$

$$1.5Ag_2O_{(s)} \rightarrow 3Ag_{(s)} + 0.75O_{2(g)} \quad (12)$$

The overall decomposition reaction for AgO_4 in air is thus

$$Ag_3O_{4(s)} \rightarrow 3Ag_{(s)} + 2O_{2(g)} \quad (13)$$

3.5.1. Vibrational spectra and thermal decomposition of Ag_3O_4 in air at 298 K

XRD, FT-IR and Raman spectroscopy were used to document the thermal decomposition of Ag_3O_4 to $1.5Ag_2O_2 + 0.5O_2$ in air at 298 K. Freshly prepared Ag_3O_4 powders were left in air at 298 K for 24 h. At regular time intervals, samples were taken and quickly analyzed using the three techniques. The data obtained is shown in Figs. 8–10, respectively.

Fig. 8a shows the XRD pattern collected for freshly prepared Ag_3O_4, and is identical to that presented in Fig. 1d. On standing in air at 298 K, the XRD peaks characteristic for Ag_3O_4 were progressively replaced by those typical for monoclinic Ag_2O_2 (Fig. 8a–f). Complete decomposition of Ag_3O_4 was achieved after about 20 h.

Fig. 9a shows the far-IR spectrum of Ag_3O_4 powder dispersed in a low-density polyethylene disk. The spectrum contains no discernable bands and was similar to that reported in Fig. 6a for metallic $Ag_7O_8NO_3$. Similarly, the Raman spectrum collected at low laser power for Ag_3O_4

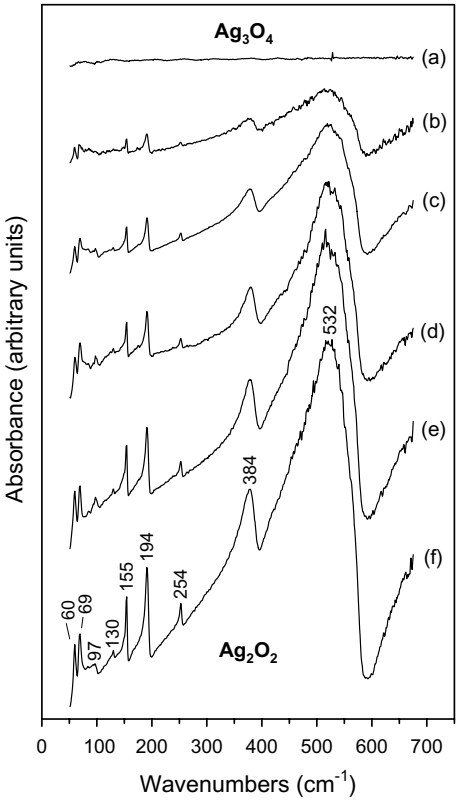


Fig. 9. FT-IR absorbance spectra for the thermal decomposition of Ag_3O_4 in air at 298 K. Time after preparation was (a) 0.5 h; (b) 4 h; (c) 8 h; (d) 12 h; (e) 16 h and (f) 20 h. The data was collected using the pressed polyethylene disk sampling method. The spectrum of the polyethylene disk was removed by subtraction.

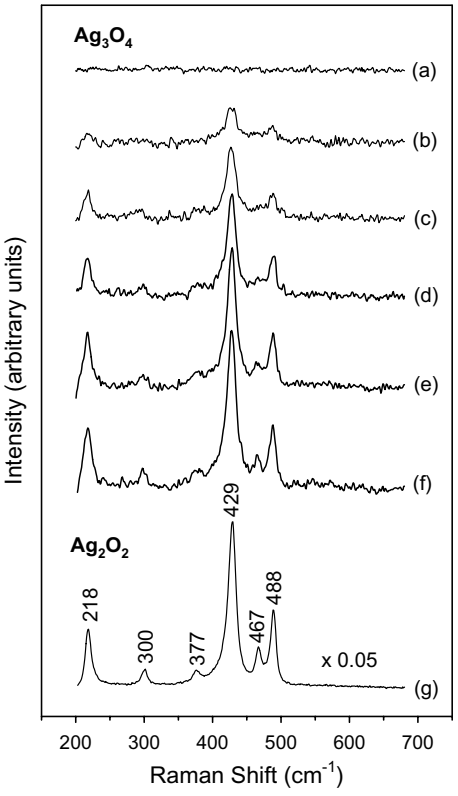


Fig. 10. Raman spectra excited at 785 nm for the thermal decomposition of Ag_3O_4 in air at 298 K. Time after preparation was (a) 0.5 h; (b) 4 h; (c) 8 h; (d) 12 h; (e) 16 h and (f) 20 h. The laser power at the sample for all measurements was ~0.3 mW. Fig. 10g was taken from the same sample as Fig. 10f, at a laser power of 5 mW.

(Fig. 10a) contained no bands. The fact that no discrete vibrational bands are observed in the FT-IR or Raman spectra for Ag_3O_4, even though some are expected based on a factor group analysis of the oxide's crystallographic structure, is clear proof that Ag_3O_4 behaves as a metal at 298 K. From the metallic properties it follows that one electron per Ag_3O_4 formula unit is delocalized over the Ag_3O_4 lattice, and the correct valence formulation for this compound is $(Ag^{2.67+})_3O_4$ rather than $Ag^{2+}(Ag^{3+})_2O_4$. The observation that Ag_3O_4 behaves as a metal is not unexpected, given that the unit cell formula for the oxide Ag_6O_8 is identical to that of the face-sharing Ag_6O_8 polyhedral units responsible for the metallic conductivity of Ag_7O_8X salts. The grey colour and metallic lustre of both Ag_3O_4 and the Ag_7O_8X salts is further evidence of similarities in the electronic structure of these compounds.

With increasing time at 298 K, the FT-IR and Raman spectra characteristic for Ag_3O_4 are slowly replaced by those of monoclinic Ag_2O_2 (Figs. 9a–f and 10a–f, respectively). Fig. 10f and g was taken sequentially from the same sample, the latter at a higher laser power and longer acquisition time to achieve a better signal-to-noise ratio. The value of using XRD and vibrational spectroscopic methods in combination to characterize silver compounds and follow their thermal decomposition is highlighted by this study.

4. Conclusions

(1) Ozonolysis of neutral or mildly acidic solutions of Ag(I) represents a simple and effective route for the sythesis of Ag_2O_2, Ag_3O_4 and Ag_7O_8X salts ($X = NO_3^-, ClO_4^-, HSO_4^-$). Previously, Ag_3O_4 and Ag_7O_8X compounds have only been accessible by electrochemical routes. Attempts to prepare Ag_2O_3 were unsuccessful.

(2) FT-IR and Raman spectra were reported for the first time for Ag_3O_4 and $Ag_7O_8NO_3$. The vibrational spectra indicate these compounds are metallic, a result also confirmed by XPS for the $Ag_7O_8NO_3$. Based on structural and spectroscopic considerations, the electron configurations of these compounds can be formulated as $(Ag^{2.67+})_3O_4$ and $(Ag^{2.67+})_6O_8 \cdot Ag^+NO_3^-$.

(3) The thermal decomposition of Ag_3O_4 and $Ag_7O_8NO_3$ powders in air was examined by DSC, XRD, FT-IR and Raman spectroscopy. The thermal stabilities of compounds prepared by ozonolysis were comparable to samples prepared by traditional electrochemical routes.

Acknowledgement

GINW thanks the Foundation for Research, Science and Technology for the award of a NZ Science and Technology Postdoctoral Fellowship (Contract # UOAX0412) and the McDiarmid Institute for Advanced Materials and Nanotechnology for financial support given to this project.

References

[1] A.P. Karpinski, S.J. Russell, J.R. Serenyi, J.P. Murphy, J. Power Sources 91 (2000) 77.
[2] D.F. Smith, J.A. Gucinski, J. Power Sources 80 (1999) 66.
[3] D.F. Smith, C. Brown, J. Power Sources 96 (2001) 121.
[4] W. Beesk, P.G. Jones, H. Rumpel, E. Schwarzmann, G.M. Sheldrick, J. Chem. Soc., Chem. Commun. (1981) 664.
[5] H.E. Swanson, Standard X-ray Diffraction Powder Patterns, Natl. Bur. Stand. Monograph 25, section 1, 45 (1962).
[6] J.A. McMillan, J. Inorg. Nucl. Chem. 13 (1960) 28.
[7] J.A. McMillan, Chem. Rev. 62 (1962) 65.
[8] V. Scatturin, P.L. Bellon, A.J. Salkind, J. Electrochem. Soc. 108 (1961) 819.
[9] K. Yvon, A. Bezinge, P. Tissot, P. Fischer, J. Solid State Chem. 65 (1986) 225.
[10] B. Standke, M. Jansen, Angew. Chem., Int. Ed. Engl. 25 (1986) 77.
[11] B. Standke, M. Jansen, J. Solid State Chem. 67 (1987) 278.
[12] B. Standke, M. Jansen, Angew. Chem., Int. Ed. Engl. 24 (1985) 118.
[13] A.N. Mansour, J. Phys. Chem. 94 (1990) 1006.
[14] S.S. Kabalkina, S.V. Popova, R.N. Serebyanaya, L.F. Verschchagin, Dokl. Akad. Nauk. SSSR 152 (1963) 853.
[15] L.H. Tjeng, M.B.J. Meinders, J. van Elp, J. Ghijsen, G.A. Sawatzky, Phys. Rev. B 41 (2001) 3190.
[16] J.S. Hammond, S.W. Gaarenstroom, N. Winograd, Anal. Chem. 47 (1975) 2193.
[17] S.W. Gaarenstroom, N. Winograd, J. Chem. Phys. 67 (1977) 3500.
[18] J.F. Weaver, G.B. Hoflund, J. Phys. Chem. 98 (1994) 8519.
[19] G.I.N. Waterhouse, G.A. Bowmaker, J.B. Metson, Appl. Surf. Sci. 183 (2001) 191.
[20] G.I.N. Waterhouse, G.A. Bowmaker, J.B. Metson, Surf. Interface Anal. 33 (2002) 401.
[21] G.I.N. Waterhouse, G.A. Bowmaker, J.B. Metson, Phys. Chem. Chem. Phys. 3 (2001) 3838.
[22] P. Behrens, S. Aßmann, U. Bilow, C. Linke, M. Jansen, Z. Anorg. Allg. Chem. 625 (1999) 111.
[23] L. van Wüllen, S. Vensky, W. Hoffbauer, M. Jansen, Solid State Sci. 7 (2005) 920.
[24] D.R. Lide (Ed.), CRC Handbook of Chemistry and Physics, 84th ed., CRC press, London, 2003.
[25] M. O'Keefe, J. Solid State Chem. 85 (1990) 108.
[26] I. Náray-Szabó, K. Popp, Z. Anorg. Allg. Chem. 322 (1963) 286.
[27] I. Náray-Szabó, G. Argay, P. Szabó, Acta Crystallogr. 19 (1965) 180.
[28] M.B. Robin, K. Andres, T.H. Geballe, N.A. Kuebler, D.B. McWhan, Phys. Rev. Lett. 17 (1966) 917.
[29] A.C. Gossard, D.K. Hindermann, M.B. Robin, N.A. Kuebler, T.H. Geballe, J. Am. Chem. Soc. 89 (1967) 7121.
[30] M.B. Robin, P. Day, Adv. Inorg. Chem. Radiochem. 10 (1967) 247.
[31] C.H. Wong, T.H. Lu, C.N. Chen, T.J. Lee, J. Inorg. Nucl. Chem. 34 (1972) 3253.
[32] M. Jansen, S. Vensky, Z. Naturforsch. 55b (2000) 882.
[33] J.C. Jack, T. Kennedy, J. Therm. Anal. 3 (1971) 25.
[34] B. Pettinger, X. Bao, I. Wilcock, M. Muhler, R. Schlögl, G. Ertl, Angew. Chem., Int. Ed. Engl. 33 (1994) 85.
[35] X. Bao, M. Muhler, Th. Schedel-Niedrig, R. Schlögl, Phys. Rev. B 54 (1996) 2249.
[36] S. Djokić, J. Electrochem. Soc. 151 (2004) C359.
[37] R. Dallenbach, J. Painot, P. Tissot, Polyhedron 1 (1982) 183.
[38] R.O. Suzuki, T. Ogawa, K. Ono, J. Am. Ceram. Soc. 82 (1999) 2033.
[39] J. Selbin, M. Usategui, J. Inorg. Nucl. Chem. 20 (1961) 91.
[40] J.A. Allen, P.H. Scaife, Aust. J. Chem. 19 (1966) 715.
[41] R.N. Hammer, J. Kleinberg, Inorg. Synth. 4 (1953) 12.

[42] Jcpds-International Centre for Diffraction Data, $Ag_7O_8No_3$, card 73-1327.
[43] Jcpds-International Centre for Diffraction Data, Ag_2O_2, card 84-1547.
[44] Jcpds-International Centre for Diffraction Data, $AgNO_3$, card 84-0713.
[45] Jcpds-International Centre for Diffraction Data, Ag_2O, card 75-1532.
[46] Jcpds-International Centre for Diffraction Data, Ag, card 04-0783.
[47] Jcpds-International Centre for Diffraction Data, Ag_3O_4, card 84-1261.
[48] A.A. Audi, P.M.A. Sherwood, Surf. Interface Anal. 29 (2000) 265.
[49] Z.X. Shen, M.H. Kuok, S.H. Tang, W.F. Sherman, Spectrochim. Acta, Part A 48 (1992) 1317.
[50] J.R. Ferraro, A. Walker, J. Chem. Phys. 42 (1965) 1273.
[51] F. Paulik, J. Paulik, M. Arnold, Thermochim. Acta 92 (1985) 787.

Available online at www.sciencedirect.com
ScienceDirect
Polyhedron 26 (2007) 3323–3335
POLYHEDRON
www.elsevier.com/locate/poly

Synthesis, photophysical and photochemical properties of tetra- and octa-substituted gallium and indium phthalocyanines

Mahmut Durmuş [a,b], Tebello Nyokong [a,*]

[a] Department of Chemistry, Rhodes University, Grahamstown 6140, South Africa
[b] Gebze Institute of Technology, Department of Chemistry, P.O. Box 141, Gebze 41400, Turkey

Received 13 February 2007; accepted 6 March 2007
Available online 12 March 2007

Abstract

The synthesis, photophysical and photochemical properties of the tetra- and octa-[4-(benzyloxyphenoxy)] substituted gallium(III) and indium(III) phthalocyanines are reported for the first time. The new compounds have been characterized by elemental analysis, IR, ^{1}H NMR spectroscopy and electronic spectroscopy. General trends are described for quantum yields of photodegredation, fluorescence quantum yields and lifetimes, triplet lifetimes and triplet quantum yields as well as singlet oxygen quantum yields of these compounds in dimethylsulfoxide (DMSO). Substituted indium phthalocyanine complexes (**7b**–**9b**) showed much higher quantum yields of triplet state and shorter triplet lifetimes, compared to the substituted GaPc derivatives due to enhanced intersystem crossing (ISC) in the former. The gallium and indium phthalocyanine complexes showed phototransformation during laser irradiation due to ring reduction. The singlet oxygen quantum yields (Φ_Δ), which give an indication of the potential of the complexes as photosensitizers in applications where singlet oxygen is required (Type II mechanism) ranged from 0.51 to 0.94. Thus, these complexes show potential as photodynamic therapy of cancer.
© 2007 Elsevier Ltd. All rights reserved.

Keywords: Phthalocyanine; Photosensitizer; Gallium; Indium; Quantum yields; Singlet oxygen; Photodegredation

1. Introduction

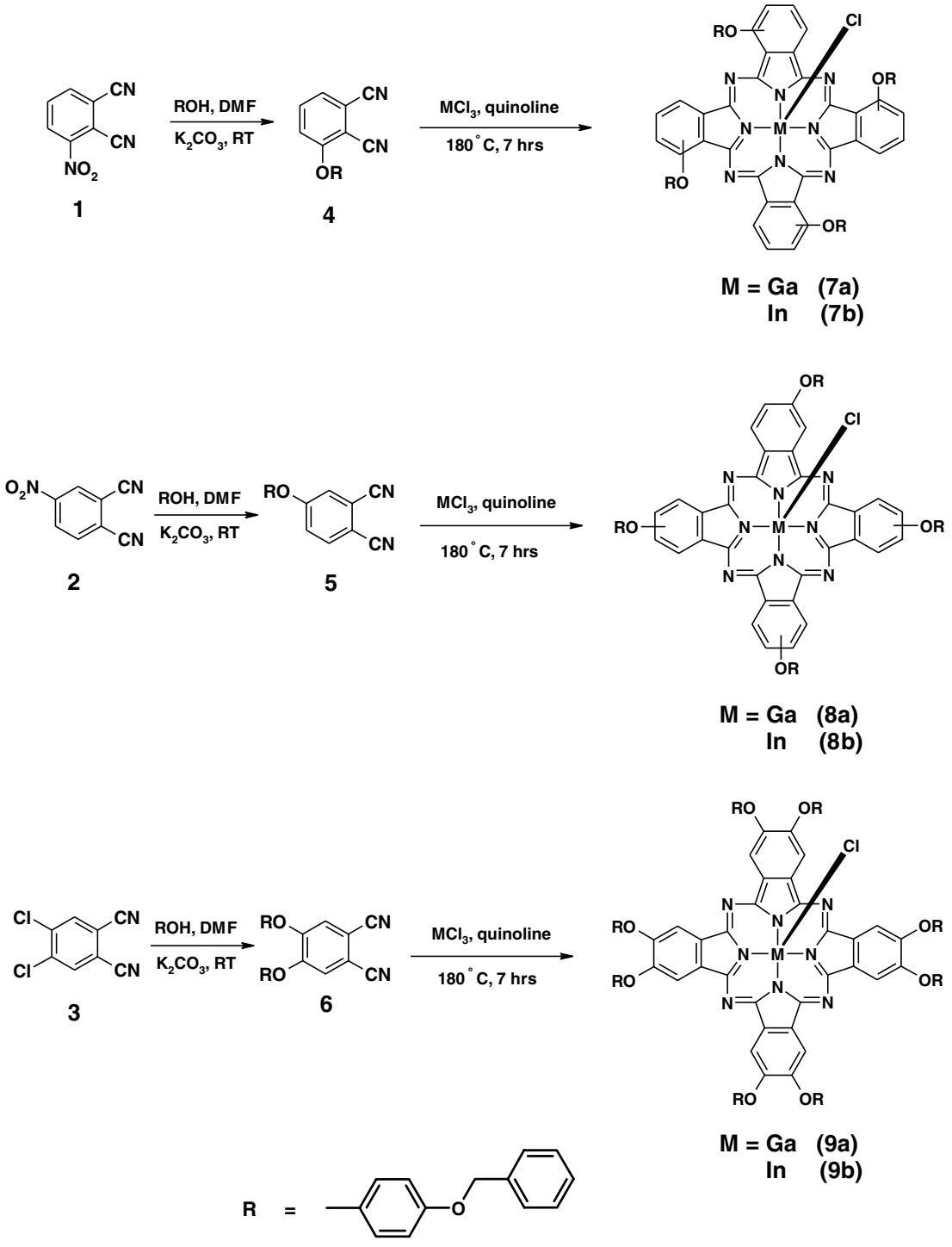
Phthalocyanines, a family of aromatic macrocycles based on an extensive delocalized 18-π electron system, are known not only as classical dyes in practical use but also as modern functional materials in scientific research [1]. There has been growing interest in the use of phthalocyanines in a variety of new high technology fields including semiconductor devices [2], Langmuir–Blodgett films [3], electrochromic display devices [4], gas sensors [5], liquid crystals [6], non-linear optics [7] and various catalytic processes [8]. The attractive characteristics of phthalocyanines in these applications arise from their great diversity, thermal and chemical stability, redox versatility and intense colour.

One of their most important applications is functioning as photosensitizers for photodynamic therapy (PDT) [9–12]. Due to the intense absorption in the visible region, high efficiency to generate reactive oxygen species (such as singlet oxygen), and low dark toxicity, phthalocyanines have been used in this avenue for the treatment of various cancers and photoinactivation of viruses [13–15]. However, their insolubility in common organic solvents causes difficulties for many applications, rendering the syntheses of soluble derivatives an important task. Phthalocyanine derivatives of increased solubility have been obtained using substituents such as alkyl, alkoxy, alkylthio chains and bulky groups. Peripheral substitution with bulky groups or long alkyl, alkoxy or alkylthio chains leads to phthalocyanine products which are soluble in apolar solvents. Sulfo or quaternary ammonium groups enhance solubility in aqueous media over a wide pH range of aqueous solutions. The size and the nature of the substituents are not

* Corresponding author. Tel.: +27 46 6038260; fax: +27 46 6225109.
E-mail address: t.nyokong@ru.ac.za (T. Nyokong).

0277-5387/$ - see front matter © 2007 Elsevier Ltd. All rights reserved.
doi:10.1016/j.poly.2007.03.007

the only criteria for the solubility of the substituted phthalocyanines; the change in symmetry caused by the substituents is also important. Generally, tetra substituted phthalocyanines are more soluble than symmetrically octa-substituted ones due to the formation of four positional isomers in the case of tetra substituted analogues [16]. According to their substituent positions two types of tetra-substituted macrocycles which show significant differences in their chemical and physical behaviour can be distinguished. Substitution at the more sterically crowded α (non-peripheral) position show reduced aggregation tendencies more than substitution at β (peripheral) position [17,18]. It has been established that non-aggregated phthalocyanines are extremely important and potentially useful for PDT applications [19]. Molecular aggregation of phthalocyanines, which is an intrinsic property of these



Scheme 1. Synthesis of 4-benzyloxyphenoxy tetra- and octa-substituted gallium and indium phthalocyanine complexes.

large πconjugated systems, provides an efficient non-radiative energy relaxation pathway, thereby shortening the excited state lifetimes and greatly reducing the photosensitizing efficiency [20,21]. The nature of peripheral substituents influences the degree of aggregation, with bulky groups reducing this phenomenon [22].

There is a continuous effort to extend the chemistry of metallophthalocyanines. Nonetheless, gallium(III) and indium(III) phthalocyanine chemistry appears not to have been fully explored especially when compared to the development of aluminium (which is the other group IIIA metal) phthalocyanine complexes. Aluminium phthalocyanine complexes have been used as PDT agents. However there are only a few studies about the photochemical and photophysical properties of gallium and indium phthalocyanine compounds [23–25]. Closed shell, diamagnetic ions, such as Zn^{2+}, Al^{3+} and Ga^{3+}, give phthalocyanine complexes with both high triplet quantum yields and long lifetimes [26].

To our knowledge, octasubstituted gallium or indium phthalocyanines have not been reported before. This is first report about synthesis of octasubstituted gallium and indium phthalocyanines. 4-Benzyloxyphenoxy substitution on gallium and indium-based phthalocyanines have not been reported before also. Thus we report on the synthesis of 4-benzyloxyphenoxy-substituted gallium (ClGaPcs) and indium (ClInPcs) phthalocyanines, tetrasubstituted at the non-peripheral (**7a**,**b**), peripheral (**8a**,**b**) positions and peripherally octasubstituted (**9a**,**b**) with 4-benzyloxyphenoxy group (Scheme 1). The development and elucidation of photophysical and photochemical properties of new phthalocyanine complexes are of fundamental importance, hence this work presents the study of these parameters. Specific phthalocyanines can thus be tailored such that they consist of certain properties which are required for various applications since the possibility of combining an unlimited number and type of substituents with a great number of central metals is infinite.

2. Experimental

2.1. Materials

Quinoline, dimethylsulfoxide (DMSO), methanol, hexane, chloroform ($CHCl_3$), dichloromethane (DCM), tetrahydrofuran (THF), acetone, ethanol and dimethylformamide (DMF) were dried as described in Perrin and Armarego [27] before use. Gallium(III) chloride, indium(III) chloride, deuterated $CDCl_3$, 1,3-diphenylisobenzofuran (DPBF) and 4-benzyloxyphenol were purchased from Aldrich. Column chromatography was performed on silica gel 60 (0.04–0.063 mm) and preparative thin layer chromatography was performed on silica gel 60 P F_{254}. 3-Nitrophthalonitrile (**1**) [28], 4-nitrophthalonitrile (**2**) [29], 4,5-dichlorophthalonitrile (**3**) [30], 3-(benzyloxyphenoxy)phthalonitrile (**4**) [31], 4-(benzyloxyphenoxy)phthalonitrile (**5**) [31], 4,5-bis-(benzyloxyphenoxy)-phthalonitrile (**6**) [31], unsubstituted gallium(III) phthalocyanine [32] and unsubstituted indium(III) phthalocyanine [32] were synthesized and purified according to literature procedures.

2.2. Equipment

UV–Vis spectra were recorded on a Cary 500 UV–Vis/NIR spectrophotometer. Fluorescence excitation and emission spectra, were recorded on a Varian Eclipse spectrofluoremeter using 1 cm pathlength cuvettes at room temperature. IR spectra (KBr pellets) were recorded on a Perkin–Elmer spectrum 2000 FTIR spectrometer. ^1H NMR spectra were recorded using a Bruker EMX 400 MHz NMR spectrometer. Elemental Analyses were performed at the University of Cape Town.

Photo-irradiations were done using a General electric Quartz line lamp (300 W). A 600 nm glass cut off filter (Schott) and a water filter were used to filter off ultraviolet and infrared radiations respectively. An interference filter (Intor, 700 nm with a band width of 40 nm) was additionally placed in the light path before the sample. Light intensities were measured with a POWER MAX5100 (Molelectron detector incorporated) power meter. Triplet absorption and decay kinetics were recorded on a laser flash photolysis system, the excitation pulses were produced by a Quanta-Ray Nd: YAG laser providing 400 mJ, 90 ns pulses of laser light at 10 Hz, pumping a Lambda-Physik FL3002 dye (Pyridin 1 dye in methanol). Single pulse energy was 7 mJ. The analyzing beam source was from a Thermo Oriel xenon arc lamp, and a photomultiplier tube was used as a detector. Signals were recorded with a two-channel digital real-time oscilloscope (Tektronix TDS 360); the kinetic curves were averaged over 256 laser pulses.

2.3. Photophysical parameters

2.3.1. Fluorescence quantum yields and lifetimes

Fluorescence quantum yields (Φ_F) were determined by the comparative method (Eq. (1)) [33,34],

$$\Phi_F = \Phi_F(\mathrm{Std})\frac{F \cdot A_{\mathrm{Std}} \cdot \eta^2}{F_{\mathrm{Std}} \cdot A \cdot \eta^2_{\mathrm{Std}}} \quad (1)$$

where F and F_{Std} are the areas under the fluorescence emission curves of the samples (**7a**,**b**, **8a**,**b** and **9a**,**b**) and the standard, respectively. A and A_{Std} are the respective absorbances of the samples and standard at the excitation wavelengths, respectively. η and η_{Std} are the refractive indexes of the solvents used for the sample and standard, respectively. Unsubstituted ZnPc (in DMSO) ($\Phi_F = 0.18$) [35] was employed as the standard. Both the samples and standard were excited at the same wavelength. The absorbance of the solutions at the excitation wavelength ranged between 0.04 and 0.05.

Fluorescence (τ_F) and natural radiative (τ_0) lifetimes were determined using PhotochemCAD program which uses the Strickler–Berg equation [36].

2.3.2. Triplet quantum yields and lifetimes

The de-aerated solutions of the respective gallium(III) and indium(III) phthalocyanine complexes were introduced into a 1 cm pathlength spectrophotometric cell and irradiated at the Q-band maxima with the laser system described above. Triplet quantum yields (Φ_T) were determined by a comparative method using triplet decay [23], Eq. (2):

$$\Phi_T^{Sample} = \Phi_T^{Std} \frac{\Delta A_T^{Sample} \cdot \varepsilon_T^{Std}}{\Delta A_T^{Std} \cdot \varepsilon_T^{Sample}} \quad (2)$$

where ΔA_T^{Sample} and ΔA_T^{Std} are the changes in the triplet state absorbances of the samples (**7a**,**b**, **8a**,**b** and **9a**,**b**) and standard, respectively; ε_T^{Sample} and ε_T^{Std}, the triplet state extinction coefficients for the samples (**7a**,**b**, **8a**,**b** and **9a**,**b**) and standard, respectively. The standard employed was ZnPc in DMSO, $\Phi_T^{Std} = 0.65$ [37].

Quantum yields of internal conversion (Φ_{IC}) were obtained from Eq. (3), which assumes that only three processes (fluorescence, intersystem crossing and internal conversion), jointly deactivate the excited singlet state of peripherally and non-peripherally tetra- and octa-substituted gallium(III) and indium(III) phthalocyanine complexes (**7a**,**b**, **8a**,**b** and **9a**,**b**):

$$\Phi_{IC} = 1 - (\Phi_F + \Phi_T) \quad (3)$$

Triplet lifetimes were determined by exponential fitting of the kinetic curves using OriginPro 7.5 software.

2.3.3. Singlet oxygen and photodegradation quantum yields

Singlet oxygen (Φ_Δ) and photodegradation (Φ_d) quantum yield determinations were carried out using the experimental set-up described above [38,39]. Typically, a 2 mL portion of the respective peripheral and non-peripheral tetra- and octa-substituted gallium(III) and indium(III) phthalocyanine (**7a**,**b**, **8a**,**b** and **9a**,**b**) solutions containing the singlet oxygen quencher was irradiated in the Q-band region with the photo-irradiation set-up described above [38,39]. Φ_Δ values were determined in air using the relative method with DPBF as singlet oxygen chemical quencher in DMSO (Eq. (4)):

$$\Phi_\Delta = \Phi_\Delta^{Std} \frac{R \cdot I_{abs}^{Std}}{R^{Std} \cdot I_{abs}} \quad (4)$$

where Φ_Δ^{Std} is the singlet oxygen quantum yield for the standard (ZnPc in DMSO, $\Phi_\Delta^{ZnPc} = 0.67$) [40], R and R_{Std} are the DPBF photobleaching rates in the presence of the respective samples (**7a**,**b**, **8a**,**b** and **9a**,**b**) and standard, respectively; I_{abs} and I_{abs}^{Std} are the rates of light absorption by the samples (**7a**,**b**, **8a**,**b** and **9a**,**b**) and standard, respectively. To avoid chain reactions induced by DPBF in the presence of singlet oxygen [41], the concentration of DPBF was lowered to $\sim 3 \times 10^{-5}$ mol dm^{-3}. Solution of sensitizer (absorbance ~1.5 at the irradiation wavelength) containing DPBF were prepared in the dark and irradiated in the Q-band region using the set-up described above. DPBF degradation at 417 nm was monitored. The light intensity used for Φ_Δ determinations was found to be 9.21×10^{15} photons s^{-1} cm^{-2}. The error in the determination of Φ_Δ was ~10% (determined from several Φ_Δ values). Photodegradation quantum yields (Φ_d) were determined using Eq. (5)

$$\Phi_d = \frac{(C_0 - C_t) \cdot V \cdot N_A}{I_{abs} \cdot S \cdot t} \quad (5)$$

where C_0 and C_t are the samples (**7a**,**b**, **8a**,**b** and **9a**,**b**) concentrations before and after irradiation respectively, V is the reaction volume, N_A the Avogadro's constant, S the irradiated cell area and t the irradiation time. I_{abs} is the overlap integral of the radiation source light intensity and the absorption of the samples (**7a**,**b**, **8a**,**b** and **9a**,**b**). A light intensity of 3.07×10^{16} photons s^{-1} cm^{-2} was employed for Φ_d determinations.

2.4. Synthesis

*2.4.1. 1,(4)-Tetrakis(4-benzyloxyphenoxyphthalocyaninato) gallium(III) (**7a**)*

A mixture of anhydrous gallium(III) chloride (0.40 g, 2.3 mmol), 3-(benzyloxyphenoxy)phthalonitrile (**4**) (1.50 g, 4.6 mmol) and quinoline (5 mL, doubly distilled over CaH_2) was stirred at 180 °C for 7 h under nitrogen atmosphere. After cooling, the solution was dropped into the ethanol. The green solid product was precipitated and collected by filtration and washed with ethanol. The crude product was dissolved in CH_2Cl_2 and then filtered. After filtering and concentrating, the dark green waxy product was purified by passing through a silica gel column, using THF as the eluting solvent. Furthermore this product was purified with preparative thin layer chromatography (silica gel) using $CHCl_3$ solvent system. Yield: 0.42 g (26%). UV–Vis (DMSO): λ_{max} nm ($\log\varepsilon$) 353 (4.62), 643 (4.48), 716 (5.20). IR [(KBr) ν_{max}/cm^{-1}]: 3055 (Ar–CH), 3027 (Ar–CH), 2945–2852 (CH), 1586 (C=C), 1194 (C–O–C). ^{1}H NMR ($CDCl_3$): δ, ppm 8.40–8.91 (4H, m, Pc–H), 7.63–7.93 (4H, m, Pc–H), 7.31–7.57 (24H, m, Phenyl–H, Pc–H), 7.04–7.28 (12H, m, Phenyl–H), 6.81–6.98 (4H, m, Phenyl–H), 5.11 (8H, m, CH_2). *Anal.* Calc. for $C_{84}H_{56}ClGaN_8O_8$: C, 71.52; H, 4.00; N, 7.94. Found: C, 71.06; H, 3.91; N, 7.81%.

*2.4.2. 1,(4)-Tetrakis(4-benzyloxyphenoxyphthalocyaninato) indium(III) (**7b**)*

Synthesis and purification was as outlined for **7a** except anhydrous $InCl_3$ was employed instead of anhydrous $GaCl_3$. The amounts of the reagents employed were: **4** (1.50 g, 4.6 mmol), indium(III) chloride (0.51 g, 2.3 mmol) and quinoline (5 ml). Yield: 0.37 g (22%). UV–Vis (DMSO): λ_{max} nm ($\log\varepsilon$) 355 (4.58), 641 (4.44), 716 (5.18). IR [(KBr) ν_{max}/cm^{-1}]: 3057 (Ar–CH), 3027 (Ar–CH), 2949–2856 (CH), 1582 (C=C), 1192 (C–O–C). ^{1}H NMR ($CDCl_3$): δ, ppm 8.79–9.18 (4H, m, Pc–H), 7.86–

8.12 (4H, m, Pc–H), 7.31–7.58 (28H, m, Phenyl–H, Pc–H), 7.23–7.28 (4H, m, Phenyl–H), 7.10–7.18 (4H, m, Phenyl–H), 6.88–6.97 (4H, m, Phenyl–H), 5.12 (8H, m, CH_2). *Anal.* Calc. for $C_{84}H_{56}ClInN_8O_8$: C, 69.31; H, 3.88; N, 7.70. Found: C, 69.19; H, 3.80; N, 7.60%.

2.4.3. 2,(3)-Tetrakis(4-benzyloxyphenoxyphthalocyaninato) gallium(III) (8a)

Synthesis and purification was as outlined for **7a** except **5** was employed instead of **4**. The amounts of the reagents employed were: **5** (1.50 g, 4.6 mmol), gallium(III) chloride (0.40 g, 2.3 mmol) and quinoline (5 ml). Yield: 0.62 g (38%). UV–Vis (DMSO): λ_{max} nm ($\log\varepsilon$) 354 (4.82), 622 (4.55), 693 (5.24). IR [(KBr) ν_{max}/cm^{-1}]: 3057 (Ar–CH), 3027 (Ar–CH), 2947–2854 (CH), 1617 (C=C), 1193 (C–O–C). ^1H NMR ($CDCl_3$): δ, ppm 8.21–8.82 (8H, m, Pc–H), 7.61–7.77 (4H, m, Pc–H), 7.36–7.58 (28H, m, Phenyl–H), 7.16–7.23 (8H, m, Phenyl–H), 5.16 (8H, m, CH_2). *Anal.* Calc. for $C_{84}H_{56}ClGaN_8O_8$: C, 71.52; H, 4.00; N, 7.94. Found: C, 71.24; H, 3.79; N, 7.96%.

2.4.4. 2,(3)-Tetrakis(4-benzyloxyphenoxyphthalocyaninato) indium(III) (8b)

Synthesis and purification was as outlined for **7a** except **5** was employed instead of **4** and anhydrous $InCl_3$ was employed instead of anhydrous $GaCl_3$. The amounts of the reagents employed were: **5** (1.50 g, 4.6 mmol), indium(III) chloride (0.51 g, 2.3 mmol) and quinoline (5 ml). Yield: 0.59 g (35%). UV–Vis (DMSO): λ_{max} nm ($\log\varepsilon$) 361 (4.78), 625 (4.46), 697 (5.16). IR [(KBr) ν_{max}/cm^{-1}]: 3056 (Ar–CH), 3027 (Ar–CH), 2950–2857 (CH), 1617 (C=C), 1192 (C–O–C). ^1H NMR ($CDCl_3$): δ, ppm 8.29–8.91 (8H, m, Pc–H), 7.58–7.77 (4H, m, Pc–H), 7.41–7.56 (28H, m, Phenyl–H), 7.15–7.22 (8H, m, Phenyl–H), 5.16 (8H, m, CH_2). *Anal.* Calc. for $C_{84}H_{56}ClInN_8O_8$: C, 69.31; H, 3.88; N, 7.70. Found: C, 69.38; H, 3.74; N, 7.49%.

2.4.5. 2,3-Octakis(4-benzyloxyphenoxyphthalocyaninato) gallium(III) (9a)

Synthesis and purification was as outlined for **7a** except **6** was employed instead of **4**. The amounts of the reagents employed were: **6** (2.00 g, 3.8 mmol), gallium(III) chloride (0.33 g, 1.9 mmol) and quinoline (5 ml). Yield: 0.84 g (40%). UV–Vis (DMSO): λ_{max} nm ($\log\varepsilon$) 358 (4.98), 620 (4.68), 692 (5.43). IR [(KBr) ν_{max}/cm^{-1}]: 3058 (Ar–CH), 3027 (Ar–CH), 2949–2857 (CH), 1602 (C=C), 1190 (C–O–C). ^1H NMR ($CDCl_3$): δ, ppm 8.62–9.16 (8H, m, Pc–H), 8.09–8.41 (8H, m, Phenyl–H), 7.36–7.61 (48H, m, Phenyl–H), 7.15–7.24 (16H, m, Phenyl–H), 5.12 (16H, d, CH_2). *Anal.* Calc. for $C_{136}H_{96}ClGaN_8O_{16}$: C, 74.13; H, 4.39; N, 5.09. Found: C, 74.01; H, 4.79; N, 5.24%.

2.4.6. 2,3-Octakis(4-benzyloxyphenoxyphthalocyaninato) indium(III) (9b)

Synthesis and purification was as outlined for **7a** except **6** was employed instead of **4** and anhydrous $InCl_3$ was employed instead of anhydrous $GaCl_3$. The amounts of the reagents employed were: **6** (2.00 g, 3.8 mmol), gallium(III) chloride (0.42 g, 1.9 mmol) in quinoline (5 ml). Yield: 0.92 g (43%). UV–Vis (DMSO): λ_{max} nm ($\log\varepsilon$) 362 (5.02), 623 (4.69), 696 (5.43). IR [(KBr) ν_{max}/cm^{-1}]: 3058 (Ar–CH), 3027 (Ar–CH), 2951–2859 (CH), 1600 (C=C), 1187 (C–O–C). ^1H NMR ($CDCl_3$): δ, ppm 8.60–9.21 (8H, m, Pc–H), 8.18–8.59 (8H, m, Phenyl–H), 7.31–7.57 (48H, m, Phenyl–H), 7.03–7.22 (16H, m, Phenyl–H), 5.15 (16H, ss, CH_2). *Anal.* Calc. for $C_{136}H_{96}ClInN_8O_{16}$: C, 72.65; H, 4.30; N, 4.98. Found: C, 72.83; H, 4.76; N, 5.05%.

3. Results and discussion

3.1. Synthesis and characterization

Phthalocyanines are prepared by cyclotetramerization of phthalonitriles or 1,3-diimino-1*H*-isoindoles. Octasubstituted phthalocyanines can be synthesized from 4,5-dichlorophthalonitriles [30]. 2(3),9(10),16(17),23(24)-Tetrasubstituted phthalocyanines can be synthesized from 4-substituted phthalonitriles while 1(4),8(11),15(18),22(25)-tetrasubstituted phthalocyanines are obtained from 3-substituted analogues [42]. In both cases a mixture of four possible structural isomers are obtained for tetrasubstituted phthalocyanines. The four probable isomers can be designed by their molecular symmetry as C_{4h}, C_{2v}, C_s and D_{2h} [43]. In this study, synthesized tetrasubstituted phthalocyanine compounds are obtained as isomer mixtures as expected. No attempt was made to separate the isomers of **7a**,**b** and **8a**,**b**.

The preparation of phthalocyanine derivatives from the aromatic nitriles occur under different reaction conditions. The syntheses of metallophthalocyanine complexes (**7a**,**b**, **8a**,**b** and **9a**,**b**) were achieved by treatment of phthalonitriles **4**, **5** and **6** with $InCl_3$ or $GaCl_3$ in freshly distilled quinoline (Scheme 1). Because gallium and indium are large atoms, high energy is required to insert the metal ion into the phthalocyanine ring, thus a high-boiling solvent (such as quinoline) is used to achieve this purpose. Complexes **7a** and **7b** are non-peripherally (α), and **8a** and **8b** are peripherally (β) tetrasubstituted, whereas complexes **9a** and **9b** are peripherally octasubstituted. Column and preparative thin layer chromatography with silica gel was employed to obtain the pure products from the reaction mixtures.

Generally, phthalocyanine complexes are insoluble in most organic solvents; however introduction of substituents on the ring increases the solubility. All complexes (**7a**,**b**, **8a**,**b** and **9a**,**b**) exhibited excellent solubility in organic solvents such as dichloromethane, chloroform, THF, toluene, DMSO. The new compounds were characterized by UV–Vis, IR and NMR spectroscopies and elemental analysis. The analyses are consistent with the predicted structures as shown in the experimental section. After conversion into gallium or indium phthalocyanines, the characteristic C≡N stretch at ~2230 cm^{-1} of

phthalonitriles **4**, **5** and **6** disappeared, indicative of metallophthalocyanine formation. The complexes showed characteristic vibrations due to ether groups (C–O–C) 1187–1194 cm^{-1}, aromatic CH stretching at ca. 3058–3027 cm^{-1} because the compounds contain different aromatic rings and aliphatic CH stretching at ca. 2949–2857 cm^{-1}.

The ^{1}H NMR spectra (Fig. 1) of tetrasubstituted phthalocyanine derivatives (**7a**,**b** and **8a**,**b**) show complex patterns due to the mixed isomer character of these compounds and they have different aromatic protons. Octasubstituted derivative (**9a**,**b**) also show complex patterns due to the different aromatic protons. The complexes were found to be pure by ^{1}H NMR with all the substituents and ring protons observed in their respective regions. The resonances belonging the phthalocyanine ring protons of non-peripherally tetrasubstituted complexes were observed between 8.40–8.91, 7.63–7.93 and 7.31–7.57 ppm (overlap with phenyl protons) for **7a**; 8.79–9.18, 7.86–8.12 and 7.31–7.58 ppm (overlap with phenyl protons) for **7b** (Fig. 1), integrating to a total of 12 protons expected for both non-peripheral and peripheral protons. The phenyl protons were observed between 7.31–7.57, 7.04–7.28 and 6.81–6.98 ppm integrating for 24 (overlap with 4 phthalocyanine ring protons), 12 and 4, respectively and totalling 36 protons as expected for **7a** and between 7.31–7.58, 7.23–7.28, 7.10–7.18 and 6.88–6.97 ppm integrating for 28 (overlap with 4 phthalocyanine ring protons), 4, 4 and 4, respectively and totally 36 protons as expected for **7b** (Fig. 1). For the peripherally tetrasubstituted complexes the resonance belonging the phthalocyanine ring protons were observed between 8.21–8.82 and 7.61–7.77 ppm for **8a** and between 8.29–8.91 and 7.58–7.77 ppm for **8b** integrating for 8 and 4 protons respectively giving a total of 12 protons as expected for both peripherally tetrasubstituted complexes. The phenyl protons were observed between 7.36–7.58 and 7.16–7.23 ppm for **8a** and between 7.41–7.56 and 7.15–7.22 ppm for **8b**, integrating for 28 and 8 protons respectively and giving a total of 36 protons for each complex as expected. The resonances belonging to phthalocyanine ring protons of octasubstituted complexes were observed between 8.62–9.16 ppm for **9a** and 8.60–9.21 ppm for **9b**, integrating 8 protons as expected. The phenyl protons for octasubstituted complexes were observed between 8.09–8.41, 7.36–7.61, 7.15–7.24 ppm for **9a** and between 8.18–8.59, 7.31–7.57, 7.03–7.22 ppm for **9b**, integrating for 8, 48 and 16, respectively, giving a total of 72 protons as expected. The methyl protons were observed at ca. 5.10 ppm, integrating 8 protons for tetrasubstituted (**7a**,**b**, **8a**,**b**) and 16 protons for octasubstituted (**9a**,**b**) complexes. The methyl protons were observed as multiplets for tetrasubstituted complexes (**7a**,**b**, **8a**,**b**) due to the mixed isomer character of these complexes. They were observed as two singlets for octasubstituted complexes (**9a**,**b**), due to the two type of CH_2 protons, with one of them near the Cl atom and the far from Cl atom.

3.1.1. Ground state electronic absorption and fluorescence spectra

The ground state electronic absorption spectra showed monomeric behaviour evidenced by a single (narrow) Q-band, typical of metallated phthalocyanine complexes (Fig. 2) [44]. In DMSO, the Q-bands were observed at: 716 (**7a**), 716 (**7b**), 693 (**8a**), 697 (**8b**), 692 (**9a**) and 696 (**9b**), Table 1. The Q-bands of the α-tetrasubstituted complexes (**7a** and **7b**) are red-shifted by 23–19 nm, when compared to the corresponding β-tetrasubstituted (**8a** and **8b**), and by 24 and 20 nm when compared with octasubstituted

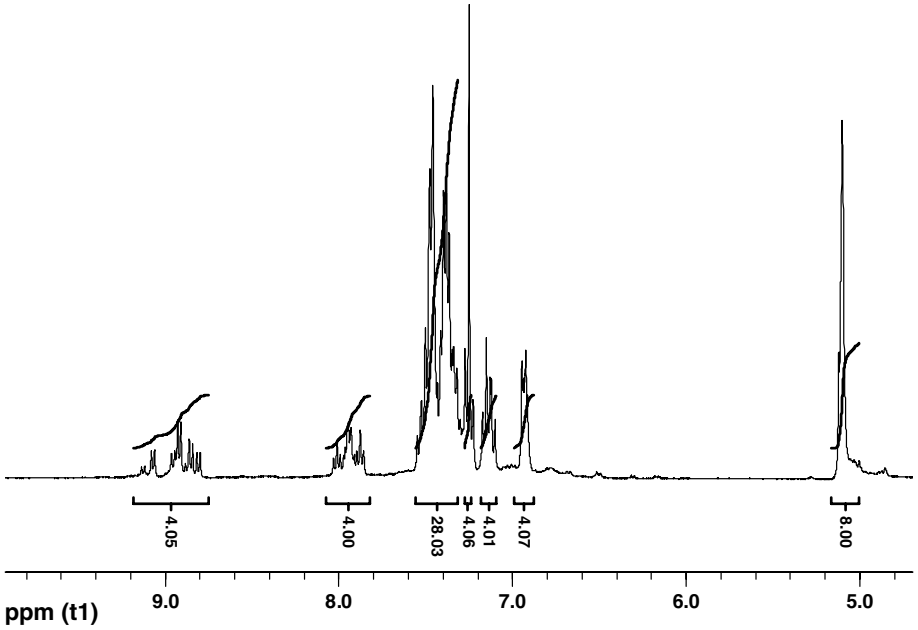


Fig. 1. ^{1}H NMR spectrum of complex **7b** in $CDCl_3$.

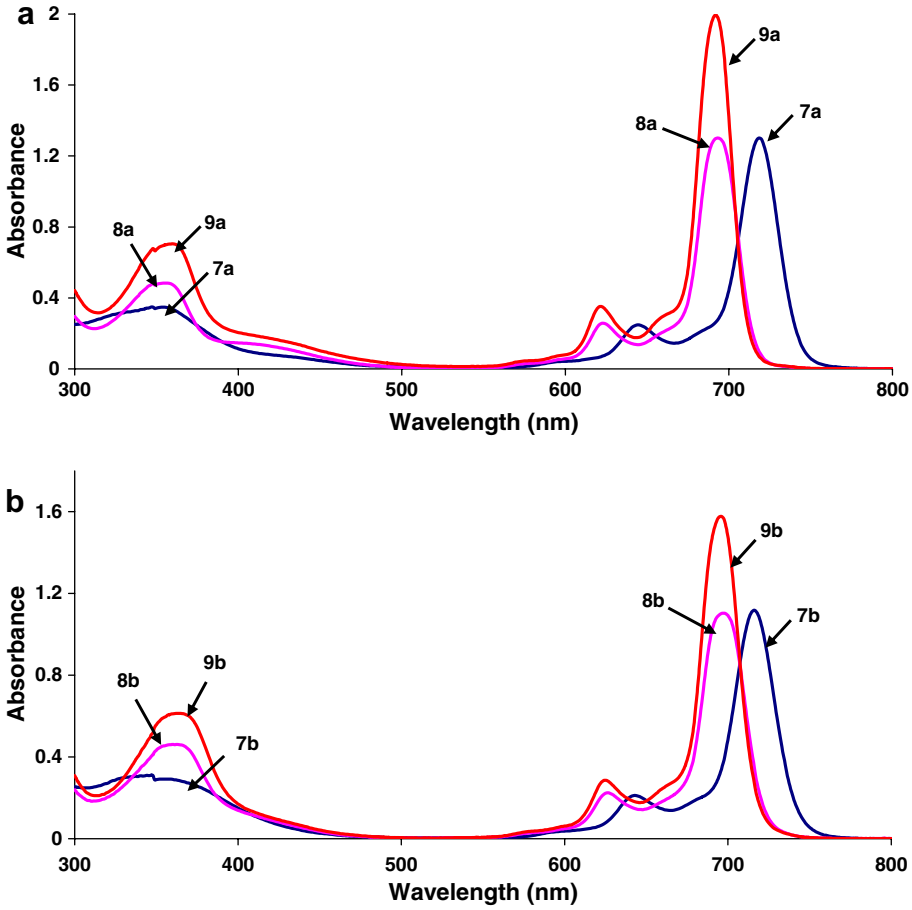


Fig. 2. Absorption spectra of: (a) **7a**, **8a** and **9a**; (b) **7b**, **8b** and **9b** in DMSO. Concentration = 4×10^{-6} mol dm^{-3}.

(**9a** and **9b**) complexes in DMSO (Table 1). The observed red spectral shift is typical of phthalocyanines with substituents at the non-peripheral positions and has been explained [45,46] to be due to linear combinations of the atomic orbitals (LCAO) coefficients at the non-peripheral positions of the HOMO being greater than those at the peripheral positions. As a result, the HOMO level is destabilized more at the non-peripheral position than it is at the peripheral position. Essentially, the energy gap (ΔE) between the HOMO and LUMO becomes smaller, resulting in a bathochromic shift. The shoulder between 400 and 450 nm may be due to charge transfer from the electron-rich ring to the electron-poor metal. The B-bands are broad due to the superimposition of the B_1 and B_2 bands in the 330–360 nm region [45].

Aggregation is usually depicted as a coplanar association of and it is dependent on the concentration, nature of the solvent, nature of the substituents, complexed metal ions and temperature [47,48]. The aggregation behaviour of the phthalocyanine complexes (**7a**,**b**, **8a**,**b** and **9a**,**b**) was also investigated at different concentrations in DMSO. In DMSO, as the concentration was increased, the intensity of absorption of the Q-band also increased and there were no new bands (normally blue shifted) due to the aggregated species for all complexes (**7a**,**b**, **8a**,**b** and **9a**,**b**) (Fig. 3 for complex **7a**). Beer–Lambert law was obeyed for all of the

Table 1
Absorption, excitation and emission spectral data for unsubstituted, tetra- and octa-substituted gallium and indium phthalocyanine compounds in DMSO

Compound	Q-band, λ_{max} (nm)	(log ε)	Excitation, λ_{Ex} (nm)	Emission, λ_{Em} (nm)	Stokes shift, Δ_{Stokes} (nm)
ClGaPc	680	5.15	680	691	11
7a	716	5.20	717	728	12
8a	693	5.24	696	704	11
9a	692	5.43	695	702	10
ClInPc	686	4.46	689	700	14
7b	716	5.18	728	739	23
8b	697	5.16	709	716	19
9b	696	5.43	707	713	17

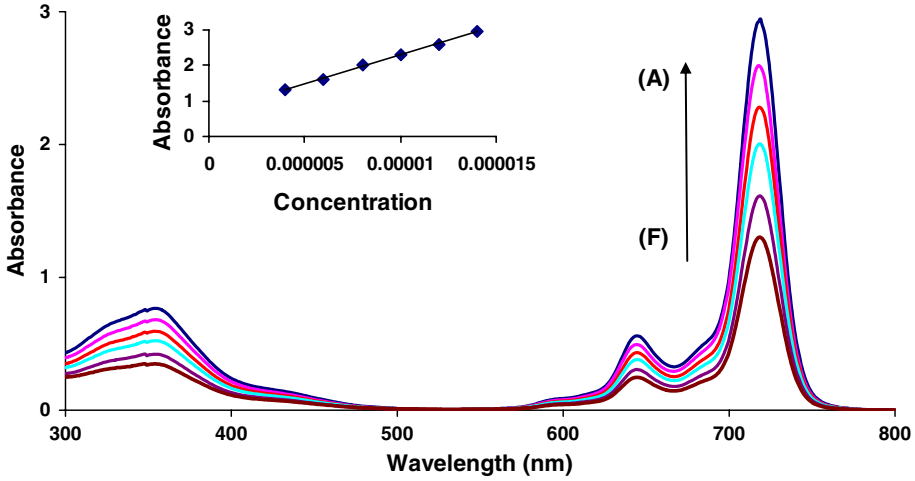


Fig. 3. Absorption spectra of **7a** in DMSO at different concentrations: 14×10^{-6} (A), $12x10^{-6}$ (B), 10×10^{-6} (C), 8×10^{-6} (D), 6×10^{-6} (E), 4×10^{-6} (F) mol dm^{-3}.

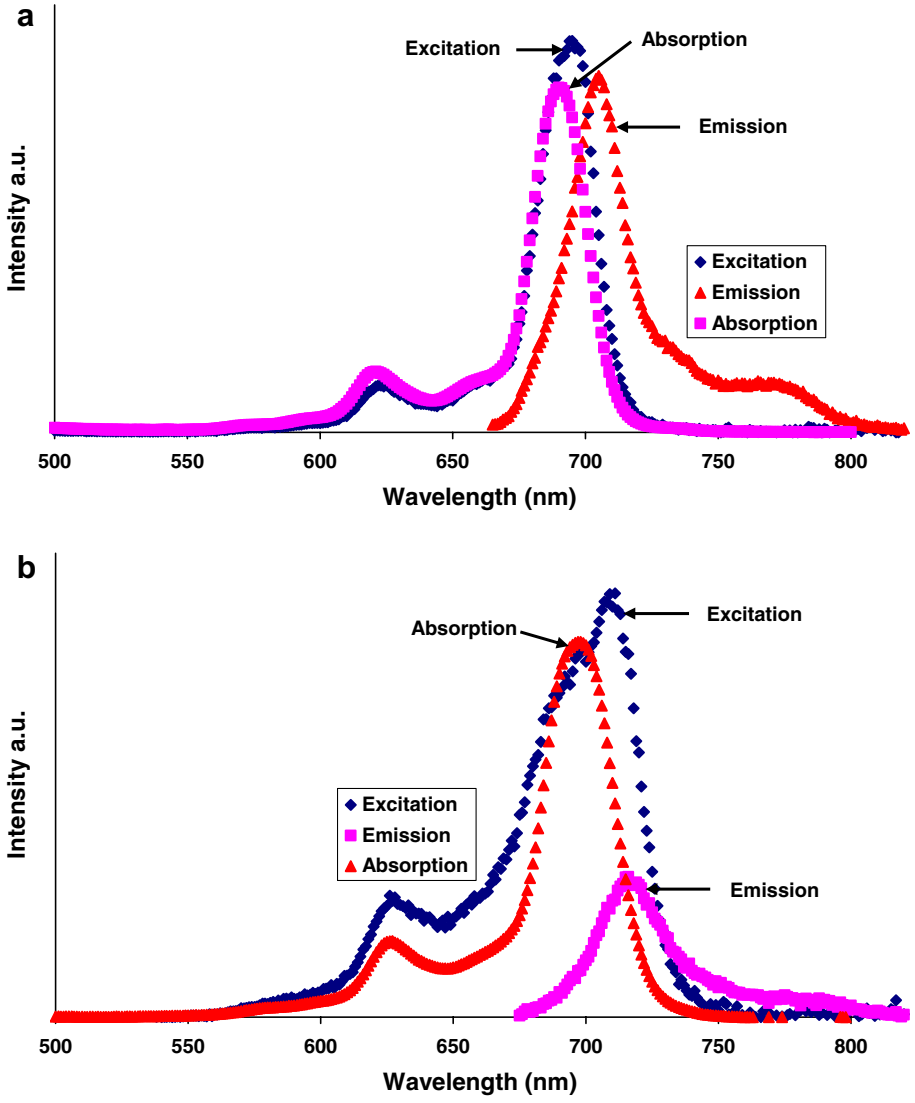


Fig. 4. Absorption, fluorescence emission and excitation spectra of (a) **8a** and (b) **8b** in DMSO. Excitation wavelength = 660 nm for **8a** and 665 nm for **8b**.

compounds in the concentrations ranging from 1.4×10^{-5} to 4×10^{-6} mol dm^{-3}.

The ClGaPc derivatives (**7a**, **8a**, **9a**) showed the same fluorescence behaviour, which was different from the ClInPc derivatives. The latter complexes (**7b**, **8b**, **9b**) also showed fluorescence behaviour which was similar to each other. Fig. 4 shows fluorescence emission, absorption and excitation spectra of complexes **8a** and **8b** as examples of the ClGaPc and ClInPc derivatives, respectively. Fluorescence emission peaks were observed at: 728 nm for **7a**, 704 nm for **8a**, 702 nm for **9a**, 739 nm for **7b**, 716 nm for **8b** and 713 nm for **9b** in DMSO (Table 1). The observed Stokes shifts are typical of MPc complexes (Table 1).

The shape of the excitation spectra were similar to absorption spectra and both were mirror images of the fluorescent spectra for the ClGaPc complexes (Fig. 4a). However in terms of wavelength, the excitation spectra was slightly red-shifted when compared to the absorption spectra, suggesting that the nuclear configurations change following excitation.

For the tetra- and octa-substituted indium phthalocyanine complexes **7b**, **8b** and **9b**, the shape of excitation spectra was different from the absorption spectra in that the Q-band of the former showed splitting, Fig. 4b, unlike the narrow Q-band of the latter. This suggests that there are changes in the molecule following excitation most likely due to loss of symmetry. The fluorescence spectra of complexes **7b**, **8b** and **9b** were also broad. Thus the Q-band maxima of the excitation and absorption spectra were different (Table 1) due to the difference in the ground and excited state species. This was however not observed for the ClGaPc complexes. The difference in the behaviours of ClGaPc and ClInPc on excitation could be due to the larger indium metal being more displaced from the core of the phthalocyanine ring, and the displacement being more pronounced on excitation hence a loss of symmetry.

Table 2
Photophysical and photochemical parameters of unsubstituted, tetra- and octa-substituted gallium and indium phthalocyanine compounds in DMSO

Compound	τ_T (μs)	Φ_F	Φ_T	Φ_{IC}	Φ_d ($\times 10^{-5}$)	Φ_Δ	S_Δ
ClGaPc	200	0.30	0.69	0.01	0.93	0.41	0.59
7a	280	0.15	0.77	0.08	0.27	0.69	0.98
8a	210	0.23	0.75	0.02	1.92	0.62	0.82
9a	200	0.13	0.74	0.13	0.50	0.51	0.69
ClInPc	50	0.018	0.91	0.07	3.43	0.61	0.67
7b	40	0.013	0.97	0.02	0.30	0.94	0.97
8b	50	0.017	0.91	0.07	0.97	0.87	0.95
9b	70	0.017	0.89	0.09	0.27	0.78	0.88

3.2. Photophysical properties

3.2.1. Fluorescence lifetimes and quantum yields

The fluorescence quantum yields (Φ_F) of ClGaPc complexes **7a**, **8a** and **9a** are typical of MPc complexes, but are lower than for the unsubstituted ClGaPc (Table 2). This suggests that the substituents quench the excited singlet state. The peripherally tetrasubstituted complex **8a** show marginally larger Φ_F values, suggesting less quenching of the excited singlet state by peripheral tetrasubstitution compared to non-peripheral tetra- and octasubstitution. For the ClInPc complexes (**7b**, **8b** and **9b**), the Φ_F values were very low due to enhancement of intersystem crossing (ISC) by the presence of a heavier indium atom in these complexes. The enhanced ISC will also result in increased triplet quantum yields and decreased triplet lifetimes as will be discussed below.

Lifetimes of fluorescence (τ_F, Table 3) were calculated using the Strickler–Berg equation. Using this equation, a good correlation has been [34] found between experimentally and the theoretically determined lifetimes for the unaggregated molecules as is the case in this work. Thus we believe that the values obtained using this equation are a good measure of fluorescence lifetimes. The τ_F values were within the range reported for MPc complexes [34]. τ_F values were lower for substituted complexes **7a**,**b**, **8a**,**b** and **9a**,**b** when compared to unsubstituted derivatives, Table 3, suggesting quenching of fluorescence by the ring substituents. For the substituted complexes, longer τ_F values were

Table 3
Rate constants for various excited state deactivation processes of unsubstituted, tetra- and octa-substituted gallium and indium phthalocyanine compounds in DMSO

Compound	Fluorescence lifetime, τ_F (ns)	Natural radiative lifetime, τ_0 (ns)	k_F^a (s^{-1}) ($\times 10^8$)	k_{ISC}^b (s^{-1}) ($\times 10^9$)	k_{IC}^c (s^{-1}) ($\times 10^8$)	k_d^d (s^{-1})
ClGaPc	3.71	11.96	0.83	0.18	0.03	4.60
7a	1.39	9.3	1.07	0.55	0.57	0.96
8a	1.90	8.26	1.21	0.39	0.10	9.10
9a	0.70	5.49	1.82	1.05	1.85	2.50
ClInPc	0.90	50.20	0.19	1.01	0.77	68.60
7b	0.12	9.03	1.07	8.08	1.14	7.50
8b	0.16	9.35	1.09	5.68	4.56	19.40
9b	0.09	5.34	1.87	9.88	10.33	3.80

[a] k_F is the rate constant for fluorescence. Values calculated using $k_F = \Phi_F/\tau_F$.
[b] k_{ISC} is the rate constant for intersystem crossing. Values calculated using $k_{ISC} = \Phi_T/\tau_F$.
[c] k_{IC} is the rate constant for internal conversion. Values calculated using $k_{IC} = \Phi_{IC}/\tau_F$.
[d] k_d is the rate constant for photodegredation. Values calculated using $k_d = \Phi_d/\tau_T$.

obtained for the peripherally tetrasubstituted complexes **8a** and **8b** compared to non-peripherally tetrasubstituted (**7a** and **7b**) and octasubstituted complexes (**9a** and **9b**), suggesting more quenching by peripheral tetrasubstitution when compared to non-peripheral ones and octasubstitution. The τ_F values ClInPc complexes were lower than for the ClGaPc complexes due to the fact that indium atom is larger than gallium atom. The natural radiative lifetime (τ_0) values of substituted complexes (**7a**,**b**, **8a**,**b** and **9a**,**b**) were lower than unsubstituted complexes (ClGaPc and ClInPc). The rate constants for fluorescence (k_F) however increased on going from unsubstituted ClGaPc (or ClInPc) to the corresponding substituted complexes **7a**,**b**, **8a**,**b** and **9a**,**b** (Table 3). There was an increase in k_F values on going from tetrasubstituted to octasubstituted ClGaPc and ClInPc complexes. Substituted complexes **7a**–**9a** and **8b**–**9b** also showed larger rate constants for internal conversion (k_{IC}, Table 3), compared to unsubstituted derivatives. There was no clear trend found for k_{IC} (Table 3) and quantum yields for internal conversion (Φ_{IC}, Table 2). In addition larger rate constants for intersystem crossing (k_{ISC}) for complexes **7a**–**9a** and **7b**–**9b** compared to the respective unsubstituted ClGaPc and ClInPc complexes confirmed improved intersystem crossing to the triplet state for the former.

3.2.2. Triplet lifetimes and quantum yields

Transient differential spectrum for complex **8a** in DMSO is shown in Fig. 5, and shows a maximum at 520 nm, hence the triplet lifetimes and yields were determined at this wavelength. Fig. 6 shows the triplet decay curves of the complexes (using complex **8a** in DMSO as an example). Table 2 shows that the triplet lifetimes for the ClGaPc complexes ranged from 200 to 280 μs, with unsubstituted ClGaPc showing the lowest triplet quantum

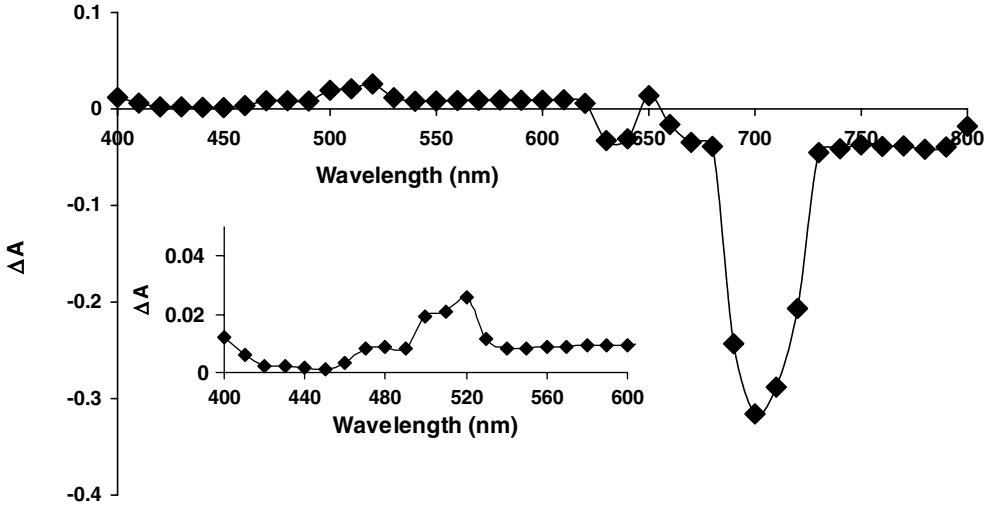


Fig. 5. Transient differential spectrum of complex **8a** in DMSO.

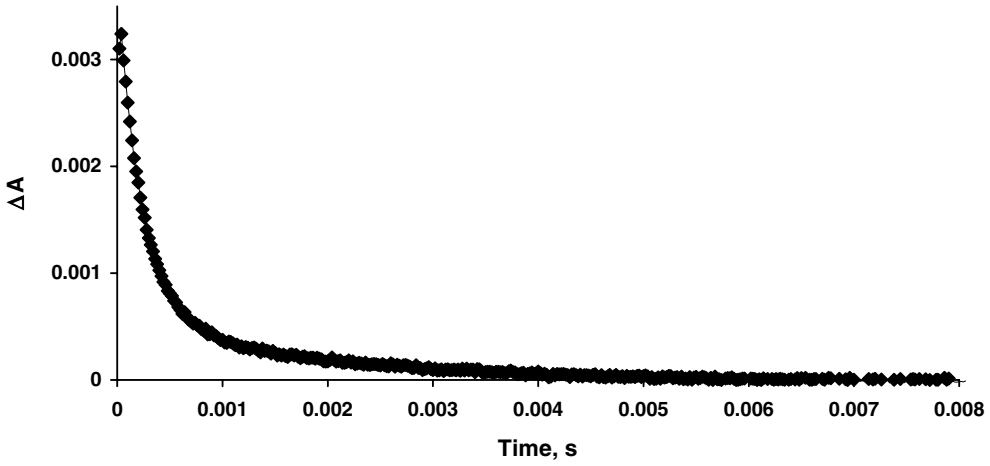


Fig. 6. Triplet decay curve of **8a** in DMSO at 520 nm. Excitation wavelength = 693 nm.

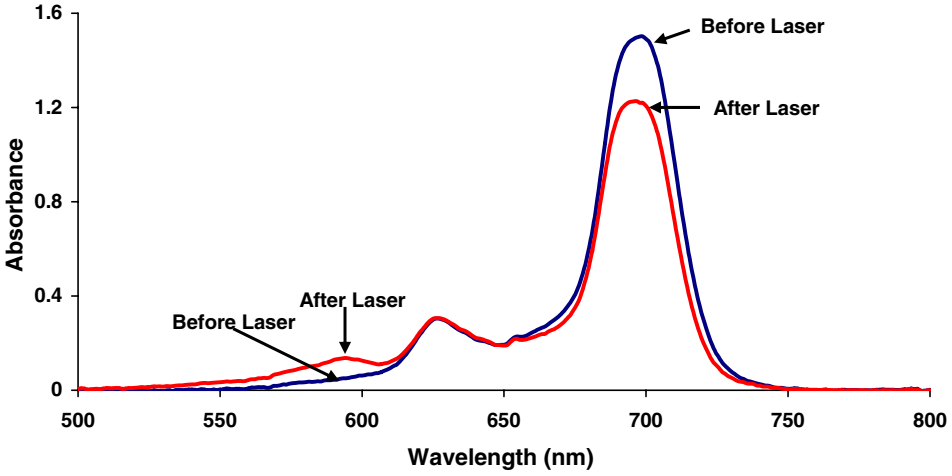


Fig. 7. Absorption spectral changes of compound **8b** before and after laser irradiation.

yield (Φ_T) when compared to substituted complexes **7a**–**9a**. Due to enhanced ISC, indium phthalocyanine complexes (ClInPc and **7b**–**9b**) showed much higher quantum yields of triplet state and shorter triplet lifetimes when compared to corresponding gallium phthalocyanine (ClGaPc and **7a**–**9a**) complexes. There is not a huge difference between Φ_T of octa- and tetra-substituted derivatives of each of ClGaPc or ClInPc.

Fig. 7 shows that for substituted complexes (**7a**–**9a** and **7b**–**9b**) and unsubstituted derivatives, there was a change is spectra following laser irradiation. The spectral changes involved the decrease in the Q-band and an increase in the absorption near 590 nm. However, on exposure of the solution to air, the Q-band increased in intensity and the band around 590 nm decreased suggesting that this band is due to a reduction products of the complexes. The first ring reduction in MPc complexes is characterized by a decrease in the Q-band and the formation of weak bands between 500 and 600 nm [49]. Thus during laser irradiation, the ClGaPc and ClInPc derivatives were partly transformed to an anion (Pc^{-3}) species. The suggested mechanism for the formation of Pc^{-3} in the presence of H donors is shown by Eqs. (6)–(8):

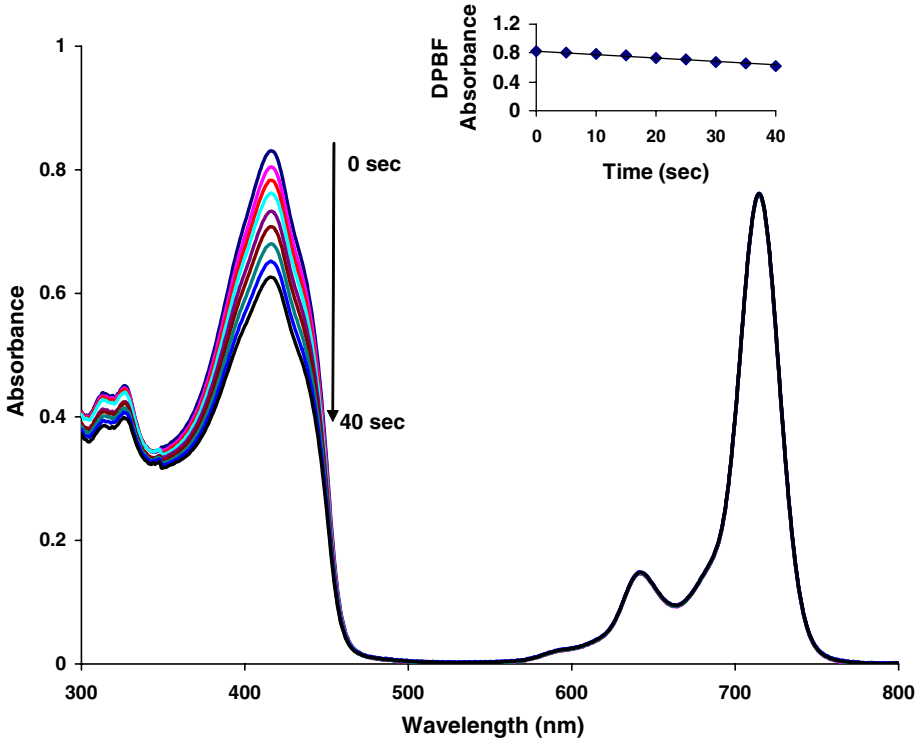


Fig. 8. A typical spectrum for the determination of singlet oxygen quantum yield. This determination was for compound **7a** in DMSO at a concentration of 3×10^{-5} mol dm^{-3}.

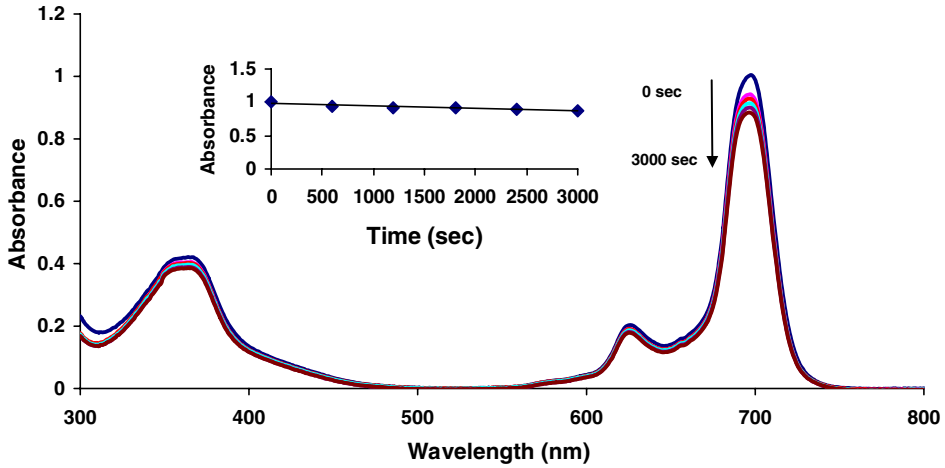


Fig. 9. The photodegredation of compound **8b** in DMSO showing the disappearance of the Q-band at 10 min intervals.

$$MPc + h\nu \rightarrow {}^{3}MPc^{*} \quad (6)$$

$${}^{3}MPc^{*} + S\text{–}H \rightarrow MPc^{\cdot -} + S\text{–}H^{\cdot +} \quad (7)$$

$$MPc^{\cdot -} + O_2 \rightarrow MPc + O_2^{\cdot -} \quad (8)$$

S = solvent

3.3. Photochemical properties

3.3.1. Singlet oxygen quantum yields

Singlet oxygen quantum yields (Φ_Δ) were determined in DMSO using DPBF as a chemical quencher. The disappearance of DBPF was monitored using UV–Vis spectrometer. Many factors are responsible for the magnitude of the determined quantum yield of singlet oxygen including; triplet excited state energy, ability of substituents and solvents to quench the singlet oxygen, the triplet excited state lifetime and the efficiency of the energy transfer between the triplet excited state and the ground state of oxygen.

Because of the presence of oxygen during the determination of singlet oxygen quantum yields (Φ_Δ) the photoreduction of complexes was not observed during singlet oxygen studies as shown by Fig. 8 for complex **7a** (as an example) in DMSO. There was no decrease in the Q-band of formation of new bands. The values of Φ_Δ were higher for complexes (**7a**,**b**, **8a**,**b** and **9a**,**b**) when compared to respective unsubstituted ClGaPc or ClInPc complexes. The trend of singlet oxygen quantum yields among the corresponding substituted complexes was non-peripherally tetrasubstituted (**7a**,**b**) > peripherally tetrasubstituted (**8a**,**b**) > octa-substituted (**9a**,**b**) for both of substituted gallium and indium phthalocyanine complexes in DMSO. The magnitude of the S_Δ ($=\Phi_\Delta/\Phi_T$) represents the efficiency of quenching of the triplet excited state by singlet oxygen. Most of the substituted complexes showed S_Δ of near unity (Table 2), suggesting efficient quenching of the triplet state by singlet oxygen. The S_Δ values were less than unity for unsubstituted ClGaPc and ClInPc complexes, suggesting inefficient quenching of the triplet state by singlet oxygen.

3.3.2. Photodegradation studies

Degradation of the molecules under irradiation can be used to study their stability and this is especially important for those molecules intended for use as photo catalysts. The collapse of the absorption spectra without any distortion of the shape confirms clean photodegradation not associated with phototransformation. The spectral changes observed for all the complexes (**7a**,**b**, **8a**,**b** and **9a**,**b**) during irradiation are as shown in Fig. 9 (using complex **8b** as an example in DMSO) and hence confirm photodegradation occurred without phototransformation.

All the complexes showed about the same stability with Φ_d of the order of 10^{-5}. Again there was no photoreduction of the complexes during photodegradation studies in the presence of oxygen, hence the magnitudes of the observed Φ_d are not due to phototransformation. The rate constant for photodegradation (k_d) values were lower for substituted indium phthalocyanine complexes **7b**, **8b** and **9b**, compared to unsubstituted ClInPc, while there was no clear trend for the ClGaPc derivatives (Table 3).

4. Conclusions

In conclusion, we have synthesized new peripherally and non-peripherally tetra-, and octa-(4-benzyloxyphenoxy) substituted gallium and indium phthalocyanines. These phthalocyanine complexes are monomeric in solution. The difference in the behaviours of ClGaPc and ClInPc complexes on excitation could be due to the larger indium metal being more displaced from the core of the phthalocyanine ring, and the displacement being more pronounced on excitation hence a loss of symmetry. Although the fluorescence quantum yields (Φ_F) of ClGaPc complexes are typical of MPc complexes, the Φ_F values for the ClInPc complexes were very low due to presence of a heavier indium atom in these complexes. 4-Benzyloxyphenoxy substituted gallium phthalocyanine complexes (**7a**–**9a**) showed long triplet lifetimes and high triplet quantum

yields. Due to enhanced ISC, 4-benzyloxyphenoxy indium phthalocyanine complexes (**7b**–**9b**) showed much higher quantum yields of triplet state and shorter triplet life times. The gallium and indium phthalocyanine complexes showed phototransformation when using laser irradiation due to the ring reduction. The substituted complexes (**7a**,**b**, **8a**,**b** and **9a**,**b**) gave good singlet oxygen quantum yields ranging from 0.51 (for **9a**) and 0.94 (for **7b**). The singlet oxygen quantum yields (Φ_Δ), which give an indication of the potential of the complexes as photosensitizers in applications where singlet oxygen is required (Type II mechanism). Thus, these complexes show potential as Type II photosensitizers for photodynamic therapy of cancer.

Acknowledgement

This work was supported by the National Research Foundation of South Africa (NRF GUN # 2053657) as well as Rhodes University.

References

[1] C.C. Leznoff, A.B.P. Lever, Phthalocyanines, Properties and Applications, vols. 1–4, VCH, New York, 1989, 1993, 1996.
[2] M. Hanack, M. Lang, Adv. Mater. 6 (1994) 819.
[3] M.J. Cook, N.B. McKeown, J.M. Simmons, A.J. Thomson, M.F. Daniel, K.J. Harrison, R.M. Richardson, S.J. Roser, J. Mater. Chem. 1 (1991) 121.
[4] D. Schlettwein, D. Wöhrle, N.I. Jaeger, J. Electrochem. Soc. 136 (1989) 2882.
[5] S. Dogo, J.P. Germain, C. Maleysson, A. Pauly, Thin Solid Films 219 (1992) 251.
[6] J. Simon, C. Sirlin, Pure Appl. Chem. 61 (1989) 1625.
[7] G. de la Torre, P. Vazquez, F. Agullo-Lopez, T. Torres, J. Mater. Chem. 8 (1998) 1671.
[8] A.B.P. Lever, M.R. Hempstead, C.C. Leznoff, W. Liu, M. Melnik, W.A. Nevin, P. Seymour, Pure Appl. Chem. 58 (1986) 1467.
[9] H. Ali, J.E. van Lier, Chem. Rev. 99 (1999) 2379.
[10] K. Katrin, A. Nihal, C. Tracy, B. David, M. Hasan, Cancer Res. 60 (2000) 5984.
[11] D. Phillips, Pure Appl. Chem. 67 (1995) 117.
[12] R. Bonnett, Chem. Soc. Rev. 24 (1995) 19.
[13] B.A. Bench, A. Beveridge, W.M. Sharman, G.J. Diebold, J.E. van Lier, S.M. Gorun, Angew. Chem., Int. Ed. 41 (2002) 747.
[14] J. Usuda, S.-M. Chiu, E.S. Murphy, M. Lam, A.-L. Nieminen, N.L. Oleinick, J. Biol. Chem. 278 (2003) 2021.
[15] I. Scalise, E.N. Durantini, Bioorg. Med. Chem. 13 (2005) 3037.
[16] C.C. Leznoff, S.M. Marcuccio, S. Grinberg, A.B.P. Lever, K.B. Tomer, Can. J. Chem. (1985) 623.
[17] R.D. George, A.W. Snow, J.S. Shirk, W.R. Barger, J. Porphyrins Phthalocyanines 2 (1998) 1.
[18] M.J. Cook, J. McMurdo, D.A. Miles, R.H. Poynter, J. Mater. Chem. 4 (1994) 1205.
[19] W. Liu, T.J. Jensen, F.R. Fronczek, R.P. Hammer, K.M. Smith, M.G.H. Vicente, J. Med. Chem. 48 (2005) 1033.
[20] L. Howe, J.Z. Zhang, J. Phys. Chem. A 101 (1997) 3207.
[21] D.K.P. Ng, C.R. Chim. 6 (2003) 903.
[22] S. FitzGerald, C. Farren, C.F. Stanley, A. Beeby, M.R. Bryce, Photochem. Photobiol. Sci. 1 (2002) 581.
[23] J.H. Brannon, D. Madge, J. Am. Chem. Soc. 102 (1980) 62.
[24] A.C. Tedesco, J.C.G. Rotta, C.N. Lunardi, Curr. Org. Chem. 7 (2003) 187.
[25] Y. Chen, Y. Araki, M. Fujitsuka, M. Hanack, O. Ito, S.M. O'Flaherty, W.J. Blau, Solid State Commun. 131 (2004) 773.
[26] J.V. Bakboord, M.J. Cook, E. Hamuryudan, J. Porphyrins Phthalocyanines 4 (2000) 510.
[27] D.D. Perrin, W.L.F. Armarego, Purification of Laboratory Chemicals, second ed., Pegamon Press, Oxford, 1989.
[28] R.D. George, A.W. Snow, J. Heterocycl. Chem. 32 (1995) 495.
[29] J.G. Young, W. Onyebuagu, J. Org. Chem. 55 (1990) 2155.
[30] D. Wöhrle, M. Eskes, K. Shigehara, A. Yamada, Synthesis (1993) 194.
[31] P. Tau, T. Nyokong, Electrochim. Acta 52 (2007) 3641.
[32] J.P. Linsky, T.R. Paul, R.S. Nohr, M.E. Kenney, Inorg. Chem. 19 (1980) 3131.
[33] S. Fery-Forgues, D. Lavabre, J. Chem. Ed. 76 (1999) 1260.
[34] D. Maree, T. Nyokong, K. Suhling, D. Phillips, J. Porphyrins Phthalocyanines 6 (2002) 373.
[35] P. Jacques, A.M. Braun, Helv. Chim. Acta 64 (1981) 1800.
[36] H. Du, R.A. Fuh, J. Li, A. Corkan, J.S. Lindsey, Photochem. Photobiol. 68 (1998) 141.
[37] T.H. Tran-Thi, C. Desforge, C. Thies, J. Phys. Chem. 93 (1989) 1226.
[38] I. Seotsanyana-Mokhosi, N. Kuznetsova, T. Nyokong, J. Photochem. Photobiol. A: Chem. 140 (2001) 215.
[39] A. Ogunsipe, T. Nyokong, J. Mol. Struct. 689 (2004) 89.
[40] N. Kuznetsova, N. Gretsova, E. Kalmykova, E. Makarova, S. Dashkevich, V. Negrimovskii, O. Kaliya, E. Luk'yanets, Russ. J. Gen. Chem. 70 (2000) 133.
[41] W. Spiller, H. Kliesch, D. Wöhrle, S. Hackbarth, B. Roder, G. Schnurpfeil, J. Porphyrins Phthalocyanines 2 (1998) 145.
[42] C.C. Leznoff, in: C.C. Leznoff, A.B.P. Lever (Eds.), Phthalocyanines: Properties and Applications, vol. 1, VCH Publishers, New York, 1989 (Chapter 1).
[43] M. Durmuş, S. Yeşilot, V. Ahsen, New J. Chem. 30 (2006) 675.
[44] M.J. Stillman, T. Nyokong, in: C.C. Leznoff, A.B.P. Lever (Eds.), Phthalocyanines: Properties and Applications, vol. 1, VCH Publishers, New York, 1989 (Chapter 3).
[45] J. Mark, M.J. Stillman, J. Am. Chem. Soc. 116 (1994) 1292.
[46] M. Konami, M. Hatano, A. Tajiri, Chem. Phys. Lett. 166 (1990) 605.
[47] H. Enkelkamp, R.J.M. Nolte, J. Porphyrins Phthalocyanines 4 (2000) 454.
[48] D.D. Dominguez, A.W. Snow, J.S. Shirk, R.G.S. Pong, J. Porphyrins Phthalocyanines 5 (2001) 582.
[49] M.J. Stillman, in: C.C. Leznoff, A.B.P. Lever (Eds.), Phthalocyanines: Properties and Applications, vol. 3, VCH Publishers, New York, 1994 (Chapter 5).

Available online at www.sciencedirect.com
ScienceDirect
Polyhedron 26 (2007) 3336–3342
POLYHEDRON
www.elsevier.com/locate/poly

X-ray structure, spectroscopic characterisation and DFT calculations of the [Re(CO)$_3$(2,2′-biquinoline)Cl] complex

B. Machura [a,*], R. Kruszynski [b]

[a] Department of Inorganic and Coordination Chemistry, Institute of Chemistry, University of Silesia, 9th Szkolna Street, 40-006 Katowice, Poland
[b] X-ray Crystallography Laboratory, Institute of General and Ecological Chemistry, Technical University of Łódź, 116 Żeromski Street, 90-924 Łódź, Poland

Received 16 February 2007; accepted 7 March 2007
Available online 20 March 2007

Abstract

The *fac*-[Re(CO)$_3$(2,2′-biquinoline)Cl] complex has been obtained in reaction of Re(CO)$_5$Cl with 2,2′-biquinoline. The compound has been studied by IR, UV–Vis spectroscopy and X-ray crystallography. The molecular orbital diagram of the tricarbonyl has been calculated with the density functional theory (DFT) method. The spin-allowed singlet–singlet electronic transitions of [Re(CO)$_3$(2,2′-biquinoline)Cl] have been calculated with the time-dependent DFT method, and the UV–Vis spectrum of the title compound has been discussed on this basis.
© 2007 Elsevier Ltd. All rights reserved.

Keywords: Rhenium carbonyl complexes; X-ray structure; UV–Vis spectra; DFT calculations

1. Introduction

For many years the diimine chelates (e.g., 2,2-bipyridine, 1,10-phenanthroline and their derivatives) of d^6 metals have been the subject of much attention. The interest of researchers has been attracted mostly by their unique photophysical and photochemical properties, crucial for numerous potential and already introduced practical applications. The most frequently studied compounds belonging to this group are complexes of general formula *fac*-[Re(CO)$_3$(diimine)(E)]$^{0/+}$, where E stands for a halogen atom or other ligand approximately axial to the heteroaromatic rings plane. The photobehaviour of the Re(I) carbonyl–diimine complexes may be discussed in terms of four types of excited states: (i) M → diimine metal-to-ligand charge transfer (MLCT) states, (ii) E → diimine ligand-to-ligand charge transfer (LLCT) states; (iii) transition from the M–E σ-bonding orbital to the diimine ligand, (iv) intraligand (IL) states. The last ones appear to lie at rather high energies in the *fac*-[Re(CO)$_3$(diimine)(E)]$^{0/+}$ complexes, and they are of little photochemical importance. The early studies has shown that the excited states of [Re(CO)$_3$(diimine)(E)]$^{0/+}$ complexes are both strong reductants and oxidants. The high reactivity of the reduced species may be utilized in photocatalysis. For example, photoexcitation of [Re(CO)$_3$(bipy)Cl] in the presence of triethylamine produces [Re(CO)$_3$(bipy)Cl]$^-$, which loses the chloride ligand. The further reaction with CO_2 results in the photocatalytic CO_2 reduction to CO. The excited states of [Re(CO)$_3$(diimine)(E)]$^{0/+}$ complexes are often sufficiently long-lived to become engaged in energy transfer reactions. Currently, several *fac*-Re(CO)$_3^+$ complexes are used as electroluminescent materials in OLED-type devices [1–12].

As the spectroscopic and redox behaviour of the Re(I) complexes are ligand dependent and can be tuned by varying the identity of their chelate ligands, there is a clear need to synthesize and investigate novel species of this type.

Here, we present the synthesis, crystal, molecular and electronic structure of the *fac*-[Re(CO)$_3$(2,2′-biquino-

* Corresponding author.
E-mail addresses: bmachura@poczta.onet.pl (B. Machura), rafal.kruszynski@p.lodz.pl (R. Kruszynski).

0277-5387/$ - see front matter © 2007 Elsevier Ltd. All rights reserved.
doi:10.1016/j.poly.2007.03.014

line)Cl] complex. The molecular orbital diagram of the title complex has been calculated with the density functional theory (DFT) calculations. This method meets with the requirements of being accurate, easy to use and fast enough to allow the study of relatively large molecules of transition metal complexes [13].

The spin-allowed singlet–singlet electronic transitions of *fac*-[Re(CO)$_3$(2,2′-biquinoline)Cl] have been calculated with the time-dependent DFT method (TDDFT method), and a good assignment with the experimental spectrum has been observed.

2. Experimental

2.1. General procedure

The reaction was performed under argon atmosphere. The solvents were dried before use, using the appropriate drying reagents. Re(CO)$_5$Cl and 2,2′-biquinoline were purchased from Aldrich, and they were used as received.

IR spectrum was recorded on a Nicolet Magna 560 spectrophotometer in the spectral range 4000–400 cm^{-1} with the samples in the form of KBr pellets. Electronic spectrum was measured on a spectrophotometer Lab Alliance UV–VIS 8500 in the range 900–200 nm in dichloromethane solution. Elemental analyses (C H N) were performed on a Perkin–Elmer CHN-2400 analyzer.

2.2. Preparation of [Re(CO)$_3$(2,2′-biquinoline)Cl]

Re(CO)$_5$Cl (0.2 g, 0.55 mmol) and 2,2′-biquinoline (0.15 g, 0.58 mmol) in toluene (50 cm^3) were refluxed for 6 h. The resulting reaction mixture was reduced in volume to ~10 ml and allowed to cool to room temperature. An off-orange solid was filtered off, washed with hexane, diethyl ether, and dried; yield 90%.

IR (KBr, cm^{-1}): ν_{NO} = 2014, 1895 and 1884 cm^{-1}; ν_{CN} and $\nu_{C=C}$ = 1616, 1595, 1578 and 1509 cm^{-1}.

Anal. Calc. for $C_{21}H_{12}N_2O_3ClRe$: C, 44.88; H, 2.15; N, 4.98. Found: C, 44.70; H, 2.20; N, 4.80%.

2.3. Crystal structures determination and refinement

Single crystals of complex [Re(CO)$_3$(2,2′-biquinoline)Cl] were grown by the slow diffusion of diethyl ether into a solution of the complex dissolved in chloroform. A orange crystal of [Re(CO)$_3$(2,2′-biquinoline)Cl]·CHCl$_3$ was mounted on a KM-4-CCD automatic diffractometer equipped with a CCD detector, and used for data collection. X-ray intensity data were collected with graphite monochromated Mo Kα radiation (λ = 0.71073 Å) at temperature of 293.0(2) K, with ω scan mode. Twenty-six-seconds exposure time was used and reflections were collected up to 2θ = 50.01°. The unit cell parameters were determined from 7044 strongest reflections respectively. Details concerning crystal data and refinement are given in Table 1. Lorentz, polarization and empirical absorption corrections [14] were applied. The structure was solved by the Patterson method and subsequently completed on the basis of the difference Fourier maps calculated after four

Table 1
Crystal data and structure refinement for [Re(CO)$_3$(2,2′-biquinoline)Cl]

Empirical formula	$C_{22}H_{13}Cl_4N_2O_3Re$
Formula weight	681.34
Temperature (K)	291.0(3)
Wavelength (Å)	0.71073
Crystal system	monoclinic
Space group	$P2_1/c$
Unit cell dimensions	
a (Å)	11.2538(9)
b (Å)	15.6386(16)
c (Å)	13.9977(13)
β (°)	109.618(8)
Volume (Å^3)	2320.5(4)
Z	4
D_{calcd} (Mg/m^3)	1.950
Absorption coefficient (mm^{-1})	5.725
F(000)	1304
Crystal size (mm)	0.47 × 0.38 × 0.28
θ Range for data collection (°)	3.09–25.14
Index ranges	$-13 \leqslant h \leqslant 12$, $-17 \leqslant k \leqslant 18$, $0 \leqslant l \leqslant 16$
Reflections collected	7746
Independent reflections [R_{int}]	4137 [0.0424]
Completeness to 2θ (%)	99.8
Maximum and minimum transmission	0.407 and 0.156
Data/restraints/parameters	4137/0/289
Goodness-of-fit on F^2	1.018
Final R indices [$I > 2\sigma(I)$]	$R_1 = 0.0424$, $wR_2 = 0.0933$
R indices (all data)	$R_1 = 0.0587$, $wR_2 = 0.1016$
Largest difference in peak and hole (e Å^{-3})	1.048 and −2.352

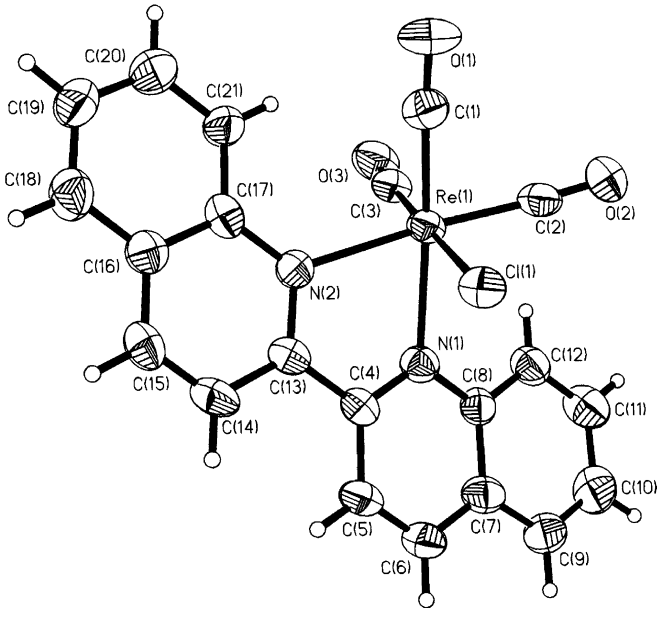


Fig. 1. Plot of [Re(CO)$_3$(2,2′-biquinoline)Cl] showing the atom numbering scheme (50% probability of displacement ellipsoids). The solvent molecule was omitted for clarity.

Table 2
The experimental and optimized bond lengths (Å) and angles (°) for [Re(CO)$_3$(2,2′-biquinoline)Cl]

	Bond lengths			Bond angles	
	Experimental	Optimized		Experimental	Optimized
Re(1)–C(1)	1.926(7)	1.927	C(1)–Re(1)–C(2)	84.0(3)	86.45
Re(1)–C(2)	1.912(8)	1.927	C(1)–Re(1)–C(3)	89.6(3)	92.23
Re(1)–C(3)	1.909(8)	1.915	C(3)–Re(1)–C(2)	88.3(3)	92.21
Re(1)–Cl(1)	2.4987(18)	2.535	C(1)–Re(1)–N(1)	169.8(2)	169.50
Re(1)–N(1)	2.243(5)	2.237	C(1)–Re(1)–N(2)	98.6(3)	99.34
Re(1)–N(2)	2.230(6)	2.237	C(1)–Re(1)–Cl(1)	90.8(2)	89.07
C(1)–O(1)	1.142(8)	1.160	C(2)–Re(1)–N(1)	102.0(2)	99.30
C(2)–O(2)	1.153(9)	1.160	C(2)–Re(1)–N(2)	174.1(2)	169.50
C(3)–O(3)	1.147(8)	1.168	C(2)–Re(1)–Cl(1)	90.0(2)	89.09
			C(3)–Re(1)–N(1)	98.8(2)	96.30
			C(3)–Re(1)–N(2)	97.0(3)	96.28
			C(3)–Re(1)–Cl(1)	178.2(2)	178.22
			N(2)–Re(1)–N(1)	74.74(19)	73.68
			N(1)–Re(1)–Cl(1)	80.98(15)	82.29
			N(2)–Re(1)–Cl(1)	84.64(14)	82.30
			O(1)–C(1)–Re(1)	176.6(7)	179.05
			O(2)–C(2)–Re(1)	175.8(6)	179.05
			O(3)–C(3)–Re(1)	176.6(6)	179.61

cycles of refinement. All the non-hydrogen atoms were refined anisotropically using full-matrix, least-squares technique. The hydrogen atoms were treated as ''riding'' on their parent carbon atoms [d(C–H$_{HCCl3}$) = 0.96 Å, d(C–H$_{2,2'\text{-biquinoline}}$) = 0.93 Å] with U_{iso}(H) = 1.2 U_{eq}(C). SHELXS97 [15], SHELXL97 [16] and SHELXTL [17] programs were used for all the calculations. Atomic scattering factors were those incorporated in the computer programs.

Table 3
The environment geometry of stacked 2,2′-biquinoline molecules distances in Å and angles in (°)

R (I)	R_2 (J)	Cg···Cg	α	β	d_p
Cg(1)	Cg(1#1)	5.7804	0.00	47.79	3.883
Cg(1)*	Cg(2#1)*	3.8386	5.93	14.34	3.749
Cg(1)*	Cg(4#1)*	4.0984	6.20	30.61	3.731
Cg(2)*	Cg(1#1)*	3.8386	5.93	12.40	3.719
Cg(2)	Cg(2#1)	5.6120	0.02	45.02	3.967
Cg(2)	Cg(3#1)	4.2103	7.43	34.47	3.657
Cg(3)	Cg(2#1)	4.2103	7.43	29.72	3.471
Cg(3)*	Cg(4#1)*	3.8569	5.77	21.49	3.491
Cg(4)*	Cg(1#1)*	4.0984	6.20	24.45	3.527
Cg(5)	Cg(3#1)	3.8569	5.77	25.16	3.589
Cg(1)	Cg(2#2)	5.3124	3.93	47.41	3.323
Cg(1)	Cg(4#2)	4.6899	5.72	40.11	3.271
Cg(3)*	Cg(2#2)*	3.9438	5.76	21.55	3.518
Cg(3)*	Cg(4#2)*	3.9392	5.19	26.86	3.487
Cg(2)	Cg(1#3)	5.3124	3.93	51.28	3.595
Cg(2)*	Cg(3#3)*	3.9438	5.76	26.87	3.668
Cg(2)	Cg(1#3)	4.6899	5.72	45.78	3.587
Cg(2)*	Cg(3#3)*	3.9392	5.19	27.73	3.514

Cg(1), Cg(2), Cg(3), Cg(4) indicates the centroids of aromatic rings containing N(1), N(2), C(12), C(21) atoms respectively, α is a dihedral angle between planes I and J, β is an angle between Cg(I)–Cg(J) vector and normal to plane I and d_p is a perpendicular distance of Cg(I) on ring J plane.
The stacked six-membered rings are indicated by (*).
Symmetry equivalent used to generate rings #1 $-x$, $-y$, $-z+1$, #2 $-x$, $y+1/2$, $-z+1/2$, #3 $-x$, $y-1/2$, $-z+1/2$.

2.4. Computational details

GAUSSIAN03 program [18] was used in the calculations. The geometry optimization was carried out with the DFT method with the use of B3LYP functional [19,20]. The electronic spectrum was calculated with the TDDFT method [21]. The calculations were performed by using ECP basis set on the rhenium atom, the standard 6-31+G** basis for chlorine, oxygen, nitrogen and carbon, and 6-31G basis for hydrogen atoms. The Xe core electrons of Re were replaced by an effective core potential and DZ quality Hay and Wadt Los Alamos ECP basis set (LANL2DZ) [22] was used for the valence electrons. Additional d function with exponent $\alpha = 0.3811$ and f function with exponent $\alpha = 2.033$ on the rhenium atom were added.

3. Results and discussion

3.1. Preparation and infrared data

The [Re(CO)$_3$(2,2′-biquinoline)Cl] complex was prepared by refluxing the [Re(CO)$_5$Cl] compound with a small

Table 4
Atomic charges and spin densities of [Re(CO)$_3$(2,2′-biquinoline)Cl]

Atom	Atomic charge
Re(1)	−0.101
Cl(1)	−0.557
N(1)	−0.448
N(2)	−0.458
C(1)	0.615
C(2)	0.615
C(3)	0.535
O(1)	−0.475
O(2)	−0.475
O(3)	−0.503

excess of 2,2′-biquinoline in toluene. The complex was isolated as air-stable, microcrystalline solid, soluble in common organic solvents. The infrared spectrum of the complex displays three bands in the carbonyl stretching region: a sharp intense band at 2014 cm^{-1} and two lower-energy bands closely spaced (1895 and 1884 cm^{-1}), typical of Re(I) diimine tricarbonyl complexes [23]. The characteristic bands of the C–C and C–N stretching modes are observed in the range 1620–1500 cm^{-1} [24].

3.2. Crystal structure

The title complex crystallises as the solvate $[Re(CO)_3$-(2,2′-biquinoline)Cl$] \cdot CHCl_3$. The crystallographic data

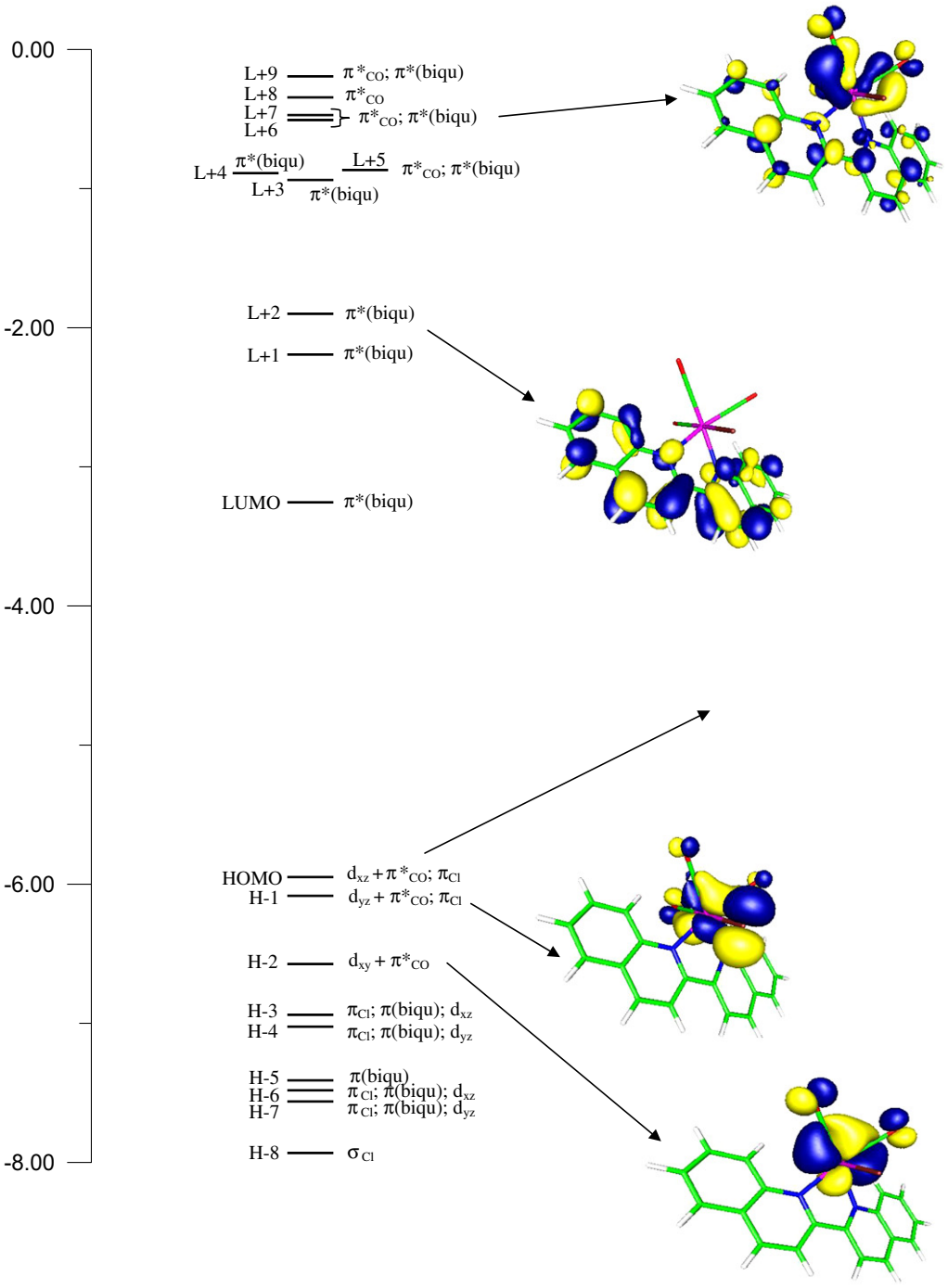


Fig. 2. The energy (eV), character and some contours of the unoccupied molecular orbitals of $[Re(CO)_3$(2,2′-biquinoline)Cl].

are given in Table 1, and the perspective drawing of [Re(CO)$_3$(2,2′-biquinoline)Cl] with atomic numbering is shown in Fig. 1. The three carbonyl ligands are arranged in a *facial* arrangement, and the rhenium coordination sphere can be described as slightly distorted tetragonal bipyramid. The deviation from ideal geometry mostly originates from geometric retrains imposed by chelating ligand (Table 2). The selected bond lengths and angles of [Re(CO)$_3$(2,2′-biquinoline)Cl] are given in Table 2. The Re–C and Re–N bond distances are close to those reported for the relative rhenium structures with 2,2′-biquinoline [25] and 2,2′-biquinoline substituted in the 3 and 3′ positions [26–28]. In the structure can not be found any intermolecular short contacts, which can be considered as classical hydrogen bonds, but one C(91)–H(91)···Cl(1) contact can be considered as very weak hydrogen bond [29,30] (D···A distance = 3.545(8) Å, H···A distance = 2.62 Å and D–H···A angle = 157.7°). Additionally in the structure exist stacked 2,2′-biquinoline molecules connected *via* π···π interactions (Table 3) [31]. These interactions expand molecules to stacked piles along crystallographic *b*0*c* plane.

3.3. Optimised geometry

The geometry of [Re(CO)$_3$(2,2′-biquinoline)Cl] was optimised in a singlet state by the DFT method with the B3LYP functional. The optimised geometric parameters are gathered in Table 2. The calculated bond lengths and angles are in agreement with the values based upon the X-ray crystal structure data, and the general trends observed in the experimental data are well reproduced in the calculations.

3.4. Charge distribution

The atomic charges from the natural population analysis (NPA) for [Re(CO)$_3$(2,2′-biquinoline)Cl] are shown in Table 4. The calculated charge on the rhenium atom of [Re(CO)$_3$(2,2′-biquinoline)Cl] is lower than the formal charge +1, as a result of significant charge donation from the ligands. The charges on the carbon atoms of the carbonyl ligands are positive, whereas the oxygen atoms are negatively charged. The carbon atom in the *trans* position to the chloride ion (π-donor ligand) has the smallest positive charge.

3.5. Electronic structure

The [Re(CO)$_3$(2,2′-biquinoline)Cl] complex is a closed-shell structure. Its molecular orbital diagram with several occupied and virtual molecular orbital contours is presented in Fig. 2. The HOMO–LUMO gap equals to 2.69 eV. The low-lying virtual orbitals correspond to π^*_{biqu} and π^*_{CO}, and the energy of the π^*_{biqu} is lower than π^*_{CO} orbitals. The three highest occupied molecular orbitals are predominately localized on the rhenium atom, corresponding to the $(5d_{xy})^2$ $(5d_{yz})^2$ $(5d_{xz})^2$ occupation of the central ion. They are, to a large extent, formed by Re 5d orbitals mixed with CO π* orbitals. The HOMO and HOMO − 1 orbitals contain also an admixture of chloride p_π orbitals.

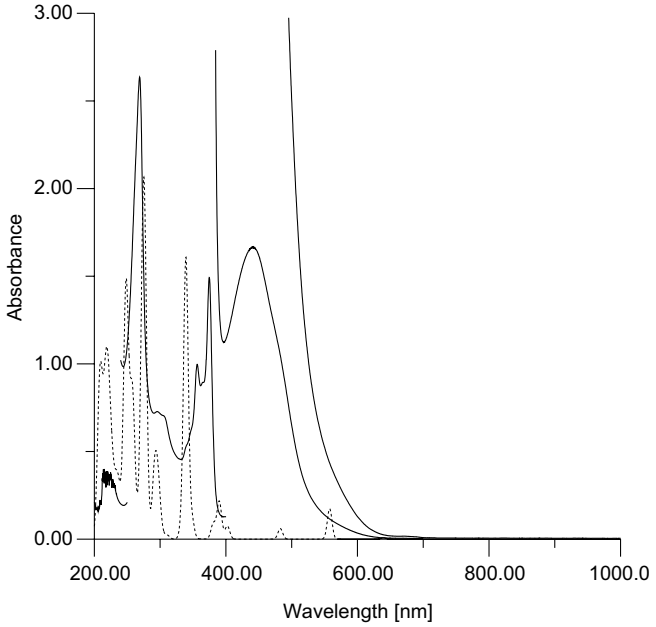


Fig. 3. The experimental (——) and calculated (----) electronic absorption spectrum of [Re(CO)$_3$(2,2′-biquinoline)Cl].

3.6. Electronic spectrum

The experimental and calculated electronic spectra of [Re(CO)$_3$(2,2′-biquinoline)Cl] are presented in Fig. 3. Each calculated transition is represented by a gaussian function $y = ce^{-bx^2}$ with the height (c) equal to the oscillator strength and b equal to 0.04 nm^{-2}.

Table 5 shows the spin-allowed singlet–singlet electronic transitions calculated with the TDDFT method for [Re(CO)$_3$(2,2′-biquinoline)Cl]. For the high energy part of the spectrum, only transitions with oscillator strengths larger than 0.010 are listed in Table 5.

The assignment of the calculated transitions to the experimental bands is based on the criterion of the energy and oscillator strength of the calculated transitions. In the description of the electronic transitions only the main components of the molecular orbital are taken into consideration.

The broad low-energy absorption band centered at 445.4 nm is attributed to *MLCT* transitions occurring from the rhenium center to the π-antibonding orbitals of the chelating ligand ($d \rightarrow \pi^*_{biqu}$). The strong experimental absorption bands in the range 400–200 nm result from *metal–ligand charge transfer* (occurring from the rhenium ion to the π-antibonding orbitals of the N–N ligand or π-antibonding orbitals of the carbonyl group) and *ligand–ligand charge transfer* transitions. The last one are of intra- and interligand character.

Table 5
The energy and molar absorption coefficients of experimental absorption bands and the electronic transitions calculated with the TDDFT method for [$Re(CO)_3$(2,2′-biquinoline)Cl]

The most important orbital excitations	Character	λ (nm)	E (eV)	f	Experimental λ (nm) [E (eV)] ε
H − 1 → L	$d \rightarrow \pi^*_{biqu}$	557.8	2.22	*0.0346*	445.4 (2.78) 8800
H − 2 → L	$d \rightarrow \pi^*_{biqu}$	482.7	2.57	*0.0120*	
H − 3 → L	$\pi_{Cl}/\pi_{biqu} \rightarrow \pi^*_{biqu}$	402.4	3.08	*0.0136*	
H − 4 → L	$\pi_{Cl}/\pi_{biqu} \rightarrow \pi^*_{biqu}$	389.9	3.18	*0.0430*	
H → L + 1	$d \rightarrow \pi^*_{biqu}$				
H − 1 → L + 1	$d \rightarrow \pi^*_{biqu}$	380.8	3.26	*0.0175*	374.6 (3.31) 98000
H − 6 → L	$\pi_{Cl}/\pi_{biqu} \rightarrow \pi^*_{biqu}$	348.2	3.56	*0.0221*	
H − 5 → L	$\pi_{biqu} \rightarrow \pi^*_{biqu}$				
H − 5 → L	$\pi_{biqu} \rightarrow \pi^*_{biqu}$	339.2	3.66	*0.3176*	356.4 (3.48) 63900
H − 6 → L	$\pi_{Cl}/\pi_{biqu} \rightarrow \pi^*_{biqu}$				
H − 2 → L + 1	$d \rightarrow \pi^*_{biqu}$	332.8	3.73	*0.0125*	
H − 3 → L + 1	$\pi_{Cl}/\pi_{biqu} \rightarrow \pi^*_{biqu}$	296.6	4.18	*0.0553*	300.0 (4.13) 45900
H − 4 → L + 1	$\pi_{Cl}/\pi_{biqu} \rightarrow \pi^*_{biqu}$	291.4	4.26	*0.0707*	
H − 3 → L + 3	$\pi_{Cl}/\pi_{biqu} \rightarrow \pi^*_{biqu}$	276.1	4.49	*0.3047*	268.8 (4.61) 150000
H − 1 → L + 4	$d \rightarrow \pi^*_{biqu}$	272.8	4.54	*0.1423*	
H − 2 → L + 6	$d \rightarrow \pi^*_{CO}/\pi^*_{biqu}$	260.3	4.76	*0.0263*	
H − 7 → L + 1	$\pi_{Cl}/\pi_{biqu} \rightarrow \pi^*_{biqu}$	257.5	4.82	*0.1288*	
H − 6 → L + 3	$\pi_{Cl}/\pi_{biqu} \rightarrow \pi^*_{biqu}$	250.0	4.96	*0.1180*	
H − 2 → L + 4	$d \rightarrow \pi^*_{biqu}$	247.6	5.01	*0.1123*	
H − 10 → L	$n_N/\pi_{biqu} \rightarrow \pi^*_{biqu}$				
H → L + 9	$d \rightarrow \pi^*_{CO}/\pi^*_{biqu}$	247.1	5.02	*0.0171*	
H − 1 → L + 9	$d \rightarrow \pi^*_{CO}/\pi^*_{biqu}$	246.5	5.03	*0.0538*	
H − 7 → L + 3	$\pi_{Cl}/\pi_{biqu} \rightarrow \pi^*_{biqu}$	236.6	5.24	*0.0344*	219.4 (5.65) 160000
H − 3 → L + 5	$\pi_{Cl}/\pi_{biqu} \rightarrow \pi^*_{CO}/\pi^*_{biqu}$	232.6	5.33	*0.0135*	
H − 1 → L + 13	$d \rightarrow \pi^*_{CO}$	229.0	5.41	*0.0185*	
H − 4 → L + 4	$\pi_{Cl}/\pi_{biqu} \rightarrow \pi^*_{biqu}$	228.5	5.43	*0.0122*	
H − 4 → L + 5	$\pi_{Cl}/\pi_{biqu} \rightarrow \pi^*_{CO}/\pi^*_{biqu}$	226.4	5.48	*0.0204*	
H − 12 → L	$n_N/\pi_{biqu} \rightarrow \pi^*_{biqu}$	223.2	5.56	*0.0812*	
H − 13 → L	$n_N/\pi_{biqu} \rightarrow \pi^*_{biqu}$	220.5	5.62	*0.0130*	
H → L + 12	$d \rightarrow \pi^*_{CO}$	219.4	5.65	*0.0297*	
H − 2 → L + 8	$d \rightarrow \pi^*_{CO}$	219.2	5.66	*0.0251*	
H − 3 → L + 4	$\pi_{Cl}/\pi_{biqu} \rightarrow \pi^*_{biqu}$				
H − 2 → L + 8	$d \rightarrow \pi^*_{CO}$	218.8	5.67	*0.0351*	
H − 9 → L + 1	$\pi_{biqu} \rightarrow \pi^*_{biqu}$	216.8	5.72	*0.0627*	
H − 4 → L + 4	$\pi_{Cl}/\pi_{biqu} \rightarrow \pi^*_{biqu}$				
H − 3 → L + 7	$\pi_{Cl}/\pi_{biqu} \rightarrow \pi^*_{CO}/\pi^*_{biqu}$	214.4	5.78	*0.0315*	
H − 3 → L + 7	$\pi_{Cl}/\pi_{biqu} \rightarrow \pi^*_{CO}/\pi^*_{biqu}$	210.8	5.88	*0.0136*	
H − 7 → L + 5	$\pi_{Cl}/\pi_{biqu} \rightarrow \pi^*_{CO}/\pi^*_{biqu}$				
H − 3 → L + 8	$\pi_{Cl}/\pi_{biqu} \rightarrow \pi^*_{CO}$	209.4	5.92	*0.0262*	
H − 5 → L + 5	$\pi_{biqu} \rightarrow \pi^*_{CO}/\pi^*_{biqu}$	208.1	5.96	*0.0841*	

biqu: 2,2′-biquinoline.

4. Conclusions

The [$Re(CO)_3$(2,2′-biquinoline)Cl] complex has been structurally and spectroscopically characterized. X-ray and IR studies confirm a *facial* geometry of the carbonyl ligands in the [$Re(CO)_3$(2,2′-biquinoline)Cl] complex. The molecular orbital diagram of the tricarbonyl has been calculated with the density functional theory (DFT) method. The HOMO, HOMO − 1 and HOMO − 2 orbitals are predominantly of d_{Re} orbital character corresponding to the $(5d_{xy})^2$ $(5d_{yz})^2$ $(5d_{xz})^2$ occupation. The low-lying virtual orbitals correspond to π^*_{biqu} and π^*_{CO}. The spin-allowed electronic transitions of *fac*-[$Re(CO)_3$(2,2′-biquinoline)Cl] have been calculated with the time-dependent DFT method (TDDFT method), and a good agreement between calculated and experimental spectra is observed.

5. Supplementary material

CCDC 623826 contains the supplementary crystallographic data for $C_{22}H_{13}Cl_4N_2O_3Re$. These data can be obtained free of charge via http://www.ccdc.cam.ac.uk/conts/retrieving.html, or from the Cambridge Crystallographic Data Centre, 12 Union Road, Cambridge CB2 1EZ, UK; fax: (+44) 1223-336-033; or e-mail: deposit@ccdc.cam.ac.uk.

Acknowledgements

The GAUSSIAN03 calculations were carried out in the Wrocław Centre for Networking and Supercomputing, WCSS, Wrocław, Poland. Crystallographic part was financed by funds allocated by the Ministry of Science and

Higher Education to the Institute of General and Ecological Chemistry, Technical University of Łódź.

References

[1] V. Balzani, A. Juris, M. Venturi, S. Campagna, S. Serroni, Chem. Rev. 96 (1996) 759.
[2] D.J. Stufkensm, A. Vlček Jr., Coord. Chem. Rev. 177 (1998) 127.
[3] I.R. Farrell, A. Vlček Jr., Coord. Chem. Rev. 208 (2000) 87.
[4] A. Vogler, H. Kunkely, Coord. Chem. Rev. 200–202 (2000) 991.
[5] D.R. Striplin, G.A. Crosby, Coord. Chem. Rev. 211 (2001) 163.
[6] A. Vlček, M. Busby, Coord. Chem. Rev. 250 (2006) 1755.
[7] S. Ranjan, S.-Y. Li, K.-C. Hwang, W.-L. Ching, C.-S. Liu, Y.-T. Tao, C.-H. Chien, S.-M. Peng, G.-H. Lee, Inorg. Chem. 42 (2003) 1248.
[8] F. Li, G. Cheng, Y. Zhao, J. Feng, S. Liu, M. Zhang, Y. Ma, J. Shen, Appl. Phys. Lett. 83 (2003) 4716.
[9] P. Christensen, A. Hamnett, A.V.G. Muir, J.A. Timney, J. Chem. Soc., Dalton Trans. (1992) 1455.
[10] H. Hori, F.P.A. Johnson, K. Koike, K. Takeuchi, T. Ibusuki, O. Ishitani, J. Chem. Soc., Dalton Trans. (1997) 1019.
[11] S.S. Jurisson, J.D. Lydon, Chem. Rev. 99 (1999) 2205.
[12] W.A. Volkert, T.J. Hoffman, Chem. Rev. 99 (1999) 2269.
[13] H. Chermette, Coord. Chem. Rev. 178–180 (1998) 699.
[14] STOE & Cie, X-RED. Version 1.18, STOE & Cie GmbH, Darmstadt, Germany, 1999.
[15] G.M. Sheldrick, Acta Crystallogr., Sect. A 46 (1990) 467.
[16] G.M. Sheldrick, SHELXL97. Program for the Refinement of Crystal Structures, University of Göttingen, Germany, 1997.
[17] G.M. Sheldrick, SHELXTL: Release 4.1 for Siemens Crystallographic Research Systems, 1990.
[18] M.J. Frisch, G.W. Trucks, H.B. Schlegel, G.E. Scuseria, M.A. Robb, J.R. Cheeseman, J.A. Montgomery Jr., T. Vreven, K.N. Kudin, J.C. Burant, J.M. Millam, S.S. Iyengar, J. Tomasi, V. Barone, B. Mennucci, M. Cossi, G. Scalmani, N. Rega, G.A. Petersson, H. Nakatsuji, M. Hada, M. Ehara, K. Toyota, R. Fukuda, J. Hasegawa, M. Ishida, T. Nakajima, Y. Honda, O. Kitao, H. Nakai, M. Klene, X. Li, J.E. Knox, H.P. Hratchian, J.B. Cross, C. Adamo, J. Jaramillo, R. Gomperts, R.E. Stratmann, O. Yazyev, A.J. Austin, R. Cammi, C. Pomelli, J.W. Ochterski, P.Y. Ayala, K. Morokuma, G.A. Voth, P. Salvador, J.J. Dannenberg, V.G. Zakrzewski, S. Dapprich, A.D. Daniels, M.C. Strain, O. Farkas, D.K. Malick, A.D. Rabuck, K. Raghavachari, J.B. Foresman, J.V. Ortiz, Q. Cui, A.G. Baboul, S. Clifford, J. Cioslowski, B.B. Stefanov, G. Liu, A. Liashenko, P. Piskorz, I. Komaromi, R.L. Martin, D.J. Fox, T. Keith, M.A. Al-Laham, C.Y. Peng, A. Nanayakkara, M. Challacombe, P.M.W. Gill, B. Johnson, W. Chen, M.W. Wong, C. Gonzalez, J.A. Pople, Gaussian 03, Revision B.03, Gaussian, Inc., Pittsburgh PA, 2003.
[19] A.D. Becke, J. Chem. Phys. 98 (1993) 5648.
[20] C. Lee, W. Yang, R.G. Parr, Phys. Rev. B 37 (1988) 785.
[21] M.E. Casida, in: J.M. Seminario (Ed.), Recent Developments and Applications in Modern Density Functional Theory, Theoretical and Computational Chemistry, vol. 4, Elsevier, Amsterdam, 1996.
[22] P.J. Hay, W.R. Wadt, J. Chem. Phys. 82 (1985) 299.
[23] P.J. Giordano, M.S. Wrighton, J. Am. Chem. Soc. 101 (1979) 2888.
[24] K. Nakamoto, Infrared and Raman Spectra of Inorganic and Coordination Compounds, 4th ed., Wiley-Interscience, New York, 1986.
[25] S.A. Moya, J. Guerrero, F.J. Rodriguez-Nieto, E. Wolcan, M.R. Feliz, R.F. Baggio, M.T. Garland, Helv. Chim. Acta 88 (2005) 2842.
[26] J. Guerrero, S.A. Moya, M.T. Garland, R.F. Baggio, Acta Crystallogr., Sect. C 54 (1998) 1592.
[27] J. Guerrero, S.A. Moya, M.T. Garland, R.F. Baggio, Acta Crystallogr., Sect. C 55 (1999) 932.
[28] S.A. Moya, J. Guerrero, R. Pastene, R. Schmidt, R. Sariego, R. Sartori, J. Sanz-Aparicio, I. Fonseca, M. Martínez-Ripoll, Inorg. Chem. 33 (1994) 2341.
[29] G.A. Jeffrey, W. Saenger, Hydrogen Bonding in Biological Structures, Springer-Verlag, 1994.
[30] G.R. Desiraju, T. Steiner, The Weak Hydrogen Bond in Structural Chemistry and Biology, Oxford University Press, 1999.
[31] C.A. Hunter, J.K.M. Sanders, J. Am. Chem. Soc. 112 (1990) 5525.

Available online at www.sciencedirect.com
ScienceDirect
Polyhedron 26 (2007) 3343–3349
POLYHEDRON
www.elsevier.com/locate/poly

Synthesis of mixed cobalt–nickel oxydiacetate compounds: The X-ray characterization of $[Co_{0.4}Ni_{0.6}(oda)(H_2O)_3]\cdot 1.5H_2O$

Abdessamad Grirrane [a], Antonio Pastor [a], Eleuterio Álvarez [b], Manuel González [a], Agustín Galindo [a,*]

[a] *Departamento de Química Inorgánica, Universidad de Sevilla, Aptdo 553, 41071 Sevilla, Spain*
[b] *Instituto de Investigaciones Químicas, CSIC-Universidad de Sevilla, Avda. Américo Vespucio 49, 41092 Sevilla, Spain*

Received 14 February 2007; accepted 7 March 2007
Available online 24 March 2007

Abstract

Mixed cobalt–nickel oxydiacetate $[Co_xNi_{1-x}(oda)(H_2O)_3]\cdot 1.5H_2O$ compounds (oda = $O(CH_2COO)_2^{2-}$; $x = 0.3$, 0.4, 0.6) were synthesized from the reaction of aqueous solutions of a mixture of nickel dichloride and cobalt dichloride with a 1:1 mixture of Na_2CO_3 and oxydiacetic acid, $O(CH_2COOH)_2$. In particular, compound $[Co_{0.4}Ni_{0.6}(oda)(H_2O)_3]\cdot 1.5H_2O$ (**1**) was characterized by single-crystal X-ray analysis. Complex **1** is a co-crystallization of $[Ni(oda)(H_2O)_3]\cdot 1.5H_2O$ and $[Co(oda)(H_2O)_3]\cdot 1.5H_2O$ compounds, the latter species being a new hydrated form of cobalt oxydiacetate that shows a *fac*-coordination for the oda ligand. These compounds can be used for the preparation of mixed metal oxides. For instance, thermal decomposition of **1**, carried out under a nitrogen atmosphere, produces essentially $Co_{0.4}Ni_{0.6}O$ oxide.
© 2007 Elsevier Ltd. All rights reserved.

Keywords: Cobalt; Nickel; Oxydiacetate; Coordination chemistry; Crystal structures; Oxides

1. Introduction

From a structural point of view, the information about oxydiacetate compounds ($O(CH_2COO)_2^{2-}$, oda) has increased significantly in recent decades. Besides the lanthanide elements, first row transition metals containing this ligand are those more studied by X-ray crystallography [1,2]. We have produced several contributions concerning the chemistry of oda complexes [3–6], and in this paper we have centred our attention on the simplest compounds of the general empirical formula $[M(oda)(H_2O)_x]\cdot nH_2O$. They are composed of a divalent first-row transition metal ion, the oda ligand and water (as a coligand or/and hydration molecule). Our interest came from the fact that these compounds are known to yield the corresponding transition metal oxides by thermal decomposition [2f,7] and, consequently, they can be selected as precursors for the synthesis of these materials.

In recent years, a renewed interest in the methodologies for the preparation of transition metal oxides has emerged, particularly nanoparticles, due to their importance in applications [8]. For instance, Pericàs and co-workers have recently described an elegant process for the room temperature synthesis of pure CoO nanoparticles [9]. These new methodologies are also applied to the preparation of mixed metal oxides (MMO) that have important practical applications in several fields [10]. A number of procedures have been employed in order to achieve precise control on the composition of the MMO powders. This is due to the influence that the homogeneous composition at the atomic length scale may have in the properties of the resulting material. A recent improvement in classical methodologies is to make use of a single source instead of a multicomponent mixture [11]. The single component may be a bimetallic compound which is capable of affording simultaneously both metal compounds into the desired final mate-

* Corresponding author. Fax: +34 954557153.
E-mail address: galindo@us.es (A. Galindo).

0277-5387/$ - see front matter © 2007 Elsevier Ltd. All rights reserved.
doi:10.1016/j.poly.2007.03.020

rial in a single step. Alternatively, the single precursor may be a solid solution of a compound with mixed metal composition, which permits the fine-tuning of properties such as magnetism [12].

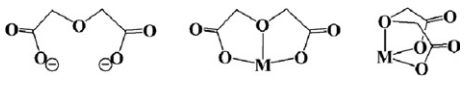
Here, we report the synthesis and properties of mixed Co–Ni oxydiacetate compounds. One of these complexes, namely $[Co_{0.4}Ni_{0.6}(oda)(H_2O)_3]\cdot 1.5H_2O$ (**1**), has been selected for study of its properties. Complex **1**, which has been characterized by single-crystal X-ray analysis, is a co-crystallization of $[Ni(oda)(H_2O)_3]\cdot 1.5H_2O$ and $[Co(oda)(H_2O)_3]\cdot 1.5H_2O$. The latter species is a new hydrated form of cobalt oxydiacetate that shows a *fac*-coordination for the oda ligand. In the absence of the Ni counterpart, the Co-oda complex displays a different $[M(oda)(H_2O)_x]\cdot nH_2O$ stoichiometry and a *mer* oda conformation. Therefore, the presence of the Ni species in **1** controls the composition of the Co complex in the crystal and also guides the conformation of the oda ligand. Furthermore, compound **1** can be used as single precursor to the mixed $Co_{0.4}Ni_{0.6}O$ oxide, which was obtained by thermal decomposition of $[Co_{0.4}Ni_{0.6}(oda)(H_2O)_3]\cdot 1.5H_2O$ (**1**) under a nitrogen atmosphere.

2. Results and discussion

2.1. Structural features of oxydiacetate $[M(oda)(H_2O)_x]\cdot nH_2O$ compounds

The oxydiacetate dianion contains five atoms as potential donors, of which four come from two carboxylate groups and one from the ether function (Scheme 1). If this ligand binds a single metal in a tridentate way, two "exo" oxygen donor atoms of the carboxylate groups remain and they are capable of additional coordination toward another metal or external electrophiles. This permits the formation of homo- and hetero-metallic extended solids or the formation of stabilizing hydrogen bonds. Concerning the tridentate coordination, two limiting situations exists (see Scheme 1): the oda ligand may be planar (*mer* coordination) or folded about the M–O vector (*fac* coordination). These two characteristics: the flexibility of oda [6] and the large capacity of this ligand to form coordination polymers (for instance, through hydrogen networks with water as a ligand or solvated [13]), make possible the formation of a rich assortment of 3D architectures notwithstanding the simplicity of a formula such as $[M(oda)(H_2O)_x]\cdot nH_2O$.

Table 1 collects the structurally characterized examples of $[M(oda)(H_2O)_x]\cdot nH_2O$ compounds and displays the corresponding oxydiacetate bonding mode. We have restricted the entries of the table to first-row transition metals, but there are also known examples of group 2 [14], cadmium [15,16] and other metals [17]. From the inspection of the table, it is evident that cobalt is the most frequent metal. In fact, there are three complexes $[Co(oda)]_n$ [7], $[\{Co(oda)(H_2O)\}\cdot H_2O]_n$ [2e,7] and $[\{Co(oda)(H_2O)_2\}\cdot H_2O]_n$ [2e,18,19], and six X-ray determinations. All of them are polymeric in nature and differ in the number of water molecules in their composition. Recently, Hung, Lu and co-workers have illustrated the influence that the water content in the synthesis reaction may have in the topology of metal frameworks based on pyridine-3,5-dicarboxylate [20]. Concerning the Co-oda system, a somewhat related relationship can be established. Scheme 2 displays a representation of the different coordination modes of oxydiacetate in structurally characterized cobalt complexes containing water. An increase in the number of water molecules that are acting as ligands produces a diminution in the connectivity of oda as a ligand. The synthesis and characterization of compound **1**, which displays a *fac*-conformation (see below), completes the series.



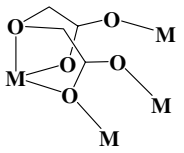
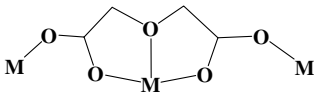
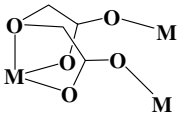
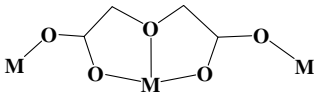
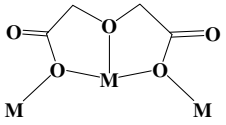
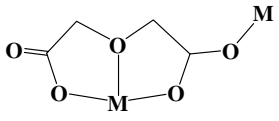
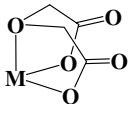
Scheme 1.

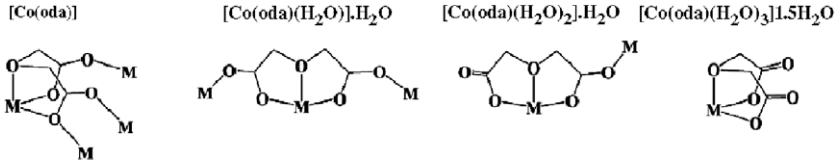
2.2. Synthesis and characterization

Following the procedure described by us for the synthesis of related oxydiacetate complexes [4], the treatment of aerobic aqueous solutions of a 1:1 mixture of nickel dichloride and cobalt dichloride with a 1:1 mixture of Na_2CO_3 and oxydiacetic acid, $O(CH_2COOH)_2$, results, after the appropriate work-up, in the formation of grey crystals of complex **1** in good yields. The chemical microanalysis indicates the composition $[M(oda)(H_2O)_3]\cdot 1.5H_2O$ for this complex. The UV–VIS spectrum of an aqueous solution of **1** (see Section 3) is the same as the spectrum of a 1:1 mixture of aqueous solutions of $[Ni(oda)(H_2O)_3]\cdot 1.5H_2O$ and $[\{Co(oda)(H_2O)_2\}\cdot H_2O]_n$ [2e,18,19]. These data suggest to us the formation of a mixed cobalt–nickel species. Similar compounds have been reported in the bibliography and some of them have been prepared by a related procedure [21]. The crystal morphology of **1** (see Fig. 1) is similar to that observed for the known complex $[Ni(oda)(H_2O)_3]\cdot 1.5H_2O$ [2f], although it differs from that observed for the related Co complex $[\{Co(oda)(H_2O)_2\}\cdot H_2O]_n$ [2e,18,19], confirming that this compound is not a mixture but a ca. 1:1 co-crystallization of $[Ni(oda)(H_2O)_3]\cdot 1.5H_2O$ and $[Co(oda)(H_2O)_3]\cdot 1.5H_2O$. The Co:Ni ratio found in **1** is $[Co_{0.4}Ni_{0.6}(oda)(H_2O)_3]\cdot 1.5H_2O$, which was determined by X-ray fluorescence and SEM microscopy (EDAX), using a crystalline-solid sample. Following the same experimental procedure, but employing mixtures of nickel dichloride and cobalt dichloride with different Co:Ni ratios, the mixed compounds $[Co_{0.6}Ni_{0.4}(oda)(H_2O)_3]\cdot 1.5H_2O$ and $[Co_{0.3}Ni_{0.7}(oda)(H_2O)_3]\cdot 1.5H_2O$ were also obtained.

The IR spectrum of $[Co_{0.4}Ni_{0.6}(oda)(H_2O)_3]\cdot 1.5H_2O$ (**1**) shows the characteristic absorptions due to the oxydiacetate ligand [22]: an intense broad band at 1605 cm^{-1}, due to the antisymmetric vibrations of the carboxylate group, and a sharp signal centred at 1091 cm^{-1} corresponding to

Table 1
Structural features of $[M(oda)(H_2O)_x]\cdot nH_2O$ compounds (M = first-row transition metal)

Formula	M	Nature	Coordination mode of oda	Ref.
[M(oda)]	Co	polymer		[7]
$[M(oda)]\cdot 0.3H_2O$	Zn	polymer		[13]
$[M(oda)]\cdot 0.5H_2O$	Cu	polymer		[2g]
$[M(oda)(H_2O)]\cdot H_2O$	Mn Co	polymer		[4,7] [2e,7]
$[M(oda)(H_2O)]_2(\mu\text{-}H_2O)$	Mn	polymer		[15]
$[M(oda)(H_2O)_2]\cdot H_2O$	Fe Co Zn	polymer		[5] [2e,18,19] [2h]
$[M(oda)(H_2O)_3]\cdot 1.5H_2O$	Ni	monomer		[2f]



Scheme 2.

the COC stretching of oda. Compounds $[Co_{0.6}Ni_{0.4}(oda)(H_2O)_3]\cdot 1.5H_2O$ and $[Co_{0.3}Ni_{0.7}(oda)(H_2O)_3]\cdot 1.5H_2O$ display similar spectra. In previous works [3,6], we have shown that the position of the latter band depends on the disposition of this ligand in the coordination sphere. Thus, when the signal appears above 1100 cm^{-1}, the oda ligand adopts a planar conformation (*mer*-disposition). In other cases, the arrangement is non-planar (*fac*-disposition). In **1**, the position of this absorption is in good agreement with the *fac*-coordination mode observed in the X-ray analysis (see below). We have realized that the IR spectrum of a compound of the type $[M(oda)(H_2O)_x]\cdot nH_2O$ can be used



Fig. 1. SEM micrograph of compound **1**.

as a fingerprint that identifies the 3D arrangement of the compound. For instance, the IR spectrum of the complex $[\{Co(oda)(H_2O)\}\cdot H_2O]_n$, structurally identified by Wang [2e] and Cheetham [7], is superimposable on that of the isomorphous Mn compound described by us, $[\{Mn(oda)(H_2O)\}\cdot H_2O]_n$ [4,7]. In addition, complex $[\{Co(oda)(H_2O)_2\}\cdot H_2O]_n$ [6], whose structure has been recently re-determined twice [2e,19], shows an identical IR spectrum to that of the isomorphous derivatives $[\{M(oda)(H_2O)_2\}\cdot H_2O]_n$ (M = Fe [5], Mg [23] and Zn [2h]). Since the IR spectra of the mixed Co–Ni compounds are identical to that recorded for $[Ni(oda)(H_2O)_3]\cdot 1.5H_2O$ [2f], we suggest that these compounds have the same structure and 3D arrangement. This proposal has been confirmed through an X-ray study of **1**.

2.3. Structural study

Compound **1** has been structurally characterized by single crystal X-ray diffraction analysis. A drawing with 50% thermal ellipsoids is shown in Fig. 2 and selected geometric parameters are collected in Table 2. X-ray diffraction cannot readily distinguish between Ni(II) and Co(II) ions and they appear delocalized on the same crystallographic site in the whole lattice. A relative ratio of 1:1 was considered, corresponding to the stoichiometry employed in the reaction from which the crystals were obtained, and refinements on the occupancies at the metal centres were carried out with this scheme (see Section 3). Compound **1** is a monomer, displaying the oda ligand in a *fac* disposition, and it is isomorphous with the Ni homologous complex. The bonding parameters around the metal centre and also the structural data within the oda ligand are similar to other characterized Ni and Co compounds [24]. For instance, the observed M–O lengths for the metal–oda moiety (M(1)–O(1) 2.0543(10), M(1)–O(2) 2.1443(11) and M(1)–O(3) 2.0223(11) Å) fit well within the range observed for oxydiacetates of Ni and Co (2.01–2.26 Å). However, the conformation of the oda ligand merits some comment. There are 17 X-ray determinations of oxydiacetate complexes of Ni and Co and only four of them display the

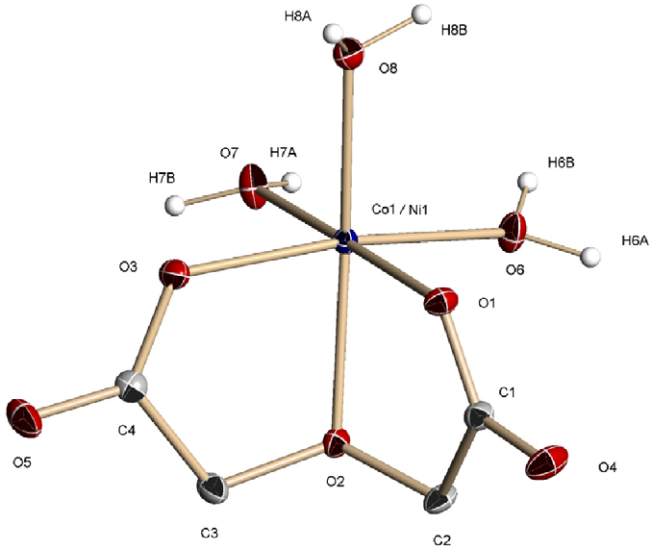


Fig. 2. ORTEP view of one of the symmetrically independent $[M(oda)(H_2O)_3]$ molecules (M = Co or Ni) present in the asymmetric unit of **1**.

fac-coordination. The remaining examples show angles between the M–O–CH_2–C(O)–O planes in the 165–180° range, a characteristic feature of a planar ligand. We have previously determined through DFT computational methods the energy differences between the two possible oda conformations in the $[Ni(oda)(H_2O)_3]$ model [6] (and also in $[VO(oda)(H_2O)_2]$ [3]). We concluded that there is a small ΔE value between the two isomers (of the order of 2 kcal mol^{-1} for the Ni compound). Under these circumstances, non-covalent interactions, such as hydrogen bond networks involving water crystallization molecules, likely determine the specific conformation of the oxydiacetate ligand. The formation of **1** is a definitive proof of the importance of the crystalline packing forces in the conformation of oda. In fact, if the synthesis of **1** is carried out under identical experimental conditions, but with the absence of Co chloride, the isolated final product is $[Ni(oda)(H_2O)_3]\cdot 1.5H_2O$ [2f]. However, if the same reaction is carried out with the absence of Ni chloride, again under identical experimental conditions, the resulting oda compound has a different formula, $[\{Co(oda)(H_2O)_2\}\cdot H_2O]_n$ [2e,18,19], displaying a planar oda ligand (*mer*-), and no evidence of the formation of $[Co(oda)(H_2O)_3]\cdot 1.5H_2O$ is found. We conclude that the presence of the Ni derivative (*fac*-) during the co-crystallization with the Co derivative specifically organizes the stoichiometry and the oda conformation in the solid state of the Co species.

2.4. Thermal decomposition of compound 1

The effect of the experimental conditions on the composition and properties of the nickel cobalt oxide series has been studied recently and several preparation techniques for getting the oxides have been evaluated [25]. The mixed

Table 2
Selected bond distances (Å) and angles (°) for compound **1**[a]

Molecule 1			
M(1)–O(3)	2.0223(11)	O(1)–C(1)	1.2696(18)
M(1)–O(7)	2.0372(11)	O(2)–C(3)	1.4356(19)
M(1)–O(6)	2.0380(11)	O(2)–C(2)	1.4418(17)
M(1)–O(1)	2.0543(10)	O(3)–C(4)	1.269(2)
M(1)–O(8)	2.0790(11)	O(4)–C(1)	1.2485(17)
M(1)–O(2)	2.1443(11)	O(5)–C(4)	1.2512(19)
O(3)–M(1)–O(7)	88.72(4)	O(6)–M(1)–O(2)	91.72(4)
O(3)–M(1)–O(6)	171.07(5)	O(1)–M(1)–O(2)	78.51(4)
O(7)–M(1)–O(6)	88.65(5)	O(8)–M(1)–O(2)	168.23(4)
O(3)–M(1)–O(1)	92.27(4)	C(3)–O(2)–C(2)	114.80(11)
O(7)–M(1)–O(1)	177.75(5)	O(4)–C(1)–O(1)	124.01(13)
O(6)–M(1)–O(1)	90.07(4)	O(4)–C(1)–C(2)	118.60(13)
O(3)–M(1)–O(8)	92.95(5)	O(1)–C(1)–C(2)	117.38(12)
O(7)–M(1)–O(8)	89.75(5)	O(2)–C(2)–C(1)	111.04(11)
O(6)–M(1)–O(8)	95.57(5)	O(2)–C(3)–C(4)	112.52(12)
O(1)–M(1)–O(8)	92.22(4)	O(5)–C(4)–O(3)	124.00(15)
O(3)–M(1)–O(2)	80.32(4)	O(5)–C(4)–C(3)	117.21(14)
O(7)–M(1)–O(2)	99.67(5)	O(3)–C(4)–C(3)	118.79(14)
Molecule 2			
M(2)–O(14)	2.0381(11)	O(9)–C(5)	1.2648(17)
M(2)–O(11)	2.0443(11)	O(10)–C(7)	1.4343(19)
M(2)–O(9)	2.0526(10)	O(10)–C(6)	1.4374(17)
M(2)–O(16)	2.0616(11)	O(11)–C(8)	1.2728(19)
M(2)–O(15)	2.0738(10)	O(12)–C(5)	1.2494(17)
M(2)–O(10)	2.1257(11)	O(13)–C(8)	1.2481(19)
O(14)–M(2)–O(11)	169.24(5)	O(9)–M(2)–O(10)	79.26(4)
O(14)–M(2)–O(9)	89.82(4)	O(16)–M(2)–O(10)	170.00(4)
O(11)–M(2)–O(9)	93.12(4)	O(15)–M(2)–O(10)	93.68(4)
O(14)–M(2)–O(16)	95.88(5)	C(7)–O(10)–C(6)	116.03(11)
O(11)–M(2)–O(16)	94.29(5)	O(12)–C(5)–O(9)	124.18(14)
O(9)–M(2)–O(16)	93.13(4)	O(12)–C(5)–C(6)	117.85(13)
O(14)–M(2)–O(15)	91.02(5)	O(9)–C(5)–C(6)	117.96(12)
O(11)–M(2)–O(15)	84.81(4)	O(10)–C(6)–C(5)	111.25(11)
O(9)–M(2)–O(15)	172.90(4)	O(10)–C(7)–C(8)	111.86(12)
O(16)–M(2)–O(15)	93.79(4)	O(13)–C(8)–O(11)	123.76(15)
O(14)–M(2)–O(10)	90.62(4)	O(13)–C(8)–C(7)	117.76(14)
O(11)–M(2)–O(10)	79.79(4)	O(11)–C(8)–C(7)	118.46(13)

[a] M = Co or Ni.

complex $[Co_{0.4}Ni_{0.6}(oda)(H_2O)_3]\cdot 1.5H_2O$ (**1**) can be a new valid precursor for the synthesis of $CoNiO_2$ oxide and thus we have studied the thermal decomposition of compound **1**, carried out under a nitrogen atmosphere in order to prevent the formation of the spinel $NiCo_2O_4$ [25]. The DTA profile essentially shows two endothermic peaks (Fig. 3). The first peak covers the 130–180 °C range and results from the loss of both coordinated and hydration water molecules, while the second at 396 °C is due to pyrolysis of the oda ligand. These observations parallel those of the isomorphous Ni species [2f] and related $[\{Co(oda)(H_2O)\}\cdot H_2O]_n$ complex [7]. The loss of hydration water molecules begins to occur at relatively low temperatures and this fact can be rationalized on the basis of the specific metal organic framework found in crystalline **1** (Fig. 4). The network of crystallization water molecules occupy channels parallel to the *a*-axis (approximate dimensions: $a = \infty$, $b = 5$ and $c = 8$ Å), which favours the removal of such molecules.

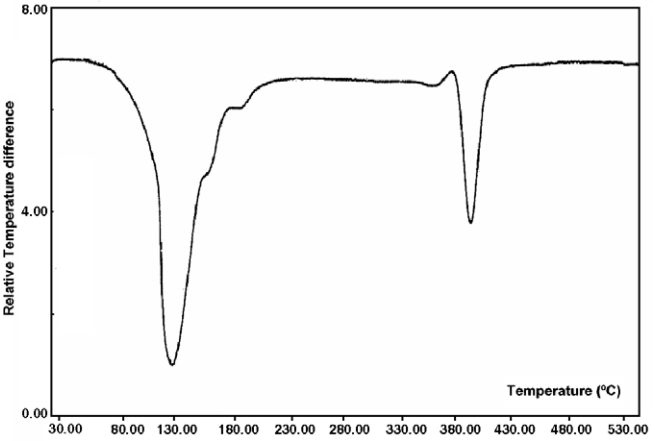


Fig. 3. DTA profile of **1**.

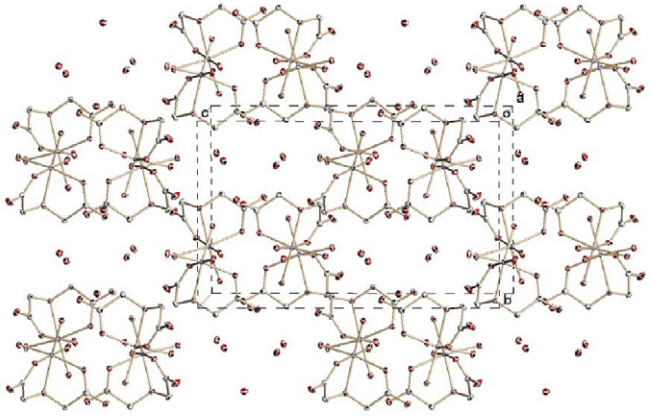


Fig. 4. Crystal packing of **1** viewed along the *a*-axis.

Chemical analysis of the sample, resulting from the thermal decomposition of **1**, (EDAX quantification by SEM and X-ray fluorescence, see details in Section 3) confirms that the composition of the solid is mainly $Co_{0.4}Ni_{0.6}O$ (a micrograph is also shown in Fig. 5), although small amounts of metallic Ni are observed by X-ray powder



Fig. 5. SEM micrograph of the mixed oxide material obtained after thermal decomposition of **1** under nitrogen.

diffraction data (peaks at 2.03 and 1.76 Å), while the oxide is rather amorphous.

3. Experimental

3.1. General

All preparations and other operations were carried out under aerobic conditions. Oxydiacetic acid and other chemicals were obtained from commercial sources and were used without further purification. The known compounds $[\{Co(oda)(H_2O)_2\}\cdot H_2O]_n$ [2e,18,19] and $[Ni(oda)(H_2O)_3]\cdot 1.5H_2O$ [2f] were prepared by the same experimental procedure described for the synthesis of **1**, but using $NiCl_2\cdot 6H_2O$ and $CoCl_2\cdot 6H_2O$, respectively.

3.2. Physical measurements

Infrared spectra were recorded on a Perkin–Elmer Model 883 spectrophotometer (Nujol emulsion in NaCl plates). Magnetic moments were measured in the solid state, at room temperature, with a Sherwood Scientific (Cambridge Research Laboratory) magnetic balance. UV–VIS spectra were recorded on a Perkin–Elmer Lambda 25 spectrophotometer. The following measurements were carried out by the "Servicios Generales de Investigación" (CITIUS) of the University of Sevilla. Microanalyses (C, H) were performed on an Elemental LECO CHNS 93 analyzer. X-ray fluorescence analyses were performed in an Axios PW4400 instrument (μSX Panalytical). SEM micrographs (SE) and chemical analysis with EDAX quantification were obtained in a Philips XL-30 instrument (silicium detector and UTW window). In both cases the samples were previously covered with graphite. Powder X-ray diffraction patterns were recorded on a Bruker D8I diffractometer.

3.3. Synthesis of $[Co_{0.4}Ni_{0.6}(oda)(H_2O)_3]\cdot 1.5H_2O$ (1) and other mixed Co–Ni compounds

To a solution of $O(CH_2COOH)_2$ (1.27 g, 12 mmol) in water (30 mL) was added a solution of Na_2CO_3 (1.61 g, 12 mmol) in water (30 mL). The mixture was stirred until the evolution of CO_2 ceased and then this mixture was added onto a 40 mL water solution of a 1:1 mixture of $NiCl_2\cdot 6H_2O$ (1.43 g; 6 mmol) and $CoCl_2\cdot 6H_2O$ (1.43 g; 6 mmol). The resulting solution was stirred for 15 min and then concentrated until ca. 40 mL. Acetone (40 mL) was added and the solution was kept at room temperature overnight. Grey crystals of complex **1** were formed, filtered off, washed with acetone, Et_2O and dried in air (2.5 g, 76%). IR (cm^{-1}): 3500–3000 br, 1605 s, 1467 s, 1431 sh, 1353 w, 1330 m, 1288 w, 1261 m, 1146 w, 1091 s, 1082 s, 1054 w, 1004 m, 967 w, 935 m, 728 s, 673 w. UV–VIS (ca. 0.05 M in water, nm): 661.1, 526.9, 398.5. $\mu_{eff} = 4.3$ μ_B at 22 °C. *Anal.* Calc. for $C_4H_{13}O_{9.5}Ni_{0.6}Co_{0.4}$: C, 17.67; H, 4.82. Found: C, 17.77; H, 4.82%. X-ray fluorescence analysis: $C_4H_{13}O_{9.5}Ni_{0.6}Co_{0.4}$: Ni/Co ratio, 1.50; found 1.51. Following the same experimental procedure, but using different ratios of $NiCl_2\cdot 6H_2O$ and $CoCl_2\cdot 6H_2O$ starting materials, the mixed compounds $[Co_{0.6}Ni_{0.4}(oda)(H_2O)_3]\cdot 1.5H_2O$ (X-ray fluorescence analysis: $C_4H_{13}O_{9.5}Ni_{0.4}Co_{0.6}$: Ni/Co ratio, 0.67; found 0.61) and $[Co_{0.3}Ni_{0.7}(oda)(H_2O)_3]\cdot 1.5H_2O$ (X-ray fluorescence analysis: $C_4H_{13}O_{9.5}Ni_{0.7}Co_{0.3}$: Ni/Co ratio, 2.33; found 2.44) were obtained, which display similar IR spectra.

3.4. Thermal analysis: synthesis of $Co_{0.4}Ni_{0.6}O$

Data were collected on a Perkin–Elmer System 714 (model 1700) instrument in flowing N_2 (40 cm^3 min^{-1}) at a heating rate of 6 °C min^{-1} by heating a crystalline solid sample of **1** (50 mg). The resulting material was identified as $Co_{0.4}Ni_{0.6}O$, according to the analysis by EDAX quantification (SEM), carried out on several particles of the oxide displaying different morphologies (average results: Co, 43; Ni, 57), and also by X-ray fluorescence: Co, 31.52; Ni, 47.09; O, 21.39. Found Co, 31.79; Ni, 43.34; O, 23.56%.

Table 3
Crystallographic data for **1**

Empirical formula	$C_4H_{13}O_{9.5}Co_{0.5}Ni_{0.5}$
Formula weight	543.93
Temperature (K)	100(2)
Wavelength (Å)	0.71073
Crystal system	orthorhombic
Space group	$Pna2_1$
Unit cell dimensions	
a (Å)	11.8336(4)
b (Å)	10.2643(4)
c (Å)	16.5393(6)
α (°)	90
β (°)	90
γ (°)	90
Volume (Å^3)	2008.92(13)
Z	4
D_{calc} (Mg m^{-3})	1.798
Absorption coefficient (mm^{-1})	1.853
$F(000)$	1124
Crystal size (mm^3)	$0.20\times 0.18\times 0.14$
θ Range for data collection (°)	2.90–30.52.
Index ranges	$-16\leqslant h\leqslant 16$, $-14\leqslant k\leqslant 14$, $-23\leqslant l\leqslant 23$
Reflections collected	26774
Independent reflections [R_{int}]	6128 [0.0304]
Completeness to $\theta = 30.52°$	99.8%
Absorption correction	semi-empirical from equivalents
Maximum and minimum transmission	0.7814 and 0.7082
Refinement method	full-matrix least-squares on F^2
Data/restraints/parameters	6128/19/317
Goodness-of-fit on F^2	1.037
Final R indices [$I > 2\sigma(I)$]	$R_1 = 0.0226$, $wR_2 = 0.0569$
R indices (all data)	$R_1 = 0.0233$, $wR_2 = 0.0572$
Absolute structure parameter	0.291(6)
Largest difference in peak and hole (e Å^{-1})	1.689 and −0.287

3.5. X-ray structural study of **1**

A summary of the crystal data of compound **1** is given in Table 3. The X-ray data were collected at 100 K on a Bruker–Nonius X8APEX-II CCD diffractometer equipped with a graphite monochromator and Mo Kα radiation. The data were reduced [26] and corrected for Lorentz polarisation effects and absorption by the multiscan method, applied by SADABS [27]. The structure was solved by direct methods (SIR-2002 [28]) and refined against all F^2 data by full-matrix least-squares techniques (SHELXTL-6.12 [29]). The occupancy factors for the Ni and Co metal sites were first refined and later both fixed to 0.5. All the non-hydrogen atoms were refined with anisotropic displacement parameters. The hydrogen atoms were included in calculated positions and refined riding on their respective carbon atoms with isotropic displacement parameters.

Acknowledgements

This work was supported by the Spanish Ministerio de Educación y Ciencia (BQU2001-3715 and CTQ2004-0084) and Junta de Andalucía. We are grateful to Raquel Moyano for the preparation of some samples.

Appendix A. Supplementary material

CCDC 631329 contains the supplementary crystallographic data for this paper. These data can be obtained free of charge via http://www.ccdc.ac.uk/conts/retrieving.html, or from the Cambridge Crystallographic Data Centre, 12 Union Road, Cambridge CB2 1EZ, UK; fax: (+44) 1223-336-033; or e-mail: deposit@ccdc.cam.ac.uk. Supplementary data associated with this article can be found, in the online version, at doi:10.1016/j.poly.2007.03.020.

References

[1] 62 hits in the Cambridge Structural Database System, Cambridge Crystallographic data Centre, 12 Union Road, Cambridge, CB2 1EZ, UK. Version 5.27, updated May 2006.
[2] Selected references: (a) Titanium: U. Thewalt, T. Guthner, J. Organomet. Chem. 379 (1989) 59;
(b) Vanadium: D. del Río, A. Galindo, J. Tejedo, F.J. Bedoya, A. Ienco, C. Mealli, Inorg. Chem. Commun. 3 (2000) 32;
(c) Manganese: C. Jiang, X. Zhu, Z.-P. Yu, Z.-Y. Wang, Inorg. Chem. Commun. 6 (2003) 706;
(d) Iron: A.K. Powell, J.M. Charnock, A.C. Flood, C.D. Garner, M.J. Ware, W. Clegg, J. Chem. Soc., Dalton Trans. (1992) 203;
(e) Cobalt: C. Jiang, Z.-Y. Wang, Polyhedron 22 (2003) 2953;
(f) Nickel: R. Baggio, M.T. Garland, M. Perec, Inorg. Chim. Acta 310 (2000) 103;
(g) Copper: S.H. Whitlow, G. Davey, J. Chem. Soc., Dalton Trans. (1975) 1228;
(h) Zinc: R. Baggio, M.T. Garland, M. Perec, Acta Crystallogr., Sect. C 59 (2003) m30.
[3] D. del Río, A. Galindo, R. Vicente, C. Mealli, A. Ienco, D. Masi, J. Chem. Soc., Dalton Trans. (2003) 1813.
[4] A. Grirrane, A. Pastor, E. Álvarez, C. Mealli, A. Ienco, P. Rosa, F. Montilla, A. Galindo, Eur. J. Inorg. Chem. (2004) 707.
[5] A. Grirrane, A. Pastor, C. Mealli, A. Ienco, P. Rosa, R. Prado-Gotor, A. Galindo, Inorg. Chim. Acta 357 (2004) 4215.
[6] A. Grirrane, A. Pastor, A. Ienco, C. Mealli, A. Galindo, J. Chem. Soc., Dalton Trans. (2002) 3771.
[7] P.M. Forster, A.K. Cheetham, Micropor. Mesopor Mater. 73 (2004) 57.
[8] See for example: Nanoparticles G. Schmid (Ed.), Wiley–VCH, New York, 2004.
[9] A. Lagunas, A. Mairata, C. Jimeno, M.A. Pericàs, Chem. Commun. (2006) 1307.
[10] See for example selected references in: G. Lu, I. Lieberwirth, G. Wegner, J. Am. Chem. Soc. 128 (2006) 15445.
[11] M. Hamid, A.A. Tahir, M. Mazhar, M. Zeller, K.C. Molloy, A.D. Hunter, Inorg. Chem. 45 (2006) 10457, and references therein.
[12] See for example: M.-H. Zeng, B. Wang, X.-Y. Wang, W.-X. Zhang, X.-M. Chen, S. Gao, Inorg. Chem. 45 (2006) 7069.
[13] R. Baggio, M.T. Garland, M. Perec, J. Chem. Soc., Dalton Trans. (1996) 2747.
[14] (a) V.A. Uchtman, R.P. Oertel, J. Am. Chem. Soc. 95 (1973) 1802;
(b) Gaduo, J.-R. Su, D.-J. Xu, Acta Crystallogr., Sect. E 61 (2005) m950;
(c) R. Baggio, M. Perec, M.T. Garland, Acta Crystallogr., Sect. C 52 (1996) 2996;
(d) R. Baggio, M.T. Garland, G. Leyva, M. Perec, G. Polla, Inorg. Chim. Acta 357 (2004) 2185.
[15] C. Jiang, X. Zhu, Z.-P. Yu, Z.-Y. Wang, Inorg. Chem. Commun. 6 (2003) 706.
[16] C.E. Boman, Acta Crystallogr., Sect. B 33 (1977) 834, 838 and 1529 (three articles).
[17] (a) For Pb metal: S. Norberg, G. Svensson, J. Albertsson, Acta Crystallogr., Sect. C 55 (1999) 356;
(b) For Eu metal: P. Starynowicz, J. Alloys Compd. 225 (1995) 406.
[18] W.E. Hatfield, J.H. Helms, B.R. Rohrs, P. Singh, J.R. Wasson, R.R. Weller, Proc. Ind. Acad. Sci., Chem. Sci. 98 (1987) 23.
[19] Z.-Y. Wu, D.-J. Xu, J.-Y. Wu, M.Y. Chiang, Acta Crystallogr., Sect. E 58 (2002) m634.
[20] Y.-L. Lu, J.-Y. Wu, M.-C. Chan, S.-M. Huang, C.-S. Lin, T.-W. Chiu, Y.-H. Liu, Y.-S. Wen, C.-H. Ueng, T.-M. Chin, C.-H. Hung, K.-L. Lu, Inorg. Chem. 45 (2006) 2430.
[21] (a) F.-T. Xie, L.-M. Duan, J.-Q. Xu, L. Ye, Y.-B. Liu, X.-X. Hu, J.-F. Song, Eur. J. Inorg. Chem. (2004) 4375;
(b) M.C. Guillem, J. Latorre, R. Martínez-Máñez, J. Payá, S. Garcia-Granda, E. Pérez-Carreño, F. Gómez-Beltrán, Polyhedron 12 (1993) 1681.
[22] H. Ramsis, E. Perez-Ruiz, J. Roger, E. Bourret, J.L. Delarbre, L. Maury, J. Raman Spectrosc. 26 (1995) 131.
[23] A. Grirrane, A. Pastor, E. Álvarez, A. Galindo, Inorg. Chem. Commun. 8 (2005) 453.
[24] For an analysis of the structural parameters of Co-oda compounds see: A. Grirrane, A. Pastor, E. Álvarez, C. Mealli, A. Ienco, P. Rosa, A. Galindo, Eur. J. Inorg. Chem. (2007) in press.
[25] D.P. Lapham, A.C.C. Tseung, J. Mat. Sci. 39 (2004) 251.
[26] SAINT 6.02, Bruker AXS, Inc., Madison, WI 53711-5373, USA, 1997–1999.
[27] G. Sheldrick, SADABS, Bruker AXS, Inc.,, Madison, WI, USA, 1999.
[28] M.C. Burla, M. Camalli, B. Carrozzini, G.L. Cascarano, C. Giacovazzo, G. Polidori, R. Spagna, J. Appl. Crystallogr. 36 (2003) 1103.
[29] SHELXTL 6.12, Bruker AXS, Inc., Madison, WI, USA, 2000–2003.

Available online at www.sciencedirect.com
ScienceDirect
Polyhedron 26 (2007) 3350–3356
POLYHEDRON
www.elsevier.com/locate/poly

Estimation of stability constants of copper(II) chelates with triamines and their mixed complexes with amino acids by using topological indices and the overlapping spheres method

Ante Miličević, Nenad Raos *

Institute for Medical Research and Occupational Health, Unit for Analytical and Physical Chemistry, Ksaverska c. 2, P.O. Box 291, HR-10000 Zagreb, Croatia

Received 15 January 2007; accepted 11 March 2007
Available online 10 April 2007

Abstract

Our two original approaches, the first based on the topological (connectivity) index $^3\chi^v$ and the second based on the model of overlapping spheres (OS), were applied for the estimation of stability constants of copper(II) complexes (CuL) with ethylenediamines ($N = 14$) and diethylenetriamines ($N = 8$), and mixed complexes (CuLA) of amino acids and diethylenetriamines ($N = 18$). The stability constants of the ethylenediamine complexes were predicted "indirectly" from calibration models developed on diethylenetriamines and vice versa, and also by a more direct method using the leave-one-out procedure of cross validation (*cv*). By averaging all the estimates, stability constants were reproduced with a *rms* error of 0.56 and 0.43 $\log K$ units for diethylenetriamines and ethylenediamines, respectively.

Stability constants of the mixed complexes (CuLA) were estimated with $S.E._{cv} = 0.69 \log K$ units (the best linear regression) and $S.E._{cv} = 0.53 \log K$ units (the best binomial regression). The best bivariate regression with the indicator variable, $\mathrm{In} = 1$ for CuLA, $\mathrm{In} = 0$ for CuL, combining stability constants of CuL and CuLA, gave $S.E._{cv} = 0.67 \log K$ units.
© 2007 Elsevier Ltd. All rights reserved.

Keywords: Copper(II) chelates; Ethylenediamines; Diethylenetriamines; Connectivity index; Molecular volumes

1. Introduction

Predicting the stability of coordination compounds is, no doubt, one of the most important problems in coordination chemistry [1]; however there is no general method for its solution. The reason for this is obvious: there are many different factors that determine the thermodynamic stability of coordination compounds. Besides electronic (strength of the metal–ligand bond), stereochemical (mode of coordination) and sterical (conformational) influences, thermodynamic stability of coordination compounds is also determined by solvation (hydration) of the metal, ligand, complex, etc. Simple empirical rules (Irving–Williams order [2], cation [3,4] and HSAB classification [5,6]) have been used in crude predictions of the stability of complexes with various metals and ligands differing in bite atoms. For structurally related complexes, models based on "interaction parameters" between the atoms in the first coordination sphere [7–9] have been used, along with methods based on a molecular mechanics [10–16] or molecular dynamics [17] approach. Also, various kinds of quantitative structure–property relationship (QSPR) models have been applied for the prediction of stability constants [18,19], along with quantum mechanical methods, i.e. model of continuous distribution of solvent [20,21] and density functional theory (DFT) [22,23].

In our study on the stability of coordination compounds, we used two new approaches. The first approach, based on the overlapping spheres (OS) model, assumes that

* Corresponding author. Tel.: +385 14673188; fax: +385 14673303.
E-mail address: raos@mimi.imi.hr (N. Raos).

0277-5387/$ - see front matter © 2007 Elsevier Ltd. All rights reserved.
doi:10.1016/j.poly.2007.03.050

the stability of coordination compounds depends on the free volume within the sphere situated at a characteristic point of the molecule (usually the central atom). The method was applied originally for the calculation of Gibbs energy of solvation [24–27]. Latter it was used in drug design [28–30], and as a tool for finding out the most stable molecular conformations [31–35]. We used the OS method for the estimation of stability constants of copper(II) chelates with amino acids and their derivatives [36], and subsequently the stability constants of copper(II) and nickel(II) complexes with 1,2-diaminoethanes [37] and mixed amino acid chelates [38]. The method was also applied for the estimation of enantioselectivity and diastereoselectivity effects in copper(II) chelates with amino acids and their *N*-alkyl derivatives [39,40].

Topological indices have found application in various fields of chemistry, starting from the classical problem of estimation of boiling points [41,42] and properties of conjugated systems [43,44] to QSAR and drug design [45,46]. We found these simple descriptors of molecular topology («constitutional formula») very suitable for the estimation of stability constants of copper(II) and nickel(II) chelates with amino acids, their *N*-alkyl derivatives and diamines [47–50]. In contrast to the method of overlapping spheres, where the three-dimensional structure (conformation) of molecule must be known, to solve a problem by the method of topological indices, only the constitution of the complex is needed. This not only facilitates the calculations, but also rules out many ambiguities that stem from the plethora of conformations attributed to the studied molecules.

In our last paper in this journal [50], it was shown that the method of topological indices yielded results of the same quality as the much more demanding OS method. It was also pointed out that both methods give in many respects complementary results, and thus the best way to estimate the stability constants appears to be the calculation of the average of the results obtained by these methods.

The aim of this paper is to take a step further; i.e. to find out whether it is possible to successfully estimate stability constants of one class of compounds from the calibration models developed on another class of complexes. For this purpose we chose copper(II) complexes with ethylenediamines and diethylenetriamines, and the mixed complexes of the later class of ligands with naturally occurring amino acids. The later chelates were studied as a model system for metal-catalyzed hydrolysis of amino acid esters [51,52], but from our point of view they are interesting for their terdentate ligand coordination and as a good model for mixed complexes of structurally unrelated ligands.

2. Methods

2.1. Method of overlapping spheres

The overlapping spheres (OS) approach is based on the evaluation of the function [53]:

$$V^* = \sum V_j(S_v \cap s_j) \tag{1}$$

where V^* is the sum of overlapping volumes of the central sphere S_v and volumes of van der Waals spheres s_j of the neighbouring atoms:

$$V_j = 1/3\pi[2R_v^3 + 2r_j^3 + r_{vj}^3] - \pi[R_v^3 x^* + (r_{vj} - x^*)(r_j^2 + r_{vj}x^*)] \tag{2}$$

where

$$x^* = (R_v^2 - r_j^2 + r_{vj}^2)/r_{vj} \tag{3}$$

In Eqs. (2) and (3) r_j stands for the van der Waals radius of atom j penetrating the central sphere with radius R_v, and r_{vj} is the distance between the centers of atom j and the central sphere. Eq. (3) holds only for a partial overlaps; otherwise $V_j = 0$ for $R_v + r_j \leqslant r_{vj}$, and $V_j = 4/3\ r_j^3\pi$ for $r_j + r_{vj} \leqslant R_v$.

The central sphere is situated at the central copper atom (Fig. 1). Usually, its value is set to 3 or 4 Å [38], but in this paper we used its best value in the range 2–5 Å. Also, as usual, we chose the conformations with the lowest V^* [36,37]. The sets of the van der Waals radii, r_j, are given elsewhere [32,53].

Calculation of the overlapping volume V^* (Eq. (1)) was performed by a special FORTRAN program. All the molecular mechanics calculations, needed to find the conformers of the copper(II) chelates, were done with the program developed by Rasmussen and co-workers [54–56], using the force field denoted as FF3 [57].

2.2. Calculation of topological indices

The calculations of topological indices were performed with a program system DRAGON 2.1, written by Todeschini and coworkers, [58] which is capable of yielding 262 topological indices in a single run, along with many other molecular descriptors. The connectivity matrix was constructed with the program CORINA, [59] developed by Sadowski, Schwab and Gasteiger.

All calculations were done with the Randić index ${}^3\chi^v$ (the valence molecular connectivity index of the 3rd order), which gives generally the most consistent results of all topological indices [48,50]:

$${}^3\chi^v = \sum_{\text{path}} \{\delta(i)\delta(j)\delta(k)\delta(l)\}^{-0.5} \tag{4}$$

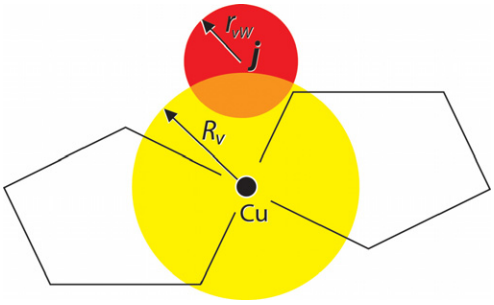


Fig. 1. General scheme of the model of overlapping spheres (cf. Eq. (1)).

where $\delta(i)$, $\delta(j)$, $\delta(k)$ and $\delta(l)$ are weights (valence-delta values) of vertices (atoms) i, j, k and l, making up the path of length 3 (three consecutive chemical bonds) in a vertex-weighted molecular graph [60,61]. The valence-delta value, $\delta(i)$, of a vertex i is defined by

$$\delta(i) = [Z^v(i) - H(i)]/[Z(i) - Z^v(i) - 1] \quad (5)$$

where $Z^v(i)$ is the number of valence electrons belonging to the atom corresponding to vertex i, $Z(i)$ is its atomic number and $H(i)$ is the number of hydrogen atoms attached to it. For instance, delta values for primary, secondary, tertiary and quaternary carbon atoms are 1, 2, 3 and 4, respectively; for oxygen in an OH group it is equal to 5, and for the NH_2 group $\delta(N) = 3$ (it has to be pointed out that $^3\chi^v$ is only a member of the family of valence connectivity indices, $^n\chi^v$, which differ from each other by path length, i.e. the number of factors δ's in the summation term, Eq. (4)).

All the diamine and triamine structures were treated as model ML^{aq} [50], i.e. assuming the binding of ligand water, up to the coordination number 4.

2.3. Regression calculations

Regression calculations, including the leave-one-out procedure of cross validation, *cv*, were done with the CROMRsel program [62]. The standard error of cross validation estimate is defined as

$$S.E._{cv} = (\sum \Delta X^2/N)^{0.5} \quad (6)$$

where ΔX and N denote *cv* residuals and number of reference points, respectively.

Because of the different coordination of diamines and triamines (2 and 3, respectively) their $\log K_1$ values were corrected if estimated "indirectly", *i.e.* from a calibration model developed on another class of compounds. The correction term is taken to be equal to −slope/3 and +slope/2 for the estimation of $\log K_1$ values of diamines and triamines, respectively ("slope" is the slope of the calibration line).

3. Results and discussion

3.1. N-Methyl and N-ethyl substituted diethylenetriamine copper(II) complexes

As the first test of the validity of our models, we chose eight copper(II) complexes with *N*-(2-aminoethyl)-1,2-ethanediamine (diethylenetriamine, dien), and its derivatives substituted at one, two or all three nitrogen atoms (Fig. 2). For all the complexes, their stability constants, K_1, were known [51]. To make a systematic comparison of both methods ($^3\chi^v$ and OS), as well as to check their predictive power for different classes of molecules, we made altogether six analogous regressions with both models (Tables 1 and 2).

Generally, the stability constants were better, but not substantially better, when estimated by the models based on connectivity indices (mean *S.E.* value is 0.60 and 0.68 $\log K$ units for all $^3\chi^v$ and OS models, respectively, Table 3). For instance, calibration lines for the diethylenetriamines yielded $S.E._{cv}$ values of 0.62 and 0.67 $\log K$ units for the $^3\chi^v$ and OS models, respectively (regr. 1 and 7, Tables 1 and 2), but the prediction of stability constants for the diamine complexes was virtually the same for both models (0.51 and 0.47 $\log K$ units, respectively, Table 3).

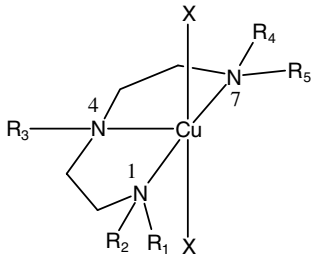


Fig. 2. General structure of copper(II) complexes with diethylenetriamines (**1**–**8**, Table 5). *X* denotes "dummy" atoms needed in molecular-mechanics calculations [57].

Table 1
Statistical parameters for linear regressions of $\log K_1$ values[a] for copper(II) complexes with triamines (cf. Table 5) and diamines (cf. Table 6) on the connectivity indices $^3\chi^v$

Regression no.	Ligands	*N*	*r*	*S.E.*	$S.E._{cv}$
1	diethylenetriamines (**1**–**8**)	8	0.965	0.45	0.62
2	ethylenediamines (**9**–**22**)	14	0.837	0.44	0.49
3	diethylenetriamine and its methyl derivatives (**1**–**5**)	5	0.965	0.34	0.61
4	diethylenetriamine and its ethyl derivatives (**1**, **6**–**8**)	4	0.976	0.43	0.82
5	all methyl derivatives (**1**–**5**, **9**, **10**, **15**)	8	0.957	0.47	0.59
6	all ethyl derivatives (**1**, **6**–**8**, **9**, **11**, **16**)	7	0.983	0.42	0.64

[a] $K_1 = [CuL][Cu]^{-1}[L]^{-1}$; L denotes the diethylenetriamine or ethylenediamine ligand.

Table 2
Statistical parameters for linear regressions of $\log K_1$ values[a] for copper(II) complexes with triamines (cf. Table 5) and diamines (cf. Table 6) on the OS volumes (V^*), $R_v = 2.1$ Å

Regression no.	Ligands	*N*	*r*	*S.E.*	$S.E._{cv}$
7	diethylenetriamines (**1**–**8**)	8	0.964	0.46	0.67
8	ethylenediamines (**9**–**22**)	14	0.872	0.39	0.46
9	diethylenetriamines and its methyl derivatives (**1**–**5**)	5	0.980	0.26	0.41
10	diethylenetriamines and its ethyl derivatives (**1**, **6**–**8**)	4	0.985	0.33	0.71
11	all methyl derivatives (**1**–**5**, **9**, **10**, **15**)	8	0.993	0.45	0.60
12	all ethyl derivatives (**1**, **6**–**8**, **9**, **11**, **16**)	7	0.998	0.30	0.45

[a] $K_1 = [CuL][Cu]^{-1}[L]^{-1}$; L denotes the diethylenetriamine or ethylenediamine ligand.

Table 3
Statistical parameters for prediction of $\log K_1$ values for copper(II) complexes with triamines (cf. Table 5) and diamines (cf. Table 6) from calibration models referred to in Tables 1 and 2

Calibration models	Ligands	N	*S.E.* ($^3\chi^v$)	*S.E.* (OS)	*rms* (mean estimates)
1 and 7	ethylenediamines (**9**–**22**)	14	0.51	0.47	0.40
2 and 8	diethylenetriamines (**1**–**8**)	8	0.83	0.56	0.50
3 and 9	ethylenediamines (**9**–**22**)	14	0.59	1.01	0.77
3 and 9	all ethyl derivatives (**1**, **6**–**8**, **9**, **11**, **16**)	7	0.56	0.88	0.70
4 and 10	ethylenediamines (**9**–**22**)	14	0.60	0.67	0.41
4 and 10	all methyl derivatives (**1**–**5**, **9**, **10**, **15**)	8	0.60	0.62	0.57
5 and 11	all ethyl derivatives (**1**, **6**–**8**, **9**, **11**, **16**)	7	0.55	0.59	0.56
6 and 12	all methyl derivatives (**1**–**5**, **9**, **10**, **15**)	8	0.54	0.64	0.58
Mean			0.60	0.68	0.56

This is also reflected in the basic calibration lines for the $^3\chi^v$ and OS models, which very closely resemble each other (Fig. 3).

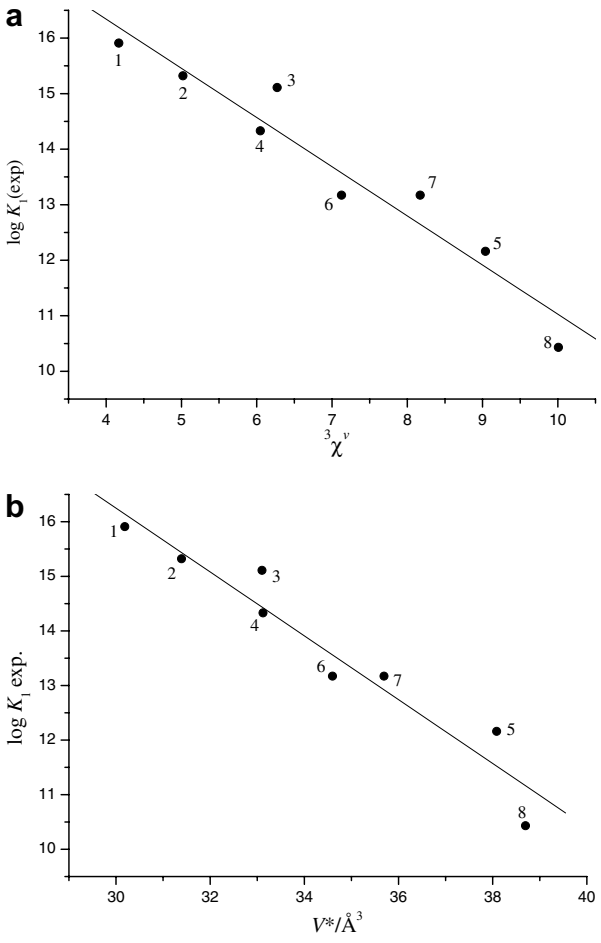


Fig. 3. The calibration lines, (a) regr. 1, Table 1 and (b) regr. 7, Table 2, for the estimation of stability constants ($\log K_1$) of copper(II) complexes with diethylenetriamines, as denoted in Table 5; (a) $\log K_1 = 19.88(71) - 0.885(98)\ ^3\chi^v$, (b) $\log K_1 = 33.8(23) - 0.585(66)\ V^*$.

Grouping of complexes with closely related ligands did not substantially enhance the results (Tables 1 and 2). For the $^3\chi^v$ variable calibration, *N*-methyl substituted diethylenetriamines ($N = 5$) yielded lines of equal quality ($S.E._{cv} = 0.61$ versus $0.62 \log K$ units), but in the case of the OS variable, substantially better results were obtained ($S.E._{cv} = 0.41$ versus $0.67 \log K$ units). It is interesting to note that calibration lines derived only from methyl derivatives were successful in the estimation of stability constants of ethyl derivatives, and vice versa (Regr. 5 and 11, 6 and 12, Table 3). This is in contrast to the simple model, $\log K_1$ versus number of methyl substitutents [51], which is intrinsically incapable of dealing with ethyl derivatives. Moreover, in spite of its very low error for diethylenetriamines ($S.E._{cv} = 0.35 \log K$ units), the model based on the number of methyl substituents yielded a very high error ($S.E. = 0.96 \log K$ units) for the prediction of the stability of copper(II) complexes with another class of ligands, methylated diaminoethanes.

3.2. Mixed copper(II) complexes with amino acids and diethylenetriamines

For the study of mixed complexes, we chose $\log \beta_2$ constants of altogether 20 mixed chelates of diethylenetriamine and its six *N*-methyl and *N*-ethyl derivatives (the same ligands as referred to in Section 3.1, cf. Table 5) with three naturally occurring α-amino acids (glycine, valine and sarcosine, i.e. *N*-methylglycine), Fig. 4 [52]. Two mixed complexes, with 1,1,4,7,7-Me_5dien and Gly or Val, were found, in contrast to the complexes of other ligands, to undergo a color change during the mixed-complex formation, which is attributed to extensive distortion of the coordination polyhedron [52]. In spite of this (quite tentative) argument, our molecular-mechanical calculation did not find any extraordinary distortion of the coordination polyhedron in the molecules of the two complexes. Moreover, the reproduction of experimental constants of these two complexes was in no way exceptional. Despite the finding that the complex with glycine shows, in regression on the OS volume ($R_v = 2.5$ Å), the highest residual ($1.34 \log K$ units), the complex with valine yielded one of the lowest

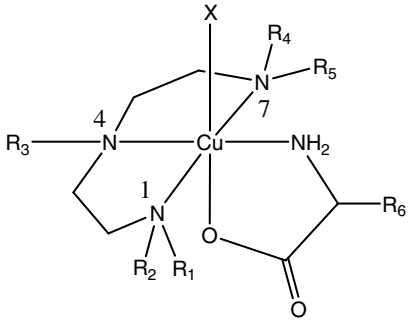


Fig. 4. General structure of mixed copper(II) complexes with amino acids and diethylenetriamines (cf. Table 5). *X* denotes "dummy" atoms needed in molecular-mechanics calculations [57].

values (0.38 log K units). In regressions with respect to $^3\chi^v$, however, residuals for these two chelates (0.73 and 1.01 log K units for the glycine and valine complexes, respectively) are close to the average value of the set ($S.E. = 0.71 \log K$ units). By discarding these two chelates, substantially better results were obtained; $S.E.$ drop from 0.71 to 0.65 and from 0.69 to 0.60 log K units for the $^3\chi^v$ and OS model, respectively (regr. 13 and 16, Table 4). All these findings strongly suggest that the stability constants for these two complexes, as referred to in Ref. [52], were poorly determined, possibly due to formation of MLA complexes of different structures.

Table 4
Statistical parameters for linear regressions of $\log\beta_2$ values[a] of copper(II) mixed complexes with amino acids (Gly, Val, Sar) and diethylenetriamines on the connectivity index $^3\chi^v$ and the OS volumes (V^*), $R_v = 2.5$ Å

Independent variable	Regression no.	Ligands	N	r	$S.E.$	$S.E._{cv}$
$^3\chi^v$	13	mixed complexes	18	0.890	0.65	0.71
	14	mixed complexes (binomial)	18	0.890	0.65	0.74
	15	mixed complexes + all diethylenetriamines	26	0.974	0.61	0.67
V^*	16	mixed complexes	18	0.908	0.60	0.69
	17	mixed complexes (binomial)	18	0.948	0.46	0.53
	18	mixed complexes + all diethylenetriamines	26	0.964	0.71	0.83
	19	mixed complexes + all diethylenetriamines ($R_v = 2.1$ Å)	26	0.940	0.91	1.00

[a] $\beta_2 = [\mathrm{CuLA}][\mathrm{Cu}]^{-1}[\mathrm{L}]^{-1}[\mathrm{A}]^{-1}$; L and A denote the diethylenetriamine and amino acid ligands, respectively.

The regressions of $\log\beta_2$ on $^3\chi^v$ and V^* for the CuLA complexes (Table 4, Fig. 5) do not differ very much, slightly favoring the OS model in respect to all parameters (r, $S.E.$ and $S.E._{cv}$). The values of the $S.E.$ parameter (0.65 and 0.60 log K units for the $^3\chi^v$ and OS models, respectively) are higher than the corresponding parameters for the ML complexes (0.45 and 0.46 log K units, for the $^3\chi^v$ and OS models, respectively; Tables 1 and 2), but not substantially. The same holds true for $S.E._{cv}$ (0.71 versus 0.62 and 0.69 versus 0.67 for the $^3\chi^v$ and OS models, respectively).

To improve the prediction power of our method, we introduced binomial regression of $\log\beta_2$ on both, $^3\chi^v$ and V^* variables (regr. 14 and 17, Table 4). For the regression on the first variable, no improvement was obtained, but the binomial regression of $\log\beta_2$ on V^* yielded substantial improvement in both $S.E.$ (0.46 versus 0.60 log K units) and $S.E._{cv}$ (0.53 versus 0.69 log K units). Regression with the indicator variable, by combining the stability constants of the ML and MLA complexes, yielded better results with $^3\chi^v$ (Fig. 6) than with the V^* variable ($S.E._{cv}$ is 0.67 and 0.83 log K units). The optimal R_v value for the mixed complexes ($R_v = 2.1$ Å) yielded results of lesser quality than the optimal value for ethylenetriaminoethanes ($R_v = 2.5$ Å).

3.3. Estimation of stability constants by combining the models

In our recent paper [50] we proposed a general method for estimation of stability constants by averaging the values obtained by all the reliable methods. To prove the validity of our approach for new systems, we estimated the $\log K_1$ values of all eight copper(II) diethylenetriamine complexes (Table 5) by using various ways of averaging. The mean of the estimated values from the calibration lines on $^3\chi^v$ and V^* (regr. 1 and 7, Tables 1 and 2) yielded a *rms* deviation

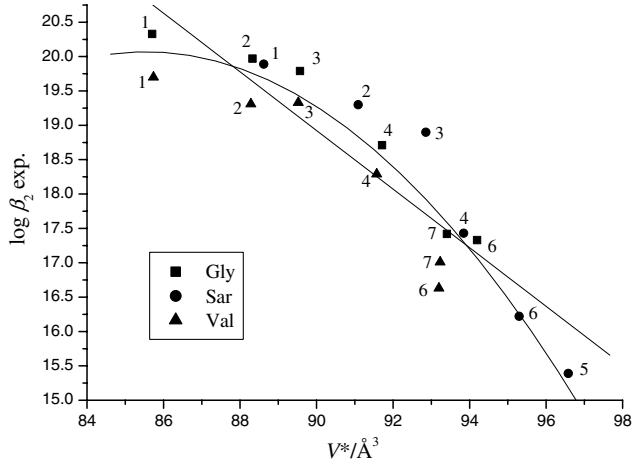


Fig. 5. The calibration models (regr. 16 and 17, Table 4) for the estimation of stability constants ($\log\beta_2$) of the mixed copper(II) complexes with amino acids and ethylenetriaminoethanes ($N = 18$). Ethylenetriaminoethanes are denoted as in Table 5, and amino acids by the graphic code presented in the picture. Regr. 16: $\log\beta_2 = 57.3(45) - 0.426(49)\ V^*$ regr. 17: $\log\beta_2 = -273(100) + 6.9(22)\ V^* - 0.040(12)\ (V^*)^2$.

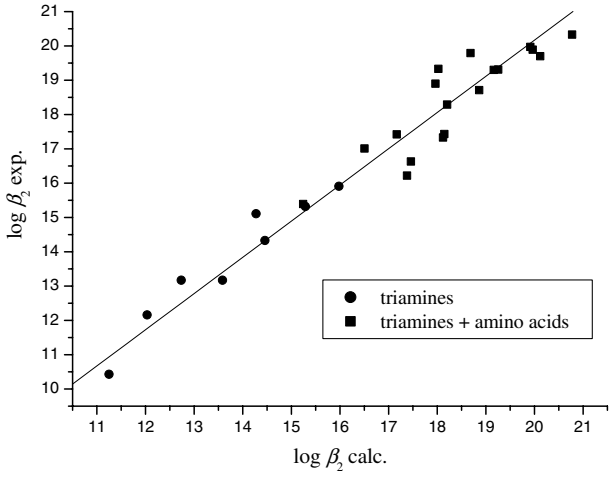


Fig. 6. Experimental vs. calculated values of stability constants ($\log\beta_2$) of copper(II) complexes with diethylenetriamines ($N = 8$, cf. Table 5) and copper(II) mixed complexes with amino acids and ethylenetriaminoethanes ($N = 18$), regr. 15, Table 4; $\log\beta_2 = 19.36(56) - 0.810(73)\ ^3\chi^v + 7.20(36)$ In, In = 1 (CuLA), In = 0 (CuL).

Table 5
Experimental values of stability constants ($\log K_1$) of copper(II) complexes with triaminoethanes and their predicted values from calibration models developed on diethylenetriamines and ethylenediamines (Tables 1 and 2)

Ligand	Exp.	Mean (regr. 1, 7)	Mean (regr. 2, 8)	Mean (regr. 1, 2, 7, 8)	Median (regr. 1, 2, 7, 8)
Dien (**1**)	15.91	16.34	16.08	16.21	16.29
1-(Me)dien (**2**)	15.32	15.48	15.43	15.45	15.48
1,4-$(Me)_2$dien (**3**)	15.11	14.26	14.48	14.37	14.32
1,1-$(Me)_2$dien (**4**)	14.33	14.50	14.56	14.53	14.53
1,1,4,7,7-$(Me)_5$dien (**5**)	12.16	11.48	12.05	11.77	11.77
1,1-$(Et)_2$dien (**6**)	13.17	13.62	13.74	13.68	13.63
1,4,7-$(Me)_3$dien (**7**)	13.17	12.71	13.05	12.88	12.88
1,1,7,7-$(Et)_4$dien (**8**)	10.43	11.60	11.52	11.56	11.56
rms		0.63	0.50	0.56	0.57
Error range		0.16–1.17	0.11–1.09	0.13–1.13	0.16–1.13

Table 6
Experimental values of stability constants ($\log K_1$) of copper(II) complexes with ethylenediamines and their predicted values from calibration models developed on diethylenetriamines and ethylenediamines (Tables 1 and 2)

Ligand	Exp.	Mean (regr. 1, 3, 4, 7, 9, 10)	Median (regr. 1, 3, 4, 7, 9, 10)	Mean (regr. 2, 8)	Mean (regr. 1–4, 7–10)	Median (regr. 1–4, 7–10)
1,2-Diaminoethane (**9**)	10.76	10.98	11.08	11.19	11.03	11.11
N-Methyl-1,2-diaminoethane (**10**)	10.55	10.15	10.18	10.29	10.18	10.22
N-Ethyl-1,2-diaminoethane (**11**)	10.19	9.94	9.88	10.12	9.98	10.01
N-Propyl-1,2-diaminoethane (**12**)	9.98	9.92	9.84	10.11	9.96	10.00
N-Butyl-1,2-diaminoethane (**13**)	9.94	9.80	9.60	10.00	9.85	9.80
N-Isopropyl-1,2-diaminoethane (**14**)	9.07	9.56	9.64	9.82	9.62	9.66
N,*N*′-Dimethyl-1,2-diaminoethane (**15**)	10.47	9.35	9.38	9.44	9.37	9.38
N,*N*′-Diethyl-1,2-diaminoethane (**16**)	9.30	8.93	8.81	9.15	8.98	8.96
N,*N*′-Dipropyl-1,2-diaminoethane (**17**)	8.79	8.88	8.73	9.22	8.96	8.97
N,*N*′-Dibutyl-1,2-diaminoethane (**18**)	8.67	8.64	8.32	9.00	8.73	8.55
1,2-Diaminopropane (**19**)	10.78	10.82	10.77	10.99	10.87	10.90
(*R*,*S*)-2,3-Diaminobutane (**20**)	10.72	10.43	10.22	10.59	10.47	10.37
(*R*,*R*)-2,3-Diaminobutane (**21**)	11.39	10.56	10.22	10.63	10.58	10.33
2-Methyl-1,2-diaminopropane (**22**)	10.53	10.54	10.51	10.71	10.58	10.64
rms		0.44	0.53	0.46	0.43	0.48
Error range		0.04–1.12	0.01–1.09	0.06–1.03	0.05–1.10	0.02–1.10

of 0.63 $\log K$ units, which is even worst than the value of 0.50 $\log K$ units obtained by the less direct method, namely from the calibration lines developed for diamine complexes (regr. 2 and 8, Table 3). Moreover, the indirect method yielded less of a maximum error than that by the direct method (1.09 versus 1.17 $\log K$ units). No improvement of estimation was obtained by calculating the mean or median value of all four estimates (*rms* is 0.56 and 0.57 $\log K$ units, for the mean and median values, respectively), as well as in terms of maximum error (1.13 $\log K$ units). The method of averaging substantially bettered extreme estimates. For instance, the error for the residual of complex **8** dropped by averaging from 1.67 to 1.09–1.13 $\log K$ units, and that of complex **4** from 0.70 to 0.17–0.23 $\log K$ units (regr. 2, Table 2).

The worst overall estimate is attributed to complex **8**, 1,1,7,7-$(Et)_4$dien, assuming it to be 1.09–1.13 $\log K$ units more stable than that found experimentally, and the best predictions were obtained for complex **2**. (By discarding complexes **8** from the set in Table 5, the *rms* error of the mean estimate for all models dropped to 0.43, and the maximum error to 0.74 $\log K$ units.) The poor estimations for complex **3** (in contrast to the fair estimation for complex **4**) could be tentatively attributed to enantioselectivity, because two epimeric complexes, 1(*S*),4(*S*) and 1(*S*),4(*R*), have the same $^3\chi^v$ and virtually the same V^* parameters.

The method of averaging was also checked on copper(II) complexes with diaminoethanes (Table 6). The indirect method of estimation of stability constants (from regr. 1, 3, 4, 7, 9, 10, Tables 1 and 2) proved even better than the direct method, based only on two values (regr. 2 and 8, Table 3). The result was further, but not substantially, improved by averaging the values calculated by all models. However, by discarding the two worst estimates (for ligands **15** and **21**) the *rms* values dropped to 0.25–0.34, and the maximum error to 0.49–0.75 $\log K$ units.

4. Conclusion

Taking into account all the presented estimates, it can be concluded that the method based on topological indices ($^3\chi^v$) leads in many cases to complementary results (cf.

Tables 1, 2, and Fig. 3) and generally to results of the same quality as the more demanding method of overlapping spheres. However, the best results were obtained by combining both methods, which is demonstrated on the copper(II) complexes with diamines and triamines (Tables 5 and 6). Also, it was shown (Table 3) that indirect estimation (from a different class of complexes) leads to results of the same quality as the estimation from the same class of compounds (Tables 1 and 2).

Despite the possible objection that our method for estimation of stability constants yields, in some cases, unacceptable estimates (cf. **15** and **21**, Table 6), the results clearly show that stability constants can be generally reproduced within the error limit of $0.5 \log K$ units, even not knowing any stability constants in the class to which the studied chelate belongs.

References

[1] R.D. Hancock, A.E. Martell, Chem. Rev. 89 (1989) 1875.
[2] I. Irving, D.R. Williams, J. Chem. Soc. (1953) 3192.
[3] G. Schwartzenbach, Anal. Chem. 32 (1960) 6.
[4] S. Ahrland, J. Chatt, N.R. Davies, Q. Rev. Chem. Soc. 12 (1958) 265.
[5] R.G. Pearson, J. Am. Chem. Soc. 85 (1963) 3533.
[6] R.G. Pearson (Ed.), Hard and Soft Acids and Bases, Hutchinson and Ross, Dowden, 1973.
[7] M. Tanaka, J. Inorg. Nucl. Chem. 35 (1973) 965.
[8] M. Tanaka, J. Inorg. Nucl. Chem. 36 (1974) 151.
[9] M. Tabata, M. Tanaka, Inorg. Chem. 27 (1988) 3190.
[10] N. Raos, S.R. Niketić, V. Simeon, J. Inorg. Biochem. 16 (1983) 1.
[11] N. Raos, V. Simeon, Croat. Chem. Acta 56 (1983) 79.
[12] N. Raos, V. Simeon, Croat. Chem. Acta 57 (1984) 1217.
[13] J. Sabolović, N. Raos, Polyhedron 9 (1990) 1277.
[14] J. Sabolović, N. Raos, Polyhedron 9 (1990) 2419.
[15] G.R. Brubaker, D.W. Johnson, Inorg. Chem. 23 (1984) 1591.
[16] B.P. Hay, D. Zhang, J.R. Rustad, Inorg. Chem. 35 (1996) 2650.
[17] A. Fedorowicz, J. Mavri, P. Bala, A. Koll, Chem. Phys. Lett. 289 (1998) 457.
[18] R.D. Hancock, J. Chem. Soc., Dalton Trans. (1980) 416.
[19] R. Svetlitski, A. Lomaka, M. Karelson, Sep. Sci. Technol. 41 (2006) 197.
[20] J. Tomasi, M. Persico, Chem. Rev. 94 (1994) 2027.
[21] R. Bonaccorsi, P. Palla, J. Tomasi, J. Am. Chem. Soc. 106 (1984) 1945.
[22] J.R. Rustad, D.A. Dixon, K.M. Rosso, A.R. Felmy, J. Am. Chem. Soc. 121 (1999) 3234.
[23] R.D. Hancock, L.J. Bartolotti, Inorg. Chem. 44 (2005) 7175.
[24] K.D. Gibbson, H.A. Scheraga, Proc. Natl. Acad. Sci. USA 58 (1967) 420.
[25] A.J. Hopfinger, Macromolecules 4 (1971) 731.
[26] K.T. No, G.S. Kim, K.H. Cho, H.A. Scheraga, Biophys. Chem. 78 (1999) 127.
[27] W. Cornell, R. Abseher, M. Nilges, D.A. Case, J. Mol. Graph. Modell. 19 (2001) 136.
[28] A.J. Hopfinger, J. Am. Chem. Soc. 102 (1980) 7196.
[29] M.H. Foglio, G. Duester, Biochim. Biophys. Acta 1432 (1999) 239.
[30] I.D. Kuntz, J.M. Blaney, S.J. Oattey, R. Langridge, T.E. Ferrin, J. Mol. Biol. 161 (1982) 269.
[31] N. Raos, Croat. Chem. Acta 72 (1999) 727.
[32] N. Raos, J. Comput. Chem. 21 (2000) 1353.
[33] N. Raos, L. Žuža-Mak, Croat. Chem. Acta 75 (2002) 909.
[34] M. Cetina, A. Hergold-Brundić, N. Raos, L. Žuža-Mak, J. Mol. Struct. 657 (2003) 145.
[35] N. Raos, L. Žuža-Mak, Croat. Chem. Acta 77 (2004) 53.
[36] N. Raos, Croat. Chem. Acta 78 (2005) 175.
[37] A. Miličević, N. Raos, Croat. Chem. Acta 78 (2005) 525.
[38] A. Miličević, N. Raos, Croat. Chem. Acta 79 (2006) 281.
[39] N. Raos, Vl. Simeon, J. Inorg. Biochem. 18 (1983) 133.
[40] N. Raos, Croat. Chem. Acta 70 (1997) 913.
[41] H. Wiener, J. Am. Chem. Soc. 69 (1947) 17.
[42] P.G. Seybold, M. May, U.A. Begal, J. Chem. Educ. 64 (1987) 575.
[43] A. Graovac, I. Gutman, N. Trinajstić, Topological approach to the chemistry of conjugated molecules, Lecture Notes in Chemistry, vol. 4, Springer-Verlag, Berlin, 1977.
[44] A. Miličević, S. Nikolić, N. Trinajstić, J. Chem. Inf. Comput. Sci. 44 (2004) 415.
[45] L.B. Kier, L.H. Hall, Molecular Connectivity and Drug Design, Academic Press, New York, 1976.
[46] A. Sabljić, N. Trinajstić, Acta Pharm. 31 (1981) 189.
[47] B. Grgas, S. Nikolić, N. Paulić, N. Raos, Croat. Chem. Acta 72 (1999) 885.
[48] S. Nikolić, N. Raos, Croat. Chem. Acta 74 (2001) 621.
[49] N. Raos, Croat. Chem. Acta 75 (2002) 117.
[50] A. Miličević, N. Raos, Polyhedron 25 (2006) 2800.
[51] J.W. Allison, R.J. Angelici, Inorg. Chem. 10 (1971) 2233.
[52] R.J. Angelici, J.W. Allison, Inorg. Chem. 10 (1971) 2238.
[53] A.J. Hopfinger, Conformational Properties of Macromolecules, Academic Press, New York, 1973.
[54] S.R. Niketić, Kj. Rasmussen, The consistent force field: a documentation, Lecture Notes in Chemistry, vol. 3, Springer-Verlag, Berlin, 1977.
[55] Kj. Rasmussen, Potential energy functions in conformational analysis, Lecture Notes in Chemistry, vol. 37, Springer-Verlag, Berlin, 1985.
[56] Kj. Rasmussen, S.B. Engelsen, J. Fabricius, B. Rasmussen, in: R. Fausto (Ed.), Proceedings of the NATO Advanced Study Institute on Molecular Spectroscopy, Ponta Delgada, Sao Miguel, Açores, Portugal, 1992, NATO ASI Series C: Mathematical and Physical Sciences, vol. 406, Kluwer Academic Publishers, Dodrecht, 1993, p. 381.
[57] B. Kaitner, B. Kamenar, N. Paulić, N. Raos, V. Simeon, J. Coord. Chem. 15 (1987) 373.
[58] <http://www.disat.unimib.it/chm/>.
[59] <http://www2.chemie.uni-erlangen.de/software/corina/index.html>.
[60] M. Randić, J. Am. Chem. Soc. 97 (1975) 6609.
[61] L.B. Kier, L.H. Hall, Molecular Connectivity in Structure–Activity Analysis, Wiley, New York, 1986.
[62] B. Lučić, N. Trinajstić, J. Chem. Inf. Comput. Sci 39 (1999) 121.

Available online at www.sciencedirect.com
ScienceDirect
Polyhedron 26 (2007) 3357–3362
POLYHEDRON
www.elsevier.com/locate/poly

Titanium(IV) complexes with monocyclopentadienyl and phenoxy-alkoxo ligands: Synthesis, structures and catalytic properties for ethylene polymerization

Tie-Qi Xu, Wei Gao, Ying Mu *, Ling Ye

Key Laboratory for Supramolecular Structure and Materials of Ministry of Education, School of Chemistry, Jilin University, 2699 Qianjin Street, Changchun 130012, People's Republic of China

Received 11 December 2006; accepted 8 March 2007
Available online 15 March 2007

Abstract

Three monochlorotitanium complexes Cp′Ti(2,4-^{t}Bu$_2$-6-(CPh$_2$O)C$_6$H$_2$O)Cl [Cp′ = η^5-C$_5$H$_5$ (**2**), η^5-C$_5$(CH$_3$)$_5$ (**3**), η^5-C$_5$H$_2$Ph$_2$CH$_3$ (**4**)] have been synthesized in high yields (>90%) by the reaction of corresponding Cp′TiCl$_3$ with the dilithium salt of ligand 2,4-^{t}Bu$_2$-6-(CPh$_2$OH)C$_6$H$_2$OH (**1**). When activated by [Ph$_3$C]$^+$[B(C$_6$F$_5$)$_4$]$^-$ and Al^{i}Bu$_3$, complexes **2**–**4** exhibit reasonable catalytic activity for ethylene polymerization, producing polyethylenes with moderate molecular weights and melting points. Addition of excess water to complex **2** gave the oxo-bridged complex [Ti(η^5-C$_5$H$_5$)(2,4-^{t}Bu$_2$-6-(CPh$_2$O)C$_6$H$_2$O)]$_2$O (**5**). Complexes **4** and **5** were characterized by single crystal X-ray diffraction.
© 2007 Elsevier Ltd. All rights reserved.

Keywords: Titanium complexes; Ethylene polymerization; Homogeneous catalysis; Metallocene catalysts

1. Introduction

Polyolefins are the largest volume synthetic materials used in the world, and have been almost applied in every aspect of our daily lives and productions. One of the most active areas of polyolefins research over the past decades has been the discovery and development of Ziegler–Natta catalysis for polymerization of ethylene and α-olefins. Since Kaminsky et. al. discovered the highly active zirconocene dichloride/methylaluminoxane (MAO) catalytic system for olefin polymerization [1], intensive research work has been focused on developing new Group 4 metallocene catalysts for improving catalytic activities and polymer properties [2,3]. Most of Group 4 metallocene and related complexes for olefin polymerization typically have two or more alkyl (or halide) groups attached to the metal. Examples of precatalysts containing only one such group are scarce [4], although they are active for olefin polymerization and are also of potential interest in the context of single-site olefin polymerization catalysis. Therefore, our current focus is the development of this class of monochlorotitanium complexes, and investigation of the influence of different substituents at cyclopentadienyl (Cp) on their catalytic activity.

In this work, a new bidentate chelating ligand 2,4-^{t}Bu$_2$-6-(CPh$_2$OH)C$_6$H$_2$OH (**1**) was firstly synthesized and introduced into the monochlorotitanium system, based on the following considerations: (i) the phenoxy-alkoxo bidentate ligand comprising the alkoxo group linked with the phenol group has two different active oxygen functionalities in the metalation reaction, therefore increasing the selectivity of forming the desired complexes in the synthetic reaction; (ii) recently, Doherty et al. have reported that introducing phenyl groups on the alkoxo ligand are able to increase catalytic activity of the precatalysts [CpTi{NC$_5$H$_4$(CR$_2$O)-2}Cl$_2$] [5], so here we choose the alkoxo ligand containing phenyl groups. With the new ligand, we successfully obtained a series of monochlorotitanium complexes

* Corresponding author. Tel.: +86 431 85168472; fax: +86 431 85193421.
E-mail address: ymu@mail.jlu.edu.cn (Y. Mu).

0277-5387/$ - see front matter © 2007 Elsevier Ltd. All rights reserved.
doi:10.1016/j.poly.2007.03.012

$Cp'Ti(2,4\text{-}^tBu_2\text{-}6\text{-}(CPh_2O)C_6H_2O)Cl$ ($Cp' = \eta^5\text{-}C_5H_5$ (**2**), $\eta^5\text{-}C_5(CH_3)_5$ (**3**), $\eta^5\text{-}C_5H_2Ph_2CH_3$ (**4**)) which have different substituents in cyclopentadienyl in high yield (>90%), and studied their application in ethylene polymerization and their hydrolysis reactions.

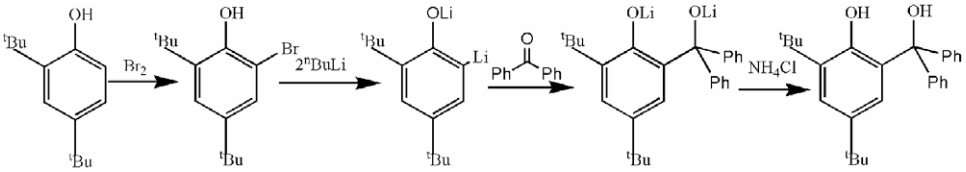
2. Results and discussion

2.1. Synthesis and characterization

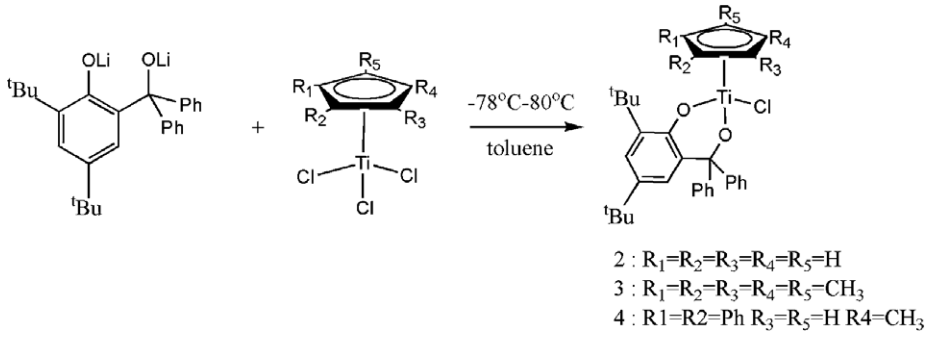
The new bidentate ligand **1** was synthesized with 2,4-di-*tert*-butylphenol as the starting material. 2-Bromo-4,6-di-*tert*-butylphenol was easily prepared from the reaction of Br_2 with 2,4-di-*tert*-butylphenol in $CHCl_3/CCl_4$ at 0 °C. The reaction of dilithium phenoxide, obtained by treating 2-bromo-4,6-di-*tert*-butylphenol with 2 equiv. of ^{n}BuLi, with benzophenone in Et_2O at −15 °C, followed by hydrolysis with saturated NH_4Cl produced the ligand **1** in a moderate yield (Scheme 1). The monochlorotitanium complexes **2**–**4** were prepared by reaction of $Cp'TiCl_3$ ($Cp' = \eta^5\text{-}C_5H_5$, $\eta^5\text{-}C_5(CH_3)_5$, $\eta^5\text{-}C_5H_2Ph_2CH_3$) with equimolar amount of dilithium salt of $2,4\text{-}^tBu_2\text{-}6\text{-}(CPh_2OH)C_6H_2OH$ in toluene in high yields (Scheme 2). These complexes were found to be easily hydrolyzed. Addition of excess water to toluene solution of complex **2** gave the oxo-bridged complex $[Ti(\eta^5\text{-}C_5H_5)(2,4\text{-}^tBu_2\text{-}6\text{-}(CPh_2O)C_6H_2O)]_2O$ (**5**) (Scheme 3). However, the same reaction with complexes **3** and **4** caused complete decomposition of both complexes to a mixture of unknown composition in which no organometallic complexes were isolated. All complexes were characterized by elemental analysis and NMR spectroscopy. Complexes **4** and **5** were characterized by single crystal X-ray diffraction.

2.2. Crystal Structures of *4* and *5*

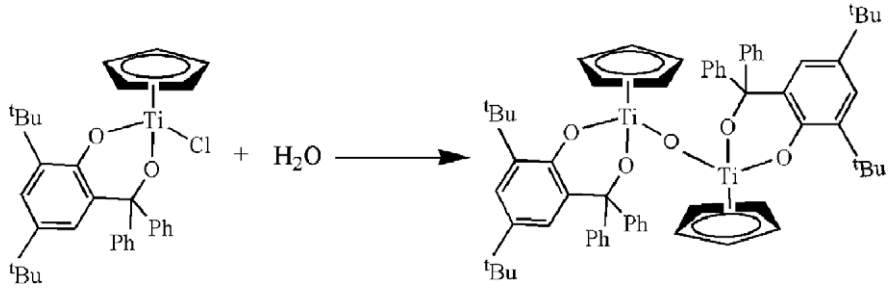
Crystals of complexes **4** and **5** suitable for single-crystal X-ray diffraction study were grown by cooling the saturated solutions of **4** and **5** in mixed CH_2Cl_2/hexane. The ORTEP drawings of the molecule structures are shown in Figs. 1 and 2. The selected bond lengths and angles are summarized in Table 1. The geometry around titanium in **4** can be described as a pseudo-tetrahedral coordination environment, which is defined by a substituted Cp ring



Scheme 1. Synthetic procedure of ligand **1**.



Scheme 2. Synthetic procedure of complexes **2**–**4**.



Scheme 3. Synthetic procedure of complex **5**.

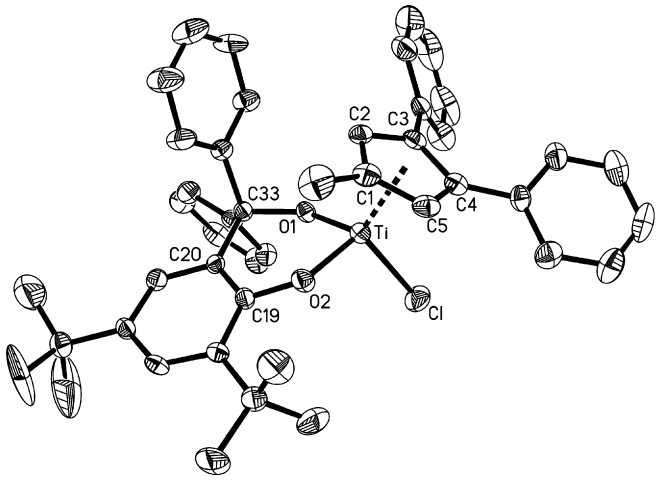


Fig. 1. Molecular structure of complex **4**.

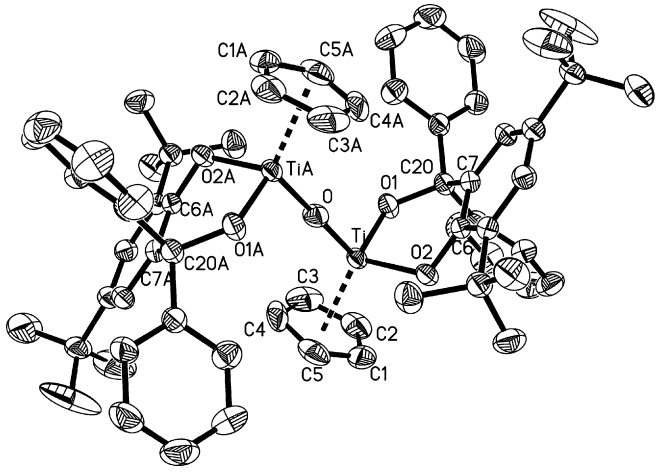


Fig. 2. Molecular structure of complex **5**.

(assuming Cp to occupy one coordination site), a chlorine atom, and two oxygen atoms from the phenol-alkoxo ligand. The phenol-alkoxo ligand adopts a puckered chelate disposition with the typical *boat* conformation. The Ti–C bond lengths range from 2.336 to 2.445 Å, and Ti–C4 (2.445 Å) are longer than those of known Ti–C (Cp ring carbon) bond lengths in similar monochlorotitanium complexes [4]. The C–C bond lengths in the substituted Cp ring range from 1.408 to 1.447 Å, and the C3–C4 (1.447 Å) bond length is the longest among these values, which could be explained by the steric and conjugate effects of the two phenyl groups on the Cp-ring.

The molecular structure of complex **5** consists of two [Ti(η^5-C_5H_5)(2,4-^{t}Bu$_2$-6-(CPh$_2$O)C$_6$H$_2$O)] units linked by Ti–O–Ti bridge. Each titanium is coordinated in a pseudo-tetrahedral geometry by a Cp ring, and three oxygen atoms (one from the oxo-bridge, and the other two from the phenoxy-alkoxo ligand). The C–C bond lengths in the Cp ring are close to the ones observed in know Ti–Cp ring carbon distances. The conformation of the phenol-alkoxo ligand 2,4-^{t}Bu$_2$-6-(CPh$_2$O)C$_6$H$_2$O in **5** is similar to complex **4**, showing a *boat* structure. The Ti–O (alkoxo) bond lengths of 1.778 Å in **4** and 1.803 Å in **5** are shorter than Ti–O (phenoxy) bond lengths of 1.831 Å in **4** and 1.848 Å in **5**, respectively, which may reflect O(pπ)–Ti(dπ) donation of alkoxo groups to the metal [5].

Table 1
Selected bond lengths and angles

Complex ***4***			
Ti–O(1)	1.778(3)	Ti–O(2)	1.831(4)
Ti–Cl	2.268(7)	Ti–C(1)	2.409(6)
Ti–C(2)	2.336(6)	Ti–C(3)	2.374(6)
Ti–C(4)	2.445(6)	Ti–C(5)	2.423(6)
O(1)–C(33)	1.428(6)	O(2)–C(19)	1.380(6)
C(1)–C(2)	1.420(8)	C(2)–C(3)	1.421(8)
C(3)–C(4)	1.447(7)	C(4)–C(5)	1.408(8)
C(1)–C(5)	1.408(7)	Cp(cent)–Ti	2.071
Cp(cent)–Ti–O(1)	121.5	Cp(cent)–Ti–O(2)	113.7
O(1)–Ti–O(2)	90.7(2)	O(1)–Ti–Cl	104.0(1)
O(2)–Ti–Cl	105.0(1)	Cp(cent)–Ti–Cl	117.7
Complex ***5***			
Ti–O(1)	1.803(2)	Ti–O	1.812(1)
Ti–O(2)	1.848(2)	Ti–C(1)	2.402(4)
Ti–C(2)	2.366(3)	Ti–C(3)	2.341(4)
Ti–C(4)	2.373(3)	Ti–C(5)	2.403(4)
O(2)–C(6)	1.377(3)	O(1)–C(20)	1.435(3)
C(1)–C(2)	1.348(7)	C(2)–C(3)	1.413(7)
C(3)–C(4)	1.408(7)	C(4)–C(5)	1.367(7)
C(1)–C(5)	1.345(6)	Cp(cent)–Ti	2.069
Cp(cent)–Ti–O(1)	119.5	Cp(cent)–Ti–O(2)	111.3
Cp(cent)–Ti–O	120.7	O(1)–Ti–O(2)	93.1(9)
O(1)–Ti–O	103.9(8)	O(2)–Ti–O	104.0(7)

2.3. Ethylene polymerization studies

The experimental results of ethylene polymerization with complexes **2**–**4** as precatalysts were summarized in Table 2. Upon activation with Al^{i}Bu$_3$ and [Ph$_3$C]$^+$-[B(C$_6$F$_5$)$_4$]$^-$, complexes **2**–**4** show good catalytic activity for ethylene polymerization, producing polyethylenes with moderate molecular weights and melting points. For complexes **2**–**4** the catalytic activity increases with the increase of Al/Ti ratio, and reaches the highest catalytic activity with the ratio Al/Ti of 150, while further increasing the Al/Ti ratio results in a decrease in catalytic activity. It is possible that excessive Al^{i}Bu$_3$ would consume so much [Ph$_3$C]$^+$[B(C$_6$F$_5$)$_4$]$^-$ that catalysts could not be efficiently activated [6]. The catalytic activity of all complexes increases with the increase of polymerization temperature, and reaches the highest value at 80 °C. Further increase in the polymerization temperature results in a decrease in the catalytic activity. The order of catalytic activity for ethylene polymerization under similar conditions (see run 2, 7 and 12 in Table 2) is **3** > **4** > **2**, which implies that both the electronic and steric factors of substituents on the cyclopentadienyl group play roles in determining catalytic activity of these complexes.

Table 2
Results of ethylene polymerization using procatalysts **2**–**4**[a]

Number	Catalyst	Al:Ti	T (°C)	Activity[b] $\times 10^{-5}$	Mη[c] $\times 10^{-5}$	T_m^d (°C)
1	2	100	80	0.64	2.12	134.7
2	2	150	80	1.32	2.32	135.2
3	2	200	80	1.16	1.98	134.2
4	2	150	60	0.44	1.86	134.0
5	2	150	100	0.92	1.71	134.5
6	3	100	80	2.88	2.89	134.6
7	3	150	80	7.22	3.11	136.3
8	3	200	80	5.16	3.37	135.8
9	3	150	60	4.04	2.74	134.9
10	3	150	100	5.12	2.88	135.1
11	4	100	80	1.82	3.67	133.7
12	4	150	80	2.52	3.01	134.2
13	4	200	80	1.76	2.76	134.1
14	4	150	60	1.52	2.52	133.6
15	4	150	100	1.74	2.34	133.3

[a] Polymerization conditions: solvent, 60 ml of toluene; catalyst, 2 μmol; B/Ti ratio, 1.3; time, 5 min.
[b] g PE (mol Ti)$^{-1}$ h^{-1} bar^{-1}.
[c] Measured in decahydronaphthalene at 135 °C.
[d] Determined by DSC at a heating rate of 10 °C min^{-1}.

3. Experimental

3.1. General comments

Reactions with organometallic reagents were carried out under an argon atmosphere (ultra-high purity) using standard Schlenk techniques [7]. Solvents were dried and distilled prior to use [8]. Polymerization grade ethylene was further purified by passage through columns of 10 Å molecular sieves and MnO. Al^{i}Bu$_3$, ^{n}BuLi and $TiCl_4$ were purchased from Aldrich. [η^5-C_5H_5]$TiCl_3$ [9], [η^5-$C_5(CH_3)_5$]$TiCl_3$ [10], [η^5-$C_5H_2Ph_2CH_3$]$TiCl_3$ [11], and $[Ph_3C]^+[B(C_6F_5)_4]^-$ [12] were prepared according to the literature procedures. NMR spectra were measured using a Varian Mercury-300 NMR spectrometer.

3.2. Synthesis of 2,4-^{t}Bu$_2$-6-(CPh_2OH)C_6H_2OH (**1**)

A solution of Br_2 (5.2 ml, 95 mmol) in $CHCl_3$ (20 ml) was added dropwise to a solution of 2,4-Di-*tert*-butylphenol (19.6 g, 95 mmol) in $CHCl_3$ (20 ml) and CCl_4 (20 ml) over 2 h at 0 °C. The mixture was stirred for 1 h at this temperature. The organic phase was separated, and washed six times with water (50 ml), dried with $MgSO_4$. Pure product (24.4 g, 90%) was obtained by column chromatography over silica (hexanes) as white crystals. A solution of 2-bromo-4,6-di-*tert*-butylphenol (5.71 g, 20 mmol) in Et_2O (40 ml) was added dropwise to a solution of ^{n}BuLi (40 mmol) in Et_2O (40 ml) at −15 °C. The mixture was slowly warmed to room temperature and stirred overnight. The solution was cooled to −15 °C, and a solution of benzophenone (7.32 g, 40 mmol) in Et_2O (20 ml) was added dropwise. The reaction mixture was stirred overnight and then quenched with 60 ml of saturated NH_4Cl (aq). The organic layer was separated, dried over $MgSO_4$, filtered, and concentrated by distillation under reduced pressure. Pure product (4.90 g, 64%) was obtained by column chromatography over silica (hexanes) as white needles. *Anal.* Calc. for $C_{27}H_{32}O_2$ (388.54): C, 83.46; H, 8.30. Found: C, 83.38; H, 8.24%. ^{1}H NMR ($CDCl_3$, 300 MHz; 298 K): δ 8.27 (s, 1H, Ph–OH), 7.17–7.35 (m, 11H, Ph), 6.33 (d, 1H, Ph), 3.47 (s, 1H, OH), 1.39 (s, 9H, Ph–^{t}Bu), 1.11 (s, 9H, Ph–^{t}Bu). C^{13} NMR ($CDCl_3$, 75.4 MHz) δ, ppm: 153.4, 145.6, 140.2, 136.9, 129.4, 128.1, 127.8, 127.7, 125.4, 124.0, 85.5, 35.5, 34.5, 31.9, 30.3.

3.3. Synthesis of [Ti(η^5-C_5H_5)(2,4-^{t}Bu$_2$-6-(CPh_2O)C_6H_2O)Cl] (**2**)

A solution of ^{n}BuLi in n-hexane (1.6 M, 1.6 ml) was added to a solution of 2,4-^{t}Bu$_2$-6-(CPh_2OH)C_6H_2OH (1.00 g, 2.57 mmol) in toluene (10 ml) at −78 °C. The reaction mixture was warmed to room temperature and stirred for 1 h to give a solution of 2,4-^{t}Bu$_2$-6-(CPh_2OLi)C_6H_2OLi. This reaction mixture was added to a solution of $CpTiCl_3$ (0.56 g, 2.57 mmol) in toluene (5 ml) at −78 °C, and the reaction mixture was warmed slowly to room temperature and then heated for another 6 h at 80 °C. After allowing the mixture to cool to room temperature, the mixture was filtered, the solution was evaporated in vacuo, and the resultant solid was extracted with *n*-hexane. The extract was concentrated and placed in the freezer. The pale yellow microcrystals were collected. Yield 91% (1.25 g, 2.34 mmol). *Anal.* Calc. for $C_{32}H_{35}ClO_2Ti$ (534.94): C, 71.85; H, 6.59. Found: C, 71.91; H, 6.49%. ^{1}H NMR ($CDCl_3$, 300 MHz; 298 K): δ 7.11–7.39 (m, 11H, Ph), 6.52 (d, 1H, Ph), 6.35 (s, 5H, Cp), 1.36 (s, 9H, Ph–^{t}Bu), 1.18 (s, 9H, Ph–^{t}Bu). C^{13} NMR ($CDCl_3$, 75.4 MHz) δ, ppm: 158.1, 147.6, 146.2, 142.9, 128.6, 128.1, 127.2, 126.5 125.4, 123.3, 118.3, 99.9, 35.3, 34.6, 31.1, 30.7.

3.4. Synthesis of [Ti(η^5-$C_5(CH_3)_5$)(2,4-^{t}Bu$_2$-6-(CPh_2O)C_6H_2O)Cl] (**3**)

Complex **3** was synthesized in the same way as described above for the synthesis of **2** with [η^5-$C_5(CH_3)_5$]$TiCl_3$ (0.74 g, 2.57 mmol) as the starting material. Pure complex **3** was obtained as yellow crystals. Yield 90% (1.40 g, 2.31 mmol). *Anal.* Calc. for $C_{37}H_{45}ClO_2Ti$ (605.07): C, 73.45; H, 7.50. Found: C, 73.37; H, 7.42%. ^{1}H NMR ($CDCl_3$, 300 MHz; 298 K): δ 7.08–7.45 (m, 11H, Ph), 6.48 (d, 1H, Ph), 1.99 (s, 15H, Cp–Me), 1.39 (s, 9H, Ph–^{t}Bu), 1.03 (s, 9H, Ph–^{t}Bu). C^{13} NMR ($CDCl_3$, 75.4 MHz) δ, ppm: 156.1, 146.3, 145.2, 141.6, 128.8, 128.5, 127.4, 126.3, 125.4, 123.6, 118.8, 98.6, 35.3, 34.9, 31.8, 30.1, 12.6.

3.5. Synthesis of [Ti(η^5-$C_5H_2Ph_2CH_3$)(2,4-^{t}Bu$_2$-6-(CPh_2O)C_6H_2O)Cl] (**4**)

Complex **4** was synthesized in the same way as described above for the synthesis of **2** with [η^5-$C_5H_2Ph_2CH_3$] $TiCl_3$

(0.99 g, 2.57 mmol) as the starting material. Pure complex **4** was obtained as yellow crystals. Yield 95% (1.71 g, 2.44 mmol). *Anal.* Calc. for $C_{45}H_{45}ClO_2Ti$ (701.16): C, 77.08; H, 6.47. Found: C, 77.14; H, 7.54%. ^{1}H NMR ($CDCl_3$, 300 MHz; 298 K): δ 7.06–7.46 (m, 21H, Ph), 6.51 (d, 1H, Ph), 6.32 (d, 1H, Cp), 6.19 (d, 1H, Cp), 1.98 (s, Cp–Me), 1.28 (s, 9H, Ph–^{t}Bu), 1.06 (s, 9H, Ph–^{t}Bu). C^{13} NMR ($CDCl_3$, 75.4 MHz) δ, ppm: 158.4, 148.2, 146.6, 143.2, 135.0, 134.2, 133.6, 132.8, 131.3, 129.7, 129.5, 129.4, 129.1, 128.8, 128.6, 128.4, 128.3, 128.2, 128.1, 128.0, 127.9, 127.7, 127.6, 127.4, 123.3, 118.9, 118.2, 99.5, 35.6, 34.5, 31.5, 30.5, 15.5.

3.6. Synthesis of [Ti(η^5-C_5H_5)(2,4-^{t}Bu$_2$-6-(CPh$_2$O)C$_6$H$_2$O)]$_2$O (5)

To a solution of complex **2** (0.60 g, 1.12 mmol) in toluene (20 ml) was added H_2O (0.04 g, 2 mmol) at room temperature. The reaction mixture was stirred for 12 h at room temperature, and the solvent was removed under vacuum. The residue was extracted with **n**-hexane. The extract was concentrated and placed in the freezer. The yellow microcrystals were collected. [Ti(η^5-C_5H_5)(2,4-^{t}Bu$_2$-6-(CPh$_2$O)-C_6H_2O)]$_2$O (**5**): Yield 80% (0.91 g, 0.90 mmol). *Anal.* Calc. for $C_{64}H_{70}O_5Ti_2$ (1014.97): C, 75.73 H, 6.95. Found: C, 75.66; H, 7.01%. ^{1}H NMR ($CDCl_3$, 300 MHz; 298 K): δ 7.06–7.46 (m, 22 H, Ph), 6.51 (d, 2H, Ph), 5.91 (s, 10H, Cp), 1.36 (s, 18H, Ph–^{t}Bu), 1.07 (s, 18H, Ph–^{t}Bu). C^{13} NMR ($CDCl_3$, 75.4 MHz) δ, ppm: 158.8, 148.1, 146.7, 142.1, 129.1, 128.5, 127.7, 126.1, 125.0, 123.1, 118.9, 107.6, 35.1, 34.2, 31.9, 30.2.

3.7. X-ray structure determinations of 4 and 5

Single crystals of complexes **4** and **5** suitable for X-ray structural analysis were obtained from the mixture of CH_2Cl_2/hexane. The data were collected at 293 K on Rigaku R-AXIS RAPID IP diffractometer for complexes **4** and **5** with Mo Kα ($\lambda = 0.71073$ Å). Details of the crystal data, data collections, and structure refinements are summarized in Table 3. Both structures were solved by direct methods [13] and refined by full-matrix least-squares on F^2. All non-hydrogen atoms were refined anisotropically and the hydrogen atoms were included in idealized position. All calculations were performed using the SHELXTL [14] crystallographic software packages.

3.8. Ethylene polymerization

A dry 250 ml steel autoclave was charged with 50 ml of toluene, thermostated at desired temperature and saturated with ethylene (1.0 bar). The polymerization reaction was started by injection of a mixture of catalyst and Al^{i}Bu$_3$ in toluene (5 ml) and a solution of $[Ph_3C]^+[B(C_6F_5)_4]^-$ in toluene (5 ml) at the same time. The vessel was repressurized to needed pressure with ethylene immediately and the pressure was kept by continuously feeding of ethylene. After 5 min, the polymerization was quenched by injecting acidified methanol [HCl (3M)/methanol = 1:1], and the polymer was collected by filtration, washed with water, methanol, and dried at 60 °C in vacuo to a constant weight.

Table 3
Crystal data and structural refinements details for **4** and **5**

	4	**5**
Molecular formula	$C_{45}H_{45}ClO_2Ti$	$C_{64}H_{70}O_5Ti_2$
Molecular weight	701.16	1015.00
Crystal system	triclinic	triclinic
Space group	$P\bar{1}$	$P\bar{1}$
a (Å)	9.174(4)	10.721(8)
b (Å)	10.511(0)	11.192(8)
c (Å)	22.379(3)	13.145(7)
α (°)	77.27(7)	103.86(7)
β (°)	82.02(0)	102.81(5)
γ (°)	68.98(0)	104.76(5)
V (Å^3)	1960.8(3)	1412.1(8)
Z	2	1
D_{calc} (g cm^{-3})	1.188	1.194
F(000)	740	538
Absorption coefficient (mm^{-1})	0.321	0.330
Collect range (°)	$0.93 \leqslant \theta \leqslant 25$	$1.67 \leqslant \theta \leqslant 27.48$
Number of independent reflections	6058	6274
R_{int}	0.0238	0.0599
Number of data/restraints/parameters	6058/0/449	6274/0/328
$R_1(I > 2\sigma)$	0.0617	0.0720
$wR_2(I > 2\sigma)$	0.1538	0.1800
Goodness-of-fit	0.997	0.958
Largest difference in peak and hole (e Å^{-3})	0.384 and −0.380	0.786 and −0.558

4. Conclusions

We have synthesized and characterized three new monochlorotitanium complexes based on mono-Cp and phenoxy-alkoxo mixed ligands. These complexes were found to be stable in air, but can be easily hydrolyzed. The reaction of complex **2** with excess water gave the oxo-bridged complex **5**. When activated with $[Ph_3C]^+[B(C_6F_5)_4]^-$ and Al^{i}Bu$_3$, these monochlorotitanium complexes exhibit good catalytic activity for ethylene polymerization and produce moderate molecular weight polyethylene. These new catalysts represent a valuable addition to the limited list of monochlorotitanium ethylene polymerization catalysts.

5. Supplementary material

CCDC 623912 and 623913 contain the supplementary crystallographic data for **4** and **5**. These data can be obtained free of charge via http://www.ccdc.cam.ac.uk/conts/retrieving.html, or from the Cambridge Crystallographic Data Centre, 12 Union Road, Cambridge CB2 1EZ, UK; fax: (+44) 1223-336-033; or e-mail: deposit@ccdc.cam.ac.uk.

Acknowledgement

This work was supported by the National Natural Science Foundation of China (Nos. 20674024 and 20374023).

References

[1] H. Sinn, W. Kaminsky, Adv. Organomet. Chem. 181 (1980) 99.
[2] (a) J. Zhang, X. Wang, G.X. Jin, Coord. Chem. Rev. 250 (2006) 95;
(b) J. Zhang, G.X. Jin, Inorg. Chem. Commum. 9 (2006) 683;
(c) V.C. Gibson, S.K. Spitzmesser, Chem. Rev. 103 (2003) 283;
(d) A.L. McKnight, R.M. Waymouth, Chem. Rev. 98 (1998) 2587;
(e) H.H. Brintzinger, D. Fischer, R. Mülhaupt, B. Rieger, R.M. Waymouth, Angew. Chem., Int. Ed. Engl. 34 (1995) 1143;
(f) T. Cuenca, Compr. Organomet. Chem. III 4 (2006) 323;
(g) L. Resconi, J.C. Chadwick, L. Cavallo, Compr. Organomet. Chem. III 4 (2006) 1005.
[3] (a) Y. Qian, J. Huang, M.D. Bala, B. Lian, H. Zhang, H. Zhang, Chem. Rev. 103 (2003) 2633;
(b) Y. Zhang, J. Wang, Y. Mu, Z. Shi, C. Lu, Y. Zhang, L. Qiao, S. Feng, Organometallics 22 (2003) 3877;
(c) H.G. Alt, A. Koppl, Chem. Rev. 100 (2000) 1205;
(d) Y. Zhang, Y. Mu, G. Li, C. Lu, T. Xiao, J. Xu, Y. Zhang, D. Zhu, S. Fen, Polyhedron 24 (2005) 1793.
[4] (a) Y. Nzkayama, K. Watanabe, N. Ueyama, A. Nakamura, A. Harada, Organometallics 19 (2000) 2498;
(b) M. Gonzalez-Maupoey, T. Cuenca, L.M. Frutos, O. Castano, E. Herdweck, Organometallics 22 (2003) 2694;
(c) F. Amor, P. Gomez-Sal, P. Royo, J. Okuda, Organometallics 19 (2000) 5168;
(d) V. Tabernero, T. Cuenca, Eur. J. Inorg. Chem. (2005) 338;
(e) J. Jin, D.R. Wilson, E.Y. Chen, Chem. Commum. (2002) 708;
(f) J. Cano, P. Royo, M. Lanfranchi, M.A. Pellinghelli, A. Tiripicchio, Angew. Chem., Ind. Ed. 40 (2001) 2495;
(g) R. Fandos, C. Hernandez, A. Otero, A. Rodriguez, M.J. Ruiz, P. Terreros, Chem. Eur. J. 9 (2003) 671.
[5] S. Doherty, R.J. Errington, A.P. Jarvis, S. Collins, W. Clegg, M.R.J. Elsegood, Organometallics 17 (1998) 3408.
[6] M. Bochmann, M.J. Sarsfield, Organometallics 17 (1998) 5908.
[7] D.F. Shriver, The Manipulation of Air-Sensitive Compounds, McGraw-Hill, New York, 1969.
[8] D.D. Perrin, W.L.F. Armarego, D.R. Perrin, The Purification of Laboratory Chemicals, Pergamon, New York, 1980.
[9] (a) R.D. Gorsich, J. Am. Chem. Soc. 80 (1958) 4744;
(b) R.D. Gorsich, J. Am. Chem. Soc. 82 (1960) 4211.
[10] G. Hidalgo, M. Mena, F. Palacios, P. Royo, R.J. Serrano, Organomet. Chem. 340 (1988) 37.
[11] Q. Wu, Q. Su, G. Li, W. Gao, Y. Mu, S. Feng, Polyhedron 25 (2006) 2565.
[12] (a) A.G. Massey, A.J. Park, J. Org. Chem. 2 (1962) 245;
(b) A.G. Massey, A.J. Park, J. Organomet. Chem. 5 (1966) 218;
(c) J.C.W. Chien, W.M. Tsai, M.D. Rasch, J. Am. Chem. Soc. 113 (1991) 8570.
[13] SHELXTL, PC Siemens Analytical X-ray Instruments, Madison WI, 1993.
[14] G.M. Sheldrick, SHELXTL Structure Determination Programs, Version 5.0, PC Siemens Analytical Systems, Madison, WI, 1994.

Available online at www.sciencedirect.com
ScienceDirect
Polyhedron 26 (2007) 3363–3372
POLYHEDRON
www.elsevier.com/locate/poly

Synthesis of novel molybdenum(V) complexes: Structural characterization of two thiosemicarbazonato complexes $[MoOCl_2\{C_6H_4(O)CH{:}NNHC{:}SNHC_6H_5\}]$ and $[MoOCl_2\{C_{10}H_6(O)CH{:}NNHC{:}SNHC_6H_5\}]\cdot CH_3CN$, and two oxohalomolybdates $NH_4[MoOCl_4(CH_3CN)]$ and $[C_5H_5NH]_2[MoOCl_5]\cdot CH_2Cl_2$

Višnja Vrdoljak, Dalibor Milić, Marina Cindrić *, Dubravka Matković-Čalogović, Dominik Cinčić

Laboratory of General and Inorganic Chemistry, Department of Chemistry, Faculty of Science, University of Zagreb, Horvatovac 102a, 10000 Zagreb, Croatia

Received 25 January 2007; accepted 8 March 2007
Available online 28 March 2007

Abstract

Mononuclear oxomolybdenum(V) complexes with thiosemicarbazonato ligands as condensation products of aldehydes (salicylaldehyde, 2-hydroxynaphthaldehyde) with thiosemicarbazides ($H_2NNHC{:}SNHR$; R = H, CH_3, C_6H_5) were prepared. The $[MoOCl_2HL]$ complexes (HL = thiosemicarbazonato ligand) were characterized by chemical analysis, IR spectroscopy, thermogravimetry and two of them, $[MoOCl_2\{C_6H_4(O)CH{:}NNHC{:}SNHC_6H_5\}]$ and $[MoOCl_2\{C_{10}H_6(O)CH{:}NNHC{:}SNHC_6H_5\}]\cdot CH_3CN$, by single-crystal X-ray structural analysis. In both complexes the MoO^{3+} core is coordinated by a monobasic tridentate ONS thiosemicarbazonato ligand and two chloro ligands. The coordination around the molybdenum atom is a distorted octahedron. $NH_4[MoOCl_4(CH_3CN)]$ and unstable $(C_5H_5NH)_2[MoOCl_5]\cdot CH_2Cl_2$ were isolated from the acetonitrile solution of $(NH_4)_2[MoOCl_5]$ and from the acetonitrile and dichloromethane (1:1) solution of $(C_5H_5NH)_2[MoOCl_5]$, respectively.

Isolation and structural characterization of $NH_4[MoOCl_4(CH_3CN)]$ from the acetonitrile solution suggests the $[MoOCl_4(CH_3CN)]^-$ anion to be the reaction intermediate in the synthesis of molybdenum(V) thiosemicarbazonato complexes.

$(C_5H_5NH)_2[MoOCl_5]\cdot CH_2Cl_2$ is a rare example of a structurally characterized simple oxohalomolybdate(V) with a six-coordinate octahedral $[MoOCl_5]^{2-}$ anion.
© 2007 Elsevier Ltd. All rights reserved.

Keywords: Oxomolybdenum(V) complexes; Thiosemicarbazone; X-ray crystal structure

1. Introduction

The chemistry of molybdenum is of great interest because its large number of accessible oxidation states offers a wide variety of complexes with diverse coordination numbers and stereochemistries [1]. Molybdenum is important in many biological processes [2,3], for example, it is well known that catalytic reactions of molybdoenzymes involve molybdenum in its +6 and +4 oxidation states. Some studies established that during the process of electron transfer to or from the redox centres, Mo(V) coexists with Mo(VI) and Mo(IV) [4–7]. In spite of the fact that investigations of oxomolybdenum(VI), (V) and

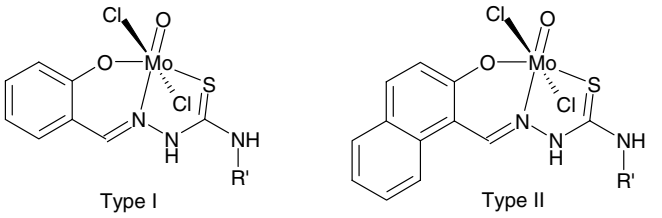
* Corresponding author. Tel.: +385 1 460 6351; fax: + 385 1 460 6341.
E-mail address: marina@chem.pmf.hr (M. Cindrić).

0277-5387/$ - see front matter © 2007 Elsevier Ltd. All rights reserved.
doi:10.1016/j.poly.2007.03.028

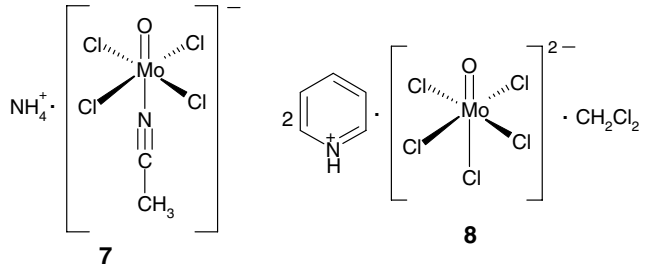
(IV) complexes with NS, SS and ONS donor ligands can give useful information on the active sites of molybdoenzymes, there are just a few studies on oxomolybdenum(V) complexes of thiosemicarbazones as NS/ONS donors [8,9].

Our interest in the chemistry of the oxomolybdenum(V) cation ligated to ONS donors has prompted us to pursue the present work. In this paper we report eight new Mo(V) complexes, six of them coordinated by monoanionic tridentate thiosemicarbazonato ligands, {C_6H_4(O)CH:NNHC:SNHR′ or $C_{10}H_6$(O)CH:NNHC:SNHR′; R′ = H, CH_3, C_6H_5}, derived from salicylaldehyde or 2-hydroxynaphthaldehyde. These ligands are of interest because their complexes with the MoO^{3+} core can be of the form MoOL, possessing coordination sites that can be utilized for substrate binding.

We obtained and characterized Mo(V) complexes of the general formula $[MoOCl_2HL]$ {HL = C_6H_4(O)CH:NNHC:SNH_2 (**1**), C_6H_4(O)CH:NNHC:$SNHCH_3$ (**2**), C_6H_4(O)CH:NNHC:$SNHC_6H_5$ (**3**), $C_{10}H_6$(O)CH:NNHC:SNH_2 (**4**), $C_{10}H_6$(O)CH:NNHC:$SNHCH_3$ (**5**)} and $[MoOCl_2HL]\cdot CH_3CN$ {HL = $C_{10}H_6$(O)CH:NNHC:$SNHC_6H_5$} (**6**).



R′	H	CH_3	C_6H_5
Type I	**1**	**2**	**3**
Type II	**4**	**5**	**6** (without cocrystallized CH_3CN)



7 **8**

Complexes **3** and **6** were also structurally characterized by single crystal X-ray diffraction. $NH_4[MoOCl_4(CH_3CN)]$ (**7**) and $[C_5H_5NH]_2[MoOCl_5]\cdot CH_2Cl_2$ (**8**), isolated and structurally characterized during our study, are part of the reaction pathway in the syntheses of the Mo(V) thiosemicarbazonato complexes.

2. Experimental

The starting molybdenum(V) salts $(NH_4)_2[MoOCl_5]$ and $(C_5H_5NH)_2[MoOCl_5]$, and the thiosemicarbazones were prepared as described in the literature [10–12]. Acetonitrile and dichloromethane were dried over phosphorus pentoxide, methanol over magnesium ethoxide.

The Analytical Services Laboratory of the Rudjer Bošković Institute provided C, H, N and S analyses. Molybdenum and chlorine were determined according to the already known methods [13,14] (Table 1). Infrared spectra were recorded in KBr discs with a Spectrum RX I spectrophotometer in the 4500–450 cm^{-1} region. Thermogravimetric analyses were measured on a Mettler TG 50 thermobalance using aluminium crucibles under oxygen atmosphere with a heating rate of 5 °C min^{-1}. In all experiments the temperature ranged from 25 to 600 °C. The results were developed by applying the Metler STAR^e 6.1 program.

2.1. Syntheses of molybdenum(V) complexes

2.1.1. Syntheses of thiosemicarbazonato molybdenum(V) complexes: *1–6*

A mixture of $(NH_4)_2[MoOCl_5]$ (0.20 g, 0.65 mmol) and the appropriate thiosemicarbazone (0.65 mmol) in dry acetonitrile (20 cm^3) (under an argon atmosphere) was heated under reflux for 4–5 h. Brown crystals of $[MoOCl_2HL]$ (**1**–**5**) or $[MoOCl_2HL]\cdot CH_3CN$ (**6**) and white NH_4Cl were deposited during the heating of the reaction mixture. The obtained products were filtered off and washed with cold water. For analytical data and selected spectroscopic data, see Table 1.

Only the crystals of **3** and **6** were suitable for single crystal X-ray structural analyses.

2.1.2. Crystallization of $NH_4[MoOCl_4(CH_3CN)]$ (7) and $(C_5H_5NH)_2[MoOCl_5]\cdot CH_2Cl_2$ (8)

The green crystalline product of **7** was deposited from a solution of $(NH_4)_2[MoOCl_5]$ (0.10 g, 0.33 mmol) in dry acetonitrile (10 cm^3), while unstable green prismatic crystals of **8** deposited from a solution of $(C_5H_5NH)_2[MoOCl_5]$ (0.10 g, 0.22 mmol) in a mixture of dry acetonitrile and dichloromethane (10 cm^3:10 cm^3). The crystalline products were obtained, filtered off and washed with cold acetonitrile (for complex **7**) or a mixture of acetonitrile and dichloromethane (for complex **8**).

2.2. X-ray crystallography

The X-ray data were collected on an Oxford Diffraction Xcalibur 3 CCD diffractometer with graphite-monochromated Mo Kα radiation ($\lambda = 0.71073$ Å). The crystallographic data are summarized in Table 2. The X-ray data for **8** were measured from a crystal coated with a thin layer of silicone grease (due to its instability). The data reduction (including the absorption correction) was performed using the CRYSALIS software package [15]. Solution, refinement and analysis of the structures were done using the programs integrated in the WINGX system [16]. The structures were solved by direct methods (SHELXS) [17] and refined by the full-matrix least-squares method based on F^2 against

Table 1
Analytical and spectral data for molybdenum(V) complexes

Formula (M_r)	Complex	Analysis found (calcd.)						Yield	Selected IR data (cm^{-1})			
		%C	%H	%Cl	%Mo	%N	%S	%	C=N	Mo=O	C=S	C–O
$[MoOCl_2(C_6H_4(O)CH:NNHC:SNH_2)]$ (377.08)	**1**	25.11 (25.44)	2.28 (2.14)	18.91 (18.80)	25.25 (25.44)	11.09 (11.14)	8.35 (8.50)	47.44 (0.11 g)	1578	948	746	1546
$[MoOCl_2(C_6H_4(O)CH:NNHC:SNHCH_3)]$ (391.10)	**2**	27.50 27.62	2.51 (2.58)	18.20 (18.13)	24.15 (24.53)	10.37 (10.74)	8.32 (8.20)	54.10 (0.13 g)	1602	939	764	1542
$[MoOCl_2(C_6H_4(O)CH:NNHC:SNHC_6H_5)]$ (453.17)	**3**	37.25 (37.11)	2.51 (2.67)	15.91 (15.64)	21.15 (21.17)	9.37 (9.27)	6.92 (7.08)	46.65 (0.13 g)	1576	968	748	1540
$[MoOCl_2(C_{10}H_6(O)CH:NNHC:SNH_2)]$ (427.15)	**4**	33.56 (33.74)	2.31 (2.36)	16.71 (16.60)	22.35 (22.46)	9.67 (9.84)	7.62 (7.51)	60.92 (0.16 g)	1618	958	766	1560
$[MoOCl_2(C_{10}H_6(O)CH:NNHC:SNCH_3)]$ (441.16)	**5**	35.25 (35.39)	2.68 (2.80)	14.21 (14.09)	19.29 (19.06)	8.18 (8.35)	6.98 (6.32)	73.89 (0.20)	1600	916	749	1536
$[MoOCl_2(C_{10}H_6(O)CH:NNHC:SNHC_6H_5)]$[a] (503.23)	**6**	43.18 (42.96)	3.01 (2.80)	13.98 (14.09)	18.80 (19.06)	8.61 (8.35)	6.09 (6.37)	47.81 (0.15 g)	1601	957	753	1538
$NH_4[MoOCl_4CH_3CN]$ (312.83)	**7**	7.44 (7.68)	2.20 (2.69)	45.42 (45.33)	30.60 (30.67)	8.79 (8.95)		89.00 (0.17 g)		975		
$[C_5H_5NH]_2[MoOCl_5]$[a] (449.41)	**8**	24.65 (26.73)	2.72 (2.69)	39.50 (39.44)	21.20 (21.35)	5.98 (6.23)		67.00 (0.13 g)		974		

[a] For complex **6** and **8** without CH_3CN and CH_2Cl_2, respectively.

all reflections (SHELXL-97) [18]. The non-hydrogen atoms were refined anisotropically. All hydrogen atoms were located in the difference Fourier maps and those attached to the nitrogen atoms were refined isotropically with restrained N–H distances; the remaining non-methyl H-atoms were refined using the riding model, with

Table 2
Crystallographic data for compounds **3**, **6**, **7** and **8**

	3	**6**	**7**	**8**
Chemical formula	$C_{14}H_{12}Cl_2MoN_3O_2S$	$C_{20}H_{17}Cl_2MoN_4O_2S$	$C_2H_7Cl_4MoN_2O$	$C_{11}H_{14}Cl_7MoN_2O$
M_r	453.17	544.28	312.84	534.33
Crystal colour	brown	brown	green	green
Habit	plate	prism	plate	prism
Crystal size (mm)	$0.75 \times 0.50 \times 0.05$	$0.30 \times 0.10 \times 0.09$	$0.45 \times 0.40 \times 0.14$	$0.25 \times 0.25 \times 0.16$
Crystal system	orthorhombic	monoclinic	orthorhombic	orthorhombic
Space group	*Pbca*	$P2_1/n$	*Cmcm*	*Pnma*
a (Å)	9.6173(8)	11.1857(4)	7.5401(6)	18.8637(13)
b (Å)	14.8577(13)	17.1942(7)	14.5150(11)	14.3845(9)
c (Å)	22.343(2)	11.7310(4)	8.4963(7)	7.0333(4)
α (°)	90	90	90	90
β (°)	90	110.005(3)	90	90
γ (°)	90	90	90	90
V (Å^3)	3192.6(5)	2120.08(14)	929.87(13)	1908.4(2)
Z	8	4	4	4
T (K)	108(2)	108(2)	100(1)	100(1)
D_{calc} (g cm^{-3})	1.886	1.705	2.235	1.860
μ(Mo Kα) (mm^{-1})	1.298	0.995	2.500	1.667
Absorption correction	numerical	multi-scan	numerical	numerical
T_{min}	0.553	0.689	0.397	0.683
T_{max}	0.928	0.914	0.740	0.781
Number of unique reflections	4633	3700	464	2868
Number of observed reflections [$I > 2\sigma(I)$]	4064	2922	464	2709
θ_{max} (°)	30.0	25.0	25.0	30.0
R_{int}	0.0284	0.0321	0.0440	0.0443
Number of parameters	216	280	40	113
Number of restraints	1	4	5	0
R_1[a] [$I > 2\sigma(I)$]	0.0357	0.0336	0.0185	0.0288
wR_2[b] (all data)	0.0862	0.0816	0.0513	0.0547

[a] $R_1 = \sum||F_o| - |F_c||/\sum|F_o|$.
[b] $wR_2 = [\sum w(|F_o| - |F_c|)^2]^{1/2}$.

$U_{iso}(H) = 1.2U_{eq}(C)$. For the methyl H-atoms in **6** only the torsion angles were refined, keeping the methyl-group geometry fixed, while the positions of the methyl H-atoms in **7** were kept fixed during refinement. The methyl H-atoms were assigned isotropic thermal parameters, $U_{iso}(H) = 1.5U_{eq}(C)$. Geometrical calculations were performed using PLATON [19]. The figures were made using ORTEP-3 [20].

3. Results and discussion

3.1. Syntheses of the complexes

The brown complexes $[MoOCl_2\{RCH{:}NNHC{:}SNHR'\}]$ [$R = C_6H_4(O)$ or $C_{10}H_6(O)$; $R' = H$, CH_3, C_6H_5] (**1**–**5**) and $[MoOCl_2\{C_{10}H_8(O)CH{:}NNHC{:}SNH{-}C_6H_5\}]\cdot CH_3CN$ (**6**) were obtained by the reaction of $(NH_4)_2[MoOCl_5]$ with a stoichiometric amount of the appropriate thiosemicarbazone (H_2L) in dry acetonitrile, under an argon atmosphere, as follows:

$$(NH_4)_2[MoOCl_5] + H_2L \xrightarrow{CH_3CN} MoOCl_2HL + 2NH_4Cl + HCl$$

All products were washed with cold water to remove ammonium chloride as the by-product of all the synthetic reactions. We were able to isolate brown single crystals of $[MoOCl_2\{C_6H_4(O)CH{:}NNHC{:}SNHC_6H_5\}]$ (**3**) and $[MoOCl_2\{C_{10}H_6(O)CH{:}NNHC{:}SNHC_6H_5\}]\cdot CH_3CN$ (**6**) from the acetonitrile solution at room temperature. In both complexes molybdenum is octahedrally coordinated by the monoprotonated tridentate ONS thiosemicarbazonato ligand, two chloro ligands and one oxygen atom. The thiosemicarbazonato complexes **1**–**6** could not be obtained if $(C_5H_5NH)_2[MoOCl_5]$ was used instead of $(NH_4)_2[MoOCl_5]$ in the synthetic trials.

All the complexes were characterized by IR spectroscopy and selected spectral data are given in Table 1. The IR spectra of complexes **1**–**6** showed characteristic vibrations for this type of compound and the data are in accordance with that in the literature [21].

The ν(OH) band at about 3440 cm^{-1} of the free ligands disappears upon the formation of the complexes and indicates that the deprotonated phenolic oxygen is involved in the molybdenum coordination. The intense bands in the region 1610–1640 cm^{-1}, associated with the C=N stretching frequency of the free ligands, are shifted to 1578 (**1**), 1602 (**2**), 1576 (**3**), 1618 (**4**), 1600 (**5**) and 1601 (**6**) cm^{-1} in the corresponding complexes and indicate coordination of the azomethine nitrogen to the molybdenum [12]. Ligand bands in the region 1515–1540 cm^{-1}, due to ν(C–O), are shifted to 1546 (**1**), 1542 (**2**), 1540 (**3**), 1560 (**4**), 1536 (**5**) and 1538 (**6**) cm^{-1} in the complexes, indicating the coordination of the oxoaryl oxygen. Appearance of a strong single band in the region 940–974 cm^{-1} confirmed the presence of $\nu(Mo{=}O_t)$. The bands at about 815–830 cm^{-1} in the free thiosemicarbazones, assigned as ν(C=S), appear at lower frequencies (760–746 cm^{-1}) in the complexes, suggesting coordination through the sulfur atom.

Isolation and structural characterization of $NH_4[MoOCl_4(CH_3CN)]$ (**7**) from an acetonitrile solution of $(NH_4)_2[MoOCl_5]$ suggests $[MoOCl_4(CH_3CN)]^-$ to be the reaction intermediate in the synthesis of the Mo(V) thiosemicarbazonato complexes. The chloro ligand *trans* to the double bonded oxygen atom in $[MoOCl_5]^{2-}$ is substituted by the acetonitrile solvent molecule, and so crystalline NH_4Cl and the $[MoOCl_4(CH_3CN)]^-$ anion are formed. The same $[MoOCl_4(CH_3CN)]^-$ anion has been found in several oxomolybdates(V), e.g. in $Tl[MoOCl_4(CH_3CN)]$ [22] and $(AsPh_4)_2[(MoOCl_4)_2(CH_3CN)]$ [23]. In the final reaction step, an acetonitrile and two mutually *trans* chloro ligands in $[MoOCl_4(CH_3CN)]^-$ are substituted by a molecule of the monodeprotonated thiosemicarbazone.

The unstable crystals of $(C_5H_5NH)_2[MoOCl_5]\cdot CH_2Cl_2$ (**8**) were obtained from an acetonitrile and dichloromethane (1:1) solution of $(C_5H_5NH)_2[MoOCl_5]$. The crystals desolvate rapidly, particularly upon prolonged exposure to air. Oxohalomolybdates(V) have been extensively studied since 1927 [24–28], however this is a rare example of a structurally characterized simple oxohalomolybdate(V) with a six-coordinated, octahedral $[MoOCl_5]^{2-}$ anion. The X-ray structure analysis of $(C_5H_5NH)_2[MoOCl_5]$ [24–28], prepared by modified literature methods [11,24–28], showed its true identity as $(C_5H_5NH)_5[MoOCl_4(H_2O)]_3Cl_2$. However, our investigation suggests that $[MoOCl_5]^{2-}$ could be one of the anions present in the acidic solution of $(C_5H_5NH)_2[MoOCl_5]$. We could further assume that the solution of $(C_5H_5NH)_2[MoOCl_5]$ in acetonitrile and dichloromethane (1:1) also contains $[MoOCl_4(CH_3CN)]^-$ anions, according to the literature data [24–28]. So, if there are $[MoOCl_4(CH_3CN)]^-$ anions in the acetonitrile solution of $(C_5H_5NH)_2[MoOCl_5]$ and these anions are the postulated reaction intermediate in the synthesis of the Mo(V) thiosemicarbazonato complexes, it is not completely obvious why the thiosemicarbazonato complexes **1**–**6** could not be obtained using this pyridinium salt as the starting material. One of the possible reasons could be the different solubility of the by-product chloride salts in acetonitrile. The low solubility of ammonium chloride in acetonitrile and the ammonium chloride crystals thus formed can act as the driving force for the removal of the chloro ligands from the $[MoOCl_4(CH_3CN)]^-$ intermediate, and the subsequent formation of the Mo(V) thiosemicarbazonato complexes. On the contrary, pyridinium chloride is much more soluble in acetonitrile, so crystals of pyridinium chloride do not occur and the chloride anions stay in the solution or bonded in the starting Mo(V) complex anions.

3.2. Thermal analysis

The thermal behaviour of the molybdenum(V) complexes **1**–**5** is in agreement with our previous findings on thiosemicarbazonato complexes of molybdenum(VI) [29,30]. The TG data of the complexes showed that their

ligands decomposed in the range 196–569 °C (**1**), 245–591 °C (**2**), 241–591 °C (**3**), 191–591 °C (**4**), 217–596 °C (**5**) and 213–588 °C (**6**).

The thermal studies of complexes **6** and **8** reveals two processes:

(1) loss of acetonitrile within the range 25–105 °C for complex **6** and loss of dichloromethane within the range 27–62 °C for complex **8**;
(2) decomposition of complex **6** within the range 213–588 °C and loss of C_5H_5NHCl for complex **8** within the range 228–557 °C.

The TG studies of complex **7** showed that it sublimates at 346 °C.

All experimental values for mass loss on the TG curve are in good agreement with the calculated values.

3.3. Structural studies

3.3.1. Structures of $[MoOCl_2\{C_6H_4(O)\text{-}CH{:}NNHC{:}SNHC_6H_5\}]$ (3) and $[MoOCl_2\{C_{10}H_6(O)\text{-}CH{:}NNHC{:}\ SNHC_6H_5\}]\cdot CH_3CN$ (6)

The molecules found in the crystal structures of **3** and **6** are shown in Figs. 1 and 2, respectively. The structures of the complex molecules in **3** and **6** are very similar and are discussed together. In **6**, complex molecules co-crystallise with molecules of acetonitrile.

In both structures, Mo(V) is coordinated by an oxo group, two chloro ligands and a monodeprotonated tridentate thiosemicarbazonato ligand. The two chloro ligands are mutually in *trans* positions, while the corresponding thiosemicarbazone molecule is meridionally bonded in its thioketo-amino tautomeric form through the thione sulfur (S), imine nitrogen (N1) and the deprotonated phenolic oxygen (O2) atoms, thus forming 5- and 6-membered chelate rings. As indicated by the bond angles (Table 3), the coordination around Mo(V) is a distorted octahedron with the Mo atom displaced from the least-squares plane of Cl1, Cl2, S and O2 atoms towards the oxo group O1 [by 0.35406(18) Å in **3** and by 0.3417(3) Å in **6**]. In both structures the bond lengths Mo = O1, Mo–Cl1 and Mo–Cl2 are similar to those found in other structures with a *trans*-$[Mo^{V}OCl_2]^{+}$ core [31–33]. The two Mo–Cl bond distances in each complex molecule are significantly different. This feature was also found in some other *trans*-$[MoOCl_2]^{+}$ complexes [31–33]. The Mo–S, Mo–N1 and Mo–O2 distances fall in the range of the corresponding bond distances observed for thiosemicarbazonato-*O*,*N*,*S* complexes with a *cis*-$[MoO_2]^{2+}$ core [29,30,34–39].

Each thiosemicarbazonato ligand in **3** and **6** consists of three planar parts: the oxoaryl (salicyl in **3**: C11–C16, C1 and O2; or 2-oxonaphthyl in **6**: C11–C20 and O2), thiosemicarbazonyl (N1, N2, C3, S and N4) and *N*-phenyl (C5–C10) moieties. Dihedral angles between the least-squares planes of the oxoaryl and the thiosemicarbazonyl fragments are 17.46(7)° and 24.22(10)° in **3** and **6**, respectively. The planarity of these two fragments allows a high

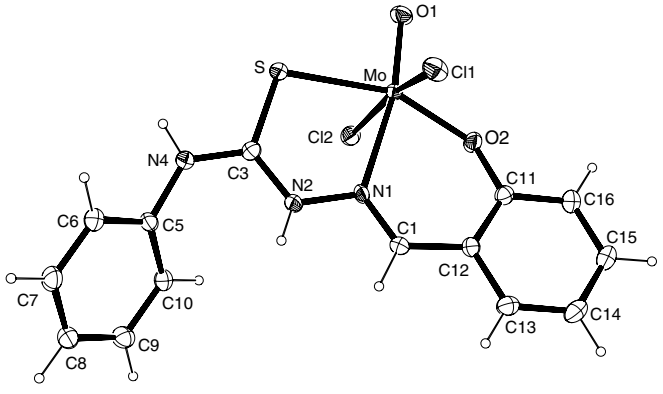


Fig. 1. The complex molecule **3** with the numbering scheme and displacement ellipsoids drawn at the 50% probability level.

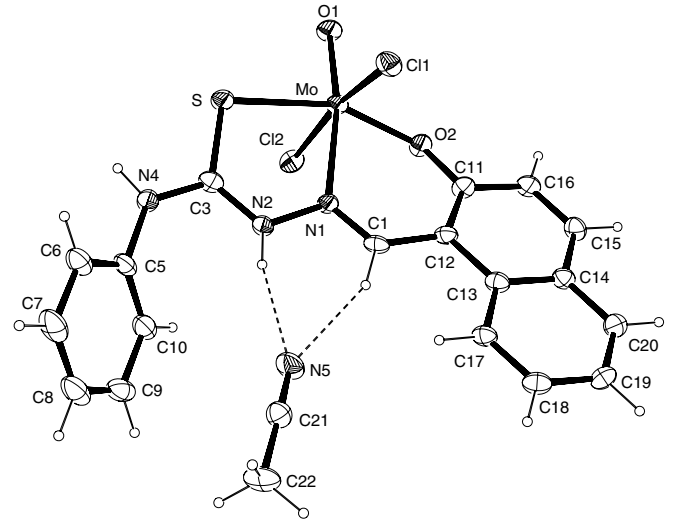


Fig. 2. The asymmetric unit of **6** with the numbering scheme and displacement ellipsoids drawn at the 50% probability level. The acetonitrile molecule is bound to the complex molecule *via* two hydrogen bonds (represented by the dashed lines).

Table 3
Selected bond distances (Å) and angles (°) for **3** and **6**

	3	**6**		**3**	**6**
Mo–O1	1.6700(18)	1.676(2)	Cl1–Mo–O2	88.74(5)	87.74(8)
Mo–Cl1	2.3834(7)	2.3944(9)	Cl1–Mo–Cl2	166.74(2)	169.29(4)
Mo–Cl2	2.4221(7)	2.4189(9)	Cl1–Mo–S	90.87(2)	92.74(3)
Mo–S	2.4521(7)	2.4640(10)	Cl1–Mo–O1	95.98(6)	95.97(9)
Mo–N1	2.3249(19)	2.294(3)	Cl2–Mo–S	86.64(2)	87.14(3)
Mo–O2	1.9406(17)	1.948(2)	Cl1–Mo–N1	83.34(5)	82.87(7)
O2–C11	1.338(3)	1.341(4)	Cl2–Mo–O1	97.09(6)	94.73(9)
C11–C12	1.415(3)	1.399(5)	Cl2–Mo–O2	88.47(5)	87.91(8)
C12–C1	1.448(3)	1.429(5)	Cl2–Mo–N1	83.42(5)	86.72(7)
C1–N1	1.293(3)	1.286(5)	S–Mo–O1	91.08(6)	92.43(8)
N1–N2	1.388(3)	1.400(3)	S–Mo–O2	156.88(5)	155.20(7)
N2–C3	1.341(3)	1.332(5)	S–Mo–N1	76.67(5)	75.94(8)
C3–S	1.714(2)	1.717(4)	O1–Mo–O2	111.95(8)	112.19(10)
C3–N4	1.329(3)	1.331(5)	O1–Mo–N1	167.71(8)	168.21(11)
N4–C5	1.432(3)	1.434(5)	O2–Mo–N1	80.32(7)	79.53(10)

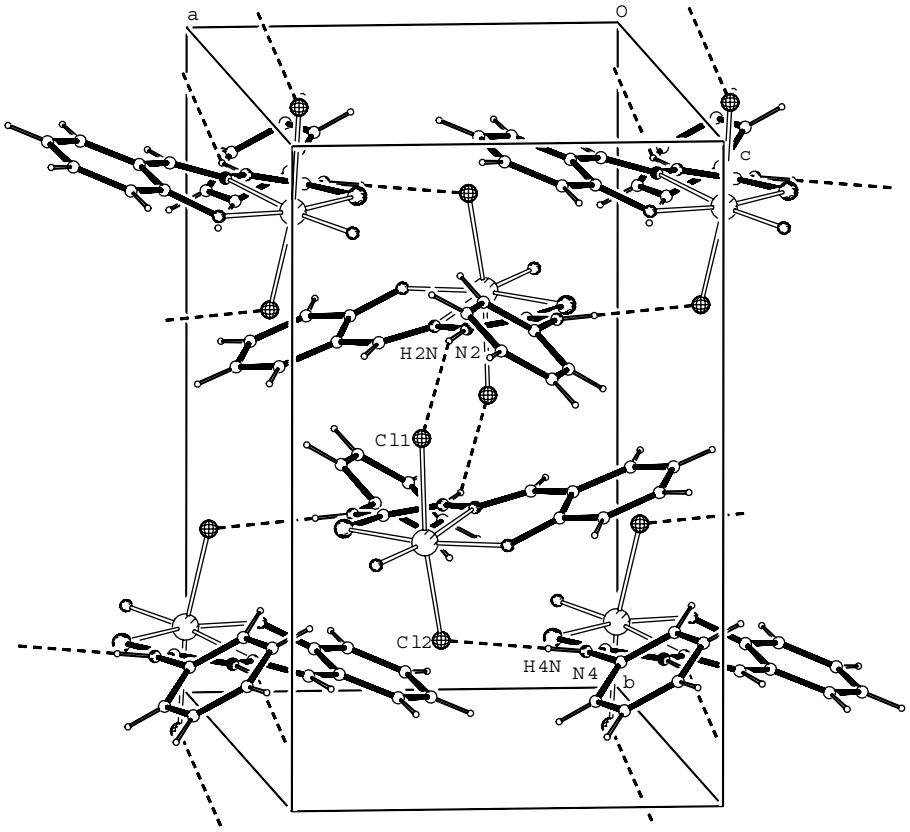


Fig. 3. The crystal packing in **3**. Each complex molecule is a part of the centrosymmetric dimer and a chain parallel to the *a* axis.

Table 4
Hydrogen bonding geometry in structures **3**, **6**, **7** and **8**

D–H···A	*d*(D–H) (Å)	*D*(H···A) (Å)	*d*(D···A) (Å)	∠(D–H···A) (°)	Symmetry operation on A
*Compound **3***					
N2–H2N···C11	0.82(3)	2.65(3)	3.343(2)	144(3)	$2-x, -y, 1-z$
C6–H6···Cg[a]	0.95	2.62	3.336(2)	132	$2-x, -y, 1-z$
N4–H4N···C12	0.840(19)	2.394(18)	3.234(2)	180(4)	$x-1/2, 1/2-y, 1-z$
C9–H9···O1	0.95	2.47	3.180(3)	131	$1/2+x, 1/2-y, 1-z$
C16–H16···O1	0.95	2.58	3.492(3)	161	$1/2+x, y, 3/2-z$
*Compound **6***					
N2–H2N···N5	0.86(4)	2.23(4)	3.069(5)	165(4)	x, y, z
C1–H1···N5	0.95	2.34	3.224(5)	155	x, y, z
N4–H4N···C12	0.86(2)	2.38(3)	3.163(4)	152(3)	$1/2+x, 1/2-y, 1/2+z$
C22–H22A···Cg	0.98	2.85	3.568(4)	131	$1-x, -y, 2-z$
*Compound **7***					
N2–H2NA···C1	0.904(19)	2.650(18)	3.3856(19)	139.1(4)	x, y, z
N2–H2NA···C1	0.904(19)	2.650(18)	3.3856(19)	139.1(4)	$x, y, 1/2-z$
N2–H2NB···C1	0.920(18)	2.651(12)	3.4064(13)	139.9(6)	$1/2+x, 1/2-y, 1-z$
N2–H2NB···C1	0.920(18)	2.651(12)	3.4064(13)	139.9(6)	$1/2-x, 1/2-y, 1-z$
N2–H2NB···O	0.920(18)	2.71(3)	3.154(4)	110.6(19)	$1/2-x, y-1/2, z$
C2–H2A···C1	0.98	2.82	3.5158(15)	129	$1/2-x, 1/2-y, z-1/2$
*Compound **8***					
N–H1N···C14	0.84(3)	2.31(3)	3.1281(16)	163(3)	x, y, z
N–H1N···C14	0.84(3)	2.31(3)	3.1281(16)	163(3)	x, y, z
C2–H2···CI2	0.95	2.78	3.6839(18)	159	$1/2-x, -y, 1/2+z$
C4–H4···C11	0.95	2.79	3.6446(19)	150	$1-x, -y, 2-z$
C4–H4···CI2	0.95	2.81	3.5517(18)	135	$1-x, -y, 2-z$
C7–H7A···O	0.99	2.51	3.252(3)	131	x, y, z
C7–H7B···C14	0.99	2.66	3.560(3)	151	$x-1/2, y, 3/2-z$

[a] Cg is the centroid of the ring C11–C12–C13–C14–C15–C16 (in both **3** and **6**).

degree of π-electron delocalization throughout them (as suggested by the corresponding bond distances; Table 3). Such π-electron delocalisation is also observed in the structures of similar free thiosemicarbazone ligand molecules [29,40–46] as well as in their *cis*-$[MoO_2]^{2+}$ complexes [29,34–39]. The π-electron delocalization is interrupted at the single N4–C5 bond [1.432(3) and 1.434(5) Å] which is, therefore, significantly longer than the (formally) single C3–N4 bond [1.329(3) and 1.331(5) Å]. Consequently, the *N*-phenyl ring is inclined to the thiosemicarbazonyl moiety [44.99(9)° in **3** and 46.97(15)° in **6**].

In **3** the two complex molecules are connected by N2–H2N···Cl1 ($2-x$, $-y$, $1-z$) hydrogen bonds, thus forming a centrosymmetrical $R_2^2(10)$ ring (Fig. 3). There is also a C6–H6···π interaction between the *N*-phenyl ring of one molecule and the salicyl ring of the other member of the centrosymmetrical dimer. Each complex molecule is also a part of a $C_1^1(6)$ chain parallel to the *a* axis formed by N4–H4N···Cl2 ($x-1/2$, $1/2-y$, $1-z$) hydrogen bonds. The salicyl ring of each molecule forms π···π interactions with the *N*-phenyl ring of the neighbouring member in the $C_1^1(6)$ chain. Additionally, the terminal oxygen atom (O1) participates in two weak C–H···O interactions (Table 4).

In **6** each acetonitrile molecule is bound to the complex molecule *via* N2–H2N···N5 and C1–H1··· N5 hydrogen bonds (Fig. 2, Table 4). Also, the acetonitrile C≡N group is involved in π···π interactions with the *N*-phenyl ring of one complex molecule and the naphthyl ring of the other, with which the acetonitrile methyl group additionally forms a C–H···π hydrogen bond. Similarly as in **3**, the complex molecules are connected into $C_1^1(6)$ chains parallel to [1 0 1] by forming N4–H4N···Cl2 ($1/2+x$, $1/2-y$, $1/2+z$) hydrogen bonds (Fig. 4). The naphthyl ring of each molecule exhibits π···π interactions with the *N*-phenyl ring of the neighbouring molecule in the $C_1^1(6)$ chain.

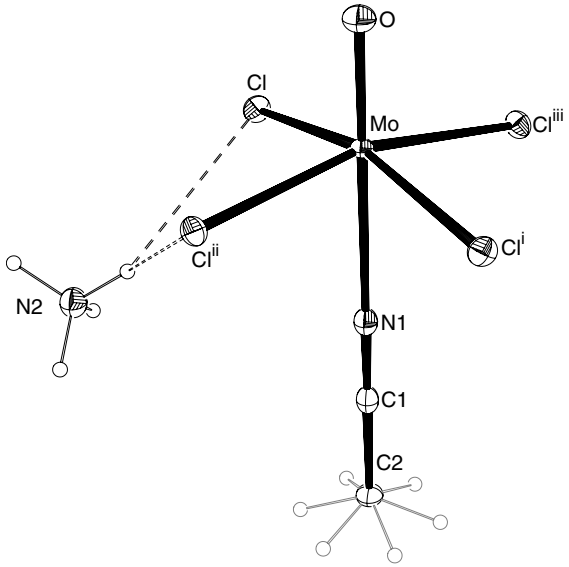


Fig. 5. The structure of $NH_4[MoOCl_4(CH_3CN)]$ (**7**) with the numbering scheme and displacement ellipsoids drawn at the 50% probability level. The methyl group is disordered between the two equally occupied sites (shown in grey). Hydrogen bonds are represented by the dashed lines. Symmetry codes: (i) $-x$, y, $z+1/2$; (ii) x, y, $-z+1/2$; (iii) $-x$, y, z.

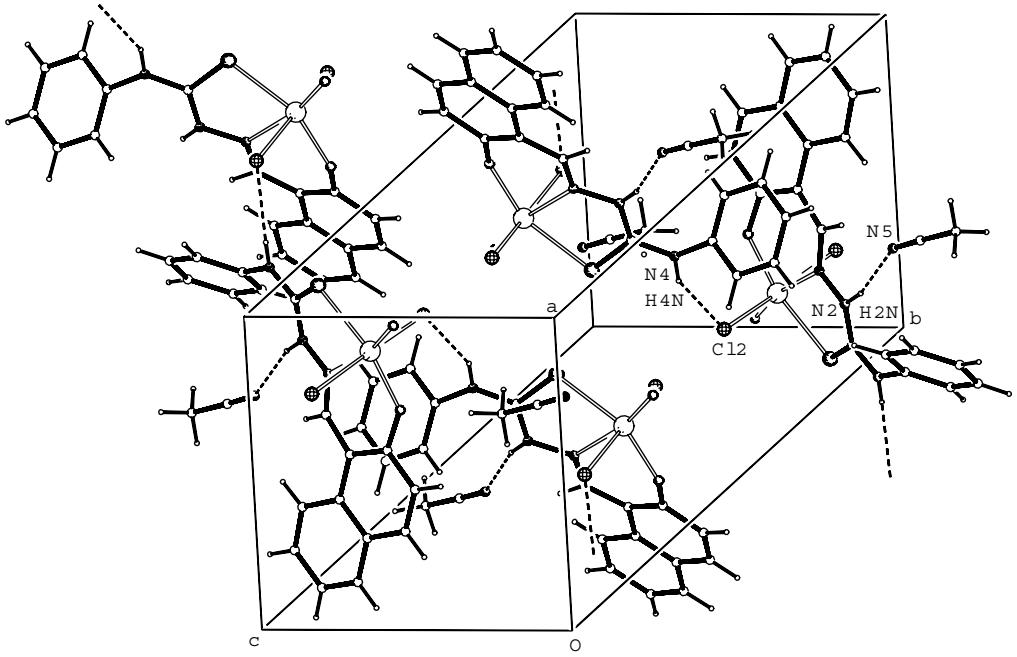


Fig. 4. The crystal packing in **6**. Each acetonitrile molecule is hydrogen-bonded to the complex molecule. Chains of the complex molecules are formed in the [1 0 1] direction.

3.3.2. Structures of $NH_4[MoOCl_4(CH_3CN)]$ (7) and $(C_5H_5NH)_2[MoOCl_5]\cdot CH_2Cl_2$ (8)

In the crystal structure of $NH_4[MoOCl_4(CH_3CN)]$ (Fig. 5) all non-hydrogen atoms lie on a twofold axis (intersection of two mirror planes), except for the chlorine atom which is in a general position. The ammonium hydrogen atoms lie in the mirror planes, while the methyl hydrogen atoms are disordered between the two equally occupied sites mutually related by the twofold axis. In the $[MoOCl_4(CH_3CN)]^-$ anion, Mo(V) is coordinated by four chloride ions, a terminal oxo group and an acetonitrile molecule, which is *trans* to the oxo group. The selected structural parameters for the $[MoOCl_4(CH_3CN)]^-$ anion are given in Table 5. Mo(V) is in a distorted octahedral environment and is displaced by 0.3697(3) Å from the plane of the four chloro ligands towards the oxo group.

Table 5
Selected bond distances (A) and angles (°) for **7**

Mo–O	1.661(3)	Cl–Mo–N1	81.06(1)
Mo–Cl	2.3789(5)	Cl–Mo–Cl^{i}	162.12(2)
Mo–N1	2.397(3)	Cl–Mo–Cl^{ii}	88.25(2)
Cl–Mo–O	98.94(1)	Cl–Mo–Cl^{iii}	88.98(2)
		O–Mo–N1	180

Symmetry codes: (i) $-x$, y, $1/2-z$; (ii) x, y, $1/2-z$; (iii) $-x$, y, z.

The bond distances Mo = O, Mo–Cl and Mo–N1 are similar to those observed in the structure of $[AlCl_2(15\text{-crown-}5)][MoOCl_4(CH_3CN)]\cdot CH_3CN$ [47] – the only other known crystal structure with the $[MoOCl_4(CH_3CN)]^-$ anion. The most striking difference between the geometries of $[MoOCl_4(CH_3CN)]^-$ anions in **7** and in $[AlCl_2(15\text{-crown-}5)][MoOCl_4(CH_3CN)]\cdot CH_3CN$ is the orientation of the bonded acetonitrile molecule: while in **7** the non-hydrogen acetonitrile atoms are in line with the Mo=O bond (as all of them lie on the twofold axis), in the latter structure an axis through the non-hydrogen atoms of the acetonitrile ligand is inclined by ~6° to the Mo=O bond.

In **7**, each NH_4^+ is connected with five $[MoOCl_4(CH_3CN)]^-$ anions (and *vice versa*) by forming a bifurcated N–H···Cl hydrogen bond with each of the four anions and a chelated N–H···O hydrogen bond with the fifth one (Table 4, Fig. 6). In addition, the methyl group of the acetonitrile ligand forms weak C–H···Cl hydrogen bonds with symmetrically related complex molecules.

The primitive orthorhombic unit cell of **8** consists of eight pyridinium cations, four $[MoOCl_5]^{2-}$ anions and four solvate CH_2Cl_2 molecules. Mo, O, Cl1, Cl3 and Cl4 atoms of $[MoOCl_5]^{2-}$ and the CH_2Cl_2 methylene group (C7 and its hydrogen atoms) lie in the mirror plane (Fig. 7). Similarly as in **7**, Mo(V) is in a distorted octahedral environ-

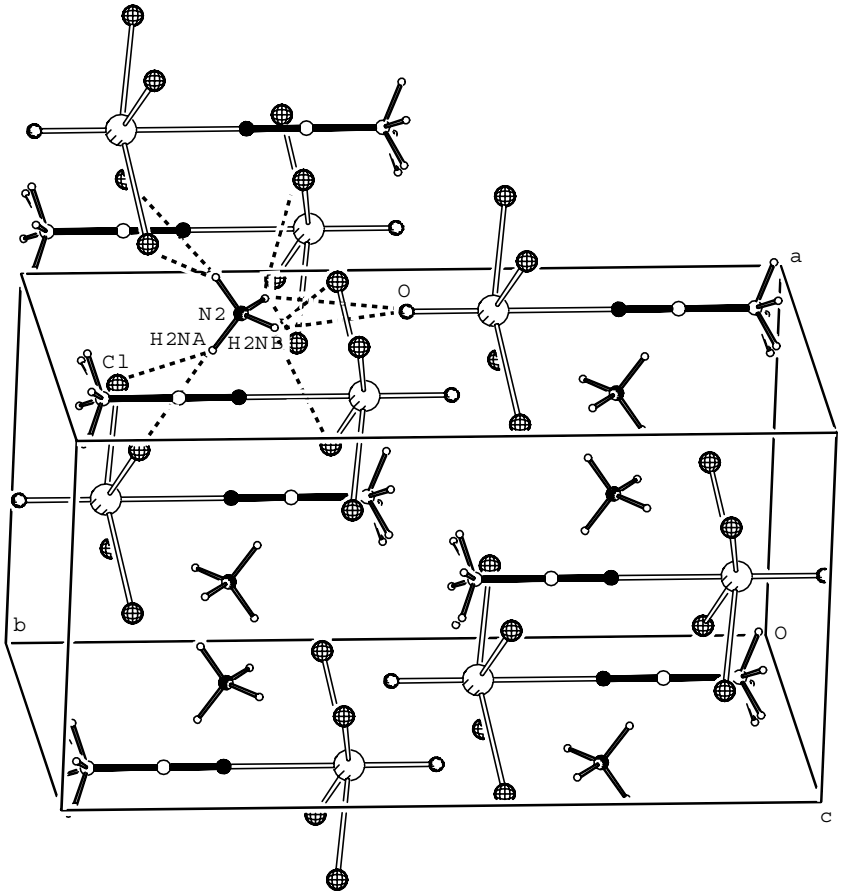


Fig. 6. The crystal packing in **7**. Each NH_4^+ cation is hydrogen-bonded to five $[MoOCl_4(CH_3CN)]^-$ anions.

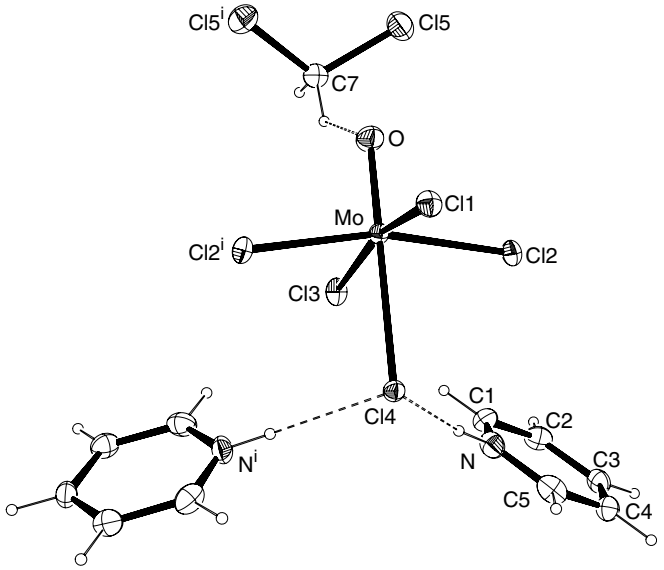


Fig. 7. The structure of $[C_5H_5NH]_2[MoOCl_5]\cdot CH_2Cl_2$ (**8**) with the numbering scheme and displacement ellipsoids drawn at the 50% probability level. Hydrogen bonds are indicated by the dashed lines. Symmetry code: (i) $x, -y+1/2, z$.

ment and is displaced by 0.2937(2) Å from the least-squares plane of four equatorial chloro ligands [Cl_{eq} = Cl1, Cl2, Cl2 ($x, -y+1/2, z$) or Cl3] towards the oxo group. The bond distances Mo = O and Mo–Cl_{eq} are similar to those found in other known structures which contain monomeric $[MoOCl_5]^{2-}$ anions [48–50]. The Mo–Cl4 bond [2.6910(6) Å] – being *trans* to the oxo group – is significantly longer than the Mo–Cl_{eq} bonds [2.3729(6)–2.4147(6) Å]. Selected geometric parameters for $[MoOCl_5]^{2-}$ are given in Table 6.

An exhaustive list of the hydrogen bonding interactions in the crystals of **8** is provided in Table 5. The axial chloro ligand (Cl4) is connected with two pyridinium cations *via* N–H···Cl hydrogen bonds (Fig. 7). These hydrogen-bonding interactions could be the reason why the Mo–Cl4 bond in the structure of **8** is longer than the corresponding bond in the other three known structures with the $[MoOCl_5]^{2-}$ anion {2.564(2) Å in $[HP(Ph)_3]_2[MoOCl_5]$ [48], 2.533(5) Å in $(PyH)_{10}[(Mo_2O_4Cl_4)_2(\mu_4\text{-hda})][MoOCl_5]Cl_2$ ($hda^{2-} = {}^{-}OOC(CH_2)_5COO^{-}$) [49], 2.5569(10) Å and 2.5790(9) Å in $[N(CH_3)_4]_2[MoOCl_5]\cdot CH_3CN$ [50]}. Namely, the chlorine atom *trans* to the oxo group in both $[HP(Ph)_3]_2[MoOCl_5]$ and $(PyH)_{10}[(Mo_2O_4Cl_4)_2(\mu_4\text{-hda})][MoOCl_5]Cl_2$ is involved in hydrogen-bonding interactions, but these are weaker than those in **8**. Additionally, each pyridinium cation forms three weak C–H···Cl interactions with the $[MoOCl_5]^{2-}$ anions. The co-crystallized CH_2Cl_2 molecules are bound to $[MoOCl_5]^{2-}$ anions by weak C–H···O and C–H···Cl hydrogen bonds. The presence of only these weak interactions between the solvent CH_2Cl_2 molecules and the other components of the crystal is the main reason why CH_2Cl_2 readily leaves the crystals of **8** and thus they rapidly disintegrate outside the mother liquor. The crystal packing of **8** is shown in Fig. 8.

Table 6
Selected bond distances (Å) and angles (°) for **8**

Mo–O	1.664(2)	Cl1–Mo–O	96.72(7)
Mo–C11	2.3729(6)	C12–Mo–$C12^{i}$	165.29(2)
Mo–C12	2.3810(5)	C12–Mo–C13	88.15(1)
Mo–C13	2.4147(6)	C12–Mo–C14	82.71(1)
Mo–C14	2.6910(6)	C12–Mo–O	97.29(1)
Cl1–Mo–C12	90.12(1)	C13–Mo–C14	83.07(2)
Cl1–Mo–C13	166.31(2)	C13–Mo–O	96.97(7)
Cl1–Mo–C14	83.24(2)	C14–Mo–O	179.96(6)

Symmetry code: (i) $x, 1/2-z$.

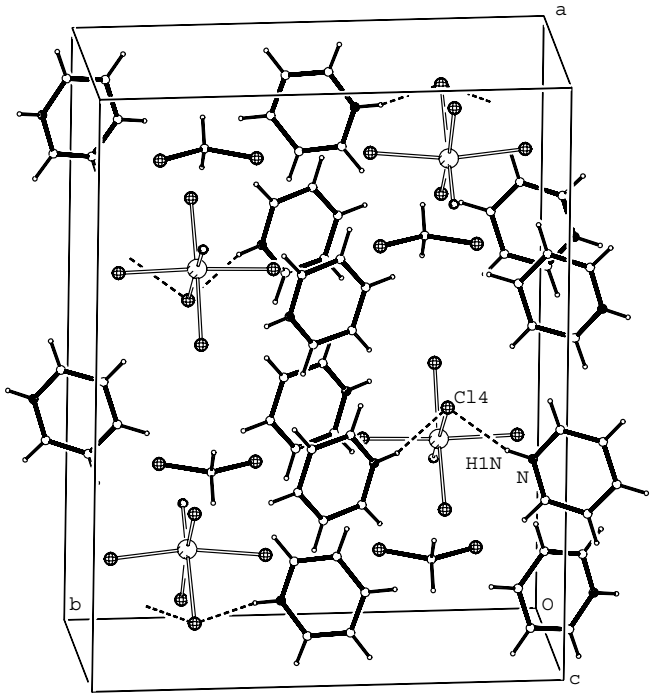


Fig. 8. The crystal packing in **8**. Each $[MoOCl_5]^{2-}$ anion is hydrogen-bonded to two $C_5H_5NH^{+}$ cations.

4. Conclusion

In this study it was shown that the thiosemicarbazones, {$C_6H_4(O)CH{:}NNHC{:}SNHR'$ or $C_{10}H_6(O)CH{:}NNHC{:}SNHR'$; R′ = H, CH_3, C_6H_5}, coordinate molybdenum(V) as monomeric tridentate ligands. The complexes **1**–**6** could not be obtained if $[C_5H_5NH]_2[MoOCl_5]$ was used instead of $[NH_4]_2[MoOCl_5]$ as the reaction precursor. One of the reasons could be the different solubility of the by-product chloride salts, ammonium chloride and pyridinium chloride, in acetonitrile. The formed ammonium chloride crystals can act as the driving force for removal of the chloro ligands from the $[MoOCl_4(CH_3CN)]^{-}$ intermediate and the subsequent formation of the mononuclear Mo(V) thiosemicarbazonato complexes. Isolation and characterization of complexes **7** and **8** suggests the presence of different oxohalomolybdate anions in acetonitrile solution, e.g. $[MoOCl_4(CH_3CN)]^{-}$ or $[MoOCl_5]^{2-}$.

Supplementary material

CCDC 625748, 625749, 625750 and 625751 contain the supplementary crystallographic data for **7**, **8**, **3** and **6**. These data can be obtained free of charge via http://www.ccdc.cam.ac.uk/conts/retrieving.html, or from the Cambridge Crystallographic Data Centre, 12 Union Road, Cambridge CB2 1EZ, UK; fax: (+44) 1223-336-033; or e-mail: deposit@ccdc.cam.ac.uk.

Acknowledgements

We thank Professor Boris Kamenar for useful discussions. This research was supported by the Ministry of Science, Education and Sports of the Republic of Croatia (Grants No. 119-1191342-1082, 119-1193079-1084 and 119-1103079-3069).

References

[1] R.R. Mendel, J. Chem. Soc., Dalton Trans. (2005) 3404.
[2] K.H. Thompson, J.H. McNeill, C. Orving, Chem. Rev. 99 (1999) 2561.
[3] Z. Afrasiabi, E. Sinn, J. Chen, Y. Ma, A.L. Rheingold, L.N. Zakharov, N. Rath, S. Padhye, Inorg. Chim. Acta 357 (2004) 271.
[4] S.K. Dutta, D.B. McConville, W.J. Youngs, M. Chaudhury, Inorg. Chem. 36 (1997) 2517.
[5] J.U. Mondal, J.G. Zamora, M.D. Kinon, F.A. Schiltz, Inorg. Chim. Acta 309 (2000) 147.
[6] R. Hahn, U. Küsthardt, W. Scherer, Inorg. Chim. Acta 210 (1993) 177.
[7] L.J. Laughlin, C.G. Young, Inorg. Chem. 35 (1996) 1050.
[8] P. Verma, K.K. Arya, S. Ahmad, J. Indian Chem. Soc. 83 (2006) 327.
[9] U.N. Shetti, V.K. Revankar, V.B. Marale, Proc. Indian Acad. Sci.: Chem. Sci. 109 (1997) 7.
[10] R.G. James, W. Wardlaw, J. Chem. Soc. (1927) 2145.
[11] G.R. Hanson, A.A. Brunette, A.C. McDonell, K.S. Murray, A.G. Wedd, J. Am. Chem. Soc. 103 (1981) 1953.
[12] S. Purohit, A.P. Koley, L.S. Prasad, P.T. Manoharan, S. Ghosh, Inorg. Chem. 28 (1989) 3735.
[13] G.A. Parker, Analytical Chemistry of Molybdenum, Springer-Verlag, New York, 1983.
[14] W.W. Scott, Standard Methods of Chemical Analysis, fifth ed., vol. 269, D. Van Nostrand Co. Inc, New York, 1961.
[15] Oxford Diffraction, Xcalibur CCD system, CRYSALIS Software system, Version 1.170, Oxford Diffraction Ltd., 2003.
[16] L.J. Farrugia, J. Appl. Crystallogr. 32 (1999) 837.
[17] G.M. Sheldrick, SHELXS97, Program for the Solution of Crystal Structures, University of Göttingen, Germany, 1997.
[18] G.M. Sheldrick, SHELXL-97, Program for the Refinement of Crystal Structures, University of Göttingen, Germany, 1997.
[19] A.L. Spek, J. Appl. Crystallogr. 36 (2003) 7.
[20] L.J. Farrugia, J. Appl. Crystallogr. 30 (1997) 565.
[21] R.A. Lal, A. Kumar, J. Chakraborty, S. Bhaumik, Trans. Metal Chem. 26 (2001) 557.
[22] J. Beck, M. Hengstmann, Z. Anorg. Allg. Chem. 624 (1998) 1943.
[23] F. Weller, U. Muller, D. Weiher, K. Dehnicke, Z. Anorg. Allg. Chem. 460 (1980) 191.
[24] B. Modec, J.V. Brenčić, Eur. J. Inorg. Chem. (2005) 1698.
[25] R.G. James, W. Wardlaw, J. Chem. Soc. (London) (1927) 2146.
[26] E.A. Allen, B.J. Brisdon, D.A. Edwards, G.W.A. Fowles, R.G. Williams, J. Chem. Soc. (1963) 4649.
[27] Y. Sasaki, A.G. Sykes, J. Chem. Soc., Dalton Trans. (1974) 1468.
[28] Y. Sasaki, R.S. Taylor, A.G. Sykes, J. Chem. Soc., Dalton Trans. (1975) 396.
[29] V. Vrdoljak, M. Cindrić, D. Milić, D. Matković-Čalogović, P. Novak, B. Kamenar, Polyhedron 24 (2005) 1717.
[30] M. Cindrić, N. Strukan, V. Vrdoljak, T. Kajfež, B. Kamenar, Z. Anorg. Allg. Chem. 628 (2002) 2113.
[31] K. Yamanouchi, S. Yamada, J.H. Enemark, Inorg. Chim. Acta 85 (1984) 129.
[32] B. Fischer, H. Schmalle, E. Dubler, A. Schafer, M. Viscontini, Inorg. Chem. 34 (1995) 5726.
[33] F.R. Fronczek, R.L. Luck, G. Wang, Inorg. Chem. Commun. 5 (2002) 384.
[34] C. Bustos, O. Burckhardt, R. Schrebler, D. Carrillo, A.M. Arif, A.H. Cowley, C.M. Nunn, Inorg. Chem. 29 (1990) 3996.
[35] G. Argay, A. Kálmán, V.M. Leovac, V.I. Češljević, B. Ribár, J. Coord. Chem. 37 (1996) 165.
[36] S.K. Dutta, D.B. McConville, W.J. Youngs, M. Chaudhury, Inorg. Chem. 36 (1997) 2517.
[37] A. Rana, R. Dinda, P. Sengupta, S. Ghosh, L.R. Falvello, Polyhedron 21 (2002) 1023.
[38] V. Vrdoljak, M. Cindrić, D. Matković-Čalogović, B. Prugovečki, P. Novak, B. Kamenar, Z. Anorg. Allg. Chem. 631 (2005) 928.
[39] M. Cindrić, V. Vrdoljak, N. Strukan, B. Kamenar, Polyhedron 24 (2005) 369.
[40] M. Soriano-García, J. Valdés-Martínez, R.A. Toscano, J. Gómez-Lara, M. Villalobos-Peñaloza, Acta Crystallogr., Sect. C 42 (1986) 623.
[41] D. Chatoapadhyay, S.K. Mazumdar, T. Banerjee, S. Gosh, T.C.W. Mak, Acta Crystallogr., Sect. C 44 (1988) 1025.
[42] M. Soriano-García, J. Valdés-Martínez, R.A. Toscano, Acta Crystallogr., Sect. C 44 (1988) 1247.
[43] J. Valdés-Martínez, M. Rubio, R. Cetina Rosado, J. Salcedo-Loaiza, R.A. Toscano, G. Espinosa-Pérez, S. Hernandez-Ortega, K. Ebert, J. Chem. Cryst. 27 (1997) 627.
[44] D. Kovala-Demertzi, N. Kourkoumelis, M.A. Demertzis, J.R. Miller, C.S. Frampton, J.K. Swearingen, D.X. West, Eur. J. Inorg. Chem. 2000 (2000) 727.
[45] S. Selvanayagam, M. Yogavel, V. Rajakannan, D. Velmurugan, S.S.S. Raj, H.-K. Fun, Acta Crystallogr., Sect. E 58 (2002) o1336.
[46] P.V. Bernhardt, L.M. Caldwell, D.B. Lovejoy, D. Richardson, Acta Crystallogr., Sect. C 59 (2003) o629.
[47] B.M. Bulychev, V.K. Bel'skii, N.R. Strel'tsova, Zh. Neorg. Khim. (Russ.) (Russ. J. Inorg. Chem.) 38 (1993) 72.
[48] P.C. Junk, J.L. Atwood, J. Coord. Chem. 46 (1999) 505.
[49] B. Modec, J.V. Brenčič, Eur. J. Inorg. Chem. 2005 (2005) 4325.
[50] S.A. Seyedsadjadi, S. Ghammamy, G. Rezaeibehbahani, Cryst. Res. Technol. 40 (2005) 727.

Available online at www.sciencedirect.com
ScienceDirect
Polyhedron 26 (2007) 3373–3378
POLYHEDRON
www.elsevier.com/locate/poly

Synthesis and characterizations of 3,3′-bis(diphenylphosphinoamine)-2,2′-bipyridine and 3,3′-bis(diphenylphosphinite)-2,2′-bipyridine and their chalcogenides

Akın Baysal [a,*], Murat Aydemir [a], Feyyaz Durap [a], Bahattin Gümgüm [a], Saim Özkar [b], Leyla Tatar Yıldırım [c]

[a] Dicle University, Department of Chemistry, 21280 Diyarbakir, Turkey
[b] Middle East Technical University, Department of Chemistry, 06531 Ankara, Turkey
[c] Hacettepe University, Department of Engineering Physics, Beytepe, 06800 Ankara, Turkey

Received 24 January 2007; accepted 9 March 2007
Available online 27 March 2007

Abstract

New bis(phosphinoamine) and bis(phosphinite) derivatives of 2,2′-bipyridine were prepared through a single step reaction of 3,3′-diamino-2,2′-bipyridine or 3,3′-dihydroxy-2,2′-bipyridine with diphenylchlorophosphine, respectively. Their P = E chalcogenides (E = O, S, Se) were also prepared. All the new compounds were characterized by elemental analysis, IR and NMR spectroscopies. The molecular structure of 3,3′-bis(diphenylthiophosphinite)-2,2′-bipyridine was elucidated by single-crystal X-ray crystallography.
© 2007 Elsevier Ltd. All rights reserved.

Keywords: Aminophosphine; Phosphinite; Diphenylchlorophosphine; X-ray diffraction; 3,3′-Bis(diphenylthiophosphinite)-2,2′-bipyridine; NMR

1. Introduction

The chemistry of aminophosphines and phosphinites has been intensively explored in recent years [1] and they have been the subject of review papers [2]. These compounds are extremely attractive as potential ligands since various structural modifications are accessible via simple P–N and P–O bond formation [3]. Many modified phosphine ligands and a variety of chiral aminophosphine–phosphinite ligands have important applications in organometallic chemistry and catalysis, giving selective catalysts for hydroformylation, hydrosilylation and asymmetric transfer hydrogenation [2c,4–6]. As the pyridylphosphine and pyridylaminophosphine derivatives can act as bidentate ligands containing both hard (nitrogen) and soft (phosphorus) donor atoms [7], their coordination chemistry has been extensively studied [8]. The catalytic activity of complexes containing phosphinopyridyl ligands has received much attention and these complexes have recently been employed as catalysts for the hydrogenation of ketones, asymmetric transfer hydrosilylation, asymmetric hydroboration, allylic substitution and carbonylation [2b,9]. While much effort has been devoted to the synthesis of chelating bis(phosphines) and their transition metal complexes, similar studies on the analogous bis(phosphinites) are less extensive [10], even though some of their complexes have proved to be efficient catalysts [11].

Herein we report the synthesis of new 3,3′-bis(diphenylphosphinoamine)-2,2′-bipyridine and 3,3′-bis(diphenylphosphinite)-2,2′-bipyridine compounds through a single step reaction of 3,3′-diamino-2,2′-bipyridine and 3,3′-dihydroxy-2,2′-bipyridine with diphenylchlorophosphine, respectively. These compounds could be isolated from the reaction solution and characterized by elemental analysis, IR and NMR spectroscopies. Furthermore, we

* Corresponding author. Tel.: +90 412 2488550; fax: +90 412 2488039.
E-mail address: akinb@dicle.edu.tr (A. Baysal).

0277-5387/$ - see front matter © 2007 Elsevier Ltd. All rights reserved.
doi:10.1016/j.poly.2007.03.027

report the crystal and molecular structure of one of the products, 3,3′-bis(diphenylthiophosphinite)-2,2′-bipyridine, $(Ph_2P(S)O)_2–C_{10}H_6N_2$, elucidated by single crystal X-ray diffraction.

2. Experimental

2.1. General remarks

All reactions and manipulations were performed under an atmosphere of dry nitrogen or argon using standard Schlenk techniques unless otherwise stated. Ph_2PCl, 2-chloro-3-nitropyridine and 2-bromo-3-hydroxypyridine were purchased from Fluka and were used as received. The starting materials 3,3′-diamino-2,2′-bipyridine [12] and 3,3′-dihydroxy-2,2′-bipyridine [13] were prepared according to previously reported procedures. Solvents were dried and distilled by standard methods prior to use. Spectra were recorded on the following instruments: NMR, Bruker Avance 400 (162.0 MHz for ^{31}P, 400.1 MHz for ^{1}H and 100.6 MHz for ^{13}C); Elemental analysis, Fisons Model EA 1108; IR, Mattson UNICAM-FTIR Model 1000 spectrometer; Melting points, Gallenkamp Model apparatus with open capilleries.

2.2. 3,3′-Bis(diphenylphosphinoamine)-2,2′-bipyridine, $(Ph_2PNH)_2–C_{10}H_6N_2$ (**1**)

Ph_2PC1 (0.59 g, 2.68 mmol) was added slowly to a solution of 3,3′-diamino-2,2′-bipyridine (0.25 g, 1.34 mmol) and Et_3N (0.29 g, 2.87 mmol) in CH_2C1_2 (45 mL) at 0 °C. The resulting yellow solution was stirred for 2 h, and the solvent was removed under reduced pressure. The residue was washed with THF and precipitated triethylamine hydrochloride was removed by filtration through a sintered Schlenk tube. THF was removed under reduced pressure, the product was washed with diethyl ether (2×20 mL) and then dried in vacuo to give a yellow solid. Yield 0.45 g, 61%. m.p. 141–143 °C; *Anal.* Calc. for $C_{34}H_{28}N_4P_2$: C, 73.65; H, 5.05; N, 10.11. Found: C, 73.40; H, 4.83; N, 10.02%. ^{1}H NMR (δ in ppm rel. to TMS, J Hz, in $CDCl_3$): 7.82 (m, H-4 and H-6, 4H), 7.57 (m, H-10, 8H), 7.36 (m, H-11 and H-12, 12H), 7.10 (dd, H-5, 2H, J 4.8 and 7.6); ^{13}C NMR (δ in ppm rel. to TMS in $CDCl_3$): 148.62 (C-3), 139.30 (C-6), 132.80 (C-12), 132.05 (C-11), 131.40 (C-9), 128.80 (C-10), 128.50 (C-12), 127.30 (C-4), 122.80 (C-5); ^{31}P NMR (δ in ppm rel. to H_3PO_4 in $CDCl_3$): 26.8 (s). Selected IR (KBr pellet in cm^{-1}): υ(N–H) 3150, υ(CN) 1561, υ(P–N) 913, υ(P–Ph) 1434.

2.3. 3,3′-Bis(diphenyloxophosphinoamine)-2,2′-bipyridine, $(Ph_2P(O)NH)_2–C_{10}H_6N_2$ (**1a**)

A THF solution (15 mL) of **1** (0.05 g, 0.09 mmol) and aqueous H_2O_2 (30% w/w, 0,018 mL) was stirred for 2 h at room temperature. The solution was filtered through Celite to remove a small amount of insoluble material. The filtrate was concentrated in vacuo to ca. 1–2 mL and addition of *n*-hexane (10 mL) gave **1a** as a bright yellow solid which was collected by suction filtration. Yield 0.038 g, 72%. m.p. 197–199 °C; *Anal.* Calc. for $C_{34}H_{28}N_4O_2P_2$: C, 69.62; H, 4.78; N, 9.55. Found: C, 69.48; H, 4.59; N, 9.42%. ^{1}H NMR (δ in ppm rel. to TMS, J Hz, in $CDCl_3$): 7.94 (m, H-10, 8H), 7.80 (m, H-6 and H-4, 4H), 7.56 (m, H-11 and H-12, 12H), 7.05 (dd, H-5, 2H, J 4.4 and 8.2); ^{13}C NMR (δ in ppm rel. to TMS in $CDCl_3$): 140.20 (C-3), 137.38 (C-6), 132.91 (C-2), 132.21 (C-11), 131.60 (C-9), 128.85 (C-10), 128.36 (C-12), 127.33 (C-4), 123.68 (C-5); ^{31}P NMR (δ in ppm rel. to H_3PO_4 in $CDCl_3$): 18.0 (s). Selected IR (KBr pellet, in cm^{-1}): υ(N–H) 3209, υ(CN) 1562, υ(P–N) 947, υ(P–Ph) 1437, υ(P═O) 1198.

2.4. 3,3′-Bis(diphenylthiophosphinoamine)-2,2′-bipyridine, $(Ph_2P(S)NH)_2–C_{10}H_6N_2$ (**1b**)

To a solution of **1** (0.05 g, 0.09 mmol) in THF (20 mL), S_8 (0.006 g, 0.18 mmol) was added and this mixture was refluxed for 6 h. The solution was filtered through Celite while hot to remove a small amount of insoluble material. The filtrate was concentrated in vacuo to ca. 1–2 mL and addition of *n*-hexane (10 mL) gave **1b** as a dark yellow solid which was collected by suction filtration. Yield 0.043 g, 77%. m.p. 251–253 °C; *Anal.* Calc. for $C_{34}H_{28}N_4S_2P_2$: C, 66.02; H, 4.53; N, 9.06; S, 10.36. Found: C, 65.88; H, 4.30; N, 8.91; S, 10.16%. ^{1}H NMR (δ in ppm rel. to TMS, J Hz, in $CDCl_3$): 8.07 (m, H-10, 8H), 7.77 (d, H-6, 2H, J 7.6), 7.67 (d, H-4, 2H, J 4.0), 7.53 (m, H-11 and H-12, 12H), 7.03 (dd, H-5, 2H, J 4.4 and 8.0); ^{13}C NMR (δ in ppm rel. to TMS in $CDCl_3$): 140.12 (C-3), 137.12 (C-6), 132.70 (C-2), 131.94 (C-11), 131.49 (C-9), 128.75 (C-10), 128.12 (C-12), 127.10 (C-4), 123.18 (C-5); ^{31}P NMR(δ in ppm rel. to H_3PO_4 in $CDCl_3$): 49.3 (s). Selected IR (KBr pellet, in cm^{-1}): υ(N–H) 3036, υ(CN) 1551, υ(P–N) 944, υ(P–Ph) 1439, υ(P═S) 649.

2.5. 3,3′-Bis(diphenylselenophosphinoamine)-2,2′-bipyridine $(Ph_2P(Se)NH)_2–C_{10}H_6N_2$ (**1c**)

Grey Se (0.014 g, 0.18 mmol) was added to a solution of **1** (0.05 g, 0.09 mmol) in THF (20 mL) and this mixture was refluxed for 6 h. The solution was filtered through Celite while hot to remove a small amount of insoluble material. The filtrate was concentrated in vacuo to ca. 1–2 mL and addition of *n*-hexane (10 mL) gave **1c** as a white solid which was collected by suction filtration. Yield 0.052 g, 81%. m.p. 233–235 °C; *Anal.* Calc. for $C_{34}H_{28}N_4Se_2P_2$: C, 57.30; H, 3.93; N, 7.87. Found: C, 57.11; H, 3.70; N, 7.64%. ^{1}H NMR (δ in ppm rel. to TMS, J Hz, in $CDCl_3$): 8.08 (m, H-10, 8H), 7.78 (d, H-6, 2H, J 8.2), 7.67 (d, H-4, 2H, J 4.0), 7.53 (m, H-11 and H-12, 12H), 7.06 (dd, H-5, 2H, J 4.4 and 7.2); ^{13}C NMR (δ in ppm rel. to TMS in $CDCl_3$): 140.20 (C-3), 136.82 (C-6), 132.71 (C-2), 131.83 (C-11), 131.40 (C-9), 128.62 (C-10), 128.09 (C-12), 127.20 (C-4), 123.22 (C-5); ^{31}P NMR (δ in ppm rel. to H_3PO_4 in

$CDCl_3$): 43.5 (s), $J(^{31}P–^{77}Se) = 756$ Hz. Selected IR (KBr pellet, in cm^{-1}): υ(N–H) 3147, υ(CN) 1551, υ(P–N) 945, υ(P–Ph) 1440, υ(P=Se) 547.

2.6. 3, 3′-Bis(diphenylphosphinite)-2,2′-bipyridine, $(Ph_2PO)_2–C_{10}H_6N_2$ (2)

Ph_2PC1 (0.53 g, 2.66 mmol) was added slowly to a solution of 3,3′-bis(dihydroxy)-2,2′-bipyridine (0.25 g, 1.33 mmol) and Et_3N (0.27 g, 2.67 mmol) in toluene (45 mL) at 0 °C. The resulting white suspension was stirred for 2 h after which time it was filtered through a sintered Schlenk tube to remove precipitated triethylamine hydrochloride. The filtrate was taken to dryness under reduced pressure, leaving a viscous material. The product was washed with diethyl ether (2 × 20 mL) and then dried in vacuo to give **2** as a white viscous material. Yield 0.51 g, 69%. *Anal.* Calc. for $C_{34}H_{26}N_2O_2P_2$: C, 73.38; H, 4.68; N, 5.04. Found: C, 73.21; H, 4.61; N, 4.92%. ^1H NMR (δ in ppm rel. to TMS, J Hz, in $CDCl_3$): 8.40 (d, H-6, 2H, J 4.2), 8.07 (dd, H-4, 2H, J 1.1 and 8.2), 7.77 (m, H-11, 8H), 7.61 (m, H-12, 4H), 7.43 (m, H-10, 8H), 7.26 (dd, H-5, 2H, J 4.6 and 8.7); ^{13}C NMR (δ in ppm rel. to TMS in $CDCl_3$):149.10 (C-3), 146.71 (C-9), 144.74 (C-6), 133.90 (C-2), 132.83 (C-4), 132.11 (C-12), 130.90 (C-11), 128,32 (C-10), 123.51 (C-5); ^{31}P NMR (δ in ppm rel. to H_3PO_4 in $CDCl_3$): 116.3 (s). Selected IR (KBr pellet, in cm^{-1}): υ(CN) 1573, υ(P–O) 952, υ(P–Ph) 1445.

2.7. 3,3′-Bis(diphenyloxophosphinite)-2,2′-bipyridine, $(Ph_2P(O)O)_2–C_{10}H_6N_2$ (2a)

A toluene solution (15 mL) of **2** (0.4 g, 0.72 mmol) and aqueous H_2O_2 (30% w/w, 0.18 mL) was stirred for 2 h at room temperature. The solution was filtered through Celite to remove a small amount of insoluble material. The filtrate was concentrated in vacuo to ca. 1–2 mL and addition of *n*-hexane (10 mL) gave **2a** as a white solid which was collected by suction filtration. Yield 0.31 g, 74%. m.p. 125–128 °C; *Anal.* Calc. for $C_{34}H_{26}N_2O_4P_2$: C, 69.39; H, 4.42; N, 4.76. Found: C, 69.18; H, 4.23; N, 4.54%. ^1H NMR (δ in ppm rel. to TMS, J Hz, in $CDCl_3$): 8.69 (d, H-6, 2H, J 4.3), 8.07 (dd, H-4, 2H, J 1.1 and 8.2), 7.73 (m, H-10, 8H), 7.58 (m, H-12, 4H), 7.45 (m, H-10, 8H), 7.30 (dd, H-5, 2H, J 4.8 and 8.4); ^{13}C NMR (δ in ppm rel. to TMS in $CDCl_3$):156.21 (C-3), 139.90 (C-9), 135.93 (C-6), 132.62 (C-2), 131.91 (C-4), 130.74 (C-12), 128.80 (C-11), 125.92 (C-10), 124.90 (C-5); ^{31}P NMR (δ in ppm rel. to H_3PO_4 in $CDCl_3$): 22.8 (s). Selected IR (KBr pellet, in cm^{-1}): υ(CN) 1574, υ(P–O) 951, υ(P–Ph) 1445, υ(P=O) 1195.

2.8. 3,3′-Bis(diphenylthiophosphinite)-2,2′-bipyridine, $(Ph_2P(S)O)_2–C_{10}H_6N_2$ (2b)

To a solution of **2** (0.4 g, 0.72 mmol) in toluene (20 mL), S_8 (0.046 g, 1.44 mmol) was added and this mixture was refluxed under argon atmosphere for 6 h. The solution was filtered through Celite while hot to remove a small amount of insoluble material. The filtrate was concentrated in vacuo to ca. 1–2 mL and addition of *n*-hexane (10 mL) gave **2b** as a dark yellow solid which was collected by suction filtration. Yield 0.34 g, 76%. m.p. 155–157 °C; *Anal.* Calc. for $C_{34}H_{26}N_2O_2S_2P_2$: C, 65.81; H, 4.19; N, 4.52; S, 10.32. Found: C, 65.63; H, 4.08; N, 4.36; S, 10.17%. ^1H NMR (δ in ppm rel. to TMS, J Hz, in $CDCl_3$): 8.40 (d, H-6, 2H, J 4.4), 7.83 (dd, H-4, 2H, J 1.2 and 8.4), 7.71 (m, H-11, 8H), 7.42 (m, H-12, 4H), 7.30 (m, H-10, 8H), 7.22 (dd, H-5, 2H, J 4.4 and 8.4); ^{13}C NMR (δ in ppm rel. to TMS in $CDCl_3$):148.35 (C-3), 146.50 (C-9), 145.05 (C-6), 134.02 (C-2), 133.10 (C-4), 132.05 (C-12), 131.27 (C-11), 128.40 (C-10), 123.68 (C-5); ^{31}P NMR (δ in ppm rel. to H_3PO_4 in $CDCl_3$): 82.8 (s). Selected IR (KBr pellet, cm^{-1}): υ(CN) 1580, υ(P–O) 913, υ(P–Ph) 1445, υ(P=S) 649.

2.9. 3,3′-Bis(diphenylselenophosphinite)-2,2′-bipyridine, $(Ph_2P(Se)O_2)–C_{10}H_6N_2$ (2c)

Grey Se (0.12 g, 1.52 mmol) was added to a solution of **2** (0.4 g, 0.72 mmol) in toluene (20 mL) and this mixture was refluxed under argon atmosphere for 6 h. The solution was filtered through Celite while hot to remove a small amount of insoluble material. The filtrate was concentrated in vacuo to ca. 1–2 mL and addition of *n*-hexane (10 mL) gave **2c** as a white solid which was collected by suction filtration. Yield 0.36 g, 72%. m.p. 134–136 °C. *Anal.* Calc. for $C_{34}H_{26}N_2O_2Se_2P_2$: C, 57.14; H, 3.64; N, 3.92. Found: C, 56.96; H, 3.54; N, 3.86%. ^1H NMR (δ in ppm rel. to TMS, J Hz, in $CDCl_3$): 8.42 (d, H-6, 2H, J 4.3), 8.08 (dd, H-4, 2H, J 1.1 and 8.1), 7.75 (m, H-11, 8H), 7.43 (m, H-12, 4H), 7.30 (m, H-10, 8H), 7.28 (dd, H-5, 2H, J 4.4 and 8.4); ^{13}C NMR (δ in ppm rel. to TMS in $CDCl_3$):157.20 (C-3), 144.43 (C-9), 134.32 (C-6), 133.31 (C-2), 132.20 (C-4), 131.43 (C-12), 130.74 (C-11), 128.21 (C-10), 124.16 (C-5); ^{31}P NMR (δ in ppm rel. to H_3PO_4 in $CDCl_3$): 86.0 (s), $J(^{31}P–^{77}Se) = 782$ Hz. Selected IR (KBr pellet, in cm^{-1}): υ(CN) 1573, υ(P–O) 887, υ(P–Ph) 1440, υ(P=Se) 547.

3. X-ray diffraction structure analysis

To determine the crystal structure of 3,3′-bis(diphenylthiophosphinite)-2,2′-bipyridine (**2b**), X-ray diffraction data were collected at room temperature with graphite monochromated Cu Kα radiation on an Enraf-Nonius CAD4 diffractometer operating in the $\omega/2\theta$ scan mode. The lattice parameters and their estimated standard deviations were determined from a least-squares refinement of 17 centered reflections in the range of $12.71 \leqslant \theta \leqslant 42.34°$ by using CAD4 Express [14]. Data reduction was carried out using XCAD4 [15]. The structure was solved by the direct method and refined by the full-matrix least-square technique using the programs SHELXS97 and SHELXL97, respectively [16].

Table 1
Crystal data and results of the structure refinement for **2b**

Formula	$[C_{17}H_{13}NOPS]_2$
Formula weight (g/mol)	620.63
Temperature (K)	293(2)
Wavelength (Å)	1.54184
Crystal system, space group	triclinic, $P\bar{1}$
Unit cell dimensions	
a (Å)	9.490(1)
b (Å)	13.031(2)
c (Å)	14.501(5)
α (°)	114.13(2)
β (°)	91.58(2)
γ (°)	106.36(1)
Cell volume (Å^3)/Z	1549.3(6)/2
Calculated density (g/cm^3)	1.33
Crystal colour/shape/size (mm)	colourless/prism/0.3 × 0.3 × 0.2
$F(000)$	644
Absorption coefficient (mm^{-1})	2.805
Absorption correction type	psi-scan
T_{max}/T_{min}	0.571/0.496
θ Range for data collection (°)	3.38–74.24
Limiting indices	$-11 \leqslant h \leqslant 11$, $-16 \leqslant k \leqslant 14$, $0 \leqslant l \leqslant 18$
Reflections collected/Unique	6085/5854 ($R_{int} = 0.0504$)
Refinement method	full-matrix least-squares on F^2
Data/parameters	5854/379
Goodness-of-fit on F^2	1.009
Final R indices ($I > 2\sigma(I)$)	$R_1 = 0.0847$, $wR_2 = 0.2159$
Largest differences in peak and hole (e/Å^3)	0.78, −0.35

Additional material available from the Cambridge Crystallographic Data Center as deposition No.: CCDC 634701 comprises H-atom coordinates, thermal parameters, and remaining bond lengths and angles.

For all non-hydrogen atoms anisotropic displacement parameters were refined and all hydrogen atoms were placed geometrically with $U_{iso}(H) = 1.2\ U_{eq}(C)$. Results of the X-ray structure determination are presented in Tables 1–3 and Figs. 1 and 2.

4. Results and discussion

The reaction of 3,3′-diamino-2,2′-bipyridine with two equivalents of diphenylchlorophosphine in the presence of triethylamine in dichloromethane affords 3,3′-bis(diphenylphosphinoamine)-2,2′-bipyridine, $(Ph_2PNH)_2$-$C_{10}H_6N_2$ (**1**), in moderate yield (Scheme 1), which was isolated from the solution as an analytically pure yellow solid. The IR spectrum of **1** shows characteristic bands at 3150, 1561, 1434 and 913 cm^{-1} due to υ(N–H), υ(CN), υ(P–Ph) and υ(P–N) stretchings, respectively. The ^{31}P–{^1H} NMR spectrum of **1** shows a single resonance at 26.8 ppm, indicating that the two phosphorus atoms in the molecule are equivalent. Treatment of **1** with H_2O_2 solution in THF affords the oxo-derivative, $(Ph_2P(O)NH)_2$–$C_{10}H_6N_2$, (**1a**). The ^{31}P NMR spectrum of **1a** shows also a singlet at 18.0 ppm, which is shielded by 8.8 ppm compared to the parent compound **1**. The reaction of **1** with two equivalents of sulfur or selenium in THF under refluxing conditions yields the corresponding sulfur, $(Ph_2P(S)NH)_2$–$C_{10}H_6N_2$ (**1b**), and selenide analogues, $(Ph_2P(Se)NH)_2$–$C_{10}H_6N_2$ (**1c**), respectively (Scheme 1). The ^{31}P NMR spectrum of **1b** shows a single resonance at 49.3 ppm. The ^{31}P NMR signal of **1c** shows a singlet at 43.5 ppm with selenium satellites, $^1J(^{31}P$–$^{77}Se) = 756$ Hz, as observed in similar tetra coordinated pentavalent phosphine selenides [7b,11a,17].

The reaction of 3,3′-dihydroxy-2,2′-bipyridine with two equivalents of diphenylchlorophosphine in the presence of triethylamine, proceeds in toluene to give 3,3′-bis(diphenylphosphinite)-2,2′-bipyridine, $(Ph_2PO)_2$–$C_{10}H_6N_2$ (**2**) in moderate yield (Scheme 1). The IR spectrum of **2** exhibits characteristic bands at 1573, 1445 and 952 cm^{-1} due to υ(CN), υ(P–Ph) and υ(P–O) stretchings, respectively. The ^{31}P–{^1H} NMR spectrum of **2** shows a single resonance at 116.3 ppm, indicating that the two phosphorus atoms in the molecule are equivalent. The oxo-deriveative, $(Ph_2P(O)O)_2$–$C_{10}H_6N_2$ (**2a**) was easily prepared by

Table 3
Structural parameters of hydrogen bonds between donor (D), acceptor (A) and hydrogen (H) in **2b**

D–H···A	D–H (Å)	A···H (Å)	D···A (Å)	D–H···A (°)
C11–H11···N2^{i}	0.93	2.58	3.434(13)	154
C12–H12···O1	0.93	2.57	2.975(10)	107
C30–H30··O2	0.93	2.50	2.904(9)	107

Symmetry codes [i: $1 + x$, y, z].

Table 2
Selected bond lengths (Å) and bond angles (°) of **2b**

P1–S1	1.915(2)	P1–O1–C13	125.6(4)	P2–O2–C19	123.7(3)
P1–O1	1.620(4)	P1–C1–C2	119.8(5)	P2–C23–C24	121.1(4)
P1–C1	1.811(6)	P1–C1–C6	121.9(5)	P2–C23–C28	120.0(4)
P1–C7	1.794(6)	P1–C7–C8	120.1(5)	P2–C29–C30	123.9(5)
P2–S2	1.908(2)	P1–C7–C12	120.7(6)	P2–C29–C34	117.1(5)
P2–O2	1.621(4)	O1–P1–S1	115.04(18)	O2–P2–S2	115.86(15)
P2–C23	1.807(5)	O1–P1–C1	100.5(2)	O2–P2–C23	104.2(2)
P2–C29	1.806(6)	O1–P1–C7	104.3(3)	O2–P2–C29	99.9(2)
N1–C16	1.320(7)	S1–P1–C1	113.73(19)	S2–P2–C23	114.1(2)
N1–C17	1.325(7)	S1–P1–C7	115.3(2)	S2–P2–C29	114.9(2)
N2–C22	1.340(8)	C7–P1–C1	106.4(3)	C29–P2–C23	106.3(3)
N2–C18	1.320(6)	C16–N1–C17	118.6(5)	C18–N2–C22	117.4(5)
O1–C13	1.387(7)	O1–C13–C17	115.8(5)	O2–C19–C20	122.0(5)
O2–C19	1.386(6)	O1–C13–C14	124.1(5)	O2–C19–C18	118.5(5)

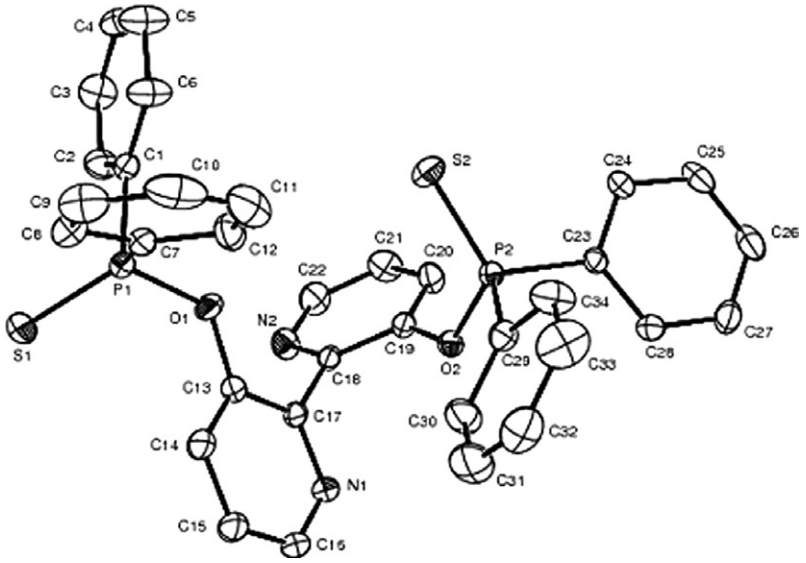


Fig. 1. ORTEP diagram of 3,3′-bis(diphenylthiophosphinite)-2,2′-bipyridine, $(Ph_2P(S)O)_2$–$C_{10}H_6N_2$ (**2b**). H atoms have been omitted for clarity.

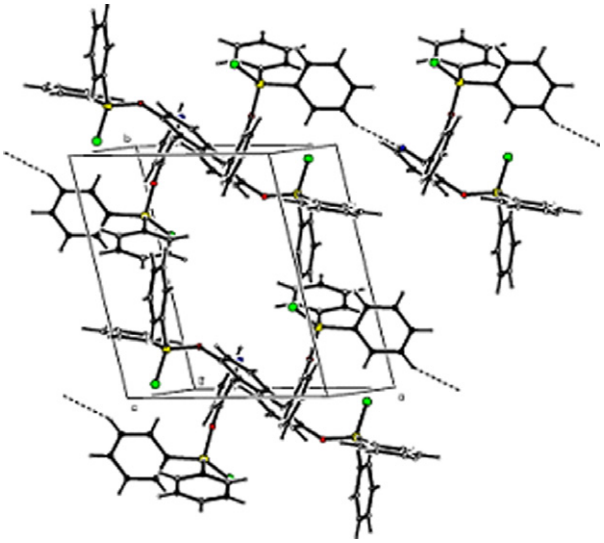
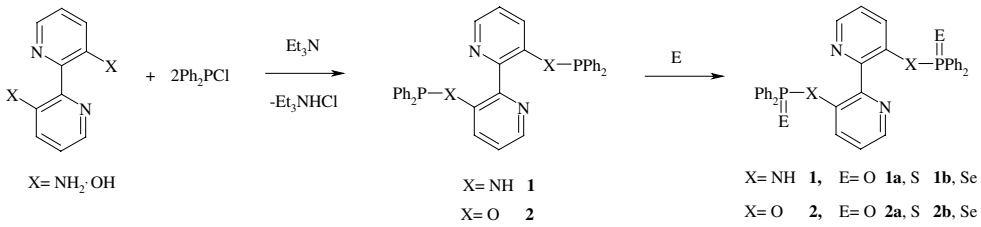


Fig. 2. Packing view of compound **2b**.

addition of excess aqueous hydrogen peroxide in toluene. The ^{31}P NMR spectrum of **2a** shows also a singlet at 22.8 ppm, remarkably shielded (by 93.5 ppm) compared to the parent compound **2**. The sulfur, $(Ph_2P(S)O)_2$–$C_{10}H_6N_2$ (**2b**), and selenide, $(Ph_2P(Se)O)_2$–$C_{10}H_6N_2$ (**2c**), analogues were prepared by addition of elemental sulfur or selenium to **2** in toluene (Scheme 1). ^{31}P–$\{^1H\}$ NMR showed single resonances at 82.6 and 86.0 ppm for the sulfide and selenide, respectively with selenium satellites ^1J (^{31}P–^{77}Se) = 782 Hz, as observed in similar P=Se compounds [7b,11a,17].

The solid-state structure of 3,3′-bis(diphenylthiophosphinite)-2,2′-bipyridine, $(Ph_2P(S)O)_2$–$C_{10}H_6N_2$ (**2b**), was determined by single-crystal X-ray diffraction study. The triclinic unit cell contains two molecules of 3,3′-bis(diphenylthiophosphinite)-2,2′-bipyridine, $[C_{17}H_{13}NOPS]_2$, with symmetry showing an inversion center (Fig. 1).

The coordination around the two phosphorus atoms (P1 and P2) are distorted tetrahedral, involving one S, one O and two C atoms from phenyl rings. In the coordination spheres, the P–S and P–O bond lengths are 1.915(2), 1.908(2) Å, and 1.620(4), 1.621(4) Å, respectively. The P–C coordination bond lengths are in the range of 1.794(6)–1.811(4) Å. The bond angles in the coordination spheres of the P1 and P2 atoms are in the range 99.9(2)–115.86(15)°, the smallest value belonging to the O2–P2–C29 angle and the largest value to the O2–P2–S2 angle. Steric effects could explain these deviations from the ideal tetrahedral angle value of 109.5°. The aromatic rings in the molecule as expected have usual bond lengths and angles. The P1…P2 distance is 5.820 Å.



Scheme 1. The formation of $(Ph_2PNH)_2$–$C_{10}H_6N_2$, $(Ph_2P(E)NH)_2$–$C_{10}H_6N_2$, $(Ph_2PO)_2$–$C_{10}H_6N_2$ and $(Ph_2P(E)O)_2$–$C_{10}H_6N_2$ (E = O, S, Se).

As shown in Fig. 2, there is an intermolecular hydrogen bonding set involving the two molecules: [C11–H11···N2]^{i} H-bond with a C11···N2 distance of 3.434(13) Å and C11–H11···N2 angle of 154° [symmetry code: (i) $1+x$, y, z]. The molecule also has two intramolecular hydrogen bonds between the oxygen atoms and one of the phenyl hydrogen atoms: [C12–H12···O1] and [C30–H30···O2] with C12···O1 and C30···O2 distances of 2.975(10), 2.904(9) Å, respectively and C12–H12···O1 and C30–H30···O2 angles of 107°. In the crystal structure, there exists a weak intermolecular interaction through hydrogen bonding involving some of the rings. The shortest intermolecular contact is observed between Cg(1)–Cg(1)^{ii} [Cg(1) = N(1)–C(16)–C(15)–C(14)–C(13)–C(17)]. The distance Cg(1)–Cg(1)^{ii} is 3.908(4) Å (symmetry code ii: $1-x$, $2-y$, $1-z$).

Acknowledgements

Partial support from Turkish Academy of Sciences, Dicle University (Project Number: DÜAPK-05-FF-27) and Hacettepe University (Scientific Research Department, Project Number: 04A602004) is gratefully acknowledged.

Appendix A. Supplementary material

CCDC 634701 contains the supplementary crystallographic data for this paper. These data can be obtained free of charge via http://www.ccdc.cam.ac.uk/conts/retrieving.html, or from the Cambridge Crystallographic Data Centre, 12 Union Road, Cambridge CB2 1EZ, UK; fax: (+44) 1223-336-033; or e-mail: deposit@ccdc.cam.ac.uk. Supplementary data associated with this article can be found, in the online version, at doi:10.1016/j.poly.2007.03.027.

References

[1] (a) Z. Fei, R. Scopelitti, P.J. Dyson, Inorg. Chem. 42 (2003) 2125;
(b) M.R. Zubiri, A.M.Z. Slawin, M. Wainwright, J.D. Woolins, Polyhedron 21 (2002) 1729;
(c) S. Priya, M.S. Balakrishma, J.T. Mague, S.M. Mobin, Inorg. Chem. 42 (2003) 1272;
(d) M.D. Rudd, M.A. Creighton, J.A. Kautz, Polyhedron 23 (2004) 1923;
(e) B. Gümgüm, O. Akba, F. Durap, L.T. Yıldırım, D. Ülkü, S. Özkar, Polyhedron 25 (2006) 3133;
(f) S.M. Aucott, A.M.Z. Slawin, J.D. Woolins, J. Organomet. Chem. 582 (1999) 83;
(g) A.M.Z. Slawin, J. Wheatly, J.D. Woolins, Polyhedron 23 (2004) 2569.

[2] (a) T. Appleby, J.D. Woollins, Coord. Chem. Rev. 235 (2002) 121;
(b) P. Espinet, K. Saulantica, Coord. Chem. Rev. 193–195 (1999) 499;
(c) F. Agbossou, J.-F. Carpentier, F. Hapiot, I. Suisse, A. Mortreux, Coord. Chem. Rev. 178–180 (1998) 1615.

[3] K.G. Gaw, M.B. Smith, J.W. Steed, J. Organomet. Chem. 664 (2002) 294.

[4] (a) M.R. Zubiri, H.L. Milton, A.M.Z. Slawin, J.D. Woollins, Inorg. Chim. Acta 357 (2004) 243;
(b) M.R. Zubiri, H.L. Milton, D.J. Cole-Hamilton, A.M.Z. Slawin, J.D. Woollins, Inorg. Chem. Commun. 7 (2004) 201;
(c) C. Saluzzo, J. Breuzard, S. Pellet-Rostaing, M. Vallet, F. Le Guyader, M. Lemaire, J. Organomet. Chem. 643–644 (2002) 98.

[5] (a) J.-X. Gao, X.-D. Yi, P.-P. Xu, C.-L. Tang, H.-L. Wan, T. Ikariya, J. Organomet. Chem. 592 (1999) 290;
(b) A.M. Maj, K.M. Pietrusiewicz, I. Suisse, F. Agbossou, A. Mortreux, J. Organomet. Chem. 626 (2001) 157.

[6] (a) R. Lou, A. Mi, Y. Jiang, Y. Qin, Z. Li, F. Fu, A.T.S.C. Chan, Tetrahedron 56 (2000) 5857;
(b) E.A. Broger, W. Burkant, M. Henning, M. Scalone, R. Schmid, Tetrahedron, Asymmetry 9 (1998) 4043;
(c) F. Agbossou-Niedercorn, I. Suisse, Coord. Chem. Rev. 242 (2003) 145;
(d) H.J. Kreuzfelt, C. Döbler, J. Mol. Cat. A: Chem. 136 (1998) 105.

[7] (a) S.M. Aucott, A.M.Z. Slawin, J.D. Woolins, J. Chem. Soc., Dalton Trans. (2000) 2559;
(b) A.M.Z. Slawin, J. Wheatley, M.V. Wheatley, J.D. Woollins, Polyhedron 22 (2003) 1397;
(c) P. Espinet, P. Gomez-Elipe, F. Villafane, J. Organomet. Chem. 450 (1993) 145;
(d) N. Biricik, Z. Fei, R. Scopelliti, P.J. Dyson, Helv. Chim. Acta 86 (2003) 3281.

[8] G. Zhang, J. Zhao, G. Raudaschl-Sieber, E. Herdtweck, F.E. Kühn, Polyhedron 21 (2002) 1737.

[9] H. Yang, M. Alvarez, N. Lugan, R. Mathieu, J. Chem. Soc., Chem. Commun. (1995) 1721.

[10] (a) M. Haiharasarma, C.H. Lake, C.L. Watkins, G.M. Gray, J. Organomet. Chem. 580 (1999) 328;
(b) P. Bergamini, V. Bertolasi, F. Milani, Eur. J. Inorg. Chem. (2004) 1277.

[11] (a) M.S. Balakrishna, P.P. George, S.M. Mobin, Polyhedron 24 (2005) 475;
(b) G.D. Cuny, S.L. Buchwald, J. Am. Chem. Soc. 115 (1993) 2066;
(c) Z. Csok, G. Szalontai, G. Czira, L. Kollar, J. Organomet. Chem. 475 (1998) 23.

[12] (a) S. Kanoktanaporn, J.A. Hugh-MacBride, J. Chem. Soc. Perkin I (1978) 1126;
(b) L. Kaczmarek, P. Nontha-Namirski, Acta Polon Pharm. XXXVI (1979) 629.

[13] C. Naumann, H. Langhals, Synthesis (1990) 279.

[14] Enraf-Nonius, CAD-4 Express Software. Version 1.1, Enraf-Nonius, Delft, Netherlands, 1993.

[15] K. Harms, S. Wocadlo, XCAD-4, Program for Processing CAD-4 Diffractometer Data, University of Marburg, Germany, 1995.

[16] G.M. Sheldrick, SHELXS97 and SHELXL97, Program for Crystal Structure Solution and Refinement, University of Göttingen, Germany, 1997.

[17] M.S. Balakrishna, P.P. George, J.T. Mague, J. Organomet. Chem. 689 (2004) 3388.

Available online at www.sciencedirect.com
ScienceDirect
Polyhedron 26 (2007) 3379–3387
POLYHEDRON
www.elsevier.com/locate/poly

Structure and magnetic properties of a double out-of-plane carboxylato-bridged Cu(II) compound with pyridine-2-carboxylate

Bogumiła Żurowska, Jerzy Mroziński *, Katarzyna Ślepokura

Faculty of Chemistry, University of Wroclaw, 14 F. Joliot Curie Street, 50-383 Wroclaw, Poland

Received 10 January 2007; accepted 11 March 2007
Available online 28 March 2007

Abstract

The spectroscopic and magnetic properties, and crystal structure of dark-blue $[Cu(2\text{-pca})_2]_n$ (**1**), (2-pca = pyridine-2-carboxylate ion) are described. The copper(II) ions are in strongly tetragonally distorted octahedral environments. They are sequentially bridged by a double out-of-plane carboxylate bridge, resulting in the formation of an infinite chain (1D). The equatorial Cu–O bonds (1.957(3) Å) are significantly shorter than the axial bonds (2.737(4) Å). The crystal structure of the compound is stabilized by interchain hydrogen bonds of the C–H···O type. The intrachain copper–copper separation is 5.178(3) Å, whereas the shortest interchain copper–copper distance is 7.614(6) Å. The magnetic properties, investigated in the temperature range 1.8–300 K, revealed the occurrence of a weak intrachain antiferromagnetic coupling, $J = -1.04\ cm^{-1}$, and an interchain exchange interaction, $zJ' = 0.34\ cm^{-1}$. The title compound appears to be a polymorphic form of the blue-violet compound (**2**) of identical stoichiometry, the X-ray structure of which was recently reported. Magneto-structural correlations in **1** have been made considering both the carboxylato bridging group and the existence of interchain hydrogen bonds. The structure and magnetic properties of **1** are compared with those of the polymorphic form **2**.
© 2007 Elsevier Ltd. All rights reserved.

Keywords: Copper(II); Pyridinecarboxylate; Crystal structure; Magnetism; Polymorphism; Hydrogen bonds

1. Introduction

Copper(II) carboxylates are structurally a very diverse group of coordination compounds due to the various coordination modes of the carboxylato ligands [1,2]. Different coordination modes of the carboxylate group lead to the formation of mononuclear and polynuclear structures. Polynuclear complexes of copper(II) with the carboxylate as a bridging group have been extensively studied in view of their interesting magnetic properties [3–5]. It is well known that the carboxylate group is able to create hydrogen bonds leading to the formation of supramolecular networks which play an important role in the transmission of magnetic interactions. Thus particular interest has also recently been focused on the development of supramolecular structures created by hydrogen bonds of different types in order to study their magnetic behaviour [6]. A variety of ligands containing N or O as donor atoms have been employed for preparation of such systems.

In our recent publications [3–5] the study of copper(II) complexes with the pyridine-2-carboxylate ligand containing N,O-donor atoms has been presented. In this work, we present the spectroscopic and magnetic properties, and the X-ray single-crystal analysis of a dark-blue form of $Cu(2\text{-pca})_2$ (**1**), where 2-pca = pyridine-2-carboxylate. We would like to emphasize that the studied compound **1** is a new crystal form of the Cu(II) compound with pyridine-2-carboxylate, structurally and magnetically characterized by us. Previously we obtained and characterized other polymorphic forms of Cu(pyridine-2-carboxylate)$_2$, namely a blue-violet (**2**) [5] and a violet (**3**) [3] form. Form **3** is a square-planar copper(II) compound in which crystal packing is due to π–π stacking and hydrogen bonds giving rise to a polymeric network arrangement. However, an interesting feature of structure **2** was found, resulting from

* Corresponding author. Tel./fax: +48 71 3757307.
E-mail address: jmroz@wchuwr.pl (J. Mroziński).

0277-5387/$ - see front matter © 2007 Elsevier Ltd. All rights reserved.
doi:10.1016/j.poly.2007.03.024

the fact that the copper(II) ions are sequentially doubly out-of plane bridged by carboxylate groups to form an infinite linear one-dimensional polymeric chain. The structure is stabilized by weak C–H···O hydrogen bonds.

Here, we describe the spectroscopic and magnetic properties of **1** in the light of the structure description. The magnitudes of the exchange interactions between neighbouring copper ions are estimated and discussed in terms of the bond properties, in particular the carboxylate bridge and the characteristics of the hydrogen bonds. In this paper we also compare the structure and magnetic properties of both **1** and **2** forms of Cu(pyridine-2-carboxylate)$_2$.

2. Experimental

2.1. Reagents and physical measurements

The starting materials and solvents for the synthesis were obtained commercially and were used as received. Metal content was determined using a Carl–Zeiss–Jena atomic absorption spectrophotometer. Elemental analyses were carried out using a Perkin–Elmer elemental analyzer 2400CHN. Infrared spectra (100–4000 cm^{-1}) were recorded on a Bruker IFS 113v spectrophotometer using KBr pellets, and solid-state electronic spectra (28000–4000 cm^{-1}) were recorded on a Cary 500 spectrophotometer. The EPR spectra of powder samples were recorded (at 295 and 77 K) on a Bruker ESP 300E spectrometer operating at X-band and equipped with a Bruker NMR gaussmeter ER 035 M and a Hewlett–Packard microwave frequency counter HP 5350B. The EPR parameters were calculated by computer simulation of the experimental spectra of the powder samples using Bruker's WIN-EPR SimFonia Version 1.25.

Magnetization measurements of polycrystalline samples were carried out with a Quantum Design SQUID magnetometer (MPMSXL-5 type) at a magnetic field of 0.5 T over the temperature range 1.8–300 K. Magnetization measurements versus magnetic field (0–5 T) were made at 2 K. The corrections for diamagnetic contributions were based on subtracting the sample-holder signal and estimating the contribution χ_D from Pascal constants [7]. The effective magnetic moments were calculated from $\mu_{eff} = 2.83(\chi_M T)^{1/2}$ using a temperature-independent paramagnetism of 60×10^{-6} cm^3 mol^{-1} for Cu(II).

2.2. X-ray crystallography of Cu(2-pca)$_2$ (*1*)

The crystallographic measurements were performed on a κ-geometry Xcalibur PX automated four-circle diffractometer with graphite–monochromatized Cu Kα radiation. The data for the crystal were collected at 100(2) K using the Oxford Cryosystems cooler. A summary of the conditions for the data collection and the structure refinement parameters are given in Table 1. The data were corrected for Lorentz and polarization effects. An analytical absorption correction was applied. Data collection, cell refinement and data reduction and analysis were carried out with the Xcalibur PX software (Oxford Diffraction Poland): CrysAlis CCD and CrysAlis RED, respectively [8a]. The structure was solved by direct methods using the SHELXS-97 program [8b] and refined by a full-matrix least-squares technique using SHELXL-97 [8c] with anisotropic thermal parameters for non-H atoms. All H atoms were found in difference Fourier maps. In the final refinement cycles, the H atoms were treated as riding atoms, with C–H distances of 0.95 Å, and with U_{iso} values of $1.2U_{eq}$(C). All figures were made using the XP program [8d].

Table 1
Crystal data and structure refinement details for Cu(2-pca)$_2$ (**1**)

Empirical formula	$C_{12}H_8CuN_2O_4$
Formula weight (g mol^{-1})	307.74
Crystal system	triclinic
Space group	$P\bar{1}$
a (Å)	5.178(3)
b (Å)	7.614(6)
c (Å)	8.109(6)
α (°)	67.06(6)
β (°)	73.81(6)
γ (°)	71.74(6)
V (Å^3)	275.1(3)
Z	1
D_{calc} (g cm^{-3})	1.858
μ (mm^{-1} for $\lambda = 1.5418$ Å)	2.951
$F(000)$	155
Crystal size (mm)	$0.10 \times 0.03 \times 0.01$
Crystal color and form	blue plates
T (K)	100(2)
θ Range (°)	6.02–75.77
h,k,l Ranges	$-6 \rightarrow 6$, $-9 \rightarrow 9$, $-6 \rightarrow 10$
Absorption correction	analytical
T_{min}/T_{max}	0.822/0.980
Measured reflections	2537
Independent reflections [R_{int}]	1006 [0.0360]
Observed reflections ($I > 2\sigma(I)$)	849
Refinement on	F^2
R ($F_o^2 > 2\sigma(F_o^2)$)	$R_1 = 0.0423$, $wR_2 = 0.1055$
R (all data)	$R_1 = 0.0514$, $wR_2 = 0.1095$
Goodness-of-fit = S	1.068
Weighting parameter a/b	0.0645/0.1022
$\Delta\rho_{max}/\Delta\rho_{min}$ (e Å^{-3})	0.62/−0.52

2.3. Synthesis of Cu(2-pca)$_2$ (*1*)

This compound was obtained from the reaction of $CuCl_2$ with the diethyl 2-pyridylmethylphosphonate ligand according to the procedure described in details elsewhere [3]. In this reaction the ligand undergoes an oxidative P-dealkylation/dephosphorylation reaction according to scheme: R–CH$_2$–P(O)(OEt)$_2$ → R–COOH + OH–P(O)(OEt)$_2$, where R = C$_5$H$_4$N The final products of this process are the complexes of composition Cu(2-pca)$_2$ and Cu(2-pca)Cl (2-pca = pyridine-2-carboxylate). Slow evaporation of the solvent led to the formation of dark-blue crystals of Cu(2-pca)$_2$, suitable for X-ray studies.

Anal. Calc. for $[C_{12}H_8N_2O_4Cu]$: C, 46.54; H, 2.63; N, 8.84; Cu 20.55; Found: C, 46.32; H, 2.58; N, 8.95; Cu, 20.79%.

3. Results and discussion

3.1. Description of the crystal structure of Cu(2-pca)$_2$ (1)

Crystallographic parameters are summarized in Table 1 and selected bond distances and angles are listed in Table 2. The structure of the Cu(2-pca)$_2$ compound with the crystallographic numbering is depicted in Fig. 1.

As can be seen from Fig. 1, the structure is a one-dimensional polymeric chain, $[Cu(2\text{-pca})_2]_n$. Each Cu(II) ion is connected to the two adjacent metal ions by two out-of-plane carboxylate bridges, creating a polymeric chain along the *a* axis in which the Cu···Cu distance within the chain is 5.178(3) Å. This distance is near the range of reported values of ca. 5 Å observed for polyatomic bridges [9]. The copper(II) atom lies on a center of symmetry. The coordination polyhedron around the copper atom can be described as a strongly distorted octahedron. The equatorial plane is composed of the oxygen and nitrogen atoms of the two chelating picolinate ions. The apical positions are occupied by two oxygen atoms [O(2)B and O(2)C] belonging to the carboxylate groups of the adjacent molecules in the chain (symmetry codes are given in Table 2). The Cu–O and Cu–N distances in the basal plane agree well with those found in other square-planar copper(II) complexes [10] but the apical distances are very long [Cu···O(2)B, O(2)C = 2.737(4) Å]. Regarding the carboxylate group, the two C–O distances are different [O(1)–C(1) 1.302(5) Å, O(2)–C(1) 1.236(4) Å], while the Cu(1)–O(1), O(1)A distances are identical (1.957(3) Å). As previously noted, each carboxylate group bridges two copper(II) ions through its O(2) oxygen atom, resulting in non-planarity of the Cu–O–C–O–Cu′ fragment. The bridging pathway is asymmetric not only in its conformation but also with respect to the C–O bond lengths. The crystal structure of compound **1** is stabilized by weak hydrogen bonds of the C–H···O type in accordance with the well-known ability of carboxylate moieties to generate hydrogen-bonding motifs in complexes. The crystal packing is shown in Fig. 2. These hydrogen bond interactions (Table 3), lead to the formation of a 2D sheet structure. The shortest interchain Cu···Cu separations are 7.614(6), 7.751(7), 8.109(6) and 8.316(7) Å (Table 2).

As mentioned earlier, the title compound **1** is a polymorphic form of Cu(pyridine-2-carboxylate)$_2$ (**2**) recently reported [5]. In both complexes the copper(II) ions are sequentially doubly bridged by carboxylate groups to form infinite one-dimensional polymeric chains. Both compounds are of parallel-planar type with out-of-plane carboxylate bridges. This type, characteristic especially for those compounds bridged by chloride ions [11], is unique among the carboxylate bridged chain compounds.

Table 2
Selected interatomic distances (Å) and valence angles (°) in Cu(2-pca)$_2$ (**1**)

Cu(1)–O(1)	1.957(3)	Cu(1)···Cu(1)C, Cu(1)D	5.178(3)
Cu(1)–N(1)	1.960(3)	Cu(1)···Cu(1)E	7.614(6)
Cu(1)–O(2)B	2.737(4)	Cu(1)···Cu(1)F	7.751(7)
O(1)–C(1)	1.302(5)	Cu(1)···Cu(1)G	8.109(6)
O(2)–C(1)	1.236(4)	Cu(1)···Cu(1)H	8.316(7)
N(1)–C(2)	1.355(4)		
O(1)–Cu(1)–N(1)	83.66(13)	O(1)–Cu(1)–O(2)C	96.14(11)
O(1)–Cu(1)–N(1)A	96.34(13)	N(1)–Cu(1)–O(2)B	91.32(12)
O(1)–Cu(1)–O(2)B	83.86(11)	N(1)–Cu(1)–O(2)C	88.68(12)

Symmetry codes: (A) $-x+1, -y+1, -z+1$; (B) $-x+2, -y+1, -z+1$; (C) $x-1, y, z$; (D) $x+1, y, z$; (E) $x, y-1, z$; (F) $x-1, y+1, z$; (G) $x, y, z-1$; (H) $x-1, y, z+1$.

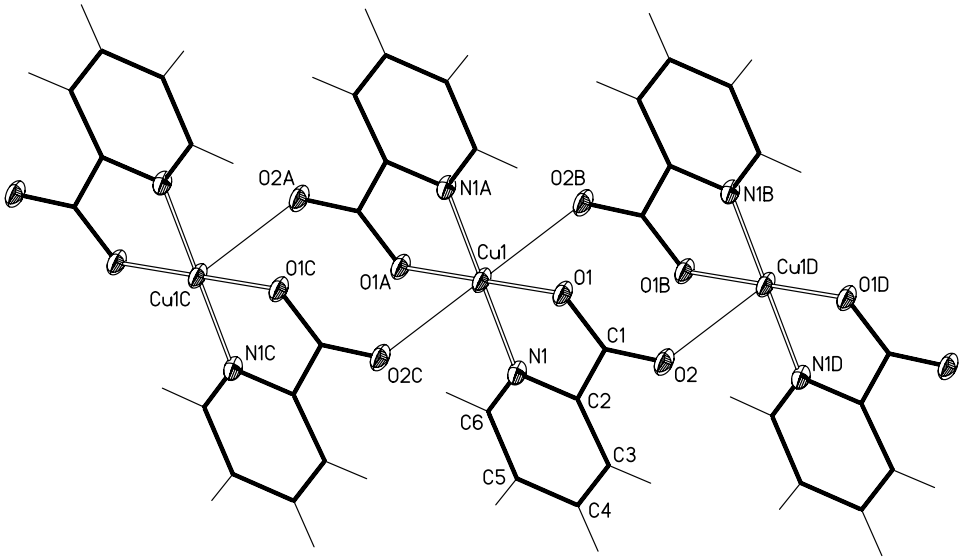


Fig. 1. The fragment of the polymeric $[Cu(2\text{-pca})_2]_n$ chain along the *a*-axis. Symmetry codes are given in Table 2.

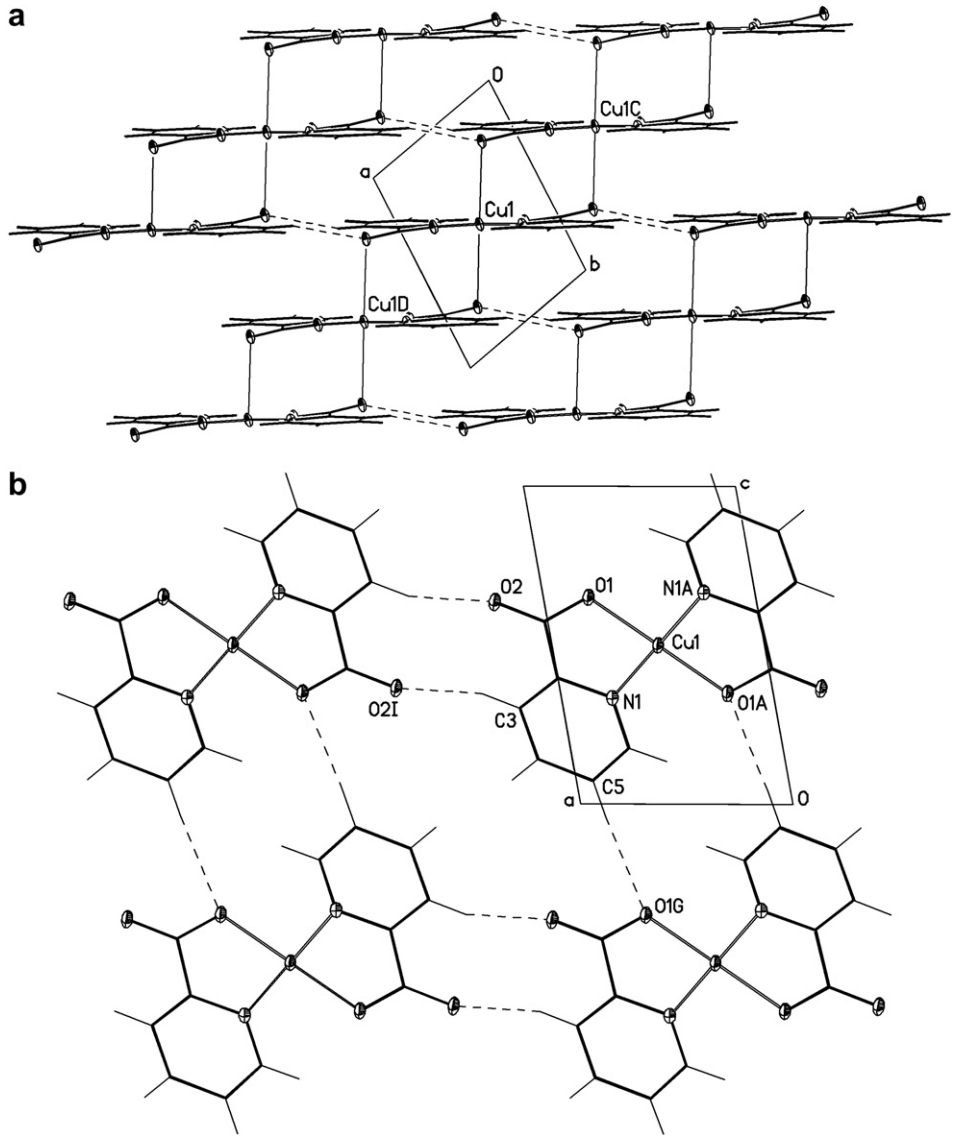


Fig. 2. (a) Crystal packing in (**1**) showing the interchain C–H···O interactions and layers formed by the planar Cu(2-pca)$_2$ fragments from adjacent chains. (b) Arrangement of Cu(2-pca)$_2$ within the 2D layer; viewed down the *b*-axis. Hydrogen contacts of the C–H···O type are shown as dashed lines. Symmetry codes are given in Tables 2 and 3.

Table 3
Geometry of C–H···O hydrogen bonds for Cu(2-pca)$_2$ (**1**)

D–H···A	D–H (Å)	H···A (Å)	D···A (Å)	D–H···A (°)
C(3)–H(3)···O(2)I	0.95	2.43	3.287(5)	150
C(5)–H(5)···O(1)G	0.95	2.49	3.419(5)	166

Symmetry codes: (G) $x, y, z-1$; (I) $-x+3, -y, -z+1$.

Bond distances and related angles in the ligand do not noticeably differ from those reported by us for **2**, in which the ligand, within the mononuclear units, is coordinated in the same fashion as in the complex discussed here.

The 1D chain structures of **1** and **2** are very similar but some subtle structural differences are observed. The Cu(II) atom in **1** lies strictly in the basal plane, whereas the copper(II) atom in **2** is displaced by 0.02 Å. The long out-of-plane Cu–O bond distance is slightly shorter (2.737(4) Å) than that reported in **2** (2.745(8)–2.770(8) Å). The in-plane Cu–O bond distance in **1** is 1.957(3) Å, however in **2** the values are 1.964(8) and 1.944(8) Å. Two related C–O distances in **1** are very different [1.302(5), 1.236(4) Å], whereas in **2** they are similar [1.270(14) and 1.267(14) Å]. The O(1)–C(1)–O(2) angle of 125° in both **1** and **2** is typical [12]. Crystal packing (H-bonds) in **1** and **2** are significantly different. Further structural parameters will be discussed in Section 3.4.

3.2. Spectroscopic properties of Cu(2-pca)$_2$ (*1*)

The earlier infrared spectroscopy study [3] on the title compound **1** indicates bond formation between the copper ion and the nitrogen atom of the pyridine ring and oxygen atom of the carboxylate group, and suggests a *trans* square-planar copper environment. The IR spectrum shows strong

asymmetric and symmetric stretching vibrations of the coordinated carboxylate groups [13], ν_{as}(COO) and ν_s(COO), at 1646 cm^{-1} and 1349 cm^{-1}, respectively with a shoulder at about 1650 cm^{-1}, overlapping with the stretching vibration of ν(C=N) of the pyridine ring. This shoulder may be the result of the presence of hydrogen bonding, as confirmed by the crystal structure [14]. The large difference between the two bands of the carboxylate group ($\Delta\nu = 297\ cm^{-1}$), as discussed earlier [5] for compound **2**, can be viewed as a pseudo-monodentate coordination, which is consistent with the structure.

A broad asymmetric band centered at 16 580 cm^{-1} observed in the ligand-field spectrum is characteristic of a tetragonally distorted octahedral complex [15], consistent with the structural analysis.

The X-band EPR spectrum of a polycrystalline sample of Cu(2-pca)$_2$ is of the axial type with g values of $g_\parallel = 2.22_0$, $g_\perp = 2.07_2$. The $g_\parallel$ value is in agreement with that observed for a CuN_2O_2 chromophore with strong planar and weaker axial bonds [5,16]. The spectra are independent of temperature. The g-values obtained from a computer simulation procedure (powder spectrum simulation) indicate basically a $d(x^2–y^2)$ ground state for Cu(II), as observed for other copper–amino acid complexes [5,17]. The hyperfine structure expected for Cu(II) ions is not observed, suggesting the existence of exchange interactions coupling the paramagnetic ions [18].

It is worth mentioning that the differences in packing arrangements of **1** and **2** are manifested mainly in their d-d spectra. The $g_\parallel$ values for both complexes are similar. However, a small shift of the d–d band observed for **1** (16 580 cm^{-1}) with respect to **2** (16 670 cm^{-1}) is in full agreement with difference in Cu–O axial bond lengths for **1** (2.737(4) Å) and for **2** (2.745(8) and 2.770(8) Å) [5].

3.3. Magnetic properties of Cu(2-pca)$_2$ (*1*)

The magnetic properties of the compound were investigated in the temperature range 1.8–300 K. The magnetic susceptibility results for the polycrystalline sample obey the Curie–Weiss law between 25 and 300 K, $\chi = C/(T-\theta)$, where χ is the magnetic susceptibility per copper atom, the Curie constant $C = Ng^2\beta^2S(S+1)/3k$ and $S = 1/2$. The best fit values of the Curie (C) and Weiss (θ) constants are equal to 0.375 $cm^3\ K\ mol^{-1}$ and −0.63 K, respectively. The negative Weiss constant value suggests a weak antiferromagnetic interaction between the copper(II) ions. The temperature variation of χT is depicted in Fig. 3.

The magnetic moment at room temperature (1.73 μ_B) is typical of the normal value for an uncoupled copper(II) system and might suggest the absence of spin exchange, but the χT value decreases slowly with temperature, lowering from 0.373 $cm^3\ K\ mol^{-1}$ at 300 K to 0.259 $cm^3\ K\ mol^{-1}$ at 1.8 K. This suggests the existence of a weak antiferromagnetic exchange interaction between the copper(II) ions at low temperatures.

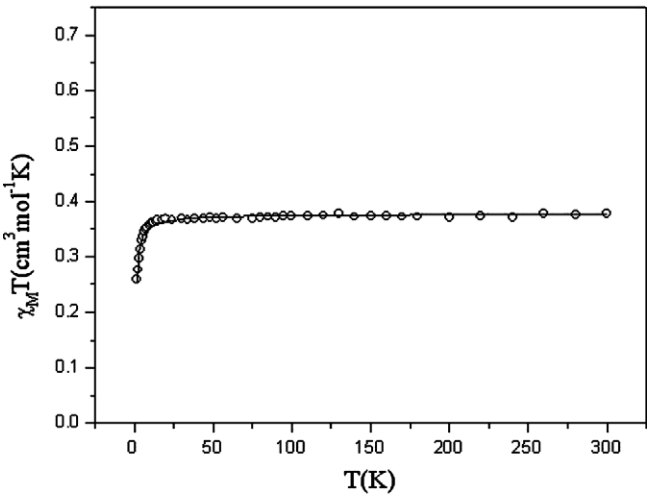


Fig. 3. Plot of $\chi_{Cu}T$ (○) vs. T for Cu(2-pca)$_2$. The solid line represents the best fit of the experimental data to the Bonner–Fisher chain model with the parameters reported in the text.

Taking into account the crystal structure of the compound, the magnetic properties could be explained by the Heisenberg linear-chain model of the magnetic interaction arising from the isotropic model $S = 1/2$ described by the Hamiltonian $H = -2J\sum_{i=1}^{n} S_i \cdot S_{i+1}$. The magnetic data were analyzed using the polynominal expression (1) developed by Hall [19] which describes well the results of Bonner and Fisher [20] on a uniformly-spaced linear chain of spin 1/2, assuming a first-order molecular-field correction (2), namely:

$$\chi_{Cu} = \frac{Ng^2\beta^2}{kT} \times \frac{0.25 + 0.14995x + 0.30094x^2}{1 + 1.9862x + 0.68854x^2 + 6.0626x^3} \quad (1)$$

$$\chi_{Cu}^{corr} = \frac{\chi_{Cu}}{1 - \frac{2zJ'}{N\beta^2 g^2}\chi_{Cu}} \quad (2)$$

where $\chi = |J|/kT$, χ_{cu} is the susceptibility of the copper(II) centers in a Heisenberg chain, zJ' is the interchain exchange, and the other parameters have their usual meanings. In the frame of this model, the best-fit parameters obtained by a least-squares fit are as follows: $J = -1.04\ cm^{-1}$, $zJ' = 0.34\ cm^{-1}$, $g = 2.01$ with $R = 4.22 \times 10^{-5}$, where R is the agreement factor defined as:

$$R = \sqrt{\sum \frac{1}{(\chi_i^{exp})^2}(\chi_i^{exp} - \chi_i^{calc})^2 \Big/ \sum \frac{1}{(\chi_i^{exp})^2}}$$

The molar magnetization M of a powder sample of the studied complex was measured as a function of the applied magnetic field H at 2 K (Fig. 4). No differences were observed between the $M(H)$ curves measured with increasing or decreasing magnetic field.

The magnetization (M Nμ_B) per Cu(II) ion at 5 T tends to 0.88 electrons (Nμ_B) and this value is less than that expected for an isolated Cu(II) ion (1 Nμ_B). The shape of the curve formed by the experimental points does not follow the Brillouin formula for an isolated Cu(II) ion and

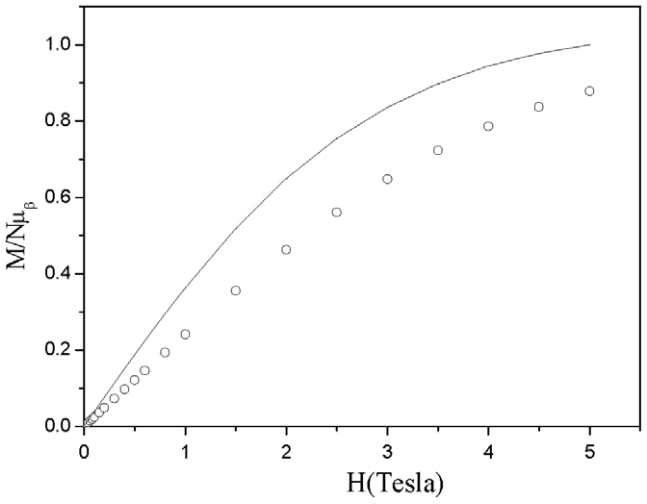


Fig. 4. A plot of the molar magnetization in $N\mu_B$ units, as a function of the magnetic field: experimental (○) and Brillouin curve for isolated Cu(II) ion (solid line).

is indicative of the dominant small antiferromagnetic coupling between the copper(II) ions.

3.4. Magneto-structural correlations

3.4.1. Intermolecular interactions through the carboxylato bridging ligand

The magnetic coupling for all known out-of-plane polynuclear copper(II)compounds is relatively weak, (J from $\sim$0.5 to ~ -1 cm^{-1}) because of the near-orthogonality of the magnetic orbitals, as has been shown for the chloro- [21], carbonato- [22] and oximato- [23] bridged compounds, and for some carboxylato-bridged complexes in which carboxylate bridges from the basal to the axial position exist with a long Cu–O distance (2.28–2.68 Å) [24]. In the case of the interactions in apical-equatorial bond modes, the orthogonality of the magnetic orbitals leads to a coupling which must be weakly antiferromagnetic, zero or weakly ferromagnetic.

For the title compound **1**, similar to compound **2**, the weak antiferromagnetic coupling observed between the copper atoms is expected in light of the same following electronic and structural features: (i) relatively long Cu–O axial distance, (ii) non-planarity of the Cu–O–C–O–Cu′ fragment (an out-of-phase exchange pathway), (iii) each carboxylate bridge involves an axial position on a copper(II) ion, where the spin density of the unpaired electron is very small (in a square-based geometry the unpaired electron is in $d(x^2-y^2)$). All these features observed in **1** and **2** are unfavorable for the propagation of strong interactions.

The magnetic behaviour of both compounds with carboxylate out-of-plane bridges can be explained as a result of the magnetic exchange within the chain through long Cu–O axial bonds (2.737(4) Å for **1** and 2.745(8)–2.770(8) Å for **2** [5]). In **1** and **2** weak antiferromagnetic interactions between the copper(II) ions through the carboxylate bridge have been found (-1.04 and -0.73 cm^{-1}, respectively).

3.4.2. Intermolecular interactions through hydrogen bonds

It is worth mentioning that studies of very weak non-covalent intermolecular interactions, such as hydrogen bonds [25a,25b,25c], stacking of aromatic rings [25d,25e,25f,25g] and intramolecular cation–π interactions [25h,25i,25j,25k], are of fundamental importance not only for further development of inorganic supramolecular chemistry and the prediction of crystal structures [25], but these contacts also generate interesting supramolecular properties, such as electrical, optical and magnetic ones [25c], and play a major role in the function of biological macromolecules. Additionally, metal–amino acid and metal–peptide complexes mimic some of the weak bonds that are important in proteins [25l,25m].

It is well known that the role played by hydrogen bonds in the transmission of magnetic interactions is still not fully understood. For many years, hydrogen bonds have been thought to propagate essentially antiferromagnetic interactions between metal centres [26], but presently, the number of ferromagnetically coupled hydrogen-bonded systems is growing [27].

In order to show which structural features may be responsible for the observed ferromagnetic coupling through hydrogen bonds in the studied compound, we decided to compare the Cu(2-pca)$_2$ complex presented here (**1**) with the other Cu(2-pic)$_2$ (**2**) previously reported by us [5]. The intermolecular hydrogen bonds for complexes **1** and **2** are listed in Tables 3 and 4, and are shown in Figs. 2 and 5.

Despite the usual weak character of the C–H···O hydrogen bonds, different superexchange couplings provided by them in **1** ($zJ' = 0.34$ cm^{-1}) and **2** ($zJ' = -0.06$ cm^{-1}) are observed. Although the ligands are the same in both complexes and the Cu(II) ions are doubly bridged by carboxylate out-of-plane bridges (1D chains), the packing of the two complexes is different. Complexes **1** and **2** form two different supramolecular structures in which the chains are linked by weak C–H···O hydrogen bonds, leading to the formation of 2D sheet structures. Therefore, in these compounds not only are the H-bonding networks different, but also their magnetic properties, generated by the hydro-

Table 4
Geometry of C–H···O hydrogen bonds and contacts for Cu(2-pca)$_2$ (**2**)

D–H···A	D–H (Å)	H···A (Å)	D···A (Å)	D–H···A (°)
C(3)–H(3)···O(2)J	0.95	2.49	3.278(14)	140
C(5)–H(5)···O(11)K	0.95	2.66	3.558(15)	157
C(5)–H(5)···O(12)K	0.95	2.54	3.391(15)	148
C(14)–H(14)···O(2)L	0.95	2.46	3.272(13)	143
C(15)–H(15)···O(12)M	0.95	2.40	3.161(14)	137

Symmetry codes: (J) $-x+2$ $-y+1$, $-z$; (K) $-x$, $y+1$, $-z+1$; (L) $x-1$, $-y+1/2$, $z+1/2$; (M) $x+1$, $-y+1/2$, $z-1/2$.

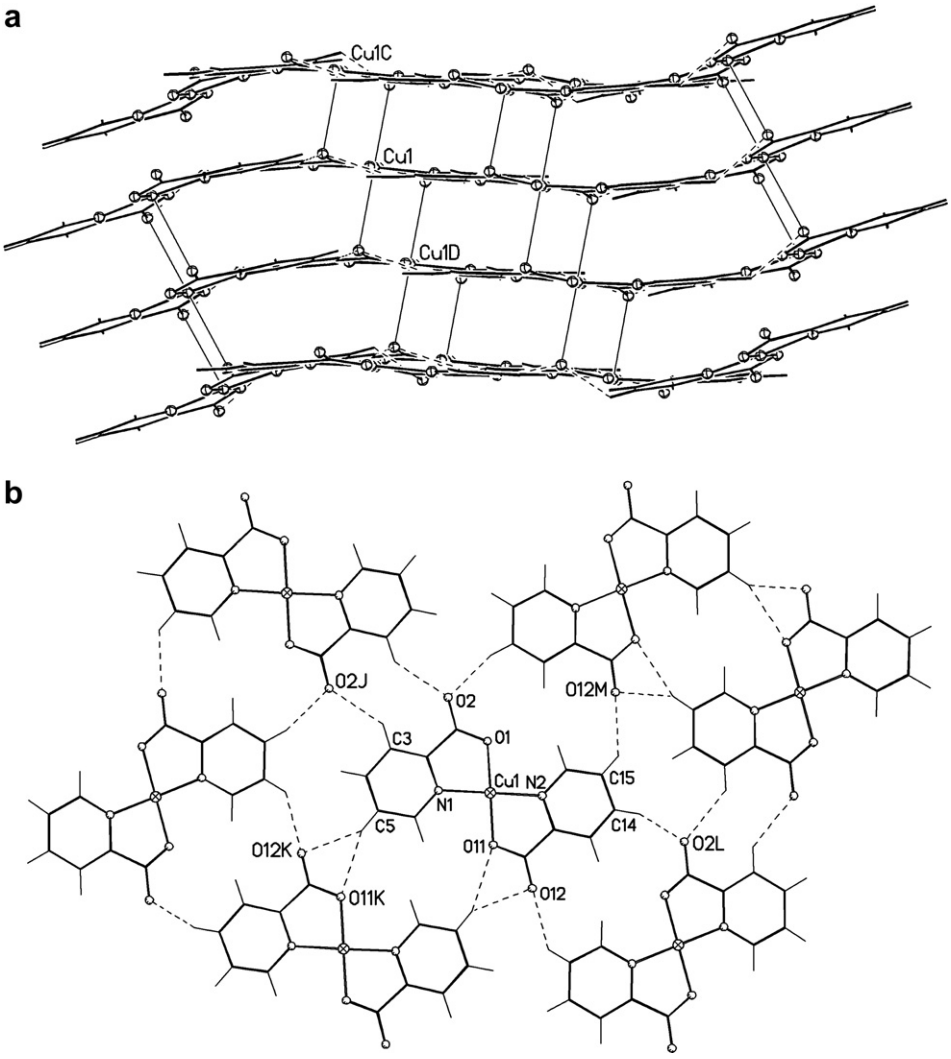


Fig. 5. (a) Crystal packing in (**2**) showing the interchain C–H···O interactions and corrugated layers formed by the planar $Cu(2\text{-pic})_2$ from adjacent chains. (b) Arrangement of $Cu(2\text{-pic})_2$ (**2**) within the 2D layer. Hydrogen contacts of the C–H···O type are shown with dashed lines [5]. Symmetry codes are given in Tables 2 and 4.

gen bonds, differ (F and AF, respectively). The shortest interchain Cu···Cu separations are 7.614(6)–8.316(7) Å in **1** and 7.43 Å and 8.09 Å in **2**.

Inspection of Tables 3 and 4 indicates some structural differences in the intermolecular C–H···O hydrogen bonds in **1** and **2**. It is worth mentioning that the H-bonds can only support very weak magnetic interactions. Because the H(5) atom in **2** is involved in weak hydrogen-bond-like contacts (three-centered bonds with a bifurcated donor) with the H···O distance >2.5 Å, the exchange interactions by these pathways are probably minor. Therefore, its possible contribution to zJ' may be neglected. Thus these contacts in **2** are excluded from the discussion. Both compounds show intermolecular hydrogen bonds with an O···H distance in the range 2.43–2.49 Å in **1** and 2.40–2.49 Å in **2**. The relative bond angles in **1**, C(3)–H(3)···O(2)I and C(5)–H(5)···O(1)G, are 150 and 166°, respectively. The relative bond angles in **2**, C(3)–H(3)···O(2)J, C(15)–H(15)···O(12)M and C(14)–H(14)···O(2)L, are 140°, 137° and 143°, respectively. Hence the binding angles in compound **1** are more favourable for transmission of the magnetic interaction through the H-bonds than those in compound **2**. On the other hand, the relative C···O separations in the C–H···O hydrogen bonds in **2** are shorter (3.161(14)–3.278(14) Å) than those (3.287(5)–3.419(5) Å) in compound **1**. This fact could explain the differences in the sign of the superexchange couplings observed in compounds **1** and **2**, because the stronger coupling corresponds to the shorter hydrogen bonded donor–acceptor distance [28]. Nevertheless, it should be underlined that other subtle structural parameters may also be responsible for the magnetic properties of copper(II) compounds with H-bond systems [25f,29].

4. Concluding remarks

The present study has provided a new example of an out-of-plane double carboxylato-bridged copper(II)

compound which is of the structurally parallel-planar type. This compound (**1**) and those (**2**) also mentioned in this work are polymorphic forms of Cu(pyridine-2-carboxylate)$_2$. The 1D chains structures in both compounds are very similar, but the deviation of the copper(II) ion from the basal plane (0.02 Å) in **2** and the small difference in Cu–O axial bond lengths observed in **1** and **2** seem to be responsible for attainment of different supramolecular structures and magnetic behaviour. Two key factors control the crystal structures of **1** and **2**, the bridging coordination and the interchain hydrogen bonds. These hydrogen bonds generate a supramolecular structure, govern the stability of the complexes and have an important role in the magnetism by a further increase in the dimensionality of the overall structure. From a magnetic point of view, it is interesting that despite the weak character of the C–H···O interactions, this magnetic pathway, as indicated by experimental results, is not negligible. The superexchange coupling provided by them may have weak antiferromagnetic or weak ferromagnetic character, as described in this work. In summary, this paper exhibits that the differences between the crystal packing of **1** and **2** are important and account for the differences in their magnetic properties.

5. Supplementary material

CCDC 626780 contains the supplementary crystallographic data for this paper. These data can be obtained free of charge via http://www.ccdc.ac.uk/conts/retrieving.html, or from the Cambridge Crystallographic Data Centre, 12 Union Road, Cambridge CB2 1EZ, UK; fax: (+44) 1223-336-033; or e-mail: deposit@ccdc.cam.ac.uk.

Acknowledgements

This work was supported by the Polish Ministry of Science and Higher Education (Grant No. 1T09A 12430). We thank Professor Julia Jezierska (Faculty of Chemistry, University of Wrocław, Wrocław, Poland) for the simulation of EPR spectra and helpful discussions.

References

[1] C. Oldham, Carboxylates, Squarates and Related Species, in: G. Wilkinson (Ed.), Comprehensive Coordination chemistry, Pergamon Press, Oxford, 1987 (Chapter 15.6).
[2] A. Caneschi, d. Gatteschi, J.P. Renard, P. Rey, R. Sessoli, J. Am. Chem. Soc. 111 (1989) 785.
[3] B. Żurowska, J. Ochocki, Z. Ciunik, J. Mroziński, J. Reedijk, Inorg. Chim. Acta 357 (2004) 755.
[4] B. Żurowska, J. Mroziński, Inorg. Chim. Acta 342 (2003) 23, and references therein.
[5] B. Żurowska, J. Mroziński, Z. Ciunik, Polyhedron 26 (2007) 1211.
[6] (a) X. Ren, Y. Chen, Ch. He, S. Gao, J. Chem. Soc. Dalton Trans. (2002) 3915, and references therein;
(b) M.S. Ray, A. Ghosh, S. Chaudhuri, M.G.B. Drew, J. Ribas, Eur. J. Inorg. Chem. (2004) 3110.
[7] E. König, Magnetic Properties of Coordination and Organometallic Transition Metal Compounds, Springer, Berlin, 1966.
[8] (a) Xcalibur PX software: CRYSALIS CCD and CRYSALIS RED, ver. 1.171, Oxford Diffraction Poland, 1995–2003;
(b) G.M. Sheldrick, SHELXS-97. Program for the Solution of Crystal Structures, University of Göttingen, Germany, 1997;
(c) G.M. Sheldrick, SHELXL-97. Program for the Refinement of Crystal Structures, University of Göttingen, Germany, 1997;
(d) XP – Interactive molecular graphics – ver. 5.1 – Bruker Analytical *X*-ray Systems, 1998.
[9] E. Colacio, J.P. Costes, R. Kivekäs, J.P. Laurent, J. Ruiz, M. Sundberg, Inorg. Chem. 30 (1991) 1475.
[10] (a) M. Melnik, M. Kabešová, M. Dunaj-Jurčo, C.E. Holloway, J. Coord. Chem. 41 (1997) 35;
(b) M.E. Bluhm, M. Ciesielski, H. Gorls, O. Walter, M. Doring, Inorg. Chem. 42 (2003) 8878;
(c) H. Masuda, A. Odani, O. Yamauchi, Inorg. Chem. 28 (1989) 624.
[11] (a) S.G.N. Roundhill, D.M. Roundhill, D.R. Bloomquist, C. Landee, R.D. Willet, D.M. Dooley, H.B. Gray, Inorg. Chem. 18 (1979) 831;
(b) J.V. Folgado, E. Coronado, D. Beltrán, J. Chem. Soc., Dalton Trans. (1986) 1061, and references therein;
(c) R. Faure, H. Loiseleur, G. Thomas-David, Acta Crystallogr. Sect. B 29 (1973) 1890;
(d) P. Segl'a, M. Jamnický, M. Koman, J. Šima, T. Głowiak, Polyhedron 17 (1998) 525.
[12] P.K. Coughlin, S.J. Lippard, J. Am. Chem. Soc. 106 (1984) 2328.
[13] (a) G.B. Deacon, R.J. Philips, Coord. Chem. Rev. 33 (1980) 227;
(b) K. Nakamoto, Infrared and Ramann Spectra of Inorganic and Coordination Compounds, Wiley, New York, 1997.
[14] G. Marcotrigiano, L. Menabue, G.C. Pellacani, J. Inorg. Nucl. Chem. 40 (1978) 165.
[15] L. Abuhijleh, C. Woods, Y. Amed, Inorg. Chim. Acta 130 (1991) 11.
[16] A.C. Fabretti, G. Franchini, P. Zannini, M. Divaira, Inorg. Chim. Acta 105 (1985) 18.
[17] O.R. Nascimento, A.J. Costa-Filho, D.I. De Morais, J. Ellena, L.F. Delboni, Inorg. Chim. Acta 312 (2001) 133.
[18] D. Gatteschi, A. Bencini, Electron Paramagnetic Resonance of Exchange Coupled Systems, Springer, Berlin, 1990.
[19] J.W.A. Hall, Ph.D. dissertation, University of North Carolins, 1977.
[20] (a) J.C. Bonner, M.E. Fisher, Phys. Rev. Sect. A. 135 (1964) 640;
(b) J.W. Stout, R.C. Chisholm, J. Chem. Phys. 36 (1962) 979.
[21] (a) J.V. Folgado, E. Coronado, D. Beltrán, J. Chem. Soc., Dalton Trans. (1986) 1061;
(b) K. Hara, M. Inoue, S. Emori, M. Kuto, J. Mag. Reson. 4 (1971) 337.
[22] S. Youngme, N. Chaichit, P. Kongsaeree, G.A. van Albada, J. Reedijk, Inorg. Chim. Acta 324 (2001) 232.
[23] B. Cervera, R. Ruiz, F. Lloret, M. Julve, J. Cano, J. Faus, C. Bois, J. Mroziński, J. Chem. Soc., Dalton Trans. (1997) 1061.
[24] P.R. Levstein, R. Calvo, Inorg. Chem. Soc. 29 (1990) 1581.
[25] (a) G.A. Jeffrey, W. Saenger, Hydrogen Bonding in Biological Structures, Springer, Berlin, 1991;
(b) G.A. Jeffrey, An Introduction to Hydrogen Bonding, Oxford, New York, 1997;
(c) H.W. Roesky, M. Andruh, Coord. Chem. Rev. 236 (2003) 91;
(d) B.E. Fisher, H. Sigel, J. Am. Chem. Soc. 102 (1980) 2998;
(e) T. Sugimori, K. Shibakawa, H. Popoić, A. Odani, O. Yamauchi, Inorg. Chem. 32 (1993) 4951;
(f) A.J. Costa-Filho, C.E. Munte, C. Barberato, E.E. Castellano, M.P.D. Mattioli, R. Calvo, O.R. Nascimento, Inorg. Chem. 38 (1999) 4413;
(g) Ch. Janiak, J. Chem. Soc., Dalton Trans. (2000) 3885;
(h) S.D. Zarić, D.M. Popoić, E-W. Knapp, Chem. Eur. J. 6 (2000) 3935;
(i) S.D. Zarić, Chem. Phys. Lett. 311 (1999) 77;

(j) M.F. Perutz, Philos. Trans. R. Soc. A 345 (1997) 105;
(k) M. Milčić, S.D. Zarić, Eur. J. Inorg. Chem. (2001) 2143;
(l) A.S. Brill, Transition metals in biochemistry, Berlin, 1977.;
(m) S.J. Lippard, J.M. Berg, Principles of Bioinorganic Chemistry, University Science Books, Mill Valley, CA, 1994.
[26] Y. Xiu, Q. Liu, H. Jiang, C. Du, X. Xu, M. Yu, Y. Zhu, New. J. Chem. 26 (2002) 176.
[27] (a) J. Tercero, C. Diaz, J. Ribaz, J. Machia, M.A. Maestro, Inorg. Chem. 41 (2002) 5373;
(b) C. Desplanches, E. Ruiz, S. Alvarez, Chem. Commun. (2002) 2614;
(c) D. Maspoch, L. Catalá, P. Gerber, D. Ruiz-Molina, J. Vidal-Gancedo, K. Wurst, C. Rovira, J. Veciana, Chem. Eur. J. 8 (2002) 3635;
(d) T.K. Payme, T. Weyhermuller, K. Wieghardt, P. Chaudhuri, Inorg. Chem. 41 (2002) 6538, and references cited therein.
[28] J.A. Bertrand, E. Fujita, D.G. VanDerveer, Inorg. Chem. 19 (1980) 2022.
[29] (a) H. Huhonen, Inorg. Chem. 25 (1986) 4692;
(b) A.J. Costa-Filho, C.E. Munte, C. Barberato, E.E. Castellano, M.P.D. Mattioli, R. Calvo, O.R. Nascimento, Inorg. Chem. 38 (1999) 4413.

Available online at www.sciencedirect.com
ScienceDirect
Polyhedron 26 (2007) 3388–3396
POLYHEDRON
www.elsevier.com/locate/poly

Syntheses, characterization and catalytic activity of Mannich aminomethylation products of bis(glycinato)metal(II) complexes

Subrahmanian Supriya [a], Aravamudhan Raghavan [a,*], V.R. Vijayaraghavan [b], J. Subramanian [c]

[a] Department of Polymer Science, University of Madras, Guindy Campus, Chennai 600 025, Tamil Nadu, India
[b] Department of Physical Chemistry, University of Madras, Guindy Campus, Chennai 600 025, Tamil Nadu, India
[c] NMR Lab, CLRI, Adyar, Chennai 600 025, Tamil Nadu, India

Received 21 January 2007; accepted 15 March 2007
Available online 24 March 2007

Abstract

Mannich aminomethylation products have been prepared from one-pot template condensation of bis(glycinato)metal(II) complexes, $M(gly)_2$, with formaldehyde and nitromethane. The synthesized compounds were characterized by suitable spectroscopic and analytical methods such as UV–Vis, infrared spectroscopy, elemental analysis, FAB mass, ESR, cyclic voltammetry, TGA and NMR. One of the synthesized products has been used as catalyst in the hydrogen peroxide induced degradation of pyrocatechol violet (PCV) dye.
© 2007 Elsevier Ltd. All rights reserved.

Keywords: Metal(II) complexes; Mannich aminomethylation; Nitromethane; Pyrocatechol violet dye

1. Introduction

Mannich aminomethylation reaction has become established as a versatile route towards synthesis of macrocyclic compounds and complexes with pendant-arm ligands [1–4]. Compounds such as amides (carboxamides and sulphoxamides), amines, diesters and nitroalkanes have been successfully used as active hydrogen containing compounds in Mannich reactions [5]. The ring-closing agents used have been dominated by nitroalkanes and malonic esters leading to nitro- and carboxylate-appended systems [6,7]. Mannich reaction involving chelated amino acids as an amine component [8,9] or as a substrate with active hydrogen has been studied extensively [10,11]. The products formed were found to vary with the pH and the α-alkyl substituents of the chelated amino acid complexes [12].

Mannich aminomethylation reaction involving nitromethane as the carbon acid has received scant attention during the past several years [13,14]. Herein, we report syntheses of new compounds using nitromethane as the carbon acid.

Use of transition metal complexes as catalysts has been the area of interest for many researchers during the past several decades. Activation of H_2O_2 by transition metal complexes has been widely applied to chemical synthesis, environmental studies, effluent treatment and sterilization processes, etc. [15–21]. This method has gained much importance, particularly in the area of oxidation of dyes [22–24], due to its technical and environmental efficiency compared to the existing physicochemical techniques that are economically unattractive.

Our attempt to use one of the synthesized Mannich aminomethylation products as catalysts in the H_2O_2 induced degradation of pyrocatechol violet dye, taken as a model compound, has been proved to be successful.

2. Experimental

Glycine (AR) and 2-propanol was supplied by SRL laboratories, nitromethane and pyrocatechol violet

* Corresponding author. Tel.: +91 4422351137.
E-mail address: doc_raghavan@rediffmail.com (A. Raghavan).

0277-5387/$ - see front matter © 2007 Elsevier Ltd. All rights reserved.
doi:10.1016/j.poly.2007.03.018

{2-[(3,4-dihydroxyphenyl)(3-hydroxy-4-oxocyclohexa-2,5-dien-1-ylidene)methyl] benzenesulphonic acid} (PCV) were obtained from Lancaster chemicals, 37% aqueous formaldehyde (HCHO) solution and AR grade hydrogen peroxide (30%) free of inhibitors were obtained from Merck. The initial concentration of H_2O_2 was determined iodometrically using a standard solution of sodium thiosulphate. Tetra(*n*-butyl)ammonium perchlorate (TBAP) was obtained from Fluka chemicals. Reference chromogen, 2,2′-azino-bis(3-ethylbenz-thiazoline)-6-sulphonate diammonium salt (ABTS), was purchased from Aldrich chemicals. $Cu(gly)_2 \cdot H_2O$, $Ni(gly)_2 \cdot 2H_2O$ and $Zn(gly)_2 \cdot H_2O$ complexes were prepared as reported in literature [25].

2.1. Physical measurements

Electronic spectra of the complexes and kinetic measurements were carried out in a Shimadzu UV-160A spectrophotometer. For the electronic and ESR spectral analysis, solutions of *ca.* 1×10^{-3} M concentration of the complexes were used and the pH was adjusted by the addition of microlitres of HCl and $HClO_4$ solutions respectively. The infrared spectra were recorded on a Thermo Mattson Satellite FT-IR spectrophotometer with KBr discs in the frequency range 4000–450 cm^{-1}. Elemental analyses were carried out using an Elementar Vario EL III Carlo Erba 1108 analyzer available at CDRI, Lucknow. FAB mass spectra were recorded on a Jeol SX-102 analyzer available at CDRI, Lucknow. ESR measurements were done using BRUKER X-Band EMX-EPR spectrometer available at CLRI, Chennai. About 3 mM solutions of the complexes in DMSO were used for ESR measurements at 77 K. Cyclic Voltammograms were obtained on CHI600A electrochemical analyzer. The measurements were carried out under oxygen-free conditions using a three-electrode cell, in which a glassy carbon electrode was the working electrode, a saturated Ag/AgCl electrode was the reference electrode and a platinum wire was used as the auxiliary electrode. TBAP was used as the supporting electrolyte. Thermogravimetric analyses (TGA) for the complexes were obtained using SDT Q600 V8.0 Build 95 thermal analyzer from 30 °C to 700 °C at a heating rate of 10 °C min^{-1} under nitrogen atmosphere. [^{1}H] and [^{13}C] NMR spectra were recorded at ambient temperature with a Jeol GSX 400 MHz and 100 MHz NMR spectrometer respectively in DMSO-d_6 with TMS as internal reference.

2.2. Reactions and syntheses

All reactions of $M(gly)_2$, where M = Cu, Ni and Zn, with formaldehyde and nitromethane were carried out in the absence of base and at pH 9.0, maintained using aqueous Na_2CO_3 solution.

2.2.1. [(1,7-dinitro-3,5-dioxa-9,12-diazabicyclo[5.3.3]-tridecane)diacetato]copper(II) (**1a**)

To a solution of $Cu(gly)_2 \cdot H_2O$ (1 g, 4.35 mmol) in 100 ml of water/methanol mixture (3:1), formaldehyde (5.2 ml, 0.07 mol) and nitromethane (0.9 ml, 17.4 mmol) were added dropwise with constant stirring. After complete addition of formaldehyde and nitromethane, the reaction mixture was stirred continuously at room temperature for another 10 h. The reaction mixture was then concentrated to one-third of its volume (~30 ml) using rotary evaporator and filtered. Purple colored product formed after several days on standing at room temperature was filtered from solution, washed with ethanol and ether and dried over $CaCl_2$. Yield: 1.22 g, 61%. *Anal.* Calc. for $C_{13}H_{18}N_4O_{10}Cu \cdot 0.5H_2O$: C, 33.72; H, 4.10; N, 12.10; O, 36.32. Found: C, 33.54; H, 4.23; N, 11.98; O, 36.94%. λ_{max}(DMSO)/nm 294 (ε/dm^3 mol^{-1} cm^{-1} 3399.9) and 638 (266.4). Selected IR peaks (cm^{-1}): 3415, 3069, 2992, 2967, 2895, 2879, 1661, 1541, 1437, 1361, 1152, 1142, 1110, 1055, 940, 906, 836, 782, 563, 509, 460. Mass (FAB) $m/z = 462$ (M^+).

2.2.2. [N,N′-1,3-(2-nitropropanediyl)bis(oxazolidine-4-carboxylato)]copper(II) (**1b**)

To a solution of $Cu(gly)_2 \cdot H_2O$ (1 g, 4.35 mmol) in 100 ml of water/methanol mixture (3:1), formaldehyde (5.2 ml, 0.07 mol) and nitromethane (0.9 ml, 17.4 mmol) were added dropwise with constant stirring. The pH of the solution was maintained at 9.0 using dilute Na_2CO_3 solution. After complete addition of formaldehyde and nitromethane, the reaction mixture was stirred continuously at room temperature for 24 h. The solution was then concentrated to one-third of its volume (~30 ml) using rotary evaporator and filtered. Blue colored product formed after several days on standing at room temperature was filtered from solution, washed with ethanol and ether and dried over $CaCl_2$. Yield: 0.92 g, 56%. *Anal.* Calc. for $C_{11}H_{15}N_3O_8Cu$: C, 34.68; H, 3.94; N, 11.03; O, 33.63. Found: C, 34.82; H, 3.89; N, 11.24; O, 33.37%. λ_{max}(DMSO)/nm 291 (ε/dm^3 mol^{-1} cm^{-1} 2100.9) and 620 (70.8). Selected IR peaks (cm^{-1}): 2923, 1655, 1606, 1553, 1464, 1394, 1349, 1256, 1138, 1104, 1084, 1019, 938, 832, 803, 750, 603, 501. FAB mass $m/z = 380$ (M^+).

2.2.3. [(1,7-dinitro-3,5-dioxa-9,12-diazabicyclo[5.3.3]-tridecane)diacetato]nickel(II) (**2a**)

To a solution of $Ni(gly)_2 \cdot 2H_2O$ (1 g, 4.12 mmol) in 100 ml of water/methanol mixture (3:1), formaldehyde (5.2 ml, 0.07 mol) and nitromethane (0.9 ml, 16.5 mmol) were added dropwise with constant stirring. After complete addition of formaldehyde and nitromethane, the reaction mixture was stirred continuously at room temperature for another 10 h. The reaction mixture was then concentrated to one-third of its volume (~30 ml) using rotary evaporator and filtered. Greenish-blue product formed after a few days on standing at room temperature was filtered from solution, washed with ethanol, ether and dried over $CaCl_2$. Yield: 1.20 g, 58%. *Anal.* Calc. for $C_{13}H_{18}N_4O_{10}Ni \cdot 3H_2O$: C, 31.03; H, 4.77; N, 11.14; O, 41.37. Found: C, 31.36; H, 4.81; N, 11.02; O, 41.55%. λ_{max}(H_2O)/nm 301 (ε/dm^3 mol^{-1} cm^{-1} 3661.9) and 638 (162.9). Selected IR peaks (cm^{-1}): 3510, 3286, 3074, 2874, 1627, 1533, 1455, 1394, 1337,

1284, 1235, 1195, 1113, 1072, 1015, 1006, 946, 909, 856, 775, 681, 612, 559, 506. No product could be isolated under alkaline condition at pH 9.0.

2.2.4. *[(1,7-dinitro-3,5-dioxa-9,12-diazabicyclo[5.3.3]-tridecane)diacetato]zinc(II) (**3a**)*

To a solution of $Zn(gly)_2 \cdot H_2O$ (1 g, 4.32 mmol) in 100 ml of water/methanol mixture (3:1), formaldehyde (5.2 ml, 0.07 mol) and nitromethane (0.9 ml, 17.3 mmol) were added dropwise with constant stirring. After complete addition of formaldehyde and nitromethane, the reaction mixture was stirred continuously at room temperature for 24 h. The reaction mixture was then concentrated to half its volume (~50 ml) using rotary evaporator and filtered. The product formed on standing at room temperature was filtered from solution, washed with ethanol, ether and dried over $CaCl_2$. Yield: 1.31 g, 62%. *Anal.* Calc. for $C_{13}H_{18}N_4O_{10}Zn \cdot 2H_2O$: C, 31.74; H, 4.47; N, 11.39; O, 39.07. Found: C, 31.88; H, 4.53; N, 11.45; O, 39.39%. $\lambda_{max}(H_2O)$/nm 290 (ε/dm^3 mol^{-1} cm^{-1} 200.3). Selected IR peaks (cm^{-1}): 3581, 3298, 2866, 1651, 1533, 1460, 1394, 1337, 1284, 1239, 1195, 1150, 1113, 1068, 1019, 995, 946, 913, 856, 775, 616, 554, 514. No product was formed under alkaline condition. ^{1}H NMR (DMSO-d_6): δ 4.47 (d, 2H, —O—CH_2—O—), 4.24 (t, 4H, —C—CH_2—O—), 3.80 (d, 2H, —N—CH_2—C—), 3.69 (s, 4H, —N—CH_2—C—), 3.60 (d, 2H, —N—CH_2—C—), 3.13 (d, 4H, —N—CH_2—C=O). ^{13}C NMR (DMSO-d_6): δ 173.80, 86.76, 82.88, 67.74, 63.98, 54.57, 52.63.

2.3. Degradation of PCV using *1a*

To a number of conical flasks of volume 100 cm^3 containing PCV/H_2O_2 mixture in double distilled water, thermostatted in water for 30 min, was added definite quantity of the catalyst and zero time was noted. The solution was stirred continuously using a magnetic stirrer. At regular time intervals, aliquots were withdrawn and the absorbance at $\lambda_{max} = 441$ nm, $\varepsilon = 15{,}766\ l\ mol^{-1}\ cm^{-1}$ was recorded. The absorbance of PCV/H_2O_2 mixture remains constant for several hours in the absence of the catalyst.

3. Results and discussion

Reactions of $M(gly)_2$ complexes with HCHO and nitromethane yielded only a single major product under the experimental conditions mentioned in this work. In the absence of a base (pH 4.5), $Cu(gly)_2$, $Ni(gly)_2$ and $Zn(gly)_2$ gave **1a**, **2a** and **3a** respectively as their products. Under alkaline condition (pH 9.0), reaction of $Cu(gly)_2$ with formaldehyde and nitromethane gave **1b** as the product and no stable product could be isolated from the reactions of $Ni(gly)_2$ and $Zn(gly)_2$ complexes.

All the synthesized complexes are stable in aqueous acid for several hours, as indicated by the electronic spectra of the complexes. The electronic spectra of the complexes do not show any shift in the position of the d–d band on lowering the pH to 2. Increased stability of bridged complexes has been proved from their constant d–d band position in the electronic spectrum at low pH values [26]. Since Cu(II) and Ni(II) complexes reported here also show constant d–d band position even at low pH values, these complexes are proposed to have a bridged structure. The ESR spectra of the copper complexes at low pH values also agree with the electronic spectral observations. The ESR spectra of the complexes **1a** and **1b** show the expected four-line ($2I + 1$) ESR pattern under both neutral and at low pH values as a result of coupling of the electron spin dipole ($s = 1/2$) with the copper nucleus dipole ($I = 3/2$). The ESR spectrum of a representative complex, **1b**, at two different pH values is shown in Fig. 1 which corroborates the results obtained for other bridged complexes [26]. Hence, both electronic and ESR spectral studies suggest a bridged structure for the complexes and the non-formation of species such as $[CuL]^+$ at lower pH values.

The IR spectra of the complexes show strong absorptions at ~1550 cm^{-1} and 1350 cm^{-1} corresponding to —NO_2 stretching vibrations. Peaks corresponding to —NH vibrations are absent in the IR spectrum of all the four complexes confirming the absence of free amino protons in the products. In the complexes **1a**, **2a** and **3a**, the

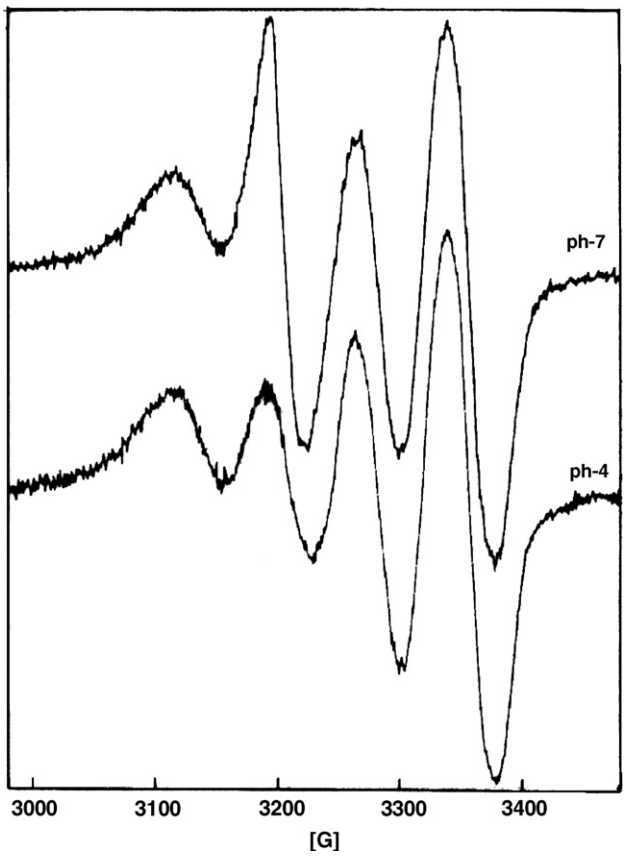


Fig. 1. Room temperature ESR spectra of **1b** at two different pHs at microwave frequency of 9.692 GHz and field modulation frequency of 100 kHz.

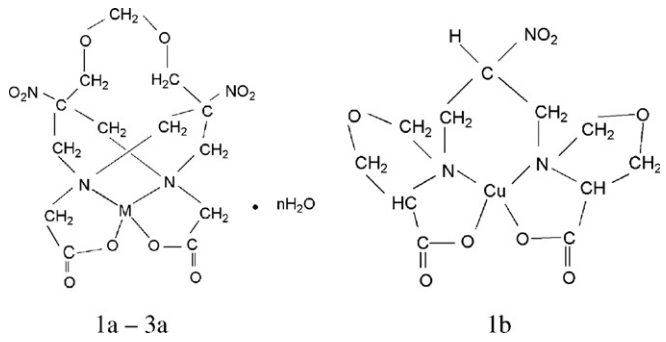


Fig. 2. Proposed structure for the synthesized complexes **1a**: M = Cu, $n = 0.5$; **2a**: M = Ni, $n = 3$; **3a**: M = Zn, $n = 2$.

peak corresponding to ether function, —CH_2—O—CH_2—, is present around ~1113 cm^{-1} and is absent in the spectrum of **1b**. The IR spectrum of **1b** shows three closely spaced peaks between ~1200 cm^{-1} −1050 cm^{-1} corresponding to oxazolidine ring [12c] and is absent in the spectra of all the other products. Based on these observations, the proposed structures of the products are shown in Fig. 2. The proposed structures of the complexes **1a**, **1b**, **2a** and **3a** are further supported by microanalysis and FAB mass spectra of the complexes.

The formation of the products from the reaction of $M(gly)_2$ with NO_2CH_3 and HCHO can be explained as follows:

In the absence of a base, $M(gly)_2$ undergoes Mannich aminomethylation reaction with nitromethane and HCHO replacing all the four amino protons of the chelated amino acid complexes. The remaining acidic protons [6] of the two nitromethane molecules react further with three other molecules of HCHO resulting in the formation of product of the type, **1a**, containing ether type linkages. Product with similar structure has also been isolated by the reaction of $Ni(gly)_2$ with HCHO and ammonia [12d]. Thus, nitromethane also undergoes active condensation reaction with chelated amino acid complexes similar to ammonia.

Under alkaline conditions, nitromethane undergoes Mannich aminomethylation reaction replacing one proton of each amino group of the metal(II) complexes. This is followed by aldol condensation of the HCHO molecules with the α-carbon protons to give oxazolidine ring containing compound **1b**.

Thermal analysis of the complexes shows weight loss at very high temperatures, all above 150 °C. Compound **1a** is found to be the most thermally stable product showing a weight loss of 1.9% above 221 °C and remains stable without any loss in weight up to 700 °C. The other three products show different percentages of weight loss at various higher temperatures. The percentage weight losses for initial decomposition of all the compounds are given in Table 1.

Table 1
Thermal decomposition of the complexes

Complexes	Range of decomposition (°C)	Weight loss (%)
1a	221–254	1.9
1b	300–350	63.4
2a	230–255	38.6
3a	188–235	42.2

3.1. ESR spectroscopy

The ESR spectrum of the product **1a** shows three hyperfine splitting lines and the fourth line is merged with the $g_\perp$ line indicating that the product exists as a monomer in solution and some slight rhombic character appears to be present. Because of the poor resolution of the ESR spectrum, computer simulation was not attempted. The spectral parameters indicate approximately square planar co-ordination around the copper(II) ion. Fig. 3a shows the ESR spectrum of the complex **1a** with $g_\parallel = 2.32$, $g_\perp = 2.06$, $A_\parallel = 175.5 \times 10^{-4}$ cm^{-1}. In the ESR spectrum of **1b**, the lines marked with arrows correspond to the triplet state ESR lines arising from dimerization of the Cu complex. We have arrived at this conclusion based on the discussion in an earlier report [27] where, a clear indication of dimeriza-

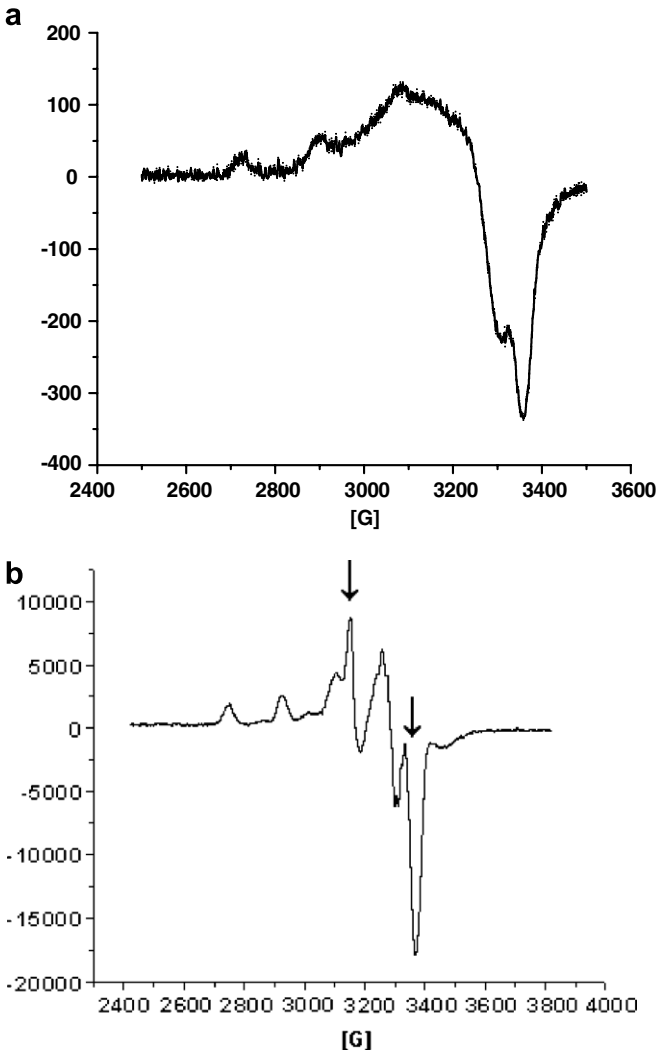


Fig. 3. X-band ESR spectrum of **1a** (a) and **1b** (b) at 77 K in DMSO at microwave frequency of 9.492 GHz and field modulation frequency of 100 kHz.

tion to form a triplet state has been shown to be present by computer simulation. From the ESR spectrum, we could clearly identify hyperfine coupling from two equivalent ^{63,65}Cu nuclei. In the ESR studies on this and related systems, we observed that the complex **1a** exists mainly as monomeric species in solution and complex **1b** exists as a mixture of monomer and dimeric units in solution. A similar identification of coexistence of monomer and dimeric Cu species in solution has been made by earlier workers [28]. Fig. 3b shows the ESR spectrum of the complex **1b** with $g_{\parallel} = 2.27$, $g_{\perp} = 2.09$ and $A_{\parallel} = 185.4 \times 10^{-4}$ cm^{-1}.

3.2. NMR spectroscopy

The ^{1}H NMR spectrum of **3a** in DMSO-d_6 shows peaks corresponding to six magnetically different protons. The assignment of the δ values for the protons is given under the experimental section. The ^{13}C NMR spectrum shows seven signals corresponding to seven different carbon atoms. The δ values exactly match that from the environment of the carbon atoms. Thus, NMR spectra of the compound lend further support to the proposed structure for the complex, **3a**.

3.3. Electrochemical studies

The electrochemical properties of the complexes were studied using cyclic voltammetry in DMSO solution containing TBAP as the supporting electrolyte. The electrochemical data of the complexes are given in Table 2. The cyclic voltammograms of the complexes are shown in Fig. 4.

All the complexes show a quasi-reversible two step electron transfer process as is evidenced from the following: The $E_{1/2}$ values are independent of scan rate; ΔE_p increases with increasing scan rate and is greater than 60 mV. The peak currents i_{pc} and i_{pa} are not equal. All complexes show metal and ligand (—NO_2) reduction peaks in the cathodic potential range −0.43 to − 0.71 V and −1.55 to −1.78 V respectively. Hence the complexes contain two reducible species which undergo reduction at two different cathodic potentials. The complexes **1a**, **2a** and **3a** show single oxidation peak at potentials +1.58, +1.19 and +1.24 V respectively. High cathodic potential values and irreversibility

Table 2
Electrochemical data[a] of the complexes

Complexes	E^1_{pc} (V)	E^1_{pa} (V)	ΔE^1_p (mV)	$E^1_{1/2}$ (V)	E^2_{pc} (V)	E^2_{pa} (V)	ΔE^2_p (mV)	$E^2_{1/2}$ (V)
1a	−0.43				−1.78			
1b	−0.71	−0.62	90	−0.66	−1.62			
2a	−0.68	−0.61	70	−0.64	−1.55	−1.44	110	−1.49
3a	−0.70				−1.77			

[a] Measured on a Pt working electrode vs. a non-aqueous Ag/Ag$^+$ reference electrode; scan rate 75 mV s^{-1}; supporting electrolyte, tetra-*N*-butylammonium perchlorate (0.1 mol dm^{-3}); complex concentration, 1 mmol dm^{-3}; E_{pc} and E_{pa} are the cathodic and anodic peak potentials for the metal (1) and ligand (2) reduction processes respectively.

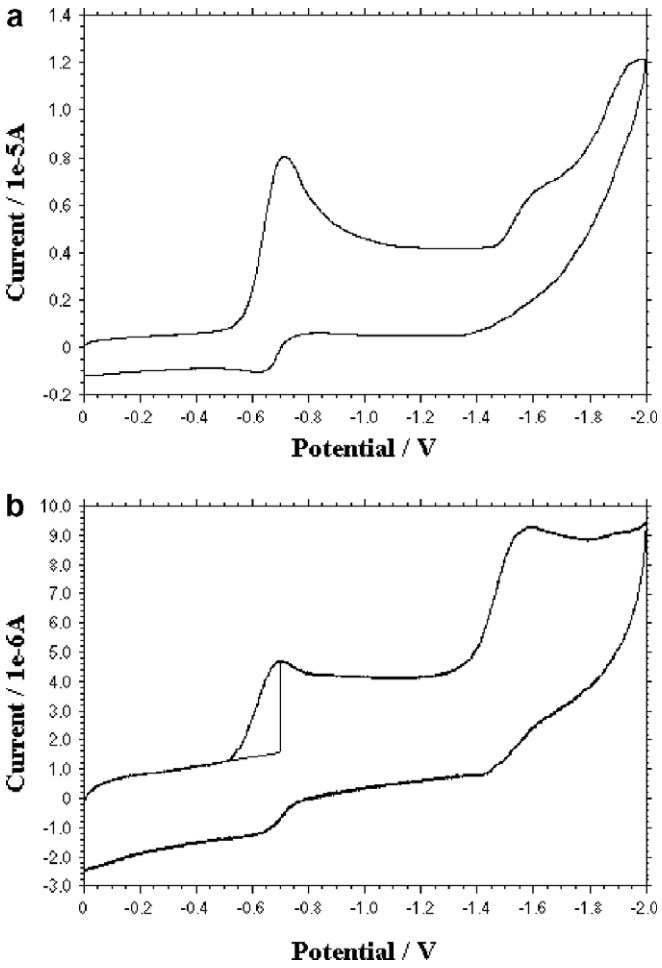


Fig. 4. Cyclic Voltammograms of the complexes **1b** (a) and **2a** (b).

of the M(II)/M(I) reduction process are characteristic of metal complexes having planar geometry [29]. Bridged complexes tend to possess planar geometry and show irreversible electrochemical metal reduction process due to stabilization of metal ion in its higher oxidation state. All the synthesized complexes reported here also show irreversible M(II)/M(I) reduction at high negative values confirming the planar geometry and a bridged structure for all the complexes.

3.4. Catalytic activity

Spectrophotometric measurements in phosphate buffer solutions showed no change in absorbance for the PCV/H_2O_2 mixture for several hours. However, an immediate decrease in absorbance at 441 nm was observed by the introduction of the catalyst (Fig. 5).

The kinetic measurements were carried out under pseudo-first-order conditions with respect to [PCV]. The value of the rate constant, k, is obtained from the slope of the straight lines of the equation, $\ln A_t = \ln A_0 - kt$, where A_t is the absorbance at time t, A_0 is the absorbance at time = 0.

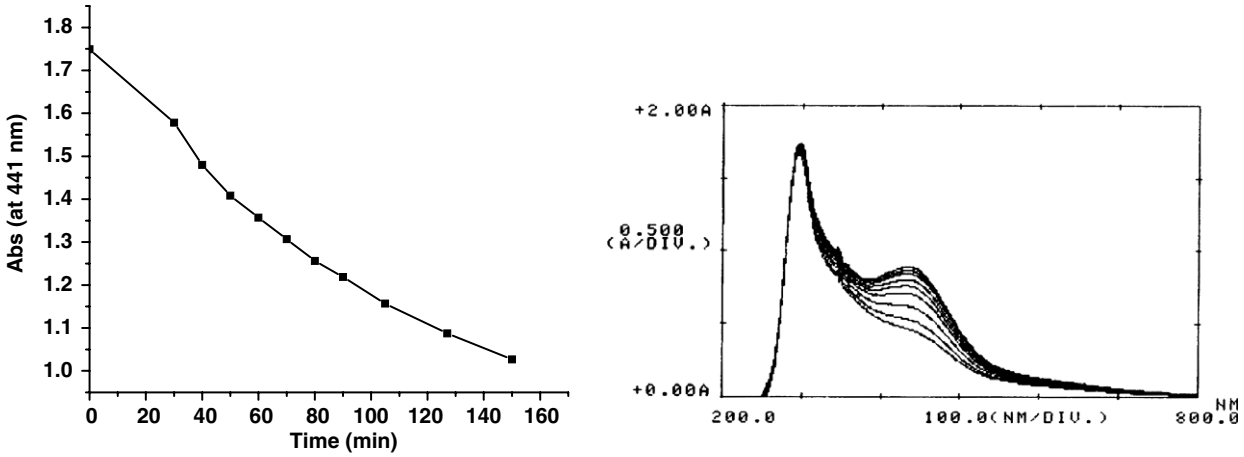


Fig. 5. The variation of absorbance for the reaction of 1.2×10^{-4} M $[PCV]_0$ with 0.01 M $[H_2O_2]_0$ in the presence of 0.01 g of the catalyst at 30 °C.

The order of the reaction with respect to $[H_2O_2]_0$ and $[PCV]_0$ was determined by carrying out experiments at constant temperature and pH. The order of the reaction was found to be one with respect to $[H_2O_2]$ by varying the concentration of $[H_2O_2]_0$ in the range 0.009–0.02 M at 30 °C (Fig. 6) at constant $[PCV]_0$. Thus the catalyst activates H_2O_2 and releases hydroxyl or perhydroxyl radical which attacks PCV leading to its degradation. The influence of [PCV] on the rate of reaction was studied by varying $[PCV]_0$ in the range $0.5–3.8 \times 10^{-4}$ M at 30 °C (Fig. 7) at constant $[H_2O_2]_0$. The reaction obeyed a first-order dependence at lower concentrations of $[H_2O_2]_0$ and $[PCV]_0$ and the rate of the reaction decreases at higher concentrations.

The rate of the reaction was found to increase with increase in the concentration of the catalyst. The effect of catalyst concentration on the degradation of the dye was studied by fixing $[PCV]_0$ and $[H_2O_2]_0$ at constant values and taking 0.01, 0.02, 0.03 g and 0.04 g of the catalyst.

The effect of pH on the reaction rate was studied using phosphate buffer solution in the pH range 5–9 and for pH > 9, drops of NaOH solution was added to the buffer solution. Under acidic condition, pH < 7, PCV exists in the form, H_3L^- (yellow), having maximum absorbance at 441 nm whereas, in alkaline medium, pH > 7, it exists as H_2L^{2-} (violet), having maximum absorbance at 596 nm [30]. The rate constant value increases with pH up to 8.0 and then starts decreasing at higher pH values (Fig. 8). The increase in the rate of the reaction under alkaline condition could be attributed to the deprotonation of H_2O_2 which effectively produce peroxo intermediate [31]. Thus rate of degradation of PCV is enhanced by the formation of the active radical species. Moreover, changes in the electronic configuration of H_2L^{2-} anion of PCV also facilitate its rapid degradation.

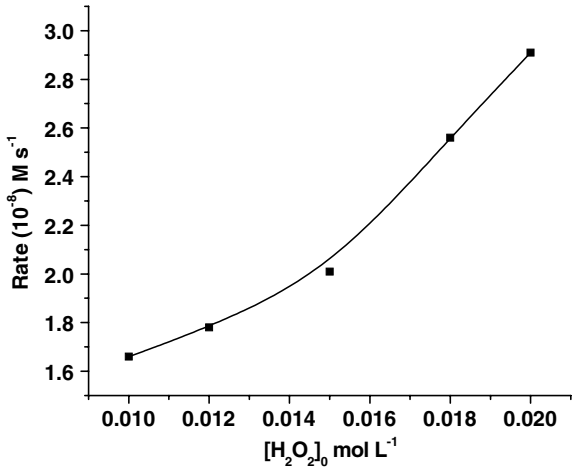


Fig. 6. Dependence of the initial rate on the $[H_2O_2]_0$ for the reaction of 1.2×10^{-4} M $[PCV]_0$ in the presence of 0.01 g of the catalyst at 30 °C.

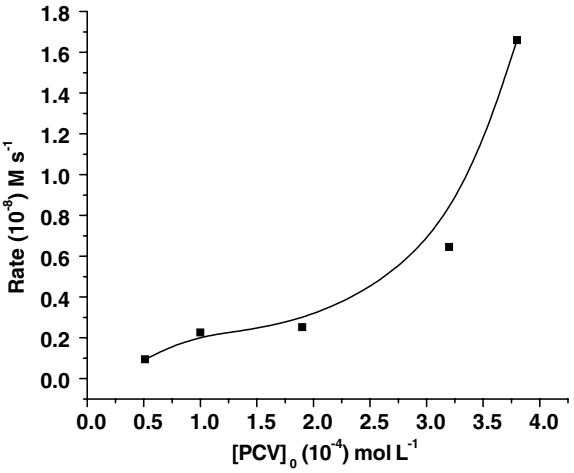


Fig. 7. Dependence of the initial rate on the $[PCV]_0$ for the reaction of 0.01 M $[H_2O_2]_0$ in the presence of 0.01 g of the catalyst at 30 °C.

The effect of chloride ions on the reaction rate was studied at fixed concentrations of $[PCV]_0$, $[H_2O_2]_0$ and the catalyst. The rate constant was found to increase with increasing [NaCl] (Fig. 9). This increase in rate can be attributed to the oxidation of chloride ions by H_2O_2 to produce other oxidizing agents such as OCl^- and Cl_2 that assist in the oxidation of PCV [32].

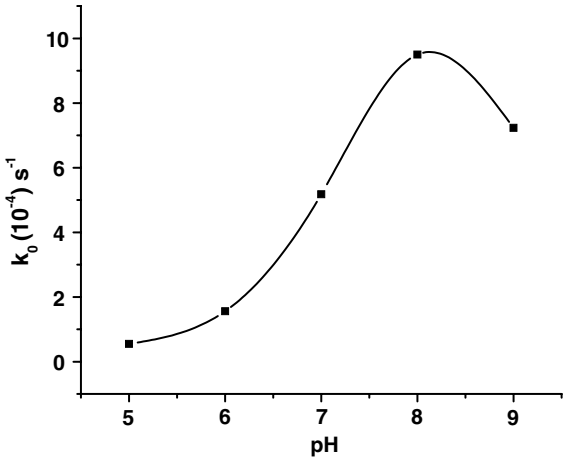


Fig. 8. Dependence of the rate constant on pH for the reaction of 1.2×10^{-4} M $[PCV]_0$ with 0.01 M $[H_2O_2]_0$ in the presence of 0.01 g of the catalyst at 30 °C.

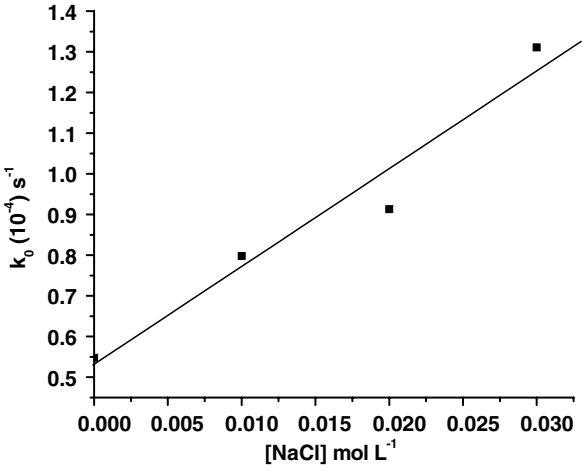


Fig. 9. Variation of rate constant with [NaCl] for the reaction of 1.2×10^{-4} M $[PCV]_0$ with 0.01 M $[H_2O_2]_0$ and 0.01 g of the catalyst at 30 °C.

Decomposition of H_2O_2 by transition metal complexes producing free radicals has already been proved by spectroscopic methods [33]. Generation of free radical species from H_2O_2 decomposition using transition metal complex has already been proved using organic radical scavenger, 2-propanol and a chromogen 2,2′-azino-bis(3-ethylbenzthiazoline)-6-sulphonate diammonium salt (ABTS) [34]. We confirmed the generation of free radical from H_2O_2 decomposition during the degradation process using different techniques. Addition of 2-propanol, a known organic radical scavenger [34d], decreased the rate of the reaction to approximately 50% of the original rate obtained without the addition of 2-propanol (Fig. 10). The decrease in the rate of the reaction is due to quenching of radicals, generated during the degradation process, by the radical scavenger.

The generation of free radical was also confirmed using the chromogen ABTS. It is known that the chromogen

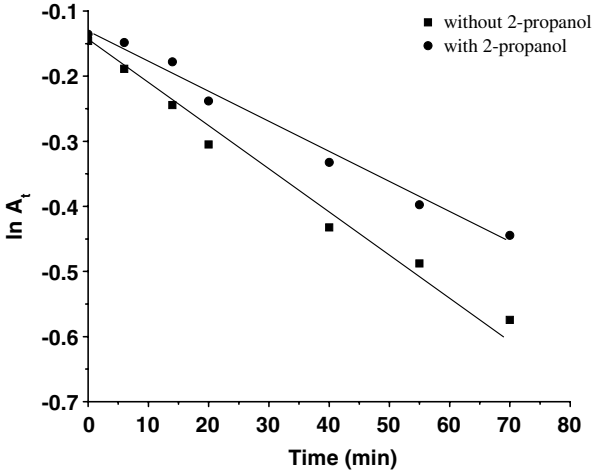


Fig. 10. Effect of addition of the radical scavenger 2-propanol on the rate of the reaction.

ABTS undergo oxidation in the presence of inorganic free radicals such as OH· [35], i.e. $ABTS + OH^{\cdot} \rightarrow ABTS^{+\cdot} + OH^-$, to give the persistent radical cation $ABTS^{+\cdot}$. In the present investigation, formation of $ABTS^{+\cdot}$ is used to confirm the generation of radical species during the degradation process. Fig. 11 shows the absorption signal of the radical cation $ABTS^{+\cdot}$ at 414 nm and 660 nm, generated in the presence of 1 mmol dm^{-3} of the complex, 4 mmol dm^{-3} ABTS and 3 mmol dm^{-3} H_2O_2. The radical cation $ABTS^{+\cdot}$ was found to be generated only when both the catalyst and H_2O_2 are present in ABTS solution.

It is well established that irradiation of H_2O_2 by UV-light leads to the formation of OH radical [36]. In the present investigation, enhancement of the reaction rate by 40% upon irradiation of the reaction mixture with UV-light ($\lambda = 254$ nm) also proves that the degradation process proceed via a free radical mechanism. The increase in the rate of the reaction by irradiation of UV-light, $\lambda = 254$ nm, is shown in Fig. 12.

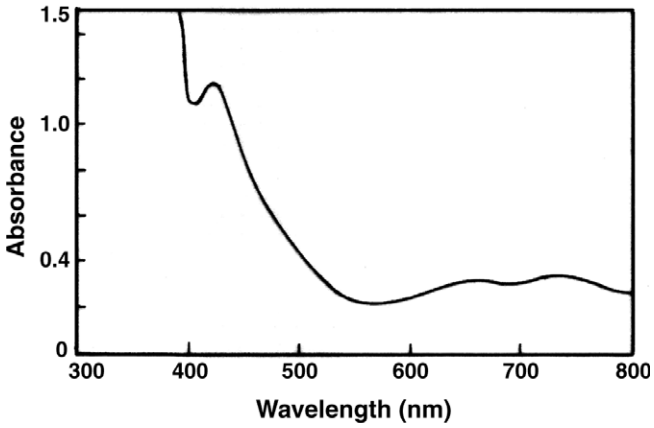


Fig. 11. Absorption spectrum of the radical cation $ABTS^{+\cdot}$ generated in the presence of 1 mmol dm^{-3} of the complex, 4 mmol dm^{-3} ABTS and 3 mmol dm^{-3} H_2O_2.

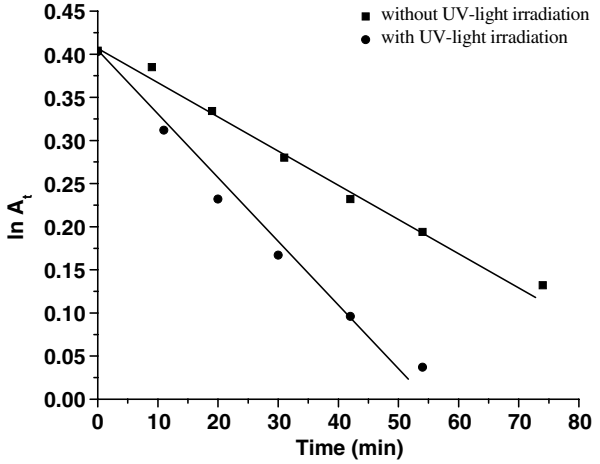


Fig. 12. Effect of irradiation of UV-light on the reaction mixture of 1.2×10^{-4} M $[PCV]_0$ with 0.01 M $[H_2O_2]_0$ in the presence of 0.01 g of the catalyst at 30 °C.

Thus, from the experimental results and discussion, it is clear that the degradation process follows a free radical mechanism involving the formation of highly active hydroxyl radical by the interaction of the catalyst with H_2O_2. These oxidizing agents attack PCV leading to its degradation and formation of other oxidation products as follows:

$$[Cu^{II}L] + H_2O_2 \underset{k_{-1}}{\overset{k_1}{\rightleftarrows}} \underset{\text{peroxo complex}}{[Cu^{II}L(HO_2^-)]} + H^+ \quad (1)$$

$$[Cu^{II}L(HO_2^-)] \xrightarrow{k_2} [Cu^{I}L] + OH^{\cdot} + \frac{1}{2}O_2 \quad (2)$$

$$PCV + HO^{\cdot} \xrightarrow{k_3} \underset{\text{Dye-radical adduct}}{[PCV(HO^{\cdot})]} \quad (3)$$

$$[PCV(HO^{\cdot})] \xrightarrow[\text{slow}]{k_4} \text{Oxidation products} \quad (4)$$

$$[Cu^{I}L] + HO^{\cdot} \xrightarrow{k_5} [Cu^{II}L] + OH^- \quad (5)$$

$$OH^- + H^+ \rightarrow H_2O \quad (6)$$

From Eq. (1), the concentration of the peroxo complex is given by

$$[[Cu^{II}L(HO_2^-)]] = K_1[[Cu^{II}L]][H_2O_2]/[H^+] \quad (7)$$

where $K_1 = k_1/k_{-1}$.

Applying steady-state approximation for the determination of $[HO^{\cdot}]$ and $[PCV(OH^{\cdot})]$,

$$\frac{d[OH^{\cdot}]}{dt} = k_2[[Cu^{II}L(HO_2^-)]] - k_3[PCV][HO^{\cdot}] - k_5[[Cu^{I}L]][OH^{\cdot}] = 0 \quad (8)$$

$$\frac{d[PCV(HO^{\cdot})]}{dt} = k_3[PCV][HO^{\cdot}] - k_4[PCV(HO^{\cdot})] = 0 \quad (9)$$

Assuming $[Cu^{II}L(HO_2^-)] = [Cu^{I}L]$ and by substituting from Eq. (7) into Eq. (8) we get,

$$[HO^{\cdot}] = \frac{k_2K_1[[Cu^{II}L]][H_2O_2]}{k_3[PCV][H^+] + k_5K_1[[Cu^{II}L]][H_2O_2]} \quad (10)$$

Substituting for $[HO^{\cdot}]$ from Eq. (10) in (9) we get,

$$[PCV(HO)^{\cdot}] = \frac{k_2k_3K_1[PCV][[Cu^{II}L]][H_2O_2]}{k_3k_4[PCV][H^+] + k_4k_5K_1[[Cu^{II}L]][H_2O_2]} \quad (11)$$

From Eq. (4),

$$\text{Rate} = k_4[PCV(HO)^{\cdot}] \quad (12)$$

Substituting for $[PCV(HO^{\cdot})]$ in Eq. (12) we get,

$$\text{Rate} = \frac{k_2k_3K_1[PCV][[Cu^{II}L]][H_2O_2]}{k_3[PCV][H^+] + k_5K_1[[Cu^{II}L]][H_2O_2]} \quad (13)$$

Expressing the initial concentration of both reactants, $[PCV]_0$ and $[H_2O_2]_0$

$$[H_2O_2]_0 = [H_2O_2] + [[Cu^{II}L(HO_2^-)]] + [OH^{\cdot}] \quad (14)$$

$$[PCV]_0 = [PCV] + [PCV(HO^{\cdot})] \quad (15)$$

Substituting from Eqs. (7) and (10) and assuming $k_3[PCV][H^+] \ll k_5K_1[[Cu^{II}L]][H_2O_2]$

$$[H_2O_2] = \frac{[H^+]\{k_5[H_2O_2]_0 - k_2\}}{k_5[H^+] + k_5K_1[[Cu^{II}L]]} \quad (16)$$

Substituting Eq. (11) in Eq. (15) and assuming $k_3k_4[PCV][H^+] \ll k_4k_5K_1[Cu^{II}L]][H_2O_2]$

$$[PCV] = \frac{k_4k_5[PCV]_0}{k_4k_5 + k_2k_3} \quad (17)$$

Substituting for $[H_2O_2]$ and $[PCV]$ in Eq. (13) we get,

$$\text{Rate} = \frac{k_2k_3k_4k_5K_1[PCV]_0[[Cu^{II}L]][H_2O_2]_0}{k_3k_4k_5[PCV]_0\{[H^+] + K_1[[Cu^{II}]]\} + K_1k_5[[Cu^{II}L]][H_2O_2]_0\{K_1k_5k_4 + k_2k_3\}}$$

Assuming $k_4k_5K_1 \gg k_2k_3$,

$$\text{Rate} = \frac{k_2k_3K_1[PCV]_0[[Cu^{II}L]][H_2O_2]_0}{k_3[PCV]_0\{[H^+] + K_1[[Cu^{II}L]]\} + K_1^2k_5[[Cu^{II}L]][H_2O_2]_0} \quad (18)$$

According to Eq. (18), the rate of the reaction is first-order with respect to $[PCV]_0$ and $[H_2O_2]_0$ at lower initial concentrations and is found to be the same experimentally, in the concentration ranges selected for the study (Figs. 6 and 7). The rate of the reaction attains a limiting value at higher concentrations. The rate also increases with increasing pH and attains a maximum value at pH 8.0 after which it decreases.

4. Conclusion

Mannich aminomethylation reactions involving $M(gly)_2$, HCHO and nitromethane have been carried out. Different products were obtained under acidic and alkaline pH conditions. Mannich aminomethylation reaction was

found to take place under both acidic and alkaline conditions, whereas, aldol condensation was found to occur only under alkaline condition, particularly with $Cu(gly)_2$ complex and not with the other glycinato complexes such as $Ni(gly)_2$ and $Zn(gly)_2$. The Mannich aminomethylation product obtained using $Cu(gly)_2$, HCHO and nitromethane under acidic condition has been used as catalyst in the H_2O_2 induced degradation of pyrocatechol violet dye and has been found to be effective. Hydrogen peroxide alone could not bring about degradation of PCV, but the addition of the catalyst increased the rate of decomposition of H_2O_2 producing hydroxyl radical which efficiently degraded the dye. The rate of degradation has also been correlated with variations in $[PCV]_0$, $[H_2O_2]_0$, pH, NaCl and catalyst concentration and a mechanism has been proposed based on the experimental observations.

Acknowledgements

We thank Dr. K. Victor Babu, Scientist, CLRI for his help in ESR interpretation.

Appendix A. Supplementary material

Supplementary data associated with this article can be found, in the online version, at doi:10.1016/j.poly.2007.03.018.

References

[1] M. Salavati-Niasari, Polyhedron 24 (2005) 1405, and references cited therein.
[2] M. Salavati-Niasari, A. Amiri, Transition Met. Chem. 30 (2005) 720.
[3] L. Shen, J. Liu, J. Gu, Z. Hu, Y. Xu, Struct. Chem. 13 (2002) 37.
[4] P.V. Bernhardt, P.C. Sharpe, Inorg. Chem. 37 (1998) 1629.
[5] L. Fabbrizzi, M. Licchelli, A.M.M. Lanfredi, O. Vassalli, F. Ugozzoli, Inorg. Chem. 35 (1996) 1582, and references cited therein.
[6] G.A. Lawrance, M. Maeder, M.A. O'leary, F. Woon, Polyhedron 9 (1990) 2227.
[7] G.A. Lawrance, T.M. Manning, M.A. O'leary, Polyhedron 7 (1988) 1263.
[8] S.B. Teo, S.G. Teoh, T.W. Hambley, M.R. Snow, J. Chem. Soc., Dalton Trans. (1986) 553.
[9] J. Balla, P.V. Bernhardt, P. Buglyo, P. Comba, T.W. Hambley, R. Schmidlin, S. Stebler, K. Varnagy, J. Chem. Soc., Dalton Trans. (1993) 1143.
[10] S.B. Teo, C.H. Ng, S.G. Teoh, H.-K. Fun, J. Coord. Chem. 24 (1991) 151.
[11] C.H. Ng, S.B. Teo, S.G. Teoh, J.P. Declercq, S.W. Ng, Aust. J. Chem. 54 (2001) 743.
[12] (a) C.H. Ng, C.M. Lin, T.M. Chang, S.G. Teoh, S.W. Yap, S.W. Ng, Polyhedron 25 (2006) 1287;
(b) C.H. Ng, Y.T. Lim, N. Moris, S.G. Teoh, Polyhedron 22 (2003) 521;
(c) C.H. Ng, T.S. Chong, S.G. Teoh, F. Adams, S.W. Ng, J. Chem. Soc., Dalton trans. (2002) 3361;
(d) S.B. Teo, S.G. Teoh, M.R. Snow, Inorg. Chim. Acta 85 (1984) L1.
[13] A.M. Sargeson, Pure Appl. Chem. 56 (1984) 1603.
[14] R.J. Geue, T.W. Hambley, J.M. Harrowfield, A.M. Sargeson, M.R. Snow, J. Am. Chem. Soc. 106 (1984) 5478.
[15] V. Conte, F.D. Furia, G. Licini, Appl. Catal. A: Gen. 157 (1997) 335.
[16] A.P. Deshmukh, V.G. Akerkar, M.M. Salunkhe, J. Mol. Catal. A: Chem. 153 (2000) 75.
[17] S. Velusamy, T. Punniamurthy, Tetrahedron Lett. 44 (2003) 8955.
[18] H.H. Monfared, Z. Amouei, J. Mol. Catal. A: Chem. 217 (2004) 161.
[19] T. Paczesniak, A. Sobkowiak, J. Mol. Catal. A: Chem. 194 (2003) 1.
[20] H.B. Dunford, Coord. Chem. Rev. 233 (2004) 311.
[21] T.-Y. Lin, C.-H. Wu, J. Catal. 232 (2005) 117.
[22] A.H. Gemeay, I.A. Mansour, R.G. El-Sharkawy, A.B. Zaki, J. Mol. Catal. A: Chem. 193 (2003) 109.
[23] A.H. Gemeay, J.A. Mansour, R.G. El-Sharkawy, A.B. Zaki, J. Colloid Interface Sci. 263 (2003) 228.
[24] I.A. Salem, Appl. Catal. B: Environ. 28 (2000) 153.
[25] (a) D.N. Sen, S. Mizushima, C. Curran, J.V. Quagliano, J. Am. Chem. Soc. 77 (1955) 211;
(b) B.W. Low, F.L. Hirshfeld, F.M. Richards, J. Am. Chem. Soc. 81 (1959) 4412.
[26] N. Arulsamy, B. Srinivas, P.S. Zacharias, Transition. Met. Chem. 15 (1990) 309.
[27] S. Supriya, A. Raghavan, V.R. Vijayaraghavan, K. Chinnakali, H.-K. Fun, J. Subramanian, Polyhedron (2007), doi:10.1016/j.poly.2007.02.017.
[28] P. Comba, T.W. Hambley, G.A. Lawrence, L.L. Martin, P. Renold, K. Varnagy, J. Chem. Soc., Dalton Trans. (1991) 277.
[29] R.D. Bereman, J.R. Dorfman, J. Bordner, D.P. Rillema, P. McCarthy, G.D. Shields, J. Inorg. Biochem. 16 (1982) 47.
[30] A. Ricciu, F. Secco, M. Venturini, B. Garcia, J.M. Leal, J. Phys. Chem. A 104 (2000) 7036.
[31] (a) I.A. Salem, Monatsh. Chem. 131 (2000) 1139;
(b) I.A. Salem, M. El-Maazawi, Chemosphere 41 (2000) 1173.
[32] I.A. Salem, Transition. Met. Chem. 25 (2000) 599.
[33] T. Ozawa, A. Hanaki, J. Chem. Soc. Chem. Commun. (1991) 330.
[34] (a) A.H. Gemeay, M.A. Salem, I.A. Salem, Colloids Surf. A 116 (1996) 277;
(b) I.A. Salem, R.I. El-hag, K.M.S. Khalil, Transition. Met. Chem. 25 (2000) 260;
(c) A.H. Gemeay, M.A. Salem, I.A. Salem, Colloids Surf. A 117 (1996) 245;
(d) M. Anbar, R.A. Munoz, P. Roma, J. Phys. Chem. 63 (1963) 2708.
[35] (a) B.S. Wolfenden, R.L. Willson, J. Chem. Soc., Perkin Trans. 2 (1982) 805;
(b) L.G. Forni, V.O. Mora-Arelano, J.E. Packer, R.L. Willson, J. Chem. Soc., Perkin Trans. 2 (1986) 1;
(c) S.L. Scott, W.-J. Chen, A. Bakac, J.H. Espenson, J. Phys. Chem. 97 (1993) 6710.
[36] (a) P.C. Selvaraj, V. Mahadevan, J. Mol. Catal. A 120 (1997) 47;
(b) E. Finkelstein, G.M. Rosen, E.J. Rauckman, J. Am. Chem. Soc 102 (1980) 4994;
(c) I.A. Alaton, I.A. Balcioglu, D.W. Bahneman, Water Res. 36 (2002) 1143;
(d) D. Georgiou, P. Melids, A. Aivasidis, K. Gimouhopoulos, Dyes and Pigments 54 (2002) 69.

Available online at www.sciencedirect.com
ScienceDirect
Polyhedron 26 (2007) 3397–3408
POLYHEDRON
www.elsevier.com/locate/poly

Aminoalkylbis(phenolate) [O,N,O] donor ligands for uranyl(VI) ion coordination: Syntheses, structures, and extraction studies

Harri Sopo, Kamal Goljahanpoor, Reijo Sillanpää *

Department of Chemistry, University of Jyväskylä, P.O. Box 35, FIN-40351, Jyväskylä, Finland

Received 16 February 2007; accepted 13 March 2007
Available online 30 March 2007

Abstract

The syntheses of five new aminoalkylbis(phenolate) ligands (as hydrochlorides) and their uranyl complexes are described. The reaction between uranyl nitrate hexahydrate and phenolic ligand [(*N*,*N*-bis(2-hydroxy-5-*tert*-butyl-3-methylbenzyl)-1-aminopropane) · HCl], $H_2L1 \cdot HCl$, forms a uranyl complex $[UO_2(HL1)_2] \cdot 2CH_3CN$ (**1**). The ligand [(*N*,*N*-bis(2-hydroxy-5-*tert*-butyl-3-methylbenzyl)-1-aminobutane) · HCl], $H_2L2 \cdot HCl$, forms a uranyl complex with a formula $[UO_2(HL2)_2] \cdot 2CH_3CN$ (**2**). The ligand [(*N*,*N*-bis(2-hydroxy-5-*tert*-butyl-3-methyl benzyl)-1-aminohexane) · HCl], $H_2L3 \cdot HCl$, yields a uranyl complex with a formula $[UO_2(HL3)_2] \cdot 2CH_3CN$ (**3**) and the ligand [(*N*,*N*-bis(2-hydroxy-5-*tert*-butyl-3-methylbenzyl)-cyclohexylamine) · HCl], $H_2L4 \cdot HCl$, yields a uranyl complex with a formula $[UO_2(HL4)_2]$ (**4**). The ligand [(*N*,*N*-bis(2-hydroxy-5-*tert*-butyl-3-methylbenzyl)-benzylamine) · HCl], $H_2L5 \cdot HCl$, forms a uranyl complex with a formula $[UO_2(HL5)_2] \cdot 2MeOH$ (**5**). The molecular structures of **1**, **2′** (**2** without methanol), **3, 4** and **5** were verified by X-ray crystallography. The complexes **1**–**5** are neutral zwitterions which form in a molar ratio of 1:2 (U to L) in the presence of a base (triethylamine) and bear similar mononuclear, distorted octahedral uranyl structures with the four coordinating phenoxo ligands forming an equatorial plane and resulting in a centrosymmetric structure for the uranyl ion. In uranyl ion extraction studies from water to dichloromethane with ligands $H_2L1 \cdot HCl$–$H_2L5 \cdot HCl$, the ligands $H_2L2 \cdot HCl$ and $H_2L4 \cdot HCl$ are the most effective ones.
© 2007 Elsevier Ltd. All rights reserved.

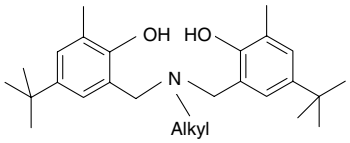
Keywords: Uranyl complex; Bisphenolate; Crystal structure; Uranyl extraction

1. Introduction

About 25–30% of the world's supply of electrical power is generated using nuclear sources [1]. This produces a vast amount of nuclear wastes to take care of and a risk of environmental contamination by radioactive material. The industrial procedure used to reprocess spent nuclear fuel is called PUREX in which the irradiated fuel is dissolved into nitric acid and an organic solvent composed of 30% tributyl phosphate in kerosene is used to recover the uranium and plutonium [2]. This liquid–liquid extraction method was developed in the 1950s and it is still the industry standard, although the process remains far from perfect [3]. The separation of uranium from sources such as phosphate rocks has been the subject of intense research worldwide [4]. In view of this extensive use of actinide extractors for different applications, it is logical to search for other options, either new methods or new selective ligands [5a–c]. For this purpose numerous kinds of solutions, e.g. expanded porphyrins [6], calixarenes [7], polyphenols [8], crown ethers [9a,9b], etc. have been presented. These types of compounds are quite bulky and some of them require the threading of the UO_2^{2+}-ion through a ring, which may be difficult. Thus there is a need for smaller and less rigid molecules containing O- or N-donor atoms or both, allowing a more flexible coordination of the UO_2^{2+}-ion. We have earlier reported that the aminoalcoholbis(phenolate) [O,N,O,O′] donor ligands of a relatively small size have good uranyl ion complexing properties [10a,10b]. Furthermore, the structure of these ligands offers a possibility to attach them on silica-gel, as described in an article

* Corresponding author. Tel.: +358 14 260 2603; fax: +358 14 260 2501.
E-mail address: resillan@jyu.fi (R. Sillanpää).

0277-5387/$ - see front matter © 2007 Elsevier Ltd. All rights reserved.
doi:10.1016/j.poly.2007.03.032



Ligand	*Alkyl*
H_2L1	propyl
H_2L2	butyl
H_2L3	hexyl
H_2L4	cyclohexyl
H_2L5	benzyl

Scheme 1. The ligands under study.

by Barbette et al. [11]. In the present study, we have prepared five new ligands by substituting the alcohol part of the aminoalcoholbis(phenolate) molecule with different alkyl groups, thus reducing the number of possible donor atoms in the coordinating molecules. This procedure also removes one polar atom (O) from the "outer sphere" of the coordinated molecule, making its exterior lipophilic after complexation and promoting the solubility of the formed complex into organic solvents which is an important feature in the extraction [2,12]. The ligand family under study is depicted in Scheme 1. Burke et al. [13] have prepared similar alkyl compounds with different phenol groups.

We have chosen 4-*tert*-butyl-2-methylphenol as a starting phenol due to the solubility behavior of the new ligands containing this phenol group. We have found that the ligands containing these groups form better crystalline solids as free ligands or uranyl complexes than the ligands containing 2,4-dimethylphenols.

The syntheses of these new ligands and their uranyl ion complexes are reported below. Also the X-ray diffraction structures are presented for the five uranyl complexes. In addition the ability of these ligands to extract uranyl ion from water to dichloromethane in different physical and chemical circumstances has been studied as it has been shown that various ligands have different optimal extraction conditions [14–18]. The effect of the anion used (uranyl nitrate versus uranyl acetate) on the extraction properties has also been studied in order to get a better understanding of the two-phase extraction system. The distribution pattern of the ligands and ions at a liquid/liquid interface may significantly contribute to the extraction rates [2,19].

2. Experimental

2.1. General information

1-Aminopropane (Sigma), 1-aminobutane (Merck), 1-aminohexane, cyclohexylamine (Fluka), benzylamine (Merck), triethylamine (Riedel-de Haën), 4-*tert*-butyl-2-methylphenol (Fluka), 37% formaldehyde (Merck), uranyl acetate dihydrate (Riedel-de Haën) and uranyl nitrate hexahydrate (Merck) were used as supplied. The ligands $H_2L1 \cdot HCl$–$H_2L5 \cdot HCl$ were synthesized by following mainly the procedure for methylamino-*N*,*N*-bis(1-methylene-2-naphthol) [13]. During the separation process the ligands were transformed to their hydrochlorides by treating them with HCl. The details of the syntheses are described below. The NMR spectra were recorded on a Bruker AVANCE DPX 250 FT NMR spectrometer or Bruker AVANCE DRX 500 FT NMR spectrometer. The ^1H and ^{13}C NMR spectra were recorded either in $CDCl_3$ or DMSO-d_6 at 30 °C. The chemical shifts are reported in ppm and referenced internally using the residual protio solvent resonances relative to tetramethylsilane ($CDCl_3$ δ 7.26, ^1H NMR; δ 77.0, ^{13}C NMR; DMSO-d_6 δ 2.50, ^1H NMR; δ 39.50, ^{13}C NMR). The mass spectrometric measurements were performed using a Micromass LCT time of flight (TOF) mass spectrometer with electrospray ionization (ESI-MS). Elemental analyses were performed using a VarioEl III elemental analyzer. The melting points were measured by Mettler Toledo FP62 Melting Point instrument and Perkin–Elmer Pyris Diamond TG/DTA Thermogravimetric/Differential Thermal Analyzer. The uranyl extraction samples were analyzed with inductively coupled plasma optical emission spectrometry (ICP-OES) at 385.958 nm using a Perkin–Elmer Optima 4300DV instrument. The pH's were measured with an Orion 720A pH-meter.

The synthesis of the ligand $H_2L1 \cdot HCl$ is described in detail below. The syntheses of the rest of the ligands followed the same procedure. Also, only the preparation of uranyl complex **1** is described in detail; the syntheses of the other complexes follow the same concept.

2.2. $H_2L1 \cdot HCl \cdot 1.5H_2O$[(*N*,*N*-bis(2-hydroxy-5-tert-butyl-3-methylbenzyl)-1-aminopropane · HCl) · $1.5H_2O$]

To a solution of 4-*tert*-butyl-2-methylphenol (3.28 g, 0.020 mol) in methanol (15 ml) (EtOH 15 ml in case of $H_2L3 \cdot HCl$, $H_2L4 \cdot HCl$ and $H_2L5 \cdot HCl$) and water (3 ml) was added aqueous formaldehyde (37%, 3.26 g, 0.040 mol), 1-aminopropane (0.60 g, 0.010 mol) and triethylamine ($V = 0.500$ ml, 0.004 mol). The resulting solution was kept in a water bath (50 °C) with stirring for 74 h (168 h in case of $H_2L2 \cdot HCl$). After that the solution was left to stand in the freezer for 24 h (48 h in case of $H_2L2 \cdot HCl$ and 94 h in case of $H_2L4 \cdot HCl$). During that time an oil phase separated from the main liquid. The liquid was decanted off and the oil was dissolved in 10 ml of cold MeOH. 4 ml of 6 M HCl was then added to the solution with stirring, leading to a formation of a white solid. The solid was filtered and washed with water (4×50 ml), recrystallized with EtOH (7 ml), washed with diethylether (10 ml) and dried. The yield was 2.15 g (45%). Mp: 156–157 °C. ^1H NMR ($CDCl_3$, 250 MHz): 0.93 (t, $J = 7.4$ Hz, 3H, alkyl CH_3), 1.25 (s, 18H, aryl *t*-butyl), 1.86 (m, 2H, $CH_3CH_2CH_2$), 2.44 (s, 6H, aryl

CH_3), 2.99 (m, 2H, NCH_2CH_2), 4.22 (d, 4H, NCH_2-aryl), 6.96 (d, 2H, aryl), 7.20 (d, 2H, aryl). ^{13}C NMR ($CDCl_3$, 63 MHz): 10.9 (alkyl CH_3), 17.2 (aryl CH_3), 17.3 ($CH_3CH_2CH_2$), 31.4 (aryl $C(CH_3)_3$), 34.0 (aryl $C(CH_3)_3$), 54.4 (NCH_2CH_2), 56.5 (NCH_2-aryl), 116.3–151.1 (aryl). ESI-MS: $m/z = 412.27$ $[H_2L1+H]^+$. The calculated value: $m/z = 412.32$ $[H_2L1+H]^+$. Elemental *Anal.* Calc. for $C_{27}H_{45}NO_{3.5}Cl$: C, 68.26; H, 9.55; N, 2.95. Found: C, 68.86; H, 9.68; N, 3.03%.

2.3. $H_2L2 \cdot HCl \cdot 1.5H_2O$ [(N,N-bis(2-hydroxy-5-tert-butyl-3-methylbenzyl)-1-aminobutane · HCl) · $1.5H_2O$]

Recrystallized with EtOH (5 ml). Yield: 2.16 g (44%). Mp: 166–168 °C. ^1H NMR ($CDCl_3$, 250 MHz): 0.82 (t, $J = 7.3$ Hz, 3H, alkyl CH_3), 1.25 (s, 18H, aryl *t*-butyl), 1.33 (m, 2H, $CH_3CH_2CH_2$), 1.75 (m, 2H, $CH_3CH_2CH_2$), 2.44 (s, 6H, aryl CH_3), 3.01 (m, 2H, NCH_2CH_2), 4.22 (s, 4H, NCH_2-aryl), 6.96 (d, 2H, aryl), 7.20 (d, 2H, aryl). ^{13}C NMR ($CDCl_3$, 63 MHz): 13.2 (alkyl CH_3), 17.2 (aryl CH_3), 19.5 ($CH_3CH_2CH_2$), 25.2 ($CH_3CH_2CH_2$), 31.4 (aryl $C(CH_3)_3$), 34.0 (aryl $C(CH_3)_3$), 52.1 (NCH_2CH_2), 56.4 (NCH_2-aryl), 116.3–151.1 (aryl). ESI-MS: $m/z = 426.29$ $[H_2L2+H]^+$. The calculated value: $m/z = 426.34$ $[H_2L2+H]^+$. Elemental *Anal.* Calc. for $C_{28}H_{47}NO_{3.5}Cl$: C, 68.75; H, 9.69; N, 2.86. Found: C, 69.05; H, 9.82; N, 2.69%.

2.4. $H_2L3 \cdot HCl \cdot 1.5H_2O$ [(N,N-bis(2-hydroxy-5-tert-butyl-3-methylbenzyl)-1-aminohexane · HCl) · $1.5H_2O$]

Recrystallized with EtOH (10 ml). Yield: 2.28 g (44%). Mp: 141–143 °C. ^1H NMR ($CDCl_3$, 250 MHz): 0.80 (t, $J = 7.0$, 3H, alkyl CH_3), 1.16 (m, 4H, $CH_3CH_2CH_2CH_2$) 1.24 (s, 18H, aryl *t*-butyl), 1.77 (m, 2H, $CH_3(CH_2)_2CH_2$), 2.08 (m, 2H, NCH_2CH_2), 2.42 (s, 6H, aryl CH_3), 3.00 (m, 2H, NCH_2CH_2), 4.23 (s, 4H, NCH_2-aryl), 6.97 (d, 2H, aryl), 7.19 (d, 2H, aryl). ^{13}C NMR ($CDCl_3$, 63 MHz): 13.8 (alkyl CH_3), 17.2 (aryl CH_3), 22.2 ($CH_3CH_2CH_2CH_2$), 23.0 ($CH_3CH_2CH_2CH_2$), 25.8 ($CH_3(CH_2)_2CH_2CH_2$), 30.8 (NCH_2CH_2), 31.4 (aryl $C(CH_3)_3$), 33.9 (aryl $C(CH_3)_3$), 52.1 (NCH_2CH_2), 56.3 (NCH_2-aryl), 116.2–151.2 (aryl). ESI-MS: $m/z = 454.34$ $[H_2L3+H]^+$. The calculated value: $m/z = 454.37$ $[H_2L3+H]^+$. Elemental *Anal.* Calc. for $C_{30}H_{51}NO_{3.5}Cl$: C, 69.67; H, 9.94; N, 2.71. Found: C, 69.22; H, 10.08; N, 2.51%.

2.5. $H_2L4 \cdot HCl$ [(N,N-bis(2-hydroxy-5-tert-butyl-3-methylbenzyl)-cyclohexylamine · HCl)]

Recrystallized with the solution of MeOH (7 ml) and EtOH (1 ml). Yield: 1.40 g (29%). Mp: 160–163 °C. ^1H NMR ($CDCl_3$, 250 MHz): 1.13–2.20 (m, 10 H, cyclohexyl-CH_2), 1.26 (s, 18H, aryl *t*-butyl), 2.47 (s, 6H, aryl CH_3), 3.14 (m, 1H, cyclohexyl-CH), 4.14 (m, 4H, NCH_2-aryl), 6.90 (d, 2H, aryl), 7.20 (d, 2H, aryl), 9.14 (s, 2H, aryl-OH), 9.32 (m, 1H, NH^+). ^{13}C NMR ($CDCl_3$, 63 MHz): 17.3 (aryl CH_3), 25.0, 25.1, 26.7, 61.1 (cyclohexyl-*C*), 31.5 (aryl $C(CH_3)_3$), 34.0 (aryl $C(CH_3)_3$), 53.0 (NCH_2-aryl), 116.1–151.1 (aryl). ESI-MS: $m/z = 452.28$ $[H_2L4+H]^+$. The calculated value: $m/z = 452.35$ $[H_2L4+H]^+$. Elemental *Anal.* Calc. for $C_{30}H_{46}NO_2Cl$: C, 73.81; H, 9.50; N, 2.87. Found: C, 73.25; H, 9.62; N, 2.68%.

2.6. $H_2L5 \cdot HCl$ [(N,N-bis(2-hydroxy-5-tert-butyl-3-methylbenzyl)-benzylamine · HCl)]

Recrystallized with MeOH (5 ml). Yield: 1.82 g (37%). Mp: 176–178 °C. ^1H NMR ($CDCl_3$, 250 MHz): 1.26 (s, 18H, aryl *t*-butyl), 2.47 (s, 6H, aryl CH_3), 4.19 (m, 6H, NCH_2-aryl), 6.93 (d, 2H, aryl), 7.19 (d, 2H, aryl), 7.45 (m, 5H, phenyl). ^{13}C NMR ($CDCl_3$, 63 MHz): 17.2 (aryl CH_3), 31.5 (aryl $C(CH_3)_3$), 34.0 (aryl $C(CH_3)_3$), 56.4 (NCH_2-aryl), 56.7 (NCH_2-phenyl), 115.9–151.1 (aryl, phenyl). ESI-MS: $m/z = 460.26$ $[H_2L5+H]^+$. The calculated value: $m/z = 460.32$ $[H_2L5+H]^+$. Elemental *Anal.* Calc. for $C_{31}H_{42}NO_2Cl$: C, 75.05; H, 8.53; N, 2.82. Found: C, 74.58; H, 8.58; N, 2.60%.

2.7. $[UO_2(HL1)_2] \cdot 2CH_3CN$ (**1**)

The complex **1** was prepared dissolving 0.040 g (0.090 mmol) of $H_2L1 \cdot HCl \cdot 1.5H_2O$, 24.8 μL (0.180 mmol) of Et_3N and 0.023 g (0.045 mmol) of $UO_2(NO_3)_2 \cdot 6H_2O$ in 10 ml of CH_3CN (15 ml of CH_3CN in the case of (**4**) and 5 ml MeOH in the case of (**2′**) and (**5**)). $H_2L1 \cdot HCl \cdot 1.5H_2O$ is not readily soluble in CH_3CN but after addition of NEt_3 it dissolves. The resulting orange solution was kept at room temperature for one week leading to the formation of the orange (red for (**5**)) crystals. The crystals were filtered off and washed twice with 5 ml of cold ethanol and air-dried. Yield: 0.035 g (66%). The crystals are very soluble in $CHCl_3$, pyridine and toluene and slightly soluble in DMSO. ^1H NMR ($CDCl_3$, 250 MHz): 0.82 (t, $J = 7.3$ Hz, 6H, $NCH_2CH_2CH_3$), 1.31 (s, 9H, aryl *t*-butyl), 1.32 (s, 27H, aryl *t*-butyl), 1.68 (m, 4H, NCH_2CH_2), 2.41 (s, 9H, aryl CH_3), 2.52 (s, 3H, aryl CH_3), 3.05 (m, 4H, NCH_2CH_2), 3.90, 4.13, 4.84, 5.22 (m, 8H, N-CH_2-aryl), 6.98, 7.28 (m, 8H, aryl), 11.71, 12.05 (m, 2H, NH^+). ^{13}C NMR ($CDCl_3$, 63 MHz): 10.9 (alkyl CH_3), 15.4 (NCH_2CH_2), 16.9, 17.2 (aryl CH_3), 31.8 (aryl $C(CH_3)_3$), 33.6 (aryl $C(CH_3)_3$, 49.9 (NCH_2CH_2), 58.3 (N-CH_2-aryl), 116.9–167.6 (aryl). ESI-MS: $m/z = 1091.71$ [(**1**)+H]$^+$. The calculated value: $m/z = 1091.66$ [(**1**)+H]$^+$. Elemental *Anal.* Calc. for $C_{54}H_{80}N_2O_6U$: C, 59.43; H, 7.39; N, 2.57. Found: C, 59.18; H, 7.41; N, 2.36%. A single crystal X-ray analysis was performed on one of these crystals.

2.8. $[UO_2(HL2)_2] \cdot 2CH_3CN$ (**2**)

Yield: 0.036 g (67%). The crystals are very soluble in $CHCl_3$, pyridine and toluene and slightly soluble in DMSO. ^1H NMR ($CDCl_3$, 250 MHz): 0.78, 0.80 (t,

$J = 7.3$ Hz, 6H, $N(CH_2)_3CH_3$), 1.26 (m, 4H, $N(CH_2)_2CH_2$), 1.31 (s, 9H, aryl *t*-butyl), 1.32 (s, 27H, aryl *t*-butyl), 1.66 (m, 4H, NCH_2CH_2), 2.41 (s, 9H, aryl CH_3), 2.52 (s, 3H, aryl CH_3), 3.07 (m, 4H, NCH_2CH_2), 3.90, 4.13, 4.84, 5.23 (m, 8H, N-CH_2-aryl), 6.99, 7.28 (m, 8H, aryl), 11.69, 12.00 (m, 2H, NH^+). ^{13}C NMR ($CDCl_3$, 63 MHz): 13.4 (alkyl CH_3), 16.9, 17.3 (aryl CH_3), 19.6 ($NCH_2CH_2CH_2$), 23.4 (NCH_2CH_2), 31.9 (aryl $C(CH_3)_3$), 33.7 (aryl $C(CH_3)_3$), 47.5 (NCH_2CH_2), 58.0 (N-CH_2-aryl), 117.6–167.7 (aryl). ESI-MS: $m/z = 1119.76$ [(**2**)+H]$^+$. The calculated value: $m/z = 1119.69$ [(**2**)+H]$^+$. Elemental *Anal.* Calc. for $C_{56}H_{84}N_2O_6U$: C, 60.09; H, 7.56; N, 2.50. Found: C, 59.55; H, 7.51; N, 2.30%. A single crystal X-ray analysis was done on one of these crystals, but the quality of the crystals from this preparation was poor. Much better crystals were obtained from methanol; the full structural analysis for a crystal obtained from methanol is labelled **2′**.

2.9. $[UO_2(HL3)_2]\cdot 2CH_3CN$ (*3*)

Yield: 0.035 g (63%). The crystals are very soluble in $CHCl_3$, pyridine and toluene and slightly soluble in DMSO. ^{1}H NMR ($CDCl_3$, 250 MHz): 0.80, 0.81 (t, $J = 6.7$ Hz, 6H, alkyl CH_3), 1.17 (m, 12H, $NCH_2CH_2CH_2CH_2CH_2$), 1.65 (m, 4H, NCH_2CH_2), 1.31 (s, 9H, aryl *t*-butyl), 1.32 (s, 27H, aryl *t*-butyl), 2.41 (s, 9H, aryl CH_3), 2.52 (s, 3H, aryl CH_3), 3.06 (m, 4H, NCH_2CH_2), 3.89, 4.13, 4.83, 5.23 (m, 8H, N-CH_2-aryl), 6.99, 7.28 (m, 8H, aryl), 11.66, 12.01 (m, 2H, NH^+). ^{13}C NMR ($CDCl_3$, 63 MHz): 13.8 (alkyl CH_3), 16.9, 17.3 (aryl CH_3), 21.3, 22.2, 25.9, 30.9 ($NCH_2CH_2CH_2$-CH_2CH_2), 31.9 (aryl $C(CH_3)_3$), 33.7 (aryl $C(CH_3)_3$), 47.9 (NCH_2CH_2), 58.1 (N-CH_2-aryl), 117.0–167.7 (aryl). ESI-MS: $m/z = 1175.99$ [(**3**)+H]$^+$, $m/z = 1198.00$ [(**3**)+Na]$^+$ and $m/z = 1214.00$ [(**3**)+K]$^+$. The calculated value: $m/z = 1175.75$ [(**3**)+H]$^+$, $m/z = 1197.74$ [(**3**)+Na]$^+$ and $m/z = 1213.71$ [(**3**)+K]$^+$. Elemental *Anal.* Calc. for $C_{60}H_{92}N_2O_6U$: C, 61.31; H, 7.89; N, 2.38. Found: C, 61.27; H, 7.89; N, 2.14%. A single crystal X-ray analysis was done on one of these crystals.

2.10. $[UO_2(HL4)_2]$ (*4*)

Yield: 0.020 g (38%). The crystals are very soluble in $CHCl_3$, pyridine and toluene and slightly soluble in DMSO. ^{1}H NMR ($CDCl_3$, 250 MHz): 1.00–2.00, 3.33 (m, 22H, cyclohexyl-*H*), 1.31 (s, 18H, aryl *t*-butyl), 1.32 (s, 18H, aryl *t*-butyl), 2.52 (s, 6H, aryl CH_3), 2.55 (s, 6H, aryl CH_3), 4.19 (m, 4H, N-CH_2-aryl), 4.81 (m, 4H, N-CH_2-aryl), 6.97 (d, 4H, aryl), 7.27 (d, 4H, aryl), 11.58 (m, 2H, NH^+). ^{13}C NMR ($CDCl_3$, 126 MHz): 17.3, 17.4 (aryl CH_3), 25.3, 25.4, 27.0, 27.1, 55.3, 60.5, 60.6 (cyclohexyl-*C*), 31.9 (aryl $C(CH_3)_3$), 33.6 (aryl $C(CH_3)_3$), 55.8 (N-CH_2-aryl), 117.3–168.0 (aryl). ESI-MS: $m/z = 1172.05$ [(**4**)+H]$^+$. The calculated value: $m/z = 1171.72$ [(**4**)+H]$^+$. Elemental *Anal.* Calc. for $C_{60}H_{88}N_2O_6U$: C, 61.52; H, 7.57; N, 2.39. Found: C, 60.65; H, 7.50; N, 2.12%. A single crystal X-ray analysis was done on one of the crystals from the synthesis vessel.

2.11. $[UO_2(HL5)_2]\cdot 2MeOH$ (*5*)

Prepared as **1**, but the solvent was methanol (5 ml). The red solution produced red crystals, which were washed twice with methanol (5 ml). Yield: 0.045 g (80%). The crystals are soluble in $CHCl_3$, pyridine, toluene and DMSO. ^{1}H NMR ($CDCl_3$, 250 MHz): 1.33 (s, 9H, aryl *t*-butyl), 1.38 (s, 27H, aryl *t*-butyl), 2.40 (s, 9H, aryl CH_3), 2.54 (s, 3H, aryl CH_3), 3.90, 4.10, 4.73, 5.09 (m, 8H, N-CH_2-aryl), 4.29 (m, 4H, N-CH_2-phenyl), 7.00, 7.07, 7.28, 7.30 (m, 8H, aryl), 7.41 (m, 10H, phenyl), 12.52, 12.80 (m, 2H, NH^+). ^{13}C NMR ($CDCl_3$, 126 MHz): 17.0, 17.3 (aryl CH_3), 31.90, 31.94 (aryl $C(CH_3)_3$), 33.68, 33.74 (aryl $C(CH_3)_3$), 51.0, 57.3, 57.8 (N-CH_2-aryl), 116.6–167.8 (aryl). ESI-MS: $m/z = 1187.93$ [(**5**)+H]$^+$, $m/z = 1209.93$ [(**5**)+Na]$^+$ and $m/z = 1225.89$ [(**5**)+K]$^+$. The calculated value: $m/z = 1187.66$ [(**5**)+H]$^+$, $m/z = 1209.64$ [(**5**)+Na]$^+$ and $m/z = 1225.62$ [(**5**)+K]$^+$. Elemental *Anal.* Calc. for $C_{62}H_{80}N_2O_6U$: C, 62.72; H, 6.79; N, 2.36. Found: C, 62.49; H, 6.81; N, 2.17%. A single crystal X-ray analysis was done on one of these crystals.

2.12. X-ray crystallography

Crystals suitable for single crystal X-ray measurements were obtained directly from the reaction vessels. The crystal data for compounds **1**–**5** are summarized in Table 1 along with other experimental details. The crystallographic data were collected at 173 K on an Enraf Nonius Kappa CCD area-detector diffractometer using graphite-monochromatized Mo Kα radiation ($\lambda = 0.71073$ Å). The data were collected using φ and ω scans and processed using a DENZO-SMN v 0.93.0 [20]. A SHELXA [21] absorption correction was applied to the data of **1**–**5**. The structures were solved by direct methods using the SHELXS-97 program [22] and full-matrix least-squares refinements on F^2 were performed using the SHELXL-97 program [22]. For all compounds the heavy atoms were refined anisotropically. The CH hydrogen atoms were included at fixed distances using fixed displacement parameters from their host atoms while other H atoms were refined using fixed displacement parameters. Structure figures were drawn using ORTEP-3 for Windows [23].

2.13. Uranyl extraction

Two-phase uranyl ion extraction studies from water to dichloromethane were performed at ambient room temperature (22–24 °C) to determine the extraction ability of the ligands and the influence of several factors on the extraction. The study consisted of six different tests: (1) the extraction ability of the prepared ligands, (2) the effect of the amount of the extractor solvent, (3) the effect of stirring

Table 1
Summary of crystallographic data for compounds **1**–**5** at 173(2) K

Compound	**1**	**2′**	**3**	**4**	**5**
Formula	$C_{58}H_{86}N_4O_6U$	$C_{56}H_{84}N_2O_6U$	$C_{64}H_{98}N_4O_6U$	$C_{60}H_{88}N_2O_6U$	$C_{64}H_{88}N_2O_8U$
Formula weight	1173.34	1119.28	1257.49	1171.35	1251.40
Crystal system	triclinic	triclinic	triclinic	monoclinic	triclinic
Space group	$P\bar{1}$ (No. 2)	$P\bar{1}$ (No. 2)	$P\bar{1}$ (No. 2)	$P\,2_1/c$ (No. 14)	$P\bar{1}$ (No. 2)
a (Å)	9.4697(2)	9.4543(3)	9.4071(2)	9.9942(2)	9.4618(2)
b (Å)	11.1762(3)	11.2111(4)	11.7023(2)	25.7977(5)	11.3751(2)
c (Å)	15.0633(4)	13.3303(5)	15.3342(4)	10.8009(3)	14.2218(4)
α (°)	94.738(1)	103.444(2)	100.565(1)	90	78.189(2)
β (°)	104.745(1)	98.870(2)	105.633(1)	98.197(1)	79.639(2)
γ (°)	111.795(1)	94.052(2)	95.305(2)	90	85.155(2)
V (Å^3)	1403.40(6)	1349.40(8)	1580.01(6)	2756.32(11)	1472.03(6)
Z	1	1	1	2	1
D_{calc} (g cm^{-3})	1.388	1.377	1.322	1.411	1.412
μ(Mo Kα) (cm^{-1})	29.42	30.55	26.18	29.95	28.12
Observed reflections	6816	6610	7729	6474	7152
R_{int}	0.0663	0.0438	0.0635	0.0593	0.0607
Parameters	326	307	353	325	415
R_1^a	0.0535 (0.0484)[b]	0.0480 (0.0471)	0.0464 (0.0436)	0.0764 (0.0435)	0.0522 (0.0464)
wR_2^c	0.0922 (0.0877)	0.0999 (0.0990)	0.0833 (0.0812)	0.0798 (0.0712)	0.0874 (0.0836)
Largest difference in peak and hole (e Å^{-3})	0.759 and −0.959	1.041 and −0.813	0.678 and −0.792	0.639 and −0.569	0.617 and −0.869

[a] $R_1 = \sum\|F_o| - |F_c\|/\sum|F_o|$.
[b] Values in parentheses for reflections with $I > 2.0\sigma(I)$.
[c] $wR_2 = \{\sum[w(F_o^2 - F_c^2)^2]/\sum[w(F_o^2)^2]\}^{1/2}$ and $w = 1/[\sigma^2(F_o^2) + (aP)^2 + bP)]$, where $P = (2F_c^2 + F_o^2)/3$.

the extractor solvent during the process, (4) the effect of the pH of the water solution, (5) the role of the uranyl salt used, and (6) the extraction ability of the known extractor, tributylphosphate (TBP), for comparative purposes. The ligands were $H_2L1 \cdot HCl$–$H_2L5 \cdot HCl$, $H_3L6 \cdot 1/3$toluene (*N*,*N*-bis(2-hydroxy-3,5-dimethylbenzyl)-2-aminoethanol · 1/3toluene), $H_3L7 \cdot HCl$ (*N*,*N*-bis(2-hydroxy-3,5-dimethylbenzyl)-4-amino-1-butanol · HCl), $H_3L8 \cdot HCl$ (*N*, *N*- bis(2-hydroxy- 5-*tert*-butyl- 3-methylbenzyl)-4-amino -1-butanol · HCl) and $H_3L9 \cdot HCl$ (*N*,*N*-bis(2-hydroxy-5-*tert*-butyl-3-methylbenzyl)-6-amino-1-hexanol · HCl). The last four ligands were prepared previously [10a,10b].

In the first experiment with ligands $H_2L1 \cdot HCl$–$H_2L5 \cdot HCl$ the experimental setup was the following: into a test tube were placed 3 ml of CH_2Cl_2 with the ligand (0.210 mmol) and NEt_3 (0.210 mmol, to neutralize HCl) and on the top of this CH_2Cl_2 layer was placed 2 ml of a water solution of uranyl nitrate hexahydrate (0.0525 mmol) leading to a U:ligand ratio of 1:4. Also one otherwise identical test tube containing no ligand and no base was prepared. The samples for ICP ($V = 50$ μL, diluted to 10 ml of H_2O) were taken from the water layer within a 480 h period of time. After taking of the samples of during hours (48 h) of extraction, 1 ml of CH_2Cl_2 was added to each test tube containing the ligand (making the total volume of CH_2Cl_2 of 4 ml) to confirm that the CH_2Cl_2 solution was not oversaturated. Finally, after taking samples during 120 h of extraction, 0.5 ml of CH_3CN was added to each test tube to provoke possible crystal formation of the extracted complexes in CH_2Cl_2. The samples were analyzed with ICP-OES at 385.958 nm using a Perkin–Elmer Optima 4300DV instrument in every experiment.

In the second experiment with ligands $H_2L2 \cdot HCl$, $H_2L4 \cdot HCl$, $H_3L7 \cdot HCl$ and $H_3L9 \cdot HCl$ the experimental setup was as follows: into a test tube was placed 6 ml of CH_2Cl_2 with the ligand (0.210 mmol) and Et_3N (0.210 mmol, to neutralize HCl) and on the top of this layer was placed 2 ml of water with uranyl nitrate (0.0525 mmol) leading to a U:ligand ratio of 1:4. One test tube containing no ligand was also prepared. The samples for ICP ($V = 50$ μL, diluted to 10 ml) were taken from the water layer during an 80 h period of time.

The third experiment was performed like the second experiment with ligands $H_2L4 \cdot HCl$ and $H_3L7 \cdot HCl$, with the exception that the test tubes were stirred with a magnetic stirrer (300–500 rpm) throughout the experiment. Before the samples were taken, the stirring was interrupted and the solutions were allowed to settle for 5 min.

The fourth experiment with ligands $H_3L6 \cdot 1/3$toluene, $H_3L7 \cdot HCl$ and $H_3L9 \cdot HCl$ was performed like the first one using 3 ml of CH_2Cl_2 without acetonitrile addition, but now uranyl acetate dihydrate was used as the uranyl salt. The samples for ICP ($V = 50$ μL, diluted to 10 ml) were taken from the water layer during a 77-h period of time.

The fifth experiment was performed like the first one using 3 ml of CH_2Cl_2 without acetonitrile addition with ligands $H_2L2 \cdot HCl$ and $H_3L8 \cdot HCl$, but now the uranyl salt (uranyl acetate dihydrate) was dissolved in an acetate buffer. The extraction effectiveness of both ligands was studied under three different buffer solutions with pH values 3.4, 4.3 and 5.2. In all cases the solutions were stirred throughout the experiment with a magnetic stirrer (300–500 rpm). The samples for ICP ($V = 50$ μL, diluted to

10 ml) were taken from the water layer during a 48 h period of time.

The sixth experiment was performed with tributylphosphate, which is used in the PUREX process, to compare the extraction ability of a known compound to our ligands in the extraction system used by us. The experimental setup was as follows: into test tube 1 was placed 2 ml of water with uranyl nitrate (0.0525 mmol) and on the top of this layer was placed 3.5 ml kerosine with 0.9 ml TBP (3.380 mmol) leading to a U:TBP ratio of 1:64. Into test tube 2 was placed 2 ml of CH_2Cl_2 with 1.0 ml TBP (3.676 mmol) and on the top of this layer was placed 2 ml of water with uranyl nitrate (0.0525 mmol) leading to a U:TBP ratio of 1:70. The samples for ICP ($V = 50$ μL, diluted to 10 ml) were taken from the water layer during a 52-h period of time.

3. Results and discussion

3.1. Syntheses of ligands and uranyl complexes

The progress of the reactions in the formation of the ligands was followed by HPLC. Generally we could observe the formation of three products: the amine with one phenol moiety (this product could be identified by ^{1}H NMR from the material obtained during the separation process of $H_2L2 \cdot HCl$ in a yield about 28%), the amine with two phenol moieties (the desired product) in a yield about 44%, and a third unidentified product, which was detected in HPLC. On the basis of our other studies we suspect that the unidentified compound is an amine with one phenol moiety with a methylene bridge between the nitrogen atom and the phenolic oxygen atom forming a six-membered ring at a yield about 16% (HPLC). Also, at the end of the reaction one could see that some unreacted phenol was present. Thus the yields of the reported ligand syntheses obtained with this method can be said to be at practical levels.

The preparation reactions for all the ligands $H_2L1 \cdot HCl$–$H_2L5 \cdot HCl$ were performed by two different methods: by refluxing at the solvent boiling temperature, and by keeping the reaction solution in a water bath at 50 °C. The progress of these reactions were followed by HPLC and from the data we could deduce that for the best yield of the desired product (amine with two phenol moieties) the method of choice was the latter one (reaction at 50 °C) with NEt_3 added as a catalyst.

The reason for lower yields of $H_2L4 \cdot HCl$ and $H_2L5 \cdot HCl$ compared to $H_2L1 \cdot HCl$–$H_2L3 \cdot HCl$ during the same reaction time (about 75 h) is the slower reaction speed. According to the HPLC reaction follow-up in the synthesis of $H_2L4 \cdot HCl$ and $H_2L5 \cdot HCl$, the compound with one phenol moiety was the main product (about 41% and 58%, respectively), and amine with two phenol moieties formed with 29% and 37% yield, respectively.

In order to make the separation process easier the reaction mixtures were treated with HCl (6 M) to form the ligand hydrochlorides, which generally solidified out as white precipitates in the reaction vessels.

Although all the ligands were dried in vacuo, $H_2L1 \cdot HCl$–$H_2L3 \cdot HCl$ contained 1.5 water molecules for one ligand unit. Those water molecules did not leave the products until the ligands were heated to their melting point. This was confirmed by TG/DTA analysis.

Generally, the complexes formed quite easily after the dissolution of the uranyl nitrate hexahydrate in acetonitrile (or in methanol or ethanol) together with an appropriate amount of the ligand and a base (triethylamine). The quick formation of the complex was clearly indicated by the immediate change in colour of the solution from yellow (uranyl nitrate) to orange or red. The crystals started to form quite quickly, but the reaction vessels were left to stand at room temperature for up to two weeks to allow for the formation of crystals. The filtrates, though, were still orange or red in colour after removal of the crystals, indicating that the crystallization was incomplete. The solutions of complexes in methanol and ethanol were much redder in colour than those in acetonitrile. The reason for the red colour is the formation of U=O···HO hydrogen bonds as shown in the structural part later. In many cases the complexes in the crystalline state formed adducts with solvents (acetonitrile, methanol or ethanol). Some of the adducts formed crystals of better quality for X-ray analysis purposes than the parent complexes without solvent molecules, but not always. Especially **4** formed methanol and ethanol adducts, which were also analysed by X-ray methods, but the calculations gave quite high *R*-values; the best results were obtained from unsolvated crystals.

The crystals of **1**, **2**, **3** and **5**, which contain solvent molecules, decompose slowly after they are removed from the reaction solution, indicating that solvent molecules are quite loosely bonded in these crystals; this is confirmed by X-ray studies.

The solubility of the complexes into organic solvents was good. The ESI-MS measurements for compounds **1**–**5** were done in a solution of $CHCl_3$ and CH_3CN (1:3) or MeOH and CH_3CN (3:1); in this procedure the compounds **1**–**5** broke down mainly into corresponding ligands but the complex ions of compounds **1**–**5** could be still identified, although the peaks were of low intensity.

3.2. NMR studies

The ^{1}H NMR spectra of the compounds **1**–**3** and **5** in $CDCl_3$ were quite similar. One of the compounds (compound 3) was completely analyzed with ^{1}H–^{1}H COSY, NOESY, ^{1}H–^{13}C HMQC and ^{1}H–^{13}C HMBC NMR techniques to find out the behavior of the complexes in $CDCl_3$. According to these data it seems that in $CDCl_3$ the conformational changes of the N-CH_2-aryl part of the compounds **1**–**3** and **5** lead to a splitting of the ^{1}H signals of the aryl ring and the N-CH_2-aryl protons in a ratio of 1:3 at 30 °C. A measurement of the ^{1}H NMR of **3** in $CDCl_3$ as a function of temperature from −60 °C to +60 °C with

increments of 10 °C (Fig. 1) verifies that the splitting pattern is due to conformational changes of the N-CH_2-aryl part of the molecule.

In compound **4** the splitting ratio of the corresponding ^{1}H signals is 1:1 at 30 °C. The reason for this difference is probably that in **4** the N-alkyl part of the molecule does not contain the flexible N-CH_2-alkyl joint which is present in the compounds **1**–**3** and **5**. Furthermore, additional NMR measurements of **1** were made in pyridine and of **3** and **5** in DMSO and toluene. From those data it is evident that in pyridine and in DMSO all these compounds break down to two components, namely $[UO_2(HLn)(Solvent)_x]^+$ (Solvent = DMSO or pyridine, and $x = 2$ or 3) and HLn^- ($n = 1$–5). Analogous results were obtained in the ^{1}H NMR studies of similar aminoalcohol substituted ligands in DMSO [10b]. The ^{1}H NMR spectra of **3** and **5** in toluene resembled those obtained in $CDCl_3$, as expected. Thus it seems that if a solvent could offer a strongly coordinating hard Lewis donor atoms (O, N), it will eject one ligand from the uranyl complex, while in the noncoordinating solvents the ligands stay attached to the uranyl ion.

3.3. Structural studies of the uranyl complexes

The solid-state structures of compounds **1**–**5** were verified by single crystal X-ray analysis. The crystals of **1, 3** and **4** were obtained from an acetonitrile solution and the crystals of **2′** and **5** from a methanol solution. The triclinic unit cells of **1** and **3** contain one complex unit with two acetonitrile molecules. The triclinic unit cell of **2′** contains one complex unit. The monoclinic unit cell of **4** contains two complex units. The triclinic unit cell of **5** contains one complex unit and two methanol molecules.

All the complexes have a centrosymmetric structure in which the uranium(VI) ion has a compressed octahedral symmetry (Figs. 2–6). Selected bond parameters for these five molecules are presented in Table 2. The asymmetric unit of all compounds contains a UO^+ unit with a negative HLn^- ligand ($n = 1$–5), which binds to the UO^+ unit via two phenoxide groups. The aliphatic nitrogen atom accepts a proton and thus it does not form a bond with the U(VI) ion. The proton on the nitrogen atom, however, forms weak intramolecular H-bonds to O2 and/or O3 (Table 3). The complexes are neutral zwitterionic units with four negative charges at the oxygen atoms, two positive charges at the uranyl ion and two positive charges on the nitrogen atoms (one per nitrogen). The overall structures are similar to the uranyl homoazacalixarene complex [24], where the uranyl ion is located inside the cage, and to the earlier reported complexes of uranyl ion with aminoalcohol ligands [10a,10b].

The U=O distances are almost the same in all compounds studied; they range from 1.789(3) to 1.808(3) Å. Only in **5** the solvent molecule (methanol) forms a hydrogen bond to O1 (see Table 3) causing a slight lengthening of the U=O bond.

The extreme values of the U–O(phenoxide) bond distances are from 2.231(3) to 2.311(3) Å in the compounds studied. These values are near the estimated "ideal" value of 2.2 Å found in U(VI) compounds with unrestricted, unidentate alkoxide ligands [25,26]. Similar values have been found also in U(VI) compounds with Schiff base

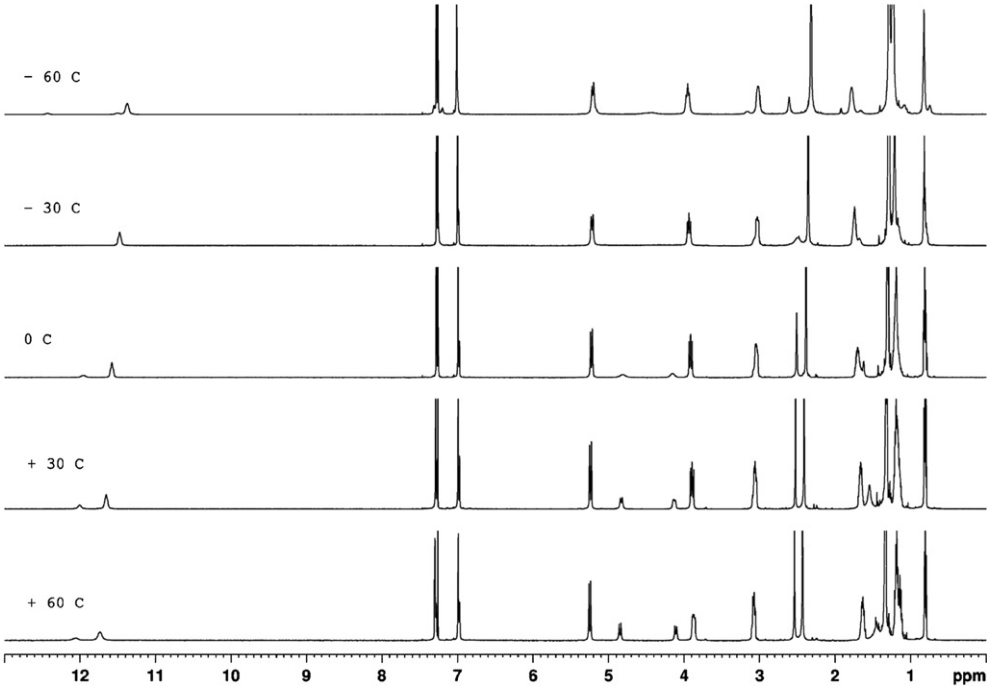


Fig. 1. The ^{1}H NMR spectrum of **3** in $CDCl_3$ as a function of temperature from −60 °C to +60 °C.

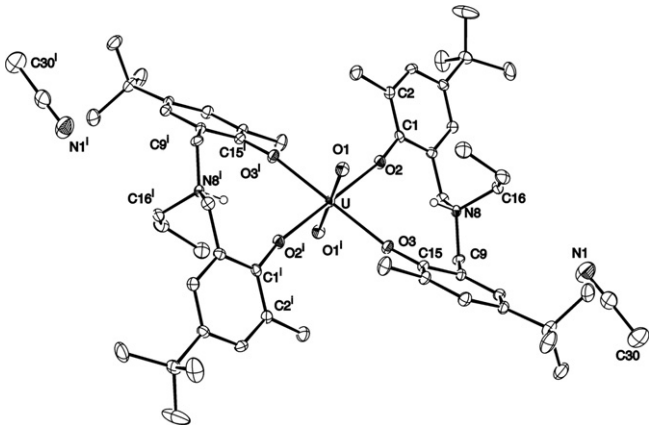


Fig. 2. Molecular structure of $[UO_2(HL1)_2]\cdot 2CH_3CN$ (**1**). Thermal ellipsoids have been drawn at 30% probability level. Symmetry operation i = −*x*, −*y*, −*z*. The CH hydrogens are not shown.

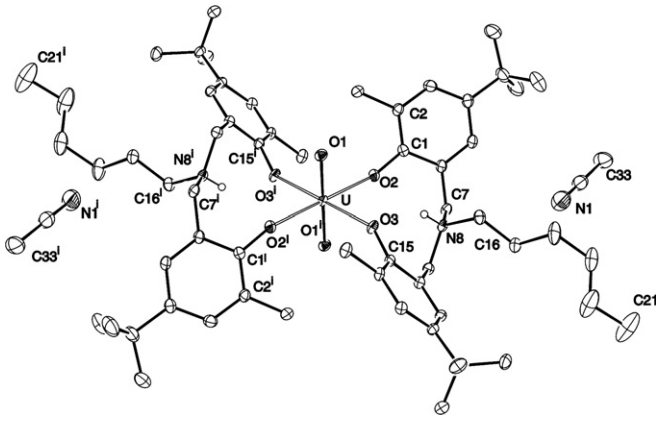


Fig. 4. Molecular structure of $[UO_2(HL3)_2]\cdot 2CH_3CN$ (**3**). Thermal ellipsoids have been drawn at 30% probability level. Symmetry operation i = −*x*, −*y*, −*z*. The CH hydrogens are not shown.

ligands [27]. This suggests that the now reported ligands bind to the UO_2^{2+} ion quite effectively.

The U–O–C angles vary from 132.0(3)° to 165.8(3)° and the corresponding U–O distances are 2.311(3) and 2.258(3) Å, respectively. These numerical values follow the general trend: the smaller is the U–O–C angle, the longer is the U–O bond.

Analysis of the bond lengths and angles in the structures **1**–**5** (see Table 2) shows only modest variations between compounds indicating that the coordination process happens quite similarly for all ligands. In the solid state the dihedral and torsion angles (see Tables 2 and 4) indicate that the ligands still have sufficient freedom to accommodate slightly different conformations for packing reasons.

3.4. Uranyl ion extraction studies

The decrease of the uranyl ion concentration in the water layer during the extraction studies at room temperature (22–24 °C) with the new ligands $H_2L1\cdot HCl$–$H_2L5\cdot HCl$ is shown in Fig. 7. The extraction was done without stirring the extraction tubes at the pH of the uranyl nitrate in water solution (around 3). The concentration ratio of the uranyl ion to the ligand was 1:4 during the extraction process. The concentration of the uranyl ion in the water layer of the control samples was constant during the follow-up.

The uranyl ion extraction efficiency of the ligands in an equilibrium situation can be described using the distribution coefficient (*D*), which expresses the ratio of the total

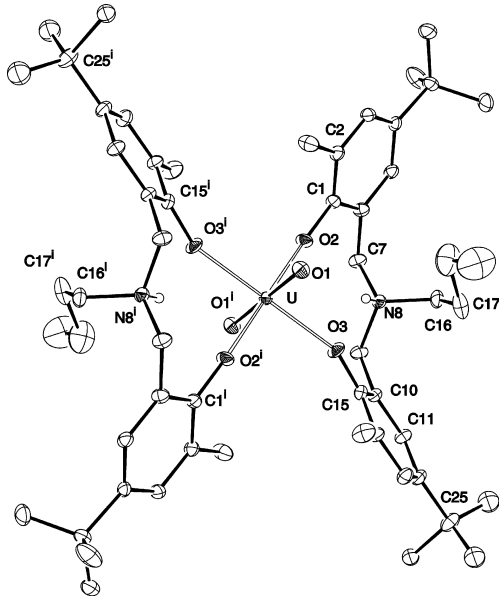


Fig. 3. Molecular structure of $[UO_2(HL2)_2]$ (**2′**). Thermal ellipsoids have been drawn at 30% probability level. Symmetry operation i = −*x*, −*y*, −*z*. The CH hydrogens are not shown.

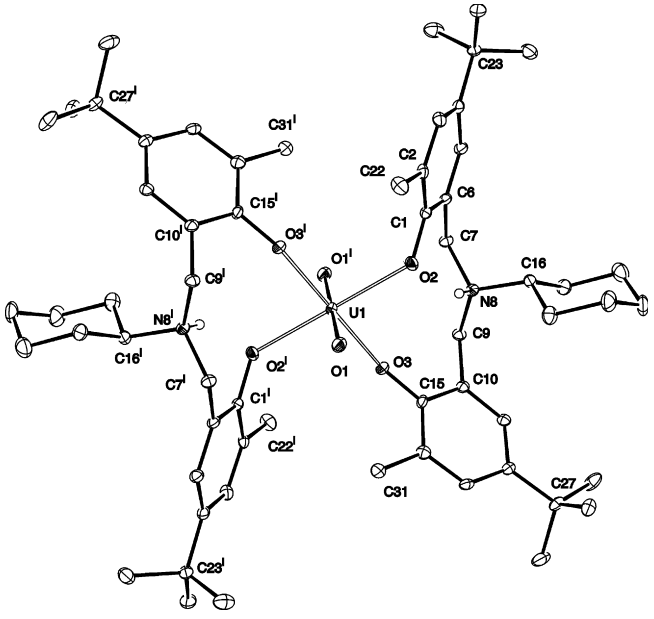


Fig. 5. Molecular structure of $[UO_2(HL4)_2]$ (**4**). Thermal ellipsoids have been drawn at 30% probability level. Symmetry operation i = −*x*, −*y*, −*z*. The CH hydrogens are not shown.

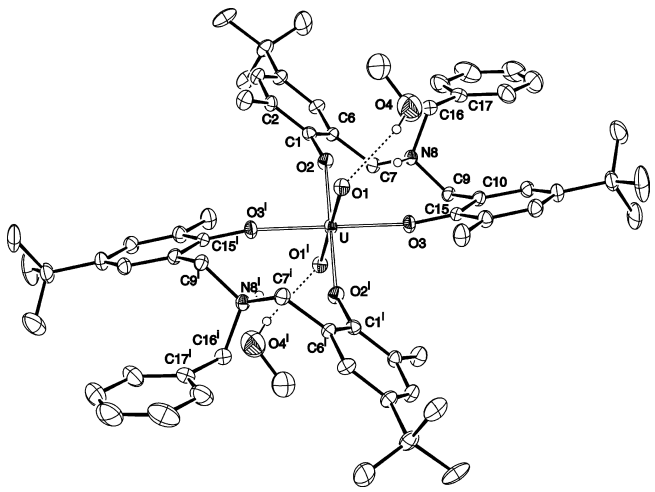


Fig. 6. Molecular structure of $[UO_2(HL5)_2]\cdot 2MeOH$ (**5**). Thermal ellipsoids have been drawn at 30% probability level. Symmetry operation i = $-x$, $-y$, $-z$. The CH hydrogens are not shown.

mass of the extracted substance in all of its possible forms in the organic and aqueous layers. It was calculated by modifying the equation given in Ref. [11]:

$$D = \frac{m(\mathrm{U})_\mathrm{o}}{m(\mathrm{U})_\mathrm{w}}, \quad (1)$$

where $m(\mathrm{U})_\mathrm{o} = m(\mathrm{U})$ in all possible forms in the CH_2Cl_2 layer at equilibrium (480 h); $m(\mathrm{U})_\mathrm{w} = m(\mathrm{U})$ in the water layer at equilibrium (480 h).

The results in Fig. 7 and in Table 5 show that the transfer of the uranyl ion from the water layer to the CH_2Cl_2 layer during 480 h was best with $H_2L2\cdot HCl$ (95%) and $H_2L4\cdot HCl$ (95%), although $H_2L1\cdot HCl$ and $H_2L3\cdot HCl$ were close to that efficiency level (92% and 94%, respectively). $H_2L5\cdot HCl$ is clearly the worst extractor.

Although ligands $H_2L1\cdot HCl$–$H_2L4\cdot HCl$ are almost equally effective in uranyl extraction and after 48 h all had transferred about 70% of uranyl ion into the organic solvent, after 120 h ligands $H_2L1\cdot HCl$, $H_2L2\cdot HCl$ and $H_2L4\cdot HCl$ had reached about 90% ($H_2L3\cdot HCl$ was still about 70%). After 480 h all ligands except $H_2L5\cdot HCl$ had reached an extraction level higher than 90%. However, the slow extraction rate is a problem with these ligands and in order to reach results in a reasonable time the extraction should be speeded up by stirring.

Table 2
Selected bond lengths (Å) and angles (°) for **1**–**5**

Compound	**1**	**2′**	**3**	**4**	**5**
Bond lengths (Å)					
U–O1	1.798(3)	1.793(3)	1.800(3)	1.789(3)	1.808(3)
U–O2	2.258(3)	2.255(3)	2.260(2)	2.311(3)	2.251(3)
U–O3	2.255(3)	2.262(3)	2.267(2)	2.244(3)	2.231(3)
C1–O2	1.333(5)	1.337(5)	1.333(4)	1.338(5)	1.341(5)
C15–O3	1.334(5)	1.327(5)	1.335(4)	1.335(5)	1.340(5)
Bond angles (°)					
O1–U–O2	90.16(14)	90.51(14)	90.71(11)	91.03(12)	89.21(12)
O1–U–O3	90.00(13)	90.43(15)	90.23(11)	90.85(13)	89.70(12)
O2–U–O3	85.07(11)	84.83(12)	84.76(9)	84.47(11)	84.60(10)
O2–U–O3[a]	94.93(11)	95.17(12)	95.24(9)	95.53(11)	95.40(10)
C1–O2–U	165.8(3)	160.2(3)	155.1(2)	132.0(3)	158.5(3)
C15–O3–U	161.1(3)	156.8(3)	147.6(2)	156.7(3)	160.4(3)
τ_1 vs. τ_2[b]	56.01(13)	53.8(2)	58.49(11)	55.22(11)	51.3(2)

[a] Atom generated by inversion.
[b] Dihedral angle between the planes of the phenyl rings: C1,...,C6 and C10,...,C15.

Table 3
Hydrogen bond parameters (Å and °)

Compound	D–H···A	*d*(D–H) (Å)	*d*(H···A) (Å)	*d*(D···A) (Å)	∠(D–H···A) (°)
1	N(8)–H(8)···O(2)	0.87(5)	2.09(5)	2.796(5)	138(4)
	N(8)–H(8)···O(3)	0.87(5)	2.35(5)	2.956(5)	127(4)
2′	N(8)–H(8)···O(2)	0.87(5)	2.26(5)	2.870(5)	127(4)
	N(8)–H(8)···O(3)	0.87(5)	2.14(5)	2.843(5)	137(5)
3	N(8)–H(8)···O(2)	0.78(4)	2.45(4)	2.978(4)	125(4)
	N(8)–H(8)···O(3)	0.78(4)	2.17(4)	2.812(4)	140(4)
4	N(8)–H(8)···O(2)	0.73(5)	2.05(5)	2.708(5)	150(5)
5	O(4)–H(4)···O(1)	0.84	2.21	3.006(6)	157
	N(8)–H(8)···O(2)	0.85(4)	2.15(4)	2.822(4)	136(4)
	N(8)–H(8)···O(3)	0.85(4)	2.29(4)	2.909(4)	130(4)

Table 4
Selected torsion angles (°) for **1**–**5**

	1	2′	3	4	5
C(5)–C(6)–C(7)–N(8)	122.0(4)	115.1(5)	112.1(4)	132.1(4)	125.1(4)
C(1)–C(6)–C(7)–N(8)	−56.3(5)	−62.8(6)	−68.1(4)	−50.7(5)	−54.2(5)
N(8)–C(9)–C(10)–C(11)	−112.2(5)	−121.4(5)	−119.6(4)	−105.0(5)	−118.1(4)
N(8)–C(9)–C(10)–C(15)	64.1(5)	58.0(6)	58.1(4)	75.0(5)	63.1(5)
C(16)–N(8)–C(7)–C(6)	−63.2(5)	−72.6(5)	−75.7(4)	−64.1(5)	−57.8(4)
C(9)–N(8)–C(7)–C(6)	169.0(3)	159.3(4)	153.6(3)	164.2(4)	171.2(3)
C(16)–N(8)–C(9)–C(10)	68.3(4)	59.7(5)	56.7(4)	77.1(5)	68.9(4)
C(7)–N(8)–C(9)–C(10)	−164.9(3)	−173.1(4)	−172.8(3)	−154.3(4)	−159.8(3)

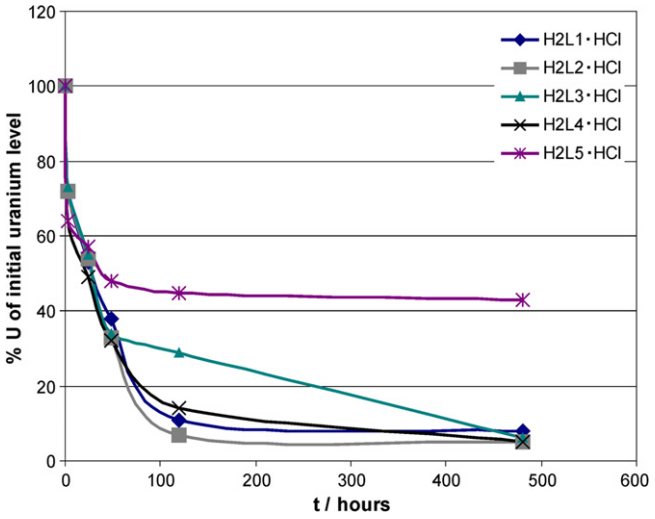


Fig. 7. Decrease of the uranium concentration (%) in the water layer as a function of time during the extraction process in experiment 1.

Table 5
Distribution coefficients (D) of the uranyl ion by the ligands $H_2L1 \cdot HCl$–$H_2L5 \cdot HCl$ ($T = 296$ K, $t = 480$ h)

	$H_2L1 \cdot HCl$	$H_2L2 \cdot HCl$	$H_2L3 \cdot HCl$	$H_2L4 \cdot HCl$	$H_2L5 \cdot HCl$
D	12.3	17.9	16.9	17.9	1.3

No crystals were formed in the CH_2Cl_2 phase during experiment 1 despite the addition of CH_3CN to the extraction solution, although uranyl complexes of ligands H_2L1–H_2L3 formed acetonitrile adducts in acetonitrile solution. In our previous extraction studies [10a] with aminoalcohol tail ligands, crystals were formed in the CH_2Cl_2 layer in some cases. This indicates that the uranyl complexes formed are more soluble in organic solvents than the uranyl complexes with similar long aminoalcohol tail ligands [10b].

The comparison of the uranyl extraction efficiency of the ligands presented in this paper with the extraction ability of the known compound (TBP) (experiment 6) revealed that during 48 h of extraction with TBP about 15% of uranyl ions (20% with TBP in kerosene) were extracted from water layer to CH_2Cl_2 layer, while the ligands $H_2L1 \cdot HCl$–$H_2L4 \cdot HCl$ extracted about 70% of uranyl ions and the ligands presented in our earlier paper [10b] extracted about 93% of uranyl ions during the same time period. Thus these new ligands are much better uranyl ion extractors than TBP in the circumstances studied.

In the extraction experiments 2 and 3 the amount of CH_2Cl_2 was increased and thus the concentration of the ligand in the organic layer was lower. Experiment 2 was done without stirring the solution and experiment 3 with stirring. Increase of the solvent led to a slower extraction rate with ligands $H_2L2 \cdot HCl$, $H_3L7 \cdot HCl$ and $H_3L9 \cdot HCl$, but to a faster rate with $H_2L4 \cdot HCl$ after 48 h of extraction (Table 6). When the solutions of ligands $H_2L4 \cdot HCl$ and $H_3L7 \cdot HCl$ were stirred during the extraction process, the system reached an equilibrium state almost within 2 h, while the process took about 80–100 h without stirring.

We also studied the influence of the uranium salt used by changing uranyl nitrate hexahydrate to uranyl acetate dihydrate in the water phase. We did the experiment with our best ligands: $H_3L6 \cdot 1/3$toluene, $H_3L7 \cdot HCl$ and $H_3L9 \cdot HCl$. This led to a better extraction efficiency with all three ligands examined: from 71% with uranyl nitrate to 92% with uranyl acetate by ligand $H_3L6 \cdot 1/3$toluene, from 93% to 98% by ligand $H_3L7 \cdot HCl$ and from 94% to

Table 6
The decrease of the uranyl ion concentration (%) in water layer (2 ml) during the extraction process (**A**: $V(CH_2Cl_2) = 3$ ml, **B**: $V(CH_2Cl_2) = 6$ ml)

Time (h)	$H_2L2 \cdot HCl$		$H_2L4 \cdot HCl$			$H_3L7 \cdot HCl$			$H_3L9 \cdot HCl$	
	A	**B**	**A**	**B**	**B′**	**A**[a]	**B**	**B′**	**A**[a]	**B**
0	100	100	100	100	100	100	100	100	100	100
3	72	70	64	32	20	23	36	10	47	80
24	54	66	49	24	21	8	15	10	10	62
48	33	60	32	14	24	7	12	11	6	42

[a] Results from Ref. [10b]. The values in B′ column were obtained by stirring the solution.

Table 7
The decrease of the uranyl ion concentration (%) in the water layer as a function of time and pH during the extraction process

Time (h)	$H_2L2 \cdot HCl$			$H_3L8 \cdot HCl$		
	pH 3.4	pH 4.3	pH 5.2	pH 3.4	pH 4.3	pH 5.2
0.0	100	100	100	100	100	100
0.5	22	10	10	21	15	10
1.0	22	10	7	20	14	8
3.0	22	11	7	20	13	8
6.0	23	12	8	20	14	8
24.0	22	12	9	23	15	8
48.0	22	13	11	20	15	7

97% by ligand $H_3L9 \cdot HCl$ after 48 h of extraction. The solutions were stirred during the extraction.

As the water solution of uranyl nitrate has a lower pH (about 2.9) than that of uranyl acetate (about 3.2), we studied the effect of pH on the extraction efficiency of ligands $H_2L2 \cdot HCl$ and $H_3L8 \cdot HCl$ in three different acetate buffers. One can clearly see from Table 7 that the extraction efficiency improves as the pH is raised from 3.4 to 5.2 (e.g. from 80% to 93% in the pH range 3.4–5.2 with $H_3L8 \cdot HCl$ after 48 h of extraction). However, high pH values can cause precipitation of uranyl hydroxide without the presence of large amounts of acetate ions and the ligand. Thus the pH value must be optimized for the best extraction results in one experiment.

4. Conclusions

The family of aminoalkylbis(phenolate) [O,N,O] donor ligands formed similar complexes with uranyl ion as the aminoalcoholbis(phenolate) [O,N,O,O′] donor ligands presented earlier [10a,10b]. The complexes presented in this paper are in the solid-state neutral uranyl complexes in which the uranyl ion is almost ideally bonded to four phenolato oxygen atoms of two ligands. The complexes formed are zwitterions, where one of the phenolic protons moves to the nitrogen atom. Changes in the aminoalkyl part of the ligand have only a minor effect on the actual coordination sphere around the uranyl ion.

The solubility of these uranyl complexes in organic solvents is very good. The uranyl extraction effectivity of these new aminoalkylbisphenolates is almost the same as that of the aminoalcoholbisphenolates, but their extraction rate is relatively slow. The reason for the slower rate compared to the aminoalcoholbisphenolates [10a,10b] is probably the higher hydrophobicity of the aminoalkylbisphenolate ligands, leading to a slower penetration rate of the ligand molecule into the water phase to react with the uranyl ion. The slow extraction rate can be compensated by mechanical stirring. However, without stirring one gets a better understanding of the effectiveness and speed of the whole extraction process.

The influence of the pH on the extraction was also studied since it is obvious that the deprotonation of the ligand influences the complex formation. We observed that when uranyl acetate dihydrate was used as uranyl salt instead of uranyl nitrate hexahydrate under the same extraction conditions, the ligands were able to extract more uranyl ions from the water phase into the CH_2Cl_2 phase. This is probably due to the fact that acetate ions in the water phase increase the pH of the solution, which increases the deprotonation of the ligand and thus improves the complexation of the uranyl ion.

According to the ^1H NMR studies in $CDCl_3$ the complexes in CH_2Cl_2 have the formula $[UO_2(HL)_2]$ (L = L1–L5). In order to get more information about the extraction process, an effort was made to find out if the uranyl complex of H_2L2 is formed in 1:1 ratio and possibly then extracted in the 1:1 form into the dichloromethane phase. This was studied by making a solution of $H_2L2 \cdot HCl$: Et_3N: $UO_2(CH_3COO)_2 \cdot 2H_2O$ in a ratio of 1:2:1 in MeOH, EtOH and acetonitrile. However, the crystals formed in these solvents were normal 1:2 complexes of UO_2^{2+} and $HL2^-$ with no indication of the formation of solid 1:1:1 complexes of UO_2^{2+}, $HL2^-$ and CH_3COO^-.

The ligands presented in this work, and also ligands studied earlier [10], are quite good uranyl ion extractors. The next phase is to study how selective these ligands are in the presence of other metal ions. Such studies are underway.

Acknowledgments

We are grateful to Prof. Matti Nurmia for correcting the language of this paper, to Elina Hautakangas for performing the elemental analyses, to Reijo Kauppinen for his assistance with NMR measurements and to Dr. Ari Väisänen for performing the ICP-measurements.

Appendix A. Supplementary material

CCDC 637167, 637168, 637169, 637170 and 637171 contain the supplementary crystallographic data (excluding structure factors) for **1**, **2**, **3**, **4** and **5**. These data can be obtained free of charge via http://www.ccdc.cam.ac.uk/conts/retrieving.html, or from the Cambridge Crystallographic Data Centre, 12 Union Road, Cambridge CB2 1EZ, UK; fax: (+44) 1223-336-033; or e-mail: deposit@ccdc.cam.ac.uk. Supplementary data associated with this article can be found, in the online version, at doi:10.1016/j.poly.2007.03.032.

References

[1] J.L. Sessler, A.E.V. Gorden, D. Seidel, S. Hannah, V. Lynch, P.L. Gordon, R.J. Donohoe, C.D. Tait, D.W. Keogh, Inorg. Chim. Acta 341 (2002) 54.
[2] M. Baaden, R. Schurhammer, G. Wipff, J. Phys. Chem. B 106 (2002) 434.
[3] J.L. Sessler, A.E. Vivian, D. Seidel, A.K. Burrell, M. Hoehner, T.D. Mody, A. Gebauer, S.J. Weghorn, V. Lynch, Coord. Chem. Rev. 216–217 (2001) 411.
[4] H. Singh, R. Vijayalakshmi, S.L. Mishra, C.K. Gupta, Hydrometallurgy 59 (2001) 69.

[5] (a) M. Sawicki, J.-M. Siaugue, C. Jacopin, C. Moulin, T. Bailly, R. Burgada, S. Meunier, P. Baret, J.-L. Pierre, F. Taran, Chem. Eur. J. 11 (2005) 3689;
(b) N. Koshino, M. Harada, Y. Morita, T. Kiikuchi, Y. Ikeda, Prog. Nucl. Energy 47 (2005) 406;
(c) A.E.V. Gorden, J. Xu, K.N. Raymond, P. Durbin, Chem. Rev. 103 (2003) 4207.
[6] J.L. Sessler, D. Seidel, A.E. Vivian, V. Lynch, B.L. Scott, D.W. Keogh, Angew. Chem., Int. Ed. 40 (2001) 591.
[7] P.D. Beer, G.D. Brindley, O.D. Fox, A. Grieve, M.I. Ogden, F. Szemes, M.G.B. Drew, J. Chem. Soc., Dalton Trans. (2002) 3101.
[8] P. Thuéry, M. Nierlich, Z. Asfari, J. Vicens, J. Chem. Soc., Dalton Trans. (2000) 1297.
[9] (a) L. Deshayes, N. Keller, M. Lance, A. Navaza, M. Nierlich, J. Vigner, Polyhedron 13 (1994) 1725;
(b) R.D. Rogers, A.H. Bond, W.G. Hipple, A.N. Rollins, R.F. Henry, Inorg. Chem. 30 (1991) 2671.
[10] (a) H. Sopo, J. Sviili, A. Valkonen, R. Sillanpää, Polyhedron 25 (2006) 1223;
(b) H. Sopo, A. Väisänen, R. Sillanpää, Polyhedron 26 (2007) 184.
[11] F. Barbette, F. Rascalou, H. Chollet, J.L. Babouhot, F. Denat, R. Guilard, Anal. Chim. Acta 502 (2004) 179.
[12] Y. Ikeda, E. Wada, M. Harada, T. Chikazawa, T. Kikuchi, H. Mineo, Y. Morita, M. Nogami, K. Suzuki, J. Alloy Compd. 374 (2004) 420.
[13] W.J. Burke, M.J. Kolbezen, C.W. Stephens, J. Am. Chem. Soc. 74 (1952) 3601.
[14] P.K. Mohapatra, V.K. Manchanda, Talanta 47 (1998) 1271.
[15] V.K. Jain, S.G. Pillai, R.A. Pandya, Y.K. Agrawal, P.S. Shrivastav, Talanta 65 (2005) 466.
[16] P. Metilda, J.M. Gladis, T.P. Rao, Anal. Chim. Acta 512 (2004) 63.
[17] M.S. El Sayed, Hydrometallurgy 68 (2003) 51.
[18] M.S. El-Shahawi, A.M. Othman, H.M. Nassef, M.A. Abdel-Fadeel, Anal. Chim. Acta 536 (2005) 227.
[19] F. Berny, R. Schurhammer, G. Wipff, Inorg. Chim. Acta 300–302 (2000) 384.
[20] Z. Otwinowski, W. Minor, in: C.W. Carter, R.M. Sweet (Eds.), Methods in Enzymology: Part A, vol. 276, Academic Press, London, 1997, pp. 307–326.
[21] G.M. Sheldrick, SHELX-97 (Release 97-2): A Program for Crystal Structure Refinement, University of Göttingen, Göttingen, Germany, 1998.
[22] G.M. Sheldrick, SHELXS-97 and SHELXL-97: Programs for Crystal Structure Refinement, University of Göttingen, Göttingen, Germany, 1997.
[23] L.J. Farrugia, J. Appl. Crystallogr. 32 (1999) 837.
[24] P. Thuéry, M. Nierlich, J. Vicens, H. Takemura, Polyhedron 20 (2001) 3183.
[25] (a) J. Harrowfield, Gazz. Chim. Ital. 127 (1997) 663;
(b) P. Thuéry, M. Nierlich, J. Harrowfield, J. Vicens (Eds.), Calixarenes 2001, Kluwert Academic Publishers, Dordrecht, 2001.
[26] D.M. Barnhart, C.J. Burns, N.N. Sauer, J.G. Watkin, Inorg. Chem. 34 (1995) 4079.
[27] D.J. Evans, P.C. Junk, M.K. Smith, Polyhedron 21 (2002) 2421.

Available online at www.sciencedirect.com
ScienceDirect
Polyhedron 26 (2007) 3409–3418
POLYHEDRON
www.elsevier.com/locate/poly

Multiple one-electron oxidation and reduction of trinuclear bis(2,4-pentanedionato)ruthenium complexes with substituted diquinoxalino[2,3-*a*:2′,3′-*c*]phenazine ligands

Sandeep Ghumaan [a], Biprajit Sarkar [b], Mahendra P. Patil [a], Jan Fiedler [c], Raghavan B. Sunoj [a,*], Wolfgang Kaim [b,*], Goutam Kumar Lahiri [a,*]

[a] *Department of Chemistry, Indian Institute of Technology – Bombay, Powai, Mumbai 400076, India*
[b] *Institut für Anorganische Chemie, Universität Stuttgart, Pfaffenwaldring 55, D – 70550 Stuttgart, Germany*
[c] *J. Heyrovský Institute of Physical Chemistry, v.v.i., Academy of Sciences of the Czech Republic, Dolejškova 3, CZ – 18223 Prague, Czech Republic*

Received 18 January 2007; accepted 15 March 2007
Available online 30 March 2007

Abstract

The complexes $(\mu_3\text{-}L^1/L^2)[Ru(acac)_2]_3$, $acac^- = 2,4$-pentanedionato, $L^1 = 2,3,8,9,14,15$-hexachlorodiquinoxalino[2,3-*a*:2′,3′-*c*]phenazine and $L^2 = 2,3,8,9,14,15$- hexamethyldiquinoxalino[2,3-*a*:2′,3′-*c*]phenazine, undergo stepwise one-electron oxidation involving a total of three electrons and stepwise one-electron reduction with three (L^2) or four electrons (L^1). All reversibly accessible states were characterized by UV–Vis–NIR spectroelectrochemistry. Oxidation leads to mixed-valent intermediates $\{(\mu_3\text{-}L)[Ru(acac)_2]_3\}^+$ and $\{(\mu_3\text{-}L)[Ru(acac)_2]_3\}^{2+}$ of which the $Ru^{III}Ru^{II}Ru^{II}$ combinations exhibit higher comproportionation constants K_c than the $Ru^{III}Ru^{III}Ru^{II}$ states – in contrast to a previous report for the unsubstituted parent systems $\{(\mu_3\text{-}L^3)[Ru(acac)_2]_3\}^{+/2+}$, $L^3 =$ diquinoxalino[2,3-*a*:2′,3′-*c*]phenazine. No conspicuous inter-valence charge transfer absorptions were observed for the mixed-valent intermediates in the visible to near-infrared regions. The monocations and monoanions were characterized by EPR spectroscopy, revealing rhombic ruthenium(III) type signals for the former. Electron addition produces ruthenium(II) complexes of the reduced forms of the ligands L, a high resolution EPR spectrum with ^{14}N and $^{35,37}Cl$ hyperfine coupling and negligible *g* anisotropy was found for $\{(\mu_3\text{-}L^1)[Ru(acac)_2]_3\}^-$. DFT calculations of $(\mu_3\text{-}L^1)[Ru(acac)_2]_3$ confirm several ligand-centered low-lying unoccupied MOs for reduction and several metal-based high-lying occupied MOs for electron withdrawal, resulting in low-energy metal-to-ligand charge transfer (MLCT) transitions.
© 2007 Elsevier Ltd. All rights reserved.

Keywords: DFT calculations; EPR; Radical complexes; Ruthenium; Electrochemistry; Spectroelectrochemistry

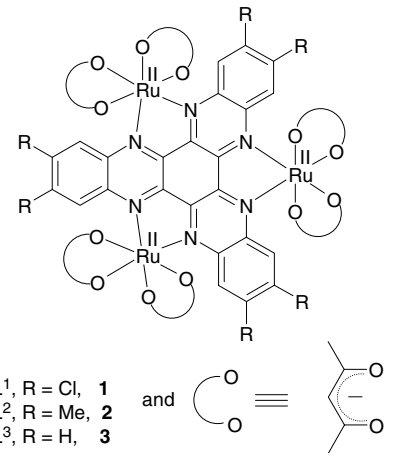
1. Introduction

In contrast to the vast number of mixed-valent ligand-bridged diruthenium complexes [1] there have been relatively few reports on the electron transfer reactivity of symmetrically trinuclear compounds [2–8]. If the common Ru^{III}/Ru^{II} redox pairs are involved, this arrangement leads to two homovalent and to two different mixed-valent states, the odd-electron form $Ru^{III}Ru^{II}Ru^{II}$ and the even-electron species $Ru^{III}Ru^{III}Ru^{II}$. Electron transfer to or from a trigonally symmetrical system can involve partial occupation of degenerate orbitals with the resulting tendency for distortion.

Following a previous report [8] on the synthesis and spectroelectrochemical characterization of unsubstituted $(\mu_3\text{-}L^3)[Ru(acac)_2]_3$ (**3**), a trinuclear complex of the extended π ligand $L^3 =$ diquinoxalino[2,3-*a*:2′,3′-*c*]phenazine, we now describe the results for the redox systems $\{(\mu_3\text{-}L^1)[Ru(acac)_2]_3\}^n$, $\mathbf{1}^n$, and $\{(\mu_3\text{-}L^2)[Ru(acac)_2]_3\}^n$, $\mathbf{2}^n$, with the hexasubstituted ligands L^1 and L^2 (Scheme 1).

* Corresponding authors. Tel.: +91 22 2576 7173; fax: +91 22 2572 3480 (R.B. Sunoj), tel.: +49 711 685 64170; fax: +49 711 685 64165 (W. Kaim), tel.: +91 22 2576 7159; fax: +91 22 2572 3480 (G.K. Lahiri).
E-mail addresses: sunoj@chem.iitb.ac.in (R.B. Sunoj), kaim@iac.uni-stuttgart.de (W. Kaim), lahiri@chem.iitb.ac.in (G.K. Lahiri).

0277-5387/$ - see front matter © 2007 Elsevier Ltd. All rights reserved.
doi:10.1016/j.poly.2007.03.030



Scheme 1.

DFT calculation results are reported for the hexachloro-substituted **1**, involving structure optimization and MO description. Voltammetric methods were employed to establish multistep reversible electron transfer while spectroelectrochemistry in the UV–Vis–NIR region as well as EPR in the X band (9.5 GHz) were used to characterize the intermediates.

2. Experimental

2.1. Materials

The precursor compounds $Ru(acac)_2(CH_3CN)_2$ [9], 2,3,8,9,14,15-hexachlorodiquinoxalino[2,3-*a*:2′,3′-*c*]phenazine (L^1) [10] and 2,3,8,9,14,15-hexamethyldiquinoxalino[2,3-*a*:2′,3′-*c*]phenazine (L^2) [11][1] were prepared according to the reported procedures. Other chemicals and solvents were reagent grade and used as received. For spectroscopic and electrochemical studies HPLC grade solvents were used.

2.2. Physical measurements

UV–Vis–NIR spectroelectrochemical studies were performed in CH_3CN/0.1 M Bu_4NPF_6 at 298 K using an optically transparent thin layer electrode (OTTLE) cell [12] in connection with a J&M TIDAS spectrophotometer. FT-IR spectra were taken on a Nicolet spectrophotometer with samples prepared as KBr pellets. Solution electrical conductivity was checked using a Systronic 305 conductivity bridge. ^1H NMR spectra were obtained with a 400 MHz Varian FT spectrometer. The EPR measurements were made in a two-electrode capillary tube [13] with an X-band Bruker system ESP300, equipped with a Bruker ER035M gaussmeter and a HP 5350B microwave counter. Cyclic voltammetric, differential pulse voltammetric and coulometric measurements were carried out using a PAR model 273A electrochemistry system. Platinum wire working and auxiliary electrodes and an aqueous saturated calomel reference electrode (SCE) were used in a three-electrode configuration. The supporting electrolyte was 0.1 M Et_4NClO_4 and the solute concentration was $\sim 10^{-3}$ M. The half-wave potential E°_{298} was set equal to $0.5(E_{pa} + E_{pc})$, where E_{pa} and E_{pc} are the anodic and cathodic cyclic voltammetric peak potentials, respectively. A platinum wire-gauze working electrode was used in the coulometric experiments. The elemental analysis was carried out with a Perkin–Elmer 240C elemental analyzer. Electrospray mass spectra were recorded on a Micromass Q-ToF mass spectrometer.

2.3. Preparation of complexes *1* and *2*

2.3.1. $[\{(acac)_2Ru^{II}\}_3(\mu\text{-}L^1)]$ (*1*)

The starting complex $Ru(acac)_2(CH_3CN)_2$ (100 mg, 0.26 mmol) and the ligand L^1 (52 mg, 0.087 mmol) were added to 20 ml of ethanol, and the mixture was heated to reflux for 6 h under a dinitrogen atmosphere. The initial orange solution gradually changed to dark green. The solvent was evaporated to dryness and the residue was purified by using a silica gel column. Initially, a red compound corresponding to $Ru(acac)_3$ was eluted by CH_2Cl_2–CH_3CN (25:1 v/v). With CH_2Cl_2–CH_3CN (20:1 v/v), a green compound corresponding to **1** was then separated. Yield: 45 mg, 35%. *Anal.* Calc. for $C_{54}H_{48}Cl_6N_6O_{12}Ru_3$: C, 43.55; H, 3.25; N, 5.65. Found: C, 43.20; H, 3.10; N, 5.32%. ^1H NMR (400 MHz) in $(CD_3)_2SO$ δ (ppm), 8.29/8.27, 8.21/8.19 (s, ($CH(L^1)$), 5.67/5.66/5.64 (s, CH(acac)), 2.34; 1.68/1.67 (s, CH_3(acac)). The positive ion electrospray mass spectrum of **1** shows the molecular ion peak centered (*m*/*z*) at 1489.58, corresponding to $\mathbf{1}^+$ (calculated molecular mass, 1488.94) and a peak centered (*m*/*z*) at 1388.53 corresponding to $\{\mathbf{1}\text{-acac}\}^+$ (calculated molecular mass, 1389.83).

2.3.2. $[\{(acac)_2Ru^{II}\}_3(\mu\text{-}L^2)]$ (*2*)

The complex $Ru(acac)_2(CH_3CN)_2$ (100 mg, 0.26 mmol) and L^2 (41 mg, 0.087 mmol) were added to 20 ml of ethanol and the mixture was heated to reflux for 12 h under a dinitrogen atmosphere. The initial orange solution gradually changed to bluish green. The solvent was evaporated and the residue purified by using a silica gel column. Initially, a red compound corresponding to $Ru(acac)_3$ was eluted by CH_2Cl_2–CH_3CN (25:1 v/v). With CH_2Cl_2–CH_3CN (5:1 v/v), a blue compound corresponding to **2** was separated. Yield: 55 mg, 46%. *Anal.* Calc. for $C_{60}H_{66}N_6O_{12}Ru_3$: C, 52.62; H, 4.86; N, 6.14. Found: C, 52.83; H, 4.85; N, 6.22%. ^1H NMR (400 MHz) in $(CD_3)_2SO$ δ (ppm), 8.34/8.28; 8.15/7.94 (s, $CH(L^2)$), 5.76/5.52 (s, CH(acac)), 2.41/2.21/1.56 (multiplet, CH_3). The positive ion electrospray mass spectrum of **2** shows the molecular ion peak centered (*m*/*z*) at 1365.95, corresponding to $\mathbf{2}^+$ (calculated molecular mass, 1366.43).

[1] The heterocyclic system was referred to as 5,6,11,12,17,18-hexaazatrinaphthalene (Ref. [11]).

2.4. Computational details

Complete geometry optimization without symmetry constraints was carried out for **1** in the Δ_3/Λ_3 configuration, using the density functional theory method at the B3LYP level. The Δ_3/Λ_3 configuration was chosen for convenience, isomerism was shown to affect the electronic structure very little [1f,1i,1j,3]. All elements except ruthenium were assigned a 6-31G* basis set. The Stuttgart–Dresden effective core potential (ECP), representing 19 core electrons, along with valence basis sets (SDD) was used for the ruthenium atoms [14a,14b]. Calculations were performed with GAUSSIAN 98 [14c]. Vertical electronic excitations based on B3LYP optimized geometries were computed using the time-dependent density functional theory (TD-DFT) formalism [14d,14e] with the B3LYP functional using the above combination of basis sets. Extinction coefficients were obtained from calculated oscillator strengths using Gaussian line shape and a full width at half maximum (fwhm) of 0.4 eV = 3228 cm^{-1} [14f]. The molecular orbital compositions have been determined using the programme AOMIX using the B3LYP/SDD,6-31G* wave function [14g]. Visual inspection of all key orbitals was done with MOLDEN [14h] to assign the nature of various electronic transitions.

3. Results and discussion

Regardless of the molar ratio of the reactants, the trinuclear complexes **1** and **2** were invariably obtained from reactions between $Ru(acac)_2(CH_3CN)_2$ and either of the free ligands. The well established [9,15] π electron donor capacity of the $Ru^{II}(acac)_2$ complex fragment is held responsible for enhancing the metal affinity of mono- and dinuclear intermediates through extensive π conjugation until full charge transfer supported coordinative saturation [16] is achieved.

Positive ion electrospray mass spectroscopy of **1** (Fig. 1a) and **2** (Fig. 1b) support the identity of the new hexasubstituted complexes. The ^1H NMR spectra of **1** and **2** exhibit two sets of signals both for the aromatic CH protons of L^1 and L^2 and for the CH/CH_3 groups of the $acac^-$ ligands (Fig. 2, Section 2). The presence of two sets of signals in each case indicates the existence of mixtures of two diastereoisomers (Δ_3/Λ_3 or $\Delta_2\Lambda/\Lambda_2\Delta$) in solution. The two closely spaced singlets for all protons involved with a particular diastereoisomeric form result from the pseudo C_3-symmetry of the molecule. In related cases such isomerism was shown to affect the electrochemical and spectroscopic response only slightly [1f,1i,1j,3], we therefore used the product distributions as obtained and as characterized by NMR (Fig. 2).

Full geometry optimization of complex **1** in the Δ_3/Λ_3 configuration was carried out at the B3LYP level of theory by using the SDD basis set for Ru and the 6-31G* basis for all other atoms (Fig. 3). Important optimized structural parameters of complex **1** are summarized in Tables S1

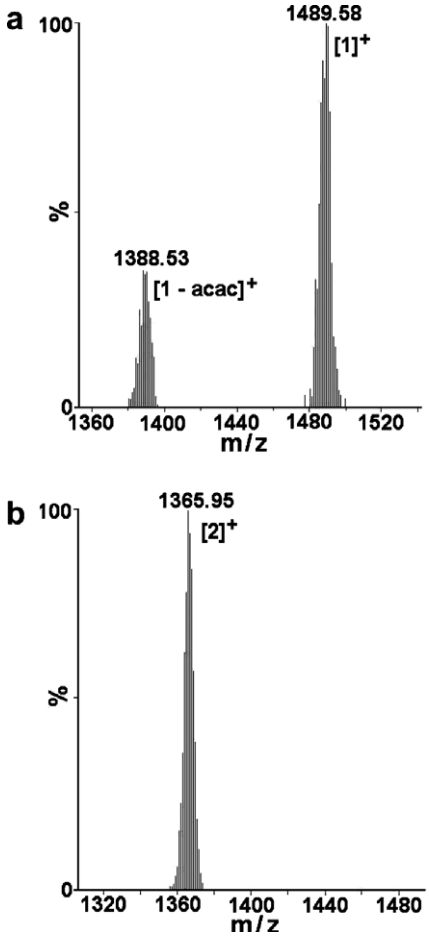


Fig. 1. Electrospray mass spectra of: (a) **1** and (b) **2** in CH_3CN.

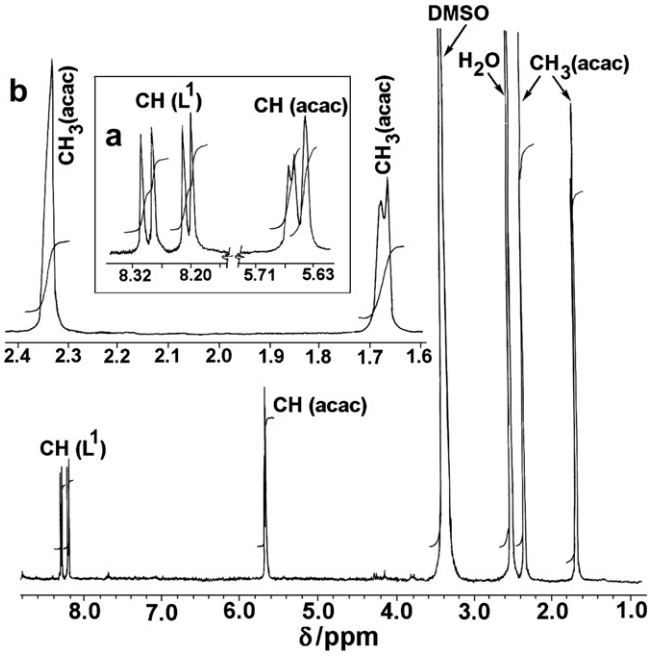


Fig. 2. ^1H NMR spectrum of **1** in $(CD_3)_2SO$. Inserts show expanded parts of the spectrum in the range of: (a) 5.5–8.5 ppm and (b) 1.5–2.5 ppm.

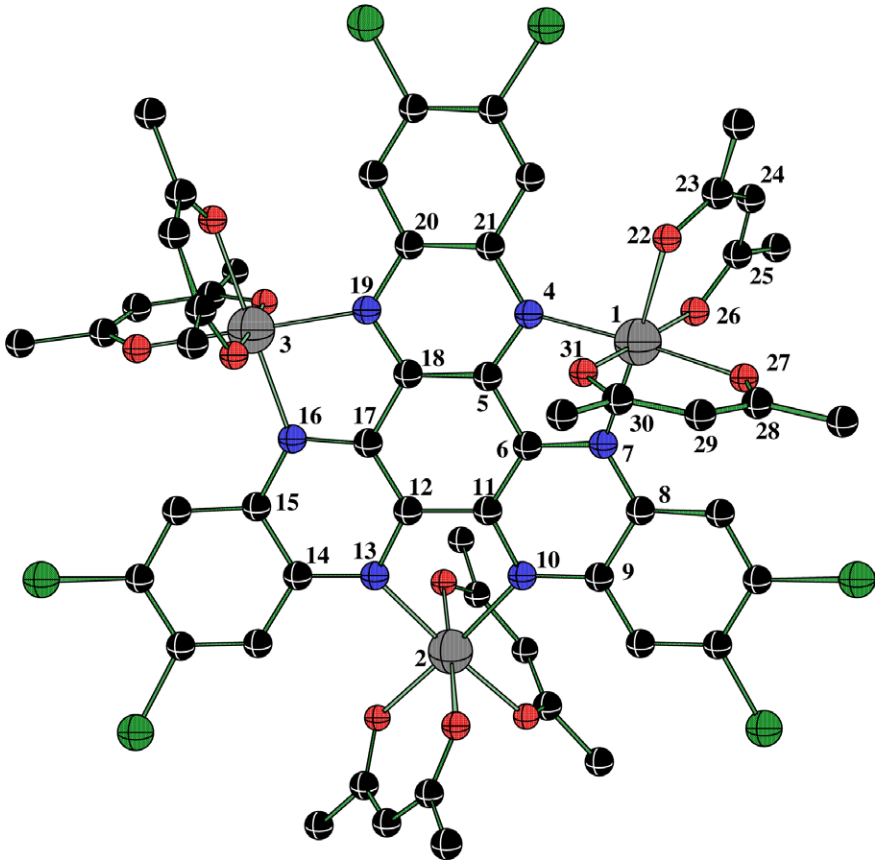


Fig. 3. Optimized structure of complex **1** at the B3LYP level of theory by using the SDD basis set for Ru and 6-31G* for all other atoms (no symmetry constraints).

and S2. The Ru–N and Ru–O(acac) distances are found to vary only slightly and range between 2.06 and 2.08 Å. The N(4)–C(5) and N(7)–C(6) π bonds are found to be elongated by about 0.023 Å in **1** as compared to the free ligand L^1, and this N–C π bond elongation is nearly the same at each ruthenium center which signifies the comparable extent of π back-bonding from each Ru^{II} ion (*vide infra*). The metal centers were found to be separated by about 6.9 Å (Table S1).

Electrochemically the complexes **1** and **2** exhibit multiple reversible one-electron reduction waves which are associated with the highly conjugated bridging ligands (L^1/L^2); the potentials also vary systematically with the electronic nature of the substituents, Me or Cl. In case of **1**, four distinct reduction processes were observed whereas only three waves were detected for **2** (Table 1, Fig. 4). In addition, **1** and **2** display three successive oxidation processes corresponding to the reversible transitions $Ru^{II}Ru^{II}Ru^{III} \rightleftharpoons Ru^{II}Ru^{II}Ru^{II}$ (couple I), $Ru^{II}Ru^{III}Ru^{III} \rightleftharpoons Ru^{II}\ Ru^{II}Ru^{III}$ (couple II), and $Ru^{III}Ru^{III}Ru^{III} \rightleftharpoons Ru^{II}Ru^{III}Ru^{III}$ (couple III) (Table 1, Fig. 4). These potentials are lower for R = Me (complex **2**) than for R = Cl (complex **1**) (Table 1), as expected from the different electron donating and withdrawing abilities. Remarkably, the separation between the redox potentials for complex oxidation leads to larger comproportionation

Table 1
Electrochemical data[a]

Compound	E°_{298}/V(ΔE_p, mV)						
	Couples						
	I	II	III	IV	V	VI	VII
1	0.16 (70)	0.56 (70)	0.79 (90)	−0.84 (70)	−0.98 (70)	−1.23 (80)	−1.71 (90)
2	0.01 (60)	0.41 (90)	0.62 (70)	−1.09 (60)	−1.20 (80)	−1.58 (100)	
3[b]	0.34 (70)	0.68 (70)	1.16 (70)	−0.46 (80)	−1.07 (70)	−1.61 (80)	

[a] In CH_3CN/0.1 M Et_4NClO_4 vs. SCE. ΔE_p: peak potential difference.
[b] Ref. [8].

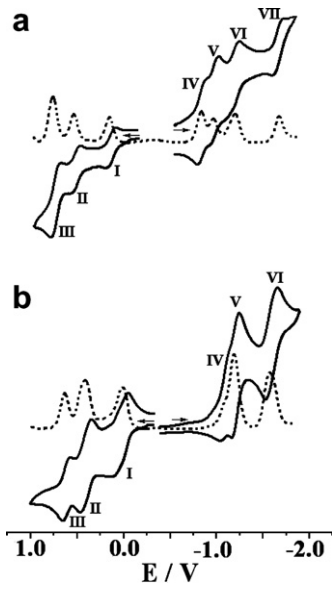


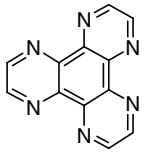
Fig. 4. Cyclic voltammograms (—) and differential pulse voltammograms (---) in CH_3CN/0.1 M Et_4NClO_4 of: (a) **1** and (b) **2**; potentials against SCE.

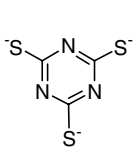
constants for the first intermediate (K_{c1}) than for the second form, $Ru^{II}Ru^{III}Ru^{III}$ (K_{c2}), both for $\mathbf{1}^{n+}$ and $\mathbf{2}^{n+}$, respectively ($RT\ln K_c = nF(\Delta E)$ [1]). Usually, the opposite is observed (Table 2) due to increasing Coulombic interactions; for instance, K_c values for the corresponding parent complex $\mathbf{3}^{n+}$ with R = H have been reported at $10^{5.7}$ (K_{c1}) < $10^{8.0}$ (K_{c2}). In comparison to $\mathbf{3}^{n}$ K_{c1} appears to be slightly greater for $\mathbf{1}^{n+}$ or $\mathbf{2}^{n+}$, however, K_{c2} is much larger for $\mathbf{3}^{n+}$ than for $\mathbf{1}^{n+}$ or $\mathbf{2}^{n+}$.

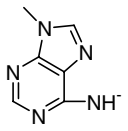
The electrolyte-dependent [17a,17b] comproportionation constants K_c reflect several different effects such as the electrostatic interaction, an inductive factor, the resonance exchange, the antiferromagnetic exchange stabilization, and ion-pairing effects [17c,17d,17e]. Their comparative interpretation is thus not always as straightforward as commonly believed. In the present case, the smaller range for the dicationic, i.e. rather highly charged $Ru^{II}Ru^{III}Ru^{III}$ forms may reflect diminished Coulombic effects due to enhanced charge delocalization by the six π donating Cl ($\mathbf{1}^{2+}$) or inductively electron donating Me substituents ($\mathbf{2}^{2+}$). Not unexpectedly, the potentials for corresponding diastereoisomers are rather similar [3,18,19]. Nevertheless, the profile of the cyclic voltammograms, in particular for **2**, suggests the existence of two diastereoisomers in solution as has also been observed by ^{1}H NMR (Fig. 2, Section 2).

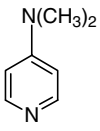
The EPR spectra taken of monocations and monoanions are in agreement with expectations [8] for the frontier orbital situation and with the DFT calculated orbital

Table 2
The variation of K_c and IVCT values in symmetrical triruthenium complexes


L^4


L^5


L^6


dmap

Formula	K_{c1}^a	K_{c2}^a	$(IVCT)_1^b$	$(IVCT)_2^b$	Ref.
			λ (nm) (ε, M^{-1} cm^{-1})	λ (nm) (ε, M^{-1} cm^{-1})	
$[\{(acac)_2Ru\}_3(\mu_3\text{-}L^1)]$ (**1**)	$10^{6.8}$	$10^{3.9}$	[c]	[c]	this work
$[\{(acac)_2Ru\}_3(\mu_3\text{-}L^2)]$ (**2**)	$10^{6.8}$	$10^{3.6}$	[c]	[c]	this work
$[\{(acac)_2Ru\}_3(\mu_3\text{-}L^3)]$ (**3**)	$10^{5.7}$	$10^{8.1}$	[c]	[c]	[8]
Δ_3/Λ_3-$[\{(bpy)_2Ru\}_3(\mu_3\text{-}L^4)]^{6+}$	$10^{3.9}$	$10^{4.1}$	2150 (3315)	2130 (2990)	[3b]
$\Delta_2\Lambda/\Lambda_2\Delta$-$[\{(bpy)_2Ru\}_3(\mu_3\text{-}L^4)]^{6+}$	$10^{3.7}$	$10^{4.1}$	2155 (4180)	2236 (2150)	[3b]
$[\{(phen)_2Ru\}_3(\mu_3\text{-}L^4)]^{6+}$	$10^{4.5}$	$10^{4.7}$	[c]	[c]	[3d]
$[\{(bpy)_2Ru\}_3(\mu_3\text{-}L^5)]^{3+}$	$10^{3.7}$	$10^{4.1}$	1900 (2300)	1900 (2400)	[4]
$[\{(phen)_2Ru\}_3(\mu_3\text{-}L^5)]^{3+}$	$10^{3.2}$	$10^{4.1}$	[d]	[d]	[4]
$[\{(pap)_2Ru\}_3(\mu_3\text{-}L^5)]^{3+}$	10^{20}	$10^{3.4}$	[d]	[d]	[5]
$[\{([9]\text{-ane-}S_3)Ru(\mu\text{-}L^6)\}_3]^{3+}$	$10^{3.0}$	$10^{6.4}$	950 (2950)	2085 (8400)	[6,7]
$[Ru_3(O)(CH_3CO_2)_6(CO)(dmap)_2]$	10^{16}	10^{27}	[d]	[d]	[2]
$[Ru_3(O)(CH_3CO_2)_6(CO)(py)_2]$	$10^{14.6}$	10^{26}	[d]	[d]	[2]
$[Ru_3(O)(CH_3CO_2)_6(CO)(CNXy)_2]$	$10^{10.2}$	10^{14}	[d]	[d]	[2]
$[Ru_3(O)(CH_3CO_2)_6(CNXy)(py)_2]$	$10^{13.5}$	10^{21}	[d]	[d]	[2]
$[Ru_3(O)(CH_3CO_2)_6(CNXy)_2(py)]$	10^{18}	10^{13}	[d]	[d]	[2]
$[Ru_3(O)(CH_3CO_2)_6(CNXy)_2(dmap)]$	10^{22}	10^{13}	[d]	[d]	[2]
$[Ru_3(O)(CH_3CO_2)_6(CNXy)_3]$	$10^{8.8}$	10^{11}	1004 (12200)	1002 (6400)	[2]

[a] K_c: comproportionation constant for $Ru_3^{III,II,II}$(K_{c1}) and $Ru_3^{III,III,II}$(K_{c2}).
[b] IVCT: inter-valence charge-transfer transitions for the $Ru_3^{II,II,III}$($IVCT_1$) and $Ru_3^{II,III,III}$ states ($IVCT_2$).
[c] Not observed.
[d] Not reported.

compositions (see Table 4). The cations exhibit rhombic Ru^{III} type signals with considerable g anisotropy in the immobilized state (Fig. 5, Table 3); this and the average g above 2 are indicative of low-spin d^5 species in a distorted octahedral situation [20].

In contrast, the monoanions exhibit EPR features without detectable g anisotropy at X band frequency (9.5 GHz), the isotropic g values near 2.00 (Table 3) signify vanishing participation of atoms with large spin–orbit coupling constants at the spin distribution [21]. The complex anion $\mathbf{1}^{\cdot-}$ was even found to exhibit hyperfine structure caused by coupling with ^{14}N ($I = 1$) and $^{35,37}Cl$ nuclei ($I = 3/2$) at the order of about 1 G (Fig. 6). These values are compatible with the composition of the lowest unoccupied MO (see Fig. 8), small, unresolved hyperfine interaction with the total of 18 methyl hydrogen atoms is likely to obscure the hyperfine structure for $\mathbf{2}^{\cdot-}$. Evidence for symmetry lowering on the EPR time scale has not been observed, there is probably rapid equilibration of any distortions.

The signal detectability at room temperature, the small line-width allowing for EPR resolution, the isotropic g factors close to the free electron value of 2.0023, and the absence of metal ($^{99,101}Ru$, $I = 5/2$) hyperfine splitting and of g anisotropy at 9.5 GHz are all in agreement with an almost exclusively ligand-centered spin [21]. In fact, the results suggest much less metal participation than in complexes of $[Ru(bpy)_2]^{2+}$ with anion radical ligands [13], probably because of the donor characteristics of $Ru(acac)_2$ in comparison to $[Ru(bpy)_2]^{2+}$.

The energies and the composition of the frontier Kohn–Sham orbitals (Figs. 7 and 8) have been examined using the AOMIX programme [14g,22]. The filled levels (between HOMO and HOMO − 6) are predominantly metal-centered orbitals with total Ru contributions of around 65% and additional mixing with the π orbitals of $acac^-$ (Table 4). The unfilled levels, on the other hand, are primarily located over the L^1 unit, having π^*

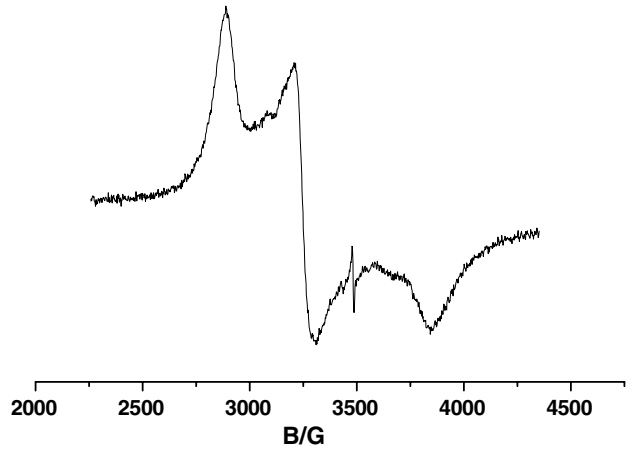


Fig. 5. EPR spectrum of $\mathbf{2}^+$ in CH_3CN/0.1 M Bu_4NPF_6 at 4 K (artefact radical signal from cavity at 3500 G).

Table 3
EPR data of monocations and monoanions

Compound	g_1	g_2	g_3	g_{iso}	Δg	Ref.
$\mathbf{1}^{\cdot-}$	[a]	[a]	[a]	2.0053	<0.10	this work
$\mathbf{1}^+$	2.398	2.140	1.815	2.131[b]	0.583	this work
$\mathbf{2}^{\cdot-}$	[a]	[a]	[a]	1.9706	<0.10	this work
$\mathbf{2}^+$	2.370	2.107	1.782	2.100[b]	0.589	this work
$\mathbf{3}^{\cdot-}$	2.058	2.058	1.924	1.969[b]	0.133	[8]
$\mathbf{3}^+$	2.332	2.154	1.877	2.128[b]	0.455	[8]

[a] Not resolved.
[b] g_{av} (calculated).

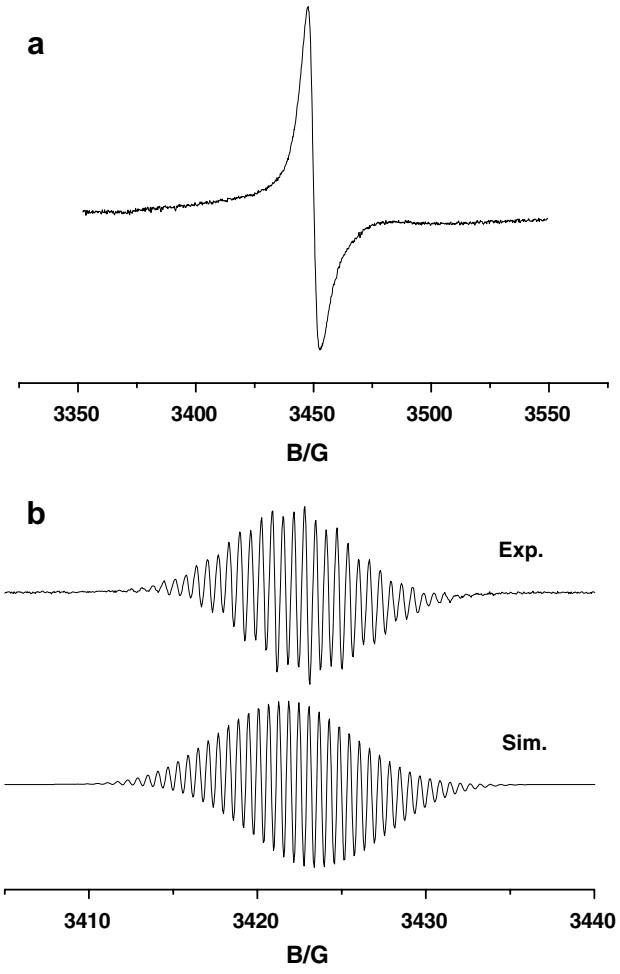
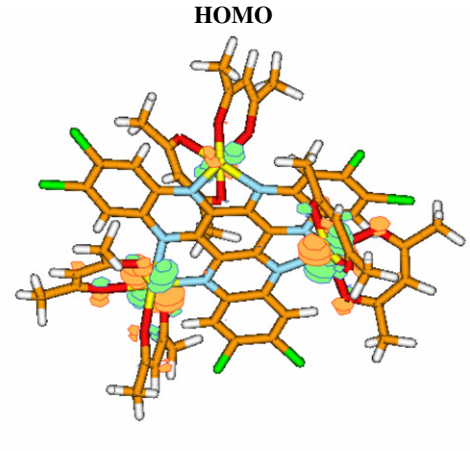
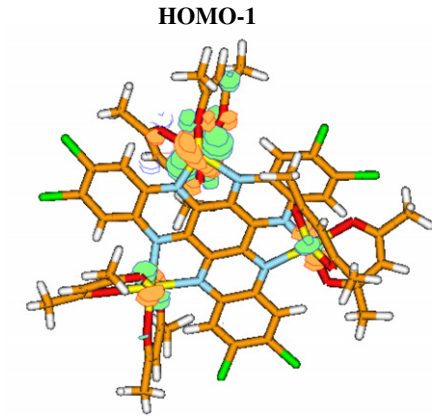


Fig. 6. EPR spectra of $\mathbf{1}^-$ at: (a) 110 K and (b) 298 K (top: experimental, bottom: simulated) in CH_3CN/0.1 M Bu_4NPF_6. Simulation parameters 1.8 G ($6\times{}^{14}N$) and 0.6/0.5 G ($6\times{}^{35}Cl/{}^{37}Cl$ in natural abundance).

characteristics[2]. Atomic orbital contributions from the metal centers towards the LUMO are successfully adopted in explaining the back-bonding within metal complexes in more quantitative fashion [23]. In the present case, the con-

[2] We have identified the π^* orbital of L^1 as the one in the xy-plane by careful analysis of the MO coefficient of the LUMO, which is mainly located on π^* of L^1 (66%) with minor contribution from dπ on Ru. Further, the d-orbital in the same plane as that of L^1 is taken as the d_{xy} and the remaining orthogonal d-orbitals as d_{xz} and d_{yz}.





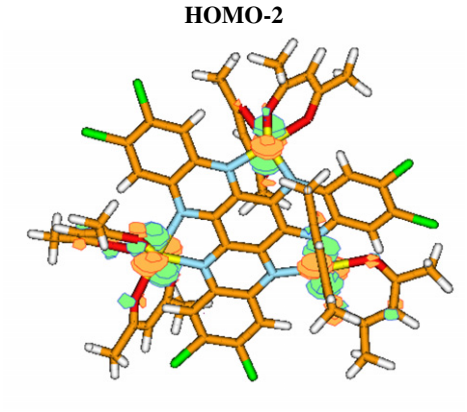
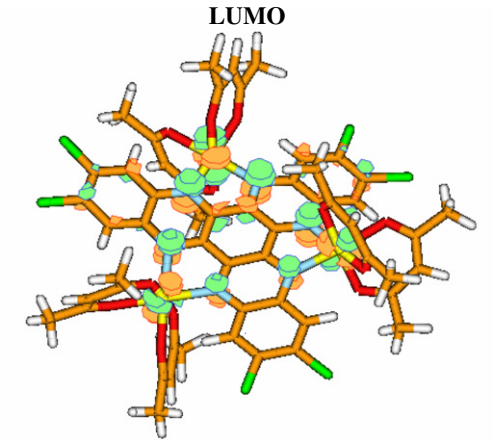
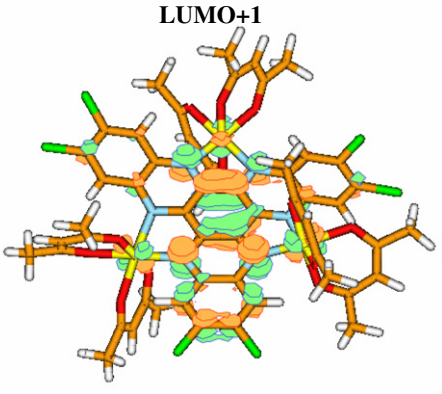


Fig. 7. Representative orbital contour diagrams of the HOMOs of **1**.





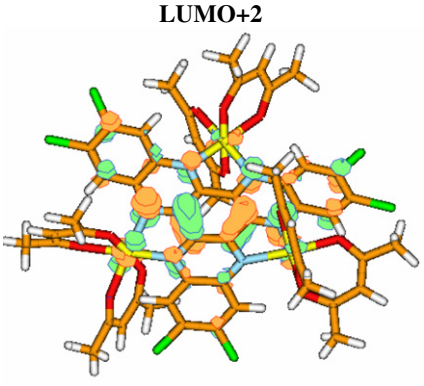


Fig. 8. Representative orbital contour diagrams of the LUMOs of **1**.

Table 4
Orbital energies and atomic orbital contributions for the frontier molecular orbitals of **1** computed without symmetry constraints

MO	Orbital energy (eV)	%Ru1	%Ru2	%Ru3	$\%Ru_{total}$	$\%L^1$	%acac
LUMO + 2	−2.95 (23790)[a]	6.5	4.6	2.9	14.0	82.7	3.3
LUMO + 1	−2.96 (23870)	5.2	6.7	3.9	15.8	81.3	2.9
LUMO	−3.16 (25490)	8.1	8.4	12.2	28.7	66.1	5.3
HOMO	−4.86 (39200)	29.1	30.3	6.5	65.9	7.2	26.9
HOMO − 1	−4.91 (39600)	10.7	8.2	47.1	66.0	5.3	29.7
HOMO − 2	−4.98 (40170)	25.5	26.6	16.1	68.2	6.6	25.2

[a] Values in parentheses indicate orbital energy in cm^{-1}.

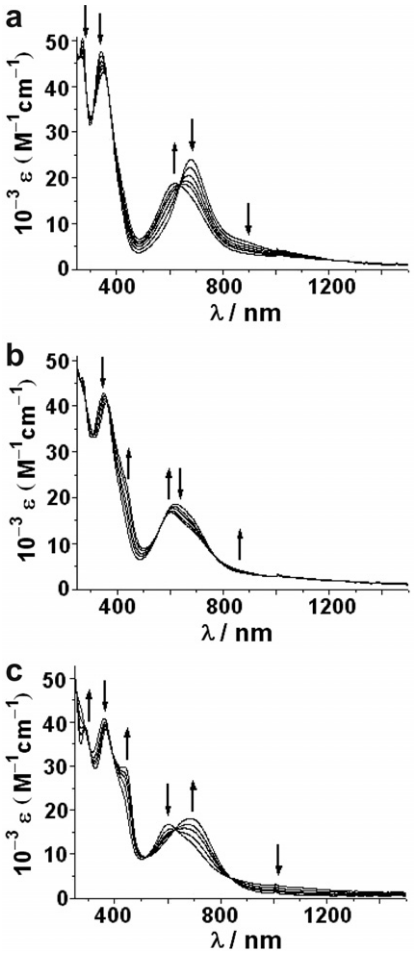


Fig. 9. UV–Vis–NIR spectroelectrochemistry for the conversions: (a) $\mathbf{1} \rightarrow \mathbf{1}^{+}$, (b) $\mathbf{1}^{+} \rightarrow \mathbf{1}^{2+}$ and (c) $\mathbf{1}^{2+} \rightarrow \mathbf{1}^{3+}$in CH_3CN/0.1 M Bu_4NPF_6.

tributions from the ruthenium atoms towards the LUMO are found to be about the same on average, the effective trigonal symmetrical situation being further confirmed by the optimized geometrical parameters around the ruthenium atoms. Nonetheless, the metals contribution especially to the calculated LUMO seems to be overestimated, considering the EPR results with their suggestion of marginal ruthenium influence.

UV–Vis–NIR absorption spectroelectrochemistry was performed for the multistep series $\mathbf{1}^{3+}$–$\mathbf{1}^{4-}$ (Figs. 9 and 10) and $\mathbf{2}^{3+}$–$\mathbf{2}^{3-}$ (Table 5).

The results show similar trends for both series in agreement with the donor effect of both kinds of substituents. The free ligands have long-wavelength π–π* absorption bands at about 412 nm (ε ca. $6 \times 10^4\ M^{-1}\,cm^{-1}$) whereas the lowest energy absorption maxima of **1** and **2** lie around 660 nm (ε ca. $1.8 \times 10^4\ M^{-1}\,cm^{-1}$). These bands are assumed to derive from allowed metal-to-ligand charge transfer (MLCT) transitions, given by the experimentally and computationally suggested presence of several high-lying occupied d levels and low-lying unoccupied ligand π* orbitals.

A selected list of computed vertical excitation energies using the time-dependent density functional theory (TD-DFT) is therefore given in Table S2. For **1**, two transitions with fairly high oscillator strengths and calculated extinction coefficients have been obtained, one at 781 nm ($\varepsilon = 2914\ M^{-1}\,cm^{-1}$) and another at 771 nm ($\varepsilon = 4993\ M^{-1}\,cm^{-1}$). The quantitative assessment of these orbital overlap-favored MLCT processes compares with experimental values for **1** of 890 nm(sh) and 680 nm ($\varepsilon = 23900\ M^{-1}\,cm^{-1}$). As must be expected for

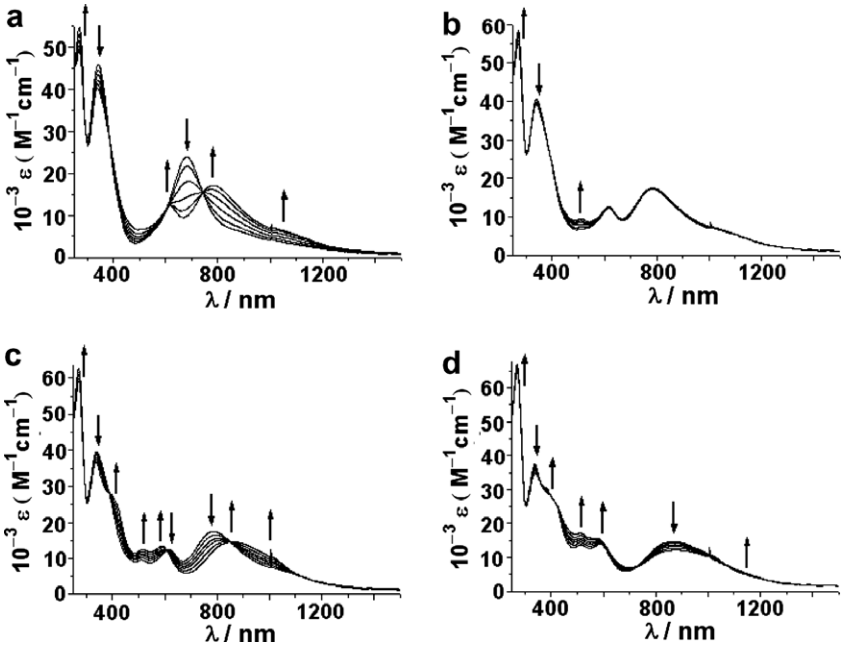


Fig. 10. UV–Vis–NIR spectroelectrochemistry for the conversions: (a) $\mathbf{1} \rightarrow \mathbf{1}^{-}$, (b) $\mathbf{1}^{-} \rightarrow \mathbf{1}^{2-}$, (c) $\mathbf{1}^{2-} \rightarrow \mathbf{1}^{3-}$ and (d) $\mathbf{1}^{3-} \rightarrow \mathbf{1}^{4-}$ in CH_3CN/0.1 M Bu_4NPF_6.

Table 5
UV–Vis–NIR data for complexes **1** and **2** from spectroelectrochemistry[a]

Complex	λ_{max} (nm) (ε, M^{-1} cm^{-1})
$\mathbf{1}^{3+}$	687 (18300), 440 (30000), 366 (38700), 290 (38600), 247 (52000)
$\mathbf{1}^{2+}$	865sh, 700sh, 602 (16800), 438sh, 362 (40900), 275sh, 248 (48400)
$\mathbf{1}^{+}$	685sh, 620 (18800), 435sh, 350 (43100), 270 (46500), 252 (46900)
1	890sh, 680 (23900), 342 (47600), 271 (50500), 250sh
$\mathbf{1}^{-}$	1060sh, 783 (17200), 616 (12300), 340 (40600), 270 (54900)
$\mathbf{1}^{2-}$	1065sh, 785 (17400), 617 (12500), 511 (9500), 339 (39200), 272 (58600)
$\mathbf{1}^{3-}$	1018 (9800), 865 (14800), 589 (13500), 515 (12600), 410 (27200), 338 (37000), 271 (63000)
$\mathbf{1}^{4-}$	1145sh, 880 (12300), 573 (15700), 512 (17100), 380sh, 340 (34900), 270 (67100)
$\mathbf{2}^{3+}$	618 (7900), 424 (20400), 350 (28900), 289sh, 243 (29400)
$\mathbf{2}^{2+}$	584 (8800), 414 (19100), 347 (29100), 326sh, 276sh, 243 (28500)
$\mathbf{2}^{+}$	614 (10700), 416sh, 334 (29100), 276 (25800), 243 (25300)
2	644 (12100), 331 (30400), 275 (27300), 242 (25700)
$\mathbf{2}^{-}$	723 (9400), 582 (8000), 337 (27400), 275 (28500), 247 (26500)
$\mathbf{2}^{2-}$	840sh, 747 (9500), 546 (7100), 415sh, 336 (25000), 274 (29800), 250sh
$\mathbf{2}^{3-}$	1017 (4700), 861 (8200), 787 (8900), 533 (8200), 411 (15800), 333 (23700), 274 (32600), 256sh

[a] In CH_3CN/0.1 M Bu_4NPF_6.

a situation with several filled d orbitals from three d^6 metal centers and a number of ligand π^* MOs (Fig. 4) there are several other MLCT transitions of lower energy but much smaller oscillator strengths (poor orbital overlap) which are not experimentally detectable (Table S2). A similar reason may preclude [8] the detection of the inter-valence charge transfer (IVCT) bands of the mixed-valent forms $\mathbf{1}^{+}$, $\mathbf{1}^{2+}$, $\mathbf{2}^{+}$ and $\mathbf{2}^{2+}$ in the typical near-infrared region [1,3]. In spite of careful spectral search even in the mid-infrared region we could not establish such bands (Table 5), although $[Ru(bpy)_2]^{2+}$ complexes of the related 1,4,5,8,9,12-hexaazatriphenylene ligands exhibit such features [3b,3c]. This absence of detectable long-wavelength absorption for otherwise clearly identified Ru^{II}/Ru^{III} mixed-valent intermediates has been noted before not only for $\mathbf{3}^{+}$ and $\mathbf{3}^{2+}$;8 dinucleating chelate acceptor bridges connecting ruthenium complex fragments, especially $Ru(acac)_2$, have previously been described to yield "IVCT silent" mixed-valent species [24]. An alternative interpretation [3a] involving the obscuring of the IVCT band by the MLCT absorptions in the visible would imply an usually strong metal–metal interaction which we consider less likely.

Within the spectroelectrochemically monitored electron transfer series (Figs. 9,10, and Table 5) it is remarkable that the second oxidation and reduction involve very little spectral changes. This may suggest spin pairing of the doubly reduced or oxidized forms in agreement with the absence of EPR triplet features. Although they can be generally assigned as MLCT and, at higher energies, as intra-ligand (IL) absorptions, the detailed identification of the major bands of the spectroelectrochemically generated complex ions (Table 5) will not be attempted and will have to await open-shell calculations. Given the photophysical and intercalating potential of such large π systems [25] further investigations of their electronic structures are warranted.

4. Conclusion

We have shown that EPR spectroscopy in conjunction with electrochemistry can provide an alternative way to identify mixed-valent intermediates, especially when the expected inter-valence CT bands in the long-wavelength region are not observable. The six fold substitution of the large heterocyclic π system clearly affects the physical properties, allowing not only for multiple oxidation at the metals but also for several ligand based reduction processes.

Acknowledgements

Financial support received from the Department of Science and Technology (DST), Council of Scientific and Industrial Research (CSIR)-New Delhi (India), the Deutsche Forschungsgemeinschaft (DFG), Fonds der Chemischen Industrie (FCI), the Deutsche Akademische Austauschdienst (DAAD) (Germany), is gratefully acknowledged.

Appendix A. Supplementary material

Supplementary data associated with this article can be found, in the online version, at doi:10.1016/j.poly.2007.03.030.

References

[1] (a) C. Creutz, Prog. Inorg. Chem. 30 (1983) 1;
(b) D.E. Richardson, H. Taube, Coord. Chem. Rev. 60 (1984) 107;
(c) K.D. Demadis, D.C. Hartshorn, T.J. Meyer, Chem. Rev. 101 (2001) 2655;
(d) J.T. Hupp, in: J.A. McCleverty, T.J. Meyer (Eds.), Comprehensive Coordination Chemistry II, Elsevier Science, Amsterdam, 2004, p. 709;
(e) M.D. Ward, Chem. Soc. Rev. 24 (1995) 121;

(f) F.R. Keene, Chem. Soc. Rev. 27 (1998) 185;
(g) G. Giuffrida, S. Campagna, Coord. Chem. Rev. 135 (1994) 517;
(h) K. Kalyanasundaram, M.K. Nazeeruddin, Inorg. Chim. Acta 226 (1994) 213;
(i) D.M. D'Alessandro, F.R. Keene, Chem. Soc. Rev. 35 (2006) 424;
(j) D.M. D'Alessandro, F.R. Keene, Chem. Rev. 106 (2006) 2270;
(k) R.J. Crutchley, in: J.A. McCleverty, T.J. Meyer (Eds.), Comprehensive Coordination Chemistry II, Vol. 2 (2004) 235;
(l) J.-P. Launay, Chem. Soc. Rev. 30 (2001) 386.

[2] K.-I. Ota, H. Sasaki, T. Matsui, T. Hamaguchi, T. Yamaguchi, T. Ito, H. Kido, C.P. Kubiak, Inorg. Chem. 38 (1999) 4070.

[3] (a) B.D. Yeomans, L.S. Kelso, P.A. Tregloan, F.R. Keene, Eur. J. Inorg. Chem. (2001) 239;
(b) D.M. D'Alessandro, F.R. Keene, Chem. Eur. J. 11 (2005) 3679;
(c) D.M. D'Alessandro, M.S. Davies, F.R. Keene, Inorg. Chem. 45 (2006) 1656;
(d) L. Jacquet, A. Kirsch-De Mesmaeker, J. Chem. Soc., Faraday Trans. 88 (1992) 2471.

[4] S. Kar, T.A. Miller, S. Chakraborty, B. Sarkar, B. Pradhan, R.K. Sinha, T. Kundu, M.D. Ward, G.K. Lahiri, Dalton Trans. (2003) 2591.

[5] S. Kar, B. Pradhan, R.K. Sinha, T. Kundu, P. Kodgire, K.K. Rao, V.G. Puranik, G.K. Lahiri, Dalton Trans. (2004) 1752.

[6] N. Shan, S.J. Vickers, H. Adams, M.D. Ward, J.A. Thomas, Angew. Chem. 116 (2004) 4028.

[7] N. Shan, S.J. Vickers, H. Adams, M.D. Ward, J.A. Thomas, Angew. Chem., Int. Ed. 43 (2004) 3938.

[8] S. Patra, B. Sarkar, S. Ghumaan, J. Fiedler, W. Kaim, G.K. Lahiri, Dalton Trans. (2004) 754.

[9] T. Kobayashi, Y. Nishina, K. Shimizu, G.P. Satô, Chem. Lett. (1988) 1137.

[10] G. Kestemont, V.D. Halleux, M. Lehmann, D.A. Ivanov, M. Watson, Y.H. Geerts, Chem. Commun. (2001) 2074.

[11] V.J. Catalano, W.E. Larson, M.M. Olmstead, H.B. Gray, Inorg. Chem. 33 (1994) 4502.

[12] M. Krejcik, M. Danek, F. Hartl, J. Electroanal. Chem. 317 (1991) 179.

[13] W. Kaim, S. Ernst, V. Kasack, J. Am. Chem. Soc. 112 (1990) 173.

[14] (a) M. Dolg, U. Wedig, H. Stoll, H. Preuss, J. Chem. Phys. 86 (1987) 866;
(b) D. Andrae, U. Haussermann, M. Dolg, H. Stoll, H. Preuss, Theor. Chim. Acta 77 (1990) 123;
(c) M.J. Frisch et al., GAUSSIAN 98, Revision A.6, Gaussian, Inc., Pittsburgh, PA, 1998;
(d) C. Lee, W. Yang, R.G. Parr, Phys. Rev. B 37 (1988) 785;
(e) M. Casida, in: D.P. Chong (Ed.), Recent Advances in Density Functional Methods, vol. 1, World Scientific Press, Singapore, 1995, p. 155;
(f) J.E. Monat, J.H. Rodriguez, J.K. McCusker, J. Phys. Chem. 106 (2002) 7399;
(g) S.I. Gorelsky, AOMIX: Program for Molecular Orbital Analysis, York University: Toronto, Canada, 1997. <http://www.sg-chem.net/>;
(h) G. Schaftenaar, J.H. Noordik, J. Comput. – Aid. Mol. Des. 14 (2000) 123.

[15] S. Patra, B. Sarkar, S. Maji, J. Fiedler, F.A. Urbanos, R. Jimenez-Aparicio, W. Kaim, G.K. Lahiri, Chem. Eur. J. 12 (2006) 489.

[16] W. Kaim, B. Olbrich-Deussner, R. Gross, S. Ernst, S. Kohlmann, C. Bessenbacher, in: M. Chanon (Ed.), Importance of Paramagnetic Organometallic Species in Activation, Selectivity and Catalysis, Kluwer Academic Publishers, Dordrecht, 1989, p. 283.

[17] (a) F. Barrière, W.E. Geiger, J. Am. Chem. Soc. 128 (2006) 3980;
(b) D.M. Alessandro, F.R. Keene, Dalton Trans. (2004) 3950;
(c) R.J. Crutchley, Adv. Inorg. Chem. 41 (1994) 273;
(d) C.E.B. Evans, M.L. Naklicki, A.R. Rezvani, C.A. White, V.V. Kondratiev, R.J. Crutchley, J. Am. Chem. Soc. 120 (1998) 13096;
(e) M. Al-Noaimi, G.P.A. Yap, R.J. Crutchley, Inorg. Chem. 43 (2004) 1770.

[18] B. Sarkar, S. Patra, J. Fiedler, R.B. Sunoj, D. Janardanan, S.M. Mobin, M. Niemeyer, G.K. Lahiri, W. Kaim, Angew. Chem. 117 (2005) 5800.

[19] B. Sarkar, S. Patra, J. Fiedler, R.B. Sunoj, D. Janardanan, S.M. Mobin, M. Niemeyer, G.K. Lahiri, W. Kaim, Angew. Chem., Int. Ed. 44 (2005) 5655.

[20] R. Hariram, B.K. Santra, G.K. Lahiri, J. Organomet. Chem. 540 (1997) 155.

[21] W. Kaim, Coord. Chem. Rev. 76 (1987) 187.

[22] S.I. Gorelsky, A.B.P. Lever, J. Organomet. Chem. 635 (2001) 187.

[23] S.I. Gorelsky, A.B.P. Lever, M. Ebadi, Coord. Chem. Rev. 230 (2002) 97.

[24] (a) S. Chellamma, M. Lieberman, Inorg. Chem. 40 (2001) 3177;
(b) See also J. Poppe, M. Moscherosch, W. Kaim, Inorg. Chem. 32 (1993) 2640;
(c) S. Patra, B. Sarkar, S. Ghumaan, J. Fiedler, W. Kaim, G.K. Lahiri, Inorg.Chem. 43 (2004) 6108.

[25] (a) A. Masschelein, A. Kirsch-De Mesmaeker, C. Verhoeven, R.N. Hinkens, Inorg. Chim. Acta 129 (1987) L13;
(b) R. Blasius, C. Moucheron, A. Kirsch-De Mesmaeker, Eur. J. Inorg. Chem. (2004) 3071.

Available online at www.sciencedirect.com
ScienceDirect
Polyhedron 26 (2007) 3419–3427
POLYHEDRON
www.elsevier.com/locate/poly

2-Hydroxy-3-carboxy-dihydrocinnamic acid: Complexation properties towards aluminium(III) and iron(III)

G. Giorgio Bombi [a], Valerio B. Di Marco [a,*], Daniele Marton [a], Stefano Moro [b], Aikebaier Reheman [a], Andrea Tapparo [a], Lisa Viero [a]

[a] Department of Chemical Sciences, University of Padova, via Marzolo 1, 35131 Padova, Italy
[b] Molecular Modeling Section, Department of Pharmaceutical Sciences, University of Padova, via Marzolo 5, 35131 Padova, Italy

Received 9 February 2007; accepted 16 March 2007
Available online 28 March 2007

Abstract

2-Hydroxy-3-carboxy-dihydrocinnamic acid (H_3L) is proposed as a simple salicylic acid derivative able to form tridentate complexes with Al(III) and Fe(III). H_3L was synthesized, and its complexation properties towards Al(III) and Fe(III) have been studied by means of potentiometric titrations, UV–Vis and NMR measurements at 25 °C in aqueous (Na)Cl 0.6 m. pK_a values of the ligand are 2.68 ± 0.02 (H_3L) and 4.49 ± 0.01 (H_2L^-). The complexes with the following stoichiometry (and stability constant, log beta values) were identified: $AlLH^+$ (3.888 ± 0.003), AlL (-0.273 ± 0.003), and AlL_2^{3-} (-2.93 ± 0.06) for Al(III), and $FeLH^+$ (6.54 ± 0.04), FeL (3.0 ± 0.1), $FeL_2H_2^-$ (10.5 ± 0.1), and FeL_2H^{2-} (7.34 ± 0.08) for Fe(III). Most of the Al(III) and Fe(III) species are either bidentate (salicylate-like), or mixed ligand-hydroxo complexes. The tridentate chelation is displayed in the AlL species. Molecular modeling confirmed experimental results.
© 2007 Elsevier Ltd. All rights reserved.

Keywords: Aluminium; Iron; Carboxylate ligands; Potentiometry; UV–Vis; Chelation therapy

1. Introduction

The therapy for metal overload pathologies usually involves the administration of suitable chelating agents to selectively remove the metal from the body. Regarding Al(III) and Fe(III), there is a need for new, safe, inexpensive, efficient, and orally effective chelators [1–8]. The chemical contribution on this topic consists in the synthesis of new ligands, and in the study of their metal–ligand complexation properties [9], especially under physiological conditions.

Hexadentate ligands possess very high selectivity towards Al(III) and Fe(III), but usually they have a poor oral bioavailability [10]. Bidentate ligands have opposite behaviour, *i.e.* lesser selectivity but higher oral bioavailability. Tridentate ligands could simultaneously display the advantages of both hexadentate and bidentate molecules, and therefore they could represent the ideal type of chelating agent. Up to now, strong tridentate ligands having three oxygen donors as chelating groups are not known [10]: at least one of the three chelating sites is a nitrogen atom. The presence of nitrogen in the metal coordination sphere, in the case of Fe(III), may favour the Fe(II) redox state and could reduce the redox potential of the complex, with possible occurrence of Fenton-type reactions in vivo and generation of hydroxyl radicals [10].

In previous works [11, and references therein] we proposed selected hydroxypyridinecarboxylic acids (Fig. 1) as new possible bidentate chelating agents for Al(III) and Fe(III) in view of several promising properties. The possibility to prepare new tridentate chelating agents by substituting the hydroxypyridinecarboxylic acid moiety is the aim of the present work. The $(CH_2)_nCOOH$ derivative in

* Corresponding author. Tel.: +39 0 498275219; fax: +39 0 498275175.
E-mail address: valerio.dimarco@unipd.it (V.B. Di Marco).

0277-5387/$ - see front matter © 2007 Elsevier Ltd. All rights reserved.
doi:10.1016/j.poly.2007.03.022

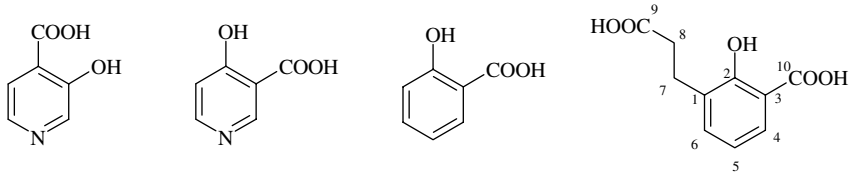


Fig. 1. From the left to the right, 3-hydroxy-4-pyridinecarboxylic acid, 4-hydroxy-3-pyridinecarboxylic acid, salicylic acid, 2-hydroxy-3-carboxy-dihydrocinnamic acid (shown in the H_3L form).

ortho with respect to the phenolic oxygen was considered in view of the relative easy of its synthesis. However, because hydroxypyridinecarboxylic acids are not commercially available, a first synthetic and complexation study attempt has been made starting with a similar, commercially available molecule, salicylic acid (Fig. 1).

A preliminary molecular modeling study allowed to individuate 2-hydroxy-3-carboxy-dihydrocinnamic acid (H_3L, Fig. 1) as the aliphatic carboxylate derivative of salicylic acid which should have the highest probability to display a tridentate chelation geometry, and therefore improved complexation affinity towards Al(III) and Fe(III). Then, because H_3L is not commercially available, it has been synthesized and characterized. In the last step, the complexation study of H_3L with Al(III) and Fe(III) has been performed by means of potentiometric titrations, UV–Vis and NMR measurements.

2. Experimental

2.1. Molecular modeling

All quantum chemistry calculations were performed by using SPARTANO2 [12] and GAUSSIAN98 [13] softwares. The ground state geometry of all, charged and uncharged, aluminium and iron complexes were fully optimized without geometry constraints using RHF/PM3 calculations. Vibrational frequency analysis was used to characterize the minima stationary points (zero imaginary frequencies). We apply the COSMO [14] using the gas phase PM3 fully optimized geometries to obtain the corresponding solvation energy ΔE_{solv}.

2.2. Synthesis and solution equilibria

2.2.1. Chemicals

All chemicals were commercially available and of pure grade. Salicylic acid, sodium hydroxide, phosphorus pentoxide, copper(II) sulphate pentahydrate, sulphuric acid (95–97% weight) and ethyl ether were Fluka (Germany) reagents. Sodium hydrogen sulphite solution (38–40% weight) and hydrochloric acid (37% weight) were purchased by Riedel de Haen (Germany). Chloroform was purchased by Janssen. Magnesium sulphate anhydrous was a Baker Analyzed Reagent (Holland) product. Ammonia solution (30%) was purchased by Carlo Erba. HCl (Prolabo), NaOH (Fluka, nominal purity 98%+, CO_2 max. 0.5%), aluminium wire (Aldrich, nominal purity 99.999%) and iron granules (Aldrich, nominal purity 99.999%) were used to prepare solutions for potentiometric and UV–Vis measurements. For the NMR measurements, D_2O (Aldrich, 99.9 atoms% D), $AlCl_3$ (Fluka, $\geqslant$99%), KOD (Aldrich, 40% sol. in D_2O, 99.9 atom% D) and DCl (Janssen, 20% wt. sol. in D_2O, 99+ atom% D) were used.

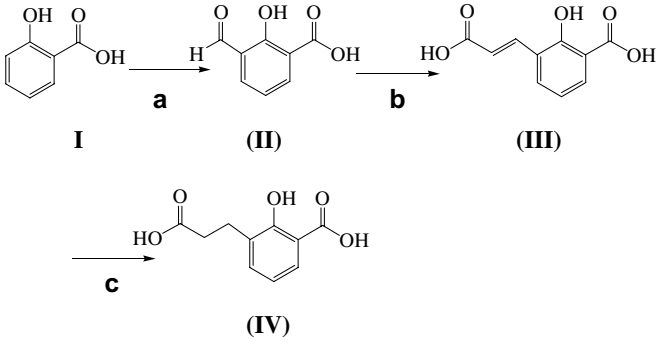
2.2.2. Apparatus

IR spectra were registered on a FT-IR Perkin–Elmer spectrophotometer mod. 237 as a nujol suspension. The ^1H and ^{13}C NMR measurements were made at room temperature with a Bruker Avance 300 operating in FT mode using 5 mm tubes. The chemical shifts were given with respect to Me_4Si (TMS) when organic deuterated solvents were employed, and to $Me_3SiCH_2CH_2COONa$ (TSP) when D_2O was used as solvent. HPLC-MS analyses were made with an Agilent instrument mod 1100 equipped with a Luna C-108 column (15 cm × 5 mm i.d.) and an ion-trap quadrupolar mass detector. The eluent was a solution of $HCOONH_4$ 2.1 mM and HCOOH 0.026 mM.

All potentiometric measurements were performed with a Metrohm 765 Dosimat apparatus. UV spectra were recorded with a Perkin–Elmer Lambda 25 spectrophotometer.

2.2.3. Synthesis of 2-hydroxy-3-carboxy-dihydrocinnamic acid (H_3L)

H_3L was prepared in three steps following the literature data.



In the first step (a), 30 g of salicylic acid (**I**) (0.27 mol) were converted to 3-formylsalycilic acid (**II**) in 15% yield by reaction with 114.7 mL $CHCl_3$ (0.68 mol) and 250 mL NaOH 1.0 M (0.25 mol) added drop wise. Reaction is com-

pleted in 5 h [15]. In step (b), 2.1 g of **II** (0.013 mol) was allowed to react with 3.0 g of malonic acid (0.028 mol) in pyridine (7.0 mL) added with three drops of aniline to form 2-hydroxy-3-carboxy-cinnamic acid (**III**) in 63% yield [16]. In the last step (c), palladium-catalyzed hydrogenation under 5 bar pressure of **III** (0.45 g, 23.7 mmol) in 30 mL of ethanol gave after four hours and crystallization with cold water the titled pure compound 2-hydroxy-3-carboxy-dihydrocinnamic acid (**IV** = H_3L) in 73% yield [16]. All the products **II**–**III**–**IV** were fully characterized by elemental analysis, melting point, IR and ^1H, ^{13}C NMR measurements and the results were in good agreement with those of literature. In addition, analysis of **II** with HPLC-MS ion-trap was used to confirm the purity of the prepared compound.

Main chemical–physical data for H_3L: Elemental *Anal.* Calc. for $C_{10}H_{10}O_5$: C, 57.14; H, 4.83. Found: C, 57.02; H, 4.50%. M.p.: 211–213 °C (literature 202–205 °C [16]); IR (KBr) = 1693 (stretching as. COO), 1637 and 1623 (stretching C=C aromatic), 1465, 1435 and 1413 cm^{-1} (stretching sim. COO). ^1H NMR in $(CD_3)_2CO$, δ: 2.61 (t, 2H, methylene protons), 2.93 (t, 2H, methylene protons), 6.87 (t, 1H, aromatic protons), 7.47 (d, 1H, aromatic proton) and 7.77 (d, 1H, aromatic proton) ppm. ^{13}C NMR in $(CD_3)_2CO$, δ (see Fig. 1): 25.98 (C-8), 33.54 (C-7), 112.56 (C-3), 119.48 (C-5), 129.31 (C-1), 136.94 (C-6), 161.04 (C-2), 173.10 (C-10) and 174.06 (C-9) ppm.

2.2.4. Synthesis of an Al–H_3L complex

An acidic solution of H_3L (105.2 mg in 10 mL, 0.05 mmol/L) was brought to pH 6.50 upon addition of KOH 0.1 M. An Al(III) solution ($AlCl_3$ 0.05 mmol/L, pH 3.37) was added drop wise under stirring (final pH 5.50). After few minutes a white precipitate formed, which was filtered, washed and dried overnight under vacuum. M.p. = 344–346 °C, IR (KBr) = 1605, 1577, 1476, 1451, 1406, 1259, 1082, 874, 765 cm^{-1}. Elemental analysis: 30.28% C, 3.85% H, 6.54% Al (by AAS). Although elemental analysis was not able to indicate the exact stoichiometry of the complex, the molar ratio Al/C = 0.216 obtained in the analysis suggests a 1:1 metal-to-ligand stoichiometric ratio (calculated ratio: 0.224). The complex is probably the neutral species $AlC_{10}H_7O_5 \cdot xH_2O$ with the copresence of some KCl.

2.2.5. Solution equilibria

The measurement method was almost the same as reported previously [17]. In the following, a summary will be given. Details are reported only when different from those already described.

All analyte concentrations were expressed in the molality scale (mol/kg of water).

For potentiometric and UV measurements, working solutions of HCl (0.1 m), NaOH (0.2 m), $AlCl_3$ (0.05 m, containing HCl 0.3 m) [17] and $FeCl_3$ (0.05 m, containing HCl 0.2 m) [18] were prepared and standardized. H_3L was used as synthesized to prepare a 0.005 m solution, brought to pH *ca.* 8.5 to ensure water solubility (at autogenic pH, *i.e.* below 3, the ligand has a too low water solubility, *ca.* 7×10^{-4} m). There was no evidence of ligand lactonization. The starting solution and all working solutions contained known amounts of NaCl to assure a constant (Na)Cl 0.6 m (0.594 M) ionic strength during the titrations. Solutions for ^1H NMR measurements were prepared by dissolving in D_2O weighed amounts of ligand, $AlCl_3$ and NaCl. The pD was adjusted by the addition of concentrated KOD and/or DCl solutions.

Potentiometric titrations are summarized in Table 1. Temperature was 25.0 ± 0.1 °C. Duplicate potentiometric measurements were executed by using two different glass electrodes (Metrohm 6.0150.100 and VWR 662-1792) and a Ag/AgCl/0.6 m NaCl reference electrode [19,20] with a J–shaped junction. Titrations were discarded if the relative e.m.f. values measured by the two electrodes differed by more than 0.2 mV (*ca.* 0.003 pH units). The acidic liquid junction potential of the reference electrode has been determined previously [18], and it can be represented by the equation [20] $E_j = -S \cdot \log(1+J \cdot C_{H^+})$, with $J = 3.69 \pm 0.08$. As a check of the accuracy of the entire experimental system, the pK_w value for water in (Na)Cl 0.6 m was computed from HCl + NaOH titrations. The values obtained from different series of experiments (pK_w = 13.699 ± 0.002, 13.701 ± 0.002, and 13.690 ± 0.003) compare well with the literature value [21] in Na(Cl) 0.6 M at 25 °C (13.727 ± 0.001). All stability constants were calculated using the computer program PITMAP [22]. The following metal-hydroxo species have been considered and the corresponding log β values kept fixed during the elaboration of the data: AlH_{-1} (logβ = −5.52), AlH_{-2} (−11.3), AlH_{-3} (−17.3), AlH_{-4} (−23.46), Al_3H_{-4} (−13.57), $Al_{13}H_{-32}$ (−109.2) [23], FeH_{-1} (logβ = −2.87), FeH_{-2} (−6.16) [18], FeH_{-3} (−12.2), FeH_{-4} (−22.2), Fe_2H_{-2} (−2.9), Fe_3H_{-4} (−6.3) [24].

UV measurements (Table 2) were carried out for solutions containing the ligand alone, and for solutions containing the ligand and the metal ion, at various pH values (cell path 1 cm). In the case of Al(III), a large metal excess was necessary to enhance the complex formation. When the pH of the solution was below 2.5, it was computed from the stoichiometric concentration of HCl, because the $[H^+]$ modifications produced by the other species (*i.e.* the free ligand, the free metal ion, and the metal–ligand complexes) were negligible under these conditions. In other cases the pH was measured with the same electrodes and procedures as for potentiometric titrations.

Table 1
Potentiometric titrations

System	Conditions			
	$C_M/10^{-3}$ m	$C_L/10^{-3}$ m	C_L/C_M	pH
(1) H_3L		0.77		2.1–11.0
(2) Al(III)/H_3L	0.28–0.77	0.77–1.13	1, 2, 3, 4	2.3–5.5
(3) Fe(III)/H_3L	0.24–0.96	0.77–1.17	1, 2, 3, 4, 5	1.8–3.7

Table 2
UV–Vis measurements

System	Conditions			
	$C_M/10^{-3}$ m	$C_L/10^{-3}$ m	pH	λ (nm) for calculation
H_3L		0.20	0.57, 1.79	
Al(III)/H_3L	1.95	0.19	1.53–2.93	265; 308
Fe(III)/H_3L	1.19	1.22	1.60–3.40	550

The $\log\beta$ values for some metal–ligand complexes were computed by the program PITMAP.

^{1}H NMR spectra of H_3L were collected at various pD values in D_2O solutions containing only the free ligand ($C_L = 0.0012$ m), and the ligand together with Al(III) at two different metal concentrations ($C_L = 0.0012$ m, $C_{Al} = 0.00052$ m and 0.0012 m). The pD was measured with a glass electrode BDH 309/1025/02 previously calibrated in buffered solutions at pH 4 and pH 7, and 0.41 pH units were added to the pH-meter readings to correct for isotopic and solvent effects [25].

3. Results and discussion

3.1. Potentiometric results

In principle H_3L is a triprotic acid (see Fig. 1). Table 3 summarizes the pK_a values obtained from our potentiometric titrations. Under the experimental conditions here used, only pK_{a1} and pK_{a2} can be detected. The former corresponds to the deprotonation of the benzoic COOH, the latter to the deprotonation of the dihydrocinnamic COOH residue. The pK_{a1} obtained by us is very similar to the one obtained for salicylic acid by Öhman et al. (p$K_{a1} = 2.724 \pm 0.001$ [26]) in very similar conditions ($T = 25$ °C, aqueous Na(Cl) 0.6 M). The pK_{a3}, which corresponds to the deprotonation of the phenol-like OH group, could be measured neither by us nor by Öhman because it is too high. Therefore, we disregarded this last proton dissociation process and considered HL as the complex-forming species in the formation equilibrium $pM + qHL + rH = M_pL_qH_{r+q}$ (for simplicity, charges will be generally omitted from the formulae, except in the Tables). In this way, more accurate formation constants were obtained, although their numerical values differ by the value of the last pK_a from those calculated in the usual way for the equilibrium $pM + qL + rH = M_pL_qH_r$.

The potentiometric titrations of solutions containing the metal and the ligand allowed the identification of the complexes AlLH, AlL, and AlL_2, for Al(III)–H_3L, and FeLH, FeL, FeL_2H_2, and FeL_2H, for Fe(III)–H_3L. The values of their stability constants are reported in Table 3. Typical distribution diagrams are reported in Fig. 2a for Al(III) and 2b for Fe(III). In the case of Al(III), a 1:1 species, probably the neutral complex AlL, was isolated as solid at slight acidic pH values.

Table 3
pK_a values of H_3L (reactions: $H_nL \rightleftharpoons H_{n-1}L + H$), and $\log\beta$ values for metal–ligand complexes at 25 °C in aqueous (Na)Cl 0.6 m (reactions: $pM + qHL + rH = M_pL_qH_{r+q}$)

Species	$\log\beta$	pK_a
H_3L		2.68 ± 0.02
H_2L^-		4.49 ± 0.01
$AlLH^+$	3.888 ± 0.003	
AlL	-0.273 ± 0.003	
AlL_2^{3-}	-2.93 ± 0.06	
$FeLH^+$	6.54 ± 0.04	
FeL	3.0 ± 0.1	
$FeL_2H_2^-$	10.5 ± 0.1	
FeL_2H^{2-}	7.34 ± 0.08	

Values are shown as the mean and standard deviation of the mean.

Some structural features of the complexes can be deduced from the stoichiometry of the species and from their stability constants. AlLH, FeLH and FeL_2H_2 likely have the dihydrocinnamic carboxylate in the protonated form, and therefore they are probably bidentate salicylate-like complexes (Fig. 3. See also UV–Vis and NMR sections).

The pK_a corresponding to the deprotonation AlLH = AlL + H ($pK_{a(AlLH)} = \log\beta_{AlLH} - \log\beta_{AlL} = 4.16$) is more

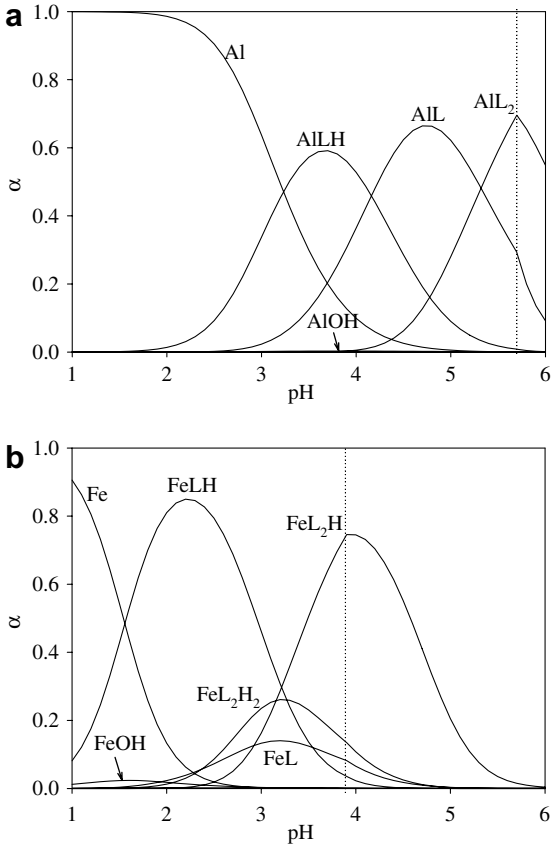


Fig. 2. Distribution diagrams of the H_3L complexes of Al(III) (a) and Fe(III) (b) in aqueous (Na)Cl 0.6 m, $T = 25$ °C; $C_M = 10^{-3}$ m, $C_L = 4 \times 10^{-3}$ m. The dotted line indicates the theoric start of metal hydroxide precipitation.

similar to the pK_{a2} of the free ligand (4.49) than to the pK_1 of $Al(H_2O)_6^{3+}$ (5.52): this suggests that the deprotonation occurs at the dihydrocinnamic carboxylic group. Moreover, as $pK_{a(AlLH)}$ is lower than the pK_{a2} of the free ligand, it is reasonable to suppose the participation of the dihydrocinnamic arm to the metal chelation (see also NMR data below).

As regards Fe(III) complexes, the pK_a values corresponding to the deprotonations $FeLH = FeL + H$ (3.54) and $FeL_2H_2 = FeL_2H + H$ (3.16) are comparable to that of $Fe(H_2O)_6^{3+}$ (2.87), and much lower than that of dihydrocinnamic carboxylate (4.49). These pK_a values could be due to the deprotonation of the dihydrocinnamic carboxylate group, its acidity being enhanced by the metal binding (thus giving rise to tridentate FeL and FeL_2H complexes). However, this pK_a enhancement is not followed by a similar increase of the stability of the complexes in comparison with those formed by salicylic acid (see below). Therefore, it is more probable that the deprotonation is due to Fe(III)-coordinated water, and FeL and FeL_2H are the mixed ligand-hydroxo-species FeLH(OH) and $FeL_2H_2(OH)$ with the dihydrocinnamic carboxylate still in the protonated form (Fig. 3).

In order to evaluate if the insertion of the dihydrocinnamic group in the salicylate moiety produced a stabilization of the metal complexes, it is necessary to compare our quantitative metal–H_3L complexation data with those of metal–salicylate. The quantitative comparison can be accomplished by computing pM (= −log [M′], with $[M'] = [M] + [MOH] + \ldots$) *versus* pH at a given metal and ligand concentration (e.g. $C_M = 10^{-6}$ m and $C_L = 5 \times 10^{-5}$ m [27]). A number of studies are available for the complexation of both metal ions with salicylate, in very different solvents and ionic media [28]. As regards Al(III), Öhman and Sjöberg [26] obtained data in Na(Cl) 0.6 M, *i.e.* in a very similar medium as ours ((Na)Cl 0.6 m), and therefore the comparison is particularly rigorous. As Fig. 4 shows, pAl values of Al(III)–H_3L are very

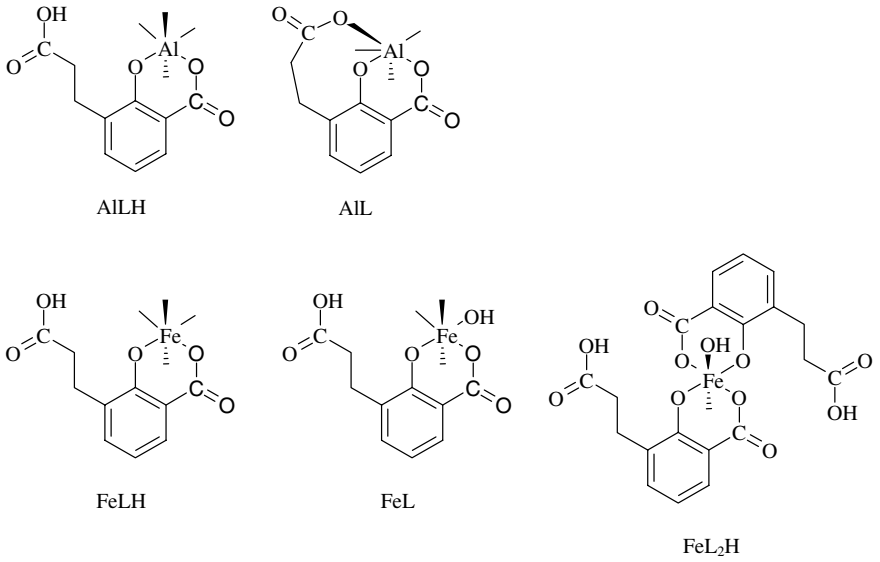


Fig. 3. Probable structures of some Al(III)–H_3L and Fe(III)–H_3L complexes.

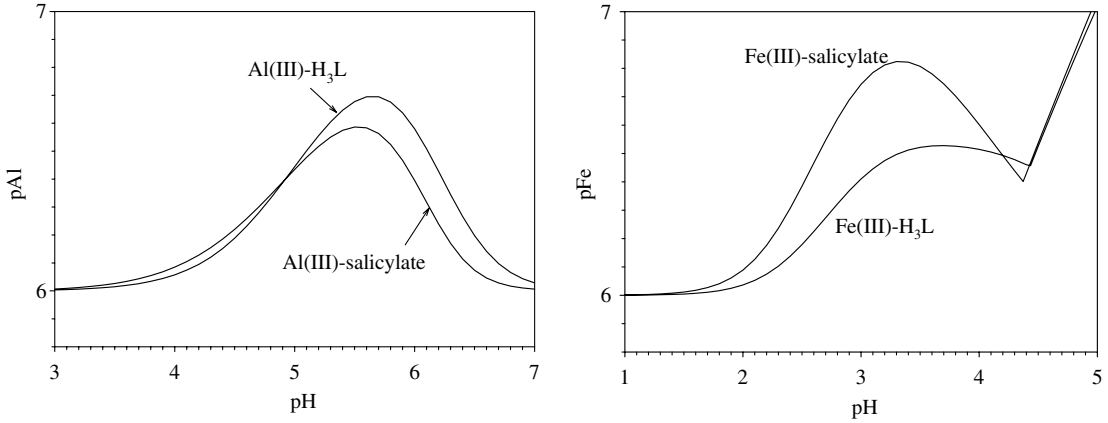


Fig. 4. pM *vs.* pH for M(III)–H_3L (present work) and M(III)–salicylate [26,29] ($C_M = 10^{-6}$ m, $C_L = 5 \times 10^{-5}$ m).

similar to those of Al(III)–salicylate. At pH values above 5 the pAl of Al(III)–H_3L is slightly higher (maximum 0.15 log units at pH ~ 6). This difference can be due to a tridentate coordination mode of AlL and AlL_2, which stabilizes Al(III)–H_3L complexes slightly more than Al(III)–salicylate ones. As regards Fe(III), the ionic medium which most closely resembles our (Na)Cl 0.6 m is KCl 0.1 M, which was used in a very old work by Akselrud and Fialkov [29]. pFe values (Fig. 4) are very similar for the two Fe(III)–ligand complexes, and slightly higher for Fe(III)–salicylate (up to 0.35 log units at pH 3). This little difference could be due to the quite different ionic strength employed to obtain the two sets of data.

In any case our potentiometric data give no evidence for a significant extra-stabilization of Al(III)- and Fe(III)–H_3L complexes with respect to the corresponding metal–salicylate ones.

3.2. Molecular modeling

To clarify the coordination geometry of Al(III) and Fe(III) complexes, a theoretical study has been carried out. In particular, the complexation reactions corresponding to the formation of tridentate ML starting from bidentate MLH were analyzed in order to take into account the interaction modes of Al(III) and Fe(III) with H_3L. The possible coordination sites of the free ligand were investigated and the interaction energies calculated in the gas phase and water solution. Quantum chemistry study confirms that the coordination of the third arm of the dihydrocinnamic ligand to both Al(III) and Fe(III) is accessible from a conformational point of view but, conversely, this additional coordination is controlled by an endothermic process. The formation of AlL seems to be, at least in water, slightly favourable with respect to the formation of the corresponding FeL derivative. The structure of fully optimized complexes and the corresponding interaction energy values are collected in Fig. 5.

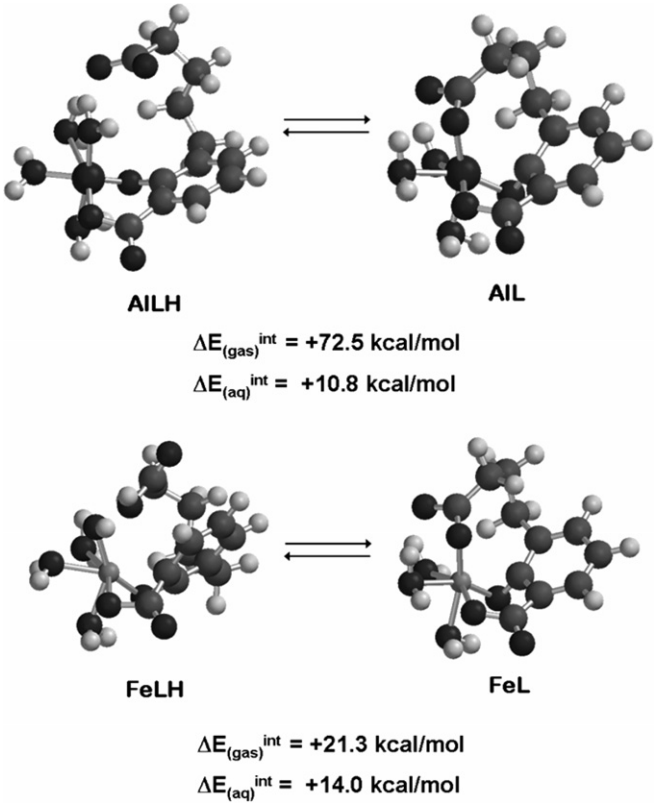


Fig. 5. PM3 fully optimized structure of the AlLH/AlL and FeLH/FeL complexes. Interaction energies (ΔE^{int}) for the complexation reaction are also reported. To simplify the picture, the water molecule replaced by the third arm of the dihydrocinnamic ligand is arbitrarily omitted.

3.3. UV–Vis results

Selected UV–Vis spectra for the Al(III)–H_3L and Fe(III)–H_3L solutions are reported in Fig. 6. In the case of Al(III)–H_3L, the increase of pH causes a slight blue shift of the main peaks and a general decrease of the absorption coefficients. These effects are in agreement with the gradual formation of the metal complexes, which are more positively charged, thus electron-poorer, than the free ligand. In the case of Fe(III)–H_3L, the metal–ligand coordination produces a charge-transfer peak centered at 550 nm ($\varepsilon = 1559\ M^{-1}\ cm^{-1}$). In the investigated pH range, the peak height is well correlated with the concentration of FeLH (compare Fig. 6b with 2b). Therefore FeLH is assumed to be the absorbing species, and the other Fe(III)–H_3L complexes do not absorb at these wavelengths. A very similar behaviour was observed for Fe(III)–salicylate complexes: the species FeL produces a charge-transfer peak (*e.g.* at 530 nm, $\varepsilon = 1660\ M^{-1}\ cm^{-1}$ in $NaClO_4$ 0.1 M [30]), and the other complexes do not absorb at the same wavelengths ([30] and references therein). Therefore, it is strongly suggested that the H_3L–FeLH species has the same bidentate structure of the salicylate–FeL species, with no role for the dihydrocinnamic arm in the metal complexation.

In the elaboration of the UV–Vis data, the formation constant of only one species could be optimized: $\log\beta_{1,1,0} = 0.5 \pm 0.3$ for Al(III)–H_3L ($\lambda = 265,\ 308$ nm), $\log\beta_{1,1,1} = 6.67 \pm 0.02$ for Fe(III)–H_3L ($\lambda = 550$ nm). The quite large error associated to the Al(III)–H_3L $\log\beta_{1,1,0}$ value, and the difference with the corresponding potentiometric constant ($\log\beta_{1,1,0} = -0.273 \pm 0.003$), are due to the similarity of the UV–Vis spectra of AlL at various pH values (Fig. 6a). The $\log\beta$ value of FeLH compares reasonably well with the corresponding potentiometric one ($\log\beta_{1,1,1} = 6.54 \pm 0.04$ for Fe(III)).

3.4. ^1H NMR results

The ^1H NMR spectra of D_2O solutions containing the free ligand and Al(III)–H_3L in a 1:1 molal ratio at two diagnostic pD values are reported in Fig. 7a and b. Proton assignments are reported (refer to Fig. 1).

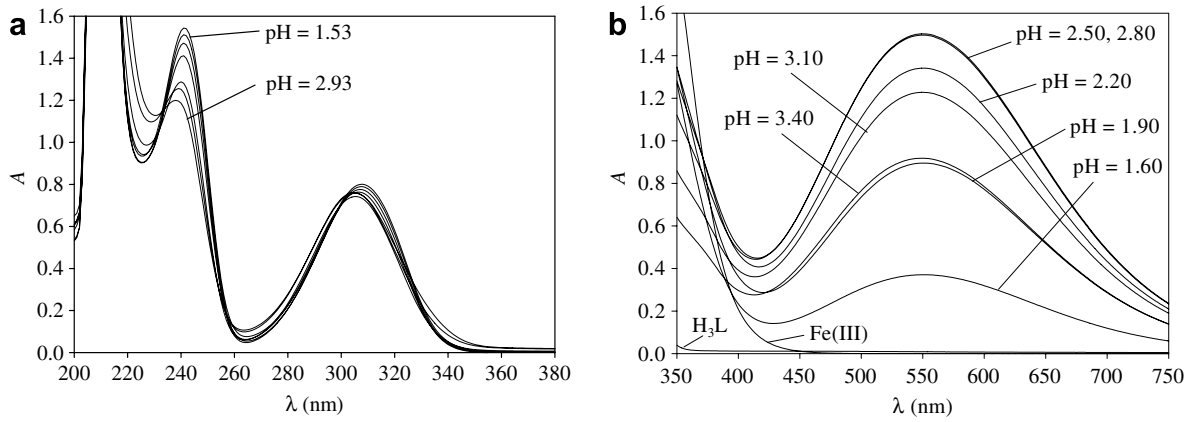


Fig. 6. UV–Vis spectra of Al(III)–H_3L (a) and Fe(III)–H_3L (b) at various pH values.

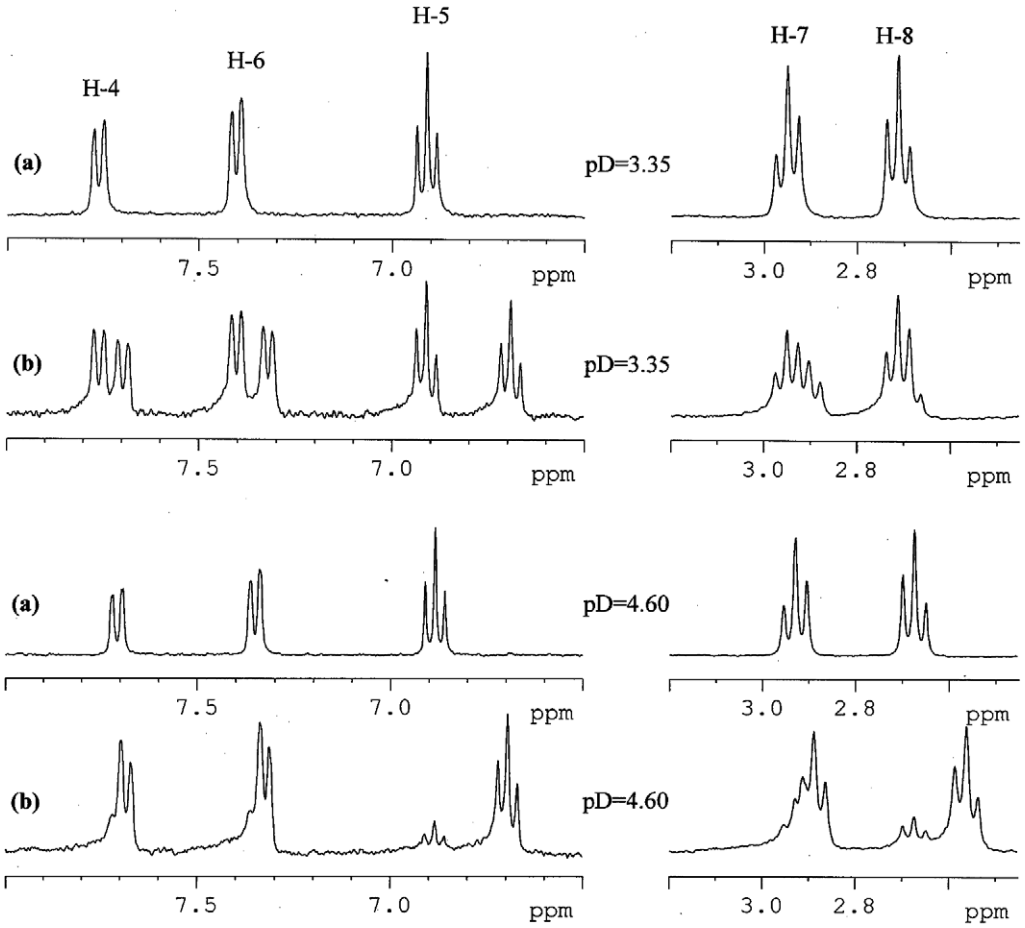


Fig. 7. ^1H NMR spectra of D_2O solutions at various pD values containing H_3L 0.0012 m (a), Al(III) 0.0012 m and H_3L 0.0012 m (b).

For the free ligand, the chemical shifts show a little pD dependence (compare Fig. 7a at pD 3.35 with Fig. 7a at pD 4.60), which is maximum for values higher than 5 (spectra not shown), where the deprotonation of dihydrocinnamic carboxylic group occurs.

Upon addition of Al(III), no modification is observed with respect of the free ligand outside the pD range 2.5–6.5, indicating that no complexation occurs at these pD values. This is in agreement with the potentiometric data, see e.g. Fig. 2a. Conversely, the appearance of new signals are observed within this pD range (compare Fig. 7a with b). At pD 3.35, a new set of signals centered at 7.70, 7.32 and 6.69 ppm is clearly visible in the aromatic region together with the signals of the free ligand. Also in the aliphatic region, new signals centered at 2.70 ppm (H-7 protons) clearly appear even if partially overlapped with

those of free ligand. These new sets of signals are assigned to the complex AlLH, which according to potentiometric data predominates at this pD value. The shift of the proton signals observed in the complex with respect to those in the free ligand indicates that the phenolic and the benzoic oxygens are involved in the metal chelation. On the other hand, the H-8 protons in AlLH must be very similar to the ones of the free ligand, as their signals are almost completely overlapped: from this it can be stated that the dihydrocinnamic carboxylate is not chelated to the metal center. This result confirms the structural hypothesis drawn for AlLH in Fig. 3.

At pD 4.60 the signals of the aromatic protons of the free ligand in the presence of Al(III) almost vanished, and the signals of the complex are predominating. By comparing this spectrum with the one a pD 3.35, also in the presence of Al(III), it can be noticed that the complex signals in the aromatic region and the signal of the H-7 protons do not shift with pD. The main change regards the appearance of a new set of signals centered at 2.55 ppm, well separated from the signals of the free ligand. Reasonably, this set can be assigned to the H-8 protons of the methylene group adjacent to the carboxylate group of the dihydrocinnamic arm (see Fig. 1). Here, it is evident that H-8 protons feel a very different chemical surrounding from those experienced by the Al(III) complex at pD 3.35, whereas all other protons have the same chemical shifts at both pD values. On the basis of potentiometric results, the NMR pattern at pD 4.60 is explained with the presence of the predominating species AlL, where also the dihydrocinnamic carboxylate is involved in the metal chelation together with the phenolate-like $-O^-$ as well as the benzoate-like COO^-. Therefore, NMR results strongly suggest a tridentate chelation at the metal in the complex AlL (this does not mean that the parallel formation of a mixed ligand-hydroxo-species AlLH(OH) is excluded, but at least that the tridentate coordinated species represents a significant fraction of AlL).

Other ^1H NMR measurements have been made for Al(III)–H_3L in a 1:2 molal ratio at several pD values (spectra not shown), in order to check the presence in solution of the complex AlL_2. We were not able to detect this species. This is due to the small amount of complex which forms in solution (apart for large excess of ligand over metal ion, and at pD values close to the start of aluminium hydroxide precipitation, see e.g. Fig. 2a).

4. Conclusions

The complexes formed in Al(III)–H_3L solutions are AlLH, AlL, and AlL_2. Potentiometric titrations allowed to obtain stoichiometry and stability constant values. UV–Vis gave a value for the stability constant of AlL, which is in fair agreement with the corresponding potentiometric result. ^1H NMR data confirmed the complex formation, and gave strong evidence of the involvement of the dihydrocinnamic carboxylate in the metal chelation. NMR and potentiometric data indicate that AlLH is a salicylate-like bidentate species, with no role of the dihydrocinnamic arm. For AlL, potentiometric data suggested and NMR supported a tridentate coordination, *i.e.* with dihydrocinnamic carboxylate chelated to the metal center together with the phenolate and the benzoate-like oxygens.

The complexes formed in Fe(III)–H_3L solutions are FeLH, FeL, FeL_2H_2, and FeL_2H. Potentiometric titrations allowed to obtain stoichiometry and stability constant values, and UV–Vis gave a value for the stability constant of FeLH, which is in reasonable agreement with the potentiometric one. The presence of an UV–Vis charge-transfer peak similar to the one encountered in Fe(III)–salicylate solutions indicates FeLH to be a salicylate-like, bidentate species. On the basis of stability constant values, it can be suggested that the dihydrocinnamic carboxylate does not chelate Fe(III) at any pH and in any complex, and that FeL and FeL_2H are mixed ligand-hydroxo-species. Anyway, the tridentate coordination, even if with a lesser relevance than in the case of Al(III), cannot be excluded.

Quantum chemistry calculations confirm experimental results: they indicate that the coordination of the third arm of the dihydrocinnamic ligand to both Al(III) and Fe(III) is accessible from a conformational point of view, and that this additional coordination is slightly more endothermic for Fe(III) than for Al(III).

As regards the chelation strength of H_3L, the presence of the dihydrocinnamic arm slightly increases the stability constant values of Al(III) complexes. The synthesis of 5-dihydrocinnamic derivatives of 3-hydroxy-4-pyridinecarboxylic acid and 4-hydroxy-3-pyridinecarboxylic acid, and the study of their Al(III) and Fe(III) complexing properties, are now in progress.

Acknowledgement

This work was supported by the University of Padova, Project TAPP PRAT 03.

References

[1] C. Hershko (Guest Editor), Sem. Hematol. 42 (2) (2005) Supplement 1.
[2] M.D. Cappellini, Best Pract. Res. Clin. Haemat. 18 (2005) 289.
[3] G.J. Kontoghiorghes, K. Pattichis, K. Neocleous, A. Kolnagou, Curr. Med. Chem. 11 (2004) 2161.
[4] G.J. Kontoghiorghes, Analyst 120 (1995) 845.
[5] G. Faa, G. Crisponi, Coord. Chem. Rev. 184 (1999) 291.
[6] R.A. Yokel, P. Ackrill, E. Burgess, J.P. Day, J.L. Domingo, T.P. Flaten, J. Savory, J. Toxicol. Environ. Health 48 (1996) 667.
[7] M.L. Albina, M. Belles, D.J. Sanchez, J.L. Domingo, Teratology 62 (2000) 86.
[8] N.F. Olivieri, G.M. Brittenham, C.E. McLaren, D.M. Templeton, R.G. Cameron, R.A. McClelland, A.D. Burt, K.A. Fleming, N. Engl. J. Med. 339 (1998) 417.
[9] R.A. Yokel, Coord. Chem. Rev. 228 (2002) 97.
[10] R.C. Hider, T. Zhouann, N.Y. Acad. Sci. 1054 (2005) 141.

[11] V.B. Di Marco, A. Dean, M.G. Ferlin, R.A. Yokel, H. Li, A. Venzo, G.G. Bombi, Eur. J. Inorg. Chem. (2006) 1284.
[12] SPARTANO2, Wavefuncion Inc., 18401 Von Karman Ave., Irvine, CA, USA.
[13] M. Frisch, G.W. Trucks, H. Schlegel, G. Scuseria, M. Robb, J. Cheeseman, V. Zakrzewski, J. Montgomery, R.E. Stratmann, J.C. Burant, S. Dapprich, J. Millam, A. Daniels, K. Kudin, M. Strain, O. Farkas, J. Tomasi, V. Barone, M. Cossi, R. Cammi, B. Mennucci, C. Pomelli, C. Adamo, S. Clifford, J. Ochterski, G.A. Petersson, P.Y. Ayala, Q. Cui, K. Morokuma, D.K. Malick, A.D. Rabuck, K. Raghavachari, J.B. Foresman, J. Cioslowski, J.V. Ortiz, B.B. Stefanov, G. Liu, A. Liashenko, P. Piskorz, I. Komaromi, R. Gomperts, R.L. Martin, D.J. Fox, T. Keith, M.A. Al-Laham, C.Y. Peng, A. Nanayakkara, C. Gonzalez, M. Challacombe, P.M.W. Gill, B.G. Johnson, W. Chen, M.W. Wong, J.L. Andres, M. Head-Gordon, E.S. Replogle, J.A. Pople, GAUSSIAN 98 (revision A.6), Gaussian, Inc, Pittsburgh, PA, 1998.
[14] A. Klant, G. Schuurmann, J. Chem. Soc., Perkin Trans. 2 (1993) 799.
[15] F. Tiemann, K.L. Reimer, Chem. Ber. 10 (1877) 1562.
[16] E. Cingolani, G. Bellomonte, F. Delle Monache, A. Sordi, Ann. Chim. (Rome) 55 (1955) 343.
[17] V.B. Di Marco, A. Tapparo, G.G. Bombi, Ann. Chim. (Rome) 89 (1999) 397.
[18] V.B. Di Marco, A. Tapparo, G.G. Bombi, Ann. Chim. (Rome) 91 (2001) 595.
[19] G.J. Janz, Silver–silver halide electrodes, in: D.J.G. Ives, G.J. Janz (Eds.), Reference Electrodes: Theory and Practice, Academic Press, New York, London, 1961.
[20] G. Biedermann, L.G. Sillén, Ark. Kemi 5 (1953) 425.
[21] S. Sjöberg, Y. Hägglund, A. Nordin, N. Ingri, Marine Chem. 13 (1983) 35.
[22] V.B. Di Marco, Ph.D. Thesis, University of Padova, 1998.
[23] L.O. Öhman, Inorg. Chem. 27 (1988) 2565.
[24] C. M Flynn Jr., Chem. Rev. 84 (1984) 31.
[25] A.K. Covington, M. Paabo, R.A. Robinson, R.G. Bates, Anal. Chem. 40 (1968) 700.
[26] L.O. Öhman, S. Sjöberg, Acta Chem. Scand. A37 (1983) 875.
[27] T. Kiss, E. Farkas, Perspec. Bioinorg. Chem. 3 (1996) 199.
[28] SCQUERY v.5.13, The Iupac Stability Constant Database, Academic Software, Copyright 2001.
[29] N. Akselrud, Y. Fialkov, Ukr. Khim. Zh. 16 (1958) 283.
[30] M.C. Chattopadhyaya, R.S. Singh, Anal. Chim. Acta 70 (1974) 49.

Available online at www.sciencedirect.com
ScienceDirect
Polyhedron 26 (2007) 3428–3436
POLYHEDRON
www.elsevier.com/locate/poly

Synthesis and characterization of novel Cd(II), Zn(II) and Ni(II) complexes with 2-quinolinecarboxaldehyde selenosemicarbazone. Crystal structure of bis(2-quinolinecarboxaldehyde selenosemicarbazonato)nickel(II)

Tamara R. Todorović [a], Alessia Bacchi [b], Nenad O. Juranić [c], Dušan M. Sladić [a], Giancarlo Pelizzi [b], Tatjana T. Božić [a], Nenad R. Filipović [d], Katarina K. Anđelković [a,*]

[a] *Faculty of Chemistry, University of Belgrade, Studentski trg 12-16, P.O. Box 158, 11001 Belgrade, Serbia*
[b] *Dipartimento di Chimica Generale ed Inorganica, Chimica Analitica, Chimica Fisica, University of Parma, Parco Area delle Scienze 17A, I-43100 Parma, Italy*
[c] *Departments of Biochemistry and Molecular Biology, Mayo College of Medicine, Mayo Clinic and Foundation, Rochester, MN 55905, USA*
[d] *Faculty of Agriculture, University of Belgrade, Nemanjina 6, 11081 Belgrade-Zemun, Serbia*

Received 17 January 2007; accepted 16 March 2007
Available online 28 March 2007

Abstract

New complexes of Cd(II), Zn(II) and Ni(II) with 2-quinolinecarboxaldehyde selenosemicarbazone (Hqasesc) were synthesized and structurally characterized. The structure of the ligand, Cd(II) and Zn(II) complexes was determined by NMR and IR spectroscopy, elemental microanalysis and molar conductivity measurements. Both complexes occur in solution in two forms, the major tetrahedral and minor octahedral. In the major Cd(II) complex one qasesc$^-$ ligand is coordinated as a tridentate, the fourth coordination site being occupied by acetate, while in the major Zn(II) complex two qasesc$^-$ ligands are coordinated as bidentates. In both minor complexes two qasesc$^-$ ligands are coordinated as tridentates forming the octahedral geometry around the central metal ion. The only paramagnetic complex in the series is Ni(II) complex for which X-ray structure analysis was performed. The complex has the angularly distorted octahedral geometry with two qasesc$^-$ ligands coordinated as tridentates, in a similar way as in the minor complexes of Cd(II) and Zn(II).
© 2007 Elsevier Ltd. All rights reserved.

Keywords: Cd(II), Zn(II) and Ni(II) complexes; Selenosemicarbazone; 2-Quinolinecarboxaldehyde; X-ray structure; NMR; Biological activity

1. Introduction

Semicarbazones and thiosemicarbazones have been extensively studied as antibacterial, antiviral and antitumor agents [1–6]. There are only few studies on biological activity of selenosemicarbazones, indicating their similar or grater activity in comparison with sulphur analogues, while oxygen analogues showed a lower activity [7–12]. Selenosemicarbazones of cinnamaldehydes, benzaldehydes and 5-hydroxy-2-formylpyridine show strong antitumor activity [7,11], selenosemicarbazones of benzaldehydes and furfural strong antimicrobial activity [9,10], and 2-acetylpyridine selenosemicarbazone antiviral activity [8]. A much greater number of complexes were synthesized with semi- and thiosemicarbazones than with selenosemicarbazones. The complexes were also studied as antibacterial, antiviral and antitumor agents [1–6].

The ligand systems used for preparation of the selenosemicarbazone complexes were selenosemicarbazones of: aliphatic acyclic and cyclic ketones [13–19], aromatic aldehydes [13,14,16,20–32], diacetyl monoxime [33–37], keto acids [32,38,39], and diketones [40–42]. Of almost

* Corresponding author. Tel.: +381 11 3336 739; fax: + 381 11 3282 750.
E-mail address: kka@chem.bg.ac.yu (K.K. Anđelković).

0277-5387/$ - see front matter © 2007 Elsevier Ltd. All rights reserved.
doi:10.1016/j.poly.2007.03.023

200 synthesized complexes, only four were characterized by X-ray structural analysis. Biological activity studies were not performed with any of the complexes.

In our previous paper, synthesis of the first heteroaromatic bis(selenosemicarbazone), 2,6-diacetylpyridine bis(selenosemicarbazone) (H_2dapsesc) and the corresponding Cd(II) and Zn(II) complexes was reported [42]. The attempted synthesis of the Ni(II) complex gave an unexpected result, namely elimination of hydrogen selenide from one side chain, affording the Ni(II) complex with the ligand 2-{1-[6-(1-selenosemicarbazonoethyl)-2-pyridyl]ethylidene}-hydrazine carbonitrile (H_2hcn), the structure of which was determined by X-ray structural analysis [42]. Such a reaction had not been reported previously.

In the present work synthesis of the heteroaromatic monoselenosemicarbazone ligand 2-quinolinecarboxaldehyde selenosemicarbazone (Hqasesc) and its Ni(II), Cd(II) and Zn(II) complexes, as well as their structure determination by X-ray crystallography and multinuclear 2D NMR spectroscopy are reported. The biological activity evaluation of the new complexes, as well as of some previously synthesized ones is also a part of this work.

2. Experimental

2.1. Materials and measurements

Selenosemicarbazide and 2-quinolinecarboxaldehyde were obtained from Acros Organics (BVBA, Geel, Belgium). $Ni(AcO)_2 \cdot 4H_2O$, $Zn(AcO)_2 \cdot 2H_2O$ and $Cd(AcO)_2 \cdot 2H_2O$ were obtained from Fluka Chemie GmbH (Germany). All solvents (ethanol, dimethyl sulfoxide, *N*,*N*-dimethylformamide) were reagent grade and used without further purification. Elemental analysis (C, H, N and S) was performed by the standard micro method using the ELEMENTARVario ELIII C.H.N.S=O analyser. IR spectra were recorded on Perkin–Elmer FT-IR 1725X spectrophotometer by the KBr technique in the region 4000–400 cm^{-1}. Molar conductivity of DMF solutions was measured at room temperature (298 K) on the digital conductometer JENWAY-4009. The magnetic measurements were performed at 298 K by the Evans' method using a MSB-MK1 balance (Sherwood Scientific Ltd.).

2.2. NMR spectroscopy

NMR spectral assignments and structural parameters were obtained by combined use of ^{1}H homonuclear spectroscopy (2D DQF-COSY, 2D TOCSY, 2D NOESY, 2D ROESY) [43–46] and multinuclear proton-detected spectroscopy (2D HSQC, 2D HMQC, 2D HMBC) [47–49]. ^{1}H homonuclear 1D and 2D spectra were obtained in DMSO-d_6 using Bruker 600 equipped with cryo-probe. 2D NOESY spectra were collected with eight scans per t1-increment and mixing time of 1 s, 2D TOCSY with mixing time of 80 ms and 2D ROESY with mixing time of 500 ms. ^{1}H–^{13}C heteronuclear 2D HSQC and HMBC experiments were obtained on the same spectrometer and samples but with an increase number of scans (64) per t1-increment. ^{1}H–^{113}Cd heteronuclear 2D HSQC spectrum was obtained on 500 MHz spectrometer equipped with a broad-band inverse probe (32 scans per 512 t1-increments). Directly detected 1D ^{113}Cd and ^{77}Se (^{113}Cd at 111 MHz, ^{77}Se at 95 MHz) spectra were obtained on the same spectrometer equipped with a broad-band direct probe (30 000 scans for ^{113}Cd and 5000 scans for ^{77}Se). Chemical shifts (δ) are given in ppm using direct (^{1}H) or indirect (hetero nuclei) referencing to tetramethylsilane as ^{1}H standard.

2.3. X-ray crystallography

Mo Kα radiation ($\lambda = 0.71073$ Å), $T = 293$ K was used on a SMART AXS 1000 CCD diffractometer for $[Ni(qasesc)_2] \cdot 2DMSO$. Lorentz, polarization, and absorption corrections were applied [50]. Structures were solved by direct methods using SIR97 [51] and refined by full-matrix least-squares on all F^2 using SHELXL97 [52] implemented in the WINGX package [53]. Hydrogen atoms were partly located on Fourier difference maps and refined isotropically and partly introduced in calculated positions. Anisotropic displacement parameters were refined for all non-hydrogen atoms. Hydrogen bonds have been analyzed with SHELXL97 [52] and PARST97 [54], and extensive use was made of the Cambridge Crystallographic Data Centre packages [55] for the analysis of crystal geometry. The bischelate $[Ni(qasesc)_2]$ complex crystallizes with two DMSO solvation molecules, for one of which the sulphur atom is disordered over two sites. Table 1 summarizes crystal data and structure determination results.

2.4. Preparation of 2-quinolinecarboxaldehyde selenosemicarbazone (Hqasesc)

To a suspension of selenosemicarbazide (0.20 g, 1.45 mmol) in ethanol (25 mL), a solution of 2-quinolinecarboxaldehyde (0.26 g, 1.65 mmol) in 6 mL ethanol–glacial acetic acid mixture (1:1) was added. The reaction mixture was refluxed with stirring for 1 h followed by cooling to a room temperature. A yellow precipitate was filtered off and washed with cold ethanol. Yield 0.34 g (86%). *Anal.* Calc. for $C_{11}H_{10}N_4Se$: C, 47.66; H, 3.64; N, 20.21. Found: C, 47.69; H, 3.48; N, 20.03%. IR (KBr, cm^{-1}): 3370 (s), 3265 (s), 3118 (s), 3003 (s), 1607 (vs), 1527 (vs), 1501 (vs), 1456 (s), 1322 (s), 1275 (s), 1101 (vs), 750 (s), 601 (s), 542 (s).

2.5. Preparation of $[Cd(qasesc)(AcO)] \cdot H_2O$ (**1**)

To a solution of Hqasesc (0.05 g, 0.18 mmol) in ethanol (10 mL), a solution of $Cd(AcO)_2 \cdot 2H_2O$ (0.05 g, 0.19 mmol) in ethanol (2 mL) was added. The reaction mixture was heated at 65 °C with stirring for 1 h followed by cooling to a room temperature. A yellow precipitate was filtered off and washed with cold ethanol. Yield 0.06 g

Table 1
Crystal data and structure refinement for $[Ni(qasesc)_2]\cdot 2DMSO$

Empirical formula	$C_{26}H_{30}N_8NiO_2S_2Se_2$
Formula weight	767.33
Temperature (K)	293(2)
Wavelength (Å)	0.71073
Crystal system	triclinic
Space group	$P\bar{1}$
Unit cell dimensions	
a (Å)	10.4907(8)
b (Å)	10.8951(8)
c (Å)	15.036(1)
α (°)	92.330(1)
β (°)	94.134(1)
γ (°)	116.412(1)
Volume (Å^3)	1530.1(2)
Z	2
D_{calc} (Mg/m^3)	1.665
Absorption coefficient (mm^{-1})	3.188
$F(000)$	772
θ Range for data collection (°)	1.36–28.29
Reflections collected	19045
Independent reflections [R_{int}]	7359 [0.0230]
Refinement method	full-matrix least-squares on F^2
Data/restraints/parameters	7359/0/467
Goodness-of-fit on F^2	0.984
Final R indices [$I > 2\sigma(I)$]	$R_1 = 0.0286$, $wR_2 = 0.0689$
R indices (all data)	$R_1 = 0.0475$, $wR_2 = 0.0748$
Largest ΔF maximum/minimum (e Å^{-3})	0.724/−0.352

(72%). *Anal.* Calc. for $C_{13}H_{14}N_4O_3SeCd$: C, 33.53; H, 3.03; N, 12.03. Found: C, 33.46; H, 3.24; N, 12.01%. IR (KBr, cm^{-1}): 3295 (s), 3071 (s), 1652 (m), 1553 (vs), 1482 (vs), 1417 (vs), 1307 (s), 1170 (vs), 757 (m), 676 (s), 626 (m). Λ_M (1×10^{-3} M, DMF): 7.79 Ω^{-1} cm^2 mol^{-1}.

2.6. Preparation of $[Zn(qasesc)_2]\cdot 3H_2O$ (2)

To a solution of Hqasesc (0.05 g, 0.18 mmol) in ethanol (10 mL), a solution of $Zn(AcO)_2\cdot 2H_2O$ (0.04 g, 0.19 mmol) in distilled water (1.5 mL) was added. The reaction mixture was heated at 65 °C with stirring for 1 h followed by cooling to a room temperature. An orange microcrystalline product was filtered off and washed with cold ethanol. Yield 0.10 g (84%). *Anal.* Calc. for $C_{22}H_{24}N_8O_3Se_2Zn$: C, 39.33; H, 3.60; N, 16.68. Found: C, 39.68; H, 3.34; N, 16.69%. IR (KBr, cm^{-1}): 3323 (s), 3291 (s), 3153 (s), 1637 (m), 1582 (s), 1472 (m), 1412 (vs), 1296 (m), 1179 (s), 1166 (s), 1120 (s), 749 (w). Λ_M (1×10^{-3} M, DMF): 5.13 Ω^{-1} cm^2 mol^{-1}.

2.7. Preparation of $[Ni(qasesc)_2]\cdot 2DMSO$ (3)

To a solution of Hqasesc (0.05 g, 0.18 mmol) in ethanol (10 mL), a solution of $Ni(AcO)_2\cdot 4H_2O$ (0.05 g, 0.19 mmol) in distilled water (2 mL) was added. The reaction mixture was heated at 65 °C with stirring for 1 h followed by cooling to a room temperature. A brown precipitate was filtered off and washed with cold ethanol. Microcrystalline product was purified by vapor diffusion using the DMSO solution as an inner solution and ethanol as an outer solvent. Yield 0.12 g (89%). *Anal.* Calc. for $C_{26}H_{30}N_8O_2Se_2S_2Ni$: C, 40.70; H, 3.94; N, 14.60; S, 8.36. Found: C, 40.60; H, 4.21; N, 14.40; S, 8.56%. IR (KBr, cm^{-1}): 3289 (m), 3169 (m), 3090 (m), 1611 (m), 1578 (m), 1410 (vs), 1305 (m), 1157 (s), 1119 (m), 1037 (m), 759 (w). Λ_M (1×10^{-3} M, DMF): 2.35 Ω^{-1} cm^2 mol^{-1}. μ (293 K) = 3.15 BM.

2.8. Preparation of H_2dapsesc, [Cd(dapsesc)] (4), [Zn(dapsesc)] (5) and [Ni(hcn)] (6)

The ligand H_2dapsesc and complexes **4–6** were prepared as described previously [42]. In short, ligand H_2dapsesc was obtained by condensation of 2,6-diacetylpyridine and selenosemicarbazide in the molar ratio of 1:2. The complexes **4–6** were synthesized by adding aqueous solution of $Cd(AcO)_2\cdot 2H_2O$, $Zn(AcO)_2\cdot 2H_2O$, or $Ni(AcO)_2\cdot 4H_2O$, respectively, into suspension of H_2dapsesc in ethanol.

2.9. Biological activity evaluation

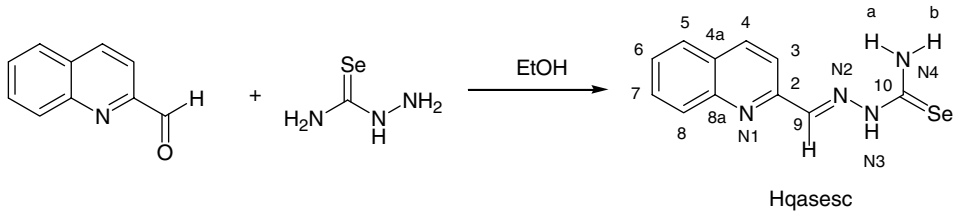
A teaspoon of lyophilized eggs of the brine shrimp *Artemia salina* was added to 1 L of the artificial sea water containing several drops of yeast suspension (3 mg of dry yeast in 5 mL distilled water), and air was passed through the suspension thermostated at 301 K, under illumination for 24 h. The tested substances were dissolved in DMSO. In a glass vial, into 1 mL of artificial sea water 1–2 drops of yeast extract solution (3 mg in 5 mL of distilled water) and 10–20 hatched nauplii were added, and finally solutions of all derivatives to the appropriate concentrations. For each concentration, two determination were performed. The vials were left at 301 K under illumination for 24 h, and afterwards live and dead nauplii were counted. $LC_{50}$was defined as the concentration of a drug that causes death of 50% nauplii. DMSO was inactive under applied conditions.

3. Results and discussion

3.1. Synthetic aspects

The new ligand system, 2-quinolinecarboxaldehyde selenosemicarbazone (Hqasesc), was obtained by condensation reaction of 2-quinolinecarboxaldehyde and selenosemicarbazide (1:1) (Scheme 1). Hqasesc is a yellow microcrystalline product soluble at room temperature in DMF and DMSO, and at elevated temperatures also in EtOH, MeOH and MeCN.

By reaction of nickel, cadmium and zinc acetates with Hqasesc in equimolar ratio (1:1) the corresponding complexes were obtained. The mole ratio of the reacting species did not influence the composition of the products. The nickel complex is soluble in MeOH, EtOH, MeCN, DMF and DMSO at room temperature, the cadmium complex



Scheme 1.

in DMSO at room temperature and in EtOH and DMF at elevated temperatures, and the zinc complex in DMSO at room temperature.

All the synthesized complexes are non-electrolytes, as determined by molar conductivity measurements.

Elemental microanalysis showed that in the molecules of Zn(II) and Ni(II) complexes there are two deprotonated ligand molecules, while in the molecule of Cd(II) complex there is only one deprotonated ligand molecule and an acetate ion.

Magnetic measurements showed that the Ni(II) complex is paramagnetic.

3.2. IR spectra

The absence of the ν(Se–H) band at 2300 cm^{-1} in the IR spectrum of the ligand is an evidence of the selenone tautomeric form. Coordination of azomethine nitrogen can be assumed on the basis of the shift of the band originating from ν(C=N) vibration toward higher frequencies in the complexes (1607 cm^{-1} in the ligand and 1637 cm^{-1}, 1614 cm^{-1} and 1611 cm^{-1} in **1**, **2** and **3**, respectively). In the Cd(II) complex, bands of the coordinated acetate (1553 cm^{-1} and 1417 cm^{-1}), and in the Ni(II) complex, band at 1037 cm^{-1} originating from non-coordinated DMSO molecules can be seen.

3.3. NMR spectral data

The (*E*)-configuration of the hydrazone moiety in the ligand can be evidenced from 2D ROESY spectrum (Fig. 1) in which protons 9 and N3 are correlated.

The Cd(II) and Zn(II) complexes are diamagnetic and their structure in solution was determined by NMR spectroscopy. The Ni(II) complex is paramagnetic.

The Cd(II) complex was characterized by ^{1}H, ^{13}C, ^{77}Se and ^{113}Cd NMR spectra as well as by two-dimensional heteronuclear correlation spectra (^{1}H–^{13}C, ^{1}H–^{113}Cd), Figs. 2–4. In all spectra there are two series of signals, indicating the presence of two complex species. Since the ratio of intensities of the signals in ^{113}Cd spectrum is 6:1, and in ^{77}Se and ^{1}H spectra 3:1, it implies that the ratio of amounts of two complexes is 6:1, whereby in the major complex one

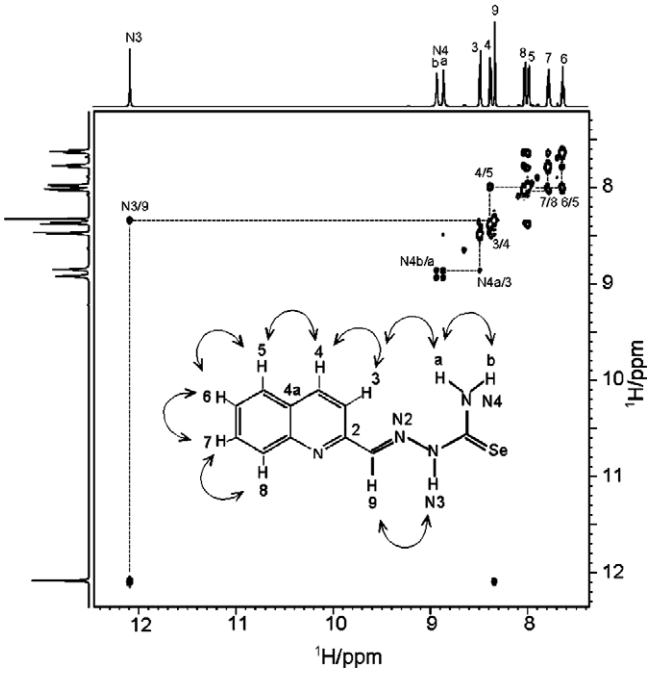


Fig. 1. 2D ROESY of Hqasesc in DMSO-d_6 at 298 K (mixing time 500 ms) recorded on Bruker 600 MHz spectrometer equipped with cryo-probe. Connectivity by spatial proximity is indicated by dashed lines in the spectrum and by arrows in the Hqasesc structure model.

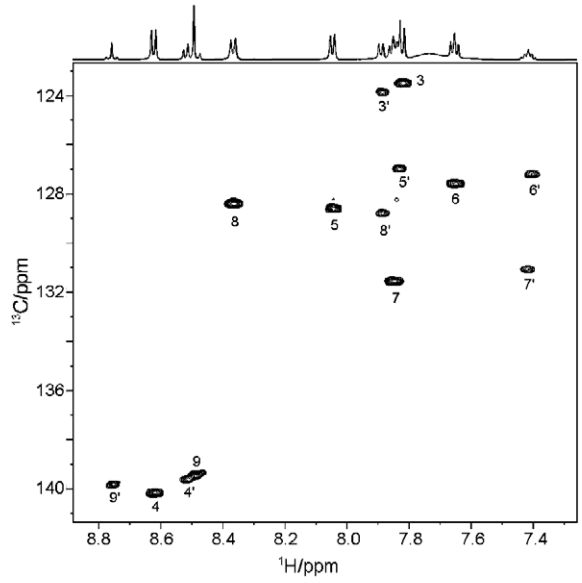


Fig. 2. {^{1}H–^{13}C}-HSQC chemical shift correlation spectrum of Cd(II) complex (DMSO-d_6, 298 K), recorded on Bruker 600 MHz spectrometer equipped with cryo-probe. Spectral peaks numbering is same as in Fig. 1; minor component is denoted by primed numbers.

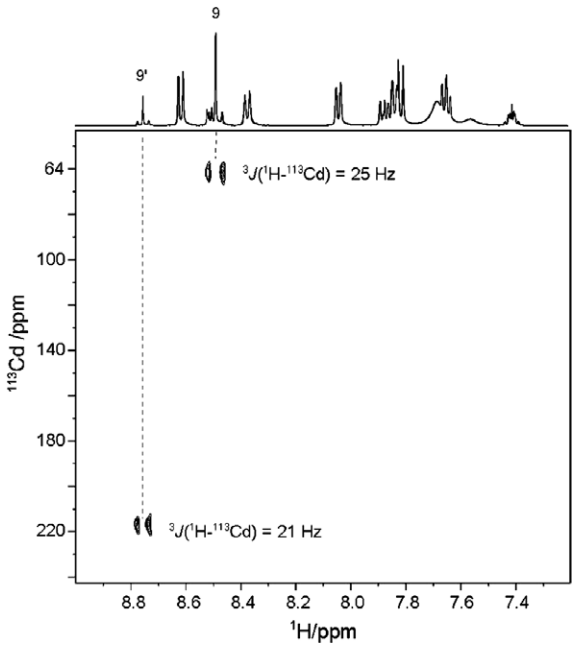


Fig. 3. {^{1}H–^{113}Cd}-HSQC chemical shift correlation spectrum of Cd(II) complex (DMSO-d_6, 298 K), recorded on Bruker 500 MHz spectrometer equipped with inverse broad-band probe. Spectral peaks numbering is same as in Fig. 1; minor component is denoted by primed numbers. Note that natural abundance of ^{113}Cd (20%) gives doublet splitting in proton spectrum at about 20% intensity.

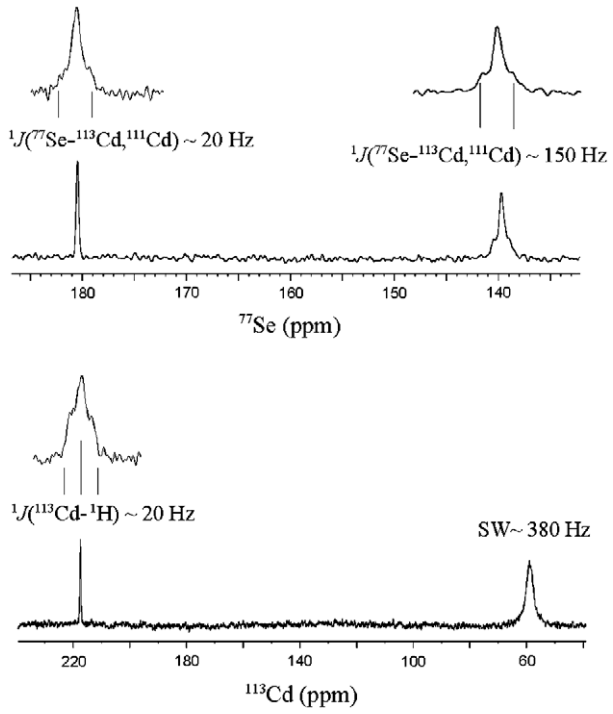


Fig. 4. ^{113}Cd (bottom) and ^{77}Se (top) spectra of Cd(II) complex (DMSO-d_6, 298 K), recorded on Bruker 500 MHz spectrometer equipped with broad-band probe. Note that natural abundance of ^{113}Cd (20%) gives doublet splitting in ^{77}Se spectrum at about 20% intensity.

ligand molecule is bound to Cd(II), while the minor one contains two ligand molecules bound to Cd(II).

The presence of two ligands in the minor complex can also be evidenced by coupling of ^{113}Cd with protons. The sharper line at 220 ppm is a triplet (Fig. 4), indicating two identical protons. When this coupling is observed in the ^{1}H spectrum (signal at 8.8 ppm), a doublet with the same coupling constant (~20 Hz) is seen (Fig. 3). That means that the minor complex has two symmetrical ligands. The chemical shifts of ^{113}Cd indicate a larger number of coordinated nitrogen atoms in the minor complex than in the major one (Cd shift of 220 ppm in the former and 60 ppm in the latter one).

The major complex has a strongly coordinated selenium, since there is a strong coupling of ^{77}Se with ^{113}Cd (a broad line at 140 ppm in 1D ^{77}Se spectrum), with a coupling constant of 150 Hz (Fig. 4). The corresponding signal in the minor complex (180 ppm) has a small $^{1}J(^{77}Se–^{113}Cd)$ coupling constant of 20 Hz, indicating a weak coordination of selenium. In both complexes azomethine nitrogen is coordinated as shown by the forementioned coupling of proton 9 (doublets with intensity of ~20%). Signal of proton 9 (Fig. 2) has a large downfield shift in comparison to the ligand. In both complexes there are large relative shifts of several protons in the quinoline molecules, indicating coordination of the quinoline nitrogen. In the major complex, quinoline nitrogen is weakly coordinated. Assignments of signals in ^{1}H and ^{13}C NMR spectra are given in Tables 2 and 3.

Based on the presented evidence, the major complex has a tetrahedral geometry with one ligand coordinated in deprotonated form *via* selenium, azomethine and quinoline nitrogens, the fourth coordination site being occupied by acetate ion (singlet at 1.79 ppm in ^{1}H spectrum) (Scheme 2). In the minor complex two deprotonated ligands are bound *via* selenium, azomethine and quinoline nitrogen atoms each, forming octahedral geometry (Scheme 3). Cadmium(II) complex with pyridine-2-carbaldehyde thiosemicarbazone, obtained from cadmium acetate, has a similar octahedral geometry, in which two deprotonated ligands are bound *via* sulphur, azomethine and pyridine nitrogen atoms [56]. Since the microanalysis is in complete accordance with the proposed structure of the major complex, it is likely that in DMSO solution the complex undergoes chemical change and a small quantity (15%) of the minor complex is formed.

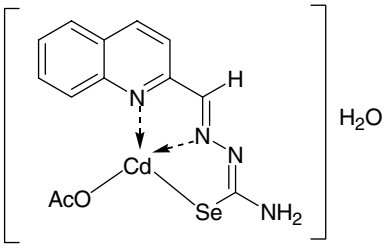
According to NMR spectral evidence (Fig. 5), the Zn(II) complex in solution also exists in two forms. Based on the intensity of the signal of C9 proton (85:15), the relative ratio of the major and minor complex is 5.7:1, assuming that in both of them there are two molecules of the ligand in one molecule of the complex. It is likely that the major complex has a tetrahedral geometry in which the ligands are coordinated *via* selenium and azomethine nitrogens (Scheme 4), while the minor complex has an octahedral geometry with two ligand molecules coordinated in the same way as in the minor Cd(II) complex (Scheme 5).

Table 2
^{1}H NMR spectral data in DMSO-d_6 at 298 K

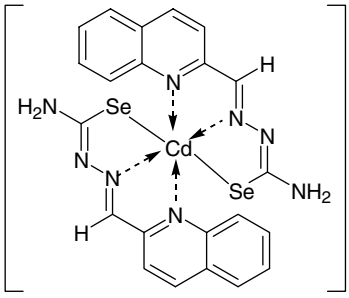
Hqasesc	δ 7.64 (t, 1H, C6, $J \sim 8.0$ Hz), 7.77 (t, 1H, C7, $J = 8.0$ Hz), 7.98 (d, 1H, C8, $J = 8.3$ Hz), 8.02 (d, 1H, C5, $J = 8.3$ Hz), 8.33 (s, 1H, C9), 8.37 (d, 1H, C4, $J = 8.6$ Hz), 8.48 (d, 1H, C3, $J = 8.6$ Hz), 8.85 (s, 1H, N4H[a]), 8.92 (s, 1H, N4H[b]), 12.08 (s, 1H, N3H)
Cd(II) complex major	δ 7.70 (t, 1H, C6, $J = 8.0$ Hz), 7.80 (d, 1H, C3, $J = 8.6$ Hz), 7.90 (t, 1H, C7, ovlp), 8.05 (d, 1H, C5, $J = 8.0$ Hz), 8.40 (d, 1H, C8, $J = 8.6$ Hz), 8.50 (s, 1H, C9), 8.62 (d, 1H, C4, $J = 8.6$ Hz)
Cd(II) complex minor	δ 7.40 (t, 1H, C6, ovlp), 7.45 (t, 1H, C7, ovlp), 7.85 (d, 1H,C5, ovlp) 7.90 (d, 1H, C3, C8, $J \sim 8.6$ Hz), 8.50 (d, 1H, C4, $J = 8.6$ Hz), 8.76 (s, 1H, C9)
Zn(II) complex major	δ 7.68 (t, 1H, C6, $J \sim 8.0$ Hz), 7.80 (d, 1H, C3, $J \sim 8.6$ Hz), 7.90 (t, 1H, C7, ovlp), 8.10 (d, 1H, C5, $J = 8.0$ Hz), 8.57 (s, 1H, C9), 8.65 (d, 1H, C4, $J = 8.5$ Hz), 8.68 (ovlp, 1H, C8)
Zn(II) complex minor	δ 7.40 (t, 1H, C7, $J \sim 8.0$ Hz), 7.70 (ovlp, 1H, C6), 7.80 (ovlp, 1H, C3), 7.85 (ovlp, 1H, C5), 7.88 (ovlp, 1H, C8), 8.50 (d, 1H, C4, $J = 8.5$ Hz), 8.80 (s, 1H, C9)

Table 3
^{13}C NMR spectral data in DMSO-d_6 at 298 K

Hqasesc	δ 118.4 (C3), 127.5 (C6), 128.1 (C4a), 128.2 (C8), 129.1 (C5), 130.2 (C7), 136.6 (C4), 144.1 (C9), 147.6 (C8a), 154.1 (C2), 174.9 (C10)
Cd(II) complex major	δ 123.5 (C3), 127.6 (C6), 128.4 (C8), 128.6 (C5), 131.5 (C7), 139.4 (C9), 140.1 (C4)
Cd(II) complex minor	δ 123.8 (C3), 126.9 (C5), 127.2 (C6), 128.8 (C8), 131.0 (C7), 139.6 (C4), 139.8 (C9)
Zn(II) complex major	δ 122.5 (C3), 127.6 (C6), 128.5 (C5), 129.0 (C8), 131.3 (C7), 139.9 (C9), 140.7 (C4)
Zn(II) complex minor	δ 123.3 (C3), 126.2 (C6), 126.9 (C7), 128.2 (C5), 128.9 (C8), 138.5 (C9), 139.9 (C4)



Scheme 2.



Scheme 3.

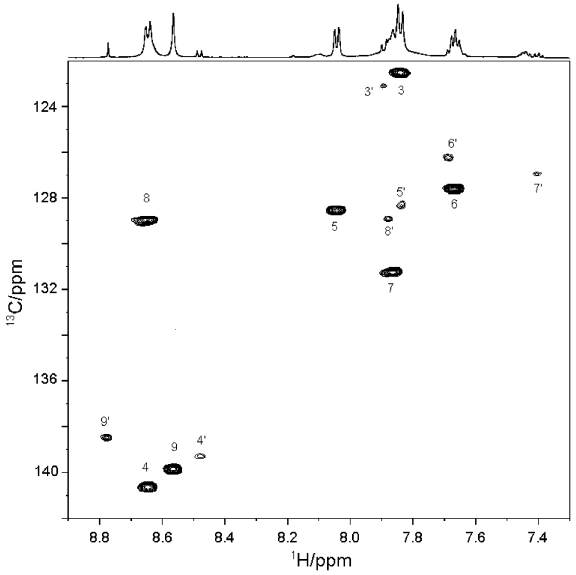
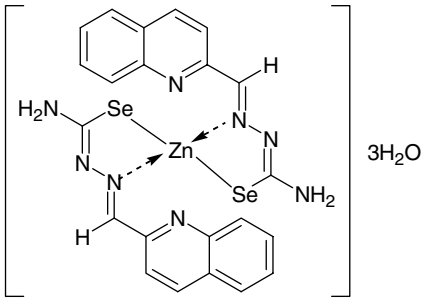


Fig. 5. {^{1}H–^{13}C}-HSQC chemical shift correlation spectrum of Zn(II) complex (DMSO-d_6, 298 K), recorded on Bruker 600 MHz spectrometer equipped with cryo-probe. Spectral peaks numbering is same as in Fig. 1; minor component is denoted by primed numbers.

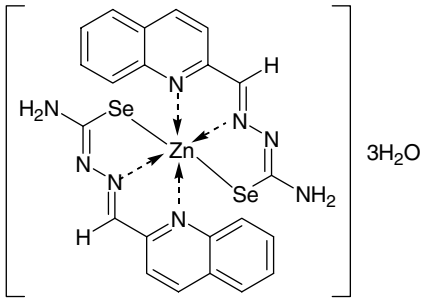
The structure in solution differs from the structure in solid state. Proton NMR spectrum of the freshly prepared solution has additional signals with fairly broad lines (Fig. 6), indicating an oligomeric structure. Since the colour changes, it is obvious that in solid state there is some (probably stacking) interaction which disappears in solution.

3.4. Crystal structure

Single crystal X-ray analysis shows that the nickel ion coordinates two deprotonated qasesc$^-$ ligands giving the octahedral bischelate complex [Ni(qasesc)$_2$]. Fig. 7 shows a perspective view of the neutral complex, and Table 4 reports the most relevant bonding parameters. The qasesc$^-$



Scheme 4.



Scheme 5.

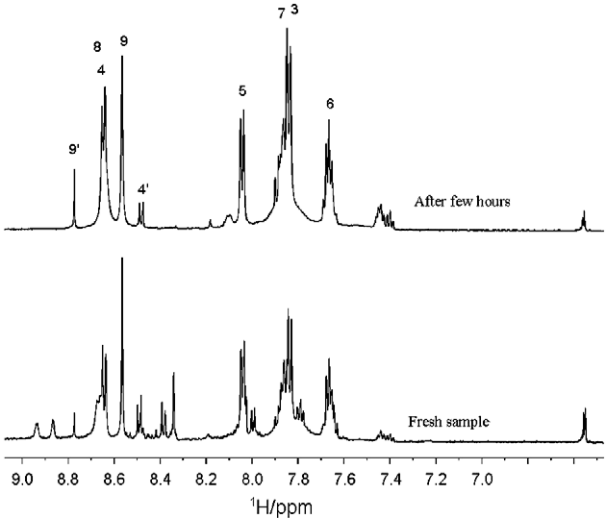


Fig. 6. ^{1}H spectrum (bottom) of freshly dissolved Zn(II) complexes and spectrum after few hours (top) (DMSO-d_6, 298 K), recorded on Bruker 600 MHz spectrometer. Spectral peaks numbering is same as in Fig. 1; minor component is denoted by primed numbers.

ligands coordinate the metal in a tridentate fashion by means of the selenium, the quinoline and the hydrazonic nitrogen atoms, forming two five membered chelate rings. The resulting octahedral coordination geometry is angularly distorted according to the bite angles of the chelate rings, ranging between 78.03(7) and 81.73(5)°. In this complex the ligand skeletons are essentially planar within 0.08 and 0.12 Å for C1–C11–N1–N4 and C12–C22–N5–N8, respectively, while the selenium atoms deviate slightly from the average planes, by 0.14 and 0.32 Å, respectively, for Se1

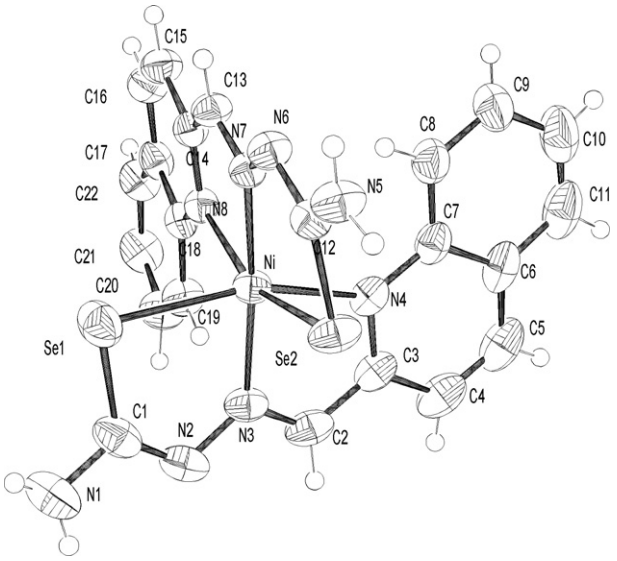


Fig. 7. Perspective view and labelling scheme of the molecular structure of [Ni(qasesc)$_2$]. Thermal ellipsoids at the 50% probability level.

Table 4
Selected bond lengths (Å) and angles (°) for [Ni(qasesc)$_2$] · 2DMSO

Ni–N(3)	2.026(2)
Ni–N(7)	2.031(2)
Ni–N(8)	2.198(2)
Ni–N(4)	2.206(2)
Ni–Se(1)	2.5221(4)
Ni–Se(2)	2.5306(4)
Se(1)–C(1)	1.886(3)
Se(2)–C(12)	1.874(2)
N(3)–Ni–N(7)	170.73(7)
N(3)–Ni–N(8)	107.36(7)
N(7)–Ni–N(8)	78.14(6)
N(3)–Ni–N(4)	78.03(7)
N(7)–Ni–N(4)	109.76(7)
N(8)–Ni–N(4)	90.67(6)
N(3)–Ni–Se(1)	81.70(6)
N(7)–Ni–Se(1)	90.93(5)
N(8)–Ni–Se(1)	90.19(4)
N(4)–Ni–Se(1)	159.01(5)
N(3)–Ni–Se(2)	93.57(5)
N(7)–Ni–Se(2)	81.73(5)
N(8)–Ni–Se(2)	158.59(4)
N(4)–Ni–Se(2)	89.31(5)
Se(1)–Ni–Se(2)	97.39(1)

and Se2. This slight distortion from planarity is due to an intramolecular repulsion between the selenium atoms, which are forced by the bischelate coordination geometry to come closer than the sum of their Van der Waals radii (Se1...Se2 = 3.795(5) Å, r_{Se} = 1.90 Å). The Ni–Se distances (Ni–Se1 = 2.5221(4) Å, Ni–Se2 = 2.5306(4) Å) are remarkably longer than the one observed in the similar isothiocyanato-[2-(diphenylphosphino)benzaldehyde selenosemicarbazonato]-nickel(II) [25] (CSD refcode: ISIPUV, Ni–Se = 2.269 Å), where the chalcogen is *trans* to a phosphine donor, and free from steric tension. Similarly, the Ni–N(quinoline) bonds (Ni–N4 = 2.206(2) Å, Ni–N8 =

2.198(2) Å) are significantly longer than the average (2.08(4) Å) found in a search on quinoline–Ni systems performed through the Cambridge Structural Database [55]. A structurally related thiosemicarbazonato *iso*-quinoline bischelate Ni(II) complex has been structurally characterized (CSD refcode: ICQTNI) [57].

The crystal packing is based on the association of pairs of neutral [Ni(qasesc)$_2$] complexes by formation of hydrogen bonds between the –NH$_2$ group of one molecule and the imminic nitrogen of the second one (N5–H...N6(i), N...N = 3.004(3) Å, N–H...N = 174(2)°, (i) = $-x$, $-y+1$, $-z+2$). A centrosymmetric dimeric pattern is obtained (Fig. 8). This molecular recognition process involves only one of the two ligands of each complex, leaving three –NH hydrogen bond donors per molecule available to interact with two DMSO guest molecules; each complex fulfills its hydrogen bonding capability by forming the contacts N1–H...O2 (N...O = 2.918(5) Å, N–H...O = 145(4)°) and N5–H...O1 (N...O = 2.895(3) Å, N–H...O = 147(2)°) (Fig. 8).

3.5. Biological activity

Biological activity of all three complexes and the corresponding ligands was tested by the brine shrimp test (toxicity to *A. salina*). This test is in good correlation with cytotoxic activity [58]. For comparison, brine shrimp test was also performed with previously synthesized complexes with H$_2$dapsesc ligand and the corresponding ligand. All the compounds showed moderate activity, the complexes being more active than the ligands (Table 5). The only exception was [Ni(hcn)], where the ligand was modified during complexation. The higher activity of the complexes is probably a consequence of the non-ionic nature of all complexes, which might facilitate their diffusion through biological membranes. The results justify further study of biological effects of the complexes.

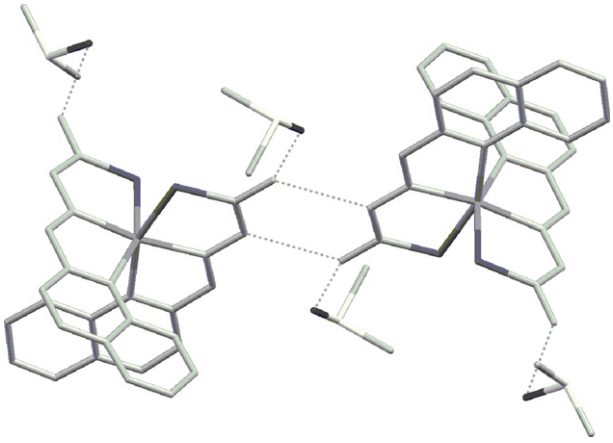


Fig. 8. Crystal association of [Ni(qasesc)$_2$] complex and DMSO guest molecules by hydrogen bonds. Hydrogen atoms omitted for clarity.

Table 5
Toxic effect (expressed as LC50 values in mM) of ligands and complexes on *Artemia salina*

Substance	LC50 (mM)
H$_2$dapsesc	35.0
[Zn(dapsesc)]	10.8
[Cd(dapsesc)]	0.9
[Ni(hcn)]	106.9
Hqasesc	33.8
[Zn(qasesc)$_2$] · 3H$_2$O	2.5
[Cd(qasesc)(AcO)] · H$_2$O	10.7
[Ni(qasesc)$_2$] · 2DMSO	1.8

Acknowledgement

This work was supported by the Ministry of Science and Environmental Protection of Serbia (Project #142026).

Appendix A. Supplementary material

CCDC 632377 contains the supplementary crystallographic data for this paper. These data can be obtained free of charge via http://www.ccdc.cam.ac.uk/conts/retrieving.html, or from the Cambridge Crystallographic Data Centre, 12 Union Road, Cambridge CB2 1EZ, UK; fax: (+44) 1223-336-033; or e-mail: deposit@ccdc.cam.ac.uk. Supplementary data associated with this article can be found, in the online version, at doi:10.1016/j.poly.2007.03.023.

References

[1] H. Beraldo, D. Gambino, Mini-Rev. Med. Chem. 4 (2004) 31.
[2] H. Beraldo, Quim. Nova 27 (2004) 461.
[3] K.H. Reddy, J. Indian Chem. Soc. 80 (2003) 69.
[4] S.N. Pandeya, J.R. Dimmock, Pharmazie 48 (1993) 659.
[5] D.X. West, A.E. Liberta, S.B. Padhye, R.C. Chikate, P.B. Sonawane, A.S. Kumbhar, R.G. Yerande, Coord. Chem. Rev. 123 (1993) 49.
[6] D.X. West, S.B. Padhye, P.B. Sonawane, Struct. Bond. 76 (1991) 1.
[7] M. Liu, P.L. Xiu, Z.J. Wang, Yaoxue Xuebao 27 (1992) 388.
[8] S.R. Turk, C. Shipman Jr., J.C. Drach, J. Gen. Virol. 67 (1986) 1625.
[9] H.G. Mautner, W.D. Kumler, Y. Okano, P. Robertson, Antibiot. Khimoter. 6 (1956) 51.
[10] K. Bednarz, Dissert. Pharm. 10 (1958) 93.
[11] K.C. Agrawal, B.A. Booth, R.L. Michaud, E.C. Moore, A.C. Sartorelli, Biochem. Pharmacol. 23 (1974) 2421.
[12] W. Brucker, H.G. Rohde, Pharmazie 23 (1968) 310.
[13] A.N. Vedyanu, N.V. Gerbeleu, Zh. Neorg. Khim. 21 (1976) 3319.
[14] A.V. Ablov, N.V. Gerbeleu, A.M. Romanov, V.M. Vlad, Zh. Neorg. Khim. 16 (1971) 1357.
[15] N.V. Gerbeleu, V.G. Bodyu, Zh. Neorg. Khim. 17 (1972) 1657.
[16] A.V. Ablov, N.V. Gerbeleu, A.M. Romanov, Zh. Neorg. Khim. 13 (1968) 787.
[17] V.G. Bodyu, N.V. Gerbeleu, Zh. Neorg. Khim. 17 (1972) 2159.
[18] D. Negoiu, I. Ghelase, Rev. Roum. Chim. 28 (1983) 225.
[19] D. Negoiu, I. Ghelase, Rev. Roum. Chim. 28 (1983) 355.
[20] I. Ghelase, D. Negoiu, Rev. Roum. Chim. 28 (1983) 463.
[21] B.T. Oloi, N.V. Gerbeleu, A.V. Ablov, Zh. Neorg. Khim. 16 (1971) 2888.
[22] A.V. Ablov, N.V. Gerbeleu, B.T. Oloi, Zh. Neorg. Khim. 16 (1971) 710.
[23] A.V. Ablov, N.V. Gerbeleu, M.V. Shopron, Zh. Neorg. Khim. 17 (1972) 734.

[24] V.F. Toropova, G.K. Amirkhanova, M.V. Shopron, Zh. Obshch. Khim. 44 (1974) 368.
[25] I.D. Brčeski, V.M. Leovac, G.A. Bogdanović, S.P. Sovilj, M. Revenco, Inorg. Chem. Commun. 7 (2004) 253.
[26] A.V. Ablov, N.V. Gerbeleu, A.M. Romanov, Zh. Neorg. Khim. 13 (1968) 3024.
[27] N.V. Gerbeleu, M.D. Revenko, A.V. Ablov, Zh. Neorg. Khim. 17 (1972) 1369.
[28] L.E. Nikolaeve, A.A. Shevyrev, T.N. Tarkhova, N.V. Belov, Kristallografiya 19 (1974) 516.
[29] T.N. Tarkhova, L.E. Nikolaeve, L.E. Simonov, A.V. Ablov, N.V. Gerbeleu, A.M. Romanov, Dokl. Akad. Nauk. 214 (1974) 1326.
[30] A.V. Ablov, N.V. Gerbeleu, A.M. Romanov, M.D. Revenko, Issled. Khim. Khelatnykh Soedin. (1971) 3.
[31] N.V. Gerbeleu, A.M. Romanov, M.D. Revenko, A.A. Desyatnik, Issled. Khim. Khelatnykh Soedin. (1971) 11.
[32] N.V. Gerbeleu, M.D. Revenko, A.V. Ablov, Zh. Neorg. Khim. 17 (1972) 136.
[33] M.G. Felin, Yu.V. Salnikov, Izv. Vyssh. Uchebn. Zaved., Khim. Khim. Tekhnol. 29 (1986) 105.
[34] A.V. Ablov, N.V. Gerbeleu, N.Ya. Negryatse, Zh. Neorg. Khim. 14 (1969) 986.
[35] V.Yu. Plotkin, M.G. Felin, N.A. Subbotina, V.V. Zelentsov, Zh. Neorg. Khim. 28 (1983) 1463.
[36] A.V. Ablov, N.V. Gerbeleu, N.Ya. Negryatse, Zh. Neorg. Khim. 16 (1971) 1069.
[37] A.V. Ablov, N.V. Gerbeleu, N.Ya. Negryatse, Zh. Neorg. Khim. 15 (1970) 119.
[38] N.Ya. Negryatse, A.V. Ablov, N.V. Gerbeleu, Zh. Neorg. Khim. 17 (1972) 124.
[39] N.V. Gerbeleu, V.G. Bodyu, Zh. Neorg. Khim. 18 (1973) 3001.
[40] N.V. Gerbeleu, M.D. Revenko, F.K. Zhovmir, B.Ya. Kuyavskaya, Zh. Neorg. Khim. 31 (1986) 2017.
[41] T.C. Castle, R.I. Maurer, F.E. Sowreym, M.J. Went, C.A. Reynolds, E.J.L. McInnes, P.J. Blower, J. Am. Chem. Soc. 125 (2003) 10400.
[42] T.R. Todorović, A. Bacchi, G. Pelizzi, N.O. Juranić, D.M. Sladić, I.D. Brčeski, K.K. Andjelković, Inorg. Chem. Commun. 9 (2006) 862.
[43] A. Woukan, R.R. Ernst, Chem. Phys. Lett. 52 (1977) 407.
[44] (a) L. Braunschweiler, R.R. Ernst, J. Magn. Reson. 53 (1983) 521;
(b) A. Bax, D.G. Davis, J. Magn. Reson. 65 (1985) 355.
[45] (a) J. Jeener, B.H. Meier, P. Bachmann, R.R. Ernst, J. Chem. Phys. 71 (1979) 4546;
(b) S. Macura, R.R. Ernst, Mol. Phys. 41 (1980) 95.
[46] (a) A.A. Bothner-By, R.L. Stephens, J.-M. Lee, C.D. Warren, R.W. Jeanloz, J. Am. Chem. Soc. 106 (1984) 811;
(b) A. Bax, D.G. Davis, J. Magn. Reson. 63 (1985) 207.
[47] G. Bodenhausen, D.J. Ruben, Chem. Phys. Lett. 69 (1980) 185.
[48] (a) L. Muller, J. Am. Chem. Soc. 101 (1979) 4481;
(b) A. Bax, S. Subramanian, J. Magn. Reson. 67 (1986) 565.
[49] A. Bax, M.F. Summers, J. Am. Chem. Soc. 108 (1986) 2093.
[50] (a) SAINT: SAX, Area Detector Integration, Siemens Analytical instruments Inc., Madison, Wisconsin, USA;
(b) G. Sheldrick, SADABS: Siemens Area Detector Absorption Correction Software, University of Goettingen, Germany, 1996.
[51] A. Altomare, M.C. Burla, M. Cavalli, G. Cascarano, C. Giacovazzo, A. Gagliardi, A.G. Moliterni, G. Polidori, R. Spagna, SIR97: A New Program For Solving and Refining Crystal Structures, Istituto di Ricerca per lo Sviluppo di Metodologie Cristallografiche CNR, Bari, 1997.
[52] G. Sheldrick, SHELXL97. Program for Structure Refinement, University of Goettingen, Germany, 1997.
[53] L.J. Farrugia, J. Appl. Crystallogr. 32 (1999) 837.
[54] M. Nardelli, J. Appl. Crystallogr. 28 (1995) 659.
[55] (a) F.H. Allen, O. Kennard, R. Taylor, Accounts Chem. Res. 16 (1983) 146;
(b) I.J. Bruno, J.C. Cole, P.R. Edgington, M. Kessler, C.F. Macrae, P. McCabe, J. Pearson, R. Taylor, Acta Crystallogr., Sect. B: Struct. Sci. 58 (2002) 389.
[56] J.S. Casas, M.V. Castano, M.S. Garcia-Taxende, I. Martinez-Santamarta, A. Sanchez, J. Sordo, E.E. Castellano, J. Zukerman-Schpector, J. Chem. Res.(S) 10 (1992) 324.
[57] M. Mathew, G.J. Palenik, J. Am. Chem. Soc. 91 (1969) 6310.
[58] B.N. Meyer, N.R. Ferrigni, J.E. Putnam, L.B. Jacobsen, D.E. Nichols, J.L. McLaughlin, Planta Med. 45 (1982) 31.

Available online at www.sciencedirect.com
ScienceDirect
Polyhedron 26 (2007) 3437–3447
POLYHEDRON
www.elsevier.com/locate/poly

Conformational study of Co(II), Ni(II), and Cr(III) complexes of the edta-type: Crystal structure of 1D polymeric *trans*(O^6)-Ba[Co(1,3-pddadp)] · $8H_2O$ complex stabilized by infinite water tapes

S. Grubišić [a,*], D.D. Radanović [a], U. Rychlewska [b,*], B. Warżajtis [b], N.S. Drašković [c], M.I. Djuran [c], S.R. Niketić [d]

[a] *Center for Chemistry, Institute of Chemistry, Technology and Metallurgy, University of Belgrade, Njegoševa 12, P.O. Box 815, 11001 Belgrade, Serbia*
[b] *Faculty of Chemistry, Adam Mickiewicz University, Grunwaldzka 6, 60-780 Poznań, Poland*
[c] *Department of Chemistry, Faculty of Science, University of Kragujevac, R. Domanovića 12, P.O. Box 60, 34000 Kragujevac, Serbia*
[d] *Department of Chemistry, Faculty of Science, University of Belgrade, Studentski trg 16, P.O. Box 158, 11001 Belgrade, Serbia*

Received 31 January 2007; accepted 22 March 2007
Available online 28 March 2007

Abstract

The *trans*(O^6) isomer of the Ba[Co(1,3-pddadp)] · $8H_2O$ complex (where 1,3-pddadp represents hexadentate 1,3-propanediamine-*N*,*N*′-diacetate-*N*,*N*′-di-3-propionate ion) has been prepared and characterized by X-ray crystallography. In the crystal structure the complex cations and anions are bridged by carboxylate oxygen atoms from the in-plane coordinated glycinate rings (G-rings) of $[Co(1,3\text{-pddadp})]^{2-}$ and by the barium-coordinated water molecules, thus forming 1D polymeric chains, separated by infinite water tapes hydrogen bonded to the $[Co(1,3\text{-pddadp})]^{2-}$ carboxylate oxygens from the out-of-plane β-alaninate rings (R-rings). Conformational analysis of the three possible geometrical isomers: *trans*(O^5), *trans*(O^5O^6), and *trans*(O^6) of the $[Co(1,3\text{-pddadp})]^{2-}$ complex, with ligand acting as hexadentate, as well as of the corresponding complexes of Ni(II) and Cr(III) has been performed using the consistent force field (CFF) method, with the parameters developed previously for edta-type complexes of chromium(III) and supplemented with new parameters for cobalt(II) and nickel(II). The energy-minimized structure of the *trans*(O^5O^6) isomer represents the global minimum for the $[M(1,3\text{-pddadp})]^{n-}$ (M = Co(II), Ni(II), and Cr(III)) species. The occurrence of the least energetically favored *trans*(O^6) isomer in a crystal and the exceptional conformation of the axially oriented β-alaninate rings can be accounted for by the stabilizing role of the infinite tapes of planar cyclic water pentamers and hexamers which act as a ''glue'' to reinforce the coordination polymeric chains.
© 2007 Elsevier Ltd. All rights reserved.

Keywords: Co(II), Ni(II), and Cr(III) complexes; Hexadentate chelates; Molecular mechanics (MM); One-dimensional Co(II)/Ba(II) coordination polymers; Infinite water tapes

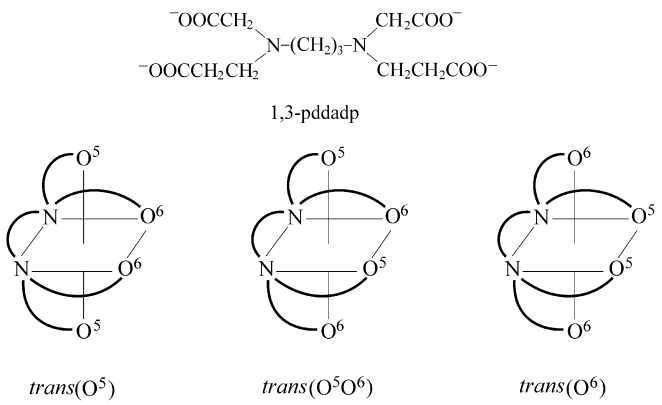
1. Introduction

The coordination chemistry of transition metal complexes with hexadentate diaminopolycarboxylate edta-type (edta = ethylenediaminetetraacetate) ligands having mixed acetate and 3-propionate carboxylate arms is attractive

* Corresponding authors. Tel.: +381 11 3336754; fax: +381 11 636061 (S. Grubišić); tel.: +48 61 8291 268; fax: +48 61 865 8008 (U. Rychlewska).
E-mail addresses: grubisic@chem.bg.ac.yu (S. Grubišić), urszular@amu.edu.pl (U. Rychlewska).

0277-5387/$ - see front matter © 2007 Elsevier Ltd. All rights reserved.
doi:10.1016/j.poly.2007.03.029

due to the fact that these complexes may have very intricate stereochemistry, particularly when the pentadentate coordination mode of the ligand is involved [1]. Complexes of 1,3-pddadp (1,3-pddadp = 1,3-propanediamine-*N*,*N*′-diacetate-*N*,*N*′-di-3-propionate ion, Scheme 1), in which 1,3-pddadp acts as a hexadentate ligand, can exist theoretically in three isomeric forms designated as *trans*(O^5), *trans*(O^5O^6), and *trans*(O^6) (where O^5 and O^6 refer to the five- and six-membered N,O rings, respectively, Scheme 1). In the synthetic reactions of Co(III), Rh(III), and Ni(II) with the 1,3-pddadp ligand, two out of three possible geometrical isomers of $[M(1,3\text{-pddadp})]^{n-}$ complex (*trans*(O^5O^6) and *trans*(O^6) for Co(III) [2–5], and *trans*(O^5) and *trans*(O^5O^6) for Rh(III) [6,7], and Ni(II) [8]) have been isolated and characterized. However, for the $[Cr(1,3\text{-pddadp})]^-$ complex all three geometrical isomers (*trans*(O^5), *trans*(O^5O^6), and *trans*(O^6)) have been reported [9]. In addition, only one dominant isomer of the 1,3-pddadp complex (*trans*(O^6)) of Cu(II) has been described [10]. In most cases, the geometry of the complex was confirmed by X-ray methods, and the X-ray data are available so far for the *trans*(O^6)-$[Cr(1,3\text{-pddadp})]^-$ [9], *trans*(O^6)-$[Co(1,3\text{-pddadp})]^-$ [3,4], *trans*(O^5O^6)-$[Co(1,3\text{-pddadp})]^-$ [5], *trans*(O^5)-$[Rh(1,3\text{-pddadp})]^-$ [7], *trans*(O^5O^6)-$[Rh(1,3\text{-pddadp})]^-$ [7], *trans*(O^5)-$[Ni(1,3\text{-pddadp})]^{2-}$ [8], and *trans*(O^6)-$[Cu(1,3\text{-pddadp})]^{2-}$ [10] structures, which were all reported by us previously except for the *trans*(O^6)-$[Cr(1,3\text{-pddadp})]^-$. Conformational analysis of the systems: $[Co(1,3\text{-pddadp})]^-$ [5] and $[Rh(1,3\text{-pddadp})]^-$ [1], with ligand acting as hexadentate, revealed that the *trans*(O^5O^6) isomer is the most stable one for either complex species. Presented in this paper are the results of X-ray structure determination of the *trans*(O^6) isomer of $[Co(1,3\text{-pddadp})]^{2-}$ complex, supplemented by a detailed stereochemical analysis of $[Co(1,3\text{-pddadp})]^{2-}$, $[Ni(1,3\text{-pddadp})]^{2-}$, and $[Cr(1,3\text{-pddadp})]^-$ complexes using the methods of molecular mechanics (MM). The obtained results are compared with those previously reported for the analogous $[Co(1,3\text{-pddadp})]^-$ [5], and $[Rh(1,3\text{-pddadp})]^-$ [1] systems.



Scheme 1.

2. Experimental

All commercially obtained reagent-grade chemicals were used without further purification. The preparation of barium 1,3-propanediamine-*N*,*N*′-diacetate-*N*,*N*′-di-3-propionate octahydrate, $Ba_2(1,3\text{-pddadp})\cdot 8H_2O$, has been reported elsewhere [2].

2.1. Preparation of barium (1,3-propanediamine-N,N′-diacetato-N,N′-di-3-propionato) cobaltate(II) octahydrate, trans(O^6)-Ba[Co(1,3-pddadp)] · 8H_2O

The *trans*(O^6)-$Ba[Co(1,3\text{-pddadp})]\cdot 8H_2O$ complex was prepared by the similar procedure as that applied for the preparation of $[Mg(H_2O)_6][Co(1,3\text{-pddadp})]\cdot H_2O$ [11].

2.81 g (0.01 mol) of $CoSO_4\cdot 7H_2O$ was dissolved in 25 cm^3 of H_2O at 60 °C. To this solution, solid $Ba_2(1,3\text{-pddadp})\cdot 8H_2O$ (7.49 g, 0.01 mol) was added and the reaction mixture was heated (60 °C) with stirring for 30 min. The precipitated $BaSO_4$ was then removed by filtration. The dark pink filtrate was poured into a 5 × 60 cm column containing Dowex 1-X8 (200–400 mesh) anion-exchange resin in the Cl^- form. After elution with 0.1 M $BaCl_2$ (*ca.* 0.5 cm^3/min) two bands were detectable on the column after two days. The second eluate, which represents the *trans*(O^6) isomer of $[Co(1,3\text{-pddadp})]^{2-}$, was reduced by evaporation to 10 cm^3 at 40 °C and desalted by passage through a G-10 Sephadex column, with distilled water as the eluant. The eluate was concentrated to a small volume, and the *trans*(O^6)-$Ba[Co(1,3\text{-pddadp})]\cdot 8H_2O$ complex was crystallized by adding of ethanol, and cooling in a refrigerator. *Anal.* Calc. for *trans*(O^6)-$Ba[Co(1,3\text{-pddadp})]\cdot 8H_2O$, $C_{13}H_{34}N_2O_{16}BaCo$ (FW = 670.69): C, 23.28; H, 5.11; N, 4.18. Found: C, 23.38; H, 5.15; N, 4.19%.

2.2. Crystallographic data collection and refinement of the structure

The crystal data for the $Ba[Co(1,3\text{-pddadp})]\cdot 8H_2O$ complex, and the parameters of data collection are summarized in Table 1. The intensity data were measured with a KM4CCD kappa-geometry diffractometer [12] using graphite monochromated Mo Kα radiation (λ = 0.71073 Å) at 295.0(2) K. The structure was solved by direct methods using SHELXS86 [13] and refined by least-squares techniques with SHELXL97 [14]. The intensity data were corrected for absorption. Anisotropic atomic displacement parameters were employed for the non-hydrogen atoms. Hydrogen atoms connected to carbon atoms have been placed at calculated positions, while those attached to the water oxygen atoms have been located on subsequent difference Fourier maps. Although refined at the earlier stages of structure determination, the hydroxyl hydrogens were eventually fixed at a distance of 0.85 Å from their respective oxygen atoms because some of the bond lengths and angles involving these hydrogens as well as their displacement parameters refined to unrea-

Table 1
Selected crystal data and structure refinement parameters for *trans*(O^6)-Ba[Co(1,3-pddadp)]·$8H_2O$ complex

Crystal data	
Chemical formula	$C_{13}H_{34}BaCoN_2O_{16}$
M_r	670.69
Cell setting	triclinic
Space group	$P\bar{1}$
Temperature (K)	295.0(2)
a (Å)	9.2344(3)
b (Å)	12.0154(5)
c (Å)	12.3048(5)
α (°)	101.874(4)
β (°)	110.034(4)
γ (°)	95.321(4)
V (Å^3)	1235.28 (8)
Z	2
D_x (Mg m^{-3})	1.803
Radiation type	Mo Kα
μ (mm^{-1})	2.33
Crystal form, color	prismatic, light burgundy
Crystal size (mm)	0.60 × 0.30 × 0.15
Data collection	
Diffractometer	Kuma KM4CCD κ-geometry diffractometer
Data collection method	ω scans
Absorption correction	numerical
T_{min}	0.411
T_{max}	0.772
Number of measured, independent, and observed reflections	10824, 5365, 4676
Criterion for observed reflections	$I > 2\sigma(I)$
R_{int}	0.031
θ_{max} (°)	27.1
Refinement	
Refinement on	F^2
$R[F^2 > 2\sigma(F^2)]$, $wR(F^2)$, S	0.025, 0.061, 1.01
Number of reflections	5365 reflections
Number of parameters	304
H-atom treatment	riding
Weighting scheme	calculated $w = 1/[\sigma^2(F_o^2) + (0.0331P)^2]$ where $P = (F_o^2 + 2F_c^2)/3$
$(\Delta/\sigma)_{max}$	0.001
$\Delta\rho_{max}$, $\Delta\rho_{min}$ (e Å^{-3})	1.03, −0.80

sonable values. All hydrogen atoms were allowed to ride on the atoms to which they were attached and their isotropic displacement parameters were given values 30% higher than the isotropic equivalent for the atom to which the H-atom was bonded. The two largest difference peaks (1.03 and 1.01 e Å^{-3}) are located in between two Ba(II) cations related by the center of symmetry at 000 and bridged by O2 carboxylate oxygens. The structure was viewed and analyzed, and drawings were prepared with Siemens computer graphics program XP [15a] and with the program MERCURY [15b].

2.3. Computational method

Molecular mechanics (MM) calculations of the three geometrical isomers of $[M(1,3\text{-pddadp})]^{n-}$ system, in which M = Co(II), Ni(II), and Cr(III) and ligand acts as hexadentate, were carried out with the consistent force field (CFF) program package [16] using the all-atom representation. The force field parameters hither used throughout the study were parameterized specifically for edta-type complexes [1,5,17,18]. Validity of the force field for the (poly)amino(poly)carboxylate modeling was proven in a number of applications [1,5,19]. The new parameters for cobalt and nickel atoms were optimized to obtain the best fit between experimental X-ray data and the modeling studies (Table 2). Potential functions for bond stretching, angle bending, torsional, non-bonded and electrostatic contributions are given in the footnote to Table 2. The force field of a maximally diagonal type is parameterized on the basis of two different types of carbon atom (sp^3 – (C) and sp^2 – (C′) carbons), two different types of oxygen atom (coordinated (O) and carbonyl (O′) oxygens), one type of hydrogen (H), nitrogen (N) and the central metal atom (Co(II) or Ni(II)). The same parameters were used for aliphatic carbons from glycinate, β-alaninate, and 1,3-propanediamine chelate rings.

Point charge parameters in the present force field were adjusted on the basis of single point DFT calculations. They were performed using the Becke three-parameter exchange (B3) [20] and the Lee–Yang–Parr correlation functional (LYP) [21]. The B3LYP calculations have been carried out with the GAUSIAN98 program [22]. The LANL2DZ basis set was chosen for all atoms. The atomic charges of Co(II) ($S = 3/2$) and Ni(II) ($S = 1$) complexes were calculated using the natural bond orbital method developed by Weinhold [23], from B3LYP optimized wave function.

MM calculations were carried out with the same molecular modeling methodology used by us in the studies of other coordination compounds [17,24]. The starting structures for geometric isomers were obtained by manipulation of the coordinates of metal complexes to generate all the permissible conformations of 1,3-propanediamine and β-alaninate rings. By this strategy we believe that we have achieved a comprehensive and reliable spanning of all geometrical isomers of the investigated complexes. Details of the procedure were described previously [17].

Geometry optimizations were carried out using a combination of the steepest-descent, Davidon–Fletcher–Powell and Newton–Raphson methods. The steepest-descent and Davidon–Fletcher–Powell methods were mostly used, in that order, for initial exploratory searches and minimizations of conformations farther from equilibrium. To approach the true minima the Newton–Raphson iterations were always employed. Geometry optimizations were carried out until convergence was attained for a gradient of $<10^{-6}$ kJ/mol Å. Siemens computer graphics program XP was used for the presentation of energy-minimized structures [15a]. Chelate ring puckering parameters were calculated using PLATON [25] and PARST [26] packages and a locally developed computer program based on the equations given by Cremer and Pople [27]. A complete list of

Table 2
Additional CFF parameters for edta-type complexes (M = Co(II) and Ni(II))[a]

Bond stretching	k_r (kcal/mol Å^2)	r_0 (Å)
M–O	500.00	2.105
M–N	500.00	2.100
Angle bending	k_θ (kcal/mol rad^2)	θ_0 (rad)
O–M–O	350.950	3.000 (3.146)
M–O–C′[b]	180.01	2.194 (2.254)
M–O–C′[c]	180.01 (480.01)	1.920 (2.264)
Electrostatic	q (esu)	
M	1.437 (1.210)	

$$E_{\text{bond}} = \sum_r \frac{1}{2}k_r(r-r^0)^2,\ E_{\text{angle}} = \sum_\theta \frac{1}{2}k_\theta(\theta-\theta^0)^2,$$

$$E_{\text{torsion}} = \sum_\phi \frac{1}{2}k_\phi(1+\cos n\phi),$$

$$E_{\text{vander waals}} = \sum_{ij}\left[\frac{2}{3}\varepsilon\left(\frac{r^*}{r}\right)^{12} - \varepsilon\left(\frac{r^*}{r}\right)^{6}\right],$$

$$E_{\text{Coulomb}} = \sum_{ij}\frac{e_i e_j}{Dr_{ij}}.$$

[a] Parameters bracketed out are for Ni(II).
[b] Parameters for M–O–C′ angles in six-membered chelate rings.
[c] Parameters for M–O–C′ angles in five-membered chelate rings.

the Cremer and Pople puckering parameters for all chelate rings together with the endocyclic torsion angles is presented in Supplementary material Tables S1–S9.

3. Results and discussion

3.1. The crystal structure of the trans(O^6)-Ba[Co(1,3-pddadp)] · 8H$_2$O complex

The ORTEP diagram of the *trans*(O^6)-[Co(1,3-pddadp)]$^{2-}$ complex anion and the coordination polyhedron around the barium cation are depicted in Fig. 1a and b, where the numbering scheme adopted for the respective atoms is also given. The basic supramolecular motifs found in the crystal lattice and the modes they bind together are illustrated in Figs. 2a–c. Selected bond distances and valence angles are listed in Table 3.

The Co(II) ion is encircled by all of the donating atoms (2N and 4O) of the 1,3-pddadp ligand to form an octahedral geometry. The complex anion [Co(1,3-pddadp)]$^{2-}$ represents the *trans*(O^6) isomer with two β-alaninate rings coordinated in the *trans* positions (R rings) and two glycinate rings coordinated in the *girdle* plane (G rings), thus making in-plane a 5–6–5 ring system (Fig. 1a). The format for describing the various chelate rings formed in these kinds of chelates is credited to Weakliem and Hoard [28]. Conformations of the six-membered chelate rings are: a nearly ideal twist-boat for the 1,3-propanediamine ring (T ring), and nearly ideal boats for both β-alaninate rings (R_1 and R_2), with the coordinated carboxylate oxygen and C_β carbon atoms in flagpole positions. The five-membered glycinate rings (G_1 and G_2) are envelope and twist,

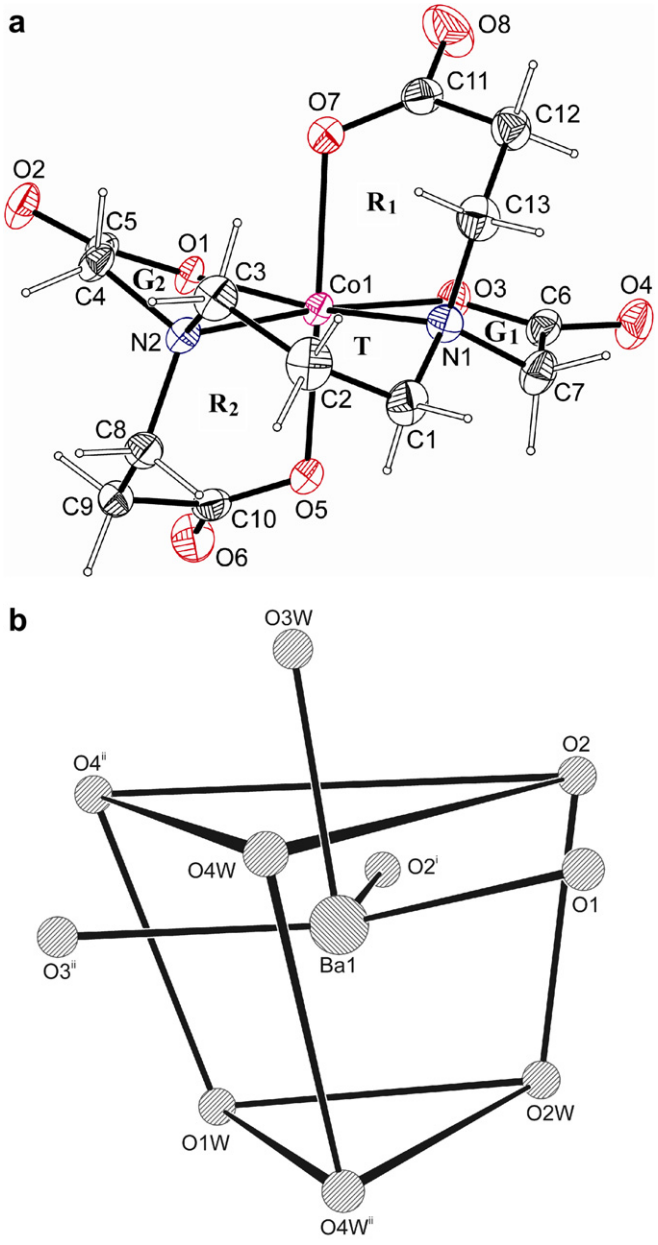


Fig. 1. (a) Molecular structure of the complex anion *trans*(O^6)-[Co(1,3-pddadp)]$^{2-}$with thermal ellipsoids drawn at the 40% probability level, (b) Tenfold coordination of barium cation (symmetry codes: (i) $-x$, $2-y$, $-z$, (ii) $1-x$, $2-y$, $-z$).

respectively (Table S3 Supplementary material). Worth to notice is the observed non-planarity of the Co–O–C=O entities belonging to the β-alaninate rings, signaled by the absolute values of the Co1–O7–C11–O8 and Co1–O5–C10–O6 torsion angles of 116.1(3)° and 116.9(2)°. A search of the Cambridge Crystallographic Data Base [29] for the M–O–C=O torsion angle magnitudes in the β-alaninate rings (M = any metal) provides 289 observations with the values in the range 107.6–180.0° but concentrated around 180°, with the mean value of 162.5(9)° and the median of 167.8°. In only 2% of cases (six observations) this torsion angle is smaller than 120.0°. This statistics illustrates that

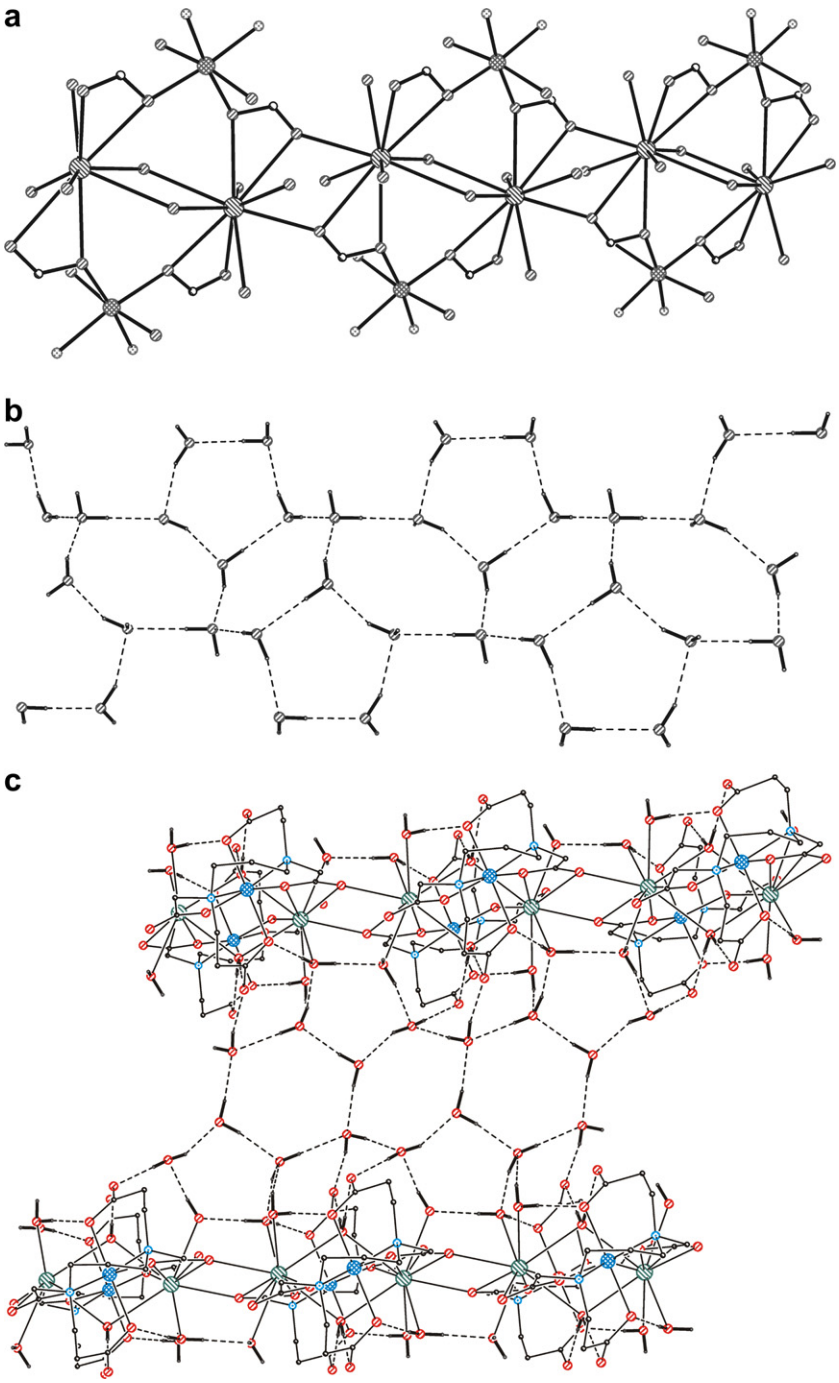


Fig. 2. Supramolecular motifs in the crystal lattice of *trans*(O^6)-Ba[Co(1,3-pddadp)] · $8H_2O$. (a) 1D coordination polymer based on the six-coordinate Co(II) and ten-coordinate Ba(II) nodes (for clarity, only atoms directly bonded to metal ions are shown), (b) tapes of water pentamers and hexamers extending along the *a*-direction, (c) illustration of the mediating role of β-alaninate carboxylates in hydrogen-bond interactions between water cluster and the metal-organic-one-dimensional framework (the only hydrogen atoms shown are those belonging to water molecules).

carboxylate groups from the β-alaninate rings generally bind metal ions in the plane of this group and in an *anti* mode, and hence the drastic non-planarity of the Co–O–C=O fragment, observed in the *trans*(O^6)-[Co(1,3-pddadp)]$^{2-}$ complex anion is exceptional. Moreover, a closer look at the six structures that possess a highly non-planar M–O–C=O fragments revealed that in all these complexes the β-alaninate rings display the bridging function. Although in the investigated crystal structure the two axially oriented β-alaninate rings are not directly involved in bridging the Co(II) and Ba(II) metal ions, they are involved in several hydrogen-bond interactions with water molecules (O1W···O5, O4W···O6, O7W···O6 and O2W···O7, O4W···O8, O6W···O8) by utilizing both carboxylate oxygens as hydrogen-bond acceptors (Table 4). Particularly important seems to be the role the two

Table 3
Selected bond distances and valence angles for *trans*(O^6)-Ba[Co(1,3-pddadp)]·$8H_2O$

Bond distances (Å)			
Ba1–O1	2.7779(15)	Co1–O1	2.0741(16)
Ba1–O2	2.9550(18)	Co1–O3	2.0813(17)
Ba1–O2^{i}	2.7140(17)	Co1–O5	2.1211(18)
Ba1–O3^{ii}	2.8477(16)	Co1–O7	2.1416(18)
Ba1–O4^{ii}	3.100(2)	Co1–N1	2.139(2)
Ba1–O1W	2.7856(19)	Co1–N2	2.138(2)
Ba1–O2W	2.8317(18)		
Ba1–O3W	2.831(2)		
Ba1–O4W	2.9719(18)		
Ba1–O4W^{ii}	2.9522(18)		
Valence angles (°)			
O1–Ba1–O2	45.20(5)	O4^{ii}–Ba1–O2W	142.24(5)
O1–Ba1–O2^{i}	107.71(5)	O4^{ii}–Ba1–O3W	55.04(6)
O1–Ba1–O3^{ii}	133.95(5)	O4^{ii}–Ba1–O4W	91.18(5)
O1–Ba1–O4^{ii}	140.83(5)	O4^{ii}–Ba1–O4W^{ii}	123.70(5)
O1–Ba1–O1W	143.31(6)	O1W–Ba1–O2W	77.36(6)
O1–Ba1–O2W	69.48(5)	O1W–Ba1–O3W	128.96(6)
O1–Ba1–O3W	86.60(6)	O1W–Ba1–O4W	123.21(5)
O1–Ba1–O4W	69.01(5)	O1W–Ba1–O4W^{ii}	71.70(6)
O1–Ba1–O4W^{ii}	82.65(5)	O2W–Ba1–O3W	134.35(6)
O2–Ba1–O2^{i}	64.19(6)	O2W–Ba1–O4W	125.93(5)
O2–Ba1–O3^{ii}	150.77(5)	O2W–Ba1–O4W^{ii}	70.65(5)
O2–Ba1–O4^{ii}	114.48(5)	O3W–Ba1–O4W	74.88(6)
O2–Ba1–O1W	132.51(5)	O3W–Ba1–O4W^{ii}	145.94(6)
O2–Ba1–O2W	67.65(5)	O4W–Ba1–O4W^{ii}	71.09(6)
O2–Ba1–O3W	67.96(6)		
O2–Ba1–O4W	103.43(5)	O1–Co1–O3	102.20(6)
O2–Ba1–O4W^{ii}	121.48(5)	O1–Co1–O5	88.62(7)
O2^{i}–Ba1–O3^{ii}	114.14(5)	O1–Co1–O7	85.12(7)
O2^{i}–Ba1–O4^{ii}	75.68(5)	O1–Co1–N1	172.35(7)
O2^{i}–Ba1–O1W	75.36(6)	O1–Co1–N2	80.72(7)
O2^{i}–Ba1–O2W	72.14(6)	O3–Co1–O5	86.95(7)
O2^{i}–Ba1–O3W	79.60(6)	O3–Co1–O7	88.79(7)
O2^{i}–Ba1–O4W	154.39(6)	O3–Co1–N1	80.96(7)
O2^{i}–Ba1–O4W^{ii}	134.46(6)	O3–Co1–N2	174.02(7)
O3^{ii}–Ba1–O4^{ii}	43.58(5)	O5–Co1–O7	171.52(7)
O3^{ii}–Ba1–O1W	68.49(5)	O5–Co1–N1	98.56(8)
O3^{ii}–Ba1–O2W	141.35(5)	O5–Co1–N2	87.91(7)
O3^{ii}–Ba1–O3W	82.91(5)	O7–Co1–N1	87.99(8)
O3^{ii}–Ba1–O4W	64.96(5)	O7–Co1–N2	96.70(7)
O3^{ii}–Ba1–O4W^{ii}	81.64(5)	N1–Co1–N2	96.80(8)
O4^{ii}–Ba1–O1W	75.84(6)		

Symmetry codes: (i) $-x, 2-y, -z$; (ii) $1-x, 2-y, -z$.

carboxylate groups play in establishing connections between metal-organic chains and infinite water tapes that propagate parallel to each other along the *a*-direction (Figs. 2a–c). More specifically, the investigated crystal structure of the *trans*(O^6)-Ba[Co(1,3-pddadp)]·$8H_2O$ complex can be considered as arising from self assembly of tetrametallic building blocks, composed of two Co(II) and two Ba(II) cations related by the center of symmetry at $\frac{1}{2}\,0\,0$ and bridged by water molecules and by the G-ring carboxylate groups. The tetrametallic units are further connected *via* the G-ring carboxylate groups (related by the center of symmetry at 0 0 0) into one-dimensional polymers (Fig. 2a). Parallel to these chains propagate infinite water tapes build of six water molecules (O2W, O3W, O5W, O6W, O7W, and O8W) forming cyclic pentamers and two distinct hexamers fused together. The rings are planar, and the average O···O distances in the three types of rings are 2.77(2), 2.81(5), 2.87(9) Å, respectively, while the average of the O···O···O angles are 108(1), 120(13), and 115(5)°. According to Infantes' classification [30] these water tapes have the symbol T5(2)6(2)6(2). Within the tapes one can distinguish the bay regions created by the T5(2)6(2)6(2)5(2) units. This is where the carboxylate groups from the β-alaninate R rings are situated, forming a hydrogen-bond linkage between the metal-organic chains and the water tapes. The coordinated and uncoordinated β-alaninate oxygen atoms act, respectively, as single and double acceptors of strong hydrogen bonds. Such extensive hydrogen-bond interactions provide explanation for the exceptional non-planarity of the Co–O–C=O fragments. The very bent Co–O–C=O moiety accompanies the boat form of the β-alaninate ring (*vide infra*).

Barium ion is deca-coordinated with five carboxylate oxygen atoms (O1, O2, O2^{i}, O3^{ii}, and O4^{ii}; where i = $-x$, $2-y$, $-z$ and ii = $1-x$, $2-y$, $-z$) and with five water molecules (O1W, O2W, O3W, O4W, and O4W^{ii}). The coordination polyhedron formed around the Ba1 is irregular four-capped trigonal prism with O1, O2^{i}, O3^{ii} and O3W constituting the caps. The uncapped trigonal prism face is one of the two triangular faces (Fig. 1b).

3.2. Strain analysis of related Co(III), Cr(III), Rh(III), Ni(II), and Co(II) edta-type chelates

The results of a comparative study of the strain characteristics of Co(III), Cr(III), Rh(III), Ni(II), and Co(II) complexes containing analogous edta-type ligands: 1,3-pddadp and 1,3-pdta (1,3-pdta = 1,3-propanediaminetetraacetate) are given in Table 5. The major contributions to strain were considered to be: (i) the octahedral angles around the metal ion, (ii) the ring angle sums of the various kinds of rings, (iii) the M–O–C bond angles, and (iv) the bond angles that the chelating nitrogen atom makes with its connectors.

The total deviation of the octahedral angles ($\sum \Delta O_h$) increases with increasing size of the metal ion radius [31] within each series of complexes ([M(1,3-pddadp)]$^{n-}$ and [M(1,3-pdta)]$^{n-}$) with exceptions for the *trans*(O^6)-[Cr(1,3-pddadp)]$^{-}$ and *trans*(O^5O^6)-[Rh(1,3-pddadp)]$^{-}$. These values vary from 36° to 67° for [M(1,3-pddadp)]$^{n-}$ and from 34° to 71° for [M(1,3-pdta)]$^{n-}$ complexes. Expanding of the two glycinate rings lowers the octahedral strain in the case of Cr(III), Rh(III), and Co(II) complexes, as can be seen while comparing the $\sum \Delta O_h$ values for the corresponding complexes (**5**) (42°) [9] *vs.* (**4**) (56°) [32]; (**7**) (42°) [7] and (**8**) (55°) [7] *vs.* (**6**) (57°) [32]; (**12**) (66°) *vs.* (**11**) (71°) [33]. However, when the two glycinate rings in [Co(1,3-pdta)]$^{-}$ system are expanded to give rise to [Co(1,3-pddadp)]$^{-}$ the opposite effect is registered (compare $\sum \Delta O_h$ values calculated for complexes (**2**) (36°) [5] and (**3**) (38°) [3] with those of (**1**) (34°) [34]). The total devi-

Table 4
Hydrogen-bond parameters for *trans*(O^6)-Ba[Co(1,3-pddadp)] · $8H_2O$

	D–H (Å)	D···A (Å)	H···A (Å)	D–H···A (°)	Symmetry operations on A
O1W–H1W···O5	0.85	2.812(3)	1.96	174	$1-x, 2-y, -z$
O1W–H2W···O5W	0.85	2.933(3)	2.20	144	
O2W–H3W···O7	0.85	2.801(3)	1.97	167	
O2W–H4W···O3W	0.85	2.789(3)	1.94	178	$-x, 2-y, -z$
O3W–H5W···O7W	0.85	2.764(3)	1.96	156	
O3W–H6W···O4	0.85	2.751(3)	2.05	139	$1-x, 2-y, -z$
O4W–H7W···O6	0.85	2.955(3)	2.11	176	
O4W–H8W···O8	0.85	3.061(3)	2.21	179	$1-x, 2-y, -z$
O5W–H9W···O2W	0.85	2.742(3)	1.91	167	
O5W–H10W···O6W	0.85	3.005(4)	2.16	179	
O6W–H11W···O7W	0.85	2.785(3)	1.95	169	$1-x, 2-y, -z$
O6W–H12W···O8	0.85	2.738(3)	1.90	168	
O7W–H13W···O6	0.85	2.701(4)	1.88	162	
O7W–H14W···O8W	0.85	2.750(4)	1.96	155	
O8W–H15W···O6W	0.85	2.820(4)	2.01	160	$x, 1+y, 1+z$
O8W–H16W···O5W	0.85	2.784(4)	1.94	170	$-x, 2-y, -z$

Table 5
Strain analysis of Co(III), Cr(III), Rh(III), Ni(II), and Co(II) complexes with hexadentate 1,3-pddadp and 1,3-pdta ligands

Complexes		r_M (Å)[a]	$\sum\Delta(O_h)$[b]	$\Delta\sum$[c]			Δ(M–O–C)[d]		$\sum\Delta$(N)[e]	Ref.
				T	R	G	R	G		
Co(III)		0.685								
$[Co(1,3\text{-pdta})]^-$	(**1**)		34	+36	+1	−12	+7	+5	15	[34]
trans(O^5O^6)-$[Co(1,3\text{-pddadp})]^-$	(**2**)		36	+34	0, +36	−9, +44	+6, +19	+5, +24	18, 14	[5]
trans(O^6)-$[Co(1,3\text{-pddadp})]^-$	(**3**)		38	+28	+33	−11	+17	+4	16	[3]
Cr(III)		0.755								
$[Cr(1,3\text{-pdta})]^-$	(**4**)		56	+35	+1	−10	+9	+7	14	[32]
trans(O^6)-$[Cr(1,3\text{-pddadp})]^-$	(**5**)		42	+26	+33	−11	+19	+5	16	[9]
Rh(III)		0.805								
$[Rh(1,3\text{-pdta})]^-$	(**6**)		57	+36	+1	−12	+6	+4	12	[32]
trans(O^5O^6)-$[Rh(1,3\text{-pddadp})]^-$	(**7**)		42	+33	+1, +32	−10, +41	+5, +14	+4, +21	13	[7]
trans(O^5)-$[Rh(1,3\text{-pddadp})]^-$	(**8**)		55	+37	−6	+27	+5	+14	7	[7]
Ni(II)		0.830								
$[Ni(1,3\text{-pdta})]^{2-}$	(**9**)		60	+33	+1	−11	+6	+6	11	[35]
trans(O^5)-$[Ni(1,3\text{-pddadp})]^{2-}$	(**10**)		60	+28	0	+36	+7	+20	8	[8]
Co(II)		0.885								
$[Co(1,3\text{-pdta})]^{2-}$[f]	(**11**)		71	+29	+1	−10	+7	+5	11	[33]
trans(O^6)-$[Co(1,3\text{-pddadp})]^{2-}$	(**12**)		67	+25	+17	−10	+4	+4	14	this work

[a] Ionic radius for C.N. = 6 [31].
[b] $\sum\Delta(O_h)$ is the sum of the absolute values of the deviations from 90° of the L–M–L′ bite angles. All values rounded off to the nearest degree.
[c] $\Delta\sum$(ring) is the deviation from the ideal of the corresponding chelate rings' bond angle sum. A mean value of the two rings (R or G) is reported for complexes having an approx. C_2 molecular symmetry.
[d] Δ(M–O–C) (ring) is the mean value of the deviation of the corresponding rings' M–O–C bond angle from 109.5°.
[e] $\sum\Delta$(N) is the sum of the absolute values of the deviations from 109.5° of the six bond angles made by the nitrogen atoms. A mean value for the two nitrogens is reported.
[f] The average values are given for the two complexes: Co[Co(1,3-pdta)] · $8H_2O$ and Mg[Co(1,3-pdta)] · $8H_2O$ that form isomorphic crystals.

ation of the octahedral angles for the $[Ni(1,3\text{-pdta})]^{2-}$ (**9**) [35] and *trans*(O^5)-$[Ni(1,3\text{-pddadp})]^{2-}$ (**10**) [8] complexes is the same and amounts 60°.

As expected, the five-membered glycinate rings of the G type are much more strained than those of the R type. The total deviation from the ideal chelate ring bond angle sum (538.5°) varies from −9° to −12° for the G rings, while for the R rings it is approx. zero except for the *trans*(O^5)-$[Rh(1,3\text{-pddadp})]^-$ [7], where this deviation of −6° av. is unusually large as far as the axially coordinated glycinates are concerned. The bond angles of the M–O–C fragment are expected to lie between 109.5° and 120°, depending on the degree of covalence of the M–O bond [36]. In general, the deviations are larger for the β-alaninate rings of the G type than for the β-alaninate rings of the R type. For edta-type chelates that are considered in this paper these values are in the range 14–24° and 4–19°, respectively (Table 5). In the reported here *trans*(O^6) isomer of $[Co(1,3\text{-pddadp})]^{2-}$ the average deviation of the Co–O–C bond angles in β-alaninate rings is very small (+4°) being of the same order of magnitude as that for the corresponding bond angles in glycinate rings.

Another important source of stain in edta-type complexes is the bonding geometry made by the chelating nitrogens. Each N atom makes four bonds with six ideally 109.5° bond angles. The greatest effect of chelation on the distortion of the tetrahedral bonding geometry of the nitrogen atoms has been registered for the Co(III) and Cr(III) complexes (Table 5).

3.3. Molecular mechanics

Energy minimization and geometry optimization procedure resulted in a few stable conformations for each geometrical isomer (*trans*(O^5), *trans*(O^5O^6), and *trans*(O^6)) of each $[M(1,3\text{-pddadp})]^{n-}$ complex (M = Co(II), Ni(II), and Cr(III)), starting from an exhaustive set of initially generated conformations [17]. Calculated energies for the most stable energy-minimized structures, as well as a comparison with the previously reported data [1,5] for the corresponding Co(III) and Rh(III) complexes are presented in Table 6. Figs. 3–5 illustrate the resulting energy-minimized structures of the three geometrical isomers of $[M(1,3\text{-pddadp})]^{n-}$ complexes (M = Co(II), Ni(II), and Cr(III)), together with the results of a least-squares fit to M (M = Co, Ni, or Cr), N1 and N2 atoms of the corresponding X-ray structures. Structural parameters for the most stable energy-minimized conformers together with the crystallographic data for the *trans*(O^6)-$[Co(1,3\text{-pddadp})]^{2-}$, *trans*($O^5$)-$[Ni(1,3\text{-pddadp})]^{2-}$ [8], and *trans*(O^6)-$[Cr(1,3\text{-pddadp})]^{-}$ [9] complexes are summarized in Tables S10 and S11 (Supplementary material). Geometries of the calculated structures are in good agreement with the corresponding values obtained from the X-ray results, if available.

Table 6
Relative energies (ΔE) and energy contributions (in kcal/mol) for the energy-minimized structures of the three geometrical isomers of $[M(1,3\text{-pddadp})]^{n-}$ complex (M = Co(II), Ni(II), Cr(III), Co(III), and Rh(III))

	ΔE	E_{total}	E_b	E_θ	E_ϕ	E_{nb}	E_c	Ref.
$[Co(1,3\text{-pddadp})]^-$								
trans(O^5O^6)	0	39	9	29	4	24	−27	[5]
trans(O^6)	3	42	9	28	8	24	−27	
trans(O^5)	5	44	10	27	7	27	−27	
$[Cr(1,3\text{-pddadp})]^-$								
trans(O^5O^6)	0	38	9	29	4	23	−27	this work
trans(O^6)	4	42	9	29	8	23	−27	
trans(O^5)	5	43	10	29	5	26	−27	
$[Rh(1,3\text{-pddadp})]^-$								
trans(O^5O^6)	0	33	7	30	3	21	−28	[1]
trans(O^5)	5	38	8	29	5	23	−27	
trans(O^6)	6	39	7	31	7	21	−27	
$[Ni(1,3\text{-pddadp})]^{2-}$								
trans(O^5O^6)	0	34	7	34	2	17	−26	this work
trans(O^5)	1	35	8	33	1	19	−26	
trans(O^6)	13	47	8	39	5	17	−22	
$[Co(1,3\text{-pddadp})]^{2-}$								
trans(O^5O^6)	0	36	6	27	12	18	−27	this work
trans(O^5)	3	39	8	30	7	22	−28	
trans(O^6)	9	45	7	32	11	17	−22	

For each $[M(1,3\text{-pddadp})]^{n-}$ system (M = Co(II), Ni(II), Cr(III), Co(III) [5], and Rh(III) [1]), the lowest energy conformer corresponds to the *trans*(O^5O^6) configuration. The total energy of the minimized structures for three geometrical isomers of $[M(1,3\text{-pddadp})]^{n-}$ (M = Co(II), Ni(II), and Rh(III)) increases in the order $E_{total}(trans(O^5O^6)) < E_{total}(trans(O^5)) < E_{total}(trans(O^6))$. However, the stability order of the two less stable isomers (*trans*(O^5) and *trans*(O^6)) for Co(III) and Cr(III) 1,3-pddadp complexes is inverse compared to the corresponding Co(II), Ni(II), and Rh(III) complexes. Analysis of the distribution of strain contributions shows that in all three isomers of $[M(1,3\text{-pddadp})]^{n-}$ (M = Co(III), Cr(III), Rh(III), Co(II), and Ni(II)) complexes the strain is mainly localized in glycinate rings i.e. in M–O–C(sp^2) bond angles, as well as in N–M–O bite angles (*trans*(O^5) isomer of Co(II) and Ni(II) complexes and *trans*(O^5O^6) isomer of Cr(III), Rh(III), Co(II), and Ni(II) complexes), and in O–M–O open angles (*trans*(O^5) isomer of Co(III) and Cr(III) complexes). The energy differences between isomers are rather small, except for the two less stable isomers of Ni(II) and Co(II) complexes (*trans*(O^5) and *trans*(O^6) isomers, respectively). For

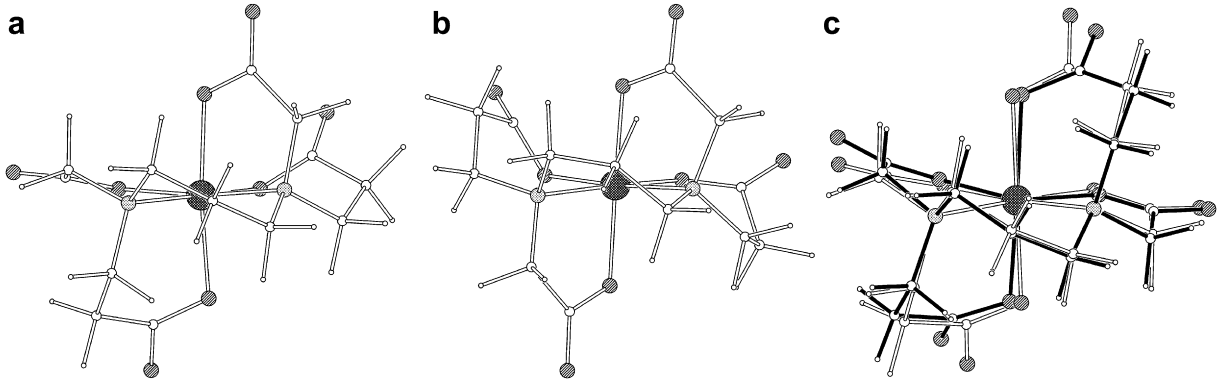


Fig. 3. Illustrations of the energy-minimized structures of the three isomers of $[Co(1,3\text{-pddadp})]^{2-}$ (open line) and X-ray crystal structure (full line): (a) *trans*(O^5O^6) isomer; (b) *trans*(O^5) isomer; (c) the result of a least-squares fit to Co1, N1 and N2 atoms of the X-ray structure and the energy-minimized structure of *trans*(O^6) isomer.

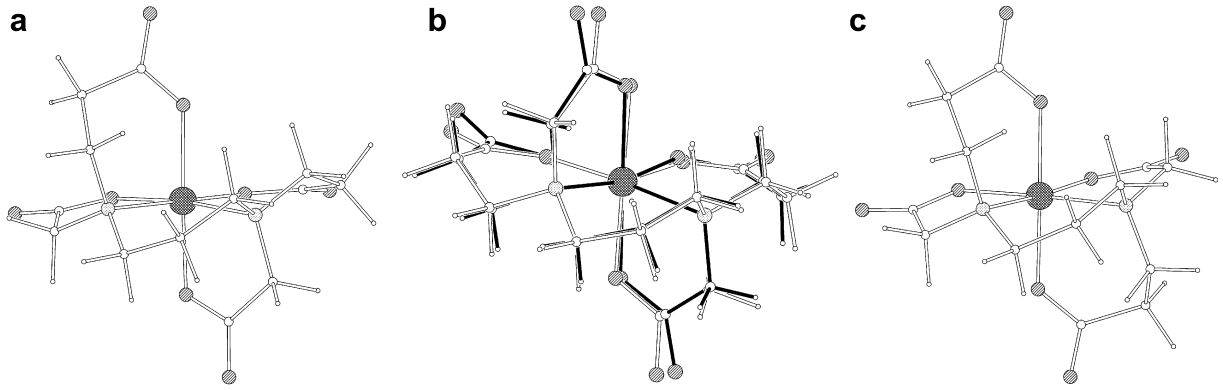


Fig. 4. Illustrations of the energy-minimized structures of the three isomers of $[Ni(1,3\text{-pddadp})]^{2-}$ (open line) and X-ray crystal structure (full line): (a) *trans*(O^5O^6) isomer; (b) the result of a least-squares fit to Ni1, N1 and N2 atoms of the X-ray structure and the energy-minimized structure of *trans*(O^5) isomer; (c) *trans*(O^6) isomer.

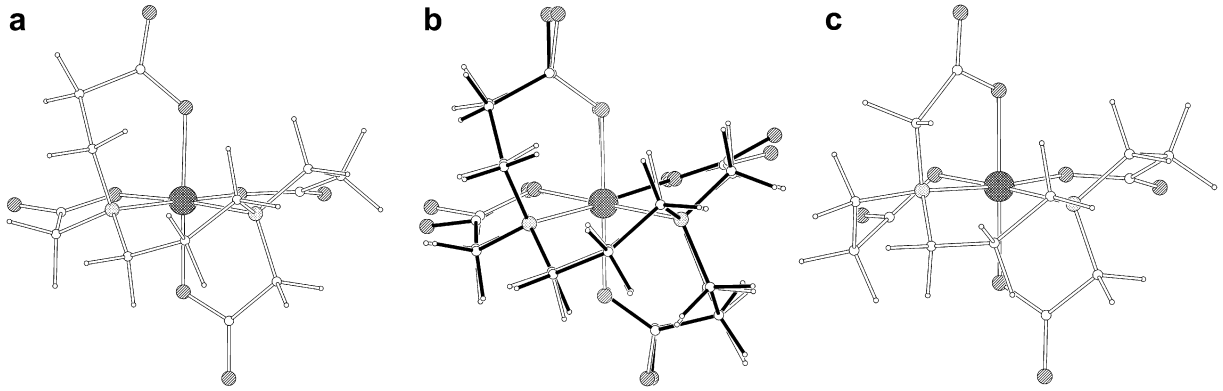


Fig. 5. Illustrations of the energy-minimized structures of the three isomers of $[Cr(1,3\text{-pddadp})]^{-}$ (open line) and X-ray crystal structure (full line): (a) *trans*(O^5O^6) isomer; (b) the result of a least-squares fit to Cr1, N1 and N2 atoms of the X-ray structure and the energy-minimized structure of *trans*(O^6) isomer; (c) *trans*(O^5) isomer.

$[M(1,3\text{-pddadp})]^{n-}$ (M = Co(III), Cr(III), Rh(III), and Co(II)) complexes energy differences between isomers originate mostly from the torsional contributions to the total energy, and in the case of Ni(II) from the angular contributions to the total energy. The analysis of the torsional contributions to the total strain shows that in Co(III), Cr(III), Rh(III), and Co(II) structures the strain is pronounced mainly in endocyclic torsions involving M–O and O–C(sp^2) bonds in the β-alaninate rings of both type (G and R).

3.4. Chelate ring conformations

In $[M(1,3\text{-pddadp})]^{n-}$ structures (M = Co(II), Ni(II), and Cr(III)) the six-membered diamine rings (T rings) adopt predominantly a twist-boat conformation except for the *trans*(O^5)-$[Co(1,3\text{-pddadp})]^{2-}$ and *trans*(O^5)-$[Cr(1,3\text{-pddadp})]^{-}$ in which boat and intermediate between boat and twist-boat forms have been observed, respectively. The axially coordinated glycinate rings (R rings) are usually almost flat while those coordinated in the equatorial plane (G rings) are highly puckered irrespective of their conformations (envelope or twist). In the case of β-alaninate rings, a twist-boat form predominates (12 out of 21 cases, see Table S12c in the Supplementary material) for both types of rings (G and R). The M–O–C=O fragments in this type of β-alaninate rings are roughly planar, as the corresponding torsion angle magnitudes span the narrow range of 144.7–155.7° (18 out of 21 cases listed in Table S12c). However, in some axially oriented β-alaninate rings (R-rings) we note a significant non-planarity of the M–O–C=O fragments, described by the values of the corresponding torsion angle magnitudes in the range of 116.1–122.5°, and associated with it pure boat conformation of the β-alaninate R-ring. This suggests that there exists a correlation between the chelate ring conformation and the M–O–C=O torsion angle magnitude. Moreover, for this pure boat conformation deviations (average value +17) from the ideal ring's bond angle sum (648) are significantly smaller than in other β-alaninate R-rings (Table 5), as are the deviations (average value +4°) of the Co–O–C bond angles from the ideal value of 109.5° (Table 5). These observations might indicate that the nearly ideal boat conformation of the β-alaninate R-ring is favored not only because it enables multiple interactions with the nearest neighbors (coordination or hydrogen bond, *vide supra*)

but also from the point of view of the ring strain. As far as the diaminopolycarboxylate edta-like complexes are concerned, the very bent M–O–C=O moiety and, connected with it, the pure boat conformation of the β-alaninate ring seem to be present only in eddadp and 1,3-pddadp types of chelates, and only in the axially oriented β-alaninate rings.

4. Conclusions

Structural preferences of transition metal complexes with diaminopolycarboxylate edta-type ligands have been compared based on our present and previous results [1,5,17,18]. For each $[M(1,3\text{-pddadp})]^{n-}$ system (M = Co(III), [5] Cr(III), Rh(III), [1] Ni(II), and Co(II)) the lowest energy conformer corresponds to the *trans*(O^5O^6) configuration with the 5–6–6 combination of the chelate rings in the G-plane. Moreover, the lowest energy isomer of the pentadentate $[Rh(1,3\text{-pddadp})Cl]^{2-}$ system (*cis*-polar, *trans*(Cl,O^5) (*N*′(R), *N*″(R)) isomer) [1] also displays the 5–6–6 configuration of the chelate rings in the G-plane, as does the lowest energy conformer of Cr(III) complex with the pentadentate 1,3-propanediamine-*N*,*N*′-diacetate-*N*-3-propionate (1,3-pddap) ligand [19]. However, the stability order of the other two isomers (*trans*(O^5) and *trans*(O^6)) is inverse for $[M(1,3\text{-pddadp})]^{-}$ (M = Co(III) and Cr(III)) with respect to the Co(II), Ni(II), and Rh(III) complexes, indicating that the effect of the metal ion size on the stability order of the two less stable isomers of $[M(1,3\text{-pddadp})]^{n-}$ system is a decisive one. The occurrence of the least energetically favored *trans*(O^6) isomer in the crystal and the unusual conformation, and geometry, of the axially oriented β-alaninate rings can be accounted for by the stabilizing role of extended tapes of planar cyclic water pentamers and hexamers which act as a "glue" to reinforce the coordination polymeric chains, consisting of complex cations and anions bridged together by carboxylate and water oxygens.

Acknowledgment

This work has been supported by the Serbian Ministry of Science and Environmental Protection through Grant No. 142017.

Appendix A. Supplementary material

CCDC 635226 contains the supplementary crystallographic data for this paper. These data can be obtained free of charge via http://www.ccdc.cam.ac.uk/conts/retrieving.html, or from the Cambridge Crystallographic Data Centre, 12 Union Road, Cambridge CB2 1EZ, UK; fax: (+44) 1223-336-033; or e-mail: deposit@ccdc.cam.ac.uk. Supplementary data associated with this article can be found, in the online version, at doi:10.1016/j.poly.2007.03.029.

References

[1] S. Grubišić, M.K. Milčić, D.D. Radanović, S.R. Niketić, J. Mol. Struct. 794 (2006) 125.
[2] D.J. Radanović, S.R. Trifunović, M.S. Cvijović, C. Maricondi, B.E. Douglas, Inorg. Chim. Acta 196 (1992) 161.
[3] M. Parvez, C. Maricondi, D.J. Radanović, S.R. Trifunović, V.D. Miletić, B.E. Douglas, Inorg. Chim. Acta 248 (1996) 89.
[4] I. Bernal, J. Cetrullo, J. Myrczek, J.S. Ricci Jr., D.J. Radanović, S.R. Trifunović, in: W. Gans, J.C.A. Boyens (Eds.), Intermolecular interactions, Plenum Press, New York, 1998, p. 155.
[5] S. Grubišić, S.R. Niketić, D.D. Radanović, U. Rychlewska, B. Warżajtis, Polyhedron 24 (2005) 1701.
[6] D.J. Radanović, M.I. Djuran, T.S. Kostić, B.E. Douglas, Inorg. Chim. Acta 211 (1993) 149.
[7] U. Rychlewska, M.I. Djuran, M.M. Vasojević, D.D. Radanović, V.M. Ristanović, D.J. Radanović, Inorg. Chim. Acta 328 (2002) 218.
[8] Z.D. Matović, S. Ianelli, G. Pelosi, S.K. Janićijević, V.M. Ristanović, G. Ponticelli, D.J. Radanović, Polyhedron 21 (2002) 2667.
[9] S. Kaizaki, M. Byakuno, M. Hayashi, J.I. Legg, K. Umakoshi, S. Ooi, Inorg. Chem. 26 (1987) 2395.
[10] D.J. Radanović, B.V. Prelesnik, D.D. Radanović, Z.D. Matović, B.E. Douglas, Inorg. Chim. Acta 262 (1997) 203.
[11] N.S. Drašković, M.I. Djuran, M.S. Cvijović, D.D. Radanović, V. Jevtović, Transition Met. Chem. 29 (2004) 874.
[12] CrysAlis CCD Software. Version 1.171 Oxford Diffraction, Oxfordshire, England, 2003.
[13] G.M. Sheldrick, Acta Crystallogr., Sect. A 46 (1990) 467.
[14] G.M. Sheldrick, SHELXL97, Program for the Refinement of Crystal Structures, University of Göttingen, Germany, 1997.
[15] (a) Stereochemical Workstation Operation Manual, Release 3.4, Siemens Analytical X-ray Instruments, Inc., Madison, WI, 1989; (b) I.J. Bruno, J.C. Cole, P.R. Edgington, M. Kessler, C.F. Macrae, P. McCabe, J. Pearson, R. Taylor, Acta Crystallogr., Sect. B 58 (2002) 389.
[16] S.R. Niketić, K. Rasmussen, The Consistent Force Field: A Documentation, Springer-Verlag, Berlin, 1977.
[17] S. Grubišić, M. Gruden, S.R. Niketić, N. Sakagami-Yoshida, S. Kaizaki, J. Mol. Struct. 609 (2002) 1.
[18] S. Grubišić, M. Gruden-Pavlović, S.R. Niketić, S. Kaizaki, N. Sakagami-Yoshida, Inorg. Chem. Commun. 6 (2003) 1180.
[19] S. Grubišić, M. Gruden-Pavlović, S.R. Niketić, N. Sakagami-Yoshida, S. Kaizaki, J. Coord. Chem., in press.
[20] A.D. Becke, J. Chem. Phys. 98 (1993) 5648.
[21] C. Lee, W. Yang, R.G. Parr, Phys. Rev. B 37 (1988) 785.
[22] M.J. Frisch, G.W. Trucks, H.B. Schlegel, G.E. Scuseria, M.A. Robb, J.R. Cheeseman, V.G. Zakrzewski, J.A. Montgomery Jr., R.E. Stratmann, J.C. Burant, S. Dapprich, J.M. Millam, A.D. Daniels, K.N. Kudin, M.C. Strain, O. Farkas, J. Tomasi, V. Barone, M. Cossi, R. Cammi, B. Mennucci, C. Pomelli, C. Adamo, S. Clifford, J. Ochterski, G.A. Petersson, P.Y. Ayala, Q. Cui, K. Morokuma, D.K. Malick, A.D. Rabuck, K. Raghavachari, J.B. Foresman, J. Cioslowski, J.V. Ortiz, B.B. Stefanov, G. Liu, A. Liashenko, P. Piskorz, I. Komaromi, R. Gomperts, R.L. Martin, D.J. Fox, T. Keith, M.A. Al-Laham, C.Y. Peng, A. Nanayakkara, C. Gonzalez, M. Challacombe, P.M.W. Gill, B. Johnson, W. Chen, M.W. Wong, J.L. Andres, M. Head-Gordon, E.S. Replogle, J.A. Pople, GAUSSIAN98, Revision A.6, Gaussian Inc., Pittsburgh, PA, 1998.
[23] A.E. Reed, L.A. Curtiss, F. Weinhold, Chem. Rev. 88 (1988) 899.
[24] M. Gruden, S. Grubišić, S.R. Niketić, A.G. Coutsolelos, J. Mol. Struct. 595 (2001) 209.
[25] A.L. Spek, Acta Crystallogr., Sect. A 46 (1990) 31.
[26] M. Nardelli, J. Appl. Crystallogr. 28 (1995) 659.
[27] D. Cremer, J.A. Pople, J. Am. Chem. Soc. 97 (1975) 1354.

[28] H.A. Weakliem, J.L. Hoard, J. Am. Chem. Soc. 81 (1959) 549.
[29] F.H. Allen, Acta Crystallogr., Sect. B 58 (2002) 380.
[30] L. Infantes, J. Chisholm, S. Motherwell, CrystEngComm 5 (85) (2003) 480.
[31] R.D. Shannon, Acta Crystallogr., Sect. A 32 (1976) 751.
[32] R. Herak, G. Srdanov, M.I. Djuran, D.J. Radanović, M. Bruvo, Inorg. Chim. Acta 83 (1984) 55.
[33] D.D. Radanović, U. Rychlewska, M.I. Djuran, N.S. Drašković, M.M. Vasojević, I.M. Hodžić, D.J. Radanović, Polyhedron 22 (2003) 2745.
[34] R. Nagao, F. Marumo, Y. Saito, Acta Crystallogr., Sect. B 28 (1972) 1852.
[35] D.J. Radanović, T. Ama, H. Kawaguchi, N.S. Drašković, D.M. Ristanović, S. Janićijević, Bull. Chem. Soc. Jpn. 74 (2001) 701.
[36] M. Parvez, C. Maricondi, D.J. Radanović, M.I. Djuran, B.E. Douglas, Inorg. Chim. Acta 182 (1991) 177.

Available online at www.sciencedirect.com
ScienceDirect
Polyhedron 26 (2007) 3448–3454
POLYHEDRON
www.elsevier.com/locate/poly

Polynuclear 3d complexes based on potentially tetra-anionic heptadentate ligands including amido, amino and phenoxo donors: Synthesis, crystal structure and magnetic properties

Samira Louhibi [a], Aicha Yacouta Nour [a,*], Laure Vendier [b], Jean-Pierre Costes [b], Jean-Pierre Tuchagues [b,*]

[a] *Département de chimie, Faculté des sciences, Université Abou Beker Belkaid, B.P. 119, 13.000 Tlemcen, Algeria*
[b] *Laboratoire de Chimie de Coordination du CNRS, UPR 8241, 205 route de Narbonne, 31077 Toulouse cedex, France*

Received 15 March 2007; accepted 22 March 2007
Available online 12 April 2007

Abstract

The synthesis and characterization of new dinuclear Mn^{III} and tetranuclear Cu^{II} complexes, $[HL^1Mn(DMSO)]_2$ (**1**) and $[H_2L^2Cu_2(MeO)_2]_2$ (**2**), are reported (H_4L^1 = 2-hydroxy-*N*-[2-({2-[(2-hydroxybenzoyl)amino]ethyl}amino)ethyl]benzamide and H_4L^2 = 2-hydroxy-*N*-[3-({3-[(2-hydroxybenzoyl)amino]propyl}(methyl)amino)propyl]benzamide). Single crystal X-ray structures have been determined for **1** and **2**. In **1** only one of the two amide functions of H_4L^1 is deprotonated in addition to the phenol ones, while in **2** all the amide functions of H_4L^2 are protonated and none of the potential nitrogen donors (amide and amine) is involved in the coordination to copper. HL^1 and H_2L^2 do not play the role of compartmental ligands and do not wrap around one Mn and one Cu ion, respectively, but embrace two metal centers yielding, with the respective assistance of auxiliary DMSO and methoxo ligands, dinuclear manganese and tetranuclear copper complexes, respectively. **1** includes two well isolated Mn^{III} ions ($Mn\cdots Mn' = 7.33$ Å) that do not interact magnetically. The intermolecular $Mn\cdots Mn''$ distance along the 1D chains (10.17 Å) is also too large to allow extended magnetic interactions. The pairwise magnetic interactions between the copper(II) ions in the tetranuclear complex **2** are so large that the $\chi_M T$ product is already equal to zero at room temperature, implying that the antiferromagnetic interaction is around $-1000\ cm^{-1}$, as observed previously for di-μ-hydroxo–dicopper complexes.
© 2007 Elsevier Ltd. All rights reserved.

Keywords: Heptadentate amide ligands; Dinuclear Mn^{III} complex; Tetranuclear Cu^{II} complex; Single-crystal X-ray structures; Magnetic studies

1. Introduction

Complexes based on polydentate ligands resulting from amide condensations are not numerous: they include different families depending on the purpose for which the complexes were prepared. In many cases, the polydentate amido ligands from which these complexes are built were purposely designed and synthesized for a given complex (or family of complexes) with specific shape, denticity, nature and functionality of donor atoms. The ligands, including amido and catecholato donors reported by Raymond et al., and their various metal complexes constitute an exemplary illustration of this approach [1]. Several other such examples are of interest in areas as diverse as catalysts, reducing or oxidizing agents, mimics of metalloproteins and enzymes, luminescent or magnetic materials. (i) From potentially tri-anionic tetradentate ligands including amido and phenoxo donors, mononuclear Mn^{IV}, Mn^{V}, Co^{III} and Co^{IV} complexes [2] as well as dicopper-(II,II), -(II,III) and -(III,III) complexes [3] were prepared. (ii) From related potentially mono-, di- or tri-anionic tetradentate ligands including amido and imidazolato and/or

* Corresponding authors. Tel.: +33 561 333154; fax: +33 561 553003.
E-mail address: jean-pierre.tuchagues@lcc-toulouse.fr (J.-P. Tuchagues).

0277-5387/$ - see front matter © 2007 Elsevier Ltd. All rights reserved.
doi:10.1016/j.poly.2007.03.051

pyridyl and/or phenoxo and/or thiolato donors, mononuclear Fe^{III} and dinuclear Ni^{II} complexes were prepared [4]. (iii) From potentially tetra-(tri-)anionic hexa-(penta-) dentate ligands including amido (imino) and phenoxo donors were prepared: a dinuclear Cr^{III} complex [5] and mononuclear Os^{II}, Os^{III}, Os^{IV} and Os^{VI} complexes as reducing and oxidizing agents [6], mononuclear Ru^{IV}, dicobalt-(II,II), -(II,III) and -(III,III) complexes as epoxidation catalysts [7], diiron(II,II) and mononuclear Bi^{III}, Cr^{III} and Fe^{III} complexes as catalysts for the controlled oxidation of organic molecules by O_2 [8], dianionic Cu^{II} ligand complexes as precursors to di- and tetra-heteronuclear 3d–3d and 3d–4f magnetic materials [9], and nitrido-Ru^{VI} and nitrido-Os^{VI} complexes as oxidizing agents [10]. (iv) From potentially tetra-anionic hexadentate ligands including amido and thiolato (or sulfinato) donors were prepared mononuclear Co^{III} [11] and Fe^{III} [12] complexes as mimics of nitrile hydratases, and a trinuclear cobalt(III,II,III) complex [13]. (v) Potentially tri-(penta-) anionic heptadentate ligands including alkoxo, amido and pyridyl (phenoxo) donors allowed the preparation of mono- and dinuclear Cu^{II}, and dinuclear Mn^{III} complexes [14]. (vi) From potentially tetra-anionic octadentate ligands including amido, amino and phenoxo donors, mononuclear Mn^{IV} [15] and dinuclear lanthanide [16] complexes were prepared for their redox, oxidizing and luminescence properties, respectively. (vii) A related potentially penta-anionic nonadentate ligand including amido, imidazolidino and phenoxo donors allowed the preparation of dinuclear Fe_2^{III} and Fe^{III},Zn^{II} complexes [17]. While all the above complexes were thoroughly characterized, most often including a single crystal molecular structure, the scarcity of Cu^{II} [18] and Fe^{III} [19] complexes prepared from related potentially tetra-anionic heptadentate ligands including amido, amino and phenoxo donors, could not be extensively characterized, and especially no single crystal molecular structure has yet been determined for any complex in this series. We have thus explored the chemistry of two such ligands (H_4L^1 = 2-hydroxy-*N*-[2-({2-[(2-hydroxybenzoyl)amino]ethyl}amino)-ethyl]benzamide and H_4L^2 = 2-hydroxy-*N*-[3-({3-[(2hydroxybenzoyl)amino]propyl}(methyl)amino)propyl]-benzamide) with transition metal complexes with the aim of exploring their nuclearities, supramolecular structure and magnetic properties. In this contribution we describe the synthesis, crystal structure and properties of two novel complexes, the dimanganese(III) and tetracopper(II) discrete species $[HL^1Mn(DMSO)]_2$ (**1**) and $[H_2L^2Cu_2(MeO)_2]_2$ (**2**), respectively.

2. Experimental

2.1. Materials

Diethylenetriamine, 3,3′-diamino-*N*-methyldipropylamine, phenylsalicylate, piperidine, triethylamine, $Cu(Ac)_2 \cdot H_2O$, $Mn(Ac)_2 \cdot 4H_2O$ (Aldrich) were used as purchased. High-grade solvents (acetonitrile, diethylether, DMSO, 2-propanol and methanol) were used for the syntheses of the ligands and complexes without further purification.

2.2. Syntheses

2.2.1. Ligands

The ligands were characterized by ^1H and by ^{13}C NMR in DMSO-d_6 (δ, ppm; s, singlet; d, doublet; dd, doublet of doublets; t, triplet ; td, triplet of doublets; q, quadruplet).

2.2.1.1. Synthesis of 2-hydroxy-N-[2-({2-[(2-hydroxybenzoyl)amino]ethyl}amino)ethyl]benzamide, H_4L^1. A mixture of phenylsalicylate (2.14 g, 1×10^{-2} mol), diethylenetriamine (0.51 g, 0.5×10^{-2} mol) and triethylamine (1 g, 1×10^{-2} mol) in 2-propanol (40 mL) was refluxed for 2 h with stirring. The white precipitate which appeared after cooling was filtered off, washed with 2-propanol and diethylether. Yield: 1.33 g (77.6%). m.p. 130 °C. *Anal.* Calc. for $C_{18}H_{21}N_3O_4$: C, 63.0; H, 6.2; N, 12.2. Found: C, 63.3; H, 6.1; N, 12.2%. ^1H NMR (250 MHz, 20 °C) δ: 9.06 (t, $J = 6.4$ Hz, 2H, OCN*H*), 7.96 (dd, $J = 1.5$ and 7.8 Hz, 2H, C(6) *H*), 7.48 (td, $J = 1.5$ and 7.8 Hz, 2H, C(4)*H*), 6.99(d, $J = 7.8$ Hz, 2H, C(3)*H*), 6.99(t, $J = 7.8$ Hz, 2H, C(5)*H*), 3.52 (q, $J = 6.4$ Hz, 4H, OCNHCH_2), 2.89 (t, $J = 6.4$ Hz, 4, NHCH_2). $^{13}C\{^1H\}$ NMR (62.896 MHz, 20°C): δ 39.1 (s, *C*H_2NHCO), 48.0 (s, *C*H_2NH), 115.7 (s, Ar*C*), 117.6 (s, Ar*C*(5)H), 118.3 (s, Ar*C*(3)H), 128.1 (s, Ar*C*(6)H), 133.6 (s, Ar*C*(4)H), 160.4 (s, Ar*C*(2)OH), 169.0 (s, O*C*NH). Characteristic IR absorptions (KBr): 3446, 3222, 1603 cm^{-1}.

2.2.1.2. Synthesis of 2-hydroxy-N-[3-({3-[(2hydroxybenzoyl)amino]propyl}(methyl)amino)propyl]benzamide] H_4L^2. The same experimental procedure as for H_4L^1, but using 3,3′-diamino-*N*-methyldipropylamine instead of diethylenetriamine, yielded H_4L^2 as an oily product. Yield: 1.0 g (52%). *Anal.* Calc. for $C_{21}H_{27}N_3O_4$: C, 65.4; H, 7.1; N, 10.9. Found: C, 65.0; H, 6.9; N, 10.5%. ^1H NMR (250 MHz, 20 °C) δ: 9.11 (s, 2H, OCN*H*), 7.94 (dd, $J = 1.5$ and 8 Hz, 2H, C(6) *H*), 7.47 (td, $J = 1.5$ and 8 Hz, 2H, C(4)*H*), 7.00 (d, $J = 8$ Hz, 2H, C(3)*H*), 6.98(t, $J = 8$ Hz, 2H, C(5)*H*), 3.46 (t, $J = 6.8$ Hz, 4H, OCNHCH_2), 2.48 (t, $J = 6.8$ Hz, 4H, CH_3NCH_2), 2.27 (s, 3H, CH_3NCH_2), 1.81 (q, $J = 6.8$ Hz, 4H, CH_2). $^{13}C\{^1H\}$ NMR (62.896 MHz, 20°C): δ 26.7 (s, *C*H_2), 37.6 (s, *C*H_2NHCO), 41.8 (s, CH_2NCH_3), 55.1 (s, *C*H_2NCH$_3$), 115.6 (s, Ar*C*), 117.6 (s, Ar*C*(5)H), 118.3 (s, Ar*C*(3)H), 127.8 (s, Ar*C*(6)H), 133.6 (s, Ar*C*(4)H), 160.6 (s, Ar*C*(2)OH), 169.0 (s, O*C*NH). Characteristic IR absorptions (thin film): 3380, 3212, 1600 cm^{-1}.

2.2.2. Complexes

*2.2.2.1. $[HL^1Mn(DMSO)]_2$ (**1**).* To a stirred methanolic solution (25 mL) of the H_4L^1 ligand (0.343 g, 1×10^{-3} mol) with piperidine (0.340 g, 4×10^{-3} mol), was added $Mn(Ac)_2 \cdot 4H_2O$ (0.245 g, 1×10^{-3} mol). The solution darkened immediately and was stirred for 3 h at

room temperature. A dark brown precipitate was then filtered off, and washed with methanol. A DMSO/acetonitrile solution of the powder yielded brown crystals 1 month later. Yield: 0.14 g (30%). *Anal.* Calc. for $C_{40}H_{48}Mn_2N_6O_{10}S_2$: C, 50.7; H, 5.1; N, 8.9; Mn, 11.6. Found: C, 50.4; H, 5.0; N, 8.8; Mn, 11.5%. Characteristic IR absorptions (KBr): 3431, 1617, 1596, 1570, 1526, 1437, 1016, 764 cm^{-1}.

*2.2.2.2. $[H_2L^2Cu_2(MeO)_2]_2$ (**2**).* To a stirred methanolic solution (25 mL) of the H_4L^2 ligand (0.385 g, 1×10^{-3} mol) was first added KOH (0.224 g, 4×10^{-3} mol) and, ten minutes later, $Cu(Ac)_2 \cdot H_2O$ (0.398 g, 2×10^{-3} mol). The mixture was stirred with heating for 2 h. A green precipitate which formed was filtered off, and washed several times with methanol. Blue–green crystals were isolated from a DMSO/methanol solution 1 month later. Yield: 0.20 g (35%). *Anal.* Calc. for $C_{46}H_{62}Cu_4N_6O_{12}$: C, 48.2; H, 5.5; N, 7.3; Cu, 22.2. Found: C, 47.9; H, 5.2; N, 7.1; Cu, 22.1%. Characteristic IR absorptions (KBr): 3305, 1609, 1579, 1538, 1526, 1241, 748 cm^{-1}.

2.3. Physical measurements

Elemental analyses were carried out on a Perkin–Elmer 2400 series II device (C, H, N) at the Microanalytical Laboratory of the Laboratoire de Chimie de Coordination in Toulouse, France, and on a Perkin–Elmer 300 Atomic Absorption Spectrophotometer (Mn, Cu) at the LCSCO laboratory of the Department of Chemistry of the University Abou Beker Belkaid in Tlemcen, Algeria. 1D ^1H and ^13C NMR spectra were recorded on an AC 250 FT spectrometer (Bruker). Chemical shifts are given in ppm versus TMS (^1H and ^{13}C) using DMSO-d_6 as the solvent. IR spectra were measured in the 400–4000 cm^{-1} range on a 9800 FTIR spectrometer (Perkin–Elmer). Samples were run as KBr pellets. Variable temperature magnetic susceptibility data were collected on powdered samples on a MPMS-55 Quantum Design SQUID magnetometer under applied magnetic fields lower than 0.5 T. Diamagnetic corrections were applied by using Pascal's constants [20].

2.4. Crystallographic data collection and structure determination for *1* and *2*

The X-ray data for compound **1** were collected on a Stoe Imaging Plate Diffractometer System (IPDS) equipped with an Oxford Cryosystems cooler device using a graphite monochromator ($\lambda = 0.71073$ Å). Data were collected [21] using φ rotation movement with the crystal-to-detector distance equal to 70 mm ($\varphi = 0.0$–$270°$, $\Delta\varphi = 1.5°$). Diffraction data for **2** were collected using an Oxford-Diffraction XCALIBUR CCD diffractometer equipped with a graphite monochromated Mo Kα radiation source. The crystal was placed 50 mm from the CCD detector. More than the hemisphere of reciprocal space was covered by a combination of four sets of exposures; each set had a different φ-angle (0, 90, 180, 270°) and each exposure of 20 s covered 0.75° in ω. Coverage of the unique set is 99.5% complete up to $2\theta = 63.22°$. The unit cell determination and data integration were carried out using the CRYSALIS package of Oxford Diffraction [22]. All structures were solved by direct methods using SIR92 [23] and refined by full-matrix least-squares on F_o^2 with SHELXL-97 [24], using anisotropic displacement parameters for non-hydrogen atoms. The hydrogen atoms were placed in calculated positions (C–H 0.96 Å) and they were included in the refinement in the riding-model approximation with $U_{iso} = 1.1\ U$(atom of attachment). Scattering factors were taken from the standard compilation [25]. The molecular plots were obtained using the CAMERON and ORTEP programs [26]. Semi-empirical absorption corrections were applied for **1** and **2** using the program DIFABS [27]. The final full-matrix least-squares refinement, minimizing $[\sum w(|F_o^2| - |F_c^2|)^2]^2$, converged at the values of R and wR listed in Table 1, presented together with the main crystallographic parameters. For both compounds, it was not possible to resolve the diffuse electron-density residuals (crystallization solvent molecules). Treatment with the SQUEEZE facility from PLATON [28] resulted in a smooth refinement. Since a few low order reflections are missing from the data set, the electron count is underestimated. Consequently, the values given for ρ_{calc}, $F(000)$ and the molecular weight are only valid for the ordered part of the structure. The relatively high R-factor for complex **1** is due to the low quality of the crystals:

Table 1
Crystallographic data collection and structure determination for complexes **1** and **2**

	1	**2**
Formula	$C_{40}H_{48}N_6O_{10}S_2Mn_2$	$C_{46}H_{62}N_6O_{12}Cu_4$
Formula weight	946.86	1145.22
Crystal system	triclinic	monoclinic
Space group	$P\bar{1}$	$P121/c1$
Crystal habit	green–brown platelets	blue–green plates
T (K)	293(2)	293(2)
a (Å)	8.1220(18)	10.2470(8)
b (Å)	10.1645(19)	17.1970(12)
c (Å)	15.213(3)	15.2080(10)
α (°)	97.84(2)	90
β (°)	103.36(3)	100.389(6)
γ (°)	101.09(2)	90
V (Å^3)	1177.4(4)	2636.0(3)
Z	1	2
λ (Å)	0.71073	0.71073
ρ_{calc} (Mg m^{-3})	1.335	1.443
Crystal size (mm)	$0.4 \times 0.25 \times 0.15$	$0.5 \times 0.4 \times 0.2$
θ Range	2.08–26.19	3.09–26.37
h	−10 to 9	−12 to 10
k	−12 to 12	−21 to 21
l	−18 to 18	−18 to 18
Reflections collected/unique	11 839/4346	19 010/5369
Data observations	1715	3378
R_1, wR_2 (all data)	0.1470, 0.1665	0.0803, 0.1260
R_1, wR_2 ($I > 2\sigma(I)$)	0.0590, 0.1299	0.0475, 0.1160

[a] $R = \sum||F_o| - |F_c||/\sum|F_o|$.
[b] $wR = [\sum w(|F_o^2| - |F_c^2|)^2/\sum w|F_o^2|^2]^{1/2}$.

among several sets of diffraction data obtained from different crystals, which all diffracted poorly, the best one was used to solve this structure. The disorder of the ligand in **2** was treated with the PART option of SHELX97.

3. Results

3.1. Syntheses

The potentially tetra-anionic heptadentate ligands H_4L^1 and H_4L^2, including two terminal phenoxo, two amido and one central amino donor, were expected to act as dinucleating ligands upon reaction with metal salts. Thus, we reacted them aerobically with Cu^{II} and Mn^{II} acetate in a 1:2 ligand/metal ratio. While the obtained Cu^{II} complex **2** had the expected 1:2 ligand/metal ratio, the Mn^{III} complex **1** was characterized by a 1:1 ligand/metal ratio. This latter reaction was then optimized by carrying it out with a 1:1 ligand/metal ratio. By carrying out these reactions in basic media we also expected to favor bridging of the metal centers through full deprotonation of the ligand. However, the analytical data, charge balance, as well as IR spectroscopy suggested the absence of bridging oxo or acetato anions or a counter-cation, implying that the ligand is not fully deprotonated in the Mn^{III} complex. This was confirmed by the single-crystal X-ray molecular structure of **1** which showed that only one of the two amide functions of H_4L^1 is deprotonated in addition to the phenol ones, yielding $[HL^1Mn(DMSO)]_2$. It is remarkable that this ligand is not fully deprotonated in spite of the propensity of amido ligands to favor high oxidation states of the metal centers to which they are coordinated [2,3,6,10,15]. On the other hand, the molecular structure of **2** confirmed another peculiarity suggested by the analytical data, charge balance and IR spectroscopy, namely none of the two amide functions of H_4L^2 are deprotonated, yielding $[H_2L^2Cu_2(MeO)_2]_2$ where the phenoxo and amido oxygen atoms of the H_2L^2 ligands are involved in the coordination to the Cu^{II} cations whilst, at variance with **1**, the central amino nitrogen atoms are not coordinated to the metal centers (see Fig. 1).

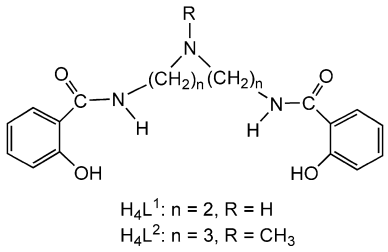


Fig. 1. Schematic representation of ligands H_4L^1 and H_4L^2.

3.2. Description of the structures

A CAMERON plot of **1** and an ORTEP plot of **2** are sketched in Figs. 2 and 3, respectively. Selected inter-atomic distances and angles are collated in Tables 2 and 3, respectively. The crystal structures confirm that HL^1 and H_2L^2 do not play the role of compartmental ligands and do not wrap around one Mn and one Cu ion, respectively. These ligands embrace two metal centers yielding, with the respective assistance of auxiliary DMSO and methoxo ligands, dinuclear manganese and tetranuclear copper complexes, respectively.

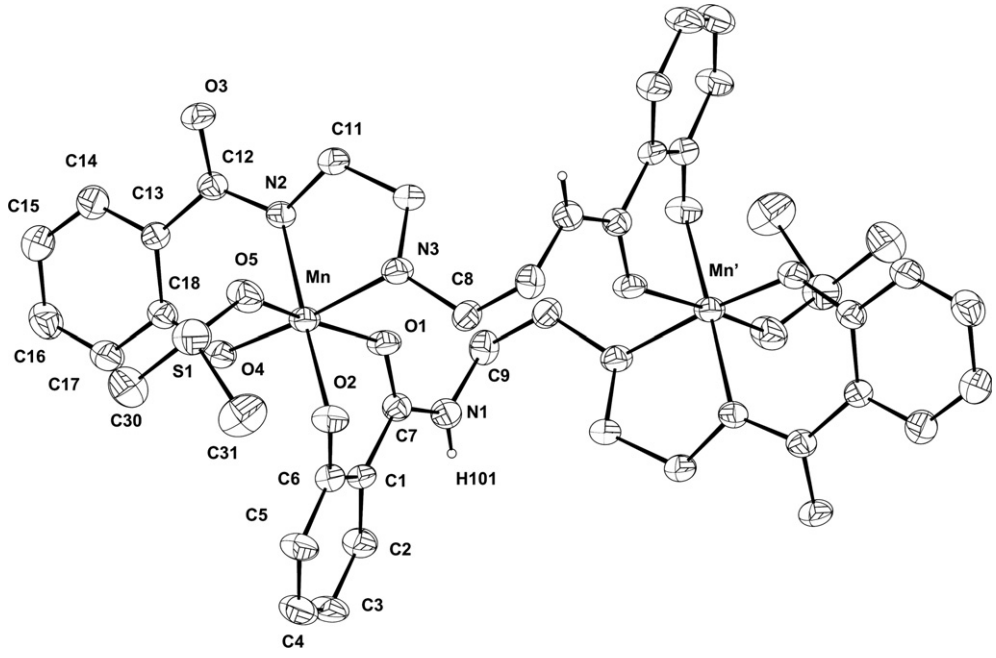


Fig. 2. ORTEP plot of the complex molecule $[HL^1Mn(DMSO)]_2$ (**1**) at the 30% probability level ($' = x + 1, -y, -z$). Carbon bonded H-atoms have been omitted for clarity.

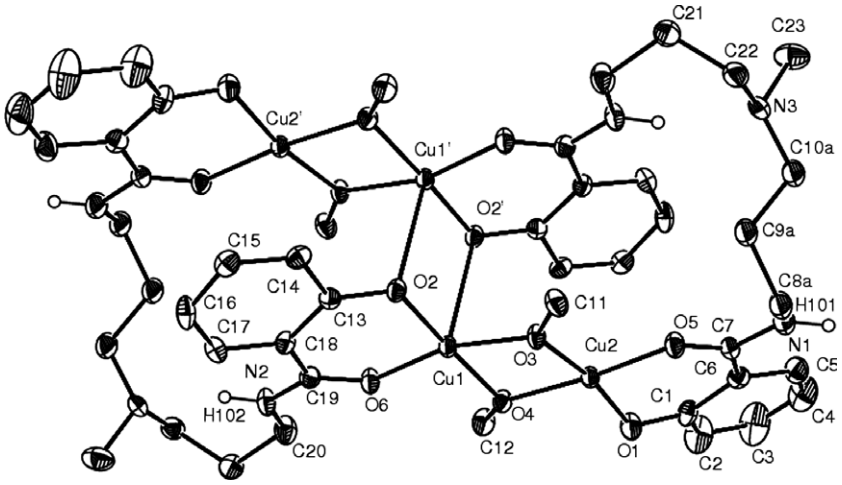


Fig. 3. ORTEP plot of $[H_2L^2Cu_2(MeO)_2]_2$ (**2**) at the 30% probability level ($' = -x+1, -y, -z$). Carbon bonded H-atoms have been omitted for clarity.

Table 2
Selected bond lengths (Å) and angles (°) for $[HL^1Mn(DMSO)]_2$ (**1**)

Mn–O1	2.198(4)	Mn–N2	1.949(4)	Mn–O2	1.894(4)	Mn–N3	2.118(5)
Mn–O4	1.863(4)	Mn–O5	2.259(4)	C7–N1	1.341(7)	C7–O1	1.246(6)
C12–N2	1.339(7)	C12–O3	1.269(6)				
O1–Mn–N2	98.10(17)	O1–Mn–N3	86.72(17)	O1–Mn–O2	83.59(16)	O1–Mn–O4	94.31(18)
O1–Mn–O5	167.80(16)	N2–Mn–O2	176.2(2)	N2–Mn–N3	83.87(18)	N2–Mn–O4	91.34(19)
N2–Mn–O5	85.89(18)	O2–Mn–O4	91.88(18)	O2–Mn–O5	91.78(17)	N3–Mn–O2	92.90(18)
N3–Mn–O4	175.19(17)	N3–Mn–O5	82.23(18)	O4–Mn–O5	97.14(18)		

Table 3
Selected bond lengths (Å) and angles (°) for $[H_2L^2Cu_2(MeO)_2]_2$ (**2**)

Cu1–O2	1.891(3)	Cu1–O3	1.926(3)	Cu1–O4	1.922(3)	Cu1–O6	1.915(3)
Cu1–O2′	2.608(3)						
Cu2–O1	1.881(3)	Cu2–O3	1.903(3)	Cu2–O4	1.918(3)	Cu2–O5	1.905(3)
O2–Cu1–O3	98.55(12)	O2–Cu1–O4	175.80(12)	O2–Cu1–O6	93.33(12)	O2–Cu1–O2′	84.38(11)
O3–Cu1–O4	77.46(11)	O3–Cu1–O6	164.16(13)	O3–Cu1–O2′	85.33 (11)	O4–Cu1–O6	90.41(11)
O4–Cu1–O2′	96.42(11)	O6–Cu1–O2′	106.21(12)	O1–Cu2–O3	170.74(13)	O1–Cu2–O4	94.41(13)
O1–Cu2–O5	92.21(13)	O3–Cu2–O4	78.12(12)	O3–Cu2–O5	95.40(12)	O4–Cu2–O5	173.28(13)

The asymmetric unit of the dinuclear complex **1** includes half the $[HL^1Mn(DMSO)]_2$ molecule. The Mn^{III} cations are thus symmetry related and each Mn^{III} is surrounded by four oxygen and two nitrogen atoms originating from two ligands and one DMSO molecule. One ligand is coordinated through one phenoxo oxygen and its deprotonated amido nitrogen atoms and the secondary amino nitrogen atom; the second ligand is chelated to the metal center through one phenoxo and one amido (belonging to the protonated amide function) oxygen atom. Consequently, each ligand is trianionic. The apical positions of the Mn coordination octahedron are occupied by the amido and the DMSO oxygen atoms. The four basal N_2O_2 donor atoms deviate from the mean coordination plane by less than 0.0138 Å. The apical Mn–O bond lengths (2.259(4) and 2.198(4) Å) are larger than the equatorial Mn–O (1.863(4) and 1.894(4) Å) and Mn–N bonds, although the $Mn–N_{amino}$ bond (2.124(5) Å) is larger than the $Mn–N_{amido}$ one (1.949(4) Å), in agreement with the Jahn–Teller elongation expected for the Mn^{III} cation. The $Mn–O_{amido}$ coordination is accompanied by a decrease of the corresponding C=O bond length (0.028 Å), more pronounced than the decrease of the C–N amido bond length following deprotonation and complexation (0.017 Å). The Mn ions belong to a 14-membered macrocycle, with a Mn···Mn′ distance of 7.330(3) Å. This dinuclear structure is reminiscent of a Cu^{II} dimer based on the pentadentate saldien ligand (2-[(*E*)-{[2′-(propylamino)ethyl]imino}methyl]phenol-2-(iminomethyl)-phenol) [29] and of the Mn^{III} dimer $[Mn_2O(5\text{-}NO_2\text{-saldien})_2]$ based on a similar 5-NO_2-salicylaldimine substituted ligand [30]. The crystal packing evidences chains of dinuclear complex molecules developing along the *b*-axis through hydrogen bonds connecting the N1(H) amide nitrogen to the O3 amide oxygen atoms of an adjacent molecule (N1–H = 0.86 Å, H(N1)···O3 = 2.18 Å, N1···O3 = 3.022(6) Å, N1–H···O3 = 165(7)° ($x, y+1, z$)). The resulting intermolecular Mn···Mn″ distance along the chains is 10.1645(19) Å.

The asymmetric unit of the tetranuclear complex **2** includes half of the $[H_2L^2Cu_2(MeO)_2]_2$ molecule. Only two Cu^{II} cations are thus crystallographically independent. Cu1 is in a square pyramidal environment: the four basal donor atoms include one amido and one phenoxo oxygen atom from H_2L^2 and two bridging methoxo oxygen atoms from the symmetry related (′) $[H_2L^2Cu_2(MeO)_2]$ half complex molecule. The apical donor is a bridging phenoxo oxygen atom from the H_2L^2 ligand of the symmetry related (′) $[H_2L^2Cu_2(MeO)_2]$ half complex molecule. Cu2 is in a square planar environment including one amido and one phenoxo oxygen atom from H_2L^2 and two bridging methoxo oxygen atoms. In complex **2**, all the amide functions are protonated and none of the potential nitrogen donors (amide and amine) are involved in the coordination to copper. Cu1 (Cu1′) is bridged to Cu2 (Cu2′) through two methoxo oxygen atoms yielding two $Cu(\mu\text{-}OMe)_2Cu$ pairs in which the Cu···Cu distance is 2.9627(7) Å. In addition, Cu1 is bridged to Cu1′ through two phenoxo oxygen atoms (one from each of the two H_2L^2 ligands in the tetranuclear $[H_2L^2Cu_2(MeO)_2]_2$ molecule) yielding one $Cu(\mu\text{-}O_{phenoxo})_2Cu$ pair in which the Cu···Cu distance is 3.3678(11) Å. The basal Cu–O bond lengths are in the tiny 1.881(3) to 1.926(3) Å range while the apical Cu–O is, as expected, significantly elongated (2.608(3) Å). Consequently, while the $Cu(\mu\text{-}OMe)_2Cu$ cores are practically perfect lozenges with equivalent Cu–OMe–Cu bridging angles (100.99(13) and 101.38(13)°), the $Cu(\mu\text{-}O_{phenoxo})_2Cu$ core is a symmetry imposed rectangle. This overall arrangement results in a 32 metalla-macrocycle, with the two phenolato rings (one from each H_2L^2 ligand) coordinated to one $Cu(\mu\text{-}OMe)_2Cu$ pair in a *trans* configuration. Two symmetry related intramolecular hydrogen bonds between N2(H) and N3 (N2–H = 0.854(10) Å, H(N2)···N3 = 2.05(2) Å, N2···N3 2.822(5) Å, N2–H···N3 = 150(4)° ($-x+1$, $-y$, $-z$)) participate in the stabilization of this tetranuclear arrangement. The crystal packing of **2** does not evidence any significant intermolecular interactions.

3.3. Magnetic studies

The thermal variation of the magnetic susceptibility χ_M has been explored for complexes **1**–**2** in the 300–2 K temperature range. The $\chi_M T$ data for complex **1** are practically constant in the 300–10 K temperature range (5.92–5.63 $cm^3\,mol^{-1}\,K$), which is close to the spin-only value for two non-interacting S = 2 metal centers (6.00 $cm^3\,mol^{-1}\,K$). Below 10 K, the $\chi_M T$ product decreases down to 3.45 $cm^3\,mol^{-1}\,K$ at 2 K. This $\chi_M T$ decrease at very low temperature results from the single ion zero field splitting associated with the Jahn–Teller elongation of the octahedral symmetry around Mn^{III}, mentioned in the molecular crystal structure section. The $\chi_M T$ data for complex **2** are virtually equal to zero in the whole temperature range suggesting strong antiferromagnetic interactions among the $Cu(\mu\text{-}OMe)_2Cu$ pairs described in the molecular crystal structure section.

4. Discussion

These results indicate that, independent of their protonation state, the diamide ligands H_4L^1 and H_4L^2, which contain seven potential donor atoms, do not wrap around the metal ions, as was the case for Ln complexes of the pentadentate saldien Schiff base $[\{Ln(saldien)(NO_3)\}_2]$ (Ln = Gd, Tb) [31] and for 3d complexes of a related Schiff base [M(mbp)] (M = Cu, Ni; mbp = *N*,*N*′-bis[(2-hydroxy-5-methyl-phenyl)phenylmethylene]-4-azaheptane-1,7-diamine) [32]. Neither do they act as common dinucleating ligands. The net result is the obtention of metalla-macrocycles (14-(HL^1 with Mn^{III}) or 32-membered macrocycles (H_2L^2 with Cu^{II})). On comparison with Schiff bases, two supplementary factors are present – the isomerism of the amide function and the number of anionic sites. It is also surprising to see that with Mn^{III} ions, three of the four possible deprotonations occurred while for Cu^{II} ions two deprotonations are observed. In both cases, neutral complexes have been isolated. The presence of methoxo bridges is also puzzling for the deprotonation of the amide function is usually easier than that for methanol. A recent example of a di-μ-methoxo bridge evidences that fairly strong basic conditions are needed for its obtention [33].

From a magnetic point of view, the complex molecule **1** includes two well isolated Mn^{III} ions (Mn···Mn′ = 7.33 Å) that do not interact magnetically. The intermolecular Mn···Mn″ distance along the 1D chains (10.17 Å) is also too large to allow extended magnetic interactions. On the contrary, the pairwise magnetic interactions between the copper(II) ions in the tetranuclear complex **2** are so large that the $\chi_M T$ product is already equal to zero at room temperature. This implies that the antiferromagnetic interaction is around $-1000\,cm^{-1}$. The Cu1–O4–Cu2 and Cu1–O3–Cu2 θ angles (101.0(2) and 101.4(2)°) are in line with previous experimental results for di-μ-hydroxo–dicopper complexes [34]. Antiferromagnetic interaction parameters J were observed for θ angles larger than 98°, their absolute value increasing with θ. Finally, it is remarkable that the magnetic behavior observed for **2** suggests a larger *J* value than those found for similar θ angles in di-μ-hydroxo–dicopper complexes [34].

Acknowledgements

S.L. and A.Y.N. acknowledge the Algerian Ministry for Education and Research for abroad Grants.

Appendix A. Supplementary material

CCDC 639533 and 639532 contain the supplementary crystallographic data for **1** and **2**. These data can be obtained free of charge via http://www.ccdc.cam.ac.uk/conts/retrieving.html, or from the Cambridge Crystallographic Data Centre, 12 Union Road, Cambridge CB2 1EZ, UK; fax: (+44) 1223-336-033; or e-mail: deposit@ccdc.cam.ac.uk. Supplementary data associated with this

article can be found in the online version, at doi:10.1016/j.poly.2007.03.051.

References

[1] (a) See for example: Z. Hou, T.D.P. Stack, C.J. Sunderland, K.N. Raymond, Inorg. Chim. Acta 263 (1997) 341;
(b) D.L. Caulder, R.E. Powers, T.N. Parac, K.N. Raymond, Angew. Chem., Int. Ed. 37 (1998) 1840;
(c) T.N. Parac, M. Scherer, K.N. Raymond, Angew. Chem., Int. Ed. 39 (2000) 1239;
(d) M. Ziegler, J.L. Brumaghim, K.N. Raymond, Angew. Chem., Int. Ed. 39 (2000) 4119;
(e) A.J. Terpin, M. Ziegler, D.W. Johnson, K.N. Raymond, Angew. Chem., Int. Ed. 40 (2001) 157;
(f) D.L. Caulder, C. Brückner, R.E. Powers, S. König, T.N. Parac, J.A. Leary, K.N. Raymond, J. Am. Chem. Soc. 123 (2001) 8923.

[2] (a) M. Koikawa, H. Okawa, S. Kida, J. Chem. Soc., Dalton Trans. (1988) 641;
(b) M. Koikawa, M. Gotoh, H. Okawa, S. Kida, J. Chem. Soc., Dalton Trans. (1989) 1613.

[3] M. Koikawa, H. Okawa, N. Matsumoto, M. Gotoh, S. Kida, T. Kohsuma, J. Chem. Soc., Dalton Trans. (1989) 2089.

[4] (a) D.S. Marlin, P.K. Mascharak, Chem. Soc. Rev. 29 (2000) 69, and references therein;
(b) T.C. Harrop, M.M. Olmstead, P.K. Mascharak, Chem. Commun. (2003) 410.

[5] T.J. Collins, B.D. Santarsiero, G.H. Spies, J. Chem. Soc. Chem. Commun. (1983) 681.

[6] F.C. Anson, J.A. Christie, T.J. Collins, R.J. Coots, T.T. Furutani, S.L. Gipson, J.T. Keech, T.E. Krafft, B.D. Santarsiero, G.H. Spies, J. Am. Chem. Soc. 106 (1984) 4460.

[7] (a) C.-M. Che, W.-K. Cheng, W.-H. Leung, T.C.W. Mak, J. Chem. Soc. Chem. Commun. (1987) 418;
(b) S. Mukerjee, K. Skogerson, S. DeGala, J.P. Caradonna, Inorg. Chim. Acta 297 (2000) 313.

[8] (a) A. Stassinopoulos, J.P. Caradonna, J. Am. Chem. Soc. 113 (1991) 8686;
(b) A. Stassinopoulos, G. Schulte, G.C. Papaefthymiou, J.P. Caradonna, J. Am. Chem. Soc. 112 (1990) 7071;
(c) S. Mukerjee, A. Stassinopoulos, J.P. Caradonna, J. Am. Chem. Soc. 119 (1997) 8097;
(d) T.L. Foster, J.P. Caradonna, J. Am. Chem. Soc. 125 (2003) 3678;
(e) M.R. Maurya, S.J.J. Titinchi, S. Chand, J. Mol. Cat. A 214 (2004) 257.

[9] (a) Y. Sunatsuki, T. Matsuo, M. Nakamura, F. Kai, N. Matsumoto, J.-P. Tuchagues, Bull. Chem. Soc. Jpn. 71 (1998) 2611;
(b) T. Kido, S. Nagasato, Y. Sunatsuki, N. Matsumoto, Chem. Commun. (2000) 2113;
(c) J.-P. Costes, F. Dahan, CR Acad. Sci. Paris, Chim. 4 (2001) 97;
(d) T. Kido, Y. Ikuta, Y. Sunatsuki, Y. Ogawa, N. Matsumoto, Inorg. Chem. 42 (2003) 398;
(e) N. Nakamura, M. Kawachi, C. Konatsu, S. Osa, T. Tarui, N. Matsumoto, N. Re, Chem. Lett. 32 (2003) 936;
(f) S. Osa, Y. Sunatsuki, Y. Yamamoto, N. Nakamura, T. Shimamoto, N. Matsumoto, N. Re, Inorg. Chem. 42 (2003) 5507;
(g) S. Osa, T. Kido, N. Matsumoto, N. Re, A. Pochaba, J. Mrozinski, J. Am. Chem. Soc. 126 (2004) 420;
(h) J.-P. Costes, F. Dahan, B. Donnadieu, M.-J. Rodriguez Douton, A. Bousseksou, J.-P. Tuchagues, Inorg. Chem. 43 (2004) 2736.

[10] (a) P.-M. Chan, W.-Y. Yu, C.-M. Che, K.-K. Cheung, J. Chem. Soc., Dalton Trans. (1998) 3183;
(b) K.L. Yip, W.-Y. Yu, P.-M. Chan, N.-Y. Zhu, C.-M. Che, J. Chem. Soc., Dalton Trans. (2003) 3556.

[11] (a) See for example: S. Chatel, M. Rat, S. Dijols, P. Leduc, J.-P. Tuchagues, D. Mansuy, I. Artaud, J. Inorg. Biochem. 80 (2000) 239;
(b) M. Rat, R. Alves de Sousa, J. Vaissermann, P. Leduc, D. Mansuy, I. Artaud, J. Inorg. Biochem. 84 (2001) 207;
(c) L. Heinrich, Y. Li, K. Provost, A. Michalowicz, J. Vaissermann, J.C. Chottard, Inorg. Chim. Acta 318 (2001) 117.

[12] S. Chatel, A.S. Chauvin, J.-P. Tuchagues, P. Leduc, E. Bill, J.C. Chottard, D. Mansuy, I. Artaud, Inorg. Chim. Acta 336 (2002) 19.

[13] M. Rat, R. Alves de Sousa, A. Tomas, Y. Frapart, J.-P. Tuchagues, I. Artaud, Eur. J. Inorg. Chem. (2003) 759.

[14] K. Bertoncello, G.D. Fallon, K.S. Murray, Polyhedron 9 (1990) 2867.

[15] (a) S.K. Chandra, S.B. Choudhury, D. Ray, A. Chakravorty, J. Chem. Soc. Chem. Commun. (1990) 474;
(b) S.K. Chandra, A. Chakravorty, Inorg. Chem. 31 (1992) 760.

[16] W.P.-W. Lai, W.-T. Wong, B.K.-F. Li, K.-W. Cheah, New J. Chem. 26 (2002) 576.

[17] P.K.S. Chowdhury, U. Mukhopadhyay, D. Ray, Indian J. Chem. 38A (1999) 1159.

[18] C.A. Sureshan, P.K. Bhattacharya, Indian J. Chem. 38A (1999) 723.

[19] A.C. Dash, R.K. Rath, Indian J. Chem. 43A (2004) 310.

[20] P. Pascal, Ann. Chim. Phys. 19 (1910) 5.

[21] STOE, IPDS Manual. Version 2.93. Stoe & Cie, Darmstadt, Germany, 1997.

[22] CRYSALIS RED, Version 1.170.32; Oxford Diffraction Ltd., Oxford, UK, 2003.

[23] A. Altomare, G. Cascarano, C. Giacovazzo, A. Guagliardi SIR92 – a program for crystal structure solution, J. Appl. Crystallogr. 26 (1993) 343.

[24] G.M. Sheldrick, SHELXL-97. Program for the Refinement of Crystal Structures from Diffraction Data. University of Göttingen, Göttingen, Germany, 1997.

[25] International Tables for Crystallography, vol. C. Kluwer Academic Publishers, Dordrecht, The Netherlands, 1992.

[26] (a) L.J. Farrugia ORTEP3 for Windows, J. Appl. Crystallogr. 30 (1997) 565;
(b) CAMERON, D.J. Watkin, C.K. Prout, L.J. Pearce, Chemical Crystallography Laboratory, Oxford, UK, 1996.

[27] N. Walker, D. Stuart, DIFABS, Acta Crystallogr. Sect. A 39 (1983) 158.

[28] A.L. Spek, Acta Crystallogr. A46 (1990) C34.

[29] E.D. McKenzie, S.J. Selvey, Inorg. Chim. Acta 18 (1976) L1.

[30] C.A. Kipke, M.J. Scott, J.W. Gohdes, W.H. Armstrong, Inorg. Chem. 29 (1990) 2193.

[31] R.C. Howell, K.V.N. Spence, I.A. Kahwa, A.J.P. White, D.J. Williams, J. Chem. Soc., Dalton Trans. (1996) 961.

[32] P.C. Healy, G.M. Mockler, D.P. Freyberg, E. Sinn, J. Chem. Soc., Dalton Trans. (1975) 691.

[33] X.H. Bu, M.L. Tong, H.C. Chang, S. Kitagawa, S.R. Batten, Angew. Chem., Int. Ed. 43 (2004) 192.

[34] V.H. Crawford, H.W. Richardson, J.R. Wasson, D.J. Hodgson, W.E. Hatfield, Inorg. Chem. 15 (1976) 2107, and references therein.

Available online at www.sciencedirect.com
ScienceDirect
Polyhedron 26 (2007) 3455–3464
POLYHEDRON
www.elsevier.com/locate/poly

New oxorhenium complexes with 2-(2′-hydroxyphenyl)-2-benzoxazolinato ligand. X-ray structure and DFT calculations for $[ReOX_2(hbo)(AsPh_3)]$ and $[ReOX_2(hbo)(PPh_3)]$ complexes

B. Machura [a,*], R. Kruszynski [b], J. Kusz [c]

[a] Department of Crystallography, Institute of Chemistry, University of Silesia, 9th Szkolna Street, 40-006 Katowice, Poland
[b] Department of X-ray Crystallography and Crystal Chemistry, Institute of General and Ecological Chemistry, Lodz University of Technology, 116 Żeromski Street, 90-924 Łódź, Poland
[c] Institute of Physics, University of Silesia, 4th Uniwersytecka Street, 40-006 Katowice, Poland

Received 24 January 2007; accepted 19 March 2007
Available online 30 March 2007

Abstract

The reactions of $[ReOX_3(AsPh_3)_2]$ and $[ReOX_3(PPh_3)_2]$ with 2-(2′-hydroxyphenyl)-2-benzoxazoline (Hhbo) have been examined and $[ReOX_2(hbo)(AsPh_3)]$ and $[ReOX_2(hbo)(PPh_3)]$ (X = Cl, Br) complexes have been obtained. The crystal and molecular structures of $[ReOCl_2(hbo)(AsPh_3)]$ (**1**) and $[ReOBr_2(hbo)(PPh_3)]$ (**4**) have been determined. The electronic structures of **1** and **4** have been calculated with the density functional theory (DFT) method. The spin-allowed electronic transitions of **1** and **4** have been calculated with the time-dependent DFT method, and the UV–Vis spectra of these complexes have been discussed.
© 2007 Elsevier Ltd. All rights reserved.

Keywords: Rhenium oxo complexes; 2-(2′-Hydroxyphenyl)-2-benzoxazoline; X-ray and electronic structure; DFT calculations; NBO analysis

1. Introduction

For many years inorganic compounds containing an oxygen atom multiply bonding to a transition metal have been in the centre of interest to those scientists engaged in basic research and to those trying to employ these complexes in catalytic processes. Oxygen atom transfer chemistry has been implicated in various reactions of industrial and biological importance, including olefin epoxidation and catalysis by cytochrome P-450 [1–3].

The chemistry of oxo rhenium complexes arouses particular interest among these compounds. It results from the favourable nuclear properties of ^{186}Re and ^{188}Re nuclides, which make the radioisotopes useful for diagnostic nuclear medicine and applications in radioimmunotherapy [4,5].

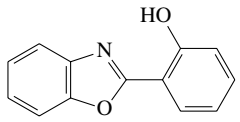
In this context, the design, synthesis and reactivity of novel rhenium oxocomplexes has become the aim of several laboratories, including ours.

Previously, we investigated the reactivity of oxorhenium(V) species-$[ReO(OEt)X_2(PPh_3)_2]$, $[ReOX_3(PPh_3)_2]$ and $[ReOX_3(AsPh_3)(OAsPh_3)]$ (X = Cl or Br) - towards pyrazole, 3,5-dimethylopyrazole and benzotriazole [6]. In this report we focus on the examinations of the reactions of $[ReOX_3(AsPh_3)_2]$ and $[ReOX_3(PPh_3)_2]$ with 2-(2′-hydroxyphenyl)-2-benzoxazoline (Hhbo, Scheme 1).

Although oxazolines have been used widely in many areas of chemistry, given the versatility of this ring which acts as a protector group, coordinating ligand, and activation moiety, studies on rhenium oxocomplexes

* Corresponding author.
E-mail addresses: basia@ich.us.edu.pl (B. Machura), rafal.kruszynski@p.lodz.pl (R. Kruszynski).

0277-5387/$ - see front matter © 2007 Elsevier Ltd. All rights reserved.
doi:10.1016/j.poly.2007.03.031



Scheme 1. Structure of Hhbo ligand.

incorporating such ligands have been relatively rare [7]. Additionally, we were encouraged by the recent reports concerning investigations of the reactivity of $[ReOCl_3(PPh_3)_2]$ towards 2-, 5-, and/or 7-substituted 8-quinolinolato and pyridinecarboxylate ligands. Several oxocomplexes of general $[ReOCl_2(O–N)(PPh_3)]$ formula have been isolated in these reactions and structurally and spectroscopically characterized [8–11]. The oxorhenium(V) chelates $[ReOCl_2(O–N)(PPh_3)]$ with pyridinecarboxylate ligands have been also examined as catalysts for the carboxylation of ethane by CO in the presence of potassium peroxodisulfate $K_2S_2O_8$ [11].

Here we present synthesis and spectroscopic data for $[ReOCl_2(hbo)(AsPh_3)]$ (**1**), $[ReOBr_2(hbo)(AsPh_3)]$ (**2**), $[ReOCl_2(hbo)(PPh_3)]$ (**3**) and $[ReOBr_2(hbo)(PPh_3)]$ (**4**) complexes. X-Ray studies have been performed for **1** and **4**, and electronic structures of **1** and **4** have been calculated with the density functional theory (DFT). The spin-allowed singlet-singlet electronic transitions of **1** have been calculated with the time-dependent DFT method (TDDFT method), and the UV–Vis spectra of these complexes have been discussed on this basis.

Currently density functional theory (DFT) is commonly used to examine the electronic structure of transition metal complexes. It meets with the requirements of being accurate, easy to use and fast enough to allow the study of relatively large molecules of transition metal complexes [12]. Recent calculations with TD-DFT method for open- and closed-shell of 5d-metal complexes (including rhenium complexes) have also supported the TD-DFT method to be applicable for such systems giving good assignment of experimental spectra [13,14].

2. Experimental

2.1. General procedure

All the reagents used to the synthesis were commercially available and were used without further purification. The $[ReOX_3(AsPh_3)_2]$ and $[ReOX_3(PPh_3)_2]$ complexes were prepared according to the literature methods [15].

IR spectra were recorded on a Nicolet Magna 560 spectrophotometer in the spectral range 4000–400 cm^{-1} with the samples in the form of KBr pellets. Electronic spectra were measured on a spectrophotometer Lab Alliance UV–Vis 8500 in the range 1000–200 nm in chloroform solution. Elemental analyses (C H N) were performed on a Perkin–Elmer CHN-2400 analyzer. ^1H NMR spectra were obtained in $CDCl_3$ using Bruker Avance 400 spectrometer.

2.2. Preparation of $[ReOCl_2(hbo)(AsPh_3)] \cdot MeCN$ (**1** · MeCN)

A mixture of $[ReOCl_3(AsPh_3)_2]$ (0.50 g, 0.54 mmol), Hhbo (0.13 g, 0.62 mmol) and acetone (70 ml) was stirred for 3 h. 50 ml of acetone was distilled off and 100 ml of diethyl ether was added. $[ReOCl_2(hbo)(AsPh_3)]$ was filtered off, washed with ethanol, diethyl ether, dried and recrystallized from acetonitrile. Yield 86%.

IR (KBr; ν/cm^{-1}): 1606 (m), 1595(sh), 1571 (w), 1538 (m) ν_{CN} and $\nu_{C=C}$; 966(s) $\nu_{Re=O}$.

UV–Vis ($CHCl_3$; λ_{max} [nm] (ε; [$dm^3\ mol^{-1}\ cm^{-1}$])): 681.0 (60), 414.3 (3010), 307.9 (2.375×10^4) and 249.5 (3.93×10^4).

^1H NMR (20 °C, $CDCl_3$, ppm); hbo related resonances: 6.80 (d, 1H); 6.89 (t, 1H); 7.10 (m, 2H); 7.40–7.55 (m, 3H) and 7.98 (d, 1H); $AsPh_3$ related resonances: 7.39–7.19 (m, 15H).

Anal. Calc. for $C_{33}H_{26}AsCl_2N_2O_3Re$: 47.72; H, 3.16; N, 3.37. Found: C, 47.80; H, 3.30; N, 3.45%.

2.3. Preparation of $[ReOBr_2(hbo)(AsPh_3)] \cdot MeCN$ (**2** · MeCN)

A procedure similar to that for $[ReOCl_2(hbo)(AsPh_3)]$ was used with $[ReOBr_3(AsPh_3)_2]$ (0.50 g, 0.47 mmol) and Hhbo (0.12 g, 0.55 mmol). Crystalline precipitate of $[ReOBr_2(hbo)(AsPh_3)] \cdot MeCN$ was collected in 88% yield.

IR (KBr; ν/cm^{-1}): 1604 (m), 1593 (sh), 1574 (w), 1538 (s) ν_{CN} and $\nu_{C=C}$; 967(s) $\nu_{Re=O}$.

UV–Vis ($CHCl_3$; λ_{max}[nm] (ε; [$dm^3\ mol^{-1}\ cm^{-1}$])): 681.5 (60), 429.5 (2.0×10^3), 310.0 (2.0×10^4) and 249.8 (5.09×10^4).

Anal. Calc. for $C_{33}H_{26}AsBr_2N_2O_3Re$: 43.11; H, 2.85; N, 3.05. Found: C, 43.25; H, 2.75; N, 2.99%.

2.4. Preparation of $[ReOCl_2(hbo)(PPh_3)] \cdot MeCN$ (**3** · MeCN)

A procedure similar to that for $[ReOCl_2(hbo)(AsPh_3)]$ was used with $[ReOCl_3(PPh_3)_2]$ (0.50 g, 0.6 mmol) and Hhbo (0.15 g, 0.7 mmol). Crystalline precipitate of $[ReOCl_2(hbo)(PPh_3)] \cdot MeCN$ was collected in 85% yield.

IR (KBr; ν/cm^{-1}): 1606 (m), 1596 (sh), 1570 (w), 1536 (s) ν_{CN} and $\nu_{C=C}$; 964 (s) $\nu_{Re=O}$.

UV–Vis ($CHCl_3$; λ_{max}[nm] (ε; [$dm^3\ mol^{-1}\ cm^{-1}$])): 681.8 (50), 400.9 (4.8×10^3), 308.7 (2.8×10^4) and 255.0 (3.6×10^4).

Anal. Calc. for $C_{33}H_{26}PCl_2N_2O_3Re$: 50.39; H, 3.33; N, 3.56. Found: C, 50.60; H, 3.25; N, 3.48%.

2.5. Preparation of $[ReOBr_2(hbo)(PPh_3)] \cdot MeCN$ (**4** · MeCN)

A procedure similar to that for $[ReOCl_2(hbo)(AsPh_3)]$ was used with $[ReOBr_3(PPh_3)_2]$ (0.50 g, 0.52 mmol) and Hhbo (0.09 g, 0.62 mmol). Crystalline precipitate of $[ReOBr_2(hbo)(PPh_3)] \cdot MeCN$ was collected in 90% yield.

Table 1
Crystal data and structure refinement for **1** and **4** complexes

	1 · MeCN	**4** · MeCN
Empirical formula	$C_{33}H_{26}AsCl_2N_2O_3Re$	$C_{33}H_{26}Br_2N_2O_3PRe$
Formula weight	830.58	875.55
Temperature (K)	295(2)	291.0(3)
Wavelength (Å)	0.71073	0.71073
Crystal system	triclinic	triclinic
Space group	$P\bar{1}$	$P\bar{1}$
Unit cell dimensions		
a (Å)	11.2153(5)	11.1711(9)
α (°)	88.159(4)	87.421(7)
b (Å)	11.3564(5)	11.5553(11)
β (°)	84.973(4)	83.772(7)
c (Å)	13.3805(6)	13.6504(7)
γ (°)	65.323(4)	65.025(9)
Volume (Å^3)	1542.60(12)	1587.9(2)
Z	2	2
D_{calc} (Mg/m^3)	1.788	1.831
Absorption coefficient (mm^{-1})	5.213	6.429
$F(000)$	808	844
Crystal size (mm)	$0.04 \times 0.14 \times 0.40$	$0.05 \times 0.22 \times 0.50$
θ Range for data collection (°)	3.35–32.86	3.34–25.10
Index ranges	$-16 \leqslant h \leqslant 16$, $-17 \leqslant k \leqslant 11$, $-19 \leqslant l \leqslant 19$	$-12 \leqslant h \leqslant 13$, $-12 \leqslant k \leqslant 13$, $-16 \leqslant l \leqslant 16$
Reflections collected	15441	16122
Independent reflections (R_{int})	9715(0.0195)	5634(0.0317)
Completeness to $2\theta = 50°$ (%)	99.3	99.6
Minimum and maximum transmission	0.427 and 0.809	0.719 and 0.204
Data/restraints/parameters	9715/0/380	5634/0/380
Goodness-of-fit on F^2	0.933	1.099
Final R indices [$I > 2\sigma(I)$] R_1	0.0245	0.0269
wR_2	0.0481	0.0617
R Indices (all data)	$R_1 = 0.0377$	$R_1 = 0.0294$
wR_2	0.0499	0.0633
Largest differences in peak and hole (e Å^{-3})	1.749 and −1.402	1.549 and −0.890

IR (KBr; ν/cm^{-1}): 1606 (s), 1595 (sh), 1575 (w), 1540 (s), ν_{CN} and $\nu_{C=C}$; 967(s) $\nu_{Re=O}$.

UV–Vis ($CHCl_3$; λ_{max}[nm] (ε; [dm^3 mol^{-1} cm^{-1}])): 663.2 (90), 410.3 (3200), 315.6 (2.43×10^3), 270.4 (3.48×10^4) and 230.0 (6.64×10^4).

^{1}H NMR (20 °C, $CDCl_3$, ppm); hbo related resonances: 6.78 (d, 1H); 6.92 (t, 1H); 7.14 (m, 2H); 7.50–7.55 (m, 3H) and 7.89 (d, 1H); PPh_3 related resonances: 7.49–7.17 (m, 15H).

Anal. Calc. for $C_{33}H_{26}PBr_2N_2O_3Re$: 45.27; H, 2.99; N, 3.20. Found: C, 45.35; H, 2.85; N, 3.29%.

2.6. Crystal structures determination and refinement

The X-ray intensity data of **1** and **4** were collected on a KM-4-CCD automatic diffractometer equipped with CCD detector and graphite monochromated Mo-Kα radiation ($\lambda = 0.71073$ Å) at room temperature. Details concerning crystal data and refinement are given in Table 1. Lorentz, polarization and absorption correction [16] were applied. The structures were solved by the Patterson method and subsequently completed by the difference Fourier recycling. All the non-hydrogen atoms were refined anisotropically using full-matrix, least-squares technique. The hydrogen atoms were treated as, riding'' on their parent carbon atoms and assigned isotropic temperature factors equal 1.2 times the value of equivalent temperature factor of the parent atom. SHELXS97 [17], SHELXL97 [18] and SHELXTL [19] programs were used for all the calculations. Atomic scattering factors were those incorporated in the computer programs.

3. Computational details

GAUSSIAN03 program [20] was used in the calculations. The geometry optimisations of **1** and **4** were carried out with the DFT method with the use of B3LYP functional [21,22]. The electronic spectra of **1** and **4** were calculated with the TDDFT method [23]. The calculations were performed by using ECP basis set on the rhenium atom, the standard 6-31+G** basis for halogen, oxygen, arsine, phosphorous and nitrogen, 6-31G* for carbon and 6-31G for hydrogen atoms. The Xe core electrons of Re were replaced by an effective core potential and DZ quality Hay and Wadt Los Alamos ECP basis set (LANL2DZ) [24] was used for the valence electrons. Additional d function with exponent $\alpha = 0.3811$ and f function with exponent $\alpha = 2.033$ on the rhenium atom were added.

Natural bond orbital (NBO) calculations were performed with the NBO code [25] included in GAUSSIAN03.

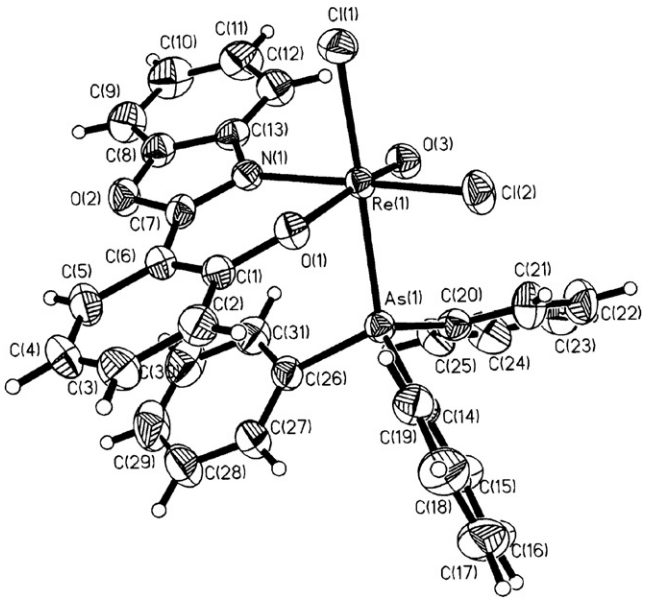


Fig. 1. The molecular structure of [$ReOCl_2$(hbo)($AsPh_3$)]. Displacement ellipsoids are drawn at 50% probability.

Table 2
The experimental and optimized bond lengths (Å) and angles (°) for **1**

Bond lengths	Experimental	Optimized	Bond angles	Experimental	Optimized
Re(1)–O(1)	1.9488(16)	2.003	O(3)–Re(1)–O(1)	165.91(7)	163.90
Re(1)–O(3)	1.6773(17)	1.681	O(3)–Re(1)–N(1)	90.34(7)	89.93
Re(1)–N(1)	2.1427(17)	2.157	O(1)–Re(1)–N(1)	81.00(7)	81.02
Re(1)–Cl(1)	2.3902(7)	2.430	O(3)–Re(1)–Cl(2)	99.49(6)	99.67
Re(1)–Cl(2)	2.3571(6)	2.422	O(1)–Re(1)–Cl(2)	89.72(5)	90.33
Re(1)–As(1)	2.5716(3)	2.641	N(1)–Re(1)–Cl(2)	169.97(5)	169.89
			O(3)–Re(1)–Cl(1)	98.72(6)	101.80
			O(1)–Re(1)–Cl(1)	92.02(5)	90.75
			N(1)–Re(1)–Cl(1)	87.43(5)	85.15
			Cl(2)-Re(1)–Cl(1)	89.08(2)	89.76
			O(3)–Re(1)–As(1)	85.00(6)	84.77
			O(1)–Re(1)–As(1)	84.39(5)	82.86
			N(1)–Re(1)–As(1)	93.09(5)	95.34
			Cl(2)–Re(1)–As(1)	89.787(18)	88.72
			Cl(1)–Re(1)–As(1)	176.241(19)	173.42

Table 3
The experimental and optimized bond lengths (Å) and angles (°) for **4**

Bond lengths	Experimental	Optimized	Bond angles	Experimental	Optimized
Re(1)–O(1)	1.957(3)	2.002	O(3)–Re(1)–O(1)	166.89(14)	165.03
Re(1)–O(3)	1.691(3)	1.680	O(3)–Re(1)–N(1)	89.84(14)	89.97
Re(1)–N(1)	2.169(3)	2.188	O(1)–Re(1)–N(1)	81.26(12)	80.60
Re(1)–Br(1)	2.5692(6)	2.586	O(3)–Re(1)–P(1)	86.17(11)	86.19
Re(1)–Br(2)	2.5073(5)	2.567	O(1)–Re(1)–P(1)	84.93(8)	83.07
Re(1)–P(1)	2.4995(10)	2.578	N(1)–Re(1)–P(1)	94.33(9)	94.82
			O(3)–Re(1)–Br(2)	98.79(11)	99.31
			O(1)–Re(1)–Br(2)	90.86(8)	91.17
			N(1)–Re(1)–Br(2)	170.47(10)	169.70
			P(1)–Re(1)–Br(2)	90.29(3)	90.28
			O(3)–Re(1)–Br(1)	98.19(11)	100.73
			O(1)–Re(1)–Br(1)	90.89(8)	90.00
			N(1)–Re(1)–Br(1)	86.42(9)	84.60
			P(1)–Re(1)–Br(1)	175.58(3)	173.04
			Br(2)–Re(1)–Br(1)	88.349(18)	89.25

Table 4
Atomic charges from the natural population analysis (NPA) for **1** and **4**

Atom	**1**	**4**
Re(1)	1.023	0.932
O(1)	−0.679	−0.686
O(3)	−0.452	−0.454
N(1)	−0.532	−0.538
X(1)	−0.414	−0.359
X(2)	−0.401	−0.327
As(1)/P(1)	1.385	1.364

4. Results and discussion

4.1. Preparation and infrared data

The $[ReOX_2(hbo)(EPh_3)]$ (X = Cl, Br; E = As, P) complexes were prepared in good yields by ligand exchange reactions starting from $[ReOX_3(EPh_3)_2]$ complexes and 2-(2′-hydroxyphenyl)-2-benzoxazoline in acetone:

$$[ReOX_3(Eph_3)_2] + Hhbo \rightarrow [ReOX_2(hbo)(Eph_3)] + HX + Eph_3 \quad X = Cl, \quad Br;\ E = As, P$$

They were isolated as green microcrystalline solids, soluble in common organic solvents.

The strong ν(Re=O) stretching band of $[ReOX_2(hbo)(EPh_3)]$ is found at 964–967 cm^{-1}, at a relatively high wavenumber, which suggests that the Re–hydroxy bond *trans* to the oxo ligand does not compete effectively for the Re_d orbitals and the bond is relatively weak. Moreover, the range in which the ν(Re=O) bands appear is very similar to those observed for Re(V)-oxo complexes with an monoanionic oxygen (RO^- and $R–COO^-$,) *trans* to the oxo group [26].

4.2. Crystal structures

Both complexes are isostructural and they crystallise as acetonitrile solvates in the triclinic space group $P\bar{1}$. No specific intermolecular interactions [27,28] with enough strength to govern molecule conformation were found in the crystals of **1** and **4**.

The molecular structure of **1** is presented in Fig. 1, and the selected bond distances and angles of **1** and **4** are collected in Tables 3 and 4, respectively.

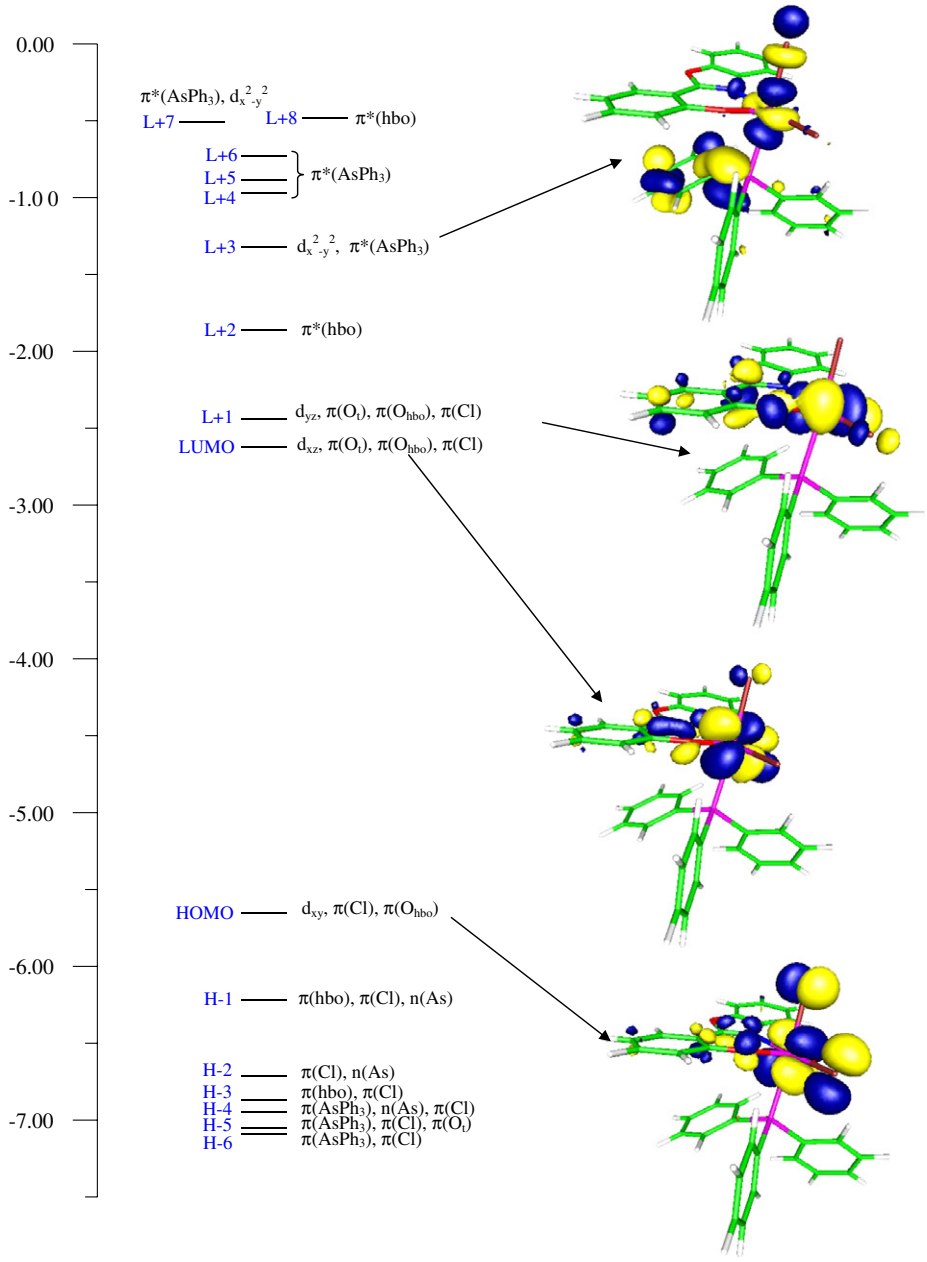


Fig. 2. The energy (eV), character and some contours of the unoccupied molecular orbitals of **1**. Positive values of the orbital contour are represented in blue (0.04 au) and negative values – in yellow (−0.04 au). (For interpretation of colour with respect to this figure caption the reader is referred to the web version of this article.)

Both complexes show octahedral geometry about the central rhenium atom defined by the terminal oxo-group, two halide ions in *cis* arrangement, the phosphorus or arsine of EPh_3 molecule, and the bidentate N,O donors of the hbo ligand. The Re(1) atoms derive 0.1326(6) and 0.1298(10) Å respectively from the equatorial N(1)/As(1)/Cl(1)/Cl(2) (compound **1**) and N(1)/P(1)/Br(1)/Br(2) (compound **4**) least squares planes. The oxygen atom of hbo is coordinated in *trans* position to the terminal oxo ligand. The multiple bonding ligand (terminal oxo) and narrow bite angle of the chelating ligand contribute to clear distortions of the pseudooctahedral environment of Re center in the $[ReOX_2(hbo)(EPh_3)]$ complexes. The high concentration of electronic density along the Re–O axis strongly influences the positions of the adjacent halogen atoms, which are pushed away.

The similar coordination geometry is observed for the other $[ReOCl_2(O–N)(PPh_3)]$ complexes with quinolinolato and pyridinecarboxylate derivatives [8–11]. Another geometry about the central atom can be noticed in dibromooxo(*N*-phenylsalicylideneaminato)(triphenylphosphine)–rhenium(V) complex [29]. Similar to the $[ReOCl_2(O–N)(PPh_3)]$ complexes with 8-quinolinolato ligands the oxygen atom of *N*-phenylsalicylideneaminato ion occupies *trans* position to the terminal oxo ligand, but bromide ions are in *trans* arrangement and PPh_3 molecule is opposite the

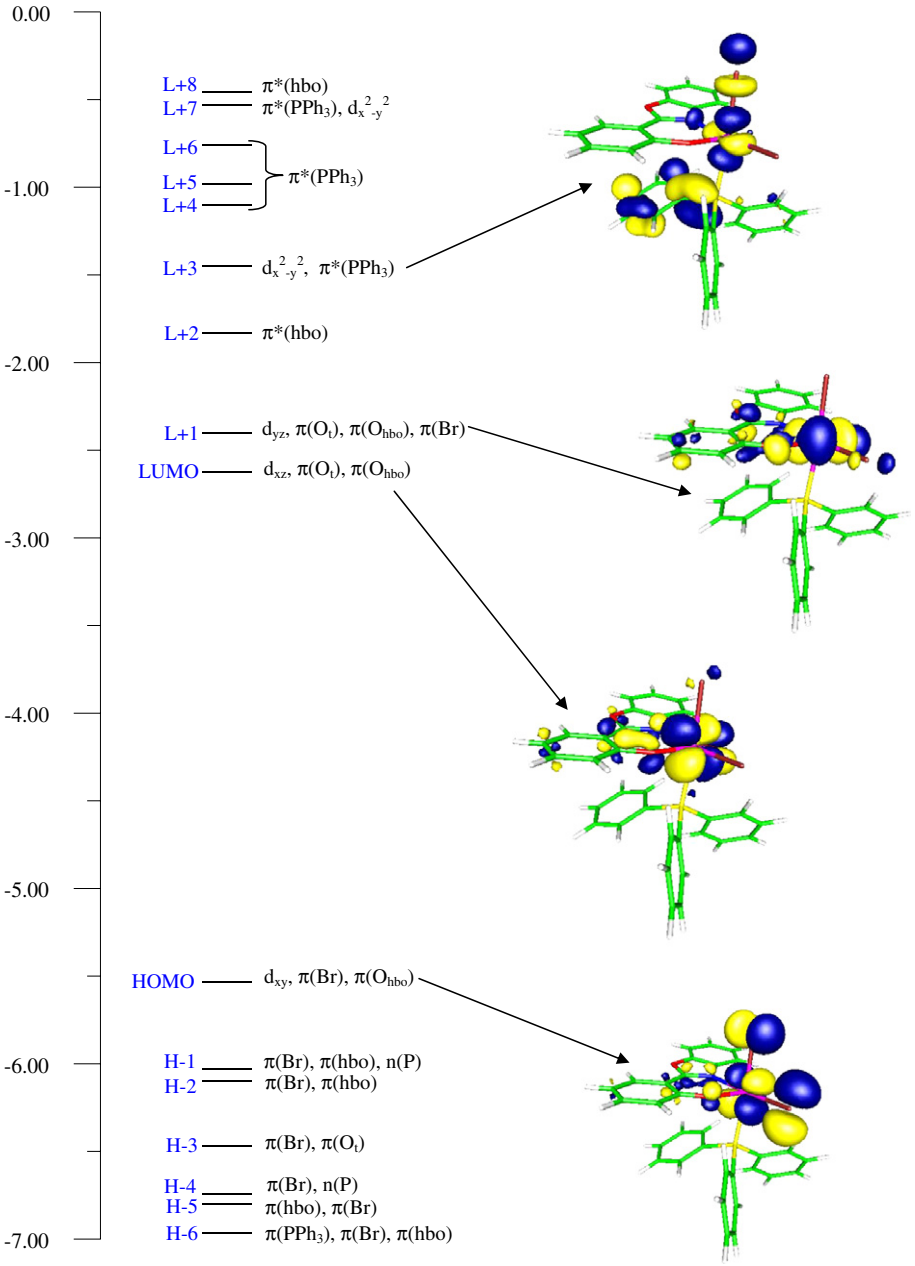


Fig. 3. The energy (eV), character and some contours of the unoccupied molecular orbitals of **4**. Positive values of the orbital contour are represented in blue (0.04 au) and negative values – in yellow (−0.04 au). (For interpretation of colour with respect to this figure caption the reader is referred to the web version of this article.)

nitrogen atom of *N*-phenylsalicylideneaminato ligand. It seems that electrostatic (not steric) factors are responsible for changing geometry about the central atom in dibromooxo(*N*-phenylsalicylideneaminato)(triphenylphosphine)–rhenium(V) in comparison with the discussed 8-quinolinolato oxocomplexes. The pyridine ring of the 8-quinolinolato ligand is good π acceptor, whereas the nitrogen atom of *N*-phenylsalicylideneaminato ion is pure donor.

The Re–O(1) and Re–O(3) distances of **1** and **4** are in good agreement with the corresponding values found for the oxorhenium(V) chelates $[ReOCl_2(O–N)(PPh_3)]$ with 2-, 5-, and/or 7-substituted 8-quinolinolato and pyridine-carboxylate ligands [8–11]. The Re–O_t bond lengths fall in the range 1.639-1.76 Å, typical of mononuclear complexes of rhenium(V) having $[ReO]^{3+}$ core, and indicate the presence of a triple bond Re≡O [30]. The interatomic distances between the rhenium atom and the oxygen atom of hbo ligand are longer the Re–O_{alkoxy} in the $[ReO(OR)X_2(PPh_3)_2]$ complexes [31], and only somewhat shorter than an ideal single Re–O bond length. The last one, predicted by the use of Pauling's covalent radius for oxygen and Cotton and Lippard's value for the octahedral covalent radius of rhenium(V), should be ca. 2.04 Å [32].

Table 5
The occupancy and composition of the calculated natural bond orbitals (NBOs) between the rhenium and the oxo ligand for **1** and **4**

BD	Occupancy	Composition of NBO	BD*	Occupancy
1				
Re–O_t	1.990	$0.564(d)_{Re} + 0.826(p)_O$	$0.826(d)_{Re} - 0.564(p)_O$	0.255
Re–O_t	1.987	$0.570(d)_{Re} + 0.822(p)_O$	$0.822(d)_{Re} - 0.570(p)_O$	0.300
4				
Re–O_t	1.993	$0.565(d)_{Re} + 0.825(p)_O$	$0.825(d)_{Re} - 0.565(p)_O$	0.269
Re–O_t	1.987	$0.571(d)_{Re} + 0.821(p)_O$	$0.821(d)_{Re} - 0.571(p)_O$	0.293

BD denotes 2-center bond.
* Denotes antibond NBO.

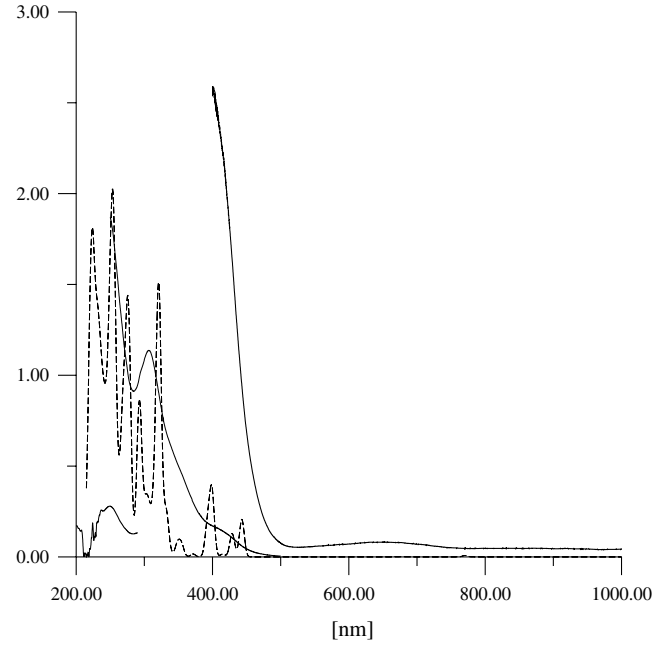


Fig. 4. The experimental (—) and calculated (---) electronic absorption spectra of **1**.

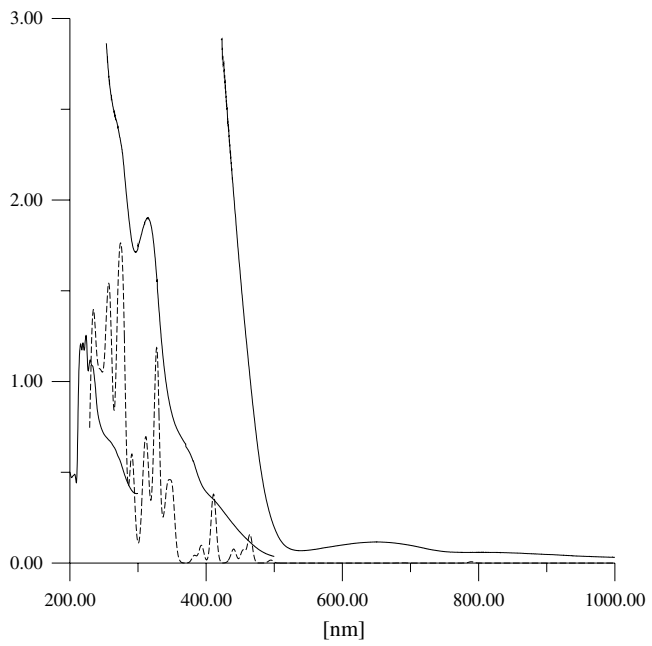


Fig. 5. The experimental (—) and calculated (---) electronic absorption spectra of **4**.

The Re1–X(1) distances *trans* to the phosphorus or arsine atom of EPh_3 molecule are slightly longer than the Re1–X(2) bonds *trans* to the nitrogen atom of the hbo^- ligand. It indicates *structural trans* effect of the EPh_3 ligands. A similar trend was observed in the oxorhenium(V) chelates $[ReOCl_2(O–N)(PPh_3)]$ with 2-, 5-, and/or 7-substituted 8-quinolinolato and pyridinecarboxylate ligands [8–11].

4.3. Geometry optimisation, charge distribution, electronic structure and NBO analysis

The geometries of **1** and **4** were optimised in a singlet state by the DFT method with the B3LYP functional. The optimized geometric parameters of **1** and **4** are gathered in Tables 2 and 3, respectively. In general, the predicted bond lengths and angles are in agreement with the values based upon the X-ray crystal structure data, and the general trends observed in the experimental data are well reproduced in the calculations.

Table 4 presents the atomic charges from the natural population analysis (NPA) for **1** and **4**. The calculated charges on the rhenium atoms in **1** and **4** are considerably lower than the formal charge 5+, and the populations of the d_{xy}, d_{xz}, d_{yz}, $d_{x^2-y^2}$ and d_{z^2} rhenium orbitals are following: 0.846, 1.044, 0.926, 1.159 and 1.543 for **1** and 0.992, 0.958, 1.128, 1.603 and 0.901 for **4**. It confirms significant charge donation from the ligands. The As and P atoms are positively charged, and the charges on the terminal oxo, halide and oxygen atom of hbo^- are significantly smaller than −2, −1 and −1, respectively. The terminal oxo ions are less negative in comparison with the oxygen atoms of hbo^-ligand. It indicates the higher electron density delocalization from the terminal ligands towards the rhenium centers and corresponds to differences in the Re–O(3) and Re–O(1) bond lengths.

The complexes **1** and **4** are closed-shell structures. Their molecular orbital diagrams with several highest HOMO and lowest LUMO contours are presented in Figs. 2 and 3, respectively. The HOMO–LUMO gaps equal to 3.03

and 2.9 eV for **1** and **4**, respectively. The highest occupied MOs of **1** and **4** are of d_{xy} type with some contributions from p_π chloride and hbo^- orbitals. The remaining four d-type orbitals of rhenium are found among unoccuppied MOs. It confirms d^2 configuration of the rhenium atoms in **1** and **4**.

The rhenium–oxygen interaction in **1** and **4** is described as a triple bond. Assuming that rhenium uses its six valence orbitals, $5d_{x^2-y^2}$, $5d_z{}^2$, 6s, $6p_x$, $6p_y$ and $6p_z$ to form σ-bonds with the six ligands, empty $5d_{xz}$ and $5d_{yz}$ orbitals are available to overlap with $2p_x$ and $2p_y$ orbitals on the terminal oxygen to form an effective triple bond. The LUMO and LUMO + 1 (Figs. 2 and 3) are ascribed as π-antibonding rhenium–oxygen molecular orbitals.

Additional information about nature rhenium–terminal oxygen bonding has been obtained by NBO analysis. The occupancy and composition of the calculated Re–O_t natural bond orbitals (NBOs) are given in Table 5.

Each natural bond orbital (NBO) σ_{AB} can be written in terms of two directed valence hybrids (NHOs) h_A and h_B on atoms A and B:

$$\sigma_{AB} = c_A h_A + c_B h_B$$

where c_A and c_B are polarization coefficients. Each valence bonding NBO must in turn be paired with a corresponding valence *anti*-bonding NBO:

$$\sigma^*_{AB} = c_B h_A - c_A h_B$$

Table 6
The energy and molar absorption coefficients of experimental absorption bands and the electronic transitions calculated with the TDDFT method for **1**

The most important orbital excitations	Character	λ [nm]	E [eV]	f	Experimental Λ [nm](E [eV])ε
H → L	d → d	770.5	1.61	0.0008	681.0 (1.82) 60
H → L + 1	d → d	678.4	1.83	0.0001	
H − 1 → L	π(hbo)/π(Cl)/n(As) → d	443.0	2.80	0.0206	414.3 (2.99) 3010
H − 1 → L + 1	π(hbo)/π(Cl)/n(As) → d	428.8	2.89	0.0128	
H → L + 2	d → π*(hbo)	399.1	3.11	0.0361	
H − 2 → L	π(Cl)/n(As) → d	392.5	3.16	0.0171	
H − 3 → L + 1	π(hbo)/π(Cl) → d	332.1	3.73	0.0142	307.9 (4.03) 23750
H − 1 → L + 2	π(hbo)/π(Cl)/n(As) → π*(hbo)	321.8	3.85	0.1000	
H − 4 → L + 1	π($AsPh_3$)/n(As)/π(Cl) → d	320.1	3.87	0.0275	
H − 7 → L	π(Cl)/π(O_t)/π($AsPh_3$)/π(hbo) → d	317.4	3.91	0.0353	
H − 8 → L	π(hbo)/π(Cl)/π($AsPh_3$) → d				
H − 8 → L	π($AsPh_3$)/π(Cl) → d	306.1	4.05	0.0119	
H − 6 → L + 1					
H − 8 → L + 1	π($AsPh_3$)/π(Cl) → d	301.9	4.11	0.0121	
H − 12 → L	π(Cl)/π($AsPh_3$) → d	293.6	4.22	0.0162	
H − 1 → L + 3	π(hbo)/π(Cl)/n(As) → d/π*($AsPh_3$)				
H − 1 → L + 3	π(hbo)/π(Cl)/n(As) → d/π*($AsPh_3$)	292.7	4.24	0.0440	
H − 3 → L + 2	π(hbo)/π(Cl) → π*(hbo)	277.2	4.47	0.0739	249.5 (4.97) 39300
H − 4 → L + 2	π($AsPh_3$)/n(As)/π(Cl) → π*(hbo)	275.5	4.50	0.0331	
H − 15 → L	π(Cl)/π(hqn)/π(O_t) → d	273.3	4.54	0.0235	
H → L + 8	d → π*(hbo)	271.4	5.57	0.0178	
H − 2 → L + 3	π(Cl)/n(As) → d/π*($AsPh_3$)	269.7	4.60	0.0163	
H − 2 → L + 3	π(Cl)/n(As) → d/π*($AsPh_3$)	268.1	4.62	0.0179	
H − 1 → L + 4	π(hbo)/π(Cl)/n(As) → π*($AsPh_3$)	266.5	4.65	0.0168	
H − 15 → L + 1	π(Cl)/π(hqn)/π(O_t) → d	255.1	4.85	0.0884	
H → L + 11	d → π*(hbo)	254.1	4.88	0.0433	
H − 9 → L + 2	π($AsPh_3$)/π(Cl) → π*(hbo)	250.5	4.95	0.0311	
H − 5 → L + 3	π(Cl)/π(O_t)π($AsPh_3$) → d/π*($AsPh_3$)	250.1	4.96	0.0339	
H − 4 → L + 3	π($AsPh_3$)/n(As)/π(Cl) → d/π*($AsPh_3$)	246.1	5.04	0.0272	
H − 16 → L + 1	π(Cl) → d	242.0	5.12	0.0199	
H − 6 → L + 3	π($AsPh_3$)/π(Cl) → d/π*($AsPh_3$)	240.3	5.16	0.0243	
H − 8 → L + 3	π(hbo)/π($AsPh_3$)/π(Cl) → d/π*($AsPh_3$)	236.0	5.25	0.0223	
H − 8 → L + 3	π(hbo)/π($AsPh_3$)/π(Cl) → d/π*($AsPh_3$)	234.6	5.29	0.0272	
H − 3 → L + 4	π(hbo)/π(Cl) → π*($AsPh_3$)	230.1	5.39	0.0534	
H − 2 → L + 6	π(Cl)/n(As) → π*($AsPh_3$)	224.2	5.53	0.0236	
H − 1 → L + 11	π(hbo)/π(Cl)/n(As) → π*(hbo)				
H − 1 → L + 11	π(hbo)/π(Cl)/n(As) → π*(hbo)	224.0	5.53	0.0276	
H − 12 → L + 3	π(Cl)/π$AsPh_3$) → d/π*($AsPh_3$)	223.8	5.54	0.0382	
H − 2 → L + 6	π(Cl)/n(As) → π*($AsPh_3$)	223.2	5.55	0.0285	
H − 6 → L + 5	π($AsPh_3$)/π(Cl) → π*($AsPh_3$)	219.5	5.65	0.0211	
H − 9 → L + 4	n(As) → d	218.9	5.66	0.0267	

ε – molar absorption coefficient [dm^3 mol^{-1} cm^{-1}]; f – oscillator strength; H – highest occupied molecular orbital; L – lowest unoccupied molecular orbital.

to complete the span of the valence space. The Lewis-type (donor) NBOs are thereby complemented by the non-Lewis-type (acceptor) NBOs that are formally empty in an idealized Lewis picture. The interactions between 'filled' Lewis-type NBOs and 'empty' non-Lewis NBOs lead to loss of occupancy from the localized NBOs of the idealized Lewis structure into the empty non-Lewis orbitals, and they are referred to as 'delocalization' corrections to the zeroth-order natural Lewis structure [33].

The detected natural Re–O_t bond orbitals of **1** and **4** complexes are orbitals of π character – the p_x and p_y oxygen orbitals and d_{xz} and d_{yz} rhenium orbitals are involved in their formation. Not detected σ_{Re-O_t} bond has character of predominant Coulomb-type interactions between the central ion and ligands [34]. Accordingly, NBO analysis confirms a triple bond between the rhenium and the terminal oxygen ligand.

4.4. Electronic spectrum

The experimental and calculated electronic spectra of **1** and **4** are presented in Figs. 4 and 5, respectively. Each calculated transition is represented by a gaussian function $y = ce^{-bx^2}$ with the height (c) equal to the oscillator strength and b equal to 0.04 nm^{-2}. The positions of absorption bands for the other [$ReOX_2$(hbo)(EPh_3)] complexes are given in the experimental part.

The spin-allowed singlet-singlet electronic transitions calculated with the TDDFT method for **1** and **4** are gathered in Tables 6 and 7, respectively. For the high energy part of the spectrum, only transitions with oscillator strengths larger than 0.015 are listed in Tables 6 and 7.

The longest wavelength experimental bands at 681.0 and 663.2 nm for **1** and **4** are attributed to the transitions of d → d character with small oscillator strengths.

Table 7
The energy and molar absorption coefficients of experimental absorption bands and the electronic transitions calculated with the TDDFT method for **4**

The most important orbital excitations	Character	λ [nm]	E [eV]	f	Experimental Λ [nm] (E [eV]) ε
H → L	d → d	779.3	1.57	0.0007	663.2 (1.87) 90
H → L + 1	d → d	689.7	1.80	0.0001	
H − 2 → L	π(Br)/π(hbo) → d	464.3	2.67	0.0157	410.3 (3.02) 3200
H − 3 → L	π(Br)/π(O_t) → d	412.8	3.00	0.0093	
H → L + 2	d → π*(hbo)	410.3	3.02	0.0304	
H − 3 → L + 1	π(Br)/π(O_t) → d	393.0	3.16	0.0097	
H − 4 → L + 1	πBr)/n(P) → d	350.3	3.54	0.0359	315.6 (3.93) 24300
H − 1 → L + 2	π(Br)/π(hbo)/n(P) → π*(hbo)	344.3	3.60	0.0201	
H − 6 → L	π(PPh_3)/π(hbo)/π(Br) → d	342.3	3.62	0.0183	
H − 5 → L + 1	π(hbo)/π(Br) → d	336.8	3.68	0.0129	
H − 8 → L	π(PPh_3)/π(hbo)/π(Br) → d	328.9	3.77	0.0218	
H − 6 → L					
H − 5 → L + 1	π(hbo)/π(Br) → d	327.7	3.78	0.0829	
H − 1 → L + 3	π(Br)/π(hbo)/n(P) → d/π*(PPh_3)	323.2	3.84	0.0199	
H − 2 → L + 3	π(Br)/ π(hbo) → d/π*(PPh_3)	313.9	3.95	0.0279	
H − 9 → L	π(PPh_3) → d	313.4	3.96	0.0137	
H − 3 → L + 2	π(Br)/π(O_t) → π*(hbo)	310.6	3.99	0.0101	
H − 7 → L + 1	π(PPh_3)/π(hbo) → d	308.4	4.02	0.0354	
H − 3 → L + 3	π(Br)/π(O_t) → d/π*(PPh_3)	291.0	4.26	0.0483	
H − 5 → L + 2	π(hbo)/π(Br) → π*(hbo)	278.7	4.45	0.0684	270.4 (4.59) 34800
H − 1 → L + 5	π(Br)/π(hbo)/n(P) → π*(PPh_3)				
H − 1 → L + 5	π(Br)/π(hbo)/n(P) → π*(PPh_3)	278.0	4.46	0.0359	
H − 4 → L + 3	π(Br)/n(P) → d/π*(PPh_3)	273.3	4.54	0.0168	
H − 16 → L	π(Br) → d	273.2	4.54	0.0298	
H − 2 → L + 5	π(Br)/π(hbo) → π*(PPh_3)	271.3	4.57	0.0448	
H − 2 → L + 5	π(Br)/π(hbo) → π*(PPh_3)	270.9	4.58	0.0262	
H − 15 → L + 1	π(hbo)/σ(Cl) → d	268.3	4.62	0.0317	
H − 5 → L + 3	π(hbo)/π(Br) → d/π*(PPh_3)	261.2	4.75	0.0157	
H − 16 → L + 1	π(Br) → d	259.9	4.77	0.0167	
H − 7 → L + 2	π(PPh_3)/π(hbo) → π*(hbo)				
H − 16 → L + 1	π(Br) → d	258.7	4.79	0.0519	
H − 7 → L + 2	π(PPh_3)/π(hbo) → π*(hbo)				
H → L + 11	d → π*(hbo)	257.3	4.82	0.0216	
H − 6 → L + 3	π(PPh_3)/π(hbo)/π(Br) → d/π*(PPh_3)	254.2	4.88	0.0328	
H − 7 → L + 3	π(PPh_3)/π(hbo) → d/π*(PPh_3)	247.2	5.02	0.0288	230.0 (5.39) 66400
H − 4 → L + 5	π(Br)/n(P) → π*(PPh_3)	241.8	5.13	0.0349	
H − 1 → L + 10	π(Br)/π(hbo)/n(P) → π*(PPh_3)	237.6	5.22	0.0167	
H − 10 → L + 3	π(PPh_3)/π(hbo) → d/π*(PPh_3)				
H − 17 → L + 1	π(hbo)/σ(Cl) → d	233.9	5.30	0.0345	
H − 6 → L + 4	π(PPh_3)/π(hbo)/π(Br) → π*(PPh_3)	232.4	5.34	0.0284	

The absorption bands with maxima at ~410 and ~310 nm are assigned to the *Metal–Ligand Charge Transfer* (occurring from the rhenium ion to the π-antibonding orbitals of the hqn ligand and EPh_3 ligands) and *Ligand–Metal Charge Transfer* ($\pi_{hqn}/\pi_{EPh_3}/\pi_{Cl}/\pi_O \rightarrow d$) transitions.

The experimental bands below 300 nm result mainly from *Ligand–Ligand Charge Transfer* and interligand (IL) transitions.

Supplementary material

CCDC 634528 and 634529 contain the supplementary crystallographic data for $C_{33}H_{26}AsCl_2N_2O_3Re$ and $C_{33}H_{26}PBr_2N_2O_3Re$. These data can be obtained free of charge via http://www.ccdc.cam.ac.uk/conts/retrieving.html, or from the Cambridge Crystallographic Data Centre, 12 Union Road, Cambridge CB2 1EZ, UK; fax: +(44) 1223-336-033; or e-mail: deposit@ccdc.cam.ac.uk.

Acknowledgement

The Gaussian03 calculations were carried out in the Wrocław Centre for Networking and Supercomputing, WCSS, Wrocław, Poland.

References

[1] R.H. Holm, Chem. Rev. 87 (1987) 1401.
[2] C.C. Romão, F.E. Kühn, W.A. Hermann, Chem. Rev. 97 (1997) 3197.
[3] S.B. Seymore, S.N. Brown, Inorg. Chem. 39 (2000) 325.
[4] W. Volkert, W.F. Goeckeler, G.J. Ehrhardt, A.R. Ketring, J. Nucl. Med. 32 (1991) 174.
[5] E.A. Deutsch, K. Libson, J.L. Vanderheyden, Technetium and Rhenium in Chemistry and Nuclear Medicine, Raven Press, New York, 1990.
[6] B. Machura, Coord. Chem. Rev. 249 (2005) 591.
[7] M. Gómez, G. Muller, M. Rocamora, Coord. Chem. Rev. 193–195 (1999) 769.
[8] X. Chen, F.J. Femia, J.W. Babich, J. Zubieta, Inorg. Chim. Acta 308 (2000) 80.
[9] Y. Miyashita, T. Ohashi, A. Imai, N. Amir, K. Fujisawa, K. Okamoto, Sci. Technol. Adv. Mater. 6 (2005) 660.
[10] O. Sigouin, A.L. Beauchamp, Can. J.Chem. 83 (2005) 460.
[11] A.M. Kirillov, M. Haukka, M.V. Kirillova, A.J.L. Pombeiro, Adv. Synth. Catal. 347 (2005) 1435.
[12] H. Chermette, Coord. Chem. Rev. 178–180 (1998) 699.
[13] M.C. Aragoni, M. Arca, T. Cassano, C. Denotti, F.A. Devillanova, F. Isaia, V. Lippolis, D. Natali, L. Niti, M. Sampietro, R. Tommasi, G. Verani, Inorg. Chem. Commun. 5 (2002) 869.
[14] P. Romaniello, F. Lelj, Chem. Phys. Lett. 372 (2003) 51.
[15] G. Rouschias, G. Wilkinson, J. Chem. Soc. A (1966) 465.
[16] (a) STOE & Cie, X-RED. Version 1.18. STOE & Cie GmbH, 1999, Darmstadt, Germany.;
(b) CrysAlis RED, Oxford Diffraction Ltd., Version 1.171.29.2.G.M. Sheldrick Acta Cryst. A 46 (1990) 467.
[17] G.M. Sheldrick, Acta Crystallogr. A 46 (1990) 467.
[18] G.M. Sheldrick, SHELXL97. Program for the Refinement of Crystal Structures, University of Göottingen, Germany, 1997.
[19] G.M. Sheldrick, SHELXTL: Release 4.1 for Siemens Crystallographic Research Systems, 1990.
[20] GAUSSIAN03, Revision B.03,M.J. Frisch, G.W. Trucks, H.B. Schlegel, G.E. Scuseria, M.A. Robb, J.R. Cheeseman, J.A. Montgomery, Jr., T. Vreven, K.N. Kudin, J.C. Burant, J.M. Millam, S.S. Iyengar, J. Tomasi, V. Barone, B. Mennucci, M. Cossi, G. Scalmani, N. Rega, G.A. Petersson, H. Nakatsuji, M. Hada, M. Ehara, K. Toyota, R. Fukuda, J. Hasegawa, M. Ishida, T. Nakajima, Y. Honda, O. Kitao, H. Nakai, M. Klene, X. Li, J.E. Knox, H.P. Hratchian, J.B. Cross, C. Adamo, J. Jaramillo, R. Gomperts, R.E. Stratmann, O. Yazyev, A.J. Austin, R. Cammi, C. Pomelli, J.W. Ochterski, P.Y. Ayala, K. Morokuma, G.A. Voth, P. Salvador, J.J. Dannenberg, V.G. Zakrzewski, S. Dapprich, A.D. Daniels, M.C. Strain, O. Farkas, D.K. Malick, A.D. Rabuck, K. Raghavachari, J.B. Foresman, J.V. Ortiz, Q. Cui, A.G. Baboul, S. Clifford, J. Cioslowski, B.B. Stefanov, G. Liu, A. Liashenko, P. Piskorz, I. Komaromi, R.L. Martin, D.J. Fox, T. Keith, M.A. Al-Laham, C.Y. Peng, A. Nanayakkara, M. Challacombe, P.M.W. Gill, B. Johnson, W. Chen, M.W. Wong, C. Gonzalez, J.A. Pople, Gaussian, Inc., Pittsburgh PA, 2003.
[21] A.D. Becke, J. Chem. Phys. 98 (1993) 5648.
[22] C. Lee, W. Yang, R.G. Parr, Phys. Rev B 37 (1988) 785.
[23] M.E. Casida, in: J.M. Seminario (Ed.), Recent developments and applications in modern density functional theory, Theor. Comput. Chem., vol.4, Elsevier, Amsterdam, 1996.
[24] P.J. Hay, W.R. Wadt, J. Chem. Phys 82 (1985) 299.
[25] E.D. Glendening, A.E. Reed, J.E. Carpenter, F. Weinhold, NBO (version 3.1).
[26] L. Wei, J. Babich, J. Zubieta, Inorg. Chim. Acta 358 (2005) 2413.
[27] G.A. Jeffrey, W. Saenger, Hydrogen Bonding in Biological Structures, Springer-Verlag, 1994.
[28] G.R. Desiraju, T. Steiner, The Weak Hydrogen Bond in Structural Chemistry and Biology, Oxford University Press, 1999.
[29] M. Sacerdoti, V. Bertolasi, G. Gilli, Acta Crystallogr. C 40 (1984) 968.
[30] J.M. Mayer, Inorg. Chem. 27 (1988) 3899.
[31] F.H. Allen, Acta Crystallogr. B 58 (2002) 380.
[32] S.R. Flechter, A.C. Skapski, J. Chem. Soc., Dalton (1972) 1073.
[33] A.E. Reed, L.A. Curtiss, F. Weinhold, Chem. Rev. 88 (1988) 899.
[34] M.L. Kuznestov, A.J.L. Pombeiro, J. Chem. Soc., Dalton Trans. (2003) 738.

Available online at www.sciencedirect.com
ScienceDirect
Polyhedron 26 (2007) 3465–3470
POLYHEDRON
www.elsevier.com/locate/poly

Synthesis and structural characterisation of new Re(III) complexes using aldimines of α-amino acids as coligands

Sucharita Basak [a], Amrita Mondal [a], Deepak Chopra [b], Kajal Krishna Rajak [a,*]

[a] Inorganic Chemistry Section, Department of Chemistry, Jadavpur University, Kolkata, 700 032, India
[b] Solid State and Structural Chemistry Unit, Indian Institute of Science, Bangalore, 560 012, India

Received 26 February 2007; accepted 21 March 2007
Available online 30 March 2007

Abstract

Complexes of the general formula $[Re^{III}(L)Cl(PPh_3)_2]$ have been synthesised by reacting H_2L and $[ReOCl_3(PPh_3)_2]$ in ethanol. Here H_2L represents imines of α-amino acids (glycine, L-alanine, L-valine, L-phenylalanine) derived from salicylaldehyde and naphthaldehyde. The crystal structure of one complex has been determined. The complexes are mononuclear, paramagnetic and display paramagnetic ^1H NMR in $CDCl_3$ solution. Their spectral and redox properties are scrutinised.
© 2007 Elsevier Ltd. All rights reserved.

Keywords: Rhenium(III); α-Amino acids; Schiff base

1. Introduction

Considerable attention has been given to the coordination chemistry of rhenium due to its widespread application in catalysis [1] as well as its β-emitting (Re^{186}, Re^{188}) isotopes which are used as therapeutic agents in nuclear medicine [2,3]. A sizable number of tridentate Schiff bases [4] have been used to investigate the chemistry of rhenium. However the chemistry of rhenium using aldimines of α-amino acids is not known. This has motivated us to initiate research of the chemistry of rhenium with the Schiff bases of α-amino acid.

The stability of α-amino acid Schiff base complexes depends on various factors, such as the amino acid side chain polarity [5], the metal, pH, solvent and temperature [6]. Moreover racemic complexes are also observed even in the case of optically active amino acid Schiff bases [5,7,8]. Herein we describe a successful synthesis of a hitherto unknown family of mononuclear Re(III) species chelated by aldimines of α-amino acids (glycine, L-alanine, L-valine, L-phenylalanine), starting from $[ReOCl_3(PPh_3)_2]$. The X-ray structure of one representative case is reported. Their spectral and redox behavior are discussed.

2. Experimental

2.1. Materials

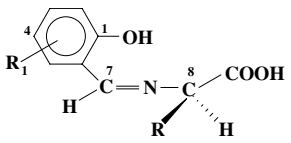
All the starting chemicals were analytically pure and were used without further purification. The Schiff bases were synthesized using the reported procedure [9].

2.2. Physical measurements

UV–Vis spectra were recorded on a Perkin–Elmer LAMBDA 25 spectrophotometer. IR spectra were measured with a Perkin–Elmer L-0100 spectrophotometer. ^1H NMR and ^{31}P spectral measurements were carried out on a Bruker FT 300 MHz spectrometer with TMS as an internal reference and Bruker FT 500 MHz spectrometer, respectively. The atom-numbering scheme used for ^1H NMR is the same as that used in the crystallography and in Chart 1. Electrochemical measurements were performed (acetonitrile solution) on a CH620 electrochemical analyzer

* Corresponding author.
E-mail address: kajalrajak@hotmail.com (K.K. Rajak).

0277-5387/$ - see front matter © 2007 Elsevier Ltd. All rights reserved.
doi:10.1016/j.poly.2007.03.036



R_1 = 4,5-Benzo , R = H ; H_2L^1
R_1 = 4,5-Benzo , R = CH_3 ; H_2L^2
R_1 = 4,5-Benzo , R = CH_2Ph ; H_2L^3
R_1 = H , R = H ; H_2L^4
R_1 = H , R = CH_3 ; H_2L^5
R_1 = H , R = CH_2Ph ; H_2L^6

$[Re(L^1)Cl(PPh_3)_2]$, 1a
$[Re(L^2)Cl(PPh_3)_2]$, 1b
$[Re(L^3)Cl(PPh_3)_2]$, 1c
$[Re(L^4)Cl(PPh_3)_2]$, 2a
$[Re(L^5)Cl(PPh_3)_2]$, 2b
$[Re(L^6)Cl(PPh_3)_2]$, 2c

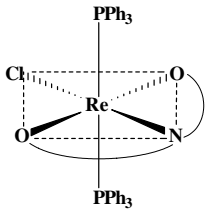


Chart 1.

using a platinum electrode under a dinitrogen atmosphere. Tetraethylammonium perchlorate (TEAP) was used as a supporting electrolyte and the potentials are referenced to the standard calomel electrode (SCE) without junction correction. Magnetic susceptibilities were measured on a PAR-155 vibrating-sample magnetometer. Microanalyses (C, H, N) were obtained from a Perkin–Elmer 2400 Series II elemental analyzer. CD spectra were recorded on a JASCO-715 polarimeter and mass spectra (70 eV) were recorded on a Qtof Micro YA263 spectrometer.

2.3. Synthesis of the complexes

The complexes $[Re^{III}(L)Cl(PPh_3)_2]$ were prepared by using a general method with $[ReOCl_3(PPh_3)_2]$ [10] as the starting material. Details are given below for one representative case (**1a**).

$[Re^{III}(L^1)Cl(PPh_3)_2]$ **1a**. 42 mg (0.18 mmol) of H_2L^1 were added to a solution of 100 mg (0.13 mmol) of $[ReOCl_3(PPh_3)_2]$ in 20 ml dry ethanol in the presence of excess PPh_3. The reaction mixture was refluxed for 6 h, producing a red precipitate. This was filtered and the solid mass was then dissolved in a minimum volume of dichloromethane and subjected to column chromatography on a silica gel column (12 × 1 cm, 60–120 mesh). A red-orange band was eluted using benzene–acetonitrile (10:1) mixture. A red-orange solid was obtained after removal of solvent from the eluate under reduced pressure. Yield: 88 mg (68%). *Anal.* Calc. for $C_{49}H_{39}NClO_3P_2Re$: C, 60.40; H, 5.04; N, 1.44. Found: C, 60.32; H, 4.98; N, 1.39%. UV–Vis (λ_{max}/nm (ε/M^{-1} cm^{-1}) CH_2Cl_2 solution): 281(20 780), 327(12 480), 365(10 695), 430(13 300), 494(4281), 1456(134). IR (KBr, cm^{-1}): ν(Re–Cl) 320; ν(C=N) 1670; $\nu(CO_2$ sym) 1310; $\nu(CO_2$ asym) 1660, 1625; ν(Re–P) 742. ^{1}H NMR ($CDCl_3$): δ 48.60 (H7, s); 9.80 (*ortho* H of PPh_3, d, J = 7.2 Hz); 8.34 (*para* H of PPh_3, t, J = 7.2 Hz); 7.87 (*meta* H of PPh_3, t, J = 7.5 Hz); −1.50 to 25.00 (ArH, 5H); −3.90 (H8, s, 2H); −23.95 (H2, d, J = 8.7 Hz). $E_{1/2}$ (Re^{III}/Re^{IV} couple): 0.33 V (ΔE_p, 80 mV); (Re^{III}/Re^{II} couple): −1.40. MS (m/z): $[M]^+$ Calcd. 973.16, 974.17, 975.17; Found: 972.89, 973.89, 974.90.

$[Re^{III}(L^2)Cl(PPh_3)_2]$ **1b**. Yield: 81 mg (62%). *Anal.* Calc. for $C_{50}H_{41}NClO_3P_2Re$: C, 60.79; H, 4.15; N, 1.41. Found: C, 60.71; H, 4.02; N, 1.38%. UV–Vis (λ_{max}/nm (ε/M^{-1} cm^{-1}) CH_2Cl_2 solution): 267(25 464), 338(11 680), 363(9585), 431(10 474), 492(3494), 1440(128). CD (λ_{max}/nm ($\Delta\varepsilon$/M^{-1} cm^{-1}) CH_2Cl_2 solution): 265(6.39), 295 (−7.65), 331(1.96), 355(−6.82), 390(1.52), 430(−19.58), 458(−10.25), 475(−10.75). IR (KBr, cm^{-1}): ν(Re–Cl) 325; ν(C=N) 1672; $\nu(CO_2$ sym) 1312; $\nu(CO_2$ asym) 1665, 1627; ν(Re–P) 747. ^{1}H NMR ($CDCl_3$): δ 47.90 (H7, s); 9.34 (*ortho* H of PPh_3, d, J = 7.8 Hz); 8.70 (*para* H of PPh_3, t, J = 7.4 Hz); 7.85 (*meta* H of PPh_3, t, J = 7.2 Hz); −1.00 to 20.00 (ArH, 5H); −5.34 (H8, d, J = 8.4 Hz); −22.22 (H2, q, J = 8.8 Hz); 1.30 (CH_3 of amino acid, d, J = 7.2 Hz, 3H). $E_{1/2}$ (Re^{III}/Re^{IV} couple): 0.44 V (ΔE_p, 80 mV); (Re^{III}/Re^{II} couple): −1.10 V. MS (m/z): $[M]^+$ Calcd. 987.46, 988.17, 985.65. Found: 987.10, 988.34, 985.70.

$[Re^{III}(L^3)Cl(PPh_3)_2]$ **1c**. Yield: 80 mg (63%). *Anal.* Calc. for $C_{56}H_{46}NClO_3P_2Re$: C, 63.19; H, 4.32; N, 1.31. Found: C, 62.89; H, 4.02; N, 1.29%. UV–Vis (λ_{max}/nm (ε/M^{-1} cm^{-1}) CH_2Cl_2 solution): 269(21 537); 332(10 752), 360(8840), 432(16 148), 489(3299), 1423(133). CD (λ_{max}/nm ($\Delta\varepsilon$/M^{-1} cm^{-1}) CH_2Cl_2): 268(10.8), 295(−14.65), 331(−3.09), 357(−9.58), 395(5.16), 427 (−22.30), 460(−17.54). IR (KBr, cm^{-1}): ν(Re–Cl) 315; ν(C=N) 1675; $\nu(CO_2$ sym) 1315; $\nu(CO_2$ asym) 1662, 1625; ν(Re–P) 748. ^{1}H NMR ($CDCl_3$): δ 49.42 (H7, s); 9.43 (*ortho* H of PPh_3, d, J = 8.4 Hz); 8.41 (*para* H of PPh_3, t, J = 8.7 Hz); 7.86 (*meta* H of PPh_3, t, J = 7.5 Hz); −1.20 to 20.00 (ArH, 10H); −5.34 (H8, d, J = 8.6 Hz); −22.25 (H2, t, J = 8.7 Hz); 0.84 (CH_2Ph, d, 2H). $E_{1/2}$ (Re^{III}/Re^{IV} couple): 0.42 V (ΔE_p, 70 mV); (Re^{III}/Re^{II} couple): −1.25 V. MS (m/z): $[M]^+$Calcd. 1063.40, 1064.20; Found: 1063.30, 1064.50.

$[Re^{III}(L^4)Cl(PPh_3)_2]$ **2a**. Yield: 78 mg (64%). *Anal.* Calc. for $C_{45}H_{35}NClO_3P_2Re$: C, 58.6; H, 3.79; N, 1.51. Found: C, 58.49; H, 3.72; N, 1.49%. UV–Vis (λ_{max}/nm (ε/M^{-1} cm^{-1}) CH_2Cl_2 solution): 275(13 585); 325(10 894), 358(8960), 410(18 067), 468(4150), 1445(125). IR (KBr, cm^{-1}): ν(Re–Cl) 332; ν(C=N) 1665; $\nu(CO_2$ sym) 1315; $\nu(CO_2$ asym) 1658, 1618; ν(Re–P) 746. ^{1}H NMR ($CDCl_3$): δ 45.50 (H7, s); 9.90 (*ortho* H of PPh_3, d, J = 7.5 Hz); 8.42 (*para* H of PPh_3, t, J = 7.3 Hz); 7.86 (*meta* H of PPh_3, t, J = 7.7 Hz); 1.00–20.00 (ArH, 3H); −8.40 (H8, s, 2H); −14.05 (H2, d, J = 7.5 Hz). $E_{1/2}$ (Re^{III}/Re^{IV} couple): 0.41 V (ΔE_p, 70 mV); (Re^{III}/Re^{II} couple): −1.15 V. MS (m/z): $[M]^+$ Calcd. 921.60, 923.20. Found: 920.80, 922.50.

$[Re^{III}(L^5)Cl(PPh_3)_2]$ **2b**. Yield: 79 mg (65%). *Anal.* Calc. for $C_{46}H_{37}NClO_3P_2Re$: C, 59.0; H, 3.95; N, 1.49. Found: C, 58.6; H, 3.88; N, 1.45%. UV–Vis (λ_{max}/nm (ε/M^{-1} cm^{-1}) CH_2Cl_2 solution): 274(20 247), 334(7457), 360

(9035), 437(13 635), 467(2742), 1453(124). CD (λ_{max}/nm ($\Delta\varepsilon$/M^{-1} cm^{-1}) CH_2Cl_2): 255(8.28), 292(−7.10), 325(0.92), 345(−4.25), 385(6.08), 415(−13.02). IR (KBr, cm^{-1}): ν(Re–Cl) 335; ν(C=N) 1669; $\nu(CO_2$ sym) 1308; $\nu(CO_2$ asym) 1661, 1618; ν(Re–P) 745. ^{1}H NMR ($CDCl_3$): δ 48.3(H7, s); 9.60 (*ortho* H of PPh_3, d, $J = 6.8$ Hz); 8.44 (*para* H of PPh_3, t, $J = 7.2$ Hz); 7.84 (*meta* H of PPh_3, t, $J = 7.5$ Hz); 1.20–20.00 (ArH, 3H); −9.80 (H8, d, $J = 8.8$ Hz); −11.85 (H2, q, $J = 7.9$ Hz), 1.42 (CH_3 of amino acid, d, $J = 6.9$ Hz, 3H). $E_{1/2}$ (Re^{III}/Re^{IV} couple): 0.42 V (ΔE_p, 80 mV); (Re^{III}/Re^{II} couple): −1.10 V. MS (*m*/*z*): $[M]^+$Calcd. 935.40, 937.80; Found: 935.60, 936.20.

$[Re^{III}(L^6)Cl(PPh_3)_2]$ **2c**. Yield: 74 mg (61%). *Anal*. Calc. for $C_{51}H_{42}NClO_3P_2Re$: C, 60.5; H, 4.15; N, 1.38. Found: C, 60.32; H, 4.08; N, 1.36%. UV–Vis (λ_{max}/nm (ε/M^{-1} cm^{-1}) CH_2Cl_2 solution): 271(18 575), 337(11 220), 365(9670), 439(10 230), 474(3982), 1437(132). CD (λ_{max}/nm ($\Delta\varepsilon$/M^{-1} cm^{-1}) CH_2Cl_2): 265(6.80), 295(−7.42), 322(0.62), 346(−6.49), 380(6.18), 418(−10.52). IR (KBr, cm^{-1}): ν(Re–Cl) 327; ν(C=N) 1676; $\nu(CO_2$ sym) 1316; $\nu(CO_2$ asym) 1659, 1622; ν(Re–P) 746. ^{1}H NMR ($CDCl_3$): δ 49.80 (H7, s); 9.50 (*ortho* H of PPh_3, d, $J = 6.6$ Hz); 8.42 (*para* H of PPh_3, t, $J = 7.2$ Hz); 7.84 (*meta* H of PPh_3, d, $J = 7.5$ Hz); 1.20–20.00 (ArH, 8H); −9.60 (H8, d, $J = 8.5$ Hz); −12.30 (H2, t, $J = 7.8$ Hz); 0.88 (CH_2Ph, d, 2H). $E_{1/2}$(Re^{III}/Re^{IV} couple): 0.45 V (ΔE_p, 80 mV); (Re^{III}/Re^{II} couple): −1.30 V. MS (*m*/*z*): $[M]^+$Calcd. 1011.80, 1009.30; Found: 1010.60, 1008.90.

2.4. X-ray structure determination

X-ray quality single crystals for the complex $[Re^{III}(L^1)Cl(PPh_3)_2]$ were grown by slow diffusion of diethyl ether into a dichloromethane solution. The X-ray intensity data were measured at 293 K on a Bruker AXS SMART APEX CCD diffractometer (Mo Kα, $\lambda = 0.71073$ Å). The detector was placed at a distance of 6.03 cm from the crystal. A total of 606 frames were collected with a scan width of 0.3° with different settings of φ. The data were reduced in SAINTPLUS [11] and an empirical absorption correction was applied using the SADABS package [12]. The metal atom was located by direct methods using SIR92 [12]. The structure was refined by the full matrix least-square method using SHELXL97 [13], that was present in the program suite WINGX (Version 1.63.04a) [14]. All non-hydrogen atoms were refined anisotropically. The azomethine hydrogen atom was directly located in difference Fourier maps and the remaining hydrogen atoms were included in calculated positions. Significant crystal data are given in Table 1.

Table 1
Crystal data and structural refinement parameters for $[Re^{III}(L^1)Cl(PPh_3)_2]\cdot CH_2Cl_2\cdot H_2O$

	$[Re^{III}(L^1)Cl(PPh_3)_2].CH_2Cl_2\cdot H_2O$
Formula	$C_{50}H_{41}Cl_2O_{0.5}NO_4P_2Re$
Formula weight	1056.60
Crystal system	orthorhombic
Space group	*F2dd*
a (Å)	17.444(3)
b (Å)	32.079(6)
c (Å)	33.483(6)
V (Å^3)	18 737(5)
Z	16
D_{calc} (Mg m^{-3})	1.498
μ (mm^{-1})	2.849
θ (°)	1.76–27.49
Measured reflections	36 191
Unique refection (R_{int})	9472 (0.0290)
Temperature (K)	293(2)
R_1,[a] wR_2[b] [$I > 2\sigma(I)$]	0.0306, 0.0719
Goodness-of-Fit on F^2	1.060

[a] $R_1 = \sum|F_o| - |F_c|/\sum|F_o|$.
[b] $wR_2 = [\sum w(F_o^2 - F_c^2)^2/\sum w(F_o^2)^2]^{1/2}$.

3. Result and discussion

3.1. Synthesis

Aldimines of four α-amino acids (glycine, L-alanine, L-valine and L-phenylalanine) have been used in the present work. The aldimine ligands will be abbreviated as H_2L (Chart 1), the two H atoms (phenolic and carboxylic) being potentially dissociable. The abbreviations for specific Schiff bases are given in Chart 1.

The stoichiometric reaction of $[ReOCl_3(PPh_3)_2]$ with the appropriate ligand in boiling ethanol afforded orange-red coloured complexes of the general formula $[Re^{III}(L)Cl(PPh_3)_2]$. It is noted that when the reaction is carried out in the presence of excess PPh_3 there is an increase in yield of $[Re^{III}(L)Cl(PPh_3)_2]$. This observation indicates that the reduction from Re(V) to Re(III) takes place via the abstraction of the Re=O oxygen atom by PPh_3 [4e].

The characterization data of the complexes are given in the Section 2. A strong C=N stretch is observed at ~1670 cm^{-1}. Carboxylate monocoordination [15,16] is consistent with the presence of one symmetric (~1310 cm^{-1}) and two asymmetric (~1620 and 1660 cm^{-1}) stretches. The Re–Cl and Re–P stretches occur at ~325 and ~745 cm^{-1} respectively.

Electro spray ionization mass spectrometry (ESI-MS) of compound **1a** displayed the highest *m*/*z* peak at 972.90, unambiguously assigned to the $[Re^{III}(L^1)Cl(PPh_3)_2]$ parent ion on the basis of the isotopic distribution of ^{35,37}Cl and ^{185,187}Re. The pattern for $(M–H)^+$ is also observed.

3.2. Crystal structure

The crystal structure of $[Re^{III}(L^1)Cl(PPh_3)_2]$ has been determined. The molecular view is shown in Fig. 1 and selected bond parameters are given in Table 2.

The tridentate meridionally disposed $[L^1]^{2-}$ contains two excellently planar segments ($OC_{10}H_6CHN$ and CCO_2; mean deviation <0.02 Å) and the dihedral angle between them is 5.8 Å. In the distorted ReO_2NClP_2 octahedral environment two oxygen atoms, one chlorine atom

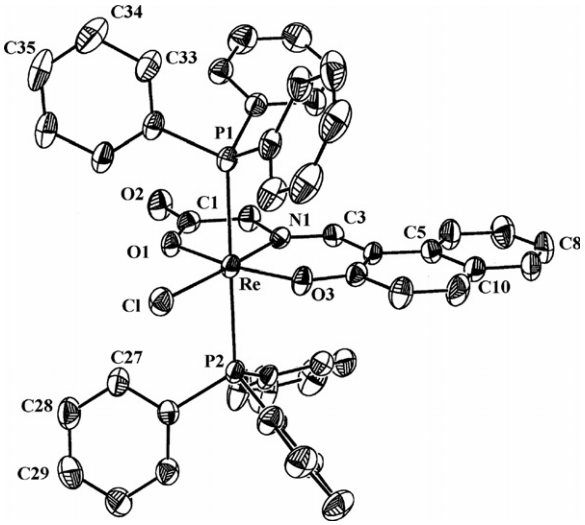


Fig. 1. Perspective view and atom-labelling scheme for the molecule $[Re^{III}(L^1)Cl(PPh_3)_2]$. All non-hydrogen atoms are represented by their 30% thermal probability ellipsoids.

and one nitrogen atom lie in the equatorial plane, whereas the axial positions are occupied by two phosphine ligands. The two Re–O bond distances are not similar and span the range 1.89–1.98 Å. The Re–P bond distances are slightly larger than for previously reported rhenium(III) mixed ligand phosphine Schiff base complexes [17]. The Re–Cl and Re–N bond distances are usual [18] (Table 2).

3.3. Electrochemical studies

The redox properties of the Re(III) α-amino acid Schiff base complexes have been examined by cyclic voltammetry using platinum as the working electrode and SCE as the reference electrode. The cyclic voltammogram was recorded at a scan rate of 50 mV/s. The relevant data are given in Section 2 and a representative voltammogram is shown in Fig. 2.

All the complexes exhibit one quasi-reversible and one irreversible one-electron wave in acetonitrile solution.

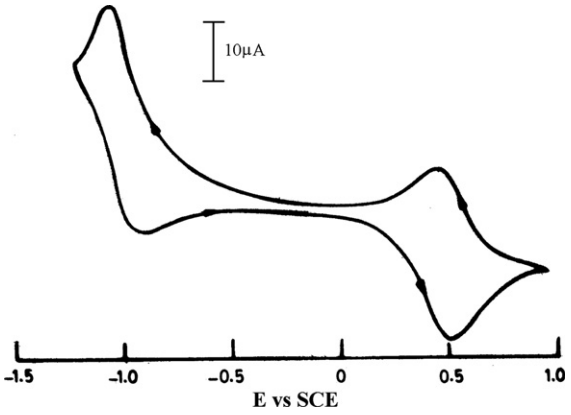


Fig. 2. Cyclic voltammogram of ca. 10^{-3} M solution of $[Re^{III}(L^2)Cl(PPh_3)_2]$ in acetonitrile.

The anodic signal (~0.50 V) at a more positive potential is assigned to the oxidation couple $Re^{IV/III}$ while the couple at ~−1.10 V is believed to be the $Re^{III/II}$ reduction. This redox behavior is consistent with previously known Re(III) complexes [17,19,20].

3.4. Magnetism and NMR spectra

The complexes show a magnetic moment value of ~1.94 BM, corresponding to mononuclear octahedral rhenium(III) d^4 species. The low value of the magnetic moment can be attributed to the large spin–orbit coupling of the rhenium(III) ion [21,22]. The complexes display well-resolved paramagnetic ^1H NMR resonances in $CDCl_3$ solution and the chemical shifts are observed within the range ~−25.00 to +50.00 ppm. The resonances are assigned on the basis of spin–spin structure and spin intensity of the respective rhenium(III) complexes.

In the present case, the absence of phosphorous-proton coupling is probably due to a rapid relaxation of the phosphorous nuclei through an electron-nuclear mechanism to the paramagnetic Re(III) center [23–28]. The paramagnetically shifted ^1H NMR spectrum of a representative case is shown in Fig. 3 and the chemical shift values of the

Table 2
Selected structural parameters for $[Re^{III}(L^1)Cl(PPh_3)_2]$ (distances in Å and angles in °)

Distances			
Re(1)–O(1)	1.896(3)	Re(1)–P(1)	2.5769(12)
Re(1)–O(2)	1.980(3)	Re (1)–P(2)	2.5807(12)
Re(1)–N(1)	2.013(4)	Re(1)–Cl(1)	2.4101(14)
Angles			
O(1)–Re(1)–O(2)	168.07(12)	O(2)–Re(1)–P(2)	92.24(10)
O(1)–Re(1)–N(1)	88.80(14)	N(1)–Re(1)–P(2)	91.54(12)
O(2)–Re(1)–N(1)	79.38(15)	N(1)–Re(1)–P(1)	91.60(12)
O(1)–Re(1)–Cl(1)	94.64(10)	N(1)–Re(1)–Cl(1)	176.56(12)
O(2)–Re(1)–Cl(1)	97.18(11)	Cl(1)–Re(1)–P(1)	88.40(5)
O(1)–Re(1)–P(1)	87.58(12)	Cl(1)–Re(1)–P(2)	88.65(5)
O(2)–Re(1)–P(1)	91.17(10)	P(1)–Re(1)–P(2)	175.74(5)
O(1)–Re(1)–P(2)	89.60(12)		

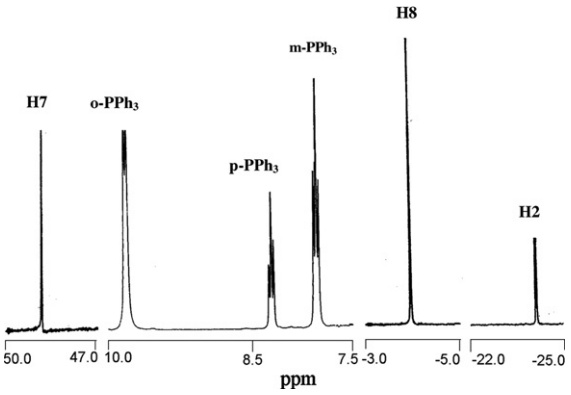


Fig. 3. ^1H NMR spectrum of $[Re^{III}(L^1)Cl(PPh_3)_2]$ in $CDCl_3$ at room temperature.

complexes are given in Section 2. The numbering scheme is as in Chart 1 and Fig. 1. In solution, the azomethine hydrogen occurs as a singlet at ~49.00 ppm. The ortho protons of the coordinated phosphine appear as a doublet at ~9.50 ppm ($J = 7$–8 Hz). The meta and para protons are observed as triplets at ~7.80 and 8.40 ppm respectively, with a coupling constant $J = 7$–9 Hz. All other aromatic H-atoms fall in the range +25.00 to −25.00 ppm. The α-hydrogen atom of the amino acid residue appears as singlet/multiplet in the negative region.

The ^{31}P NMR signals for the phosphines coordinated to the Re(III) center were not observed and the result is consistent with previously reported paramagnetic Re(III) complexes [26,29,30].

3.5. Electronic and CD spectra

The electronic and CD spectra were recorded in dichloromethane solution. The electronic and CD spectral data are given in Section 2. The CD spectra of the Re(III) chelates of amino acid Schiff bases below 550 nm are given in Fig. 4.

The low energy d–d absorption of the complexes is found near 1000 and 1470 nm. A moderately intense absorption band is observed at ~360 nm and this can be attributed to the π–π* transition originating mainly from the azomethine chromophore. The bathochromic shift of this band compared to the free amino acid Schiff bases [31]is due to the increase of conjugation in the molecule upon coordination. The intense absorption band at higher energy, ~270 nm, is presumably from the π–π* transition of the benzene/naphthalene ring of the Schiff bases. The CD spectra are more informative than the corresponding absorption spectra. A careful comparison of the CD spectra of the Re(III) amino acid Schiff base complexes reveal that the sign and pattern of three bands or shoulder in the UV region as well as the Cotton effect is same within the entire family. This observation clearly indicates that the coordinating ligands adopt a common conformation. It has been recognized that a negative azomethine CD band corresponds to the L-absolute configuration of the amino acid residue. The present results are consistent with previously reported complexes using aldimines of α-amino acids [6,32].

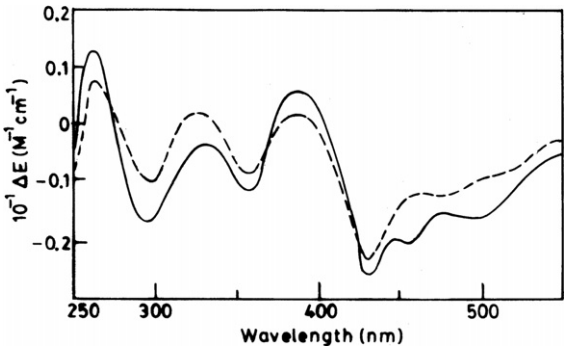


Fig. 4. Circular dichroism spectra of **1b** (——) and **1c** (—) in dry dichloromethane solution.

4. Conclusion

The Schiff bases of salicyladehyde/naphthaldehyde and α-amino acids (glycine, L-alanine, L-valine, L-phenylalanine) react with $[ReOCl_3(PPh_3)_2]$ toafford Re(III) complexes of the general formula $[Re^{III}(L)Cl(PPh_3)_2]$. The species $[Re^{III}(L)Cl(PPh_3)_2]$ represent the first example of structurally characterized Re(III) complexes incorporating α-amino acid Schiff bases as a coligand. The CD spectra confirm the L-absolute configuration of the amino acids in the complexes. Our search for new rhenium complexes of Schiff bases of different amino acids and peptides are in progress.

Acknowledgements

Financial support from the University Grant Commission, New Delhi, India, Department of Science and Technology, New Delhi, India and from the Council of Scientific and Industrial Research, New Delhi, India is greatly acknowledged. We are also thankful to the DST for data collection on the CCD facility setup (Indian Institute of Science, Bangalore, India) under the IRHPA-DST program.

Appendix A. Supplementary material

CCDC 285571 contains the supplementary crystallographic data for this paper. These data can be obtained free of charge via http://www.ccdc.cam.ac.uk/conts/retrieving.html, or from the Cambridge Crystallographic Data Centre, 12 Union Road, Cambridge CB2 1EZ, UK; fax: (+44) 1223-336-033; or e-mail: deposit@ccdc.cam.ac.uk. Supplementary data associated with this article can be found, in the online version, at doi:10.1016/j.poly.2007.03.036.

References

[1] (a) A.M. Santos, C.C. Romao, F.E. Kuhn, J. Am. Chem. Soc. 125 (2003) 2414;
(b) W.A. Hermann, F.E. Kuhn, Acc. Chem. Res. 30 (1997) 169;
(c) T.B. Towne, F.E. Mc Donald, J. Am. Chem. Soc. 119 (1997) 6022.
[2] (a) E. John, M.L. Thakur, J. De Fulvio, M.R. McDevitt, I. Dajanov, J. Nucl. Med. 34 (1993) 260;
(b) J.P. DiZio, C.J. Anderson, A. Davison, G.J. Ehrhardt, K.E. Carlson, M.J. Welch, J.A. Katzenellenbogen, J. Nucl. Med. 33 (1992) 558;
(c) H.J. Lee, W.M. Partridge, Bioconjugate Chem. 14 (2003) 546, and references therein;
(d) M. Nicolini, G. Bandoli, U. Mazzi (Eds.), Technetium and Rhenium in Nuclear Medicine, vol. 4, S.G. Editoriali, Padova, Italy, 1995.
[3] (a) S.S. Jurisson, J.D. Lydon, Chem. Rev. 99 (1999) 2205;
(b) W.A. Volkert, T.J. Hoffman, Chem. Rev. 99 (1999) 2269.
[4] (a) U. Mazzi, F. Refosco, Transition Met. Chem. 10 (1985) 121;
(b) S.M. Harben, P.D. Smith, R.L. Beddoes, D. Collison, C.D. Garner, J. Chem. Soc., Dalton Trans. (1997) 2777;
(c) F. Tisato, F. Refosco, A. Moresco, G. Bandoli, U. Mazzi, M. Nicolini, J. Chem. Soc., Dalton Trans. (1990) 2225;

(d) M. Shivakumar, S. Banerjee, M. Menon, A. Chakravorty, Inorg. Chim. Acta 275–276 (1998) 546;
(e) S. Sengupta, J. Gangopadhayay, A. Chakravorty, J. Chem. Soc., Dalton Trans. (2003) 4635.
[5] L. Casella, M. Gullotti, Inorg. Chem. 22 (1983) 2259.
[6] M.R. Wagner, F.A. Walker, Inorg. Chem. 22 (1983) 3021.
[7] R.D. Gillard, R. Woottan, J. Chem. Soc. B (1970) 364.
[8] V. Kettmann, E. Fresova, Acta Crystallogr. C49 (1993) 1932.
[9] I. Sakiyan, E. Logoglu, S. Arstan, N. Sari, N. Sakiyan, BioMetals 17 (2004) 115.
[10] J. Chatt, G.A. Rowe, J. Chem. Soc. 2 (1962) 4019.
[11] Bruker, SMART, SAINT, SADABS, XPREP, SHELXTL, Bruker AXS Inc., Madison.WI, USA, 1998.
[12] A. Altomare, G. Cascarano, C. Giacovazzo, J. Appl. Crystallogr. 26 (1993) 343.
[13] G.M. Sheldrick, SHELXL97, Program for crystal structure refinement, University of Gottingen, Germany, 1997.
[14] L.J. Farrugia, WINGXJ, Appl. Crystallogr. 32 (1999) 837.
[15] B. Kavanagh, J.W. Steed, D.A. Toecher, J. Chem. Soc. Dalton Trans. (1993) 327.
[16] K.K. Rajak, S.P. Rath, S. Mondal, A. Chakravorty, Inorg. Chem. 38 (1999) 3283.
[17] P.D. Benny, J.L. Green, H.P. Engelbrecht, C.L. Barnes, S.S. Jurisson, Inorg. Chem. 44 (2005) 2381.
[18] (a) A. Mondal, S. Sarkar, D. Chopra, T.N. Guru Row, K.K. Rajak, J. Chem. Soc., Dalton Trans. (2004) 3244;
(b) A. Mondal, S. Sarkar, D. Chopra, K.K. Rajak, Inorg. Chim. Acta 359 (2006) 2141.
[19] G. Battistuzzi, M. Borsari, R. Battistuzzi, Polyhedron 16 (1997) 2093.
[20] S.R. Banerjee, L. Wei, M.K. Levadala, N. Lazarova, V.O. Golub, C.J. O'Connor, K.A. Stephenson, J.F. Valliant, J.W. Babich, J. Zubieta, Inorg. Chem. 41 (2002) 5795.
[21] J.E. Fergusson, Coord. Chem. Rev. 1 (1966) 459.
[22] A. Earnshaw, B.N. Figgis, J. Lewis, R.D. Peacock, J. Chem. Soc. (1961) 3132.
[23] D. Shaw, E.W. Randall, J. Chem. Soc., Chem. Commun. (1965) 82.
[24] E.W. Randall, D. Shaw, Mol. Phys. 10 (1965) 41.
[25] J. Chatt, G.J. Leigh, D.M.P. Mingos, E.W. Randall, D. Shaw, J. Chem. Soc., Chem. Commun. (1968) 419.
[26] F.A. Cotton, R.L. Luck, Inorg. Chem. 28 (1989) 2181.
[27] S. Bhattacharyya, S. Banerjee, B.K. Dirghangi, M. Menon, A. Chakravorty, J. Chem. Soc., Dalton Trans. (1999) 155.
[28] C.A. Mitsopoulou, N. Mahieu, M. Motevalli, E.W. Randall, J. Chem. Soc., Dalton Trans. (1996) 4563.
[29] E.W. Randall, D. Shaw, J. Chem. Soc. A (1969) 2867.
[30] C. Pearson, A.L. Beauchamp, Inorg. Chim. Acta 237 (1995) 13.
[31] Y. Matsushima, A.E. Martell, J. Am. Chem. Soc. 89 (1967) 1322.
[32] (a) I. Cavaco, J.C. Pessoa, M.T. Duarte, R.T. Henriques, P.M. Matias, R.D. Gillard, J. Chem. Soc., Dalton Trans. (1996) 1989;
(b) L. Casella, M. Gullotti, Inorg Chem. 25 (1986) 1294;
(c) L. Casella, M. Gullotti, G. Pacchioni, J. Am. Chem. Soc. 104 (1982) 2386.

Available online at www.sciencedirect.com
ScienceDirect
Polyhedron 26 (2007) 3471–3477
POLYHEDRON
www.elsevier.com/locate/poly

The synthesis, characterization and melting properties of thiophene-containing dithiocarboxylate complexes of nickel(II)

Mary S. Thomas [a], Marilé Landman [b,*], Simon Lotz [b,*], Elizabeth M. van der Merwe [c]

[a] Department of Chemistry, University of Limpopo, Turfloop Campus, P. Bag X 1106, Sovenga 0727, South Africa
[b] Department of Chemistry, University of Pretoria, Pretoria 0002, South Africa
[c] Department of Chemistry, University of South Africa, P. O. Box 392, Pretoria 0003, South Africa

Received 16 February 2007; accepted 22 March 2007
Available online 12 April 2007

Abstract

The reactions of a series of 5-alkyl-2-thiophenedithiocarboxylates with nickel(II) chloride afforded two types of complexes, blue nickel(II) complexes with two terminal dithiocarboxylate ligands, $[Ni(S_2CTR)_2]$ and violet nickel(II) complexes with perthio- and dithiocarboxylate ligands, $[Ni(S_2CTR)(S_3CTR)]$ (where T = 2,5-disubstituted thiophene, R = C_nH_{2n+1}, $n = 4, 6, 8, 12, 16$). The blue monomers are preferred for the shorter chains (C_4 and C_6) and the violet compounds form exclusively for the longer chains (C_8, C_{12}, and C_{16}) in the alkylthiophene complexes. In addition to the above series, $[Ni(S_2CTCH_3)_2]$, was prepared in a one-pot reaction in THF and both the blue and violet products were isolated. It was possible to convert the blue complexes $[Ni(S_2CTR)_2]$ (R = butyl, hexyl) into the corresponding violet complexes $[Ni(S_2CTR)(S_3CTR)]$ after stirring in THF solutions for prolonged periods of time. Liquid-crystalline properties of these complexes were examined by DSC and POM. The violet complexes with C_8 and C_{12} alkyl chains showed liquid-crystalline properties.
© 2007 Elsevier Ltd. All rights reserved.

Keywords: Nickel; Thiophene; Liquid crystal; Dithiocarboxylate ligands

1. Introduction

An important class of nickel(II) complexes are those with sulfur donor-atoms such as thiols, dithiolene and dithiocarboxylate as ligands [1,2]. Earlier literature (1963–1975) has revealed nickel(II) complexes displaying a variety of coordination numbers and many different coordination modes for thiol, dithiocarboxylate, dithiocarbamate and trithiocarboxylate ligands [1]. Square-planar, tetrahedral, 5-coordinate, and octahedral geometries are known for nickel(II) with dithiocarboxylate ligands. It has been widely demonstrated that square-planar or square-pyramidal coordination leads to the appearance of liquid-crystalline properties, whereas tetrahedral geometry, it was assumed, inhibits mesophase formation. This assumption has recently been refuted [3]. Examples of complexes with two bidentate dithiocarboxylate or dithiocarbamate ligands surrounding one nickel(II) metal have been documented before and a crystal structure determination of $[Ni\{S_2CPh\}_2]$ revealed a flat, square-planar mononuclear nickel(II) complex [4].

Nickel(II) ions in complexes containing different coordination modes and structural features must not be underestimated for potential applications as liquid-crystalline materials [5,6]. The first mesogenic nickel(II) complexes were those with dithiolene ligands and were studied by Giroud and Müller-Westerhoff in [7]. The nickel(II) complexes displayed enantiotropic mesophases, which were nematic for the shorter chains and smectic for the longer alkyl chains. In addition to the calamitic (rod-like) metallomesogens, Ohta and co-workers reported disc-shaped

* Corresponding authors. Tel.: +27 12 420 2527; fax: +27 12 3625297.
E-mail address: marile.landman@up.ac.za (M. Landman).

0277-5387/$ - see front matter © 2007 Elsevier Ltd. All rights reserved.
doi:10.1016/j.poly.2007.03.056

metallomesogens for nickel(II) with dithiolenes [8]. Of the piperazine dithiocarbamate complexes of palladium, nickel, copper and zinc only the nickel and copper derivatives showed liquid-crystalline behaviour [9]. The mesogenic properties of bis(*p*-alkylphenyldithiolate) complexes of nickel(II) and platinum(II) were reported by Müller-Westerhoff in [10].

Adams and co-workers synthesized the mesomorphic 4-alkyloxydithiobenzoate derivatives of Ni(II), Pd(II) and Zn(II) [11]. The mesomorphism of nickel(II) and palladium(II) complexes were similar, showing smectic C phases for longer alkyl chains. Later on Ohta and co-workers employed alkyldithiocarboxylate as ligands to form dimeric nickel(II) complexes that exhibited monotropic smectic phases [12].

In this study, the reactions of a series of 5-alkyl-2-thiophenedithiocarboxylates with nickel(II) chloride were investigated to see if the inclusion of thiophene in the chain would affect the outcome of the reactions and play a role in determining the melting point behaviour and properties of mesophases. It is envisaged that the geometry of the rod-like structures of the complexes will be affected by the presence of thiophene in the molecule in stead of benzene and that the electronic properties of these complexes will be different than the benzene analogues in their electronic influence on the CS_2 moiety.

2. Experimental

2.1. General

Solvents were dried and distilled under nitrogen prior to use. Diethyl ether, tetrahydrofuran and hexane were distilled from sodium metal, with benzophenone as indicator in the case of ethereal solvents. Dichloromethane was distilled from phosphorus pentoxide. Thiophene was purified as described by Spies and Angelici [13]. Reactions were performed in an inert atmosphere of either nitrogen or argon using standard Schlenk and vacuum-line techniques. Column chromatography was carried out under a nitrogen-atmosphere using silica gel (particle size 0.063–0.200 nm) as stationary phase. All other reagents were purchased from commercial suppliers and used without further purification. All NMR spectra were recorded in degassed deuterated chloroform on a Bruker ARX-300 spectrometer. Chemical shifts were referenced to chloroform. ^{1}H and ^{13}C NMR spectra were measured at 300.133 and 75.469 MHz, respectively. Infrared spectra were recorded on a Perkin–Elmer Spectrum RX1 FT-IR spectrophotometer with a NaCl cell using hexane as solvent. Liquid-crystalline properties were examined on a differential scanning calorimeter (DSC) Q 100 V8.2 Build 268 and hot-stage polarising optical microscope (POM) Olympus BX60 equipped with a Linkam THMS600 hot stage and a Linkam TMS93 programmable temperature controller.

2.2. Synthesis

2.2.1. Synthesis of 5-alkyl-2-thiophenedithiocarboxylate ligands

2.2.1.1. Preparation of 2-alkylthiophene (RT). The procedure used was similar to the one described by Brandsma [14]. *n*-Butyl lithium (15.6 mL, 25.0 mmol) was added to a mixture of THF (50.0 mL) and hexane (30.0 mL), which was cooled to −20 °C. Thiophene (1.68 g, 20.0 mmol) was introduced over 10 min with cooling between 0 °C and 10 °C. The cooling bath was removed and the mixture was allowed to warm to room temperature. The alkyl bromide (2.74 g for butyl bromide, 20.0 mmol) was added in one portion without external cooling. The temperature of the solution was raised to 50 °C and kept at this temperature for a further 30 min. The rest of the procedure was carried out in air. Ice water (100 ml) was added with vigorous stirring. Two layers formed and were separated. Two further extractions with 20 mL diethyl ether of the aqueous phase gave a combined organic solution that was dried over anhydrous $MgSO_4$. The mixture was concentrated in a rotary evaporator to afford the crude product. Yield = 2.38 g; 85% for R = butyl.

2.2.1.2. Preparation of 5-alkyl-2-thiophenedithiocarboxylic acid ($RTCS_2H$). *n*-Butyl lithium (12.5 mL, 20.0 mmol) was added to a solution of THF (50.0 mL) and hexane (30.0 mL), which was cooled to −20 °C. 2-Alkyl thiophene (R = butyl, 2.38 g, 17.0 mmol) was introduced over 10 min with cooling between 0 °C and 10 °C. The cooling bath was removed and the mixture that warmed to room temperature was stirred for a further 10 min. The solution was cooled to 0 °C and copper(I) bromide (0.10 g) added. Carbon disulfide (1.29 g, 17.0 mmol) was added drop-wise to the stirred mixture. The colour of the reaction mixture changed to deep-red. The cooling bath was removed and the mixture was allowed to warm to room temperature while stirring was continued for a further 1 h. Ice water (100.0 mL) was added followed by dilute hydrochloric acid (20.0 mL, 1 mol/dm^3). The organic layer was separated in air and the product extracted into diethyl ether (70.0 mL) and washed with 2 × 50.0 mL of water. The product was dried over $MgSO_4$ and the solvent removed *in vacuo*. Yield = 3.30 g; 89.8% for R = butyl.

2.2.1.3. Preparation of sodium 5-butyl-2-thiophenedithiocarboxylate ($C_4H_9TCS_2Na$). Sodium metal (0.35 g, 15.3 mmol) was added over 10 min to vigorously stirred methanol (50.0 mL) to form sodium methoxide. When all the sodium had dissolved, additional (20.0 mL) methanol was added. 5-Alkyl-2-thiophenedithiocarboxylic acid (for R = butyl, 3.30 g, 15.3 mmol) was added over 5 min to the mixture and left stirring for 30 min. The solvent was removed under reduced pressure, affording, for R = butyl, the sodium 5-butyl-2-thiophenedithiocarboxylate as an orange-brown solid. Yield = 3.09 g; 85%.

*2.2.2. Synthesis of bis(5-butyl-2-thiophenedithiocarboxylato) nickel(II) [$Ni(S_2CTC_4H_9)_2$] (**1a**)*

The procedure was similar to that of Adams et al. [15], who prepared dithiobenzoate complexes. The reaction was done in air. To a stirred solution of sodium 5-butyl-2-thiophenedithiocarboxylate (1.55 g, 6.5 mmol) in water (25.0 mL) was added, drop-wise, a pale green solution of $NiCl_2 \cdot 6H_2O$ (0.71 g, 3.0 mmol) in water (10.0 mL) at room temperature. The colour of the solution turned blue-violet and the mixture was left to stir for 3 h. The mixture was concentrated to 25.0 mL on a rotary evaporator and 20.0 mL of methanol was added. The precipitate was separated by filtration and dried. Further purification was done on a silica gel column and the product was purified with hexane/CH_2Cl_2 (4:1) as the eluent. A blue powder was obtained on evaporation of the solvent. Yield = 0.49 g; 66%.

1a, R = C_4H_9: ^{1}H NMR (300 MHz, $CDCl_3$, 25 °C, δ in ppm; J in Hz) 7.73 (d, 2H, H3, $J = 3.9$), 6.83 (d, 2H, H4, $J = 3.6$), 2.79 (t, 4H, H6, $J = 7.2$), 1.66 (m, 4H, H7), 1.37 (m, 4H, H8), 0.92 (t, 6H, H9, $J = 7.2$); ^{13}C NMR (ppm) $^*S_2C$ (C1) n.o., 159.3 (C2), 148.8 (C5), 129.8 (C3), 127.0 (C4), 33.1, 30.8, 22.7, 13.6 (C6–C9); IR (cm^{-1}) 2918 (vs), 1458 (vs), 1375 (s), 1049 (m), 977 (m), 721 (s).

2.2.3. The synthetic route for the other four complexes was similar

2a, R = C_6H_{13}: ^{1}H NMR (300 MHz, $CDCl_3$, 25 °C, δ in ppm; J in Hz) 7.72 (d, 2H, H3, $J = 4.1$), 6.82 (d, 2H, H4, $J = 3.9$), 2.78 (t, 4H, H6, $J = 7.7$), 1.68 (m, 4H, H7), 1.30 (m, 12H, H8–H10), 0.87 (t, 6H, H11, $J = 7.5$); ^{13}C NMR (ppm) $^*S_2C$ (C1) n.o., 159.4 (C2), 148.8 (C5), 129.6 (C3), 127.0 (C4), 31.4, 31.2, 29.7, 28.7, 22.5, 14.0 (C6–C11), IR (cm^{-1}) 2920 (s), 1461 (vs), 1375 (s), 1050 (m), 978 (m), 721 (s).

3b, R = C_8H_{17}: *Anal.* Calc. for $C_{26}H_{38}S_7Ni$: C, 49.28; H, 6.05. Found: C, 49.67; H, 6.25%. ^{1}H NMR (300 MHz, $CDCl_3$, 25 °C, δ in ppm; J in Hz) 7.77 (d, 2H, H3, $J = 4.0$), 7.49 (d, 2H, H3′, $J = 3.7$), 6.86 (d, 2H, H4, $J = 3.8$), 6.75 (d, 2H, H4′, $J = 3.8$), 2.79 (t, 4H, H6, $J = 7.8$), 2.74 (t, 8H, H6′, $J = 7.2$), 1.67 (m, 8H, H7 and H7′), 1.62 (m, 40H, H8–H12 and H8′–H12′), 0.87 (t, 12H, H13 and H13′, $J = 6.5/7.2'$); ^{13}C NMR (ppm) 227.8, 214.8 (C1 and C1′), 159.0 , 156.2 (C2 and C2′), 148.4, 139.3 (C5 and C5′), 129.8, 129.1 (C3 and C5′), 127.1, 127.0 (C4 and C4′), 31.8, 31.1, 30.7, 29.7, 29.2, 29.0, 22.6, 14.1 (C6–C13 and C6′–C13′); IR (cm^{-1}) 2920 (vs), 1461 (vs), 1375 (s), 1067 (w), 1048 (m), 999 (m), 970 (m), 721 (s).

4b, R = $C_{12}H_{25}$: ^{1}H NMR (300 MHz, $CDCl_3$, 25 °C, δ in ppm; J in Hz) 7.78 (d, 2H, H3, $J = 4.0$), 7.48 (d, 2H, H3′, $J = 3.9$), 6.86 (d, 2H, H4, $J = 3.9$), 6.75 (d, 2H, H4′, $J = 3.9$), 2.79 (t, 4H, H6, $J = 7.6$), 2.73 (t, 4H, H6′, $J = 7.5$), 1.67 (m, 8H, H7 and H7′), 1.29 (m, 72H, H8–H16 and H8′–H16′), 0.87 (t, 12H, H17 and H17′, $J = 7.2$); ^{13}C NMR (ppm) 227.8, 214.8 (C1 and C1′), 159.0, 156.2, 148.4, 139.3, 129.8, 129.2, 127.1, 127.0 (C2–C5 and C2′–C5′), 31.9, 31.8, 31.4, 31.1, 30.7, 29.7, 29.6, 29.6, 29.5, 29.3, 29.1, 29.0, 22.7, 14.1 (C6–C17 and C6′–C17′); IR (cm^{-1}) 2921 (vs), 1460 (vs), 1375 (s), 1049 (m), 994 (w), 980 (m), 720 (s).

5b, R = $C_{16}H_{33}$: ^{1}H NMR (300 MHz, $CDCl_3$, 25 °C, δ in ppm; J in Hz) 7.70 (d, 2H, H3, $J = 3.9$), 7.48 (d, 2H, H3′, $J = 3.9$), 6.86 (d, 2H, H4, $J = 3.9$), 6.75 (d, 2H, H4′, $J = 3.9$), 2.76 (dt, 8H, H6 and H6′, $J = 7.8/7.5$), 1.69 (m, 8H, H7 and H7′), 1.28 (m, 104H, H8–H20 and H8′–H20′), 0.86 (t, H21 and H21′, $J = 6.5/7.0$); ^{13}C NMR (ppm) 227.9, 214.9 (C1 and C1′), 159.0, 156.2, 139.3, 129.8, 129.2, 127.1, 127.0 (C2–C5 and C2′–C5′), 31.9, 31.1, 31.0, 30.7, 30.6, 30.2, 29.9, 29.8, 29.7, 29.7, 29.7, 29.6, 29.5, 29.4, 29.2, 29.2, 29.0, 22.7, 14.1 (C6–C21 and C6′–C21′); IR (cm^{-1}) 2922 (vs), 1458 (vs), 1375 (s), 1049 (m) 977 (m), 925 (w), 720 (s).

*2.2.4. Second method of synthesis (one-pot reaction) for **6a** and **6b***

In a second method (one-pot reaction), 2-methylthiophene (1.96 g, 20.0 mmol) was lithiated by the addition of *n*-butyl lithium (13.8 mL, 22.0 mmol) at −20 °C in THF. The colour of the solution immediately changed to orange on addition of the BuLi, but changed gradually to yellow after stirring for 30 min. The mixture was cooled to −50 °C and carbon disulfide (1.52 g, 20.0 mmol) was added. The mixture became dark red in colour and was stirred for 30 min. Anhydrous nickel(II) chloride (1.30 g, 10.0 mmol) was added in small portions and the mixture was allowed to reach room temperature. The yellow solid material gradually dissolved on reacting and the solution changed first to green then to blue and thereafter to violet over a period of 3 h. The blue-violet product was purified by filtration of the reaction mixture through a plug of silica gel once the solvent was changed to dichloromethane and afforded **6** in very high yield (the yield was more than 80%). From this mixture both blue and violet compounds were isolated by column chromatography with mixtures of hexane and dichloromethane as eluents. The blue compound **6a** was less soluble in organic solvents compared to the violet compound **6b**.

6a, R = CH_3: *Anal.* Calc. for $C_{12}H_{10}S_6Ni$: C, 35.56; H, 2.49. Found: C, 35.71; H, 2.63%. ^{1}H NMR (300 MHz, $CDCl_3$, 25 °C, δ in ppm; J in Hz) 7.72 (d, 2H, H3, $J = 4.0$), 6.82 (d, 2H, H4, $J = 3.9$), 2.43 (s, 3H, Me); ^{13}C NMR (ppm) 228.0 (C1), 159.0, 139.3, 129.2, 127.1 (C2–C5), 14.1 (C6); IR (cm^{-1}) 2919 (vs), 1460 (vs), 1375 (s), 1049 (m), 978 (m), 721 (s).

6b, R = CH_3: *Anal.* Calc. for $C_{12}H_{10}S_7Ni$: C, 32.95; H, 2.30. Found: C, 33.17; H, 2.52%. ^{1}H NMR (300 MHz, $CDCl_3$, 25 °C, δ in ppm; J in Hz) 7.76 (d, 2H, H3, $J = 3.8$), 7.47 (d, 2H, H3′, $J = 3.6$), 6.85 (d, 2H, H4, $J = 3.7$), 6.74 (d, 2H, H4′, $J = 3.6$), 2.47 (s, 3H, Me), 2.43 (s, 3H, Me′); ^{13}C NMR (ppm) 227.9, 214.9 (C1 and C1′), 159.0, 156.2, 140.1, 139.3, 129.8, 129.2, 127.1, 127.0 (C2–C5 and C2′–C5′), 14.2, 14.1 (C6 and C6′); IR (cm^{-1})

2920 (vs), 1458 (vs), 1375 (s) 1046 (m), 999 (w), 978 (m), 721 (s).

2.2.5. Conversion of *1a* and *2a* into *1b* and *2b*

The blue complexes **1a** and **2a** were converted to the violet complexes **1b** and **2b**, respectively, by stirring 0.5 g of the blue complex, **1a** or **2a**, in 20 mL of THF for 12 h at room temperature.

1b, R = C_4H_9: ^{1}H NMR (300 MHz, $CDCl_3$, 25 °C, δ in ppm; J in Hz) 7.78 (d, 2H, H3, $J = 3.9$), 7.49 (d, 2H, H3′, $J = 4.1$), 6.87 (d, 2H, H4, $J = 3.9$), 6.75 (d, 2H, H4′, $J = 3.9$), 2.80 (t, 4H, H6, $J = 7.2$), 2.74 (t, 4H, H6′, $J = 7.2$), 1.67 (q, 4H, H7, $J = 7.5'$), 1.66 (q, 4H, H7′, $J = 7.5$), 1.40 (m, 4H, H8, $J = 7.4$), 1.39 (m, 4H, H8′, $J = 7.4$), 0.93 (t, 6H, H9, $J = 7.2$), 0.92 (t, 6H, H9′, $J = 7.2$); ^{13}C NMR (ppm) 227.9, 214.9 (C1 and C1′), 160.1, 158.2, 149.4, 148.6, 131.3, 129.8, 127.6, 127.2 (C2–C5 and C2′–C5′), 33.6, 31.4, 22.6, 13.9 (C6–C9 and C6′–C9′); IR (cm^{-1}) 2921 (vs), 1461 (vs), 1375 (s), 1049 (m), 970 (m), 925 (w), 721 (s).

2b, R = C_6H_{13}: ^{1}H NMR (300 MHz, $CDCl_3$, 25 °C, δ in ppm; J in Hz) 7.77 (d, 2H, H3, $J = 3.2$), 7.48 (d, 2H, H3′, $J = 3.2$), 6.86 (d, 2H, H4, $J = 3.1$), 6.75 (d, 2H, H4′, $J = 3.1$), 2.82 (dt, 8H, H6 and H6′, $J = 7.2$), 1.71 (m, 8H, H7 and H7′), 1.32 (m, 24H, H8–H10 and H8′–H10′), 0.91 (t, 12H, H11 and H11′, $J = 7.2$); ^{13}C NMR (ppm) 227.8, 214.8 (C1 and C1′), 159.0, 156.2, 147.4, 144.6, 139.3, 128.8, 127.1, 127.0 (C2–C5 and C2′–C5′), 30.8, 29.9, 28.9, 27.9, 21.6, 13.1 (C6–C11 and C6′–C11′); IR (cm^{-1}) 2920 (vs), 1460 (vs), 1375 (s), 1097 (m), 1050 (m) 978 (m), 720 (s).

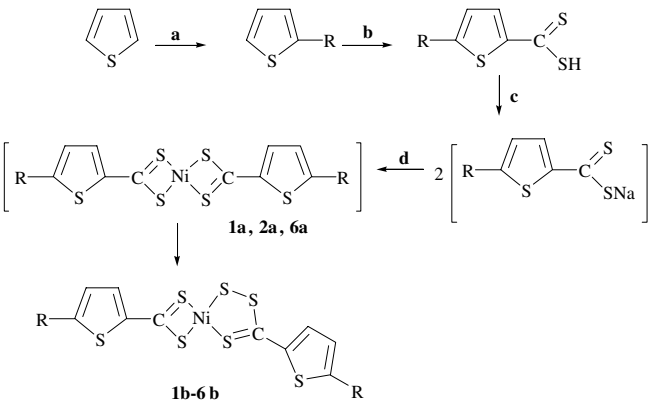
3. Results and discussion

3.1. Synthesis and characterization

Five complexes of the type $[Ni(S_2CTR)_2]$ (where T = 2,5-disubstituted thiophene, R = alkyl group; C_4H_9 (**1**), C_6H_{13} (**2**), C_8H_{17} (**3**), $C_{12}H_{25}$ (**4**), $C_{16}H_{33}$ (**5**)) were synthesized via a four-step reaction sequence as shown in Scheme 1.

The sodium 5-alkyl-2-thiophenedithiocarboxylate precursors were synthesized according to the literature procedures [14]. The final step was similar to that of Adams and co-workers who prepared complexes with dithiobenzoate ligands [15].

The formation of violet vs blue compounds in this study was dependent on the solvent, as well as the length of the alkyl chain. Using the first method of synthesis, the blue monomers are preferred for the shorter chains (C_4 and C_6) and the violet compounds for the longer chains (C_8, C_{12} and C_{16}). In a third experiment, pure blue complex **1a** was dissolved in THF and stirred at room temperature. A sample was taken after 1 h and the ^{1}H NMR spectrum was recorded in deuterated chloroform. The solution consisted of 83% blue and 17% violet complex by comparing the integration ratios of the different signals.



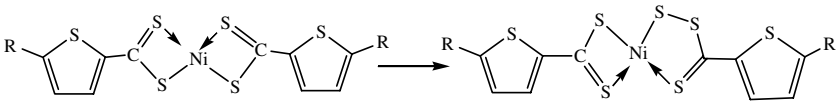
Scheme 1. Reagents: **a** *n*-BuLi, RBr; **b** *n*-BuLi, CS_2, HCl; **c** Na/MeOH; **d** $NiCl_2 \cdot H_2O$.

As stirring continued the colour of the reaction mixture gradually changed from blue to violet. After 12 h the conversion was complete and only the violet complex could be isolated from the reaction mixture. A similar result was achieved after stirring **2** for 10 h. The blue compound converted into the violet compound. The mass peak at m/z-value of 632 (^{58}Ni, 3%) corresponds to the mass of **3b** and represents the molecular ion, $[Ni(S_3CTR)(S_2CTR)]^+$ (R = C_8H_{17}). Chemical analysis supported the structures proposed for the violet complexes. Based on the physical and spectroscopic data and literature results, it was concluded that **1b–6b** were the mononuclear nickel(II) complexes with perthio- and dithiocarboxylate ligands as shown in Scheme 2. The only outstanding issue was the source of additional sulfur for insertion. The formation of perthiocarboxylate complexes of nickel(II) have previously been achieved by thermal conditions and the addition of polysulfides, elemental sulfur or by a photolytic procedure in dichloromethane or chloroform [16,17].

It is unclear how the sulfur-inserted ligand was formed under such mild reaction conditions, and in the absence of an oxidant and warrants further investigations. Studies involving the mechanism of the sulfur insertion process using labeled ^{34}S revealed that the sulfur atom is inserted between a C–S bond and not between a M–S bond [18,19]. Based on this, an intermolecular mechanism whereby a sulfur atom from one dithiocarboxylate molecule was inserted into a second one to form perthiocarboxylate, was proposed by Fackler and Fetchin [19]. It was previously noted that temperature plays an important role for the transformation of a dithiocarboxylate into a perthiocarboxylate ligand, and in this study it can be assumed that the thiophene facilitated the sulfur inclusion under the mild reaction conditions. This could be achieved by the stabilization of the electrophilic CS_2-carbon in the intermediate by electron charge transfer from the thiophene ring.

3.2. Characterization of the complexes

The complexes were characterized by NMR and infrared spectroscopy and representative examples by mass



Scheme 2. Structures of novel nickel(II) complexes.

spectra, uv and elemental analysis [20]. The blue complexes, **1a**, **2a** and **6a**, displayed two doublets in the thiophene region of the spectra, while the violet complexes, **1b**–**6b**, displayed four doublets in this area. This can be ascribed to the difference in electronic environment of the thiophene protons in the unsymmetrical perthio-, thiocarboxylate complexes compared to the symmetrical dithiocarboxylate complexes. For **3b**, the four doublets are at 7.77, 7.49, 6.86 and 6.75 ppm, respectively. Interestingly, the triplet of the CH_2 group attached to the thiophene of the octyl chain is also duplicated for the two types of ligands emphasising the large differences in the coordination modes of the perthio- and dithiocarboxylato ligands (see Fig. 1). The resonances in the ^{13}C NMR spectra of **1**–**6b** were assigned based on a 2D HETCOR spectrum recorded for **3b.** The ^{13}C NMR spectrum of **3b** showed the resonances of CS_2 as one peak for **1a**, **2a** and **6a** and two peaks for **1**–**6b**. The lower chemical shift value was assigned to the CS_2 of the perthiocarboxylate ligand. These resonances are typically at 228 ppm for identical dithiocarboxylate ligands and at 214 and 227 ppm for the complexes with mixed dithio- and perthiocarboxylate ligands. The thiophene resonances as well as the carbon atoms of the alkyl chain are also duplicated for the two different ligands in **1b**–**6b** and are unique for both types of complexes.

The infrared data supported the structures of the complexes and compared well with literature values [21–23]. The peaks at 1049 and 977 cm^{-1} were assigned for C–S stretching frequencies. Usually the stretching frequencies of the dithiocarboxylic acid are around 1100 and 900 cm^{-1} for the C=S and C–S stretching frequencies. We ascribe the lowering of the higher wave number and the increase in the lower wave number to the transfer of charge from the thiophene unit to the coordinating CS_2-moiety. In the electronic spectrum of the blue complex **1a** the d–d transitions of nickel(II) was at 602 nm and the value is similar to that reported by Furlani for monomeric dithiocarboxylate complexes of nickel(II) [24]. The d–d transitions of nickel(II) in the violet complex **1b** was at 551 nm and this value is similar to the literature value of a mixed dithiobenzoato and perthiobenzoato nickel(II) complex [25].

3.3. Thermal properties

Thermal properties of the complexes were investigated by using differential scanning calorimetry (DSC) and hot-stage polarising optical microscopy (POM). All the complexes were subjected to thermal analysis by DSC. The scanning rate was 10 °C per minute. No double melting behaviour was observed for **1a**, **1b**, **2a**, **2b** and **5b** whereas double melting behaviour was observed for **3b** and **4b**. Two endothermic peaks could be observed at 77 °C and 88 °C for **3b**. The peak at 88 °C is compatible with the melting point and the peak at 77 °C is for crystal-to-crystal transition. The clearing point was not observed in the DSC. Complex **4b** also showed two endothermic peaks at 102 °C and 117 °C.

Complexes **3b**, **4b** and **5b** were also examined using hot-stage polarising optical microscopy. Complex **3b** (Fig. 2) is an enantiotropic liquid crystal and it exhibits a nematic phase. Enantiotropic liquid crystals show mesomorphism upon heating the solid as well as on cooling the isotropic liquid. The transition temperature of **3b** was between 92 °C and 116 °C.

The optical texture of **3b** is similar to the nematic phase of 4-nonyloxybenzoic acid [26]. Complex **4b** was a mixture of dark highly viscous liquid and opaque crystals. The liquid was not birefringent and therefore it was not a liquid crystal. The opaque crystals however melted to a nematic phase. Transition temperatures of the complexes **1**–**5** are given in Table 1. It is shown that the melting temperatures increase from the shortest chain to C_{12} and then decreases sharply for C_{16}.

Complexes **1**, **2** and **5b** directly melted to the isotropic liquids without passing through any mesophases. The transition temperature range for **3b** was between 92 °C and 116 °C (N → I) whereas for the benzene analogue [Ni(8-ottb)$_2$], the range was between 122 °C and 186 °C (N → I) [15]. The lower transition temperature observed for **3b** may be ascribed to the thiophene in the complex, due to the greater disorder in the packing of this complex compared to the rod-like benzene analogues. The thiophene complexes are not straight rods but have more of a ''step-rod'' structure [27]. This deviation from linearity may be the reason for the lower transition temperatures observed. It was reported that thiophene systems have generally lower melting points than their benzene counter parts due to reduced packing efficiency in the molecules [28].

Complexes **1a**, **1b**, **2a**, **2b** and **5b** had no mesogenic behaviour whereas complexes **3b** and **4b** showed nematic mesophases. The optimum chain length suitable for mesomorphism for the alkyl thiophene dithiocarboxylate complexes was C_8.

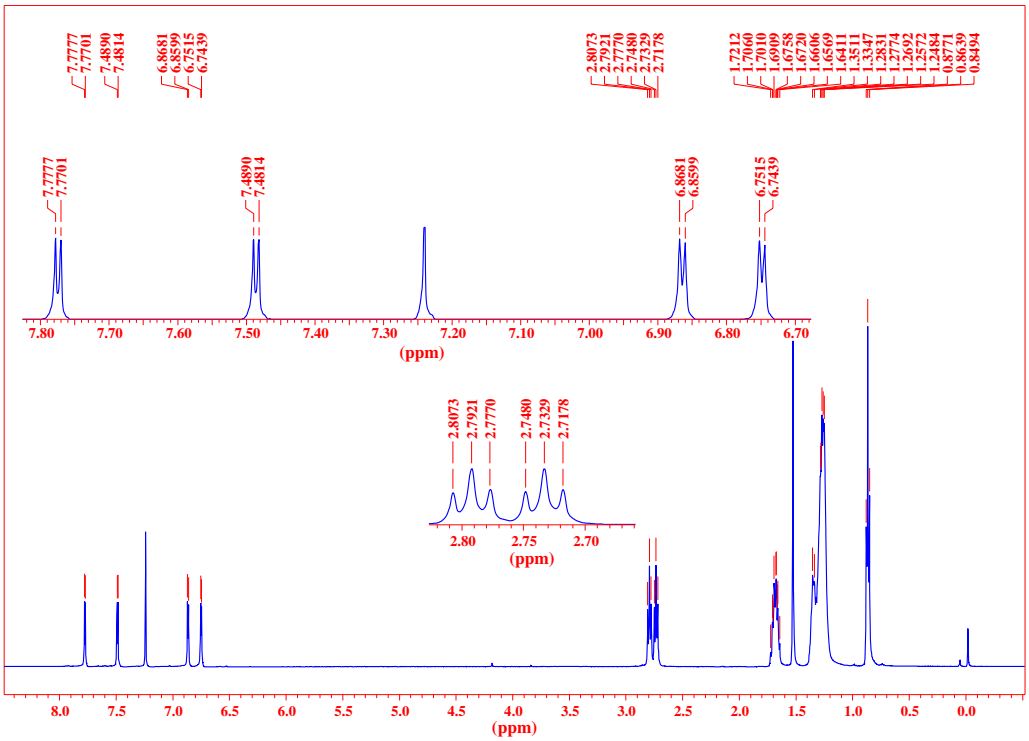


Fig. 1. The ^{1}H NMR spectrum ($CDCl_3$) of **3b**.

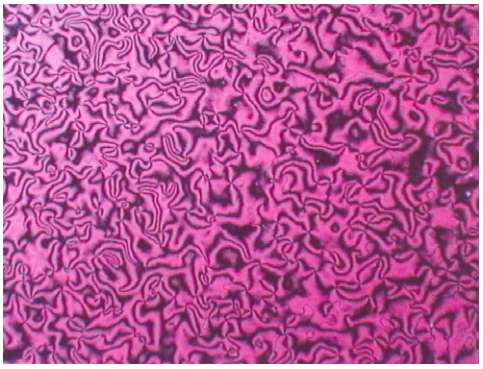


Fig. 2. Nematic phase of [Ni($S_3CTC_8H_{17}$)($S_2CTC_8H_{17}$)] **3b** at 105 °C (200× magnification).

Table 1
Transition temperatures of **1**–**5**

Complex	Chain	Transition	Temperature (°C)
1a	C_4H_9	Cr → I	52
2a	C_6H_{13}	Cr → I	65
3b	C_8H_{17}	Cr → N	92
		N → I	116
4b	$C_{12}H_{25}$	Cr → N	117
		N → I	102
5b	$C_{16}H_{33}$	Cr → I	61

Cr, crystal; N, nematic phase; and I, isotropic liquid.

4. Conclusion

The reactions of a series of 5-alkyl-2-thiophenedithiocarboxylates with nickel(II) chloride formed two types of complexes, mononuclear nickel(II) complexes with two terminal dithiocarboxylate ligands (blue) and mononuclear nickel(II) complexes with perthio- and dithiocarboxylate ligands (violet). The formation of violet vs blue compounds in this study was dependent not only on the properties of the solvent, but also by the length of the alkyl chain and the conversion from **a**- to **b**-type products enhanced by the presence of thiophene in the chain. Using the first method of synthesis the blue monomers are preferred for the shorter chains (C_4 and C_6) and violet compounds for the longer chains (C_8, C_{12} and C_{16}). It was previously noted that temperature plays an important role for the transformation of dithiocarboxylate to a perthiocarboxylate ligand [19]. The blue compounds are less soluble than the violet compounds. Thermal studies with DSC and POM showed that the complexes with C_8 and C_{12} alkyl chains are liquid crystals (metallomesogens). The mesomorphism of the two complexes was similar, as both complexes showed nematic phases. Unfortunately it was not possible to obtain **a**-type complexes of **3** and **4** to compare and study their melting behaviours. The dark colour of the complexes made phase characterization very difficult. The transition temperatures of these complexes are lower than the benzene analogues, as predicted [15]. Complexes **3b** and **4b** are the first examples of metallomesogens of nickel(II) complexes with 5-alkyl-2-thiophenedithiocarboxylate as ligands. In future, further work will be done on the optical and conducting properties of these complexes.

Acknowledgements

The authors would like to thank Prof. Koen Binnemans for POM measurements and helpful discussions. The National Research Foundation of South Africa for financial support.

Appendix A. Supplementary material

Supplementary data associated with this article can be found, in the online version, at doi:10.1016/j.poly.2007.03.056.

References

[1] D. Coucouvanis, Prog. Inorg. Chem. 11 (1970) 233.
[2] R.P. Burns, F.P. McCullong, C.A. McAuliffe, Adv. Inorg. Rad. Chem. 23 (1980) 211.
[3] (a) R. Gimenez, A.B. Manrique, S. Uriel, J. Barbera, J.L. Serrano, Chem. Commun. (2004) 2064;
(b) G. Barberio, A. Bellusci, A. Crispini, M. Ghedini, A. Golemme, P. Prus, D. Pucci, Eur. J. Inorg. Chem. (2005) 181.
[4] M. Bonamico, G. Dessy, V. Fares, L. Scaramuzza, J. Chem. Soc., Dalton Trans. (1975) 2250.
[5] P. Espinet, M.A. Esteruelas, L.A. Oro, J.L. Serrano, E. Sola, Coord. Chem. Rev. 117 (1992) 215.
[6] D.W. Bruce, J. Chem. Soc., Dalton Trans. (1993) 2983.
[7] A.M. Giroud, U.T. Müller-Westerhoff, Mol. Cryst. Liq. Cryst. 41 (1977) 11.
[8] K. Ohta, H. Hasebe, H. Ema, T. Fugimoto, I. Yamamoto, J. Chem. Soc., Chem. Commun. (1989) 1610.
[9] N. Hoshino-Miyajima, J. Chem. Soc., Chem. Commun. (1993) 1442.
[10] U.T. Müller-Westerhoff, A. Nazzal, R.J. Cox, A.M. Giroud, Mol. Cryst. Liq. Cryst. 56 (1980) 249.
[11] H. Adams, N.A. Bailey, D.W. Bruce, R. Dhillon, D.A. Dunmur, S.E. Hunt, E. Lalinde, A.A. Maggs, R. Orr, P. Styring, M.S. Wragg, P.M. Maitlis, Polyhedron 7 (1988) 1861.
[12] K. Ohta, H. Ema, I. Yamamoto, K. Matsuzaki, Liq. Cryst. 3 (1988) 1671.
[13] G.H. Spies, R.J. Angelici, Organometallics 6 (1987) 1902.
[14] (a) L. Brandsma, H.D. Verkruijsse, Preparative Polar Organometallic Chemistry, vol. 1, Springer Verlag, Heidelberg, 1987, p. 124;
(b) M. Landman, H. Görls, S. Lotz, Eur. J. Inorg. Chem. (2001) 233;
(c) M. Landman, H. Görls, S. Lotz, J. Organomet. Chem. 617–618 (2001) 280.
[15] H. Adams, A.C. Albeniz, N.A. Bailey, D.W. Bruce, A.S. Cherodian, R. Dhillon, D.A. Dunmur, P. Espinet, J.L. Feijoo, E. Lalinde, P.M. Maitlis, R.M. Richardson, G. Ungar, J. Mater. Chem. 1 (1991) 843.
[16] J.P. Fackler Jr., J.A. Fetchin, J.A. Smith, J. Am. Chem. Soc. 92 (1970) 2910.
[17] J.P. Fackler Jr., D. Coucouvanis, J.A. Fetchin, W.C. Seidel, J. Am. Chem. Soc. 90 (1968) 2784.
[18] D. Coucouvanis, J.P. Fackler Jr., J. Am. Chem. Soc. 89 (1967) 1346.
[19] J.P. Fackler Jr., J.A. Fetchin, J. Am. Chem. Soc. 92 (1970) 2912.
[20] R.J. Abraham, J. Fischer, P. Lottus, Introduction to NMR Spectroscopy, John Wiley & Sons, 1998, p. 30.
[21] M.L. Shankaranarayana, C.C. Patel, Can. J. Chem. 39 (1961) 1633.
[22] J.M. Burke, J.P. Fackler Jr., Inorg. Chem. 11 (1972) 3000.
[23] D.H. Busch, Adv. Chem. 1 (1963) 37.
[24] C. Furlani, O. Piovesana, A.A.G. Tomlinson, J. Chem. Soc., Dalton Trans. (1972) 212.
[25] K. Ohta, H. Ema, Y. Morizumi, T. Watanabe, T. Fugimoto, I. Yamamoto, Liq. Cryst. 8 (1990) 311.
[26] R. Van Deun, Liquid Crystals with Lanthanides, PhD thesis, Katholieke Universiteit Leuven, Belgium, 2001.
[27] M.S. Thomas, D.C. Liles, M. Landman, E.M. van der Merwe, S. Lotz, Polyhedron 25 (2006) 3562.
[28] L.H. Wu, Y.C. Wang, C.S. Hsu, Liq. Cryst. 27 (2000) 1503.

Available online at www.sciencedirect.com
ScienceDirect
Polyhedron 26 (2007) 3479–3490
POLYHEDRON
www.elsevier.com/locate/poly

Adsorption and intercalation of Acid Blue 9 on Mg–Al layered double hydroxides of variable metal composition

Anthony R. Auxilio [a], Philip C. Andrews [a], Peter C. Junk [a], Leone Spiccia [a,*], Daniel Neumann [b], Warwick Raverty [b], Nafty Vanderhoek [b]

[a] CRC Smartprint and School of Chemistry, Monash University, Victoria 3800, Australia
[b] CRC Smartprint and CSIRO Ensis Papro, Clayton, Victoria 3169, Australia

Received 23 January 2007; accepted 7 March 2007
Available online 24 March 2007

Abstract

Layered double hydroxides (LDHs) of the type $[Mg_{1-X}Al_X(OH)_2]^{X+}[(CO_3^{2-})_{X/2} \cdot mH_2O]$ with variable Mg/Al molar ratios have been prepared by co-precipitation of Mg^{2+} and Al^{3+} ions at constant pH. The ability of these compounds to adsorb Acid Blue 9 has been evaluated by UV–Vis spectrophotometry, FT-IR spectroscopy, powder X-ray diffraction analysis, N_2 adsorption/desorption analysis, scanning electron microscopy, energy-dispersive X-ray analysis, X-ray photoelectron spectroscopy and atomic absorption spectroscopy. Optimum adsorption of Acid Blue 9 (AB9) was achieved for LDHs produced from mixtures containing Mg and Al in molar ratios varying from 3.1 to 4.4. LDHs with such compositions giving an equilibrium binding constant (K_a) of ca. $1.2 \times 10^5\ M^{-1}$ with a maximum monolayer coverage (C_m) of ca. 7.6×10^{-2} mmol g^{-1}. This observation was correlated to the surface area, phase purity, pore size and volume, particle size and the surface morphology of the LDHs. Powder XRD analysis after adsorption of 1.85 mM Acid Blue 9 in 20% (v/v) glycerol–H_2O solvent system indicated that the dye was not intercalated between the brucite-like layers as no change was evident in the $d_{(003)}$ spacing. Thus, at this low concentration surface adsorption of the dye is occurring. Powder XRD analysis revealed that intercalation was achieved at 76 mM dye concentration in the same solvent system for materials with Mg:Al molar ratios between 3.1 and 5.6. This results in an expansion of the interlayer spacing from ca. 8 Å to 19 Å to accommodate the AB9 anion. For the sample produced from a 3:1 mixture of Mg/Al, thermal gravimetric and elemental/micro analyses revealed that the new hybrid material has the composition $[Mg_{3.0}Al_{1.0}(OH)_{7.5}][(CO_3)_{0.62} \cdot 3.2H_2O \cdot 1.5\text{Glycerol} \cdot 0.1\text{Acid Blue 9}]$.
© 2007 Elsevier Ltd. All rights reserved.

Keywords: Layered double hydroxides; Adsorption; Intercalation; Acid Blue 9; Co-precipitation

1. Introduction

Layered solids have attracted the attention of many researchers because of their possible use in a variety of applications [1–3]. These compounds may be classified as neutral layers which are held together by van der Waals interactions, negatively charged layers which are separated by mobile cations, and positively charged layers which are separated by anions [4]. They have distinctive properties that are characterized by the strong intralayer bonds and weak interlayer interactions.

Positively charged layer compounds are known as layered double hydroxide (LDH), or hydrotalcite-like compounds. Their empirical formula is $[M^{2+}_{1-X}M^{3+}_X\text{-}(OH)_2]^{X+}[(A^{n-})_{X/n} \cdot mH_2O]$ where M^{2+} and M^{3+} are di- and trivalent cations, respectively, A^{n-} is an exchangeable anion, and x is the molar ratio, $M^{3+}/(M^{2+} + M^{3+})$, that determines layer charge density [5,6]. These compounds exist in two dimorphic forms, rhombohedral hydrotalcite and hexagonal manasseite. In the hydrotalcite structure, three double-layers are present per unit cell, whilst in the manasseite structure, two double-layers are present [7].

* Corresponding author. Tel.: +61 3 9905 4526; fax: +61 3 9905 4597.
E-mail address: leone.spiccia@sci.monash.edu.au (L. Spiccia).

0277-5387/$ - see front matter © 2007 Elsevier Ltd. All rights reserved.
doi:10.1016/j.poly.2007.03.019

The crystal structure consists of positively charged brucite-like octahedral hydroxide layers due to the isomorphous replacement of some divalent metal cation by trivalent metal cation [8]. Positive charges on the surface of the layer are neutralised by interlayer anions. When LDHs are immersed in aqueous solutions some of the interlayer anions can move into the solution and can be exchanged with other ions [9].

There have been many studies focussing on the application of layered double hydroxides as adsorbent material using different interlayer anions [10–15] and as a host for intercalation chemistry [16–21]. Remarkably absent in the literature is the optimisation of adsorption and intercalation properties through fine tuning of the divalent/trivalent metal molar ratios. In this paper, we report the adsorption affinity of Acid Blue 9 (AB9) to hydrotalcite-like compounds of the type $[Mg_{1-X}Al_X(OH)_2]^{X+}[(CO_3^{2-})_{X/2}\cdot mH_2O]$ herein referred to as Mg–Al–LDH–CO_3 (Fig. 1) in which the Mg/Al content was varied with a view to improving the adsorption (surface) and intercalation (interlamellar) properties of the LDH material (in the context of this study, adsorption is taken to indicate chemisorption since the exact nature of binding is not known). We demonstrate that anion exchange can still be achieved even if the original interlayer anion is carbonate – an ion that can be difficult to exchange from the LDH interlayer region.

AB9 was chosen as the dye for our investigation as it has many important practical applications. For example, it is used in textile industry for dyeing textile fibres and, as a consequence, studies [22,23] have been conducted to reduce the colour of the dye-containing effluents through treatments involving adsorption onto low-cost materials, such as LDHs. Intercalation of this dye into an LDH could also be used for slow-dying process technology, i.e., slow release of the dye from the inorganic lamella into a solution [13]. AB9 has also been studied [24] as film dopant to act as photosensitive chromophore for optics and laser technology application. Finally, AB9 has also been used for ink jet technology [25] so its adsorption and/or intercalation into LDHs is of commercial significance.

2. Experimental

2.1. Synthesis

Mg–Al–LDH–CO_3 materials were prepared by the co-precipitation method described previously [26]. Solution A containing $Mg(NO_3)_2\cdot 6H_2O$ and $Al(NO_3)_3\cdot 9H_2O$ (Sigma–Aldrich) with Mg^{2+}/Al^{3+} molar ratios varying from 2.0 to 10.0 were dissolved in 150 mL of distilled water to give solutions with a Mg^{2+} concentration of 1.6 M. Solution B containing NaOH and Na_2CO_3 (Merck) was prepared by dissolving the salts in 150 mL distilled water. The concentrations of reagents in solution B were related to the concentrations of metal ions in solution A as follows: $[NaOH] = 1.6[Mg^{2+}+Al^{3+}]$ and $[Na_2CO_3] = 2.0[Al^{3+}]$.

Solution A (150 mL) and solution B (150 mL) were added dropwise to a vessel containing stirred distilled water (120 mL) at such a rate that the pH of the reaction mixture was maintained at 9.5 (±0.05). The addition process was controlled by a Metrohm 736 GP Titrino auto titrator and carried out at room temperature. The resulting slurry was aged at 100 °C for 16 h. The precipitate was then filtered, washed three times with distilled water, and dried at 100 °C for 24 h. All products were then ground with an agate mortar and pestle prior to analysis and use in dye adsorption testing. Hydromagnesite ($Mg_5(CO_3)_4(OH)_2\cdot 5H_2O$; Sigma–Aldrich) was included in the analysis for discussion purposes.

A typical intercalation reaction leading to sample 5 (see Table 5) was performed based on a modified method [27] that involved reacting 0.5 g of Mg–Al–LDH–CO_3 (Mg/Al = 3.1 and without prior removal of CO_3^{2-} ions) with 5 mL, 76 mM disodium salt of Acid Blue 9 (disodium α-(4-(*N*-ethyl-3-sulfonatobenzylamino)phenyl)-alpha-(4-*N*-thyl-3-sulfonatobenzylamino,cyclohexa-2,5-dienylidene)toluene-2-sulfonate) (Fig. 2; Saujanya Dyechem company) in a 5:1 (v/v) H_2O:glycerol solvent system. The overall process is the same as the dye affinity test outlined below. The molecular structure and size of the dye was estimated in the gas phase using the Hyperchem software. This was

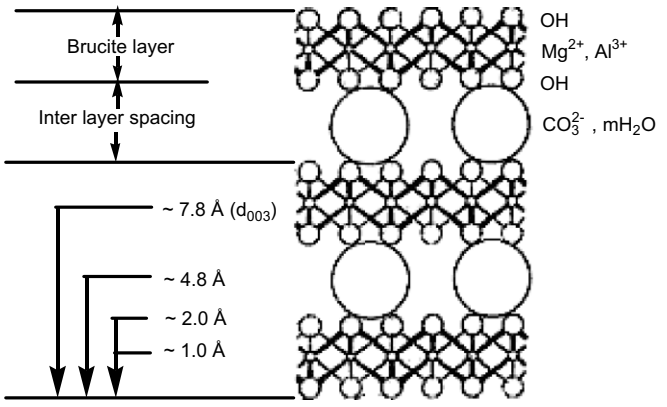


Fig. 1. 2D – Schematic representation of Mg–Al–LDH–CO_3 system [10].

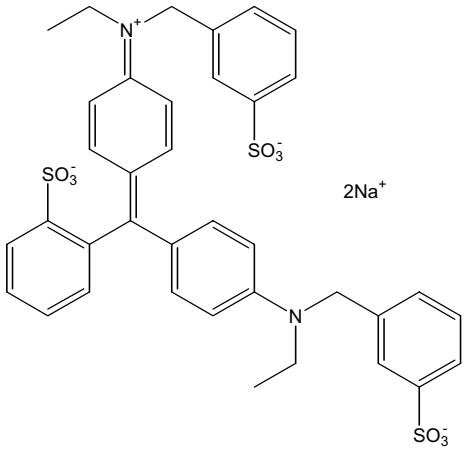


Fig. 2. Disodium salt of Acid Blue 9.

done by finding the lowest energy conformation prior to energy minimization. It should be pointed out that single crystal X-ray analysis of the dye could not be done due to the amorphous nature of Acid Blue 9. The solid produced was recovered by centrifugation and dried under air atmosphere for 24 h at 100 °C.

2.2. Dye affinity test

The change in the adsorbed amounts of Acid Blue 9 with time was measured for up to 7 days. It was found that the adsorbed amount was the same after mixing (vortex) for 1 min. and after vigorous stirring (magnetic stirrer) for 7 days. On the basis of these results, the adsorption for the determination of adsorption isotherms was carried out for 1 min. using a vortex (2500 rpm).

A 9.23×10^{-6} M solution of the dye prepared in 20% glycerol/Milli-Q water solvent mixture was found to exhibit a λ_{max} at 629 nm and $\varepsilon = 1.37 \times 10^5\ M^{-1}\ cm^{-1}$. The Mg–Al–LDH–$CO_3$ with different Mg/Al ratios were then subjected to a dye affinity test (three replicates) according to published methodologies [28], using Acid Blue 9 solution (1.85 mM). The dye solution (5 mL) was added to the Mg–Al–LDH–CO_3 system (0.5 g) in a centrifuge tube. The tube was agitated using a vortex mixer for 1 min followed by centrifugation (4600 rpm, 5 min.). The supernatant liquid was removed carefully and the mass of liquid was recorded. An aliquot of supernatant liquid (25 μL) was diluted with Milli-Q water (5 mL) giving a ratio of 1:200 and analysed using CARY 100 Bio UV–Vis spectrophotometer. It should be pointed out that for Mg–Al–LDH–CO_3 with Mg:Al ratios of 3.0, 3.1, 4.4, and 5.6, a dilution factor lower than 200 was used so that the final absorbance reading was in the range of 0.5–1.0.

The absorbance of the diluted supernatant was recorded at the wavelength of maximum absorption (629 nm). The value was then divided by the absorbance for the untreated dye, giving a relative absorbance value. A ratio greater than one indicates that the supernatant has a high dye concentration post treatment whilst a ratio of less than one indicates good affinity of the dye for the Mg–Al–LDH–CO_3 system.

For Mg–Al–LDH–CO_3 systems that exhibited the best affinity of Acid Blue 9, adsorption isotherms were measured and the Langmuir equation [14], originally derived for gas adsorption on planar surfaces [29], was then used to estimate the dye adsorption properties of the material, $C_s = C_m K_a C_p/(1 + K_a C_p)$, where C_s (mmol/g) is the amount of dye adsorbed to the surface, C_p (mmol/mL) is the amount of dye remaining in the solution, C_m (mmol/g) is the maximum adsorption capacity at a monolayer coverage, and K_a ($M^{-1} = (mmol/mL)^{-1}$) is the equilibrium binding constant.

2.3. Characterization

The synthesized LDH materials were analysed by powder X-ray diffraction using a Philips 1140 diffractometer under the following conditions: 40 kV, 25 mA, Cu Kα ($\lambda = 0.15406$ nm) radiation. The samples, as unoriented powders, were scanned in steps of 0.02° (2θ) in the range from 2° to 70° at a speed of 2°/min.

Metal analyses were carried out using three different techniques. Energy dispersive X-ray spectroscopy at a voltage of 15 kV using Link ISIS manufactured by Oxford Instruments. X-ray photoelectron spectroscopy using Kratos AXIS HSi spectrometer with a monochromated Al Kα source at a power of 180 W (12 kV × 15 mA) and a hemispherical analyser operating in the fixed analyser transmission mode. The total pressure in the main vacuum chamber during analysis was $\sim 10^{-8}$ mbar. Each sample was analysed at an electron take-off angle of 90° relative to the sample surface. The Mg 2s and Al 2p photoelectrons were identified and quantified from survey spectra acquired at 320 eV pass energy. Atomic absorption spectroscopy analyses were conducted using a VARIAN SpectrAA-400 spectrophotometer.

Elemental analysis was performed by the Campbell Microanalytical Laboratory, University of Otago, New Zealand and Chemical & MicroAnalytical Services Pty. Ltd., Australia.

Infrared experiments were carried out using EQUINOX–IFS 55 spectrometer. Samples were mixed with KBr to produced a disc with a 1% compound loading. The spectra was recorded between 4000 and 400 cm^{-1}. Fifty scans were recorded with a resolution of 2 cm^{-1}.

Thermogravimetric analyses were performed on a Perkin–Elmer Pyris 1 TGA instrument. Ten to twenty milligrams of samples was heated in a platinum crucible between 25 and 800 °C at a heating rate of 10 °C/min under a stream of air.

Surface morphologies and particle size distribution were studied using Philips XL30 field emission scanning electron microscope manufactured by Oxford Instruments at a voltage of 5 kV.

Surface area, pore size, and pore volume were studied using an Omnisorp 360 CX manufactured by Coulter using nitrogen adsorption–desorption at 77 K.

The density was determined by helium pycnometry technique using AccuPyc 1330 gas displacement pycnometer manufactured by Micromeritics.

3. Results and discussion

3.1. Surface adsorption studies

Three different methods were utilized to determine the metal content as well the Mg to Al molar ratio of the synthetic Mg–Al–LDH–CO_3 materials. These methods were in close agreement to each other giving a relative standard deviation (RSD) of <0.2 for LDHs with Mg:Al molar ratios of less than 5.0. Higher RSD were observed for Mg:Al molar ratio of 6.0 and above (Table 1) due to the aluminium content being below the threshold that can be accurately measured by EDX and XPS techniques. AAS values are used throughout the discussion of the results

Table 1
Mg/Al ratios using energy dispersive X-ray spectroscopy (EDX), X-ray photoelectron spectroscopy (XPS) and atomic absorption spectroscopy (AAS)

Calculated Mg:Al molar ratio[a]	Experimental			RSD
	EDX	XPS	AAS	
2.0	2.1	2.2	1.9	0.15
3.0	3.3	3.1	3.0	0.15
4.0	3.2	3.4	3.1	0.12
			3.0[b]	
5.0	4.2	4.4	4.4	0.12
6.0	5.8	4.8	5.6	0.53
7.0	7.7	6.3	7.6	0.78
8.0	9.6	5.7	8.0	1.96
9.0	8.0	6.7	9.3	1.30
10.0	9.4	8.0	10.7	1.35

[a] Based on the ratio of reagent added in the synthesis of the LDHs.
[b] Determined by Campbell microanalytical laboratory.

Table 2
Dye adsorbed calculated as the number of Acid Blue 9 molecules per surface area of LDHs and amount of Acid Blue 9 left in the solution (initial dye concentration = 1.85 mM)

Mg:Al molar ratio	Adsorbed dye (# Dye/nm^2)[a]	Dye remaining in solution (mM)
1.9	0.26	9.9×10^{-2}
3.0	0.09	7.3×10^{-3}
3.1	0.09	2.9×10^{-3}
4.4	0.10	2.9×10^{-3}
5.6	0.14	2.9×10^{-3}
7.6	0.37	4.4×10^{-2}
8.0	0.45	1.2×10^{-1}
9.3	0.43	1.4×10^{-1}
10.7	0.47	2.2×10^{-1}

[a] Calculated according to the formula: 6.02×10^{23} (moldye$_{total}$–moldye$_{supernatant}$)/(0.5 g × surface area)/1×10^{-18}.

presented herein. At the higher Mg/Al molar ratio ($\geqslant 5$) some of the Mg must come from hydromagnesite that formed during the synthesis.

The results of the dye affinity test shown in Fig. 3, indicate that the Mg–Al–LDH–CO_3 system exhibits excellent dye affinity for samples with composition in the range of Mg/Al molar ratios of 3.1–5.6. Above and below these values the dye affinity decreases. The equilibrium concentration of Acid Blue 9 left in the supernatant was subtracted from the initial Acid Blue 9 concentration to determine the adsorbed dye in a given fixed amount of LDH as a function of the surface area of LDH (Table 2). No change in the interlayer spacing as measured by powder XRD was observed indicating that the Acid Blue 9 is adsorbed onto the surface of the material and not intercalated between the interlayer.

It is apparent from Table 2 that Mg/Al molar ratios of 3.1–5.6 adsorbed almost all the dye from the solution (<0.3% remaining solution). Even though most of the dye is adsorbed from solution, the surface coverage of the adsorbed dye is low (~0.10 mol/nm^2) for these ratios. This is due to higher surface area (see Table 4) of these materials plus the fact that the concentration (1.85 mM) of dye used was fixed and insufficient to achieve monolayer coverage for Mg:Al molar ratios of 3.1–5.6.

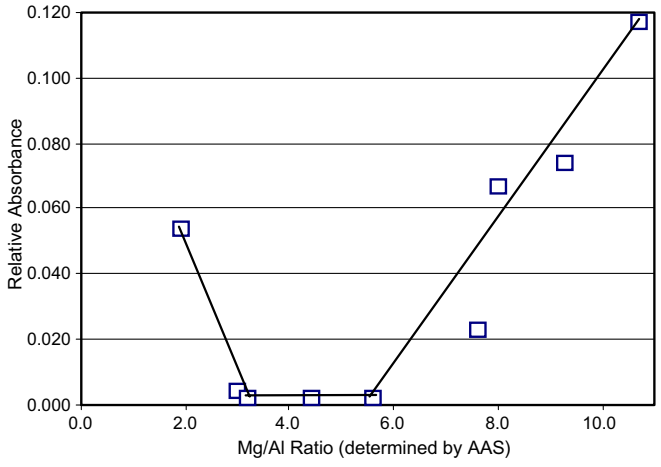


Fig. 3. Relative absorbance of solutions used to adsorb Acid Blue 9 on Mg–Al–LDH–CO_3 system with varying Mg/Al ratios.

The maximum adsorption capacity and binding constants of these materials were determined by measuring the amount of dye adsorbed as a function of concentration of Acid Blue 9. The data, shown in Fig. 4, could be fitted very well using the Langmuir model. According to Giles et al. [30] these are of L-2 curves which indicates that the Acid Blue 9 molecules are most likely to be adsorbed to the surface of the LDH by very strong intermolecular interactions. It should be noted, however, that since the initial part of the isotherm is nearly vertical, one may consider such a curve as belonging also to an H-2 class which is a special case of the L curves. This further demonstrates that Acid Blue 9 has such a high affinity for the LDH that it is adsorbed even from dilute solutions. The plateau may represent the formation of a complete monolayer coverage from which maximum adsorption capacity can be derived. The long plateau of these materials suggest that after the surface has been saturated to the first degree a high energy barrier needs to be overcome before additional adsorption can occur on new sites, or even the interlayer region.

The Langmuir model parameters (C_m and K_a) are listed in Table 3 and reveal interesting trends. These three LDH materials have much the same affinity for Acid Blue 9 as indicated by the similar K_a values of ca. 1.2×10^5 M^{-1}. However, the optimum adsorption was exhibited by the materials with Mg/Al molar ratios of 3.1 and 4.4, both of which gave C_m values of ca. 7.6×10^{-2} mmol/g. A significant decrease in the C_m value was observed for the material with a molar ratio 5.6 and it can be concluded that this type of LDH material exhibits the best adsorption properties for metal molar ratios in the range 3.1–4.4.

To rationalize this behavior, the powder X-ray diffractograms (Fig. 5) of these compounds were closely examined.

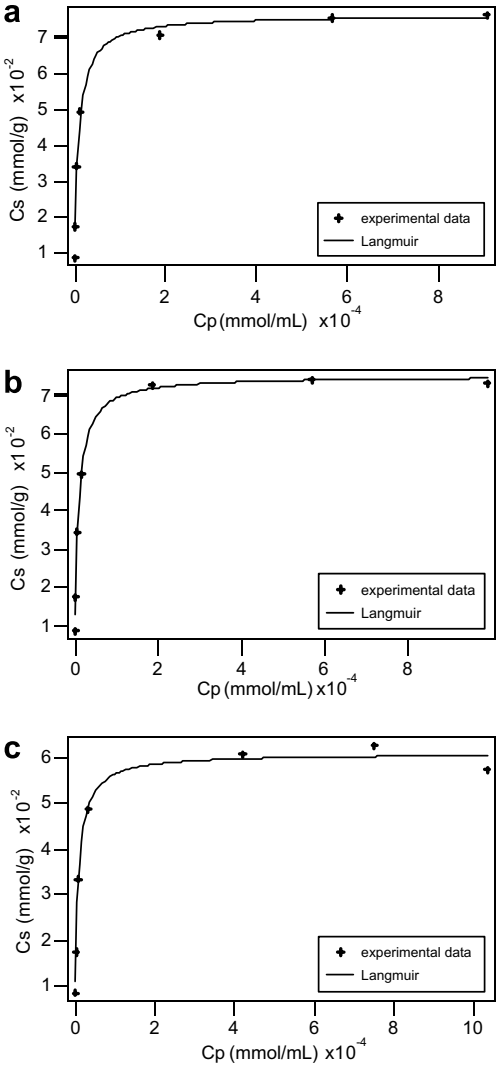


Fig. 4. Adsorption isotherms for Acid Blue 9 binding to Mg–Al–LDH–CO_3 system at a Mg/Al (a) 3.1; (b) 4.4 and (c) 5.6. Fitting of the data to the Langmuir equation is represented by the full line.

Table 3
Langmuir model parameters for Acid Blue 9 binding to the Mg–Al–LDH–CO_3 system at ratios 3.1, 4.4, and 5.6

Mg:Al molar ratio	C_m (mmol/g)	K_a (M^{-1})
3.1	$7.62\ (\pm 0.29) \times 10^{-2}$	$1.18\ (\pm 0.20) \times 10^{5}$
4.4	$7.51\ (\pm 0.16) \times 10^{-2}$	$1.19\ (\pm 0.11) \times 10^{5}$
5.6	$6.09\ (\pm 0.12) \times 10^{-2}$	$1.24\ (\pm 0.13) \times 10^{5}$

It was found that a pure hydrotalcite-like compound can only be produced within a very narrow range of x values ($M^{3+}/[M^{2+} + M^{3+}]$), between 0.24 (Mg/Al = 3.1) and 0.34 (Mg/Al = 1.9) which is within the range of most reliable limits reported in previous studies (viz. $0.2 \leqslant x \leqslant 0.4$) [5,7,31,32].

Fig. 5 shows that the (hkl) reflections where $l \neq 0$ of the hydrotalcite-like phase are slightly shifted to the lower 2θ as the x value is decreased. This is due to an increase in the interlayer spacing, as evident from a change in c values,

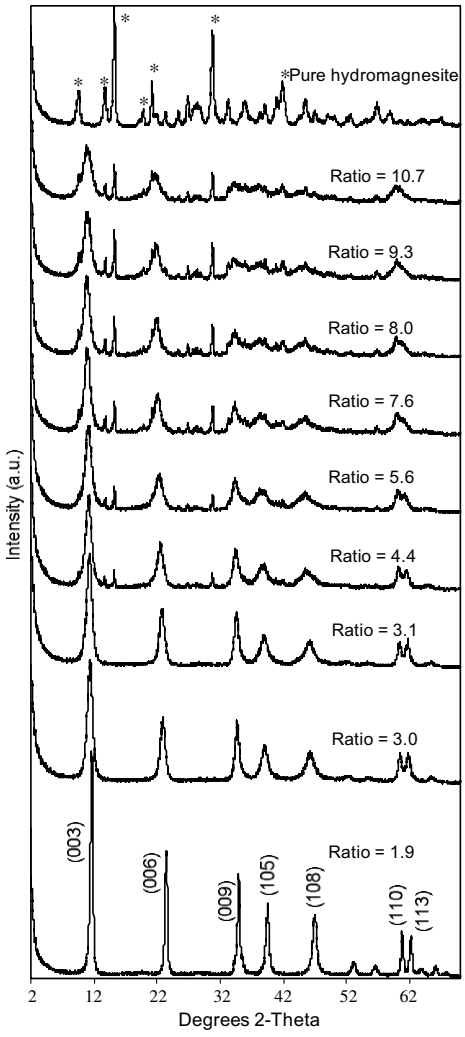


Fig. 5. X-ray powder diffractograms of Mg–Al–LDH–CO_3 system at different Mg/Al values and for pure hydromagnesite.

i.e., from $c = 7.6$ Å for $x = 0.34$ (ratio = 1.9) up to $c = 8.1$ Å for $x = 0.09$ (ratio = 10.7) (see Supplementary material, Table S1). Therefore, a less compact Mg–Al–LDH–CO_3 system results at a lower value of x. This has been proposed [31] to be due to the decrease in charge density which consequently results in a lower electrostatic attraction between positive brucite-like layers and negative interlayer species. This less compact textural property could be contributing for the better dye affinity of these materials but other factors like surface area (vide infra) will be more important. We note also that this will be valid only if the compound in question is hydrotalcite-like. As can be seen from Fig. 5, starting from a Mg:Al molar ratio of 4.4, a new phase can be observed in the powder XRD as revealed in the emergence of new set of reflections in the diffraction pattern, notably at 2θ values of 9.6°, 13.8°, 15.2°, 19.9°, 21.2°, 30.8° and 41.9° (*shown in asterisks*). At the same time the reflections for hydrotalcite-like phase becomes less intense. Analysis of these new reflections revealed that it is a hydromagnesite compound which has the formula of $Mg_5(CO_3)_4(OH)_2 \cdot 5H_2O$ (*JCPDS #:*

70-1177). This compound may be formed via the following reactions:

$$Mg^{2+} + 2OH^- \Longleftrightarrow Mg(OH)_2 \quad (1)$$

$$5Mg(OH)_2 + 4CO_2 + H_2O \rightarrow Mg_5(CO_3)_4(OH)\cdot 5H_2O \quad (2)$$

The formation of this compound at a molar ratio of 4.4 is probably triggered by two factors: (1) the interlayer spacing (7.9 Å) is already too high such that interlamellar anions are no longer effective in holding the brucite layers, leading to a collapse of some interlamellar domains of the hydrotalcite-like compound [31] favoring the formation of a new phase, and (2) the deficiency of trivalent metal ions necessary in the formation of hydrotalcite-like compounds. Interestingly, as the Mg/Al molar ratio is further increased (lower x value) the adsorption ability of the material decreases. This suggests that the good adsorption behavior can be ascribed to the presence of a hydrotalcite phase and not of the hydromagnesite phase. The materials with Mg:Al molar ratios of 4.4 and 5.6 still exhibit good dye adsorption properties due to the fact that they consist predominantly of the hydrotalcite phase. In this context, the dye affinity of the material with Mg:Al molar ratio of 5.6 is excellent, but the capacity to adsorb the dye has dropped by ca. 25% (see Table 3).

The (003), (006) and (009) reflections of the hydrotalcite-like phase get broader as the x value gets smaller (Fig. 5). Application of the Scherrer equation [33], $t = 0.9\lambda/B\cos\theta_B$, where t is the crystallite size, λ is the wavelength of the radiation used, B is the full width at half maximum (FWHM) and θ_B is the Bragg diffraction angle, leads to the conclusion that the average crystallite size of the hydrotalcite phase material is decreasing. This implies that the material has a greater surface area, and consequently, better adsorbance.

Table 4 summarizes the surface area, pore diameter/pore volume and density of Mg–Al–LDH–CO_3 system at different Mg/Al molar ratios as determined using the BET (Brunauer, Emmett and Teller) theory, B.J.H. (Barret, Joyner and Halenda) method and helium pycnometry, respectively. It is clear that the adsorptive capacity of these materials increases with the surface area reaching a maximum that has a Mg/Al molar ratio of 3.1 (SA = 123 m^2/g). The surface area value at Mg/Al = 3.1 is in excellent agreement with that reported by Reichle [34] of 120 m^2/g, although the crystallization temperature used in this study was 100 °C (24 h) (cf. 65–75 °C (18 h) by Reichle). Beyond a Mg/Al molar ratio of 4.4, the surface area starts to decrease and so does the adsorptive capacity (see Table 3). It can be concluded that as hydromagnesite starts to form, dye adsorption by the material decreases, due to a decrease in surface area and for the poorer dye adsorptive properties of hydromagnesite.

The change in surface area influences the pore volume of these materials. Obviously, the larger the volume, the larger the surface area, and therefore more dye would be needed to achieve monolayer adsorption on the surface can take place. In fact, the highest pore volumes were measured for materials with the best dye affinity, i.e., at Mg:Al molar ratios of 3.1 and 4.4.

Table 4
Textural properties of Mg–Al–LDH–CO_3 materials at different Mg/Al values

Mg/Al[a]	Surface area[c] (m^2/g)	Ave. pore diameter[d] (Å)	Corrected pore vol.[e] (cm^3/g)	Ave. density[f] (g/cm^3)
1.9	40	284	0.28	2.10
3.0	118	263	0.78	2.00
3.1	123	266	0.82	2.03
4.4	110	264	0.72	2.01
5.6	81	225	0.45	1.99
7.6	29	236	0.17	1.99
8.0	23	271	0.16	2.01
9.3	24	263	0.16	2.01
10.7	21	293	0.15	1.99
PHM[b]	18	322	0.14	2.17

[a] Mg/Al molar ratio determined by AAS analysis of the LDH.
[b] Pure hydromagnesite (included for comparison).
[c] BET method.
[d] BJH method.
[e] BJH method.
[f] Helium density.

With respect to the pore diameter, there was no correlation with adsorptive capacity of the material. It is clear however, that all of these materials can be considered mesoporous, i.e., having pores at 2–50 nm [35]. It should also be noted that, despite the significant change in surface area and pore size, all of the materials studied have much the same average density of ca. 2 g cm^{-3}. Fig. 6 shows the adsorption and desorption isotherms of selected materials and they can be classified as type IV isotherms which are typical of mesoporous materials [31,36] such as hydrotalcite and hydromagnesite. The same type of isotherms were exhibited by the other materials prepared in this study. The shapes of pores can usually be inferred from the form of the adsorption–desorption isotherm. All synthesised materials including the pure hydromagnesite do not show a limiting adsorption capacity at high relative pressures, thus, according to Sing et al. [37] this is a H3 type hysteresis which is characteristic of aggregates of plate-like particles leading to slit-shaped pores. This conclusion is supported by scanning electron microscope analysis (Fig. 7).

For the material with Mg/Al = 1.9, the SEM shows a hexagonal platelet morphology consistent with previous studies [34,38]. It appears also that the average particle size ($\sim 50 \times 250$ nm) is quite uniform, implying a narrow particle size distribution. However, starting from a molar ratio of 3.0 and up to a molar ratio of 9.3, mixing of a coral-like morphology with large lamellar shaped materials is evident, the latter becoming more pronounced as the Mg/Al molar ratio increases. A closer examination of the coral-like surface micrographs reveal that these are just plate-like

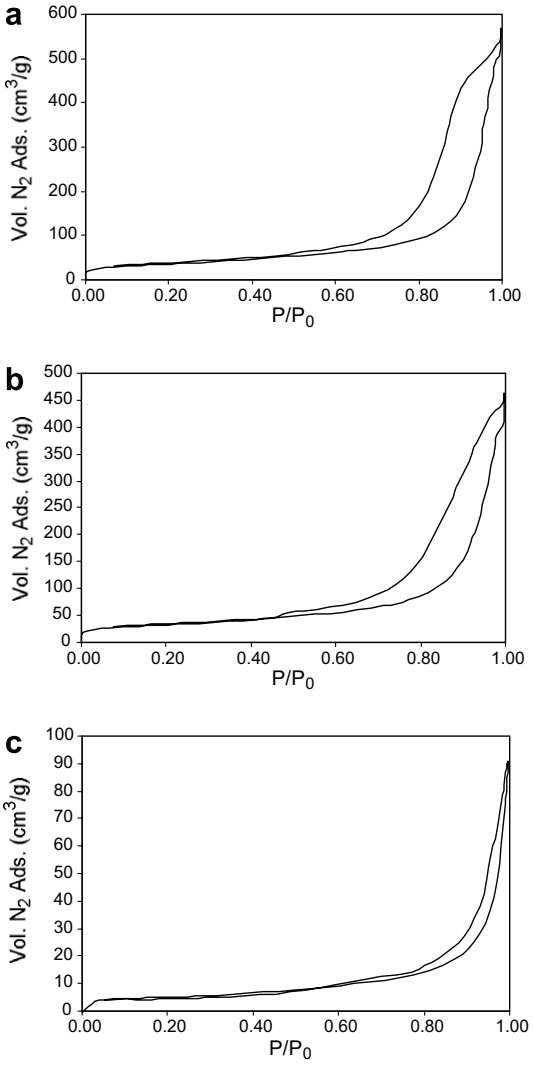


Fig. 6. N_2 Adsorption–desorption isotherms of: (a) Mg–Al–LDH–CO_3 at ratio 3.1 (b) Mg–Al–LDH–CO_3 at ratio 4.4 and (c) pure hydromagnesite (PHM).

particles arranged in a "hollow-block" fashion (see Fig. 7). Interestingly, this hollow-block fashion arrangement becomes most evident at Mg/Al = 3.1 and decrease in prominence above Mg/Al = 5.6. At and above this molar ratio, a wide particle size distribution (100–670 nm in diameter) is more evident. At Mg/Al = 10.7, the surface morphology becomes more characteristic of hydromagnesite, that is, lamellar plates are stacked parallel to each other. Since pure hydromagnesite was found to exhibit the least adsorptive capacity of all the materials studied (not shown in Fig. 3), it can be concluded that the presence of hydromagnesite is a further factor (in addition to a reduction in surface area) causing reduction in the dye adsorption properties of the materials. In fact, hydromagnesite exhibited the least surface area (18 m^2/g) and pore volume (0.14 cm^3/g) of all materials studied and the presence of this material is likely to be contributing to a reduction in surface area.

3.2. Intercalation (interlamellar anionic exchange)

Previous studies [27,39] showed that the use of a swelling agent, such as glycerol, assists the intercalation of Keggin-type polyoxometalate anions into layered double hydroxides. In such studies glycerol (1:2 (v/v) H_2O:glycerol) was used to increase the interlayer spacing prior to the intercalation reaction. Carbonates were also removed before intercalation by heating the LDH material to 500 °C and then reconstructing it under N_2 atmosphere. The possibility of whether anion intercalation can occur in our dye affinity test procedure was examined using a 5:1 (v/v) H_2O:glycerol (low glycerol loading) in the presence of carbonate and hydroxide anions. To probe whether Acid Blue 9 molecules are intercalated between the interlayer spacing or just a surface adsorption, the dye treated pigment during the dye affinity test was collected. This pigment was then dried at 100 °C for 24 h, ground with an agate mortar and pestle and subjected to PXRD analysis. Acid Blue 9 in its original form was also subjected for PXRD analysis. Fig. 8 shows the diffractograms of Mg–Al–LDH–CO_3 system at different Mg/Al molar ratios treated with 1.85 mM dye showed no change in the $d_{(003)}$ basal spacing (see Supplementary material, Table S1) of the LDH before and after dye treatment. This means that Acid Blue 9 was not intercalated. However, two important observations can be made from the diffraction peaks. Firstly, the appearance of a broad background peak at 2θ of ca. 20° is due to Acid Blue 9 which exhibits a diffuse or amorphous X-ray pattern. Most likely, the dye has precipitated as microcrystals on the surface. Secondly, the reflection at $2\theta = 9.6°$ (*for hydromagnesite*) that starts to appear for a Mg:Al molar ratio of 4.4 for untreated LDH, disappears for the treated LDH as the Mg:Al molar ratio increases (e.g., at Mg:Al molar ratio of 9.3 and 10.7). This reflection and the (0 0 3) reflection of hydrotalcite results in one broadened diffraction line which is the only one experimentally observable. The transformation of symmetric and sharp reflections into broad and asymmetric diffraction bands after treatment with glycerol (see also Fig. 9a) is an indication of the presence of stacking faults. Although incorporation of glycerol into the hydrotalcite did not increase the gallery height, it is believed, however, that uneven expansion leads to planar defects (i.e. stacking faults) that may facilitate the intercalation of bulky anions, such as Acid Blue 9.

One could argue that intercalation is still possible considering especially that the dye has the same charge as the carbonate ion. Since preliminary investigations have shown that Mg:Al molar ratios of 3.1–5.6 exhibit the best dye adsorption properties on these materials. These were treated with a more concentrated (76 mM; 1.5 meq/g ion-exchange capacity) Acid Blue 9 solution. This concentration is ten times greater than that needed for a complete monolayer coverage (7.6×10^{-2} mmol/g) for the material that exhibits the best adsorption properties. Fig. 9b shows the diffractograms of Mg:Al molar ratios of 3.1–5.6 treated

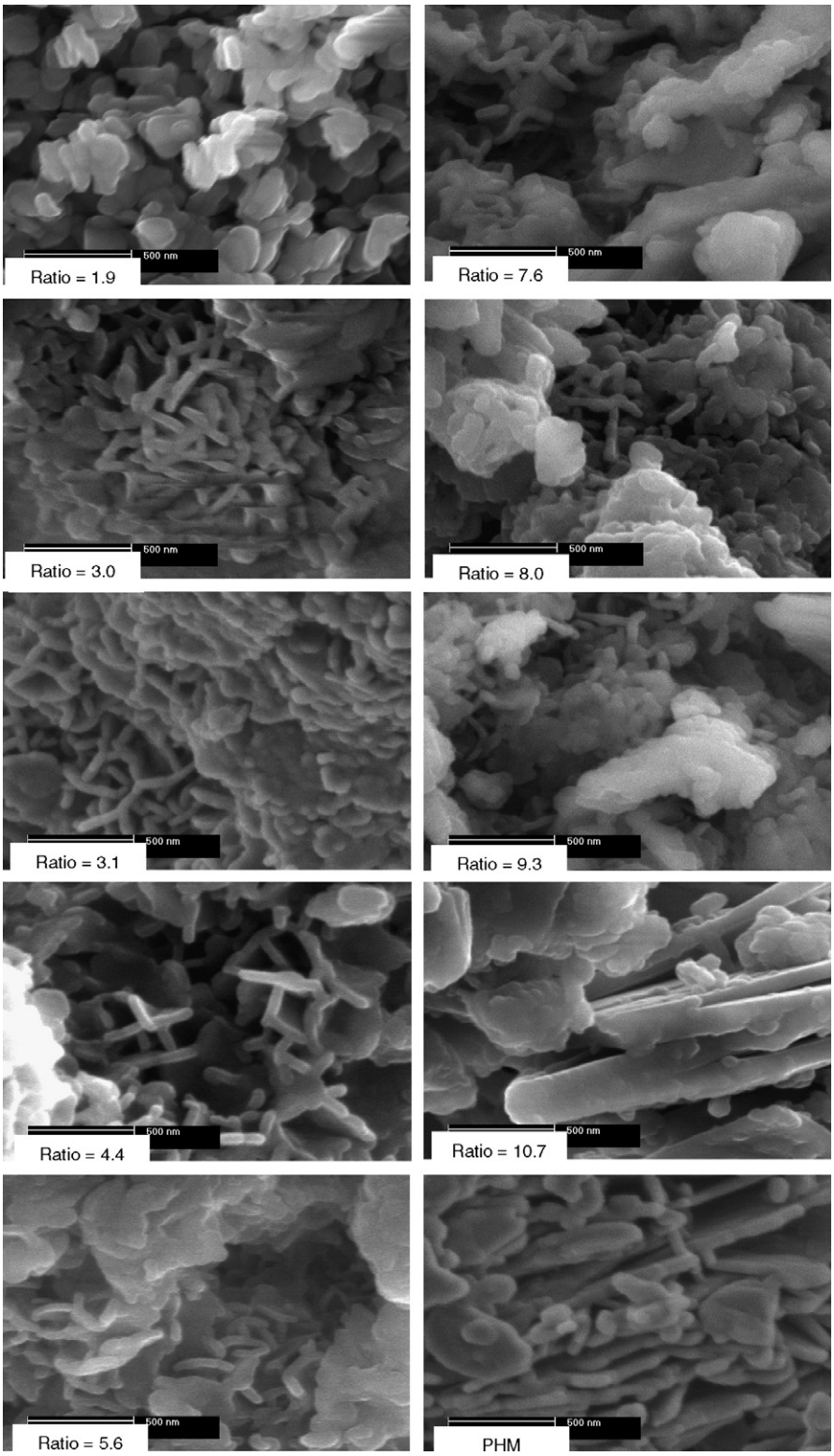


Fig. 7. Scanning electron micrographs of Mg–Al–LDH–CO_3 systems at varying ratios and pure hydromagnesite compound (PHM).

with 76 mM Acid Blue 9 in pure H_2O solvent. Clearly, no evidence of intercalation can be observed as there are no changes in peak position and intensity (cf. original hydrotalcite materials, Fig. 5). This is despite an increase in the Acid Blue 9 content of the materials (see Table 5).

Since this amount (76 mM) of dye is less than the specific ion-exchange capacity of LDH used that is 2.2 meq/g, the LDH was treated with more concentrated aqueous solutions of AB9 having an ion-exchange capacities of 3.0 and 6.1 meq/g. Again, there was no sign of intercalation

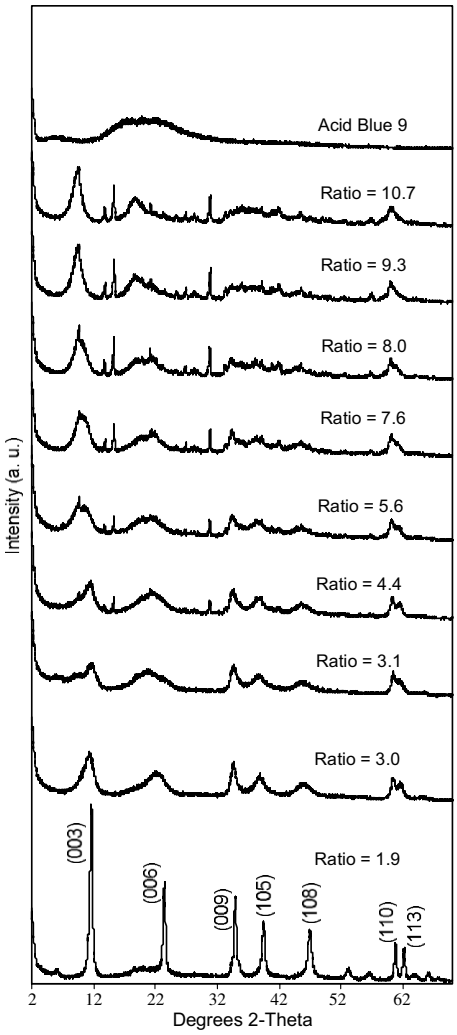


Fig. 8. X-ray powder diffractograms of Mg–Al–LDH–CO_3 system at different Mg/Al values after dye (1.85 mM) treatment and for Acid Blue 9.

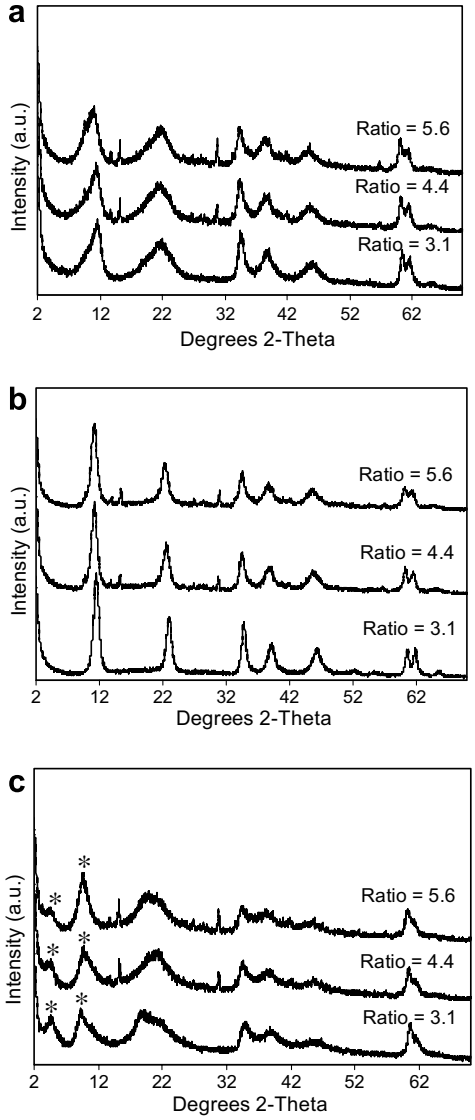


Fig. 9. X-ray powder diffractograms of Mg–Al–LDH–CO_3 system at Mg/Al values of 3.1, 4.4 and 5.6 upon treatment of: (a) 20% (v/v) glycerol–H_2O; (b) Acid Blue 9 solution. (76 mM) in pure H_2O solvent; (c) Acid Blue 9 solution. (76 mM) in 20% (v/v) glycerol–H_2O solvent system. *New reflections at 2θ of 4.6° and 9.5° indicating a d spacing of 19.3 Å and 9.3 Å, respectively.

as shown by the diffractograms (see Supplementary Material, Figure S1). This indeed shows that CO_3^{2-} is very strongly held within the interlayer [40] and that this, and the small interlayer spacing, prevents exchange of AB9 ions for the carbonate precursor anion [41].

Interestingly, when the same materials were treated with only 76 mM Acid Blue 9 in 20% (v/v) glycerol–H_2O solvent system, intercalation was observed (Fig. 9c). New reflections were found at 2θ of ca. 4.6 and 9.5θ (*shown in asterisks*) that gave a d spacing of ca. 19.0 Å (1.9 nm) and 9.5 Å (1.0 nm) respectively. The d spacing at $2\theta = 4.6°$ could correspond to the basal spacing of a new less ordered layered material being formed through intercalation of the dye which is topotactic to the Mg–Al–LDH–CO_3 system precursor. At Mg:Al molar ratio of 3.1, this less ordered intercalate is more dominant, but at Mg:Al molar ratios of 4.4 and 5.6, it is less evident due to the presence of hydromagnesite in the starting material. A basal spacing of 19.0 Å corresponds to an interlayer spacing of 14 Å. This corresponds extremely well to the length of the Acid Blue 9, which in the gas phase has the dimensions of a nanosized molecular box of $x = 10.3$ Å; $y = 10.0$ Å; $z = 12.8$ Å. In addition two of the sulfonate groups are approximately located along the z-axis. For intercalation to occur, the SO_3^- ends of the guest are likely to orient themselves towards the metal cations of the host so as to maximise electrostatic interactions. Consequently, the z and y axes of the molecular box would be slightly tilted in a counter clockwise direction (Fig. 10). This orientation of AB9 in the interlayer of LDH was inferred only based on X-ray data on the AB9 intercalated LDH material and the 3D-structure of AB9 calculated using computational chemistry. Hansen and Taylor [42] have proposed three hypotheses of how the presence of glycerol may facilitate easy intercalation of anions with lower charge density using Mg(II)–

Table 5
Variation in composition and basal spacing of Mg–Al–LDH–CO_3 with a Mg/Al = 3.1 with treatment conditions

Sample	Treatment	Composition[a]	d_{003} (Å)[b]
1	untreated	$[Mg_{3.0}Al_{1.0}(OH)_{7.5}][(CO_3)_{0.72} \cdot 3.0\ H_2O]$	7.8
2	treated w/20% glycerol–H_2O solvent system	$[Mg_{3.0}Al_{1.0}(OH)_{7.5}][(CO_3)_{0.72} \cdot 4.5H_2O \cdot 2.1(C_3O_3H_8)]$	7.6
3	treated w/1.85 mM AB9 in 20% glycerol–H_2O solvent system	$[Mg_{3.0}Al_{1.0}(OH)_{7.5}][(CO_3)_{0.71} \cdot 5.0H_2O \cdot 1.9(C_3O_3H_8) \cdot 0.015(C_{37}H_{34}S_3N_2O_9)]$	7.7
4	treated w/76 mM AB9 in pure H_2O	$[Mg_{3.0}Al_{1.0}(OH)_{7.5}][(CO_3)_{0.62} \cdot 3.8H_2O \cdot 0.1(C_{37}H_{34}S_3N_2O_9)]$	7.7
5	treated w/76 mM AB9 in 20% glycerol–H_2O solvent system	$[Mg_{3.0}Al_{1.0}(OH)_{7.5}][(CO_3)_{0.62} \cdot 3.2H_2O \cdot 1.5(C_3O_3H_8) \cdot 0.1(C_{37}H_{34}S_3N_2O_9)]$	19.0

[a] From elemental/micro and thermo gravimetric analyses.
[b] Powder-XRD analysis.

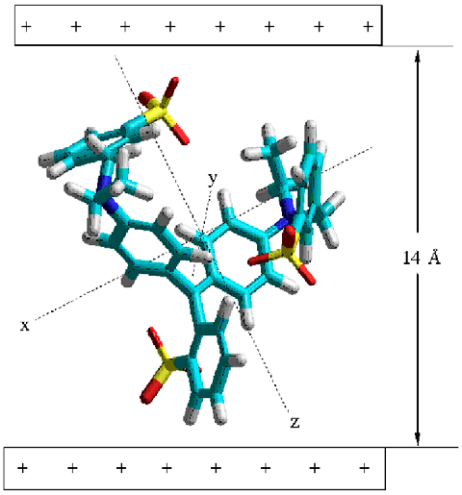


Fig. 10. Acid Blue 9 ion intercalated between Mg–Al–LDH–CO_3 layers.

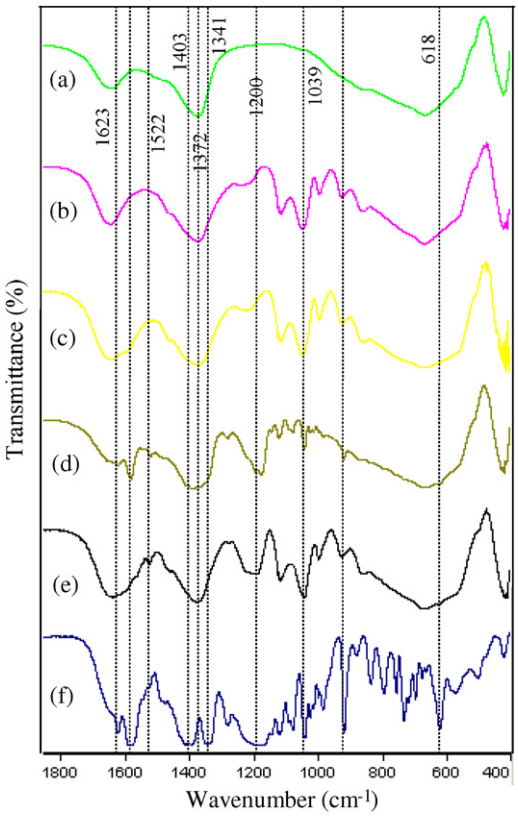


Fig. 11. FT-IR spectra of the (a) Pure Mg–Al–LDH–CO_3 with Mg/Al = 3.1, (b) Mg–Al–LDH–CO_3 added with 20% (v/v) glycerol–H_2O system, (c) Mg–Al–LDH–CO_3 added with 1.85 mM Acid Blue 9 in 20% (v/v) glycerol–H_2O solvent system, (d) Mg–Al–LDH–CO_3 added with 76 mM Acid Blue 9 in pure water, (e) Mg–Al–LDH–CO_3 added with 76 mM Acid Blue 9 in 20% (v/v) glycerol–H_2O solvent system, and (f) Acid Blue 9.

Fe(III) hydroxycarbonate as LDH, some of which could be used to explain how bulky anions, such as AB9, can be exchanged into the Mg(II)–Al(III) LDH in the presence of glycerol and even when carbonate is the interlayer anion. Firstly, swelling of the interlayer between the brucite-like sheets, following penetration by glycerol into the interlayer, decreases the strength of the electrostatic and H-bonding interactions between carbonate and the brucite layers. This anion is then exchangeable with anions present in high concentrations outside the interlayer region. Secondly, negatively charged glycerolate anions, could form under dehydrating conditions in reactions involving the interlayer CO_3^{2-}, e.g. when the materials are treated with liquid glycerol as represented in Eq. (3)

$$2(CH_2OH\text{–}CHOH\text{–}CH_2OH) + CO_3^{2-} \Longleftrightarrow CO_{2(g)} + 2(CH_2OH\text{–}CHOH\text{–}CH_2O)^- + H_2O \quad (3)$$

With the decomposition of the CO_3^{2-} and its liberation as CO_2, it has been suggested that the glycerolate anions are retained in the interlayer as the charge compensating anion.

Table 5 shows the calculated compositions based on elemental/micro and TGA analyses data, (see Supplementary material, Table S2 and Figures S2–S7) as well as the corresponding basal spacings of Mg–Al–LDH–CO_3 (Mg/Al ~ 3.1) at different treatment conditions. As pointed out previously, no change in the basal spacings were observed in any conditions employed except when a more concentrated (76 mM) solution of Acid Blue 9 in a 20% glycerol–H_2O was used to treat the layered double hydroxides. This results in ca. 14% Acid Blue 9 (surface and interlamellar) loading of the new material. Although the amount of added Acid Blue 9 is insufficient to replace all

the carbonates originally present in the system (also confirmed via FT-IR analyses), it does cause a major change in the basal spacing from 7.8 Å to 19.0 Å (see Fig. 8c).

Fig. 11 shows the IR spectra of pure Mg–Al–LDH–CO_3 with Mg/Al = 3.1, Mg–Al–LDH–CO_3 treated with 20% (v/v) glycerol–H_2O solution, Mg–Al–LDH–CO_3 treated 1.85 mM Acid Blue 9 in 20% (v/v) glycerol–H_2O solvent system, Mg–Al–LDH–CO_3 treated with 76 mM Acid Blue 9 in pure water, Mg–Al–LDH–CO_3 intercalated with Acid Blue 9, and Acid Blue 9. Pure Mg–Al–LDH–CO_3 (Fig. 11a) exhibited peaks at 691 and 1372 cm^{-1} which are due to vibration of the interlayer CO_3^{2-}.

When Mg–Al–LDH–CO_3 is treated with 20% glycerol (Fig. 11b), the C–O stretches of glycerol between 1000 and 1210 cm^{-1} are evident indicating a high loading of glycerol, which is consistent with the elemental analyses. Fig. 11c shows the spectra of Mg–Al–LDH–CO_3 treated 1.85 mM Acid Blue 9 in 20% (v/v) glycerol–H_2O solvent system. Vibrations due to glycerol still dominate the spectrum but vibrations between 1522 and 1623 cm^{-1} starts to appear that could be due to C=C ring stretches of surface bound Acid Blue 9. When Mg–Al–LDH–CO_3 is treated with a higher concentration of Acid Blue 9 in water (Fig. 11d), vibrations due to Acid Blue 9 becomes more apparent in the 1522–1623 cm^{-1} and additional C–N and S–O stretches are also evident in the range 1039–1150 cm^{-1}. It should be noted that although Acid Blue 9 vibrations are so evident, powder X-ray analyses (see Fig. 9b) indicated that intercalation had not occurred. Fig. 11e shows the spectra of Mg–Al–LDH–CO_3 intercalated with Acid Blue 9 (see Fig. 9c also) in which vibrations due to Acid Blue 9 are evident, In particular, the strong absorption centered at 1200 cm^{-1} is present and could only be due to SO_3^- vibration of Acid Blue 9 species.

Intercalation of a negatively charged species in a layered double hydroxide system can occur in three ways: reconstruction method [8], self-assembly technique [10,12] and anion exchange methods [43]. Anion exchange follows the order, $CO_3^{2-} > SO_4^{2-} \gg OH^- > F^- > Cl^- > Br^- > NO_3^- > ClO_4^-$. In keeping with this, we have further demonstrated here that carbonate-LDHs are excellent precursors for surface adsorption since the interlayer carbonates will not be involved in the exchange process, whereas, the surface carbonates or hydrogen carbonates are easily replaced by anionic dyes [27].

4. Conclusions and future studies

In this study, surface adsorption of Acid Blue 9 to Mg–Al–LDH–CO_3 materials was observed when a 1.85 mM dye solution in a 20% (v/v) glycerol–H_2O mixture was used. This system exhibited excellent surface adsorption (chemisorption) properties when the Mg/Al molar ratios were between 3.1 and 4.4, the compositions corresponding to the pure hydrotalcite phase. The adsorption behaviour correlates with the surface area, phase purity, surface morphology, particle size distribution and packing density. Interlamellar anion exchange was observed using 76 mM Acid Blue 9 solution in the same glycerol/water solvent system but was not observed when pure water was used as the solvent. This means that, through the use of glycerol, partial intercalation of bulky anions can take place even when carbonates are used as interlayer anions and even when the amount of anions added is well below the specific ion-exchange capacity of the LDH material. This method affords a facile synthesis of organic–inorganic hybrid materials using a very stable and easy to produce type of layered double hydroxide. To our knowledge, this is the first work that demonstrates the use of the anion exchange method to intercalate bulky anionic molecules into Mg–Al layered double hydroxides with carbonate as interlayer anions. However, in order to achieve this, an agent such as glycerol is needed to assist in the expansion of the hydrotalcite interlayer. Further studies aimed at improving the dye adsorption characterization of the LDH material are in progress.

Acknowledgement

This work was supported by the Smartprint Cooperative Research Centre (CRC), Australia.

Appendix A. Supplementary material

Supplementary data available: (1) Basal spacings for Mg–Al–LDH–CO_3; (2) CHN analyses; (3) PXRD diffratograms of Mg–Al–LDH–CO_3 (Mg/Al = 3.1) treated with amounts of AB9 higher than the anionic exchange capacities of LDH used in pure H_2O solvent; and (4) Thermal gravimetric analysis curves. Supplementary data associated with this article can be found, in the online version, at doi:10.1016/j.poly.2007.03.019.

References

[1] F. Millange, R.I. Walton, D. O'Hare, J. Mater. Chem. 10 (2000) 1713.
[2] A. Vaccari, Appl. Clay Sci. 14 (1999) 161.
[3] D.G. Evans, X. Duan, Chem. Commun. (2006) 485.
[4] U. Schubert, N. Husing, Synthesis of Inorganic Materials, Weinhem, Wiley-VCH, Germany, 2000.
[5] F. Cavani, F. Trifiro, A. Vaccari, Catal. Today 11 (1991) 173.
[6] M. Wei, S. Shi, J. Wang, Y. Li, X. Duan, J. Solid State Chem. 177 (2004) 2534.
[7] I. Pausch, H. Lohse, K. Schurmann, R. Allmann, Clays Clay Min. 34 (1986) 507.
[8] T. Sato, A. Okuwaki, Solid State Ionics 45 (1991) 43.
[9] R.R. Delgado, M.A. Vidaurre, C.P.D. Pauli, M.A. Ulibarri, M.J. Avena, J. Colloid Interf. Sci. (2004) 431.
[10] Y. You, G.F. Vance, D.L. Sparks, J. Zhuang, Y. Jin, J. Environ. Quality 32 (2003) 2046.
[11] M.Z.b. Hussein, A.H. Yahaya, L.M. Ping, Dyes Pigments 63 (2004) 135.
[12] F. Li, Y. Wang, Q. Yang, D.G. Evans, C. Forano, X. Duan, J. Hazard. Mater. B 125 (2005) 89.
[13] M.Z.b. Hussein, Z. Zainal, A.H. Yahaya, A.b.A. Aziz, Mater. Sci. Eng. B 88 (2002) 98.

[14] M.A. Ulibarri, I. Pavlovic, C. Barriga, M.C. Hermosin, J. Cornejo, Appl. Clay Sci. 18 (2001) 17.
[15] M.A. Ulibarri, I. Pavlovic, M.C. Hermosin, J. Cornejo, Appl. Clay Sci. 10 (1995) 131.
[16] G.R. Williams, T.G. Dunbar, A.J. Beer, A.M. Fogg, D. O'Hare, J. Mater. Chem. 16 (2006) 1222.
[17] G.R. Williams, T.G. Dunbar, A.J. Beer, A.M. Fogg, D. O'Hare, J. Mater. Chem. 16 (2006) 1231.
[18] F. Yongjun, L. Dianqing, W. Yuan, D.G. Evans, D. Xue, Poly. Deg. Stabil. 91 (2006) 789.
[19] S. Sasaki, S. Aisawa, H. Hirahara, A. Sasaki, H. Nakayama, E. Narita, J. Solid State Chem. 179 (2006) 1129.
[20] L. Lei, Z. Nan, L. Shi-Jun, C. Da-Zhou, J. Phys. Chem. Solids 66 (2005) 1844.
[21] Z. Hui, Z. Kang, S. Hui, D. Xue, J. Solid State Chem. 178 (2005) 3485.
[22] W.T. Tsai, C.Y. Chang, C.H. Ing, C.F. Chang, J. Colloid Interf. Sci. (2004) 72.
[23] Y. Li, C. Liu, C. Chiou, Bull. Environ. Contam. Toxicol. 70 (2003) 1112.
[24] T. Geethakrishnan, P.K. Palanisamy, J. Mod. Opt. 53 (2006) 1131.
[25] I. Kengo, F. Yoshio, US Patent, US6281270, 2001.
[26] Z. Yun, L. Feng, Z. Rui, D.G. Evans, D. Xue, Chem. Mater. 14 (2002) 4286.
[27] E.D. Dimotakis, T.J. Pinnavaia, Inorg. Chem. Commun. 29 (1990) 2393.
[28] D. Neumann, S. Loffler, W. Raverty, N. Vanderhoek, P. Andrews, P. Junk, L. Spiccia. Pigments for ink receptor layers – characterisation and assessment, in: 58th Appita Conference Proceedings 2003; Australia, 2003, pp. 383–386.
[29] I. Langmuir, J. Am. Chem. Soc. 40 (1918) 1361.
[30] C.H. Giles, T.H. MacEwan, S.N. Nakhwa, D. Smith, J. Chem. Soc. (1960) 3973.
[31] V. Rives (Ed.), Layered Double Hydroxides: Present and Future, Nova Science Publishers, New York, 2001.
[32] O. Marino, G. Mascolo, Thermochim. Acta 55 (1982) 377.
[33] B.D. Cullity, S.R. Stock, Elements of X-ray Diffraction, 3rd ed., PEARSON Prentice Hall, Upper Saddle River, NJ, 2001.
[34] W.T. Reichle, Solid State Ionics 22 (1986) 135.
[35] P.A. Webb, C. Orr, Analytical Methods in Fine Particle Technology, first ed., Micromeritics Instrument Corp., USA, 1997.
[36] M.A. Aramendia, V. Borau, C. Jimenez, J.M. Marinas, J.R. Ruiz, F.J. Urbano, J. Solid State Chem. 168 (2002) 156.
[37] K.S.W. Sing, D.H. Everett, R.A.W. Haul, L. Moscou, R.A. Pierotti, J. Rouquerol, T. Siemieniewska, Pure Appl. Chem. 57 (1985) 603.
[38] J.M. Fernandez, C. Barriga, M.-A. Ulibarri, F.M. Labajos, V. Rives, J. Mater. Chem. 4 (1994) 1117.
[39] T.J. Pinnavaia, T. Kwon, E.D. Dimotakis, J. Amarasekera, US Patent, PCT US91/03110, 1991.
[40] S. Miyata, Clays Clay Miner. 31 (1983) 305.
[41] A.d. Roy, C. Forano, J.P. Besse, Layered double hydroxides: synthesis and post-synthesis modification, in: V. Rives (Ed.), Layered Double Hydroxides: Present and Future, Nova Science Publishers, New York, 2001.
[42] H.C.B. Hansen, R.M. Taylor, Clay Miner. 26 (1991) 311.
[43] N.H. Gutmann, L. Spiccia, T.W. Turney, J. Mater. Chem. 10 (2000) 1219.

Available online at www.sciencedirect.com
ScienceDirect
Polyhedron 26 (2007) 3491–3495
POLYHEDRON
www.elsevier.com/locate/poly

Reactivity of mercury(II) halides with the unsymmetrical phosphorus ylide $Ph_2PCH_2CH_2PPh_2$=C(H)C(O)Ph: Crystal structure of $\{HgI_2[PPh_2CH_2CH_2PPh_2$=C(H)C(O)Ph$]\}_n$

Mothi Mohamed Ebrahim [a,b], Helen Stoeckli-Evans [a,*], Krishnaswamy Panchanatheswaran [b,*]

[a] *Institute of Microtechnology, University of Neuchâtel, Neuchâtel, Switzerland*
[b] *School of Chemistry, Bharathidasan University, Tiruchirappalli, India*

Received 14 December 2006; accepted 21 March 2007
Available online 14 April 2007

Abstract

The unsymmetrical phosphorus ylide, $Ph_2PCH_2CH_2PPh_2$=C(H)C(O)Ph is shown to react with Hg(II) halides to form polymeric products with the composition $\{HgX_2[PPh_2CH_2CH_2PPh_2C(H)C(O)Ph]\}_n$, where X = Cl (**1**), Br (**2**), I (**3**). The complexes have been characterized by elemental analysis, IR, ^1H, ^{31}P NMR spectra as well as by ESI mass spectra. In product **1** the ylide exhibits a P, C-bridging mode of coordination, while in **2** and **3** it shows a monodentate P-coordination with the dangling ylide. The structure of complex **3** has been characterized crystallographically. The monomeric –Hg–I–Hg– bridging in **3** leads to a zig-zag polymeric chain in which mercury assumes a distorted tetrahedral geometry.
© 2007 Elsevier Ltd. All rights reserved.

Keywords: Phosphorus ylides; Resonance stabilization; Coordination polymer; Mercury(II) complexes

1. Introduction

Resonance stabilized phosphorus ylides are versatile ligands for heavy metal ions [1–5]. The α-keto stabilized ylides derived from bisphosphines, viz., $Ph_2PCH_2PPh_2$=C(H)C(O)R, $Ph_2PCH_2CH_2PPh_2$=C(H)C(O)R (R=Me, Ph or OMe) [6] and PhC(O)C(H)=$PPh_2CH_2CH_2PPh_2$=C(H)C(O)Ph [7] form an important class of such ligands which can exist in ylidic and enolate forms. These ligands can therefore engage in different types of bonding as illustrated in Chart 1 for $Ph_2PCH_2CH_2PPh_2$=C(H)C(O)Ph.

The bonding mode (f) had been previously observed for Pd(II), Pt(II) and Rh(I) [6–13]. In addition, Rh(I) was shown to exhibit the P-bonding mode (a) [13]. We have been interested in investigating the different bonding modes adopted by ylides when ligated to Hg(II) and U(VI) [14]. Hg(II) forms C-coordinated complexes with Ph_3P=C(H)C(O)Ph [15,16] and Ph_3P=C(H)CO(OEt) [17]. On the other hand, regiospecific O-coordination of the acetyl oxygen has been observed for the reaction of Hg(II) halides with Ph_3P=C(COPh)(COMe). The remarkable change in reactivity arises from a subtle variation in the molecular-electronic structure of the ylide due to the presence of additional keto stabilization. Further, although $HgBr_2$ and HgI_2 form 1:1 dimeric halobridged complexes with the above ylide, $HgCl_2$ forms a 1:2 monomeric square planar complex [18]. Motivated by the above chemistry, we decided to study the interaction of Hg(II) halides with mixed ylide-phosphine ligands. In this paper, we report the reactivity of the ligand $Ph_2PCH_2CH_2PPh_2$=C(H)C(O)Ph, Benzoylmethylenediphenyl-2-diphenylphosphinoethylphosphorane (BDEP), towards mercury(II) halides.

* Corresponding authors. Tel.: +91 431 2407053; fax: +91 431 2407045.
E-mail address: panch_45@yahoo.co.in (K. Panchanatheswaran).

0277-5387/$ - see front matter © 2007 Elsevier Ltd. All rights reserved.
doi:10.1016/j.poly.2007.03.059

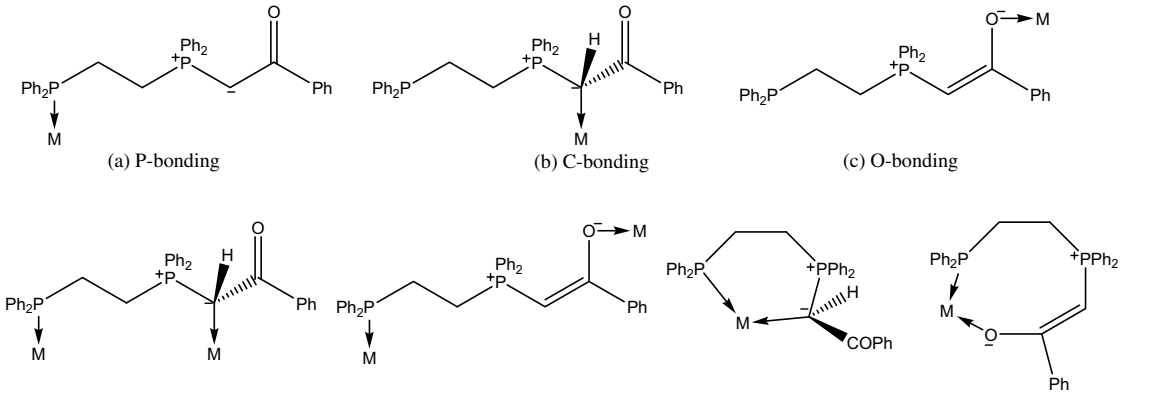


Chart 1. The possible bonding modes of $Ph_2PCH_2CH_2PPh_2$=C(H)C(O)Ph to metal M.

2. Experimental

All reactions were carried out under an atmosphere of dry nitrogen. Reactants and reagents were obtained from Aldrich Chemical Company and used without further purification. The solvents were dried and distilled using standard methods [19].

2.1. Instrumentation

The ^1H and ^{31}P–{^1H} NMR spectra were recorded on a Bruker DPX400 or Varian Gemini 200 spectrometer, referenced relative to residual solvent and external 85% H_3PO_4, respectively. The IR spectra in the interval of 4000–400 cm^{-1} were recorded on a Perkin–Elmer 1720X FT-IR spectrophotometer using KBr pellets. ESI-mass spectra were measured on a Bruker FTMS 4.7T BioAPEX II instrument using the solution of the complexes in acetonitrile. Elemental analyses were performed at the Ecole d'ingénieurs de Fribourg, Switzerland.

2.2. Synthesis of compounds

2.2.1. $Ph_2PCH_2CH_2PPh_2$=C(H)C(O)Ph

The ligand was prepared by the treatment of triethylamine on the monophosphonium bromide derived from 1,2-bis(diphenylphosphino)ethane (dppe) as reported previously [6]. IR (cm^{-1}): 3054, 2912, 1585, 1521, 1482, 1434, 1396, 1308, 1175, 1108, 1061, 1025, 998, 898, 882, 794, 746, 739, 722, 701, 653, 507, 490. ^1H NMR (200 MHz, $CDCl_3$): 2.20–2.33 (m, 2H), 2.79–2.94 (m, 2H), 4.26 (d, 1H, $^2J_{P-H} = 23.0$), 7.33–8.01 (m, 25H). ^{31}P NMR (162 MHz, $CDCl_3$): −12.20 (d, $^3J_{P-P} = 47.5$), 17.54 (d, $^3J_{P-P} = 47.5$).

2.2.2. Synthesis of $\{HgX_2[PPh_2CH_2CH_2PPh_2C(H)C(O)Ph]\}_n$ {X = Cl (1), Br (2), I (3)}

The following general procedure was used for preparing the complexes. To a solution of HgX_2 (0.38 mmol) in methanol (10 ml), a solution of $PPh_2CH_2CH_2PPh_2CHCOPh$ (0.2 g, 0.38 mmol) also in methanol (10 ml) was added dropwise at 0 °C and stirred for 2 h. The resulting solid, admixed with grey material was treated with dichloromethane (25 ml) and filtered through celite. Addition of excess methanol to the concentrated filtrate caused the precipitation of the products as white solids. The complexes were purified by repeating the precipitation three times and the solid dried under vacuum.

1. Yield: 0.16 g (56%). M.p. 142–144 °C. *Anal.* Calc. for $C_{34}H_{30}Cl_2HgOP_2$: C, 51.82; H, 3.84. Found: C, 51.26; H, 3.78%. IR (cm^{-1}): 3055, 2910, 1637, 1594, 1577, 1483, 1436, 1403, 1322, 1289, 1189, 1105, 998, 841, 778, 733, 688, 509, 481. ^1H NMR (200 MHz, DMSO-d_6): 3.18–3.47 (br, 4H merged with residual H_2O), 5.15 (d, 1H, $^2J_{P-H} = 9.4$), 7.47–8.07 (m, 25H). ^{31}P NMR (81 MHz, DMSO-d_6): 23.78 (br, d), 35.88 (br, d). Mass spectrum: ESI [*m*/*z*, ion, %]: 753 $[M-Cl]^+$(100), 1269 $[M^*-Cl]$ (83), where $M^* = [HgCl_2(PPh_2CH_2CH_2PPh_2C(H)C(O)Ph)_2]$.
2. Yield: 0.18 g (54%). M.p. >120 °C (decomposes). *Anal.* Calc. for $C_{34}H_{30}Br_2HgOP_2$: C, 46.57; H, 3.45. Found: C, 46.62; H, 3.40%. IR (cm^{-1}): 3053, 2920, 1584, 1511, 1484, 1436, 1391, 1182, 1107, 998, 1025, 894, 734, 723, 704, 691, 509, 491. ^1H NMR (200 MHz, DMSO-d_6): 3.06–3.36 (br, 4H merged with residual H_2O), 4.68 (d, 1H, $^2J_{P-H} = 19.4$), 7.18–7.79 (m, 25H). ^{31}P NMR (81 MHz, DMSO-d_6): 20.27 (br, d), 30.12 (br). Mass spectrum: ESI [*m*/*z*, ion, %]: 797 $[M-Br]^+$ (23).
3. Yield: 0.25 g (68%). M.p. >152 °C (decomposes). *Anal.* Calc. for $C_{34}H_{30}HgI_2OP_2$: C, 42.06; H, 3.11. Found: C, 41.85; H, 3.08%. IR (cm^{-1}): 3053, 1629, 1585, 1504, 1482, 1435, 1398, 1181, 1110, 1026, 998, 891, 727, 706, 690, 506, 493. ^1H NMR (400 MHz, $CDCl_3$): 3.16 (br, 2 H), 3.37 (br, 2H), 4.34 (d, 1H, $^2J_{P-H} = 21.7$), 7.39–8.01 (m, 25H). ^{31}P NMR (162 MHz, $CDCl_3$): 6.46 (br), 19.33 (d, $^3J_{P-P} = 57.1$). Mass spectrum: ESI [*m*/*z*, ion, %]: 845 $[M-I]^+$ (16).

Table 1
Selected IR, ^{1}H and ^{31}P NMR spectral data [δ (ppm), J (Hz)]

	ν (C=O)	δ PC*H* ($^2J_{P-H}$)	δ *P*Ph$_2$ ($^3J_{P-P}$)	δ *P*CHCOPh ($^3J_{P-P}$)
BDEP	1521	4.26 (23.0)	−12.20 (47.5)	17.54 (47.5)
1	1637	5.15 (9.4)	35.88	23.78
2	1511	4.68 (19.4)	30.12	20.27 (55.6)
3	1504	4.34 (21.7)	6.46	19.33 (57.1)

Table 2
Crystal data and refinement details for complex **3**

Empirical formula	$C_{34}H_{30}HgI_2$ OP_2,0.5($C_4H_{10}O$)
Formula weight	1007.97
Crystal system	monoclinic
Space group	$P2_1/c$
a (Å)	22.9215(13)
b (Å)	8.3325(3)
c (Å)	19.8801(11)
β (°)	111.565(4)
V (Å^3)	3531.2(3)
Z	4
Absorption coefficient (mm^{-1})	6.226
Collected reflections	49879
Independent reflections	9565
R(int)	0.0917
Observed reflections [$I > 2\sigma(I)$]	7035
R_1 (observed data)	0.0500
wR_2 (all data)	0.1185

2.3. X-ray crystallography

Single crystals of **3** were obtained as colourless needles, when a hot 1-butanol solution containing the complex was allowed to stand at room temperature for a week. The intensity data were collected at 173 K (−100 °C) on a Stoe Mark II-Image Plate Diffraction System [20] equipped with a two-circle goniometer using Mo Kα graphite monochromated radiation. Image plate distance 100 mm, ω rotation scans 0–180° at ϕ 0°, and 0–20° at ϕ 90°, step $\Delta\omega = 1.0°$, 2θ range 2.29–59.53°, d_{min}–d_{max} = 17.779–0.716 Å. The structure was solved by direct methods using the program SHELXS-97 [21]. The refinement and all further calculations were carried out using SHELXL-97 [22]. The H-atoms were included in calculated positions and treated as riding atoms using SHELXL default parameters. The non-H atoms were refined anisotropically, using weighted full-matrix least-squares on F^2. An empirical absorption correction was applied using the MULscanABS routine in PLATON [23]; transmission factors: $T_{min}/T_{max} = 0.2744/0.6083$. A region of disordered electron density was squeezed out using the SQUEEZE routine in PLATON; 68 electrons for a volume of 346.9 Å^3, which was equated to 0.5 molecule of 1-butanol per asymmetric unit. Further crystallographic data are given in Table 2.

3. Results and discussion

The reactions of mercury(II) halides with unsymmetrical phosphorus ylide, $Ph_2PCH_2CH_2PPh_2$=C(H)C(O)Ph in 1:1 molar ratio yield two different polymeric products. While mercury(II) chloride forms a P, C-coordinated bridging complex [type (d), Chart 1], the mercury(II) bromide, and iodide, produce monodentate P-coordinated complexes with dangling ylide [type (a), Chart 1].

Complexes **1** and **2** are moderately soluble in acetonitrile and DMSO whereas the solubility of the complex **3** is higher in chloroform than in DMSO or acetonitrile. The yields of **1** and **2** are low due to some decomposition during the reaction. The IR spectrum of **1** shows the ν(CO) absorption at 1637 cm^{-1}, in the region typical for the C-bonded phosphonium ylides [24]. Similarly, in the ^{1}H NMR spectrum, both the downfield shift of the signal due to the PCH group and the decrease in the coupling constant are ascribed to C-coordination of the ylide (Table 1). The ^{31}P NMR spectrum of **1** exhibits two broad doublets at 23.78 and 35.88 ppm, which are assigned to the coordinated P=CHCOPh and PPh_2 groups, respectively. The spectral data thus indicate the bidentate coordination of the ligand through both P and C atoms. Although, complex **1** gives satisfactory elemental analysis for the 1:1 metal to ligand stoichiometry, the ESI-mass spectrum in acetonitrile solvent shows, in addition to the parent pseudomolecular ion, $[HgCl_2L–Cl]^+$ observed at m/z 753 as the base peak, another peak at m/z 1269 (83%) which is attributed to an $[HgCl_2(L)_2–Cl]^+$ ion. Such an observation is best explained by the polymeric structure with bridging mode of coordination of the ylide where both 1:1 and 1.2 (metal: ligand) fragmentation is possible.

In the IR spectra of **2** and **3**, the ν(CO) absorptions are shifted only slightly from that of the free ligand (Table 1). As noted previously [15], the coordination of the ylide through carbon or oxygen causes a significant increase or decrease, respectively, in the ν(CO) frequency. In the ^{1}H NMR spectra of **2** and **3**, the doublets due to the methine proton at 4.68 and 4.34 ppm, respectively, appear in the same region as observed for the free ligand (4.26 ppm). The ^{31}P NMR signals due to P=CHCOPh group are not much shifted from the corresponding value for the free ylide (Table 1). However, the signals due to PPh_2 group exhibit the expected downfield shifts for coordination. Thus, IR and NMR data indicate that interaction of ligand to $HgBr_2$ and HgI_2 is only through the phosphine part, as proved for the crystal structure of **3**. This is corroborated by the absence of any species containing two ligands in the ESI Mass spectra in acetonitrile for both **2** and **3**. The absence of ^{199}Hg satellites in the ^{31}P NMR spectra of all the complexes can be attributed to the fast exchange of ligand with metal, as noted previously for Hg(II)–phosphine complexes [25,26].

3.1. Crystal structure of complex 3

The molecular structure of **3** is shown in Fig. 1 and selected bond lengths and angles are given in Table 3. The X-ray analysis reveals the coordination of the ligand through the phosphorus atom only. The Hg(II) atom is

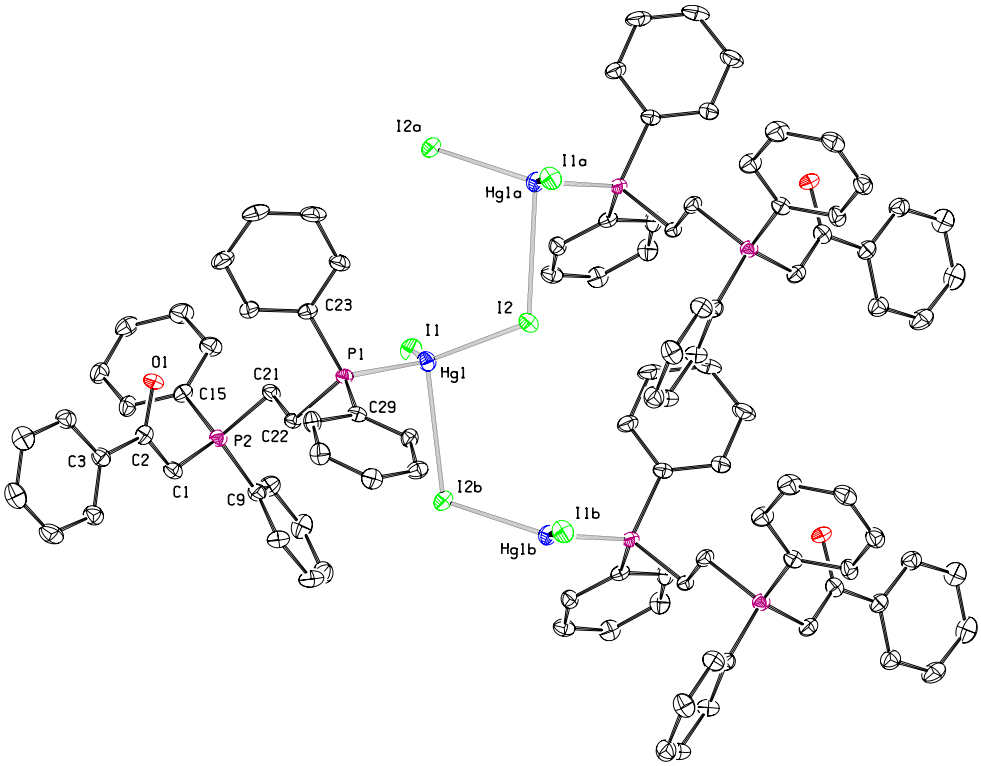


Fig. 1. Polymeric structure of **3** showing part of the chain running parallel to *b*-axis. The hydrogen atoms have been omitted for clarity. (*Symmetry codes*: $a = -x, -1/2 + y, 1/2-z$; $b = -x, 1/2 + y, 1/2-z$.)

located in a distorted tetrahedral environment with one 'P', one terminal 'I' and two bridging 'I' atoms, resulting in an one-dimensional polymeric chain. The Hg–P bond length of 2.472(2) Å is consistent with the values reported for monomeric mercury(II)–phosphine complexes [27]. However, this distance is shorter when compared to those in the polymeric complex, $[Hg(CN)_2dppe]_n$ [2.606(3) Å and 2.534(4) Å] containing the bridging phosphine ligand [28]. The Hg–I(terminal) bond distance [2.705(1) Å] is comparable to those of 2.727(2) and 2.693(2) Å found in $[Hg\{Ph_2P(S)CH_2PPh_2\}I_2]$ [29]. The asymmetric bridging nature of the other two iodo ligands is indicated by the two different Hg–I(bridging) distances of 2.728(1) and 3.321(1) Å. The latter distance being rather long, indicates a weak Hg–I(bridging) interaction. The bond angles around Hg atom (Table 3) indicate a severe distortion from ideal tetrahedral geometry. The deviation of atom Hg1 from the best least-squares plane defined by atoms I1, I2 and P1, is only 0.254 Å. This is comparable to the previous observations in the complexes $[HgX_2\{Ph_2PCH_2CH_2P(O)Ph_2\}]_n$ (X = Br, I) [30] and $[HgI_2\{Ph_2P(S)CH_2PPh_2\}]$ [29], where a weak coordination of the one of the ligands lead to a flattened tetrahedral geometry as shown by the small deviations (ranging from 0.244 to 0.406 Å) of the Hg atom from the plane defined by other three strongly bonded atoms. On the basis of the high solubility of complex **3** in most of the solvents and the long Hg–I(bridging) distance, it is possible that the polymer could dissociate to form a monomeric species in solution as indicated by the ESI mass spectral data. The ylidic moiety shows no interaction with mercury. The bond angles around C1 (~120°) and the P2–C1 distance [1.716(7) Å] indicate that the ylidic carbon remains unprotonated. Similarly, the short C1–C2 and long C=O distances show the resonance delocalization in the free ylide. As observed previously for α-stabilized phosphorus ylides [31], the phosphorus and oxygen atoms are *cis* oriented due to significant interaction between P^+ and O^- centres, as shown by the appropriate length and torsion angle (Table 3).

Table 3
Selected geometric parameters for **3**

Bond lengths (Å)			
Hg(1)–P(1)	2.472(2)	P(2)–C(15)	1.810(6)
Hg(1)–I(1)	2.706(1)	P(2)–C(9)	1.810(7)
Hg(1)–I(2)	2.728(1)	P(2)–C(21)	1.830(6)
Hg(1)–I(2^i)	3.321(1)	O(1)–C(2)	1.283(8)
P(2)–C(1)	1.716(7)	C(1)–C(2)	1.392(9)
P(1)–C(29)	1.805(6)	C(2)–C(3)	1.480(9)
P(1)–C(23)	1.819(6)	C(21)–C(22)	1.522(8)
P(1)–C(22)	1.827(6)	P2···O1	2.828(7)
Angles (°)			
P(1)–Hg(1)–I(1)	120.11(4)	C(2)–C(1)–P(2)	116.6(5)
P(1)–Hg(1)–I(2)	122.07(4)	C(2)–C(1)–H(1)	121.7
I(1)–Hg(1)–I(2)	115.04(2)	P(2)–C(1)–H(1)	121.7
P(1)–Hg(1)–I(2^i)	90.57(3)	P(2)–C(1)–C(2)–O(1)	−3.1(8)
I(1)–Hg(1)–I(2^i)	91.12(2)	P(2)–C(21)–C(22)–P(1)	−178.3(3)
I(2)–Hg(1)–I(2^i)	105.06(1)		

Symmetry transformation: (i) $-x, y + 1/2, -z + 1/2$.

4. Conclusions

In this study, we have shown that Hg(II) halides react with the unsymmetrical phosphorus ylide, Ph_2PCH_2-CH_2PPh_2=C(H)C(O)Ph, to form complexes in which the ylide exhibits different coordination modes. The difference can be accounted for by hardness associated with $HgCl_2$ compared to the softness of other two mercuric halides. Further, it is interesting to note that the monodentate P-coordination to mercury in the complexes **2** and **3**, with dangling ylide moiety, is in stark contrast to the product of the same ligand with $UO_2(NO)_2 \cdot 6H_2O$. The latter displays a monodentate O-coordination with the dangling phosphino group [32].

Acknowledgements

M.M.E. thank the Swiss Federal Commission for a scholarship to study at the University of Neuchâtel. K.P. thanks the Department of Science and Technology, New Delhi, India for financial assistance (SERC-SR/S1/IC-29/2003).

Appendix A. Supplementary material

CCDC 630609 contains the supplementary crystallographic data for **3**. These data can be obtained free of charge via http://www.ccdc.cam.ac.uk/conts/retrieving.html, or from the Cambridge Crystallographic Data Centre, 12 Union Road, Cambridge CB2 1EZ, UK; fax: (+44) 1223-336-033; or e-mail: deposit@ccdc.cam.ac.uk. Supplementary data associated with this article can be found, in the online version, at doi:10.1016/j.poly.2007.03.059.

References

[1] L.R. Falvello, J.C. Gines, J.J. Carbo, A. Lledos, R. Navarro, T. Soler, E.P. Urriolabeitia, Inorg. Chem. 45 (2006) 6803.
[2] U. Belluco, R.A. Michelin, M. Mozzon, R. Bertani, G. Facchin, L. Zanotto, L. Pandolfo, J. Organomet. Chem. 557 (1998) 37.
[3] O.I. Kolodiazhnyi, Tetrahedron 52 (1996) 1855.
[4] R. Navarro, E.P. Urriolabeitia, J. Chem. Soc., Dalton Trans. (1999) 4111.
[5] M. Taillefer, H.-J. Cristau, Top. Curr. Chem. 229 (2003) 41.
[6] Y. Oosawa, H. Urabe, T. Saito, Y. Sasaki, J. Organomet. Chem. 122 (1976) 113.
[7] A. Spannenberg, W. Baumann, U. Rosenthal, Organometallics 19 (2000) 3991.
[8] R. Uson, J. Fornies, R. Navarro, A.M. Ortega, J. Organomet. Chem. 334 (1987) 389.
[9] L.R. Falvello, S. Fernandez, R. Navarro, E.P. Urriolabeitia, Inorg. Chem. 39 (2000) 2957.
[10] H. Takahashi, Y. Oosawa, A. Kobayashi, T. Saito, Y. Sasaki, Chem. Lett. (1976) 15.
[11] H. Takahashi, Y. Oosawa, A. Kobayashi, T. Saito, Y. Sasaki, Bull. Chem. Soc. Jpn. 50 (1977) 1771.
[12] I.J.B. Lin, H.C. Shy, C.W. Liu, L.-K. Liu, S.-K. Yeh, J. Chem. Soc., Dalton Trans. (1990) 2509.
[13] D. Saravanabharathi, T.S. Venkatakrishnan, M. Nethaji, S.S. Krishnamurthy, Proc. Ind. Acad. Sci. (Chem. Sci.) 115 (2003) 741.
[14] E.C. Spencer, B. Kalyanasundari, M.B. Mariyatra, J.A.K. Howard, K. Panchanatheswaran, Inorg. Chim. Acta 359 (2006) 35.
[15] M. Kalyanasundari, K. Panchanatheswaran, W.T. Robinson, H. Wen, J. Organomet. Chem. 491 (1995) 103.
[16] B. Kalyanasundari, K. Panchanatheswaran, V. Parthasarathi, W.T. Robinson, Bull. Chem. Soc. Jpn. 72 (1999) 33.
[17] E.C. Spencer, M.B. Mariyatra, J.A.K. Howard, A.M. Kenwright, K. Panchanatheswaran, J. Organomet. Chem. 692 (2007) 1081.
[18] P. Laavanya, U. Venkatasubramanian, K. Panchanatheswaran, J.A.K. Bauer, Chem. Commun. (2001) 1660.
[19] W.L.F. Armarego, D.D. Perrin, Purification of Laboratory Chemicals, fourth ed., Butterworth-Heinemann, Oxford, 1996.
[20] Stoe, X-Area V1.17 & X-RED32 V1.04 Software, Stoe & Cie GmbH, Darmstadt, Germany, 2002.
[21] G.M. Sheldrick, SHELXS-97 program for crystal structure determination, Acta Crystallogr., Sect. A A46 (1990) 467.
[22] G.M. Sheldrick, SHELXL-97, Universität Göttingen, Göttingen, Germany, 1999.
[23] A.L. Spek, J. Appl. Crystallogr. 36 (2003) 7.
[24] L.R. Falvello, S. Fernandez, R. Navarro, E.P. Urriolabeitia, New J. Chem. 21 (1997) 909.
[25] B. Hoge, C. Thosen, I. Pantenburg, Inorg. Chem. 40 (2001) 3084.
[26] F. Cecconi, C.A. Ghilardi, P. Innocenti, S. Midollini, A. Orlandini, A. Ineco, A. Vacca, J. Chem. Soc., Dalton Trans. (1996) 2821.
[27] N.A. Bell, T.D. Dee, M. Goldstein, P.J. McKenna, I.W. Nowell, Inorg. Chim. Acta 71 (1983) 135.
[28] M. Camalli, F. Caruso, L. Zambonelli, Acta Crystallogr., Sect. A B38 (1982) 2468.
[29] T.S. Lobana, M.K. Sandhu, M.J. Liddell, E.R.T. Tiekink, J. Chem. Soc., Dalton Trans. (1990) 691.
[30] M.M. Ebrahim, A. Neels, H. Stoeckli-Evans, K. Panchanatheswaran, Polyhedron 26 (2007) 1277.
[31] A. Lledos, J.J. Carbo, E.P. Urriolabeitia, Inorg. Chem. 40 (2001) 4913.
[32] M. Kalyanasundari, Ph.D. Thesis, Bharathidasan University, Tiruchirappalli, India, 1998.

Available online at www.sciencedirect.com
ScienceDirect
Polyhedron 26 (2007) 3496–3504
POLYHEDRON
www.elsevier.com/locate/poly

Novel diaminoaluminum halides and a diaminoaluminum hydride: 1,3,2-Diazaalumina-[3]ferrocenophanes

Bernd Wrackmeyer *, Elena V. Klimkina, Wolfgang Milius

Anorganische Chemie II, Universität Bayreuth, D-95440 Bayreuth, Germany

Received 13 February 2007; accepted 24 March 2007
Available online 30 March 2007

Abstract

The dilithiated derivative **2** of 1,1′-bis(trimethylsilylamino)ferrocene (**1**) reacts with the pyridine adducts of the aluminum trihalides AlX_3 (X = Cl, Br, I) to give the respective 1,3,2-diazaalumina-[3]ferrocenophanes (**4b**, **c**, **d**) as pyridine adducts. The fluoride **4a** could not be obtained in this way. The reaction of 1,1′-bis(trimethylsilylamino)ferrocene (**1**) with the dimethyl(ethyl)amine- or pyridine adduct of aluminium trihydride gave the 1,3,2-diazaalumina-[3]ferrocenophanes (**5**) and (**6**) as the amine and pyridine adducts, respectively. Treatment of **5** with trimethyltin fluoride afforded the adduct **7** with an Al–F function. Addition of pyridine converted **7** into the desired pyridine adduct of the fluoride (**4a**). The molecular structures of the pyridine adducts **4a**, **4b**, **4c** and **6** were determined by X-ray analysis. The pyridine is in the *trans*-position relative to the N–Si bond vectors, and temperature dependent solution-state NMR spectra prove that prominent structural features are retained in solution.
© 2007 Elsevier Ltd. All rights reserved.

Keywords: Aluminum amides; [3]Ferrocenophanes; NMR; X-ray structure

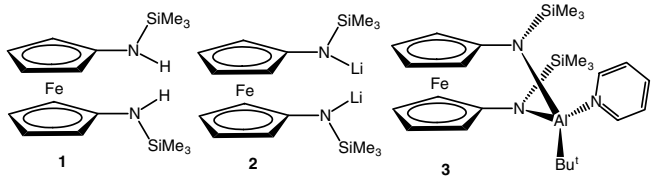
1. Introduction

The principle structures as well as the reactivity of neutral aluminum amides can be tuned by the appropriate choice of the amino groups. There are rare structurally characterised examples containing tri-coordinate aluminum linked to rather bulky amino groups [1]. On the other hand, there are numerous examples containing penta-coordinate [2] or tetra-coordinate aluminum [1a,3]. In the latter cases, the majority of the compounds are either dimers [1c,4], in which two amino groups form bridges between the aluminum atoms, or intramolecular coordination takes place [4a,5]. Alternatively, the structures of few examples of tetra-coordinate aluminum amides with intermolecular coordination have been studied with suitable donors such as trimethylamine [6], pyridine [7] or some other Lewis bases [3c,6b,7b]. There is also some structural information available on tetra-coordinate aluminum amides with *N*-silylamino groups, again with intramolecular [4a,4b,4f,5a,5b,5d] or intermolecular coordination [1e,4a,4c,4d,4e,4f,6c,8]. The presence of amino groups together with halogeno or hydrido functions at aluminum deserves interest, since such compounds are known as catalysts for various organic transformations [5a,5b,5c,9] or as hydroaluminating [10] or selective reducing reagents [11].

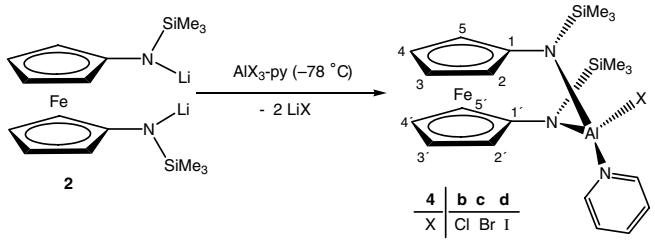
We are interested in the conversion of 1,1′-diaminoferrocene [12] into suitable chelating ligands in order to build [3]ferrocenophanes containing the N–M–N bridge. For this purpose, the 1,1′-bis(trimethylsilylamino)ferrocene **1** is a useful starting compound [13], since it can be readily metalated e.g. to give the dilithiated derivative **2** (Scheme 1). The latter reacts with numerous dihalides to give the corresponding [3]ferrocenophanes containing the $N(SiMe_3)$–M–$N(SiMe_3)$ bridge, where M can be a main group element [14–18] or a transition metal [13,19]. Alternatively, **1** can react with metal hydrides to give the desired products by elimination of H_2, as known for other amines and aluminum hydrides [3d,5a,6a,6b,20].

* Corresponding author. Tel.: +049 921 552542; fax: +049 921 552157.
E-mail addresses: b.wrack@uni-bayreuth.de, wrackmeyer@superkabel.de (B. Wrackmeyer).

0277-5387/$ - see front matter © 2007 Elsevier Ltd. All rights reserved.
doi:10.1016/j.poly.2007.03.035



Scheme 1.



Scheme 2.

Recently, we have reported on the first examples of 1,3,2-diazaalumina-[3]ferrocenophanes bearing a bulky organyl group at aluminum such as **3** [21] (Scheme 1). Certainly, the introduction of an exocyclic function at the site of aluminum is an attractive object. Indeed, the formation of the chloride **4b** (Scheme 2), as a side product has already been observed in the course of the previous study [21]. This prompted us to attempt the direct synthesis of such aluminum halides and of the hydride as adducts.

2. Experimental

2.1. General

The syntheses of starting materials and products as well as all handling of the samples were carried out observing necessary precautions to exclude traces of air and moisture. Carefully dried solvents and oven-dried glassware were used throughout. The deuterated solvents CD_2Cl_2 and $CDCl_3$ were distilled over CaH_2 in an atmosphere of Ar. All other solvents were distilled from Na metal in an atmosphere of argon. The starting materials were prepared as described in the literature, i.e. 1,1′-bis(trimethylsilylamino)ferrocene (**1**) [13], *N*,*N*′-dilithio-1,1′-bis(trimethylsilylamino)ferrocene (**2**) ($fc(NSiMe_3)_2Li_2$) [16]. Trimethyltin fluoride, Me_3SnF [22], was sublimed at 130–135 °C (0.02 Torr) prior to use. NMR measurements: Bruker ARX 250: ^1H, ^{13}C, ^{27}Al, ^{29}Si NMR (refocused INEPT [23] based on $^2J(^{29}Si,^1H) = 7$ Hz); Varian INOVA 400: ^1H, ^{13}C, ^{19}F NMR; Bruker DRX 500: ^{15}N NMR; chemical shifts are given with respect to Me_4Si [$\delta^1H(CHDCl_2)$ 5.33, $(C_6D_5CD_2H) = 2.08$; $\delta^{13}C(CD_2Cl_2) = 53.8$, $(C_6D_5CD_3) = 20.4$; $\delta^{29}Si = 0$ for $\Xi(^{29}Si) = 19.867184$ MHz]; external neat $CFCl_3$ [$\delta^{19}F = 0$ for $\Xi(^{19}F) = 94.094003$ MHz]; external neat $MeNO_2$ [$\delta^{15}N = 0$ for $\Xi(^{15}N) = 10.136767$ MHz]; external 1.1 M $Al(NO_3)_3$ in D_2O [$\delta^{27}Al = 0$ for $\Xi(^{27}Al) = 26.056890$ MHz]. In the cases of the compounds **4b**, **4c**, **6**, the crystalline solids as well as reaction solutions were studied by NMR. For **4a**, **4d**, **5**, **7** NMR spectra of reaction solutions were measured. EI-MS spectra: Finnigan MAT 8500 spectrometer (ionisation energy 70 eV) with direct inlet; the *m*/*z* data refer to the isotopes ^1H, ^{12}C, ^{14}N, ^{27}Al, ^{28}Si, and ^{56}Fe. IR spectra: Perkin–Elmer Spectrum 2000 FTIR. The melting points (uncorrected) were determined using a Büchi 510 melting point apparatus.

2.2. 1,3-Bis(trimethylsilyl)-2-halogeno-2-pyridine-1,3,2-diazaalumina-[3]ferrocenophanes (**4**)

2.2.1. 1,3-Bis(trimethylsilyl)-2-chloro-2-pyridine-1,3,2-diazaalumina-[3]ferrocenophane (**4b**)

Freshly prepared $fc(NSiMe_3)_2Li_2$ (**2**) (292 mg, 0.78 mmol) was taken up in toluene (20 mL); the solution was cooled to −78 °C, and a solution of freshly prepared $AlCl_3$-py [from $AlCl_3$ (105 mg, 0.78 mmol) and pyridine (0.063 mL, 0.78 mmol) in toluene (10 mL)] was added drop wise. After stirring the reaction mixture for 1 h at −78 °C and then for 18 h at ambient temperature, insoluble materials were separated by centrifugation, and the clear liquid was collected. Volatile materials were evaporated and the remaining oil was washed with hexane (10 mL), and a solid was obtained. Thus was dried in a vacuum to give **4b** as a brown powder (236 mg; 60%). Crystallisation from toluene-[d_8], after 2 days at −20 °C, gave orange crystals of **4b** (132 mg; 34%); m.p. >260 °C (decomposition). ^1H NMR (250.1 MHz; CD_2Cl_2; 25 °C): $\delta = -0.10$ (s, 18H, Me_3Si), 3.72 (br) (m, 4H, $H^{2,2',5,5'}$), 3.81 (m, 4H, $H^{3,3',4,4'}$), 7.78 (m, 2H, H_β), 8.20 (m, 1H, H_γ), 9.09 (d, 2H, H_α, $J = 4.5$ Hz). ^1H NMR (250.1 MHz; CD_2Cl_2; −50 °C): $\delta = -0.20$ (s, 18H, Me_3Si), 3.38, 3.86 (m, m, 2H, 2H, $H^{2,2'}$, $H^{5,5'}$), 3.70, 3.78 (m, m, 2H, 2H, $H^{3,3'}$, $H^{4,4'}$), 7.80 (m, 2H, H_β), 8.23 (m, 1H, H_γ), 8.94 (m, 2H, H_α).

2.2.2. 1,3-Bis(trimethylsilyl)-2-bromo-2-pyridine-1,3,2-diazaalumina-[3]ferrocenophane (**4c**)

Freshly prepared $fc(NSiMe_3)_2Li_2$ (**2**) (260 mg, 0.70 mmol) was taken up in toluene (20 mL); the solution was cooled to −78 °C, and $AlBr_3$ (186 mg, 0.70 mmol) and pyridine (0.060 mL, 0.75 mmol) was added. After stirring the reaction mixture for 1 h at −78 °C and then for 14 h at ambient temperature, insoluble materials were separated by centrifugation, and the clear liquid was collected. Volatile materials were removed in vacuo (0.001 torr) to give **4c** as a brown solid (358 mg; 94%). Crystallisation from toluene-[d_8], after 2 days at −20 °C, gave red-orange crystals of **4c** (195 mg; 51%); m.p. >270 °C (decomposition). ^1H NMR (250.1 MHz; CD_2Cl_2; 25 °C): $\delta = -0.18$ (s, 18H, Me_3Si), 3.83 (br) (m, 4H, $H^{2,2',5,5'}$), 3.87 (m, 4H, $H^{3,3',4,4'}$), 7.85 (br) (m, 2H, H_β), 8.22 (m, 1H, H_γ), 9.18 (br) (m, 2H, H_α). ^1H NMR (250.1 MHz; CD_2Cl_2; −40 °C): $\delta = -0.27$ (s, 18H, Me_3Si), 3.61, 3.86 (m, m, 2H, 2H, $H^{2,2'}$, $H^{5,5'}$), 3.77, 3.80 (m, m, 2H, 2H, $H^{3,3'}$, $H^{4,4'}$), 7.80 (m, 2H, H_β), 8.23 (m, 1H, H_γ), 9.01 (m, 2H,

H_α). EI-MS (70 eV) for $C_{21}H_{32}N_3AlSi_2Fe$ (465.13): *m/z* (%) = 360 (100) [fc(N(H)SiMe$_3$)$_2$], 328 (53), 288 (55), 272 (5), 256 (25), 216 (15), 194 (8), 178 (6), 147 (50), 136 (8), 103 (13).

2.2.3. 1,3-Bis(trimethylsilyl)-2-iodo-2-pyridine-1,3,2-diazaalumina-[3]ferrocenophane (*4d*)

The synthesis was carried out in the same way as for **4c**, starting from 164 mg (0.44 mmol) of fc(NSiMe$_3$)$_2$Li$_2$ (**2**), AlI_3 (180 mg, 0.44 mmol) and pyridine (0.05 mL, 0.62 mmol), to give 287 mg of a mixture containing **4d** (ca. 70%) and several unidentified side products as brown oily material. ^{1}H NMR (250.1 MHz; CD_2Cl_2; 25 °C): $\delta = -0.28$ (s, 18H, Me_3Si), 3.81, 3.98 (br) (m, m, 2H, 2H, $H^{2,2'}$, $H^{5,5'}$), 3.87 (br) (m, 4H, $H^{3,3',4,4'}$), 7.81 (br) (m, 2H, H_β), 8.25 (m, 1H, H_γ), 9.22 (br) (m, 2H, H_α). ^{1}H NMR (250.1 MHz; CD_2Cl_2; −40 °C): $\delta = -0.40$ (s, 18H, Me_3Si), 3.81, 3.95 (m, m, 2H, 2H, $H^{2,2'}$, $H^{5,5'}$), 3.83 (m, m, 2H, 2H, $H^{3,3'}$, $H^{4,4'}$), 7.80 (m, 2H, H_β), 8.25 (m, 1H, H_γ), 9.13 (m, 2H, H_α).

The products **4b**, **c**, **d** decompose slowly as solids under Ar at room temperature to green-black powders, which are insoluble in CD_2Cl_2 and inaccessible for NMR spectroscopic characterisation.

2.2.4. Reaction of the N,N′-dilithio-1,1′-bis(trimethylsilylamino)ferrocene (*2*) with AlF_3 and pyridine

When the synthesis was carried out as described for **4c**, starting from 216 mg (0.58 mmol) of fc(NSiMe$_3$)$_2$Li$_2$ (**2**), AlF_3 (49 mg, 0.58 mmol) and pyridine (0.05 mL, 0.62 mmol), a crude reaction mixture (248 mg) was obtained containing **1** (ca. 70%) and fc(NSiMe$_3$)$_2$Li$_2$-2py (ca. 30%) as a brown, oily-material. The absence of ^{19}F NMR signals indicated that an appreciable amount of soluble fluorine-containing materials was not present.

2.3. 1,3-Bis(trimethylsilyl)-2-hydro-1,3,2-diazaalumina-[3]ferrocenophane adducts (*5*) and (*6*)

2.3.1. 1,3-Bis(trimethylsilyl)-2-dimethyl(ethyl)amine-2-hydro-1,3,2-diazaalumina-[3]ferrocenophane (*5*)

A solution of 1,1′-bis(trimethylsilylamino)ferrocene (**1**) (176 mg, 0.49 mmol) in toluene (10 mL) was cooled to 0 °C, and a solution of AlH_3-N(Et)Me$_2$ (0.98 mL of a 0.5 M solution in toluene, 0.49 mmol) was added drop wise. While stirring, gas evolution was observed. The reaction mixture was stirred at 0 °C for 1 h, then allowed to reach ambient temperature and kept stirring for 20 h. Volatile materials were removed *in vacuo*, the remaining yellow-green oil was dissolved in hexane (20 mL) and centrifugated. Then, the solvent was removed *in vacuo* to give 190 mg (85%) of **5** as a yellow-orange oil. ^{1}H NMR (250.1 MHz; toluene-[d_8]; 25 °C; *J*/Hz): $\delta = 0.26$ (s, 18H, Me_3Si), 0.63 (t, 3H, CCH_3, $J = 7.3$ Hz), 2.08 (s, 6H, NCH_3), 2.70 (q, 2H, NCH_2), 3.44 (m, 2H, $H^{2,2'}$), 3.86 (m, 4H, $H^{3,3',4,4'}$), 4.00 (m, 2H, $H^{5,5'}$). IR (toluene-[d_8]) ν(Al–H) = 1818 (br) cm^{-1}.

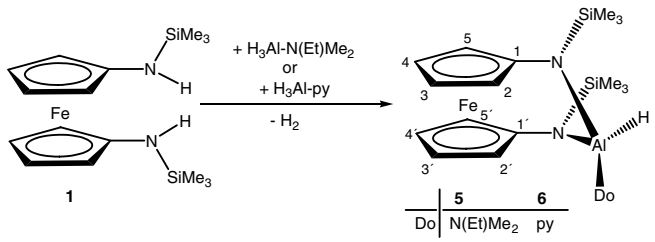
2.3.2. 1,3-Bis(trimethylsilyl)-2-hydro-2-pyridine-1,3,2-diazaalumina-[3]ferrocenophane (*6*)

The synthesis was carried out as described for **5**, starting from 216 mg (0.60 mmol) of fc(N(H)SiMe$_3$)$_2$ (**1**) and a

Table 1
Crystallographic data of the 1,3-bis(trimethylsilyl)-2-X-2-pyridine-1,3,2-diazaalumina-[3]ferrocenophane (**4a**–**4c**, and **6**)

	6 X = H	**4a** X = F	**4b** X = Cl	**4c** X = Br
Formula	$C_{21}H_{32}AlFeN_3Si_2$	$C_{21}H_{31}AlFFeN_3Si_2$	$C_{21}H_{31}AlClFeN_3Si_2$	$C_{21}H_{31}AlBrFeN_3Si_2$
Crystal	orange prism	orange prism	red-orange prism	red-orange prism
Dimensions (mm)	0.22 × 0.16 × 0.07	0.26 × 0.20 × 0.18	0.20 × 0.15 × 0.12	0.18 × 0.15 × 0.12
Crystal system	triclinic	triclinic	triclinic	monoclinic
Space group	$P\bar{1}$	$P\bar{1}$	$P\bar{1}$	$P2(1)/n$
Lattice parameters				
a (pm)	1062.7(2)	1077.3(2)	880.90(18)	1037.6(2)
b (pm)	1093.3(2)	1101.9(2)	1076.7(2)	1372.0(3)
c (pm)	1232.0(3)	1221.0(2)	1405.2(3)	1809.8(4)
α (°)	67.42(3)	66.49(3)	90.99(3)	
β (°)	86.42(3)	86.50(3)	103.97(3)	92.61(3)
γ (°)	72.20(3)	71.42(3)	106.17(3)	
Z	2	2	2	4
Absorption coefficient μ (mm^{-1})	0.742	0.750	0.863	2.278
Diffractometer	STOE IPDS I	STOE IPDS I	STOE IPDS II	STOE IPDS I
	Mo Kα, λ = 71073 pm, graphite monochromator			
Measuring range (ϑ) (°)	1.8–26.0	1.8–26.0	1.5–24.7	1.9–26.0
Reflections collected	8254	9302	14809	17620
Independent reflections ($I > 2\sigma(I)$)	4527	4538	4164	4777
Absorption correction[a]	none	none	none	none
Refined parameters	253	262	262	262
wR_2/R_1 ($I > 2\sigma(I)$)	0.154/0.065	0.101/0.046	0.077/0.030	0.111/0.046
Maximum/minimum residual electron density (e pm^{-3} 10^{-6})	0.863/−0.344	0.547/−0.207	0.348/−0.132	0.630/−0.408

[a] Absorption correction did not improve the data set.

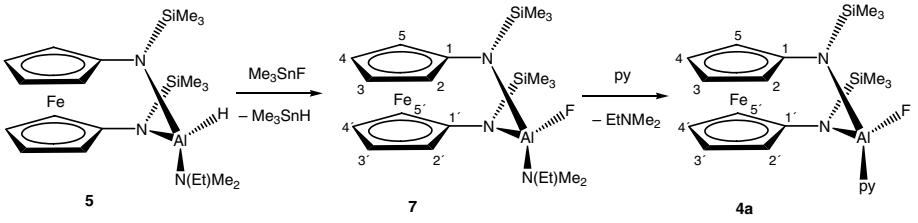


Scheme 3.

solution of freshly prepared AlH_3-py [from AlH_3-$N(Et)Me_2$ (1.20 mL of a 0.5 M solution in toluene, 0.60 mmol) and pyridine (0.048 mL, 0.60 mmol) in toluene (10 mL)], to give 303 mg of a mixture containing **6** (70%) and **1** (ca. 30%). Crystallisation from CD_2Cl_2, after 2 days at −20 °C, gave orange crystals of **6** (115 mg, 41%); m.p. 170 °C (decomposition). The product decomposes slowly as a solid under Ar at room temperature to green-black powder, which is insoluble in CD_2Cl_2 and inaccessible for NMR spectroscopic characterisation. ^{1}H NMR (250.1 MHz; CD_2Cl_2; 25 °C): $\delta = 0.05$ (s, 18H, Me_3Si), 3.54 (br) (m, 4H, $H^{2,2',5,5'}$), 3.70 (m, 4H, $H^{3,3',4,4'}$), 7.74 (m, 2H, H_β), 8.13 (m, 1H, H_γ), 8.96 (d, 2H, H_α, $J = 3.5$ Hz). ^{1}H NMR (250.1 MHz; CD_2Cl_2; −60 °C): $\delta = 0.002$ (s, 18H, Me_3Si), 3.42 (br) (m, 4H, $H^{2,2',5,5'}$), 3.61 (m, 4H, $H^{3,3',4,4'}$), 3.95 (br) (s, 1H, AlH), 7.73 (m, 2H, H_β), 8.13 (m, 1H, H_γ), 8.76 (m, 2H, H_α). EI-MS (70 eV) for $C_{21}H_{32}N_3AlSi_2Fe$ (465.13): m/z (%) = 392 (1) [M^+−$SiMe_3$], 360 (100) [$fc(N(H)SiMe_3)_2]^+$, 288 (20).

2.4. 1,3-Bis(trimethylsilyl)-2-fluoro-1,3,2-diazaalumina-[3]ferrocenophane adducts (7) and (4a)

A solution of **5** (120 mg; 0.26 mmol) in toluene-[d_8] (1 mL) was added to Me_3SnF (64 mg; 0.35 mmol). The mixture was stirred for 2 h and centrifugated to separate the excess of Me_3SnF. The resulting mixture contained about 70% of the dimethyl(ethyl)amine adduct **7** together



Scheme 4.

Table 2
^{13}C, ^{27}Al, ^{19}F and ^{29}Si NMR data[a] of the 1,3-bis(trimethylsilyl)-2-X-2-pyridine-1,3,2-diazaalumina-[3]ferrocenophane (**4a**–**4d** and **6**)

Compound R	**6**[b,c] X = H	**4a** X = F	**4b** X = Cl		**4c** X = Br		**4d** X = I	
	298 K	298 K	298 K	223 K	298 K	233 K	298 K	233 K
δ^{13}C(N-$SiMe_3$)	2.2 (55.4)	1.7 (56.1) [1.8]	1.8 (56.3)	0.8	1.5 (56.1)	0.6 (56.1)	1.3 (56.3)	0.4 (56.4)
δ^{13}C(fc-C^1)	106.4	103.7 [0.7]	104.1	102.8	103.8	102.7	103.3	102.4
δ^{13}C(fc-$C^{2,5}$)	67.6 (br)	68.1	68.4 (br)	65.9, 68.4	68.5 (br)	67.3, 68.0	68.4 (br), 69.0 (br)	67.5, 68.8
δ^{13}C(fc-$C^{3,4}$)	64.3	65.2	65.1	63.1	65.1	64.2, 64.3	65.3 (br)	64.5, 64.8
X	3.95 (δ^1H, 213 K) (br)	−154.6 (δ^{19}F)(br)						
Pyridine	126.1 (C_β)	124.7 (C_β) (br)	126.3 (C_β)	125.7 (C_β)	126.4 (C_β) (br)	125.7 (C_β)	126.2 (C_β) (br)	125.8 (C_β)
	141.5 (C_γ)	137.7 (C_γ) (br)	142.5 (C_γ)	142.3 (C_γ)	143.1 (C_γ)	142.7 (C_γ)	143.5 (C_γ)	143.4 (C_γ)
	148.4 (C_α)	149.2 (C_α) (br)	148.7 (C_α)	147.0 (C_α)	149.7 (C_α) (br)	147.5 (C_α)	149.0 (C_α) (br)	148.0 (C_α)
δ^{27}Al	120 ($h_{1/2}$ = 4050 Hz)	105 ($h_{1/2}$ = 3500 Hz)	95 ($h_{1/2}$ = 4500 Hz)		110 ($h_{1/2}$ = 6000 Hz)		n.o.[d,e]	
δ^{29}Si	2.9 (55.5)	3.8 (56.1){1.1}	4.0 (56.1)	4.8	3.6 (56.1)	3.9	2.7 (56.2)	2.6

[a] In CD_2Cl_2 (**6**, **4b**, **4c**, **4d**), toluene-[d_8] (**4a**); coupling constants (±0.5 Hz) $^1J(^{29}Si, ^{13}C)$ are given in parentheses; $^nJ(^{19}F, ^{13}C)$ in brackets; $^3J(^{29}Si, ^{19}F)$ in braces.

[b] No changes in the NMR spectra at 213 K, except of δ^1H(Al–H).

[c] δ^{15}N −343.4 (NSi).

[d] n.o. = not observed.

[e] Signal overlaps strongly with the artefact arising from the probe head material.

with **1**, Me_3SnH and several unidentified side products (about 30%) (^1H, ^{13}C and ^{29}Si NMR). ^1H NMR (399.8 MHz; toluene-[d_8]; 25 °C; J/Hz): $\delta = 0.26$ (s, 18H, Me_3Si), 0.31 (t, 3H, CCH_3, $J = 4.0$ Hz), 2.10 (s, 6H, NCH_3), 2.78 (q, 2H, NCH_2), 3.41 (m, 2H, $H^{2,2'}$), 3.85 (m, 4H, $H^{3,3',4,4'}$), 4.00 (m, 2H, $H^{5,5'}$).

Then pyridine (0.015 mL, 0.19 mmol) was added to this reaction mixture at −78 °C. The solution was stirred for 20 min. The resulting mixture contained the pyridine adduct **4a** (about 70%), **1**, Me_3SnH, free dimethyl(ethyl)amine and several unidentified side products. Single orange crystals of **4a** for X-ray analysis were grown from toluene-[d_8] solution after 5 days at −20 °C; m.p. >240 °C (decomposition). ^1H NMR (399.8 MHz; toluene-[d_8]; 25 °C): $\delta = 0.18$ (s, 18H, Me_3Si), 3.69 (br) (m, 4H, $H^{2,2',5,5'}$), 3.80 (m, 4H, $H^{3,3',4,4'}$), 6.65 (br) (m, 2H, H_β), 6.91 (br) (m, 1H, H_γ), 8.62 (br) (m, 2H, H_α).

Table 3
^{13}C, ^{27}Al, ^{15}, ^{19}F and ^{29}Si NMR data[a] of the 1,3-bis(trimethylsilyl)-2-dimethyl(ethyl)amine-2-X-1,3,2-diazaalumina-[3]ferrocenophanes (**5**) and (**7**)

Compound	**5** X = H	**7** X = F
$\delta^{13}C$(N-$SiMe_3$)	3.0 (56.1)	2.3 (56.1) [2.3]
$\delta^{13}C$(fc-C^1)	106.4	103.6 [1.3]
$\delta^{13}C$(fc-$C^{2,5}$)	66.8 (C^2), 69.8 (C^5)	66.8 (C^2), 69.9(C^5)
$\delta^{13}C$(fc-$C^{3,4}$)	64.5, 65.0	64.9, 65.3
X	n.o.[b] (δ^1H)	−155.9 ($\delta^{19}F$)
N(Et)Me_2	52.5, 6.0 (NCH_2CH_3) 43.5 (CH_3N)	52.7 [1.4], 3.0 (NCH_2CH_3)43.8 [1.8] (CH_3N)
$\delta^{27}Al$	125 ($h_{1/2} = 3350$ Hz)	110 ($h_{1/2} = 3300$ Hz)
$\delta^{29}Si$	2.7 (56.1)	4.1 (56.1) {0.8}
$\delta^{15}N$	−353.7 (NSi) −346.7 (NEt)	

[a] Measured in toluene-[d_8] at 25 °C; coupling constants (±0.5 Hz) $^1J(^{29}Si, ^{13}C)$ are given in parentheses, $^nJ(^{19}F, ^{13}C)$ in brackets; $^3J(^{29}Si, ^{19}F)$ in braces.
[b] n.o. = not observed.

2.5. Crystal structure determinations of the 1,3-bis(trimethylsilyl)-1,3,2-diazaalumina-[3]ferrocenophane pyridine adducts (*4a*, *4b*, *4c*, and *6*)

Details pertinent to the crystal structure determinations are listed in Table 1. Crystals of appropriate size were sealed under Ar in Lindemann capillaries. The data collections were carried out at 20 °C.

3. Results and discussion

3.1. Synthesis

The reaction of the aluminum trihalides in the presence of pyridine (py) with **2** (Scheme 2) provides a straightforward route to the chloride **4b**, bromide **4c** and iodide **4d**, whereas the formation of the fluoride **4a** was not observed. The dilithiated species **2** did not react with aluminum trifluoride, and the reaction solution contained only **1**, as a result of hydrolysis, and **2**, shown by ^{29}Si NMR, and ^{19}F

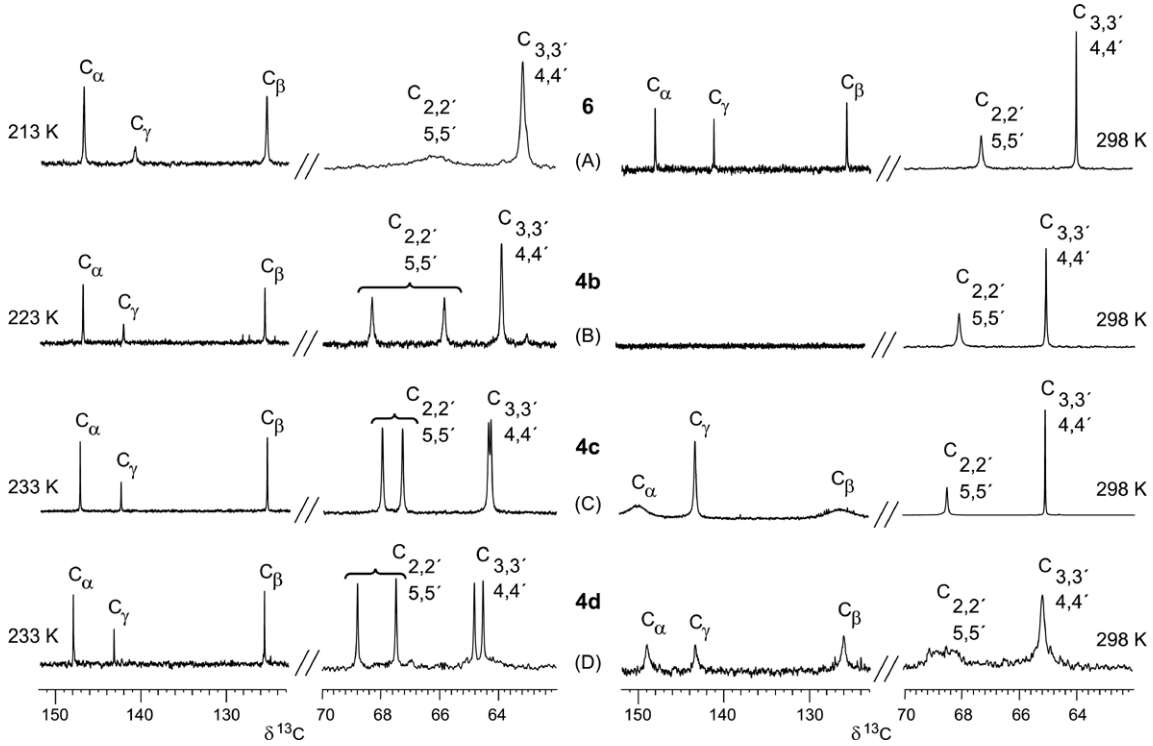


Fig. 1. Parts of the room temperature (right trace) and low temperature (left trace) 62.9 MHz $^{13}C\{^1H\}$ NMR spectra of the 1,3-bis(trimethylsilyl)-2-X-2-pyridine-1,3,2-diazaalumina-[3]ferrocenophane (**6**, **4b**, **4c**, and **4d**) (CD_2Cl_2). (A) **6** (R = H). (B) **4b** (R = Cl). (C) **4c** (R = Br). (D) **4d** (R = I).

NMR indicated the absence of any soluble aluminum fluoride.

The compounds **4b**, **c**, **d** are orange solids, extremely sensitive towards traces of moisture. Crystalline materials suitable for X-ray analysis were obtained for the chloride **4b** and the bromide **4c** (*vide infra*).

The reaction of aluminum trihydride adducts with **1** opens the most convenient way to the hydride adducts **5** and **6** (Scheme 3), of which **6** could be isolated for single crystal X-ray diffraction studies (*vide infra*). Both **5** and **6** are sensitive to moisture, appear to be very reactive, and the ease of their essentially quantitative formation is promising for further applications.

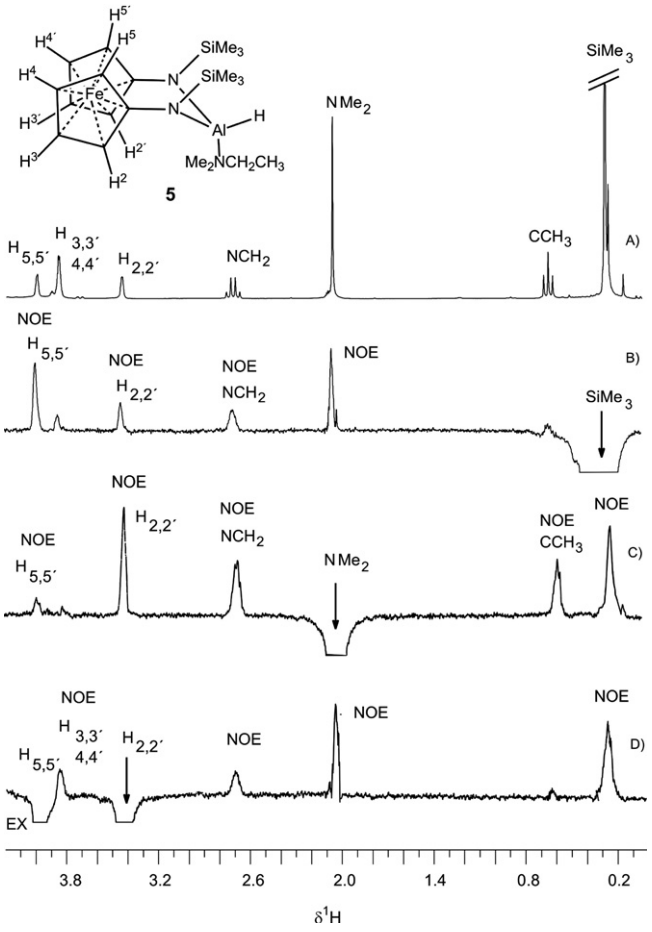


Fig. 2. 400 MHz $^{1}H\{^{1}H\}$ NOE difference spectra (gradient enhanced [27]) of **5** (10% in toluene-[d_8] at 23 °C; relaxation delay 1.5 s; mixing time 0.6 s; 30 min of spectrometer time). The irradiated resonance signals are marked by arrows; the resulting intensities arising from NOE or EXchange are marked. (A) Normal ^{1}H NMR spectrum. (B) The $NSiMe_3$-resonance was irradiated and response is shown: $H^{5,5'}$(++) and $H^{2,2'}$(+) of the cyclopentadienyl groups, NCH_2 and NMe_2 of the dimethyl(ethyl)amine ligand. (C) The NMe_2-resonance of the dimethyl(ethyl)amine ligand was irradiated and response is shown: $H^{5,5'}$(+) and $H^{2,2'}$(++) of the cyclopentadienyl groups, NCH_2CH_3 of the dimethyl(ethyl)amine ligand, and the $SiMe_3$ group. (D) The $H^{2,2'}$-resonance of the cyclopentadienyl groups was irradiated and response is shown: magnetisation transfer [25] takes place between $H^{2,2'}$ and $H^{5,5'}$, whereas NOE is observed for $H^{3,3',4,4'}$(+) of the cyclopentadienyl groups, NCH_2 and NMe_2 of the dimethyl(ethyl)amine ligand, and the $SiMe_3$ group.

The reaction of **5** with Me_3SnF in toluene-[d_8] leads to the aluminium monofluoride adduct **7** in moderate to good yields [6a,24]. The formation of some side products may arise because of reactions of the tin hydride with **5** or **7**. Pyridine displaces the amine from the adduct **7**, and the pyridine adduct **4a** is formed and crystallises from the reaction solution (see Scheme 4).

3.2. NMR spectroscopy

The NMR data given in Tables 2 and 3 and in Section 2 are in support of the proposed structures for the compounds **4**–**7**. The Fe, C^1, $C^{1'}$, *N*, *N*′, Al atoms form non-planar rings, and the ring inversion becomes slow as compared to the NMR time scale at lower temperatures for the pyridine adducts (Fig. 1), and is already slow at room temperature for the amine adduct **5** (Fig. 2). However, the structure of **5** in solution is not rigid as shown by magnetisation transfer [25] (Fig. 2D), and this is also evident from the 2D $^{13}C/^{13}C$ EXSY experiment (Fig. 3) [26]. Apparently, the bulky amine prevents fast inversion at the site of the aluminium. $^{1}H/^{1}H$ NOE difference spectra [27] indicate that the position of the pyridine or the amine $Me_2(Et)N$ is opposite to the N-$SiMe_3$ groups, as found for the solid state (*vide infra*). This is exactly the other way round when compared with **3** (Scheme 1), where the bulky *tert*-butyl group avoids close contacts with the $SiMe_3$

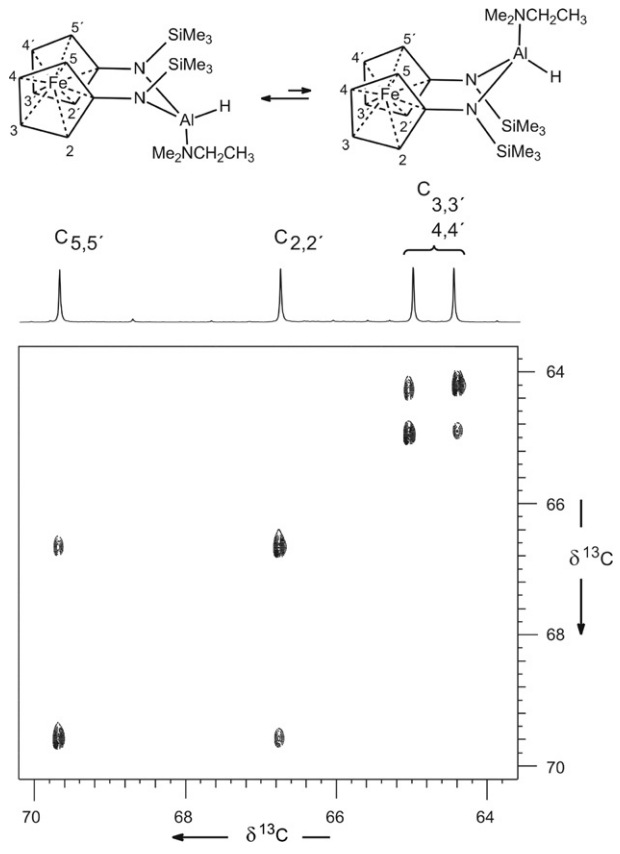


Fig. 3. ^{13}C 2D EXSY NMR spectrum [26] of compounds **5** (100.5 MHz, 10% in toluene-[d_8], at 23 °C), relaxation delay 2.0 s; mixing time 1.0 s.

groups, both in solution and in the solid state [21]. The NOE experiments, together with 2D $^{1}H/^{13}C$ shift correlations, also serve conveniently for the assignment of ^{1}H and ^{13}C NMR signals of the cyclopentadienyl groups.

Frequently, ^{1}H NMR signals of aluminum hydrides are not reported, since these signals tend to be weak and broad, and may be hidden underneath other intense signals. This is also true for **5**, whereas in the case of **6**, the signal could be observed at low temperature in the range typical of other ^{1}H(Al–H) NMR signals [5a,6b,6c]. Similarly, the ^{19}F NMR signals of **4a** and **7** are broad and fit into the range known for terminal Al–F bonds ($\delta^{19}F$ −145 to −180) [6a,24].

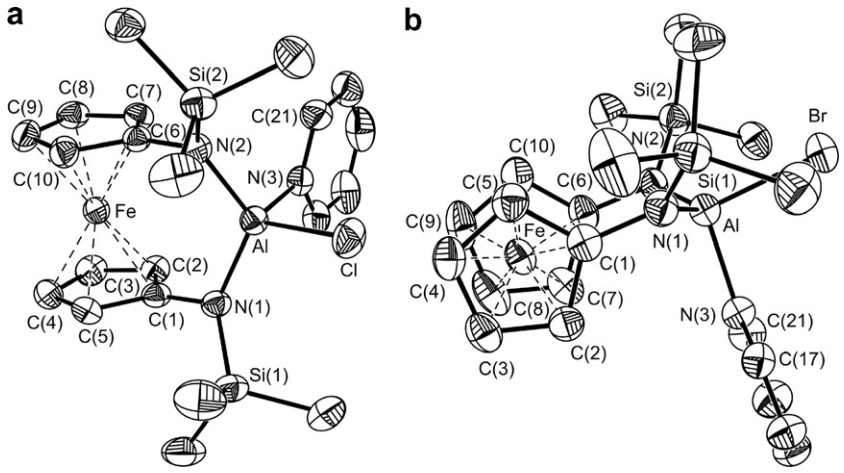


Fig. 4. Molecular structures of **4b** (a) and **4c** (b) (ORTEP plot, 40% probability, hydrogen atoms are omitted for clarity), see Table 4 for structural parameters. The molecular structures of **4a** and **6** are analogous.

Table 4
Selected bond lengths (pm) and angles (°)[a] of the 1,3-bis(trimethylsilyl)-1,3,2-diazaalumina-[3]ferrocenophane pyridine adducts **4a**–**4c**, and **6**

	6 X = H	**4a** X = F	**4b** X = Cl	**4c** X = Br
Al–N(1)	183.7(4)	183.4(3)	182.45(19)	183.0(4)
Al–N(2)	184.0(4)	183.0(3)	181.91(19)	182.4(4)
Al–N(3) (from py)	199.7(4)	197.5(3)	197.4(2)	197.8(3)
Al–X	[b]	166.9(2)	215.08(13)	233.41(15)
N(1)–Si(1)	173.9(4)	173.9(3)	173.70(19)	174.0(4)
N(2)–Si(2)	173.4(4)	174.1(3)	173.90(19)	174.8(3)
N(1)···N(2)	316.7	318.2	316.7	317.7
C(1)···C(6)	324.3	326.5	323.6	324.8
Fe···Al	351.1	346.3	342.7	342.2
N(1)–Al–N(2) (*endo*)	118.91(16)	120.55(12)	120.75(9)	120.86(17)
N(1)–Al–X	109.3	111.09(12)	110.69(7)	110.61(13)
N(2)–Al–X	118.9	110.35(13)	110.68(7)	111.61(12)
N(1)–Al–N(3) (from py)	104.19(16)	105.71(12)	108.27(9)	106.53(15)
N(2)–Al–N(3) (from py)	105.30(16)	107.09(12)	105.08(9)	106.71(16)
C(1)–N(1)–Si(1)	119.1(3)	119.1(2)	116.83(14)	118.0(3)
C(6)–N(2)–Si(2)	116.5(3)	116.8(2)	118.02(14)	117.9(3)
Al–N(1)–C(1)	116.3(2)	115.0(2)	113.64(13)	113.3(3)
Al–N(2)–C(6)	116.7(3)	115.6(2)	113.01(13)	113.6(2)
Al–N(1)–Si(1)	122.4(2)	123.51(15)	126.50(11)	127.5(2)
Al–N(2)–Si(2)	124.3(2)	124.93(16)	126.97(10)	127.1(2)
Fe–C(1)–N(1)–Al–N(2)–C(6)$\overline{\Delta}$ (pm)[c]	12.8	13.3	14.6	14.9
Distance of Al from the plane Fe–C(1)–N(1)–N(2)–C(6) (pm)[c]	51.8	53.4	59.0	59.4
C_5/C_5 (α)	2.3	1.9	3.3	3.3
C_5/N(1) (β_1)	1.6	1.8	0.4	0.8
C_5/N(2) (β_2)	0.2	1.2	0.1	0.6
	towards iron	towards iron	bent away from iron	towards iron
C_5–Fe–C_5 (γ)	176.7	177.0	176.8	177.1
C_5/C_5 (twist) (τ)	5.1	4.6	3.5	2.2
Fe–C_5 (centre)	164.3	164.4	164.6	164.6
	164.5	164.5	164.8	164.7

[a] The definition of the angles α, β, γ and τ is given in Ref. [28].
[b] If the H-atom was refined without restraints, the distance Al–H is 161(4) pm.
[c] Mean deviation from plane.

3.3. X-ray crystallography

The molecular structures of the adducts **4b** and **4c** (all molecular structures of **4a**, **b**, **c** and **6** are analogous) are shown in the Fig. 4, and selected structural parameters are compiled in Table 4. Intermolecular interactions appear to be negligible. The tetrahedral surroundings of the aluminum atoms enforce non-planar arrangements in the cycles containing the atoms Al, N(1), C(1), Fe, C(6), N(2), and the pyridine ligand avoids contacts with the $SiMe_3$ groups in all cases studied here. Thus, these structures differ from that of **3** (Scheme 1), where the steric interactions pyridine/$SiMe_3$ are less repulsive than for *tert*-Bu/$SiMe_3$ groups. Expectedly, the Al–N(amino) are shorter than Al–N(pyridine) bonds. The surroundings of the amino nitrogen atoms deviate slightly from trigonal planarity as shown by the respective sum of the bond angles: 357.6°, 357.3° for **4a**, 356.9°, 358.0° for **4b**, 358.8°, 358.6° for **4c**, and 357.8°, 257.5° for **6**. Remarkably, changes in all Al–N bond lengths in the series **4a**, **b**, **c** and **6** are rather small, almost within the error limits. Reported Al–N(pyridine) bond lengths of pyridine adducts range from 186.3(4) to 203.0(4) pm [7b,7c], and it appears that steric repulsion is the major influence for extended bond lengths, as in the cases of **3** 202.7(4) pm [21], tmp_2AlBr(py) (203.0(4) pm [7b]) or tmp_2AlI(py) (202.2(3) pm [7b]).

The cyclopentadienyl rings adopt almost exactly eclipsed conformations, and the rings differ only slightly from a parallel orientation [28] which appears to be typical for these [3]ferrocenophanes [13–19,21]. In **4a**, the distances F···C(Si) (327.2, 317.8 pm) indicate for the carbon atoms being closest in space to the Al–F unit that attractive Al–F···H–C interactions [29] may have to be considered.

4. Supplementary material

CCDC 634696, 634693, 634694, and 634695 contain the supplementary crystallographic data for **4a**, **4b**, **4c**, and **6**. These data can be obtained free of charge via http://www.ccdc.cam.ac.uk/conts/retrieving.html, or from the Cambridge Crystallographic Data Centre, 12 Union Road, Cambridge CB2 1EZ, UK; fax: (+44) 1223-336-033; or e-mail: deposit@ccdc.cam.ac.uk.

Acknowledgement

This work was supported by the Deutsche Forschungsgemeinschaft.

References

[1] (a) I. Krossing, H. Nöth, C. Tacke, M. Schmidt, H. Schwenk, Chem. Ber. 130 (1997) 1047, and Refs. therein;
(b) K. Knabel, I. Krossing, H. Nöth, H. Schwenk-Kircher, M. Schmidt-Amelunxen, T. Seifert, Eur. J. Inorg. Chem. (1998) 1095;
(c) K. Knabel, H. Nöth, T. Seifert, Z. Naturforsch., B: Chem. Sci. 57 (2002) 830;
(d) D. Chakraborty, E.Y.-X. Chen, Organometallics 21 (2002) 1438, and Refs. therein;
(e) S.D. Waezsada, C. Rennekamp, H.W. Roesky, C. Röpken, E. Parisini, Z. Anorg. Allg. Chem. 624 (1998) 987.

[2] (a) M.P. Donzello, R. Agostinetto, S.S. Ivanova, M. Fujimori, Y. Suzuki, H. Yoshikawa, J. Shen, K. Awaga, C. Ercolani, K.M. Kadish, P.A. Stuzhin, Inorg. Chem. 44 (2005) 8539, and Refs. therein;
(b) J.-H. Huang, H.-J. Chen, J.-C. Chang, C.-C. Zhou, G.-H. Lee, S.-M. Peng, Organometallics 20 (2001) 2647;
(c) M.D. Fryzuk, G.R. Giesbrecht, S.J. Rettig, Inorg. Chem. 37 (1998) 6928;
(d) M.D. Fryzuk, G.R. Giesbrecht, S.J. Rettig, G.P.A. Yap, J. Organomet. Chem. 591 (1999) 63;
(e) L.M. Engelhardt, M.G. Gardiner, C. Jones, P.C. Junk, C.L. Raston, A.H. White, Dalton Trans. (1996) 3053.

[3] (a) K. Knabel, H. Nöth, Z. Naturforsch., B: Chem. Sci. 60 (2005) 155;
(b) S.G. Nelson, B.-K. Kim, T.J. Peelen, J. Am. Chem. Soc. 122 (2000) 9318;
(c) H. Hohmeister, H. Wessel, P. Lobinger, H.W. Roesky, P. Müller, I. Usón, H.-G. Schmidt, M. Noltemeyer, J. Magull, J. Fluorine Chem. 120 (2003) 59;
(d) C. Klein, H. Nöth, M. Tacke, M. Thomann, Angew. Chem. 105 (1993) 923;
Angew. Chem., Int. Ed. 32 (1993) 886.

[4] (a) J.-P. Bezombes, B. Gehrhus, P.B. Hitchcock, M.F. Lappert, P.G. Merle, Dalton Trans. (2003) 1821;
(b) V. Passarelli, F. Benetollo, P. Zanella, Dalton Trans. (2004) 1424;
(c) C.-C. Chang, M.-D. Li, M.Y. Chiang, S.-M. Peng, Y. Wang, G.-H. Lee, Inorg. Chem. 36 (1997) 1955;
(d) U. Wannagat, T. Blumenthal, D.J. Brauer, H. Bürger, J. Organomet. Chem. 249 (1983) 33;
(e) T. Blumenthal, U. Wannagat, D.J. Brauer, H. Bürger, Monatsh. Chem. 114 (1983) 1271;
(f) S. Schulz, F. Thomas, W.M. Priesmann, M. Nieger, Organometallics 25 (2006) 1392;
(g) M.G. Gardiner, S.M. Lawrence, C.L. Raston, Inorg. Chem. 38 (1999) 4467.

[5] (a) N. Emig, H. Nguyen, H. Krautscheid, R. Réau, J.-B. Cazaux, G. Bertrand, Organometallics 17 (1998) 3599;
(b) N. Emig, R. Réau, H. Krautscheid, D. Fenske, G. Bertrand, J. Am. Chem. Soc. 118 (1996) 5822;
(c) S.G. Nelson, T.J. Peelen, Z. Wan, J. Am. Chem. Soc. 121 (1999) 9742;
(d) C.H. Lee, Y.-H. La, S.J. Park, J.W. Park, Organometallics 17 (1998) 3648;
(e) S. Singh, H.-J. Ahn, A. Stasch, V. Jancik, H.W. Roesky, A. Pal, M. Biadene, R. Herbst-Irmer, M. Noltemeyer, H.-G. Schmidt, Inorg. Chem. 45 (2006) 1853.

[6] (a) H. Zhu, J. Chai, H.W. Roesky, M. Noltemeyer, H.-G. Schmidt, D. Vidovic, J. Magull, Eur. J. Inorg. Chem. (2003) 3113;
(b) T. Bauer, S. Schulz, H. Hupfer, M. Nieger, Organometallics 21 (2002) 2931;
(c) U. Fooken, M.A. Khan, R.J. Wehmschulte, Inorg. Chem. 40 (2001) 1316.

[7] (a) K. Ouzounis, H. Riffel, H. Hess, U. Kohler, J. Weidlein, Z. Anorg. Allg. Chem. 504 (1983) 67;
(b) I. Krossing, H. Nöth, H. Schwenk-Kircher, Eur. J. Inorg. Chem. (1998) 927;
(c) K. Hensen, A. Lemke, T. Stumpf, M. Bolte, H. Fleischer, C.R. Pulham, R.O. Gould, S. Harris, Inorg. Chem. 38 (1999) 4700;
(d) J.R. Gardinier, F.P. Gabbaï, New J. Chem. 25 (2001) 1567.

[8] J.F. Janik, R.L. Wells, A.L. Rheingold, I.A. Guzei, Polyhedron 17 (1998) 4101.

[9] (a) A. Mitra, L.J. DePue, S. Parkin, D.A. Atwood, J. Am. Chem. Soc. 128 (2006) 1147, and Refs. therein;
(b) B. Saito, T. Katsuki, Angew. Chem. 117 (2005) 4676;
Angew. Chem., Int. Ed. 44 (2005) 4600, and Refs. therein;
(c) P. Chen, M.H. Chisholm, J.C. Gallucci, X. Zhang, Z. Zhou, Inorg. Chem. 44 (2005) 2588;

(d) A. Saito, H. Yanai, T. Taguchi, Tetrahadron Lett. 45 (2004) 9439;
(e) S.G. Nelson, C. Zhu, X. Shen, J. Am. Chem. Soc. 126 (2004) 14, and Refs. therein;
(f) K. Kamahori, S. Tada, K. Ito, S. Itsuno, Macromolecules 32 (1999) 541;
(g) R.L. Halterman, S.-T. Jan, H.L. Nimmons, D.J. Standlee, M.A. Khan, Tetrahedron 53 (1997) 11257;
(h) Y.C. Park, H.G. Na, Main Group Met. Chem. 20 (1997) 269.

[10] (a) C.-Y. Lin, C.-F. Tsai, H.-J. Chen, C.-H. Hung, R.-C. Yu, P.-C. Kuo, H.M. Lee, J.-H. Huang, Chem. Eur. J. 12 (2006) 3067;
(b) G.C. Welch, W.E. Piers, M. Parvez, R. McDonald, Organometallics 23 (2004) 1811;
(c) E.C. Ashby, S.A. Noding, J. Org. Chem. 45 (1980) 1035;
(d) E.C. Ashby, S.A. Noding, J. Org. Chem. 44 (1979) 4364;
(e) E.C. Ashby, S.R. Noding, J. Organomet. Chem. 177 (1979) 117.

[11] (a) J.S. Cha, S.H. Jang, S.Y. Kwon, Bull. Korean Chem. Soc. 23 (2002) 1697, and Refs. therein;
(b) J.S. Cha, S.J. Moon, Bull. Korean Chem. Soc. 23 (2002) 1340, and Refs. therein;
(c) J.S. Cha, J.C. Lee, Y.C. Ju, Bull. Korean Chem. Soc. 18 (1997) 890, and Refs. therein;
(d) N.M. Yoon, Pure Appl. Chem. 68 (1996) 843, and Refs. therein;
(e) J.S. Cha, H.C. Brown, J. Org. Chem. 58 (1993) 3974, and Refs. therein;
(f) M. Muraki, T. Mukaiyama, Chem. Lett. (1975) 875, and Refs. therein;
(g) T. Sato, Y. Gotoh, M. Watanabe, T. Fujisawa, Chem. Lett. (1983) 1533.

[12] (a) G.R. Knox, Proc. Chem. Soc. London (1959) 56;
(b) J.M. Osgerby, P.L. Pauson, J. Chem. Soc. (1961) 4615;
(c) A.N. Nesmeyanov, V.N. Drozd, V.A. Sazonova, Dokl. Akad. Nauk SSSR 150 (1963) 321;
(d) A. Shafir, M.P. Power, G.D. Whitener, J. Arnold, Organometallics 19 (2000) 3978.

[13] A. Shafir, M.P. Power, G.D. Whitener, J. Arnold, Organometallics 20 (2001) 1365.

[14] B. Wrackmeyer, H.E. Maisel, W. Milius, M. Herberhold, J. Organomet. Chem. 680 (2003) 271.

[15] B. Wrackmeyer, W. Milius, H.E. Maisel, H. Vollrath, M. Herberhold, Z. Anorg. Allg. Chem. 629 (2003) 1169.

[16] B. Wrackmeyer, E.V. Klimkina, H.E. Maisel, W. Milius, M. Herberhold, Inorg. Chim. Acta 357 (2004) 1703.

[17] B. Wrackmeyer, E.V. Klimkina, W. Milius, O.L. Tok, M. Herberhold, Inorg. Chim. Acta 358 (2005) 1420.

[18] B. Wrackmeyer, E.V. Klimkina, W. Milius, Z. Anorg. Allg. Chem. 632 (2006) 2331.

[19] A. Shafir, J. Arnold, J. Am. Chem. Soc. 123 (2001) 9212.

[20] M.C. Hodgson, M.A. Khan, R.J. Wehmschulte, J. Cluster Sci. 13 (2002) 503.

[21] B. Wrackmeyer, E.V. Klimkina, W. Milius, Inorg. Chem. Commun. 9 (2006) 716.

[22] (a) E. Krause, Ber. Dtsch. Chem. Ges. 51 (1918) 1447;
(b) J. Vela, J.M. Smith, Y. Yu, N.A. Ketterer, C.J. Flaschenriem, R.J. Lachicotte, P.L. Holland, J. Am. Chem. Soc. 127 (2005) 7857.

[23] (a) G.A. Morris, R. Freeman, J. Am. Chem. Soc. 101 (1979) 760;
(b) G.A. Morris, J. Am. Chem. Soc. 102 (1980) 428;
(c) J. Schraml, in: Z. Rappoport, Y. Apeloig (Eds.), The Chemistry of Organic Silicon Compounds, vol. 3, Wiley, Chichester, 2001, pp. 223–339.

[24] (a) J. Pinkas, H.W. Roesky, J. Fluorine Chem. 122 (2003) 125;
(b) Y. Peng, J. Rong, D. Vidovic, H.W. Roesky, T. Labahn, J. Magull, M. Noltemeyer, H.-G. Schmidt, J. Fluorine Chem. 125 (2004) 951.

[25] A.E. Derome, Modern NMR Techniques for Chemistry research, Pergamon, Oxford, 1987, pp. 188–190.

[26] (a) Y. Huang, S. Macura, R.R. Ernst, J. Am. Chem. Soc. 103 (1981) 5327;
(b) R. Willem, Prog. NMR Spectrosc. 20 (1988) 1;
(c) C.L. Perrin, T.J. Dwyer, Chem. Rev. 90 (1990) 935.

[27] K. Stott, J. Keeler, Q.N. Van, A.J. Shaka, J. Magn. Reson. 125 (1997) 302.

[28] M. Herberhold, Angew. Chem. 107 (1995) 1985;
Angew. Chem., Int. Ed. 34 (1995) 1837.

[29] (a) J.A.K. Howard, V.J. Hoy, D. O'Hagan, G.T. Smith, Tetrahedron 52 (1996) 12613;
(b) J.D. Dunitz, R. Taylor, Chem. Eur. J. 3 (1997) 89;
(c) G.R. Desiraju, Acc. Chem. Res. 35 (2002) 565;
(d) J.D. Dunitz, A. Gavezzotti, Angew. Chem. 117 (2005) 1796;
J.D. Dunitz, A. Gavezzotti, Angew. Chem., Int. Ed. 44 (2005) 1766;
(e) K. Reichenbächer, H.I. Süss, J. Hulliger, Chem. Soc. Rev. 34 (2005) 22;
(f) M.C.W. Chan, S.C.F. Kui, J.M. Cole, G.J. McIntyre, S. Matsui, N. Zhu, K.-H. Tam, Chem. Eur. J. 12 (2006) 2607.

Available online at www.sciencedirect.com
ScienceDirect
Polyhedron 26 (2007) 3505–3512
POLYHEDRON
www.elsevier.com/locate/poly

Synthesis, characterization, and electrochemical and electrical properties of novel mononuclear and binuclear ball-type Zn(II) and Co(II) phthalocyanines substituted with 1a,8b-dihydronaphtho[*b*]naphthofuro-[3,2-*d*]furan-7,10-diyl

Zafer Odabaş [a], Ahmet Altındal [b], Ali Rıza Özkaya [a], Mustafa Bulut [a], Bekir Salih [c], Özer Bekaroğlu [d,*]

[a] *Department of Chemistry, Marmara University, Faculty of Science and Letters, 34722, Göztepe, Istanbul, Turkey*
[b] *Department of Physics, Marmara University, Faculty of Science and Letters, 34722, Göztepe, Istanbul, Turkey*
[c] *Department of Chemistry, Hacettepe University, 06532 Ankara, Turkey*
[d] *Department of Chemistry, Technical University of İstanbul, Maslak-İstanbul, Turkey*

Received 14 February 2007; accepted 24 March 2007
Available online 10 April 2007

Abstract

New mononuclear phthalocyanines [Zn(II) **4** and Co(II) **6**] and ball-type bisphthalocyanines [Zn(II) **5** and Co(II) **7**] have been synthesized from the corresponding compound **3**, which can be obtained from the reaction of 4-nitrophthalonitrile **1** with 1a,8b-dihydronaphtho[*b*]naphthofuro[3,2-*d*]furan-7,10-diol **2**. The novel compounds have been characterized by elemental analysis, UV/Vis, IR, ^{1}H NMR and MASS spectroscopy. The electrochemical measurements show the formation of various mixed-valence oxidized and reduced species, due to intramolecular interactions between the two phthalocyanine units in the ball-type binuclear metallophthalocyanines. Detailed studies of the effect of temperature on the electronic properties of the films were investigated by dc conductivity and impedance spectroscopy techniques at temperatures between 290 K and 460 K. Thermally activated conductivity dependence on temperature was observed from the dc measurements. The ac results give a power law behavior in which the frequency exponent decreases with temperature. It was observed that the impedance spectra consist of a curved line at low temperature. These curved lines transform into a full semicircle with increasing temperature.
© 2007 Elsevier Ltd. All rights reserved.

Keywords: Ball-type; Mononuclear; Bisphthalocyanine; Synthesis; Electrochemistry, Electrical conductivity

1. Introduction

Binuclear phthalocyanines (Pcs) have attracted great attention because of their unique spectroscopic, electrochemical and electrical properties. In this respect, binuclear Pcs linked by various kinds of bridges, i.e., lanthanoid and actinoid sandwich dimmers [1–3], covalently linked cofacial dimmers [4–6], planar homo- and hetero-dimers sharing a common aromatic ring or linked by other units [7–11] and linear dimers linked by flexible alkyl chains [12,13] have been synthesized. These dimers and multimers, especially those with rigid cofacial configurations, usually show spectroscopic electrochemical and electrical properties which differ significantly from the parent monomers. A strong interaction between the halves of the molecule is usually detected in electronic absorption and MCD spectroscopy and electrochemistry. The redox couples observed in monomeric species are usually split into two couples. It

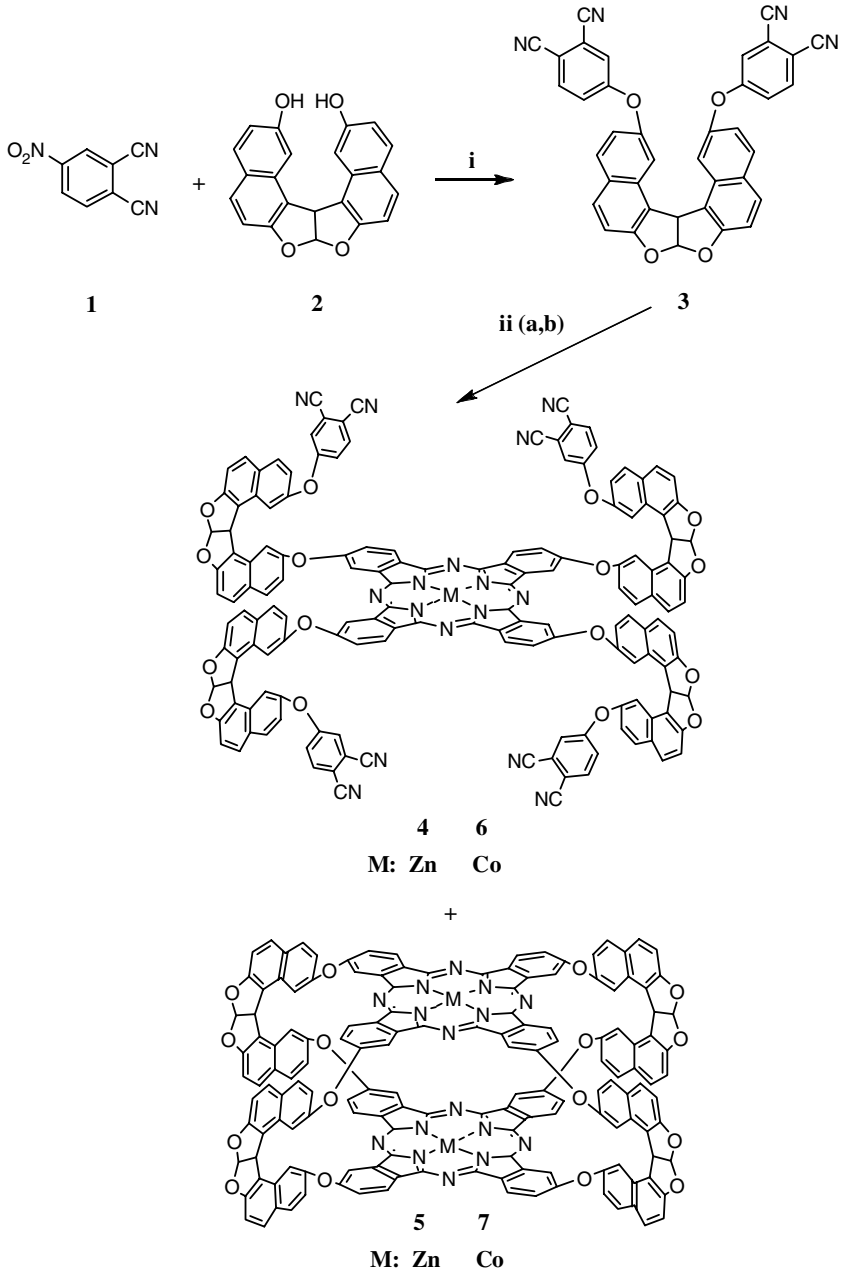
* Corresponding author. Address: Bilim Sokak, Kardesler Apt., No. 6/9, Erenköy, Istanbul, Turkey. Tel.: +90 216 359 01 30; fax: +90 216 386 08 24.
E-mail address: obekaroglu@gmail.com (Ö. Bekaroğlu).

0277-5387/$ - see front matter © 2007 Elsevier Ltd. All rights reserved.
doi:10.1016/j.poly.2007.03.047

was suggested that electron cloud overlap is important for a strong interaction.

The first synthesis of ball-type binuclear Pcs was reported in 2003 by the Zefirov group [14]. However, the studies on this type of Pc did not continue until we recently reported the synthesis, characterization and electrical, electrochemical and gas sensing properties of ball-type *t*-butylcalix-[4]arene bridged [15] and 1,1′-methylene-di-naphthalen-2-ol bridged [16] metal free and/or metallophthalocyanines. These novel compounds showed interesting mixed-valence behavior.

For a long time, binuclear Pcs have been obtained by the tetramerization of phthalonitrile (or its derivatives) with basic catalysts in a suitable solvent such as pentanol, hexanol, dimethylformamide or *o*-dichlorobenzene at 180–200 °C. Recently investigators have used new reaction techniques such as microwawe irradiation or heating of the solid phase to obtain binuclear Pcs. In this paper, in our continuing efforts, we have used the "heating of the solid phase" method for the synthesis of novel ball-type four 1a,8b-dihydronaphtho[*b*]naphthofuro-[3,2-*d*]furan-7,10-diol bridged zinc(II) and cobalt(II) phthalocyanines (Scheme 1).



Scheme 1. (i) K_2CO_3, DMSO; (ii) a: $Zn(CH_3COO)_2 \cdot 2H_2O$, 300 °C; b: $Co(CH_3COO)_2 \cdot 4H_2O$, 280 °C.

The electrical and electrochemical properties of the compounds are also presented.

2. Experimental

The starting materials **1** and **2** were synthesized by the methods described previously in the literature [17–20]. IR spectra were recorded on a Shimadzu FTIR-8300 spectrophotometer as KBr pellets. Electronic spectra were recorded on a Shimadzu UV-1601 spectrophotometer. Elemental analyses were performed by the Instrumental Analysis Laboratory of Tubitak–Ankara. ^{1}H NMR spectra were recorded in *d*-chloroform, *d*-dimethylsulfoxide and *d*-acetone with a Mercury-Vx 400 MHz instrument. Mass spectra were acquired on a Voyager-DE™ PRO MALDI-TOF mass spectrometer (Applied Biosystems, USA) equipped with a nitrogen UV-Laser operating at 337 nm. Spectra were recorded either in reflectron and linear modes with an average of 50 shots.

2.1. Synthesis

2.1.1. 4,4′-(1a,8b-Dihydronaphtho[b]naphthofuro[3,2-d]-furan-7,10-diyl)bis(oxy)diphthalonitrile (3)

A mixture of 4-nitro-1,2-dicyanobenzene **1** (0.657 g, 3.8×10^{-3} mol) and 4,4′-(1a,8b-dihydronaphtho[*b*]naphthofuro[3,2-*d*]furan-7,10-diyl)bis(oxy)diphthalonitrile **2** (0.650 g, 1.9×10^{-3} mol) in 20 mL dry dimethylsulfoxide (DMSO) was stirred at room temperature under N_2. K_2CO_3 (0.828 g, 6×10^{-3} mol) was added into the mixture over a period of 2 h. After stirring the reaction mixture for a further 24 h, the undissolved salt was removed by filtration. The reaction mixture was poured into water (100 mL) and stirred. The precipitate was filtered and washed with water. The residue was chromatographed by silica gel and eluted with CH_2Cl_2 (DCM). Yield: 1.14 g (96%). This compound is soluble in $CHCl_3$, DCM, tetrahydrofuran (THF), dimethylformamide (DMF), acetone and acetonitrile. Mp: 152 °C. IR (KBr pellet) ν_{max}/cm^{-1}: 833, 968, 1056, 1134, 1184, 1249, 1280, 1307, 1361, 1419, 1454, 1485, 1519, 1593, 1631, 2229, 3082. *Anal.* Calc. for $C_{38}H_{18}N_4O_4$: C, 76.76; H, 3.05; N, 9.42. Found: C, 76.33; H, 2.95; N, 9.83%. ^{1}H NMR (chloroform-*d*) δ, ppm: 5.4 (d, $J=5.85$ Hz 1H), 7.01 (d, $J=8.58$ Hz, 2H), 7.01 (d, $J=8.19$ Hz, 2H), 7.15 (s, 2H), 7.27 (d, $J=5.85$ Hz, 1H), 7.29 (d, $J=8.58$ Hz, 2H), 7.60 (d, $J=8.19$ Hz, 2H), 7.65 (br ds, 2H), 7.84 (d, $J=8.97$ Hz, 2H), 7.95 (d, $J=8.97$ Hz, 2H).

2.1.2. [2,10,16,24-Tetrakis(1a-hydronaphtho[b]-naphthofuro[3,2-d]-7,10-dyl-4-oxyphthalo-nitrile)-phthalocynaninatozinc(II)] (4) and [1′a,8′b-tetrakis-bis{(2′,10′,16^I,24′)-phthalocyaninatozinc(II)}dioxynaphtho-[b]-naphthofuro[3,2-d]furan-7,10-diyl] (5)

A mixture of compound **3** (0.2 g, 0.3×10^{-3} mol) and $Zn(OAc)_2\cdot2H_2O$ (0.100 g, 2.4×10^{-3} mol) was powdered in a quartz crucible and heated in a sealed glass tube for 5 min under dry N_2 atmosphere at 300 °C. After cooling to room temperature, 5 mL of DMF was added to the residue to dissolve the product. The reaction mixture was precipitated by adding water. The precipitate was filtered, multiply washed at first with hot water and then with hot ethanol in order to eliminate the unreacted starting materials, and dried *in vacuo*. Then, the crude product was washed with acetic acid, methanol, ethanol, acetonitrile and acetone for 12 h, respectively, in a soxhlet apparatus. The residue was coarsely fractionated on a silica gel column eluting with chloroform and a gradient of chloroform–THF up to 100% THF. This compound is soluble in chloroform (slightly), THF, DMF and DMSO. Mp > 350 °C. Yield of **4**: 6 mg (5%). Yield of **5**: 30 mg (15%).

Compound **4** is slightly soluble in DCM and $CHCl_3$, and soluble in THF, DMF and DMSO. Mp > 350 °C. IR (KBr pellet) ν_{max}/cm^{-1}: 835, 945, 1041, 1085, 1184, 1220, 1249, 1332, 1394, 1446, 1487, 1514, 1606, 1722, 2231, 2850, 2925, 3066. *Anal.* Calc. for $C_{152}H_{72}N_{16}O_{16}Zn$: C, 74.71; H, 2.97; N, 9.17. Found: C, 74.02; H, 3.02; N, 9.21%. ^{1}H NMR (DMSO-d_6) δ, ppm: 8.25–7.60 (m, 32H, arom.), 7.50–6.85 (m, 32H, arom.), 7.32 (m, 4H, O–CH–O), 5.80 (m, 4H, Ar–CH–Ar). MS (MALDI-TOF): *m*/*z* 2446 (M+H).

Compound **5** is soluble in THF, DMF and DMSO. Mp > 350 °C. IR (KBr pellet) ν_{max}/cm^{-1}: 834, 946, 1042, 1094, 1179, 1223, 1257, 1361, 1394, 1454, 1476, 1517, 1606, 1654, 2850, 2925, 3025. *Anal.* Calc. for $C_{152}H_{72}N_{16}O_{16}Zn_2$: C, 72.76; H, 2.89; N, 8.93. Found: C, 72.53; H, 3.08; N, 9.23%. ^{1}H NMR (DMSO-d_6) δ, ppm: 8.18–6.80 (m, 64H, arom.), 6.85 (m, 4H, O–CH–O), 5.70 (m, 4H, Ar–CH–Ar). MS (MALDI-TOF): *m*/*z* 2510 (M+H).

2.1.3. [2,10,16,24-Tetrakis(1a-hydronaphtho-[b]naphthofuro[3,2-d]-7,10-dyl-4-oxyphthalo-nitrile)-phthalocynaninatocobalt(II)] (6) and [1′a,8′btetrakis-bis{(2′,10′,16^I,24′)-phthalocyaninatocobalt(II)}-dioxynaphtho-[b]-naphthofuro[3,2-d]furan-7,10-diyl] (7)

A mixture of compound **3** (0.200 g, 0.337 mmol) and $Co(OAc)_2\cdot4H_2O$ (0.130 g, 0.522 mmol) was powdered in a quartz crucible and heated in a sealed glass tube for 5 min under dry N_2 atmosphere at 280 °C. After cooling to room temperature, the blue-green reaction product was obtained, isolated and purified with using the same procedure explained above for **4** and **5**. Yield of **6**: 5 mg (4.5%). Yield of **7**: 28 mg (14%).

Compound **6** is slightly soluble in DCM and $CHCl_3$, and is soluble in THF, DMF and DMSO. Mp > 350 °C. IR (KBr pellet) ν_{max}/cm^{-1}: 752, 956, 1053, 1090, 1179, 1228, 1253, 1361, 1453, 1476, 1517, 1610, 1628, 2231, 2850, 2925, 3059. *Anal.* Calc. for $C_{152}H_{72}N_{16}O_{16}Co$: C, 74.91; H, 2.98; N, 9.20. Found: C, 74.77; H, 2.87; N, 9.15%. MS (MALDI-TOF): *m*/*z* 2438 (M+H).

Compound **7** is soluble in chloroform (slightly), THF, DMF and DMSO. Mp > 350 °C. IR (KBr pellet) ν_{max}/

cm^{-1}: 833, 956, 1056, 1094, 1118, 1181, 1226, 1253, 1363, 1407, 1452, 1473, 1518, 1609, 1655, 2850, 2925, 3059. *Anal.* Calc. for $C_{152}H_{72}Co_2N_{16}O_{16}$: C, 73.14; H, 2.91; N, 8.98. Found: C, 73.05; H, 2.88; N, 8.73%. MS (MALDI-TOF): *m*/*z* 2496 (M+H).

2.2. Electrochemical measurements

The cyclic voltammetry (CV) and controlled potential coulometry (CPC) measurements were carried out with a Princeton Applied Research Model VersaStat II potentiostat/galvanostat controlled by an external PC and utilizing a three-electrode configuration at 25 °C. The working electrode was a Pt plate with a surface area of 0.10 cm^2. The surface of the working electrode was polished with a H_2O suspension of Al_2O_3 before each run. The last polishing was done with a particle size of 50 nm. A Pt wire served as the counter electrode. A saturated calomel electrode (SCE) was employed as the reference electrode and separated from the bulk of the solution by a double bridge. The ferrocene/ferrocenium couple (Fc/Fc^+) was also used as an internal standard. Electrochemical grade tetrabutylammonium perchlorate (TBAP) in extra pure DMSO and DCM was employed as the supporting electrolyte at a concentration of 0.10 mol dm^{-3}. High purity N_2 was used for deoxygenating the solution at least 20 min prior to each run and to maintain a nitrogen blanket during the measurements. For controlled (CPC) studies, a Pt gauze working electrode (10.5 cm^2 surface area), Pt wire counter electrode, separated by a glass bridge, and a SCE as the reference electrode were used.

2.3. Electrical conductivity and impedance measurements

For the electrical characterization, an interdigital comb structure with 100 μm gap on a glass substrate was used. Thin films of the compounds were obtained by the spin-coating method. The substrate temperature was kept constant at 290 K during deposition of the materials over the electrodes. Dc conductivity and impedance spectra measurements were performed between 290 and 460 K using a Keithley 617 electrometer. Ac conductivity and impedance measurements were carried out with a Keithley 3330 LCZ meter in the frequency range 40 Hz to 10^5 Hz, in the temperature range from 290 to 460 K. Both dc and ac conductivity measurements were performed under 10^{-3} mbar in the dark. The conductivity data were recorded using an IEEE 488 data acquisition system incorporating a personal computer.

3. Results and discussion

3.1. Synthesis

The synthesis of the bisphthalodinitriles is based on the reaction of diols with an excess of compound **1** (DMF or DMSO in the presence of dry K_2CO_3 as a base, at 25 °C, 20–96 h) [17]. Our key starting material is compound **3** which can be obtained via the reaction of compound **1** and **2**, in dry DMSO in the presence of dry K_2CO_3. **4**, **5** and **6**, **7** were synthesized by heating **3** with $Zn(OAc)_2 \cdot 2H_2O$ and $Co(OAc)_2 \cdot 4H_2O$, respectively, in a sealed tube under a N_2 atmosphere (Scheme 1).

Elemental analysis, IR, ^{1}H NMR, MASS and UV/Vis spectra confirm the proposed structures of the compounds. Compounds **3**, **4** and **6** show a sharp intense CN vibration band at 2229–2231 cm^{-1} in the IR spectra. The spectra of compounds **3**–**7** showed Ar–O–Ar peaks at 1220–1285 cm^{-1}, C=C (in the phenyl and naphthalene rings) peaks at 1560–1655 cm^{-1}, C=N peaks at 1670–1720 cm^{-1}, aromatic CH peaks at 3060–3070 cm^{-1} and aliphatic CH peaks at 2840–2945 cm^{-1}. The ^{1}H NMR spectra were also in good correlation with the structure of the synthesized compounds. In the ^{1}H NMR spectrum of compound **3**, which was taken in chloroform-*d*, the phenyl protons appeared at 7.65 (br s), 7.60 (d) and 7.13 (br d) ppm, naphthalene protons at 7.95 (d), 7.84 (d), 7.29 (d), 7.15 (s) and 7.01 (br d) ppm, and CH protons at 7.27 (d) and 5.40 (d) ppm. In addition, in the ^{1}H NMR spectra of **4** and **5**, which were taken in DMSO-d_6, the aromatic protons appeared in the range 8.25–6.80 (m) ppm and the aliphatic CH peaks 5.70–5.80 (m) ppm.

The UV–Vis spectra of **4**–**7** in DMF showed characteristic absorptions between 610 and 710 nm in the Q-band region. The Q-band observed for the compounds was attributed to the $\pi \rightarrow \pi^*$ transition from the highest occupied molecular orbital (HOMO) to the lowest unoccupied molecular orbital (LUMO) of the Pc ring. The other bands (B) in the UV region at 300–350 nm were observed due to transitions from the deeper π levels to the LUMO (Table 1).

An α-cyano-4-hydroxycinnamic acid (ACCA) (10 mg/mL in acetonitrile–water mixture, 1:1 v/v) matrix for **6** and 2,5-dihydroxy benzoic acid (DHB) (20 mg/mL acetonitrile) MALDI matrices were prepared. MALDI samples were prepared by mixing the complex (2 mg/mL in tetrahydrofuran for **6** and **7**, and in dichloromethane for **4** and **5**) with the matrix solution (1:20 v/v) in a 0.5 mL eppendorf® micro tube. Finally 1 μL of this mixture was deposited on

Table 1
UV–Vis data for **4**–**7** in DMF

Compound	λ, nm (log ε, M^{-1} cm^{-1})		
4	704 (4.169), 618[a] (3.786)	673 (4.178), 339 (4.218)	647 (3.930)
5	684 (3.358), 339 (3.390)	620 (2.818)	
6	672 (4.258), 332[a] (4.208)	611[a] (3.734), 304 (4.264)	
7	705 (3.799), 620[a] (3.801)	674 (3.843), 339 (4.248)	646 (3.901)

[a] = Shoulder.

the sample plate, dried at room temperature and then analyzed.

3.2. Electrochemistry

The redox properties of the complexes were examined by cyclic voltammetry, differential pulse voltammetry and controlled potential coulometry in DMSO/TBAP. A summary of the relevant electrochemical data is given in Table 2. Typical voltammograms for the mononuclear metallophthalocyanines [Zn(II)Pc(−2) **4**, Co(II)Pc(−2) **6**] and ball-type dinuclear phthalocyanines {[Zn(II)Pc(−2)]$_2$ **5**, [Co(II)Pc(−2)]$_2$ **7**} are shown in Figs. 1 and 2. The CPC studies showed that all the redox processes for the complexes involve the transfer of one electron.

Complex **4** displayed three quasi-reversible reduction waves at $E_{1/2} = -0.69$, $E_{1/2} = -1.00$ and $E_{1/2} = -1.35$ V vs. SCE, with considerably high anodic to cathodic peak separations, and a nearly reversible oxidation peak with a relatively low peak separation, Fig. 1A. These phthalocyanine ring-based redox processes were examined as a function of potential scan rate in order to determine the mode of mass transport. The peak currents for the processes R1, R2, R3 and O1 increased in direct proportion to the square root of the scan rate between 0.025 and 0.500 V/s, thus suggesting that the relevant reactions are controlled by diffusion.These redox processes are probably ligand based since zinc is not redox active in phthalocyanine complexes. The redox potentials measured for **4** are consistent with the general redox characteristics reported previously for similar Pcs [21].

The voltammogram for **5** at 0.100 V s^{-1} is shown in Fig. 1B. It appears that characteristic Pc(−2)/Pc(−3) redox process of monophthalocyanines is not well-split due to

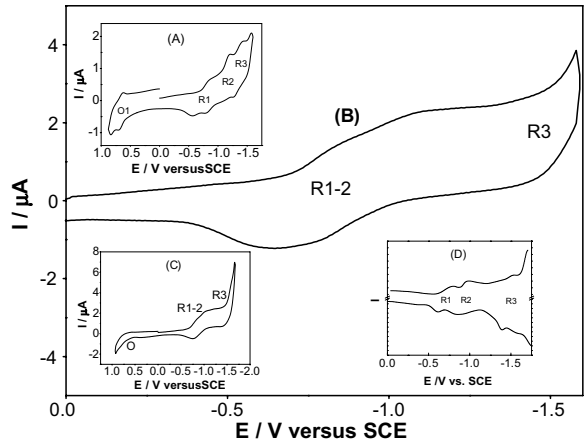


Fig. 1. Voltammograms of **4** and **5** in DMSO/TBAP. A: CV of **4** at 0.100 V s^{-1}. B: CV of **5** at 0.100 V s^{-1}. C: CV of **5** at 0.010 V s^{-1}. D: DPV of **5** at 0.100 V s^{-1}.

weak interactions between the two cofacial phthalocyanine rings in **5**, and thus a rounded-shaped voltammogram is observed. The redox processes of this complex are better defined in the voltammogram recorded at 0.010 V s^{-1}, Fig. 1C. Unfortunately, the oxidation process/processes are still ill-defined. However, the differential pulse voltammogram of the complex enabled us to detect the splitting of the first reduction process clearly, Fig. 1D. The observed redox potentials suggest that the mixed-valence splitting energy for the Pc(−2)/Pc(−3) process in **5** (0.22 V) is lower as compared with that reported recently (0.43 V) for ball-type four 1,1′-methylenedinaphthalen-2-ol bridged metallophthalocyanine, [Zn(II)Pc(−2)]$_2$ [16]. This provides additional support for relatively weak interactions between the phthalocyanine rings in **5**, and is consistent with the

Table 2
The electrochemical data for **1**–**4** in DMSO[a]

Complex	Redox processes		$E_{1/2}$ (V)	ΔE_p (V)	ΔE (V)	ΔE_s (V)
4	$[Zn(II)Pc(-1)]^+/Zn(II)Pc(-2)$	O1	0.66	0.06	1.35	
	$Zn(II)Pc(-2)/[Zn(II)Pc(-3)]^-$	R1	−0.69	0.26		
	$[Zn(II)Pc(-3)]^-/[Zn(II)Pc(-4)]^{2-}$	R2	−1.00	0.40		
	$[Zn(II)Pc(-4)]^{2-}/[Zn(II)Pc(-5)]^{3-}$	R3	−1.35	0.14		
6	$[Co(III)Pc(-2)]^+/Co(II)Pc(-2)$	O1	0.43	0.14	0.82	
	$Co(II)Pc(-2)/[Co(I)Pc(-2)]^-$	R1	−0.39	0.10		
	$[Co(I)Pc(-2)]^-/[Co(I)Pc(-3)]^{2-}$	R2	−1.33	0.08		
5	$[Zn(II)Pc(-2)]_2/[Zn(II)Pc(-2)\cdot Zn(II)Pc(-3)]^-$	R1	−0.69[b]	0.18[b]		0.22[b]
	$[Zn(II)Pc(-2)\cdot Zn(II)Pc(-3)]^-/[Zn(II)Pc(-3)]_2^{2-}$	R2	−0.91[b]	0.10[b]		
	$[Zn(II)Pc(-3)]_2^{2-}/[Zn(II)Pc(-3)\cdot Pc(-4)]^{3-}$	R3	−1.46[b]	0.12[b]		
7	$[Co(II)Pc(-2)\cdot Co(III)Pc(-2)]^+/[Co(II)Pc(-2)]_2$	O1	0.50	0.08	0.86	
	$[Co(II)Pc(-2)]_2/[Co(II)Pc(-2)\cdot Co(I)Pc(-2)]^-$	R1	−0.36	0.20		0.39
	$[Co(II)Pc(-2)\cdot Co(I)Pc(-2)]^-/[Co(I)Pc(-2)]_2^{2-}$	R2	−0.75	0.34		
	$[Co(I)Pc(-2)]_2^{2-}/[Co(I)Pc(-2)\cdot Co(I)Pc(-3)]^{3-}$	R3	−1.34	0.08		

[a] Half-wave potentials in DMSO versus the Fc/Fc$^+$ couple correspond approximately with the above **4**–**7** data minus 0.50 V. $E_{1/2}$ values were measured by cyclic voltammetry [$E_{1/2} = (E_{pa} + E_{pc})/2$. The peak separation values ($\Delta E_p = E_{pa} - E_{pc}$) are reported at 0.100 V s^{-1}. ΔE is the potential difference between the first oxidation and first reduction potentials. It represents the HOMO–LUMO gap for **4** and **5**, but the charge transfer transition for **6** and **7** involving redox-active metal centers. ΔE_s indicates the mixed-valence splitting energy for the relevant split redox couple.

[b] Measured by differential pulse voltammetry.

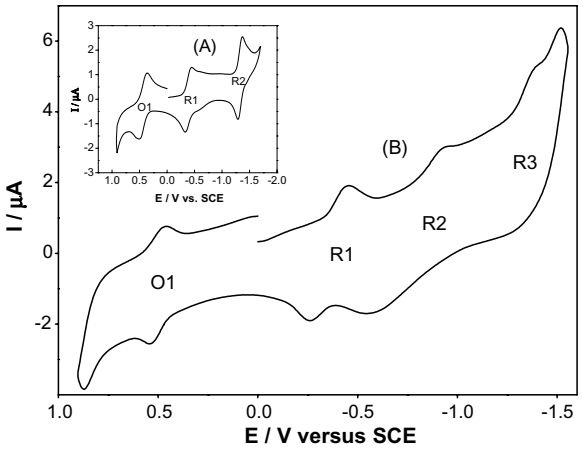


Fig. 2. Cyclic voltammograms of **6** (A) and **7** (B) at $0.100\ \mathrm{V\ s^{-1}}$ in DMSO/TBAP.

difference in the bridges in **5** and the recently reported [Zn(II)Pc(−2)]$_2$. It is expected that the distance between the cofacial phthalocyanine rings is higher in **5** than that in [Zn(II)Pc(−2)]$_2$.

Voltammetric behavior of **6** is different from that of **4**, in terms of redox potentials. It indicates two well-defined one-electron reduction processes at $E_{1/2} = -0.39$ and $E_{1/2} = -0.67$ V versus SCE, and a one-electron oxidation process at $E_{1/2} = 0.43$ V versus SCE, Fig. 2A. Some metallophthalocyanines vary in their electrochemical behavior according to their environment, i.e., the oxidation of Co(II)Pc(−2) can lead to [Co(III)Pc(−2)]$^+$ or [Co(II)Pc(−1)]$^+$ depending on whether there are any available suitable coordinating species that would stabilize the Co(II) center [21]. Such electrochemistry, especially of Co(II)Pc(−2) and Fe(II)Pc(−2) is split into two sections, that referring to donor solvents and that referring to non-donor solvents. The main difference lies in whether the metal or the ring is oxidized first. Donor solvents strongly favor Co(III)Pc(−2) by coordinating along the axis to form six coordinate species. If such donor solvents are absent, then oxidation to Co(III) is inhibited and ring oxidation occurs first. Thus, the first oxidation and the first reduction processes of **6** are probably metal based and correspond to Co(II)Pc(−2)/[Co(III)Pc(−2)]$^+$ and Co(II)Pc(−2)/[Co(I)Pc(−2)]$^-$, respectively,while the second reduction is ring based, since the voltammetric measurements were carried out in DMSO/TBAP.

The ball-type **7** displays three one-electron quasi-reversible reduction couples and a reversible one-electron oxidation couple within the potential limits of the DMSO/TBAP medium, Fig. 2B. A comparison of the first two reduction potentials of **7** with those of **6** clearly suggests the formation of mixed valence species. The difference between the first and second reduction potentials of **7** is 0.39 V, whilst it is 0.92 V for **6**. The two one-electron reduction couples can be attributed to the stepwise reduction of the two Co(II) centers in **7**, and thus to the formation of mixed valence [Co(II)Pc(−2) · Co(I)Pc(−2)]$^-$ species in the first step and doubly oxidized [Co(I)Pc(−2)]$_2^{2-}$ species in the second step. The splitting observed for the Co(II)/Co(I) process in this study may be attributed to the interactions between the two cobalt centers, which are probably held in close proximity by the cofacial ligand geometry, resulting in overlap of their d_{z^2} orbitals along the cobalt–cobalt axis. The third reduction and the first oxidation couples can be assigned to the formation of [Co(I)Pc(−2) · Co(I)Pc(−3)]$^{3-}$ and [Co(II)Pc(−2) · Co(III)Pc(−2)]$^+$ respectively, since all redox couples involve the transfer of one electron. The formation of a fully reduced ligand and a fully oxidized metal species could not be observed. These processes appear to be out of the available solvent/electrolyte limited potential range. The splitting of metal or phthalocyanine based redox processes as a result of the interaction between the cofacial phthalocyanine units has also been reported recently for ball-type four 1,1′-methylenedinaphthalen-2-ol bridged [Co(II)Pc(−2)]$_2$ [16]. The observed redox potentials suggest that the mixed-valence splitting energy, ΔE_s, for the Co(II)/Co(I) process in **7** (0.39 V) is smaller as compared with that reported recently for ball-type four 1,1′-methylenedinaphthalen-2-ol bridged [Co(II)Pc(−2)]$_2$ (0.44 V). This implies relatively weak interactions between the phthalocyanine rings in **7**, and is consistent with the difference between the bridges in **7** and the recently reported [Co(II)Pc(−2)]$_2$. It may be concluded that the distance between the cofacial phthalocyanine rings or metal centers in **7** is higher than that in [Co(II)Pc(−2)]$_2$. Moreover, it appears that Co(II)/Co(I) mixed-valence species in **7** are more stable than the Pc(−2)/Pc(−3) mixed-valence species in **5**.

3.3. Electrical conductivity and impedance spectroscopy

The temperature dependent dc behavior of the films was determined from the slope of the current–voltage (*I–V*) measurements by using the following relation:

$$\sigma_{dc} = \frac{I}{V}\frac{d}{(2n-1)l \cdot h}$$

where I is the measured current, V is the bias voltage, d is the electrode spacing, n is the number of electrode finger pairs, l is the overlap length of the electrode fingers and h is the thickness of the electrodes. A linear *I–V* behavior was found in the voltage range of −1 V to 1 V, indicating no rectifying properties. Well defined straight lines were obtained from Arrhenius plots (logarithms of dc conductivity versus inverse temperature). This linear temperature dependence of the dc conductivity suggest the presence of only one conduction mechanism, assuming that the dominant levels are the conduction and valence bands in the whole temperature range for the films of **4**–**7**. The observed electrical conductivity values at room temperature for **4**–**7** are 2.7×10^{-12}, 5.1×10^{-12}, 4.2×10^{-12} and 1.6×10^{-12} S/cm, respectively. The order of dc conductivities observed for these compounds are **5** > **6** > **4** > **7** for all temperatures investigated. The value of the activation energy was derived

from the slope of the $\log \sigma_{dc}$ vs. $1/T$ graph, and is 0.67 eV for **4**, 0.75 eV for **5**, 0.83 eV for **6** and 0.55 eV for **7**.

The ac conductivity and impedance spectrum measurements were performed in the temperature range 290–460 K and for frequencies between 40 and 10^5 Hz. Fig. 3 shows the frequency dependence of the measured ac conductivity at 373 K for films of **4**–**7**. The figure indicates the strong conductivity dependence on frequency at around room temperature, with weaker frequency dependence at high temperatures for the films. It can be seen from Fig. 3 that the ac conductivity increases with frequency. The frequency dependence of the conductivity can be represented by the universal power law for all compounds

$$\sigma_{ac} = A\omega^s \quad (1)$$

where ω is the angular frequency, A and the frequency exponent, s, are material dependent constants. This type of frequency dependent ac conduction has been explained on the basis of two distinct mechanisms for carrier conduction. One of them is the Quantum Mechanical Tunelling model (QMT). According to this model, the conduction occurs by means of thermally assisted Quantum Mechanical Tunelling. The other model, which is also known as the Correlated Barrier Hopping (CBH) model, is based on the concept of charged defects and in this method bipolarons hop between two charged defect states D^+ and D^- over the barrier separating them, rather than tunneling through the barrier. In these two models, the frequency exponent s is found to have two different trends with temperature and frequency [22]. Our calculations showed that s is definitely a function of temperature for all compounds and shows a general tendency to increase with decreasing temperature. This is in agreement with the prediction of the CBH model. The decrease in s with temperature is in contradiction with the QMT model.

To ensure complete electrical properties of the compounds, the impedance spectroscopy technique was used in the frequency range 40–10^5 Hz. Fig. 4 shows the temperature dependence of the real part of the impedance, $Z(\omega) = R(\omega) + iX(\omega)$, at indicated frequencies for compound **5**. The observed $R(T)$ reveals that there is an obviously different tendency for different ranges of temperature. Namely, over the temperature range from 290 K to the critical temperature there appears a positive temperature coefficient (PTC), and a negative temperature coefficient (NTC) is seen above this temperature. The crossover occurs between 375 and 411 K. It is clear from Fig. 4 that in the transition region from PTC to NTC, there is a peak of $R(T)$. At a frequency of 2 kHz, it is clearly found that a peak of $R(T)$ displays at about 411 K, which is considered as a switching point from PTC to NTC. This peak weakens slowly and shifts to the low temperature region with increasing frequency. On the other hand, it was found from the analysis of the temperature dependence of the imaginary part of the impedance that $X(T)$ displays a negative temperature coefficient for all frequencies. Similar results of the impedance spectra were obtained for all temperatures investigated. The measured impedance curves are composed of a not fulfilled quasi-vertical line at low

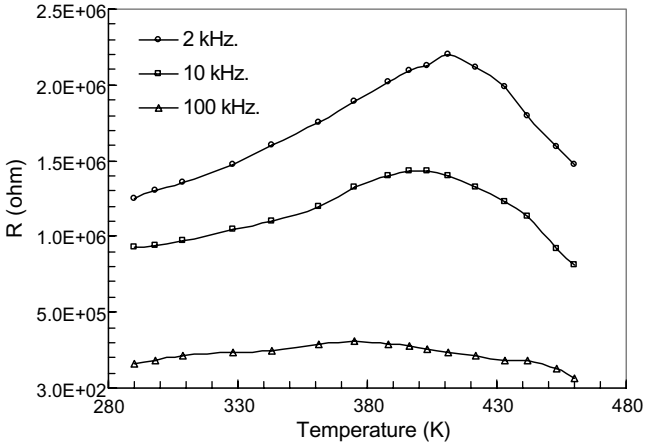


Fig. 4. Temperature dependence of the real part of the impedance for compound **5**.

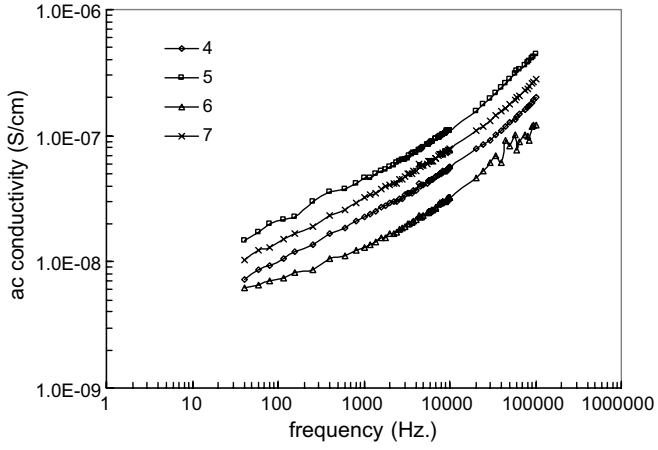


Fig. 3. Frequency dependence of the ac conductivity at 373 K for the films of **4**–**7**.

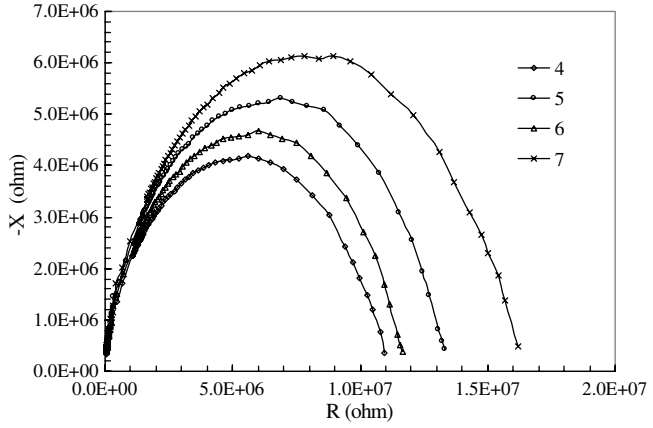


Fig. 5. Impedance spectra of the compounds at 400 K.

temperatures, suggesting pure capacitive behavior. On the complex plane plot at high temperatures, only a depressed semicircle with different radii were observed, Fig. 5, for compounds **4**–**7** at higher temperatures, indicating deviation from the Debye dispersion relation. In the case of a depressed semicircle in the impedance spectra, the relaxation time is considered as a distribution of values, rather than a single relaxation time.

Acknowledgements

This work was supported partly by the Turkish Academy of Sciences (TUBA), The State Planning Organization (Project Number: 2003 K 120810) and The Research Fund of Marmara University.

Appendix A. Supplementary material

Supplementary data associated with this article can be found, in the online version, at doi:10.1016/j.poly.2007.03.047.

References

[1] Ş. Merey, Ö. Bekaroğlu, J. Chem. Soc. (1999) 4503.
[2] N. Koike, H. Uekusa, Y. Ohashi, C. Harnoode, F. Kitamura, T. Ohsaka, K. Tokuda, Inorg. Chem. 35 (1996) 5798.
[3] J. Jiang, D.P. Arnold, H. Yu, Polyhedron 18 (1999) 2129.
[4] (a) C.C. Leznoff, H. Lam, W.A. Nevin, N. Kobayashi, P. Janda, A.B.P. Lever, Angew. Chem., Int. Engl. 26 (1987) 1021;
(b) H. Lam, S.M. Marcuccio, P.I. Svirskaya, S. Greenberg, C.C. Leznoff, R. L Cerny, Can. J. Chem. 67 (1989) 1087.
[5] N. Kobayashi, Y. Yanagisawa, T. Osa, H. Lam, C.C. Leznoff, Anal. Chem. 6 (1990) 813.
[6] N. Kobayashi, H. Lam, W.A. Nevin, P. Janda, C.C. Leznoff, A.B.P. Lever, Inorg. Chem. 29 (1990) 3415.
[7] N. Kobayashi, H. Lam, W.A. Nevin, P. Janda, C.C. Leznoff, T. Koyama, A. Monden, H. Shirai, J. Am. Chem. Soc. 116 (1994) 879.
[8] N. Kobayashi, M. Numao, R. Kondo, S. Nakajima, T. Osa, Inorg. Chem. 30 (1991) 2241.
[9] N. Kobayashi, J. Chem. Soc., Chem. Commun. (1991) 1203.
[10] N. Kobayashi, Y. Higashi, T. Osa, Chem. Lett. (1994) 1813.
[11] E.M. Garcia-Frutos, F. Fernandez-Lazaro, E.M. Maya, P. Vazquez, T. Torres, J. Org. Chem. 65 (2000) 6841.
[12] S. Vigh, H. Lam, P. Janda, A.B.P. Lever, C.C. Leznoff, R.L. Cerny, Can. J. Chem. 69 (1991) 1457.
[13] (a) E.M. Maya, P. Vazquez, T. Torres, Chem. Eur. J. 5 (1999) 2004;
(b) K. H Schweikart, M. Hanack, Eur. J. Org. Chem. (2000) 2551;
(c) E.M. Maya, P. Vazquez, T. Torres, L. Gobbi, F. Diedrich, S. Pyo, L. Echegoyen, J. Org. Chem. 65 (2000) 823.
[14] A.Y. Tolbin, A.V. Ivanov, L.G. Tomilova, N.S. Zefirov, J. Porphyrins Phthalocyanines 7 (2003) 162.
[15] T. Ceyhan, A. Altındal, A.R. Özkaya, M.K. Erbil, B. Salih, Ö. Bekaroğlu, Chem. Commun. (2006) 320.
[16] Z. Odabaş, A. Altındal, B. Salih, M. Bulut, Ö. Bekaroğlu, Polyhedron 26 (2007) 695.
[17] C.C. Leznoff, S.M. Marcuccio, S. Greenberg, A.B.P. Lever, K.B. Tomer, Can. J. Chem. (1965) 623.
[18] J.G. Young, W. Onyebuago, J. Org. Chem. 55 (1990) 2155.
[19] A. Acuner Tunca, N. Talınlı, A. Akar, Tetrahedron 51 (1995) 2109.
[20] Z. Odabaş, N. Talınlı, Heterocycl. Commun. 6 (2000) 437.
[21] A.B.P. Lever, E.R. Milaeva, G. Speier, in: C.C. Leznoff, A.B.P. Lever (Eds.), Phthalocyanines: Properties and Applications, vol. 3, VCH, New York, 1993, p. 1.
[22] S.R. Elliot, Adv. Phys. 36 (1987) 135.

molar ratios of diamine and carbonyl compounds is not the only determining factor for mono-condensation or di-condensation of such Schiff bases. However, an explanation for such hydrolytic behaviour is still lacking.

In the present paper, we report the synthesis, structural features and spectroscopic characterization of some new complexes of Ni(II) perchlorate and Ni(II) thiocyanate with neutral mono-Schiff bases or di-Schiff bases derived from the condensation of 1,2-propanediamine or 1,3-propanediamine with pyridine-2-carboxaldehyde or 2-acetylpyridine. Here, we observe that the formation of tetradentate or tridentate ligands is directed by the counter anions. We attempt to rationalise the syntheses in the light of anion modulation of cation templating effect. Although, templated reactions are known for many years, the use of anions as templates is still a relatively young [10] and to our knowledge, there is no report where an anion directed cation templating effect has been taken into account to provide an explanation for the synthesis of complexes of tridentate and tetradentate Schiff bases.

2. Experimental

All chemicals were of reagent grade and used without further purification.

Caution!!! Although no problems were encountered in this work, perchlorate salts containing organic ligands are potentially explosive. Only a small amount of the material should be prepared and they should be handled with care.

2.1. Preparations

2.1.1. Synthesis of ligands

Two sets of ligands, set-1 and set-2 were prepared by refluxing the respective diamine (1,3-diaminopropane or 1,2-diaminopropane) (10 mmol) with 2-acetylpyridine or pyridine-2-carboxaldehyde (10 mmol for set-1 and 20 mmol for set-2) in methanol solution (20 cm^3) for ca. 3 h. The ligands were not isolated. The methanol solutions were used for the syntheses of the complexes.

2.1.2. Synthesis of the complexes $[Ni(L^1)_2](ClO_4)_2$ (**1**) {L^1 = N^1-(1-pyridin-2-yl-ethylidine)-propane-1,3-diamine}, $[Ni(L^2)_2](ClO_4)_2$ (**2**) {L^2 = N^1-pyridine-2-ylmethylene-propane-1,3-diamine} and $[Ni(L^3)_2](ClO_4)_2$ (**3**) {L^3 = N^1-(1-pyridine-2-yl-ethylidine)-propane-1,2-diamine}

To prepare complexes **1**–**3**, a methanol solution (20 cm^3) of Ni(II) perchlorate hexahydrate (5 mmol, 1.825 g) was added to the methanol solution (10 mmol) of the respective set-1 ligands (1,3-diaminopropane and 2-acetylpyridine for **1**; 1,3-diaminopropane and pyridine-2-aldehyde for **2**; 1,2-diaminopropane and 2-acetylpyridine for **3**) and refluxed for 1 h. Orange red precipitate was separated in each case on cooling the mixture and was collected by filtration. Diffraction quality single crystals were obtained after a few days by slow evaporation of an orange acetonitrile solution of compound **1** and **3** in open atmosphere, but all efforts to grow suitable single crystals of **2** failed.

Complex **1** (Yield: 2.14 g, 70%). *Anal.* Calc. for $C_{20}H_{30}Cl_2N_6NiO_8$: C, 39.25; H, 4.94; N, 13.73; Ni, 9.59. Found: C, 39.5; H, 4.8 ; N,13.4; Ni, 10.8%; UV–Vis, λ_{max} (nm), (ε_{max} ($dm^3\,mol^{-1}\,cm^{-1}$)) (acetonitrile), 519 (109), 795 (197). Magnetic moment, $\mu_{eff} = 3.1$ BM.

Complex **2** (Yield: 1.99 g, 68%). *Anal.* Calc. for $C_{18}H_{26}Cl_2N_6NiO_8$: C, 37.02; H, 4.49; N, 14.39; Ni, 10.05. Found: C, 37.1; H, 4.6; N, 13.8; Ni, 10.6%; UV–Vis, λ_{max} (nm), (ε_{max} ($dm^3\,mol^{-1}\,cm^{-1}$)) (acetonitrile), 514 (118), 795 (129). Magnetic moment, $\mu_{eff} = 3.2$ BM.

Complex **3** (Yield: 1.68 g, 55%). *Anal.* Calc. for $C_{20}H_{30}Cl_2N_6NiO_8$: C, 39.25; H, 4.94; N, 13.73; Ni, 9.59. Found: C, 37.5; H, 3.8; N,11.4; Ni, 11.6%; UV–Vis, λ_{max} (nm), (ε_{max} ($dm^3\,mol^{-1}\,cm^{-1}$)) (acetonitrile), 508 (109), 797 (163). Magnetic moment, $\mu_{eff} = 3.1$ BM.

2.1.3. Synthesis of the complexes $[Ni(L^4)](SCN)_2$ (**4**) {L^4 = N,N′-bis-(1-pyridine-2-yl-ethylidine)-propane-1,3-diamine}, $[Ni(L^5)](SCN)_2$ (**5**) {L^5 = N,N′-bis(pyridine-2-ylmethyline)-propane-1,3-diamine} and $[Ni(L^6)](SCN)_2$ (**6**) {L^6 = N,N′-bis-(1-pyridine-2-yl-ethylidine)-propane-1,2-diamine}

A methanol solution (20 cm^3) of nickel thiocyanate tetrahydrate (10 mmol, 2.47 g) was added to the methanol solution (10 mmol) of respective set-2 ligands (1,3-diaminopropane and 2-acetylpyridine for **4**; 1,3-diaminopropane and pyridine-2-aldehyde for **5**; 1,2-diaminopropane and 2-acetylpyridine for **6**) and refluxed for 2 h. Pale yellowish green crystals were separated in each case on cooling the mixture and were collected by filtration. Complexes **4** and **5** were re-crystallised from methanol solution to obtain needle shaped greenish yellow single crystals suitable for X-ray diffraction. No suitable single crystals could be obtained for complex **6**.

Complex **4** (Yield: 2.96 g, 65%). *Anal.* Calc. for $C_{19}H_{20}N_6NiS_2$: C, 50.13; H, 4.43; N, 18.46; Ni, 12.89. Found: C, 50.2 ; H, 4.7; N,17.9; Ni, 11.9%; UV–Vis, λ_{max} (nm), (ε_{max} ($dm^3\,mol^{-1}\,cm^{-1}$)) (acetonitrile), 505 (118), 795 (129). Magnetic moment, $\mu_{eff} = 3.1$ BM.

Complex **5** (Yield: 3.16 g, 74%). *Anal.* Calc. for $C_{17}H_{16}N_6NiS_2$: C, 47.8; H, 3.78; N, 19.67; Ni, 13.74. Found: C, 47.6; H, 4.1; N, 19.5; Ni, 13.9%; UV–Vis, λ_{max} (nm), (ε_{max} ($dm^3\,mol^{-1}\,cm^{-1}$)) (acetonitrile), 501 (198), 872 (178). Magnetic moment, $\mu_{eff} = 3.1$ BM.

Complex **6** (Yield: 2.50 g, 55%). *Anal.* Calc. for $C_{19}H_{20}N_6NiS_2$: C, 50.13; H, 4.43; N, 18.46; Ni, 12.89. Found: C, 50.2 ; H, 4.7; N,18.4; Ni, 13.1%; UV–Vis, λ_{max} (nm), (ε_{max} ($dm^3\,mol^{-1}\,cm^{-1}$)) (acetonitrile), 514 (164), 881 (213). Magnetic moment, $\mu_{eff} = 3.1$ BM.

2.2. Physical measurements

Elemental analyses (carbon, hydrogen and nitrogen) were performed using a Perkin–Elmer 240C elemental analyzer. The nickel content in all the complexes was estimated

Table 1
Crystal data and refinement details of complexes **1**, **3**–**5**

Crystal data	**1**	**3**	**4**	**5**
Formula	$C_{20}H_{30}Cl_2N_6NiO_8$	$C_{20}H_{30}Cl_2N_6NiO_8$	$C_{19}H_{20}N_6NiS_2$	$C_{17}H_{16}N_6NiS_2$
F_w	612.09	612.11	455.24	427.19
Temperature (K)	150	150	150	150
Space group	*Pbca*	*Pbca*	$P\bar{1}$	$P\bar{1}$
Crystal system	orthorhombic	orthorhombic	triclinic	triclinic
Crystal dimensions (mm)	0.23 * 0.20 * 0.17	0.26 * 0.03 * 0.02	0.27 * 0.04 * 0.03	0.28 * 0.24 * 0.03
a (Å)	14.937(1)	18.766(1)	7.997(1)	6.790(1)
b (Å)	18.009(1)	16.325(1)	11.152(1)	11.934(1)
c (Å)	36.886(2)	34.157(2)	12.327(1)	12.184(3)
α (°)	(90)	(90)	78.40(1)	80.73(1)
β (°)	(90)	(90)	80.67(1)	74.07(2)
γ (°)	(90)	(90)	76.15(1)	87.03(1)
V (Å^3)	10191.4(9)	10463.8(11)	1038.0(2)	936.9(3)
Z	16	16	2	2
D_{calc} (g/cm^3)	1.596	1.554	1.457	1.514
μ (mm^{-1})	1.029	1.002	1.153	1.272
F(000)	5088	5088	472	440
Total reflections	68 542	70 204	7324	5808
Unique reflections	14 914	15 354	5792	4614
Observed data [$I > 2\sigma(I)$]	7424	4570	3855	3182
Number of parameters refined	667	668	253	235
R(int)	0.081	0.089	0.018	0.036
R indices (all data)	$R_1 = 0.1027$, $wR_2 = 0.1276$	$R_1 = 0.1640$, $wR_2 = 0.1679$	$R_1 = 0.0628$, $wR_2 = 0.0975$	$R_1 = 0.1305$, $wR_2 = 0.3159$
R indices [$I > 2\sigma(I)$]	$R_1 = 0.0512$, $wR_2 = 0.1196$	$R_1 = 0.0618$, $wR_2 = 0.1553$	$R_1 = 0.0373$, $wR_2 = 0.0931$	$R_1 = 0.1067$, $wR_2 = 0.3059$

gravimetrically using DMG. IR spectra in KBr (4500–500 cm^{-1}) were recorded using a Perkin–Elmer RXI FT-IR spectrophotometer. Electronic spectra in acetonitrile (1200–350 nm) were recorded in a Hitachi U-3501 spectrophotometer. The magnetic susceptibility measurements were done with an EG & PAR vibrating sample

Table 2
Selected bond lengths and bond angles in complexes **1** and **3**

	1 ($n = 2$)		**3** ($n = 1$)	
	Molecule 1	Molecule 2	Molecule 1	Molecule 2
Ni–N(11)	2.103(2)	2.083(2)	2.104(4)	2.095(4)
Ni–N(18)	2.099(2)	2.096(3)	2.021(3)	2.011(4)
Ni–N(2n)	2.089(2)	2.087(3)	2.130(3)	2.117(4)
Ni–N(31)	2.090(2)	2.110(2)	2.089(4)	2.125(4)
Ni–N(38)	2.088(2)	2.080(2)	2.030(4)	2.004(4)
Ni–N(4n)	2.096(2)	2.103(2)	2.142(4)	2.135(4)
N(38)–Ni–N(2n)	90.78(10)	92.18(10)	99.77(14)	99.22(15)
N(38)–Ni–N(31)	78.76(10)	78.45(10)	77.72(16)	77.54(16)
N(2n)–Ni–N(31)	89.11(10)	90.14(10)	90.09(14)	94.40(14)
N(38)–Ni–N(4n)	95.73(10)	95.28(10)	79.60(15)	82.08(15)
N(2n)–Ni–N(4n)	96.15(10)	91.85(10)	92.88(14)	93.07(15)
N(31)–Ni–N(4n)	172.46(10)	173.50(10)	157.30(15)	159.17(15)
N(38)–Ni–N(18)	173.33(10)	167.68(10)	174.78(15)	176.63(16)
N(2n)–Ni–N(18)	94.18(10)	95.52(10)	80.95(14)	80.96(15)
N(31)–Ni–N(18)	96.84(9)	91.90(10)	107.47(15)	99.08(15)
N(4n)–Ni–N(18)	88.18(9)	94.06(10)	95.22(14)	101.28(14)
N(38)–Ni–N(11)	95.88(9)	93.56(9)	101.27(14)	101.47(14)
N(2n)–Ni–N(11)	169.87(10)	173.77(10)	158.95(14)	159.07(15)
N(31)–Ni–N(11)	84.74(9)	88.63(9)	94.49(14)	87.05(14)
N(4n)–Ni–N(11)	90.78(10)	90.04(9)	90.77(14)	92.84(14)
N(18)–Ni–N(11)	78.63(9)	78.42(10)	78.08(14)	78.19(15)

magnetometer, model 155 at room temperature and diamagnetic corrections were made using Pascal's constants. Electrochemical measurements were performed under a dry nitrogen atmosphere in a three-electrode configuration using Pt disc working electrode, Pt auxiliary electrode and standard calomel reference electrode on a PAR Versastat-2 electrochemistry system in this work and were uncorrected for junction contribution. The value for the ferrocenium–ferrocene couple under our conditions is 0.42 V.

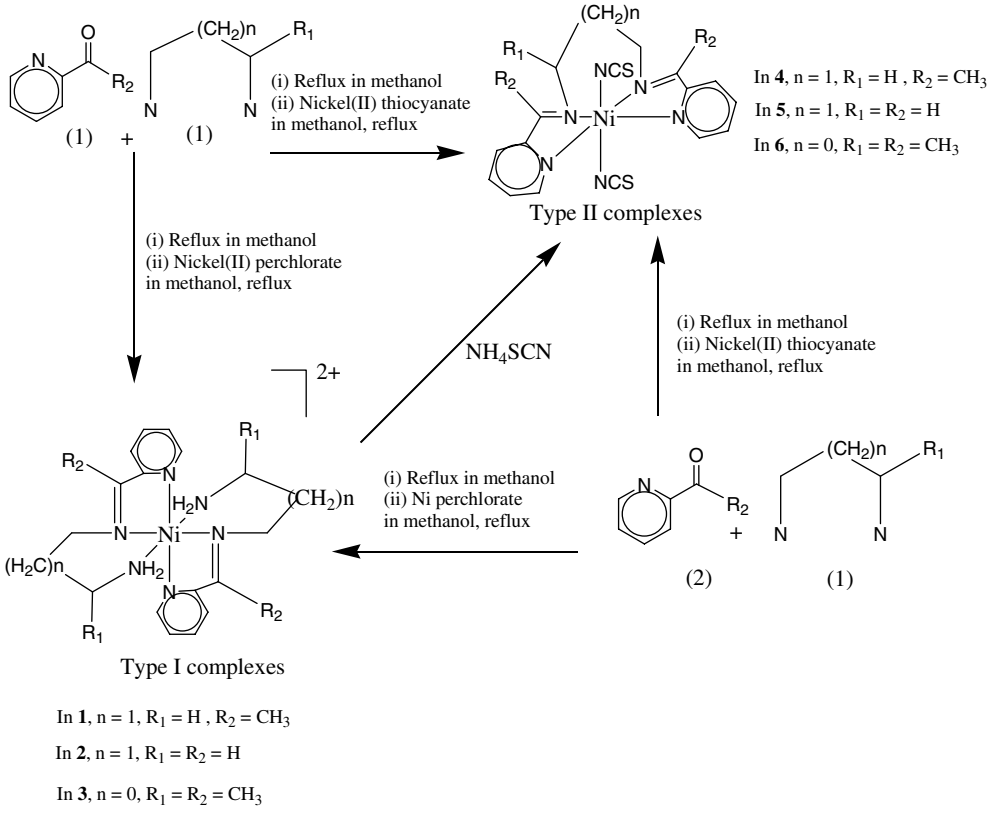
2.3. X-ray crystallography

Crystal data are given in Tables 1 and 2. Intensity data were measured at 150 K using the Oxford X-Calibur CCD System with Mo Kα radiation. The crystals were positioned at 50 mm from the CCD. 321 frames were measured with a counting time of 3 s. Data analyses were carried out with the CRYSALIS program [11]. The structures were solved using direct methods with the SHELX97 program [12]. The non-hydrogen atoms were refined with anisotropic thermal parameters. The hydrogen atoms bonded to carbon were included in geometric positions and given thermal parameters equivalent to 1.2 times those of the atom to which they were attached. Absorption corrections were carried out using the ABSPACK program [13]. The structures were refined on F^2 using SHELX97 [12]. The R value of **5** is rather high because of the poor quality of the crystals. In **5**, all four perchlorates were disordered and two sets of oxygen tetrahedra were refined with occupancies of x and $1-x$ with $x = 0.62(1)$, $0.60(1)$, $0.58(1)$, $0.57(1)$, respectively. Also one of the carbon atoms in one of the two independent cations was disordered and two sets of positions were refined similarly with x converging to 0.51(1).

3. Results and discussion

3.1. Syntheses

Two sets of ligands (Set-1: L^1, L^2 and L^3 and Set-2: L^4, L^5 and L^6) have been employed for the synthesis of complexes with Ni(II) perchlorate and Ni(II) thiocyanate (Scheme 1). For the set-1 and set-2 ligands, the respective diamine and carbonyl compounds were mixed in 1:1 and 1:2 ratios, respectively in methanol and refluxed for 3 h. The ligands were not isolated and the methanol solutions were used for the synthesis of complexes. When the methanol solution of any of the set-1 ligands is added to methanol solution of Ni(II) perchlorate bis-complexes (type-1; **1**–**3**) of the respective tridentate ligands are produced in high yield. Similarly, set-2 ligands yield type-2 complexes of tetradentate di-Schiff base ligands; **4**–**6**, when methanol solution of Ni(II) thiocyanate is added. From these results one may assume that the diamine:carbonyl compound ratio is the only important factor to determine the nature of the products formed. In fact, during the synthesis of Cu(II) complexes of such ligands, we isolated the



Scheme 1.

complexes of mono- and di-Schiff bases simply by changing the diamine carbonyl compound ratios [14,6c]. However, in the present systems when we add set-1 ligands to methanol solution of $Ni(SCN)_2$ we do not obtain any type-1 complex; type-2 compounds are the sole products. Similarly, set-2 ligands on addition to methanol solution of Ni(II) perchlorate yield exclusively type-1 complexes. Thus, it is obvious that the nature of Schiff bases present in the complexes does not depend upon the ratios of the diamine:carbonyl compounds (set-1 or set-2) used for their preparation; instead the counter anions present in the Ni(II) salt dictate their composition. Another interesting observation is that when a methanol solution of ammonium thiocyanate is added to the solution of type 1 complexes (2:1 molar ratio), they transform into type-2 complexes i.e. complexes of mono-Schiff base transforms into di-Schiff base complexes in presence of thiocyanate confirming the importance of anion on the type of Schiff base complexes formed.

The formation of the Schiff base complexes can be rationalised in the light of templating effect of Ni(II) modulated by the counter anions. A templating agent can be said to contain the required information to organize a collection of building blocks so that they can be linked together in a specific manner [10]. The nitrogen donor ligands usually form octahedral Ni(II) complexes. In perchlorate salts, Ni(II) prefers to be coordinated with two tridentate ligands to satisfy its six coordination sites leaving the weakly coordinating perchlorate as counter ion. On the other hand, the thiocyanate ions that have similar crystal field stabilization energy as the Schiff base occupy two coordination sites leaving the other four sites to be coordinated by the Schiff base and that can be achieved most efficiently by a tetradentate Schiff base ligand. The driving force for the formation of tetradentate Schiff base in presence of Ni(II) and thiocyanate is also obvious when addition of thiocyanate ion to complexes **1**, **2** or **3** transforms them to **4**, **5** or **6**, respectively. The lower solubility of **4**, **5** or **6** compare to **1**, **2**, **3** in methanol seems also contribute positively in this transformation.

However, during the synthesis of Cu(II) complexes, we observed that the ratio of carbonyl compound and diamine was important for the formation of complexes of tridentate or tetradentate Schiff bases as mentioned earlier [14,6c]. When the ratio was 1:1, complexes of tridentate and when 1:2, complexes of tetradentate Schiff bases were formed irrespective of the nature of the anions present. The apparent anomaly may be rationalized considering the active Jahn–Teller effect present in Cu(II) that makes its coordination number and geometry much more flexible.

3.2. Description of the structures

3.2.1. Complex *1*

The structure of **1** together with the atomic numbering scheme is shown in Fig. 1. The structure consists of discrete $[NiL^1_2]^{2+}$ cations together with perchlorate anions. There

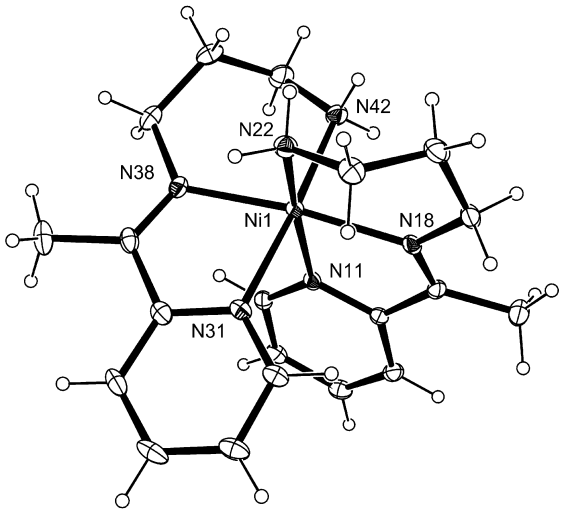


Fig. 1. The structure of one of the $[NiL^1_2]^{2+}$ independent cations in **1**, ellipsoids at 25% probability. Only the coordinating atoms along with central metal are labelled for clarity. The second molecule in the asymmetric unit has an equivalent geometry.

are two cations in the asymmetric unit with equivalent geometries, together with four perchlorate anions, one of which is shown in Fig. 1. The metal atoms are in six-coordinate octahedral environments being bonded to the two tridentate ligands which occupy mer positions. The Ni(1)–N bond lengths are all equivalent ranging from 2.083(2) to 2.110(2) Å. Selected bond lengths and bond angles are given in Table 2. The conformations of the six membered saturated rings of both the molecules present in the asymmetric unit are intermediate between boat and twist boat.

There are eight available H atoms on the four NH_2 groups (N22, N42 in molecule 1 and N62, N82 in molecule 2) for H-bond formation. Amongst them, H42b, attached to N42 in molecule 1 is involved in a strong H-bond with symmetry related $(x-1/2,-y+1/2,-z)$ perchlorate oxygen ($O33^c$). Another O atom of the same perchlorate ($O34^c$) forms a relatively weak H bond with H62b (N62) of molecule 2. H62a and H82a form H bonds with O41 and O43 respectively, whereas H42a, H22a, H22b and H82b are involved in H bonding with symmetry related perchlorate oxygen atoms $O11^a$ $(-x+1/2,y-1/2,z)$, $O12^a$ $(-x+1/2,y-1/2,z)$, $O21^b$ $(x-1/2,y,-z+1/2)$ and $O32^d$ $(-x+2,-y,-z)$, respectively (Fig. 2). The details of hydrogen bonds are given in Table 4.

3.2.2. Complex *3*

The structure of **3** contains discrete $[NiL^3_2]^{2+}$ cations together with perchlorate anions. There are two cations with equivalent geometries, one of which is shown in Figure S1 (Supplementary material), together with four anions in the asymmetric unit. Selected bond lengths and bond angles are given in Table 2. The conformations of the five membered saturated rings of both the molecules present in

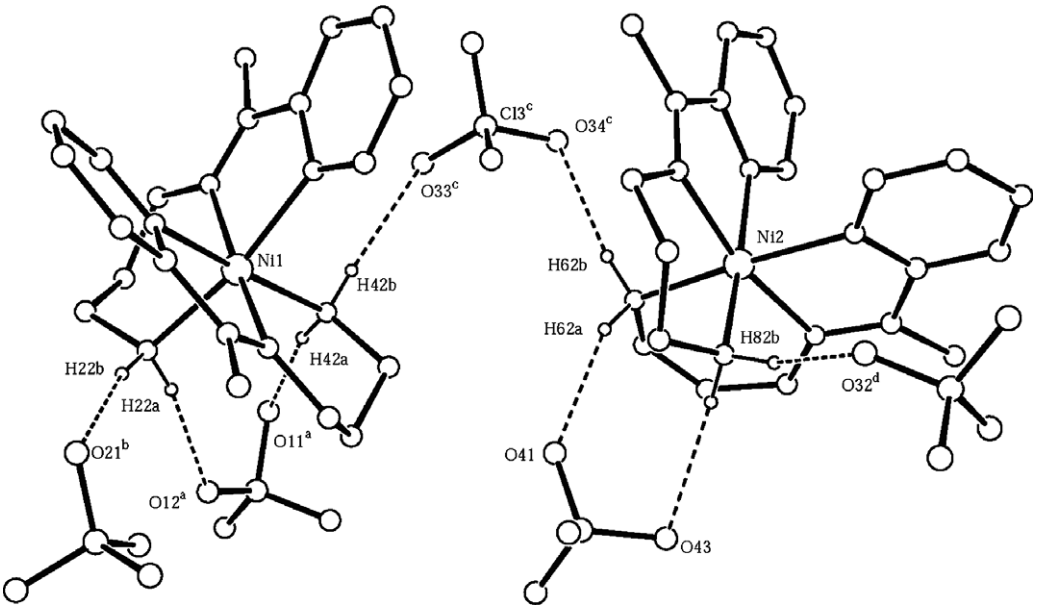


Fig. 2. The packing of **1** showing how the two independent cations are linked by hydrogen bonds to bridging perchlorate anions.

the asymmetric unit are intermediate between boat and twist boat.

The metal atoms are bonded to two tridentate ligands in the mer conformation and the structure is therefore similar to **1**. This environment of the metal atom is more distorted from octahedral than in **1**, presumably because there are only two carbon atoms between the donor nitrogen atoms N(18) and N(21) and also N(38) and N(41) thus forming two five-membered chelate rings compared to three carbon atoms between the donor nitrogen atoms N(18) and N(22) and also N(38) and N(42) which form six-membered chelate rings in **1**. The geometries of the two cations are compared in Table 3 and one obvious difference is that the chelating angles in **3** average to 81° compared to 95° in **1**. Also the bond lengths to the imine nitrogens N(18) and N(38) are much shorter in **3** than in **1** averaging at 2.016 Å compared to 2.091 Å. It would appear therefore that the lengthening of these bonds in **1** is due to the steric strain of the extra carbon atom creating the six-member chelate ring. The Ni–N distances to the NH_2 groups in **3** are slightly longer (average 2.132 Å) compared to the analogous distances in **1** (average 2.094 Å). However the distances to the pyridine nitrogen atom N(11) are equivalent.

The hydrogen bond pattern in the structure is complicated because of the disorder in one of the cations and in all four perchlorates. Because of the former disorder, there are two sets of alternate positions for the two hydrogens bonded to N21, namely H21a, H21b and H21c and H21d and because of the anion disorder there are alternate hydrogen bonds for most of the amines. Details are pro-

Table 3
Selected bond lengths and bond angles in **4** and **5**

	4	**5**
Ni(1)–N(1)	2.066(2)	2.025(8)
Ni(1)–N(2)	2.086(2)	2.153(9)
Ni(1)–N(11)	2.121(2)	2.115(8)
Ni(1)–N(18)	2.069(2)	2.078(9)
Ni(1)–N(22)	2.076(2)	2.076(9)
Ni(1)–N(29)	2.120(2)	2.127(9)
N(1)–Ni(1)–N(2)	179.50(8)	178.2(4)
N(1)–Ni(1)–N(11)	90.15(7)	92.8(3)
N(1)–Ni(1)–N(18)	90.89(7)	94.4(4)
N(1)–Ni(1)–N(22)	87.46(8)	93.9(4)
N(1)–Ni(1)–N(29)	88.90(7)	94.2(4)
N(2)–Ni(1)–N(11)	89.70(7)	85.4(3)
N(2)–Ni(1)–N(18)	89.54(7)	85.7(3)
N(2)–Ni(1)–N(22)	92.75(7)	87.8(3):
N(2)–Ni(1)–N(29)	90.70(7)	86.0(3)
N(11)–Ni(1)–N(18)	77.66(7)	78.9(3)
N(11)–Ni(1)–N(22)	172.89(7)	169.5(3)
N(11)–Ni(1)–N(29)	108.76(7)	108.6(3)
N(18)–Ni(1)–N(22)	95.68(7)	92.6(3)
N(18)–Ni(1)–N(29)	173.57(8)	168.3(3)
N(22)–Ni(1)–N(29)	77.90(7)	78.9(3)
Ni(1)–N(1)–C(1)	158.08(19)	177.9(9)
Ni(1)–N(2)–C(2)	178.08(18)	135.7(8)

Table 4
Hydrogen bond distances (Å) and angles (°) for complex **1**

D–H···A	D···A	H···A	∠D–H···A
N22–H22A···O12[a]	3.114(4)	2.22	170
N22–H22B···O21[b]	3.480(4)	2.59	168
N42–H42A···O11[a]	3.174(5)	2.29	167
N42–H42B ···O33[c]	3.378(4)	2.48	177
N62–H62A···O41	3.074(4)	2.27	148
N62–H62B···O34[c]	3.305(4)	2.43	165
N82–H82A···O43	3.340(4)	2.46	168
N82–H82B···O32[d]	3.173(3)	2.37	149

(Symmetry transformation: [a] $= -x+1/2, y-1/2, z$; [b] $= x-1/2, y, -z+1/2$; [c] $= x-1/2, -y+1/2, -z$; [d] $= -x+2, -y, -z$). D, donor; H, hydrogen; A, acceptor.

Table 5
Hydrogen bond distances (Å) and angles (°) for complex **3**

D–H···A	D···A	H···A	∠D–H···A
N21–H21A···O43	3.263(9)	2.41	159
N21–H21B···O47[a]	2.933(14)	2.16	143
N21–H21C···O48	3.160(11)	2.29	162
N21–H21D···O47[a]	2.933(14)	2.05	166
N41–H41A···O42	3.223(8)	2.39	154
N41–H41A···O48	3.113(9)	2.25	159
N41–H41B···O54[b]	3.085(8)	2.19	174
N41–H41B···O58[b]	3.086(9)	2.19	172
N61–H61A···O35[A]	3.271(13)	2.51	143
N61–H61B···O41	3.242(9)	2.51	139
N61–H61B···O45	3.119(11)	2.50	127
N81–H81D···O32	3.035(10)	2.16	162
N81–H81D···O35	3.115(11)	2.25	161
N81–H81E···O55	3.157(11)	2.26	171
N81–H81E···O53	3.187(9)	2.44	140

Note that because of the disorder in the perchlorates there are two alternate positions for each perchlorate oxygen atom and therefore for each hydrogen bond.
(Symmetry transformation: [a] $= -x+1, -y+1, -z+1$; [b] $= x+1/2, y, -z+3/2$). D, donor; H, hydrogen; A, acceptor.
[A] In this case only, the alternative oxygen atom does not form a hydrogen bond.

vided in Table 5 and illustrated in Fig. 3. Again the hydrogen bonds between the cations and anions allow the perchlorates to bridge between the cations.

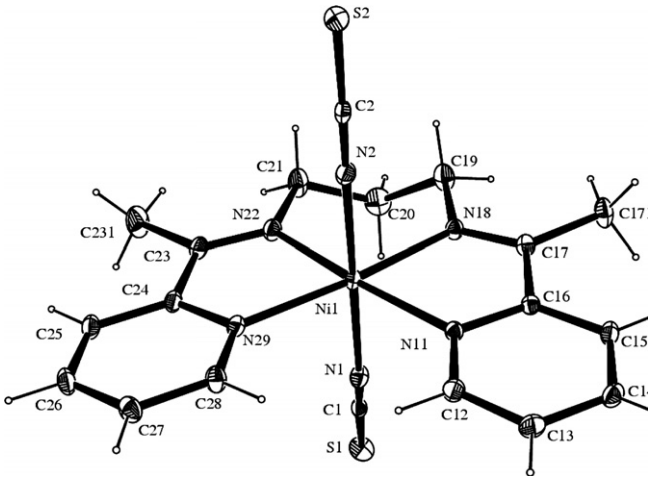


Fig. 4. The structure of **4** together with the atom numbering scheme, ellipsoids at 20% probability.

3.2.3. Complexes *4* and *5*

The structure of **4** is shown in Fig. 4 together with the atom numbering scheme (complex **5** has very similar molecular structure: Figure S2, Supplementary material). The structures of **4** and **5** consist of discrete $NiL^4(NCS)_2$ and $NiL^5(NCS)_2$ molecules, respectively.

The nickel atom is in a slightly distorted octahedral site in **4** with the ligand (L^4) occupying the equatorial plane and the N-bonded thiocyanate anions in axial positions at

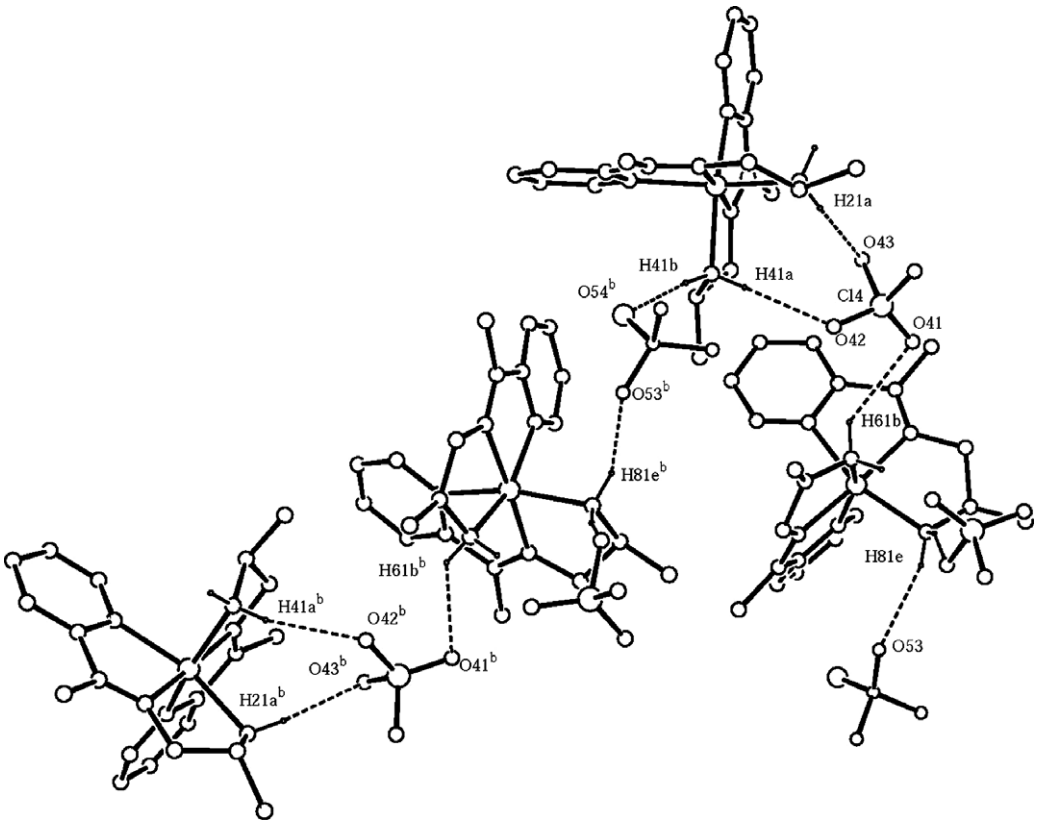


Fig. 3. H-bonds in complex **3**. Only one tetrahedron of the disordered perchlorates is shown.

distances of 2.066(2), 2.086(2) Å. The Ni–N bond lengths to the pyridine nitrogen atoms are slightly longer [2.119(2), 2.120(2) Å] than those to the imino nitrogens [2.076(2), 2.069(2) Å]. The CuN_4 equatorial plane has an r.m.s. deviation of 0.021 Å. The saturated six membered ring [Ni(1)–N(18)–C(19)–C(20)–C(21)–N(22)–Ni(1)] has an envelope conformation with puckering parameters [15] $Q = 0.563(3)$, $\theta = 119.6(3)$, $\phi = 354.1(3)$.

The metal atom in **5** is also six-coordinate being bonded to the tetradentate ligand (L^5) which occupies an equatorial plane together with two iso-thiocyanate groups in axial positions. The Ni(1)–N bond lengths to ligand donor atoms are to N(11) 2.115(8), N(18) 2.078(9), N(22) 2.076(9), N(29) 2.127(9) Å. The Ni(1)–N(1) and Ni(1)–N(2) bond lengths to the axial thiocyanate [2.025(8) and 2.153(9) Å] differ significantly and this difference in axial bond lengths may be correlated with the difference in Ni(1)–N–C angles which are 177.9(9) for Ni(1)–N(1)–C(1) and 135.7(8)° for Ni(1)–N(2)–C(2). The saturated six member ring [Ni(1)–N(18)–C(19)–C(20)–C(21)–N(22)–Ni(1)] has an envelope conformation with puckering parameters [15] $Q = 0.575(11)$, $\theta = 127.4(10)$, $\phi = 359.3(13)$. Selected bond lengths and bond angles of **4** and **5** are given in Table 3.

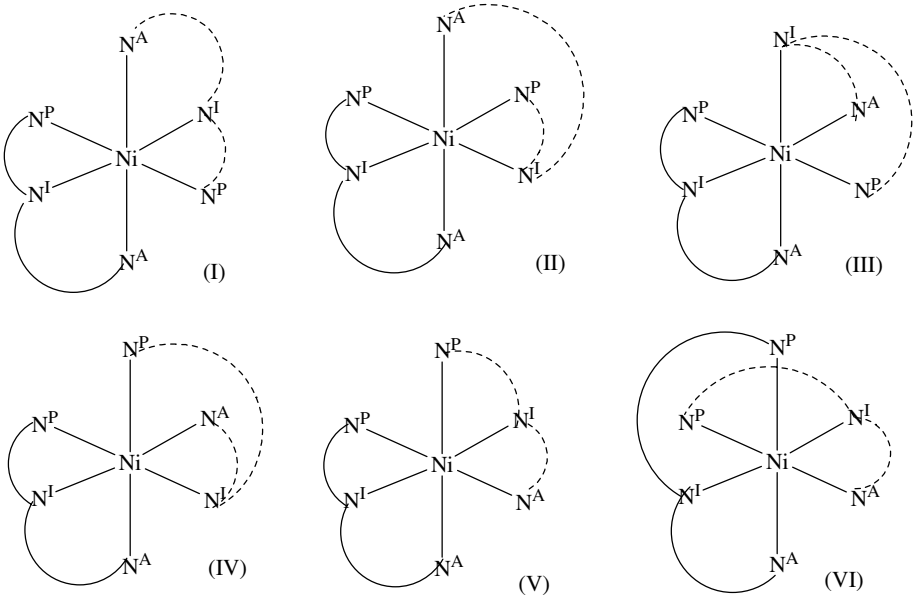
3.3. Geometrical preferences

The four complexes whose structures have been determined are found to have distorted octahedral geometry. In type 1 complexes (**1** and **3**) two tridentate ligands encapsulate Ni(II) through six ligating nitrogen atoms from one pyridyl, one imine and one amino group of each ligand. In the bis complexes of such asymmetric tridentate ligands there is possibility of formation of six geometrical isomers – one meridional and five facial (Scheme 2). However, only the meridional one which has the pyridyl nitrogen atoms in the cis positions, the imine nitrogen atoms in the trans positions and amino nitrogen atoms in cis positions has been formed exclusively for both the complexes as is confirmed by X-ray analysis. Electronic factor cannot explain the stability of the mer isomer as here the trans disposition of two imine groups causes competition between them for the same metal d-orbitals, minimizing the back-bonding stabilization. However, the non-bonding interaction in the mer isomer is expected to be low (as two chelate rings are orthogonal to each other) and this along with the requirement of efficient crystal packing seems to be responsible for its exclusive formation.

In case of complexes **4** and **5**, the tetradentate Schiff base encapsulates the equatorial plane leaving the two axial trans positions to be coordinated by the thiocyanate group and this trans isomer is the exclusive product in both cases. The extra stability of this isomer probably comes from both steric and electronic effects as in this configuration, the cis orientation of the two imine groups allows maximized back-bonding stabilization (as evident from the Ni–N^i bond shortening) from 2.099(2), 2.096(3) Å for Ni–N(18); 2.088(2), 2.080(2) Å for Ni–N(38) in the two molecules of **1** to 2.069(2) Å for Ni–N(18) and 2.076(2) for Ni–N(22) in **4** and at the same time, steric repulsion is minimized by the trans disposition of two NCS moieties.

3.4. Electronic and IR spectra

The electronic spectra of all the six complexes (**1**–**6**) were recorded in acetonitrile solution. A broad band is observed near 800 nm, well separated from the second transition at about 510 nm for all the complexes. The third d–d band



Scheme 2. Possible geometrical isomers of the complexes $[NiL_2]^{2+}$ ($L = L^1$, L^2, and L^3); I–V are facial isomers, whereas VI is the meridional one (N^I, N^A and N^P indicate imine, amine and pyridyl nitrogen atoms, respectively).

at lower wavelength cannot be observed as it is obscured by a strong charge transfer transition in each case. The two absorption peaks are assigned to as $^3T_{2g} \leftarrow {}^3A_{2g}$ and $^3T_{1g}(F) \leftarrow {}^3A_{2g}$ transitions. The calculated values of Dq lie in the ranges 1250–1260 cm^{-1} for all complexes and are in good agreement with literature values [16].

In the IR spectra of all the six complexes, the imine (C=N) stretch appears at about 1650 cm^{-1}. The two NH_2 stretching modes are observed in complexes of tridentate ligands (**1**–**3**) near 3340 and 3290 cm^{-1} as sharp bands (doublet) for the asymmetric and symmetric stretching vibrations, respectively. Concerning the ClO_4^- anion, the ν_3 mode at 1089, 1088 and 1093 cm^{-1} for **1**–**3** respectively, is somewhat broadened, but the ν_4 band at 622.4, 622 and 622.3, respectively, is devoid of any splitting and are consistent with the IR active normal modes for T_d symmetry suggesting that these anions are not coordinated to the nickel ions as substantiated by the crystal structures of **1** and **3**. The strong bands at 2009, 2006 and 2001 cm^{-1} in the IR spectra of **4**–**6**, respectively, indicate the presence of N-bonded thiocyanate [17].

3.5. Luminescence studies

Complexes **1**–**3** do not display any fluorescence probably because the small energy gap between the ground state and first excited state favouring non-radiative decay. On the other hand, complexes **4**–**6** show fluorescence. These are assigned as intra-ligand fluorescence $^1(\pi \rightarrow \pi^*)$. The spectroscopic data are given in Table 6 (without solvent correction).

3.6. Electrochemistry

The redox behaviour of all the complexes were studied by using cyclic voltammetry (CV) in acetonitrile (0.1 M NEt_4ClO_4) in the potential range ±2 V by using platinum auxiliary electrode and Pt disc working electrode at ambient temperature (300 K) with no trace of decomposition as reflected in smooth curve. The reported potentials (Tables 7 and 8) are referenced to the saturated calomel electrode (SCE).

Complexes **1**–**3** displayed two one electron cyclic voltammetric responses at about 0.95 and 1.70 V. The irreversible redox signal encountered near 1.70 V is attributable to the $Ni^{4+/3+}$ response, whereas quasi reversible ($\Delta E_p \sim 118$ mV) one electron oxidative response at about 0.95 V is attributable to the $Ni^{3+/2+}$ couple. The absence of any satellite response is consistent with the exclusive occurrence of single isomer in the solution. No voltammetric response consistent with $Ni^{2+/+}$ reduction is observed.

Table 6
Photophysical data for the complexes **1**–**6**

Complex	Absorption	Emission
1	376	
2	367	
3	405	
4	280	458
5	281	435
6	280	449

Table 7
Electrochemical data for complexes **1**–**3**

Compound	$E_{1/2}$/V (ΔE_p/mV)[a]	
	$Ni^{III/II}$ couple	$Ni^{IV/III}$ couple
1	0.97(110)	1.69
2	0.95(115)	1.71
3	0.96(118)	1.68

[a] $E_{1/2}$ is calculated as the average of anodic (E_{pa}) and cathodic (E_{pc}) peak potentials; $\Delta E_p = (E_{pa} - E_{pc})$.

Table 8
Electrochemical data for complexes **4**–**6**

Compound	$E_{1/2}$/V (ΔE_p/mV)[a]	
	$Ni^{II/I}$	couple $Ni^{III/II}$ couple
4	−0.95(60)	0.64(120)
5	−0.95(78)	0.70(130)
6	−0.90(82)	0.61(125)

[a] $E_{1/2}$ is calculated as the average of anodic (E_{pa}) and cathodic (E_{pc}) peak potentials; $\Delta E_p = (E_{pa} - E_{pc})$.

Complexes **4**–**6** do not follow a similar trend as that of **1**–**3**. Compound **4** shows two quasi reversible redox couples at $E_{1/2} = 0.64$ and −0.95 V (vs. SCE). The redox reaction at $E_{1/2} = +0.64$ V corresponds to the first electron abstraction from the complex and is consistent with $[NiL^2(SCN)_2]^+/[NiL^2(SCN)_2]$ couple. The redox couples at $E_{1/2} = -0.95$ can be assigned to the electron addition to Ni^{II} complex to form Ni^{I} species. The similar pattern of cyclic voltammogram of **4**–**6** indicates the similarity of their structures (Table 8).

All the redox signals remain virtually invariant under different scan rates (0.01–1.0 V s^{-1}) in the temperature range 300–280 K. Solvent dependent shift and change in electrochemical reversibility of redox couples are not significant.

3.7. Magnetic properties

The effective magnetic moments (ranging from 3.03 to 3.12 BM) of the complexes **1**–**6** clearly confirm the presence of two unpaired electrons ($S = 1$) in a pseudo-octahedral environment, in agreement with a high-spin configuration ($t_{2g}^6 e_g^2$) as was also observed in similar systems [6f].

4. Conclusion

The syntheses of Ni(II) complexes with mono-condensed tridentate or tetradentate di-Schiff base have been rationalised by anion directed cation templating effect. When all six coordination numbers of the Ni(II) are to

be fulfilled by the Schiff base ligand, the tridentate mono-Schiff base is formed so that two such ligands can result in discrete octahedral complex. But when two of the coordination sites are occupied by strongly coordinating anions, tetra-coordinated di-Schiff base is formed to satisfy the remaining four coordination sites.

Acknowledgments

We thank EPSRC and the University of Reading for funds for the X-Calibur system.

Appendix A. Supplementary material

CCDC 625792, 625795, 625793 and 625794 contain the supplementary crystallographic data for **1**, **3**, **4** and **5**. These data can be obtained free of charge via http://www.ccdc.cam.ac.uk/conts/retrieving.html, or from the Cambridge Crystallographic Data Centre, 12 Union Road, Cambridge CB2 1EZ, UK; fax: (+44) 1223-336-033; or e-mail: deposit@ccdc.cam.ac.uk. Supplementary data associated with this article can be found, in the online version, at doi:10.1016/j.poly.2007.03.037.

References

[1] (a) B.L. Small, R. Schmidt, Chem. Eur. J. 10 (2004) 1014;
(b) A.S. Ionkin, W.J. Marshall, J. Organomet. Chem. 689 (2004) 1057;
(c) V.C. Gibson, S.K. Spitzmesser, Chem. Rev. 103 (2003) 283;
(d) D.S. McGuiness, P. Wasserscheid, W. Keim, D. Morgan, J.T. Dixon, A. Bollman, H. Maumela, F. Hess, U. Englert, J. Am. Chem. Soc. 125 (2003) 5272;
(e) S. Mecking, Coord. Chem. Rev. 203 (2000) 325;
(f) T.R. Younkin, E.F. Connor, J.I. Henderson, S.K. Friedrich, R.H. Grubbs, D.A. Bansleben, Science 288 (2000) 1750.

[2] S.J. Coles, M.B. Hursthouse, D.G. Kelley, A.J. Toner, N.M. Walker, J. Chem. Soc., Dalton Trans. (1998) 3489.

[3] (a) H. Schiff, Ann. Suppl. 3 (1864) 343;
(b) M. Calligaris, L. Randaccio, in: G. Wilkinson, R.D. Gillard, J.A. McCleverty (Eds.), Comprehensive Coordination Chemistry, vol. 2, Pergamon Press, Oxford, 1987, p. 727;
(c) M. Kojima, H. Taguchi, M. Tsuchimoto, K. Nakajima, Coord. Chem. Rev. 237 (2003) 183;
(d) E. Tsuchida, K. Oyaizu, Coord. Chem. Rev. 237 (2003) 213;
(e) N.S. Venkataramanan, G. Kuppuraj, S. Rajagopal, Inorg. Chim. Acta 249 (2005) 1249;
(f) T. Katsuki, Chem. Soc. Rev. 7 (2004) 437;
(g) P.G. Cozzi, Chem. Soc. Rev. 7 (2004) 410;
(h) C. Baleizao, H. Garcia, Chem. Rev. 106 (2006) 3987.

[4] (a) M.S. Ray, S. Chattopadhyay, M.G.B. Drew, A. Figuerola, J. Ribas, C. Diaz, A. Ghosh, Eur. J. Inorg. Chem. (2005) 4562;
(b) J.P. Costes, F. Dahan, J.P. Laurent, Inorg. Chem. 25 (1986) 413;
(c) M. Kwiatkowski, E. Kwiatkowski, A. Olechnowicz, D.M. Ho, E. Deutsch, Inorg. Chim. Acta 150 (1988) 65;
(d) H.-D. Bian, J.-Y. Xu, W. Gu, S.-P. Yan, P. Cheng, D.-Z. Liao, Z.-H. Jiang, Polyhedron 22 (2003) 2927;
(e) M. Mikuriya, Y. Hatano, E. Asato, Bull. Chem. Soc. Jpn. 70 (1997) 2495;
(f) J.P. Costes, J.-F. Sehera, F. Dahan, J.P. Laurent, Polyhedron 25 (1986) 2790;
(g) M. Kwiatkowski, E. Kwiatkowski, A. Olechnowiez, G. Bandoli, Inorg. Chim. Acta 182 (1991) 117;
(h) E. Kwiatkowski, M. Kwiatkowski, A. Olechnowiez, J. Mrozinski, D.M. Ho, E. Deutsch, Inorg. Chim. Acta 158 (1989) 37;
(i) S. Banerjee, P.-G. Lassahn, C. Janiak, A. Ghosh, Polyhedron 24 (2005) 2963;
(j) M.S. Ray, G.C. Mukhopadhyay, M.G.B. drew, T.-H. Lu, S. Chaudhuri, A. Ghosh, Inorg. Chim. Acta, Inorg. Chem. Commun. 6 (2003) 961.

[5] (a) J.P. Costes, G. Cros, M.H. Darbieu, J.P. Laurent, Inorg. Chim. Acta 60 (1982) 111;
(b) S. Chattopadhyay, M.S. Ray, S. Chaudhuri, G.C. Mukhopadhyay, G. Bocelli, A. Cantoni, A. Ghosh, Inorg. Chim. Acta 269 (2006) 1367;
(c) M. Kwiatkowski, G. Bandoli, J. Chem. Soc., Dalton Trans. (1992) 379;
(d) M. Kwiatkowski, E. Kwiatkowski, A. Olechnowiez, D.M. Ho, E. Deutsch, J. Chem. Soc., Dalton Trans. (1990) 2497;
(e) E. Kwiatkowski, M. Klein, G. Romanowski, Inorg. Chim. Acta 293 (1999) 115;
(f) J.P. Costes, F. Dahan, A. Dupuis, J.P. Laurent, J. Chem. Soc., Dalton Trans. (1998) 1307.

[6] (a) T.G. Campbell, F.L. Urbach, Inorg. Chem. 12 (1973) 1836, and references therein;
(b) W.C. Potter, L.T. Taylor, Inorg. Chem. 15 (1976) 1329;
(c) S. Chattopadhyay, M.G.B. Drew, A. Ghosh, Inorg. Chim. Acta 359 (2006) 4519;
(d) S.H. Rahaman, R. Ghosh, T.H. Lu, B.K. Ghosh, Polyhedron 24 (2005) 1525;
(e) C.M. Liu, R.G. Xiong, J.L. Zuo, X.Z. You, X.Y. Huang, Polyhedron 15 (1996) 2051;
(f) S. Banerjee, J. Gangopadhyay, C.Z. Lu, J.T. Chen, A. Ghosh, Eur. J. Inorg. Chem. (2004) 2533.

[7] (a) M. Linss, U. Weser, Inorg. Chim. Acta 125 (1986) 117;
(b) Q. Lu, C.-Y. Shen, Q.-H. Luo, Polyhedron 12 (1993) 2005;
(c) Q. Luo, Q. Lu, A. Dai, L. Huang, J. Inorg. Biochem. 51 (1993) 655;
(d) J. Muller, K. Felix, C. Maichle, E. Lengfelder, J. Strahle, U. Weser, Inorg. Chim. Acta 233 (1995) 11;
(e) C.-M. Liu, R.-G. Xiong, X.-Z. You, Y.-J. Liu, K.-K. Cheung, Polyhedron 15 (1996) 4565;
(f) C.-M. Liu, R.-G. Xiong, X.-Z. You, H.-K. Fun, K. Sivakumar, Polyhedron 16 (1997) 119;
(g) P.A. Cerutti, Science 277 (1985) 375.

[8] M. Hanack, S. Deger, A. Lange, Coord. Chem. Rev. 83 (1988) 115.

[9] S. Gourbatsis, S.P. Perlepes, I.S. Butler, N. Hadjiliadis, Polyhedron 18 (1999) 2369.

[10] N. Gimeno, R. Vilar, Coord. Chem. Rev. 250 (2006) 3161, and references therein.

[11] Crysalis, Oxford Diffraction Ltd., Version 1, 2005.

[12] G.M. Sheldrick, Shelx97, Program for Crystal Structure Calculations, University of Gottingen, 1997.

[13] Abspack, Oxford Diffraction Ltd., 2005.

[14] S. Chattopadhyay, M.S. Ray, M.G.B. Drew, A. Figuerola, C. Diaz, A. Ghosh, Polyhedron 25 (2006) 2241.

[15] (a) D. Cramer, J.A. Pople, J. Am. Chem. Soc. 97 (1975) 1354;
(b) J.C.A. Boyens, J. Cryst. Mol. Struct. 8 (1978) 31.

[16] R.S. Drago, in: Physical Methods in Chemistry, Saunders, Philadelphia, 1977 (Chapter 11).

[17] K. Nakamoto, Infrared and Raman Spectra of Inorganic and Coordination Compounds, third ed., Wiley-Interscience, New York, 1978, p. 275.

temperature range of 1 or 2 K. Abrupt transitions in particular can also exhibit thermal hysteresis when measured in warming and cooling modes. An abrupt transition reflects cooperativity between the spin centres in the solid, which are in close proximity to each other [13]. As such, this is a reflection of the intermolecular packing within the solid material; different crystal polymorphs of the same compound can exhibit very different thermal spin-crossover regimes. It is an open question to what degree it should be possible to control the form of a spin transition, by manipulating the crystal packing of the solid [14]. Such considerations are very important for producing materials that could be used for the applications listed in the previous paragraph [9].

Although thermal spin-transitions are most heavily-studied, spin crossover in transition metal compounds can also be induced by other physical stimuli. The first to be discovered chronologically was that a high → low spin change can be effected by the application of pressure to the sample [3]. This depends on the fact that the volume of the low-spin state of a molecule is always smaller than its high-spin form. Since this is favoured at higher pressures, increasing pressure results in the thermal transition temperature $T_{1/2}$ being shifted to higher temperature as the low-spin state is stabilised [16,17]. More recently, it was noted that placing a sample in a very strong magnetic field has the reverse effect of stabilising its high-spin state [18]. The field can interact more strongly with the high-spin form of the compound, which is always more paramagnetic, causing $T_{1/2}$ to shift to lower temperature as the field strength is increased [19]. Very high magnetic fields of 30 T or above are required to decrease $T_{1/2}$ by more than a fraction of a degree, however.

More importantly, it was discovered in 1984 that spin-state conversions can also be induced in the solid by laser irradiation [20–22]. Most commonly the low-spin form of a spin-transition compound is converted using a green laser to its high-spin form, which is metastable at the temperature of the experiment, typically below 30 K. If the temperature is held below its activation barrier for thermal relaxation, then the sample can only relax back to its low-spin ground state by quantum-mechanical tunnelling. Since tunnelling is slow when the ground and excited states of a compound have very different structures, some samples can retain their excited spin-state for weeks at low enough temperatures. This has been termed the "light-induced excited spin-state trapping" (LIESST) effect [23]. It is not unusual for photogenerated high-spin forms of iron(II) materials to be long-lived below 50 K, but examples are also known where excited spin-states remain trapped at higher temperatures [24–28], the current record for a molecular species being 130 K [28]. The thermal stability of LIESST excited states in the solid state is inversely related to their thermal crossover temperature $T_{1/2}$, and seems to be controlled more by the molecular structure of the materials studied, than by any longer range cooperativity phenomena. This opens interesting possibilities that spin-crossover molecular materials showing light-induced bistability at higher temperatures might be designed [29].

Metastable high-spin forms of spin-transition materials at low temperature can also sometimes be trapped by thermal quenching; that is, very rapid cooling of the sample to ca. 5 K [30]. They can also be observed following nuclear decay of a ^{57}Co nucleus in a high-spin cobalt(II) complex, to the metastable high-spin form of the corresponding ^{57}Fe compound, in a Mössbauer emission spectroscopy experiment (the "nuclear decay-induced excited spin-state trapping" or NIESST effect) [31]. The resultant metastable high-spin states formed by both techniques usually exhibit the same thermal stability and relaxation kinetics as their light-induced counterparts for a given material, where these have been compared.

The low temperatures required for the observation of spin-state trapping phenomena might restrict their practical application. However, switching spin states at higher temperatures by irradiation can also be achieved, for materials that are genuinely bistable at the temperature of measurement. That is, if the experiment is performed at a temperature inside the thermal hysteresis loop of a cooperative spin-transition. This phenomenon has been observed occasionally at low temperatures [32,33], but very recently the first fully reversible, room temperature light-activated switch of this type was attained. That is, a material that can be shuttled between its bistable low- and high-spin forms at room temperature, by pulses of the *same* laser radiation [34]. This is not a spin-trapping process, but is a genuine, reversible light-induced colour switch that has clear potential applications.

By far the majority of known spin-transition compounds are octahedral iron(II) compounds, of general formula $[FeL_6]^{n+}$ or $[Fe(NCX)_2L_4]$. The 'L' ligand here is a nitrogen donor, usually from a heterocyclic group which may be monodentate or part of a larger polydentate ligand framework, while NCX^- is isothiocyanate (X = S) or, sometimes, isoselenocyanate (X = Se) or a related pseudohalide. Of all the metal ions [35] and ligands that are known to give spin-crossover complexes, the iron(II)/N–ligand combination leads to the greatest change in metal–ligand bond lengths between the high- and low-spin states [36]. Greater structural changes induce larger cooperativity between spin centres during spin-crossover, leading to more abrupt thermal transitions that may show hysteresis. Hence abrupt spin-transitions that take place within a temperature range of <5 K, are well-known for solid iron(II)/N–ligand complexes but rare for compounds of other metal ions or ligand types [37]. Similarly, iron(II) compounds with N-donor ligands give by far the longest-lived photochemical excited spin-states, since the large structural changes involved inhibit relaxation of these excited states by quantum mechanical tunnelling. For example, the rate of tunnelling relaxation of photogenerated high-spin states of spin-crossover iron(II) complexes in low-temperature matrices is ca. 10^7 times slower than for comparable iron(III) compounds [38].

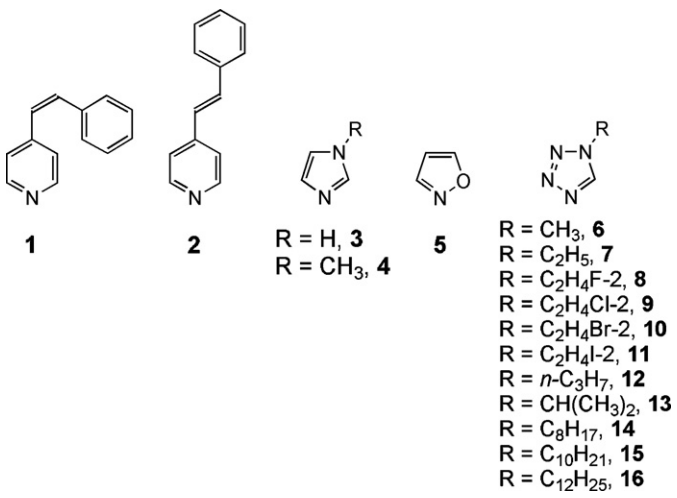
The potential applications of spin-crossover materials, and the range of physical phenomena they can exhibit,

mean that the synthesis and structural and physical chemistry of new spin-crossover compounds is of great current interest worldwide. Reflecting its current popularity, the chemistry and physics of spin-crossover phenomena has been reviewed extensively in recent years [1,13,17,18,23,29,35,39–44]. These literature articles mostly describe the novel structural [12,35,40] and physical [17,18,23,41–44] chemistry that has been discovered in spin-transition materials; or, efforts to design new spin-transition materials de novo to have technologically useful thermochromic or photochromic properties [13,29,40]. Ref. [1] is particularly highlighted as an accessible, general introduction to spin-crossover phenomena, and Ref. [39] as a recent series of three volumes covering all aspects of spin-transition chemistry. Several individual chapters from Ref. [39] are also cited during this review.

The aim of this article is different, being to survey the range of metal complexes that have been shown to exhibit spin-transitions. This will provide a convenient guide to what materials have been made before (and which have not), highlighting those that exhibit interesting spin-transitions or structural chemistry. Since most spin-crossover chemistry has been achieved using mononuclear iron(II) complexes with N-donor ligation (see above), the review concentrates on that class of compounds. The discussion is organised by ligand type, and described in order of increasing ligand donacity. Polynuclear and polymeric iron(II) spin-transition compounds are not described here, but have been reviewed elsewhere [13,40,44].

2. Monodentate ligands

The solid compounds "$Fe(py)_6X_2$" (py = pyridine; $X^- = Br^-$, I^- or NCO^-) in fact have the composition $[FeX_2(py)_4]\cdot 2py$ [45]. However, three solid salts of the $[Fe(py)_6]^{2+}$ dication have been isolated, namely $[Fe(py)_6]X_2$ ($X^- = PF_6^-$, [46], picrate [47] and $1/2[Fe_4(CO)_{13}]^{2-}$ [48]). A crystal structure of the latter compound at room temperature shows a high-spin, centrosymmetric octahedral iron centre. $[Fe(py)_6][picrate]_2$ is also high-spin at room temperature, as are its 4-picoline and 3-picoline-containing analogues [47]. The PF_6^- salt loses pyridine in MeCN solution, forming $[Fe(py)_x(NCMe)_{6-x}]^{2+}$ ($x \approx 5$) [46]. Interestingly these solutions are thermochromic, changing from pale yellow at room temperature to dark red when frozen. It is uncertain whether this reflects the onset of a spin-state transition, however. Molecular mechanics calculations suggest that the apparent instability of octahedral $[Fe(py)_6]^{2+}$ is a consequence of steric hindrance between the 2- and 6-H atoms on adjacent pyridine ligands [49]. No other homoleptic Fe(II) complexes of six-membered azinyl ligands have yet been synthesised. While $[Fe(NCS)_2(py)_4]$ is high-spin at ambient pressure, a partial spin-crossover can be induced in this compound under 5–7 GPa pressure at room temperature [50]. Although $[Fe(NCB\{C_6H_5\}_3)_2(\mathbf{1})_4]$ is also high-spin, $[Fe(NCB\{C_6H_5\}_3)_2(\mathbf{2})_4]$ undergoes a quite abrupt thermal spin-transition centred at 190 K. Irradiation of these compounds in a cellulose acetate film at 140 K causes their interconversion through photoisomerisation of the ligand styryl group, with a concomitant change in the spin-state of the iron centre [51]. This was the first time a ligand-driven, light-induced spin-transition had been demonstrated. Several related complexes containing other 4-(*trans*-styryl)pyridine derivatives also undergo more gradual thermal spin-crossover, with $155 < T_{1/2} < 200$ K [51].



A much larger number of complexes containing monodentate azole ligands have been prepared. All known $[FeL_6]^{2+}$ or $[Fe(NCS)_2L_4]$ complexes of pyrazole [52,53], imidazole [46,52,54–57] or thiazole [58] ligands are high-spin at room temperature. Of these only $[Fe(\mathbf{3})_6][NO_3]_2$, $[Fe(\mathbf{4})_6]Cl_2$ [54], $[Fe(\mathbf{4})_6]S_8$ [56] and some $[Fe(NCS)_2L_4]$ (L = pyrazole or a 5-alkylpyrazole) compounds [53] have been shown to remain high-spin on cooling, however. In contrast, all known $[FeL_6]^{2+}$ salts of *iso*-oxazole (**5**) or 1-alkyltetrazole (**6**–**16**) 'L' ligands undergo spin-state transitions at low temperatures (Table 1) [59]. This apparent ordering of ligand donor strengths:

[tetrazole,*iso*-oxazole] > imidazole

does not correspond to the ordering of pK_as of the conjugate acids of the free heterocycles:

imidazole > tetrazole > *iso*-oxazole.

Molecular mechanics calculations on $[Fe(pz)_6]^{2+}$ (pz = pyrazole) suggest that it instead reflects intramolecular, interligand steric hindrance between the C–H or N–H groups adjacent to the coordinated N-donor on each ligand [49]. This disfavours the Fe–N bond contraction associated with a spin-state transition. Such steric repulsion will be less significant for *iso*-oxazole or tetrazole complexes, which have only one C–H or N–H group adjacent to their ligand N-donors, than for imidazoles which have two. All known iron(II) complexes of 1,2,4-triazoles have polynuclear or polymeric structures and are outside the scope of this article, but have been reviewed in [59].

Table 1
Iron(II) complexes of isooxazole and 1-alkyltetrazole derivatives

	Spin-state or $T_{1/2}$ (K)	Form of spin-state transition	Spin states of crystal structure(s)	Other measurements[f]	Refs.
$[Fe(\mathbf{5})_6][BF_4]_2$	91, 192	gradual, 2 steps, 87% complete	HS, 1:2 HS:LS	Cal, Mag, Vis	[60,61]
$[Fe(\mathbf{5})_6][ClO_4]_2$	213	abrupt, 9 K hysteresis	HS	Cal, DFT, Mag, Möss, T_1, Vis	[60–64]
$[Fe(\mathbf{5})_6][Fe(\mathbf{5})_4(OH_2)_2][BF_4]_4$	173	n/a	HS, LS	Mag	[59]
$[Fe(\mathbf{6})_6][BF_4]_2$	75	gradual, 50% complete	$3 \times$ HS, 1:1 HS:LS, LS	IR, LIESST, Mag, Möss, Pos, Quen, T_1, Vis	[66,67,69–74]
$[Fe(\mathbf{6})_6][ClO_4]_2$	66	gradual, 50% complete	HS	LIESST, Möss	[68,69]
$[Fe(\mathbf{6})_6][PF_6]_2$	207	gradual		Möss	[77]
$[Fe(\mathbf{6})_6][CF_3SO_3]_2$	173	abrupt, 12 K hysteresis, 33% complete		Mag, Möss, Quen	[78,79]
$[Fe(\mathbf{7})_6][BF_4]_2$	105	gradual, 67% complete	HS	IR, LIESST, Mag, Möss, Pos, Press, T_1, Vis	[32,66,68,73,74,80]
$[Fe(\mathbf{8})_6][BF_4]_2$	108, 137	gradual, 2 steps, 67% complete		IR, Mag, Möss	[84]
$[Fe(\mathbf{8})_6][ClO_4]_2$	130	gradual		IR, Mag, Möss	[84]
$[Fe(\mathbf{9})_6][BF_4]_2$	142, 190[a] 108, 190[b]	gradual, 2 steps	HS[e], LS[e]	Mag, Möss, PD, Vis	[81,82]
$[Fe(\mathbf{9})_6][ClO_4]_2$	135[a], 177[a] or 177[b]	gradual, 2 steps, 17 K hysteresis on first step.[a] gradual, 50% complete[b]	HS[e], LS[e]	Mag, Möss, PD, Vis	[81,83]
$[Fe(\mathbf{9})_6][PF_6]_2$	121, 185	gradual, 2 steps		Mag, Möss, PD, Vis	[81]
$[Fe(\mathbf{10})_6]X_2$ ($X^- = BF_4^-$, ClO_4^-)	150–166	both gradual	HS[e], LS[e] (BF_4^-)	IR, Mag, Möss, PD	[84,85]
$[Fe(\mathbf{11})_6]X_2$ ($X^- = BF_4^-$, ClO_4^-)	150–205	both gradual, 2 steps (ClO_4^-)	HS[e], LS[e] (BF_4^-)	IR, Mag, Möss, PD	[84,85]
$[Fe(\mathbf{12})_6][BF_4]_2$	125[c] or 131[d]	abrupt, 7 K hysteresis[d]	$3 \times$ HS, LS[e]	Brill, DFT, EPR, INS, IR, LIESST, Mag, Möss, Pos, PD, PND, Press, Raman, T_1, XAS	[20,22,65–67,69,73,74,87–93,95–106]
$[Fe(\mathbf{12})_6][ClO_4]_2$	150	gradual	HS	Brill, Mag, Möss, μSR	[69,94,104]
$[Fe(\mathbf{12})_6][PF_6]_2$	74	abrupt	$2 \times$ HS	LIESST, Mag, Möss, Press, Vis	[107]
$[Fe(\mathbf{12})_6][CF_3SO_3]_2 \cdot 2(\mathbf{12})$	178	abrupt		Cal, Mag, Möss, Vis	[71]
$[Fe(\mathbf{13})_6][BF_4]_2$	72	ca. 30% complete		IR, Mag, Möss	[67]
$[Fe(\mathbf{14})_6][BF_4]_2$	148	gradual		IR, LIESST, Mag, Möss, Vis	[66,108]
$[Fe(\mathbf{15})_6][BF_4]_2$	120	gradual, 85% complete		IR, LIESST, Mag, Möss, Vis	[66,108]
$[Fe(\mathbf{16})_6][BF_4]_2$	152	gradual		IR, LIESST, Mag, Möss, Vis	[66,108]

See also Ref. [66] for some additional examples.

[a] Powder sample.

[b] Crystalline sample.

[c] Rapid Cooling.

[d] Slow Cooling.

[e] Structure refinement from powder diffraction data.

[f] Brill = Brillouin spectroscopy; Cal = calorimetry; Dielec = variable temperature dielectric constant measurements; DFT = density functional calculations; EPR = variable temperature EPR of trace copper(II) or manganese(II) dopant ions; HF-EPR = high-frequency EPR of the high-spin iron(II) complex; HF-Mag = low → high spin conversion using a very strong magnetic field; IE = deuterium isotope effect measurements; INS = inelastic neutron scattering; IR = variable temperature infrared spectroscopy; LIESST = light-induced excited spin state trapping experiments; Mag = variable temperature magnetic susceptibility; MM = molecular mechanics calculations; Möss = Mössbauer spectroscopy; μSR = muon spin resonance; PND = polarised neutron diffraction; Pos = positronium annihilation lifetime measurements; PD = variable temperature powder diffraction; Press = magnetic susceptibility or Mössbauer spectroscopy measurements under high pressure; Quen = thermal trapping of high-spin state at low temperatures by rapid cooling; Sol = spin-crossover temperature determination in solution by variable temperature UV/Vis or Evans method measurements; stress = magnetic susceptibility measurements under mechanical stress; T_1 = variable temperature solid-state NMR T_1 measurements; TEM = transmission electron microscopy; Vis = diffuse reflectance or single crystal absorption UV/Vis/NIR; XAS = X-ray absorption spectroscopy (EXAFS or XANES).

Single crystals of $[Fe(\mathbf{5})_6][BF_4]_2$ (space group $P\bar{3}$) contain two independent complex dications, both with crystallographic C_3-symmetry, one of which has twice the occupancy of the other [59]. This compound shows a gradual, two-step spin-state transition; two-thirds of the iron centres become low-spin at 192 K, and the other one-third at 91 K [60,61], leaving a 13% residual high-spin content below 50 K. At 130 K the crystalline compound has undergone a crystallographic phase transition to $P\bar{1}$ [60]. The low temperature phase contains three independent complex molecules, all now on general positions: two of these contain low-spin iron centres, while

the third one is high-spin. Interestingly, while $[Fe(\mathbf{5})_6][ClO_4]_2$ is isostructural with the BF_4^- salt at room temperature [60], it undergoes a very different spin-crossover. This proceeds in a single abrupt step with a 9 K hysteresis loop centred at 213 K, to 94% completeness [61,62]. Single crystals of this material do not undergo the crystallographic phase transition that operates for the BF_4^- salt [60], and clearly all the iron centres in $[Fe(\mathbf{5})_6][ClO_4]_2$ that undergo a spin-state transition, do so at the same time. The $[Fe(\mathbf{5})_6]^{2+}$ moieties in the double salt $[Fe(\mathbf{5})_6][Fe(\mathbf{5})_4(OH_2)_2][BF_4]_4$ undergo spin-crossover at 173 K [59]. Density functional (DF) [63] and hybrid density functional/molecular mechanics (DF/MM) calculations [64] have both predicted a high-spin ground state for $[Fe(\mathbf{5})_6]^{2+}$ at 0 K, contrary to what is observed.

The spin-crossover behaviour of homoleptic Fe(II) 1-alkyltetrazole complexes has been heavily studied [59,65]. A complete list of known materials of this type is given in Table 1. Only those examples that show unusual structural or physical chemistry will be discussed in detail, however. In addition to the compounds in Table 1, seven other $[Fe(Rtz)_6][BF_4]_2$ (Rtz = a 1-alkyltetrazole with R ranging from *n*-butyl to *n*-octadecyl) complexes have been studied by variable temperature IR spectroscopy with a view to determining their spin transition temperatures. However, while the spectra are described in detail, the measured $T_{1/2}$ values were not reported [66].

The salts $[Fe(\mathbf{6})_6]X_2$ ($X^- = BF_4^-$ [67] and ClO_4^- [68]) exhibit very similar spin-transitions, which occur gradually at very low temperatures, centred near 70 K. In both cases, the transition only proceeds to 50% completeness. Crystalline $[Fe(\mathbf{6})_6][BF_4]_2$ and $[Fe(\mathbf{6})_6][ClO_4]_2$ are isostructural, containing two unique centrosymmetric half-molecules in their asymmetric unit that are both high-spin at higher temperatures [69]. At 10 K, however, one of the two iron sites in the BF_4^- salt has become low-spin while the other remains high-spin [70]. The spin-states of each iron site in both salts at 10 K can be shuttled between their different spin-states by irradiation with the appropriate laser wavelength, selectively affording fully high-spin and fully low-spin forms of the materials [68,70,71]. Single crystal structures of all three forms of the compound (high-spin, low-spin and mixed) were obtained at 10 K [70]. The relaxation of both forms of $[Fe(\mathbf{6})_6][BF_4]_2$ back to their 1:1 high:low-spin ground state shows complicated kinetics, consistent with a high degree of cooperativity between the two sites. The different zero-point energy differences between the high- and low-spin states ($\Delta E^0_{HL} = E^0_{HS} - E^0_{LS}$) for the two molecules in the BF_4^- crystal at 20 K was determined, at $+120\ cm^{-1}$ for the low-spin site and $-60\ cm^{-1}$ for the high-spin one [71]. The fully high-spin form of $[Fe(\mathbf{6})_6][BF_4]_2$ can also be trapped quantitatively at 10 K by thermal quenching [72]. Thermal spin-crossover and LIESST phenomena in the diluted materials $[Fe_xM_{1-x}(\mathbf{6})_6][ClO_4]_2$ (M = Zn [75] and Ni [76]) have also been studied.

At room temperature, $[Fe(\mathbf{6})_6][CF_3SO_3]_2$ contains a single, unique high-spin iron environment [78,79] which, between 175 and 195 K, undergoes a change to a second high-spin crystallographic phase of unknown structure that also only contains one iron site [78]. Upon further cooling, a cooperative spin-transition is observed centered at 173 K with a 12 K hysteresis loop is observed that is only 33% complete [78,79]. No structural information below the transition temperature is available. While $[Fe(\mathbf{6})_6][CF_3SO_3]_2$ does not exhibit a LIESST effect, its fully high-spin form can be trapped by thermal quenching to 5 K. The quenched metastable material has an indefinite lifetime below the unusually high temperature of 103 K [79].

Only the BF_4^- salt of $[Fe(\mathbf{7})_6]^{2+}$ has been described to date [67]. At room temperature the crystalline material contains two different complex molecule environments: one centrosymmetric half-molecule, and one whole molecule on a general crystallographic site [80]. Upon cooling, the wholly occupied molecular site undergoes a gradual high → low-spin transition centred at 105 K; the second, half-occupied molecule remains high-spin at all temperatures. Spin-crossover in the bulk material is therefore only 67% complete at 5 K [67,80]. The high-spin site remains high-spin at 60 K, under applied pressures of up to 1.2 kbar [80]. As for $[Fe(\mathbf{6})_6][BF_4]_2$ (see above), however, metastable fully high-spin *and* fully low-spin forms of $[Fe(\mathbf{7})_6][BF_4]_2$ can be produced by laser irradiation at 20 K [32,80]. This implies that spin-crossover at the half-occupied iron site is thermodynamically accessible, but may exhibit too wide a thermal hysteresis to be observed on thermal cooling. Analysis of the relaxation kinetics of this site implies that its thermal transition temperature in warming mode is ca. 77 K [32].

Powder diffraction has shown that $[Fe(\mathbf{9})_6]X_2$ ($X^- = BF_4^-$ and ClO_4^-), $[Fe(\mathbf{10})_6][BF_4]_2$ and $[Fe(\mathbf{11})_6][BF_4]_2$ are all isostructural [81–84], and the structures of the high-spin and low-spin forms of all four salts have been solved and refined from synchrotron powder diffraction data [82–84]. These compounds retain the same unit cell and crystal symmetry at all temperatures, and contain a single centrosymmetric half-molecule in their asymmetric unit. It is therefore unusual that $[Fe(\mathbf{9})_6]X_2$ ($X^- = BF_4^-$, ClO_4^- and PF_6^-) [81] and the BF_4^- and ClO_4^- salts of $[Fe(\mathbf{8})_6]^{2+}$, $[Fe(\mathbf{10})_6]^{2+}$ and $[Fe(\mathbf{11})_6]^{2+}$ [85] all undergo gradual thermal spin-crossover, many of which show pronounced plateaus at around 50% conversion. The appearance of this transition is very dependent on the form of the solid samples for the $[Fe(\mathbf{9})_6]^{2+}$ salts [81]. Most dramatically, $[Fe(\mathbf{9})_6][ClO_4]_2$ undergoes a complete, two-step thermal spin-crossover as a powder, one of which shows a pronounced hysteresis loop; but only the first of these steps is observed in crystalline samples of the same material, whose transition is therefore only 50% complete [81]. No sample-dependent behaviour for the other compounds in this series was reported [85]. The different types of thermal spin-crossover shown by these isostructural complexes have been reproduced theoretically, by models describing

the effects of small changes in elastic intermolecular interactions between each molecule and its two nearest neighbours in the solid [86].

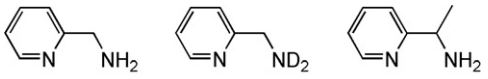
High-spin, crystalline $[Fe(\mathbf{12})_6][BF_4]_2$ contains a single one-third-occupied molecule site lying on a site of $\bar{3}$ crystal symmetry [69]. Rapid cooling of the sample retains this crystal form, producing an isostructural low-spin material [87,88] whose structure has been refined from powder diffraction data [89]. Under these conditions, spin-crossover occurs abruptly at 125 K without hysteresis [90]. However, cooling the sample more slowly to below 135 K over a 30 min period causes a small upward shift in $T_{1/2}$ with the appearance of a small hysteresis loop [67]. The low-spin form of the material under these conditions has greatly reduced crystallinity and cannot be solved by diffraction methods [69], although it may have lowered crystallographic symmetry [91]. The ''ordered'', super-cooled low-spin form can be converted to this ''disordered'' phase by annealing above 120 K [65], or by exposure to a synchrotron X-ray beam below a certain critical incident wavelength [88]. LIESST and reverse-LIESST interconversion of the spin-states in ''ordered'' low-spin $[Fe(\mathbf{12})_6][BF_4]_2$ (see below) does not convert it to its ''disordered'' phase, however [92]. Interestingly, rewarming the ''disordered'' low-spin phase cleanly regenerates the fully crystalline high-spin material [65]. Doped materials $[Fe_xZn_{1-x}(\mathbf{12})_6][BF_4]_2$ show the same cooling-controlled spin-crossover as the neat iron material for $x > 0.44$, but more dilute solids with $x < 0.44$ form the ''ordered'' low-spin phase only [90,93]. While $[Fe(\mathbf{12})_6][ClO_4]_2$ is isostructural with the BF_4^- salt at room temperature [69], its thermal spin transition is much more gradual [94].

Despite its complex behaviour, $[Fe(\mathbf{12})_6][BF_4]_2$ is one of the best characterised of all molecular spin-crossover compounds (Table 1), as it has often been used as a prototype material in the development of new physical techniques relating to spin-crossover. In particular, the first demonstration of the LIESST effect employed this compound (its relaxation temperature is 60 K) [20,22,24], as did the first ''reverse-LIESST'' high → low-spin photoconversion experiment [95]. These and other experiments on it provided the basis for interpretation of the physics of trapped spin-state relaxation [96]. More recently, the same compound has provided the first demonstration of optical hysteresis in the rates of laser-induced interconversion of high- and low-spin states [97]; and, the only spin-density map of a spin-crossover compound (by single crystal polarised neutron diffraction) obtained to date [98].

3. Bidentate ligands

3.1. 2-(Aminomethyl)pyridine

The salts $[Fe(\mathbf{17})_3]X_2$ ($X^- = Cl^-$, Br^- and I^-) were some of the first spin-crossover iron(II) compounds to be discovered (Table 2) [5]. The unsolvated chloride and bromide salts both show a relatively gradual spin-transition centred near 110 K, which proceeds to completion for the chloride salt but is only ca. 60% complete for the bromide. The iodide salt exists as an approximately 1:1 high-spin:low-spin mixture below ca. 250 K, but a small increase in μ_{eff} at 300 K implies the existence of a thermal spin-transition centred above room temperature [5]. A room temperature crystal structure determination of $[Fe(\mathbf{17})_3]I_2$ showed that its asymmetric unit contains a 1:1 mixture of the *fac* and *mer* isomers of the complex [109]. The *mer* molecule in the crystal is high-spin, while the Fe–N bond lengths in the *fac* molecule imply that it is predominantly low-spin, but with a significant high-spin fraction that was estimated at 30%.



17 **18** **19**

Much more heavily studied have been the hydrates and alcohol solvates of the chloride and bromide salts of the $[Fe(\mathbf{17})_3]^{2+}$ cation (Table 2). The monohydrate $[Fe(\mathbf{17})_3]Cl_2 \cdot H_2O$ exhibits an abrupt spin-transition centred at 250 K, with a very wide thermal hysteresis loop of 91 K by Mössbauer spectroscopy [110]. Although structural data from this phase are not available, a recent adiabatic heat capacity calorimetry study has implied that the initial high → low-spin transition in cooling mode at 199 K initially affords a metastable low-spin phase, which undergoes the reverse low → high-spin conversion in warming mode at 211 K [111]. Hence, rapid scanning of the spin-transition with descending–ascending temperature ramp gives a thermal hysteresis loop of only 12 K. However, the metastable low-spin material transforms slowly to a second, stable low-spin structure when annealed at 200 K for two weeks. This new, stable low-spin phase undergoes the reverse low → high-spin conversion in warming mode at 280 K, similar to that observed in the earlier Mössbauer study. Hence, the width of the thermal hysteresis loop shown by $[Fe(\mathbf{17})_3]Cl_2 \cdot H_2O$ depends on the conditions used to measure it. In contrast to this behaviour, the dihydrate $[Fe(\mathbf{17})_3]Cl_2 \cdot 2H_2O$ is low-spin at room temperature and below [110]. Crystals of this compound contain the *fac* isomer of the complex dication [109,113].

Although they are not perfectly isostructural, the solvates $[Fe(\mathbf{17})_3]Cl_2 \cdot MeOH$ and $[Fe(\mathbf{17})_3]Cl_2 \cdot EtOH$ adopt the same *mer* geometry at their iron site and essentially identical intermolecular hydrogen bonding networks in the crystal [14,114]. The methanol solvate exhibits a gradual thermal spin-crossover centred at 153 K [14,110,113,114], and does not undergo a crystallographic phase change during the transition [113,115]. Spin-crossover in the ethanol solvate is more abrupt, and is notable

Table 2
Iron(II) complex salts of 2-(aminomethyl)pyridine and related ligands

	Spin-state or $T_{1/2}$ (K)	Form of spin-state transition	Spin states of crystal structure(s)	Other measurements	Refs.
$[Fe(\mathbf{17})_3]Cl_2$	≈110	gradual		Mag, Möss, Sol	[5,145]
$[Fe(\mathbf{17})_3]Cl_2 \cdot H_2O$	250[a] or 205[b]	abrupt, 91 K[a] or 12 K[b] hysteresis		Cal, Möss, Press, XAS	[110–112]
fac-$[Fe(\mathbf{17})_3]Cl_2 \cdot 2H_2O$	LS		2 × LS	Mag, Möss	[109,110,113]
mer-$[Fe(\mathbf{17})_3]Cl_2 \cdot MeOH$	153	gradual	HS, 4 × mixed-spin, LS	Cal, IE, LIESST, Mag, Möss, T_1, XAS	[14,110,113–121]
mer-$[Fe(\mathbf{17})_3]Cl_2 \cdot EtOH$	114, 121	abrupt, 2 steps	8 × HS, 5 × 1:1 HS:LS, 6 × LS	Cal, EPR, IE, INS, IR, LIESST, Mag, Möss, NIESST, PES, Press, Raman, T_1, XAS	[14,110,112,114,115, 117,118,120–142]
mer-$[Fe(\mathbf{17})_3]Cl_2 \cdot CH_2{=}CHCH_2OH$	92, 131	gradual, 2 steps. discontinuity when sample is ≈35% HS	HS	Mag	[14]
mer-$[Fe(\mathbf{17})_3]Cl_2 \cdot n$PrOH	HS		HS	Mag	[14]
mer-$[Fe(\mathbf{17})_3]Cl_2 \cdot i$PrOH	145,[c] 177	gradual, 2 steps. 7 K hysteresis on first step.	HS	Mag	[14]
mer-$[Fe(\mathbf{17})_3]Cl_2 \cdot t$BuOH	HS		HS	Mag	[14]
$[Fe(\mathbf{17})_3]Br_2$	110	gradual, ca. 60% complete		Mag, Möss, Sol	[5,114,145]
$[Fe(\mathbf{17})_3]Br_2 \cdot MeOH$	120	gradual		Mag	[114]
mer-$[Fe(\mathbf{17})_3]Br_2 \cdot EtOH$	123[d]	gradual, 2K hysteresis	HS	Mag, Möss	[114,143,144]
1:1 *fac*:*mer*-$[Fe(\mathbf{17})_3]I_2$	>300	gradual, 50% complete	ca. 65% HS	Mag, Möss	[5,109]
$[Fe(\mathbf{17})_3][ClO_4]_2$	234	gradual, ca. 85% complete		Mag, Möss, Sol	[145,147,148]
$[Fe(\mathbf{17})_3][PF_6]_2$	179	gradual		Mag, Möss, Press, Sol	[145,149,150]
$[Fe(R\text{–}\mathbf{19})_3][ClO_4]_2$	90	gradual		Mag	[147]

Where known, the geometric isomer adopted by the iron centres in these compounds is given. See also Ref. [146] for an additional example, and Table 1 for the abbreviations of physical techniques.
[a] Rapid temperature scanning.
[b] Slow temperature scanning.
[c] Hysteresis only observed when high-spin fraction of the sample is between ca. 70% and 90%.
[d] Hysteresis only observed when high-spin fraction of the sample is >50%.

for being the first example of a discontinuous spin-crossover to be discovered [122]. The transition proceeds over two steps at 114 and 121 K, with a plateau between them corresponding to 50% spin conversion [123]. This narrow discontinuity had been missed in earlier studies of this material [110,114,118]. Statistical modelling predicted that the plateau region corresponds to an intermediate state containing short-range ordering of high-spin/low-spin pairs of molecules [124]. Consistent with this, early crystallographic studies [114,115,125], including one determination within the plateau region at 115 K [115], had indicated that the spin-transition in $[Fe(\mathbf{17})_3]Cl_2 \cdot EtOH$ proceeds without any change in crystal symmetry. However, a more recent variable temperature study using synchrotron radiation detected a discreet, long-range-ordered intermediate crystal phase within the plateau region, that has the same $P2_1/c$ space group as the fully high- and low-spin material, but a unit cell that has doubled along the c direction so that Z has increased from 4 to 8 [126]. The asymmetric unit of the intermediate phase contains one high-spin and one low-spin molecular environment, alternating within the 2D hydrogen-bonded layers in the lattice. The intermolecular processes responsible for ordering the high-spin/low-spin molecular pairs in the intermediate phase have been modelled theoretically [127]. Thermal spin-crossover in the doped materials $[Fe_xCo_{1-x}(\mathbf{17})_3]Cl_2 \cdot EtOH$ ($x \leqslant 0.65$) [128] and $[Fe_{0.73}Zn_{0.27}(\mathbf{17})_3]Cl_2 \cdot EtOH$ [123] proceeds smoothly and without any apparent discontinuity.

The LIESST effect has been demonstrated in $[Fe(\mathbf{17})_3]Cl_2 \cdot EtOH$, although its trapped high-spin state is only long-lived below 25 K [21]. The metastable high-spin state of a single crystal of the compound at 10 K has the same structure as the fully high- and low-spin material, and appears to decay back to its low-spin state without passing through the ordered intermediate crystal phase [129,130]. The kinetics of this LIESST relaxation imply that short-range correlations between high-spin/low-spin molecular pairs play a significant role in this process, however [131]. Continuous irradiation of the

crystal in its intermediate phase at 118 K also appears to yield the fully high-spin phase, although a full crystallographic determination was not possible [130]. While the Fe–N vibrations in the far-IR spectra of the thermal and photochemical high-spin states of $[Fe(\mathbf{17})_3]Cl_2 \cdot EtOH$ are similar [132], their ligand vibrations in the IR fingerprint region show significant differences [133]. In the light of the above crystallographic results, this has been ascribed to local differences in intermolecular interactions between ligands in the two materials [132]. The quantum efficiency of the low → high-spin conversion in $[Fe(\mathbf{17})_3]Cl_2 \cdot EtOH$ under LIESST conditions has been measured as being almost 100% [134]. Although its thermal spin-transition temperature is barely perturbed inside a strong, 7 T magnetic field, the lifetime of the LIESST excited state of $[Fe(\mathbf{17})_3]Cl_2 \cdot EtOH$ at 10 K is increased by 50% under these conditions [135]. The LIESST effect in $[Fe(\mathbf{17})_3]Cl_2 \cdot EtOH$ has also been studied by non-resonant inelastic neutron scattering [136], EXAFS [137], photoelectron spectroscopy [138], X-ray spectroscopy [139] and EPR (of cobalt(II) ions doped into the iron(II) host material) [140].

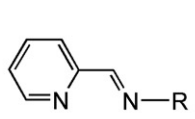
The spin transitions undergone by the deuterated materials $[Fe(\mathbf{18})_3]Cl_2 \cdot CH_3OD$ [118] and $[Fe(\mathbf{18})_3]Cl_2 \cdot C_2H_5OD$ [118,141] both take place at ca. 15 K higher temperature than for their protio-congeners, while exhibiting a similar degree of cooperativity [118]. This was the first time that an isotope effect on spin-crossover had been detected. The origin of the effect was unclear, but may reflect the influence of M–L vibrational modes in the cooperativity of the transitions; or, a change in the intermolecular hydrogen bond geometry in the crystals upon deuteration. Consistent with these explanations, deuteration at the methylene group or pyridine ring of $[Fe(\mathbf{17})_3]Cl_2 \cdot C_2H_5OH$ had a much smaller effect on $T_{1/2}$ [18]. Measurements of thermal spin-transitions [119,123,128], and rates of relaxation of the LIESST metastable high-spin states at low temperatures [120,121], in a series of doped solids $[Fe_xM_{1-x}(\mathbf{17})_3]Cl_2 \cdot MeOH$ and $[Fe_xM_{1-x}(\mathbf{17})_3]Cl_2 \cdot EtOH$ (M = Zn, Co or Mn) have been used to develop theories of cooperative transitions in bulk materials [96].

Four other alcohol solvates $[Fe(\mathbf{17})_3]Cl_2 \cdot ROH$ (R = *n*Pr, *i*Pr, allyl and *t*Bu) have also been prepared [14]. The propan-1-ol, propan-2-ol and allyl alcohol solvates are isostructural with $[Fe(\mathbf{17})_3]Cl_2 \cdot EtOH$ above, while the *t*-butanol solvate is not but shows the same 2D layered hydrogen-bonded network structure as the others. Intriguingly, the spin-transition regimes exhibited by these materials, and the methanol and ethanol solvates, are very different. The allyl alcohol solvate shows a gradual transition in two steps, centred at 92 and 131 K, with no plateau between them. Spin-crossover in the $[Fe(\mathbf{17})_3]Cl_2 \cdot i$PrOH is triggered by a crystallographic phase transition at 196 K to an intermediate phase, that also contains a doubled unit cell but differs from the one in $[Fe(\mathbf{17})_3]Cl_2 \cdot EtOH$. This intermediate phase undergoes a gradual high → low-spin conversion upon cooling to 157 K (where the material is still ca. 90% high-spin), when the original unit cell of the material is restored and the remaining transition proceeds much more rapidly on further cooling to 90 K. A narrow hysteresis loop is observed where the high-spin fraction of the material is between ca. 70% and 90% only. Finally, the propan-1-ol and *tert*-butanol solvates remain fully high-spin on cooling to 5 K. Given the near-identical crystal packing in these compounds, their very different spin-transition regimes led to the conclusion that it is currently impossible to engineer a spin-crossover compound from first principles, based purely on its molecular and long-range structure [14]. The bromide salt $[Fe(\mathbf{17})_3]Br_2 \cdot EtOH$ [114] is also isostructural with its chloride-containing congener [143] and shows an apparently smooth spin-transition from magnetic measurements, in one step centred at 123 K [114,144]. However, a narrow thermal hysteresis loop of 2 K was revealed from Mössbauer measurements, which is only present when the sample is >50% high-spin. A variable temperature unit cell study did not reveal the source of this anomaly, but showed that the low-spin and high-spin forms of the compound were isostructural [144].

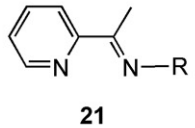
Spin-crossover in several salts of $[Fe(\mathbf{17})_3]^{2+}$ has also been measured in solution. The thermodynamics of this transition differ to a small extent in different solvents, with more polar solvents stabilising the high-spin state by accepting stronger hydrogen bonds from the complex amino groups [145,146]. The solution-phase spin-crossover does not depend on the identity of the counterions present, however [145].

3.2. 2-(Carbaldimino)pyridine derivatives and related ligands

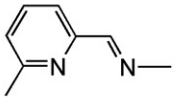
Nearly all known salts of type $[Fe(\mathbf{20})_3]^{2+}$ [151–156] and $[Fe(\mathbf{21})_3]^{2+}$ [155–158] are low-spin at room temperature, whether 'R' is H, or an alkyl or aryl group. Only one such compound has been crystallographically characterised, which contains a *mer* iron(II) complex dication [155]. However, NMR data imply that both *fac* and *mer* isomers are present in solutions of this class of complex [154,155] which, in one case, have been separated by chromatography [158]. The compound $[Fe(\mathbf{22})_3][ClO_4]_2$ shows a gradual thermal spin-transition centred near 160 K, that is 70% complete at 5 K from susceptibility and Mössbauer measurements [159]. Interestingly, $[Fe(\mathbf{23})_3]I_2 \cdot 2H_2O$ [152] and $[Fe(\mathbf{24})_3][ClO_4]_2$ [153] are both high-spin at room temperature, although no variable temperature studies were undertaken.



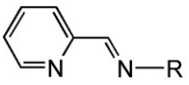
20



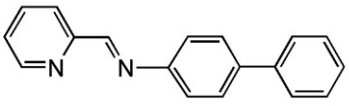
21



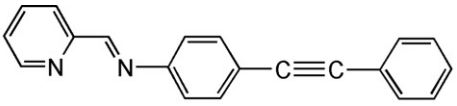
22



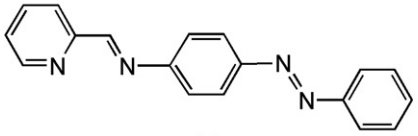
R=NMe_2, **23**
R = C_6H_4I-4, **24**
R = CH_3, **25**
R = *i*-C_3H_7, **26**
R = C_6H_5, **27**
R = $C_6H_4CH_3$-2, **28**
R = $C_6H_4CH_3$-4, **29**
R = $C_6H_3(CH_3)_2$-2,6, **30**
R = C_6H_4Cl-4, **31**
R = $C_6H_4OCH_3$-4, **32**
R = $C_6H_4OC_{16}H_{33}$-4, **33**
R = $C_6H_4(OC_{16}H_{33})_2$-3,4, **34**
R = $C_6H_4(OC_{16}H_{33})_3$-3,4,5, **35**



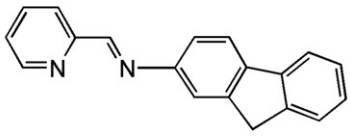
36



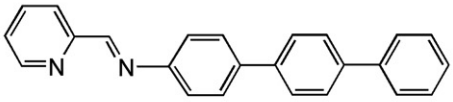
37



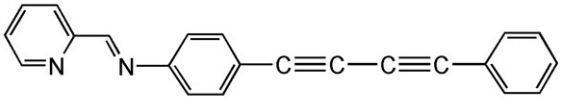
38



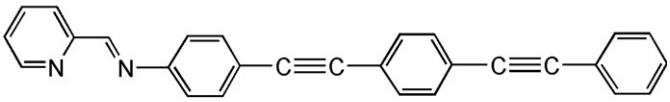
39



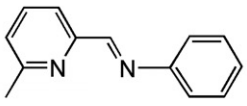
40



41



42



43

While a large number of complexes of type $[Fe(NCS)_2L_2]$ and $[Fe(NCSe)_2L_2]$ (L = a ligand of type **20**) have been shown to undergo thermal spin-transitions, only a few of them have been characterised in detail (Table 3). Most heavily studied have been complexes with ligands bearing extended aromatic Schiff base substituents like **36**–**38** and **40** [160]. All examples of this type that have been structurally characterised crystallise in one of two closely related crystal forms, in the space groups $P2_1/c$ or *Pccn*. Indeed, $[Fe(NCS)_2(\mathbf{37})_2]$ undergoes a crystallographic phase change from one form to the other during its spin transition (which contributes to the unusually wide thermal hysteresis loop shown by this compound [187]), while $[Fe(NCS)_2(\mathbf{36})_2]$ can be obtained in either polymorph from methanol solution, depending on the rate of crystallisation [181]. The α-form (*Pccn*) [30,179,180] undergoes a very abrupt thermal transition at 170 K, with a 6 K hysteresis loop [179], while the β-form ($P2_1/c$) [182] exhibits a much more gradual spin-crossover, centred at a higher temperature of 198 K [181]. The same trend does not extend to other compounds in the series, however, since $[Fe(NCS)_2(\mathbf{38})_2]$

Table 3
Iron(II) isothiocyanato and isoselenocyanato complexes of 2-(carbaldimino)pyridine derivatives

	Spin-state or $T_{1/2}$ (K)	Form of spin-state transition	Spin states of crystal structure(s)	Other measurements	Refs.
$[Fe(NCS)_2(\mathbf{25})_2]$	ca. 35:65 HS:LS[a]			Mag, Möss	[161]
$[Fe(NCS)_2(\mathbf{26})_2]$	270	gradual	HS, LS	Mag, Möss	[161–166]
$[Fe(NCSe)_2(\mathbf{26})_2]$	375	gradual	2 × LS	Mag	[166]
$[Fe(NCS)_2(\mathbf{27})_2]$	140	gradual, 45% complete		LIESST, Mag, Möss, NLO, Press	[153,162,168–176]
$[Fe(NCS)_2(\mathbf{28})_2]$	150	gradual, 35% complete at 80 K		Möss	[162,172,173]
$[Fe(NCS)_2(\mathbf{29})_2]$	186	gradual		LIESST, Mag, Möss	[24,162,165,172]
$[Fe(NCS)_2(\mathbf{30})_2]$	HS			Mag, Möss, Press	[173,175]
$[Fe(NCS)_2(\mathbf{31})_2]$	150	gradual, 35% complete at 80 K		Möss	[162,172]
$[Fe(NCS)_2(\mathbf{32})_2]$	165	gradual, 80% complete at 80 K		Möss	[162,172]
$[Fe(NCS)_2(\mathbf{33})_2]$	HS			Mag, PD	[177]
$[Fe(NCS)_2(\mathbf{34})_2]$	130	gradual, 15% complete		Cal, Mag, PD	[177]
$[Fe(NCS)_2(\mathbf{35})_2]$	217	gradual, 85% complete		Cal, Mag, PD	[177,178]
α-$[Fe(NCS)_2(\mathbf{36})_2]$	170	abrupt, 5 K hysteresis	2 × HS, 2 × LS	Cal, EPR, LIESST, Mag, Möss, NLO, Press, Quen	[24,30,33,172,175,176,179–181,183–186]
β-$[Fe(NCS)_2(\mathbf{36})_2]$	198	gradual	HS, LS	LIESST, Mag, Möss	[181,182]
$[Fe(NCS)_2(\mathbf{37})_2]$	225	abrupt, 60 K hysteresis	HS, LS	EPR, LIESST, Mag, μSR, NLO, Press	[175,176,183,187–191]
$[Fe(NCS)_2(\mathbf{38})_2]$	189	gradual, 6 K hysteresis	HS, 2 × LS	LIESST, Mag, μSR, Press	[24,166,175,180,183,188,191]
$[Fe(NCSe)_2(\mathbf{38})_2]$	255	gradual		LIESST, Mag	[24,166,188]
$[Fe(NCS)_2(\mathbf{39})_2]$	165	abrupt		LIESST, Mag	[24,183]
$[Fe(NCSe)_2(\mathbf{39})_2]$	236	gradual		LIESST, Mag	[24,183]
$[Fe(NCS)_2(\mathbf{40})_2]$	140	gradual, 60% complete	HS, 2 × mixed-spin	Mag, NLO, Press	[176,180,188]
$[Fe(NCS)_2(\mathbf{41})_2]$	HS		HS	Mag	[160]
$[Fe(NCS)_2(\mathbf{42})_2]$	n/a	25 % complete at 77 K		Mag, NLO	[176]
$[Fe(NCS)_2(\mathbf{43})_2]$	HS			Möss	[153,173]

All compounds in this series that have been crystallographically characterised contain *cis*-isothiocyanate ligands. See also Refs. [162,167,169–173] for more examples, and Table 1 for the abbreviations of physical techniques.

[a] The high-spin:low-spin ratio in the sample was essentially invariant between 78 and 298 K by Mössbauer spectroscopy and/or susceptibility measurements.

and $[Fe(NCS)_2(\mathbf{40})_2]$ respectively adopt the $P2_1/c$ and *Pccn* crystal forms, but both exhibit very gradual thermal spin-crossover [188]. Rather, the width of the thermal spin-transition in these compounds appears to correlate with two structural parameters. First, the transition becomes more cooperative as intermolecular steric contacts to the thiocyanate ligand S atoms become shorter [160,182]. Second, the cooperativity also increases with increasing trigonal distortion of the octahedral N_6 donor sphere about the high-spin iron atom (see below) [182,192].

The α- and β-forms of $[Fe(NCS)_2(\mathbf{36})_2]$ also show different LIESST behaviour, with the metastable high-spin state of the β-form being formed less efficiently under irradiation at 10 K, and less thermally stable [180]. The metastable high-spin state of α-$[Fe(NCS)_2(\mathbf{36})_2]$ can also be generated by thermal quenching, and has been crystallographically characterised in this way [30]. Comparison of their crystal structures with those of other $[Fe(NCS)_2L_2]$ complexes (L = **37**, **38**, **40**, **41** or another bidentate N-donor chelate) implied that the thermal stability of their trapped high-spin states and, by extension, their thermal spin-crossover temperatures $T_{1/2}$ are controlled by the degree of structural rearrangement of the ligand sphere taking place during spin conversion. This was quantified by an angle ('Θ') defining the degree of trigonal distortion of the six N donor atoms away from an ideal octahedral geometry [192]. A large angular rearrangement of the ligand sphere during spin-crossover results in a large difference in Θ between the low- and

Table 4
Homoleptic iron(II) complexes of *bis*-heterocyclic ligands

	Spin-state or $T_{1/2}$ (K)	Form of spin-state transition	Spin states of crystal structure(s)	Other measurements	Refs.
mer-[Fe(**47**)$_3$]X$_2$ (X$^-$ = BF_4^-, ClO_4^-)	<89	both gradual	HS (ClO_4^-)[a]	Mag, Möss, PD, Vis	[64,194]
[Fe(**47**)$_3$][PF_6]$_2$	HS			Mag, Möss	[194]
[Fe(**48**)$_3$][BF_4]$_2$ · 1/2**48**	<89	gradual		Mag, Möss	[195]
[Fe(**49**)$_3$][ClO_4]$_2$	HS			Mag, Möss	[195]
[Fe(**50**)$_3$]X$_2$ (X$^-$ = ClO_4^-, PF_6^-)	310–345	both gradual	ca. 50% HS (ClO_4^-)	Mag, Möss	[196]
[Fe(**51**)$_3$][BPh_4]$_2$	>313	gradual		Mag, Möss	[195]
[Fe(**52**)$_3$]X$_2$ (X$^-$ = BF_4^-, ClO_4^-)	250–>333	both gradual		Mag, Möss, Sol	[195]
[Fe(**69**)$_3$]X$_2$ (X$^-$ = I^-, BF_4^-, PF_6^-)	<91–150	all gradual		Mag, Möss	[197–200]
[Fe(**69**)$_3$][ClO_4]$_2$	150	gradual		IR, LIESST, Mag, Möss, NIESST	[197,199–206]
mer-[Fe(**69**)$_3$][$B(C_6H_5)_4$]$_2$	≈180	gradual	HS	LIESST, Möss	[198,203,207]
[Fe(**70**)$_3$][ClO_4]$_2$	HS	gradual		Mag, Möss	[208]
[Fe(**71**)$_3$][ClO_4]$_2$ · H_2O	205	gradual		IR, LIESST, Mag, Möss, NIESST	[203,209]
[Fe(**72**)$_3$][ClO_4]$_2$	HS			Mag, Möss	[195]
[Fe(**73**)$_3$]X$_2$ · $x$$H_2O$ (X$^-$ = BF_4^-, ClO_4^-)	137–170 or HS	gradual, sample-dependent (ClO_4^-)		Mag, Möss, PD, Vis	[194,200]
[Fe(**75**)$_3$]X$_2$ (X$^-$ = Cl^-, ClO_4^-), $CF_3SO_3^-$	all LS		LS (ClO_4^-, $CF_3SO_3^-$)	Mag, Möss	[64,211]
[Fe(**76**)$_3$]X$_2$ (X$^-$ = BF_4^-, ClO_4^-, $FeCl_4^{2-}$, $Fe(NCS)_4^{2-}$)	all LS		LS (ClO_4^-)	Mag	[212]
[Fe(**77**)$_3$][NCS]$_2$	380	gradual		Mag	[322]
[FeL$_3$]X$_2$ (L = **84**–**86**; X = PF_6^- + NCS^-, BF_4^-, $CF_3SO_3^-$ {**85** only})	all LS			Mag	[213–215]
[Fe(**87**)$_3$]X$_2$ (X$^-$ = BF_4^-, ClO_4^-)	both LS			Mag, Möss	[216]
[Fe(**88**)$_3$]X$_2$ · $n$$H_2O$ (X$^-$ = I^-, BF_4^-, ClO_4^-)	345–365	all gradual	<50% HS, LS (ClO_4^-)	Mag, Möss, Vis (BF_4^-)	[217]
[Fe(**89**)$_3$]X$_2$ · $t$$H_2O$ (X$^-$ = BF_4^-, ClO_4^-, PF_6^-)	265–>363	all gradual		Mag, Möss	[216]
[Fe(**89**)$_3$][CF_3SO_3]$_2$	235	abrupt, 12 K hysteresis		Mag, Möss	[218]
mer-[Fe(**89**)$_3$][CF_3SO_3]$_2$ · 2H_2O	350	gradual	mostly LS	Mag, Möss	[218]
[Fe(**90**)$_3$][ClO_4]$_2$	HS at RT			Mag	[219]
[Fe(**91**)$_3$][ClO_4]$_2$	225	gradual		Mag	[220]
[Fe(**92**)$_3$]X$_2$ · $n$$H_2O$ (X$^-$ = Cl^-, ClO_4^-, PF_6^-, 1/2SO_4^{2-})	140–210	all gradual		Mag and/or Möss	[221,222,224]
mer-[Fe(**92**)$_3$][BF_4]$_2$ · 2H_2O	135	gradual, 70% complete	HS, ca. 30% HS	Cal, LIESST, Mag, Möss, Quen	[221–224]
[Fe(**92**)$_3$][SO_4]$_{0.4}$[BF_4]$_{1.2}$ · 3H_2O	170	gradual		LIESST, Mag	[224]
[Fe(**93**)$_3$]X$_2$ · $n$$H_2O$ (X$^-$ = BF_4^-, ClO_4^-, PF_6^-)	HS or <89–245	gradual, sample-dependent		Mag, Möss	[222,225]
[Fe(**94**)$_3$][PF_6]$_2$ · H_2O	250	Incomplete at 78 K		Möss	[225]
mer-[Fe(**95**)$_3$]X$_2$ (X$^-$ = BF_4^-, ClO_4^-, PF_6^-)	160 (BF_4^-)	all gradual	HS (BF_4^-)	Mag, Möss	[222]
[Fe(**96**)$_3$][PF_6]$_2$ · H_2O	LS			Möss	[222,225]
[Fe(**97**)$_3$]X$_2$ (X$^-$ = BF_4^-, ClO_4^-)	both LS			Mag, Möss	[226,227]
[Fe(**98**)$_3$][BF_4]$_2$	175–235	gradual (BF_4^-), abrupt (ClO_4^-)	HS, LS (ClO_4^-)[b]	Mag, Möss, Vis	[228]
[Fe(**99**)$_3$][ClO_4]$_2$	HS			Mag	[228]
[Fe(**100**)$_3$][$B(C_6H_5)_4$]$_2$	180	gradual, 65% complete at 99 K		Mag, Vis	[229]
mer-[Fe(**101**)$_3$]X$_2$ · H_2O (X$^-$ = BF_4^-, ClO_4^-)	both LS		LS (BF_4^-)	Mag, Möss	[227,230]
[Fe(**102**)$_3$] X$_2$ · $n$$H_2O$ (X$^-$ = BF_4^-, n = 0; X$^-$ = ClO_4^-, n = 1)	260–265	both gradual		Mag, Möss, Vis	[228]
[Fe(**103**)$_3$]X$_2$ · $n$$H_2O$ (X$^-$ = Cl^-, NCS^-, ClO_4^-, 1/2SeO_4^{2-}, 1/2$S_2O_3^{2-}$, 1/2SeO_4^{2-})	243–>293	all gradual		Mag, Möss	[231–235]
[Fe(**103**)$_3$][$B(C_6H_5)_4$]$_2$ · 3H_2O	>293	gradual		ISC, Mag, Möss	[231,236–238,518]
[Fe(**104**)$_3$] X$_2$ (X$^-$ = I^-, BF_4^-, ClO_4^-, BPh_4^-)	LS, >373 (BPh_4^-)	gradual (BPh_4^-)		Mag, Möss	[239]
[Fe(**105**)$_3$][ClO_4]$_2$ · H_2O	HS			Mag, Möss	[234]
[Fe(**106**)$_3$]X$_2$ · $n$$H_2O$ (X$^-$ = Br^-, I^-, NO_3^-, BF_4^-, [BPh_4]$^-$, [$Cr(NH_3)_2(NCS)_4$]$^-$)	<80–>300	all gradual		ISC (BPh_4^-), Mag, Möss, Vis (Br^-, NO_3^-, BF_4^-)	[235,236,240–245]

(*continued on next page*)

Table 4 (*continued*)

	Spin-state or $T_{1/2}$ (K)	Form of spin-state transition	Spin states of crystal structure(s)	Other measurements	Refs.
mer-[Fe(**106**)$_3$][ClO$_4$]$_2$ · nH$_2$O (n = 1, 2)	141–230	both gradual	HS (n = 2)	Cal, IR, Mag, Möss, PD, Vis, XAS	[234,240–242,246,247]
[Fe(**107**)$_3$]X$_2$ · nH$_2$O (X$^-$ = I$^-$, BF$_4^-$, ClO$_4^-$)	all >300	all gradual		Mag, Möss	[239,248,466]
[FeL$_3$][ClO$_4$]$_2$ (L = **108**, **109**)	both HS			Mag, Möss (**108**)	[245,249]
[Fe(**110**)$_3$][ClO$_4$]$_2$ (2 phases)	LS or 110	abrupt, ca. 75% complete at 83 K		Mag, Möss	[250]
mer-[Fe(**111**)$_3$][BF$_4$]$_2$	LS		LS		[251]
fac-[Fe(**116**)$_3$][BF$_4$]$_2$ · 2H$_2$O	LS		2 × LS	Mag	[252]
mer-[Fe(**116**)$_3$][ClO$_4$]$_2$ · H$_2$O	LS		LS	Mag	[252]
[Fe(**117**)$_3$][ClO$_4$]$_2$	277	gradual, ca. 68% complete		Mag	[253]
[Fe(**118**)$_3$] X$_2$ · nH$_2$O (X$^-$ = BF$_4^-$, ClO$_4^-$, PF$_6^-$, 1/2SO$_4^{2-}$)	HS or 182–>350	all gradual	<50% HS, LS (ClO$_4^-$)	Mag	[253]
[Fe(**119**)$_2$(**119**–H)]X · 2H$_2$O (X$^-$ = BF$_4^-$, ClO$_4^-$)	130–150	both gradual		Mag, Möss	[218]
mer-[Fe(**119**)$_3$][BF$_4$]$_2$ · 1.5H$_2$O	HS at RT		HS		[218]
[Fe(**120**)$_3$][BF$_4$]$_2$	310	gradual		Mag, Möss, Vis	[254]
[Fe(**120**)$_3$][ClO$_4$]$_2$ (3 phases)[c]	LS, 232, or >323	abrupt, 5 K hysteresis (232) or gradual (>323)		Mag, Möss	[227,254]
[Fe(**121**)$_3$]X$_2$ (X$^-$ = BF$_4^-$, ClO$_4^-$)	≈340	both gradual	LS (BF$_4^-$)	Mag, Möss, Sol	[254,255]
[Fe(**122**)$_3$]X$_2$ (X$^-$ = ClO$_4^-$, FeCL$_4^{2-}$)	both LS			Mag	[256]
[FeL$_3$][ClO$_4$]$_2$ (L = **123**, **124**)	both LS			Mag	[256]
[Fe(**126**)$_3$]X$_2$ (X$^-$ = ClO$_4^-$, [BPh$_4$]$^-$)	both LS			Mag	[256]
[Fe(**127**)$_3$]X$_2$ · nCH$_3$OH (X$^-$ = BF$_4^-$, 1/2CO$_3^{2-}$)	both HS		HS (CO$_3^{2-}$)	Mag, Möss	[257,258]
[Fe(**128**)$_3$]X$_2$ · nH$_2$O (X$^-$ = Cl$^-$, ClO$_4^-$)	both HS		HS (Cl$^-$, ClO$_4^-$)	Mag	[259,260]
[Fe(**129**)$_3$]X$_2$ (X$^-$ = ClO$_4^-$, BPh$_4^-$)	HS, 116 (ClO$_4^-$)	abrupt (ClO$_4^-$)		Mag, Möss	[261]
[Fe(**130**)$_3$]X$_2$ (X$^-$ = ClO$_4^-$, BPh$_4^-$)	<93–310	both gradual		ISC (ClO$_4^-$), Mag, Möss	[238,261,262]
[FeL$_3$][ClO$_4$]$_2$ (L = **131**–**134**)	all HS			Mag, Möss	[216,255,261]

Where it is known, the geometric isomer adopted by the iron centres in those compounds containing unsymmetric chelate ligands is given. Homoleptic complexes of unhindered 2,2′-bipyridines (e.g. **44**–**46** and related ligands) and 1,10-phenanthrolines (e.g. **80**–**97** and related ligands), which are all low-spin [193], are not listed. See Ref. [248] for an additional example, and Table 1 for the abbreviations of physical techniques.

[a] Crystals contained half an equivalent of uncoordinated ligand.

[b] Crystallographic disorder of the coordinated ligands meant that it could not be determined whether the compound adopts the *fac* or *mer* geometric isomer.

[c] The "gradual" phase of this compound transforms to the "abrupt" phase upon heating to 323 K.

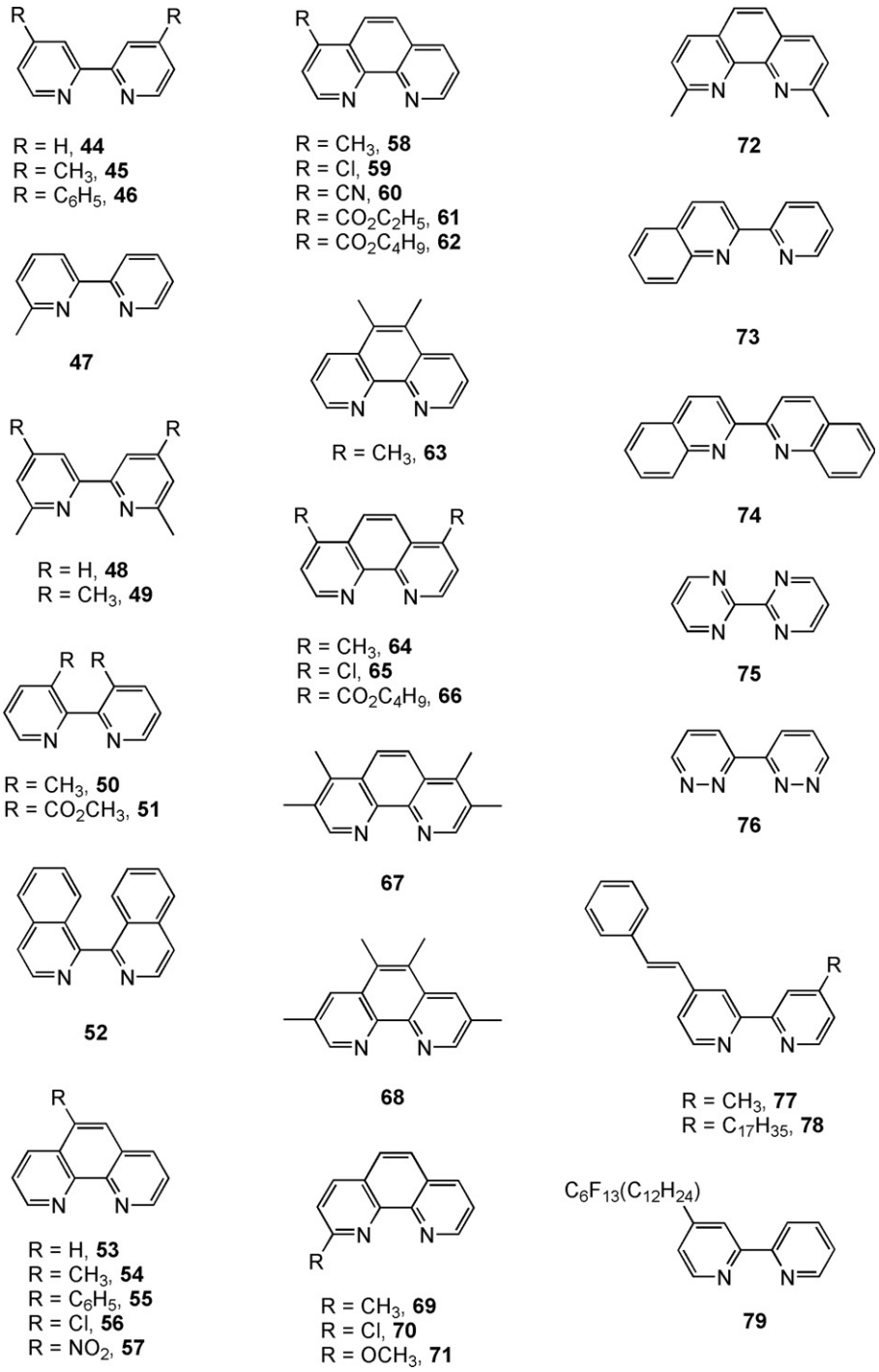
high-spin forms ('$\Delta\Theta$'). There is an almost linear correlation of $\Delta\Theta$ with $T_{1/2}$ in this series of materials [192]. The low → high-spin conversion of α-[Fe(NCS)$_2$(**36**)$_2$] has also been achieved by irradiation at 170 K, inside its thermal spin-transition hysteresis loop where the high- and low-spin forms of the compound are indefinitely stable [33]. However, [Fe(NCS)$_2$(**26**)$_2$] does not undergo the LIESST effect upon laser irradiation at 10 K [166].

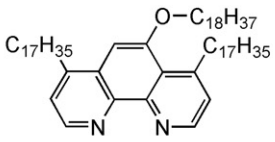
The compounds [M(NCS)$_2$(**36**)$_2$] and [M(NCS)$_2$(**37**)$_2$] (M = Mn, Fe, Co, Ni and Zn) show second-order hyperpolarisabilities β of up to 800×10^{-30} esu in acetonitrile solution [176]. The magnitude of β increases in the order Mn > Fe > Co > Ni > Zn, correlating with the number of unpaired electrons at the metal ion (assuming they are all high-spin in solution; [Fe(NCS)$_2$(**39**)$_2$] is high-spin at room temperature at room temperature in this solvent). The iron compounds [Fe(NCS)$_2$L$_2$] with different 'L' ligands show the trends in β of **40** > **36** > **27**; and, **42** > **37** > **27** [176]. Acetonitrile solutions of [Fe(NCS)$_2$(**36**)$_2$] at room temperature also show a very high third-order non-linear optical susceptibility γ, of -130000×10^{-36} esu [186].

3.3. Bipyridines and other, directly linked, bis-heterocyclic ligands

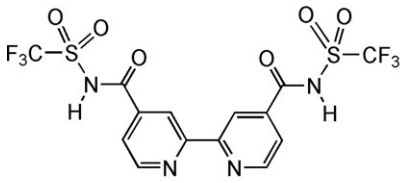
As for [Fe(**20**)$_3$]$^{2+}$ in the previous section, many [FeL$_3$]$^{2+}$ complexes with *bis*-pyridyl donor 'L' ligands are low-spin [193]. The reduction in ligand field required to afford a spin-transition centre with this ligand type has been achieved in three ways, however. First, is by substitution at the 6-position of *one* of the pyridyl rings, as in [FeL$_3$]$^{2+}$ (L = **47** and **69**–**71**). This induces steric repulsion within the coordination shell, making the high-spin state (with its longer Fe–N bonds) more favourable. Bipyridyls disubstituted at the 6 and 6′ positions (as in **48**, **49** and **74** for example) are too bulky for a homoleptic [FeL$_3$]$^{2+}$ complex to form [195,200]. Second, is by inducing conformational strain into the bipyridyl backbone. Hence, salts

of $[FeL_3]^{2+}$ with L = **50**–**52** all undergo thermal spin-transitions centred at 250 K or above, which has been ascribed to sterically-induced twisting of the bipyridyl ligands [195,196]. This reduces covalent overlap between the metal ion and the ligand lone pairs, which are no longer oriented towards the metal d-orbitals. Finally, replacement of one or both pyridyl donors in the bidentate ligand by a less basic heterocycle (usually an azole) can also afford a homoleptic iron(II) spin-crossover complex. The majority of the compounds listed in Table 4 are of this type. A transient high-spin state of $[Fe(\mathbf{44})_3]^{2+}$ doped into other $[M(\mathbf{44})_3]^{2+}$ hosts can be photogenerated, if the host metal centre 'M' is larger than iron(II), since the reduced chemical pressure of the lattice surrounding each iron centre will favour its larger high-spin form. The (rapid) high → low-spin relaxation rates of the resultant high-spin $[Fe(\mathbf{44})_3]^{2+}$ centres correlate perfectly with the radius of the host metal 'M' [424]. High-spin states

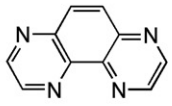




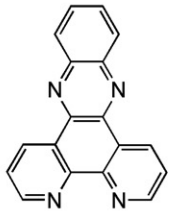
80



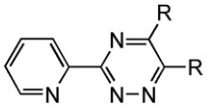
81



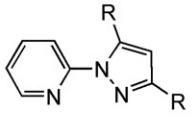
82



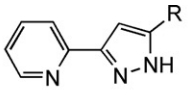
83



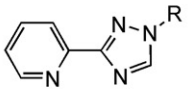
R = CH_3, **84**
R = C_6H_5, **85**
R = C_5H_4N-2, **86**



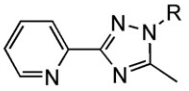
R = H, **87**
R = CH_3, **88**



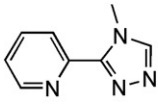
R = H, **89**
R = CH_3, **90**
R = C_6H_5, **91**



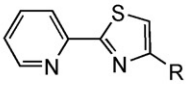
R = H, **92**
R = CH_3, **93**



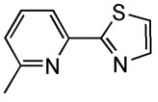
R = H, **94**
R = CH_3, **95**



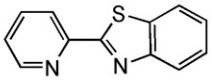
96



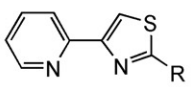
R = H, **97**
R = CH_3, **98**



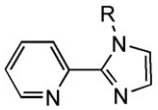
99



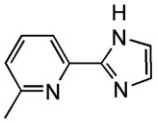
100



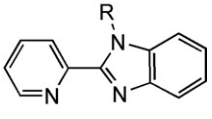
R = H, **101**
R = CH_3, **102**



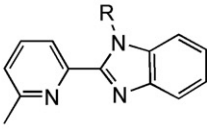
R = H, **103**
R = CH_3, **104**



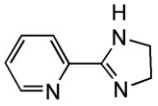
105



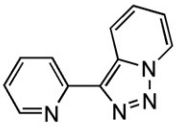
R = H, **106**
R = CH_3, **107**



R = H, **108**
R = CH_3, **109**



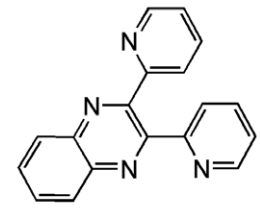
110



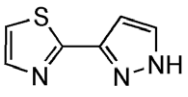
111

of $[Fe(\mathbf{44})_3]^{2+}$ and $[Fe(\mathbf{53})_3]^{2+}$ have also been detected by Mössbauer emission spectroscopy following nuclear decay of their corresponding, high-spin ^{57}Co analogues (the NIESST effect) [31,210].

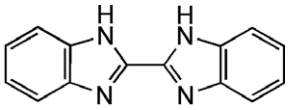
Only five $[FeL_3]^{2+}$ complex salts in Table 4 have been reported to undergo a cooperative thermal spin-transition, namely: anhydrous $[Fe(\mathbf{89})_3][CF_3SO_3]_2$ [218]; $[Fe(\mathbf{98})_3][ClO_4]_2$ [228]; one of the two solid forms of $[Fe(\mathbf{110})_3][ClO_4]_2$ [250]; one of three apparently different crystal phases of $[Fe(\mathbf{120})_3][ClO_4]_2$ [254]; and, $[Fe(\mathbf{129})_3][ClO_4]_2$ [261]. The only one of these compounds to exhibit significant thermal hysteresis in its spin transition is $[Fe(\mathbf{89})_3][CF_3SO_3]_2$. A crystallographic study of $[Fe(\mathbf{98})_3][ClO_4]_2$ showed that its abrupt spin-crossover is not mediated by a crystallographic phase change [228]; no structural data are available for the rest of the compounds. Aerial oxidation of $[Fe(\mathbf{129})_3][ClO_4]_2$ yields the iron(III), mono-deprotonated ligand complex $[Fe(\mathbf{129}–H)(\mathbf{129})_2][ClO_4]_2$ which also undergoes a



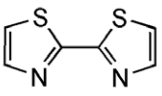
112



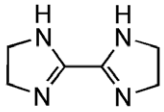
119



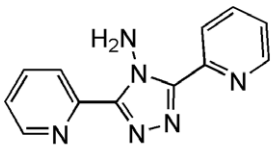
128



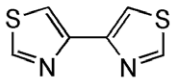
120



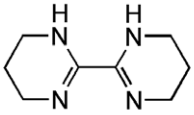
129



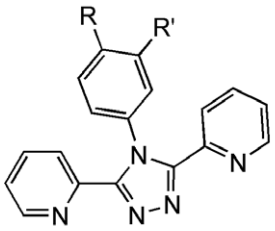
113



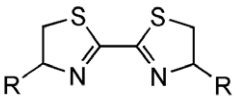
121



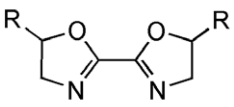
130



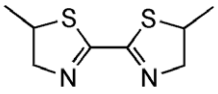
R = H, R' = CH_3, **114**
R = CH_3, R' = H, **115**



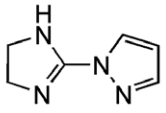
R = H, **122**
R = CH_3, **123**
R = C_2H_5, **124**



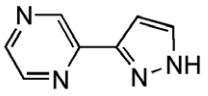
R = H, **131**
R = CH_3, **132**



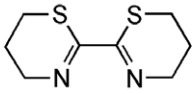
125



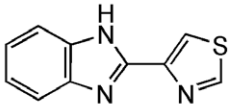
133



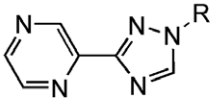
116



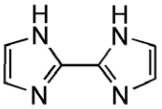
126



134



R = H, **117**
R = CH_3, **118**



127

thermal spin-transition [261]. Self-exchange between these two compounds, and oxidation of TEMPO by the iron(II) complex, both proceed by hydrogen-atom transfer [262].

All the other complexes in Table 4 that undergo spin-crossover do so in a gradual and often incomplete manner, that in at least some cases varies significantly between samples. Complex salts of **92**–**96** exhibit heterogeneous iron environments by Mössbauer spectroscopy in the solid, which undergo spin-crossover at different rates, or to differing degrees, upon cooling [220,223,225]. In only one case has this information been combined with a variable temperature crystallographic investigation, for $[Fe(\mathbf{92})_3][BF_4]_2 \cdot 2H_2O$, which undergoes a gradual spin-crossover centred at 135 K that is only 70% complete [221,223,224]. Crystals of this compound contain just one unique iron site, with anions and solvent molecules that are very badly disordered in layers between the complex dications. The

symmetry and intermolecular packing of this structure do not change across the temperature range of the spin-transition, which led to the conclusion that the multiple iron sites detected in this material by Mössbauer spectroscopy simply reflect local heterogeneities in their intermolecular environments, caused by the aforementioned anion and solvent disorder [223]. It is unclear whether this conclusion can be generalised towards other complexes of **92**–**96**, or to other compounds in Table 4 that show poorly-defined spin-transitions, most of which have only a single type of iron site by Mössbauer (see e.g. [195,216,218,228,239,254]). Other possible origins of the gradual, often incomplete spin-crossover in the compounds in Table 4 could include: the co-crystallisation of *fac* and *mer* isomers in the bulk material; linkage isomerism (for ligands like **92**–**95**, **117** and **118** for example, which could coordinate through the triazole *N*2 or *N*4 atoms); and/or, co-crystallisation of racemic and optically pure polymorphs of these chiral molecules.

Bidentate ligands that form low-spin $[FeL_3]^{2+}$ complexes can often yield compounds of the $[Fe(NCS)_2L_2]$ type that do show spin-crossover (Table 5). The compounds $[Fe(NCS)_2(\mathbf{44})_2]$ [263] and $[Fe(NCX)_2(\mathbf{53})_2]$ (X = S and Se) [4] were among the first iron(II) spin-crossover compounds to be identified. Early reports described that the appearance of the thermal spin-transition in all these materials varies considerably between samples, which led to the suggestion that these materials crystallise as more than one polymorph [4,263,264]. Since more recent studies showed that their spin-crossover is very dependent on sample history [269,287,289], and there are no structural data from a putative second polymorph, this remains an open question [50,112,304]. The spin-transition in unground samples of each compound is very abrupt, and shows a small hysteresis loop of no more than 1 K. The crystal forms that have been characterised for all three compounds are all isostructural (in the orthorhombic space group *Pbcn*), contain *cis*-octahedral iron(II) centres, and do not undergo a crystallographic phase change during spin-crossover [275,276,285,286,308]. While the unit cell of a second orthorhombic polymorph of $[Fe(NCS)_2(\mathbf{44})_2]$ has also been reported [263], no more detailed structural information on this form is available. Attempts to synthesise $[Fe(NCSe)_2(\mathbf{44})_2]$ yielded instead a product of formula $[Fe_3(\mathbf{44})_7(NCSe)_6]$, whose structure is uncertain but which contains two low-spin and one high-spin iron centres [277].

Both $[Fe(NCS)_2(\mathbf{44})_2]$ and, in particular, $[Fe(NCS)_2(\mathbf{53})_2]$ are some of the best characterised spin-crossover complexes (Table 5), and have often been used as prototype materials in the demonstration of new aspects of the spin-crossover phenomenon. Particular highlights in their chemistry include some of the first studies of the LIESST phenomenon [21,271]; the first demonstration of the NIESST effect in a spin-crossover compound [270,287]; the first conclusive observation of the perturbation of a thermal spin-transition by a strong, continuous or pulsed, magnetic field [291]; and, the demonstration that spin-crossover in $[Fe(NCS)_2(\mathbf{53})_2]$ (and $[Fe(NCS)_2(\mathbf{122})_2]$) is also reflected in changes in their dielectric constants, leading to potential applications in dielectric memory devices [11]. The low- and (trapped) high-spin forms of $[Fe(NCS)_2(\mathbf{53})_2]$ [286] and $[Fe(NCSe)_2(\mathbf{53})_2]$ [308] have been crystallographically characterised at very low temperatures. Interestingly, the metastable high-spin forms of both compounds at ca. 30 K show small, but significant, differences from their thermally stabilised high-spin forms at room temperature, particularly in the Fe–NCX bond length and the intermolecular contacts in the crystal. That has been attributed to anisotropic contraction of their crystals on cooling between the two very different temperatures of the experiments. This leads to different intermolecular crystal pressures in the two structures, resulting in changes in the way the molecules pack together and deformation of the ligand shell about the rather plastic high-spin iron(II) ions.

Like $[Fe(NCS)_2(\mathbf{44})_2]$ and $[Fe(NCS)_2(\mathbf{53})_2]$, most of the other complexes in Table 5 that have been crystallographically characterised also have *cis*-isothiocyanate (or analogous) ligands. However, all except one example [340] of complexes of the (pyrid-2-yl)triazolyl-donor ligands **111** and **113**–**115** instead adopt a *trans* stereochemistry [251,334–340]. Most heavily studied of these is the series $[FeX_2(\mathbf{113})_2]$ ($X^- = NCS^-$, $NCSe^-$, $\{NC\}_2N^-$, $tcnq^-$). The thiocyanate and selenocyanate compounds both crystallise in two different unsolvated polymorphs with the same $P2_1/n$ crystal symmetry. The α-polymorph of both compounds undergoes a relatively gradual but well-defined thermal spin-crossover on cooling [334,335], but the β-polymorph remains high-spin at all temperatures [337]. While the geometries of the complex molecules in the two polymorphs are very similar, it is noteworthy that the Fe–N bonds in the β-crystals are consistently longer than in the α-form, by up to 0.04 Å [337]. The increased structural rearrangement that would be required to produce a putative low-spin form of the β-polymorph may be responsible for its remaining high-spin on cooling. A similar polymorphism between spin-crossover and high-spin crystal forms is also shown by $[Fe(NCS)_2(\mathbf{112})_2]$, although this compound adopts the *cis*-geometric isomer [348].

The thermal spin-transition in $[Fe(N\{CN\}_2)_2(\mathbf{113})_2]$ has very low $T_{1/2}$ of 86 K, with a pronounced discontinuity at around 50% conversion, and only proceeds to 63% completeness at a normal rate of cooling [338]. The discontinuity may reflect the fact that two distinct crystal phases of this material have been identified, which could both be present in the bulk material [339]. The high-spin state of this material can be trapped at low temperatures by irradiation or thermal quenching. Importantly, the thermally trapped material relaxes to a fully low-spin form upon rewarming to ca. 50 K, showing that the low-spin state of this material is accessible. This implies that its incomplete spin-crossover reflects partial kinetic trapping of the high-spin state at the very low temperatures involved. Single crystal structures of the trapped metastable high-spin state of $[Fe(N\{CN\}_2)_2(\mathbf{113})_2]$ at 15 K have been reported, by

Table 5
Iron(II) isothiocyanato and isoselenocyanato complexes of *bis*-heterocyclic ligands, and related compounds

	Spin-state or $T_{1/2}$ (K)	Form of spin-state transition	Spin states of crystal structure(s)	Other measurements	Refs.
cis-[Fe(NCS)$_2$(**44**)$_2$]	212	abrupt, <1K hysteresis, sample-dependent	HS, 3 × LS	Cal, IR, LIESST, Mag, Möss, NIESST, Press, T_1	[62,263–276]
cis-[Fe(NCS)$_2$(**44**)$_2$] · py	260–360	gradual	2 × LS	Mag, Möss	[a]
[Fe(NCE)$_2$(**45**)$_2$] (E = S, Se)	≈320	both gradual		Mag, Möss, Press (S), XAS (S)	[112,278]
[Fe(NCE)$_2$(**46**)$_2$] (E = S, Se)	140—180, >380	both gradual, 2 steps		IR, Mag, Möss	[279]
cis-[Fe(NCS)$_2$(**53**)$_2$]	177	abrupt, <1K hysteresis, sample-dependent	2 × HS, 2 × LS	Cal, DFT, Dielec, HF-Mag, INS, IR, LIESST, Mag, Möss, μSR, NIESST, PES, Pos, Press, Raman, Stress, T_1, TEM, XAS	[4,11,21,24,50,63,73,112,117,265,266,269–274,280–306]
[Fe(NCS)$_2$(**53**)$_2$] · H$_2$O	179 or LS	abrupt, sample-dependent		Cal, Mag, Möss	[274,278,307]
cis-[Fe(NCSe)$_2$(**53**)$_2$]		abrupt, sample-dependent	2 × HS, 3 × LS	Cal, DFT, IR, LIESST, Mag, Möss, Press, T_1	[4,62,63,266,274,271,280,281,284,290,292,308]
[Fe(NCBR$_3$)$_2$(**53**)$_2$] (R = H, Ph)	LS, 355 (R = H)	gradual (R = H)		IR, Mag, Möss	[292,309,310]
[Fe(NCS)$_2$(py)$_2$(**53**)] · 1/2py	106	abrupt		Cal, IR, LIESST, Mag, Möss, Press, XAS	[50,112,271,272,293,311]
[Fe(NCS)$_2$(**44**)(**53**)]	177	gradual, sample-dependent		Mag, Möss	[312]
[Fe(NCS)$_2$L$_2$] · H$_2$O (L = **54**–**57**)	95–>292	all gradual, sample-dependent (**56**)		Cal (**54**), Mag, Möss, Press (**54**, **56**, **57**)	[278,294]
[Fe(NCS)$_2$L$_2$] (L = **58**–**61**)	145–265	all gradual		Mag, Möss	[313,314]
[Fe(NCS)$_2$L$_2$] (L = **62**, **66**)	>370	both very gradual		Mag, Möss	[161]
[Fe(NCS)$_2$(**63**)$_2$]	221	gradual		IR, LIESST, Mag, Möss, Press	[294,315]
[Fe(NCS)$_2$(**64**)$_2$]	120	abrupt, 3 K hysteresis		Möss, Mag, IR, PD, XPS, Press	[274,294,316,317]
[Fe(NCS)$_2$(**64**)$_2$] · (C$_5$H$_4$NCH$_3$-2)	174	abrupt, 56 K hysteresis		Mag, Möss, PD	[313,318]
[Fe(NCS)$_2$(**64**)$_2$] · x(C$_5$H$_5$N)	HS			Mag, Möss	[313]
[Fe(NCS)$_2$L$_2$] (L = **65**, **67**)	both HS			IR (**67**), Mag, Möss	[278,313,314]
[Fe(NCS)$_2$L$_2$] (L = **68**, **69**)	both HS			Mag (**69**), Möss, Press	[294,319]
cis-[Fe(NCS)$_2$(**72**)$_2$] · 1/4H$_2$O	HS		HS	IR, Mag, Möss, Press	[294,314,320,321]
[Fe(NCS)$_2$(**73**)$_2$]	HS			Mag	[200]
cis-[Fe(NCS)$_2$(py)$_2$(**75**)] · 1/4py	115	abrupt, 3 K hysteresis	HS	Cal, Mag, Möss, Press, XAS	[50,112,311]
[Fe(NCS)$_2$(**76**)$_2$]	LS			Mag	[212]
[Fe(NCS)$_2$L$_2$] (L = **77**–**79**)	230–295	all gradual		LIESST (**79**), Mag	[322–328]
[Fe(NCS)$_2$(**80**)$_2$]	HS above 77 K			IR	[295]
cis-[Fe(NCS)$_2$(**82**)$_2$] · xCH$_3$CN (x = 1/2, 1)	HS (x = 1/2), 168 (x = 1)	gradual (x = 1)	HS, mostly LS (x = 1)	Mag	[329]
cis-[Fe(NCS)$_2$(**83**)$_2$]	143	abrupt, 40 K hysteresis	HS	Mag, Möss, Quen	[330,331]
[Fe(NCS)$_2$L$_2$] · xH$_2$O (L = **87**, **88**)	both HS			Mag, Möss (**87**)	[216,332]
[Fe(NCE)$_2$(**89**)$_2$] · xH$_2$O (E = S, Se)	all HS		HS (S, x = 1)	Mag	[217,333]
cis-[Fe(NCE)$_2$(**89**)$_2$] · 2 H$_2$O · 1/2CH$_3$OH (E = S, Se)	HS (S), 125 (Se)	gradual, ca. 65% complete (Se)	HS, ca. 35% HS (Se)	Mag	[333]
cis-[Fe(NCS)$_2$(**103**)$_2$] · 2CH$_3$OH	HS		HS	Mag	[333]
[Fe(NCS)$_2$(**106**)$_2$]	HS			Mag, Möss	[242]
[Fe(NCS)$_2$(**141**)$_2$] · H$_2$O	118	gradual		LIESST, Mag	[251]
trans-[Fe(NCS)$_2$(**141**)$_2$] · 2CHCl$_3$	108	gradual, 20% complete	HS	Mag	[251]
[Fe(NCSe)$_2$(**111**)$_2$]	251	gradual		Cal, Mag	[251]
cis-[Fe(NCS)$_2$(**112**)$_2$]	HS		HS[b]	Mag	[334]
trans-[Fe(NCE)$_2$(**113**)$_2$] (E = S, Se; both 2 phases)	HS or 180–224	both gradual	HS (S, Se; both phases)	Cal, LIESST, Mag, Möss, Press	[24,334–337]
trans-[Fe(N{CN}$_2$)$_2$(**113**)$_2$] (2 phases)	86[c]	gradual, 2 steps, 63% complete[b]	HS (both phases) LS (1 phase only)	Mag, LIESST, Quen	[338,339]

(*continued on next page*)

Table 5 (*continued*)

	Spin-state or $T_{1/2}$ (K)	Form of spin-state transition	Spin states of crystal structure(s)	Other measurements	Refs.
trans-[Fe(tcne)$_2$(**113**)$_2$]	280	gradual	ca. 50% HS, LS	EPR, Mag, Möss	[340]
cis-[Fe(NCS)$_2$(**114**)$_2$]	HS		HS	Mag	[341]
trans-[Fe(NCS)$_2$(**115**)$_2$]	231	abrupt	HS	IR, Mag, XAS	[341]
cis-[Fe(NCS)$_2$(**122**)$_2$] (2 phases)	HS or 177	abrupt, 10 K hysteresis	HS (both phases) LS (one phase)	Cal, Dielec, EPR, HF-EPR, HF-Mag, IR, LIESST, Mag, Möss, PD, Press, T_1	[11,296,342–352]
[Fe(NCSe)$_2$(**122**)$_2$]	223	abrupt, 4 K hysteresis		Cal, IR, LIESST, Mag, Möss, PD	[343,347,349,353]
[Fe(NCS)$_2$L$_2$] (L = **123**, **124**)	both HS			Mag, Möss	[343]
[Fe(NCS)$_2$(**125**)$_2$]	205	gradual		Cal, Mag, Möss	[343,347]
cis-[Fe(NCE)$_2$(**126**)$_2$] (E = S, Se)	225 (E = S), LS (E = Se)	gradual	HS and LS (E = S)	Mag, Möss, Press (S)	[298,299,343]

Where it is known, the disposition of the isothiocyanate (or similar) ligands about the iron centres in these compounds is indicated. See Refs. [161,215,274,278] for more examples, and Table 1 for the abbreviations of physical techniques.

[a] N. Sinclair, S. R. Batten, B. Moubaraki, K. S. Murray, private communication.

[b] From a solvated crystal structure.

[c] The bulk material probably contains a mixture of both crystal phases, accounting for its spin-crossover discontinuity.

both irradiation and thermal quenching of a single crystal [339]. While its spin-transition is unexceptional in itself, [Fe(tcnq)$_2$(**113**)$_2$] is unusual as a spin-crossover compound containing two organic radical anion [tcnq$^{\bullet}$]$^-$ ligands [340].

UV irradiation of the *trans*-styryl group in CH_3CN solutions of [Fe(NCS)$_2$(**77**)$_2$] at room temperature results in its photoisomerisation to the *cis*-geometric isomer. UV/Vis spectra show that this change is accompanied by the appearance of an increased high-spin iron fraction in the solution, the first time that a ligand-driven, light-induced spin-crossover (LD-LISC) had been demonstrated at room temperature [322,323]. Gradual thermal spin-crossover in Langmuir–Blodgett films of [Fe(NCS)$_2$(**78**)$_2$] [323–326], [Fe(NCS)$_2$(**79**)$_2$] [327] and [Fe(NCS)$_2$(**80**)$_2$] [295] has been observed. The spin-transition in monolayer samples [Fe(NCS)$_2$(**78**)$_2$] [325] and [Fe(NCS)$_2$(**79**)$_2$] [327] closely resembles that in the neat solid, although in the latter compound spin-crossover is only achieved if the film is first annealed at 370 K, the melting point of the semi-fluorinated chain substituents. However, although Langmuir–Blodgett films of [Fe(NCS)$_2$(**80**)$_2$] undergo a gradual thermal spin-transition centred at 260 K, the neat solid complex is high-spin above liquid nitrogen temperatures [295]. Laser irradiation of unannealed Langmuir–Blodgett films of [Fe(NCS)$_2$(**79**)$_2$] results in ca. 20% photoconversion to its metastable high-spin form [328]. The LIESST excited state in the film decays more rapidly than in the neat solid compound, which may reflect the different pressure experienced by molecules in a monolayer compared to the solid state. The complex [Fe(NCS)$_2$(**81**)$_2$] has been patented for use as a dye in solar cells, although its spin-state properties were not recorded [354].

Several other [Fe(NCS)$_2$L$_2$] compounds, not listed in Table 5, exhibit magnetic moments of intermediate value at room temperature, that often do not vary significantly on cooling. This led to several early suggestions that they adopt an intermediate, $S = 1$ spin state [161,274,278,279,309]. Although intermediate-spin iron(III) complexes are well-established [355], genuine $S = 1$ iron(II) compounds are very rare and none of the established examples is octahedral [356]. It was subsequently shown that one of the putative intermediate-spin iron(II) compounds in Table 5 in fact contains a mixture of high- and low-spin iron sites that interconvert rapidly on the Mössbauer timescale, leading to a single averaged Mössbauer doublet for the material near room temperature [309] (see also Section 7). More generally, an intermediate spin-state would imply that the energy gap between the $d_{x^2-y^2}$ and d_{z^2} orbitals is large enough to overcome the unfavourable electron pairing energy (to prevent a high-spin state from forming), but that Δ_{oct} is small so the compound is not low-spin. That requirement implies that the $\Delta E\{d_{x^2-y^2} \rightarrow d_{z^2}\} > \Delta_{oct}$, which is extremely unlikely in an octahedral ligand field. Hence, reports of putative $S = 1$ [Fe(NCS)$_2$L$_2$] compounds should be treated with caution.

3.4. Selected complexes of other bidentate ligands

The compounds [Fe(**44**)(**135**)$_2$] and [Fe(**53**)(**135**)$_2$] are isostructural at room temperature, and undergo abrupt thermal spin-transitions at almost the same temperature with $160 \leqslant T_{1/2} \leqslant 163$ K [357]. However, [Fe(**53**)(**135**)$_2$] undergoes a crystallographic phase change upon spin-crossover, from $C2/c$ (high-spin) to $P\bar{1}$ (low-spin), while [Fe(**44**)(**135**)$_2$] retains the $C2/c$ crystal form in both spin states [358]. This different phase behaviour is also probably retained in these two compounds during spin-crossover under pressure [359]. Laser irradiation of [Fe(**53**)(**135**)$_2$] at 30 K produces a metastable high-spin form of its low-

temperature $P\bar{1}$ phase. That explains the lower LIESST relaxation temperature exhibited by this complex (44 K) compared to [Fe(**44**)(**135**)$_2$] (52 K), since the metastable high-spin state of the latter adopts the $C2/c$ crystal form [358]. The homoleptic complex [Fe(**135**)$_3$]$^-$ can only be isolated in the presence of a large excess of **135**$^-$ ligand; its tetraethylammonium salt is high-spin at 300 K [360]. The only other homoleptic iron(II) complexes of *bis*-pyrazolylborate ligands have a [FeL$_2$] stoichiometry [361,362] and are often very air-sensitive. They have been assigned tetrahedral structures from their IR spectra [363]. The *bis*-pyrazolylmethane complexes *trans*-[Fe(NCS)$_2$(**136**)$_2$] [364] and [Fe(NCS)$_2$(**137**)$_2$] [365] are high-spin at room temperature, although the visible spectrum of the latter compound implies that it may undergo a spin-crossover equilibrium in CH_3NO_2 solution.

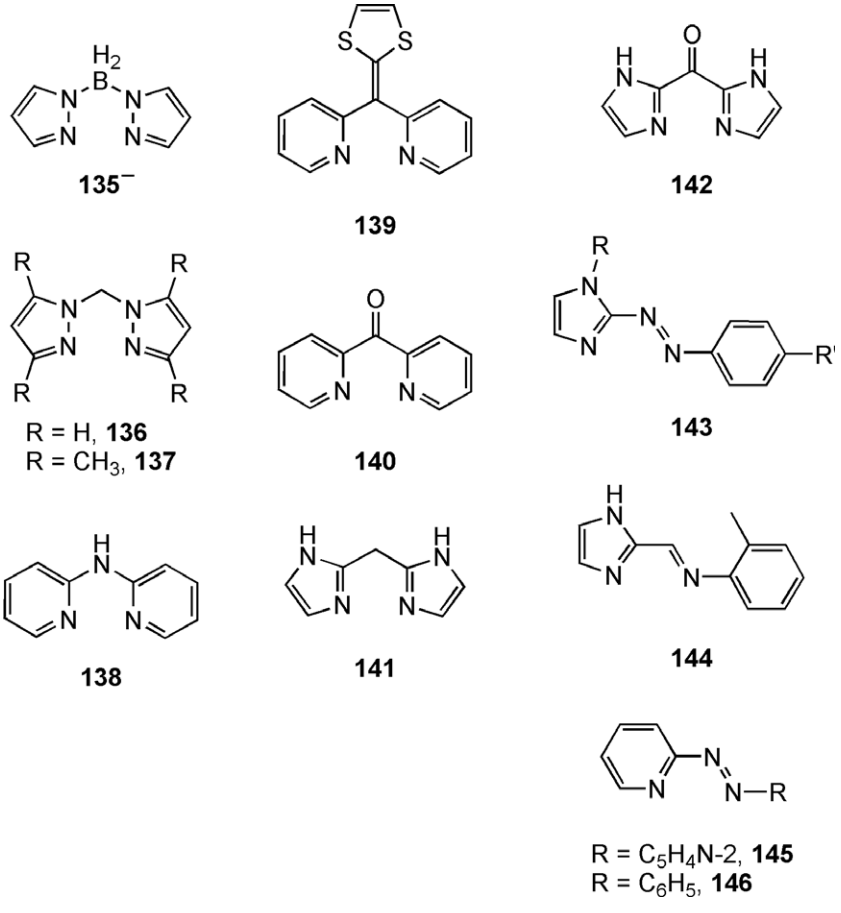
While [Fe(N{CN}$_2$)$_2$(**138**)$_2$] is high-spin [366], *cis*-[Fe(NCS)$_2$(**138**)$_2$] shows a gradual thermal spin-transition upon cooling, centred at the low temperature of 88 K [366,367]. In contrast, *cis*-[Fe(NCS)$_2$(**139**)$_2$]·1/2CH_3OH exhibits a very abrupt spin-crossover at 132 K, which was attributed to lattice cooperativity mediated by intermolecular S···S contacts in the crystal [368]. The compound undergoes quantitative photoconversion to a trapped high-spin form at 5 K, which relaxes upon rewarming to 66 K. The related complex [Fe(NCS)$_2$(**140**)$_2$] is low-spin at room temperature [369]. [Fe(**141**)$_3$][ClO_4]$_2$ is high-spin, and is oxidised to [Fe(**142**)$_3$][ClO_4]$_2$ upon exposure to air [370]. The latter compound appears to undergo a thermal spin-crossover in solution by Evans' method, being almost fully high-spin at 307 K.

While complexes of type [Fe(**143**)$_3$]$^{2+}$ (R = H or alkyl, R′ = H, alkyl or Cl) are all low-spin [371], [Fe(NCS)$_2$(**143**)$_2$] are high-spin at room temperature [372]. A full variable temperature magnetic study of the thiocyanato complex with R = CH_3 and R′ = C_2H_5 confirmed that it remains high-spin on cooling to 5 K. [Fe(NCS)$_2$(**144**)$_2$] is also high-spin, and has *cis*-isothiocyanate ligands in the crystal [373]. The dipyridylhydrazone ligands in low-spin [Fe(NCS)$_2$(**145**)$_2$] chelate to the metal through one pyridyl and one azo N donor [374]. Salts of homoleptic [Fe(**146**)$_3$]$^{2+}$ are also low-spin [375].

4. Tridentate ligands

4.1. Tripodal ligands

Several iron(II) complexes of *tris*-pyrazolyl-borate and methane ligands exhibit thermal spin-transitions (Table 6) [376]. The parent compound [Fe(**147**)$_2$] is low-spin at room



temperature, but undergoes a complete low → high spin-crossover on warming [377]. An initial heating:cooling cycle shows a gradual transition with a 33 K hysteresis loop, with $T_{1/2}\uparrow = 393$ K and $T_{1/2}\downarrow = 360$ K [377,378]. Subsequent heating:cooling cycles on the same sample follow the pathway of the cooling curve, with no hysteresis now being observed. DSC measurements suggested that [Fe(**147**)$_2$] undergoes an irreversible crystallographic phase transition upon initial heating to 393 K; consistent with this, its single crystals shatter at this temperature [378].

Table 6
Iron(II) complexes of *tris*-pyrazolylborate, *tris*-pyrazolylmethane and related ligands

	Spin-state or $T_{1/2}$ (K)	Form of spin-state transition	Spin states of crystal structure(s)	Other measurements	Refs.
[Fe(**147**)$_2$]	393 on 1st scan, 360 on subsequent scans	gradual	LS	Cal, IR, Mag, Möss, PES, Press, Sol, Stress, XAS	[302,377–390]
[Fe(**148**)$_2$]	HS at RT, 60% HS at 4 K	n/a	HS	Möss, XAS	[385–387,391]
[Fe(**149**)$_2$]	135	gradual, 50% complete	HS	Mag, Möss	[392,393]
[FeL$_2$] (L = **150**–**152**)	all HS		HS (**150**,[a] **152**)	Möss (**151**, **152**) , XAS (**152**)	[387,394,395]
[FeL$_2$] (L = **153**, **154**)	both LS			Möss	[387–389]
[Fe(**155**)$_2$]	195	gradual	HS	Mag, Möss, MM, Press, Sol, XAS	[379,382–387,389,396,397]
[Fe(**156**)$_2$]	HS		HS	Mag, Möss, Press, Sol, XAS	[361,382,383,389,393,396]
[Fe(**159**)$_2$]	LS		LS	MM, Möss, PES, Sol, XAS	[49,382,385,386,396,397]
[Fe(**160**)$_2$]	173	gradual, 50% complete	HS, 1:1 HS:LS[a]	Mag, Möss	[392,393]
[FeL$_2$] (L = **162**–**164**)	all LS			Mag (**164**), Möss (**162**, **164**), MM (**163**)	[49,387,396,399]
[Fe(**165**)$_2$]	HS		HS	Mag, Möss	[400]
[Fe(**166**)$_2$] (2 phases)	HS or 131		HS (both phases), LS	Mag, Möss	[399]
[Fe(**166**)$_2$] · 2CH$_2$Cl$_2$	≈185	gradual	HS, LS	Mag, Möss	[399]
[Fe(**167**)$_2$]	275, 114	2 steps, gradual then abrupt	HS, 1:1 HS:LS, LS	Mag, Möss	[401]
[Fe(**168**)$_2$]	173	abrupt, 50% complete	HS	Mag, Möss	[401]
[Fe(**169**)$_2$]	178	gradual, 30 K hysteresis	HS	Mag, Möss	[401]
[FeL$_2$] (L = **170**, **172**)	LS		LS[a]	Möss (**171**)	[402,405]
[Fe(**171**)$_2$]	310	gradual	LS[a]	Mag, Möss, PES, Sol	[381,385,403,404]
[Fe(**173**)$_2$]	HS			Möss	[385]
[Fe(**174**)$_2$]Br$_2$	LS			Mag	[365]
[Fe(**174**)$_2$]X$_2$ (X$^-$ = NO$_3^-$,[b] ClO$_4^-$, PF$_6^-$)	all > RT	all gradual	LS (NO$_3^-$)	ISC, Mag (NO$_3^-$, ClO$_4^-$), Möss	[409,411,412]
[Fe(**174**)$_2$][BF$_4$]$_2$	420	gradual	LS	Mag, Möss, XAS	[384,410]
[Fe(**175**)$_2$]X$_2$ (X$^-$ = BF$_4^-$, ClO$_4^-$)	175–220	both gradual		Mag, Möss	[408]
[Fe(**175**)$_2$][PF$_6$]$_2$	HS			Mag, Möss	[408]
[Fe(**176**)$_2$][PF$_6$]$_2$	280	gradual		Mag, Möss	[408]
[Fe(**177**)$_2$][ClO$_4$]$_2$	355	gradual		Mag, Möss	[408]
[Fe(**178**)$_2$][BF$_4$]$_2$	206	abrupt, 50% complete	2 × HS, 1:1 HS:LS	Mag, Möss, Press, XAS	[384,410,413,414]
[Fe(**178**)$_2$]I$_2$[c]	203	abrupt, 15 K hysteresis, ca. 80% complete	HS	Mag, Möss, Press, XAS	[414,416]
[Fe(**178**)$_2$]I$_2$ · 4CH$_2$Cl$_2$	HS above 110 K		HS		[416]
[Fe(**178**)$_2$][ClO$_4$]$_2$	HS			Mag, Möss	[408]
[Fe(**179**)$_2$][BF$_4$]$_2$	129	abrupt, 38 K hysteresis	HS	Mag, Möss	[417]

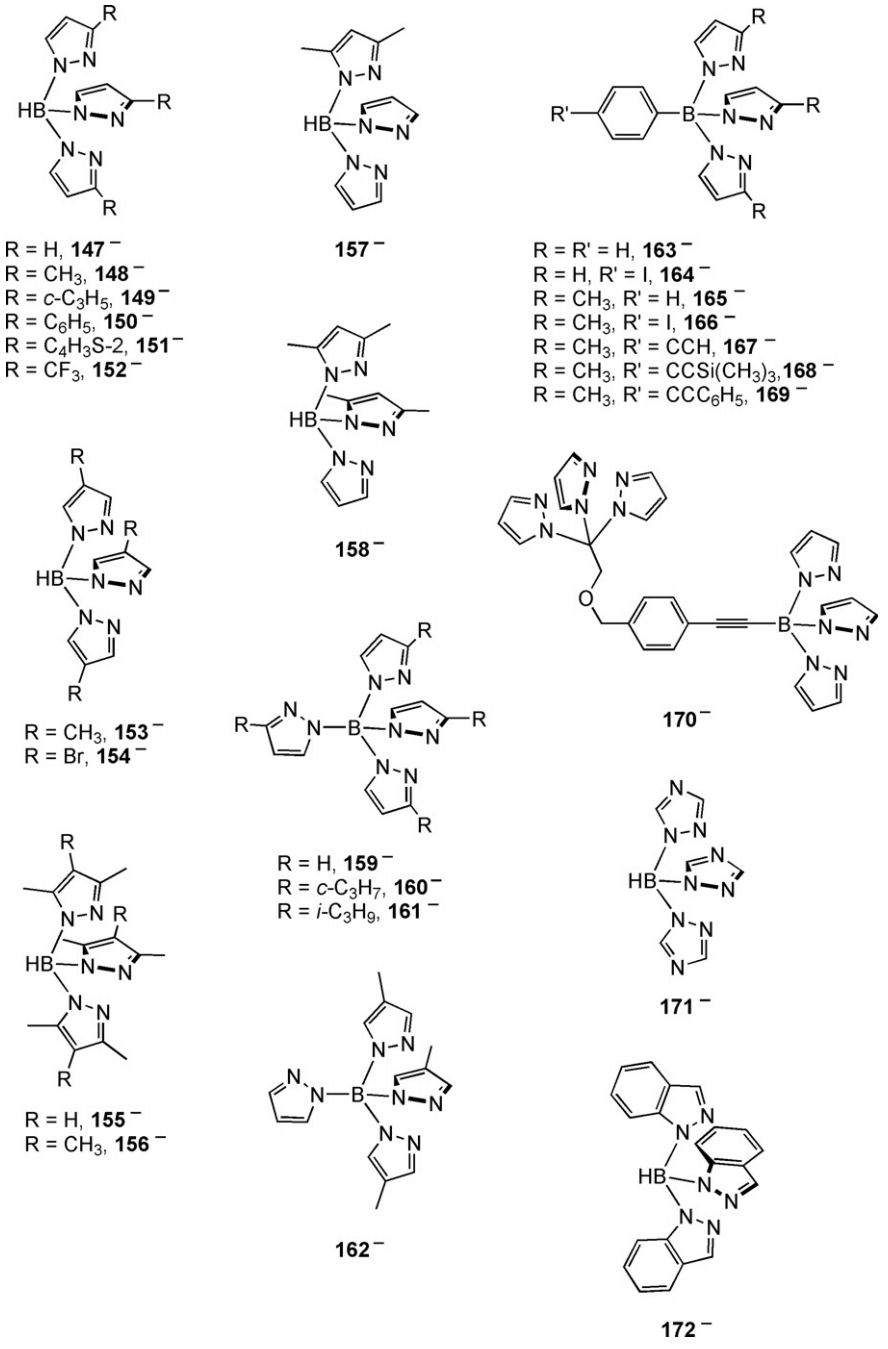
See also Refs. [361,385,401,406] for additional examples, and Table 1 for the abbreviations of physical techniques.

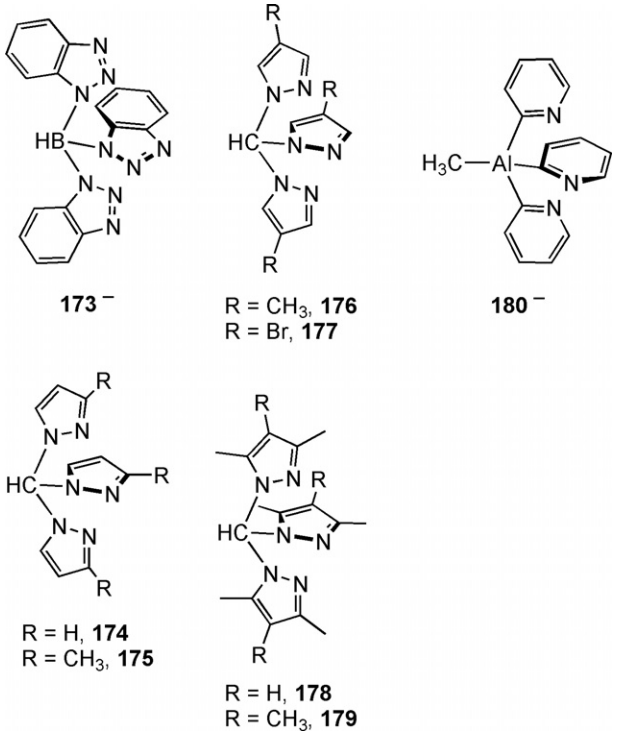
[a] From a solvated crystal structure.

[b] Compound forms two crystalline polymorphs, which have similar magnetic behaviour and were both crystallographically characterised.

[c] Powder precipitated from CH$_2$Cl$_2$. The same compound precipitated from acetone, undergoes a similar spin-state transition that is only 12% complete.

The methylated complex [Fe(**148**)$_2$] undergoes a partial spin-state transition upon cooling by Mössbauer spectroscopy, from HS at room temperature to a 3:2 HS:LS ratio at 4.2 K [385]. This may reflect that crystals of the material contain two independent molecules per asymmetric unit, both of which are high-spin at room temperature. It is possible that one of these molecules undergoes a partial spin-crossover upon cooling while the other does not, although this remains to be investigated further. Solid [Fe(**155**)$_2$] undergoes a gradual, complete spin-state transition centred at 195 K [389], while [Fe(**149**)$_2$] and [Fe(**160**)$_2$] also exhibit gradual spin-transitions at slightly lower temperatures, that are only 50% complete. This reflects the fact that the crystalline compounds both contain two distinct iron sites [393]. In chlorinated solvents [Fe(**147**)$_2$] ($T_{1/2} \approx 340$ K), [Fe(**157**)$_2$] ($T_{1/2} > 290$ K), [Fe(**158**)$_2$] ($T_{1/2} \approx 290$ K) and [Fe(**155**)$_2$] (HS above 215 K) show sequentially lowered spin-crossover temperatures [396,398], which reflects steadily increasing steric hindrance between the pyrazole-3-methyl substituents in the methylated complexes [49]. Consistent with this explanation, the fully methylated compound [Fe(**156**)$_2$] is high-spin in the solid above 4.2 K [390,393], while [Fe(**153**)$_2$] is low-spin at room temperature [387].





The compounds [Fe(**159**)$_2$] [49,382], [Fe(**163**)$_2$] [49] and [Fe(**164**)$_2$] [399] are all low-spin at room temperature in the solid and in solution. Crystal structures and molecular mechanics calculations on [Fe(**163**)$_2$] have implied that this reflects steric repulsion between the non-coordinated pyrazolyl or phenyl boron substituent and the coordinated pyrazole rings, which enforces narrow N–B–N angles between the coordinated pyrazole groups [49]. Interestingly, however, photoelectron spectroscopy on [Fe(**159**)$_2$] has implied that this compound is high-spin in the gas phase below 290 K [397]. The compound [Fe(**166**)$_2$] has been isolated as two unsolvated polymorphs, and one CH_2Cl_2 solvate [399]. One of the unsolvated forms is high-spin, while the other undergoes an abrupt thermal spin-transition at 131 K. This behaviour was attributed to the different patterns of intermolecular π–π interactions between the pendant iodophenyl groups in the crystal. These are clearly more geometrically favourable in the high-spin polymorph, which may result in a higher activation barrier for the structural rearrangement required for spin-crossover in this form. In addition to the compounds listed in Table 6, several other homoleptic iron(II) complexes of sterically hindered *tris*- or *tetrakis*-pyrazolylborates are known that are presumably high-spin or low-spin at room temperature from their colouration and/or NMR behaviour [361,401,406]. However, Mössbauer spectra and EXAFS studies imply that [Fe(**161**)$_2$] instead adopts a tetrahedral structure with bidentate ligands [407].

Where they undergo spin-crossover (see below), *bis*-(*tris*pyrazolylmethane) complexes of iron(II) undergo spin-state transitions at generally similar temperatures to their *bis*-(*tris*pyrazolylborate) analogues containing the same pattern of pyrazole substitution (Table 6). This shows that the zwitterionic nature of iron *tris*pyrazolylborate compounds has little effect on the electronic character of the iron centre. The preference of [Fe(**174**)$_2$]$^{2+}$ for a low-spin state at 0 K has been successfully reproduced by density functional (DF) calculations incorporating non-hybrid BLYP or PW91 basis sets [63]. The same BLYP DF method correctly predicted that [Fe(**174**)$_2$]$^{2+}$ and [Fe(**177**)$_2$]$^{2+}$ should undergo spin-crossover at similar temperatures [408].

The salt [Fe(**178**)$_2$][BF$_4$]$_2$ undergoes an abrupt spin-state transition at 206 K, without hysteresis, that is only 50% complete [410]. This is a result of a crystallographic phase change at this temperature [413]: from a high-temperature form in $C2/c$ that contains one formula unit per asymmetric unit, that is fully high-spin at 220 K; to a low-temperature form in $P\bar{1}$ containing two crystallographically independent molecules, one of which is low-spin at 173 K while the other is apparently fully high-spin. The analogous complexes [M(**178**)$_2$][BF$_4$]$_2$ (M = Co, Ni, Cu) are isomorphous with the iron compound at room temperature and also undergo the same phase transition upon cooling, although this has no impact on their variable temperature magnetic moment [415]. [Fe(**178**)$_2$]I$_2$, when crystallised from CH_2Cl_2, undergoes a spin-state transition at 203 K that is ca. 80% complete; the remaining 20% of the sample become low-spin upon further cooling to ca. 60 K. In contrast, the same compound when crystallised from acetone undergoes spin-crossover at the same temperature, but that is only about 12% complete [416]. The trapping of some forms of [Fe(**178**)$_2$]$^{2+}$ in the high-spin state was rationalised by comparing crystal structures of two polymorphs of [Fe(**178**)$_2$]I$_2$ that crystallise from CH_2Cl_2. These were a solvent-free form, that undergoes spin-crossover at 195 K, at which point the crystals shatter; and, a solvate of formula [Fe(**178**)$_2$]I$_2$ · 4CH_2Cl_2 that remains high-spin at 110 K [416]. The main difference between these two compounds at room-temperature lies in the pitch of their pyrazole rings, as expressed by the Fe–N–N–C torsion angles. In the unsolvated crystals of [Fe(**178**)$_2$]I$_2$ this torsion averages to 171° for the six pyrazole groups, while for the solvate the average torsion is 161° [416]. A similarly low average Fe–N–N–C torsion of 162° is seen in the molecule in the low-temperature polymorph of [Fe(**178**)$_2$][BF$_4$]$_2$, that is trapped in a high-spin state. In contrast, the low-spin molecule in the same structure shows an average torsion of 179°, reflecting the smaller size of the low-spin Fe(II) ion [413]. Apparently, in a crystalline environment molecules of [Fe(**178**)$_2$]$^{2+}$ with strongly tilted pyrazole rings are insufficiently flexible to accommodate the change in size of the coordinated iron ion, that would accompany a spin-state transition. Similar conclusions about the influence of pyrazole ring pitch on spin-state were drawn from a survey of known high-spin iron(II) *tris*pyrazolylborate complexes [393,400].

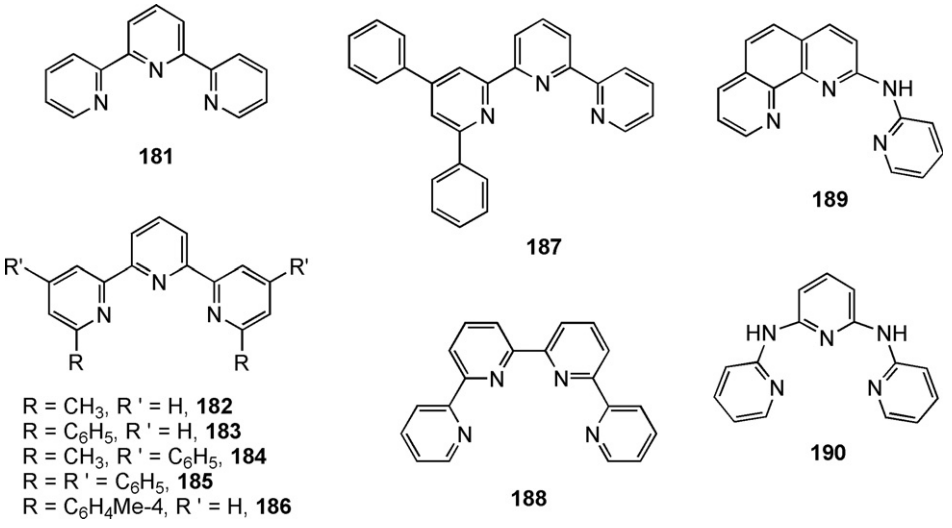
Homoleptic iron(II) complexes of several other tripodal ligands containing three pyrid-2-yl, pyrazol-1-yl or imidazol-2-yl donors in various combinations have also been reported, and are nearly all low-spin [409,410,418]. One possible exception is [Fe(**180**)$_2$], which is 'paramagnetic at room temperature' but shows a unique Fe–N bond length of 2.054(3) Å at 180 K that would indicate a predominantly low-spin state at that temperature [419].

4.2. Terpyridines

All $[FeL_2]^{2+}$ salts, where L is **181** or a derivative substituted at the 4- or 5-positions of one or more of the pyridine rings, are low-spin [420,421]. However, metastable high-spin states of $[^{57}Fe(\mathbf{181})_2]Cl_2 \cdot 5H_2O$ and $[^{57}Fe(\mathbf{181})_2][ClO_4]_2 \cdot 1/2H_2O$ have been detected at low temperatures by Mössbauer emission spectroscopy, as intermediates in the nuclear decay of the corresponding salts of $[^{57}Co(\mathbf{181})_2]^{2+}$ [422]. The rates of relaxation of these metastable high-spin $[Fe(\mathbf{181})_2]^{2+}$ species, down to their low-spin ground state, are inversely proportional to the ligand field strength experienced by the Co(II) ions in the starting materials [422]. This is the same trend as seen in the relaxation of photogenerated metastable high-spin species (Sections 1 and 8). Irradiation of a doped solid $[Fe_{0.02}Mn_{0.98}(\mathbf{181})_2][ClO_4]_2$ converts the (low-spin) Fe fraction of the material into its metastable high-spin state that is indefinitely long lived at 10 K [423]. In contrast, pure $[Fe(\mathbf{181})_2][ClO_4]_2$ does not undergo spin-conversion upon irradiation under the same conditions. This is the first time that a low-spin complex has been fully activated towards the LIESST spin-trapping effect by doping into a host material (although an increase in the lifetime of the transient photogenerated high-spin form of a low-spin complex, doped it into a host lattice, had been demonstrated before [424]).

In contrast, $[FeL_2]^{2+}$ complexes of 6-substituted-2,2′:6′,2″-terpyridines have more varied electronic structures. The complexes of **182**–**185** are high-spin in solution, while $[Fe(\mathbf{185})_2][ClO_4]_2 \cdot CH_3CN \cdot H_2O$ is high-spin in the crystal at 223 K [425]. Salts of $[Fe(\mathbf{186})_2]^{2+}$ undergo spin-crossover on cooling in CH_3CN, but show more complex behaviour in the solid state: $[Fe(\mathbf{186})_2]PF_6]_2$ is completely high-spin above 5 K, while $[Fe(\mathbf{186})_2][ClO_4]_2$ is low-spin at room temperature [425]. This dichotomy was explained by structure determinations of solvated crystals of these compounds. Low-spin $[Fe(\mathbf{186})_2][ClO_4]_2$ has a fairly regular octahedral geometry with near-perpendicular terpyridyl ligands, that shows only small deviations from local D_{2d}-symmetry if the ligand phenyl substituents are ignored. However (high-spin) $[Fe(\mathbf{187})_2][PF_6]_2 \cdot 2(CH_3)_2CO$ has an unusual, twisted coordination geometry, in which the dihedral angle between the terpyridyl frameworks of the two ligands is only 64.0°. The same twisted high-spin structure is also shown by $[Fe(\mathbf{185})_2][ClO_4]_2 \cdot CH_3CN \cdot H_2O$ [425] and $[Fe(\mathbf{186})_2][FeCl_4]_2$ [426]. A theoretical study on a related system (Section 4.3) has shown that this structure corresponds to an angular Jahn–Teller distortion of the high-spin d^6 ^5E configuration (in O_h symmetry), which traps the iron centre in a high-spin state [15].

The crystal structure of $[Fe(\mathbf{188})_2][ClO_4]_2$ at room temperature shows a high spin Fe(II) centre with each quaterpyridyl ligand binding in a tridentate manner [427]. The coordination geometry of this compound is highly distorted, in a manner that partly resembles that of $[Fe(\mathbf{187})_2][PF_6]_2$ [424]. In $[Fe(\mathbf{188})_2][ClO_4]_2$, however, this distorted structure leaves space for an additional long Fe···N contact of 2.819(9) Å to the fourth pyridyl ring of one of the two ligands, resulting in a [6+1] coordination geometry overall. No low temperature crystallographic or



magnetic investigation of this compound was undertaken. Solid [Fe(**189**)$_2$]X$_2$ (X$^-$ = NO$_3^-$ and BF$_4^-$), [Fe(**189**–H)$_2$] [428] and [Fe(**190**)$_2$]Cl$_2$ · 2MeOH [429] are all low-spin.

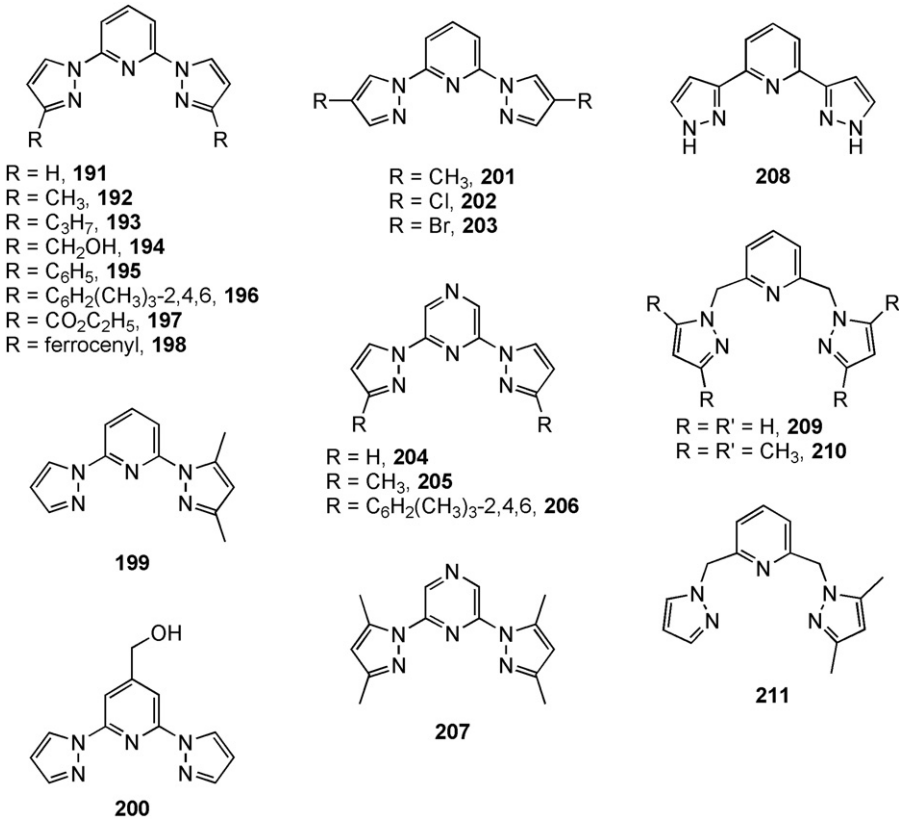
4.3. 2,6-Di(pyrazolyl)pyridines and related ligands

Iron(II) complexes of **191** and several of its substituted derivatives have been prepared (Table 7) [430]. Solid [Fe(**191**)$_2$][BF$_4$]$_2$ exhibits an abrupt spin transition at 261 K in the solid [15,26,431–433], but the ClO$_4^-$ [434], PF$_6^-$ [15] and SbF$_6^-$ [434] salts of the same complex, which are isostructural with each other, remain fully high-spin above 5 K. This behaviour is explained by the crystal structures of the two compounds: while [Fe(**191**)$_2$][BF$_4$]$_2$ has a six-coordinate geometry at iron with near-regular D_{2d} symmetry, the other salts adopt an unusual C_2-distorted, twisted molecular structure that traps the complex in a high-spin state. DF calculations showed that the C_2 structure represents an angular Jahn-Teller distortion of the high-spin d^6 manifold [15]. The same structural distortion is also exhibited, to differing degrees, by high-spin [Fe(**191**)$_2$]I$_{0.5}$[I$_3$]$_{1.5}$ [435], [Fe(**194**)$_2$]X$_2$ (X = BF$_4^-$ [434] and ClO$_4^-$ [437]), [Fe(**195**)$_2$][BF$_4$]$_2$ [434] and [Fe(**204**)$_2$]-[SbF$_6$]$_2$ [442], and by high-spin iron(II) complexes of three terpyridine derivatives (Section 4.2) [425,426]. The salt [Fe(**191**)$_2$][Co(C$_2$B$_9$H$_{11}$)$_2$]$_2$ is also notable, in containing equal numbers of angularly distorted and undistorted molecules in the crystal [435]. As expected, this material undergoes a thermal spin transition that is only 50% complete. Interestingly, recrystallisation of [Fe(**191**)$_2$][BF$_4$]$_2$ at a temperature below its thermal spin-transition yielded a different low-spin phase [Fe(**191**)$_2$][BF$_4$]$_2$ · xCH$_3$NO$_2$ ($x \approx 3$) Crystals of this material become high-spin, with concomitant decomposition, at essentially the same temperature as the spin-transition undergone by the solvent-free material [15].

Table 7
Iron(II) complexes of 2,6-di(pyrazol-1-yl)pyridine and 2,6-di(pyrazol-1-yl)pyrazine derivatives

	Spin-state or $T_{1/2}$ (K)	Form of spin-state transition	Spin states of crystal structure(s)	Other measurements	Refs.
[Fe(**191**)$_2$][BF$_4$]$_2$	261	abrupt, 3 K hysteresis	3 × HS, 3 × LS	Cal, DFT, LIESST, Mag, Möss, Sol	[15,26,64,431–433]
[Fe(**191**)$_2$]X$_2$ (X$^-$ = ClO$_4^-$, PF$_6^-$, SbF$_6^-$; 2X$^-$ = 1/2I$^-$ · 3/2I$_3^-$)	all HS		HS	Mag, Möss (ClO$_4^-$)	[15,434,435]
[Fe(**191**)$_2$][Co(C$_2$B$_9$H$_{11}$)$_2$]$_2$	318	gradual, 50% complete	ca. 65% HS, 1:1 HS:LS[a]	Mag	[435]
[Fe(**192**)$_2$][SbF$_6$]$_2$	HS		HS	Mag	[435]
[Fe(**193**)$_2$]X$_2$ (X$^-$ = BF$_4^-$, PF$_6^-$)	HS		HS (PF$_6^-$)[a]	Mag	[434,436]
[Fe(**194**)$_2$]X$_2$ (X$^-$ = BF$_4^-$, ClO$_4^-$)	HS		HS	Mag (BF$_4^-$), Möss (BF$_4^-$)	[434,437]
[Fe(**195**)$_2$][BF$_4$]$_2$ (2 phases)	both HS		HS (both phases)	Mag, Möss	[434,436]
[Fe(**196**)$_2$]X$_2$ (X$^-$ = BF$_4^-$, PF$_6^-$, 1/2FeCl$_4^{2-}$)	LS		LS (FeCl$_4^{2-}$, PF$_6^-$)[a]	Mag	[426,436]
[FeL$_2$][BF$_4$]$_2$ (L = **197**, **198**)	both HS		HS	Mag, Möss (**228**)	[434,438]
[Fe(**199**)$_2$][BF$_4$]$_2$	LS		LS	Mag	[430]
[Fe(**200**)$_2$]X$_2$ (X$^-$ = BF$_4^-$, ClO$_4^-$)	271–284	both abrupt	HS, 2 × LS	LIESST, Mag	[433,439]
[Fe(**201**)$_2$][BF$_4$]$_2$	LS		LS	Mag	[433]
[Fe(**201**)$_2$][ClO$_4$]$_2$	232	abrupt, 3 K hysteresis	HS, LS	LIESST, Mag	[433]
[Fe(**202**)$_2$][BF$_4$]$_2$	202	abrupt, 2 K hysteresis	HS, LS	Mag	[440]
[Fe(**203**)$_2$][BF$_4$]$_2$	253	abrupt, 3 K hysteresis	HS	Mag	[440]
[Fe(**204**)$_2$]X$_2$ (X$^-$ = BF$_4^-$, ClO$_4^-$)	206–223	both abrupt, 3–5 K hysteresis	HS (ClO$_4^-$)[b]	LIESST, Mag, PD (ClO$_4^-$)	[26,433,441,442]
[Fe(**204**)$_2$][BF$_4$]$_2$ · 3CH$_3$NO$_2$	198	abrupt	HS, LS		[441]
[Fe(**204**)$_2$][SbF$_6$]$_2$	HS		HS	Mag	[443]
[Fe(**205**)$_2$][BF$_4$]$_2$	240	gradual, 2 steps	HS, 1:1 HS:LS, LS	LIESST, Mag	[441,444]
[Fe(**205**)$_2$][ClO$_4$]$_2$	196, 133	abrupt then gradual, 2 steps	HS, 1:1 HS:LS, LS	LIESST, Mag	[441,444]
[FeL$_2$]X$_2$ (L = **206**, **207**; X$^-$ = BF$_4^-$, ClO$_4^-$)	all LS		LS (both BF$_4^-$)[a]	Mag	[441]

See Table 1 for the abbreviations of physical techniques.
[a] From a solvated crystal structure.
[b] Structure refinement from powder diffraction data.



Unlike the solvent-free material (see above), crystalline $[Fe(\mathbf{194})_2][ClO_4]_2 \cdot x$MeCN ($x \approx 0.75$) is high-spin at 200 K but undergoes a partial spin-state transition upon cooling to 100 K, resulting in a colour change and the appearance of ligand conformational disorder [437]. Refinement of this disorder implied that the transition was 42% complete at this temperature. The packing diagram at 100 K revealed that one of the disordered ligand hydroxyl groups is only 1.456(17) Å from its nearest neighbour when both molecules are low-spin. This steric clash implies that only one complex molecule in this pair can be low-spin, and places a natural limitation of 50% completeness on the spin-state transition.

The salts $[Fe(\mathbf{204})_2]X_2$ ($X = BF_4^-$ and ClO_4^-) both show abrupt high $\rightarrow$ low spin-state transitions upon cooling, with $T_{1/2} = 223$ K and 206 K, respectively [441]. Powder diffraction measurements showed that $[Fe(\mathbf{204})_2][ClO_4]_2$ is isostructural with $[Fe(\mathbf{191})_2][BF_4]_2$ at room temperature but, unlike the latter compound, it undergoes a crystallographic phase change at the spin-crossover temperature [442]. The high- and low-spin forms have the same apparent crystal symmetry, but the unit cell *a* axis has doubled in length in the low-temperature phase. The similarly abrupt nature of the spin-transitions exhibited by these three compounds, and by $[Fe(\mathbf{201})_2][ClO_4]_2$, $[Fe(\mathbf{202})_2][BF_4]_2$ and $[Fe(\mathbf{203})_2][BF_4]_2$ has been attributed to the layered "terpyridine embrace" crystal packing motif that they all adopt [440]. Thermal spin-crossover in $[Fe(\mathbf{205})_2]X_2$ ($X = BF_4^-$ and ClO_4^-) involves two discrete steps [441], despite their only containing a single unique iron environment [444]. The first part of the transition is triggered by an ordering of an anion site in the crystal, which allows an apparently random distribution of half the iron centres to undergo spin-crossover without causing a change in crystal symmetry. The remaining high-spin fraction then undergoes spin-crossover much more gradually as the temperature is further lowered [444].

Several compounds in Table 7 exhibit quantitive photoconversion to their LIESST high-spin states, which have relaxation temperatures of up to 100 K [26,433]. The trapped high-spin forms of $[Fe(\mathbf{191})_2][BF_4]_2$ [432] and $[Fe(\mathbf{200})_2]X_2$ ($X = BF_4^-$ [439] and ClO_4^- [433]) have also been crystallographically characterised at 30 K. In contrast to $[Fe(NCX)_2(\mathbf{53})_2]$ ($X = S$ [286] and Se [308]; Section 3.3), for all these compounds the thermally populated high-spin state at room temperature and the photochemically trapped high-spin state at 30 K show no significant structural differences at the iron centre. The reason why these two sets of crystalline materials behave differently in the LIESST experiment may be related to the different crystal packing motifs they adopt.

Many hydrated and anhydrous salts of $[Fe(\mathbf{208})_2]^{2+}$ also undergo thermal spin-crossover (Table 8). The highly hydrated salts are low-spin at room-temperature, but often become high-spin on heating with concomitant water loss. The less hydrated or anhydrous materials usually undergo

Table 8
Iron(II) complexes of 2,6-di(pyrazol-3-yl)pyridine

	Spin-state or $T_{1/2}$ (K)	Form of spin-state transition	Spin states of crystal structure(s)	Other measurements	Refs.
[Fe(**208**)$_2$]Cl$_2$ · xH$_2$O (x = 0, 6.5)	both LS		LS (x = 6.5)	Mag	[445]
[Fe(**208**)$_2$]Br$_2$	252	abrupt, 4 K hysteresis		LIESST, Mag	[25,446]
[Fe(**208**)$_2$]Br$_2$ · 5H$_2$O[a]	340	gradual		LIESST, Mag	[25,446]
[Fe(**208**)$_2$]I$_2$	203	abrupt, 2 K hysteresis		Mag, Sol	[446]
[Fe(**208**)$_2$]I$_2$ · 2H$_2$O	256	abrupt		LIESST, Mag	[25]
[Fe(**208**)$_2$]I$_2$ · 4H$_2$O[a]	330	gradual	LS	Mag, Möss	[25,446]
[Fe(**208**)$_2$][NCS]$_2$ · 2H$_2$O	205, 252	gradual, 2 steps, both steps show hysteresis	HS	Cal, LIESST, Mag, Möss, PD	[25,447,448]
[Fe(**208**)$_2$][NCSe]$_2$	231	abrupt, 2K hysteresis	HS	LIESST, Mag, Möss	[25,447]
[Fe(**208**)$_2$][NO$_3$]$_2$ · 2H$_2$O	>353	gradual		Möss, Mag	[446]
[Fe(**208**)$_2$][BF$_4$]$_2$	176	abrupt, 10 K hysteresis		Möss, Mag, Vis, DFT, EPR, INS, LIESST, Quen, Sol	[25,63,446,449–452]
[Fe(**208**)$_2$][BF$_4$]$_2$$xH_2$O ($x$ = 2,[a] 3)	288–>300	both gradual	LS (x = 3)	LIESST (x = 3), Mag, Möss (x = 2)	[25,446]
[Fe(**208**)$_2$][ClO$_4$]$_2$ · xH$_2$O (x = 0, 1, 3[a])	220–330	all gradual		Mag	[449]
[Fe(**208**)$_2$][PF$_6$]$_2$	171	abrupt, 2 K hysteresis, 50% complete		LIESST, Mag, Möss, Sol	[25,446]
[Fe(**208**)$_2$][PF$_6$]$_2$ · xH$_2$O (x = 1, 2, 3[a])	177–355	all gradual, discontinuous (x = 1, 2)		Mag, Möss (x = 2)	[25,446]
[Fe(**208**)$_2$][CF$_3$SO$_3$]$_2$	230	gradual, 50% complete		Mag, Möss	[453]
[Fe(**208**)$_2$][CF$_3$SO$_3$]$_2$ · H$_2$O	140↓ 170, 285↑	abrupt, discontinuous in warming mode		EPR, Mag, Möss, Quen	[451,453,454]
[Fe(**208**)$_2$][CF$_3$SO$_3$]$_2$ · 3H$_2$O[a]	355	gradual	LS	Mag, Möss	[453]
[Fe(**208**)$_2$][Fe(CN)$_5$(NO)]	182	abrupt, 3 K hysteresis	HS, LS	Mag, Möss	[455]
[Fe(**208**)$_2$]$_2$[Cr(C$_2$O$_4$)$_3$]ClO$_4$ · 5H$_2$O[a]	375	gradual, 20 K hysteresis	LS	Mag	[456]
[Fe(**208**)$_2$]$_2$[Cr(**44**)(C$_2$O$_4$)$_2$]$_2$	361	abrupt, 16 K hysteresis		Cal, Mag	[457]
[Fe(**208**)$_2$]$_2$[Cr(**44**)(C$_2$O$_4$)$_2$]$_2$ · 2H$_2$O[a]	380	gradual, 50% complete	1:1 HS:LS	Cal, Mag	[457]

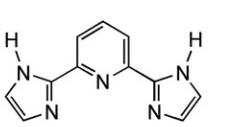
See Table 1 for the abbreviations of physical techniques.
[a] Transition is accompanied by water loss from the sample.

spin-crossover below room-temperature. Anhydrous [Fe(**208**)$_2$][BF$_4$]$_2$ exhibits an abrupt spin transition at 176 K, with a hysteresis loop of between 10 and 16 K depending on the measurement [25,449,450]. The trapped high-spin state of [Fe(**208**)$_2$][BF$_4$]$_2$ can be generated below 80 K by thermal quenching or irradiation; this was the first compound whose LIESST thermal relaxation was shown to deviate from first-order kinetics owing to cooperativity in the solid [450]. In contrast, [Fe(**208**)$_2$][CF$_3$SO$_3$]$_2$ · H$_2$O exhibits in cooling mode an abrupt and complete high → low-spin transition at 140 K. However, upon rewarming the low → high-spin conversion takes place in two steps: a gradual transition centred at 170 K during which ca. 1/3 of the sample becomes high-spin; and, a more abrupt change at 285 K [454]. This leads to the bulk of the sample showing a very wide spin-crossover hysteresis width of ca. 140 K. The high-spin form of [Fe(**208**)$_2$][CF$_3$SO$_3$]$_2$ · H$_2$O can also be generated at 77 K by thermal trapping or irradiation although, unlike the BF_4^- salt, the thermal relaxation kinetics of these two forms of the metastable high-spin state are very different [454]. This implies that freeze-quenching the sample preserves the high-temperature crystallographic phase, while LIESST excitation generated a metastable high-spin form of the low-temperature phase. Consistent with this suggestion, an EPR study implied that spin-crossover in both [Fe(**208**)$_2$][BF$_4$]$_2$ and [Fe(**208**)$_2$][CF$_3$SO$_3$]$_2$ · H$_2$O is accompanied by a change in crystallographic symmetry [451].

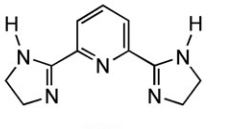
The gradual thermal spin-transition in [Fe(**208**)$_2$][NCS]$_2$ · 2H$_2$O is split into two steps which, unusually, both exhibit pronounced hysteresis [447,448]. Repeated cycling through this transition changes its form to a single, more abrupt spin-crossover at 232 K; annealing of the sample at room temperature for 24 h led to its reversion to the original behaviour. Powder diffraction measurements showed that this reflects a sample-dependent distribution of two crystal phases in the bulk material, which can be thermally interconverted [448]. Spin-crossover in three different salts of $[Fe(\mathbf{208})_2]^{2+}$ in acetone solution is essentially independent of the anion present, occurring at $T_{1/2} \approx 260$–270 K [446].

Eight different hydrated or anhydrous salts of $[Fe(\mathbf{208})_2]^{2+}$ exhibit efficient LIESST excitation on irradiation at 10 K, yielding trapped high-spin materials with relaxation temperatures of between 40 and 110 K [25]. LIESST relaxation in a $[Fe(\mathbf{208})_2]^{2+}$/Nafion film takes place in the same temperature range as the neat solids, showing that intermolecular cooperativity has only a minor influence on the stability of a metastable high-spin state [458].

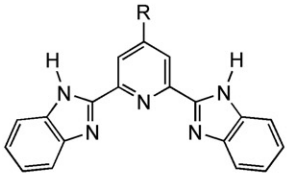
$[Fe(\mathbf{209})_2][ClO_4]_2 \cdot H_2O$ undergoes a gradual thermal spin-transition centred near 250 K [459,460]. Salts of $[Fe(\mathbf{210})_2]^{2+}$ [459,461] and $[Fe(\mathbf{211})_2]^{2+}$ [459,462] are high-spin, which probably reflects steric crowding about the iron centres [462]. A small low-spin population was detected in $[Fe(\mathbf{210})_2][ClO_4]_2 \cdot CH_3CN$ and $[Fe(\mathbf{210})_2][B(C_6H_5)_4]_2 \cdot 2CH_3CN$, however, whose relative abundance varies with temperature in a manner inconsistent with a simple spin-crossover equilibrium. This was attributed to a thermally induced interconversion of spin-states in a fraction of the sample, triggered by a change in ligand conformation [461]. Photoexcitation of $[Fe(\mathbf{209})_2][ClO_4]_2 \cdot H_2O$ at 10 K affords its trapped high-spin state, which decays at the relatively low temperature of 38 K [463]. The high → low-spin reverse-LIESST effect in $[Fe(\mathbf{210})_2][ClO_4]_2 \cdot CH_3CN$ has also been demonstrated, albeit with a conversion efficiency of <30% [464]. Relaxation of the trapped excited spin-states in both materials occurs via a distribution of rate constants rather than simple sigmoidal kinetics, which was suggested to reflect the presence in the bulk solid of both *fac* and *mer* complex isomers, and/or different conformers of the unusually flexible tridentate ligand [463,464].



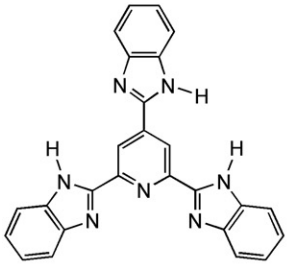
212



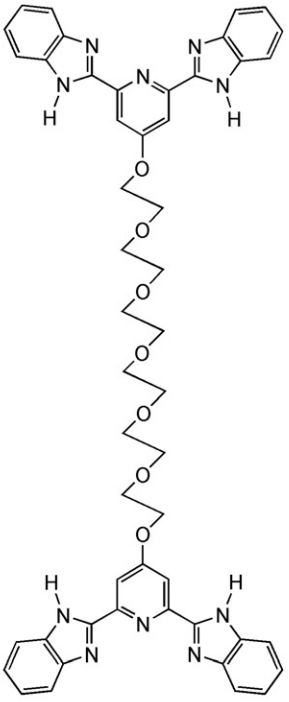
213



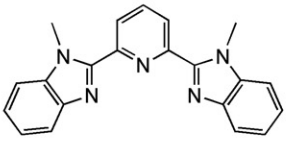
R = H, **214**
R = CH_3, **215**
R = Cl, **216**
R = OH, **217**
R = $OC_{12}H_{25}$, **218**



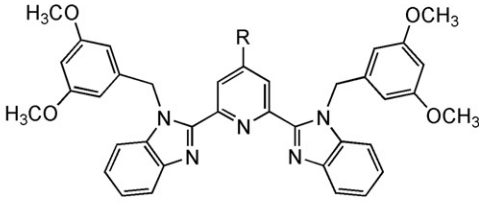
219



220



221



R = H, **222**
R = C_6H_5, **223**
R = $C_6H_4NO_2$-4, **224**

4.4. 2,6-Di(imidazolyl)pyridines, 2,6-di(benzimidazolyl)pyridines and related ligands

The complex $[Fe(\mathbf{212})_2][ClO_4]_2$ undergoes a spin-transition in CD_3OD solution upon cooling from room temperature to 200 K, although no further magnetochemical characterisation of this material was reported. Basic, aerobic methanol solutions of this compound rapidly convert to a low-spin iron(III) complex of the deprotonated ligand, isolated as $Na[Fe(\mathbf{212}\text{–}2H)_2]\cdot 2H_2O$ [465]. The salt $[Fe(\mathbf{213})_2][ClO_4]_2$ is low-spin [466].

Freshly prepared crystalline samples of $[Fe(\mathbf{214})_2][ClO_4]_2\cdot 1/4H_2O$ undergo an abrupt spin-crossover at 403 K with a 12 K hysteresis loop [467–470]. However, susceptibility measurements of rapidly precipitated or aged samples exhibit a variable, reduced population of this transition, superimposed onto a much broader feature centred at lower temperature [469]. These effects do not appear to reflect loss of the water content of the aged and powder samples [469], but may be caused by the presence of iron(III) contaminants [467]. These observations may explain the somewhat variable behaviour found in earlier reports of this material [471,472]. Solid $[Fe(\mathbf{214})_2][BPh_4]_2\cdot xH_2O$ is high-spin when $x = 0$ and 2, but undergoes a gradual spin-crossover centred near 325 K when $x = 4$ [468,473]. The crystalline complex $[Fe(\mathbf{214}\text{–}H)_2]\cdot H_2O$ can be precipitated from aqueous ethanol in the presence of NEt_3, and also exhibits a gradual spin-transition centred at 424 K [474,475]. Further heating results in loss of water from the solid, accompanied by a stabilisation of the high-spin state. Several other solid salts of $[Fe(\mathbf{214})_2]^{2+}$ also undergo spin-crossover above room-temperature, but have been less well characterised [471,473]. Polyethene [476] and polyvinylalcohol [477,478] films containing $[Fe(\mathbf{214})_2][ClO_4]_2$ also undergo spin-crossover by far-IR and UV/Vis spectroscopy. Stretching the PVA films causes the complex molecules to orient themselves within the polymer, allowing their polarisation absorption spectra to be obtained [478].

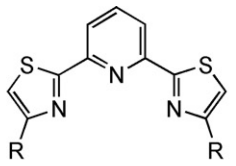
Spin crossover of $[Fe(\mathbf{214})_2]^{2+}$ in solution is complicated by ligand dissociation equilibria, ligand deprotonation and the formation of $[Fe(\mathbf{214})_3]^{2+}$, all of which has been studied in some detail [12,479–481]. Although the mid-point temperature of this transition in all solvents is >350 °C [480,481], the room temperature magnetic moment of this compound depends strongly on concentration and solvent used [480]. The high- and low-spin states of $[Fe(\mathbf{214})_2]^{2+}$ and $[Fe(\mathbf{214}\text{–}H)_2]$ in methanol/ethanol mixtures show different fluorescence maxima, whose relative intensities change as the temperature is lowered and spin-crossover progresses [478]. The energy difference of the two fluorescence peaks implied that the high- and low-spin states in $[Fe(\mathbf{214})_2]^{2+}$ are separated by ca. 350 cm^{-1}. Although $[Fe(\mathbf{216})_2]^{2+}$ and $[Fe(\mathbf{217})_2]^{2+}$ are high-spin in MeOH solution [481,482], solid-state far-IR spectra show that $[Fe(\mathbf{215})_2][ClO_4]_2$ is high-spin and $[Fe(\mathbf{216})_2][ClO_4]_2$ low-spin, while $[Fe(\mathbf{216})_2][ClO_4]_2\cdot 3H_2O$ shows thermal spin-crossover [483]. In contrast, $[Fe(\mathbf{216}\text{–}H)_2]\cdot 2C_2H_5OH\cdot H_2O$ and $[Fe(\mathbf{217}\text{–}H)_2]\cdot 2C_2H_5OH\cdot H_2O$ are predominantly low-spin in solution [484] and the solid state [485]. The complex $[Fe(\mathbf{219})_2][ClO_4]_2\cdot 2H_2O$ undergoes a very abrupt spin-crossover at 323 K, with a 35 K hysteresis loop. The morphology of this material prevented its structural characterisation, however [475]. The stability constants of the 1:1 and 2:1 iron(II) complexes of **218** and **220** have been communicated [486]. The *N*,*N*′-dialkylated ligand complexes $[FeL_2][ClO_4]_2$ (L = **221** [471] and **222**–**224** [487]) are all low-spin.

4.5. Selected complexes of other tridentate ligands

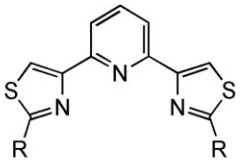
While $[Fe(\mathbf{225})_2][ClO_4]_2$is low-spin, steric repulsion from the ligand methyl groups reduces the ligand field in $[Fe(\mathbf{226})_2][ClO_4]_2$ so that it exhibits a gradual thermal spin-crossover centred below 91 K [465]. Similar behaviour is shown by $[Fe(\mathbf{227})_2]X_2$ (low-spin) and $[Fe(\mathbf{228})_2]X_2$ (spin-crossover; $X^- = BF_4^-$ and ClO_4^-), with $T_{1/2}$ for the latter being 350–360 K [488]. Solid $[Fe(\mathbf{229})_2][ClO_4]_2$shows sample-dependent behaviour, sometime undergoing a gradual spin-transition and sometimes remaining high-spin [470,471,489]. A Mössbauer study identified four different iron environments in the solid compound, whose relative distributions varied between samples and appeared to be very dependent on the solvent content [471]. The salts $[Fe(\mathbf{229})_2]Br[FeBr_4]$ [489], $[Fe(\mathbf{229})_2][BPh_4]_2$ [490] and $[Fe(\mathbf{230})_2][ClO_4]_2$ [471] are high-spin although, interestingly, the susceptibility of five-coordinate $[Fe(\mathbf{53})(\mathbf{229})][ClO_4]_2$ is consistent with a partial spin-transition near 170 K [490].

The hydrates $[Fe(\mathbf{231})_2]Cl_2\cdot 6H_2O$ [443] and $[Fe(\mathbf{231})_2]Cl_2\cdot 3H_2O$ [491] are both high-spin, but the anhydrous compound is low-spin and hygroscopic [491]. The latter has been proposed as a moisture detector, particularly for use in space probes [492]. Five other hydrated salts of $[Fe(\mathbf{231})_2]^{2+}$ are high-spin, as are salts of $[Fe(\mathbf{232})_2]^{2+}$ and $[Fe(\mathbf{234})_2]^{2+}$. However, $[Fe(\mathbf{233})_2]X_2\cdot H_2O$ ($X^- = BF_4^-$ and ClO_4^-) both show gradual thermal spin-crossover centred above 80 K [491]. A high-spin state is enforced in $[Fe(\mathbf{235})_2][PF_6]_2$ [493] and $[Fe(\mathbf{236}\text{–}H)_2]$ [494] by conformational strain, associated with the central five-membered ring in the ligands. However, the BF_4^- and ClO_4^- salts of $[Fe(\mathbf{237})_2]^{2+}$ [495,496] both show gradual spin-transitions by susceptibility and Mössbauer measurements, although these were only ca. 60% complete at the lowest temperature measured, 77 K [497].

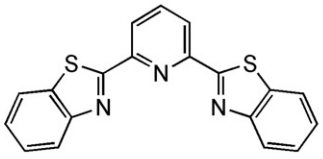
Different salt hydrates of $[Fe(\mathbf{238})_2]^{2+}$ [495] are either high-spin [498,499], or undergo gradual spin-crossover with $T_{1/2}$ ranging from ca. 250 to >400 K [498,500]. A more thorough study of $[Fe(\mathbf{238})_2][NO_3]_2$ showed that its spin-transition is inhibited by a significant activation energy of 18.8 kJ mol^{-1} below 190 K [501]. If the sample is cooled slowly, the transition is centred at 246 K and proceeds to completeness, with a pronounced hysteresis loop of 34 K. More gradual and incomplete spin-crossover is observed with more rapid temperature ramps, as in earlier studies [498,500]. Unfortunately the structural basis for this unu-



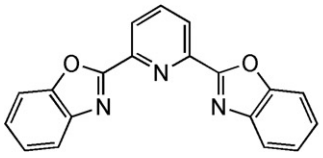
R = H, **225**
R = CH_3, **226**



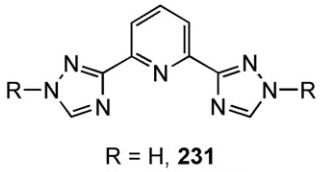
R = H, **227**
R = CH_3, **228**



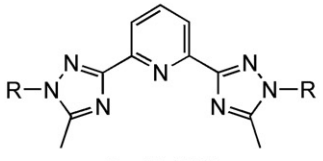
229



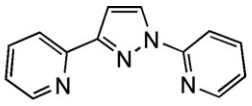
230



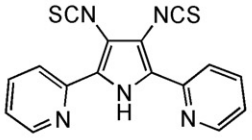
R = H, **231**
R = CH_3, **232**



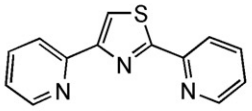
R = H, **233**
R = CH_3, **234**



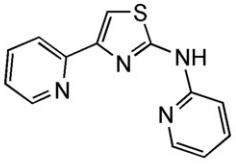
235



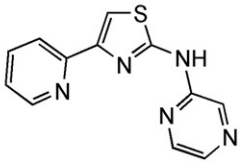
236



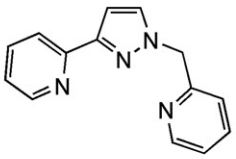
237



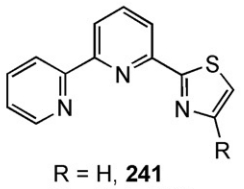
238



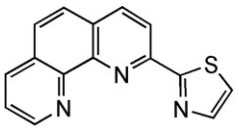
239



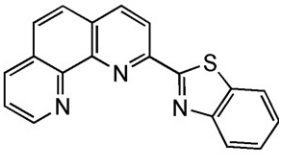
240



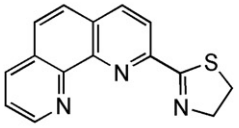
R = H, **241**
R = CH_3, **242**



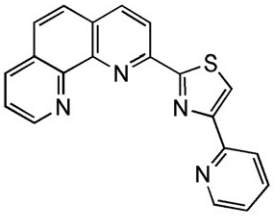
243



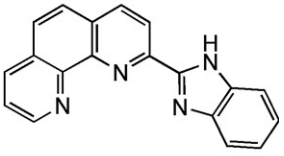
244



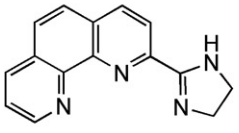
245



246

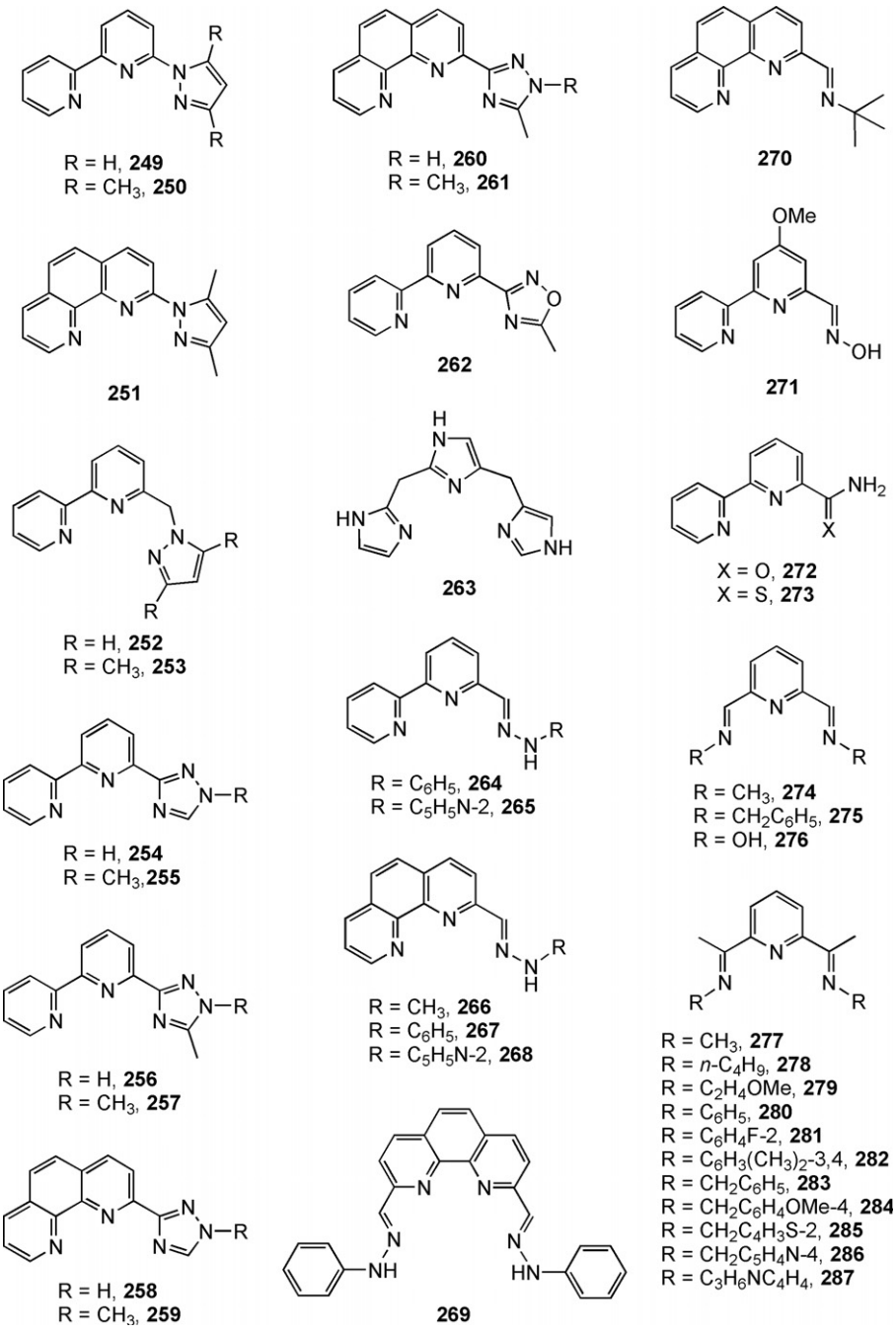


247



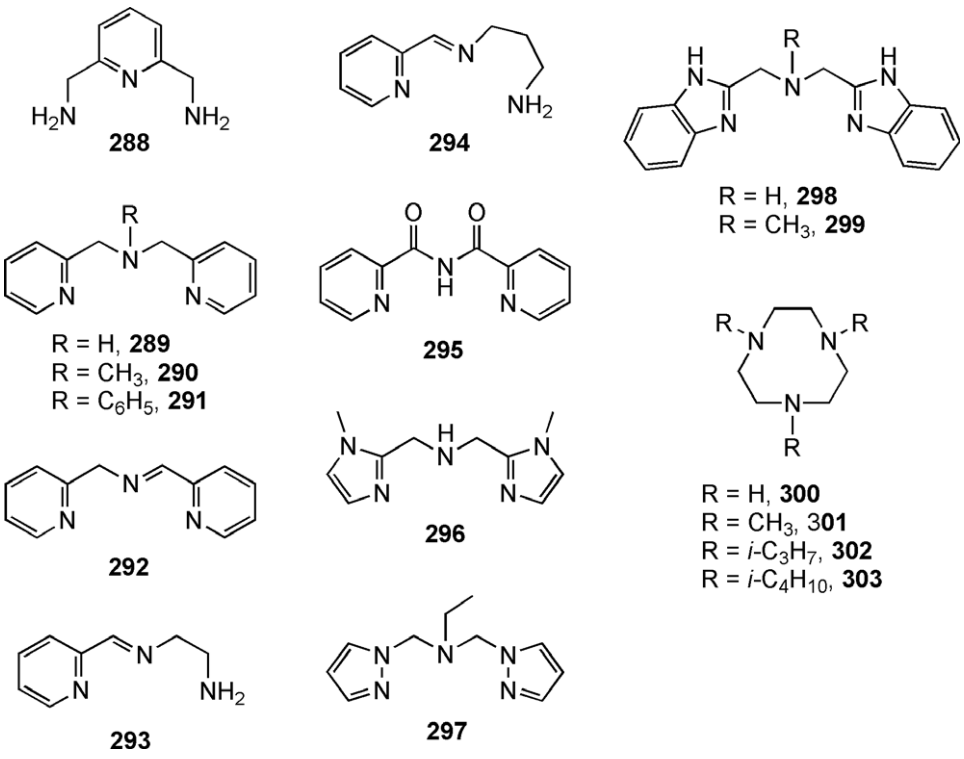
248

sual behaviour is unknown. Aqueous solutions of [Fe(**238**)$_2$]Cl_2 undergo spin-crossover, with a mid-point below 287 K [502]. Interestingly, neutral [Fe(**238**–H)$_2$] also undergoes gradual, incomplete thermal spin-crossover, at temperatures rather lower than the dicationic species [503,504]. The form of this transition is very dependent on the presence or absence of solvent in the material, with $T_{1/2}$ varying from ca. 210 to <83 K [504]. The NO_3^- and BF_4^- salts of $[Fe(\mathbf{239})_2]^{2+}$ undergo spin-crossover above room temperature when hydrated, and below room temperature when anhydrous, while the $CF_3SO_3^-$ salt also shows $T_{1/2} > 383$ K [505]. Spin-crossover in [Fe(**239**–H)$_2$] resembles that in [Fe(**238**–H)$_2$], with a similar dependence on solvent content and sample history [506]. Comparison of the cationic and neutral complexes of **238** and **239** shows that the pyrazine ring in the latter tends to stabilise the



low-spin form of its compounds. This is particularly obvious in solution, when comparing $T_{1/2}$ of [Fe(**238**–H)$_2$] (215 K) and [Fe(**239**–H)$_2$] ($\gg$299 K) in CD_3OD [506].

Solid [Fe(**240**)$_2$][ClO_4]$_2$ exhibits a gradual thermal spin-crossover centred at 173 K [507]. Susceptibility measurements on [Fe(**242**)$_2$]X_2 ($X^- = BF_4^-$ and PF_6^-) [496], [Fe(**243**)$_2$][BF_4]$_2$, [Fe(**244**)$_2$][BF_4]$_2$ [508], [Fe(**247**)$_2$][BF_4]$_2 \cdot 2H_2O$, [Fe(**247**–H)$_2$]$\cdot CHCl_3$ and [Fe(**248**)$_2$][BF_4]$_2 \cdot H_2O$ [509] all show gradual spin-transitions on heating, mostly centred significantly above 363 K. The magnetic moment of [Fe(**245**)$_2$][BF_4]$_2$ decreases very slowly on cooling from 4.8 BM at 363 K to 4.2 BM at 83 K, while [Fe(**241**)$_2$][BF_4]$_2$ is low-spin [496] and [Fe(**246**)$_2$][BF_4]$_2$ (which presumably contains tridentate **246** ligands) is high-spin [508]. Solid [Fe(**249**)$_2$]$X_2 \cdot H_2O$ ($X^- = BF_4^-$ and ClO_4^-) are predominantly low-spin at room temperature [510], while the PF_6^- salts of [Fe(**249**)$_2$]$^{2+}$ [511] and [Fe(**250**)$_2$]$^{2+}$ [512] are both low-spin in acetone solution. However, three different salt hydrates of [Fe(**251**)$_2$]$^{2+}$ exhibit gradual spin-transitions centred at, or slightly above, room temperature [513]. Acetone solutions of [Fe(**252**)$_2$][PF_6]$_2$ are low-spin, but those of [Fe(**253**)$_2$][PF_6]$_2$ give $\mu_{eff} = 4.1$ BM at room temperature, indicating spin-equilibrium behaviour [512].



Hydrated or anhydrous salts of $[FeL_2]^{2+}$ (L = **254**–**257** [514] and **262** [517]) are high-spin at room temperature, although in each case a small low-spin population appears on heating to up to 383 K. While the complexes of **254**–**257** are all low-spin in solution as well [514], the high-spin state of $[Fe(\mathbf{262})_2]^{2+}$ predominates in acetone at room temperature, allowing the activation volume for its spin-transition to be determined [518]. Solid salts of $[FeL_2]^{2+}$ (L = **258**–**261**) show more variable behaviour, with nearly all of those examined exhibiting gradual thermal spin-crossover, albeit at widely variable $T_{1/2}$ values ranging from <89 to >373 K [515,516]. Best studied is $[Fe(\mathbf{261})_2][ClO_4]_2$, whose spin-transition is centred near 265 K when anhydrous but which crystallises in two different hydrated forms. Crystal structures showed that $[Fe(\mathbf{261})_2][ClO_4]_2 \cdot H_2O$ exists as a mixture of high- and low-spin molecules at room temperature, consistent with the magnetic and Mössbauer spectroscopic data from the anhydrous material, but that $[Fe(\mathbf{261})_2][ClO_4]_2 \cdot 2/3H_2O$ is low-spin [516]. $[FeL_2][ClO_4]_2$ (L = **258**–**261**) also undergo spin-transitions in acetone solution, mostly centred near room-temperature [515].

While $[Fe(\mathbf{263})_2]F_2$ is essentially high-spin [519,520], a gradual spin-transition involving 6% of the sample was detected at low temperatures. A theoretical study implied that the ground-state of the molecule is in fact high-spin, but that the energy gap between the high- and low-spin states of the compound is unusually small at ca. 40 cm^{-1}. The weak spin-crossover in this system is therefore driven by transitions between molecular vibrational energy levels with temperature, rather than by the usual factors [519]. Several other salts of $[Fe(\mathbf{263})_2]^{2+}$ undergo complete gradual thermal spin-transitions on cooling [520–523]. A comprehensive study of the four halide salts of this cation showed that $T_{1/2}$ followed the trend in counterion of $I^- > Br^- > Cl^- > F^-$. DF calculations implied that this trend reflects the different electronegativities of the anions, which interact with the iron centres through strong N–H···X (X^- = halide) hydrogen bonds [520]. Relaxation of the LIESST excited state of $[Fe(\mathbf{263})_2]Cl_2$ [520,522] takes place at 42 K, and displays complicated kinetics below 30 K implying that a range of quantum mechanical tunneling frequences are involved in the relaxation process [524].

Although $[Fe(\mathbf{266})_2]^{2+}$ is low-spin [525], salts of $[Fe(\mathbf{267})_2]^{2+}$ and $[Fe(\mathbf{268})_2]^{2+}$ do undergo thermal spin-transitions. The behaviour of $[Fe(\mathbf{267})_2][BF_4]_2$ [525–557] and $[Fe(\mathbf{267})_2][ClO_4]_2$ [344,527,528] is very similar, each compound undergoing abrupt spin-crossover centred at 283 K ($X^- = BF_4^-$) and 252 K ($X^- = ClO_4^-$) with a hysteresis loop of 8 K. Powder diffraction measurements showed that both transitions are accompanied by a crystallographic phase change, although single crystal data are not available. The width of the hysteresis in these spin-transitions *increases* with increasing pressure, contrary to the expectations of mean field theory. This anomaly can be accounted for if the bulk modulus of the material varies with pressure [529]. Iron(II) complexes of *N*′,*N*′-disubstituted hydrazones related to **266**–**268** [525], and of **265** [530] and **269** (which was proposed to contain tridentate **269** ligands) [531] are all high-spin, while those of $[Fe(\mathbf{264})_2]^{2+}$ are low-spin [530]. Solid $[Fe(\mathbf{270})_2][BF_4]_2$ exhibits a gradual, complete thermal spin-crossover centred around 220 K, but iron(II) complexes of related Schiff

bases with smaller imino *N*-substituents are all low-spin [532]. The pK_a of [Fe(**271**)$_2$]$^{2+}$ has been determined, but no solid state properties of this complex were reported [533]. Ligands **272**, **273** and their *N*-substituted derivatives form low-spin complexes with iron(II), where the ligands afford a *N*,*N*,*O* or *N*,*N*,*S* donor set [534].

The complexes [Fe(**274**)$_2$][ClO$_4$]$_2$ [535] and [Fe(**275**)$_2$]Br$_2$ [536] are low-spin, as are salts of [FeL$_2$]$^{2+}$ (L = **277**–**287**, and related diimines derived from 2,6-diacetylpyridine) [537]. The pK_as and electrochemistry of [Fe(**276**)$_2$]$^{2+}$ and [Fe(**276**–H)$_2$] have been reported, but not their solid-state behaviour [538]. Coordination polymers with tridentate metal-binding domains related to **274** have been prepared by reacting 2,6-pyridinedicarbaldehyde with a range of straight-chain diaminoalkanes in the presence of iron(II) salts. These are structurally amorphous and contain a mixture of low-spin iron(II) and high-spin iron(III) centres [536]. Similar iron(II) polymers, with metal binding sites related to **277**, have also been prepared from 2,6-diacetylpyridine and four different diaminoalkanes [539]. Despite its dark brown colouration, [Fe(**288**)$_2$]Cl$_2$ · 2 H$_2$O is high-spin at room temperature by crystallography [540]. The synthesis of iron(II) catenanes containing tridentate metal-binding motifs related to **274** [541] and rotaxanes related to **288** [542] have been reported but no characterisation data were provided.

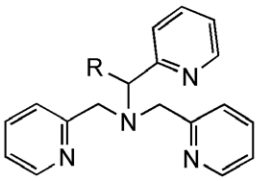
Salts of [Fe(**289**)$_2$]$^{2+}$ [471,543,544] and [FeL$_2$][ClO$_4$]$_2$ (L = **292**–**294**) [535] are low-spin, but [Fe(NCS)$_2$(py)(**289**)] is predominantly high-spin at 80 K and above [545] and [Fe(**290**)$_2$][PF$_6$]$_2$ [544,546] and [Fe(**291**)$_2$][ClO$_4$]$_2$ [546] are high-spin at room temperature. The iron centre in [Fe(**295**–H)$_2$] is low-spin [547], and remains low-spin when additional metal ions are coordinated to its O-donors [548]. Its iron(III) congener [Fe(**295**–H)$_2$]$^+$ is a spin-crossover system, however [547]. The complex [Fe(**296**)$_2$]Cl$_{1.3}$Br$_{0.7}$ is high-spin above 30 K [64,549], while [Fe(**297**)$_2$][ClO$_4$]$_2$ has been synthesised but its spin-state was not reported [550]. The voltammograms of [Fe(**298**)$_2$]Cl$_3$ and [Fe(**299**)$_2$]Cl$_3$ in MeCN show iron(III/II) couples of −0.21 and −0.74 V versus Ag/Ag$^+$ respectively, suggesting that their iron(II) congeners (which have not been reported) might not be air-stable [551]. While salts of [Fe(**300**)$_2$]$^{2+}$ are low-spin in the solid state [552], in solution the complex dication undergoes thermal spin-crossover centred at 335 K in (CD$_3$)$_2$NCDO, and 349 K in D$_2$O [553]. More sterically encumbered 1,4,7-triazacyclononanes like **301**–**303** only form 1:1 metal:ligand complexes with iron(II) [554]. While several larger ring triazamacrocycles are known, their iron(II) complexes have not been described.

5. Tetradentate ligands

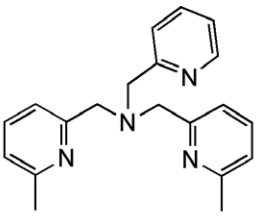
The complexes [Fe(NCS)$_2$(**304**)] and [Fe(NCS)$_2$(**305**)] undergo a very gradual thermal spin-transition centred near 150 K [545]. The fully low-spin state of [Fe(NCS)$_2$(**304**)] can be prepared following slow cooling to 5 K [555], and its spin-crossover has been studied by variable temperature Mössbauer [555,556] and FTIR [555] spectroscopies, EXAFS [557], nuclear resonant and inelastic scattering [557,558] and DF calculations [63]. The LIESST excited state of [Fe(NCS)$_2$(**304**)] is generated quantitatively at 10 K, and relaxes back to its near 50 K [559]. Spin-crossover in [Fe(NCS)$_2$(**308**)] is similarly gradual, being centred near 190 K [560], but [Fe(NCS)$_2$(**307**)] is high-spin [545]. Spin-crossover in [Fe(NCS)$_2$(**315**)] occurs abruptly, without hysteresis, at 138 K [561]. Three polymorphs of [Fe(NCS)$_2$(**317**)] can be crystallised. One of these undergoes a quite gradual thermal spin-transition centred at 176 K (polymorph A, space group $P\bar{1}$ at 298 K), one is high-spin (polymorph B, $P2_1/c$) while the third exhibits an abrupt transition at 116 K, with a hysteresis width of 8 K (polymorph C, *Pbca*) [562]. Room-temperature crystal structures of the three polymorphs show that the same geometric isomer was present in all three structures, with *cis*-pyridyl donors, but that the Fe–N{pyridyl} distances increase in the trend A < C < B. That is consistent with the observed increasing stabilisation of the high-spin state along this series. This structural difference can also be reproduced theoretically, if the different Madelung constants of the three lattices are considered in the calculation [563]. Solid [Fe(NCS)$_2$(**320**)] is high-spin at room temperature [564].

Salts of [Fe(NCCH$_3$)$_2$L]$^{2+}$ are low-spin when L is **304** [565–567], **309** and **310** [566], but high-spin when L is **306** [566,567], **307** [568], **311** and **312** [566,567]. Solutions of [Fe(NCCH$_3$)$_2$L]$^{2+}$ (L = **313**, **314** [566], **316** and **318** [569]) in CD$_3$CN are high-spin, although these were not isolated as solids, while [Fe(NCCH$_3$)$_2$(**304**)]$^{2+}$ apparently undergoes a thermal spin-transition upon warming in the same solvent [565]. The crystalline triflate salt of the *bis*-ligand complex [Fe(**304**)$_2$]$^{2+}$ is octahedral and high-spin at 173 K, with one dangling pyridyl donor per ligand (cf. [Fe(**290**)$_2$]$^{2+}$ and [Fe(**291**)$_2$]$^{2+}$, Section 4.5) but the [B(C$_6$H$_5$)$_4$]$^-$ salt of the same compound is eight-coordinate [565].

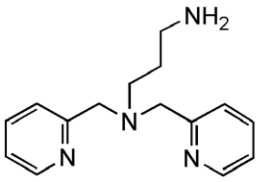
Solid [Fe(**127**)(**315**)][ClO$_4$]$_2$ · 1/2H$_2$O exhibits a rather gradual spin-transition in two distinct steps, centred at 171 and 218 K. These steps are explained by the presence of two independent complex molecule sites observed in the crystalline compound [570]. While the trapped LIESST excited state of [Fe(**127**)(**315**)][ClO$_4$]$_2$ · 1/2 H$_2$O can be generated, the photoconversion is only 40% efficient. Decay of the resultant trapped high-spin content of the sample upon warming also occurs in two steps, at 21 and 36 K. In contrast, spin-crossover in [Fe(**113**)(**319**)][ClO$_4$]$_2$ takes place abruptly at 176 K with a 10 K hysteresis loop. This hysteresis is not caused by a crystallographic phase change during the spin-transition. Rather, it may reflect the extensive hydrogen bonding and π–π stacking in the structure, or an order/disorder transition of one of the **319** ligand propyl groups that was observed to take place on cooling [571]. DF calculations implied that both ligand conformations in this complex should give rise to similar spin-transition temperatures [572].



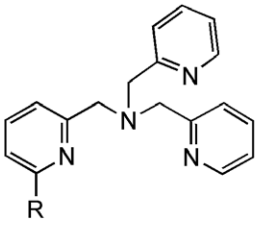
R = H, **304**
R = CH_3, **305**



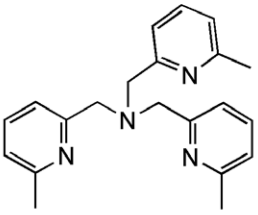
311



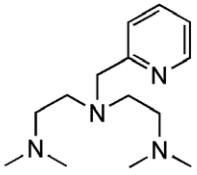
317



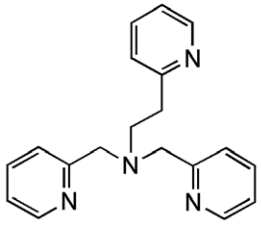
R = CH_3, **306**
R = C_6H_5, **307**



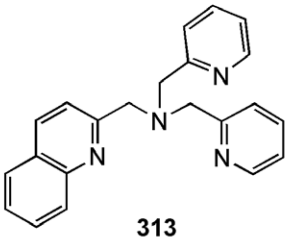
312



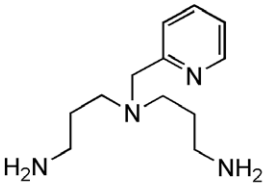
318



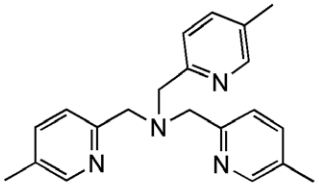
308



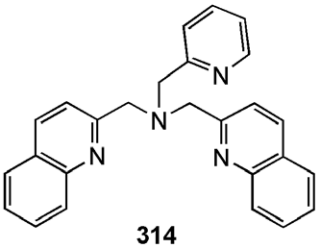
313



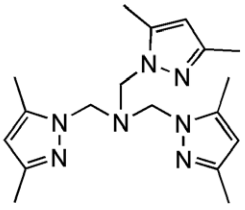
319



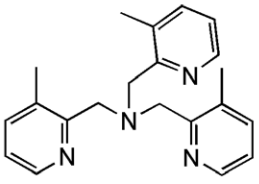
309



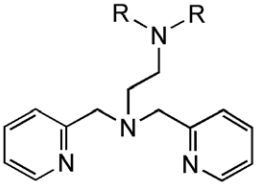
314



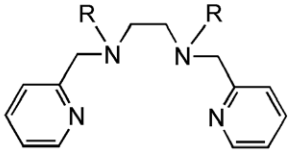
320



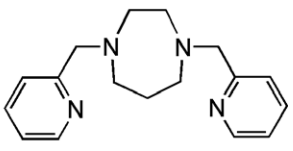
310



R = H, **315**
R = CH_3, **316**

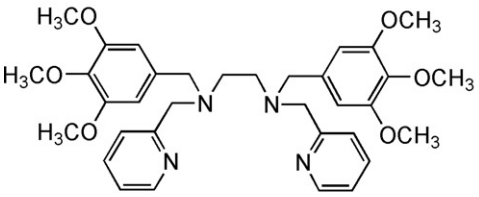


R = H, **321**
R = CH_3, **322**

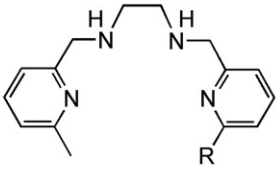


323

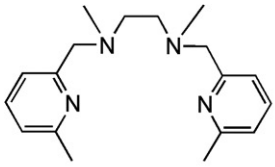
(*continued on next page*)



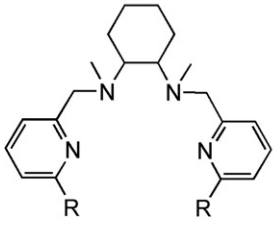
324



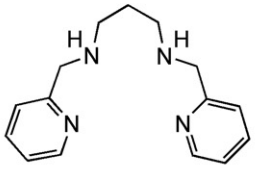
R = H, **325**
R = CH_3, **326**



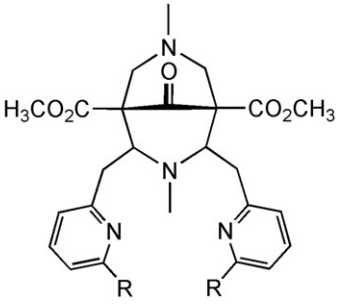
327



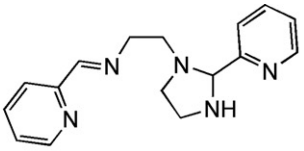
R = H, **328**
R = CH_3, **329**



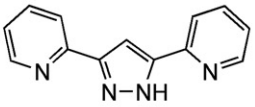
330



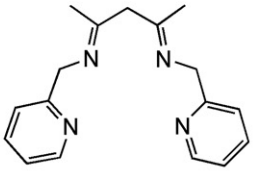
R = H, **331**
R = CH_3, **332**



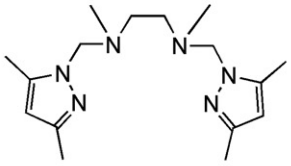
333



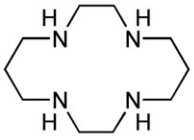
334



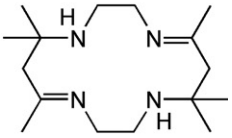
335



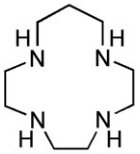
336



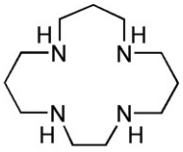
337



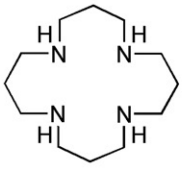
338



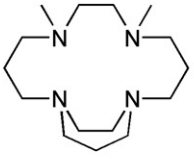
339



340



341



342

suggestion, ca. 70% of the iron content in the powder can be trapped in its high-spin state by rapid quenching from 150 to 20 K; the yield of trapped high-spin material following laser irradiation at 20 K was only 40%, however [573]. The LIESST relaxation temperature of the compound is around 40 K. $[Fe(NCSe)_2(\mathbf{321})]$ [573] and $[Fe(NCBH_3)_2(\mathbf{321})]$ [575] undergo spin-crossover at progressively higher temperatures, of 181 and 362 K respectively; the former compound does not exhibit the LIESST phenomenon [573]. Powdered $[Fe(NCS)_2L]$ (L = **322**, **325**, **326** [574], **331** and **332** [576]) are all high-spin, but $[Fe(NCS)_2(\mathbf{333})]$ is low-spin [577] and $[Fe(NCS)_2(\mathbf{330})]$ exhibits a very gradual spin crossover with a midpoint near 185 K [63,555,574,578]. Although no magnetic data are available, the C≡N vibrations in the IR spectrum of $[Fe(NCS)_2(\mathbf{336})]$ (at 2069 and 2077 cm^{-1}) imply it is high-spin at room temperature [579].

The complex $[Fe(NCCH_3)_2(\mathbf{322})][ClO_4]_2$ undergoes a spin-transition in CD_3CN solution, centred at around 290 K [569,580,581]. The anomalously high enthalpy of this transition (40 kJ mol^{-1}) implies that the spin-transition competes with ligand substitution equilibria in solution, possibly involving coordination of the perchlorate anions [581]. The same compound is low-spin in the crystal with *cis*-MeCN ligands [582], as is $[Fe(NCCH_3)_2(\mathbf{324})][ClO_4]_2$ [583]. Other $[Fe(NCCH_3)_2L]^{2+}$ complexes with L = **327** [579], **328** and **329** [584] have been reported to be paramagnetic in CD_3CN solution, but have not been isolated as solids, while $[Fe(NCCH_3)_2(\mathbf{323})]^{2+}$ (which should contain *trans*- rather than *cis*-MeCN ligands) has also been briefly mentioned [585]. A theoretical study implied that $[Fe(NCCH_3)_2L]^{2+}$ should be a spin-crossover compound when L = **322** (as observed), but will be high-spin when L = **327** or one of several other 6,6″-disubstituted derivatives of **322** [586]. The solid complex $[Fe(\mathbf{334})(\mathbf{321})][BF_4]_2 \cdot 2H_2O \cdot 1/2(C_2H_5)_2O$ exhibits a thermal spin-transition on heating, with a midpoint above 400 K [587], while crystalline $[Fe(\mathbf{45})(\mathbf{335})][ClO_4]_2$ [588] and *trans*-$[Fe(NCCH_3)_2(\mathbf{335})][ClO_4]_2$ [589] are both low-spin. The latter compound rapidly reacts with CH_3CN or other nitriles to form a tripodal pentadentate ligand complex (Section 6), through nucleophilic attack of the (transiently) deprotonated β-diimine moiety at the C≡N bond [588,589]. The quaterpyridine complex $[Fe(\mathbf{188})_2]^{2+}$, which contains tridentate **188**, has been discussed in Section 4.2.

Macrocyclic complexes of type $[FeL_2(\mathbf{337})]^{n+}$ (L = NCS^-, CN^-, $n = 0$; L = CH_3CN, $n = 2$) are all low-spin [590], as are analogues with C-alkylated or unsaturated 14-membered macrocycles [591–594]. One possible exception to that is $[Fe(\mathbf{53})(\mathbf{338})][ClO_4]_2$, which exhibits an intermediate magnetic moment at room temperature (although its instability made characterisation difficult) [591]. However, increasing or decreasing the macrocycle ring size, as in $[Fe(NCS)_2L]$, (L = **339**–**341**) and $[Fe(NCCH_3)_2L][PF_6]_2$ (L = **340** and **341**) affords compounds that are high-spin at room temperature [593]. Only one six-coordinate complex of this type with an *N*-alkylated cyclam appears to have been reported, namely high-spin $[Fe(NCS)_2(\mathbf{342})]$ [595]; 1,4,8,11-tetramethylcyclam itself forms high-spin five-coordinate complexes with iron(II) [596]. Six-coordinate iron(II) porphyrin [597] and phthalocyanine [598] complexes with axial amine or imine bases are low-spin, while most other classes of tetrapyrrole macrocycle (including corrins and corroles) favour higher oxidation states of iron.

6. Pentadentate ligands

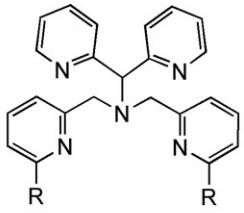
Several complexes of type $[Fe(NCCH_3)L]^{2+}$ (L = **343**–**346** and related derivatives substituted at one, two or four pyridine rings) have been synthesised, as pro-catalysts for organic oxidation reactions. All are low-spin in the solid and solution phases, where this has been determined [599,600]. The spin-state of $[FeL(\mathbf{348})]^{n+}$ depends on L, being low-spin when L = CH_3CN, pyridine or CN^- but high-spin when L is an O-donor [601,602]. Crystalline $[FeN_3(\mathbf{348})]CF_3SO_3 \cdot 2H_2O$ undergoes a gradual thermal spin-crossover with a mid-point of 156 K, that is 80% complete at low temperatures [602]. Crystallographic studies showed that this spin-transition is accompanied by contraction of the five Fe–N bonds to ligand **348**, but apparently not the Fe–N_3 bond. Interestingly, after mild grinding the spin-transition is lost and the material remains high-spin on cooling. The same compound also undergoes spin-crossover in CD_3OD, with $T_{1/2} = 207$ K. Crystalline $[Fe(HOCH_3)(\mathbf{348})][CF_3SO_3]_2$ [603] undergoes a more abrupt spin-crossover at 90 K, which is <50% complete below that temperature and shows significant sample-dependent hysteresis [602]. Water-soluble $[Fe(NCCH_3)(\mathbf{347})]^{2+}$ has been prepared, but its spin-state was not determined [604].

The UV/Vis spectrum of $[Fe(NCS)(\mathbf{349})]PF_6$ has been reported, which does not unequivocally establish its spin-state [605]. However, $[Fe(N\{CN\}_2)(\mathbf{350})]PF_6 \cdot CH_3OH$ is low-spin in the solid state, while dinuclear $[\{Fe(\mathbf{350})\}_2(\mu\text{-}N\{CN\}_2)][PF_6]_2 \cdot xH_2O$ undergoes an abrupt spin-transition that is sample-dependent and only 50% complete when $x = 1$, but which proceeds to completion in two discrete steps when $x = 0$ [606]. Salts of $[Fe(NCCH_3)L]^{2+}$ (L = **351** [607], **352** [608], **353**, **354** [589], **356** [609] and **357** [600]) and $[Fe(NCS)L]^+$ (L = **355** [577], **356** [609], **358** [610]) are all low-spin, while $[\{Fe(NCS)\}_2(\mu\text{-}\mathbf{359})][ClO_4]_2$ is high-spin at room temperature [610]. Quinquepyridines **360** and **361** afford seven-coordinate high-spin iron(II) complexes with two axial acetonitrile ligands [604]. In contrast, $[Fe(NCS)_2L]$ (L = **362**–**364**) are all high-spin and six-coordinate, with tetradentate bispidene ligands [576].

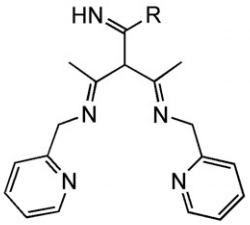
Solid $[Fe(CN)_2(\mathbf{365})] \cdot H_2O$ exhibits very complex and sample-dependent spin-crossover and LIESST behaviour. Powder samples of this compound show an abrupt thermal spin-transition that is 50% complete, centred at 212 K with a hysteresis width of 25 K [28,611,612]. However, an initial

cooling/warming scan of the crystalline high-spin compound [28,613] instead results in a 100% complete, abrupt spin-crossover at 166 K, with a 13 K hysteresis loop [28,614]. Subsequent scans of the crystalline sample instead resemble the data from the powder material, as the crystals decompose during the spin-transition [28]. However, if the same sample is stored at room temperature for 8 h before re-examination, the original complete spin-crossover behaviour is restored [614].

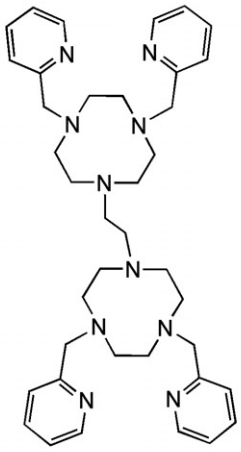
Since crystalline $[Fe(CN)_2(\mathbf{365})] \cdot H_2O$ is seven-coordinate at room-temperature [613], this behaviour may reflect a geometry change during spin-crossover, from seven-coordinate high-spin to six-coordinate low-spin iron centres [611,612]. Such a structure change would also have to involve a change in crystal symmetry [613]. Rewarming the low-spin complex would initially generate a six-coordinate high-spin form, which could only revert slowly to its original seven-coordinate phase. It is the six-coordinate



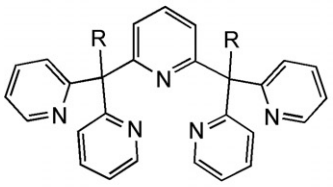
R = H, **343**
R = OCH_3, **344**
R = Br, **345**
R = CO_2CH_3, **346**



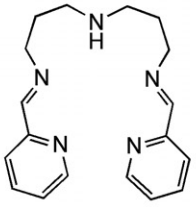
R = CH_3, **353**
R = C_6H_5, **354**



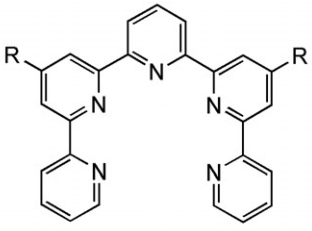
359



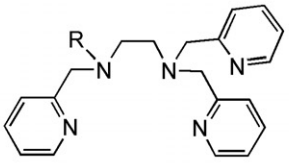
R = OH, **347**
R = OCH_3, **348**



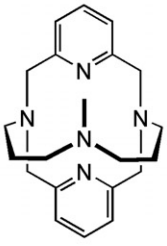
355



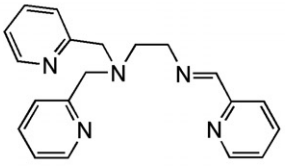
R = H, **360**
R = C_6H_5, **361**



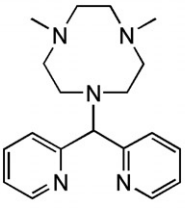
R = CH_3, **349**
R = $CH_2C_6H_5$, **350**



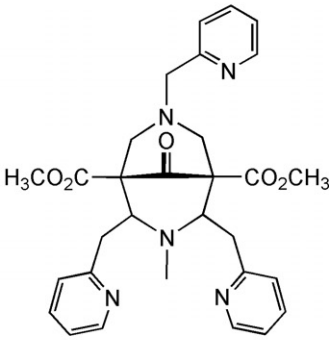
356



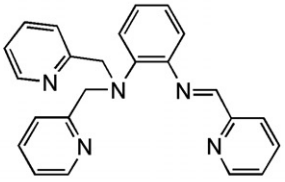
351



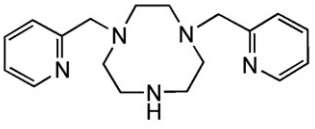
357



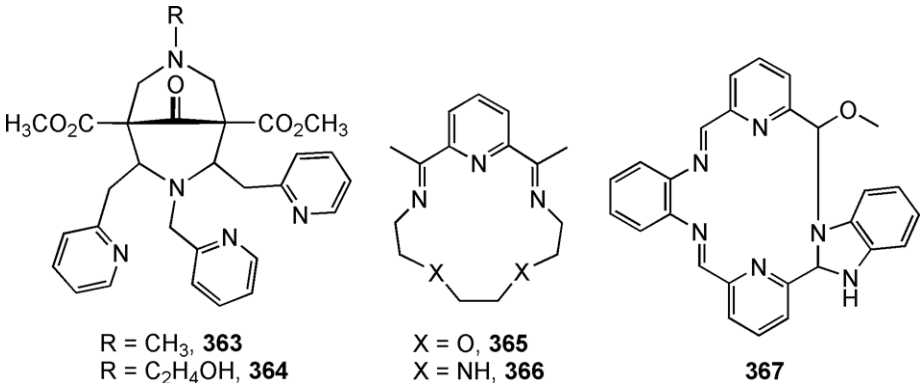
362



352



358



high-spin phase that undergoes the incomplete thermal spin-transition observed in powder samples. Both the low-spin, and 1:1 high:low-spin, low-temperature phases of $[Fe(CN)_2(\mathbf{365})] \cdot H_2O$ exhibit the LIESST effect, undergoing relaxation at 132 and 73 K, respectively [28,614–616]. The former temperature is the highest T(LIESST) value yet recorded in a molecular species [29]. The 1:1 high:low-spin phase also undergoes the reverse-LIESST effect, albeit with only ca. 15% conversion efficiency [615]. Laser irradiation of the 1:1 high:low-spin material at 216 K generates a high-spin species, which decays *irreversibly* back to a partially low-spin form upon annealing at 203 K for 2 h [617]. A 1-D chain complex was produced by linking $[Fe(CN)_2(\mathbf{365})]$ centres with $[Mn(hfac)_2]$ moieties (hfacH = 1,1,1,5,5,5-hexafluoro-2,4-pentanedione), which also undergoes a 50% complete spin-transition, at 110 K, albeit this time gradually and without hysteresis [618]. $[Fe(CN)_2(\mathbf{366})]$ and related complexes of pentaaza macrocycles are low-spin [611], but $[Fe(NCS)_2L]$ (L = **365** [619], **366** [620] and **367** [621]) are all high-spin at room temperature, and also seven-coordinate.

7. Hexadentate ligands

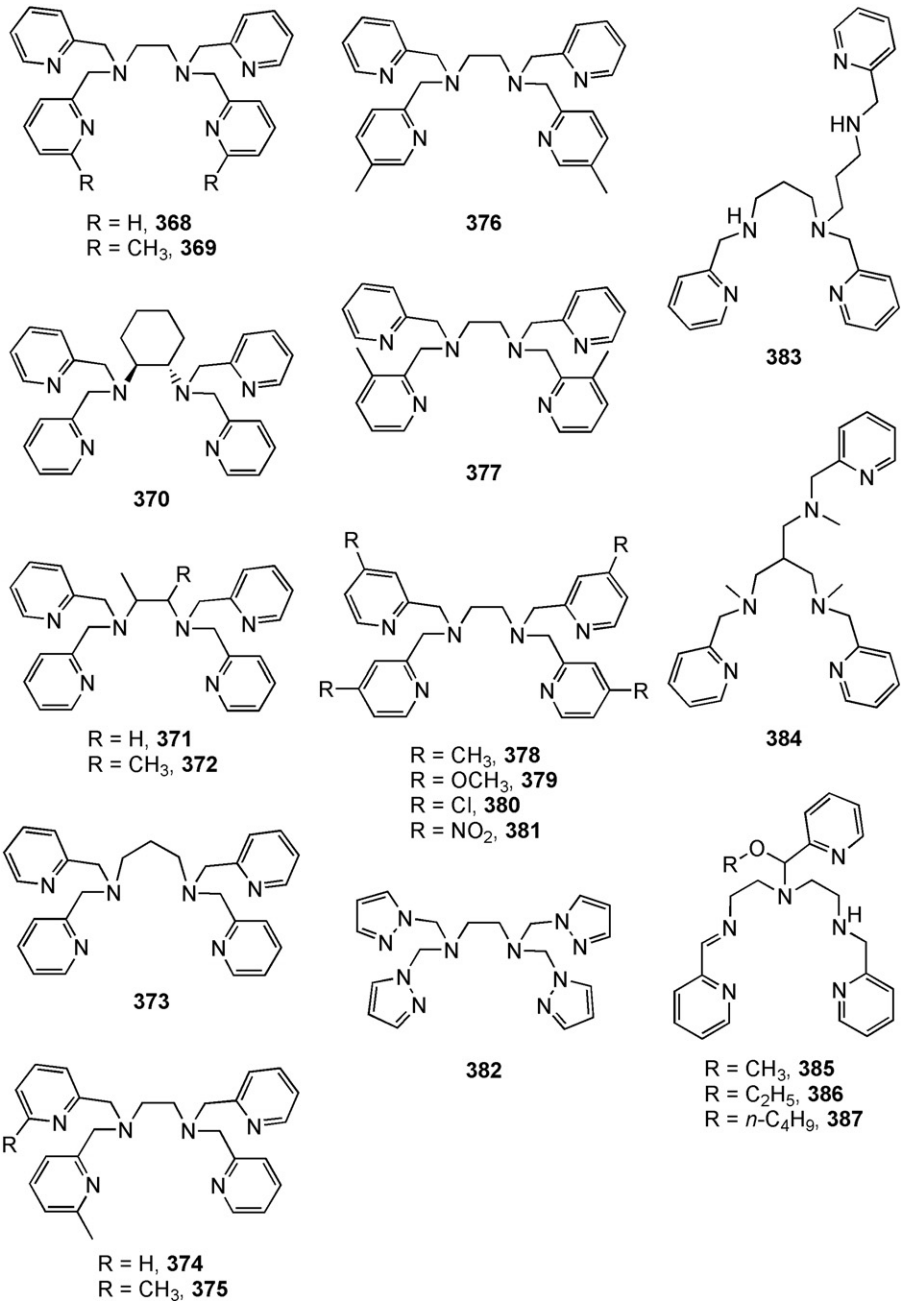
Solid $[Fe(\mathbf{368})][ClO_4]_2 \cdot xH_2O$ ($x = 1/2$–1) has a slightly variable water content, and exhibits a gradual, complete spin transition with a midpoint near 365 K [622–624]. Unusually, only a single, temperature-dependent Mössbauer doublet is observed in this compound at all temperatures, showing that its high- and low-spin states interconvert more quickly that the Mössbauer timescale [623]. Photolysis experiments established that this spin-state exchange takes place on a sub-picosecond timescale in aqueous solution [625]. This rapid spin-interconversion was suggested to reflect a trigonal twist in the six-coordinate coordination sphere, leading to an increase in spin–orbit interaction between the different spin-states of the molecule [623]. While the kinetics of light-induced spin-interconversion in $[Fe(\mathbf{368})][ClO_4]_2$ in solution have been studied in some detail [625,626], its LIESST properties in the solid state have not been reported. An anhydrous material, $[Fe(\mathbf{368})][ClO_4]_2$, has also been described, whose spin-transition is still gradual and shifted to significantly higher temperatures than the hydrate [623,626], while its $T_{1/2}$ for spin-crossover in dmf solution has been measured at 363 K. The $[Fe(\mathbf{368})]^{2+}$ dication has been used as a model in several theoretical studies of spin-crossover systems [63,64,627]. The complex $[Fe(NCS)(\mathbf{369})]PF_6$ is high-spin at room temperature by IR ($\nu_{C\equiv N} = 2055\ cm^{-1}$), with one dangling 6-methylpyridyl group [605].

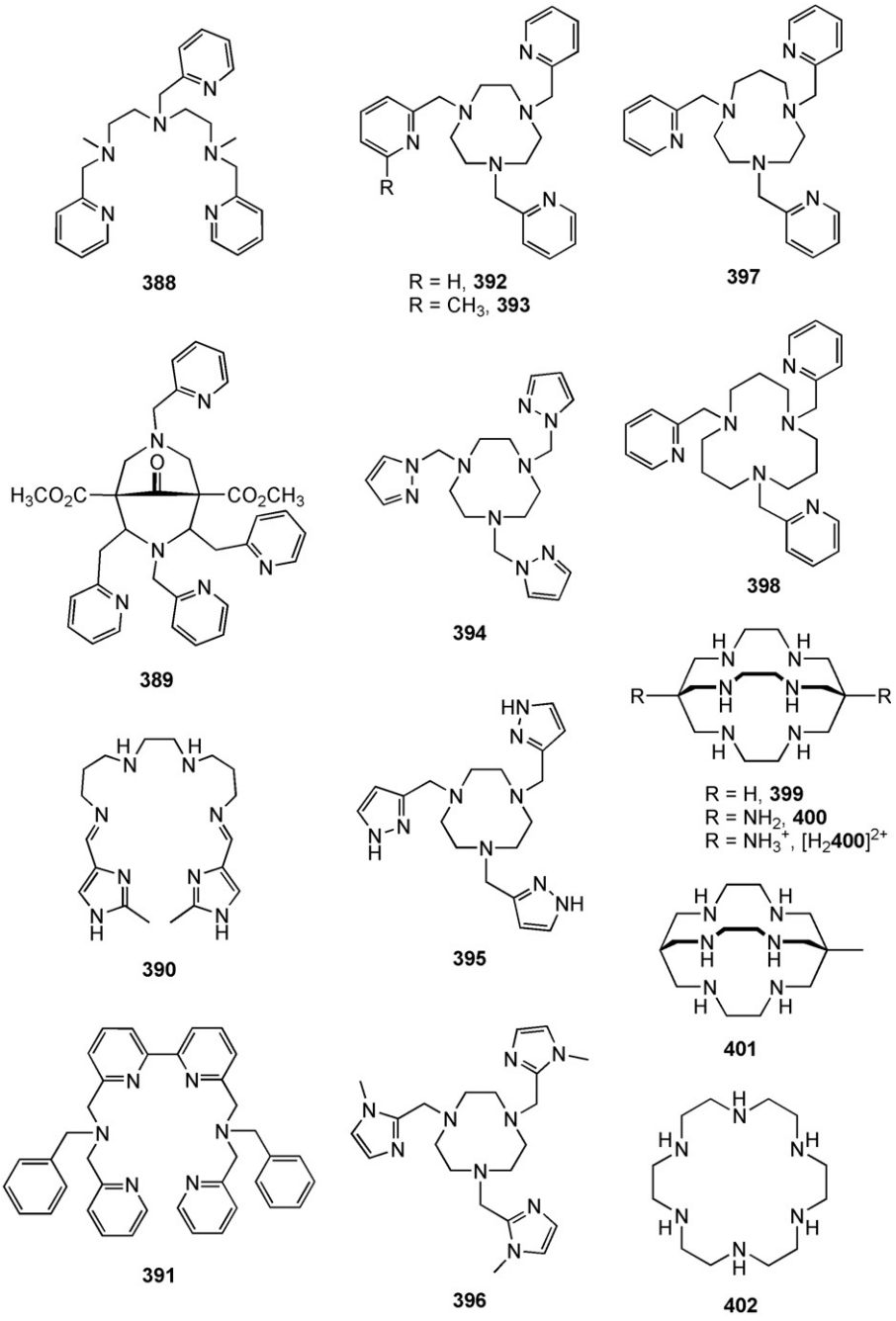
Spin-crossover in $[Fe(\mathbf{370})][ClO_4]_2 \cdot 2H_2O$ [622,628] and $[Fe(\mathbf{371})][ClO_4]_2 \cdot xH_2O$ ($x = 2/3$–1) [622,627] is gradual and centred significantly above 400 K, while $[Fe(\mathbf{373})][ClO_4]_2 \cdot H_2O$ is low-spin, and $[Fe(\mathbf{369})][ClO_4]_2 \cdot H_2O$ [622] and $[Fe(\mathbf{374})][ClO_4]_2 \cdot xH_2O$ ($x = 2/3$–1) [622,627] are high-spin. $[Fe(\mathbf{372})][ClO_4]_2$ undergoes thermal spin-crossover in dmf solution (as do $[Fe(\mathbf{370})][ClO_4]_2$ and $[Fe(\mathbf{371})][ClO_4]_2$), but its solid state properties were not reported [236]. Spin-interconversion in $[Fe(\mathbf{370})][ClO_4]_2$ in methanol solution shows biphasic kinetics, which was attributed to the existence of two conformations of the ligand cyclohexyl ring [236,628]. Interestingly, all other known examples of this phenomenon (discussed below) also involve iron complexes of hexadentate ligands that completely encapsulate the metal ion. Iron(II) complexes of **375**–**381** have been synthesised, but their spin-states were not recorded [629]. In contrast to the six-coordinate complexes of the tetrapyridyl ligands, $[FeX(\mathbf{382})]X \cdot H_2O$ ($X^- = BF_4^-$ and ClO_4^-) are seven-coordinate and high-spin above 4 K [630].

Spin-crossover in $[Fe(\mathbf{383})][BF_4]_2$ is discontinuous. The first step is gradual, centred at 181 K and involves 50% of the sample. The second step is abrupt, at 121 K with a 4 K hysteresis; below that temperature, about 90% of the material is in its low-spin state. The high- and low-spin forms of the compound are isostructural, but differ in that one of the amino donors is disordered in the high-spin crystal, but crystallographically ordered in the low-spin state. This order:disorder transition is probably the cause of the cooperativity in the low-temperature spin-crossover step [631]. Stereochemically similar $[Fe(\mathbf{384})][ClO_4]_2$ is also a spin-crossover compound, exhib-

iting a gradual, complete transition centred at 196 K in the solid state and 230 K in propionitrile [632]. An inelastic neutron scattering study has been performed on this complex [633]. Crystalline $[FeL][B(C_6H_5)_4]_2$ (L = **385**–**387**) are all low-spin [634], while $[Fe(\mathbf{388})][BF_4]_2$ [635] and $[Fe(NCS)_2(\mathbf{389})]$ [576] are high-spin, the latter compound having a tetradentate bispidene ligand with two dangling pyridyl donors.

The compound $[Fe(\mathbf{390})][ClO_4]_2$ undergoes an abrupt thermal spin-transition, with $T = 172$ K and a 5 K hysteresis loop [636]. This reflects a crystallographic phase change during spin-crossover, caused by a conformational change in one of the the six-membered chelate rings. The bipyridyl-containing ligand complex $[Fe(\mathbf{391})][PF_6]_2$ exists as an approximately 1:3 high:low-spin mixture, which is almost invariant between 77 and 293 K. Its crystal structure reveals two independent iron sites, one of which is low-spin while the other suffers strongly from disorder and was proposed to contain a mixture of high- and low-spin centres [637].





Salts of the macrocylic complexes $[Fe(\mathbf{392})]^{2+}$ [64,635,638], and $[Fe(\mathbf{395})]FeCl_4$ [639] and $[Fe(\mathbf{396})][B(C_6H_5)_4]_2$ [640], are all low-spin. However, $[Fe(\mathbf{393})][ClO_4]_2$ exhibits a very gradual spin-transition centred significantly above room temperature [641], while salts of $[Fe(\mathbf{394})]^{2+}$ are high-spin at room temperature [639,640]. Although it is low-spin in the solid state, $[Fe(\mathbf{397})][ClO_4]_2$ shows a thermal spin-transition in $MeCN/H_2O$ mixed solvent systems. Transient spin-interconversion in this solvent exhibits biphasic kinetics, the rate of one of the processes being invariant with temperature (that is, it has no activation barrier) [642]. This was proposed to reflect the conformational stiffness of the macrocyclic ligand framework (cf. $[Fe(\mathbf{370})][ClO_4]_2$, see above). The larger, 12-membered macrocycle **398** forms high-spin iron(II) complexes [635,643]. The solid macrobicyclic complexes $[FeL][CF_3SO_3]_2$ (L = **399** and **401**) and $[Fe(H_2\mathbf{400})]Cl_2Br_2 \cdot 4H_2O$ are high-spin, but $[Fe(\mathbf{400})][CF_3SO_3]_2$ is low-spin [644,645]. All three of the triflate salts undergo spin-transitions in CD_3CN, however [644]. The magnetic moment of the high-spin compound $[Fe(\mathbf{402})][B(C_6H_5)_4]_2$ is slightly temperature-dependent, which was interpreted on the basis of partial electron transfer between the iron(II) dications and tetraphenylborate anions [646].

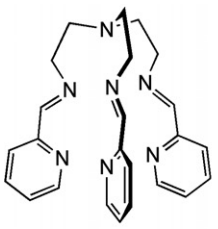
8. Higher denticity ligands

Iron(II) complexes of heptadentate Schiff bases derived from *tris*-(2-aminoethyl)amine (tren) have been heavily studied (Table 9). The high-spin forms of these compounds typically adopt [6+1] coordination geometries, with the tertiary amino donor capping one face of a compressed octahedron with a Fe–N distance of 2.5–3.3 Å (tabulated in [678]). The stereochemistries of the low-spin forms of these compounds tend to be more rigorously octahedral, with the capping N donor being >3.4 Å from the iron atom [648,649,657,665,670–674]. There is no apparent correlation between the distance of this additional ligand donor from the iron centre, and whether or not the compound undergoes spin-crossover [678].

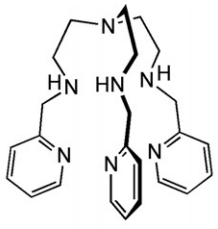
Table 9
Iron(II) complex salts of potentially heptadentate Schiff bases derived from *tris*-(2-aminoethyl)amine and related ligands

	Spin-state or $T_{1/2}$ (K)	Form of spin-state transition	Spin states of crystal structure(s)	Other measurements	Refs.
[Fe(**403**)]X_2 ($X^- = BF_4^-$, ClO_4^-)	LS		RT (LS, both salts)	Mag, Möss	[647–650]
[Fe(**403**)][PF_6]$_2$ (2 phases)	LS or 150	gradual, 50% complete	LS or HS	DFT, Mag, Möss, PES, Raman, Sol, XAS	[651–658]
[Fe(**404**)]X_2 $X^- = ClO_4^-$, PF_6^-	⩾400	both gradual		Mag, Möss, PES (PF_6^-), Raman (PF_6^-), Sol	[650–654,660,661,663]
[Fe(**405**)]X_2 ($X^- = ClO_4^-$, PF_6^-)	290–320	both gradual		Mag, Möss, PES (PF_6^-), Raman (PF_6^-), Sol	[650–654,660–663]
[Fe(**406**)]X_2 ($X^- = ClO_4^-$, PF_6^-) 654,656,660,662,663]	210–240	both gradual		Mag, Möss, PES (PF_6^-), Press (PF_6^-), Raman (PF_6^-), Sol, XAS	[150,650–
[Fe(**407**)][ClO_4]$_2$	HS at RT		HS	Mag	[658]
[Fe(**408**)]X_2 ($X^- = ClO_4^-$, BPh_4^-)	⩽293	both complete at 77 K	LS (ClO_4^-)[a]	Möss	[665]
[Fe(**408**–2H)] · H_2O	HS at RT		HS		[666]
[Fe(**409**)][BF_4]$_2$ · $3H_2O$	210	gradual	HS, LS	LIESST, Mag, Möss	[669,670]
[Fe(**409**)][ClO_4]$_2$	<293	50% complete at 77 K		Möss	[665]
				[Fe(**409**)]$Cl_{0.5}$[PF_6]$_{1.5}$ · $2H_2O$	LS
	LS		[666]		
[Fe(**409**)][Fe(**409**–3H)]BF_4	RT	gradual, sample-dependent	HS, LS	LIESST, Mag, Möss	[670]
[Fe(**409**)][Fe(**409**–3H)]X_2 ($X^- = NO_3^-$, BF_4^-)	160–190 Fe(II) >300 Fe(III)	both abrupt Fe(II) gradual Fe(III)	HS:LS, LS:LS	LIESST, Mag, Möss	[670,671]
[Fe(**410**)]I_2 · CH_3OH	HS			Mag	[672]
[Fe(**410**)]Cl[I_3]	113	abrupt	HS, LS	LIESST, Mag, Möss, Quen	[672]
[Fe(**410**)]Cl[PF_6]	122	abrupt, 50% complete	HS, 1:1 HS:LS	Mag, Möss	[673]
[Fe(**410**)]Cl[AsF_6]	82, 112	abrupt, 2 steps	HS, 1:1 HS:LS, LS	Mag, Möss, Quen	[673]
[Fe(**410**)]Cl[SbF_6]	117	gradual	HS, LS	Mag, Möss	[673]
[Fe(**410**)]Cl[CF_3SO_3]	82	abrupt, 4 K hysteresis	HS	Mag, Möss, Quen	[673]
[Fe(**410**)][NO_3]$_2$ · $1.5H_2O$	HS			Mag, Möss	[674]
[Fe(**410**)][Fe(**410**–3H)]X ($X^- = NO_3^-$, BF_4^-, ClO_4^-)	85–150, 160–220	both gradual, 2 steps	HS, 1:1 HS:LS, mostly LS (all NO_3^-)	LIESST (NO_3^-, BF_4^-), Mag, Möss (NO_3^-, ClO_4^-)	[674,675]
[Fe(**410**)][Fe(**410**–3H)]X ($X^- = PF_6^-$, AsF_6^-)	160–165, 235–250	both abrupt then gradual; 2 steps	HS, 1:1 HS:LS, mostly LS (all PF_6^-)	LIESST (AsF_6^-), Mag, Möss (PF_6^-)	[675]
[Fe(**410**)][Fe(**410**–3H)][NO_3]$_2$	HS Fe(II) ≈240 Fe(III)	very gradual		LIESST, Mag, Möss	[674]
[Fe(**411**)][NO_3]$_2$ · CH_3OH	HS		HS	Mag	[676]
[Fe(**412**)][ClO_4]$_2$	>77	>50% complete at 77 K	HS, <50% HS	Möss	[668]
[Fe(**413**)][PF_6]$_2$	HS		HS	Mag	[677]
[Fe(**414**)]X_2 · H_2O ($X^- = BF_4^-$, ClO_4^-)	both HS		HS (both salts)	Mag	[678]
[Fe(**415**)][ClO_4]$_2$ · H_2O	HS		HS	Mag, Möss	[679]

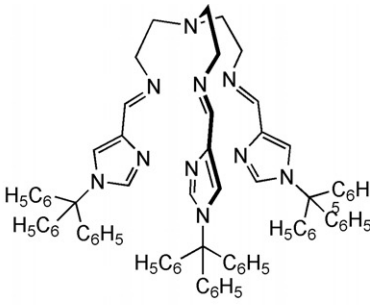
See Refs. [659,660,667,668] for additional examples, and Table 1 for the abbreviations of physical techniques.
[a] From a solvated crystal structure.



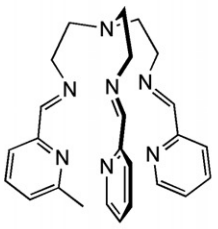
403



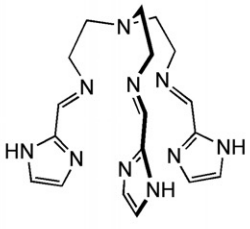
407



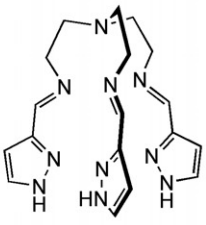
413



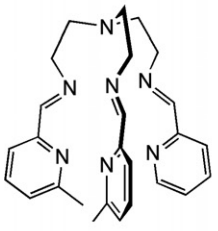
404



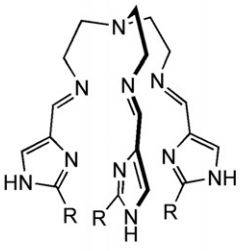
408



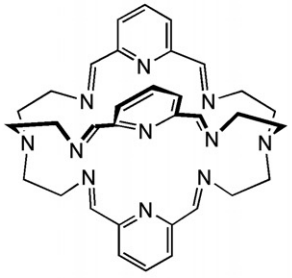
414



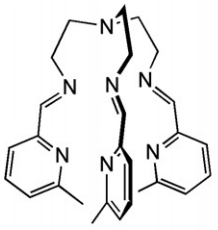
405



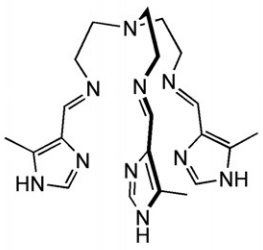
R = H, **409**
R = CH_3, **410**
R = C_6H_5, **411**



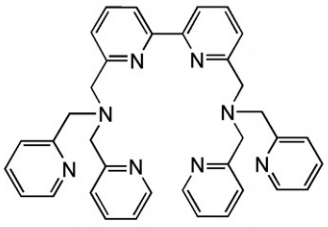
415



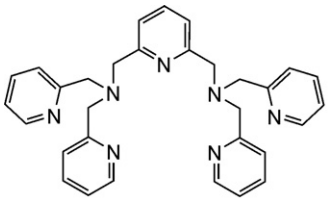
406



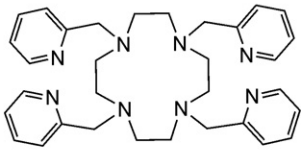
412



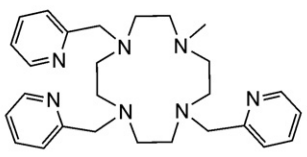
416



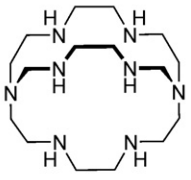
417



419



418



420

Two crystal phases of [Fe(**403**)][PF_6]$_2$ have been isolated [658]. One of these is low-spin (as are other salts of this cation), but the other undergoes a gradual spin-transition centred near 150 K that is about 50% complete. The spin-crossover $T_{1/2}$ in acetone and DMSO solutions for [Fe(**404**)][PF_6]$_2$ and [Fe(**405**)][PF_6]$_2$ is almost identical to their solid state values but [Fe(**406**)][PF_6]$_2$ is high-spin in these solvents [651,653], despite also being a spin-crossover compound in the sold state. The kinetics of light-induced spin-interconversion and decay in [Fe(**405**)][ClO_4]$_2$ doped into polymer films [661], solutions of [Fe(**404**)]$^{2+}$, [Fe(**405**)]$^{2+}$ and [Fe(**406**)]$^{2+}$ [662], and the doped solids [Fe_xZn_{1-x}L][PF_6]$_2$ (L = **403**–**406**; $x = 0.00025$–0.0005) [120,664], have been studied in detail. The first of these

studies provided the first direct experimental evidence for the involvement of quantum mechanical tunnelling in the relaxation of metastable spin-states [661]. Ultrafast EXAFS measurements in solution have revealed that the low → high-spin conversion in [Fe(**403**)][PF_6]$_2$ is complete within 70 ps following laser irradiation [656]. The complex [Fe(**407**)]$^{2+}$ is air-sensitive, and undergoes conversion to [Fe(**403**)]$^{2+}$ in aerobic solution [658].

A series of salts of [Fe^{II}L][Fe^{II}(L–3H)]$^+$ and [Fe^{II}L]-[Fe^{III}(L–3H)]$^{2+}$ (L = **409** and **410**) have been studied in detail. While [Fe(**409**)][Fe(**409**–3H)]BF_4 undergoes spin-crossover in one gradual step centred near room temperature [670], the spin-transitions of [Fe(**410**)][Fe(**410**–3H)]X (X$^-$ = NO_3^-, BF_4^-, ClO_4^-, PF_6^-, AsF_6^- and SbF_6^-) all show two discrete steps arising from the [Fe(**410**)]$^{2+}$ and [Fe(**410**–3H)]$^-$ sites in the lattice [674,675]. The iron(III) sites in the mixed-valent compounds [Fe(**409**)][Fe(**409**–3H)]X_2 (X$^-$ = NO_3^- [671] and BF_4^- [670]) exhibit gradual spin-transitions centred above room temperature, while their iron(II) centres show a more abrupt transition at 160–190 K. Iron(III) spin-crossover in [Fe(**410**)][Fe(**410**–3H)][NO_3]$_2$ is similarly broad but shifted to lower temperature, as expected on steric grounds, while its iron(II) content remains high-spin [674]. All these compounds crystallise in the chiral space groups *P*3 or *R*3, with two distinct iron environments lying on C_3 axes. Both iron centres in [Fe(**410**)][Fe(**410**–3H)]BF_4 exhibit the LIESST effect, giving ca. 75% total photoconversion at 5 K and a relaxation temperature near 50 K [675]. Conversely, only the iron(II) content of [Fe(**409**)][Fe(**409**–3 H)][NO_3]$_2$ undergoes LIESST photoconversion, relaxing between 50 and 100 K [671]. The LIESST phenomenon was also detected in [Fe(**409**)]-[Fe(**409**–3H)]BF_4 [670] and [Fe(**410**)][Fe(**410**–3H)]AsF_6 [675], but was much less efficient. Thermal and photochemical spin-crossover has also been studied in several salts of the simple mononuclear analogues [Fe(**409**)]$^{2+}$ [665,669,670] and [Fe(**410**)]$^{2+}$ [672,673].

Crystals of the potentially octadentate complex [Fe(**416**)][PF_6]$_2$ contain two unique iron sites. One of these is octahedral with two dangling pyridyl groups, while the other is best described as having a [6+1] coordination geometry with one long Fe···N pyridyl interaction of 3.1 Å [637]. The complex is predominantly high-spin in the solid state and in CD_3CN solution, but with a ca. 25% low-spin fraction that does not change significantly with temperature. The kinetics of high → low-spin state relaxation of [Fe(**416**)][PF_6]$_2$ in solution are biphasic, demonstrating that the two high-spin coordination geometries found in the solid state are also present in solution [637]. Crystals of [Fe(**417**)][ClO_4]$_2$ contain seven-coordinate complex molecules that appear to remain high-spin on cooling to 80 K. As for [Fe(**416**)]$^{2+}$, its UV/Vis spectrum suggests the presence of a six-coordinate iron centre in solution, however [680]. The crystal structure of [Fe(**418**)][ClO_4]$_2$ at room temperature is seven-coordinate and high-spin [681], while eight-coordinate [Fe(**419**)]-[ClO_4]$_2$ remains high-spin on cooling to 5 K [682]. Solid [Fe(**420**)][ClO_4]$_2$ · 3H_2O is also high-spin at room temperature; although no crystal structure is available, its manganese(II) analogue is only six-coordinate [683]. A small number of other iron(II) complexes with potential, or actual, [FeN_7]$^{2+}$ or [FeN_8]$^{2+}$ donor sets have also been reported but their spin-state behaviour was not described [684].

References

[1] P. Gütlich, Y. Garcia, H.A. Goodwin, Chem. Soc. Rev. 29 (2000) 419.
[2] (a) L. Cambi, A. Cagnasso, Atti Accad. Naz. Lincei 13 (1931) 809;
(b) L. Cambi, L. Szegö, Ber. Dtsch. Chem. Ges. 64 (1931) 2591;
(c) L. Cambi, L. Szegö, A. Cagnasso, Atti Accad. Naz. Lincei 15 (1932) 266;
(d) L. Cambi, L. Szegö, A. Cagnasso, Atti Accad. Naz. Lincei 15 (1932) 329;
(e) L. Cambi, L. Szegö, Ber. Dtsch. Chem. Ges. 66 (1933) 656.
[3] A.H. Ewald, R.L. Martin, I.G. Ross, A.H. White, Proc. Roy. Soc. London Ser. A 280 (1964) 235.
[4] (a) W.A. Baker Jr., H.M. Bobonich, Inorg. Chem. 3 (1964) 1184;
(b) E. König, K. Madeja, Inorg. Chem. 6 (1967) 48.
[5] G.A. Renovitch, W.A. Baker Jr., J. Am. Chem. Soc. 89 (1967) 6377.
[6] J. Kröber, E. Codjovi, O. Kahn, F. Grolière, C. Jay, J. Am. Chem. Soc. 115 (1993) 9810.
[7] (a) O. Kahn, C.J. Martinez, Science 179 (1998) 44;
(b) O. Kahn, Chem. Br. 35 (2) (1999) 24.
[8] A. Bousseksou, C. Vieu, J.-F. Létard, P. Demont, J.-P. Tuchagues, L. Malaquin, J. Menegotto, L. Salmon, Molecular memory and method for making same, PCT Int. WO 2003019695, 2003, 22pp.
[9] J.-F. Létard, P. Guionneau, L. Goux-Capes, Top. Curr. Chem. 235 (2004) 221.
[10] R.N. Muller, L. van der Elst, S. Laurent, J. Am. Chem. Soc. 125 (2003) 8405.
[11] A. Bousseksou, G. Molnár, P. Demont, J. Menegotto, J. Mater. Chem. 13 (2003) 2069.
[12] M. Enamullah, W. Linert, Thermochim. Acta 388 (2002) 401.
[13] J.A. Real, A.B. Gaspar, V. Niel, M.C. Muñoz, Coord. Chem. Rev. 236 (2003) 121.
[14] M. Hostettler, K.W. Toernroos, D. Chernyshov, B. Vangdal, H.-B. Bürgi, Angew. Chem., Int. Ed. 43 (2004) 4589.
[15] J.M. Holland, J.A. McAllister, C.A. Kilner, M. Thornton-Pett, A.J. Bridgeman, M.A. Halcrow, J. Chem. Soc., Dalton Trans. (2002) 548.
[16] V. Ksenofontov, A.B. Gaspar, P. Gütlich, Top. Curr. Chem. 235 (2004) 23.
[17] P. Gütlich, V. Ksenofontov, A.B. Gaspar, Coord. Chem. Rev. 249 (2005) 1811.
[18] P. Gütlich, A. Hauser, H. Spiering, Angew. Chem., Int. Ed. 33 (1994) 2024.
[19] A. Bousseksou, F. Varret, M. Goiran, K. Boukheddaden, J.-P. Tuchagues, Top. Curr. Chem. 235 (2004) 65.
[20] S. Decurtins, P. Gütlich, C.P. Köhler, H. Spiering, A. Hauser, Chem. Phys. Lett. 105 (1984) 1.
[21] S. Decurtins, P. Gütlich, C.P. Köhler, H. Spiering, J. Chem. Soc., Chem. Commun. (1985) 430.
[22] S. Decurtins, P. Gütlich, K.M. Hasselbach, A. Hauser, H. Spiering, Inorg. Chem. 24 (1985) 2174.
[23] (a) P. Gütlich, Y. Garcia, T. Woike, Coord. Chem. Rev. 219–221 (2001) 839;
(b) A. Hauser, Top. Curr. Chem. 234 (2004) 155.
[24] J.-F. Létard, L. Capes, G. Chastanet, N. Moliner, S. Létard, J.A. Real, O. Kahn, Chem. Phys. Lett. 313 (1999) 115.

[25] S. Marcen, L. Lecren, L. Capes, H.A. Goodwin, J.-F. Létard, Chem. Phys. Lett. 358 (2002) 87.
[26] V.A. Money, J.S. Costa, S. Marcén, G. Chastanet, J. Elhaïk, M.A. Halcrow, J.A.K. Howard, J.-F. Létard, Chem. Phys. Lett. 391 (2004) 273.
[27] N. Shimamoto, S.-S. Ohkoshi, O. Sato, K. Hashimoto, Inorg. Chem. 41 (2002) 678.
[28] S. Hayami, Z.-Z. Gu, Y. Einaga, Y. Kobayasi, Y. Ishikawa, Y. Yamada, A. Fujishima, O. Sato, Inorg. Chem. 40 (2001) 3240.
[29] (a) J.-F. Létard, P. Guionneau, O. Nguyen, J.S. Costa, S. Marcen, G. Chastanet, M. Marchivie, L. Capes, Chem. Eur. J. 11 (2005) 4582;
(b) J.-F. Létard, J. Mater. Chem. 16 (2006) 2550.
[30] M. Marchivie, P. Guionneau, J.-F. Létard, D. Chasseau, J.A.K. Howard, J. Phys. Chem. Solids 65 (2004) 17, and refs. therein.
[31] P. Gütlich, Top. Curr. Chem. 234 (2004) 231.
[32] R. Hinek, H. Spiering, P. Gütlich, A. Hauser, Chem. Eur. J. 2 (1996) 1435.
[33] E. Freysz, S. Montant, S. Létard, J.-F. Létard, Chem. Phys. Lett. 394 (2004) 318.
[34] (a) S. Bonhommeau, G. Molnár, A. Galet, A. Zwick, J.A. Real, J.J. McGarvey, A. Bousseksou, Angew. Chem., Int. Ed. 44 (2005) 4069;
(b) S. Cobo, G. Molnár, J.A. Real, A. Bousseksou, Angew. Chem., Int. Ed. 45 (2006) 5786.
[35] (a) P.J. van Koningsbruggen, Y. Maeda, H. Oshio, Top. Curr. Chem. 233 (2004) 259;
(b) H.A. Goodwin, Top. Curr. Chem. 234 (2004) 23;
(c) Y. Garcia, P. Gütlich, Top. Curr. Chem. 234 (2004) 49.
[36] E. König, Prog. Inorg. Chem. 35 (1987) 527.
[37] See e.g. (a) S. Hayami, Z.-Z. Gu, H. Yoshiki, A. Fujishima, O. Sato, J. Am. Chem. Soc. 123 (2001) 11644;
(b) M. Zerara, A. Hauser, ChemPhysChem 5 (2004) 395.
[38] S. Schenker, A. Hauser, R.M. Dyson, Inorg. Chem. 35 (1996) 4676.
[39] P. Gütlich, H.A. Goodwin (Eds.), Top. Curr. Chem. 233–235 (2004).
[40] J.A. Real, A.B. Gaspar, V. Niel, M.C. Muñoz, Dalton Trans. (2005) 2062.
[41] O. Sato, Acc. Chem. Res. 36 (2003) 692.
[42] P. Gütlich, P.J. van Koningsbruggen, F. Renz, Struct. Bonding (Berlin) 107 (2004) 27.
[43] A.B. Gaspar, V. Ksenofontov, M. Seredyuk, P. Gütlich, Coord. Chem. Rev. 249 (2005) 2661.
[44] (a) Y. Garcia, V. Niel, M.C. Muñoz, J.A. Real, Top. Curr. Chem. 233 (2004) 229;
(b) A.B. Gaspar, M.C. Muñoz, J.A. Real, J. Mater. Chem. 16 (2006) 2522.
[45] C.D. Burbridge, D.M.L. Goodgame, Inorg. Chim. Acta 4 (1971) 231.
[46] B.D. Pandey, D.C. Rupainwar, Transition Met. Chem. 6 (1981) 249.
[47] W. Hieber, R. Werner, Chem. Ber. 90 (1957) 286.
[48] R.J. Doedens, L.F. Dahl, J. Am. Chem. Soc. 88 (1966) 4847.
[49] Y. Sohrin, H. Kokusen, M. Matsui, Inorg. Chem. 34 (1995) 3928.
[50] C. Roux, J. Zarembowitch, J.-P. Itie, A. Polian, M. Verdaguer, Inorg. Chem. 35 (1996) 574.
[51] (a) C. Roux, J. Zarembowitch, B. Gallois, T. Granier, R. Claude, Inorg. Chem. 33 (1994) 2273;
(b) M.-L. Boillot, C. Roux, J.-P. Audière, A. Dausse, J. Zarembowitch, Inorg. Chem. 35 (1996) 3975.
[52] (a) J. Reedijk, Recl. Trav. Chim. Pays-Bas 88 (1969) 1451;
(b) J. Reedijk, Recl. Trav. Chim. Pays-Bas 90 (1971) 1285.
[53] (a) J. Reedijk, J.A. Smit, Recl. Trav. Chim. Pays-Bas 90 (1971) 1135;
(b) J. Reedijk, D.W. Engelfriet, Recl. Trav. Chim. Pays-Bas 91 (1972) 883.
[54] (a) E.G. Pavel, N. Kitajima, E.I. Solomon, J. Am. Chem. Soc. 120 (1998) 3949;
(b) G. Carver, P.L.W. Tregenna-Piggott, A.-L. Barra, A. Neels, J.A. Stride, Inorg. Chem. 42 (2003) 5771.
[55] T.E. Westre, P. Kennepohl, J.G. DeWitt, B. Hedman, K.O. Hodgson, E.I. Solomon, J. Am. Chem. Soc. 119 (1997) 6297.
[56] S. Dev, E. Ramli, T.B. Rauchfuss, S.R. Wilson, Inorg. Chem. 30 (1991) 2514.
[57] (a) J. Reedijk, Recl. Trav. Chim. Pays-Bas 90 (1971) 1249;
(b) J. Reedijk, J. Inorg. Nucl. Chem. 33 (1971) 179;
(c) F. Seel, R. Lehnert, E. Bill, A. Trautwein, Z. Naturforsch., Teil B 35 (1980) 631;
(d) R.J. Broekema, P.F.M. Durville, J. Reedijk, J.A. Smit, Transition Met. Chem. 7 (1982) 25;
(e) L.L. Miller, R.A. Jacobson, Y.-S. Chen, D.M. Kurtz jr, Acta Crystallogr., Sect. C 45 (1989) 527;
(f) T.B. Rauchfuss, S. Dev, S.R. Wilson, Inorg. Chem. 31 (1992) 153;
(g) R.C. Scarrow, M.G. Trimitsis, C.P. Buck, G.N. Grove, R.A. Cowling, M.J. Nelson, Biochemistry 33 (1994) 15023;
(h) C.R. Randall, L. Shu, Y.-M. Chiou, K.S. Hagen, M. Ito, N. Kitajima, R.J. Lachicotte, Y. Zang, L. Que Jr., Inorg. Chem. 34 (1995) 1036;
(i) J.A. García-Vázquez, J. Romero, A. Sousa-Pedrares, A. Sousa, A .D. Garnovskii, D.A. Garnovskii, J. Chem. Cryst. 30 (2000) 23.
[58] M. James, H. Kawaguchi, K. Tatsumi, Polyhedron 16 (1997) 4279.
[59] P.J. van Koningsbruggen, Top. Curr. Chem. 233 (2004) 123.
[60] (a) W. Hibbs, A.M. Arif, P.J. van Koningsbruggen, J.S. Miller, CrystEngComm (1999) 12;
(b) W. Hibbs, P.J. van Koningsbruggen, A.M. Arif, W.W. Shum, J.S. Miller, Inorg. Chem. 42 (2003) 5645.
[61] W.L. Driessen, P.H. van der Voort, Inorg. Chim. Acta 21 (1977) 217.
[62] B. Maiti, B.R. McGarvey, P.S. Rao, L.C. Stubbs, J. Magn. Reson. 54 (1983) 99.
[63] H. Paulsen, L. Duelund, H. Winkler, H. Toftlund, A.X. Trautwein, Inorg. Chem. 40 (2001) 2201.
[64] M.B. Darkhovskii, A.L. Tchougréeff, J. Phys. Chem. A 108 (2004) 6351.
[65] J. Kusz, P. Gütlich, H. Spiering, Top. Curr. Chem. 234 (2004) 129.
[66] P. Weinberger, M. Grunert, Vibr. Spectrosc. 34 (2004) 175.
[67] (a) P.L. Franke, J.G. Haasnoot, A.P. Zuur, Inorg. Chim. Acta 59 (1982) 5;
(b) E.W. Mueller, J. Ensling, H. Spiering, P. Gütlich, Inorg. Chem. 22 (1983) 2074.
[68] P. Poganiuch, P. Gütlich, Hyperfine Interact. 40 (1988) 331.
[69] L. Wiehl, Acta Crystallogr., Sect. B 49 (1993) 289.
[70] J. Kusz, H. Spiering, P. Gütlich, J. Appl. Cryst. 34 (2001) 229.
[71] R. Hinek, P. Gütlich, A. Hauser, Inorg. Chem. 33 (1994) 567.
[72] O. Roubeau, A.F. Stassen, I.F. Gramage, E. Codjovi, J. Linares, F. Varret, J.G. Haasnoot, J. Reedijk, Polyhedron 20 (2001) 1709.
[73] A. Vértes, M. Bokor, K. Süvegh, T. Marek, Z. Nemes-Vetéssy, I. Labádi, K. Burger, J. Phys. Chem. Solids 59 (1998) 1235.
[74] T. Marek, M. Bokor, K. Tompa, A. Vértes, K. Süvegh, Z. Nemes-Vetéssy, K. Burger, Struct. Chem. 14 (2003) 349.
[75] T. Buchen, P. Poganiuch, P. Gütlich, J. Chem. Soc., Dalton Trans. (1994) 2285.
[76] T. Buchen, D. Schollmeyer, P. Gütlich, Inorg. Chem. 35 (1996) 155.
[77] P. Adler, P. Poganiuch, H. Spiering, Hyperfine Interact. 52 (1989) 47.
[78] P. Gütlich, P. Poganiuch, Angew. Chem., Int. Ed. 30 (1991) 975.
[79] A.F. Stassen, O. Roubeau, I.F. Gramage, J. Linarès, F. Varret, I. Mutikainen, U. Turpeinen, J.G. Haasnoot, J. Reedijk, Polyhedron 20 (2001) 1699.
[80] R. Hinek, H. Spiering, D. Schollmeyer, P. Gütlich, A. Hauser, Chem. Eur. J. 2 (1996) 1427.
[81] A.F. Stassen, E. Dova, J. Ensling, H. Schenk, P. Gütlich, J.G. Haasnoot, J. Reedijk, Inorg. Chim. Acta 335 (2002) 61.
[82] (a) E. Dova, A.F. Stassen, R.A.J. Driessen, E. Sonneveld, K. Goubitz, R. Peschar, J.G. Haasnoot, J. Reedijk, H. Schenk, Acta Crystallogr., Sect. B 57 (2001) 531;
(b) E. Dova, R. Peschar, M. Takata, E. Nishibori, H. Schenk, A.F. Stassen, J.G. Haasnoot, Chem. Eur. J. 11 (2005) 5855.

[83] E. Dova, R. Peschar, M. Sakata, K. Kato, H. Schenk, Chem. Eur. J. 12 (2006) 5043.
[84] E. Dova, R. Peschar, M. Sakata, K. Kato, A.F. Stassen, H. Schenk, J.G. Haasnoot, Acta Crystallogr., Sect. B 60 (2004) 528.
[85] A.F. Stassen, M. Grunert, E. Dova, M. Müller, P. Weinberger, G. Wiesinger, H. Schenk, W. Linert, J.G. Haasnoot, J. Reedijk, Eur. J. Inorg. Chem. (2003) 2273.
[86] (a) A.B. Koudriavtsev, A.F. Stassen, J.G. Haasnoot, M. Grunert, P. Weinberger, W. Linert, Phys. Chem. Chem. Phys. 5 (2003) 3666;
(b) A.B. Koudriavtsev, A.F. Stassen, J.G. Haasnoot, M. Grunert, P. Weinberger, W. Linert, Phys. Chem. Chem. Phys. 5 (2003) 3676.
[87] J. Kusz, H. Spiering, P. Gütlich, J. Appl. Cryst. 33 (2000) 201.
[88] Y. Moritomo, K. Kato, A. Kuriki, A. Nakamoto, N. Kojima, M. Takata, M. Sakata, J. Phys. Soc. Jpn. 71 (2002) 2609.
[89] Y. Moritomo, K. Kato, A. Nakamoto, N. Kojima, E. Nishibori, M. Takata, M. Sakata, J. Phys. Soc. Jpn. 71 (2002) 1015.
[90] (a) J. Jung, H. Spiering, Z. Yu, P. Gütlich, Hyperfine Interact. 95 (1995) 107;
(b) J. Jung, G. Schmitt, L. Wiehl, A. Hauser, K. Knorr, H. Spiering, P. Gütlich, Z. Phys. B 100 (1996) 523;
(c) J. Jeftić, A. Hauser, J. Phys. Chem. B 101 (1997) 10262.
[91] L. Wiehl, H. Spiering, P. Gütlich, K. Knorr, J. Appl. Cryst. 23 (1990) 151.
[92] N.O. Moussa, G. Molnár, X. Ducros, A. Zwick, T. Tayagaki, K. Tanaka, A. Bousseksou, Chem. Phys. Lett. 402 (2005) 503.
[93] J. Jeftić, H. Romstedt, A. Hauser, J. Phys. Chem. Solids 57 (1996) 1743.
[94] S.J. Campbell, V. Ksenofontov, Y. Garcia, J.S. Lord, Y. Boland, P. Gütlich, J. Phys. Chem. B 107 (2003) 14289.
[95] A. Hauser, Chem. Phys. Lett. 124 (1986) 543.
[96] A. Hauser, Coord. Chem. Rev. 111 (1991) 275, and refs. therein.
[97] X.J. Liu, Y. Moritomo, T. Kawamoto, A. Nakamoto, N. Kojima, Phys. Rev. B 67 (2003) 012102.
[98] (a) J. Jeftić, B. Gillon, A. Goujon, Q. Nau, A. Gukasov, E. Codjovi, F. Varret, Polyhedron 22 (2003) 2155, and 3555 (correction);
(b) A. Goujon, B. Gillon, A. Gukasov, J. Jeftic, Q. Nau, E. Codjovi, F. Varret, Phys. Rev. B 67 (2003) 220401.
[99] L.H. Böttger, A.I. Chumakov, M.C. Grunert, P. Gütlich, J. Kusz, H. Paulsen, U. Ponkratz, V. Rusanov, A.X. Trautwein, J.A. Wolny, Chem. Phys. Lett. 429 (2006) 189.
[100] Y. Nagai, H. Saito, T. Hyodo, A. Vértes, K. Süvegh, Phys. Rev. B 57 (1998) 14119.
[101] (a) M. Bokor, T. Marek, K. Tompa, J. Mag. Reson. A 122 (1996) 157;
(b) M. Bokor, T. Marek, K. Tompa, P. Gütlich, A. Vértes, Eur. Phys. J. D 7 (1999) 567;
(c) T. Marek, M. Bokor, G. Lasanda, K. Tompa, L. Párkányi, J. Buschmann, J. Phys. Chem. Solids 61 (2000) 621.
[102] J. Jeftić, M. Matsarski, A. Hauser, A. Goujon, E. Codjovi, J. Linares, F. Varret, Polyhedron 20 (2001) 1599.
[103] A. Goujon, B. Gillon, A. Debede, A. Cousson, A. Gukasov, J. Jeftić, G.J. McIntyre, F. Varret, Phys. Rev. B 73 (2006) 104413.
[104] J. Jung, F. Bruchhaeuser, R. Feile, H. Spiering, P. Gütlich, Z. Phys. B 100 (1996) 517.
[105] A. Ozarowski, B.R. McGarvey, Inorg. Chem. 28 (1989) 2262.
[106] A. Michalowicz, J. Moscovici, O. Kahn, J. Phys. IV 7 (1997) 633.
[107] J. Jeftić, R. Hinek, S.C. Capelli, A. Hauser, Inorg. Chem. 36 (1997) 3080.
[108] T. Buchen, P. Gütlich, Chem. Phys. Lett. 220 (1994) 262.
[109] B.A. Katz, C.E. Strouse, Inorg. Chem. 19 (1980) 658.
[110] M. Sorai, J. Ensling, K.M. Hasselbach, P. Gütlich, Chem. Phys. 20 (1977) 197.
[111] T. Nakamoto, A. Bhattacharjee, M. Sorai, Bull. Chem. Soc. Jpn. 77 (2004) 921.
[112] M.-L. Boillot, J. Zarembowitch, J.-P. Itie, A. Polian, E. Bourdet, J.G. Haasnoot, New J. Chem. 26 (2002) 313, and 27 (2003) 663 (correction).
[113] A.M. Greenaway, E. Sinn, J. Am. Chem. Soc. 100 (1978) 8080.
[114] A.M. Greenaway, C.J. O'Connor, A. Schrock, E. Sinn, Inorg. Chem. 18 (1979) 2692.
[115] B.A. Katz, C.E. Strouse, J. Am. Chem. Soc. 101 (1979) 6214.
[116] (a) T. Nakamoto, Z.-C. Tan, M. Sorai, Inorg. Chem. 40 (2001) 3805;
(b) H. Oyanagi, T. Tayagaki, K. Tanaka, J. Luminesc. 119-120 (2006) 361.
[117] P.S. Rao, P. Ganguli, B.R. McGarvey, Inorg. Chem. 20 (1981) 3682.
[118] P. Gütlich, H. Köppen, H.G. Steinhäuser, Chem. Phys. Lett. 74 (1980) 475.
[119] P. Adler, L. Wiehl, E. Meissner, C.P. Köhler, H. Spiering, P. Gütlich, J. Phys. Chem. Solids 48 (1987) 517.
[120] A. Hauser, A. Vef, P. Adler, J. Chem. Phys. 95 (1991) 8710.
[121] A. Vef, U. Manthe, P. Gütlich, A. Hauser, J. Chem. Phys. 101 (1994) 9326.
[122] H. Köppen, E.W. Müller, C.P. Köhler, H. Spiering, E. Meissner, P. Gütlich, Chem. Phys. Lett. 91 (1982) 348.
[123] R. Jakobi, H. Spiering, P. Gütlich, J. Phys. Chem. Solids 53 (1992) 267.
[124] (a) T. Kohlhaas, H. Spiering, P. Gütlich, Z. Phys. B 102 (1997) 455;
(b) H. Romstedt, H. Spiering, P. Gütlich, J. Phys. Chem. Solids 59 (1998) 1353.
[125] (a) M. Mikami, M. Konno, Y. Saito, Chem. Phys. Lett. 63 (1979) 566;
(b) M. Mikami, M. Konno, Y. Saito, Acta Crystallogr., Sect. B 36 (1980) 275.
[126] D. Chernyshov, M. Hostettler, K.W. Törnroos, H.-B. Bürgi, Angew. Chem., Int. Ed. 42 (2003) 3825.
[127] (a) Y. Ogawa, S. Koshihara, K. Koshino, T. Ogawa, C. Urano, H. Takagi, Phys. Rev. Lett. 84 (2000) 3181;
(b) T. Luty, K. Yonemitsu, J. Phys. Soc. Jpn. 73 (2004) 1237.
[128] I. Sanner, E. Meissner, H. Köppen, H. Spiering, P. Gütlich, Chem. Phys. 86 (1984) 227.
[129] N. Huby, L. Guerin, E. Collet, L. Toupet, J.-C. Ameline, H. Cailleau, T. Roisnel, T. Tayagaki, K. Tanaka, Phys. Rev. B 69 (2004) 020101.
[130] J. Kusz, D. Schollmeyer, H. Spiering, P. Gütlich, J. Appl. Cryst. 38 (2005) 528.
[131] H. Romstedt, A. Hauser, H. Spiering, J. Phys. Chem. Solids 59 (1998) 265.
[132] H. Okamura, M. Matsubara, T. Nanba, T. Tayagaki, S. Mouri, K. Tanaka, Y. Ikemoto, T. Moriwaki, H. Kimura, G. Juhasz, Phys. Rev. B 72 (2005) 073108.
[133] (a) T. Tayagaki, K. Tanaka, Phys. Rev. Lett. 86 (2001) 2886;
(b) T. Tayagaki, K. Tanaka, J. Luminesc. 94–95 (2001) 537;
(c) T. Tayagaki, K. Tanaka, N. Yonemura, M. Shirai, K. Kan'no, Int. J. Mod. Phys. B 15 (2001) 3709;
(d) H. Okamura, M. Matsubara, T. Tayagaki, K. Tanaka, Y. Ikemoto, H. Kimura, T. Moriwaki, T. Nanba, J. Phys. Soc. Jpn. 73 (2004) 1355;
(e) T. Tayagaki, K. Tanaka, H. Okamura, Phys. Rev. B 69 (2004) 064104.
[134] C. Enachescu, U. Oetliker, A. Hauser, J. Phys. Chem. B 106 (2002) 9540.
[135] Y. Ogawa, T. Ishikawa, S. Koshihara, K. Boukheddaden, F. Varret, Phys. Rev. B 66 (2002) 073104.
[136] G. Juhasz, M. Seto, Y. Yoda, S. Hayami, Y. Maeda, Chem. Commun. (2004) 2574.
[137] (a) L.X. Chen, Z. Wang, J.K. Burdett, P.A. Montano, J.R. Norris, J. Phys. Chem. 99 (1995) 7958;
(b) K. Okamoto, K. Kohdate, K. Nagai, J. Miyawaki, H. Kondoh, T. Yokoyama, A. Nojima, T. Ohta, J. Synchrotron Rad. 10 (2003) 242;
(c) K. Okamoto, K. Nagai, J. Miyawaki, H. Kondoh, T. Ohta, Chem. Phys. Lett. 371 (2003) 707;
(d) H. Oyanagi, T. Tayagaki, K. Tanaka, J. Phys. Chem. Solids 65 (2004) 1485.
[138] M. Kamada, T. Takahashi, Y. Doi, K. Fukui, T. Tayagaki, K. Tanaka, Phase Transitions 75 (2002) 847.

[139] H. Osawa, T. Iwazumi, H. Shoji, E. Hirai, T. Nakamura, Y. Ogawa, T. Ishikawa, S. Koshihara, Y. Isozumi, S. Nanao, Phase Transitions 75 (2002) 919.
[140] M. Shirai, N. Yonemura, T. Tayagaki, K. Kan'no, K. Tanaka, J. Luminesc. 94-95 (2001) 529.
[141] H. Köppen, E. Meissner, L. Wiehl, H. Spiering, P. Gütlich, Hyperfine Interact. 52 (1989) 29.
[142] (a) J. Fleisch, P. Gütlich, H. Köppen, Radiochem. Radioanal. Lett. 42 (1980) 279;
(b) P.E. Doan, B.R. McGarvey, Inorg. Chem. 29 (1990) 874.
[143] L. Wiehl, G. Kiel, P. Gütlich, Z. Kristallogr. 170 (1985) 195.
[144] L. Wiehl, G. Kiel, C.P. Köhler, H. Spiering, P. Gütlich, Inorg. Chem. 25 (1986) 1565.
[145] H.L. Chum, J.A. Vanin, M.I.D. Holanda, Inorg. Chem. 21 (1982) 1146.
[146] W. Linert, B. Pauresmaeil, Oriental J. Chem. 7 (1991) 56.
[147] H. Toftlund, Coord. Chem. Rev. 94 (1989) 67.
[148] Y. Umemura, Y. Minai, T. Tominaga, J. Phys. Chem. B 103 (1999) 647.
[149] P. Adler, H. Spiering, P. Gütlich, Inorg. Chem. 26 (1987) 3840.
[150] P. Adler, H. Spiering, P. Gütlich, J. Phys. Chem. Solids 50 (1989) 587.
[151] (a) D.H. Busch, J.C. Bailar jr., J. Am. Chem. Soc. 78 (1956) 1137;
(b) R.K. Murmann, A.E. Healy, J. Am. Chem. Soc. 83 (1961) 2092;
(c) L.M. Epstein, J. Chem. Phys. 40 (1964) 435;
(d) J. Burgess, R.H. Prince, J. Chem. Soc. A (1967) 434;
(e) E.J.S. Vichi, P. Krumholz, J. Chem. Soc., Dalton Trans. (1975) 1543;
(f) J. Burgess, M.V. Twigg, Transition Met. Chem. 3 (1978) 88;
(g) H.H. Wei, C.S. Hsiao, J. Chin. Chem. Soc. 28 (1981) 69;
(h) W.H. Batschelet, N.J. Rose, Inorg. Chem. 22 (1983) 2078.
[152] M.A. Robinson, D.H. Busch, Inorg. Chem. 2 (1963) 1171.
[153] P. Barth, G. Schmauss, H. Specker, Z. Naturforsch., Teil B 27 (1972) 1149.
[154] L.J. Wilson, I. Bertini, J. Coord. Chem. 1 (1972) 237.
[155] M.J. Blandamer, J. Burgess, D.L. Elvidge, P. Guardado, A.W. Hakin, L.J.S. Prouse, S. Radulovic, D.R. Russell, Transition Met. Chem. 16 (1991) 82.
[156] (a) K. Schlosser, E. Hoyer, J. Inorg. Nucl. Chem. 33 (1971) 4370;
(b) K. Schlosser, E. Hoyer, D. Arnold, Spectrochim. Acta A 30 (1974) 1431;
(c) H.L. Chum, T. Rabockai, Inorg. Chim. Acta 19 (1976) 145;
(d) E. Baggio-Saitovitch, N.G. De Souza, E.J.S. Vichi, Inorg. Chim. Acta 25 (1977) L23;
(e) H.L. Chum, M. Rock, Inorg. Chim. Acta 37 (1979) 113;
(f) H.L. Chum, D. Koran, R.A. Osteryoung, Inorg. Chem. 20 (1981) 3304.
[157] S. Alshehri, J. Burgess, Transition Met. Chem. 23 (1998) 689.
[158] G.B. Kauffman, B.H. Gump, G.L. Anderson, B.J. Stedjee, J. Chromatogr. 117 (1976) 455.
[159] Y. Maeda, S. Shite, Y. Takashima, Y. Nishida, Bull. Chem. Soc. Jpn. 50 (1977) 2902.
[160] P. Guionneau, M. Marchivie, G. Bravic, J.-F. Létard, D. Chasseau, Top. Curr. Chem. 234 (2004) 97.
[161] K. Madeja, W.H. Böhmer, N.-T. Thúy, G. Oehme, A.A. El-Saghier, A. Vertes, K. Burger, Z. Anorg. Allg. Chem. 447 (1978) 5.
[162] Y. Maeda, Y. Takashima, Y. Nishida, Bull. Chem. Soc. Jpn. 49 (1976) 2427.
[163] D. Cower, R.H. Herber, Inorg. Chem. 26 (1987) 1642.
[164] D.C. Figg, R.H. Herber, Hyperfine Interact. 62 (1990) 99.
[165] R. Saint-James, C. R. Acad. Sci., Ser. C 273 (1971) 485.
[166] S. Hayami, R. Kawajiri, G. Juhasz, T. Kawahara, K. Hashiguchi, O. Sato, K. Inoue, Y. Maeda, Bull. Chem. Soc. Jpn. 76 (2003) 1207.
[167] H.H. Wei, B.J. Chiou, J. Chin. Chem. Soc. 33 (1986) 267.
[168] E. König, G. Ritter, R. Schnakig, Chem. Phys. Lett. 27 (1974) 23.
[169] S.P. Kao, Y.C. Jean, H.H. Wei, Hyperfine Interact. 28 (1986) 711.
[170] H.H. Wei, C.S. Hsiao, J. Chin. Chem. Soc. 29 (1982) 147.
[171] (a) H.H. Wei, Y.C. Jean, Chem. Phys. Lett. 106 (1984) 523;
(b) Y.C. Jean, H.H. Wei, Hyperfine Interact. 28 (1986) 705.
[172] H.H. Wei, S.P. Kao, J. Chin. Chem. Soc. 32 (1985) 399.
[173] H.H. Wei, S.P. Kao, Y.C. Jean, Transition Met. Chem. 11 (1986) 405.
[174] Z. Yu, H. Spiering, P. Gütlich, Transition Met. Chem. 21 (1996) 472.
[175] V. Ksenofontov, G. Levchenko, H. Spiering, P. Gütlich, J.-F. Létard, Y. Bouhedja, O. Kahn, Chem. Phys. Lett. 294 (1998) 545.
[176] J.-B. Gaudry, L. Capes, P. Langot, S. Marcen, M. Kollmannsberger, O. Lavastre, E. Freysz, J.-F. Létard, O. Kahn, Chem. Phys. Lett. 324 (2000) 321.
[177] S. Hayami, K. Danjobara, S. Miyazaki, K. Inoue, Y. Ogawa, Y. Maeda, Polyhedron 24 (2005) 2821.
[178] S. Hayami, K. Danjobara, K. Inoue, Y. Ogawa, N. Matsumoto, Y. Maeda, Adv. Mater. 16 (2004) 869.
[179] J.-F. Létard, P. Guionneau, L. Rabardel, J.A.K. Howard, A.E. Goeta, D. Chasseau, O. Kahn, Inorg. Chem. 37 (1998) 4432.
[180] P. Guionneau, C. Brigouleix, Y. Barrans, A.E. Goeta, J.-F. Létard, J.A.K. Howard, J. Gaultier, D. Chasseau, C. R. Acad. Sci., Ser. IIc 4 (2001) 161.
[181] J.-F. Létard, G. Chastanet, O. Nguyen, S. Marcen, M. Marchivie, P. Guionneau, D. Chasseau, P. Gütlich, Monats. Chem. 134 (2003) 165.
[182] M. Marchivie, P. Guionneau, J.-F. Létard, D. Chasseau, Acta Crystallogr., Sect. B 59 (2003) 479.
[183] L. Capes, J.-F. Létard, O. Kahn, Chem. Eur. J. 6 (2000) 2246.
[184] (a) J. Degert, N. Lascoux, S. Montant, S. Létard, E. Freysz, G. Chastanet, J.-F. Létard, Chem. Phys. Lett. 415 (2005) 206;
(b) K. Ichiyanagi, J. Hebert, L. Toupet, H. Cailleau, P. Guionneau, J.-F. Létard, E. Collet, Phys. Rev. B 73 (2006) 060408;
(c) C. Enachescu, R. Tanasa, A. Stancu, G. Chastanet, J.-F. Létard, J. Linares, F. Varret, J. Appl. Phys. 99 (2006) 08J504.
[185] (a) J.-F. Létard, H. Daubric, C. Cantin, J. Kliava, Y.A. Bouhedja, O. Nguyen, O. Kahn, Mol. Cryst. Liq. Cryst. Sci. Tech., Sect. A 335 (1999) 1207;
(b) H. Daubric, J. Kliava, P. Guionneau, D. Chasseau, J.-F. Létard, O. Kahn, J. Phys.: Condens. Matter 12 (2000) 5481;
(c) H. Daubric, R. Berger, J. Kliava, G. Chastanet, O. Nguyen, J.-F. Létard, Phys. Rev. B 66 (2002) 054423.
[186] J.-F. Létard, S. Montant, P. Guionneau, P. Martin, A. Le Calvez, E. Freysz, D. Chasseau, R. Lapouyade, O. Kahn, Chem. Commun. (1997) 745.
[187] J.-F. Létard, P. Guionneau, E. Codjovi, O. Lavastre, G. Bravic, D. Chasseau, O. Kahn, J. Am. Chem. Soc. 119 (1997) 10861.
[188] P. Guionneau, J.-F. Létard, D.S. Yufit, D. Chasseau, G. Bravic, A.E. Goeta, J.A.K. Howard, O. Kahn, J. Mater. Chem. 9 (1999) 985.
[189] H. Daubric, C. Cantin, C. Thomas, J. Kliava, J.-F. Létard, O. Kahn, Chem. Phys. 244 (1999) 75.
[190] (a) S.J. Blundell, F.L. Pratt, I.M. Marshall, C.A. Steer, W. Hayes, J.-F. Létard, S.L. Heath, A. Caneschi, D. Gatteschi, Synth. Met. 133–134 (2003) 531;
(b) S.J. Blundell, F.L. Pratt, T. Lancaster, I.M. Marshall, C.A. Steer, S.L. Heath, J.-F. Létard, T. Sugano, D. Mihailovic, A. Omerzu, Polyhedron 22 (2003) 1973.
[191] S.J. Blundell, F.L. Pratt, C.A. Steer, I.M. Marshall, J.-F. Létard, J. Phys. Chem. Solids 65 (2004) 25.
[192] M. Marchivie, P. Guionneau, J.-F. Létard, D. Chasseau, Acta Crystallogr., Sect. B 61 (2005) 25.
[193] H.A. Goodwin, Top. Curr. Chem. 233 (2004) 59.
[194] D. Onggo, J.M. Hook, A.D. Rae, H.A. Goodwin, Inorg. Chim. Acta 173 (1990) 19.
[195] D. Onggo, H.A. Goodwin, Aust. J. Chem. 44 (1991) 1539.
[196] D.C. Craig, H.A. Goodwin, D. Onggo, Aust. J. Chem. 41 (1988) 1157.
[197] H.A. Goodwin, R.N. Sylva, Aust. J. Chem. 21 (1968) 83.
[198] E. König, G. Ritter, B. Braunecker, K. Madeja, H.A. Goodwin, F.E. Smith, Ber. Bunsen-Ges. Phys. Chem. 76 (1972) 393.

[199] E. König, S. Kremer, Chem. Phys. Lett. 8 (1971) 312.
[200] C.M. Harris, S. Kokot, H.R.H. Patil, E. Sinn, H. Wong, Aust. J. Chem. 25 (1972) 1631.
[201] E. König, G. Ritter, H.A. Goodwin, J. Inorg. Nucl. Chem. 39 (1977) 1773.
[202] J. Fleisch, P. Gütlich, K.M. Hasselbach, E.W. Müller, Inorg. Chem. 15 (1976) 958.
[203] P. Poganiuch, P. Gütlich, Inorg. Chem. 26 (1987) 455.
[204] A. Hauser, J. Adler, P. Gütlich, Chem. Phys. Lett. 152 (1988) 468.
[205] K. Endo, M. Amano, H. Sano, Radioisotopes 28 (1979) 215.
[206] D.W. Fink, W.E. Ohnesorge, J. Am. Chem. Soc. 91 (1969) 4995.
[207] H.A. Goodwin, E.S. Kucharski, A.H. White, Aust. J. Chem. 36 (1983) 1115.
[208] (a) E.J. Halbert, C.M. Harris, E. Sinn, G.J. Sutton, Aust. J. Chem. 26 (1973) 951;
(b) W.M. Reiff, G.J. Long, Inorg. Chem. 13 (1974) 2150;
(c) J. Fleisch, P. Gütlich, K.M. Hasselbach, Inorg. Chim. Acta 17 (1976) 51.
[209] (a) J. Fleisch, P. Gütlich, K.M. Hasselbach, Inorg. Chem. 16 (1977) 1979;
(b) J. Fleisch, P. Gütlich, Chem. Phys. Lett. 45 (1977) 29.
[210] (a) J. Ensling, B.W. Fitzsimmons, P. Gütlich, K.M. Hasselbach, Angew. Chem., Int. Ed. Engl. 9 (1970) 637;
(b) J.P. Sanchez, Y. Llabador, J.M. Friedt, J. Inorg. Nucl. Chem. 35 (1973) 3557.
[211] (a) R.R. Ruminski, K.D. Van Tassel, J.D. Petersen, Inorg. Chem. 23 (1984) 4380;
(b) R.R. Ruminski, J.D. Petersen, Inorg. Chim. Acta 97 (1985) 129;
(c) P.S. Braterman, J.I. Song, R.D. Peacock, Inorg. Chem. 31 (1992) 555;
(d) G. De Munno, M. Julve, J.A. Real, Inorg. Chim. Acta 255 (1997) 185;
(e) G.A. Van Albada, W.J.J. Smeets, A.L. Spek, J. Reedijk, J. Chem. Cryst. 30 (2000) 441.
[212] D. Onggo, A.D. Rae, H.A. Goodwin, Inorg. Chim. Acta 178 (1990) 151.
[213] R. Hage, J.G. Haasnoot, J. Reedijk, Inorg. Chim. Acta 172 (1990) 19.
[214] H.A. Goodwin, F.E. Smith, Inorg. Chim. Acta 7 (1973) 541.
[215] A. El Jammal, E. Graf, M. Gross, J. Electroanal. Chem. Interfac. Electrochem. 245 (1988) 201.
[216] K.H. Sugiyarto, H.A. Goodwin, Aust. J. Chem. 41 (1988) 1645.
[217] A.T. Baker, N.J. Ferguson, H.A. Goodwin, A.D. Rae, Aust. J. Chem. 42 (1989) 623.
[218] L.S. Harimanow, K.H. Sugiyarto, D.C. Craig, M.L. Scudder, H.A. Goodwin, Aust. J. Chem. 52 (1999) 109.
[219] B. Chiswell, Inorg. Chim. Acta 6 (1972) 629.
[220] H. Hennig, M. Benedix, R. Benedix, Z. Chem. 11 (1971) 188.
[221] P. Stupik, J.H. Zhang, M. Kwiecien, W.M. Reiff, J.G. Haasnoot, R. Hage, J. Reedijk, Hyperfine Interact. 28 (1986) 725.
[222] K.H. Sugiyarto, D.C. Craig, A.D. Rae, H.A. Goodwin, Aust. J. Chem. 48 (1995) 35.
[223] A.F. Stassen, M. de Vos, P.J. van Koningsbruggen, F. Renz, J. Ensling, H. Kooijman, A.L. Spek, J.G. Haasnoot, P. Gütlich, J. Reedijk, Eur. J. Inorg. Chem. (2000) 2231.
[224] O. Roubeau, M. de Vos, A.F. Stassen, R. Burriel, J.G. Haasnoot, J. Reedijk, J. Phys. Chem. Solids 64 (2003) 1003.
[225] P. Stupik, W.M. Reiff, R. Hage, J. Jacobs, J.G. Haasnoot, J. Reedijk, Hyperfine Interact. 40 (1988) 343.
[226] L.J. Fitzpatrick, H.A. Goodwin, Inorg. Chim. Acta 61 (1982) 229.
[227] D. Onggo, M.L. Scudder, D.C. Craig, H.A. Goodwin, Aust. J. Chem. 53 (2000) 153.
[228] A.T. Baker, H.A. Goodwin, A.D. Rae, Inorg. Chem. 26 (1987) 3513.
[229] A.T. Baker, H.A. Goodwin, Aust. J. Chem. 37 (1984) 1157.
[230] A.T. Baker, H.A. Goodwin, A.D. Rae, Aust. J. Chem. 37 (1984) 2431.
[231] R.J. Dosser, W.J. Eilbeck, A.E. Underhill, P.R. Edwards, C.E. Johnson, J. Chem. Soc. A (1969) 810.
[232] D.M.L. Goodgame, A.A.S.C. Machado, Inorg. Chem. 8 (1969) 2031.
[233] R.K. Boggess, J.W. Hughes, C.W. Chew, J.J. Kemper, J. Inorg. Nucl. Chem. 43 (1981) 939.
[234] Y. Sasaki, T. Shigematsu, Bull. Chem. Soc. Jpn. 46 (1973) 3438.
[235] R. Vijayalakshmi, S.M. Yusuf, S.K. Kulshreshtha, J. Phys. Chem. Solids 65 (2004) 975.
[236] J.J. McGarvey, I. Lawthers, K. Heremans, H. Toftlund, Inorg. Chem. 29 (1990) 252.
[237] (a) K.A. Reeder, E.V. Dose, L.J. Wilson, Inorg. Chem. 17 (1978) 1071;
(b) E.V. Dose, M.A. Hoselton, N. Sutin, M.F. Tweedle, L.J. Wilson, J. Am. Chem. Soc. 100 (1978) 1141;
(c) J.J. McGarvey, I. Lawthers, K. Heremans, H. Toftlund, J. Chem. Soc., Chem. Commun. (1984) 1575;
(d) J.K. Beattie, K.J. McMahon, Aust. J. Chem. 41 (1988) 1315.
[238] J.J. McGarvey, I. Lawthers, J. Chem. Soc., Chem. Commun. (1982) 906.
[239] K.H. Sugiyarto, H.A. Goodwin, Aust. J. Chem. 40 (1987) 775.
[240] J.R. Sams, J.C. Scott, T.B. Tsin, Chem. Phys. Lett. 18 (1973) 451.
[241] S.P. Ghosh, L.K. Mishra, Inorg. Chim. Acta 7 (1973) 545.
[242] J.R. Sams, T.B. Tsin, J. Chem. Soc., Dalton Trans. (1976) 488.
[243] J.R. Sams, T.B. Tsin, Inorg. Chem. 15 (1976) 1544.
[244] R.L. Martin, I.A.G. Roos, D.L. Goodgame, A.A.S.C. Machado, Aust. J. Chem. 31 (1978) 487.
[245] A.T. Baker, H.A. Goodwin, Aust. J. Chem. 30 (1977) 771.
[246] (a) R. Boča, P. Baran, L. Dlhan, J. Sima, G. Wiesinger, F. Renz, U. El-Ayaan, W. Linert, Polyhedron 16 (1997) 47;
(b) R. Boča, M. Vrbová, R. Werner, W. Haase, Chem. Phys. Lett. 328 (2000) 188;
(c) R. Boča, M. Boča, H. Ehrenberg, H. Fuess, W. Linert, F. Renz, I. Svoboda, Chem. Phys. 293 (2003) 375.
[247] S.M. Peng, H.F. Chen, Bull. Inst. Chem., Acad. Sin. 37 (1990) 49.
[248] S.G. Telfer, B. Bocquet, A.F. Williams, Inorg. Chem. 40 (2001) 4818.
[249] L.J. Charbonniere, A.F. Williams, C. Piguet, G. Bernardinelli, E. Rivara-Minten, Chem. Eur. J. 4 (1998) 485.
[250] D.M.L. Goodgame, A.A.S.C. Machado, J. Chem. Soc. D (1969) 1420.
[251] V. Niel, A.B. Gaspar, M.C. Muñoz, B. Abarca, R. Ballesteros, J.A. Real, Inorg. Chem. 42 (2003) 4782.
[252] R.J. Smithson, C.A. Kilner, A.R. Brough, M.A. Halcrow, Polyhedron 22 (2003) 725.
[253] F.E. Bradford, L.P. Connor, C.A. Kilner, M.A. Halcrow, Polyhedron 23 (2004) 2141.
[254] D.C. Craig, H.A. Goodwin, D. Onggo, A.D. Rae, Aust. J. Chem. 41 (1988) 1625.
[255] A.T. Baker, H.A. Goodwin, Aust. J. Chem. 38 (1985) 851.
[256] J. Nelson, S.M. Nelson, W.D. Perry, J. Chem. Soc., Dalton Trans. (1976) 1282.
[257] (a) A.S. Abushamleh, H.A. Goodwin, Aust. J. Chem. 32 (1979) 513;
(b) R.B. Lauffer, B.C. Antanaitis, P. Aisen, L. Que Jr., J. Biol. Chem. 258 (1983) 14212.
[258] M.A. Martinez Lorente, F. Dahan, V. Petrouleas, A. Bousseksou, J.-P. Tuchagues, Inorg. Chem. 34 (1995) 5346.
[259] D. Boinnard, P. Cassoux, V. Petrouleas, J.-M. Savariault, J.-P. Tuchagues, Inorg. Chem. 29 (1990) 4114.
[260] C.H. Lai, S.S. Chern, S.M. Peng, Bull. Inst. Chem., Acad. Sin. 35 (1988) 31.
[261] M.G. Burnett, V. McKee, S.M. Nelson, J. Chem. Soc., Dalton Trans. (1981) 1492.
[262] (a) J.C. Yoder, J.P. Roth, E.M. Gussenhoven, A.S. Larsen, J.M. Mayer, J. Am. Chem. Soc. 125 (2003) 2629;
(b) E.A. Mader, A.S. Larsen, J.M. Mayer, J. Am. Chem. Soc. 126 (2004) 8066.
[263] E. König, K. Madeja, K.J. Watson, J. Am. Chem. Soc. 90 (1968) 1146.
[264] A.T. Casey, Aust. J. Chem. 21 (1968) 2291.

[265] J.H. Takemoto, B. Hutchinson, Inorg. Chem. 12 (1973) 705.
[266] J.R. Ferro, J. Takemoto, Appl. Spectrosc. 28 (1974) 66.
[267] E. König, G. Ritter, Phys. Lett. A 43 (1973) 488.
[268] S.K. Kulshreshtha, R.M. Iyer, Chem. Phys. Lett. 108 (1984) 501.
[269] E.W. Müller, H. Spiering, P. Gütlich, Chem. Phys. Lett. 93 (1982) 567.
[270] J. Ensling, P. Gütlich, K.M. Hasselbach, B.W. Fitzsimmons, Chem. Phys. Lett. 42 (1976) 232.
[271] R.H. Herber, Inorg. Chem. 26 (1987) 173.
[272] A.A. Yousif, R.H. Herber, Hyperfine Interact. 36 (1987) 13.
[273] S. Usha, T. Srinivasan, C.N.R. Rao, Chem. Phys. 100 (1985) 447.
[274] W.H. Böhmer, K. Madeja, G. Oehme, A. Vertes, K. Burger, Z. Anorg. Allg. Chem. 486 (1982) 153.
[275] E. König, K.J. Watson, Chem. Phys. Lett. 6 (1970) 457.
[276] M. Konno, M. Mikami-Kido, Bull. Chem. Soc. Jpn. 64 (1991) 339.
[277] (a) E. König, K. Madeja, W.H. Böhmer, J. Am. Chem. Soc. 91 (1969) 4582;
(b) E. König, G. Ritter, J. Phys. Chem. Solids 33 (1972) 327.
[278] A.J. Cunningham, J.E. Fergusson, H.K. Powell, E. Sinn, H. Wong, J. Chem. Soc., Dalton Trans. (1972) 2155.
[279] D.C. Figg, R.H. Herber, I. Felner, Inorg. Chem. 30 (1991) 2535.
[280] E. König, K. Madeja, Spectrochim. Acta A 23 (1967) 45.
[281] (a) D.C. Fisher, H.G. Drickamer, J. Chem. Phys. 54 (1971) 4825;
(b) A. Bousseksou, G. Molnár, J.-P. Tuchagues, N. Menéndez, E. Codjovi, F. Varret, C. R. Chimie 6 (2003) 329.
[282] J.H. Takemoto, B. Hutchinson, Inorg. Nucl. Chem. Lett. 8 (1972) 769.
[283] M. Sorai, S. Seki, J. Phys. Soc. Jpn. 33 (1972) 575.
[284] M. Sorai, S. Seki, J. Phys. Chem. Solids 35 (1974) 555.
[285] (a) P. Spacu, D. Ciomartan, M. Teodorescu, Rev. Roum. Chim. 17 (1972) 977;
(b) B. Gallois, J.A. Real, C. Hauw, J. Zarembowitch, Inorg. Chem. 29 (1990) 1152.
[286] M. Marchivie, P. Guionneau, J.A.K. Howard, G. Chastanet, J.-F. Létard, A.E. Goeta, D. Chasseau, J. Am. Chem. Soc. 124 (2002) 194.
[287] A.G. Maddock, J.J. Schleiffer, J. Chem. Soc., Dalton Trans. (1977) 617.
[288] (a) S. Vasudevan, H.N. Vasan, C.N.R. Rao, Chem. Phys. Lett. 65 (1979) 444;
(b) K. Burger, C. Furlani, G. Mattogno, J. Electron. Spectrosc. Relat. Phenom. 21 (1980) 249.
[289] P. Ganguli, P. Gütlich, E.W. Müller, W. Irler, J. Chem. Soc., Dalton Trans. (1981) 441.
[290] (a) D.M. Adams, G.J. Long, A.D. Williams, Inorg. Chem. 21 (1982) 1049;
(b) J. Pebler, Inorg. Chem. 22 (1983) 4125.
[291] (a) Y. Qi, E.W. Müller, H. Spiering, P. Gütlich, Chem. Phys. Lett. 101 (1983) 503;
(b) A. Bousseksou, N. Negre, M. Goiran, L. Salmon, J.-P. Tuchagues, M.-L. Boillot, K. Boukheddaden, F. Varret, Eur. Phys. J. B 13 (2000) 451;
(c) N. Negre, C. Consejo, M. Goiran, A. Bousseksou, F. Varret, J.-P. Tuchagues, Physica B 294–295 (2001) 91.
[292] K.F. Purcell, M.P. Edwards, Inorg. Chem. 23 (1984) 2620.
[293] (a) P. Spacu, M. Teodorescu, D. Ciomartan, Monatsh. Chem. 103 (1972) 1;
(b) P. Spacu, M. Teodorescu, G. Filotti, P. Telnic, Z. Anorg. Allg. Chem. 392 (1972) 88.
[294] C.B. Bargeron, H.G. Drickamer, J. Chem. Phys. 55 (1971) 3471.
[295] (a) A. Ruaudel-Teixier, A. Barraud, P. Coronel, O. Kahn, Thin Solid Films 160 (1988) 107;
(b) P. Coronel, A. Barraud, R. Claude, O. Kahn, A. Ruaudel-Teixier, J. Zarembowitch, J. Chem. Soc., Chem. Commun. (1989) 193.
[296] B.R. McGarvey, J. Mag. Reson. 82 (1989) 253.
[297] (a) C. Cartier dit Moulin, P. Rudolf, A.-M. Flank, C.T. Chen, J. Phys. Chem. 96 (1992) 6196;
(b) V. Briois, C. Cartier dit Moulin, P. Sainctavit, C. Brouder, A.-M. Flank, J. Am. Chem. Soc. 117 (1995) 1019;
(c) G. Sankar, J.M. Thomas, V. Varma, G.U. Kulkarni, C.N.R. Rao, Chem. Phys. Lett. 251 (1996) 79;
(d) J.-J. Lee, H.-S. Sheu, C.-R. Lee, J.-M. Chen, J.-F. Lee, C.-C. Wang, C.-H. Huang, Y. Wang, J. Am. Chem. Soc. 122 (2000) 5742.
[298] J.A. Real, B. Gallois, T. Granier, F. Suez-Panama, J. Zarembowitch, Inorg. Chem. 31 (1992) 4972.
[299] T. Granier, B. Gallois, J. Gaultier, J.A. Real, J. Zarembowitch, Inorg. Chem. 32 (1993) 5305.
[300] (a) N. Shioyasu, K. Kagetsu, K. Mishima, M.K. Kubo, T. Tominaga, K. Nishiyama, K. Nagamine, Hyperfine Interact. 84 (1994) 477;
(b) Y. Garcia, V. Ksenofontov, S.J. Campbell, J.S. Lord, Y. Boland, P. Gütlich, J. Phys. Chem. B 108 (2004) 17838.
[301] (a) A. Bousseksou, J.J. McGarvey, F. Varret, J.A. Real, J.-P. Tuchagues, A.C. Dennis, M.-L. Boillot, Chem. Phys. Lett. 318 (2000) 409;
(b) G. Brehm, M. Reiher, S. Schneider, J. Phys. Chem. A 106 (2002) 12024;
(c) K.L. Ronayne, H. Paulsen, A. Höfer, A.C. Dennis, J.A. Wolny, A.I. Chumakov, V. Schünemann, H. Winkler, H. Spiering, A. Bousseksou, P. Gütlich, A.X. Trautwein, J.J. McGarvey, Phys. Chem. Chem. Phys. 8 (2006) 4685.
[302] N. Tsuchiya, A. Tsukamoto, T. Ohshita, T. Isobe, M. Senna, N. Yoshioka, H. Inoue, Solid State Sci. 3 (2001) 705.
[303] M. Gasgnier, M.-L. Boillot, O. Kaitasov, J. Mater. Sci. Lett. 21 (2002) 599.
[304] V. Ksenofontov, A.B. Gaspar, G. Levchenko, B. Fitzsimmons, P. Gütlich, J. Phys. Chem. B 108 (2004) 7723.
[305] (a) M. Reiher, Inorg. Chem. 41 (2002) 6928;
(b) Y. Zhang, E. Oldfield, J. Phys. Chem. A 107 (2003) 4147.
[306] H. Paulsen, A.X. Trautwein, J. Phys. Chem. Solids 65 (2004) 793.
[307] M. Teodorescu, Rev. Roum. Chim. 21 (1976) 1031.
[308] E.J. MacLean, C.M. McGrath, C.J. O'Connor, C. Sangregorio, J.M.W. Seddon, E. Sinn, F.E. Sowrey, S.J. Teat, A.E. Terry, G.B.M. Vaughan, N.A. Young, Chem. Eur. J. 9 (2003) 5314.
[309] (a) K.F. Purcell, S.M. Yeh, J.S. Eck, Inorg. Chem. 16 (1977) 1708;
(b) M.P. Edwards, C.D. Hoff, B. Curnutte, J.S. Eck, K.F. Purcell, Inorg. Chem. 23 (1984) 2613.
[310] K.F. Purcell, J.P. Zapata, J. Chem. Soc., Chem. Commun. (1978) 497.
[311] R. Claude, J.A. Real, J. Zarembowitch, O. Kahn, L. Ouahab, D. Grandjean, K. Boukheddaden, F. Varret, A. Dworkin, Inorg. Chem. 29 (1990) 4442, and 30 (1991) 2578 (correction).
[312] H. Inoue, H. Nakajima, T. Takahashi, H. Uchida, T. Shirai, E. Fluck, Bull. Chem. Soc. Jpn. 59 (1986) 3483.
[313] E. König, G. Ritter, K. Madeja, W.H. Böhmer, Ber. Bunsen-Ges. Phys. Chem. 77 (1973) 390.
[314] E. König, G. Ritter, W. Irler, B. Kanellakopulos, J. Phys. C 10 (1977) 603.
[315] D.C. Figg, R.H. Herber, J.A. Potenza, Inorg. Chem. 31 (1992) 2111.
[316] (a) E. König, G. Ritter, R. Zimmermann, Chem. Phys. Lett. 26 (1974) 425;
(b) E. König, G. Ritter, B. Kanellakopulos, J. Phys. C 7 (1974) 2681;
(c) E. König, G. Ritter, Solid State Commun. 18 (1976) 279;
(d) E. König, G. Ritter, W. Irler, Chem. Phys. Lett. 66 (1979) 336.
[317] K. Burger, H. Ebel, Inorg. Chim. Acta 53 (1981) L105.
[318] E. König, G. Ritter, S.K. Kulshreshtha, N. Csatary, Inorg. Chem. 23 (1984) 1903.
[319] E. König, G. Ritter, K. Madeja, A. Rosenkranz, J. Inorg. Nucl. Chem. 34 (1972) 2877.
[320] B.W. Dockum, W.M. Reiff, Inorg. Chim. Acta 35 (1979) 285.
[321] E. König, G. Ritter, K. Madeja, J. Inorg. Nucl. Chem. 43 (1981) 2273.
[322] M.-L. Boillot, S. Chantraine, J. Zarembowitch, J.-Y. Lallemand, J. Prunet, New J. Chem. 23 (1999) 179.

[323] M.-L. Boillot, A. Sour, P. Delhaes, C. Mingotaud, H. Soyer, Coord. Chem. Rev. 190–192 (1999) 47.
[324] M.-L. Boillot, H. Soyer, New J. Chem. 21 (1997) 889.
[325] (a) H. Soyer, C. Mingotaud, M.-L. Boillot, P. Delhaes, Thin Solid Films 327–329 (1998) 435;
(b) H. Soyer, C. Mingotaud, M.-L. Boillot, P. Delhaes, Langmuir 14 (1998) 5890.
[326] H. Soyer, E. Dupart, C. Mingotaud, C.J. Gomez-Garcia, P. Delhaes, Colloids Surf. A 171 (2000) 275.
[327] H. Soyer, E. Dupart, C.J. Gomez-Garcia, C. Mingotaud, P. Delhaes, Adv. Mater. 11 (1999) 382.
[328] J.-F. Létard, O. Nguyen, H. Soyer, C. Mingotaud, P. Delhaes, O. Kahn, Inorg. Chem. 38 (1999) 3020.
[329] J.A. Real, M.C. Muñoz, E. Andres, T. Granier, B. Gallois, Inorg. Chem. 33 (1994) 3587.
[330] Z.J. Zhong, J.-Q. Tao, Z. Yu, C.-Y. Dun, Y.-Y. Liu, X.-Z. You, J. Chem. Soc., Dalton Trans. (1998) 327.
[331] Z. Yu, K. Liu, J.Q. Tao, Z.J. Zhong, Z.X. You, G.G. Siu, Appl. Phys. Lett. 74 (1999) 4029.
[332] N. Saha, S.K. Kar, J. Ind. Chem. Soc. 66 (1989) 521.
[333] B.A. Leita, B. Moubaraki, K.S. Murray, J.P. Smith, Polyhedron 24 (2005) 2165.
[334] N. Moliner, M.C. Muñoz, P.J. Van Koningsbruggen, J.A. Real, Inorg. Chim. Acta 274 (1998) 1.
[335] N. Moliner, M.C. Muñoz, S. Létard, J.-F. Létard, X. Solans, R. Burriel, M. Castro, O. Kahn, J.A. Real, Inorg. Chim. Acta 291 (1999) 279.
[336] P. Gütlich, A.B. Gaspar, V. Ksenofontov, Y. Garcia, Yann. J. Phys.: Condens. Matter 16 (2004) S1087–S1108.
[337] A.B. Gaspar, M.C. Muñoz, N. Moliner, V. Ksenofontov, G. Levchenko, P. Gütlich, J.A. Real, Monatsh. Chem. 134 (2003) 285.
[338] N. Moliner, A.B. Gaspar, M.C. Muñoz, V. Niel, J. Cano, J.A. Real, Inorg. Chem. 40 (2001) 3986.
[339] S. Pillet, C. Lecomte, C.F. Sheu, Y.C. Lin, I.J. Hsu, Y. Wang, J. Phys. Conf. Ser. 21 (2005) 221.
[340] (a) J.P. Cornelissen, J.H. Van Diemen, L.R. Groeneveld, J.G. Haasnoot, A.L. Spek, J. Reedijk, Inorg. Chem. 31 (1992) 198;
(b) P.J. Kunkeler, P.J. van Koningsbruggen, J.P. Cornelissen, A.N. van der Horst, A.M. van der Kraan, A.L. Spek, J.G. Haasnoot, J. Reedijk, J. Am. Chem. Soc. 118 (1996) 2190.
[341] D. Zhu, Y. Xu, Z. Yu, Z. Guo, H. Sang, T. Liu, X. You, Chem. Mater. 14 (2002) 838.
[342] V. McKee, S.M. Nelson, J. Chem. Soc., Chem. Commun. (1976) 225.
[343] G. Bradley, V. McKee, S.M. Nelson, J. Nelson, J. Chem. Soc., Dalton Trans. (1978) 522.
[344] W. Irler, G. Ritter, E. König, H.A. Goodwin, S.M. Nelson, Solid State Commun. 29 (1979) 39.
[345] (a) E. König, G. Ritter, W. Irler, S.M. Nelson, Inorg. Chim. Acta 37 (1979) 169;
(b) E.W. Müller, H. Spiering, P. Gütlich, J. Chem. Phys. 79 (1983) 1439;
(c) E. König, B. Kanellakopulos, B. Powietzka, J. Nelson, J. Chem. Phys. 99 (1993) 9195.
[346] S.K. Kulshreshtha, R. Sasikala, E. König, Chem. Phys. Lett. 123 (1986) 215.
[347] S.K. Kulshreshtha, R.M. Iyer, E. König, J. Phys. Chem. Solids 53 (1992) 39.
[348] (a) A. Ozarowski, B.R. McGarvey, A.B. Sarkar, J.E. Drake, Inorg. Chem. 27 (1988) 628, and 2560 (correction);
(b) A. Galet, A.B. Gaspar, M.C. Muñoz, G. Levchenko, J.A. Real, Inorg. Chem. 45 (2006) 9670.
[349] D.C. Figg, R.H. Herber, Inorg. Chem. 29 (1990) 2170.
[350] E. König, G. Ritter, H. Gruensteudel, J. Dengler, J. Nelson, Inorg. Chem. 33 (1994) 837.
[351] A.G.M. Jansen, J. Lejay, H. Wiegelmann, P. Wyder, W. Bronger, Z. Phys. Chem. 182 (1993) 1.
[352] A. Ozarowski, S.A. Zvyagin, W.M. Reiff, J. Telser, L.-C. Brunel, J. Krzystek, J. Am. Chem. Soc. 126 (2004) 6574.
[353] E. König, G. Ritter, J. Dengler, J. Nelson, Inorg. Chem. 28 (1989) 611.
[354] T. Watanabe, Metal complex dye for a dye sensitized solar cell, Eur. Pat. Appl. EP 1213776, 2002, 35pp.
[355] See e.g. (a) D. Niarchos, A. Kostikas, A. Simopoulos, D. Coucouvanis, D. Piltingsrud, R.E. Coffman, J. Chem. Phys. 69 (1978) 4411;
(b) D.P. Riley, D.H. Busch, Inorg. Chem. 23 (1984) 3235;
(c) K. Shelly, T. Bartczak, W.R. Scheidt, C.A. Reed, Inorg. Chem. 24 (1985) 4325;
(d) J.P. Fitzgerald, G.P.A. Yap, A.L. Rheingold, C.T. Brewer, L. May, G.A. Brewer, J. Chem. Soc., Dalton Trans. (1996) 1249;
(e) N. Moliner, J.A. Real, M.C. Muñoz, R. Martinez-Manez, J.M.C. Juan, J. Chem. Soc., Dalton Trans. (1999) 1375;
(f) T. Sakai, Y. Ohgo, T. Ikeue, M. Takahashi, M. Takeda, M. Nakamura, J. Am. Chem. Soc. 125 (2003) 13028;
(g) M.P. Shaver, L.E.N. Allan, H.S. Rzepa, V.C. Gibson, Angew. Chem., Int. Ed. 45 (2006) 1241.
[356] See e.g. (a) J.P. Collman, J.L. Hoard, N. Kim, G. Lang, C.A. Reed, J. Am. Chem. Soc. 97 (1975) 2676;
(b) P. Hamon, L. Toupet, J.R. Hamon, C. Lapinte, J. Chem. Soc., Chem. Commun. (1994) 931.
[357] (a) J.A. Real, M.C. Muñoz, J. Faus, X. Solans, Inorg. Chem. 36 (1997) 3008;
(b) N. Moliner, L. Salmon, L. Capes, M.C. Muñoz, J.-F. Létard, A. Bousseksou, J.-P. Tuchagues, J.J. McGarvey, A.C. Dennis, M. Castro, R. Burriel, J.A. Real, J. Phys. Chem. B 106 (2002) 4276.
[358] A.L. Thompson, A.E. Goeta, J.A. Real, A. Galet, M.C. Muñoz, Chem. Commun. (2004) 1390.
[359] A. Galet, A.B. Gaspar, G. Agusti, M.C. Muñoz, G. Levchenko, J.A. Real, Eur. J. Inorg. Chem. (2006) 3571.
[360] F. Mani, Inorg. Chim. Acta 117 (1986) L1.
[361] S. Trofimenko, J. Am. Chem. Soc. 89 (1967) 6288.
[362] (a) S. Trofimenko, J. Am. Chem. Soc. 89 (1967) 3170;
(b) T.R. Belderraín, M. Paneque, E. Carmona, E. Gutiérrez-Puebla, M.A. Monge, C. Ruiz-Valero, Inorg. Chem. 41 (2002) 425.
[363] J.P. Jesson, S. Trofimenko, D.R. Eaton, J. Am. Chem. Soc. 89 (1967) 3148.
[364] L.D. Field, B.A. Messerle, L.P. Soler, T.W. Hambley, P. Turner, J. Organomet. Chem. 655 (2002) 146.
[365] F. Mani, Inorg. Nucl. Chem. Lett. 15 (1979) 297.
[366] A.B. Gaspar, G. Agustí, V. Martínez, M.C. Muñoz, G. Levchenko, J.A. Real, Inorg. Chim. Acta 358 (2005) 4089.
[367] C.D. Burbridge, D.M.L. Goodgame, J. Chem. Soc. A (1967) 694.
[368] K. Takahashi, T. Kawakami, Z.-Z. Gu, Y. Einaga, A. Fujishima, O. Sato, Chem. Commun. (2003) 2374.
[369] V. Rattanaphani, W.R. McWhinnie, Inorg. Chim. Acta 9 (1974) 239.
[370] G. Guillot, E. Mulliez, P. Leduc, J.-C. Chottard, Inorg. Chem. 29 (1990) 577.
[371] U.S. Ray, D. Banerjee, C. Sinha, Proc. Ind. Acad. Sci., Chem. Sci 115 (2003) 169.
[372] U. Ray, D. Banerjee, J.-C. Liou, C.-N. Lin, T.-H. Lu, C. Sinha, Inorg. Chim. Acta 358 (2005) 1019.
[373] C.F. Shue, Z.C. Lee, H.H. Wei, M.C. Cheng, Y. Wang, Polyhedron 13 (1994) 2259.
[374] D.A. Baldwin, A.B.P. Lever, R.V. Parish, Inorg. Chem. 8 (1969) 107.
[375] (a) S. Gupta, A. Chakravorty, Inorg. Nucl. Chem. Lett. 9 (1973) 109;
(b) A. Saha, P. Majumdar, S.-M. Peng, S. Goswami, Eur. J. Inorg. Chem. (2000) 2631.
[376] G.J. Long, F. Grandjean, D.L. Reger, Top. Curr. Chem. 233 (2004) 91.

[377] B. Hutchinson, L. Daniels, E. Henderson, P. Neill, G.J. Long, L.W. Becker, J. Chem. Soc., Chem. Commun. (1979) 1003.
[378] F. Grandjean, G.J. Long, B.B. Hutchinson, L. Ohlhausen, P. Neill, J.D. Holcomb, Inorg. Chem. 28 (1989) 4406.
[379] J.D. Oliver, D.F. Mullica, B.B. Hutchinson, W.O. Milligan, Inorg. Chem. 19 (1980) 165.
[380] G. Bruno, G. Centineo, E. Ciliberto, S. Di Bella, I. Fragala, Inorg. Chem. 23 (1984) 1832.
[381] C. Janiak, T.G. Scharmann, J.C. Green, R.P.G. Parkin, M.J. Kolm, E. Riedel, W. Mickler, J. Elguero, R.M. Claramunt, D. Sanz, Chem. Eur. J. 2 (1996) 992.
[382] G.J. Long, B.B. Hutchinson, Inorg. Chem. 26 (1987) 608.
[383] C. Hannay, M.-J. Hubin-Franskin, F. Grandjean, V. Briois, J.-P. Itié, A. Polian, S. Trofimenko, G.J. Long, Inorg. Chem. 36 (1997) 5580.
[384] V. Briois, P. Sainctavit, G.J. Long, F. Grandjean, Inorg. Chem. 40 (2001) 912.
[385] S. Calogero, G.G. Lobbia, P. Cecchi, G. Valle, J. Friedl, Polyhedron 13 (1994) 87.
[386] S. Zamponi, G. Gambini, G.G. Lobbia, R. Marassi, M. Berrettoni, P. Cecchi, Polyhedron 14 (1995) 1929.
[387] P. Cecchi, M. Berrettoni, M. Giorgetti, G.G. Lobbia, S. Calogero, L. Stievano, Inorg. Chim. Acta 318 (2001) 67.
[388] (a) G.G. Lobbia, B. Bovio, C. Santini, C. Pettinari, F. Marchetti, Polyhedron 16 (1997) 671;
(b) G.G. Lobbia, B. Bovio, C. Santini, P. Cecchi, C. Pettinari, F. Marchetti, Polyhedron 17 (1998) 17.
[389] J.P. Jesson, J.F. Weiher, S. Trofimenko, J. Chem. Phys. 48 (1968) 2058.
[390] G.J. Long, L.W. Becker, W. Laurie, B.B. Hutchinson, Adv. Chem. Ser. 194 (1981) 453.
[391] P. Cecchi, G.G. Lobbia, F. Marchetti, G. Valle, S. Calogero, Polyhedron 13 (1994) 2173.
[392] A.L. Rheingold, G.P.A. Yap, L.M. Liable-Sands, I.A. Guzei, S. Trofimenko, Inorg. Chem. 36 (1997) 6261.
[393] D.L. Reger, J.R. Gardinier, J.D. Elgin, M.D. Smith, D. Hautot, G.J. Long, F. Grandjean, Inorg. Chem. 45 (2006) 8862.
[394] D.M. Eichorn, W.H. Armstrong, Inorg. Chem. 29 (1990) 3607.
[395] J.C. Calabrese, P.J. Domaille, S. Trofimenko, G.J. Long, Inorg. Chem. 30 (1991) 2795.
[396] J.P. Jesson, S. Trofimenko, D.R. Eaton, J. Am. Chem. Soc. 89 (1967) 3158.
[397] A. Gulino, E. Ciliberto, S. Di Bella, I. Fragala, Inorg. Chem. 32 (1993) 3759.
[398] T. Buchen, P. Gütlich, Inorg. Chim. Acta 231 (1995) 221.
[399] D.L. Reger, J.R. Gardinier, M.D. Smith, A.M. Shahin, G.J. Long, L. Rebbouh, F. Grandjean, Inorg. Chem. 44 (2005) 1852.
[400] D.L. Reger, J.D. Elgin, M.D. Smith, F. Grandjean, L. Rebbouh, G.J. Long, Polyhedron 25 (2006) 2616.
[401] D.L. Reger, J.R. Gardinier, W.R. Gemmill, M.D. Smith, A.M. Shahin, G.J. Long, L. Rebbouh, F. Grandjean, J. Am. Chem. Soc. 127 (2005) 2303.
[402] D.L. Reger, J.R. Gardinier, S. Bakbak, R.F. Semeniuc, U.H.F. Bunz, M.D. Smith, New J. Chem. 29 (2005) 1035.
[403] (a) C. Janiak, J. Chem. Soc., Chem. Commun. (1994) 545;
(b) C. Janiak, Chem. Ber. 127 (1994) 1379.
[404] C. Janiak, T.G. Scharmann, T. Bräuniger, J. Holubova, M. Nadvornik, Z. Anorg. Allg. Chem. 624 (1998) 769.
[405] C. Janiak, S. Temizdemir, S. Dechert, W. Deck, F. Girgsdies, J. Heinze, M.J. Kolm, T.G. Scharmann, O.M. Zipffel, Eur. J. Inorg. Chem. (2000) 1227.
[406] (a) S. Trofimenko, J.C. Calabrese, P.J. Domaille, J.S. Thompson, Inorg. Chem. 28 (1989) 1091;
(b) J.C. Calabrese, P.J. Domaille, J.S. Thompson, S. Trofimenko, Inorg. Chem. 29 (1990) 4429;
(c) M. Cano, J.V. Heras, S. Trofimenko, A. Monge, E. Gutierrez, C.J. Jones, J.A. McCleverty, J. Chem. Soc., Dalton Trans. (1990) 3577;
(d) J.C. Calabrese, S. Trofimenko, Inorg. Chem. 31 (1992) 4810;
(e) F. Jäkle, K. Polborn, M. Wagner, Chem. Ber. 129 (1996) 603;
(f) F.F. de Biani, F. Jäkle, M. Spiegler, M. Wagner, P. Zanello, Inorg. Chem. 36 (1997) 2103;
(g) A.L. Rheingold, B.S. Haggerty, G.P.A. Yap, S. Trofimenko, Inorg. Chem. 36 (1997) 5097;
(h) S.L. Guo, F. Peters, F.F. de Biani, J.W. Bats, E. Herdtweck, P. Zanello, M. Wagner, Inorg. Chem. 40 (2001) 4928.
[407] (a) G.J. Long, F. Grandjean, S. Trofimenko, Inorg. Chem. 32 (1993) 1055;
(b) C. Hannay, R. Thissen, V. Briois, M.-J. Hubin-Franskin, F. Grandjean, G.J. Long, S. Trofimenko, Inorg. Chem. 33 (1994) 5983.
[408] H. Paulsen, L. Duelund, A. Zimmermann, F. Averseng, M. Gerdan, H. Winkler, H. Toftlund, A.X. Trautwein, Monatsh. Chem. 134 (2003) 295.
[409] P.A. Anderson, T. Astley, M.A. Hitchman, F.R. Keene, B. Moubaraki, K.S. Murray, B.W. Skelton, E.R.T. Tiekink, H. Toftlund, A.H. White, J. Chem. Soc., Dalton Trans. (2000) 3505.
[410] D.L. Reger, C.A. Little, A.L. Rheingold, M. Lam, L.M. Liable-Sands, B. Rhagitan, T. Concolino, A. Mohan, G.J. Long, V. Briois, F. Grandjean, Inorg. Chem. 40 (2001) 1508.
[411] J.J. McGarvey, H. Toftlund, A.H.R. Al-Obaidi, K.P. Taylor, S.E.J. Bell, Inorg. Chem. 32 (1993) 2469.
[412] H. Winkler, A.X. Trautwein, H. Toftlund, Hyperfine Interact. 70 (1992) 1083.
[413] D.L. Reger, C.A. Little, V.G. Young Jr., M. Pink, Inorg. Chem. 40 (2001) 2870.
[414] C. Piquer, F. Grandjean, O. Mathon, S. Pascarelli, D.L. Reger, C.A. Little, G.J. Long, Inorg. Chem. 42 (2003) 982.
[415] D.L. Reger, C.A. Little, M.D. Smith, G.J. Long, Inorg. Chem. 41 (2002) 4453.
[416] D.L. Reger, C.A. Little, M.D. Smith, A.L. Rheingold, K.-C. Lam, T.L. Concolino, G.J. Long, R.P. Hermann, F. Grandjean, Eur. J. Inorg. Chem. (2002) 1190.
[417] D.L. Reger, J.D. Elgin, M.D. Smith, F. Grandjean, L. Rebbouh, G.J. Long, Eur. J. Inorg. Chem. (2004) 3345.
[418] See e.g. (a) J.C. Lancaster, W.R. McWhinnie, J. Chem. Soc. A (1970) 2673;
(b) E. Larsen, G.N. LaMar, B.E. Wagner, J.E. Parks, R.H. Holm, Inorg. Chem. 11 (1972) 2652;
(c) W.M. Reiff, J. Am. Chem. Soc. 95 (1973) 3048;
(d) E.S. Kucharski, W.R. McWhinnie, A.H. White, Aust. J. Chem. 31 (1978) 53;
(e) R.K. Boggess, S.J. Boberg, J. Inorg. Nucl. Chem. 42 (1980) 21;
(f) R.K. Boggess, J.W. Hughes, C.W. Chew, J.J. Kemper, J. Inorg. Nucl. Chem. 43 (1981) 939;
(g) T. Astley, A.J. Canty, M.A. Hitchman, G.L. Rowbottom, B.W. Skelton, A.H. White, J. Chem. Soc., Dalton Trans. (1991) 1981;
(h) P.V. Bernhardt, P. Comba, A. Mahu-Rickenbach, S. Stebler, S. Steiner, K. Varnagy, M. Zehnder, Inorg. Chem. 31 (1992) 4194;
(i) L.P. Wu, Y. Yamagiwa, I. Ino, K. Sugimoto, T. Kuroda-Sowa, T. Kamikawa, M. Munakata, Polyhedron 18 (1999) 2047.
[419] C.S. Alvarez, F. García, S.M. Humphrey, A.D. Hopkins, R.A. Kowenicki, M. McPartlin, R.A. Layfield, R. Raja, M.C. Rogers, A.D. Woods, D.S. Wright, Chem. Commun. (2005) 198.
[420] E.C. Constable, Adv. Inorg. Chem. Radiochem. 30 (1986) 69.
[421] For selected recent examples see e.g. (a) N. Belfrekh, C. Dietrich-Buchecker, J.-P. Sauvage, Inorg. Chem. 39 (2000) 5169;
(b) G. Pickaert, M. Cesario, L. Douce, R. Ziessel, Chem. Commun. (2000) 1125;
(c) A.C. Benniston, L.J. Farrugia, P.R. Mackie, P. Mallinson, W. Clegg, S.J. Teat, Aust. J. Chem. 53 (2000) 707;
(d) N.W. Alcock, P.R. Barker, J.M. Haider, M.J. Hannon, C.L. Painting, Z. Pikramenou, E.A. Plummer, K. Rissanen, P. Saarenketo, J. Chem. Soc., Dalton Trans. (2000) 1447;
(e) E.C. Constable, C.E. Housecroft, M. Neuburger, D. Phillips, P.R. Raithby, E. Schofield, E. Sparr, D.A. Tocher, M. Zehnder, Y. Zimmermann, J. Chem. Soc., Dalton Trans. (2000) 2219;

(f) H. Krass, E.A. Plummer, J.M. Haider, P.R. Barker, N.W. Alcock, Z. Pikramenou, M.J. Hannon, D.G. Kurth, Angew. Chem., Int. Ed. 40 (2001) 3862;
(g) C.B. Smith, E.C. Constable, C.E. Housecroft, B.M. Kariuki, Chem. Commun. (2002) 2068;
(h) E.C. Constable, B. Kariuki, A. Mahmood, Polyhedron 22 (2003) 687;
(i) G.J.E. Davidson, S.J. Loeb, Dalton Trans. (2003) 4319;
(j) J.S. Choi, C.W. Kang, K. Jung, J.W. Yang, Y.-G. Kim, H. Han, J. Am. Chem. Soc. 126 (2004) 8606;
(k) C. Alonso, L. Ballester, A. Gutiérrez, M.F. Perpiñán, A.E. Sánchez, M.T. Azcondo, Eur. J. Inorg. Chem. (2005) 486;
(l) S. Hayami, K. Danjobara, Y. Shigeyoshi, K. Inoue, Y. Ogawa, Y. Maeda, Inorg. Chem. Commun. 8 (2005) 506;
(m) J.P. López, W. Kraus, G. Reck, A. Thünemann, D.G. Kurth, Inorg. Chim. Acta 358 (2005) 3384.
[422] H. Oshio, H. Spiering, V. Ksenofontov, F. Renz, P. Gütlich, Inorg. Chem. 40 (2001) 1143.
[423] F. Renz, H. Oshio, V. Ksenofontov, M. Waldeck, H. Spiering, P. Gütlich, Angew. Chem., Int. Ed. 39 (2000) 3699.
[424] A. Hauser, N. Amstutz, S. Delahaye, A. Sadki, S. Schenker, R. Sieber, M. Zerara, Struct. Bonding (Berlin) 106 (2004) 81, and refs. therein.
[425] E.C. Constable, G. Baum, E. Bill, R. Dyson, R. van Eldik, D. Fenske, S. Kaderli, D. Morris, A. Neubrand, M. Neuburger, D.R. Smith, K. Wieghardt, M. Zehnder, A.D. Zuberbühler, Chem. Eur. J. 5 (1999) 498.
[426] F. Pelascini, M. Wesolek, F. Peruch, A. De Cian, N. Kyritsakas, P.J. Lutz, J. Kress, Polyhedron 23 (2004) 3193.
[427] D.B. Dell' Amico, F. Calderazzo, U. Englert, L. Labella, F. Marchetti, J. Chem. Soc., Dalton Trans. (2001) 357.
[428] (a) A.S. Abushamleh, H.A. Goodwin, C.G. Benson, G.J. Long, Aust. J. Chem. 37 (1984) 281;
(b) D.C. Craig, M.L. Scudder, W.-A. McHale, H.A. Goodwin, Aust. J. Chem. 51 (1998) 1131.
[429] M.-H. Yang, C.-C. Chou, H.-C. Lee, G.-H. Lee, M.-K. Leung, S.-M. Peng, Chem. Commun. (1997) 2279.
[430] M.A. Halcrow, Coord. Chem. Rev. 249 (2005) 2880.
[431] J.M. Holland, J.A. McAllister, Z. Lu, C.A. Kilner, M. Thornton-Pett, M.A. Halcrow, Chem. Commun. (2001) 577.
[432] V.A. Money, I. Radosavljevic Evans, M.A. Halcrow, A.E. Goeta, J.A.K. Howard, Chem. Commun. (2003) 158.
[433] C. Carbonera, J.S. Costa, V.A. Money, J. Elhaïk, J.A.K. Howard, M.A. Halcrow, J.-F. Létard, Dalton Trans. (2006) 3058.
[434] J. Elhaïk, D.J. Evans, C.A. Kilner, M.A. Halcrow, Dalton Trans. (2005) 1693.
[435] J. Elhaïk, C.A. Kilner, M.A. Halcrow, Dalton Trans. (2006) 823.
[436] J.M. Holland, S.A. Barrett, C.A. Kilner, M.A. Halcrow, Inorg. Chem. Commun. 5 (2002) 328.
[437] J. Elhaïk, C.A. Kilner, M.A. Halcrow, CrystEngComm 7 (2005) 151.
[438] L. Han, M. Nihei, K. Oshio, Polyhedron 24 (2005) 2409.
[439] V.A. Money, J. Elhaïk, M.A. Halcrow, J.A.K. Howard, Dalton Trans. (2004) 1516.
[440] R. Pritchard, C.A. Kilner, M.A. Halcrow, Chem. Commun. (2007) 577.
[441] J. Elhaïk, V.A. Money, S.A. Barrett, C.A. Kilner, I. Radosavljevic Evans, M.A. Halcrow, Dalton Trans. (2003) 2053.
[442] V.A. Money, I. Radosavljevic Evans, J. Elhaïk, M.A. Halcrow, J.A.K. Howard, Acta Crystallogr., Sect. B 60 (2004) 41.
[443] C.A. Kilner, M.A. Halcrow, Polyhedron 25 (2006) 235.
[444] V.A. Money, J. Elhaïk, I. Radosavljevic Evans, M.A. Halcrow, J.A.K. Howard, Dalton Trans. (2004) 65.
[445] M.L. Scudder, D.C. Craig, H.A. Goodwin, CrystEngComm 7 (2005) 642.
[446] K.H. Sugiyarto, D.C. Craig, A.D. Rae, H.A. Goodwin, Aust. J. Chem. 47 (1994) 869.
[447] K.H. Sugiyarto, M.L. Scudder, D.C. Craig, H.A. Goodwin, Aust. J. Chem. 53 (2000) 755.
[448] (a) A. Bhattacharjee, V. Ksenofontov, K.H. Sugiyarto, H.A. Goodwin, P. Gütlich, Adv. Funct. Mater. 13 (2003) 877;
(b) A. Bhattacharjee, J. Kusz, V. Ksenofontov, K.H. Sugiyarto, H.A. Goodwin, P. Gütlich, Chem. Phys. Lett. 431 (2006) 72.
[449] K.H. Sugiyarto, H.A. Goodwin, Aust. J. Chem. 41 (1988) 1645.
[450] (a) H.A. Goodwin, K.H. Sugiyarto, Chem. Phys. Lett. 139 (1987) 470;
(b) T. Buchen, P. Gütlich, H.A. Goodwin, Inorg. Chem. 33 (1994) 4573.
[451] R.C.W. Sung, B.R. McGarvey, Inorg. Chem. 38 (1999) 3644.
[452] A.I. Chumakov, R. Rueffer, O. Leupold, I. Sergueev, Struct. Chem. 14 (2003) 109.
[453] K.H. Sugiyarto, K. Weitzner, D.C. Craig, H.A. Goodwin, Aust. J. Chem. 50 (1997) 869.
[454] T. Buchen, P. Gütlich, K.H. Sugiyarto, H.A. Goodwin, Chem. Eur. J. 2 (1996) 1134.
[455] K.H. Sugiyarto, W.-A. McHale, D.C. Craig, A.D. Rae, M.L. Scudder, H.A. Goodwin, Dalton Trans. (2003) 2443.
[456] E. Coronado, M.C. Giménez-López, C. Gimenez-Saiz, J.M. Martínez-Agudo, F.M. Romero, Polyhedron 22 (2003) 2375.
[457] M.C. Giménez-López, M. Clemente-León, E. Coronado, F.M. Romero, S. Shova, J.-P. Tuchagues, Eur. J. Inorg. Chem. (2005) 2783.
[458] J.-F. Létard, J.S. Costa, S. Marcen, C. Carbonera, C. Desplanches, A. Kobayashi, N. Daro, P. Guionneau, J.-P. Ader, J. Phys. Conf. Ser. 21 (2005) 23.
[459] (a) S. Mahapatra, N. Gupta, R.N. Mukherjee, J. Chem. Soc., Dalton Trans. (1991) 2911, and (1992) 3401 (correction);
(b) S. Mahapatra, R.N. Mukherjee, Polyhedron 12 (1993) 1603.
[460] S. Mahapatra, R.J. Butcher, R.N. Mukherjee, Ind. J. Chem. A 40 (2001) 973.
[461] P. Manikandan, K. Padmakumar, K.R.J. Thomas, B. Varghese, H. Onodera, P.T. Manoharan, Inorg. Chem. 40 (2001) 6930.
[462] S. Mahapatra, R.J. Butcher, R.N. Mukherjee, J. Chem. Soc., Dalton Trans. (1993) 3723.
[463] C. Enachescu, J. Linares, F. Varret, K. Boukheddaden, E. Codjovi, S.G. Salunke, R. Mukherjee, Inorg. Chem. 43 (2004) 4880.
[464] C. Enachescu, F. Varret, E. Codjovi, J. Linares, S. Floquet, P. Manikandan, P.T. Manoharan, J. Phys. Chem. B 110 (2006) 5883.
[465] R.F. Carina, L. Verzegnassi, A.F. Williams, G. Bernardinelli, Chem. Commun. (1998) 2681.
[466] A.T. Baker, P. Singh, V. Vignevich, Aust. J. Chem. 44 (1991) 1041.
[467] R. Boča, P. Baran, L. Dlháň, H. Fuess, W. Haase, F. Renz, W. Linert, I. Svoboda, R. Werner, Inorg. Chim. Acta 260 (1997) 129.
[468] R. Boča, M. Boča, R. Jaroščiak, M. Vrbová, Mol. Cryst. Liq. Cryst. Sci. Tech., Sect. A 335 (1999) 1263.
[469] R. Boča, M. Boča, L. Dlháň, K. Falk, H. Fuess, W. Haase, R. Jaroščiak, B. Papánková, F. Renz, M. Vrbová, R. Werner, Inorg. Chem. 40 (2001) 3025.
[470] B. Papánková, M. Vrbová, R. Boča, P. Simon, K. Falk, G. Miehe, H. Fuess, J. Therm. Anal. Calor. 67 (2002) 721.
[471] (a) A.W. Addison, S. Burman, C.G. Wahlgren, O.A. Rajan, T.M. Rowe, E. Sinn, J. Chem. Soc., Dalton Trans. (1987) 2621;
(b) S. Ruettimann, C.M. Moreau, A.F. Williams, G. Bernardinelli, A.W. Addison, Polyhedron 11 (1992) 635.
[472] B. Strauss, V. Gutmann, W. Linert, Monatsh. Chem. 124 (1993) 391.
[473] R. Boča, P. Baran, M. Boča, L. Dlháň, H. Fuess, W. Haase, W. Linert, B. Papánková, R. Werner, Inorg. Chim. Acta 278 (1998) 190.
[474] M. Enamullah, W. Linert, V. Gutmann, R.F. Jameson, Monatsh. Chem. 125 (1994) 1301.
[475] R. Boča, F. Renz, M. Boča, H. Fuess, W. Haase, G. Kickelbick, W. Linert, M. Vrbová-Schikora, Inorg. Chem. Commun. 8 (2005) 227.
[476] F. Renz, U. El-Ayaan, W. Linert, Y. Fukuda, Mol. Cryst. Liq. Cryst. Sci. Tech., Sect. A 335 (1999) 1233.
[477] F. Renz, M. Hasegawa, T. Hoshi, U. El-Ayaan, W. Linert, Y. Fukuda, Mol. Cryst. Liq. Cryst. Sci. Tech., Sect. A 335 (1999) 1243.

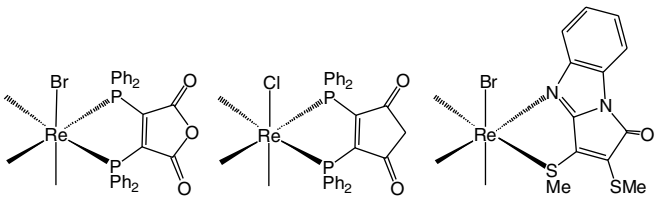
[478] M. Hasegawa, F. Renz, T. Hara, Y. Kikuchi, Y. Fukuda, J. Okubo, T. Hoshi, W. Linert, Chem. Phys. 277 (2002) 21.
[479] (a) B. Strauss, W. Linert, V. Gutmann, R.F. Jameson, Monatsh. Chem. 123 (1992) 537;
(b) M. Enamullah, J. Coord. Chem. 42 (1997) 231.
[480] B. Strauss, V. Gutmann, W. Linert, Monatsh. Chem. 124 (1993) 515.
[481] W. Linert, M. Konecny, F. Renz, J. Chem. Soc., Dalton Trans. (1994) 1523.
[482] W. Linert, M. Enamullah, V. Gutmann, R.F. Jameson, Monatsh. Chem. 125 (1994) 661.
[483] (a) M. Enamullah, W. Linert, J. Coord. Chem. 35 (1995) 325;
(b) M. Enamullah, W. Linert, J. Coord. Chem. 38 (1996) 337.
[484] M. Enamullah, F. Renz, U. El-Ayaan, G. Wiesinger, W. Linert, Vibr. Spectrosc. 14 (1997) 95.
[485] M. Enamullah, W. Linert, V. Gutmann, Vibr. Spectrosc. 9 (1995) 265.
[486] S.J. Rowan, J.B. Beck, J.S. Chen, Polymer Preprints 45 (2004) 494.
[487] C.G. Bochet, C. Piguet, A.F. Williams, Helv. Chim. Acta 76 (1993) 372.
[488] A.T. Baker, H.A. Goodwin, Aust. J. Chem. 39 (1986) 209.
[489] S.E. Livingstone, J.D. Nolan, J. Chem. Soc., Dalton Trans. (1972) 218.
[490] M. Boča, R. Boča, G. Kickelbick, W. Linert, I. Svoboda, H. Fuess, Inorg. Chim. Acta 338 (2002) 36.
[491] K.H. Sugiyarto, D.C. Craig, A.D. Rae, H.A. Goodwin, Aust. J. Chem. 46 (1993) 1269.
[492] F. Renz, A.P. de Souza, G. Klingelhöfer, H.A. Goodwin, Hyperfine Interact. 139/140 (2002) 699.
[493] A.T. Baker, D.C. Craig, G. Dong, A.D. Rae, Aust. J. Chem. 48 (1995) 1071.
[494] J.W. Ciszek, Z.K. Keane, L. Cheng, M.P. Stewart, L.H. Yu, D. Natelson, J.M. Tour, J. Am. Chem. Soc. 128 (2006) 3179, and 6264 (correction).
[495] H.A. Goodwin, Aust. J. Chem. 17 (1964) 1366.
[496] B.J. Childs, D.C. Craig, M.L. Scudder, H.A. Goodwin, Inorg. Chim. Acta 274 (1998) 32.
[497] (a) H.A. Goodwin, R.N. Sylva, Aust. J. Chem. 21 (1968) 2881;
(b) E. König, G. Ritter, H.A. Goodwin, Chem. Phys. 1 (1973) 17.
[498] R.N. Sylva, H.A. Goodwin, Aust. J. Chem. 20 (1967) 479.
[499] A.T. Baker, H.A. Goodwin, A.D. Rae, Aust. J. Chem. 37 (1984) 443.
[500] E. König, G. Ritter, H.A. Goodwin, Chem. Phys. Lett. 44 (1976) 100.
[501] G. Ritter, E. König, W. Irler, H.A. Goodwin, Inorg. Chem. 17 (1978) 224.
[502] J.K. Beattie, R.A. Binstead, R.J. West, J. Am. Chem. Soc. 100 (1978) 3044.
[503] (a) R.N. Sylva, H.A. Goodwin, Aust. J. Chem. 21 (1968) 1081;
(b) H.J. Keller, K.E. Schwarzhans, H.A. Goodwin, R.N. Sylva, Z. Naturforsch., Teil B 24 (1969) 1058;
(c) E. König, G. Ritter, W. Irler, H.A. Goodwin, B. Kanellakopulos, J. Phys. Chem. Solids 39 (1978) 521.
[504] (a) E. König, G. Ritter, H.A. Goodwin, Chem. Phys. 5 (1974) 211;
(b) E. König, G. Ritter, R. Zimmermann, H.A. Goodwin, J. Chem. Phys. 61 (1974) 3197.
[505] B.J. Childs, J.M. Cadogan, D.C. Craig, M.L. Scudder, H.A. Goodwin, Aust. J. Chem. 50 (1997) 129.
[506] B.J. Childs, D.C. Craig, K.A. Ross, M.L. Scudder, H.A. Goodwin, Aust. J. Chem. 47 (1994) 891.
[507] S. Singh, V. Mishra, R. Mukherjee, N. Seethalekshmi, R. Mukherjee, Dalton Trans. (2003) 3392.
[508] H.A. Goodwin, D.W. Mather, F.E. Smith, Aust. J. Chem. 28 (1975) 33.
[509] D.W. Mather, H.A. Goodwin, Aust. J. Chem. 28 (1975) 505.
[510] A.T. Baker, J.P. Matthews, Aust. J. Chem. 52 (1999) 339.
[511] T. Ayers, S. Scott, J. Goins, N. Caylor, D. Hathcock, S.J. Slattery, D.L. Jameson, Inorg. Chim. Acta 307 (2000) 7.
[512] T. Ayers, R. Turk, C. Lane, J. Goins, D.L. Jameson, S.J. Slattery, Inorg. Chim. Acta 357 (2004) 202.
[513] A.S. Abushamleh, H.A. Goodwin, Aust. J. Chem. 41 (1988) 873.
[514] B.J. Childs, D.C. Craig, M.L. Scudder, H.A. Goodwin, Aust. J. Chem. 51 (1998) 895.
[515] K.H. Sugiyarto, D.C. Craig, A.D. Rae, H.A. Goodwin, Aust. J. Chem. 49 (1996) 505.
[516] K.H. Sugiyarto, D.C. Craig, H.A. Goodwin, Aust. J. Chem. 49 (1996) 497.
[517] B.J. Childs, D.C. Craig, M.L. Scudder, H.A. Goodwin, Aust. J. Chem. 52 (1999) 673.
[518] J. DiBenedetto, B. Arkle, H.A. Goodwin, P.C. Ford, Inorg. Chem. 24 (1985) 455.
[519] A. Bousseksou, M. Verelst, H. Constant-Machado, G. Lemercier, J.-P. Tuchagues, F. Varret, Inorg. Chem. 35 (1996) 110.
[520] G. Lemercier, N. Brefuel, S. Shova, J.A. Wolny, F. Dahan, M. Verelst, H. Paulsen, A.X. Trautwein, J.-P. Tuchagues, Chem. Eur. J. 12 (2006) 7421.
[521] G. Lemercier, A. Bousseksou, S. Seigneuric, F. Varret, J.-P. Tuchagues, Chem. Phys. Lett. 226 (1994) 289.
[522] G. Lemercier, A. Bousseksou, M. Verelst, F. Varret, J.-P. Tuchagues, J. Magn. Magn. Mater. 150 (1995) 227.
[523] A. Thiel, A. Bousseksou, M. Verelst, F. Varret, J.-P. Tuchagues, Chem. Phys. Lett. 302 (1999) 549.
[524] S. Bonhommeau, N. Brefuel, V.K. Palfi, G. Molnár, A. Zwick, L. Salmon, J.-P. Tuchagues, J.S. Costa, J.-F. Létard, H. Paulsen, A. Bousseksou, Phys. Chem. Chem. Phys. 7 (2005) 2909.
[525] H.A. Goodwin, D.W. Mather, Aust. J. Chem. 27 (1974) 965.
[526] E. König, G. Ritter, A.K. Kulshreshtha, J. Waigel, H.A. Goodwin, Inorg. Chem. 23 (1984) 1896.
[527] (a) S.K. Kulshreshtha, R.M. Iyer, Chem. Phys. Lett. 134 (1987) 239;
(b) E. König, B. Kanellakopulos, B. Powietzka, H.A. Goodwin, Inorg. Chem. 29 (1990) 4944.
[528] E. König, G. Ritter, W. Irler, H.A. Goodwin, J. Am. Chem. Soc. 102 (1980) 4681.
[529] (a) E. König, G. Ritter, J. Waigel, H.A. Goodwin, J. Chem. Phys. 83 (1985) 3055;
(b) V. Ksenofontov, H. Spiering, A. Schreiner, G. Levchenko, H.A. Goodwin, P. Gütlich, J. Phys. Chem. Solids 60 (1999) 393.
[530] D. Onggo, D.C. Craig, A.D. Rae, H.A. Goodwin, Aust. J. Chem. 44 (1991) 331.
[531] A.S. Abushamleh, H.A. Goodwin, Aust. J. Chem. 33 (1980) 2171.
[532] H.A. Goodwin, D.W. Mather, Aust. J. Chem. 27 (1974) 2121.
[533] S. Dholakia, R.D. Gillard, J. Chem. Soc., Dalton Trans. (1984) 2245.
[534] See e.g. (a) H.A. Goodwin, F.E. Smith, E. König, G. Ritter, Aust. J. Chem. 26 (1973) 521;
(b) H.A. Goodwin, D.W. Mather, F.E. Smith, Aust. J. Chem. 26 (1973) 2623;
(c) B.J. Childs, J.M. Cadogan, D.C. Craig, M.L. Scudder, H.A. Goodwin, Aust. J. Chem. 51 (1998) 273;
(d) B.J. Childs, H.A. Goodwin, Aust. J. Chem. 54 (2001) 685.
[535] E. Baggio-Saitovitch, M.A. De Paoli, Inorg. Chim. Acta 27 (1978) 15.
[536] T. Sugano, M. Nomura, K. Awaga, P.L. Kieng, T. Ohta, M. Kinoshita, Bull. Chem. Soc. Jpn. 59 (1986) 2615.
[537] See e.g. (a) S. Alshehri, M.J. Blandamer, J. Burgess, P. Guardado, C.D. Hubbard, Polyhedron 12 (1993) 445;
(b) C. Scheer, P. Chautemps, I. Gautier-Luneau, J.-L. Pierre, G. Serratric, E. Saint-Aman, Polyhedron 15 (1996) 219;
(c) H.E. Toma, T.E. Chavez-Gil, Inorg. Chim. Acta 257 (1997) 197;
(d) B. De Bruin, E. Bill, E. Bothe, T. Weyhermüller, K. Wieghardt, Inorg. Chem. 39 (2000) 2936;
(e) Y. Chen, R. Chen, C. Qian, X. Dong, J. Sun, Organometallics 22 (2003) 4312;
(f) G. Chiericato Junior, A.P.S. Silva, L.S. Guinesi, Polyhedron 23 (2004) 1953;

(g) G.J.P. Britovsek, J. England, S.K. Spitzmesser, A.J.P. White, D.J. Williams, Dalton Trans. (2005) 945.
[538] G.I.H. Hanania, M.S. Michailides, D.H. Irvine, J. Phys. Chem. 81 (1977) 1382, and refs. therein.
[539] H.E. Toma, T.E. Chavez-Gil, R.C. Rocha, H.R. Rechenberg, J. Incl. Phenom. Macrocycl. Chem. 34 (1999) 57.
[540] P. Bonhôte, M. Ferigo, H. Stoeckli-Evans, W. Marty, Acta Crystallogr., Sect. C 49 (1993) 2102, and C50 (1994) 470 (correction).
[541] D.A. Leigh, P.J. Lusby, S.J. Teat, A.J. Wilson, J.K.Y. Wong, Angew. Chem., Int. Ed. 40 (2001) 1538.
[542] L. Hogg, D.A. Leigh, P.J. Lusby, A. Morelli, S. Parsons, J.K.Y. Wong, Angew. Chem., Int. Ed. 43 (2004) 1218.
[543] R.J. Butcher, A.W. Addison, Inorg. Chim. Acta 158 (1989) 211.
[544] S.M. Nelson, J. Rodgers, J. Chem. Soc. A (1968) 272.
[545] F. Hojland, H. Toftlund, S. Yde-Andersen, Acta Chem. Scand. A 37 (1983) 251.
[546] A. Hazell, C.J. McKenzie, L.P. Nielsen, Polyhedron 19 (2000) 1333.
[547] S. Wocadlo, W. Massa, J.-V. Folgado, Inorg. Chim. Acta 207 (1993) 199.
[548] (a) T. Kajiwara, T. Ito, J. Chem. Soc., Dalton Trans. (1998) 3351; (b) A. Kamiyama, T. Noguchi, T. Kajiwara, T. Ito, Inorg. Chem. 41 (2002) 507.
[549] H. Ierno, J. Jordanov, New J. Chem. 21 (1997) 241.
[550] J.B.J. Veldhuis, W.L. Driessen, J. Reedijk, J. Chem. Soc., Dalton Trans. (1986) 537.
[551] R. Viswanathan, M. Palaniandavar, T. Balasubramanian, P.T. Muthiah, J. Chem. Soc., Dalton Trans. (1996) 2519.
[552] (a) K. Wieghardt, W. Schmidt, W. Herrmann, H.J. Küppers, Inorg. Chem. 22 (1983) 2953; (b) J.C.A. Boeyens, A. Forbes, R.D. Hancock, K. Wieghardt, Inorg. Chem. 24 (1985) 2926.
[553] (a) J.W. Turner, F.A. Schultz, Inorg. Chem. 38 (1999) 358; (b) J.W. Turner, F.A. Schultz, Inorg. Chem. 40 (2001) 5296.
[554] (a) D.W. Blakesley, S.C. Payne, K.S. Hagen, Inorg. Chem. 39 (2000) 1979; (b) A. Diebold, A. Elbouadili, K.S. Hagen, Inorg. Chem. 39 (2000) 3915.
[555] A.A. Yousif, H. Winkler, H. Toftlund, A.X. Trautwein, R.H. Herber, J. Phys.: Condens. Matter 1 (1989) 7103.
[556] Z. Yu, G. Schmitt, S. Hofmann, H. Spiering, Y.F. Hsia, P. Gütlich, Hyperfine Interact. 93 (1994) 1459.
[557] H. Paulsen, H. Grunsteudel, W. Meyer-Klaucke, M. Gerdan, H.F. Grunsteudel, A.I. Chumakov, R. Ruffer, H. Winkler, H. Toftlund, A.X. Trautwein, Eur. Phys. J. B 23 (2001) 463.
[558] H. Paulsen, H. Winkler, A.X. Trautwein, H. Grunsteudel, V. Rusanov, H. Toftlund, Phys. Rev. B 59 (1999) 975.
[559] Z. Yu, Y.F. Hsia, X.Z. You, H. Spiering, P. Gütlich, J. Mater. Sci. 32 (1997) 6579.
[560] G. Brehm, M. Reiher, B. Le Guennic, M. Leibold, S. Schindler, F.W. Heinemann, S. Schneider, J. Raman Spectrosc. 37 (2006) 108.
[561] G.S. Matouzenko, A. Bousseksou, S. Lecocq, P.J. van Koningsbruggen, M. Perrin, O. Kahn, A. Collet, Inorg. Chem. 36 (1997) 2975.
[562] G.S. Matouzenko, A. Bousseksou, S. Lecocq, P.J. van Koningsbruggen, M. Perrin, O. Kahn, A. Collet, Inorg. Chem. 36 (1997) 5869.
[563] S. Zein, G.S. Matouzenko, S.A. Borshch, J. Phys. Chem. A 109 (2005) 8568.
[564] F. Mani, G. Scapacci, Inorg. Chim. Acta 38 (1980) 151.
[565] A. Diebold, K.S. Hagen, Inorg. Chem. 37 (1998) 213.
[566] K. Chen, L. Que Jr., J. Am. Chem. Soc. 123 (2001) 6327.
[567] Y. Zang, J. Kim, Y. Dong, E.C. Wilkinson, E.H. Appelman, L. Que Jr., J. Am. Chem. Soc. 119 (1997) 4197.
[568] M.P. Jensen, S.J. Lange, M.P. Mehn, E.L. Que, L. Que Jr., J. Am. Chem. Soc. 125 (2003) 2113.
[569] G.J.P. Britovsek, J. England, A.J.P. White, Inorg. Chem. 44 (2005) 8125.
[570] G.S. Matouzenko, J.-F. Létard, S. Lecoeq, A. Bousseksou, L. Capes, L. Salmon, M. Perrin, O. Kahn, A. Collet, Eur. J. Inorg. Chem. (2001) 2935.
[571] G.S. Matouzenko, A. Bousseksou, S.A. Borshch, M. Perrin, S. Zein, L. Salmon, G. Molnár, S. Lecocq, Inorg. Chem. 43 (2004) 227.
[572] S. Zein, G.S. Matouzenko, S.A. Borshch, Chem. Phys. Lett. 397 (2004) 475.
[573] T. Buchen, H. Toftlund, P. Gütlich, Chem. Eur. J. 2 (1996) 1129.
[574] H. Toftlund, E. Pedersen, S. Yde-Andersen, Acta Chem. Scand. A 38 (1984) 693.
[575] K. Nakano, N. Suemura, S. Kawata, A. Fuyuhiro, T. Yagi, S. Nasu, S. Morimoto, S. Kaizaki, Dalton Trans. (2004) 982.
[576] H. Börzel, P. Comba, K.S. Hagen, Y.D. Lampeka, A. Lienke, G. Linti, M. Merz, H. Pritzkow, L.V. Tsymbal, Inorg. Chim. Acta 337 (2002) 407.
[577] N. Brefuel, C. Lepetit, S. Shova, F. Dahan, J.-P. Tuchagues, Inorg. Chem. 44 (2005) 8916.
[578] (a) H. Winkler, A. Sawaryn, A.X. Trautwein, A.S. Yousif, C. Hermes, H. Toftlund, R.H. Herber, Hyperfine Interact. 42 (1988) 921; (b) Z. Yu, G. Schmitt, N. Boeres, H. Spiering, P. Gütlich, J. Phys.: Condens. Matter 7 (1995) 777.
[579] F. Paap, W.L. Driessen, J. Reedijk, B. Kojic-Prodic, A.L. Spek, Inorg. Chim. Acta 104 (1985) 55.
[580] M. Costas, A.K. Tipton, K. Chen, D.-H. Jo, L. Que Jr., J. Am. Chem. Soc. 123 (2001) 6722.
[581] K.P. Bryliakov, E.A. Duban, E.P. Talsi, Eur. J. Inorg. Chem. (2005) 72.
[582] K. Chen, L. Que Jr., Chem. Commun. (1999) 1375.
[583] Y. Mekmouche, S. Ménage, J. Pécaut, C. Lebrun, L. Reilly, V. Schuenemann, A. Trautwein, M. Fontecave, Eur. J. Inorg. Chem. (2004) 3163.
[584] M. Costas, L. Que Jr., Angew. Chem., Int. Ed. 41 (2002) 2179.
[585] K. Chen, L. Que Jr., Angew. Chem., Int. Ed. 38 (1999) 2227.
[586] D. Quinonero, D.G. Musaev, K. Morokuma, Inorg. Chem. 42 (2003) 8449.
[587] K. Ni-iya, A. Fuyuhiro, T. Yagi, S. Nasu, K. Kuzushita, S. Morimoto, S. Kaizaki, Bull. Chem. Soc. Jpn. 74 (2001) 1891.
[588] H. Kurosaki, Y. Ishikawa, T. Ishihara, T. Yamamoto, Y. Yamaguchi, M. Goto, Dalton Trans. (2005) 1086.
[589] (a) M. Goto, Y. Ishikawa, T. Ishihara, C. Nakatake, T. Higuchi, H. Kurosaki, V.L. Goedken, Chem. Commun. (1997) 539; (b) M. Goto, Y. Ishikawa, T. Ishihara, C. Nakatake, T. Higuchi, H. Kurosaki, V.L. Goedken, J. Chem. Soc., Dalton Trans. (1998) 1213.
[590] J.C. Dabrowiak, P.H. Merrell, D.H. Busch, Inorg. Chem. 11 (1972) 1979.
[591] V.L. Goedken, P.H. Merrell, D.H. Busch, J. Am. Chem. Soc. 94 (1972) 3397.
[592] J.C. Dabrowiak, P.H. Merrell, J.A. Stone, D.H. Busch, J. Am. Chem. Soc. 95 (1973) 6613.
[593] D.D. Watkins Jr., D.P. Riley, J.A. Stone, D.H. Busch, Inorg. Chem. 15 (1976) 387.
[594] J.W. Koch, M. Hanack, Chem. Ber. 120 (1987) 1853.
[595] S.R. Collinson, N.W. Alcock, T.J. Hubjn, D.H. Busch, J. Coord. Chem. 52 (2001) 317.
[596] K.D. Hodges, R.G. Wollmann, E.K. Barefield, D.N. Hendrickson, Inorg. Chem. 16 (1977) 2746.
[597] F.A. Walker, Chem. Rev. 104 (2004) 589.
[598] (a) V.N. Nemykin, A.E. Polshina, V.Y. Chernii, E.V. Polshin, N. Kobayashi, Dalton Trans. (2000) 1019; (b) V.N. Nemykin, N. Kobayashi, V.Y. Chernii, V.K. Belsky, Eur. J. Inorg. Chem. (2001) 733.
[599] (a) G. Roelfes, M. Lubben, K. Chen, R.Y.N. Ho, A. Meetsma, S. Genseberger, R.M. Hermant, R. Hage, S.K. Mandal, V.G. Young Jr., Y. Zang, H. Kooijman, A.L. Spek, L. Que, B.L. Feringa, Inorg. Chem. 38 (1999) 1929; (b) G. Roelfes, M.E. Branum, L. Wang, L. Que Jr., B.L. Feringa, J. Am. Chem. Soc. 122 (2000) 11517; (c) M. van den Heuvel, T.A. van den Berg, R.M. Kellogg, C.T. Choma, B.L. Feringa, J. Org. Chem. 69 (2004) 250.
[600] G. Roelfes, V. Vrajmasu, K. Chen, R.Y.N. Ho, J.-U. Rohde, C. Zondervan, R.M. la Crois, E.P. Schudde, M. Lutz, A.L. Spek, R.

Hage, B.L. Feringa, E. Münck, L. Que Jr., Inorg. Chem. 42 (2003) 2639.
[601] (a) M.E. De Vries, R.M. La Crois, G. Roelfes, H. Kooijman, A.L. Spek, R. Hage, B.L. Feringa, Chem. Commun. (1997) 1549; (b) C.R. Goldsmith, R.T. Jonas, A.P. Cole, T.D.P. Stack, Inorg. Chem. 41 (2002) 4642.
[602] D.J. Rudd, C.R. Goldsmith, A.P. Cole, T.D.P. Stack, K.O. Hodgson, B. Hedman, Inorg. Chem. 44 (2005) 1221.
[603] R.T. Jonas, T.D.P. Stack, J. Am. Chem. Soc. 119 (1997) 8566.
[604] E.L.-M. Wong, G.-S. Fang, C.-M. Che, N. Zhu, Chem. Commun. (2005) 4578.
[605] I. Bernal, I.M. Jensen, K.B. Jensen, C.J. McKenzie, H. Toftlund, J.-P. Tuchagues, J. Chem. Soc., Dalton Trans. (1995) 3667.
[606] N. Ortega-Villar, A.L. Thompson, M.C. Muñoz, V.M. Ugalde-Saldívar, A.E. Goeta, R. Moreno-Esparza, J.A. Real, Chem. Eur. J. 11 (2005) 5721.
[607] A.K. Patra, M.M. Olmstead, P.K. Mascharak, Inorg. Chem. 41 (2002) 5403.
[608] A. Machkour, D. Mandon, M. Lachkar, R. Welter, Eur. J. Inorg. Chem. (2005) 158.
[609] S. Collinson, N.W. Alcock, A. Raghunathan, P.K. Kahol, D.H. Busch, Inorg. Chem. 39 (2000) 757.
[610] L. Spiccia, G.D. Fallon, M.J. Grannas, P.J. Nichols, E.R.T. Tiekink, Inorg. Chim. Acta 279 (1998) 192.
[611] S.M. Nelson, P.D.A. McIlroy, C.S. Stevenson, E. König, G. Ritter, J. Waigel, J. Chem. Soc., Dalton Trans. (1986) 991.
[612] E. König, G. Ritter, J. Dengler, S.M. Nelson, Inorg. Chem. 26 (1987) 3582.
[613] P. Guionneau, J.S. Costa, J.-F. Létard, Acta Crystallogr., Sect. C 60 (2004) m587.
[614] J.S. Costa, P. Guionneau, J.-F. Létard, J. Phys. Conf. Ser. 21 (2005) 67.
[615] H. Liu, A. Fujishima, O. Sato, Appl. Phys. Lett. 85 (2004) 2295.
[616] S. Bonhommeau, T. Guillon, L.M.L. Daku, P. Demont, J.S. Costa, J.-F. Létard, G. Molnár, A. Bousseksou, Angew. Chem., Int. Ed. 45 (2006) 1625.
[617] H. Liu, A. Fujishima, O. Sato, Appl. Phys. Lett. 86 (2005) 122511.
[618] S. Hayami, G. Juhasz, Y. Maeda, T. Yokoyama, O. Sato, Inorg. Chem. 44 (2005) 7289.
[619] M.G.B. Drew, A.H. bin Othman, S.G. McFall, P.D.A. McIlroy, S.M. Nelson, J. Chem. Soc., Dalton Trans. (1977) 1173.
[620] (a) M.G.B. Drew, J. Grimshaw, P.D.A. McIlroy, S.M. Nelson, J. Chem. Soc., Dalton Trans. (1976) 1388; (b) M.G.B. Drew, A.H. bin Othman, S.M. Nelson, J. Chem. Soc., Dalton Trans. (1976) 1394.
[621] S.M. Nelson, F.S. Esho, M.G.B. Drew, P. Bird, J. Chem. Soc., Chem. Commun. (1979) 1035.
[622] H. Toftlund, S. Yde-Andersen, Acta Chem. Scand. A 35 (1981) 575.
[623] H.R. Chang, J.K. McCusker, H. Toftlund, S.R. Wilson, A.X. Trautwein, H. Winkler, D.N. Hendrickson, J. Am. Chem. Soc. 112 (1990) 6814.
[624] X. Solans, L. Ruiz-Ramirez, R. Moreno-Esparza, M. Labrador, A. Escuer, J. Solid State Chem. 109 (1994) 315.
[625] J.K. McCusker, K.N. Walda, R.C. Dunn, J.D. Simon, D. Magde, D.N. Hendrickson, J. Am. Chem. Soc. 115 (1993) 298.
[626] J.K. McCusker, A.L. Rheingold, D.N. Hendrickson, Inorg. Chem. 35 (1996) 2100.
[627] (a) G. Chen, G. Espinosa-Perez, A. Zentella-Dehesa, I. Silaghi-Dumitrescu, F. Lara-Ochoa, Inorg. Chem. 39 (2000) 3440; (b) G. Chen, R. Liu, I. Silaghi-Dumitrescu, G. Espinosa-Perez, A. Zentella-Dehesa, F. Lara-Ochoa, Int. J. Quant. Chem. 83 (2001) 60.
[628] J.K. McCusker, H. Toftlund, A.L. Rheingold, D.N. Hendrickson, J. Am. Chem. Soc. 115 (1993) 1797.
[629] M. Tamura, Y. Urano, K. Kikuchi, T. Higuchi, M. Hirobe, T. Nagano, Chem. Pharm. Bull. 48 (2000) 1514.
[630] F.B. Hulsbergen, W.L. Driessen, J. Reedijk, G.C. Verschoor, Inorg. Chem. 23 (1984) 3588.
[631] G.S. Matouzenko, D. Luneau, G. Molnár, N. Ould-Moussa, S. Zein, S.A. Borshch, A. Bousseksou, F. Averseng, Eur. J. Inorg. Chem. (2006) 2671.
[632] A.H.R. Al-Obaidi, K.B. Jensen, J.J. McGarvey, H. Toftlund, B. Jensen, S.E.J. Bell, J.G. Carroll, Inorg. Chem. 37 (1996) 5055.
[633] H. Paulsen, R. Benda, C. Herta, V. Schunemann, A.I. Chumakov, L. Duelund, H. Winkler, H. Toftlund, A.X. Trautwein, Phys. Rev. Lett. 86 (2001) 1351.
[634] (a) V.M. Ugalde-Saldívar, M.E. Sosa-Torres, L. Ortiz-Frade, S. Bernès, H. Höpfl, J. Chem. Soc., Dalton Trans. (2001) 3099; (b) V.M. Ugalde-Saldívar, H. Höpfl, N. Farfán, A.R. Toscano, M.E. Sosa-Torres, Inorg. Chim. Acta 358 (2005) 3545.
[635] L. Christiansen, D.N. Hendrickson, H. Toftlund, S.R. Wilson, C.L. Xie, Inorg. Chem. 25 (1986) 2813.
[636] N. Brefuel, S. Imatomi, H. Torigoe, H. Hagiwara, S. Shova, J.-F. Meunier, S. Bonhommeau, J.-P. Tuchagues, N. Matsumoto, Inorg. Chem. 45 (2006) 8126.
[637] (a) S. Schenker, P.C. Stein, J.A. Wolny, C. Brady, J.J. McGarvey, H. Toftlund, A. Hauser, Inorg. Chem. 40 (2001) 134; (b) C. Brady, P.L. Callaghan, Z. Ciunik, C.G. Coates, A. Døssing, A. Hazell, J.J. McGarvey, S. Schenker, H. Toftlund, A.X. Trautwein, H. Winkler, J.A. Wolny, Inorg. Chem. 43 (2004) 4289.
[638] K. Wieghardt, E. Schöffmann, B. Nuber, J. Weiss, Inorg. Chem. 25 (1986) 4877.
[639] M. Di Vaira, F. Mani, P. Stoppioni, J. Chem. Soc., Dalton Trans. (1997) 1375.
[640] G. De Martino Norante, M. Di Vaira, F. Mani, S. Mazzi, P. Stoppioni, J. Chem. Soc., Dalton Trans. (1992) 361.
[641] M. Koikawa, K.B. Jensen, H. Matsushima, T. Tokii, H. Toftlund, J. Chem. Soc., Dalton Trans. (1998) 1085.
[642] A.H.R. Al-Obaidi, J.J. McGarvey, K.P. Taylor, S.E.J. Bell, K.B. Jensen, H. Toftlund, J. Chem. Soc., Chem. Commun. (1993) 536.
[643] (a) D. Zhang, D.H. Busch, Inorg. Chem. 33 (1994) 5138; (b) N.W. Alcock, D. Zhang, D.H. Busch, Acta Crystallogr., Sect. C 55 (1999) 886.
[644] L.L. Martin, K.S. Hagen, A. Hauser, R.L. Martin, A.M. Sargeson, J. Chem. Soc., Chem. Commun. (1988) 1313.
[645] L.L. Martin, R.L. Martin, K.S. Murray, A.M. Sargeson, Inorg. Chem. 29 (1990) 1387.
[646] M. Miteva, P. Bonchev, V. Russanov, E. Zhecheva, D. Mekhandzhiev, K. Kabassanov, Polyhedron 10 (1991) 763.
[647] (a) E. Larsen, G.N. LaMar, B.E. Wagner, J.E. Parks, R.H. Holm, Inorg. Chem. 11 (1972) 2652; (b) W.M. Reiff, J. Am. Chem. Soc. 95 (1973) 3048.
[648] C. Mealli, E.C. Lingafelter, J. Chem. Soc. D (1970) 885.
[649] G. Brewer, C. Luckett, L. May, A.M. Beatty, W.R. Scheidt, Inorg. Chim. Acta 357 (2004) 2390.
[650] A.J. Conti, C.L. Xie, D.N. Hendrickson, J. Am. Chem. Soc. 111 (1989) 1171.
[651] M.A. Hoselton, L.J. Wilson, R.S. Drago, J. Am. Chem. Soc. 97 (1975) 1722.
[652] M.S. Lazarus, M.A. Hoselton, T.S. Chou, Inorg. Chem. 16 (1977) 2549.
[653] L.J. Wilson, D. Georges, M.A. Hoselton, Inorg. Chem. 14 (1975) 2968.
[654] K.M. Kadish, C.H. Su, D. Schaeper, C.L. Merrill, L.J. Wilson, Inorg. Chem. 21 (1982) 3433.
[655] W.H. Batschelet, N.J. Rose, Inorg. Chem. 22 (1983) 2078.
[656] M. Khalil, M.A. Marcus, A.L. Smeigh, J.K. McCusker, H.H.W. Chong, R.W. Schoenlein, J. Phys. Chem. A 110 (2006) 38.
[657] K. Boubekeur, A. Deroche, F. Lambert, I. Morgenstern-Badarau, Acta Crystallogr., Sect. C 51 (1995) 2244.
[658] I. Morgenstern-Badarau, F. Lambert, J.P. Renault, M. Cesario, J.-D. Marechal, F. Maseras, Inorg. Chim. Acta 297 (2000) 338.
[659] A. Alousy, J. Burgess, D. Elvidge, C.D. Hubbard, S. Radulovic, Inorg. React. Mech. 2 (2000) 249.
[660] W.H. Batschelet, N.J. Rose, Inorg. Chem. 22 (1983) 2083.

[661] C.L. Xie, D.N. Hendrickson, J. Am. Chem. Soc. 109 (1987) 6981.
[662] M.A. Hoselton, R.S. Drago, L.J. Wilson, N. Sutin, J. Am. Chem. Soc. 98 (1976) 6967.
[663] W.S. Hammack, A.J. Conti, D.N. Hendrickson, H.G. Drickamer, J. Am. Chem. Soc. 111 (1989) 1738.
[664] (a) W. Wang, I.Y. Chan, S. Schenker, A. Hauser, J. Chem. Phys. 106 (1997) 3817;
(b) S. Schenker, A. Hauser, W. Wang, I.Y. Chan, J. Chem. Phys. 109 (1998) 9870.
[665] C. Brewer, G. Brewer, C. Luckett, G.S. Marbury, C. Viragh, A.M. Beatty, W.R. Scheidt, Inorg. Chem. 43 (2004) 2402.
[666] F. Lambert, C. Policar, S. Durot, M. Cesario, Y. Lu, H. Korri-Youssoufi, B. Keita, L. Nadjo, Inorg. Chem. 43 (2004) 4178.
[667] (a) S.-P. Yang, Y.-X. Tong, H.-L. Zhu, H. Cao, X.-M. Chen, L.-N. Ji, Polyhedron 20 (2001) 223;
(b) H.M. Chen, S.P. Yang, Q.Q. Chen, J.M. Chen, X.B. Yu, Acta Crystallogr., Sect. E 61 (2005) m1277.
[668] C. Brewer, G. Brewer, G. Patil, Y. Sun, C. Viragh, R.J. Butcher, Inorg. Chim. Acta 358 (2005) 3441.
[669] H. Ohta, Y. Sunatsuki, M. Kojima, S. Iijima, H. Akashi, N. Matsumoto, Chem. Lett. (2004) 350.
[670] Y. Sunatsuki, H. Ohta, M. Kojima, Y. Ikuta, Y. Goto, N. Matsumoto, S. Iijima, H. Akashi, S. Kaizaki, F. Dahan, J.-P. Tuchagues, Inorg. Chem. 43 (2004) 4154.
[671] Y. Sunatsuki, Y. Ikuta, N. Matsumoto, H. Ohta, M. Kojima, S. Iijima, S. Hayami, Y. Maeda, S. Kaizaki, F. Dahan, J.-P. Tuchagues, Angew. Chem., Int. Ed. 42 (2003) 1614.
[672] M. Yamada, E. Fukumoto, M. Ooidemizu, N. Brefuel, N. Matsumoto, S. Iijima, M. Kojima, N. Re, F. Dahan, J.-P. Tuchagues, Inorg. Chem. 44 (2005) 6967.
[673] M. Yamada, Yamada, H. Hagiwara, H. Torigoe, N. Matsumoto, M. Kojima, F. Dahan, J.-P. Tuchagues, N. Re, S. Iijima, Chem. Eur. J. 12 (2006) 4536.
[674] Y. Ikuta, M. Ooidemizu, Y. Yamahata, M. Yamada, S. Osa, N. Matsumoto, S. Iijima, Y. Sunatsuki, M. Kojima, F. Dahan, J.-P. Tuchagues, Inorg. Chem. 42 (2003) 7001.
[675] M. Yamada, M. Ooidemizu, Y. Ikuta, S. Osa, N. Matsumoto, S. Iijima, M. Kojima, F. Dahan, J.-P. Tuchagues, Inorg. Chem. 42 (2003) 8406.
[676] S. Nagasato, I. Katsuki, Y. Motoda, Y. Sunatsuki, N. Matsumoto, M. Kojima, Inorg. Chem. 40 (2001) 2534.
[677] I. Morgenstern-Badarau, F. Lambert, A. Deroche, M. Cesario, J. Guilhem, B. Keita, L. Nadjo, Inorg. Chim. Acta 275–276 (1998) 234.
[678] (a) M.J. Hardie, C.A. Kilner, M.A. Halcrow, Acta Crystallogr., Sect. C 60 (2004) m177;
(b) M.A. Halcrow, unpublished data.
[679] A.F. Deeney, C.J. Harding, G.G. Morgan, V. McKee, J. Nelson, S.J. Teat, W. Clegg, J. Chem. Soc., Dalton Trans. (1998) 1837.
[680] D.G. Lonnon, D.C. Craig, S.B. Colbran, Inorg. Chem. Commun. 5 (2002) 958.
[681] X.-H. Bu, W. Chen, Z.-H. Zhang, R.-H. Zhang, S.-M. Kuang, T. Clifford, Inorg. Chim. Acta 310 (2000) 110.
[682] X.-H. Bu, S.-L. Lu, R.-H. Zhang, H. Liu, H.-P. Zhu, Q.-T. Liu, Polyhedron 19 (2000) 431.
[683] J. Coyle, M.G.B. Drew, C.J. Harding, J. Nelson, R.M. Town, J. Chem. Soc., Dalton Trans. (1997) 1123.
[684] See e.g. (a) M. Di Vaira, F. Mani, P. Stoppioni, J. Chem. Soc., Chem. Commun. (1989) 126;
(b) G. De Martino Norante, M. Di Vaira, F. Mani, S. Mazzi, P. Stoppioni, Inorg. Chem. 29 (1990) 2822;
(c) R. Ziessel, J.-M. Lehn, Helv. Chim. Acta 73 (1990) 1149;
(d) M. Di Vaira, F. Mani, P. Stoppioni, J. Chem. Soc., Dalton Trans. (1992) 1127;
(e) W.O. Koch, A. Barbieri, M. Grodzicki, V. Schünemann, A.X. Trautwein, H.-J. Krüger, Angew. Chem., Int. Ed. 35 (1996) 422.

(bma) [4], 4,5-bis(diphenylphosphino)-4-cyclopenten-1,3-dione (bpcd) [5], and 2,3-bis(methylthio)pyrrolo[1,2-a]benzimidazol-1-one (bmpb) [6], the structures of which are shown below.



fac-BrRe(CO)$_3$(bma) *fac*-ClRe(CO)$_3$(bpcd) *fac*-BrRe(CO)$_3$(bmpb)

In terms of the diphosphine ligand bpcd, we recently confirmed that facile and significant structural modifications of the central dione platform could easily be achieved through Knoevenagel condensation reactions. Two such reactions involving the union of 9-anthracenecarboxaldehdye and ferrocenecarboxaldehyde are depicted in Scheme 1 [7,8]. The resulting second-generation ligands derived from bpcd can be custom- or fine-tuned to produce compounds that have a fixed or specific redox potential(s) by simply controlling the extent of π-electron delocalization within the diphosphine ligand platform. With the attachment of suitable donor–acceptor groups to the original dione scaffold, new ligands with the ability to function as directed energy transfer agents can be expected.

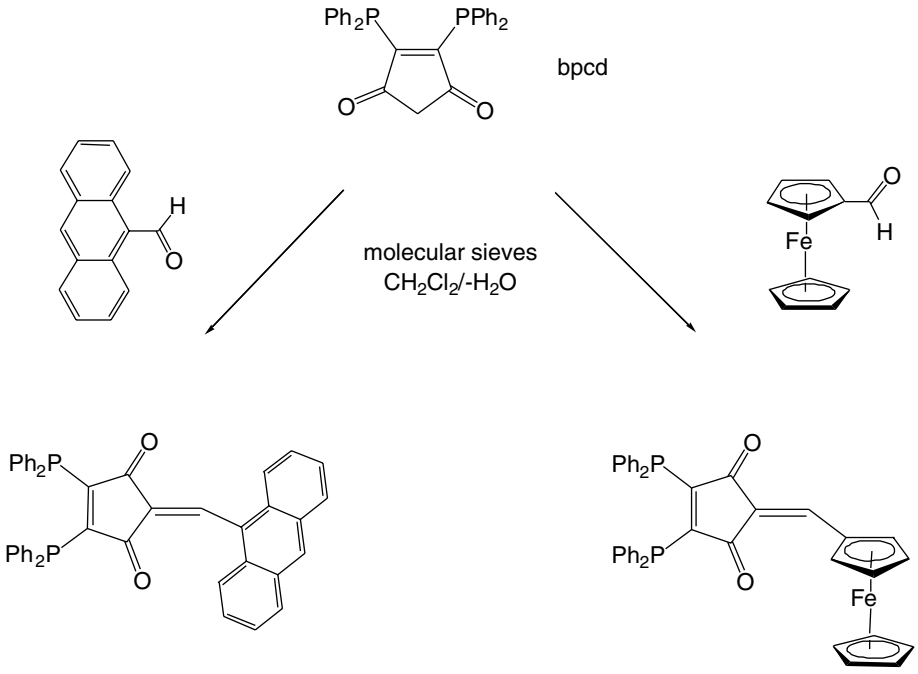
Wishing to extend our functionalization studies of the bcpd ligand to other aldehydes that could, in principle, function as multidentate ligand systems, we have studied the condensation reaction between thiophene-2-carboxaldehyde and bpcd. Herein we present our data on the synthesis of the new diphosphine ligand 2-(2-thienylidene)-4,5-bis(diphenylphosphino)-4-cyclopenten-1,3-dione (tbpcd). The reactivity of this ligand with BrRe(CO)$_5$ and BrRe(CO)$_3$(THF)$_2$ has been examined and found to give *fac*-BrRe(CO)$_3$(tbpcd) in high yield. Both new compounds have isolated and their solid-state structures determined. The redox properties and photophysics of the tbpcd ligand and its rhenium(I) complex have been investigated and the results are discussed relative to MO calculations at the extended Hückel level.

2. Experimental

2.1. General

The starting diphosphine ligand bpcd was prepared from 4,5-dichloro-4-cyclopenten-1,3-dione and Ph_2PSiMe_3 [9], while BrRe(CO)$_3$(THF)$_2$ was synthesized from BrRe(CO)$_5$ [10]. The thiophene-2-carboxaldehyde was purchased from Aldrich Chemical Co. and used as received. All reaction and NMR solvents were distilled from an appropriate drying agent using Schlenk techniques and stored under argon in storage vessels equipped with high-vacuum Teflon stopcocks [11]. The tetra-*n*-butylammonium perchlorate (TBAP) electrolyte was purchased from Johnson Matthey Electronics and was recrystallized from ethyl acetate/hexane, followed by drying under high vacuum for at least 36 h.

The IR spectral data were recorded on a Nicolet 20 SXB FT-IR spectrometer in sealed 0.1 mm NaCl cells, while the



Scheme 1.

^{1}H spectral data were recorded at 200 MHz on a Varian Gemini-200 spectrometer. The ^{31}P NMR spectra were collected in the proton-decoupled mode on a Varian 300-VXR spectrometer at 121 MHz, with the reported chemical shifts referenced to external H_3PO_4 (85%), taken to have $\delta = 0$. The absorption spectra were recorded on a HP 8453 ChemStation (Marshall) or a HP 8425A diode array spectrometer (UNT). The emission data were recorded on a Jobin Fluorolog FL 3-22 spectrometer equipped with DataMax software. The ESI-APCI mass spectra were recorded at the University of the Pacific in the positive ionization mode for **1** and the negative ionization mode for **2**.

2.2. Synthesis of tbpcd (*1*)

To a small Schlenk vessel was added 0.20 g (0.43 mmol) of bpcd, followed by 25 mL of CH_2Cl_2, 0.39 mL (excess) thiophene-2-carboxaldehyde, and ca. 4.0 g of molecular sieves (4 Å). Stirring over night under argon led to the complete consumption of the bpcd ligand, as assessed by TLC analysis. The presence of the desired product was confirmed by TLC examination of the reaction solution. Here the tbpcd ligand was observed as an orange spot having a $R_f = 0.30$ using CH_2Cl_2/petroleum ether (3:2) as the eluent. The molecular sieves were filtered away and the solution concentrated to ca. 0.5 mL, after which the crude product was subjected to chromatographic separation over silica gel using the aforementioned solvent system to give tbpcd as an orange solid in 90% yield (0.22 g). IR (CH_2Cl_2): ν(CO) 1719 (m, symm dione), 1673 (vs, antisymm dione) cm^{-1}. ^{1}H NMR ($CDCl_3$): δ 7.05 (dd, 1H, thiophene, $^3J_{H-H} = 7$, 5 Hz), 7.22–7.46 (m, 20H, phenyls), 7.56 (s, 1H, vinyl), 7.68 (d, 1H, thiophene, $^3J_{H-H} = 7$ Hz), 7.90 (d, 1H, thiophene, $^3J_{H-H} = 5$ Hz). ^{31}P NMR ($CDCl_3$): δ −24.23 (AB quartet, $J_{P-P} = 25$ Hz). ESI-APCI MS (*m*/*z*): 581.086 [**1**+Na]$^+$, 558.995 [**1**]$^+$.

2.3. Synthesis of fac-BrRe(CO)$_3$(tbpcd) (*2*) from tbpcd and BrRe(CO)$_3$(THF)$_2$

To a Schlenk tube under argon was charged 0.10 g (0.20 mmol) of $BrRe(CO)_3(THF)_2$ and 0.11 g (0.20 mmol) of **1**, after which 20 mL of CH_2Cl_2 was added via cannula. The contents were stirred at room temperature for 3 h and examined by TLC, which revealed the complete consumption of the starting materials and only the presence of the desired product as a yellow spot at $R_f = 0.20$ using CH_2Cl_2 as the mobile phase. The solvent was concentrated and compound **2** subsequently isolated by column chromatography over silica gel using CH_2Cl_2. Yield of **2**: 0.14 g (80%). IR (CH_2Cl_2): ν(CO) 2039 (s), 1966 (s), 1912 (s), 1728 (vw, symm dione), 1684 (s, antisymm dione) cm^{-1}. ^{1}H NMR ($CDCl_3$): δ 7.21 (dd, 1H, thiophene, $^3J_{H-H} = 7$, 5 Hz), 7.32–7.90 [m, 22H, vinyl (1H), thiophene (1H), and phenyls (20H)], 8.06 (d, 1H, thiophene, $^3J_{H-H} =$ 5 Hz). ^{31}P NMR ($CDCl_3$): δ 18.09 (s, 1P), 19.18 (s, 1P). ESI-APCI MS (*m*/*z*): 907.821 [**2**]$^-$, 938.922 [**2**+MeO]$^-$.

2.4. X-ray diffraction structures

Single crystals of the tbpcd ligand were grown from a CH_2Cl_2 solution containing tbpcd that had been layered with hexane, while X-ray quality crystals of *fac*-BrRe(CO)$_3$(tbpcd) were grown from an acetone solution containing *fac*-BrRe(CO)$_3$(tbpcd) that was layered with Et_2O. The reported X-ray data for both compounds were collected on a Bruker SMART™ 1000 CCD-based diffractometer at 213 K. The frames were integrated with the available SAINT software package using a narrow-frame algorithm [12], and the structures were solved and refined using the SHELXTL program package [13]. The molecular structures were checked by using PLATON [14], and solved by direct methods with all nonhydrogen atoms refined anisotropically. All carbon-bound hydrogen atoms were assigned calculated positions and allowed to ride on the attached heavy atom, unless otherwise noted. Refinement for tbpcd converged at $R = 0.0641$ and $R_w = 0.1187$ for 6379 independent reflections with $I > 2\sigma(I)$, with **2** · acetone yielding convergence values of at $R = 0.0358$ and $R_w = 0.0873$ for 8558 independent reflections with $I > 2\sigma(I)$. Tables 1 and 2 summarize the pertinent X-ray data for compounds **1** and **2** · acetone.

2.5. Electrochemistry

The cyclic voltammetric data were recorded on a PAR Model 273 potentiostat/galvanostat, equipped with positive feedback circuitry to compensate for *i*R drop. The

Table 1
X-ray crystallographic data and processing parameters for the ligand tbpcd (**1**) and *fac*-BrRe(CO)$_3$(tbpcd) · acetone (**2** · acetone)

Compound	**1**	**2** · acetone
CCDC entry no.	623341	623342
Crystal system	monoclinic	monoclinic
Space group	$P2_1/c$	$P2_1/c$
a (Å)	13.049(2)	15.986(3)
b (Å)	10.878(2)	15.761(3)
c (Å)	19.582(2)	14.522(3)
β (°)	93.461(3)	95.267(3)
V (Å^3)	2774.5(7)	3643(1)
Molecular formula	$C_{34}H_{24}O_2P_2S$	$C_{37}H_{24}BrO_5P_2ReS$ · acetone
Formula weight	558.53	966.75
Formula units per cell (Z)	4	4
D_{calc} (Mg/m^3)	1.337	1.763
λ (Mo Kα) (Å)	0.71073	0.71073
μ (mm^{-1})	0.263	4.625
R_{merge}	0.0550	0.0783
Absorption correction	empirical	empirical
Absorption correction factor	0.8149/0.6572	1.0000/0.4525
Total reflections	21 540	38 899
Independent reflections	6379	8558
Data/restraints/parameters	6379/0/353	8558/0/462
R	0.0641	0.0358
R_w	0.1187	0.0873
Goodness-of-fit on F^2	1.005	0.993
$\Delta\rho_{maximum}$, $\Delta\rho_{minimum}$ (e/Å^3)	0.490 and −0.261	1.978 and −1.290

Table 2
Selected bond distances (Å) and angles (°) in ligand tbpcd (**1**) and *fac*-$BrRe(CO)_3$(tbpcd) · acetone (**2** · acetone)

*tbpcd (**1**)*			
Bond distances			
S(1)–C(34)	1.693(3)	S(1)–C(31)	1.727(3)
C(1)–C(30)	1.352(3)	C(1)–C(5)	1.466(4)
C(1)–C(2)	1.473(3)	C(2)–C(3)	1.514(4)
C(3)–C(4)	1.355(3)	C(4)–C(5)	1.526(3)
C(30)–C(31)	1.436(3)	C(31)–C(32)	1.411(4)
C(32)–C(33)	1.398(4)	C(33)–C(34)	1.351(4)
P(1)···P(2)	3.330(1)	S(1)···O(2)	2.861(2)
Bond angles			
C(34)–S(1)–C(31)	91.5(1)	C(30)–C(1)–C(5)	131.1(2)
C(30)–C(1)–C(2)	121.9(2)	C(5)–C(1)–C(2)	107.0(2)
C(4)–C(3)–P(2)	121.7(2)	C(2)–C(3)–P(2)	128.4(2)
C(3)–C(4)–P(1)	122.9(2)	C(5)–C(4)–P(1)	128.2(2)
C(1)–C(30)–C(31)	132.8(2)	C(30)–C(31)–S(1)	127.6(2)
*fac-BrRe(CO)$_4$(tbpcd) · acetone (**2** · acetone)*			
Bond distances			
Re(1)–P(2)	2.449(1)	Re(1)–P(1)	2.468(1)
Re(1)–Br(1)	2.6530(6)	S(1)–C(37)	1.676(5)
S(1)–C(34)	1.714(5)	C(1)–C(2)	1.342(5)
C(1)–C(5)	1.526(5)	C(2)–C(3)	1.513(6)
C(3)–C(4)	1.473(6)	C(4)–C(33)	1.365(6)
C(4)–C(5)	1.469(6)	C(33)–C(34)	1.430(6)
C(34)–C(35)	1.467(6)	C(35)–C(36)	1.355(7)
C(36)–C(37)	1.361(8)	P(1)···P(2)	3.213(2)
S(1)···O(2)	2.912(3)		
Bond angles			
C(32)–Re(1)–C(31)	91.0(2)	C(32)–Re(1)–C(30)	88.1(2)
C(31)–Re(1)–C(30)	90.1(2)	C(32)–Re(1)–P(2)	95.6(1)
C(31)–Re(1)–P(2)	92.5(1)	C(30)–Re(1)–P(2)	175.4(1)
C(32)–Re(1)–P(1)	95.4(1)	C(31)–Re(1)–P(1)	171.7(1)
C(30)–Re(1)–P(1)	95.4(1)	P(2)–Re(1)–P(1)	81.59(3)
C(32)–Re(1)–Br(1)	178.3(1)	C(31)–Re(1)–Br(1)	89.5(1)
C(30)–Re(1)–Br(1)	93.5(1)	P(2)–Re(1)–Br(1)	82.69(3)
P(1)–Re(1)–Br(1)	83.95(3)	C(37)–S(1)–C(34)	91.7(3)
C(2)–C(1)–P(1)	120.2(3)	C(5)–C(1)–P(1)	130.5(3)
C(1)–C(2)–P(2)	121.2(3)	C(3)–C(2)–P(2)	126.6(3)
C(5)–C(4)–C(3)	107.9(3)		

homemade three-electrode cell that was used allowed the cyclic voltammograms to be recorded under oxygen- and moisture-free conditions. A platinum disk (area = 0.0079 cm^2) was employed as the working and auxiliary electrode. The reference electrode utilized a silver wire as a quasi-reference electrode, with the reported potential data standardized against the formal potential of the Cp_2Fe/Cp_2Fe^+ (internally added) redox couple, taken to have $E_{1/2} = 0.307$ V [15].

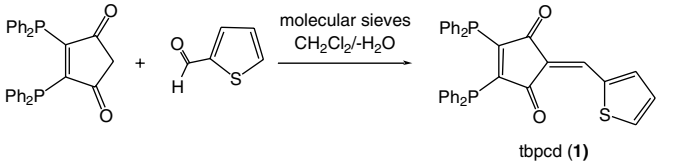
2.6. Extended Hückel MO calculations

The extended Hückel calculations on tbpcd and *fac*-$BrRe(CO)_3$(tbpcd) were carried out using the original program developed by Hoffmann [16], as modified by Mealli and Proserpio [17]. The weighted H_{ij}'s contained in the program were used in the calculations. The input *Z*-matrices for the model compounds tbpcd-H_4 and *fac*-$BrRe(CO)_3$(tbpcd-H_4) were constructed from the X-ray data of **1** and **2** · acetone, employing hydrogens in the place of the four ancillary phenyl groups and setting the P–H bond distances to 1.41 Å [18].

3. Results and discussion

3.1. Synthesis, spectroscopic data, and X-ray diffraction structure of tbpcd (*1*)

Knoevenagel condensation of the diphosphine ligand bpcd with thiophene-2-carboxaldehyde (excess) proceeds readily in CH_2Cl_2 at room temperature in the presence of added molecular sieves to afford the new diphosphine ligand 2-(2-thienylidene)-4,5-bis(diphenylphosphino)-4-cyclopenten-1,3-dione (tbpcd) in near quantitative yield. Simply stirring the two reagents without added molecular sieves showed no evidence for the formation of tbpcd (**1**), as assessed by TLC and IR analyses, which clearly underscores the need to drive the reaction to completion through the removal of the water that accompanies the Knoevenagel reaction. Compound **1** was subsequently isolated as a relatively air-stable orange solid after chromatographic separation over silica using CH_2Cl_2/petroleum ether (3:2) as the eluent. Eq. (1) illustrates the reaction leading to the tbpcd ligand.



(1)

The tbpcd ligand was fully characterized in solution by IR and NMR spectroscopies, ESI mass spectrometry, and X-ray diffraction analysis. The ^{1}H NMR spectrum of **1** confirmed the loss of the methylene hydrogens from the bpcd ligand and the formyl hydrogen from the thiophene-2-carboxaldehyde. The ^{31}P NMR spectrum displays a classic four-line AB quartet centered at δ −24.23 in keeping with the inequivalent phosphine moieties in **1**. The vibrationally coupled dione carbonyl groups of the tbpcd ligand give rise to symmetric and antisymmetric ν(CO) bands at 1719 (m) and 1673 (vs) cm^{-1} [19], that are 23 and 32 cm^{-1} lower in energy, respectively, relative to the ν(CO) bands of bpcd ligand [9,20], which in turn indicates that the tbpcd ligand is slightly more electron rich than the bpcd ligand. The UV-vis spectrum of **1** in CH_2Cl_2 is shown in Fig. 1, where a single absorbance at 374 nm ($\varepsilon = 18\,000$) is observed. The absorbance is insensitive to the nature of the solvent as the UV–vis band exhibits a small shift to 371 nm ($\varepsilon = 20\,000$) when the spectrum was recorded in MeCN solvent. The ESI mass spectrum of **1** that was recorded in the positive ion mode revealed *m*/*z* peaks at 581.086 and 558.995 for the singly charged sodium adduct of tbpcd $[\mathbf{1} + Na]^+$ and the parent ion of $[\mathbf{1}]^+$, respectively, consistent with the proposed ligand product.

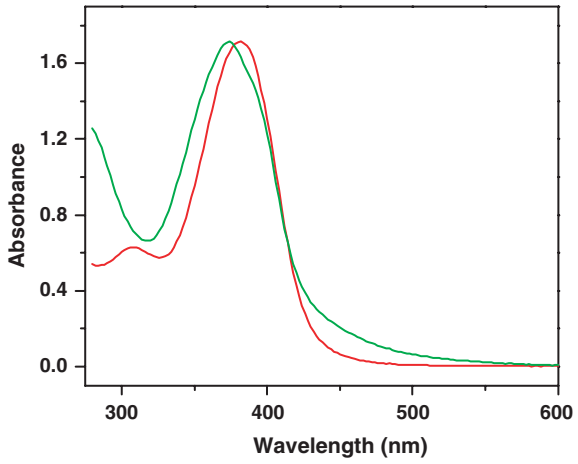


Fig. 1. UV–Vis spectra of the tbpcd ligand (green) and *fac*-BrRe(CO)$_3$(tbpcd) (red) in CH_2Cl_2 at room temperature. Both compounds were recorded at a concentration of ca. 10^{-4} M. (For interpretation of the references to colour in this figure legend, the reader is referred to the web version of this article.)

The solid-state structure of tbpcd was determined by single-crystal X-ray diffraction analysis, with the thermal ellipsoid plot of **1** shown in Fig. 2. The union of the bpcd ligand to the formyl carbon atom of the thiophene-2-carboxaldehyde is confirmed by the presence of the exocyclic alkene moiety defined by the C(1)–C(30) vector, whose 1.352(3) Å bond length is in excellent agreement with the 1.355(3) Å bond distance found for the C(3)–C(4) π bond in the dione platform. The internuclear P(1)···P(2) bond distance of 3.330(1) Å is slightly longer than the 3.278(3) Å P···P distance reported for unsaturated diphosphine ligand (*Z*)-$Ph_2PCH{=}CHPPh_2$ [21], while the O(2)···S(2) internuclear distance of 2.861(2) Å is shorter than the sum of the van der Waals radii for oxygen and sulfur atoms by ca. 0.36 Å [22]. These structural trends indicate that the molecule is not subject to significant adverse perturbations. The two five-membered rings are essentially coplanar based on an interplanar angle of 9.1(1)°. The remaining bond distances and angles are unremarkable and require no comment.

3.2. Syntheses, spectroscopic data, and X-ray diffraction structure of *fac*-BrRe(CO)$_3$(tbpcd) (**2**)

The reactivity of the tbpcd ligand was next examined with the rhenium(I) compounds $BrRe(CO)_5$ and $BrRe(CO)_3(THF)_2$ given our aforementioned interest in ligand-substituted rhenium compounds [4,6]. Our initial substitution studies employed $BrRe(CO)_5$ as a starting material. Heating an equimolar mixture of $BrRe(CO)_5$ and tbpcd at ca. 60–70 °C in either toluene or 1,2-dichloroethane furnished *fac*-$BrRe(CO)_3$(tbpcd) in good yields. TLC and IR analyses confirmed that **2** was formed as the major product. The same product was also obtained using the labile compound $BrRe(CO)_3(THF)_2$ in place of $BrRe(CO)_5$. In the case of $BrRe(CO)_3(THF)_2$, the reaction with added tbpcd ligand proceeded rapidly at room temperature to produce **2** in quantitative yield. While both rhenium starting materials give compound **2**, the use of the $BrRe(CO)_3(THF)_2$ has a slight advantage in that the reaction is cleaner and the solvent can be removed directly to give pure **2** for immediate use, if desired. The thermolysis reactions were accompanied by small amounts of unreacted

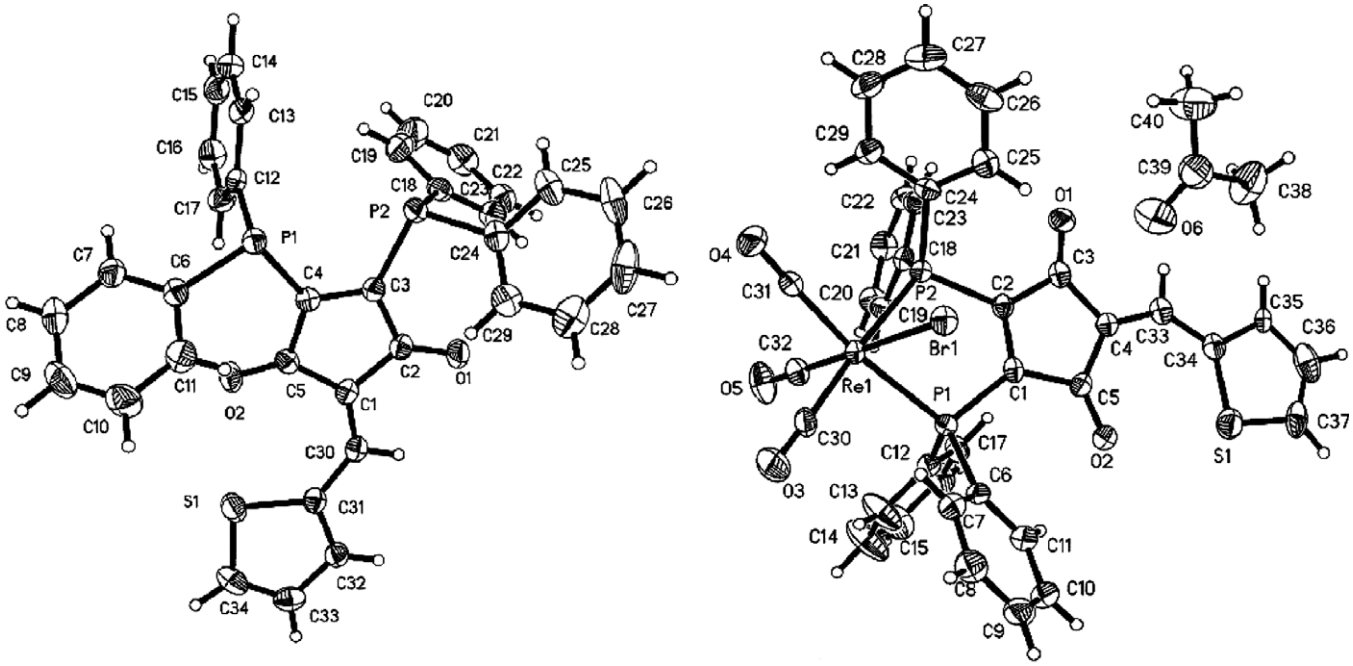


Fig. 2. Thermal ellipsoid plots of the ligand tbpcd (left) and *fac*-BrRe(CO)$_3$(tbpcd) · acetone (right) showing the thermal ellipsoids at the 50% probability level.

starting materials and unknown material(s) that remained at the origin of the TLC, necessitating a chromatographic separation. Compound **2** is air stable in the solid state, but solutions containing **2** that have been exposed to the atmosphere exhibit signs of decomposition on standing for several hours.

2 was characterized in solution by traditional spectroscopic methods, mass spectrometry (negative-ion mode), and X-ray crystallography. The IR spectrum exhibits three terminal rhenium carbonyl stretching bands at 2039 (s), 1966 (s), and 1912 (s) cm^{-1}, whose frequencies and symmetry closely match the IR data reported by us for the related compounds *fac*-$BrRe(CO)_3$(bma) and *fac*-$ClRe(CO)_3$(bpcd) [4,5]. Coordination of the tbpcd ligand to the $BrRe(CO)_3$ fragment is accompanied by a slight decrease in the electron density associated with tbpcd ligand based on the ca. 10 cm^{-1} shift of the dione ν(CO) bands to higher energy. The symmetric and antisymmetric dione carbonyl stretching bands appear at 1728 and 1684 cm^{-1}, respectively. The ^1H NMR data are fully consistent with the coordination of the tbpcd ligand to the *fac*-$BrRe(CO)_3$ fragment, as is the ^{31}P NMR spectrum, where two down-field singlets at δ 18.09 and 19.18 support the existence of a chelating tbpcd ligand that binds the rhenium atom via the two phosphorus moieties [23]. The UV–Vis spectrum of **2** shown in Fig. 1 exhibits a strong absorbance at 383 nm (ε = 28 000) and a weaker band at 308 (ε = 9500). The UV–vis spectrum recorded in MeCN afforded the same two-band pattern [378 nm (ε = 35 000), 308 (ε = 13 000)] for **2** as found in CH_2Cl_2. The ESI mass spectrum of **2** run in MeOH solvent revealed *m*/*z* peaks at 907.821 and 938.922 for the parent compound $[\mathbf{2}]^-$ and its methoxide adduct $[\mathbf{2} + MeO]^-$, respectively, in agreement with the formulated structure for **2**.

The adopted coordination mode of the tbpcd ligand in **2** was established by X-ray diffraction analysis. Single crystals of **2**, as the acetone solvate, were found to exist as discrete molecules in the unit cell. The thermal ellipsoid plot of **2** is shown in the right-hand side of Fig. 1, where the chelation of the tbpcd ligand to the rhenium center by the two phosphine moieties is confirmed. The rhenium atom is six-coordinate and possesses a distorted octahedral geometry. The Re(1)–P(1) and Re(1)–P(2) distances of 2.468(1) and 2.449(1) Å, respectively, and the observed bond angle of 81.59(3)° for the P(2)–Re(1)–P(1) linkage exhibit acceptable values in comparison to those bond distances and angles in related rhenium compounds structurally characterized by us [24]. The P(1)···P(2) [3.213(2) Å] and S(1)···O(2) [2.912(3) Å] bond distances and the interplanar angle of 5.8(2)° are in agreement with those values of the free tbpcd ligand and confirm that the ancillary ligand does not experience any major structural perturbations upon coordination to the rhenium center. The remaining bond distances and angles are unexceptional and require no comment.

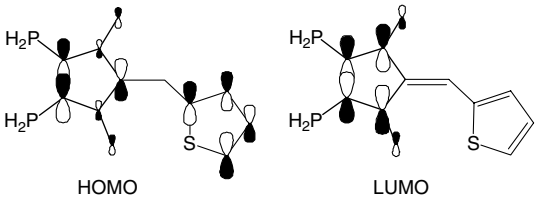
3.3. Cyclic voltammetry, MO calculations, and emission spectroscopy data

The cyclic voltammetric properties of the tbpcd ligand and compound **2** were next probed at a platinum disk electrode in CH_2Cl_2 solvent containing 0.2 M TBAP as the supporting electrolyte. Initially scanning a tbpcd sample at room temperature at a rate of 0.5 V/s over the potential range of 1.2 to −1.8 V revealed the presence of two reduction processes attributed to the $0/1^-$ and $1^-/2^-$ redox couples. The latter reduction exhibits a forward wave at $E_p^c = -1.45$ with no accompanying reverse wave (E_p^a), leading to an irreversible reduction under these conditions. Narrowing the potential window to 0 to −1.3 V and scanning just over the first reduction wave confirmed that $0/1^-$ redox couple, which displays an $E_{1/2} = -1.09$ V, is fully reversible when analyzed by standard electrochemical criteria [15]. The electron stoichiometry for the first reduction process (1e−) was also verified by comparison of the current function of the known one-electron standard ferrocene with that from tbpcd ligand. The recorded $E_{1/2}$ value for the tbpcd ligand closely matches that cyclic voltammetically determined $E_{1/2}$ value for the diphosphine ligand bpcd by Tyler and co-worker and the anthracene-functionalized bpcd ligand ($E_{1/2} = -1.01$ V) prepared by us and depicted in Scheme 1 [7,20,25].

The CV of compound **2** was recorded under identical conditions to those employed for **1**. Here the two reversible one-electron waves found at $E_{1/2} = -0.68$ and −1.39 V are readily assignable to the $0/1^-$ and $1^-/2^-$ redox couples, respectively, and parallel those data reported earlier by us for the related diphosphine complex *fac*-$BrRe(CO)_3$(bma) and the compound *fac*-$BrRe(CO)_3$(bpcd) [4,26]. It is interesting to note that the coordination of the tbpcd ligand to the rhenium center in **2** leads to enhanced stability of the $1^-/2^-$ redox couple.

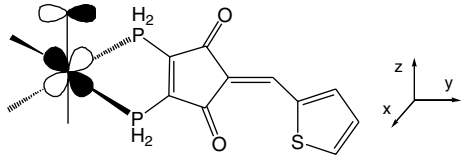
That the CV data from **1** and **2** are similar and in concert with the UV–vis data for both compounds suggest that the free ligand and its rhenium complex possess common HOMO and LUMO levels. This premise was established by carrying out extended Hückel MO calculations on compounds **1** and **2**. Here the model compound 2-(2-thienylidene) -4,5-bis(diphenylphosphino-H_4)-4-cyclopenten -1, 3-dione (tbpcd-H_4) was employed in our calculations, where the four ancillary phenyl groups were replaced with hydrogen atoms. The HOMO for tbpcd-H_4 occurs at −12.00 eV and is confined to the π system of the dione and thiophene rings, as shown below. The dominant contributions from the C=C π bond of the dione moiety and the carbon framework of the thiophene ring, the latter which displays a strong resemblance to ψ_2 of cyclopentadiene and other four-π-electron systems, are evident. The LUMO occurs at −10.45 eV and is strongly π^* in character and exclusively localized on the four carbon and two oxygen atoms associated with the dione platform. The nodal pattern of the LUMO is consistent with theoretical expec-

tations for a six-π-electron system and the MO results from maleic anhydride [7,27].



HOMO LUMO

The HOMO and LUMO levels in *fac*-BrRe(CO)$_3$(tbpcd-H$_4$) were next determined so that a direct MO comparison with the free tbpcd-H$_4$ ligand could made. The calculated energies and orbital composition of the important HOMO and LUMO levels in *fac*-BrRe(CO)$_3$(tbpcd-H$_4$) were unchanged relative to the free ligand tbpcd-H$_4$. The presence of a low-lying π^* LUMO that is localized on the dione moiety in *fac*-BrRe(CO)$_3$(tbpcd-H$_4$) is expected and has been theoretical and experimentally confirmed in all compounds containing an ancillary bpcd ligand investigated to date [20,28]. The surprising feature here was the composition of the HOMO level in **2** since our earlier report on *fac*-BrRe(CO)$_3$(bma) revealed that the HOMO was associated with an out-of-phase interaction involving the rhenium d_{yz} and bromine p_y orbitals with no contribution from the bma π system. Accordingly, we ran comparative Hückel calculations on *fac*-BrRe(CO)$_3$(bpcd-H$_4$) and confirmed that the LUMO (−10.44 eV) was identical to that calculated for *fac*-BrRe(CO)$_3$(bma-H$_4$) and *fac*BrRe(CO)$_3$(tbpcd-H$_4$). The HOMO in the unfunctionalized diphosphine compound *fac*-BrRe(CO)$_3$(bpcd-H$_4$) occurs at −12.35 eV and exhibits the same antibonding rhenium d_{yz} and bromine p_y interaction as found in *fac*-BrRe(CO)$_3$(bma-H$_4$) [26]. The dichotomy in the HOMO composition between *fac*-BrRe(CO)$_3$(tbpcd-H$_4$) and the corresponding bma and bpcd derivatives is readily traced to π interactions between the dione and thiophene rings in the tbpcd ligand. The extended π conjugation in the functionalized or second-generation tbpcd ligand leads to a high-lying π orbital that has no counterpart in the simple bpcd ligand. Examination of the subjacent highest-occupied molecular orbital (sHOMO) at −12.35 eV in *fac*-BrRe(CO)$_3$(tbpcd-H$_4$), which is depicted below, reveals the presence of the expected metal-based rhenium d_{yz} and bromine p_y antibonding orbital in excellent agreement with the MO data from *fac*-BrRe(CO)$_3$(bma-H$_4$) [4] and *fac*-BrRe(CO)$_3$(bpcd-H$_4$) [26].



sHOMO in *fac*-BrRe(CO)$_3$(tbpcd-H$_4$)

Finally, the photophysics for compounds **1** and **2** were explored through the use of emission spectroscopy as this would allow us to corroborate experimentally the $\pi \rightarrow \pi^*$ HOMO/LUMO transition indicated by the extended Hückel calculations. The emissive properties of compounds **1** and **2** were examined at room temperature in both CH_2Cl_2 and MeCN with excitation into the long wavelength band at ca. 380 nm. However, any emission displayed from either compound was not resolvable from the baseline, indicating very weak emission at best and fully consistent with the proposed intraligand $\pi \rightarrow \pi^*$ transition in the free ligand and its rhenium(I) compound [29].

4. Conclusions

The synthesis of the new unsaturated diphosphine ligand 2-(2-thienylidene)-4,5-bis(diphenylphosphino)-4-cyclopenten-1,3-dione (tbpcd) from 4,5-bis(diphenylphosphino)-4-cyclopenten-1,3-dione (bpcd) and thiophene- 2-carboxaldehyde is described. The ligand substitution chemistry of the tbpcd ligand with the rhenium compounds BrRe(CO)$_5$ and BrRe(CO)$_3$(THF)$_2$ has been examined and found to furnish *fac*-BrRe(CO)$_3$(tbpcd) as the sole observable reaction product. Both new compounds have been fully characterized and their physical properties studied by a combination of methods including cyclic voltammetry, emission spectroscopy, and MO calculations.

5. Supplementary material

CCDC 623341 and 623342 contain the supplementary crystallographic data for tbpcd and *fac*-BrRe(CO)$_3$(tbpcd). These data can be obtained free of charge via http://www.ccdc.cam.ac.uk/conts/retrieving.html, or from the Cambridge Crystallographic Data Centre, 12 Union Road, Cambridge CB2 1EZ, UK; fax: (+44) 1223-336-033; or e-mail: deposit@ccdc.cam.ac.uk.

Acknowledgements

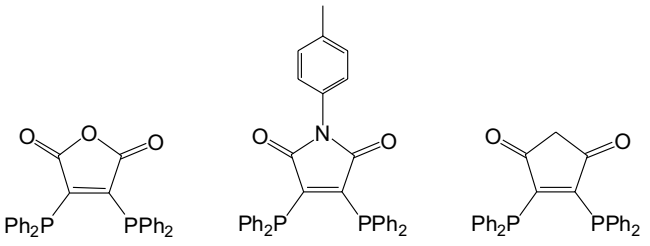
Financial support from the Robert A. Welch Foundation (Grants P-0074-WHW and B-1093-MGR) is appreciated. Prof. Andreas H. Franz (University of the Pacific) is thanked for recording the ESI-ACPI mass spectral data for the tbpcd ligand and *fac*-BrRe(CO)$_3$(tbpcd).

References

[1] (a) J.C. Luong, L. Nadjo, M.S. Wrighton, J. Am. Chem. Soc. 100 (1978) 5790;
(b) V.W.W. Yam, V.C.Y. Lau, K.K. Cheung, Orgonometallics 14 (1995) 2749;
(c) A. Vogler, H. Kunkely, Coord. Chem. Rev. 200–202 (2000) 991;
(d) D.R. Striplin, G.A. Crosby, Coord. Chem. Rev. 211 (2001) 163;
(e) J.M. Villegas, S.R. Stoyanov, W. Huang, D.R. Rillema, Inorg. Chem. 44 (2005) 2297;
(f) H. Tsubaki, A. Sekine, Y. Ohashi, K. Koike, H. Takeda, O. Ishitani, J. Am. Chem. Soc. 127 (2005) 15544.

[2] (a) P. Belser, S. Bernhard, C. Blum, A. Beyeler, L. De Cola, V. Balzani, Coord. Chem. Rev. 190–192 (1999) 190;
(b) A. Beyeler, P. Belser, L. De Cola, Angew. Chem., Int. Ed. Engl. 36 (1997) 2779;
(c) W. Belliston-Bittner, R. Alexander, Y.H.L. Nguyen, D.J. Stuehr, J.R. Winkler, H.B. Gray, J. Am. Chem. Soc. 127 (2005) 15907.
[3] (a) S.Y. Reece, D.G. Nocera, J. Am. Chem. Soc. 127 (2005) 9448;
(b) S.Y. Reece, M.R. Seyedsayamdost, J. Stubbe, D.G. Nocera, J. Am. Chem. Soc. 128 (2006) 13654.
[4] K. Yang, S.G. Bott, M.G. Richmond, Organometallics 14 (1995) 2387.
[5] W.H. Watson, S. Kandala, M.G. Richmond, J. Chem. Crystallogr. 36 (2006) 77.
[6] G. Wu, D.R. Glass, D. May, W.H. Watson, D. Wiedenfeld, M.G. Richmond, J. Organomet. Chem. 690 (2005) 4993.
[7] W.H. Watson, B. Poola, M.G. Richmond, J. Chem. Crystallogr. 36 (2006) 715.
[8] For an earlier report describing Knoevenagel-type condensation reactions with 4,5-dichloro- 4-cyclopenten-1,3-dione, the starting material for the ligand bpcd, see: R. Alfred, Z. Hellmut, Chem. Ber. 94 (1961) 1800.
[9] (a) D. Fenske, H. Becher, Chem. Ber. 107 (1974) 117;
(b) D. Fenske, Chem. Ber. 112 (1979) 363.
[10] (a) D. Vitali, F. Calderazzo, Gazz. Chim. Ital. 102 (1972) 587;
(b) F. Calderazzo, I.P. Mavani, D. Vatali, I. Bernal, J.D. Korp, J.L. Atwood, J. Organomet. Chem. 160 (1978) 207.
[11] D.F. Shriver, The Manipulation of Air-Sensitive Compounds, McGraw-Hill, New York, 1969.
[12] SAINT Version 6.02, Bruker Analytical X-ray Systems Inc., Copyright 1997–1999.
[13] SHELXTL Version 5.1, Bruker Analytical X-ray Systems Inc., Copyright 1998.
[14] A.L. Spek, PLATON – A Multipurpose Crystallographic Tool, Utrecht University, Utrecht, The Netherlands, 2001.
[15] A.J. Bard, L.R. Faulkner, Electrochemical Methods, Wiley, New York, 1980.
[16] (a) R. Hoffmann, W.H. Lipscomb, J. Chem. Phys. 36 (1962) 2179;
(b) R. Hoffmann, J. Chem. Phys. 39 (1963) 1397.
[17] C. Mealli, D.M. Proserpio, J. Chem. Ed. 67 (1990) 399.
[18] R.C. Weast (Ed.), Handbook of Chemistry and Physics, 56th ed., CRC Press, Cleveland, OH, 1975.
[19] N.B. Coltrup, L.H. Daly, S.E. Wiberley, Introduction to Infrared and Raman Spectroscopy, Academic Press, New York, 1990.
[20] R. Meyer, D.M. Schut, K.J. Keana, D.R. Tyler, Inorg. Chim. Acta 240 (1995) 405.
[21] S.J. Berners, L.A. Colquhoun, P.C. Healy, K.A. Byriel, J.V. Hanna, J. Chem. Soc., Dalton Trans. (1992) 3357.
[22] A. Bondi, J. Phys. Chem. 68 (1968) 441.
[23] P.E. Garrou, Chem. Rev. 81 (1981) 229.
[24] (a) S.G. Bott, K. Yang, M.G. Richmond, J. Organomet. Chem. 689 (2004) 791;
(b) S.G. Bott, K. Yang, M.G. Richmond, J. Chem. Crystallogr. 35 (2005) 709;
(c) C.-G. Xia, S.G. Bott, M.G. Richmond, Inorg. Chim. Acta 230 (1995) 45.
[25] For an earlier electrochemical investigation of the bpcd ligand using polarographic methods, see: H.J. Becher, D. Fenske, M. Heyman, Z. Anorg. Allg. Chem. 475 (1981) 27.
[26] Unpublished results.
[27] (a) T.A. Albright, J.K. Burdett, M.H. Whangbo, Orbital Interactions in Chemistry, Wiley-Interscience, New York, 1985;
(b) K. Hayakawa, N. Mibu, E. Osawa, K. Kanematsu, J. Am. Chem. Soc. 104 (1982) 7136.
[28] (a) H. Shen, S.G. Bott, M.G. Richmond, Organometallics 14 (1995) 4625;
(b) N.W. Duffy, R.R. Nelson, M.G. Richmond, A.L. Rieger, P.H. Rieger, B.H. Robinson, D.R. Tyler, J.C. Wang, K. Yang, Inorg. Chem. 37 (1998) 4849;
(c) S.G. Bott, H. Shen, M.G. Richmond, J. Organomet. Chem. 689 (2004) 3426.
[29] G.L. Geoffroy, M.S. Wrighton, Organometallic Photochemistry, Academic Press, New York, 1979.

manner analogous to that displayed by CO ligands [4]. The structures of these three diphosphine ligands are shown below.



Wishing to explore further the chemistry of organometallic compounds with structurally more diverse diphosphine ligands that possess highly conjugated π arrays and well-defined redox and photochemically sensitive moieties, we have instituted studies on the modification of the bpcd ligand. The successful synthesis of such second-generation diphosphine ligands would allow us the opportunity to study heretofore novel cluster-ligand systems as redox relays, energy-storage devices, and photochemical and/or redox sensing components [5,6]. Early results using bpcd as a platform for the construction of new diphosphine ligands have been encouraging, and significant structural modifications of the parent diphosphine with the aldehydes 9-anthracenecarboxaldehyde and thiophene-2-carboxaldehyde have produced the new ligands 2-(anthracenyl-9-ylidene)-4,5-bis(diphenylphosphino)-4-cyclopenten-1,3-dione and 2-(2-thienylidene)-4,5-bis(diphenylphosphino)-4-cyclopenten-1,3-dione, respectively, through a Knoevenagel condensation route [7,8]. Scheme 1 depicts the synthetic protocol and structures of these new diphosphine ligands.

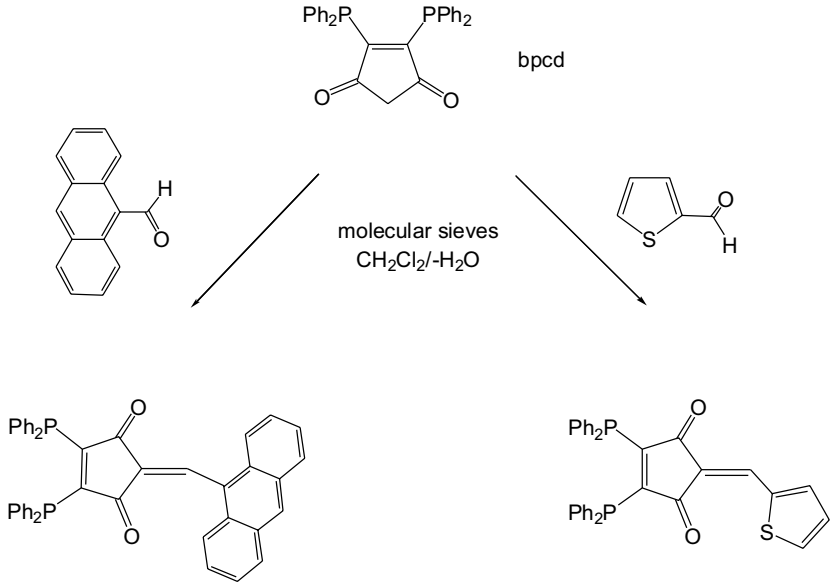
Herein we present our results on the condensation of bpcd with ferrocenecarboxaldehyde to give the new diphosphine ligand 2-(ferrocenylidene)-4,5-bis(diphenylphosphino)-4-cyclopenten-1,3-dione (fbpcd). The reactivity of the fbpcd ligand with the triosmium cluster 1,2-$Os_3(CO)_{10}(MeCN)_2$ has been examined, and the kinetics for the isomerization of the fbpcd ligand in 1,2-$Os_3(CO)_{10}$(fbpcd) (**2b**) to 1,1-$Os_3(CO)_{10}$(fbpcd) (**2c**) are discussed. Near-UV irradiation of cluster **2c** leads to CO loss and production of the hydride-bridged cluster $HOs_3(CO)_9[\mu\text{-}PhP(C_6H_4)\text{-}C{=}C(PPh_2)C(O)C{=}CH(C_5H_4FeCp)C(O)]$ (**3**). The *ortho*-metalation of one of the aryl groups of the fbpcd ligand in **3** has been structurally confirmed.

2. Experimental

2.1. General

The starting cluster 1,2-$Os_3(CO)_{10}(MeCN)_2$ was prepared from $Os_3(CO)_{12}$ [9], which was in turn was obtained from the carbonylation of OsO_4 using a 450 mL Parr Series 4560 bench-top mini reactor [10]. The bpcd ligand was synthesized from hexachlorocyclopentadiene [11]. The chemicals hexachlorocyclopentadiene, ferrocenecarboxaldehyde, and $Me_3NO \cdot 2H_2O$ were purchased from Aldrich Chemical Co. The latter chemical was dried by azeotropic distillation from benzene and stored under argon when not in use. All reaction and NMR solvents were distilled from an appropriate drying agent using Schlenk techniques and stored under argon in storage vessels equipped with high-vacuum Teflon stopcocks [12]. The combustion analysis was performed by Atlantic Microlab, Norcross, GA.

All IR spectra were recorded on a Nicolet 20 SXB FT-IR spectrometer in sealed 0.1 mm NaCl cells, while the



Scheme 1.

^{1}H spectra were recorded at 200 MHz on a Varian Gemini-200 spectrometer. The ^{31}P NMR spectra were collected in the proton-decoupled mode on a Varian 300-VXR spectrometer at 121 MHz, with the reported chemical shifts referenced to external H_3PO_4 (85%), taken to have $\delta = 0$. The MALDI-TOF mass spectra for the fbpcd ligand and cluster **3** were recorded at the University of the Pacific in the positive ion mode.

2.2. Synthesis of the diphosphine ligand fbpcd

To a Schlenk tube containing 0.20 g (0.43 mmol) of bpcd dissolved in 30 mL of CH_2Cl_2 at room temperature was added 92 mg of ferrocenecarboxaldehyde (0.43 mmol) and ca. 5 g of 4 Å molecular sieves. The introduction of the molecular sieves was accompanied by an immediate color change from the orange–yellow color of the two starting reagents to that of purple, signifying the presence of the desired product. The vessel was sealed and stirring was continued overnight. TLC examination of the reaction solution the following day revealed the complete consumption of the starting materials and the presence of a single purple spot at $R_f = 0.50$ using CH_2Cl_2/hexane (1:1) as a mobile phase. The crude reaction was filtered to remove the molecular sieves and the solvent concentrated down to ca. 0.5 mL, after which the product was run across a short column of silica gel using a 40:60 mixture of CH_2Cl_2/hexane as the eluent. Yield of purple fbpcd: 0.28 g (97%). IR (CH_2Cl_2): ν(CO) 1717 (w, symm dione), 1671 (vs, antisymm dione) cm^{-1}. ^{1}H NMR ($CDCl_3$): δ 4.13 (s, 5H, Cp), 4.67 (br, 2H, Cp), 5.16 (br, 2H, Cp), 7.27–7.44 (m, 21H, aryls and alkenyl). ^{31}P NMR ($CDCl_3$): δ −23.49 (AB quartet, $^3J_{P-P} = 60$ Hz). MALDI-TOF MS (m/z): 660.7 [fbpcd]$^+$.

2.3. Preparation of 1,2-$Os_3(CO)_{10}$(fbpcd) (**2b**) from 1,2-$Os_3(CO)_{10}(MeCN)_2$ and fbpcd

To 0.25 g (0.27 mmol) of 1,2-$Os_3(CO)_{10}(MeCN)_2$ in 30 mL of CH_2Cl_2 was added 0.18 g (0.27 mmol) of fbpcd under argon. The solution was stirred at room temperature, and the progress of the reaction was monitored by TLC analysis, which confirmed the consumption of both starting materials after 3 h and the presence of a new dark blue spot corresponding to the clusters **2b**, **2c**, and **3**. The solvent was evaporated under vacuum and the residue passed over a short column of silica gel using a 70:30 mixture of hexane/CH_2Cl_2 to furnish 0.30 g of a dark blue solid. The composition of the isolated cluster mixture was analyzed by using ^{1}H and ^{31}P NMR spectroscopies, which revealed the product distribution: **2b** (80%), **2c** (19%), and **3** (1%).

NMR spectroscopic data for **2b**: ^{1}H NMR (toluene-d_8): δ 3.54 (s, 5H, Cp), 4.20 (br, 2H, Cp), 4.64 (br, 2H, Cp), 6.95–7.25 (m, 12H, aryl), 7.55 (s, 1H, vinyl), 7.70–7.95 (m, 8H, aryl). ^{31}P NMR (toluene-d_8): δ −18.0 (AB quartet, $J_{P-P} = 17$ Hz).

2.4. Thermal isomerization of **2b** to **2c**

To a Schlenk vessel under argon was charged 0.10 g of the previous cluster mixture, followed by 25 mL of toluene via cannula. The solution was next saturated with CO, after which the vessel was sealed and removed from the vacuum line and placed in a thermostated bath at 315 K. The solution was heated for several days and the progress of the reaction was periodically checked by NMR spectroscopy, which revealed the complete consumption of **2b** and a concomitant increase in the amount of cluster **2c** and only a trace amount of cluster **3**. Heating the same sample for an additional 45 days showed only the presence of cluster **2c**. The solvent was removed and cluster **2c** was run across a short column of silica gel and then recrystallized from benzene/CH_2Cl_2. Yield: 95 mg (95%). IR (CH_2Cl_2): ν(CO) 2095 (s), 2046 (s), 2010 (vs), 1975 (s), 1961 (m), 1926 (m), 1719 (w, symm dione), 1675 (m, antisymm dione) cm^{-1}. ^{1}H NMR (toluene-d_8): δ 3.71 (s. 5H, Cp), 4.26 (br, 2H, Cp), 4.95 (br, 2H, Cp), 7.05–7.29 (m, 12H, aryl), 7.63 (s, 1H, vinyl), 7.83–8.00 (m, 8H, aryl). ^{31}P NMR (toluene-d_8): δ 19.8 (AB quartet, $J_{P-P} = 21$ Hz). *Anal.* Calc. for $C_{50}H_{30}FeO_{12}Os_3P_2 \cdot CH_2Cl_2$: C, 38.38; H, 2.02. Found: C, 37.99; H, 1.95%.

2.5. Photochemical preparation of **3** from **2c**

To 50 mg (0.033 mmol) of **2c** in a Schlenk tube was added 20 mL of toluene, after which the vessel was freeze–pump–thaw degassed three times and sealed. The solution was irradiated at room temperature using two GE Blacklights having a maximum output of 366 ± 20 nm for an extended period of time, with periodic removal of the liberated CO through additional freeze–pump–degas cycles. Depending on the thickness of the Schlenk tube, near quantitative conversion to the desired hydride-bridged cluster **3** was typically achieved after two weeks of continuous irradiation. The sample of **3** was passed across a short column of silica gel using CH_2Cl_2 and then recrystallized from benzene/CH_2Cl_2. Yield: 40 mg (82%). IR (CH_2Cl_2): ν(CO) 2085 (vs), 2041 (vs), 2015 (vs), 1986 (vs), 1967 (sh), 1720 (w, symm dione), 1676 (m, antisymm dione) cm^{-1}. ^{1}H NMR (toluene-d_8): δ −15.87 (t, hydride, $J_{P-H} = 14$ Hz), 3.61 and 3.65 (s, 5H each, Cp), 4.19 and 4.32 (br, 2H each, Cp), 4.56 and 4.85 (br, 1H each, Cp), 4.93 and 4.91 (br, 1H each, Cp), 6.90–8.30 (overlapping m, aryls and vinyl). ^{31}P NMR (toluene-d_8): δ 21.40 (d, $J_{P-P} = 13$ Hz), 22.11 (d, $J_{P-P} = 13$ Hz), 30.64 (t, $J_{P-P} = 13$ Hz). MALDI-TOF MS (m/z): 1457.7 [M−CO]$^+$.

2.6. X-ray diffraction data for cluster **3**

Tables 1 and 2 contain the X-ray data and processing parameters and selected bond distances and angles, respectively, for cluster **3**. Single crystals of **3** suitable for X-ray diffraction analysis were grown at room temperature from a CH_2Cl_2 solution containing **3** that had been layered with

Table 1
X-ray crystallographic data and processing parameters for cluster **3**

CCDC Entry no.	628577
Crystal system	triclinic
Space group	$P\bar{1}$
a (Å)	11.275(3)
b (Å)	14.681(4)
c (Å)	16.557(4)
α (°)	100.085(4)
β (°)	91.507(4)
γ (°)	101.870(4)
V (Å)^3	2635(1)
Molecular formula	$C_{49}H_{30}FeO_{11}Os_3P_2$ + disordered C_5H_{12}
Fw	1555.26
Formula units per cell (Z)	2
D_{calc} (Mg/m^3)	1.959
λ (Mo Kα) (Å)	0.71073
μ (mm^{-1})	7.598
R_{merge}	0.0603
Absorption correction	empirical
Absorption correction factor	0.9223/0.2490
Total reflections	21587
Independent reflections	11383
Data/restraints/parameters	11383/0/617
R	0.0455
R_w	0.0992
Goodness-of-fit on F^2	0.959
$\Delta\rho$(max), $\Delta\rho$(min) (e/Å^3)	2.503, −1.662

Table 2
Selected bond distances (Å) and angles (°) in cluster **3**

Bond distances			
Os(1)–Os(3)	2.9132(7)	Os(1)–Os(2)	2.9441(8)
Os(2)–Os(3)	2.8666(8)	Os(1)–P(1)	2.365(2)
Os(1)–P(2)	2.305(2)	P(1)···P(2)	3.184(3)
Os(2)–C(24)	2.165(9)	C(1)–C(2)	1.32(1)
C(1)–C(5)	1.54(1)	C(2)–C(3)	1.50(1)
C(3)–C(4)	1.47(1)	C(4)–C(6)	1.37(1)
C(4)–C(5)	1.45(1)	C(6)–C(7)	1.44(1)
Cp(centroid)–Fe[a]	1.646(4)	Cp′(centroid)–Fe[b]	1.655(6)
Bond angles			
C(41)–Os(1)–C(42)	92.4(4)	C(41)–Os(1)–P(2)	87.0(3)
C(42)–Os(1)–P(2)	94.7(3)	C(41)–Os(1)–P(1)	168.9(3)
C(42)–Os(1)–P(1)	96.7(3)	P(2)–Os(1)–P(1)	85.95(7)
C(42)–Os(1)–Os(3)	86.5(3)	P(2)–Os(1)–Os(3)	172.47(6)
P(1)–Os(1)–Os(3)	86.52(5)	P(2)–Os(1)–Os(2)	120.63(5)
P(1)–Os(1)–Os(2)	86.66(5)	C(44)–Os(2)–Os(3)	87.1(3)
C(43)–Os(2)–Os(1)	117.2(3)	C(23)–P(1)–Os(1)	115.0(3)
C(1)–P(1)–Os(1)	105.1(3)	C(2)–P(2)–Os(1)	107.3(3)
C(6)–C(4)–C(5)	121.0(7)	C(6)–C(4)–C(3)	131.2(7)
C(5)–C(4)–C(3)	107.8(6)	C(4)–C(6)–C(7)	133.0(8)
C(24)–C(23)–P(1)	119.7(6)		

[a] Cp centroid defined by the atoms C(7)–C(11).
[b] Cp′ centroid defined by the atoms C(12)–C(16).

pentane. The reported X-ray data were collected on a Bruker SMART™ 1000 CCD-based diffractometer at 211 K. The frames were integrated with the available SAINT software package using a narrow-frame algorithm, [13] and the structure was solved and refined using the SHELXTL program package. [14] The molecular structure was checked by using PLATON [15] and solved by direct methods with all nonhydrogen atoms refined anisotropically. All carbon-bound hydrogen atoms were assigned calculated positions and allowed to ride on the attached heavy atom, unless otherwise noted. The hydride ligand that bridges the Os(1)–Os(2) vector could not be located and the presence of a disordered pentane solvent molecule that resisted refinement was also noted. Convergence for **3** was achieved at $R = 0.0455$ and $R_w = 0.0992$ for 11383 independent reflections with $I > 2\sigma(I)$.

2.7. Kinetic studies

The UV–vis studies were carried out using a mixture of clusters **2b** and **2c** at a concentration of ca. 10^{-4} M using 1.0 cm quartz UV–vis cells that were equipped with a high-vacuum Teflon stopcock to facilitate handling on the vacuum line. Solutions containing the isomeric mixture of clusters **2b** and **2c** were prepared under 1 atm CO and used immediately before each kinetic measurement. The role of CO is to suppress the formation of the hydride-bridged cluster **3** from cluster **2c** at elevated temperature. The Hewlett–Packard 8452A diode array spectrometer employed in our studies was configured with a variable-temperature cell holder and was connected to a VWR constant temperature circulator, allowing for the quoted temperatures to be maintained within ±0.5 K. The UV–vis kinetics for the transformation of **2b** → **2c** were monitored by following the increase of the 360 nm absorbance band as a function of time typically for 4–6 half-lifes. The rate constants quoted in Table 3 were determined by non-linear regression analysis using the single exponential function[1]:

$$A(t) = A_\infty + \Delta A * \ e^{(-kt)}$$

The ^{1}H NMR kinetic experiment was conducted under CO (1 atm) in a 5 mm NMR tube possessing a J. Young valve and was monitored for slightly over 2 half-lifes. The concentration of the initial ca. 70/30 mixture of **2b**/**2c** was ca. 10^{-2} M and the solvent used was toluene-d_8. The extent of the reaction was determined by following the decrease in the intensity of the Cp singlet of **2b** at δ 3.54, as quantified against the methoxy resonance of the internal standard *p*-dimethoxybenzene.

The activation parameters for the isomerization of **2b** to **2c** were calculated from a plot of $\ln(k/T)$ versus T^{-1} [16], with the error limits representing deviation of the data points about the least-squares line of the Eyring plot.

[1] The rate calculations were performed by using the Agilent ChemStation software package configured to the spectrometer or the commercially available program ORIGIN6.0. Here the initial (A_0) and final (A_∞) absorbances and the rate constant (k) were floated to give the quoted least-squares value for first-order rate constant k.

Table 3
Experimental rate constants for the isomerization of **2b** to **2c**[a]

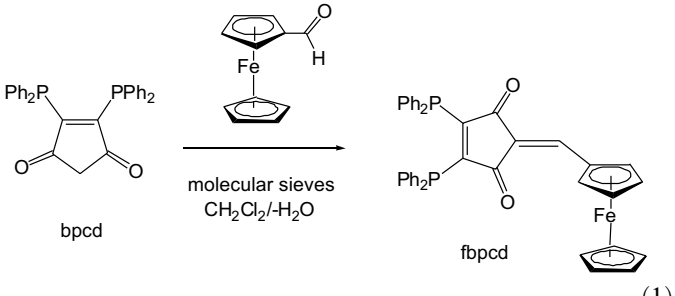
Entry number	Temperature (K)	Solvent	10^5k (s^{-1})
1	313.0	toluene	2.07 ± 0.04
2	318.0	toluene	3.21 ± 0.08
3	323.0	toluene	4.90 ± 0.09
4	323.0	toluene	5.9 ± 0.1[b]
5	323.0	toluene-d_8	7.0 ± 0.5[c]
6	328.0	toluene	9.8 ± 0.1
7	333.0	toluene	18.5 ± 0.4
8	338.0	toluene	29 ± 1
9	343.0	toluene	54.1 ± 0.2

[a] The UV–vis kinetic data were collected in ca. 10^{-4} M solution containing a ca. 70/30 mixture of clusters **2b** and **2c** under 1 atm CO by following the increase in the absorbance of the 360 nm band.
[b] Reaction performed in the presence of PPh_3 (25 equivalents).
[c] Reaction analyzed by ^{1}H NMR spectroscopy using ca. 10^{-2} M solution containing a ca. 70/30 mixture of **2b/2c**.

3. Results and discussion

3.1. Synthesis and spectroscopic characterization of the diphosphine ligand fbpcd

Knoevenagel condensation of ferrocenecarboxaldehdye with the diphosphine ligand bpcd proceeds rapidly in CH_2Cl_2 at room temperature in the presence of added molecular sieves (4 Å) to afford the new diphosphine ligand 2-(ferrocenylidene)-4,5-bis(diphenylphosphino)-4-cyclopenten-1,3-dione (fbpcd) in 97% yield. The role of the molecular sieves is to drive the condensation reaction to completion through the removal of the accompanying H_2O. This latter aspect was verified by a control experiment where the ferrocenecarboxaldehdye and bpcd reagents were stirred for a period of several days in the absence of molecular sieves. No fbpcd ligand was observed, as assessed by TLC and IR analyses. However, the addition of the molecular sieves to this solution led to the immediate formation of the desired ligand. The fbpcd ligand was subsequently isolated as an air-sensitive purple solid after chromatographic separation over silica using CH_2Cl_2/petroleum ether (3:2) as the eluent. The following equation illustrates the reaction leading to the fbpcd ligand.

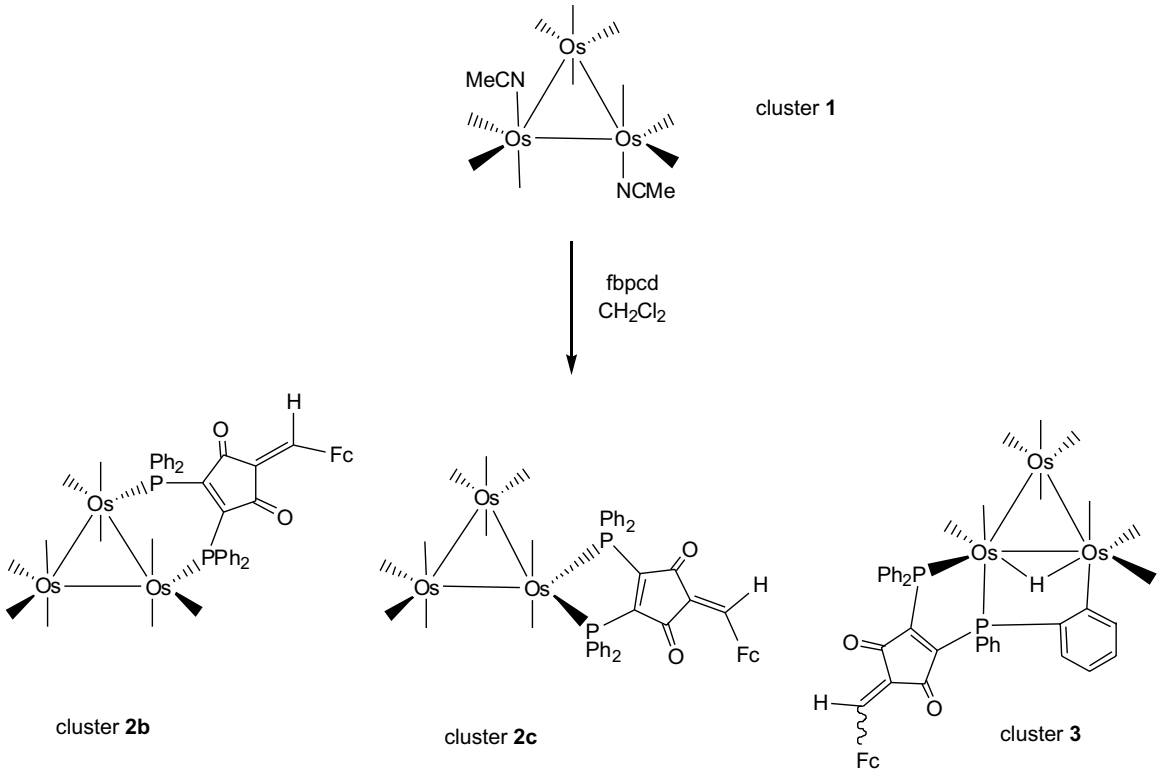


(1)

The fbpcd ligand was fully characterized in solution by IR and NMR spectroscopies, and by MALDI-TOF mass spectrometry. The IR spectrum showed the vibrationally coupled symmetric and antisymmetric ν(CO) bands belonging to the dione moiety at 1717 and 1671 cm^{-1} [17]. These carbonyl stretching bands are 25 and 34 cm^{-1} lower in energy, respectively, relative to the ν(CO) bands of the starting bpcd ligand [11,18], supporting the fact that the fbpcd ligand is more electron rich than the parent diphosphine ligand. The ^{1}H NMR spectrum confirmed the loss of the methylene hydrogens of the bpcd ligand and the formyl hydrogen of the ferrocenecarboxaldehyde substrate. A singlet at δ 4.13 (5H) and two broadened resonances at δ 4.67 and 5.16, each of which integrates for 2H, are readily assigned to the intact ferrocene Cp ring and the functionalized Cp ring that is attached to the dione platform. The vinyl hydrogen associated with the ferrocenylidene moiety and the aromatic hydrogens from the four phenyl groups appear as a multiplet from δ 7.27–7.44. The two inequivalent ^{31}P groups in the fbpcd ligand appear as a classic AB quartet centered at δ −23.49 with a $J/\Delta\nu$ value of 0.30 [19]. The MALDI-TOF mass spectrum of the diphosphine ligand revealed a strong m/z peak at 660.7 for the singly charged parent $[fbpcd]^+$ ion consistent with the proposed formulation of the fbpcd ligand.

3.2. Reaction of 1,2-$Os_3(CO)_{10}(MeCN)_2$ with the ligand fbpcd

Treatment of the activated cluster 1,2-$Os_3(CO)_{10}(MeCN)_2$ (**1**) with an equimolar amount of the fbpcd ligand at 293 K in CH_2Cl_2 leads to the rapid consumption of **1** and the fbpcd ligand (<1 h) and formation of a new dark blue spot ($R_f = 0.60$ using a 1:1 mixture of CH_2Cl_2/hexane as the eluent), as determined by TLC analysis. NMR analysis (^{1}H and ^{31}P) of the reaction solution before a formal work-up revealed the presence of three species assignable to 1,2-$Os_3(CO)_{10}$(fbcpd) (**2b**), 1,1-$Os_3(CO)_{10}$(fbpcd) (**2c**), and $HOs_3(CO)_9[\mu$-$PhP(C_6H_4)C{=}C(PPh_2)C(O)C{=}CH(C_5H_4FeCp)C(O)]$ (**3**). These three products showed no discernable separation on silica gel and neutral alumina when analyzed with sundry different mobile phases. The diphosphine-bridged cluster **2b** is formed as the major product in ca. 80% yield, with cluster **2c** present in ca. 18–19% and the hydride-bridged cluster **3** accounting for the reminder of the ternary mixture. The observed product distribution is reminiscent of that found by us in the reaction between cluster **1** and the related diphosphine ligand bmi [2a]. These data are in accord with cluster **1** serving as an independent platform for the formation of clusters **2b** and **2c** and not a process involving the isomerization of **2b** to **2c** since our extrapolated rate data for such an isomerization at 293 K would occur with a half-life on the order of 42 h (vide infra). The bimodal substitution behavior exhibited in the reaction of cluster **1** and fbpcd is not without precedent, as we have found that the reaction of cluster **1** with the diphosphine ligand 1,2-bis(dimethylphosphino)ethane (dmpe) affords the isomeric clusters 1,2-$Os_3(CO)_{10}$(dmpe) and 1,1-$Os_3(CO)_{10}$(dmpe) as a noninterconverting mixture [20]. Scheme 2 illustrates the course of this substitution reaction using the fbpcd ligand.



Scheme 2.

Given the nature of the product mixture and the fact that both **2b** and **2c** possess overlapping carbonyl bands, the IR spectral data for pure **2b** cannot be reported with certainty.[2] Fortunately, the NMR data for **2b** could be extracted from the crude reaction mixture due to sufficient resolution of the two major components. The ^{1}H NMR spectrum of **2b** recorded in toluene-d_8 exhibits three distinct sets of cyclopentadienyl resonances at δ 3.54 (5H), 4.20 (2H), and 4.64 (2H) that are similar to the pattern displayed by the free fbpcd ligand. The aromatic hydrogens appear as two sets of multiplets from δ 6.95–7.25 (m, 12H, aryl) and 7.70–7.95 (m, 8H, aryl), with a vinyl singlet for the ferrocenylidene moiety appearing at δ 7.55. The ^{31}P NMR spectrum of **2b** reveals the presence of an AB quartet centered at δ −18.0 with $J_{P-P} = 17$ Hz. The high-field location of the bridging fbpcd ligand in **2b** is in keeping with the general trend found in other diphosphine-bridged clusters vis-á-vis the corresponding chelating isomer (vide infra) [21].

3.3. Synthesis of *2c* and isomerization kinetics

The thermally promoted isomerization of the fbpcd ligand about the triosmium frame in **2b** was next explored as part of our interest in the coordinative flexibility exhibited by rigid unsaturated diphosphine ligands [2a,3c,22]. Heating the initially formed cluster mixture under 1 atm CO produced clear spectroscopic changes in the ^{1}H and ^{31}P NMR spectra in concert with the conversion of **2b** and **3** to the chelating cluster **2c**. Provided these reactions were conducted in the dark or under red-light conditions, the formation of **2c** from **2b** was found to be quantitative. Pure **2c** was subsequently isolated via recrystallization and characterized in solution by traditional spectroscopic methods and combustion analysis.

The IR spectrum of **2c** recorded in CH_2Cl_2 revealed terminal Os–CO carbonyl stretching bands at 2095 (s), 2046 (s), 2010 (vs), 1975 (s), 1961 (m), and 1926 (m) cm^{-1}, with the two dione carbonyl bands appearing at 1719 (w) and 1675 (m) cm^{-1}. The symmetry and frequencies of the terminal carbonyl stretching bands closely match those IR data reported by us for the diphosphine-chelated clusters 1,1-$Os_3(CO)_{10}$(bpcd) and 1,1-$Os_3(CO)_{10}$(bmi) [2a,3c]. The chelation of the fbpcd ligand in **2c** is accompanied by a down-field shift of the signature cyclopentadienyl ^{1}H resonances relative to **2b** and appear at δ 3.71 (5H), 4.26 (2H), and 4.95 (2H). The resonances belonging to the aromatic hydrogens [δ 7.05–7.29 (12H) and 7.83–8.00 (8H)] and the lone ferrocenylidene hydrogen (δ 7.63) are relatively unchanged from that of cluster **2b**. Finally, the ^{31}P NMR spectrum displays an AB quartet at δ 19.8 for the diphosphine ligand. The large nuclear deshielding exhibited by

[2] The spectral contributions from the hydride cluster **3** (<1%) did not offer significant interference in comparison to the carbonyl frequencies from cluster **2c**.

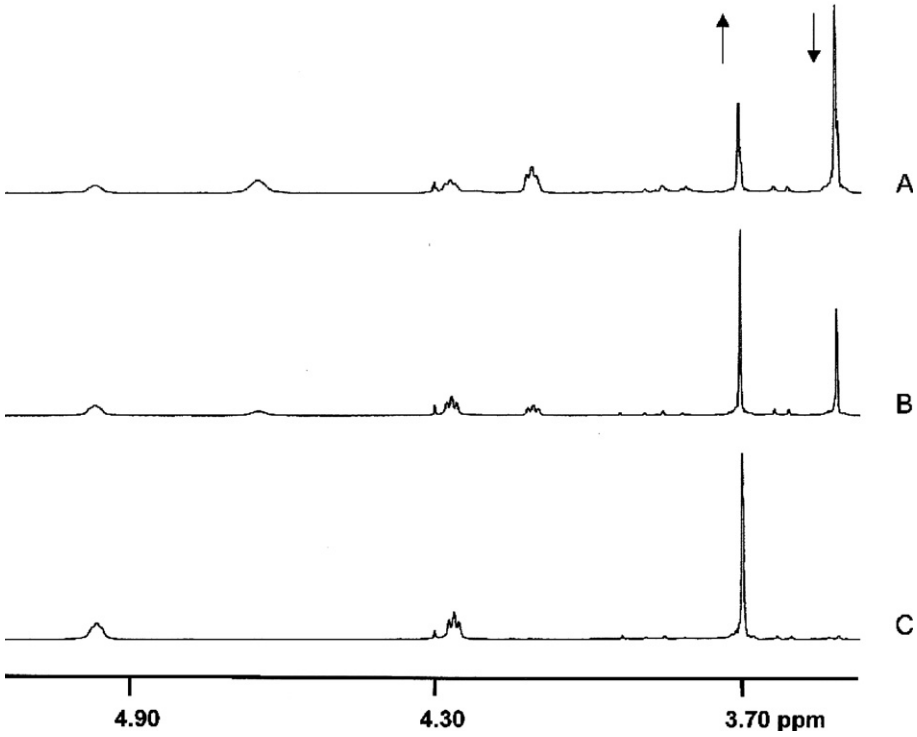


Fig. 1. ^{1}H NMR kinetic data for the isomerization of **2b** → **2c** in toluene-d_8 at 323 K in the cyclopentadienyl region at (A) 0 h, (B) 3 h, and (C) 20 h.

the fbpcd ligand in **2c** relative to the bridging analogue is consistent with the adoption of a chelating coordination mode [21].

The isomerization kinetics for **2b** → **2c** were initially examined by ^{1}H NMR spectroscopy in toluene-d_8 at 323 K. Here a cluster mixture that contained ca. a 70/30 composition of **2b** to **2c** was employed.[3] Representative spectral changes in the cyclopentadienyl region from δ 3.00–5.20 are illustrated in Fig. 1. Here the growth of the three cyclopentadienyl resonances belonging to the chelating isomer was found to be proportional to the rate of consumption of the Cp resonances belonging to **2b**. A traditional plot of ln [**2b**] versus time furnished the first-order rate constant quoted in Table 3 (entry 5), which agrees nicely with the two other rate constants measured by UV–vis spectroscopy at the same temperature (entries 3 and 4). The clean conversion to **2c** found by NMR spectroscopy underscores the fact that the isomerization is not accompanied by the formation of extraneous material(s) and is unidirectional unlike the isomerization reactions in the diphosphine-substituted clusters $Os_3(CO)_{10}$-[(*Z*)$PPh_2CH{=}CHPPh_2$] and $H_4Ru_4(CO)_{10}$(dppe) that give rise to an equilibrium mixture of bridging and chelating isomers [22,23].

[3] The trace amount of cluster **3**, which is initially present and ultimately converted to **2c** under CO, can be ignored as it does not adversely affect the data analysis.

The kinetics for the isomerization of **2b** → **2c** were also investigated by UV–vis spectroscopy in toluene solution over the temperature range 313–343 K. The first-order rate constants for these reactions are reported in Table 3, while Fig. 2a shows the spectral changes that accompany the isomerization at 323 K. The rate of the reaction was easily assessed by following the increase in the absorbance of the 360 nm belonging to **2c**. The isomerization was judged to be free from kinetic complications and negligible material loss based on the isosbestic point at 390 nm that is maintained throughout the course of the reaction. Fig. 2b shows the fit between the absorbance data and the least-squares regression curve that affords the quoted rate constant in Table 3. The effect of added PPh_3 on the reaction at 323 K was also examined (Table 3, entry 4), yielding a rate constant of $5.9 \pm 0.1\ s^{-1}$ that is essentially indistinguishable with the rate constant measured under CO (entry 3). These data argue against a rate-limiting dissociative process that yields a long-lived unsaturated intermediate. The kinetic data for the conversion of **2b** → **2c** strongly support the involvement of a unimolecular process whereby one of the phosphine moieties and two CO groups undergo an equatorial permutation about the cluster polyhedron via a μ-phosphine/μ-CO intermediate. The Eyring plot of ln(k/T) versus T^{-1} shown in Fig. 3 afforded activation parameters ($\Delta H^{\ddagger} = 23.1 \pm 0.3$ kcal/mol and $\Delta S^{\ddagger} = -7 \pm 1$ eu) consistent with the structural rearrangement exemplified by the "merry-go-process" that is depicted in the following equation [2a,3c,22]:

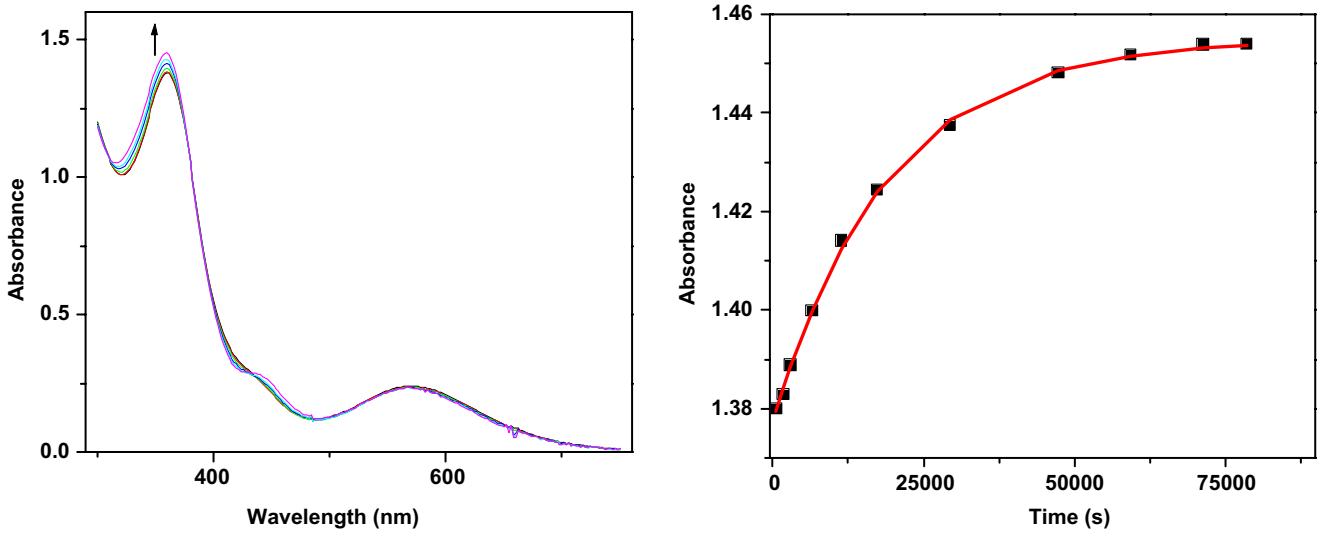
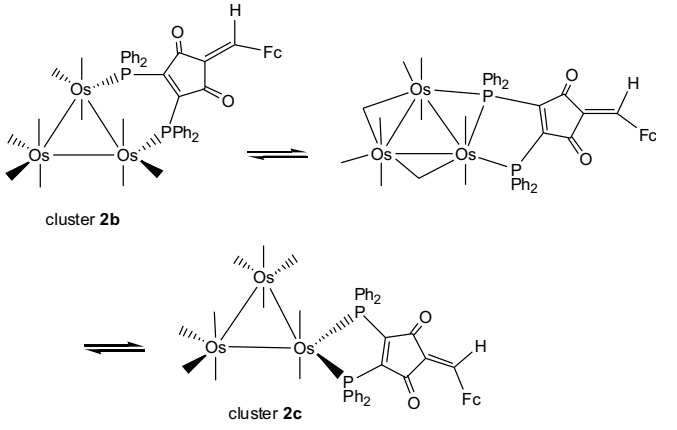


Fig. 2. UV-vis spectral changes for the isomerization of **2b** → **2c** in toluene at 323 K (left) and the absorbance changes at 360 nm versus time curve for the experimental data (■) and the least-squares fit of k (—, right).



(2)

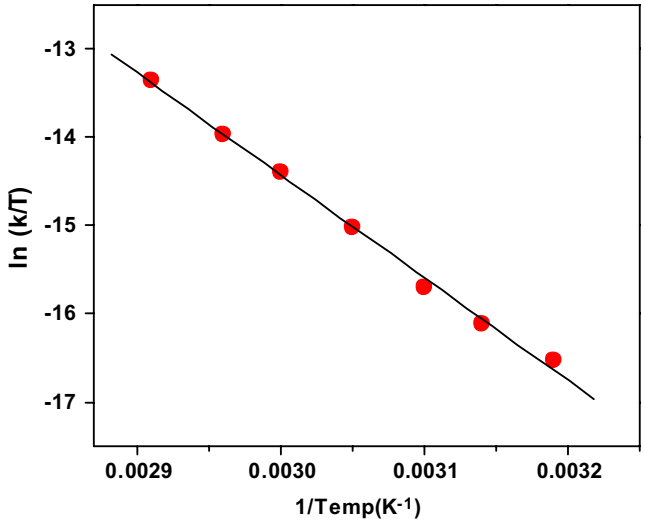


Fig. 3. Eyring plot for the conversion of **2b** → **2c** in toluene over the temperature range of 313–343 K.

3.4. Synthesis of the hydride-bridged cluster 3 from 2c

The photochemical reactivity of **2c** was examined given our interest in diphosphine ligand activation at metal clusters through *ortho*-metalation [2a,3c,22]. We have previously demonstrated the photoefficient CO loss and C–H bond activation of an ancillary aryl ligand in the diphosphine-chelated clusters $Os_3(CO)_{10}$(bpcd) and $Os_3(CO)_{10}$(bmi) to give the hydride-bridged clusters $HOs_3(CO)_9[\mu\text{-}Ph_2PC{=}C(PhP\{C_6H_4\})C(O)CH_2C(O)]$ and $HOs_3(CO)_9[\mu\text{-}Ph_2PC{=}C(PhP\{C_6H_4\})C(O)N(p\text{-tolyl})C(O)]$, respectively. Irradiation of cluster **2c** using 366 nm light leads to the slow loss of CO and *ortho*-metalation of one of the phenyl ligands to give the cluster $HOs_3(CO)_9[\mu\text{-}PhP(C_6H_4)C{=}C(PPh_2)C(O)C{=}CH(C_5H_4FeCp)C(O)]$ (**3**). In comparison to our earlier studies on $Os_3(CO)_{10}$(bpcd) and $Os_3(CO)_{10}$(bmi), the photochemically promoted *ortho*-metalation of **2c** is exceeding slow, as assessed by NMR analysis. Depending upon the amount of **2c** employed, good yields of **3** could be achieved by prolonged photolysis for several weeks with frequent removal of the liberated CO. Optical excitation of $Os_3(CO)_{10}$(bpcd) has been shown to furnish the unsaturated cluster $Os_3(CO)_9$(bpcd), followed by an intermediate π-aryl complex that precedes the formal *ortho*-metalation step. The π-aryl complex is sensitive to extraneous CO, which upon capture regenerates the starting cluster $Os_3(CO)_{10}$(bpcd) [3c]. The same scenario is assumed to be operative in the case of cluster **2c**, which accounts of the observed sensitivity to CO. Photolysis of a CO-saturated solution of **2c** shows no evidence for the formation of the desired hydride-bridged cluster **3**. Controlled thermolysis of **3** with CO (1 atm) regenerates **2c** in quantitative yield, as determined by NMR spectroscopy. Cluster **3** was isolated by column chromatography, followed by recrystallization, as an air-sensitive, blue solid. Eq. (3) illustrates the reaction of **2c** to **3**:

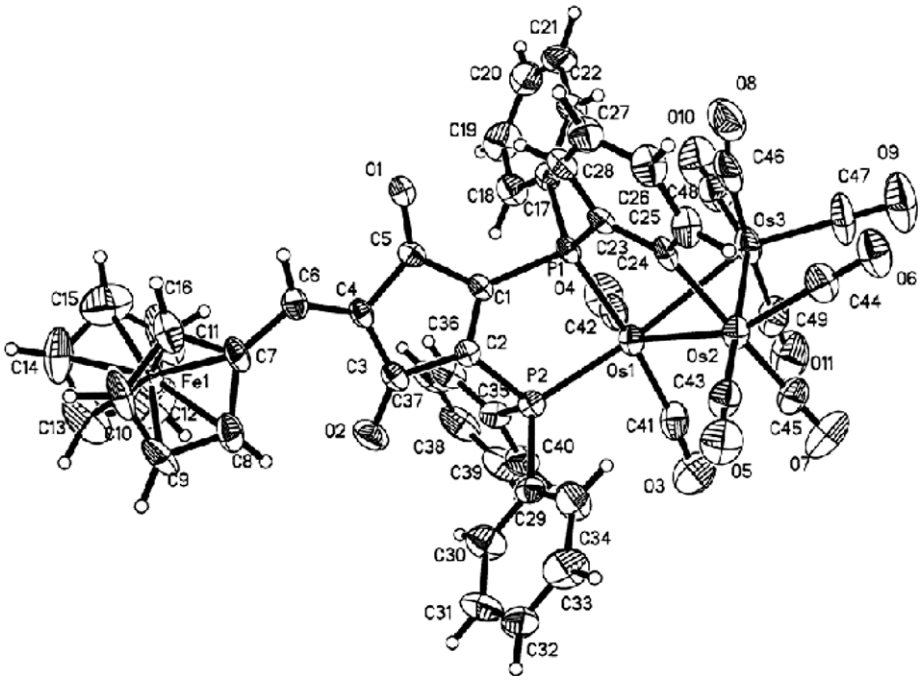
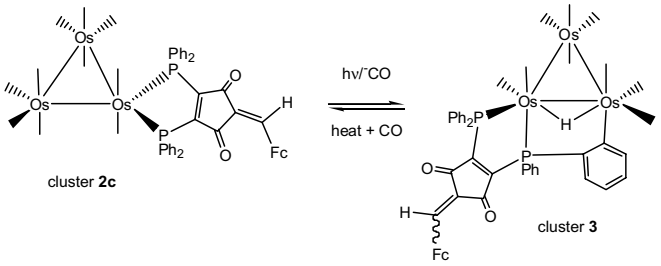


Fig. 4. Thermal ellipsoid plot of cluster **3** showing the thermal ellipsoids at the 50% probability level. The pentane solvent molecule has been omitted for clarity.



(3)

Cluster **3** was characterized in solution by IR and NMR spectroscopies. The *ortho*-metalation attendant on photolysis was confirmed by ^{1}H NMR spectroscopy. The observation of a high-field triplet at δ −15.87 provides unequivocal evidence for the presence of an edge-bridged cluster hydride. Particularly informative were the NMR data that revealed the existence of a 45:55 mixture diastereomers for **3**, whose origin derives from the proximal and distal orientations of the ferrocene moiety relative to the *ortho*-metalated aryl group. The nonfunctionalized Cp ring in the ^{1}H NMR spectrum of **3** appears as two singlets at δ 3.61 and 3.65, while the other Cp ring exhibits three sets of broadened multiplets at δ 4.19 and 4.32 (br, 2H each), 4.56 and 4.85 (br, 1H each), and 4.93 and 4.91 (br, 1H each). The essentially equimolar composition of diastereomers was corroborated by ^{31}P NMR spectroscopy. The presence of two distinct high-field doublets recorded at δ 21.40 and 22.11 and one triplet at δ 30.64, which results from overlapping doublets, is consistent with this formulation. No attempts have been made to assign these resonances to specific phosphine moieties. The MALDI-TOF mass spectrum showed a weak peak centered on *m*/*e* 1457.7 for the loss of one CO group from of **3**, as well as ions for the loss of seven additional CO groups.

The molecular composition of one of the diastereomers of **3** was established by X-ray diffraction analysis. Fig. 4 shows the thermal ellipsoid plot **3** and ascertains the activation of one of the aryl rings via *ortho*-metalation. The Os–Os bond distances range from 2.866(8) Å [Os(2)–Os(3)] to 2.9441(8) Å [Os(1)–Os(2)], with an mean distance of 2.908 Å that parallels those Os–Os single-bond distances reported for other Os_3 clusters. Despite the fact that the bridging hydride was not located during the crystallographic refinement, its location may be confidently assigned to the Os(1)–Os(2) vector [24]. Here the formation of an edge-bridging hydride leads to an elongation of the Os(1)–Os(2) bond length relative to the other two Os–Os bonds in **3**. Both phosphorus atoms of the fbpcd ligand coordinate to the Os(1) center in a chelating fashion and exhibit distinct axial [P(1)] and equatorial [P(2)] dispositions. This represents a change in the phosphine disposition from **2c** where both phosphine moieties were initially situated at equatorial sites. Presumably, the stereochemical change facilitates the ensuing *ortho*-metalation. The P(1)–Os(1)–P(2) angle of 85.95(7)° and the two Os–P distances of 2.305(2) Å [Os(1)–P(2)] and 2.365(2) Å [Os(1)–P(1)] exhibit values unremarkable to those angles and distance found by us in related compounds [1–3]. The Os(2)–C(24) bond distance of 2.165(9) Å is in excellent agreement with those metal-carbon sigma bond distances found in di- and trinuclear osmium compounds containing an *ortho*-metalated aryl ligand [25]. The nine CO groups are

linear and exhibit distances and angles consistent with such linkages. The ferrocene and dione ring moieties are unexceptional and require no comment.

4. Conclusions

The synthesis and properties of the new diphosphine ligand fbpcd are described. The kinetics for the bridge-to-chelate isomerization of the fbpcd ligand in $Os_3(CO)_{10}$(fbpcd) have been measured, with a sequence involving a nondissociative ''merry-go-round'' migration of the ancillary fbpcd ligand and two CO groups supported by a moderately negative entropy of activation. The chelating isomer of $Os_3(CO)_{10}$(fbpcd) losses CO upon 366 nm irradiation, leading to the *ortho*-metalation of the one of the aryl groups and formation of the hydride-bridged cluster $HOs_3(CO)_9[\mu\text{-}PhP(C_6H_4)C{=}C(PPh_2)C(O)C{=}CH(C_5H_4FeCp)C(O)]$, whose molecular structure has been crystallographically determined.

Acknowledgements

Financial support from the Robert A. Welch Foundation (Grants P-0074-WHW and B-1093-MGR) is much appreciated, and Professor. Andreas H. Franz (University of the Pacific) is thanked for recording the MALDI-TOF mass spectra.

Appendix A. Supplementary material

CCDC 628577 contains the supplementary crystallographic data for **3**. These data can be obtained free of charge via http://www.ccdc.cam.ac.uk/conts/retrieving.html, or from the Cambridge Crystallographic Data Centre, 12 Union Road, Cambridge CB2 1EZ, UK; fax: +(44) 1223-336-033; or e-mail: deposit@ccdc.cam.ac.uk. Supplementary data associated with this article can be found, in the online version, at doi:10.1016/j.poly.2007.03.057.

References

[1] (a) For bma ligand reactivity studies, see: K. Yang, J.M. Smith, S.G. Bott, M.G. Richmond, Organometallics 12 (1993) 4779;
(b) S.G. Bott, K. Yang, K.A. Talafuse, M.G. Richmond, Organometallics 22 (2003) 1383;
(c) S.G. Bott, K. Yang, M.G. Richmond, J. Organomet. Chem. 690 (2005) 3067; 691 (2006) 3771.
[2] (a) For bmi and related ligand reactivity studies, see: W.H. Watson, B. Poola, M.G. Richmond, J. Organomet. Chem. 691 (2006) 4676;
(b) K. Ejsmont, W.H. Watson, J. Liu, M.G. Richmond, J. Chem. Crystallogr. 33 (2003) 541.
[3] (a) For bpcd ligand reactivity studies, see: H. Shen, S.G. Bott, M.G. Richmond, Organometallics 14 (1995) 4625;
(b) S.G. Bott, H. Shen, R.A. Senter, M.G. Richmond, Organometallics 22 (2003) 1953;
(c) W.H. Watson, G. Wu, M.G. Richmond, Organometallics 25 (2006) 930;
(d) W.H. Watson, S.G. Bodige, K. Ejsmont, J. Liu, M.G. Richmond, J. Organomet. Chem. 691 (2006) 3609;
(e) W.H. Watson, B. Poola, M.G. Richmond, J. Organomet. Chem. 691 (2006) 5579.
[4] (a) F.A. Cotton, B.E. Hanson, in: P. de Mayo (Ed.), Rearrangements in Ground and Excited States, Academic Press, New York, 1980 [Chapter 12];
(b) S. Aime, L. Milone, Prog. NMR Spectrosc. 11 (1977) 183.
[5] (a) M. Hissler, J.E. McGarrah, W.B. Connick, D.K. Geiger, S.D. Cummings, R. Eisenberg, Coord. Chem. Rev. 208 (2003) 115;
(b) C.J. McAdam, J.L. Morgan, B.H. Robinson, J. Simpson, P.H. Rieger, A.L. Rieger, Organometallics 22 (2003) 5126.
[6] For a report on Knoevenagel condensation reactions using 4,5-dichloro-4-cyclopenten-1,3-dione, the direct precursor in the synthesis of the diphosphine ligand bpcd, see: R. Alfred, Z. Hellmut, Chem. Ber. 94 (1961) 1800.
[7] W.H. Watson, B. Poola, M.G. Richmond, J. Chem. Crystallogr. 36 (2006) 715.
[8] W.H. Watson, D. Wiedenfeld, A. Pingali, B. Poola, M.G. Richmond, Polyhedron (2007) in press.
[9] J.N. Nicholls, M.D. Vargas, Inorg. Synth. 26 (1989) 289.
[10] S.R. Drake, P.A. Loveday, Inorg. Synth. 28 (1990) 230.
[11] (a) D. Fenske, H. Becher, Chem. Ber. 107 (1974) 117;
(b) D. Fenske, Chem. Ber. 112 (1979) 363.
[12] D.F. Shriver, The Manipulation of Air-Sensitive Compounds, McGraw-Hill, New York, 1969.
[13] Saint Version 6.02, Bruker Analytical X-ray Systems, Inc. Copyright 1997–1999.
[14] SHELXTL Version 5.1, Bruker Analytical X-ray Systems, Inc. Copyright 1998.
[15] PLATON - A Multipurpose Crystallographic Tool, Utrecht University, Utrecht, The Netherlands, A.L. Spek (2001).
[16] B.K. Carpenter, Determination of Organic Reaction Mechanisms, Wiley-Interscience, New York, 1984.
[17] N.B. Coltrup, L.H. Daly, S.E. Wiberley, Introduction to Infrared and Raman Spectroscopy, Academic Press, New York, 1990.
[18] R. Meyer, D.M. Schut, K.J. Keana, D.R. Tyler, Inorg. Chim. Acta 240 (1995) 405.
[19] F.A. Bovey, Nuclear Magnetic Resonance Spectroscopy, Academic Press, New York, 1969.
[20] W.H. Watson, B. Poola, M.G. Richmond, J. Chem. Crystallogr. 36 (2006) 123.
[21] (a) P.E. Garrou, Chem. Rev. 81 (1981) 229;
(b) M.G. Richmond, J.K. Kochi, Organometallics 6 (1987) 254.
[22] W.H. Watson, G. Wu, M.G. Richmond, Organometallics 24 (2005) 5431.
[23] S. Kandala, M.G. Richmond, Inorg. Chem. 45 (2006) 5976.
[24] D.M.P. Mingos, D.J. Wales, Introduction to Cluster Chemistry, Prentice-Hall, Englewood Cliffs, NJ, 1990.
[25] (a) A.J. Deeming, S.E. Kabir, N.I. Powell, P.A. Bates, M.B. Hursthouse, J. Chem. Soc., Dalton Trans. (1987) 1529;
(b) A.J. Deeming, K.I. Hardcastle, S.E. Kabir, J. Chem. Soc., Dalton Trans. (1988) 827;
(c) S.E. Kabir, K.M.A. Malik, E. Molla, M.A. Mottalib, J. Organomet. Chem. 616 (2000) 157;
(d) R.D. Adams, J.E. Cortopassi, J. Cluster Sci. 6 (1995) 437;
(e) S.B. Colbran, P.T. Irele, B.F.G. Johnson, F.J. Lahoz, J. Lewis, P.R. Raithby, J. Chem. Soc., Dalton Trans. (1989) 2023.

and spectral characterization of dioxomolybdenum(VI) complexes of N(4)-substituted ONS donor ligands. The single crystal X-ray diffraction studies of three of the synthesized complexes are also described.

2. Experimental

2.1. Materials

$MoO_2(acac)_2$ (Sigma–Aldrich) and pyridine (S.D. Fine Chemicals) were used without further purification. All compounds used for the synthesis of the thiosemicarbazone ligands were purified by standard methods and solvents were purified by distillation. The ligands were recrystallized from ethanol/methanol and dried in vacuo before complexation.

2.2. Synthesis

The ligands H_2L^1 and H_2L^2 were synthesized by the earlier reported methods [5,6].

*[(MoO$_2$L^1)$_2$] (**1**)*. To a hot methanolic solution of the ligand H_2L^1 (2 mmol, 0.582 g), was added a methanolic solution of $MoO_2(acac)_2$ (2 mmol, 0.652 g) with constant stirring. The orange solution obtained was refluxed for about 3 h and allowed to cool. The orange crystals which formed were separated and dried. *Anal*. Calc. for $C_{30}H_{38}N_6O_6S_2Mo_2$: C, 43.17; H, 4.59; N, 10.07. Found: C, 43.05; H, 4.52; N, 10.04%.

*[MoO$_2$L^{1}py] (**2**)*. To a hot methanolic solution of complex **1** (0.5 mmol, 0.417 g), was added 2 mL of pyridine and the mixture was heated until a clear deep yellow solution was produced. The above solution was refluxed for about 3 h and allowed to cool. Slow evaporation of the reaction mixture over 3 days produced yellow crystals. *Anal*. Calc. for $C_{20}H_{24}N_4O_3SMo$: C, 48.39; H, 4.87; N, 11.29. Found: C, 48.16; H, 4.70; N, 11.12%.

*[(MoO$_2$L^2)$_2$] (**3**)*. To a hot ethanolic solution of the ligand H_2L^2 (1.5 mmol, 0.428 g), was added an ethanolic solution of $MoO_2(acac)_2$ (1.5 mmol, 0.489 g) with constant stirring. The orange solution obtained was refluxed for about 3 h and the orange compound formed was filtered, washed with ethanol and ether and dried in vacuo over P_4O_{10}. *Anal*. Calc. for $C_{30}H_{32}N_6O_6S_2Mo_2$: C, 43.80; H, 3.19; N, 10.22. Found: C, 43.69; H, 3.02; N, 10.13%.

*[MoO$_2$L^{2}py] (**4**)*. To a hot ethanolic solution of complex **3** (0.5 mmol, 0.205 g), was added 2 mL of pyridine and the mixture was heated until a clear deep yellow solution was produced. The above solution was refluxed for

Table 1
Crystal data and structure refinement parameters for [$(MoO_2L^1)_2$] (**1**), [MoO_2L^1py] (**2**) and [MoO_2L^2py] (**4**)

Compound	**1**	**2**	**4**
Empirical formula	$C_{30}H_{38}Mo_2N_6O_6S_2$	$C_{20}H_{24}MoN_4O_3S$	$C_{20}H_{18}MoN_4O_3S$
Formula weight	834.68	496.43	490.38
Temperature (K)	293(2)	293(2)	293(2)
Wavelength (Å)	0.71073	0.71073	0.71073
Crystal system	monoclinic	triclinic	triclinic
Space group	$P2_1/c$	$P\bar{1}$	$P\bar{1}$
Unit cell dimensions			
a (Å)	9.499(2)	8.9127(7)	8.7464(16)
b (Å)	12.3649(7)	10.424(3)	10.879(3)
c (Å)	14.488(2)	11.726(3)	11.098(2)
α (°)	90	75.15(2)	95.178(19)
β (°)	96.506(15)	87.531(11)	100.563(16)
γ (°)	90	86.643(12)	103.999(19)
Volume (Å^3)	1690.8(5)	1050.7(4)	997.2(4)
Z	2	2	2
D_{calc} (Mg/m^3)	1.639	1.569	1.633
Absorption coefficient (mm^{-1})	0.916	0.752	0.792
F(000)	848	508	496
Crystal size (mm)	$0.25 \times 0.20 \times 0.20$	$0.30 \times 0.25 \times 0.20$	$0.33 \times 0.21 \times 0.17$
θ Range for data collection (°)	3.17–30.09	2.95–25.00	3.15–25.00
Index ranges	$-13 \leqslant h \leqslant 11$, $-15 \leqslant k \leqslant 17$, $-20 \leqslant l \leqslant 19$	$-10 \leqslant h \leqslant 10$, $-12 \leqslant k \leqslant 12$, $-13 \leqslant l \leqslant 13$	$-10 \leqslant h \leqslant 10$, $-12 \leqslant k \leqslant 12$, $-13 \leqslant l \leqslant 13$
Reflections collected	15752	8911	10402
Independent reflections (R_{int})	4891 (0.0207)	3670 (0.0142)	3511 (0.0212)
Refinement method	full-matrix on F^2	full-matrix on F^2	full-matrix on F^2
Data/restraints/parameters	4891/0/217	3670/0/266	3511/0/267
Goodness-of-fit on F^2	1.071	1.063	1.073
Final R indices [$I > 2\sigma(I)$]	$R_1 = 0.0229$, $wR_2 = 0.0558$	$R_1 = 0.0388$, $wR_2 = 0.1099$	$R_1 = 0.0228$, $wR_2 = 0.0505$
R indices (all data)	$R_1 = 0.0297$, $wR_2 = 0.0579$	$R_1 = 0.0429$, $wR_2 = 0.1132$	$R_1 = 0.0271$, $wR_2 = 0.0514$
Largest difference in peak and hole (e Å^{-3})	0.428 and −0.452	1.864 and −0.627	0.348 and −0.331

$R_1 = \sum \| F_o | - | F_c \| / \sum | F_o |$, $wR_2 = \{\sum [w(F_o^2 - F_c^2)^2] / \sum [w(F_o^2)^2]\}^{1/2}$.

about 3 h and allowed to cool. Slow evaporation of the reaction mixture over 5 days produced yellow crystals. *Anal*. Calc. for $C_{20}H_{24}N_4O_3SMo$: C, 48.98; H, 3.70; N, 11.43. Found: C, 48.82; H, 3.65; N, 11.24%.

2.3. Physical measurements

Elemental analyses of C, H and N were done on a Vario EL III elemental analyzer and FT-IR spectra were recorded on a Thermo Nicolet AVATAR 370 DTGS FT-IR spectrophotometer instrument using KBr pellets in the 4000–400 cm^{-1} region at SAIF, Cochin University of Science and Technology, Kochi 22, India. Electronic spectra in solutions were recorded on a Spectro UV–VIS Double Beam UVD-3500 spectrophotometer at the Department of Applied Chemistry, CUSAT, Kochi 22 in the 200–900 nm range. Magnetic susceptibility measurements were carried out at IIT, Roorkee, in the polycrystalline state at room temperature on a Par model 155 Vibrating Sample Magnetometer at 5 kOe field strength. Single crystal X-ray crystallographic analysis of the compounds were carried out using a CrysAlis CCD diffractometer, Oxford Diffraction Ltd., at the Single Crystal X-ray Diffraction Facility, IIT, Bombay.

2.4. Crystallography

The crystallographic data and structure refinement parameters for complexes **1**, **2** and **4** are given in Table 1. An orange block crystal of compound **1**, a golden yellow crystal of **2** and an yellow crystal of **4** were measured at 293(2) K on a CrysAlis CCD diffractometer with graphite-monochromated Mo Kα radiation ($\lambda = 0.71073$ Å). The program CrysAlis RED was used for data reduction and cell refinement [7]. The structure was solved by direct methods using SHELXS [8] and refined by full-matrix least-squares refinement on F^2 using SHELXL [8]. The N–H hydrogen atoms were located from difference Fourier maps and refined isotropically. The remainder of the H-atoms were included in calculated positions and refined as riding atoms using default SHELXL parameters. For compound **1**, the final refinement cycle was based on all 4891 independent reflections and 217 variables with $R_1 = 0.0229$, $wR_2 = 0.0558$. For compounds **2** and **4**, the final refinement cycles were based on all 3670 and 3511 independent reflections and 266 and 267 variables, respectively, with $R_1 = 0.0388$, $wR_2 = 0.1099$ for **2** and $R_1 = 0.0228$, $wR_2 = 0.0505$ for **4**.

3. Results and discussion

3.1. Synthesis

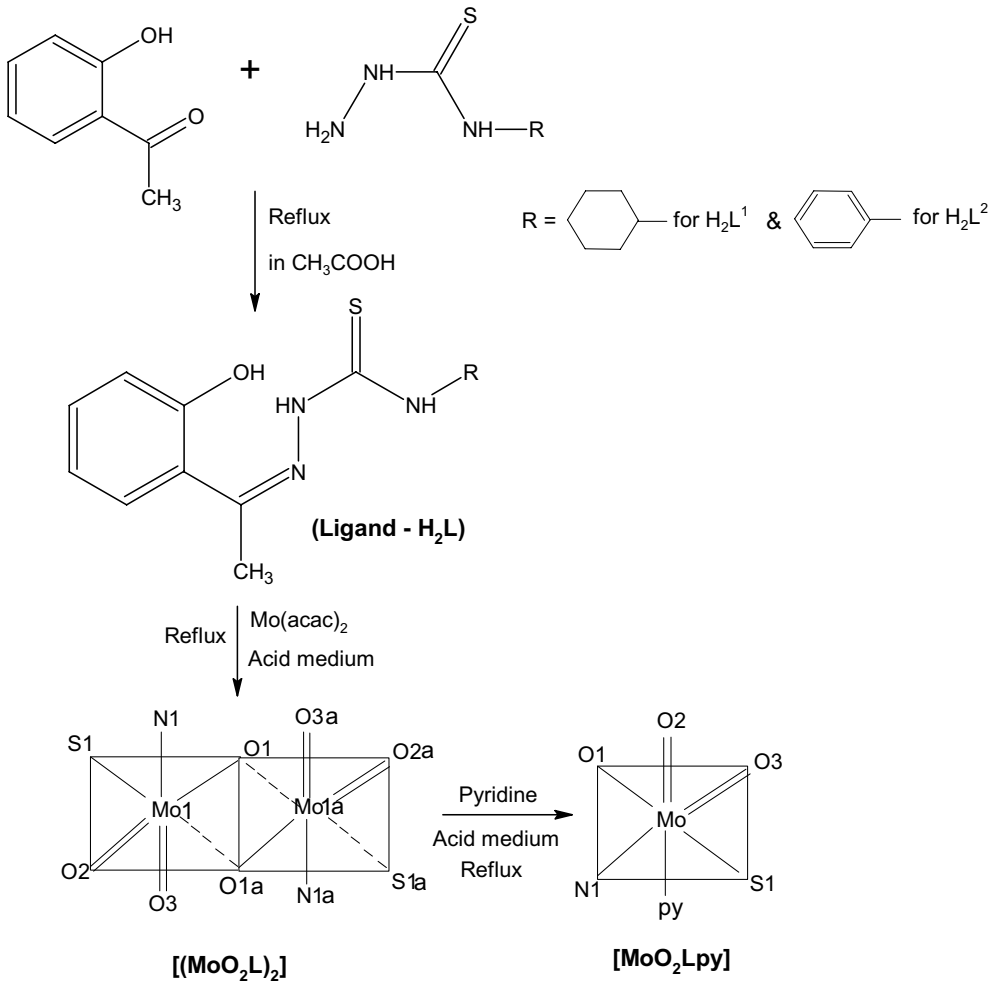
2-Hydroxyacetophenone N(4)-cyclohexyl and N(4)-phenyl thiosemicarbazones (H_2L^1 and H_2L^2) were used as the ligands. The crystal structures of both ligands were published earlier by us [9,10]. These are found to act as dianionic tridentate ONS donors in this work. The stoichiometric reaction (Scheme 1) of bis(acetylacetonato)dioxomolybdenum(VI) with H_2L in refluxing methanol/ethanol afforded the orange six-coordinated complexes of the type $[(MoO_2L)_2]$ (**1** and **3**). The $[MoO_2L(B)]$ complexes **2** and **4** were prepared by reaction of $[(MoO_2L)_2]$ with a heterocyclic base {B = pyridine (py)} in methanol/ethanol. Magnetic susceptibility and molar conductivity data indicate that these MoO_2^{2+} complexes are diamagnetic and electrically non-conducting in solution. These complexes are soluble in DMF and DMSO.

3.2. Spectral characteristics

Selected spectroscopic data of the complexes are summarized in Tables 2 and 3. Table 2 lists the tentative assignments of the main IR bands of the dioxomolybdenum(VI) complexes for the ligands H_2L^1 and H_2L^2 in 4000–50 cm^{-1} region. The free ligands H_2L^1 and H_2L^2 show bands at ca. 3374 and 3060 cm^{-1}, which are due to the stretching modes of the –OH and –NH groups, respectively. These bands are absent in the complexes which suggests deprotonation of the phenolic group, indicating coordination through the phenolic oxygen, and enolization of the thione sulfur followed by deprotonation. On coordination of the azomethine nitrogen, ν(C=N) shifts to lower wavenumbers by 10–20 cm^{-1} as the band shifts from ca. 1608 to 1592 cm^{-1} in the spectra of the four dioxomolybdenum(VI) complexes. The ν(N–N) of the thiosemicarbazone is found at ca. 1118 cm^{-1}. The increase in the frequency of this band in the spectra of the complexes, due to an increase in the bond strength, again confirms coordination via the azomethine nitrogen [11,12].

The decrease in the stretching frequency of the ν(CS) band from ca. 841 cm^{-1} in the thiosemicarbazones by 80–90 cm^{-1} upon complexation indicates coordination via the thiolato sulfur [13,14]. IR spectra of complexes **1**–**4** show sharp bands at ca. 1540 cm^{-1} due to the newly formed ν(N=C) bond, indicating the coordination of sulfur in the enolate form rather than the keto form [15,16]. In all the complexes, the phenolic oxygen is coordinated to molybdenum by the loss of the OH proton. The ligands have a band at ca. 1279 cm^{-1}, which is due to ν(C–O). This band is shifted to ca. 1244 cm^{-1} in the complexes, indicating the coordination of O^- [17]. It was reported that structurally characterized polymeric dioxomolybdenum(VI)-tridentate complexes have sharp bands in the 810–820 cm^{-1} region [18]. Here, in complexes **1** and **3** a strong band is observed at 821 and 810 cm^{-1}, respectively, suggesting the presence of Mo–O···Mo bridging in their structures [19,20]. All complexes (**1**–**4**) exhibit two bands at ca. 891 and 927 cm^{-1} assigned to symmetric and antisymmetric vibrations, respectively, of the *cis*-MoO_2^{2+} core [21,22].

The electronic absorption bands of the dioxomolybdenum(VI) complexes recorded in DMF solution, are given in Table 3. The thiosemicarbazones (H_2L^1 and H_2L^2) have a ring $\pi \rightarrow \pi^*$ band at ca. 36 690 cm^{-1} and a band at ca. 31 050 cm^{-1} due to $n \rightarrow \pi^*$ transitions associated with the azomethine linkage. These bands suffer marginal shifts on



Scheme 1. Reaction diagram for the isolation of the dioxomolybdenum(VI) complexes.

Table 2
Selected IR bands (cm^{-1}) with tentative assignments of the dioxomolybdenum(VI) complexes

Compound	ν(C=N)	ν(N=C)	ν(N–N)	ν(C–S)	ν(C–O)	ν(Mo=O)
H_2L^1	1613		1111	1358, 846	1263	
$[(MoO_2L^1)_2]$	1585	1549	1142	1352, 768	1240	897, 943
$[MoO_2L^1py]$	1596	1543	1136	1357, 757	1252	886, 926
H_2L^2	1603		1160	1362, 835	1295	
$[MoO_2L^2]$	1590	1538	1136	1311, 751	1246	886, 914
$[MoO_2L^2py]$	1597	1532	1130	1316, 751	1240	898, 926

Table 3
Electronic spectral data (cm^{-1}) of the dioxomolybdenum(VI) complexes

Compound	$[(MoO_2L^1)_2]$ (**1**)	$[MoO_2L^1py]$ (**2**)	$[MoO_2L^2]$ (**3**)	$[MoO_2L^2py]$ (**4**)
λ_{max} (cm^{-1})	34240	33890	34360	34120
	27020	28010	29940	28320
	23310	23750	24270	24150

complexation. The complexes **1**–**4** display a broad band in the 25000–23250 cm^{-1} region and two strong absorptions in the 30300–27020 and 35710–33890 cm^{-1} regions, which are assignable to L → Mo(dπ) LMCT and intraligand transitions, respectively [23–25].

3.3. Description of the crystal structures of the compounds $[(MoO_2L^1)_2]$ (**1**), $[MoO_2L^1py]$ (**2**) and $[MoO_2L^2py]$ (**4**)

The molecular structure and the atom numbering scheme for complexes **1**, **2** and **4** are shown in Figs. 1–3, respectively, and relevant bond distances and angles are presented in Tables 4 and 5. The coordination geometry around molybdenum can be described as distorted octahedral in the three dioxomolybdenum(VI) complexes **1**, **2** and **4**, the ligand $(L)^{2-}$ acting as a tridentate ligand forming a six-membered metallocycle involving the MoO_2^{2+} moiety. In complex **1**, the principal ligand is bonded to *cis*-MoO_2^{2+} in a planar fashion, coordinating through the nitrogen N(1), sulfur S(1) and oxygen O(1) atoms.

Compound **1** is a binuclear dioxomolybdenum(VI) complex, in which structural evidence for the achievement of hexacoordination through Mo–O···Mo bridging is observed. The Mo–O···Mo bridging is effected by one of the carboxylate oxygen atoms with a threefold coordinated oxygen atom C–O–Mo2. Three atoms O(1), N(1) and S(1) of the doubly deprotonated thiosemicarbazone ligand and one terminal oxo atom, O(3), occupy the meridional plane and lie at 0.0599, 0.0983, 0.0105 and 0.0720 Å, respectively,

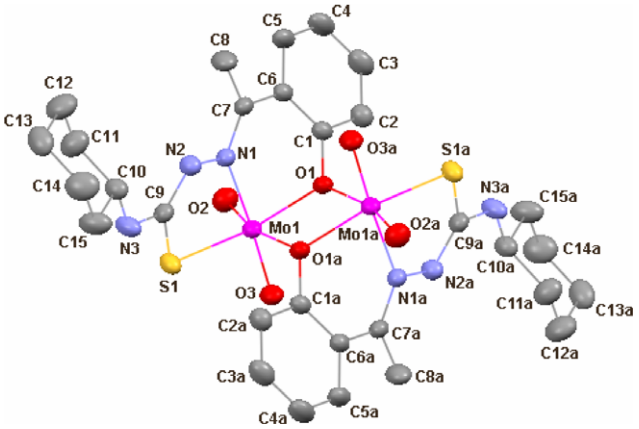


Fig. 1. Ellipsoidal plot of compound **1** (hydrogen atoms are omitted) with the atom labelling scheme.

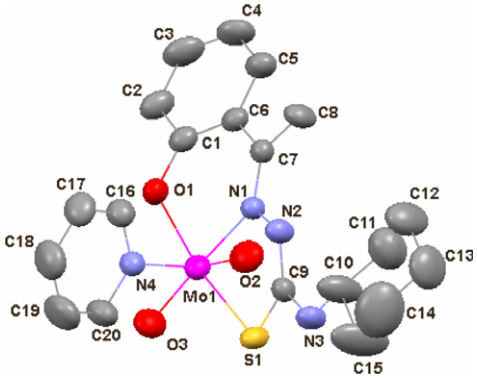


Fig. 2. Ellipsoidal plot of compound **2** (hydrogen atoms are omitted) with the atom labelling scheme.

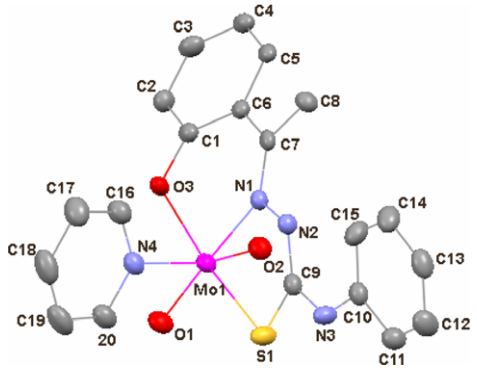


Fig. 3. Ellipsoidal plot of compound **4** (hydrogen atoms are omitted) with the atom labelling scheme.

out of the least squares plane through them, and the Mo atom lies 0.4164 Å out of this plane in the direction of the O(2) atom, the other terminal oxygen. Both oxygen atoms O(2) and O(1a) occupy the axial positions and form an O(2)–Mo(1)–O(1a) angle of 166.97(5)°. The Mo(1)–O(1a) bond [2.4241(12) Å] is significantly longer than the other Mo–O bonds [Mo(1)–O(2), 1.6845(13) Å; Mo(1)–O(3), 1.7075(12) Å; Mo(1)–O(1), 1.9977(11) Å], indicating that O(1a) is weakly bonded to the MoO_2^{2+} moiety. The Mo(1)–O(2) and Mo(1)–O(3) bond distances of the MoO_2^{2+} group are unexceptional and are almost equal [Mo(1)–O(2), 1.6845(13) Å; Mo(1)–O(3), 1.7075(12) Å]. Compound **1** is centrosymmetric, therefore, Mo1 and Mo1a are crystallographically equivalent.

From a comparison of the bond distances and angles of the ligand (H_2L^1) and compound **1**, it is clear that the ligand coordinates to the MoO_2^{2+} core in the deprotonated thiolate form because in compound **1** the C–S bond distance [C(9)–S(1)] exhibits the value 1.7632(16) Å which is nearer to a C–S single bond [1.81 Å] than a C–S double bond distance [1.60 Å] [26]. However, it falls short of the pure C–S single bond distance. The reason for such shortening may be attributed to electron delocalization in the coordinated ligand [27]. The adjacent C(9)–N(2) bond now displays a typical double bond distance [1.299(2) Å] and a N(1)–N(2) bond distance of 1.3851(19) Å is also apparent for compound **1**. In the uncomplexed H_2L^1 ligand, the similar bonds C(8)–N(2) and N(1)–N(2) are 1.351(2) Å and 1.392(2) Å, respectively. The C(7)–N(1) bond distance in compound **1** is close to the usual C=N bond length [C(7)–N(1), 1.3078(19) Å]. The N–N–C bond angle of the ligand (H_2L^1) [N(1)–N(2)–C(8), 119.95(17)°] is reduced by a few degrees [N(1)–N(2)–C(9), 113.28(13)° in **1**] on complex formation. These changes are directly due to coordination of the ligand to the MoO_2^{2+} moiety when it becomes a delocalized system [28–30].

In complexes **2** and **4**, the sixth coordination position is occupied by the heterocyclic base, pyridine coordinating through its nitrogen N(4). The large Mo–N(4) distances [2.433(3) Å in **2**; 2.4380(19) Å in **4**] reveal that the pyridine moiety is rather weakly coordinated to the MoO_2^{2+} core. In complexes **2** and **4**, the Mo–O bond distances of the MoO_2^{2+} core are almost equal [Mo–O(2), 1.688(3) and Mo–O(3), 1.713(3) Å in **2** and Mo–O(2), 1.7070(15) and Mo–O(1), 1.7121(15) Å in **4**]. These observations raise an interesting point about the suspected inherent weakness of the sixth position in the coordination octahedron of the MoO_2^{2+} core, *trans* to the Mo=O(2) bond [31,32].

By comparing the bond distances and angles of ligands (H_2L^1 and H_2L^2) with their respective complexes **2** and **4**, it is clear that the ligands coordinate to the MoO_2^{2+} core in the doubly deprotonated enolate form [C(8)–S(1), 1.688(2) Å in H_2L^1 and 1.6653(17) Å in H_2L^2; C(9)–S(1), 1.746(4) Å in **2** and 1.766(2) Å in **4**; C(8)–N(2), 1.351(2) Å in H_2L^1 and 1.363(2) Å in H_2L^2; C(9)–N(2), 1.299(5) Å in **2** and 1.304(3) Å in **4**; N(1)–N(2)–C(8), 119.95(17)° in H_2L^1 and 118.60(15)° in H_2L^2; N(1)–N(2)–C(9), 113.4(3)° in **2** and 113.35(16)° in **4**].

Ring puckering analyses and least-square plane calculations show that the rings Cg(2) in complex **1** and Cg(1) in complex **2** and Cg(1) in complex **4**, comprising of atoms Mo(1), S(1), C(9), N(2) and N(1), adopt an envelope on Mo(1) and the ring Cg(5) in complexes **1** and **2**, comprising of atoms C(10), C(11), C(12), C(13), C(14) and C(15) adopt chair conformations [33].

Table 4
Selected bond lengths (Å) for compounds **1**, **2** and **4**

	1	**2**		**4**	
Mo(1)–O(2)	1.6845(13)	Mo(1)–O(2)	1.688(3)	Mo(1)–O(2)	1.7070(15)
Mo(1)–O(3)	1.7075(12)	Mo(1)–O(3)	1.713(3)	Mo(1)–O(1)	1.7121(15)
Mo(1)–O(1)	1.9977(11)	Mo(1)–O(1)	1.939(3)	Mo(1)–O(3)	1.9479(15)
Mo(1)–N(1)	2.2801(13)	Mo(1)–N(1)	2.294(3)	Mo(1)–N(1)	2.3094(17)
Mo(1)–S(1)	2.4090(5)	Mo(1)–S(1)	2.4258(12)	Mo(1)–S(1)	2.4257(8)
Mo(1)–O(1a)	2.4241(12)	Mo(1)–N(4)	2.433(3)	Mo(1)–N(4)	2.4380(19)
S(1)–C(9)	1.7632(16)	S(1)–C(9)	1.746(4)	S(1)–C(9)	1.766(2)
N(1)–C(7)	1.3078(19)	N(1)–C(7)	1.300(5)	N(1)–C(7)	1.312(3)
N(1)–N(2)	1.3851(19)	N(1)–N(2)	1.387(4)	N(1)–N(2)	1.397(2)
N(2)–C(9)	1.299(2)	N(2)–C(9)	1.299(5)	N(2)–C(9)	1.304(3)
O(1)–C(1)	1.3841(17)	N(3)–C(9)	1.344(5)	N(3)–C(9)	1.356(3)
O(1)–Mo(1a)	2.4241(12)				

Table 5
Selected bond angles (°) for compounds **1**, **2** and **4**

	1	**2**		**4**	
O(2)–Mo(1)–O(3)	105.45(6)	O(2)–Mo(1)–O(3)	105.79(15)	O(2)–Mo(1)–O(1)	106.05(7)
O(2)–Mo(1)–O(1)	99.41(6)	O(2)–Mo(1)–O(1)	96.23(13)	O(2)–Mo(1)–O(3)	96.63(7)
O(3)–Mo(1)–O(1)	105.79(5)	O(3)–Mo(1)–O(1)	107.72(13)	O(1)–Mo(1)–O(3)	107.45(7)
O(3)–Mo(1)–N(1)	158.27(5)	O(3)–Mo(1)–N(1)	159.03(13)	O(2)–Mo(1)–N(1)	91.11(7)
O(2)–Mo(1)–S(1)	103.18(5)	O(2)–Mo(1)–S(1)	99.85(11)	O(1)–Mo(1)–N(1)	160.00(7)
O(3)–Mo(1)–S(1)	91.75(4)	O(3)–Mo(1)–S(1)	90.94(11)	O(1)–Mo(1)–S(1)	90.64(6)
O(1)–Mo(1)–S(1)	146.45(4)	O(1)–Mo(1)–S(1)	150.99(8)	O(3)–Mo(1)–S(1)	150.25(5)
O(2)–Mo(1)–O(1a)	166.97(5)	O(2)–Mo(1)–N(4)	169.42(13)	O(2)–Mo(1)–N(4)	168.87(6)
N(2)–N(1)–Mo(1)	122.16(9)	N(2)–N(1)–Mo(1)	122.0(2)	N(2)–N(1)–Mo(1)	122.06(12)
C(9)–N(2)–N(1)	113.28(13)	C(9)–N(2)–N(1)	113.4(3)	C(9)–N(2)–N(1)	113.35(16)

In the crystal packing, the molecules of **1** are intermolecularly hydrogen bonded through N(3)–H(3N) and O(3). In molecule **2**, hydrogen bonding interactions are between C(3)–H(3) and O(3) and between C(17)–H(17) and O(2), and the molecules are arranged in an opposite manner and the pyridyl rings are anti-parallel to each other. The molecules of **4** are arranged in an opposite manner and the phenyl rings are parallel to each other. Intermolecular hydrogen bonding interactions are observed between C(13)–H(13) and O(1) and between C(5)–H(5) and O(2).

4. Conclusion

Preparation and characterization of dioxomolybdenum(VI) complexes involving a dianionic tridentate ONS donor in the form of 2-hydroxyacetophenone N(4)-cyclohexyl and N(4)-phenyl thiosemicarbazones are reported. In all these complexes, the main complex MoO_2L is a structurally characterized pentacoordinate species with one vacant position. This vacant position is found to act as a substrate-binding site. Complexes **1** and **3** are binuclear and the vacant position is occupied by an oxygen atom from the second unit, while complexes **2** and **4** are mononuclear and these six coordinate adducts are easily formed by the attachment of pyridine to the sixth position.

Acknowledgements

The authors are indebted to SAIF, Cochin University of Science and Technology, Kochi, Kerala, India for elemental analyses and IR spectral analyses. We are thankful to the National Single Crystal X-ray diffraction Facility, IIT, Bombay, India for providing single crystal XRD results. The financial support by DST, New Delhi, India (No. SR/SI/IC-31/2002) is gratefully acknowledged.

Appendix A. Supplementary material

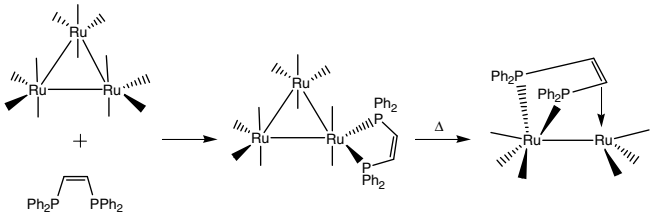
CCDC 603959, 603960 and 609175 contain the supplementary crystallographic data for **1**, **2** and **4**. These data can be obtained free of charge via http://www.ccdc.cam.ac.uk/conts/retrieving.html, or from the Cambridge Crystallographic Data Centre, 12 Union Road, Cambridge CB2 1EZ, UK; fax: (+44) 1223-336-033; or e-mail: deposit@ccdc.cam.ac.uk. Supplementary data associated with this article can be found, in the online version, at doi:10.1016/j.poly.2007.03.046.

References

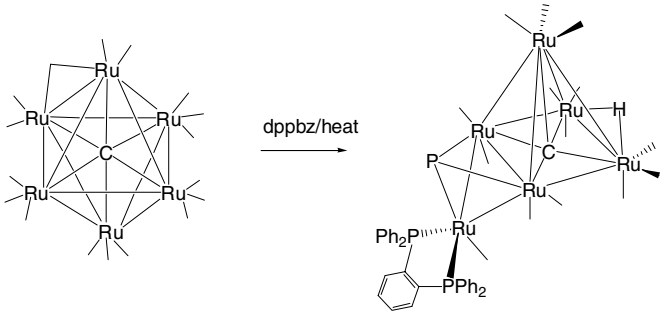
[1] I.K. Dhavan, J.H. Enemark, Inorg. Chem. 35 (1996) 4873.
[2] S.J.N. Burgmayer, E.I. Stiefel, J. Chem. Educ. 62 (1985) 943.
[3] S.B. Kumar, M. Chaudhuri, J. Chem. Soc., Dalton Trans. (1992) 269.

[4] Z. Afrasiabi, E. Sinn, J. Chen, Y. Ma, A.L. Rheingold, L.N. Zakharov, N. Rath, S. Padhye, Inorg. Chim. Acta 357 (2004) 271.
[5] P. Bindu, M.R.P. Kurup, Transition Met. Chem. 22 (1997) 578.
[6] G.F. de Sousa, R.H.P. Francisco, M.T.P. Gambardella, R.H. de A. Santos, A. Abras, J. Braz. Chem. Soc. 12 (2001) 722.
[7] B.V. Nonius, Nonius, MACH3 Software, Delft, The Netherlands, 1997.
[8] G.M. Sheldrick, SHELXL-97 and SHELXS-97, University of Göttingen, Göttingen, Germany, 1997.
[9] E.B. Seena, B.N. Bessy Raj, M.R.P. Kurup, E. Suresh, J. Chem. Crystallogr. 36 (2006) 189.
[10] E.B. Seena, E. Manoj, M.R.P. Kurup, Acta Crystallogr., Sect. C 62 (2006) o486.
[11] A. Syamal, K.S. Kale, Inorg. Chem. 4 (1965) 867.
[12] B.S. Garg, M.R.P. Kurup, S.K. Jain, Y.K. Bhoon, Transition Met. Chem. 13 (1988) 309.
[13] L.J. Willis, J.M. Loehr, K.F. Miller, A.E. Bruce, E.I. Stiefel, Inorg. Chem. 25 (1986) 4289.
[14] M. Joseph, M. Kuriakose, M.R.P. Kurup, E. Suresh, A. Kishore, S.G. Bhat, Polyhedron 25 (2006) 61.
[15] S. Bhattacharjee, R. Bhattacharyya, J. Chem. Soc., Dalton Trans. (1993) 1151.
[16] E.B. Seena, M.R.P. Kurup, Polyhedron 26 (2007) 829.
[17] O.A. Rajan, A. Chakravarthy, Inorg. Chem. 20 (1981) 660.
[18] R.A. Lal, A. Kumar, J. Chakraborty, S. Bhaumik, Transition Met. Chem. 26 (2001) 557.
[19] J.M. Berg, R.H. Holm, Inorg. Chem. 22 (1983) 1768.
[20] M. Cindric, V. Vrdoljak, N. Strukan, B. Kamenar, Polyhedron 24 (2005) 369.
[21] F.J. Arnaiz, R. Aguado, M.R. Podrosa, A.D. Cian, J. Fischer, Polyhedron 19 (2000) 2141.
[22] A. Rana, R. Dinda, P. Sengupta, L.R. Falvello, S. Ghosh, Polyhedron 21 (2002) 1023.
[23] S. Purohit, A.P. Koley, L.S. Prasad, P.T. Manoharan, S. Ghosh, Inorg. Chem. 28 (1989) 3735.
[24] C.S.J. Chang, J.H. Enemark, Inorg. Chem. 30 (1991) 683.
[25] S. Gupta, A.K. Barik, S. Pal, A. Hazra, S. Roy, R.J. Butcher, S.K. Kar, Polyhedron 26 (2007) 133.
[26] M. Joseph, V. Suni, M.R.P. Kurup, M. Nethaji, A. Kishore, S.G. Bhat, Polyhedron 23 (2004) 3069.
[27] M.W. Bishop, J. Chatt, J.R. Dilworth, M.B. Hursthouse, M. Motevalli, J. Chem. Soc., Dalton Trans. (1979) 1603.
[28] R. Dinda, P. Sengupta, S. Ghosh, H.M. Figge, W.S. Sheldrick, J. Chem. Soc., Dalton Trans. (2002) 4434.
[29] A. Lehtonen, R. Sillanpaa, Polyhedron 24 (2005) 257.
[30] A. Lehtonen, M. Wasberg, R. Sillanpaa, Polyhedron 25 (2006) 767.
[31] S.K. Dutta, D.B. McConville, W.J. Youngs, M. Chaudhury, Inorg. Chem. 36 (1997) 2517.
[32] R. Dinda, P. Sengupta, S. Ghosh, H.M. Figge, W.S. Sheldrick, Eur. J. Inorg. Chem. (2003) 363.
[33] D. Cremer, J.A. Pople, J. Am. Chem. Soc. 97 (1975) 1354.

with dppbz. It is believed that the chelation of the dppbz ligand to $Ru_6(\mu_6\text{-}C)(CO)_{17}$ leads to a polyhedral expansion of the ruthenium core, coupled with the scavenging of phosphorus and hydrogen atoms from an additional dppbz ligand to furnish the edge-bridged cluster $HRu_6(\mu_5\text{-}C)(\mu_3\text{-}P)(CO)_{14}$(dppbz) [4]. These novel reactions are depicted in Eqs. (1) and (2).

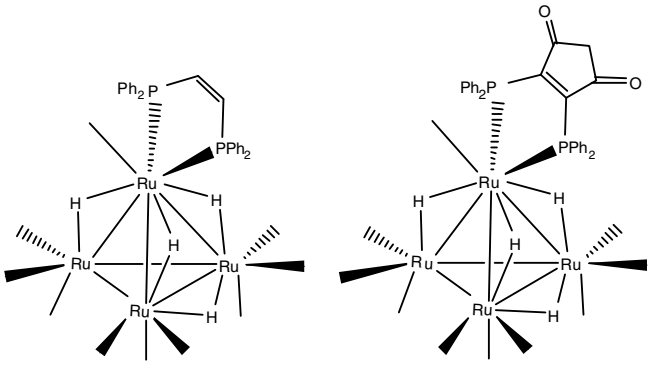


(1)



(2)

The reaction between the ruthenium cluster $Ru_3(CO)_{12}$ and myriad diphosphine ligands has been thoroughly explored over the last three decades [5]. The formal replacement of two carbonyl groups by the diphosphine ligand affords the corresponding cluster $Ru_3(CO)_{10}$(P–P), where the diphosphine ligand (P–P) may be coordinated to the cluster frame across adjacent ruthenium centers (bridging) or at a single metal center (chelating). Numerous examples exist for both P–P ligand coordination modes. The study of $Ru_3(CO)_{10}$(P–P) clusters has provided valuable insight into the stability of diphosphine ligands (P–P) relative to deleterious ligand decomposition through P–C bond cleavage, C–H bond ortho metalation, and cyclometalation pathways [6]. The observed degradation of phosphine ligands at well-defined metal complexes provides crucial evidence that debunks the innocent or spectator status of such ligands [7]. In comparison, the reactivity of diphosphine ligands with the hydride-bridged cluster $H_4Ru_4(CO)_{12}$ (**1**) has received scant attention vis-a-vis $Ru_3(CO)_{12}$. Other than our recent report on the synthesis and structural characterization of 1,1-$H_4Ru_4(CO)_{10}$[(*Z*)-$Ph_2PCH{=}CHPPh_2$] and 1,1-$H_4Ru_4(CO)_{10}$(bpcd), whose structures are shown below, there exist no other examples for the reaction of $H_4Ru_4(CO)_{12}$ with rigid, unsaturated diphosphine ligands [8,9]. The diphosphine ligands (*Z*)-$Ph_2PCH{=}CHPPh_2$ and bpcd react with cluster **1** to give the diphosphine-chelated clusters without any sign of the corresponding diphosphine-bridged species.



Wishing to establish the generality of ligand chelation at cluster **1** with other unsaturated diphosphine ligands, we have investigated the thermal and Me_3NO oxidative-decarbonylation activation of cluster **1** in the presence of the ligands 1,2-bis(diphenylphosphino)-benzene (dppbz) and 1,8-bis(diphenylphosphino)naphthalene (dppn). The course of these substitution reactions has been established through NMR spectroscopies and X-ray crystallographic analyses of the cluster compounds $H_4Ru_4(CO)_{10}$(dppbz) (**2**) and $H_4Ru_4(CO)_{10}$(dppn) (**3**). The thermal and photochemical stability of both product clusters have been investigated, with the results discussed relative to other diphosphine-substituted ruthenium clusters.

2. Experimental

2.1. General

The starting hydride cluster $H_4Ru_4(CO)_{12}$ (**1**) was prepared from $Ru_3(CO)_{12}$ and H_2 according to the published procedure [10], with the $Ru_3(CO)_{12}$ synthesized from hydrated $RuCl_3$ and CO using a 1l Parr Series 4000 rocking autoclave [11]. The dppn ligand was prepared from 1-bromonaphthalene and Ph_2PCl [12]. The chemicals 1-bromonaphthalene, dppbz, and $Me_3NO \cdot nH_2O$ were purchased from Aldrich Chemical Co. The $Me_3NO \cdot nH_2O$ was dried by azeotropic distillation from benzene and the anhydrous Me_3NO was stored in a Schlenk tube under argon. All reaction, IR, and NMR solvents were of reagent grade and were distilled from a suitable drying agent and stored in Schlenk vessels equipped with Teflon stopcocks [13]. The combustion analyses were performed by Atlantic Microlab, Norcross, GA.

The IR spectral data were recorded on a Nicolet 20 SXB FT-IR spectrometer in sealed 0.1 mm NaCl cells, while the ^1H NMR (200 MHz) and ^{31}P NMR (121 MHz) spectra were recorded on Varian Gemini-200 and 300-VXR spectrometers, respectively. The ^{31}P NMR spectra were collected in the proton-decoupled mode with the reported chemical shifts referenced to external H_3PO_4 (85%), taken to have $\delta = 0$.

2.2. Synthesis of 1,1-$H_4Ru_4(CO)_{10}$(dppbz) (2)

(A) Me_3NO activation: To 0.10 g (0.13 mmol) of cluster **1** and 68 mg (0.14 mmol) of dppbz in a 100-mL Schlenk flask under argon was added 20 mL of CH_2Cl_2, followed by 21 mg (0.28 mmol) of Me_3NO. The solution was stirred at room temperature for 1 h and then examined by TLC analysis using CH_2Cl_2/hexane (1:1) as the eluent, which revealed the presence of a new orange spot at $R_f = 0.55$ corresponding to the desired cluster **2**, in addition to a small amount of unreacted starting cluster **1**. After an initial preparative separation of cluster **2** by column chromatography, the crude product was re-crystallized from CH_2Cl_2/hexane to afford 75 mg of **2** (48%). IR (CH_2Cl_2): ν(CO) 2073 (s), 2043 (vs), 2022 (vs), 1982 (m) cm^{-1}. ^1H NMR ($CDCl_3$): δ 7.80–7.20 (m, 24H, aryl groups), −15.70 (b, 3H), −18.84 (b, 1H). ^{31}P NMR ($CDCl_3$): δ 66.50. *Anal.* Calc. for $C_{40}H_{28}O_{10}P_2Ru_4 \cdot CH_2Cl_2$: C, 40.27; H, 2.47. C, 40.28; H, 2.43%.

(B) Thermolysis reaction: This reaction was carried out in a Schlenk tube containing 50 mg (0.067 mmol) of $H_4Ru_4(CO)_{12}$ and 34 mg (0.070 mmol) of dppbz in 15 mL of 1,2-dichloroethane (DCE). The vessel was heated at ca. 65 °C over night and worked up in a manner similar to that described above. Yield of cluster **2**: 37 mg (48%).

2.3. Synthesis of 1,1-$H_4Ru_4(CO)_{10}$(dppn) (3)

(A) Me_3NO activation: To a Schlenk tube under argon was charged 0.10 g (0.13 mmol) of $H_4Ru_4(CO)_{12}$, 73 mg (0.14 mmol) of dppn, and 21 mg (0.28 mmol) of Me_3NO, after which 25 mL of CH_2Cl_2 was added by syringe. The solution was stirred for 1 h at room temperature and the progress of the reaction was checked by TLC analysis, which confirmed the presence of cluster **3** ($R_f = 0.45$ in 3:2 CH_2Cl_2/hexane) and a trace of unreacted **1**. The desired cluster **3** was isolated by flash-column chromatography employing 3:2 CH_2Cl_2/hexane as the eluent. Crude **3** was re-crystallized from benzene/hexane to afford pure **3** in 38% yield (60 mg). IR (CH_2Cl_2): ν(CO) 2072 (s), 2043 (vs), 2020 (vs), 1998 (s) cm^{-1}. ^1H NMR ($CDCl_3$): δ 7.50–6.50 (m, 26H, aryl groups), −15.70 (b, 3H), −17.20 (b, 1H). ^{31}P NMR ($CDCl_3$): δ 34.90. *Anal.* Calc. for $C_{44}H_{30}O_{10}P_2Ru_4$: C, 44.60; H, 2.55. C, 44.69; H, 3.07%.

(B) Thermolysis reaction: This reaction was conducted in a manner identical to that described for the earlier thermolysis reaction. Here 50 mg (0.067 mmol) of cluster **1** and 37 mg (0.070 mmol) of dppn were heated at ca. 70 °C in DCE solvent overnight. Cluster **3** was isolated by flash-column chromatography in 35% yield (28 mg).

2.4. X-ray diffraction data

Tables 1 and 2 contain the X-ray data and processing parameters and selected bond distances and angles, respectively, for clusters **2** and **3**. Single crystals of clusters **2** and **3** suitable for X-ray crystallography were grown from a CH_2Cl_2 solution containing each cluster that had been layered with hexane. The X-ray data for **2** (TCU) and **3** · 1/2hexane (NMHU) were collected on APEX II CCD-based diffractometers at 213 K and 295 K, respectively. The frames were integrated with the available SAINT [14] and APEX2 [15] software packages using a narrow-frame algorithm, and each structure was solved and refined using the SHELXTL program package [16]. The molecular structures were checked using PLATON [17], and all non-hydrogen atoms were refined anisotropically. All carbon-bound hydrogen atoms were assigned calculated positions and allowed to ride on the attached heavy atom, while the four bridging hydrides associated with the tetraruthenium core of both clusters were located and refined isotropically. The refinement for **2** converged at $R = 0.0374$ and $R_w = 0.0758$ for 9281 independent reflections with $I > 2\sigma(I)$ and for **3** · 1/2hexane at $R = 0.0249$ and $R_w = 0.0563$ for 13172 independent reflections with $I > 2\sigma(I)$.

Table 1
X-ray crystallographic data and processing parameters for the tetraruthenium clusters **2** and **3** · 1/2hexane

Cluster	**2**	**3** · 1/2hexane
CCDC entry number	627941	627940
Molecular formula	$C_{40}H_{28}O_{10}P_2Ru_4$	
$C_{44}H_{30}O_{10}P_2Ru_4 \cdot 1/2$hexane		
Formula weight	1134.84	1227.99
Crystal system	triclinic	monoclinic
Space group	$P\bar{1}$	$P2_1/n$
a (Å)	11.224(2)	12.5564(3)
b (Å)	12.574(2)	18.8149(4)
c (Å)	15.265(2)	19.7648(4)
α (°)	83.613	
β (°)	88.076(2)	91.831(1)
γ (°)	74.434(2)	
V (Å^3)	2062.4(5)	4667.0(2)
T (K)	213	295
Formula units per cell (Z)	2	4
D_{calc} (Mg/m^3)	1.827	1.748
λ (Mo Kα) (Å)	0.71073	0.71073
μ (mm^{-1})	1.569	1.394
R_{merge}	0.0549	0.0221
Absorption correction	empirical	empirical
Absorption correction factor	0.9136/0.6769	0.9594/0.8731
Total reflections	17861	51707
Independent reflections	9181	13172
Data/restrain/parameters	9181/0/522	13172/0/585
R	0.0374	0.0249
R_w	0.0758	0.0563
Goodness-of-fit on F^2	0.950	1.006
$\Delta\rho_{max}$ and $\Delta\rho_{min}$ (e/Å^3)	0.652 and −0.912	0.493 and −0.308

3. Results and discussion

3.1. Syntheses and spectroscopic data for clusters 2 and 3

The formal replacement of two carbonyl groups in $H_4Ru_4(CO)_{12}$ by the ligands dppbz and dppn is readily achieved by controlled thermolysis of cluster **1** in the presence of the desired ligand in toluene or DCE solution over

Table 2
Selected bond distances (Å) and angles (°) in the tetraruthenium clusters **2** and **3** · 1/2hexane

Cluster **2**			
Bond distances (Å)			
Ru(1)–C(31)	1.873(4)	Ru(1)–P(1)	2.297(1)
Ru(1)–P(2)	2.304(1)	Ru(1)–Ru(3)	2.9467(6)
Ru(1)–Ru(2)	2.9776(5)	Ru(1)–Ru(4)	3.0091(6)
Ru(2)–C(33)	1.889(5)	Ru(2)–C(34)	1.910(5)
Ru(2)–C(32)	1.927(5)	Ru(2)–Ru(3)	2.8029(6)
Ru(2)–Ru(4)	2.9286(6)	Ru(3)–C(35)	1.892(5)
Ru(3)–C(37)	1.907(5)	Ru(3)–C(36)	1.911(5)
Ru(3)–Ru(4)	2.7904(6)	Ru(4)–C(38)	1.886(5)
Ru(4)–C(40)	1.904(6)	Ru(4)–C(39)	1.932(6)
P(1)···P(2)	3.066(1)		
Bond angles (°)			
C(31)–Ru(1)–P(1)	89.7(1)	C(31)–Ru(1)–P(2)	93.7(1)
P(1)–Ru(1)–P(2)	83.60(4)	C(31)–Ru(1)–Ru(3)	90.6(1)
P(1)–Ru(1)–Ru(3)	111.60(3)	P(2)–Ru(1)–Ru(3)	164.26(3)
C(31)–Ru(1)–Ru(2)	97.7(1)	P(1)–Ru(1)–Ru(2)	165.75(3)
P(2)–Ru(1)–Ru(2)	107.89(3)	C(31)–Ru(1)–Ru(4)	145.4(1)
P(1)–Ru(1)–Ru(4)	109.11(3)	P(2)–Ru(1)–Ru(4)	116.51(3)
C(2)–P(1)–Ru(1)	107.6(1)	C(1)–P(2)–Ru(1)	107.6(1)
Cluster **3** · 1/2hexane			
Bond distances (Å)			
Ru(1)–C(36)	1.889(3)	Ru(1)–C(37)	1.907(3)
Ru(1)–C(38)	1.923(2)	Ru(1)–Ru(4)	2.7871(2)
Ru(1)–Ru(2)	2.9337(2)	Ru(1)–Ru(3)	3.0331(2)
Ru(2)–C(40)	1.884(2)	Ru(2)–C(41)	1.901(3)
Ru(2)–C(39)	1.924(2)	Ru(2)–Ru(4)	2.7707(2)
Ru(2)–Ru(3)	3.0422(2)	Ru(3)–C(35)	1.861(2)
Ru(3)–P(1)	2.3025(5)	Ru(3)–P(2)	2.3150(5)
Ru(3)–Ru(4)	2.9776(2)	Ru(4)–C(42)	1.877(2)
Ru(4)–C(43)	1.890(3)	Ru(4)–C(44)	1.903(3)
P(1)···P(2)	3.141(2)		
Bond angles (°)			
C(35)–Ru(3)–P(1)	90.98(7)	C(35)–Ru(3)–P(2)	90.52(7)
P(1)–Ru(3)–P(2)	85.74(2)	C(35)–Ru(3)–Ru(4)	94.33(6)
P(1)–Ru(3)–Ru(4)	113.64(1)	P(2)–Ru(3)–Ru(4)	159.88(2)
C(35)–Ru(3)–Ru(1)	103.21(7)	P(1)–Ru(3)–Ru(1)	162.14(1)
P(2)–Ru(3)–Ru(1)	104.64(1)	C(35)–Ru(3)–Ru(2)	148.82(7)
P(1)–Ru(3)–Ru(2)	104.69(1)	P(2)–Ru(3)–Ru(2)	116.98(1)
C(1)–P(1)–Ru(3)	113.31(7)	C(9)–P(2)–Ru(3)	116.09(7)

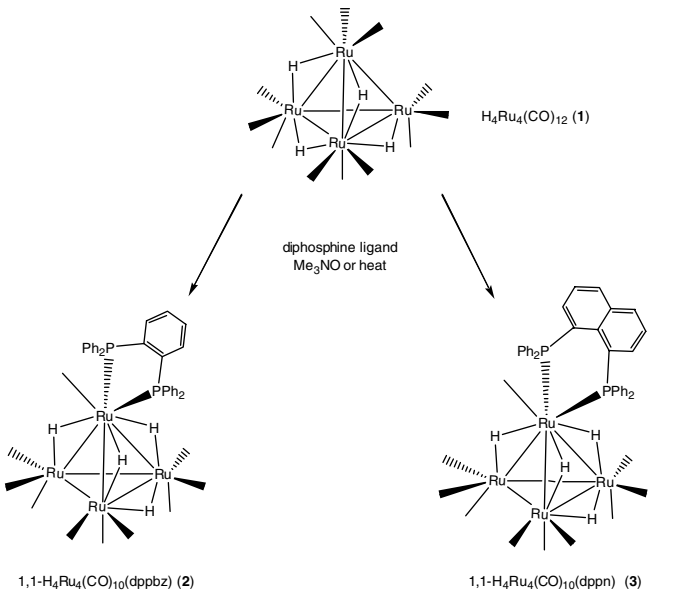
a temperature range of 65–70 °C. There is no noticeable solvent dependence on the reaction, as both toluene and DCE solvents afford comparable yields of clusters **2** and **3**. The same diphosphine-substituted clusters are also produced when a mixture of **1** and diphosphine ligand is treated with a slight excess of the oxidative-decarbonylation reagent Me_3NO [18]. Scheme 1 illustrates the reactions under consideration. Monitoring these reactions by TLC confirmed the near complete consumption of cluster **1** (>95%) and the presence of the desired product as an orange-yellow spot [**2**: $R_f = 0.55$ using CH_2Cl_2/hexane (1:1); **3**: $R_f = 0.45$ using CH_2Cl_2/hexane (3:2)]. Also accompanying each reaction was the presence of an unknown black material at the origin of the TLC plate that is attributed to decomposed cluster. No attempts were made to characterize this material since it remained irreversibly bound to the chromatographic support. Clusters **2** and **3** were subsequently isolated by column chromatography over silica gel as mildly air-sensitive solids. While clusters **2** and **3** may be handled for short periods of time as solids in the atmosphere, solutions containing these clusters appear to be more oxygen sensitive, exhibiting noticeable decomposition upon exposure to oxygen after only a few hours.

Both **2** and **3** were characterized in solution by IR and NMR spectroscopies. Terminal carbonyl stretching bands observed at 2073 (s), 2043 (vs), 2022 (vs), 1982 (m) cm^{-1} for **2** and 2072 (s), 2043 (vs), 2020 (vs), 1998 (s) cm^{-1} for **3** are in excellent agreement with those data reported by us for the cluster compounds 1,1-$H_4Ru_4(CO)_{10}$[(*Z*)-$Ph_2PCH{=}CHPPh_2$] and 1,1-$H_4Ru_4(CO)_{10}$(bpcd) [8]. The ^1H NMR spectrum of **2** reveals a multiplet for the aromatic hydrogens at δ 7.80–7.20 and two high-field hydrides at δ −15.70 and −18.84 in a 3:1 integral ratio. The ^1H NMR spectrum of **3** mirrors that of cluster **2**, which in turn suggests a common coordination mode of the ancillary diphosphine ligand in both products. The recorded ^{31}P NMR spectra for **2** and **3** exhibit singlets at δ 66.50 and 34.90, respectively, that are consistent with rapid edge-terminal-edge scrambling of the four hydrides, as first put forth by Shapley and Churchill in the chelating isomer of 1,1-$H_4Ru_4(CO)_{10}$(dppe) [19].

3.2. X-ray diffraction data for clusters 2 and 3 · 1/2hexane

The molecular structure of each product was determined by single-crystal X-ray diffraction analysis. Single crystals of both clusters exist as discrete molecules in the unit cell with no unusually short inter- or intramolecular contacts. Fig. 1 shows the thermal ellipsoid plots for clusters **2** and **3**, the latter as a hexane solvate, where the chelation of the dppbz and dppn ligands to their respective cluster core is definitively established. The crystallographically located hydrides in **2** that are associated with the Ru(1)–Ru(4), Ru(1)–Ru(2), Ru(1)–Ru(3), and Ru(2)–Ru(4) vectors range from 3.009(6) Å [Ru(1)–Ru(4)] to 2.9286(6) Å [Ru(2)–Ru(4)] and exhibit a mean distance of 2.9655 Å. The two shorter, non-hydride-bridged Ru–Ru vectors involving the Ru(2)–Ru(3) [2.8029(6) Å] and Ru(3)–Ru(4) [2.7904(6) Å] bonds exhibit a mean distance of 2.7967 Å that is ca. 0.17 Å shorter than the corresponding hydride-bridged Ru–Ru bonds. These bond-length trends are in keeping with those found in related hydride-bridged clusters [19,20,21]. The P(1)···P(2) distance of 3.066(1) Å is slightly smaller compared to the 3.1629(5) Å internuclear P···P distance found by us for the free dppbz ligand.[1] The Ru(1)–P(2) [2.304(1) Å] and Ru(1)–P(1) [2.297(1) Å] bond distances and the bond angle of 83.60(4)° for the P(1)–Ru(1)–P(2) atoms are not unreasonable relative to those values reported for the dppbz-substituted clusters $Ir_4(CO)_7(\mu\text{-}CO)_3$(dppbz) and $HRu_6(\mu_5\text{-}C)(\mu_3\text{-}P)(CO)_{14}$-

[1] Unpublished structural data for the free dppbz ligand.



Scheme 1.

(dppbz) [4,22]. While structurally characterized mononuclear compounds that possess a dppbz ligand are numerous, to our knowledge, the aforementioned Ir_4 and Ru_6 clusters represent the only polynuclear examples containing this diphosphine ligand. The 10 carbonyl groups in **2** are all linear and exhibit a mean Ru–C distance of 1.90 Å. The remaining bond distances and angles are unexceptional and require no comment.

The coordination mode adopted by the dppn ligand and the disposition of the hydrides and carbonyl groups about cluster **3** are similar to that of **2**. The four long Ru–Ru bonds belonging to the Ru(1)–Ru(2), Ru(3)–Ru(4), Ru(1)–Ru(3), and Ru(2)–Ru(3) atoms exhibit a mean distance of 2.9967 Å in excellent agreement with those bond distances found in other hydride-bridged Ru–Ru bonds and the positions associated with the crystallographically located hydrides in **3**. The two shorter bonds defined by the Ru(2)–Ru(4) [2.7707(2) Å] and Ru(1)–Ru(4) [2.7871(2) Å] vectors exhibit an average distance of 2.7789 Å. The chelation of the dppn ligand to the Ru(3) center gives rise to Ru(3)–P(1) and Ru(3)–P(2) distances of 2.3025(5) Å and 2.3150(5) Å, respectively, and an internuclear P(1)···P(2) distance of 3.141(2) Å. The observed angle of 85.74(2)° for the P(1)–Ru(3)–P(2) atoms is slightly smaller than the analogous angle found in the dppn-chelated clusters $Ru_3(CO)_8(\mu\text{-dppm})$(dppn) [89.62(4)°] [23] and $PhCCo_3(CO)_4(\mu\text{-}CO)_3$(dppn) [88.62(3)°] [24], which to date represent the only other structurally characterized clusters containing an intact dppn ligand. Finally, the 10 carbonyl groups in **3** are all linear, with distances and angles consistent with such linkages.

3.3. Thermal and photochemical stability studies of clusters *2* and *3*

Due to our long-term interest in the study of ligand degradation reactions at polynuclear clusters [7], we next examined the temperature and photochemical stability of the new clusters **2** and **3**. Heating sealed NMR tubes containing **2** and **3** in toluene-d_8 at temperatures up to 125 °C for a period of several days showed no evidence for any reaction, as assessed by ^1H and ^{31}P NMR spectroscopies. Noticeable decomposition of both clusters was observed at temperatures above 140 °C, paralleling our earlier stability studies on 1,1-$H_4Ru_4(CO)_{10}$[(*Z*)-$Ph_2PCH{=}CHPPh_2$] and 1,1-$H_4Ru_4(CO)_{10}$(bpcd) [8]. The decomposition of **2** and **3** is accompanied by a broadening of the NMR resonances, which may signal the intervention of radical species, and the deposit of an insoluble dark brown solid. These results stand in contrast to the limited thermal stability of the tetraruthenium cluster $H_4Ru_4(CO)_{10}$-

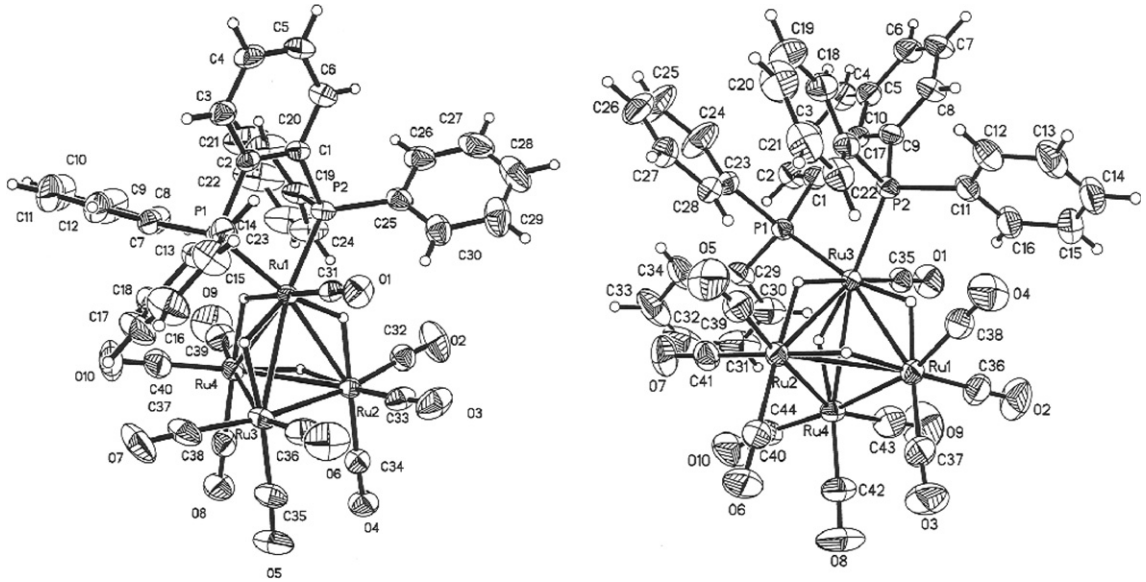


Fig. 1. Thermal ellipsoid plots of clusters **2** (left) and **3** · 1/2hexane (right) showing the thermal ellipsoids at the 50% probability level.

[(*S*)-BINAP], which undergoes facile decarbonylation at 70 °C to afford the face-bridged cluster $H_4Ru_4(CO)_9[\mu_3$-(*S*)-BINAP] [25], as well as the cluster fragmentation exhibited by the trinuclear clusters $Ru_3(CO)_{10}[(Z)$-$Ph_2PCH{=}CHPPh_2]$ (see Eq. (1)) and $Ru_3(CO)_{10}$-(bpcd) to the diruthenium donor–acceptor compounds $Ru_2(CO)_6[(Z)$-$Ph_2PCH{=}CHPPh_2]$ and $Ru_2(CO)_6$-(bpcd) [1a,2].

Whereas the photochemical activation of the parent cluster **1** has been thoroughly examined and shown to undergo CO loss, albeit with low quantum efficiency ($\Phi \approx 10^{-3}$) [26], analogous studies using diphosphine-substituted clusters derived from **1** are scarce [8]. The photochemical reactivity of **2** and **3** was probed in toluene-d_8 and CD_2Cl_2 solvents in sealed NMR tubes. Here the samples were irradiated using 366 nm light for two weeks and periodically monitored by NMR spectroscopy. No reaction was observed under these conditions, signaling the high stability of these particular clusters. The inert behavior of **2** and **3** under these conditions is not surprising since optical excitation of these clusters should be confined to a manifold largely involving the population of ruthenium–ruthenium antibonding σ^* orbitals. Efficient reformation of an optically cleaved ruthenium–ruthenium σ bond is apparently the dominant pathway, accounting for the absence of net photochemical reactivity. Similar results have been found by us for the clusters 1, 1-$H_4Ru_4(CO)_{10}[(Z)$-$Ph_2PCH{=}CHPPh_2]$ and 1,1-H_4Ru_4-$(CO)_{10}$(bpcd) [8].

4. Conclusions

The new cluster compounds 1,1-$H_4Ru_4(CO)_{10}$(dppbz) and 1,1-$H_4Ru_4(CO)_{10}$(dppn) have been synthesized from $H_4Ru_4(CO)_{12}$ and the respective diphosphine ligand. The chelating coordination mode adopted by the ancillary diphosphine ligand in each product has been established by NMR spectroscopy and X-ray crystallography. The thermal and photochemical stability of these clusters parallel related tetraruthenium clusters already prepared by us.

Acknowledgments

Financial support from the Robert A. Welch Foundation (Grants P-0074-WHW and B-1093-MGR) is much appreciated, and the NSF/DMR (Grant 0420863-VNN) is thanked for the purchase of the single-crystal X-ray diffractometer.

Appendix A. Supplementary material

CCDC 627941 and 627940 contain the supplementary crystallographic data for **2** and **3** · 1/2hexane. These data can be obtained free of charge via http://www.ccdc.cam.ac.uk/conts/retrieving.html, or from the Cambridge Crystallographic Data Centre, 12 Union Road, Cambridge CB2 1EZ, UK; fax: (+44) 1223-336-033; or e-mail: deposit@ccdc.cam.ac.uk.Supplementary data associated with this article can be found, in the online version, at doi:10.1016/j.poly.2007.03.034.

References

[1] (a) H. Shen, S.G. Bott, M.G. Richmond, Organometallics 14 (1995) 4625;
(b) S.G. Bott, H. Shen, R.A. Senter, M.G. Richmond, Organometallics 22 (2003) 1953;
(c) W.H. Watson, K. Ejsmont, J. Liu, M.G. Richmond, J. Chem. Crystallogr. 33 (2003) 541;
(d) S.G. Bott, H. Shen, M.G. Richmond, J. Organomet. Chem. 689 (2004) 3426, 690 (2005) 3838;
(e) S. Kandala, M.G. Richmond, Inorg. Chem. 45 (2006) 5976.
[2] M.I. Bruce, M.L. Williams, B.W. Skelton, A.H. White, J. Organomet. Chem. 306 (1986) 115.
[3] The reaction between $Ru_3(CO)_{12}$ and the unsaturated diphosphine ligand 3,4-bis(diphenylphosphino)-5-methoxy-2(5*H*)furanone (bmf) proceeds in a manner identical to that described in Ref. [2] to afford the donor–acceptor compound $Ru_2(CO)_6$(bmf) as a 1:1 mixture of diastereomers. S.G. Bott, K. Yang, M.G. Richmond, J. Coord. Chem. (2007) in press.
[4] W.H. Watson, S. Kandala, M.G. Richmond, J. Organomet. Chem. 692 (2007) 1648.
[5] (a) F.-E. Hong, Y.-C. Chang, C.-P. Chang, Y.-L. Huang, J. Chem. Soc., Dalton Trans. (2004) 157;
(b) G. Lavigne, J.-J. Bonnet, Inorg. Chem. 20 (1981) 2713;
(c) M.I. Bruce, T.W. Hambley, B.K. Nicholson, M.R. Snow, J. Organomet. Chem. 235 (1982) 83;
(d) S.E. Kabir, S.J. Ahmed, M.I. Miah, D.W. Bennett, D.T. Haworth, T.A. Siddiquee, E. Rosenberg, J. Organomet. Chem. 689 (2004) 3412;
(e) G. Gervasio, R. Gobetto, P.J. King, D. Marabello, E. Sappa, Polyhedron 17 (1998) 2937;
(f) A.W. Coleman, D.F. Jones, P.H. Dixneuf, C. Brisson, J.-J. Bonnet, G. Lavigne, Inorg. Chem. 23 (1984) 952;
(g) E.-L. Diz, A. Neels, H. Stoeckli-Evans, G. Süss-Fink, Polyhedron 20 (2001) 2771.
[6] (a) G. Lavigne, N. Lugan, J.-J. Bonnet, Organometallics 1 (1982) 1040;
(b) M.M. Harding, B.S. Nicholls, A.K. Smith, J. Orgaomet. Chem. 226 (1982) C17;
(c) N. Lugan, J.-J. Bonnet, J.A. Ibers, J. Am. Chem. Soc. 107 (1985) 4484;
(d) W.R. Cullen, S.T. Chacon, M.I. Bruce, F.W.B. Einstein, R.H. Jones, Organometallics 7 (1988) 2273;
(e) S.E. Kabir, T.A. Siddiquee, E. Rosenberg, R. Smith, M.B. Hursthouse, K.M.A. Malik, K.I. Hardcastle, M. Visi, J. Cluster Sci. 9 (1998) 185;
(f) M.I. Bruce, P.A. Humphrey, O.B. Shawkataly, M.R. Snow, E.R.T. Tiekink, W.R. Cullen, Organometallics 9 (1990) 2910.
[7] W.H. Watson, G. Wu, M.G. Richmond, Organometallics 25 (2006) 930, and references cited therein.
[8] W.H. Watson, S. Kandala, M.G. Richmond, J. Chem. Crystallogr. 36 (2006) 813.
[9] For structures of related Ru_4 clusters with ancillary BINAP and biphenyl-based diphosphines, see: D. Braga, U. Matteoli, P. Sabatino, A. Scrivanti, J. Chem. Soc., Dalton Trans. (1995) 419.
[10] M.I. Bruce, M.L. Williams, Inorg. Synth. 28 (1990) 219.
[11] M.I. Bruce, C.M. Jensen, N.L. Jones, Inorg. Synth. 26 (1989) 259.
[12] (a) R.D. Jackson, S. James, A.G. Orpen, P.G. Pringle, J. Organomet. Chem. 458 (1993) C3;
(b) A. Karacar, H. Thönnessen, P.G. Jones, R. Bartsch, R. Schmutzler, Heteroatom. Chem. 8 (1997) 539.

[13] D.F. Shriver, The Manipulation of Air-Sensitive Compounds, McGraw-Hill, New York, 1969.
[14] SAINT Version 6.02, Bruker Analytical X-ray Systems, Inc. Copyright 1999, Madison, WI.
[15] APEX2 Version 2.02, Bruker Analytical X-ray Systems, Inc. Copyright 2005, Madison, WI.
[16] SHELXTL Version 6.14, Bruker Analytical X-ray Systems, Inc. Copyright 2003, Madison, WI.
[17] A.L. Spek, PLATON – A Multipurpose Crystallographic Tool, Utrecht University, Utrecht, The Netherlands, 2001.
[18] (a) U. Koelle, J. Organomet. Chem. 133 (1977) 53;
(b) M.O. Albers, N. Coville, Coord. Chem. Rev. 53 (1984) 227.
[19] (a) J.R. Shapley, S.I. Richter, M.R. Churchill, R.A. Lashewycz, J. Am. Chem. Soc. 99 (1977) 7384;
(b) M.R. Churchill, R.A. Lashewycz, J.R. Shapley, S.I. Richter, Inorg. Chem. 19 (1980) 1277.
[20] (a) L.J. Pereira, W.K. Leong, J. Organomet. Chem. 691 (2006) 2448;
(b) R.D. Adams, B. Captain, W. Fu, Organometallics 19 (2000) 3670;
(c) R.G. Teller, R. Bau, Struct. Bond. 44 (1981) 1.
[21] D.M.P. Mingos, D.J. Wales, Introduction to Cluster Chemistry, Prentice-Hall, Englewood Cliffs, NJ, 1990.
[22] B.K. Park, M.A. Miah, H. Kang, K. Lee, Y.-J. Cho, D.G. Churchill, S. Park, M.-G. Choi, J.T. Park, Organometallics 24 (2005) 675.
[23] M.I. Bruce, P.A. Humphrey, S. Okucu, R. Schmutzler, B.W. Skelton, A.H. White, Inorg. Chim. Acta 357 (2004) 1805.
[24] W.H. Watson, S. Kandala, M.G. Richmond, J. Organomet. Chem. 692 (2007) 968.
[25] S.P. Tunik, T.S. Pilyugina, I.O. Koshevoy, S.I. Selivanov, M. Haukka, T.A. Pakkanen, Organometallics 23 (2004) 568.
[26] (a) J.L. Graff, M.S. Wrighton, J. Am. Chem. Soc. 102 (1980) 2123;
(b) J.L. Graff, M.S. Wrighton, Inorg. Chim. Acta 63 (1982) 63;
(c) J.G. Bentsen, M.S. Wrighton, J. Am. Chem. Soc. 106 (1984) 4041.

dimensionality and control of supramolecular topology. The use of the terephthalate (tp) ligand has frequently been made in the construction of such complexes owing to its diverse binding modes as a linker, and that allows it to assume a variety of structures from discrete molecules to one- (1D), two- (2D), or three-dimensional (3D) networks [18–22]. It is noteworthy that the molecular dimensionality of coordination polymers bridged by tp can be raised by hydrogen bond and other intermolecular contacts, such as face-to-face π–π and edge-to-face CH–π interactions [23,24]. The former is realized when lattice water molecules acting as hydrogen donors and acceptors are present in the crystal structure [25]. A considerable amount of work has been reported in the literature about the binding properties of dicyanamide (dca). It can act as in uni-, bi-, tridentate manner, and both of its homo- and heteroleptic complexes have rich topologies and magnetic properties [26–34]. When co-ligands are introduced, a large number of networks of varied dimensions are obtained and characterized. In short, the principles set forth by organic crystal engineering, especially regarding the reliability of hydrogen bonds, can be applied to the assembly of coordination networks. The controlled synthesis and characterization of different forms has thus become a major issue of solid-state chemistry.

We report herein the syntheses, structures and magnetic properties of three new nickel complexes [Ni(3,2,3-tet)-$\{Ag(CN)_2\}_2$] (**1**), $[Ni(3,2,3\text{-tet})(\mu\text{-tp})]_n \cdot 1.5nH_2O$ (**2**) and $\{[Ni(3,2,3\text{-tet})(\mu_{1,5}\text{-dca})](ClO_4)\}_n$ (**3**). The details of the structural features vary because one is dealing here with intermolecular interactions arising from different hydrogen bonding substituents.

2. Experimental

2.1. Materials

The ligand *N*,*N*′-bis(3-aminopropyl)ethylenediamine was purchased from Aldrich and used as received. Terephthalic acid, and sodium dicyanamide were of analytical reagent grade (Fluka). Ni(II) salts were purchased from commercial sources and used as received. Sodium terephthalate was readily prepared by the reaction of terephthalic acid with a stoichiometric amount of NaOH in water. All other chemicals, e.g. sodium hydroxide, $AgNO_3$ and NaCN were of reagent grade. Methanol and *N*,*N*-dimethylformamide were of reagent grade and were used without further purification. Double distilled water was used throughout.

2.2. Physical measurements

Microanalysis (CHN) was performed in a Perkin–Elmer 240C elemental analyzer. FT-IR spectra were obtained on a Nicolet, MAGNA- IR 750 spectrometer with samples prepared as KBr pellets. Cyclic voltammetry (scan rate of 0.02 V s^{-1}) was performed at a platinum electrode using an EG&G PARC electrochemical analysis system (model 250/5/0) in DMF under dry nitrogen atmosphere in conventional three-electrode configurations. Absorption spectra were carried out on Shimadzu UV2100 UV–Vis recording spectrophotometer. Thermal stability (TG-DTA) studies were carried out on a Mettler Toledo TGA/SDTA 851^e instrument with a heating rate of 10 °C min^{-1} in a nitrogen atmosphere. Magnetic susceptibility measurements of **2** and **3** were carried out with a Quantum Design MPMS XL SQUID magnetometer under an applied magnetic field of 10 000 Oe. The temperature dependence of molar susceptibility, χ_M, for both the complexes was measured on crystalline samples in the temperature range 2–300 K.

2.3. Synthesis of complexes

2.3.1. Synthesis of $[Ni(3,2,3\text{-tet})\{Ag(CN)_2\}_2]$ (*1*)

To an (10 cm^3) aqueous solution of 0.149 g (0.6 mmol) nickel(II) acetate tetrahydrate was added a methanolic solution of 3,2,3-tet (0.6 mmol) to give a pink-violet solution. To this mixture, an aqueous solution of 0.110 g (0.6 mmol) sodium dicyanoargentate(I) (cyano complexes of silver and nickel are toxic!) was added and the solution was stirred for an hour. Upon standing for 8 days at room temperature, pink-violet crystals were separated out. These were filtered off, washed successively with mother liquor and diethyl ether, and dried in vacuo. Yield: 40% (based on nickel). *Anal.* Calc. for **1**: C, 26.00; H, 3.98; N, 20.30. Found: C, 25.80; H, 4.00; N, 20.20%. Selected IR data (cm^{-1}, KBr pellet): 3300 (m), 2163 (s, ν(C≡N)), 2135 (s, ν(C≡N)). UV–Vis (DMF) [λ_{max}, nm]: 350, 555, 806.

2.3.2. Synthesis of $[Ni(3,2,3\text{-tet})(\mu\text{-tp})]_n \cdot 1.5nH_2O$ (*2*)

Nickel(II) perchlorate hexahydrate (0.293 g, 0.8 mmol) was dissolved in 10 cm^3 of water. To this green solution was added a (5 cm^3) DMF solution of 3,2,3-tet (0.8 mmol). The resulting pink-violet solution was stirred for 10 min and filtered off to remove any suspended material. To the filtrate, 5 cm^3 aqueous solution of Na_2-tp (0.168 g, 0.8 mmol) was added and the solution was stirred for 30 min at room temperature. Light pink-violet crystals suitable for X-ray diffraction were obtained after 5 days. Yield: 60% (based on nickel). *Anal.* Calc. for **2**: C, 45.60; H, 6.17; N, 13.30. Found: C, 45.67; H, 6.14; N, 13.40%. Selected IR data (cm^{-1}, KBr pellet): 3300 (m), 2900 (m), 1673 (w, HOH bendings), 1572 (s, $\nu_{asym}(COO^-)$), 1354 (m, $\nu_{sym}(COO^-)$). UV–Vis (H_2O) [λ_{max}, nm]: 275, 350, 555, 806.

2.3.3. Synthesis of $\{[Ni(3,2,3\text{-tet})(\mu_{1,5}\text{-dca})](ClO_4)\}_n$ (*3*)

DMF solution (10 cm^3) containing sodium dicyanamide (0.071 g, 0.8 mmol) and 3,2,3-tet (0.8 mmol) was added to 10 cm^3 of an aqueous solution of nickel(II) perchlorate hexahydrate (0.293 g, 0.8 mmol). The mixture was stirred for 20 min, then filtered off to remove any suspended material. The filtrate was kept at room temperature. Slow evaporation of the resulted purple solution led to purple crystals

of complex **3**. Yield: 65% (based on nickel). *Anal.* Calc. for **3**: C, 30.11; H, 5.52; N, 24.59. Found: C, 30.13; H, 5.55; N, 24.61%. Selected IR data (cm^{-1}, KBr pellet): 3300 (m), 2275 (m, $\nu_{sym}(C{\equiv}N) + \nu_{asym}(C{\equiv}N)$), 2249 (m, $\nu_{asym}(C{\equiv}N) + \nu_{sym}(C{\equiv}N)$), 2161 (s, $\nu_{asym}(C{\equiv}N) + \nu_{sym}(C{\equiv}N)$). UV–Vis (DMF) [$\lambda_{max}$, nm]: 350, 555, 806.

2.4. Crystal structure determination and structural refinement of complexes *1,2* and *3*

Single crystals of compound **1** were grown from an MeOH–H_2O medium whereas those of compound **2** and **3** were grown from a DMF–H_2O medium. The X-ray single crystal data for complexes **1**–**3** were collected on a Siemens P4 4-circle-diffractometer. Crystal size: $0.18 \times 0.37 \times 0.58$, $0.22 \times 0.23 \times 0.38$ and $0.30 \times 0.35 \times 0.36$ mm for complexes **1**, **2** and **3** respectively. Unit cell dimensions and intensity data were measured at 293 K for **1, 2** and **3**. The crystallographic data, conditions used for the intensity data collection and some features of the structure refinement are listed in Table 1. Graphite-monochromated Mo Kα radiation ($\lambda = 0.71073$ Å) was used to collect the data sets for **1**–**3**. Unit cell dimensions and intensity data were measured at 293 K for **1** and **2** and 294 K for **3**. For **1**, **2** and **3** the accurate unit cell parameters were determined from automatic centering of 17, 25 and 31 reflections respectively, and refined by least-square methods. 3344 independent reflections were collected for **1** in the range $2.5° < \theta < 25.0°$, 3579 such reflections for **2** in the range $2.1° < \theta < 25.2°$ and 6000 reflections in the range $1.8° < \theta < 25.0°$ for **3**. 2405, 2587 and 2425 reflections were assumed as observed applying the condition $I > 2\sigma(I)$] for complexes **1**, **2** and **3** respectively. All calculations for data reduction, structure solution and refinement were done by standard procedures (SHELXS-97) [35] and (SHELXL-97) [36]. All non-hydrogen atoms were refined anisotropically by full-matrix least-squares techniques on F^2. All the hydrogen atoms of the complexes were constrained to idealized positions and refined using a riding model, with C–H = 0.97 and N–H = 0.90 Å, and with U_{ISO} (H) = 1.2 U_{eq} (C) or 1.2U_{eq} (N). The relatively high values of R_1 (0.086) and wR_2 (0.167) for **3** are due to the low scattering power of the crystal, for which only 2425 of 6000 independent reflections were observed on the basis of the criteria $I > 2\sigma(I)$.

3. Results and discussion

3.1. Description of the crystal structures

3.1.1. Description of the structure of *[Ni(3,2,3-tet){Ag(CN)$_2$}$_2$] (1)*

The molecular structure of the trinuclear complex is shown in Fig. 1. Selected bond distances and angles are listed in Table 2. The nickel atom exhibits a slightly deformed octahedral coordination with one chelate N-bonded 3,2,3-tet molecule placed in the equatorial plane

Table 1
Crystal data and refinement details of complexes **1**, **2** and **3**

	1	**2**	**3**
Formula	$C_{12}H_{22}N_8Ag_2Ni$	$C_{32}H_{52}N_8O_{11}Ni_2$	$C_{20}H_{44}Cl_2N_{14}O_8Ni_2$
Formula weight	552.83	842.24	797.01
Crystal system	orthorhombic	triclinic	orthorhombic
Space group	*Pbca* (No. 61)	$P\bar{1}$ (No. 2)	*Pbca* (No. 61)
a (Å)	8.2713(17)	9.331(4)	14.122(4)
b (Å)	16.678(3)	10.419(4)	21.596(8)
c (Å)	28.055(6)	11.353(2)	22.591(8)
α (°)	90	96.51(3)	90
β (°)		100.58(3)	
γ (°)		109.71(7)	
V (Å^3)	3870.2(13)	1002.9(8)	6890(4)
Z	8	1	8
D_{calc} (g/cm^3)	1.898	1.395	1.537
μ (mm^{-1})	2.976	1.003	1.311
F(000)	2176	444	3328
Temperature (K)	293	293	294
λ (Å)	0.71073 (Mo Kα)	0.71073 (Mo Kα)	0.71073 (Mo Kα)
$\theta_{minimum-maximum}$ (°)	2.5–25.0	2.1–25.2	1.8–25.0
Reflections collected	4260	3777	7224
Independent reflections	3344	3579	6000
Observed data [$I > 2\sigma(I)$]	2405	2587	2425
Data/restraints/parameters	3344/0/209	3579/0/241	6000/0/415
Goodness-of-fit on F^2	0.991	1.026	0.914
Final *R* indices [$I > 2\sigma(I)$]	$R_1 = 0.0370$, $wR_2 = 0.0869$	$R_1 = 0.0481$, $wR_2 = 0.1016$	$R_1 = 0.0859$, $wR_2 = 0.1667$
R indices (all data)	$R_1 = 0.0640$, $wR_2 = 0.0957$	$R_1 = 0.0802$, $wR_2 = 0.1110$	$R_1 = 0.2224$, $wR_2 = 0.2081$
Maximum/minimum residues (e Å)	0.59, −0.61	0.54, −0.42	0.69, −0.57

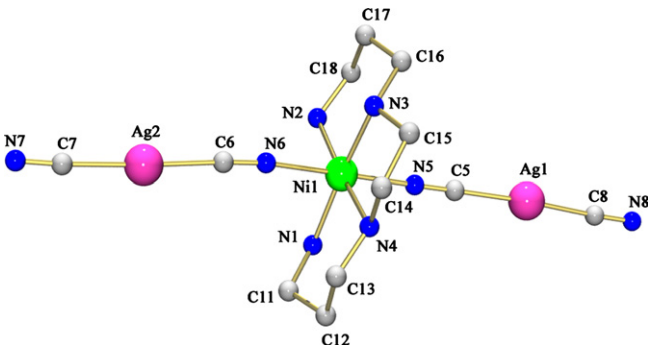


Fig. 1. Molecular structure of complex [Ni(3,2,3-tet){Ag(CN)$_2$}$_2$] (**1**). All hydrogen atoms have been omitted for clarity.

Table 2
Selected bond lengths (Å) and angles (°) in compound [Ni(3,2,3-tet)-{Ag(CN)$_2$}$_2$] (**1**)

Bond lengths			
Ni1–N1	2.079(4)	Ni1–N6	2.103(5)
Ni1–N2	2.102(5)	Ag1–C5	2.051(5)
Ni1–N3	2.092(4)	Ag1–C8	2.045(5)
Ni1–N4	2.098(5)	Ag2–C6	2.056(5)
Ni1–N5	2.101(5)	Ag2–C7	2.043(6)
Bond angles			
N1–Ni1–N2	95.20(18)	N2–Ni1–N6	89.63(19)
N1–Ni1–N3	174.90(18)	N3–Ni1–N4	84.34(19)
N1–Ni1–N4	90.57(18)	N3–Ni1–N5	91.28(18)
N1–Ni1–N5	88.47(17)	N3–Ni1–N6	88.52(18)
N1–Ni1–N6	91.75(17)	N4–Ni1–N5	90.26(18)
N2–Ni1–N3	89.90(18)	N5–Ni1–N6	179.65(18)
N2–Ni1–N4	174.23(19)	C5–Ag1–C8	177.8(2)
N2–Ni1–N5	90.09(18)	C6–Ag2–C7	176.3(2)

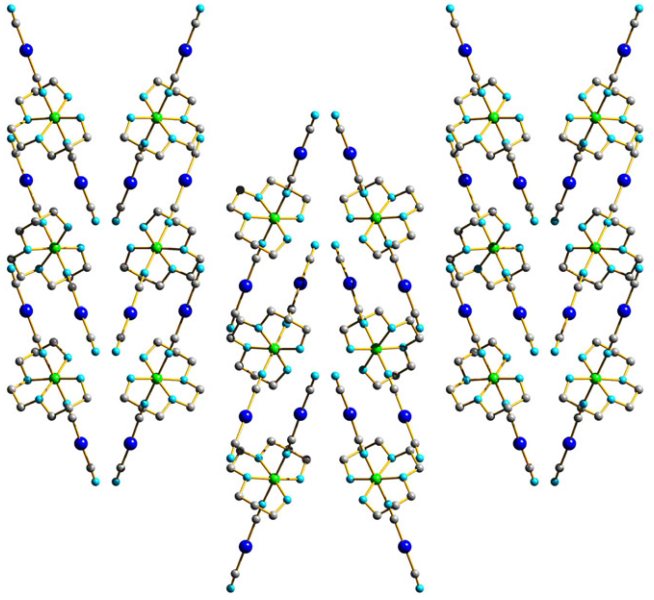


Fig. 2. A view of the packing diagram of complex **1**.

and two N-bonded dicyanoargentate anions as ligands placed in the axial positions. Similar bonding of dicyanoargentate anions has already been observed for other metal complexes, e.g. in the tin complex [N(Ph$_4$)][Cl(Ph$_3$)Sn-(μ-NC)Ag(CN)$_2$] (Ph = phenyl) exhibiting a discrete molecular structure [37] and in the chain-like structure of [Mn^{III}(salen)Ag(CN)$_2$] [38]. The packing diagram (Fig. 2) reveals that the discrete trinuclear heterobimetallic units are packed together with very weak argentophilic interactions as evidenced by the Ag–Ag contact (3.508 Å) that is comparable to the summed van der Waals radii of two silver atoms (3.440 Å). This distance is shorter than the Ag–Ag distances (3.5607(6) and 3.7125(6) Å) found in another Ni complex [Ni(tren)Ag(CN)$_2$][Ag(CN)$_2$] [39] where there are no significant metallophilic interactions. In this compound, [Ag(CN)$_2$]$^-$ building block acts as a monodentate ligand. The bond angles C5–Ag1–C8 (177.8(2)°) and C6–Ag2–C7 (176.3(2)°) deviate slightly from linearity.

3.1.2. Description of the structure of [Ni(3,2,3-tet)-(μ-tp)]$_n$ · 1.5nH$_2$O (2)

A perspective view of complex **2** with the atom-numbering scheme is shown in Fig. 3. Selected bond distances and angles are reported in Table 3. The Ni1 atom shows six coordination, with the four nitrogen atoms of the 3,2,3-tet moiety coordinated in the same equatorial plane while the oxygen atoms O1 and O2 of two bridging terephthalate anions complete the coordination sphere with same Ni–O distances [2.100(3) Å]. The latter distance is slightly longer with respect to those in the basal plane [range 2.075(4)–2.096(3) Å]. Along a chain, the terephthalate anions having the phenyl ring located about a crystallographic symmetry center connect Ni-3,2,3-tet units in a bismonodentate fashion. The bisbidentate fashion of the terephthalate anion has been ruled out due to longer interatomic distance [Ni1–O10 = 3.359 Å] as well as larger Ni1–O1–O10 bond angle (104.16°). The dihedral angle formed by the anion with the equatorial plane is 76.95°; the carboxylate group O1/C10/O10 deviates slightly form coplanarity with the phenyl ring (8.24°) whereas the other carboxylate group O2/C20/O20 deviates from coplanarity with the same phenyl ring by 9.10°. These deviations are uniform throughout the chain. Within a linear chain Ni···Ni is separated by 11.404 Å. This distance is comparable with other terephthalato bridged nickel complexes, 11.446(2) Å in

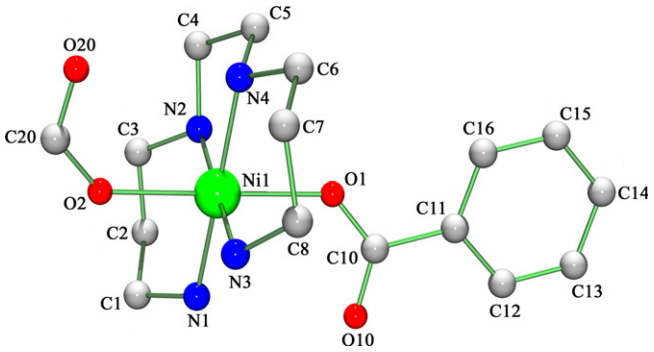


Fig. 3. Molecular structure of complex [Ni(3,2,3-tet)(μ-tp)]$_n$ · 1.5nH$_2$O (**2**). All hydrogen atoms have been omitted for clarity.

Table 3
Selected bond lengths (Å) and angles (°) in compound [Ni(3,2,3-tet)-(μ-tp)]$_n \cdot 1.5nH_2O$ (**2**)

Bond lengths			
Ni1–O1	2.100(3)	Ni1–N4	2.096(3)
Ni1–O2	2.100(3)	O1–C10	1.223(5)
Ni1–N1	2.089(4)	O2–C20	1.249(5)
Ni1–N2	2.092(4)	O10–C10	1.215(6)
Ni1–N3	2.075(4)	O20–C20	1.250(6)
Bond angles			
O1–Ni1–O2	178.14(13)	O2–Ni1–N4	93.69(13)
O1–Ni1–N1	93.57(14)	N1–Ni1–N2	89.49(17)
O1–Ni1–N2	89.02(15)	N1–Ni1–N3	95.03(18)
O1–Ni1–N3	92.39(16)	N1–Ni1–N4	173.14(17)
O1–Ni1–N4	85.00(13)	N2–Ni1–N3	175.17(16)
O2–Ni1–N1	87.88(14)	N2–Ni1–N4	83.79(15)
O2–Ni1–N2	92.15(15)	N3–Ni1–N4	91.74(16)
O2–Ni1–N3	86.32(16)	Ni1–O1–C10	131.4(3)

Hydrogen bonds (Å, °)

D–H–A	D···A	H···A	∠D–H···A
N1–H1A[a]···O10	2.894(6)	2.2200	131.00
N1–H1B···O10	3.097(6)	2.2500	156.00
N2–H2···OW1	3.042(3)	2.1700	160.00
N3–H3B···O10	2.948(6)	2.1200	152.00
N4–H4···O20	2.848(5)	2.0100	153.00

[a] Symmetry transformations used to generate equivalent atoms: A = 1 + *x*, 1 + *y*, *z*; B = 1 − *x*, −*y*, −*z*.

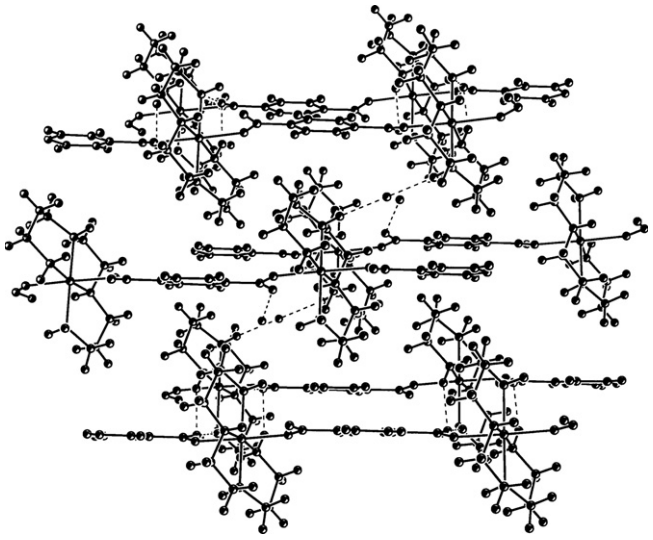


Fig. 4. A view of the packing diagram of **2** showing two-dimension sheet-like network.

[Ni(pyrazole)$_4$(tp)]$_n$ [40], 11.514(1) Å in [Ni($C_{12}H_{30}N_6O_2$)-($C_8H_4O_4$)]$_n \cdot 4nH_2O$ [41] and 11.379(10) Å in (μ-terephthalato)[Ni(dca)(dpt)(H_2O)]$_2$ [34].

The packing diagram of **2** (Fig. 4) consists of 1D polymeric chains formed by Ni-3,2,3-tet moieties bridged by terephthalate units. In addition, hydrogen bonds make the one-dimensional entity extending toward a higher dimensional system. Linkage between the 1D arrays is formed by intermolecular hydrogen bonds. The lattice water molecule OW1 connects two 3,2,3-tet neighboring units via hydrogen bonds (N2···OW1 = 3.042(3) Å). The free carboxylate oxygen atom O10 is additionally hydrogen bonded to another amine group of the 3,2,3-tet moiety (N3···O10 = 2.948(6) Å). Therefore, two C–O bond distances of the carboxylate group have practically no difference although one is coordinated (C10–O1 = 1.223(5) Å) and the other is uncoordinated (C10–O10 = 1.215(6) Å). In general, coordinated C–O bond distances of carboxylate groups range 1.266–1.279 Å which are longer than free carbonyl C–O bond distances of 1.226–1.255 Å when terephthalate coordinates a metal ion in a monodentate fashion [42–46]. As a consequence, these intermolecular hydrogen bonds extend the 1D coordination network into a 2D sheet-like network. No significant π–π interaction between the phenyl rings is observed and hence the formation of any 3D network has been ruled out.

3.1.3. Description of the structure of {[Ni(3,2,3-tet)-($\mu_{1,5}$-dca)](ClO_4)}$_n$ (**3**)

The labeled diagram for complex **3** is shown in Fig. 5 and selected bond lengths and angles are listed in Table 4. The coordination sphere of Ni(II) is defined by four nitrogen atoms of the tetradentate N_4 ligand 3,2,3-tet situated in the equatorial plane and two *trans*-dca nitrogen atoms at the axial positions resulting in a distorted octahedral coordination environment. The Ni(II) is displaced 0.060 Å out of the equatorial plane. The Ni–$N_{3,2,3\text{-tet}}$ and Ni–N_{dca} bond lengths are in the range 2.107(8)–2.118(8) Å and 2.074(8)–2.112(8) Å, respectively. The dca groups are non-linear with C20–N6–C21 and C20′–N6′–C21′ bond angles of 124.6(9) and 120.2(8)° respectively. To achieve internal charge balance there is a perchlorate counter anion outside the coordination sphere. It should be emphasized that the

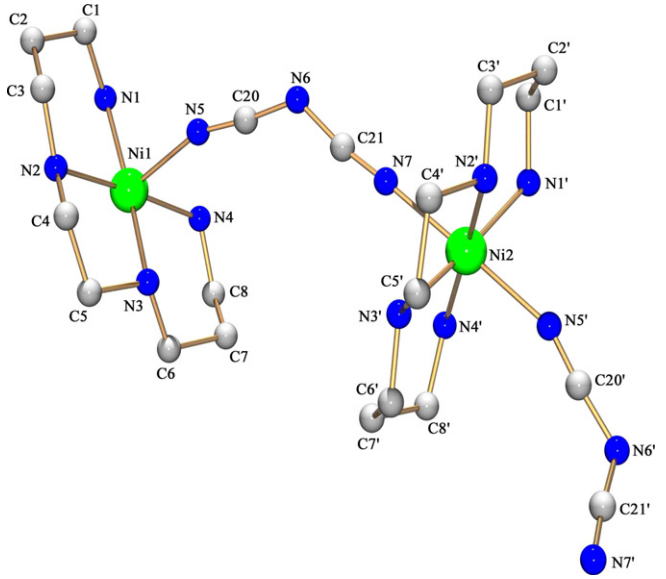


Fig. 5. A perspective view of complex {[Ni(3,2,3-tet)($\mu_{1,5}$-dca)](ClO_4)}$_n$ (**3**). All hydrogen atoms and the perchlorate anions have been omitted for clarity.

Table 4
Selected bond lengths (Å) and angles (°) for compound {[Ni(3,2,3-tet)-($\mu_{1,5}$-dca)](ClO$_4$)}$_n$ (**3**)

Bond lengths			
Ni1–N1	2.090(9)	Ni2–N1′	2.109(8)
Ni1–N2	2.095(9)	Ni2–N2′	2.108(9)
Ni1–N3	2.124(9)	Ni2–N3′	2.118(8)
Ni1–N4	2.114(8)	Ni2–N4′	2.107(8)
Ni1–N5	2.107(9)	Ni2–N5′	2.122(8)
Bond angles			
N1–Ni1–N2	90.4(3)	N3–Ni1–N5	86.2(4)
N1–Ni1–N3	172.8(4)	N4–Ni1–N5	87.9(3)
N1–Ni1–N4	93.6(3)	N1′–Ni2–N2′	92.1(3)
N1–Ni1–N5	91.9(4)	N1′–Ni2–N3′	174.8(3)
N2–Ni1–N3	82.7(3)	N1′–Ni2–N4′	92.9(3)
N2–Ni1–N4	175.9(3)	N1′–Ni2–N5′	90.9(3)
N2–Ni1–N5	92.6(3)	N1′–Ni2–N7	90.1(3)
N3–Ni1–N4	93.3(3)	N2′–Ni2–N3′	83.2(3)

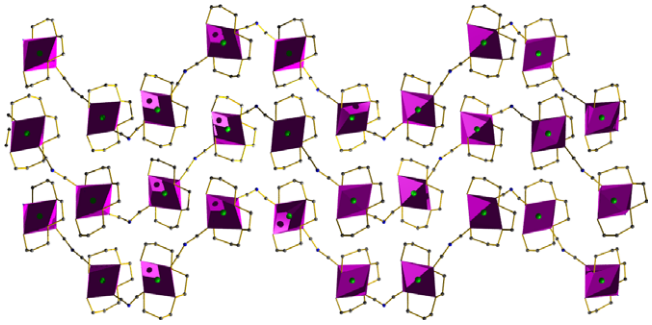


Fig. 6. The packing diagram of complex **3** showing one-dimensional network.

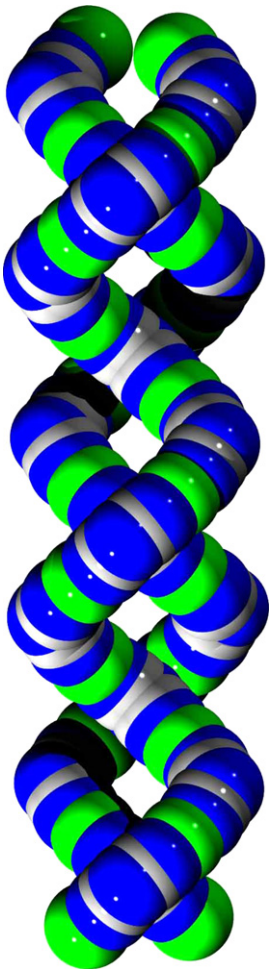


Fig. 7. A perspective view of the double-helical structure.

dca acts as a $\mu_{1,5}$-bridging ligand and links two neighboring Ni^{II}-3,2,3-tet moieties forming an infinite one-dimensional system (Fig. 6). Interestingly, when viewed along the crystallographic *a*-axis, such a 1D chain propagates in a helical fashion. Also, each adjacent chain is composed of an alternating assembly of left-hand (M) and right-hand (P) helices (Fig. 7). A twisting is observed between two successive dca ligands with a dihedral angle of 68.42° which leads to the formation of the helical column in which the repeating period is 13.652 Å. To our knowledge there is no such example of this $\mu_{1,5}$-type of dicyanamide helical bridging in any Ni(II) complexes. An earlier report shows that in the complex [Ni(tmeda)(dca)$_2$] [47], a helical 3D structure is formed but each helical chain is not 'stitched' whereas in complex **3**, the linking mode and structural characteristics are different. The most common 1,5-bridging mode comprises of either a zig-zag or a straight chain-like network [48,49]. No classical hydrogen bond is operative in the packing structure. It may be pointed out that diffraction from the crystal of **3** was apparently rather weak owing to the intrinsic problem of the crystal. Despite the low precision of the structural parameters, the main framework of the 1D chain is clearly revealed. The relevant bond distances and angles are comparable to other reported systems [48,49].

3.2. Cyclic voltammetry

The cyclic voltammogram of complex **1** was recorded in DMF solution with TBAP as supporting electrolyte in the potential range −1.8 to +1.2 V versus SCE. The voltammogram is characterized by a well-defined oxidation wave with $E_{1/2} = 0.86$ V (Fc/Fc$^+$) and $\Delta E = 50$ mV. This anodic response corresponds to the $[Ni^{II}(3,2,3\text{-tet})\{Ag(CN)_2\}_2] - e \rightarrow [Ni^{III}(3,2,3\text{-tet})\{Ag(CN)_2\}_2]^+$ reaction and this is a quasireversible one. In the cathodic region, a quasireversible reduction of Ni^{III} to Ni^{II} for the reaction $[Ni^{III}(3,2,3\text{-tet})\{Ag(CN)_2\}_2]^+ + e \rightarrow [Ni^{II}(3,2,3\text{-tet})\{Ag(CN)_2\}_2]$ with an $E_{1/2}$ value of −0.93 V and $\Delta E = 390$ mV is observed. The quasireversibility of the couples might be due to the instability of the formally Ni^{III} species. In the said potential range no anodic wave for the oxidation of the ligand is observed.

The cyclic voltammogram of complex **3** was recorded in DMF solution with TBAP as supporting electrolyte in the potential range −1.6 to +1.6 V versus SCE. The cyclic voltammogram exhibits two quasireversible waves. The redox couple with the anodic peak $E_{1/2} = 0.79$ V (Fc/Fc$^+$) and $\Delta E = 130$ mV, may be assigned to the reaction

$[Ni^{II}(3,2,3\text{-tet})(\mu_{1,5}\text{-dca})]^{+} - e \rightarrow [Ni^{III}(3,2,3\text{-tet})(\mu_{1,5}\text{-dca})]^{2+}$. In the cathodic wave, a quasireversible reduction with an $E_{1/2}$ value of -0.83 V and $\Delta E = 190$ mV is observed and may be assigned to the reaction $[Ni^{III}(3,2,3\text{-tet})(\mu_{1,5}\text{-dca})]^{2+} + e \rightarrow [Ni^{II}(3,2,3\text{-tet})(\mu_{1,5}\text{-dca})]^{+}$. No anodic wave for the oxidation of the ligands is featured. For both the complexes the chemical environment is not suitable to stabilize the Ni(I) state and hence no Ni^{II}/Ni^{I} couple is observed in the cyclic voltammograms.

3.3. Thermal studies

TG-DTA plots of **1** clearly shows four weight loss steps. The first mass loss in the region 60–130 °C corresponds to the loss of one cyanide unit from one argentocyanide moiety of the complex. The observed weight loss of 5.14% is in agreement with the calculated one (4.70%). The second step (150–300 °C) reveals that rest of the three cyanide moieties are decomposed and the observed mass loss (13.99%) corroborates well with the calculated one (14.11%). The third and fourth steps in the temperature range 300–450 °C are composite in nature and correspond to the complete decomposition of the 3,2,3-tet ligand with the observed weight loss of 32.09%, accompanied by a sharp exothermic peak in the DTA curve. The total weight loss of 51.22% matches fairly with the calculated one (50.29%) if the final product is assumed to be a mixture of metallic nickel and silver.

The TG-DTA curves of complex **2** show two steps corresponding to the decomposition process. The compound is stable up to 80 °C. The weight loss (6.61%) from 80–120 °C corresponds to the loss of all the water molecules (6.37%) from the complex. Meanwhile, in this temperature region, the DTA curve shows an endothermic peak showing energy absorption. The next step (240–440 °C) is attributed to framework decomposition of the 3,2,3-tet and the terephthalate moieties into gaseous products. The observed weight loss (80.01%) matches well with the calculated one (79.78%). The total weight loss of 86.62% is agreeable to the calculated weight loss of 86.15% and the residue is assumed to be metallic nickel.

As complex **3** contains perchlorate as the counter anion, no attempt has been made for the thermal study owing to its possible explosive nature.

3.4. Magnetic properties of 2 and 3

Magnetic susceptibility data for polycrystalline samples were collected in the temperature range 2–300 K and 2–200 K for **2** and **3**, respectively in an applied magnetic field of 1T. The magnetic behavior ($\chi_M T$ versus T) of the complexes **2** and **3** is shown in Fig. 8. Complex **2** displays a temperature-independent $\chi_M T$ value of 1.11 ± 0.01 cm^3 mol^{-1} K in the temperature range 300–15 K. Similarly, complex **3** shows a temperature-independent $\chi_M T$ value of 1.13 ± 0.05 cm^3 mol^{-1} K in the range 200–10 K. The values are expected for magnetically isolated $S = 1$ spin

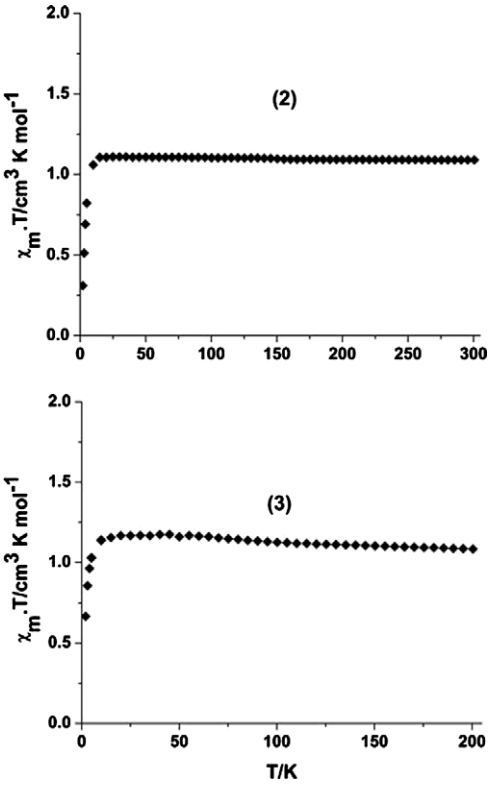


Fig. 8. Plots of $\chi_M T$ vs. T for complexes **2** and **3**.

system with $g = 2.11$ and 2.13 for complexes **2** and **3**, respectively. At lower temperature, they decrease slowly to 0.31 cm^3 mol^{-1} K at 2.0 K for **2** and to 0.66 cm^3 mol^{-1} K at 2.0 K for **3**. This behavior is typical of very weak intermolecular interaction between the magnetic centers. This is expected for a complex where two magnetic centers are quite far from each other for any magnetic exchange. In other Ni(II) complexes reported in literature [50,51], this behavior is also observed. In both cases, the $\chi_M T$ values obey the Curie–Weiss law $\chi = C/(T - \theta)$ giving Weiss constant θ values of -0.51 K and -0.32 K for **2** and **3**, respectively. Several factors that could act simultaneously here are (i) antiferromagnetic intramolecular coupling, (ii) antiferromagnetic intermolecular coupling and (iii) the D (ZFS) parameter intrinsic to the nickel(II) ion. It is difficult to evaluate these parameters since the couplings are small.

4. Conclusion

This paper describes three Ni(II) complexes having 3,2,3-tet as the primary ligand with argentocyanide, terephthalate and dicyanamide as the co-ligands. The complex **1** with argentocyanide is a discrete molecule. This is a rare case where $Ag(CN)_2^-$ does not act as a bridging unit. Complex **2** forms a 2D sheet-like architecture involving the bridging terephthalate and intermolecular hydrogen bonding (N–H···O and O–H···O). A novel 1D helical network with Ni(II) and the dicyanamide is found in the complex **3**.

There are many reports on coordination complexes of Ni(II) with the N_4 donor ligands and dicyanamide as the bridging ligand but our work seems to be the first one where a 1D helical network is characterized. Complex **2** displays a temperature-independent $\chi_M T$ value of $1.11 \pm 0.01\ cm^3\ mol^{-1}\ K$ in the temperature range 300–15 K whereas that of complex **3** is found to be $1.13 \pm 0.05\ cm^3\ mol^{-1}\ K$ in the range 200–10 K. The values are expected for magnetically isolated $S = 1$ spin system with $g = 2.11$ and 2.13 for both the complexes.

Acknowledgements

We thank Dr. A. Ghosh (Department of Chemistry, University of Calcutta) for assistance in getting the measurements of thermal studies. We record our sincere thanks to Dr. T. K. Paine of our Department for useful discussions on magnetic susceptibility results.

Appendix A. Supplementary material

CCDC 628854, 628853 and 628856 contain the supplementary crystallographic data for **1**, **2** and **3**. These data can be obtained free of charge via http://www.ccdc.cam.ac.uk/conts/retrieving.html, or from the Cambridge Crystallographic Data Centre, 12 Union Road, Cambridge CB2 1EZ, UK; fax: (+44) 1223-336-033; or e-mail: deposit @ccdc.cam.ac.uk. Supplementary data associated with this article can be found, in the online version, at doi:10.1016/j.poly.2007.03.040.

References

[1] S.R. Batten, R. Robson, Angew. Chem., Int. Ed. 37 (1998) 1460.
[2] R. Sekiya, S. Nishikiori, Chem. Eur. J. 8 (2002) 4803.
[3] M. Munakata, L.P. Wu, T. Kuroda-Sowa, Adv. Inorg. Chem. 46 (1999) 173.
[4] O.M. Yaghi, H. Li, C. Davis, D. Richardson, T.L. Groy, Acc. Chem. Res. 31 (1998) 474.
[5] P.J. Hagrman, D. Hagrman, J. Zubieta, Angew. Chem., Int. Ed. 38 (1999) 2638.
[6] X.-H. Bu, W. Chen, S.-L. Lu, R.-H. Zhang, D.-Z. Liao, W.-M. Bu, M. Shionoya, F. Brisse, J. Ribas, Angew. Chem., Int. Ed. 40 (2001) 3201.
[7] R. Boča, M. Gembický, R. Herchel, W. Haase, L. Jäger, C. Wagner, H. Ehrenberg, H. Fuess, Inorg. Chem. 42 (2003) 6965.
[8] F. Březina, Z. Smékal, Z. Trávníček, Z. Šindelář, R. Pastorek, J. Marek, Polyhedron 16 (1997) 1331.
[9] J. Chakraborty, N. Shaikh, H. Mayer-Figge, W.S. Sheldrick, P. Vojtíšek, P. Banerjee, Struct. Chem., in press.
[10] P. Román, C. Guzmán-Mirallels, A. Luque, J.I. Beitia, J. Cano, F. Lloret, M. Julve, S. Alvarez, Inorg. Chem. 35 (1996) 3741.
[11] Z. Smékal, P. Thornton, Z. Šindelář, R. Klička, Polyhedron 17 (1998) 1631.
[12] C.-H. Kwak, J. Kim, Inorg. Chem. Commun. 3 (2000) 550.
[13] A. Escuer, R. Vicente, J. Ribas, M. Salah El Fallah, X. Solans, M. Font-Bardia, Inorg. Chim. Acta 216 (1994) 5.
[14] A. Escuer, R. Vicente, J. Ribas, M. Salah El Fallah, X. Solans, M. Font-Bardía, Inorg. Chem. 32 (1993) 3727.
[15] J. Do, A.J. Jacobson, Inorg. Chem. 40 (2001) 2468.
[16] (a) H. Schmidbaur, Chem. Soc. Rev. (1995) 391;
(b) P. Pyykkö, Chem. Rev. 97 (1997) 597;
(c) B.-C. Tzeng, A. Schier, H. Schmidbaur, Inorg. Chem. 38 (1999) 3978.
[17] M. Bardaji, A. Laguna, J. Chem. Educ. 76 (1999) 201.
[18] J. Cano, G.D. Munno, J.L. Sanz, R. Ruiz, J. Faus, F. Lloret, M. Julve, A. Caneschi, J. Chem. Soc., Dalton Trans. (1997) 1915.
[19] C.S. Hong, Y.S. You, Polyhedron 23 (2004) 3043.
[20] L. Li, Z. Liu, S.S. Turner, D. Liao, Z. Jiang, S. Yan, Eur. J. Inorg. Chem. (2003) 62.
[21] X. Shi, G. Zhu, Q. Fang, G. Wu, G. Tian, R. Wang, D. Zhang, M. Xue, S. Qiu, Eur. J. Inorg. Chem. (2004) 185.
[22] C.S. Hong, Y. Do, Inorg. Chem. 36 (1997) 5684.
[23] Y. Go, X. Wang, E.V. Anokhina, A.J. Jacobson, Inorg. Chem. 43 (2004) 5360.
[24] C. Ma, Y. Han, R. Zhang, D. Wang, Eur. J. Inorg. Chem. (2005) 1649.
[25] C.S. Hong, Y.S. You, Polyhedron 23 (2004) 1379.
[26] S.R. Batten, P. Jensen, B. Moubaraki, K.S. Murray, R. Robson, J. Chem. Soc., Chem. Commun. (1998) 439.
[27] M. Kurmoo, C.J. Kepert, New J. Chem. 22 (1998) 1515.
[28] P. Jensen, S.R. batten, G.D. Fallon, B. Moubaraki, K.S. Murray, D.J. Price, J. Chem. Soc., Chem. Commun. (1999) 177.
[29] J.L. Manson, C.R. Kmety, A.J. Epstein, J.S. Miller, Inorg. Chem. 38 (1999) 2552.
[30] A. Escuer, F.A. Mautner, N. Saz, R. Vicente, Inorg. Chem. 39 (2000) 1668.
[31] P.M. van der Werff, S.R. batten, P. Jensen, B. Moubaraki, K.S. Murray, Inorg. Chem. 40 (2001) 1718.
[32] S. Martin, M.G. Barandika, J.I.R. Larramendi, R. Cortes, M. Font-Bardía, L. Lezama, Z.E. Serna, X. Solans, T. Rojo, Inorg. Chem. 40 (2001) 3687.
[33] Z.M. Wang, B.W. Sun, J. Luo, S. Gao, C.S. Liao, C.H. Yan, Y. Li, Inorg. Chim. Acta 332 (2002) 127.
[34] D. Ghoshal, H. Bialas, A. Escuer, M. Font-Bardía, T.K. Maji, J. Ribas, X. Solans, R. Vicente, E. Zangrando, N. Ray Chaudhuri, Eur. J. Inorg. Chem. (2003) 3929.
[35] G.M. Sheldrick, Acta Crystallogr., Sect. A 46 (1990) 467.
[36] G.M. Sheldrick, SHELXL-97, Program for Crystal Structure Refinement, University of Göttingen, 1997.
[37] M. Carcelli, C. Ferrari, C. Pelizzi, G. Pelizzi, G. Predieri, C. Solinas, J. Chem. Soc., Dalton Trans. (1992) 2127.
[38] A. Panja, N. Shaikh, P. Vojtíšek, S. Gao, P. Banerjee, New J. Chem. 26 (2002) 1025.
[39] C.J. Shorrock, B.-Y. Xue, P.B. Kim, R.J. Batchelor, B.O. Patrick, D.B. Leznoff, Inorg. Chem. 41 (2002) 6743.
[40] C.S. Hong, J.H. Yoon, J.H. Lim, H.H. Ko, Eur. J. Inorg. Chem. (2005) 4818.
[41] H.J. Choi, M.P. Suh, Inorg. Chem. 38 (1999) 6309.
[42] P. Chaudhuri, K. Oder, K. Wieghart, S. Gehring, W. Haase, B. Nuber, J. Weiss, J. Am. Chem. Soc. 110 (1988) 3657.
[43] M. Verdaguer, J. Gouteron, S. Jeannin, Y. Jeannin, O. Kahn, Inorg. Chem. 23 (1984) 4291.
[44] E. Bakalbassis, P. Bergerat, O. Kahn, S. Jeannin, Y. Jeannin, Y. Dromzee, M. Guillot, Inorg. Chem. 31 (1992) 625.
[45] C.E. Xanthopoulos, M.P. Sigalas, G.A. Katsoulos, C.A. Tsipis, A. Terzis, M. Mentzafos, A. Hountas, Inorg. Chem. 32 (1993) 5423.
[46] E. Bakalbassis, A.P. Bozopoulos, J. Mrozinski, P. Rentzeperis, C.A. Tsipis, Inorg. Chem. 27 (1988) 529.
[47] J. Luo, X.-G. Zhou, S. Gao, L.-H. Weng, Z.-H. Shao, C.-M. Zhang, Y.-R. Li, J. Zhang, R.-F. Cai, Inorg. Chem. Commun. 7 (2004) 669.
[48] E. Colacio, I.B. Maimoun, R. Kivekas, R. Sillanpaa, J. Suarez-Varela, Inorg. Chim. Acta 357 (2004) 1465.
[49] R. Boča, M. Boča, M. Gembický, L. Jäger, C. Wagner, H. Fuess, Polyhedron 23 (2004) 2337.
[50] K.-Y. Choi, K.-M. Chun, K.-C. Lee, J. Kim, Polyhedron 21 (2002) 1913.
[51] S. Sen, P. Talukder, S. Mitra, G. Rosair, G. Yap, V. Gramlich, J. Kim, T. Matsushita, C. Desplanches, J.-P. Sutter, Inorg. Chim. Acta 358 (2005) 4534.

and structural properties [9]. Complexes of **1** were screened for their antitumor and antimicrobial activities [10], but their luminescence properties have barely been investigated [11]. In the present investigation we have synthesized a series of novel blue luminescent high-spin ($s = 5/2$) iron(III) complexes using ligand **1** as the blue light emitting species [11a]. Interestingly, the photophysical and chemical properties of the iron(III) complex can be modulated by controlling the degree of protonation of the ligand or by insertion of a nucleophile. Emphasis will be given to understanding the binding phenomenon via the binding constant and thermodynamic calculations for the complexation equilibrium. Other important features scrutinized include absorption, emission, redox and magnetic studies. The X-ray structure of one of the iron(III) complexes authenticates an FeN_4O_2 coordination with interesting Cl···H–O bonding [12].

2. Experimental

2.1. Materials

All starting materials and solvents were purchased from Aldrich Chemical Company and were used without further purification unless otherwise stated.

2.2. Physical measurements

A Perkin–Elmer 2400 C Elemental Analyzer was used to collect microanalytical data (C, H, N). A Sartorius CP64 balance was used for weighing purposes. IR data were collected with the help of a FTIR Perkin–Elmer L 120-000 A. The UV–Vis spectra of the ligand and its complexes were measured on a Shimadzu UV-1601 spectrophotometer and corrected for backgrounds due to solvent absorption. Fluorescence spectra were recorded with a Perkin–Elmer LS 50B Luminescence Spectrometer. For binding constant measurements, solutions were prepared at a fixed concentration of H_2L^1 (1.0×10^{-5} M) and at a concentration of the metal ions ranging from 1.0×10^{-6} M to 10.0×10^{-6} M at room temperature. Electrochemical measurements were performed under a nitrogen atmosphere on a Versastat II PAR Electrochemistry system using solvents and supporting electrolyte (TEAP) prepared and purified as before [13]. The reference electrode was a saturated calomel electrode (SCE). Solution electrical conductivities were measured with the help of a Philips PR 9500 bridge, the solute concentration being 10^{-3} M. For spectroscopic and electrochemical studies HPLC grade solvents were used.

2.3. X–ray crystallography

Single crystals of $[Fe^{III}(HL^1)_2]Cl \cdot H_2O$ (**2**), were grown by slow diffusion of hexane into a dichloromethane solution of the complex, followed by slow evaporation. A rod shaped crystal was mounted on a glass fiber. Intensity data for complex **2** was collected at 173 K (−100 °C) by the ω-scan method over the 2θ range 1.78–29.27° on a Stoe Mark II-Image Plate Diffraction System [14a] equipped with a two-circle goniometer and using Mo Kα graphite monochromated radiation ($\lambda = 0.71073$ Å). Structure solution and refinement were done by direct methods using SHELXS-97 and SHELXL-97 programs [14b,14c]. The structure was successfully solved in the space group $P2_1/c$. Of the 5990 independent reflections, 5006 satisfying $I > 2\sigma(I)$ were used for the structure solution. The NH H atoms were located from Fourier difference maps and refined isotropically. The water H atoms were located from Fourier difference maps. They were refined isotropically with the O–H bond lengths restrained to be 0.82(2) Å. The remainders of the H atoms were included in calculated positions and treated as riding atoms using SHELXL default parameters. All non-hydrogen atoms were refined anisotropically. An absorption correction was applied using MULscanABS in PLATON [14d]. The molecular structure and crystallographic numbering scheme are illustrated in the PLATON drawing [14d].

Molecular formula $C_{24}H_{22}ClFeN_6O_3$, M 533.78, monoclinic, space group $P2_1/c$, $a = 11.9163(6)$ Å, $b = 20.4137(9)$ Å, $c = 9.4770(5)$ Å, $\beta = 106.028(4)°$, $V = 2215.72(19)$ Å^3, $Z = 4$, $D_{calc} = 1.600$ g cm^{-3}, absorption coefficient $\mu = 0.844$ mm^{-1}, crystal dimensions: $0.39 \times 0.36 \times 0.25$ mm, $F(000)$: 1100, θ range for data collection: 1.78–29.27 (°), index ranges: $-16 \leqslant h \leqslant 16$, $-27 \leqslant k \leqslant 27$, $-13 \leqslant l \leqslant 12$, reflections collected/unique: 31 762/5990, significant unique reflections: 5006 with $I > 2\sigma(I)$, refinement method: full-matrix least-squares on F^2, data/parameters/restraints: 5990/332/2, goodness-of-fit on F^2: 1.045, final R indices $[I > 2\sigma(I)]$: $R_1 = 0.0348$, $wR_2 = 0.0797$, R indices (all data): $R_1 = 0.0454$, $wR_2 = 0.0856$, weighting scheme: $w = 1/[(\sigma F_o)^2 + (0.0395P)^2 + 0.9534P]$, where $P = (F_o^2 + 2F_c^2)/3$, largest difference peak and hole (e/Å^3): 0.542 and −0.584.

$R_1 = [\sum||F_o| - |F_c||]/\sum|F_o|$ (based on F), $wR_2 = [[\sum w(|F_o^2 - F_c^2|)^2]/[\sum w(F_o^2)^2]]^{1/2}$ (based on F^2), GOF $= ((\sum(|F_o| - |F_c|)^2)/(N_o - N_v))^{1/2}$ with N_o = number of observed reflections and N_v = number of parameters.

2.4. Syntheses

2.4.1. Salicylaldehyde 2-pyridyl hydrazone H_2L^1 (**1**)

The ligand was prepared by the same general procedure as before [15].

2.4.2. Iron complexes

$[Fe^{III}(HL^1)_2]Cl$ (**2**): To a stirred methanolic solution of anhydrous ferric chloride (0.03 g, 0.2 mmol) was added a solution of H_2L^1 (**1**), (0.085 g, 0.4 mmol) in methanol (5 ml) and the resulting brown solution was stirred for 0.5 h. The solvent was evaporated on a rotary evaporator, and on recrystallization from methanol deep brown crystals of $[Fe^{III}(HL^1)_2]Cl$ (**2**), were obtained. Yield 89%. Selected FTIR data, ν (cm^{-1}): 3356, 1623, 1594, 1574,

1537, 1515, 1376, 1355, 1332, 1287, 1250, 1205, 1150, 1139, 1103, 1121, 1030, 1003, 933, 880, 858, 794, 766, 753, 655, 604, 522, 469, 426. *Anal.* Calc. for $C_{24}H_{20}N_6O_2FeCl \cdot H_2O$: C, 54.01; H, 4.12; N, 15.75. Found: C, 54.02; H, 4.14; N, 15.74%.

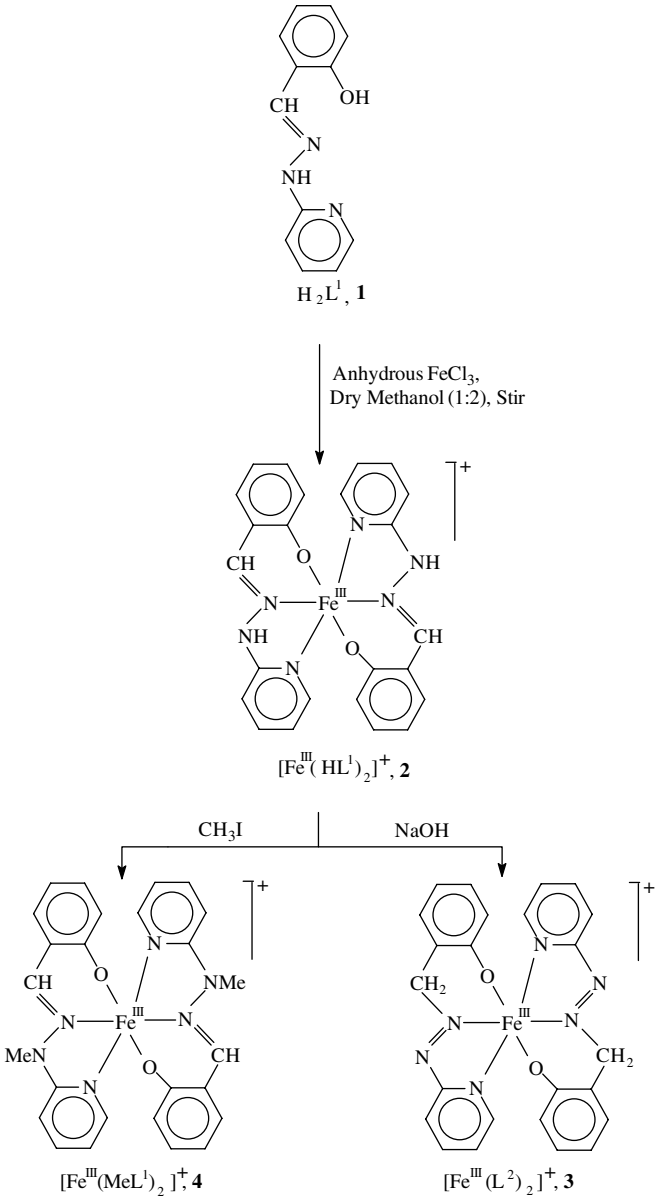
[$Fe^{III}(L^2)_2$]Cl (**3**): Anhydrous ferric chloride (0.03 g, 0.2 mmol) in methanol (5 ml) was added to a methanolic solution (5 ml) of **1** (0.085 g, 0.4 mmol), previously deprotonated by adding NaOH (0.016 g, 0.4 mmol). A green colored solution was obtained which on evaporation yielded shining greenish brown crystalline solids of $[Fe^{III}(L^2)_2]Cl$ (**3**). Yield 85%. Selected FTIR data, ν (cm^{-1}): 3362, 3011, 2921, 2842, 1614, 1538, 1482, 1469, 1427, 1328, 1285, 1202, 1150, 1100, 1058, 1031, 1008, 931, 881, 848, 753, 604, 429, 469. *Anal.* Calc. for $C_{24}H_{18}N_6O_2FeCl$: C, 56.11; H, 3.50; N, 16.36. Found: C, 55.12; H, 3.56; N 16.38%.

[$Fe^{III}(MeL^1)_2$]Cl (**4**): To a methanolic solution of $[Fe^{III}(HL^1)_2]Cl$ (**2**), (0.1 g, 0.2 mmol) 1 ml methyl iodide was added and stirred for 0.5 h at room temperature resulting in a reddish brown solution. The solvent was evaporated and the complex was recrystallized from methanol and finally dried over fused calcium chloride to obtain $[Fe^{III}(MeL^1)_2]Cl$ (**4**), as reddish brown crystalline solids. Yield 80%. Selected FTIR data, ν (cm^{-1}): 3383, 1621, 1538, 1496, 1358, 1324, 1286, 1148, 1105, 855, 765, 694, 526, 430, 376. *Anal.* Calc. for $C_{26}H_{24}N_6O_2FeCl$: C, 57.43; H, 4.41; N, 15.46. Found: C, 57.42; H, 4.40; N, 15.44%.

3. Results and discussion

3.1. Syntheses and characterization

The ligand system H_2L^1 (**1**), used in the present work is tridentate in nature, incorporating imine, phenolic and pyridyl functions as potential donor sites. The 1:2 reaction of H_2L^1 with anhydrous ferric chloride in methanol at room temperature afforded deep brown colored blue luminescent $[Fe^{III}(HL^1)_2]Cl$ (**2**), in excellent yields, which can subsequently be deprotonated into luminescent green colored $[Fe^{III}(L^2)_2]Cl$ (**3**), followed by methylation leading to another luminescent reddish brown complex, $[Fe^{III}(MeL^1)_2]Cl$ (**4**). The synthetic routes for complexes **2**, **3** and **4** are depicted in Scheme 1. All the complexes are highly soluble in acetonitrile, methanol and ethanol. They are 1:1 electrolytes ($\Lambda = 130$–$134\ \Omega^{-1}\ cm^2\ M^{-1}$) in acetonitrile. The room temperature (298 K) magnetic moments of complexes **2**, **3** and **4** lie in the range 5.56–5.84 μ_B, indicating a high-spin configuration (d^5, $t_{2g}^3e_g^2$, $s = 5/2$) with FeN_4O_2 coordination.



Scheme 1.

3.2. Absorption and Emission Spectra of H_2L^1 and its Iron(III) Complexes

All the spectroscopic measurements were carried out in degassed methanol at room temperature. The bands appearing in the UV region (240–395 nm) are characteristic of the ligand H_2L^1 (**1**) (Fig. 1). In the complexes these

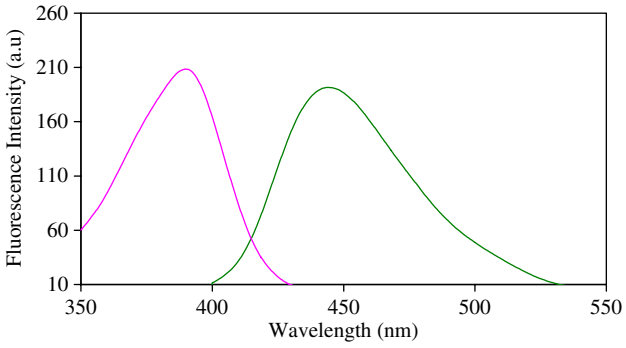


Fig. 1. Excitation (—) and emission (—) spectra of H_2L^1 (**1**), in degassed methanol at 298 K.

ligand centred bands are accompanied by multiple bands extending into the visible region (400–460 nm). The excitation and emission spectra of the ligand and the complexes are listed in Table 1. On excitation at 390 nm, the ligand H_2L^1 (**1**), strongly fluoresces in the blue region (444 nm) due to an intraligand $^1(\pi–\pi^*)$ transition [11a]. Upon complexation with iron(III), the emission peak is slightly red shifted with a significant quenching in emission intensity, as observed in $[Fe^{III}(HL^1)_2]Cl$ (**2**). Subsequent quenching is observed in the deprotonated complex, $[Fe^{III}(L^2)_2]Cl$ (**3**), and the methylated complex, $[Fe^{III}(MeL^1)_2]Cl$ (**4**), with a slight shift in emission wavelength (Table 1). Thus all the complexes **2**, **3** and **4** emit strongly in the blue region (400–460 nm) of the spectrum (Fig. 2). During excitation, the ligand **1** and complex **2** undergo an auto increment in fluorescence intensity at room temperature, without the influence of any external reagent, viz. acid, alkali, excess metal or ligand, possibly due to the internal photo induced azo-imine tautomerism (Scheme 2) [16,17]. The rate of increment is the highest for ligand **1**.

Deprotonation of the imine form, $[Fe^{III}(HL^1)_2]Cl$ (**2**), stabilizes the azo form, $[Fe^{III}(L^2)_2]Cl$ (**3**), with a decreased rate of increment. Complex **3** was isolated and characterized (FTIR $\nu_{N=N} \sim 1450\ cm^{-1}$). Interestingly, the increment is totally stopped in the methyl substituted complex, $[Fe^{III}(MeL^1)_2]Cl]$ (**4**), due to the unavailability of the –NH proton required for the intramolecular tautomerism [16,17].

3.3. Thermodynamics of binding

The association constant (K_{ass}) of complex **2** can be estimated spectrophotometrically (Fig. 3) according to Eq. (1) [18], where X represents the absorption intensity, C_H and C_G are the corresponding concentrations of the ligand and the metal ion.

The K_{ass} (UV–Vis) was found to be 4.6421×10^4 at 298 K. The temperature dependence of the binding constant was studied between 298 and 308 K, and the values of the

$$X = X_0 + (X_{lim} - X_0)/2C_0\{C_H + C_G + 1/K_{ass} - [(C_H + C_G + 1/K_{ass})^2 - 4C_HC_G]^{1/2}\} \quad (1)$$

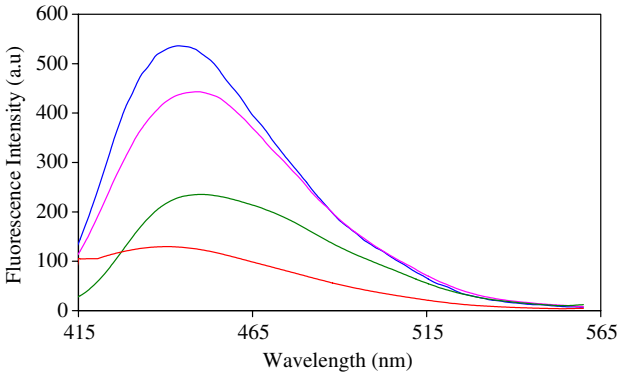
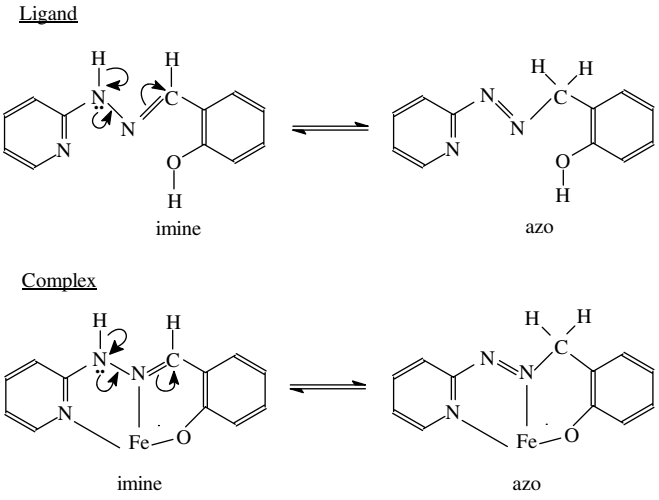


Fig. 2. Emission spectra of ligand **1** (—) and complexes **2** (—), **3** (—), **4** (—), (1×10^{-5} M) in degassed methanol (pH = 7.0), $\lambda_{exc} = 390$ nm, at 298 K.



Scheme 2.

thermodynamic parameters ($\Delta G^0 = -6401.04$ cal/M, $\Delta H^0 = -636.36$ cal/M, $\Delta S^0 = 23.62$ cal/M/deg) were obtained at 298 K in degassed methanol. It is seen that the binding process is favoured by a negative ΔH^0 and positive ΔS^0. A variable temperature UV–Vis titration was performed to monitor the variation of the dissociation constant with temperature, which often gives clues as to the nature of the forces involved in the interaction.

Table 1
Spectral characteristics of iron(III) complexes of H_2L^1

Compounds	Excitation		Emission		F/F_o[a]
	λ_{exc} (nm)	log ε	λ_{em} (nm)	Intensity (a.u)	
H_2L^1 (**1**)	390	5.10	444.49	536.84	
$[Fe^{III}(HL^1)_2]^+$ (**2**)	390	4.58	449.04	438.51	0.81
$[Fe^{III}(L^2)_2]^+$ (**3**)	390	4.32	451.32	235.18	0.47
$[Fe^{III}(MeL^1)_2]^+$ (**4**)	390	4.39	444.11	129.54	0.24

[a] The ratio of fluorescence intensity of the metal complexes of H_2L^1 in the presence of metal (F) and in the absence of metal (F_o). The concentrations of metal and H_2L^1 being 10^{-6} mol/L and 10^{-5} mol/L respectively.

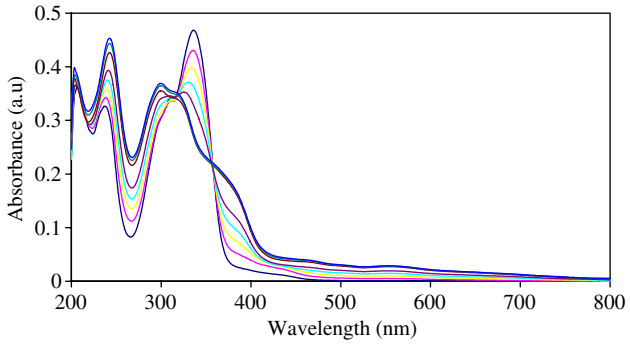


Fig. 3. UV absorbance spectra of H_2L^1 (1.0×10^{-5} M) upon addition of iron(III) (1.0×10^{-6} M – 1.0×10^{-5} M) in degassed methanol (pH = 7.0) at 298 K.

3.4. Electrochemistry

The redox properties of the complexes have been studied in acetonitrile (0.1 M TEAP) solution by cyclic voltammetry (CV) using a platinum-working electrode. $[Fe^{III}(HL^1)_2]Cl$ (**2**), displays a quasi-reversible (ΔE_p = 140 mV) one-electron cyclic response near – 0.15 V versus the saturated calomel electrode (SCE). The response is assigned to the $[Fe^{III}(HL^1)_2]^+/[Fe^{II}(HL^1)_2]$ reduction. Isolation of $[Fe^{II}(HL^1)_2]$ in the pure state is difficult due to rapid air oxidation of the bivalent species. In the deprotonated complex $[Fe^{III}(L^2)_2]Cl$ (**3**), an irreversible couple is observed at a lower potential, possibly due to the predominance of the azo tautomer over the imine form [19].

3.5. X-ray structure of $[Fe^{III}(HL^1)_2]Cl \cdot H_2O$

The molecular structure of complex **2** has been established by single crystal X-ray diffraction. A view of $[Fe^{III}(HL^1)_2]Cl \cdot H_2O$ (**2**), is shown in Fig. 4. The water molecules and chloride ions occur as discrete entities in the lattice and participate in intermolecular hydrogen bonding. The two ligands span meridionally, binding the metal in a hexadentate FeN_4O_2 fashion, utilizing pairs of pyridyl-N, phenolato-O and imine-N, resulting in a *cis* configuration for the FeN_4O_2 sphere. The angles at the metal centre between the *cis* positioned donor pairs span the range 73.27(5)–97.58(5)° and those between *trans* positioned pairs are 154.08(5)–155.30(5)°. The two tridentate ligands have the same gross structures with little conformational change. The five-membered FeN_3C chelate rings are relatively planar. The r.m.s. deviations of the five fitted atoms are 0.0535 for ring [Fe1, N1, C5, N2, N3] and 0.0164 for ring [Fe1, N4, C17, N5, N6]. The six-membered FeC_3NO chelate rings are also relatively planar, with the

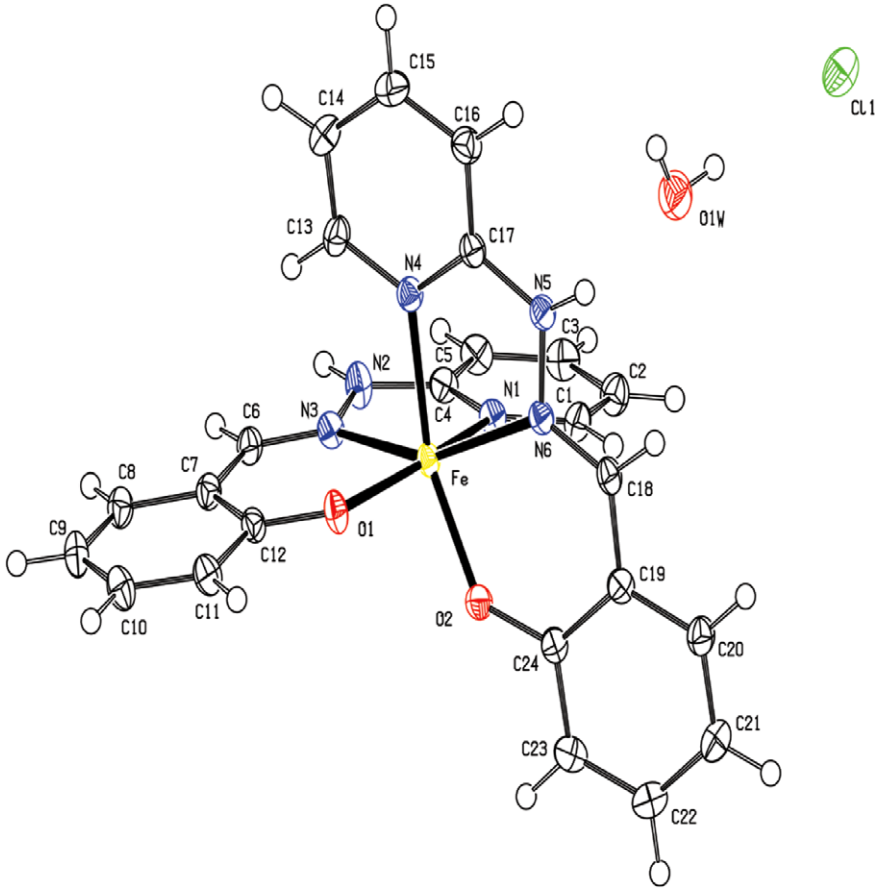


Fig. 4. Perspective view and atom labelling scheme for $[Fe^{III}(HL^1)_2]Cl \cdot H_2O$ (**2**). All atoms are represented by their 50% thermal probability ellipsoids.

r.m.s deviations of the six fitted atoms being 0.0124 for ring [Fe1, O1, C12, C7, C6, N3], and 0.0759 for ring [Fe1, O2, C24, C19, C18, N6]. The four Fe–N lengths are virtually same, the average value being 2.159(1) Å, as expected for high-spin iron(III) complexes (2.1 Å) [20]. The Fe–$O_{phenolate}$, bond length, 1.9041(12) Å, is almost equal to other high-spin iron(III) complexes (~1.89 Å) [21]. The two imine (–NH) bond lengths are almost the same, the average value is 1.373(2) Å, longer than the N=N bond length, 1.28 Å [22]. The bond distance of N(3)–C(6) is 1.295(2) Å and that of N(6)–C(18) is 1.296(2) Å, which is normal for C=N [23] (See Tables 2 and 3).

3.6. Hydrogen bonding

In complex **2**, there is one strong N(5)–H(5A)···O(1w), 2.841(2) Å, and one weak N(2)–H(2A)···Cl(1), 3.111(2) Å intermolecular hydrogen bond, as expected for N–H···O (~2.90 Å) [24] and N–H···Cl (~3.08 Å) [12]. These N–H···O and N–H···Cl hydrogen bonds undergo weak interactions with chloride and water molecules present in the crystal lattice. The crystal packing diagram (Fig. 5) clearly shows this interlayer O–H···Cl bridging (O(1w)–H(1wA)–Cl(1), 3.162(2) Å; O(1w)–H(1wB)–Cl(1), 3.199(2) Å) at the interface of the main molecule [12].

Table 2
Selected bond lengths (Å) and bond angles (°) for $[Fe^{III}(HL^1)_2]Cl \cdot H_2O$ (**2**)

Bond lengths			
Fe–N(1)	2.1583(14)	Fe–O(1)	1.9069(12)
Fe–N(3)	2.1551(13)	Fe–O(2)	1.9013(12)
Fe–N(4)	2.1590(14)	N(2)–N(3)	1.3730(20)
Fe–N(6)	2.1672(13)	N(5)–N(6)	1.3742(19)
N(2)–H(2A)–Cl(1^a)	3.1107(15)	N(5)–H(5A)···O(1W)	2.8410(20)
O(1W)–H(1WA)–Cl(1)	3.1623(18)	O(1W)–H(1WB)···Cl(1^b)	3.1991(18)
Bond angles			
N(1)–Fe–N(4)	97.58(5)	O(1)–Fe–N(4)	90.74(5)
N(1)–Fe–N(6)	90.41(5)	O(1)–Fe–N(6)	114.28(5)
N(3)–Fe–N(1)	73.43(5)	O(2)–Fe–N(1)	91.62(6)
N(3)–Fe–N(4)	88.98(5)	O(2)–Fe–N(3)	116.90(5)
N(3)–Fe–N(6)	154.39(5)	O(2)–Fe–N(4)	154.08(5)
N(4)–Fe–N(6)	73.27(5)	O(2)–Fe–N(6)	82.52(5)
O(1)–Fe–N(1)	155.30(5)	O(2)–Fe–O(1)	90.86(5)
O(1)–Fe–N(3)	83.56(5)		

Symmetry transformations used to generate equivalent atoms: [a] $x-1, y, z$; [b] $x, -y+1/2, z+1/2$.

Table 3
Hydrogen-bonds for $[Fe^{III}(HL^1)_2]Cl \cdot H_2O$ (**2**) [(Å) and (°)]

D–H···A	*d*(D–H)	*d*(H···A)	*d*(D···A)	∠(DHA)
N(2)–H(2A)···Cl(1^i)	0.87(2)	2.24(2)	3.1107(15)	172(2)
N(5)–H(5A)···O(1W)	0.82(2)	2.05(2)	2.841(2)	162(2)
O(1W)–H(1WA)···Cl(1)	0.775(17)	2.395(18)	3.1623(18)	171(3)
O(1W)–H(1WB)···Cl(1^{ii})	0.798(18)	2.406(18)	3.1991(18)	173(3)

Symmetry transformations used to generate equivalent atoms: (i) $x-1, y, z$; (ii) $x, -y+1/2, z+1/2$.

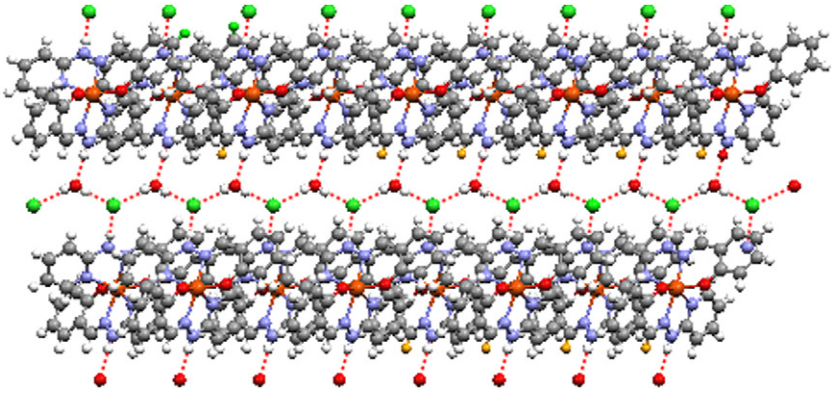


Fig. 5. Packing diagram along the *b* axis exhibiting alternate Cl(●)···H–O(●) bonding in $[Fe^{III}(HL^1)_2]Cl \cdot H_2O$ (**2**).

4. Conclusion

A series of blue luminescent high-spin ($s = 5/2$) iron(III) complexes of H_2L^1 have been successfully designed and synthesized. Deprotonation and insertion of a nucleophile into the parent complex significantly modulates the photophysical and chemical properties. Moreover, the ligand and its iron(III) complex undergo photoinduced intramolecular azo-imine tautomerism. The association constant (K_{ass}) and thermodynamic calculations clearly revealed that the binding process is favoured by a negative ΔH^0 and positive ΔS^0. The X-ray structure of complex **2** shows that the acyclic tridentate H_2L^1 (**1**), span meridionally, binding the metal in a hexadentate FeN_4O_2 fashion, utilizing pairs of pyridyl-N, phenolato-O and imine-N, resulting in a *cis* configuration for the FeN_4O_2 coordination sphere. The complex also displays bridging interlayer hydrogen bonding.

Acknowledgements

Financial support received from the Department of Science and Technology, New Delhi, and the Council of Scientific and Industrial Research, New Delhi, are gratefully acknowledged. We are grateful to the University of Kalyani for providing infrastructural facilities.

Appendix A. Supplementary material

CCDC 632086 contains the supplementary crystallographic data for $[Fe^{III}(HL^1)_2]Cl \cdot H_2O$ (**2**). These data can be obtained free of charge via http://www.ccdc.cam.ac.uk/conts/retrieving.html, or from the Cambridge Crystallographic Data Centre, 12 Union Road, Cambridge CB2 1EZ, UK; fax: (+44) 1223-336-033; or e-mail: deposit@ccdc.cam.ac.uk. Supplementary data associated with this article can be found, in the online version, at doi:10.1016/j.poly.2007.03.053.

References

[1] (a) S.S. Sun, A.J. Lees, Coord. Chem. Rev. 230 (2002) 171;
(b) C. Bargossi, M.C. Fiorini, M. Montalti, L. Prodi, N. Zaccheroni, Coord. Chem. Rev. 208 (2000) 17;
(c) E. Kimura, S. Aoki, BioMetals 14 (2001) 191, and references cited therein;
(d) L. Fabbrizzi, G. Francese, M. Licchelli, A. Perotti, A. Taglietti, Chem. Commun. (1997) 581;
(e) L. Fabrizzi, M. Licchelli, L. Parodi, A. Poggi, A. Taglietti, Eur. J. Inorg. Chem. (1999) 35;
(f) G. De Santis, L. Fabbrizzi, M. Licchelli, A. Poggi, A. Taglietti, Angew. Chem., Int. Ed. Engl. 35 (1996) 202.

[2] (a) V. Balzani, P. Ceroni, S. Gestermann, C. Kauffmann, M. Gorka, F. Vogtle, Chem. Commun. (2000) 853;
(b) R.Y. Tsien, Biochemistry 19 (1980) 2396;
(c) G. Grynkiewicz, M. Poenie, R. Y Tsien, J. Biol. Chem. 260 (1985) 3440;
(d) A. Minta, J. Kao, R.Y. Tsien, J. Biol. Chem. 264 (1989) 8171.

[3] (a) C.-H. Chen, J. Shi, Coord. Chem. Rev. 171 (1998) 161;
(b) C.W. Tang, S.A. Van Slyke, Appl. Phys. Lett. 51 (1987) 913;
(c) C.W. Tang, S.A. Van Slyke, C.H. Chen, J. Appl. Phys. 65 (1989) 3610;
(d) S. Miyata, S. Nalwa, Org. Electroluminescent Materials and Devices, Gordon and Breach, Japan, 1997.

[4] (a) A.P. de Silva, H.Q.N. Gunaratne, T. Gunlaugsson, A.J.M. Huxley, C.P. McCoy, J.T. Rademacher, T.E. Rice, Chem. Rev. 97 (1997) 1515;
(b) A.W. Czarnik, Chem. Biol. 2 (1995) 423;
(c) A.W. Czarnik, Fluorescent chemosensors for ion and molecule recognition, ACS Symposium Series, vol. 538, Am. Chem. Soc., Washington, DC, 1993;
(d) L. Fabbrizzi, A. Poggi, Chem. Soc. Rev. 24 (1995) 197;
(e) J.P. Desvergne, A.W. Czarnik, in: Chemosensors for Ion and Molecule Recognition, Kluwer Academic Publishers, Boston, 1997;
(f) A.P. de Silva, D.B. Fox, A.J.M. Huxley, T.S. Moody, Coord. Chem. Rev. 205 (2000) 41;
(g) D.T. Mc Quade, A.E. Pullen, T.M. Swager, Chem. Rev. 100 (2000) 2537;
(h) G. Klein, D. Kaufmann, S. Schurch, J. Reymond, Chem. Commun. (2001) 561, and references cited therein;
(i) L. Wang, X. Zhu, W. Wang, J. Guo, W. Wong, Z. Li, J. Chem. Soc., Dalton Trans. (2005) 3235;
(j) V. Amendola, L. Fabbrizzi, P. Pallavicini, Coord. Chem. Rev. 216–217 (2001) 435.

[5] (a) L. Fabbrizzi, M. Licchelli, P. Pallavicini, A. Perotti, D. Sacchi, Angew. Chem., Int. Ed. Engl. 33 (1994) 1975;
(b) L. Fabbrizzi, M. Licchelli, P. Pallavicini, A. Perotti, A. Taglietti, D. Sacchi, Chem. Eur. J. 2 (1996) 75;
(c) A.P. de Silva, H.Q.N. Gunaratne, C.P. McCoy, J. Am. Chem. Soc. 119 (1997) 7891;
(d) B. Ramchandran, A. Samanta, Chem. Commun. (1997) 1037;
(e) G.E. Collins, L.S. Choi, Chem. Commun. (1997) 1135;
(f) J. Yoon, N.E. Ohler, D.H. Vance, W.D. Aumiller, A.W. Czarnik, Tetrahedron Lett. 38 (1997) 3845;
(g) U. Oguz, E.U. Akkaya, Tetrahedron Lett. 38 (1997) 4509;
(h) E. Brunet, M.T. Alonso, O. Juanes, R. Sedano, J.C. Rodriguez-Ubis, Tetrahedron Lett. 38 (1997) 4459;
(i) L. Fabbrizzi, M. Licchelli, P. Pallavicini, L. Parodi, Angew. Chem. 110 (1998) 838;
(j) G. Hennrich, H. Sonnenschein, U. Resch-Genger, J. Am. Chem. Soc. 121 (1999) 5073;
(k) W.S. Xia, R.H. Schmehl, C.J. Li, J. Am. Chem. Soc. 121 (1999) 5599;
(l) H.F. Ji, G.M. Brown, R. Debestani, Chem. Commun. (1999) 609;
(m) K. Rurack, M. Kollmannsberger, U. Retsch-Genger, J. Duab, J. Am. Chem. Soc. 122 (2000) 968;
(n) G.K. Walkup, S.C. Burdette, S.J. Lippard, R.Y. Tsien, J. Am. Chem. Soc. 122 (2000) 5644;
(o) L. Prodi, C. Bargossi, M. Montalti, N. Zaccheroni, N. Su, J.S. Bradshaw, R.M. Izzat, P.B. Savage, J. Am. Chem. Soc. 122 (2000) 6769;
(p) H.F. Ji, R. Debestani, G.M. Brown, R.A. Sachleben, Chem. Commun. (2000) 833;
(q) W.X. Xia, R.H. Schmehl, C.J. Li, Chem. Commun. (2000) 695;
(r) W.X. Xia, R.H. Schmehl, C.J. Li, Eur. J. Org. Chem. (2000) 387.

[6] (a) I.R. Laskar, S. Hsu, T. Chen, Polyhedron 24 (2005) 189;
(b) R.J. Holmes, W.D. Andrade, S.R. Forest, X. Ren, .J. Li, M. Thompson, Appl. Phys. Lett. 83 (2003) 3818;
(c) S. Tokito, T. Iijima, Y. Suzuri, H. Kita, T. Tsuzuki, F. Sato, Appl. Phys. Lett. 83 (2003) 569;
(d) K.Y. Ho, W.Y. Yu, K.K. Cheung, C.M. Che, Chem. Commun. (1998) 2101;
(e) La M. Deda, I. Aiello, A. Grisolia, M. Ghedini, M. Amati, F. Lelj, J. Chem. Soc., Dalton Trans. (2006) 330;
(f) A.B. Tamayo, B.D. Alleyne, P.I. Djurovich, S. Lamansky, I. Tsyba, N.N. Ho, R. Bau, M.E. Thompson, J. Am. Chem. Soc. 125 (2003) 7377.

[7] F. Thomas, G. Serratrice, Claude Beguin, E.S. Aman, J.L. Pierre, M. Fontecave, J.P. Laulhere, J. Biol. Chem. 274 (1999) 13375.

[8] (a) A. Ali, Q. Zhang, J. Dai, X. Huang, BioMetals 12 (2003) 285;
(b) T. Palanché, F. Marmolle, M.A. Abdallah, A. Shanzer, A.M. Albrecht-Gary, J. Biol. Inorg. Chem. 4 (1999) 188;
(c) Y. Sugiura, J. Kuwahara, T. Nagasawa, H. Yamada, J. Am. Chem. Soc. 109 (1987) 5848;
(d) S.D. Lytton, B. Mester, J. Libman, A. Shenzer, Z. Ioav, Anal. Biochem. 205 (1992) 326.
[9] (a) V. Sadus, Trans. Met. Chem. 20 (1995) 256;
(b) A. Zuhri, Z.A. Ali, Maher A. Eid, S. Shalabi, Mikrochim. Acta. 20 (1987) 153;
(c) A. Zuhri, Z.A. Ali, Maher A Eid, M. Foua'd, Anal. Lett. 19 (1986) 1881;
(d) K. Bhoon, V. Coll, in: Proceedings of the Indian National Science Academy, Part A, Physical Sc., vol. 49, 1983, p. 118;
(e) F.Z. Mona, L. John, J. Org. Chem. 41 (1976) 2491.
[10] (a) M. Mohan, N.S. Gupta, C. Lakhami, N.K. Jha, J. Inorg. Biochem. 31 (1987) 7;
(b) S. Uday, S. Padhye, B. David, R. Daniel, F. Scott, E.A. Christopher, K.P. Annie, J. Inorg. Biochem. 90 (2002) 127.
[11] (a) M.R. Ceba, C. Blanco, F.G. Sánchez, J. Photochem. 30 (1985) 353;
(b) C. Blanco, F.G. Sánchez, Anal. Chem. 56 (1984) 2035.
[12] (a) G. Desiraju, T. Steiner, The Weak Hydrogen Bond in Structural Chemistry and Biology, Oxford University Press, Oxford, 1999;
(b) G. Desiraju, T. Steiner, The Weak Hydrogen Bond, Oxford University Press, Oxford, 1997;
(c) P. Drevenšek, I. Leban, I. Turel, G. Giester, E. Tillmanns, Acta Crystallogr., Sect. C 59 (2003) m376;
(d) T. Steiner, G.R. Desiraju, Revi. Chem. Commun. (1998) 891;
(e) P.M. Bhatt, G.R. Desiraju, Acta Crystallogr., Sect. E 63 (2007) o771;
(f) R. Banerjee, B.K. Saha, G.R. Desiraju, Acta Crystallogr., Sect. C 62 (2006) o346;
(g) P.M. Bhatt, G.R. Desiraju, Acta Crystallogr., Sect. C 62 (2006) o362;
(h) B.K. Saha, R. Banerjee, A. Nangia, G.R. Desiraju, Acta Crystallogr., Sect. E 62 (2006) o2283.
[13] (a) B.K. Lahiri, S. Bhattacharya, B. Ghosh, A. Chakravorty, Inorg. Chem. 26 (1987) 4324;
(b) P. Basu, S.B. Choudhury, S. Pal, A. Chakravorty, Inorg. Chem. 28 (1989) 2680.
[14] (a) Stoe. 2005. X-Area V1.26 & X-RED32 V1.26 Softwarem, Stoe & Cie GmbH, Darmstadt, Germany;
(b) G.M. Sheldrick, SHELXS-97 Program for Crystal Structure Determination, Acta Crystallogr., Sect. A 46 (1990) 467, 473;
(c) G.M. Sheldrick, SHELXL-97, Universität Göttingen, Göttingen, Germany, 1999;
(d) A.L. Spek, J. Appl. Cryst. 36 (2003) 7.
[15] J.F. Geldard, F. Lions, Inorg. Chem. 2 (1963) 270.
[16] (a) H. Görner, S. Khanra, T.W. Müller, P. Chaudhuri, J. Phys. Chem. A 110 (2006) 2587;
(b) A. Akai, T. Harada, K. Ya, K. Ohno, M. Aida, J. Phys. Chem. A 110 (2006) 6016.
[17] B. Mondal, S. Chakraborti, P. Munshi, M.G. Walawalkar, G.K. Lahiri, J. Chem. Soc., Dalton Trans. (2000) 2327.
[18] (a) J. Valeur, J. Pouger, J. Bourson, J. Phys. Chem. 96 (1992) 6545;
(b) Y. Liu, B. Li, C. You, J. Org. Chem. 66 (2001) 225.
[19] A. Wood, W. Aris, D.J.R. Brook, Inorg. Chem. 43 (2004) 8355.
[20] W. Lin, W.J. Welsh, W.R. Harris, Inorg. Chem. 33 (1994) 884.
[21] M. Lanznaster, A. Neves, A.J. Bortuluzzi, B. Szpoganicz, E. Schwingel, Inorg. Chem. 41 (2002) 5641.
[22] S. Karmakar, A. Chakravorty, Inorg. Chem. 35 (1996) 1935.
[23] N. Bag, S.B. Chowdhury, A. Pramanik, G.K. Lahiri, A. Chakravorty, Inorg. Chem. 29 (1990) 5013.
[24] M. Pecul, J. Leszczynski, J. Sadlej, J. Phys. Chem. A 104 (2000) 8105.

(apical) position of this subsite is occupied by a third non-bridging solvent molecule coordinated to the dimanganese cluster. Terminally bound water molecules are easily displaced from the metal complexes and this apical site likely serves as the initial substrate binding site during catalysis. The other subsite (Mn2) has a bidentate (chelating) coordination mode for glutamate, which may prevent exogenous ligands from binding and makes each of the manganese ions six-coordinate in the cluster, with approximately octahedral geometry at each subsite. The Mn–Mn separation in the resting state of the enzyme is 3.03 Å and both manganese centres are in the three oxidation state. The EXAFS analysis of the same protein predicted a Mn–Mn separation of 3.53 Å in the fully reduced state, i.e. 2,2 oxidation state [5]. It is well known that the azide ion acts as an inhibitor of *L. plantarum* catalase forming an active site complex. The crystal structure of the azide coordinated protein is virtually indistinguishable from the native structure except in the vicinity of the active site, where significant differences occur. In the azide complex of the oxidized form of the enzyme, the anion occupies a terminal position on the Mn1 subsite, replacing the solvent present in the native structure. Since azide is an analog of hydrogen peroxide, this mode of bonding is likely to mimic that of the coordinated substrate. The X-ray structure of azide bonded catalase in the oxidized state revealed the terminal bonding mode for the coordinated azide, however the coordination mode of azide in the reduced state of the enzyme is not definitely known.

Carboxylato bridged dinuclear Mn complexes have attracted much attention in recent years because of their potential biological relevance [6] in different manganese containing enzymes [7]. While several dinuclear Mn complexes having (μ-oxo)bis(μ-carboxylato) [8], (μ-hydroxo)-bis(μ-carboxylato) [9], (μ-hydroxo)(μ-acetato) [10], (μ-hydroxo)bis(μ-acetato) [11] bridges are known, no example exist of dinuclear manganese complexes with a (μ-azido)(μ-carboxylato) bridging unit. As a part of our synthetic effort towards modelling the active site of Mn-containing protein by using the hindered tris(pyrazolyl)borate as a supporting ligand, we now report on dinuclear complexes bridged with a single carboxylato and a single azido unit along with other carboxylate complexes of manganese (II), and their catalytic activity.

2. Experimental

2.1. Materials

All solvents used were purified by the literature methods [12]. Reagents of the highest grade commercially available were used without further purification. All manipulations were carried out under a nitrogen atmosphere using standard Schlenk tube techniques unless otherwise stated. 3,5-iPr_2pzH [$Pz^{iPr2}H$] (**1**), KHB(3,5-$iPr_2pz)_3$ [Tp^{iPr2}] (**2**) [13], KHB(3-Ph,5-Mepz)$_3$ [$Tp^{Ph,Me}$] (**3**) [14] and Tp^{iPr2}MnCl (**4**) [15] were synthesized by the literature methods.

2.2. Physical methods

IR spectra were obtained on a Thermo Nikolet Nexus FT-IR spectrometer in KBr discs. Room temperature magnetic susceptibility measurements were done on a Princeton applied research vibrating sample magnetometer Model 155 whereas the magnetic susceptibility measurements at variable temperature (from liquid helium to room temperature) were performed on a Quantum Design Squid Magnetometer Model MPMS. The X-ray data collection and processing for **6** and **9** were performed on a Kappa Apex Bruker CCD detector with Mo Kα radiation ($\lambda = 0.71070$ Å). In the reduction of data, Lorentz and polarization corrections, and empirical absorption corrections were made. All non-hydrogen atoms were refined aniostropically. The structures were solved by Patterson methods and refined anisotropically with the SHELX program suite [16]. Hydrogen atoms were constrained by a rigid model.

2.3. Synthesis of the complexes

2.3.1. [$Tp^{Ph,Me}$MnCl] (**5**)

$MnCl_2 \cdot 4H_2O$ (0.198 g, 1.0 mmol) was stirred with **3** (0.521 g, 1.0 mmol) in 10 mL CH_3OH and 20 mL CH_2Cl_2 for 1 h. The solution was filtered over celite and the solvent was evaporated to dryness under vacuum. Crystallization of complex **5** from acetonitrile yielded a colorless solid in 89% (0.51 g, 0.89 mmol.) yield. *Anal.* Calc. for $C_{30}H_{28}N_6BClMn$: C, 62.79; H, 4.91; N, 14.64; Cl, 6.17. Found: C, 63.00; H, 4.82; N, 14.36; Cl, 6.21%. IR (KBr, cm^{-1}): ν(BH) 2541.

2.3.2. [$Tp^{Ph,Me}$Mn(acac)] (**6**)

To an acetonitrile (30 mL) solution of complex **5**, one equivalent of sodium acetylacetonate (0.109 g, 0.89 mmol) was added and the resulting solution was stirred for 8 h. The reaction mixture was filtered over celite and the solvent was evaporated to dryness under vacuum. Crystals suitable for X-ray data collection were obtained by slow cooling of the compound in a mixture of CH_2Cl_2 and CH_3CN in 75% (0.43 g, 0.67 mmol.) yield. *Anal.* Calc. for $C_{35}H_{36}N_6O_2BMn$: C, 65.84; H, 5.68; N, 13.16. Found: C, 66.00; H, 5.82; N 13.06%. IR (KBr, cm^{-1}): ν(BH) 2539, ν(CO) 1594. Magnetic moment μ_{eff} (295 K) = 5.78 BM.

2.3.3. [$Tp^{Ph,Me}$Mn(μ-N_3) (μ-acac)Mn $Tp^{Ph,Me}$] (**7**)

The reaction of complex **6** (0.427 g, 0.67 mmol) in dichloromethane (20 mL) and sodium azide (0.043 g, 0.67 mmol) in methanol (10 mL) for 3 h followed by filtration over celite and evaporation to dryness under vacuum resulted in the formation of compound **7** in 77% (0.35 g, 0.52 mmol) yield. *Anal.* Calc. for $C_{65}H_{64}N_{15}O_2B_2Mn_2$: C, 64.05; H, 5.29; N, 17.23. Found: C, 63.90; H, 5.22; N, 17.16%. IR (KBr, cm^{-1}): ν(BH) 2514, ν(CO) 1596, $\nu(N_3)$ 2075. Magnetic moment μ_{eff} (295 K) = 5.57 BM/Mn^{2+}.

*2.3.4. [Tp^{ipr2}Mn(pic)] (**8**)*

To a dichloromethane (20 mL) solution of **4** (0.556 g, 1.0 mmol) was added a 10 mL methanolic solution of potassium picolinate (0.161 g, 1.0 mmol), and the resulting solution was stirred for 3 h. After this time, the reaction mixture was filtered over celite. The evaporation of solvent under vacuum resulted in a white crystalline compound in 64% (0.41 g, 0.64 mmol) yield. *Anal.* Calc. for $C_{33}H_{50}N_7O_2BMn$: C, 61.68; H, 7.84; N, 15.23. Found: C, 61.59; H, 7.94; N, 15.43%. IR (KBr, cm^{-1}), ν(BH) 2538, ν_{as}(COO) 1592, ν_s(COO) 1470. Magnetic moment μ_{eff} (295 K) = 5.83 BM.

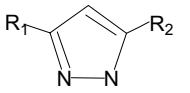
*2.3.5. [Tp^{ipr2}Mn(μ-N$_3$)(μ-pic)Mn(Pz^{ipr2})Tp^{ipr2}] (**9**)*

The reaction of complex **8** (0.411 g, 0.64 mmol), Pz^{ipr2}H (0.097 g, 0.64 mmol) and sodium azide (0.041 g, 0.64 mmol) in 20 mL dichloromethane and 10 mL methanol for 3 h resulted in the formation of complex **9**. The resulting solution was filtered over celite and evaporated to dryness under vacuum. The solid was dissolved in a mixture of dichloromethane and acetonitrile (1:1 ratio) and a crystalline compound was obtained by slow cooling of the solution at 4 °C in 36% (0.310 g, 0.23 mmol) yield. *Anal.* Calc. $C_{69}H_{112}N_{18}O_2B_2Mn_2$: C, 61.06; H, 8.32; N, 18.57. Found: C, 61.39; H, 8.56; N 18.69%. IR (KBr, cm^{-1}), ν(BH) 2545, ν_{as}(COO) 1593, ν_s(COO) 1469, ν(N$_3$) 2077. Magnetic moment μ_{eff} (295 K) = 5.68 BM/Mn^{2+}.

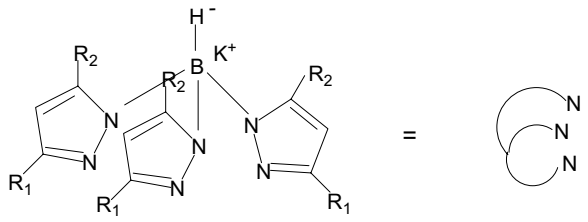
3. Results and discussion

As reported in our previous work [17], the reaction of a binuclear Mn(II) di(μ-hydroxo) complex with one equivalent of benzoic acid results in the replacement of one hydroxide ligand to give the corresponding bimetallic (μ-hydroxo)(μ-benzoato) complex. Further replacement of the bridging hydroxide with azide gave a binuclear Mn(II) complex [18]. Due to the high solubility of this compound in the majority of organic solvents, we could not get a suitable single crystal for X-ray structure determination. However on the basis of IR and other spectroscopic techniques, a (μ-azido)(μ-benzoato) bridged manganese (II) dimer complex was proposed.

In our effort to prepare a model compound for Mn-containing pseudocatalase, first we prepared the starting complexes Tp^{iPr2}MnCl (**4**) and Tp^{Ph,Me}MnCl (**5**). The starting materials were prepared by reacting manganese (II) chloride with both 3-phenyl,5-methyl and 3,5-diisopropyl-substituted pyrazolylborate ligands (Fig. 1). The starting materials viz., **4** and **5** (Fig. 2) when treated with sodium acetylacetonate/sodium picolinate gave 5-coordinated manganese (II) complexes Tp^{Ph,Me}Mn(acac) (**6**) and Tp^{iPr2}Mn(pic) (**8**) (Fig. 3). The IR data suggested that both acac and pic are coordinated in a bidentate manner. The single crystal X-ray study of **6** suggested that the manganese ion is coordinated by three nitrogen atoms of Tp^{Ph,Me} and two oxygen atoms of acetylacetonate (Fig. 4). The Mn–N bond distances range from 2.178(2) to 2.230(2) Å



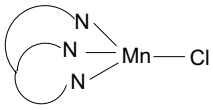
R$_1$, R$_2$ = (CH$_3$)$_2$CH- 1



R$_1$, R$_2$ = (CH$_3$)$_2$CH- 2

R$_1$ = CH$_3$ R$_2$ = C$_6$H$_5$- 3

Fig. 1. Chemdraw structures of **1**, **2** and **3**.



R$_1$, R$_2$ = (CH$_3$)$_2$CH- 4

R$_1$ = CH$_3$ R$_2$ = C$_6$H$_5$- 5

Fig. 2. Chemdraw structures of **4** and **5**.

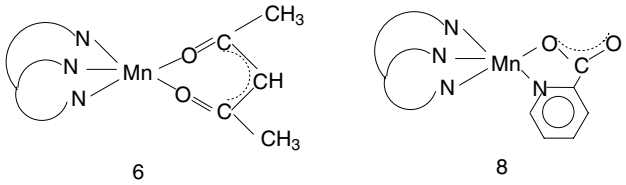


Fig. 3. Chemdraw structures of **6** and **8**.

and fall in the range of reported Mn–N bond distances of manganese complexes having other Tp ligands [19]. The Mn–O bond distances of the coordinated acetylacetonate, Mn(1)–O(1), Mn(1)–O(2), are 2.078(2) Å. These Mn–O bond distances are well within the range of other Mn–O bond distances [20]. The IR band at 1592, (ν_{as}(COO)) and 1470, (ν_s(COO)) cm^{-1} in the picolinate complex suggest the bidentate coordination mode of the ligand. Although, a crystal structure is not available for complex **8**, other data suggest the same structure with a 5-coordinated manganese center as is seen for **6**. Both complexes **6** and **8** were used for the synthesis of the corresponding azido complexes. When complexes **6** and **8** in dichloromethane solvent were treated with a methanolic solution of sodium azide for 3 h, **7** and **9** (Fig. 5) were formed, respectively. Although both these reaction were carried out in the presence of an excess amount of azide, no detectable amount of [TpMn(N$_3$)] was formed. Thus, the formation of **7** and **9** is a thermodynamically favorable reaction. Detailed characterization of these

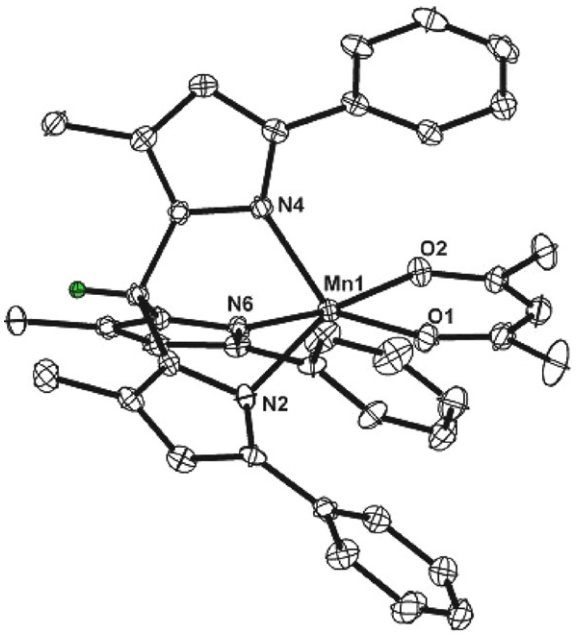
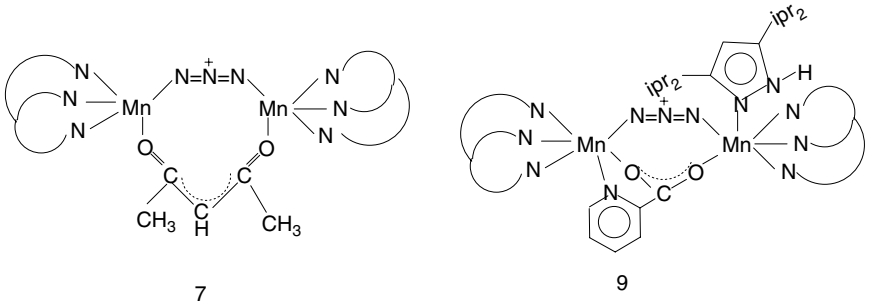


Fig. 4. Thermal ellipsoid view of complex **6** drawn at the 30% probability level. All hydrogen atoms have been omitted for clarity.

complexes revealed that both complexes have azide coordination where each metal center is 6-coordinated in **9** and 5-coordinated in complex **7**. IR data demonstrated that in both **7** and **9**, the azide ligands are coordinated in a μ-1,3-fashion. Complex **7** could not be crystallized as single crystals, but slow recrystallization of **9** from dichloromethane and acetonitrile at 4 °C gave single crystals suitable for X-ray studies. The X-ray data collection for **9** was performed at 100 K (Table 1) and a thermal ellipsoid view is given in Fig. 6. The molecular structure of **9** (Fig. 6) represents a novel (μ-1,3-azido)(μ-picolinato) bridging core. This is the first example of such a structure, while a (μ-hydroxo)(μ-1,3-azido) binuclear copper complex with Tp^{iPr2} was reported previously [21].

As shown in Fig. 6, each manganese is in a 6-coordination sphere as is present in Mn-containing catalase/pseudocatalase. The most interesting feature of this structure is that the picolinate ligand is behaving as a tridentate ligand in this complex, where one nitrogen and one oxygen is coordinated with one manganese center and only one oxygen is coordinated with the other manganese center in an asymmetric manner. The tridentate coordination nature



7 9

Fig. 5. Chemdraw structures of **7** and **9**.

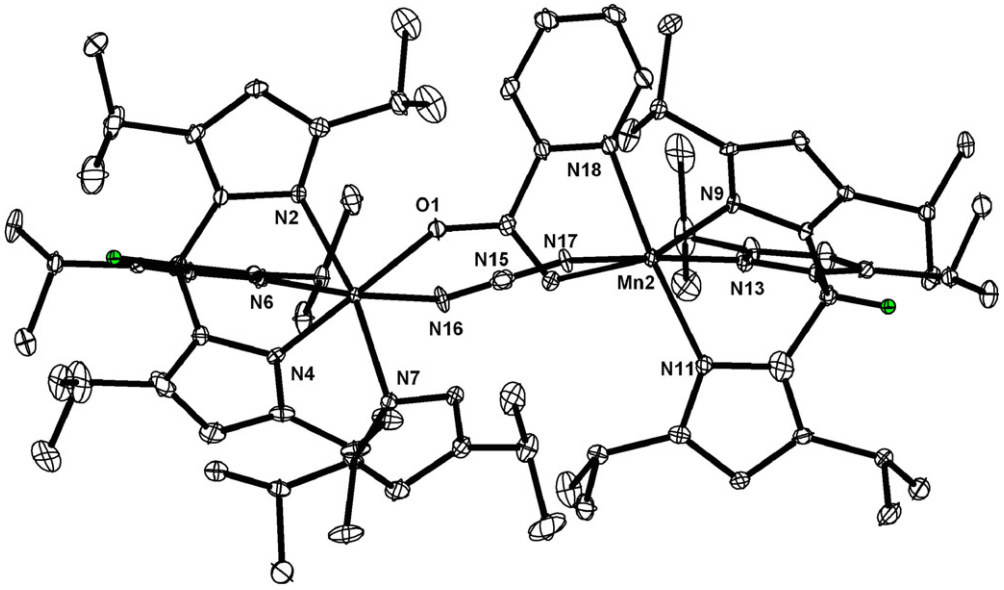


Fig. 6. Thermal ellipsoid view of complex **9** drawn at the 30% probability level. All hydrogen atoms have been omitted for clarity.

Table 1
Crystallographic data for [$Tp^{Ph,Me}$Mn(acac)] (**6**) and [Tp^{ipr2}Mn(μ-N_3)-(μ-pic)Mn(Pz^{ipr2})Tp^{ipr2}] (**9**)

	6	**9**
Formula weight	723.37	1496.44
Crystal system	triclinic	monoclinic
Space group	$P\bar{1}$	$P21/n$
Lattice parameters		
a (Å)	11.7457(17)	13.290(2)
b (Å)	11.8283(17)	31.649(5)
c (Å)	15.670(2)	21.206(3)
α (°)	101.839(2)	90.00
β (°)	94.360(2)	106.881(7)
γ (°)	119.440(2)	90.00
V (Å^3)	1815.2(4)	8535(2)
Z	2	4
D_{calc} (g/cm^3)	1.324	1.165
Data collection		
μ (Mo Kα) (cm^{-1})	0.551	0.352
θ_{max} (°)	28.79	25.55
Number of parameters refined	433	978
R	0.0758	0.0542
R_w	0.1966	0.0854

Table 2
Selected bond lengths (Å) and angles (°) for [$Tp^{Ph,Me}$Mn(acac)] (**6**) and [Tp^{ipr2}Mn(μ-N_3)(μ-pic)Mn(Pz^{ipr2}) Tp^{ipr2}] (**9**)

*$Tp^{Ph,Me}$Mn(acac) (**6**)*			
Bond lengths (Å)			
Mn(1)–O(1)	2.078(2)	Mn(1)–O(2)	2.078(2)
Mn(1)–N(2)	2.202(2)	Mn(1)–N(4)	2.178(2)
Mn(1)–N(6)	2.230(2)		
Bond angles (°)			
O(2)–Mn(1)–O(1)	85.16(8)	O(2)–Mn(1)–N(4)	111.93(9)
O(1)–Mn(1)–N(4)	108.30(8)	O(2)–Mn(1)–N(2)	156.95(9)
O(1)–Mn(1)–N(2)	93.25(8)	N(4)–Mn(1)–N(2)	90.44(8)
O(2)–Mn(1)–N(6)	92.12(8)	O(1)–Mn(1)–N(6)	157.69(9)
N(4)–Mn(1)–N(6)	93.29(8)	N(2)–Mn(1)–N(6)	80.67(8)
*Tp^{ipr2}Mn(μ-pic)(μ-N_3)Mn(Pz^{ipr2})Tp^{ipr2} (**9**)*			
Bond lengths (Å)			
Mn(1)–N(2)	2.281(5)	Mn(1)–N(4)	2.231(5)
Mn(1)–N(6)	2.253(5)	Mn(1)–N(7)	2.313(5)
Mn(1)–N(16)	2.183(5)	Mn(1)–O(1)	2.231(4)
Mn(2)–N(9)	2.216(5)	Mn(2)–N(11)	2.208(5)
Mn(2)–N(13)	2.262(5)	Mn(2)–N(17)	2.207(5)
Mn(2)–N(18)	2.297(5)	Mn(2)–O(2)	2.251(4)
Bond angles (°)			
N(16)–Mn(1)–O(1)	85.29(17)	N(16)–Mn(1)–N(4)	90.14(19)
O(1)–Mn(1)–N(4)	174.35(17)	N(16)–Mn(1)–N(6)	173.7(2)
O(1)–Mn(1)–N(6)	93.97(16)	N(4)–Mn(1)–N(6)	90.20(17)
N(16)–Mn(1)–N(2)	92.54(19)	O(1)–Mn(1)–N(2)	95.22(16)
N(4)–Mn(1)–N(2)	81.64(18)	N(6)–Mn(1)–N(2)	81.25(18)
N(16)–Mn(1)–N(7)	97.42(19)	O(1)–Mn(1)–N(7)	89.81(16)
N(4)–Mn(1)–N(7)	94.08(18)	N(6)–Mn(1)–N(7)	88.86(17)
N(2)–Mn(1)–N(7)	169.18(17)	N(11)–Mn(2)–N(17)	95.59(19)
N(11)–Mn(2)–N(9)	87.13(18)	N(17)–Mn(2)–N(9)	91.31(18)
N(11)–Mn(2)–O(2)	108.76(16)	N(17)–Mn(2)–O(2)	81.93(16)
N(9)–Mn(2)–O(2)	163.19(17)	N(11)–Mn(2)–N(13)	80.72(19)
N(17)–Mn(2)–N(13)	175.9(2)	N(9)–Mn(2)–N(13)	86.84(18)
O(2)–Mn(2)–N(13)	100.80(16)	N(11)–Mn(2)–N(18)	171.39(19)
N(17)–Mn(2)–N(18)	93.01(19)	N(9)–Mn(2)–N(18)	93.03(18)
O(2)– Mn(2)–N(18)	72.10(16)	N(13)–Mn(2)–N(18)	90.69(19)

of picolinate is not uncommon and a few examples have been reported earlier [22], but to the best of our knowledge this is the first report of a (μ-azido)(μ-picolinato) binuclear manganese (II) complex where picolinate is showing tridentate behavior. Mn1 is coordinated with three nitrogen atoms of Tp^{iPr2} and one nitrogen of free pyrazole whereas Mn2 is coordinated with only three nitrogen atoms of Tp^{iPr2} ligand. The azide molecule is coordinated with both manganese centres, bridging in a η-1,3-fashion. The striking feature of the tridentate behaviour of picolinate is that in this complex the coordination sphere of both manganese ions are six, as in native catalase/pseudocatalase enzyme, with a slight difference of the coordinating ligands in the vicinity of the metal ions. In the native enzyme it has been reported that the azide ions act as inhibitors and the crystal structure of the azide bonded catalase demonstrated that the binding of azide is terminal where as in complex **9** the azide is bonded in a bridging mode. Binuclear transition metal complexes with (μ-azido)(μ-carboxylato) are very rare in the literature [23]. The coordination mode of the azide ligand in the oxidized state of catalase is well known, but still there is speculation about the binding mode of this ligand in the reduced state. Also it has been reported in the literature that the metal–metal separation in the reduced state of the enzyme is more than that of the oxidized form and there is strong belief that the binding mode of the azide ligand may also change to bridging in the reduced form, which may be responsible for the large separation of the manganese ions. In fact the Mn–Mn separation in binuclear complexes is very much dependent on the presence of bridging ligands as evident from the Mn–Mn separation in different complexes with the Tp^{iPr2} ligand (Table 3). The Mn–Mn separation in di(μ-hydroxo) dimanganese (II) (3.33 Å), changes to 3.603(2) Å in (μ-hydroxo)(μ-pyrazolato) dimanganese(II) [24], 2.706 Å in di(μ-oxo)(μ-acetato) dimanganese (III,IV) [10] and 2.70 Å in di(μ-oxo) dimanganese (III) [15]. This distance further increases when azide is present in the bridging mode. In complex **9**, the Mn–Mn separation is 5.355 Å. The Mn–Mn separation of 5.355 Å in complex **9** gives us strong support to propose that the terminal mode of azide in the oxidized form of pseudocatalase changes to a bridging mode in the reduced form. The Mn–N bond distances of both coordinated Tp^{iPr2} ligands are in the range 2.208–

Table 3
The distances between Mn–Mn ions in different binuclear complexes of the hydrotris(3,5-diisopropyl-pyrazol-1-yl)borate ligand

Complex	Mn1–Mn2 distance (Å)	Reference
$TpMn^{II}(\mu\text{-}OH)_2Mn^{II}Tp$	3.314(1)	[15]
$TpMn^{III}(\mu\text{-}O)_2Mn^{III}Tp$	2.696(2)	[15]
$TpMn^{II}(\mu\text{-}OH)(\mu\text{-}3,5\text{-}Pr^i_2pz)Mn^{II}Tp$	3.603(2)	[24]
$TpMn^{II}(\mu\text{-}OBz)_3Mn^{II}$ $(3,5\text{-}Pr^i_2pz)_2$	3.753(2)	[19]
$TpMn^{III}(\mu\text{-}O)_2(\mu\text{-}OAc)Mn^{IV}Tp$	2.709(1)	[10]
$TpMn^{II}(\mu\text{-}OBz)_3Mn^{II}$ (Tp^iPr_2)	4.006(1)	[17]

2.281 Å, as reported for other complexes of this ligand. The bond distance of coordinated 3,5-diisopropylpyrazole (Mn1–N7, 2.313 Å) is larger than the Mn–N bond distance of Tp^{iPr2} (Table 2). The Mn–N bond distances of the coordinated azide (Mn1–N16, 2.183; Mn1–N17, 2.207 Å) are very similar to the Cu–N bond distance in the azide bridged dinuclear copper complex (Cu–N4, 2.06 Å) [21].

In complex **9**, both manganese centres (Mn1 and Mn2) are also linked to each other by a μ-1,3-OCO bridge, whereas the nitrogen of picolinate is coordinated to Mn2 only, forming a five coordinate ring as shown in Fig. 6. Fig. 7 shows the interaction between two independent molecules and Fig. 8 shows the packing diagram of the compound. As shown in Fig. 7, a CH_3–π interaction appears

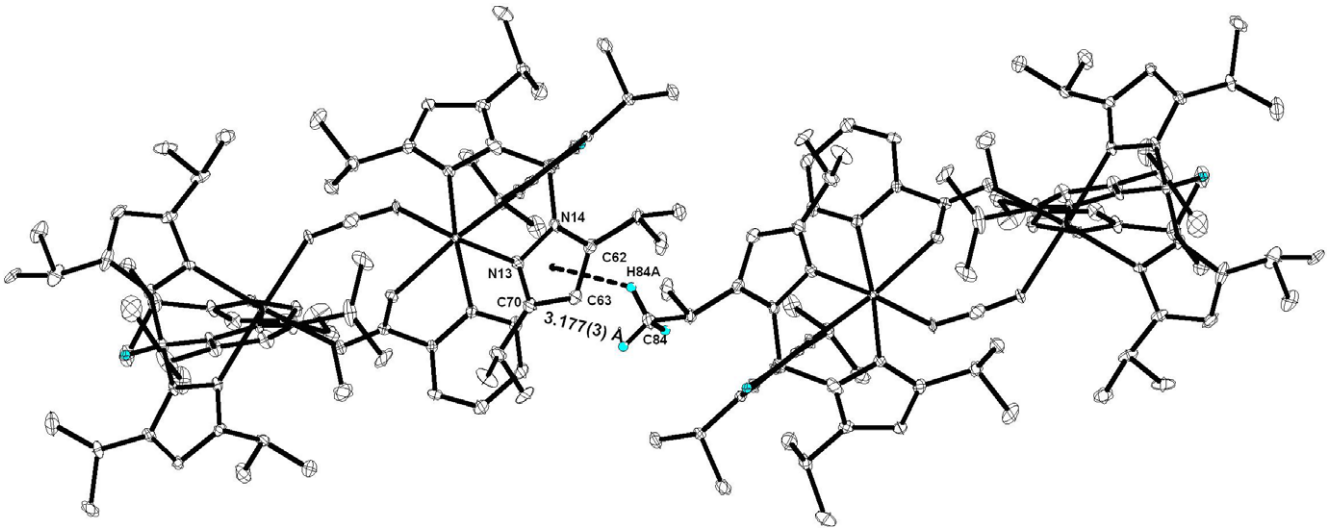


Fig. 7. Molecular structure showing CH_3–π interaction in complex **9**.

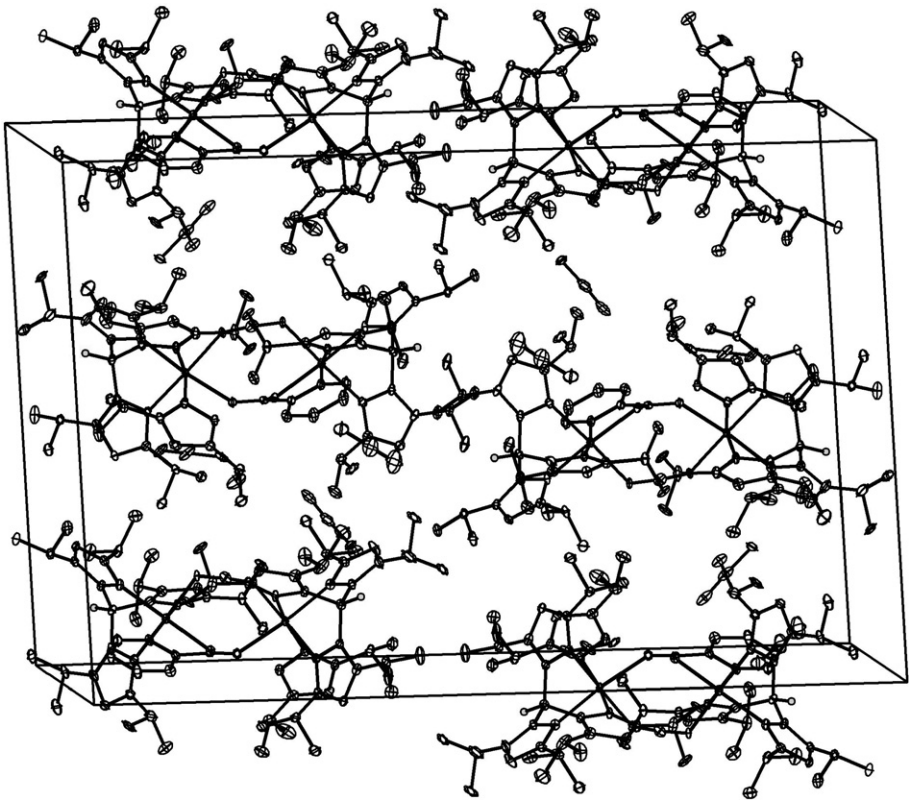


Fig. 8. Packing view of complex **9**.

to exist between the two independent molecules with a separation of 3.177(3) Å.

3.1. Magnetic studies

The room temperature magnetic moment for all the reported complexes are well within the range of magnetic moment reported for manganese (II) complexes [25,26]. Since the coordination structure of complex **9** is very close to the active site structure of manganese containing catalase/pseudocatalase, its magnetic properties has been reported at variable temperatures ranging from helium to room temperature. Fig. 9 shows the temperature dependence plot of μ_{eff} (○) and χ_M (△). The value of μ_{eff} at 300 K amounts to 5.69 μ_B, close to the spin-only value of 5.92 μ_B for $S = 1/2$. The effective magnetic moment smoothly decreases with temperature. The χ_M versus T curve shows maxima at approximately 44 K and then declines rapidly to zero at 6 K, indicating the presence of weak antiferromagnetic coupling between the manganese ions [26].

3.2. Catalytic activity studies

3.2.1. Electronic spectra

Complexes **7** and **9** exhibit no absorption band in the visible region, suggesting that both manganese ions in these complexes are in the two oxidation state. In order to get an insight into the disproportionation of H_2O_2 catalyzed by complexes **7** and **9**, the reaction was monitored by absorption spectroscopy. The UV–vis absorption spectra of these complexes (showing no bands) are very similar to the optical spectrum (lack of visible absorption) of manganese catalase from *T. thermophilus* (TTC) in the reduced (II, II) state [27]. During the reaction of **9** with H_2O_2 in methanol, a new band at 379 nm wavelength appeared and the intensity of this band increases with increasing concentration of hydrogen peroxide until the reaction is completed.

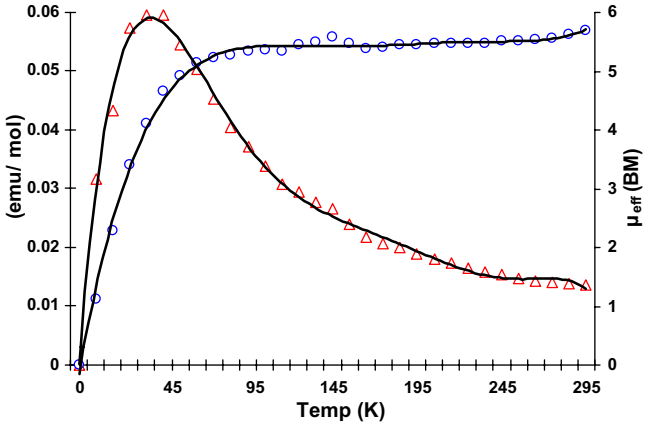


Fig. 9. Plot of μ_{eff} (○) and χ (△) vs. temperature for complex **9**.

3.2.2. Kinetics

Since the coordination geometry of complex **9** is very similar to the active site structure of pseudocatalase, the kinetic experiment of complex **9** with H_2O_2 was performed in detail. An excess concentration of H_2O_2 was used in the reaction to measure the initial rate of oxygen evolution and formation of new manganese species in methanol at room temperature. The order of the reaction with respect to the catalyst was measured by varying the catalyst concentration at a constant concentration of H_2O_2. The initial rate versus catalyst concentration showed a good linear correlation (Fig. 10). The linear dependence of the rate with respect to the catalyst revealed that the reaction is first order. The slope of the line gives a first order rate constant $(k) = 9.725 \times 10^{-4}\ s^{-1}$ for a H_2O_2 concentration of 24.47 mM. The rate constant for complex **9** is slower as compared to other model compounds reported in the literature [28,29]. At a constant concentration, complex **9** exhibits saturation kinetics with H_2O_2 and follows the Michaelis–Menten equation. The catalytic turnover number $(k_{cat}) = 6.676 \times 10^{-3}\ s^{-1}$ and the Michaelis constant (K_M) is 114 mM (Fig. 11). As reported in the literature, some catalases whose activity was not inhibited by CN^- or azide (N_3^-) are called pseudocatalase. The interesting aspect of **9** is that in spite of azide binding, it exhibits catalytic activity and catalyses the disproportionation of hydrogen peroxide.

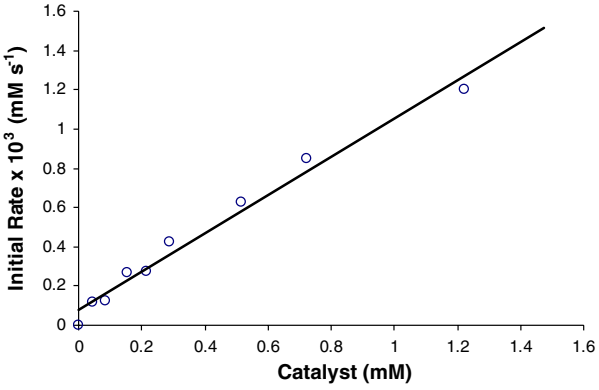


Fig. 10. Effect of the [catalyst] on the initial rate of H_2O_2 disproportionation at 25 °C and $[H_2O_2] = 24.47$ mM in methanol.

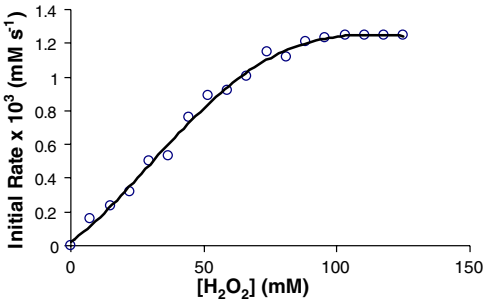


Fig. 11. Effect of the $[H_2O_2]$ on the initial rate of H_2O_2 disproportionation at 25 °C and [catalyst] = 368 μM in methanol.

4. Conclusion

In conclusion, we have reported the synthesis, structural as well as catalytic studies of some manganese compounds as suitable models for manganese-containing pseudocatalase. To the best of our knowledge complex **9** is the first manganese complex that is a μ-1,3-azido bridged dimer having picolinate as a bridging ligand. The most striking feature of this complex is that the picolinate is behaving as tridentate ligand, which is not very common. Due to the tridentate nature of picolinate, each manganese center is 6-coordinated which is very important for the catalytic activity of pseudocatalase. The coordination number of each manganese ion in **7** is five where the acetylacetonate behaves as a bidentate ligand. The interesting observation is that complex **9** has the capability for disproportionation of hydrogen peroxide but complex **7** does not because the coordination geometry of this complex is not very similar to the active site structure of the native enzyme. Thus, complex **9** may be a true model for manganese-containing pseudocatalase both structurally as well as functionally.

Acknowledgements

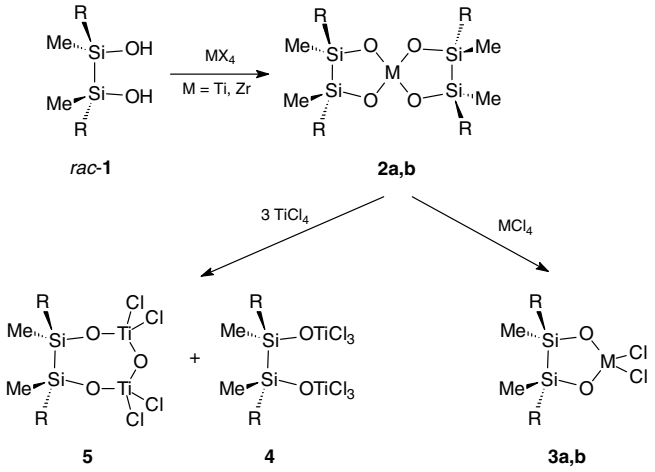
This research was supported by DST, New Delhi. The authors are grateful to Dr. W. Thomas, Max-Planck Institute for Bioinorganic Chemistry, Muelheim, Germany for fruitful discussion on the X-ray structure. We are also thankful to the Head, Institute Instrumentation Centre, Indian Institute of Technology Roorkee, for the single crystal X-ray facility.

Appendix A. Supplementary material

CCDC 633945 and 633946 contain the supplementary crystallographic data for this paper. These data can be obtained free of charge via http://www.ccdc.cam.ac.uk/conts/retrieving.html, or from the Cambridge Crystallographic Data Centre, 12 Union Road, Cambridge CB2 1EZ, UK; fax: (+44) 1223-336-033; or e-mail: deposit@ccdc.cam.ac.uk. Supplementary data associated with this article can be found, in the online version, at doi:10.1016/j.poly.2007.03.049.

References

[1] G.S. Waldo, J.E. Penner-Hahn, Biochemistry 34 (1995) 1507.
[2] J.E. Penner-Hahn, in: V.L. Pecoraro (Ed.), Manganese Redox Enzymes, VCH Publishers, Inc., New York, 1992.
[3] (a) Y. Kono, I. Fridovich, J. Biol. Chem. 258 (1983) 6015;
(b) G.S. Algood, J.J. Perry, J. Bacteriol. 168 (1986) 563;
(c) S.V. Khangulov, V.V. Barynin, A.V.R. Grebenko, A.I. Grebenko, N.V. Voevodskaya, L.A. Blyumenfel'd, S.N. Dobryakov, V.B. Il'yasova, Bioorg. Khim. 12 (1986) 741.
[4] V.V. Barynin, M.M. Whittaker, S.V. Antonyuk, V.S. Lamzin, P.M. Harrison, P.J. Artymiuk, J.W. Whittaker, Structure 9 (2001) 725.
[5] T. L Stemmler, J.E. Penner-Hahn, Biochemistry 36 (1997) 9847.
[6] (a) K. Wieghardt, Angew. Chem., Int. Ed. Engl. 28 (1989) 1153;
(b) J.B. Vincent, G. Christou, Adv. Inorg. Chem. 33 (1989) 137;
(c) L. Que Jr., A.E. True, Prog. Inorg. Chem. 38 (1990) 97;
(d) V.L. Pecoraro, M.J. Baldwin, A. Gelasco, Chem. Rev. 94 (1994) 807;
(e) W. Ruttinger, G.C. Dismukes, Chem. Rev. 97 (1997) 1;
(f) J.P. McEvoy, G.W. Brudwig, Chem. Rev. 108 (2006) 4455.
[7] (a) Y. Kono, I. Fridovich, J. Biol. Chem. 258 (1983) 6015;
(b) V.V. Barynin, A.A. Vagin, V.R. Melik-Adamyan, A.I. Grebenko, S.V. Khangulov, A.N. Popov, M.E. Andrianova, B.K. Vainshtein, Sov. Phys. Dokl. 31 (1986) 877;
(c) G.C. Dismukes, Chem. Rev. 96 (1996) 2909;
(d) A.E. Meier, M.M. Whittaker, J.W. Whittaker, Biochemistry 35 (1996) 348.
[8] (a) K. Wieghardt, U. Bossek, D. Ventur, J. Weiss, J. Chem. Soc., Chem. Commun. (1985) 347;
(b) J.E. Sheats, R.S. Czernuszewiez, G.C. Dismukes, A.L. Rheingold, V. Petrouleas, J. Stubbe, W.H. Armstrong, R.H. Beer, S.J. Lippard, J. Am. Chem. Soc. 109 (1987) 1435;
(c) J.B. Vincent, K. Folting, J.C. Huffman, G. Christou, Biochem. Soc. Trans. 16 (1988) 822;
(d) S. Menage, J.-J. Girerd, A. Gleizes, Chem. Commun. (1998) 431;
(e) U. Bossek, K. Wieghardt, B. Nuber, J. Weiss, Inorg. Chim. Acta 165 (1989) 123.
[9] K. Wieghardt, U. Bossek, B. Nuber, J. Weiss, J. Bonvoisin, M. Corbella, S.E. Vitols, J.-J. Girerd, J. Am. Chem. Soc. 110 (1988) 7398.
[10] M. Osawa, K. Fujisawa, N. Kitajima, Y. Moro-oka, Chem. Lett. (1997) 919.
[11] N. Kitajima, M. Osawa, S. Imai, Y. Moro-oka, K. Heerwegh, C.A. Reed, P. Boyd, Inorg. Chem. 33 (1994) 4613.
[12] D.D. Perrin, W.L. Armarego, D.R. Perrin, Purification of Laboratory Chemicals, second ed., Pergamon, New York, 1980.
[13] N. Kitajima, K. Fujisawa, C. Fujimoto, Y. Moro-oka, S. Hashimoto, T. Kitagawa, K. Toriumi, K. Tatsumi, A. Nakamura, J. Am. Chem. Soc. 114 (1992) 1277.
[14] S. Imai, K. Fujisawa, T. Kobayashi, N. Shirasawa, H. Fujii, T. Yoshimura, N. Kitajima, Y. Moro-oka, Inorg. Chem. 37 (1998) 3066.
[15] N. Kitajima, U.P. Singh, H. Amagai, M. Osawa, Y. Moro-oka, J. Am. Chem. Soc. 113 (1991) 7757.
[16] (a) G.M. Sheldrick, Acta Cryst. A. 46 (1990) 467;
(b) G.M. Sheldrick, SHELXTL – NT 2000 version 6.12, reference manual, University of Göttingen, Göttingen, Germany.
[17] U.P. Singh, R. Singh, S. Hikichi, M. Akita, Y. Moro-oka, Inorg. Chim. Acta 310 (2000) 273.
[18] R. Singh, Ph.D. dissertation 2001, Indian Institute of Technology Roorkee, Roorkee 247 667, India.
[19] M. Osawa, U.P. Singh, M. Tanaka, Y. Moro-oka, N. Kitajima, J. Chem. Soc., Chem. Commun. (1993) 943.
[20] D.M. Hong, H.H. Wei, K.H. Chang, G.H. Lee, Y. Wang, J. Chin. Chem. Soc. 45 (1998) 701.
[21] N. Kitajima, K. Fujisawa, S. Hikichi, Y. Moro-oka, J. Am. Chem. Soc. 115 (1993) 7874.
[22] (a) C.J. Milios, E. Kefalloniti, C.P. Raptopoulou, A. Terzis, A. Es Cuer, R. Vicente, S.P. Perlepes, Polyhedron 23 (2004) 83;
(b) D. Huang, W. Wang, X. Zhang, C. Chen, F. Chen, Q. Liu, D. Liao, L. Li, L. Sun, Eur. J. Inorg. Chem. (2004) 1454.
[23] U.P. Singh, P. Babbar, A.K. Sharma, Inorg. Chim. Acta 358 (2005) 271.
[24] H. Komatsuzaki, S. Ichikawa, S. Hikichi, M. Akita, Y. Moro-oka, Inorg. Chem. 37 (1998) 3652.
[25] U.P. Singh, A.K. Sharma, P. Tyagi, S. Upreti, R.K. Singh, Polyhedron 25 (2006) 3628.
[26] A. Grirrane, A. Pastor, A. Galindo, A. Ienco, C. Mealli, P. Rosa, Chem. Commun. (2003) 512.
[27] M.M. Whittaker, V.V. Barynin, S.V. Antonyuk, J.W. Whittaker, Biochemistry 38 (1999) 9126.
[28] C. Palopoli, B. Chansou, J.-P. Tuchagues, S. Signorella, Inorg. Chem. 39 (2000) 1458.
[29] D. Moreno, C. Palopoli, V. Daier, S. Shova, L. Vendier, M.G. Sierra, J.-P. Tuchagues, S. Signorella, J. Chem. Soc., Dalton Trans. (2006) 5156.



Scheme 1. Synthesis of the titanium and zirconium disiloxides **2**–**5**.

the ^{29}Si NMR spectra showed only one signal for the $SiMe_3$ silicon atoms.

In addition, the structure of **2a** was investigated by X-ray crystallography; suitable crystals were grown from *n*-heptane (Fig. 1). Although the quality of the data (*R* value ca. 0.16) was insufficient to make any commentary on the structural parameters in detail, the orientation and connectivity of the located silicon, oxygen and titanium atoms reveals, however, a spirocyclic disilane-1,2-diolate complex with a distorted tetrahedral geometry around the central titanium.

When 3 equiv. of $TiCl_4$ were reacted with **2a**, a ring opening reaction occurs, which results in the formation of the dinuclear complex **4** (Scheme 1). The reaction is almost complete within minutes as indicated by NMR spectroscopy, and the isolated yields were within 80–85% following crystallization from pentane. The composition of the thermally stable but moisture sensitive compound corresponds well to the results of an elemental analysis. An analogous ring opening reaction has been observed previously for the six-membered spirocyclic compound $\{SiMe_2[(Me_3Si)_2SiO]_2\}_2Ti$ [6e]. The formation of **4** can simply be understood as an insertion reaction of $TiCl_4$ into the Ti–O bond sequence of **3a** that is intermediately formed during the course of the reaction. The fact that **2a** rapidly undergoes ring opening to **4** even at low temperatures clearly reflects the constrained nature of these five-membered ring systems relative to larger ring compounds [7]. It should be noted that a similar reaction of the corresponding Zr derivative **2b** with an excess of $ZrCl_4$ did not occur. Besides **4**, small amounts (ca. 5%) of a new species could be detected by NMR spectroscopy. The structural characterization of this compound was accomplished by single-crystal X-ray crystallography; suitable crystals were obtained from pentane solutions in a freezer. The analysis of the X-ray data revealed the compound to be the oxo bridged dinuclear titanium complex **5** (Fig. 2). In the solid state, **5** adopts a dimeric structure in which the two seven-membered ring fragments are linked by Ti–O dative bonds resulting in a planar four-membered ring. Distances from the titanium to the bridging oxygen [Ti1A–O3A 1.9826(18); Ti2–O3 1.9161(19) and Ti1A–O3 1.9529 (19) Å] are strongly elongated compared to the titanium to non-bridging O atom [Ti1A–O2A 1.738(2); Ti2–O1 1.7442(19) Å] within the seven-membered ring, indicating only weak interactions in this dimeric structure. The Ti–O distances of **5** are similar to those found in the closely related six-membered ring compound $SiMe_2[(Me_3Si)_2SiO]_2$-$TiCl_2$ [6e] and the dinuclear species $[(O^tBu_2SiO)TiCl_2]_2$ [8]. The five-coordinated Ti centers of **5** exhibit highly distorted trigonal bipyramidal geometries. Further dative bonds are observed between the non-oxygen bridging Ti2 and the Cl3 that is attached to the oxygen bridging Ti1 [Ti2–Cl3,

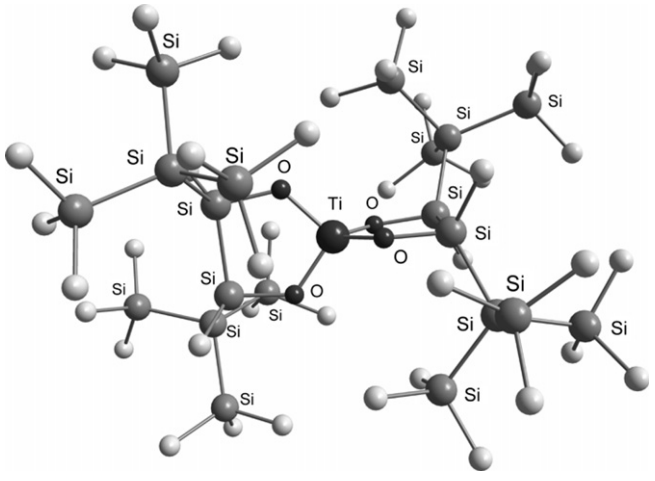


Fig. 1. Structural model of compound **2a**.

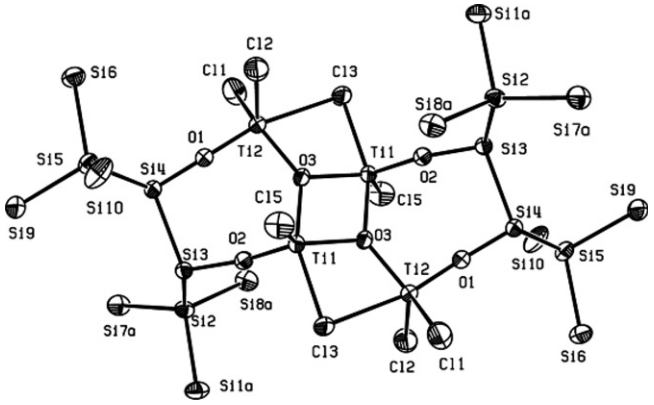
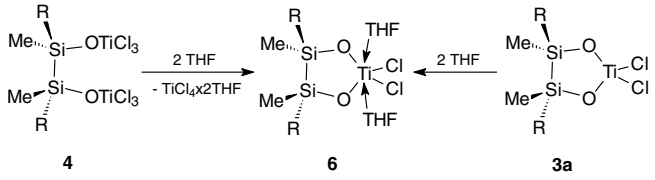


Fig. 2. Molecular structure of **5** in the crystal. The thermal ellipsoids correspond to 50% probability. Methyl groups are omitted for clarity. Selected bond lengths (Å) and angles (°): Si3–Si4 2.3904(10), Si4–O1 1.695(2), Si3–O2A 1.703(2), Ti2–O1 1.7442(19), Ti1A–O2A 1.738(2), Ti2–O3 1.9161(19), Ti1A–O3 1.9529(19), Ti1A–O3A 1.9826(18), Ti2–Cl2 2.1984(10), Ti2–Cl1 2.2356(10), Ti2–Cl3 2.6309(9), Ti1A–Cl5A 2.1918(9), Ti1A–Cl3A 2.3589(9), Si4–O1–Ti2 161.60(14), Si3–O2A–Ti1A 158.11(14), Ti2–O3–Ti1A 134.85(10), Ti2–O3–Ti1 121.39(10), Ti1A–O3–Ti1 103.66(8), O1–Ti2–O3 96.46(8), O2A–Ti1A–O3 97.68(9), O2A–Ti1A–O3A 130.47(9), O3A–Ti1–O3 76.34(8), Cl2–Ti2–Cl1 110.46(4), Cl2–Ti2–Cl3 92.21(4), Cl1–Ti2–Cl3 82.51(3), Cl5A–Ti1A–Cl3A 96.63(4), Ti1–Cl3–Ti2 85.72(3).

2.6309(9); Ti1–Cl3, 2.3589(9) Å]. The unusual formation of this compound can be explained by the fact that $TiCl_4$ stock solutions that have been used for the synthesis of **4** might be contaminated by small amounts of oxo containing titanium species arising from partial hydrolysis. In fact, careful NMR-spectroscopic investigations have shown that also the titanium dichloride **3a** is slightly contaminated by **5**.

Interestingly, upon addition of THF-d_8 the dinuclear titanium disilane-1,2-diolate **4** reacted cleanly within minutes, resulting in the quantitative formation of a new complex. However, the reaction did not yield the expected THF complex of **4**: rather, the quantitative product of $TiCl_4$ elimination, the THF complex **6** was formed as evidenced by multinuclear NMR spectral data (Scheme 2). The structural interpretation has been confirmed by the independent reaction of THF-d_8 with **3a** at room temperature. From the reaction of the dinuclear complex **4** with THF-d_8 single-crystals of $TiCl_4 \cdot 2THF$-d_8, suitable for X-ray crystallography, were obtained. The structure is shown in Fig. 3 and reveals an octahedral titanium center being coordinated by two molecules of THF-d_8.



Scheme 2. Reaction of **3a** and **4** with THF-d_8.

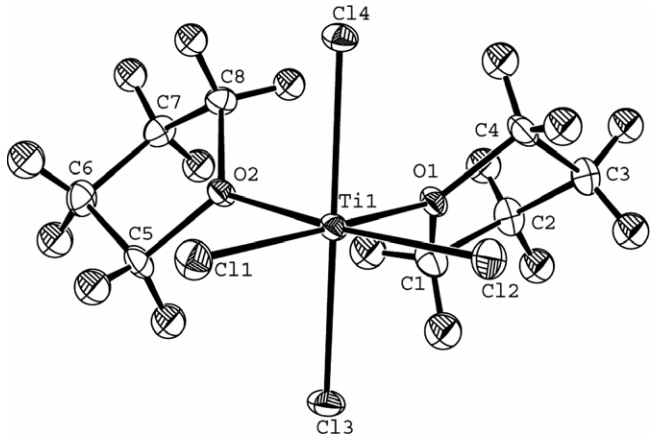


Fig. 3. Molecular structure of $TiCl_4 \cdot 2THF$-d_8 in the crystal. The thermal ellipsoids correspond to 50% probability. Selected bond lengths (Å) and angles (°): Ti1–O2 2.1050(10), Ti1–O1 2.1112(10), Ti1–Cl1 2.2497(4), Ti1–Cl2 2.2616(4), Ti1–Cl3 2.2909(4), Ti1–Cl4 2.2939(4), O1–C4 1.4754(17), O1–C1 1.4758(18), O2–C5 1.4768(16), O2–C8 1.4792(17), O2–Ti1–O1 81.80(4), O2–Ti1–Cl1 91.38(3), O1–Ti1–Cl1 172.92(3), O2–Ti1–Cl2 171.03(3), O1–Ti1–Cl2 89.38(3), Cl1–Ti1–Cl2 97.486(18), O2–Ti1–Cl3 88.00(3), O1–Ti1–Cl3 86.62(3), Cl1–Ti1–Cl3 91.283(17), Cl2–Ti1–Cl3 93.136(18), O2–Ti1–Cl4 86.10(3), O1–Ti1–Cl4 87.33(3), Cl1–Ti1–Cl4 94.115(16), Cl2–Ti1–Cl4 91.886(16), Cl3–Ti1–Cl4 172.093(18).

3. Conclusion

The synthesis of the strained five-membered ring compounds $\{(E)$-$[Me(Me_3Si)_3SiSiO]_2\}_2M$ (**2a**,**b**) and (E)-$[Me(Me_3Si)_3SiSiO]_2MCl_2$(**3a**,**b**) derived from the bidentate disilane-1,2-diolate ligand *rac*-$[Me(Me_3Si)_3SiSiO]_2^{2-}$ (**1**)-H_2 has been reported. In the presence of $TiCl_4$, **2a** rapidly undergoes a ring opening reaction to (E)-$[Me(Me_3Si)_3SiSiO]_2Ti_2Cl_6$ (**4**), which clearly reflects the constrained nature of the chelating disilane-1,2-diolate framework.

4. Experimental

4.1. General procedure

All manipulations of air- and/or moisture-sensitive compounds were carried out under an atmosphere of argon using standard Schlenk and Glove Box techniques. THF, *n*-heptane and *n*-pentane were distilled under argon from alkali metals prior to use. Benzene-d_6 and THF-d_8 were dried over activated molecular sieves and stored in the glove box. The racemic ligand **1** was prepared as previously described [6b]. NMR: Bruker AC 250, Bruker ARX 300, Bruker ARX 500 IR: Nicolet 205 FT-IR. MS: Intectra AMD 402, chemical ionization with isobutane as the reactant gas.

4.1.1. $\{(E)$-$[Me(Me_3Si)_3SiSiO]_2\}_2Ti$ (**2a**)

Freshly distilled $Ti(OEt)_4$ (0.45 ml, 2.13 mmol) was added to a stirred solution of rac-**1** (2.5 g, 4.07 mmol) in 20 ml heptane at room temperature. After stirring for 30 min, a yellow microcrystalline material started to precipitate from the solution. After refluxing for 2 h, the resulting solution was concentrated to a volume of ca. 15 ml and slowly cooled to −40 °C for 2 days. The yellow crystals that formed were filtered, washed twice with cold *n*-heptane, and dried under vacuum. Yield 2.34 g (86%). Mp > 230 °C. ^{1}H NMR (C_6D_6, 250 MHz): $\delta = 0.44$ (s, $SiMe_3$, 54H), 1.05 (s, OSiMe, 6H) ppm. ^{13}C NMR (C_6D_6, 62.9 MHz): $\delta = 3.66$ (s, $SiMe_3$), 10.12 (s, OSiMe) ppm. ^{29}Si NMR (C_6D_6, 59.6 MHz): δ −125.59 ($Si(SiMe_3)_3$), −9.42 ($SiMe_3$), 44.90 (SiO). MS: (70 eV, *m*/*z* in %): 1275 (100) [M^+], 1260 (17) [M^+-CH_3]. *Anal.* Calc. for $C_{40}H_{120}O_4Si_{20}Ti$ (1275.02): C, 37.68, H 9.49. Found: C, 36.48, H, 9.34%.

4.1.2. (E)-$[Me(Me_3Si)_3SiSiO]_2TiCl_2$ (**3a**)

To a stirred solution of **2a** (1.0 g, 0.79 mmol) in 30 ml pentane was added a toluene solution of $TiCl_4$ (0.82 ml, 1 M) at room temperature. After stirring for one day, the solution was concentrated to a volume of ca. 15 ml and slowly cooled to −40 °C. The red-orange crystals that formed were filtered, washed twice with cold pentane and dried under vacuum. Yield 0.46 g (40%). Mp 155–157 °C. ^{1}H NMR (THF-d_8, 300 MHz): $\delta = 0.30$ (s, $SiMe_3$, 54H), 1.04 (s, OSiMe, 6H) ppm. ^{1}H NMR (C_6D_6, 250 MHz): $\delta = 0.34$ (s, $Si(SiMe_3)_3$, 54H), 1.09 (s, SiMe, 6 H) ppm.

^{13}C NMR (THF-d_8, MHz): $\delta = 3.75$ ($SiMe_3$), 7.79 (OSiMe) ppm. ^{13}C NMR (C_6D_6, 62.9 MHz): $\delta = 3.5$ ($Si(SiMe_3)_3$), 9.5 (SiMe) ppm. ^{29}Si NMR (THF-d_8, MHz): $\delta = -124.25$ ($Si(SiMe_3)_3$), −9.70 ($SiMe_3$), 65.39 (SiO) ppm. ^{29}Si NMR (C_6D_6, 59.6 MHz): $\delta = -122.3$ ($Si(SiMe_3)_3$), −9.9 ($SiMe_3$), 75.4 (SiO) ppm. MS (70 eV, *m/z* in %): 732 (15) [M^+], 717 (9) [M^+−Me]. *Anal.* Calc. for $C_{20}Cl_2H_{60}O_2Si_{10}Ti$ (732.33): C, 32.80; H, 8.36, Cl, 9.68. Found: C, 32.49; H, 7.96; Cl, 9.75%.

4.1.3. (E)-[Me(Me$_3$Si)$_3$SiSiO]$_2$ZrCl$_2$ · 2THF (3b)

$Zr(NEt_2)_4$ (0.3 ml, 0.85 mmol) was added to a stirred solution of rac-**1** (1.0 g, 1.61 mmol) in *n*-heptane (30 ml) at room temperature. After stirring for 2 h at 95 °C, the solvent and other volatiles were removed under vacuum to leave {(*E*)-[$Me(Me_3Si)_3SiSiO]_2$}$_2$Zr × $HNEt_2$ (**2b**) as a crystalline material (an analytically pure sample can be obtained by recrystallization from *n*-pentane at −40 °C). The residue was dissolved in THF (90 ml) and transferred via cannula into a THF solution of $ZrCl_4$ (0.219 g, 0.94 mmol) at −78 °C. After being stirred for 24 h at room temperature, the solvent was replaced by *n*-pentane and the resulting suspension was filtered and washed twice with *n*-pentane. Then the volume of the combined filtrates was reduced and the solution was kept in a freezer. The colorless crystals that formed were filtered, washed with cold *n*-pentane and dried under vacuum. Yield 0.31 g (40%). Mp > 85 °C (dec.). ^{1}H NMR (C_6D_6, 250 MHz): $\delta = 0.48$ (s, $SiMe_3$, 54H), 1.22 (s, SiMe, 6H), 1.37, 4.07 (2m, THF, 2 × 8H) ppm. ^{13}C NMR (C_6D_6, 62.9 MHz): $\delta = 3.7$ ($SiMe_3$), 9.1 (SiMe), 25.3, 72.9 (THF) ppm. ^{29}Si NMR (C_6D_6, 59.6 MHz): $\delta = -126.2$ ($Si(SiMe_3)_3$), −9.7 ($SiMe_3$), 42.8 (SiO) ppm. *Anal.* Calc. for $C_{20}H_{60}Cl_2O_2Si_{10}Zr \times C_8H_{16}O_2$ (919.58): C 36.57; H, 8.33. Found: C, 34.96; H, 8.29%.

Analytical data of **2b**: Yield 0.41 g (36%); Mp 188–190 °C. ^{1}H NMR (C_6D_6, 250 MHz): $\delta = 0.45$ (s, $Si(SiMe_3)_3$, 108H) 1,02 (s, SiMe, 12H), 1.06 (br, $HNEt_2$, 6H), 2.54 (br, $HNEt_2$, 4H) ppm. ^{13}C NMR (C_6D_6, 75.5 MHz): $\delta = 4.1$ ($SiMe_3$), 10.9 (SiMe), 14.7, 43.2 ($HNEt_2$) ppm. ^{29}Si NMR (C_6D_6, 59.6 MHz): $\delta = -126.9$ ($Si(SiMe_3)_3$), −9.7 ($SiMe_3$), 30.3 (SiO) ppm. MS (70 eV, *m/z* in %): 1316 (100) [M^+−$HNEt_2$], 1244 (14) [M^+−$SiMe_3$], 1072 (20) [M^+−$Si(SiMe_3)_3$]. *Anal.* Calc. for $C_{40}H_{120}O_4Si_{20}Zr \times C_4H_{11}$ N (1391.45): C, 37.98; H, 9.49; N, 1.01. Found: C, 36.69; H, 9.50; N, 0.96%.

4.1.4. Synthesis of (E)-[Me(Me$_3$Si)$_3$SiSiO]$_2$Ti$_2$Cl$_6$ (4) and (E)-[Me(Me$_3$Si)$_3$SiSiO]$_2$Ti$_2$OCl$_4$ (5)

A toluene solution of $TiCl_4$ (2.5 ml, 1 M) was added to a stirred solution of **2a** (0.5 g, 0.79 mmol) in pentane (30 ml) at room temperature. After stirring for 1 day the red solution was concentrated to a volume of ca. 15 ml. Crystallization in a freezer at −40 °C afforded complex **4** as red-orange crystals contaminated by red crystals of **5**. Yield 0.56 g (77%).

Analytical data of (E)-[Me(Me$_3$Si)$_3$SiSiO]$_2$Ti$_2$Cl$_6$ (**4**): ^{1}H NMR (C_6D_6, 250 MHz): $\delta = 0.37$ (s, $SiMe_3$, 54H), 1.13 (s, SiMe, 6H) ppm. ^{13}C NMR (C_6D_6, 62.9 MHz): $\delta = 3.9$ ($SiMe_3$), 9.3 (SiMe) ppm. ^{29}Si NMR (C_6D_6, 59.6 MHz): $\delta = -118.5$ ($Si(SiMe_3)_3$), −9.4 ($SiMe_3$), 56.5 (SiO) ppm. MS (70 eV, *m/z* in %): 732 (24) [M^+−$TiCl_4$], 717 (6) [M^+−$TiCl_4$−Me], 424 (40) [M^+−Me −4 $SiMe_3$], 291 (52) [M^+−Me−4 × $SiMe_3$−$OTiCl_2$], 188 (18) [$TiCl_4$]. *Anal.* Calc. for $C_{20}H_{60}Cl_6O_2Si_{10}Ti_2$ (922.03): C, 26.05; H, 6.56. Found: C, 25.06, H, 6.66%.

Analytical data of (E)-[Me(Me$_3$Si)$_3$SiSiO]$_2$Ti$_2$OCl$_4$ (**5**): ^{1}H NMR (C_6D_6, 250 MHz): $\delta = 0.32$ (s, $SiMe_3$, 54H), 1.09 (s, SiMe, 6H) ppm. *Anal.* Calc. for $C_{20}H_{60}Cl_4O_3Si_{10}Ti_2$ (867.09): C, 27.70; H, 6.97. Found: C, 27.46, H, 6.66%.

4.1.5. Reaction of 3a and 4 with THF-d_8

A J. Young NMR tube was charged in the glove box with **3a** (30 mg) or **4** (30 mg) and dissolved in THF-d_8 (0.5 ml). The progress of the reaction was monitored by ^{1}H NMR spectroscopy and complete conversion of the starting materials into the THF-d_8 adduct **6** was observed immediately. ^{1}H NMR (THF-d_8, 250 MHz): $\delta = 0.30$ (s, $SiMe_3$, 54H), 1.04 (s, SiMe, 6H) ppm. ^{13}C NMR (THF-d_8, 62.9 MHz): $\delta = 3.6$ ($SiMe_3$), 7.7 (SiMe) ppm. ^{29}Si NMR (THF-d_8, 59.6 MHz): $\delta = -124.1$ [$Si(SiMe_3)_3$], −9.6 ($SiMe_3$), 65.6 (SiO) ppm.

5. Crystal structure determination of 5 and $TiCl_4$ · 2THF-d_8

5.1. Crystal data of 5, CCDC 615442

The crystal was fixed with perfluoropolyether on the tip of a thin glass rod. Intensity data of this crystal were then collected at 173(2) K on a Bruker X8 APEX-diffractometer with a CCD camera, Mo Kα-radiation ($\lambda = 0.71073$ Å) and graphite monochromator. Formula $C_{20}H_{60}Cl_4O_3Si_{10}Ti_2$ M = 867.18, monoclinic, $P2_1/n$, $a = 9.6229(2)$ Å, $b = 25.4548(5)$ Å, $c = 19.2748(4)$ Å, $\alpha = \gamma = 90.00°$, $\beta = 98.8450(10)°$, $V = 4665.20(16)$ Å^3, $Z = 4$, $\rho_{calc} = 1.235$ g cm^{-3}, $\mu = 0.849$ m^{-1}, 67 045 measured reflections, 10 684 independent reflections ($R_{int} = 0.0590$), 401 parameters, $R_1(F) = 0.0469$ for 8361 reflections with $I > 2\sigma(I)$ and $wR_2(F^2) = 0.1081$ for all data, residual electron density highest peak 0.528 and deepest hole −0.384 e$^-$/Å^3.

5.2. Crystal data of $TiCl_4$ · 2THF-d_8, CCDC 619743

The crystal was fixed with perfluoropolyether on the tip of a thin glass rod. Intensity data of this crystal were then collected at 173(2) K on a Bruker X8 APEX-diffractometer with a CCD camera, Mo Kα-radiation ($\lambda = 0.71073$ Å) and graphite monochromator. Formula $C_8D_{16}O_2Cl_4Ti$, M = 350.00, orthorhombic, $P2_12_12_1$, $a = 7.7878(3)$ Å, $b = 12.6128(5)$ Å, $c = 13.8568(5)$ Å, $\alpha = \beta = \gamma = 90.00°$, $V = 1361.10(9)$ Å^3, $Z = 4$, $\rho_{calc} = 1.708$ g cm^{-3}, $\mu = 1.393$ mm^{-1}, 8702 measured reflections, 3120 independent reflections ($R_{int} = 0.0252$), 136 parameters, $R_1(F) = 0.0191$ for 3032 reflections with $I > 2\sigma(I)$ and $wR_2(F^2)$

$= 0.0473$ for all data, residual electron density highest peak 0.204 and deepest hole -0.299 e^{-}/Å^{3}.

Acknowledgements

We thank Prof. Dr. H. Oehme for his generous support and we gratefully acknowledge the support of our research by the Fonds der Chemischen Industrie.

Appendix A. Supplementary material

CCDC 615442 and 619743 contain the supplementary crystallographic data for **4b** and **3**. These data can be obtained free of charge via http://www.ccdc.cam.ac.uk/conts/retrieving.html, or from the Cambridge Crystallographic Data Centre, 12 Union Road, Cambridge CB2 1EZ, UK; fax: (+44) 1223-336-033; or e-mail: deposit@ccdc.cam.ac.uk. Supplementary data associated with this article can be found, in the online version, at doi:10.1016/j.poly.2007.03.043.

References

[1] M.H. Chisholm, Inorg. Chem. 4 (1992) 273.
[2] R. Duchateau, H.C.L. Abbenhuis, R.A. van Santen, A. Meetsma, S.K.-H. Thiele, M.F.H. van Tol, Organometallics 17 (1998) 5663.
[3] For spirocyclic siloxandiolate complexes see: (a) K.A. Andrianov, N.A. Kurasheva, L.I. Kuteinikova, Zh. Obshch. Khim. 46 (1976) 1533;
(b) K.A. Andrianov, N.A. Kurasheva, L.I. Kuteinikova, Izv. Akad. Nauk SSSR, Ser. Khim. 10 (1977) 2314;
(c) M.A. Hossain, M.B. Hursthouse, Inorg. Chim. Acta 44 (1980) L259;
(d) M.A. Hossain, M.B. Hursthouse, M.A. Mazid, A.C. Sullivan, J. Chem. Soc., Chem. Commun. (1988) 1305;
(e) M.A. Hossain, M.B. Hursthouse, A. Ibrahim, M. Mazid, A.C. Sullivan, J. Chem. Soc., Dalton Trans. (1989) 2347;
(f) M. Motevalli, D. Shah, A.C. Sullivan, J. Chem. Soc., Dalton Trans. (1993) 2849;
(g) M. Lazell, M. Motevalli, S.A.A. Shah, C.K.S. Simon, A.C. Sullivan, J. Chem. Soc., Dalton Trans. (1996) 1449.
[4] For reviews see: (a) H.-H. Brintzinger, R. Mülhaupt, D. Fischer, B. Rieger, R.M. Waymouth, Angew. Chem. 107 (1995) 1255;
(b) H.-H. Brintzinger, R. Mülhaupt, D. Fischer, B. Rieger, R.M. Waymouth, Angew. Chem., Int. Ed. Engl. 34 (1995) 1143;
(c) G. Erker, Acc. Chem. Res. 34 (2001) 309;
(d) J.C. Green, Chem. Soc. Rev. 27 (1998) 263;
(e) H.G. Alt, E. Samuel, Chem. Soc. Rev. 27 (1998) 323;
(f) P.J. Shapiro, Coord. Chem. Rev. 231 (2002) 67;
(g) J. Gromada, J.-F. Carpentier, A. Mortreux, Coord. Chem. Rev. 248 (2004) 397.
[5] Reviews: (a) A.L. McKnight, R.M. Waymouth, Chem. Rev. 98 (1998) 2587;
(b) J. Okuda, T. Eberle, Half-sandwich complexes as metallocene analogues, in: A. Togni, A.L. Haltermann (Eds.), Metallocenes – Synthesis, Reactivity, Applications, vol. 1, Wiley-VCH, Weinheim, 1998, p. 415.
[6] For monocyclic five and six-membered silandiolate complexes see: (a) D. Martineau, P. Dumas, P. Sigwalt, Makromol. Chem. 184 (1983) 1397;
(b) D. Hoffmann, H. Reinke, C. Krempner, J. Organomet. Chem. 662 (2002) 1;
(c) D. Hoffmann, H. Reinke, C. Krempner, in: N. Auner, J. Weis (Eds.), Organosilicon Chemistry V, VCH, Weinheim, 2003, p. 420;
(d) C. Krempner, H. Reinke, K. Weichert, in: N. Auner, J. Weis (Eds.), Organosilicon Chemistry, vol. VI, VCH, Weinheim, 2005, p. 344;
(e) C. Krempner, M. Köckerling, H. Reinke, K. Weichert, Inorg. Chem. 45 (2006) 3203.
[7] For example, hexamethylcyclotrisiloxane (D3), a six-membered ring compound, can readily be polymerized by ring opening polymerization using anionic or cationic initiators, while octamethylcyclotetrasiloxane (D4), an eight-membered ring, is much less reactive towards ring opening reactions, see: (a) L.M. Terman, L.G. Klapshina, Y.A. Kurskii, S.S. Zislmina, Polym. Sci. USSR 29 (1987) 1330;
(b) M.J. Ziemelis, J.C. Saam, Macromolecules 22 (1989) 2111;
(c) J.M. Yu, D. Teyssle', R.B. Khalifa, S. Boilleau, Polym. Bull. 32 (1994) 35.
[8] A. Haoudi-Mazzah, A. Mazzah, H.G. Schmidt, M. Noltemeyer, H.W. Roesky, Z. Naturf, B: Chem. Sci. 46 (1991) 587.

In this paper, as a part of our continuing study, we would like to report the synthesis and characterization of new cationic cyclopentadienyl (Cp) ruthenium(II), osmium(II) and pentamethylcyclopentadienyl (Cp*) iridium(III) complexes with chelating N ∩ N-donor ligands [L_1 = 2-(2′-pyridyl)imidazole, L_2 = 2-(2′-pyridyl)benzimidazole, L_3 = 2-(2′-pyridyl)-4,5-dimethylimidazole, L_4 = 2-(2′-pyridyl)-4,5-diphenylimidazole (Scheme 1). In order to confirm the nature of bonding, the molecular structures of [CpRu{2-(2′-pyridyl)imidazole}(PPh_3)]PF_6 ([**1**]PF_6), [CpRu{2-(2′-pyridyl)benzimidazole}(PPh_3)]PF_6 ([**2**]PF_6) and [Cp*Ir{2-(2′-pyridyl)imidazole}Cl] PF_6 ([**7**]PF_6) have been solved by X-ray crystallography.

2. Experimental

Elemental analyses were performed on a Perkin–Elmer-2400 CHN/O analyzer. Infrared spectra were recorded on a Perkin–Elmer Model 983 spectrophotometer with the sample prepared as KBr pellets. The ^{1}H NMR spectra were recorded on a Bruker ACF-300 (300 MHz) spectrometer in $CDCl_3$ solvents with TMS as internal reference. All chemicals used were of reagent grade. All reactions were carried out in distilled and dried solvents. Ruthenium trichloride, iridium trichloride and osmium tetraoxide were purchased from Arora Matthey Ltd. and Aldrich. The 2-(2′-pyridyl)imidazole and its derivatives were prepared by following a literature procedure [10]. 2-(2′-Pyridyl)benzimidazole (Aldrich), pyridine-2-aldehyde (Fluka), glyoxal (Aldrich), 2,3-butanedione (Aldrich) and benzyl (Sd Fine) were used as received. The precursor's complexes [$CpRu(PPh_3)_2Cl$], [$CpOs(PPh_3)_2Br$] [11] and [Cp*Ir(μ-Cl)Cl]$_2$ [12] were prepared by following the reported literature methods.

2.1. Synthesis of [CpRu(N ∩ N)(PPh_3)]PF_6

The following general procedure was used for the preparation of complexes [**1**]PF_6 to [**4**]PF_6.

2.1.1. Preparation of [1]PF_6

A mixture of [$CpRu(PPh_3)_2Cl$] (0.1 g, 0.14 mmols), 2-(2′-pyridyl)imidazole (0.04 g, 0.28 mmols) and NH_4PF_6 (0.046 g, 0.28 mmols) was refluxed in dry methanol (20 ml) under a nitrogen atmosphere for 6 h. The yellow suspension turns to a light yellow color. The solvent is evaporated at reduced pressure. Then the residue is dissolved in dichloromethane (5 ml), and the solution filtered to remove ammonium chloride. The yellow solution is concentrated (2 ml) and by addition of an excess of hexane the orange yellow product precipitates. The compound is filtered and dried under vacuum to give [**1**]PF_6.

Complex [CpRu{2-(2′-pyridyl)imidazole}(PPh_3)]PF_6 [**1**]PF_6 (Yield: 63 mg, 64%). Elemental *Anal.* Calc. for $C_{31}H_{27}N_3F_6P_2Ru$: C, 51.81; H, 3.76; N, 5.85. Found: C, 51.54; H, 4.17; N, 5.44%. IR (KBr pellets, cm^{-1}): 1606 ($\nu_{C=C}$), 1480, 1440 ($\nu_{C=N}$), 857 (ν_{PF6}), ^{1}H NMR ($CDCl_3$, δ): 12.01 (s, 1H, NH); 9.04 (d, J_{H-H} = 5.74 Hz, 1H, H_6); 8. 75 (d, J_{H-H} = 6.08 Hz, H_7); 8.50 (d, J_{H-H} = 6.02 Hz, H_8); 8.00 (d, J_{H-H} = 5.12 Hz, 1H, H_3); 7.78 (m, 15H, Ph); 7.70 (t, 1H, H_4); 7.32 (t, 1H, H_5); 4.68 (s, 5H, C_5H_5).

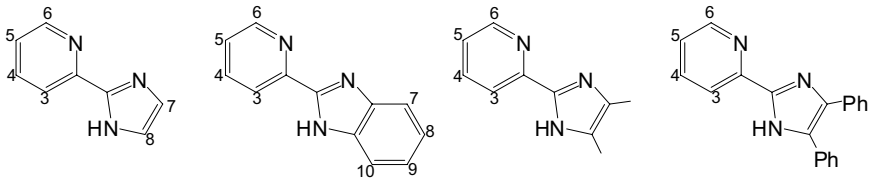
Complex [CpRu{2-(2′-pyridyl)benzimidazole}(PPh_3)]-PF_6 [**2**]PF_6 (Yield: 65 mg, 62%). Elemental *Anal.* Calc. for $C_{35}H_{29}F_6P_2N_3Ru$: C, 54.69; H, 3.78; N, 5.47. Found: C, 54.87; H, 4.12; N, 5.67%. IR (KBr pellets, cm^{-1}): 1613 ($\nu_{C=C}$), 1447 ($\nu_{C=N}$), 850 (ν_{PF6}), ^{1}H NMR ($CDCl_3$, δ): 12.01 (s, 1H, NH); 8.94 (d, J_{HH} = 5.42 Hz, 1H, H_6); 8.07 (d, J_{HH} = 5.80 Hz, 1H, H_3); 7.98 (t, 1H, H_4); 7.90 (t, 1H, H_5); 7.48 (m, 15H, Ph); 7.32 (m, 4H H_{7-10}); 4.64 (s, 5H, C_5H_5).

Complex [CpRu{2-(2′-pyridyl)-4,5-dimethylimidazole}-(PPh_3)]PF_6 [**3**]PF_6 (Yield: 64 mg, 62%). Elemental *Anal.* Calc. for $C_{33}H_{31}F_6P_2N_3Ru$: C, 53.08; H, 4.16; N, 5.63. Found: C, 53.28; H, 4.66; N, 5.77%. IR (KBr pellets, cm^{-1}): 1604 ($\nu_{C=C}$), 1480, 1447 ($\nu_{C=N}$); 855 (ν_{P-F}), ^{1}H NMR ($CDCl_3$, δ): 12.10 (s, 1H, NH); 8.50 (d, J_{H-H} = 5.74 Hz, 1H, H_6); 8.18 (d, J_{H-H} = 5.00 Hz, 1H, H_3); 7.53 (m, 15H, Ph); 7.39 (t, 1H, H_4); 7.28 (t, 1H, H_5); 4.67 (s, 5H, C_5H_5); 3.21 (s, 6H, CH_3).

Complex [CpRu{2-(2′-pyridyl)-4,5-diphenylimidazole}-(PPh_3)]PF_6 [**4**]PF_6 (Yield: 70 mg, 60%). Elemental *Anal.* Calc. for $C_{43}H_{35}N_3P_2F_6Ru$: C, 59.31; H, 4.02; N, 4.83. Found: C, 60.23; H, 4.23; N, 5.13%. IR (KBr pellets, cm^{-1}): 1600 ($\nu_{C=C}$), 1480, 1440 ($\nu_{C=N}$), 850 (ν_{P-F}), ^{1}H NMR ($CDCl_3$, δ): 8.50 (d, J_{H-H} = 5.0 Hz, 1H, H_6); 8.27 (d, J_{H-H} = 5.73 Hz, 1H, H_3), 7.92 (m, 25H, Ph); 7.60 (t, 1H, H_4); 7.37 (t, 1H, H_5); 4.62 (s, 5H, C_5H_5).

2.2. Synthesis of [CpM(N ∩ N)(PPh_3)]PF_6

These complexes were prepared by the same method given in Section 2.1 using of [$CpOs(PPh_3)_2(CH_3CN)$]PF_6 instead of [$CpRu(PPh_3)_2Cl$].



Scheme 1. Ligands and numbering scheme used in this study.

Complex [CpOs{2-(2′-pyridyl)imidazole}(PPh_3)]PF_6 [**5**]PF_6 (Yield: 48 mg, 57%). Elemental *Anal.* Calc. for $C_{31}H_{27}N_3P_2F_6Os$: C, 46.09; H, 3.35; N, 5.21. Found: C, 46.36; H, 4.03; N, 5.65%. IR (KBr pellets, cm^{-1}): 1600 ($\nu_{C=C}$), 1480, 1440 (s, $\nu_{C=N}$), 885 (s, br, ν_{PF6}) ^1H NMR ($CDCl_3$, δ): 8.95 (d, $J_{H-H} = 5.7$ Hz, 1H, H_6); 8.78 (d, $J_{H-H} = 6.05$ Hz, 1H, H_3); 8.63 (d, $J_{H-H} = 6.12$ Hz, 1H, H_7); 8.59 (d, $J_{H-H} = 5.52$ Hz, 1H, H_8); 7.89 (m, 15H, Ph); 7.75 (t, 1H, H_4); 7.48 (t, 1H, H_5); 4.59 (s, 5H, C_5H_5).

Complex [CpOs{2-(2′-pyridyl)benzimidazole}(PPh_3)]-PF_6 [**6**]PF_6 (Yield: 46 mg, 52%). Elemental *Anal.* Calc. for $C_{35}H_{29}N_3P_2F_6Os$: C, 49.01; H, 3.38; N, 4.90. Found: C, 49.15; H, 3.56; N, 5.15%. IR (KBr pellets, cm^{-1}): 1613 ($\nu_{C=C}$), 1447 ($\nu_{C=N}$), 885 (s, br, ν_{PF6}). ^1H (NMR, $CDCl_3$, δ): 8.50 (d, $J_{H-H} = 5.2$ Hz, 1H, H_6); 8.10 (d, $J_{H-H} = 5.2$ Hz, 1H, H_3); 7.93 (m, 15H, Ph); 7.78 (t, 1H, H_4); 7.56 (t, 1H, H_5); 7.37 (m, 4H H_{7-10}); 4.65 (s, 5H, C_5H_5).

2.3. Synthesis of [Cp*Ir(N ∩ N)Cl]PF_6

These complexes were prepared by the same method given in Section 2.1 using 0.5 equiv. of [Cp*Ir(μ-Cl)Cl]$_2$ instead of 1 equiv. of [CpM(PPh_3)$_2$Cl].

Complex [Cp*Ir{2-(2′-pyridyl)imidazole}Cl]PF_6 [**7**]PF_6 (Yield: 52 mg, 64%). Elemental *Anal.* Calc. for $C_{18}H_{22}ClN_3F_6PIr$: C, 33.13; H, 3.37; N, 6.44. Found: C, 32.87; H, 3.88; N, 6.23%. IR (KBr pellets, cm^{-1}): 1600 ($\nu_{C=C}$), 1460–1327 ($\nu_{C=N}$), 850 (ν_{P-F}), ^1H NMR ($CDCl_3$, δ): 8.94 (d, $J_{H-H} = 6.4$ Hz, 1H, H_6); 8.50 (d, $J_{H-H} = 6.12$ Hz, 1H, H_3); 8.00 (d, $J_{H-H} = 6.03$ Hz, 1H, H_7); 7.90 (d, $J_{H-H} = 5.23$ Hz, 1H, H_8); 7.73 (t, 1H, H_4); 7.43 (t, 1H, H_5); 1.86 (s, 15H, C_5Me_5).

Complex [Cp*Ir{2-(2′-pyridyl)benzimidazole}Cl]PF_6 [**8**]PF_6 (Yield: 54 mg, 62%). Elemental *Anal.* Calc. for $C_{22}H_{24}ClN_3F_6PIr$: C, 37.61; H, 3.42; N, 5.98. Found: C, 37.52; H, 3.87; N, 6.15%. IR (KBr pellets, cm^{-1}): 1600 ($\nu_{C=C}$), 1474–1407 ($\nu_{C=N}$), 850 (ν_{P-F}), ^1H NMR ($CDCl_3$, δ): 8.97 (d, $J_{H-H} = 5.63$ Hz, 1H, H_6); 8.90 (d, $J_{H-H} = 5.29$ Hz, 1H, H_3); 7.85 (t, 1H, H_4); 7.43 (t, 1H, H_5); 7.24 (m, 4H, H_{7-10}); 1.82 (s, 15H, C_5Me_5).

2.4. Single-crystal X-ray structures analyses

Crystal suitable for X-ray diffraction study for compound [**1**]PF_6, [**2**]PF_6 and [**7**]PF_6 were grown by slow diffusion of diethylether into dichloromethane solution of complexes [**1**]PF_6, [**2**]PF_6 and [**7**]PF_6, respectively. The orange reddish crystals of compound [**1**]PF_6 and [**7**]PF_6 were mounted on a Stoe Image Plate Diffraction system equipped with a ϕ circle goniometer, using Mo Kα graphite monochromated radiation ($\lambda = 0.71073$ Å) with ϕ range 0–200°, increment of 1.2°, D_{max}–$D_{min} = 12.45$–0.81 Å. Whereas crystal of [**2**]PF_6 was mounted on a Bruker Apex CCD diffractometer in a full reciprocal sphere equipped with a CCD detector, X-ray intensity data were collected with Mo Kα graphite monochromated radiation at 120(2) K, with 0.3°ω scan mode and 10 second per frame. The intensity data were corrected for Lorenz and polarization effects. The structures were solved by direct methods using the program SHELXS-97 [13]. Refinement and all further calculations were carried out using SHELXL-97 [14]. The H-atoms were included in calculated positions and treated as riding atoms using the SHELXL default parameters. The non-H-atoms were refined anisotropically, using weighted full-matrix least-square on F^2. In [**2**]$PF_6 \cdot H_2O$, the $-C_5H_4NC_3N_2H-$ fragment of the 2-(2′-pyridyl)benzimidazole was found to be disordered over two positions and the partial occupancy factor was refined at 76:24. Crystallographic details are summarized in Table 1. Figs. 1, 2 and 4 are drawn with ORTEP32 [15] while Figs. 3 and 5 are drawn with MERCURY [16].

3. Results and discussion

The reactions in dry methanol of [CpRu(PPh_3)$_2$Cl] and [CpOs(PPh_3)$_2$Br] (Cp = η^5-C_5H_5) with an excess of chelating N ∩ N-ligands and NH_4PF_6 result, under refluxing conditions, in the dissociation of one triphenylphosphine and the halide ligands to yield the monocationic complexes [CpM(N ∩ N)(PPh_3)]$^+$ (**1**: M = Ru, N ∩ N = 2-(2′-pyridyl) imidazole; **2**: M = Ru, N ∩ N = 2-(2′-pyridyl)benzimidazole; **3**: M = Ru, N ∩ N = 2-(2′-pyridyl)-4,5-dimethylimidazole; **4**: M = Ru, N ∩ N = 2-(2′-pyridyl)-4,5-diphenylimidazole; **5**: M = Os, N ∩ N = 2-(2′-pyridyl)imidazole; **6**: M = Os, N ∩ N = 2-(2′-pyridyl)benzimidazole), see Scheme 2. The compounds are isolated and characterized as hexafluorophosphate salts.

In the case of the reaction of the dinuclear iridium(III) complex [Cp*Ir(μ-Cl)Cl]$_2$ (Cp = η^5-C_5Me_5) with 2 equiv. of chelating N ∩ N-ligands in the presence of NH_4PF_6, cleavage of the chloro-bridge followed by dissociation of one chloride ligand, affords the complexes [Cp*Ir{2-(2′-pyridyl)imidazole}Cl]PF_6([**7**]PF_6) and [Cp*Ir{2-(2′-pyridyl)benzimidazole}Cl]PF_6 ([**8**]PF_6), see Scheme 3.

The complexes **1–8** are pale yellow to orange reddish colored. They are highly soluble in polar solvents such as chloroform, acetone, methanol, dichloromethane *etc.*, but insoluble in non-polar solvents such as hexane, pentane *etc.*, C, H, N analyses, IR, ^1H NMR spectroscopic data were given in the experimental section, which supported the formation of these complexes. The X-ray structures of representative complexes **1**, **2** and **7** were determined to confirm the structure of the complexes (**1–8**). The infrared spectra of complexes **1–6** exhibited very strong bands at 1613–1600 cm^{-1} and 1480–1440 cm^{-1}corresponding to phenyl groups of triphenylphosphine and N-bases, while in complexes **7** and **8** prominent peaks were observed at 1600 cm^{-1} and 1474–1327 cm^{-1}. The counter ion (PF_6) exhibit a strong band around 845 cm^{-1} for ν_{PF6} group.

The protons' corresponding to the cyclopentadienyl ligands appear in the region of 4.6–4.7 ppm while the triphenylphosphine peaks are observed as a multiplet in the aromatic region between 7 and 8 ppm. The chemical shifts of cyclopentadienyl groups appear downfield as compared

Table 1
Crystallographic and structure refinement parameters for complexes [**1**]PF_6, [**2**]$PF_6 \cdot H_2O$ and [**7**]PF_6

	[**1**]PF_6	[**2**]$PF_6 \cdot H_2O$	[**7**]PF_6
Chemical formula	$C_{31}H_{27}F_6N_3P_2Ru$	$C_{35}H_{31}F_6N_3OP_2Ru$	$C_{18}H_{22}ClF_6N_3PIr$
Formula weight	718.57	786.64	653.01
Crystal system	monoclinic	triclinic	triclinic
Space group	$P2_1/c$ (no. 14)	$P\bar{1}$ (no. 2)	$P\bar{1}$ (no. 2)
Crystal colour and shape	orange block	red block	red block
Crystal size	$0.32 \times 0.20 \times 0.20$	$0.28 \times 0.23 \times 0.18$	$0.35 \times 0.26 \times 0.21$
a (Å)	13.552(3)	10.379(4)	8.0428(9)
b (Å)	14.582(3)	11.285(4)	11.4031(14)
c (Å)	17.920(6)	15.601(6)	11.7074(13)
α (°)	90	108.602(5)	93.585(14)
β (°)	126.31(2)	91.211(5)	96.862(14)
γ (°)	90	104.887(5)	98.154(14)
V (Å^3)	2853.6(13)	1663.0(10)	1051.8(2)
Z	4	2	2
T (K)	173(2)	120(2)	173(2)
D_c (g cm^{-3})	1.673	1.571	2.062
μ (mm^{-1})	0.729	0.635	6.613
Scan range (°)	$1.86 < \theta < 29.24$	$1.98 < \theta < 28.23$	$2.58 < \theta < 26.03$
Unique reflections	6277	7437	3821
Reflections used [$I > 2\sigma(I)$]	4388	6379	3518
R_{int}	0.0588	0.0261	0.0501
Final R indices [$I > 2\sigma(I)$][a]	0.0387, wR_2 0.0860	0.0457, wR_2 0.1073	0.0323, wR_2 0.0782
R indices (all data)	0.0605, wR_2 0.0926	0.0543, wR_2 0.1131	0.0373, wR_2 0.0884
Goodness-of-fit	0.910	1.016	1.112
Maximum and minimum $\Delta\rho$ (e Å^{-3})	0.763, −1.038	0.754, −0.530	1.775, −1.850

[a] Structures were refined on F_o^2: $wR_2 = [\sum[w(F_o^2 - F_c^2)^2]/\sum w(F_o^2)^2]^{1/2}$, where $w^{-1} = [\sum(F_o^2) + (aP)^2 + b]$ and $P = [\max(F_o^2, 0) + 2F_c^2]/3$.

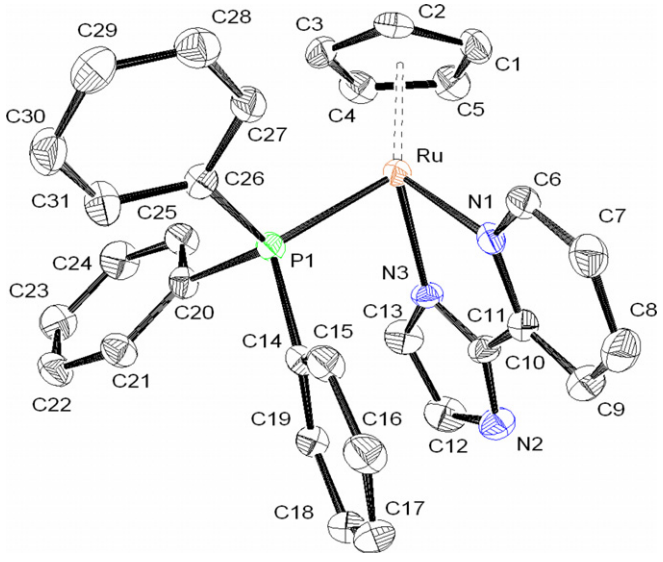


Fig. 1. ORTEP diagram with labelling scheme for [CpRu{2-(2′-pyridyl)imidazole}(PPh_3)]$^+$ ([**1**]PF_6), at 50% probability level, H-atoms and PF_6 anion omitted for clarity.

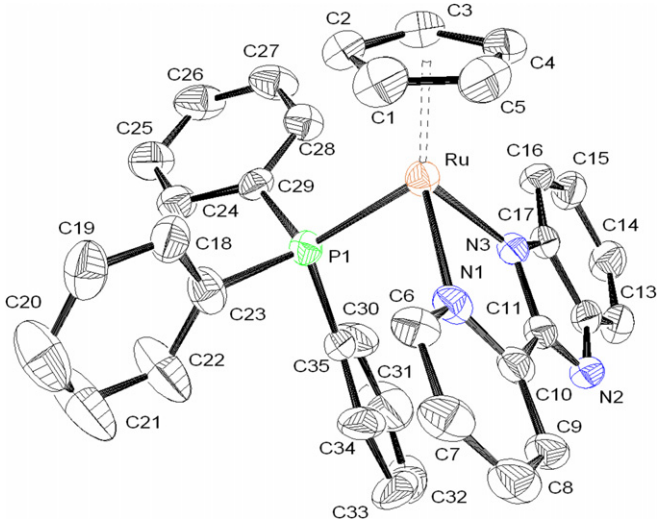


Fig. 2. ORTEP diagram with labelling scheme for [CpRu{2-(2′-pyridyl)benzimidazole}(PPh_3)]$^+$ ([**2**]$PF_6 \cdot H_2O$) at 50% probability level, H-atoms, PF_6 anion and water molecule omitted for clarity.

to the precursor complexes (4.43–4.31 ppm). The downfield shift position of the cyclopentadienyl protons in complexes **1–6**, which might results from the change in electron density on the metal center due to chelation of the nitrogen base ligands through the nitrogen atoms of the 2-(2′-pyridyl)imidazole derivatives ligands. The ^{1}H NMR spectra of complexes **1–6** also showed two pseudo-triplets in the range of 7.85–6.32 ppm due to the pyridine protons (H4 and H5) of the N ∩ N-donor ligands, a singlet at 12.01 ppm corresponds to the NH protons of the ligands. The spectra of the Cp* complexes **7** and **8** showed resonance for the methyl protons of the Cp* ligand as singlets at 1.86 ppm and 1.82 ppm, respectively.

Molecular structure of the representative hexafluorophosphates salts [**1**]PF_6, [**2**]PF_6 and [**7**]PF_6 are presented in Figs. 1, 2 and 4, respectively. Selected bond lengths and angles are recorded in Table 2. The molecular

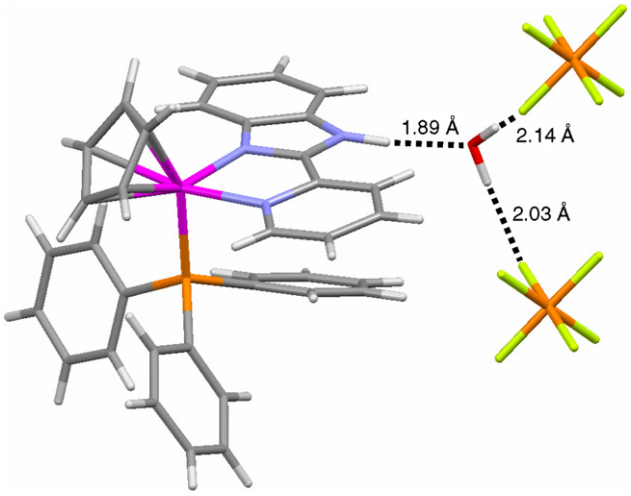
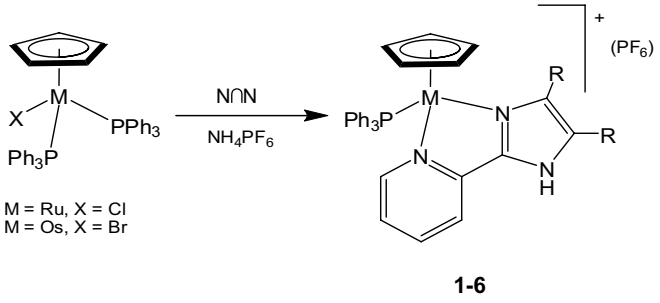
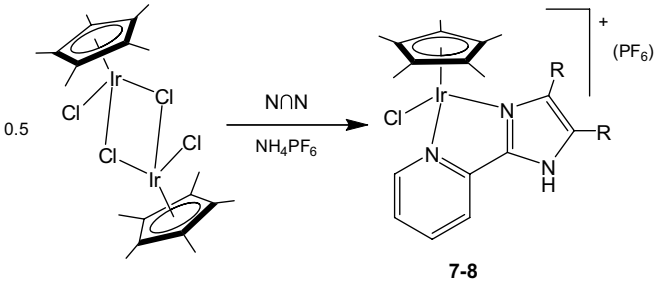


Fig. 3. Hydrogen-bonded system observed in $[\mathbf{2}]PF_6 \cdot H_2O$.



Scheme 2.



Scheme 3.

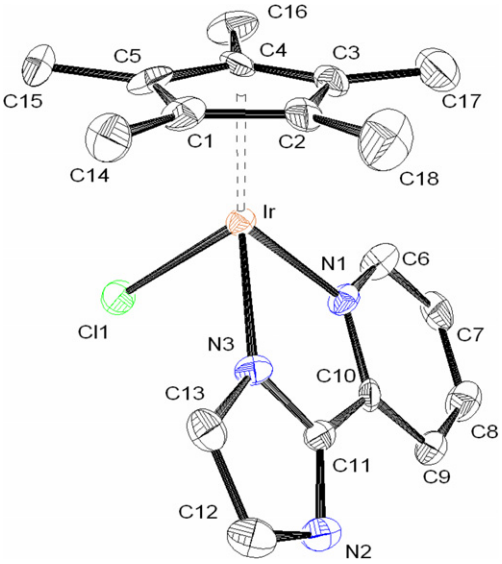


Fig. 4. ORTEP diagram with labelling scheme for [Cp*Ir{2-(2′-pyridyl)imidazole}Cl]$^+$ ([**7**]PF_6) at 50% probability level, H-atoms and PF_6 anion omitted for clarity.

Table 2
Selected bond lengths and angles for complexes [**1**]PF_6, [**2**]$PF_6 \cdot H_2O$ and [**7**]PF_6

	1	**2**	**7**
Distances (Å)			
Ru–P	2.316(1)	2.325(1)	
Ir–Cl			2.4183(14)
M–N1	2.113(3)	2.1169(17)	2.106(5)
M–N3	2.093(3)	2.0939(15)	2.080(5)
M–C1	2.208(4)	2.109(4)	2.178(6)
M–C2	2.177(4)	2.157(3)	2.149(5)
M–C3	2.150(4)	2.226(3)	2.158(6)
M–C4	2.180(4)	2.219(3)	2.144(6)
M–C5	2.215(4)	2.146(4)	2.164(6)
Angles (°)			
N1–M–N3	75.98(10)	76.08(17)	76.48(19)
N1–M–P1	90.12(8)	92.15(6)	
N3–M–P1	87.66(8)	89.02(6)	
N1–Ir–Cl1			84.60(14)
N3–Ir–Cl1			86.95(14)

structures of $[CpRu\{2\text{-}(2'\text{-pyridyl})imidazole\}(PPh_3)]^+$ (**1**) and $[CpRu\{2\text{-}(2'\text{-pyridyl})benzimidazole\}(PPh_3)]^+$ (**2**) have been established by single-crystal X-ray structure analysis of [**1**]PF_6 and [**2**]$PF_6 \cdot \cdot \cdot H_2O$, respectively. Both complexes show typical piano-stool geometry with the metal center coordinated by a cyclopentadienyl ligand, a PPh_3 ligand and a chelating N ∩ N-ligand, see Figs. 1 and 2.

The Ru–N bond distances [2.113(3) and 2.093(3) Å in **1**; 2.117(2) and 2.094(2) in **2**] are comparable to those in $[(\eta^6\text{-}p\text{-}Pr^iC_6H_4Me)RuCl(2,3\text{-bis}(2\text{-pyridyl})pyrazine)]BF_4$[17] and $[(\eta_6\text{-}C_6H_6)RuCl(2\text{-}(1\text{-imidazole-2-yl})pyridine)]PF_6$ [18a]. Accordingly, there is no significant difference in the Ru–P bond length in **1** [2.316(1) Å] or **2** [2.325(1) Å] with reported values [9d,19]. The N(1)–Ru–N(3) bond angle in complexes **1** [76.0(1)°] and **2** [76.1(2)°] are similar to those of compounds $[(\eta^6\text{-}p\text{-}Pr^iC_6H_4Me)RuCl(2,3\text{-bis}(2\text{-pyridyl})pyrazine)]^+$ [N–Ru–N = 76.5(2)°] [17] and $[(\eta^6\text{-}p\text{-}Pr^iC_6H_4Me)RuCl(2,3\text{-bis}(\alpha\text{-pyridyl})quinoxaline)]^+$ [N–Ru–N = 76.2(2)°] [18b]. The angles between the least-square planes of $\eta^5\text{-}C_5H_5$ and that of the N ∩ N-ligand are 57.8(2)° in **1** and 55.3(2)° in **2**.

Complex [**2**]PF_6 crystallizes with one molecule of water per asymmetric unit, which forms a hydrogen-bonded network with two hexafluorophosphate anions and the N–H group of the N ∩ N ligand, see Fig. 3. The N–O and O–F distances of the hydrogen bonds are, respectively, 2.820(3) Å for the N–H of the 2-(2′-pyridyl)benzimidazole

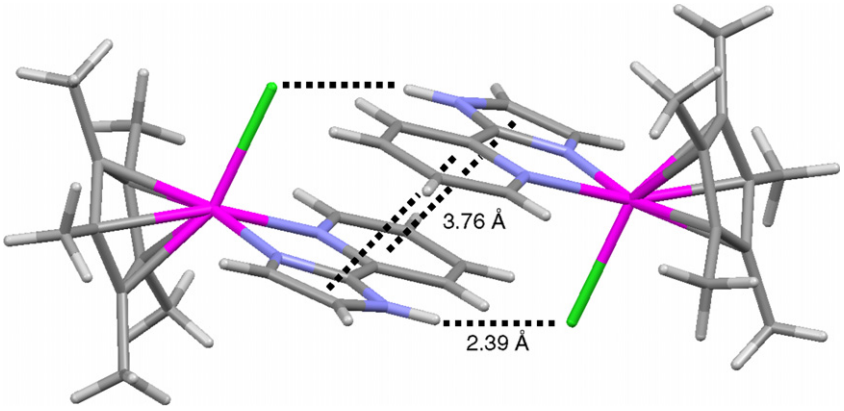


Fig. 5. Dimeric structure of [**7**]PF_6 showing the intermolecular NH···Cl hydrogen contacts and π–π interacting system.

ligand and H_2O, and 2.941(4) and 2.907(4) Å between the hexafluorophosphate anions and the water molecule. The N–H···O angle is 167.1° while the O–H···F angles are 178° and 153°, respectively.

The molecular structure of [Cp*Ir{2-(2′-pyridyl)imidazole}Cl]$^+$ (**7**) has been established by single-crystal X-ray structure analysis of [**7**]PF_6 (see Fig. 4). The complex shows a typical piano-stool geometry with the metal center coordinated by the pentamethylcyclopentadienyl ligand, a terminal chloride and the 2-(2′-pyridyl)imidazole ligand. The Ir–N bond distances [2.106(5) and 2.080(5) Å] are slightly shorter to those in [**1**]PF_6 and [**2**]PF_6. The average distance between the metal atom and the carbon atoms of the η^5-C_5Me_5 ring is 2.16 Å. This average bond length is comparable to that in the related η^5-C_5Me_5 iridium complex [(η^5-C_5Me_5)IrCl((*S*)-1-phenylethylsalicylaldiimine)] [2.17 Å] [20]. The Ir–Cl bond length is 2.4183(14) Å in **7**, which is slightly longer to the reported iridium complex [(η^5-C_5Me_5)IrCl((*S*)-1-phenylethylsalicylaldiimine)] [2.4017(16) Å] [20].

In the crystal packing of [**7**]PF_6, two molecules of **7** form a dimer through N–H···Cl contacts and π-stacking interactions, see Fig. 5. The N–Cl separation is 3.254(5) Å with an N–H···Cl angle of 162.1°. The distance observed between the π-stacking interacting systems (centroid···centroid 3.76 Å) is in good agreement with the theoretical value calculated for this stacking mode [21]. The distance observed between the two iridium centers of the dimer is 7.841(1) Å and excludes any possible metal–metal interactions.

4. Conclusions

The present study describes the synthesis of eight new CpRu, CpOs and Cp*Ir complexes containing 2-(2′-pyridyl)imidazole ligands. Representative complexes have been characterized by single X-ray study. In the crystal packing of [**7**]PF_6, two molecules of **7** form a dimer through N–H···Cl contacts and π-stacking interactions.

Acknowledgements

Mohan Rao Kollipara greatly acknowledges the *Department of Science and Technology, New Delhi* (Sanction Order No. SR/S1/IC-11/2004) for financial support. We also thank Míriam Pérez, Servei RMN Universitat Autònoma de Barcelona 08193 Bellaterra, Barcelona for providing the NMR facility.

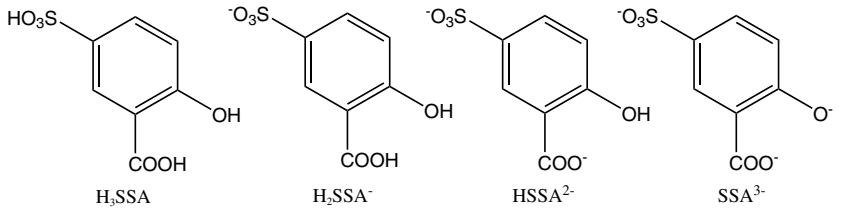
Appendix A. Supplementary material

CCDC 637370, 637371 and 637372 contain the supplementary crystallographic data for [**1**]PF_6, [**2**]$PF_6 \cdot H_2O$ and [**7**]PF_6. These data can be obtained free of charge via http://www.ccdc.cam.ac.uk/conts/retrieving.html, or from the Cambridge Crystallographic Data Centre, 12 Union Road, Cambridge CB2 1EZ, UK; fax: (+44) 1223-336-033; or e-mail: deposit@ccdc.cam.ac.uk. Supplementary data associated with this article can be found, in the online version, at doi:10.1016/j.poly.2007.03.055.

References

[1] (a) W. Baratta, E. Herdtweck, W.A. Hermann, P. Rigo, J. Schwarz, Organometallics 21 (2002) 2101;
(b) M.A. Bennett, K. Khan, E. Wenger, in: G. Wilkinson, F.G.A. Stone, E.W. Abel (Eds.), Comprehensive Organometallic Chemistry II, second ed., vol. 7, Elsevier, Oxford, 1995, Chapter 8 and references cited therein.
[2] (a) S.G. Davies, J.P. McNally, J. Smallridge, Adv. Organomet. Chem. 30 (1991) 1;
(b) B.M. Trost, J.A. Marting, R.J. Kulawiec, A.F. Indolese, J. Am. Chem. Soc. 115 (1993) 10402;
(c) P. Pertici, V. Ballantini, P. Salvadori, M.A. Bennett, Organometallics 14 (1995) 2565;
(d) D.L. Davies, J. Fawcett, R. Krafczyk, D.R. Russell, J. Organomet. Chem. 545–546 (1997) 581.
[3] (a) B.M. Trost, M.U. Frederiksen, M.T. Rudd, Angew. Chem., Int. Ed. Eng. 44 (2005) 6630, and references cited therein;
(b) W. Baratta, A.D. Zotto, P. Rigo, Chem. Commun. (1997) 2163;
(c) A.D. Zotto, W. Baratta, G. Verardo, P. Rigo, Eur. J. Org. Chem. (2000) 2795.
[4] M.A. Esteruelas, E.G. Puebla, A.M. López, E. Oñate, J.I. Tolosa, Organometallics 19 (2000) 275.

[5] (a) R. Lalrempuia, H. Yennawar, Y.A. Mozharivskyj, K. Mohan Rao, J. Organomet. Chem. 689 (2004) 539;
(b) T. Wilczewski, J. Organomet. Chem. 317 (1986) 307;
(c) T. Wilczewski, J. Organomet. Chem. 297 (1985) 331;
(d) M.I. Bruce, G.A. Koutsantonis, M.J. Liddel, B.K. Nicholson, J. Organomet. Chem. 320 (1987) 217, and references cited therein.
[6] (a) P. Govindaswamy, K. Mohan Rao, J. Coord. Chem. 59 (2006) 663;
(b) P. Govindaswamy, Y.A. Mozharivskyj, K. Mohan Rao, Polyhedron 24 (2005) 1710;
(c) H. Aneetha, P.S. Zacharias, B. Srinivas, G.H. Lee, Y. Wang, Polyhedron 18 (1999) 299.
[7] (a) T. Blackmore, M.I. Bruce, F.G.A. Stone, J. Chem. Soc. A (1971) 2376;
(b) G.S. Ashby, M.I. Bruce, I.B. Tomkins, R.C. Wallis, Aust. J. Chem. 32 (1979) 1003;
(c) S.G. Davies, S.J. Simpson, H. Felkin, T. Fillebeen-Khan, Organometallics 2 (1983) 539;
(d) S.G. Davies, S.J. Simpson, H. Felkin, T. Fillebeen-Khan, F. Tadjand, O. Watts, J. Chem. Soc., Chem. Commun. (1981) 341;
(e) M.I. Bruce, S.F. Wong, B.W. Skelton, A.H. White, J. Chem. Soc., Dalton Trans. (1981) 1398.
[8] (a) J.P. Selegue, Organometallics 1 (1982) 217;
(b) J.P. Selegue, J. Am. Chem. Soc. 105 (1983) 5921.
[9] (a) R. Lalrempuia, P. Govindaswamy, Y.A. Mozharivskyj, K. Mohan Rao, Polyhedron 23 (2004) 1069;
(b) K. Mohan Rao, E.K. Rymmai, Polyhedron 22 (2003) 307;
(c) K. Sarjit Singh, P.J. Carroll, K. Mohan Rao, Polyhedron 24 (2005) 391;
(d) K. Sarjit Singh, Y.A. Mozharivskyj, C. Thone, K. Mohan Rao, J. Organomet. Chem. 690 (2005) 3720.
[10] B. Chiswell, F. Lions, B.S. Morris, Inorg. Chem. 31 (1964) 110.
[11] (a) M.I. Bruce, N.J. Windsor, Aust. J. Chem. 30 (1977) 1601;
(b) M.I. Bruce, P.J. Low, B.W. Skelton, E.R.T. Tiekink, A. Werth, A.H. White, Aust. J. Chem. 48 (1995) 1887.
[12] (a) J.W. Kang, K. Moseley, P.M. Maitlis, J. Am. Chem. Soc. 91 (1969) 5970;
(b) C. White, A. Yates, P.M. Maitlis, Inorg. Synth. 29 (1992) 228.
[13] M. Sheldrick, Acta Crystallogr., Sect. A 46 (1990) 467.
[14] M. Sheldrick, SHELXL-97, University of Göttingen, Göttingen, Germany, 1999.
[15] L.J. Farrugia, J. Appl. Cryst. 30 (1997) 565.
[16] I.J. Bruno, J.C. Cole, P.R. Edgington, M. Kessler, C.F. Macrae, P. Mc Cabe, J. Pearson, R. Taylor, Acta Crystallogr., Sect. B 58 (2002) 389.
[17] A. Singh, N. Singh, D.S. Pandey, J. Organomet. Chem. 642 (2002) 48.
[18] (a) H. Mishra, R. Mukherjee, J. Organomet. Chem 691 (2006) 3545;
(b) R. Lalrempuia, K. Mohan Rao, Polyhedron 22 (2003) 3155.
[19] P. Govindaswamy, C. Sinha, K. Mohan Rao, J. Organomet. Chem. 690 (2005) 3465.
[20] H. Brunner, A. Köllnberger, T. Burgemeister, M. Zabel, Polyhedron 19 (2000) 1519.
[21] S. Tsuzuki, K. Honda, T. Uchimura, M. Mikami, K. Tanabe, J. Am. Chem. Soc. 124 (2002) 104.



Scheme 1. The 5-sulfosalicylic acid species.

$(H_2O)]_n$ [6,7], $[K(H_2SSA)(H_2O)_2]_n$ [8], $[Rb(H_2SSA)(H_2O)]_n$ [9], $[Cs(H_2SSA)]_n$ [10], $[Ca(HSSA)(H_2O)_3]_n$ [8], $\{[Sr(H_2SSA)_2(H_2O)] \cdot H_2O\}_n$ [11], $[Ba(H_2SSA)_2(H_2O)_5]_n$ [12], $\{[La(SSA)(H_2O)_8] \cdot H_2O\}_n$ [13], $[Eu(H_2SSA)_2(H_2O)_5]_n$ [14], $\{[Yb(SSA)_3(H_2O)_8] \cdot H_2O\}_n$ [15], $[Sm(HSSA)_2(H_2O)_6]_n$ [16], and $[Nd(SSA)(H_2O)]_n$ [17]. Also, examples with mixed-metal species are known, e.g. $[NaCu(SSA)(H_2O)_4]_n$ [6], $[Na_3La_2Tb(SSA)_4(H_2O)_{26}]_n$ [18] and $[Na_3La_2Y(SSA)_4(H_2O)_{26}]_n$ [19]. Among the known examples are occasional complexes with mixed mono- and dianionic ligand species, e.g. $\{[Na_3(H_2SSA)(HSSA) \cdot H_2O]\}_n$ [20]. Also, in a number of these complexes the 5-sulfosalicylate species act as counter-anions without participating in coordination, e.g. the Yb^{III} complex which has the actual structural formula $\{[Yb(H_2O)_8(H_2SSA)_3] \cdot H_2O\}_n$ [15], while a series of first-row transition metal(II) complexes have a similar type of constitution, with a general formula $[M(H_2O)_6(H_2SSA)_2 \cdot nH_2O]$ [M = Mn, $n = 2$; M = Co, $n = 4$; M = Ni, $n = 4$; M = Cu, $n = 2$; M = Zn, $n = 4$ [21]. These differ from the polymeric structures shown in the Group 1 complexes and in the silver(I) complexes $[Ag_4(HSSA)_2(H_2O)_2]_n$ and $[Ag_2(HSSA)(H_2O)–Ag_2(H_2SSA)_2(H_2O)_3] \cdot H_2O\}_n$ [22].

In an investigation of the complexes of sulfosalicylic acid with the Group 1 metal ions, it was found that not only were the reported complexes with K^I, Rb^I and Cs^I [8–10] isolated, a second presumably efflorescent form of the Rb complex, $[Rb_3(H_2SSA)(HSSA)(H_2O)_4]_n$ (**1**), was formed and its structure is reported here. This complex also has both H_2SSA^- and $HSSA^{2-}$ ligand species. A parallel determination using 5-sulfosalicylic acid and CsOH similarly gave an unstable compound which when recrystallized from water surprisingly gave the previously reported [10] anhydrous compound $[Cs(H_2SSA)]_n$ (**2**) confirmed by both elemental analysis and a low-temperature single-crystal X-ray diffraction analysis. The structure of the stable hydrated lead(II) complex $[Pb(H_2SSA)_2(H_2O)]_n$ (**3**) is also reported here, the only previous structure of a compound of lead(II) with 5-sulfosalicylic acid being a dimeric mixed-ligand complex with 1,10-phenanthroline, $[Pb_2(HSSA)_2(phen)_2(H_2O)_2]$ [23].

2. Experimental

2.1. Synthesis of compounds

Compound **1** $[Rb_3(H_2SSA)(HSSA)(H_2O)_4]_n$ was synthesized by adding 0.23 g (1 mmol) of 4-carboxy-3-hydroxybenzenesulfonic acid (5-sulfosalicylic acid) to 30 mL of an aqueous solution containing 0.10 g (1 mmol) of rubidium hydroxide. The mixture was heated for ca. 10 min at 90° and the resultant hot-filtered solution was then allowed to evaporate at room temperature. The colourless prisms of **1** which were obtained after several weeks were unstable in air, deteriorating slowly to a white powder, presumably due to loss of water of solvation, prompting the low-temperature X-ray diffraction analysis. No elemental analysis was therefore performed.

Compound **2** $[Cs(H_2SSA)]_n$ was synthesized using a parallel procedure to that in **1**, by adding 0.23 g (1 mmol) of 5-sulfosalicylic acid to 30 mL of an aqueous solution containing 0.15 g (1 mmol) of cesium hydroxide. The crystals obtained after several weeks of room temperature evapora-

Table 1
Cell data for compounds **1**–**3**

	Compound **1**	Compound **2**	Compound **3**
CCDC reference	637681	641976	637682
Formula	$C_{14}H_{19}O_{17}Rb_3S_2$	$C_7H_5CsO_6S$	$C_{14}H_{12}O_{13}PbS_2$
M_r	761.81	350.08	659.58
Crystal class	monoclinic	monoclinic	monoclinic
Space group	$P2_1/c$	$P2_1/c$	$P2_1/m$
a (Å)	15.0117(10)	9.6336(6)	8.5751(7)
b (Å)	23.0776(16)	7.1404(4)	5.9654(5)
c (Å)	7.0560(5)	14.3617(9)	17.8447(13)
β (°)	93.415(1)	91.842(1)	101.040(1)
V (Å^3)	2440.1(3)	987.4(1)	896.53(12)
$D_{calc.}$ (g cm^{-3})	2.074	2.355	2.436
Z	4	4	2
λ (Mo Kα) (mm^{-1})	6.238	3.966	9.716
Temperature (K)	130(2)	130(2)	130(2)
$2\theta_{max}$ (°)	50	50	50
Crystal size (mm)	0.30 × 0.30 × 0.30	0.45 × 0.25 × 0.15	0.25 × 0.15 × 0.10
Total data	12 575	4986	4513
Collection range	$-17 \leqslant h \leqslant 17$, $-21 \leqslant k \leqslant 27$, $-8 \leqslant l \leqslant 7$	$-10 \leqslant h \leqslant 11$, $-8 \leqslant k \leqslant 8$, $-10 \leqslant l \leqslant 17$	$-10 \leqslant h \leqslant 9$, $-7 \leqslant k \leqslant 7$, $-14 \leqslant l \leqslant 21$
Unique data	4303	1742	1744
R_{int}	0.050	0.020	0.022
N [$I > 2.0\sigma(I)$]	3577	1683	1716
R_1^a	0.066	0.023	0.022
wR_2^a	0.168	0.061	0.060
S^a	1.09	1.09	1.12
A,B^b	0.052, 34.4	0.037, 0.998	0.035, 0.018

[a] $R_1 = (\sum||F_o| - |F_c||)/\sum|F_o|$; $wR_2 = \{\sum w[(F_o^2 - F_c^2)]^2/\sum[w(F_o^2)^2]\}^{1/2}$; $S = \{\sum[w(F_o^2 - F_c^2)^2]/(n-p)\}^{1/2}$; $w = [\sigma^2(F_o^2) + (AP)^2 + BP]^{-1}$ {where $P = [(\text{max. } F_o^2, 0) + 2(F_c^2)]/3$}.

[b] Cell parameters from Ref. [10] at 298 K: $a = 9.682(3)$, $b = 7.317(2)$, $c = 14.358(4)$ (Å), $\beta = 90.641(14)°$, $V = 1017.2(5)$ Å^3.

tion of the solvent were found to be unstable in air but on recrystallization from water gave stable prismatic crystals of **2**, the previously reported structurally characterized anhydrous complex [10], confirmed here by elemental analysis (*Anal*. Calc. for $C_7H_5CsO_6S$: C, 24.0; H, 1.44. Found: C, 24.2; H, 1.5%) and low-temperature single-crystal X-ray diffraction (see Table 1).

Compound **3** $[Pb(H_2SSA)_2(H_2O)]_n$ was synthesized by mixing together in the solid state, 0.33 g (1 mmol) of lead nitrate and 0.46 g (2 mmol) of 5-sulfosalicylic acid, then extracting with gentle heating for ca. 10 min with 30 mL of 80% water–ethanol. Room-temperature evaporation of the hot-filtered solution gave colourless crystal prisms of **3** (m.p. >281 °C), which darkened on exposure to air. No elemental analysis was performed.

2.2. X-ray structure determinations

X-ray diffraction data for compounds **1**–**3** were collected at 130(2) K on an Bruker CCD-equipped diffractometer by using monochromatized Mo Kα X-radiation ($\lambda = 0.71073$ Å). No significant crystal decomposition in the X-ray beam was in evidence for any compound. Data were corrected for Lorentz and polarization effects (SMART and SAINT [24]), and for absorption (SADABS [24]). The structures were solved by direct methods and refined using full-matrix least-squares (SHELX-97 [25]), with anisotropic thermal parameters for all non-hydrogen atoms. With **1**, three of the water molecules were found to be disordered over similar split sites [O21W, O22W; O31W, O32W; O41W, O42W: site occupancy factors 0.65:0.35] and were refined separately. Hydrogen atoms were either located by difference methods or included in the refinements at calculated positions with coordinates and isotropic thermal parameters fixed or treated as riding models (**1**) or with **2** and **3** the interactive H atom/s were refined isotropically. Cell data and general details of data collection and structure refinement for compounds **1**–**3** are given in Table 1. Bond distances and angles about the metal coordination polyhedra in **1** and **3** are given in Tables 2 and 3, but since there are no significant differences between the 130 K structure of **2** and the previously reported room-temperature structure, details are not considered in any detail here. It should also be noted that in the discussion and the bond distance and angle tables for **1**, only the major-occupancy components of the three split-site water molecules are considered.

Table 2
Bond distances (Å) and angles (°) about the coordination polyhedra for **1**

Distances					
Rb1–O53A	3.031(7)		Rb2–O51A^{c}	2.995(6)	
Rb1–O2A^{a}	2.879(5)		Rb2–O51B^{d}	2.871(7)	
Rb1–O51A^{b}	2.934(6)		Rb2–O52B^{f}	2.796(7)	
Rb1–O52A^{b}	3.152(6)		Rb3–O1W	2.889(7)	
Rb1–O53A^{c}	2.855(6)		Rb3–O31W	2.953(15)	
Rb1–O51B^{d}	3.046(6)		Rb3–O41W	3.151(13)	
Rb1–O52B^{d}	2.881(8)		Rb3–O71A	2.938(7)	
Rb2–O1W	3.075(7)		Rb3–O71B^{g}	3.063(7)	
Rb2–O2B	2.992(7)		Rb3–O72B^{h}	2.976(6)	
Rb2–O21W	3.01(2)		Rb3–O72A^{i}	2.988(7)	
Rb2–O52A^{e}	2.958(7)				
Angles					
O53A–Rb1–O2A^{a}	169.43(17)	O1W–Rb2–O2B	109.56(19)	O1W–Rb3–O31W	95.0(3)
O53A–Rb1–O51A^{b}	99.38(18)	O1W–Rb2–O21W	78.8(7)	O1W–Rb3–O41W	85.7(3)
O53A–Rb1–O52A^{b}	113.15(18)	O1W–Rb2–O52A^{e}	85.94(19)	O1W–Rb3–O71A	116.43(19)
O53A–Rb1–O53A^{c}	85.93(18)	O1W–Rb2–O51A^{c}	110.31(19)	O1W–Rb3–O71B^{g}	135.9(2)
O53A–Rb1–O51B^{d}	80.88(18)	O1W–Rb2–O51B^{d}	76.73(19)	O1W–Rb3–O72B^{h}	144.9(2)
O53A–Rb1–O52B^{d}	84.08(18)	O1W–Rb2–O52B^{f}	171.0(2)	O1W–Rb3–O72A^{i}	74.4(2)
O2A^{a}–Rb1–O51A^{b}	86.16(18)	O2B–Rb2–O21W	66.6(4)	O31W–Rb3–O41W	73.0(5)
O2A^{a}–Rb1–O52A^{b}	64.39(17)	O2B–Rb2–O52A^{e}	154.71(18)	O31W–Rb3–O71A	126.7(4)
O2A^{a}–Rb1–O53A^{c}	85.04(18)	O2B–Rb2–O51A^{c}	115.31(19)	O31W–Rb3–O71B^{g}	110.6(3)
O2A^{a}–Rb1–O51B^{d}	104.00(17)	O2B–Rb2–O51B^{d}	73.92(18)	O31W–Rb3–O72B^{h}	67.4(4)
O2A^{a}–Rb1–O52B^{d}	106.19(18)	O2B–Rb2–O52B^{f}	74.20(19)	O31W–Rb3–O72A^{i}	154.4(4)
O51A^{b}–Rb1–O52A^{b}	46.70(16)	O21W–Rb2–O52A^{e}	98.5(5)	O41W–Rb3–O71A	68.1(3)
O51A^{b}–Rb1–O53A^{c}	152.11(18)	O21W–Rb2–O51A^{c}	168.1(8)	O41W–Rb3–O71B^{g}	135.2(3)
O51A^{b}–Rb1–O51B^{d}	121.52(17)	O21W–Rb2–O51B^{d}	122.3(7)	O41W–Rb3–O72B^{h}	60.6(3)
O51A^{b}–Rb1–O52B^{d}	73.91(18)	O21W–Rb2–O52B^{f}	95.8(7)	O41W–Rb3–O72A^{i}	127.8(3)
O52A^{b}–Rb1–O53A^{c}	106.01(17)	O52A^{e}–Rb2–O51A^{c}	75.15(18)	O71A–Rb3–O71B^{g}	76.45(19)
O52A^{b}–Rb1–O51B^{d}	161.50(18)	O52A^{e}–Rb2–O51B^{d}	130.40(19)	O71A–Rb3–O72B^{h}	62.27(18)
O52A^{b}–Rb1–O52B^{d}	119.22(17)	O52A^{e}–Rb2–O52B^{f}	87.82(19)	O71A–Rb3–O72A^{i}	78.58(19)
O53A^{c}–Rb1–O51B^{d}	86.31(17)	O51A^{c}–Rb2–O51B^{d}	68.43(17)	O71B^{g}–Rb3–O72B^{h}	79.19(18)
O53A^{c}–Rb1–O52B^{d}	133.98(18)	O51A^{c}–Rb2–O52B^{f}	74.2(2)	O71B^{g}–Rb3–O72A^{i}	67.08(17)
O51B^{d}–Rb1–O52B^{d}	47.76(17)	O51B^{d}–Rb2–O52B^{f}	112.3(2)	O72B^{h}–Rb3–O72A^{i}	133.27(19)

$a = -x, 1/2 + y, 1/2 - z$; $b = -x, 1 - y, -z$; $c = -x, 1 - y, 1 - z$; $d = x, 11/2 - y, -1/2 + z$; $e = x, y, 1 - z$; $f = x, 11/2 + y, 1/2 - z$; $g = 1 - x, -1/2 + y, 11/2 - z$; $h = 1 - x, 1 - y, 1 - z$; $i = x, 1/2 - y, 1/2 + z$.

Table 3
Bond distances (Å) and angles (°) about the coordination polyhedron in **3**

Distances			
Pb1–O1W	2.407(4)	Pb1–O51B^{b}	2.580(3)
Pb1–O51A	2.561(3)	Pb1–O51B^{c}	2.580(3)
Pb1–O52B	2.717(4)	Pb1–O51A^{d}	2.561(3)
Pb1–O52A^{a}	2.675(4)		
Angles			
O1W–Pb1–O51A	73.31(8)	O52B–Pb1–O52A^{a}	76.86(11)
O1W–Pb1–O52B	141.30(12)	O52B–Pb1–O51B^{b}	130.30(7)
O1W–Pb1–O52A^{a}	141.84(11)	O52B–Pb1–O51B^{c}	130.30(7)
O1W–Pb1–O51B^{b}	72.31(8)	O52B–Pb1–O51A^{d}	79.22(8)
O1W–Pb1–O51B^{c}	72.31(8)	O52A^{a}–Pb1–O51B^{b}	80.46(8)
O1W–Pb1–O51A^{d}	73.31(8)	O52A^{a}–Pb1–O51B^{c}	80.46(8)
O51A–Pb1–O52B	79.22(8)	O52A^{a}–Pb1–O51A^{d}	129.21(7)
O51A–Pb1–O52A^{a}	129.21(7)	O51B^{b}–Pb1–O51B^{c}	87.55(9)
O51A–Pb1–O51B^{b}	82.05(9)	O51B^{b}–Pb1–O51A^{d}	145.61(8)
O51A–Pb1–O51B^{c}	145.61(8)	O51B^{c}–Pb1–O51A^{d}	82.05(9)
O51A–Pb1–O51A^{d}	88.27(9)		

$a = 1 - x, -1/2 + y, -z$; $b = 1 - x, 1/2 + y, -z$; $c = 1 - x, -y, -z$; $d = x, 1/2 - y, z$.

3. Results and discussion

3.1. The structural chemistry of *1*–*3*

3.1.1. Compound *1*

The structure of the rubidium complex with 5-sulfosalicylic acid, $[Rb_3(H_2SSA)(HSSA)(H_2O)_4]_n$ (**1**) reported here, represents an unstable hydrate variant of the previously reported polymeric complex, the monohydrate $[Rb(H_2SSA)(H_2O)]_n$ [9]. In **1**, there are two ligand species, one a dianion $(HSSA)^{2-}$ (A), the other a monoanionic $(H_2SSA)^{-}$ (B) and both are involved, along with a bridging water molecule (O1W) in linking the three Rb^{+} centres (Rb1–Rb3) (Fig. 1). The three independent coordination centres are irregular seven-coordinate but differ in their makeup (Table 2). The coordination sphere about Rb1 comprises six sulfonate-O donors and one phenate-O donor [Rb–O range: 2.855(6)–3.152(6) Å]. The coordination sphere about Rb2 consists of four sulfonate-O and one phenolate-O donors and two water molecules, one bridging to Rb3 (O1W), the other monodentate and having split occupancy (O21W, O22W: site occupancy factors 0.65, 0.35) [Rb–O range: 2.796(7)–3.031(7) Å]. The third centre about Rb3 has no sulfonate-O involvement but has four carboxylate-O donors together with three water molecules, the previously mentioned bridging one, and two monodentate ones, both having split sites similar to O2W [O31W, O32W and O41W, O42W, both with site occupancy factors of 0.65, 0.35, respectively] [Rb–O range: 2.889(7)–3.151(13) Å]. The metal coordination as well as the three-dimensional framework polymeric structure generated (Fig. 2) is common in the Group 1 metal complexes of 5-sulfosalicylic acid, including that of $[Rb(H_2SSA)(H_2O)]_n$ [9], which has 7-coordination about the metal [Rb–O, 2.847(5)–3.110(5) Å] but has the single coordinated water non-bridging. In that structure the water acts as an acceptor in a strong hydrogen bond with the carboxylic acid proton of the H_2SSA^{-} ligand whereas in **1**, the acid proton of the B ligand is strongly hydrogen-bonded to a carboxylate-O of the A ligand [O71B···O71A, 2.467(9) Å].

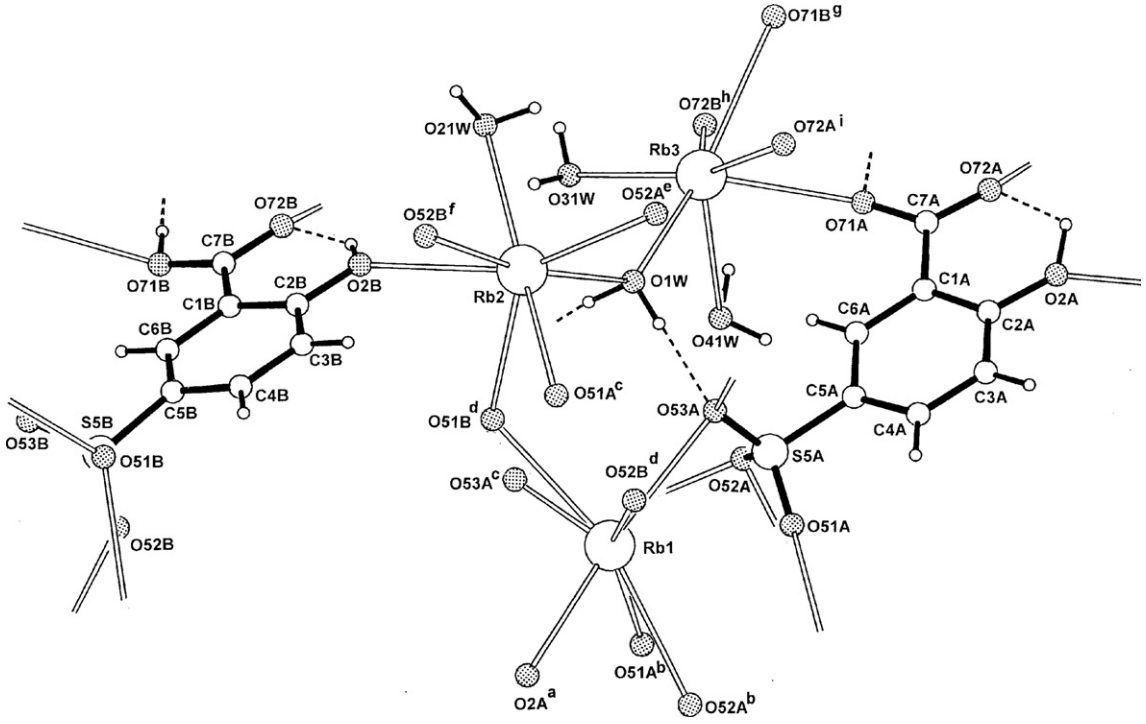


Fig. 1. A general view of the coordination about the three interlinked Rb centres (Rb1–Rb3) in **1** including the atom numbering scheme. Partial hydrogen-bonding interactions are shown as broken lines. The smaller-occupancy components of the split-site water molecules O21W, O31W and O41W (O22W, O32W, O42W) are not shown. For symmetry operators, see Table 2.

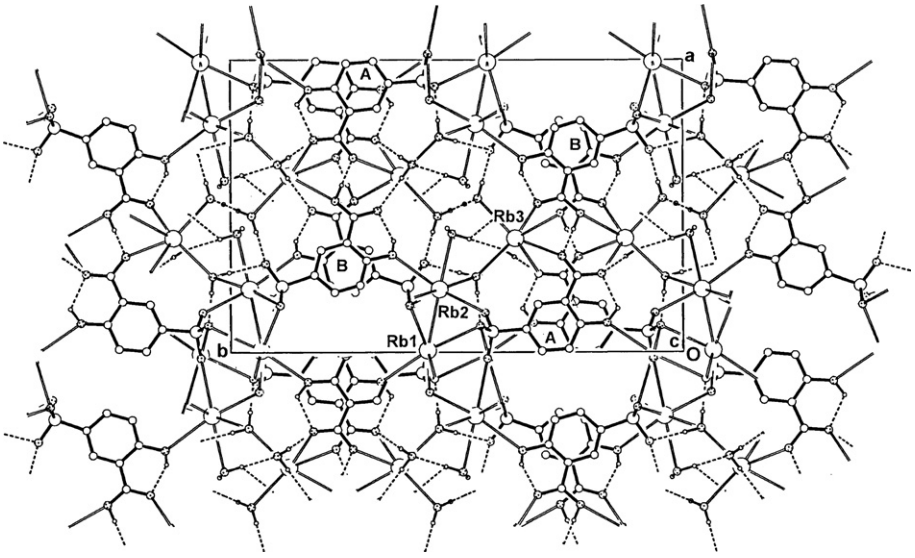


Fig. 2. The three-dimensional framework polymer structure of **1** viewed down the *c* axial direction of the unit cell.

Also present but expected in both ligand species is the intramolecular hydrogen bond linking the phenolic group to the carboxyl-O [O2–H2···O72: 2.552(9) Å (A) and 2.565(10) Å (B)]. This bond is found in the hydrate pseudo-polymorphs of the acid [1–5] as well as in the mono- and dianionic species of the acid found in its salts [26], and in complexes **2** and **3**.

The presence of large number of oxygen acceptor and water hydrogen-donor sites means that there are also a number of hydrogen-bonding associations which stabilize the structure of 1 including an intramolecular water···sulfonate interaction [O1W–H···O53A, 2.792(10) Å]. Although a 1:1 reactant stoichiometry was used in the synthesis of **1**, it would appear that its formation is the result of favoured conditions within the crystallizing product. The presence of water in the crystallization has an obvious influence upon the composition of the crystal in which significant water lability is inherent.

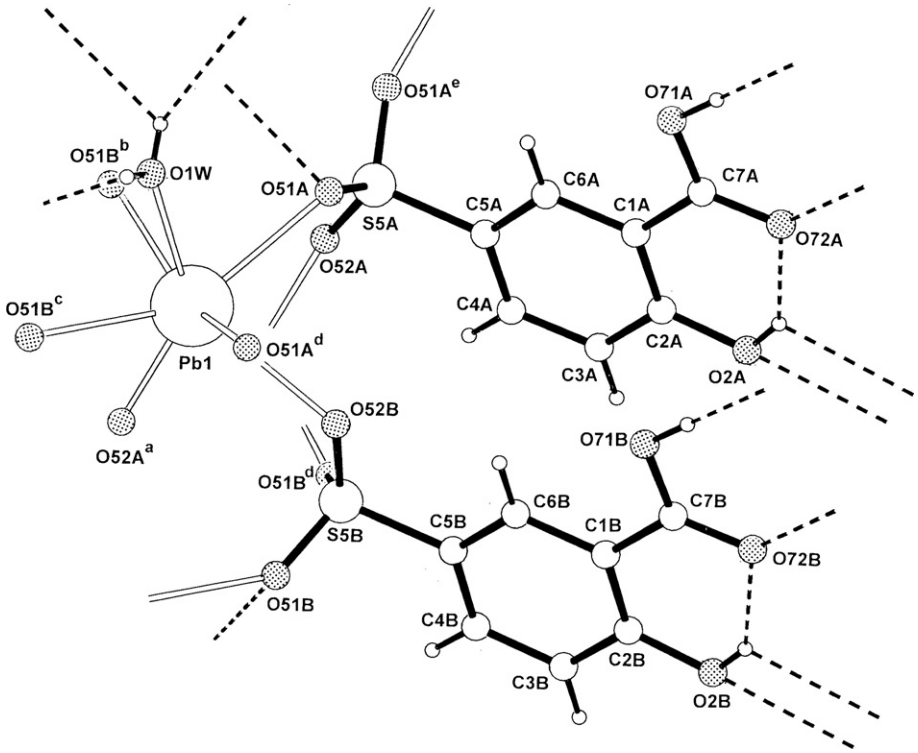


Fig. 3. The stereochemistry about the PbO_7 coordination polyhedron in **3**, including the atom numbering scheme. The atoms O51A^{e} in ligand A and O51B^{d} in ligand B lie across crystallographic mirror planes and are generated by the operators $d = x, 1/2 - y, z$ and $e = x, 11/2 - y, z$. For other operators, see Table 3.

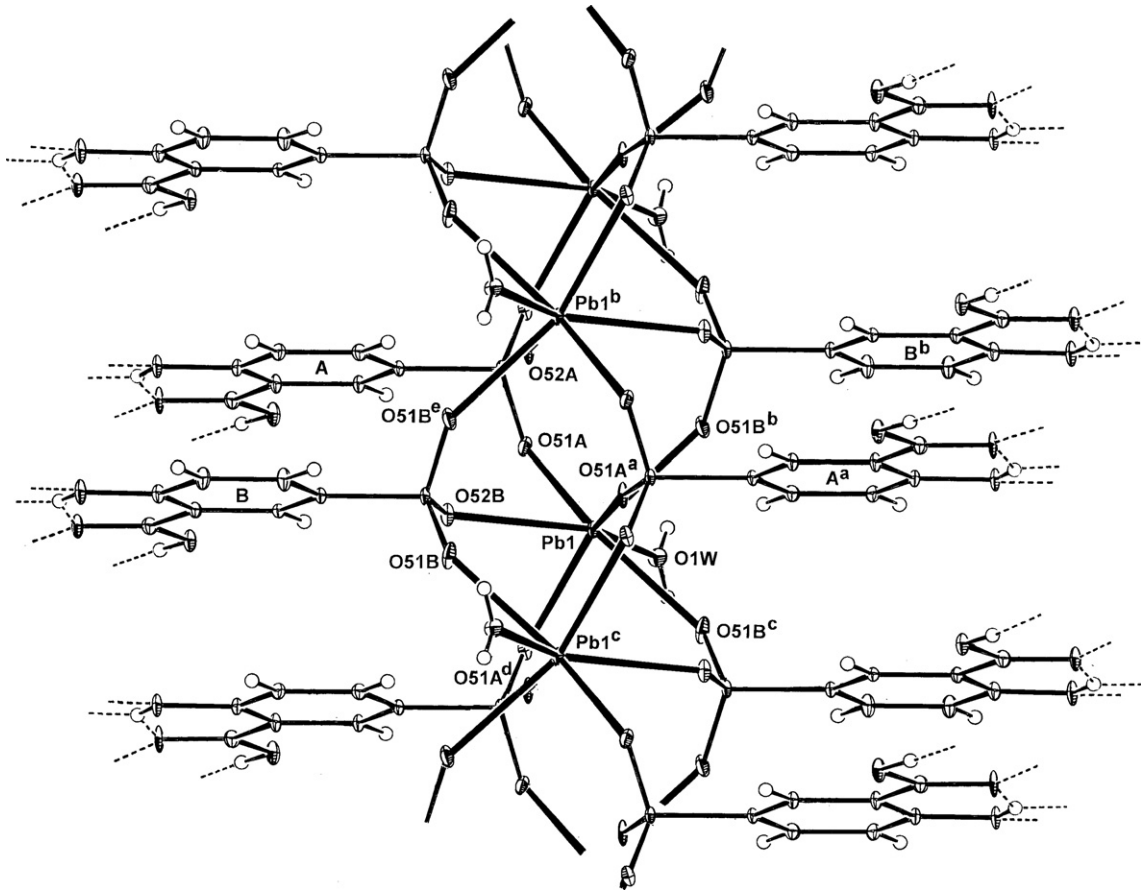


Fig. 4. The helical substructure in **3** extending along the *b* axial direction. The structure is further extended peripherally through head-to-head hydrogen-bonding interactions (shown as broken lines) involving the carboxylic acid and phenolic substituent groups of the SSA ligands. Atoms are shown as 30% probability ellipsoids [33].

3.1.2. Compound *2*

The room-temperature (298 K) structure of the anhydrous caesium complex with 5-sulfosalicylic acid, $[Cs(H_2SSA)]_n$ (**2**), has been previously described [10], and is a three-dimensional framework coordination polymer having an irregular Cs–O9 repeat (the asymmetric unit) which involves all oxygen donor atoms of eight independent H_2SSA^- ligands. Comparative cell parameters for this previous determination are given in Table 1 but the basic structural description remains the same, except for the minor changes in cell dimension-dependent values e.g. Cs–O bond distance range: 2.963(2)–3.434(2) Å (130 K) cf. 3.093(3)–3.449(3) Å (298 K).

3.1.3. Compound *3*

The lead(II) complex with 5-sulfosalicylic acid, $[Pb(H_2SSA)_2(H_2O)]_n$ (**3**), shows a three-dimensional structure based on coordination step-polymer ribbons interlinked by hydrogen-bonding interactions involving the carboxylic acid groups of the H_2SSA^- ligand species. The basic repeat unit (the asymmetric unit) in the helical ribbons is an irregular PbO_7 coordination centre [Pb–O range: 2.407(4)–2.717(4) Å] (Table 3), comprising the single monodentate water and six separate sulfonate oxygen donor atoms (Figs. 3 and 4). Each sulfonate group bridges three lead centres giving Pb···Pb repeats of 4.4747(4) Å down the *b*-axial direction in the unit cell. This is different from the discrete dimer formed in the mixed-ligand [1,10-phenanthroline-($HSSA^{2-}$)] lead complex [23] in which the two six-coordinate lead centres are bridged by the $HSSA^{2-}$ ligands through both the sulfonate and carboxylate groups. However, polymeric $Pb^{(II)}$ carboxylates and sulfonates are very common, as are irregular coordination polyhedra, and although Pb may assume regular octahedral, tetrahedral and square planar stereochemistry [27], irregular systems such as that found in **3** are well documented in the literature [28–32]. In **3**, most atoms including the Pb, the water-O and all atoms of the SSA ligand species, with the exception of two of the sulfonate-O atoms (O51A and O51B and their mirror-related pairs) lie in crystallographic mirror planes in the unit cell at $y = 1/4, 3/4$. The carboxylic acid groups link the coordination chains peripherally in characteristic intermolecular head-to-head cyclic hydrogen-bonding associations [O71A–H···O72B, 2.655(6) Å and O71B–H···O72A, 2.605(5) Å]. In addition, the substituent phenolic groups give a side-to-side interaction [O···O, 2.700(5) Å], closing the steps in the layered framework polymer (Fig. 5). The coordinated water molecule

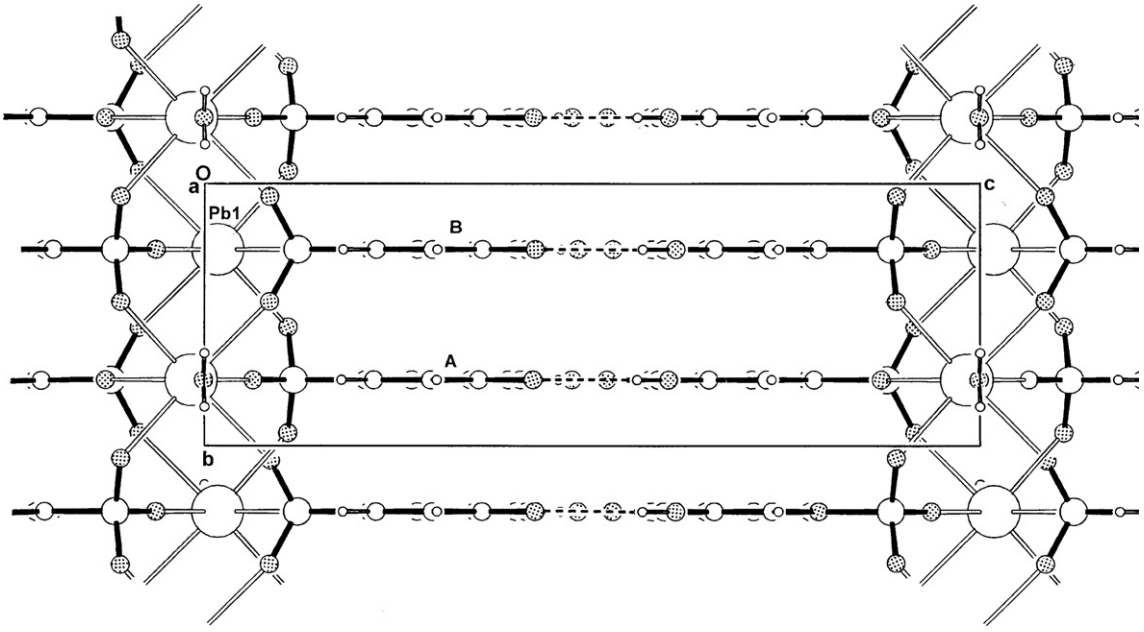


Fig. 5. The step-polymer structure and layering in **3** viewed down the crystallographic mirror planes showing the hydrogen-bonding extensions along the *c* axial direction.

also gives stability to the complex through hydrogen bonding, while within the ligand species the expected [26] intramolecular phenolic O–H···O(carboxylate) hydrogen bond is found [O···O, 2.602, 2.609(6) Å].

3.2. Conclusions

It has been further demonstrated that the 5-sulfosalicylic acid molecule is particularly efficient as a ligand for metal complexation, giving in most compounds (e.g. compounds **2** and **3**) chemically stable polymeric materials. This utility of this compound as a ligand is the result of a number of factors including: (1) The desirable stereochemical features presented by its substituent donor groups providing for multidentate coordination and polymeric structure extension. (2) The inherent selectivity achievable through pH and reactant stoichiometry in the control of ligand speciation (i.e. mono-, di- or trianionic species): mixed-species in complexes such as found in compound **1** are also possible, although uncommon. (3) The proton-acceptor properties of the oxygen atoms of the substituent groups, which allow for secondary hydrogen-bonding associations, commonly with incorporated water molecules (both coordinated and solvated). However, as is demonstrated in the rubidium(I) complex **1** and reinforced by a number of other examples from the crystallographic literature, there is a higher incidence of structures having hydrate lability in complexes of 5-sulfosalicylate with higher atomic number metallic elements.

Acknowledgements

The authors acknowledge financial support from the School of Physical and Chemical Sciences, Queensland University of Technology, the School of Biomolecular and Physical Sciences, Griffith University and the School of Chemistry, the University of Melbourne.

Appendix A. Supplementary material

CCDC 637681, 641976 and 637682 contain the supplementary crystallographic data for **1**, **2** and **3**. These data can be obtained free of charge via http://www.ccdc.cam.ac.uk/conts/retrieving.html, or from the Cambridge Crystallographic Data Centre, 12 Union Road, Cambridge CB2 1EZ, UK; fax: (+44) 1223-336-033; or e-mail: deposit @ccdc.cam.ac.uk. Supplementary data associated with this article can be found, in the online version, at doi:10.1016/j.poly.2007.03.044.

References

[1] R. Attig, D. Mootz, Acta Crystallogr., Sect. B 33 (1977) 2422.
[2] Z.G. Aliev, L.O. Atovmyan, T.A. Baranova, A.E. Ukshe, Zh. Strukt. Khim. 36 (1995) 947.
[3] R. Attig, J.M. Williams, J. Chem. Phys. 66 (1977) 1389.
[4] D. Mootz, J. Fayoz, Acta Crystallogr., Sect. B 26 (1970) 2046.
[5] A. Merschenz-Quack, D. Mootz, Acta Crystallogr., Sect. C 46 (1990) 1478.
[6] A. Marzotto, D.A. Clemente, T. Gerola, G. Valle, Polyhedron 20 (2001) 1079.
[7] Z.G. Aliev, L.O. Atovmyan, J. Struct. Chem. 42 (2001) 506, Na.
[8] Y. Li, L. Deng, X. Zhou, S. Zhang, Q. Yang, Wuli Huaxue Zhubao 14 (1998) 778.
[9] M. Hu, Y. Du, S. Li, Y. Jiang, Z. Liu, C. Geng, Acta Crystallogr., Sect. E 61 (2005) m15.
[10] M. Hu, C. Geng, S. Li, Y. Du, Y. Jiang, Z. Liu, J. Organomet. Chem. 690 (2005) 3118.
[11] S. Gao, L.-H. Huo, Z.-B. Zhu, J.-R. Li, Acta Crystallogr., Sect. E 61 (2005) m417.

[12] J.-F. Ma, J. Yang, L. Li, G.-L. Zheng, J.-F. Liu, Inorg. Chem. Commun. 6 (2003) 581.
[13] Z.G. Aliev, L.O. Atovmyan, T.A. Baranova, S.B. Pirkes, Koord. Khim. 17 (1991) 1282.
[14] P. Starynowicz, J. Alloys Comp. 305 (2000) 117.
[15] A. Rohde, W. Urland, Acta Crystallogr., Sect. E 62 (2006) m1210.
[16] Z.G. Aliev, T.A. Baranova, L.O. Atovmyan, S.B. Pirkes, Koord. Khim. 20 (1994) 150.
[17] X.Q. Wang, J. Zhang, Z.J. Li, Y.H. Wen, J.K. Cheng, Y.G. Yao, Acta Crystallogr., Sect. C 60 (2004) m657.
[18] H.-Y. Sun, C.-H. Huang, X.-H. Jin, G.-X. Xu, Polyhedron 14 (1995) 1201.
[19] H.-Y. Sun, C.-H. Huang, L.-B. Gan, G.-X. Xu, Z.-S. Ma, N.-C. Shi, Chin. J. Chem. 13 (1995) 150.
[20] Z.-B. Zhu, S. Gao, L.-H. Huo, S.W. Ng, Acta Crystallogr., Sect. E 61 (2006) m192.
[21] J.-F. Ma, J. Yang, J.-F. Liu, Acta Crystallogr., Sect. E 59 (2003), m478 (Mn); m481 (Co); m483 (Ni); m485 (Cu); m487 (Zn).
[22] S. Gao, Z.-B. Zhu, L.-H. Huo, S.W. Ng, Acta Crystallogr., Sect. E 61 (2005) m279, m282.
[23] J.-F. Li, Y.-J. Zhao, X.-H. Li, M.-L. Hu, Acta Crystallogr., Sect. E 60 (2004) m1210.
[24] SMART, ver. 5.55 (2000); SAINT, ver. 5.01 (1998); SADABS, (1999), ver 2.03. Bruker AXS Inc., Madison, USA.
[25] SHELX-97, Program for Crystal Structure Determination, University of Göttingen, Germany, 1997.
[26] G. Smith, U.D. Wermuth, J.M. White, Acta Crystallogr., Sect. C 61 (2005) o105.
[27] M.R.St J. Foreman, T. Gelbrick, M.B. Hursthouse, M.J. Plater, Inorg. Chem. Commun. (2000) 234.
[28] X.-H. Li, S.-Z. Yang, Acta Crystallogr., Sect. E 60 (2004) m423, Pb-SCA.
[29] B. Bridgewater, G. Parkin, Inorg. Chem. Commun. 3 (2000) 534.
[30] F. Cecconi, C.A. Ghilardi, S. Midollini, A. Orlandini, Inorg. Chem. 6 (2003) 546.
[31] S.M. Ying, J.G. Mao, B.P. Yang, Inorg. Chem. Commun. 6 (2003) 1319.
[32] X.-F. Zhang, S. Gao, L.-H. Huo, H. Zhao, Acta Crystallogr., Sect. C 62 (2006) m617.
[33] PLATON, A Multipurpose Crystallographic Tool, University of Utrech, The Netherlands, 2007.

at least reveal whether intermolecular or intramolecular forces are most important for determining cluster structure.

2. Experimental

2.1. Synthesis

2.1.1. Preparation of Liq

This material is prepared by treating 8-hydroxyquinoline with either *n*-butyllithium [9] or lithium hydroxide [10]; it readily sublimes under reduced pressure to give a pale yellow, highly crystalline material.

2.1.2. Preparation of MeLiq

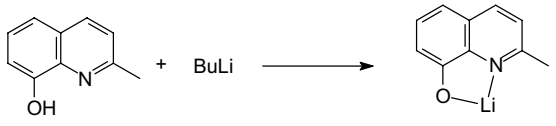
This compound was prepared by the reaction of 2-methyl-8-hydroxyquinoline with *n*-butyllithium in anhydrous toluene at 0 °C or in hexane at 20 °C [11] as shown in Scheme 1. The MeLiq was formed as a white precipitate and collected by filtration. The crude material was purified by sublimation to give colorless crystals.

2.1.3. Preparation of PhLiq

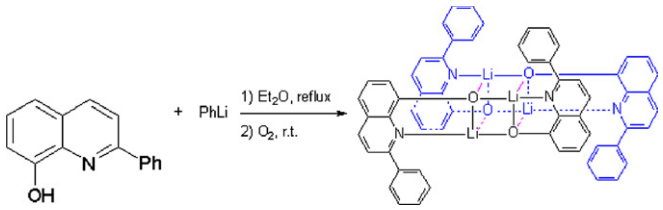
This compound was prepared by the reaction of 8-hydroxy-2-phenylquinoline with two equivalents of *n*-phenyllithium in anhydrous diethyl ether [12], as shown in Scheme 2. The product was isolated as a green powder, which was then sublimed to purify.

2.2. Crystal structure determination

The crystals suitable for single-crystal X-ray quality were obtained by sublimation. Single-crystal structure determination by X-ray diffraction was performed using a Nonius KappaCCD [13] diffractometer, equipped with a normal focus, sealed-tube X-ray source (Mo Kα radiation, $\lambda = 0.71073$ Å). All data sets were collected at room temperature. The first ten frames were used for indexing reflections using the DENZO package [14] and refined to obtain final cell parameters. Data reductions were performed using DENZO-SMN. The structures were solved by direct methods and refined by full-matrix least squares on F^2 with anisotropic displacement parameters for the non-hydrogen atoms using the Bruker, Shelxtl suite of programs [15]. The hydrogen atoms were incorporated into idealized positions. Details of cell data, data collection, and structure refinement are summarized in Table 1. Structure determination details for Liq are described in detail in Ref. [8]. High R_{merg} values and weak diffraction in the case of the MeLiq and PhLiq indicates that the crystal quality was not good. However, even after several attempts, we were unable to get better quality crystals. Liq and MeLiq both crystallize in the triclinic space group, $P\bar{1}$, whereas PhLiq crystallizes in the monoclinic space group, $P2_1/c$. ORTEP diagrams for asymmetric units are illustrated in Fig. 1. There was slight disorder in PhLiq structure, which was left untreated.



Scheme 1.



Scheme 2.

2.3. Computational methods

Geometry optimizations were performed using the Gaussian 03 [16] and the B3LYP hybrid DFT method

Table 1
Crystal data and structure refinement for Lithium quinolate complexes

	MeLiq	PhLiq
Empirical formula	$C_{10}H_8LiNO$	$C_{60}H_{40}Li_4N_4O_4$
Formula weight	165.11	908.72
Crystal system	triclinic	monoclinic
Space group	$P\bar{1}$	$P2(1)/c$
Unit cell dimensions		
a (Å)	9.6894(7)	10.4420(3)
b (Å)	12.8165(7)	24.1250(5)
c (Å)	12.9557(10)	19.5230(8)
α (°)	119.336(3)	90.0
β (°)	98.094(3)	94.1850
γ (°)	100.313(3)	90.0
Volume (Å$^{3)}$	1330.03(16)	4905.0(3)
Z	6	4
Density (Mg/m^3)	1.237	1.231
Absorption coefficient (mm^{-1})	0.079	0.076
F(000)	516	1888
Crystal size (mm)	$0.35 \times 0.17 \times 0.07$	$0.27 \times 0.22 \times 0.12$
θ Range (°)	1.87 to 27.39	1.34 to 27.43
Index ranges	$-12 \leqslant h \leqslant 12$, $-16 \leqslant k \leqslant 15$, $-16 \leqslant l \leqslant 16$	$-12 \leqslant h \leqslant 13$, $-31 \leqslant k \leqslant 30$, $-25 \leqslant l \leqslant 24$
Reflections collected	21 609	34 832
Independent reflections	5922	10 638
R(int)	0.2153	0.3468
Completeness to θ (°)	27.39, 97.7%	27.43, 95.0%
Data/restraints/parameters	5922/0/355	10638/0/649
Goodness-of-fit on F^2	0.899	0.868
Final R indices [$I > 2\sigma(I)$],		
R_1	0.0759	0.0773
R_2	0.1344	0.1259
Largest difference in peak and hole (e Å^{-3})	0.225 and −0.206	0.165 and −0.214

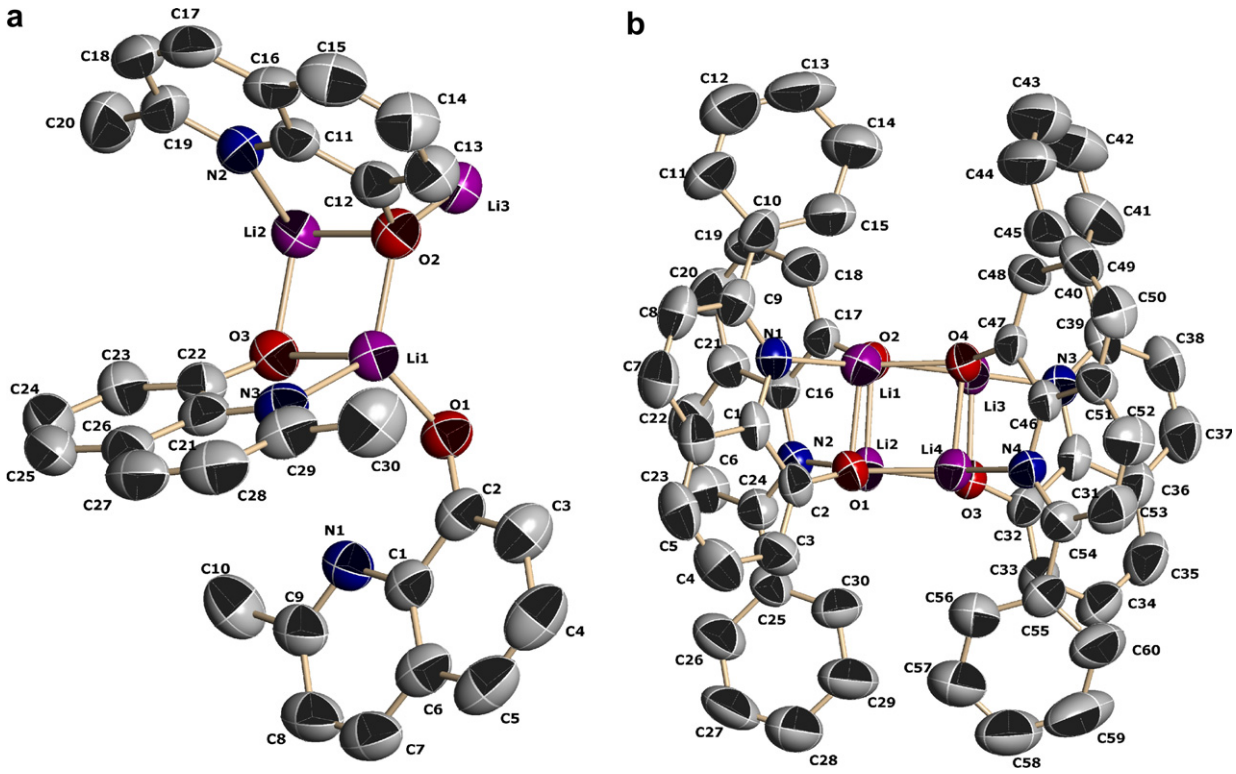


Fig. 1. ORTEP diagrams showing asymmetric units of: (a) MeLiq and (b) PhLiq, with atomic numbering scheme. H atoms are omitted for clarity. Thermal ellipsoids are drawn at 50% probability level.

[17]. The DGDZVP DFT-optimized basis set [18] was used on the Li, N, and O atoms because these are directly involved in coordination, while the MIDI! basis set [19] was used for the remaining (C and H) atoms. Use of a smaller basis set of C and H was mostly helpful for some of the relatively large PhLiq calculations, containing many C atoms; but due to the known good performance of MIDI! on hydrocarbon geometries [19], a mixed basis was used throughout in order to maintain a consistent level of theory across all structures. Structures were optimized in C_1 symmetry, although most structures approached idealized symmetry.

In the MeLiq and PhLiq cases, factors such as phenyl torsions and ligand/ligand steric interactions sometimes played a role in the geometry optimizations. Rather than compute multiple trivially different structures using DFT, a prescreening process was done. In these cases, the starting geometry was taken from the corresponding DFT-optimized Liq structure, then the Me or Ph groups were added as appropriate, using the builder in SPARTAN [20]. Any resulting close contacts were relieved if necessary, for example, by permitting some motion of the ligands with respect to the nearby Li–O bonds while maintaining all Li and O atoms at fixed positions. In the case of PhLiq structures, the phenyl torsions were optimized (keeping Li and O atoms still fixed, and N–Li bond distances were constrained to less than 3 Å) using the systematic conformational search algorithm implemented in SPARTAN, using a molecular mechanics force field. If necessary, this step was repeated using HF/PM3 [21], while maintaining the same constraints, in order to identify one or two most favored candidates for subsequent DFT structure and energy refinement.

3. Results and discussion

Liq and MeLiq molecules crystallize as hexamers, whereas PhLiq crystallizes as a tetramer (Fig. 2). For Liq and MeLiq, the asymmetric units are trimers, with each half of the hexamer related to the other half by symmetry, whereas the asymmetric unit of PhLiq is the tetramer itself. In all three cases, in addition to the oxygen of the 8-hydroxyquinolinate, the quinolinate nitrogen is also involved in coordination to the lithium, resulting in a coordination number of four for each lithium atom in the structure. Liq, a hexamer represented by the formula Li_6q_6, can be described as a doubly stacked trimer. Each trimer is composed of a six-membered ring of alternating oxygen and lithium atoms with the second ring rotated 60° relative to the first ring, allowing for alternating oxygen and lithium atoms between the rings. Essentially, each six-membered ring is planar, resulting in a hexagonal prism of alternating lithium and oxygen atoms that represent the base structure. Whereas, the MeLiq structure can best be described as a paddle-wheel structure, with methyl quinolate rings attached edgewise (perpendicular to the plane) onto the hexagonal prism of alternating lithium and oxygen atoms representing base structure. The PhLiq structure

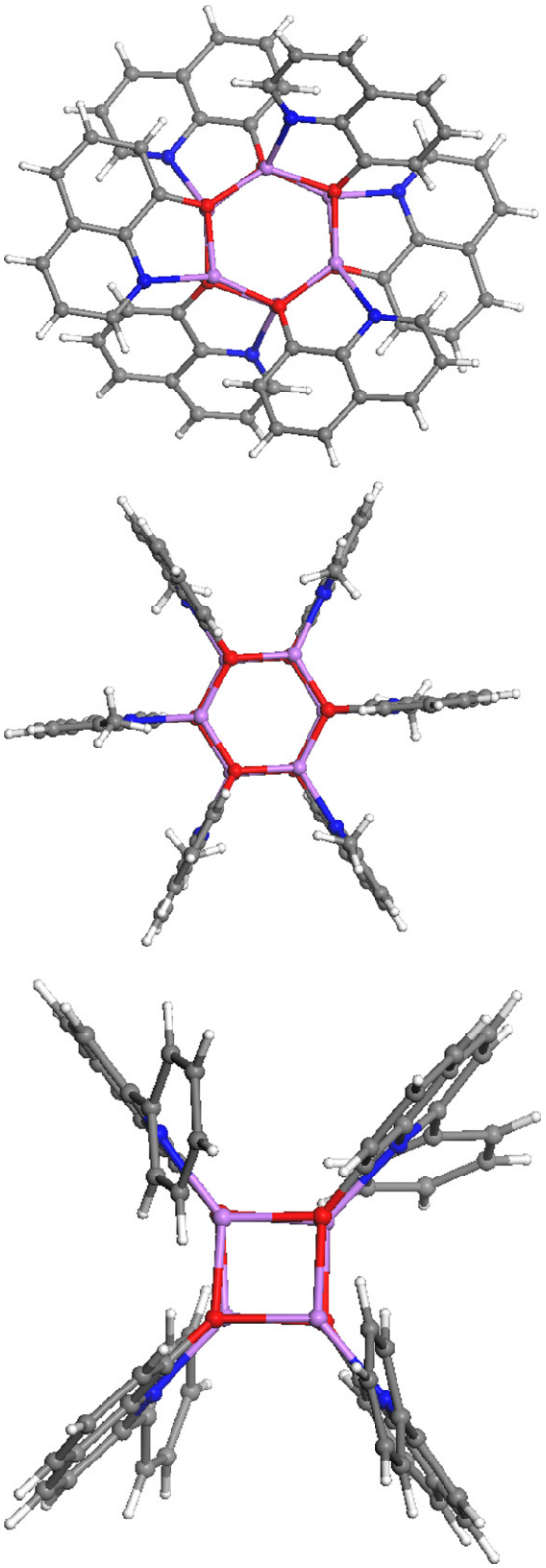


Fig. 2. An illustration of different coordination geometries between hexamers Liq and MeLiq, and tetramer PhLiq.

is described as an eclipsed-form tetramer, with a ring attachment arrangement similar to that for the MeLiq structure. A comparison of the Li–O bond lengths in Table 2 shows a range of 1.892–2.100 Å for the Li–O bond lengths. As expected in case of Liq (and also in MeLiq), the Li–O bond lengths within the trimer are much shorter than those between two stacked trimers in a hexamer. The Li–N bond lengths are in the range of 1.986–2.071 Å (Table 3). The Li–N bond lengths in MeLiq (2.040–2.071) are significantly longer than those in Liq (1.992–2.023). In the Liq and PhLiq crystal packing, intermolecular π–π stacking is evident between the quinoline ring of one molecule and the quinoline ring of the adjacent molecule. In case of MeLiq, there is minimal intramolecular π overlap, instead there seem to be multiple phenyl–phenyl embrace type [22] and C–H···π interactions [23,24].

One of the goals of the computational studies was to evaluate energetic preferences for certain lithium quinolinate structures. Theoretical methods are capable of directly evaluating whether the observed structural variations are due to differences in the inherent stability of various cluster geometries that arise from intracluster steric (and perhaps also electronic) effects from substitution at the quinoline 2-position. If such stability differences are trivial, or poorly match the observations, it would suggest that intercluster factors, such as crystal-packing effects, might better explain the observed structural variations (the observation that these are sublimable compounds seemingly suggests that crystal-packing forces are not unusually strong). The approach we use is similar in principle to the theoretical work previously carried out on oligomeric lithium–oxygen species, [25–29] most notably the studies carried out by Armstrong, Wheatley, and coworkers [26,28] on lithium–oxygen clusters comprising nitrogen-containing ligands. We first geometry-optimize various observed and hypothetical Li_nquinoline$_n$ structures ($n = 1$, 2, 3, 4, and 6) to determine their DFT energy. We are less interested in the total energy of the clusters than the average binding energy (ABE) per monomer. The ABE of a given Li_nquinoline$_n$ structure was obtained by dividing its SCF energy by n and subtracting from that value of the SCF energy for the corresponding monomer ($n = 1$). This was done separately for each case: H, Me, and Ph. The ABE of each Li_1quinoline$_1$ structure is thus by definition 0; and for the clusters ($n = 2$, 3, 4, and 6), relatively negative ABEs imply relatively favored cluster geometries (see Table 4).

The computations were done systematically on Liq, MeLiq, and PhLiq monomers and clusters. The various structures are most easily visualized using the Liq case (Fig. 3), described below, as to their approximate symmetry. One Li_1q_1 (C_s) and one Li_2q_2 (D_{2h}) structure are found (Fig. 3a); the dimer contains a Li_2O_2 four-membered ring core. Two Li_3q_3 structures are found (Fig. 3b): one is a D_{3h} structure with a six-membered ring Li_3O_3 core, and the other is a C_1 structure with a compact polyhedral Li_3O_3 core that could be considered a collapsed or folded ring-ladder structure [30]. While interesting, this polyhedral structure is not conceptually a building block for the $n = 6$ structures, so this structure was not recalculated for the Me and Ph cases. For the Li_4q_4 case, two structures are found (Fig. 3c), each containing similar cubic Li_4O_4 cores. These

Table 2
A comparison of Li–O bond lengths (Å) in Liq, MeLiq, and PhLiq

	Liq		MeLiq		PhLiq
O(1)–Li(2)	1.939(4)	O(1)–Li(2)#2	1.903(6)	O(1)–Li(4)	1.921(8)
O(1)–Li(1)	1.937(4)	O(1)–Li(1)	1.907(6)	O(1)–Li(2)	1.949(8)
O(1)–Li(3)#1	1.996(4)	O(1)–Li(3)#2	2.029(6)	O(1)–Li(1)	1.990(7)
O(2)–Li(3)	1.930(4)	O(2)–Li(3)	1.906(6)	O(2)–Li(1)	1.892(8)
O(2)–Li(1)#1	2.058(4)	O(2)–Li(1)	1.921(7)	O(2)–Li(3)	1.905(7)
O(2)–Li(2)	1.918(4)	O(2)–Li(2)	2.051(6)	O(2)–Li(2)	2.015(7)
O(3)–Li(2)#1	2.100(4)	O(3)–Li(2)	1.911(6)	O(3)–Li(4)	1.902(8)
O(3)–Li(3)	1.901(4)	O(3)–Li(3)#2	1.932(6)	O(3)–Li(2)	1.929(7)
O(3)–Li(1)	1.919(4)	O(3)–Li(1)	2.027(6)	O(3)–Li(3)	1.977(7)
				O(4)–Li(1)	1.942(8)
				O(4)–Li(3)	2.004(9)
				O(4)–Li(4)	2.018(7)

#1 $-x, -y+1, -z+1$ #2 $-x+1, -y+1, -z+1$.

Table 3
A comparison of Li–N bond lengths (Å) in Liq, MeLiq, and PhLiq

	Liq		MeLiq		PhLiq
N(1)–Li(1)	2.023(4)	N(1)–Li(3)#2	2.040(7)	N(1)–Li(1)	1.988(8)
N(2)–Li(2)	1.992(4)	N(2)–Li(2)	2.071(6)	N(2)–Li(2)	2.007(8)
N(3)–Li(3)	2.019(4)	N(3)–Li(1)	2.057(6)	N(3)–Li(3)	2.006(8)
				N(4)–Li(4)	1.986(8)

#1 $-x, -y+1, -z+1$ #2 $-x+1, -y+1, -z+1$.

Table 4
Calculated DFT energies, in hartrees (B3LYP: DGDZVP basis set for Li, N, and O; MIDI! basis set for C and H) for Liq, MeLiq, and PhLiq clusters

Structure	Liq	MeLiq	PhLiq
Monomer	−482.139017 (Fig. 3a)	−521.228548	−711.850832
Dimer	−964.363997 (Fig. 3a)	−1042.544277	−1423.786326
Cyclic trimer	−1446.572202 (Fig. 3b	−1563.840032	−2135.700551
Polyhedral trimer	−1446.554880 (Fig. 3b)		
Cubic, eclipsed	−1928.791360 (Fig. 3c)	−2085.153551	−2847.640154
Cubic, staggered	−1928.791377 (Fig. 3c)	−2085.152824	−2847.641796[a]
Hex. prism, paddlewheel	−2893.206419 (Fig. 3d)	−3127.759645[a]	−4271.472095
Hex. prism, eclipsed	−2893.212954 (Fig. 3d)	−3127.742586	−4271.453732
Hex. prism, staggered	−2893.213972 (Fig. 3d)[a]	−3127.746714 (Fig. 5)	−4271.456305 (Fig. 5)

[a] Corresponds to an experimentally observed structure (see Ref. [8] for Liq and Fig. 2 for MeLiq and PhLiq).

might be described as two dimers that are stacked such that the quinoline rings are either eclipsed (D_{2d}) or staggered (D_2) with respect to the opposite dimer. Finally, three Li_6q_6 structures were found (Fig. 3d) containing similar hexagonal prism-shaped Li_6O_6 cores and possessing D_3 symmetry. These structures can be considered "paddle wheel", eclipsed, and staggered. Stacking two trimers results in a hexamer that may be either staggered or eclipsed (depending on the directional sense of how they are stacked). Analogous eclipsed hexamers have also been termed "trilobate" [31].

When we compare the ABEs (Fig. 4) of all of the computed clusters, we see that the rough trend of stability is dimer ≪ trimer ≪ tetramers < hexamers. Dimers and trimers seem unlikely as independent lithium quinolinate structures, but it is interesting to note that the polyhedral Li_3q_3 structure is nearly as stable as the isomeric six-membered ring Li_3q_3. For the tetramers, the energy differences between the staggered and eclipsed forms are small, as well as similar in magnitude for the H, Me, and Ph cases. This is because the quinolines splay away from each other on non-adjacent edges of the Li_4O_4 cube, thereby minimizing steric interactions. The energy preferences of the hexagonal-prism hexamers are more complicated. In the absence of Me or Ph steric interactions, the paddle-wheel structure is less favored than the eclipsed or staggered forms. The staggered hexamers are slightly more stable than the isomeric eclipsed forms, but the energy differences are small, again because the three quinolines on one half of the stacked trimer splay away from the three quinolines on the other half of the stack. However, because the MeLiq and PhLiq hexamers do have unfavorable steric interactions between neighboring ligands (i.e., on the same side of the stack) in the eclipsed and staggered forms, the paddle-wheel isomers have the lowest ABEs in the Me and Ph cases. These steric interactions are shown in Fig. 5.

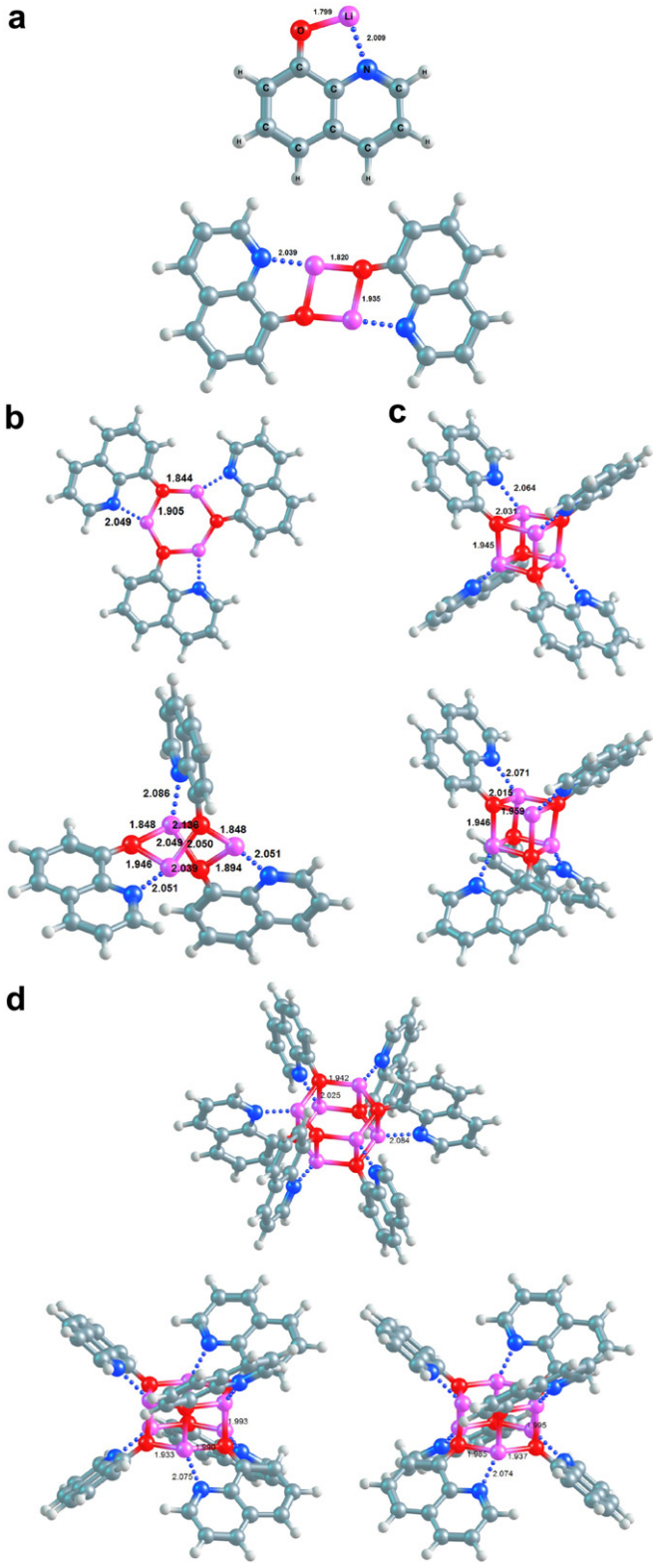


Fig. 3. (a) DFT-computed Liq monomer (top) and dimer (bottom) structures, with unique Li–O and Li–N bond lengths (Å) shown. (b) Isomeric DFT-computed Liq trimer structures. Flat form (top); polyhedral form (bottom), with unique Li–O and Li–N bond lengths (Å) shown. (c) Isomeric DFT-computed Liq tetramer structures. Eclipsed form (top); staggered form (bottom), with unique Li–O and Li–N bond lengths (Å) shown. (d) Isomeric DFT-computed Liq hexamer structures. Paddle-wheel form (top); eclipsed form (bottom left); staggered form (bottom right), with unique Li–O and Li–N bond lengths (Å) shown.

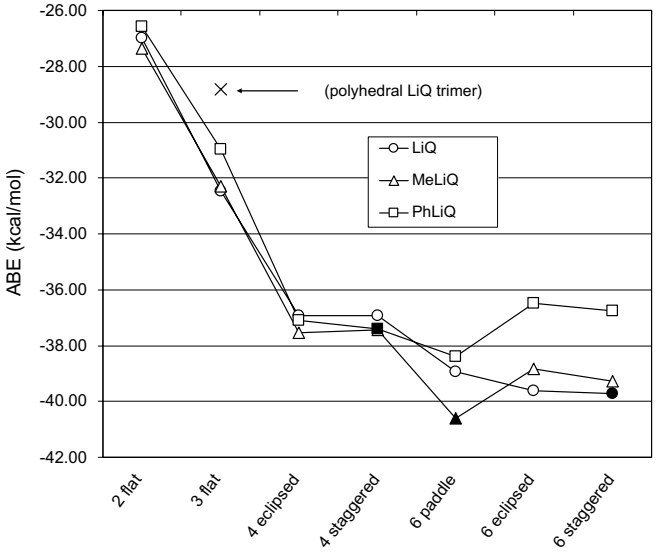


Fig. 4. B3LYP computed average binding energies (ABE, kcal/mol) for Liq, MeLiq, and PhLiq structures, $n = 2$, 3, 4, and 6. Relatively more negative ABEs indicate more stable structures. The "flat", "polyhedral", etc., structures are described in the text and Fig. 3a–c. The filled circle, triangle, and square represent computed models of experimentally observed structures. For Liq and MeLiq, these are also the points with the most favorable ABEs; whereas for PhLiq, the $n = 6$ "paddle" structure has a lower ABE than the observed structure.

The computational results point to crystal-packing effects, rather than inherent favorability of the isolated tetramer, as favoring the observed PhLiq structure. This seems reasonable in as much as the phenyl groups are relatively large substituents that do not directly participate in lithium binding, yet can participate in π-stacking effects (e.g., with neighboring molecules in the crystal lattice, see Fig. 3).

A caveat with respect to the present calculated results is that the level of computed accuracy is unknown, especially because the trustworthiness of computations on lithium alkoxides may be less well established by reference to experimental data than computations of hydrocarbons, for example. Fortunately structural isomers have the same number and type of bonds and lone pairs and therefore benefit from systematic cancellation of errors [32]. Still, errors may be as great as ±2 kcal/mol and perhaps twice that when comparing similar but non-isomeric structures, such as dimer vs. trimer ABEs. This is on the order of the computed ABE differences between the various hexamers and tetramers. Thus we cannot rule out the possibility that it is only coincidental that the calculations point to the observed structures as lowest-energy in both the Liq and MeLiq cases, and in the PhLiq case point to the observed structure as the lowest energy tetramer (and second most stable PhLiq structure overall).

4. Conclusions

A comparison of the solid-state structures of Li complexes, Liq, MeLiq, and PhLiq, illustrates steric effects on the coordination chemistry of lithium. Replacement of

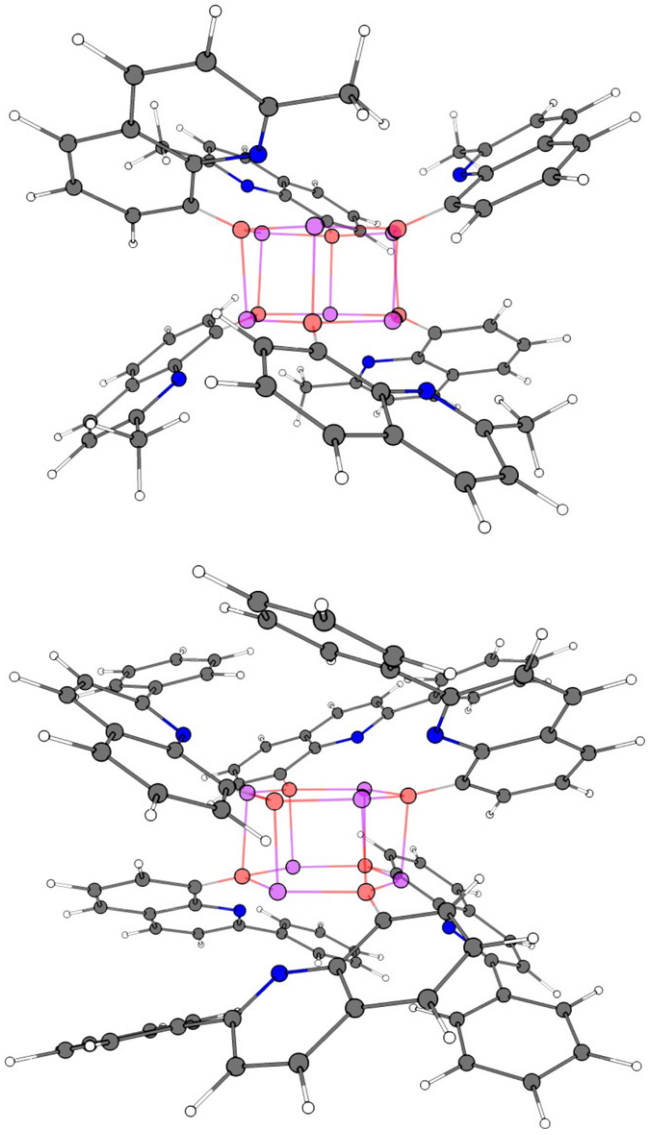


Fig. 5. DFT-computed staggered forms of hexameric MeLiq (top) and PhLiq (bottom), in a perspective view that emphasizes the interligand steric interactions. The N–Li bonds are omitted for clarity. Considering the hexamers as stacked trimers, the important steric interactions between ligands involve methyl or phenyl groups approaching neighboring quinoline rings on the same side of the stack, whereas the steric interactions with ligands on the opposite side of the stack are relatively insignificant.

the 2-hydrogen in 8-hydroxyquinoline with a methyl or phenyl changes the crystal structure from a doubly stacked trimer to a paddle-wheel hexamer to a tetramer. Thus, substitution at the 2-position of the 8-hydroxyquinoline ligand has significant impact on the aggregation of the lithium complex in the crystalline state, indicating different coordination geometries, and coordination numbers may be found when small changes in remote organic substituents are made. The possible influence of crystal-packing forces on the preferred cluster structure was probed using density functional theory calculations on a systematically varied set of Liq, MeLiq, and PhLiq clusters. For all three cases, the order of stabilization energy (per monomer) is dimer < trimer < tetramer ≈ hexamer. For Liq and MeLiq the observed structures match the most stable computed structures. In the PhLiq case, the observed tetrameric structure is computed to be less stable (+1.2 kcal/mol/monomer) than the lowest energy structure, a hexamer. The computational results suggest that crystal-packing effects, rather than the inherent favorability of the isolated tetramer, likely favor the observed PhLiq structure.

Appendix A. Supplementary material

CCDC 633214, 633215 contain the supplementary crystallographic data for this paper. These data can be obtained free of charge via www.ccdc.ac.uk/conts/retrieving.html, or from the Cambridge Crystallographic Data Centre, 12 Union Road, Cambridge CB2 1EZ, UK; fax: (+44) 1223-336-033; or e-mail: deposit@ccdc.cam.ac.uk. Supplementary data associated with this article can be found, in the online version, at doi:10.1016/j.poly.2007.03.054.

References

[1] P. Kathirgamanathan, EP Patent EP1458834, 2003.
[2] S.A. Van Slyke, P.S. Bryan, F.V. Lovecchio, US Patent 5150006, 1992.
[3] P. Kathirgamanathan, US Patent Application US200441015 A1, 2004.
[4] J. Endo, T. Matsumoto, J. Kido, Jpn. J. Appl. Phy. Part 2: Lett. 41 (7A) (2002) L800.
[5] Y.Z. Wu, R.G. Sun, X.Y. Zheng, W.Q. Zhu, X.Y. Jiang, Z.L. Zhang, S.H. Xu, J. Soc. Info. Display 12 (4) (2004) 501.
[6] F.A. Cotton, G. Wilkinson, C.A. Murillo, M. Bochmann, Advanced Inorganic Chemistry, sixth ed., Wiley, New York, 1999.
[7] A.F. Holleman, E.W. Wilberg, Inorganic Chemistry, thirty-fourth ed., Academic Press, New York, 2001.
[8] W.J. Begley, M. Rajeswaran, Acta Crystallogr. Sect. E E62 (2006) m1200.
[9] P. Kathirgamanathan, US Patent Application US20060003089 A1, 2006.
[10] S.G. Schulman, M.S. Rietta, J. Pharm. Sci. 60 (11) (1971) 1762.
[11] X. Bei, D.C. Swenson, R.F. Jordon, Organometallics 16 (15) (1997) 3282.
[12] C. Wang, Z. Yu, Anhui Gongcheng Keji Xueyuan Xuebao, Ziran Kexueban 20 (3) (2005) 21.
[13] Nonius, KappaCCD, Nonius, Delft, The Netherlands, 2001.
[14] Z. Otwinowski, W. Minor, in: C.W. Carter Jr., R.M. Sweet (Eds.), Methods in Enzymology, vol. 276, Academic Press, New York, 1997, p. 307.
[15] Bruker, SHELXTL: Structure Analysis Program, version 5.10, BRUKER AXS Inc., Madison, WI, USA, 1999.
[16] M.J. Frisch, G.W. Trucks, H.B. Schlegel, G.E. Scuseria, M.A. Robb, J.R. Cheeseman, J.A. Montgomery Jr., J.T. Vreven, K.N. Kudin, J.C. Burant, J.M. Millam, S.S. Iyengar, J. Tomasi, V. Barone, B. Mennucci, M. Cossi, G. Scalmani, N. Rega, G.A. Petersson, H. Nakatsuji, M. Hada, M. Ehara, K. Toyota, R. Fukuda, J. Hasegawa, M. Ishida, T. Nakajima, Y. Honda, O. Kitao, H. Nakai, M. Klene, X. Li, J.E. Knox, H.P. Hratchian, J.B. Cross, V. Bakken, C. Adamo, J. Jaramillo, R. Gomperts, R.E. Stratmann, O. Yazyev, A.J. Austin, R. Cammi, C. Pomelli, J.W. Ochterski, P.Y. Ayala, K. Morokuma, G.A. Voth, P. Salvador, J.J. Dannenberg, V.G. Zakrzewski, S. Dapprich, A.D. Daniels, M.C. Strain, O. Farkas, D.K. Malick, A.D. Rabuck,

K. Raghavachari, J.B. Foresman, J.V. Ortiz, Q. Cui, A.G. Baboul, S. Clifford, J. Cioslowski, B.B. Stefanov, G. Liu, A. Liashenko, P. Piskorz, I. Komaromi, R.L. Martin, D.J. Fox, T. Keith, M.A. Al-Laham, C.Y. Peng, A. Nanayakkara, M. Challacombe, P.M.W. Gill, B. Johnson, W. Chen, M.W. Wong, C. Gonzalez, J.A. Pople, GAUSSIAN 03, Revision C.02, Gaussian, Inc., Wallingford CT, 2004.
[17] A.D. Becke, J. Chem. Phys. 98 (1993) 5648.
[18] N. Godbout, D.R. Salahub, J. Andzelm, E. Wimmer, Can. J. Chem. 70 (1992) 560.
[19] R.E. Easton, D.J. Giesen, A. Welch, C.J. Cramer, D.G. Truhlar, Theor. Chim. Acta 93 (1996) 281.
[20] Spartan '02 for Linux, Wavefunction Inc., Irvine, CA, 2002.
[21] (a) J.J.P. Stewart, J. Comp. Chem. 10 (1989) 209;
(b) J.J.P. Stewart, J. Comp. Chem. 10 (1989) 221.
[22] I. Dance, M. Scudder, Polyhedron 16 (20) (1997) 3545.
[23] C. Janiak, J. Chem. Soc. Dalton Trans. (2000) 3885.
[24] H. Suezawa, S. Ishihara, Y. Umezawa, S. Tsuboyama, M. Nishio, Eur. J. Org. Chem. 2004 (23) (2004) 4816.
[25] B. Goldfuss, P.v.R. Schleyer, F.J. Hampel, Organometallics 16 (1997) 5032.
[26] D.R. Armstrong, W. Clegg, S.M. Hodgson, R. Snaith, A.E.H. Wheatley, J. Organomet. Chem. 550 (1998) 233.
[27] A. Yakimansky, A.H.E. Muller, Macromolecules 32 (1999) 1731.
[28] D.R. Armstrong, R.P. Davies, P.R. Raithby, R. Snaith, A.E.H. Wheatley, New J. Chem. 23 (1999) 499.
[29] C. Strohmann, T. Seibel, D. Schildbach, J. Am. Chem. Soc. 126 (2004) 9876.
[30] R.E. Mulvey, Chem. Soc. Rev. 27 (1998) 339.
[31] T. Chivers, A. Downard, G.P.A. Yap, Inorg. Chem. 37 (1998) 5708.
[32] W.J. Hehre, L. Radom, P. v. R. Schleyer, J.A. Pople, Ab Initio Molecular Orbital Theory, Wiley-Interscience, New York, 1986 (Chapter 6).

ruthenium(III) compound to successfully complete phase I clinical trials [21]. The main feature of the majority of these complexes is the presence of four chlorides, one DMSO, and one N-donor ligand in the coordination sphere. At present, very few examples of such ruthenium(III) complexes exist that have been structurally characterized by X-ray diffraction methods. These include complexes, for example, where the N-donor ligand is ammonia [22], thiazole [23], guaninium [24], imidazole [22], pyridine [25], triazole [26] as well as symmetrical ruthenium dimers with pyrazine, pyrimidine, and bipyridine [27], and the unsymmetrical dimer with bridging pyrazine [28]. Here we report the synthesis and characterization of several ruthenium(III) complexes with dimethylsulfoxide and heterocyclic dinitrogen ligands as well as the crystal structures of the $[Ru(DMSO)(pz)Cl_4]^-$ (pz = pyrazine) monoanion with two different cations, tetraphenylphosphonium (PPh_4) and Na. These cations are quite different and the architectures of the crystal structures were expected to differ considerably. These two compounds are the first two Ru(III) species containing a terminal pyrazine ligand to be characterized structurally.

2. Experimental

Ethanol (100%) was purchased from Pharmaco Products Inc. All other reagents and solvents were purchased from Sigma Aldrich Inc. IR spectra were recorded in the solid state on a Nicolet 4700 FTIR spectrometer between 4000 and 250 cm^{-1}. ^1H NMR spectra were measured in D_2O, acetone-d_6, $CDCl_3$, and CD_3CN on a Varian Gemini 300 MHz spectrometer. The solvent peaks at 4.80 ppm, 2.05 ppm, 7.26 ppm, and 1.94 ppm for D_2O, CD_3COCD_3, $CDCl_3$, and CD_3CN, respectively, were used as internal standards for the ^1H NMR spectra. Spectral abbreviations used below: br (broad), vbr (very broad), s (strong), m (medium), w (weak), sh (shoulder).

2.1. Synthesis

$[(DMSO)_2H]$*trans*-$[Ru(DMSO)_2Cl_4]$, $[Na]$*trans*-$[Ru(DMSO)_2Cl_4]$, and $[NBu_4]$*trans*-$[RuCl_4(DMSO)_2]$ (Bu = *n*-butyl) were synthesized according to the literature methods [27,29].

*[PPh₄]trans-[Ru(DMSO)₂Cl₄] (**1**).* Tetraphenylphosphonium chloride (0.34 g, 0.92 mmol) dissolved in 6 mL of H_2O was added to a solution of $[(DMSO)_2H]$*trans*-$[Ru(DMSO)_2Cl_4]$ (0.34 g, 0.61 mmol) dissolved in 3 mL of H_2O, while stirring. A yellow precipitate formed within minutes. The precipitate was collected by filtration, washed with diethylether and vacuum dried. Yield: 89%. IR (cm^{-1}): 1107s ν(DMSO–S), 416w ν(Ru–S), 339, 319s ν(Ru–Cl). ^1H NMR (CD_3CN/ppm): −13.0 (DMSO–S), 7.95, 7.74 (phenyl protons).

*[PPh₄]trans-[Ru(DMSO)(pz)Cl₄] (**2**).* $[PPh_4]$*trans*-$[Ru(DMSO)_2Cl_4]$ (**1**) (0.30 g, 0.40 mmol) was dissolved in a mixture of 7 mL acetone and 4 mL acetonitrile, while 0.16 g of pyrazine (pyz) (2.0 mmol) was dissolved in 1 mL of acetone. The ruthenium solution was added slowly to the pyrazine solution to form a clear orange mixture. After several hours the product precipitated as orange crystals. The crystals were collected by filtration, washed with cold diethylether and vacuum dried. Yield: 73%. Alternatively, complex **2** can be synthesized from complex **3** by the addition of $[PPh_4]Br$ or $[PPh_4]Cl$ in aqueous solution. IR (cm^{-1}): 1588 (pz), 1108s (DMSO–S), 420m ν(Ru–S), 342, 328s ν(Ru–Cl). ^1H NMR (CD_3CN/ppm): −12.6 (br, DMSO–S), −5.6 (vbr, pz $H^{2,6}$), −1.6 (br, pz $H^{3,5}$), 7.95, 7.74 (phenyl protons). *Anal.* Calc. for $C_{30}H_{30}Cl_4N_2OPSRu$: C, 48.6; H, 4.05; N 3.78. Found: C, 48.4; H, 3.84; N, 3.87%.

*[Na]trans-[Ru(DMSO)(pz)Cl₄] · DMSO (**3**).* The synthesis of this compound was similar to that reported [27] with some changes. Pyrazine (80.2 mg, 1.00 mmol) dissolved in 5 mL of acetone was added to a solution of 82.5 mg (0.198 mmol) of $[Na]$*trans*-$[Ru(DMSO)_2Cl_4]$ dissolved in 2 mL of DMSO. The resulting mixture was filtered and the filtrate was stirred at room temperature for 1.5 h. A 50/50 acetone/diethylether solution (5.0 mL) was added to the reaction mixture followed by an additional 5.0 mL of diethylether. The mixture was then placed at 4 ° C. Orange crystals appeared within 48 h. The mother liquor was decanted and the crystals washed with diethylether. Yield: 67%. ^1H NMR (D_2O/ppm): −13.9 (br), (DMSO–S), −7.5 (vbr, $H^{3,5}$ pyz), −2.1 (br, $H^{2,6}$ pyz). This compound was reported, but the solvate molecules appear different [27].

*[NBu₄]trans-[RuCl₄(DMSO)(bpy)] (bpy = 4,4′-bipyridine) (**4**).* 0.63 g of $[NBu_4]$*trans*-$[RuCl_4(DMSO)_2]$ (0.98 mmol) was dissolved in 15 mL of acetone and 0.60 g of 4,4-bipyridine (3.8 mmol) was dissolved in 4 mL of acetone. The ruthenium solution was added to the 4,4-bipyridine solution to form a clear orange solution. After several hours of stirring, the product was precipitated after the addition of 10 mL of cold diethylether. The yellow precipitate was collected by filtration, washed with cold diethylether and vacuum dried. Yield: 86% (0.60 g). IR (cm^{-1}): 1595, 1612w (bpy), 1109s (DMSO–S), 422m ν(Ru–S), 349, 325s ν(Ru–Cl). ^1H NMR (acetone/ppm): −12.2 (br, DMSO–S), 7.5 (br, bpy $H^{2',6'}$), 6.0 (br, bpy $H^{3',5'}$), −1.2 (br, bpy $H^{3,5}$), −6.0 (vbr, bpy $H^{2,6}$).

*[PPh₄]trans-[RuCl₄(DMSO)(bpy)] (**5**).* 0.50 g of $[PPh_4]$*trans*-$[RuCl_4(DMSO)_2]$ (0.68 mmol) was dissolved in 15 mL of CH_2Cl_2 and 0.40 g of 4,4-bipyridine (2.6 mmol) was dissolved in 6 mL of CH_2Cl_2. The ruthenium solution was added to the 4,4-bipyridine solution to form a clear orange solution. After several hours of stirring, the product was precipitated after the addition of 10 mL of cold diethylether. The yellow precipitate was collected by filtration, washed with cold diethylether, and vacuum dried. Yield: 82% (0.45 g). IR (cm^{-1}): 1595, 1612w (bpy), 1107s (DMSO–S), 422m ν(Ru–S), 331s,br ν(Ru–Cl). ^1H NMR ($CDCl_3$/ppm): −12.8 (br, DMSO–S), 7.5 (br, bpy $H^{2',6'}$), 5.5 (br, bpy $H^{3',5'}$), −1.7 (br, bpy $H^{3,5}$), 8.06 (br, phenyl protons). *Anal.* Calc. for $C_{36}H_{34}Cl_4N_2OPSRu$: C, 52.9; H, 4.17; N 3.43. Found: C, 52.6; H, 3.94; N, 3.23%.

*[PPh4]trans-[RuCl4(DMSO)(pym)] (pym = pyrimidine) (**6**).* 0.20 g of [PPh_4]*trans*-[$RuCl_4(DMSO)_2$] (0.27 mmol) was dissolved in 5 mL of CH_2Cl_2 and 0.15 g of pyrimidine (0.98 mmol) was dissolved in 1 mL of acetone. The ruthenium solution was added to the pyrimidine solution to form a clear orange solution. After several hours of stirring, the product was precipitated with the addition of 10 mL of diethylether. The yellow precipitate was collected by filtration, washed with diethylether, and vacuum dried. Yield: 67% (0.133 g). IR (cm^{-1}): 1585, 1560 (pym), 1107s (DMSO–S), 421m ν(Ru–S), 339, 324sh ν(Ru–Cl). ^1H NMR (CD_3CN/ppm): −13.0 (br, DMSO–S), 6.34 (pym H^4), −0.58 (br, pym H^5), −1.7 (vbr, pym H^6), −6.5 (vbr, pym H^2), 7.96, 7.78 (br, phenyl protons); ($CDCl_3$/ppm): −12.7 (br, DMSO–S), 6.32 (br, bpy H^4), −0.52 (br, H^5), 8.16 (br, phenyl protons). *Anal.* Calc. for $C_{30}H_{30}Cl_4N_2OPSRu$: C, 48.6; H, 4.05; N 3.78. Found: C, 48.4; H, 3.78; N, 3.77%.

2.2. Crystallographic measurements and structure resolution

The crystallographic measurements of crystals **2** and **3** were done on a Bruker P4 diffractometer using graphite-monochromatized Mo Kα ($\lambda = 0.71073$ Å) radiation. The cell dimensions were determined at room temperature, from a least-squares refinement of the angles 2θ, ω and χ obtained for well-centered reflections. The data collection was made by the $2\theta/\omega$ scan technique using the XSCANS program [30]. The background time to scan time ratio was 0.5.

Table 1
Crystallographic data and experimental details

Crystal	**2**	**3**
Name	PPh_4[Ru(DMSO)(pz)Cl_4]	Na[Ru(DMSO)(pz)Cl_4]·DMSO
Chemical formula	$C_{30}H_{30}Cl_4N_2OPRuS$	$C_8H_{16}Cl_4N_2NaO_2RuS_2$
M_w	740.46	502.21
Space group	$P2_1/n$ (No. 14)	$P\bar{1}$ (No. 2)
a (Å)	13.161(3)	7.0972(7)
b (Å)	17.070(4)	10.6838(15)
c (Å)	14.826(4)	12.379(2)
α (°)	90.	91.164(14)
β (°)	104.65(2)	93.48(12)
γ (°)	90.	105.83(11)
Volume (Å^3)	3222.5(14)	900.7(2)
Z	4	2
ρ_{calc} (g cm^{-3})	1.526	1.852
μ(Mo Kα) (mm^{-1})	0.959	1.718
F(000)	1500	498
Reflections collected	12656	10499
Observed Reflections ($I > 2\sigma(I)$)	4778	4284
R_1 ($I > 2\sigma(I)$)	0.0327	0.0307
wR_2 (all data)	0.0748	0.0770
S	1.049	1.023

$R_1 = \sum(|F_o - F_c|)/\sum|F_o|$, $wR_2 = [\sum(w(F_o^2 - F_c^2)^2)/\sum(w(F_o^2)^2)]^{1/2}$.

The coordinates of the Pt atom were determined by direct methods and all the other non-hydrogen atoms were found by the usual Fourier methods. The refinement of the structure was done on F^2 by full matrix least-squares analysis. The hydrogen atom positions were fixed in their calculated positions with $U_{eq} = 1.2\ U_{eq}$ (or 1.5 for methyl groups) of the carbon to which they are bonded. Corrections were made for absorption (semi-empirical from psi-scans for **2** and integration for **3**), Lorentz and polarization effects. The calculations were done using the Bruker SHELXTL system [30]. The crystallographic data and details are shown in Table 1.

3. Results and discussion

3.1. [PPh4]trans-[Ru(DMSO)2Cl4] (1)

This yellow compound was synthesized from the aqueous reaction of [$(DMSO)_2H$]*trans*-[$Ru(DMSO)_2Cl_4$] with tetraphenylphosphonium chloride.

$$[(DMSO)_2H]trans\text{-}[Ru(DMSO)_2Cl_4] + [PPh_4]Cl \xrightarrow[H_2O]{} [PPh_4]trans\text{-}[Ru(DMSO)_2Cl_4]$$

The synthesis and characterization of this ionic complex has not been reported yet in the literature, therefore we give a brief description. The IR spectrum of the compound shows a ν(S–O) vibration at 1107 cm^{-1}. Absorption at 416 cm^{-1} was assigned to the metal stretching vibration ν(Ru–S) while those at 339 and 319 cm^{-1} were attributed to ν(Ru–Cl). The NMR spectrum of **1** and all of the complexes reported here show peaks that are characteristic of complexes containing paramagnetic ruthenium(III). Protons close to the paramagnetic center have large line-width (often some peaks are too wide to be observable) and are shifted greatly upfield [31–33]. The peak at −13.0 ppm is assigned to the coordinated DMSO (through the S atom).

3.2. [PPh4][Ru(DMSO)(pyrazine)Cl4] (2)

This new ionic complex was synthesized from the reaction of the bis-DMSO Ru(III) ionic complex **1** with pyrazine (pz) as shown in the following equation:

$$[PPh_4]trans\text{-}[Ru(DMSO)_2Cl_4] + pz \xrightarrow[\text{acetone/acetonitrile}]{} [PPh_4]trans\text{-}[Ru(DMSO)(pz)Cl_4]$$

Alternatively, compound **2** was also synthesized from the aqueous reaction of compound **3** with tetraphenylphosphonium chloride or tetraphenylphosphonium bromide.

The IR spectrum of **2** shows a ν(S–O) vibration at 1108 cm^{-1}, a ν(Ru–S) band at 420 cm^{-1} and ν(Ru–Cl) vibrations at 342 and 328 cm^{-1}. The NMR spectrum shows a peak at −12.6 ppm integrating to six protons assigned to the coordinated DMSO, while the peak at −1.6 ppm integrating to two protons is assigned to the protons (H^3 and H^5) on the pyrazine ring. The protons on the pyrazine ring

(H^2 and H^6) closest to the paramagnetic ruthenium center are seen in a very broad peak at −5.6 ppm (for labeling see Chart 1).

Compound **2** was recrystallized from acetone/diethylether and the crystals were studied by crystallographic methods. The results have shown that the orange crystals consist of discrete complexed anions, $[Ru(DMSO)(pz)Cl_4]^-$ (Fig. 1) and $[PPh_4]^+$ cations. The complexed anion is the *trans* isomer and the coordination around the Ru(III) center is octahedral. The bond distances and angles are shown in Table 2. The *cis* angles around the metal vary between 87.73(7)° and 92.66(3)°, while the *trans* angles are between 177.32(3)° and 179.07(7)°. The Ru–Cl bond distances range from 2.3425(9) to 2.3589(10) Å, the Ru–S bond is 2.2941(9) Å and the Ru–N distance is 2.118(2) Å. These values are in agreement with published values found in a few related structures [22,24,27,28,34].

The environment around the S atom in the DMSO ligand is approximately tetrahedral but there are small deformations. The O–S–C angles are larger (ave. 107.18(17)°) than the C–S–C angle (98.77(18)°) as expected. The Ru–S–O angle (117.98(10)°) is also larger than the Ru–S–C angles (ave. 111.95(13)°). The average angle Ru–N–C is 121.9(2)°. The N1–C bond lengths (ave. 1.332(4) Å) are not different from those of N4–C (ave. 1.328(5) Å), but the angles C–N–C are different. The internal ring angle at the metal-bonded N1 atom is larger (116.3(3)°) than the angle of the non-bonded N4 atom (114.7(3)°) as observed in Pt(II) compounds of the type *cis*- and *trans*-$Pt(R_2SO)(pz)Cl_2$ where the bonded angle C2–N1–C6 is slightly larger than the C3–N4–C5 angle [35].

In order to minimize the interactions with the rest of the molecule, the pyrazine ligand is at ≈45° to the different Ru square planes. Here, the dihedral angle between the pyrazine and the RuN1S1Cl1Cl3 plane is 47.65(11)°, while it is 42.36(10)° with the RuN1S1Cl2Cl4 plane. In the DMSO ligand, the O atom of DMSO was found almost in the RuS1N1Cl1Cl3 plane, which reduces steric hindrance in the complexed ion, since the larger methyl groups are far from the four *cis* chloro ligands. The torsion angles Cl1–Ru–S–O and Cl3–Ru–S–O are −7.14(15)° and 172.94(15)°, respectively. In this conformation of the DMSO and pyrazine ligands, the energy of the molecular ion is close to a minimum.

The PPh_4 cations are normal. The average P–C bond distance is 1.800(3) Å with an average C–P–C angle of 109.48(13)°. No H-bonds are expected in this crystal. The ions are held together in the crystal by electrostatic forces and by van der Waals interactions.

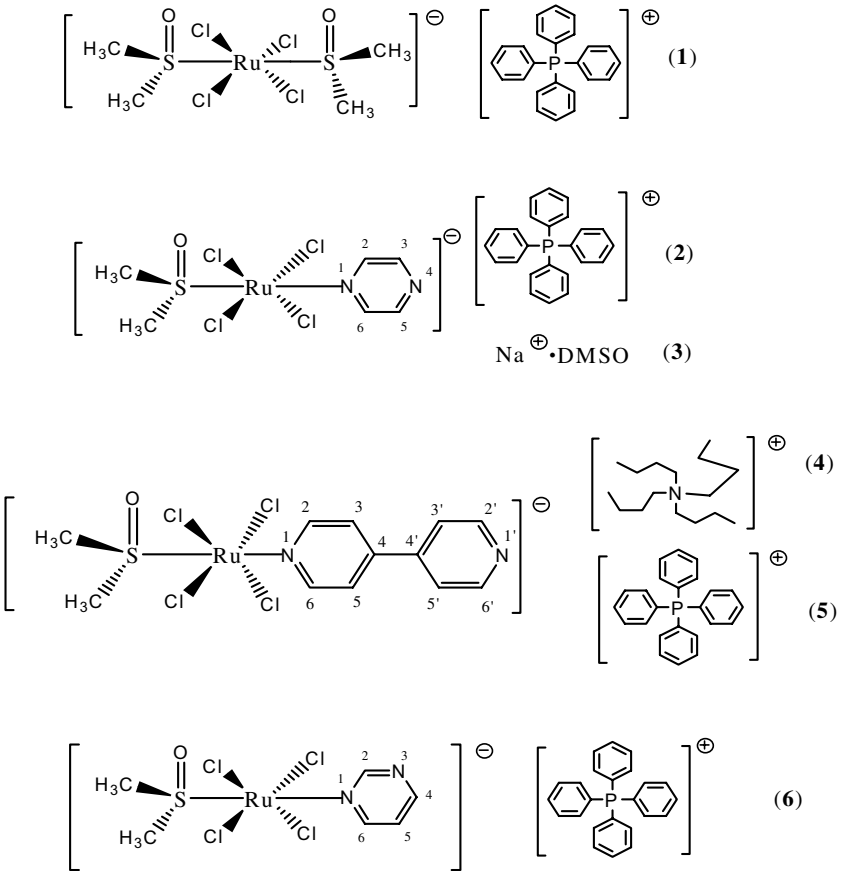


Chart 1. Ruthenium(III) molecular structures.

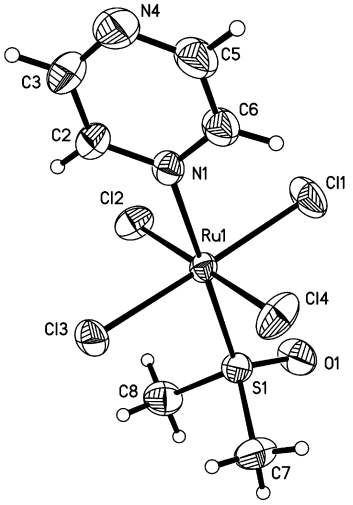


Fig. 1. ORTEP view of the $[Ru(DMSO)(pz)Cl_4]^-$ anion in crystal **2**. Ellipsoids are shown at 40% probability level and the H atoms are of arbitrary size.

3.3. *[Na][Ru(DMSO)(pyrazine)Cl$_4$] · DMSO (**3**)*

This compound was synthesized from the reaction of $[Na][Ru(DMSO)_2Cl_4]$ with pyrazine in acetone and DMSO similar to the procedure already reported.

$$[Na][Ru(DMSO)_2Cl_4] + pz \xrightarrow[DMSO]{acetone} [Na][Ru(DMSO)(pz)Cl_4]\cdot DMSO$$

The orange compound was crystallized in a mixture of acetone and diethylether and the crystals were studied by X-ray diffraction methods. The results have shown that the compound crystallized with a molecule of solvent (DMSO). The reported compound [27], which was not studied by crystallographic methods, contained 1.5 molecule of DMSO and 0.5 molecule of H_2O, although it was crystallized from the same solvents.

Fig. 2 shows the labeling scheme of the asymmetric unit in crystal **3**. The complexed anion is the *trans* isomer and the coordination around the Ru(III) center is octahedral. The bond distances and angles are shown in Table 2. The *cis* angles around the metal vary between 87.95(3)° and 93.96(3)°, while the *trans* angles are between 176.43(2)° and 177.74(2)°. The Ru–Cl bond distances range from 2.3395(8) to 2.3754(7) Å, the Ru–S bond is 2.3027(7) Å and the Ru–N distance is 2.1257(19) Å. These values are very similar to those observed in crystal **2** described above and they are in agreement with published values found in a few related structures [22,24,27,28].

The environment around the bonded S atom in the DMSO ligand is approximately tetrahedral but there are small deformations. The O–S1–C angles are larger (ave. 106.39(17)°) than the C–S1–C angle (100.4(2)°) as expected. The Ru–S–O angle (117.73(8)°) is also larger than the Ru–S–C angles (ave. 112.15(17)°). The average angle Ru–N–C is 121.64(16)°. The N1–C bonds (ave. 1.343(3) Å) are not very different from the N4–C bonds (ave. 1.333(3) Å), but the angles C–N–C are slightly different. The internal ring angle at the metal-bonded N1 atom is slightly larger (116.7(2)°) than the angle of the non-bonded

Table 2
Bond distances (Å), bond and torsion angles (°)

	2	**3**
Ru–Cl1	2.3425(9)	2.3754(7)
Ru–Cl2	2.3449(9)	2.3458(7)
Ru–Cl3	2.3520(8)	2.3395(8)
Ru–Cl4	2.3589(10)	2.3684(7)
Ru–N1	2.118(2)	2.1257(19)
Ru–S1	2.2941(9)	2.3027(7)
S1–O1	1.468(2)	1.4705(19)
S1–C (ave.)	1.787(3)	1.770(3)
S2–O2		1.496(2)
S2–C (ave.)		1.784(3)
N1–C (ave.)	1.332(4)	1.343(3)
N4–C (ave.)	1.328(5)	1.333(3)
P1–C (ave.)	1.800(3)	
N1–Ru–S1	179.07(7)	177.68(6)
N1–Ru–Cl1	88.27(7)	88.35(6)
N1–Ru–Cl2	90.08(7)	89.98(6)
N1–Ru–Cl3	89.91(7)	89.29(6)
N1–Ru–Cl4	87.73(7)	89.25(6)
S1–Ru–Cl1	92.66(3)	93.96(3)
S1–Ru–Cl2	90.02(4)	89.86(3)
S1–Ru–Cl3	89.16(3)	88.40(3)
S1–Ru–Cl4	92.15(4)	91.04(2)
Cl1–Ru–Cl2	91.08(4)	87.95(3)
Cl1–Ru–Cl3	178.18(3)	177.74(2)
Cl1–Ru–Cl4	90.39(4)	88.55(2)
Cl2–Ru–Cl3	89.00(4)	92.14(3)
Cl2–Ru–Cl4	177.32(3)	176.43(2)
Cl3–Ru–Cl4	89.46(4)	91.34(3)
Ru–N1–C (ave.)	121.4(2)	121.64(16)
Ru–S1–O1	117.98(10)	117.73(8)
Ru–S1–C (ave.)	111.95(13)	112.15(12)
O1–S1–C (ave.)	107.18(17)	106.39(17)
C–S1–C	98.77(18)	100.4(2)
O1–S2–C (ave.)		105.99(15)
C–S2–C		98.49(17)
C2–N1–C6	116.3(3)	116.7(2)
C3–N4–C5	114.7(3)	115.2(2)
C–P–C (ave.)	109.48(13)	
Cl1–Ru–S1–O1	−7.14(15)	−161.74(11) (Cl2)
Cl3–Ru–S1–O1	172.94(15)	21.71(11) (Cl4)
Cl–Ru–N1–C (ave.)	≈45	≈45

*Distances and angles around the Na atom in **3***

Na–O1	2.303(2)	Na–O2	2.324(2)
Na–N4′	2.519(2)	Na–Cl1′	2.7760(13)
Na–Cl4	2.9222(12)	Na–Cl4′	2.8404(13)
O1–Na–O2	92.97(9)	O1–Na–N4′	86.13(8)
O1–Na–Cl1′	175.65(8)	O1–Na–Cl4	76.74(6)
O1–Na–Cl4′	104.86(7)	O2–Na–N4′	92.89(8)
O2–Na–Cl1′	89.89(6)	O2–Na–Cl4	106.54(7)
O2–Na–Cl4′	162.13(7)	N4′–Na–Cl1′	92.00(6)
N4′–Na–Cl4	154.51(7)	N4′–Na–Cl4′	87.33(6)
Cl1′–Na–Cl4	104.10(4)	Cl1′–Na–Cl4′	72.25(3)
Cl4–Na–Cl4′	79.17(3)	Na–N4–C (ave.)	122.08(16)
Na–O1–S1	135.34(13)	Na–O2–S2	124.79(12)
Na′–Cl1–Ru	100.17(3)	Na′–Cl4–Ru	98.55(3)
Na–Cl4–Ru	111.28(3)	Na–Cl4–Na′	100.83(3)

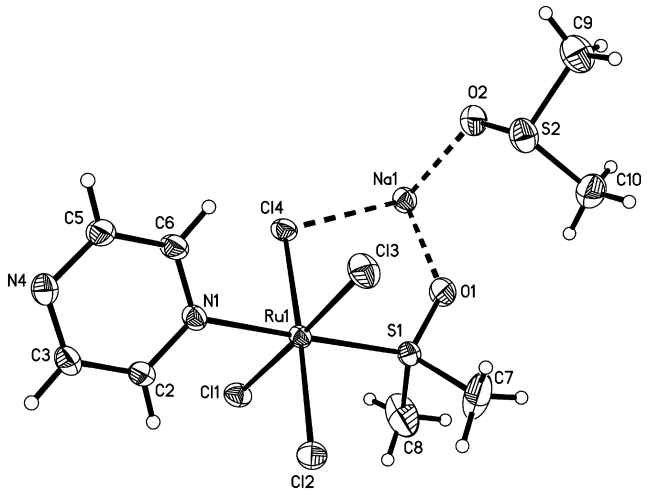


Fig. 2. ORTEP view of [Na][Ru(DMSO)(pz)Cl_4] · DMSO (**3**) showing the labelling scheme of the asymmetric unit. Ellipsoids are shown at 40% probability level and the H atoms are of arbitrary size.

N4 atom (115.2(2)°), as observed in crystal **2**, which also contains a monodentate pyrazine ligand.

Complex **3** crystallized with a molecule of DMSO which is not bonded to the Ru(III) atom. The S2–O2 bond is longer (1.496(2) Å) than the S1–O1 bond distance in crystals **2** and **3** (ave. 1.469(2) Å) as expected when the S atom is not coordinated to a metal. When the binding site of DMSO is the S atom, the order of the S–O bond increases when compared to the free molecule, while it is reduced if the molecule is bonded to the metal atom through its O atom. The NMR and IR spectra are in agreement with the published data. Only one ν(S–O) band was observed at 1104 cm^{-1} [27].

The O atom of the bonded DMSO ligand was found close to the RuS1N1Cl2Cl4 plane, which reduces steric hindrance in the complexed anion, since the larger methyl groups are far for the four *cis* chloro ligands. The torsion angles Cl2–Ru–S1–O1 and Cl4–Ru–S1–O1 are −161.74(11)° and 21.71(11)°, respectively. The plane of pyrazine is located at about ≈45° from the two different Ru(III) square planes. The dihedral angle between the pyrazine and the RuN1S1Cl2Cl4 plane is 41.56(6)°, while it is 48.18(7)° with the RuN1S1Cl1Cl4 plane. This conformation of the molecular ion is similar to the one observed in crystal **2** and corresponds approximately to the one of lowest energy.

The environment around the Na atoms was closely examined. There are six atoms in its close environment. The distances and angles are shown in Table 2. The geometry is a distorted octahedron. Three of the close contacts are shown in Fig. 2. The Na–O1 (from bonded DMSO) and Na–O2 (unbonded DMSO) distances are 2.303(2) and 2.324(2) Å, respectively. The Na–Cl4 distance is 2.9222(12) Å. There are three other short contacts with the following: N4′ (2.519(2) Å), Cl1′ (2.7760(13) Å), and Cl4′ (2.8404(13) Å). The chloro ligand Cl4 forms a bridge between two Na atoms, while Cl1 forms a bridge between a Na and a Ru atom. The two other Cl ligands are not involved with the Na atoms. The DMSO ligand forms a bridge between a Ru (through its S atom) atom and a Na (through its O) atom, while the S atom of the second DMSO molecule is free, but its O atom is in the close environment of the Na atom. There are important distortions from the octahedral structure around the Na atom. The *cis* angles vary between 72.25(3)° (Cl′–Na–Cl4′) and 106.54(7)° (O2–Na–Cl4), while the *trans* angles are between 154.51(7)° and 175.65(8)°.

The Na atom has a very important role in this structure. It bridges the different complexed ions to form infinite polymeric chains or ribbons parallel to the *b* axis. One of these is shown in Fig. 3. The two ligands Cl2 and Cl3, which are not involved with the Na atoms point towards the outside of the chain, along with S2 and the two C atoms of the free DMSO molecule. Several cycles are formed, ranging from four atoms (Ru, Cl1, Na, Cl4) to seven atoms (Ru, Cl1, Na, Cl4, Na, O1, S1). These neutral ribbons are held together by van der Waals forces. There may be weak π–π stacking

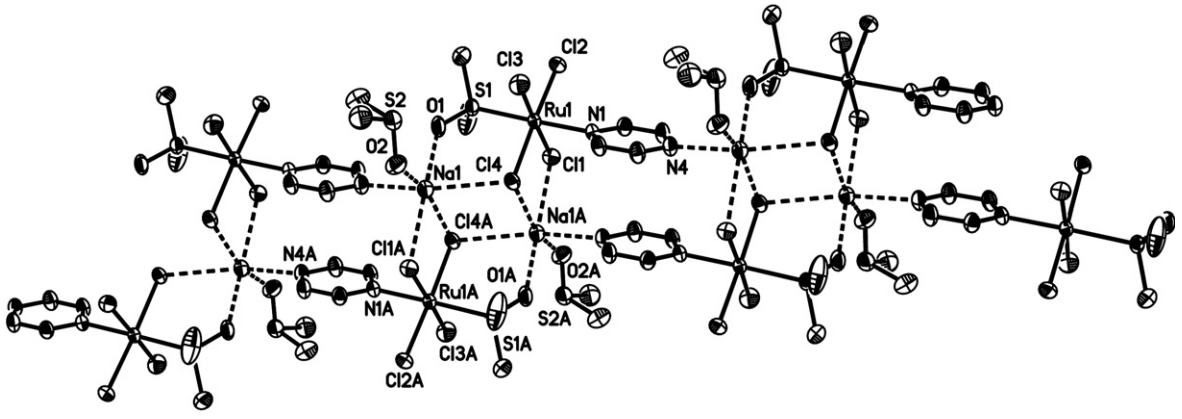


Fig. 3. ORTEP view of a ribbon in compound **3** showing the octahedral environment around the Na atom (---), which bridges the anions [Ru(DMSO)(pz)Cl_4]$^-$.

interactions of the pyrazine ligands, as the distance between pyrazine pairs shown in Fig. 3 is 3.548(16) Å [36].

A few related structures were reported with the sodium cation. In $[Na][Ru(DMSO)(NH_3)Cl_4]\cdot 2DMSO$ and $[Na][Ru(DMSO)(Im)Cl_4]\cdot H_2O$, CH_3COCH_3 [22], the environment around the Na atom is tetrahedral with four Na–O distances between 2.272(4) and 2.489(3) Å. But the long-range arrangement in the crystal was not discussed. A few other related structures containing Na ions were published, but the environment around the Na atom was not considered [27]. In these structures, the role of the Na ions in the architecture, besides its counterion function, was not studied.

In crystal **3**, the unbonded DMSO molecule plays also a very important role in the formation of the chains. In a few reported structures containing the same cation, the chains are not formed, but rather shorter oligomers [22] containing two Ru(III) and two Na atoms were produced. For the latter structures, the tetrahedral environment around the Na atoms is formed with four O atoms from DMSO or H_2O molecules.

3.4. [NBu4]trans-[RuCl4(DMSO)(bpy)] (4) and [PPh4]trans-[RuCl4(DMSO)(bpy)] (5)

$[PPh_4]$*trans*-$[Ru(DMSO)(bpy)Cl_4]$ (**5**) (bpy = 4,4′-bipyridine) was prepared from $[PPh_4]$*trans*-$[Ru(DMSO)_2Cl_4]$ in methylene chloride as shown in the following equation:

$$[PPh_4]\textit{trans}\text{-}[Ru(DMSO)_2Cl_4] + 4,4'\text{-bpy} \xrightarrow[\text{methylene chloride}]{} [PPh_4][Ru(DMSO)(bpy)Cl_4]$$

The NMR spectrum of compound **5** showed, along with signals for the tetraphenyl phosphonium cation, several peaks for the protons of the coordinated ligands. The signal at −12.8 ppm is assigned to the coordinated DMSO while the peak at −1.7 ppm is assigned to the protons (H^3 and H^5) on the coordinated pyridine ring but furthest from the paramagnetic ruthenium(III) center. The protons closest to the ruthenium center (H^2 and H^6, Chart 1) are not observed due to a line-width that is too broad for the peak to be seen. The protons on the second pyridine ring are observed at 5.5 ($H^{3'}$ and $H^{5'}$) and 7.5 ppm ($H^{2'}$ and $H^{6'}$) for the two pairs closer and further from the ruthenium atom, respectively. The IR spectrum of **5** shows a terminal bpy mode at 1595 cm^{-1} along with a ν(S–O) vibration at 1107 cm^{-1}, a ν(Ru–S) band at 422 cm^{-1}, and a ν(Ru–Cl) vibration at 331 cm^{-1}.

$[NBu_4]$*trans*-$[Ru(DMSO)(bpy)Cl_4]$ (**4**) was prepared similarly to complex **5**, however the reaction was done in acetone solution. The NMR and IR spectral characterization and signal assignments were also similar, except in the proton NMR, where all four sets of bpy proton pairs were observed in this case. The protons closest to the ruthenium atom (H^2 and H^6), unobservable for complex **5** are seen as a very broad peak at −6.0 ppm.

3.5. [PPh4]trans-[Ru(DMSO)(pym)Cl4] (6)

$[PPh_4]$*trans*-$[Ru(DMSO)(pym)Cl_4]$ (**6**) was prepared from $[PPh_4]$*trans*-$[Ru(DMSO)_2Cl_4]$ in methylene chloride as shown in the following equation:

$$[PPh_4]\textit{trans}\text{-}[Ru(DMSO)_2Cl_4] + \text{pyrimidine} \xrightarrow[\text{methylene chloride}]{} [PPh_4][Ru(DMSO)(pym)Cl_4]$$

The NMR spectrum of compound **6** in acetonitrile solution showed, along with signals for the tetraphenylphosphonium cation, five peaks for the protons of the coordinated ligands. The signal at −13.0 ppm is assigned to the coordinated DMSO as expected. There are four peaks seen for the pyrimidine ligand as each proton is unique in this case due to the loss of symmetry in the ligand once it has coordinated. The peak at 6.34 ppm has the narrowest line-width and is therefore assigned to the proton furthest from the paramagnetic center, H^4 [31]. The peak at −0.58 ppm is assigned to the H^5 proton similar to complex **3.** Two very broad peaks are observed at −1.7 and −6.5 ppm and are assigned to H^6 and H^2, respectively, those closest to the paramagnetic ruthenium center. In chloroform solution the peaks were observed at 6.32, −0.52, and −12.7 for the H^4, H^5, and DMSO protons, respectively. The H^2 and H^6 protons were too broad to be seen. The IR spectrum of **6** shows a terminal pym mode at 1585 cm^{-1} along with a ν(S–O) vibration at 1107 cm^{-1}, a ν(Ru–S) band at 421 cm^{-1}, and ν(Ru–Cl) vibrations at 339 and 324 cm^{-1}.

4. Conclusion

A library search in the Cambridge data file has revealed no Ru complexes containing both a sulfoxide and a monodentate pyrazine ligand. The two structures are also the first examples of Ru(III) compounds containing a monodentate pyrazine ligand. Three structures containing the pyrazine ligand bridging two Ru(III) atoms were found. These are the symmetric dimers $Na[(DMSO)Cl_4Ru(\mu\text{-}pz)RuCl_4(DMSO)]\cdot H_2O\cdot DMSO$ [27] and $(TMSO)_2H[(TMSO)Cl_4Ru(\mu\text{-}pz)RuCl_4(TMSO)]\cdot CH_3COCH_3$ (where TMSO = tetramethylenesulfoxide) [34], and the unsymmetrical $NH_4[(DMSO)Cl_4Ru(\mu\text{-}pz)RuCl_3(S\text{–}DMSO)(O\text{–}DMSO)]\cdot CH_3OH$ dimer [28]. It seems that pyrazine usually function as a bridging ligand and it is more difficult to prepare complexes containing monodentate pyrazine ligands. In the preparation of these types of complexes, the potential bridging ligand was added in a large excess, in order to reduce the formation of pyrazine-bridged oligomeric species. The same is true for the bipyridine and pyrimidine complexes.

The use of cations like PPh_4^+ or NR_4^+ which do not form H-bonds or other strong electrostatic attractions like alkali metals should prevent the formation of infinite chains or other materials with extended structures. In the few published structures containing Na cations with a tetrahedral environment, small oligomers are formed [22]. In the case of crystal **3**, the Na^+ cations have an octahedral

environment and it can form bridges between the Ru(III) complexed anions to form a ID extended structure. It might be interesting to replace the Na atom by a larger metal like Ba, which could accept a larger environment, for example, a coordination number of 8 and form multidimensional (2D or 3D) materials. The formation of such species is an area of current interest in supramolecular chemistry. The study of multidimensional compounds is important in material science, especially for paramagnetic species.

Acknowledgements

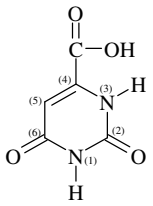
The authors are grateful to the Natural Science and Engineering Research Council of Canada for financial support. We also thank Orgometa, Skylar Ferrara, and Bard College.

Appendix A. Supplementary material

CCDC 637826 and 637827 contain the supplementary crystallographic data for this paper. These data can be obtained free of charge via http://www.ccdc.cam.ac.uk/conts/retrieving.html, or from the Cambridge Crystallographic Data Centre, 12 Union Road, Cambridge CB2 1EZ, UK; fax: (+44) 1223-336-033; or e-mail: deposit@ccdc.cam.ac.uk. Supplementary data associated with this article can be found, in the online version, at doi:10.1016/j.poly.2007.03.041.

References

[1] N. Farrell, Transition Metal Complexes as Drugs and Chemotherapeutic Agents, Kluwer, Dordrecht, 1989, pp. 44–46.
[2] P.J. O'Dwyer, J.P. Stevenson, S.W. Johnson, Clinical status of cisplatin, carboplatin, and other platinum-based antitumor drugs, in: B. Lippert (Ed.), Cisplatin: Chemistry and Biochemistry of a Leading Anticancer Drug, Verlag, Zurich, Helvetica Chimica Acta (1999) 31–72.
[3] C.X. Zhang, S.J. Lippard, Curr. Opin. Chem. Biol. 7 (2003) 481.
[4] E.R. Jamieson, S.J. Lippard, Chem. Rev. 99 (1999) 2467.
[5] Z. Suo, S.J. Lippard, K.A. Johnson, Biochemistry 38 (1999) 715.
[6] S. Komeda, G.V. Kalayda, M. Lutz, A.L. Spek, Y. Yamanaka, T. Sato, M. Chikuma, J. Reedijk, J. Med. Chem. 46 (2003) 1210.
[7] S. Komeda, M. Lutz, A.L. Spek, M. Chikuma, J. Reedijk, Inorg. Chem. 39 (2000) 4230.
[8] S. van Zutphen, E. Pantoja, R. Soriano, C. Soro, D.M. Tooke, A.L. Spek, H. den Dulk, J. Brouwer, J. Reedijk, Dalton Trans. (2006) 1020.
[9] V. Brabec, O. Novakova, Drug Resist. Updat. 9 (2006) 111.
[10] E. Alessio, G. Mestroni, A. Bergamo, G. Sava, Met. Ions Biol. Syst. 42 (2004) 323.
[11] I. Kostova, Curr. Med. Chem. 13 (2006) 1085.
[12] M.J. Clarke, in: A. Sigel, H. Sigel (Eds.), Metal Ions in Biological Systems, Marcel Dekker, New York, 1979, pp. 231–283.
[13] E. Alessio, G. Balducci, M. Calligaris, G. Casta, W. Attia, G. Mestroni, Inorg. Chem. 30 (1991) 609.
[14] G. Mestroni, E. Alessio, G. Sava, International Patent PCT C 07F 15/00, A61K 31/28, WO 98/00431, 1998.
[15] C.G. Hartinger, S. Zorbas-Seifried, M.A. Jakupec, B. Kynast, H. Zorbas, B.K. Keppler, J. Inorg. Biochem. 100 (2006) 891.
[16] M. Cocchietto, G. Sava, Pharmacol. Toxicol. 87 (2000) 193.
[17] S. Zorzet, A. Sorc, C. Casarsa, M. Cocchietto, G. Sava, Met.-Based Drugs 8 (2001) 1.
[18] G. Sava, A. Bergamo, M. Cocchietto, Clin. Cancer Res. 6 (2000) 4566.
[19] G. Sava, I. Capozzi, V. Clerici, G. Gagliardi, E. Alessio, G. Mestroni, Clin. Exp. Metastasis 16 (1998) 371.
[20] M.J. Clarke, Coord. Chem. Rev. 236 (2003) 209.
[21] J.M. Rademaker-Lakhai, D. Van den Bongard, D. Pluim, J.H. Beijnen, J.H. Schellens, Clin. Cancer Res. 10 (2004) 3717.
[22] E. Alessio, G. Balducci, G. Lutman, G. Mestroni, M. Calligaris, W.M. Attia, Inorg. Chim. Acta 203 (1993) 205.
[23] P. Mura, M. Camalli, L. Messori, F. Piccioli, P. Zanello, M. Corsini, Inorg. Chem. 43 (2004) 3863.
[24] I. Turel, M. Pecanac, A. Golobic, E. Alessio, B. Serli, A. Bergamo, G. Sava, J. Inorg. Biochem. 98 (2004) 393.
[25] Q.A. de Paula, A.A. Batista, O.R. Nascimento, A.J. da Costa-Filho, M.S. Schultz, M.R. Bonfadini, G. Oliva, J. Braz. Chem. Soc. 11 (2000) 530.
[26] E. Reisner, V.B. Arion, M.F.C. Guedes da Silva, R. Lichtenecker, A. Eichinger, B.K. Keppler, V. Kukushkin, A.J.L. Pombeiro, Inorg. Chem. 43 (2004) 7083.
[27] E. Allesio, G. Mestroni, S. Geremia, M. Calligaris, E. Iengo, Dalton Trans. (1999) 3361.
[28] B. Serli, E. Iengo, T. Gianferrara, E. Zangrando, E. Alessio, Met.-Based Drugs 8 (2001) 9–18.
[29] E. Alessio, M. Bolle, B. Milani, G. Mestroni, P. Faleschini, S. Geremia, M. Calligaris, Inorg. Chem. 34 (1995) 4716.
[30] XSCANS and SHELXTL Programs (PC, version 5), Bruker Analytical X-ray Systems, Madison, WI, 1995.
[31] C. Anderson, A.L. Beauchamp, Inorg. Chem. 34 (1995) 6065.
[32] C. Anderson, A.L. Beauchamp, Can. J. Chem. 73 (1995) 471.
[33] C. Anderson, Can. J. Chem. 79 (2001) 1477.
[34] R.S. Srivastava, F.R. Fronczek, L.M. Romero, Inorg. Chim. Acta 357 (2004) 2410.
[35] F.D. Rochon, J.R.L. Priqueler, Can. J. Chem. 82 (2004) 649.
[36] W. Lu, M.C.W. Chan, K. Cheung, Chi-Ming Che, Organometallics (2001) 2477.



Scheme 1. Orotic acid.

equally important complexes of the orotate counter anion [36–39]. To our surprise, no reported data were found for either a bis(orotate) complex or a cadmium complex with the orotate ligand. Recently, we have reported some transition metal-orotate complexes with various *N*-donor ligands [19–24,38–41] and the first neutral orotic acid complexes [42]. Polydentate amine ligands generally coordinate to metal ions using all of the available N atoms as donors. Ethylenediamine (en) acts as a bidentate ligand in the majority of its complexes, chelating to one metal ion through both N atoms, and there are a few complexes in which it coordinates as a monodentate ligand [43,44]. Despite the importance of the en ligand in Co(III) chemistry, the first X-ray structure of monodentate en coordinated to Co(III) has been described only recently [45]. The study of Cd-en formation dates back to 1945, when three complexes were shown to form in aqueous solution [46], and only limited structural information is available in the literature [47–50]. Orotic acid complexes with 1,10-phenanthroline are also interesting due to their roles in biological systems such as binding of small molecules to DNA [51].

As a part of our continuing research on the synthesis and characterization of complexes of orotic acid with *N*-donor ligands, we describe in this study, the synthesis, spectroscopic, thermal characterization and crystal structure of the first bis(orotato)cadmium(II) complex with monodentate protonated ethylenediamine ligands, *trans*-$[Cd(HOr)_2(enH)_2]\cdot 2H_2O$ (**1**) and the crystal structure of the diaquabis(1,10-phenanthroline)cadmium(II) complex with two orotate counter ions, *cis*-$[Cd(H_2O)_2(phen)_2]$-$(H_2Or)_2\cdot 2H_2O$ (**2**).

2. Experimental

2.1. Preparation of *1*

A solution of ethylenediamine (0.25 g, 4 mmol) in water (10 mL) was dropped into a stirred solution of $3CdSO_4\cdot 8H_2O$ (1.54 g, 2 mmol) and orotic acid monohydrate (0.70 g, 4 mmol) in water (25 mL). The solution was heated to 60 °C in a temperature-controlled bath and stirred for 10 h at 60 °C. The crystals that formed after cooling to room temperature were filtered off and washed with 10 mL portions of distilled water and ethanol and dried in air. *cis*-$[Cd(H_2O)_2(phen)_2](H_2Or)_2\cdot 2H_2O$ was also prepared according to the method of Yesilel and Ölmez [39].

2.2. Materials and measurements

All used chemicals were analytical reagent products. Elemental analyses for C, H and N were carried out at the TÜBİTAK Marmara Research Centre. The IR spectrum was recorded in the 4000–500 cm^{-1} region with a Mattson 1000 FT-IR spectrometer using KBr pellets. Magnetic susceptibility measurement at room temperature was performed using a Sherwood Scientific MXI model Gouy magnetic balance. Thermal analysis curves (TG, DTG and DTA) were recorded simultaneously in a static air atmosphere with a Rigaku TG8110 thermal analyzer. The heating rate was 10 °C min^{-1} and the DTG sensitivity was 0.05 mg s^{-1}. The conductance value was measured on a 522 CRISON conductimeter.

The intensity data were collected at room temperature using an Enraf-Nonius CAD4 diffractometer [52] with Mo Kα radiation using the $w/2q$ scan mode. The cell parameters were determined from least-squares analysis using 25 centered reflections in the range $2.4° \leqslant \theta \leqslant 26.3°$. Three standard reflections were periodically measured (every 120 min) during data collection and showed no significant intensity variations. The structure was solved by direct methods using the solution program SHELXS97 [53] in the WINGX package [54] and refined on F_0^2 using SHELXL97 [53]. Absorptions corrections were applied using the integration method. All non-hydrogen atoms were refined, first with isotropic and then with anisotropic thermal displacement parameters by full matrix least squares. All H atoms on N and O atoms except C6 and C7 hydrogens were located from a difference Fourier map and freely refined, C6 and C7 hydrogens were treated using a riding model. An ORTEP drawing [55] of the molecule and the atomic numbering scheme is shown in Figs. 1–3. The crystal and experimental data are given in Table 1. Values of

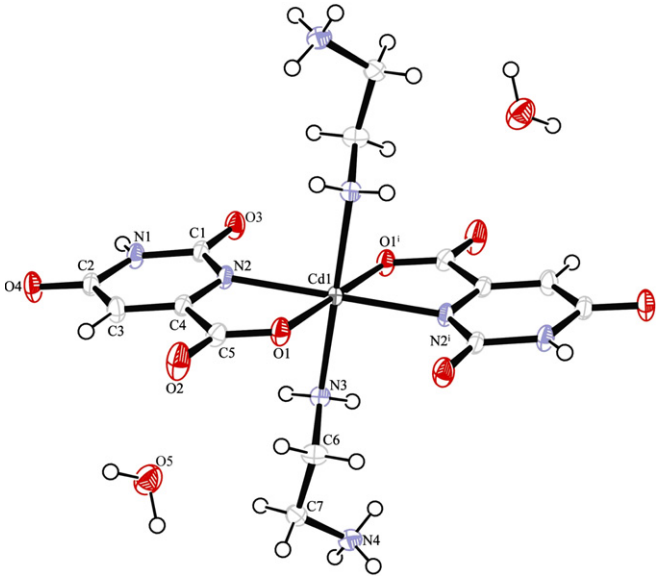


Fig. 1. The molecular structure of **1**.

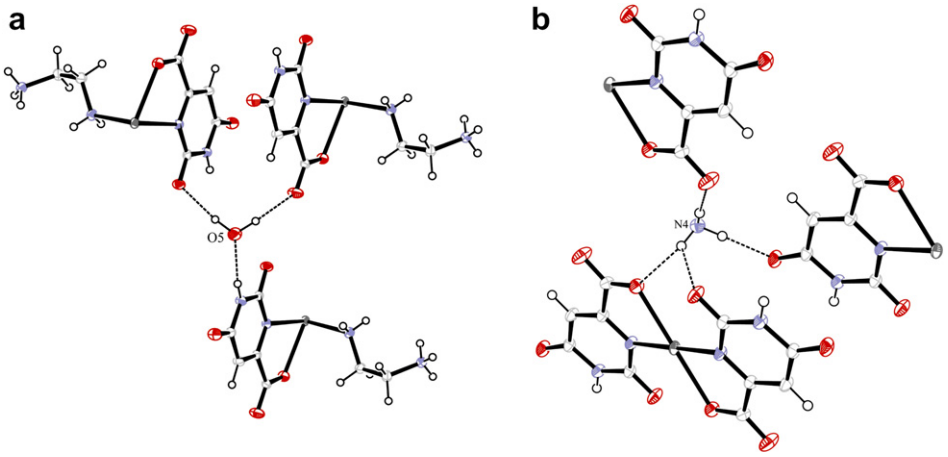


Fig. 2. The hydrogen bonding geometry of **1**.

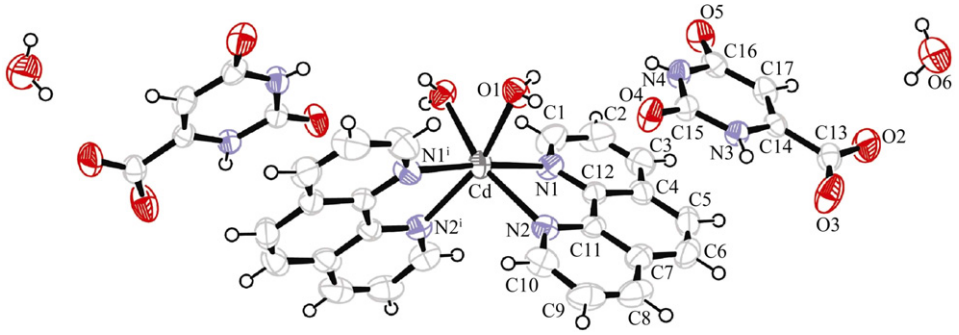


Fig. 3. The molecular structure of **2**.

selected bond lengths and angles, and hydrogen bonding geometries are given in Tables 2 and 3, respectively.

3. Results and discussion

The molar conductance value of the cadmium complex ($\Lambda_M = 40$ ohm^{-1} cm^2 mol^{-1}) indicates that *trans*-[Cd(HOr)$_2$(enH)$_2$]$\cdot$ 2H$_2$O is a non-electrolyte and the magnetic moment measurement shows that complex **1** is diamagnetic as expected.

3.1. IR spectrum of 1

In the IR spectrum of **1**, the crystal water stretching mode appears at 3506 cm^{-1}. The absorption bands in the frequency range 3400–3163 cm^{-1} are attributed to ν(NH) vibrations of the amine group of the HOr and en ligands. The bands with medium intensities at 3400 and 3315 cm^{-1}correspond to the NH_2 and NH_3 stretching vibration of the protonated en ligand. The $N_{(3)}$–H stretching bands at 3147 cm^{-1} of orotic acid [56] disappeared with complex **1** formation. This indicates the deprotonation of the N(3) atom and coordination to the cadmium(II) ion. Stretching of the carbonyl groups of polycrystalline H_3Or give rise to three strong and overlapped bands, at 1729 ($66\%\nu_{C=O(carboxylic)} + 17\%\nu_{C5=O4,in\text{-}phase}$), 1719 ($56\%\nu_{C5=O4} + 19\%\nu_{C=O(carboxylic),out\text{-}of\text{-}phase}$) and 1700 cm^{-1} ($73\%\nu_{C4=O3} + 11\%\nu_{ring}$) [56]. In the infrared spectrum of [CuHOr(H$_2$O)-en]$\cdot$ H$_2$O [19], a complex band at 1655 cm^{-1} appears. Three carbonyl bands were observed on the bis(deprotonation) of HOr, with a red-shift of all three bands. The carbonyl stretchings are overlapped with the water bending band and give two very strong broadened absorptions at 1635 and 1618 cm^{-1}. From the IR spectrum of **1**, it can be assumed that the orotate residues, HOr^{2-}, are coordinated as bidentate ligands to the metal through the carboxylic oxygen and N(3) from the pyrimidine ring. The medium-intense band at 1492 cm^{-1} is assigned to the C–N stretching of the uracilate ring.

3.2. Thermal studies

The endothermic peak ($DTG_{max} = 188$ °C) in the temperature range 149–217 °C corresponds to the loss of two crystal water molecules. In the second and third stages, in the temperature range 218–324 °C, the Cd(II) complex is involved in the decomposition of the two enH ligand molecules, giving an endothermic effect ($DTG_{max} = 232$ and 296 °C). In the following stages CO_2/CO is released from the orotate and the residual organic matter burns. The

Table 1
The details of crystal and experimental data for **1** and **2**

Empirical formula	$C_{14}H_6N_8O_{10}Cd$ (**1**)	$C_{34}H_{30}N_8O_{12}Cd$ (**2**)
Formula weight	578.83	855.06
Temperature (K)	293(2)	293(2)
Wavelength (Å)	0.71073	0.71073
Crystal system	triclinic	monoclinic
Space group	$P\bar{1}$	$C2/c$
Unit cell dimensions		
a (Å)	7.699(1)	16.125(5)
b (Å)	8.543(1)	12.625(5)
c (Å)	9.061(1)	16.753(5)
α (°)	80.76(1)	
β (°)	70.40(1)	92.637(5)
γ (°)	67.41(1)	
V (Å^3)	517.9(1)	3407(2)
Z	1	4
μ (mm^{-1})	1.13	0.72
D_{calc} (Mg m^{-3})	1.856	1.667
θ Range (°)	2.4–26.3	2.4–26.3
Measured reflections	2239	3484
Independent reflections	2099	3368
Absorption correction	integration	integration
Refinement method	full-matrix least-squares on F^2	full-matrix least-squares on F^2
Final R indices [$I > 2\sigma(I)$]	0.019	0.035
R indices (all data)	0.053	0.096
Goodness-of-fit on F^2	1.19	1.06
Largest difference peak and hole (e Å^{-3})	0.75 and −0.64	0.69 and −0.78

Table 2
Selected bond distances (Å) and angles (°) in **1** and **2**

Bond distances (Å)			
Complex ***1***			
Cd–N2	2.284(2)	C1–O3	1.238(2)
Cd–N3	2.344(2)	C2–O4	1.252(2)
Cd–O1	2.385(2)	C5–O1	1.261(2)
		C5–O2	1.243(2)
Complex ***2***			
Cd–O1	2.305(3)	C13–O2	1.229(4)
Cd–N1	2.313(3)	C13–O3	1.244(4)
Cd–N2	2.327(3)	C15–O4	1.219(3)
		C16–O5	1.238(4)
Bond angles (°)			
Complex ***1***			
N2–Cd–N3	89.7(6)	N3–Cd–O1	91.8(6)
N2–Cd–O1	70.0(5)		
Complex ***2***			
O1–Cd–N1	95.14(9)	O1^i–Cd–N1	95.17(10)
O1–Cd–N2	93.39(9)	N1–Cd–N2	72.23(9)
O1–Cd–O1^i	82.24(9)	N1–Cd–N1^i	175.03(9)
O1–Cd–N1^i	88.61(9)	N1–Cd–N2^i	104.34(9)
O1–Cd–N2^i	159.95(9)	N2–Cd–N2^i	96.98(9)

isoorotic acid and 2-thioisoorotic acid complexes [57,58] and $[Co(HOr)(H_2O)(4\text{-Meim})_3]$ [40] decompose by releasing CO/CO_2. The final solid product of thermal decomposition was identified as CdO (Found: 79.73, calc. 80.58%).

Table 3
Hydrogen bonding interactions for **1** and **2** (Å, °)

D–H···A	d(D–H)	d(H···A)	d(D···A)	< (DHA)
Complex **1**				
N1–H1···O5^i	0.81(3)	2.10(3)	2.903(3)	169(3)
N3–H13···O4^i	0.86(3)	2.14(3)	2.984(3)	167(2)
N4–H14···O4^{ii}	0.89(3)	1.94(3)	2.831(3)	179(3)
O5–H15···O3^{iii}	0.95(2)	1.92(2)	2.851(3)	170(4)
N3–H23···O4^{ii}	0.85(3)	2.18(3)	3.007(3)	163(2)
N4–H24···O1^{iv}	0.84(3)	2.18(3)	2.941(3)	151(3)
N4–H24···O3^{v}	0.84(3)	2.37(3)	2.833(3)	115(2)
O5–H25···O2^{vi}	0.95(2)	2.04(2)	2.972(3)	170(3)
N4–H34···O2^{vii}	0.84(3)	1.96(3)	2.799(3)	176(3)
C7–H7A···O3^{iii}	0.97	2.59	3.407(3)	142.0
C7–H7A···O1^{vi}	0.97	2.55	3.296(3)	133.4
Complex **2**				
C6–H6···O6^i	0.93	2.42	3.264(5)	151
O1–H1A···O3^{ii}	0.73(5)	2.02(5)	2.722(4)	60(5)
N3–H3N···O4^{ii}	0.88(3)	2.02(3)	2.866(3)	163(3)
C3–H3···O2^{iii}	0.93	2.35	3.234(4)	160
O1–H1B···O5^{iv}	0.81(5)	2.02(5)	2.828(3)	173(5)
N4–H4N···O5^{iv}	0.72(3)	2.18(3)	2.899(4)	178(4)
O6–H6B···O4^{v}	0.90(6)	2.48(6)	3.205(5)	138(5)
O6–H6A···O2	0.82(5)	1.97(5)	2.781(5)	167(5)

Symmetry codes (**1**): (i) $-x-1, -y, -z+1$, (ii) $x, y, z-1$, (iii) $x, y-1, z$, (iv) $x-1, y, z$, (v) $-x-1, -y, -z$, (vi) $-x, -y-1, -z+1$, (vii) $-x, -y-1, -z$.

Symmetry codes (**2**): (i) $-x+3/2, y+1/2, -z-1/2$, (ii) $-x+3/2, -y+1/2, -z$, (iii) $-x+2, y, -z-1/2$, (iv) $-x+2, -y, -z$ (v) $x, -y, z-1/2$.

3.3. Crystallographic analysis

3.3.1. trans-$[Cd(HOr)_2(enH)_2]\cdot 2H_2O$

The molecular structure of **1** with the atom labelling is shown in Fig. 1. Selected bond lengths and angles and hydrogen bonding geometries are given in Tables 2 and 3, respectively. The compound crystallizes in the triclinic space group $P\bar{1}$. Each orotic acid molecule has donated one H atom to the ethylenediamine N atom of a ethylenediammonium molecule, forming the bis(ethylenediammonium)bis(orotate)cadmium(II) dihydrate complex. The Cd(II) ion in *trans*-$[Cd(HOr)_2(enH)_2]\cdot 2H_2O$ is in a distorted octahedral configuration, coordinated by two molecules of orotato and two molecules of enH ligands. The bis(deprotonated) orotato ligands coordinate to the cadmium atom through both the heterocyclic N2 atom and the adjacent carboxylate group O1 atom, creating a chelate ring, while the protonated en ligands behave as a unusual monodentate ligand through the N3 atom. As there is just one HOr ligand in the other bidentate orotate complexes [6–25], the en ligands in the $[Co(HOr)(en)_2]H_2Or\cdot 5H_2O$, $[Cu(HOr)(en)(H_2O)]\cdot H_2O$ [19] and $[Pd(HOr)(en)]\cdot 0.5H_2O$ [10] complexes bond in a bidentate manner. The two N atoms of HOr and two O atoms of the carboxylate group of HOr form the equatorial plane, whereas the N atoms of the enH ligands are in the apical positions. The Cd1–N3 bond distance of 2.344(2) Å is similar to that found in $\{[Cd(barb)_2(\mu\text{-en})]\cdot 2H_2O\}_n$ (2.281(1) Å) [50] and $[Cd_2(en)_5](ClO_4)_4$ (2.324(5) Å) [47]. The Cd–N2 and

Cd–O1 bond distances of 2.284(2) and 2.385(2) Å, respectively, are significantly longer than that found in $[Co(HOr)(en)_2]H_2Or \cdot 5H_2O$ (1.974(4) and 1.914(4) Å), $[Cu(HOr)(en)(H_2O)] \cdot H_2O$ (1.986(3) and 1.990(2) Å) [19], $[Pd(HOr)(en)] \cdot 0.5H_2O$ (2.011(4) and 2.012(3) Å) [10], $[Cu(HOr)(NH_3)_2]$ (2.005(3) and 1.962(3) Å) [11] and $[Cu(HOr)(tea)] \cdot H_2O$ (2.007(2) and 1.944(2) Å) [20]. The HOr ligand is essentially planar with a r.m.s. deviation of 0.0361 Å, and the largest deviation from the mean plane is −0.0787 (13) Å for the O1 atom. The carboxylate C–O distances in the orotate anion also display some variability, depending on their environment. The C–O distances are practically equal in the H_2Or^- anion acting as a counter ion [37]. In **1**, the oxygen atoms of the orotate ligand have different environments; while the carboxylate O1 atom coordinates to the Cd atom, O2 acts as an acceptor for two hydrogen bonds, O5–H25···O2 and N4–H34···O2, the O3 and O4 atoms of the orotate ligand making hydrogen bonds via O5–H15, C7–H7A, N4–H24 and N4–H14, N3–H23, N3–H13, respectively. Therefore, the C–O bond lengths are in the range 1.238(2)–1.261(2) Å [C1–O3 = 1.238(2), C2–O4 = 1.252(2), C5–O1 = 1.261(2) and C5–O2 = 1.243(2) Å], which are comparable with those in similar Co(II), Ni(II) and Cu(II) complexes [19,24].

The crystal packing was formed by intermolecular hydrogen bonding. The hydrogen bonds observed are: (i) hydrogen bonding among water molecule O5 and carboxylate oxygen O2 (O5···O2 = 2.972(3) Å, at $x-1, y, z$), carbonyl oxygen O3 (O5···O3 = 2.851(3) Å, $x, y-1, z$) and pyrimidine nitrogen N1 (N1···O5 = 2.903(3) Å, $-x-1, -y, -z+1$) (Fig. 2), (ii) hydrogen bonding of the amine group of the protonated en ligand and orotate oxygens $O1^{iv}$, $O2^{vii}$, $O3^{v}$ and $O4^{ii}$ atoms [N4···O1 = 2.941(3) Å, (iv) $x-1, y, z$, N4···O2 = 2.799(3) Å, (vii) $-x, -y-1, -z$, N4···O3 = 3.407(3) Å, (v) $-x-1, -y, -z$, N4···O4 = 2.831(3) Å, (ii) $x, y, z-1$] (Fig. 2). There are also hydrogen bonds between the NH_2 group of the enH ligand which is coordinated to a Cd atom and the carbonyl oxygen O4 of orotate and also the orotate C7 atom and the carbonyl oxygen O3 and the carboxylate oxygen O1. The details for hydrogen bond geometries are given in Table 3.

3.3.2. *cis*-$[Cd(H_2O)_2(phen)_2](H_2Or)_2 \cdot 2H_2O$

A view of the molecule and its atom numbering scheme are shown in Fig. 3 and selected bond lengths and bond angles are given in Table 2. In the *cis*-$[Cd(H_2O)_2(phen)_2](H_2Or)_2 \cdot 2H_2O$ complex, the Cd atom exhibits a distorted octahedral coordination geometry defined by four nitrogen atoms from two chelating phen ligands together with two aqua ligands. The coordinated water molecule [Cd1–O1 = 2.305(3) Å] and two phen N atoms [Cd1–N1 = 2.313(3), Cd1–N2 = 2.327(3) Å] and the symmetry related N atom (symmetry codes: $2-x, y, 1/2-z$) form the equatorial plane with bond angles of $O1–Cd–N2^{i} = 159.95(9)°$ and $N1–Cd–N1^{i} = 175.03(9)°$, whereas the symmetry related fourth phen N atom and the second water molecule are in apical positions with an $O1–Cd1–N1^{i}$ angle of 160.1(1)°. These values are in agreement with those previously reported for other phen containing metal orotate complexes [23,38]. The equatorial plane and the phen ligand are approximately planar. The carboxylate C–O distances are practically equal when the orotate ligand acts as a counter ion [C13–O2 = 1.229(4), C13–O3 = 1.244(4), C15–O4 = 1.219(3), C16–O5 = 1.238(4) Å].

The complex **2** exhibits intramolecular and intermolecular hydrogen bonds as listed in Table 3. The coordinated water molecules link the orotate ions to the metal complex via $O1–H1A···O3^{ii}$ and $O1–H1B···O5^{iv}$ hydrogen bonds ((ii) $-x+3/2, -y+1/2, -z$ and (iv) $-x+2, -y, -z$). Each uncoordinated water molecule (O6) is hydrogen bonded to orotate ions through $O6–H6B···O4^{v}$ and O6–H6A···O2 hydrogen bonds. Furthermore, the symmetry related orotate ions are linked by $N3–H3N···O4^{iii}$ and $N4–H4···O5^{iv}$ hydrogen bonds to form chains (see Table 2 for symmetry codes).

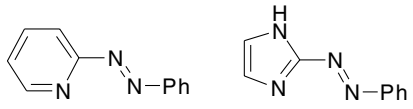
Appendix A. Supplementary material

CCDC 630739 and 630738 contain the supplementary crystallographic data for **1** and **2**. These data can be obtained free of charge via http://www.ccdc.cam.ac.uk/conts/retrieving.html, or from the Cambridge Crystallographic Data Centre, 12 Union Road, Cambridge CB2 1EZ, UK; fax: (+44) 1223-336-033; or e-mail: deposit@ccdc.cam.ac.uk. Supplementary data associated with this article can be found, in the online version, at doi:10.1016/j.poly.2007.03.060.

References

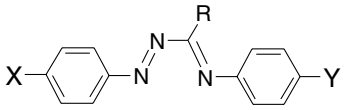
[1] D.D. Genchev, Dokl. Bolg. Akad. Nauk. 23 (1970) 435.
[2] N. Lalioti, C.P. Raptopoulou, A. Terzis, A. Panagiotopoulos, S.P. Perlepes, E. Manessi-Zoupa, J. Chem. Soc., Dalton Trans. 8 (1998) 1327.
[3] G. Maistralis, A. Koutsodimou, N. Katsaros, Transit. Met. Chem. 25 (2000) 166.
[4] D. Mentzafos, N. Katsaros, A. Terzis, Acta Crystallogr., Sect. C 43 (1987) 1905.
[5] D.J. Darenbourg, D.L. Larkins, J.H. Reibenspies, Inorg. Chem. 37 (1998) 6125.
[6] X. Li, Q. Shi, D. Sun, W. Bi, R. Cao, Eur. J. Inorg. Chem. (2004) 2747.
[7] A. Karipides, B. Thomas, Acta Crystallogr., Sect. C 42 (1986) 1705.
[8] O. Kumberger, J. Riede, H. Schmidbaur, Chem. Ber. 124 (1991) 2739.
[9] A.D. Burrows, D.M.P. Mingos, A.J.P. White, D.J. Williams, J. Chem. Soc., Dalton Trans. (1996) 149.
[10] P. Castan, T. Ha, Inorg. Chim. Acta 221 (1994) 173.
[11] I. Mutikainen, P. Lumme, Acta Crystallogr., Sect. B 36 (1980) 2233.
[12] I. Mutikainen, R. Hämäläinen, M. Klinga, U. Turpeinen, Z. Kristallogr. 212 (1997) 65.
[13] I. Mutikainen, R. Hämäläinen, M. Klinga, O. Orama, U. Turpeinen, Acta Crystallogr., Sect. C 52 (1996) 2480.
[14] T. Solin, K. Matsumoto, K. Fuwa, Bull. Chem. Soc. Jpn. 54 (1981) 3731.
[15] M. Sabat, D. Zglinska, B. Jezowska-Trzebiatowska, Acta Crystallogr., Sect. B 36 (1980) 1187.
[16] I. Mutikainen, Inorg. Chim. Acta 136 (1987) 155.
[17] X. Li, W. Bi, D. Yuan, R. Cao, Acta Crystallogr., Sect. E 59 (2003) m470.

[18] X. Li, R. Cao, W. Bi, D. Sun, M. Hong, Acta Crystallogr., Sect. E 59 (2003) m228.
[19] H. İçbudak, H. Ölmez, O.Z. Yeşilel, F. Arslan, P. Naumov, G. Jovanovski, A.R. Ibrahim, A. Usman, H.K. Fun, S. Chantrapromma, S.W. Ng, J. Mol. Struct. 657 (2003) 255.
[20] H. Olmez, H. Icbudak, O.Z. Yesilel, C. Arici, D. Ulku, Z. Kristallogr. 219 (2004) 300.
[21] I. Ucar, A. Bulut, O.Z. Yesilel, H. Olmez, O. Büyükgüngör, Acta Crystallogr., Sect. C 60 (2004) m563.
[22] O.Z. Yeşilel, F. Tezcan, H. Ölmez, H. Paşaoğlu, O. Büyükgüngör, Z. Anorg. Allg. Chem. 631 (2005) 2497.
[23] O.Z. Yeşilel, I. Uçar, A. Bulut, H. Ölmez, O. Büyükgüngör, Z. Naturforsch. 61b (2006) 147.
[24] O.Z. Yeşilel, H. Ölmez, I. Uçar, A. Bulut, C. Kazak, Z. Anorg. Allg. Chem. 631 (2005) 3100.
[25] M.J. Plater, M.R.J. Foreman, J.M.S. Skakle, R.A. Howie, Inorg. Chim. Acta 332 (2002) 135.
[26] I. Mutikainen, Finn. Chem. Lett. (1985) 193.
[27] X. Li, R. Cao, D. Sun, Q. Shi, M. Hong, Y. Ling, Inorg. Chem. Commun. 5 (2002) 589.
[28] T.T.B. Ha, A.M. Larsonneur-Galibert, P. Castan, J. Jaud, J. Chem. Crystallogr. 29 (1999) 565.
[29] D. Sun, R. Cao, Y. Liang, M. Hong, Y. Zhao, J. Weng, Aust. J. Chem. 55 (2002) 681.
[30] W. Brockner, R. Branscheid, M. Gjikaj, A. Adam, Z. Naturforsch. 60b (2005) 175.
[31] O. Kumberger, J. Riede, H. Schmidbaur, Chem. Ber. 124 (1991) 2739.
[32] F. Nepveu, N. Gaultier, N. Korber, J. Jaud, P. Castan, J. Chem. Soc., Dalton Trans. 24 (1995) 4005.
[33] I. Mutikainen, Recl. Trav. Chim. Pays-Bass 106 (1987) 438.
[34] X. Li, R. Cao, D. Sun, Q. Shi, W. Bi, M. Hong, Inorg. Chem. Commun. 6 (2003) 815.
[35] A.Q. Wu, F.K. Zheng, X. Liu, G.C. Guo, L.Z. Cai, Z.C. Dong, Y. Takano, J.S. Huang, Inorg. Chem. Commun. 9 (2006) 347.
[36] I. Bach, O. Kumberger, H. Schmidbaur, Chem. Ber. 123 (1990) 2267.
[37] L.R. Falvello, D. Ferrer, T. Soler, M. Tomás, Acta Crystallogr., Sect. C 59 (2003) m149.
[38] A. Bulut, H. İçbudak, O.Z. Yeşilel, H. Ölmez, O. Büyükgüngör, Acta Crystallogr., Sect. E 59 (2003) m736.
[39] O.Z. Yeşilel, H. Ölmez, J. Therm. Anal. Calorim. 86 (2006) 211.
[40] O.Z. Yeşilel, M.S. Soylu, H. Ölmez, O. Büyükgüngör, Polyhedron 25 (2006) 2985.
[41] O.Z. Yeşilel, H. Ölmez, H. Icbudak, J. Therm. Anal. Calorim., in press.
[42] O.Z. Yesilel, H. Ölmez, Trans. Met. Chem. 30 (2005) 992.
[43] F.A. Cotton, G. Wikinson, C.A. Murillo, M. Bochmann, Advanced Inorganic Chemistry, sixth ed., Wiley, New York, 1980, pp. 27–29.
[44] R.L. Fanshawe, A. Mobinikhaledi, C.R. Clark, A.G. Blackman, Inorg. Chim. Acta 307 (2000) 26.
[45] D.A. House, P.J. Steel, Inorg. Chim. Acta 288 (1999) 53.
[46] G.A. Carlson, J.P. McReynolds, F.H. Verhoek, J. Am. Chem. Soc. 67 (1945) 1334.
[47] G. Ma, A. Fischer, R. Nieuwendaal, K. Ramaswamy, S.E. Hayes, Inorg. Chim. Acta 358 (2005) 3165.
[48] N.V. Podberezskaya, V.V. Bakakin, S.V. Borisov, Zh. Struk. Khim. 10 (1969) 847.
[49] L. Li, B. Chen, Y. Song, G. Li, H. Hou, Y. Fan, L. Mi, Inorg. Chim. Acta 344 (2003) 95.
[50] F. Yilmaz, V.T. Yilmaz, C. Kazak, Z. Anorg. Allg. Chem. 631 (2005) 1536.
[51] C.V. Sastri, D. Eswaramoorthy, L. Giribabu, B.G. Maiya, J. Inorg. Biochem. 94 (2003) 138.
[52] Enraf Nonius: Cad-4 Express Version 1.1. Delft, The Netherlands, 1993.
[53] G.M. Sheldrick, SHELXS-97 and SHELXL-97. Program for Crystal Structure Solution and Refinement, University of Göttingen, Germany, 1997.
[54] L.J. Farrugia, WINGX. Program for Crystallography Package, J. Appl. Crystallogr. 32 (1999) 837.
[55] L.J. Farrugia, ORTEP. Program for Crystal Molecular Drawing, J. Appl. Crystallogr. 30 (1997) 565.
[56] A. Hernanz, F. Billes, I. Bratu, R. Navarro, Biopolymers 57 (2000) 187.
[57] F. Hueso-Urena, M.N. Moreno-Carretto, Thermochim. Acta 182 (1991) 9.
[58] F. Hueso-Ureña, M.N. Moreno-Carretto, J.M. Salas-Peregrín, Thermochim. Acta 170 (1990) 225.



I II

Recently, there has been an increasing interest in azomethine ligands, due to the photochromatic, redox active, pH responsive and photo-redox activity of this functional moiety [10,11]. Excellent examples of such predesigned molecular materials are 1-arylimino-l-arylhydrazono-propan-2-one (**III**) [12]. The arylamidrazones (**III**) are new class of bidentate ligands having a low-lying π^*(CN) MOs conjugated with π^*(N=N) MOs.



III

The conjugation shown in the structure of (**III**) is expected to create an extremely strong electron acceptor situation when they are bound to Ru(II). In this study, we extend our synthesis of azomethine ligands to include several new bidentate ligands and their Ru(II) complexes. Changing the substituents (X, Y and R) is expected to vary the π-acceptor ligands properties on these new bidentate ligands and thus "tune" the electronic properties of the ruthenium and consecutively the energy of MLCT bands. The spectral studies, redox properties and single crystal X-ray structures (for two representative examples) of these new families are described in this work.

2. Experimental

2.1. Materials

The reagents, aniline derivatives, α-chloroacetylacetone, α-chloroacetoacetate, ruthenium trichloride, 2,2′-bipyridine (bpy), lithium chloride and solvents (reagent grade), were purchased from Aldrich and were used as received. Tetrabutylammonium hexafluorophosphate (TBAH), purchased from Aldrich, was recrystallized twice from 1:1 ethanol/water solution and then vacuum dried at 110 °C. Hydrazonyl chlorides were prepared according to reported procedures [13]. The synthesis and the physical characterization of the ligand, 1-(4-chlorophenylimino)-l-(phenylhydrazono)-propan-2-one (**6c**) and the complex *trans*-[Ru(bpy)-(**6c**)Cl_2] (**11**) have been described previously [12]. Elemental analysis was performed by Canadian Microanalytical Services Ltd. (Canada).

2.2. General procedure for syntheses of arylamidrazones (*L*)

A solution of arylamine (20 mmol) and triethylamine (2.4 g, 24 mmol) in 5.0 mL ethanol was added to a 10 mL solution of the appropriate hydrazonyl chloride (20 mmol). The resulted reaction mixture was refluxed for 2 h. Condensing the solution followed by cooling produce a yellow solid which was collected by filtration, washing with water and recrystallizing from 2-propanol.

2.2.1. 1-(Phenylimino)-1-(phenylhydrazono)-propan-2-one (*6a*)

Yield: 2.6 g (52%). *Anal.* Calc. for $C_{15}H_{13}N_3O$: C, 71.7; H, 5.21; N, 16.7. Found. C, 72.3; H, 5.10; N, 16.9%. UV–Vis in acetonitrile: λ_{max} (ε_{max}): 352 (8.83×10^4), 294 (5.24×10^4), 214 (6.90×10^4). IR: ν(N=N) 1496, ν(C=N) 1601, ν(C=O) 1668. ^{1}H NMR (in $CDCl_3$, δ ppm): 6.64 (2H, d, H3), 6.92 (2H, t, H4), 7.05 (2H, d, H2), 7.31 (4H, m, H1, HX, HY), 2.63 (3H, s, HR). M.p. is 132–134 °C.

2.2.2. 1-(4-Methylphenylimino)-1-(phenylhydrazono)-propan-2-one (*6b*)

Yield: 3.0 g (57%). *Anal.* Calc. for $C_{16}H_{15}N_3O$: C, 72.4; H, 5.70; N, 15.8. Found: C, 72.1; H, 5.21; N, 15.5%. UV–Vis in acetonitrile: λ_{max} (ε_{max}): 353 (8.09×10^4), 294 (4.69×10^4), 240 (6.24×10^4). IR: ν(N=N) 1478, ν(C=N) 1599, ν(C=O) 1664. ^{1}H NMR (in $CDCl_3$, δ ppm): 6.58 (2H, d, H2), 6.97 (1H, t, HX), 7.07 (2H, d, H1), 7.09 (2H, d, H4), 7.27 (2H, d, H3) 2.31 (3H, s, HR), 2.63 (3H, s, HY). M.p. is 132–134 °C.

2.2.3. 1-(4-Bromophenylimino)-1-(phenylhydrazono)-propan-2-one (*6d*)

Yield: 4.0 g (60%). *Anal.* Calc. for $C_{15}H_{12}BrN_3O$: C, 54.6; H, 3.66; N, 12.7. Found: C, 54.2; H, 3.88; N, 12.5%. UV–Vis in acetonitrile: λ_{max} (ε_{max}): 351 (8.92×10^4), 294 (5.32×10^4), 243 (6.98×10^4). IR: ν(N=N) 1478, ν(C=N) 1596, ν(C=O) 1675. ^{1}H NMR (in $CDCl_3$, δ ppm): 6.51 (2H, d, H2), 6.987 (1H, t, HX), 7.1 (2H, d, H3), 7.31 (2H, t, H4), 7.35 (2H, d, H1), 2.6 (3H, s, HR). M.p. is 144–146 °C.

2.2.4. 1-(Naphthylimino)-1-(phenylhydrazono)-propan-2-one (*6e*)

Yield: 3.8 g (63%). *Anal.* Calc. for $C_{19}H_{15}N_3O$: 75.7; H, 5.02; N, 13.9. Found: C, 75.6; H, 5.21; N, 13.7%. UV–Vis in acetonitrile: λ_{max} (ε_{max}): 358 (8.80×10^4), 294 (5.20×10^4), 210 (6.86×10^4). IR: ν(N=N) 1504, ν(C=N) 1600, ν(C=O) 1673. ^{1}H NMR (in $CDCl_3$, δ ppm): 6.34 (1H, d, H (naphthyl proton)), 6.91 (1H, t, HX), 7.04 (2H, d, H (naphthyl proton)), 7.31 (3H, m, H4, H (naphthyl proton)), 7.6 (3H, m, H3), 7.9 (1H, d, H (naphthyl proton)), 8.1 (1H, d, H (naphthyl proton)), 2.71 (3H, s, HR). M.p. is 148–150 °C.

2.2.5. 1-(4-Methyloxyphenylimino)-1-(phenylhydrazono)-propan-2-one (*6f*)

Yield: 3.1 g (55%). *Anal.* Calc. for $C_{16}H_{15}N_3O_2$: C, 68.3; H, 5.37; N, 14.9. Found: C, 68.1; H, 5.21; N, 15.1%. UV–Vis in acetonitrile: λ_{max} (ε_{max}): 357 (8.75×104), 297 (5.0×104), 240 (6.78×10^4). IR: ν(N=N) 1504, ν(C=N)

1618, ν(C=O) 1660. ^{1}H NMR (in $CDCl_3$, δ ppm): 6.62 (2H, d, H1), 6.80 (2H, d, H2), 6.92 (1H, t, HX), 7.03 (2H, t, H4), 7.25 (2H, d, H3), 3.75 (3H, s, HY), 2.75 (3H, s, HR). M.p. is 98–100 °C.

2.2.6. 1-(4-Nitrophenylimino)-1-(phenylhydrazono)-propan-2-one (**6g**)

Yield: 3.1 g (51%). *Anal.* Calc. for $C_{15}H_{14}N_4O_3$: C, 60.4; H, 4.73; N, 18.8. Found: C, 60.1; H, 4.51; N, 18.5%. UV–Vis in acetonitrile: λ_{max} (ε_{max}): 338 (8.81×10^4), 297 (5.20×10^4), 231 (6.85×10^4). IR: ν(N=N) 1505, ν(C=N) 1602, ν(C=O) 1667. ^{1}H NMR (in $CDCl_3$, δ ppm): 6.34 (2H, d, H2), 7.02 (1H, t, HX), 7.13 (2H, d, H3), 7.31 (2H, t, H4) 8.16 (2H, d, H1), 2.60 (3H, s, HR). M.p. is 174–176 °C.

2.2.7. Methyl-1-(phenylimino)-1-(phenylhydrazono)-acetate (**7a**)

Yield: 3.2 g (59%). *Anal.* Calc. for $C_{15}H_{13}N_3O_2$: C, 67.4; H, 4.90; N, 15.7. Found: C, 67.1; H, 5.21; N, 15.5%. UV–Vis in acetonitrile: λ_{max} (ε_{max}): 335 (8.85×10^4), 291 (5.23×10^4), 234 (6.91×10^4). IR: ν(N=N) 1504, ν(C=N) 1600, ν(C=O) 1696. ^{1}H NMR (in $CDCl_3$, δ ppm): 6.66 (2H, d, H1), 6.9 (2H, t, H2), 7.09 (2H, t, H4), 7.25 (4H, m, H3, HX, HY), 3.9 (3H, s, HR). M.p. is 134–136 °C.

2.2.8. Methyl-1-(4-chlorophenylimino)-1-(phenylhydrazono)-acetate (**7c**)

Yield: 3.1 g (51%). *Anal.* Calc. for $C_{15}H_{12}N_3O_2Cl$: C, 59.7; H, 4.01; N, 13.9. Found: C, 59.5; H, 4.21; N, 13.5%. UV–Vis in acetonitrile: λ_{max} (ε_{max}): 345 (8.79×10^4), 294 (5.18×10^4), 240 (6.89×10^4). IR: ν(N=N), 1489 ν(C=N), 1593, ν(C=O) 1705. ^{1}H NMR (in $CDCl_3$, δ ppm): 6.54 (2H, d, H1), 6.9 (1H, t, HX), 7.09 (2H, t, H4), 7.18 (2H, d, H2), 7.27 (2H, d, H3), 3.9 (3H, s, HR). M.p. is 87–89 °C.

2.2.9. Methyl-1-(phenylimino)-1-(4-chlorophenylhydrazono)-acetate (**8a**)

Yield: 3.6 g (60%). *Anal.* Calc. for $C_{15}H_{12}N_3O_2Cl$: C, 59.7; H, 4.01; N, 11.8. Found: C, 59.6; H, 4.20; N, 11.6%. UV–Vis in acetonitrile λ_{max} (ε_{max}): 340 (8.7×10^4), 275 (5.17×10^4), 211 (6.89×10^4). IR: ν(N=N), 1490 ν(C=N), 1598, ν(C=O) 1705. ^{1}H NMR (in $CDCl_3$, δ ppm): 6.65 (1H, t, HX), 6.9 (2H, d, H4), 7.0 (2H, d, H2), 7.2 (2H, t, H1), 7.3 (2H, d, H3), 3.8 (3H, s, HR). m.p. is 104–106 °C.

2.2.10. Methyl-1-(4-chlorophenylimino)-1-(4-chlorophenylhydrazono)-acetate (**8c**)

Yield: 3.7 g (55%). *Anal.* Calc. for $C_{15}H_{11}N_3O_2Cl_2$: C, 53.6; H, 3.30; N, 12.5. Found: C, 53.9; H, 3.50; N, 12.2%. UV–Vis in acetonitrile: λ_{max} (ε_{max}): 342 (8.89×10^4), 300 (5.29×10^4), 246 (6.94×10^4). IR: ν(N=N) 1488, ν(C=N) 1588, ν(C=O) 1706. ^{1}H NMR (in $CDCl_3$, δ ppm): 6.55 (2H, d, H2), 7.03(2H, d, H4), 7.25 (2H, d, H1), 7.38 (2H, d, H3), 3.87(3H, s, HR). M.p. is 84–86 °C.

2.2.11. Methyl-1-(4-bromophenylimino)-1-(4-chlorophenylhydrazono)-acetate (**8d**)

Yield: 4.7g (62%). *Anal.* Calc. for $C_{15}H_{11}N_3O_2ClBr$: C, 47.3; H, 2.91; N, 11.0. Found: C, 47.5; H, 3.20; N, 10.9%. UV–Vis in acetonitrile: λ_{max} (ε_{max}): 340 (8.81×10^4), 305 (5.22×10^4), 246 (6.88×10^4). IR: ν(N=N) 1484, ν(C=N) 1599, ν(C=O) 1712. ^{1}H NMR (in $CDCl_3$, δ ppm): 6.51 (2H, d, H1), 7.02 (2H, d, H4), 7.21 (2H, d, H2), 7.39 (2H, d, H3), 3.93 (3H, s, HR). M.p. is 97–99 °C.

2.3. General procedure for the syntheses of trans-[Ru(bpy)(**L**)Cl_2]

Ruthenium trichloride trihydrate (261 mg, 1.0 mmol) and (1.0 mmol) of (**L**) were dissolved in 100 mL of absolute ethanol. After refluxing for 1 h, 1.0 mmol of bpy was added to the solution. The reaction was heated for an additional 2 h then an excess amount of LiCl (500 mg, 11.8 mmol) was added. After allowing the reaction mixture to reflux for an additional 1 h, the solvent was then removed by rotary evaporator. The crude product was dissolved in dichloromethane, filtered and washed with water to remove the unreacted ruthenium trichloride and lithium chloride. The filtrate was reduced to 20 mL and purified by chromatography (50×3 cm) column containing 250 g alumina grade (III). The first pale yellow band, thought to be the azomethine ligand (**L**) was eluted with hexane. Acetone was used to elute the second dark-red band of the product.

2.3.1. trans-[Ru(bpy)(**6a**)Cl_2] · 0.5H_2O (**9**)

Yield: 301 mg (52%). *Anal.* Calc. for $RuC_{25}H_{21}N_5OCl_2\cdot0.5H_2O$: C, 51.0; H, 3.77; N, 11.9. Found: C, 51.0; H, 3.65; N, 11.9.%. UV–Vis in DMF: λ_{max} (ε_{max}): 509 (13.1×10^3). ^{1}H NMR (in $CDCl_3$, δ ppm): 6.98 (1H, t, H8′), 7.03 (1H, t, H8), 7.10 (1H, d, H9), 7.51 (6H, m, H2, H4, H7′, HX), 7.74 (1H, t, HY), 7.79 (3H, m, H3, H7), 7.83 (1H, d, H9′), 7.93 (1H, d, H6), 7.97 (1H, d, H6′), 8.06 (2H, d, H1), 2.79 (3H, s, HR).

2.3.2. trans-[Ru(bpy)(**6b**)Cl_2] (**10**)

Yield. 231 mg (39%). *Anal.* Calc. for $RuC_{26}H_{23}N_5OCl_2$: C, 52.6; H, 3.91; N, 11.8. Found: C, 51.3; H, 3.19; N, 11.4%. UV–Vis in DMF: λ_{max} (ε_{max}): 513 (10.5×10^3). ^{1}H NMR (in $CDCl_3$, δ ppm): 7.01 (1H, t, H8), 7.05 (1H, t, H8′), 7.23 (1H, d, H9), 7.3 (2H, d, H1), 7.4 (2H, d, H2), 7.5 (2H, t, H4), 7.72 (1H, t, HX), 7.82 (3H, m, H9, H6, H6′), 7.93 (1H, d, H7′), 7.97 (1H, d, H7), 8.06 (2H, d, H3), 2.49 (3H, s, HY), 2.78 (3H, s, HR).

2.3.3. trans-[Ru(bpy)(**6d**)Cl_2] · CH_2Cl_2 (**12**)

Yield: 311 mg (47%). *Anal.* Calc. for $RuC_{25}H_{20}N_5OCl_2Br\cdot CH_2Cl_2$: C, 42.0; H, 2.98; N, 9.42. Found: C, 42.4; H, 2.69; N, 9.25%. UV–Vis in DMF: λ_{max} (ε_{max}): 508 (11.6×10^3). ^{1}H NMR (in $CDCl_3$, δ ppm): 6.97 (1H, t, H8′), 7.15 (1H, t, H8), 7.22 (1H, d, H9), 7.38 (2H, d, H1), 7.5 (2H, t, H4), 7.67 (2H, d, H2), 7.71 (1H, t, HX),

7.76 (1H, d, H9), 7.8 (1H, t, H7′), 7.87 (1H, t, H7), 7.94 (1H, d, H6′), 7.99 (1H, d, H6), 8.04 (2H, d, H3), 2.07 (3H, s, HR).

*2.3.4. trans-[Ru(bpy)(**6e**)Cl$_2$] · 0.25C$_7$H$_8$ (**13**)*

Yield: 294 mg (45%). *Anal.* Calc. for $RuC_{29}H_{23}N_5OCl_2.0.25C_7H_8$: C, 56.6; H, 3.86; N, 10.7. Found: C, 56.4; H, 3.52; N, 10.4%. UV–Vis in DMF: λ_{max} (ε_{max}): 508 (10.57×10^3). ^{1}H NMR (in $CDCl_3$, δ ppm): 6.74 (1H, t, H8), 6.98 (1H, d, H8′), 7.04 (1H, d, H9), 7.43 (1H, t, H7), 7.54 (3H, m, naphtyl protons), 7.68 (1H, t, HX), 7.7 (4H, m, H7, naphtyl protons), 7.86 (3H, m, H4, H9′), 7.96 (1H, d, H6), 8.03 (1H, d, H6′), 8.19 (2H, d, H3), 2.72 (3H, s, HR).

*2.3.5. trans-[Ru(bpy)(**6f**)Cl$_2$] (**14**)*

Yield: 257 mg (42%). *Anal.* Calc. for $RuC_{26}H_{23}N_5O_2Cl_2$: C, 51.2; H, 3.80; N, 11.5. Found: C, 51.4; H, 3.95; N, 11.2%. UV–Vis in DMF: λ_{max} (ε_{max}): 514 (10.5×10^3). ^{1}H NMR (in $CDCl_3$, δ ppm):, 6.97 (1H, t, H8′), 7.00 (1H, t, H8) 7.20 (1H, d, H9), 7.26 (2H, d, H1), 7.38 (2H, d, H2), 7.48 (2H, t, H4), 7.68 (1H, t, HX)7.65 (1H, d, H9′), 7.75 (2H, m, H7, H7′), 7.79 (1H, d, H6′), 7.94 (1H, d, H6), 8.03 (2H, d, H3), 2.74 (3H, s, HY), 2.45 (3H, s, HR).

*2.3.6. trans-[Ru(bpy)(**6g**)Cl$_2$] · CH$_2$Cl$_2$ (**15**)*

Yield: 309 mg (42%). *Anal.* Calc. for $RuC_{25}H_{22}N_6O_3Cl_2 \cdot CH_2Cl_2$: C, 43.9; H, 3.40; N, 11.8%. Found: C, 43.5; H, 3.29; N, 11.5%. UV–Vis in DMF: λ_{max} (ε_{max}): 504 (10.6×10^3). ^{1}H NMR (in $CDCl_3$, δ ppm): 7.02 (1H, t, H8), 7.14 (1H, t, H8′), 7.24 (1H, d, H9), 7.5 (2H, t, H4),7.65 (2H, d, H1), 7.75 (1H, d, H9), 7.8 (1H, t, HX), 7.87 (1H, t, H7′), 7.94 (1H, t, H7), 8.01 (1H, d, H6′), 8.04 (1H, d, H6), 8.14 (2H, d, H2), 8.32 (2H, d, H3) 2.83 (3H, s, HR).

*2.3.7. trans-[Ru(bpy)(**7a**)Cl$_2$] (**16**)*

Yield: 258 mg (43%). *Anal.* Calc. for $RuC_{25}H_{21}N_5O_2Cl_2$: C, 50.4; H, 3.55; N, 11.8. Found: C, 49.1; H, 3.49; N, 11.4%. UV–Vis in DMF: λ_{max} (ε_{max}): 500 (10.6×10^3). ^{1}H NMR (in $CDCl_3$, δ ppm): 6.9 (1H, t, H8), 7.02 (1H, t, H8′), 7.2 (1H, d, H9), 7.42 (2H, t, H4), 7.54 (4H, m, HY, H2, H9′), 7.68 (1H, t, HX), 7.74 (1H, t, H7′), 7.80 (1H, t, H7), 7.88 (1H, d, H6′), 7.94 (1H, d, H6), 8.00 (2H, d, H3), 3.83 (3H, HR).

*2.3.8. trans-[Ru(bpy)(**7c**)Cl$_2$] (**17**)*

Yield: 321 mg (51%). *Anal.* Calc. for $RuC_{25}H_{20}N_5O_2Cl_3$: C, 47.7; H, 3.20; N, 11.1. Found: C, 47.6; H, 3.39; N, 11.3%. UV–Vis in DMF: λ_{max} (ε_{max}): 500 (10.5×10^3). ^{1}H NMR (in $CDCl_3$, δ ppm): 6.92 (1H, t, H8), 7.12 (1H, t, H8′), 7.29 (1H, d, H9), 7.46 (7H, m, H1, H2, H4, HX), 7.56 (1H,d, H9′), 7.66 (1H, t, H7′), 7.73 (1H, t, H7), 7.86 (1H, d, H6′), 7.89 (1H, d, H6), 7.98 (2H, d, H3), 3.85 (3H, s, HR).

*2.3.9. trans-[Ru(bpy)(**8a**)Cl$_2$] · 0.5acetone (**18**)*

Yield: 323 mg (47%). *Anal.* Calc. for $RuC_{25}H_{20}N_5O_2Cl_3 \cdot 0.5C_3H_6O$: C, 48.3; H, 3.52; N, 10.6. Found: C, 48.4; H, 3.62; N, 10.3%. UV–Vis in DMF: λ_{max} (ε_{max}): 499 (12.6×10^3). ^{1}H NMR (in $CDCl_3$, δ ppm): 7.07 (1H, t, H8), 7.1 (1H, t, H8′), 7.21 (1H, d, H9), 7.49 (7H, m, H1, H4), 7.58 (4H, m, H2, HY, H9′), 7.87 (2H, m, H7, H7′), 8.0 (2H, m, H6, H6′), 8.08 (2H, d, H3), 3.88 (3H, s, HR).

*2.3.10. trans-[Ru(bpy)(**8c**)Cl$_2$] (**19**)*

Yield: 332 mg (50%). *Anal.* Calc. for $RuC_{25}H_{19}N_5O_2Cl_4$: C, 45.2; H, 2.88; N, 10.5. Found: C, 46.4; H, 3.62; N, 10.3%. UV–Vis in DMF: λ_{max} (ε_{max}): 501 (12.4×10^3). ^{1}H NMR (in $CDCl_3$, δ ppm): 7.08 (1H, t, H8), 7.17 (1H, t, H8′), 7.35 (1H, d, H9), 7.46 (4H, m, H1, H4), 7.63 (2H, d, H2), 7.79 (1H, d, H9), 7.88 (2H, m, H7, H7′), 7.94 (1H, d, H6′), 8.03 (1H, d, H6), 8.05 (2H, d, H3), 3.88 (3H, s, HR).

*2.3.11. trans-[Ru(bpy)(**8d**)Cl$_2$] (**20**)*

Yield: 370 mg (52%). *Anal.* Calc. for $RuC_{25}H_{19}N_5O_2Cl_3Br$: C, 42.4; H, 2.70; N, 9.88. Found: C, 42.6; H, 3.01; N, 9.65%. UV–Vis in DMF: λ_{max} (ε_{max}): 502 (12.0×10^3). ^{1}H NMR (in $CDCl_3$, δ ppm): 7.09 (1H, t, H8), 7.16 (1H, t, H8′), 7.36 (1H, d, H9), 7.48 (4H, m, H1, H4), 7.60 (1H, d, H9′), 7.82 (2H, d, H2), 7.9 (2H, m, H7, H7′), 8.02 (2H, m, H6, H6′), 8.05 (2H, d, H3), 3.89 (3H, s, HR).

2.4. Instrumentation

Cyclic voltammetry studies were performed in 99.8% anhydrous acetonitrile (Aldrich, HPLC grade) using a BAS CV-27W voltammetric analyzer and plotted on a BAS XY recorder. Three electrodes were utilized in this system, two platinum-disk working and counter (auxiliary) electrodes (BAS, 1.6-mm diameter), and a silver wire pseudo-reference electrode with ferrocene (0.665 V versus NHE) as an internal reference [14]. To control the temperature, a Haake D8-G refrigerated bath and circulator was used to maintain the cell temperature at 25.0 ± 0.1 °C. Tetrabutylammonium hexafluorophosphate (0.1 M) was twice recrystallized and vacuum dried at 110 °C, and used as the supporting electrolyte. Spectroscopic data were obtained using the following instruments Cary 5 spectrophotometer; IR spectra (KBr disk, 4000–200 cm), FT-IR JASCO model 420; H NMR spectra (Bruker (AC) 300 MHz FT NMR spectrometer). Spectroelectrochemistry for complex **18** was performed using an optically transparent thin layer electrochemistry (OTTLE) cell [15]. The cell had interior dimensions of roughly 1×2 cm with a path length of 0.2 cm and was fitted with an Ag/AgCl reference electrode. ITO (indium-tin oxide) coated glass served as working and counters electrodes and was purchased from Delta-Technologies. Spectra were obtained on Cary 5 spectrophotometer versus appropriate background of solvent and electrolyte at scan rate of 1800 nm/min. The potential was controlled by the same BAS CV-27 which was used for cyclic voltammetry. At any given potential, the system was allowed to come to equilibrium ($i \approx 0$ μA) before the spectrum was taken.

Table 1
Crystallographic data and structure refinement parameters for **13** and **18**

Compound	**13**	**18**
Formula	$C_{61.5}H_{50}Cl_4N_{10}O_2Ru_2$	$C_{26.5}H_{23}Cl_3N_5O_{2.5}Ru$
Molecular weight	1305.06	658.92
Crystal system	triclinic	monoclinic
Space group	$P\bar{1}$	$P2_1/c$
a (Å)	14.6230(2)	12.2391(11)
b (Å)	15.6896(2)	11.3273(10)
c (Å)	15.6905(3)	21.0382(19)
α (°)	89.3012(13)	90
β (°)	66.9141(12)	100.5510(10)
γ (°)	66.5962(12)	90
V (Å^3)	2994.87(9)	2867.3(4)
Z	2	4
T (K)	298(2)	296(2)
λ (Å)	0.71073	0.71073
ρ_{calc} (Mg/m^3)	1.447	1.526
μ (mm^{-1})	0.734	0.861
$F(000)$	1322	1328
Crystal size (mm)	$0.36 \times 0.19 \times 0.12$	$0.30 \times 0.20 \times 0.06$
θ Range (°)	1.43–25.25	1.69–25.25
Index ranges	$-17 \leqslant h \leqslant 17$, $-18 \leqslant k \leqslant 18$, $-18 \leqslant l \leqslant 18$	$-14 \leqslant h \leqslant 14$, $-13 \leqslant k \leqslant 13$, $-25 \leqslant l \leqslant 25$
Number of reflections collected	34887	45319
Number of independent reflections (R_{int})	10836 (0.0523)	5188 (0.0373)
Data/restraints/parameters	10836/0/694	5188/4/333
Goodness-of-fit	1.038	1.073
R_1^a [$I > 2\sigma(I)$]	0.0589	0.0470
wR_2^b [$I > 2\sigma(I)$]	0.1655	0.1380
Largest difference in peak and hole (e Å^{-3})	1.401 and −0.586	1.522 and −1.312

[a] $R_1 = \sum||F_o| - |F_c||/\sum|F_o|$.
[b] $wR_2 = \{\sum[w(F_o^2 - F_c^2)^2]/\sum[w(F_o^2)^2]\}^{1/2}$.

2.5. Computational methods

The crystallographic geometry of Ru(II) complex **18** was used as a representative example for our calculations. All calculations were carried out with GAUSSIAN-03 program package [16]. The Becke three parameters hybrid exchange [17] and the Lee–Yang–Parr correlation functionals [18] (B3LYP) were used. Time-dependent density functional theory (TD-DFT) [19,20] was used for the calculation of the lowest 10 singlet to singlet excitation energy.

2.6. Crystallography

Crystallographic data of crystals of compound **13** or **18** were collected at 298(2) K using a Bruker/Siemens SMART APEX instrument (Mo Kα radiation, $\lambda = 0.71073$ Å). Data were measured using phi and omega scans of 0.5° per frame for 20 {10} s, and a full sphere of data were collected. A total of 1282 {1464} frames were collected with a final resolution of 0.83 Å. Cell parameters were retrieved using APEX2 [21] software and refined using SAINTPlus on all observed reflections [22]. Data reduction and correction for Lp and decay were performed using the SAINTPlus software. Absorption corrections were applied using SADABS [23]. The structure was solved by direct methods and refined by least squares method on F^2 using the SHELXTL program package [24]. The structure was solved in the space group $P\bar{1}$ for **13** and $\{P2_1/c\}$ for **18** by analysis of systematic absences. In **13** the disordered toluene solvent (50% occupied, modeled as a rigid group from coordinates from the Cambridge Database) was held isotropic. In complex **17**, the disordered methyl ester group (50%) and the acetone solvent (50%) were held isotropic. All other non-hydrogen atoms were refined anisotropically. No decomposition was observed during data collection for both structures. Details of the data collection and refinement of **13** and **18** are given in Table 1. Selected bond lengths and angles for **13** and **18** are given in Table 2.

3. Results and discussion

3.1. Synthesis

The new ligands (**6**–**8**) used in this study were prepared in a two-step sequence starting with commercially

Table 2
Selected bond lengths (Å) and angles (°) for complexes **13** and **18**

13				**18**	
Conformer 1		Conformer 2			
Ru1–Cl1	2.3725(16)	Ru2–Cl4	2.3879(16)	Ru1–Cl2	2.3539(12)
Ru1–Cl2	2.3725(14)	Ru2–Cl3	2.3746(17)	Ru1–Cl1	2.3904(12)
Ru1–N19	1.945(4)	Ru2–N54	1.946(4)	Ru1–N24	1.956(3)
Ru1–N25	2.154(4)	Ru2–N60	2.014(5)	N23–N24	1.321(5)
N19–N20	1.299(6)	N54–N55	1.323(6)	C20–N23	1.359(6)
N20–C21	1.359(7)	N55–C56	1.352(7)	N19–C20	1.438(6)
C21–N25	1.299(7)	C56–N60	1.306(7)	Ru1–N19	2.024(4)
N19–Ru1–N25	75.55(19)	N54–Ru2–N60	76.23(18)	N1–Ru1–N12	76.64(14)
N19–Ru1–N1	103.67(18)	N54–Ru2–N47	103.19(18)	N24–Ru1–N19	75.98(15)
N25–Ru1–N1	175.04(18)	N60–Ru2–N47	169.32(19)	N24–Ru1–N1	103.08(14)
N19–Ru1–N12	175.78(17)	N54–Ru2–N36	173.47(19)	N19–Ru1–N1	173.13(14)
N25–Ru1–N12	104.84(19)	N60–Ru2–N36	105.38(19)	N24–Ru1–N12	178.46(14)
N1–Ru1–N12	76.32(18)	N47–Ru2–N36	76.43(19)	N19–Ru1–N12	104.47(14)

Table 3
Cyclic voltammetry and electronic spectroscopy data of *trans*-[Ru(bpy)(**L**)Cl_2] complexes

Complex number	Cyclic voltammetric data $E_{1/2}$ (V)[a]					Electronic spectroscopic data[b]
	$(E^{M}_{1/2})$[c]	Calculated E_L(L)[d]	Cathodic peak maximum for L[e]		bpy(0/−1)	λ_{max} (nm) (E_{MLCT})[f]
			L(0/−1)	L(−1/−2)		
9	1.1800	0.42	−0.48	−0.88	−1.71	(510) 56.06
10	1.1600	0.40	−0.51	−0.88	−1.70	(513) 55.73
11	1.1700	0.41	−0.49	−0.85	−1.60	(511) 55.95
12	1.2100	0.45	−0.45	−0.83	−1.55	(508) 56.28
13	1.2000	0.44	−0.44	−0.84	−1.60	(506) 56.50
14	1.1400	0.38	−0.41	−0.76	−1.53	(514) 55.62
15	1.2300	0.47	−0.44	−0.80	−1.60	(504) 56.73
16	1.2500	0.49	−0.42	−0.75	−1.52	(500) 57.18
17	1.2300	0.47	−0.39	−0.76	−1.52	(500) 57.18
18	1.2500	0.49	−0.40	−0.75	−1.53	(499) 57.30
19	1.2600	0.50	−0.41	−0.77	−1.58	(499) 57.30
20	1.2500	0.49	−0.40	−0.76	−1.55	(500) 57.18

[a] Solvent MeCN, supporting electrolyte Bu_4NPF_6 (0.1 M), scan rate 0.1 V/s, Pt-disk working electrode, Pt-wire auxiliary electrode, reference electrode Ag at 25 °C.
[b] Solvent MeCN.
[c] $E^{M}_{1/2} = (E_{pa} + E_{pc})/2$.
[d] $E_{Ru(III/II)} = 0.97\left[\sum E_L\right] + 0.4$ in V vs. NHE (1)
[e] The L(0/−1) and L(−1/−2) are irreversible. The cathodic peak maximum are reported here.
[f] $E_{MLCT} = [28\,591/\lambda_{max}\ (nm)]$ kcal mol^{-1}.

available aniline derivatives (**1**) and β-diketone or β-diketoester (**2**) as shown in Scheme 1. Reaction of the hydrazonyl chloride **3** with the appropriate aniline derivatives (**4**), followed by air oxidation for the intermediate (**5**) in refluxing ethanol gave the azomethine ligands (**6**–**8**) (Scheme 1). The structures of these ligands were conformed by ^{1}H NMR, mass spectra and elemental analysis.

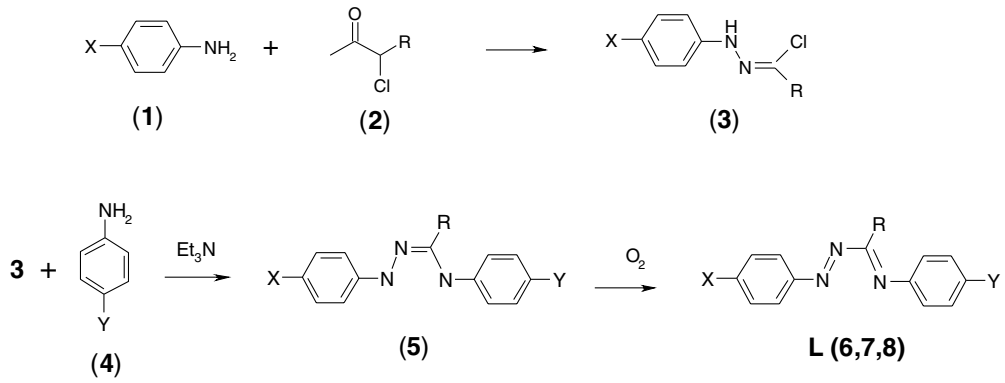
The synthesis of *trans*-[Ru(bpy)LCl_2] was achieved by the stepwise equimolar addition of ruthenium trichloride hydrate, azoimine ligands, bpy and then an excess of lithium chloride (Scheme 2).

These neutral complexes are air stable, soluble in several organic solvents and were recrystallized easily as dark red platelets from slowly evaporating solutions of a mixture of dichloromethane/toluene or acetone. The structures of the diamagnetic complexes were confirmed by ^{1}H NMR spectra and crystallography. The chemical shifts (see Section 2) were assigned on the basis of the literature values and spin–spin interactions. Electron donating or withdrawing substituents on **L** had a respective shielding or deshielding effect on chemical shifts.

The IR spectra of the ligands (see Section 2) exhibit a sharp band at 1660–1712 cm^{-1} corresponds to C=O stretching frequency of the acetyl or the ester group. The formation of the azoimine ligand was confirmed by the intense bands at 1580–1600 and 1470–1490 cm^{-1} which correspond to C=N and N=N stretching bands, respectively. In all complexes, ν(N=N) is red-shifted by 25–30 cm^{-1} compared to that of the ligands, which is a good indication of N-coordination [25].

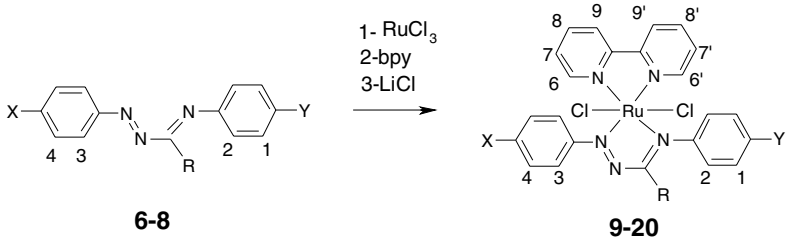
3.2. Crystal structures

Crystallographic data for complexes **13** and **18** are compiled in Table 1 and ORTEP figures of **13** and **18** are shown in Figs. 1 and 2, respectively. In addition, selected inner coordination sphere bond parameters of **13** and **18** are listed in Tables 2. Complex **13** crystallizes in two conformations with some minor differences in bond lengths and angles (see Table 2). The presence of two conformers is suggested to be due the crystallization of toluene in the lattice and to crystal packing forces. The Ru–N [N(azo): N(19) and N(54)] bond distances (average, 1.946 Å) are shorter than the Ru–N [N(methine): N(25) and N(60)] (average, 2.017 Å) bond distance by 0.07 Å and shorter than those of Ru–N(azo) (1.971, 2.014 Å) in other azo-pyridines complexes [25,26]. This shortening may be due to greater π-back donation from Ru-d orbital to the empty π* orbital of the azoimine ligand, and this comes as an indication that the M–L π interaction is localized in the M–azo fragment [9,27]. For complex (**18**), Ru–N(azo) bond distance is 1.959 Å and is shorter than Ru–N(methine) bond distance of 2.024 Å with both slightly longer than the average bond distance of Ru–N(azo) (1.946 Å) and Ru–N(methine) (2.017 Å) of complex (**13**). This is probably due to the electron withdrawing ester group which is attached to azomethine moiety in complex (**18**). As shown in Figs. 1 and 2, the Ru(II) ion of complex **13** and **18** occupies a distorted octahedral coordination sphere in which the chloride ligands are trans to each other and the azomethine and bipyridine nitrogen donor atoms are



L	X	R		Y
6	H	$COCH_3$	a	H
			b	CH_3
			c	Cl
			d	Br
			e	$C_{10}H_7$
			f	OMe
			g	NO_2
7	H	CO_2CH_3	a c	
8	Cl	CO_2CH_3	a c d	

Scheme 1.



Scheme 2.

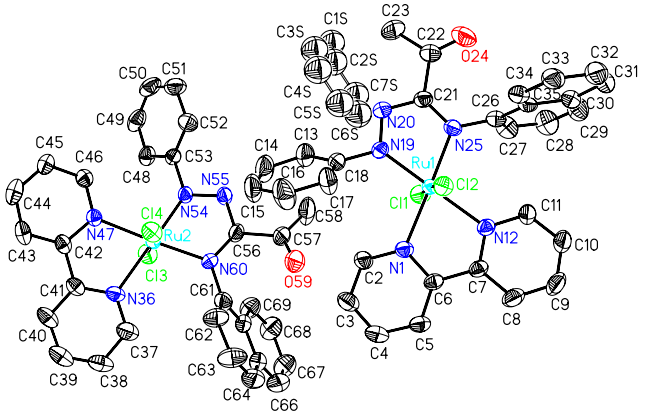


Fig. 1. Thermal ellipsoid drawing (30%) of complex **13** showing the two independent conformations of the Ru complex and the solvent toluene molecule (0.5 occupancy). Hydrogen atoms have been omitted for clarity.

equatorially coordinated. In the equatorial plane, the five-membered rings described by the coordination of an azomethine ligand and of bpy to ruthenium have approximately equivalent coordination bite-angles (Table 2) and deviate considerably from ideal octahedral geometry.

For complexes **13** and **18**, the Ru–N(azo) and Ru–N(methine) distances are shorter than corresponding lengths in similar reported ruthenium azo-imine complexes $(tcc\text{-}Ru(papm)_2Cl_2$ [26] and $tcc\text{-}Ru(aai\text{-}Bz)_2Cl_2$ [25]). This is due to the greater π-back bonding of d(Ru)–π*(azo) and this suggests that the new azomethine bidentate ligands are stronger π-acceptor ligands compared to reported azo-imine ligands [25,26]. The strong π-acidity for these new bidentate ligands are supported by the large positive shift of the Ru(III/II) couple (Table 3) as discussed below.

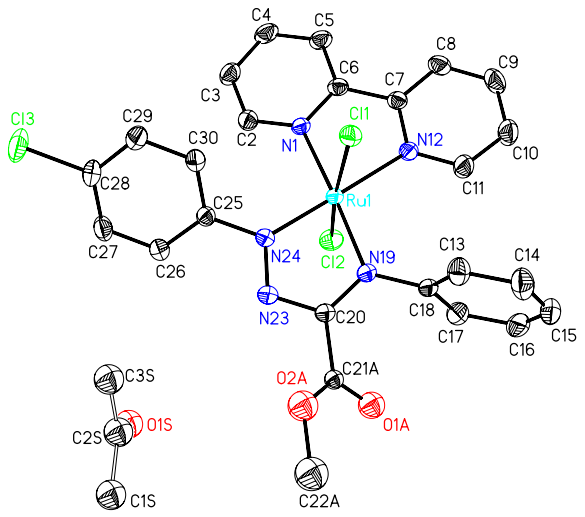


Fig. 2. Thermal ellipsoid plot (30%) of complex **18**. Hydrogen atoms omitted for clarity. The ester group is shown in only one of the disordered conformations (acetone 0.5 occupancy).

3.3. Electrochemistry

The electrochemical behavior of the complexes in acetonitrile was examined by cyclic voltammetry. The results are summarized in Table 3. As a representative example, the cyclic voltammogram for complex **18** is shown in Fig. 3. At positive potentials, the single wave between 1.0 and 1.30 V is assigned to a reversible Ru(III/II) couple. These couples were determined from the average of the anodic and cathodic peak potentials ($E_{1/2}$), where $E_{1/2} = (E_{pa} + E_{pc})/2$ at scan rate of 100 mV. This couple occurs at more positive potentials compared to many dihalide ruthenium(II) complexes [27]. At negative potentials, three one-electron ligand reduction waves were observed between −0.4 and −2.0 V. The two irreversible waves between −0.56 and −0.88 V versus NHE (cathodic wave peak maxima) are assigned to the two electron reduction of the azo group analogous to the azopyridine systems. The LUMO of **L** can accommodate up to two electrons and the reduction may be represented by the following equation [26]:

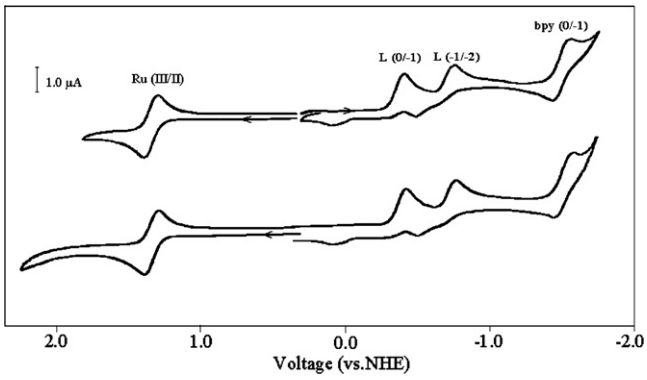
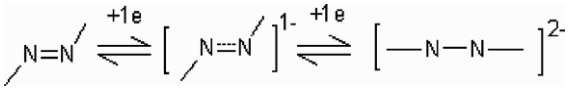


Fig. 3. Cyclic voltammogram for **18** in acetonitrile 0.1 M TBAH at 25 °C, data reported in V vs. NHE with scan rate of 0.1 V/s.



(1)

The wave at the most negative potential scanned (less than −1.60 versus NHE) is assigned to the reduction of bpy. The difference in the ligand reduction potentials can be explained by the greater stability of azo group orbitals compared to that of bpy (see theoretical calculations below). Both Ru(III/II) and the reduction potential for the auxiliary ligand were shifted to more positive potentials upon replacing the acetyl group attached to azomethine moieties with the more withdrawing ester group.

Lever [29] has developed an electrochemical parameterization method to calculate ruthenium(III/II) couples of complexes with octahedral geometry as shown in the following equation:

$$E_{Ru(III/II)} = 0.97\left[\sum E_L\right] + 0.04 \quad \text{in V versus NHE} \qquad (2)$$

where $\sum E_L$ is the sum of electrochemical parameters for each ligand in the complex. The parameter E_L is a measure of the stabilizing effect a ligand has on the Ru(II) state and so the greater the magnitude of positive E_L the more positive the Ru(III/II) couple. For *trans*-[Ru(bpy)LCl$_2$], the E_L of **L** was calculated and listed in Table 3. It is observed that the magnitude of E_L increases as the number of electron withdrawing substituents attached to the azoimine moiety increases. These parameters are approximately the same as those reported for phenylazopyridine ($E_L = 0.40$) and tolylazopyridine ($E_L = 0.41$) but significantly higher than that for the weaker π-acid bpy ($E_L = 0.259$) or for the π-donor chloride ($E_L = -0.24$) [29].

3.4. Electronic structure

Theoretical calculations were performed on **18** using GAUSSIAN-03 program package [16]. Relative percentages of atomic contributions to the lowest unoccupied and highest occupied molecular orbitals have been placed in Table 4. Moreover, the isodensity plots for the HOMOs and LUMOs orbitals of **18** are shown in Fig. 4. Results indicate that the LUMO is constructed mainly from the

Table 4
Relative percentages of atomic contributions to the lowest unoccupied and highest occupied molecular orbitals (LUMO and HOMO) of **18**

MO	Energy (eV)	Ru	bpy	Azo-imine ring	Cl	Others[a]
LUMO − 4	−6.50	5	4	9	57	26
LUMO − 3	−6.47	3	5	6	84	2
LUMO − 2	−6.00	73	2	6	4	15
LUMO − 1	−5.43	33	1	17	45	3
HOMO	−4.93	61	2	5	31	0
LUMO	−2.85	21	20	41	6	12
LUMO + 1	−2.12	10	80	7	3	2
LUMO + 2	−1.39	2	94	0	0	3
LUMO + 3	−1.18	2	96	1	0	2
LUMO + 4	−0.66	14	3	24	5	54

[a] Group attached to azo-imine ring (Cl-Ph, Ph, CO_2CH_3).

π^* orbital of azoimine together with a small contribution from π^* orbital of bpy. In addition, the LUMO has 21% metal d-orbital character which suggests significant back donation [30]. The LUMO + 1, LUMO + 2 and LUMO + 3 are mainly bpy in character. For the HOMOs, the three highest energy orbitals (HOMO, HOMO − 1 and HOMO − 2) have a significant contributions of Ru(dπ) orbitals.

The lowest 10 singlet-to-singlet spin-allowed excitation states were taken into account for the calculation of the electronic absorption spectrum by using TD-DFT method. The calculated energy of excitation states and transition oscillator strength (f) (only $f > 0.005$ is listed) of **18** are shown in Table 5. The absorption spectrum of **18** was simulated using GAUSSSUM software [31] based on the obtained TD-DFT results. Each excited state was interpolated by a Gaussian convolution with the full-width at half-maximum (FWHM) of 3000 cm^{-1}. In good agreement, both simulated absorption spectrum of **18**, Fig. 5, and experimental spectrum, in Fig. 7, show two visible region absorptions. The computed spectrum is for gas phase complexes and shows a moderate red-shift to lower energy transitions because of the absence of solvation effects. For the lower energy band ($\lambda_{max} = 499$ (experimental) and 563 (calculated) nm), the initial states are HOMO − 1 and HOMO − 2 orbitals (Table 5), which have sizable contributions of Ru(dπ) orbitals. The LUMO possesses a significant contribution from the π^* orbital of azomethine and because of this, the lower energy band is assigned to MLCT (Ru(dπ) → π^* azomethine). The shoulder centered at 390 (experimental) and 447 (calculated) nm is assigned to overlapping MLCT and ligand–ligand transitions. The MLCT transition results from Ru(dπ) → bpy(π^*) (or HOMO → LUMO + 2), while the ligand–ligand transition result mainly from the HOMO − 3 and HOMO − 4 which is mainly chloride in character to the azomethine π^* orbital (LUMO).

3.5. Spectroelectrochemistry

The MLCT bands of the complexes exhibit relatively little solvatochromism with a shift to higher values in the hydroxylic solvents compared with nonhydroxylic solvents. This can be attributed to significant metal–ligand orbital mixing [30] while the small shift for MLCT to higher energy can be attributed to more solvation of the dipolar ground state relative to less dipolar excited state by the polar solvent [32].

Spectroelectrochemistry of **11** and **18** in DMF solution (Figs. 6 and 7, respectively) was performed in order to obtain the visible electronic absorption spectra of the Ru(III) oxidation state. Reversibility was indicated by the maintenance of the isosbestic points in the absorption spectrum for both forward (oxidation) and reverse (reduction)

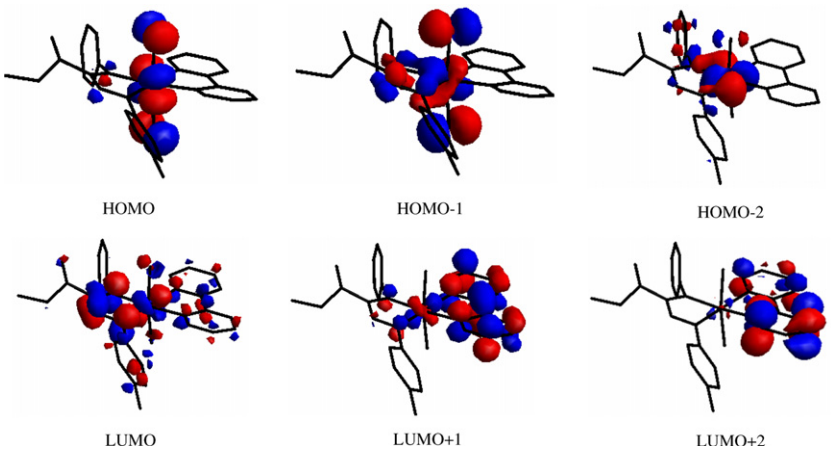


Fig. 4. Isodensity plots (isodensity contour = 0.04) of the HOMO and LUMO orbitals of complex **18**.

Table 5
Computed excitation energies (eV), electronic transition configurations and oscillator strengths (f) for the optical transitions in the visible region of **18** (transitions with $f > 0.005$ are listed)

eV (nm)	f	Composition
1.911 (649)	0.0051	91% HOMO → LUMO + 1, 6% HOMO → LUMO
2.203 (563)	0.0496	38% HOMO − 1 → LUMO, 33% HOMO − 2 → LUMO, 10% HOMO − 1 → LUMO + 1
2.577 (481)	0.0068	75% HOMO − 1 → LUMO + 1, 8% HOMO − 2 → LUMO
2.776 (447)	0.0083	65% HOMO − 3 → LUMO, 14% HOMO → LUMO + 2, 10% HOMO − 4 → LUMO
2.797 (443)	0.0074	77% HOMO → LUMO + 2, 7% HOMO − 4 → L, 6% HOMO − 3 → LUMO
2.804 (442)	0.0115	59% HOMO − 4 → LUMO, 19% HOMO − 3 → LUMO, 11% others

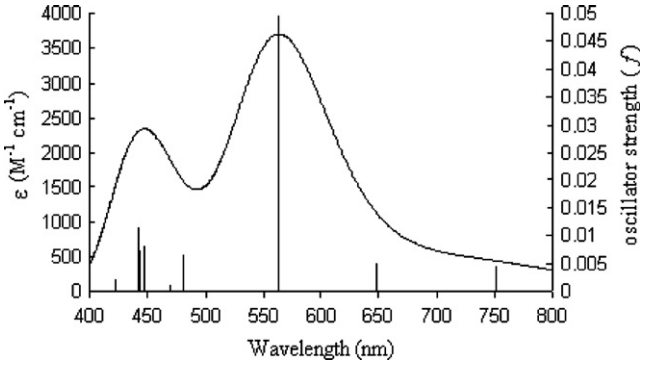


Fig. 5. Simulated absorption spectrum (black line) for **18** based on TD-DFT calculations, compared to excitation energies and oscillator strengths.

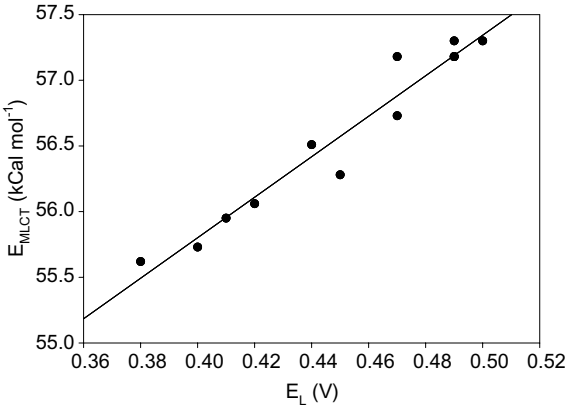


Fig. 8. The correlation between the ligand electrochemical parameter, E_L, and MLCT energy, E_{MLCT}.

processes and the greater than 95% recovery of the Ru(II) complex spectrum. As shown in Figs. 6 and 7, oxidation of these complexes results in a decrease in the intensity of the lower energy band that we have assigned to a MLCT transition. The concomitant growth of absorbance at $\lambda > 550$ nm is assigned to chloride-to-Ru(III) ($p\pi \rightarrow d\pi^*$) ligand-to-metal charge transfer LMCT transitions. The higher energy band at 368 nm ($\varepsilon = 9810\ M^{-1}\ cm^{-1}$) in the absorption spectrum of $\mathbf{11}^+$ (Fig. 6), is only a shoulder in the spectrum of $\mathbf{18}^+$ (Fig. 7), suggesting that the acetyl group of the ligand **6c** participates in the state descriptions responsible for this absorption.

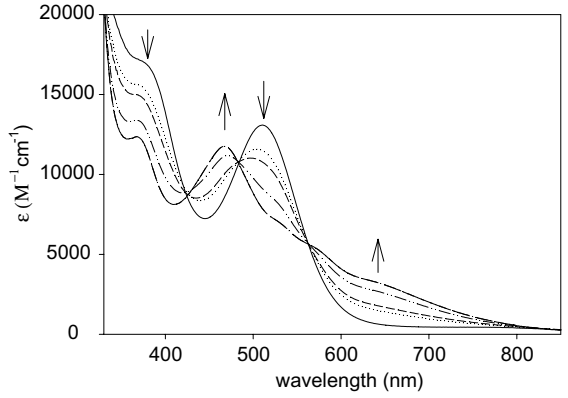


Fig. 6. Spectroelectrochemical oxidation of complex **11** in DMF, 0.1 M TBAH, 25 °C.

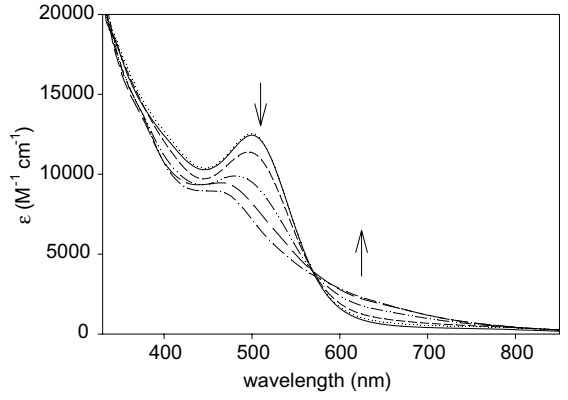


Fig. 7. Spectroelectrochemical oxidation of complex **18** in DMF, 0.1 M TBAH, 25 °C.

The MLCT band of a Ru(II) mononuclear complex and its electrochemistry provide information about the relative energies of the complex's metal and ligand-based orbitals. The change in dπ-orbital energy can be measured experimentally by measuring the potential of the Ru(III/II) couple. For the complexes of this study, acetate azomethine ligands shift the Ru(III/II) couple approximately 100 mV positive relative to their propanone analogues. This can be explained by the enhanced π-acceptor properties of acetate azomethine ligands which originate from the inductive effect of the carboxy methyl ester group. The relationship between MLCT band energy and the ligand electrochemical parameter, E_L(L), for the azomethine ligands (Table 3) is revealed by Fig. 8. The linear correlation that is observed strongly suggests that substitution of the azomethine ligand provides researchers with a useful tool for the fabrication of novel ruthenium(II)–polypyridine complexes that have specific electronic and structural properties.

4. Conclusions

Ten ruthenium(II) complexes, *trans*-[Ru(bpy)LCl_2], where bpy is 2,2′-bipyridine and **L** is a substituted azomethine ligand, were synthesized and characterized by crystallography and spectroscopic and electrochemical methods. Crystallographic studies of **13** and **18** show that bidentate azomethine ligands are strong π-acceptors that coordinate via imine and azo nitrogens. Cyclic voltammetric studies of *trans*-[Ru(bpy)LCl_2] complexes show reversible ruthenium-based oxidation–reduction processes and irreversible ligand-based redox reactions. The electronic effect of the azomethine substituents was seen in the ruthenium and ligand couples, which shifted to more positive values when stronger electron-withdrawing substituents were introduced. The high degree of metal-to-azomethine back dona-

tion is evident from the diminished solvatochromism of the MLCT band which suggests considerable mixing of metal and ligands orbitals [28]. The electronic absorption spectra of these complexes show a strong band in the visible region which is assigned to a $d\pi$-to-$p\pi^*$ (Ru(II)-to-azomethine) MLCT transition based on TD-DFT calculations and spectroelectrochemical correlations. Azomethine ligands are a useful tool for the fabrication of novel ruthenium(II)–polypyridine complexes with specific electronic and structural properties.

5. Supplementary material

CCDC 638037 and 638038 contain the supplementary crystallographic data for **13** and **18**. These data can be obtained free of charge via http://www.ccdc.cam.ac.uk/conts/retrieving.html, or from the Cambridge Crystallographic Data Centre, 12 Union Road, Cambridge CB2 1EZ, UK; fax: (+44) 1223-336-033; or e-mail: deposit@ccdc.cam.ac.uk.

Acknowledgements

Mousa Al-Noaimi thanks the Hashemite University (Jordan) for research support. R.J.C. is grateful to Natural Sciences and Engineering Research Council of Canada for financial support. The Bruker (Siemens) SMART APEX diffraction facility was established at the University of Idaho with the assistance of the NSF-EPSCoR program and the M.J. Murdock Charitable Trust, Vancouver, WA, USA. This work is supported in part by the Deanship of Academic Research, The University of Jordan.

References

[1] J. Reedijk, in: G. Wilkinson, R.D. Gillard, J.A. McCleverty (Eds.), Comprehensive Coordination Chemistry, vol. 2, Pergamon Press, Oxford, 1987, p. 73.
[2] E.C. Constable, P.J. Steel, Coord. Chem. Rev. 106 (1990) 227.
[3] T. Yamato, Z. Zhou, T. Kanbara, M. Shimura, K. Kizu, T. Maryyama, T. Takamura, T. Fukuida, B. Lee, N. Ooba, S. Tomaru, T. Kurihara, T. Kaino, K. Kubota, S. Sasaki, J. Am. Chem. Soc. 118 (1996) 10389.
[4] F. Casalboni, Q.G. Mulazzani, C.D. Clark, M.Z. Hoffman, P.L. Orizando, M.W. Perkovic, D.P. Rillema, Inorg. Chem. 36 (1997) 2252.
[5] R. Llanguri, J.J. Morris, W.C. Stanley, E.T. Bell-Loncella, M. Turner, W.J. Boyko, C.A. Bessel, Inorg. Chim. Acta 315 (2001) 53.
[6] X.-J. Yang, C. Janiak, J. Heinze, F. Drepper, P. Mayer, H. Piotrowski, P. Klufers, Inorg. Chim. Acta 318 (2001) 103.
[7] J. Sherborne, S.M. Scott, K.C. Gordon, Inorg. Chim. Acta 260 (1997) 199.
[8] K.R. Barqawi, A. Llobet, T.J. Meyer, J. Am. Chem. Soc. 110 (1988) 7751.
[9] W. Kaim, Coord. Chem. Rev. 219–221 (2001) 463.
[10] J. Otsuki, K. Sato, M. Tsvjino, N. Okuda, K. Araki, M. Seno, Chem. Lett. (1996) 847.
[11] V.W.-W. Yam, V.C.-Y. Lau, K.-K. Cheung, J. Chem. Soc., Chem. Commun. (1995) 259.
[12] M. Al-Noaimi, R.J. Abdel-Jalil, S. Haddad, R. Al-Far, R.J. Crutchley, Inorg. Chim. Acta 359 (2006) 2395.
[13] N.F. Eweiss, A. Osman, J. Heterocycl. Chem. 17 (1980) 1713.
[14] T. Gennett, D.F. Milner, M.J. Weaver, J. Phys. Chem. 89 (1985) 2787.
[15] (a) M. Kejeik, M. Danek, F. Hartl, J. Electroanal. Chem. 317 (1991) 179;
(b) C. Evans, Ph.D. Thesis Carleton University, 1997.
[16] M.J. Frisch et al., GAUSSIAN-03, Revision B.03, Gaussian Inc., Pittsburgh, PA, 2003.
[17] A.D. Becke, J. Chem. Phys. 98 (1993) 5648.
[18] C. Lee, W. Yang, R.G. Parr, Phys. Rev. B 37 (1988) 785.
[19] E. Runge, E.K.U. Gross, Phys. Rev. Lett. 52 (1984) 997.
[20] M.K. Casida, in: D.P. Chong (Ed.), Recent Advances in Density Functional Methods, vol. 1, World Scientific, Singapore, 1995, p. 155.
[21] APEX2: v2.1-RC12, Bruker AXS, Madison, WI, 2006.
[22] SAINTPlus: v. 7.23a, Data Reduction and Correction Program, Bruker AXS, Madison, WI, 2004.
[23] SADABS: v.2004/1, An Empirical Absorption Correction Program, Bruker AXS Inc., Madison, WI, 2004.
[24] G.M. Sheldrick, SHELXTL: v. 6.14. Structure Determination Software Suite, Bruker AXS Inc., Madison, WI, 2004.
[25] P.K. Santra, T.K. Misra, D. Das, C. Sinha, A.M.Z. Slawin, J.D. Woollins, Polyhedron 18 (1999) 2869.
[26] T.K. Misra, D. Das, C. Sinha, P. Ghosh, C.K. Pal, Inorg. Chem. 37 (1998) 1672.
[27] S. Goswami, L.F. Falvello, A. Chakravorty, Inorg. Chem. 26 (1987) 3365.
[28] B.K. Ghosh, A. Mukhopadhyay, S. Goswami, S. Ray, A. Chakravorty, Inorg. Chem. 23 (1984) 4633.
[29] A.B.P. Lever, Inorg. Chem. 29 (1990) 1271.
[30] S.I. Gorelsky, A.B.P. Lever, M. Ebadi, Coord. Chem. Rev. 230 (2002) 97.
[31] N.M. O'Boyle, GAUSSSUM 2.0, 2006. Available from: <http://gausssum.sf.net>.
[32] (a) P. Byabartta, Transition Met. Chem. 30 (2005) 738;
(b) B.K. Santra, G.A. Thakur, P. Ghosh, A. Pramanik, G.K. Lahiri, Inorg. Chem. 35 (1996) 3050;
(c) A. Saha, P. Majumdar, S.-M. Peng, S. Goswami, Eur. J. Inorg. Chem. (2000) 2631;
(d) N.C. Pramanik, S. Bhattacharya, Transition Met. Chem. 22 (1997) 524;
(e) M. Shivakumar, K. Pramanik, I. Bhattacharya, A. Chakravorty, Inorg. Chem. 39 (2000) 4332.

with quinoline-2-carboxylic acid. Quinoline-2-carboxylic acid is the biological compound involved in the metabolism of tryptophan. It is a strong chelator providing the donor set similar to that responsible for binding metal ion in PQQ (pyrroloquinilnequinone) cofactor of quinoprotein family [9].

Here, we present synthesis and spectroscopic data for $[ReOCl_2(quin\text{-}2\text{-}c)(PPh_3)]$ (**1**), $[ReOBr_2(quin\text{-}2\text{-}c)(PPh_3)]$ (**2**), $[ReOCl_2(quin\text{-}2\text{-}c)(AsPh_3)]$ (**3**) and $[ReOBr_2(quin\text{-}2\text{-}c)(AsPh_3)]$ (**4**) complexes. X-ray studies have been performed for **1** and **4**, and electronic structure of **1** has been calculated with the density functional theory (DFT). The singlet–singlet electronic transitions of **1** have been calculated with the time-dependent DFT method (TD-DFT method), and the UV–Vis spectra of these complexes have been discussed on this basis.

Currently, density functional theory (DFT) is commonly used to examine the electronic structure of transition metal complexes. It meets with the requirements of being accurate, easy to use and fast enough to allow the study of relatively large molecules of transition metal complexes [10]. Recent calculations with TD-DFT method for open- and closed-shell of 5d-metal complexes (including rhenium complexes) have also supported the TD-DFT method to be applicable for such systems giving good assignment of experimental spectra [11,12].

Some theoretical investigations have been carried out on rhenium compounds. The electronic structures of nitrido, oxo, carbonyl, nitrosyl and nitrile rhenium complexes, as well as their spectroscopic properties, bonding and reactivity have been theoretically studied at the HF, MP2, EHT and DFT levels of theory using various basis sets [13–22]. Gancheff and co-workers [15] have performed extended tests of the ability of the B3LYP method in LANL2DZ basis set for rhenium compounds in a geometry optimization and calculation of spectral properties. Although this is not a very extended basis set, its use with DFT has shown to be sufficient for the geometry optimization and calculation of spectral properties. It gives good agreement with the experimental data and its use is justified in the case of large molecules.

2. Experimental

2.1. General procedure

The reagents used to the synthesis were commercially available and were used without further purification. The $[ReOX_3(AsPh_3)_2]$ and $[ReOX_3(PPh_3)_2]$ complexes were prepared according to the literature methods [23].

IR spectra were recorded on a Nicolet Magna 560 spectrophotometer in the spectral range 4000–400 cm^{-1} with the samples in the form of KBr pellets. Electronic spectra were measured on a spectrophotometer Lab Alliance UV–VIS 8500 in the range 1000–180 nm in chloroform solution. Elemental analyses (C,H,N) were performed on a Perkin-Elmer CHN-2400 analyzer.

2.2. Preparation of $[ReOCl_2(quin\text{-}2\text{-}c)(PPh_3)]$ (**1**)

A mixture of $[ReOCl_3(PPh_3)_2]$ (0.50 g, 0.6 mmol), quinoline-2-carboxylic acid (0.12 g, 0.69 mmol) and acetone (50 ml) was stirred at room temperature for 3 h. Half of the solvent was removed and diethyl ether (50 ml) was added to precipitate the product as a green solid, which was filtered off and dried. Yield: 85%. Crystals suitable for X-ray investigation were obtained by recrystallization from acetonitrile.

Anal. Calc. for $C_{28}H_{21}Cl_2NO_3PRe$: C, 47.53; H, 2.99; N, 1.98. Found: C, 47.70; H, 3.06; N, 2.05%.

2.3. Preparation of $[ReOBr_2(quin\text{-}2\text{-}c)(PPh_3)]$ (**2**)

A procedure similar to that for $[ReOCl_2(quin\text{-}2\text{-}c)(PPh_3)]$ was used with $[ReOBr_3(PPh_3)_2]$ (0.50 g, 0.52 mmol and quinoline-2-carboxylic acid (0.10 g, 0.58 mmol). Crystalline precipitate of $[ReOBr_2(quin\text{-}2\text{-}c)(PPh_3)]$ was collected in 80% yield.

Anal. Calc. for $C_{28}H_{21}Br_2NO_3PRe$: C, 42.22; H, 2.66; N, 1.76. Found: C, 42.35; H, 2.72; N, 1.84%.

2.4. Preparation of $[ReOCl_2(quin\text{-}2\text{-}c)(AsPh_3)]$ (**3**)

A procedure similar to that for $[ReOCl_2(quin\text{-}2\text{-}c)(PPh_3)]$ was used with $[ReOCl_3(AsPh_3)_2]$ (0.50 g, 0.54 mmol) and quinoline-2-carboxylic acid (0.11 g, 0.64 mmol). Crystalline precipitate of $[ReOCl_2(quin\text{-}2\text{-}c)(AsPh_3)]$ was collected in 80% yield.

Anal. Calc. for $C_{28}H_{21}Cl_2NO_3AsRe$: C, 44.75; H, 2.82; N, 1.86. Found: C, 44.68; H, 2.92; N, 1.85%.

2.5. Preparation of $[ReOBr_2(quin\text{-}2\text{-}c)(AsPh_3)]$ (**4**)

A procedure similar to that for $[ReOCl_2(quin\text{-}2\text{-}c)(PPh_3)]$ was used with $[ReOBr_3(AsPh_3)_2]$ (0.50 g, 0.47 mmol) and quinoline-2-carboxylic acid (0.10 g, 0.58 mmol). Yield: 85%. Crystals suitable for X-ray investigation were obtained by recrystallization from acetonitrile.

Anal. Calc. for $C_{28}H_{21}Br_2NO_3AsRe$: C, 40.02; H, 2.52; N, 1.67. Found: C, 40.22; H, 2.63; N, 1.69%.

2.6. Crystal structures determination and refinement

The X-ray intensity data of **1** and **4** were collected on a KM-4-CCD automatic diffractometer equipped with CCD detector and graphite monochromated Mo Kα radiation ($\lambda = 0.71073$ Å) at room temperature. Details concerning crystal data and refinement are given in Table 1. Lorentz, polarization and absorption correction [24] were applied. The structures were solved by the Patterson method and subsequently completed by the difference Fourier recycling. All the non-hydrogen atoms were refined anisotropically using full-matrix, least-squares technique. The hydrogen atoms were treated as "riding" on their parent carbon atoms and assigned isotropic temperature factors equal

Table 1
Crystal data and structure refinement for **1** and **4** complexes

	1	**4**
Empirical formula	$C_{28}H_{21}Cl_2NO_3PRe$	$C_{28}H_{21}Br_2NO_3AsRe$
Formula weight	707.53	840.40
Temperature (K)	291.0(3)	291.0(3)
Wavelength (Å)	0.71073	0.71073
Crystal system	monoclinic	monoclinic
Space group	$P2_1/c$	$P2_1/c$
Unit cell dimensions		
a (Å)	9.8397(2)	10.4564(4)
b (Å)	31.9248(4)	15.5067(7)
β (°)	109.087(2)	96.508(4)
c (Å)	8.7523(2)	16.9885(8)
Volume (Å^3)	2598.21(9)	2736.8(2)
Z	4	4
D_{calc} (Mg/m^3)	1.809	2.040
Absorption coefficient (mm^{-1})	4.975	8.590
F(000)	1376	1592
Crystal size (mm)	$0.081 \times 0.080 \times 0.077$	$0.579 \times 0.262 \times 0.133$
θ Range for data collection (°)	2.53–25.17	3.21–25.12
Index ranges	$-11 \leqslant h \leqslant 11$, $-38 \leqslant k \leqslant 38$, $-10 \leqslant l \leqslant 10$	$-12 \leqslant h \leqslant 12$, $-18 \leqslant k \leqslant 18$, $-20 \leqslant l \leqslant 20$
Reflections collected	28075	28206
Independent reflections [R_{int}]	4661 [0.0254]	4876 [0.0374]
Completeness to $2\theta = 50°$ (%)	99.8	99.7
Minimum and maximum transmission	0.677 and 0.684	0.091 and 0.376
Data/restraints/parameters	4661/0/325	4876/0/325
Goodness-of-fit on F^2	1.065	1.160
Final R indices [$I > 2\sigma(I)$]	$R_1 = 0.0201$ $wR_2 = 0.0411$	$R_1 = 0.0251$ $wR_2 = 0.0495$
R indices (all data)	$R_1 = 0.0301$ $wR_2 = 0.0445$	$R_1 = 0.0289$ $wR_2 = 0.0508$
Largest difference in peak and hole (e Å^{-3})	0.959 and −0.710	0.499 and −0.842

1.2 times the value of equivalent temperature factor of the parent atom. SHELXS 97 [25], SHELXL 97 [26] and SHELXTL [27] programs were used for all the calculations. Atomic scattering factors were those incorporated in the computer programs.

3. Computational details

GAUSSIAN 03 program [28] was used in the calculations. The geometry of **1** was optimized in singlet state with the DFT method with the use of B3LYP functional [29,30]. The electronic spectrum of **1** was calculated with the TDDFT method [31]. The calculations were performed by using ECP basis set on the rhenium atom, and the standard 6-31G basis set for others. For chloride, oxygen, phosphorous and nitrogen atoms, diffuse and polarization functions were added [32,33]. The Xe core electrons of Re were replaced by an effective core potential and DZ quality Hay and Wadt Los Alamos ECP basis set (LANL2DZ) [34] was used for the valence electrons. Additional d function with exponent $\alpha = 0.3811$ and f function with exponent $\alpha = 2.033$ on the rhenium atom were added [35].

Natural bond orbital (NBO) calculations were performed with the NBO code [36] included in GAUSSIAN 03.

4. Results and discussion

4.1. Preparation and infrared data

The $[ReOX_2(quin\text{-}2\text{-}c)(EPh_3)]$ (X = Cl, Br; E = As, P) complexes were prepared in good yields by ligand exchange reactions starting from $[ReOX_3(EPh_3)_2]$ complexes and quinoline-2-carboxylic acid in acetone:

$$[ReOX_3(EPh_3)_2] + \text{quin-2-cH} \rightarrow [ReOX_2(\text{quin-2-c})(EPh_3)] + HX + EPh_3, \quad X = Cl, Br; E = As, P$$

They were isolated as green microcrystalline solids, soluble in common organic solvents.

The selected frequencies observed in the IR spectra of $[ReOX_2(quin\text{-}2\text{-}c)(EPh_3)]$ complexes are collected in Table 2. The values of $\Delta\nu(CO_2) = \nu_{as}(CO_2) - \nu_s(CO_2)$ are equal to ≈370 cm^{-1} for $[ReOX_2(quin\text{-}2\text{-}c)(EPh_3)]$ compounds, and indicate that the carboxylate group binds in a monodentate fashion [37].

The strong ν(Re=O) stretching bands of $[ReOX_2(quin\text{-}2\text{-}c)(EPh_3)]$ compounds are in the higher end of the range observed for $\{ReO\}^{3+}$ core complexes. This suggests that the Re-carboxylate bond *trans* to the oxo ligand does not compete effectively for the d_{Re} orbitals and the bond is relatively weak. Moreover, the narrow range in which the ν(Re=O) bands appear is very similar to those observed for Re(V)-oxo complexes with an monoanionic oxygen (RO^- and $R\text{–}COO^-$,) *trans* to the oxo group [38].

Table 2
Selected IR frequencies (cm^{-1}) values of $[ReOX_2(qiun\text{-}2\text{-}c)(EPh_3)]$ complexes

Complex	ν(Re=O)	ν_{as}(COO)	ν_s(COO)
1	996	1689	1318
2	990	1693	1320
3	987	1691	1319
4	988	1692	1320

Table 3
Analysis of short contacts between the quinoline rings and triphenyl phospine ring (distances in Å and angles in °)

R(I)	R(J)	Cg···Cg	α	β	d_p
1					
Cg(1)	Cg(3)	3.7306	11.61	23.38	3.183
Cg(2)	Cg(3)	5.2775	3.32	53.90	3.034
2					
Cg(1)	Cg(4)	3.9641	26.29	16.07	3.146
Cg(2)	Cg(4)	5.1335	24.82	41.08	2.249

R_1, R_2, R_3, R_4 indicates the centroids of aromatic rings containing N(1), C(24), C(13), C(1) atoms, respectively, α is a dihedral angle between planes I and J, β is an angle between Cg(I)–Cg(J) vector and normal to plane I and d_p is a perpendicular distance of Cg(I) on ring J plane.

4.2. Crystal structures

Both complexes crystallise in the monoclinic space group $P2_1/c$. Although the crystal packing motives are different in compounds **1** and **4**, both molecules are isomorphic in solid state.

The classical hydrogen bonds cannot be found in the structures **1** and **4**, only some C–H···O weak inter- and intramolecular hydrogen bonds exist [39]. Additionally in

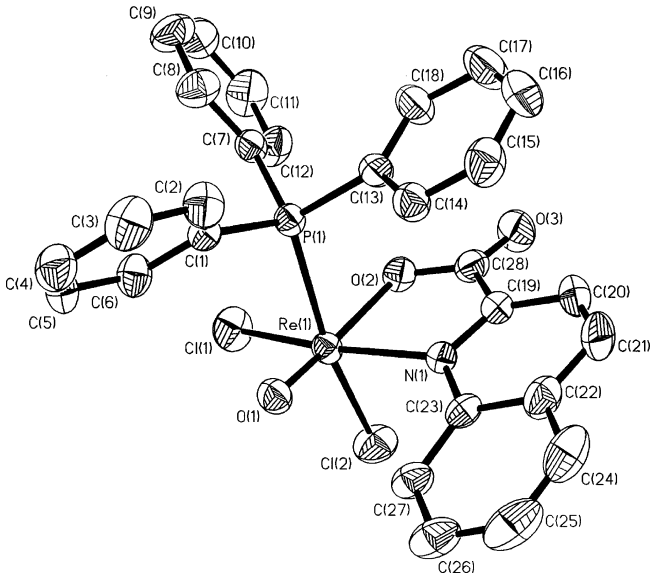


Fig. 1. The molecular structure of **1**. Displacement ellipsoids are drawn at 50% probability.

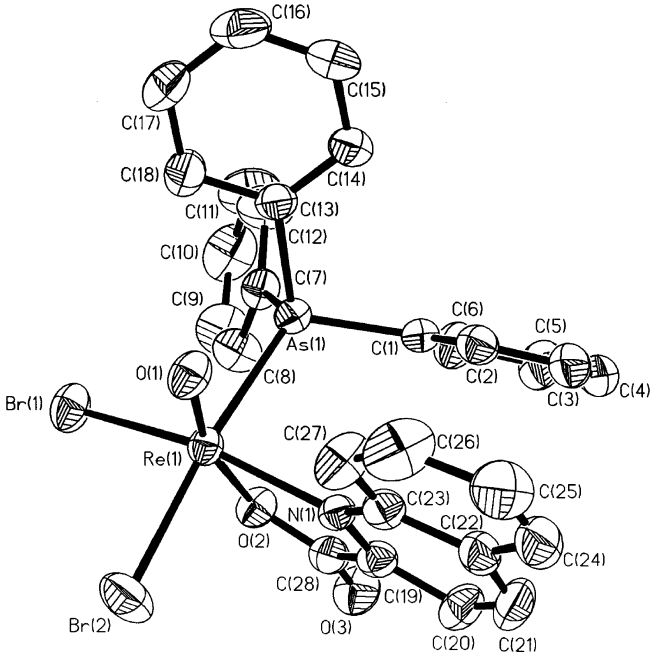


Fig. 2. The molecular structure of **4**. Displacement ellipsoids are drawn at 50% probability.

Table 4
The experimental and optimized bond lengths (Å) and angles (°) for **1**

Bond lengths	Experimental	Optimized
Re(1)–O(1)	1.6679(19)	1.677
Re(1)–O(2)	2.048(2)	2.047
Re(1)–N(1)	2.168(3)	2.218
Re(1)–Cl(1)	2.3368(9)	2.395
Re(1)–Cl(2)	2.3601(8)	2.422
Re(1)–P(1)	2.4839(8)	2.556
O(1)–Re(1)–O(2)	161.91(9)	159.36
O(1)–Re(1)–N(1)	93.07(9)	93.29
O(2)–Re(1)–N(1)	75.22(8)	74.36
O(1)–Re(1)–Cl(1)	100.78(7)	102.85
O(2)–Re(1)–Cl(1)	91.89(6)	91.24
N(1)–Re(1)–Cl(1)	165.93(7)	163.33
O(1)–Re(1)–Cl(2)	105.20(7)	104.78
O(2)–Re(1)–Cl(2)	87.90(6)	90.43
N(1)–Re(1)–Cl(2)	85.68(7)	83.42
Cl(1)–Re(1)–Cl(2)	88.28(3)	88.42
O(1)–Re(1)–P(1)	87.42(7)	86.87
O(2)–Re(1)–P(1)	79.62(6)	78.63
N(1)–Re(1)–P(1)	93.02(6)	97.54
Cl(1)–Re(1)–P(1)	90.10(3)	87.56
Cl(2)–Re(1)–P(1)	167.36(3)	168.26

Table 5
The experimental bond lengths (Å) and angles (°) for **4**

Bond lengths	Experimental
Re(1)–O(1)	1.675(2)
Re(1)–O(2)	2.061(2)
Re(1)–N(1)	2.185(3)
Re(1)–Br(1)	2.4872(4)
Re(1)–Br(2)	2.4992(5)
Re(1)–As(1)	2.5807(4)
O(1)–Re(1)–O(2)	164.05(12)
O(1)–Re(1)–N(1)	96.90(11)
O(2)–Re(1)–N(1)	75.24(10)
O(1)–Re(1)–Br(1)	100.52(9)
O(2)–Re(1)–Br(1)	88.15(7)
N(1)–Re(1)–Br(1)	162.53(7)
O(1)–Re(1)–Br(2)	103.54(10)
O(2)–Re(1)–Br(2)	89.80(7)
N(1)–Re(1)–Br(2)	85.25(7)
Br(1)–Re(1)–Br(2)	89.387(16)
O(1)–Re(1)–As(1)	86.78(10)
O(2)–Re(1)–As(1)	79.79(7)
N(1)–Re(1)–As(1)	92.25(7)
Br(1)–Re(1)–As(1)	90.050(14)
Br(2)–Re(1)–As(1)	169.591(15)

Table 6
Atomic charges from the natural population analysis (NPA) for **1**

Atom	Charge
Re(1)	1.025
O(1)	−0.453
O(2)	−0.715
N(1)	−0.458
Cl(1)	−0.350
Cl(2)	−0.400
P(1)	1.399

the structures **1** and **4** exist π···π stacking interactions between the quinoline rings and one of the triphenyl phospine rings. (Table 3) [40].

The molecular structures of **1** and **4** are presented in Figs. 1 and 2, and the selected bond distances and angles are collected in Tables 4 and 5, respectively.

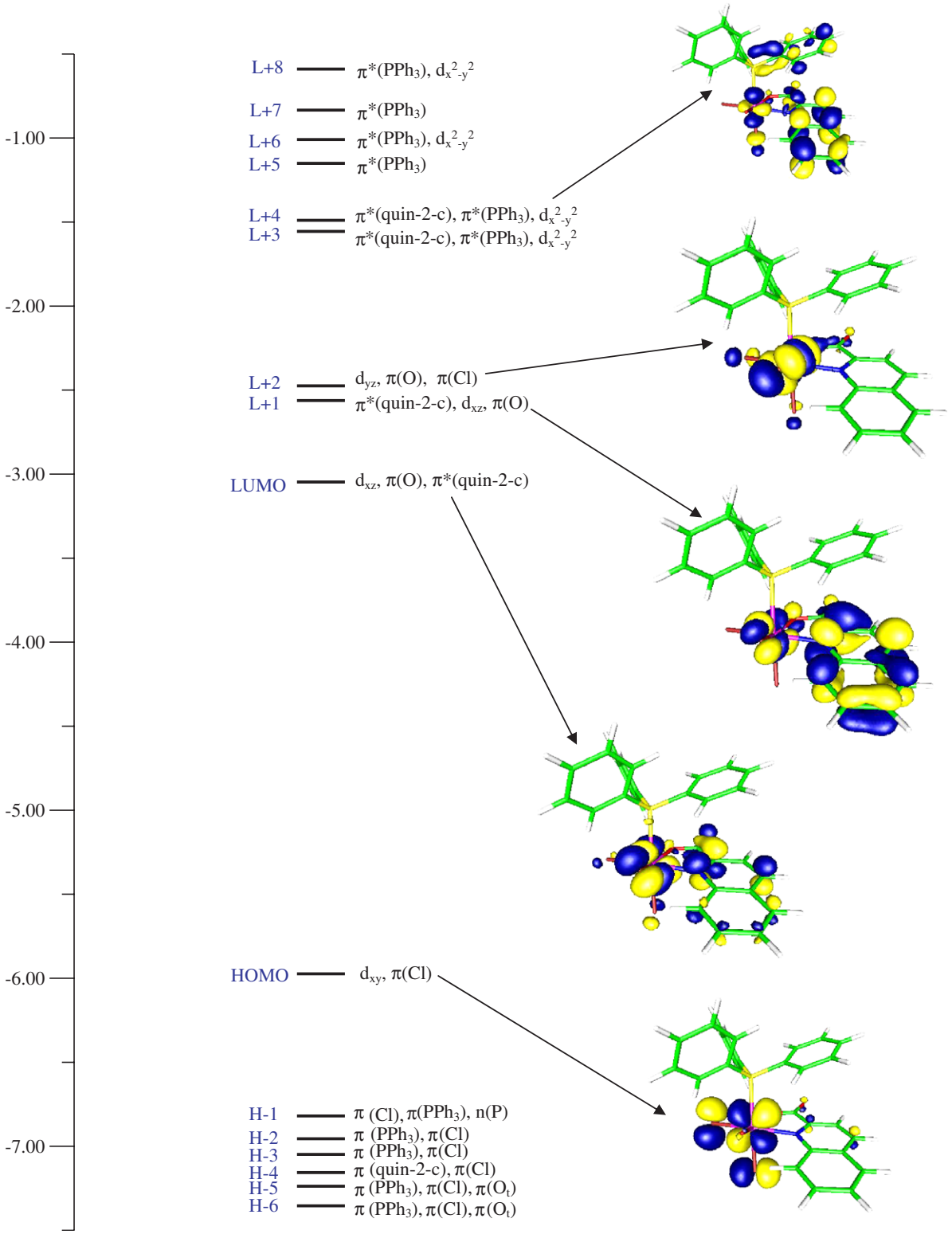


Fig. 3. The energy (eV), character and some contours of the unoccupied molecular orbitals of **1**. Positive values of the orbital contour are represented in blue (0.04 au) and negative values – in yellow (−0.04 au). (For interpretation of the references to colour in this figure legend, the reader is referred to the web version of this article.)

Table 7
The occupancy of the calculated natural bond orbitals (NBOs) between the rhenium and the oxo ligand for **1**

BD	Occupancy	BD	BD*	Occupancy
Re–O_t	1.989	$0.558(d)_{Re} + 0.830(p)_O$	$0.830(d)_{Re} - 0.558(p)_O$	0.271
Re–O_t	1.982	$0.573(d)_{Re} + 0.820(p)_O$	$0.820(d)_{Re} - 0.573(p)_O$	0.272

BD denotes 2-center bond.
* Denotes antibond NBO.

The geometry of $[ReOX_2(quin\text{-}2\text{-}c)(EPh_3)]$ compounds reveals typical features of quasi-octahedral oxorhenium(V)complexes with oxygenated bidentate ligands. For complex **1**, the rhenium atom is displaced 0.2234(7) Å from the plane formed by the two chloride, one nitrogen and one phosphorous atoms (plane A) and 0.0919(8) and 0.0654(10) Å from the planes formed respectively by the two oxygen, one chloride and one phosphorous atoms (plane B) and two oxygen, one chloride and one nitrogen atoms (plane C). Least squares plane A is inclined at 87.52(5)° to plane B and at 88.29(4)° to plane C. Planes B and C are inclined at 89.41(23)°. These values in **4** are respectively, 0.2869(7), 0.0748(9), and 0.0751(12) Å, 87.95(6)°, 88.68(6)° and 89.14(4)°. The deformation of the octahedron is caused by the presence multiple bonding ligand (terminal oxo) and narrow bite angle of the chelating ligand. The high concentration of electronic density along the Re—O_t axis strongly influences the positions of the adjacent halogen atoms, which are pushed away. In each complex, the rhenium atom is coordinated by a terminal oxygen atom (O_t), two halide ions in *cis* arrangement, the phosphorus or arsine atom from EPh_3 molecule, and the bidentate *N*,*O* donors of the carboxylate ligand. The oxygen atom of *quin-2-c* ligand lies in *trans* position to the terminal oxo ion.

The Re–O_t bond lengths of $[ReOX_2(quin\text{-}2\text{-}c)(EPh_3)]$ complexes fall in the range 1.639–1.76 Å, typical of mononuclear complexes of rhenium(V) having $[ReO]^{3+}$ core, and indicate the presence of a triple bond Re≡O [41]. The interatomic distances between the rhenium atom and the oxygen atom of carboxylate ligand are almost equal to an ideal single Re–O bond length. The last one, predicted by the use of Pauling's covalent radius for oxygen and Cotton and Lippard's value for the octahedral covalent radius of rhenium(V), should be ca. 2.04 Å [42].

Table 8
Band position [nm] and molar absorption coefficient [$dm^3\,mol^{-1}\,cm^{-1}$] (in brackets) of $[ReOX_2(qiun\text{-}2\text{-}c)(EPh_3)]$ complexes

1	2	3	4
856.3 (55)	827.1 (80)	847.1 (75)	898.8 (60)
692.7 (130)	694.4 (170)	706.9 (185)	708.5 (180)
429.6 (3520)	430.7 (4320)	430.4 (2770)	420.4 (2880)
376.7 (4060)	370.3 (5680)	370.0 (3060)	369.9 (3220)
274.8 (20550)	285.2 (16900)	314.8 (13515)	286.0 (13200)
238.5 (175200)	241.5 (128320)	239.9 (14130)	239.9 (117380)
207.9 (180750)	210.7 (176670)	207.4 (190225)	210.8 (165650)

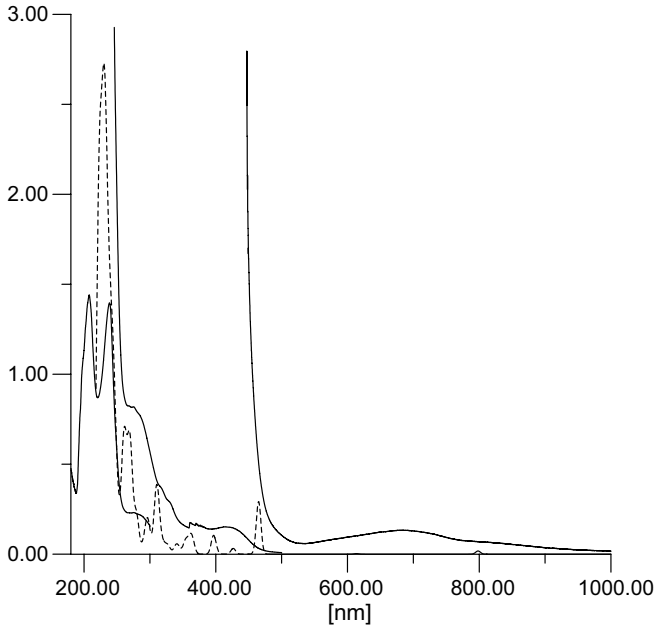


Fig. 4. The experimental (——) and calculated (----) electronic absorption spectra of **1**.

The Re(1)–X(1) distances *trans* to the phosphorus or arsine atom of EPh_3 molecule are slightly longer than the Re(1)–X(2) bonds *trans* to the nitrogen atom of the *quin-2-c* ligand. It indicates *structural trans* effect of the EPh_3 ligands.

4.3. Geometry optimisation, charge distribution, electronic structure and NBO analysis

The geometry of **1** was optimised in a singlet state by the DFT method with the B3LYP functional. The optimized geometric parameters of **1** are gathered in Table 4. In general, the predicted bond lengths and angles are in agreement with the values based upon the X-ray crystal structure data, and the general trends observed in the experimental data (discussed above) are well reproduced in the calculations. The plane A is inclined at 87.96° to plane B and at 89.00° to plane C. Planes B and C are inclined at 87.23°.

Table 6 presents the atomic charges from the Natural Population Analysis (NPA) for **1**. The calculated charge on the rhenium atom in **1** is considerable lower than the formal charge +5, corresponding d^2 configuration of the central ion. The populations of the d_{xy}, d_{xz}, d_{yz}, $d_{x^2-y^2}$ and d_{z^2} rhenium orbitals equal to 1.071, 0.842, 0.824,

1.898 and 0.883 also significantly differ from the formal d^2 configuration of the rhenium atom in **1**. It results from charge donation from the oxo ligands, halide ions and phosphine molecule. ligands. The P atom is positively charged, and the charges on the terminal oxo, halide and oxygen atom of *quin-2-c* are significantly smaller than −2, −1 and −1, respectively. The terminal oxo ions are less negative in comparison with the oxygen atoms of *quin-2-c* ligand. It indicates the higher electron density delocalization from the terminal ligand towards the rhenium center and corresponds to differences in the Re–O(1) and Re–O(2) bond lengths.

The $[ReOX_2(quin\text{-}2\text{-}c)(EPh_3)]$ complexes are closed-shell structures. The molecular orbital diagram of **1** with several occupied and unoccupied molecular orbital contours is presented in Fig. 3. The local symmetry of the rhenium centre has been considered in the discussion: *z*-axis goes along the O–Re–O linkage, and *x*-axis – through the P–Re–Cl bonds. The HOMO–LUMO gap equals to 2.93 eV. The highest occupied MO is of d_{xy} type with some contributions from p_π chloride orbitals. The remaining four d-type orbitals of rhenium are found among unoccupied MOs. It confirms d^2 configuration of the rhenium atoms in $[ReOX_2(quin\text{-}2\text{-}c)(EPh_3)]$ complexes.

The rhenium–terminal oxygen interaction in **1** is described as a triple bond. Assuming that rhenium uses its six valence orbitals, $5d_{x^2-y^2}$, $5d_{z^2}$, 6s, $6p_x$, $6p_y$ and $6p_z$ to form σ-bonds with the six ligands, empty $5d_{xz}$ and $5d_{yz}$ orbitals are available to overlap with $2p_x$ and $2p_y$ orbitals on the terminal oxygen to form an effective triple bond. The LUMO and LUMO + 2 (Fig. 3) are ascribed as π-antibonding rhenium–oxygen molecular orbitals.

Additional information about nature rhenium-terminal oxygen bonding has been obtained by NBO analysis. The occupancy and composition of the calculated $Re–O_t$ natural bond orbitals (NBOs) are given in Table 7.

Table 9
The energy and molar absorption coefficients of experimental absorption bands and the electronic transitions calculated with the TDDFT method for **1**

The most important orbital excitations	Character	λ (nm)	*E* (eV)	*f*	Experimental Λ (nm) (*E* (eV))ε
H → L	d → d/π*(quin-2-c)	798.3	1.55	0.0025	856.3 (1.45) 55
H → L+2	d → d	613.7	2.02	0.0004	692.7 (2.02) 130
H → L+1	d → π*(quin-2-c)/d	465.0	2.67	0.0417	429.6 (2.89) 3520
H−1 → L	π(Cl)/π(PPh_3)/n(P) → d/π*(quin-2-c)	426.4	2.91	0.0045	
H−2 → L	π(Cl)/π(PPh_3) → d/π*(quin-2-c)	396.4	3.13	0.0141	376.7 (3.29) 4060
H−1 → L+2	π(Cl)/π(PPh_3)/n(P) → d	365.2	3.39	0.0058	
H−3 → L	π(PPh_3)/π(Cl) → d/π*(quin-2-c)	362.6	3.42	0.0073	
H−4 → L	π(quin-2-c)/π(Cl) → d/π*(quin-2-c)				
H−3 → L	π(PPh_3)/π(Cl) → d/π*(quin-2-c)	359.3	3.45	0.0066	
H−4 → L	π(quin-2-c)/π(Cl) → d/π*(quin-2-c)				
H−5 → L	π(PPh_3)/π(Cl)/π(O) → d/π*(quin-2-c)	353.7	3.51	0.0095	
H−4 → L+1	π(quin-2-c)/π(Cl) → π*(quin-2-c)/d	312.0	3.97	0.0218	274.8 (4.51) 20550
H−11 → L	π(quin-2-c)/π(Cl) → d/π*(quin-2-c)	309.6	4.00	0.0244	
H−11 → L+1	π(quin-2-c)/π(Cl) → π*(quin-2-c)/d	279.6	4.44	0.0252	
H−1 → L+3	π(Cl)/π(PPh_3)/n(P) → π*(quin-2-c)/π*(PPh_3)	268.9	4.61	0.0583	
H−13 → L+1	π(Cl)/π(PPh_3)/n(P) → π*(quin-2-c)/d	261.9	4.73	0.0297	
H−1 → L+4	π(Cl)/π(PPh_3)/n(P) → π*(quin-2-c)/π*(PPh_3)	259.2	4.78	0.0454	
H−1 → L+5	π(Cl)/π(PPh_3)/n(P) → π*(PPh_3)	246.9	5.02	0.0239	239.9 (5.17) 75200
H−1 → L+5	π(Cl)/π(PPh_3)/n(P) → π*(PPh_3)	245.5	5.05	0.0454	
H−5 → L+3	π(PPh_3)/π(Cl)/π(O) → π*(quin-2-c)/π*(PPh_3)				
H−16 → L+1	π(Cl)/π(quin-2-c)/π(O) → π*(quin-2-c)/d	244.2	5.08	0.0182	
H−3 → L+4	π(PPh_3)/π(Cl) → π*(quin-2-c)/π*(PPh_3)	242.1	5.12	0.0265	
H → L+11	d → π*(PPh_3)	239.2	5.18	0.0512	
H → L+11	d → π*(PPh_3)	237.7	5.22	0.0247	
H-2 → L+5	π(PPh_3)/π(Cl) → π*(PPh_3)	237.1	5.23	0.0265	
H-9 → L+4	π(Cl)/π(quin-2-c)/π(O) → π*(quin-2-c)/π*(PPh_3)	233.7	5.31	0.0578	
H−6 → L+4	π(PPh_3)/π(Cl)/π(O) → π*(quin-2-c)/π*(PPh_3)	233.0	5.32	0.0842	
H−15 → L+1	π(Cl)/π(quin-2-c)/π(O) → π*(quin-2-c)/d	229.5	5.40	0.1772	
H−10 → L+3	π(PPh_3)/π(quin-2-c)/π(Cl) → π*(quin-2-c)/π*(PPh_3)	228.5	5.43	0.0235	
H−16 → L+2	π(Cl)/π(quin-2-c)/π(O) → d	224.8	5.52	0.0346	
H−1 → L+8	π(Cl)/π(PPh_3)/n(P) → π*(PPh_3)/d	223.3	5.55	0.0189	
H−4 → L+5	π(quin-2-c)/π(Cl) → π*(PPh_3)	222.9	5.56	0.1511	
H−6 → L+5	π(PPh_3)/π(Cl)/π(O) → π*(PPh_3)	221.5	5.60	0.0175	
H−3 → L+7	π(PPh_3)/π(Cl) → π*(PPh_3)	218.9	5.66	0.0207	207.9 (5.96) 80.750

ε, molar absorption coefficient ($dm^3\ mol^{-1}\ cm^{-1}$); *f*, oscillator strength; H, highest occupied molecular orbital; L, lowest unoccupied molecular orbital.

Each natural bond orbital (NBO) σ_{AB} can be written in terms of two directed valence hybrids (NHOs) h_A and h_B on atoms A and B:

$$\sigma_{AB} = c_A h_A + c_B h_B$$

where c_A and c_B are polarization coefficients. Each valence bonding NBO must in turn be paired with a corresponding valence *anti*-bonding NBO:

$$\sigma^*_{AB} = c_B h_A - c_A h_B$$

to complete the span of the valence space. The Lewis-type (donor) NBOs are thereby complemented by the non-Lewis-type (acceptor) NBOs that are formally empty in an idealized Lewis picture. The interactions between 'filled' Lewis-type NBOs and 'empty' non-Lewis NBOs lead to loss of occupancy from the localized NBOs of the idealized Lewis structure into the empty non-Lewis orbitals, and they are referred to as 'delocalization' corrections to the zeroth-order natural Lewis structure [36].

Two detected natural Re–O_t bond orbitals of **1** are π orbitals – the p_x and p_y oxygen orbitals and d_{xz} and d_{yz} rhenium orbitals are involved in their formation. Not detected $\sigma_{Re–Ot}$ bond has character of predominant Coulomb-type interactions between the central ion and ligands [43]. The terminal oxo ligand of **1** has two lone pair orbitals, and electron density from one of them is strongly delocalized into non-Lewis rhenium orbital. Accordingly, NBO analysis confirms a triple bond between the rhenium and the terminal oxygen ligand.

4.4. Electronic spectra

The electronic spectra of $[ReOX_2(quin\text{-}2\text{-}c)(EPh_3)]$ complexes are very similar in terms of the position, intensity and shape of the bands in the whole region 1000–180 nm. The positions and molar absorption coefficients of electronic bands for $[ReOX_2(quin\text{-}2\text{-}c)(EPh_3)]$ complexes are given in Table 8.

The experimental and calculated electronic spectra of **1** are presented in Fig. 4. Each calculated transition is represented by a gaussian function $y = ce^{-bx^2}$ with the height (c) equal to the oscillator strength and b equal to 0.04 nm^{-2}. Table 9 presents the calculated singlet–singlet electronic transitions of **1** and their assignments to the experimental bands. For the high energy part of the spectrum, only transitions with oscillator strengths larger than 0.015 are listed in Table 9.

The longest wavelength experimental bands at 856.3 and 692.7 nm can be attributed to the transitions of d → d character. However, due to some participation of π^* orbitals of the *quin-2-c* ligand in the LUMO orbital, character of the H → L electronic transition is ascribed as d → d/π^*(quin-2-c). The metal-ligand charge transfer (d → π^*quin-2-c) makes the largest contribution into the experimental band at 429.6 nm. The absorption band at 376.7 nm is assigned to ligand-metal charge transfer ($\pi_{quin\text{-}2\text{-}c}/\pi_{EPh3}/\pi_{Cl}/\pi_O$ → d) transitions, whereas the experimental bands at 274.8 and 239.9 nm result mainly from the ligand–ligand charge transfer and interligand (IL) transitions.

5. Supplementary material

CCDC 639645 and 639646 contain the supplementary crystallographic data for this paper. These data can be obtained free of charge via http://www.ccdc.cam.ac.uk/conts/retrieving.html, or from the Cambridge Crystallographic Data Centre, 12 Union Road, Cambridge CB2 1EZ, UK; fax: (+44) 1223-336-033; or e-mail: deposit@ccdc.cam.ac.uk.

Acknowledgement

The GAUSSIAN 03 calculations were carried out in the Wrocław Centre for Networking and Supercomputing, WCSS, Wrocław, Poland.

References

[1] R.H. Holm, Chem. Rev. 87 (1987) 1401.
[2] C.C. Romão, F.E. Kühn, W.A. Hermann, Chem. Rev. 97 (1997) 3197.
[3] S.B. Seymore, S.N. Brown, Inorg. Chem. 39 (2000) 325.
[4] F.E. Kühn, A. Scherbaum, W.A. Herrmann, J. Organomet. Chem. 689 (2004) 4149.
[5] A.M. Kirillov, M. Haukka, M.V. Kirillova, A.J.L. Pombeiro, Adv. Synth. Catal. 347 (2005) 1435.
[6] W. Volkert, W.F. Goeckeler, G.J. Ehrhardt, A.R. Ketring, J. Nucl. Med. 32 (1991) 174.
[7] E.A. Deutsch, K. Libson, J.L. Vanderheyden, Technetium and Rhenium in Chemistry and Nuclear Medicine, Raven Press, New York, 1990.
[8] B. Machura, Coord. Chem. Rev. 249 (2005) 591.
[9] D. Dobrzyńska, T. Lis, L.B. Jerzykiewicz, Inorg. Chem. Commun. 8 (2005) 1090.
[10] H. Chermette, Coord. Chem. Rev. 178–180 (1998) 699.
[11] M.C. Aragoni, M. Arca, T. Cassano, C. Denotti, F.A. Devillanova, F. Isaia, V. Lippolis, D. Natali, L. Niti, M. Sampietro, R. Tommasi, G. Verani, Inorg. Chem. Commun. 5 (2002) 869.
[12] P. Romaniello, F. Lelj, Chem. Phys. Lett. 372 (2003) 51.
[13] A. Voigt, U. Abram, R. Böttcher, U. Richter, J. Reinhold, R. Kirmse, Chem. Phys. 253 (2000) 171.
[14] M. Lipowska, L. Hansen, R. Cini, X. Xu, H. Choi, A.T. Taylor, L.G. Marzilli, Inorg. Chim. Acta 339 (2002) 327.
[15] J. Gancheff, C. Kremer, E. Kremer, O.N. Ventura, J. Mol. Struct. (Theochem) 580 (2002) 107.
[16] M.L. Kuznestov, E.A. Klestova-Nadeeva, A.I. Dement'ev, J. Mol. Struct. (Theochem) 671 (2004) 229.
[17] N. Psaroudakis, K. Mertis, D.G. Liakos, E.D. Simandiras, Chem. Phys. Lett. 369 (2003) 490.
[18] X.-Y. Liu, S. Bouherour, H. Jacobsen, H.W. Schmalle, H. Berke, Inorg. Chim. Acta 330 (2002) 250.
[19] É. Bencze, J. Mink, I. Pápai, I.S. Butler, D. Lafleur, D.F.R. Gilson, J. Organomet. Chem. 616 (2000) 1.
[20] W.-Y. Wong, S.-H. Cheung, X. Huang, Z. Lin, J. Organomet. Chem. 655 (2002) 39.
[21] B. Machura, R. Kruszynski, M. Jaworska, Polyhedron 25 (2006) 1111.
[22] B. Machura, R. Kruszynski, Polyhedron 25 (2006) 1985.
[23] G. Rouschias, G. Wilkinson, J. Chem. Soc. A (1966) 465.
[24] STOE & Cie, X-RED. Version 1.18, STOE & Cie GmbH, Darmstadt, Germany, 1999.

[25] G.M. Sheldrick, Acta Crystallogr., Sect. A 46 (1990) 467.
[26] G.M. Sheldrick, SHELXL 97. Program for the Refinement of Crystal Structures, University of Göottingen, Germany, 1997.
[27] G.M. Sheldrick, SHELXTL: Release 4.1 for Siemens Crystallographic Research Systems, 1990.
[28] M.J. Frisch, G.W. Trucks, H.B. Schlegel, G.E. Scuseria, M.A. Robb, J.R. Cheeseman, J.A. Montgomery, Jr., T. Vreven, K.N. Kudin, J.C. Burant, J.M. Millam, S.S. Iyengar, J. Tomasi, V. Barone, B. Mennucci, M. Cossi, G. Scalmani, N. Rega, G.A. Petersson, H. Nakatsuji, M. Hada, M. Ehara, K. Toyota, R. Fukuda, J. Hasegawa, M. Ishida, T. Nakajima, Y. Honda, O. Kitao, H. Nakai, M. Klene, X. Li, J.E. Knox, H.P. Hratchian, J.B. Cross, C. Adamo, J. Jaramillo, R. Gomperts, R.E. Stratmann, O. Yazyev, A.J. Austin, R. Cammi, C. Pomelli, J.W. Ochterski, P.Y. Ayala, K. Morokuma, G.A. Voth, P. Salvador, J.J. Dannenberg, V.G. Zakrzewski, S. Dapprich, A.D. Daniels, M.C. Strain, O. Farkas, D.K. Malick, A.D. Rabuck, K. Raghavachari, J.B. Foresman, J.V. Ortiz, Q. Cui, A.G. Baboul, S. Clifford, J. Cioslowski, B.B. Stefanov, G. Liu, A. Liashenko, P. Piskorz, I. Komaromi, R.L. Martin, D.J. Fox, T. Keith, M.A. Al-Laham, C.Y. Peng, A. Nanayakkara, M. Challacombe, P.M.W. Gill, B. Johnson, W. Chen, M.W. Wong, C. Gonzalez, J.A. Pople, GAUSSIAN 03, Revision B.03, Gaussian, Inc., Pittsburgh, PA, 2003.
[29] A.D. Becke, J. Chem. Phys. 98 (1993) 5648.
[30] C. Lee, W. Yang, R.G. Parr, Phys. Rev. B 37 (1988) 785.
[31] M.E. Casida, in: J.M. Seminario (Ed.), Recent Developments and Applications in Modern Density Functional Theory, Theoretical and Computational Chemistry, vol. 4, Elsevier, Amsterdam, 1996.
[32] P.C. Hariharan, J.A. Pople, Theor. Chim. Acta 28 (1973) 213.
[33] V.A. Rassolov, M.A. Ratner, J.A. Pople, P.C. Redfern, L.A. Curtiss, J. Comp. Chem. 22 (2001) 976.
[34] P.J. Hay, W.R. Wadt, J. Chem. Phys. 82 (1985) 299.
[35] K. Eichkorn, F. Weigend, O. Treutler, R. Ahlrichs, Theor. Chem. Acc. 97 (1997) 119.
[36] E.D. Glendening, A.E. Reed, J.E. Carpenter, F. Weinhold, NBO (version 3.1). A.E. Reed, L.A. Curtiss, F. Weinhold, Chem. Rev. 88 (1988) 899.
[37] G.B. Deacon, R.J. Phillips, Coord. Chem. Rev. 33 (1980) 227.
[38] L. Wei, J. Babich, J. Zubieta, Inorg. Chim. Acta 358 (2005) 2413.
[39] G.R. Desiraju, T. Steiner, The Weak Hydrogen Bond in Structural Chemistry and Biology, Oxford University Press, 1999.
[40] C.A. Hunter, J.K.M. Sanders, J. Am. Chem. Soc 112 (1990) 5525.
[41] J.M. Mayer, Inorg. Chem. 27 (1988) 3899.
[42] S.R. Fletcher, A.C. Skapski, J. Chem. Soc. Dalton (1972) 1073.
[43] M.L. Kuznetsov, A.J.L. Pombeiro, J. Chem. Soc. Dalton Trans. (2003) 738.

was prepared as previously reported [3]. Elemental analyses (C, H, N, S) were performed on a LECO CHNS-932 analyzer. Molybdenum was determined by titration with lead(II) nitrate [9]. IR spectra (KBr dispersion, 4000–400 cm^{-1} range) were recorded on a Nicolet Impact 410 (Software Omnic for Windows) spectrometer. NMR spectra were recorded on a Varian Mercury-plus 300 spectrometer (300 MHz for ^1H) at 20 °C, and Varian Unity Inova 400 spectrometer (400 MHz for ^1H and 161.92 MHz for ^{31}P) for variable temperature experiments. Chemical shifts are relative to TMS (^1H), or external 85% H_3PO_4 (^{31}P), with downfield values reported as positive. Coupling constants *J* are given in Hertz.

2.2. Preparation of compounds $Mo_2O_5(acac)_2L_2$

2.2.1. Preparation of $Mo_2O_5(acac)_2(H_2O)_2$

$MoO_2(acac)_2$ (0.326 g, 1 mmol) was dissolved in 96% ethanol (15 ml). The resulting solution was stirred for 45 min at r.t. and concentrated under vacuum nearly to dryness. Then diethyl ether (20 ml) was added and the mixture was stirred for 10 min. The white precipitate that formed was collected by filtration, washed with diethyl ether (3 × 3 ml) and dried under vacuum. Yield: 0.223 g (88%). IR (cm^{-1}): *ν*(Mo=O) 903(s), 949(s), *ν*(Mo–O–Mo) 766(s). ^1H NMR (methanol-d_4, 300 MHz, *δ*, ppm): 5.85 (s, 2H, CH), 4.90 (s, 4H, H_2O), 2.11 (br, 12H, CH_3). *Anal.* Calc. for $C_{10}H_{18}Mo_2O_{11}$: C, 23.73; H, 3.58; Mo, 37.91. Found: C, 23.45; H, 3.69; Mo, 37.83%.

2.2.2. Preparation of $Mo_2O_5(acac)_2(D_2O)_2$

$MoO_2(acac)_2$ (0.065 g, 0.2 mmol) was dissolved in 96% EtOD (EtOD/D_2O, 96/4, v/v, 5 ml). The resulting solution was stirred for 15 min at r.t. and concentrated under vacuum nearly to dryness. Then diethyl ether (8 ml) was added and the mixture was stirred for 5 min. The white precipitate that formed was collected by filtration, washed with diethyl ether (3 × 3 ml) and dried under vacuum. Yield: 0.035 g (68%). IR (cm^{-1}): *ν*(O–D) 2427(s), *ν*(Mo=O) 904(s), 949(s), *ν*(Mo–O–Mo) 768(s). ^1H NMR (methanol-d_4, 300 MHz, *δ*, ppm): 5.85 (s, 2H, CH), 2.11 (br, 12H, CH_3). *Anal.* Calc. for $C_{10}H_{14}D_4Mo_2O_{11}$: C, 23.54; H, 2.77; Mo, 37.61. Found: C, 23.41; H, 2.05; Mo, 37.74%.

2.2.3. Preparation of $Mo_2O_5(acac)_2L_2$ [L = DMSO, p-Tol_2 SO, DMF, DMA, DMBA, TMU, $OPPh_3$, HMPA]

A mixture of $MoO_2(acac)_2$ (0.326 g, 1 mmol) and L (1.1 mmol) in 96% ethanol (15 ml) was stirred for 45 min at r.t. The resulting solution was concentrated under vacuum to approximately 2 ml. Then diethyl ether (20 ml) was added and the precipitate that formed was filtered, washed with diethyl ether (3 × 3 ml) and dried under vacuum.

$Mo_2O_5(acac)_2(DMSO)_2$: Yield: 0.304 g (97%). M.p. (dec.) 142–144 °C. IR (cm^{-1}): *ν*(Mo=O) 902(s), 928(s), *ν*(Mo–O–Mo) 780(s). ^1H NMR (methanol-d_4, 300 MHz, *δ*, ppm): 5.85 (s, 2H, CH), 2.66 (s, 12H, S–CH_3), 2.11 (br, 12H, CH_3). *Anal.* Calc. for $C_{14}H_{26}Mo_2O_{11}S_2$: C, 26.85; H, 4.18; S, 10.24. Found: C, 26.89; H, 4.21; S, 10.47%.

$Mo_2O_5(acac)_2$(*p*-$Tol_2SO)_2$: Yield: 0.442 g (95%). IR (cm^{-1}): *ν*(Mo=O) 907(s), 938(s), *ν*(Mo–O–Mo) 771(s). ^1H NMR (methanol-d_4, 300 MHz, *δ*, ppm): 7.56–7.50 (m, 8H, Ph), 7.37–7.31 (m, 8H, Ph), 5.84 (s, 2H, CH), 2.37 (s, 12H, *Ph*–CH_3), 2.11 (br, 12H, CH_3). *Anal.* Calc. for $C_{38}H_{42}Mo_2O_{11}S_2$: C, 49.04; H, 4.55; S, 6.89. Found: C, 49.26; H, 4.63; S, 7.09%.

$Mo_2O_5(acac)_2(DMF)_2$: Yield: 0.300 g (98%). IR (cm^{-1}): *ν*(Mo=O) 906(s), 941(s), *ν*(Mo–O–Mo) 752(s). ^1H NMR (methanol-d_4, 300 MHz, *δ*, ppm): 7.98 (s, 2H, CO–H), 5.85 (s, 2H, CH), 3.00 (s, 6H, N–CH_3), 2.86 (s, 6H, N–CH_3), 2.11 (br, 12H, CH_3). *Anal.* Calc. for $C_{16}H_{28}Mo_2N_2O_{11}$: C, 31.18; H, 4.58; N, 4.55. Found: C, 30.87; H, 4.56; N, 4.35%.

$Mo_2O_5(acac)_2(DMA)_2$: Yield: 0.306 g (95%). M.p. (dec.) 129–131 °C. IR (cm^{-1}): *ν*(Mo=O) 903(s), 938(s), *ν*(Mo–O–Mo) 748(s). ^1H NMR (methanol-d_4, 300 MHz, *δ*, ppm): 5.85 (s, 2H, CH), 3.06 (s, 6H, N–CH_3), 2.92 (s, 6H, N–CH_3), 2.11 (br, 12H, CH_3), 2.07 (s, 6H, N–CO–CH_3). *Anal.* Calc. for $C_{18}H_{32}Mo_2N_2O_{11}$: C, 33.55; H, 5.01; N, 4.35. Found: C, 33.21; H, 4.98; N, 4.62%.

$Mo_2O_5(acac)_2(DMBA)_2$: Yield: 0.356 g (93%). IR (cm^{-1}): *ν*(Mo=O) 908(s), 940(s), *ν*(Mo–O–Mo) 738(s). ^1H NMR (methanol-d_4, 300 MHz, *δ*, ppm): 7.48–7.38 (m, 10H, Ph), 5.85 (s, 2H, CH), 3.10 (s, 6H, N–CH_3), 2.99 (s, 6H, N–CH_3), 2.11 (br, 12H, CH_3). *Anal.* Calc. for $C_{28}H_{36}Mo_2N_2O_{11}$: C, 43.76; H, 4.72; N, 3.65. Found: C, 43.85; H, 4.83; N, 3.74%.

$Mo_2O_5(acac)_2(TMU)_2$: Yield: 0.320 g (91%). IR (cm^{-1}): *ν*(Mo=O) 907(s), 936(s), *ν*(Mo–O–Mo) 742(s). ^1H NMR (methanol-d_4, 300 MHz, *δ*, ppm): 5.85 (s, 2H, CH), 2.81 (s, 24H, N–CH_3), 2.11 (br, 12H, CH_3). *Anal.* Calc. for $C_{20}H_{38}Mo_2N_4O_{11}$: C, 34.20; H, 5.45; N, 7.98. Found: C, 33.98; H, 5.24; N, 8.09%.

$Mo_2O_5(acac)_2(OPPh_3)_2$: Yield: 0.483 g (94%). M.p. (dec.) 122–124 °C. IR (cm^{-1}): *ν*(Mo=O) 897(s), 928(s). ^1H NMR (methanol-d_4, 300 MHz, *δ*, ppm): 7.69–7.51 (m, 30H, Ph), 5.84 (s, 2H, CH), 2.10 (br, 12H, CH_3). *Anal.* Calc. for $C_{46}H_{44}Mo_2O_{11}P_2$: C, 53.81; H, 4.32; Mo, 18.69. Found: C, 53.89; H, 4.29; Mo, 17.87%.

$Mo_2O_5(acac)_2(HMPA)_2$: Yield: 0.369 g (89%). IR (cm^{-1}): *ν*(Mo=O) 902(s), 938(s), *ν*(Mo–O–Mo) 773(s). ^1H NMR (methanol-d_4, 300 MHz, *δ*, ppm): 5.85 (s, 2H, CH), 2.64 (d, $^3J_{P-H} = 9.4$ Hz, 36H, N–CH_3), 2.11 (br, 12H, CH_3). *Anal.* Calc. for $C_{22}H_{50}Mo_2N_6O_{11}P_2$: C, 31.89; H, 6.08; N, 10.14. Found: C, 31.63; H, 5.94; N, 10.47%.

2.2.4. Preparation of $Mo_2O_5(acac)_2L_2$ [L = Bu_2SO, $OPBu_3$]

A mixture of $MoO_2(acac)_2$ (0.326 g, 1 mmol) and L (1.1 mmol) in 96% ethanol (15 ml) was stirred for 45 min at r.t. The resulting solution was concentrated under vacuum near to dryness, *ca.* 1 ml, then a mixture of diethyl

ether:hexane (1:1, v/v, 20 ml) was added. The precipitate that formed was collected by filtration, washed with diethyl ether:hexane (1:1, 3 × 3 ml) and dried under vacuum.

$Mo_2O_5(acac)_2(Bu_2SO)_2$: Yield: 0.344 g (87%). IR (cm^{-1}): ν(Mo=O) 904(s), 934(s), ν(Mo–O–Mo) 755(s). ^1H NMR (methanol-d_4, 300 MHz, δ, ppm): 5.85 (s, 2H, CH), 2.88–2.69 (m, 8H, $CH_{2\alpha}$), 2.11 (br, 12H, CH_3), 1.80–1.78 (m, 8H, $CH_{2\beta}$), 1.60–1.41 (m, 8H, $CH_{2\gamma}$), 0.99 (t, $^3J_{H-H} = 7.3$ Hz, 12H, CH_2–CH_3). *Anal.* Calc. for $C_{26}H_{50}Mo_2O_{11}S_2$: C, 39.30; H, 6.34; S, 8.07. Found: C, 39.52; H, 6.74; S, 8.49%.

$Mo_2O_5(acac)_2(OPBu_3)_2$: Yield: 0.377 g (83%). IR (cm^{-1}): ν(Mo=O) 903(s), 938(s), ν(Mo–O–Mo) 753(s). ^1H NMR ($CDCl_3$, 300 MHz, δ, ppm): 5.83 (s, 2H, CH), 2.21 (s, 6H, CH_3), 2.14 (s, 6H, CH_3), 1.76–1.34 (m, 36H, CH_2), 0.93 (t, $^3J_{H-H} = 7.3$ Hz, 18H, CH_2–CH_3). *Anal.* Calc. for $C_{34}H_{68}Mo_2O_{11}P_2$: C, 45.04; H, 7.56; Mo, 21.16. Found: C, 45.24; H, 7.68; Mo, 19.99%.

2.3. Crystal-structure determinations

Suitable single crystals of $Mo_2O_5(acac)_2(D_2O)_2$ were grown by cooling an acetone-d_6 solution of this compound in a freezer. Single crystals of $Mo_2O_5(acac)_2(DMF)_2$ were grown by slow evaporation of a solution of the complex in 96% ethanol. Crystal data for the compounds were collected using a Bruker SMART CCD area-detector diffractometer with Mo Kα radiation. Intensities were integrated [10] from several series of exposures, each exposure covering 0.3° in ω, and the total data set being a sphere. All non-hydrogen atoms were assigned anisotropic displacement parameters and refined without positional constraints. For $Mo_2O_5(acac)_2(D_2O)_2$ deuterium atoms D(4A) and D(4B) were located in the electron density difference map, assigned isotropic displacement parameters and refined without positional constraints. All other hydrogen atoms were constrained to ideal geometries and refined with fixed isotropic displacement parameters. Table 1 provides the crystallographic details for these compounds.

2.4. Catalytic activity

The measurement of the catalytic activity of $Mo_2O_5(acac)_2(DMSO)_2$ in the oxidation of PPh_3 with DMSO was monitored by ^{31}P NMR (161.92 MHz) spectroscopy as previously reported [11], and compared with that of $MoO_2(acac)_2$ under the same conditions. We carried out experiments at 25 and 75 °C, for $[Mo]_0 = 0.02$ mol dm^{-3} and $[PPh_3]_0/[Mo] = 20$.

3. Results and discussion

3.1. Synthesis and characterization of the complexes

It is well known that $MoO_2(acac)_2$ can be easily prepared by treating acidic solutions of molybdates with acetylacetone [3]. However, it is somewhat difficult to purify it by re-crystallization from common solvents because of its propensity to hydrolyze with any adventitious water. This hydrolysis should lead to the final product $MoO_3 \cdot nH_2O$, but it is not always immediately formed.

While we were carrying out studies on the reactivity of $MoO_2(acac)_2$ with a variety of chiral acids it was soon evident that the diketonate was hydrolyzed in solution very quickly. This process seemed to proceed in two consecutive well differentiated steps. Indeed, we were able to obtain the hydrate $Mo_2O_5(acac)_2(H_2O)_2$ without significant difficulty, which strongly supports the idea that the hydrolytic removal of acetylacetonate from $MoO_2(acac)_2$ takes place in this way, the second step occurring very slowly at room temperature (Scheme 1).

Table 1
Crystal data and summary of intensity data collection and structure refinement of complexes $Mo_2O_5(acac)_2(D_2O)_2$ and $Mo_2O_5(acac)_2(DMF)_2$

	$Mo_2O_5(acac)_2(D_2O)_2$	$Mo_2O_5(acac)_2(DMF)_2$
Empirical formula	$C_{10}H_{14}D_4Mo_2O_{11}$	$C_{16}H_{28}Mo_2N_2O_{11}$
Formula weight	510.15	616.28
Crystal system	monoclinic	monoclinic
Space group	*C*2/*c*	*C*2/*c*
a (Å)	13.589(3)	14.024(5)
b (Å)	8.194(2)	8.6500(16)
c (Å)	15.294(3)	19.849(5)
β (°)	100.575(13)	93.77(3)
V (Å)^3	1674.1(7)	2402.6(12)
Z	4	4
Color	yellow	colourless
Crystal size (mm)	0.30 × 0.20 × 0.20	0.60 × 0.20 × 0.15
D_{calc} (g cm^{-3})	2.024	1.704
Temperature (*K*)	293(2)	293(2)
Wavelength (Å)	0.71073	0.71073
Diffractometer	Bruker SMART CCD	Bruker SMART CCD
Scan mode	omega scans	omega scans
hkl Limits	−16,16/ −9,9/ −18,18	−16,16/−10,10/ −23,23
θ Range for data collection (°)	2.71–25.09	2.06–25.00
Reflections collected	7941	11,176
Independent reflections [R_{int}]	1497 [0.0268]	2111 [0.0397]
Reflections with ($I > 2\sigma(I)$)	1383	1858
Data/restraints/ parameters	1497/0/113	2111/0/145
R indices (for reflections with $I > 2\sigma(I)$)	$R_1 = 0.0208$, $wR_2 = 0.0534$	$R_1 = 0.0281$, $wR_2 = 0.0703$
R indices (for independent reflections)	$R_1 = 0.0231$, $wR_2 = 0.0545$	$R_1 = 0.0334$, $wR_2 = 0.0726$
Goodness-of-fit on F^2	$S = 1.087$	$S = 1.073$
Largest difference in peak and hole (e Å^{-3})	0.417 and −0.433	0.347 and −0.312
Completeness to θ	$\theta = 25.09°$, 100.0%	$\theta = 25.00°$, 99.8%
Absorption correction	semi-empirical from equivalents	semi-empirical from equivalents
Maximum and minimum transmission	0.734 and 0.648	0.848 and 0.728
Refinement method	full-matrix least-squares on F^2	full-matrix least-squares on F^2

This assumption is in accordance with the behavior observed for $MoO_2(acac)_2$ in 96% ethanol. Thus, when the ^1H NMR of $MoO_2(acac)_2$ is recorded in 96% ethanol-d_6, from the outset the spectrum shows the same amount of acacH and coordinated acac. This indicates that the hydrolysis of the first acetylacetonate takes place quickly, and that the dinuclear dioxomolybdenum species are present in solution from the beginning. However, the hydrolysis of the second acetylacetonate is a slow process.

Thus, $Mo_2O_5(acac)_2(H_2O)_2$, and the closely related $Mo_2O_5(acac)_2(D_2O)_2$, could be obtained by treating $MoO_2(acac)_2$ with mixtures of ethanol–water close to the azeotropic composition, as described in the experimental part. Then we attempted to prepare the anhydrous parent compound $Mo_2O_5(acac)_2$ by warming up $Mo_2O_5(acac)_2(H_2O)_2$ smoothly under vacuum, and by treating it with 2,2-dimethoxypropane, although without success. We also failed to obtain satisfactory results by reacting MoO_3 with $MoO_2(acac)_2$ in several solvents, including the molten diketonate.

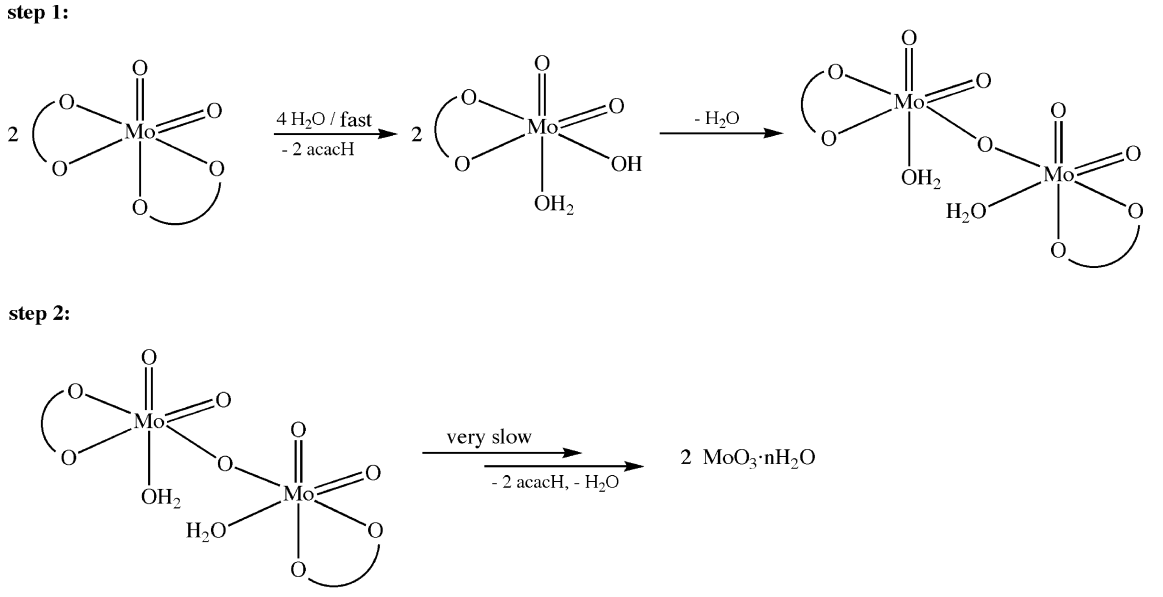
As previously reported [11–13], a wide number of dioxomolybdenum(VI) compounds could be readily prepared from $MoO_2X_2(H_2O)_2$ (X = Cl, Br) *via* substitution of water with ligands able to displace it from the coordination sphere of molybdenum. Based on these results we treated $Mo_2O_5(acac)_2(H_2O)_2$ with representative monodentate tertiary amines, amides, sulfoxides and phosphine oxides and could prepare the above mentioned $Mo_2O_5(acac)_2L_2$ compounds. Higher yields were obtained in a simpler manner by carrying out the reactions of $MoO_2(acac)_2$ with the corresponding ligand in 96% ethanol, as an one-pot synthesis. It is likely that other compounds with common amides, sulfoxides and phosphine oxides might be similarly prepared. However, we were unable to isolate the related compounds with N-donor ligands such as tributylamine and 4-methylpyridine. With these bases we always obtained ill-defined products without characteristic IR bands attributable to *cis*-dioxomolybdenum and acetylacetonate groups. This result was not surprising at all since we had observed in other dioxomolybdenum(VI) complexes that amines, in presence of water, induce complete hydrolysis leading to alkylammonium molybdates.

The analytical data (C, H, N, S, Mo) for these compounds were in good agreement with those expected for products with the formulation $Mo_2O_5(acac)_2L_2$. All the compounds are colorless or white, though they slowly develop a blue coloration when left in air. They are insoluble in diethyl ether and hydrocarbons, somewhat soluble in tetrahydrofuran and acetone, and soluble in lighter alcohols, solvents from which they could be re-crystallized.

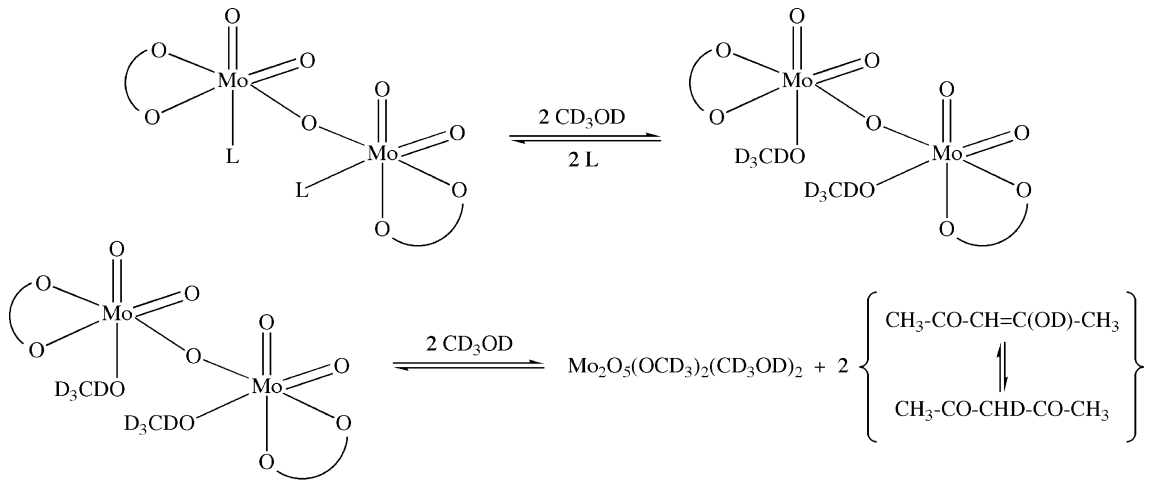
The derivatives of DMSO, DMA and $OPPh_3$ melt with decomposition in the range 122–144 °C while all the other products decompose before melting. However they can be stored for months, in a dry atmosphere in the dark and at room temperature, without noticeable decomposition.

We have found that these dioxomolybdenum complexes react with common organophosphines and phosphites (PPh_3, PBu_3, $P(OBu)_3$, $P(OPh)_3$) leading to brown solutions. It is likely that, at least in part, new dinuclear complexes with a $[Mo_2O_4]^{2+}$ core might be formed in this process, though we do not have confident analytical data to support this assumption.

The IR spectra of the compounds are characterized by two strong bands in the region 880–950 cm^{-1} which indicate that, as usual for dioxomolybdenum(VI) species, the *cis*-MoO_2 moiety is present in all products [14]. We find it difficult to establish correlations between the position of these bands and the nature of the ligands. The com-



Scheme 1.



Scheme 2.

pounds also show a band in the range 735–780 cm^{-1}, characteristic of ν(Mo–O–Mo) [15]; this band is not easy to assign in the $OPPh_3$ complex, since the ligand also absorbs in this region.

The ^1H NMR spectra for $Mo_2O_5(acac)_2(OPBu_3)_2$ has been recorded using $CDCl_3$ as solvent, and is characterized by two singlets of equal intensity for the methyl groups and another singlet for the CH group from the acac ligand. The signals characteristic for the free neutral ligand are shifted, as usual, to lower fields due to coordination. The ^1H NMR spectra for all the others complexes have been recorded in methanol-d_4 because of their low solubility in other common deuterated solvents. These NMR spectra show the signals corresponding to the neutral ligands in the same positions as the free ligands. The signals for the acac group are similar to those found for the coordinated acac in the above mentioned $MoO_2(acac)_2$. At room temperature there is only one broad signal for the methyl groups from the acac ligand, solved as two singlets (2.16 and 2.06 ppm) at low temperature (−40 °C), which is consistent with a dynamic equilibrium in solution. The intensity of the singlet at 5.85 ppm assigned to the CH group decreases slowly with time, supporting the idea of exchange between hydrogen and deuterium atoms. Taking into account both facts, a possible explanation is an exchange between the deuterium of methanol-d_4 and the methynic hydrogen of acetylacetonate *via* coordination and de-coordination to the molybdenum center as shown in Scheme 2.

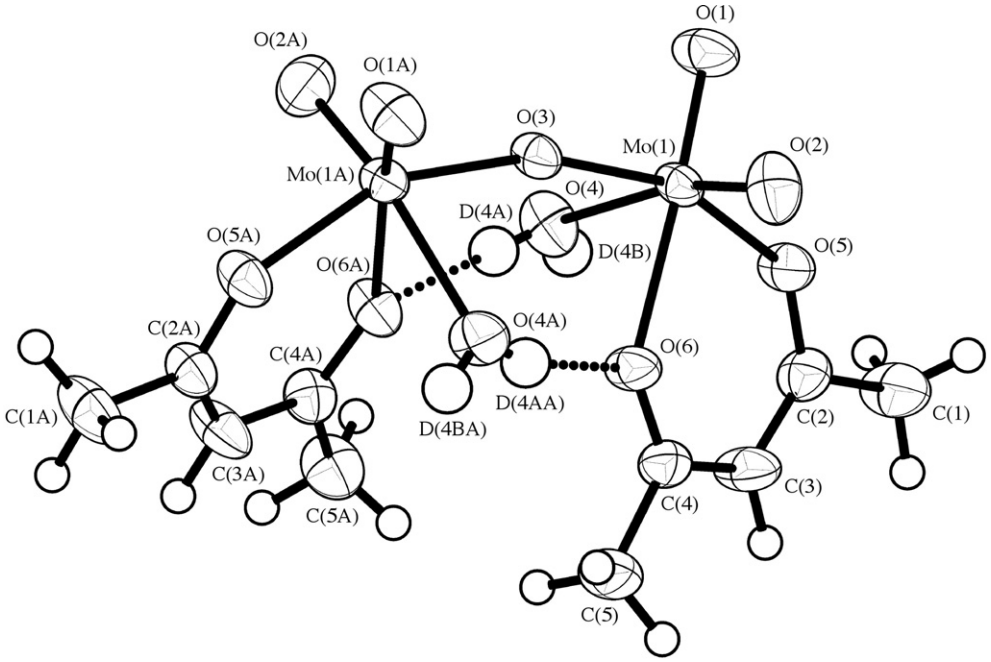


Fig. 1. Molecular structure and atom-labelling scheme for $Mo_2O_5(acac)_2(D_2O)_2$ with thermal ellipsoids at the 50% probability level, showing hydrogen bonds involving deuterium.

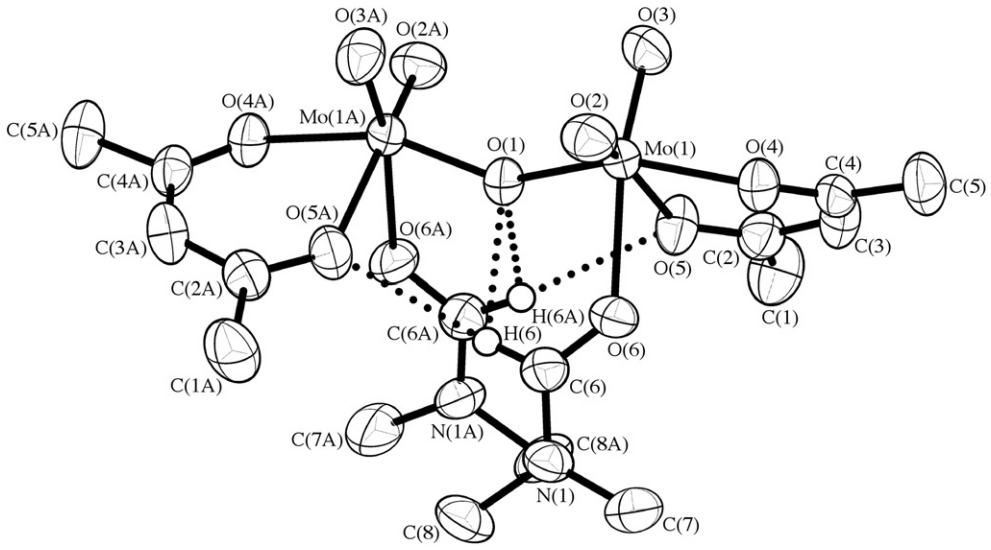


Fig. 2. Molecular structure and atom-labelling scheme for $Mo_2O_5(acac)_2(DMF)_2$ with thermal ellipsoids at the 50% probability level, showing hydrogen bonds; hydrogen atoms are omitted for clarity.

3.2. Molecular structures

Dinuclear compounds with a $[Mo_2O_5]^{2+}$ core have been known for a long time. They can have a single, double or triple bridge, the former being the most common [16]. To the best of our knowledge, the compounds presented here are the first examples of complexes with this core and the acetylacetonate ligand. The molecular structures for $Mo_2O_5(acac)_2(L)_2$ (L = D_2O, DMF) were determined by single-crystal X-ray diffraction analysis. Views of $Mo_2O_5(acac)_2(D_2O)_2$ and $Mo_2O_5(acac)_2(DMF)_2$ are shown in Figs. 1 and 2. Selected bond lengths and angles are listed in Table 2, and hydrogen contacts for $Mo_2O_5(acac)_2(D_2O)_2$ and $Mo_2O_5(acac)_2(DMF)_2$ in Tables 3 and 4, respectively.

In both complexes the molybdenum atom is coordinated in a pseudo-octahedral fashion, as expected, with distortions from the ideal geometry mainly arising from the different nature of the O-donor atom set and the bite of the acac ligand. The two terminal oxo ligands on molybdenum are mutually *cis*, and *cis* to the bridging oxo. One acetylacetonate and one water-d_2 (or dimethylformamide) ligand complete the six-coordination sphere of molybdenum.

The Mo–Ot distances, ranging from 1.678 to 1.703 Å, are within the range usually found in dioxomolybdenum(VI) compounds (1.65–1.75 Å) [17]. The Mo–Ob distances are practically equivalent in both compounds, 1.888 Å. The two sets of Mo–O distances to the acetylacetonate ligands, 2.040 and 2.058 Å (*trans* to Ob), and 2.202 and 2.207 Å (*trans* to Ot), indicate that Ot has a larger *trans*-weakening effect than Ob. The long Mo–OD_2 and Mo–$OCHNMe_2$ (*trans* to Ot), distances of 2.284 and 2.270 Å illustrate the large structural *trans* effect of the Ot ligand.

The angles subtended by the atoms coordinated to molybdenum are also in the range of those found for similar complexes [18]. The largest *cis* O–Mo–O bond angles correspond to the shortest Mo–O bond distances, in agreement with the idea that interligand or interbond repulsions determine such coordination spheres.

With regard to the Mo–O–Mo angles, 160° and 149° for $Mo_2O_5(acac)_2(D_2O)_2$ and $Mo_2O_5(acac)_2(DMF)_2$ respectively, the values are very likely determined by the nature of the neutral ligands. Indeed, in complexes with a $[Mo_2O_5]^{2+}$ core and a single bridging oxo ligand, the

Table 2
Selected bond lengths (Å) and angles (°) for $Mo_2O_5(acac)_2(D_2O)_2$ and $Mo_2O_5(acac)_2(DMF)_2$

$Mo_2O_5(acac)_2(D_2O)_2$		$Mo_2O_5(acac)_2(DMF)_2$	
Bond lengths			
Mo(1)–O(2)	1.678(2)	Mo(1)–O(2)	1.683(2)
Mo(1)–O(1)	1.7028(19)	Mo(1)–O(3)	1.687(2)
Mo(1)–O(3)	1.8879(6)	Mo(1)–O(1)	1.8870(10)
Mo(1)–O(5)	2.0402(19)	Mo(1)–O(4)	2.058(2)
Mo(1)–O(6)	2.2022(19)	Mo(1)–O(5)	2.207(2)
Mo(1)–O(4)	2.284(2)	Mo(1)–O(6)	2.270(2)
Bond angles			
O(2)–Mo(1)–O(1)	103.75(11)	O(2)–Mo(1)–O(3)	103.30(12)
O(2)–Mo(1)–O(3)	101.35(8)	O(2)–Mo(1)–O(1)	102.39(9)
O(1)–Mo(1)–O(3)	101.76(9)	O(3)–Mo(1)–O(1)	100.50(11)
O(2)–Mo(1)–O(5)	95.81(10)	O(2)–Mo(1)–O(4)	90.99(11)
O(1)–Mo(1)–O(5)	91.24(9)	O(3)–Mo(1)–O(4)	93.73(11)
O(2)–Mo(1)–O(6)	89.28(10)	O(3)–Mo(1)–O(5)	91.09(11)
O(1)–Mo(1)–O(6)	164.99(9)	O(2)–Mo(1)–O(5)	163.50(10)
O(1)–Mo(1)–O(4)	88.40(10)	O(2)–Mo(1)–O(6)	88.51(10)
O(2)–Mo(1)–O(4)	167.18(10)	O(3)–Mo(1)–O(6)	166.42(11)
O(5)–Mo(1)–O(6)	79.89(7)	O(4)–Mo(1)–O(5)	79.90(9)
O(3)–Mo(1)–O(6)	82.57(8)	O(1)–Mo(1)–O(5)	82.52(8)
O(3)–Mo(1)–O(5)	155.22(9)	O(1)–Mo(1)–O(4)	157.54(12)
O(5)–Mo(1)–O(4)	79.63(8)	O(4)–Mo(1)–O(6)	79.19(8)
O(6)–Mo(1)–O(4)	78.16(8)	O(5)–Mo(1)–O(6)	76.33(9)
O(3)–Mo(1)–O(4)	79.74(7)	O(1)–Mo(1)–O(6)	83.16(10)
Mo(1)–O(3)–Mo(1A)	160.01(14)	Mo(1)–O(1)–Mo(1A)	149.21(19)

Symmetry transformations used to generate equivalent atoms: #1 $-x+2$, y, $-z+1/2$; #1 $-x+2$, y, $-z+3/2$.

Table 3
Hydrogen contacts for $Mo_2O_5(acac)_2(D_2O)_2$ (Å and °), involving D_2O

A–D···B	*d*(A–D)	*d*(D···B)	*d*(A···B)	∠(AD···B)
Hydrogen bonds – intramolecular				
O(4)–D(4A)···O(6A)	0.74(3)	2.032	2.726	155.995
O(4A)–D(4AA)···O(6)	0.74(3)	2.032	2.726	155.995
Hydrogen bonds – intermolecular				
O(4)–D(4B)···O(1A)′	0.77(3)	1.946	2.716	174.162
O(4A)–D(4BA)···O(1)′	0.77(3)	1.946	2.716	174.162

Symmetry transformations used to generate equivalent atoms: #1 $-x+2$, y, $-z+1/2$.

Table 4
Hydrogen contacts for $Mo_2O_5(acac)_2(DMF)_2$ (Å and °)

A–H···B	*d*(A–H)	*d*(H···B)	*d*(A···B)	∠(AH···B)
Hydrogen bonds				
C(6)–H(6)···O(1)	0.930	2.420	2.912	112.966
C(6)–H(6)···O(5A)	0.930	2.544	3.468	171.865
C(6A)–H(6A)···O(1)	0.930	2.420	2.912	112.966
C(6A)–H(6A)···O(5)	0.930	2.544	3.468	171.865

Symmetry transformations used to generate equivalent atoms: #1 $-x+2$, y, $-z+3/2$.

Mo–O–Mo angle varies from 136° to 180° [16]; the fact that in the compound $Mo_2O_5(SCN)_2L_2$ (L = 4,4′-di-*tert*-butyl-2,2′-bipyridine) [19] molecules with linear and angular (156°) Mo–O–Mo arrangements coexist in the crystal, suggest that, in the absence of steric hindrance, the value of this angle plays a minor role in the stability of the compound. Thus in the D_2O complex the moderate intramolecular hydrogen bonds (Table 3 and Fig. 1) involving coordinated water-d_2 might be responsible for the bending of the Mo–O–Mo unit. Similarly, the intramolecular hydrogen contacts of the methynic hydrogen from the coordinated dimethylformamide and oxygen atoms in acetylacetonate (Table 4 and Fig. 2) might be of sufficient relevance to determine the Mo–O–Mo angle in $Mo_2O_5(acac)_2(DMF)_2$.

It should be noted that in these compounds the unit cell contains both enantiomers. The crystal is racemic, with opposite enantiomers related by a crystallographic inversion center.

The crystal packing in both compounds can be described as stacking of alternate planes, each of them formed by one of the enantiomers, linked only by Van der Waals forces. Hydrogen bonds also play a significant role in the packing for $Mo_2O_5(acac)_2(D_2O)_2$; in a given plane each molecule is linked to four others by hydrogen bonds as shown in Fig. 3.

Based on the nature of the ligands and the structures found for the D_2O and DMF derivatives it is probable that

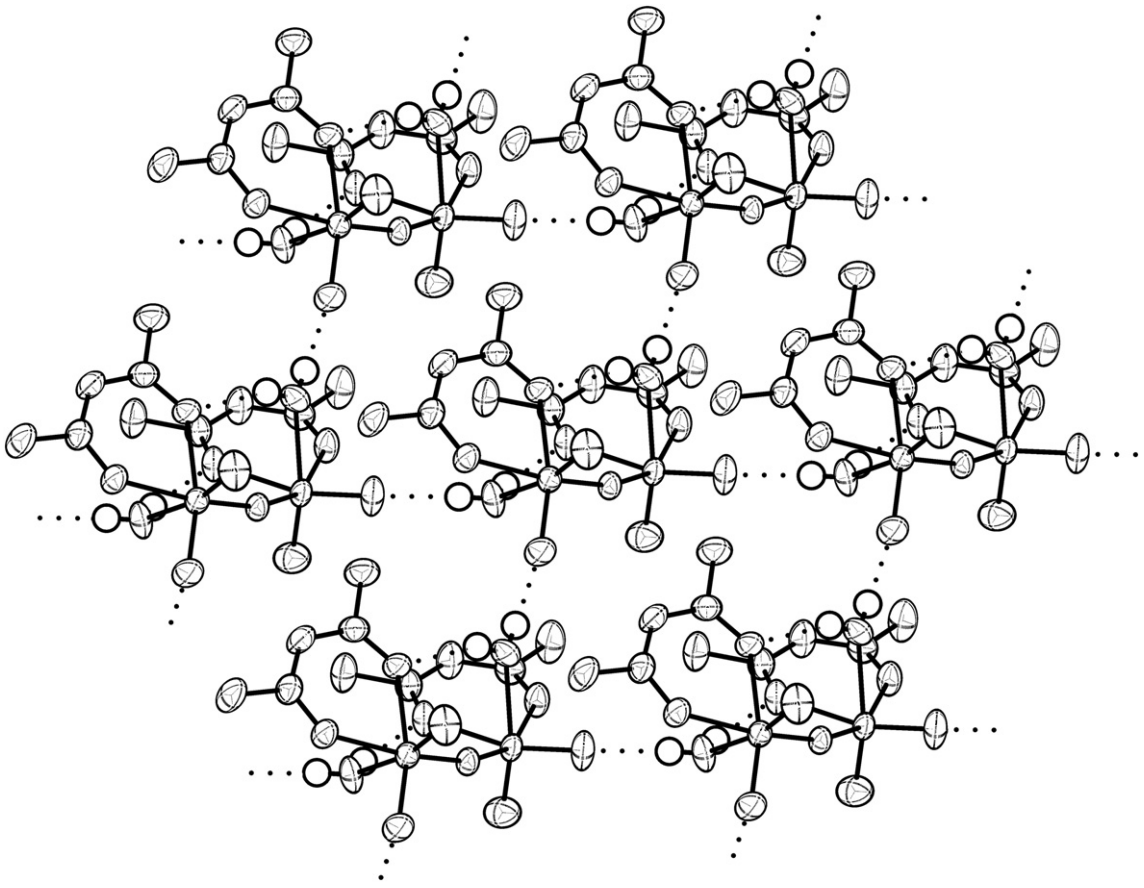


Fig. 3. Crystal structure for $Mo_2O_5(acac)_2(D_2O)_2$ with thermal ellipsoids at the 50% probability level, showing hydrogen bonds; hydrogen atoms are omitted for clarity.

all the compounds possess similar related structures. However, it is also probable that some of them, especially those containing large neutral ligands, might be formed by centrosymmetric molecules to minimize repulsions.

3.3. Catalytic tests in oxotransfer reactions

The behavior of these compounds toward phosphines and phosphites is indicative of oxotransfer processes from the dioxomolybdenum center to the P oxoacceptor. The slow discoloration of the resulting products when DMSO was added and the evolution of the foul-smelling dimethyl sulfide after several hours are indicative of oxo-transference from DMSO to the reduction products. These observations suggest that the compounds possess a low ability to work as oxotransfer catalysts at temperatures near to room temperature. In view that $MoO_2(acac)_2$ has been recently used to catalyze a few relevant oxotransfer processes [6–8], we have measured the rate of oxidation of PPh_3 to $OPPh_3$ by DMSO in presence of $Mo_2O_5(acac)_2(DMSO)_2$ and $MoO_2(acac)_2$, and confirmed that the transformation goes very slowly at room temperature in both cases (24 h, 3% conversion). However the activity increases significantly with temperature. The behavior of the compounds is very similar and *ca.* 24 h are required at 75 °C to get 95% conversion.

Acknowledgements

We thank the Junta de Castilla y León (BU033A06 and BU012A06) for financial support. Jaime Escribano thanks Junta de Castilla y León for a fellowship.

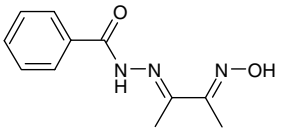
Appendix A. Supplementary material

CCDC 634857 and CCDC 634858 contains the supplementary crystallographic data for $[Mo_2O_5(acac)_2(D_2O)_2]$ and $[Mo_2O_5(acac)_2(DMF)_2]$ respectively. These data can be obtained free of charge via http://www.ccdc.cam.ac.uk/conts/retrieving.html, or from the Cambridge Crystallographic Data Centre, 12 Union Road, Cambridge CB2 1EZ, UK; fax: (+44) 1223-336-033; or e-mail: deposit@ ccdc.cam.ac.uk. Supplementary data associated with this article can be found, in the online version, at doi:10. 1016/j.poly.2007.03.062.

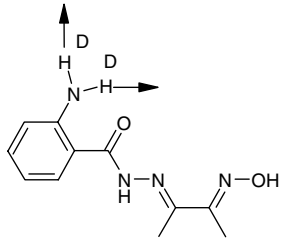
References

[1] M.M. Jones, J. Am. Chem. Soc. 81 (1959) 3188.
[2] M.C. Chakravorti, D. Bandyopadhyay, in: R.N. Grimes (Ed.), Inorg. Synth, vol. 29, Wiley–Interscience, New York, 1992, p. 129, Chapter 3.
[3] F.J. Arnáiz, J. Chem. Educ. 72 (1995) A7.
[4] J.A. Craig, E.W. Harlan, B.S. Snyder, M.A. Whitener, R.H. Holm, Inorg. Chem. 28 (1989) 2082.
[5] A. Lehtonen, M. Wasberg, R. Sillanpää, Polyhedron 25 (2006) 767.
[6] A.U. Barlan, A. Basak, H. Yamamoto, Angew. Chem., Int. Ed. 45 (2006) 5849.
[7] S. Velusamy, M. Ahamed, T. Punniyamurthy, Org. Lett. 6 (2004) 4821.
[8] C.Y. Lorber, J.A. Osborn, Tetrahedron Lett. 37 (1996) 853.
[9] R. Pürschel, E. Lassner, R. Scharf, Zeitschr. Anal. Chem. 163 (1958) 104.
[10] SAINT integration software, Siemens Analytical X-ray Instruments Inc., Madison, WI, 2000.
[11] F.J. Arnáiz, R. Aguado, J.M. Martínez-Ilarduya, Polyhedron 13 (1994) 3257.
[12] F.J. Arnáiz, R. Aguado, M.R. Pedrosa, J. Mahía, M.A. Maestro, Polyhedron 21 (2002) 1635.
[13] F.J. Arnáiz, R. Aguado, M.R. Pedrosa, A. De Cian, Inorg. Chim. Acta 347 (2003) 33.
[14] J.H. Enemark, C.G. Young, Adv. Inorg. Chem. 40 (1994) 2.
[15] P.C.H. Mitchell, Quart. Rev. 20 (1966) 103.
[16] E.I. Stiefel, in: G. Wilkinson, R.D. Gillard, J.A. McCleverty (Eds.), Comprehensive Coordination Chemistry, vol. 3, Pergamon Press, Oxford, 1987, p. 1375, Chapter 36.5.
[17] W.A. Nugent, J.M. Mayer, Metal–Ligand Multiple Bonds, Wiley, New York, 1988.
[18] R.H. Holm, Chem. Rev. 87 (1987) 1401.
[19] H. Arzoumanian, R. Bakhtchadjian, G. Agrifoglio, H. Krentzien, J-C. Daran, Eur. J. Inorg. Chem. (1999) 2255.

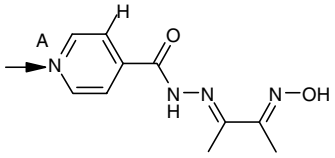
largely uninvestigated. As a ligand, the oxime moiety is potentially ambidentate [15] and can coordinate either through the nitrogen or oxygen atom. The vast literature on structural studies of oxime complexes reveals some interesting features of its coordination behavior. It may coordinate to one metal ion through the nitrogen atom and another metal ion through the oxygen atom. Thus it can form a $\mu_{1,2}(N,O)$ oximato-bridged extended network [16]. In the majority of complexes only the nitrogen atom coordinates to the metal center, and the oxygen atom does not take part in coordination [17]. The hydrogen atom of the oxime –OH group can form potentially strong intra- or intermolecular hydrogen bonds [18] with other donor atoms or groups. Thus metal complexes bearing non-deprotonated oximes may be considered as supramolecular synthons, capable of forming extended supramolecular networks via intermolecular hydrogen bonds. The orientation of the oxime group in these molecules plays a major role in determining the dimensionality of the extended network. Keeping this in mind, we have synthesized Schiff bases of diacetyl monooxime with benzoyl hydrazide, salicyloyl hydrazide, anthraniloyl hydrazide and isonicotinoyl hydrazide, to study the supramolecule forming abilities of these Schiff bases. These aroyl hydrazones have been chosen in such a way that the aroyl moiety varies from being a H-bond donor as well as acceptor (salicyloyl), only a H-bond donor (anthraniloyl) and only a H-bond acceptor (isonicotinoyl). We shall show below that such a systematic variation of the H-bond forming ability has a profound effect on the supramolecular structures of these molecules (see Scheme 1).



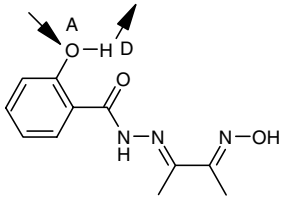
dmoBH : *The aroyl moiety has no H bond forming capability*



dmoAH :*The aroyl moiety is a H-bond donor only*



dmoInH :*The aroyl moiety is a H-bond acceptor only*



dmoSH :*The aroyl moiety is both a H-bond donor and H-bond acceptor*

Scheme 1. A graphical representation of the ligands showing the possible hydrogen bond donor and acceptor sites on the aroyl moiety.

2. Experimental

2.1. Materials

Diacetyl monooxime and methyl/ethyl esters of benzoic, salicylic, anthranilic and isonicotinic acids were obtained from Aldrich and were used without further purification. Organic solvents were purified following published procedures [19]. TEAP was prepared following the literature procedure [20].

2.2. Physical measurements

Elemental analyses were performed on a Perkin–Elmer 2400 C,H,N analyzer. UV–Vis spectra were recorded using a JASCO 7850 spectrophotometer. ^{1}H NMR spectra were recorded on a Bruker 500 MHz spectrometer using $Si(CH_3)_4$ as an internal standard. Cyclic voltammetry was carried out using a PAR Versastat instrument driven by E-chem software. A three-electrode configuration with Pt working and auxiliary electrodes, Ag/AgCl reference electrode and tetraethylammonium perchlorate (TEAP) as the supporting electrolyte was used. The potentials were calibrated against the ferrocene/ferrocenium couple.

2.3. Synthesis of the ligands

All the four aroyl hydrazides were prepared by known methods [21]. The four Schiff base ligands used in this study were prepared by refluxing an equimolar mixture of diacetyl monooxime and the respective hydrazide in methanolic medium. A typical synthesis is described below.

2.3.1. Benzoyl hydrazone of diacetyl monooxime (dmoBH)

To a 30 ml methanolic solution of diacetyl monooxime (1.01 g, 10 mmol), benzoyl hydrazide (1.36 g, 10 mmol) dissolved in 50 ml methanol was added and refluxed for 2.5 h. On reducing the volume to ~30 ml, a white solid appeared. The solid was filtered and thoroughly washed with ethanol (2×5 ml) followed by diethyl ether (2×5 ml). Yield: 1.58 g, 72%. The solid was recrystallised from hot ethanol. *Anal.* Calc. for $C_{11}H_{13}N_3O_2$: C, 60.27; H, 5.94; N, 19.18. Found: C, 60.71, H, 5.85; N, 18.98%. M.p. 190 °C. Selected IR bands (cm^{-1}): 3190 b (ν_{O-H}), 1671 ($\nu_{C=O}$), 1580 ($\nu_{C=N}$), 1024 (ν_{N-O}). ^{1}H NMR (DMSO-d_6, δ ppm): 2.15 (s, 3H), 3.29 (s, 3H), 7.49–7.50 (t, 2H), 7.56 (m, 1H), 7.82 (m, 2H), 10.68 (s, 1H), 11.57 (s, 1H).

2.3.2. Salicyloyl hydrazone of diacetyl monooxime (dmoSH)

Anal. Calc. for $C_{11}H_{13}N_3O_3$: C, 56.17; H, 5.53; N, 17.87. Found: C, 56.03; H, 5.42; N, 17.96%. M.p. 199 °C. Selected IR bands (cm^{-1}): 3286 b (ν_{O-H}), 1655($\nu_{C=O}$), 1608 ($\nu_{C=N}$), 1024 (ν_{N-O}). ^1H NMR (DMSO-d_6, δ ppm): 2.03 (s, 3H), 2.12 (s, 3H), 6.96–7.02 (m, 2H), 7.41 (t, 1H), 7.96 (d, 1H), 11.29 (s, 1H), 11.60 (s, 1H), 11.70 (s, 1H).

2.3.3. Anthraniloyl hydrazone of diacetyl monooxime (dmoAH)

Anal. Calc. for $C_{11}H_{14}N_4O_2$: C, 56.41; H, 5.98; N, 23.93. Found: C, 56.57; H, 5.87; N, 23.78%. M.p. 177 °C. Selected IR bands (cm^{-1}): 3190 b (ν_{O-H}), 1671 ($\nu_{C=O}$), 1580 ($\nu_{C=N}$), 1024 (ν_{N-O}). ^1H NMR (DMSO-d_6, δ ppm): 1.99 (s, 3H), 2.13 (s, 3H), 6.15 (s, 2H), 6.55 (t, 1H), 6.74 (d, 1H), 7.18 (t, 1H), 7.51 (d, 1H), 10.43 (s, 1H), 11.53 (s, 1H).

2.3.4. Isonicotinoyl hydrazone of diacetyl monooxime (dmoInH)

Anal. Calc. for $C_{10}H_{12}N_4O_2$: C, 54.55; H, 5.45; N, 25.45. Found: C, 54.82; H, 5.37; N, 25.67%. M.p. >250 °C. Selected IR bands (cm^{-1}): 3175 b (ν_{O-H}), 1675 ($\nu_{C=O}$), 1605 ($\nu_{C=N}$), 1026 (ν_{N-O}). ^1H NMR (DMSO-d_6,δ ppm): 2.03 (s, 3H), 2.17 (s, 3H), 7.70–7.75 (m, 2H), 8.68–8.69 (m, 2H), 10.92 (s, 1H), 11.67 (s, 1H).

2.4. Syntheses of the complexes

All the complexes were prepared following a similar method of reacting a methanolic solution of the metal salt, ligand and Et_3N in a 1:2:2 ratio. Preparation of one of the nickel complexes is described below.

*2.4.1. $Ni^{II}(dmoS)_2$ (**1**) · 2DMF*

To a 50 ml methanolic solution of the ligand dmoSH (0.235 g, 1 mmol) Et_3N (0.101 g, 1 mmol) was added with stirring when the initially colorless solution turned yellow. Addition of $Ni(ClO_4)_2.6H_2O$ (0.183 g, 0.5 mmol) to the yellow solution produced a light brown colored solution. After 5 h of stirring the volume of the solution was reduced to ~20 ml and filtered. A light brown colored solid was obtained. The residue was thoroughly washed with methanol (3 × 3 ml), followed by diethyl ether (2 × 5 ml). The crude product was recrystallised from a solution in a DMF–diethyl ether mixture. Yield 0.229 g, 68%. *Anal.* Calc. for $C_{28}H_{38}N_8NiO_8$: C, 49.89; H, 5.64; N, 16.63. Found: C, 50.02; H, 5.67; N, 16.71%. Selected IR bands (cm^{-1}): 3234 b (ν_{O-H}), 1496 s ($\nu_{C=N}$), 1057 s ($\nu_{C\text{-}Oenol}$), 977, 910 (ν_{N-O}). Electronic spectrum in DMSO solution, λ nm (ε M^{-1} cm^{-1}): 868 (24), 385sh (14474), 355 (24234), 318sh (20105), 287 (26205).

*2.4.2. $Ni^{II}(dmoA)_2$ (**2**) · 2DMF*

Yield: 72%. *Anal.* Calc. for $C_{28}H_{40}N_{10}NiO_6$: C, 50.15; H, 5.97; N, 20.89. Found: C, 50.39; H, 6.02; N, 20.78%. Selected IR bands (cm^{-1}): 3368 b (ν_{O-H}), 1488 s ($\nu_{C=N}$), 1056 s ($\nu_{C\text{-}Oenol}$), 1008 w, 965 w (ν_{N-O}). Electronic spectrum in DMSO solution, λ nm (ε M^{-1} cm^{-1}): 857 (31), 390sh (12578), 347 (23557).

*2.4.3. $Ni^{II}(dmoB)_2$ (**3**)*

Yield: 77%. *Anal.* Calc. for $C_{22}H_{24}N_6NiO_4$: C, 53.44; H, 4.86; N, 17.00. Found: C, 53.59; H, 4.90; N, 16.91%. Selected IR bands (cm^{-1}): 3420 b (ν_{O-H}), 1498 s ($\nu_{C=N}$), 1056 s ($\nu_{C\text{-}Oenol}$), 1008 w, 972 w (ν_{N-O}). Electronic spectrum in DMSO solution, λ nm (ε M^{-1} cm^{-1}): 470sh (709), 400 (2174), 350 (5561), 282 (26939).

*2.4.4. $Ni^{II}(dmoIn)_2$ (**4**)*

Yield: 69%. *Anal.* Calc. for $C_{20}H_{22}N_8NiO_4$: C, 48.38; H, 4.43; N, 22.58. Found: C, 48.51; H, 4.39; N, 22.72%. Selected IR bands (cm^{-1}): 3434 b (ν_{O-H}), 1489 s ($\nu_{C=N}$), 1055 s ($\nu_{C\text{-}Oenol}$), 1005 w, 965 w (ν_{N-O}). Electronic spectrum in DMSO solution, λ nm (ε M^{-1} cm^{-1}): 868 (27), 376 (15455), 284 (10213).

*2.4.5. $Zn^{II}(dmoS)_2$ (**5**)*

Yield: 75%. *Anal.* Calc. for $C_{22}H_{24}N_6Zn\ O_6$: C, 49.45; H, 4.49; N, 15.74. Found: C, 49.62; H, 4.44; N, 15.82%. Selected IR bands (cm^{-1}): 3185 b (ν_{O-H}), 1604 s ($\nu_{C=N}$), 1060 s ($\nu_{C\text{-}Oenol}$), 1016 w, 978 w (ν_{N-O}). Electronic spectrum in DMSO solution, λ nm (ε M^{-1} cm^{-1}): 389sh (13551), 379 (7331), 354 (25981), 315sh (21926), 286 (28077).

*2.4.6. $Zn^{II}(dmoA)_2$ (**6**)*

Yield: 62%. *Anal.* Calc. for $C_{22}H_{26}N_8ZnO_4$: C, 49.72; H, 4.89; N, 21.09. Found: C, 49.96; H, 4.92; N, 20.98%. Selected IR bands (cm^{-1}): 3435 b (ν_{O-H}), 1502 s ($\nu_{C=N}$), 1063 s ($\nu_{C\text{-}Oenol}$), 1006 w, 974 w (ν_{N-O}). Electronic spectrum in DMSO solution, λ nm (ε M^{-1} cm^{-1}): 422 (7360), 413sh (13413), 391(17807).

*2.4.7. $Zn^{II}(dmoB)_2$ (**7**)*

Yield: 69%. *Anal.* Calc. for $C_{22}H_{24}N_6ZnO_4$: C, 52.69; H, 4.79; N, 16.77. Found: C, 52.25; H, 4.75; N, 16.98%. Selected IR bands (cm^{-1}): 3421 b (ν_{O-H}), 1485 s ($\nu_{C=N}$), 1079 s ($\nu_{C\text{-}Oenol}$), 1002 w, 967w (ν_{N-O}). Electronic spectrum in DMSO solution, λ nm (ε M^{-1} cm^{-1}): 410 (7867), 370 (22209).

*2.4.8. $Zn^{II}(dmoIn)_2$ (**8**)*

Yield : 48%. *Anal.* Calc. $C_{20}H_{22}N_8ZnO_4$: C, 47.64; H, 4.37; N, 22.23. Found: C, 47.36; H, 4.32; N, 22.42%. Selected IR bands (cm^{-1}): 3420 b (ν_{O-H}), 1490 s ($\nu_{C=N}$), 1055 s ($\nu_{C\text{-}Oenol}$), 1000 w, 956 w (ν_{N-O}). Electronic spectrum in DMSO solution, λ nm (ε M^{-1} cm^{-1}): 376 (15103), 372 (6109).

2.5. X-ray crystallographic studies

X-ray quality single crystals were obtained by diffusion of a DMF (for **1** and **2**)/DMSO (for **5** and **8**) solution of the compound into liquid diethyl ether. Data were collected

on a Bruker Smart CCD area detector diffractometer at 93(2) K, using graphite monochromated Mo Kα radiation for **1**, **2** and **5** and using Cu Kα radiation at 293(2) K for **8**. The use of Cu Kα radiation for **8** was not for any scientific necessity but because of the limitations of the facility available at that point in time. The data were solved by direct methods and refined by the full matrix least squares method using SHELX-97 [22]. The non-hydrogen atoms were refined with anisotropic displacement parameters. All hydrogen atoms were placed at calculated positions and refined as riding atoms using isotropic displacement parameters. Corrections for Lorentz polarization effects and a semi empirical absorption were applied. The refinements converged with residuals summarized in Table 1.

2.6. Computational studies

All calculations were performed using the HYPERCHEM 7.01 program [23], using the default parameters of the program. The structure of the ligands were optimized first with MM^+, followed by the PM3 method [24]. Single point calculations on the hydrazone ligands in their coordination conformation were performed using the PM3 method, which includes configuration interaction arising from singly excited states arising from the 20 highest occupied and 20 lowest unoccupied molecular orbitals.

3. Results and discussion

3.1. Syntheses

The Schiff base ligands dmoBH, dmoSH, dmoAH and dmoInH were prepared according to the method described above. All the ligands were obtained in good yield and high purity, as confirmed by the spectroscopic data (IR and ^{1}H NMR spectra). All the complexes were obtained easily by stirring the reactants at room temperature in methanol. Use of one equivalent of base for each equivalent of ligand

Table 1
Crystal data and structure refinement for **1** · 2DMF, **2** · 2DMF, **5** and **8**

	1· 2DMF	**2** · 2DMF	**5**	**8**
Empirical formula	$C_{28}H_{38}N_8NiO_8$	$C_{28}H_{40}N_{10}NiO_6$	$C_{22}H_{24}N_6O_6Zn$	$C_{20}H_{22}N_8O_4Zn$
Formula weight	673.37	671.39	533.84	503.83
Temperature (K)	93(2)	93(2)	93(2)	293(2)
Wavelength (Å)	0.71073	0.71073	0.71073	1.54178
Crystal system	monoclinic	triclinic	orthorhombic	monoclinic
Space group	$P2_1/c$	$P\bar{1}$	*Aba*2	$C2/c$
Unit cell dimensions				
a (Å)	11.064(4)	11.735(5)	12.368(2)	20.738(6)
b (Å)	28.562(10)	12.424(5)	17.715(2)	8.594(2)
c (Å)	11.027(4)	12.990(5)	10.288(2)	13.615(4)
α (°)	90	90.339(7)	90	90
β (°)	114.112(6)	110.941(6)	90	114.54(2)
γ (°)	90	112.898(6)	90	90
Volume (Å^3)	3180.4(18)	1606.1(11)	2254.1(7)	2207.3(10)
Z	4	2	4	4
D_{calc} (Mg/m^3)	1.406	1.388	1.573	1.516
Absorption coefficient (mm^{-1})	0.671	0.661	1.143	1.939
F(000)	1416	708	1104	1040
Crystal size (mm)	$0.45 \times 0.35 \times 0.25$	$0.88 \times 0.20 \times 0.15$	$0.42 \times 0.40 \times 0.30$	$0.56 \times 0.25 \times 0.15$
θ Range for data collection (°)	1.43–28.19	1.70–28.63	2.30–28.31	5.66–68.48
Index ranges	$12 \leqslant h \leqslant 14$, $-37 \leqslant k \leqslant 37$, $-14 \leqslant l \leqslant 14$	$-15 \leqslant h \leqslant 14$, $-16 \leqslant k \leqslant 16$, $-17 \leqslant l \leqslant 14$	$-16 \leqslant h \leqslant 16$, $-23 \leqslant k \leqslant 23$, $-13 \leqslant l \leqslant 12$	$0 \leqslant h \leqslant 24$, $-10 \leqslant k \leqslant 0$, $-16 \leqslant l \leqslant 14$
Reflections collected	21 642	11 584	7919	2080
Independent reflections [R_{int}]	7459 [0.1001]	7384 [0.0434]	2327 [0.0346]	2022 [0.0630]
Maximum and minimum transmission	1.0000 and 0.5392	1.0000 and 0.5662	1.0000 and 0.7143	0.7995 and 0.4086
Data/restraints/parameters	7459/0/418	7384/0/420	2327/1/164	2022/0/153
Goodness-of-fit on F^2	1.015	1.022	1.079	1.036
Final R indices [$I > 2\sigma(I)$]	$R_1 = 0.0681$, $wR_2 = 0.1497$	$R_1 = 0.0602$, $wR_2 = 0.1338$	$R_1 = 0.0319$, $wR_2 = 0.0759$	$R_1 = 0.0621$, $wR_2 = 0.1474$
R indices (all data)	$R_1 = 0.1496$, $wR_2 = 0.1800$	$R_1 = 0.1014$, $wR_2 = 0.1510$	$R_1 = 0.0357$, $wR_2 = 0.0777$	$R_1 = 0.1228$, $wR_2 = 0.1834$
Largest difference in peak and hole (e Å^{-3})	0.796 and −0.734	0.817 and −0.776	0.957 and −0.224	0.249 and −0.444

left the oxime –OH unaffected. So this hydrogen can play an important role in determining the supramolecular architecture through hydrogen bonding.

3.2. Structures of Ni(dmoS)$_2$ (**1**) · 2DMF and Ni(dmoA)$_2$ (**2**) · 2DMF

The molecular structures of **1** and **2** are shown in Figs. 1 and 2, respectively. Selected bond distances and angles of the two molecules are collected in Table 2. The Ni(II) centers in both molecules are in a distorted octahedral geometry with a N_4O_2 donor environment. Each ligand is coordinated through the oxime nitrogen, the imine nitrogen and the enolate oxygen. The oxime oxygen does not participate in coordination. All the six bonds formed by the Ni(II) center are different and they vary in the following order for both molecules: Ni–N_{imine}(hydrazone) < Ni–O < Ni–N_{oxime}. This order is in agreement with earlier reports [25], where, for a tridentate ligand, the metal ligand bonds involving the terminal donors were found to be longer than that involving the central donor. The main reason behind this observation is probably the relatively small bite angles of the chelates which results in a bending away of the terminal donors from the metal d_σ and p_σ orbitals. The average Ni–N_{oxime} and Ni–O bond lengths for the two molecules are very close to each other, while the average Ni–N_{imine} bond length for **2** is larger than that of **1**. A plot of the lone pair energy of the donor atom (L), obtained by PM3 calculation on the deprotonated ligands, versus Ni–L distance was found to be linear (Fig. 3;

Table 2
Bond lengths (Å) and angles (°) for **1** · 2DMF and **2** · 2DMF

	1 · 2DMF	**2** · 2DMF
Ni–N(2A)	1.984(3)	1.985(3)
Ni–N(2B)	1.997(3)	1.982(3)
Ni–O(2A)	2.083(3)	2.076(2)
Ni–O(2B)	2.090(3)	2.110(2)
Ni–N(1A)	2.132(4)	2.135(3)
Ni–N(1B)	2.121(4)	2.195(3)
N(2A)–Ni–N(2B)	172.27(15)	177.94(12)
N(2A)–Ni–O(2A)	77.82(13)	76.35(11)
N(2B)–Ni–O(2A)	94.45(12)	102.49(11)
N(2A)–Ni–O(2B)	101.40(13)	102.24(10)
N(2B)–Ni–O(2B)	78.04(12)	76.06(10)
O(2A)–Ni–O(2B)	90.84(12)	93.23(10)
N(2A)–Ni–N(1B)	104.77(14)	106.17(11)
N(2B)–Ni–N(1B)	76.01(13)	75.53(11)
O(2A)–Ni–N(1B)	94.42(13)	93.56(10)
O(2B)–Ni–N(1B)	153.83(12)	151.58(10)
N(2A)–Ni–N(1A)	76.94(14)	76.16(11)
N(2B)–Ni–N(1A)	110.78(13)	105.00(11)
O(2A)–Ni–N(1A)	154.76(12)	152.50(10)
O(2B)–Ni–N(1A)	94.13(13)	93.30(11)
N(1B)–Ni–N(1A)	91.95(14)	93.29(11)

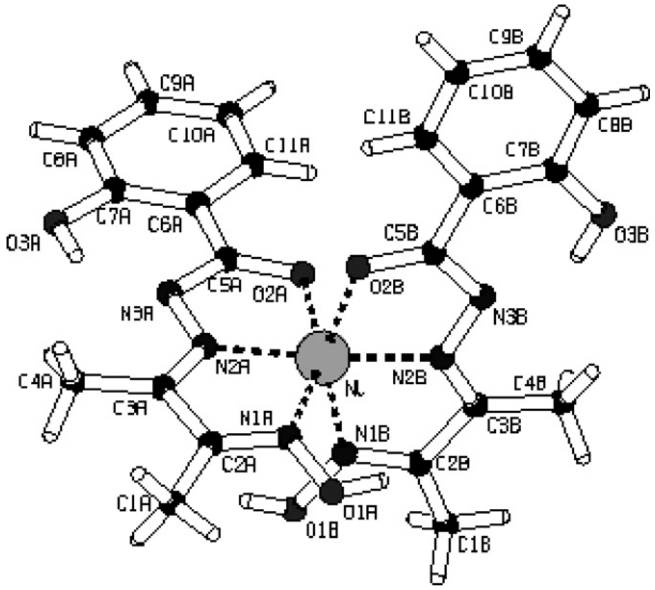


Fig. 1. PLUTON [26] diagram for the Ni(II) coordination sphere of $Ni^{II}(dmoS)_2$ (**1**) · 2DMF along with atom numbering scheme.

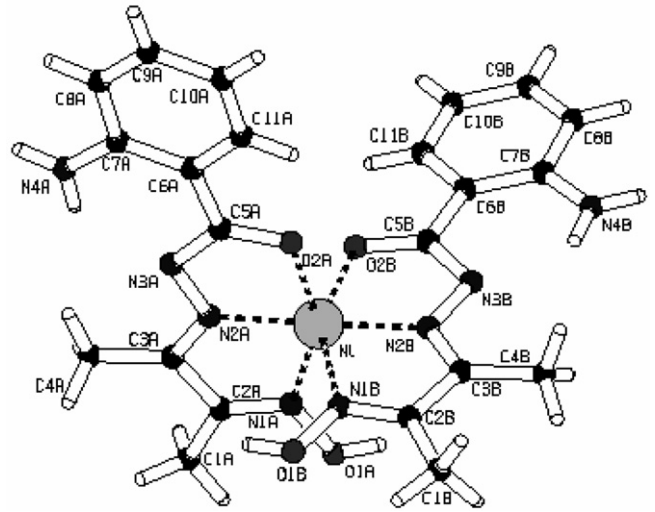


Fig. 2. PLUTON diagram for the Ni(II) coordination sphere of $Ni^{II}(dmoA)_2$ (**2**) · 2DMF along with atom numbering scheme.

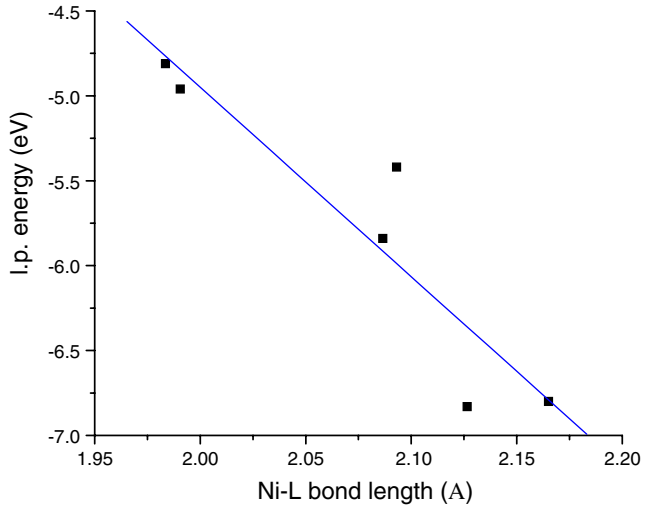


Fig. 3. Plot of lone pair energy of the donor atoms (L) vs. Ni–L bond length.

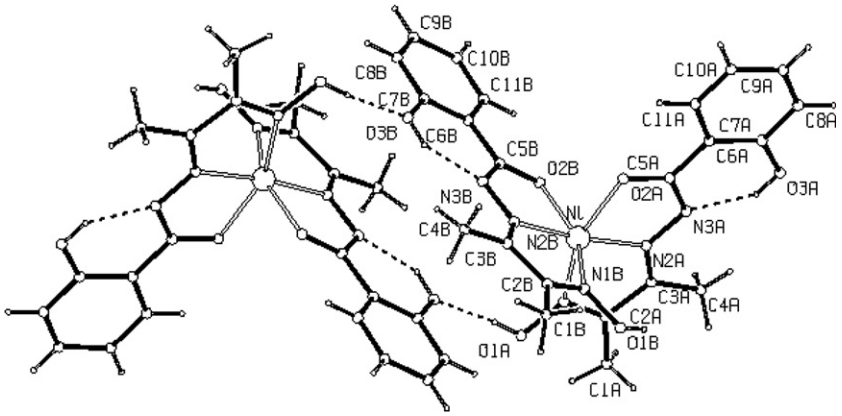


Fig. 4. H-bonded dimer formation for **1**.

|R| = 0.92). Each ligand forms two planar chelate rings and the dihedral angle between these two rings is between 0.90° and 1.34°, suggesting overall planarity of the tridentate ligands which favors substantial electron delocalization over the ligand backbone.

The chelate rings formed by the second ligand are almost orthogonal to those formed by the first. For both **1** and **2** there are two intramolecular hydrogen bonds, formed between N3A and N3B and the phenolic hydrogens H3AA and H3BA for **1** and between N3A and N3B and the aniline hydrogens H4AE and H4BE for **2**.

Though the molecular structures of **1** and **2** are very similar, the three-dimensional supramolecular structures of **1** and **2** are radically different, because of the different H-bonding abilities of the pendant phenolic –OH (for **1**) and anilinic $-NH_2$ (for **2**). Both the compounds contain two co-crystallized DMF molecules in the asymmetric unit, and these co-crystallized solvent molecules play vital roles in linking the close packed individual residues in the crystal into a supramolecular network.

In **1** there are a pair of hydrogen bonds between the oxime hydrogen H1AD and the phenolic oxygen O3B of an adjacent molecule and the oxime hydrogen H1AD of the second molecule with the phenolic oxygen O3B of the first molecule, resulting in formation of self assembled complementary hydrogen bonded dimers (Fig. 4). There are two sets of DMF molecules in the lattice. One set of DMF molecules, whose oxygen and nitrogen atoms are designated as O2S and N2S, respectively (residue 3), are involved in connecting the dimers along the '*b*' axis via O(1B)–H(1BD)···O(2S) and C(12S)–H(12A)···O(1B)[a] hydrogen bonds (Fig. 5, Table 3), resulting in a zig-zag pattern along this axis (symmetry code for a is $1-2x$, $1-2y$, $1-2z$). The other set of DMF molecules, whose oxygen and nitrogen atoms are designated as O1S and N1S (residue 2), connect the dimeric units along the '*a*' axis through C–H···O hydrogen bonds. The C4B–H4BB of one molecule of a dimer is hydrogen bonded to O1S, while the hydrogen of C(22S)–H(22C) bond of the same DMF is weakly hydrogen bonded to the oxime oxygen O1B of an adjacent dimer. Thus each dimer unit is connected to its adjacent two dimer units via a pair of H-bonding DMF molecules, resulting in a one dimensional chain (along the '*a*' axis) of dimers (Fig. 6). Apart from hydrogen bond-

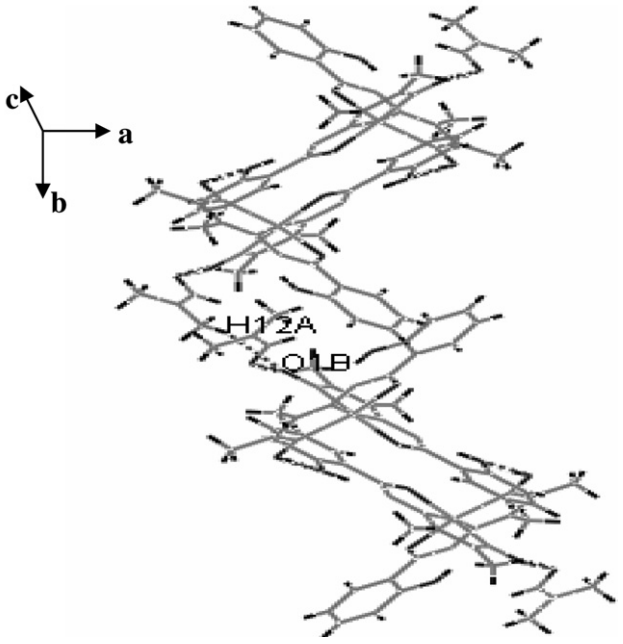


Fig. 5. Propagation of H-bonded dimers of **1** along the '*b*' axis'' view along c^* (perpendicular to the *ab* plane).

Table 3
Hydrogen bonds for Ni(dmoS)$_2$ (**1**) · 2DMF (Å and °)

D–H···A	*d*(D–H)	*d*(H···A)	*d*(D···A)	∠(DHA)
O(1A)–H(1AD)···O(3B)#1	0.84	1.78	2.620(4)	172.9
O(3A)–H(3AA)···N(3A)	0.84	1.85	2.583(5)	145.4
O(1B)–H(1BD)···O(2S)	0.84	1.79	2.607(4)	165.1
O(3B)–H(3BA)···N(3B)	0.84	1.78	2.515(4)	145.9
C(4B)–H(4BB)···O(1S)	0.98	2.44	3.247(7)	139.0
C(22S)–H(22A)···O(1S)	0.98	2.41	2.794(10)	103.0
C(12S)–H(12A)···O(1B)[a]	0.98	2.52	3.236(8)	130.0
C(22S)–H(22C)···O(1B)[b]	0.98	2.62	3.539(8)	156.0

Symmetry transformations: #1 = $-x+1$, $-y+1$, $-z+1$; a = $1-2x$, $1-2y$, $1-2z$; b = $-1+x$, y, z.

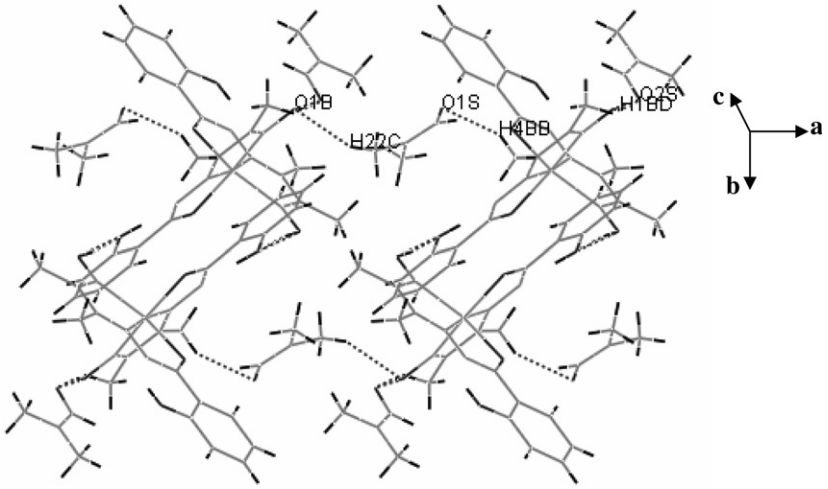


Fig. 6. Propagation of the dimers units of **1** along the '*a*' axis (view along c^*).

ing DMF molecules described above, that bind pairs of adjacent dimers along the '*a*' axis, the adjacent dimers are also connected to each other via complementary C–H···O hydrogen bonds involving the C–H protons H4AB and H1AC of the CH_3 fragments of one dimeric unit and the oxime and amide oxygens O1A and O2B respectively of the other dimeric unit (Supplementary Figure, SF 1). Different parallel one dimensional chains (along the '*a*' axis) are interconnected along the '*c*' axis through C(13S)–H(13C)···O(1S)^b hydrogen bonds (symmetry code for b is $1 + x$, y, $1 + z$) (Supplementary Figure, SF 2).

Unlike **1** · 2DMF, where there are discrete hydrogen bonded dimers in the solid state, there is no such dimer formation in the crystal structure of **2** · 2DMF. Moreover, the oxime oxygens or hydrogens of a given Ni(II) complex moiety (residue 1) do not participate in hydrogen bonding with the adjacent Ni(II) complex moieties, rather they only form hydrogen bonds with nearby solvent molecules.

There are two pendant anilinic $-NH_2$ moieties in a given asymmetric unit. As mentioned earlier each one of these $-NH_2$ groups forms one intramolecular hydrogen bond with the corresponding amide nitrogen. The two intramolecular hydrogen bonds are N(4A)–H(4AE)···N(3A) and N(4B)–H(4BD)···N(3B). Apart from these intramolecular hydrogen bonds, each anilinic $-NH_2$ moiety is also involved in one intermolecular hydrogen bond formation using its own hydrogen atom and the amide oxygen of a neighboring unit (Fig. 7). Thus N4A is connected to O2B

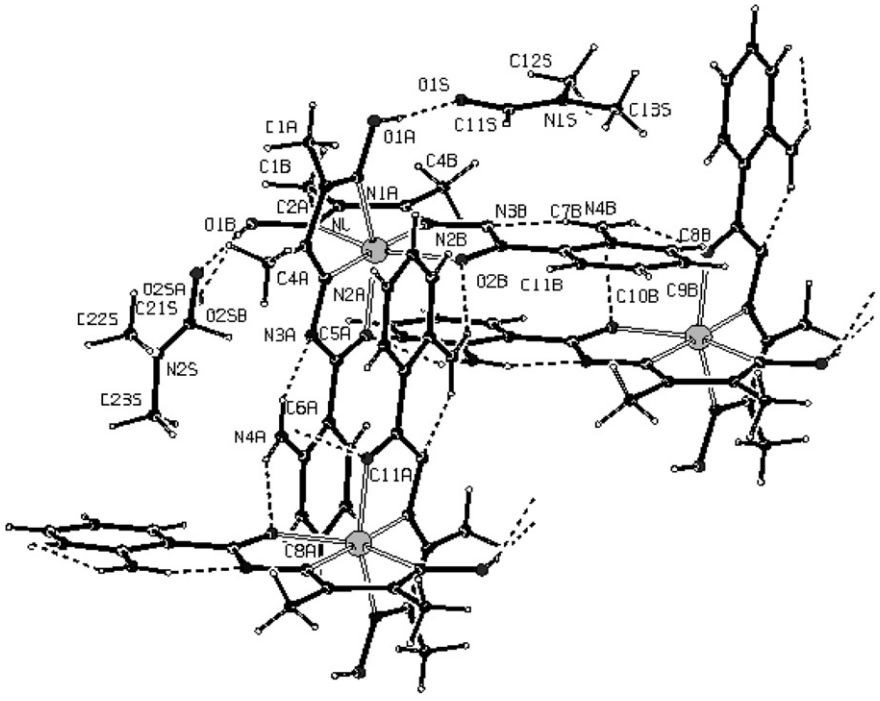


Fig. 7. Complementary hydrogen bonds with the adjacent units in a three-dimensional supramolecular assembly of **2** · 2DMF.

Table 4
Hydrogen bonds for Ni(dmoA)$_2$ (**2**) · 2 DMF (Å and °)

D–H···A	*d*(D–H)	*d*(H···A)	*d*(D···A)	∠(DHA)
O(1A)–H(1AD)···O(1S)	0.84	1.79	2.612(4)	164.1
O(1B)–H(1BD)···O(2SA)	0.84	1.78	2.595(5)	162.0
O(1B)–H(1BD)···O(2SB)	0.84	1.86	2.488(13)	130.3
N(4A)–H(4AD)···O(2B)^{c}	0.88	2.18	2.976(3)	150.9
N(4A)–H(4AE)···N(3A)	0.88	2.06	2.709(4)	129.4
N(4B)–H(4BE)···O(2A)^{d}	0.88	2.11	2.919(4)	153.1
N(4B)–H(4BD)···N(3B)	0.88	2.03	2.673(4)	129.4
C(8A)–H(8AA)···O(2B)	0.95	2.59	3.337(4)	136.0
C(9A)–H9AA···O(1A)^{e}	0.95	2.43	3.358(5)	165.0

Symmetry transformations: c = 1 − *x*, 1 − *y*, −*z*; d = 1 − *x*, 1 − *y*, −1 − *z*; e = −1 + *x*, −1 + *y*, *z*.

of a neighboring unit via N(4A)–H(4AD)···O(2B)^{c} while N4B is connected to O2A of another neighboring unit via N(4B)–H(4BE)···O(2A)^{d} hydrogen bonds (symmetry code for c is 1 − *x*, 1 − *y*, −*z*; and that for d is 1 − *x*, 1 − *y*, −1 − *z*; Table 4). An identical pair of hydrogen bonds connects O2A and O2B of the first unit with the N4B^{d} and N4A^{c} of the other two units, respectively. N4A^{d}, O2B^{d} and N4B^{c} and O2A^{c} are then involved in similar hydrogen bonding interactions with their adjacent units resulting in the propagation of a complementary hydrogen bonded self assembled infinite zig-zag chain along the '*c*' axis (Supplementary Figure SF4). Apart from the N–H···O bonds described above, which are responsible for the propagation of the infinite chain, there are also complementary C–H···O contacts lending additional stability to the chain. The major such contacts are: C(8A)–H(8AA)···O(2B)^{c} and C(8A)–H(8AA)^{c}···O(2B); C(8B)–H(8BA)···O(2A)^{d} and C(8B)–H(8BA)^{d}···O(2A). Two neighboring chains are connected by C(9A)–H(9AA)···O(1A)^{e} hydrogen bonds (symmetry code for e is −1 + *x*, −1 + *y*, *z*). The co-crystallized DMF molecules are hydrogen bonded to their parent Ni(II) complex unit via O(1A)–H(1AD) ···O(1S) and O(1B)–H(1BD)···O(2SA) interactions.

3.3. Structures of Zn(dmoS)$_2$ (5) and Zn(dmoIn)$_2$ (8)

The Zn(II) complexes **5** and **8** crystallize without incorporating any solvent molecules in their lattice. The molecular structures of both the Zn(II) complexes possess a C_2 symmetry which makes the two ligands coordinated to a given metal ion equivalent (Figs. 8 and 9). Zn(II) is in a highly distorted octahedral environment in both molecules, however in **8** the distortion of the Zn(II) coordination polyhedron is much more severe than that in **5**. Thus in **5** the *cis*-angles vary between 73.47(8)° and 119.10(8)°, while the *trans*-angles are in the range 148.31(7)–162.81(12)° (Table 5). In **8**, the *cis*-angles are in the range 68.19(17)–129.17(18)°, while the *trans*-angles are in the range 142.2(3)–146.17(15)°. The Zn–N(2) and Zn–O(2) distances are shorter in **8** compared to those in **5**, however the Zn–N(1) distance is considerably shorter in **5** than that in **8**. In **5** the five-membered chelate rings involving the oxime nitrogen and imine nitrogen constitute good least square planes (planes containing the atoms Zn, N(1), C(2), C(3) and N(2) and their symmetry related counterparts, $\chi^2 = 53.2$), while the planarity of the chelate rings involving the hydrazone fragments only (i.e. planes containing Zn,

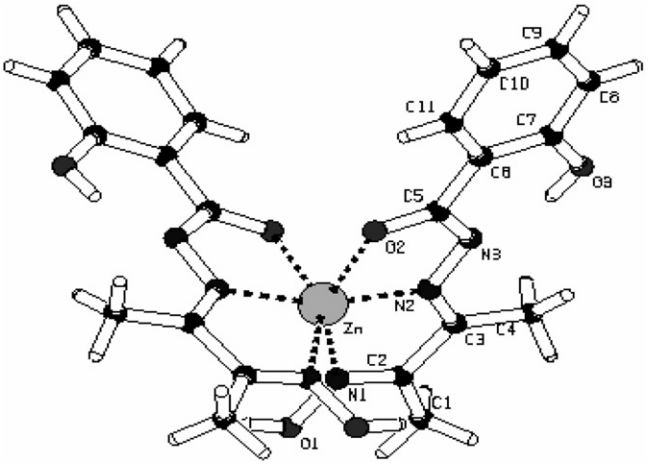


Fig. 8. PLUTON diagram of Zn^{II}(dmoS)$_2$ (**5**) with the atom numbering scheme.

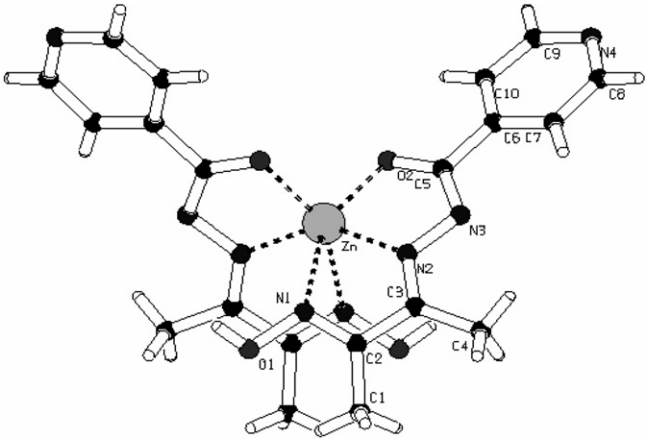


Fig. 9. PLUTON diagram of Zn^{II}(dmoIn)$_2$ (**8**) with the atom numbering scheme.

Table 5
Bond lengths (Å) and angles (°) for **5** and **8**

	5	**8**
Zn–N(2)	2.051(2)	2.015(5)
Zn–O(2)	2.172(2)	2.020(4)
Zn–N(1)	2.228(2)	2.575(5)
N(2)–Zn–N(2)#1	162.81(12)	142.2(3)
N(2)–Zn–O(2)	75.56(7)	78.63(17)
N(2)#1–Zn–O(2)	92.59(8)	129.17(18)
O(2)–Zn–O(2)#1	93.81(11)	95..9(2)
N(2)–Zn–N(1)#1	119.10(8)	83.49(17)
O(2)–Zn–N(1)#1	94.11(8)	99.88(17)
O(2)–Zn–N(1)	148.31(7)	146.17(15)
N(2)–Zn–N(1)	73.47(8)	68.19(17)

Symmetry transformation to get the equivalent position #1: for **5** is −*x*, −*y*, *z*; for **8** is −*x*, *y*, −*z* + 3/2.

N(2), N(3), C(5) and O(2) and their symmetry related counterparts, $\chi^2 = 3108.0$), are relatively poor. The dihedral angle between the two chelate planes formed by a given ligand is ~5°, which may be compared with the value of ~1° found in the corresponding Ni(II) complex **1** · 2DMF, containing the same ligand, indicating the ligand is more puckered in the Zn(II) complex. The metal ligand distances in the Ni(II) complex are also much shorter than the corresponding Zn(II) complex, probably because of the crystal field stabilization energy of Ni(II) as well as due to its more regular geometry. In contrast to **5**, no reasonably good least square plane can be described which includes the oxime nitrogen N(1) or its symmetric equivalent N(1A) for compound **8**, though the hydrazone fragment consisting of N(2), N(3), C(5), O(2) or its symmetrically equivalent counterpart along with Zn form a least square plane with $\chi^2 = 432.0$. The dihedral angle between the chelate planes involving the hydrazone fragment of the two ligands is only 68.5(2)° in **8**, compared to the near ideal value of 88.10(10)° for **5**.

Whereas the Ni(II) complex (**1**) of the salicyloyl hydrazone ligand of DAMO (dmoSH) forms self assembled complementary H-bonded dimers in the solid state, the corresponding Zn(II) complex (**5**) of the same ligand is connected to four similar neighboring units through H-bonds (Table 6). The two pendant phenolic oxygens O3 and O3#1 of each complex unit are H-bonded to the oxime oxygens $O1^f$ and $O1^g$ of two neighboring units via O(1)–$H(1D)^f\cdots O(3)$ and O(1)–$H(1D)^g\cdots O(3\#1)$ ($f = 1/2 + x$, $-y$, $-1/2 + z$, $g = -1/2 - x$, y, $-1/2 + z$). Again the two pendant oxime hydrogens O(1)–H(1D) and O(1#1)–H(1D#1) connect the first unit with two other neighboring units via O(1)–H(1D)···$O(3)^h$ and O(1#1)–H(1D#1)···$O(3)^i$ ($h = -1/2 + x$, $-y$, $1/2 + z$; $i = 1/2 - x$, y, $1/2 + z$). The phenolic oxygens of the complex units f and g and the oxime hydrogens of complex units h and i then participate in further hydrogen bonding to form a layer structure (Figs. 10 and 11). Several such layers are then arranged along the *b* axis to produce a three-dimensional array.

The molecules of **8** self organize into two interpenetrating one-dimensional zig-zag chains through complementary pairs of hydrogen bonding (Fig. 12, Table 7). Each complex moiety is connected to two adjacent moieties (of symmetry $j = x + 1/2$, $-y + 1/2$, $z + 1/2$ and $\mathbf{k} = -x$, y, $-z + 3/2$) via O(1)–H(1D)···$N(4)^j$ and O(1)–$H(1D)^k\cdots$N(4) hydrogen bonds, where any given complex unit acts as an acceptor of two hydrogen bonds (from one oxime hydrogen of each of the two adjacent units) using its two isonicotinic nitrogens N4 and N4#1, and using two of its own oxime hydrogens H1D and H1D#1 to act as donors

Table 6
Hydrogen bonds for $Zn(dmoS)_2$ (**5**) (Å and °)

D–H···A	*d*(D–H)	*d*(H···A)	*d*(D···A)	∠(DHA)
O(1)–H(1D)···$O(3)^h$	0.84	1.74	2.580(3)	172.8
O(3)–H(3O)···N(3)	0.84	1.69	2.443(3)	148.7

Symmetry transformations: $h = -1/2 + x$, $-y$, $1/2 + z$.

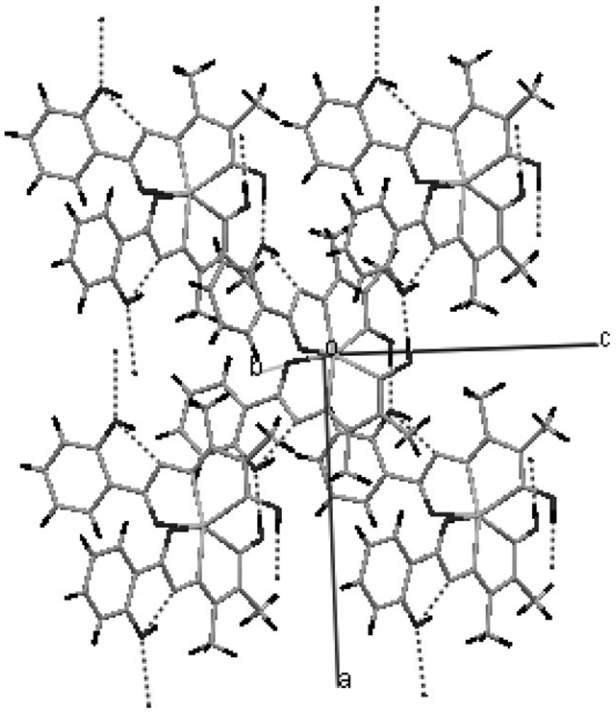


Fig. 10. Layer structure of **5**.

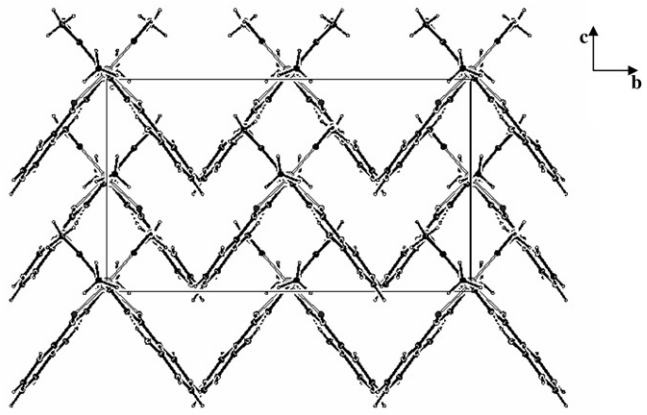


Fig. 11. Packing diagram of **5**.

of two hydrogen bonds, one each to two of its adjacent units described above. As a result of the formation of these hydrogen bonded zig-zag chains, the isonicotinic rings of two adjacent moieties become parallel to each other. These two rings have a C_g–C_g distance of 3.843(4) Å (C_g is the centroid of the ring [26]), resulting in appreciable π–π interactions between them.

3.4. IR spectra

In all the ligands and the corresponding complexes, a broad band in the region 3100–3300 cm^{-1} indicates the presence of hydrogen bonded –OH groups. The ν_{N-H} band for the amide functionality (in the free ligand) and that of the $-NH_2$ group (for anthraniloyl hydrazone) is buried under the broad band of –OH. In all the ligands a strong

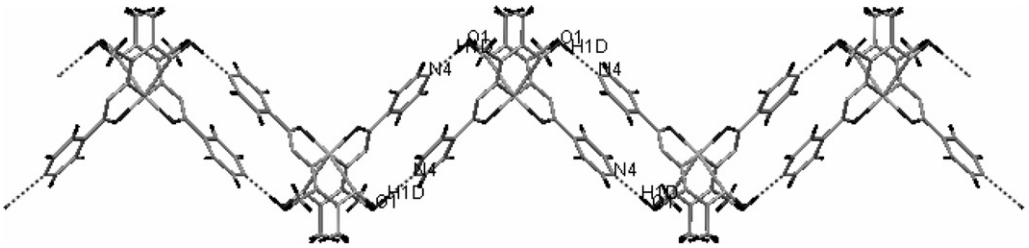


Fig. 12. Two interpenetrating one-dimensional zig-zag chains through complementary pairs of hydrogen bonding in **8** (view along the '*c*' axis).

Table 7
Hydrogen bonds for $Zn(dmoIn)_2$ (**8**) (Å and °)

D–H···A	*d*(D–H)	*d*(H···A)	*d*(D···A)	∠(DHA)
O(1)–H(1D)···N(4)^{j}	0.82	1.87	2.686(7)	171.5

Symmetry transformations: j = $x + 1/2$, $-y + 1/2$, $z + 1/2$.

sharp band is observed spanning the region 1648–1675 cm^{-1}, due to C=O stretching. This band disappears in the complexes and a new band develops around 1050 cm^{-1}. This is a clear evidence of enolization of the ligands during complexation. A moderately strong band in the ligands between 1580 and 1608 cm^{-1} due to $\nu_{C=N}$ shifts to lower energy in the complexes, indicating the participation of the imine nitrogen in coordination. All the ligands and the complexes show one or more weak bands in the region 1050–900 cm^{-1} due to oxime N–O stretching.

3.5. Electronic spectra

Electronic spectra of the nickel complexes in DMSO solution show a broad band of very low intensity ($\varepsilon \sim 30\ M^{-1}\ cm^{-1}$) around ~850 nm. This band seems to be an overlapping of the spin allowed transition $^3A_2 \rightarrow {}^3T_1$ (ν_2) with the spin forbidden transition $^3A_2 \rightarrow {}^1E$ [27]. The ν_3 band is masked by a high intensity charge transfer band around ~380 nm, while the ν_1 band is probably located above 1000 nm, which is beyond the detection range of our instrument. Additionally, there are charge transfer bands and intraligand transitions present in the UV region for all the complexes (Supplementary Figure SF6 and SF7) .

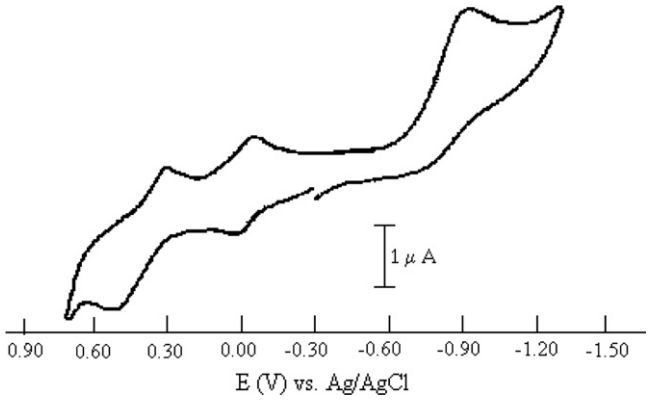


Fig. 13. Cyclic voltammogram (scan rate 10 mV s^{-1}) of $Ni(dmoA)_2$ (**2**) · 2DMF in DMSO solution at a platinum electrode at 298 K.

3.5.1. Electrochemical properties

Anodic scans of all the Ni(II) and Zn(II) complexes show an irreversible or quasi-reversible oxidation in the region 0.40–0.70 V (Table 8). So this oxidation is definitely a ligand based oxidation. The Ni(II) complexes **2** and **3** show a reversible oxidative Ni^{II}/Ni^{III} couple with $E_{1/2}$ values of 0.14 and 0.07 V respectively (Fig. 13). An irreversible reduction peak in the region −0.8 to 1.0 V is obtained for most of the complexes on a cathodic scan. This peak has been assigned to reduction of the ligand.

4. Conclusions

We have designed four ligands in such a way that they can have different types of hydrogen bonding ability. All the ligands contain the oxime moiety, which can be a

Table 8
Cyclic voltammetric data

Compounds	Metal centered oxn.			Ligand based oxn.			Ligand based redn.
	E_{pa} (V)	E_{pc} (V)	ΔE_p (mV)	E_{pa} (V)	E_{pc} (V)	ΔE_p (mV)	E_{pc} (V)
1 · 2DMF				0.511	0.411	100	
2 · 2DMF	0.048	−0.016	64	0.542	0.365	177	−0.878
3	0.106	0.036	70				−0.869
4				0.438	0.358	80	−0.854
5				0.685			
6				0.690			−0.795
7				0.671			−0.940
8							

hydrogen bond donor as well as an acceptor. In the salicyloyl hydrazide Schiff bases, the salicyl –OH group can also function as a hydrogen bond donor as well as acceptor. The aromatic $–NH_2$ group in anthraniloyl hydrazone has two hydrogen atoms for donation but it cannot act as a hydrogen bond acceptor. On the other hand, the isonicotinoyl nitrogen can only act as an H-bond acceptor. In $Ni(dmoS)_2$ (**1**) · 2DMF and $Zn(dmoS)_2$ (**5**) the salicyloyl hydrazone moiety forms two different types of hydrogen bonding pattern; in $Ni(dmoS)_2$ (**1**) · 2DMF it forms a linear chain of dimers, whereas in $Zn(dmoS)_2$ (**5**) it forms a hydrogen bonded layer structure. Thus the metal ions can be used to control the stereochemical orientation of the ligands which in turn determine the nature of the hydrogen bonded supramolecular network. In $Ni(dmoA)_2$ (**2**) · 2DMF each $–NH_2$ group in anthraniloyl hydrazone acts as one intramolecular and one intermolecular hydrogen bond donor, leading to the formation of a one dimensional zig-zag chain. A zig-zag chain is also formed in $Zn(dmoIn)_2$ (**8**). In $Ni(dmoS)_2$ (**1**) · 2DMF, $Ni(dmoA)_2$ (**2**) · 2DMF and $Zn(dmoIn)_2$ (**8**) the supramolecular network is obtained via self assembly through complementary hydrogen bonding, however such complementary hydrogen bonding is absent in $Zn(dmoS)_2$ (**5**). As the compounds are soluble only in DMF or DMSO and **1** and **2** only crystallize from DMF while for **5** and **8** crystals were obtained only from a DMSO solution, we cannot investigate the role of the solvent in determining the supramolecular structure, particularly for **1** and **2**.

Acknowledgments

This work has been supported by grants from AICTE and UGC, Government of India, New Delhi. S.N. acknowledges UGC, Government of India, for financial support. We also acknowledge the use of IR and UV–Vis spectrophotometers of our department purchased from a DST (India)-FIST grant.

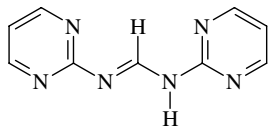
Appendix A. Supplementary material

CCDC 287946, 287947, 287948 and 287945 contain the supplementary crystallographic data for **1** · 2DMF, **2** · 2DMF, **5** and **8**. These data can be obtained free of charge via http://www.ccdc.cam.ac.uk/conts/retrieving.html, or from the Cambridge Crystallographic Data Centre, 12 Union Road, Cambridge CB2 1EZ, UK; fax: (+44) 1223-336-033; or e-mail: deposit@ccdc.cam.ac.uk. Supplementary data associated with this article can be found, in the online version, at doi:10.1016/j.poly.2007.03.063.

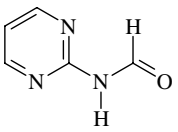
References

[1] D. Braga, F. Grepioni, G.R. Desiraju, Chem. Rev. 98 (1998) 1375.
[2] D. Braga, F. Grepioni, Coord. Chem. Rev. 183 (1999) 19.
[3] D. Braga, F. Grepioni, Acc. Chem. Res. 33 (2000) 601.
[4] N.J. Burke, A.D. Burrows, A.S. Donovan, R.W. Harrington, M.F. Mahon, C.E. Price, Dalton Trans. (2003) 3840.
[5] D.M.P. Mingos, M. Alajarin, A.E. Aliev, A.D. Burrows, K.D.M. Harris, A. Pastor, J.W. Steed, D.R. Turner, Supramolecular Assembly via Hydrogen Bonds, vol. 1, Springer, Berlin, 2004.
[6] (a) S.S.M. Chung, W.S. Li, M. Schröder, Chem. Commun. (1997) 1005;
(b) A.J. Blake, N.R. Champness, A.N. Khlobystov, D.A. Lemenovskii, W.S. Li, M. Schröder, Chem. Commun. (1997) 1339.
[7] (a) L. Carlucci, G. Ciani, D.W.V. Gudenberg, D.M. Proserpio, Inorg. Chem. 36 (1997) 3812;
(b) D. Wang, K. Kim, J. Am. Chem. Soc. 119 (1997) 451.
[8] (a) M. Fujita, Y.J. Kwon, O. Sasaki, K. Yamaguchi, K. Ogura, J. Am. Chem. Soc. 117 (1995) 7287;
(b) H.J. Choi, M.P. Suh, J. Am. Chem. Soc. 120 (1998) 10622.
[9] (a) T.L. Hennigar, D.C. MacQuarrie, P. Losier, R.D. Rogers, M.J. Zaworotko, Angew. Chem., Int. Ed. Engl. 36 (1997) 972;
(b) A.J. Blake, N.R. Champness, A.N. Khlobystov, D.A. Lemenovskii, W.S. Li, M. Schröder, Chem. Commun. (1997) 2027;
(c) Y.-B. Dong, R.C. Layland, M.D. Smith, N.G. Pschirer, U.H.F. Bunz, H.-C. zur Loye, Inorg. Chem. 38 (1999) 3056.
[10] (a) M. Fujita, Y.J. Kwon, S. Wsahizu, K. Ogura, J. Am. Chem. Soc. 116 (1994) 1151;
(b) F. Lloret, G.D. Munno, J. Miguel, J. Cano, R. Ruiz, A. Canesschi, Angew. Chem., Int. Ed. Engl. 37 (1998) 135;
(c) G.A. Doyle, D.M.L. Goodgame, S.P.W. Hill, D.J. Williams, J. Chem. Soc., Chem. Commun. (1993) 207;
(d) Y.-B. Dong, R.C. Layland, N.G. Pschirer, M.D. Smith, U.H.F. Bunz, H.-C. zur Loye, Chem. Mater. 11 (1999) 1415.
[11] (a) M. Ruben, J.-M. Lehn, G. Vaughan, Chem. Commun. (2003) 1338;
(b) L.H. Uppadine, J.-P. Gisselbrecht, J.-M. Lehn, Chem. Commun. (2004) 718.
[12] S. Naskar, D. Mishra, S.K. Chattopadhyay, M. Corbella, A.J. Blake, Dalton Trans. (2005) 2428.
[13] S. Naskar, M. Corbella, A.J. Blake, S.K. Chattopadhyay, Dalton Trans. (2007) 1150.
[14] S. Naskar, S. Biswas, D. Mishra, B. Adhikary, L.R. Falvello, T. Soler, C.H. Schwalbe, S.K. Chattopadhyay, Inorg. Chim. Acta 357 (2004) 4257.
[15] A. Chakravorty, Coord. Chem. Rev. 13 (1974) 1.
[16] (a) S. Sreerama, S. Pal, Inorg. Chem. 41 (2002) 4843;
(b) D. Datta, A. Chakravorty, Inorg. Chem. 21 (1982) 363;
(c) S. Ross, T. Weyhermüller, E. Bill, E. Bothe, U. Flörke, K. Wieghardt, P. Chaudhuri, Eur. J. Inorg. Chem. (2004) 984;
(d) S. Wan, W. Mori, S. Yamada, S.I. Murahashi, Bull. Chem. Soc. Jpn. 62 (1989) 435.
[17] (a) J. Korvenranta, H. Saarinen, M. Näsäkkälä, Inorg. Chem. 21 (1982) 4296;
(b) J.G. Mohanty, R.P. Singh, A. Chakravorty, Inorg. Chem. 14 (1975) 2178;
(c) A.N. Singh, R.P. Singh, J.G. Mohanty, A. Chakravorty, Inorg. Chem. 16 (1977) 2597;
(d) J.G. Mohanty, A. Chakravorty, Inorg. Chem. 15 (1976) 2912;
(e) A.G. Lappin, M.C.M. Laranjeira, R.D. Peacock, Inorg. Chem. 22 (1983) 786.
[18] (a) V.Y. Kukuskin, T. Nishioka, T. Tudela, K. Isobe, I. Kinoshita, Inorg. Chem. 36 (1997) 6157;
(b) R.S. Bendre, R.J. Butcher, A.S. Kuwar, Acta Cryst. E 61 (2005) 3511.
[19] D.D. Perrin, W.L.F. Armarego, P.R. Perrin, Purification of Laboratory Chemicals, Pergamon Press, Oxford, 1966.
[20] D.T. Sawyer, A. Sobkowiak, J.L. Roberts Jr., Electrochemistry for Chemists, second ed., Wiley, New York, 1995, p. 333.
[21] E.H. Rodd, Chemistry of Carbon Compounds, vol. 3, part A, Elsevier, London, 1954, p. 556.
[22] G.M. Sheldrick, SHELX97 [Includes SHELXS97, SHELXL97, CIFTAB], Program for Crystal Structure Analysis (Release 97-2), Göttingen, Germany, 1998.

[23] Hyperchem for Windows, Release 7.01, Hypercube Inc., 115 NW, 4th Street, Gainesville, FL 32601.
[24] (a) J.J.P. Stewart, J. Comput. Chem. 12 (1991) 320;
(b) J.J.P. Stewart et al. QCPE# 50.
[25] (a) D. Mishra, S. Naskar, S.K. Chattopadhyay, M. Maji, P. Sengupta, R. Dinda, S. Ghosh, T.C.W. Mak, Transition Met. Chem. 30 (2005) 352;
(b) R.P. Thummel, Y. Jahng, Inorg. Chem. 25 (1986) 2527;
(c) H. Sugimoto, K. Tsuge, K. Tanaka, J. Chem. Soc., Dalton Trans. (2001) 57.
[26] A.L. Spek, PLATON, A Multiple Crystallographic Tool, Utrecht University, Utrecht, The Netherlands, 2005.
[27] A.B.P. Lever, Inorganic Electronic Spectroscopy, second ed., Elsevier, Amsterdam, 1984, p. 507.



HL1



HL2

2. Experimental

2.1. General procedures

All manipulations were carried out under dry, oxygen-free nitrogen by using Schlenk techniques, unless otherwise noted. Diethyl ether, hexanes and tetrahydrofuran were purified by distillation from sodium/benzophenone. NMR spectra were measured on a Bruker Avance 300 MHz spectrometer. UV–Vis spectra were obtained from a Shimadzu UV-2450 spectrometer. Elemental analyses were obtained from a PE 2400 series II CHNS/O analyzer or Perkin–Elmer CHN-2400.

2.2. Materials

Molybdenum carbonyl was purchased from Strem Chemical Co. and used as received. $Mo_2(O_2CCH_3)_4$ [9], *N*,*N*′-bis(pyrimidine-2-yl)formamidine (H**L1**) [10] and *N*-(2-pyrimidinyl)formamide (H**L2**) [11] were prepared according to the previously reported procedures.

2.3. Preparations of $Mo_2(O_2CCH_3)$(**L1**) $_2$(**L2**) (**1**)

H**L1** (0.40 g, 2.0 mmol) and H**L2** (0.12 g, 1.0 mmol) were placed in a flask containing $Mo_2(O_2CCH_3)_4$ (0.44 g, 1.0 mmol) in 15 mL THF. The mixture was then stirred at room temperature for 1 h to yield a red solution. The solvent was reduced and ether added to induce precipitation. The solid was filtered, washed with ether and then dried under reduced pressure. Yield: 0.23 g (23%). *Anal.* Calc. for $C_{33}H_{34}Mo_2N_{15}O_5$ (MW = 912.61): C, 43.43; H, 3.76; N, 23.02. Found: C, 43.02; H, 3.57; N, 23.42%. ^{1}H NMR (300 MHz, DMSO-d_6): δ 2.53 (s, 3H, CH_3), 6.77 (t, 1H, H^{para}, $^3J_{H-H} = 4.41$ Hz), 7.03 (t, 2H, H^{para}, $^3J_{H-H} = 4.70$ Hz), 7.06 (t, 2H, H^{para}, $^3J_{H-H} = 4.70$ Hz), 8.20 (dd, 1H, H^{meta}, $^3J_{H-H} = 2.35$ Hz), 8.32 (d, 1H, H^{meta}, $^3J_{H-H} = 4.70$ Hz), 8.42 (d, 4H, H^{meta}, $^3J_{H-H} = 4.70$ Hz), 8.48 (d, 4H, H^{meta}, $^3J_{H-H} = 5.00$ Hz), 9.99 (s, 1H, CH), 10.41 (s, 2H, CH). IR (cm^{-1}, KBr disk): 1698(m), 1637(m), 1560(m), 1521(m), 1387(s), 1307(m), 1285(m), 1243(w), 1098(w), 965(w), 882(w), 811(m), 677(w), 641(w), 482(w), 459(w), 442(w). UV–Vis (λ_{max}, nm (ε, M^{-1} cm^{-1})): 453 (3802). Crystals suitable for X-ray crystallography were obtained by layering a THF solution of **1** with hexanes.

2.4. Preparation of trans-Mo_2(**L1**)$_2$ (**L2**)$_2$ (**2**)

H**L1** (0.40 g, 2.0 mmol) and H**L2** (0.24 g, 2.0 mmol) were placed in a flask containing $Mo_2(O_2CCH_3)_4$ (0.44 g, 1.0 mmol) in 15 mL CH_3CN. The mixture was then stirred at room temperature for 1 h to yield a red solution. The solvent was reduced and ether added to induce precipitation. The red solid was filtered, washed with ether and then dried under reduced pressure. The ^{1}H NMR spectrum shows that only one complex form was obtained, which was characterized as *trans*-Mo_2 (**L1**)$_2$(**L2**)$_2$ by X-ray crystallography. Plate red crystals were obtained by layering the red solution of *trans*-Mo_2(**L1**)$_2$(**L2**)$_2$ in CH_3CN with ether. 0.30 g (31%). *Anal.* Calc. for $C_{28}H_{22}Mo_2N_{18}O_3$ (MW = 834.52): C, 44.14; H, 4.01; N, 25.73. Found: C, 44.17; H, 3.72; N, 26.12%. ^{1}H NMR (300 MHz, DMSO-d_6): δ 6.86 (t, 2H, H^{para}, $^3J_{H-H} = 4.41$ Hz), 7.03 (t, 4H, H^{para}, $^3J_{H-H} = 4.70$ Hz), 8.45 (d, 10H, H^{meta}, $^3J_{H-H} = 4.70$ Hz), 8.75 (dd, 2H, H^{meta}, $^3J_{H-H} = 2.35$ Hz), 10.01 (s, 2H, CH), 10.36 (s, 2H, CH). IR (cm^{-1}, KBr disk): 1660(m), 1581(m), 1560(m), 1534(m), 1516(s), 1426(s), 1385(s), 1351(s), 1301(w), 1288(s), 1258(m), 1205(w), 1185(w), 1100(w), 1016(w), 991(w), 976(m), 939(m), 882(m), 817(m), 790(m), 735(w), 705(w), 652(w), 640(w), 606(w), 531(w), 440(w). UV–Vis (λ_{max}, nm (ε, M^{-1} cm^{-1})): 538 (1419).

2.5. Preparation of cis-Mo_2(**L1**)$_2$ (**L2**)$_2$ (**3**)

When the reaction described for the preparation of **2** was carried out in 15 mL MeOH, a red solid was obtained. The ^{1}H NMR spectrum shows that two complexes were formed in about equal amounts. By layering the solution of the red solid in THF with ether, both plate and hexagonal crystals were formed and were separated manually. The plate crystals were characterized as **2**, while the hexagonal ones as **3** by X-ray crystallography. Yield for **3**: 0.12 g (14%). *Anal.* Calc. for $C_{28}H_{22}Mo_2N_{18}O_3$ (MW = 834.52): C, 44.14; H, 4.01; N, 25.73. Found: C, 44.22; H, 3.82; N, 26.01%. ^{1}H NMR (300 MHz, DMSO-d_6): δ 6.81 (t, 2H, H^{para}, $^3J_{H-H} = 4.70$ Hz), 6.97 (t, 2 H, H^{para}, $^3J_{H-H} = 4.41$ Hz), 7.00 (t, 2H, H^{para}, $^3J_{H-H} = 4.70$ Hz), 8.11 (d, 4H, H^{meta}, $^3J_{H-H} = 4.70$ Hz), 8.45 (d, 4H, H^{meta}, $^3J_{H-H} = 4.70$ Hz), 8.53 (dd, 2H, H^{meta}, $^3J_{H-H} = 2.35$ Hz), 8.65 (dd, 2H, H^{meta}, $^3J_{H-H} = 2.35$ Hz), 10.08 (s, 2H, CH), 10.37 (s, 2 H, CH). IR (cm^{-1}, KBr disk): 1650(m), 1519(m), 1427(m), 1388(s), 1288(m), 1245(w), 1188(w), 995(s), 875(s), 767(m), 640(w), 601(w). UV–Vis (λ_{max}, nm (ε, M^{-1} cm^{-1})): 533 (1790).

2.6. Preparations of Mo_2(**L2**)$_4$ (**4**)

A solution of Na**L2** was prepared by stirring $NaNH_2$ (0.078 g, 2.0 mmol) and H**L2** (0.25 g, 2.0 mmol) in THF (20 mL) at room temperature for 1 h. The resulting solution was then transferred to a flask containing a solution of $Mo_2(O_2CCH_3)_4$ (0.22 g, 0.5 mmol) in 20 mL THF. A

Table 1
Crystal data for complexes **1**–**4**

Compound	**1**	**2**	**3**	**4**
Formula	$C_{25}H_{21}Mo_2N_{15}O_3$	$C_{36}H_{38}Mo_2N_{18}O_4$	$C_{28}H_{22}Mo_2N_{18}O_2$	$C_{20}H_{16}Mo_2N_{12}O_4$
Fw	771.45	978.72	834.52	680.33
Crystal system	orthorhombic	monoclinic	monoclinic	tetragonal
Space group	*Pnma*	*P*2(1)/*c*	*P*2(1)/*c*	$P\bar{4}c2$
a (Å)	27.689(5)	8.7663(13)	9.8328(7)	17.3458(15)
b (Å)	15.407(3)	11.206(2)	12.9195(9)	17.3458(15)
c (Å)	10.0355(16)	20.821(3)	33.666(2)	33.104(4)
α (°)	90	90	90	90
β (°)	90	96.221(3)	91.1570(10)	90
γ (°)	90	90	90	90
V (Å^3)	4281.2(13)	2033.2(5)	4275.9(5)	9960.1(18)
Z	4	2	4	14
D_{calc} (g/cm^3)	1.197	1.600	1.296	1.588
F(000)	1536	992	1664	4704
Crystal size (mm)	0.1 × 0.4 × 0.2	0.1 × 0.4 × 0.2	0.1 × 0.1 × 0.2	0.30 × 0.45 × 0.50
Data collections and instruments	Siemens P4	Siemens CCD	Siemens CCD	Siemens P4
Range (2θ) for data collection (°)	3.96 ⩽ 2 ⩽ 49.98	3.94 ⩽ 2 ⩽ 55.16	3.38 ⩽ 2 ⩽ 57.64	3.32 ⩽ 2 ⩽ 50.00
Limiting indices *hkl*	−1 to 32, −18 to 1, −1 to 11	−11 to 10, −9 to 14, −26 to 24	−13 to 13, −17 to 17, −45 to 45	0–20, 0–20, 0–39
Reflections collected	5867	12280	59545	8844
Independent reflections (R_{int})	3867 (0.0678)	4650 (0.0632)	11153 (0.0647)	8679 (0.0333)
Data/restraints/parameters	3867/0/226	4650/0/269	11153/0/451	8679/0/602
Goodness of fit indicator[c]	1.054	1.006	1.010	1.023
Final *R* indices [$I > 2\sigma(I)$][a,b]	$R_1 = 0.0699$, $wR_2 = 0.1177$	$R_1 = 0.0495$, $wR_2 = 0.0788$	$R_1 = 0.0355$, $wR_2 = 0.0674$	$R_1 = 0.0521$, $wR_2 = 0.0881$
R indices (all data)	$R_1 = 0.1632$, $wR_2 = 0.1307$	$R_1 = 0.1599$, $wR_2 = 0.0847$	$R_1 = 0.0668$, $wR_2 = 0.0707$	$R_1 = 0.0929$, $wR_2 = 0.0974$
Largest difference in peak and hole (e/Å^{-3})	0.856 and −1.200	0.694 and −0.458	0.523 and −0.494	0.492 and −0.405

$a = 0.0177$, $b = 5.9520$, **1**; $a = 0.0080$, $b = 0$, **2**; $a = 0.0252$, $b = 0$, **3**; $a = 0.0100$, $b = 0$, **4**.

[a] $R_1 = \Sigma\|F_o| - |F_c\|/\Sigma|F_o|$.

[b] $wR_2 = [w(F_o^2F_c^2)^2/w(F_o^2)^2]^{1/2}$. $w = 1/[\sigma^2(F_o^2) + (ap)^2 + (bp)], p = [\max(F_o^2 \text{ or } 0) + 2(F_c^2)]/3$.

[c] Goodness-of-fit = $[\Sigma w(F_o^2F_c^2)^2/N_{observed} - N_{parameters}]^{1/2}$.

red solution formed immediately, which was stirred until some yellow solid began to precipitate. The solid was filtered and dried under vacuum to give a yellow powder. Yield: 0.23 g (67%). *Anal*. Calc. for $C_{20}H_{16}Mo_2N_{12}O_4$ (MW = 680.33): C, 35.30; H, 2.37; N, 24.69. Found: C, 34.97; H, 2.17; N, 25.01%. ^{1}H NMR (300 MHz, DMSO-d_6): δ 7.12 (t, 4 H, H^{para}, $^3J_{H-H} = 4.70$ Hz), 8.08 (dd, 4H, H^{meta}, $^3J_{H-H} = 2.35$ Hz), 8.66 (dd, 4H, H^{meta}, $^3J_{H-H} = 2.35$ Hz), 10.01 (s, 4H, CH). IR (cm^{-1}, KBr disk): 1626(m), 1580(m), 1542(m), 1450(s), 1288(m), 1188(m), 947(w), 797(w), 506(w). UV–Vis (λ_{max}, nm (ε, M^{-1} cm^{-1})): 550 (1620). Crystals suitable for X-ray crystallography were obtained by slow diffusion of ether into a THF solution of **4**.

3. X-ray crystallography

The diffraction data of complexes **1**–**4** were collected at 22 °C on a Siemens P4 diffractometer or Siemens SMART CCD diffractometer, which was equipped with graphite-monochromated Mo Kα ($K_\alpha = 0.71073$ Å) radiation. The crystals suitable for X-ray crystallography were sealed inside the capillary. Data reduction was carried by standard methods with use of well-established computational procedures [12]. The structure factors were obtained after Lorentz and polarization correction. The structure of complex **1** was solved by a direct method and refined by using least-squares refinements [13]. The final agreement factors were $R_1 = 0.0699$, w$R_2 = 0.1177$. The crystallographic procedures for complexes **2**–**4** were similar to those for **1**. Disordered solvent molecules, presumabled to be THF, are presented in complexes **1**, **3** and **4,** and the PLATON/

Table 2
Selected bond distances (Å) and angles (°) for **1**

Distances			
Mo(1)–Mo(2)	2.0951(17)	Mo(1)–N(3)	2.145(6)
Mo(1)–N(7)	2.140(11)	Mo(2)–N(4)	2.147(6)
Mo(2)–N(8)	2.159(9)	Mo(2)–O(2)	2.155(8)
Mo(1)–O(1)	2.121(9)		
Angles			
Mo(2)–Mo(1)–O(1)	90.0(2)	Mo(1)–Mo(2)–O(2)	92.7(3)
Mo(1)–Mo(2)–N(4)	91.5(2)	Mo(1)–Mo(2)–N(8)	92.7(3)
Mo(2)–Mo(1)–N(3)	91.8(2)	Mo(2)–Mo(1)–N(7)	92.0(3)
O(1)–Mo(1)–N(3)	89.93(19)	O(1)–Mo(1)–N(7)	177.9(4)
O(2)–Mo(2)–N(4)	91.14(18)	O(2)–Mo(2)–N(8)	174.6(4)
N(3)–Mo(1)–N(3A)	176.4(4)	N(7)–Mo(1)–N(3)	90.00(19)
N(4A)–Mo(2)–N(4)	176.1(4)	N(4)–Mo(2)–N(8)	88.72(18)

Table 3
Selected bond distances (Å) and angles (°) for **2**

Distances			
Mo–Mo(A)	2.103(1)	Mo–N(3A)	2.130(5)
Mo–N(4)	2.144(5)	Mo–N(7)	2.130(6)
Mo–N(9A)	2.113(7)		
Angles			
Mo(A)–Mo–N(9A)	88.8(2)	Mo(A)–Mo–N(3A)	92.5(2)
N(9A)–Mo–N(3A)	92.6(2)	Mo(A)–Mo–N(7)	94.1(2)
N(9A)–Mo–N(7)	177.1(3)	N(3A)–Mo–N(7)	87.4(2)
Mo(A)–Mo–N(4)	92.5(2)	N(9A)–Mo–N(4)	89.9(2)
N(3A)–Mo–N(4)	174.5(2)	N(7)–Mo–N(4)	89.9(2)

SQUEEZE tool was applied [14]. Large solvent void volumes were observed for these structures. The relative percentages per unit cell are 40.4% for **1** (1730.8 out of 4281.2 $Å^3$), 32.4% for **3** (1386.8 out of 4275.9 $Å^3$) and 20.4% for **4** (2029.7 out of 9960 $Å^3$). Where relevant, data cited are given without disordered solvent contributions. Basic information pertaining to the crystal parameters and structure refinement is summarized in Table 1. Selected bond distances and angles for **1**–**4** are given in Tables 2–5.

4. Results and discussion

4.1. Syntheses and spectroscopic studies

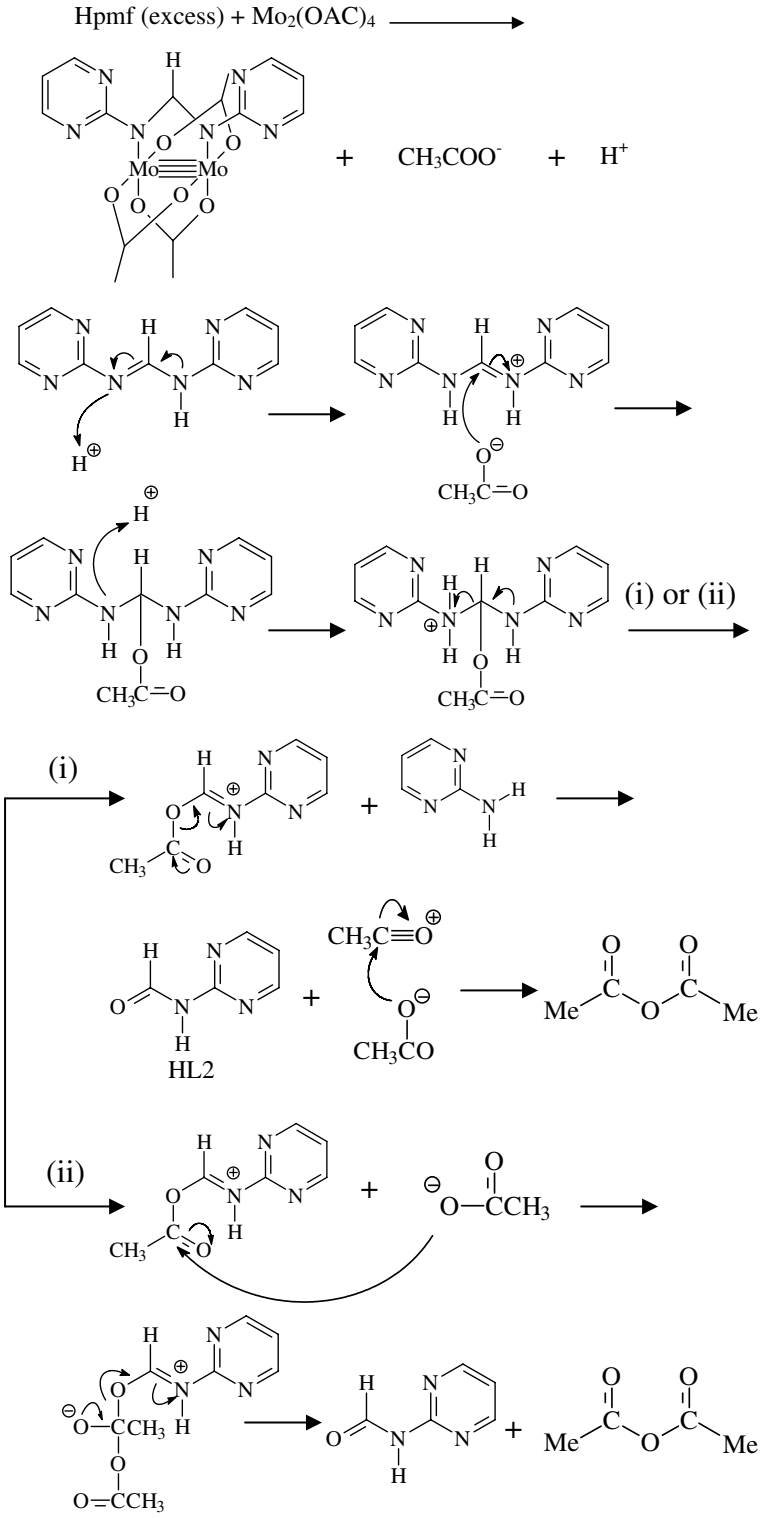
By the reaction of 2 equiv. of *N*,*N*′-bis(pyrimidyl-2-yl)formamidine (H**L1**) and 1 equiv. of *N*-(2-pyrimidinyl)formamide (H**L2**) with 1 equiv. of $Mo_2(O_2CCH_3)_4$ in THF, the complex $Mo_2(O_2CCH_3)(\mathbf{L1})_2(\mathbf{L2})$ (**1**) was obtained. When the reaction was carried out in a 2:2:1 ratio in CH_3CN, the complex *trans*-$Mo_2(\mathbf{L1})_2(\mathbf{L2})_2$ (**2**) was isolated. Both complexes **2** and *cis*-$Mo_2(\mathbf{L1})_2(\mathbf{L2})_2$ (**3**) can be prepared if the reaction in a 2:2:1 ratio was carried out in CH_3OH. The plate and hexagonal crystals which were obtained for **2** and **3**, respectively, were separated manually. To our best knowledge, it is the first time that both *cis* and *trans* forms of dimolybdenum complexes containing formamidinate ligands are able to be separated by using different solvents. The complex $Mo_2(\mathbf{L2})_4$ (**4**) was prepared by reacting the sodium salt of *N*-(2-pyrimidinyl)formamide (H**L2**) with $Mo_2(O_2CCH_3)_4$ in THF. These complexes were characterized by spectroscopic methods and their structures determined by X-ray crystallography. There were distinct color changes from yellow to red in these reactions. These complexes are air-sensitive and decompose in air after several days. In the UV–Vis spectra, complexes **1**–**4** show the lowest energy bands at 453, 538, 533 and 530 nm, respectively, which can be assigned to the $\delta \rightarrow \delta^*$ excitations of the Mo–Mo quadruple bonds. For the two isomers **2** and **3**, the *trans* form is red-shifted by 5 nm from the *cis* form. Complexes **1**–**3** were first obtained unexpectedly with low yields in the reactions of $Mo_2(O_2CCH_3)_4$with excess H**L1** in different solvents, presumably due to the decomposition of H**L1** to H**L2**. Two possible decomposition pathways

Table 5
Selected bond distances (Å) and angles (°) for one of the three independent molecules of **4**, which contains Mo(1) and Mo(2) atoms

Distances			
Mo(1)–Mo(2)	2.0866(10)	Mo(1)–N(1)	2.145(7)
Mo(1)–N(7)	2.148(7)	Mo(1)–N(11)	2.161(7)
Mo(1)–N(5)	2.177(7)	Mo(2)–N(4)	2.151(7)
Mo(2)–N(10)	2.138(7)	Mo(2)–N(8)	2.158(7)
Mo(2)–N(2)	2.183(8)		
Angles			
Mo(2)–Mo(1)–N(1)	92.47(19)	Mo(2)–Mo(1)–N(7)	91.6(2)
N(1)–Mo(1)–N(7)	176.0(3)	Mo(2)–Mo(1)–N(11)	93.78(18)
N(1)–Mo(1)–N(11)	88.0(3)	N(7)–Mo(1)–N(11)	91.8(3)
Mo(2)–Mo(1)–N(5)	94.24(18)	N(1)–Mo(1)–N(5)	87.2(3)
N(7)–Mo(1)–N(5)	92.5(3)	N(11)–Mo(1)–N(5)	170.8(3)
Mo(1)–Mo(2)–N(4)	91.70(19)	Mo(1)–Mo(2)–N(10)	91.39(19)
N(4)–Mo(2)–N(10)	176.9(3)	Mo(1)–Mo(2)–N(8)	94.38(19)
N(4)–Mo(2)–N(8)	91.0(3)	N(10)–Mo(2)–N(8)	89.3(3)
Mo(1)–Mo(2)–N(2)	93.5(2)	N(4)–Mo(2)–N(2)	89.5(3)
N(10)–Mo(2)–N(2)	89.9(3)	N(8)–Mo(2)–N(2)	172.1(3)

Table 4
Selected bond distances (Å) and angles (°) for **3**

Distances			
Mo(1)–Mo(2)	2.1017(3)	Mo(1)–N(3)	2.1632(19)
Mo(1)–N(9)	2.1520(19)	Mo(1)–N(13)	2.197(2)
Mo(1)–N(18)	2.1524(19)	Mo(2)–N(4)	2.1427(18)
Mo(2)–N(10)	2.1615(19)	Mo(2)–N(15)	2.1463(18)
Mo(2)–N(16)	2.1817(19)		
Angles			
Mo(2)–Mo(1)–N(9)	92.94(5)	Mo(2)–Mo(1)–N(18)	91.65(5)
N(9)–Mo(1)–N(18)	172.13(7)	Mo(2)–Mo(1)–N(3)	90.37(5)
N(9)–Mo(1)–N(3)	94.44(7)	N(18)–Mo(1)–N(3)	91.92(8)
Mo(2)–Mo(1)–N(13)	93.06(5)	N(9)–Mo(1)–N(13)	86.33(7)
N(18)–Mo(1)–N(13)	87.04(7)	N(3)–Mo(1)–N(13)	176.45(8)
Mo(1)–Mo(2)–N(15)	91.90(5)	Mo(1)–Mo(2)–N(4)	93. 93(5)
N(15)–Mo(2)–N(4)	173.40(7)	Mo(1)–Mo(2)–N(10)	91.98(5)
N(15)–Mo(2)–N(10)	90.09(7)	N(4)–Mo(2)–N(10)	92.80(7)
Mo(1)–Mo(2)–N(16)	93.3(1)	N(15)–Mo(2)–N(16)	86.22(7)
N(4)–Mo(2)–N(16)	90.36(7)	N(10)–Mo(2)–N(16)	173.64(7)



Scheme 1. Two possible decomposition pathways for the formation of H**L2**.

are proposed, Scheme 1, involving the attack of the hydroxyl oxygen atom of the CH_3COO^- anion obtained from the reaction of $Mo_2(O_2CCH_3)_4$ with excess H**L1** to the methine carbon atom of the protonated H**L1** ligand, followed by breaking of the N–C bond to give H**L2**, 2-aminopyrimidine and acetic anhydride. The acetic anhydride was characterized by its IR spectrum. The acetyl cation, CH_3CO^+, has been used in the acetylation of benzene [15] and the formation of acetic anhydride by decomposition of acetic acid adsorbed on Ni(111) has been reported [16].

4.2. Structure of *1*

Red crystals of **1** conform to the space group *Pnma* with eight molecules in a unit cell. Fig. 1a shows the ORTEP diagram for **1**. The molecular structure of **1** consists of two molybdenum atoms [Mo–Mo = 2.0951(17) Å] which are spanned by one bridging acetate, two **L1** and one **L2** ligand. The **L1** ligands are coordinated to the molybdenum centers through the two central nitrogen atoms, leaving the pyrimidyl nitrogen atoms uncoordinated and resulting in Mo···N intra-molecular interactions of 3.067 and 3.114 Å to the pyrimidyl nitrogen atoms. The **L2** ligand is coordinated to the metal centers through one of the pyrimidyl nitrogen atoms and the amine nitrogen atom, resulting in a Mo···O distance of 3.174 Å to the uncoordinated oxygen atom. The observed Mo–N distances fall in a wide range from 2.140 to 2.159 Å in **1**. The molecules of **1** are interlinked through extensive C–H···N (H···N = 2.536 Å, ∠C–H···

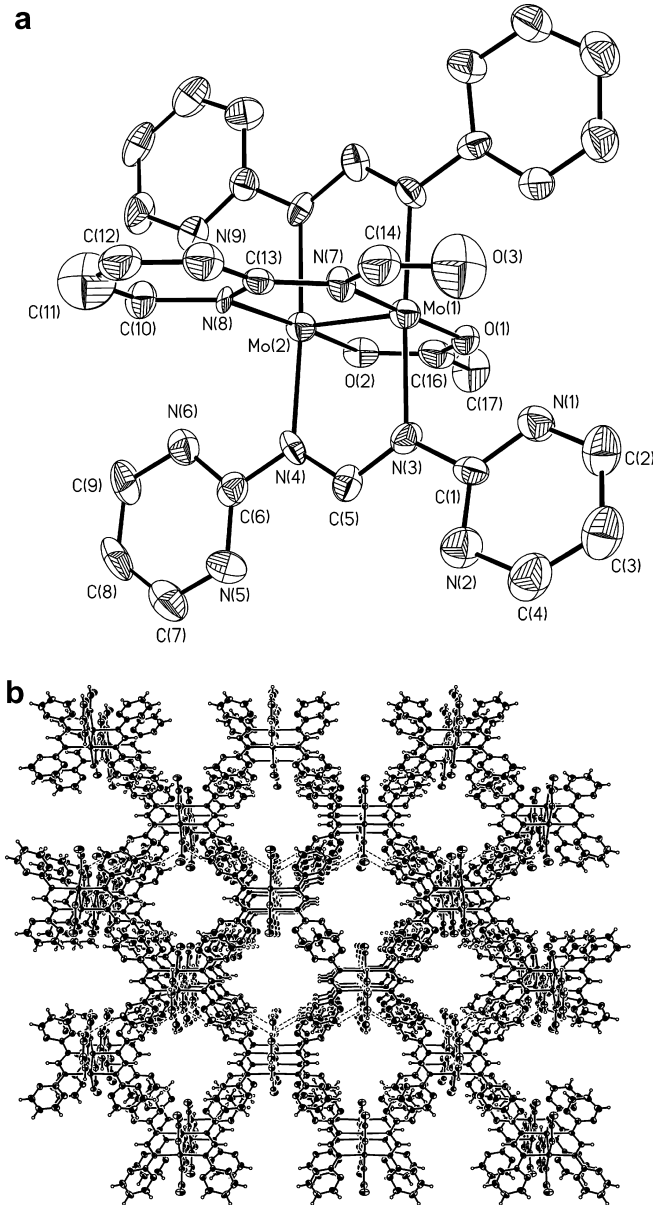


Fig. 1. (a) An ORTEP diagram showing the structure of **1**. Thermal ellipsoids are shown at the 30% probability level for the molecular structure. (b) The packing diagram of **1**.

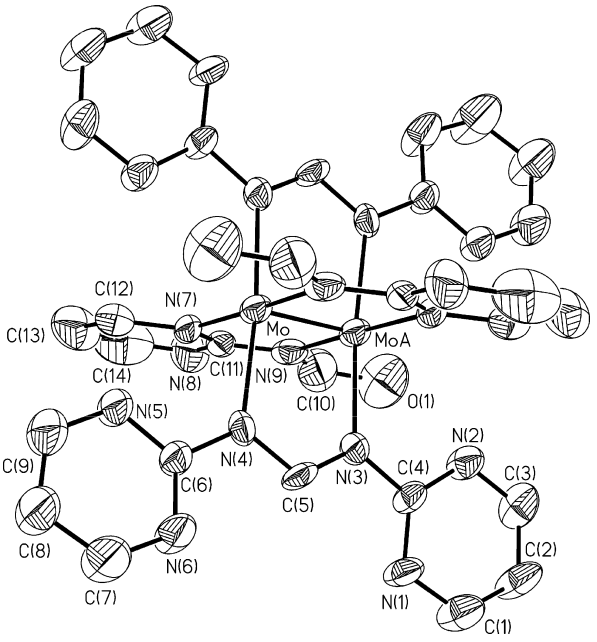


Fig. 2. An ORTEP diagram showing the structure of **2**. Thermal ellipsoids are shown at the 30% probability level for the molecular structure.

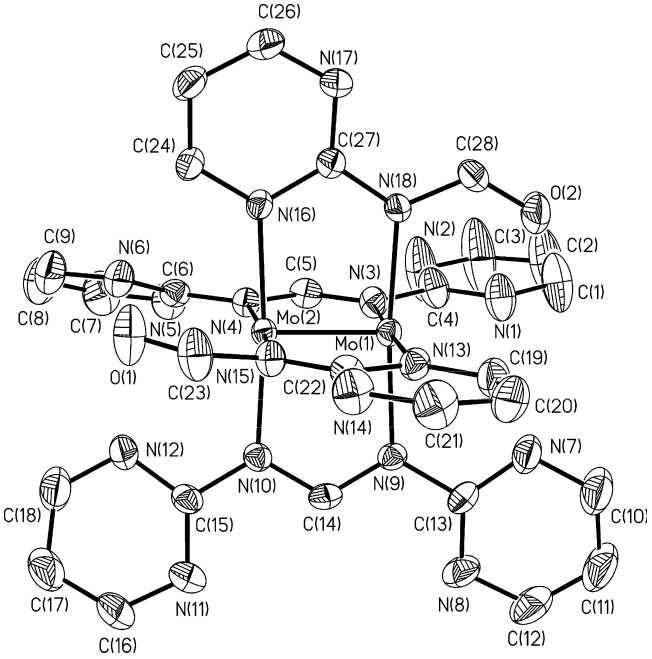


Fig. 3. An ORTEP diagram showing the structure of **3**. Thermal ellipsoids are shown at the 30% probability level for the molecular structure.

N = 162.9°) and C–H···O (H···O = 2.346 Å, ∠C–H ···O = 174.2°) interactions to form a 3-D structure, Fig. 1b. Intermolecular π–π interactions through the pyrimidyl rings with interplanar distances of 3.598 Å between the pyrimidyl rings are also found.

4.3. Structures of *2* and *3*

Red crystals of **2** and **3** conform to the space group $P2_1/c$ with two and four molecules in a unit cell, respectively. Figs. 2 and 3 show the ORTEP diagrams for **2** and **3**, respec-

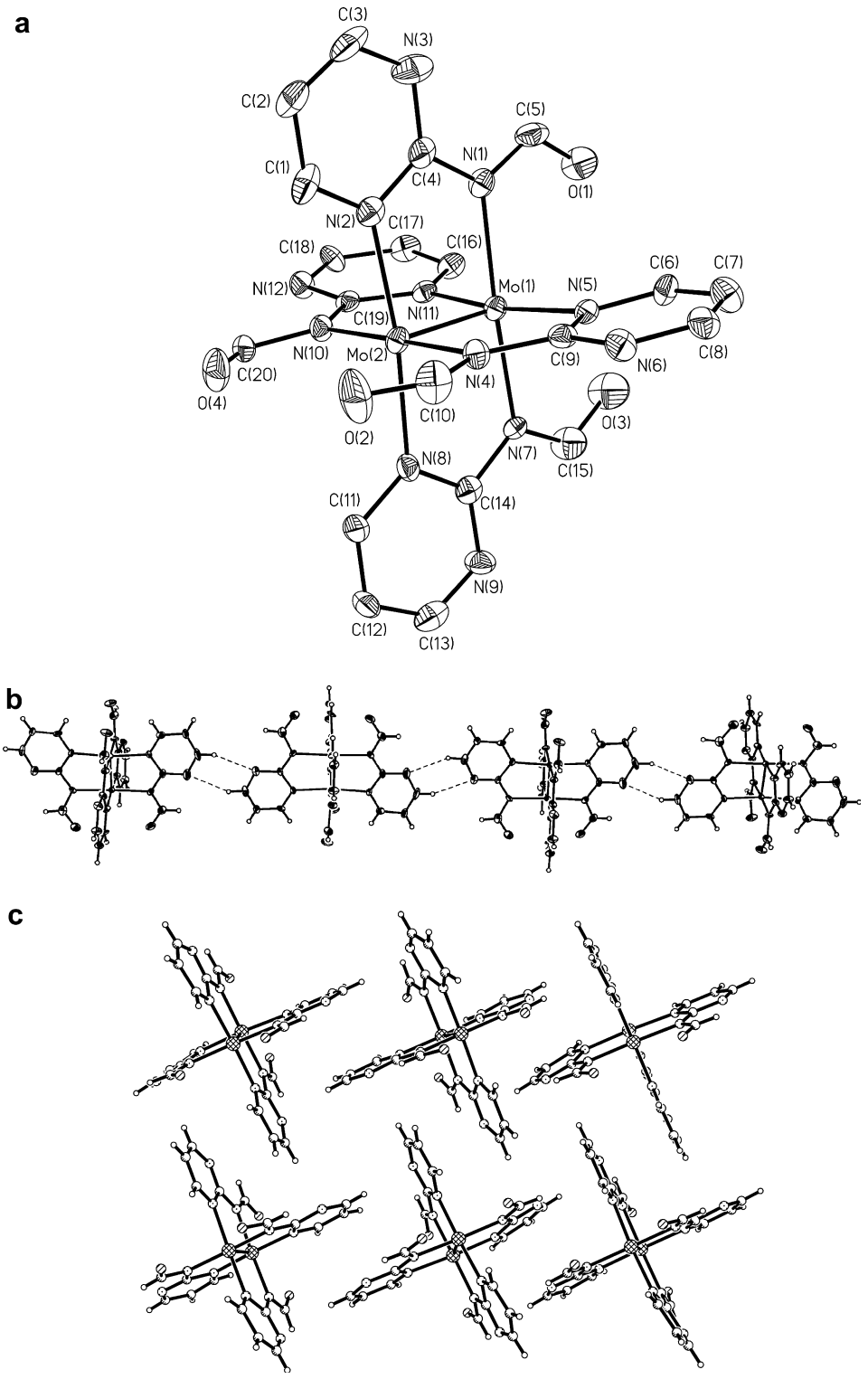


Fig. 4. (a) An ORTEP diagram showing one of the three independent molecules of **4**, which contains Mo(1) and Mo(2) atoms. Thermal ellipsoids are shown at the 30% probability level for the molecular structure. (b) A diagram showing the linear chain of the molecules linked by the self-complementary double C–H···N hydrogen bonds. (c) A diagram showing the intermolecular π–π and C–H···π interactions of **4**.

tively. The molecular structure of **2** consists of two molybdenum atoms [Mo–Mo = 2.103(1) Å] which are spanned by two *trans* **L1** and two *trans* **L2** ligands, while the two molybdenum atoms [Mo–Mo = 2.1017(3) Å] of **3** are spanned by two *cis* **L1** and two *cis* **L2** ligands. The **L1** and **L2** ligands in **2** and **3** are coordinated to the molybdenum centers with bridging modes similar to those in **1**, resulting in Mo···N and Mo···O intra-molecular interactions in the range of 3.118–3.220 and 3.096–3.191 Å, respectively. The Mo–N bond distances fall in the range from 2.146 to 2.200 Å in **2** and 2.142 to 2.197 Å in **3**. The cis–trans isomerism does not lead to significant differences in the Mo–Mo and Mo–N distances. While the molecules of **2** are interlinked through π–π interactions with interplanar distances of 3.672 Å between the pyrimidyl rings, those of **3** are interlinked through both C–H···O (H···O = 2.415, 2.388 Å, ∠C–H···O = 158.5°, 163.1°) and intermolecular π–π interactions with interplanar distances of 3.682 Å.

Complexes **2** and **3** establish the first pair of *trans* and *cis* forms of dimolybdenum complexes containing formamidinate ligands. For comparison it is noted that a pair of dimolybdenum complexes containing benzanidinate and acetate ligands, *trans*- and *cis*-$Mo_2(O_2CCH_3)_2$[PhC(NSi$(CH_3)_3)_2]_2$, have been reported, where the benzamidinates adopt bridging and chelating bonding modes, respectively [17].

4.4. Structure of 4

Red crystals of **4** conform to the space group $P\bar{4}c2$ with 14 molecules in a unit cell. Each asymmetric unit contains one and three quarters of the dinuclear molecules, including a full molecule [Mo(1)–Mo(2)], a half molecule [Mo(3)–Mo(4)] and a quarter of the molecule [Mo(5)–Mo(5A)]. Fig. 4a shows the ORTEP diagram of one of the three independent molecules containing the Mo(1) and Mo(2) atoms. The molecular structure of **4** consist of two molybdenum atoms which are spanned by four **L2** ligands. The Mo–Mo separations are 2.0866 (10), 2.0826 (12) and 2.084 (2) Å, and the observed Mo–N distances fall in a wide range from 2.138(7) to 2.183(8) Å. The **L2** ligands are coordinated to the metal centers through the two nitrogen atoms, resulting in Mo···O intra-molecular interactions in the range from 3.039–3.116 Å. Noticeably, the molecules of **4** are interlinked though self-complementary double C–H···N (H···N = 2.519 Å, ∠C–H···N = 154.7°) hydrogen bonds to form linear chains, Fig. 4b, which are linked through C–H···O (H···O = 2.513 Å, ∠C–H···O = 98.7°) hydrogen bonds. These molecules are also linked through intermolecular π–π and C–H···π interactions through the pyrimidyl rings and the pyrimidyl hydrogen atoms. The interplanar distances between the pyrimidyl rings are 3.716 and 3.891 Å, while the C–H···π distances are 2.898 and 3.280 Å, Fig. 4c.

Complex **4** invites comparisons with Mo_2[pyNC(O)$CH_3]_4$ [18] and Mo_2[pyNC(O)$CH_2CH_3]_4$ [Mo–Mo = 2.0806(4), 2.0826(6) and 2.0869(4) Å] [19]. The structure of the complex Mo_2[pyNC(O)$CH_3]_4$ was solved in the space group $I4/m$ by using a disordered model and thus its ligand arrangements cannot be certain [18]. While the amido oxygen atoms in the ligands of the three forms of Mo_2[pyNC(O)$CH_2CH_3]_4$ are either toward the axial position of the Mo_2 unit or away from that position [19], all the amido oxygen atoms in the three independent molecules of **4** are toward the axial positions. Since the ligands in Mo_2[pyNC(O)$CH_2CH_3]_4$ and **4** are similar in nature, no significant difference in their Mo–Mo distances are observed.

4.5. Structural comparisons

The pmf^- ligands in complexes **1**–**3** are not flat but are twisted about the C–N bonds, with dihedral angles of 17.2 for **1**, 10.7 for **2** and 19.8 and 26.0° for **3** between the two pyrimidyl rings of the pmf^- ligands, presumably due to the formation of Mo···N and Mo···O axial interactions. It is noted that complex **3** shows the largest dihedral angle, which can be ascribed to the fact that the*cis* form adopts the more sterically crowded environment for the

Table 6
Structural comparisons for complexes **1**–**4**, units in Å

Compound	Mo–Mo	Mo–N	Mo···N	Mo–O	Mo···O	π–π interaction	C–H···π interaction
1	2.0951(17)	2.140–2.159	3.067 3.114	2.124 2.154	3.174	3.598	
2	2.103(1)	2.146–2.200	3.118 3.220		3.163	3.672	
3	2.1017(3)	2.142–2.197	3.120 3.126 3.173 3.173		3.096 3.191	3.682	
4	2.0866(10) 2.0826(12) 2.084(2)	2.138–2.183			3.039–3.116	3.716, 3.891	2.898, 3.280

pairs of **L1** and **L2** ligands. However, no significant relationship between the dihedral angles and the Mo···N distances is observed, indicating that the nature of the weak interactions such as C–H···O, C–H···N hydrogen bonds and π–π interactions, which appear frequently in these complexes to self-assemble their molecules, play an important role in determining these angles and distances.

A comparison of then structural parameters for complexes **1**–**4** is listed in Table 6. The Mo–Mo distances are typical for complexes containing a quadruple bond and fall into the 'normal' range of 2.06–2.17 Å for the quadruply bonded dimolybdenum complexes [18]. It is also seen that complexes **1**–**3**, which contain both Mo···N and Mo···O axial interactions, show significantly longer Mo–Mo distances than complex **4** which has only Mo···O interactions.

Acknowledgement

We thank the National Science Council of the Republic of China for support.

Appendix A. Supplementary material

CCDC 637191, 637192, 637193 and 637194 contain the supplementary crystallographic data for this paper. These data can be obtained free of charge via http://www.ccdc.cam.ac.uk/conts/retrieving.html, or from the Cambridge Crystallographic Data Centre, 12 Union Road, Cambridge CB2 1EZ, UK; fax: (+44) 1223-336-033; or e-mail: deposit@ccdc.cam.ac.uk. Supplementary data associated with this article can be found, in the online version, at doi:10.1016/j.poly.2007.03.061.

References

[1] F.A. Cotton, C.A. Murillo, R.A. Walton, Multiple Bonds between Metal Atoms, third ed., Springer Science and Business Media, Inc., New York, 2005.
[2] (a) C. Lin, J.D. Protasiewicz, T. Ren, Inorg. Chem. 35 (1996) 7455; (b) C. Lin, J.D. Protasiewicz, E.T. Smith, T. Ren, Inorg. Chem. 35 (1996) 6422.
[3] T. Ren, C. Lin, P. Amalberti, D. Macikenas, J.D. Protasiewicz, J.C. Baum, T.L. Gibson, Inorg. Chem. Commun. 1 (1998) 23.
[4] M.H. Chisholm, F.A. Cotton, L.M. Daniels, K. Folting, J.C. Huffman, S.S. Iyer, C. Lin, A.M. Macintosh, C.A. Murillo, J. Chem. Soc., Dalton Trans. (1999) 13872.
[5] R. Clérac, F.A. Cotton, K.R. Dunbar, C.A. Murillo, X. Wang, Inorg. Chem. 40 (2001) 420.
[6] T. Ren, Coord. Chem. Rev. 175 (1998) 43.
[7] Y.-Y. Wu, J.-D. Chen, L.-S. Liou, J.-C. Wang, Inorg. Chim. Acta 336 (2002) 71.
[8] Y.-Y. Wu, Y.-C. Kao, J.-D. Chen, C.-H. Hung, Inorg. Chim. Acta 357 (2004) 1002.
[9] A.B. Brignole, F.A. Cotton, Inorg. Synth. 13 (1972) 81.
[10] G.A. van Albada, P.J. van Koningsbruggen, I. Mutikainen, U. Turpeinen, J. Reedijk, Eur. J. Inorg. Chem. (1999) 2269.
[11] R.S. Hosmane, F.N. Burnett, M.S. Albert, J. Org. Chem. 49 (1984) 1212.
[12] (a) SMART/SAINT/ASTRO, Release, 4.03, Siemens Energy & Automation, Inc, Madison, WI, USA, 1995.;
(b) XSCANS, Release, 2.1, Siemens Energy & Automation, Inc, Madison, WI, USA, 1995.
[13] SHELXTL 5.10. Bruker Analytical X-ray Instruments Inc., Karlsruche, Germany, 1997.
[14] A.L. Spek, J. Appl. Cryst. 36 (2003) 7.
[15] Y. Sato, M. Yato, T. Ohwada, S. Saito, K. Shudo, J. Am. Chem. Soc. 117 (1995) 3037.
[16] W. Erley, J.G. Chen, D. Sander, J. Vac. Sci. Technol. A. 8 (1990) 976.
[17] G. Zou, T. Ren, Inorg. Chim. Acta 304 (2000) 305.
[18] F.A. Cotton, W.H. Ilsley, W. Kaim, Inorg. Chem. 18 (1979) 2717.
[19] F.A. Cotton, L.M. Daniels, E.A. Hillard, C.A. Murillo, Inorg. Chem. 41 (2002) 2466.

[16,17], Burns and Hill [18] and Mereiter [19]. Mereiter [19] studied the crystal structure of natural and synthetic curite. Dissolution experiments on crystals of synthetic curite were recently described by Schindler et al. [20]. Infrared spectrum of curite was described without any details by Gevork'yan et al. (together with curite thermal decomposition) [21,22]. Thermal analysis and infrared spectra of curite were published by Čejka et al. [23] and reviewed in detail by Čejka [24]. Kubatko et al. [25,26] recently described the thermodynamics of curite formation.

The sheet structure of curite crystals has orthorhombic symmetry, space group *Pnam*, and unit-cell parameters: *a*, 12.53–12.58; *b*, 13.01–13.03; *c*, 8.39–8.40 Å, $Z = 2$ [3,16,17]. Compositional variability has been observed in curite [14,16,17]. The structure of curite contains three symmetrically unique uranium atoms in form of the $(UO_2)^{2+}$ units, forming $UO_2\Phi_4$ and $UO_2\Phi_5$ polyhedra ($\Phi = O^{2-}$ or OH^-). One uranium cation $U^{6+}(1)$ is coordinated by three atoms of O^{2-} and one OH^-units at the equatorial position of a tetragonal bipyramid, while the other two uranium cations $U^{6+}(2)$ and $U^{6+}(3)$ are both coordinated by three O^{2-} and two OH^- units thus forming uranyl pentagonal bipyramids. There are two structurally distinct Pb^{2+} in the curite structure, both coordinated by six uranyl oxygens, one equatorial O^{2-} of uranyl polyhedra and two water molecules. One symmetrically distinct H_2O site is present [3,16,17].

According to Li and Burns, the geometries of the Pb polyhedra are distorted owing to the electron lone pair stereo activity of Pb^{2+} [16,17]. Because of Pb content variability in the interlayer (some Pb sites are not fully occupied), the charge-balancing mechanism $O^{2-} \Longleftrightarrow OH^-$ was assumed in the uranyl anion sheets in the crystal structure of curite. Li and Burns studied 14 crystals of natural curite and one crystal of synthetic curite and concluded that the structural formula of curite may be written as $Pb_{3+x}(H_2O)[(UO_2)_4O_{4+x}(OH)_{3-x}]_2$. From the bond-valence parameters point of view, some O^{2-} ions may be under bonded. The structure of curite contains water molecules and hydroxyl ions. An appropriate arrangement of hydrogen-bonding network present in the curite structure is therefore expected.

Raman spectroscopy has proven very useful for the study of minerals [27–34]. Indeed Raman spectroscopy has proven most suitable for the study of diagentically related minerals as often occurs with uranyl minerals [29–31,33,35]. Some previous studies have been undertaken by the authors using Raman spectroscopy to study complex secondary minerals formed by crystallisation from concentrated sulphate solutions [36]. The significance of this work rests with the use of Raman spectroscopy to analyse complex mixtures of diagenetically related minerals. Often when studying secondary minerals of uranium, complex mixtures occur. Raman spectroscopy can focus on individual crystals and analyse these individual crystals. This paper forms a part of our Raman and infrared spectroscopy research of secondary minerals including uranyl minerals.

2. Experiments

2.1. Minerals

The curite samples used in this work were obtained from the Mineralogical Research Company and originated from Shinkolobwe Mine and The Ranger Uranium Mine, Northern Territory, Australia. The minerals were analysed by X-ray diffraction for phase purity and for chemical composition by energy dispersive X-ray analysis (EDX).

2.2. Raman spectroscopy

Crystals of curite were placed on the stage of an Olympus BHSM microscope, equipped with 10× and 50× objectives and part of a Renishaw 1000 Raman microscope system, which also includes a monochromator, a filter system and a charge coupled device (CCD). Raman spectra were excited by a HeNe laser (633 nm) at a resolution of 2 cm^{-1} in the range between 100 and 4000 cm^{-1}. Repeated acquisition using the highest magnification was accumulated to improve the signal to noise ratio. Spectra were calibrated using the 520.5 cm^{-1} line of a silicon wafer. In

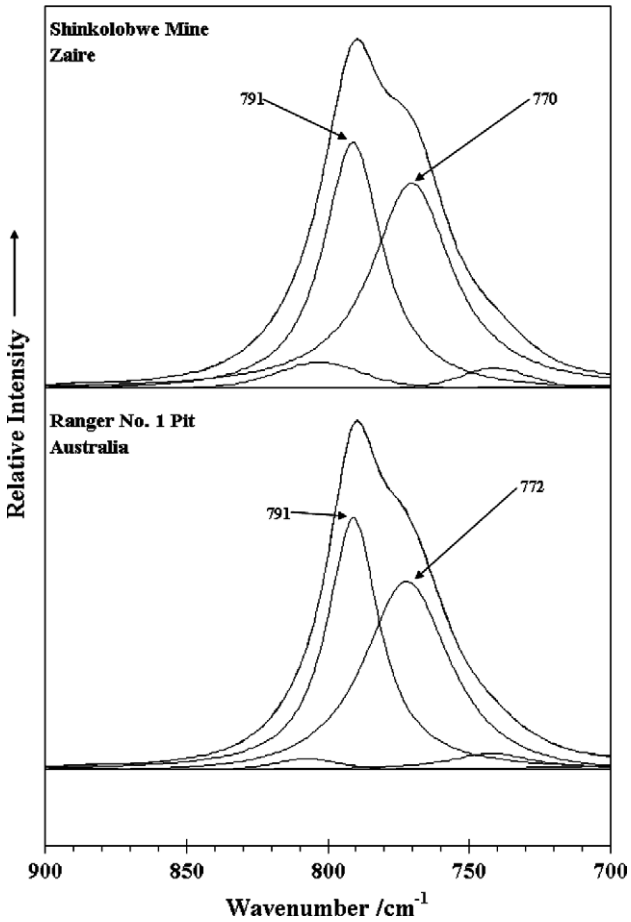


Fig. 1. Raman spectra of curite in the 700–900 cm^{-1} region from The Ranger Uranium Mine and Shinkolobwe Mine.

order to ensure that the correct spectra are obtained, the incident excitation radiation was scrambled. Previous studies by the authors provide more details of the experimental technique [37–41].

Spectral manipulation such as baseline adjustment, smoothing and normalisation were performed using the Spectracalc software package GRAMS (Galactic Industries Corporation, NH, USA). Band component analysis was undertaken using the Jandel 'PEAKFIT' software package which enabled the type of fitting function to be selected and allows specific parameters to be fixed or varied accordingly. Band fitting was done using a Lorentz–Gauss cross-product function with the minimum number of component bands used for the fitting process. The Gauss–Lorentz ratio was maintained at values greater than 0.7 and fitting was undertaken until reproducible results were obtained with squared correlations of $r^2 > 0.995$.

2.3. Infrared spectroscopy

Infrared spectra were obtained using a Nicolet Nexus 870 FTIR spectrometer with a smart endurance single bounce diamond ATR cell. Spectra over the 4000–525 cm^{-1} range were obtained by the co-addition of 64

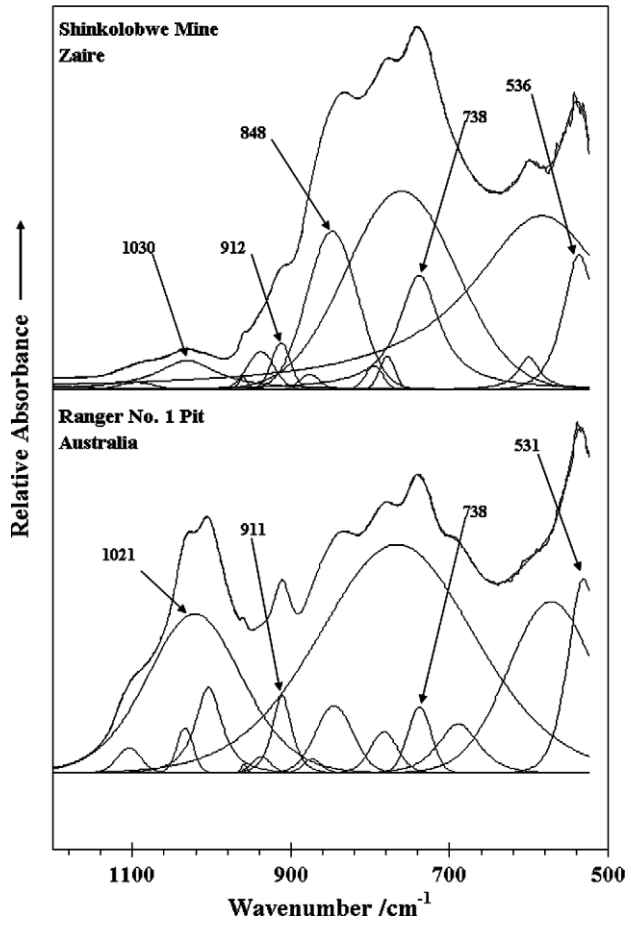


Fig. 2. Infrared spectra of curite in the 500–1200 cm^{-1} region from The Ranger Uranium Mine and Shinkolobwe Mine.

Table 1
Results of the Raman and infrared spectral analysis of curite

Shinkolobwe Mine		Ranger no. 1 pit	
Center (cm^{-1})	FWHM (cm^{-1})	Center (cm^{-1})	FWHM (cm^{-1})
IR			
		3696.9	23.1
		3663.5	46.4
		3622.2	40.7
3530.7	35.4	3528.3	27.7
3492.8	63.3		
3417.8	134.4	3408.9	93.0
3291.6	301.9	3297.6	530.6
3074.9	507.4		
2102.1	62.1		
		1798.0	241.7
		1638.3	90.8
1597.3	101.0		
1592.8	20.0	1593.0	18.9
		1575.1	75.7
1521.0	141.5		
		1475.7	236.1
1370.3	259.9		
1094.5	49.5	1104.0	35.8
1030.8	93.2	1033.5	24.1
		1021.2	140.7
		1003.7	39.4
959.8	11.3	958.9	7.4
937.7	39.9	937.2	27.4
912.3	28.8	911.0	28.6
876.1	28.7	872.9	26.7
847.8	74.9	845.2	55.2
795.0	25.7		
778.3	23.0	782.5	39.8
760.3	163.4	766.2	230.9
737.9	61.7	737.6	34.7
		688.5	60.2
599.6	32.8		
583.4	218.9	571.5	127.8
536.2	47.2	530.9	45.8
Raman			
3532.0	48.9		
3479.7	49.7		
3429.1	86.6	3436.8	112.5
3311.8	210.2		
		3297.1	164.0
1597.2	49.0		
1551.8	7.8		
1519.5	94.8	1530.2	112.1
885.5	18.6	886.2	20.7
803.0	35.1	807.2	26.2
791.1	24.7	791.0	22.1
770.3	34.2	772.0	35.6
740.8	27.8	742.1	34.7
649.1	58.4	649.8	73.9
575.0	13.7		
558.3	47.0	560.9	46.7
527.1	20.3		
503.4	42.4	503.3	50.2
475.9	31.2	474.6	19.7
454.7	33.7	454.8	34.3
393.7	29.4	393.2	27.8
366.8	30.7	366.9	22.9
341.3	44.3	340.4	44.7
300.1	10.7	300.8	22.3
272.3	21.2	272.5	23.2

Table 1 (*continued*)

Shinkolobwe Mine		Ranger no. 1 pit	
Center (cm^{-1})	FWHM (cm^{-1})	Center (cm^{-1})	FWHM (cm^{-1})
Raman			
249.8	18.7	249.6	19.2
		224.6	17.5
212.7	35.1	211.6	18.5
210.6	8.4		
182.8	14.6	184.4	15.9
161.1	13.7	162.9	9.5
150.6	10.2	153.5	18.6
143.1	12.2	143.9	10.9

scans with a resolution of 4 cm^{-1} and a mirror velocity of 0.6329 cm/s. Spectral manipulation such as baseline adjustment, smoothing and normalisation was performed using the GRAMS® software package (Galactic Industries Corporation, Salem, NH, USA).

3. Results and discussion

As mentioned above, the space group of curite is $D_{2h}{}^{16}$–*Pnam*: $C_1(8)$, $2C_i(4)$, $C_s(4)$, $Z = Z_p = 2$. In the unit cell, there are three different types of uranium: U(1) in $C_s(4)$ position forms one kind of tetrahedral bipyramidal polyhedra [$(UO_2)O_3(OH)$], while U(2) and U(3) in $C_s(4)$ and $C_1(8)$ positions thus form two kinds of pentagonal bipyramidal polyhedra [$(UO_2)O_3(OH)_2$] [14–16,19,42]. Factor group analysis of the nonsymmorphic space group, in which curite crystallizes, is isomorphous with point group D_{2h}. The symmetry lowering is accompanied with infrared activation of the ν_1 $(UO_2)^{2+}$ symmetric stretching vibration and splitting of the ν_2 (δ) $(UO_2)^{2+}$ bending vibration [14,23,24]. Thus, all (UO_2) vibrations are both Raman and infrared active.

3.1. Raman spectrum of curite

The Raman spectra of curite from The Ranger Uranium Mine and Shinkolobwe Mine in the 700–900 cm^{-1} region are shown in Fig. 1. Fig. 2 displays the infrared spectra of curite in the 500–1200 cm^{-1}. Results of the Raman spectral analysis are reported in Table 1. Bands at 885 cm^{-1} (1.795 Å) and 886.2 (1.795 Å) cm^{-1}, respectively, are attributed to the ν_3 $(UO_2)^{2+}$ antisymmetric stretching vibrations (Fig. 1). Bands at 803 (1.808 Å) and 791.1 (1.82 Å) cm^{-1} and 807.2 (1.803 Å) and 791 (1.82 Å) cm^{-1}, respectively, are assigned to the ν_1 $(UO_2)^{2+}$ symmetric stretching vibrations. As in the case of corresponding infra-

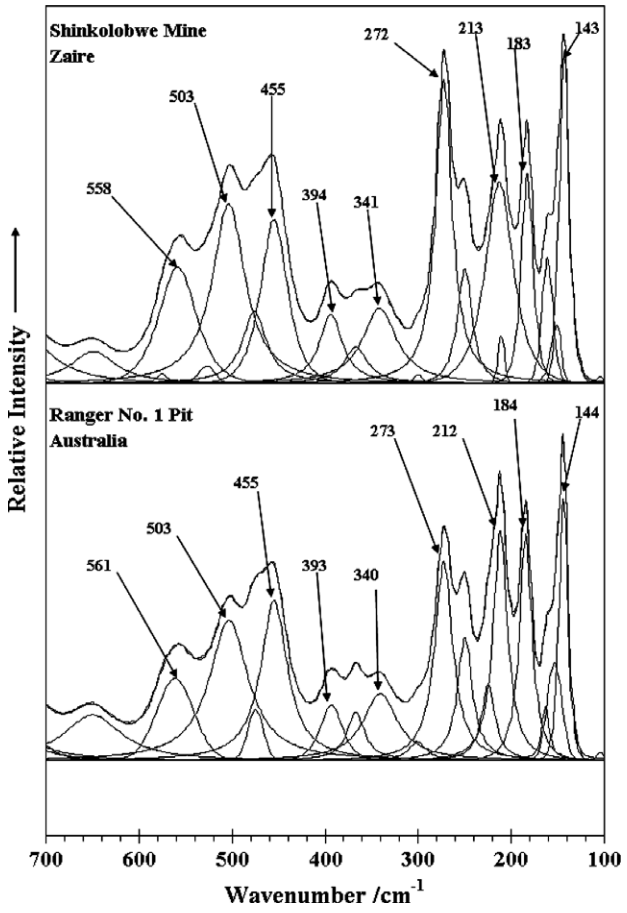


Fig. 3. Raman spectra of curite in the 100–700 cm^{-1} region from The Ranger Uranium Mine and Shinkolobwe Mine.

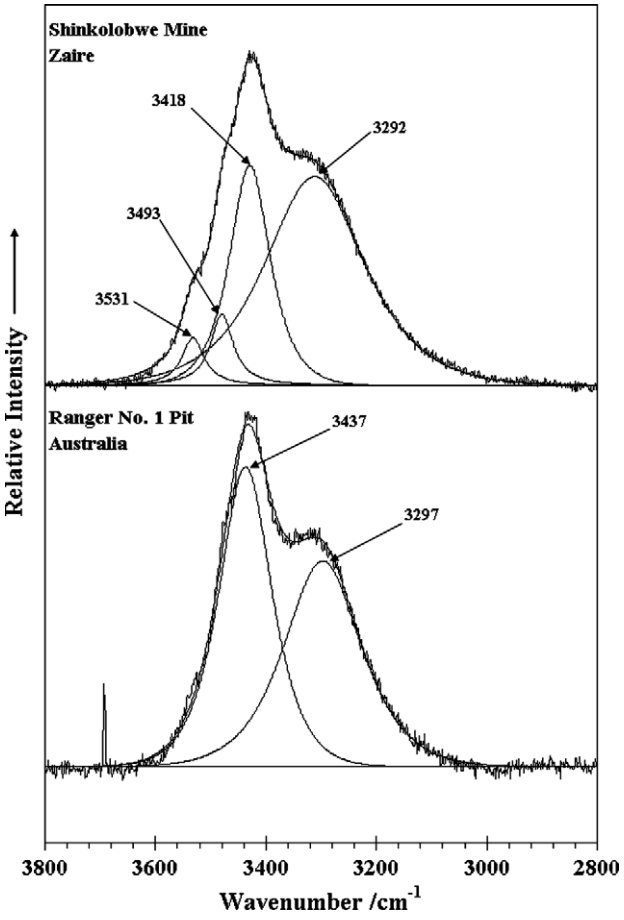


Fig. 4. Raman spectra of curite in the 2800–3800 cm^{-1} region from The Ranger Uranium Mine and Shinkolobwe Mine.

red bands, U–O bond lengths in uranyls were calculated with two empirical relations by Bartlett and Cooney [43]. Obtained values are in agreement with the data from single crystal structure analyses of curite [15,17,19].

Bands in the range 772–649 cm^{-1} may be connected with the molecular water librations modes and/or out-of-plane γ U–OH bending vibrations (Fig. 3). Bands in the range 454–575 cm^{-1} are related to the ν (U_3O) bridge elongation, 340–394 cm^{-1} to the ν $U_3(OH)_3$ elongation, 249–301 cm^{-1} to the γ (U_3O) out-of-plane bending and/or ν_2 (δ) $(UO_2)^{2+}$ bending vibrations, 161–210 cm^{-1} to the (UO_2) translations, and 143–154 cm^{-1} to the $(UO_2)^{2+}$ rotations [14,23,44–46].

3.2. Infrared spectrum of curite

U–O bond lengths for uranyls (Å) calculated with the empirical relation by Bartlett and Cooney [43] are given in parentheses. Bands at 912.3 (1.776 Å) and 876.1 (1.802 Å) cm^{-1} (Shinkolobwe sample), and 911.0 (1.777 Å) and 872.9 (1.805 Å) cm^{-1} (Ranger sample) are attributed to the ν_3 $(UO_2)^{2+}$ antisymmetric stretching vibrations. Bands at 959.8 (1.743 Å) and 937.7 (1.758 Å) cm^{-1} and 958.9 (1.744 Å) and 937.2 (1.758 Å) cm^{-1} may be also attributed to the ν_3 $(UO_2)^{2+}$ vibrations, however, calculated U–O bond lengths are much lower than those inferred from the X-ray single crystal structure analysis of natural and synthetic curite (average values 1.84 Å (see for example, Mereiter [19]); 1.79 Å, Taylor et al. [15]; 1.844 Å, Li and Burns [17]). These bands are connected with the δ U–OH bending vibrations. The ν_1 $(UO_2)^{2+}$ symmetric stretching vibration may be infrared active. According to empirical relations ν_1 $(UO_2)^{2+} = 0.94\nu_3$ $(UO_2)^{2+}$ Å and $\nu_1 = 0.89\nu_3$ $(UO_2)^{2+} + 21$ Å [for details see Čejka 1999 and references therein], this vibration should be located in the region 860–820 cm^{-1} and 833–798 cm^{-1}, respectively. Bands at 847.8 (1.764 Å) and 795 (1.816 Å) cm^{-1} and 845.2 (1.766 Å) cm^{-1}, respectively, are therefore attributed to the ν_1 $(UO_2)^{2+}$ vibrations. Bands in the range 1576–1003 cm^{-1} are assigned to the δ U–OH bending vibrations, while those in the range 783–688 cm^{-1} with the γ U–OH vibrations and/or libration modes of water molecules. According to Dothée [44,45], bands in the range 600–530 are assigned to the ν U_3O bridge elongation.

Fig. 4 displays the Raman spectra in the 2400–3800 cm^{-1} region of curite. Figs. 5 and 6 display the Infra-

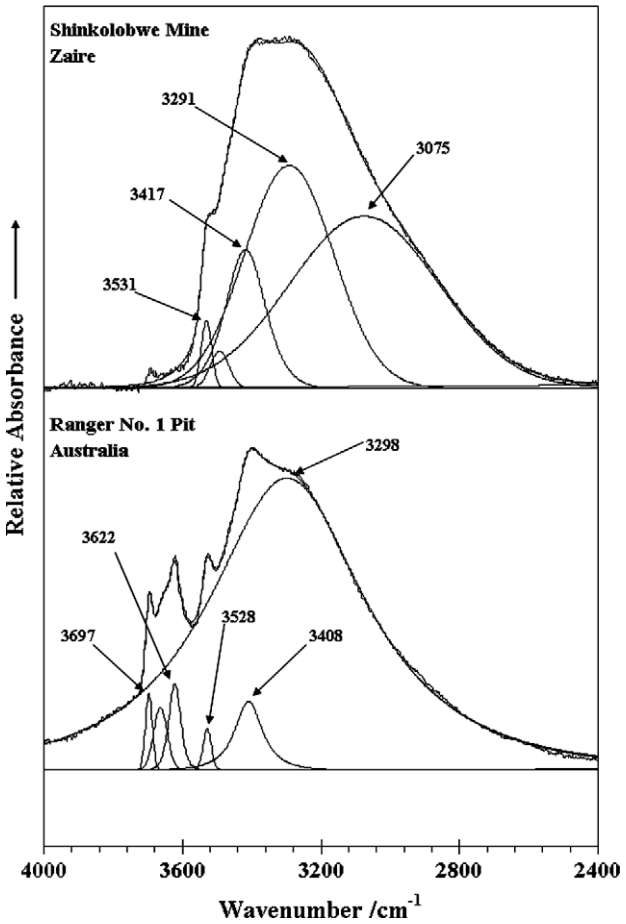


Fig. 5. Infrared spectra of curite in the 2400–4000 cm^{-1} region from The Ranger Uranium Mine and Shinkolobwe Mine.

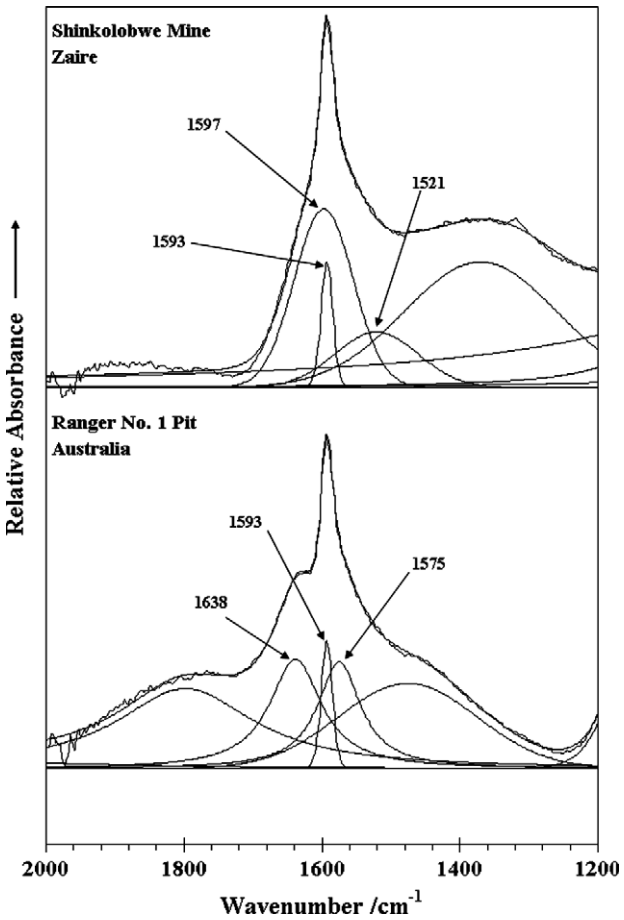


Fig. 6. Infrared spectra of curite in the 1200–2000 cm^{-1} region from The Ranger Uranium Mine and Shinkolobwe Mine.

red spectra of curite in the 2400–4000 cm^{-1} and 1200–2000 cm^{-1} regions from The Ranger Uranium Mine and Shinkolobwe Mine. Bands in the range 3531–3074 cm^{-1} (Shinkolobwe sample) are connected to the νOH stretching vibrations of water molecules and hydroxyls. It may be inferred that the wavenumbers correspond to weak to strong hydrogen bonds in the crystal structure of curite from Shinkolobwe [47]. A somewhat different arrangement of water molecules was observed in the infrared spectrum of the curite sample from Ranger Mine (3696.9–3297.7 cm^{-1}). It may be inferred that in the crystal structure of this sample practically free hydroxyls and weakly hydrogen bonded hydroxyls and water molecules are present [47]. This is in agreement with two bands observed close to 1595 cm^{-1} (Shinkolobwe sample) and bands at 1638.3 and 1593 cm^{-1} (Ranger sample) attributed to the δ H_2O bending vibrations. Bands at 2102.1 cm^{-1} and 1798.0 cm^{-1}, respectively, may be assigned to overtones and/or combination bands. Bands in the range 3297–3532 cm^{-1} are assigned to the ν OH stretching vibrations of water molecules and hydroxyl ions (Figs. 4 and 5). The wavenumbers prove the presence of relatively strong to weak hydrogen bonds in the crystal structure of curite. This does not fully agree with the observed infrared bands. Only a band at 1597.2 cm^{-1} (Shinkolobwe sample) was observed (Fig. 6). It may be assigned to the δ H_2O bending vibration. This band corresponds to water molecules relatively weakly bonded in the structure of curite. Bands in the range 1519–1552 cm^{-1} are connected with the δ U–OH bending vibration.

4. Conclusions

(a) Raman and infrared spectra of two curite samples were studied.
(b) Bands connected with the $(UO_2)^{2+}$ and $(OH)^-$ stretching and bending vibrations were attributed respecting their number as a result of FGA-correlation.
(c) Coincidence of some of the bands of the $(UO_2)^{2+}$ stretching vibrations with the bands assigned to U–OH bending vibrations was examined.
(d) U–O bond lengths in uranyls were calculated and compared with the X-ray single crystal structure data. Both data are in good agreement.
(e) The presence of free or weakly hydrogen bonded symmetrically distinct hydroxyls located in the sheets were inferred from the infrared spectrum of curite sample from Ranger Mine. This is in agreement with the crystal structure of curite.
(f) Water molecules of the interlayer together with hydroxyls from the uranyl anion sheet participate in a set of hydrogen bonds forming thus a complex hydrogen-bonding network which influences the origin, formation and stability of the mineral. This is supported by the fact that infrared and Raman spectra of the both curite samples somewhat differ in the regions of OH stretching and H_2O bending vibrations.

References

[1] P.C. Burns, K.M. Deely, Can. Mineralogist 40 (2002) 1579.
[2] Y. Li, P.C. Burns, R.A. Gault, Can. Mineralogist 38 (2000) 153.
[3] Y. Li, University of Notre Dame, University of Notre Dame, 2002.
[4] A.J. Locock, P.C. Burns, T.M. Flynn, Am. Mineralogist 90 (2005) 240.
[5] P.C. Burns, Canadian Mineralogist 43 (2005) 1839.
[6] P.C. Burns, Reviews in Mineralogy 38 (1999) 23.
[7] P.C. Burns, R. Finch, (Eds.), Uranium: Mineralogy, Geochemistry and the Environment. Proceedings of a Short Course held 22–23 October 1999 in Golden, CO.) (Rev. Mineral., 1999; 38), 1999.
[8] K.S.V. Brugger, P. Berlepsch, N. Meisser, S. Ansermet, T. Armbruster, Am. Miner. 89 (2004) 339.
[9] A. Schoep, Compt. Rend. 173 (1921) 1186.
[10] J. Protas, Compt. Rend. 257 (1963) 1919.
[11] A. Courtois, Université de Nancy, 1968.
[12] R. Sobry, Am. Miner. 56 (1971) 1065.
[13] P. Piret, B. Mineral. 108 (1985) 659.
[14] J. Cejka, J. Cejka, R. Skala, J. Sejkora, A. Muck, Neues Jahrbuch fuer Mineralogie, Monatshefte (1998) 385.
[15] J.C. Taylor, W.I. Stuart, I.A. Mumme, J. Inorg. Nucl. Chem. 43 (1981) 2419.
[16] Y. Li, P.C. Burns, Can. Mineral. 38 (2000) 1433.
[17] Y. Li, P.C. Burns, Can. Mineral. 38 (2000) 727.
[18] P.C. Burns, F.C. Hill, Can. Mineral. 38 (2000) 163.
[19] K. Mereiter, TMPM, Tscher. Miner. Petrog. 26 (1979) 279.
[20] M. Schindler, P. Mandaliev, F.C. Hawthorne, A. Putnis, Can. Mineral. 44 (2006) 415.
[21] S.V. Gevork'yan, A.S. Povarennykh, D.I. Rakovich, Konstitutsiya i Svoistva Mineralov 7 (1973) 99.
[22] A.S. Povarennykh, Konstitutsiya i Svoistva Mineralov 13 (1979) 78.
[23] J. Cejka Jr., A. Muck, Z. Urbanec, J. Cejka, Thermochim. Acta 93 (1985) 637.
[24] J. Cejka, Rev. Miner. 38 (1999) 521.
[25] K.-A. Kubatko, K. Helean, A. Navrotsky, P.C. Burns, Am. Mineral. 91 (2006) 658.
[26] K.A. Kubatko, University of Notre Dame, 2005.
[27] R.L. Frost, D.A. Henry, K. Erickson, J. Raman Spectrosc. 35 (2004) 255.
[28] R.L. Frost, J. Cejka, M.L. Weier, W. Martens, D.A. Henry, Vib. Spectrosc. 39 (2005) 131.
[29] R.L. Frost, M.L. Weier, W.N. Martens, J.T. Kloprogge, J. Kristof, J. Raman Spectrosc. 36 (2005) 797.
[30] R.L. Frost, J. Cejka, M.L. Weier, W. Martens, J. Raman Spectrosc. 37 (2006) 538.
[31] R.L. Frost, M.L. Weier, B.J. Reddy, J. Cejka, J. Raman Spectrosc. 37 (2006) 816.
[32] R.L. Frost, J. Cejka, M. Weier, G.A. Ayoko, Spectrochim. Acta A 65 (2006) 529.
[33] R.L. Frost, J. Cejka, M. Weier, W.N. Martens, J. Raman Spectrosc. 37 (2006) 879.
[34] R.L. Frost, J. Cejka, M. Weier, G.A. Ayoko, J. Raman Spectrosc. 37 (2006) 1362.
[35] R.L. Frost, M.L. Weier, J. Cejka, J.T. Kloprogge, J. Raman Spectrosc. 37 (2006) 585.
[36] R.L. Frost, R.-A. Wills, M.L. Weier, W. Martens, J. Raman Spectrosc. 36 (2005) 435.
[37] R.L. Frost, J. Raman Spectrosc. 37 (2006) 910.
[38] R.L. Frost, D.A. Henry, M.L. Weier, W. Martens, J. Raman Spectrosc. 37 (2006) 722.
[39] R.L. Frost, M.L. Weier, J. Raman Spectrosc. 34 (2003) 776.

[40] W. Martens, R.L. Frost, J.T. Kloprogge, P.A. Williams, J. Raman Spectrosc. 34 (2003) 145.
[41] R.L. Frost, P.A. Williams, W. Martens, J.T. Kloprogge, J. Raman Spectrosc. 33 (2002) 752.
[42] P.C. Burns, F.C. Hill, Can. Mineral. 38 (2000) 175.
[43] J.R. Bartlett, R.P. Cooney, J. Mol. Struct. 193 (1989) 295.
[44] D. Dothee, Vibrational spectroscopy of hydrated potassium hexauranate for the phase study of the uranium(VI) oxide–potassium chloride–water system. Univ. Besancon, Fr., 1980, p. 148.
[45] D.G. Dothee, M.M. Camelot, J.L. Bernard, B. Soc. Chim. Fr. (1980) 221.
[46] J. Protas, Bull. Soc. Franc. Mineral. Crist. 82 (1959) 239.
[47] E. Libowitzky, Monatsh. Chem. 130 (1999) 1047.

$M(Haap)_2(H_2O)_2](NO_3)_2$ (with $M = Co^{2+}$, Ni^{2+}, Zn^{2+}) and for $Pd(aap)_2$ [5].

The ligand Haap might have biological interest, while as a free ligand it was tested as an inducer for the Friend Leukemia cells [6]. Very recently the pair wise arrangement of a donor and acceptor H-bond group was realized and the molecule was used as a highly effective co-crystallising agent for carboxylate acids [7].

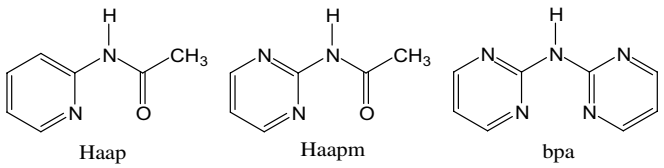
This paper focuses on amides monofunctionalized at the N site to form a chelating ligand, like in the ligand *N*-(pyridin-2-yl)acetamide [4]. With one of the N–H groups now available at the backside of the ligand, lattice stabilisation and even lattice engineering becomes possible with the counter anions, or other H-bond acceptors outside the coordination sphere. The phenomenon is well known for lattice stabilisation of coordination compounds. However, to use more than one function at the backside of the ligand is relatively rare.

In fact, the ligand bis(pyrimidyl)amine (bpa), see Scheme 1, has recently been introduced by us [8,9] and we have shown several cases of special lattice stabilisations by this type of hydrogen bonding [10–13]. This bpa ligand, however, has the structure A–D–A (where A is H-bond acceptor, and D stands for H-bond donor), allowing only asymmetric self-association yielding pairs A–**D**–**A**/**A**–**D**–A, where bold means involved in H-bond interaction.

We now have used the substituted amine, to generate the pair of ligands *N*-(pyridin-2-yl)acetamide (Haap) and the newly designed *N*-(pyrimidin-2-yl)acetamide (Haapm), as shown in Scheme 1. In the second case, a matching pair **A**–**D**/**A**–**D** would be available. The normal pyridine ligand (Haap) has been used as a reference, where only the amide H-bond donor is available.

To select a proper metal, we have chosen Cu(II), due to its plasticity in the coordination sphere and its preference for a trans geometry of weakly coordinating anions. This paper describes 10 new Cu(II) coordination compounds with the above ligand pair Haap and Haapm; we have chosen the anions: chloride, nitrate, tetrafluoridoborate, perchlorate, and triflate, to simultaneously study the effect of the decreasing capacity of the anions to coordinate. Characterisation of the new compounds has been performed by Infrared, ligand field and EPR spectroscopy. In addition 3D structures for five different compounds have been determined, which all proved the coordination mode of the ligand to be bis-bidentate (N,O).

It turned out that in all cases the N–H group of the ligand takes part in lattice stabilisation via extensive intermolecular hydrogen bonding. However, most surprisingly, the second N atom in the heterocyclic ring of Haapm does not take part in any hydrogen bond acceptance, contrary to the earlier reported, related bpa ligand.



Scheme 1. The ligands Haap, Haapm and for comparison bpa.

2. Experimental

2.1. Syntheses

The ligand Haap was synthesized according to the literature [4], by refluxing equimolar amounts of 2-aminopyridine and acetic anhydride for 2 h. Purification of the ligand was performed by distillation [4].

The new ligand Haapm was synthesized according to the same procedure as for Haap, but now using 2-aminopyrimidine in stead of 2-aminopyridine. The remaining brown solid was purified first by drying in an oven at 120 °C and then by recrystallisation from a mixture of toluene/hexane (1:1). Yield: 85%. *Anal.* Calc. for $C_6H_7N_3O$: C, 52.5; H, 5.2; N, 30.6. Found: C, 52.4; H, 5.2; N, 30.6%. NMR: 8.6 (doublet, phenyl) 7.0 (triplet, phenyl); 2.49 (methyl); 8.8 (NH).

Synthesis of the Cu(II) coordination compounds: 0.1 mmol of the Cu(II) salt and 0.2 mmol of the ligand were each dissolved in methanol. The solutions were slowly put together and filtered to remove any non-dissolved precipitate. After a few days the blue crystalline, or microcrystalline product separated. Yields are 50% or higher. The same compounds were obtained when using ethanol in stead of methanol. All new compounds show satisfactory elemental analyses as seen in Table 1.

2.2. Physical measurements

C, H, N determinations were performed on a Perkin–Elmer 2400 Series II analyzer. UV–Vis–NIR spectra were obtained on a Perkin–Elmer Lambda900 spectrophotometer using the diffuse reflectance technique, with MgO as a reference.

X-band powder EPR spectra were obtained on a Jeol RE2x electron spin resonance spectrometer at RT and at 77 K, using DPPH ($g = 2.0036$) as a standard.

FTIR spectra were obtained on a Perkin–Elmer Paragon 1000 FTIR spectrophotometer equipped with a Golden Gate ATR device, using the reflectance technique (4000–300 cm^{-1}, res. 4 cm^{-1}).

2.3. Crystal structure determination and refinement of the structures

A suitable crystal of each of the five compounds was selected from their mother liquids and mounted to a glass fibre using the oil-drop method [14]; data were collected on a Nonius Kappa CCD diffractometer (graphite-monochromated Mo Kα radiation). The intensity data were corrected for Lorentz and polarisation effects, for absorption and extinction. The structures were solved by direct methods.

The programs COLLECT [15], SHELXS-97 [16], SHELXL-97 [17] were used for data reduction, structure solution and structure refinement, respectively. Refinement of F^2 was done against all reflections. All non-hydrogen atoms were refined anisotropically. All H atoms were introduced in calculated positions and refined with fixed geometry with respect to their carrier atoms. Selected bond distances and angles are given in Table 2. Crystallographic data of the compounds are summarized in Table 3.

3. Results and discussion

3.1. General structure and stoichiometry, and molecular structure

For all the five different counter ions, in all cases a similar stoichiometry was obtained, i.e. $Cu(LL)_2(anion)_2$, with similar colours and spectra properties. Table 1 lists some major properties of all 10 compounds, and explains the used code. A listing of major IR amide bands is given in Supplementary Table S1. No solvent molecules were found to be present in the lattice, irrespective of the used synthesis in all 10 compounds. In several cases crystals suitable for single-crystal structure determination were obtained, and five of these with high-quality crystals are included in this paper, including each of the five different anions.

A thermal ellipsoid plot, together with the used numbering scheme is shown in Fig. 1, for compound $Cu(Haap)_2(ClO_4)_2$ (**2**), whereas Fig. 2 shows the structure of $Cu(Haapm)_2(CF_3SO_3)_2$ (**6**). Projections of the structures for compounds **5**, **8** and **9**, respectively, are given in Supplementary figures S1–S3. Selected bond lengths and bond angles for all five compounds are given in Table 2.

The Cu(II) ion has a distorted octahedral geometry with the basal plane formed by two nitrogen atoms and two oxygen atoms of two bischelating ligands with Cu–N distances which vary from 2.005(2) to 2.042(2) Å and Cu–O distances which vary from 1.930(2) to 1.960(2) Å. All five compounds have basically the same overall structure, compounds **2**, **5**, **6** and **9** also have a centre of symmetry locating through the Cu(II) ion, while compound **8** has no

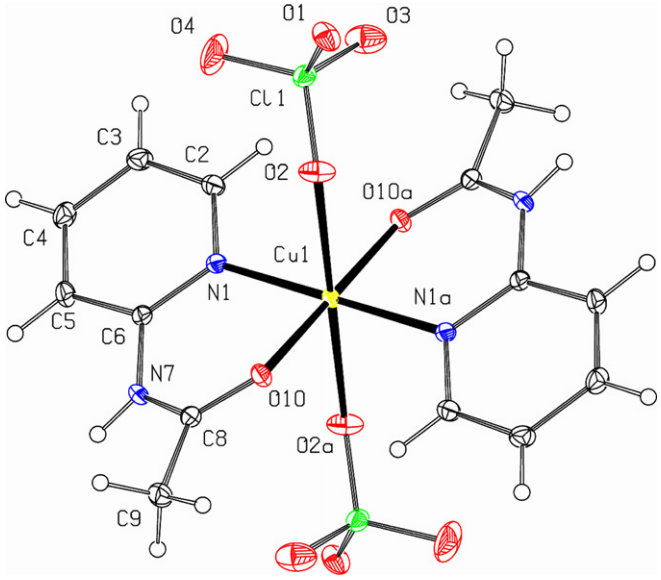


Fig. 1. Thermal ellipsoid plot (50% probability) of compound **2** with the used atom-labelling scheme.

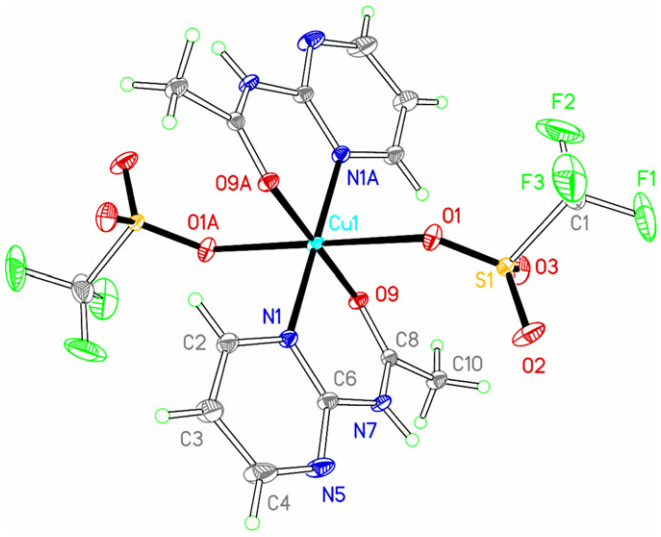


Fig. 2. Thermal ellipsoid plot (50% probability) of compound **6** with the used atom-labelling scheme.

Table 1
Cu(II) compounds with Haap and Haapm

Number and formula of the compound	Colour	Ligand field maximum (10^3 cm^{-1})	EPR parameters[a]
1. $Cu(Haap)_2(CF_3SO_3)_2$	blue	15.6	$g_\parallel = 2.28$, $g_\perp = 2.06$, $A_\parallel = 15.6$
2. $Cu(Haap)_2(ClO_4)_2$[b]	blue	15.0	$g_\parallel = 2.26$(vw), $g_\perp = 2.06$
3. $Cu(Haap)_2(NO_3)_2$	blue	15.8	$g_\parallel = 2.27$, $g_\perp = 2.07$
4. $Cu(Haap)_2(BF_4)_2$	blue	16.0	$g_\parallel = 2.27$(vw), $g_\perp = 2.07$
5. $Cu(Haap)_2Cl_2$[b]	blue	14.8	$g_{av} = 2.11$
6. $Cu(Haapm)_2(CF_3SO_3)_2$[b]	blue	15.5	$g_\parallel = 2.31$(vw,br), $g_\perp = 2.07$
7. $Cu(Haapm)_2(ClO_4)_2$	blue	16.0	$g_\parallel$ 2.27, $g_\perp = 2.07$
8. $Cu(Haapm)_2(NO_3)_2$[b]	blue	14.6	$g_\parallel = 2.28$, $g_\perp = 2.08$, $A_\parallel = 16.2$(vw)
9. $Cu(Haapm)_2(BF_4)_2$[b]	blue	15.7	$g_\parallel = 2.23$(vw,br), $g_\perp = 2.07$
10. $Cu(Haapm)_2Cl_2$	blue	14.3 (9.6)	$g_\parallel = 2.27$, $g_\perp = 2.08$

[a] $A_\parallel$ in mT; vw, very weak; br, broad.
[b] X-ray structure solved.

Table 2
Selected bond distances, angles and H-bond information for the Cu(II) compounds

Compound	**2** (ClO_4)	**5** (Cl)	**6** (CF_3SO_3)	**8** (NO_3)	**9** (BF_4)
Distances					
$Cu–O_{ligand}$	1.938(2)	1.957(2)	1.960(2)	1.926(2) 1.948(2)	1.930(2)
$Cu–N_{ligand}$	2.008(2)	2.004(2)	2.005(2)	2.019(2) 2.042(2)	2.010(2)
$Cu–O/F/Cl_{anion}$	2.476(2)	2.815(1)	2.417(2)	2.421(2) 2.463(2)	2.476(2)
$O_{ligand}–Cu–O_{ligand}$	180.0	180.0	180.0	174.84(7)	180.0
$N_{ligand}–Cu–N_{ligand}$	180.0	180.0	180.0	174.00(7)	180.0
$X_{anion}–Cu–X_{anion}$	180.0	180.0	180.0	159.92(7)	180.0
		D–H	H···A	D···A	D–H···A
Hydrogen bond parameters					
Structure (**2**) perchlorate					
N7–H7A···O1 [x, y, $-1+z$]		0.88	2.12	2.954(3)	158
Structure (**5**) chloride					
N7–H7A···Cl1 [$1/2-x$, $-1/2+y$, z]		0.88	2.30	3.156(3)	165
Structure (**6**) triflate					
N7–H7A···O2 [$-x+1$, y, $-z+3/2$]		0.88	1.96	2.832(2)	167
Structure (**8**) nitrate					
N17–H17A···O11 [$-x$, $1-y$, $-z$]		0.88	2.17	3.003(3)	157[a]
N17–H17A···O13 [$-x$, $1-$y, $-z$]		0.88	2.28	3.047(3)	146[a]
N27–H27A···O22 [$1-x$, $1-y$, $1-z$]		0.88	1.96	2.776(3)	153[a]
Structure (**9**) tetrafluoridoborate					
N7–H7A···F2 [$-x$, $-y$, $1-z$]		0.88	2.01	2.881(3)	173

NB: D–H have been fixed at 0.88 Å.
[a] Bifurcated H atom.

centre of symmetry. Therefore, in compounds **2**, **5**, **6** and **9** the basal trans angles are 180°, while in compound **8** the basal trans angles are 174.84(7)° and 174.00(7)°.

The axial positions are occupied by an atom of an anion with semi-coordination distances of 2.476(2) Å ($Cu–O_{ClO_4}$), 2.815(1) Å (Cu–Cl), 2.417(2) Å ($Cu–O_{CF_3SO_3}$), 2.421(2) and 2.463(2) Å ($Cu–O_{NO_3}$) and 2.476(2) Å ($Cu–F_{BF_4}$).

3.2. Lattice structures and hydrogen bonding

A point of special interest is the intermolecular H-bond pattern for these compounds, as five of them have just the N–H donor group, whereas the other five have the imine-N as a possible N–H acceptor in the lattice, in analogy to the bis(pyrimidin-2-yl)amine complexes. In fact all five compounds do show only a clear N–H··· anion hydrogen bond, which is quite strong given the geometries (see Table 2). In compounds **2**, **6** and **9** which have the ClO_4^-, $CF_3SO_3^-$ and BF_4^- as an anion the H-bonds are formed by the amine N–H donor and one atom of the anion with distances of 2.954(3), 2.832(2) and 2.881(3) Å, respectively, providing a 1D polymeric double-chain type array. In Fig. 3 an example is shown for one of these compounds. The nitrate compound **8** also gives a quite similar polymeric array, but in this case the H-bond between the N–H and the nitrate oxygen atoms are alternating with distances of 2.776(3) Å and (bifurcated H-bonds of) 3.003(3) and 3.046(3) Å with the other nitrate oxygen (see figure S4 for details). Compound **5** differs from the other ones, as the H-bond between the amine N–H and the Cl^- ion provides an zigzag 2D-based polymeric array with N–H···. Cl contact distance of 3.156(3) Å, as shown in Fig. 4. Most surprisingly, and in fact not predicted, the other N atom of the pyrimidine ring, in compounds **6**, **8** and **9**, which has a lone pair, and which is know to take part in H bonding in the ligand bpa (see Scheme 1), does not take part in any hydrogen bonding in these compounds. The shortest contacts with any intermolecular atom are all over 4 Å. The reasons for this are not understood at the moment, but future studies are planned to use counter anions, like hydrogencarbonate and hydrogensulfate, that would provide a N–H donor, while at the same time using one O atom to bind to the metal.

3.3. Electronic and infrared spectroscopy

The diffuse reflectance spectra of the powdered solids are summarized in Table 1. All compounds (**1**–**10**) show a ligand field spectrum with a strong broad tail-shaped band with a centre around $14.3–16.0 \times 10^3$ cm^{-1}, values which are consistent with a (distorted) octahedral geometry [18]. No attempts were undertaken to a detailed analysis on the very small different peaks in the LF spectra.

In Table S1, selected infrared bands are given. The amide I band consists mainly of $\nu_{(C=O)}$ and the amide II bands arise mainly of $\nu_{(C=N)}$ [4]. When an amide group coordinates through the oxygen atom, the amide I band will shift to lower frequency and the amide II band to

Table 3
Crystal and refinement data for the five compounds

Compound	**2** (ClO_4)	**5** (Cl)	**6** (CF_3SO_3)	**8** (NO_3)	**9** (BF_4)
Molecular formula	$C_{14}H_{16}Cl_2CuN_4O_{10}$	$C_{14}H_{14}Cl_2CuN_4O_2$	$C_{14}H_{14}CuF_6N_6O_8S_2$	$C_{12}H_{14}CuN_8O_8$	$C_{12}H_{14}B_2CuF_8N_6O_2$
Molecular weight	534.75	406.75	635.97	461.85	511.45
T (K)	173(2)	173(2)	173(2)	173(2)	173(2)
Crystal system	triclinic	orthorhombic	monoclinic	monoclinic	triclinic
Space group	$P\bar{1}$	*Pbca*	*C*2/*c*	*P*21/*c*	$P\bar{1}$
a (Å)	7.640(2)	12.792(3)	19.719(4)	14.034(3)	7.399(2)
b (Å)	7.804(1)	8.109(2)	14.163(3)	8.726(3)	7.502(2)
c (Å)	9.292(2)	15.070(3)	8.863(2)	15.445(3)	9.516(1)
α (°)	65.45(2)	90.0	90.0	90.0	81.53(3)
β (°)	81.44(2)	90.0	106.21(3)	113.15(3)	73.80(3)
γ (°)	85.33(2)	90.0	90.0	90.0	67.85(3)
V (Å^3)	498.2(2)	1563.2(5)	2376.9(8)	1739.1(8)	469.3(2)
Z	1	4	4	4	1
F_{000}	271	828	1276	940	255
D_{cal} (Mg m^{-3})	1.782	1.728	1.777	1.764	1.810
μ (mm^{-1})	1.427	1.753	1.195	1.321	1.265
Crystal size (mm)	0.10 × 0.05 × 0.04	0.06 × 0.04 × 0.04	0.20 × 0.20 × 0.20	0.10 × 0.10 × 0.10	0.06 × 0.04 × 0.04
Colour, shape	blue, needle	blue, prismatic	blue, block	blue, block	blue, prismatic
θ range (°)	2.70–27.50	2.70–27.61	3.22–26.00	2.68–27.51	2.93–27.48
Number of reflections collected	7741	20208	8808	24070	6324
Number of independent reflections [R_{int}]	2268 [0.0471]	1803 [0.0471]	2232 [0.0166]	3983 [0.0406]	2156 [0.0461]
Number of refined parameters	143	107	169	262	142
S[a] (Goodness-of-fit)	1.059	0.826	1.04	1.030	1.057
Final R indices [$I > 2\sigma(I)$]	$R_1 = 0.0346$	$R_1 = 0.0368$	$R_1 = 0.0291$	$R_1 = 0.03061$	$R_1 = 0.0291$
	$wR_2 = 0.0858$	$wR_2 = 0.0820$	$wR_2 = 0.0701$	$wR_2 = 0.0817$	$wR_2 = 0.1057$
R indices (all data)	$R_1 = 0.0434$	$R_1 = 0.0673$	$R_1 = 0.0344$	$R_1 = 0.0404$	$R_1 = 0.0526$
	$wR_2 = 0.0891$	$wR_2 = 0.0959$	$wR_2 = 0.0730$	$wR_2 = 0.0872$	$wR_2 = 0.1094$
Largest difference minimum, maximum (e Å^{-3})	−0.598, 0.520	−0.439, 0.372	−0.469, 0.464	−0.508, 0.534	−0.7000, 0.864

$R = \sum ||F_o| - |F_c|| / \sum |F_o||$, $R_w = [\sum w\{|F_o| - |F_c|\}^2 / w|F_o|^2]^{1/2}$.
[a] Goodness-of-fit $S = [\sum w(F_o^2 - F_c^2)^2/(n-p)]^{1/2}$, where n is the number of reflections and p the number of parameters.

higher frequency [4]. As can be seen in Table S1 the amide bands shift indeed to lower, respectively. higher frequency, which confirms that the coordination in all compounds is through the oxygen and the nitrogen atom. The anion bands are observed at the normal frequencies for mono-coordinated anions [19]. The $\nu_{as(S=O)}$ stretching bands in the triflate compounds (compounds **1** and **6**) are observed at 1275, 1249 cm^{-1} and 1276, 1244 cm^{-1}, respectively. All these bands are in agreement with the literature for mono-dentate and/or H-bonded triflate absorptions [20,21].

The N–H stretch vibrations of the amide groups nicely correlate with the known basicity of the anions and the bands vary from 3340 cm^{-1} (for BF_4^-, the weakest acceptor) to 2700 cm^{-1} (for Cl^-, the strongest acceptor), see Table S1. As can be seen from the infrared spectra of the NH/CH regions of the compounds (figure S5 for compounds **1**–**5** and figure S6 for compounds **6**–**10**) the strength of the H

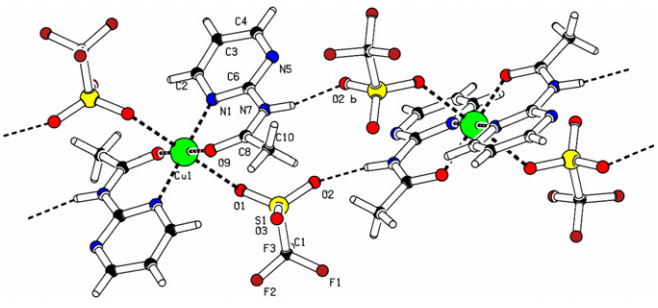


Fig. 3. 1D polymeric antiparallel chain array formed by intermolecular hydrogen bonds via Cu, triflate and NH groups (compound **6**).

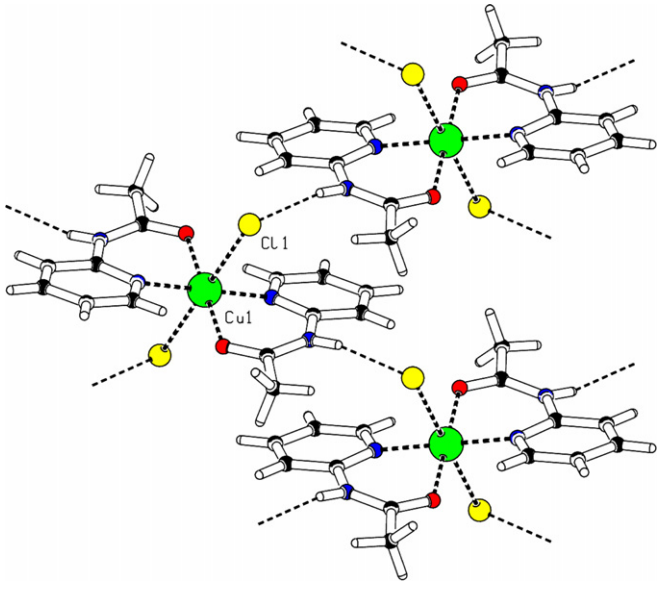


Fig. 4. Zigzag polymeric 2D array formed by lattice hydrogen bonding via Cu–Cl–NH groups (compound **5**).

bonds, as measured by the N–H centre of gravity, nicely follows the order of: $BF_4 < ClO_4 < CF_3SO_3 < NO_3 < Cl$.

3.4. Magnetic properties

X-band EPR spectra of polycrystalline powders of the complexes (**1**–**10**) were recorded at room temperature. As shown in Table 1 the compounds **2**, **7**, **9** and **10** show an axial $S = 1/2$ signal with a $g_\perp$ at 2.06–2.08 and with an unresolved (often weak to very weak) $g_\parallel$ values of 2.23–2.31. Compounds **1** and **8** show resolved hyperfine splitting on $g_\parallel$ with a value of 2.28 and an $A_\parallel$ of 15.6 mT and 16.2 mT, respectively. These g values are in the usual range for copper in a (distorted) elongated octahedral environment [18]. The other compounds do not show this hyperfine splitting, which is ascribed to exchange narrowing by too close intermolecular contacts.

4. Concluding remarks

All above, new mononuclear-based Cu(II) compounds with the known ligand Haap and with the newly designed ligand Haapm appeared to be easy to synthesize and have been characterized by standard methods, as well as by X-ray structure determinations. Different anions have been used and in all cases, irrespective of solvent and ratio M:L the same stoichiometry, i.e. $M(LL)_2(anion)_2$, was found, suggesting a stable lattice energy. All compounds have an elongated octahedral geometry.

As predicted with the design of the ligands and the complexes, the rear side of the ligand with the N–H group, plays a key role in the formation of the 3D structure and the formation of chains of the type –**Cu**–**anion**–**NH-(ligand)**–**Cu**– . Only in the case of the small chloride anion, a different packing (2D), but also based on the N–H groups at the rear side of the ligand is found. The strength of the hydrogen bonding, as measured by the lowering of the N–H stretch, runs parallel with the basic properties of the anions. Surprisingly, the second ring nitrogen in the ligand Haapm does not appear to play a role at all in the hydrogen bonding, despite the availability and exposure of its lone pair to the lattice. Further studies with different anions, i.e. those that contain a NH donor, should shed further light on this interesting lattice engineering problem.

Acknowledgements

The work described in the present paper has been supported by the Leiden University Study group WFMO (Werkgroep Fundamenteel Materialenonderzoek). Financial support and coordination by the FP6 Network of Excellence ''Magmanet'' (Contract number 515767) is kindly acknowledged.

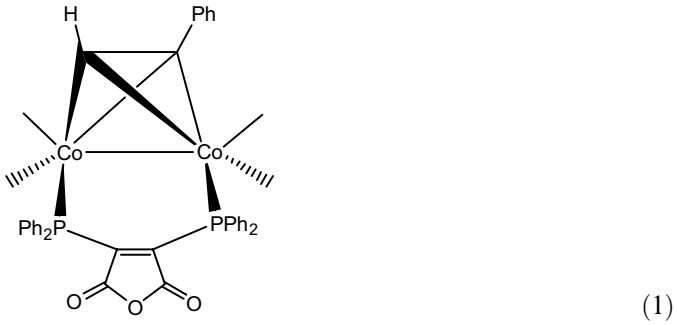
Appendix A. Supplementary material

CCDC 637247, 637248, 637249, 637250, 637251 contain the supplementary crystallographic data for **2**, **5**, **6**, **8** and **9**. These data can be obtained free of charge via http://www.ccdc.cam.ac.uk/conts/retrieving.html, or from the Cambridge Crystallographic Data Centre, 12 Union Road, Cambridge CB2 1EZ, UK; fax: (+44) 1223-336-033; or e-mail: deposit@ccdc.cam.ac.uk. Supplementary data associated with this article can be found, in the online version, at doi:10.1016/j.poly.2007.04.035.

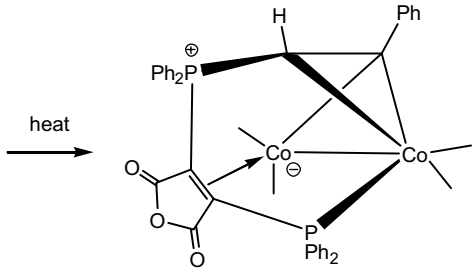
References

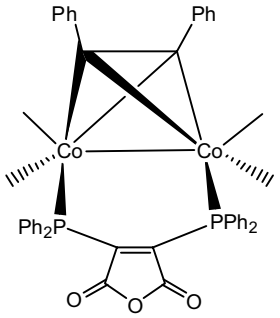
[1] M. Mikami, I. Nakagawa, T. Shimanou, Spectrochim. Acta A 25 (1969) 365.
[2] M. Sekizaki, Acta Crystallogr., Sect. B 29 (1973) 327.
[3] M. Sekizaki, K. Yamasaki, Inorg. Chim. Acta 4 (1970) 296.
[4] M. Nonoyama, S. Tomita, K. Yamasaki, Inorg. Chim. Acta 12 (1975) 33.
[5] V. Scheller-Krattiger, K.H. Scheller, E. Sinn, R.B. Martin, Inorg. Chim. Acta 60 (1982) 45.
[6] C.D. Li, L.S. Rittmann, A.S. Tsiftsoglou, K.K. Bhargava, A.C. Sartorelli, J. Med. Chem. 21 (1978) 874.
[7] C.B. Aakeroy, I. Hussain, J. Desper, Cryst. Growth Des. 6 (2006) 474.
[8] G.A. van Albada, I. Mutikainen, U. Turpeinen, J. Reedijk, Polyhedron 23 (2004) 993.
[9] G.A. van Albada, O. Roubeau, I. Mutikainen, U. Turpeinen, J. Reedijk, New J. Chem. 27 (2003) 1693.
[10] G.A. van Albada, I. Mutikainen, U. Turpeinen, J. Reedijk, Inorg. Chem. Commun. 9 (2006) 1067.
[11] G.A. van Albada, A. Mohamadou, A.M.M. Lanfredi, I. Mutikainen, U. Turpeinen, F. Ugozzoli, J. Reedijk, J. Chem. Crystallogr. 35 (2005) 541.
[12] G.A. van Albada, I. Mutikainen, U. Turpeinen, J. Reedijk, J. Chem. Crystallogr. 34 (2004) 613.
[13] G.A. van Albada, O. Roubeau, P. Gamez, H. Kooijman, A.L. Spek, J. Reedijk, Inorg. Chim. Acta 357 (2004) 4522.
[14] T. Kottke, D. Stalke, J. Appl. Crystallogr. 26 (1993) 615.
[15] Nonius, COLLECT, Nonius BV, Delft, The Netherlands, 2002.
[16] G.M. Sheldrick, SHELXS-97, Program for Crystal Structure Solution, University of Göttingen, Germany, 1997.
[17] G.M. Sheldrick, SHELXL-97. Program for Crystal Structure Refinement, University of Göttingen, Germany, 1997.
[18] B.J. Hathaway, Comprehensive Coordination Chemistry, Pergamon Press, Oxford, 1987.
[19] K. Nakamoto, Infrared and Raman Spectra of Inorganic and Coordination Compounds, Wiley, New York, 1978.
[20] G.A. van Albada, W.J.J. Smeets, A.L. Spek, J. Reedijk, J. Chem. Crystallogr. 28 (1998) 427.
[21] G.A. van Albada, W.J.J. Smeets, A.L. Spek, J. Reedijk, Inorg. Chim. Acta 260 (1997) 151.

anhydride ligand. These reactions are depicted in Eqs. (1) and (2), respectively.

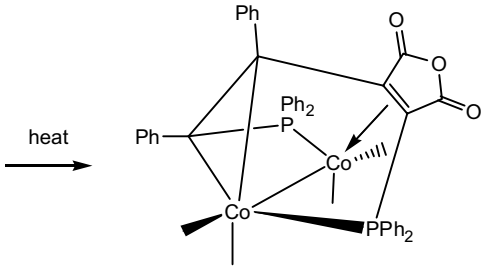


(1)





(2)



Wishing to further explore the chemistry of our zwitterionic hydrocarbyl complexes, we have investigated the substitution reactivity of $Co_2(CO)_4$[μ-PhC=C(H)PPh_2C=C(PPh_2)C(O)OC(O)] (**1**) with PMe_3 [5]. The addition of PMe_3 to **1** is shown to trigger the insertion of a CO group into one of the Co–C(hydrocarbyl) bonds to give the acyl species $Co_2(CO)_3(PMe_3)$[μ-PhC(CO)=C(H)PPh_2C= C(PPh_2)C(O)OC(O)] (**2**). Compound **2** undergoes a formal CO deinsertion upon thermolysis to afford the simple PMe_3-substituted derivative $Co_2(CO)_3$(P-Me_3)[μ-PhC=C(H)PPh_2C=C(PPh_2)C(O)OC (O)] (**3**). The course of these substitution reactions has been established through NMR spectroscopy and X-ray crystallographic analyses of compounds **2** and **3**.

2. Experimental

2.1. General

The starting dicobalt compound $Co_2(CO)_4$[μ-PhC=C(H)PPh_2C=C(PPh_2)C(O)OC(O)] was prepared from $Co_2(CO)_6$(μ-PhCCH) and bma accordingly to the published procedure [2]. The alkyne compound $Co_2(CO)_6$-(μ-PhCCH) was synthesized from $Co_2(CO)_8$ and phenylacetylene [6], while the diphosphine ligand bma was synthesized from 2,3-dichloromaleic anhydride and Ph_2PSiMe_3 [7]. PMe_3 was prepared from $P(OPh)_3$ and MeMgI [8]. The chemicals phenylacetylene, $P(OPh)_3$, and MeI were purchased from Aldrich Chemical Co. and used as received. $Co_2(CO)_8$ was purchased from Strem Chemicals and stored under CO and in the refrigerator when not in use. The ^{13}CO (99%) used in the preparation of the ^{13}C-enriched sample of $Co_2(CO)_6$(μ-PhCCH) was obtained from Isotec. All reaction and NMR solvents were distilled from an appropriate drying agent using Schlenk techniques and stored under argon in storage vessels equipped with high-vacuum Teflon stopcocks [9]. The combustion analyses were performed by Atlantic Microlab, Norcross, GA.

The IR spectral data were recorded on a Nicolet 20 SXB FT-IR spectrometer in sealed 0.1 mm NaCl cells, while the ^{13}C spectral data were recorded at 50 MHz on a Varian Gemini-200 spectrometer. The ^{31}P NMR spectra were collected in the proton-decoupled mode on a Varian 300-VXR spectrometer at 121 MHz, with the reported chemical shifts referenced to external H_3PO_4 (85%), taken to have $\delta = 0$.

2.2. Synthesis of $Co_2(CO)_3(PMe_3)$[μ-PhC(CO)=C(H)PPh_2C=C(PPh_2)C(O)OC(O)] (2)

To a small Schlenk tube containing 0.20 g (0.20 mmol) of **1** in 15 mL of CH_2Cl_2 at room temperature was added 1.05 equiv. of PMe_3 (0.42 mL of a 0.5 M solution of PMe_3 in CH_2Cl_2). The reaction was instantaneous based on TLC and IR analyses of the reaction solution, which revealed the complete consumption of **1** and the formation of **2**. The solvent was removed under vacuum and the residue was passed across a short column of silica gel using CH_2Cl_2/acetone (95:5) as the eluent. Recrystallization of crude **2** from CH_2Cl_2/heptane afforded the analytical sample and single crystals of **2** suitable for X-ray diffraction analysis. Yield of black-green **2**: 0.18 g (85%). IR (CH_2Cl_2): ν(CO) 2022 (vs), 1985 (vs), 1777 (m, symm anhydride), 1719 (m, antisymm anhydride), 1590 (bw, acyl) cm^{-1}. ^{13}C NMR (THF, 178 K): δ 197.83 (d, 1C, $J_{P-C} = 23$ Hz), 206.65 (s, 2C), 234.50 (d, 1C, $J_{P-C} = 15$ Hz). ^{31}P NMR (THF, 178 K): δ 14.90 (overlapping resonances, 2P), 19.21 (d, 1P, $J_{P-P} = 61$ Hz, phosphonium moiety). *Anal.* Calc. for $C_{43}H_{35}Co_2O_7P_3$: C, 59.06; H, 4.03. Found: C, 59.36; H, 4.38%.

2.3. Thermolysis of $Co_2(CO)_3(PMe_3)[\mu\text{-}PhC(CO)=C(H)PPh_2C=C(PPh_2)C(O)OC(O)]$ and formation of $Co_2(CO)_3(PMe_3)[\mu\text{-}PhC=C(H)PPh_2C=C(PPh_2)C(O)OC(O)]$ (3)

To a Schlenk tube under argon was charged 0.20 g (0.23 mmol) of **2**, followed by the addition of 20 mL of 1,2-dichloroethane (DCE) via syringe. The vessel was sealed and then heated at 60 °C for 1 h, at which time TLC analysis confirmed the presence of compounds **1**, **2**, and **3**. Heating was continued for another hour and the solution examined again by TLC. At this point, only compounds **1** (minor) and **3** (major) were observed ($R_f = 0.80$ for **1** and $R_f = 0.65$ for **3** using CH_2Cl_2 as the eluent). The desired compound **3** was isolated after solvent removal and purification by column chromatography over silica gel using CH_2Cl_2 as the mobile phase. Crude **3** was subsequently recrystallized from CH_2Cl_2/hexane to furnish the combustion sample and the single crystals of **3** suitable for X-ray crystallography. Yield of **3**: 82% (0.16 g). IR (CH_2Cl_2): ν(CO) 2001 (s), 1958 (s), 1777 (m, symm anhydride), 1721 (m, antisymm anhydride) cm^{-1}. ^{13}C NMR (THF, 178 K): δ 202.07 (d, 1C, $J_{P-C} = 20$ Hz), 207.37 (d, 1C, $J_{P-C} = 21$ Hz), 211.89 (s, 1C). ^{31}P NMR (THF, 178 K): δ 10.80 (overlapping resonances, 2P), 33.78 (d, 1P, $J_{P-P} = 67$ Hz, phosphonium moiety). *Anal.* Calc. for for $C_{42}H_{35}Co_2O_6P_3$: C, 59.59; H, 4.13. Found: C, 59.29; H, 4.26%.

2.4. X-ray diffraction data

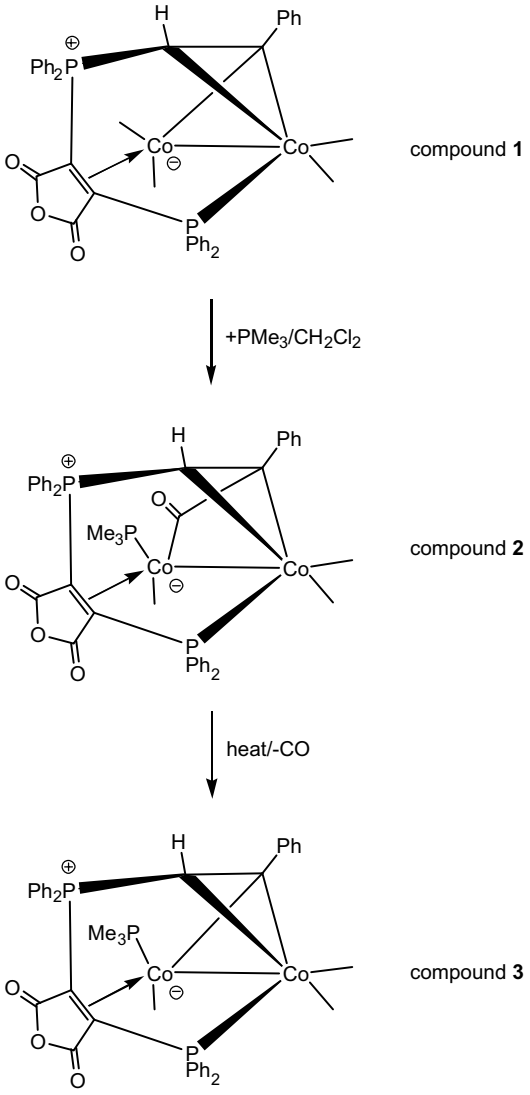
Tables 1 and 2 contain the X-ray data and processing parameters and selected bond distances and angles, respectively, for compounds **2** and **3**. A suitable crystal was selected and sealed inside a Lindemann capillary, followed by mounting on an Enraf-Nonius CAD-4 diffractometer. After the cell constants were obtained, intensity data in the range of $2° \leqslant 2\theta \leqslant 44°$ (**2**) and $2° \leqslant 2\theta \leqslant 40°$ (**3**) were collected at 298 K and were corrected for Lorentz, polarization, and absorption (DIFABS). The structures of compounds **2** and **3** were solved using SHELX-86. All non-hydrogen atoms were located with difference Fourier maps and full-matrix least-squares refinement in both compounds. In the case of **2**, the cobalt, phosphorus, oxygen, and the carbonyl carbon atoms were refined anisotropically, with the phenyl, hydrocarbyl, and maleic anhydride ring carbon atoms refined isotropically. Due to the poor scattering displayed by the crystal of **3**, only the Co and P atoms were refined anisotropically. All hydrogen atoms were assigned calculated positions and allowed to ride on the attached heavy atom. Refinement on **2** converged at $R = 0.0427$ and $R_w = 0.0460$ for 2127 unique reflections

Table 1
X-ray crystallographic data and processing parameters for the dicobalt compounds **2** and **3**

Compound	**2**	**3**
Crystal system	orthorhombic	monoclinic
Space group	$P2_12_12_1$	$P2_1/n$
a (Å)	10.2936(7)	9.189(3)
b (Å)	17.471(1)	19.254(4)
c (Å)	22.294(2)	21.702(4)
β (°)		92.00(2)
V (Å^3)	4009.3(5)	3837(2)
Molecular formula	$C_{43}H_{35}Co_2O_7P_3$	$C_{42}H_{35}Co_2O_6P_3$
Fw	874.54	846.53
Formula units per cell (Z)	4	4
D_{calc} (g/mm^3)	1.449	1.465
λ (Mo Kα), Å	0.71073	0.71073
μ (cm^{-1})	9.91	10.32
R_{merge}	n/a	0.037
Absorption correction	Fourier	Fourier
Absorption correction factor	0.90/1.13	0.69/1.32
Total reflections	2811	4000
Independent reflections	2127	1375
Data/residual/parameters	2127/0/301	1375/0/238
R	0.0427	0.0620
R_w	0.0460	0.0715
Goodness of fit on F^2	0.76	0.72
$\Delta\rho$(maximum), $\Delta\rho$(minimum) (e/Å^{-3})	0.45 near Co(1)	0.52 near C(2)

Table 2
Selected bond distances (Å) and angles (°) in the dicobalt compounds **2** and **3**

Compound 2			
Bond distances			
Co(1)–Co(2)	2.650(2)	Co(1)–P(1)	2.187(3)
Co(1)–C(1)	1.77(1)	Co(1)–C(2)	1.79(1)
Co(1)–C(16)	2.030(9)	Co(1)–C(17)	2.022(9)
Co(2)–P(3)	2.239(3)	Co(2)–C(3)	1.73(1)
Co(2)–C(4)	1.944(9)	Co(2)–C(11)	2.095(9)
Co(2)–C(15)	2.006(9)	P(2)–C(15)	1.776(9)
O(4)–C(4)	1.23(1)	C(4)–C(17)	1.48(1)
C(11)–C(12)	1.44(1)	C(11)–C(15)	1.47(1)
C(14)–C(15)	1.47(1)	C(16)–C(17)	1.43(1)
Bond angles			
Co(2)–Co(1)–P(1)	70.08(8)	Co(2)–Co(1)–C(1)	91.8(3)
Co(2)–Co(1)–C(2)	173.1(3)	Co(2)–Co(1)–C(16)	83.7(3)
Co(2)–Co(1)–C(17)	75.2(3)	C(16)–Co(1)–C(17)	41.5(4)
Co(1)–Co(2)–P(3)	159.7(1)	Co(1)–Co(2)–C(3)	93.1(4)
Co(1)–Co(2)–C(4)	65.7(3)	Co(1)–Co(2)–C(11)	81.8(3)
Co(1)–Co(2)–C(15)	89.5(3)	C(4)–Co(2)–C(11)	135.2(4)
C(4)–Co(2)–C(15)	105.3(4)	C(11)–Co(2)–C(15)	41.9(4)
Co(2)–C(4)–O(4)	123.7(7)	Co(2)–C(4)–C(17)	114.7(6)
P(2)–C(16)–C(17)	124.5(7)		
Compound 3			
Bond distances			
Co(1)–Co(2)	2.553(4)	Co(1)–P(1)	2.197(6)
Co(1)–C(1)	1.80(2)	Co(1)–C(2)	1.69(3)
Co(1)–C(16)	2.09(2)	Co(1)–C(17)	1.98(2)
Co(2)–P(3)	2.210(6)	Co(2)–C(3)	1.74(2)
Co(2)–C(11)	2.05(2)	Co(2)–C(15)	2.06(2)
Co(2)–C(17)	2.00(2)	C(11)–C(12)	1.43(3)
C(11)–C(15)	1.39(3)	C(14)–C(15)	1.47(3)
C(16)–C(17)	1.40(3)		
Bond angles			
Co(2)–Co(1)–P(1)	70.9(2)	Co(2)–Co(1)–C(1)	101.5(8)
Co(2)–Co(1)–C(2)	164.6(9)	Co(2)–Co(1)–C(16)	75.2(6)
Co(2)–Co(1)–C(17)	50.4(5)	C(16)–Co(1)–C(17)	40.1(7)
Co(1)–Co(2)–P(3)	154.0(2)	Co(1)–Co(2)–C(3)	92.6(7)
Co(1)–Co(2)–C(11)	84.8(5)	Co(1)–Co(2)–C(15)	89.0(5)
Co(1)–Co(2)–C(17)	49.6(4)	C(11)–Co(2)–C(15)	39.5(7)



Scheme 1.

with $I > 3\sigma(I)$, while **3** afforded convergence values of $R = 0.0620$ and $R_w = 0.0715$ for 1375 unique reflections with $I > 3\sigma(I)$.

3. Results and discussion

3.1. Synthesis, spectroscopic data, and X-ray diffraction structure of 2

Treatment of **1** with a slight excess of PMe_3 at room temperature leads to a rapid reaction based on the brown to black-green color change exhibited by the reaction solution. TLC examination confirmed the complete consumption of brown **1** and the presence of a slower moving black-green spot corresponding to **2** at $R_f = 0.50$ using CH_2Cl_2/acetone (95:5) as the eluent. No reaction between **1** and PMe_3 was observed at 0 °C, while the reaction between **1** and PPh_3 conducted at room temperature showed no sign for the formation of any product. This latter observation suggests that the CO insertion reaction that affords **2** is sensitive to the nucleophilicity of incoming ligand and does not proceed via a pre-equilibrium involving the unsaturated acyl species $Co_2(CO)_3$[μ-PhC(CO)=C(H)PPh_2C=C(PPh_2)C(O)OC(O)], as added phosphine would be captured without complications under these circumstances. Compound **2** was subsequently isolated in high yield as a mildly air-sensitive solid after chromatographic separation over silica using the aforementioned eluent. Scheme 1 depicts the transformation of **1** to **2**.

Compound **2** was characterized by IR and NMR spectroscopies, elemental analysis, and X-ray crystallography. The IR spectrum displays terminal Co–CO bands 2022 (vs) and 1985 (vs) cm^{-1} and two ν(CO) bands for the kinematically coupled carbonyl groups associated with the anhydride ring at 1777 (m) and 1719 (m) cm^{-1} [10]. The shift to lower energy by both sets of carbonyl groups in **2** relative to **1** is consistent with the addition of an electron-rich PMe_3 ligand to **1**. The acyl band in **2** appears as a broad, weak band at 1590 cm^{-1}, in agreement with the reported frequencies in other such acyl derivatives [11]. The low-temperature ^{13}C NMR spectrum of a ^{13}CO-enriched sample of **2** exhibits two terminal Co–CO resonances at δ 197.83 (1C) and 206.65 (2C) and an acyl CO resonance at δ 234.50 [12], while the ^{31}P NMR spectrum reveals an overlapping singlet and doublet at δ 14.90 for the cobalt-bound phosphine groups and a down-field doublet at δ 19.21 belonging to the phosphonium moiety. The ^{31}P NMR data recorded for **2** parallel those data reported by us for compound **1**, which displays ^{31}P chemical shifts at δ 4.70 and 31.30 for the phosphine and phosphonium groups, respectively [2].

The solid-state structure of **2** was determined by single-crystal X-ray diffraction analysis [13].[1] Single crystals of **2** exist as discrete molecules in the unit cell with no unusually short inter- or intramolecular contacts. The ORTEP diagram of **1**, shown in Fig. 1, confirms the regiospecific addition of the PMe_3 ligand to the Co(2) atom and the insertion of the C(4)O(4) carbonyl group into the Co(2)–C(17) bond of **1**. The Co(1)–Co(2) bond distance of 2.650(2) Å is 0.101 Å longer than the cobalt–cobalt bond length reported for compound **1**. This lengthening is attributed to the presence of the ancillary PMe_3 ligand. The Co(1)–P(1) and Co(2)–P(3) distances of 2.187(3) Å and 2.239(3) Å, respectively, fall within acceptable ranges for such linkages [14]. The Co(2)–C(4) and C(4)–C(17) distances of 1.944(9) Å and 1.48(1) Å, respectively, and the angles associated with the Co(2)–C(4)–C(17) [114.7(6)°] and Co(2)–C(4)–O(4) [123.7(7)°] linkages exhibit values consistent with other acyl-substituted cobalt compounds

[1] The chiral space group $P2_12_12_1$ exhibited by compound **2** presumably reflects a spontaneous separation of one of the enantiomers from the bulk sample whose composition consists of a racemic mixture of **2**. Unfortunately, the absolute chirality associated with the two stereocenters in the X-ray structure **2** cannot be definitively ascertained based on the available X-ray data.

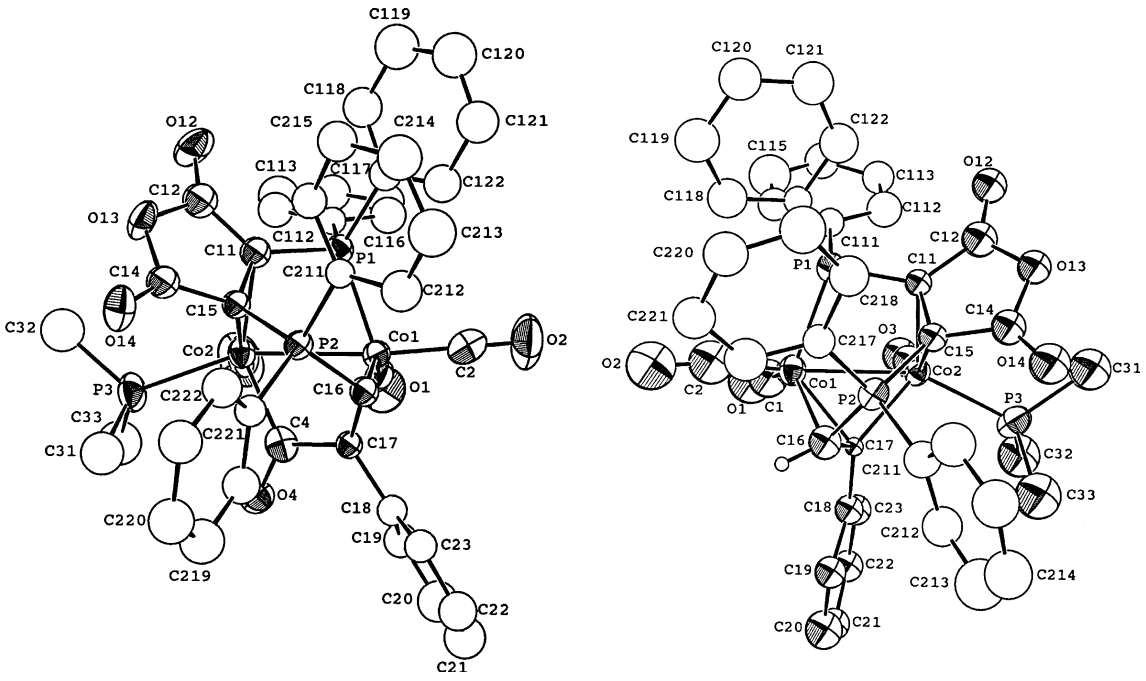


Fig. 1. ORTEP diagrams of compounds **2** (left) and **3** (right) showing the thermal ellipsoids at the 30% probability level.

[15]. The three terminal CO groups display distances and angles consistent with such groups. The remaining bond distances and angles are unremarkable and require no comment.

3.2. Synthesis, spectroscopic data, and X-ray diffraction structure of 3

The temperature sensitivity of **2** was subsequently verified during a routine thermolysis study. Heating **2** in either DCE or toluene solution over the temperature range of 50–75 °C leads to the consumption of **2** and concurrent formation of the simple phosphine-substituted compound **3** as the major product, as assessed by TLC and IR analyses. TLC examination also revealed the presence of a small amount of compound **1** and some decomposed material that remained irreversibly bound to the TLC plate irrespective of the mobile phase employed. The observation of **1** during the thermolysis reaction raises an interesting aspect concerning the route leading to **3**. It is possible that **1** serves as the principal product from the acyl-deinsertion reaction, which in turn requires the expulsion of the PMe_3 ligand from **2**. Once regenerated **1** could again react with the liberated PMe_3 to furnish **2** and then ultimately produce **3** through a slower secondary event(s). The observation of both **1** and **3** from **2** is also consistent with a dual reaction manifold, where the amount of each product (**1** and **3**) reflects a kinetic preference associated with the acyl-deinsertion step [16]. Of these two general paths, we favor the latter one based on the results obtained from the thermolysis of a toluene solution of **2** that was purged with argon in order to remove the liberated CO and PMe_3. Under such conditions, the back reaction between **1** and PMe_3 would be eliminated. Accordingly, **1** would be observed as the dominant product, provided that the expulsion of PMe_3 from **2** is favored over CO dissociation. The significant amount of **3** that accompanies this particular experiment (TLC monitoring) indicates that the conversion of **2** to **3** proceeds primarily through the liberation of CO and not PMe_3. The bottom portion of Scheme 1 shows the conversion of **2** to **3**.

Compound **3** was isolated by column chromatography in 82% yield and characterized by traditional spectroscopic methods, combustion analysis, and X-ray crystallography. The IR spectrum of **3** showed two strong carbonyl stretching bands at 2001 and 1958 cm^{-1} belonging to the terminal Co–CO groups and two anhydride carbonyl bands at 1777 (m) and 1721 (m) cm^{-1} that represent the vibrationally coupled symmetric and antisymmetric anhydride stretches, respectively. The presence of three terminal Co–CO groups in **3** was verified by ^{13}C NMR spectroscopy of a ^{13}CO-enriched sample of **3**. Here, ^{13}C resonances recorded at δ 202.07, 207.37, and 211.89 support the formulated structure of **3** and the loss of the acyl moiety. The ^{31}P NMR spectrum of **3** exhibits a high-field resonance at δ 10.80 for the overlapping cobalt-bound phosphine moieties and the hydrocarbyl-bound phosphonium ligand at δ 33.78. These data are similar to those chemical shifts recorded for compound **2**.

The molecular composition of **3** was established by X-ray diffraction analysis. The ORTEP diagram of **3** depicted in the right-hand portion of Fig. 1 confirms the loss of the acyl moiety in the conversion of **2** to **3**. With the exception of the ancillary PMe_3 group at Co(2), the overall structure of **3** is comparable to the published structure of **1** [2]. The 2.553(4) Å bond distance for the Co(1)–Co(2) vector is in

keeping with its single-bond designation and consistent with those Co–Co bond lengths found in other dinuclear cobalt compounds [17]. The cobalt-bound alkene moieties defined by the atoms C(11)–C(15) and C(16)–C(17) exhibit bond distances of 1.39(3) and 1.40(3) Å, respectively, that are slightly shorter than those distances found in **2**. The remaining bond distances and angles are unexceptional and require no comment.

4. Conclusions

The addition of PMe_3 to $Co_2(CO)_4$[μ-PhC= C(H)PPh_2 C=C(PPh_2)C(O)OC(O)] (**1**) promotes the regiospecific CO insertion into one of the Co-C(hydrocarbyl) bonds and production of the acyl compound $Co_2(CO)_3$-(PMe_3)[μ-PhC(CO)=C(H)PPh_2C=C(PPh_2)C(O)OC(O)] (**2**). This represents the first example of a phosphine-induced CO-insertion reaction in a zwitterionic hydrocarbyl compound of this genre. Compound **2** is thermally unstable and undergoes decarbonylation to furnish the PMe_3-substituted compound $Co_2(CO)_3(PMe_3)$[μ-PhC=C(H)PPh_2C= C(PPh_2)C(O)OC(O)] (**3**) and **1**, as the major and minor products, respectively. Our future endeavors will explore the generality of this reaction with isonitrile ligands and different phosphines, and the kinetics for the CO insertion reaction will be investigated using low-temperature spectroscopic techniques.

Acknowledgement

Financial support from the Robert A. Welch Foundation (Grant B-1093-M.G.R) is much appreciated.

Appendix A. Supplementary material

CCDC 627411 and 627412 contain the supplementary crystallographic data for **2** and **3**. These data can be obtained free of charge via http://www.ccdc.cam.ac.uk/conts/retrieving.html, or from the Cambridge Crystallographic Data Centre, 12 Union Road, Cambridge CB2 1EZ, UK; fax: (+44) 1223-336-033; or e-mail: deposit@ccdc.cam.ac.uk. Supplementary data associated with this article can be found, in the online version, at doi:10.1016/j.poly.2007.04.004.

References

[1] (a) S.J. Trepanier, J.N.L. Dennett, B.T. Sterenberg, R. McDonald, M. Cowie, J. Am. Chem. Soc. 126 (2004) 8046;
(b) J.R. Wigginton, A. Chokshi, T.W. Graham, R. McDonald, M.J. Ferguson, M. Cowie, Organometallics 24 (2005) 6398;
(c) S. Yoshimitsu, S. Hikichi, M. Akita, Organometallics 21 (2002) 3762;
(d) C.S.-W. Lau, W.-T. Wong, J. Chem. Soc., Dalton Trans. (1999) 2511;
(e) R.D. Adams, L. Chen, M. Huang, Organometallics 13 (1994) 2696.

[2] (a) K. Yang, S.G. Bott, M.G. Richmond, Organometallics 13 (1994) 3767;
(b) K. Yang, S.G. Bott, M.G. Richmond, J. Organomet. Chem. 516 (1996) 65.

[3] (a) For examples involving intermolecular phosphine attack on a coordinated alkyne ligand, see D.M. Hoffman, J.C. Huffman, D. Lappas, D.A. Wierda, Organometallics 12 (1993) 4312;
(b) J. Takats, J. Washington, B.D. Santarsiero, Organometallics 13 (1994) 1078;
(c) T. Mao, Z. Zhang, J. Washington, J. Takats, R.B. Jordan, Organometallics 18 (1999) 2331.

[4] K. Yang, S.G. Bott, M.G. Richmond, Organometallics 13 (1994) 3788.

[5] For related substitution studies from our labs, see K. Yang, S.G. Bott, M.G. Richmond, Organometallics 14 (1995) 919, 2718.

[6] H. Greenfield, H.W. Sternberg, R.A. Friedel, J.H. Wotiz, R. Markby, I. Wender, J. Am. Chem. Soc. 78 (1956) 120.

[7] F. Mao, C.E. Philbin, T.J.R. Weakley, D.R. Tyler, Organometallics 9 (1990) 1510.

[8] M.L. Luetkens Jr., A.P. Sattelberger, H.H. Murray, J.D. Basil, J.P. Fackler Jr., Inorg. Synth. 26 (1989) 7.

[9] D.F. Shriver, The Manipulation of Air-Sensitive Compounds, McGraw-Hill, New York, 1969.

[10] N.B. Coltrup, L.H. Daly, S.E. Wiberley, Introduction to Infrared and Raman Spectroscopy, Academic Press, New York, 1990.

[11] C.P. Horwitz, D.F. Shriver, Adv. Organomet. Chem. 23 (1984) 219.

[12] All NMR spectrum were recorded at low temperature in order to minimize undesirable ^{59}Co broadening of the ^{13}C and ^{31}P resonances. No noticeable fluxional behavior was observed for the CO and phosphine ligands in **2** and **3**. See M. Schwartz, M.G. Richmond, A.F.T. Chen, G.E. Martin, J.K. Kochi, Inorg. Chem. 27 (1988) 4698.

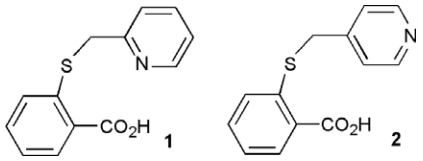
[13] (a) For reports of spontaneous resolution of racemic mixtures, see R. Clérac, F.A. Cotton, K.R. Dunbar, T. Lu, C.A. Murillo, X. Wang, Inorg. Chem. 39 (2000) 3065;
(b) A. Johansson, M. Håkansson, S. Jagner, Chem. Eur. J. 11 (2005) 5311;
(c) H. Okazaki, Y. Kushi, H. Yoneda, J. Am. Chem. Soc. 107 (1985) 4183.

[14] A.G. Orpen, L. Brammer, F.H. Allen, O. Kennard, D.G. Watson, R.J. Taylor, Chem. Soc., Dalton Trans. (1989) S1.

[15] (a) A.J.M. Caffyn, M.J. Mays, G.A. Solan, D. Braga, P. Sabatino, G. Conole, M. McPartlin, H.R. Powell, J. Chem. Soc., Dalton Trans. (1991) 3103;
(b) I. Moldes, J. Ros, M.R. Torres, A. Perales, R. Mathieu, J. Organomet. Chem 464 (1994) 219;
(c) J.D. King, M.J. Mays, G.E. Pateman, G.A. Solan, G. Conole, M. McPartlin, J. Chem. Soc., Dalton Trans. (2001) 202;
(d) E. Champeil, S.M. Draper, J. Chem. Soc., Dalton Trans. (2001) 1440.

[16] For a classical study demonstrating this phenomenon, see C.P. Casey, D.M. Scheck, J. Am. Chem. Soc. 102 (1980) 2723.

[17] (a) T.J. Snaith, P.J. Low, R. Rousseau, H. Puschmann, J.A.K. Howard, J. Chem. Soc., Dalton Trans. (2001) 292;
(b) M.J. Mays, P.R. Raithby, M.-A. Rennie, V. Sarveswaran, G.A. Solan, Inorg. Chim. Acta 277 (1998) 186;
(c) F.A. Cotton, J.D. Jamerson, B.R. Stults, J. Am. Chem. Soc. 98 (1976) 1774;
(d) C.-G. Xia, S.G. Bott, G. Wu, M.G. Richmond, J. Chem. Crystallogr. 34 (2004) 513.



Scheme 1. The structures of pyridylmethylthiobenzoic acid **1** and **2**.

2. Results and discussion

2.1. Reaction of 2-(2-pyridylmethylthio)benzoic acid (*1*) with R_2SnO (R = Et or ^nBu)

Upon treatment of 2-(2-pyridylmethylthio)benzoic acid with R_2SnO (R = Et or ^nBu) in a 1:1 molar ratio in anhydrous benzene, dimeric compounds $\{[(2\text{-}PyCH_2SC_6H_4CO_2)SnR_2]_2O\}_2$ [R = Et (**3**) and ^nBu (**4**)] were yielded, which have been characterized by elemental analyses, IR as well as NMR spectra. The NMR spectra of these two compounds are consistent with their structures as dimeric distannoxanes. For instance, the ^{119}Sn spectra of these compounds verify the presence of *endo*- and *exo*-cyclic tin atoms. A pair of resonances of equal intensities is observed at −207.92 and −209.58 ppm for **3** as well as at −194.13 and −193.13 ppm for **4**. These values are comparable with those reported for other dimeric distannoxanes with cyclic Sn_2O_2 units [13,21–23], and correspond to a five-coordinated or weakly six-coordinated tin atom. In addition, the ^1H and ^{13}C NMR spectra of these two compounds also support the suggested structures, and exhibit two sets of ethyl signals for **3** and butyl signals for **4**.

In order to prove the role of these heteroatoms in the carboxylate ligands, the structure of **4** has also been confirmed further by X-ray crystallography, and presented in Fig. 1. Selected bond distances and angles are listed in Table 1. As seen in Fig. 1, the pyridyl nitrogen atoms do not coordinate to the tin atoms. The crystallographically unique carboxylic ligands display different coordination

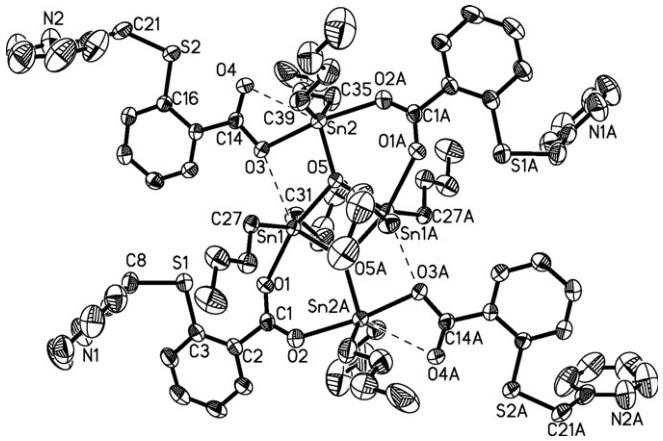


Fig. 1. The molecular structure of **4** with the thermal ellipsoids at the 30% probability level. Hydrogen atoms are omitted for clarity. Symmetric operation of "A" is 1 − *x*, 2 − *y*, 1 − *z*.

Table 1
Selected bond distances (Å) and angles (°) for compounds **4** and **5**

Compound **4**[a]		Compound **5**[b]	
Sn1–O1	2.257(3)	Sn1–O1	2.161(2)
Sn1–O5	2.166(3)	Sn1–O1A	2.034(2)
Sn1–O5A	2.043(3)	Sn1–O5A	2.253(3)
Sn1···O3	2.83(1)	Sn1···O2	3.045(4)
Sn1···Sn1A	3.302(4)	Sn1···Sn1A	3.300(1)
Sn2–O5	2.045(3)	Sn2–O1	2.045(2)
Sn2–O2A	2.266(4)	Sn2–O2	2.213(2)
Sn2–O3	2.195(3)	Sn2–O4	2.253(3)
Sn2···O4	2.77(1)	Sn2–O3	2.531(2)
C3–S1	1.780(6)	C11–S1	1.768(3)
C8–S1	1.815(6)	C16–S1	1.823(4)
C1–O1	1.264(6)	C9–O2	1.294(4)
C1–O2	1.260(6)	C9–O3	1.244(4)
C14–O3	1.311(6)	C22–O4	1.258(4)
C14–O4	1.223(6)	C22–O5	1.240(4)
C27–Sn1–C31	139.3(2)	C1–Sn1–C3	137.0(1)
O1–Sn1–O5	165.1(1)	O1–Sn1–O5A	165.7(1)
O5A–Sn1–C27	107.9(1)	O1A–Sn1–C3	109.7(1)
C27–Sn1–O5	99.7(1)	C1–Sn1–O1	94.8(1)
C31–Sn1–O1	83.5(1)	C1–Sn1–O5A	82.9(1)
C35–Sn2–C39	141.7(3)	C5–Sn2–C7	146.9(1)
O3–Sn2–O2A	170.4(1)	O2–Sn2–O4	171.6(1)
O5–Sn2–C35	112.6(2)	O1–Sn2–C7	109.4(1)
O5–Sn2–C39	105.0(1)	O1–Sn2–O3	139.11(8)
C3–S1–C8	103.5(3)	C11–S1–C16	103.4(1)
Sn1–O5–Sn2	120.8(1)	Sn1A–O1–Sn2	133.2(1)
Sn1–O5–Sn1A	103.3(1)	Sn1A–O1–Sn1	103.71(9)
O1–C1–O2	123.9(5)	O2–C9–O3	120.2(3)
O3–C14–O4	120.2(5)	O4–C22–O5	123.8(3)

[a] Symmetry code of "A" is 1 − *x*, 2 − *y*, 1 − *z*.
[b] Symmetry code of "A" is 1 − *x*, −*y*, 2 − *z*.

modes. One acts as a monodentate ligand by the carboxylate oxygen, while the other is a bridging bidentate ligand by two oxygen atoms of the carboxyl group. Each tin atom adopts a five-coordinate distorted trigonal bipyramidal geometry with two oxygen atoms (O1 and O5 for Sn1 as well as O3 and O2A for Sn2) occupying the axial positions. The axial O–Sn–O angles (O1–Sn1–O5 165.1(1)° and O3–Sn2–O2A 170.4(1)°) significantly derivate from 180°. Some weak intramolecular Sn···O interactions are also observed. The Sn···O distances (Sn1···O3 2.83(1) Å, Sn2···O4 2.77(1) Å) are significantly shorter than the sum of the van der Waal's radii for the Sn and O atom of 3.57 Å [9], but are markedly longer than the covalent Sn–O distance, such as Sn1–O1 (2.257(3) Å) and Sn1–O5 (2.166(3) Å).

2.2. Reaction of 2-(4-pyridylmethylthio)benzoic acid (*2*) with R_2SnO (R = Et or ^nBu)

The reaction of 2-(4-pyridylmethylthio)benzoic acid with Et_2SnO in a 1:1 molar ratio in anhydrous benzene also gives a dimeric compound, $\{[(4\text{-}PyCH_2SC_6H_4CO_2)SnEt_2]_2O\}_2$ (**5**). Although its ^{119}Sn NMR spectrum only shows a broad single resonance peak at −193.17 ppm (possibly owing to coincidental overlapping), the ^{13}C NMR spectrum clearly shows two sets of signals for the ethyl

carbons, consistent with the structure of a dimeric distannoxane, like in **4**. However, treatment of 2-(4-pyridylmethylthio)benzoic acid with $^{n}Bu_2SnO$ in a 1:1 molar ratio under similar reaction conditions only yields the diorganotin dicarboxylate $(4\text{-}PyCH_2SC_6H_4CO_2)_2Sn(^{n}Bu)_2$ (**6**). Its ^{1}H and ^{13}C NMR spectra exhibit only one set of butyl signals. In addition, the ^{119}Sn NMR spectrum of **6** displays one resonance at −155.56 ppm, markedly different from those of **3**–**5**, but comparable with those reported for related diorganotin dicarboxylates [10,22,23]. Although the tin atom in this compound is seven-coordinate in the solid state (see Fig. 3), this ^{119}Sn NMR chemical shift is not consistent with that of a seven-coordinate tin centre [8,16], suggesting that the seven-coordinate structure of tin is not retained, and extensive dissociation may occur in solution. It is known that the steric hindrance of the carboxylic acid or alkyl groups of tin significantly affects the coordinate environment of the tin atom in organotin carboxylates [8,9,24]. So the greater bulkiness of the butyl group compared to that of the ethyl group possibly plays a key role in the formation of **6** in this reaction.

The distannoxane structure for **5** and dicarboxylate structure for **6** are also supported by their X-ray diffraction analyses. The molecular structure of **5** is presented in Fig. 2, and selected bond distances and angles are listed in Table 1. To a first approximation, the molecular structure of **5** is similar to that of **4**. For instance, they both have tetranuclear distannoxane structures, and the pyridyl nitrogen atoms do not participate in coordination to the tin atoms in either of these two compounds. On the other hand, some noticeable differences exist between **4** and **5**. In **5**, one tin atom (Sn1) adopts a five-coordinate distorted trigonal bipyramidal geometry, while the other tin (Sn2) is in a six-coordinate distorted octahedral geometry. The coordination modes of the carboxylic ligands are also different in these two compounds. One carboxylic ligand in **5** acts as a bidentate bridging ligand, while the other is a bidentate chelating ligand. In addition, the Sn1···O2 distance (3.045(4) Å) in **5** is longer than the corresponding Sn1···O3 distance (2.83(1) Å) in **4**, implying weaker nonbonded Sn···O interactions in **5**. Additionally, it is noteworthy pointing out these two compounds have short Sn1···Sn1A separations (3.302(4) Å in **4** and 3.300(1) Å in **5**) [12,25].

The molecular structure of **6** is presented in Fig. 3, and selected bond distances and angles are listed in Table 2. The tin atom has a seven-coordinate distorted pentagonal-bipyramidal geometry, with four oxygen atoms of two chelating carboxylate ligands and the pyridyl nitrogen atom occupying the equatorial plane and two butyl groups lying in axial positions with an axial angle C27–Sn1–C31of 167.0(1)°. The Sn1 atom lies in the plane formed by the Sn1

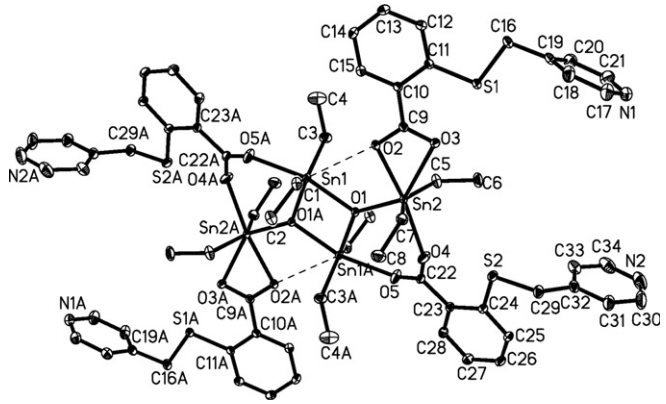


Fig. 2. The molecular structure of **5** with the thermal ellipsoids at the 30% probability level. Hydrogen atoms are omitted for clarity. Symmetric operation of "A" is $1-x, -y, 2-z$.

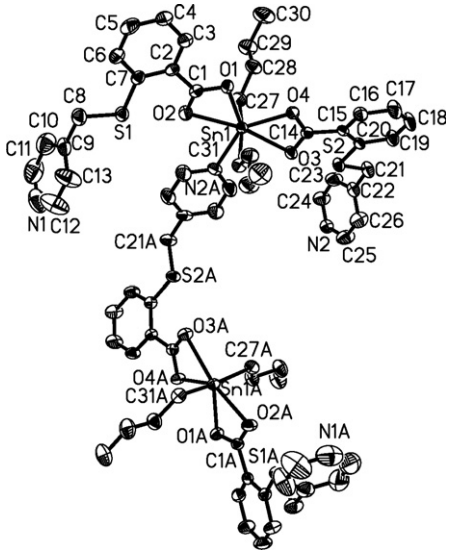


Fig. 3. The molecular structure of **6** with the thermal ellipsoids at the 30% probability level. Hydrogen atoms are omitted for clarity. Symmetric operation of "A" is $0.5-x, 0.5+y, 0.5-z$.

Table 2
Selected bond distances (Å) and angles (°) for compounds **6** and **8**

Compound **6**[a]		Compound **8**[b]	
Sn1–O1	2.227(3)	Sn1–O2	2.149(2)
Sn1–O2	2.420(3)	Sn1···O1	3.040(3)
Sn1–N2A	2.510(4)	Sn1–N1A	2.524(2)
S(1)–C(7)	1.771(5)	C6–S1	1.816(3)
S(1)–C(8)	1.812(5)	C7–S1	1.768(3)
C1–O1	1.267(5)	C13–O1	1.224(4)
C1–O2	1.251(5)	C13–O2	1.300(4)
C27–Sn1–C31	167.0(1)	C14–Sn1–C20	124.2(1)
C27–Sn1–O4	95.6(1)	C20–Sn1–C26	112.6(1)
C31–Sn1–O3	90.3(1)	C26–Sn1–O2	90.1(1)
O4–Sn1–O1	84.2(1)	C20–Sn1–N1A	85.7(1)
O4–Sn1–O2	140.0(1)	O2–Sn1–N1A	175.27(9)
O2–Sn1–O3	164.4(1)	C6–S1–C7	102.3(1)
C31–Sn1–N2A	83.2(1)	O1–C13–O2	123.1(3)
O4–Sn1–N2A	138.3(1)		
C7–S1–C8	103.2(2)		
O1–C1–O2	120.2(4)		

[a] Symmetry code of "A" is $0.5-x, 0.5+y, 0.5-z$.
[b] Symmetry code of "A" is $-0.5+x, 0.5-y, 0.5+z$.

O1, O2, O3, O4 and N2A atoms, and only deviates from the plane by 0.0101 Å. Furthermore, this compound forms a linkage coordination polymer through the interactions of the pyridyl nitrogen atoms with the adjacent tin atoms. The Sn1–N2A bond distance is 2.510(4) Å, comparable with those reported in other related seven-coordinate organotin dicarboxylates [8,12,16].

2.3. Reaction of 1 and 2 with $(Ph_3Sn)_2O$

Reaction of pyridylmethylthiobenzoic acids **1** and **2** with $(Ph_3Sn)_2O$ in a 2:1 molar ratio gives triphenyltin carboxylates (2-$PyCH_2SC_6H_4CO_2$)$SnPh_3$ (**7**) and (4-$PyCH_2SC_6H_4CO_2$)$SnPh_3$ (**8**), which have also been characterized by elemental analyses, IR, NMR spectra and X-ray crystallography. The molecular structure of **7** is presented in Fig. 4, and indicates that the tin is in a distorted tetrahedral geometry. The carboxylate group acts as unidentate ligand. Like **4** and **5**, the pyridyl nitrogen atom in **7** does not participate in coordination to the tin atom. Additionally, other weak non-bonded interactions, such as intramolecular Sn···O (Sn1···O2 2.737(3) Å) and intermolecular S···S (S1···$S1^i$ 3.617(4) Å, symmetry code: i = 1 − *x*, 2 − *y*, 2 − *z*) interactions, have also been observed in this compound.

Like compound **6**, **8** forms a linkage coordination polymer through the interactions of the pyridyl nitrogen atoms with the adjacent tin atoms, as shown in Fig. 5. In **8**, however, the tin atom adopts a five-coordinate distorted trigonal bipyramidal geometry with one oxygen atom and the pyridyl nitrogen atom occupying the axial positions with an axial angle O2–Sn1–N1A of 175.27(9)° (see Table 2). The non-bonded Sn···O distance (Sn1···O1 3.040(3) Å) is significantly longer than the corresponding Sn···O distances in **4** and **7** (Sn1···O3 2.83(1) Å in **4** and Sn1···O2 2.737(3) Å in **7**), but is similar to that in **5** (Sn1···O2 3.045(4) Å). The Sn–N distance is 2.524(2) Å, also similar with that in **6** (2.510(4) Å) and other related polymeric triphenyltin derivatives containing pyridyl carboxylate ligands, such as 4-$PyCO_2SnPh_3$ (2.512(6) Å) [26,27].

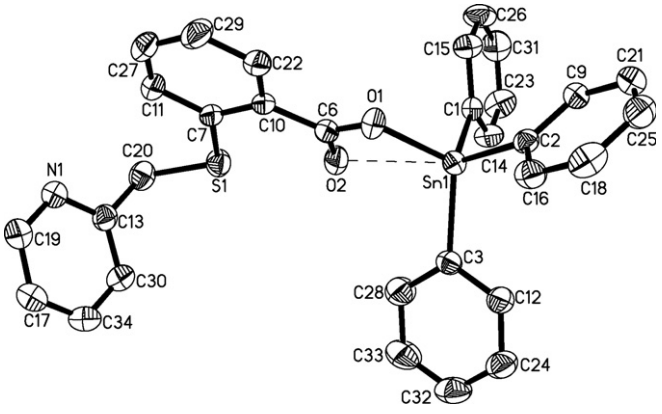


Fig. 4. The molecular structure of **7** with the thermal ellipsoids at the 30% probability level. Hydrogen atoms are omitted for clarity. Selected bond distances [Å] and angles [°]: Sn1–O1 = 2.058(2), Sn1···O2 = 2.737(3), Sn1–C1 = 2.120(3), Sn1–C2 = 2.127(3), Sn1–C3 = 2.126(3), C6–O1 = 1.304(4), C6–O2 = 1.237(4), C20–S1 = 1.819(4), S1···$S1^i$ = 3.617(4) Å; C1–Sn1–C3 = 119.4(1), C2–Sn1–O1 = 98.6(1), C1–Sn1–O1 = 106.4(1), O1–C6–O2 = 120.2(3), C7–S1–C20 = 104.3(1)° (symmetry code: i = 1 − *x*, 2 − *y*, 2 − *z*).

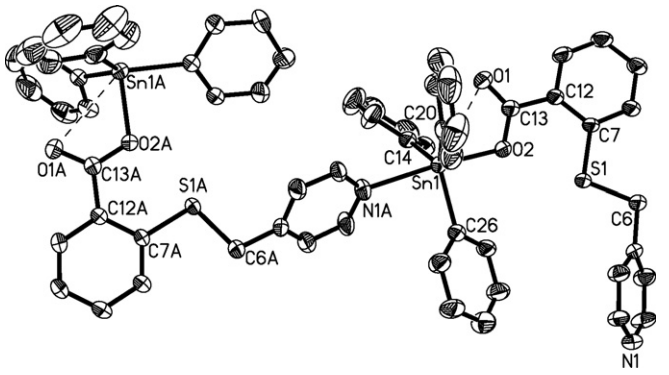


Fig. 5. The molecular structure of **8** with the thermal ellipsoids at the 30% probability level. Hydrogen atoms are omitted for clarity. Symmetric operation of "A" is −0.5 + *x*, 0.5 − *y*, 0.5 + *z*.

The IR and NMR spectra of compounds **7** and **8** are also consistent with their structures. For instance, the considerable differences between the asymmetric and symmetric stretching vibrations of the carboxylate groups (292 cm^{-1} in **7** and 301 cm^{-1} in **8**) indicate that they act as unidentate ligands [27,28]. The ^{119}Sn NMR spectrum of **7** displays one resonance at −103.44 ppm, very close to the values reported for the corresponding four-coordinated triphenyltin carboxylates, such as 105.97 ppm in $Ph_3SnO_2CCH_2CH_2COC_6H_4C_6H_5$ [29]. Although the tin atom in **8** is five-coordinate in the solid state (see Fig. 5), its ^{119}Sn NMR chemical shift (−107.52 ppm) is similar to that of **7**, indicating that the polymeric five-coordinate organotin structure is lost in solution. This result has also been observed in **6** and other polymeric or oligomeric organotin derivatives [30].

2.4. Biological activity

Preliminary *in vitro* tests for fungicidal activity of compounds **3**–**8** have been carried out by the fungi growth inhibition method [31]. These compounds are dissolved in DMF at a concentration of 50 ppm. The data are summarized in Table 3, and show that all compounds display certain activity to *Physolospora piricola* at a low concentration. Moreover, the triphenyltin carb-

Table 3
The fungicidal activities of compounds **3**–**8**

Compound	Inhibition ratio (%) (50 ppm)					
	3	**4**	**5**	**6**	**7**	**8**
Gibbereila zeae	0	0	0	0	60.8	47.8
Alternaria solani	0	0	0	23.5	70.0	23.5
Cercospora arachidicola	0	0	0	0	50.0	56.3
Physolospora piricola	45.6	39.7	39.7	51.4	70.6	85.2
Fusarium oxysporum	0	0	0	0	64.0	64.0

oxylates **7** and **8** are more active than the other diorganotin derivatives, similar to the results reported previously by Alt [32]. In addition, compound **8** shows the highest inhibition percentage for *Physolospora piricola* (85.2%) *in vitro*.

3. Experimental

Multinuclear NMR spectra were obtained with a Bruker AV300 or Mercury 300BB spectrometer using $CDCl_3$ as solvent unless otherwise noted, and the chemical shifts were reported in ppm with respect to reference standards (internal $SiMe_4$ for ^1H NMR and ^{13}C NMR spectra, external $SnMe_4$ for ^{119}Sn NMR). IR spectra were obtained on a Bio-Rad FTS 6000 spectrometer using KBr discs. Elemental analyses were carried out on a Perkin–Elmer 2400C analyzer. Melting points were measured with an X-4 digital micro melting-point apparatus and were uncorrected.

3.1. Preparation of pyridylmethylthiobenzoic acids

These acids were prepared by a slight modification of the method in the literature [20]. To a solution of KOH (0.241 mol) in 50 ml of EtOH and 10 ml of water, thiosalicylic acid (73.1 mmol) and chloromethylpyridine–HCl (73.2 mmol) were added. The reaction mixture was stirred at room temperature for 2 h, and then water (100 ml) was added. The water solution was extracted with diethyl ether (3×50 ml), and the organic phase was discarded to remove unreacted starting materials. The water phase was acidified to a pH value of 4 with 2 M HCl to give a white precipitate, which was filtered off, washed by water, and dried in air to yield pyridylmethylthiobenzoic acid, which could be crystallized with a large amount of alcohol.

3.1.1. Preparation of 2-(2-pyridylmethylthio)benzoic acid (*1*)

This acid was obtained by the reaction of thiosalicylic acid with 2-chloromethylpyridine–HCl. Yield: 72%; mp 173 °C (dec.). ^1H NMR (DMSO): $\delta = 8.53$ (d, 1H, C_5H_4N), 7.89 (d, 1H, C_5H_4N), 7.77–7.48, 7.28–7.20 (m, m, 4H, 2H, C_5H_4N and C_6H_4), 4.31 (s, 2H, CH_2) ppm. ^{13}C NMR (DMSO): $\delta = 167.3$ (CO_2H), 157.1, 149.0, 140.8, 136.9, 132.3, 130.9, 127.8, 125.8, 124.0, 123.3, 122.3 (C_5H_5N and C_6H_4), 37.8 (CH_2) ppm. IR (cm^{-1}): ν(C=O) 1688.8 s.

3.1.2. Preparation of 2-(4-pyridylmethylthio)benzoic acid (*2*)

This acid was obtained similarly to **1** using thiosalicylic acid and 4-chloromethylpyridine–HCl. Yield: 70%; mp 180 °C (dec.). ^1H NMR (DMSO): $\delta = 8.48$ (d, 2H, C_5H_4N), 7.87 (d, 2H, C_5H_4N), 7.48–7.39, 7.21–7.17 (m, m, 3H, 1H, C_6H_4), 4.23 (s, 2H, CH_2) ppm. ^{13}C NMR (DMSO): $\delta = 167.3$ (CO_2H), 149.6, 146.3, 140.0, 132.3, 130.9, 128.1, 125.9, 124.3, 124.1 (C_5H_5N and C_6H_4), 34.3 (CH_2) ppm. IR (cm^{-1}): ν(C=O) 1690.1 s.

3.2. Reaction of pyridylmethylthiobenzoic acid with R_2SnO ($R = {}^nBu$ or Et)

A mixture of pyridylmethylthiobenzoic acid **1** or **2** (1 mmol) and R_2SnO (1 mmol) in anhydrous benzene (40 ml) was stirred and heated at reflux for 8 h to yield a clear solution. After removing the benzene *in vacuo*, the crude product was recrystallized from a suitable solvent.

3.2.1. Preparation of $\{[(RCO_2)SnEt_2]_2O\}_2$ (R = 2-(2-pyridylmethylthio)phenyl) (*3*)

This compound was obtained by the reaction of **1** with Et_2SnO. The reaction time was 15 h. The crude product was recrystallized from benzene/hexane to afford white crystals of **3**. Yield: 65%; mp 167–169 °C. ^1H NMR: $\delta = 8.54$ (d, 2H, C_5H_4N), 7.90, 7.60–7.52, 7.36–7.14 (d, m, m, 2H, 4H, 8H, C_5H_4N and C_6H_4), 4.30 (s, 4H, CH_2), 1.67–1.61, 1.41–1.33 (m, m, 8H, 12H, $SnCH_2CH_3$) ppm. ^{13}C NMR: $\delta = 173.13$ (COO), 157.96, 153.17, 151.99, 149.29, 137.01, 131.82, 131.59, 126.16, 124.18, 123.18, 122.26 (C_5H_4N and C_6H_4), 39.24 (CH_2), 23.17, 21.28, 10.31, 10.06 (ethyl carbons) ppm. ^{119}Sn NMR: $\delta = -207.92$, -209.58 ppm. IR (cm^{-1}): ν_{as} (COO) 1591, 1572, ν_s (COO) 1399, 1346. *Anal.* Calc. for $C_{34}H_{40}N_2O_5S_2Sn_2$: C, 47.58; H, 4.70; N, 3.26. Found: C, 47.26; H, 4.25; N, 3.15%.

3.2.2. Preparation of $\{[(RCO_2)Sn({}^nBu)_2]_2O\}_2$ (R = 2-(2-pyridylmethylthio)phenyl) (*4*)

This compound was obtained by the reaction of **1** with $^nBu_2SnO$, and was recrystallized from ether to afford white crystals of **4**. Yield: 62%; mp 92–94 °C. ^1H NMR: $\delta = 8.55$ (d, 2H, C_5H_4N), 7.85–7.10 (m, 14H, C_5H_4N and C_6H_4), 4.30 (s, 4H, CH_2), 1.77–1.55, 1.34–1.21 (m, m, 16H, 8H, $SnCH_2CH_2CH_2$), 0.85–0.73 (m, 12H, CH_3) ppm. ^{13}C NMR: $\delta = 172.98$ (COO), 157.81, 157.51, 149.09, 139.91, 136.68, 131.27, 131.03, 126.21, 124.05, 122.97, 121.98 (C_5H_4N and C_6H_4), 39.14 (CH_2), 30.08, 28.47, 27.64, 27.37, 26.87, 26.82, 13.59, 13.53 (butyl carbons) ppm. ^{119}Sn NMR: $\delta = -194.13$, -195.13 ppm. IR (cm^{-1}): ν_{as} (COO) 1591, 1575, ν_s (COO) 1406, 1346. *Anal.* Calc. for $C_{42}H_{56}N_2O_5S_2Sn_2$: C, 51.98; H, 5.82; N, 2.89. Found: C, 51.67; H, 5.89; N, 2.70%.

3.2.3. Preparation of $\{[(RCO_2)SnEt_2]_2O\}_2$ (R = 2-(4-pyridylmethylthio)phenyl) (*5*)

This compound was obtained by the reaction of **2** (1 mmol) with Et_2SnO (1 mmol), and was recrystallized from benzene/hexane to afford white crystals of **5**. Yield: 64%; mp 174–177 °C. ^1H NMR: $\delta = 8.46$ (d, 4H, C_5H_4N), 7.81 (d, 2H, C_6H_4), 7.29–7.19, 7.09–7.03 (m, m, 6H, 4H, C_5H_4N and C_6H_4), 4.03 (s, 4H, CH_2), 1.59–1.46, 1.33–1.25 (m, m, 8H, 12H, $SnCH_2CH_3$) ppm. ^{13}C NMR: $\delta = 172.90$ (COO), 150.21, 148.61, 136.37, 132.67, 131.48, 128.33, 126.32, 124.49, 123.42 (C_5H_4N and C_6H_4), 34.67 (CH_2), 22.92, 20.97, 10.03, 9.76 (ethyl carbons) ppm. ^{119}Sn NMR: $\delta = -193.17$ (br) ppm. IR (cm^{-1}): ν_{as} (COO) 1592, 1573, ν_s (COO) 1459, 1398. *Anal.* Calc. for

$C_{34}H_{40}N_2O_5S_2Sn_2$: C, 47.58; H, 4.70; N, 3.26. Found: C, 47.62; H, 4.57; N, 3.23%.

3.2.4. Preparation of $(RCO_2)_2Sn(^nBu)_2$ (R = 2-(4-pyridylmethylthio)phenyl) (6)

This compound was obtained by the reaction of **2** (1 mmol) with $^nBu_2SnO$ (1 mmol), and was recrystallized from ethyl acetate/hexane to afford white crystals of **6**. Yield: 68%; mp 174–176 °C. ^{1}H NMR: $\delta = 8.58$ (d, 4H, C_5H_4N), 8.17 (d, 2H, C_6H_4), 7.44–7.38, 7.24–7.19 (m, m, 6H, 4H, C_5H_4N and C_6H_4), 4.15 (s, 4H, CH_2), 1.90–1.84, 1.80–1.73, 1.44–1.37 (m, m, m, 4H, 4H, 4H, $SnCH_2CH_2CH_2$), 0.88 (t, 6H, CH_3) ppm. ^{13}C NMR: $\delta = 175.58$ (*C*OO), 149.89, 146.11, 140.30, 132.60, 132.52, 128.62, 125.92, 124.62, 124.03 (C_5H_4N and C_6H_4), 36.23 (CH_2), 26.73, 26.26, 26.19, 13.57 (butyl carbons) ppm. ^{119}Sn NMR: $\delta = -155.56$ ppm. IR (cm^{-1}): ν_{as} (COO) 1615, ν_s (COO) 1401. *Anal.* Calc. for $C_{34}H_{38}N_2O_4S_2Sn$: C, 56.60; H, 5.31; N, 3.88. Found: C, 56.39; H, 5.20; N, 3.64%.

3.3. Reaction of pyridylmethylthiobenzoic acid with $(Ph_3Sn)_2O$

A mixture of pyridylmethylthiobenzoic acid **1** or **2** (2 mmol) and $(Ph_3Sn)_2O$ (1 mmol) in anhydrous benzene (40 ml) was stirred and heated at reflux for 6 h to yield a clear solution. After removing the benzene *in vacuo*, the crude product was recrystallized from a suitable solvent.

3.3.1. Preparation of RCO_2SnPh_3 (R = 2-(2-pyridylmethylthio)phenyl) (7)

This compound was obtained by the reaction of **1** with $(Ph_3Sn)_2O$, and recrystallized from ether/hexane to afford white crystals of **7**. Yield: 78%; mp 103–105 °C. ^{1}H NMR: $\delta = 8.57$, 8.15 (d, d, 1H, 1H, C_5H_4N), 7.97–7.76 (m, 6H, C_6H_5), 7.61, 7.52–7.33, 7.19–7.12 (t, m, m, 1H, 12H, 2H, C_6H_5, C_5H_4N and C_6H_4), 4.34 (s, 2H, CH_2) ppm. ^{13}C NMR: $\delta = 172.87$ (*C*OO), 157.62, 149.10, 141.11, 138.48, 137.43, 137.04, 136.91, 132.93, 132.38, 130.15, 128.93, 126.08, 124.17, 122.98, 122.14 (C_6H_5, C_5H_4N and C_6H_4), 38.97 (CH_2) ppm. ^{119}Sn NMR: $\delta = -103.44$ ppm. IR (cm^{-1}): ν_{as} (COO) 1622, ν_s (COO) 1330. *Anal.* Calc. for $C_{31}H_{25}NO_2SSn$: C, 62.65; H, 4.24; N, 2.36. Found: C, 62.38; H, 4.55; N, 2.43%.

3.3.2. Preparation of RCO_2SnPh_3 (R = 2-(4-pyridylmethylthio)phenyl) (8)

This compound was obtained by the reaction of **2** with $(Ph_3Sn)_2O$, and recrystallized from benzene/hexane to afford slight yellow crystals of **8**. Yield: 80%; mp 186–188 °C. ^{1}H NMR: $\delta = 8.49$, 7.18 (d, d, 2H, 2H, C_5H_4N), 8.11 (d, 1H, C_6H_4), 7.95–7.74 (m, 6H, C_6H_5), 7.47–7.29 (m, 12H, C_6H_5 and C_6H_4), 4.08 (s, 2H, CH_2) ppm. ^{13}C NMR: $\delta = 172.38$ (*C*OO), 149.88, 146.24, 139.88, 138.43, 137.00, 132.61, 132.03, 130.16, 128.92, 128.35, 126.38, 124.72, 124.02 (C_6H_5, C_5H_4N and C_6H_4), 36.49 (CH_2) ppm. ^{119}Sn NMR: $\delta = -107.52$ ppm. IR (cm^{-1}): ν_{as} (COO) 1632, ν_s (COO) 1331. *Anal.* Calc. for $C_{31}H_{25}NO_2SSn$: C, 62.65; H, 4.24; N, 2.36. Found: C, 62.58; H, 4.47; N, 2.24%.

4. Crystal structure determinations

Crystals of **4** and **7** suitable for X-ray analyses were obtained by slowly cooling their hot ether/hexane solutions. Crystals of **6** suitable for X-ray analysis were

Table 4
Crystal data and refinement parameters for compounds **4**–**8**

Compound	4	5	6	7	8
Formula	$C_{84}H_{112}N_4O_{10}S_4Sn_4$	$C_{68}H_{80}N_4O_{10}S_4Sn_4$	$C_{34}H_{38}N_2O_4S_2Sn$	$C_{31}H_{25}NO_2SSn$	$C_{31}H_{25}NO_2SSn$
Formula weight	1940.78	1716.36	721.47	594.27	594.27
Crystal size (mm)	$0.22 \times 0.20 \times 0.04$	$0.34 \times 0.28 \times 0.10$	$0.20 \times 0.16 \times 0.10$	$0.22 \times 0.20 \times 0.12$	$0.28 \times 0.22 \times 0.20$
T (K)	294(2)	113(2)	294(2)	293(2)	293(2)
λ (Mo Kα) (Å)	0.71070	0.71070	0.71073	0.71073	0.71073
Crystal system	triclinic	monoclinic	monoclinic	triclinic	monoclinic
Space group	$P\bar{1}$	$P2_1/c$	$C2/c$	$P\bar{1}$	$P2_1/n$
a (Å)	12.122(5)	14.740(2)	32.462(4)	9.289(1)	9.7463(7)
b (Å)	13.418(5)	17.587(3)	10.067(1)	9.466(1)	16.939(1)
c (Å)	16.026(6)	15.064(2)	20.558(3)	16.039(3)	16.117(1)
α (°)	100.607(2)	90	90	95.858(3)	90
β (°)	106.862(4)	117.268(2)	92.845(2)	102.746(3)	91.455(1)
γ (°)	109.755(5)	90	90	99.226(3)	90
V (Å^3)	2229.7(15)	3471.0(9)	6710.0(15)	1343.9(4)	2659.9(3)
Z	1	2	8	2	4
D_{calc} (g cm^{-3})	1.445	1.642	1.428	1.469	1.484
F(000)	988	1720	2960	600	1200
μ (mm^{-1})	1.256	1.602	0.925	1.056	1.068
Number of unique reflections (R_{int})	10039(0.0396)	8972(0.0420)	5914(0.0419)	5418(0.0244)	4703(0.0269)
Number of observed reflections ($I > 2\sigma(I)$)	6317	8074	3947	3895	3501
Number of parameters	479	422	390	325	408
Goodness of fit	1.033	1.087	1.042	1.039	1.010
Residuals R, Rw	0.0497, 0.1165	0.0389, 0.1032	0.0386, 0.0889	0.0385, 0.0650	0.0300, 0.0782

obtained by slow diffusion of hexane into its CH_2Cl_2 solution at room temperature. Crystals of **5** and **8** suitable for X-ray analyses were obtained by slowly cooling their hot benzene/hexane solutions. Intensity data were collected on a Rigaku Saturn CCD detector for **4** and **5**, and a Bruker SMART CCD diffractometer for **6**–**8**. One carbon (C4) of an ethyl group at the tin atom in **5** is disordered and was refined over two sites with occupancies of 0.41 for C4 and 0.59 for C4′. The pyridyl carbons (C1–C4) and the phenyl carbons (C27, C28, C30 and C31) in **8** are also disordered. The site occupation factors of these disordered atoms were adjusted (0.63 for C1–C4 atoms and 0.59 for C27, C28, C30 and C31 atoms) to give reasonable thermal parameters. The structures were solved by direct methods and refined by full-matrix least-squares on F^2. All non-hydrogen atoms were refined anisotropically. A summary of the fundamental crystal data for **4**–**8** is listed in Table 4.

Acknowledgements

This work is supported by the National Natural Science Foundation of China (No. 20421202) and the Ministry of Education of China (NCET-04-0227).

Appendix A. Supplementary materials

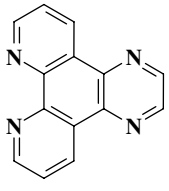
CCDC 636064, 636065, 636066, 636067 and 636068 contain the supplementary crystallographic data for **4**, **5**, **6**, **7** and **8**. The data can be obtained free of charge via http://www.ccdc.cam.ac.uk/conts/retrieving.html, or from the Cambridge Crystallographic Data Centre, 12 Union Road, Cambridge CB2 1EZ, UK; fax: (+44) 1223-336-033; or e-mail: deposit@ccdc.cam.ac.uk. Supplementary data associated with this article can be found, in the online version, at doi:10.1016/j.poly.2007.04.029.

References

[1] M. Gielen, Appl. Organomet. Chem. 16 (2002) 481.
[2] M. Gielen, Coord. Chem. Rev. 151 (1996) 41.
[3] E.R.T. Tiekink, Appl. Organomet. Chem. 5 (1991) 1.
[4] V. Chandrasekhar, S. Nagendran, V. Baskar, Coord. Chem. Rev. 235 (2002) 1.
[5] V. Dokorou, M.A. Demertzis, J.P. Jasinski, D. Kovala-Demertzi, J. Organomet. Chem. 689 (2004) 317.
[6] G. Prabusankar, R. Murugavel, Organometallics 23 (2004) 5644.
[7] C. Ma, Q. Zhang, R. Zhang, D. Wang, Chem. Eur. J. 12 (2006) 420.
[8] A. Szorcsik, L. Nagy, J. Sletten, G. Szalontai, E. Kamu, T. Fiore, L. Pellerito, E. Kalman, J. Organomet. Chem. 689 (2004) 1145.
[9] A. Szorcsik, L. Nagy, A. Deák, M. Scopelliti, Z.A. Fekete, A. Császár, C. Pellerito, L. Pellerito, J. Organomet. Chem. 689 (2004) 2762.
[10] Y. Zhou, J. Tao, S. Ren, J. Yu, Z. Xia, J. Organomet. Chem. 690 (2005) 2186.
[11] F. Benetollo, G.G. Lobbia, M. Mancini, M. Pellei, C. Santini, J. Organomet. Chem. 690 (2005) 1994.
[12] T.S.B. Baul, W. Rynjah, E. Rivarola, A. Lyčka, M. Holčapek, R. Jirásko, D. de Vos, R.J. Butcher, A. Linden, J. Organomet. Chem. 691 (2006) 4850.
[13] A. Szorcsik, L. Nagy, M. Scopelliti, A. Deák, L. Pellerito, G. Galbács, M. Hered, J. Organomet. Chem. 691 (2006) 1622.
[14] M.I. Khan, M.K. Baloch, M. Ashfaq, Obaidullah, Appl. Organomet. Chem. 20 (2006) 463.
[15] T.S.B. Baul, A. Mizar, X. Song, G. Eng, R. Jirásko, M. Holčapek, R. Willem, M. Biesemans, I. Verbruggen, R. Butcher, J. Organomet. Chem. 691 (2006) 2605.
[16] H.D. Yin, G.L. Zhong, J. Gao, H.L. Xu, J. Organomet. Chem. 691 (2006) 1235.
[17] C. Di Nicola, A. Galindo, J.V. Hanna, F. Marchetti, C. Pettinari, R. Pettinari, E. Rivarola, B.W. Skelton, A.H. White, Inorg. Chem. 44 (2005) 3094.
[18] R. García-Zarracino, H. Höpfl, J. Am. Chem. Soc. 127 (2005) 3120.
[19] H. Takahiro, T. Hisashi, S. Yoshimasa, K. Kenji, O. Kazuyoshi, Y. Minoru, B. Masakazu, PCT Int. Appl., WO 2004078723, CA 141:260553, 2004.
[20] Y. Sadakazu, H. Masatoshi, H. Katsuo, S. Kaoru, JP 63253073, CA 110:173237, 1988.
[21] Z.-K. Wen, H.-B. Song, M. Du, Y.-P. Zhai, L.-F. Tang, Appl. Organomet. Chem. 19 (2005) 1055.
[22] J.-T. Lu, S.-S. Chen, M. Du, L.-F. Tang, Appl. Organomet. Chem. 20 (2006) 448.
[23] S.G. Teoh, S.H. Ang, E.S. Looi, C.A. Keok, S.B. Teo, J.P. Declercq, J. Organomet. Chem. 523 (1996) 75.
[24] M.S. Kumar, S. Upreti, H.P. Gupta, A.J. Elias, J. Organomet. Chem. 691 (2006) 4708.
[25] R. Zhang, Y. Han, C. Ma, J. Inorg. Organomet. Polym. Mater. 16 (2006) 25.
[26] S.-G. Teoh, S.-H. Ang, H.-C. Lim, H.-K. Fun, A.R. Ibrahim, J. Coord. Chem. 46 (1998) 87.
[27] H.-D. Yin, C.-H. Wang, Q.-J. Xing, Polyhedron 23 (2004) 1805.
[28] Q. Duong, X. Song, E. Mitrojorgji, S. Gordon, G. Eng, J. Organomet. Chem. 691 (2006) 1775.
[29] L. Tian, Q. Yu, X. Zheng, Z. Shang, X. Liu, B. Qian, Appl. Organomet. Chem. 19 (2005) 672.
[30] M. Gielen, A. El Khloufi, M. Biesemans, F. Kayser, R. Willem, B. Mahieu, D. Maes, J.N. Lisgarten, L. Wyns, A. Moreira, T.K. Chattopadhay, R. Palmer, Organometallics 13 (1994) 2849.
[31] F. Junich, U. Yasuhiko, I. Kouzou, Method of Pesticide Experiment – Fungicide, Agricultural Press of China, Beijing, 1991, Translated by S. Li, D. Wang, S. Jiao.
[32] M. Danish, H.G. Alt, A. Badshah, S. Ali, M. Mazhar, J. Organomet. Chem. 486 (1995) 51.

undergo significant changes in coordination geometry during the redox process. The ability to deliberately control the microstructure of a coordination polymer by using macroscopic principles, through dissociation/binding of ligands from/to metal centres by an applied potential can have numerous material applications [15]. Copper(I) polypyridine complexes also display interesting photoluminescent properties. There has been considerable interest to harness the photophysical properties of copper(I) polypyridines for many practical applications, such as light harvesters, molecular sensors and switches [16]. The excellent photophysical properties of copper(I) polypyridines have opened a new area of study involving their intercalation with biological systems, in particular DNA intercalation and cleavage [17].

Phenanthroline based ligands, such as dipyrido[3,2-*f*:2′,3′-*h*]-quinoxaline (dpq), dipyridophenazine (dppz) and 7,8-dimethylpyridophenazine (dppx) with an extended planar quinoxaline moiety, can act as good bidentate ligands as well as good binders to DNA. Several ruthenium(II) complexes, such as $[RuL_2(dpq)]^{2+}$ (L = bpy or phen), have been synthesized because they bind to DNA strongly by intercalating the aromatic dpq ligand between the base pair. Moreover, on binding to DNA they strongly luminesce, acting as "light switches" [18]. More recently, the synthesis, structure and DNA binding of a copper(I) complex of dpq has been reported [19]. It has also been shown that copper(II) complexes having photoactive and DNA binding ligands cleave DNA on irradiation with red light [20]. Ternary copper(II) complexes derived from tridentate ONO and ONS ligands and the DNA binding ligand dpq cleaves DNA on exposure to red light [21]. In view of the growing interest in the use of the ligand dpq, which besides the studies made above has not been used extensively, we have been interested to explore the coordination chemistry of the dpq transition metal complexes in greater detail. Herein we report the synthesis, X-ray crystal structures, spectroscopic properties and redox activities of zinc(II), copper(I), copper(II), nickel(II), cobalt(II), cobalt(III), iron(II) and manganese(II) complexes of dpq.



dpq

2. Experimental

2.1. Materials

All chemicals were obtained from commercial sources and were used as received. Solvents were dried and purified according to standard methods [22]. 1,2-Diaminoethane was dried over potassium hydroxide before vacuum distillation. 1,10-Phenanthroline-5,6-dione was prepared according to the reported method [23].

Caution: The perchlorate salts reported here are potentially explosive and, therefore, should be handled with care.

2.2. Preparation of dipyrido[3,2-f:2′,3′-h]-quinoxaline (dpq)

The ligand was prepared by the condensation of 1,10-phenanthroline-5,6-dione and 1,2-diaminoethane in a modified method [24]. To an acetonitrile solution (20 mL) of 1,10-phenanthroline-5,6-dione (1.05 g, 5 mmol), an acetonitrile solution (10 mL) of 1,2-diaminoethane (0.30 g, 5 mmol) was added. The mixture was refluxed for 3 h after which it was cooled to room temperature. A black resinous precipitate was removed by filtration and the filtrate was dried on a rotary evaporator. The crude product thus obtained was recrystallized from acetonitrile to get the white crystalline pure compound. Yield: 2.5 g (70%). *Anal.* Calc. for $C_{14}H_8N_4$: C, 72.40; H, 3.47; N, 24.12. Found: C, 72.40; H, 3.48; N, 24.08%. IR (KBr): 3446br, 1635w, 1577m, 1519w, 1467m, 1392s, 1207w, 1116w, 1080m, 870w, 1212m, 808s, 740s, 686w, 621m. ^{1}H NMR ($CDCl_3$, 300 MHz): δ 9.45 (d, 2H), 9.23 (d, 2H), 8.93 (s, 2H), 7.74 (m, 2H).

2.3. Preparation of the metal complexes

2.3.1. $[Cu^I(dpq)_2](ClO_4)$ (1)

To a solution of dpq (0.46 g, 2 mmol) in dry methanol (10 mL) was added a solution of $[Cu(CH_3CN)_4](ClO_4)$ (0.33 g, 1 mmol) in dry methanol (10 mL) under a nitrogen atmosphere. The resulting dark red solution was refluxed for 0.5 h, during which time a dark maroon microcrystalline compound was deposited. The product was collected by filtration and washed with methanol. Yield: 0.50 g (80%). *Anal.* Calc. for $C_{28}H_{16}N_8O_4ClCu$: C, 53.59; H, 2.57; N, 17.86. Found: C, 53.50; H, 2.60; N, 17.78%. ESI-MS (positive, in acetonitrile): $m/z = 527.08$ (100%) $[Cu(dpq)_2]^+$. IR (KBr): 3434br, 3085w, 1627w, 1576m, 1470m, 1434w, 1420s, 1384s, 1275w, 1085s, 839w, 734m, 630m cm^{-1}. ^{1}H NMR (DMSO-d_6, 300 MHz): δ 9.65 (d, 2H), 9.31 (s, 2H), 9.14 (d, 2H), 8.18 (dd, 2H). UV–Vis–NIR (λ_{max}/nm (ε/M^{-1} cm^{-1})): 215 (62000), 255 (100000), 300 (34000), 445 (4700).

2.3.2. $[Cu^{II}(dpq)_2(H_2O)](ClO_4)_2 \cdot H_2O$ (2)

To a solution of dpq (0.46 g, 2 mmol) in methanol (15 mL) was added a methanol solution (10 mL) of $Cu(ClO_4)_2 \cdot 6H_2O$ (0.37 g, 1.0 mmol). The resulting blue solution was stirred at room temperature for 0.5 h. On concentration of the solution to ca. 10 mL on a hot plate, a crystalline product was deposited. This was filtered and recrystallized from 1:1 acetonitrile–ethanol to obtain single crystals of a bluish-green colour. Yield: 0.60 g (75%). *Anal.*

Calc. for $C_{28}H_{20}N_8O_{10}Cl_2Cu$: C, 44.08; H, 2.64; N, 14.69. Found: C, 44.18; H, 2.62; N, 14.65%. ESI-MS (positive, in acetonitrile): $m/z = 626.03$ (15%) $[Cu(dpq)_2(ClO_4)]^+$; 264.55 (100%) $[Cu(dpq)_2]^{2+}$. IR (KBr): 3403br, 3085w, 1626w, 1582m, 1532m, 1488s, 1428s, 1388s, 1282w, 1087s, 818m, 731s, 622m cm^{-1}. UV–Vis–NIR (λ_{max}/nm (ε/$M^{-1}\,cm^{-1}$)): 215 (63000), 260 (100000), 295 (35000), 700 (100), 900 (115).

2.3.3. $[Cu^{II}(dpq)_2](ClO_4)_2$ (3)

A dry acetonitrile solution (15 mL) of $Cu(ClO_4)_2 \cdot 6H_2O$ (0.37 g, 1.0 mmol) and a solution of dpq (0.46 g, 2 mmol) in the same solvent were mixed together. The resulting solution was refluxed for 0.5 h, during which period a clear blue solution was obtained. The solution was filtered and the filtrate was concentrated on a water bath to ca. 5 mL. On slow evaporation of the solvent at room temperature, a blue crystalline product was deposited. This was filtered and washed with 1:1 acetonitrile–diethyl ether. Yield: 0.58 g (80%). *Anal.* Calc. for $C_{28}H_{16}N_8O_8Cl_2Cu$: C, 46.26; H, 2.22; N, 15.41. Found: C, 46.18; H, 2.20; N, 15.36%. ESI-MS (positive, in acetonitrile): $m/z = 626.03$ (20%) $[Cu(dpq)_2(ClO_4)]^+$; 264.55 (100%) $[Cu(dpq)_2]^{2+}$. IR (KBr): 3078w, 1619w, 1582m, 1531w, 1485m, 1407s, 1387m, 1308m, 1213w, 1088s, 818m, 731s, 625m cm^{-1}. UV–Vis–NIR (λ_{max}/nm (ε/$M^{-1}\,cm^{-1}$)): 215 (63000), 260 (100000), 295 (35000), 700 (50), 900 (55).

2.3.4. $[\{Cu^{II}(dpq)_2(H_2O)\}\{Cu^{II}(dpq)_2(ClO_4)\}](ClO_4)_3$ (4)

To a dry acetonitrile solution (15 mL) of compound 1,10-phenanthroline-5,6-dione (0.42 g, 2 mmol) was added an acetonitrile solution (10 mL) of $Cu(ClO_4)_2 \cdot 6H_2O$ (0.37 g, 1.0 mmol) and the resulting green solution was set to reflux. A solution of 1,2-diaminoethane (0.12 g, 2 mmol) in 10 mL of dry acetonitrile was gradually added to the reaction mixture under refluxing conditions. The solution became reddish-brown and the reflux was continued for 2 h during which time a dark maroon microcrystalline compound was deposited. The product was collected by filtration and was identified to be copper(I) compound **1**. The green filtrate on standing at room temperature produced bright green single crystals of compound **4**. These were filtered and washed with 1:1 acetonitrile–diethyl ether. Yield: 0.45 g (60%). *Anal.* Calc. for $C_{56}H_{34}N_{16}O_{17}Cl_4Cu_2$: C, 45.70; H, 2.33; N, 15.23. Found: C, 45.65; H, 2.30; N, 15.17%. ESI-MS (positive, in acetonitrile): $m/z = 626.03$ (15%) $[Cu(dpq)_2(ClO_4)]^+$; 264.55 (100%) $[Cu(dpq)_2]^{2+}$. IR (KBr): 3407br, 3081w, 1615w, 1581m, 1531w, 1486m, 1407s, 1388m, 1308w, 1214w, 1088s, 818m, 732m, 625m cm^{-1}. UV–Vis–NIR (λ_{max}/nm (ε/$M^{-1}\,cm^{-1}$)): 215 (63000), 260 (100000), 295 (35000), 700 (190), 900 (200).

2.3.5. $[Zn^{II}(dpq)_2(ClO_4)_2]$ (5)

A solution of $Zn(ClO_4)_2 \cdot 6H_2O$ (0.34 g, 1 mmol) in 10 mL of dry acetonitrile was added to a solution of dpq (0.46 g, 2 mmol) in acetonitrile (10 mL) and the mixture was refluxed for 1 h. The solution was filtered and the filtrate was concentrated to ca. 5 mL on a hot plate. On slow evaporation of the solvent at the room temperature, light yellow crystals deposited. The product was filtered and washed with 1:1 acetonitrile–diethyl ether. Yield: 0.55 g (75%). *Anal.* Calc. for $C_{28}H_{16}N_8O_8Cl_2Zn$: C, 46.14; H, 2.21; N, 15.38. Found: C, 46.11; H, 2.19; N, 15.41%. ESI-MS (positive, in acetonitrile): $m/z = 627.03$ (20%) $[Zn(dpq)_2(ClO_4)]^+$; 265.05 (100%) $[Zn(dpq)_2]^{2+}$. IR (KBr): 3423br, 3052w, 1613w, 1582m, 1529w, 1481m, 1446w, 1403s, 1388s, 1338w, 1262w, 1212w, 1084s, 925w, 873w, 827m, 737m, 630s cm^{-1}. ^1H NMR (DMSO-d_6, 300 MHz): δ 9.74 (d, 2H), 9.17 (s, 2H), 8.38 (d, 2H), 7.95 (dd, 2H). UV–Vis–NIR (λ_{max}/nm (ε/$M^{-1}\,cm^{-1}$)): 225 (46600), 255 (92000), 300 (28600).

2.3.6. $[Ni^{II}(dpq)_3](ClO_4)_2$ (6)

To a methanol solution of dpq (0.35 g, 1.5 mmol) was added a solution (10 mL) of $Ni(ClO_4)_2 \cdot 6H_2O$ (0.16 g, 0.5 mmol) in methanol. The pink coloured solution was refluxed for 0.5 h and the microcrystalline product that deposited was filtered and recrystallized from 1:1 acetonitrile–ethanol. Yield: 0.38 g (85%). *Anal.* Calc. for $C_{42}H_{24}N_{12}O_8Cl_2Ni$: C, 52.86; H, 2.53; N, 17.70. Found: C, 52.76; H, 2.50; N, 17.61%. ESI-MS (positive, in acetonitrile): $m/z = 378.09$ (100%) $[Ni(dpq)_3]^{2+}$. IR (KBr): 3419br, 3091w, 1613w, 1581m, 1530w, 1481m, 1446w, 1388s, 1338w, 1304w, 1262w, 1212m, 1084s, 925w, 873w, 827m, 737m, 630m cm^{-1}. ^1H NMR (DMSO-d_6, 300 MHz): δ 50.30 (2H), 17.93 (2H), 10.14 (2H). UV–Vis–NIR (λ_{max}/nm (ε/$M^{-1}\,cm^{-1}$)): 215 (60000), 260 (110000), 300 (4000), 785 (11), 855 (9).

2.3.7. $[Co^{II}(dpq)_3](ClO_4)_2$ (7)

This compound was prepared in the same way as described for **6**, using $Co(ClO_4)_2 \cdot 6H_2O$ instead of $Ni(ClO_4)_2 \cdot 6H_2O$. Yield: 85%. *Anal.* Calc. for $C_{42}H_{24}N_{12}O_8Cl_2Co$: C, 52.85; H, 2.53; N, 17.61. Found: C, 52.79; H, 2.51; N, 17.55%. ESI-MS (positive, in acetonitrile): $m/z = 378.59$ (100%) $[Co(dpq)_3]^{2+}$. IR (KBr): 3415br, 3083w, 1611w, 1581m, 1530m, 1481m, 1404s, 1389s, 1314w, 1282w, 1213m, 1088s, 816m, 735m, 623m cm^{-1}. ^1H NMR (DMSO-d_6, 300 MHz): δ 99.88 (2H), 49.84 (2H), 18.14 (2H), 13.63 (2H). UV–Vis–NIR (λ_{max}/nm (ε/$M^{-1}\,cm^{-1}$)): 210 (58000), 250 (107000), 290 (52000), 910 (10).

2.3.8. $[Co^{III}(dpq)_3](ClO_4)_3$ (8)

Compound **7** (0.48 g, 0.5 mmol) was dissolved in 15 mL of dry methanol and a mixture of $(C_4H_9)_4NBr$ (0.16 g, 0.5 mmol) and Br_2 (80 mg, 0.5 mmol) in methanol (2 mL) was added to it over a period of 0.5 h. A pink coloured compound of the composition $[Co^{III}(dpq)_3]Br_3$ that deposited was collected by filtration and washed thoroughly with methanol. The product was suspended in methanol (20 mL) and a methanol (5 mL) solution of $AgClO_4$ (3 mmol) was added to it. The mixture was stirred for 1 h

and the precipitated AgBr was removed by filtration. The filtrate on concentration produced bright pink crystals. Yield: 85%. *Anal*. Calc. for $C_{42}H_{24}N_{12}O_{12}Cl_3Co$: C, 47.86; H, 2.29; N, 15.95. Found: C, 47.78; H, 2.25; N, 15.89%. ESI-MS (positive, in acetonitrile): $m/z = 426.06$ (80%) $[Co(dpq)_3(ClO_4)]^{2+}$; 252.73 (100%) $[Co(dpq)_3]^{3+}$. IR (KBr): 3415br, 3078br, 1619w, 1582m, 1531w, 1485m, 1407s, 1387m, 1213w, 1088s, 818m, 731s, 625m cm^{-1}. ^1H NMR (DMSO-d_6, 300 MHz): δ 9.86 (d, 2H), 9.50 (s, 2H), 8.14 (dd, 2H), 7.88 (d, 2H). UV–Vis–NIR (λ_{max}/nm ($\varepsilon/M^{-1}\,cm^{-1}$)): 210 (66000), 250 (95000), 290 (sh, 34000), 460 (210).

2.3.9. $[Fe(dpq)_3](ClO_4)_2$ (**9**)

To a methanol solution of dpq (0.35 g, 1.5 mmol) was added solid $Fe(ClO_4)_2 \cdot 6H_2O$ (0.16 g, 0.5 mmol) under nitrogen. The solution was heated under reflux for 0.5 h, during which time a deep red crystalline compound was deposited. This was collected by filtration and recrystallized from 1:1 ethanol–acetonitrile. Yield: 0.35 g, 85%. *Anal*. Calc. for $C_{42}H_{24}N_{12}O_8Cl_2Fe$: C, 53.02; H, 2.54; N, 17.66. Found: C, 52.97; H, 2.48; N, 17.60%. ESI-MS (positive, in acetonitrile): $m/z = 378.59$ (100%) $[Fe(dpq)_3]^{2+}$. IR (KBr): 3415br, 3083w, 1632m, 1580w, 1483m, 1406s, 1385s, 1260w, 1210w, 1107s, 1088s, 813m, 733m, 627m cm^{-1}. ^1H NMR (DMSO-d_6, 300 MHz): δ 9.55 (d, 2H), 9.37 (s, 2H), 7.94 (d, 2H), 7.88 (dd, 2H). UV–Vis–NIR (λ_{max}/nm ($\varepsilon/M^{-1}\,cm^{-1}$)): 255 (144000), 295 (54000), 440 (7100), 520 (10600), 850 (5).

2.3.10. $[Mn^{II}(dpq)_3](ClO_4)_2$ (**10**)

This compound was prepared in the same way as described for **6**, using $Mn(ClO_4)_2 \cdot 6H_2O$ instead of $Ni(ClO_4)_2 \cdot 6H_2O$. Yield: 0.38 g (80%). *Anal*. Calc. for $C_{42}H_{24}N_{12}O_8Cl_2Mn$: C, 53.07; H, 2.54; N, 17.68. Found: C, 53.00; H, 2.50; N, 17.68%. ESI-MS (positive, in acetonitrile): $m/z = 376.59$ (100%) $[Mn(dpq)_3]^{2+}$. IR (KBr): 3421br, 3098w, 1646w, 1581m, 1529w, 1478m, 1436w, 1389s, 1307w, 1213w, 1085s, 878w, 737m, 627m cm^{-1}. UV–Vis–NIR (λ_{max}/nm ($\varepsilon/M^{-1}\,cm^{-1}$)): 225 (58300), 255 (115000), 295 (35000).

2.4. Physical measurements

The C, H and N analyses were performed on a Perkin–Elmer 2400 II elemental analyzer. IR spectra were recorded using KBr disks on a Shimadzu FTIR 8400S spectrometer. The electronic absorption spectra were obtained with a Perkin–Elmer 950 UV/Vis/NIR spectrophotometer. The electrospray ionization mass spectra (ESI-MS) were measured on a Micromass Qtof YA 263 mass spectrometer. The electrochemical measurements were carried out with a BAS 100 B electrochemistry system using a three-electrode assembly comprising a glassy carbon working electrode, Pt auxiliary electrode and an aqueous Ag/AgCl reference electrode. The cyclic voltammetric (CV) and square wave voltammetric (SWV) measurements were carried out at 25 °C under a nitrogen atmosphere at room temperature. The solutions were 1 mmol dm^{-3} in complexes and 0.1 mol dm^{-3} in tetraethylammonium perchlorate (TEAP) as the supporting electrolyte. The reference electrode was separated from the bulk electrolyte by a salt bridge containing the supporting electrolyte in nitromethane solutions. IR compensation was made automatically during each run. Under the experimental conditions the $E_{1/2}$ values of the ferrocene/ferrocenium couple were observed at 435 and 410 mV in acetonitrile and nitromethane, respectively.

2.5. Crystallography

Crystals suitable for structure determinations of $[Cu^{II}(dpq)_2(H_2O)](ClO_4)_2 \cdot H_2O$ (**2**), $[Cu^{II}(dpq)_2](ClO_4)_2$ (**3**), $[\{Cu^{II}(dpq)_2(H_2O)\}\{Cu^{II}(dpq)_2(ClO_4)\}](ClO_4)_3$ (**4**) and $[Zn^{II}(dpq)_2(ClO_4)_2]$ (**5**) were obtained by slow evaporation of their acetonitrile–ethanol solutions. The crystals were mounted on glass fibres using perfluoropolyether oil. Intensity data were collected on a Bruker AXS SMART APEX diffractometer at 153(2) K for **2**, **4** and **5** and at 223(2) K for **3** using graphite-monochromated Mo Kα radiation ($\lambda = 0.71073$ Å). The data were processed with SAINT [25] and absorption corrections were made with SADABS [25] The structures were solved by direct and Fourier methods and refined by full-matrix least-squares methods based on F^2 using SHELX-97 [26]. For the structure solutions and refinements the SHELX-TL software package [27] was used. The non-hydrogen atoms were refined anisotropically, while the hydrogen atoms were placed at geometrically calculated positions with fixed thermal parameters. Crystal data and details of data collection are listed in Table 1.

3. Results and discussion

3.1. Synthesis and characterization

The ligand dipyrido[3,2-*f*:2′,3′-*h*] quinoxaline, abbreviated as dpq, has been obtained by [1+1] cyclocondensation between 1,10-phenanthroline-5,6-dione and 1,2-diaminoethane. The ligand dpq readily reacts with $[Cu(CH_3CN)_4](ClO_4)$ in acetonitrile under nitrogen to produce the copper(I) complex $[Cu^{I}(dpq)_2](ClO_4)$ (**1**). The reaction with $Cu(ClO_4)_2 \cdot 6H_2O$ under slightly different conditions, however, gives rise to three different products **2**–**4**, all of which have been structurally characterized. For example, the reaction between the ligand and the metal salt in methanol produces the bluish-green compound $[Cu^{II}(dpq)_2(H_2O)](ClO_4)_2 \cdot H_2O$ (**2**), while the reaction carried out in dry acetonitrile produces blue crystals of composition $[Cu^{II}(dpq)_2](ClO_4)_2$ (**3**). In contrast, if the condensation reaction between 1,10-phenanthroline-5,6-dione and 1,2-diaminoethane is carried out in acetonitrile in the presence of $Cu(ClO_4)_2 \cdot 6H_2O$, initially the copper(I) complex **1** is deposited and from the filtrate a green coloured co-crystal-

Table 1
Crystallographic data and structure refinement parameters for $[Cu^{II}(dpq)_2(H_2O)](ClO_4)_2 \cdot H_2O$ (**2**), $[Cu^{II}(dpq)_2](ClO_4)_2$ (**3**), $[\{Cu^{II}(dpq)_2(H_2O)\}\{Cu^{II}(dpq)_2(ClO_4)\}](ClO_4)_3$ (**4**) and $[Zn^{II}(dpq)_2(ClO_4)_2]$ (**5**)

Compound	**2**	**3**	**4**	**5**
Empirical formula	$C_{28}H_{20}Cl_2N_8O_{10}Cu$	$C_{28}H_{16}Cl_2N_8O_8Cu$	$C_{56}H_{34}Cl_4N_{16}O_{17}Cu_2$	$C_{28}H_{16}Cl_2N_8O_8Zn$
Formula weight	762.96	726.9	1471.87	728.76
Temperature (K)	153(2)	223(2)	153(2)	153(2)
Crystal system	triclinic	monoclinic	triclinic	monoclinic
Space group	$P\bar{1}$	$C2/c$	$P\bar{1}$	$C2/c$
Unit cell dimensions				
a (Å)	8.5250(5)	29.9863(14)	13.6639(11)	8.4231(6)
b (Å)	12.2436(8)	13.7129(7)	14.3677(11)	13.8767(6)
c (Å)	14.1431(9)	14.4062(7)	14.8581(11)	23.9103(13)
α (°)	94.583(1)	90	98.110(1)	90
β (°)	91.130(1)	110.202(1)	100.885(1)	96.110(1)
γ (°)	100.944(1)	90	93.983(1)	90
Volume (Å^3)	1443.81(16)	5559.4(5)	2821.9(4)	2778.9(3)
Z	2	8	2	4
D_{calc} (Mg/m^3)	1.755	1.737	1.732	1.742
$F(000)$	774	2936	1488	1472
Crystal size (mm)	$0.30 \times 0.20 \times 0.20$	$0.40 \times 0.35 \times 0.32$	$0.40 \times 0.36 \times 0.20$	$0.35 \times 0.35 \times 0.30$
Reflections collected	9210	17184	17664	8703
Data/restraints/parameters	6390/8/454	6306/51/451	12471/0/856	3260/21/213
Goodness-of-fit on F^2	0.892	1.034	0.866	1.045
R indices (all data)	$R_1^a = 0.0384$, $wR_2^b = 0.0938$	$R_1 = 0.0371$, $wR_2 = 0.0976$	$R_1 = 0.0643$, $wR_2 = 0.1775$	$R_1 = 0.0464$, $wR_2 = 0.1249$
Final R indices $[I > 2\sigma(I)]$	$R_1 = 0.0501$, $wR_2 = 0.1000$	$R_1 = 0.0455$, $wR_2 = 0.1025$	$R_1 = 0.1033$, $wR_2 = 0.1936$	$R_1 = 0.0493$, $wR_2 = 0.1275$

[a] $R_1 = \sum||F_o| - |F_c||/\sum|F_o|$.
[b] $wR_2(F^2)[\sum w(F_o^2 - F_c^2)^2/\sum w(F_o^2)^2]^{1/2}$.

lized compound of composition $[\{Cu^{II}(dpq)_2(H_2O)\}\{Cu^{II}(dpq)_2(ClO_4)\}](ClO_4)_3$ (**4**) is isolated. The reaction between dpq and $Zn(ClO_4)_2 \cdot 6H_2O$ in a 2:1 ratio in methanol leads to the formation of $[Zn^{II}(dpq)_2(ClO_4)_2]$ (**5**). The tris-dpq complexes $[M^{II}(dpq)_3](ClO_4)_2$ (M = Ni (**6**), Co (**7**), Fe (**9**) and Mn (**10**)) are obtained by the direct reaction between the ligand and the metal salt in a 1:3 ratio. The cobalt(II) complex on oxidation with bromine produces the corresponding cobalt(III) complex as the bromide salt, which on treatment with a stoichiometric amount of silver perchlorate affords the cobalt(III) compound $[Co^{III}(dpq)_3](ClO_4)_3$ (**8**).

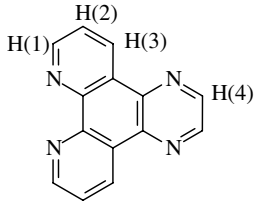
In all the perchlorate compounds, characteristic ClO_4^- vibrations for ionic perchlorate are observed at about 1085–1090 and 625–630 cm^{-1}.

Compounds **1**–**10** have been characterized by their ESI (positive) mass spectra measurements in acetonitrile. Complex $[Cu^{I}(dpq)_2](ClO_4)$ (**1**) exhibits a single peak at 527.08 due to the unipositive cation $[Cu^{I}(dpq)_2]^+$. For complexes **2**–**5**, similar spectral features have been observed. They are characterized by the observation of both unipositively charged $[M^{II}(dpq)_2(ClO_4)]^+$ and doubly-positively charged $[M^{II}(dpq)_2]^{2+}$ (M = Cu and Zn) species. For the tris-dpq compounds **6**, **7**, **9** and **10** only one peak is observed due to the dication $[M^{II}(dpq)_3]^{2+}$ (M = Ni, Co, Fe and Mn). The mass spectra of the cobalt(III) complex $[Co(dpq)_3](ClO_4)_3$ (**8**) exhibits the features expected for the doubly-positively charged $[Co(dpq)_3(ClO_4)]^{2+}$ and triply-positively charged $[Co(dpq)_3]^{3+}$ species. As examples, the observed and the simulated spectra of compounds **8** and **10** are shown in Fig. S1a and b.

3.2. ^1H NMR spectra

^{1}H NMR spectroscopic studies were carried out for complexes **1**, **5**, **6**, **7**, **8** and **9** in $(CD_3)_2SO$. The observed chemical shifts along with the spectral assignments are given in Section 2.

For the diamagnetic complexes **1**, **5**, **8** and **9** the ligand resonances are expected to be observed as a doublet H(1), doublet of doublet H(2), doublet H(3) and a singlet H(4) (the numbering scheme for the protons is shown in Scheme 1). For complex **1**, the two doublets are observed at 9.65 ($J = 8.3$ Hz) and 9.14 ($J = 5.2$ Hz) ppm for H(1) and H(3), respectively, while the singlet and the doublet of doublet appear at 9.31 and 8.18 ($J = 5.1$, 2.9 Hz) ppm. The spectral features exhibited by **5** and **9** are quite similar. The H(4) proton is observed as a sharp singlet at $\delta = 9.17$ ppm for **5** and at 9.37 ppm for **9**. Complex **5** exhibits two doublets for H(1) and H(3) at $\delta = 9.73$ ($J = 8.8$ Hz) and 8.37 ($J = 4.8$ Hz) ppm, respectively; however, for **9** these two peaks are observed at $\delta = 9.55$ ($J = 8.2$ Hz) and 7.95 ($J = 5.2$ Hz) ppm. The H(2) proton



Scheme 1.

appears as a doublet of doublet at $\delta = 7.94$ ppm ($J = 4.9$, 3.3 Hz) in **5** and at 7.87 ppm ($J = 5.2$,2.8 Hz) in **9**. The spectrum of **9** is shown in Fig. S2a. Finally, $[Co^{III}(dpq)_3](ClO_4)_3$ (**8**) exhibits a doublet at 9.88 ppm ($J = 8.2$ Hz), the singlet at 9.49 ppm, the doublet of doublet at 8.13 ppm ($J = 5.8$, 2.4 Hz) and a doublet at 7.87 ppm ($J = 5.6$ Hz), which are due to the H(1), H(4), H(2) and H(3) protons, respectively (Fig. S2b).

Studies on the paramagnetic ^{1}H NMR spectroscopic behaviour of the two complexes **6** and **7** have been carried out in $(CD_3)_2SO$ solution. In paramagnetic compounds, hyperfine-shifted resonances are observed due to interactions between nuclear spin and unpaired electron spins, in addition to the normal diamagnetic nuclear spin interactions. Electron and nuclear spin interactions occurring through bonds give rise to the Fermi contact shift, while those interactions occurring through space give rise to a dipolar or pseudocontact shift. The dipolar shift depends on the magnetic anisotropy of the system and the position in space of a given proton. The contribution of contact shift decreases rapidly with the increase of the number of bonds connecting the proton with the paramagnetic centre, and vanishes after three or four bond separations. However, when the unpaired electron spin is delocalized the interaction remains significant for protons many bonds away from the metal centre. For assignment of signals in paramagnetic compounds, measurement of longitudinal relaxation times (T_1) and transverse relaxation times (T_2) are particularly important. T_1 correlates with the proximity of proton to paramagnetic centre, while $T_2 = 1/\tau(\text{fwh})$, where fwh is the full width of a signal at its half-height, correlates the line width to the proximity of a proton to the paramagnetic site. Closer proximity of a proton to the metal centre gives rise to a shorter T_1 and broader line width.

Fig. S2c shows the spectrum observed for the high-spin cobalt(II) complex **7**. Of the four observed resonances, the three signals that are observed at 49.84, 18.14 and 13.63 ppm are sharp, while the one observed at 99.90 ppm is broader. The assignments made for these signals from T_1 values, line widths and integration of protons are given in Table 2. The spectrum of the high-spin nickel(II) complex (**6**), however, exhibits (Fig. S2d) only three signals at 50.30 H(2), 17.90 H(3) and 10.15 H(4) ppm, all having the same areas of integration. The assignment of the signals of structurally related nickel(II) compound **6** has been made straightforward by comparison with **7**. As may be noted, the broadening of the resonances increases as they are shifted to lower fields. It seems that the missing resonance H(1) is lost due to line broadening and its shift to a considerably lower field.

Table 2
Chemical shifts, T_1 values, line widths and spectral assignments for $[Co^{II}(dpq)_3](ClO_4)_2$ (**7**) in DMSO-d_6

δ (ppm)	Relative area	T_1 (ms)	$\Delta_{1/2}$ (Hz)[a]	Assignment[b]
99.89	1	<1	305	H(1)
49.84	1	29.77	45	H(2)
18.14	1	51.64	25	H(3)
13.77	1	359.17	20	H(4)

[a] Full width at half-height.
[b] Proton sites are illustrated in Scheme 1.

3.3. Crystal structures

3.3.1. $[Cu^{II}(dpq)_2(H_2O)](ClO_4)_2 \cdot H_2O$ (2)

The ORTEP representation of the cation $[Cu(dpq)_2(H_2O)]^{2+}$ in **2** is shown in Fig. 1a and the relevant bond distances and angles are given in Table 3. The five-coordinated copper(II) centre $[CuN_4O]$ adopts a distorted trigonal bipyramidal geometry. The atoms N(1), N(2) and O(WA1) form an exact trigonal plane on which the copper atom lies. The nitrogen atoms N(2) and N(4) are *trans*-axially disposed. The distances of the copper centre from the donor atoms in the trigonal plane are unequal; the Cu–N(1) [2.105(2) Å] and Cu–O(WA1) [2.142(2) Å] distances are considerably longer than the Cu–N(3) distance [2.029(2) Å]. The two axial distances Cu–N(2) [1.966(2) Å] and Cu–N(4) [1.972(2) Å], however, are very close and are shorter than the equatorial bond lengths. Considerable departure of the relevant angles in the equatorial plane [N(1)–Cu–N(3) = 125.55(8)°, N(1)–Cu–O(WA1) = 95.24(7)° and N(3)–Cu–O(WA1) = 139.21(7)°] from the desired angle of 120° are indicative of distortion from ideal tbp geometry. The *trans*-axial N(2)–Cu–N(4) angle is 172.21(8)°. The indicator of a five-coordinated geometry τ in this case is 0.55 ($\tau = 0$ for sp and 1 for tbp) [28].

An interesting array of intra and intermolecular hydrogen bonds is observed in compound **2** (Fig. 1b and Table S1). The two hydrogen atoms of the coordinated water (WA1) are bridged with a perchlorate oxygen O(23) and the oxygen atom of the solvated water (WA2), whose hydrogen atoms in turn are bridged with a perchlorate oxygen O(11) and a quinoxaline nitrogen atom N(6) of a symmetry related adjacent molecule. In effect, the two adjacent complex molecules form a dimeric unit by involving the ionic perchlorates and the solvated water in the hydrogen bonding network.

It should be mentioned that after determination of the structures of the copper(II) compounds **2**–**4**, we found that the X-ray structure of **2** has been reported by another group [20]. While the structure determination of **2** by us has been made at 153 K, the reported one was made at 293 K. Accordingly, the unit cell parameters found in the present case are relatively shorter as compared to the earlier reported values [20]. The influence of temperature can be appreciated by comparing the unit cell volume, which is 1443.81(2) Å^3 at 153 K as against 1481.7(8) Å^3 at 293 K. In terms of Cu–N distances, the difference observed in the two sets of studies are insignificant, albeit the Cu–O(W) distance reported here [2.1236(18) Å] is somewhat shorter compared to the reported value [2.145(3) Å]. As

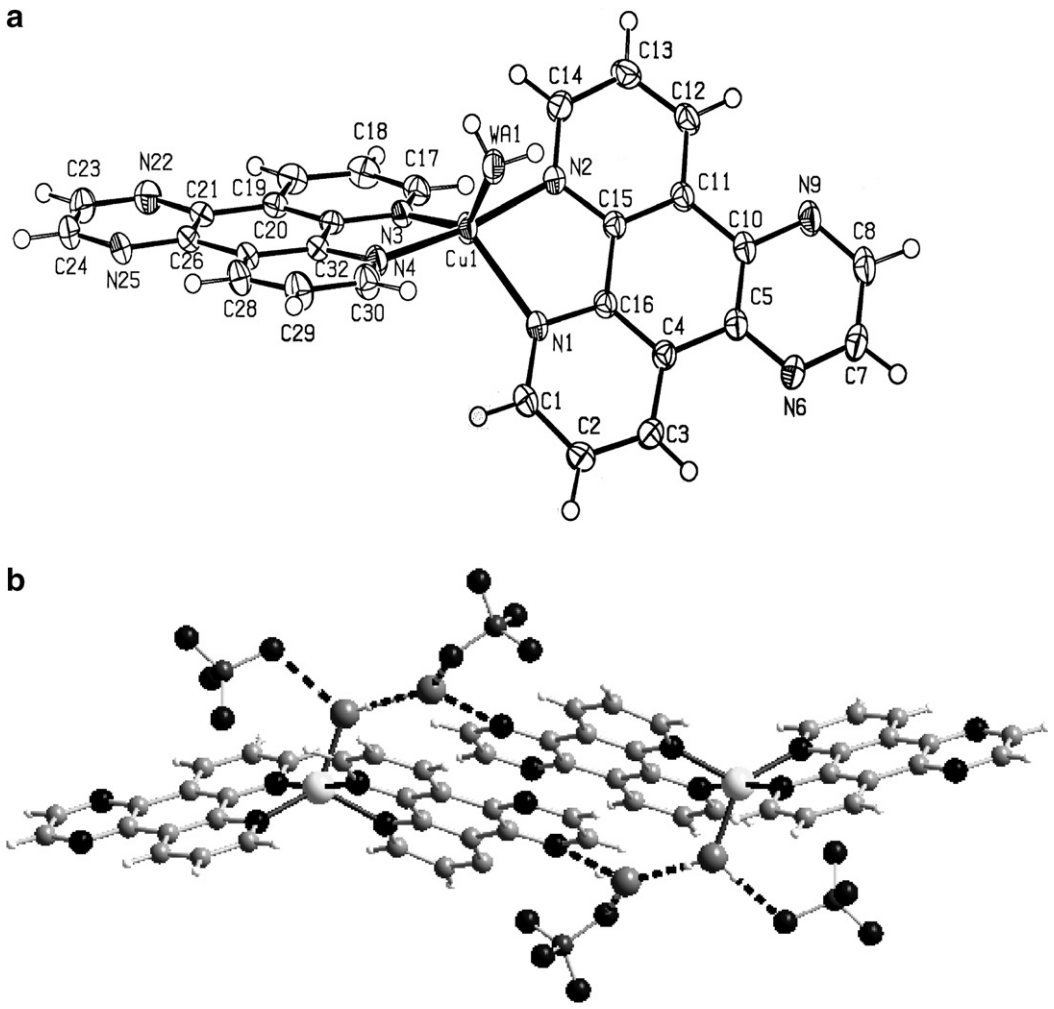


Fig. 1. (a). An ORTEP representation of the molecule $[Cu^{II}(dpq)_2(H_2O)](ClO_4)_2 \cdot H_2O$ (**2**) showing 50% probability displacement ellipsoids. (b) Dimeric structures formed by the intermolecular hydrogen bonding network involving the perchlorate ion and solvated water molecule in complex $[Cu^{II}(dpq)_2(H_2O)](ClO_4)_2 \cdot H_2O$ (**2**).

expected, the influence of temperature becomes more conspicuous in the relatively weaker hydrogen bridged distances. Since with the lowering of temperature the thermal vibration gets reduced, accordingly O···O and O···N distances at 153 K are found to be shorter by 0.03–0.09 Å relative to those reported at 293 K.

3.3.2. *[Cu(dpq)$_2$](ClO$_4$)$_2$ (**3**)*

In complex **3**, one of the perchlorate anions is disordered, whose three oxygen atoms O(22), O(23) and O(24) have double occupancy (0.55:0.55), while O(21) and Cl(2) have unique occupancy. The ORTEP projection of the cation $[Cu(dpq)_2]^{2+}$ is shown in Fig. 2. The four-coordinated CuN_4 core, in terms of a square planar description, does not turn out to be satisfactory because the donor atoms involved are alternatively displaced above and below the least-squares plane by 0.40 Å, albeit the copper centre is lying exactly on the mean plane. The alternative description in terms of a tetrahedral configuration is also unsatisfactory because the dihedral angle θ between the opposing CuN_2 planes is 37.9° ($\theta = 0°$ for square planar and 90° for tetrahedral). In **3**, the distances Cu–N(1) [2.022(2) Å] and Cu–N(2) [1.992(2) Å] are nearly equal, as are the complimentary distances Cu–N(3) [2.026(2) Å] and Cu–N(4) [1.987(2) Å]. The *transoid* angles N(1)–Cu–N(3) [146.40(7)°] and N(2)–Cu–N(4) [167.54(8)°] deviate considerably from the values expected for a square planar geometry. The *cisoid* angles N(1)–Cu–N(2) and N(3)–Cu–N(4) are equal [82.20(7)°], while the two other opposing angles N(1)–Cu–N(4) and N(2)–Cu–N(3) are 100.14(7)° and 102.70(7)°, respectively. Clearly, the tetrahedral description is worse relative to the square planar description.

A consideration of the proximities of the oxygen atoms of one of the perchlorate anions to the copper centre reveals that the disordered oxygen O(22) is 2.427(4) Å away from the metal atom. If this distance is reckoned as a bond, Fig. S3 provides another ORTEP representation of the $[Cu(dpq)_2(ClO_4)]^+$ cation. In the five-coordinated environment $[CuN_4O]$, the geometry of the copper centre may be either trigonal bipyramidal (tbp) or square pyramidal

Table 3
Selective bond distances (Å) and angles (°) for compounds **2**–**5**

$[Cu^{II}(dpq)_2(H_2O)](ClO_4)_2 \cdot H_2O$ (**2**)		$[Cu^{II}(dpq)_2](ClO_4)_2$ (**3**)		$[\{Cu^{II}(dpq)_2(H_2O)\}\{Cu^{II}(dpq)_2(ClO_4)\}](ClO_4)_3$ (**4**)			
Cu(1)–N(1)	2.1047(19)	Cu(1)–N(1)	2.0225(18)	Cu(1)–N(11)	2.042(4)	Cu(2)–N(21)	1.982(4)
Cu(1)–N(2)	1.9660(19)	Cu(1)–N(2)	1.9918(18)	Cu(1)–N(12)	1.982(4)	Cu(2)–N(22)	2.046(4)
Cu(1)–N(3)	2.0288(19)	Cu(1)–N(3)	2.0265(17)	Cu(1)–N(13)	2.043(4)	Cu(2)–N(23)	2.041(4)
Cu(1)–N(4)	1.9715(15)	Cu(1)–N(4)	1.9875(18)	Cu(1)–N(14)	1.981(3)	Cu(2)–N(24)	1.977(4)
Cu(1)–WA(1)	2.1236(18)	Cu(1)–O(221A)	2.427(4)	Cu(1)–O(1)	2.427(4)	Cu(2)–O(42)	2.540(4)
						Cu(2)–O(44)	2.510(5)
N(1)–Cu(1)–N(2)	81.40(8)	N(1)–Cu(1)–N(2)	82.19(7)	N(11)–Cu(1)–N(12)	81.71(15)	N(21)–Cu(2)–N(22)	82.01(17)
N(3)–Cu(1)–N(4)	82.39(8)	N(3)–Cu(1)–N(4)	82.21(7)	N(13)–Cu(1)–N(14)	82.00(15)	N(23)–Cu(2)–N(24)	83.01(14)
N(1)–Cu(1)–N(3)	125.55(8)	N(1)–Cu(1)–N(3)	146.40(7)	N(11)–Cu(1)–N(13)	135.76(14)	N(21)–Cu(2)–N(23)	98.18(16)
N(1)–Cu(1)–N(4)	105.04(8)	N(1)–Cu(1)–N(4)	100.14(7)	N(11)–Cu(1)–N(14)	100.11(15)	N(21)–Cu(2)–N(24)	171.00(16)
N(2)–Cu(1)–N(3)	97.52(8)	N(2)–Cu(1)–N(3)	102.70(7)	N(12)–Cu(1)–N(13)	101.24(15)	N(22)–Cu(2)–N(23)	137.32(15)
N(2)–Cu(1)–N(4)	172.21(8)	N(2)–Cu(1)–N(4)	167.45(8)	N(12)–Cu(1)–N(14)	173.32(15)	N(22)–Cu(2)–N(24)	103.21(15)
N(1)–Cu(1)–WA(1)	95.24(8)	N(1)–Cu(1)–O(221A)	95.34(16)	N(11)–Cu(1)–O(1)	115.29(18)	O(42)–Cu(2)–O(44)	52.02(15)
N(2)–Cu(1)–WA(1)	87.59(7)	N(2)–Cu(1)–O(221A)	90.81(11)	N(12)–Cu(1)–O(1)	85.33(14)	N(21)–Cu(2)–O(42)	89.53(17)
N(3)–Cu(1)–WA(1)	139.21(7)	N(3)–Cu(1)–O(221A)	117.56(16)	N(13)–Cu(1)–O(1)	108.93(18)	N(22)–Cu(2)–O(42)	82.85(14)
N(4)–Cu(1)–WA(1)	87.45(8)	N(4)–Cu(1)–O(221A)	76.82(11)	N(14)–Cu(1)–O(1)	88.09(14)	N(23)–Cu(2)–O(42)	139.70(13)
						N(24)–Cu(2)–O(42)	83.92(17)
						N(21)–Cu(2)–O(44)	83.95(18)
						N(22)–Cu(2)–O(44)	132.68(13)
						N(23)–Cu(2)–O(44)	89.35(14)
						N(24)–Cu(2)–O(44)	87.15(16)

$[Zn^{II}(dpq)_2(ClO_4)_2]$ (**5**)[a]					
Zn(1)–N(1)	2.127(2)	N(1)–Zn(1)–N(2)	77.92(8)	N(1)–Zn(1)–O(14A)	89.54(9)
Zn(1)–N(1A)	2.127(2)	N(1)–Zn(1)–N(2A)	95.45(8)	N(2)–Zn(1)–O(14A)	161.42(8)
Zn(1)–N(2)	2.120(2)	N(2)–Zn(1)–N(2A)	102.21(11)	N(1A)–Zn(1)–O(14)	89.54(9)
Zn(1)–N(2A)	2.120(2)	N(2)–Zn(1)–N(1A)	95.45(8)	N(2A)–Zn(1)–O(14)	161.42(8)
Zn(1)–O(14)	2.1899(19)	N(2A)–Zn(1)–N(1A)	77.92(8)	N(1A)–Zn(1)–O(14A)	98.72(8)
Zn(1)–O(14A)	2.1899(19)	N(1)–Zn(1)–N(1A)	169.57(11)	N(2A)–Zn(1)–O(14A)	92.49(8)
		N(1)–Zn(1)–O(14)	98.72(8)	O(14)–Zn(1)–O(14A)	75.75(12)
		N(2)–Zn(1)–O(14)	92.49(8)		

[a] For **5** 'A' indicates: $-x, y, -z + 1/2$.

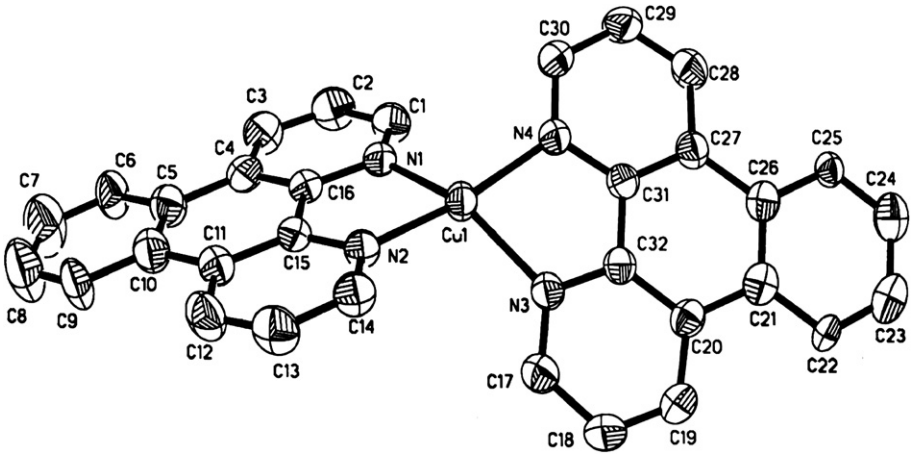


Fig. 2. A four-coordinated ORTEP projection of the molecule $[Cu^{II}(dpq)_2](ClO_4)_2$ (**3**) showing 50% probability displacement ellipsoids.

(sp). To consider the tbp geometry, the atoms N(1), N(3) and O(221) form the trigonal plane and the atoms N(2) and N(4) are *trans*-axially disposed. However, the angles N(1)–Cu–N(3) [146.40(7)°], N(1)–Cu–O(221) [95.34(16)°] and N(3)–Cu–O(221) [117.56(16)°] all deviate from the ideal angle of 120°. The *trans* angles N(2)–Cu–N(4) [167.54(8)°] also deviates from 180°. Moreover, the value of $\tau = 0.35$ falls short of that to be a tbp candidate. In favor or against the alternative sp geometry with a Cu–O(221) apical distance of 2.427(4) Å, the same arguments made for the square planar geometry apply.

3.3.3. $[\{Cu^{II}(dpq)_2(H_2O)\}\{Cu^{II}(dpq)_2(ClO_4)\}](ClO_4)_3$ (**4**)

Complex **4** is a co-crystallized compound in which the asymmetric unit contains two cationic species viz.

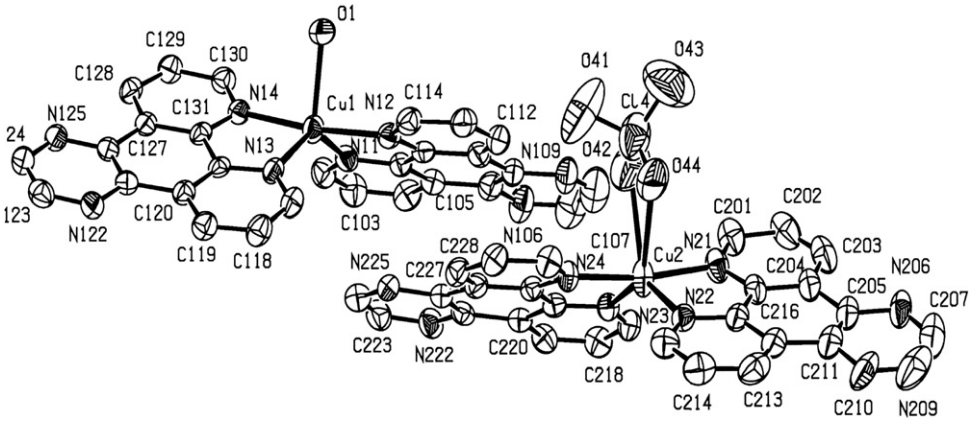


Fig. 3. An ORTEP representation of the cation of the complex $[\{Cu^{II}(dpq)_2(H_2O)\}\{Cu^{II}(dpq)_2(ClO_4)\}](ClO_4)_3$ (**4**) showing 50% probability displacement ellipsoids.

$\{Cu(dpq)_2(H_2O)\}^{2+}$ and $\{Cu(dpq)_2(ClO_4)\}^{+}$, and three perchlorate anions. An ORTEP projection of the cations in **4** is shown in Fig. 3. It may be noted that **4** can be considered as the 1:1 co-crystals of **2** and **3**. However, it will be evident that notwithstanding the same composition, the cationic species of **4** have subtle structural differences from **2** and **3**.

In **4**, the five-coordinated copper(II) centre in $[Cu(dpq)_2(H_2O)]^{2+}$ cation obtains a tbp geometry with N(11), N(13) and O(1) forming the trigonal plane and N(12) and N(14) occupying the axial positions. Unlike **3**, in which the two equatorial Cu–N distances are significantly different, in **6** the two equatorial Cu–N(11) and Cu–N(13) distances are equal [2.043(4) Å]. The third equatorial Cu–O(1) bond length, however, is long [2.144(3) Å]. The *trans* axially disposed Cu–N(12) and Cu–N(14) bond distances are also equal [1.982(4) Å]. The N–Cu–N and N–Cu–O bond angles in the trigonal plane lie in the range 109–136°. The *trans* N(12)–Cu–N(14) angle is 173.32(14)°. The value of τ in this case (0.63) is greater than that of **3** (0.55), indicating lesser distortion in the present case.

The ORTEP projection of the cation $[Cu(dpq)_2(ClO_4)]^{+}$ in **4** (Fig. 4) shows that the two perchlorate oxygens O(42) and O(44) are bound to the copper(II) centre in a bidentate fashion. For a better view of the six-coordinated metal core $[CuN_4O_2]$ another ORTEP projection is shown in Fig. S4. It may be noted that in terms of an octahedral description, the metal centre is located in the basal plane formed by the atoms N(22), N(23), O(44) and O(42). However, these atoms are displaced from the least-squares plane by ±0.215(5) Å for the oxygen atoms and ±0.123(4) Å for the nitrogen atoms. Since the Cu–N(22)/N(23) distances [2.046(4) and 2.041(4) Å] are much shorter as compared to the Cu–O(42)/O(44) distances [2.540(4) and 2.510(5) Å], the metal atom in the N_2O_2 plane is located closer to the nitrogen atoms. The *trans*-axial Cu–N(21)/N(24) distances are 1.982(4) and 1.977(4) Å, and are even shorter than the equatorial distances, indicating a distorted compressed geometry.

3.3.4. *[Zn(dpq)$_2$(ClO$_4$)$_2$] (**5**)*

The molecular structure of the zinc(II) complex $[Zn(dpq)_2(ClO_4)_2]$ (**5**) is shown in Fig. 4. A twofold axis passes mid-way through the metal-bound perchlorate oxygens O(14) and O(14A). The coordination environment around the six-coordinated metal centre $[ZnN_4O_2]$ may be considered as distorted octahedral. The atoms N(2), N(2A), O(14A) and O(14) form the best plane, although the atoms N(2)/N(2A) are displaced from the mean plane by ±0.214(2) Å and O(14)/O(14A) by ±0.265(2) Å. The metal atom lies exactly on the mean plane. The nitrogen atoms N(1) and N(1A) are *trans*-axially disposed to the metal centre. The equatorial and axial Zn–N distances [2.120(2) and 2.127(2) Å] are almost equal, while the equatorial Zn–O distances [2.190(2) Å] are slightly longer. The *trans*-axial N(1)–Zn–N(1A) angle is 169.57(11)°, while the *trans*-equatorial N(2)–Zn–O(14A) angle is 161.42(8)°. The trigonal planes N(1)O(14A)N(2A) and N(1A)O(14)-N(2) are inclined to each other by 50.0°, again indicating a distorted octahedral geometry. The relevant bond distances and bond angles are listed in Table 3.

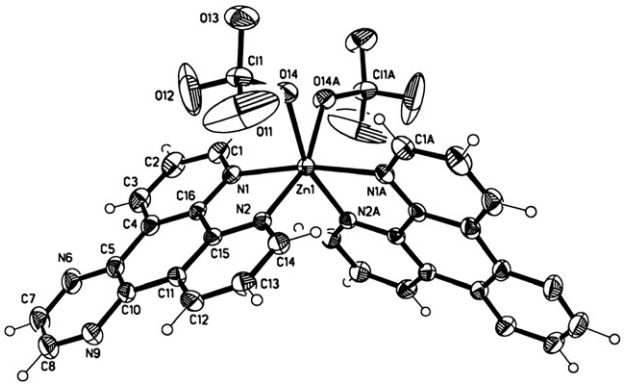


Fig. 4. An ORTEP projection of the complex $[Zn^{II}(dpq)_2(ClO_4)_2]$ (**5**) showing 50% probability displacement ellipsoids. 'A' indicates the symmetry operation $(1-x, y, -z+1/2)$.

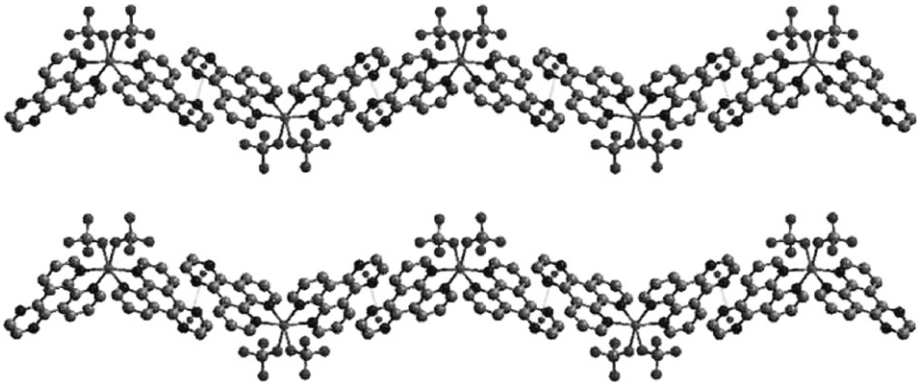


Fig. 5. An 1-D growth of the molecule $[Zn^{II}(dpq)_2(ClO_4)_2]$ (**5**) through π–π stacking interactions.

Another interesting structural feature of this compound is the presence of a π–π interaction between the pyrazine ring C(5)N(6)C(7)C(8)C(9)C(10) of the adjacent molecule, forming a sinusoidal pattern, as shown in Fig. 5. The distance between the centroid of the pyrazine rings is 3.542 Å.

3.4. Electronic spectra

The absorption spectroscopic behaviour of compounds **1**–**10** have been studied in acetonitrile. In addition, the spectra of compounds **2**–**4** have been obtained in nitromethane. The UV–Vis–NIR spectral data for theses compounds in acetonitrile are given in Section 2.

All of the complexes exhibit three very strong absorption bands at 215–225 nm, 250–260 nm and 290–300 nm, due to the ligand centred π–π* transitions. In the case of the copper(I) complex **1**, a strong band observed at 415 nm ($\varepsilon = 4700\ M^{-1}\ cm^{-1}$) is due to a metal-to-ligand charge transfer (MLCT) transition. This charge transfer transition occurs from the filled metal orbital (d^{10}) to the empty π* antibonding orbital of the bipyridine ligand. Although the solid state structures of the three copper(II) complexes $[Cu^{II}(dpq)_2(H_2O)](ClO_4)_2$ (**2**), $[Cu^{II}(dpq)_2](ClO_4)_2$ (**3**) and $[\{Cu^{II}(dpq)_2(H_2O)\}\{Cu^{II}(dpq)_2(ClO_4)\}](ClO_4)_3$ (**4**) are different, in acetonitrile solution they exhibit similar spectral features in the visible and near IR region. Two broad absorption bands are observed at 700 and 900 nm. It is documented, especially for copper(II) complexes, that a single d–d band with a high energy shoulder is indicative of a trigonal bipyramidal stereochemistry around the metal centre, while an absorption envelop with a low energy shoulder is characteristic of a square pyramidal geometry. Some penta-coordinated copper(II) complexes with two d–d bands of equal intensity appear to possess an intermediate distorted geometry [29]. The broadness of these bands are indicative of the presence of more than two transitions at lower energies as expected for copper(II) in a distorted trigonal bipyramidal environment. Indeed, deconvolution of the absorption spectrum of **2** in acetonitrile by Gaussian line-shape analysis gives rise to three peaks (shown in Fig. S5), which are due to the $d_{x^2-y^2} \rightarrow d_{z^2}$, $d_{xy} \rightarrow d_{z^2}$ and d_{xz}, $d_{yz} \rightarrow d_{z^2}$ transitions in ascending order of energies. It appears that the identical spectra observed for complexes **2**–**4** in acetonitrile is due the presence of the same penta-coordinated species, $[Cu^{II}(dpq)_2(CH_3CN)]^{2+}$, in all three cases. However, in nitromethane, which is a non-coordinating solvent, some variation in positions and intensities of these bands in the three cases becomes evident. This is illustrated in Fig. S6a–c by deconvoluting the absorption spectra observed for **2**–**4** in nitromethane. The spectral data and the deconvoluted peak positions of **2**–**4** in nitromethane are listed in Table 4.

The absorption spectrum of the nickel(II) complex $[Ni(dpq)_3](ClO_4)_2$ (**6**) shows the presence of bands at 215 ($\varepsilon = 60\,000\ M^{-1}\ cm^{-1}$), 260 ($\varepsilon = 110\,000\ M^{-1}\ cm^{-1}$), 300 nm ($\varepsilon = 40\,000\ M^{-1}\ cm^{-1}$), 785 ($\varepsilon = 11\ M^{-1}\ cm^{-1}$) and 855 nm ($\varepsilon = 9\ M^{-1}\ cm^{-1}$). In octahedral nickel(II) complexes three spin-allowed transitions $^3A_{2g} \rightarrow {}^3T_{2g}$, $^3T_{1g}$, $^3T_{1g}(P)$ are normally observed. Because the separation of the energy between the $^3A_{2g} \rightarrow {}^3T_{2g}$ and $^3A_{2g} \rightarrow {}^3T_{1g}$ transitions in a wide variety of octahedral nickel(II) complexes lies in the range 5000–8000 cm^{-1}, it is highly unlikely that the two absorption peaks observed as a doublet at 855 nm (11 700 cm^{-1}) and 785 nm (12 750 cm^{-1}), which differ only by 1000 cm^{-1}, could be assigned due to these transitions. On the other hand, when Dq/B approaches unity the ^1E_g state lies close to $^3T_{1g}$, and due to their extensive mixing the spin forbidden $^3A_{2g} \rightarrow {}^1E_g$ transitions steals intensity from the spin-allowed $^3A_{2g} \rightarrow {}^3T_{1g}$ transition, being observed as a doublet.

Table 4
UV–Vis and deconvoluted absorption peaks for complexes **2**–**4** in nitromethane

Compound	λ_{max}/nm (ε/$M^{-1}\ cm^{-1}$)	Deconvoluted peaks (nm)
$[Cu^{II}(dpq)_2(H_2O)](ClO_4)_2 \cdot H_2O$ (**2**)	740 (140), 870 (115)	695, 865, 935
$[Cu^{II}(dpq)_2](ClO_4)_2$ (**3**)	710 (150), 840 (120)	685, 835, 940
$[\{Cu^{II}(dpq)_2(H_2O)\}\{Cu^{II}(dpq)_2(ClO_4)\}](ClO_4)_3$ (**4**)	725 (150), 870 (115)	695, 880, 950

The tris-dpq cobalt(II) complex **7** exhibits a lone d–d band at 910 nm ($\varepsilon = 10\ M^{-1}\ cm^{-1}$) in addition to the internal ligand transitions observed at 210 ($\varepsilon = 58\,000\ M^{-1}\ cm^{-1}$), 250 ($\varepsilon = 107\,000\ M^{-1}\ cm^{-1}$) and 290 nm ($\varepsilon = 52\,000\ M^{-1}\ cm^{-1}$). The observed d–d band is due to the $^4T_{1g} \rightarrow {}^4T_{2g}$ transition. A second band, which is expected to be observed at ca. 500 nm in octahedral cobalt(II) complexes due to the $^4T_{1g} \rightarrow {}^4T_{1g}$ (P) transition, is not seen in the present case. In the cobalt(III) complex $[Co(dpq)_3]^{3+}$ ($\mathbf{9}^{3+}$), aside from the bands observed at 210 ($\varepsilon = 66\,000\ M^{-1}\ cm^{-1}$), 250 ($\varepsilon = 95\,000\ M^{-1}\ cm^{-1}$) and 290 nm ($\varepsilon = 34\,000\ M^{-1}\ cm^{-1}$), a band due to the $^1A_{1g} \rightarrow {}^1T_{1g}$ transition is observed at 460 nm ($\varepsilon = 210\ M^{-1}\ cm^{-1}$). The higher energy $^1A_{1g} \rightarrow {}^1T_{2g}$ transition is apparently masked by the intense band observed at 290 nm. Since the energy of the $^1T_{1g}$ state is $10Dq - C$ ($C \approx 4B \approx 2000\ cm^{-1}$) [9], the value of $10Dq$ is estimated to be $24\,200\ cm^{-1}$.

The low-spin iron(II) complex **10** exhibits MLCT absorptions at 440 and 520 nm and a d–d transition at 850 nm.

3.5. Electrochemistry

The electrochemical characteristics of complexes **1, 2**, **3**, **4**, **7** and **8** have been examined by CV and SWV and the observed redox potentials are given in Table 5.

The copper(I) complex $[Cu(dpq)_2](ClO_4)$ (**1**) undergoes a one electron quasireversible ($\Delta E_p = 120$ mV) oxidation at $E_{1/2} = 110$ mV in acetonitrile. As mentioned earlier, the absorption spectra of the copper(II) complexes (**2**–**4**) have been examined in acetonitrile and nitromethane, hence, the electrochemical behaviour of these compounds have also been studied in those two solvents. In acetonitrile, similar to the absorption spectral behaviour, all the three compounds (**2**–**4**) exhibit identical electrochemical responses with $E_{1/2} = 120$ mV and $\Delta E_p = 150$ mV. Cyclic voltammograms of these compounds, however, differ significantly in nitromethane, as observed in their electronic spectra. In nitromethane, the $E_{1/2}$ value of $[Cu(dpq)_2(H_2O)](ClO_4)_2 \cdot H_2O$ (**2**) is 325 mV ($\Delta E_p = 70$ mV) (Fig. S7a), that of $[Cu(dpq)_2](ClO_4)_2$ (**3**) is 355 mV ($\Delta E_p = 70$ mV) (Fig. S7b) and finally for $[\{Cu^{II}(dpq)_2(H_2O)\}\{Cu^{II}(dpq)_2(ClO_4)\}](ClO_4)_3$ (**4**) (Fig. S7c) the $E_{1/2}$ and ΔE_p values are 350 mV and 70 mV. As expected, the redox behaviour of the cobalt(II) complex **7** in the oxidative mode and the cobalt(III) complex **8** in the reductive mode are identical. The $E_{1/2}$ value of the fully reversible ($\Delta E_p = 70$ mV) Co^{II}/Co^{III} couple is 540 mV (shown in Fig. S8).

Table 5
Electrochemical data[a] for complexes **1**–**4**, **7** and **8**

Compound	Acetonitrile		Nitromethane	
	$E^b_{1/2}$ (mV)	ΔE^c_p	$E_{1/2}$ (mV)	ΔE_p
$[Cu^I(dpq)_2](ClO_4)$ (**1**)	110	120	330	70
$[Cu^{II}(dpq)_2(H_2O)](ClO_4)_2$ (**2**)	110	130	325	70
$[Cu^{II}(dpq)_2](ClO_4)_2$ (**3**)	105	120	355	70
$[\{Cu^{II}(dpq)_2(H_2O)\}\{Cu^{II}(dpq)_2(ClO_4)\}](ClO_4)_3$ (**4**)	100	120	350	70
$[Co^{II}(dpq)_3](ClO_4)_2$ (**7**)	535	70		
$[Co^{III}(dpq)_3](ClO_4)_3$ (**8**)	540	70		

[a] All the potentials are against Ag/AgCl reference electrode.
[b] $E_{1/2}$ values are the average of those obtained from cyclic voltammetric and square wave voltammetric measurements, which are within ±5 mV.
[c] ΔE_p refers to the peak to peak separation at a scan rate of 100 mV s^{-1}.

4. Conclusion

Copper(I), copper(II), zinc(II), nickel(II), cobalt(II), cobalt(III), manganese(II) and iron(II) complexes (**1**–**10**) of dipyrido[3,2-*f*:2′,3′-*h*]-quinoxaline (dpq) have been synthesized and structurally characterized. Various spectroscopic and electrochemical properties of these compounds have been studied.

The most significant aspect of the study is the isolation and structural characterization of three copper(II) complexes of dpq. The compound of composition $[Cu^{II}(dpq)_2(H_2O)](ClO_4)_2$ (**1**) has been obtained by reacting $Cu(ClO_4)_2 \cdot 6H_2O$ with dpq in methanol. The structure determination of this bluish-green compound has revealed that copper(II) has a highly deformed penta-coordinated geometry and can be best described as a distorted trigonal bipyramid with a τ value of 0.55. When the reaction between $Cu(ClO_4)_2 \cdot 6H_2O$ and dpq is carried out in dry acetonitrile, the blue coloured product isolated has the composition $[Cu(dpq)_2](ClO_4)_2$ (**3**). This compound has an irregular geometry. As such, the $[Cu(dpq)_2]^{2+}$ cation deviates from a square planar configuration to a tetrahedral geometry, although the extent of tetrahedral distortion is rather less (dihedral angle $\theta = 38°$). The close proximity of an oxygen atom of a distorted perchlorate (Cu–$OClO_3 = 2.43$ Å) confers a five-coordinate geometry, which again is neither square planar nor trigonal bipyramidal. In the third method of preparation, the condensation reaction between 1,10-phenanthroline-5,6-dione and 1,2-diaminoethane has been carried out in the presence of $Cu(ClO_4)_2 \cdot 6H_2O$ in methanol. Initially, a dark coloured copper(I) complex of composition $[Cu(dpq)_2](ClO_4)$ (**1**) gets deposited and from the solution a second green coloured complex of copper(II) having the composition $[\{Cu(dpq)_2(H_2O)\}\{Cu(dpq)_2(OClO_3)\}](ClO_4)_3$ (**4**) has been isolated. The structure determination of this compound has established the presence of the two different complex cations in the asymmetric unit. It may therefore be considered as a co-crystal. The structure of the $[Cu(dpq)_2(H_2O)]^{2+}$ cation is not exactly the same as the earlier described compound. The tbp geometry is more regular ($\tau = 0.63$) in this case. In the cation $[Cu(dpq)_2(ClO_4)]^+$, the perchlorate is bound to the metal centre in a bidentate fashion [Cu–O = 2.51 and 2.54 Å], thus conferring a six-coordinate geometry to the copper. Similar to the other structures, in this case the metal centre also obtains a highly irregular geometry which is intermediate between octahedral and trigonal prismatic (the angle between the two trigonal faces is 32°).

The zinc compound $[Zn(dpq)_2(OClO_3)_2]$ (**5**) also shows an interesting structure. Because the two perchlorates are unidentately coordinated to the metal centre, the zinc(II) centre obtains a distorted octahedral geometry. In the crystal lattice, the quinoxaline ring of the complex unit is involved in an intermolecular π–π interaction which leads to the generation of a sinusoidal chain.

The proton NMR spectra of the complexes, including those of the paramagnetic complexes $[Ni^{II}(dpq)_3](ClO_4)_2$ (**6**) and $[Co^{II}(dpq)_3](ClO_4)_2$ (**7**) have been studied. The assignment of protons for complex **7** has been made on the basis of their T_1 and T_2 values. The redox behaviour of copper(II) complexes **2**–**4** in acetonitrile is identical but in nitromethane they exhibit different behaviour from each other. The cobalt(II) and cobalt(III) complexes **7** and **8** undergo a reversible electron transfer reaction and the $E_{1/2}$ values of the Co^{II}/Co^{III} couple in acetonitrile is 540 mV.

Acknowledgements

We gratefully acknowledge Prof. K. Nag for his invaluable help and suggestions during the course of this work and in the preparation of the manuscript. M.G. and P.B. are also thankful to CSIR, India for the award of a research fellowship.

Appendix A. Supplementary material

CCDC 637011, 637012, 637013 and 637014 contain the supplementary crystallographic data for **2**, **3**, **4** and **5**. These data can be obtained free of charge via http://www.ccdc.cam.ac.uk/conts/retrieving.html, or from the Cambridge Crystallographic Data Centre, 12 Union Road, Cambridge CB2 1EZ, UK; fax: (+44) 1223-336-033; or e-mail: deposit@ccdc.cam.ac.uk. ESI-MS (positive) for complexes **8** and **10** (Fig. S1a and b), ^1H NMR spectra of **6**, **7**, **8**, **9** (Fig. S2a–d), ORTEP representation of cation $[Cu(dpq)_2(ClO_4)]^+$ in complex **3** (Fig. S3), six-coordinated metal core $[CuN_4O_2]$ in one of the units of the complex **4** (Fig. S4), UV–Vis–NIR spectra of **2** in acetonitrile (Fig. S5) and **2**–**4** in nitromethane (Fig. S6a–c) with deconvolution, cyclic voltammogram of complexes **2**–**4** and ferrocene in nitromethane (Fig. S7a–c) and cyclic voltammogram of complexes **7** and **8** (Fig. S8). Supplementary data associated with this article can be found, in the online version, at doi:10.1016/j.poly.2007.04.014.

References

[1] J. Reedijk, in: G. Wilkinson, R.D. Gillard, J.A. McCleverty (Eds.), Comprehensive Coordination Chemistry, vol. 2, Pergamon Press, Oxford, 1987, p. 73.
[2] (a) L.Y. Chung, A.C. Constable, M.S. Khan, J. Lewis, Inorg. Chim. Acta 185 (1991) 93;
(b) G.R. Newkome, D.K. Kohli, F. Fronczek, J. Chem. Soc., Chem. Commun. (1980) 9;
(c) E.C. Constable, S.M. Elder, J. Healy, D.A. Tocher, J. Chem. Soc., Dalton Trans. (1990) 1669;
(d) E.C. Constable, R. Chotalia, J. Chem. Soc., Chem. Commun. (1992) 64;
(e) A.S. Abushamleh, H.A. Goodwin, Aust. J. Chem. 41 (1988) 873;
(f) C.J. Chandler, L.W. Deady, J.A. Reiss, J. Heterocycl. Chem. 18 (1981) 599.
[3] (a) T. Garber, S.V. Wallendael, D.P. Rillema, M. Kirk, W.E. Hatfield, J.H. Welch, P. Singh, Inorg. Chem. 29 (1990) 2863;
(b) Y. Yao, M.W. Perkovic, D.P. Rillema, C. Woods, Inorg. Chem. 31 (1992) 3956.
[4] (a) M. Athar Masood, P.S. Zacharias, J. Chem. Soc., Dalton Trans. (1991) 111;
(b) M. Athar Masood, D.J. Hodgson, Inorg. Chem. 32 (1993) 4839.
[5] (a) P.J. Burke, K. Henrick, D.R. McMillin, Inorg. Chem. 21 (1982) 1881;
(b) R.J. Crutchley, R. Hynes, E.J. Gabe, Inorg. Chem. 29 (1990) 4921;
(c) J.F. Dobson, B.E. Green, P.C. Healy, H.L. Colin Kennard, C. Pakawatchai, A.H. White, Aust. J. Chem. 37 (1984) 649;
(d) R.N. Williams, L.D. Cola, F. Hartl, J.J. Hagref, J.N. Planeix, A.D. Cian, N.W. Hosseini, Coord. Chem. Rev. 230 (2002) 253;
(e) J. Wang, J. Reibenspies, R.J. Motekaitis, A.E. Martell, J. Chem. Soc., Dalton Trans. (1995) 1511;.
[6] (a) M.T. Miller, P.K. Gantzel, T.B. Karpishin, Inorg. Chem. 38 (1999) 3414;
(b) M.T. Miller, P.K. Gantzel, T.B. Karpishin, Inorg. Chem. 38 (1999) 5246;
(c) D.H. Lee, N.N. Murthy, K.D. Karlin, Inorg. Chem. 36 (1997) 5785;
(d) N.K. Eggleston, D.R. McMillin, K.S. Koenig, A.J. Pallenberg, Inorg. Chem. 36 (1997) 172;
(e) C.T. Cunningham, J.J. Moore, K.L.H. Cunningham, P.E. Fanwick, Inorg. Chem. 39 (2000) 3638.
[7] (a) G.A.V. Albada, I. Mutikainen, O. Roubeau, U. Turpeinen, J. Reedijk, Inorg. Chim. Acta 331 (2002) 208;
(b) G.A.V. Albada, A. Mohamadou, I. Mutikainen, U. Turpeinen, J. Reedijk, Eur. J. Inorg. Chem. (2004) 3733.
[8] (a) R.D. Willett, G. Pon, C. Nagy, Inorg. Chem. 40 (2001) 4342;
(b) T. Pintauer, J. Qiu, G. Kickelbick, K. Matyjaszewski, Inorg. Chem. 40 (2001) 2818;
(c) J. Cody, J. Dennisson, J. Gilmore, D.G. VanDerveer, M.M. Henary, A. Gabrielli, C.D. Sherrill, Y. Zhang, C.-P. Pan, C. Burda, C.J. Fahrni, Inorg. Chem. 42 (2003) 4918.
[9] S. Itoh, N. Kishikawa, T. Suzuki, H.D. Takagi, J. Chem. Soc., Dalton Trans. (2005) 1066.
[10] (a) T. Otsuka, N. Takahashi, N. Fujigasaki, A. Sekine, Y. Ohashi, Y. Kaizu, Inorg. Chem. 38 (1999) 1340;
(b) T. Wada, K. Tsuge, K. Tanaka, Inorg. Chem. 39 (2000) 1340;
(c) M. Sjodin, S. Styring, B. Akermark, L. Sun, L. Hammarstrom, J. Am. Chem. Soc. 122 (2000) 3932;
(d) F.G. Gao, A.J. Bard, J. Am. Chem. Soc. 12 (2000) 7426;
(e) E. Garribba, G. Micera, D. Sanna-Erre, Inorg. Chim. Acta 299 (2000) 253;
(f) J. Guo, Z. Han, P.J. Wu, Mol. Catal. A 159 (2000) 77.
[11] D.O. Bucher, J.P. Sauvage, J.M. Kern, J. Am. Chem. Soc. 111 (1989) 7791.
[12] M. Athar Masood, R. Jagannathan, P.S. Zacharias, J. Chem. Soc., Dalton Trans. (1991) 2553.
[13] (a) K.E. Erkkila, D.T. Odom, J.K. Barton, Chem. Rev. 99 (1999) 2777;
(b) H.T. Chifotides, K.R. Dunbar, Acc. Chem. Res. 38 (2005) 146.
[14] E.I. Solomon, U.N. Sundaram, T.E. Machonkin, Chem. Rev. 96 (1996) 2563.
[15] (a) E.I. Solomon, D.W. Randall, T. Glaser, Coord. Chem. Rev. 200 (2000) 595;
(b) P. Comba, R. Remenyi, Coord. Chem. Rev. 228 (2003) 9.
[16] (a) E. Baranoff, J.P. Coli, Y. Furusho, A.C. Laemmel, J.P. Sauvage, Chem. Commun. (2000) 1935;

(b) F.N. Castellano, G.J. Meyer, Prog. Inorg. Chem. 44 (1997) 167;
(c) M.T. Miller, T.B. Karpishin, Sensor Actuator 61 (1999) 222.
[17] D.R. McMillin, K.N. McNett, Chem. Rev. 98 (1998) 1201.
[18] (a) I. Greguric, J.R. Aldrich-Wright, J.G. Collins, J. Am. Chem. Soc. 119 (1997) 3621;
(b) J.G. Collins, A.D. Sleeman, J.R. Aldrich-Wright, I. Greguric, T.W. Hambley, Inorg. Chem. 37 (1998) 3133;
(c) J.G. Collins, J.R. Aldrich-Wright, I.D. Greguric, P.A. Pellegrini, Inorg. Chem. 38 (1999) 5502;
(d) P.A. Pellegrini, J.R. Aldrich-Wright, J. Chem. Soc., Dalton Trans. (1988) 2341;
(e) N. Gupta, N. Grover, G.A. Neyhart, W. Liang, P. Singh, H.H. Thorp, Angew. Chem., Int. Ed. 31 (1992) 1048;
(f) J.-G. Liu, Q.-L. Zhang, X.-F. Shi, L.-N. Ji, Inorg. Chem. 40 (2001) 5045;
(g) A. Greguric, I.D. Greguric, T.W. Hambley, J.R. Aldrich-Wright, J.G. Collins, J. Chem. Soc., Dalton Trans. (2002) 849;
(h) J.R. Aldrich-Wright, R.F. Fenton, I.D. Greguric, T.W. Hambley, P.A. Williams, J. Chem. Soc., Dalton Trans. (2002) 4666.
[19] P.A.N. Reddy, B.K. Santra, M. Nethaji, A.R. Chakravarty, Indian J. Chem., Sect. A 42 (2003) 2185.
[20] (a) B.K. Santra, P.A.N. Reddy, G. Neelakanta, S. Mahadevan, M. Nethaji, A.R. Chakravarty, J. Inorg. Biol. Chem. 89 (2002) 191;
(b) A.M. Thomas, M. Nethaji, S. Mahadevan, A.R. Chakravarty, J. Inorg. Biol. Chem. 94 (2003) 171;
(c) S. Dhar, D. Senapati, P.A.N. Reddy, P.K. Das, A.R. Chakravarty, Chem. Commun. (2003) 2452;
(d) A.M. Thomas, G. Neelakanta, S. Mahadevan, M. Nethaji, A.R. Chakravarty, Eur. J. Inorg. Chem. (2002) 2720.
[21] (a) S. Dhar, M. Nethaji, A.R. Chakravarty, Inorg. Chem. 44 (2005) 8876;
(b) S. Dhar, M. Nethaji, A.R. Chakravarty, Inorg. Chem. 44 (2005) 2582;
(c) S. Dhar, M. Nethaji, A.R. Chakravarty, Inorg. Chem. 45 (2006) 11043.
[22] D.D. Perrin, W.L. Armarego, D.R. Perrin, Purification of Laboratory Chemicals, 2nd ed., Pergamon Press, Oxford, 1980.
[23] (a) M. Yamada, Y. Tanaka, Y. Yoshimoto, S. Kurda, I. Shimao, Bull. Chem. Soc. Jpn. 65 (1992) 1006;
(b) J.E. Dichson, L.A. Summers, Aust. J. Chem. 23 (1970) 1023.
[24] J.E. Dickeson, L.A. Summers, Aust. J. Chem. 23 (1970) 1023.
[25] SAINT, version 6.02, SADABS, version 2.03, Bruker AXS Inc., Madison, WI, 2002.
[26] G.M. Sheldrick, SHELXL-97: Program for the Refinement of Crystal Structures, University of Göttingen, Göttingen, Germany, 1997.
[27] SHELXTL, version 6.10; Bruker AXS Inc., Madison, WI, 2002.
[28] A.W. Addison, T.N. Rao, J. Reedijk, J. van Rijn, G.C. Vershoor, J. Chem. Soc., Dalton Trans. (1984) 1349.
[29] A.B.P. Lever, Inorganic Electronic Spectroscopy, 2nd ed., Elsevier, Amsterdam, 1984.

Herein, we report on the synthesis and characterization of **L2**, as well as on its thiol-protected precursor **L1**. Protonation constants of **L2** and its stability constants with Cu^{2+}, Zn^{2+} and Cd^{2+} will also be reported. An analysis of the protonation scheme of **L2** is discussed, as well as the structural environment in solution of Cu(II) and Zn(II) in the complexes with **L2**.

2. Experimental

2.1. Reagents

Chemicals and solvents were of reagent grade and were used without further purification, unless stated otherwise. 1,4,7,10-tetraazacyclododecane (cyclen) was purchased from Strem (New-Buryport, MA, USA). Sodium hydride, triphenylmethane-thiol, tetrahydrofuran, dibromoethane, toluene, sodium hydroxide, methanol, dichloromethane, ammonium, hydrochloride acid, deuterated water and chloroform were obtained from Aldrich Chemical Co. Silica gel 60 (70–230 mesh, pH range = 6.5–7.5) was obtained from Merck.

2.2. Analytical methods

^{1}H (300 MHz) and ^{13}C (75.5 MHz) NMR spectra were recorded in a Varian Unit Inova-300 spectrometer at a probe temperature of about 20°C. The spectra were performed in $CDCl_3$ (δ/ppm: ^{1}H: 7.24; ^{13}C: 77.00) or D_2O versus an external reference of 1,4-dioxane (δ/ppm: ^{1}H: 3.75; ^{13}C: 69.20). Positive-ion mass spectra were obtained in a Finnigan FT/MS 2001-DT FTICR mass spectrometer by laser desorption ionization. pH measurements were performed in a ORION SA 720. UV–Vis spectra were done in a Cary 500. EPR spectroscopic measurements of the copper complex were recorded with a Bruker ESP 380 spectrometer equipped with continuous-flow cryostats for liquid nitrogen, operating at X-band.

2.3. Synthesis of 2-[1,4,7,10-tetraazacyclododecan-1-yl]-ethanetritylthiol (*L1*)

To a solution of cyclen (285 mg, 1.5 mmol) in hot toluene (50 cm^3) was slowly added bromoethyl tritylthiol [7] (210 mg; 0.5 mmol) dissolved in toluene (50 cm^3). The reaction mixture was refluxed overnight and then a solution of NaOH (20%) added. The organic phase was separated and the solvent evaporated under vacuo. The solid obtained was purified by silica-gel chromatography using as eluent a mixture of $CHCl_3$/MeOH/aq. NH_3 (gradient 100:0:0 → 0:100:0 → 0:80:20, $R_f = 0.2$ in 80:20 MeOH/ aq. NH_3 solution) **L1** (100 mg, 43%); δ_H/(300 MHz, $CDCl_3$): 7.37 (6 H, d, aromatic protons), 7.26–7.14 (9 H, m, aromatic protons), 2.89–2.84 (4 H, m), 2.52–2.48 (8 H, m), 2.36–2.32 (8 H, m); δ_C(75.5 MHz, $CDCl_3$): 144.9 (Ph), 129.6 (Ph), 127.8 (Ph), 126.5 (Ph), 66.8 ($SCPh_3$), 53.5 ($CH_2CH_2SCPh_3$), 50.80 (C_{ring}), 46.9 (C_{ring}), 46.1 (C_{ring}), 44.9 (C_{ring}), 29.4 ($CH_2CH_2SCPh_3$).

2.4. Synthesis of 2-[1,4,7,10-tetraazacyclododecan-1-yl]-ethanethiol (*L2*)

Compound **L1** was refluxed in 20% HCl, for 2 h. After cooling to room temperature, the resulting solution was washed with dichloromethane, the aqueous extracts separated and vacuum dried yielding a white solid **L2** (75 mg, 80%). δ_H (300 MHz, D_2O, pD 1.05): 2.54 (2 H, t, C(1)H); 2.70 (2 H, t, C(2)H); 2.84 (4 H, t, C(3)H); 2.97 (4 H, br m, C(6)H); 3.07 (8 H, br m, C(4)H + C(5)H); δ_C (75.5 MHz, D_2O/ 1,4-dioxane, pD 1.05): 56.8 (*C2*); 50.3 (*C3*); 45.6 (*C4*); 44.4 (*C6*); 43.9 (*C5*); 22.0 (*C1*); *m/z* (LDI): calc. for $[^{12}C_{10}{}^1H_{25}{}^{14}N_4{}^{32}S]^+$: 233.179, $[^{12}C_{10}{}^1H_{24}{}^{14}N_4{}^{32}S^{23}Na]^+$: 255.161, $[^{12}C_{10}{}^1H_{25}{}^{14}N_4{}^{32}S^{39}K]^+$: 271.135; found: $[M+H]^+$: 233.191, $[M+Na]^+$: 255.156, $[M+K]^+$: 271.118.

2.5. X-ray crystal analyses

Crystal data for **L1**: $C_{29}H_{52}N_4O_{10}S_2$, $M_r = 680.87$, triclinic, space group $P\bar{1}$, $a = 8.1242(1)$, $b = 8.8600(1)$, $c = 27.0151(4)$ Å, $\alpha = 81.8670(10)$, $\beta = 82.1130(10)$, $\gamma = 63.9020(10)°$, $U = 1722.57(4)$ Å^3, $Z = 2$, $D_c = 1.313$ g cm^{-3}, μ (Mo Kα) = 1.260 mm^{-1}. Suitable colourless prismatic crystals (0.40 × 0.32 × 0.06 mm) were mounted in air on a goniometer head. X-ray diffraction experiments were performed with a Bruker AXS APEX CCD detector diffractometer using graphite monochromated Mo Kα radiation ($\lambda = 0{:}71073$ Å), at 150 K in the ϕ and ω scans mode. A semi empirical absorption correction was carried out using SADABS [8].

Data collection, cell refinement and data reduction were done with the SMART and SAINT programs [9]. The structures were solved by direct methods using SIR97 [10] and refined by fullmatrix least-squares methods using the program SHELXL97 [11] using the winGX software package [12]. Non-hydrogen atoms were refined with anisotropic thermal parameters. The H atoms of the CH and CH_2 were placed at calculated positions using a riding model, with distances C–H = 0.95 Å (aromatic) and C–H = 0.99 Å (CH_2) and with Uiso(H) = 1.2Ueq(C) of the parent atom. The H atoms in the water, NH_2 and NH were located in difference Fourier maps and its coordinates and isotropic thermal parameters were refined.

The residual electronic density ranging from 0.393 to −0.392 e Å^{-3} was within expected values. The final refinement of 472 parameters converged to final R and R_W indices $R_1 = 0.0408$ and $wR_2 = 0.0972$ for 7020 reflections with $I > 2\sigma(I)$. Molecular graphics were prepared using ORTEP 3 [13].

2.6. Potentiometric studies

2.6.1. Reagents and solutions

Metal ion solutions were prepared at about 2.5×10^{-3} mol dm^{-3} from the nitrate salts of the metals and were titrated using standard methods [14]. Deionized

(Millipore/Milli-Q System) distilled water was used. Carbonate-free solutions of the KOH titrant were obtained, maintained and discarded when the percentage of carbonate was about 0.5% of the total amount of base [15].

2.6.2. Equipment and work conditions

The equipment was used as described before [16]. The temperature was kept at 25.0 ± 0.1 °C, atmospheric CO_2 was excluded from the cell during the titrations by passing purified nitrogen across the top of the experimental solution in the reaction cell. The ionic strength of the solutions was kept at 0.10 mol dm^{-3} with KNO_3.

2.6.3. Measurements

The $[H^+]$ of the solutions was determined by the measurement of the electromotive force (emf) of the cell, $E = E^{\circ\prime} + Q\log[H^+] + E_j$. $E^{\circ\prime}$, Q, E_j and $K_w = ([H^+][OH^-])$ were obtained as described previously [17]. The value of K_w was found equal to $10^{-13.80}$ (mol dm^{-3})^2. The potentiometric equilibrium measurements were made on 25.00 cm^3 of $\approx 2.00 \times 10^{-3}$ mol dm^{-3} ligand solutions diluted to a final volume of 30.00 cm^3, in the absence of metal ions and in the presence of each metal ion for which the C_M:C_L ratio was 1:1. A minimum of two replicate measurements was taken.

The emf data were taken after additions of 0.050 cm^3 increments of standard KOH solution, and after stabilization in this direction, equilibrium was then approached from the other direction adding standard nitric acid.

For determination of the stability constants, out-of-cell titrations were performed in the pH region from which the direct and back titrations were not superimposed. In such regions, independent vials each one at different pH were prepared and left to equilibrate in a water bath at 25.0 °C and the corresponding pH values checked every week till stabilization of the pH, which occurred generally within 2–4 weeks.

2.6.4. Calculation of equilibrium constants

Overall protonation constants, β_i^H were calculated by fitting the potentiometric data obtained for the free ligand with HYPERQUAD program [18]. Stability constants of the various species formed in solution were obtained from the experimental data corresponding to the titration of solutions of the different metal ions, each of them with different metal to ligand ratios, also using the HYPERQUAD program. The initial computations were obtained in the form of overall stability constants, $\beta_{M_mH_hL_l}$ values, $\beta_{M_mH_hL_l} = [M_mH_hL_l]/([M]_m \times [H]_h \times [L]_l)$. Differences, in log units, between the values $\beta_{M(HL)}$ (or $\beta_{MLH_{-1}}$) and β_{ML} provide the stepwise reaction constants. The species considered in a particular model were those that could be justified by the principles of co-ordination chemistry. The errors quoted are the standard deviations of the overall stability constants given directly by the program for the input data, which include all the experimental points of all titration curves. The hydrolysis constants of the metal ions were taken from the literature and kept constant for the calculations [19].

2.7. NMR studies

2.7.1. ^{13}C NMR titration

The electrode was calibrated with standard buffer solutions and the final pD was calculated according to the equation $pD = pH^* + (0.40 \pm 0.02)$ [20], where pH^* corresponds to the reading of the pH meter. The solutions ($\approx 2 \times 10^{-3}$ M) used for the NMR titration measurements were made up in D_2O and the pD value was adjusted by adding DCl or CO_2-free KOD. The solutions were allowed to stabilize and the pD values were measured directly in the NMR-tube with a combination microelectrode Mettler-Toledo U402-M3-S7/200.

2.7.2. EPR studies

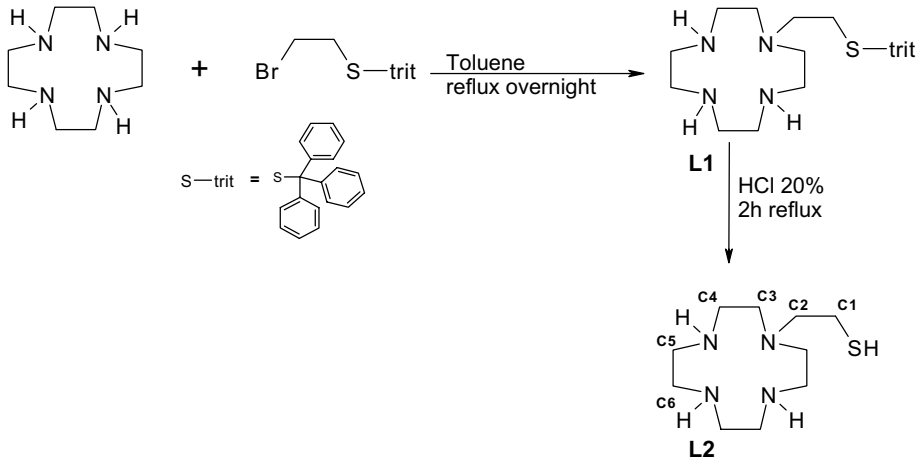
The Cu^{2+}/**L2** complexes ($\approx 1.6 \times 10^{-3}$ mol dm^{-3} in 40% DMSO/H_2O solution) were prepared at pH 5, 8 and 12 and were recorded at 104 K. The EPR spectra of Cu^{2+}/cyclen complexes were also recorded at the same pH values and conditions for comparison.

3. Results and discussion

3.1. Synthesis and characterization

Different synthetic procedures have been described to prepare mono-substitued tetraazamacrocycles, namely the introduction of the side chain on the amine before cyclization [21–23], pH controlled reactions [24], protection/deprotection methods [25] or alkylation of the macrocycle using an excess of the ligand versus the desired alkylating agent [26]. It has also been reported that it was possible to introduce one oxygen or sulphur pendant arm in the cyclen backbone by reacting cyclen with stoichiometric amounts of trimethylene oxide or ethylene sulphide, respectively [27,4,5a,5b,5c]. Following our previous work on tetraazamacrocycles, we have tried the synthesis of the mono-*N*-(2-ethanethiol) cyclen derivative (**L2**) following the described methodology [4]. In our hands, such synthetic procedure has never worked properly and compound **L2** could never be isolated. **L2** was synthesized in 40% overall yield, by slow addition of bromoethyl tritylthiol [7] to cyclen, in a 1:3 molar ratio, followed by acidic deprotection of the thiol group (Scheme 1).

Compound **L1** was also isolated and characterized by ^1H and ^{13}C NMR spectroscopy and by X-ray crystallography, upon purification by column chromatography using MeOH/NH_3 as eluent. Slow concentration of the fractions containing **L1** led to crystals suitable for X-ray crystallography. Compound **L1** crystallizes on the triclinic system, $P\bar{1}$ space group, with cell parameters $a = 8.1242(1)$ Å, $b = 8.8600(1)$ Å, $c = 27.0151(4)$ Å, $\alpha = 81.867(1)°$ $\beta = 82.113(1)°$ $\gamma = 63.902(1)°$ and $V = 1722.57(4)$ Å^3. The asymmetric unit contains one molecule of diprotonated



Scheme 1. Syntheses of **L1** and **L2**.

L1 ($C_{29}H_{40}N_4S$), one sulphate dianion $(SO_4)^{2-}$ and six water molecules, given the molecular formula $[C_{29}H_{40}N_4S]\cdot SO_4\cdot 6H_2O$. In Fig. 1 is presented an ORTEP diagram showing the numbering scheme of the asymmetric unit.

Some selected bond lengths (Å) and angles (°) for the dication $[C_{29}H_{40}N_4S]^{2+}$ are listed in Table 1.

The macrocycle was found to be protonated in the amines N2 and N4. The average $C–N_{protonated}$ bond distances (1.490 Å) are slightly longer than the average $C–N_{unprotonated}$ ones (1.467 Å). These differences compare well with the values previously reported for other protonated macrocyclic ligands [28]. The four nitrogen atoms of the macrocycle are coplanar with an rms of 0.0306, the CH_2 groups of the backbone are below this plane, while the sulphur arm is above the plane, pointing in the opposite direction. The calculated torsion angle N1–C2–C1–S1 of 178.1° shows the relative position of the pendant arm towards the macrocycle cavity.

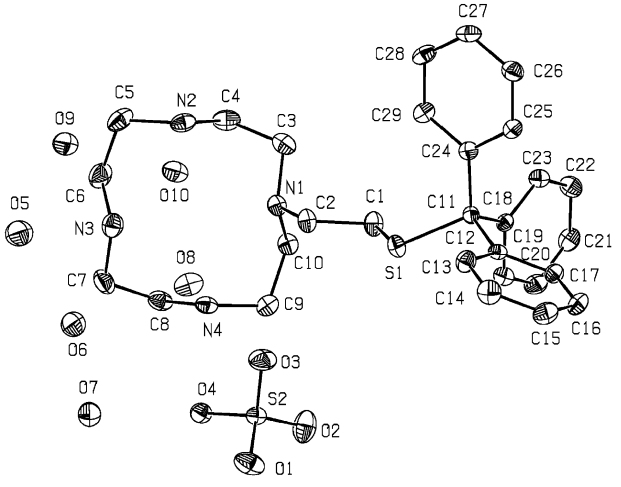


Fig. 1. ORTEP diagram with atomic numbering scheme of asymmetric unit with thermal ellipsoids at 50% probability level. Hydrogen atoms are omitted for clarity.

Table 1
Selected bond lengths (Å) and angles (°) for the dication $[C_{29}H_{40}N_4S]^{2+}$

S(1)–C(1)	1.822(2)	N(2)–C(4)	1.484(3)
S(1)–C(11)	1.862(2)	N(2)–C(5)	1.497(3)
C(1)–C(2)	1.531(2)	N(3)–C(6)	1.459(3)
N(1)–C(2)	1.470(2)	N(3)–C(7)	1.471(3)
N(1)–C(3)	1.472(2)	N(4)–C(8)	1.483(2)
N(1)–C(10)	1.467(2)	N(4)–C(9)	1.497(2)
C(1)–S(1)–C(11)	105.14(8)	C(2)–C(1)–S(1)	105.56(12)
C(10)–N(1)–C(3)	111.02(14)	N(1)–C(2)–C(1)	116.56(15)
C(5)–N(2)–C(4)	117.13(16)	C(3)–N(1)–C(2)	113.99(15)
C(7)–N(3)–C(6)	113.57(16)	C(10)–N(1)–C(2)	115.64(14)
C(8)–N(4)–C(9)	114.98(15)		

The crystal packing of compound **L1** is characterized (Fig. 2) by the formation of a bidimensional layer parallel to the bc plane due to several hydrogen bonds between the water molecules and due to intermolecular short N···O and C···O contacts between SO_4^{2-} units and the macrocycle (Table 2).

Compound **L2** is quite soluble in water and stable under aerobic conditions. The formulation of **L2** was mainly based on multinuclear NMR spectroscopy (^1H, ^{13}C, $^1H,^1H$ COSY, $^1H,^{13}C$ HSQC) at different pD values (range 1–14) and also on mass spectrometry. In the LDI-positive mass spectrum three main peaks were found at $m/z =$ 233.191, 255.156 and 271.118 corresponding to $[M+H]^+$, $[M+Na]^+$ and $[M+K]^+$, respectively.

In the pD range studied, the ^{13}C NMR spectra recorded exhibit six resonances, a pattern consistent with the two-fold symmetry expected for **L2**: four resonances were assigned to the carbon atoms of the backbone and the other two to the carbon atoms of the pendant arm. The ^1H NMR spectra at pD 1.05 presented five resonances with different multiplicities at 2.54, 2.70, 2.84, 2.97, 3.07 ppm in an intensity ratio of 2:2:4:4:8. At higher pD values, the ^1H NMR spectra became less clear due to the overlapping of some resonances. 2D NMR studies ($^1H,^1H$ and $^1H,^{13}C$ correlations) were performed at pD 1.05. In Fig. 3 is shown

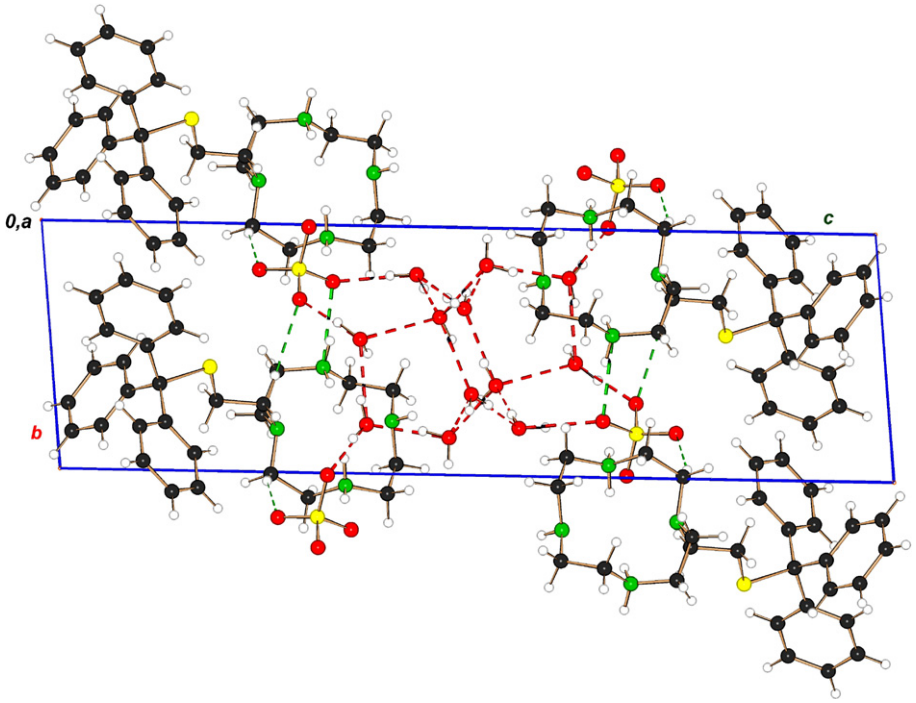


Fig. 2. Crystal structure of **L1** viewed along *a*.

Table 2
Selected hydrogen bonds and short contacts in the crystal structure of compound **L1**

	Distance (Å)
$O_{sulphate}\cdots N$	
O4···N4	2.766(2)
O4···N2	2.764(3)
$O_{sulphate}\cdots H–C_{backbone}$	
O1···H4b–C4	2.612(2)
O1···H6b–C6	2.381(2)
O3···H2a–C2	2.564(1)
$O_{sulphate}\cdots H–C_{aromatic}$	
O2···H14–C14	2.456(2)
O2···H28–C28	2.688(2)

the g-COSY $^{1}H,^{1}H$ and the g-HSQC $^{1}H,^{13}C$ 2D correlations. From these studies it was possible to conclude that the triplets centered at 2.54 and 2.70 ppm correlate with the carbons at 22.03 and 56.81 ppm, respectively. Based on the carbon and proton NMR data of the free arm and on literature data, the resonances at 22.03 and 56.81 ppm were assigned to the α (C1) and β (C2) carbon atoms of the pendant arm, respectively (Scheme 1). The triplet centred at 2.84 ppm (4 H) correlates with the carbon atoms at 50.26 ppm, assigned to C3. The multiplet at 2.97 ppm (4 H) correlates with the carbon atom at 44.39 ppm and correlates with the multiplet at 3.07 ppm (8 H). Based on these data the resonance at 44.39 ppm was assigned to the C6 carbon atoms and the multiplet at 3.07 ppm (8 H) was assigned to the protons bound to the C4 and C5 atoms which appear at 45.64 and 43.92 ppm, respectively. In Table 3 are presented the chemical shifts and the corresponding assignment of the resonances of **L2** at pD 1.05.

3.2. Acid–base behaviour

The protonation constants of **L2** were determined by potentiometry at 25.0 °C and 0.10 mol dm^{-3} KNO_3 ionic strength. The values found are summarized in Table 4. Compound **L2** has five protonation constants, from which four could be determined by potentiometry, but the remaining one is too low to be determined by this technique. Just for comparison, in Table 4 are also shown the protonation constants for cyclen, 2-hydroxyethyl cyclen (**L3**) and 3-hydroxypropyl cyclen (**L4**) (Fig. 4) [27,29].

Based on the values of Table 4 it is difficult to ascribe the protonation sequence of **L2**. In order to understand this sequence a ^{13}C NMR titration was performed. These studies were carried out at 20 °C without controlling the ionic strength [30]. In Fig. 5 are shown the ^{13}C NMR titration curves.

The ^{13}C NMR spectra recorded for **L2** exhibit six resonances in the entire pD range. For each magnetically equivalent carbon atom, single resonances have been observed, indicating a rapid exchange between protonated species. For the interpretation of these data, the pK_H values determined for **L2** (Table 4) were converted in terms of pK_D, using the correlation $pK_D = 0.11 + 1.10\,pK_H$, determined for polyaza and polyoxa–polyaza macrocyclic compounds by Delgado et al. [31]: $pK_{D1} = 12.19$, $pK_{D2} = 11.09$, $pK_{D3} = 9.08$ and $pK_{D4} = 2.62$. From the analysis of the

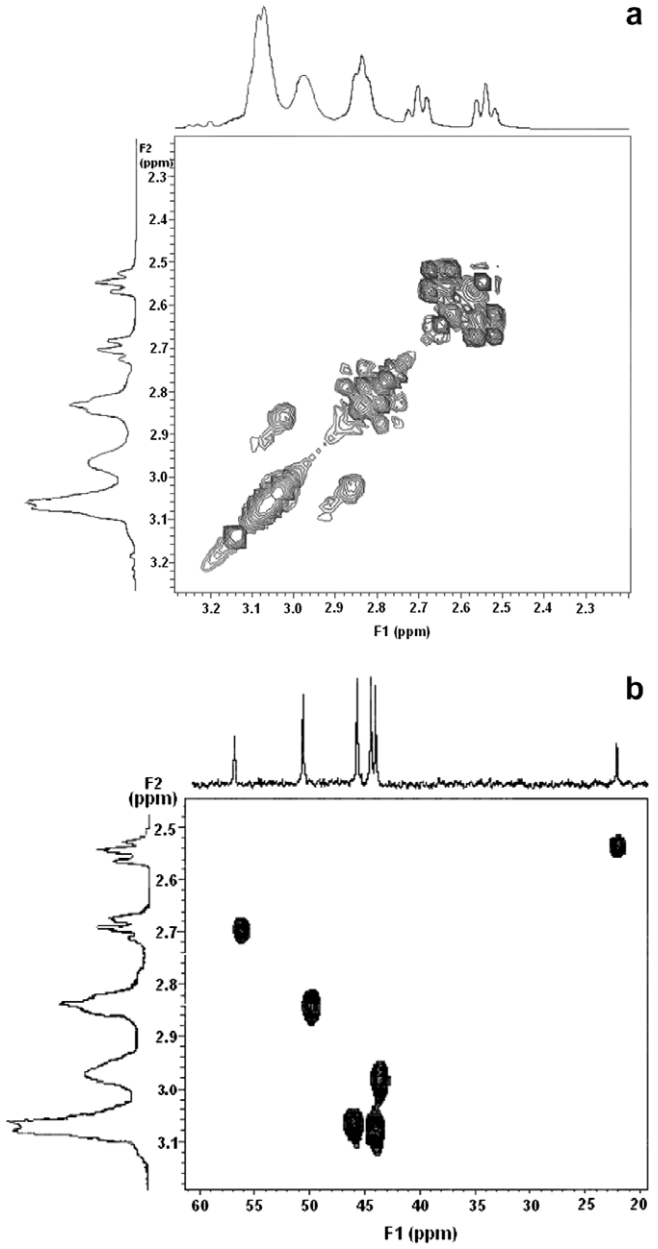


Fig. 3. g-Cosy $^{1}H,^{1}H$ (a) and g-HSQC $^{1}H,^{13}C$ (b) 2D correlations for **L2** at pD 1.05.

Table 3
^{1}H and ^{13}C NMR data for **L2** at pD 1.05

Assignment	Chemical shift (ppm)	
	^{1}H	^{13}C
C1	2.54 (t, 2 H)	22.03
C2	2.70 (t, 2 H)	56.81
C3	2.84 (t, 4 H)	50.26
C4	3.07 (m, 8 H)	45.64
C5		43.92
C6	2.97 (m, 4 H)	44.39

NMR titration curves, three pD regions were defined, one comprising two protonation constants ($13.0 \geqslant pD \geqslant 10.5$), and the other two comprising one protonation constant each ($10.5 \geqslant pD \geqslant 8.0$ and $pD \leqslant 3.0$). The high symmetry of **L2** makes difficult to predict the protonation sequence, but an attempt has been made taking into account that when a protonation occurs at a given site the β-carbons are upfield shifted [32]. In the $13.0 \geqslant pD \geqslant 10.5$ region two protonations occur, and their constant values differ only by one log unit, which makes difficult to distinguish the effect of each one. However, taking into account that in this range the resonances ***C2***, ***C4*** and ***C5*** are upfield shifted, while ***C1*** shifts downfield, it seems that the thiolate group is protonated and a second proton may be shared by the $\mathbf{N}_{I}$ and $\mathbf{N}_{III}$ amines. In the region $10.5 \geqslant pD \geqslant 8.0$ a third protonation occurs on one amine of the macrocyclic ring, and this proton together with the one already existing in the macrocycle backbone will be shared by the $\mathbf{N}_{I}/\mathbf{N}_{II}/\mathbf{N}_{II}$ amines centres. This is supported by the upfield shift of the resonances ***C1***, ***C3***, and ***C6***. In the pD range 8.0–3.0 no significant changes were observed, but for $pD \leqslant 3.0$ the ***C1***, ***C4*** and ***C5*** carbon atoms are upfield shifted, being ***C1*** the most significantly shifted (ca. 1 ppm), which may indicate the protonation of the $\mathbf{N}_{I}$ centre.

Table 4
Protonation constants (log units) of **L2** and other related macrocyclic ligands

Species h,l	L2[a]		Cyclen[b]	L3[c]	L4[d]
	$\log \beta_{H_iL}$	$\log K_{H_iL}$	$\log K_{H_iL}$	$\log K_{H_iL}$	$\log K_{H_iL}$
11	10.98(2)	10.98	10.97	10.72	10.56(4)
12	20.96(2)	9.98	9.87	9.28	9.14(4)
13	29.11(4)	8.15	1.6	<2	<2.3
14	31.39(6)	2.28	0.8	<2	<2.3
Overall basicity		31.39	23.24	<24	<24.4

Values in parentheses are standard deviations in the last significant figures.
[a] $T = 25.0$ °C, $I = 0.10$ mol dm^{-3} in KNO_3, this work.
[b] $I = 0.50$ mol dm^{-3} in KNO_3, Ref. [29a] and $I = 0.20$ mol dm^{-3} in $NaClO_4$, Ref. [29b].
[c] $I = 0.10$ mol dm^{-3} NEt_4ClO_4, Ref. [29c].
[d] $I = 0.10$ mol dm^{-3} in $NaClO_4$, Ref. [27].

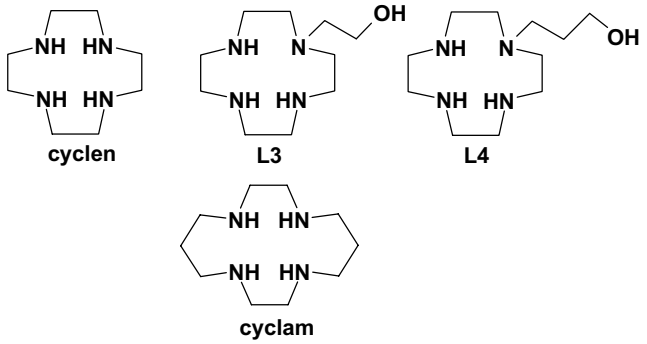


Fig. 4. Structure of the ligands used for comparison: cyclen, 2-hydroxyethyl cyclen (**L3**), 3-hydroxypropyl cyclen (**L4**) and cyclam.

3.3. Stability constants

The complexation of **L2** with Cu^{2+}, Zn^{2+} and Cd^{2+} was followed by potentiometry, at 25.0 °C and 0.1 mol dm^{-3}

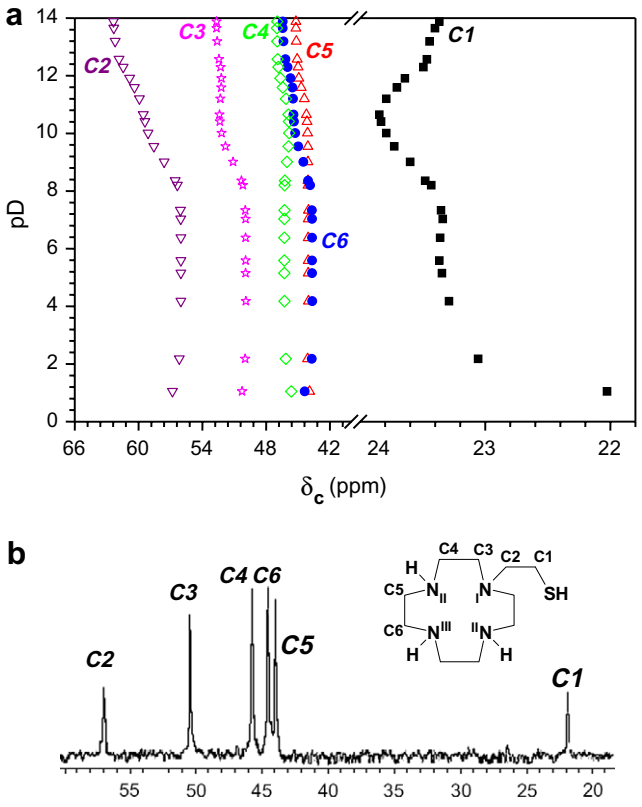


Fig. 5. (a) ^{13}C NMR titration curves for **L2** (chemical shift (δ_C) in function of pD): ■, *C1*; ▽, *C2*; ☆, *C3*; ♦, *C4*; △, *C5* and ●, *C6*. (b) ^{13}C NMR spectrum of **L2** (D_2O, pD 1.05).

KNO_3, and the corresponding stability constants were determined. The kinetics of formation of the complexes of **L2** with the transition metal ions studied is relatively slow. The stability constants were determined by the use of a batch method in the pH regions where complexation equilibrium was not attained during in-cell titrations, leading to stability constants with relatively high standard deviations. In Table 5 are listed the stability constants of the complexes of **L2** with Cu^{2+}, Zn^{2+} and Cd^{2+}, together with the constants for the corresponding complexes with related tetraazmacrocycles. Cyclam was included due to its very high affinity for copper(II) [33].

Only mononuclear species were formed with the studied metal ions, namely [ML], [M(HL)], [M(H_2L)], [M(L(OH))] and [M(L(OH)$_2$)]. The latter species is only formed for Cd^{2+}, while [M(H_2L)] only exists when $M = Cu^{2+}$. At physiological pH, the [ML] complex is formed at about 100% for Cu^{2+}, while for Cd^{2+} and for Zn^{2+} only above pH 8 this is the main species (Fig. 6).

The trend found for the stability of the complexes studied, [CuL] > [ZnL] ≈ [CdL], follows the usual order for cyclen derivatives. However the $\log K_{CuL}/\log K_{ZnL}$ and $\log K_{CuL}/\log K_{CdL}$ ratios are smaller than usually found for ligands having only amine donor atoms, such as cyclen and cyclam. This feature, together with the larger values of K_{ML} observed for **L2**, when compared to cyclen, strongly suggests the involvement of the arm in the coordination sphere of the metal centre. For all the metal ions, completely different direct and backtitration potentiometric curves were obtained, suggesting structural rearrangements, may be related with the formation and break of the M–S bond.

A direct comparison of stability constants of **L2** and those reported for cyclen, **L3**, **L4** and cyclam can only be made using the pM ($-\log[M^{2+}]$) values (Table 6) [35], due to the different basicity of the ligands.

These data indicate that compound **L2** has higher affinity for the transition metal ions studied than the tetraaza-

Table 5
Stability constants (log units) for complexes of **L2** and other related ligands with Cu^{2+}, Zn^{2+} and Cd^{2+} ions

Metal	Species *mhl*	L2[a]		Cyclen[b]	L4[c]	Cyclam[d]
		$\log \beta_{MH_iL}$	$\log K_{MH_iL}$	$\log K_{MH_iL}$	$\log K_{MH_iL}$	$\log K_{MH_iL}$
Cu^{2+}	101	21.19(6)	21.17	23.29	17.3(1)	26.5
				24.8		27.2
	111	27.45(4)	6.26			
	121	30.47(7)	3.02			
	1−11	12.2(1)	−8.99		10.2	
Zn^{2+}	101	18.6(1)	18.6	16.2	13.7(1)	15.5
	111	25.60(2)	7.00	5.74		3.99
	1−11	8.8(1)	−9.8		−8.3	
Cd^{2+}	101	18.8(1)	18.8	14.3	13.0(1)	11.23
	111	25.51(5)	6.71			
	121				9.8	
	1−11	9.2(1)	−9.6			
	1−21	−1.7(1)	−10.9			

Values in parentheses are standard deviations in the last significant figures.
[a] This work, $T = 25.0$ °C, $I = 0.10$ mol dm^{-3} KNO_3.
[b] $I = 0.1$ mol dm^{-3} $NaNO_3$, Ref. [29a].
[c] $T = 25.0$ °C , $I = 0.1$ mol dm^{-3} NEt_4ClO_4, Ref. [27].
[d] Refs. [33,34].

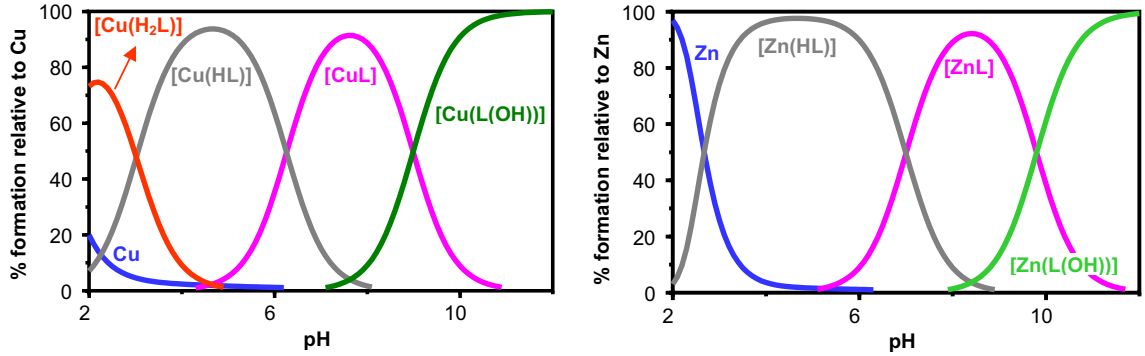


Fig. 6. Species distribution diagrams for the Cu^{2+} and Zn^{2+} complexes with **L2** in water, $C_L = C_M = 4.0 \times 10^{-5}$ mol dm^{-3} (charges were omitted).

Table 6
pM values[a] calculated for **L2** and other related ligands (pH 7.4)

Ion	L2	Cyclen	L4	Cyclam
Cu^{2+}	14.24	9.27, 10.02	11.59	10.19, 10.54
Cd^{2+}	11.91	4.73	7.29	2.57
Zn^{2+}	11.77	5.68	7.99	2.42

[a] The values were calculated for 100% excess of free ligand, using the program HySS [35], $C_L = 2C_M = 1 \times 10^{-5}$ mol dm^{-3} and the stability constants given in Table 5.

macrocycles considered for comparison. For the same cavity size, the presence of a coordinating pendant arm increases significantly the stability of the complexes. A decrease of the pM values is found when the cavity size increases. However, **L2** shows a low selectivity for Cu over Zn and Cd.

3.4. Structural studies in solution

3.4.1. NMR studies of zinc(II) complexes

To assess the nature of the inner sphere of the zinc, the ^{13}C NMR spectra of solutions containing Zn^{2+} and **L2** (1:1 molar ratio) have been recorded at different pD values. Based on the species distribution diagram (Fig. 6), we have chosen the 5.6, 7.6 and 11.6 pH values, which correspond to the [Zn(HL)], [ZnL] and [Zn(L(OH))] species, respectively. In Table 7 are collected the chemical shifts of the carbon atoms of the Zn^{2+}/**L2** species formed as well as those for the free **L2**, recorded in the same experimental conditions.

Table 7
Chemical shift (δ/ppm) of the carbon atoms of **L2** and of the species Zn/**L2** at pD 6, 8 and 12

	pD ≈ 6		pD ≈ 8		pD ≈ 12	
	L2	**Zn/L2**	**L2**	**Zn/L2**	**L2**	**Zn/L2**
C1	23.36	26.37	23.43	26.02	23.64	25.97
C2	56.02	55.07	56.36	57.22	60.84	57.18
C3	49.93	51.66	50.20	52.22	52.22	52.18
C4	46.30	46.54	46.26	47.22	46.66	47.19
C5	44.04	45.64	44.05	46.18	44.93	44.45
C6	43.69	44.40	43.87	44.49	45.71	46.14

Most of the carbon atoms of **L2** are significantly downfield shifted upon coordination to the Zn^{2+}. These results are consistent with the formation of a Zn^{2+}/**L2** complex and seem to indicate that all the donor atoms are coordinated to the metal. The significant downfield shift observed for ***C2***, when pD increases from 6 to 8, may be correlated to the deprotonation followed by coordination of the thiol group, in agreement with the potentiometric studies (Table 5).

3.4.2. UV–Vis and EPR spectroscopic studies of copper(II) complexes

The UV–Vis–NIR and the EPR spectra of Cu^{2+}/**L2** and Cu^{2+}/cyclen complexes were recorded at pH 5, 8 and 12, which for Cu^{2+}/**L2** corresponds to about 100% of the [Cu(HL)], [CuL] and [Cu(L(OH))] species, respectively (Fig. 6). As can be seen in Table 8, the electronic spectra of the Cu^{2+} complexes with **L2** and cyclen exhibit two well defined bands, one in the UV–Vis range and another in the charge transfer region. A red-shift of the band in the UV–Vis is expected when the geometry of a Cu^{2+} complex changes from a square planar to a penta-coordinated one. For Cu^{2+}/cyclam [36] and Cu^{2+}/1,4,8-trimethyl-11-(2-thioethyl)-1,4,8,11-tetraazacyclotetradecane [5a], which have been considered to be four and five-coordinated, the maximum absorption of the bands has been reported to be at $\lambda_{max} = 513$ nm and 622 nm, respectively. Our data for Cu^{2+}/**L2** and Cu^{2+}/cyclen seem to indicate that in the complexes studied in this work the copper centre is five-coordinated. In the pH range studied, both complexes present the same pattern for the UV–Vis spectra and the maximum of absorption does not change significantly with the pH. These results may suggest that the environment around the Cu is the same, independently of the protonation of the corresponding ligand. However, the molar absorptivity of the complex Cu^{2+}/**L2** increases with pH, indicating a highest distortion for the complex, most probably due to the deprotonation of the sulphur atom and formation of a strong apical Cu–S bond.

In Fig. 7 are shown the X-band EPR spectra of Cu^{2+}/**L2** and Cu^{2+}/cyclen complexes and their simulated spectra, at different pH values. All the spectra indicated the presence

Table 8
Spectroscopic data for the copper(II) complexes of **L2** and other related ligands taken from literature

Ligands or Cu(II) complexes (pH)	UV–Vis–near IR	EPR ($10^4 A_i$/cm^{-1})					
	λ/nm (ε/mol^{-1} dm^3 cm^{-1})	g_x	g_y	g_z	A_x	A_y	A_z
L2 (5)[a,b]	612 (112); 277 (4×10^4)			2.198			182.14
L2 (8)[a]	615 (132); 270 (6×10^4)	2.040	2.055	2.198	16.88	17.68	182.41
L2 (12)[a]	620 (220); 273 (8×10^4)	2.041	2.082	2.200	1.92	7.68	186.98
Cyclen (5)[a]	579 (56); 282 (1×10^4)	2.040	2.055	2.197	16.88	21.02	181.97
Cyclen (8)[a]	578 (56); 274 (3×10^4)	2.040	2.055	2.196	16.88	21.02	181.99
Cyclen (12)[a]	581 (80); 274 (3×10^4)	2.052	2.060	2.212	2.30	10.33	180.23
[Cu(cyclen)Cl]$^+$[c]	599 (220)	2.057		2.198	24.1		184.2
[Cu(cyclam)]Cl$_2$[c]	513 (100)	2.049		2.186	38.7		205.0
[Cu(H$_2$O)$_6$]$^{2+}$[d]		2.08		2.4			134.0

[a] This work.
[b] Species A: $g_z = 2.410$ and $A_z = 131.92$.
[c] Ref. [36].
[d] Ref. [38].

of only one species, except for Cu^{2+}/**L2** at pH 5, which revealed the presence of two species. All the spectra showed the expected four well-resolved lines at low field, due to the interaction of the unpaired electron spin with the copper nucleus. The hyperfine coupling constants (A) and g values obtained by the simulation of the spectra [37] are shown in Table 8, together with those of other copper(II) complexes taken from literature, for comparison [36,38]. The simulation of the spectra revealed three different g values with $g_z > (g_x + g_y)/2$ and the lowest $g \geqslant 2.04$, which is characteristic of mononuclear copper(II) complexes having rhombic-octahedral with elongation of the axial bonds or distorted square-based pyramidal symmetries, and $d_{x^2-y^2}$ ground state.

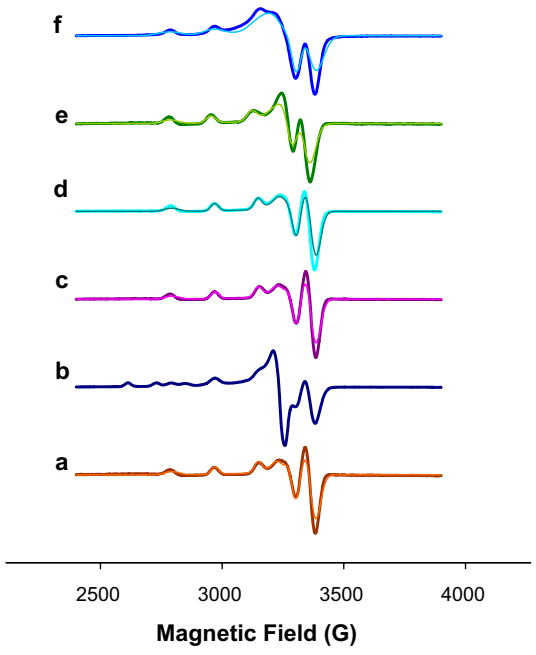


Fig. 7. X-band EPR spectra of copper complexes of **L2** and cyclen in $\approx 1.5\times10^{-3}$ mol dm^{-3} and 40% DMSO/H$_2$O solutions (strong lines) and the simulated spectra (smooth lines) at different pH values: (a) Cu^{2+}/Cyclen, pH 5, at 114.5 K; (b) Cu^{2+}/**L2**, pH 5, at 111.6 K; (c) Cu^{2+}/Cyclen, pH 8, at 105.9 K; (d) Cu^{2+}/**L2**, pH 8, at 112.2 K; (e) Cu^{2+}/Cyclen, pH 12, at 119.4 K and (f) Cu^{2+}/**L2**, pH 12, at 107.6 K. All spectra were recorded with microwave power of 2.0 mW, modulation amplitude of 1 mT, and frequency of 9.41 GHz.

The two species present, at pH 5, in the EPR spectrum of Cu^{2+}/**L2** are in about the same proportion, based on the intensity of the bands. The simulation of this spectrum could not be obtained and so is not presented. Nevertheless, the direct analysis of the spectrum and the estimated g_z and A_z parameters suggest that one species (species A) corresponds to the aqua-complex [Cu(H$_2$O)$_6$]$^{2+}$, and the other to the species found at pH 8 (species B).

The EPR parameters of the Cu^{2+}/**L2** and Cu^{2+}/cyclen complexes (at pH $\geqslant$ 5) are similar, pointing to identical coordination environments. The g_i and A_i values are related to the electronic transitions by the factors derived from the ligand field theory [39]: the g_i values increase and the A_i values decrease as the equatorial ligand field becomes weaker or the axial ligand field stronger and this occurs with the simultaneous red-shift of the d–d absorption bands in the electronic spectra [39,40].

Additionally the EPR data obtained in this work for the copper(II) complexes of **L2** and cyclen are quite different from those for Cu^{2+}/cyclam also collected in Table 8. In the latter complex the copper has a square planar geometry, with the equatorial plane formed by the four nitrogen atoms of the macrocycle and the metal centre included into the cavity [41]. Indeed, the 12-membered cavity of **L2** and cyclen is too small for the copper centre, and therefore the macrocycle take a folded arrangement with the metal out of the cavity. In the cyclen complex a water molecule or other solution ion completes a five-coordination geometry, while in the Cu^{2+}/**L2** the sulphur of the arm certainly do the same effect. A square-pyramidal geometry is expected for **L2** complexes since in the case of a trigonal-bipyramidal a $g_\perp > g_\parallel$ and a UV–Vis band in the region 800–850 nm would be observed [42]. Thus, considering the UV–Vis and the EPR data, a square pyramidal geometry

is expected for all the complexes studied in this work, and the small changes observed for Cu^{2+}/**L2** versus Cu^{2+}/cyclen can be most probably only assigned to distortions in the structure, promoted by a stronger coordination of the thiol group at higher pH.

4. Concluding remarks

A mono-N-substituted cyclen derivative with a 2-ethanethiol pendant arm, 2-[1,4,7,10-tetraazacyclododecan-1-yl]-ethanethiol (**L2**), has been successfully synthesized, being its thiol-protected precursor (**L1**) also characterized in solution and in the solid state. Compound **L2** was characterized by 2D NMR studies and its protonation constants were determined by potentiometry. An analysis of the protonation scheme of **L2** was discussed based on ^{13}C NMR titration. The stability constants of **L2** with Cu^{2+}, Zn^{2+} and Cd^{2+} were determined by potentiometry, and their values follow the usual trend found for cyclen derivatives: [Cu**L2**] > [Zn**L2**] ≈ [Cd**L2**]. At physiological pH, the pM values calculated for the metal complexes of **L2** have shown that this ligand is less selective for Cu^{2+} over Zn^{2+} and Cd^{2+}, compared to cyclen and cyclam. Spectroscopic data indicate that **L2** forms penta-coordinated complexes with Cu^{2+} and Zn^{2+}.

In summary, the introduction of a thiol pendant arm in the cyclen backbone has improved the affinity for Cu^{2+} but its selectivity has decreased. Radioactive studies with copper are underway to evaluate the possible use of this ligand for biological applications.

5. Supplementary material

CCDC 636011 contains the supplementary crystallographic data (excluding structure factors) for **L1**. These data can be obtained free of charge via http://www.ccdc.cam.ac.uk/conts/retrieving.html, or from the Cambridge Crystallographic Data Centre, 12 Union Road, Cambridge CB2 1EZ, UK; fax: (+44) 1223-336-033; or e-mail: deposit@ccdc.cam.ac.uk.

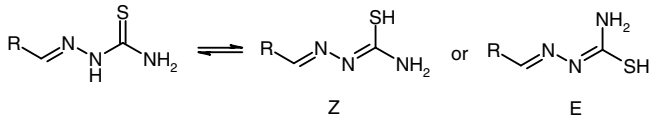
Acknowledgements

S. Lacerda thanks FCT for the Ph.D. Grant (SFRH/BD/19168/2004). S. Lacerda, M.P. Campello and I. Santos thank Prof. J. Ascenso for NMR discussions. The authors also thank Dr. J. Marçalo for MS measurements and S. Carvalho for the EPR measurements.

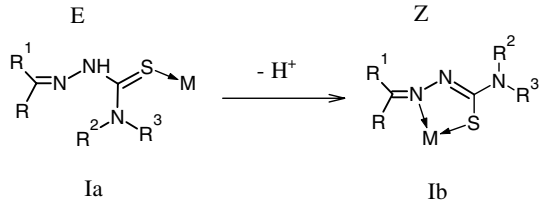
References

[1] (a) C.J. Anderson, in: M.J. Welch, C.S. Redvanly (Eds.), Handbook of Radiopharmaceuticals: Radiochemistry and Applications, Wiley, New York, 2003, pp. 401–422 (Chapter 12);
(b) C.J. Anderson, M.J. Welch, Chem. Rev. 99 (1999) 2219;
(c) P.J. Blower, J.S. Lewis, J. Zweit, Nucl. Med. Biol. 23 (1996) 957.
[2] (a) L.J. Ackerman, D.X. West, C.J. Mathias, M.A. Green, Nucl. Med. Biol. 26 (1999) 551, and references therein;
(b) J.S. Lewis, A. Srinivasan, M.A. Schmidt, C.J. Anderson, Nucl. Med. Biol. 26 (1999) 267;
(c) B.E. Rogers, H.M. Bigott, D.W. McCarthy, D.D. Manna, J. Kim, T.L. Sharp, M.J. Welch, Bioconj. Chem. 14 (2003) 756;
(d) X. Chen, R. Park, M. Tohme, A.H. Shahinian, J.R. Badind, P.S. Conti, Bioconj. Chem. 15 (2004) 41;
(e) X. Liang, P. Sadler, Chem. Soc. Rev. 33 (2004) 246.
[3] L.A. Bass, M. Wang, M.J. Welch, C.J. Anderson, Bioconj. Chem. 11 (2000) 527.
[4] A. Lewin, J.P. Hill, R. Boetzel, T. Georgiou, R. James, C. Kleanthous, G.R. Moore, Inorg. Chim. Acta 331 (2002) 123.
[5] (a) D. Tschudin, A. Basak, T.A. Kaden, Helv. Chim. Acta 71 (1988) 100;
(b) R. Ma, M.J. Welch, J. Reibenspies, A.E. Martell, Inorg. Chim. Acta 236 (1995) 75;
(c) R.P. Houser, J.A. Halfen, V.G. Young Jr., N.J. Blackburn, W.B. Tolman, J. Am. Chem. Soc. 117 (1995) 10745;
(d) T. Gyr, H.R. Mäcke, M. Herming, Angew. Chem., Int. Ed. Engl. 36 (1977) 24.
[6] (a) L. Maria, A. Paulo, I.C. Santos, I. Santos, P. Kurtz, B. Spingler, R. Alberto, J. Am. Chem. Soc. 128 (2006) 14590;
(b) R. Garcia, L. Gano, L. Maria, A. Paulo, I. Santos, H. Spies, J. Biol. Inorg. Chem. 11 (2006) 769;
(c) S. Alves, J.D.G. Correia, I. Santos, B. Veerendra, G.L. Sieckman, T.J. Hoffman, T. Rold, L. Retzloff, J. McCrate, A. Prasanphanich, C.J. Smith, J. Nucl. Med. Biol. 33 (2006) 625;
(d) F. Marques, L. Gano, M. Paula Campello, S. Lacerda, I. Santos, L.M.P. Lima, J. Costa, R. Delgado, J. Inorg. Biochem. 100 (2006) 270;
(e) S. Alves, J.D.G. Correia, A. Paulo, L. Gano, J. Smith, I. Santos, Bioconj. Chem. (2005) 438;
(f) C. Fernandes, S. Seifert, H. Spies, R. Syhre, R. Bergman, L. Gano, I. Santos, Bioconj. Chem. 16 (2005) 660;
(g) I. Santos, A. Paulo, J.D.G. Correia, Top. Curr. Chem. 252 (2005) 45, Contrast Agents III: Radiopharmaceuticals–From Diagnostics to Therapeutics, Springer, Berlin, Heidelberg 2005.
[7] S. Meegalla, K. Plössl, M.-P. Kung, S. Chumpradit, D.A. Stevenson, D. Frederick, H.F. Kung, Bioconj. Chem. 7 (1996) 421.
[8] G.M. Sheldrick, SADABS, Bruker AXS Inc., Madison, WI, USA, 2004.
[9] Bruker, SMART and SAINT, Bruker AXS Inc., Madison, WI, USA, 2004.
[10] A. Altomare, M.C. Burla, M. Camalli, G. Cascarano, G. Giacovazzo, A. Guagliardi, A.G.G. Moliterni, G. Polidori, R. Spagna, J. Appl. Cryst. 32 (1999) 115.
[11] G.M. Sheldrick, SHELXL97, Program for Crystal Structure Refinement, University of Göttingen, Germany, 1997.
[12] L.J. Ferrugia, J. Appl. Cryst. 32 (1999) 837.
[13] L.J. Ferrugia, J. Appl. Cryst. 30 (1997) 565.
[14] G. Shwardzenbach, W. Flaschka, Complexometric Titrations, Methuen & Co, London, 1969.
[15] G. Shwardzenbach, W. Biedermann, Helv. Chim. Acta 31 (1948) 331.
[16] (a) P. Antunes, P.M. Campello, R. Delgado, M.G.B. Drew, V. Félix, I. Santos, J. Chem. Soc., Dalton Trans. (2003) 1852;
(b) K.P. Guerra, R. Delgado, L.M.P. Lima, M.G.B. Drew, V. Félix, J. Chem. Soc., Dalton Trans. (2004) 1812;
(c) F. Marques, K.P. Guerra, L. Gano, J. Costa, M.P. Campello, L.M.P. Lima, R. Delgado, I. Santos, J. Biol. Inorg. Chem. 9 (2004) 859.
[17] (a) J. Costa, R. Delgado, M.G.B. Drew, V. Félix, A. Saint-Maurice, J. Chem. Soc., Dalton Trans. 12 (2000) 1907;
(b) J. Costa, R. Delgado, M.G.B. Drew, V. Félix, R.T. Henriques, J.C. Waerenborgh, J. Chem. Soc., Dalton Trans. 18 (1999) 3253.
[18] P. Gans, A. Sabatini, A. Vacca, Talanta 43 (1996) 1739.
[19] NIST Standard Reference Database 46, NIST Critically Selected Stability Constants of Metal Complexes Database, Version 5.0, Data collected and selected by R.M. Smith and A.E. Martell, US Department of Commerce, National Institute of Standards and Technology, 1998.

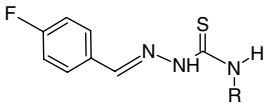
[20] A.K. Covington, M. Paabo, R.A. Robison, R.G. Bates, Anal. Chem. 40 (1968) 700.
[21] T.J. Lotz, T.A. Kaden, J. Chem. Soc., Chem. Commun. (1977) 15.
[22] T.J. Lotz, T.A. Kaden, Helv. Chim. Acta 61 (1978) 1376.
[23] N.W. Alcock, H.A. Omar, P. Moore, C. Pierpoint, J. Chem. Soc., Dalton Trans. (1985) 219.
[24] Z. Kovacs, D. Sherry, Synthesis (1996) 759.
[25] (a) K. Malesse, A. Loos, Liebigs Ann. (1996) 935;
(b) M. Woods, G.E. Kiefer, S. Bott, A. Castillo-Muzquiz, C. Eshelbrenner, L. Michaudet, K. McMillan, S.D.K. Mudigunda, D. Ogrin, G. Tircsó, S. Zang, P. Zhao, D. Sherry, J. Am. Chem. Soc. 126 (2004) 9248;
(c) G. Hervé, H. Bernard, N. Le Bris, M. Le Baccon, J.-J. Yaouanc, H. Handel, Tetrahedron Lett. 41 (1999) 2571;
(d) J. Rohovec, R. Gyepes, I. Císařová, J. Rudovský, I. Lukeš, Tetrahedron Lett. 41 (2000) 1249.
[26] M. Studer, T.A. Kaden, Helv. Chim. Acta 69 (1986) 2081.
[27] P.J. Davies, K.P. Wainwright, Inorg. Chim. Acta 294 (1999) 103.
[28] (a) W. Clegg, P.B. Iveson, J.C. Lockhart, J. Chem. Soc., Dalton Trans. (1992) 3291, and references therein;
(b) E. Kimura, H. Kitamura, T. Koike, M. Shiro, J. Am. Chem. Soc. 119 (1997) 10909;
(c) C. Bazzicalupi, A. Bencini, E. Berni, A. Bianchi, S. Ciattini, C. Giorgi, S. Maoggi, P. Paoletti, B. Valtancoli, J. Org. Chem. 67 (2002) 9107.
[29] (a) A.P. Leugger, L. Hertli, T.A. Kaden, Helv. Chim. Acta 61 (1978) 2296;
(b) M. Kodama, E. Kimura, J. Chem. Soc., Dalton Trans. (1980) 327;
(c) T. Koike, S. Kajitani, I. Nakamura, E. Kimura, J. Am. Chem. Soc. 117 (1995) 1210.
[30] C. Frassineti, L. Alderighi, P. Gans, A. Sabatini, A. Vacca, S. Ghelli, Anal. Bioanal. Chem. 376 (2003) 1041.
[31] R. Delgado, J.J.R.F. Da Silva, M.T.S. Amorim, M.F. Cabral, S. Chaves, J. Costa, Anal. Chim. Acta 245 (1991) 271.
[32] (a) Ryszard Nazarski, Magn. Reson. Chem. 41 (2003) 70, and references cited therein;
(b) R. Clay, S. Corr, M. Micheloni, P. Paoletti, Inorg. Chem. 24 (1985) 3330;
(c) A. Bianchi, B. Escuder, E. Garcia-España, S.V. Luis, V. Marcelino, J.F. Miravet, J.A. Ramírez, J. Chem. Soc., Perkin Trans. 2 (1994) 1253;
(d) C.N. Reilley, Anal. Chem. 47 (1975) 2116;
(e) M. Ciampolini, M. Micheloni, N. Nardi, P. Paoletti, P. Dapporto, F. Zanobini, J. Chem. Soc., Dalton Trans. (1984) 1357.
[33] V.J. Thöm, G.D. Hosken, R.D. Hancock, Inorg. Chem. 24 (1985) 3378.
[34] (a) M. Kodama, E. Kimura, J. Chem. Soc., Dalton Trans. 116 (1976) 1720;
(b) M. Kodama, E. Kimura, J. Chem. Soc., Dalton Trans. (1977) 1473;
(c) M. Micheloni, A. Sabatini, P. Paoletti, J. Chem. Soc., Perkin Trans. 2 (1978) 828.
[35] L. Alderighi, P. Gans, A. Ienco, D. Peters, A. Sabatini, A. Vacca, Coord. Chem. Rev. 184 (1999) 311.
[36] K. Miyoshi, H. Tanaka, E. Kimura, S. Tsuboyama, S. Murata, H. Shimizu, K. Ishizu, Inorg. Chim. Acta 78 (1983) 23.
[37] F. Neese, Diploma Thesis, University of Konstanz, Germany, 1993.
[38] E.I. Solomon, K.W. Penfield, D.E. Wilcox, Struct. Bonding 53 (1983) 1.
[39] (a) A.W. Addison, M. Carpenter, L.K.-M. Lau, M. Wicholas, Inorg. Chem. 17 (1978) 1545;
(b) M.J. Maroney, N.J. Rose, Inorg. Chem. 23 (1984) 2252.
[40] P.W. Lau, W.C. Lin, J. Inorg. Nucl. Chem. 37 (1975) 2389.
[41] (a) P.A. Tasker, L. Sklar, J. Cryst. Mol. Struct. 5 (1975) 329;
(b) J.C.A. Boeyens, S.M. Dobson, in: Ivan Bernal (Ed.), Stereochemical and Stereophysical Behaviour of Macrocycles, vol. 2, Elsevier, Amsterdam, 1987, pp. 1–102.
[42] M.C. Styka, R.C. Smierciak, E.L. Blinn, R.E. DeSimone, J.V. Passariello, Inorg. Chem. 17 (1978) 82.



Scheme 1. Thione/thiol equilibrium and conventional nomenclature for the two thiolic forms.



Scheme 2. R^1, R^2 and R^3 can be either H or organic radicals.



Scheme 3. Chemical drawing of Hfbt ligand (R = H) and Me-Hfbt ligand ($R = CH_3$).

electronic configuration Cu(I) ions do not have an energetically preferred geometry and their coordination is therefore mainly governed by steric repulsions. Aside from the two donor species P and S the remaining space around the copper ion is usually occupied by a fourth ligand, usually a halide. In our experiments we have decided to verify if the absence of other soft species can influence the coordination and in particular if in these conditions the imino nitrogen becomes a suitable donor for coordination. In this paper, the complexes of 4-fluorobenzaldehyde thiosemicarbazones (Hfbt and Me-Hfbt, Scheme 2) with Cu(I) nitrate, sulphate and acetate in the presence of triphenylphosphine (Ph_3P) are reported. The choice of these oxoanions was envisaged to stabilize the ligand in the *Z* conformation thank to their capability to form concerted hydrogen bonds while the *N*-methylated derivative was used for comparison to verify if the terminal amino hydrogen, not involved in the aforementioned hydrogen bonds, can influence the crystal packing. All of these compounds have been characterized by elemental analysis, IR, ^{1}H NMR spectroscopy and compounds **1**, **5** and **6** also by X-ray crystallography Scheme 3.

2. Experimental

2.1. Materials and techniques

$[Cu(PPh_3)_2NO_3]$, $[Cu_2(PPh_3)_4SO_4]$ and $[Cu(PPh_3)_2(CH_3COO)]$ were prepared by reduction of the corresponding Cu(II) salt using a fourfold excess of PPh_3 in CH_3OH at reflux temperature for 1, 2 and 3 h, respectively. The white powder formed in the reaction flask was filtered to separate the product from Ph_3PO and washed first with EtOH and then with diethyl ether. $Cu(NO_3)_2 \cdot 3H_2O$, $CuSO_4 \cdot 5H_2O$, $Cu(CH_3CCO)_2 \cdot H_2O$ were procured from Carlo Erba while PPh_3 was purchased from Aldrich. C, H, N, S analyses were obtained with a Carbo-Erba 1108 instrument. IR spectra were recorded using KBr pellets on a Nicolet 5PC FTIR spectrophotometer in the 4000–400 cm^{-1} range. ^{1}H NMR spectra were recorded on a Bruker AC300 spectrometer at 300 MHz in DMSO with TMS as the internal reference.

2.2. Preparation of the ligands and of their complexes

4-Fluorobenzaldehyde thiosemicarbazone was prepared by condensation of 4-fluorobenzaldehyde with thiosemicarbazide or N^1-methylthiosemicarbazide in a 1:1 molar ratio in ethanol using the procedure reported in the literature [18].

2.2.1. Synthesis of $[Cu(PPh_3)_2(Hfbt)]NO_3$ (1)

To a stirred solution of $[Cu(PPh_3)_2NO_3]$ (1.650 g, 2.54 mmol) in methanol (30 mL) was added an equimolar amount of the ligand (0.502 g, 2.54 mmol) dissolved in methanol (30 mL). The contents were stirred for 2 h at room temperature. The clear solution was allowed to evaporate at room temperature and a yellow colored crystalline product was formed. The isolated powder was recrystallized from EtOH 95% and crystals apt for X-ray diffraction were obtained (yield: 1.400 g, 65%; m.p.: 184 °C). The complex is soluble in DMSO, $CHCl_3$ and CH_2Cl_2. *Anal.* Calc. for $C_{44}H_{38}CuFN_4O_3P_2S$: C, 62.37; H, 4.52; N, 6.61; S, 3.78. Found: C, 62.45; H, 4.17; N, 6.64; S, 3.81%. Main IR peaks (KBr, cm^{-1}): $\nu_{as}(NH_2)$ 3442 m; $\nu_s(NH_2)$ 3118 m; ν(N–H) 3284 w, $\nu(C–H_{aromatic})$ 3054 w, $\nu(C–C_{aromatic})$ 1627 s, 1506 s and 1480 s; ν(C=N) 1602 s; ν(C–P) 1433 vs; $\nu(NO_3)$ 1384 vs and 1293 s; ν(C–F) 1234 s; $\delta(C–H_{aromatic})$ 1156 m and 1093 m; ν(C=S) 827 m; $\gamma(C–H_{aromatic})$ 745 vs and 695 vs. ^{1}H NMR data (δ, ppm; DMSO-d_6): 7.25 (t, b, 8H, overlapped ligand H_m and PPh_3H_p); 7.37 (t, 12H, PPh_3H_m); 7.87 (dd, 2H, ligand H_o); 7.99 (s, 1H, C*H*=N); 8.29 and 8.39 (2 s, 1H each, NH_2); 11.61 (s, 1H, C(S)N*H*).

2.2.2. Synthesis of $[Cu(PPh_3)_2(Hfbt)]_2SO_4 \cdot CH_3OH$ (2)

To a stirred solution of $[Cu_2(PPh_3)_4SO_4]$ (0.662 g, 0.52 mmol) in methanol (20 mL) was added a twofold molar amount of the ligand (0.205 g, 1.04 mmol) dissolved in methanol (20 mL). The contents were stirred for 2 h at room temperature. A yellow powder was formed and the product was filtered (yield: 0.600 g, 68%; m.p.: 132 °C). The complex is soluble in DMSO, $CHCl_3$ and CH_2Cl_2. *Anal.* Calc. for $C_{89}H_{80}Cu_2F_2N_6O_5P_4S_3$: C, 62.93; H, 4.75; N, 4.95; S, 5.66. Found: C, 62.51; H, 4.49; N, 4.83; S, 5.50%. Main IR peaks (KBr, cm^{-1}): $\nu_{as}(NH_2)$ 3377 s; $\nu_s(NH_2)$ 3143 m; ν(N–H) 3289 m, $\nu(C–H_{aromatic})$ 3052 m, $\nu(C–C_{aromatic})$ and overlapped ν(C=N) 1602 vs, $\nu(C–C_{aromatic})$

1507 vs and 1480 s; ν(C–P) 1434 vs; ν(C–F) 1234 s; δ(C–$H_{aromatic}$) 1155 s and 1094 s; $\nu(SO_4)$ 1121 s; ν(C=S) 833 m; γ(C–$H_{aromatic}$) 745 vs and 696 vs. ^{1}H NMR data (δ, ppm; DMSO-d_6): 7.24 (t, b, 8H, overlapped ligand H_m and PPh_3H_p); 7.36 (t, 12H, PPh_3H_m); 7.45 (t, 12H, PPh_3H_o); 7.86 (bs, 2H, ligand H_o); 7.99 (s, 1H, C*H*=N); 8.29 and 8.39 (2s, 1H each, NH_2); 11.58 (s, 1H, C(S)N*H*).

2.2.3. Synthesis of $[Cu(PPh_3)_2(Hfbt)]CH_3COO$ (3)

To a stirred solution of $[Cu(PPh_3)_2(CH_3COO)]$ (0.672 g, 1.04 mmol) in methanol (25 mL) was added an equimolar amount of the ligand (0.205 g, 1.04 mmol) dissolved in methanol (25 mL). The contents were stirred for 2 h at room temperature. The clear solution was allowed to evaporate and a yellow product was afforded (yield: 0.650 g, 76%; dec.: 178 °C). The complex is soluble in DMSO, $CHCl_3$ and CH_2Cl_2. *Anal.* Calc. for $C_{46}H_{41}CuFN_3O_2P_2S$: C, 65.43; H, 4.89; N, 4.98; S, 3.80. Found: C, 65.84; H, 4.78; N, 5.01; S, 3.69%. Main IR peaks (KBr, cm^{-1}): $\nu(NH_2)$ 3481 m, 3382 m, 3141 w; ν(NH) 3293 m, 3238 w; ν(C–$H_{aromatic}$) 3052 m; ν_{as}(COO) 1580 s; ν(C–$C_{aromatic}$) 1596 s and 1478 s; ν(C–P) 1434 vs; ν(C–F) 1229 s; δ(C–$H_{aromatic}$) 1156 m and 1094 m; ν(C=S) 834 m; γ(C–$H_{aromatic}$) 746 vs and 696 vs. ^{1}H NMR data (δ, ppm; DMSO-d_6): 2.10 (bs, 3H, CH_3COO); 7.26 (t, b, 8H, overlapped ligand H_m and PPh_3H_p); 7.40 (t, 12H, PPh_3H_m); 7.52 (t, 12H PPh_3H_o); 7.95 (dd, 2 H, ligand H_o); 8.06 (s, 1H, C*H*=N); 8.30 and 8.41 (2s, 1H each, NH_2); 11.54 (s, 1H, C(S)N*H*).

2.2.4. Synthesis of $[Cu(PPh_3)_2(Me\text{-}Hfbt)]NO_3 \cdot CH_3OH$ (4)

To a stirred solution of $[Cu(PPh_3)_2NO_3]$ (1.134 g, 1.75 mmol) in methanol (25 mL) was added an equimolar amount of the ligand (0.368 g, 1.74 mmol) dissolved in methanol (20 mL). The contents were stirred for 2 h at room temperature. The clear solution was allowed to evaporate at room temperature and a yellow colored powder was obtained (yield: 1.078 g, 69%; m.p.: 100 °C). The complex is soluble in DMSO, $CHCl_3$ and CH_2Cl_2. *Anal.* Calc. for $C_{46}H_{44}CuFN_4O_4P_2S$: C, 61.84; H, 4.96; N, 6.27; S, 3.59. Found: C, 61.72; H, 4.65; N, 6.31; S, 3.53%. Main IR peaks (KBr, cm^{-1}): ν(N–H) 3382 m, 3239 m, ν(C–$H_{aromatic}$) 3052 w; ν(C–$H_{aliphatic}$) 2998 m; ν(C–$C_{aromatic}$) 1601 s, 1507 s and 1480 s; ν(C=N) 1566 s; ν(C–P) 1434 vs; $\nu(NO_3)$ 1384 vs and 1292 s; ν(C–F) 1234 s; δ(C–$H_{aromatic}$) 1156 m and 1093 m; ν(C=S) 834 w; γ(C–$H_{aromatic}$) 746 vs and 696 vs. ^{1}H NMR data (δ, ppm; DMSO-d_6): 2.99 (d, 3H, NCH_3); 7.24 (t, b, 8H, overlapped ligand H_m and PPh_3 H_p); 7.37 (t, 12H, PPh_3H_m); 7.47 (t, 12H PPh_3H_o); 7.86 (dd, 2H, ligand H_o); 7.99 (s, 1H, C*H*=N); 8.56 (s, 1H, N*H*CH_3); 11.44 (s, 1H, C(S)N*H*).

2.2.5. Synthesis of $[Cu(PPh_3)_2(Me\text{-}Hfbt)]_2SO_4$ (5)

To a stirred solution of $[Cu_2(PPh_3)_4SO_4]$, (0.631 g, 0.50 mmol) in methanol (35 mL) was added a twofold molar amount of the ligand (0.209 g, 1.00 mmol) dissolved in methanol (15 mL). The contents were stirred for 2 h at room temperature. The clear solution was allowed to evaporate at room temperature and a yellow colored crystalline product was formed. The isolated powder was dissolved in warm EtOH 95% and crystals apt for X-ray diffraction were obtained (yield: 1.050 g, 62%; m.p.: 143 °C). The complex is soluble in DMSO, $CHCl_3$ and CH_2Cl_2. *Anal.* Calc. for $C_{90}H_{80}Cu_2F_2N_6O_4P_4S_3$: C, 63.78; H, 4.76; N, 4.96; S, 5.68. Found: C, 63.55; H, 4.68; N, 4.91; S, 5.51%. Main IR peaks (KBr, cm^{-1}): ν(NH) 3446 w, 3378 w, 3226 w; ν(C–$H_{aromatic}$) 3051 m; ν(C–$H_{aliphatic}$) 2934 m; ν(C–$C_{aromatic}$) 1602 s, 1508 vs and 1480 s; ν(C=N) 1567 m; ν(C–P) 1435 vs; ν(C–N) 1329 m; ν(C–F) 1233 s; δ(C–$H_{aromatic}$) 1156 m and 1093 m; $\nu(SO_4)$ 1118 s; ν(C=S) 831 m; γ(C–$H_{aromatic}$) 746 vs and 697 vs. ^{1}H NMR data (δ, ppm; DMSO-d_6): 2.08 (s, 3H, NCH_3); 7.25 (t, b, 8H, overlapped ligand H_m and PPh_3 H_p); 7.37 (t, 12H, PPh_3H_m); 7.44 (t, 12H PPh_3H_o); 7.86 (dd, 2H, ligand H_o); 8.00 (s, 1H, C*H*=N); 8.27 (s, 1H, N*H*CH_3); 11.54 (s, 1H, C(S)N*H*).

2.2.6. Synthesis of $\{[Cu(PPh_3)_2(Me\text{-}Hfbt)]CH_3COO\}_2 \cdot 2EtOH \cdot H_2O$ (6)

To a stirred solution of $[Cu(PPh_3)_2(CH_3COO)]$ (0.619 g, 0.96 mmol) in ethanol 95% (25 mL) was added an equimolar amount of the ligand (0.202 g, 0.96 mmol) dissolved in ethanol (15 mL). The contents were stirred for 2 h at reflux temperature. The clear solution was allowed to evaporate at room temperature and yellow-brown crystals suitable for X-ray diffraction were afforded (yield: 1.280 g, 74%; m.p.: 144 °C). The complex is soluble in DMSO, $CHCl_3$ and CH_2Cl_2. *Anal.* Calc. for $C_{98}H_{100}Cu_2F_2N_6O_7P_4S_2$: C, 64.42; H, 5.52; N, 4.60; S, 3.51. Found: C, 64.45; H, 5.55; N, 4.62; S, 3.53%. Main IR peaks (KBr, cm^{-1}): ν(NH) 3378 w, 3238 w; ν(C–$H_{aromatic}$) 3053 m; ν(C–$H_{aliphatic}$) 2970 m; ν_{as}(COO) 1619 vs; ν_s(COO) 1396 s; ν(C–$C_{aromatic}$) 1599 vs, 1507 vs and 1480 vs; ν(C–P) 1434 vs; ν(C–F) 1232 s; δ(C–$H_{aromatic}$) 1156 m and 1093 m; ν(C=S) 832 m; γ(C–$H_{aromatic}$) 746 vs and 697 vs. ^{1}H NMR data (δ, ppm; DMSO-d_6): 1.18 (t, 3H, CH_3CH_2OH), 2.10 (bs, 6H, NCH_3 + CH_3COO); 3.72 (q, 2H, CH$_3$CH_2OH), 7.28 (t, b, 8H, overlapped ligand H_m and PPh_3 H_p); 7.39 (t, 12H, PPh_3H_m); 7.48 (t, 12H PPh_3H_o); 7.91 (dd, 2H, ligand H_o); 8.04 (s, 1H, C*H*=N); 8.34 (s, 1H, N*H*CH_3); 11.58 (s, 1H, C(S)N*H*).

2.3. Crystallography

Relevant data concerning data collection and details of structure refinement are summarized in Table 1. Intensity data were collected on a Philips PW1100 (compounds **1** and **6**) and on a SMART 1000 Bruker AXS diffractometer (compound **5**) with Mo Kα radiation. Data from crystals of compounds **1** and **6** collected on the Philips diffractometer were non corrected for absorption while for compound **5** an absorption correction was carried out using the SADABS [19] procedure. The WINGX [20] package was used all through the refinement and completion of the structure. The structures were solved using direct methods (SIR-97 [21]). Refinements were carried out by full matrix least-

Table 1
Experimental data for crystallographic analyses

Compound	1	2	3
Chemical formula	$C_{44}H_{38}CuFN_4O_3P_2S$	$C_{90}H_{80}Cu_2F_2N_6O_4P_4S_3$	$C_{98}H_{100}Cu_2F_2N_6O_7P_4S_2$
Formula weight	847.32	1694.74	1827.01
Space group (no.)	$P\bar{1}(2)$	$P2_1/c(14)$	$P\bar{1}(2)$
a (Å)	13.490(3)	18.117(3)	14.168(1)
b (Å)	14.064(3)	18.336(3)	17.550(1)
c (Å)	11.318(3)	25.211(4)	20.231(1)
α (°)	94.36(2)	90.0	108.638(1)
β (°)	106.47(3)	91.830(3)	94.385(1)
γ (°)	96.37(2)	90.0	90.019(1)
V (Å^3)	2033.4(9)	8371(2)	4751.0(5)
Z	2	4	2
$F(000)$	876	3512	1908
T (K)	298.15	298.15	298.15
D_{calc} (Mg/m^3)	1.384	1.345	1.277
μ (cm^{-1})	7.17	7.18	6.19
λ (Å)	0.71069	0.71069	0.71069
R	0.056	0.0548	0.0486
Rw_2	0.1021	0.1184	0.0992

$R = \sum\|F_o\| - F_c\|/\sum|F_o|$.
$Rw_2 = \left\{\sum[w(F_o^2 - F_c^2)^2]/\sum[w(F_o^2)^2]\right\}^{1/2}$.

squares cycles SHELXL97 [22] for all compounds. The hydrogen atoms were calculated with standard geometry and refined in riding position. Atomic scattering factors were taken from the International Tables for Crystallography [23]. The program PARST [24] was employed for the geometrical description and ORTEP [25] and MERCURY [26] for the drawings.

3. Results and discussion

3.1. Synthesis and spectroscopy

Compounds (**1**), (**5**) and (**6**) afforded crystals suitable for X-ray diffraction studies and structural data allow for a correlation between structures and spectroscopic data. As for complexes obtained from NO_3^- is concerned, the IR spectral behaviour of (**1**) and (**4**) is very similar in all the observed range. This allows to suppose that the Me-Hfbt ligand of complex (**4**) is in the same environment of complex (**1**). It is useful to note that the same differences found between complex (**1**) and its free ligand are also found between (**4**) and its free ligand. The IR absorptions of the C=S groups are shifted at lower frequencies with respect to the free ligand (827 cm^{-1} for (**1**) versus 836 cm^{-1} and 834 cm^{-1} for (**4**) versus 837) indicating the weakening of the C=S bond after coordination. Changes in the spectral ranges between 1500 and 1600 cm^{-1} (νC=N) and between 1130 and 1340 cm^{-1} (NC(=S)N absorptions) indicate the C=N involvement in coordination. It can also be generally observed a broadening of the ν(NH) absorptions, showing a different behaviour of the hydrogen bonding network in the complexes with respect to the free ligands. This can be due to the fact that also in the free ligands at the solid state N–H bonds are involved in strong hydrogen bonds. For this reason it is not always observed in the IR spectra of complexes a shift to lower frequencies with respect to the free ligand. The absorption at *ca.* 1394 and 1293 cm^{-1} are assigned to the absorptions of the non coordinated inorganic ligand. NMR data suggest that also in solution ligands are in their neutral form as can be observed from the presence at 11.61 ppm for (**1**) and 11.44 ppm for (**4**). With respect of NMR data of the free ligands, a slight shift to low field of N–H protons is observed (up to 0.20 ppm).

Similar considerations can be also drawn for complexes (**2**) and (**5**) obtained from SO_4^{2-} and (**3**) and (**6**) from CH_3COO^- anions. In particular for (**2**) and (**5**) can be observed the presence at 1120 cm^{-1} strong absorption of ionic SO_4^{2-}. The IR spectra of complexes (**3**) and (**6**) result more complicated because of the presence of CH_3COO^- asymmetric and symmetric stretchings.

In this way for all complexes a tetrahedral coordination by means of S,N, P, P can be assumed.

3.2. Crystal structures of the complexes

The syntheses allowed to isolate in crystalline form complexes (**1**), (**5**) and (**6**) and in order to establish their structural features, single crystal X-ray crystallography experiments were carried out (Table 2).

In Fig. 1 is reported the ORTEP view of complex $Cu(PPh_3)_2(Hfbt)]NO_3$ (**1**). The structure can be described as formed by a cationic complex molecule with a nitrate as a counterion and the copper(I) ion coordinates two triphenylphosphines and a parafluorobenzaldehyde thiosemicarbazone molecule in its neutral form. The thiosemicarbazone binds to the metal through the sulfur and the iminic nitrogen and forms a five-term chelation ring with an angle N–Cu–S of 85.13(5)°. The P–Cu–P angle is rather

Table 2
Selected bond distances (Å) and angles (°) for compounds **1**, **5** and **6**

	1	**5**		**6**	
Cu(1)–P(1)	2.3056(7)	2.273(2)	2.261(2)	2.294(1)	2.284(1)
Cu(1)–P(2)	2.2521(7)	2.295(2)	2.286(2)	2.293(1)	2.260(1)
Cu(1)–S(1)	2.3482(8)	2.354(2)	2.337(3)	2.337(1)	2.338(1)
Cu(1)–N(3)	2.136(2)	2.164(6)	2.117(8)	2.162(4)	2.171(4)
N(2)–N(3)	1.380(2)	1.387(8)	1.350(9)	1.386(5)	1.376(5)
C(1)–N(1)	1.327(3)	1.338(9)	1.331(10)	1.330(6)	1.329(5)
C(1)–N(2)	1.337(3)	1.341(9)	1.331(12)	1.349(6)	1.345(5)
C(1)–S(1)	1.693(2)	1.685(8)	1.709(9)	1.688(5)	1.689(4)
C(2)–N(3)	1.286(2)	1.290(9)	1.323(10)	1.282(5)	1.293(5)
C(2)–C(3)	1.454(3)	1.457(11)	1.425(12)	1.462(6)	1.453(7)
C(3)–C(8)	1.381(3)	1.374(11)	1.363(13)	1.385(6)	1.372(7)
C(3)–C(4)	1.380(3)	1.352(11)	1.425(13)	1.388(6)	1.395(7)
C(4)–C(5)	1.374(3)	1.374(12)	1.419(14)	1.376(7)	1.374(9)
C(5)–C(6)	1.356(3)	1.318(13)	1.355(15)	1.362(7)	1.345(10)
C(6)–F(1)	1.352(3)	1.382(10)	1.370(13)	1.362(6)	1.359(7)
C(6)–C(7)	1.357(4)	1.336(13)	1.324(17)	1.363(7)	1.363(9)
C(7)–C(8)	1.375(4)	1.385(12)	1.380(16)	1.380(6)	1.374(7)
C(9)–N(1)		1.440(10)	1.444(11)	1.441(6)	1.444(6)
N(3)–Cu(1)–P(2)	125.07(5)	102.6(2)	114.8(2)	113.9(1)	122.8(1)
N(3)–Cu(1)–P(1)	99.64(5)	114.9(2)	108.1(2)	116.3(1)	104.1(1)
P(2)–Cu(1)–P(1)	126.83(3)	135.39(8)	128.52(9)	121.20(5)	123.15(5)
N(3)–Cu(1)–S(1)	85.13(5)	83.9(2)	85.8(2)	84.8(1)	83.8(1)
P(2)–Cu(1)–S(1)	110.68(3)	104.65(8)	107.46(9)	108.15(5)	106.55(5)
P(1)–Cu(1)–S(1)	99.21(3)	102.69(8)	102.65(9)	104.93(5)	108.88(5)
C(1)–N(1)–C(9)		122.3(7)	123.5(9)	124.7(5)	124.3(4)
C(1)–N(2)–N(3)	122.8(2)	121.1(6)	123.1(8)	122.7(4)	123.0(4)
C(2)–N(3)–N(2)	112.9(2)	113.7(6)	113.0(8)	113.8(4)	114.1(4)
C(2)–N(3)–Cu(1)	133.5(1)	132.8(5)	134.3(6)	134.4(3)	131.4(3)
N(2)–N(3)–Cu(1)	111.6(1)	112.9(5)	112.6(6)	111.8(3)	111.4(3)
N(1)–C(1)–N(2)	115.1(2)	113.1(7)	116.0(9)	114.4(4)	115.0(4)
N(1)–C(1)–S(1)	121.1(2)	123.1(7)	120.8(8)	122.4(4)	122.7(4)
N(2)–C(1)–S(1)	123.7(2)	123.7(6)	123.2(7)	123.1(4)	122.3(4)
N(3)–C(2)–C(3)	125.4(2)	122.4(8)	124.5(9)	126.1(4)	124.8(5)
C(8)–C(3)–C(4)	117.7(2)	117.5(8)	116.9(10)	118.0(5)	118.4(5)
C(8)–C(3)–C(2)	117.7(2)	119.9(8)	116.2(11)	123.9(4)	123.8(5)
C(4)–C(3)–C(2)	124.6(2)	122.6(8)	126.6(10)	118.1(4)	117.8(5)
C(5)–C(4)–C(3)	121.8(2)	122.3(9)	121.8(10)	121.1(5)	119.9(6)
C(6)–C(5)–C(4)	118.3(2)	118.1(10)	116.8(12)	118.8(5)	119.5(6)
F(1)–C(6)–C(5)	119.1(2)	119.0(11)	115.7(13)	119.4(5)	119.1(7)
F(1)–C(6)–C(7)	118.6(2)	117.7(10)	119.6(13)	118.2(5)	118.3(8)
C(5)–C(6)–C(7)	122.2(2)	123.2(9)	124.6(13)	122.4(5)	122.6(6)
C(6)–C(7)–C(8)	118.9(3)	118.5(9)	118.7(13)	118.4(5)	118.0(6)
C(7)–C(8)–C(3)	121.0(3)	120.3(9)	121.0(12)	121.4(5)	121.6(5)

wide (125.07(5)°) and the copper tetrahedral coordination is therefore strongly distorted. The coordination bonds have distances that range from 2.136(2) Å for the Cu1–N3 bond to 2.3482(8) Å for the Cu1–S1 bond. The nitrate ion forms a strong charge assisted H-bonding with the thiosemicarbazone NH groups through two of its oxygens (see Table 3). The thiosemicarbazone moiety, that should be expected to be planar because of the extended conjugated system of double bonds, is significantly distorted: the angle between the average plane of the 4-fluorobenzaldehyde ring and that of the thiosemicarbazide moiety is 23.63(7)°. This distortion can be interpreted as a double interaction of the fluorophenyl moiety with two phenyls belonging to two different triphenylphosphines.

The main feature that characterizes the packing of these molecules is a so-called sixfold phenyl embrace (6PE) [27a,27b,27c,27d] (P1...P1^{I} $I = (1 - x, -y, -z)$ distance 6.979 Å) (see Fig. 2) between two centrosymmetrically related molecules. The phenyls of the triphenylphosphines involved in this interaction present what the aforementioned paper calls a "good rotor" conformation with torsion angles (defined by the copper, the phosphorus, the ipso carbon and the next carbon atom of the phenyl group which gives the torsion angle in the range 90°, −90°) of 43.53°, 45.69° and 49.21° while the other triphenylphosphine has a more irregular conformation (torsion angles of 23.90°, 37.31°, 78.23°) due to an edge-to-face interaction between the fluorobenzene group with a tpp phenyl group.

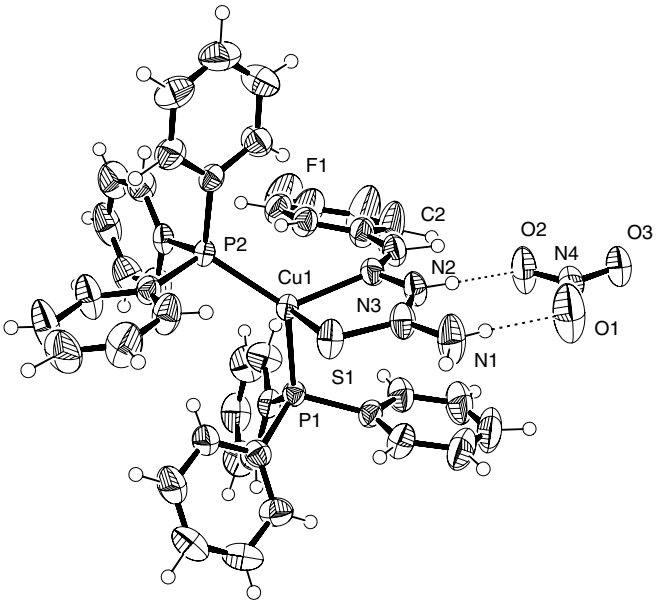


Fig. 1. ORTEP drawing of complex $Cu(PPh_3)_2(Hfbt)]NO_3$ (**1**) showing thermal ellipsoids at the 50% probability level.

Table 3
Relevant hydrogen bonds (Å, °) found in molecule **1**, **5** and **6**

Compound **1**	N1…O1(nitrate)	2.906(3)	N1–H…O1	178(3)
	N2…O2(nitrate)	2.717(2)	N2–H…O2	166(3)
Compound **5**	N1…O4(sulfate)	2.751(9)	N1–H…O4	135.5(5)
	N2…O3(sulfate)	2.740(9)	N2–H…O3	156.4(5)
	N4…O2(sulfate)	2.757(10)	N4–H…O2	153.4(5)
	N5…O1(sulfate)	2.902(10)	N5–H…O1	170.2(5)
Compound **6**	N1…O2(acetate 1)	2.701(7)	N1–H…O2	168.6(3)
	N2…O1(acetate 1)	2.746(6)	N2–H…O1	160.1(3)
	N4…O4(acetate 2)	2.805(6)	N4–H…O4	165.4(3)
	N5…O3(acetate 2)	2.720(6)	N5–H…O3	168.6(3)
	O5(ethanol)…O1 (acetate)	2.645(6)	O5–H…O1	145.4(4)
	O6(ethanol)…O4 (acetate)	2.792(9)	O6–H…O4	154.6(6)

To complete the description of the packing it is noteworthy to observe the presence of two longer P…P distances due to the presence of two pairs of phenyls belonging to two centrosymmetrically related molecules that interact edge-to-face (see Fig. 2). The other N terminal hydrogen atom seem to play no role in the packing.

The structure of compound **5**, $[Cu(PPh_3)_2(Me\text{-}Hfbt)]_2SO_4$, is reported in Fig. 3. The asymmetric unit is formed by two complex $[Cu(PPh_3)_2(Me\text{-}Hfbt)]^+$ cations bridged by a sulfate anion. The two cationic moieties differ significantly in their geometrical features. One of the thiosemicarbazone ligand (molecule A) presents a marked dihedral angle (43.6(3)°) between the average plane of the thiosemicarbazide moiety and that of the fluorobenzyl ring, while in the other (molecule B) is almost planar (the same dihedral angle is 2.91(3)°). The sulfate ion forms two

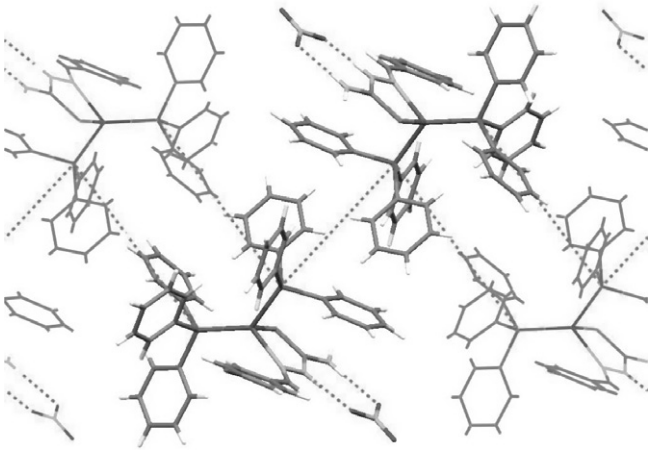


Fig. 2. MERCURY drawing of the packing of compound (**1**) showing the two molecules (capped sticks) involved in the six phenyl embrace and the looser pheny–phenyl interactions between adjacent molecules (in wireframe).

charge assisted H-bonds connecting the two complex molecules A and B (see Table 3).

Also this packing is determined by a very tight six-atom phenyl embrace characterized by a P4…$P4^I$ ($I = -x$, $1-x$, $-z$) interaction with a distance of 6.645 Å (see Fig. 4), much shorter than that observed in the previous one. A looser sixfold phenyl embrace is observed between P2 and $P3^I$ ($I = -x$, $-1/2+y$, $1/2-z$) (distance 7.66 Å) and this interaction together with the previously described contact form a bidimensional layer of molecules that lie on the *yz* plane. These layers are connected by a third interaction between two tpp that is characterized by a longer P…P distance of 7.785 Å [P1…$P3^I$ $I = 1+x$, y, z].

The crystal structure of compound **6** $\{[Cu(PPh_3)_2(Me\text{-}Hfbt)]CH_3COO\}_2 \cdot 2EtOH \cdot H_2O$ is reported in Fig. 5. In the asymmetric unit are present two independent complex cations, two acetate ions, two ethanol molecules and a water. The carboxyl group of the acetate forms two hydrogen bonds (see Table 3) with the NH groups of the thiosemicarbazide moiety in a way analogous to that observed in the nitrate derivative previously discussed (**1**). Moreover one of the two carboxylic oxygens (different in molecule A and in molecule B, see Fig. 6) in both acetates is also involved in a bifurcated but strong hydrogen bond with the ethanols (see Table 3). As in the previous case in the two complex molecules the thiosemicarbazone ligands have different planarities and precisely a dihedral angle between the thiourea moiety and the aromatic ring of 8.5(2)° in molecule A and 37.0(2)° in molecule B. Noteworthy the P–Cu–P angles [121.20(5)° and 123.15(5)°] that are by far smaller than those found in the other two complexes [126.83(3)° in compound **1** and 135.39(8)° and 128.52(9)° in compound **5**].

A series of considerations must be done on the hydrogen bonding system found in these compounds. A common feature is the strong charge assisted hydrogen bondings that stabilize the ligand in its neutral form. In particular some

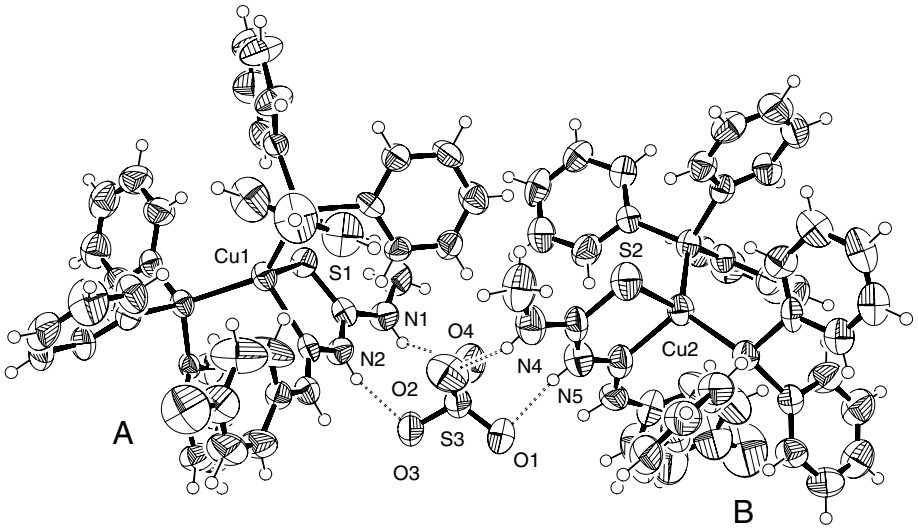


Fig. 3. ORTEP drawing of complex $[Cu(PPh_3)_2(Me\text{-}Hfbt)]_2SO_4$ (**5**) showing thermal ellipsoids at the 50% probability level.

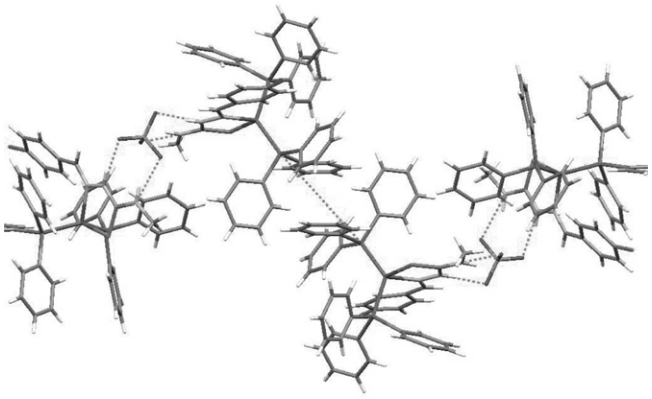


Fig. 4. MERCURY drawing of the packing of compound (**5**) showing two sulphate bridged dimeric molecules involved in the P4...P4 six phenyl embrace.

of these hydrogen bonds formed with the acidic hydrazinic nitrogen are among the shortest observed in the literature. Using a thiourea moiety as a reference we have found in the CSD [28a,28b] that the average N–H...O distance is 2.918(8) Å for the nitrate ion, 2.872(12) Å for the sulfate ion and 2.882(9) Å for the acetate that are comparable with the distances observed for the aminic NH in compound **1** (2.906(3) Å) while those found in complex **5** (2.751(33) and 2.757(10) Å) and in compound **6** (2.701(7) and 2.805(6) Å) are remarkably shorter. The hydrogen bonds that involve the hydrazinic nitrogen are very strong with distances of 2.717(2) Å for **1**, 2.740(9) Å in **5** and 2.746(6) Å and 2.720(6) Å in **6**. The only exception is the hydrazinic N of molecule B of compound **5** (2.902(9) Å) in which the distance is larger than the average and this distortion is probably due to the packing.

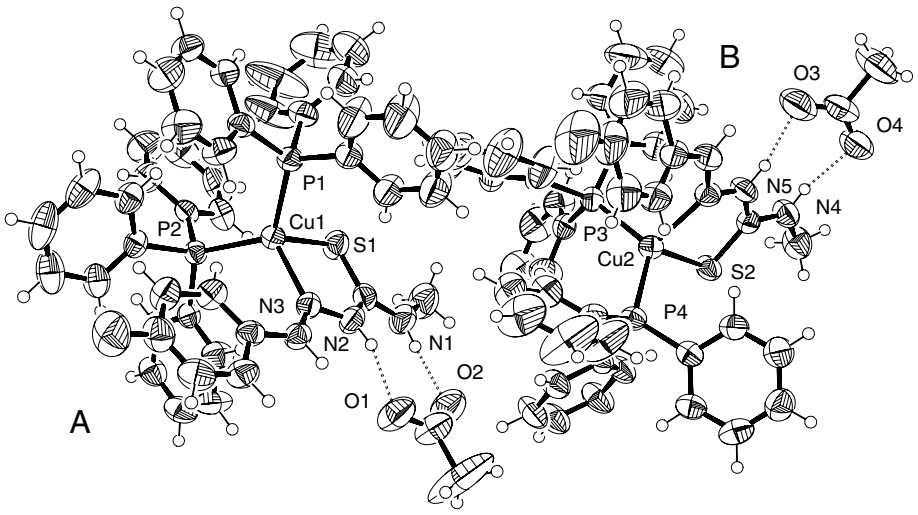


Fig. 5. ORTEP drawing of the moiety $\{[Cu(PPh_3)_2(Me\text{-}Hfbt)]CH_3COO\}_2$ of complex (**6**) showing thermal ellipsoids at the 50% probability level.

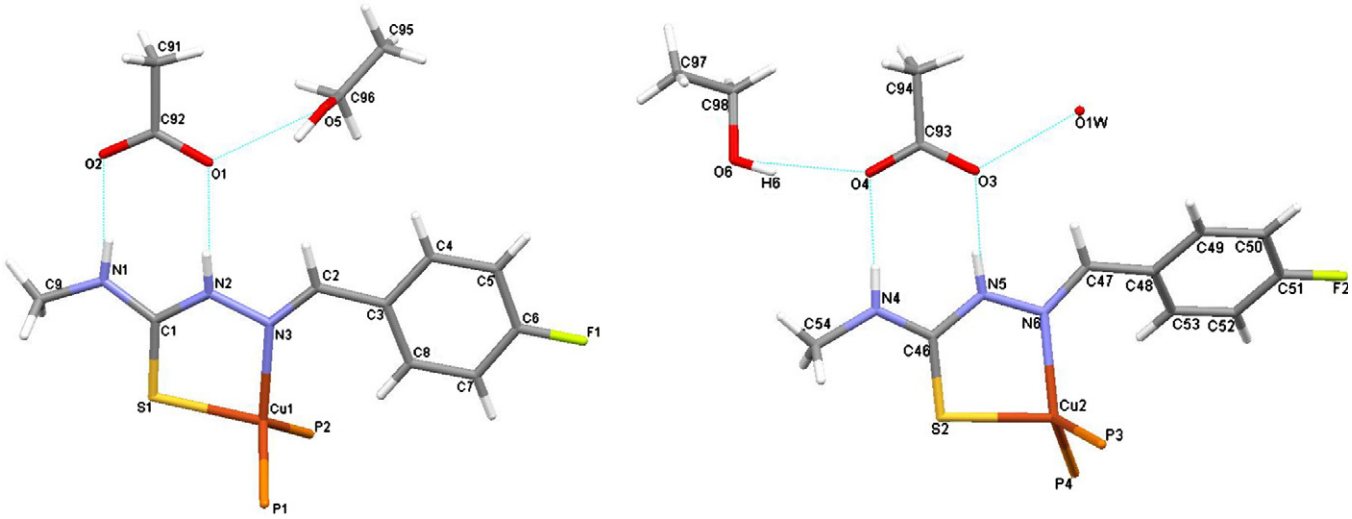


Fig. 6. MERCURY drawings of the hydrogen bond patterns around the acetate ion in the two independent molecules in compound **6**.

4. Conclusions

As hypothesized in the introduction the main features presented by these copper(I) complex molecules are determined by three factors: (a) the absence of soft donor atoms, besides P and S, that force the imino nitrogen to coordinate to the metal center; (b) the overall flatness of the thiosemicabazone moiety that allows its insertion in the cleft formed by the bulky blob of the two triphenylphosphines and, (c) the presence of the charged assisted hydrogen bonds formed by the anions that contribute to the *Z* configuration of the ligand. A contribution that is not predictable in the detail but that is decisive in understanding the overall packing and some distortions in the planarity of the thiosemicarbazone ligand in the crystal is the extended system of weak interactions among the aromatic rings.

Appendix A. Supplementary material

CCDC 640078, 640079 and 640080 contain the supplementary crystallographic data for **1**, **5** and **6**. These data can be obtained free of charge via http://www.ccdc.cam.ac.uk/conts/retrieving.html, or from the Cambridge Crystallographic Data Centre, 12 Union Road, Cambridge CB2 1EZ, UK; fax: (+44) 1223-336-033; or e-mail: deposit@ccdc.cam.ac.uk. Supplementary data associated with this article can be found, in the online version, at doi:10.1016/j.poly.2007.04.026.

References

[1] T.S. Lobana, Rekha, A.P.S. Pannu, G. Hundal, R.J. Butcher, A. Castineiras, Polyhedron (2007), doi:10.1016/j.poly.2006.12.044.
[2] T.S. Lobana, Rekha, R.J. Butcher, Trans. Met. Chem. 29 (2004) 291.
[3] T.S. Lobana, Rekha, R.J. Butcher, A. Castineiras, E. Bermejo, P.V. Bharatam, Inorg. Chem. 45 (2006) 1535.
[4] D.X. West, S.B. Padhye, P.B. Sonawane, Struct. Bond. (Berlin) 76 (1991) 4.
[5] D.R. Smith, Coord. Chem. Rev. 164 (1997) 575.
[6] A.R. Cowley, J.R. Dilworth, P.S. Donnelly, E. Labisbal, A. Sousa, J. Am. Chem. Soc. 124 (2002) 5270.
[7] D.B. Lovejoy, D.R. Richardson, Blood 100 (2002) 666.
[8] L.-J. Ming, Med. Res. Rev. 23 (2003) 697.
[9] M. Belicchi-Ferrari, G. Gasparri-Fava, C. Pelizzi, P. Tarasconi, Inorg. Chim. Acta 97 (1985) 99.
[10] M. Belicchi-Ferrari, G. Gasparri-Fava, M. Lanfranchi, C. Pelizzi, P. Tarasconi, Inorg. Chim. Acta 181 (1991) 253.
[11] X.-H. Zhou, T. Wu, D. Li, Inorg. Chim. Acta 359 (2006) 1442.
[12] V.W.W. Yam, W.K. Lee, K.K. Cheun, J. Chem. Soc., Dalton Trans. (1996) 2335.
[13] V.W.W. Yam, K.K.W. Lo, Chem. Soc. Rev. 28 (1999) 323.
[14] D. Li, W.J. Shi, L. Hou, Inorg. Chem. 44 (2005) 3907.
[15] J.A. Simon, W.E. Palke, P.C. Ford, Inorg. Chem. 35 (1996) 6413.
[16] (a) P. Souza, A.I. Matesanz, C. Pastor, Inorg. Chem. Commun. 5 (2002) 344;
(b) R. Pedrido, M.R. Bermejo, M.J. Romero, A.M. González-Noya, M. Maneiro, M.I. Fernández, Inorg. Chem. Commun. 8 (2005) 1036.
[17] (a) J.S. Casas, M.S. Garcia-Tasende, J. Sordo, Coord. Chem. Rev. 209 (2000) 197;
(b) M.J.M. Campbell, Coord. Chem. Rev. 15 (1975) 279;
(c) S.B. Padhye, G. Kauffman, Coord. Chem. Rev. 63 (1985) 127;
(d) D.X. West, A.E. Liberta, S.B. Padhye, R.C. Chikate, P.B. Sonawane, A.S. Kumbhar, R.G. Yerande, Coord. Chem. Rev. 123 (1993) 49;
(e) R.L. De Lima, L.R.D. Teixeira, T.M.G. Carneiro, H. Beraldo, J. Braz. Chem. Soc. 10 (1999) 184;
(f) N.T. Akinchan, R. Akinchan, P.M. Drozdewski, Y.H. Yang, T.L. Klein, D.X. West, Synth. React. Inorg. Met.-Org. Chem. 26 (1996) 1735;
(g) H.G. Zheng, D.X. Zeng, X.Q. Xin, W.T. Wong, Polyhedron 16 (1997) 3499;
(h) S. Lhuachan, S. Siripaisarnpipat, N. Chaichit, Eur. J. Inorg. Chem. (2003) 263;
(i) L.J. Ashfield, A.R. Cowley, J.R. Dilworth, P.S. Donnelly, Inorg. Chem. 43 (2004) 4121;
(j) M. Belicchi-Ferrari, A. Bonardi, G. Gasparri-Fava, C. Pelizzi, P. Tarasconi, Inorg. Chim. Acta 223 (1994) 77;
(k) T.S. Lobana, Rekha, B.S. Sidhu, A. Castineiras, E. Bermejo, T. Nishioka, J. Coord. Chem. 58 (2005) 803;
(l) T.S. Lobana, S. Khanna, R.J. Butcher, A.D. Hunter, M. Zeller, Polyhedron 25 (2006) 2755.
[18] M. Belicchi-Ferrari, S. Capacchi, G. Reffo, G. Pelosi, P. Tarasconi, R. Albertini, S. Pinelli, P. Lunghi, J. Inorg. Biochem. 81 (2000) 89.
[19] G.M. Sheldrick, SADABS. Program for Empirical Absorption correction of Area Detector Data, University of Gottingen, Germany, 1996.

[20] L.J. Farrugia, J. Appl. Cryst. 32 (1999) 837–838.
[21] A. Altomare, M.C. Burla, M. Camalli, G. Cascarano, C. Giacovazzo, A. Guagliardi, A.G.G. Moliterni, G. Polidori, R. Spagna, SIR 97, J. Appl. Cryst. 32 (1999) 115.
[22] G. Sheldrick, SHELXL 97 A Program for Structure Refinement, University of Gottingen, Germany, 1997.
[23] International Tables for X-ray Crystallography, vol. 4, Kynoch Press, Birmingham, UK, 1974.
[24] M. Nardelli, PARST95. An update to PARST: a system of Fortran routines for calculating molecular structure parameters from the results of crystal structure analyses, J. Appl. Cryst. 28 (1995) 659.
[25] C.K. Johnson, M.N. Burnett, ORTEPIII. Report ORNL-6895, Oak Ridge National Laboratory, TN, USA, 1996.
[26] C.F. Macrae, P.R. Edgington, P. McCabe, E. Pidcock, G.P. Shields, R. Taylor, M. Towler, J. van de Streek, J. Appl. Cryst. 39 (3) (2006) 453.
[27] (a) I.G. Dance, M.L. Scudder, J. Chem. Soc., Chem. Commun. (1995) 1039;
(b) Chem. Eur. J. 2 (1996) 481;
(c) I. Dance, M. Scudder, J. Chem. Soc., Dalton Trans. 10 (2000) 1579;
(d) I. Dance, M. Scudder, J. Chem. Soc., Dalton Trans. 10 (2000) 1587.
[28] (a) F.H. Allen, Acta Crystallogr., Sect. B 58 (2002) 380;
(b) I.J. Bruno, J.C. Cole, P.R. Edgington, M. Kessler, C.F. Macrae, P. McCabe, J. Pearson, R. Taylor, Acta Crystallogr., Sect. B 58 (2002) 389.

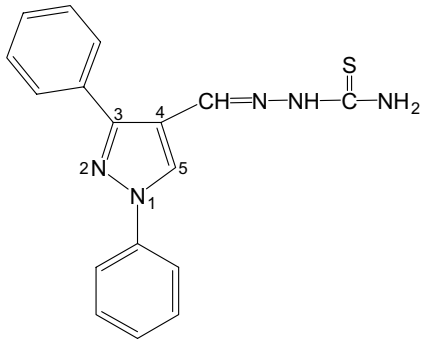


Fig. 1. Chemical structure of Ph_2PzTSC.

structural variation on the heterocyclic ring might bring out significant enhancement in their biological effects, especially in corresponding metal complexes, often with novel structural information. Synthesis and spectroscopic characterization of nickel(II) complexes with some pyrazolyl thiosemicarbazones, such as 5-methyl-3-formylpyrazole-3-substituted thiosemicarbazones have been reported by other authors [14–16]. As a part of our investigation toward synthesis and structural characterization of new compounds containing biorelevant pyrazolyl thiosemicarbazones, the present paper reports the synthesis, spectroscopic, and structural properties of 1,3-diphenylpyrazole-4-carboxaldehyde thiosemicarbazone ligand (Ph_2PzTSC, Fig. 1) and its nickel(II) complex.

2. Experimental

2.1. Reagents and starting materials

Solvents and reagents were obtained from commercial sources. The solvents were purified using the established method [17]. Thiosemicarbazide and nickel(II) acetate tetrahydrate were purchased from Aldrich Chemicals, USA. 1,3-Diphenylpyrazole-4-carboxaldehyde was synthesized according to Rathelot et al. procedure [18].

2.2. Preparation of Ph_2PzTSC

The Ph_2PzTSC ligand was prepared by refluxing the mixture of the 1,3-diphenylpyrazole-4-carboxaldehyde (1.24 g, 5 mmol) and thiosemicarbazide (0.45 g, 5 mmol) in ethanol (20 cm^3) for 4 h. One drop of glacial acetic acid was previously added into the mixture. After cooling, the white precipitate was filtered, washed with cold chloroform in order to remove the traces of unchanged aldehyde, and dried over anhydrous calcium chloride. Yield: 1.25 g, 78%. The suitable crystals for X-ray analysis were obtained by recrystallization of the ligand from the mixture of acetone and methanol (1:1 v/v).

Anal. Calc. for $C_{17}H_{15}N_5S$: C, 63.53; H, 4.70; N, 21.79. Found: C, 63.75; H, 4.62; N, 21.55%. UV–Vis spectra (cm^{-1}/log ε): 31950 (4.0); ~30 000 (4.0).

^1H NMR (200 MHz, DMSO-d_6): 7.38–7.70, m (8H, Ar); 7.80, br s (1H, NH_2); 7.90, d (2H, Ar, $J = 7.86$ Hz, *ortho*-H, N-substituted phenyl); 8.22, s (1H, Pz); 8.27, br s (1H, NH_2); 9.19, s (1H, CH=N); 11.34, br s (1H, NH).

^{13}C NMR (200 MHz, DMSO-d_6): 117.43; 118.66; 127.15; 127.85; 128.30; 128.75; 128.91; 129.85; 132.28; 135.10; 139.20; 151.52; 177.72.

IR (KBr pellets): 3326, 3257, 3140, 1618, 1598, 1543, 1500, 1221, 1098, 1064, 831, 807, 755, 704, 687 cm^{-1}.

2.3. Preparation of $[Ni(Ph_2PzTSC\text{-}H)_2]$

$Ni(CH_3COO)_2 \cdot 4H_2O$ (0.25 g, 1 mmol) was dissolved in methanol (10 cm^3) under heating and the solution was mixed with a warm solution of Ph_2PzTSC (0.32 g, 1 mmol) in acetone (20 cm^3). The heating was continuated for several minutes. After 10 h of standing, the brown crystals were filtered and washed with acetone and dried over anhydrous calcium chloride Yield: 0.16 g, 46%.

Anal. Calc. for $C_{34}H_{28}N_{10}NiS_2$: C, 58.38; H, 4.03; N, 20.02; Ni, 8.39. Found: C, 58.42; H, 3.98; N, 20.12; Ni, 8.42%. $\lambda_M(DMF) = 3.3$ S cm^2 mol^{-1}. UV–Vis: (cm^{-1}/log ε): ~33 300 (4.0); 30 210 (4.3); 25 500 sh (3.7); 19 300 sh (2.1). sh (shoulder).

^1H NMR (200 MHz, DMSO-d_6): 6.97–7.19, m (7H; 5H, phenyl and 2H, NH_2); 7.49, s (1H, Pz); 7.50, d (1H, Ar, $J = 7.36$Hz, *para*-H, N-substituted phenyl); 7.65, t, (2H, Ar, $J = 7.66$Hz, *meta*-H, N-substituted phenyl); 8.03, d, (2H, $J = 7.77$Hz, *ortho*-H, N-substituted phenyl); 9.84, s (1H, CH=N, azomethine).

^{13}C NMR (200 MHz, DMSO-d_6): 114.29; 119.89; 127.62; 127.86; 128.44; 128.83; 129.88; 130.10; 130.89; 139.23; 150.17; 152.68; 173.46.

IR (KBr pellets): 3466, 3284, 3067, 1626, 1596, 1526, 1513, 1504, 1219, 956, 705, 672 cm^{-1}.

2.4. Physical measurements

Elemental (C, H, N) analysis of the samples was carried out by standard micromethods in the Center for Instrumental Analysis, Faculty of Chemistry, Belgrade. Nickel content was determined by the complexometric titration with EDTA method, upon the destruction of complex with the mixture of concentrated H_2SO_4 and HNO_3. Molar conductivity of freshly prepared 1×10^{-3} mol dm^{-3} solution was measured on a Jenway 4010 conductivity meter. IR spectra were recorded on a Perkin Elmer Spectrum One FT-IR spectrometer with a KBr disc. ^1H and ^{13}C NMR spectra were obtained using a Varian Gemini 200 spectrometer. Electronic spectra were recorded on a Secomam (Anthelie 2, Advanced, for the range 270–900 nm) and on a Thermo Nicolet instrument (NEXUS 670 FT-IR, for the range 900–1400 nm) in $(1–2) \times 10^{-3}$ mol dm^{-3} DMF solutions of the ligand and complex. Thermal analysis in argon and air gas carriers with a 15 dm^3/min flowing rate and a heating rate of 10 K/min were carried out using a DuPont 1090 TA system. For thermogravimetric

measurements platinum crucible was employed. DSC curves were recorded in open aluminum sample pans. As a reference an empty pan was used. The sample masses were about 5 mg.

2.5. X-ray data collection and structure refinement

The diffraction data for both compounds were collected on an Enraf-Nonius CAD4 diffractometer [19] by using graphite-monochromated Mo Kα (0.71073 Å) radiation at 293(2) K. The data were corrected for Lorentz and polarization effects [20]. Cell constants and the orientation matrix for data collection, obtained from 25 centered reflections in the θ range of 13.17–15.81° for the ligand, corresponded to an orthorhombic cell. In the case off the complex, the 25 centered reflections in the θ range 13.97–17.25° led to a triclinic cell. Both structures were solved by direct methods and difference Fourier methods and refined on the F^2 by full-matrix least-square method [21]. In both cases the all H atoms were determined from ΔF maps but at the final stage of the refinement they were placed at geometrically calculated positions (in purpose to decrease the number of refined parameters). The calculated C–H and N–H distances were 0.93 and of 0.86 Å respectively, and the isotropic displacement parameters are equal to 1.5 and 1.2 times of the equivalent isotropic displacement parameters of the C and N atoms. The software used for the publication are: PLATON [22], WinGX [23], PARST [24] and ORTEPIII [25]. Crystal and structure refinement data for Ph_2PzTSC and $[Ni(Ph_2PzTSC\text{-}H)_2]$ are summarized in Table 1.

Table 1
Crystal and structure refinement data for Ph_2PzTSC and $[Ni(Ph_2PzTSC\text{-}H)_2]$

Empirical formula	$C_{17}H_{15}N_5S$	$C_{34}H_{28}N_{20}NiS_2$
Formula weight	321.40	699.49
Color	white	brown
Temperature (K)	293(2)	293(2)
Crystal size (mm)	$0.025 \times 0.014 \times 0.010$	$0.300 \times 0.026 \times 0.020$
Crystal system	orthorhombic	triclinic
Space group	*Pbca*	$P\bar{1}$
Unit cell		
a (Å)	8.458(4)	12.364(6)
b (Å)	17.476(6)	12.451(5)
c (Å)	21.986(5)	12.478(5)
α (°)	90	103.27(4)
β (°)	90	92.86(6)
γ (°)	90	115.59(3)
Volume (Å^3)	3249.8(14)	1661.7(12)
Z	8	2
Calculated density, ρ (g cm^{-3})	1.314	1.398
θ Range for data collection (°)	1.58–25.97	2.44–25.98
Absorption coefficient (mm^{-1})	0.206	0.751
$F(000)$	1344	724
Index ranges	$0 \leqslant h \leqslant 10$, $0 \leqslant k \leqslant 21$, $0 \leqslant l \leqslant 27$	$0 \leqslant h \leqslant 15$, $-15 \leqslant k \leqslant 14$, $-15 \leqslant l \leqslant 15$
Reflections collected	3617	6832
Independent reflections	3617	6511
Parameters	208	424
Goodness-of-fit	0.914	1.004
R_1 [$I > 2\sigma(I)$]	0.0636	0.0472
Largest difference in peak and hole	0.273 and −0.241	0.383 and −0.338

3. Results and discussion

3.1. Syntheses and general properties of ligand and complex

The title ligand, 1,3-diphenylpyrazole-4-carboxaldehyde thiosemicarbazone (Ph_2PzTSC) was synthesized in good yield (78%) by condensation from warm ethanolic solutions of the corresponding aldehyde and thiosemicarbazide in an 1:1 mole ratio, in the presence of a small quantity of the glacial acetic acid. The white crystals of the ligand are stable at room temperature. The ligand is very soluble in Me_2CO and DMF, soluble in MeOH, less soluble in aqueous EtOH, and practically insoluble in Et_2O and water.

The brown single crystals of the *cis*-square-planar $[Ni(Ph_2PzTSC\text{-}H)_2]$ complex were obtained by reaction of the warm methanolic solution of $Ni(CH_3COO)_2 \cdot 4H_2O$ with acetone solution of the ligand in mole ratio of 1:1. The complex is soluble in DMF, less soluble in Me_2CO, and insoluble in Et_2O, MeOH, EtOH, and water.

The ligand participates in coordination with nickel(II) ion in its monoanionic form after deprotonation of the hydrazine nitrogen, due to the presence of acetate ion as a Brönsted base, resulting in complex of non-electrolyte type. This is in the agreement with its low molar conductivity. The diamagnetism of the complex is in the accordance with its square-planar structure confirmed by X-ray analysis. The diamagnetic property of the complex is also retained in DMF solution.

3.2. IR spectral studies

A comparative study of the IR spectral data of the complex with that of the ligand gives valuable information regarding bonding sites of the ligand molecule.

The IR spectra of compounds with C=S group attached to a nitrogen show an absorption band due to ν(C=S) stretching in the region between 1020 and 1250 cm^{-1}. In principle, the ligand can exhibit thione/thiol tautomerism, since it contains a thioamide NH–C=S functional group [26]. The missing ν(S–H) band between 2600 and 2800 cm^{-1} indicates that the ligand remains in its thione form. The ligand exhibits a strong band at 1098 and a medium one at 1064 cm^{-1} due to ν(C=S) stretches [27]. Also, two bands at 831 and 807 cm^{-1} in the spectrum of the free ligand can be attributed to vibrations involving interaction between ν(C=S) stretching and ν(C–N) stretchings [28]. The appearance of these bands indicates the existence of ligand in its thione form in the solid state. The disappear-

ance of the ν(C=S) band in this region and the appearance of a medium intensity band at 672 cm^{-1} in the spectrum of the complex suggests the thioenolization of the C=S group and coordination of the thiolate sulfur to nickel [29].

In the spectrum of the ligand three bands appear in the frequency range 3000–4000 cm^{-1}. Two of them, at 3327 and 3257 cm^{-1}, belong to are due to asymmetrical and symmetrical $\nu(NH_2)$ stretching, respectively, and one to the hydrazine ν(NH) at 3159 cm^{-1} [30]. The spectral ν(N–H) band of thiosemicarbazone disappears in the complex indicating the deprotonation of the NH group and coordination via the thiolate sulfur. On the other hand, the bands in the region attributed to symmetrical and asymmetrical stretching modes $\nu(NH_2)$ in the spectrum of the ligand, undergo a change in the spectrum of the complex. This is explained by the coordination of sulfur from C=S(NH_2) group as reported earlier [31,32].

In the ligand spectrum, the strong band observed at 1618 cm^{-1} is assigned to ν(C=N) stretching vibrations [33]. This band shifts to higher wavenumbers at 1626 cm^{-1} in the spectrum of the complex, indicating the coordination of nitrogen of the azomethine group to the central metal ion [31,34].

According to the literature data [15,16], IR bands assigned to $\nu(C{=}N_{pz})$ (pyrazole ring) have been found to shift to the higher frequency region in the nickel complexes referring to the participation of the ring nitrogen atom as a potential bonding site. The negative shift of the very strong $\nu(C{=}N_{pz})$ frequencies from 1543 cm^{-1} in the spectrum of the free Ph_2PzTSC to 1526 cm^{-1} after complexation with nickel(II) ion does not indicate the involvement of pyrazole nitrogen in bonding. This band shifting to lower wavenumbers could be explained by resonance effects through the all conjugated system after the deprotonation and complexation with nickel(II) ion.

3.3. NMR spectral studies

The assignment of all reported signals (^{1}H and ^{13}C) was carried out by means of 1D and 2D homo- and heteronuclear correlated NMR spectroscopy.

3.3.1. ^{13}C NMR spectra

The carbon C=S signal appears at higher field in the spectrum of the complex compared to that in the ligand. This behavior suggests thione-to-thiol evolution in the ligand, an increase in the thiocarbonyl-deprotonated nitrogen bond order [35] and possible coordination of the nickel ion to the thiolic sulfur atom.

^{13}C NMR spectrum shows an unexpectedly low positive $\Delta\delta = \delta$(complex) − δ(free ligand) shift of only 2.0 ppm for the azomethine carbon. In the earlier reports, the complexation through azomethine nitrogen causes a great positive chemical shift of the azomethine carbon in the ^{13}C NMR spectra of complexes [35,36]. On the other side, the C-5 pyrazole carbon exhibits a great positive shift of 15.0 ppm, while the C-4 carbon is shifted to higher field for 3.1 ppm. This behavior of the C-5 pyrazole carbon is probably caused by the positive resonance effect of the phenyl-substituted pyrazole nitrogen, due to the delocalization of π-electrons through C-5, C-4, azomethine carbon, and thiosemicarbazone part of the molecule after the deprotonation of hydrazine nitrogen and complexation. Thus, the reduced electron density of the azomethine carbon after coordination is compensated by resonance effect which results in low difference in the chemical shift of the azomethine carbon in the spectrum of the free ligand compared to that in the complex. In this way the electron density of the azomethine nitrogen is significantly increased as well as its nucleophility facilitating its coordination to nickel(II). The practically same δ-value for C-3 pyrazole carbon (139.2 ppm) in the ^{13}C NMR spectrum of the free ligand compared to the corresponding shift in the complex confirms this hypothesis. The chemical shifts of the other carbon atoms undergo no significant changes upon complexation.

3.3.2. ^{1}H NMR spectra

The ^{1}H NMR spectrum of Ph_2PzTSC ligand show a broad singlet at 11.34 ppm relative to the NH next to C=S, while the signal of the azomethine proton appears at 9.19 ppm. The sharp singlet of the pyrazole proton appears at 8.22 ppm while the aromatic protons occur in 7.38–7.92 ppm range. It is interesting to notice the presence of two broad singlets for two NH_2 protons, at 8.27 and 7.80 ppm respectively. These two protons are different which means that the free rotation around C–N bond is hindered because of its partial double bond character [37].

The coordinating mode of the ligand was confirmed by comparing ^{1}H NMR spectral data of the ligand with the corresponding ones in the complex. The absence of the NH proton signal in the spectrum of the complex suggests the thioenolization and subsequently, the replacement of a proton by the metal ion. This replacement with nickel(II) induces the shift of NH_2 protons to lower δ-values in the spectrum of the complex (overlapped with the aromatic protons shifts in 6.97–7.19 ppm region).

A significant downfield shift of the azomethine proton signal in the complex ($\Delta\delta = 0.65$ ppm) with respect to the corresponding free ligand confirms the coordination of azomethine nitrogen [15,27].

It is interesting to emphasize that C-5 pyrazole proton shifts to lower δ-value from 8.22 ppm in the spectrum of the ligand to 7.49 ppm in the spectrum of the complex. On the other hand, the doublet assigned to *ortho*-N-substituted phenyl protons at 7.90 ppm (center of doublet) is shifted to lower field in the spectrum of the complex at 8.03 ppm, together with *meta* and *para* protons. These shifts are induced by positive resonance effect of phenyl-substituted pyrazole nitrogen and the participation of its electron pair in the delocalization of π-electrons after coordination, which is in the accordance with ^{13}C NMR spectral data for the free ligand and its nickel complex. The

other aromatic proton shifts of the ligand and those in the complex appear in the expected region.

3.4. Electronic spectra

Similarly to the ligand, the red-brownish DMF solution of the Ni(II) complex absorbs in the UV range in several unresolved bands belonging to intraligand transitions. A shoulder appearing at about 25 500 cm^{-1} is probably CT band.

The only one d–d band at about 19 000 cm^{-1} appearing as a shoulder of this CT band is consistent with the assumption of a preserved square-planar geometry in DMF solution. In the near IR region, under 10 000 cm^{-1} no bands were observed, as is usual in complexes with this geometry [38].

3.5. Crystal structures

3.5.1. Crystal structure of Ph_2PzTSC

Fig. 2. shows an ORTEP plot of Ph_2PzTSC ligand with the atomic numbering scheme. Relevant bond distances and angles are listed in Table 2. The thiosemicarbazone moiety of the ligand shows E configuration around the C2–N1 and C1–N2 bond as found in most of the thiosemicarbazones. As confirmed by the C=S bond distance of 1.692(5) Å, the ligand is present in its thione form. The partial double bond characters in formally single bonds of thiosemicarbazone moiety suggest the extensive electron delocalization. Consequently, this part of molecule exhibits considerable planarity. The moiety comprising C2, N1, N2, C1, S1, and N3 atoms has a mean plane deviation of 0.036 Å with the N1 showing the greatest displacement of 0.082 Å. The formally single C2–C3 bond (1.453(7) Å) which connects the thiosemicarbazone fragment to the rest of the molecule allows its free rotation, thus the dihedral angle formed between the best planes of the thiosemicarbazone fragment and the central pyrazole ring achieves 48.3°.

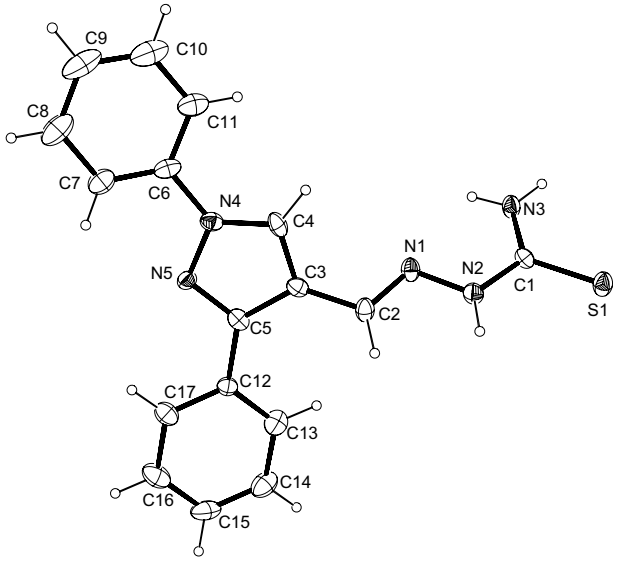


Fig. 2. Crystal structure of Ph_2PzTSC with the atomic numbering scheme. Ellipsoids are drawn at the 50% probability level.

Table 2
Selected bond lengths (Å) and angles (°)

	Ph_2PzTSC	$[Ni(Ph_2PzTSC\text{-}H)_2]$	
		A	B
Ni1–N1		1.914(3)	1.921(3)
Ni1–S1		2.141(2)	2.148(2)
N1–N2	1.387(5)	1.424(4)	1.410(4)
C1–N2	1.344(6)	1.289(5)	1.304(4)
C1–N3	1.315(6)	1.352(5)	1.349(4)
C1–S1	1.692(5)	1.744(4)	1.737(4)
C2–N1	1.279(6)	1.282(4)	1.296(4)
C2–C3	1.453(7)	1.449(5)	1.446(5)
N4–C5	1.432(7)	1.438(5)	1.435(5)
C5–C12	1.483(7)	1.470(5)	1.463(5)
N1–Ni1–S1		86.1(2)	85.51(9)
Ni1–N1–C2		128.3(3)	130.8(2)
Ni–N1–N2		117.7(2)	118.3(2)
Ni–S1–C1		94.4(2)	95.1(2)
N1a–Ni–N1b		102.5(2)	
S1a–Ni–S1b		90.1(1)	
N1a–Ni–S1b		162.9(3)	
N1b–Ni–S1a		163.8(3)	
N2–N1–C2	114.3(5)	113.9(3)	110.8(3)
N1–C2–C3	119.0(5)	124.3(3)	127.6(3)
N1–N2–C1	119.7(4)	110.9(3)	111.4(3)
N2–C1–S1	119.7(4)	123.9(3)	122.9(3)
N2–C1–N3	117.4(4)	119.4(4)	118.3(3)
N5–N4–C6	119.5(5)	120.5(3)	120.2(3)
N5–C5–C12	118.4(5)	119.4(4)	121.3(3)

The bond lengths within the aromatic parts of the molecule are normal [39]. The phenyl rings are titled in the same direction relative to the central pyrazole moiety. The dihedral angles formed between the best planes of the pyrazole and the two phenyl rings are similar, 18.1° and 19.1° with the C6–C11 and C12–C17 rings respectively. The dihedral angle between the titled phenyls is 6.0°.

The three intramolecular hydrogen bonds of the very bent character (D–H···A ≈ 100°) stabilize the geometry of Ph_2PzTSC (Table 3). The strongest intermolecular N3–H3···N5 hydrogen bond connects the centrosymmetrically related molecules into the cyclic dimers. Since this interaction is formed between the thiosemicarbazone and pyrazole moieties it probably causes the above mentioned twisting of the thiosemicarbazone fragment. The two interactions of the N–H···S type (Table 3) further connect the molecules of the ligand into the 2D structures parallel to the *ac* crystallographic plane. The segment of this 2D hydrogen bonded pattern is shown in Fig. 3.

3.5.2. Crystal structure of $[Ni(Ph_2PzTSC\text{-}H)_2]$

In $[Ni(Ph_2PzTSC\text{-}H)_2]$ complex the Ni(II) ion lies in an approximately square-planar coordination environment formed by two hydrazine N1 and two thiol S1 atoms from

Table 3
Geometry of hydrogen bonds

D–H···A	D–H (Å)	H···A (Å)	D···A (Å)	D–H···A (°)
Ph_2PzTSC				
N3–H3a···N1^{i}	0.86	2.29	2.642(2)	104.7(3)
C7–H7···N5^{i}	0.93	2.48	2.801(2)	100.1(4)
C17–H17···N5^{i}	0.93	2.53	2.836(2)	99.8(4)
N3–H3a···N5^{ii}	0.86	2.31	3.079(2)	140.1(3)
N2–H2n···S1^{iii}	0.86	2.68	3.312(4)	131.1(5)
N3–H3b···S1^{iv}	0.86	2.63	3.421(3)	155.2(5)
[Ni(Ph_2PzTSC-H)$_2$]				
C7a–H7a···N5a^{v}	0.93	2.57	2.853(2)	98.2(3)
C7b–H7b···N5b^{v}	0.93	2.54	2.830(2)	98.5(3)
C17a–H17a···N5a^{v}	0.93	2.61	2.883(2)	97.5(3)
C17b–H7b···N5b^{v}	0.93	2.67	2.930(2)	93.6(3)
N3a–H3a···N2a^{vi}	0.86	2.14	3.003(3)	178.3(3)
N3b–H3b···N2b^{vii}	0.86	2.12	2.968(2)	168.9(3)

Symmetry codes: (i) x, y, z; (ii) $-x+2$, $-y$, $-z+2$; (iii) $x+1.5$, y, $-z+2.5$; (iv) $x+0.5$, y, $-z+2.5$; (v) x, y, z; (vi) $-x$, $-y$, $-z+2$; (vii) $-x+1$, $-y$, $-z+1$.

the deprotonated thiosemicarbazone ligands (Fig. 4). The molecules of L have the *cis* mutual arrangement. The four donor atoms are significantly displaced from the mean coordination plane with the maximum deviation of atom N1a (0.471 Å).

The deviation from the regular square-planar geometry is also indicated by the coordination angles (Table 2). The N1a–Ni–N1b angle of 102.5(2)° shows significant disagreement with the theoretical value (90°) probably due to the steric effects between the bulky fragments attached to N1 atoms. The S1a–Ni–S1b angle shows almost ideal value of 90.1(1)°. The coordination bond distances Ni–N and Ni–S are comparable to those found in similar neutral square-planar complexes of Ni(II). Comparison of the remaining bonds in [Ni(Ph_2PzTSC-H)$_2$] to those of the uncoordinated ligand Ph_2PzTSC shows marked differences probably originated by the ligand's deprotonation and coordination. The most significant difference is found in the C–S bond which increases its length upon the ligand complexation for an average value of 0.048 Å. On the contrary, C1–N2 bond decreases its length for the similar average value.

Five membered chelate rings assume envelope conformation (the puckering parameters are: $q_2 = 0.324(3)$ Å, $\phi_2 = 181.0(7)°$, $q_2 = 0.320(2)$ Å, $\phi_2 = 182.5(7)°$ for the branches A and B respectively) and form the dihedral angle of 20.4°. The thiosemicarbazide moiety upon complexation retains its planarity, however it is worth mentioning that the dihedral angle between its best plane and central pyrazole ring decrease from the value of 48.3° to the values of 19.2° and 16.9° in the A and B branch respectively. This change in the ligand geometry is probably caused by the

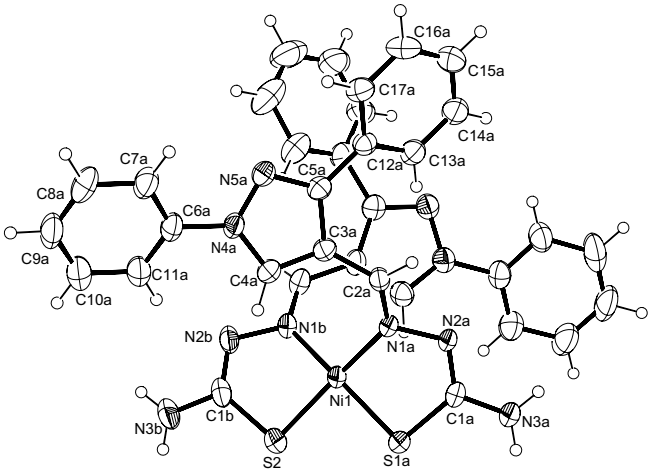


Fig. 4. Crystal structure of [Ni(Ph_2PzTSC-H)$_2$] with the atomic numbering scheme (the atomic numbering in the branch B is equivalent to A and is partly excluded for the sake of clarity). Ellipsoids are drawn at the 50% probability level.

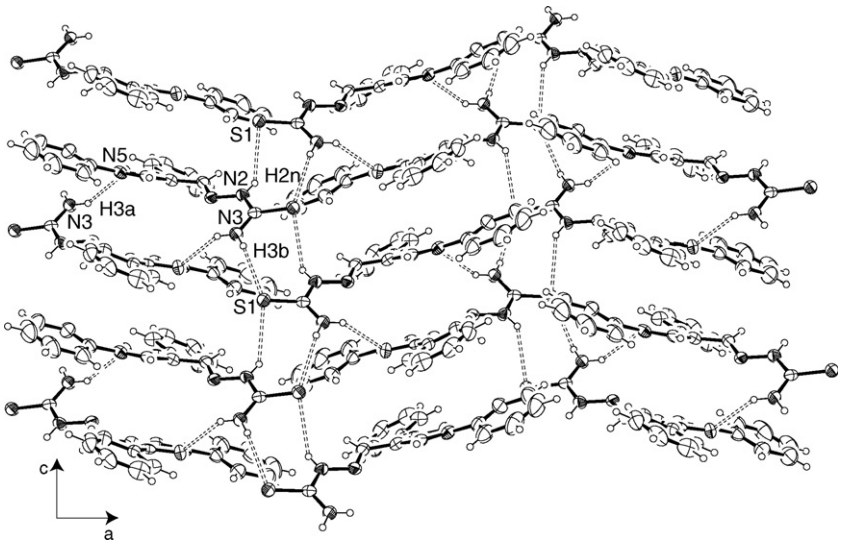


Fig. 3. View of the 2D hydrogen bonding linkage in Ph_2PzTSC.

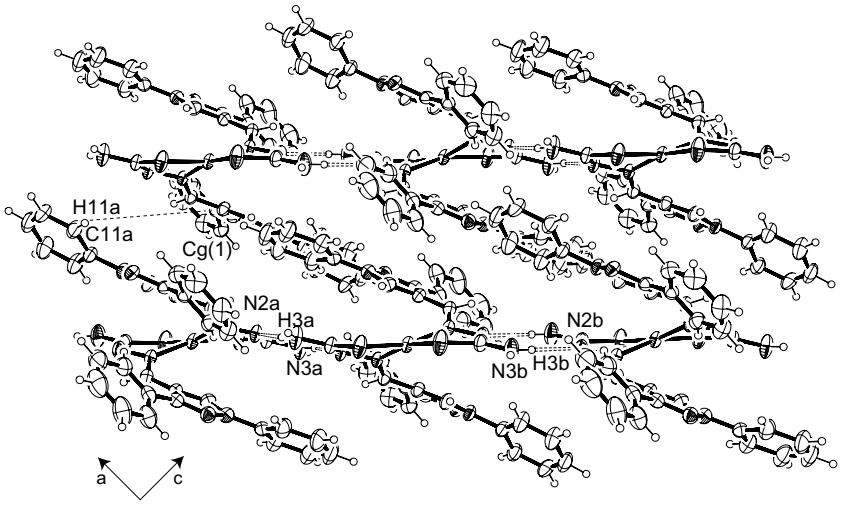


Fig. 5. Segment of the 2D molecular arrangement in [Ni(Ph_2PzTSC-H)$_2$].

braking of the N3–H3···N5 hydrogen bond, which plays a key role in the ligand's crystal arrangement. In the molecule of complex, the atom N5 remains only as an acceptor in the two intramolecular C–H···N bonds also present in the molecule of the free ligand (Table 3).

The molecules of complex are interconnected by the two pairs of N–H···N hydrogen bonds acting on each side of the molecule and connecting the [Ni(Ph_2PzTSC-H)$_2$] into the chains parallel to the diagonal of the *ac* plane. There is no further hydrogen bonding in this crystal structure; however the arrangement of the bulky carbonyl fragments provides the additional stabilizing contacts of the C–H···π type (C13a–H13a···Cg(1)^{i}: H13a···Cg = 2.92 Å, C13a–H13a···Cg = 140.1°; C11a–H11a···Cg(2)^{ii}: H11a···Cg = 2.88 Å, C11a–H11a···Cg = 137.1°; C17b–H17b···Cg(1)^{iii}: H17b···Cg = 2.99 Å, C17b–H17b···Cg = 102.3°. Cg(1) and Cg(2) are the centers of the rings N4b–C5b and C12a–C17a respectively. Symmetry codes: (i) x, y, z; (ii): $-x+1$, $-y$, $-z+2$; (iii) $-x$, $-y-1$, $-z+1$). It is interesting to notice that the dihedral angles formed between the central pyrazole moiety and the phenyl rings increase, compared to the corresponding angles in the ligand molecule (from 18.1° and 19.0° in HL to 27.0° and 27.2° (branch A) and 26.2° and 27.2° (B branch) of [Ni(Ph_2PzTSC-H)$_2$] respectively). However, in contrast to the branch B where the phenyl rings are as in the case of the ligand titled in the same direction regarding the pyrazole ring (the dihedral angle between the phenyls is 16.7°), in the A branch the phenyl rings are titled in the mutually opposite directions regarding the pyrazole (the dihedral angle between the phenyls is 49.3°). Namely, the C6a–C11a phenyl has the orientation which is different from those present in the free ligand and the branch B. It appears that in the absence of the other intermolecular interactions the C11a–H···π interaction in which this phenyl is involved has the decisive role in its final orientation. The segment of the 2D molecular arrangement is given in Fig. 5.

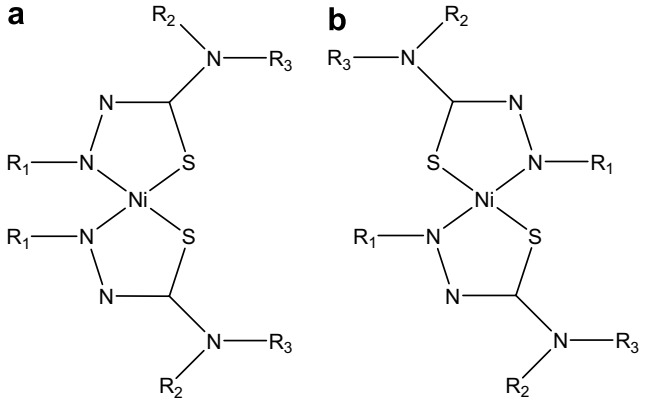


Fig. 6. Bis (bidentate) *cis*- and *trans*-Ni(II) complexes with thiosemicarbazide-based ligands.

3.5.3. Comparative database study of the similar bis(bidentate) Ni(II) complexes with the thiosemicarbazide-based ligands

As the X-ray analysis of [Ni(Ph_2PzTSC-H)$_2$] has shown, the square-planar geometry of this complex is rather tetrahedrally deformed (NNSS donor atoms deviate for 0.27 Å in average from the mean plane defined with these atoms). To compare its structural parameters and the coordination geometry to those of the similar bis(bidentate) Ni(II) complexes with the thiosemicarbazide-based ligands (Fig. 6) the CSD [40] search has been included. There are 37 crystal structures with the coordination number four extracted from the CSD and their refcodes are listed in Table 4.[1] The fact that only one (NIEPZF) of these structures shows the tetrahedral arrangement of the ligands can be explained by known preference of the Ni(II) ions to form square-planar complexes. From the remaining crystal structures, only

[1] List of references for all crystal structures extracted from CSD is given in the Supplementary material.

Table 4
Selected geometrical parameters for four-coordinated Ni(II) complexes with bidentate thiosemicarbazide-based ligands

Refcode[a]	P1/P2 (°)	Ni_P3 (Å)	Ni_P4 (Å)
NIEPZF	75.5	0.170	0.171
cis			
JEYPOS*	24.6	0.639	0.629
[Ni(Ph_2PzTSC-H)$_2$]*	22.7	0.602	0.596
XARWOC*	20.6	0.717	0.573
QEBDEG*	19.5	0.591	0.621
QEBDEG*	12.7	0.723	0.764
NIDTSS10	6.6	0.093	0.093
QEBDAC*	5.8	0.759	0.758
CNITSC	1.1	0.010	0.010
ALAHIE	0.2	0.112	0.074
WERNIQ	0.2	0.027	0.027
trans			
WUHQEV	4.2	0.491	0.191
XENNIN	3.9	0.249	0.162
BAKBUL	0.1	0.295	0.297
TCARNI01	0.0	0.213	0.213
EHAZOC	0.0	0.409	0.409
KUXLEU	0.0	0.232	0.232
ABECOA	0.0	0.108	0.108
ZOJXIF	0.0	0.089	0.089
BAKBIZ	0.0	0.219	0.219
RONDUT	0.0	0.419	0.419
WABHOX	0.0	0.277	0.277
BAKBOF	0.0	0.133	0.133
FIBWIX	0.0	0.205	0.205
TCARNI	0.0	0.198	0.198
FUTRAN	0.0	0.191	0.191
NIDTSS10	0.0	0.061	0.061
NIPTCZ10	0.0	0.008	0.008
BAKBEV	0.0	0.170	0.170
HOPCEU	0.0	0.386	0.386
VOGVIW	0.0	0.292	0.292
EHAZUI	0.0	0.146	0.146
EBEHEZ	0.0	0.351	0.351
KOMGAU	0.0	0.512	0.512
QOVGAJ	0.0	0.272	0.272
NSEMSU	0.0	0.002	0.002
ABECOA	0.0	0.133	0.133
FACKIE	0.0	0.569	0.569
IHAXAQ	0.0	0.445	0.445
TIFTUX	0.0	0.281	0.281
TNITSC	0.0	0.282	0.282

The complexes with the *cis*-positioned voluminous ligands are labeled by asterisk (*).

[a] List of references for all crystal structures extracted from CSD is given in the Supplementary material.

eight show the *cis* mutual arrangement (Fig. 6a) of the bidentate ligands, suggesting that this configuration is generally less favorable than *trans* (Fig. 6b). As expected, due to the steric hindrance the interligand N–Ni–N angle is larger in the *cis*-complexes with bulky carbonyl moieties attached to N donor atoms and it is ranging from 99.7° to 103.8°. Corresponding geometrical parameters calculated for [Ni(Ph_2PzTSC-H)$_2$] correlate very well with these values.

To compare the extent of the tetrahedral distortion on the same level (from the ideal square-planar geometry) in each of the listed complexes, we have analyzed the values of the dihedral angles formed between two N–Ni–S best planes. In Table 4. this angle is assigned as P1/P2. Because the N–Ni–S planes contain the central metal ion and a whole set of the donor atoms, the angle between them is sufficient to define the degree of the deformation of the coordination geometry from the ideal square-planar (P1/P2 = 0°) toward the tetrahedral one (P1/P2 = 90°). The structures in Table 4 are sorted with the reference to P1/P2 parameter. According to it the greatest deformations from the regular square-planar geometry are found in the complexes with the *cis*-positioned voluminous ligands as it is the case in the novel [Ni(Ph_2PzTSC-H)$_2$] which is the second most deformed. Interesting is the case of QEBDAC structure which exhibits somewhat less deformed square-planar geometry (P1/P2 parameter) but the most deformed chelate rings (based on parameters Ni_P3 and Ni_P4 which represent the displacement of the Ni atom from the best planes of the rest of the chelate rings). These observations suggest that there are two ways in which the geometry of the *cis*-Ni(II) square-planar complexes adopts to the requirements of the voluminous ligands: (1) through the distortion of the coordination geometry around the metal ion; (2) through the deformation of the preferentially planar five membered chelate rings.

It is evident that the *trans*-complexes have more regular square-planar geometry which is reflected in very low values of the P1/P2 parameter (Table 4) with NNSS donor atoms being practically in coplanar position. If voluminous substituents in these complexes exist they are also in *trans* position and from that reason they are not able to form intramolecular steric interactions. It seems however that in some cases (KOMGAU and FACKIE) they still affect the chelate rings conformation.

3.6. Thermal analysis

The decomposition curves of Ph_2PzTSC refer to the melting of the compound which is accompanied by its decomposition with an onset temperature of 490 K (217 °C). The fragmentation steps are superposed avoiding thus the determination of the decomposition mechanism. Some coke residue is observed in argon above 1000 K.

The decomposition of [Ni(Ph_2PzTSC-H)$_2$] begins at the same temperature (490 K) as that of the ligand with a low mass loss of about 2% (repeated measurements with samples from different synthesis). This means that the complex formation does not raise the thermal stability of the compound as is usual. On the basis of the mass loss, taking into account the short range interactions in the crystal, the leaving fragment is most probable an ammonia molecule (Calc. 2.4%). In IR spectrum of the intermediate the band of the original complex, assigned to $\nu(NH_2)$ vibration, has almost completely vanished, supporting the proposition of the departure of an ammonia molecule during the thermal decomposition up to 520 K. The deep purple color of the complex has also changed to dark brown.

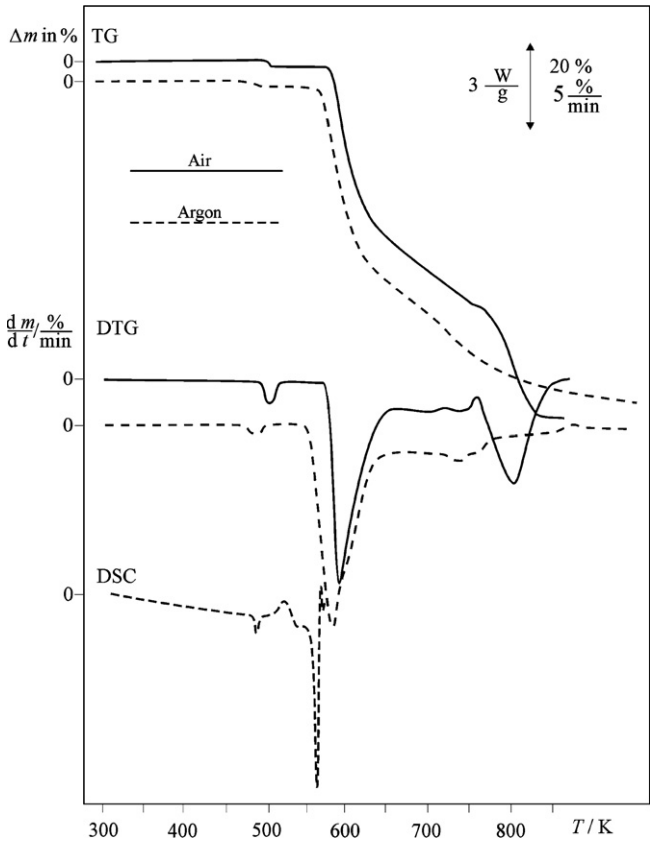


Fig. 7. Thermal decomposition curves of [Ni(Ph_2PzTSC-H)$_2$].

The mass loss is accompanied with an endothermic DSC peak which is followed by an exothermic one in a temperature range of 510–530 K. For this DSC peak no corresponding DTG peak is observed (see Fig. 7). Namely, in 510–560 K temperature range DTG curve falls to zero referring to formation of a stable intermediate. The exothermic process may be the consequence of a spontaneous intra- or intermolecular rearrangement [41], due to the loss of NH_3 molecule. According to the observation with a hot-stage microscope, there is no melting of the intermediate up to 550 K. The melting with an onset temperature at 550 K is immediately followed by an exothermic decomposition.

The decomposition of the complex begins at somewhat higher temperature in air, being continuous above 560 K in both atmospheres (Fig. 7). There is no possibility thus to determine the decomposition mechanism. As in sulfur containing complexes in air, in a platinum crucible, uncontrollable oxidation processes are taking place [42,43], it is meaningless to analyze the composition of the residue. In argon the decomposition is not finished up to 1000 K.

Acknowledgments

This work was supported by the Ministry of Science and Environmental Protection of the Republic of Serbia (Project No. 142028B) and the Provincial Secretariat for Science and Technological Development of Vojvodina.

Appendix A. Supplementary material

CCDC 633472 and 633473 contain the supplementary crystallographic data for Ph_2PzTSC and [Ni(Ph_2PzTSC-H)$_2$]. These data can be obtained free of charge via http://www.ccdc.cam.ac.uk/conts/retrieving.html, or from the Cambridge Crystallographic Data Centre, 12 Union Road, Cambridge CB2 1EZ, UK; fax: (+44) 1223-336-033; or e-mail: deposit@ccdc.cam.ac.uk. Supplementary data associated with this article can be found in the online version, at doi:10.1016/j.poly.2007.04.012.

References

[1] D.L. Klayman, J.F. Bartosevich, T.S. Griffin, C.J. Mason, J.P. Scovill, J. Med. Chem. 22 (1979) 855.
[2] D.X. West, S.B. Padhye, P.B. Sonawane, Struct. Bond. 76 (1991) 1.
[3] A.E. Liberta, D.X. West, Biometals 5 (1992) 121.
[4] F.A. French, E.J. Blanz, J.R. Do Amaral, D.A. French, J. Med. Chem. 13 (1970) 1117.
[5] H. Beraldo, D. Gambino, Mini. Rev. Med. Chem. 4 (2004) 31.
[6] W.L. John, R.M. Patera, M.J. Plummer, B.P. Halling, D.A. Yuhas, Pest. Sci. 42 (1994) 29.
[7] M.J. Genin, C. Biles, B.J. Keiser, S.M. Poppe, S.M. Swaney, W.G. Tarplay, Y. Yagi, D.L. Romero, J. Med. Chem. 43 (2000) 1034.
[8] H. Hashimoto, K. Imamura, J.I. Haruta, K. Wakitani, J. Med. Chem. 45 (2002) 1511.
[9] A.G. Habeeb, P.N.P. Rao, E.E. Knaus, J. Med. Chem. 44 (2001) 3039.
[10] M.L.P. Price, W.L. Jorgensen, J. Am. Chem. Soc. 122 (2000) 9455.
[11] R.R. Ranatunge, R.A. Earl, D.S. Garvey, D.R. Janero, L.G. Letts, A.M. Martino, M.G. Murty, S.K. Richardson, D.J. Schwalb, D.V. Young, I.S. Zemtseva, Bioorg. Med. Chem. Lett. 14 (2004) 6049.
[12] E. Elzein, R. Kalla, X. Li, T. Perry, E. Parkhill, V. Palle, V. Varkhedkar, A. Gimbel, D. Zeng, D. Lustig, D. Leung, J. Zablocki, Bioorg. Med. Chem. Lett. 16 (2006) 302.
[13] D.X. West, A.E. Liberta, S.B. Padhye, R.C. Chikate, P.B. Sonawane, A.S. Kumbhar, R.G. Yerande, Coord. Chem. Rev. 123 (1993) 49.
[14] A.K. Barik, S. Paul, S.K. Kar, R.J. Butcher, J.C. Bryan, Polyhedron 18 (1998) 571.
[15] N.C. Saha, R.J. Butcher, S. Chaudhuri, N. Saha, Polyhedron 22 (2003) 383.
[16] N.C. Saha, R.J. Butcher, S. Chaudhuri, N. Saha, Polyhedron 24 (2005) 1015.
[17] D.D. Perrin, W.L.F. Armarego, D.R. Perrin, Purification of Laboratory Chemicals, second ed., Pergamon Press, Oxford, 1980.
[18] P. Rathelot, N. Azas, H. El-Kashef, F. Delmas, C. Di Giorgio, P. Timon-David, J. Maldonado, P. Vanelle, Eur. J. Med. Chem. 37 (2002) 671.
[19] Enraf-Nonius CAD4 Software, Version 5.0, Enraf-Nonius, Delft, The Netherlands, 1989.
[20] CAD-4 Express Software. Enraf-Nonius, Delft, The Netherlands, 1994.
[21] (a) G.M. Sheldrick, SHELXS97. Program for the Solution of Crystal Structures, University of Göttingen, Germany, 1997;
(b) G.M. Sheldrick, SHELXL97. Program for the Refinement of Crystal Structures, University of Göttingen, Germany, 1997.
[22] (a) A.L. Spek, Acta Crystallogr., Sect. A 46 (1990) C34;
(b) A.L. Spek, PLATON, A Multipurpose: Crystallographic Tool, Utrecht University, Utrecht, The Netherlands, 1998.
[23] L.J. Farrugia, J. Appl. Crystallogr. 32 (1999) 837.
[24] M. Nardelli PARST, J. Appl. Crystallogr. 28 (1995) 659.
[25] L.J. Farrugia ORTEPIII for Windows, J. Appl. Crystallogr. 30 (1997) 565.
[26] Y. Tian, C. Duan, C. Zhao, X. You, Inorg. Chem. 36 (1997) 1247.

[27] M.R. Maurya, A. Kumar, M. Abid, A. Azam, Inorg. Chim. Acta 359 (2006) 2439.
[28] R.M. Silverstein, C.G. Bassler, T.C. Morrill, Spectrometric Identification of Organic Compounds, third ed., John Wiley and Sons Inc., New York, 1974, p. 113.
[29] P. Bera, N. Saha, S. Kumar, D. Banerjee, R. Bhattacharya, Transition Met. Chem. 24 (1999) 425.
[30] M.B. Ferrari, S. Capacchi, G. Reffo, G. Pelosi, P. Tarasconi, R. Albertini, S. Pinelli, P. Lunghi, J. Inorg. Biochem. 81 (2000) 89.
[31] P. Bindu, M.R.P. Kurup, T.R. Satyakeerty, Polyhedron 18 (1999) 321.
[32] E.M. Jouad, M. Allain, M.A. Khan, G.M. Bouet, Polyhedron 24 (2005) 327.
[33] E.M. Jouad, M. Allain, M.A. Khan, G.M. Bouet, J. Mol. Struct. 604 (2002) 205.
[34] M. Rodriguez-Argüelles, M.B. Ferrari, G.G. Fava, G. Pelizzi, G. Pelosi, R. Albertini, A. Bonati, P.P. Dall' Aglio, P. Lunghi, S. Pinelli, J. Inorg. Biochem. 66 (1997) 7.
[35] J.S. Casas, M.C. Rodriguez-Argüelles, U. Russo, A. Sanchez, J. Sordo, A. Vazquez-Lopez, S. Pinelli, P. Lunghi, A. Bonati, R. Albertini, J. Inorg. Biochem. 69 (1998) 283.
[36] M.R. Maurya, A. Kumar, A.R. Bhat, A. Azam, C. Bader, D. Rehder, Inorg. Chem. 45 (2006) 1260.
[37] M. Belicchi Ferrari, A. Bonardi, G. Gaspari Fava, C. Pelizzi, P. Tarasconi, Inorg. Chim. Acta 223 (1994) 77.
[38] A.B.P. Lever, Inorganic Electronic Spectroscopy, Russian Edition., Mir, Moscow, 1987, p. 2.
[39] M. Dincer, N. Ozdemir, I. Yildirim, E. Demir, Y. Akcamur, S. Isik, Acta Crystallogr., Sect. E 60 (2004) o317.
[40] F.H. Allen, Acta Crystallogr., Sect. B 58 (2002) 380.
[41] H.A. El-Boraey, J. Therm. Anal. Cal. 81 (2005) 339.
[42] K. Mészáros Szécsényi, V.M. Leovac, Ž.K. Jaćimović, G. Pokol, J. Therm. Anal. Cal. 74 (2003) 943.
[43] A. Kovács, D. Nemcsok, G. Pokol, K. Mészáros Szécsényi, V.M. Leovac, Ž.K. Jaćimović, I. Radosavljević Evans, J.A.K. Howard, Z.D. Tomić, G. Giester, New J. Chem. 29 (2005) 833.

a small amount of $(PMe_3)_2B_{12}H_{10}$ [6]. These compounds were characterized by elemental analysis only. The possibility of isomers of $(PMe_3)_2B_{12}H_{10}$ was not addressed.

During our studies of the syntheses of pallada-diarsaboranes, we obtained some products having charge-compensating Lewis base ligands bonded to cage boron atoms [8]. Many other transition metal-mediated substitution reactions of phosphines (PR_3) onto boron atoms of polyhedral cage molecules have been reported. For example, reaction of $PdI_2(PPh_3)_2$ with $Cs[TeB_{10}H_{11}]$ in refluxing toluene formed 2-I-2-PPh_3-*closo*-2,1-$PdTeB_{10}H_9(PPh_3)$ in good yield [9]. Another example is the conversion of 8,8-$(PMe_2Ph)_2$-*nido*-8,7-$PtCB_9H_{11}$ in refluxing toluene to 6-PMe_2Ph-*closo*-1-CB_9H_8 in good yield [10]. These results lead us to study more generally some palladium-assisted substitution reactions of $B_{10}H_{10}(-2)$ and $B_{12}H_{12}(-2)$ ions, including a brief mention of 1,7-$(PMe_2Ph)_2B_{12}H_{10}$ [11]. Recently, the synthesis and crystal structure determination of $N(n\text{-}Bu)_4[PPh_3\text{-}B_{12}H_{11}]$ was reported [12]. This derivative was prepared by reaction of $[N(n\text{-}Bu)_4]_2[B_{12}H_{11}I]$ with $Pd(Ph_3)_4$.

In this report, we describe in detail the reaction of $(PMe_2Ph)_2PdCl_2$ with $Na_2[B_{12}H_{12}]$ and also with K[7,8-$C_2B_9H_{12}$] to give several charge-compensated products in moderate yields.

2. Experimental

2.1. Physical measurements

Boron (^{11}B) NMR spectra were obtained at 115.85 MHz (21 °C) with a Nicolet NT-360 spectrometer and were externally referenced to $BF_3(OEt_2)$. Phosphorus (^{31}P) NMR spectra were obtained at 146.2 MHz (21 °C) and externally referenced to 85% H_3PO_4. Proton (^1H) NMR spectra were obtained at 361.1 MHz (21 °C) and internally referenced to trace protonated solvent. In all NMR spectra, positive chemical shifts were downfield. Melting points were obtained in sealed, evacuated capillaries and are uncorrected.

2.2. Materials

All reactions were performed under an atmosphere of prepurified nitrogen. Tetrahydrofuran (THF) was freshly distilled from sodium benzophenone ketyl. Dichloromethane (CH_2Cl_2) was distilled from P_2O_5. Potassium dodecahydro-7,8-dicarba-*nido*-undecaborate(1−), K[7,8-$C_2B_9H_{12}$], was prepared by a literature method [13]. Bis(dimethylphenylphosphine) palladium(II) chloride was prepared by the method of Wild et al. [14].

2.3. $(PMe_2Ph)_2$-*closo*-$B_{12}H_{10}$ isomers and $Na[(PMe_2Ph)$-*closo*-$B_{12}H_{11}]$

In a typical reaction scheme, $Na_2B_{12}H_{12}$ (1.81 g, 9.6 mmol) was placed in a 500 mL round-bottom flask equipped with a magnetic stir bar and dissolved in 40 mL dry THF. In a separate flask, $(PMe_2Ph)_2PdCl_2$ (4.35 g, 9.6 mmol) was dissolved in 240 mL of dry THF and then transferred slowly via cannula to the stirred solution of $Na_2B_{12}H_{12}$. The mixture was stirred at room temperature for 1 day during which time the color changed from orange to brown. The mixture was vacuum filtered to remove solid material. To the clear THF solution was added an excess of $NaBH_4$ to reduce all remaining palladium species to Pd^0. Vigorous gas evolution occurred as the mixture was brought to reflux, which was continued for 6 h. The mixture was left at room temperature over night to complete the reduction. The mixture was filtered through a coarse-fritted filter under nitrogen to remove the reduced metal solids (*Caution:* The filtered solids may spontaneously ignite if exposed to air). The THF was removed from the filtrate by rotary evaporation leaving a thick white oil. This crude mixture was dissolved in CH_2Cl_2 and mixed with 3 g of silica gel (Merck grade 60, 230–400 mesh, 60 Å). The CH_2Cl_2 was removed in vacuo and the solids were packed on a 35 cm × 2.4 cm silica gel chromatography column, and eluted initially with 1:1 (v/v) toluene:CH_2Cl_2. There were four bands. Band I, $R_f = 0.96$ by TLC (CH_2Cl_2 mobile phase, I_2 development) was determined by ^{11}B NMR to be $(PMe_2Ph)BH_3$, $^{11}B\{^1H\}$, −38 ppm, $J_{B-P} = 61$ Hz [15] Band II, $R_f = 0.85$ was a white solid (353 mg, 8.82% yield) and $R_f = 0.6$ was determined to be 1,12-$(PMe_2Ph)_2$-$B_{12}H_{10}$ by ^{11}B NMR (see Table 1). Band III, 1,7-$(PMe_2Ph)_2$-$B_{12}H_{10}$, a white solid, m.p. 202–206 °C (1.201 g, 30.14% yield). And band IV was eluted with 1:1 CH_2Cl_2:CH_3CN and was found to be a relatively insoluble compound, whose ^{11}B NMR spectrum was consistent with Na-[(PMe_2Ph)-$B_{12}H_{11}$] (see Table 2–6).

2.4. PMe_2Ph-*nido*-7,8-$C_2B_9H_{11}$ isomers

In a two-neck, round-bottom flask equipped with a septum and nitrogen inlet were placed K[*nido*-7,8-$C_2B_9H_{12}$] (172 mg, 0.998 mmol) and $(PMe_2Ph_2PdCl_2$ (226 mg, 0.498 mmol), and 25 mL dry distilled CH_2Cl_2. The dicarbollide salt did not fully dissolve. The solution gradually darkened from yellow to orange to brown while stirring overnight. The reaction mixture was filtered on a coarse-fritted funnel, to leave behind some gray solids. The brown filtrate was rotary evaporated, and the remaining solids extracted with benzene. An excess of $NaBH_4$ was added to the benzene solution to reduce all remaining palladium species to Pd^0. The solution was brought to reflux for 4 h. The mixture was filtered through a coarse-fritted funnel to remove fluffy grayish solids, resulting in a nearly colorless filtrate. The benzene was rotary evaporated to a yellow oil (221 mg, 81.9% crude yield). ^{11}B NMR indicated that the oil consisted of a mixture of 9-PMe_2Ph-*nido*-7,8-$C_2B_9H_{11}$ (major product) and 10-PMe_2Ph-*nido*-7,8-$C_2B_9H_{11}$ (minor product). Subsequent crystallization from CH_2Cl_2/pentane at 5 °C yielded pale yellow needles of 9-PMe_2Ph-*nido*-7,8-$C_2B_9H_{11}$.

Table 1
^{11}B NMR data

Compound	Chemical shift (ppm), (relative intensities) [$J_{^{11}B-H}$ (Hz)]
1,12-$(PMe_2Ph)_2$-$B_{12}H_{10}$	−13.8, (10B) [129]; −16.1, (2B) [$J_{^{11}B-^{31}P} \cong 230$ Hz]
1,7-$(PMe_2Ph)_2$-$B_{12}H_{10}$	−11.9, (4B); −13.6, (4B) [159]; −15.3, (2B); −16.2, (2B) [$J_{^{11}B-^{31}P} \cong 150$ Hz]
Na[(PMe_2Ph)-$B_{12}H_{11}$]	−11.1, (1B) [132]; −13.4, (5B) [138]; −14.9, (5B) [141] −17.6, (1B) [$J_{^{11}B-^{31}P} = 141$ Hz]
N(*n*-Bu)$_4$[PPh_3-$B_{12}H_{11}$][a]	−8.4, (1B); −12.3 (5B); −13.5, (5B); −17.9 (1B) [$J_{^{11}B-^{31}P} = 134$ Hz]
9-PMe_2Ph-7,8-$C_2B_9H_{11}$	−4.1 (1B), [138]; −10.1 (1B), [145]; −15.6 (1B), [$J_{^{11}B-^{31}P} = 155$ Hz]; −16.1 (1B); −18.0 (1B); −23.6 (1B) [156]; −25.5 (1B) [145] −28.3 (1B) [129]; −36.2 (1B) [143]
10-PMe_2Ph-7,8-$C_2B_9H_{11}$	−11.0 (2B); −15.0 (1B); −16.1 (2B); −20.7 (2B) [154]; −34.5 (1B) [$J_{^{11}B-^{31}P} \cong 145$ Hz] −36.1 (1B)
9-PPh_3-7,8-$C_2B_9H_{11}$[b]	−2.97 (1B); −9.26 (1B); −14.89 (1B) [$J_{^{11}B-^{31}P} = 155$ Hz]; −16.37 (1B) −17.80 (1B); −23.46 (1B), −25.50 (1B) −26.89 (1B); −36.04 (1B)
9-PPh_3-7,8-$C_2B_9H_{11}$[c]	−1.42 (1B); −7.76 (1B); −12.98 (1B) [$J_{^{11}B-^{31}P} = 149$ Hz] −14.58 (1B); −16.20 (1B); −21.86 (1B) −23.78 (1B); −25.33 (1B); −34.47 (1B)
10-PPh_3-7,8-$C_2B_9H_{11}$[c]	−9.86 (2B); 14.16 (3B); −19.02 (2B) −32.18 (1B) [$J_{^{11}B-^{31}P} = 150$ Hz]; −35.83 (1B)
9-PPh_2Me-7,8-$C_2B_9H_{11}$[c]	−2.34 (1B); −8.56 (1B); −12.61 (1B) [$J_{^{11}B-^{31}P} = 164$ Hz] −15.12 (1B); −16.60 (1B); −22.13 (1B); −23.90 (2B); −26.52 (1B); −35.04 (1B)
10-PPh_2Me-7,8-$C_2B_9H_{11}$[c]	−9.72 (2B); −14.50 (3B); −19.25 (2B) −33.02 (1B) [$J_{^{11}B-^{31}P} = 150$ Hz]; −36.05 (1B)

[a] Ref. [12], $CHCl_3$ solvent.
[b] Ref. [22], solvent, CH_2Cl_2.
[c] Refs. [20,21].

Table 2
^{1}H NMR data

Compound	Chemical shift (ppm), (relative intensities) assignt, multiplicity, $^2J_{H-P}$ (Hz)
1,7-$(PMe_2Ph)_2$-$B_{12}H_{10}$[a]	1.78, (12H), P*Me*$_2$, doublet, 12.2 7.4–7.6, (10H), P*Ph*, multiplet
1,12-$(PMe_2Ph)_2$-$B_{12}H_{10}$	1.56, (12H), P*Me*$_2$, doublet, 10.3 7.4–7.6, (10H), P*Ph*, multiplet
9-PMe_2Ph-7,8-$C_2B_9H_{11}$	1.81, (3H), PMe_2, doublet, 11.9 1.89, (3H), PMe_2, doublet, 12.1 2.23 (2H), *H*-Carb. 7.58–7.77, (5H) P*Ph*, multiplet

[a] $CDCl_3$ solvent.

Table 3
^{31}P{^{1}H} NMR data

Compound	Chemical shift (ppm), multiplicity, J_{B-P} (Hz)
1,7-$(PMe_2Ph)_2$-$B_{12}H_{10}$	−8.9, 1:1:1:1 quartet, 150
9-PMe_2Ph-7,8-$C_2B_9H_{11}$	−7.8, 1:1:1:1 quartet, 151

Table 4
Crystallographic data

Compound	1,7-(PMe_2Ph)-$B_{12}H_{10}$	9-PMe_2Ph-7,8-$C_2B_9H_{11}$
Molecular weight	416.10	270.55
Crystal system, *Z*	triclinic, $P\bar{1}$, 2	monoclinic, *C*2/*c*, 8
Unit cell		
A (Å)	9.607(1)	29.978(9)
B (Å)	14.997(2)	6.769(2)
C (Å)	8.934(1)	17.063(5)
α (°)	99.32(0)	
β (°)	109.86(0)	115.02(1)
γ (°)	88.05(0)	
V (Å^3)	1194.31	3137.44
ρ_{calc} (g cm^{-3})	1.157	1.146
λ (Å)	0.71069	0.71069
μ (cm^{-1})	1.799	1.481
Det-samp distance (cm)	22.5	22.5
Samp-source distance (cm)	23.5	23.5
Takeoff angle (°)	2.0	2.0
Average ω scan width at half-height (°)	0.25	0.25
Scan speed (°/min)	4.0	10.0
Scan width (°)	2.0 + dispersion	1.8 + dispersion
Single bkgd time at extremes of scan (s)	4	4
Aperture size (mm)	3.0 × 4.0	3.0 × 4.0
Collection limit (2θ, °)	6–45	6–45
Total number of reflections	3384	2296
Number of unique intensity	3133	2059
Number with $F > 0.0$	3018	1927
Number with $F > 2.33^*\sigma(F)$	2714	1626
R for averaging	0.011	0.032
Final residuals		
R(*F*)	0.0338	0.0403
$R_w(F)$	0.0366	0.0425
Goodness-of-fit for last cycle	1.938	1.334
Maximum Δ/σ for last cycle	0.05	0.11

Det-samp dist, detector to sample distance; Samp-source distance, sample to X-ray source distance; Single bkgd time at extremes of scan, single background time at extremes of scan.

2.5. Crystal structure determinations – general

The diffractometer utilized for data collection was designed and constructed locally. The apparatus comprised a Picker X-ray generator and Picker four-circle goniostat equipped with a Furnas Monochromater (HOG crystal) was modified by addition of stepping motors (Slo-Syn) on each of the four axes, and a fifth motor drives a 20-position filter/attenuator wheel. The latter allows top/bottom-left/right alignment of reflections. All motors are driven by a locally designed ISA board in an IBM-PC compatible computer. The computer also has a timer/scaler board which is used to accumulate the counts from the scintillation counter

Table 5
Selected bond distances (Å) for 1,7-$(PMe_2Ph)_2$-*closo*-$B_{12}H_{10}$

P(13)–B(1)	1.9055(25)	B(4)–B(9)	1.787(4)
P(22)–B(7)	1.9113(25)	B(5)–B(6)	1.792(4)
B(1)–B(2)	1.768(3)	B(5)–B(9)	1.776(4)
B(1)–B(3)	1.760(3)	B(5)–B(10)	1.785(4)
B(1)–B(4)	1.769(3)	B(6)–B(10)	1.788(4)
B(1)–B(5)	1.765(4)	B(6)–B(11)	1.780(4)
B(1)–B(6)	1.775(3)	B(7)–B(8)	1.770(3)
B(2)–B(3)	1.804(3)	B(7)–B(11)	1.778(3)
B(2)–B(6)	1.794(4)	B(7)–B(12)	1.772(3)
B(2)–B(7)	1.769(3)	B(8)–B(9)	1.787(4)
B(2)–B(11)	1.789(3)	B(8)–B(12)	1.799(4)
B(3)–B(4)	1.789(3)	B(9)–B(10)	1.802(4)
B(3)–B(7)	1.763(3)	B(9)–B(12)	1.787(4)
B(3)–B(8)	1.791(4)	B(10)–B(11)	1.783(4)
B(4)–B(5)	1.790(4)	B(10)–B(12)	1.790(4)
B(4)–B(8)	1.773(4)	B(11)–B(12)	1.795(4)

Table 6
Selected bond distances (Å) for 9-(PMe_2Ph)-*nido*-7,8-$C_2B_9H_{11}$

P(12)–B(9)	1.905(3)	B(3)–C(8)	1.735(4)
B(1)–B(2)	1.745(5)	B(4)–B(5)	1.762(5)
B(1)–B(3)	1.774(5)	B(4)–C(8)	1.738(4)
B(1)–B(4)	1.780(5)	B(4)–B(9)	1.761(4)
B(1)–B(5)	1.781(4)	B(5)–B(6)	1.811(5)
B(1)–B(6)	1.811(5)	B(5)–B(9)	1.752(5)
B(2)–B(3)	1.760(5)	B(5)–B(10)	1.798(5)
B(2)–B(6)	1.758(5)	B(6)–B(10)	1.800(5)
B(2)–C(7)	1.694(4)	B(6)–B(11)	1.799(5)
B(2)–B(11)	1.796(5)	C(7)–C(8)	1.534(4)
B(3)–B(4)	1.779(4)	C(7)–B(11)	1.630(5)
B(3)–C(7)	1.705(4)	C(8)–B(9)	1.589(5)
B(10)–B(11)	1.870(5)	B(9)–B(10)	1.792(5)

used with the goniostat. The control software, PCPS.EXE, is the Picker software written by W. E. Streib of the Indiana University Molecular Structure Center (IUMSC). The software for structure solution and refinement include SHELXTL-PC and other versions of SHELX, as well as the XTEL program library.

2.6. Crystal structure determination of 1,7-$(PMe_2Ph)_2B_{12}H_{10}$

A typical crystal of 1,7-$(PMe_2Ph)_2$-$B_{12}H_{10}$ was grown by slow evaporation from a 1:1 solution of toluene and CH_2Cl_2. The crystal was affixed to the end of a glass fiber using silicone grease and transferred to the goniostat where it was cooled to −174 °C for characterization and data collection.

A systematic search of a limited hemisphere of reciprocal space located a set of diffraction maxima with no symmetry or systematic absences, corresponding to a triclinic space group. Subsequent solution and refinement of the structure confirmed the centrosymmetric choice, $P\bar{1}$.

All hydrogen atoms were clearly visible in a difference Fourier phased on the nonhydrogen atoms, and were refined isotropically in the final cycles of refinement. A final difference Fourier was essentially featureless, the largest peak being 0.34 e/Å^3.

2.7. Crystal structure determination of 9-(PMe_2Ph)-7,8-$C_2B_9H_{11}$

Pale yellow crystals of a 9-$PPhMe_2$-7,8-$C_2B_9H_{11}$ were grown from a solution of CH_2Cl_2/pentane held at 5 °C. A small, well-formed fragment of a larger crystal was affixed to the end of a glass fiber using silicone grease and transferred to the goniostat where it was cooled to −174 °C for characterization and data collection.

A systematic search of a limited hemisphere of reciprocal space located a set of diffraction maxima with monoclinic symmetry and systematic absences corresponding to one of the centered space groups $C2/c$ or Cc. Subsequent solution and refinement confirmed the centrosymmetric choice, $C2/c$.

Data were collected using a continuous θ, 2θ scan technique with fixed backgrounds at each extreme of the scan. Data were corrected for Lorentz and polarization effects. The structure was solved by direct methods (MULTAN 78) and standard Fourier techniques. All hydrogen atoms were clearly visible in a difference Fourier phased on the nonhydrogen atoms, and were included in the least squares refinement.

A final difference Fourier was essentially featureless, the largest peak being 0.32 e/Å^3. It was observed that this peak was near the bridging hydride in the B_9C_2 cage, and in fact would appear to bridge the two carbon atoms. Attempts to model this as a partial occupancy bridging hydrogen (with the occupancy of the located bridge allowed to vary also) did not lead to a successful convergence. In all probability, the hydrogen may "float" on the face of the carborane, but the crystallographic evidence is lacking.

The structure is essentially the same as that reported for 9-PPh_3-*nido*-7,8-$C_2B_9H_{11}$ [22] and 9-$PMePh_2$-*nido*-7,8-$C_2B_9H_{11}$ [20,21]. The diphenylmethyl phosphine structure reported by Zakharkin et al. is remarkably similar, and is nearly isostructural [20,21].

3. Results and discussion

3.1. PMe_2Ph derivatives of the $B_{12}H_{12}^{-2}$ ion

Reaction of $Na_2[B_{12}H_{12}]$ with $(PMe_2Ph)_2PdCl_2$ at ambient temperature gave three phosphine-substituted products, each in low yield, namely $Na[(PMe_2Ph)B_{12}H_{11}]$, 1,7-$(PMe_2Ph)_2B_{12}H_{10}$ (30% yield, approx.) and 1,12-$(PMe_2Ph)_2B_{12}H_{10}$ (8% yield, approx.). The crude reaction mixture was subsequently treated with excess sodium borohydride to reduce all palladium-containing intermediates, "L_nPdX_m" to palladium metal. The first band to be eluted during column chromatography on silica gel, 1:1 (v/v) toluene:CH_2Cl_2 was $(PMe_2Ph)BH_3$ identified by ^{11}B NMR, $\delta_{^{11}B} = -38$ ppm, $J_{B-P} = 61$ Hz [15]. The boron in this compound originated from $NaBH_4$, added to the reaction mixture during workup and was not due to degradation of the $B_{12}H_{12}(-2)$ ion.

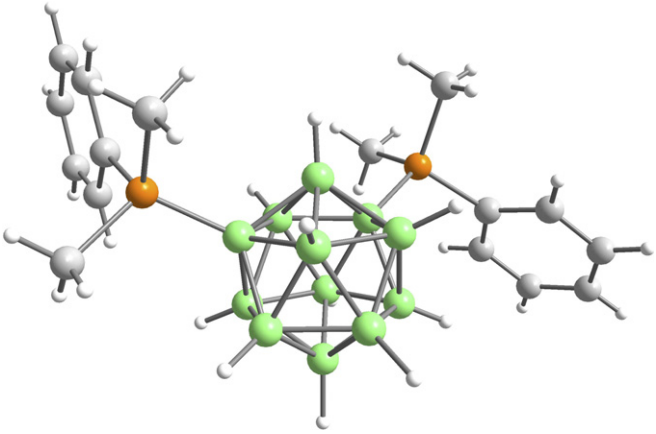


Fig. 1. X-ray structure of 1,7-$(PMe_2Ph)_2$-*closo*-$B_{12}H_{10}$.

The 1,12-$(PMe_2Ph)_2B_{12}H_{10}$ isomer was identified by its ^{11}B NMR spectrum (see Table 1), which indicates a high symmetry (D_{5h}) and excludes the 1,2- or 1,7-isomer configuration for this product.

An X-ray structural determination (Fig. 1) has been undertaken on the other bis-phosphine isomer which was isolated and it conclusively proves it to be the 1,7-isomer.

The 1,7-$(PMe_2Ph)_2B_{12}H_{10}$ product was obtained in the higher yield and is statistically the most favored bis-phosphine derivative. Note that steric factors may be important in this substitution process since to-date no 1,2-bis-phosphine product has been observed.

The X-ray structure (Fig. 1) shows no anomalous distances or angles. The B–P distances, 1.9055 and 1.9113 Å are quite usual, as are the B–B distances, which all are in the range 1.760–1.804 Å. This compares favorably with the B–P distance of 1.928 Å found for $[N(n\text{-}Bu)_4][(PPh_3)\text{-}B_{12}H_{11}]$ [12].

The B–P coupling constant for the 1,7-disubstituted product as determined by ^{31}P NMR was 150 Hz. This is within the range of values observed for similar phosphine-borane compounds (118–200 Hz) [16,17]. The value could not be corroborated by ^{11}B NMR, however, because the doublet was not well-enough resolved for accurate measurement. The B–P coupling constant observed for $Na[(PMe_2Ph)\text{-}B_{12}H_{11}]$ in the ^{11}B NMR spectrum was 141 Hz. This agreed well with the B–P value reported previously for $N(n\text{-}Bu)_4\text{-}[PPh_3\text{-}B_{12}H_{11}]$ of 134 Hz [12].

3.2. PMe_2Ph-*nido*-7,8-$C_2B_9H_{11}$ isomers

Reaction of *nido*-7,8-$C_2B_9H_{12}(-1)$ ion with $(PMe_2Ph)_2\text{-}PdCl_2$ at ambient temperature yielded two isomers of (PMe_2Ph)-*nido*-7,8-$C_2B_9H_{11}$. The combined crude yield of both the asymmetric 9-isomer and symmetric 10-isomer was 82%. The ^{11}B NMR spectrum of the mixture suggested that the 9-isomer predominated by approximately 2:1. Preference for reaction at the 9 position has been observed in electrophilic substitution reaction of *nido*-7,8-$C_2B_9H_{12}(-1)$ ion by I_2 [18], by $(C_5H_5)Fe(CO)_2$(alkene)(+1) ion [19] and by Ph_2PCl [20,21]. The ^{11}B NMR spectra of 9- and 10-PMe_2Ph-*nido*-7,8-$C_2B_9H_{11}$ agree with those of the two isomers of the previously-reported (PPh_3)-*nido*-7,8-$C_2B_9H_{11}$ [20–23] and $(PMePh_2)$-*nido*-7,8-$C_2B_9H_{11}$ [20,21] (see Table 1). The asymmetric 9-isomer has nine distinct resonances in its spectrum, whereas the C_s symmetric 10-isomer has six resonances in a 2:2:2:1:1:1 area ratio. In each of the 9-isomer derivatives, the resonance at approximately −12.6 to −15.6 ppm displayed $^{11}B\text{–}^{31}P$ spin–spin coupling of 149–164 Hz. For the 10-isomer derivatives, the resonance at −32.1 to −34.5 ppm displayed $^{11}B\text{–}^{31}P$ coupling of 145–150 Hz.

The X-ray structure (Fig. 2) shows no anomalous distances or angles. The B–P distance of 1.905 Å is typical of

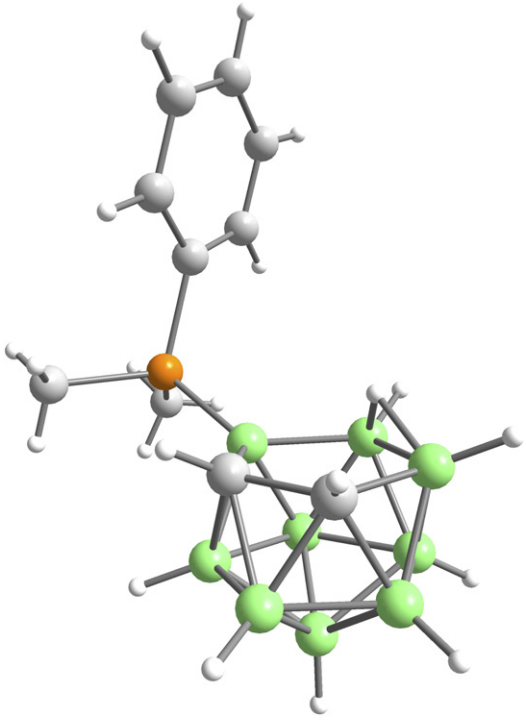


Fig. 2. X-ray structure of 9-(PMe_2Ph)-*nido*-7,8-$C_2B_9H_{11}$.

phosphine boranes; the B–B distances are all in the range 1.745–1.870 Å, and the B–C distances are slightly shorter at 1.589–1.738 Å which is typical of carborane species.

Appendix A. Supplementary material

CCDC 634413 and 634414 contain the supplementary crystallographic data for this paper. These data can be obtained free of charge via http://www.ccdc.cam.ac.uk/conts/retrieving.html, or from the Cambridge Crystallographic Data Centre, 12 Union Road, Cambridge CB2 1EZ, UK; fax: (+44) 1223-336-033; or e-mail: deposit@ccdc.cam.ac.uk. Supplementary data associated with this article can be found, in the online version, at doi:10.1016/j.poly.2007.04.025.

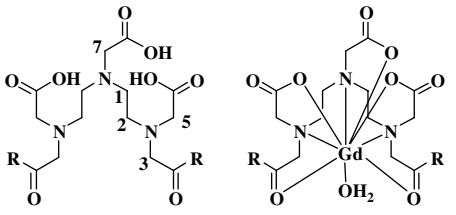
References

[1] R.F. Heck, Palladium Reagents in Organic Syntheses, Academic Press, London, 1985.
[2] A. Suzuki, J. Orgmet. Chem. 576 (1999) 147.
[3] S.R. Chemler, D. Trauner, S.J. Danishefsky, Angew. Chem., Int. Ed. 40 (2001) 4544.
[4] L. Eriksson, I.P. Beletskaya, V.I. Bregadze, I.B. Sivaev, S. Sjoberg, J. Organomet. Chem. 657 (2002) 267.
[5] E.W. Corcoran Jr., L.G. Sneddon, in: J.F. Liebman, A. Greenberg, R.E. Williams (Eds.), Advances in Boron and the Boranes, VCH Publishers, Inc., NewYork, 1988, pp. 71–89.
[6] H.C. Miller, N.E. Miller, E.L. Muetterties, Inorg. Chem. 3 (1964) 1456.
[7] W.H. Knoth, W.R. Hertler, E.L. Muetterties, Inorg. Chem. 4 (1965) 280.
[8] S.A. Jasper Jr., S. Roach, J.N. Stipp, J.C. Huffman, L.J. Todd, Inorg. Chem. 32 (1993) 3072.
[9] G. Ferguson, J.F. Gallagher, M. McGrath, J.P. Sheehan, T.R. Spalding, J.D. Kennedy, J. Chem. Soc., Dalton Trans. (1993) 27.
[10] J.H. Jones, B. Stibr, J.D. Kennedy, M. Thornton-Pett, Coll. Czech. Chem. Commun. 58 (1993) 2924.
[11] S.A. Jasper Jr., R.B. Jones, J. Mattern, J.C. Huffman, L.J. Todd, Inorg. Chem. 33 (1994) 5620.
[12] R. Bernard, D. Cornu, D. Luneau, D. Naoufal, J.P. Scharff, P. Miele, J. Organomet. Chem. 690 (2005) 2745.
[13] J. Plesek, S. Hermanek, B. Stibr, Inorg. Synth. 22 (1983) 231.
[14] N.K. Roberts, B.W. Skelton, A.H. White, S.B. Wild, J. Chem. Soc., Dalton Trans. (1982) 2093.
[15] G.R. Eaton, W.N. Lipscomb, NMR Studies of Boron Hydrides and Related Compounds, W.A. Benjamin, Inc., New York, 1969, p. 460.
[16] J. Bould, P. Brint, J.D. Kennedy, M. Thornton-Pett, J. Chem. Soc., Dalton Trans. (1993) 2335.
[17] G. Ferguson, J.F. Gallagher, J.P. Sheehan, T.R. Spalding, J.D. Kennedy, R. Macias, J. Chem. Soc., Dalton Trans. (1993) 3147.
[18] F.P. Olsen, M.F. Hawthorne, Inorg. Chem. 4 (1965) 1839.
[19] F. Sato, T. Yamamoto, J.R. Wilkinson, L.J. Todd, J. Organomet. Chem. 86 (1975) 243.
[20] L.I. Zakharkin, V.A. Olśhevskaya, G.G. Zhigareva, V.A. Antonovich, P.V. Perovskii, A.I. Yanovskii, A.V. Polyakov, Yu T. Struchkov, Metallorg. Khim. 2 (1989) 1274.
[21] L.I. Zakharkin, V.A. Olśhevskaya, G.G. Zhigareva, V.A. Antonovich, P.V. Perovskii, A.I. Yanovskii, A.V. Polyakov, Yu T. Struchkov, Organomet. Chem. USSR 2 (1989) 671.
[22] K.M. Kim, Y. Do, C.B. Knobler, M.F. Hawthorne, Bull. Kor. Chem. Soc. 10 (1989) 321.
[23] L.I. Zakharkin, N.V. Granberg, V.A. Antonovich, Izv. Akad. Nauk. SSSR, Ser. Khim. 8 (1976) 1830.

may be assumed that, although the dissociation of [Gd(DTPA-BMA)(H_2O)] is fast and a complexation equilibrium exists in body fluids, the high selectivity of the DTPA-BMA ensures sufficient *in vivo* safety of the injected CA [5–7]. More recently, however, it was found that the kinetic stability of [Gd(DTPA-BMA)(H_2O)] and related [Gd(DTPA-bis(amide))(H_2O)] complexes is high enough to be compared with that of $[Gd(DTPA)(H_2O)]^{2-}$ [8,9]. This finding also implies that stability constants and selectivities play a minor role in determining the non-toxicity of a CA; the crucial factor is undoubtedly the high kinetic stability. In other words, toxicity of the Gd(III) complexes is an intrinsic property and cannot be directly related to the thermodynamic or kinetic stabilities. The knowledge of the thermodynamic stability, conditional stability, and selectivity helps to understand the *in vivo* stability of the complexes [10,11].

There are now known a variety of DTPA-bis(amide) ligands, many of which carry aromatic or large aliphatic substituents, thus resulting in poor solubility in water upon complexation with Gd [12–18]. High solubility in water along with non-toxicity is an essential criterion for practical application as MRI CA. Despite the availability of such a great number of DTPA-bis(amides), little synthetic attempt has been made for the modification of the terminal bis(amide) groups with additional alkyl carboxylate sidearms such as seen in Chart 1.

Intrigued by these observations and motivated by our continued search for novel DTPA-bis(amide) ligands, [19] we have designed and synthesized a new class of DTPA-bis(amide) ligands (**1a**–**1l**) and their Gd(III) complexes of the type [Gd(**1**)(H_2O)] · xH_2O (**2a**–**2l**). In addition, with a potential application for as MRI CA in mind, some relevant physicochemical properties were measured. They are (i) the protonation constants of **1a**–**1l**, (ii) thermodynamic and conditional stability constants of **2a**–**2l**, (iii) the selectivity of **1a**–**1l** for the Gd(III) ion over the endogenous metal ions such as Zn(II), Ca(II), and Cu(II), and (iv) relaxivities (R_1 and R_2) of **2a**–**2l** both in aqueous and hydroxypropyl-β-cyclodextrin (HP-β-CD) solutions. These and comparative results will be presented in this paper.



R =		
OH	H_5[DTPA]	$[Gd(DTPA)(H_2O)]^{2-}$
$NHCH_3$	H_3[DTPA-BMA]	[Gd(DTPA-BMA)(H_2O)]
$NH(CH_2)_2CO_2H$	**1a**	**2a**
$NH(CH_2)_3CO_2H$	**1b**	**2b**
$NH(CH_2)_4CO_2H$	**1c**	**2c**
$NH(CH_2)_5CO_2H$	**1d**	**2d**
$NH(CH_2)_2CO_2Me$	**1e**	**2e**
$NH(CH_2)_3CO_2Me$	**1f**	**2f**
$NH(CH_2)_4CO_2Me$	**1g**	**2g**
$NH(CH_2)_5CO_2Me$	**1h**	**2h**
$NH(CH_2)_2CO_2Et$	**1i**	**2i**
$NH(CH2)_3CO_2Et$	**1j**	**2j**
$NH(CH2)_4CO_2Et$	**1k**	**2k**
$NH(CH_2)_5CO_2Et$	**1l**	**2l**

Chart 1.

2. Experimental

2.1. General remarks

All reactions were carried out under an atmosphere of dinitrogen using the standard Schlenk techniques. Solvents were purified and dried using standard procedures. All commercial reagents were purchased from Aldrich and used as received unless otherwise stated. Deionized water was used for all experiments. Hydroxypropyl-β-cyclodextrin (HP-β-CD) was obtained from TCI and used without further purification. The ^1H and ^{13}C NMR experiments were performed on a Bruker Advance 400 or 500 Spectrometer by Korea Basic Science Institute (KBSI). Chemical shifts were given as δ values with reference to tetramethylsilane (TMS) as an internal standard. Coupling constants are in Hz. FAB-mass spectra were obtained by using a JMS-700 model (Jeol, Japan) mass spectrophotometer. IR spectra were run on a Mattson FT-IR Galaxy 6030E spectrophotometer by KBSI. Elemental analyses were performed by Center for Instrumental Analysis, KNU. T_1 measurements were carried out using an inversion recovery method with a variable inversion time (TI) at 1.5 T (64 MHz). The magnetic resonance (MR) images were acquired at 35 different TI values ranging from 50 to 1750 ms. T_1 relaxation times were obtained from the non-linear least square fit of the signal intensity measured at each TI value. For T_2 measurements the CPMG (Carr–Purcell–Meiboon–Gill) pulse sequence was adapted for multiple spin-echo measurements. Thirty four images were acquired with 34 different echo time (TE) values ranging from 10 to 1900 ms. T_2 relaxation times were obtained from the non-linear least squares fit of the mean pixel values for the multiple spin-echo measurements at each echo time. Relaxivities (R_1 and R_2) were then calculated as an inverse of relaxation time per mM.

2.2. Potentiometric measurements

Potentiometric titrations were performed with an automatic titrator to determine the protonation constants of the DTPA-bis(amide) ligands and the stability constants of corresponding metal complexes. The autotitrating system consists of a 798 MPT Titroprocessor, a 728 stirrer and a PT-100 combination pH electrode (Metrohm). The pH electrode was calibrated using standard buffer solutions. All calibrations and titrations were carried out under a CO_2-free nitrogen atmosphere in a sealed glass vessel (50 cm^3) thermostatted at 25 ± 0.1 °C at an ionic strength of 0.10 mol/dm^3 KCl. The concentrations of metal ion

and amide solutions were maintained at approximately 0.6 mmol/dm^3. A CO_2-free KOH solution (0.100 mol/dm^3) was used as a titrant to minimize the changes in ionic strength during the titration. Dioxygen and carbon dioxide were excluded from the reaction mixtures by maintaining a positive pressure of purified nitrogen in the titration cell. The electromotive force of the cell is given by $E = E^{0} + Q\log[H^+] + E_j$, and both E^{0} and Q were determined by titrating a solution with a known hydrogen-ion concentration at the same ionic strength, using the acid range of the titration. The liquid-junction potential (E_j) was found to be negligible under the experimental conditions employed.

2.3. Computational method

The protonation constants of the ligands and the overall stability constants of various metal complexes formed in aqueous solutions were determined from the titration data using the computer program HYPERQUAD [20]. The accuracy of this method was verified by measuring the protonation and the stability constants for Ca(II), Zn(II), Cu(II), and Gd(III) complexes of [DTPA-BMA]$^{3-}$. The results were compared with the literature values [7].

2.4. Syntheses

2.4.1. Diethylenetriamine-N,N′,N″-triacetic-N,N′-dianhydride

The title compound was prepared according to the literature method with a slight modification [21]. The product was obtained as a white solid. Yield 33.2 g (93%). ^{1}H NMR [DMSO-d_6, 400 MHz], δ 3.70 (s, 8H, terminal NCH_2CO$_2$), 3.30 (s, 2H, central NCH_2CO$_2$), 2.75 (t, $J = 7.6$, 4H, NCH_2) and 2.59 (t, $J = 7.6$, 4H, NCH_2).

2.4.2. Syntheses of methyl and ethyl esters of the amino acids

2.4.2.1. Methyl-3-aminopropionate hydrochloride. To a stirred suspension of 3-aminopropionic acid (2.23 g, 25 mmol) in methanol (50 mL) was added thionyl chloride (3.57 g, 30 mmol) for 10 min at 0 °C. The reaction mixture was then left under reflux for 2 h, after which the mixture was cooled to RT. The solvent was removed under a reduced pressure, and the residue triturated thrice with hexane (30 mL). The resulting solid was dried under vacuo for 6 h. Yield 3.32 g (95%). ^{1}H [DMSO-d_6, 400 MHz], $\delta = 8.36$ (br s, 3H, NH_2HCl), 3.69 (s, 3H, OCH_3), 3.05 (m, 2H, H3), 2.80 (t, $J = 7.04$, 2H, H2). ^{13}C [DMSO-d_6, 100 MHz], $\delta = 171.04$ (C1), 52.09 (*C*H$_3$), 34.87 (C3), 31.52 (C2). *Anal.* Calc. for $C_4H_{10}ClNO_2$: C, 34.42; H, 7.22; N, 10.03. Found: C, 34.47; H, 7.28; N, 10.17%.

2.4.2.2. Methyl-4-aminobutanoate hydrochloride. The title compound was obtained by following the same procedure for methyl-3-aminopropionate hydrochloride by replacing 3-aminopropionic acid with 4-aminobutanoic acid. Yield 3.69 g (96%). ^{1}H [DMSO-d_6, 400 MHz], $\delta = 8.23$ (br s, 3H, NH_2HCl), 3.59 (s, 3H, OCH_3), 2.77 (m, 2H, H4), 2.44 (t, $J = 7.52$, 2H, H2), 1.81 (m, 2H, H3). ^{13}C [DMSO-d_6, 100 MHz], $\delta = 173.00$ (C1), 51.75 (*C*H$_3$), 38.29 (C4), 30.53 (C2), 22.67 (C3). *Anal.* Calc. for $C_5H_{12}ClNO_2$: C, 39.10; H, 7.87; N, 9.12. Found: C, 38.70; H, 8.05; N, 9.00%.

2.4.2.3. Methyl-5-aminopentanoate hydrochloride. The title compound was obtained by following the same procedure for methyl-3-aminopropionate hydrochloride by replacing 3-aminopropionic acid with 5-aminopentanoic acid. Yield 3.94 g (94%). ^{1}H [DMSO-d_6, 400 MHz], $\delta = 8.17$ (br s, 3H, NH_2HCl), 3.57 (s, 3H, OCH_3), 2.73 (m, 2H, H5), 2.32 (t, $J = 6.54$, 2H, H2), 1.56 (m, 4H, H3, H4). ^{13}C [DMSO-d_6, 100 MHz], $\delta = 173.42$ (C1), 51.62 (*C*H$_3$), 38.60 (C5), 33.00 (C2), 26.34 (C4), 21.72 (C3). *Anal.* Calc. for $C_6H_{14}ClNO_2$: C, 42.99; H, 8.42; N, 8.36. Found: C, 42.63; H, 8.55; N, 8.28%.

2.4.2.4. Methyl-6-aminohexanoate hydrochloride. The title compound was obtained by following the same procedure for methyl-3-aminopropionate hydrochloride by replacing 3-aminopropionic acid with 6-aminohexanoic acid. Yield 4.32 g (95%). ^{1}H [DMSO-d_6, 400 MHz], $\delta = 8.14$ (br s, 3H, NH_2HCl), 3.57 (s, 3H, OCH_3), 2.71 (t, $J = 7.52$, 2H, H6), 2.29 (t, $J = 7.28$, 2H, H2), 1.53 (m, 4H, H3, H5), 1.29 (m, 2H, H4). ^{13}C [DMSO-d_6, 100 MHz], $\delta = 173.56$ (C1), 51.58 (*C*H$_3$), 38.77 (C6), 33.35 (C2), 26.88 (C5), 25.63 (C3), 24.22 (C4). *Anal.* Calc. for $C_7H_{16}ClNO_2$: C, 46.28; H, 8.88; N, 7.71. Found: C, 45.89; H, 9.15; N, 7.69%.

2.4.2.5. Ethyl-3-aminopropionate hydrochloride. The title compound was obtained by following the same procedure for methyl-3-aminopropionate hydrochloride by replacing methanol with ethanol. Yield 3.57 g (93%). ^{1}H [DMSO-d_6, 400 MHz], $\delta = 8.29$ (br s, 3H, NH_2HCl), 4.07 (q, $J = 7.00$ 2H, OCH_2), 2.97 (t, $J = 7.04$, 2H, H3), 2.71 (t, $J = 7.04$, 2H, H2), 1.18 (t, $J = 7.00$, 3H, CH_3). ^{13}C [DMSO-d_6, 100 MHz], $\delta = 170.57$ (C1), 60.75 (*C*H$_2$), 34.85 (C3), 31.65 (C2), 14.32 (*C*H$_3$). *Anal.* Calc. for $C_5H_{12}ClNO_2$: C, 39.10; H, 7.87; N, 9.12. Found: C, 38.79; H, 8.03; N, 9.00%.

2.4.2.6. Ethyl-4-aminobutanoate hydrochloride. The title compound was obtained by following the same procedure for methyl-3-aminopropionate hydrochloride by replacing 3-aminopropionic acid with 4-aminobutanoic acid and methanol with ethanol. Yield 3.94 g (94%). ^{1}H [DMSO-d_6, 400 MHz], $\delta = 8.24$ (br s, 3H, NH_2HCl), 4.04 (q, $J = 7.04$, 2H, OCH_2), 2.77 (m, 2H, H4), 2.41 (t, $J = 7.54$, 2H, H2), 1.81 (qn, $J = 7.52$, 2H, H3), 1.16 (t, $J = 7.04$, 3H, CH_3). ^{13}C [DMSO-d_6, 100 MHz], $\delta = 172.52$ (C1), 60.29 (*C*H$_2$), 38.29 (C4), 30.75 (C2), 22.68 (C3), 14.43 (*C*H$_3$). *Anal.* Calc. for $C_6H_{14}ClNO_2$: C, 42.99; H, 8.42; N, 8.36. Found: C, 42.72; H, 8.62; N, 8.28%.

2.4.2.7. Ethyl-5-aminopentanoate hydrochloride. The title compound was obtained by following the same procedure for methyl-3-aminopropionate hydrochloride by replacing 3-aminopropionic acid with 5-aminopentanoic acid and methanol with ethanol. Yield 4.22 g (93%). ^{1}H [DMSO-d_6, 400 MHz], $\delta = 8.18$ (br s, 3H, NH_2HCl), 4.03 (q, $J = 7.00$, 2H, OCH_2), 2.73 (m, 2H, H5), 2.29 (t, $J = 6.52$, 2H, H2), 1.56 (m, 4H, H3, H4), 1.16 (t, $J = 7.00$, 3H, CH_3). ^{13}C [DMSO-d_6, 100 MHz], $\delta = 172.93$ (C1), 60.12 (CH_2), 38.62 (C5), 33.23 (C2), 26.62 (C4), 21.75 (C3), 14.44 (CH_3). *Anal.* Calc. for $C_7H_{16}ClNO_2$: C, 46.28; H, 8.88; N, 7.71. Found: C, 45.82; H, 9.12; N, 7.61%.

2.4.2.8. Ethyl-6-aminohexanoate hydrochloride. The title compound was obtained by following the same procedure for methyl-3-aminopropionate hydrochloride by replacing 3-aminopropionic acid with 6-aminohexanoic acid and methanol with ethanol. Yield 4.65 g (95%). ^{1}H [DMSO-d_6, 400 MHz], $\delta = 8.16$ (br s, 3H, NH_2HCl), 4.03 (q, $J = 7.00$, 2H, OCH_2), 2.71 (m, 2H, H6), 2.26 (t, $J = 7.28$, 2H, H2), 1.53 (m, 4H, H3, H5), 1.29 (m, 2H, H4), 1.16 (t, $J = 7.00$, 3H, CH_3). ^{13}C [DMSO-d_6, 100 MHz], $\delta = 173.09$ (C1), 60.05 (CH_2), 38.77 (C6), 33.56 (C2), 26.85 (C5), 25.61 (C3), 24.23 (C4), 14.44 (CH_3). *Anal.* Calc. for $C_8H_{18}ClNO_2$: C, 49.10; H, 9.27; N, 7.16. Found: C, 48.89; H, 9.54; N, 7.12%.

2.4.3. Syntheses of the DTPA-bis(amide) ligands

*2.4.3.1. Compound **1a** · 3.5H$_2$O.* To a suspension of DTPA-bis(anhydride) (1.79 g, 5 mmol) in dry DMF (15 mL) was added 3-aminopropionic acid (0.891 g, 10 mmol). The mixture was stirred at 65 °C for 4 h. The solvent was removed from the reaction mixture under reduced pressure, and the residue dissolved in methanol (10 mL). The solution was passed through a short column of silica gel (60 mesh) with methanol as an eluent. The residue obtained after removal of the solvent from the eluate was triturated with a mixture of acetone and diethylether (30:70 v/v, 150 mL). The solid product was isolated by filtration, washed with acetone (3×30 mL) and dried under vacuo at 70 °C for 8 h. Yield 2.21 g (74%). ^{1}H [DMSO-d_6, 400 MHz], $\delta = 7.97$ (s, 2H, CH_2CONH), 3.34 (s, 2H, H7), 3.18 (s, 4H, H5), 3.12 (m, 4H, H1′), 3.08 (s, 4H, H3), 2.87 (s, 4H, H2), 2.70 (s, 4H, H1), 2.24 (t, $J = 6.56$ 4H, H2′). ^{13}C [DMSO-d_6, 100 MHz], $\delta = 171.92$ (C3′), 171.70 (C8/C6), 169.04 (C6/C8), 168.83 (C4), 56.32 (C7), 54.00 (C5), 51.05 (C3), 49.15 (C2), 33.60 (C1), 32.85 (C2′), 30.97 (C1′). *Anal.* Calc. for $C_{20}H_{33}N_5O_{12} \cdot 3.5H_2O$: C, 40.13; H, 6.74; N, 11.70. Found: C, 40.16; H, 6.69; N, 11.66%. FAB-MS (*m*/*z*): Calc. for $C_{20}H_{34}N_5O_{12}$: 536.22 $[MH]^+$; $C_{20}H_{33}N_5NaO_{12}$: 558.20 $[MNa]^+$. Found: 536.07 ($[MH]^+$); 558.07 ($[MNa]^+$).

*2.4.3.2. Compound **1b** · 2H$_2$O.* This compound was obtained essentially by following the same procedure as that for **1a** by replacing 3-aminopropionic acid with 4-aminobutanoic acid. Yield 2.40 g (80%). ^{1}H [DMSO-d_6, 400 MHz], $\delta = 7.87$ (s, 2H, CH_2CONH), 3.30 (s, 2H, H7), 3.07 (s, 4H, H5), 3.01 (s, 4H, H3), 2.84 (m, 8H, H1′,H2), 2.66 (s, 4H, H1), 1.97 (t, $J = 7.28$ 4H, H3′), 1.40 (m, 4H, H2′). ^{13}C [DMSO-d_6, 100 MHz], $\delta = 174.74$ (C4′), 173.48 (C8/C6), 170.56 (C6/C8), 149.88 (C4), 57.95 (C7), 55.92 (C5), 50.48 (C3), 48.93 (C2), 38.17 (C1), 31.74 (C1′), 31.07 (C3′), 24.95 (C2′). *Anal.* Calc. for $C_{22}H_{37}N_5O_{12} \cdot 2H_2O$: C, 44.07; H, 6.89; N, 11.68. Found: C, 43.92; H, 7.16; N, 11.58%. FAB-MS (*m*/*z*): Calc. for $C_{22}H_{38}N_5O_{12}$: 564.25 $[MH]^+$; $C_{22}H_{37}N_5NaO_{12}$: 586.23 $[MNa]^+$. Found: 564.13 ($[MH]^+$); 586.11 ($[MNa]^+$).

*2.4.3.3. Compound **1c** · 3H$_2$O.* This compound was obtained essentially by following the same procedure as that for **1a** by replacing 3-aminopropionic acid with 5-aminopentanoic acid. Yield 2.49 g (77%). ^{1}H [DMSO-d_6, 400 MHz], $\delta = 7.84$ (s, 2H, CH_2CONH), 3.28 (s, 2H, H7), 3.12 (s, 4H, H5), 3.04 (s, 4H, H3), 2.84 (m, 8H, H1′,H2), 2.65 (s, 4H, H1), 1.99 (t, $J = 7.04$ 4H, H4′), 1.23 (m, 8H, H2′, H3′). ^{13}C [DMSO-d_6, 100 MHz], $\delta = 174.82$ (C5′), 173.06 (C8/C6), 170.45 (C6/C8), 149.91 (C4), 57.72 (C7), 55.45 (C5), 52.48 (C3), 50.71 (C2), 48.94 (C1), 38.30 (C1′), 33.75 (C4′), 28.92 (C2′), 22.30 (C3′). *Anal.* Calc. for $C_{24}H_{41}N_5O_{12} \cdot 3H_2O$: C, 44.65; H, 7.34; N, 10.85. Found: C, 44.50; H, 7.07; N, 10.85%. FAB-MS (*m*/*z*): Calc. for $C_{24}H_{42}N_5O_{12}$: 592.28 $[MH]^+$; $C_{24}H_{41}N_5NaO_{12}$: 614.26 $[MNa]^+$. Found: 592.12 ($[MH]^+$); 614.11 ($[MNa]^+$).

*2.4.3.4. Compound **1d** · 3H$_2$O.* This compound was obtained essentially by following the same procedure as that for **1a** by replacing 3-aminopropionic acid with 6-aminohexanoic acid. Yield 2.80 g (83%). ^{1}H [DMSO-d_6, 400 MHz], $\delta = 8.08$ (s, 2H, CH_2CONH), 3.83 (s, 2H, H7), 3.42 (s, 4H, H5), 3.32 (s, 4H, H3), 3.20 (s, 4H, H2), 3.06 (m, 4H, H1′) 2.95 (s, 4H, H1), 2.19 (t, $J = 7.26$ 4H, H5′), 1.47 (m, 4H, H2′), 1.41 (m, 4H, H3′), 1.24 (m, 4H, H4′). ^{13}C [DMSO-d_6, 100 MHz], $\delta = 174.83$ (C6′), 172.81 (C8/C6), 170.57 (C6/C8), 149.83 (C4), 57.12 (C7), 55.03 (C5), 52.44 (C3), 49.99 (C2), 48.91 (C1), 38.63 (C1′), 33.99 (C5′), 29.09 (C2″), 26.27 (C3′), 24.54 (C4′). *Anal.* Calc. for $C_{26}H_{45}N_5O_{12} \cdot 3H_2O$: C, 46.35; H, 7.63; N, 10.40. Found: C, 46.57; H, 7.49; N, 10.45%. FAB-MS (*m*/*z*): Calc. for $C_{26}H_{46}N_5O_{12}$: 620.31 $[MH]^+$; $C_{26}H_{45}N_5NaO_{12}$: 642.29 $[MNa]^+$. Found: 620.16 ($[MH]^+$); 642.17 ($[MNa]^+$).

*2.4.3.5. Compound **1e** · 1.5H$_2$O.* This compound was obtained essentially by following the same procedure as that for **1a** by replacing 3-aminopropionic acid with methyl-3-aminopropionate hydrochloride. Yield 1.95 g (66%). ^{1}H [DMSO-d_6, 400 MHz], $\delta = 8.14$ (s, 2H, CH_2CONH), 3.78 (s, 2H, H7), 3.59 (s, 4H, H5), 3.40 (m, 4H, H1′), 3.29 (m, 8H, H3, H2′), 3.17 (s, 6H, COOCH_3), 3.13 (s, 4H, H2), 2.92 (s, 4H, H1). ^{13}C [DMSO-d_6, 100 MHz], $\delta = 171.70$ (C3′), 171.26 (C8/C6), 170.57 (C6/C8), 169.22 (C4), 55.60 (C7), 53.55 (C5), 50.94 (C3), 50.22 (COOCH_3), 48.50 (C2), 47.41 (C1), 33.56 (C1′), 32.67 (C2′). *Anal.* Calc. for $C_{22}H_{37}N_5O_{12} \cdot 1.5H_2O$: C,

44.74; H, 6.83; N, 11.86. Found: C, 44.83; H, 6.99; N, 12.16%. FAB-MS (*m*/*z*): Calc. for $C_{22}H_{38}N_5O_{12}$: 564.25 $[MH]^+$; $C_{21}H_{36}N_5O_{12}$: 550.23 $[MH-(CH_3)]^+$; $C_{20}H_{34}N_5O_{12}$: 536.22 $[MH-2(CH_3)]^+$. Found: 564.13 ($[MH]^+$); 550.13 $[MH-(CH_3)]^+$; 536.08 $[MH-2(CH_3)]^+$.

2.4.3.6. Compound ***1f*** $\cdot$ *1.75H_2O.* This compound was obtained essentially by following the same procedure as that for **1a** by replacing 3-aminopropionic acid with methyl-4-aminobutanoate hydrochloride. Yield 2.15 g (69%). ^{1}H [DMSO-d_6, 400 MHz], $\delta = 8.05$ (s, 2H, CH_2CONH), 3.62 (s, 2H, H7), 3.58 (s, 4H, H5), 3.39 (m, 8H, H2, H1′), 3.28 (m, 8H, H3, H1), 2.89 (s, 6H, $COOCH_3$), 2.23 (t, $J = 7.28$, 4H, H3′), 1.65 (m, 4H, H2′). ^{13}C [DMSO-d_6, 100 MHz], 174.70 (C4′), 173.54 (C8/C6), 170.97 (C6/C8), 168.75 (C4), 56.94 (C7), 55.20 (C5), 54.82 (C3), 52.97 ($COOCH_3$), 52.37 (C2), 49.88 (C1), 47.04 (C1′), 25.25 (C3′), 22.94 (C2′). *Anal.* Calc. for $C_{24}H_{41}N_5O_{12} \cdot 1.75H_2O$: C, 46.26; H, 7.20; N, 11.24. Found: C, 46.15; H, 7.16; N, 11.63%. FAB-MS (*m*/*z*): Calc. for $C_{24}H_{42}N_5O_{12}$: 592.28 $[MH]^+$; $C_{23}H_{40}N_5O_{12}$: 578.26 $[MH-(CH_3)]^+$; $C_{22}H_{38}N_5O_{12}$: 564.25 $[MH-2(CH_3)]^+$. Found: 592.13 ($[MH]^+$); 578.13 $[MH-(CH_3)]^+$; 564.12 $[MH-2(CH_3)]^+$.

2.4.3.7. Compound ***1g*** $\cdot$ *3H_2O.* This compound was obtained essentially by following the same procedure as that for **1a** by replacing 3-aminopropionic acid with methyl-5-aminopentanoate hydrochloride. Yield 2.53 g (75%). ^{1}H [DMSO-d_6, 400 MHz], $\delta = 8.09$ (s, 2H, CH_2CONH), 3.77 (s, 2H, H7), 3.48 (s, 4H, H5), 3.32 (s, 4H, H3), 3.17 (s, 6H, $COOCH_3$), 3.07 (m, 4H, H2), 2.93 (m, 4H, H1), 2.21 (t, $J = 7.02$, 4H, H1′), 1.48 (m, 12H, H2′, H3′, H4′). ^{13}C [DMSO-d_6, 100 MHz], $\delta = 174.91$ (C5′), 173.78 (C8/C6), 173.03 (C6/C8), 170.77 (C4), 57.42 (C7), 55.34 (C5), 54.85 (C3), 52.63 ($COOCH_3$), 51.72 (C2), 50.39 (C1), 49.12 (C1′), 33.87 (C4′), 29.07 (C2′), 22.47 (C3′). *Anal.* Calc. for $C_{26}H_{45}N_5O_{12} \cdot 3H_2O$: C, 46.35; H, 7.63; N, 10.40. Found: C, 46.40; H, 7.65; N, 10.76%. FAB-MS (*m*/*z*): Calc. for $C_{26}H_{46}N_5O_{12}$: 620.31 $[MH]^+$; $C_{25}H_{44}N_5O_{12}$: 606.29 $[MH-(CH_3)]^+$; $C_{24}H_{42}N_5O_{12}$: 592.28 $[MH-2(CH_3)]^+$. Found: 620.17 ($[MH]^+$); 606.15 $[MH-(CH_3)]^+$; 592.14 $[MH-2(CH_3)]^+$.

2.4.3.8. Compound ***1h*** $\cdot$ *2H_2O.* This compound was obtained essentially by following the same procedure as that for **1a** by replacing 3-aminopropionic acid with methyl-6-aminohexanoate hydrochloride. Yield 2.53 g (74%). ^{1}H [DMSO-d_6, 400 MHz], $\delta = 8.11$ (s, 2H, CH_2CONH), 4.01 (s, 2H, H7), 3.45 (s, 4H, H5), 3.35 (s, 4H, H3), 3.29 (m, 4H, H2), 3.04 (m, 10H, $COOCH_3$, H1), 2.19 (t, $J = 7.52$, 4H, H1′), 1.39 (m, 16H, H2′, H3′, H4′, H5′). ^{13}C [DMSO-d_6, 100 MHz], $\delta = 173.27$ (C6′), 172.15 (C8/C6), 171.47 (C6/C8), 169.01 (C4), 55.41 (C7), 53.46 (C5), 50.88 (C3), 50.01 ($COOCH_3$), 48.18 (C2), 37.17 (C1), 32.48 (C1′), 32.03 (C5′), 27.58 (C2′), 24.79 (C3′), 23.05 (C4′). *Anal.* Calc. for $C_{28}H_{49}N_5O_{12} \cdot 2H_2O$: C, 49.18; H, 7.81; N, 10.24. Found: C, 48.93; H, 7.86; N, 10.63%. FAB-MS (*m*/*z*): Calc. for $C_{28}H_{50}N_5O_{12}$: 648.34 $[MH]^+$; $C_{27}H_{48}N_5O_{12}$: 634.32 $[MH-(CH_3)]^+$; $C_{26}H_{46}N_5O_{12}$: 620.31 $[MH-2(CH_3)]^+$. Found: 648.22 ($[MH]^+$); 634.19 $[MH-(CH_3)]^+$; 620.16 $[MH-2(CH_3)]^+$.

2.4.3.9. Compound ***1i*** $\cdot$ *3H_2O.* This compound was obtained essentially by following the same procedure as that for **1a** by replacing 3-aminopropionic acid with ethyl-3-aminopropionate hydrochloride. Yield 2.29 g (71%). ^{1}H [DMSO-d_6, 400 MHz], $\delta = 8.18$ (s, 2H, CH_2CONH), 3.96 (s, 2H, H7), 3.61 (m, 4H, H1′), 3.51 (s, 4H, H5), 3.29 (m, 8H, H3, $COOCH_2CH_3$), 3.12 (m, 4H, H2′), 2.88 (s, 4H, H2), 2.72 (s, 4H, H1), 2.42 (t, $J = 7.02$, 6H, $COOCH_2CH_3$). ^{13}C [DMSO-d_6, 100 MHz], $\delta = 173.19$ (C3′), 172.74 (C8/C6), 172.22 (C6/C8), 170.75 (C4), 56.92 (CH_2CH_3), 54.97 (C7), 54.18 (C5), 52.34 (C3), 49.67 (C2), 48.89 (C1), 35.06 (C1′), 34.14 (C2′), 31.81 (CH_2CH_3). *Anal.* Calc. for $C_{24}H_{41}N_5O_{12} \cdot 3H_2O$: C, 44.65; H, 7.34; N, 10.85. Found: C, 44.48; H, 7.42; N, 10.66%. FAB-MS (*m*/*z*): Calc. for $C_{22}H_{38}N_5O_{12}$: 564.25 $[MH-(C_2H_5)]^+$; $C_{20}H_{34}N_5O_{12}$: 536.22 $[MH-2(C_2H_5)]^+$. Found: 564.13 $[MH-(C_2H_5)]^+$; 536.08 $[MH-2(C_2H_5)]^+$.

2.4.3.10. Compound ***1j*** $\cdot$ *3.75H_2O.* This compound was obtained essentially by following the same procedure as that for **1a** by replacing 3-aminopropionic acid with ethyl-4-aminobutanoate hydrochloride. Yield 2.16 g (63%).^{1}H [DMSO-d_6, 400 MHz], $\delta = 7.99$ (s, 2H, CH_2CONH), 3.91 (s, 2H, H7), 3.34 (s, 4H, H5), 3.20 (m, 12H, H3, H2, H1′), 2.99 (m, 4H, CH_2CH_3), 2.88 (m, 4H, H1), 2.12 (t, $J = 7.26$, 4H, H3′), 1.54 (m, 4H, H2′), 1.13 (t, $J = 7.00$, 6H, CH_2CH_3). ^{13}C [DMSO-d_6, 100 MHz], $\delta = 174.53$ (C4′), 173.00 (C8/C6), 170.79 (C6/C8), 168.52 (C4), 60.11 (CH_2CH_3), 56.84 (C7), 55.00 (C5), 53.92 (C3), 52.30 (C2), 49.56 (C1), 31.51 (C1′), 24.79 (C3′), 22.79 (C2′), 14.40 (CH_2CH_3). *Anal.* Calc. for $C_{26}H_{45}N_5O_{12} \cdot 3.75H_2O$: C, 45.44; H, 7.70; N, 10.19. Found: C, 45.45; H, 7.51; N, 9.97%. FAB-MS (*m*/*z*): Calc. for $C_{26}H_{46}N_5O_{12}$: 620.31 $[MH]^+$; $C_{24}H_{42}N_5O_{12}$: 592.28 $[MH-(C_2H_5)]^+$; $C_{22}H_{38}N_5O_{12}$: 564.25 $[MH-2(C_2H_5)]^+$. Found: 620.16 ($[MH]^+$); 592.13 $[MH-(C_2H_5)]^+$; 564.13 $[MH-2(C_2H_5)]^+$.

2.4.3.11. Compound ***1k*** $\cdot$ *3.75H_2O.* This compound was obtained essentially by following the same procedure as that for **1a** by replacing 3-aminopropionic acid with ethyl-5-aminopentanoate hydrochloride. Yield 2.50 g (70%). ^{1}H [DMSO-d_6, 400 MHz], $\delta = 8.13$ (s, 2H, CH_2CONH), 4.03 (m, 4H, CH_2CH_3), 3.50 (s, 2H, H7), 3.45 (s, 4H, H5), 3.35 (s, 4H, H3), 3.28 (m, 4H, H2), 3.06 (m, 4H, H1′), 2.99 (m, 4H, H1), 2.25 (m, 4H, H4′), 1.46 (m, 8H, H2′, H3′), 1.17 (t, $J = 7.00$, 6H, CH_2CH_3). ^{13}C [DMSO-d_6, 100 MHz], $\delta = 174.74$ (C5′), 173.12 (C8/C6), 172.85 (C6/C8), 170.55 (C4), 60.03 (CH_2CH_3), 57.32 (C7), 55.17 (C5), 52.44 (C3), 50.37 (C2), 50.07 (C1), 33.69 (C1′), 33.43 (C4′), 28.90 (C2′), 22.28 (C3′), 14.47

(CH_2CH_3). *Anal.* Calc. for $C_{28}H_{49}N_5O_{12}\cdot 3.75H_2O$: C, 47.02; H, 7.96; N, 9.79. Found: C, 46.97; H, 7.79; N, 9.68%. FAB-MS (*m*/*z*): Calc. for $C_{28}H_{50}N_5O_{12}$: 648.34 $[MH]^+$; $C_{26}H_{46}N_5O_{12}$: 620.31 $[MH-(C_2H_5)]^+$; $C_{24}H_{42}N_5O_{12}$: 592.28 $[MH-2(C_2H_5)]^+$. Found: 648.20 ($[MH]^+$); 620.14 $[MH-(C_2H_5)]^+$; 592.10 $[MH-2(C_2H_5)]^+$.

2.4.3.12. Compound ***1l*** $\cdot$ *4.75H_2O.* This compound was obtained essentially by following the same procedure as that for **1a** by replacing 3-aminopropionic acid with ethyl-6-aminohexanoate hydrochloride. Yield 2.66 g (70%). ^1H [DMSO-d_6, 400 MHz], $\delta = 8.12$ (s, 2H, CH_2CONH), 4.03 (m, 4H, CH_2CH_3), 3.51 (s, 2H, H7), 3.45 (s, 4H, H5), 3.35 (s, 4H, H3), 3.29 (m, 4H, H2), 3.06 (m, 4H, H1′), 2.99 (m, 4H, H1), 2.23 (m, 4H, H5′), 1.48 (m, 4H, H4′), 1.41 (m, 4H, H2′), 1.26 (m, 4H, H3′), 1.18 (t, $J = 7.02$, 6H, CH_2CH_3). ^{13}C [DMSO-d_6, 100 MHz], $\delta = 173.06$ (C6′), 172.76 (C8/C6), 170.61 (C6/C8), 168.55 (C4), 60.01(CH_2CH_3), 56.87 (C7), 54.87 (C5), 53.85 (C3), 52.38 (C2), 49.66 (C1), 33.97 (C1′), 29.10 (C5′), 26.29 (C2′), 24.55 (C3′), 24.30 (C4′), 14.46 (CH_2CH_3). *Anal.* Calc. for $C_{30}H_{53}N_5O_{12}\cdot 4.75H_2O$: C, 47.33; H, 8.27; N, 9.20. Found: C, 47.31; H, 7.91; N, 9.03%. FAB-MS (*m*/*z*): Calc. for $C_{28}H_{50}N_5O_{12}$: 648.34 $[MH-(C_2H_5)]^+$; $C_{26}H_{46}N_5O_{12}$: 620.31 $[MH-2(C_2H_5)]^+$. Found: 648.21 $[MH-(C_2H_5)]^+$; 620.16 $[MH-2(C_2H_5)]^+$.

2.4.4. Syntheses of the Gd(III) complexes

2.4.4.1. Compound ***2a*** $\cdot$ *7H_2O.* To a solution of **1a** (1.20 g, 2 mmol) in deionized water (10 mL) was added Gd_2O_3 (0.36 g 1 mmol). The suspension was stirred for 6 h at 100 °C during which time a pale yellow solution resulted. The reaction mixture was cooled to RT and passed through a Celite column to remove any solid impurities. The solvent was removed and the residue taken up in methanol (3 mL). The methanolic solution was added drop wise into acetone at 0 °C with stirring to precipitate the product as a white solid. The product was isolated by filtration, washed with acetone, dried under vacuo at 80 °C for 6 h. Yield 1.37 g (82%). *Anal.* Calc. for $C_{20}H_{32}GdN_5O_{13}\cdot 7H_2O$: C, 28.81; H, 5.56; N, 8.40. Found: C, 28.73; H, 5.38; N, 8.45%. FABMS (*m*/*z*): Calc. for $C_{20}H_{31}GdN_5O_{12}$: 691.12 $[MH-(H_2O)]^+$. Found: 691.18 $[MH-(H_2O)]^+$.

2.4.4.2. Compound ***2b*** $\cdot$ *5H_2O.* This compound was obtained essentially by following the same procedure as that for **2a** by replacing **1a** with **1b**. Yield 1.50 g (91%). *Anal.* Calc. for $C_{22}H_{36}GdN_5O_{13}\cdot 5H_2O$: C, 31.99; H, 5.61; N, 8.48. Found: C, 32.03; H, 5.50; N, 8.47%. FABMS (*m*/*z*): Calc. for $C_{22}H_{35}GdN_5O_{12}$: 719.15 $[MH-(H_2O)]^+$. Found: 719.21 $[MH-(H_2O)]^+$.

2.4.4.3. Compound ***2c*** $\cdot$ *4H_2O.* This compound was obtained essentially by following the same procedure as that for **2a** by replacing **1a** with **1c**. Yield 1.45 g (87%). *Anal.* Calc. for $C_{24}H_{40}GdN_5O_{13}\cdot 4H_2O$: C, 34.48; H, 5.79; N, 8.38. Found: C, 34.51; H, 5.72; N, 8.43%. FABMS (*m*/*z*): Calc. for $C_{24}H_{39}GdN_5O_{12}$: 747.18 $[MH-(H_2O)]^+$. Found: 747.24 $[MH-(H_2O)]^+$.

2.4.4.4. Compound ***2d*** $\cdot$ *3H_2O.* This compound was obtained essentially by following the same procedure as that for **2a** by replacing **1a** with **1d**. Yield 1.39 g (82%). *Anal.* Calc. for $C_{26}H_{44}GdN_5O_{13}\cdot 3H_2O$: C, 36.91; H, 5.96; N, 8.28. Found: C, 37.01; H, 6.22; N, 8.36%. FABMS (*m*/*z*): Calc. for $C_{26}H_{43}GdN_5O_{12}$: 775.21 $[MH-(H_2O)]^+$. Found: 775.27 $[MH-(H_2O)]^+$.

2.4.4.5. Compound ***2e*** $\cdot$ *6H_2O.* This compound was obtained essentially by following the same procedure as that for **2a** by replacing **1a** with **1e**. Yield 1.38 g (82%). *Anal.* Calc. for $C_{22}H_{36}GdN_5O_{13}\cdot 6H_2O$: C, 31.31; H, 5.73; N, 8.30. Found: C, 31.28; H, 5.34; N, 8.73%. FABMS (*m*/*z*): Calc. for $C_{22}H_{35}GdN_5O_{12}$: 719.15 $[MH-(H_2O)]^+$; $C_{21}H_{33}GdN_5O_{12}$: 705.14 $[MH-(H_2O+CH_3)]^+$; $C_{20}H_{31}GdN_5O_{12}$: 691.12 $[MH-(H_2O+2CH_3)]^+$. Found: 719.17 ($[MH-(H_2O)]^+$); 705.14 $[MH-(H_2O+CH_3)]^+$; 691.14 $[MH-(H_2O+2CH_3)]^+$.

2.4.4.6. Compound ***2f*** $\cdot$ *5H_2O.* This compound was obtained essentially by following the same procedure as that for **2a** by replacing **1a** with **1f**. Yield 1.32 g (77%). *Anal.* Calc. for $C_{24}H_{40}GdN_5O_{13}\cdot 5H_2O$: C, 33.76; H, 5.90; N, 8.20. Found: C, 33.42; H, 5.65; N, 8.62%. FABMS (*m*/*z*): Calc. for $C_{24}H_{39}GdN_5O_{12}$: 747.18 $[MH-(H_2O)]^+$; $C_{23}H_{37}GdN_5O_{12}$: 733.17 $[MH-(H_2O+CH_3)]^+$; $C_{22}H_{35}GdN_5O_{12}$: 719.15 $[MH-(H_2O+2CH_3)]^+$. Found: 747.24 ($[MH-(H_2O)]^+$); 733.22 $[MH-(H_2O+CH_3)]^+$; 719.19 $[MH-(H_2O+2CH_3)]^+$.

2.4.4.7. Compound ***2g*** $\cdot$ *8H_2O.* This compound was obtained essentially by following the same procedure as that for **2a** by replacing **1a** with **1g**. Yield 1.67 g (89%). *Anal.* Calc. for $C_{26}H_{44}GdN_5O_{13}\cdot 8H_2O$: C, 33.36; H, 6.46; N, 7.48. Found: C, 33.27; H, 6.68.; N, 7.92%. FABMS (*m*/*z*): Calc. for $C_{26}H_{43}GdN_5O_{12}$: 775.21 $[MH-(H_2O)]^+$; $C_{25}H_{41}GdN_5O_{12}$: 761.20 $[MH-(H_2O+CH_3)]^+$; $C_{24}H_{39}GdN_5O_{12}$: 747.18 $[MH-(H_2O+2CH_3)]^+$. Found: 775.27 ($[MH-(H_2O)]^+$); 761.24 $[MH-(H_2O+CH_3)]^+$; 747.24 $[MH-(H_2O+2CH_3)]^+$.

2.4.4.8. Compound ***2h*** $\cdot$ *8H_2O.* This compound was obtained essentially by following the same procedure as that for **2a** by replacing **1a** with **1h**. Yield 1.54 g (80%). *Anal.* Calc. for $C_{28}H_{48}GdN_5O_{13}\cdot 8H_2O$: C, 34.88; H, 6.69; N, 7.26. Found: C, 34.75; H, 6.37; N, 7.59%. FABMS (*m*/*z*): Calc. for $C_{27}H_{45}GdN_5O_{12}$: 789.23 $[MH-(H_2O+CH_3)]^+$; $C_{26}H_{43}GdN_5O_{12}$: 775.21 $[MH-(H_2O+2CH_3)]^+$. Found: 789.27 $[MH-(H_2O+CH_3)]^+$; 775.25 $[MH-(H_2O+2CH_3)]^+$.

2.4.4.9. Compound ***2i*** $\cdot$ *10H_2O.* This compound was obtained essentially by following the same procedure as that for **2a** by replacing **1a** with **1i**. Yield 1.72 g (91%).

Anal. Calc. for $C_{24}H_{40}GdN_5O_{13}\cdot 10H_2O$: C, 30.54; H, 6.41; N, 7.42. Found: C, 30.88; H, 6.17; N, 7.13%. FABMS (*m*/*z*): Calc. for $C_{24}H_{39}GdN_5O_{12}$: 747.18 $[MH-(H_2O)]^+$; $C_{22}H_{35}GdN_5O_{12}$: 719.15 $[MH-(H_2O+C_2H_5)]^+$; $C_{20}H_{31}GdN_5O_{12}$: 691.12 $[MH-(H_2O+2C_2H_5)]^+$. Found: 747.58 ($[MH-(H_2O)]^+$); 719.54 $[MH-(H_2O+C_2H_5)]^+$; 691.49 $[MH-(H_2O+2C_2H_5)]^+$.

2.4.4.10. Compound ***2j*** $\cdot 8H_2O$. This compound was obtained essentially by following the same procedure as that for **2a** by replacing **1a** with **1j**. Yield 1.63 g (87%). *Anal.* Calc. for $C_{26}H_{44}GdN_5O_{13}\cdot 8H_2O$: C, 33.36; H, 6.46; N, 7.48. Found: C, 33.29; H, 6.26; N, 7.29%. FABMS (*m*/*z*): Calc. for $C_{24}H_{39}GdN_5O_{12}$: 747.18 $[MH-(H_2O+C_2H_5)]^+$; $C_{22}H_{35}GdN_5O_{12}$: 719.15 $[MH-(H_2O+2C_2H_5)]^+$. Found: 747.58 $[MH-(H_2O+C_2H_5)]^+$; 719.54 $[MH-(H_2O+2C_2H_5)]^+$.

2.4.4.11. Compound ***2k*** $\cdot 5H_2O$. This compound was obtained essentially by following the same procedure as that for **2a** by replacing **1a** with **1k**. Yield 1.51 g (83%). *Anal.* Calc. for $C_{28}H_{48}GdN_5O_{13}\cdot 5H_2O$: C, 36.95; H, 6.42; N, 7.70. Found: C, 36.87; H, 6.17.; N, 8.12%. FABMS (*m*/*z*): Calc. for $C_{28}H_{47}GdN_5O_{12}$: 803.25 $[MH-(H_2O)]^+$; $C_{26}H_{43}GdN_5O_{12}$: 775.21 $[MH-(H_2O+C_2H_5)]^+$; $C_{24}H_{39}GdN_5O_{12}$: 747.18 $[MH-(H_2O+2C_2H_5)]^+$. Found: 803.65 ($[MH-(H_2O)]^+$); 775.62 $[MH-(H_2O+C_2H_5)]^+$; 747.61 $[MH-(H_2O+2C_2H_5)]^+$.

2.4.4.12. Compound ***2l*** $\cdot 8H_2O$. This compound was obtained essentially by following the same procedure as that for **2a** by replacing **1a** with **1l**. Yield 1.83 g (92%). *Anal.* Calc. for $C_{30}H_{52}GdN_5O_{13}\cdot 8H_2O$: C, 36.32; H, 6.91; N, 7.06. Found: C, 36.21; H, 6.69.; N, 7.33%. FABMS (*m*/*z*): Calc. for $C_{30}H_{51}GdN_5O_{12}$: 831.28 $[MH-(H_2O)]^+$; $C_{28}H_{47}GdN_5O_{12}$: 803.25 $[MH-(H_2O+C_2H_5)]^+$; $C_{26}H_{43}GdN_5O_{12}$: 775.21 $[MH-(H_2O+2C_2H_5)]^+$. Found: 831.66 ($[MH-(H_2O)]^+$); 803.65 $[MH-(H_2O+C_2H_5)]^+$; 775.62 $[MH-(H_2O+2C_2H_5)]^+$.

3. Results and discussion

3.1. Synthesis and characterization

Chart 1 shows a list of new Gd(III) complexes of DTPA-bis-amides derivatized by alkyl carboxylic acids (or esters) on the amide side-arms. The new series of ligands are obtainable from the simple condensation of DTPA-bis(anhydride) with corresponding aminocarboxylic acid (or esters) in an 1:2 molar ratio in DMF. The complex formation can be carried out by the reaction with Gd_2O_3 ([Gd]/[L] = 1/2) under reflux in deionized water. The complexes are obtained as white solids, yet isolated as hydrated forms due to their highly hygroscopic nature. Naturally they are soluble almost indefinitely in water and some organic solvents such as alcohol, DMF, and DMSO.

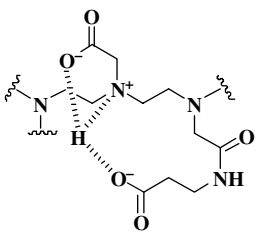
The complex formation can be confirmed straightforwardly by analytical and various spectroscopic techniques (^1H and ^{13}C NMR, FAB-mass). As stated above, it is quite common for these complexes to exist as hydrated solids thus to be formulated as $[Gd(\mathbf{1})(H_2O)]\cdot xH_2O$. Although attempted crystallization for further structural confirmation has so far been futile, the coordination of one water molecule can be deduced from the X-ray crystal structure of a related Gd-complex reported earlier by us [19].

3.2. Protonation constants

The protonation constants of **1a**–**1l** were determined by potentiometric titration in the pH range 2–11. The protonation constants (K_i^H) are defined in Eq. (1), where $i = 1,2,\ldots$

$$K_i^H = [H_iL]/[H_{i-1}L][H^+] \quad (1)$$

The calculated protonation constants are presented in Table 1 along with those for DTPA-BMA and DTPA for comparative purposes. It is known that for the DTPA-bis(amide) ligands the first protonation takes place at the central nitrogen atom, while the second and the third at the terminal amine nitrogen atoms [22]. Table 1 shows that all but **1i** exhibit higher first protonation constants ($\log K_1^H$) than DTPA-BMA. Some of the ligands such as **1a**–**1c** show even higher values than the parent DTPA. When the comparison is made within the present series, those carrying carboxylic acids in the amide side-arms (**1a**–**1d**) reveal higher protonation constants than those carrying carboxylic esters (**1e**–**1l**). It seems quite obvious then that the presence of the carboxylic acid in the amide side-arm renders the protonation of the central amine nitrogen facile by some co-operative interaction, possibly by hydrogen bonding between the carboxylic acid in the amide side-arm and the acetate arm on the central amine nitrogen as proposed in the structure **A** (*vide infra*). Yet, such a co-operative interaction seems to be less conspicuous or even negligible in the case of those carrying alkyl carboxylate side-arms as observed with **1e**–**1l** exhibiting relatively lower $\log K_1^H$ values.



(A)

The length of alkyl chain in the amide side-arm also seems to play a role, as evidenced by a little lower $\log K_1^H$ value for **1d** as compared with those for **1a**–**1c**. These

Table 1
Protonation constants ($\log K_i^H$) of **1a**–**1l** ($I = 0.10$ mol/dm^3)

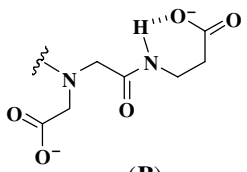
Equilibrium	$\log K$ (25 °C, $\mu = 0.10$ M (KCl))													
	1a	**1b**	**1c**	**1d**	**1e**	**1f**	**1g**	**1h**	**1i**	**1j**	**1k**	**1l**	DTPA-BMA[a]	DTPA[b]
[HL]/[L][H]	10.88	10.98	10.97	9.79	9.44	9.77	9.87	9.88	9.34	9.4	9.55	9.44	9.37	10.49
[H_2L]/[HL][H]	6.76	6.45	6.53	5.74	5.17	5.74	5.74	5.59	5.27	5.29	5.49	5.40	4.38	8.60
[H_3L]/[H_2L][H]	4.4	4.62	4.61	4.58	4.21	4.74	3.93	5.01	5.20	4.02	4.38	4.81	3.31	4.28
[H_4L]/[H_3L][H]														2.64
$\sum pK_a$	22.04	22.05	22.11	20.11	18.82	20.25	19.54	20.48	19.81	18.71	19.42	19.65	17.06	26.01

[a] Data obtained from Ref. [7].
[b] Ref. [36].

observations may be attributed to the long distance between the central amine nitrogen and the carboxylic acid in the side-arm.

A drastic decrease in the second protonation constant ($\log K_2^H$) is found with DTPA-BMA as well as the present series although the decrease is relatively small with DTPA. These observations indicate that the second protonation becomes much more difficult with DTPA-bis(amides) than with DTPA. This is because the terminal amine nitrogen of DTPA-BMA, for example, is strongly involved in the hydrogen bonding interaction with the acetate as well as the amide proton on the same terminal nitrogen, thus making the terminal nitrogen less basic [22–25]. However, such an interaction seems to be less pronounced in the present series than that in DTPA-BMA, as demonstrated in Table 1. A little higher affinity for the second protonation with the present series may be explained in terms of the structure **B**, where the terminal nitrogen becomes more prone towards protonation because of the hydrogen bonding interaction taking place within the amide side-arm. Yet, the basicity of the terminal amine nitrogen can be decreased by the presence of the vicinal electron-withdrawing amide functionality in the DTPA-bis(amide) series [18]. With DTPA, however, such an induction effect is absent.

In the same vein, the hydrogen bonding interaction proposed here may also account for higher third protonation constants ($\log K_3^H$) for the present series than that for DTPA-BMA (Table 1). Here again, the inductive effect of the vicinal amide group may by operative.



(**B**)

3.3. Thermodynamic stability constants

The thermodynamic stability constants ($K_{ML(therm)}$) are described by Eq. (2), where M is the free unhydrolyzed aqua metal ion, L the totally deprotonated free ligand, and ML the nonprotonated and nonhydrolyzed complex.

$$K_{ML(therm)} = [ML]/[M][L] \quad (2)$$

The direct potentiometric titration method cannot be applied for the measurement of the stability constants of Gd(III) complexes of bis(amides) since they are formed at low pH. Instead, they were determined by employing the method of ligand–ligand competition potentiometric titration between EDTA and bis(amide) ligands (L) for Gd(III) ion [26–28]. Yet, the stability constants of Cu(II), Zn(II), and Ca(II) complexes were measured by direct titration of the ligands.

In Table 2 are listed the thermodynamic stability constants for the complexes of **1a**–**1l** along with DTPA-BMA and DTPA for comparison. Quite obviously and expectedly, the stability constants of not only DTPA-BMA but also **1a**–**1l**are significantly lower than that of DTPA. The DTPA-bis(amide) type ligands are in general a weaker base than DTPA due to the presence of amide oxygens, a weaker donor than carboxylate oxygens of DTPA towards coordination with the Gd(III) ion [19]. When the comparison is made between DTPA-BMA and **1a**–**1l**, the former exhibits somewhat lower or comparable $\log K_{GdL(therm)}$ values than the latter except for **1e**, **1f**, and **1h**. Of the twelve ligands in the present series, the first three (**1a**–**1c**) show the highest stability than any of the rest in the series, the observation being consistent with the order of ligand basicity as shown in Table 1. Here again, as is the case with protonation constants, not only carboxylic acid groups but also the length of alkyl chain in the amide side-arms seem to be essential. For instance, it is those carrying carboxylic acids on the amide side-arm (**1a**–**1d**) that demonstrate the highest thermodynamic stability in the series. The exact role of the carboxylic acids has yet to be clarified although some sort of coordinative interaction with the central Gd(III) ion may be taken into consideration as a partial explanation for the increased stability. Therefore, relatively lower stability constants found with **1e**–**1l** are naturally the consequences of ester formation. As for the influence of the alkyl chain in the amide side-arm, it is best illustrated by the lowest stability constant of **1d** possessing the longest alkyl chain among the four carboxylic acid derivatives (**1a**–**1d**).

Table 2
Stability constants and selectivity constants of Gd(III), Zn(II), Ca(II), and Cu(II) complexes of **1a**–**1l** ($I = 0.10$ mol/dm^3)

Equilibrium	log K (25 °C, $\mu = 0.10$ M (KCl))													
	1a	**1b**	**1c**	**1d**	**1e**	**1f**	**1g**	**1h**	**1i**	**1j**	**1k**	**1l**	DTPA-BMA[a]	DTPA[b]
[GdL]/[Gd][L]	19.05	17.89	17.78	17.18	16.87	14.49	17.66	14.73	16.46	17.44	16.95	16.18	16.85	22.46
[GdHL]/[GdL][H]	4.15	5.41	5.48	4.94	4.13	6.77	3.93	6.79	4.31	4.00	4.59	4.94	[c]	2.39
{log $K_{GdL'}$(pH 7.4)}	15.37	14.25	14.15	14.78	14.82	12.11	15.18	12.24	14.51	15.43	14.79	14.13	14.84	18.14
[CaL]/[Ca][L]	8.28	9.11	9.94	7.9	7.04	7.76	7.73	7.59	7.64	7.08	7.33	7.35	7.17	10.75
[CaHL]/[CaL][H]	7.58	6.6	6.71	5.64	5.19	5.93	5.93	5.69	5.90	5.05	5.51	5.24	4.45	6.11
{log $K_{CaL'}$(pH 7.4)}	4.71	5.48	6.31	5.50	4.99	5.38	5.25	5.10	5.69	5.07	5.17	5.30	5.11	6.43
[ZnL]/[Zn][L]	12.59	13.35	13.13	11.67	11.50	11.40	13.06	11.13	10.72	11.21	11.55	10.42	12.04	18.70
[ZnHL]/[ZnL][H]	6.39	5.65	5.83	5.34	4.87	5.59	4.74	5.73	5.32	5.15	5.35	5.55	4.04	5.60
{log $K_{ZnL'}$(pH 7.4)}	9.02	9.72	9.50	9.27	9.45	9.02	10.58	8.64	8.77	9.20	9.39	8.37	10.02	14.38
[CuL]/[Cu][L]	13.09	13.88	13.61	11.76	11.95	11.98	13.57	11.91	11.23	11.9	11.81	10.83	13.03	21.38
[CuHL]/[CuL][H]	6.38	5.73	5.93	5.4	4.83	5.69	4.51	5.65	5.33	4.94	5.36	5.59	3.36	4.81
{log $K_{CuL'}$(pH 7.4)}	9.52	10.25	9.98	9.36	9.90	9.60	11.09	9.42	9.28	9.89	9.65	8.78	11.06	17.06
[log K_{sel}(Gd/Ca)]	10.66	8.77	7.84	9.28	9.83	6.73	9.93	7.14	8.82	10.36	9.62	8.83	9.68	11.71
[log K_{sel}(Gd/Zn)]	6.35	4.53	4.65	5.51	5.37	3.09	4.60	3.60	5.74	6.23	5.40	5.76	4.81	3.76
[log K_{sel}(Gd/Cu)]	5.85	4.0	4.17	5.42	4.92	2.51	4.09	2.28	5.23	5.54	5.14	5.35	3.82	1.08
log K'_{sel}	10.62	8.80	8.93	9.80	9.65	7.36	8.87	8.56	10.01	10.49	9.69	10.04	9.03	7.04

[a] Data obtained from Ref. [7].
[b] Ref. [36].
[c] Not reported.

3.4. Conditional stability constants and selectivity constants

The conditional stability constants reveal the extent of complexation at the given pH. To understand the stability of the complexes at the physiological pH, the stability constants of the complexes have been evaluated at pH 7.4 using Eq. (3), [7,29] where K_n^H ($n = 1, 2, 3, \ldots$) are the stepwise protonation constants of the ligands.

$$K_{ML(cond)} = K_{ML(therm)}(1 + K_1^H[H] + K_1^H K_2^H[H]^2 + K_1^H K_2^H K_3^H[H]^3 + \cdots)^{-1} \quad (3)$$

In Table 2 are also listed conditional stability constants of Gd(III), Zn(II), Ca(II), and Cu(II) complexes of **1a**–**1l**. Here again, the most obvious observation is that DTPA exhibits the highest conditional stability constants than any of DTPA-bis(amides) regardless of metals. All but **1f** and **1h** among the DTPAbis(amide) ligands described here, form Gd(III) complexes with slightly higher or comparable conditional stability than DTPA-BMA at pH 7.4 (Table 2).

The logarithmic selectivity constant (log K_{sel}) of a ligand for Gd(III) over Ca(II), Zn(II), or Cu(II) is defined as the difference between $K_{GdL(therm)}$ and $K_{ML(therm)}$ (M = Ca(II), Zn(II) and Cu(II)). In other words, these constants are a measure of affinity of the ligands towards Gd(III) over other metal ions. Table 2 shows that all ligands demonstrate favorable selectivity towards Gd(III) over Zn(II) and Cu(II), and even greater selectivity than DTPA-BMA and DTPA except for **1f** and **1h**. In the case of Ca(II), DTPA shows the highest affinity towards Gd(III) than other ligands.

The modified selectivity constants (K'_{sel}) are better employed to have a deeper insight into the stability of Gd(III) complexes as compared with other endogenous metal complexes of Ca(II), Zn(II), Cu(II), and proton at the physiological pH. They can be calculated using the following Eqs. (4)–(8) and $K_{ML(therm)}$ values in Eq. (4). Here α's are the side reaction coefficients.

$$K'_{sel} = K_{ML(therm)}(\alpha_{H^{-1}} + \alpha_{CaL^{-1}} + \alpha_{CuL^{-1}} + \alpha_{ZnL^{-1}})^{-1} \quad (4)$$

$$\alpha_{H^{-1}} = 1 + K_1^H[H] + K_1^H K_2^H[H]^2 + K_1^H K_2^H K_3^H[H]^3 + \cdots \quad (5)$$

$$\alpha_{CaL^{-1}} = 1 + K_{CaL}[Ca^{2+}] \quad (6)$$

$$\alpha_{CuL^{-1}} = 1 + K_{CuL}[Cu^{2+}] \quad (7)$$

$$\alpha_{ZnL^{-1}} = 1 + K_{ZnL}[Zn^{2+}] \quad (8)$$

The log K'_{sel} values at pH 7.4 for the Gd(III) complexes of **1a**–**1l** were calculated using the in vivo concentrations of $[Cu(II)] = 1.0 \times 10^{-3}$ mM, $[Ca(II)] = 2.5$ mM, and $[Zn(II)] = 5.0 \times 10^{-2}$ mM, [7] and are collected in Table 2. The table shows all DTPA-bis(amides) reveal greater selectivity (higher log K'_{sel} values) towards Gd(III) than DTPA. Yet, further significant observations other than the one stated above can hardly be made, although those amides carrying ethyl carboxylates in the amide side-arm seem to impart some extra in vivo stability for the Gd(III) complexes (Table 2).

In Table 3 are shown the pM values, total metal ion sequestering ability of a ligand, for the complexes of Gd(III), Zn(II), Ca(II), and Cu(II) incorporating **1a**–**1l**, DTPA-BMA, and DTPA as ligands. The larger pM values reflect a higher affinity of the ligand for the metal ion under the specified conditions [30]. The table indicates that most of the ligands of the present series are much stronger Gd(III) chelating agent than DTPA-BMA. The higher pGd values compared to the corresponding pCa, pZn and pCu values reflect the Gd(III) complexes are stable enough to avoid interference by other endogenously available metal ions. Different pGd values among **1a**–**1l** seem to indicate that here again the presence of carboxylic acid

Table 3
The pM[a] values of the complexes of Gd(III), Zn(II), Ca(II) and Cu(II) at pH 7.4

Ligands	pGd	pCa	pZn	pCu
1a	17.71	7.05	11.36	11.86
1b	16.65	7.88	12.12	12.65
1c	16.52	8.68	11.87	12.35
1d	16.18	6.90	10.50	10.95
1e	15.87	6.04	10.50	10.95
1f	13.49	6.76	10.40	10.98
1g	16.66	6.73	12.06	12.57
1h	13.72	6.58	10.12	10.90
1i	15.46	6.64	9.72	10.23
1j	16.44	6.08	10.21	10.90
1k	15.95	6.33	10.55	10.81
1l	15.18	6.35	9.42	9.83
DTPA-BMA	13.88	4.19	9.06	10.05
DTPA	17.14	5.45	13.39	16.06

[a] $pM = -\log[M]_{free}$ at pH 7.4; $[\text{metal ion}]_{total} = 1\ \mu mol/dm^3$; $[ligand]_{total} = 1.1\ \mu mol/dm^3$.

groups as well as the length of alkyl chains in the amide side-arms play certain roles.

3.5. Relaxometric studies

The relaxivities R_1 and R_2 of **2a**–**2l** in aqueous and aqueous HP-β-CD solutions are collected in Table 4. In aqueous solutions, the complexes show significantly lower relaxivities than analogous Gd(III) complexes of DTPA-BMA and DTPA. Yet, it is known that a significant increase in relaxivity is established when "host–guest" inclusion complexes are formed between the hydrophobic β-cyclodextrin cavity of hydroxypropyl-β-cyclodextrin (HP-β-CD) and Gd(III) complexes [10,31,32]. Such inclusion becomes possible through non-covalent interactions between β-cyclodextrin cavities and the substituents of ligands coordinated to the Gd(III) ion. Thus, hydrophobicity of the substituents in the ligand determines the stability of the inclusion complex [33]. In addition, HP-β-CD is biocompatible and has been used in the preparation of aqueous solution of water-insoluble drugs [34–36]. In this regard, the aliphatic amide side-arms in **2a**–**2l** are expected to interact with the hydrophobic cavities of the β-CD moieties of HP-β-CD thus leading to the formation of "host–guest" complexes. Indeed, dramatic increases in R_1 and R_2 values are to be noted. These observations demonstrate that the inclusion has truly taken place between **2** and HP-β-CD.

Table 4
Relaxivity data of **2a**–**2l** in aqueous and aqueous HP-β-CD solutions

Complexes	R_1 ($mM^{-1}\ s^{-1}$)	R_2 ($mM^{-1}\ s^{-1}$)	R_1^a in HP-β-CD ($mM^{-1}\ s^{-1}$)	R_2^a in HP-β-CD ($mM^{-1}\ s^{-1}$)
2a	1.58	1.50	9.4	9.7
2b	1.43	1.23	10.4	11.0
2c	1.31	1.00	8.6	8.7
2d	1.44	1.23	11.6	12.1
2e	1.59	1.71	8.7	8.8
2f	1.54	1.35	8.8	8.9
2g	1.47	1.31	9.1	9.2
2h	1.65	1.52	12.6	13.0
2i	1.95	1.94	10.1	10.4
2j	1.71	1.63.	12.2	12.5
2k	1.68	1.65	10.4	10.5
2l	1.54	1.40	10.5	10.8
Gd(DTPA-BMA)	4.58	4.76		
$[Gd(DTPA)]^{2-}$[b]	3.40	3.80		

[a] [HP-β-CD] = 50 mM.
[b] $[Gd(DTPA)]^{2-}$, R_1 and R_2 measured at $B_0 = 1.0$ T.

References

[1] P. Caravan, Chem. Soc. Rev. 35 (2006) 512.
[2] S. Aime, S.G. Crich, E. Gianolio, G.B. Giovenzana, L. Teia, E. Terreno, Coord. Chem. Rev. 250 (2006) 1562.
[3] É. Tóth, A.E. Merbach (Eds.), The Chemistry of Contrast Agents in Medical Magnetic Resonance Imaging, Wiley, Chichester, 2001.
[4] P. Caravan, J.J. Ellison, T.J. McMurry, R.B. Lauffer, Chem. Rev. 99 (1999) 2293.
[5] A.D. Sherry, W.P. Cacheris, K.-T. Kuan, Magn. Reson. Med. 8 (1988) 191.
[6] C. Paul-Roth, K.N. Raymond, Inorg. Chem. 34 (1995) 1408.
[7] W.P. Cacheris, S.C. Quay, S.M. Rocklage, Magn. Reson. Imag. 8 (1990) 467.
[8] G.L. Rothermel, E.N. Rizkalla Jr., G.R. Choppin, Inorg. Chim. Acta 262 (1997) 133.
[9] L. Sarka, L. Burai, R. Király, L. Zékány, E. Brücher, J. Inorg. Biochem. 91 (2002) 320.
[10] Z. Jászberényi, É. Tóth, T. Kálai, R. Király, L. Burai, E. Brücher, A.E. Merbach, K. Hideg, J. Chem. Soc., Dalton Trans. (2005) 694.
[11] Y.-M. Wang, T.-H. Cheng, G.-C. Liu, R.-S. Sheu, J. Chem. Soc., Dalton Trans. (1997) 833.
[12] S.W.A. Bligh, A.H.M.S. Chowdhury, M. McPartlin, I.J. Scowen, R.A. Bulman, Polyhedron 14 (1995) 567.
[13] H. Lammers, F. Maton, D. Pubanz, M.W. van Laren, H. Van Bekkum, A.E. Merbach, R.N. Muller, J.A. Peters, Inorg. Chem. 36 (1997) 2527.
[14] S. Aime, F. Benetollo, G. Bombieri, S. Colla, M. Fasano, S. Paoletti, Inorg. Chim. Acta 254 (1997) 63.
[15] X. Zhao, R. Zhuo, Z. Lu, W. Liu, Polyhedron 16 (1997) 2755.
[16] H. Lammers, A.M. van der Heijden, H. van Bekkum, C.F.G.C. Geraldes, J.A. Peters, Inorg. Chim. Acta 268 (1998) 249.
[17] S.W.A. Bligh, A.H.M.S. Chowdhury, D. Kennedy, C. Luchinat, G. Parigi, Magn. Reson. Med. 41 (1999) 767.
[18] Y.-M. Wang, Y.-J. Wang, R.-S. Sheu, G.-C. Liu, W.-C. Liu, J.-H. Liao, Polyhedron 18 (1999) 1147.
[19] S. Dutta, S.-K. Kim, E.J. Lee, T.-J. Kim, D.-S. Kang, Y. Chang, S.O. Kang, W.-S. Han, Bull. Korean Chem. Soc. 27 (2006) 1038.
[20] P. Gans, A. Sabatini, A. Vacca, Talanta 43 (1996) 1739.
[21] W.C. Eckelman, S.M. Karesh, R.C. Reba, J. Pharm. Sci. 64 (1975) 704.
[22] C.F.G.C. Geraldes, A.M. Urbano, M.C. Alpoim, A.D. Sherry, K.-T. Kuan, R. Rajagopalan, F. Maton, R.N. Muller, Magn. Reson. Imag. 13 (1995) 401.
[23] J.L. Sudmeier, C.N. Reilley, Anal. Chem. 36 (1964) 1698.
[24] Y. Fujiwara, C.N. Reilley, Anal. Chem. 40 (1968) 890.
[25] P. Letkeman, A.E. Martell, Inorg. Chem. 18 (1979) 1284.
[26] W.R. Harris, A.E. Martell, Inorg. Chem. 15 (1976) 713.
[27] Y. Li, A.E. Martell, R.D. Hancock, J.H. Reibenspies, C.J. Anderson, M.J. Welch, Inorg. Chem. 35 (1996) 404.
[28] C.H. Taliaferro, R.J. Motekaitis, A.E. Martell, Inorg. Chem. 23 (1984) 1188.

[29] K. Kumar, M.F. Tweedle, M.F. Malley, J.Z. Gougoutas, Inorg. Chem. 34 (1995) 6472.
[30] C.J. Bannochie, A.E. Martell, Inorg. Chem. 30 (1991) 1385.
[31] S. Aime, M. Botta, D. Parker, J.A.G. Williams, J. Chem. Soc., Dalton Trans. (1995) 2259.
[32] S. Aime, M. Botta, M. Panero, M. Grandi, F. Uggeri, Magn. Reson. Chem. 29 (1991) 923.
[33] S. Aime, M. Botta, L. Frullano, S.G. Crich, G.B. Giovenzana, R. Pagliarin, G. Palmisano, M. Sisti, Chem. Eur. J. 5 (1999) 1253.
[34] T. Loftsson, M.E. Brewster, J. Pharm. Sci. 85 (1996) 1012.
[35] R.A. Rajewski, V.J. Stella, J. Pharm. Sci. 85 (1996) 1142.
[36] A.E. Martell, R.M. Smith, Critical Stability Constants, vol. 1, Plenum, New York, 1974.

nal residual solvent peaks. Elemental analyses were performed by the Analytical Chemistry Division of Bhabha Atomic Research Centre, Mumbai. The TG/DTA for **7** and **8** were recorded on a Mettler TGA-851E instrument under the flow of an air.

2.2. Synthesis of (3,5-dimethyl,N,N-dibutyl, carbamoyl methyl pyrazole (*L₁*)

3,5-Dimethyl pyrazole (4.6 g, 0.048 mol), $ClCH_2CONBu_2$ (10.0 g, 0.048 mol) and triethylamine (10 ml) were refluxed in 1,2-dichloroethane for 80 h and the resulting solution was treated with 100 ml of 20% HCl solution. The organic layer was separated, dried over anhydrous Na_2SO_4, filtered and dried. The resulting colorless solid was recrystallized from hot hexane as a white solid. Yield: 12.0 g (94%). Elemental *Anal*. Calc. for $C_{15}H_{27}N_3O$: C, 67.9; H, 10.2; N, 15.8. Found: C, 67.8; H, 10.0; N, 15.6%. IR (KBr, Nujol): ν/cm^{-1} 1653 (CO). ^1H NMR (25 °C, $CDCl_3$): δ 0.92 (t, 6 Hz, CH_3, Bu), 0.95 (t, 6 Hz, CH_3, Bu), 1.32–1.40 (m, CH_2, Bu), 1.47–1.52 (m, CH_2, Bu), 2.18 (s, CH_3, dmPz), 2.19 (s, CH_3, dmPz), 3.28 (m, NCH_2, Bu), 4.81 (s, NCH_2CO), 5.83 (s, dmPz). (25 °C, CD_3OD): δ 0.92 (t, 6 Hz, CH_3, Bu), 0.99 (t, 6 Hz, CH_3, Bu), 1.32 (m, CH_2, Bu), 1.42 (m, CH_2, Bu), 1.52 (m, CH_2, Bu), 1.62 (m, CH_2, Bu), 2.18 (s, CH_3, dmPz), 2.19 (s, CH_3, dmPz), 3.35 (m, NCH_2, Bu), 4.97 (s, NCH_2CO), 5.94 (s, dmPz).

2.3. Synthesis of (3,5-dimethyl,N,N-di-isobutyl carbamoyl methyl pyrazole (*L₂*)

This was prepared similarly to $\mathbf{L_1}$ by taking 3,5-dimethyl pyrazole (3.7 g, 0.039 mol), $ClCH_2CON^iBu_2$ (8.0 g, 0.039 mol) and triethylamine (10 ml). The final product was obtained as white needles. Yield: 9.7 g (94%). Elemental *Anal*. Calc. for $C_{15}H_{27}N_3O$: C, 67.9; H, 10.2; N, 15.8. Found: C, 67.7; H, 10.1; N, 15.5%. IR (KBr, Nujol): ν/cm^{-1} 1655 (CO); ^1H NMR (25 °C, $CDCl_3$): δ 0.85 (d, 7 Hz, CH_3, ^{i}Bu), 0.95 (d, 7 Hz, CH_3, ^{i}Bu), 1.99 (m, CH, ^{i}Bu), 2.18 (s, CH_3, dmPz), 2.19 (s, CH_3, dmPz), 3.16 (d, 7.5 Hz, NCH_2, ^{i}Bu), 3.28 (d, 7.5 Hz, NCH_2, ^{i}Bu), 4.83 (s, NCH_2CO), 5.82 (s, dmPz).

2.4. Synthesis of (N,N-dibutyl, carbamoyl methyl pyrazole (*L₃*)

This was prepared similarly to $\mathbf{L_1}$ by taking pyrazole (3.3 g, 0.049 mol), $ClCH_2CONBu_2$ (10.0 g, 0.049 mol) and triethylamine (10 ml). The final product was obtained as a semi-solid. Yield: 10.0 g (90%). Elemental *Anal*. Calc. for $C_{13}H_{23}N_3O$: C, 65.8; H, 9.7; N, 17.7. Found: C, 65.4; H, 10.0; N, 17.4%. IR (KBr, Nujol): ν/cm^{-1} 1655 (CO). ^1H NMR (25 °C, $CDCl_3$): δ 0.88 (t, 6 Hz, CH_3, Bu), 0.94 (t, 6 Hz, CH_3, Bu), 1.3 (m, CH_2, Bu), 1.52 (m, CH_2, Bu), 3.28 (m, NCH_2, Bu), 4.96 (s, NCH_2CO), 6.28 (t, 2 Hz, Pz), 7.50 (d, 2 Hz, Pz), 7.52 (d, 2 Hz, Pz).

2.5. Synthesis of N,N-diisobutyl, carbamoyl methyl pyrazole (*L₄*)

This was prepared similarly to $\mathbf{L_1}$ by taking pyrazole (3.0 g, 0.044 mol), $ClCH_2CON^iBu_2$ (9.2 g, 0.044 mol) and triethylamine (10 ml). The final product was obtained as a semi-solid. Yield: 9.6 g (91%). Elemental *Anal*. Calc. for $C_{15}H_{27}N_3O$: C, 65.8; H, 9.7; N, 17.7. Found: C, 65.7; H, 10.1; N, 17.5%. IR (KBr, Nujol): ν/cm^{-1} 1654 (CO). ^1H NMR (25 °C, $CDCl_3$): δ 0.82 (d, 7 Hz, CH_3, ^{i}Bu), 0.94 (d, 7 Hz, CH_3, ^{i}Bu), 1.99 (m, CH, ^{i}Bu), 3.13 (d, 7 Hz, NCH_2, ^{i}Bu), 3.18 (d, 7 Hz, NCH_2, ^{i}Bu), 4.98 (s, NCH_2CO), 6.28 (t, 2 Hz, Pz), 7.49 (d, 2 Hz, Pz), 7.52 (d, 2 Hz, Pz).

2.6. Synthesis of 3,5-dimethyl,N,N-dioctyl, carbamoyl methyl pyrazole (*L₅*)

This was prepared similarly to $\mathbf{L_1}$ by taking 3,5-dimethyl pyrazole (3.0 g, 0.031 mol), $ClCH_2CON(C_8H_{17})_2$ (10.0 g, 0.031 mol) and triethylamine (10 ml). The final product was obtained as a pasty liquid. Yield: 11.0 g (93%). Elemental *Anal*. Calc. for $C_{23}H_{43}N_3O$: C, 73.2; H, 11.4; N, 11.1. Found: C, 72.7; H, 10.4; N, 10.5%. IR (KBr, Nujol): ν/cm^{-1} 1654 (CO). ^1H NMR (25 °C, $CDCl_3$): δ 0.84 (m, CH_3, C_8H_{17}), 1.2–1.3 (br, CH_2, C_8H_{17}), 2.16 (s, CH_3, dmPz), 2.18 (s, CH_3, dmPz), 3.25 (m, NCH_2, C_8H_{17}), 3.77 (m, NCH_2, C_8H_{17}), 4.78 (s, NCH_2CO), 5.83 (s, dmPz).

2.7. Synthesis of [$UO_2(NO_3)_2$*L₁*] (*6*)

To a solution of $\mathbf{L_1}$ (550 mg, 2.08 mmol) in $CHCl_3$, solid $[UO_2(NO_3)_2 \cdot 6H_2O]$ (502 mg, 1.0 mmol) was added and stirred for few minutes until all $[UO_2(NO_3)_2 \cdot 6H_2O]$ dissolves to give clear solution. This solution was filtered and allowed to stand for over night in a closed vial. This process deposited yellow crystalline solid, which was filtered, washed with $CHCl_3$ and dried. Yield: 600 mg (91%). Elemental *Anal*. Calc. for $[UO_2(NO_3)_2C_5H_7N_2CH_2CON(C_4H_9)_2]$, $C_{15}H_{27}N_5O_9U$: C, 27.3; H, 4.1; N, 10.6. Found: C, 27.0; H, 4.0; N, 10.1%. IR (KBr, Nujol): ν/cm^{-1} 1614 (CO), 930 (O=U=O). ^1H NMR (25 °C, CD_3COCD_3): δ 0.97 (t, 7 Hz, CH_3, Bu), 1.07 (t, 7 Hz, CH_3, Bu), 1.47 (m, CH_2, Bu), 1.60 (m, CH_2, Bu), 1.88 (m, CH_2, Bu), 2.48 (s, CH_3, dmPz), 2.72 (s, CH_3, dmPz), 3.97 (br, NCH_2, Bu), 4.13 (br, NCH_2, Bu), 5.47 (s, NCH_2CO), 6.51 (s, dmPz).

2.8. Synthesis of [$UO_2(NO_3)_2$*L₂*] (*7*)

It was prepared similarly to **6** by taking $\mathbf{L_2}$ (500 mg, 1.89 mmol) and $[UO_2(NO_3)_2 \cdot 6H_2O]$ (450 mg, 0.89 mmol). Yield: 550 mg (93%). Elemental *Anal*. Calc. for $[UO_2(NO_3)_2C_5H_7N_2CH_2CON(^iC_4H_9)_2]$, $C_{15}H_{27}N_5O_9U$: C, 27.3; H, 4.1; N, 10.6. Found: C, 27.1; H, 3.9; N, 10.3%. IR (KBr, Nujol mull): ν/cm^{-1} 1600 (CO), 939 (O=U=O). ^1H NMR (25 °C, CD_3COCD_3): δ 0.93 (d, 7 Hz, CH_3, ^{i}Bu), 1.08 (d, 7 Hz, CH_3, ^{i}Bu), 2.21 (m, CH,

^{i}Bu), 2.45 (s, CH_3, dmPz), 2.70 (s, CH_3, dmPz), 3.84 (br, NCH_2, ^{i}Bu), 4.06 (br, NCH_2, ^{i}Bu), 5.52 (s, NCH_2CO), 6.49 (s, dmPz).

2.9. Synthesis of $[UO_2(NO_3)_2\mathbf{L_3}]$ (**8**)

It was prepared similarly to **6** by taking $\mathbf{L_3}$ (500 mg, 2.11 mmol) and $[UO_2(NO_3)_2 \cdot 6H_2O]$ (502 mg, 1.0 mmol). Yield: 600 mg (95%). Elemental *Anal.* Calc. for $[UO_2(NO_3)_2C_3H_3N_2CH_2CON(C_4H_9)_2]$, $C_{13}H_{23}N_5O_9U$: C, 24.7; H, 3.6; N, 11.1. Found: C, 24.5; H, 3.3; N, 10.7%. IR (KBr, Nujol): ν/cm^{-1} 1612 (CO), 929 (O=U=O). ^{1}H NMR (25 °C, CD_3COCD_3): δ 0.98 (t, 7 Hz, CH_3, Bu), 0.99 (t, 6 Hz, CH_3, Bu), 1.48 (m, CH_2, Bu), 1.62 (m, CH_2, Bu), 1.89 (m, CH_2, Bu), 3.98 (br, NCH_2, Bu), 4.20 (br, NCH_2, Bu), 5.62 (s, NCH_2CO), 6.40 (br, Pz), 7.71 (br, Pz), 7.83 (br, Pz).

2.10. Synthesis of $[UO_2(NO_3)_2\mathbf{L_4}]$ (**9**)

It was prepared similarly to **6** by taking $\mathbf{L_4}$ (500 mg, 2.11 mmol) and $[UO_2(NO_3)_2 \cdot 6H_2O]$ (400 mg, 0.79 mmol). Yield: 502 mg (93%). Elemental *Anal.* Calc. for $[UO_2(NO_3)_2C_3H_3N_2CH_2CON(^{i}C_4H_9)_2]$, $C_{13}H_{23}N_5O_9U$: C, 24.7; H, 3.6; N, 11.1. Found: C, 24.4; H, 3.5; N, 10.9%. IR (KBr, Nujol): ν/cm^{-1} 1595 (CO), 941 (O=U=O). ^{1}H NMR (25 °C, CD_3COCD_3): δ 0.93 (d, 7 Hz, CH_3, ^{i}Bu), 1.01 (d, 7 Hz, CH_3, ^{i}Bu), 2.24 (m, CH, ^{i}Bu), 3.87 (br, NCH_2, ^{i}Bu), 4.08 (br, NCH_2, ^{i}Bu), 5.63 (s, NCH_2CO), 6.42 (br, Pz), 7.67 (br, Pz), 7.82 (br, Pz).

2.11. Synthesis of $[La(NO_3)_3(\mathbf{L_4})_2]$ (**10**)

To a solution of $\mathbf{L_4}$ (700 mg, 2.97 mmol) in ethyl acetate, solid $[La(NO_3)_3 \cdot 6H_2O]$ (400 mg, 0.92 mmol) was added and refluxed for 2 h. The resulting white solid was filtered, washed with ethyl acetate, hexane and dried. Yield: 680 mg (92%). Elemental *Anal.* Calc. for $[La(NO_3)_3\{C_3H_3N_2CH_2CON(^{i}C_4H_9)_2\}_2]$, $C_{26}H_{46}N_9O_{11}La$: C, 39.1; H, 5.8; N, 15.8. Found: C, 38.7; H, 5.4; N, 15.2%. IR (KBr, Nujol): ν/cm^{-1} 1615, 1603 (CO). ^{1}H NMR (25 °C, CD_3COCD_3): δ 0.84 (d, 7 Hz, CH_3, ^{i}Bu), 0.99 (d, 7 Hz, CH_3, ^{i}Bu), 2.12 (m, CH, ^{i}Bu), 3.32 (d, NCH_2, ^{i}Bu), 3.50 (d, NCH_2, ^{i}Bu), 5.37 (s, NCH_2CO), 6.34 (t, Pz), 7.68 (d, Pz), 7.84 (d, Pz).

2.12. Synthesis of $[Ce(NO_3)_3(\mathbf{L_4})_2]$ (**11**)

To a solution of $\mathbf{L_4}$ (650 mg, 2.75 mmol) in ethyl acetate, solid $[Ce(NO_3)_3 \cdot 6H_2O]$ (400 mg, 0.92 mmol) was added and refluxed for 2 h. The resulting white solid was filtered, washed with ethyl acetate, hexane and dried. Yield: 650 mg (88%). Elemental *Anal.* Calc. for $[Ce(NO_3)_3\{C_3H_3N_2CH_2CON(^{i}C_4H_9)_2\}_2]$, $C_{26}H_{46}N_9O_{11}Ce$: C, 39.0; H, 5.7; N, 15.7. Found: C, 38.6; H, 5.5; N, 15.4%. IR (KBr, Nujol): ν/cm^{-1} 1613, 1603 (CO). ^{1}H NMR (25 °C, CD_3COCD_3): δ 0.85 (d, CH_3, ^{i}Bu), 1.00 (d, CH_3, ^{i}Bu), 2.12 (m, CH, ^{i}Bu), 3.31 (d, NCH_2, ^{i}Bu), 3.49 (d, NCH_2, ^{i}Bu), 5.34 (m, NCH_2CO), 6.32 (m, Pz), 7.66 (br, Pz), 7.82 (m, Pz).

2.13. Solvent extraction studies

Distribution studies were performed by using a solution of $\mathbf{L_5}$ in toluene (as such, without any pre-equilibration for the acidity variation experiments and pre-equilibrated with 3 M HNO_3 for the slope measurements) with the required aqueous phase spiked with ^{233}U, ^{239}Pu or ^{241}Am tracers in a thermostated water bath for 1 h at 25 ± 0.1 °C. Assay of organic and aqueous phases were done in duplicate by alpha counting using a dioxane based liquid scintillator for ^{233}U and ^{239}Pu and direct γ counting for ^{241}Am. The distribution ratio (D) is defined as the ratio of the concentration of uranium in the organic phase to that of the aqueous phase.

2.14. X-ray diffraction studies of **6**, **7** and **11**

Data for the crystals **6**, **7** and **11** were measured with the Mo Kα radiation ($\lambda = 0.71073$ Å) using the MARresearch Image Plate System. The crystals were positioned at 70 mm from the Image Plate. Ninety-five frames were measured at 2° intervals with a counting time of 2 min. Data analysis was carried out with the XDS program [36a]. The structures were solved using direct methods with the SHELXS program [36b]. In **11** one of the alkyl chains was disordered with three of the carbon atoms refined over two sites. Apart from these disordered atoms, all non-hydrogen atoms in all these structures were refined with anisotropic thermal parameters. The hydrogen atoms bonded to carbon atoms were included in the geometric positions and given thermal parameters equivalent to 1.2 times those of the atoms to which they attached. Empirical absorption corrections were carried out using the DIFABS program [36c]. The struc-

Table 1
Crystal and structural refinement details for **7** and **11**

Compound	**7**	**11**
Empirical formula	$C_{15}H_{27}N_5O_9U$	$C_{26}H_{46}N_9O_{11}Ce$
Formula weight	659.45	800.84
Crystal system	monoclinic	monoclinic
Space group	$P2_1/c$	$C2/c$
a (Å)	8.130(11)	13.611(15)
b (Å)	15.437(17)	13.049(15)
c (Å)	18.93(2)	22.41(2)
β (°)	96.905(10)	106.600(10)
Volume (Å^3)	2359(5)	3815(7)
Z (formula unit)	4	4
D_{calc} (g/cm^3)	1.857	1.394
Reflections collected/unique	10387/4120	9519/3558
Data/restraints/parameters	3249/0/278	3558/0/218
Goodness of fit on F^2	1.145	1.282
Final R indices [$I > 2\sigma(I)$]	0.0600	0.0500
R indices (all data)	0.0830	0.0550

$w = 1/[\sigma^2(F_o^2) + (0.0122P)^2 + 18.3632P]$ for **7**, $w = 1/[\sigma^2(F_o^2) + (0.0253P)^2 + 19.30227P]$ for **11**. where $P = (F_o^2 + 2F_c^2)/3$ for **7** and **11**.

tures were refined to convergence on F^2 using SHELXL [36d]. Selected crystallographic data for **7** and **11** are summarized in Table 1 and for **6** given as Supplementary material (Table 2).

3. Results and discussion

3.1. Synthesis and characterization of CMPz ligands

The reaction of pyrazole or dimethyl pyrazole with various monochloroacetyl amides yielded the corresponding carbamoyl methyl pyrazoles [37] $\mathbf{L_1}$ to $\mathbf{L_5}$ (Scheme 1). The IR spectra of $\mathbf{L_1}$ to $\mathbf{L_5}$ showed the presence of a carbamoyl group in all these ligands. The ^{1}H NMR spectra of $\mathbf{L_1}$ to $\mathbf{L_5}$ showed the expected peaks and multiplicities. The –NCH_2CO– protons of all these ligands showed a single resonance around 4.8–4.9 ppm and are deshielded about 0.8–0.9 ppm with respect to the starting chloroacetyl amides.

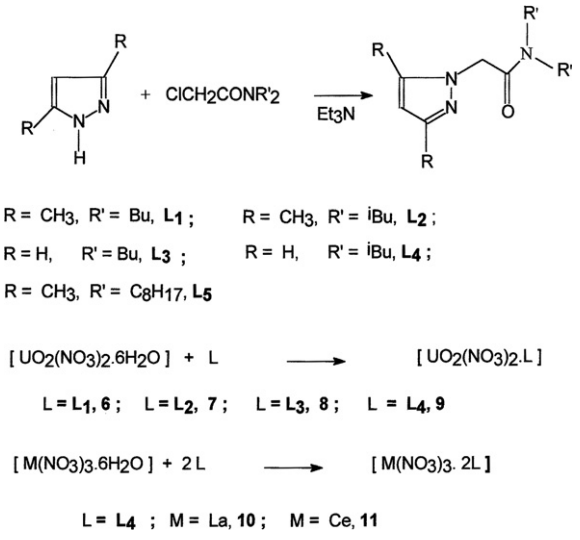
3.2. Complexation study of L_1, L_2, L_3 and L_4 with uranyl nitrate

The complexing ability of $\mathbf{L_1}$, $\mathbf{L_2}$, $\mathbf{L_3}$ and $\mathbf{L_4}$ with uranyl nitrate was studied by using elemental analysis, IR and NMR spectroscopic techniques. The reaction of $[UO_2(NO_3)_2 \cdot 6H_2O]$ with $\mathbf{L_1}$, $\mathbf{L_2}$, $\mathbf{L_3}$ or $\mathbf{L_4}$, yielded the compounds **6–9** (Scheme 1). The C, H and N analysis revealed that the ratio of ligand to uranyl nitrate is 1:1 in all these compounds. The IR spectra of **6–9** show that the water molecules from the starting compound $[UO_2(NO_3)_2 \cdot 6H_2O]$ are completely replaced by the ligand and that the ligand is bonded through the carbamoyl oxygen atom to the uranyl group.

The observed frequency differences for a carbamoyl ($\Delta\nu_{CO} = 35–50\ cm^{-1}$, where $\Delta\nu_{CO} = \nu_{CO(free\ ligand)} - \nu_{CO(coordinated)}$) [14–28] group are consistent with the supposition that the carbamoyl group is bonded to the uranyl group directly in the reported compounds. Similar differences are also observed in the compounds of CMP, CMPO or CMSO with uranyl nitrate such as, $[UO_2(NO_3)_2(^iC_3H_7O)_2POCH_2CONEt_2]$ [14], $[UO_2(NO_3)_2(C_6H_5)_2POCH_2CONEt_2]$ [17] or $[UO_2(NO_3)_2\ C_6H_5SOH_2CONBu_2]$ [28]. The ^{1}H NMR spectra of **6–9** show that both the NCH_2CO (ca. 0.5–0.6 ppm) and pyrazole (ca. 0.3–0.7 ppm) protons are deshielded with respect to the free ligand, indicating that the ligand is bonded to the uranyl group in solution. It is apparent from the elemental analysis and IR spectral results that ligands $\mathbf{L_1}$–$\mathbf{L_4}$ are acting as bidentate chelating ligand in compounds **6–9** in the solid state to give similar structures to those observed in the compounds of CMPO, CMP or CMSO with uranyl nitrate. Structures of compounds **6** and **7** have been determined by single crystal X-ray diffraction methods and show the bidentate chelating mode of bonding for the ligand in the solid state.

3.3. Molecular structures of 6 and 7

The molecular structure of **6** is shown in Supplementary material (Fig. 1) and that of **7** is shown in Fig. 2. The selected interatomic bond distances and angles for **7** are given in Table 3 and those of **6** Supplementary material (Table 4). The structures of **6** and **7** are similar and show that the uranium atom is surrounded by seven oxygen atoms and one nitrogen atom in a hexagonal bi-pyramidal geometry. Four oxygen atoms of the two nitrate groups, together with one oxygen and one nitrogen atoms of the CMPz ligand form the equatorial hexagonal plane. The five oxygen and one nitrogen atoms (O5N) are coplanar to within 0.14 Å in **6** and 0.13 Å in **7**. The two uranyl oxygen atoms occupy the axial positions. Two nitrate groups act as bidentate chelating ligands and bonded through the oxygen atoms to the uranyl group. The CMPz ligand acts as a



Scheme 1.

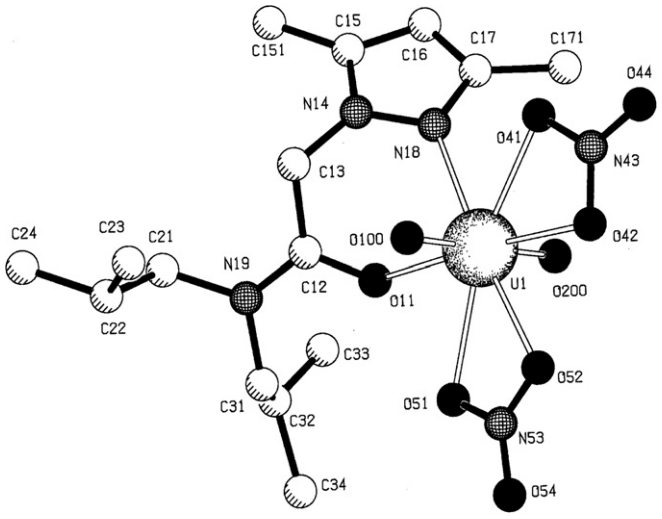


Fig. 2. Molecular structure of **7**, hydrogen atoms omitted for clarity.

Table 3
Important bond distances (Å) and angles (°) for **7** and **11**

Compound 7			
U1–O100	1.748(9)	U1–O11	2.364(7)
U1–O200	1.759(8)	U1–O52	2.517(8)
U1–O41	2.511(8)	U1–O42	2.521(9)
U1–O51	2.549(8)	U1–N18	2.554(9)
O100–U1–O200	178.7(4)	O11–U1–N18	67.2(3)
O41–U1–O42	50.5(3)	O42–U1–O52	60.5(3)
O52–U1–O51	50.3(3)	O51–U1–O11	65.1(3)
N18–U1–O41	67.7(3)		
*Compound **11***			
Ce1–O41	2.660(5)	O11–Ce1–O11	71.94(19)
Ce1–O42	2.651(5)	O51–Ce1–O51	47.40(19)
Ce1–O51	2.650(5)	O42–Ce1–O41	47.73(14)
Ce1–O11	2.477(4)	O11–Ce1–O41	72.08(16)
Ce1–N18	2.732(5)	O42–N43–O41	116.1(5)

bidentate chelating ligand and is bonded through both the pyrazolyl nitrogen and carbamoyl oxygen atoms to the uranyl group.

This is a similar type of co-ordination to that observed in the compounds of the bi-functional ligands, CMP, CMPO, *β*-Sulfoxo phosphine oxide, malonamide and CMSO with uranyl nitrate such as, $[UO_2(NO_3)_2Ph\{EtO\}POCH_2CONEt_2]$, $[UO_2(NO_3)_2Ph_2POCH_2CONEt_2]$ [17], $[UO_2(NO_3)_2(^iC_3H_7O)_2\ POCH_2SO(p\text{-}CH_3C_6H_4)]$ [20],$[UO_2(NO_3)_2(^iC_3H_7)_2NCO)_2CH_2]$ [27] and $[UO_2(NO_3)_2C_6H_5SOH_2CONBu_2]$ [28]. The observed U–N(pyrazolyl) bond distances (2.551(19) Å) in **6** and (2.554(9) Å) in **7** are very close to the values observed in $[UO_2(NO_3)_2(C_{12}H_8N_2)]$ ($C_{12}H_8N_2$ = phenanthroline) (2.556(2) Å) [31,32] and $[UO_2(C_{15}H_{11}N_3)_2(OTf)_2]$ ($C_{15}H_{11}N_3$ = terpyridine) (2.567(6), 2.592(6) Å) [33,34]. The U–O(amide) distances (2.377(9) Å) in **6** and (2.364(7) Å) in **7** are slightly shorter than the values observed in $[UO_2(NO_3)_2Ph\{EtO\}POCH_2CONEt_2]$ (2.426(8) Å), $[UO_2(NO_3)_2Ph_2POCH_2CONEt_2]$ (2.404(5) Å) [17], $[UO_2(NO_3)_2(^iC_3H_7)_2NCOCH_2CON(^iC_3H_7)_2]$ (2.41(2) Å) [27] and $[UO_2(NO_3)_2C_6H_5SOH_2CONBu_2]$ (2.442(9) Å) [28]. The observed average U–O(NO_3) bond distance 2.524(8) Å is normal [17,20,27,28]. The angles subtended at the metal atom show that the uranium atom has a slightly distorted hexagonal bi-pyramidal geometry.

3.4. Complexation study of L_4 with lanthanum(III) and cerium(III) Nitrates

The reaction of L_4 with $La(NO_3)_3 \cdot 6H_2O$ or $Ce(NO_3)_3 \cdot 6H_2O$ yielded **10** or **11** (Scheme 1). The C, H, N analysis revealed that the ratio of ligand to metal is 2:1 in both the compounds. The IR spectra of **11** and **12** show that the water molecules from the starting compounds $[M(NO_3)_3 \cdot 6H_2O]$ are replaced completely by the ligands. The spectra show further that the ligands are bonded through the carbamoyl oxygen atoms to the metal ion. ($\Delta\nu_{CO} = 41$–$53\ cm^{-1}$, where $\Delta\nu_{CO} = \nu_{CO\ (free\ ligand)} - \nu_{CO(coordinated)}$). This arrangement is similar to that observed in the compounds of CMPO, CMP, CMSO or malonamide with lanthanide(III) nitrate compounds such as: $[Gd(NO_3)_3\{(^iC_3H_7O)_2POCH_2SO(p\text{-}CH_3C_6H_4)\}_2]$ [19], $[Ce(NO_3)_3(TMSA)_2]$, $[Ce(NO_3)_3(TMSA)_2]_\alpha$ [25] and $[Ce(NO_3)_3\{C_6H_5SOH_2CONBu_2\}_2]$ [28]. The ^1H NMR of the compounds show that both the NCH_2CO (ca. 0.4 ppm) and pyrazole (ca. 0.2–0.3 ppm) protons of the CMPz ligand are deshielded with respect to the free ligand, indicating that the ligand is bonded to the lanthanide ion in solution. The structure of compound **11** has been determined by single crystal X-ray diffraction methods and showing the bidentate chelating mode of bonding for the carbamoyl methyl pyrazole ligand.

3.5. Molecular structure of 11

The molecular structure of **11**, which contains a crystallographic twofold axis is shown in Fig. 3 together with the numbering scheme and selected interatomic bond distances and angles are given in Table 3. The structure shows that the cerium(III) ion is bonded to two CMPz ligands and three nitrate groups to give a coordination number of ten. Both CMPz ligands are bidentate being bonded through both the pyrazolyl nitrogen and carbamoyl oxygen atoms to the cerium(III) nitrate. Six oxygen atoms from three nitrate groups, two oxygen and two nitrogen atoms from two CMPz ligands form a bi-capped square anti-prismatic geometry around the cerium ion. Similar structures are also observed in the compounds of CMP, CMPO, CMSO or bis(diphenylphosphino methane) dioxide with lanthanide (III) nitrates, viz., $[Sm(NO_3)_3\{(^iPrO)_2POCH_2CONEt_2\}_2]$ [15][$Nd(NO_3)_3\{Ph_2POCH_2CONEt_2\}_2$] [16][$Ce(NO_3)_3(C_6H_5SOCH_2CONBu_2)_2$] [28] and $[M(NO_3)_3(DPPMO)_2]$ (M = La or Ce) [38]. The observed metal to oxygen and metal to nitrogen bond distances are in the range of (2.650(4)–2.660(5) Å) for Ce–O(nitrate) [28,38], 2.477(4) Å for Ce–O(amide) [15,28,39] and 2.732(5) Å for

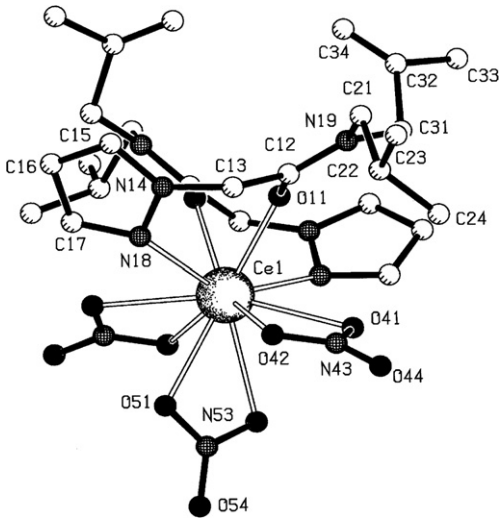


Fig. 3. Diagram of the structure of **11**, hydrogen atoms omitted for clarity.

Ce–N(pyrazole) [40] and agree well with those found previously.

3.6. Thermal studies of the compounds 6 and 7

Thermogravimetric (TG) and differential thermal analyses (DTA) of **6** and **7** (see Supplementary material) were carried out to see whether the bonded ligands can be destroyed completely on heating or not. These compounds decompose in two steps to give U_3O_8 as a final product (identified from the powder X-ray diffraction pattern of the decomposition product), without any other impurities. However, the decomposition of phosphine oxide compounds of uranyl nitrate yielded the corresponding uranyl phosphate as a final product [41]. This observation clearly shows that the CMPz ligands can be completely destroyed on incineration, as indeed can the amide ligands [8b].

3.7. Extraction studies of U(VI), Pu(IV) and Am(III) with L_5 from nitric acid medium

The extraction studies were carried out by using the ligand $\mathbf{L_5}$ in toluene with the U(VI), Pu(IV) and Am(III) ions in tracer level (using the ^{233}U, ^{239}Pu and ^{241}Am tracers) from nitric acid medium to assess the feasibility of using these ligands (0.2F for U(VI) and Am(III) and 0.004F for Pu(IV), where F = weight dissolved in 1 l of the solvent/formula weight) for extraction purposes. Distribution ratios (D) for U(VI), Pu(IV) and Am(III) as a function of nitric acid concentrations (Fig. 4) show clearly that U(VI) and Pu(IV) are extracted significantly from nitric acid at concentrations of 1–10 M. However, Am(III) did not show appreciable extraction under the conditions studied. The observed distribution ratios follow the order of: $D_{Pu(IV)} \gg D_{U(VI)} \gg D_{Am(III)}$ and are similar to those observed for the CMP, CMPO, CMSO or malonamide ligands with these metal ions [28,42].

In order to establish the nature of species extracted during the solvent extraction process, the distribution ratios for the U(VI) and Pu(IV) were measured as a function of $\mathbf{L_5}$ concentrations. The plots of $\log D$ versus $\log[\mathbf{L_5}]$ for U(VI) and Pu(IV) show straight lines with slopes between 1 and 2 (1.5 and 1.9 for U(VI), Pu(IV), respectively, see Supplementary material (Figs. 5 and 6)) indicating, that the species extracted under the solvent extraction conditions are a mixture of $UO_2(NO_3)_2 \cdot CMPz$ and $UO_2(NO_3)_2 \cdot 2CMPz$ and just $Pu(NO_3)_4 \cdot 2CMPz$ for U(VI) and Pu(IV), respectively.

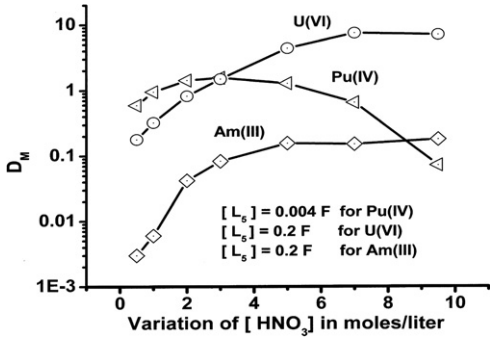


Fig. 4. Extraction data for $\mathbf{L_5}$ with U(VI), Pu(IV) and Am(III).

4. Conclusions

Studies on the coordination ability of the carbamoyl methyl pyrazole ligands with uranyl (VI), lanthanum(III) and cerium(III) nitrates show that the ligands act as bidentate chelating ligands in all these compounds. Preliminary extraction studies of $\mathbf{L_5}$ with the U(VI), Pu(IV) and Am(III) at tracer level show that they can extract U(VI) and Pu(IV) from HNO_3 of concentrations from 1 to 10 M. TG/DTA experiments show that the CMPz ligands can be destroyed easily on incineration.

Acknowledgements

We thank, the Head, Analytical Chemistry Division, BARC, for carbon, hydrogen and nitrogen analysis, the Head, National NMR facilities, TIFR, Mumbai for NMR spectra and the Head, Fuel Chemistry Division for his support. We also thank the EPSRC (UK) and the University of Reading for funds for the Image Plate system.

Appendix A. Supplementary material

CCDC 619366, 619367 and 619368 contain the supplementary crystallographic data for **6**, **7** and **11**. These data can be obtained free of charge via http://www.ccdc.cam.ac.uk/conts/retrieving.html, or from the Cambridge Crystallographic Data Centre, 12 Union Road, Cambridge CB2 1EZ, UK; fax: (+44) 1223-336-033; or e-mail: deposit@ccdc.cam.ac.uk. X-ray crystallographic files in CIF format for **6**, **7**, and **11**, molecular structure for **6** (Fig. 1), crystal and structural refinement details for **6** (Table 2), important bond lengths and bond angles for **6** (Table 4), TG/DTA for **6** and **7** and $\log D$ vs. $\log[\mathbf{L_5}]$ plots for uranium(VI) and plutonium(IV) (Figs. 5 and 6) are deposited with the editor as supplementary material. Supplementary data associated with this article can be found, in the online version, at doi:10.1016/j.poly.2007.04.005.

References

[1] L.R. Morss, N.M. Edelstein, J. Fuger, J.J. Katz, The Chemistry of the Actinide and Transactinide Elements, Springer, The Netherlands, 2006.
[2] C.J. Burns, M.P. Neu, H. Boukhalfa, K.E. Gutowshi, N.J. Bridges, R.D. Rogers, in: J.A. McCleverty, T.J. Meyer, G.F.R. Parkin (Eds.), Comprehensive Coordination Chemistry II, vol. 3, Elsevier, Oxford, 2004, p. 189.
[3] E.P. Horwitz, H. Diamond, A. Martin, Solv. Extr. Ion Exch. 5 (1987) 447.
[4] W.W. Schulz, E.P. Horwitz, Sep. Sci. Technol. 23 (1988) 1191.
[5] K.L. Nash, G.R. Choppin, Sep. Sci. Technol. 32 (1997) 255.

[6] J.N. Mathur, M.S. Murali, K.L. Nash, Solv. Extr. Ion Exch. 19 (2001) 357.
[7] G.R. Choppin, A. Morgenstern, J. Radioanal. Nucl. Chem. 243 (2000) 45.
[8] (a) C. Musikas, Inorg. Chim. Acta 140 (1987) 197;
(b) C. Madic, M.J. Hudson, High level liquid waste partitioning by means of completely incinerable extractants, European Commission, Nuclear Science and Technology, EU18038EN, Luxembourg, 1998.
[9] L. Nigond, C. Musikas, C. Cullerdier, Solv. Extr. Ion Exch. 12 (1994) 261.
[10] L. Nigond, N. Condamines, P.Y. Cordier, J. Livert, C. Madic, C. Cullerdier, C. Musikas, Sep. Sci. Technol. 30 (1995) 2075.
[11] Y. Sasaki, Y. Sugo, S. Suzuki, S. Tachimori, Solv. Extr. Ion Exch. 19 (2001) 91.
[12] S. Tachimori, Y. Sasaki, S. Suzuki, Solv. Extr. Ion Exch. 20 (2002) 687.
[13] Z. Zhu, Y. Sasaki, H. Suzuki, S. Suzuki, T. Kimura, Anal. Chim. Acta 527 (2004) 163.
[14] S.M. Bowen, E.N. Duesler, R.T. Paine, Inorg. Chem. 21 (1982) 261.
[15] S.M. Bowen, E.N. Duesler, R.T. Paine, Inorg. Chim. Acta 61 (1982) 155.
[16] L.J. Caudle, E.N. Duesler, R.T. Paine, Inorg. Chem. 24 (1985) 4441.
[17] L.J. Caudle, E.N. Duesler, R.T. Paine, Inorg. Chim. Acta 110 (1985) 91.
[18] D.J. McCabe, A.A. Russell, S. Karthikeyan, R.T. Paine, R.R. Ryan, B. Smith, Inorg. Chem. 26 (1987) 1230.
[19] S. Karthikeyan, R.R. Ryan, R.T. Paine, Inorg. Chem. 28 (1989) 2783.
[20] D.T. Cromer, R.R. Rayan, S. Karthikeyan, R.T. Paine, Inorg. Chim. Acta 172 (1990) 165.
[21] P. Byers, M.G.B. Drew, M.J. Hudson, N.S. Isaacs, C. Madic, Polyhedron 13 (1994) 349.
[22] G.Y.S. Chan, M.G.B. Drew, M.J. Hudson, P.B. Iveson, J.O. Liljenzin, M. Skalberg, L. Spjuth, C. Madic, J. Chem. Soc., Dalton Trans. (1997) 649.
[23] P. Thuery, M. Nierlich, M.C. Charbonnel, C. Den Auwer, J.P. Dognon, Polyhedron 18 (1999) 3599.
[24] P.B. Iveson, M.G.B. Drew, M.J. Hudson, C. Madic, J. Chem. Soc., Dalton Trans. (1999) 3605.
[25] B.M. Rapko, B.K. McNamara, R.D. Rogers, G.J. Lumetta, B.P. Hay, Inorg. Chem. 38 (1999) 4585.
[26] C. Den Auwer, M.C. Charbonnel, M.G.B. Drew, M. Grigoriev, M.J. Hudson, P.B. Iveson, C. Madic, M. Nierlich, M.T. Presson, R. Revel, M.L. Russell, P. Thuery, Inorg. Chem. 39 (2000) 1487.
[27] G.J. Lumetta, B.K. McNamara, B.M. Rapko, R.L. Sell, R.D. Rogers, G. Broker, J.E. Hutchison, Inorg. Chim. Acta 309 (2000) 103.
[28] S. Kannan, K.V. Chetty, V. Venugopal, M.G.B. Drew, Dalton Trans. (2004) 3604.
[29] G. Tian, J. Xu, L. Rao, Angew. Chem., Int. Ed. 44 (2005) 6200.
[30] K. Matloka, A. Gelis, M. Regalbuto, G. Vanfegrify, M.J. Scott, Dalton Trans. (2005) 3719.
[31] N.W. Alcock, D.J. Flanders, D. Brown, J. Chem. Soc., Dalton Trans. (1985) 1001.
[32] N.W. Alcock, D.J. Flanders, M. Pennington, D. Brown, Acta Crystallogr., Sect. C 44 (1988) 247.
[33] J.C. Berthet, M. Nierlich, M. Ephritikhine, Chem. Commun. (2003) 1660.
[34] J.C. Berthet, M. Nierlich, M. Ephritikhine, Dalton Trans. (2004) 2814.
[35] A.J. Speziale, P.C. Hamn, J. Am. Chem. Soc. 78 (1956) 2556.
[36] (a) W. Kabsch, J. Appl. Crystallogr. 21 (1988) 916;
(b) G.M. Sheldrick, SHELXS: Program for Crystal Structure Solution, University of Göttingen, Göttingen, Germany, 1993;
(c) N. Walker, D. Stuart, Acta Crystallogr., Sect. A 39 (1983) 158;
(d) G.M. Sheldrick, SHELXL: Program for Crystal Structure Refinement, University of Göttingen, Göttingen, Germany, 1993.
[37] B. Govind, T. Satyanarayana, K.V. Reddy, Polyhedron 15 (1996) 1009.
[38] M. Lees, A.W.G. Platt, Inorg. Chem. 42 (2003) 4673.
[39] J.C. Berthet, P. Thuery, M. Ephritikhine, Polyhedron 25 (2006) 1700.
[40] (a) L.I. Semenova, A.N. Sobolev, B.W. Skelton, A.H. White, Aust. J. Chem. 52 (1999) 519;
(b) M. Grigoriev, C. Den Auwer, C. Madic, Acta Crystallogr., Sect. C 57 (2001) 1141.
[41] A.R. de Aquino, G. Bombieri, P.C. Isolani, G. Vicentini, J. Zukerman-Schpector, Inorg. Chim. Acta 306 (2000) 101.
[42] E.P. Horwitz, K.A. Martin, H. Diamond, L. Kaplan, Solv. Extr. Ion Exch. 4 (1986) 449.

2. Experimental

2.1. General procedures

All experiments were carried out under purified argon using standard Schlenk techniques or in a glove box (<1 ppm O_2, 5 ppm H_2O). Diethyl ether and tetrahydrofuran were distilled from Na/benzophenone, toluene and pentane were distilled from Na/K alloy under nitrogen and degassed by freeze-thaw-vacuum cycles prior to use. Chlorinated solvents were distilled from calcium hydride. Deuterated solvents were purchased from Eurisotop and purified before use. *rac*-Lactide (Aldrich) was sublimed twice before use. Mg(*n*Bu)$_2$, *i*-PrMgCl and MeMgI (all Aldrich) were used as received. Bis[2-(3,5-dimethyl-1-pyrazolyl)ethyl]amine (**1**) was synthesized according to the literature [7].

NMR spectra were recorded on Bruker AC-200, AC-300 and AM-500 spectrometers in Teflon-valved NMR tubes at 23 °C otherwise stated. ^{1}H and ^{13}C NMR chemical shifts were determined using residual solvent resonances and are reported versus $SiMe_4$. Assignment of signals was made from ^{1}H–^{13}C HMQC and ^{1}H–^{13}C HMBC 2D NMR experiments. Coupling constants are given in Hertz. Elemental analyses (C, H, N) were performed by the Microanalytical Laboratory at the Institute of Chemistry of Rennes and are the average of two independent determinations. Molecular weights of PLA were determined by gel permeation chromatography (GPC) at room temperature on a Waters apparatus equipped with five PL gel columns (Polymer Laboratories Ltd.), an autosampler Waters WISP 717, and a differential refractometer Shimadzu RID 6A. THF was used as eluent at a flow rate of 1.0 mL min^{-1}. Polystyrene standards were used for molecular weight universal calibration. The microstructure of polymers was determined by ^{1}H NMR in $CDCl_3$.

2.2. [Bis[2-(3,5-dimethyl-1-pyrazolyl)ethyl]amide]$_2$Mg (**3**)

To a solution of pro-ligand **1** (0.301 g, 1.15 mmol) in toluene (5 mL) was slowly added Mg(*n*-Bu)$_2$ (0.58 mL of a 1.0 M solution in heptane, 0.58 mmol) at room temperature. The reaction mixture was stirred for 2 h. Volatiles were removed under vacuum, and the residue was recrystallized from toluene/pentane (ca. 1:3) at −34 °C to give block colorless crystals of **3** (0.22 g, 70%). A suitable crystal was selected for X-ray diffraction analysis. ^{1}H NMR (C_6D_6, 300 MHz): δ 5.66 (s, 4H, pyrazole-*H*), 4.23 (m br, 8H, NCH$_2$C*H*$_2$-pyrazole), 3.48 (m, 8H, NC*H*$_2$CH$_2$-pyrazole), 2.01 (s, 12H, pyrazole-C*H*$_3$), 1.78 (s, 12H, pyrazole-C*H*$_3$). ^{13}C{^{1}H} NMR (C_6D_6, 300 MHz): δ 148.64 (pyrazole-*C*CH$_3$), 137.28 (pyrazole-*C*CH$_3$), 104.62 (pyrazole-*C*H), 60.71 (N*C*H$_2$CH$_2$-pyrazole), 48.18 (NCH$_2$*C*H$_2$-pyrazole), 10.45 (pyrazole-*C*H$_3$), 9.81 (pyrazole-*C*H$_3$). *Anal.* Calc. for $C_{28}H_{44}MgN_{10}$ (545.02): C, 61.70; H, 8.14; N, 25.70. Found: C, 61.52; H, 8.32; N, 25.47%.

2.3. [Bis[2-(3,5-dimethyl-1-pyrazolyl)ethyl]amide]MgCl (**4**)

A 100 mL Schlenk flask was charged with *i*PrMgCl (0.57 mL of a 2.0 M solution in Et_2O, 1.14 mmol) and Et_2O (10 mL). A solution of pro-ligand **1** (298 mg, 1.14 mmol) in Et_2O (10 mL) was added dropwise in at −78 °C, and the mixture was allowed to warm to room temperature and stirred overnight. A large amount of white precipitate formed, which was separated off and recrystallized from CH_2Cl_2/THF (1:10), to give **4** as colorless crystals (0.30 g, 82%). A suitable crystal was selected for X-ray diffraction analysis. ^{1}H NMR (CD_2Cl_2, 300 MHz): δ 5.84 (s, 2H, pyrazole-*H*), 3.98 (t, $^3J = 4.7$, 4H, NCH$_2$C*H*$_2$-pyrazole), 2.76 (m br, 4H, NC*H*$_2$CH$_2$-pyrazole), 2.40 (s, 6H, pyrazole-C*H*$_3$), 2.17 (s, 6H, pyrazole-C*H*$_3$). ^{1}H NMR ($CDCl_3$, 300 MHz): δ 5.84 (s, 2H, pyrazole-*H*), 3.99 (t, $^3J = 3.8$, 4H, NCH$_2$C*H*$_2$-pyrazole), 3.15 (m br, 4H, NC*H*$_2$CH$_2$-pyrazole), 2.57 (s, 6H, pyrazole-C*H*$_3$), 2.09 (s, 6H, pyrazole-C*H*$_3$). ^{13}C{^{1}H} NMR (CD_2Cl_2, 300 MHz): δ149.26 (pyrazole-*C*CH$_3$), 139.29 (pyrazole-*C*CH$_3$), 105.96 (pyrazole-*C*H), 55.25 (N*C*H$_2$CH$_2$-pyrazole), 50.28 (NCH$_2$*C*H$_2$-pyrazole), 13.63 (pyrazole-*C*H$_3$), 10.69 (pyrazole-*C*H$_3$). *Anal.* Calc. for $C_{14}H_{22}ClMgN_5$ (320.12): C, 52.53; H, 6.93; N, 21.88. Found: C, 52.05; H, 6.82; N, 21.34%.

2.4. [Bis[2-(3,5-dimethyl-1-pyrazolyl)ethyl]amide]MgI (**5**)

The same procedure was used as for **4**, starting from **1** (528 mg, 2.02 mmol) and MeMgI (0.67 mL of a 3.0 M solution in Et_2O, 2.02 mmol), to give complex **5** as colorless crystals (0.64 g, 77%). A suitable crystal was selected for X-ray diffraction analysis. ^{1}H NMR (CD_2Cl_2, 300 MHz): δ 6.01 (s, 2H, pyrazole-*H*), 4.04 (m, 4H, NCH$_2$C*H*$_2$-pyrazole), 3.16 (m, 4H, NC*H*$_2$CH$_2$-pyrazole), 2.29 (s, 6H, pyrazole-C*H*$_3$), 2.03 (s, 6H, pyrazole-C*H*$_3$). ^{13}C{^{1}H} NMR (CD_2Cl_2, 300 MHz): δ149.34 (pyrazole-*C*CH$_3$), 143.05 (pyrazole-*C*CH$_3$), 107.03 (pyrazole-*C*H), 53.48 (N*C*H$_2$-CH$_2$-pyrazole), 48.35 (NCH$_2$*C*H$_2$-pyrazole), 13.14 (pyrazole-*C*H$_3$), 11.23 (pyrazole-*C*H$_3$). *Anal.* Calc. for $C_{14}H_{22}IMgN_5$ (411.57): C, 40.86; H, 5.39; N, 17.02. Found: C, 40.53; H, 5.42; N, 16.85%.

2.5. Solid state structure determination of complexes **3**–**5**

A suitable single crystal of **3**–**5** was mounted onto a glass fiber using the "oil-drop" method. Diffraction data were collected at 100 K using either an ENRAF NONIUS Kappa CCD diffractometer (complex **3**) or an APEXII Bruker-AXS CCD plate diffractometer (complexes **4** and **5**) with graphite monochromatized Mo Kα radiation ($\lambda = 0.71073$ Å). A combination of ω- and ϕ-scans was carried out to obtain at least a unique data set. Crystal structures were solved by means of the Patterson method, remaining atoms were located from difference Fourier synthesis, followed by full-matrix least-squares refinement

Table 1
Crystal data and structure refinement for complexes **3**–**5**

	3	**4** · $2CH_2Cl_2$	**5**[a]
Empirical formula	$C_{28}H_{44}MgN_{10}$	$C_{30}H_{48}Cl_6Mg_2N_{10}$	$C_{28}H_{44}I_2Mg_2N_{10}$
fw/g mol^{-1}	545.04	810.10	823.15
Temperature (K)	120(2)	100(2)	100(2)
Wavelength (Å)	0.71073	0.71073	0.71073
Crystal system	monoclinic	monoclinic	monoclinic
Space group	$P2_1/c$	$P2_1/n$	$P2_1/n$
a (Å)	14.5479(2)	14.6786(15)	11.9898(7)
b (Å)	9.9538(2)	8.6878(8)	9.2075(5)
c (Å)	20.2878(4)	16.5985(17)	18.1210(10)
α (°)	90	90	90
β (°)	91.0450(10)	112.150(4)	94.259(3)
γ (°)	90	90	90
Volume (Å^3)	2937.32(9)	1960.5(3)	1994.96(19)
Z	4	2	2
D_{calc} (Mg m^{-3})	1.233	1.372	1.370
Absorption coefficient (mm^{-1})	0.097	0.507	1.638
$F(000)$	1176	848	824
Crystal size (mm)	$0.5 \times 0.35 \times 0.29$	$0.45 \times 0.2 \times 0.1$	$0.04 \times 0.11 \times 0.30$
θ Range for data collection (°)	2.68–27.48	2.34–27.45	1.97–27.48
Index ranges	$-18 \leqslant h \leqslant 18$, $-12 \leqslant k \leqslant 12$, $-26 \leqslant l \leqslant 26$	$-19 \leqslant h \leqslant 17$, $-10 \leqslant k \leqslant 11$, $-19 \leqslant l \leqslant 21$	$-15 \leqslant h \leqslant 14$, $-11 \leqslant k \leqslant 11$, $-23 \leqslant l \leqslant 23$
Reflections collected	12621	20436	42210
Independent reflection [R_{int}]	6712 [0.0254]	4466 [0.0366]	4566 [0.0307]
Absorption correction	none	semi-empirical from equivalents	semi-empirical from equivalents
Refinement method	full-matrix least-squares on F^2	full-matrix least-squares on F^2	full-matrix least-squares on F^2
Data/restraints/parameters	6712/0/353	4466/0/217	4566/0/190
Goodness-of-fit on F^2	0.998	1.059	1.104
Final R indices [$I > 2\sigma(I)$]	$R_1 = 0.0555$, $wR_2 = 0.1462$	$R_1 = 0.0603$, $wR_2 = 0.1602$	$R_1 = 0.0238$, $wR_2 = 0.0696$
R indices (all data)	$R_1 = 0.0758$, $wR_2 = 0.1585$	$R_1 = 0.0707$, $wR_2 = 0.1684$	$R_1 = 0.0284$, $wR_2 = 0.0711$
Largest differences in peak and hole (e Å^{-3})	0.435 and −0.306	2.143 and −1.688	0.723 and −0.489

[a] Disordered solvent molecules have been removed using the SQUEEZE function; see Section 2.

based on F^2 (programs SHELXS-97 and SHELXL-97) [10]. Many hydrogen atoms could be found from the Fourier difference. Carbon-bound hydrogen atoms were placed at calculated positions and forced to ride on the attached carbon atom. The hydrogen atom contributions were calculated but not refined. All non-hydrogen atoms were refined with anisotropic displacement parameters. Crystals of compound **5** were found to contain lattice disordered solvent molecules, which could not be sufficiently modeled in the refinement cycles. These molecules were of no chemical/crystallographical importance and were therefore removed using the SQUEEZE procedure implemented in PLATON package. Crystal data and details of data collection and structure refinement are given in Table 1. Crystallographic data for **3**–**5** are also available as cif files (see Supplementary data).

2.6. Typical procedure for rac-lactide polymerization

To a 10 mL Schlenk flask equipped with a magnetic stirrer, and containing the catalyst (0.01 mmol) in toluene or THF (2.5 mL), was introduced the proper amount of *rac*-lactide rapidly. The polymerization was carried out for a given time period and the reaction was then quenched by addition of acidified methanol (3% HCl, 200 mL). The precipitated polymer was filtered, washed with methanol and dried overnight under vacuum at 60 °C.

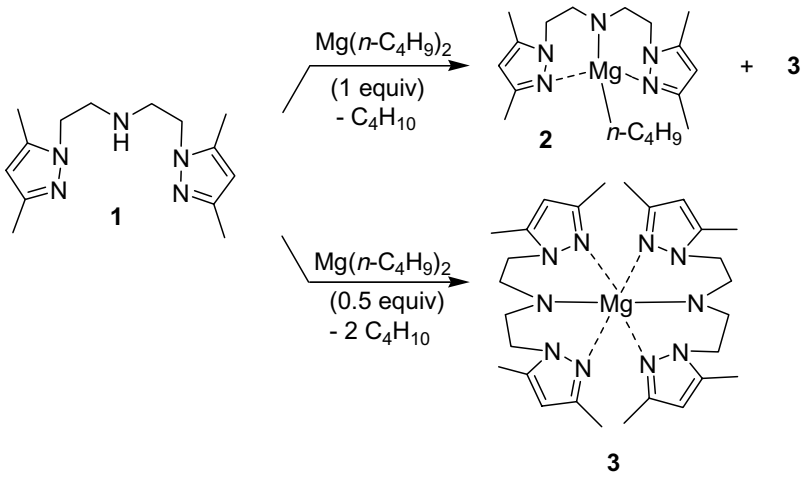
3. Results and discussion

3.1. Syntheses of Mg–NNN complexes

Combination of Mg(nBu)$_2$ with 1 equiv. of pro-ligand **1** (LH) in toluene leads, by alkane elimination, to a mixture of the mono-ligand complex [L]Mg(nBu) (**2**) and bis-ligand complex [L]$_2$Mg (**3**), which could not be efficiently separated (Scheme 1).[1] Attempts to prepare selectively heteroleptic complex **2** by adjusting reaction parameters (temperature, concentration, slow addition of reagents) failed.[2] On the other hand, upon using 2 equiv. of

[1] Key NMR data for **2**: ^{1}H NMR (C_6D_6, 300 MHz): δ 5.52 (s, 2H, pyrazole-*H*), 4.05 (t, $^3J = 6.1$ Hz, 4H, NCH$_2$C*H*$_2$-pyrazole), 3.26 (t, $^3J = 6.1$ Hz, 4H, NC*H*$_2$CH$_2$-pyrazole), 2.28 (s, 6H, pyrazole-C*H*$_3$), 1.69 (s, 6H, pyrazole-C*H*$_3$), 1.16 (m, 7H, MgCH$_2$C*H*$_2$C*H*$_2$C*H*$_3$), 0.08 (m, 2H, MgC*H*$_2$CH$_2$CH$_2$CH$_3$).

[2] Alternative synthesis of **2** via treatment of chloro complex **4** with n BuLi led to complicated mixtures of products, including **2**, **3** and several other unidentified species, which could not be purified.



Scheme 1.

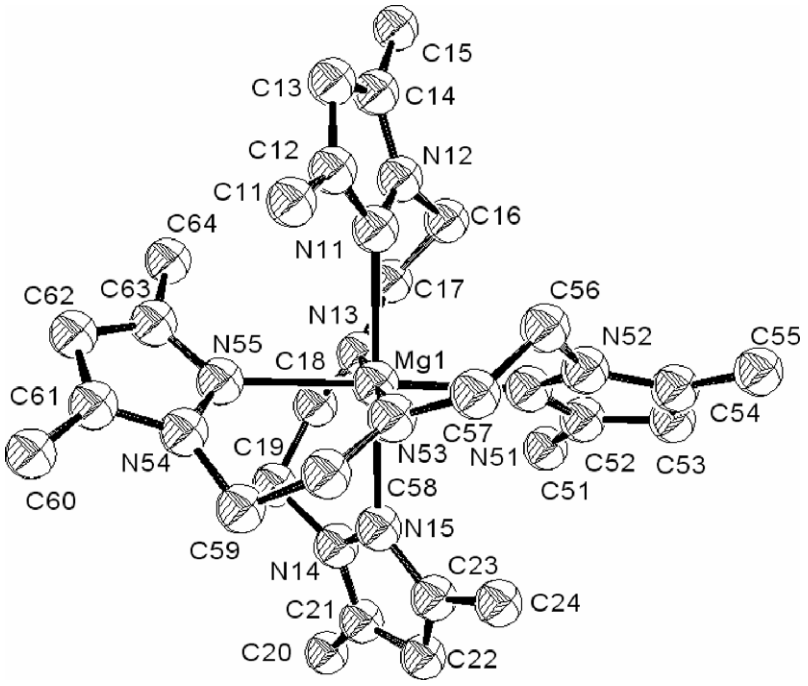
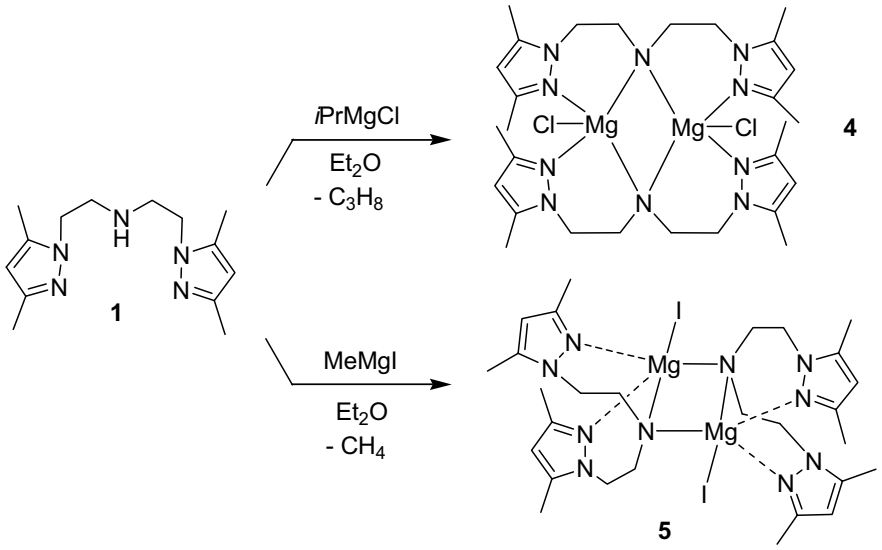


Fig. 1. Solid-state structure of **3** (ellipsoids drawn at the 50% probability; hydrogen atoms omitted for clarity). Selected bond lengths (Å) and angles (deg): Mg(1)–N(13), 2.093(2); Mg(1)–N(11), 2.2965(19); Mg(1)-N(15), 2.2911(19); Mg(1)–N(53), 2.095(2); Mg(1)–N(55), 2.3256(19); Mg(1)–N(51), 2.2897(19); N(13)–C(17), 1.443(3); N(12)–C(16), 1.470(3); N(11)–Mg(1)–N(15), 170.50(7); N(11)–Mg(1)–N(13), 85.36(7); N(13)–Mg(1)–N(15), 85.44(7); N(11)–Mg(1)–N(53), 95.19(7); N(15)–Mg(1)–N(53), 94.03(7); C(17)–N(13)–C(18), 107.17(16); C(17)–N(13)–Mg(1), 127.09(13); C(18)–N(13)–Mg(1), 125.74(14).

pro-ligand **1** (versus Mg), bis-ligand complex **3** was produced selectively and isolated in good yield (70%). Complex **3** was fully characterized by multinuclear NMR in solution and an X-ray diffraction analysis in the solid state (Scheme 1, Fig. 1). Similarly, the reaction of pro-ligand **1** with 1 equiv. of *i*PrMgCl or MeMgI at low temperature cleanly afforded the expected magnesium halide complexes [L]MgX (X = Cl, **4**; I, **5**) in high yields (Scheme 2), which contains either a small (Cl) or large (I) size halide atom for the purpose of comparison.

3.2. Solid-state structures of Mg–NNN complexes

Complexes **3**–**5** have been characterized by single-crystal X-ray diffraction studies. Crystallographic details are reported in Table 1, and the molecular structures as well as selected bond lengths and angles are given in Figs. 1–3. Complex **3** is monomeric in the solid state, while complexes **4** and **5** feature a dimeric structure. As anticipated, the pyrazolyl nitrogen atoms in **3** coordinate to the Mg center, which is six-coordinated showing a slightly dis-



Scheme 2.

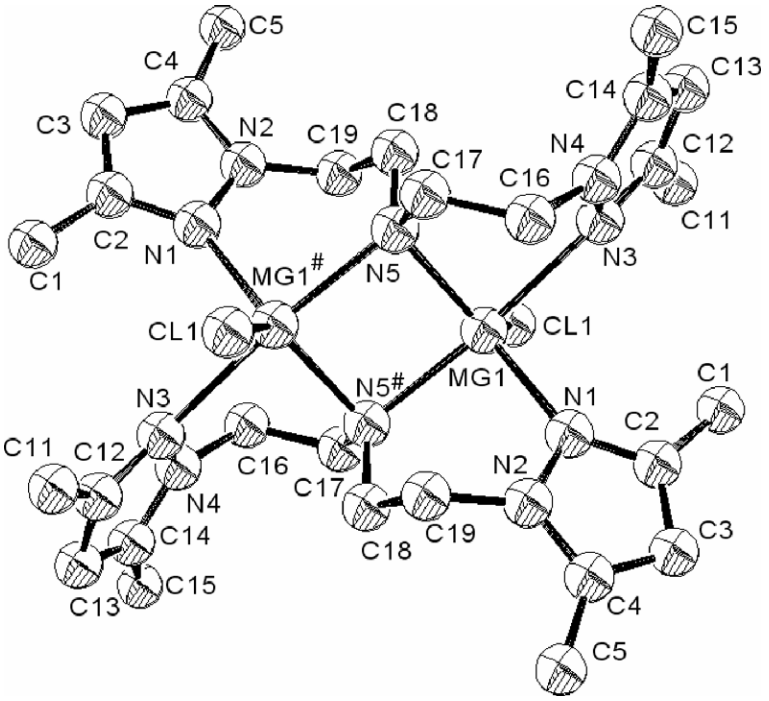


Fig. 2. Solid-state structure of **4** (ellipsoids drawn at the 50% probability; hydrogen atoms omitted for clarity). Selected bond lengths (Å) and angles (deg): Mg(1)–Cl(1), 2.3600(10); Mg(1)–N(5), 2.159(2); Mg(1)-N(3), 2.365(2); Mg(1)–N(5$^{\#}$), 2.205(2); Mg(1)–N(1), 2.161(2); C(16)–N(4), 1.454(3); C(17)–N(5), 1.484(3); Cl(1)–Mg(1)–N(1), 112.16(7); Cl(1)–Mg(1)–N(5), 121.48(7); N(1)–Mg(1)–N(5), 125.81(9); Mg(1)–N(5)–C(17), 114.28(15); Mg(1)–N(5)–C(18), 105.43(16); C(17)–N(5)–C(18), 109.8(2); N(5)–Mg(1)–N(5$^{\#}$), 87.18(9).

torted octahedral environment. The nitrogen atoms of a given ligand (i.e., N11–N13–N15 and N51–N53–N55) and the corresponding pyrazolyl rings are almost individually co-planar with the metal center, while the two pyrazolyl rings are perpendicular to each other. The Mg–N(amido) bond distances (average 2.094(2) Å) involving the sp^2-hybridized N bridge atoms in complex **3** (sum of angles around N(13) and N(53) = 359.96 and 360.00°) are ca. 0.2 Å shorter than the Mg–N(amino) bonds (average 2.3007(19) Å) involving the pyrazolyl N atoms. Those values fall in the usual ranges observed for Mg–N(amido) bonds (2.0040(1)–2.0314(1) Å) [2e] and related coordinating Mg–N bonds (2.2247(18) Å) [4a], respectively.

The solid state structures of complexes **4** and **5** feature two five-coordinated Mg centers, with μ-bonding via the N atom of the ligand bridge (Figs. 2 and 3). The overall structures of **4** and **5** are centrosymmetric around the Mg_2N_2 square plane and the two Mg–X bonds (X = Cl,

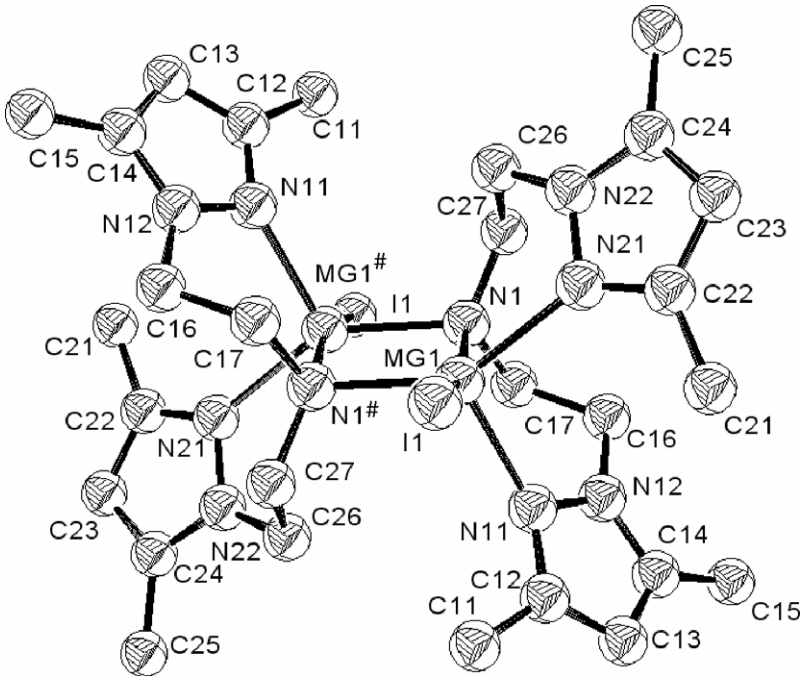


Fig. 3. Solid-state structure of **5** (ellipsoids drawn at the 50% probability; hydrogen atoms omitted for clarity). Selected bond lengths (Å) and angles (deg): Mg(1)–I(1), 2.9540(7); Mg(1)–N(1), 2.1477(18); Mg(1)-N(1#), 2.1153(18); Mg(1)–N(11), 2.1493(19); Mg(1)–N(21), 2.1659(19); N(1)–C(27), 1.477(3); N(22)–C(26), 1.460(3); I(1)–Mg(1)–N(1), 162.47(6); I(1)–Mg(1)–N(11), 103.01(5); I(1)–Mg(1)–N(21), 86.14(5); C(27)–N(1)–C(17), 108.56(15); C(27)–N(1)–Mg(1), 117.50(13); C(17)–N(1)–Mg(1), 110.71(12); Mg(1)–N(1)–Mg(1#), 93.43(7); N(1)–Mg(1)–N(1#), 86.57(7).

I) are therefore transoid. The Mg–N(μ-amido) bond distances (2.159(2)–2.205(2) Å) in **4** are similar to those in **5** (2.1153(18)–2.1477(18) Å), and are logically slightly longer than the Mg–N(amido) bonds (2.093(2)–2.095(2) Å) in **3**. The Mg–I bond distance of 2.9540(7) Å in **5** is much longer than that reported for $MgI_2(THF)_3$ (2.7458(14) Å) [2a]; on the other hand, the Mg–Cl bond distance (2.3600(10) Å) in **4** is very close to the value reported for other five-coordinated complex (2.3652(14) Å) [5c]. Interestingly, the coordination mode of the $[NNN]^-$ ligand is quite different in the chloride and iodide complexes; i.e., in **4**, each ligand wraps the two Mg metal centers, adopting a "spanned" coordination, while in **5**, each ligand wraps only one metal center. This provides an interesting example of ligand coordination selectivity via external control. Considering the relatively small size Cl atom and larger I atom [11], one may speculate that this difference arises from a steric control. Though, it is difficult to establish unambiguously whether those differences in ligation arise from intrinsic molecular features or from crystal packing forces.[3]

3.3. Polymerization catalysis

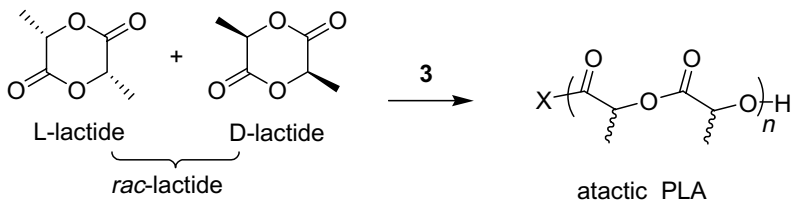
Complex **3** was evaluated in the polymerization of *rac*-lactide at room temperature (Scheme 3) [3f,3h,3t,5c]. Representative results are summarized in Table 2. Complex **3** proved significantly active both in toluene and THF solutions, with full conversion of 100 equiv. of monomer observed within 10 min. The produced polylactides (PLAs) had a relatively narrow molecular weight distribution ($M_w/M_n = 1.28$–1.34)[4] and the experimental (corrected) [12] number-average molecular weights were in close agreement with the calculated values, assuming that **3** acts a di-initiator; i.e., both amido groups of bis(ligand) complex **3** initiates a polymer chain.[5] This assumption is supported by the observation in the ^{1}H NMR spectrum of a precipitated PLA sample of resonances attributable to bis[2-(3,5-dimethyl-1-pyrazolyl)ethyl]amido end groups (see Supplementary data). Furthermore, the M_n values of the PLAs increased linearly with the [*rac*-LA]/[**3**] ratio (entries 2–4), indicating overall a well-controlled polymerization. However, the homo-decoupled ^{1}H NMR spectra of the methine regions of PLAs, both prepared in THF and toluene, showed an atactic microstructure.[6]

[3] NMR data for **4** and **5** are uninformative about the actual solution structures of these species; however, it is unlikely that the solution structures deviate much from those in the solid state.

[4] These polydispersity values are usual for amido [–$N(SiMe_3)_2$, –$N(SiHMe_2)_2$]-metal initiators, which are known to be less nucleophilic than other initiating groups such as alkoxides; see Ref. [5b].

[5] For a similar initiation process of lactide polymerization via one ligand of a bis(ligand) magnesium complex, see Ref. [4c].

[6] We speculate that the absence of stereocontrol may be attributed to the initiation of two polymer chains per Mg complex, which rejects the ligand at the termini of growing polymer chains and de facto enables effective chain-end control.



Scheme 3.

Table 2
Rac-Lactide polymerization initiated by complex **3**[a]

Entry	[LA]/[**3**]	Solvent	Time (min)[b]	Yield (%)	$M_{n,calc}^{c}$ (g mol^{-1})	$M_{n,exp}^{d,e}$ (g mol^{-1})	M_w/M_n[d]
1	100	toluene	10	97	7200	11300	1.28
2	100	THF	10	95	7200	10000	1.29
3	200	THF	60	97	14400	19500	1.33
4	300	THF	60	95	21600	31500	1.34

[a] $T = 20$ °C, solvent = 2.5 mL, **3** = 0.01 mmol.
[b] Reaction time was not optimized.
[c] Calculated $M_{n,calc}$ values considering two polymer chains per Mg complex.
[d] Experimental M_n and M_w/M_n values as determined by GPC in THF vs. PS standards.
[e] Using a correcting factor 0.58 for M_n; see Ref. [12].

Acknowledgements

We thank Total and Arkema Co. (Grant to B.L.) and the Centre National de la Recherche Scientifique for financial support of this work. We gratefully thank Dr. C. Navarro, Dr. M. Glotin, and Dr. G. Meunier (Arkema Co.) for valuable discussions.

Appendix A. Supplementary material

CCDC 642128, 642129, and 642130 contain the supplementary crystallographic data for **3**, **4**, and **5**. These data can be obtained free of charge via http://www.ccdc.cam.ac.uk/conts/retrieving.html, or from the Cambridge Crystallographic Data Centre, 12 Union Road, Cambridge CB2 1EZ, UK; fax: (+44) 1223-336-033; or e-mail: deposit@ccdc.cam.ac.uk. Supplementary data associated with this article can be found, in the online version, at doi:10.1016/j.poly.2007.04.022.

References

[1] (a) H.G. Richey Jr. (Ed.), Grignard Reagents, John Wiley and Sons Ltd., Chichester, 2000;
(b) B.J. Wakefield, Organomagnesium Methods in Organic Synthesis, Academic Press, London, 1995.
[2] (a) R.J. Wehmschulte, B. Twamley, M.A. Khan, Inorg. Chem. 40 (2001) 6004;
(b) D.R. Armstrong, W. Clegg, R.E. Mulvey, R.B. Rowlings, J. Chem. Soc., Dalton Trans. (2001) 409;
(c) Y. Sarazin, M. Schormann, M. Bochmann, Organometallics 23 (2004) 3296;
(d) S.C. Cole, M.P. Coles, P.B. Hitchcock, Organometallics 23 (2004) 5159;
(e) Y. Tang, L.N. Zakharov, A.L. Rheingold, R.A. Kemp, Organometallics 24 (2005) 836;
(f) B. Conway, E. Hevia, A.R. Kennedy, R.E. Mulvey, S. Weatherstone, J. Chem. Soc., Dalton Trans. (2005) 1532.
[3] (a) S. Westhusin, P. Gantzel, P.J. Walsh, Inorg. Chem. 37 (1998) 5956;
(b) V.C. Gibson, J.A. Segal, A.J.P. White, D.J. Williams, J. Am. Chem. Soc. 122 (2000) 7120;
(c) P.J. Bailey, C.M.E. Dick, S. Fabre, S. Parsons, J. Chem. Soc., Dalton Trans. (2000) 1655;
(d) P.J. Bailey, R.A. Coxall, C.M. Dick, S. Fabre, S. Parsons, Organometallics 20 (2001) 798;
(e) A.R. Sadique, M.J. Heeg, C.H. Winter, Inorg. Chem. 40 (2001) 6349;
(f) B.M. Chamberlain, M. Cheng, D.R. Moore, T.M. Ovitt, E.B. Lobkovsky, G.W. Coates, J. Am. Chem. Soc. 123 (2001) 3229;
(g) M.H. Chisholm, J.C. Huffman, K. Phomphrai, J. Chem. Soc., Dalton Trans. (2001) 222;
(h) M.H. Chisholm, J. Gallucci, K. Phomphrai, Inorg. Chem. 41 (2002) 2785;
(i) A.P. Dove, V.C. Gibson, E.L. Marshall, A.J.P. White, D.J. Williams, Chem. Commun. (2002) 1208;
(j) H. Sachdev, C. Wagner, C. Preis, V. Huch, M. Veith, J. Chem. Soc., Dalton Trans. (2002) 4709;
(k) S. Harder, Organometallics 21 (2002) 3782;
(l) P.J. Bailey, R.A. Coxall, C.M. Dick, S. Fabre, L.C. Henderson, C. Herber, S.T. Liddle, D. Loroño-González, A. Parkin, S. Parsons, Chem. Eur. J. 9 (2003) 4820;
(m) A.P. Dove, V.C. Gibson, P. Hormnirun, E.L. Marshall, J.A. Segal, A.J.P. White, D.J. Williams, J. Chem. Soc., Dalton Trans. (2003) 3088;
(n) H.M. El-Kaderi, A. Xia, M.J. Heeg, C.H. Winter, Organometallics 23 (2004) 3488;
(o) Y. Tang, L.N. Zakharov, A.L. Rheingold, R.A. Kemp, Organometallics 23 (2004) 4788;
(p) T. Chivers, C. Fedorchuk, M. Parvez, Organometallics 24 (2005) 580;
(q) R.A. Layfield, S.M. Humphrey, Organometallics 24 (2005) 6063;
(r) M.-L. Hsueh, B.-T. Ko, T. Athar, C.-C. Lin, T.-M. Wu, S.-F. Hsu, Organometallics 25 (2006) 4144;
(s) D. Zhang, H. Kawaguchi, Organometallics 25 (2006) 5506;
(t) L.F. Sánchez-Barba, D.L. Hughes, S.M. Humphrey, M. Bochmann, Organometallics 25 (2006) 1012;

(u) P.J. Bailey, C.M. Dick, S. Fabre, S. Parsons, L.J. Yellowlees, J. Chem. Soc., Dalton Trans. (2006) 1602.
[4] (a) A. Xia, M.J. Heeg, C.H. Winter, Organometallics 21 (2002) 4718;
(b) P. Wei, D.W. Stephan, Organometallics 22 (2003) 601;
(c) J. Ejfler, M. Kobylka, L.B. Jerzykiewicz, P. Sobota, J. Chem. Soc., Dalton Trans. (2005) 2047;
(d) I.J. Blackmore, V.C. Gibson, P.B. Hitchcock, C.W. Rees, D.J. Williams, A.J.P. White, J. Am. Chem. Soc. 127 (2005) 6012.
[5] (a) A.D. Pajerski, E.P. Squiller, M. Parvez, R.R. Whittle, H.G. Richey Jr., Organometallics 24 (2005) 809;
(b) M.H. Chisholm, J.C. Gallucci, K. Phomphrai, Inorg. Chem. 44 (2005) 8004;
(c) L.E. Breyfogle, C.K. Williams, V.G. Young Jr., M.A. Hillmyer, W.B. Tolman, J. Chem. Soc., Dalton Trans. (2006) 928;
(d) Y. Xiao, Z. Wang, K. Ding, Macromolecules 39 (2006) 128.
[6] (a) T.P. Hanusa, Chem. Rev. 93 (1993) 1023;
(b) J.L. Sebestl, T.T. Nadasdi, M.J. Heeg, C.H. Winter, Inorg. Chem. 37 (1998) 1289.
[7] N. Ajellal, M.C.A. Kuhn, A.D.G. Boff, M. Hoerner, C.M. Thomas, J.-F. Carpentier, O.L. Casagrande Jr., Organometallics 25 (2006) 1213.
[8] F. Junges, M.C.A. Kuhn, A.H.D.P. dos Santos, C.M. Thomas, J.-F. Carpentier, O.L. Casagrande Jr., in preparation.
[9] B. Lian, C.M. Thomas, O.L. Casagrande Jr., C.W. Lehmann, T. Roisnel, J.-F. Carpentier, Inorg. Chem. 47 (2007) 328.
[10] (a) G.M. Sheldrick, SHELXS-97, Program for the Determination of Crystal Structures, University of Goettingen, Germany, 1997;
(b) G.M. Sheldrick, SHELXL-97, Program for the Refinement of Crystal Structures, University of Goettingen, Germany, 1997.
[11] M.P. LoCoco, R.F. Jordan, J. Am. Chem. Soc. 126 (2004) 13918.
[12] H. Ma, J. Okuda, Macromolecules 38 (2005) 2665.

synthesize particular supramolecular systems with diverse architectures and dimensions for exploring new functional materials [18–20]. One of them consists of the ingenious use of compartmental ligands, which are organic molecules able to hold together two or more metal ions. The Schiff's bases derived from 2-formyl-4-methylphenol and 2,6-diformyl-4-methylphenol are among the most popular ligands belonging to this family [21,22].

In earlier literature reports [23,24], several N-substituted macropolycyclic systems were discussed (Chart 1). The macrobicyclic system II (Chart 1) contains two ether O atoms and two tertiary N atoms, the second compartment (N_2O_2) contains two tertiary N atoms and two phenolic O atoms, and the third compartment (N_2O_2) is composed of two phenolic O atoms and two imine N atoms. We have now introduced nitrogen donor atoms instead of the ether oxygens in the macrobicyclic system III. This work focuses on the synthesis of binuclear copper(II) complexes with dissimilar compartmental macrobicyclic ligands containing N-substituted "tet *a*" groups (Scheme 1). The resulting compounds have one hexadentate compartment (N_4O_2) comprised of four "tet *a*" nitrogens and two phenolic oxygens, and one tetradentate compartment (N_2O_2) comprised of two phenolic oxygens and two imine nitrogen. The special feature of this ligand is that the macrocyclic ring size can be varied, which allows more insight to recognize and further understand DNA cleavage.

2. Experimental

2.1. Materials

5-methylsalicylaldehyde, 3-chloromethyl-5-methylsalicylaldehyde [25], 1,4,8,11-tetraazatricyclo[9.3.1.1^{4,8}]hexadecane [26,27] and 1,8[*N*,*N*′-bis{(3-formyl-2-hydroxy-5-methyl)benzyl}]-1,4,8,11-tetraaza-5,5,7,12,12,14-hexamethylcyclotetra decane – precursor compound (PC) [28] were prepared from the literature methods. Tetra(*n*-butyl)ammonium perchlorate (TBAP) was used as the supporting electrolyte.

Caution! TBAP is potentially explosive; hence care should be taken in handling the compound. All other solvents and reagents were of the highest grade available and were found to be sufficiently pure for use as supplied.

Elemental analysis was carried out on a Carlo Erba Model 1106 elemental analyzer. The copper content was analyzed using a Varian Spectra 200 atomic absorption spectrometer. Electronic spectral studies were carried out on a Hitachi 320 spectrophotometer in DMF. IR spectra were recorded on a Hitachi 270-50 spectrophotometer on KBr disks in the range of 400–4000 cm^{-1}. FAB mass spectra of the complexes were obtained on a JEOL SX 102/DA-6000; *m*-nitrobenzyl alcohol (NBA) was used as the matrix. The molar conductivity of a freshly prepared solution of the complexes in DMF was measured using an Elico Model SX80 conductivity bridge. Cyclic voltammograms were

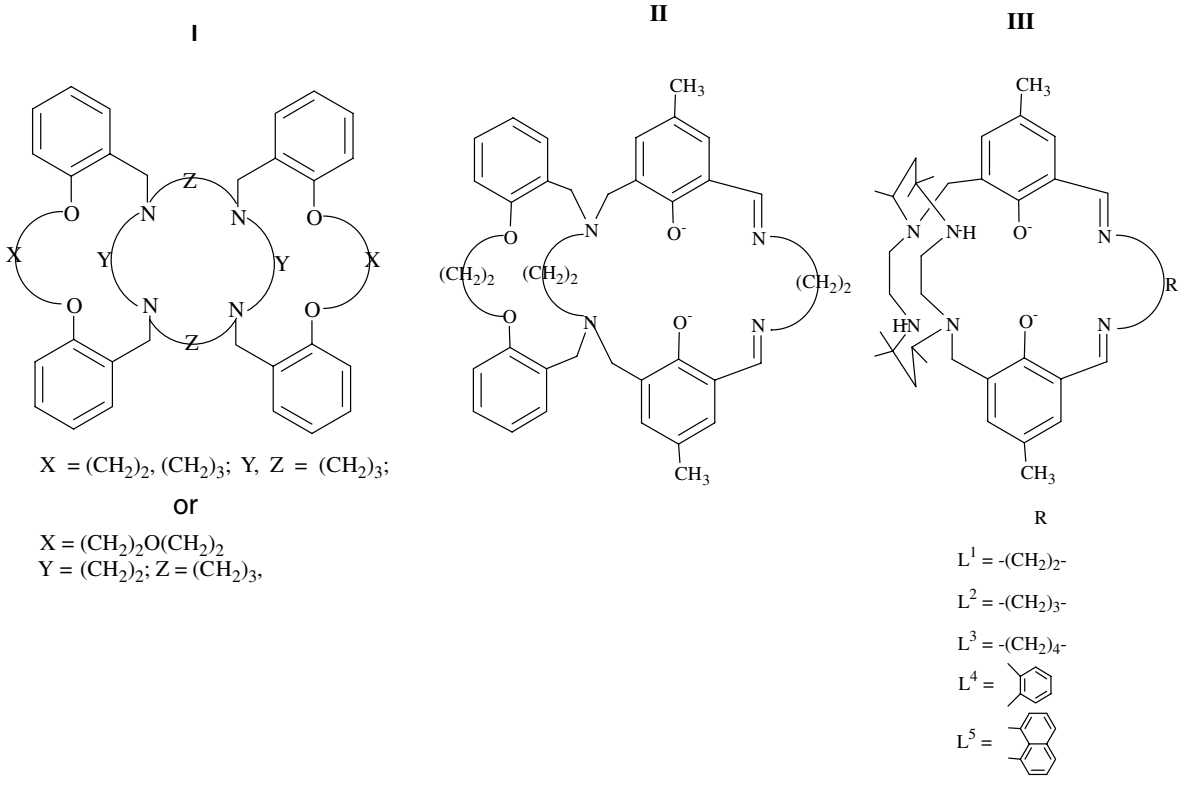
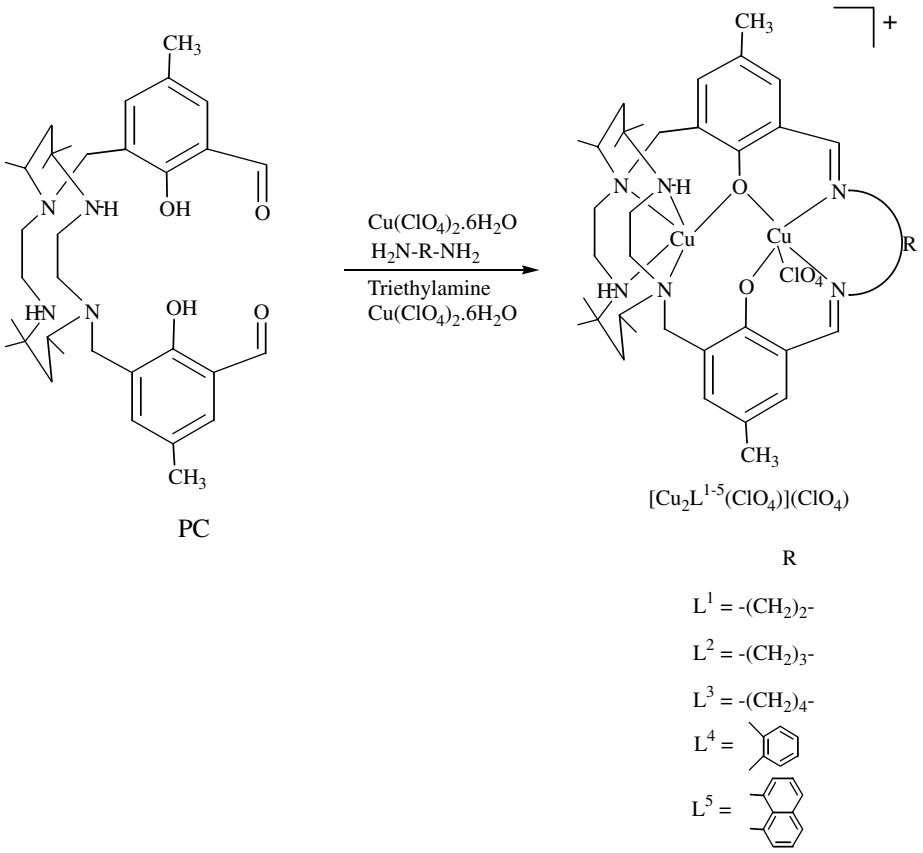


Chart 1.



Scheme 1. Synthesis of the macrobicyclic binuclear copper(II) complexes.

obtained on a CHI600A electrochemical analyzer using a three-electrode cell in which a glassy carbon electrode was the working electrode, a saturated Ag/AgCl electrode was the reference electrode and a platinum wire was used as an auxiliary electrode under oxygen-free conditions. The concentration of the complexes was 10^{-3} M. Tetra(butyl)ammonium perchlorate (10^{-1} M) was used as the supporting electrolyte. A ferrocene/ferrocenium (1+) couple was used as an internal standard and $E_{1/2}$ of the ferrocene/ferrocenium (Fc/Fc^{+}) couple under the experimental conditions was 470 mV in DMF, and ΔE_p for Fc/Fc^{+} was 70 mV. The room-temperature magnetic moment was measured on a PAR vibrating sample magnetometer (Model-155). Variable-temperature magnetic studies were performed on a PAR model 155 vibrating sample magnetometer in the temperature range 77–300 K, and the instrument was calibrated using metallic nickel as supplied with the instrument. X-band ESR spectra of the Cu(II) complexes were recorded using DMF as a solvent at liquid-nitrogen temperature on a Varian EPR-E 112 spectrometer with diphenylpicrylhydrazine (DPPH) as the reference.

The catalytic oxidation of 3,5-di-tertiarybutylcatechol to the corresponding *o*-quinone was studied using 10^{-3} M of the copper(II) complexes in acetonitrile solution. The reaction was followed spectrophotometrically by choosing the strongest absorbance of the product, 3,5-di-tertiarybutyl-*o*-benzoquinone, around 390 nm and monitoring the increase in the absorbance at this wavelength over time intervals of 10 min. Initial rates (dc/dt) (<2% conversion of 3,5-ditertiarybutylcatechol) were determined by spectrophotometric determination of the released *o*-quinone. The initial reaction rates were also determined from the slope of the trace at 390 nm during the first 30 min of the reactions, when the absorption at 390 nm increases linearly. The kinetic activity of the metal complexes towards the hydrolysis of 4-nitrophenyl phosphate was examined in the presence of tetramethylammonium hydroxide in DMF solvent. Equimolar concentrations (10^{-3} M) of the complex and tetramethylammonium hydroxide were used. The concentration of 4-nitrophenyl phosphate was 10^{-1} M. The initial reaction rates were determined from the slope of the trace at 425 nm during the first 30 min of the reactions, when the absorption at 425 nm increases linearly.

The DNA cleavage was monitored by agarose gel electrophoresis on plasmid pBR 322 DNA. The tests were performed under aerobic conditions with H_2O_2 as a reducing agent. Each reaction mixture contained 1 μg of supercoiled pBR 322 DNA, 10^{-4} to 10^{-6} M of complex, 2 μl of DMSO (1%) and 5 μl of hydrogen peroxide (40 mmol l^{-1}). The reaction was incubated at 37 °C for 2 h. After incubation, 1 μl of loading buffer (0.25% bromophenol blue, 0.25% xylene cyanol, 30% glycerol in H_2O) was added to each tube and the mixed samples were loaded on 1% agarose

gel. The electrophoresis was carried out for 2 h at 50 V in TBE buffer (89 mM tris-borate, pH 8.3, 1 mmol l^{-1} EDTA). Gels were stained with ethidium bromide (1 μg ml^{-1}) for 30 min prior to being photographed under UV light.

2.2. Synthesis of the macrobicyclic binuclear copper(II) complexes

$[Cu_2L^1(ClO_4)](ClO_4)$: A methanolic solution of copper(II) perchlorate hexahydrate (0.63 g, 1.7 mmol) was added to a hot solution of PC (1.00 g, 1.7 mmol) in methanol, followed by the addition of 1,2-diaminoethane (0.11 g, 1.7 mmol) and triethylamine (0.47 g, 3.4 mmol) in methanol. After an hour, another 1 mol of copper(II) perchlorate (0.63 g, 1.7 mmol) was added and the solution was refluxed in a water bath for 24 h. The resulting solution was filtered whilst still hot and allowed to stand at room temperature. After slow evaporation of the solvent at 25 °C, an air-stable dark green compound was collected by filtration, which was washed with methanol and dried in vacuum.

Yield: 1.03 g (65%). *Anal.* Calc. for $C_{36}H_{54}N_6O_{10}Cl_2Cu_2$: C, 46.55; H, 5.81; N, 9.05; Cu, 13.69. Found: C, 46.58; H, 5.75; N, 9.02; Cu, 13.66%. FAB mass (NBA matrix, *m/z* (%)): 307, 345, 446, 571, 599, 636, 700, 636, 728, 828 Conductance (Λ_m, S cm^2 mol^{-1}) in DMF: 80. Selected IR data (KBr)(*ν*, cm^{-1}): 3409, 3230, 1612, 1114, 1098, 1087, 625. λ_{max}, nm (ε, M^{-1} cm^{-1}) in DMF: 755 (sh), 552 (130), 365 (14800), 275 (17200). $g = 2.10$; μ_{eff}: 1.50 BM.

The complexes $[Cu_2L^2(ClO_4)](ClO_4)$, $[Cu_2L^3(ClO_4)](ClO_4)$, $[Cu_2L^4(ClO_4)](ClO_4)$ and $[Cu_2L^5(ClO_4)](ClO_4)$ were synthesized by following the above procedure using 1,3-diaminopropane (0.14 g, 1.7 mmol), 1,4-diaminobutane (0.17 g, 1.7 mmol), 1,2-diaminobenzene (0.18 g, 1.7 mmol) and 1,8-diaminonaphthalene (0.26 g, 1.7 mmol) respectively, instead of using 1,2-diaminoethane.

$[Cu_2L^2(ClO_4)](ClO_4)$: Dark green compound. Yield: 0.92 g (58%). *Anal.* Calc. for $C_{37}H_{56}N_6O_{10}Cl_2Cu_2$: C, 47.13; H, 5.94; N, 8.91; Cu, 13.49. Found: C, 47.08; H, 5.89; N, 8.85; Cu, 13.52%. FAB mass (NBA matrix, *m/z* (%)): 307, 345, 446, 504, 552, 571, 613, 650, 738, 744. Conductance (Λ_m, S cm^2 mol^{-1}) in DMF: 87. Selected IR data (KBr)(*ν*, cm^{-1}): 3452, 3225, 1642, 1105, 1092, 1088, 626. λ_{max}, nm (ε, M^{-1} cm^{-1}) in DMF: 765 (sh), 580 (130), 359 (16300), 276 (20400). $g = 2.11$; μ_{eff}: 1.53 BM.

$[Cu_2L^3(ClO_4)](ClO_4)$:Dark green compound. Yield: 0.97 g (60%). *Anal.* Calc. for $C_{38}H_{58}N_6O_{10}Cl_2Cu_2$: C, 47.69; H, 6.06; N, 8.78; Cu, 13.29. Found: C, 47.65; H, 5.97; N, 8.75; Cu, 13.24%. Conductance (Λ_m, S cm^2 mol^{-1}) in DMF: 79. Selected IR data (KBr) (*ν*, cm^{-1}): 3440, 3220, 1632, 1116, 1093, 1087, 625. λ_{max}, nm (ε, $M^{-1}cm^{-1}$) in DMF: 785 (sh), 590 (160), 377 (18500), 264 (24300). $g = 2.11$; μ_{eff}: 1.59 BM.

$[Cu_2L^4(ClO_4)](ClO_4)$: Brown color compound. Yield: 1.06 g (64%). *Anal.* Calc for $C_{40}H_{54}N_6O_{10}Cl_2Cu_2$: C, 49.18; H, 5.53; N, 8.60; Cu, 13.02. Found: C, 49.14; H, 5.48; N, 8.56; Cu, 12.97%. Conductance (Λ_m, S cm^2 mol^{-1}) in DMF: 64. Selected IR data (KBr) (*ν*, cm^{-1}): 3448, 3225, 1612, 1140, 1096, 1087, 624. λ_{max}, nm (ε, M^{-1} cm^{-1}) in DMF: 774 (sh), 568 (140), 437 (10100), 397 (28400), 357 (34500), 273 (46400). $g = 2.10$; μ_{eff}: 1.54 BM.

$[Cu_2L^5(ClO_4)](ClO_4)$: Dark green color compound. Yield: 1.12 g (64%). *Anal.* Calc. $C_{44}H_{56}N_6O_{10}Cl_2Cu_2$: C, 51.46; H, 5.45; N, 8.18; Cu, 12.38. Found: C, 51.39; H, 5.43; N, 8.13; Cu, 12.32%. Conductance (Λ_m, S cm^2 mol^{-1}) in DMF: 80. Selected IR data (KBr) (*ν*, cm^{-1}): 3425, 3225, 1620, 1141, 1096, 1087, 632. λ_{max}, nm (ε, M^{-1} cm^{-1}) in DMF: 780 (sh), 575 (145), 408 (14800), 381 (30200), 270 (52300). $g = 2.11$; μ_{eff}: 1.46 BM.

3. Results and discussion

A series of macrobicyclic binuclear copper(II) complexes were synthesized by Schiff base condensation of the pendant substituted ''tet *a*'' compound (PC) with various diamines in the presence of a copper(II) ion. The synthetic pathway of the complexes is shown in Scheme 1.

Molar conductivity measurements of the copper(II) complexes in DMF resulted in Λ_m values in the range 69–100 S cm^2 mol^{-1}, which indicate that the complexes are 1:1 electrolytes [29]. The positive ion FAB mass spectrum of the complex $[Cu_2L^1(ClO_4)](ClO_4)$ showed a peak at $m/z = 828$, corresponding to the $[Cu_2L^1(ClO_4)]^+$ ion, and the complex $[Cu_2L^2(ClO_4)](ClO_4)$ showed a peak at $m/z = 744$, corresponding to the $[Cu_2L^2–2ClO_4]^+$ ion. The positive ion FAB mass spectral data of the copper(II) complexes confirm the proposed formulation of the complexes.

3.1. Spectral studies

The IR spectra of the binuclear copper(II) complexes showed bands in the region 3220–3260 cm^{-1}, indicating the presence of NH groups, and a peak [30] in the range 1608–1642 cm^{-1} is due to *ν*(C=N). The peak at 1674 cm^{-1} due to *ν*(C=O) of the PC disappeared in the complexes and the formation of a new peak for *ν*(C=N) indicates effective Schiff's base condensation [31]. The binuclear copper(II) complexes showed two peaks near 1100 cm^{-1} and one peak near 620 cm^{-1}. Of the two peaks around 1100 cm^{-1} one is split, indicating the presence of a coordinated perchlorate ion, while the other peak does not show any splitting, indicating the presence of an uncoordinated perchlorate ion [32].

Electronic spectra of all the complexes were obtained in DMF medium. The copper(II) complexes exhibit an absorption maximum in the range 550–610 nm and a shoulder band in the range 755–785 nm, due to a d–d transition of the copper(II) ion [33,34], indicating that the geometry around the copper ion is square-pyramidal. On moving from the complexes of ligands L^1 to L^3, an increase in λ_{max} (red shift) of the d–d transition of the metal ion was observed, which indicates that the distortion of the coordi-

nation geometry around the metal ion increases [35]. A moderate intense band observed in the range 350–400 nm is due to a ligand to metal charge transfer transition and the strong band observed in the range 260–280 nm is due to an intraligand charge transfer transition. The intraligand charge transfer band may be due to the precursor compound which forms part of the ligand and shows a band at 270 nm. Apart from these, additional peaks are observed for the complexes of ligands L^4 to L^5 due to the presence of the aromatic ring in the imine nitrogen compartment.

3.2. Electrochemistry

The electrochemical properties of the copper(II) complexes reported in the present work were studied by cyclic voltammetry and the electrochemical data are summarized in Table 1. Cyclic voltammograms of the copper(II) complexes are shown in Fig. 1.

The binuclear copper(II) complexes of ligands L^1 to L^5 show two irreversible reduction waves in the potential ranges $E^1_{pc} = -0.70$ to -1.10 V and $E^2_{pc} = -0.98$ to -1.36 V. Controlled potential electrolysis indicates that each process corresponds to one electron transfer processes. The two redox processes are assigned as follows:

Table 1
Electrochemical data of the copper(II) complexes

Complexes	E^1_{pc} (V)	E^2_{pc} (V)
$[Cu_2L^1(ClO_4)](ClO_4)$	−0.95	−1.18
$[Cu_2L^2(ClO_4)](ClO_4)$	−0.81	−1.05
$[Cu_2L^3(ClO_4)](ClO_4)$	−0.70	−0.98
$[Cu_2L^4(ClO_4)](ClO_4)$	−1.10	−1.36
$[Cu_2L^5(ClO_4)](ClO_4)$	−1.02	−1.32

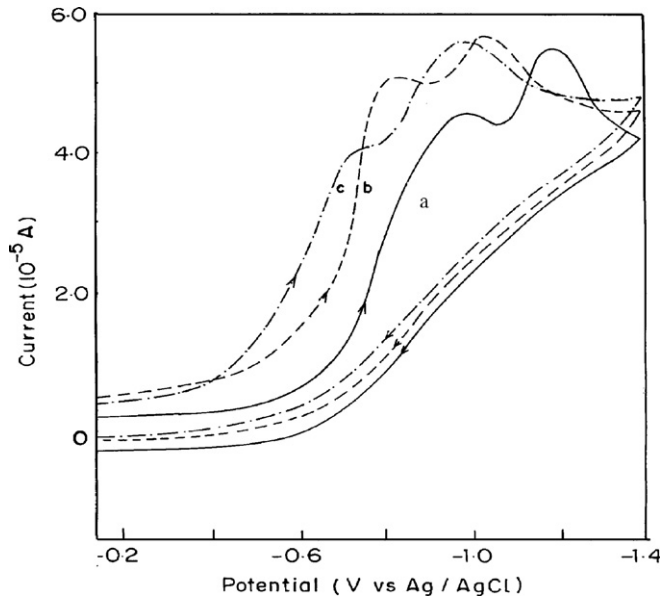


Fig. 1. Cyclic voltammograms of the copper(II) complexes: (a) $[Cu_2L^1(ClO_4)](ClO_4)$; (b) $[Cu_2L^2(ClO_4)](ClO_4)$ and (c) $[Cu_2L^3(ClO_4)](ClO_4)$.

$$Cu^{II}Cu^{II} \rightarrow Cu^{II}Cu^{I} \rightarrow Cu^{I}Cu^{I}$$

The complexes of ligands L^1 to L^3, which contain an aliphatic diamine, have reduction potentials E^1_{pc} in the range -0.70 to -0.95 V, which is close to the reduction potential of the copper(II) ion in the complex [Cu(salen)] [36], and E^2_{pc} values in the range -0.98 to -1.18 V, which is close to the reduction potential of the complex $[Cu(tet\ a)]^{2+}$ ($E_{pc} = -1.08$ V) [37]. Thus, the first reduction potential (E^1_{pc} is ascribed to the metal ion in the imine nitrogen compartment (N_2O_2) while the second reduction potential (E^2_{pc}) is assigned to the metal ion in the "tet *a*" compartment (N_4O) site. On going from ligand L^1 to L^3, the first and second reduction potentials of the corresponding binuclear copper(II) complexes undergo an anodic shift, with $E^1_{pc} = -0.95$ to -0.70 V and $E^2_{pc} = -1.18$ to -0.98 V as the number of methylene groups increase. As the chain length of the imine compartment increases, the entire macrocyclic ring becomes more flexible, which causes easier reduction [38–40]. The same tendencies were observed for the complexes of ligands L^4 and L^5, which contain aromatic diamines. As the chelate ring size increases, the reduction potential shifts from $E^1_{pc} = -1.10$ to -1.02 V and $E^2_{pc} = -1.36$ to -1.32 V. The complexes with aromatic diimines are reduced at higher potentials than the complexes with aliphatic diimines. The reason for this may be due to the greater planarity and electronic properties that are associated with aromatic rings [41]. Whatever the precise interpretation of the bimetallic redox process, it is clear that their magnitude is subject to variation due to changes caused by the nature of the ligand, geometry and by the presence of the other metal [42].

3.3. Magnetic studies

The ESR spectra of the copper(II) complexes were recorded in frozen dilute DMF solution. The ESR spectra of the copper(II) complexes showed a broad band, centered around $g = 2.10$. The broad ESR spectra of the complexes indicate the presence of an antiferromagnetic interaction between the two copper(II) ions in the complexes [43]. Bimetallic copper(II) complexes containing two contiguous paramagnetic ions give magnetic moments of 1.50 to 1.59 B.M., which are less than the total spin-only values. Presumably the lowering of these magnetic moments is due to antiferromagnetic coupling by superexchange through the phenolic oxygen atoms [44]. To evaluate the singlet–triplet energy separation ($-2J$), variable temperature magnetic studies for the complexes $[Cu_2L^3(ClO_4)](ClO_4)$ and $[Cu_2L^4(ClO_4)](ClO_4)$ were performed in the temperature range 78–298 K, and the experimental magnetic susceptibility values were fitted to the modified Bleaney–Bowers equation [45].

$$\chi_{cu} = (Ng^2\beta^2)/(3kT)[3 + \exp(-2J/kT)]^{-1}(1-\rho) + 0.45(\rho/T) + N_\alpha$$

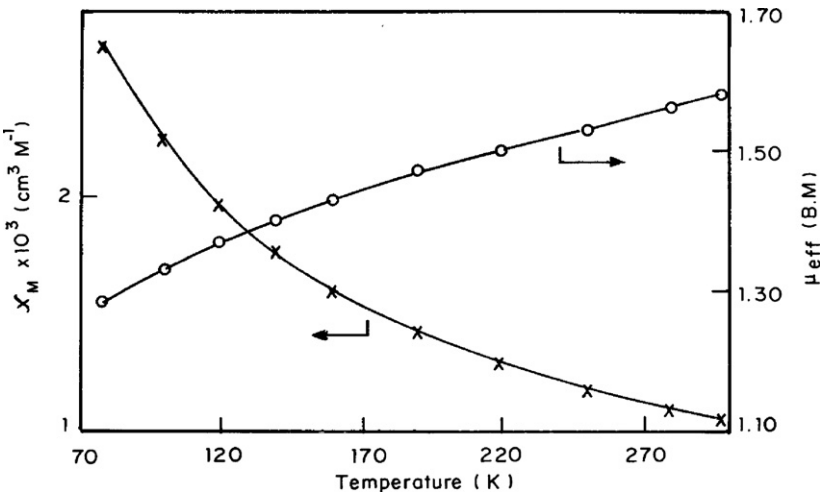


Fig. 2. Temperature dependence of the magnetic properties of the binuclear copper(II) complex $[Cu_2L^3(ClO_4)](ClO_4)$.

where χ_{cu} is the paramagnetic susceptibility per metal atom after correction for diamagnetism, N is Avogadro's number, β is the Boltzmann constant, g is the average gyromagnetic ratio and ρ is the percentage of monomeric impurities, $-2J$ is the singlet-triplet separation, N_α is the temperature independent paramagnetism (60×10^6 $cm^3\,M^{-1}$). A non-linear least-square fitting program was employed to calculate $-2J$, g and ρ. Plots of χ_{Cu} vs T and μ_{Cu} vs T for the complex $[Cu_2L^3(ClO_4)](ClO_4)$ is shown in Fig. 2. A significantly higher $-2J$ value is observed for the complex of L^4 when compared to the complex of L^3. The most probable reason for the strong antiferromagnetic exchange interaction in the L^4 complex may be the greater planarity due to the aromatic diamine ($-2J = 216\ cm^{-1}$) when compared with complex L^3 which contains an aliphatic diamine ($-2J = 144\ cm^{-1}$) and also due to ring size. Studies on magnetostructural correlations for phenoxo-bridged binuclear copper complexes show that the major factor that controls the exchange interactions is the Cu–O–Cu bridge angle; however other factors such as the degree of distortion from planarity and reduction in electron density on the copper atoms reduce the effective overlap of the metal orbitals with those of the bridging ligand, and hence reduce the antiferromagnetic spin exchange between the metal centers [46]. Ruiz et al. [47] found that for hydroxo- and alkoxobridged copper(II) complexes the displacement of the O–R bond in Cu_2O_2 framework also influences the extent of the exchange interaction. If there is out-of-plane displacement of R in O–R, then the antiferromagentic exchange interaction is found to be less. In our earlier complex $[Cu_2L^{1\ b}](ClO_4)_2$ (Chart 1), the observed exchange-interaction value was $-2J = 214\ cm^{-1}$. The possible reason for this low value compared to the present system may be the extent of the out-of-plane displacement of the phenyl ring from the O atom within the Cu_2O_2 framework and deviation from coplanarity as Ruiz et al., already reported [48].

3.4. Kinetic studies of hydrolysis of 4-nitrophenyl phosphate

The hydrolytic activity of the binuclear copper(II) complexes towards 4-nitrophenyl phosphate has been examined spectrophotometrically in DMF. An absorption band typical of the *p*-nitrophenolate ion appeared at 425 nm, the intensity of which increased with time. No significant hydrolysis of the test substrate was observed when the metal complex was absent. The initial rate values for catalytic hydrolysis of 4-nitrophenyl phosphate by the binuclear copper(II) complexes are given in Table 2. The initial rate values are in the range 1.8×10^{-5} to $2.1 \times 10^{-5}\ Ms^{-1}$.

The structural features and electrochemical properties are important factors in determining the catalytic activity of the complexes. Increasing the ring size, varying the donor atoms and changing from a mononuclear to a binuclear system all lead to significant differences in the catalytic properties of the complexes. It is seen that the reactivity of the complexes differs significantly as the size of the macrocycle increases. Comparison of the catalytic activities of the complexes of ligands L^1 and L^2 clearly evinces that the complex of ligand L^2 has enhanced catalytic activity. It is indeed noteworthy to say that the increase in flexibility due to the increase in the ring size of the macrocycle is the possible reason for the observed higher initial rate value of the complex of ligand L^2 because

Table 2
(a) Hydrolysis of 4-nitrophenylphosphate by the copper(II) complexes and (b) catecholase activity of the copper(II) complexes

Complexes	Hydrolysis of 4-nitrophenyl phosphate V_{in} (Ms^{-1})	Catecholase activity V_{in} (Ms^{-1})
$[Cu_2L^1(ClO_4)](ClO_4)$	1.8×10^{-5}	2.7×10^{-5}
$[Cu_2L^2(ClO_4)](ClO_4)$	2.0×10^{-5}	3.1×10^{-5}
$[Cu_2L^3(ClO_4)](ClO_4)$	2.1×10^{-5}	3.5×10^{-5}
$[Cu_2L^4(ClO_4)](ClO_4)$	1.7×10^{-5}	2.4×10^{-5}
$[Cu_2L^5(ClO_4)](ClO_4)$	1.9×10^{-5}	2.6×10^{-5}

the metal ion can more easily get reduced and bind with the substrate. The same was supported by both spectral and electrochemical studies. It was seen that if the reduction potential is too negative, the complex has a decreased catalytic activity due to a more difficult reduction to copper(I), and a more positive reduction potential of the complex gives a higher catalytic activity since the donor atoms stabilize copper(I) at the expense of copper(II). A macrocyclic ring size increase produces a distortion in the geometry around the metal ion, which enhances the accessibility of the metal ion for the bonding of phosphate and OH groups [49]. It can be stated that the planarity that is associated with the aromatic ring imparts a lower catalytic efficiency due to the rigidity of the systems, as observed in the case of the electrochemical reduction of the complexes.

3.5. Kinetic studies of oxidation of catechol (catecholase activity)

The copper(II) complexes were tested for catecholase activity. The amount of DTBQ formed with respect to time is given in Fig. 3. The rate values are also reported in Table 2. The initial rate values for the binuclear copper(II) complexes range from 2.7×10^{-5} to 3.5×10^{-5} Ms^{-1}. The initial rate values of the binuclear complexes are found to increase as the macrocyclic ring size increases. The increase in ring size makes the systems more flexible, which results in easier reduction of the metal ion. It is evidenced from the literature, [23,50] that the initial rate values for the more distorted complexes are higher than those of the less-distorted complexes.

3.6. DNA cleavage studies

The naturally occurring supercoiled DNA form (Form I), when nicked, gives rise to an open circular relaxed form (Form II) and upon further cleavage, results in the linear form (Form III). No cleavage occurs in the absence of

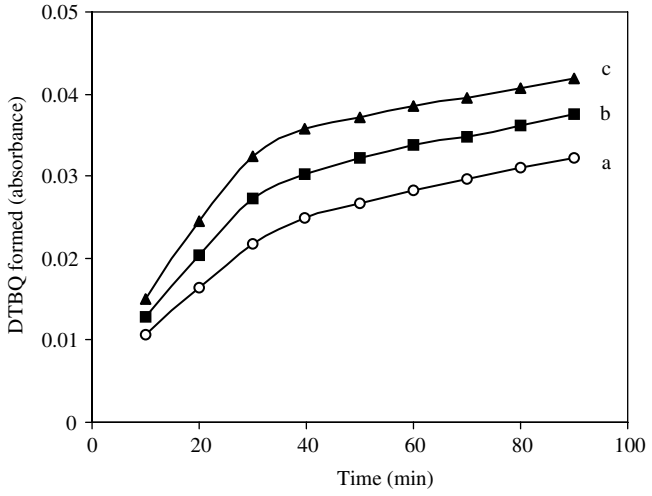


Fig. 3. Catecholase activity of the copper(II) complexes: (a) $[Cu_2L^1(ClO_4)](ClO_4)$; (b) $[Cu_2L^2(ClO_4)](ClO_4)$ and (c) $[Cu_2L^3(ClO_4)](ClO_4)$.

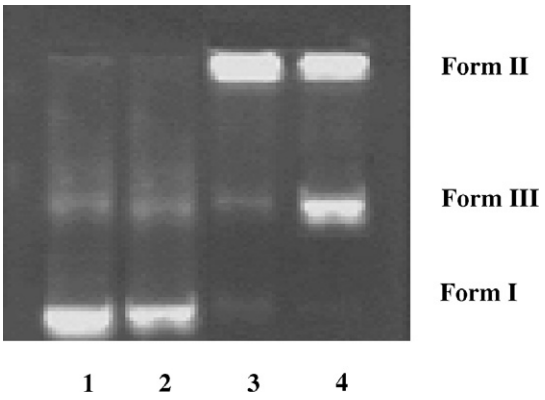


Fig. 4. Cleavage of pBR322 DNA by the copper(II) complexes: Lane 1. DNA control; Lane 2. DNA + H_2O_2; Lane 3. DNA + H_2O_2 + complex $[Cu_2L^1(ClO_4)](ClO_4)$ 20 μmol l^{-1}; Lane 4. DNA + H_2O_2 + complex $[Cu_2L^1(ClO_4)](ClO_4)$ 50 μmol l^{-1}.

H_2O_2 and complexes. As shown in Fig. 4, the complexes can effectively cleave duplex DNA in the presence of H_2O_2. The copper(II) complexes show a very remarkable cleaving ability at very low concentrations. In the presence of the copper(II) complex $[Cu_2L^1(ClO_4)](ClO_4)$ (20 μmol l^{-1}), plasmid DNA was nicked as is evident from the formation of Form II and the disappearance of the supercoiled form in the electrophoretic experiment (lanes 3 and 4). At a slightly higher concentration of then dinuclear complex $[Cu_2L^1(ClO_4)](ClO_4)$ (50 μmol l^{-1}), the cleavage is found to be much more efficient, as is seen from the formation of linear form (Form III) in lane 4. As the complex concentration increases, the probability of double strand scissions is enhanced once the DNA has undergone a single strand break. It is clear that the cleavage of pBR 322 DNA is highly dependent on the concentration of the complexes. The different DNA cleavage efficiency of the complexes was due to the different binding affinity of the complexes to DNA. It is thought that most cleavage cases are caused by copper ions reacting with H_2O_2 to produce the diffusible hydroxyl radical (·OH) or molecular oxygen, which may damage DNA through Fenton type chemistry [51,52].

4. Conclusion

Catechol oxidation and phosphate hydrolysis studies observed that the complex $[CuL^3(ClO_4)](ClO_4)$ has a higher catalytic activity than the other corresponding complexes. The ligand L^3 has a larger chelate ring size and is more flexible when compared to the other ligand systems, which leads to distortion in the geometry of the complex. This distorted complex has a higher catalytic activity than the other rigid complexes and the same was supported by spectral, magnetic and electrochemical studies.

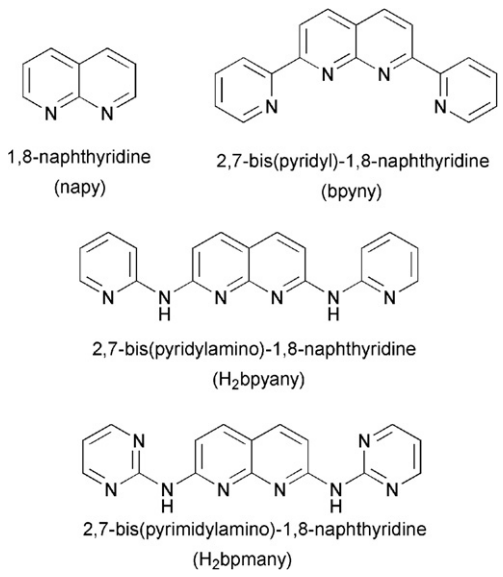
Acknowledgements

The author N.S. gratefully acknowledges for the financial support received from the SCIENCE CITY, Chennai,

India. We are thankful to Dr. P. Srinivasan for fruitful discussions on DNA cleavage studies.

References

[1] P.A. Vigato, S. Tamburini, D.E. Fenton, Coord. Chem. Rev. 106 (1990) 25.
[2] J.A. Ibers, R.H. Holm, Science 109 (1980) 223.
[3] K. Wieghardt, Angew. Chem. Int. Ed. Engl. 28 (1989) 1153.
[4] D.W. Stephan, Coord. Chem. Rev. 95 (1989) 41.
[5] N.W. Alcock, K.P. Balakrishnan, P. Moore, G.A. Pike, J. Chem. Soc. Dalton Trans. (1987) 889.
[6] K.R. Adam, I.M. Atkinson, L.F. Lindoy, Inorg. Chem. 36 (1997) 480.
[7] K.P. Wainwright, Coord. Chem. Rev. 35 (1997) 166.
[8] P.V. Berhardt, G.A. Lawrance, Coord. Chem. Rev. 104 (1990) 297.
[9] E. Maimon, I. Zilbermann, G. Golub, A. Ellern, A.I. Shames, H.A. Cohen, D. Meyerstein, Inorg. Chim. Acta 324 (2001) 65.
[10] M. Rodriguez, A. Liobet, M. Corbella, P. Muller, M.A. Uson, A.E. Martell, J. Reibenspies, J. Chem. Soc. Dalton Trans. (2002) 2900.
[11] E. Kimura, H. Kitamura, T. Koike, M. Shiro, J. Am. Chem. Soc. 119 (1997) 10909.
[12] M. Demeunynck, C. Baily, W.D. Wilson (Eds.), Small Molecule DNA and RNA Binders: From Synthesis to Nucleic Acid Complexes, Wiley VCH Weinheim, 2002, p. 754.
[13] D.S. Sigman, D.R. Graham, V. D'Aurora, A.M. Stern, J. Biol. Chem. 254 (1979) 12269.
[14] D.S. Sigman, Acc. Chem. Res. 19 (1986) 180.
[15] J. Chin, Curr. Opin. Chem. Biol. 1 (1997) 514.
[16] E. Kimura, S. Aoki, T. Koike, M. Shiro, J. Am. Chem. Soc. 119 (1997) 3068.
[17] R.H. Holm, P. Kenneohl, E.I. Solomon, Chem. Rev. 96 (1996) 2239.
[18] P.J. Stang, B. Olenyuk, Acc. Chem. Res. 30 (1997) 502.
[19] M. Fujita, Chem. Soc. Rev. 27 (1998) 417.
[20] M.J. Zaworotko, Nature 402 (1999) 242.
[21] A.J. Atkins, D. Black, A.J. Blake, A.M. Beceraa, S. Parsons, L.R. Ramirez, M. Schroder, Chem. Commun. (1996) 457.
[22] P. Zanello, S. Tamburini, P.A. Vigato, G.A. Mazzocchin, Coord. Chem.Rev. 77 (1987) 165.
[23] M. Thirumavalavan, P. Akilan, M. Kandaswamy, K. Chinnakali, G. Senthilkumar, H.K. Fun, Inorg. Chem. 42 (2003) 3308.
[24] T.H. Ahn, J. Kim, L.F. Lindoy, J. Wang, Aust. J. Chem. 52 (1999) 1139.
[25] J.C. Duff, J. Chem. Soc. (1941) 547.
[26] J.D. Crane, D.E. Fenton, J.M. Latour, A.J. Smith, J. Chem. Soc., Dalton Trans. (1991) 2279.
[27] N.W. Alcock, P. Moore, K.F. Mok, J. Chem. Soc., Perkin Trans. II (1980) 1186.
[28] N. Sengottuvelan, D. Saravanakumar, V. Narayanan, M. Kandaswamy, K. Chinnakali, G. Senthilkumar, Bull. Chem. Soc. Jpn. 77 (2004) 1153.
[29] W.J. Geary, Coord. Chem. Rev. 7 (1971) 81.
[30] K. Nakamoto, Infrared and Raman Spectra of Inorganic and Coordination Compounds, Wiley Interscience, New York, 1978.
[31] G. Das, R. Shukala, S. Mandal, R. Singh, P.K. Bharadwaj, J.V. Singh, K.V. Whitemire, Inorg. Chem. 36 (1997) 323.
[32] M. Lachkar, R. Guilard, A. Atmani, A.D. Cian, J. Fischer, R. Weiss, Inorg. Chem. 37 (1998) 1575.
[33] B.J. Hathway, in: G. Wilkinson (Ed.), Comprehensive Coordination Chemistry Vol. 5, Pergamon Press, NewYork, 53, 1987, p. 674.
[34] M.R. Malachowski, H.B. Huynh, L. Tomlinson, R.S. Kelly, J.W. FurbeeJun, J. Chem. Soc., Dalton Trans. (1995) 31.
[35] R. Bhalla, M. Helliwell, C.D. Garner, Inorg. Chem. 36 (1997) 2944.
[36] F. Abba, G.D. Santis, L. Fabbrizzi, M. Licchelli, A.M.M. Lanfredi, P. Pallavicini, A. Poggi, F. Ugozzoli, Inorg. Chem. 33 (1994) 1366.
[37] D.C. Olson, J. Vasilevskis, Inorg. Chem. 8 (1969) 1611.
[38] E.V.R. Akimova, N.W. Alcock, D.H. Busch, Inorg. Chem. 37 (1998) 1563.
[39] E. Gao, W. Bu, G. Yang, D. Liao, Z. Jiang, S. Yan, G. Way, J. Chem. Soc., Dalton Trans. (2000) 1431.
[40] J. Manonmani, R. Thirumurugan, M. Kandaswamy, V. Narayanan, S. Shanmuga Sundara Raj, M.N. Ponnuswamy, G. Shanmugam, H.K. Fun, Polyhedron 20 (2001) 3039.
[41] .M. Thirumavlavan, P. Akilan, M. Kandaswamy, Supramolecular Chemistry 16 (2004) 137.
[42] C. Belle, C. Beguin, I. Gautier-luneau, S. Hamman, C. Philouze, J.L. Pierre, F. Thomas, S. Torelli, Inorg. Chem. 41 (2002) 479.
[43] W.B. Tolman, R.L. Rardin, S.J. Lippard, J. Am. Chem. Soc. 111 (1989) 4532.
[44] H. Okawa, M. Tadokora, T.Y. Aratake, M. Ohba, K. Shindom, M. Mitsumi, M. Koikawa, M. Tomono, D.E. Fenton, J. Chem. Soc., Dalton Trans. (1993) 253.
[45] B. Bleaney, K.D. Bowers, Proc. R. Soc. London Ser. A 214 (1952) 415.
[46] M. Lubben, R. Hage, A. Meetsma, B.L. Feringa, Inorg. Chem. 34 (1995) 2217.
[47] E. Ruiz, P. Alemany, S. Alvarez, J. Cano, J. Am. Chem. Soc. 119 (1997) 1297.
[48] E. Ruiz, P. Alemany, S. Alvarez, J. Cano, Inorg. Chem. 36 (1997) 3683.
[49] K. Moore, G.S. Vigee, Inorg. Chim. Acta 66 (1982) 125.
[50] B. Bosnich, Inorg. Chem. 38 (1999) 2554.
[51] A. Sreedhara, J.A. Cowan, Chem. Commun. (1998) 1737.
[52] C. Wailling, Acc. Chem. Res. 8 (1975) 125.



Scheme 1. Structure of 1,8-naphthyridine and its derivatives.

isolated in which each nickel ion has a formal charge of +1.5. The magnetic properties of $[Ni_2(napy)_4Br_2]^+$ reveal that the ground spin-state of the system is in a quartet state. Recently, we have reported the synthesis and structural studies of linear hexa-cobalt and -nickel complexes, in which the metal chain is supported by four 1,8-naphthyridine-based $bpyany^{2-}$ ligands (Scheme 1) [18,19]. On the basis of the X-ray structure analysis, the $Co_6^{11+/12+}$ complexes have delocalized electronic structures whereas the $Ni_6^{11+/12+}$ complexes can be regarded as localized ones.

Here we describe the synthesis, crystal structures, and electrochemical and magnetic properties of novel linear hexanickel string complexes $[Ni_6(\mu_6\text{-bpmany})_4X_2]Cl$ (X = Cl (**1**); X = NCS (**2**)), and their singly oxidized products $[Ni_6(\mu_6\text{-bpmany})_4X_2](BF_4)_2$ (X = Cl (**3**); X = NCS (**4**)), where bpmany is the dianion of 2,7-bis(α-pyrimidylamino)-1,8-naphthyridine.

2. Results and discussion

2.1. Synthesis

The new ligand, 2,7-bis(α-pyrimidylamino)-1,8-naphthyridine (H_2bpmany), was prepared in good yield by palladium-catalyzed cross-coupling of 2-aminopyrimidine with 2,7-dichloro-1,8-naphthyridine, and characterized by ^{1}H NMR and FAB mass spectrometry. The reaction of H_2bpmany with $Ni(OAc)_2 \cdot 4H_2O$ in a 4:6 ratio in refluxing naphthalene, followed by addition of excess LiCl or NaSCN generates $[Ni_6(\mu_6\text{-bpmany})_4X_2]Cl$ (X = Cl (**1**); X = NCS (**2**)). The presence of the Cl^- counter anion in **2** may be explained by the presence of a small amount of Cl^- anion produced by dissociation of CH_2Cl_2 [20], which is the only source of chloride ion in the synthesis of this compound. In this reaction, the desired product was expected to be a hexanickel complex with six Ni^{2+} ions. However, the reaction gave a mixed valence species that has five Ni^{2+} ions and one Ni^+ ion. Based on the electrochemical data, as will be discussed later on, one of the redox potentials was observed at about 0.00 V vs. Ag/AgCl. This indicates that the form $[Ni_6(\mu_6\text{-bpmany})_4X_2]^{2+}$ is relatively easy to reduce to $[Ni_6(\mu_6\text{-bpmany})_4X_2]^+$. Under the reaction conditions, any reagents in an excess amount or even the solvent could be the source of reducing agent. Treatment of **1** or **2** with $[Cp_2Fe]BF_4$ in CH_2Cl_2 gives dark brown crystals of the singly oxidized complexes $[Ni_6(\mu_6\text{-bpmany})_4X_2](BF_4)_2$ (X = Cl (**3**); X = NCS (**4**)). It should be mentioned that complexes **1**–**4** can be prepared under air, and are found to be air-stable in the solid state. The IR active C≡N stretching vibration was observed at 2067 cm^{-1} for both **2** and **4**.

Table 1
Crystallographic data for complexes **1**, **2** and **4**

	1 · $4.5CH_2Cl_2 \cdot 0.5H_2O$	**2** · $5CH_2Cl_2 \cdot 0.5CH_3CN$	**4** · $2CH_3CN \cdot 2Et_2O$
Formula	$C_{68.5}H_{50}N_{32}Cl_{12}Ni_6O_{0.5}$	$C_{72}H_{51.5}Cl_{11}N_{34.5}Ni_6S_2$	$C_{78}H_{66}B_2F_8N_{36}Ni_6O_2S_2$
Formula weight	2107.06	2206.31	2129.67
Crystal size (mm)	0.50 × 0.18 × 0.03	0.50 × 0.15 × 0.10	0.37 × 0.10 × 0.10
Crystal system	monoclinic	tetragonal	monoclinic
Space group	*C*2/*c*	*P*4/*n*	$P2_1/c$
a (Å)	31.0776(10)	28.7185(5)	11.1541(1)
b (Å)	16.1371(5)	28.7185(5)	16.7568(2)
c (Å)	34.2316(11)	11.0775(2)	23.2990(3)
β (°)	105.2450(12)		91.0548(7)
V (Å^3)	16563.1(9)	9136.2(3)	4354.01(9)
Z	8	4	2
ρ (Mg m^{-3})	1.690	1.604	1.624
θ Range for collection (°)	1.23–25.00	1.42–25.00	1.50–27.50
Absorption coefficient (mm^{-1})	1.788	1.641	1.406
Maximum, minimum transmission	0.934, 0.674	0.869, 0.666	0.875, 0.736
Measured reflections	67,846	43,566	50,910
Unique reflections [R_{int}]	14,500 [0.0790]	8026 [0.0677]	9996 [0.0585]
R_1, wR_2 ($I > 2\sigma(I)$)[a]	0.1156, 0.3488	0.1085, 0.3117	0.0765, 0.2366
R_1, wR_2 (all data)[a]	0.1824, 0.3940	0.1625, 0.3575	0.1258, 0.2722

[a] $R_1 = \sum|F_o - F_c|/\sum|F_o|$; $wR_2 = [\sum w|F_o^2 - F_c^2|^2/\sum wF_o^4]^{1/2}$.

2.2. Structures

Complex **1** crystallizes in space group $C2/c$ and the structure consists of the hexanickel cation $[Ni_6(bpmany)_4Cl_2]^+$ and a Cl^- anion. Complex **2** crystallizes in space group $P4/n$ and the cation resides on an inversion center with 50% disorder of a spiral set of four $bpmany^{2-}$ ligands. The $[Ni_6(\mu_6\text{-}bpmany)_4]^{3+}$ cation in both complexes **1** and **2** is roughly in a D_4 symmetry and the linear Ni_6 unit is supported by four $bpmany^{2-}$ ligands in a spiral configuration (Figs. 1 and 2). Thus, the average bond lengths for complexes **1** and **2** were calculated by a D_4 symmetry (Table 2). In the hexanickel chain of compounds **1** and **2**, the terminal nickel ions (Ni(1) and Ni(6)) are square pyramidal whereas Ni(2)–Ni(5) are square planar. The redox active center should be Ni(3) and Ni(4) which gives a Ni_2^{3+} unit. The average Ni–Ni distances from outer to inner are 2.409(2), 2.289(2) and 2.221(2) Å for **1**, and 2.408(2), 2.304(2) and 2.218(2) Å for **2**. The average Ni–Cl bond distance of 2.307(3) Å in **1** is in the range of Ni–Cl bond lengths for the analogous complexes $[Ni_nL_4Cl_2]$ where L is an oligo-(α-pyridyl)amido ligand. The Ni–N_{pm} distance is 2.08(1) Å, which is longer by about 0.20 Å than Ni–N_{amido} and Ni–N_{napy} distances, suggesting that the terminal Ni^{II} ions are in a high-spin state and the internal ones in a low-spin state.

Table 2
Average bond distances (Å) and torsion angles (°) for complexes **1**, **2** and **4**

	1	2	4
Ni(1)–Ni(2)	2.409(2)	2.408(2)	2.404(1)
Ni(2)–Ni(3)	2.289(2)	2.304(2)	2.306(1)
Ni(3)–Ni(4)	2.221(2)	2.218(2)	2.275(1)
Ni–X	2.307(3)	1.988(9)	2.063(5)
Ni(1)–N_{pm}	2.08(1)	2.08(1)	2.08(1)
Ni(2)–N_{amido}	1.93(1)	1.92(2)	1.89(1)
Ni(3)–N_{napy}	2.01(1)	2.03(2)	1.92(1)
N_{pm}–Ni–Ni–N_{amido} torsion	23.96	24.52	22.47
N_{amido}–Ni–Ni–N_{napy} torsion	15.19	14.03	16.44
N_{napy}–Ni–Ni–N_{napy} torsion	13.79	13.15	15.32

The singly oxidized complex **4** crystallizes in the monoclinic space group $P2_1/c$ with $Z = 2$. The dication resides on an inversion center with 50% disorder of a spiral set of four $bpmany^{2-}$ ligands, and the positive charges are compensated by two BF_4^- ions (Fig. 3). The Ni–Ni distances of **4** from outer to inner are 2.404(1), 2.306(1) and

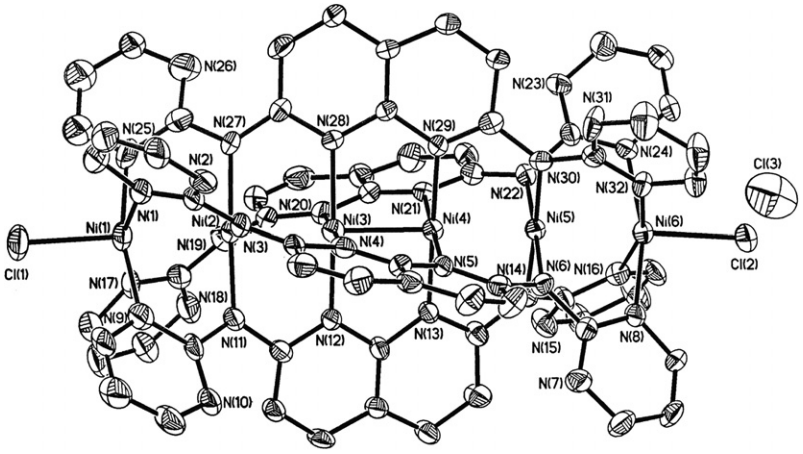


Fig. 1. ORTEP drawing of complex **1**. Thermal ellipsoids are drawn at the 30% probability level. Hydrogen atoms are omitted for clarity.

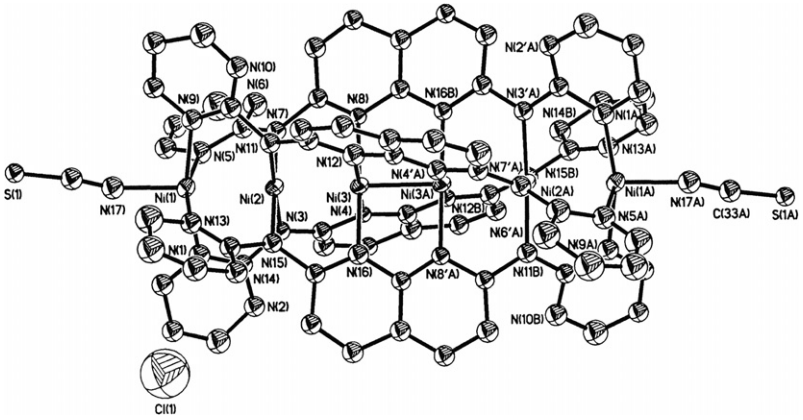


Fig. 2. ORTEP drawing of complex **2**. Thermal ellipsoids are drawn at the 30% probability level. Hydrogen atoms are omitted for clarity.

2.275(1) Å. Removal of one electron from **2** results in an increase in the central Ni–Ni distance from 2.218(2) to 2.275(1) Å and a decrease in the Ni–N_{napy} distance from 2.03(2) to 1.92(1) Å. This indicates that the electron is abstracted from the central Ni_2 unit. In the analoguous complex $[Ni_6(bpyany)_4(NCS)_2](PF_6)$ [19], a similar trend in the structural changes has also been observed when an electron was removed from the Ni_6 chain.

To get further insight on the structures of these complexes, EPR measurements have been performed. The X-band EPR spectra of frozen **1** and **2** are illustrated in Fig. 4, and show signals at $g_\perp = 2.34$ and $g_\parallel = 2.14$ for **1**, and $g_\perp = 2.31$ and $g_\parallel = 2.14$ for **2**, which are consistent with the expected spin-state of $S = 1/2$ in the central Ni_2^{3+} unit. In contrast, no EPR signals were observed for **3** and **4**, consistent with antiferromagnetic coupling of the unpaired electrons in the molecules.

To see if the symmetrical structure of the Ni_6^{11+} complexes persist in solution, the ^1H NMR spectrum of **2** was examined. For a symmetrical molecule, three peaks for the eight equivalent pyrimidyl groups and two peaks for the four equivalent naphthyridyl groups should be observed. As shown in Fig. 5, the spectrum consists of five signals at 72.66, 20.89, 18.81, 15.64 and 12.86 ppm corresponding to the $bpmany^{2-}$ protons, and is consistent with a D_4 symmetry for the $[Ni_6(\mu_6\text{-bpmany})_4(NCS)_2]^+$ core and paramagnetism of the complex.

As mentioned, the Ni_6^{n+} complexes can be considered as roughly D_4. The central Ni_2N_8 unit is practically half way between the eclipsed and staggered conformations. The mixed-valence $[Ni_2(napy)_4X_2]^+$ (X = halogen) cations have a spin state of $S = 3/2$. In contrast, the dinickel unit of **1** and **2** is in a spin-state of $S = 1/2$. A qualitative MO energy-level diagram for the central $Ni_6^{3+/4+}$ units of our complexes in a square planar coordination environment is shown in Scheme 2. This MO picture can be used to rationalize the observed magnetic properties which correspond to a system with one unpaired electron.

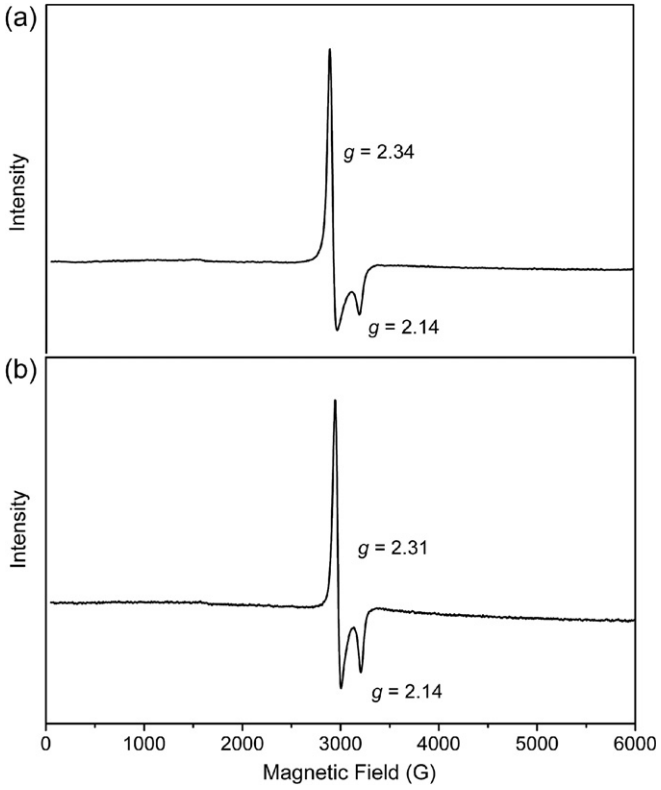


Fig. 4. X-band EPR spectrum of (a) **1** and (b) **2** taken in dichloromethane glass at 77 K.

2.3. Magnetic properties

The magnetic susceptibility of **1**–**4** were measured in the temperature range of 2–300 K. Compounds **1** and **2** exhibit similar magnetic properties. As an example, Fig. 6 shows the magnetic behavior of **2**. At 300 K the effective magnetic moments of 4.54 and 4.58 μ_B for **1** and **2**, respectively, are close to the spin-only value of 4.36 μ_B expected for a system with three spin states of $S = 1$, 1/2 and 1. The μ_{eff} values in the range 30–300 K decrease gradually with decreasing

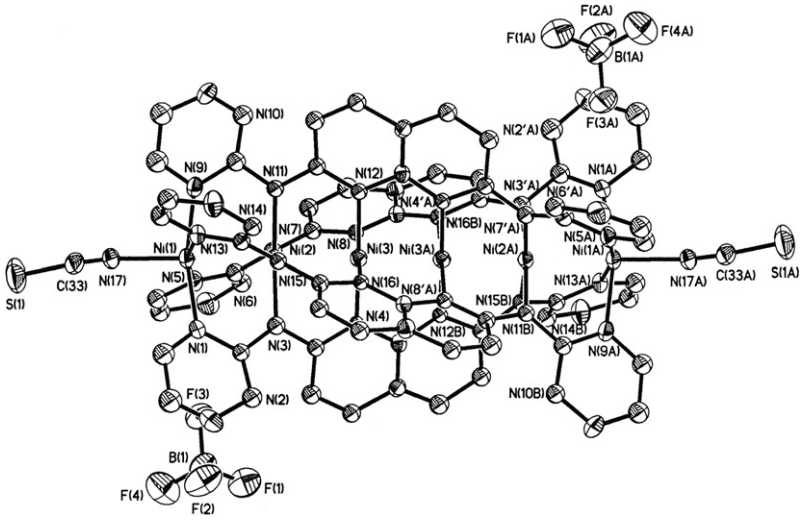


Fig. 3. ORTEP drawing of complex **4**. Thermal ellipsoids are drawn at the 30% probability level. Hydrogen atoms are omitted for clarity.

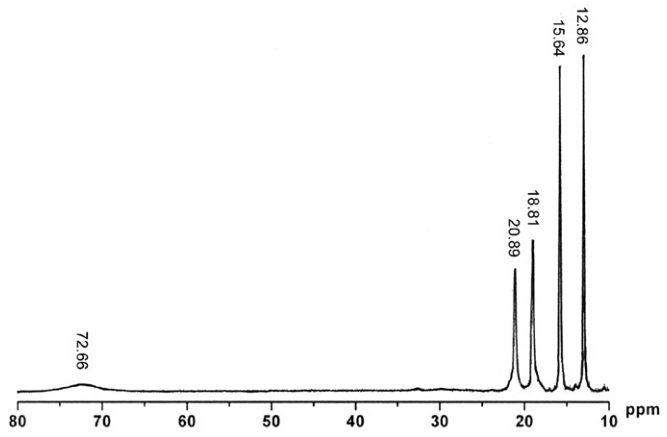
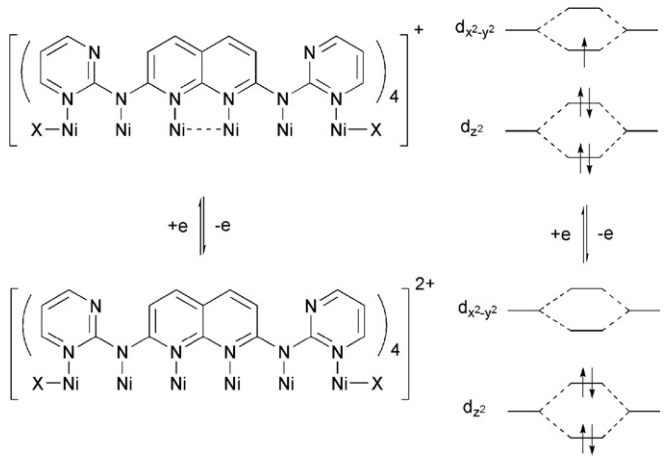


Fig. 5. ^{1}H NMR spectrum of **2** taken at 400 MHz in d_6-DMSO at room temperature.



Scheme 2. The energy level scheme for the central $Ni_2^{3+/4+}$ units in square planar coordination environments in the active electron approximation.

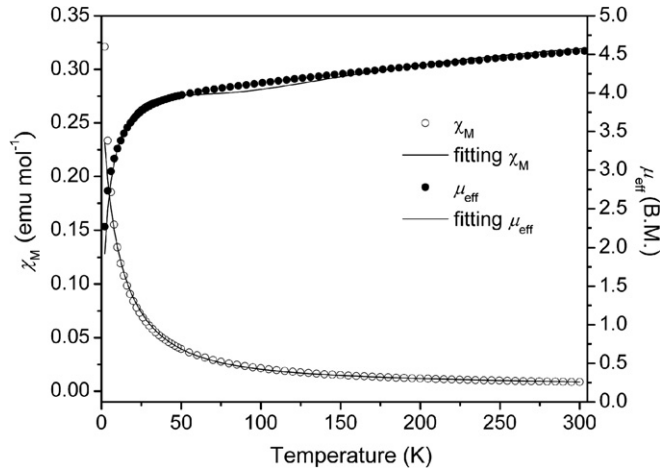


Fig. 6. The magnetic behavior for **2**: molar magnetic susceptibility χ_M (○) and effective magnetic moments μ_{eff} (●). The solid lines are the best-fit curves.

temperature and then decrease sharply to 2.26 and 1.77 μ_B for compounds **1** and **2** at 2 K. These data suggest antiferromagnetic interactions between the terminal Ni^{2+} ion and the central Ni_2^{3+} unit. Taking into account the structural data of this complex, the isotropic spin-exchange for Ni_6^{11+} complex can be given as

$$H = -2J(\widehat{S}_1 \cdot \widehat{S}_{34} + \widehat{S}_6 \cdot \widehat{S}_{34}) - 2J'\widehat{S}_1 \cdot \widehat{S}_6 \quad (1)$$

where J represents the coupling constant to between the terminal Ni^{2+} and central Ni_2^{3+}, and J' is the coupling constant between the two terminal Ni^{2+} ions. Assuming $J' = 0$, the Hamiltonian in Eq. (1) gives rise to five spin states corresponding to the total spin operator $\widehat{S}_T = \widehat{S}_{16} + \widehat{S}_{34}$, i.e., two doublets ($S_T = 1/2$), two quartets ($S_T = 3/2$) and one sextet ($S_T = 5/2$). The molar magnetic susceptibility expression shown in Eq. (2) was then obtained by substituting the energies given in the Heisenberg–Dirac–van Vleck equation [21]

$$\chi_M = \frac{Ng^2\beta^2}{4kT} \times \frac{10 + e^{J/kT} + e^{3J/kT} + 10e^{4J/kT} + 35e^{5J/kT}}{2 + e^{J/kT} + e^{3J/kT} + 2e^{4J/kT} + 3e^{5J/kT}} \quad (2)$$

When impurities are taken into account, χ_M with the Weiss constant is expressed by the following:

$$\chi_M = \frac{Ng^2\beta^2}{4k(T-\theta)} \times \frac{10 + e^{J/kT} + e^{3J/kT} + 10e^{4J/kT} + 35e^{5J/kT}}{2 + e^{J/kT} + e^{3J/kT} + 2e^{4J/kT} + 3e^{5J/kT}} \times (1-\rho) + \frac{2Ng^2\beta^2}{3kT} \times \rho + \chi_{TIP} \quad (3)$$

where N is Avogadro's number, g is the Landé factor, β is the Bohr magneton of the electron, k is the Boltzmann constant, θ is the Weiss constant and T is the temperature in Kelvin. Least-square fitting of the experimental data leads to $J = -46.64\ cm^{-1}$, $g = 2.37$, $\theta = -14.28$ K, $\rho = 0$ and TIP = 0 with a correlation coefficient of 0.9976 for **1** and $J = -47.27\ cm^{-1}$, $g = 2.34$, $\theta = -9.13$ K, $\rho = 0$ and TIP = 0 with a correlation coefficient of 0.9976 for **2**. The negative Weiss constants indicate the presence of a dominant antiferromagnetic exchange interaction between the spin carriers. The g values obtained by magnetic measurements are very close to the EPR results of 2.34 for **1** and 2.31 for **2**.

It should be mentioned that under the limiting conditions, Eq. (2) gives a limiting moment of 3.87 BM. Compounds **1** and **2** have magnetic moments of 2.26 and 1.77 BM at 2 K, which is below the limiting moment. Considering the antiferromagnetic interaction between terminal and central spin centers ($J = -46.64\ cm^{-1}$ and $-47.27\ cm^{-1}$ for **1** and **2**, respectively), the ground state should be a quartet state ($S = 3/2$). The theoretical value of μ_{eff} would be expected to be 3.87 BM at low temperatures. However, the relatively strong intermolecular interactions in **1** and **2** ($\theta = zJS(S+1)/3k = -14.28$ K and -9.13 K) should also be taken into account. Thus, the μ_{eff} values of **1** and **2** decrease significantly at low temperatures.

Such a spin-state structure for compounds **1** and **2** is similar to those in the heterotrinuclear $Ni^{II}Cu^{II}Ni^{II}$ species reported by Kahn [22] and Liao [23]. For example, in Kahn's complex, $\{[Ni(bapa)(H_2O)]_2Cu(pba)\}(ClO_4)_2$ where bapa = bis(3-aminopropyl) and pba = 1,3-propylenebis(oxamato), the two high local spins exhibit an antiferromagnetic interaction with the small local spin and the small central spin polarizing the two high terminal spins in a ferromagnetic-like fashion.

Based on the structural analysis, there are no Ni–Ni bonds in **3** and **4**. The inner Ni^{2+} ions lie in a square planar coordination, and are therefore diamagnetic. The terminal Ni^{2+} ions are in a high-spin state and in a square pyramidal geometry, and have two unpaired electrons each. Fig. 7 shows the molar magnetic susceptibility and effective magnetic moments with respect to absolute temperature (K) for **4**. At 300 K the effective magnetic moment of 4.08 μ_B is close to the expected value of 4.00 μ_B for two non-interacting $S = 1$ spin states. When the temperature is lowered the value steadily decreases and reaches 2.52 μ_B at 2 K. This behavior is indicative of two antiferromagnetically coupled high-spin Ni^{2+} ions in the terminal positions of the Ni_6^{12+} chain. Therefore, Eq. (4) can be used to fit the data for **3** and **4**:

$$\chi_M = \frac{Ng^2\beta^2}{k(T-\theta)} \times \frac{2e^{2J/kT} + 10e^{6J/kT}}{1 + 3e^{2J/kT} + 5e^{6J/kT}} \times (1-\rho) + \frac{2Ng^2\beta^2}{3kT} \times \rho + \chi_{TIP} \quad (4)$$

This equation is based on an isotropic interaction between two $S = 1$ centers with the spin Hamiltonian, $H = -2J\hat{S}_1 \cdot \hat{S}_6$, and taking into account paramagnetic $S = 1$ impurities. The symbol J is the coupling constant between two terminal Ni^{2+} ions and the other symbols have been defined above. Both Ni_6^{12+} complexes reveal weak antiferromagnetic coupling of ca. $-5\ cm^{-1}$ between two terminal Ni^{2+} ions, consistent with our previous reports on multinuclear nickel complexes [14].

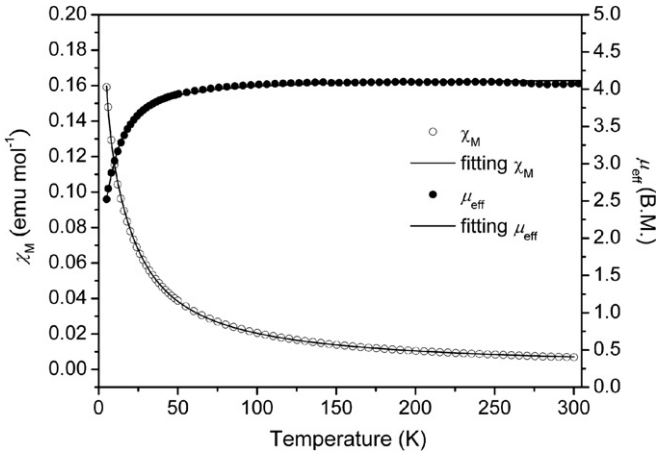


Fig. 7. The magnetic behavior for **4**: molar magnetic susceptibility χ_M (○) and effective magnetic moments μ_{eff} (●). The solid lines are the best-fit curves.

2.4. Electrochemical measurements

The electrochemical properties of **1** and **2** were investigated by cyclic voltammetry in CH_2Cl_2 solution with 0.1 M TBAP as the supporting electrolyte at a scan rate of 100 mV s^{-1}. The cyclic voltammograms exhibit three reversible redox waves at $E_{1/2}^{(1)} = +0.87$, $E_{1/2}^{(2)} = -0.02$ and $E_{1/2}^{(3)} = -0.46$ V for **1**, and $E_{1/2}^{(1)} = +0.96$, $E_{1/2}^{(2)} = -0.01$ and $E_{1/2}^{(3)} = -0.41$ V for **2**, where $E_{1/2}^{(1)}$, $E_{1/2}^{(2)}$ and $E_{1/2}^{(3)}$ correspond to Ni_6^{13+}/Ni_6^{12+}, Ni_6^{12+}/Ni_6^{11+} and Ni_6^{11+}/Ni_6^{10+}, respectively (Table 3). As an example, Fig. 8 shows the cyclic voltammogram of **1**. All of these electrochemical reactions involve one-electron processes, as judged by thin-layer spectroelectrochemical techniques. The oxidation observed at $E_{1/2}^{(2)} = -0.02$ can be assigned to one-electron abstraction from Ni_6^{11+} to generate the corresponding Ni_6^{12+} species. By comparison with the reported values of the analogous complexes $[Ni_6(\mu_6\text{-bpyany})_4X_2](PF_6)_2$ [19], the redox waves of **1** and **2** at $E_{1/2}^{(2)}$ and $E_{1/2}^{(3)}$ are anodically shifted in the range 210–270 mV. The significant difference in the redox potentials can be explained by the electron-withdrawing nature of the pyrimidyl groups of the supporting ligands. The smaller $E_{1/2}^{(2)}$ values for complexes **1** and **2** reflects their good stability under air. Thus, substitution of pyridyl with pyrimidyl groups allows us to fine-tune the redox properties of the complexes.

Spectroelectrochemistry was also conducted to confirm the oxidation states at a certain potential for **1** and **2**. Fig. 9 illustrates the absorption spectral changes of **2** at various applied potentials from −0.10 to +0.20 V in CH_2Cl_2 containing 0.1 M TBAP. As the applied potential

Table 3
Half-wave potentials of the redox couples

	$E_{1/2}^{(1)}$ (V)	$E_{1/2}^{(2)}$ (V)	$E_{1/2}^{(3)}$ (V)	
$[Ni_6(\mu_6\text{-bpmany})_4Cl_2]^+$ (**1**)	+0.87	−0.02	−0.46	this work
$[Ni_6(\mu_6\text{-bpmany})_4(NCS)_2]^+$ (**2**)	+0.96	−0.01	−0.41	this work
$[Ni_6(\mu_6\text{-bpyany})_4Cl_2]^+$	+1.12	−0.23	−0.73	Ref. [19]
$[Ni_6(\mu_6\text{-bpyany})_4(NCS)_2]^+$	+1.08	−0.22	−0.70	Ref. [19]

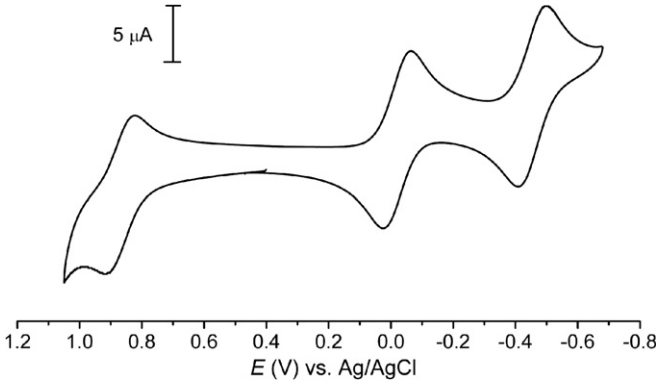


Fig. 8. The cyclic voltammograms of **1** in CH_2Cl_2 containing 0.1 M TBAP with a scan rate of 100 mV s^{-1}.

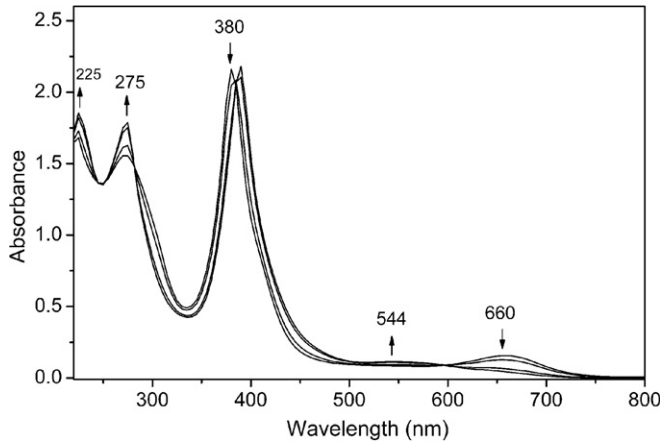


Fig. 9. Electronic absorption spectral changes for the first oxidation of **2** in CH_2Cl_2 containing 0.1 M TBAP at various applied potentials from −0.10 to +0.20 V.

increases, the peaks at 380 and 660 nm decrease in their absorption intensity whereas those at 225, 275, 390 and 544 nm increase with clear isosbestic points. The resulting spectrum is identical with that of complex **4** obtained by chemical methods.

3. Conclusions

The novel linear hexanickel string complexes **1**–**4** have been synthesized, and their magnetic and electrochemical properties have been investigated. Complexes **1**, **2** and **4** were structurally characterized. In the structures, the linear Ni_6 chain is helically wrapped by four all-*syn* type $bpmany^{2-}$ ligands. The two terminal Ni^{2+} ions in all the complexes are in a high-spin state ($S = 1$). While complexes **3** and **4** (Ni_6^{12+}) do not show metal–metal bonding for the adjacent Ni^{2+} ions, the reduced forms **1** and **2** (Ni_6^{11+}) exhibit short Ni–Ni distances for the Ni_2 unit coordinated to the 1,8-naphthyridyl groups, indicating the presence of metal–metal interactions. The magnetic susceptibility and X-band EPR spectra agree well with the electronic structures in that one unpaired electron is located at the central Ni_2 unit for complexes **1** and **2**. These $Ni_6^{11+/12+}$ complexes may be used as molecular switches, since their electronic structure changes drastically upon oxidation or reduction. The STM (scanning tunneling microscopy) studies of complexes **2** and **4**, and the preparation of compounds containing $[M_6(bpmany)_4]^{n+}$ cores with other metal atoms or heterometal string complexes are underway in our laboratory.

4. Experimental

4.1. Materials

All Reagents were obtained from commercial suppliers and were used without further purification unless otherwise noted. The compounds 2-aminopyrimidine, naphthalene, *t*-BuONa and NaSCN were purchased from Acros. Ferrocenium tetrafluoroborate and tetra-*n*-butylammonium perchlortae (TBAP) were purchased from Aldrich. Nickel acetate tetrahydrate, sodium tetrafloroborate, 1,3-bis(diphenylphosphino)propane (dppp) and $Pd_2(dba)_3$ were from Strem Chemicals. 2,7-Dichloro-1,8-naphthyridine was prepared according to literature procedures and modifications thereof [24].

4.2. Physical measurements

^1H NMR measurements were performed with a Varian 400 spectrometer with $SiMe_4$ as the internal reference. Magnetic susceptibility measurements on polycrystalline samples were carried out with a Quantum Design MPMS-7 SQUID magnetometer in the range of 2–300 K and using an applied field of 2000 G. Experimental data were corrected for the diamagnetic contribution calculated from Pascal's constants. Frozen solution X-band EPR spectra were recorded using a Bruker EMX-10 spectrometer. Electronic absorption spectra were measured in CH_2Cl_2 with a Hitachi U-3010 spectrophotometer. Infrared spectra were recorded on a Nicolet Magan 550 FT-IR spectrophotometer using KBr pellets. Elemental analyses were performed on a Perkin–Elmer CHN 2400. FAB mass spectra were obtained with a Hewlett–Packard 5890A spectrophotometer operating in the positive ion detection mode. Electrochemistry was carried out on a CHI 750A potentiostat in CH_2Cl_2 with 0.1 M TBAP. The cyclic voltammograms were recorded with a home-made three-electrode cell equipped with a BAS glassy carbon (0.07 cm^2) disk as the working electrode, a platinum wire as the auxiliary electrode and a home-made Ag/AgCl (saturated) reference electrode. The reference electrode was separated from the bulk solution by a double junction filled with electrolyte solution. Potentials are reported vs. Ag/AgCl (saturated) and referenced to the ferrocene–ferrocenium ($[Cp_2Fe]/[Cp_2Fe]^+$) couple which occurs at $E_{1/2} = +0.54$ V vs. Ag/AgCl (saturated). The working electrode was polished with 0.03 μm aluminium on Buehler felt pads and was subjected to ultrasound for 1 min prior to each experiment. The reproducibility of individual potential values was within ±5 mV. Optical thin layer electrochemical (OTTLE) spectra were accomplished with the use of a 1 mm cuvette, a 100 mesh platinum gauze as the working electrode, a platinum wire as the auxiliary electrode and a Ag/AgCl (saturated) reference electrode.

4.3. Synthesis

4.3.1. 2,7-Bis(α-pyrimidylamino)-1,8-naphthyridine ($H_2bpmany$)

$H_2bpmany$ was synthesized following the reported procedure using palladium catalyst [25]. To a mixture of 2-aminopyrimidine (4.18 g, 44 mmol), 2,7-dichloro-1,8-naphthyridine (3.98 g, 20 mmol) and *t*-BuONa (4.22 g, 44 mmol) in toluene (250 mL) were added $Pd_2(dba)_3$

(549 mg, 0.6 mmol) and 1,3-bis(diphenylphosphino)propane (dppp, 495 mg, 1.2 mmol). This mixture was stirred at 160 °C under an argon atmosphere for 2 d. After cooling to room temperature, the mixture was filtered, and then washed with toluene (3 × 50 mL), H_2O (3 × 100 mL) and MeOH (3 × 50 mL). The product was obtained as pale yellow solid, which was dried under vacuum (5.62 g, 89%). ^1H NMR (400 MHz, d_6-DMSO, 298 K, TMS): δ 10.24 (s, 2H; N*H*), 8.61 (d, $J = 4.8$ Hz, 4H; Pym*H*), 8.38 (d, $J = 8.8$ Hz, 2H; 4,5-Napy*H*), 8.21 (d, $J = 8.8$ Hz, 2H; 3,6-Napy*H*), 7.03 (t, $J = 4.8$ Hz, 2H; Pym*H*); IR (KBr): 3067, 3229, 3415 cm^{-1} (NH); ESI-MS: *m*/*z* (%): 317.31 (100) $[M+H]^+$; Elemental *Anal*. Calc. for $C_{16}H_{12}N_8$: C, 60.75; H, 3.82; N, 35.42. Found: C, 60.84; H, 3.72; N, 35.28%.

4.3.2. $[Ni_6(\mu_6\text{-bpmany})_4Cl_2]Cl$ (1)

A 125 mL Erlenmeyer flask was charged with H_2bpmany (316 mg, 1 mmol), $Ni(OAc)_2 \cdot 4H_2O$ (373 mg, 1.5 mmol) and naphthalene (20 g). The mixture was heated at 200–210 °C for 3 h, and then excess LiCl (84 mg, 2 mmol) was carefully added, during which time the mixture became dark green. After the mixture was cooled to about 60 °C, *n*-hexane (3 × 100 mL) was used to remove naphthalene. The dry solid was extracted with CH_2Cl_2 and crystallized from CH_2Cl_2 and Et_2O to give dark green crystals (173 mg, 40%). UV/Vis (CH_2Cl_2): λ_{max} (ε) 232 (115,700), 278 (130,500), 382 (161,700), 656 nm (8500); FAB-MS: *m*/*z* (%): 1680.1 (40) $[M]^+$, 1644.9 (10) $[M-Cl]^+$, 1176.1 (100); Elemental *Anal*. Calc. for $C_{64}H_{40}Cl_3N_{32}Ni_6$: C, 44.80; H, 2.35; N, 26.12. Found: C, 44.54; H, 2.22; N, 26.28%.

4.3.3. $[Ni_6(\mu_6\text{-bpmany})_4(NCS)_2]Cl$ (2)

Complex **2** was synthesized using a procedure similar to that for **1** except that NaSCN (162 mg, 2 mmol) was used instead of LiCl. Dark green crystals were obtained by slow diffusion of Et_2O into the solution of product in CH_2Cl_2 and CH_3CN (124 mg, 28%). IR (KBr): 2067 cm^{-1} (C≡N); UV/Vis (CH_2Cl_2): λ_{max} (ε) 232 (136,800), 274 (137,800), 384 (172,400), 654 nm (9300); FAB-MS: *m*/*z* (%): 1724.4 (25) $[M]^+$, 1667.4 (20) $[M-NCS]^+$, 1176.5 (100); Elemental *Anal*. Calc. (%) for $C_{66}H_{40}ClN_{34}Ni_6S_2$: C, 45.01; H, 2.29; N, 27.04. Found: C, 44.74; H, 2.42; N, 26.49%.

4.3.4. $[Ni_6(\mu_6\text{-bpmany})_4Cl_2](BF_4)_2$ (3)

A 50 mL round-bottomed flask containing **1** (86 mg, 0.05 mmol) and ferrocenium tetrafluoroborate (14 mg, 0.05 mmol) was charged with CH_2Cl_2 (20 mL) at room temperature. The initially dark green solution became dark brown upon stirring. The solution was stirred for 1 h, and then Et_2O were added to precipitate a dark brown solid. The solid was extracted with CH_2Cl_2 and crystallized from MeCN and Et_2O to give dark brown crystals (26 mg, 28%). UV/Vis (CH_2Cl_2): λ_{max} (ε) 230 (124,700), 274 (136,400), 388 (164,300); FAB-MS: *m*/*z* (%): 1680.0 (50) $[M]^+$, 1645.0 (10) $[M-Cl]^+$, 1176.1 (100); Elemental *Anal*. Calc. for $C_{64}H_{40}B_2Cl_2F_8N_{32}Ni_6$: C, 41.46; H, 2.17; N, 24.18. Found: C, 42.04; H, 2.43; N, 24.71%.

4.3.5. $[Ni_6(\mu_6\text{-bpmany})_4(NCS)_2](BF_4)_2$ (4)

A procedure similar to that for complex **3** was employed. Dark brown crystals were obtained by slow diffusion of Et_2O into the solution of the product in CH_3CN (32 mg, 34%). IR (KBr): 2067 cm^{-1} (C≡N); UV/Vis (CH_2Cl_2): λ_{max} (ε) 232 (117,300), 274 (131,600), 388 (166,100); FAB-MS: *m*/*z* (%): 1723.9 (25) $[M]^+$, 1666.9 (15) $[M-NCS]^+$, 1176.0 (100); Elemental *Anal*. Calc. for $C_{66}H_{40}B_2F_8N_{34}Ni_6S_2$: C, 41.74; H, 2.12; N, 25.08. Found: C, 42.10; H, 2.41; N, 25.43%.

4.4. X-ray crystallographic determinations

Crystallographic information for **1**, **2** and **4** are summarized in Table 1. The chosen crystals were mounted on a glass fiber. X-ray diffraction data for **1**, **2** and **4** were collected at 150 K on a NONIUS Kappa CCD diffractometer installed with monochromatized Mo Kα radiation, $\lambda = 0.71073$ Å. Cell parameters were retrieved and refined using DENZO-SMN software on all observed reflections [26]. Data reduction was performed with the DENZO-SMN software [27]. An empirical absorption was based on the symmetry-equivalent reflections and absorption corrections were applied with the SORTAV program. All the structures were solved by using SHELXS-97 [28] and refined with SHELXL-97 [29] by full-matrix least squares on F^2 values. Hydrogen atoms were fixed at calculated positions and refined using a riding model.

Acknowledgements

We thank the National Science Council of Taiwan and the Ministry of Education of Taiwan for financial support of this work.

Appendix A. Supplementary material

CCDC 626037, 626038 and 626039 contain the supplementary crystallographic data for **1**, **2** and **4**. These data can be obtained free of charge via http://www.ccdc.cam.ac.uk/conts/retrieving.html, or from the Cambridge Crystallographic Data Centre, 12 Union Road, Cambridge CB2 1EZ, UK; fax: (+44) 1223-336-033; or e-mail: deposit@ccdc.cam.ac.uk. Supplementary data associated with this article can be found, in the online version, at doi:10.1016/j.poly.2007.04.036.

References

[1] (a) L.-P. Wu, P. Field, T. Morrissey, C. Murphy, P. Nagle, B. Hathaway, C. Simmons, P. Thornton, J. Chem. Soc., Dalton Trans. (1990) 3835;
(b) G.J. Pyrka, M. El-Mekki, A.A. Pinkerton, J. Chem. Soc., Chem. Commun. (1991) 84.
[2] S. Aduldecha, B. Hathaway, J. Chem. Soc., Dalton Trans. (1991) 993.

[3] (a) F.A. Cotton, L.M. Daniels, C.A. Murillo, I. Pascual, J. Am. Chem. Soc. 119 (1997) 10223;
(b) R. Clérac, F.A. Cotton, L.M. Daniels, K.R. Dunbar, C.A. Murillo, I. Pascual, Inorg. Chem. 39 (2000) 748;
(c) R. Clérac, F.A. Cotton, L.M. Daniels, K.R. Dunbar, C.A. Murillo, I. Pascual, Inorg. Chem. 39 (2000) 752;
(d) F.A. Cotton, L.M. Daniels, P. Lei, C.A. Murillo, X. Wang, Inorg. Chem. 40 (2001) 2778;
(e) J.F. Berry, F.A. Cotton, C.A. Murillo, B.K. Roberts, Inorg. Chem. 43 (2004) 2277.

[4] (a) F.A. Cotton, L.M. Daniels, G.T. Jordan IV, C.A. Murillo, J. Am. Chem. Soc. 119 (1997) 10377;
(b) M. Rohmer, M. Bénard, J. Am. Chem. Soc. 120 (1998) 9372;
(c) F.A. Cotton, C.A. Murillo, X. Wang, J. Chem. Soc., Dalton Trans. (1999) 3327;
(d) F.A. Cotton, C.A. Murillo, X. Wang, Inorg. Chem. 38 (1999) 6294;
(e) R. Clérac, F.A. Cotton, K.R. Dunbar, T. Lu, C.A. Murillo, X. Wang, Inorg. Chem. 39 (2000) 3065;
(f) R. Clérac, F.A. Cotton, K.R. Dunbar, T. Lu, C.A. Murillo, X. Wang, J. Am. Chem. Soc. 122 (2000) 2272;
(g) R. Clérac, F.A. Cotton, L.M. Daniels, K.R. Dunbar, K. Kirschbaum, C.A. Murillo, A.A. Pinkerton, A.J. Schultz, X. Wang, J. Am. Chem. Soc. 122 (2000) 6226;
(h) R. Clérac, F.A. Cotton, L.M. Daniels, K.R. Dunbar, C.A. Murillo, X. Wang, Inorg. Chem. 40 (2001) 1256;
(i) R. Clérac, F.A. Cotton, S.P. Jeffery, C.A. Murillo, X. Wang, Inorg. Chem. 40 (2001) 1265.

[5] (a) R. Clérac, F.A. Cotton, K.R. Dunbar, C.A. Murillo, I. Pascual, X. Wang, Inorg. Chem. 38 (1999) 2655;
(b) J.F. Berry, F.A. Cotton, L.M. Daniels, C.A. Murillo, J. Am. Chem. Soc. 124 (2002) 3212;
(c) J.F. Berry, F.A. Cotton, C.A. Murillo, J. Chem. Soc., Dalton Trans. (2003) 3015;
(d) J.F. Berry, F.A. Cotton, L.M. Daniels, C.A. Murillo, X. Wang, Inorg. Chem. 42 (2003) 2418.

[6] J.F. Berry, F.A. Cotton, P. Lei, C.A. Murillo, Inorg. Chem. 42 (2003) 377.

[7] (a) J.-T. Sheu, C.-C. Lin, I. Chao, C.-C. Wang, S.-M. Peng, Chem. Commun. (1996) 315;
(b) C.-K. Kuo, J.-C. Chang, C.-Y. Yeh, G.-H. Lee, C.-C. Wang, S.-M. Peng, J. Chem. Soc., Dalton Trans. (2005) 3696.

[8] S.-Y. Lai, T.-W. Lin, Y.-H. Chen, C.-C. Wang, G.-H. Lee, M.-H. Yang, M.-K. Leung, S.-M. Peng, J. Am. Chem. Soc. 21 (1999) 250.

[9] (a) F.A. Cotton, L.M. Daniels, T. Lu, C.A. Murillo, X. Wang, Chem. Commun. (1999) 2461;
(b) F.A. Cotton, L.M. Daniels, T. Lu, C.A. Murillo, X. Wang, J. Chem. Soc., Dalton Trans. (1999) 517;
(c) H.-C. Chang, J.-T. Li, C.-C. Wang, T.-W. Lin, H.-C. Lee, G.-H. Lee, S.-M. Peng, Eur. J. Inorg. Chem. (1999) 1243.

[10] (a) S.-J. Shieh, C.-C. Chou, G.-H. Lee, C.-C. Wang, S.-M. Peng, Angew. Chem., Int. Ed. Engl. 36 (1997) 56;
(b) C.-Y. Yeh, C.-H. Chou, K.-C. Pan, C.-C. Wang, G.-H. Lee, Y.O. Su, S.-M. Peng, J. Chem. Soc., Dalton Trans. (2002) 2670.

[11] (a) C.-C. Wang, W.-C. Lo, C.-C. Chou, G.-H. Lee, J.-M. Chen, S.-M. Peng, Inorg. Chem. 37 (1998) 4059;
(b) C.-Y. Yeh, Y.-L. Chiang, G.-H. Lee, S.-M. Peng, Inorg. Chem. 41 (2002) 4096.

[12] Y.-H. Chen, C.-C. Lee, C.-C. Wang, S.-Y. Lai, F.-Y. Li, C.-Y. Mou, S.-M. Peng, Chem. Commun. (1999) 1667.

[13] S.-Y. Lai, C.-C. Wang, Y.-H. Chen, C.-C. Lee, Y.-H. Liu, S.-M. Peng, J. Chin. Chem. Soc. 46 (1999) 477.

[14] S.-M. Peng, C.-C. Wang, Y.-L. Jang, Y.-H. Chen, F.-Y. Li, C.-Y. Mou, M.-K. Leung, J. Magn. Magn. Mater. 209 (2000) 80.

[15] (a) A. Clearfield, P. Singh, I. Bernal, J. Chem. Soc., Chem. Commun. (1970) 389;
(b) P. Singh, A. Clearfield, I. Bernal, J. Coord. Chem. 1 (1971) 29;
(c) A. Døssing, S. Larsen, A.V. Lelieveld, R.M. Bruun, Acta Chem. Scand. 53 (1999) 230.

[16] (a) D. Gatteschi, C. Mealli, L. Sacconi, J. Am. Chem. Soc. 95 (1973) 2736;
(b) L. Sacconi, C. Mealli, D. Gatteschi, Inorg. Chem. 13 (1974) 1985;
(c) A. Bencini, D. Gatteschi, L. Sacconi, Inorg. Chem. 17 (1978) 2670;
(d) A. Bencini, E. Berti, A. Caneschi, D. Gatteschi, E. Giannasi, I. Invernizzi, Chem. Eur. J. 8 (2002) 3660.

[17] (a) W.R. Tikkanen, E. Binamira-Soriaga, W.C. Kaska, P.C. Ford, Inorg. Chem. 22 (1983) 1147;
(b) W.R. Tikkanen, E. Binamira-Soriaga, W.C. Kaska, P.C. Ford, Inorg. Chem. 23 (1984) 141;
(c) W.R. Tikkanen, C. Krüger, K.D. Bomben, W.L. Jolly, W.C. Kaska, P.C. Ford, Inorg. Chem. 23 (1984) 3633;
(d) E. Binamira-Soriaga, N.L. Keder, W.C. Kaska, Inorg. Chem. 29 (1990) 3167.

[18] C.-H. Chien, J.-C. Chang, C.-Y. Yeh, G.-H. Lee, J.-M. Fang, S.-M. Peng, J. Chem. Soc., Dalton Trans. (2006) 2106.

[19] C.-H. Chien, J.-C. Chang, C.-Y. Yeh, G.-H. Lee, J.-M. Fang, Y. Song, S.-M. Peng, J. Chem. Soc., Dalton Trans. (2006) 3249.

[20] T.S. Calderwood, T.C. Bruice, Inorg. Chem. 25 (1986) 3722.

[21] O. Kahn, Molecular Magnetism, Wiley-VCH, New York, 1993.

[22] (a) Y. Pei, Y. Journaux, O. Kahn, Inorg. Chem. 27 (1988) 399;
(b) J. Ribas, C. Diaz, R. Costa, Y. Journaux, C. Mathoniere, O. Kahn, A. Gleizes, Inorg. Chem. 29 (1990) 2042.

[23] (a) E.-Q. Gao, J.-K. Tang, D.-Z. Liao, Z.-H. Jiang, S.-P. Yan, G.-L. Wang, Inorg. Chem. 40 (2001) 3134;
(b) Q.-L. Wang, L.-N. Zhu, D.-Z. Liao, S.-P. Yan, Z.-H. Jiang, P. Cheng, G.-M. Yang, J. Mol. Struct. 754 (2005) 10.

[24] G.R. Newkome, S.J. Garbis, V.K. Majestic, F.R. Fronczek, G. Chiari, J. Org. Chem. 46 (1981) 833.

[25] S. Wagaw, S.L. Buchwald, J. Org. Chem. 61 (1996) 7240.

[26] Z. Otwinowski, W. Minor, Methods Enzymol. 276 (1997) 307.

[27] R.H. Blessing, Acta. Crystallogr., Sect. A 51 (1995) 33.

[28] G.M. Sheldrick, Acta. Crystallogr., Sect. A 46 (1990) 467.

[29] G.M. Sheldrick, SHELXL-97, University of Göttingen, Germany, 1997.

2. Experimental

2.1. General procedures and measurements

All operations were carried out under dry oxygen-free nitrogen atmosphere using standard Schlenck techniques. Diethyl ether and tetrahydrofuran (THF) were distilled over Na-benzophenone ketyl prior to use. Dimethylformamide was dried with barium oxide and distilled under reduced pressure. Amines for the preparation of amine complexes were distilled immediately before use. Triphenylphosphine was recrystallized prior to use and checked by ^{31}P NMR and melting point for purity. All other reagents were commercial products and used without further purification. Elemental analyses (C, H, N) were performed on a LECO CHNS-932 analyzer (Module VTF-900 for O). Chlorine was eventually determined by gravimetry as AgCl and molybdenum by titration with lead(II) nitrate [21]. IR spectra (KBr dispersion, 4000–400 cm^{-1} range) were recorded on a Nicolet Impact 410 (Software Omnic for Windows) spectrometer. NMR spectra were recorded on a Varian Unity Inova-400 spectrometer (400 MHz for ^1H and 161.92 MHz for ^{31}P) at 20 °C. Chemical shifts are relative to TMS (^1H), or external 85% H_3PO_4 (^{31}P), with downfield values reported as positive. Coupling constants *J* are given in Hertz.

2.2. Preparation of the complexes

2.2.1. Preparation of $Mo_2O_3Cl_4(DMF)_4$

To a solution of 0.315 g (1.2 mmol) of PPh_3 in 8 ml of DMF, 0.690 g (2 mmol) of $MoO_2Cl_2(DMF)_2$, dissolved in 4 ml of DMF, was added. The mixture was stirred under nitrogen at room temperature for 10 h to obtain a dark brown solution, then 60 ml of diethyl ether was added. After stirring the mixture for 6 h the brown precipitate was filtered, washed with three 5-ml portions of diethyl ether and dried under vacuum.

$Mo_2O_3Cl_4(DMF)_4$: Yield 0.540 g (80.4%). IR(cm^{-1}): *ν*(Mo=O) 972(s); *ν*(Mo–O–Mo) 794(s). ^1H NMR (acetone-d_6): 8.09 ppm (s, 1H, H–CO); 3.01 ppm (s, 3H, $–CH_3$); 2.84 ppm (s, 3H, $–CH_3$). *Anal.* Calc. for $C_{12}H_{28}Mo_2Cl_4N_4O_7$: C, 21.38; H, 4.19; N, 8.31; Cl, 21.04; Mo, 28.47. Found: C, 21.86; H, 4.07; N, 8.35; Cl, 21.95; Mo, 28.61%.

2.2.2. Preparation of $Mo_2O_3Cl_4(L)_4$ (L = HMPA, $OPPh_3$, py, 1/2 bipy, 1/2 1,10-phen, 1/2 $dppmO_2$)

To a solution of 0.134 g (0.2 mmol) of [$Mo_2O_3Cl_4(DMF)_4$] in 30 ml of THF, a solution of 0.8 mmol of L in 5 ml THF was added with stirring. The resulting mixture was stirred for 5 min and the microcrystalline precipitate filtered, washed with three 3-ml portions of THF and dried under vacuum. The complexes were brownish for O-donor and reddish for N-donor ligands.

$Mo_2O_3Cl_4(HMPA)_4$: Yield 0.192 g (88%). IR(cm^{-1}): *ν*(Mo=O) 961(s); *ν*(Mo–O–Mo) 799(m). ^1H NMR (acetone-d_6): 2.86 ppm (d, $^3J_{H–P} = 9.9$ Hz, 18H, $–CH_3$). $^{31}P\{^1H\}$ NMR (acetone-d_6): 29 ppm. *Anal.* Calc. for $C_{72}H_{60}Mo_2Cl_4O_7P_4$: C, 26.24; H, 6.61; N, 15.30. Found: C, 26.01; H, 6.43; N, 14.98%.

$Mo_2O_3Cl_4(OPPh_3)_4$: Yield 0.236 g (79%). IR(cm^{-1}): *ν*(Mo=O) 974(s); *ν*(Mo–O–Mo) 768(m). ^1H NMR (acetone-d_6): 8.10–7.38 ppm (m, 15H, –Ph). $^{31}P\{^1H\}$ NMR (acetone-d_6): 40.2 ppm. *Anal.* Calc. for $C_{72}H_{60}Mo_2Cl_4O_7P_4$: C, 57.85; H, 4.05; Cl, 9.49; Mo, 12.84. Found: C, 58.05; H, 4.07; Cl, 9,80; Mo, 12.54%.

$Mo_2O_3Cl_4(py)_4$: Yield 0.144 g (81%). IR(cm^{-1}): *ν*(Mo=O) 953(s); *ν*(Mo–O–Mo) 764(m). ^1H NMR (acetone-d_6): 8.83 ppm (br s, 2H, for protons on C_2 and C_6); 8.35 ppm (t, $^3J_{H–H} = 6.5$ Hz, 1H, for proton on C_4); 7.92 ppm (br s, 2H, for protons on C_3 and C_5). *Anal.* Calc. for $C_{20}H_{20}Mo_2Cl_4N_4O_3$: C, 34.41; H, 2.89; N, 8.03. Found: C, 34.14; H, 2.93; N, 8.18%.

$Mo_2O_3Cl_4(bipy)_2$: Yield 0.118 g (85%). IR(cm^{-1}): *ν*(Mo=O) 955(s); *ν*(Mo–O–Mo) 770(s). ^1H NMR (acetone-d_6): 9.65–8.41 ppm (m, 8H, bipy). *Anal.* Calc. for $C_{20}H_{16}Mo_2Cl_4N_4O_3$: C, 34.61; H, 2.32; N, 8.07. Found: C, 34.59; H, 2.61; N, 8.11%.

$Mo_2O_3Cl_4$ (1,10-phen)$_2$: Yield 0.130 g (87%). IR(cm^{-1}): *ν*(Mo=O) 961(s); *ν*(Mo–O–Mo) 775(m). ^1H NMR (acetone-d_6): 9.23–8.15 ppm (tm,8H, phen). *Anal.* Calc. for $C_{24}H_{16}Mo_2Cl_4N_4O_3$: C, 38.84; H, 2.17; N, 7.55. Found: C, 38.75; H, 2.85; N, 7.17%.

$Mo_2O_3Cl_4(dppmO_2)_2$: Yield 0.188 g (78%). IR(cm^{-1}): *ν*(Mo=O) 975(s); *ν*(Mo–O–Mo) 785(m). ^1H NMR (acetone-d_6): 8.03–7.81 ppm (m, 8H, Ph); 7.60–7.32 ppm (m, 12H, Ph); 3.9 ppm (t, $^2J_{H–P} = 12.5$ Hz, 2H, $–CH_2$). $^{31}P\{^1H\}$ NMR (acetone-d_6): 39.9 ppm. *Anal.* Calc. for $C_{50}H_{44}Mo_2Cl_4O_7P_4$: C, 49.45; H, 3.65; Cl, 11.68; Mo, 15.80. Found: C, 49.78; H, 3.41; Cl, 11.05; Mo, 16.01%.

2.2.3. Preparation of $Mo_2O_3Cl_4(L)_4$ (L = isoquin, 4-pic)

To a solution of 0.134 g (0.2 mmol) of [$Mo_2O_3Cl_4(DMF)_4$] in 30 ml of THF, a solution of 0.8 mmol of L in 60 ml of diethyl ether was added with stirring. The resulting mixture was stirred for 15 min and the reddish precipitate filtered, washed with three 5-ml portions of diethyl ether and dried under vacuum.

$Mo_2O_3Cl_4(isoquin)_2$: Yield 0.164 g (91%). IR(cm^{-1}): *ν*(Mo=O) 947(s); *ν*(Mo–O–Mo) 800(m). ^1H NMR (acetone-d_6): 9.61 ppm (s, 1H, for protons on C_1); 8.62–8.21 ppm (qd, $^3J_{H–H} = 7.9$ Hz, 4H, for protons on C_3, C_4, C_5 and C_8); 8.16–7.92 ppm (dt, $^3J_{H–H} = 7.9$ Hz, 2H, for protons on C_6 and C_7). *Anal.* Calc. for $C_{36}H_{28}Mo_2Cl_4N_4O_3$: C, 48.13; H, 3.14; N, 6.24. Found: C, 47.98; H, 2.96; N, 6.51%.

$Mo_2O_3Cl_4(4\text{-pic})_2$: Yield 0.140 g (93%). IR(cm^{-1}): *ν*(Mo=O) 935(s); *ν*(Mo–O–Mo) 795(m). ^1H NMR (acetone-d_6): 8.65 ppm (d, $^3J_{H–H} = 6.5$ Hz, 2H, for protons on C_2 and C_6); 7.84 ppm (d, $^3J_{H–H} = 6.5$ Hz, 2H, for protons on C_3 and C_5); 2.65 ppm (s, 3H, $–CH_3$). *Anal.* Calc. for $C_{24}H_{28}Mo_2Cl_4N_4O_3$: C, 38.22; H, 3.74; N, 7.43. Found: C, 38.51; H, 3.84; N, 7.63%.

2.2.4. Formation of $Mo_2O_4Cl_2(L)_4$ (L = DMF, 1/2 bipy)

Single crystals of $Mo_2O_4Cl_2(DMF)_4$ and $Mo_2O_4Cl_2(bipy)_2$ were grown by slow diffusion of diethyl ether, and a solution of 0.156 g (1 mmol) of bipy in 20 ml of diethyl ether, respectively, on a solution containing 0.345 g (1 mmol) of $MoO_2Cl_2(DMF)_2$ and 0.158 g (0.6 mmol) of PPh_3 in 4 ml of DMF.

2.3. Crystal-structure determinations

Crystal data for the complexes $Mo_2O_4Cl_2(DMF)_4$ and $Mo_2O_4Cl_2(bipy)_2$ were collected using a KappaCCD diffractometer with graphite-monochromated Mo Kα radiation. Hydrogen atoms positions were located from difference Fourier maps. Both structures were solved using OpenMoleN 2.2. Table 1 provides crystallographic details for these compounds.

Table 1
Crystal data and summary of intensity data collection and structure refinement of complexes $Mo_2O_4Cl_2(DMF)_4$ and $Mo_2O_4Cl_2(Bipy)_2$

	$Mo_2O_4Cl_2(DMF)_4$	$Mo_2O_4Cl_2(Bipy)_2$
Empirical formula	$C_{12}H_{28}Cl_2Mo_2N_4O_8$	$C_{20}H_{16}Cl_2Mo_2N_4O_4 \cdot C_3H_7NO$
Molecular weight	619.16	712.26
Crystal system	monoclinic	monoclinic
Space group	*C*1*c*1	$P12_1/n1$
a (Å)	10.4920(5)	13.3350(3)
b (Å)	14.5400(9)	14.7780(5)
c (Å)	14.7840(5)	14.1980(4)
β (°)	92.534(3)	111.021(2)
V (Å^3)	2253.1(3)	2611.7(3)
Z	4	4
Color	yellow	red
Crystal dimension (mm)	0.16 × 0.14 × 0.10	0.20 × 0.16 × 0.12
D_{calc} (g cm^{-3})	1.83	1.81
F(000)	1240	1416
μ (mm^{-1})	1.394	1.209
Temperature (K)	173	173
Wavelength (Å)	0.71073	0.71073
Radiation	Mo Kα graphite monochromated	Mo Kα graphite monochromated
Diffractometer	KappaCCD	KappaCCD
Scan mode	phi scans	phi scans
hkl Limits	−10,15/−12,20/−15,16	0,18/0,21/−20,19
Θ Limits (°)	2.5/32.33	2.5/32.44
Number of data measured	6599	15606
Number of data with $I > 3\sigma(I)$	2801	6122
Weighting scheme	$4F_o^2/(\sigma^2(F_o^2) + 0.0064F_o^4)$	$4F_o^2/(\sigma^2(F_o^2) + 0.0064F_o^4)$
Number of variables	251	334
R	0.039	0.041
Rw	0.056	0.065
Goodness-of-fit (GOF)	1.004	1.279
Largest peak in final difference (e Å^{-3})	0.311	0.623

3. Results and discussion

3.1. Synthesis and characterization of the dinuclear (μ-oxo)oxomolybdenum(V) chlorocomplexes

The complexes of Mo(V), containing the Mo_2O_3 unit, that have been structurally characterized possess one Mo–O–Mo bridge and two terminal oxygen atoms in either *cis* or *trans* configuration with respect to the Mo centers. They are usually prepared via reduction of the corresponding dioxomolybdenum(VI) compounds with P oxo-acceptors followed by comproportion and, more rarely, by substitution in other Mo(V) species [22] and oxidation of compounds with molybdenum in lower oxidation states [23].

As part of our studies [24,25] on molybdenum complexes in oxotransfer reactions, we have examined the behavior of several addition compounds of MoO_2Cl_2 with common phosphines and phosphites in several solvents.

Phosphites, such as $P(OBu)_3$ and $P(OPh)_3$, were thought to be superior to phosphines for reduction due to the fact that the resulting phosphates are considerably less basic than the corresponding phosphine oxides, and so they were initially investigated. As expected, the formation of dinuclear (μ-oxo)oxomolybdenum(V) complexes was observed. However, we were unable to obtain pure products in a wide range of conditions. A similar result was obtained in most cases when using PBu_3 and PPh_3.

However, we found that $Mo_2O_3Cl_4(DMF)_4$ could be prepared, in a pure form and in high yield, by reacting $MoO_2Cl_2(DMF)_2$ with PPh_3 in DMF as solvent. This compound was always obtained whenever the ratio $PPh_3/MoO_2Cl_2(DMF)_2$ was 0.5 or superior and the reactions were carried out at room temperature. This is consistent with the well known fact that, in absence of serious steric restrictions, oxomolybdenum(IV) and dioxomolybdenum(VI) species have a strong tendency to associate leading to stable comproportion products of oxomolybdenum(V), which are considerably more resistant to reduction [26]. As could be expected, the use of pure MoO_2Cl_2 instead of $MoO_2Cl_2(DMF)_2$ gave rise to similar results. However, the readily available air stable $MoO_2Cl_2(DMF)_2$ complex [24] is more appropriate for this synthesis by cost and resistance to hydrolysis.

When the reduction was performed in THF the originally green solution changed to brown and the composition of the isolated solid was consistent with a mixture of $Mo_2O_3Cl_4(OPPh_3)_4$ and $Mo_2O_3Cl_4(DMF)_4$ complexes. An excess of additional $OPPh_3$ was required to avoid the formation of the DMF adduct.

Taking into account the easy formation of $Mo_2O_3Cl_4(DMF)_4$, we investigated the possibility of using it as starting material for the preparation of other addition

compounds of $Mo_2O_3Cl_4$, having in mind the limitations derived from the basicity of the amide.

In this way we were able to prepare in good yield a number of $Mo_2O_3Cl_4$ derivatives with phosphine oxides and aromatic amines by mixing solutions of $Mo_2O_3Cl_4(DMF)_4$ and the corresponding ligand in THF. However, it should be noted, that the yield obtained for the isoquinoline and 4-picoline derivatives could be significantly improved by using diethyl ether.

The analytical data (C, H, N, Cl, Mo) for the products were in agreement with those expected for dinuclear (μ-oxo)oxomolybdenum(V) chlorocomplexes.

Not surprisingly, tertiary aliphatic amines afforded ill-defined products, even operating in strictly anhydrous conditions. This fact had been previously observed in substitution reactions on $MoO_2Cl_2(DMF)_2$ and in the catalytic deoxigenation of *N*-oxides [25].

As could be expected, sulfoxides which are also usually able to displace DMF from the coordination sphere of molybdenum, led to slow re-oxidation of $\{Mo_2O_3\}^{4+}$ to $\{MoO_2\}^{2+}$ species. Thus, solutions of $Mo_2O_3Cl_4(DMF)_4$ slowly decolorized when treated with sulfoxides at room temperature.

The compounds here reported are insoluble in hexane and diethyl ether; moderately soluble in THF, acetone and acetonitrile, solvents from which they could be recovered; and very soluble in DMF and DMSO, usually with reaction. They can be stored for months, at room temperature and in a dry atmosphere, without noticeable decomposition.

No relevant features are observed in the IR spectra of these compounds. They are characterized by one strong band in the region 930–980 cm^{-1} that has been assigned to ν(Mo=O) [27], and another band in the region 750–810 cm^{-1} similarly assigned to ν(Mo–O–Mo) in the $\{Mo_2O_3\}^{4+}$ core [5]. The position of the band ν(Mo=O) seems to be sensitive to the nature of the coordinated ligands. As could be expected, the value for ν(Mo=O) appears at lower wavelength for oxygen- than for nitrogen-coordinated ligands. This behavior is similar to that observed in several dioxomolybdenum(VI) complexes [19,20].

With regard to ^1H and ^{31}P NMR spectra of these complexes, the characteristic signals for the free ligands are shifted, as usual, to lower fields upon coordination. It should be noted that the ^{31}P NMR spectra for $Mo_2O_3Cl_4(dppmO_2)_2$ shows only one signal at 39.9 ppm for the coordinated ligand, a similar position to that found in $MoO_2Br_2(dppmO_2)$ [19].

3.2. Formation of the dinuclear bis (μ-oxo)oxomolybdenum(V) chlorocomplexes

To the best of our knowledge there are no reports on rational syntheses for this kind of molecular complexes. However, Mitchell postulated the formation of several Mo(V) oxochlorocomplexes depending on the extent of the hydrolysis of $MoCl_5$ during the synthetic procedure [27].

This fact prompted us to attempt the preparation of dinuclear bis(μ-oxo)oxomolybdenum(V) species from $Mo_2O_3Cl_4(L)_4$ by adding controlled amounts of water to the dinuclear bis(μ-oxo)oxomolybdenum(V) chlorocomplexes. However, we are unable to obtain the desired products.

Then, we also tried to remove one chlorine atom from $MoO_2Cl_2(DMF)_2$ using metals, namely copper, silver and magnesium. In all runs we observed reduction, but were unable to get well defined products, except in the case of copper with $MoO_2Cl_2(DMF)_2$ in DMSO at 70 °C, where we isolated the previously reported, yet here undesired, $(Cu_4Cl_6O)(DMSO)_4$ [28].

However, while attempting to grow crystals of $Mo_2O_3Cl_4(DMF)_4$ a mixture of compounds was obtained. This mixture consisted of a brown microcrystalline precipitate of the starting product along with pale yellow crystals, corresponding to $Mo_2O_4Cl_2(DMF)_4$. Similar procedure with $Mo_2O_3Cl_4(bipy)_2$ yielded red crystals of $Mo_2O_4Cl_2(bipy)_2$, which crystallized as the dimethylformamide monosolvate. These compounds are presumably formed by hydrolysis of the parent $Mo_2O_3Cl_4(L)_4$ compounds with traces of water.

3.3. Molecular structure of dinuclear bis (μ-oxo)oxomolybdenum(V) chlorocomplexes

The molecular structure for $Mo_2O_4Cl_2(DMF)_4$ and $Mo_2O_4Cl_2(bipy)_2$ was determined from single-crystal X-ray diffraction analysis. The molecular structure of $Mo_2O_4Cl_2(DMF)_4$ (CC enantiomer) is shown in Fig. 1, and that of $Mo_2O_4Cl_2(bipy)_2$ (CC enantiomer) in Fig. 2. Selected bond lengths and angles are listed in Table 2.

The compounds are dinuclear species, with the two molybdenum atoms linked through two μ-oxo bridges and a Mo–Mo interaction. The geometry around each

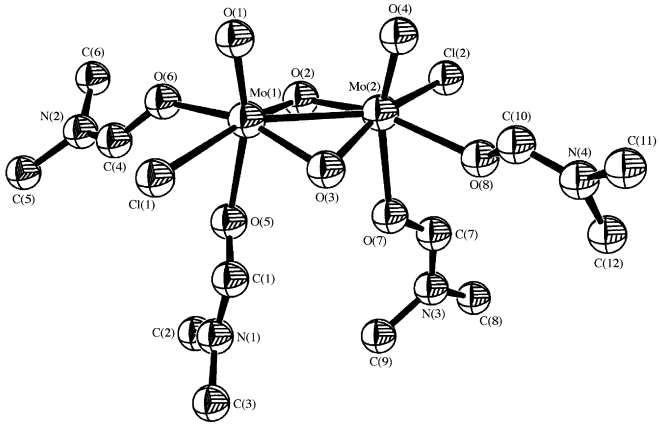


Fig. 1. Molecular structure and atom-labeling scheme for $Mo_2O_4Cl_2(DMF)_4$, CC enantiomer, with thermal ellipsoids at the 50% probability level; hydrogen atoms are omitted.

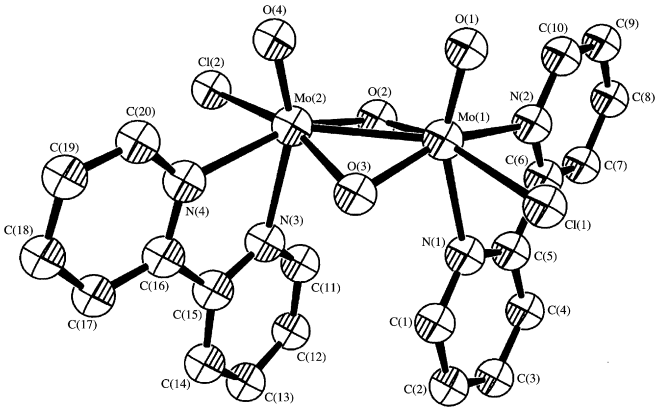


Fig. 2. Molecular structure and atom-labeling scheme for $Mo_2O_4Cl_2(Bipy)_2$, CC enantiomer, with thermal ellipsoids at the 50% probability level; hydrogen atoms are omitted.

molybdenum atom is best described as a distorted octahedron formed by an oxo terminal group *cis* with respect to the two oxo bridges, a chloride *cis vs.* the oxo terminal group and two *cis* positions for neutral ligands. Distortions from the theoretical octahedral geometry are explained in terms of interligand repulsions and Mo–Mo interaction.

Selected bond lengths and angles are listed in Table 2. The bond length for Mo(1)–Mo(2) is indicative of a Mo–Mo single bond resulting from a d^1–d^1 interaction, in good agreement with those previously reported (2.541–2.690 Å) [11,29]. All distances Mo=O are similar, considering the experimental error, and within the narrow range usually found for oxomolybdenum compounds (1.65–1.75 Å).

The strong interaction of the molybdenum atom with the terminal oxo ligand is shown by a pronounced *trans* influence with the Mo–(O or N) distances *trans* to the Mo=O, longer than the *cis* Mo–(O or N) distance.

The bond lengths for Mo–Cl are slightly different, shorter in the bipy derivative than in the DMF analogous. In the $Mo_2O_4Cl_2(DMF)_4$ complex the bond lengths for Mo–Cl (2.474 and 2.507 Å) are longer than in $MoO_2Cl_2(DMF)_2$ (2.341 Å) [30] probably due to the *trans* influence of the bridging oxygen atom in the dinuclear complex.

The molecular structure of $Mo_2O_4Cl_2(bipy)_2 \cdot DMF$ here reported, shows some differences with respect to the previously described $Mo_2O_4Cl_2(bipy)_2 \cdot CH_3NO_2$ [13]. In our compound the bond lengths Mo=O are slightly longer (1.69 Å) than those in the nitromethane solvate (1.60 Å) and the bond lengths Mo–N (2.22 and 2.32 Å) are markedly different. Also, in $Mo_2O_4Cl_2(bipy)_2 \cdot DMF$ the two pyridine rings are not coplanar, forming an angle of 12°.

It should be noted that in the crystal packing of $Mo_2O_4Cl_2(DMF)_4$ the unit cell contains two pairs of enantiomers. The crystal structure can be described as formed by the stacking of alternate planes, each of them formed by one of the enantiomers in the same relative orientation, linked only by Van der Waals forces.

Table 2
Selected bond lengths (Å) and angles (°) of complexes $Mo_2O_4Cl_2(DMF)_4$ and $Mo_2O_4Cl_2(Bipy)_2$

$Mo_2O_4Cl_2(DMF)_4$		$Mo_2O_4Cl_2(Bipy)_2$	
Bond lengths			
Mo(2)–Mo(1)	2.5517(7)	Mo(1)–Mo(2)	2.5649(3)
Mo(2)–O(4)	1.697(5)	Mo(1)–O(1)	1.690(2)
Mo(1)–O(1)	1.700(5)	Mo(2)–O(4)	1.697(2)
Mo(2)–O(3)	1.951(5)	Mo(1)–O(2)	1.957(2)
Mo(2)–O(2)	1.919(5)	Mo(1)–O(3)	1.923(2)
Mo(1)–O(3)	1.930(5)	Mo(2)–O(2)	1.925(2)
Mo(1)–O(2)	1.915(5)	Mo(2)–O(3)	1.953(2)
Mo(2)–Cl(2)	2.474(2)	Mo(1)–Cl(1)	2.4593(9)
Mo(1)–Cl(1)	2.507(2)	Mo(2)–Cl(2)	2.4739(8)
Mo(2)–O(7)	2.258(5)	Mo(1)–N(1)	2.330(2)
Mo(2)–O(8)	2.178(5)	Mo(1)–N(2)	2.233(3)
Mo(1)–O(5)	2.277(5)	Mo(2)–N(3)	2.325(3)
Mo(1)–O(6)	2.144(5)	Mo(2)–N(4)	2.222(3)
Bond angles			
Mo(2)–Mo(1)–O(1)	97.9(2)	Mo(1)–Mo(2)–O(4)	99.91(8)
Mo(1)–Mo(2)–O(4)	98.0(2)	Mo(2)–Mo(1)–O(1)	99.65(8)
Mo(2)–Mo(1)–Cl(1)	138.38(5)	Mo(1)–Mo(2)–Cl(2)	137.86(2)
Mo(1)–Mo(2)–Cl(2)	134.35(5)	Mo(2)–Mo(1)–Cl(1)	136.01(2)
O(1)–Mo(1)–Cl(1)	89.9(2)	O(4)–Mo(2)–Cl(2)	89.91(8)
O(4)–Mo(2)–Cl(2)	92.3(2)	O(1)–Mo(1)–Cl(1)	92.96(8)
O(1)–Mo(1)–O(3)	107.6(2)	O(4)–Mo(2)–O(2)	113.03(9)
O(1)–Mo(1)–O(2)	104.2(2)	O(4)–Mo(2)–O(3)	106.1(1)
O(4)–Mo(2)–O(2)	108.5(2)	O(1)–Mo(1)–O(3)	112.9(1)
O(4)–Mo(2)–O(3)	103.3(2)	O(1)–Mo(1)–O(2)	105.8(1)
O(1)–Mo(1)–O(6)	92.8(2)	O(4)–Mo(2)–N(4)	90.7(1)
O(4)–Mo(2)–O(8)	89.7(2)	O(1)–Mo(1)–N(2)	89.5(1)
O(1)–Mo(2)–O(5)	164.2(3)	O(4)–Mo(2)–N(3)	157.1(1)
O(4)–Mo(2)–O(7)	162.7(2)	O(1)–Mo(1)–N(1)	157.8(1)
O(6)–Mo(1)–O(3)	159.5(2)	N(4)–Mo(2)–O(2)	156.27(9)
O(8)–Mo(2)–O(2)	160.8(2)	N(2)–Mo(1)–O(3)	157.50(9)
O(2)–Mo(1)–Cl(1)	163.8(1)	O(3)–Mo(2)–Cl(2)	162.27(7)
O(3)–Mo(2)–Cl(2)	163.7(1)	O(2)–Mo(1)–Cl(1)	160.08(6)
O(3)–Mo(2)–O(2)	92.8(2)	O(2)–Mo(1)–O(3)	91.44(8)
O(3)–Mo(1)–O(2)	93.6(2)	O(2)–Mo(2)–O(3)	91.48(8)
O(5)–Mo(1)–O(6)	75.4(2)	N(3)–Mo(2)–N(4)	70.86(9)
O(7)–Mo(2)–O(8)	73.5(2)	N(1)–Mo(1)–N(2)	70.44(9)
O(4)–Mo(2)–Mo(1)–O(1)	5.68	O(1)–Mo(1)–Mo(2)–O(4)	9.55

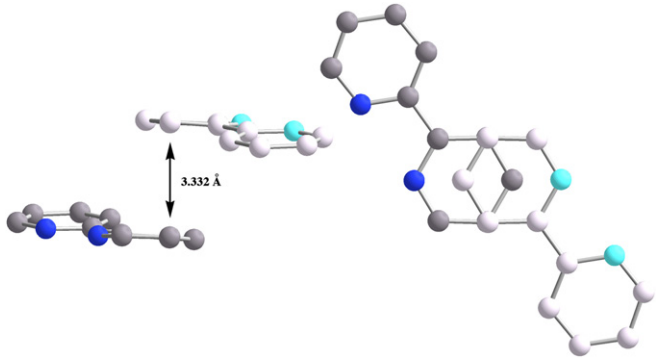


Fig. 3. Details of π–π stacking interactions in $[MoO_2Cl(Bipy)]_2$.

In the case of $Mo_2O_4Cl_2(bipy)_2 \cdot DMF$ the crystal is also racemic, but with opposite enantiomers related by a crystallographic inversion center. The crystal structure can be

Table 3
π–π Stacking interactions between pyridinic rings for $[MoO_2Cl(Bipy)]_2$

i	*j*	DC	ANG	DZ	DXY	DZ′	DXY′	DS	CC	CC′
1	2	3.54	0.75	3.36	1.34	3.31	1.32	3.58	21	21
Reported [33]		3.80		3.57	1.30	3.57	1.30		27	27

Ring 1: N(1)–C(1)–C(2)–C(3)–C(4)–C(5). Ring 2: N(1A)–C(1A)–C(2A)–C(3A)–C(4A)–C(5A). DC, distance between the centroids of the aromatic rings *i* and *j*; ANG, angle between the least-squares planes; DZ, distance between the centroid of *j* ring and the least-squares of *i* ring; ; DZ′, distance between the centroid of *i* ring and the least-squares of *j* ring; DXY, distance between the centroids of *i* and *j* projected onto the least-squares plane of *i*; DXY′, distance between the centroids of *j* and *i* projected onto the least-squares plane of *j*; DS, distance from the centroid of *j* to the nearest hydrogen atom of *i* ring; CC, the angle formed between the vector between the ring centroids and the ring normal to the least-squares plane of *j*; CC′, the angle formed between the vector between the ring centroids and the ring normal to the least-squares plane of *i*.

viewed as an alternating sequence of parallel planes, each of them formed by only one enantiomer. The arrangement into each plane is better described as formed by couples of molecules of the same enantiomer, twisted one with respect to the other, repeated along the plane to form the 2D structure. It is noteworthy that, the shortest C(2)···C(4A) and C(4)···C(2A) distances between the pyridine rings involving N(1) from two molecules of different enantiomers (3.332 Å), and the disposition of the planes of these two pyridine fragments (closely parallel, with an angle between the pyridinic ring planes of ca. 1°) suggest the existence of π–π stacking interactions between the aromatic rings. Also, the coordination of a metal center to the nitrogen heteroatom from pyridines and other heterocycles enhances the electron-withdrawing effect through its positive charge, so that the stability of the π–π interaction increases [31,32]. In addition, the stacking does not exhibits a perfect face-to-face alignment of the atoms, as shown in Fig. 3, but can be described as a slipped packing [33]. The results of the structural analysis shown in Table 3 are in good agreement with the presence of strong π–π stacking interactions [34,35], where both molecules from the couple are linked in this way (involving the N(1) pyridinic ring), one of them to another molecule in the upper plane whereas the other one is linked similarly to the lower plane.

Acknowledgement

J. Escribano thanks Junta de Castilla y León for a predoctoral fellowship. This work was supported by the Junta de Castilla y León (Grants BU033A06 and BU012A06).

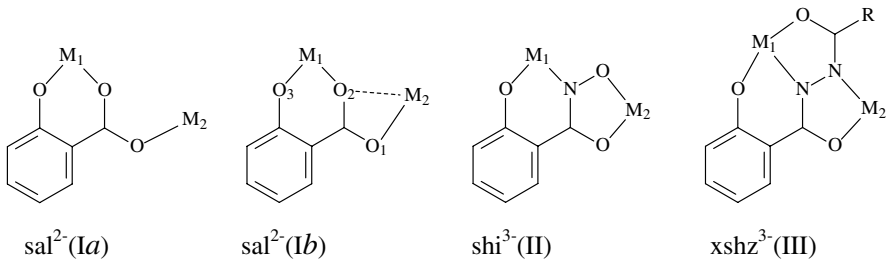
Appendix A. Supplementary material

CCDC 233642 and 233641 contain the supplementary crystallographic data for $[Mo_2O_4Cl_2(DMF)_4]$ and $[Mo_2O_4Cl_2(bipy)_2]$. These data can be obtained free of charge via http://www.ccdc.cam.ac.uk/conts/retrieving.html, or from the Cambridge Crystallographic Data Centre, 12 Union Road, Cambridge CB2 1EZ, UK; fax: (+44) 1223-336-033; or e-mail: deposit@ccdc.cam.ac.uk. Supplementary data associated with this article can be found, in the online version, at doi:10.1016/j.poly.2007.04.013.

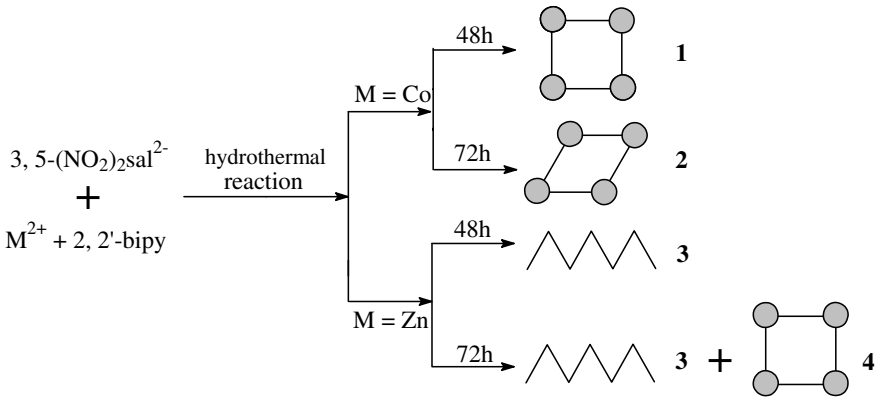
References

[1] C.D. Garner, J.M. Charnock, in: G. Wilkinson, R.D. Gillard, J.A. McCleverty (Eds.), Comprehensive Coordination Chemistry, vol. 3, Pergamon Press, Oxford, 1987, p. 1329 (Chapter 36.4).
[2] J.H. Enemark, C.G. Young, Adv. Inorg. Chem. 40 (1994) 2.
[3] N. Manwani, R. Ratnani, R.N. Prasad, J.E. Drake, M.B. Hurthouse, M.E. Light, Inorg. Chim. Acta 351 (2003) 49 (and references therein).
[4] J.A. Craig, E.W. Harlan, B.S. Snyder, M.A. Whitener, R.H. Holm, Inorg. Chem. 28 (1985) 2082.
[5] M.M. El-Essawi, F. Weller, K. Stahl, M. Kersting, Q. Dehnicke, Z. Anorg. Allg. Chem. 542 (1986) 175.
[6] F.A. Cotton, L.M. Daniels, S. Herrero, Acta Crystallogr., Sec. C: Cryst. Struct. Commun. 55 (1999) IUC9900018.
[7] K. Wieghardt, M. Guttmann, P. Chaudhuri, W. Gebert, M. Minelli, C.G. Young, J.H. Enemark, Inorg. Chem. 24 (1985) 3151.
[8] B. Zhuang, L. Zuang, L. He, Y. Yang, J. Lu, Inorg. Chim. Acta 145 (1988) 225.
[9] B. Modec, J.V. Brencic, J. Koller, Eur. J. Inorg. Chem. (2004) 1611.
[10] H. Lang, P.E. Fanwick, R.A. Walton, Inorg. Chim. Acta 328 (2002) 232.
[11] S. Takekuma, K. Tomoda, M. Sasaki, T. Minematsu, H. Takekuma, Bull. Chem. Soc. Jpn. 77 (2004) 1935.
[12] L. Xu, E. Wang, C. Hu, R. Huang, Transition Met. Chem. 26 (2001) 563.
[13] J. Beck, W. Hiller, E. Schweda, J. Strahle, Z. Naturforsch., B: Chem. Sci. 39 (1984) 1110.
[14] J.I. Dulebohn, T.C. Stamatakos, D.L. Ward, D.G. Nocera, Polyhedron 10 (1991) 2813.
[15] F.J. Arnáiz, R. Aguado, J. Sanz-Aparicio, M. Martínez-Ripoll, Polyhedron 13 (1994) 2745.
[16] F.J. Arnáiz, R. Aguado, J.M. Martínez-Ilarduya, Polyhedron 13 (1994) 3257.
[17] R. Sanz, R. Aguado, M.R. Pedrosa, F.J. Arnáiz, Synthesis (2002) 856.
[18] F.J. Arnáiz, R. Aguado, M.R. Pedrosa, J. Mahía, M.A. Maestro, Polyhedron 20 (2001) 2781.
[19] F.J. Arnáiz, R. Aguado, M.R. Pedrosa, J. Mahía, M.A. Maestro, Polyhedron 21 (2002) 1635.
[20] F.J. Arnáiz, R. Aguado, M.R. Pedrosa, A. De Cian, Inorg. Chim. Acta 347 (2003) 33.
[21] R. Pürschel, E. Lassner, R. Scharf, Zeitschr. Anal. Chem. 163 (1958) 104.
[22] B. Kamenar, M. Penavic, B. Korpar-Colig, B. Markovic, Inorg. Chim. Acta 65 (1982) L245.
[23] S.D. Perera, B.L. Shaw, M. Thornton-Pett, Inorg. Chim. Acta 234 (1995) 185.
[24] R. Sanz, J. Escribano, R. Aguado, M.R. Pedrosa, F.J. Arnáiz, Synthesis (2004) 1629.
[25] R. Sanz, J. Escribano, Y. Fernández, R. Aguado, M.R. Pedrosa, F.J. Arnáiz, Synlett (2005) 1389.
[26] R.H. Holm, Chem. Rev. 87 (1987) 1401.

[27] P.C.H. Mitchell, J. Inorg. Nucl. Chem. 25 (1963) 963.
[28] S. Brownstein, N.F. Han, E. Gabe, F. Lee, Can. J. Chem. 67 (1989) 551.
[29] D. Saurenz, F. Demirhan, P. Richard, R. Poli, H. Sitzmann, Eur. J. Inorg. Chem. (2002) 1415.
[30] L.R. Florian, E.R. Corey, Inorg. Chem. 7 (1968) 722.
[31] C.A. Hunter, J.K.M. Sanders, J. Am. Chem. Soc. 112 (1990) 5525.
[32] F. Cozzi, M. Cinquini, R. Annunziata, J.S. Siegel, J. Am. Chem. Soc. 115 (1993) 5330.
[33] C. Janiak, J. Chem. Soc., Dalton Trans. (2000) 3885.
[34] A. Albert, F.H. Cano, Cristalografía, publiciones CSIC, Madrid, 1995.
[35] I. Unamuno, J.M. Gutierrez-Zorrilla, A. Luque, P. Roman, L. Lezama, R. Calvo, T. Rojo, Inorg. Chem. 37 (1998) 6452.



Scheme 1. Binding models of sal^{2-} in complexes **1**–**4** and binding mode of shi^{3-} and $xshz^{3-}$ ligands.



Scheme 2. Formation pathways of complexes **1**–**4**.

to $xshz^{3-}$ (*N*-substituted salicylhydrazidate, H_3xshz) or shi^{3-} (substituted salicylhydroxamic acid, H_3shi) [1a,6,7]. There is a weak coordination between M2 and O2 in model I*b*. The alternation between the existence and the non-existence of weak coordination may lead to polymorphs.

As a continuation of our effort in the formation of metallamacrocycles, we attempted to explore the assembly of metallamacrocycles by hydrothermal reactions, using 3d-series metals M(II), 3,5-dinitrosalicylate (3,5-$(NO_2)_2$sal) and 2,2′-bipyridine (2,2′-bipy). Herein, we report the syntheses, crystal structures and properties of four Co/Zn 3,5-$(NO_2)_2$sal complexes. Among the four title compounds, the cyclic tetranuclear cobalt compounds **1** and **2** are polymorphic, and the zinc compounds **3** and **4** are polymorphic too. Complex **3** has a 1D chain structure while the complex **4** has a cyclic tetranuclear structure. Compounds **1** and **4** form an isomorphous pair. The title complexes **1**, **2** and **4** are the first examples of a 3,5-$(NO_2)_2$sal complex with a metallamacrocyclic structure. The formation pathway of the title compounds **1**–**4** is shown in Scheme 2. This research represents an interesting fact that different isomeric complexes can be obtained by a simple change of the reaction time.

2. Experimental

2.1. Materials and general procedures

All of the chemicals were obtained from commercial sources and were used without further purification. Elemental analyses were conducted on a Perkin-Elmer 2400 CHN elemental analyzer. Magnetic measurements were carried out in the "Servei de Magnetoquímica (Universitat de Barcelona)" on polycrystalline samples (30 mg) with a Quantum Design SQUID MPMS-XL magnetometer working in the 2–300 K range. The magnetic field was 0.1 T. The diamagnetic corrections were evaluated from Pascal's constants. Fluorescence spectroscopy was performed on a Perkin-Elmer LS 55 luminescence spectrometer.

2.2. Synthesis of complexes

2.2.1. Synthesis of $Co_4(2,2'\text{-bipy})_4\{3,5\text{-}(NO_2)_2sal\}_4$ (*1*)

A mixture of $Co(OAc)_2 \cdot 4H_2O$ (0.1 mmol), 2,2′-bipy (0.1 mmol), 3,5-dinitrosalicylic acid (0.2 mmol) and distilled water (10 ml), with the pH value adjusted to 7 by addition of 1 M NaOH solution, was put into a Teflon-lined autoclave (20 mL) and then heated at 180 °C for 48 h. Deep brown block-like crystals of **1** in 93% yield based on Co were obtained. *Anal.* Calc. for $C_{68}H_{40}N_{16}O_{28}Co_4$: C, 46.27; H, 2.2; N, 12.70. Found: C, 46.22; H, 2.25; N, 12.75%.

2.2.2. Synthesis of $Co_4(2,2'\text{-bipy})_4\{3,5\text{-}(NO_2)_2sal\}_4$ (*2*)

The same mixture as that for **1** was used, with the reaction at 180 °C for 72 h, resulting in deep brown block-like crystal of **2** in 92% yield based on Co. *Anal.* Calc. for $C_{68}H_{40}N_{16}O_{28}Co_4$: C, 46.27; H, 2.2; N, 12.70. Found: C, 46.19; H, 2.23; N, 12.76%.

*2.2.3. Synthesis of [Zn(2,2′-bipy){3,5-(NO_2)$_2$sal}]$_n$ (**3**)*

The same synthetic procedure as that for **1** was used except that $Co(OAc)_2 \cdot 4H_2O$ was replaced by $Zn(NO_3)_2 \cdot 6H_2O$, giving yellow block-like crystals of **3** in 92% yield based on Zn. *Anal*. Calc. for $C_{17}H_{10}N_4O_7Zn$: C, 45.61; H, 2.25; N, 12.52. Found: C, 45.55; H, 2.30; N, 12.54%.

*2.2.4. Synthesis of Zn$_4$(2,2′-bipy)$_4${3,5-(NO_2)$_2$sal}$_4$ (**4**)*

The same mixture as that for **3** was used, with the reaction at 180 °C for 72 h, resulting in **3** in about 70% yield and light yellow block-like crystals of **4** in about 15% yield based on Zn. *Anal*. Calc. for $C_{68}H_{40}N_{16}O_{28}Zn_4$: C, 45.61; H, 2.25; N, 12.52. Found: C, 45.52; H, 2.26; N, 12.48%.

2.3. X-ray crystallography

X-ray diffraction measurements were carried out at 293 K with graphite monochromated Mo Kα radiation ($\lambda = 0.71073$ Å) on a Bruker SMART CCD 1000 diffractometer for **2** and on a Rigaku R-AXIS RAPID Weissenberg IP diffractometer for **1**, **3** and **4**. The structures were solved by direct methods (SHELXTL-97) and refined on F^2 by full-matrix least-squares techniques. The high values of the thermal parameters of the oxygen atoms of the NO_2 groups in complexes **1**, **2** and **4** suggest disordered positions of these oxygen atoms. Therefore, these oxygen atoms are in disordered positions and were refined isotropically. The crystallographic data for **1**–**4** are summarized in Table 1.

3. Results and discussion

3.1. Structural description

As illustrated in Fig. 1, the centrosymmetrical molecular square structure of **1** is built up of four cobalt(II) cations (Co1, Co2, Co1A and Co2A, symmetry code A, $-x+1$, $-y$, $-z+1$), four bridging 3,5-(NO_2)$_2$sal ligands and four 2,2′-bipy ligands. Selected bond lengths and angles are listed in Table 2.

Each Co^{II} ion is pentacoordinated by three oxygen atoms from two 3,5-(NO_2)$_2$sal ligands and two nitrogen atoms from a 2,2′-bipy ligand. The Co1 atom has a distorted square-pyramidal geometry with a τ value of 0.03 [8]. However, the coordination sphere of Co2 is between square-pyramidal and the trigonal bipyramidal, with a τ value of 0.40. When the Co1–O9 and Co2–O2A distances (2.504(1) Å and 2.705(4) Å) are considered as weak coordination, the Co1 and Co2 centers may be regarded as having distorted octahedral conformations.

Every one of the four 3,5-(NO_2)$_2$sal ligands exhibits a bichelating coordination mode (Scheme 1(I*b*)). Therefore, neighboring cobalt atoms are connected by one 3,5-

Table 1
Crystallographic data for complexes **1**–**4**

Compound	**1**	**2**	**3**	**4**
Formula	$C_{68}H_{40}N_{16}O_{28}Co_4$	$C_{68}H_{40}N_{16}O_{28}Co_4$	$C_{17}H_{10}N_4O_7Zn$	$C_{68}H_{40}N_{16}O_{28}Zn_4$
Formula weight	1764.88	1764.88	447.66	1790.64
Crystal system	monoclinic	monoclinic	monoclinic	monoclinic
Space group	$P2_1/c$	$P2_1/c$	$P2_1/c$	$P2_1/c$
a (Å)	13.015(3)	14.715(2)	12.411(5)	12.2799(1)
b (Å)	12.842(3)	21.907(3)	16.008(5)	13.5024(3)
c (Å)	21.541(6)	21.593(3)	8.721(3)	22.1376(6)
α (°)	90	90	90	90
β (°)	103.235(9)	94.865(2)	93.84(2)	102.282(2)
γ (°)	90	90	90	90
V (Å^3)	3505(2)	6936(1)	1729.8(1)	3586.6(1)
Z	2	4	4	2
D_{calc} (g/cm^{-3})	1.672	1.690	1.473	1.658
T (K)	293(2)	293(2)	293(2)	293(2)
μ (mm^{-1})	1.031	1.042	1.473	1.420
F(000)	1784	3568	904	1808
$\theta_{minimum}$, $\theta_{maximum}$(°)	3.17, 27.47	1.86, 25.00	3.03, 27.47	1.70, 27.48
$h_{minimum–maximum}$	−15 → 16	−17 → 17	−16 → 16	0 → 15
$k_{minimum–maximum}$	−16 → 16	−26 → 25	−20 → 20	0 → 17
$l_{minimum–maximum}$	−27 → 27	−24 → 25	−10 → 11	−28 → 28
R_{int}	0.0359	0.0538	0.0235	0.0538
Number of unique data	7979	11595	3954	8200
Number of observed	5784	6468	3448	4145
Number of variables	517	1041	262	515
R_1 [$I > 2\sigma(I)$]	0.0550	0.0439	0.0258	0.0565
wR_2 [$I > 2\sigma(I)$]	0.1516	0.1054	0.0666	0.1441
Goodness-of-fit	1.063	0.944	1.032	0.949
$(\Delta\rho)_{maximum,minimum}$ (e/Å^3)	0.792 (−0.638)	0.690 (−0.432)	0.316 (−0.238)	0.674 (−0.570)
$(\Delta/\sigma)_{maximum}$, $(\Delta/\sigma)_{minimum}$	0.001, 0.000	0.001, 0.000	0.000, 0.000	0.001, 0.000

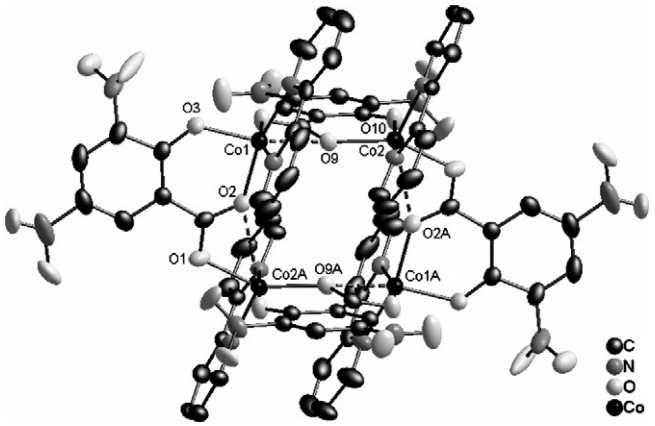


Fig. 1. Molecular structure of complex **1** with 30% probability ellipsoids, hydrogen atoms are omitted for clarity. Symmetry code A, $-x+1$, $-y$, $-z+1$. Only one orientation of the disordered NO_2 groups is presented.

Table 2
Selected bond lengths (Å) and angles (°) for complexes **1** and **4**[a]

Complex **1**		Complex **4**	
Co(1)–O(2)	2.026(3)	Zn(1)–O(2)	2.041(3)
Co(1)–O(3)	1.995(3)	Zn(1)–O(3)	1.979(3)
Co(1)–O(8)	2.078(3)	Zn(1)–O(8)	2.003(3)
Co(1)–N(3)	2.115(3)	Zn(1)–N(4)	2.154(4)
Co(1)–N(4)	2.116(3)	Zn(1)–N(3)	2.095(4)
Co(2)–O(9)	2.027(2)	Zn(2)–O(9)	2.013(3)
Co(2)–O(10)	1.978(3)	Zn(2)–O(10)	2.016(4)
Co(2)–O(1A)	2.010(3)	Zn(2)–O(1A)	2.025(4)
Co(2)–N(7)	2.108(3)	Zn(2)–N(7)	2.153(5)
Co(2)–N(8)	2.064(3)	Zn(2)–N(8)	2.072(4)
O(3)–Co(1)–O(2)	90.6(1)	O(3)–Zn(1)–O(2)	90.1(1)
O(3)–Co(1)–O(8)	96.2(1)	O(3)–Zn(1)–O(8)	105.9(2)
O(2)–Co(1)–O(8)	91.4(1)	O(2)–Zn(1)–O(8)	95.2(1)
O(3)–Co(1)–N(3)	97.5(1)	O(3)–Zn(1)–N(3)	112.6(2)
O(2)–Co(1)–N(3)	92.2(1)	O(2)–Zn(1)–N(3)	92.2(2)
O(8)–Co(1)–N(3)	165.8(1)	O(8)–Zn(1)–N(3)	140.8(2)
O(3)–Co(1)–N(4)	102.0(1)	O(3)–Zn(1)–N(4)	97.2(2)
O(2)–Co(1)–N(4)	164.0(1)	O(2)–Zn(1)–N(4)	169.0(2)
O(8)–Co(1)–N(4)	97.0(1)	O(8)–Zn(1)–N(4)	90.8(2)
N(3)–Co(1)–N(4)	76.5(1)	N(3)–Zn(1)–N(4)	77.4(2)
O(9)–Co(2)–O(10)	88.5(1)	O(9)–Zn(2)–O(10)	87.8(1)
O(9)–Co(2)–O(1A)	151.4(1)	O(9)–Zn(2)–O(1A)	144.0(2)
O(10)–Co(2)–O(1A)	91.7(1)	O(10)–Zn(2)–O(1A)	90.9(2)
O(9)–Co(2)–N(7)	90.7(1)	O(9)–Zn(2)–N(7)	92.9(2)
O(10)–Co(2)–N(7)	175. 4(1)	O(10)–Zn(2)–N(7)	173.5(2)
O(1)A–Co(2)–N(7)	91.2(1)	O(1)A–Zn(2)–N(7)	92.3(2)
O(9)–Co(2)–N(8)	115.9(1)	O(9)–Zn(2)–N(8)	118.8(2)
O(10)–Co(2)–N(8)	98.5(1)	O(10)–Zn(2)–N(8)	96.5(2)
O(1)A–Co(2)–N(8)	92.4(1)	O(1)A–Zn(2)–N(8)	97.0(2)
N(7)–Co(2)–N(8)	77.8(1)	N(7)–Zn(2)–N(8)	77.6(2)

[a] Symmetry code: A, $-x+1$, $-y$, $-z+1$.

$(NO_2)_2$sal ligand through the bridging oxygen atoms (O9, O2A, O9A and O2), generating a Co_4O_4 core of the molecular square. The four Co^{II} ions in the core are exactly coplanar. The Co…Co distances in the core are 4.319(2) and 4.617(9) Å along the side and 6.594(19) and 6.038(1) Å across the diagonal. The angles Co2–Co1–Co2A and Co1–Co2–Co1A in the core are 84.95(1)° and 95.05(1)°, respectively, indicating a slight deviations from an ideal square geometry.

Adjacent tetranuclear metallamacrocycles are further connected to each other by C–H…O hydrogen bonds [9] between the C–H group of the 2,2′-bipy ligand and the oxygen atom in the NO_2 groups of the 3,5-$(NO_2)_2$sal ligand, resulting in an extended 3D network structure (Fig. S1). The H…O distances are in the range of 2.43–2.53 Å. Detailed data are given in Table S1.

On comparison with the many substituted salicylhydroxamic acid and *N*-substituted salicylhydrazidate complexes, only a few 3,5-$(NO_2)_2$sal complexes have been found [10]. There are two types of structure for the known five 3,5-$(NO_2)_2$sal complexes, i.e. a 1D structure for $[Co^{II}(phen)\{3,5\text{-}(NO_2)_2sal^{2-}\}]$ [10b] and $[Mn(phen)\{3,5\text{-}(NO_2)_2sal^{2-}\}]$ [10c] and a discrete multinuclear structure for the other three complexes. To our knowledge, the title complexes **1**, **2** and **4** are the first examples of any 3,5-$(NO_2)_2$sal complex with a metallamacrocycle structure.

The molecular structure of complex **2** is shown in Fig. 2. Selected bond lengths and angles are listed in Table 3. The cyclic tetranuclear complex molecule Co_4(2,2′-bipy)$_4$-$\{3,5\text{-}(NO_2)_2sal\}_4$ (**2**) contains four cobalt(II) cations (Co1, Co2, Co3 and Co4), four 3,5-$(NO_2)_2$sal ligands and four 2,2′-bipy ligands. Two of the four 3,5-$(NO_2)_2$sal ligands bridge two neighboring $[Co(2,2'\text{-bipy})]^{2+}$ corners through one bridging carboxylate oxygen atom (O2 or O16). For the other two 3,5-$(NO_2)_2$sal ligands, each one bridges two neighboring $[Co(2,2'\text{-bipy})]^{2+}$ corners through two oxygen atoms (O8 and O9 or O22 and O23) in the carboxylate group. Therefore, four cobalt cations and four 3,5-$(NO_2)_2$sal ligands construct a molecular rhomboid structure with a $Co_4O_6C_2$ core. The molecular rhomboid structure in **2** is different from the molecular square structure in **1**. The four neighboring Co…Co distances in the $Co_4O_6C_2$ core are 5.116(1), 4.247(1), 5.209(2) and 4.370(1) Å. The Co–Co–Co angles in the core are 101.10(1)°, 79.83(1)°, 101.35(1)° and 77.71(1)°.

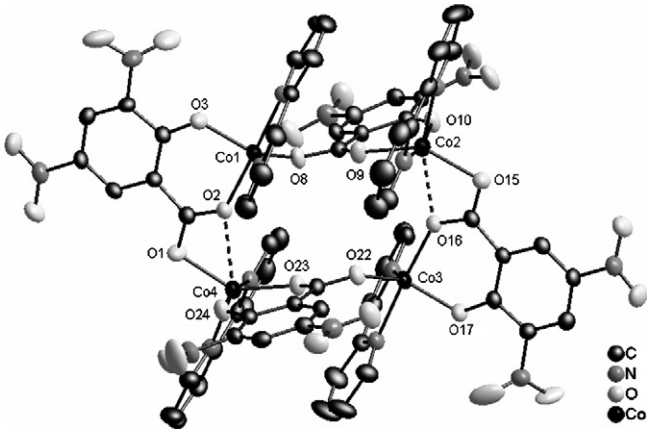


Fig. 2. Molecular structure of complex **2** with 30% probability ellipsoids, hydrogen atoms are omitted for clarity. Only one orientation of the disordered NO_2 groups is presented.

Table 3
Selected bond lengths (Å) and angles (°) for **2**

Co(1)–O(8)	1.968(3)	Co(3)–O(17)	1.971(3)
Co(1)–O(3)	1.970(3)	Co(3)–O(22)	1.986(3)
Co(1)–O(2)	2.036(3)	Co(3)–O(16)	2.024(3)
Co(1)–N(3)	2.056(3)	Co(3)–N(11)	2.067(3)
Co(1)–N(4)	2.127(3)	Co(3)–N(12)	2.107(3)
Co(2)–O(10)	1.975(3)	Co(4)–O(24)	1.974(3)
Co(2)–O(9)	2.001(3)	Co(4)–O(23)	1.995(3)
Co(2)–N(8)	2.092(3)	Co(4)–O(1)	2.061(3)
Co(2)–O(15)	2.098(3)	Co(4)–N(16)	2.087(3)
Co(2)–N(7)	2.114(3)	Co(4)–N(15)	2.103(3)
O(8)–Co(1)–O(3)	119.2(1)	O(10)–Co(2)–O(9)	88.8(1)
O(8)–Co(1)–O(2)	91.8(1)	O(10)–Co(2)–N(8)	93.9(1)
O(3)–Co(1)–O(2)	89.4(1)	O(9)–Co(2)–N(8)	110.5(1)
O(8)–Co(1)–N(3)	129.6(1)	O(10)–Co(2)–O(15)	102.4(1)
O(3)–Co(1)–N(3)	110.0(1)	O(9)–Co(2)–O(15)	146.5(1)
O(2)–Co(1)–N(3)	99.5(1)	N(8)–Co(2)–O(15)	100.3(1)
O(8)–Co(1)–N(4)	91.8(1)	O(10)–Co(2)–N(7)	167.0(1)
O(3)–Co(1)–N(4)	89.7(1)	O(9)–Co(2)–N(7)	86.3(1)
O(2)–Co(1)–N(4)	176.3(1)	N(8)–Co(2)–N(7)	76.6(1)
N(3)–Co(1)–N(4)	77.5(1)	O(15)–Co(2)–N(7)	88.2(1)
O(17)–Co(3)–O(22)	123.5(1)	O(24)–Co(4)–N(15)	168.3(1)
O(17)–Co(3)–O(16)	89.6(1)	O(23)–Co(4)–N(15)	86.8(1)
O(22)–Co(3)–O(16)	93.3(1)	O(1)–Co(4)–N(15)	89.3(1)
O(17)–Co(3)–N(11)	111.2(1)	N(16)–Co(4)–N(15)	77.4(1)
O(22)–Co(3)–N(11)	122.4(1)	O(24)–Co(4)–O(23)	89.8(1)
O(16)–Co(3)–N(11)	104.5(1)	O(24)–Co(4)–O(1)	100.0 (1)
O(17)–Co(3)–N(12)	87.1(1)	O(23)–Co(4)–O(1)	143.7(1)
O(22)–Co(3)–N(12)	87.9(1)	O(24)–Co(4)–N(16)	94.4(1)
O(16)–Co(3)–N(12)	176.7(1)	O(23)–Co(4)–N(16)	117.4(1)
N(11)–Co(3)–N(12)	77.4(1)	O(1)–Co(4)–N(16)	96.8(1)

There are two kinds of coordination modes for the four 3,5-$(NO_2)_2$sal ligands in complex **2**; the two of four ligands act in the monochelating-bridging mode (Scheme 1a), and the other two act in the bichelating mode (Scheme 1b), to give the $Co_4O_6C_2$ core of the molecular rhomboid.

The coordination geometry of two cobalt atoms, Co1 and Co3, is distorted trigonal bipyramidal, with τ values of 0.78 and 0.90, respectively. However, the coordination geometry of Co2 and Co4 can be described as a distorted octahedron because of the weak coordination (Co2–O16 = 2.431(3) Å, Co4–O2 = 2.518(3) Å).

There are some intermolecular C–H...O hydrogen bonds which form an extended 3D structure (Fig. S2). The H...O distances are in the range 2.396–2.523 Å (Table S1).

The 1D chain structure of complex **3** is given in Fig. 3. Selected bond lengths and angles are illustrated in Table 4. Each Zn^{II} ion is pentacoordinated by three oxygen atoms of two 3,5-$(NO_2)_2$sal ligands and two nitrogen atoms of a 2,2′-bipy ligand. The coordination sphere is between square-pyramidal and trigonal bipyramidal, with a τ value of 0.32. Each 3,5-$(NO_2)_2$sal ligand adopts a monochelating-bridging mode (Scheme 1(I*a*)) and links two Zn^{II} ions into a 1D chain structure along the *c* axis. The chain core is with a $[–Zn–O–C–O–]_n$ repeat. The neighboring Zn1...Zn1A distance (Symmetry code: A x, $-y+1/2$, $z-1/2$) is 5.132(1) Å, and the Zn–Zn–Zn angle is 116.35(1)°. The 1D chains are further connected by C–H...O hydrogen bonds, resulting in a 3D supramolecular network structure (Fig. S3). The H...O distances are in the range 2.602–2.670 Å (Table S1).

The zinc compound **4** and the cobalt compound **1** are isomorphous. The centrosymmetrical molecular square structure in **4** (Fig. S4) is the same as that in **1**. Selected bond lengths and angles of complex **4** are listed in Table 2. In compound **4**, each one of four bridging oxygen atoms (O2, O9, O2A and O9A, symmetry code A, $-x+1$, $-y$, $-z+1$) of the carboxylate groups from four 3,5-$(NO_2)_2$sal ligands bridges two zinc(II) cations to form an Zn_4O_4 core in the molecular square structure. The Zn...Zn distances in **4** are 4.746(4) and 4.663(2) Å along the side and 6.558(4) and 6.747(1) Å across the diagonal. The vertex angles for Zn2–Zn1–Zn2A and Zn1–Zn2–Zn1A are 91.63(1)° and 88.37(1)°, respectively. It indicates a quite ideal square geometry.

The coordination geometry for the four zinc(II) cations in **4** is between square-pyramidal and the trigonal bipyramidal, the τ values of the Zn1 and Zn2 polyhedra being 0.47 and 0.49, respectively. The Zn1–O9 distance is 2.881(4) Å, and the Zn2–O2A distance is 2.744(4) Å. When Zn1–O9 and Zn2–O2A are considered as weakly coordi-

Table 4
Selected bond lengths (Å) and angles (°) for **3**[a]

Zn(1)–O(1)A	1.983(1)	Zn(1)–N(4)	2.086(2)
Zn(1)–O(3)	1.994(1)	Zn(1)–N(3)	2.107(1)
Zn(1)–O(2)	2.019(1)	O(2)–Zn(1)–N(4)	91.29(5)
O(1)A1–Zn(1)–O(3)	93.72(6)	O(3)–Zn(1)–N(3)	92.16(5)
O(1)A1–Zn(1)–O(2)	93.92(5)	O(2)–Zn(1)–N(3)	163.17(5)
O(3)–Zn(1)–O(2)	88.87(5)	N(4)–Zn(1)–N(3)	78.03(5)
O(1)A–Zn(1)–N(4)	122.34(5)	O(1)A–Zn(1)–N(3)	102.77(5)
O(3)–Zn(1)–N(4)	143.82(5)		

[a] Symmetry code: A, x, $-y+1/2$, $z-1/2$.

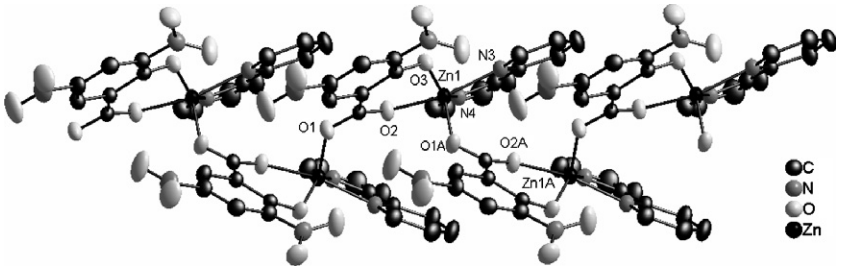


Fig. 3. 1D chain of complex **3** with 30% probability ellipsoids. Symmetry code A, x, $-y+1/2$, $z-1/2$.

nating, the coordination geometries of the Zn^{II} ions can be described as distorted octahedra. Each 3,5-$(NO_2)_2$sal ligand exhibits a bichelating coordination mode (Scheme 1 I*b*).

The C–H...O hydrogen bonds in complex **4** (Table S1) bridge the adjacent tetranuclear metallamacrocycles to create an extended 3D network structure (Fig. S5).

3.2. Weak coordination interactions and coordination orientations

There exist weak coordination interactions M2...O2 between the O,O′,O″-tridentate ligand 3,5-$(NO_2)_2$sal and the metal cation (I*b* in Scheme 1) in compounds **1**, **2** and **4**. As shown in Table 5, the absolute value of the torsion angles O2–C–O1–M2 are between 0.2° and 8.7°, and the C–O1–M2 bridging angles are in the range 100.2–115.5°. When there are no weak coordination interactions of M2...O2 (I*a* in Scheme 1), the torsion angles O2–C–O1–M2 in **2** and **3** are between 26.7° and 33.4°, and the C–O1–M2 bridging angles are in the range 125.6-128.1°. The strength of the weak coordination interactions among the four title compounds is of the following order: **1**, **4** > **2** > **3**. Coincidentally, compounds **1** and **4** have the molecular square structure, compound **2** has the molecular rhomboid structure while compound **3** has the chain structure. This suggests that the weak coordination interactions have significant influence on the space orientations of the 3,5-$(NO_2)_2$sal ligand, and may affect the crystallization processes and solid state architectures.

3.3. Magnetism

The temperature dependences of $\chi_M T$ (χ_M being the magnetic susceptibility for four Co^{II}ions) in complexes **1** and **2** are shown in Figs. 4 and 5 (from 300 K to 2 K), respectively. $\chi_M T$ at 300 K in **1** and **2** is close to 9 and 10.5 $cm^3\,mol^{-1}\,K$, respectively, and these values are as expected for four isolated pentacoordinated Co^{II} ions. $\chi_M T$ in **1** monotonously decreases to reach 0.2 $cm^3\,mol^{-1}\,K$ at 2.00 K. $\chi_M T$ in **2** monotonously decreases to reach 1.0 $cm^3\,mol^{-1}\,K$ at 2.00 K. The shape of these curves for complexes **1** and **2** is characteristic of the occurrence of weak antiferromagnetic interactions between the Co^{II} centres. The antiferromagnetic behaviour in the two complexes is corroborated by plotting the reduced magnetization (M/Nβ) versus H at 2 K. In both cases the shape of the curve is typical for an antiferromagnetic coupling, not very strong, and the values at 5 T are close to 4 Nβ instead of 12 (the theoretical values assuming $g = 2.00$ for four Co^{II} ions fully isolated). The pentacoordinated Co^{II} ion does not present spin–orbit coupling, such as occurs with the octahedral analogues. Thus, they can be treated as systems with $S = 3/2$ with the spin-hamiltonian formalism. Taking into account the tetranuclear character of **1** and **2** we have done the fit assuming two different J values (alternated) by means of the CLUMAG program [11]. The best fit is given by the exchange parameters $J_1 = -0.41\ cm^{-1}$, $J_2 = -0.33\ cm^{-1}$ and $g = 2.21$ for **1** and $J_1 = -0.36\ cm^{-1}$, $J_2 = -0.23\ cm^{-1}$ and $g = 2.30$ for **2**. The two set of values are similar, it being interesting to emphasize that for complex **1** the two J values are more similar, which agrees with

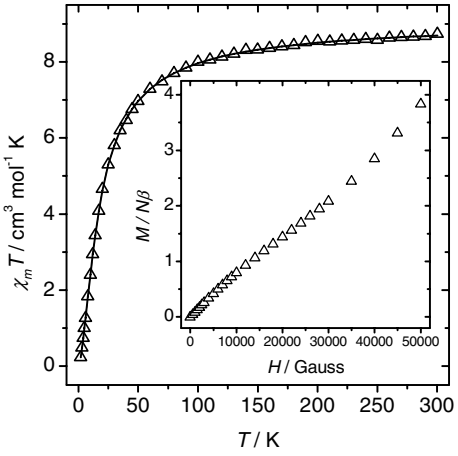


Fig. 4. Plot of $\chi_M T$ vs. T for complex **1**. The solid line represents the best fit. Inset: plot of the reduced magnetization (M/Nβ) at 2 K.

Table 5
A comparison between weak coordination, torsion angles and bridging angles in complexes **1**–**4**

Complex	M2[a]	M2...O2 distance (Å)	Weak coordination	O2–C–O1–M2 torsion angle (°)	C–O1–M2 bridging angle (°)	Structure type
1	Co1	2.50(1)	yes	–0.2(4)	103.2(2)	molecular square
	Co2	2.705(4)	yes	8.7(4)	110.0(2)	
2	Co1	3.170(3)	no	26.7(5)	125.6(3)	molecular rhomboid
	Co2	2.431(3)	yes	4.8(4)	100.2(2)	
	Co3	3.251(3)	no	−31.7(5)	127.8(3)	
	Co4	2.518(3)	yes	−2.5(4)	103.2(3)	
3	Zn1	3.280(2)	no	−33.4(2)	128.1(1)	1D chain
4	Zn1	2.881(4)	yes	8.7(6)	115.5(3)	molecular square
	Zn2	2.744(4)	yes	−1.6(6)	111.0(3)	

[a] The symbols M2, O2, C, and O1 are the same as those in Scheme 1(I*b*).

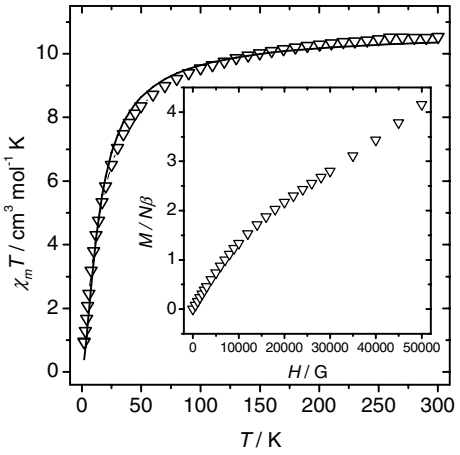


Fig. 5. Plot of $\chi_M T$ vs. T for complex **2**. The solid line represents the best fit. Inset: plot of the reduced magnetization (M/Nβ) at 2 K.

a structure that it is more square-like in **1** and more rhomboid-like in **2**. The small J values are due, in both cases, to the magnetic pathway created by the carboxylate bridging groups in a *syn–anti* configuration. The small overlap between the magnetic orbitals accounts for the weak coupling observed. This qualitative approach was already introduced by Kahn when studying this kind of *syn–anti* coordination mode [12].

3.4. Photoluminescence

The emission spectra of complex **3** and the free 3,5-$(NO_2)_2$sal ligand in the solid state at room temperature have been investigated. Complex **3** exhibits blue fluorescent emission bands at ca. 485 nm upon excitation at ca. 360 nm (Fig. S6). These emissions are assigned to the intraligand fluorescent emission because similar emissions are observed for the free 3,5-$(NO_2)_2$sal (Fig. S7) [13].

4. Conclusion

In summary, three cyclic tetranuclear complexes and one 1D chain structure complex have been prepared by the hydrothermal reactions of $Co(OAc)_2 \cdot 4H_2O$/$Zn(NO_3)_2 \cdot 6H_2O$, 3,5-$(NO_2)_2$sal and 2,2′-bipy with different reaction times. The cobalt complexes **1** and **2** constitute a pair of polymorphs. There is a molecular square structure with a Co_4O_4 core in **1** and a molecular rhomboid structure with a $Co_4O_6C_2$ core in **2**. The zinc complexes **3** and **4** constitute a pair of polymorphs too. There is a 1D structure in **3** and a molecular square structure in **4**. Our results demonstrate an interesting fact that polymorphic compounds with different structure types can be obtained by a simple change of the reaction time. Compounds **1** and **4** form an isomorphous pair.

The weak coordination interactions have a significant influence on the space orientations of the 3,5-$(NO_2)_2$sal ligand. There are antiferromagnetic interactions in the cyclic tetranuclear pentacoordinated cobalt(II) complexes **1** and **2**.

Acknowledgements

This project was financially supported by the Natural Science Foundation of China (Nos. 20431010 and 20171012), the Natural Science Foundation of Fujian Province, China (E0110010), and the Spanish Government (Grant BQU2003/00539).

Appendix A. Supplementary material

CCDC 617368, 617369, 617370 and 617371 contain the supplementary crystallographic data for **1**, **2**, **3** and **4**. These data can be obtained free of charge via http://www.ccdc.cam.ac.uk/conts/retrieving.html, or from the Cambridge Crystallographic Data Centre, 12 Union Road, Cambridge CB2 1EZ, UK; fax: (+44) 1223-336-033; or e-mail: deposit@ccdc.cam.ac.uk. Supplementary data associated with this article can be found, in the online version, at doi:10.1016/j.poly.2007.04.028.

References

[1] (a) V.L. Pecoraro, A.J. Stemmler, B.R. Gibney, J.J. Bodwin, H. Wang, J.W. Kampf, A. Barwinski, in: K.D. Karlin (Ed.), Prog. Inorg. Chem, vol. 45, Wiley, New York, 1997, p. 83;
(b) J.A.R. Navarro, B. Lippert, Coord. Chem. Rev. 185–186 (1999) 653;
(c) S. Leininger, B. Olenyuk, P.J. Stang, Chem. Rev. 100 (2000) 853;
(d) F.A. Cotton, C. Lin, C.A. Murillo, Acc. Chem. Res. 34 (2001) 759;
(e) P.H. Dinolfo, J.T. Hupp, Chem. Mater 13 (2001) 3113;
(f) F. Würthner, C.-C. You, C.R. Saha-Möller, Chem. Soc. Rev. 33 (2004) 133;
(g) C.H.M. Amijs, G.P.M. van Klink, G. van Koten, J. Chem Soc. Dalton Trans. (2006) 308.

[2] (a) M.S. Lah, V.L. Pecoraro, J. Am. Chem. Soc. 111 (1989) 7258;
(b) R.-D. Schnebeck, E. Fresisinger, B. Lippert, J. Am. Chem. Soc. 122 (2000) 1381;
(c) D.S. Cati, J. Ribas, J.R. Ariño, H.S. Evans, Inorg. Chem. 43 (2004) 1021;
(d) P.S. Mukherjee, K.S. Min, A.M. Arif, P.J. Stang, Inorg. Chem. 43 (2004) 6345;
(e) Z. He, C. He, Z.-M. Wang, E.-Q. Gao, Y. Liu, C.-H. Yan, J. Chem Soc., Dalton Trans. (2004) 502;
(f) M.A. Galindo, J.A.R. Navarro, M.A. Romero, M. Quirós, J. Chem Soc., Dalton Trans. (2004) 1563;
(g) Y. Wang, M. Odoko, N. Okabe, Acta Crystallogr., Sect. C 60 (2004) m479;
(h) J.-P. Zhang, Y.-Y. Lin, X.-C. Huang, X.-M. Chen, Chem. Commun. (2005) 1258;
(i) F.A. Cotton, C.-Y. Liu, C.A. Murillo, X.-P. Wang, Inorg. Chem. 45 (2006) 2619.

[3] (a) B. Moulton, M.J. Zaworotko, Chem. Rev. 101 (2001) 1629;
(b) D. Braga, F. Grepioni, Chem. Commun (2005) 3635;
(c) J.-P. Zhang, X.-M. Chen, Chem. Commun. (2006) 1689;
(d) T.L. Hennigar, D.C. MacQuarrie, P. Losier, R.D. Rogers, M.J. Zaworotko, Angew. Chem., Int. Ed. Engl. 36 (1997) 972;
(e) S. Masaoka, D. Tanaka, Y. Nakanishi, S. Kitagawa, Angew. Chem., Int. Ed. 43 (2004) 2530.

[4] (a) E. Lozano, M. Nieuwenhuyzen, S.L. James, Chem. Eur. J. 7 (2001) 2644;
(b) H. Abourahma, B. Moulton, V. Kravtsov, M.J. Zaworotko, J. Am. Chem. Soc. 124 (2002) 9990;
(c) M.C. Brandys, R.J. Puddephatt, J. Am. Chem. Soc. 124 (2002) 3946;
(d) Z.-Q. Qin, M.C. Jennings, R.J. Puddephatt, Chem. Eur. J. 8 (2002) 735;
(e) C.-Y. Su, A.M. Goforth, M.D. Smith, H.-C. zur Loye, Inorg. Chem. 42 (2003) 5685;
(f) X.-C. Huang, J.-P. Zhang, X.-M. Chen, J. Am. Chem. Soc. 126 (2004) 13218;
(g) L. Jiang, T.-B. Lu, X.-L. Feng, Inorg. Chem. 44 (2005) 7056.

[5] (a) B. Zhao, X.-Y. Chen, P. Cheng, D.-Z. Liao, S.-P. Yan, Z.-H. Jiang, J. Am. Chem. Soc. 126 (2004) 15394;
(b) C.-F. Wang, E.-Q. Gao, Z. He, C.-H. Yan, Chem. Commun. (2004) 720;
(c) F.E. Jacobsen, S.M. Cohen, Inorg. Chem. 43 (2004) 3038;
(d) J.H. Thurston, A. Kumar, C. Hofmann, K.H. Whitmire, Inorg. Chem. 43 (2004) 8427;
(e) J. Lu, J.-H. Yu, X.-Y. Chen, P. Cheng, X. Zhang, J.-Q. Xu, Inorg. Chem. 44 (2005) 5978;
(f) N. L Rosi, J. Kim, M. Eddaoudi, B. Chen, M. O'Keeffe, O.M. Yaghi, J. Am. Chem. Soc. 127 (2005) 1504;
(g) X.-J. Li, X.-Y. Wang, S. Gao, R. Cao, Inorg. Chem. 45 (2006) 1508.

[6] (a) S.-X. Liu, S. Lin, B.-Z. Lin, C.-C. Lin, J.-Q. Huang, Angew. Chem., Int. Ed. 40 (2001) 1084;
(b) S. Lin, S.-X. Liu, J.-Q. Huang, C.-C. Lin, J. Chem. Soc., Dalton Trans. (2002) 1595;
(c) S. Lin, S.-X. Liu, Z. Chen, B.-Z. Lin, S. Gao, Inorg. Chem. 43 (2004) 2222.

[7] R.P. John, K. Lee, B.J. Kim, B.J. Suh, H. Rhee, M.S. Lah, Inorg. Chem. 44 (2005) 7109 (and references therein).

[8] A.W. Addison, T.N. Rao, J. Reedjik, J. van Rijn, C.G. Verschoor, J. Chem. Soc., Dalton Trans. (1984) 1349.

[9] (a) S. Varughese, V.R. Pedireddi, Chem. Commun. (2005) 1824;
(b) K. Biradha, K.V. Domasevitch, B. Moulton, C. Seward, M.J. Zaworotko, Chem.Commun. (1999) 1327.

[10] (a) D. Valigura, M. Melník, M. Koman, L. Martiśka, M. Korabik, J. Mroziński, T. Glowiak, Polyhedron 23 (2004) 2447;
(b) X. He, Y.-N. Li, G.-H. Li, Y.-Z. Li, P. Zhang, J.-N. Xu, Y. Wang, Inorg. Chem. Commun. 8 (2005) 983;
(c) X. He, M.-H. Bi, K.-Q. Ye, Q.-R. Fang, P. Zhang, J.-N. Xu, Y. Wang, Inorg. Chem. Commun. 9 (2006) 1165;
(d) A.H. bin Othman, Effendy, B.W. Skelton, A.H. White, Aust. J. Chem. 56 (2003) 719.

[11] The series of calculations were made using the computer program CLUMAG, which uses the irreducible tensor operator (ITO) formalism: D. Gatteschi, L. Pardi, Gazz. Chim. Ital. 123 (1993) 231.

[12] Y. Pei, K. Nakatani, O. Kahn, J. Sletten, J.P. Renard, Inorg. Chem. 28 (1989) 3170.

[13] (a) L.-L. Wen, D.-B. Dang, C.-Y. Duan, Y.-Z. Li, Z.-F. Tian, Q.-J. Meng, Inorg. Chem. 44 (2005) 7161;
(b) X.-X. Xu, Y. Lu, E.-B. Wang, Y. Ma, X.-L. Bai, J. Mol. Struct. 825 (2006) 124.

phenylboronic acid. In addition, the Heck reaction of bromobenzene with styrene catalyzed by these palladacycles, as mentioned above, will also be discussed.

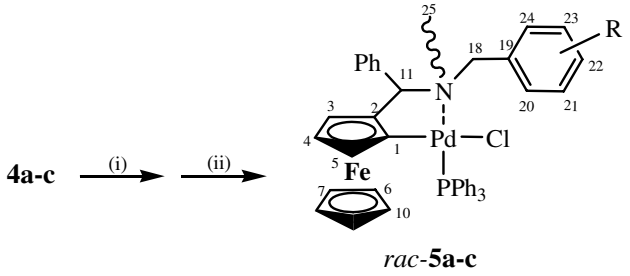
2. Results and discussion

2.1. Synthesis of ferrocenylamines 4a–c and their cyclopalladated complexes 5a–c

The preparation of *tert*-ferrocenylamines **4a–c** is shown in Scheme 1. Condensation of benzoylferrocene and 4 equiv. of benzylamine catalyzed by titanium tetrachloride [8] in toluene produced the dark-red ferrocenylketimines **2a–c** in good yields. Reduction of **2a–c** with $LiAlH_4$-$AlCl_3$ [9] in THF gave *sec*-amines **3a–c**, respectively in moderate yields. An attempt at the synthesis of **4a–c** from **3a–c** by our earlier used protocol, i.e. using aqueous HCHO, $NaCNBH_3$ in HOAc, [10] was unsuccessful due to the easier debenzylation of the former reactant [9,11] under such reaction conditions. Thus, CH_3I was chosen as the methylation reagent and *t*-BuOK as the base to synthesize **4a–c** from **3a–c** (Scheme 1). **4a–c** were finally obtained as orange solids in yields of 50–65%.

The synthesis of palladacycles **5a–c** is outlined in Scheme 2. Treatment of **4a–c** with 1 equiv. of Na_2PdCl_4–PPh_3 in methanol produced red-brown solids **5a–c** in 70–80% yields after purification by column chromatography (see Section 4). Similar to our earlier obtained palladacycles [7a,7b,7c], **5a–c** are very stable in air and easily soluble in CH_2Cl_2, $CHCl_3$, ethyl acetate, acetone and benzene, but are insoluble in ethanol and hexane.

Compounds **2–5** were characterized by elemental analysis, IR and ^1H NMR. Elemental analyses of **2–5** are in good agreement with their proposed formula. The IR and ^1H NMR spectra of **2–4** are very similar to those observed in imines, *sec*-amines and *tert*-amines derived from the starting materials formylferrocene and benzylamines [7b,7c]. The IR spectra of **5a–c** show two medium absorption bands at $\nu \sim 1100$ and 1000 cm^{-1}, implying that each of these palladacycles contains a free cyclopentadienyl (Cp) ring [12]. The ^1H NMR spectra of **5a–c**clearly demonstrate that the chemical shifts of N–CH_3 are located downfield ($\delta \sim 2.80$ ppm) compared to those of the free *tert*-amines **4a–c** ($\delta \sim 1.99$ ppm). This change can be rationalized by N–Pd coordination, which decreases the electron density



Scheme 2. (i) Na_2PdCl_4/NaOAc/CH_3OH. (ii) PPh_3/CH_3OH. R = H (a), 4-OCH_3 (b), 4-CH_3 (c).

of the N atom and causes the δ-values of N–CH_3 to shift downfield. In addition, the satellites of H20–H24 in the phenyl ring all exhibit their unique AA′XX′ splitting patterns (except **5a**), indicating that palladacycles **5a–c** are formed *via* the activation of the $C_{Ferrocenyl}$–H bond rather than the C_{phenyl}–H bond [13].

Since the nitrogen atom in **4a–c** connects directly to three different groups and a rapid N-inversion [14] exists, after the coordination of the nitrogen atom with palladium, the forms of the N–Pd coordinated intermediates (Fig. 1) can be simplified as two kinds, i.e., one has a R_N configuration, and another has the opposite, regardless of the chirality of C11. Accordingly, the following activation of the C–H bond in the Cp ring will produce theoretically four isomeric palladacycles (two pairs of racemes, *i.e.*, R_NR_P and S_NS_P, S_NR_P and R_NS_P). Similar to our earlier observations [7], only one pair of raceme R_NR_P and S_NS_P was found to dominate in these reactions, the other pair of raceme R_NS_P and S_NR_P was observed in trace amounts and can be easily removed by

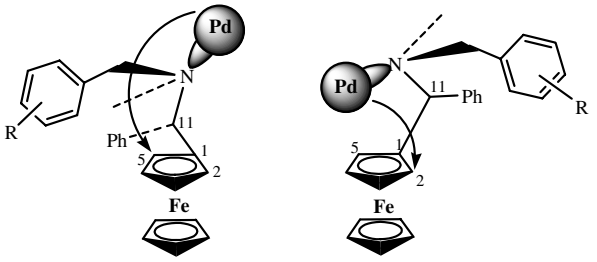
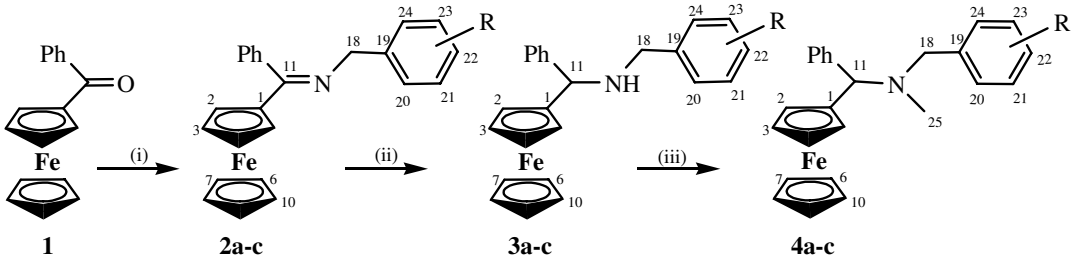


Fig. 1. The possible activation modes of C–H bonds in the Cp ring for N–Pd coordinated intermediates (left: R_N, right: S_N).



Scheme 1. (i) $RC_6H_4CH_2NH_2$/$TiCl_4$/toluene, reflux. R = H (a), 4-OCH_3 (b), 4-CH_3 (c). (ii) $LiAlH_4$/$AlCl_3$/THF. (iii) CH_3I/*t*-BuOK, THF.

chromatography. This stereoselective C–H bond activation is probably attributed to the preferred N–Pd orientations in the intermediates (Fig. 1), which allow the palladium atom to approach preferably to the C2–H or C5–H bond and then activate each of them. To some extent, the preferred N–Pd orientations in these intermediates are relevant to the geometries of the *tert*-ferrocenylamines [15]. In addition, zero optical rotations of **5a**–**c** measured at the given conditions ($\lambda = 5893$ Å, CH_2Cl_2, 293 K) also indicate that these palladacycles consist of racemes.

The structure of **5a** was determined by single crystal X-ray analysis (Fig. 2, S_NS_P). Crystallographic data for **5a** are given in Table 1, selected bond lengths and angles are listed in Table 2. X-ray diffraction studies demonstrates that **5a** consists of the discrete molecule {Pd[(η^5-C_5H_5)Fe(η^5-C_5H_3CHPhN(CH_3)$CH_2C_6H_5$)](PPh$_3$)Cl} separated by van der Waals contacts. The palladium atom is in a slightly distorted square-planar environment, bonded to Cl(1), P(1), N(1) and C(1). The deviation of each atom from the mean plane is Pd(1), −0.1015; Cl(1), −0.0489; P(1), 0.1071; N(1), 0.1149; C(1), −0.0716 Å, respectively. **5a** contains a bicycle, which is formed by the substituted Cp ring of the ferrocenyl fragment and a five-membered palladacycle with an envelope-like conformation. The N(1)–Pd(1) bond length of 2.224(3) Å is slightly longer than those observed in cyclopalladated [(*N*,*N*-dimethylamino)methyl]ferrocene (FcN, 2.170 Å) [16] and [({*N*-methyl-*N*-4-nitrobenzyl}-amino)methyl]ferrocene (BFcN, 2.195 Å) [7c]. In addition, the PPh$_3$ moiety in **5a** adopts a *trans*-configuration to N(1), with a N(1)–Pd(1)–P(1) bond angle of 167.53(7)°, which is slightly less than that in cyclopalladated BFcN (169.00(9)°). The Pd(1)–C(1) bond length of 2.002(3) Å is nearly the same as those observed in cyclopalladated FcN (1.983(1) Å) and BFcN (1.988(4) Å). The average C–C bond length (1.418 Å) in the ferrocenyl moiety is very close to the reported values of other ferrocene derivatives [17]. The Fe–C (Cp ring) bond lengths range from 2.036 to 2.082 Å. The eclipsed two Cp rings are planar and nearly parallel (interplanar angle of 2.2°).

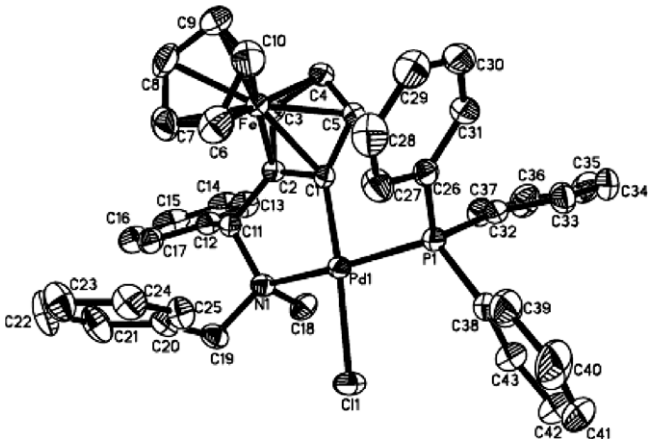


Fig. 2. X-ray crystal structure of **5a** (H atoms are all omitted for clarity).

Table 1
Crystallographic data for **5a**

Compound	**5a**
Empirical formula	$C_{43}H_{39}ClFeNPPd$
Formula weight	798.42
Crystal dimensions (mm)	$0.28 \times 0.22 \times 0.20$
Crystal system, space group	monoclinic, $P2(1)/n$
a (Å)	10.716(8)
b (Å)	17.638(1)
c (Å)	19.259(2)
α (°)	90
β (°)	94.153(1)
γ (°)	90
V (Å^3)	3631(5)
Z	4
ρ_{calc} (g cm^{-3})	1.461
μ (mm^{-1})	1.044
θ Range for data collection	$2.23 \leqslant \theta \leqslant 24.08°$
Limiting indices	$-10 \leqslant h \leqslant 12$, $-20 \leqslant k \leqslant 20$, $-21 \leqslant l \leqslant 22$
Reflections collected/unique [R_{int}]	19259/6383 [0.0375]
Data/restraints/parameters	6383/0/434
Final R_1, wR_2	0.0323, 0.0768
Largest difference in peak and hole (e Å^{-3})	0.542 and −0.345

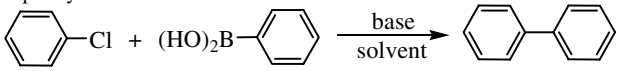
Table 2
Selected bond lengths and angles for **5a**

Bond lengths (Å)			
Pd(1)–P(1)	2.2401(1)	C(1)–C(2)	1.431(4)
Pd(1)–Cl(1)	2.3920(2)	N(1)–C(11)	1.524(4)
C(2)–C(11)	1.520(4)	N(1)–C(19)	1.499(4)
Bond angles (°)			
C(1)–Pd(1)–N(1)	82.18(1)	C(18)–N(1)–C(19)	107.5(2)
N(1)–Pd(1)–Cl(1)	91.24(7)	C(1)–Pd(1)–P(1)	91.67(9)
C(11)–N(1)–Pd(1)	109.92(2)	C(1)–Pd(1)–Cl(1)	173.25(8)
C(19)–N(1)–C(11)	110.2(2)	P(1)–Pd(1)–Cl(1)	94.51(5)
C(18)–N(1)–C(11)	112.1(2)	C(2)–C(1)–Pd(1)	114.15(2)

2.2. Suzuki coupling

Before investigation of the Suzuki coupling for aryl chlorides, the coupling of bromobenzene and phenylboronic acid catalyzed by **5a**–**c** (under the conditions K_2CO_3, THF) was studied. The coupling results showed that 100% of biphenyl was obtained, indicating that palladacycles **5a**–**c** are excellent catalysts for activation of the C_{phenyl}–Br bond. To examine the catalytic efficiency of **5** for the coupling of aryl chlorides, a quick survey of solvents including dioxane, toluene, THF and DMF/H_2O was made (Table 3). Table 3 revealed that using K_2CO_3 as the base and 0.1 mol% of **5a** as the catalyst the coupling reaction in dioxane gave the best results (Entry 1, 89%, Table 3). We further investigated the effect of the bases, e.g., K_2CO_3, Cs_2CO_3, K_3PO_4 and *t*-BuOK in the same reaction (Table 3). It was found that K_2CO_3 was better than the others (Entries 4–7). Therefore, K_2CO_3 was ultimately chosen as the base for this system.

Table 3
Influence of solvents and bases on the Suzuki coupling of chlorobenzene with phenyl-boronic acid[a]



Entry	Solvent	Base	Yield (%)[b]
1	dioxane	K_2CO_3	89.1
2	toluene	K_2CO_3	45.9
3	THF	K_2CO_3	51.3
4	DMF/H_2O	K_2CO_3	36.2
5	dioxane	Cs_2CO_3	67.6
6	dioxane	K_3PO_4	15.0
7	dioxane	*t*-BuOK	26.7

[a] Reaction conditions: catalyst *rac*-**5a** (0.1 mol%), PhCl (1 mmol), $PhB(OH)_2$ (1.5 mmol), base (2 mmol), solvent (10 cm^3), reflux, 10 h.
[b] Determined by GC, based on PhCl, average of two runs.

Under the optimized conditions as mentioned above, the relative activities of **5a**–**c** for the Suzuki coupling of aryl chlorides and phenylboronic acid were studied (Table 4). When the reactions were carried out at 100 °C for 10 h, **5a**–**c** all exhibited good activity with the loading as low as 0.1 mol % (Entries 1–3). However, when 0.01% of **5a** was used, the coupling yield was lower (Entry 4, 22.3%). Under the optimized reaction conditions (K_2CO_3, dioxane, 100 °C, 10 h) phenylboronic acid could couple efficiently with the aryl chlorides ranging from electron-donating to electron-withdrawing groups (Entries 5–10). In particular, for 4-$CH_3C_6H_5Cl$ the coupling yield was up to 98.0% (Entry 6). Even for the bulky 2,4-dinitrophenyl chloride, its coupling with phenylboronic acid was also achieved and the resulting biaryl yield was moderate.

2.3. Heck reaction

We initially examined the Heck reaction of chlorobenzene with styrene catalyzed by **5a**–**c**. Unfortunately the product yields were much lower (yield < 3%), and these results were consistent with the another group's observations [6]. Later we paid attention to the reaction of bromobenzene with styrene, and the results are summarized in Table 5. It was found that using DMF as the solvent and K_2CO_3 as the base at 140 °C for 7 h, an excellent yield of product could be obtained when the loading of palladacycle **5b** was as low as 0.1 mol% (Entry 6). Similar to the Suzuki coupling, when 0.01% of catalyst was used, the coupling yield was lower (Entry 8, 39%).

3. Conclusions

tert-Ferrocenylamines were easily synthesized by *N*-methylation of the corresponding *sec*-amines with CH_3I. Treatment of these *tert*-amines with Na_2PdCl_4 afforded racemic palladacycles with a σ Pd–C_{sp^2}, Ferrocenyl bond. These palladacycles have been proven to be highly efficient catalysts for the Suzuki coupling of aryl chlorides with phenylboronic acid and the Heck reaction of bromobenzene with styrene under the given conditions.

4. Experimental

4.1. Materials and instruments

Benzoylferrocene, enzylamines, $TiCl_4$, $LiAlH_4$, $AlCl_3$, CH_3I, *t*-BuOK, NaOAc, PPh_3 were obtained commercially and were used without further purification. Na_2PdCl_4 was prepared in our laboratory. All of the solvents were purified with standard methods prior to use. Melting points were obtained on a Yanaco micro melting point apparatus and were uncorrected. Elemental analyses were measured on a Carlo Erba 1106 Elemental analyzer. ^1H NMR spectra were obtained with Bruker AV-400 spectrometer using $CDCl_3$ as the solvent and TMS as the internal standard. IR spectra were recorded on a BIO-RAD 3000 spectrophotometer.

4.2. Preparation of ferrocenylketimines (*2*)

General procedure: **2a**–**c** were prepared according to the literature method [8].

4.2.1. $\{(\eta^5\text{-}C_5H_5)Fe(\eta^5\text{-}C_5H_4C(C_6H_5)=NCH_2C_6H_5)\}$ (*2a*)

Yield: (80%); a dark-red liquid; *Anal.* Calc. for $C_{24}H_{21}FeN$: C, 76.00; H, 5.58; N, 3.69. Found, C, 76.08; H, 5.69; N, 3.90%. FT-IR (KBr): 3084(w), 3027(w), 2856(w), 1614(vs), 1494(s), 1453(m), 1343(m), 1289(s), 1181(m), 1106(s), 1026(s), 1003(s), 822(s),703(s) cm^{-1}. ^1H NMR ($CDCl_3$): δ 3.81 (bs, 2H, H2, H5), 4.08 (bs, 2H, H3, H4), 4.14 (s, 5H, η^5-C_5H_5), 4.50 (s, 2H, H18), 7.45–7.89 (m, 10H, Ph).

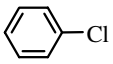
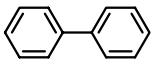
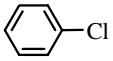
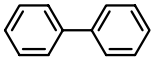
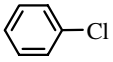
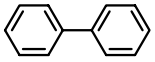
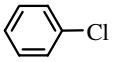
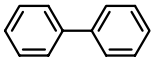
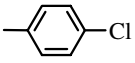
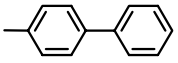
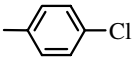
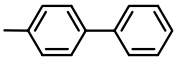
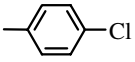
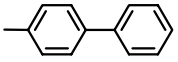
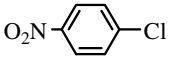
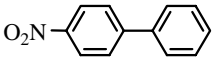
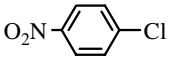
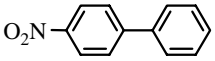
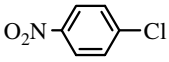
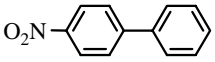
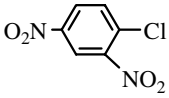
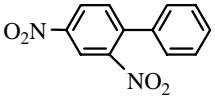
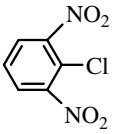
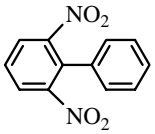
4.2.2. $\{(\eta^5\text{-}C_5H_5)Fe(\eta^5\text{-}C_5H_4C(C_6H_5)=NCH_2C_6H_4\text{-}OCH_3\text{-}4)\}$ (*2b*)

Yield: (76%); a dark-red liquid; *Anal.* Calc. for $C_{25}H_{23}FeNO$: C, 73.36; H, 5.66; N, 3.42. Found, C, 73.25; H, 5.73; N, 3.19%. FT-IR (KBr): 3088(w), 3022(w), 2909(w), 1611(vs), 1511(vs), 1462(s), 1291(s), 1245(vs), 1173(m), 1101(s), 1035(s), 818(s), 702(s) cm^{-1}. ^1H NMR ($CDCl_3$): δ 3.82 (s, 3H, OCH_3), 3.87 (bs, 2H, H2, H5), 4.11 (bs, 2H, H3, H4), 4.17 (s, 5H, η^5-C_5H_5), 4.55 (s, 2H, H18), 6.99–7.50 (m, 4H, H20, H21, H23, H24), 7.25–7.38 (m, 5H, Ph).

4.2.3. $\{(\eta^5\text{-}C_5H_5)Fe(\eta^5\text{-}C_5H_4C(C_6H_5)=NCH_2C_6H_4CH_3\text{-}4)\}$ (*2c*)

Yield: (85%); a dark-red liquid; *Anal.* Calc. for $C_{25}H_{23}FeN$: C, 76.35; H, 5.89; N, 3.56. Found: C, 76.21; H, 5.56; N, 3.81%. FT-IR (KBr): 3093(w), 3021(w), 2922(w), 1614(vs), 1515(s), 1480(s), 1290(vs), 1179(w), 1106(s), 1002(s), 820(vs), 703(vs) cm^{-1}. ^1H

Table 4
Palladacycles-catalyzed conversion of aryl chlorides to biaryls[a]

Entry	Aryl halide	Catalyst (mol%)	Product	Yield (%)[b]
1		*rac*-**5a**(0.1)		89.1
2		*rac*-**5b**(0.1)		86.5
3		*rac*-**5c**(0.1)		85.2
4		*rac*-**5a**(0.01)		22.3
5		*rac*-**5a**(0.1)		91.7
6		*rac*-**5b**(0.1)		98.0
7		*rac*-**5c**(0.1)		95.1
8		*rac*-**5a**(0.1)		72.4
9		*rac*-**5b**(0.1)		78.7
10		*rac*-**5c**(0.1)		80.6
11		*rac*-**5c**(0.1)		68.5
12		*rac*-**5b**(0.1)		45.3

[a] Reaction conditions: ArCl (1 mmol), $PhB(OH)_2$ (1.5 mmol), K_2CO_3 (2 mmol), dioxane (10 cm^3), 100 °C, 10 h.
[b] Determined by GC, based on aryl chloride used, average of two runs.

NMR ($CDCl_3$): δ 2.15 (s, 3H, CH_3), 3.85 (bs, 2H, H2, H5), 4.10 (bs, 2H, H3, H4), 4.16 (s, 5H, η^5-C_5H_5), 4.53 (s, 2H, H18), 7.13–7.25 (m, 4H, H20, H21, H23, H24), 7.43–7.55 (m, 5H, Ph).

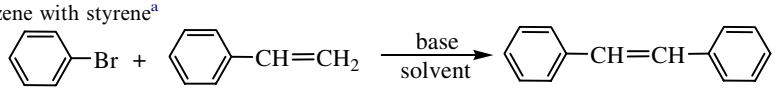
4.3. Preparation of sec-ferrocenylamines (*3*)

General procedure: **3a**–**c** were prepared with a modification of the 'Cais' method [8]. The difference was the reduction conditions. In our experiment, 3% mmol of $AlCl_3$ was used as the catalyst and THF as the solvent.

4.3.1. {(η^5-C_5H_5)Fe(η^5-$C_5H_4CH(C_6H_5)NHCH_2C_6H_5$)} (*3a*)

Yield: (77%); an orange solid; m.p. 68–70 °C. *Anal.* Calc. for $C_{24}H_{23}FeN$: C, 75.60; H, 6.08; N, 3.67. Found: C, 75.63; H, 6.25; N, 3.82%. FT-IR (KBr): 3328(s), 3084(m), 3022(m), 2948(m), 2857(m), 1598(m), 1493(vs),

Table 5
The Heck reaction of bromobenzene with styrene[a]



Entry	Solvent	Catalyst (mol%)	T (°C)	Base	Yield (%)[b]
1	1,4-dioxane	*rac*-**5b**(0.1)	80	K_2CO_3	3.0
2	1,4-dioxane	*rac*-**5b**(1)	100	K_2CO_3	5.0
3	toluene	*rac*-**5b**(1)	100	K_2CO_3	3.0
4	DMF	*rac*-**5b**(0.1)	100	K_2CO_3	22.0
5	DMF	*rac*-**5b**(1)	140	K_2CO_3	100
6	DMF	*rac*-**5b**(0.1)	140	K_2CO_3	100
7	DMF	*rac*-**5b**(0.1)	140	*t*-BuOK	87.0
8	DMF	*rac*-**5b**(0.01)	140	K_2CO_3	39.0
9	DMF	*rac*-**5a**(0.1)	140	K_2CO_3	96.0
10	DMF	*rac*-**5c**(0.1)	140	K_2CO_3	98.0

[a] All reactions were carried out with 1 mmol of PhBr, 1.5 mmol of styrene and 2 mmol of base in 10 cm^3 of solvent for 7 h.
[b] Determined by GC, based on PhBr, average of two runs.

1452(vs), 1283(m), 1197(m), 1105(vs), 1022(s), 996(s), 820(vs), 699(vs) cm^{-1}. ^1H NMR ($CDCl_3$): δ 2.17 (s, 1H, NH), 3.58–3.80 (q, 2H, H18) 4.06 (s, 1H, H11), 4.04 (s, 5H, η^5-C_5H_5), 4.30 (bs, 2H, H2, H5), 4.48 (bs, 2H, H3, H4), 7.23–7.43 (m, 10H, Ph).

4.3.2. {(η^5-C_5H_5)Fe(η^5-$C_5H_4CH(C_6H_5)NHCH_2C_6H_4$-$OCH_3$-4)} (**3b**)

Yield: (72%); a yellow solid; m.p. 57–60 °C. *Anal*. Calc. for $C_{25}H_{25}FeNO$: C, 73.00; H, 6.13; N, 3.41. Found: C, 73.09; H, 6.31; N, 3.55%. FT-IR (KBr): 3324(m), 3083(m), 3022(m), 2954(s), 2827(m), 1610(vs), 1512(vs), 1452(s), 1300(m), 1247(vs), 1174(s), 1105(vs), 1036(s), 1001(s), 821(vs), 700(vs) cm^{-1}. ^1H NMR ($CDCl_3$): δ 2.17 (s, 1H, NH), 3.51–3.74 (q, 2H, H18), 3.82 (s, 3H, OCH_3), 4.04 (s, 5H, η^5-C_5H_5), 4.05 (s, 1H, H11), 4.30 (bs, 2H, H2, H5), 4.46 (bs, 2H, H3, H4), 6.90–7.41 (m, 4H, H20, H21, H23, H24), 7.23–7.34 (m, 5H, Ph).

4.3.3. {(η^5-C_5H_5)Fe(η^5-$C_5H_4CH(C_6H_5)NHCH_2C_6H_4$-$CH_3$-4)} (**3c**)

Yield: (81%); a yellow solid; m.p. 93–94 °C. *Anal*. Calc. for $C_{25}H_{25}FeN$: C, 75.96; H, 6.37; N, 3.54. Found: C, 75.89; H, 6.15; N, 3.90%. FT-IR (KBr): 3324(m), 3073(m), 3013(m), 2924(m), 2821(m), 1597(m), 1508(vs), 1451(s), 1333(m), 1179(m), 1104(vs), 1021(s), 996(s), 817(vs), 699(vs) cm^{-1}. ^1H NMR ($CDCl_3$) δ 2.17 (s, 1H, NH), 2.14 (s, 3H, CH_3), 3.54–3.76 (q, 2H, H18), 4.04 (s, 5H, η^5-C_5H_5), 4.05 (s, 1H, H11), 4.30 (bs, 2H, H2, H5), 4.47 (bs, 2H, H3, H4), 7.12–7.21 (m, 4H, H20, H21, H23, H24), 7.41–7.53 (m, 5H, Ph).

4.4. Synthesis of tert-ferrocenylamines (**4**)

General procedure: To a stirred solution of **3** (2 mmol) in 20 cm^3 of THF was added CH_3I (3 mmol) in 5 cm^3 THF and *t*-BuOK (3 mmol). The mixture was kept in the dark at room temperature and stirred for 48 h. TLC monitored the reaction progress until it was complete. The solvent was removed under reduced pressure and 30 cm^3 of water was then added. The mixture was extracted with diethyl ether (3×20 cm^3) and separated. The extracts were combined, dried over Na_2SO_4 and removed to give crude products which were purified by column chromatography (silica gel, ethyl acetate/hexane = 1:5, v/v) to afford **4a**–**c**.

4.4.1. {(η^5-C_5H_5)Fe(η^5-$C_5H_4CH(C_6H_5)N(CH_3)CH_2$-$C_6H_5$)} (**4a**)

Yield: (58%); an orange solid; m.p. 64–66 °C. *Anal*. Calc. for $C_{25}H_{25}FeN$: C, 75.96; H, 6.37; N, 3.54. Found: C, 75.88; H, 6.60; N, 3.81%. FT-IR (KBr): 3081(s), 3019(s), 2957(s), 2783(s), 1596(s), 1493(vs), 1452(vs), 1366(m), 1286(m), 1106(vs), 1002(vs), 818(vs) cm^{-1}. ^1H NMR ($CDCl_3$): δ 1.95 (s, 3H, H25), 3.22–3.51 (q, 2H, H18), 3.79 (s, 5H, η^5-C_5H_5), 4.13 (s, 1H, H11), 4.11 (bs, 2H, H2, H5), 4.34 (bs, 2H, H3, H4), 7.19–7.52 (m, 10H, Ph).

4.4.2. {(η^5-C_5H_5)Fe(η^5-C_5H_4 $CH(C_6H_5)N(CH_3)CH_2$-$C_6H_4OCH_3$-4)} (**4b**)

Yield: (50%); an orange solid; m.p. 72–73 °C. *Anal*. Calc. for $C_{26}H_{27}FeNO$: C, 73.42; H, 6.40; N, 3.29. Found: C, 73.37; H, 6.58; N, 3.36%. FT-IR (KBr): 3088(m), 3024(m), 2953(s), 2831(m), 2775(m), 1605(vs), 1510(vs), 1452(vs), 1296(m), 1242(vs), 1106(vs), 1002(vs), 818(vs) cm^{-1}. ^1H NMR ($CDCl_3$): δ 1.98 (s, 3H, H25), 3.23–3.51 (q, 2H, H18), 3.85 (s, 3H, OCH_3), 3.81 (s, 5H,η^5-C_5H_5), 4.14 (s, 1H, H11), 4.13 (bs, 2H, H2, H5), 4.36 (bs, 2H, H3, H4), 6.91–7.42 (m, 4H, H20, H21, H23, H24), 7.26–7.35 (m, 5H, Ph).

4.4.3. {(η^5-C_5H_5)Fe(η^5-$C_5H_4CH(C_6H_5)N(CH_3)CH_2$-$C_6H_4CH_3$-4)} (**4c**)

Yield: (65%); an orange solid; m.p. 70–72 °C. *Anal*. Calc. for $C_{26}H_{27}FeN$: C, 76.29; H, 6.65; N, 3.42. Found: C, 76.23; H, 6.43; N, 3.60%. FT-IR (KBr): 3091(m),

3023(m), 2956(s), 2776(m), 1600(m), 1513(vs), 1452(vs), 1286(m), 1106(vs), 1002(vs), 805(vs) cm^{-1}. ^1H NMR ($CDCl_3$): δ 1.99 (s, 3H, H25), 2.35 (s, 3H, CH_3), 3.24–3.52 (q, 2H, H18), 3.83 (s, 5H, η^5-C_5H_5), 4.16 (s, 1H, H11), 4.15 (bs, 2H, H2, H5), 4.38 (bs, 2H, H3, H4), 7.13–7.22 (m, 4H, H20, H21, H23, H24), 7.44–7.55 (m, 5H, Ph).

4.5. Synthesis of cyclopalladated tert-ferrocenylamines (5)

General procedure: To a stirred solution of **4** (1 mmol), sodium acetate (82 mg, 1 mmol) in 30 cm^3 of methanol was added dropwise a solution of Na_2PdCl_4 (0.29 g, 1 mmol) in 15 cm^3 of methanol. The mixture was stirred for 4 h at room temperature under argon and TLC monitored the reaction's progress. Then PPh_3 (0.41 g, 1.5 mmol) was added and the mixture was stirred for another 30 min. The solvent was removed in vacuo, and the residues were purified by column chromatography (silica gel, ethyl acetate/hexane = 1:2, v/v) to give **5**.

4.5.1. [PdCl(PPh$_3$){(η^5-C$_5$H$_5$)Fe(η^5-C$_5$H$_3$CH(C$_6$H$_5$)N-(CH$_3$)CH$_2$C$_6$H$_5$)}] (5a)

Yield: (72%); a red solid; m.p. > 193 °C (dec.). *Anal.* Calc. for $C_{43}H_{39}ClFeNPPd$: C, 64.68; H, 4.92; N, 1.75. Found: C, 64.60; H, 4.89; N, 1.82%. FT-IR (KBr): 3054(w), 2955(w), 2922(w), 1486(m), 1450(m), 1435(vs), 1095(s), 999(s), 823(m), 752(s), 701(vs) cm^{-1}. ^1H NMR($CDCl_3$): δ 2.88 (m, 2H, H18), 3.21 (s, 3H, H25), 4.84 (s, 1H, H11), 3.85 (s, 5H, η^5-C_5H_5), 3.76 (d, 1H, H5), 4.08 (m, 1H, H4), 4.16 (d, 1H, H3), 7.73–7.82 (m,10H, 2Ph), 7.35–7.54 (m, 15H, PPh_3).

4.5.2. [PdCl(PPh$_3$){(η^5-C$_5$H$_5$)Fe(η^5-C$_5$H$_3$CH(C$_6$H$_5$)N-(CH$_3$)CH$_2$C$_6$H$_4$OCH$_3$-4)}] (5b)

Yield (80%); a red solid; m.p. > 189 °C (dec.). *Anal.* Calc. for $C_{44}H_{41}ClFeNOPPd$: C, 63.79; H, 4.99; N, 1.69. Found: C, 63.72; H, 4.81; N, 1.96%. FT-IR (KBr): 3045(w), 2954(w), 1512(vs), 1454(m), 1435(vs), 1246(s), 1178(s), 1100(s), 995(m), 816(s), 747(s), 702(vs) cm^{-1}. ^1H NMR ($CDCl_3$): δ 2.79 (s, 3H, H25), 3.24 (m, 2H, H18), 3.43 (s, 3H, OCH_3), 3.73 (s, 5H, η^5-C_5H_5), 3.74 (m, 1H, H5), 3.80 (m, 1H, H4), 3.95 (d, 1H, H3), 4.96 (s, 1H, H11), 6.90–7.05 (m, 4H, H20, H21, H23, H24), 7.39–7.66 (m, 15H, PPh_3), 7.70–7.85 (m, 5H, Ph).

4.5.3. [PdCl(PPh$_3$){(η^5-C$_5$H$_5$)Fe(η^5-C$_5$H$_3$CH(C$_6$H$_5$)N-(CH$_3$)CH$_2$C$_6$H$_4$ CH$_3$-4)}] (5c)

Yield (70%); a red solid; m.p. > 172 °C (dec.). *Anal.* Calc. for $C_{44}H_{41}ClFeNPPd$: C, 65.04; H, 5.09; N, 1.72. Found: C, 65.12; H, 4.85; N, 1.65%. FT-IR (KBr): 3051(w), 2954(w), 2920(w), 1484(s), 1455(s), 1437(vs), 1185(m), 1103(s), 1002(m), 823(m), 751(s), 693(vs) cm^{-1}. ^1H NMR ($CDCl_3$): δ 2.43 (s, 3H, CH_3), 2.79 (s, 3H, H25), 3.21 (m, 2H, H18), 3.50 (s, 5H, η^5-C_5H_5), 5.16 (s, 1H, H11), 3.73 (m, 1H, H5), 3.82 (d, 1H, H3), 4.10 (m, 1H, H4), 7.13–7.22 (m, 4H, H20, H21, H23, H24), 7.39–7.56 (m, 15H, PPh_3), 7.70–7.85 (m, 5H, Ph).

4.6. General procedure for the Suzuki coupling

Palladacycles **5** (0.1 mmol%), aryl chlorides (1.0 mmol), phenylboronic acid (1.5 mmol), K_2CO_3 (2 mmol), dioxane (10 cm^3) were added to a 25 cm^3 round-bottomed flask and the mixture was heated at 100 °C for 10 h. Upon cooling, the reaction mixture was poured into water and extracted with CH_2Cl_2, concentrated and purified by flash chromatography on silica gel. The purity of the compounds was checked by GC and yields are based on aryl chlorides.

4.7. General procedure for the Heck reaction

Palladacycles **5** (0.1 mmol%), bromobenzene (1.0 mmol), styrene (1.5 mmol), K_2CO_3 (2 mmol), DMF (10 cm^3) were added to a 25 cm^3 round-bottomed flask and the mixture was heated at 140 °C for 7 h. Upon cooling, the reaction mixture was poured into water and extracted with CH_2Cl_2, concentrated and purified by flash chromatography on silica gel. The purity of the compounds was checked by GC and yields are based on bromobenzene.

4.8. X-ray crystallographic study of 5a

Crystals of **5a** were grown at room temperature by slow evaporation of a mixture of hexane and ethyl acetate over a period of one week. A single crystal of this complex was mounted on a Bruker SMART CCD diffractometer equipped with monochromated graphite Mo Kα (λ = 0.71073 Å) radiation at ambient temperature (T = 293 K) using the ω–2θ multi-scans technique for data collection. Semi-empirical absorption corrections were applied using the SABABS program [18]. The structure was solved by direct methods and refined by the full-matrix least-squares procedure on F^2 using the SHELX suite of programs [19]. The values of R_1 were given based on F_o with a typical threshold of $F^2 \geqslant 2\sigma(F^2)$. The weighted R-factors wR were based on F^2 with calc. $w = 1/[\sigma^2(F_o^2) + (0.0000P)^2 + 0.0827P]$ where $P = (F_o^2 + 2F_c^2)/3$ for **5a**. Crystallographic data for **5a** are summarized in Table 1. Selected bond lengths and angles for **5a** are presented in Table 2.

5. Supplementary material

CCDC 603093 contains the supplementary crystallographic data for **5a**. These data can be obtained free of charge via http://www.ccdc.cam.ac.uk/conts/retrieving.html, or from the Cambridge Crystallographic Data Centre, 12 Union Road, Cambridge CB2 1EZ, UK; fax: (+44) 1223-336-033; or e-mail: deposit@ccdc.cam.ac.uk.

Acknowledgements

We are indebted to the Natural Science Foundation of Tianjin Metropolitan Council (Project No. 033609011) and the State Key Laboratory of Elemento-organic Chemistry, Nankai University, People's Republic of China for financial support of this project.

References

[1] (a) S. Yonezawa, T. Komurasaki, K. Kawada, T. Tsuri, M. Fuji, A. Kugimiwa, N. Haga, S. Mitsumori, M. Inagaki, T. Nakadani, Y. Tamura, S. Takechi, T. Taishi, M. Ohatani, J. Org. Chem. 63 (1998) 5831;
(b) D.E. Zembower, H. Zhang, J. Org. Chem. 63 (1998) 9300;
(c) G. Lin, A. Zhang, Tetrahedron 56 (2000) 7163;
(d) S. Kumar, J. Chem. Soc., Perkin Trans. 1 (1998) 3157;
(e) G.R. Gree, I.S. Mann, M.V. Mullane, A. Mckillop, Tetrahedron 54 (1998) 9875;
(f) H. Koyama, T. Kamikawa, Tetrahedron Lett. 38 (1997) 3973;
(g) G. Bringmann, R. Gotaz, P.A. Keller, R. Walter, M.R. Boyd, F. Lang, A. Garcia, J.J. Walsh, I. Tellitu, K.V. Bhaskar, T.R. Kelly, J. Org. Chem. 63 (1998) 1090;
(h) K.C. Nicolaou, A.E. Koumbis, M. Takayagagi, S. Natarajan, N.F. Jain, T. Bando, H. Liu, R. Hughes, Chem. Eur. J. 5 (1999) 2622.

[2] (a) L. Yin, J. Liebscher, Chem. Rev. 107 (2007) 133;
(b) J.P. Corbet, G. Mignani, Chem. Rev. 106 (2006) 2651;
(c) R.B. Bedford, C.S.J. Cazin, D. Holder, Coord. Chem. Rev. 248 (2004) 2283.

[3] (a) E. Peris, R.H. Crabtree, Coord. Chem. Rev. 248 (2004) 2239;
(b) O. Navarro, N. Marion, J. Mei, S.P. Nolan, Chem. Eur. J. 12 (2006) 5142;
(c) O. Navarro, N. Marion, Y. Oonishi, R.A. Kelly, S.P. Nolan, J. Org. Chem. 71 (2006) 685;
(d) F.E. Hahn, M.C. Jahnke, T. Pape, Organometallics 26 (2007) 150.

[4] (a) N.T.S. Phan, M. van der Sluys, C.W. Jones, Adv. Synth. Catal. 348 (2006) 609;
(b) J. Dupont, C.S. Consorti, J. Spencer, Chem. Rev. 105 (2005) 2527;
(c) L.F. Tietze, H. Ila, H.P. Bell, Chem. Rev. 104 (2004) 3453;
(d) J. Hassan, M. Sevignon, C. Gozzi, E. Schulz, M. Lemaire, Chem. Rev. 102 (2002) 1359;
(e) A. Zapf, M. Beller, Chem. Commun. (2005) 431;
(f) A. Suzuki, Chem. Commun. (2005) 4759;
(g) I.P. Beletskaya, A.V. Cheprakov, J. Organomet. Chem. 689 (2004) 4055.

[5] (a) R.B. Bedford, C.S.J. Cazin, Chem. Commun. (2001) 1540;
(b) R.C. Huang, K.H. Shaughnessy, Organometallics 25 (2006) 4105;
(c) J.L. Zhang, L. Zhao, M.P. Song, T.C.W. Mak, Y.J. Wu, J. Organomet. Chem. 691 (2006) 1301;
(d) J.F. Gong, G.Y. Liu, C.X. Du, Y. Zhu, Y.J. Wu, J. Organomet. Chem. 690 (2005) 3963;
(e) I.J.S. Fairlamb, A.R. Kapdi, A.F. Lee, G. Sanchez, G. Lopez, J.L. Serrano, L. Garcıa, J. Perez, E. Perez, J. Chem. Soc., Dalton Trans. (2004) 3970;
(f) J. Ruiz, C. Vicente, N. Cutillas, J. Perez, J. Chem. Soc., Dalton Trans. (2005) 1999;
(g) D.A. Alonso, C. Najera, M.C. Pacheco, J. Org. Chem. 67 (2002) 5588;
(h) D.A. Alonso, C. Najera, M.C. Pacheco, Org. Lett. 2 (2000) 1823;
(i) R.B. Bedford, C.S.J. Cazin, S.J. Coles, T. Gelbrich, M.B. Hursthouse, V.J.M. Scordia, J. Chem. Soc., Dalton Trans. (2003) 3350;
(j) S.W. Lee, J. Organomet. Chem. 691 (2006) 1347;
(k) C.L. Chen, Y.H. Liu, S.M. Peng, S.T. Liu, Organometallics 24 (2005) 1075;
(l) C. Xu, J.F. Gong, Y.H. Zhang, Y. Zhu, Y.J. Wu, Australian J. Chem. 60 (2007) 190.

[6] (a) M. Ohff, A. Ohff, D. Milstein, Chem. Commun. (1999) 357;
(b) F. Yang, Y.M. Zhang, R. Zheng, J. Tang, M.Y. He, J. Organomet. Chem. 651 (2002) 146;
(c) K. Takenaka, M. Minakawa, Y. Uozumi, J. Am. Chem. Soc. 127 (2005) 12273;
(d) X.J. Gai, R. Grigg, M.I. Ramzan, V. Sridharan, S. Collard, J.E. Muir, Chem. Commun. (2000) 2053;
(e) M. Nowotny, U. Hanefeld, H. van Koningsveld, T. Maschmeyer, Chem. Commun. (2000) 1877;
(f) C. Rocaboy, J.A. Gladysz, New J. Chem. 27 (2003) 39;
(g) C.C. Cassol, A.P. Umpierre, G. Machado, S.I. Wolke, J. Dupont, J. Am. Chem. Soc. 127 (2005) 3298;
(h) S.G. Fiddy, J. Evans, M.A. Newton, T. Neisius, R.P. Tooze, R. Oldman, Chem. Commun. (2003) 2682;
(i) B.L. Shaw, S.D. Perera, E.A. Staley, Chem. Commun. (1998) 1361;
(j) M.R. Eberhard, Org. Lett. 13 (2004) 2125;
(k) D.E. Bergbreiter, S. Furyk, Green Chem. 6 (2004) 280.

[7] (a) H.X. Wang, Y.J. Li, R.Q. Gao, H.F. Wu, F.Y. Geng, R. Jin, Inorg. Chem. Commun. 9 (2006) 685;
(b) H.X. Wang, H.F. Wu, R.Q. Gao, X.L. Yang, L. Wan, W.Q. Zhang, R. Jin, Inorg. Chem. Commun. 9 (2006) 1235;
(c) H.X. Wang, H.F. Wu, H.C. Zhou, F.Y. Geng, R.Q. Gao, X.L. Yang, L. Wan, W.Q. Zhang, R. Jin, Inorg. Chim. Acta 359 (2006) 4114;
(d) H.X. Wang, H.F. Wu, H.C. Zhou, R. Jin, R.Q. Gao, F.Y. Geng, J. Xu, Y.J. Li, W.Q. Zhang, Polyhedron 25 (2006) 2530.

[8] M. Cais, P. Ashkenazi, S. Dani, J. Gottlieb, J. Organomet. Chem. 124 (1997) 49.

[9] H.X. Wang, R.Q. Gao, X.L. Yang, L. Wan, H.F. Wu, F.Y. Geng, R. Jin, Polyhedron 26 (2007) 1037.

[10] R.F. Borch, A.I. Hassid, J. Org. Chem. 37 (1972) 1673.

[11] M.A. Carroll, A.J.P. White, D.A. Widdowson, D.J. Williams, J. Chem. Soc., Perkin Trans. 1 (2000) 1551.

[12] M. Rosenblum, R.B. Woodward, J. Am. Chem. Soc. 80 (1958) 5443.

[13] (a) R. Bosque, C. Lopez, J. Sales, J. Organomet. Chem. 498 (1995) 147;
(b) C. Lopez, J. Sales, X. Solans, R. Zquiak, J. Chem. Soc., Dalton Trans. (1992) 2321;
(c) R. Bosque, C. Lopez, J. Sales, X. Solans, M. Font-Bardia, J. Chem. Soc., Dalton Trans. (1994) 735.

[14] V.I. Sokolov, L.L. Troitskaya, T.A. Sorokina, Izv. Akad. Nauk SSSR. (1971) 2612.

[15] (a) H.X. Wang, Y.J. Li, R. Jin, J.R. Niu, H.F. Wu, H.C. Zhou, J. Xu, R.Q. Gao, F.Y. Geng, J. Organomet. Chem. 691 (2006) 987;
(b) H.F. Wu, H.X. Wang, J. Xu, F.Y. Geng, R.Q. Gao, X.L. Yang, Anal. Sci. 22 (2006) 197.

[16] C. Lopez, R. Bosque, X. Solans, M. Font-Bardia, New. J. Chem. 22 (1998) 977.

[17] T.H. Allen, O. Kennard, Chem. Des. Autom. News 8 (1993) 146.

[18] G.M. Sheldrick, SADABS, University of Göttingen, 1996.

[19] G.M. Sheldrick, SHELXS-97 and SHELXL-97, Programs for Crystal Structure Solution and Refinement, University of Göttingen, 1997.

2. Results and discussion

2.1. Syntheses of tetra(tert-butyl)metallate complexes of lanthanide elements

The preparation of the salt $[Li(THF)_4][Er(t\text{-}Bu)_4]$ has been reported previously [19]. In our hands, the reported preparation proceeded as described, but we were not able to obtain analytically pure material. Instead, we obtained materials with low carbon and hydrogen analyses that retained chloride. Attempts to prepare the terbium analog $[Li(THF)_4][Tb(t\text{-}Bu)_4]$ gave similar results.

In order to obtain crystalline and analytically pure samples, we have investigated the corresponding $[Li(DME)_3^+]$ salt, where DME is 1,2-dimethoxyethane. Thus, slow addition of a pentane solution of *tert*-butyllithium to a suspension of anhydrous erbium trichloride in DME/pentane at −78 °C, followed by warming to room temperature gives a pink solution, from which pink crystals of $[Li(DME)_3][Er(t\text{-}Bu)_4]$ (**1**) can be obtained by layering a saturated ether solution with pentane and cooling to −20 °C. The material so obtained is analytically pure. The corresponding Tb complex $[Li(DME)_3][Tb(t\text{-}Bu)_4]$ (**2**) can be made similarly, but the cerium analog could not be successfully isolated by the same route.

The IR spectrum of the erbium complex **1** shows ν_{CH} bands due to the *tert*-butyl groups at 2753, 2724, and 2667 cm^{-1}. In comparison, for the $[Li(THF)_4^+]$ salt of this same anion, Evans et al. reported similar bands at 2760, 2730, 2670 and 2620 cm^{-1} [19]. The low frequencies of these C–H modes are characteristic of *tert*-butyl groups [26,27], and are not consequences of CH_3–Li or agostic interactions, as verified by the X-ray structure (see below). The IR spectrum of the terbium analog **2** is essentially identical to that of **1**. ^1H NMR spectra of paramagnetic **1** and **2** contain broad resonances for the *tert*-butyl groups at δ −11 and −76.6, respectively.

2.2. Molecular structure of [Li(DME)$_3$][Er(t-Bu)$_4$] (1)

General crystallographic data, selected bond lengths and angles for **1** are listed in Tables 1 and 2, respectively; views of one of the cations and one of the anions are given in Fig. 1. In the asymmetric unit there are two anions, one full cation, and two half-cations. Except for some disordering of the *tert*-butyl groups on Er(2), the two crystallographically inequivalent anions have very similar metric parameters. The DME ligands about one of the lithium centers are also disordered, but again the coordination geometries of all three independent cations are very similar.

The erbium(III) center in **1** is ligated by four *tert*-butyl groups in an approximately tetrahedral arrangement. The C–Er–C angles between the *tert*-butyl groups range from 108.4(3)° to 111.2(3)° and the Er–C distances range from 2.352(6) to 2.395(6) Å. These values are similar to those seen for the $[Lu(t\text{-}Bu)_4^-]$ anion [18], in which the C–Lu–C angles range from 107.3° to 109.8° and the Lu–C distances range from 2.32(2) to 2.43(2) Å. In $Cp_2Lu(t\text{-}Bu)(THF)$ [28], the Lu–C distance to the *tert*-butyl group was much longer at 2.47(2) Å, probably because the coordination number of this compound is higher.

Each lithium cation in **1** is surrounded by three DME molecules, which form a distorted octahedral coordination

Table 1
Crystal Data for $[Li(DME)_3][Er(t\text{-}Bu)_4]$ (**1**)

Empirical formula	$C_{28}H_{66}ErLiO_6$
Formula weight	673.01
Temperature (K)	193(2)
λ (Å)	0.71073
Crystal system	monoclinic
Space group	*C*2/*c*
a (Å)	27.309(9)
b (Å)	19.177(6)
c (Å)	27.818(9)
(β) (°)	94.614(6)
V (Å^3)	14521(8)
Z	16
ρ (Mg/m^3)	1.231
Absorption coefficient (mm^{-1})	2.343
F(000)	5648
Crystal size (mm)	0.08 × 0.14 × 0.14
θ Range for data collection (°)	1.92–25.38
Reflections collected	74312
Refinement method	full-matrix least-squares on F^2
Data/restraints/parameters	72825/649/625
Goodness-of-fit on F^2	0.907
$R^a[I > 2\sigma(I)]$	0.0955
wR_2^b (all data)	0.2459
Largest peak and hole (e Å^{-3})	2.689 and −1.158

[a] $R = \sum||F_o| - |F_c||/\sum|F_o|$.
[b] $wR_2 = \{\sum w[(F_o^2 - F_c^2)^2]/\sum[w(F_o^2)^2]\}^{1/2}$.

Table 2
Selected bond distances (Å) and angles (°) for $[Li(DME)_3][Er(t\text{-}Bu)_4]$ (**1**)

Distances			
Er(1)–C(1)	2.378(6)	C(9)–C(11)	1.493(14)
Er(1)–C(5)	2.352(6)	C(9)–C(12)	1.480(14)
Er(1)–C(9)	2.395(6)	C(13)–C(14)	1.477(14)
Er(1)–C(13)	2.378(6)	C(13)–C(15)	1.501(14)
C(1)–C(2)	1.509(14)	C(13)–C(16)	1.488(14)
C(1)–C(3)	1.500(14)	Li(1)–O(41)	2.089(14)
C(1)–C(4)	1.491(14)	Li(1)–O(42)	2.077(14)
C(5)–C(6)	1.471(14)	Li(1)–O(51)	2.144(15)
C(5)–C(7)	1.485(14)	Li(1)–O(52)	2.083(15)
C(5)–C(8)	1.478(14)	Li(1)–O(61)	2.113(14)
C(9)–C(10)	1.497(14)	Li(1)–O(62)	2.066(15)
Angles			
C(1)–Er(1)–C(5)	108.8(3)	O(42)–Li(1)–O(51)	90.5(6)
C(1)–Er(1)–C(9)	109.3(3)	O(42)–Li(1)–O(52)	163.4(8)
C(1)–Er(1)–C(13)	109.6(3)	O(42)–Li(1)–O(61)	93.8(6)
C(5)–Er(1)–C(9)	111.2(3)	O(42)–Li(1)–O(62)	100.26(6)
C(5)–Er(1)–C(13)	108.4(3)	O(51)–Li(1)–O(52)	77.4(5)
O(41)–Li(1)–O(42)	77.7(5)	O(51)–Li(1)–O(61)	91.2(6)
O(41)–Li(1)–O(51)	100.5(6)	O(51)–Li(1)–O(62)	164.8(7)
O(41)–Li(1)–O(52)	93.2(6)	O(52)–Li(1)–O(61)	97.8(6)
O(41)–Li(1)–O(61)	165.5(8)	O(52)–Li(1)–O(62)	93.9(6)
O(41)–Li(1)–O(62)	92.3(6)	O(61)–Li(1)–O(62)	77.6(5)

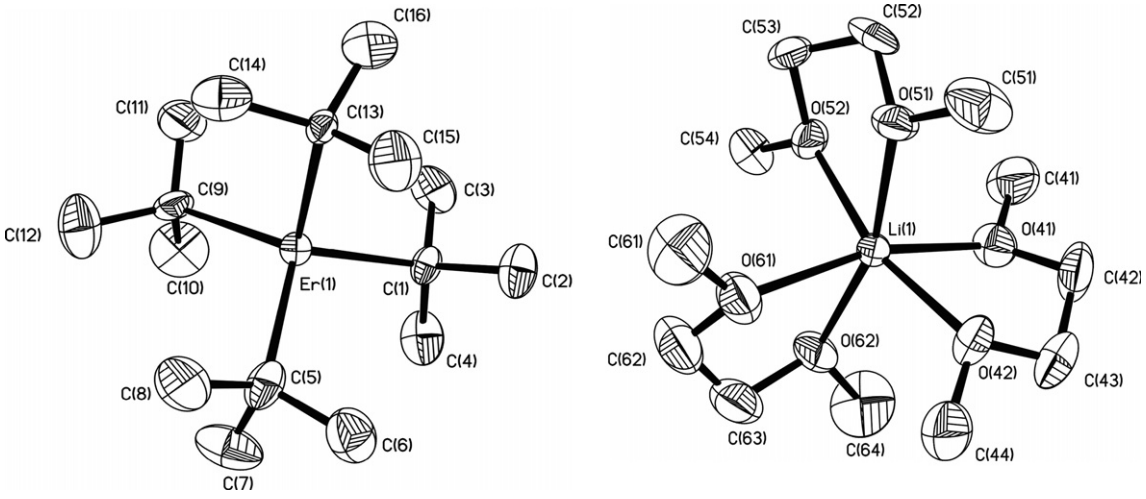


Fig. 1. Molecular structure of $[Li(DME)_3][Er(t\text{-}Bu)_4]$ (**1**); anion at left, cation at right.

sphere. The Li–O distances, which lie between 2.07(2) and 2.14(2) Å, agree with the 2.07(1)–2.17(1) Å range found in $[Li(DME)_3][(Cp_3Sm)_2(\mu\text{-}Cl)]$ [29] and the 2.12(1) Å value in $[Li(DME)_3][Zr(SCMe_3)_5]$ [30]. Some $[Li(DME)_3^+]$ cations are known in which the Li–O distances vary over a wider range: from 2.03(2) to 2.37(2) Å in $[Li(DME)_3][(C_5H_4Me)La(NPh_2)_3]$ [31] and from 2.07(2) to 2.34(2) Å in $[Li(DME)_3][Cp_2Nd(NPh_2)_2]$ [32]. The O–Li–O angles in **1** range from 77.4(5)° to 77.7(5)°, a range that is consistent with previous values for this cation.

Colorless crystals of the terbium analog **2** were also obtained by diffusion of pentane into an ether solution at −20 °C. The crystals were twinned and the diffraction data set, which approximated to cubic symmetry, could not be solved.

2.3. Attempts to prepare tetra(alkyl)lanthanide(IV) species

Alkyl groups are reasonably strongly donating and are well-known to stabilize higher oxidation states of transition metals [33]. Among alkyl groups, *tert*-butyl substituents are among the most strongly donating [34]. In addition, because four *tert*-butyl groups are able to saturate the coordination sphere of a Ln^{3+} metal – as the existence of $[Ln(t\text{-}Bu)_4^-]$ anions shows – they should also be able to saturate the coordination sphere of a somewhat smaller Ln^{4+} metal center. Such Ln^{4+} centers are still large enough to accommodate four *tert*-butyl substituents, as shown by the existence of a tetra(*tert*-butyl) complex of an even smaller ion: the Cr^{4+} center in $Cr(t\text{-}Bu)_4$ [35].

Of all the lanthanide elements, cerium has the most accessible tetravalent oxidation state and is the natural starting point for efforts to prepare a tetra(alkyl) derivative. Although we were unable to isolate pure salts of the tetra(*tert*-butyl)cerate(III) ion (see above), we attempted to prepare this species and oxidize it *in situ*. After treatment of $CeCl_3$ with 4 equivalents of *tert*-butyllithium in THF/ pentane at −78 °C, the mixture was exposed to dry O_2 at −40 °C. No color change occurred. Filtration and removal of the solvent gave an oily liquid, from which no organometallic species could be isolated.

The significance of this result is unclear, in part because the organocerium(III) starting material was not isolated but prepared *in situ*. To complement this result, we investigated whether pure samples of the anionic terbium(III) compound $[Li(DME)_3][Tb(t\text{-}Bu)_4]$ (**2**) react with oxidants to generate $Tb(t\text{-}Bu)_4$. Terbium (along with Pr) has the most accessible +4 oxidation state after cerium, its stability deriving in part from its f^7 electronic configuration.

Injection of 4 equivalents of dioxygen into solutions of **2** immediately caused a color change from colorless to yellow. When this reaction was followed by NMR spectroscopy, the broad ^1H NMR resonance at δ −76.6 due to the starting material disappeared after the addition of oxygen. Two new resonances appeared at δ 0.88 and 4.62, which are due to *iso*-butane (1.67 mol/mol Tb), and *iso*-butene (0.80 mol/mol Tb), respectively [36–38]; these assignments were confirmed by GC analysis. No new NMR resonances appeared that could be ascribed to an organolanthanide product. Similar addition of O_2 to the erbium complex **1** caused an exotherm but did not result in a change in the solution color. The broad ^1H NMR peak at δ −11 due to the starting material disappeared after dioxygen was added, but no peaks due to new organolanthanide species were apparent.

We also examined the action of one-electron chemical oxidants on the terbium compound **2**. Addition of silver acetate or silver chloride to a solution of **2** in diethyl ether resulted in the immediate precipitation of silver metal and a color change similar to that seen upon the addition of oxygen. Neither of these reactions resulted in the formation of pentane-soluble organolanthanide species. Addition of one equivalent of 1,1′-dimethylferrocenium tetrakis[3,5-bis(trifluoromethyl)phenyl]borate to **2** in diethyl ether caused the solution to change color from blue (the color of the ferrocenium salt) to yellow (the color of dimethylferrocene),

but again there was no evidence from the NMR spectra of the formation of a new organolanthanide species.

The present studies suggest that Ln(*t*-butyl)$_4$ species, if they exist, are not readily obtained by direct oxidation of their [Ln(*t*-butyl)$_4^-$] analogs with common oxidizing agents, possibly because the alkyl groups are more easily oxidized than the metal center.

3. Experimental

All syntheses were carried out under an argon atmosphere, using a glove box and Schlenk techniques. Solvents were dried over Na/benzophenone and distilled under nitrogen immediately before use. The starting materials $ErCl_3$ and $TbCl_3$ (99.9% pure, Alfa-Aesar), pentane solutions of *tert*-butyllithium (Aldrich), and oxygen gas (S. J. Smith) were used as received. Microanalyses were performed by the University of Illinois Microanalytical Laboratory. The IR spectra were recorded on a Nicolet Impact 410 instrument as Nujol mulls between KBr plates. The gas chromatographs were recorded on an Agilent 6890/5973 GCMS equipped with FID and TCD detectors; the inlet temperature was 250 °C, the oven temperature was 275 °C, the carrier gas was He (20.0 mL/min), and the separations were carried out on a 30 m long, 0.32 mm diameter, 1.5 μm thick carbon PLOT column with a deactivated SiO_2 guard column (J&W Scientific). The ^{1}H NMR data were collected on a Varian Unity U400 instrument at 400 MHz. Chemical shifts are reported in δ units (positive shifts to high frequency) relative to tetramethylsilane.

3.1. Tris(1,2-dimethoxyethane)lithium tetra(tert-butyl)erbate, [Li(DME)$_3$][Er(t-Bu)$_4$] (1)

To a slurry of $ErCl_3$ (0.30 g, 1.10 mmol) suspended in 1,2-dimethoxyethane (9 mL) and pentane (5 mL) at −78 °C was added a solution of *tert*-butyllithium (2.82 mL of a 1.7 M solution in pentane, diluted to 35 mL with pentane) dropwise over 90 min. The mixture was stirred for two hours at −78 °C and then slowly warmed to room temperature. After two hours at room temperature, the mixture had separated into a colorless layer (pentane and DME), a pink suspension (crude product), and a white powder (LiCl). The colorless layer was carefully decanted and the solid was washed with pentane (30 mL) and extracted with diethyl ether (2 × 30 mL). The bright pink extract was filtered, concentrated to about 30 mL, layered with pentane (~10 mL), and cooled to −20 °C. The pink prisms were isolated and dried in vacuum. Yield: 0.3 g (40%). Mp: 105 °C (dec). *Anal.* Calc. for $C_{28}H_{66}LiO_6Er$: C, 49.9; H, 9.88; Li, 1.03; Er, 24.9. Found: C, 49.1; H, 9.69; Li, 1.02; Er, 24.1%. ^{1}H NMR (d_8-THF): δ −11 (s, fwhm = 680 Hz, *t*-Bu), δ 3.2 (br, DME). IR (cm^{-1}): 2753 s, 2724 s, 2667 s, 2615 w, 1267 m, 1194 m, 1127 m, 1085 s, 1031 m, 870 s, 784 s.

3.2. Tris(1,2-dimethoxyethane)lithium tetra(tert-butyl)terbate, [Li(DME)$_3$][Tb(t-Bu)$_4$] (2)

The procedure is the same as that for the preparation of **1** except that the reagents used were $TbCl_3$ (0.30 g, 1.13 mmol) and *tert*-butyllithium (2.9 mL of a 1.7 M solution in pentane). The product was isolated as colorless prisms. Yield: 0.31 g (41%). Mp: 80 °C (dec). *Anal.* Calc. for $C_{28}H_{66}LiO_6Tb$: C, 50.6; H 10.0; Li, 1.04; Tb, 23.9. Found. C, 49.8; H, 9.78; Li, 1.02; Tb, 23.4%. ^{1}H NMR (d_8-THF): δ −76.6 (s, fwhm = 300 Hz, *t*-Bu) δ 3.3 (s, MeO), 3.4 (s, OCH_2). IR (cm^{-1}): 2752 s, 2722 s, 2668 s, 1246 s, 1195 s, 1130 s, 1088 s, 1030 m, 985 m, 871 s, 777 s.

3.3. Attempts to oxidize tetra(tert-butyl)terbate, [Li(DME)$_3$][Tb(t-Bu)$_4$] (2)

Colorless crystals of **2** (0.31 g, 0.47 mmol) were dissolved in diethyl ether (30 mL) and O_2 gas (45 mL, 1.85 mmol) was injected by syringe into the solution at room temperature. The solution color changed from colorless to yellow and a small amount of a flocculent precipitate formed. An aliquot was removed for analysis by GCMS, which showed the presence of *iso*-butene and *iso*-butane, in addition to peaks for the solvent and 1,2-dimethoxyethane.

In a separate experiment, a sample of **2** was placed in a 5 mm diameter NMR tube capped with a rubber septum, and the crystals were dissolved in d_8-THF (1 mL) to give a colorless solution. O_2 gas was bubbled into the solution until the solution color became yellow. ^{1}H NMR spectra were taken before and after the introduction of O_2. ^{1}H NMR (d_8-THF): δ 0.88 (s, CH*Me*$_3$), δ 4.62 (s, *CH*$_2$=CMe$_2$). The methine peak of *iso*-butane and the methyl peak of iso-butene were obscured by the resonance at δ 1.72 due to the solvent; peaks at δ 3.44 and 3.28 due to 1,2-dimethoxyethane were also present. By assuming that the 1,2-dimethoxyethane peaks corresponded to 3 mol/(mol Tb), the peak integrations suggested that 1.67 mol of *iso*-butane and 0.80 mol of *iso*-butene were formed per mol of Tb.

3.4. X-ray crystallographic studies [39]

Pink crystals of [Li(DME)$_3$][Er(*t*-Bu)$_4$] (**1**) were grown by diffusion of pentane into a diethyl ether solution at −20 °C. The crystal was twinned but the twinning was non-merohedral, and the two partially overlapping diffraction patterns were indexed separately. Systematic absences for *hkl* ($h + k \neq 2n$), and *h*0*l* ($l \neq 2n$) were consistent with the space groups *Cc* and *C*2/*c*. The structure was solved in *Cc* and later symmetrized to *C*2/*c*, which is correct space group. No corrections for crystal decay were necessary and, owing to the twinning, no absorption correction was applied. Systematically absent reflections were deleted.

The structure was solved using direct methods by using the SHELXTL software package. The correct positions for the

erbium atoms were deduced by direct-methods from an E-map. Subsequent least-squares refinement and difference Fourier calculations revealed the positions of the remaining non-hydrogen atoms. Non-hydrogen atoms were refined with independent anisotropic displacement parameters. Hydrogen atoms were fixed in "idealized" positions and their displacement parameters were tied to those of the attached non-hydrogen atom. The $Li(DME)_3$ cation centered on Li(3) was disordered about the two-fold axis. The disorder involved overlapping atoms, and was modeled in terms of three complete DME molecules, the atoms of which were assigned site occupancy factors of exactly 0.5. In addition, two of the *tert*-butyl groups on Er(2) were disordered over two rotameric conformations. The site occupancy factors for these groups were initially refined, but later set equal to exactly 0.5.

At this point, it became clear that several classes of reflections were affected by the twinning. Reflections with $|l| = 0$, 1, 11, 12, 13, 14, 24, 25, and 26 were systematically more intense than calculated. For reflections with these values of l, the calculated intensity was set equal to the formula $I_{calc} = xI_{hkl} + (1 - x)I_{h'k'l'}$, where $h' = -h - \mathrm{rnd}(l/6)$, $k' = -k$, and $l' = l$, and x is the volume fraction of the major twin individual; "rnd" indicates that the quotient $l/6$ was rounded to the nearest integer. About 100 of the reflections with $|l| = 1$, 11, and 14 were not modeled well by this function ($F^2 > 4.5F^2$), evidently because the two reciprocal lattices were sometimes distinguishable and only one reflection had been measured; such reflections were either reassigned calculated intensities based solely on the major twin, or deleted from the reflection file. The intensities of symmetry-equivalent reflections were *not* averaged, and 72 825 unique reflections were used in the least-squares refinement. The twin ratio refined to 0.682(1) for the major twin individual.

Similarity constraints were imposed on the Li–O, C–O, and C–C distances of the disordered DME ligands attached to Li(3), on the C–C distances in the disordered *tert*-butyl groups on Er(2), and on the displacement parameters of adjacent atoms. In the final cycle of least squares, anisotropic displacement factors were refined for all erbium and for all ordered oxygen carbon atoms; isotropic displacement parameters were refined for the lithium atoms and all disordered oxygen and carbon atoms. Hydrogen atoms were placed in idealized positions (for methyl protons, they were placed in positions staggered with respect to the substituents on the vicinal atom). The displacement parameters for methylene hydrogens were set equal to 1.2 times U_{eq} for the attached carbon; those for methyl hydrogens were set to 1.5 times U_{eq}. Successful convergence was indicated by the maximum shift/error of −0.009 for the last cycle. Final refinement parameters are given in Table 1. The largest peak in the final Fourier difference map (2.69 e $Å^{-3}$) was located 1.2 Å from Er(2). A final analysis of variance between observed and calculated structure factors showed that the intensities of many of the reflections with $|l| = 1$, 11, and 14 (and some with $|l| = 2$) were still not modeled well; otherwise, there were no systematic errors.

4. Supplementary material

CCDC 635390 contains the supplementary crystallographic data for this paper. These data can be obtained free of charge via http://www.ccdc.cam.ac.uk/conts/retrieving.html, or from the Cambridge Crystallographic Data Centre, 12 Union Road, Cambridge CB2 1EZ, UK; fax: (+44) 1223-336-033; or e-mail: deposit@ccdc.cam.ac.uk.

Acknowledgments

We thank the National Science Foundation for support of this research under Grant Nos. DMR03-54060 and DMR04-20768, and Scott R. Wilson and Teresa Prussak-Wieckowska for collecting the X-ray crystallographic data.

References

[1] F.T. Edelmann, in: E.W. Abel, F.G.A. Stone, G. Wilkinson, M.F. Lappert (Eds.), Comprehensive Organometallic Chemistry II, vol. 4, Pergamon, New York, 1995, pp. 11–212.
[2] R. Anwander, in: S. Kobayashi (Ed.), Topics in Organometallic Chemistry, vol. 2, Springer, Berlin, 1999, pp. 1–62.
[3] J-C.G. Bünzli, Acc. Chem. Res. 39 (2006) 53.
[4] P. Dorenbos, Chem. Mater. 17 (2005) 6452.
[5] Y.M. Kiselev, Y.D. Tret'yakov, Russ. Chem. Rev. 68 (1999) 365.
[6] M.N. Bochkarev, Coord. Chem. Rev. 248 (2004) 835.
[7] W.J. Evans, J. Organomet. Chem. 647 (2002) 2.
[8] S. Cotton, in: J.A. McCleverty, T.J. Meyer (Eds.), Comprehensive Coordination Chemistry II, vol. 3, Pergamon, New York, 2003, pp. 93–187.
[9] P.B. Hitchcock, M.F. Lappert, A.V. Protchenko, Chem. Commun. (2006) 3546.
[10] Z.W. Hu, G. Kaindl, B.G. Muller, J. Alloys Comp. 246 (1997) 177.
[11] M. Josse, M. Dubois, M. El-Ghozz, J. Cellier, D. Avignant, Acta Crystallogr., Sect. B 61 (2005) 1.
[12] D. Avignant, E. Largeau, V. Gaumet, P. Dugat, M. El-Ghozzi, J. Alloys Comp. 277 (1998) 1.
[13] Y. Hinatsu, Y. Doi, J. Alloys Comp. 418 (2006) 155.
[14] W.J. Liu, M. Dolg, P. Fulde, Inorg. Chem. 37 (1998) 1067.
[15] F.T. Edelmann, D.M.M. Freckmann, H. Schumann, Chem. Rev. 102 (2002) 1851.
[16] A. Streitwieser, S.A. Kinsley, C.H. Jenson, J.T. Rigsbee, Organometallics 23 (2004) 5169.
[17] H.D. Amberger, H. Reddmann, F.T. Edelmann, J. Organomet. Chem. 690 (2005) 2238.
[18] H. Schumann, W. Genthe, E. Hahn, J. Pickardt, J. Organomet. Chem. 306 (1986) 215.
[19] A.L. Wayda, W.J. Evans, J. Am. Chem. Soc. 100 (1978) 7119.
[20] H. Schumann, J. Muller, N. Bruncks, H. Lauke, J. Pickardt, H. Schwarz, K. Eckart, Organometallics 3 (1984) 69.
[21] J.L. Atwood, W.E. Hunter, R.D. Rogers, J. Holton, J. McMeeking, R. Pearce, M.F. Lappert, J. Chem. Soc., Chem. Commun. (1978) 140.
[22] H. Schumann, J. Müller, J. Organomet. Chem. 169 (1979) C1.
[23] F.A. Hart, A.G. Massey, M.S. Saran, J. Organomet. Chem. 21 (1970) 147.
[24] S.A. Cotton, F.A. Hart, M.B. Hursthouse, A.J. Welch, J. Chem. Soc., Chem. Commun. (1972) 1225.
[25] W.J. Evans, A.L. Wayda, J. Organomet. Chem. 202 (1980) C6.
[26] G.S. Girolami, C.G. Howard, G. Wilkinson, J. Chem. Soc., Dalton Trans. (1985) 921.

[27] G.E. Coates, P.D. Robers, A.J. Downs, J. Chem. Soc. A (1967) 1085.
[28] W.J. Evans, A.L. Wayda, J. Chem. Soc., Chem. Commun. (1981) 292.
[29] H. Schumann, S. Nickel, J. Loebel, J. Pickardt, Organometallics 7 (1988) 2004.
[30] H. Kawaguchi, K. Tatsumi, R.E. Cramer, Inorg. Chem. 35 (1996) 4391.
[31] J. Guan, S. Jin, Y. Lin, Q. Shen, Organometallics 11 (1992) 2483.
[32] J. Guan, Q. Shen, S. Jin, Y. Lin, Polyhedron 13 (1994) 1695.
[33] B.K. Bower, H.G. Tennent, J. Am. Chem. Soc. 94 (1972) 2512.
[34] C.A. Tolman, Chem. Rev. 77 (1977) 313.
[35] W. Kruse, J. Organomet. Chem. 42 (1972) C39.
[36] E. Pretsch, P. Bühlmann, C. Affolter, Structure Determination of Organic Compounds: Tables of Spectral Data, Springer, New York, 2000.
[37] S.A. Cheema, K.A. Holbrook, G.A. Oldershaw, D.P. Starkey, R.W. Walker, Phys. Chem. Chem. Phys. 1 (1999) 3243.
[38] S.L. Suib, J.F. Tanguay, M.L. Occelli, J. Am. Chem. Soc. 108 (1986) 6972.
[39] J.L. Brumaghim, J.G. Priepot, G.S. Girolami, Organometallics 18 (1999) 2139.

known for their analogues $[Cu(PhCN)_4][BF_4]$ (**2**) and $[Cu(BzCN)_4][BF_4]$ (**3**). In fact, to the best of our knowledge, no report has been given regarding the characterization of the complex **3**. We started our studies motivated by the possibility of using such compounds as starting materials for the preparation of new Cu(I) complexes. In addition, the evaluation of the factors that can affect detection of copper by NMR spectroscopy on these related systems will enlarge the application of this tool for the study of copper(I)-containing materials.

2. Experimental

2.1. General

Solvents and starting materials were used as received from the suppliers. Preparation of complex **2** was conducted using standard Schlenk techniques, under argon atmosphere.

2.2. Instrumentation

Elemental analyses (C, H, N) were performed on a Fisions MOD EA 1108 analyser. The infrared spectra (4000–400 cm^{-1}) were recorded on BOMEM BM 100 FT-IR spectrometer. NMR spectra were recorded on a Varian MERCURY plus spectrometer 7.05 T, operating at 300.07 MHz for ^{1}H, 96.27 MHz for ^{11}B, 75.46 MHz for ^{13}C, 282.31 MHz for ^{19}F and 79.58 MHz for ^{63}Cu. The ^{1}H, $^{11}B\{^{1}H\}$, $^{13}C\{^{1}H\}$, and ^{19}F NMR spectra were obtained in acetone-d_6 as solvent at room temperature. Chemical shifts (δ) are given in ppm relative to $SiMe_4$ (internal reference for ^{1}H and ^{13}C), neat $BF_3 \cdot OEt_2$ (external reference for ^{11}B) and CCl_3F (external reference for ^{19}F), respectively. The solution NMR studies were performed using broad band probe heads equipped with a variable-temperature unity precise to 0.5 °C. ^{63}Cu NMR spectra were acquired at 300 K (unless otherwise stated) in a 5 mm tube (o.d.) and were externally referenced to a 0.1 mol/L solution of **1** in CD_3CN by using a capillary ($\delta = 0$). A single pulse sequence was used. Typical NMR parameters were the following: spectroscopic window 55 866 Hz, pulse 10.7 μs (π/2 pulse length), acquisition time 0.293 s, 2048 scans, FT size 65 536 points. An exponential function Lb = 10 has been applied before Fourier transform. The ^{63}Cu line width at half-height, $\Delta\nu_{1/2}$, was determined by fitting it to Gaussian line shape using the VNMR 6.1C software. The $\Delta\nu_{1/2}$ for **1** was determined to be 530 Hz in accord with previous results [10].

2.3. Preparation of the complexes

The copper-nitrile complexes have been obtained based on the reported method for the preparation of **1** [11]. Typically, the complex $[Cu(BzCN)_4][BF_4]$ (**3**) was prepared as follows: Cu_2O (72 mg, 0.5 mmol) was suspended in phenylacetonitrile – BzCN (5 mL). Under continuous stirring, HBF_4 40% (0.16 mL, 1.0 mmol) was added at once. The red suspension was stirred until the color has discharged (approximately 1 h). After that, the product started to crystallize from the medium and the crystallization process was completed by adding toluene (1:1 v/v). The microcrystalline solid was filtered off, washed with ethyl ether and vacuum dried. Yield 405 mg (65%). M.p. 90–92 °C. *Anal.* Calc. for $C_{32}H_{28}BCuF_4N_4$: C, 62.10; H, 4.56; N, 9.05; Cu, 10.27. Found: C, 62.61; H, 4.50; N, 8.84; Cu, 9.48%. NMR (acetone-d_6) ^{1}H δ 7.31–7.16 (m, 20H, CH arom.), 3.95 (s, 8H, CH_2); $^{13}C\{^{1}H\}$ δ 130.8, 129.2, 128.3, 128.0, 118.5 (broad, CN), 23.0; $^{11}B\{^{1}H\}$ δ 2.2; ^{19}F δ −146.7. Selected IR bands (Nujol mull): 2284 (ν CN), 1050 cm^{-1} (br, ν_{asym} BF_4^-).

The complex $[Cu(PhCN)_4][BF_4]$ (**2**) was prepared as described above but in argon atmosphere to prevent its decomposition.

NMR (acetone-d_6) ^{1}H δ 7.8–7.6 (m); $^{13}C\{^{1}H\}$ δ 132.3, 130.7, 127.9, 109.3 (broad, CN); $^{11}B\{^{1}H\}$ δ 0.2; ^{19}F δ −147.1.

2.4. Crystallographic determination of 3

Suitable crystal of **3** for X-ray diffraction studies was grown by slow diffusion of ethyl ether into its BzCN solution.

Crystallographic measurements were made on a Bruker Kappa X8 Apex II CCD area detector with graphite monochromatized Mo Kα radiation ($\lambda = 0.71073$ Å) at 100(1) K. Raw image data were processed with SAINT and SADABS [12] to produce the final intensity data corrected for polarization, Lorentz and absorption effects. The structure was solved by direct methods (SHELXS-97) and additional atoms were located in the difference Fourier map and refined on F^2 (SHELXL-97) [13]. Hydrogen atoms were refined using a riding model.

Crystal data for **3** $C_{32}H_{28}BCuF_4N_4$: $M = 618.93$, colorless plate, $0.09 \times 0.43 \times 0.44$ mm^3, monoclinic, $P2(1)/n$ (no. 14 alternate), $a = 9.9620(11)$ Å, $b = 29.881(3)$ Å, $c = 10.2236(12)$ Å, $\beta = 90.363(5)°$, $V = 3043.3(6)$ $Å^3$, $Z = 4$, $D_{calc} = 1.351$ g cm^{-3}, $F_{000} = 1272$, $2\theta_{max} = 30.48°$, 53 060 reflection collected, 9250 independent, $R_{int} = 4.58\%$. Final goodness-of-fit = 1.036, R_1 [$I > 2\sigma(I)$] = 0.0367, wR_2 [all data] = 0.096, 380 parameters, $\Delta\rho_{min} = -0.52$, $\Delta\rho_{max} = 0.71$ e $Å^{-3}$.

3. Results and discussion

3.1. Solution ^{63}Cu NMR

3.1.1. Concentration effect

A stock solution of **2** 0.50 mol/L in benzonitrile, PhCN, was prepared and used to make the desired solutions for ^{63}Cu NMR studies. A dependence of the line width at half-height ($\Delta\nu_{1/2}$) on the concentration of **2** has been noticed (Fig. 1). It is worth mentioning that a 1.0 mol/L solution of **2** shows no ^{63}Cu NMR signal i.e. the bandwidth is so broad that it is beyond detection.

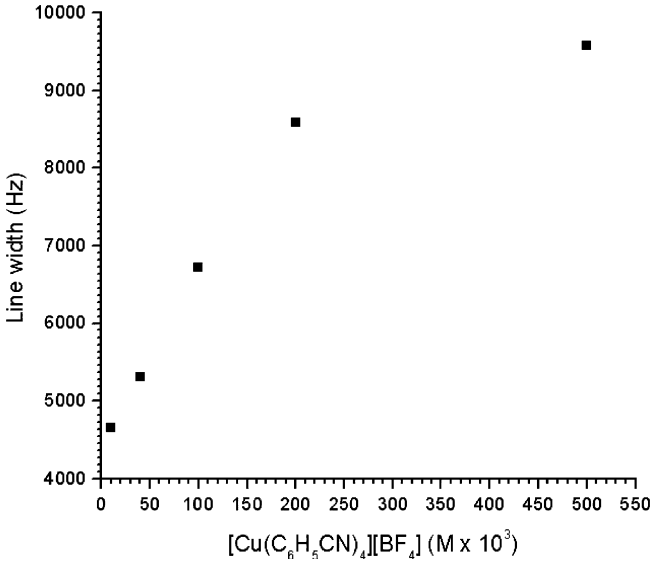


Fig. 1. Dependence of line width of the ^{63}Cu resonance on the concentration of $[Cu(PhCN)_4][BF_4]$ (**2**) in benzonitrile solution.

3.1.2. Temperature effect

The effect of the temperature on the ^{63}Cu chemical shift has been known to depend on the complex studied. For **1**, a negative effect of −0.75 ppm/K has been observed with the temperature increase [3]. A larger effect of about −1.0 ppm/K has been observed for **2** within the temperature range of 268–343 K (Fig. 2). As can be seen in Fig. 3, a line width minimum is observed at 313 K.

3.2. Solid-state ^{63}Cu NMR

While the solution of **3** could not be studied by ^{63}Cu NMR spectroscopy since its resonance is extremely broad, the ^{63}Cu MAS NMR spectrum of microcrystalline **3** (Fig. 4) shows a resonance whose line width is comparable to that of the standard CuCl.

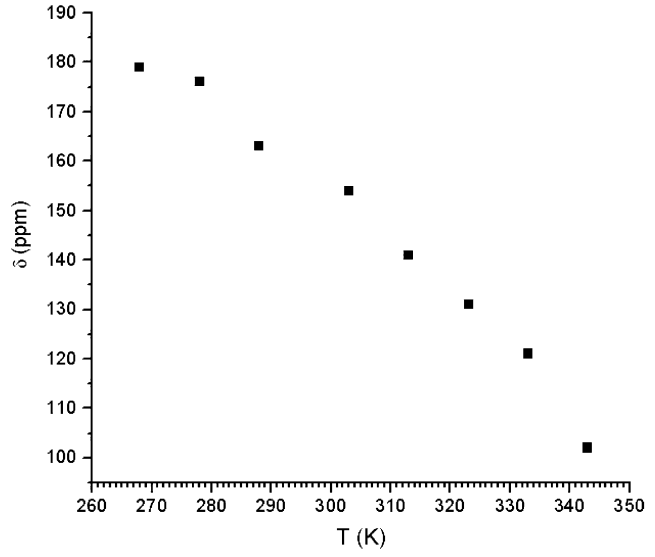


Fig. 2. Dependence of the ^{63}Cu chemical shift on the temperature of a 0.05 mol/L solution of $[Cu(PhCN)_4][BF_4]$ (**2**) in benzonitrile solution.

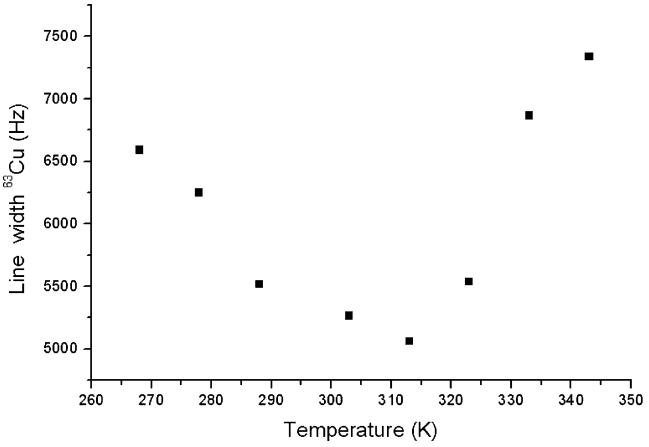


Fig. 3. Dependence of the ^{63}Cu line width on the temperature of a 0.05 mol/L solution of $[Cu(PhCN)_4][BF_4]$ (**2**) in benzonitrile solution.

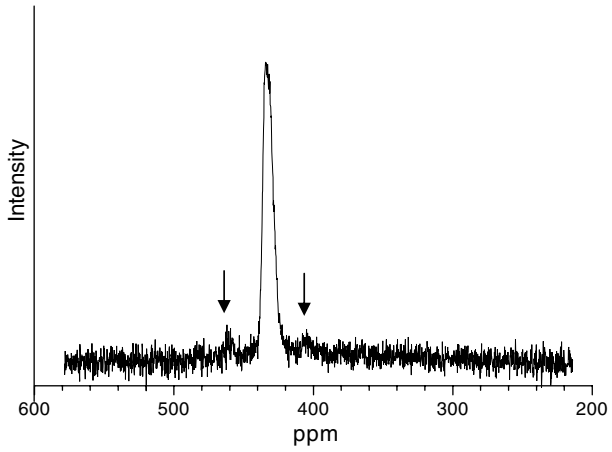


Fig. 4. ^{63}Cu MAS NMR spectrum of complex $[Cu(BzCN)_4][BF_4]$ (**3**) referenced against static CuCl ($\delta = 0$) [20]. Spectroscopic window 100 kHz, pulse width 5.5 μs, acquisition time 0.05 s, 256 scans, FT size 32768, spin rate 4 kHz. An exponential function Lb = 10 has been applied before Fourier transform. The two arrows point to spinning sidebands.

3.3. Solution structure by ^{63}Cu spectroscopy

It has been known that detectable narrow lines for ^{63}Cu NMR are usually obtained if the coordination sphere around Cu(I) is rigorously tetrahedral. These line widths are governed essentially by the quadrupolar relaxation rate, $(1/T_2)_Q$ [7], which depends on the symmetry. The $(1/T_2)_Q$ depends, in addition to some other parameters, on the reorientational correlation time, τ_R, which in turns depends on the viscosity of the solvent, η_S, and the radius of the complex, r_c, (Stokes–Einstein model).

$$\tau_R \propto \eta_S r_c^3 \quad (1)$$

In complex **2**, an increase in the ^{63}Cu line width occurs with the increase of the complex concentration. This result is in line with previous reports concerning the complexes [Cu

$(MeCN)_4]X$, where $X = BF_4^-$, ClO_4^- in acetonitrile as solvent [2,8,10]. It is also known that a dramatic increase of the line width occurs with an increase of the mole ratio benzonitrile/acetonitrile [7]. This phenomenon has been interpreted as a consequence of an increase of the viscosity of the medium as the concentration of the complex increases (Eq. 1). Attempts to acquire ^{63}Cu NMR spectra of **2** in $(CD_3)_2CO$ were unsuccessful. It is concluded that the ligand benzonitrile tends to dissociate giving the three-coordinate, or even two-coordinate, species as depicted below (Eq. 2). When benzonitrile is employed as solvent such dynamic equilibrium favors the tetra-coordinated species and so the signal can be detected.

$$[Cu(PhCN)_4]^+ = [Cu(PhCN)_{(4-n)}]^+ + n\text{PhCN} \quad (2)$$

Complex **2** exhibited an anomalous profile in the variable-temperature ^{63}Cu spectra above 213 K, since decreasing of the line width would be expected with increasing temperature for quadrupolar relaxation. This same profile has been observed for $[Cu(MeCN)_4]X$ although their line width minimum is located at about 268 K [2]. Such anomaly has been interpreted based on ligand exchange becoming more severe with increasing temperature.

In the case of **3**, no signal could be detected either in the phenylacetonitrile solution 0.05–0.2 mol/L range or in acetone-d_6 as solutions in the 0.005–0.25 mol/L range, in spite of much effort devoted to this task. Since compound **3** is much more inert in the air compared to **2**, its reluctance to give NMR signal should not be attributed to the presence of Cu^{2+}. The white solid **3** has been kept in a stopped vessel for about two years with no apparent change although it has been opened a couple of times. We hypothesized that this behavior is a consequence of dynamic equilibrium taking place in solution between the tetra- three- and two-coordinated species, with exchange rate in the order of the NMR time scale. Even MeCN, which is less crowding compared to BzCN, can form low-coordinated copper(I) complexes, demonstrated recently by the X-ray structure of two-coordinated $[Cu(MeCN)_2][B(C_6F_5)_4]$ [14]. In order to confirm our hypothesis we set out to study **3** by solid-state ^{63}Cu NMR spectroscopy and X-ray crystallography. Accordingly, ^{63}Cu MAS NMR spectrum has been acquired for the microcrystalline solid **3** and it turned out to give a reasonably sharp resonance, namely, $\Delta\nu_{1/2}$ 1.06 kHz (Fig. 4) which is comparable to the reference's line width obtained at the same speed. The NMR data of **3** suggest that the copper atom is tetra-coordinated in the solid-state while in solution an equilibrium between tetra- and lower coordinated species is operative. In fact, the X-ray diffraction study confirmed that the copper(I) atoms is tetra-coordinated by four nitrile ligands in a slightly distorted tetrahedral geometry (Fig. 5).

The ^1H and $^{13}C\{^1H\}$ NMR of **2** and **3** spectra show no indication of free nitrile in acetone-d_6 solution at room temperature. It can be concluded that one only see averaged signals in such conditions, consistent with the proposed equilibrium depicted in (2).

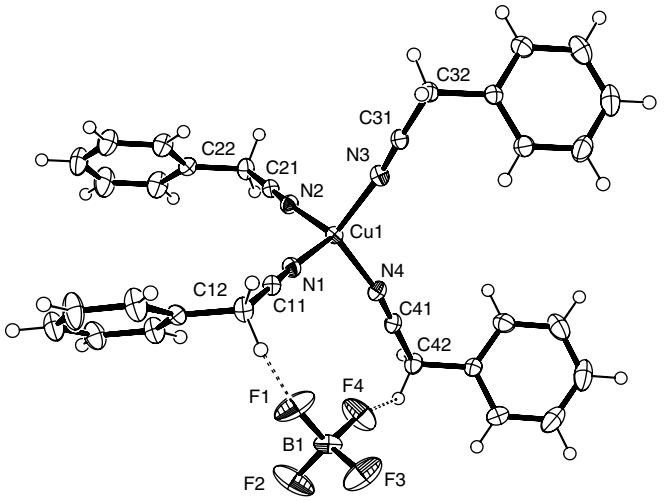


Fig. 5. ORTEP [21] plot of $[Cu(BzCN)_4][BF_4]$ (**3**) with the atom numbering. Thermal ellipsoids are scaled at 50%. Selected bond distances (Å) and bond angles (°): Cu(1)–N(1), 1.9828(12); Cu(1)–N(2), 1.9869(12); Cu(1)–N(3), 1.9815(12); Cu(1)–N(4), 1.9838(12); N(3)–Cu(1)–N(1), 102.14(5); N(3)–Cu(1)–N(4), 114.74(5); N(1)–Cu(1)–N(4), 111.90(5); N(3)–Cu(1)–N(2), 110.78(5); N(1)–Cu(1)–N(2), 114.89(5); N(4)–Cu(1)–N(2), 102.85(5); C(11)–N(1)–Cu(1), 170.74(12); C(21)–N(2)–Cu(1), 170.72(12); C(31)–N(3)–Cu(1), 169.69(12); C(41)–N(4)–Cu(1), 168.37(12).

3.4. X-ray structure of 3

The X-ray crystallographic study of the complex $[Cu(BzCN)_4][BF_4]$ (**3**) reveals a slightly distorted tetrahedral copper(I) center with four BzCN ligands coordinated via their nitrogen atoms. The Cu–N distances, which are almost equal varying from 1.9815(12) Å to 1.9869(12) Å, are close to the average found for similar compounds, 1.99(3) Å for 47 compounds found in the Cambridge Structural Database [15]. The angle between the planes N1–Cu1–N4 and N2–Cu1–N3 is 81.42(3)° showing a slightly flattening of the tetrahedron; the N–Cu–N bond angles range from 102.85(5)° to 114.89(5)°. The Cu–N–C angles fall between 168.37(12)° and 170.74(12)°, which is normal compared to the average for the similar compounds, 172(4)°. The geometry of the BzCN ligands is not remarkable. No π–π interactions are seen in the structure of **3**, unlike those of similar $[Cu(NCPh)_4]^+$ compounds [16–18] where the Cu–N–C angles are much more distorted from the average and the geometry around the copper(I) atom is more flattened. There are non-classic hydrogen bonding interactions between one hydrogen atom of each methylene

Table 1
Non-classic hydrogen bonds for **3**, $[Cu(BzCN)_4][BF_4]$ (Å and °)

D–H···A	d(D–H)	d(H···A)	d(D···A)	∠(DHA)
C(12)–H(12B)···F(1)	0.99	2.62	3.1777(19)	115.7
C(42)–H(42B)···F(4)	0.99	2.67	3.248(2)	117.7
C(32)–H(32B)···F(3)[a]	0.99	2.61	3.2010(19)	118.3
C(22)–H(22B)···F(2)[a]	0.99	2.59	3.1891(19)	119.2

Symmetry transformations used to generate equivalent atoms.
[a] $x, y, z-1$.

group of the BzCN ligands and the fluorine atoms of the BF_4 anion, Table 1, to form a continuous chain along the crystallographic *z* direction.

3.5. Chemical properties of $[Cu(PhCN)_4][BF_4]$ (2) and $[Cu(BzCN)_4][BF_4]$ (3)

Crystalline **3** can be handled on a bench top since it is more air-stable copper(I) complex compared to **1** or **2**. It is also stable in BzCN solution. Apparently, the benzyl groups block more effectively the access of dioxygen molecule compared to methyl groups, for example. Compound **3** seems to be a more convenient starting material for the preparation of copper(I) complexes since it is: (i) easily prepared, (ii) safely handled, and (iii) labile regarding ligand displacement. For instance, the reaction of **3** with 4,6-dimethylpyrimidine-2-thione (dmpymtH) proceeds in phenylacetonitrile/toluene mixture (1:1), under reflux, with displacement of all BzCN molecules by the heterocyclic ligand giving the already known complex $[Cu(dmpymtH)_3]_2[BF_4]_2 \cdot 2H_2O$ [19]. The lability of **3** is also supported by the fact that when it was treated with a coordinating anion containing salt, i.e., KSCN, pure CuSCN precipitated, confirmed by comparison of its infrared spectrum with that of an authentic sample.

Acknowledgement

Financial support from FINEP CT-INFRA (970/01) is gratefully acknowledged.

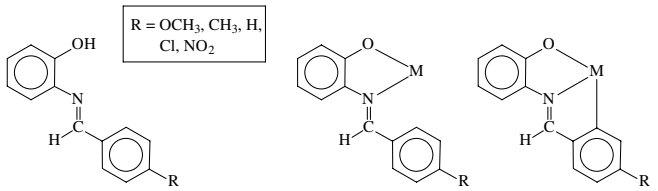
Appendix A. Supplementary material

CCDC 632661 contains the supplementary crystallographic data for this paper. These data can be obtained free of charge via http://www.ccdc.cam.ac.uk/conts/retrieving.html, or from the Cambridge Crystallographic Data Centre, 12 Union Road, Cambridge CB2 1EZ, UK; fax: (+44) 1223-336-033; or e-mail: deposit@ccdc.cam.ac.uk. Supplementary data associated with this article can be found, in the online version, at doi:10.1016/j.poly.2007.04.007.

References

[1] C. Borriello, M.E. Cucciolito, A. Panunzi, F. Ruffo, Tetrahedron: Asymmetry 12 (2001) 2467.
[2] J.K. Irangu, R.B. Jordan, Inorg. Chem. 42 (2003) 3934, and references cited therein.
[3] P. Granger, in: P.S. Pregosin (Ed.), Transition Metal Nuclear Magnetic Resonance, vol. 13, Elsevier, Amsterdan, 1991, p. 265.
[4] J. Malito, Annu. Rep. NMR Spectrosc. 38 (1999) 265.
[5] J.R. Black, W. Levason, M.D. Spicer, M. Webster, J. Chem. Soc., Dalton Trans. (1993) 3129.
[6] D.S. Gill, L. Rodehüser, J.-J. Delpuech, J. Chem. Soc., Faraday Trans. 86 (1990) 2847.
[7] D.S. Gill, L. Rodehüser, P. Rubini, J.-J. Delpuech, J. Chem. Soc., Faraday Trans. 91 (1995) 2307.
[8] U. Ochsenbein, C.W. Schläpfer, Helv. Chim. Acta 63 (1980) 1926.
[9] O. Lutz, H. Oehler, P. Kroneck, Z. Phys. A: Hadrons Nucl. 288 (1978) 17.
[10] P. Kroneck, J. Kodweiss, O. Lutz, A. Nolle, D. Zepf, Z. Naturforsch. 37a (1982) 186.
[11] G.J. Kubas, B. Monzyk, A.L. Crumbliss, in: R.J. Angelici (Ed.), Inorg. Synth. 28 (1991) 68.
[12] Bruker AXS Inc., SAINT (version 7.06A) and SADABS (version 2.10), Madison, Wisconsin, USA, 2005.
[13] G.M. Sheldrick, SHELXS97 and SHELXL97, University of Göttingen, Göttingen, Germany, 1997.
[14] H.-C. Liang, E. Kim, C.D. Incarvito, A.L. Rheingold, K.D. Karlin, Inorg. Chem. 41 (2002) 2209.
[15] F.H. Allen, Acta Crystallogr., Sect. B 58 (2002) 380.
[16] S. Brownstein, N.F. Han, E. Gabe, Y. Le Page, Can. J. Chem. 67 (1989) 2222.
[17] G.A. Bowmaker, D.S. Gill, B.W. Skelton, N. Somers, A.H. White, Z. Naturforsch. B 59 (2004) 1307.
[18] J.M. Knaust, D.A. Knight, S.W. Keller, J. Chem. Crystallogr. 33 (2003) 813.
[19] V.A.S. Falcomer, S.S. Lemos, A.A. Batista, J. Ellena, E.E. Castellano, Inorg. Chim. Acta 359 (2006) 1064.
[20] S. Sakida, N. Kato, Y. Kawamoto, Mater. Res. Bull. 37 (2002) 2263.
[21] L.J. Farrugia, J. Appl. Cryst. 30 (1997) 565.

accommodate tridentate ligands via displacement of three pre-coordinated ligands and, more importantly, its proven efficiency to bring about C–H activation of organic molecules [2b,2c,2i]. Reaction of the *N*-(2′-hydroxyphenyl)benzaldimines (**1**) with $[Ru(PPh_3)_2(CO)_2Cl_2]$ has indeed been observed to afford a family of organoruthenium complexes containing chelate **3** (M = Ru). An account of the chemistry of these organoruthenium complexes is presented here, with special reference to their formation, structure and, spectral and electrochemical properties.



2. Experimental

2.1. Materials

Commercial ruthenium trichloride was purchased from Arora Matthey, Kolkata, India. Triphenylphosphine, 2-aminophenol and the *para*-substituted benzaldehydes were obtained from Merck, India. All other chemicals and solvents were reagent grade commercial materials and were used as received. $[Ru(PPh_3)_2(CO)_2Cl_2]$ was prepared following a reported procedure [8]. The *N*-(2′-hydroxyphenyl)-benzaldimines (**1**) were prepared by reacting equimolar amounts of respective *para*-substituted benzaldehyde and 2-aminophenol in ethanol. Purification of acetonitrile and dichloromethane, and preparation of tetrabutylammonium perchlorate (TBAP) for electrochemical work were performed as reported in the literature [9].

2.2. Synthesis

The $[Ru(PPh_3)_2(CO)(L\text{-}R)]$ complexes were synthesized by following a general procedure. Specific details are given below for a particular complex.

[Ru(PPh$_3$)$_2$(CO)(L-OCH$_3$)]: *N*-(2′-hydroxyphenyl)-4-methoxybenzaldimine (30 mg, 0.13 mmol) was dissolved in 2-methoxyethanol (40 mL) and triethylamine (30 mg, 0.30 mmol) was added to it followed by $[Ru(PPh_3)_2(CO)_2Cl_2]$ (100 mg, 0.13 mmol). The resulting mixture was then refluxed for 24 h, whereby a violet solution was obtained. Evaporation of the solution gave a violet solid, which was subjected to purification by thin layer chromatography on a silica plate. Using benzene as the eluant a violet band separated, which was extracted with acetonitrile. On evaporation of the acetonitrile extract $[Ru(PPh_3)_2(CO)(L\text{-}OCH_3)]$ was obtained as crystalline solid. Yield: 70%. *Anal.* Calc. C, 69.70; H, 4.66; N, 1.59. Found: C, 69.79; H, 4.64; N, 1.57%. ^{1}H NMR in $CDCl_3$, δ ppm[2]: 3.48 (OCH_3); 5.72 (t, 1H, $J = 7.1$); 5.90 (d, H, $J = 6.0$); 6.07 (d, 2H)*; 6.37 (s, 1H); 6.46 (t, 1H, $J = 7.2$); 6.73 (d, 1H, $J = 8.2$); 7.15–7.49 ($2PPh_3$). IR: 1919 cm^{-1} (ν_{CO}).

[Ru(PPh$_3$)$_2$(CO)(L-CH$_3$)]: Yield: 80%. *Anal.* Calc. C, 70.99; H, 4.75; N, 1.62. Found: C, 71.01; H, 4.72; N, 1.59%. ^{1}H NMR in $CDCl_3$, δ ppm: 1.89 (CH_3); 5.70 (t, 1H, $J = 7.1$); 5.90 (d, 1H, $J = 7.9$); 6.08 (d, 1H, $J = 8.2$); 6.29 (d, 1H, $J = 7.4$); 6.46 (t, 1H, $J = 7.6$); 6.69 (2H)*; 7.15–7.61 ($2PPh_3$). IR: 1920 cm^{-1} (ν_{CO}).

[Ru(PPh$_3$)$_2$(CO)(L-H)]: Yield: 75%. *Anal.* Calc. C, 70.75; H, 4.59; N, 1.65. Found: C, 70.78; H, 4.57; N, 1.64%. ^{1}H NMR in $CDCl_3$, δ ppm: 5.30 (s, 1H); 5.70 (t, 1H, $J = 7.3$); 5.91 (d, 1H, $J = 7.9$); 6.03 (d, 1H, $J = 8.3$); 6.44 (t, 2H); 6.74 (d , 1H, $J = 7.2$); 7.03 (d, 1H, $J = 7.4$); 7.13–7.70 ($2PPh_3$). IR: 1917 cm^{-1} (ν_{CO}).

[Ru(PPh$_3$)$_2$(CO)(L-Cl)]: Yield: 74%. *Anal.* Calc. C, 67.98; H, 4.30; N, 1.58. Found: C, 68.02; H, 4.28; N, 1.55%. ^{1}H NMR in $CDCl_3$, δ ppm: 5.71 (t, 1H, $J = 7.4$); 5.91 (d, 1H, $J = 7.8$); 6.05 (d, 1H, $J = 8.3$); 6.46 (t, 1H, $J = 9.4$); 6.65 (d, 1H, $J = 7.9$); 6.83 (s, 1H); 7.17–7.66 ($2PPh_3$). IR: 1921 cm^{-1} (ν_{CO}).

[Ru(PPh$_3$)$_2$(CO)(L-NO$_2$)]: Yield: 78%. *Anal.* Calc. C, 67.19; H, 4.66; N,1.59. Found: C, 67.21; H, 4.64; N, 1.57%. ^{1}H NMR in $CDCl_3$, δ ppm: 5.71 (d, 2H)*; 5.89 (d, 1H, $J = 8.17$); 6.11 (t, 1H, $J = 10.12$); 6.28 (s, 1H); 6.35 (d, 1H, $J = 7.57$); 6.79 (t, 1H, $J = 9.99$); 6.91 (s, 1H); 7.16–7.37 ($2PPh_3$). IR: 1920 cm^{-1} (ν_{CO}).

2.3. Physical measurements

Microanalyses (C, H, N) were performed using a Heraeus Carlo Erba 1108 elemental analyzer. ^{1}H NMR spectra were recorded in $CDCl_3$ solution on a Bruker Avance DPX 300 NMR spectrometer using TMS as the internal standard. IR spectra were obtained on a Shimadzu FTIR-8300 spectrometer with samples prepared as KBr pellets. Electronic spectra were recorded on a JASCO V-570 spectrophotometer. Electrochemical measurements were made using a CH Instruments model 600A electrochemical analyzer. A platinum disc working electrode, a platinum wire auxiliary electrode and an aqueous saturated calomel reference electrode (SCE) were used in the cyclic voltammetry experiments. All electrochemical experiments were performed under a dinitrogen atmosphere. All electrochemical data were collected at 298 K and are uncorrected for junction potentials.

2.4. X-ray crystallography

Single crystals of $[Ru(PPh_3)_2(CO)(L\text{-}H)]$ were obtained by slow evaporation of an acetonitrile solution of the complex. Selected crystal data and data collection parameters

[2] Chemical shifts are given in ppm and multiplicity of the signals along with the associated coupling constants (*J* in Hz) are given in parentheses. Overlapping signals are marked with an asterisk.

are given in Table S1. Data were collected on a Bruker SMART APEX CCD area detector system using graphite monochromated Mo Kα radiation ($\lambda = 0.71073$ Å). X-ray data reduction, structure solution and refinement were done using SHELXS-97 and SHELXL-97 programs [10]. The structure was solved by the direct methods. The absolute configuration of the $[Ru(PPh_3)_2(CO)(L\text{-}H)]$ complex was determined by Flack parameter 0.12(4). Expected values of Flack parameter are 0 for correct and +1 for inverted structure. Using the option TWIN/BASF, the refined BASF is found to be identical with the Flack parameter, which confirmed the correct enantiomer.

Crystal data for $C_{50}H_{39}NO_2P_2Ru$, $M = 848.83$, $0.08 \times 0.11 \times 0.18$ mm^3, monoclinic, space group Cc, $a = 23.531(4)$ Å, $b = 8.988(2)$ Å, $c = 20.553(4)$ Å, $\beta = 115.15(2)°$, $V = 3934.8(15)$ Å^3, $Z = 4$, $D_{calc} = 1.433$ Mg m^{-3}, $F(000) = 1744$, $\lambda = 0.71073$ Å, $T = 293$ K, $\mu = 0.523$ mm^{-1}, 19 776 reflections collected, 7677 unique ($R_{int} = 0.019$). Final goodness-of-fit = 1.07, $R_1 = 0.0543$, $wR_2 = 0.1258$, R indices based on 7024 reflections with $I > 2\sigma(I)$.

3. Results and discussion

3.1. Synthesis and crystal structure

Five *N*-(2′-hydroxyphenyl)benzaldimines (**1**) have been used in the present study, differing in the inductive effect of the *para*-substituents (R), in order to observe their influence, if any, on the redox properties of the complexes. These ligands are in general abbreviated as H_2L-R, where H_2 stands for the two protons, the phenolic proton and one ortho proton of the phenyl ring in the benzaldehyde fragment, which are expected to undergo dissociation upon formation of chelate **3** and R for the *para*-substituent. Reactions of the *N*-(2′-hydroxyphenyl)benzaldimines (**1**) with $[Ru(PPh_3)_2(CO)_2Cl_2]$ proceed smoothly in refluxing 2-methoxyethanol in the presence of triethylamine, affording a family of violet complexes of type $[Ru(PPh_3)_2(CO)(L\text{-}R)]$ in good yields. Microanalytical (C, H, N) data of

Table 1
Selected bond distances (Å) and angles (°) for complex $[Ru(PPh_3)_2(CO)(L\text{-}H)]$

Bond distances (Å)			
Ru(1)–C(52)	2.089(8)	C(46)–N(1)	1.336(9)
Ru(1)–N(1)	1.992(5)	C(40)–N(1)	1.470(10)
Ru(1)–O(2)	2.107(6)	C(45)–O(2)	1.343(9)
Ru(1)–P(1)	2.401(2)	C(39)–O(1)	1.057(8)
Ru(1)–P(2)	2.354(3)		
Ru(1)–C(39)	1.860(6)		
Bond angles (°)			
C(52)–Ru(1)–O(2)	154.7(2)	C(52)–Ru(1)–N(1)	77.2(3)
P(1)–Ru(1)–P(2)	177.76(7)	N(1)–Ru(1)–O(2)	77.5(2)
N(1)–Ru(1)–C(39)	172.5(3)	Ru(1)–C(39)–O(1)	168.0(8)

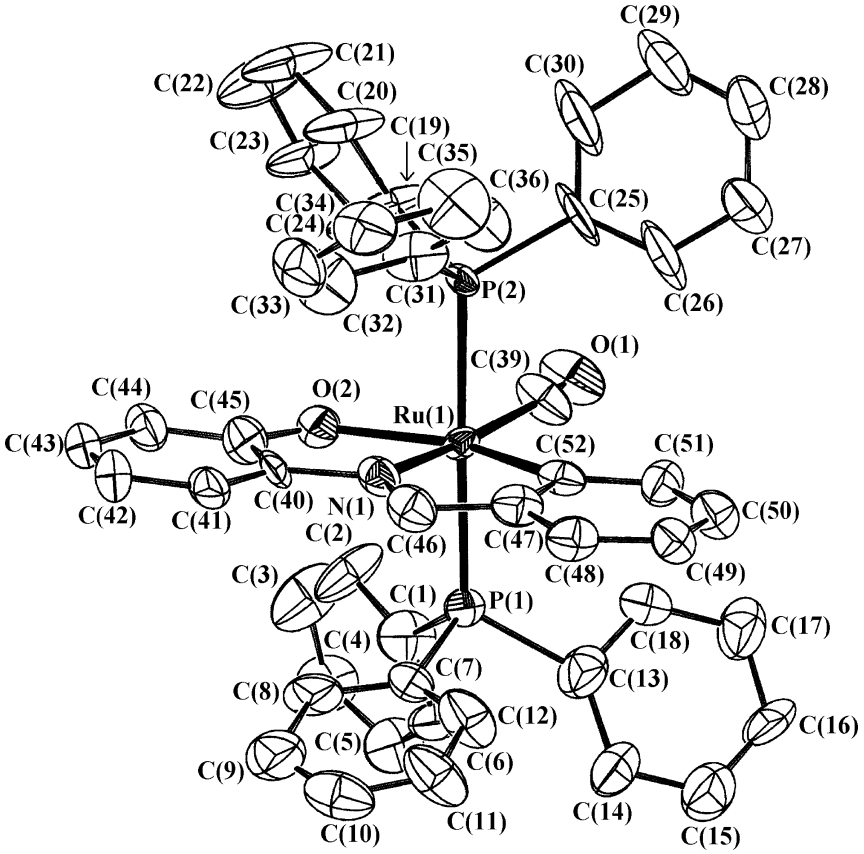


Fig. 1. Structure of the $[Ru(PPh_3)_2(CO)(L\text{-}H)]$ complex. The thermal ellipsoids of several carbon atoms are not of proper shape, probably due to overestimated empirical absorption correction.

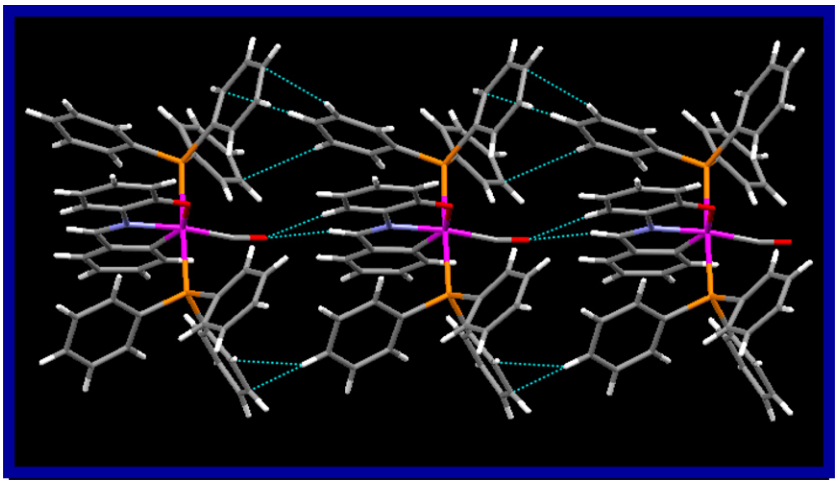
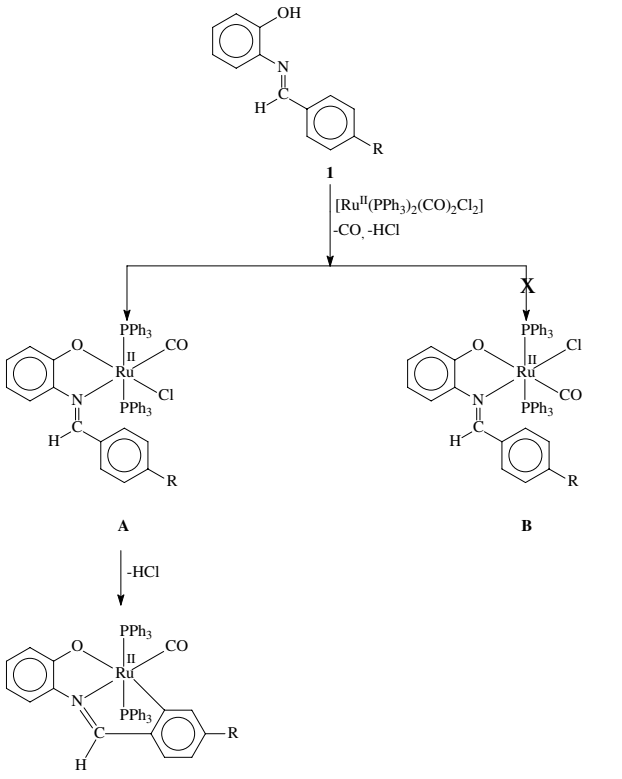


Fig. 2. The hydrogen bonding interactions in the crystal lattice of $[Ru(PPh_3)_2(CO)(L\text{-}H)]$.

the complexes are in well agreement with their compositions. The complexes are diamagnetic, which corresponds to the bivalent state of ruthenium (low-spin d^6, $S = 0$). These preliminary characterization data of the complexes indicate that the benzaldimines are probably serving as dianionic tridentate ligands in them. In order to authenticate the coordination mode of the benzaldimines in these complexes, as well as to find out their stereochemistry, structure of a representative member of this family, *viz.* $[Ru(PPh_3)_2(CO)(L\text{-}H)]$, has been determined by X-ray crystallography. The structure is shown in Fig. 1, and selected bond parameters are listed in Table 1. The structure shows that the *N*-(2′-hydroxyphenyl)benzaldimine is coordinated to ruthenium in the tridentate C,N,O-fashion (**3**, M = Ru), via loss of the phenolic proton and another proton from one ortho position of the phenyl ring in the benzaldehyde fragment. Thus two adjacent five-membered rings are formed with O–Ru–N and N–Ru–C bite angles of 77.5° and 77.2°, respectively. Two triphenylphosphines and a carbonyl are also coordinated to the metal center. Ruthenium is therefore sitting in a C_2NOP_2 coordination environment, which is distorted octahedral in nature as reflected in all the bond parameters around ruthenium. The coordinated benzaldimine ligand and the carbonyl have constituted one equatorial plane with the metal at the center, while the PPh_3 ligands have occupied the remaining axial positions and hence they are mutually trans. The Ru–P and Ru–C (carbonyl) and C–O (carbonyl) distances are all quite normal [2b,2c,2i]. Within the Ru-(L-H) fragment, the Ru–C, Ru–N and Ru–O distances are also quite usual [2b,2c,2i,11] and so are the C–O and C–N distances [4]. However, the Ru–C–O angle (168.0°) in the Ru-carbonyl fragment is found to deviate significantly from linearity. The absence of any solvent of crystallization in the crystal lattice of $[Ru(PPh_3)_2(CO)(L\text{-}H)]$ indicates possible existence of non-covalent interaction(s) between the individual complex molecules. A closer look at the packing pattern of the crystal reveals that non-covalent interactions of two types, viz. C–H···O and C–H···π interactions, are active in the lattice, which are illustrated in Fig. 2. The carbonyl oxygen in each complex molecule is hydrogen-bonded simultaneously to a phenyl C–H and the azomethine C–H of the benzaldimine ligand belonging to an adjacent complex molecule. Several phenyl C–H fragments of the triphenyl phosphines are involved in hydrogen-bonding with the π-cloud over the phenyl rings of the triphenylphosphines of neighboring complex molecules. Each complex molecule is thus linked with the surrounding complex molecules through C–H···O and C–H···π interactions, and this extended intermolecular hydrogen-bonding interactions seem to be responsible for holding the crystal together. As all the $[Ru(PPh_3)_2(CO)(L\text{-}R)]$ complexes have been synthesized similarly and they show similar properties (*vide infra*), the other four $[Ru(PPh_3)_2(CO)(L\text{-}R)]$ ($R \neq H$) complexes are assumed to have similar structures as the $[Ru(PPh_3)_2(CO)(L\text{-}H)]$ complex.

Although the exact mechanism behind formation of the $[Ru(PPh_3)_2(CO)(L\text{-}R)]$ complexes is not completely clear to us, the sequences shown in Scheme 1 seem probable. In the first step the benzaldimine ligand binds to ruthenium, via loss of the phenolic proton, as a bidentate N,O-donor with simultaneous dissociation of a carbon monoxide and a chloride ion from $[Ru(PPh_3)_2(CO)_2Cl_2]$, thereby producing a reactive intermediate (**A**). In **A** the coordinated chloride and the pendent phenyl ring of the benzaldimine are appropriately disposed for the C–H activation to occur at the ortho position of the phenyl ring and hence it is believed to undergo the expected cyclometallation via elimination of HCl to produce the final organoruthenium complex, $[Ru(PPh_3)_2(CO)(L\text{-}R)]$. Presence of triethylamine seems to have facilitated initial dissociation of the phenolic proton, as well as elimination of HCl during orthometallation.[3] Attempts to isolate the intermediate **A** have failed, probably because it

[3] From the same reactions the complexes are obtained in very poor yield in the absence of triethylamine.



Scheme 1. Probable steps of the formation of the $[Ru(PPh_3)_2(CO)(L\text{-}R)]$ complexes.

undergoes rapid cyclometallation to afford the $[Ru(PPh_3)_2(CO)(L\text{-}R)]$ complex. Formation of another stereoisomer of the intermediate (**B**), keeping the *trans* disposition of the two triphenylphosphines unaltered and differing only in the relative disposition of carbonyl and chloride, is, in principle, possible. This stereoisomer **B** is unlikely to undergo a similar cyclometallation due to unfavorable disposition of the chloride. However, this isomer **B** has never been obtained from the synthetic reactions, which suggests that isomer **A** is the only intermediate formed under the prevailing reaction conditions.

3.2. Spectral properties

Infrared spectra of the $[Ru(PPh_3)_2(CO)(L\text{-}R)]$ complexes show many bands of varying intensities within 4000–400 cm^{-1}. Assignment of each individual band to a specific vibration has not been attempted. However, three strong bands observed around 518, 695 and 743 cm^{-1} in all the complexes are attributable to the coordinated triphenylphosphines, and a very intense band observed near 1920 cm^{-1} to the coordinated carbonyl. Comparison with the spectrum of $[Ru(PPh_3)_2(CO)_2Cl_2]$ shows presence of some new bands (*viz*. 1090, 1314, 1434, 1462, 1566, 1588 cm^{-1}) in the spectra of the $[Ru(PPh_3)_2(CO)(L\text{-}R)]$ complexes, which are probably due to the coordinated benzaldimine ligand.

^1H NMR spectra of the $[Ru(PPh_3)_2(CO)(L\text{-}R)]$ complexes, recorded in $CDCl_3$ solution, show broad signals for the coordinated triphenylphosphines within 7.1–7.6 ppm. The methyl signals of the benzaldimine ligand in the $[Ru(PPh_3)_2(CO)(L\text{-}CH_3)]$ and $[Ru(PPh_3)_2(CO)(L\text{-}OCH_3)]$ complexes are observed, respectively, at 1.89 and 3.48 ppm. However, signal for the azomethine proton could not be identified probably due to its overlap with the triphenylphosphine signals. All other signals expected for the coordinated benzaldimine ligand are observed clearly in all the complexes. Thus the infrared and ^1H NMR spectral data of the $[Ru(PPh_3)_2(CO)(L\text{-}R)]$ complexes are found to be consistent with their compositions.

All the $[Ru(PPh_3)_2(CO)(L\text{-}R)]$ complexes are readily soluble in dichloromethane, chloroform, acetone, etc., and sparingly soluble in methanol, ethanol, acetonitrile, etc., producing violet solutions. Electronic spectra of the complexes have been recorded in dichloromethane solution. Spectral data are presented in Table 2. Each complex shows several intense absorptions in the visible and ultraviolet region. The absorptions in the ultraviolet region are believed to be due to transitions within the ligand orbitals. To have an insight into the nature of absorptions in the visible region, semi-empirical EHMO calculations have been performed on computer-generated models of all the complexes [12], where phenyl rings of the triphenylphosphines have been replaced by hydrogens. The results are found to be qualitatively similar for all the complexes.[4] Compositions of some selected molecular orbitals are given in Table 3 and partial MO diagram of a representative complex is shown in Fig. 3. The calculations show that the highest occupied molecular orbital (HOMO) and the next two filled molecular orbitals, viz. HOMO − 1 and HOMO − 2, have major contribution (>47%) from the metal d-orbitals and hence they may be considered as ruthenium t_2 orbitals. The lowest unoccupied molecular orbital (LUMO) is localized almost entirely on the benzaldimine ligand and is concentrated mostly (>50%) on the imine fragment. The next two vacant molecular orbitals, viz. LUMO + 1 and LUMO + 2, are localized on different parts of the coordinated benzlaldimine ligand. Hence the lowest energy absorption in the visible region may be assigned to an electronic transition from the filled ruthenium t_2 orbital (HOMO) to the vacant π^*(imine) orbital of the benzaldimine ligand (LUMO). The other absorptions in the visible region are attributable to transitions occurring from the ruthenium t_2 orbitals to the higher energy vacant orbitals.

3.3. Electrochemical properties

Electrochemical properties of the $[Ru(PPh_3)_2(CO)(L\text{-}R)]$ complexes have been studied by cyclic voltammetry in 1:9

[4] In the $[Ru(PPh_3)_2(CO)(L\text{-}NO_2)]$ complex, the LUMO has significant contribution (57%) from the NO_2 group.

Table 2
Electronic spectral and cyclic voltammetric data

Compound	Electronic spectral data[a] λ_{max}, nm (ε, $M^{-1}\,cm^{-1}$)	Cyclic voltammetric data[b]	
$[Ru(PPh_3)_2(CO)(L\text{-}OCH_3)]$	269[c](11 000), 308[c](7000), 380(2500), 551(2000)	0.38[d](70)[e], 1.09[f]	−1.09[g]
$[Ru(PPh_3)_2(CO)(L\text{-}CH_3)]$	267[c](22 000), 307[c](13 000), 385(3800), 564(3000)	0.41[d](80)[e], 1.17[f]	−1.10[g]
$[Ru(PPh_3)_2(CO)(L\text{-}H)]$	262[c](24 000), 302[c](14 000), 386(6000), 563(4000)	0.45[d](80)[e], 1.27[f]	−1.07[g]
$[Ru(PPh_3)_2(CO)(L\text{-}Cl)]$	263[c](23 000), 307[c](13 000), 388(5000), 567(4000)	0.51[d](70)[e], 1.27[f]	−1.10[g]
$[Ru(PPh_3)_2(CO)(L\text{-}NO_2)]$	264[c](47 000), 323[c](24 000), 379[c](17 000), 489(8000), 577(5000)	0.68[d](80)[e]	−1.13[g]

[a] In dichloromethane solution.
[b] Solvent, 1:9 dichloromethane–acetonitrile; supporting electrolyte, TBAP; reference electrode, SCE.
[c] Shoulder.
[d] $E_{1/2} = 0.5(E_{pa} + E_{pc})$, where E_{pa} and E_{pc} are anodic and cathodic peak potentials, scan rate, 50 mV s^{-1}.
[e] $\Delta E_p = E_{pa} - E_{pc}$.
[f] E_{pa} value.
[g] E_{pc} value.

Table 3
Composition of selected molecular orbitals of the complexes

Compounds	Contributing fragments	% Contribution of fragments to					
		HOMO	HOMO − 1	HOMO − 2	LUMO	LUMO + 1	LUMO + 2
$[Ru(PPh_3)_2(CO)(L\text{-}OCH_3)]$	Ru	53	57	53	3	2	
	$L\text{-}OCH_3$	40	27	38	89 (C=N, 54)	96	93
	CO		14				
$[Ru(PPh_3)_2(CO)(L\text{-}CH_3)]$	Ru	54	56	54	3	2	
	$L\text{-}CH_3$	41	29	39	91 (C=N, 53)	95	94
	CO		13				
$[Ru(PPh_3)_2(CO)(L\text{-}H)]$	Ru	56	47	54	3	2	
	L-H	41	29	36	91 (C=N, 53)	95	94
	CO		13				
$[Ru(PPh_3)_2(CO)(L\text{-}Cl)]$	Ru	48	56	52	3	2	
	L-Cl	43	28	40	91 (C=N, 54)	96	94
	CO		13				
$[Ru(PPh_3)_2(CO)(L\text{-}NO_2)]$	Ru	56	56	54	2	2	
	$L\text{-}NO_2$	37	28	37	94 (C=N, 15)	92	96
	CO		13				

dichloromethane–acetonitrile solution (0.1 M TBAP).[5] Voltammetric data are presented in Table 2 and a representative voltammogram is deposited as supplementary data (Fig. S1). All the complexes show two oxidative responses on the positive side of SCE[6] and a reductive response on the negative side. The first oxidative response is reversible in nature, characterized by a peak-to-peak separation (ΔE_p) of 70–80 mV, which remains unchanged upon changing the scan rate and the anodic peak-current (i_{pa}) is almost equal to the cathodic peak-current (i_{pc}). The other two responses are irreversible in nature. In view of the composition of the HOMO, the first reversible oxidation, observed within 0.3–0.7 V, is assigned to Ru(II)–Ru(III) oxidation. However, the second irreversible oxidation, observed within 1.0–1.3 V, is tentatively attributed to oxidation of the C,N,O-coordinated benzaldimine ligand.[6] Based on the composition of the LUMO, the irreversible reductive response observed around −1.1 V may be assigned to reduction of the imine fragment in the coordinated benzaldimine ligand. One-electron nature of the two oxidative responses has been verified by comparing their current heights with that of ferrocene–ferrocenium couple under identical experimental conditions. However, the irrerversible reductive response shows non-stoichiometric current (i_{pc}). Potential of the first oxidation is found to be sensitive to the nature of the substituent R in the coordinated benzaldimine ligand. The potential increases with increasing electron-withdrawing character of the substituent R. The plot of $E_{1/2}$ versus σ [σ = Hammett constant of R [13], $OCH_3 = -0.27$, $CH_3 = -0.17$, $H = 0.00$, $Cl = 0.23$ and $NO_2 = 0.78$] is linear (Fig. S2) with a slope (ρ) of 0.28 V

[5] A little dichloromethane was necessary to take the complex into solution. Addition of large excess of acetonitrile was necessary to record the redox responses in proper shape.
[6] The second irreversible oxidation has not been observed in the $[Ru(PPh_3)_2(CO)(L\text{-}NO_2)]$ complex.

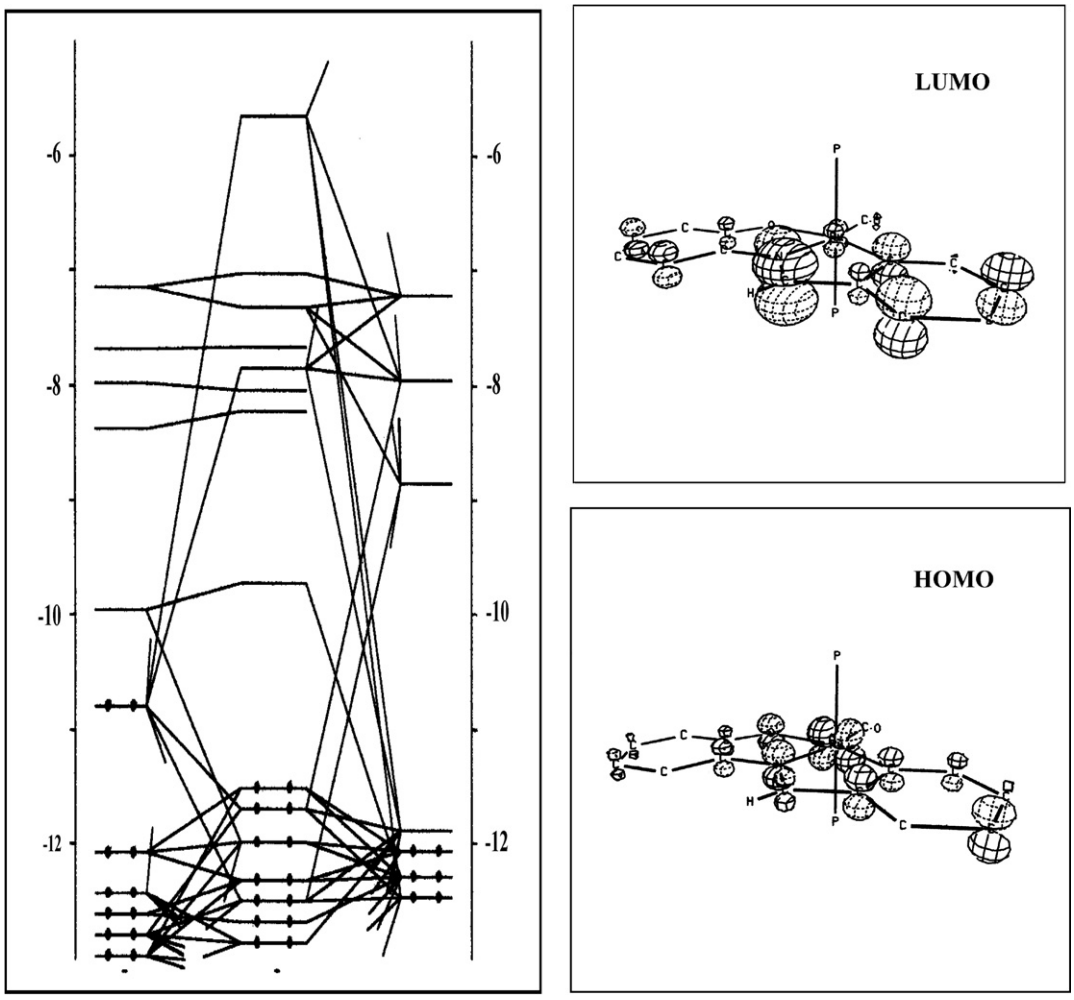


Fig. 3. Partial molecular orbital diagram of $[Ru(PPh_3)_2(CO)(L\text{-}H)]$ complex.

(ρ = reaction constant of this couple [14]), which shows that the substituent (R) on the coordinated benzaldimine ligand, which is four-bonds away from the metal center, can still influence the metal-centered oxidation potential in a predictable manner.

4. Conclusions

The present study shows that the *N*-(2′-hydroxyphenyl)benzaldimines (**1**) can undergo facile C–H activation at one ortho position of the aryl ring in the benzaldimine fragment, mediated by $[Ru(PPh_3)_2(CO)_2Cl_2]$. This study also indicates that similar C–H activation of organic molecules having structural similarity with the *N*-(2′-hydroxyphenyl)benzaldimines may also be possible upon their reaction with $[Ru(PPh_3)_2(CO)_2Cl_2]$ and other suitable transition metal complexes, and such possibilities are currently under exploration.

Acknowledgements

Financial assistance received from the Department of Science and Technology New Delhi, [Grant No. SR/S1/IC-15/2004] is gratefully acknowledged. The authors thank Professor Saswati Lahiri of the Department of Organic Chemistry, Indian Association for the Cultivation of Science, Kolkata, for her help. Thanks are also due to the School of Chemistry, University of Hyderabad, for X-ray diffraction data collection on the crystal. Swati Dutta thanks the Council of Scientific and Industrial Research, New Delhi, for her fellowship [Grant No. 9/96(410)/2003-EMR-I] and Chhandasi GuhaRoy thanks the University Grants Commission, New Delhi, for her fellowship [Grant No. 10-2(5)/2005(I)-E.U.II].

Appendix A. Supplementary material

CCDC 626175 contains the supplementary crystallographic data for this paper. These data can be obtained free of charge via http://www.ccdc.cam.ac.uk/conts/retrieving.html, or from the Cambridge Crystallographic Data Centre, 12 Union Road, Cambridge CB2 1EZ, UK; fax: (+44) 1223-336-033; or e-mail: deposit@ccdc.cam.ac.uk. Supplementary data associated with this article can be found, in the online version, at doi:10.1016/j.poly.2007.04.020.

References

[1] (a) R. Drozdzak, B. Allaert, N. Ledoux, I. Dragutan, V. Dragutan, F. Verpoort, Coord. Chem. Rev. 249 (2005) 3055;
(b) .K. Nazeeruddin, C. Klein, P. Liska, M. Grätzel, Coord. Chem. Rev. 249 (2005) 1460;
(c) J.K. Hurst, Coord. Chem. Rev. 249 (2005) 313;
(d) M.K. Nazeeruddin, S.M. Zakeeruddin, J.J. Lagref, P. Liska, P. Comte, C. Barolo, G. Viscardi, K. Schenk, M. Graetzel, Coord. Chem. Rev. 248 (2004) 1317;
(e) L. Spiccia, G.B. Deacon, C.M. Kepert, Coord. Chem. Rev. 248 (2004) 1329;
(f) Y. Saito, T. Azechi, T. Kitamura, Y. Hasegawa, Y. Wada, S. Yanagida, Coord. Chem. Rev. 248 (2004) 1469;
(g) B. Serli, E. Zangrando, T. Gianferrara, L. Yellowless, E. Alessio, Coord. Chem. Rev. 245 (2003) 73;
(h) M.J. Clarke, Coord. Chem. Rev. 236 (2003) 209;
(i) E. Tfouni, M. Krieger, B.R. McGarvey, D.W. Franco, Coord. Chem. Rev. 236 (2003) 57;
(j) M.J. Clarke, Coord. Chem. Rev. 232 (2002) 69;
(k) C.M. Che, J.S. Huang, Coord. Chem. Rev. 231 (2002) 51;
(l) F. Hartl, M.P. Aarnts, H.A. Nieuwenhuis, J. van. Slageren, Coord. Chem. Rev. 230 (2002) 106;
(m) S.I. Gorelsky, A.B.P. Lever, M. Ebadi, Coord. Chem. Rev. 230 (2002) 97;
(n) J.F. Endicott, H.B. Schlegel, M.J. Uddin, D.S. Seniveratne, Coord. Chem. Rev. 229 (2002) 95;
(o) H. Yersin, C. Kratzer, Coord. Chem. Rev. 229 (2002) 75;
(p) G. Simonneaux, P.L. Maux, Coord. Chem. Rev. 228 (2002) 43;
(q) L.N. Ji, X.H. Zou, J.G. Liu, Coord. Chem. Rev. 216–217 (2001) 513;
(r) M. Turki, C. Daniel, Coord. Chem. Rev. 216–217 (2001) 31;
(s) N.A.P. Kane-Maguire, J.F. Wheeler, Coord. Chem. Rev. 211 (2001) 145;
(t) B.Z. Shan, Q. Zhao, N. Goswami, D.M. Eichhom, D.P. Rillema, Coord. Chem. Rev. 211 (2001) 117;
(u) V. Balzani, A. Juris, Coord. Chem. Rev. 211 (2001) 97.

[2] (a) S. Halder, R. Acharyya, S.M. Peng, G.H. Lee, M.G.B. Drew, S. Bhattacharya, Inorg. Chem. 45 (2006) 9654;
(b) P. Gupta, S. Dutta, F. Basuli, S.M. Peng, G.H. Lee, S. Bhattacharya, Inorg. Chem. 45 (2006) 460;
(c) S. Nag, P. Gupta, R.J. Butcher, S. Bhattacharya, Inorg. Chem. 43 (2004) 4814;
(d) P.K. Sinha, L.R. Falvello, S. Bhattacharya, Indian J. Chem. 43A (2004) 1846;
(e) A. Das, S.M. Peng, G.H. Lee, S. Bhattacharya, New J. Chem. 28 (2004) 712;
(f) R. Acharyya, S.M. Peng, G.H. Lee, S. Bhattacharya, Inorg. Chem. 42 (2003) 7378;
(g) P. Gupta, F. Basuli, S. Bhattacharya, C.G. Pierpont, Inorg. Chem. 41 (2002) 5810;
(h) K. Majumder, R.J. Butcher, S. Bhattacharya, Inorg. Chem. 41 (2002) 4605;
(i) F. Basuli, S.M. Peng, S. Bhattacharya, Inorg. Chem. 40 (2001) 1126;
(j) P.K. Sinha, L.R. Falvello, S.M. Peng, S. Bhattacharya, Polyhedron 19 (2000) 1673.

[3] (a) Y.Z. Shen, H. Gu, Y. Zhu, Y. Pan, J. Organomet. Chem. 691 (2006) 1817;
(b) A.P. Mishra, L.R. Pandey, Ind. J. Chem. Sec. A 44A (2005) 94;
(c) Y. Long, T. Cai, Z. Peng, Q. Li, Jingni Huagong Zhongjianti 32 (2002) 30.

[4] (a) S. Basu, S. Dutta, M.G.B. Drew, S. Bhattacharya, J. Organomet. Chem. 691 (2006) 3581;
(b) C. Lopez, A. Caubet, S. Perez, X. Solans, M.F. Bardia, J. Organomet. Chem. 681 (2003) 82;
(c) P. Ghosh, A. Pramanik, N. Bag, G.K. Lahiri, A. Chakravorty, J. Organomet. Chem. 454 (1993) 237;
(d) A. Albinati, C. Arz, P.S. Pregosin, J. Organomet. Chem. 335 (1987) 379.

[5] (a) U. Jaeger-Fiedle, P. Arndt, W. Baumann, A. Spannenberg, V.V. Burlakov, U. Rosenthal, Eur. J. Inorg. Chem. 14 (2005) 2842;
(b) K.J. Keuseman, I.P. Smolinkova, V.V. Dunina, Organometallics 24 (2005) 4159;
(c) L. Shi, Y.Q. Tu, M. Wang, F.M. Zhao, C.A. Fan, Y.M. Zhao, W.J. Xia, J. Am. Chem. Soc. 127 (2005) 10836;
(d) R.K. Thalji, K.A. Ahrendt, R.G. Bergman, J.A. Ellman, J. Org. Chem. 70 (2005) 6775;
(e) Y. Fan, M.B. Hall, Organometallics 24 (2005) 3827;
(f) M.A. Esteruelas, A.M. Lopez, Organometallics 24 (2005) 3584;
(g) T.G. Driver, M.W. Day, J.A. Labinger, J.E. Bercaw, Organometallics 24 (2005) 3644;
(h) B. Rybtchinski, R. Cohen, M.L. Jan, D. Milstein, J. Am. Chem. Soc. 125 (2003) 11041;
(i) C.B. Pamplin, P. Legzdins, Acc. Chem. Res. 36 (2003) 223;;
(j) R.H. Crabtree, J. Chem. Soc., Dalton Trans. (2003) 3985;
(k) V. Ritleng, C. Sirlin, M. Pfeffer, Chem. Rev. 102 (2002) 1731;
(l) B. Rybtchinski, S. Oevers, M. Montag, A. Vigalok, A. Rozenberg, J.M. L Martin, D. Milstein, J. Am. Chem. Soc. 123 (2001) 9064;
(m) A. Vigalok, D. Milstein, Acc. Chem. Res 34 (2001) 798;
(n) C. Slugovc, I. Padilla-Martnez, S. Sirol, E. Carmona, Coord. Chem. Rev. 213 (2001) 129;
(o) C. Jia, T. Kitamura, Y. Fujiwara, Acc. Chem. Res. 34 (2001) 633;
(p) A. Sundermann, O. Uzan, D. Milstein, J.M.L. Martin, J. Am. Chem. Soc. 122 (2000) 7095.

[6] (a) A. Egger, V.B. Arion, E. Reisner, B.C. Losantos, S. Shova, G. Trettenhahn, B.K. Keppler, Inorg. Chem. 44 (2005) 122;
(b) P. Mura, F. Piccioli, C. Gabbiani, M. Camalli, L. Messori, Inorg. Chem. 44 (2005) 4897;
(c) A. Chouai, S.E. Wicke, C. Turro, J. Bacsa, K.R. Dunbar, D. Wang, R.P. Thummel, Inorg. Chem. 44 (2005) 5996;
(d) E. Reisner, V.B. Arion, A. Eichinger, N. Kandler, G. Giester, A.J.L. Pombeiro, B.K. Keppler, Inorg. Chem. 44 (2005) 6704;
(e) B. Serli, E. Zangrando, T. Gianferrara, L. Yellowlees, E. Alessio, Coord. Chem. Rev. 245 (2003) 73.

[7] (a) J. Tsuji, Transition Metal Reagents and Catalysts, Wiley-VCH, Weinheim, 2000;
(b) M. Bellar, C. Bolm, Transition Metals for Organic Synthesis 1-2, Wiley-VCH, Weinheim, 1998;
(c) L.S. Hegedus, Coord. Chem. Rev. 168 (1998) 49;
(d) L.S. Liebeskind (Ed.), Advances in Metal-Organic Chemistry, Jai Press, Greenwich, CT, 1996;
(e) B. Cornils, W.A. Hermann (Eds.), Applied Homogenous Catalysis with Organometallic Compounds: A Comprehensive Handbook in Two Volumes, VCH, Weinheim, 1996;
(f) E. Abel, F.G.A. Stone, G. Wilkinson (Eds.), Comprehensive Organometallic Chemistry, vol. 12, Pergamon Press, Oxford, 1995;
(g) L.S. Hegedus, Transition Metals in the Synthesis of Complex Organic Molecules, Mill Valley, CA, 1994;
(h) J.P. Collman, L.S. Hegedus, J.R. Norton, R.G. Finke, Principles and Applications of Organotransition Metal Chemistry, Mill Valley, CA, 1987;
(i) B.M. Trost, T.R. Verhoeven, in: E. Abel, F.G.A. Stone, G. Wilkinson (Eds.), Comprehensive Organometallic Chemistry, vol. 8, Pergamon Press, Oxford, 1982.

[8] N. Ahmad, S.D. Robinson, M.F. Uttley, J. Chem. Soc., Dalton Trans. (1972) 843.

[9] (a) M. Walter, L. Ramaley, Anal. Chem. 45 (1973) 165;
(b) D.T. Sawyer, J.L. Roberts Jr., Experimental Electrochemistry for Chemists, Wiley, New York, 1974.

[10] G.M. Sheldrick, SHELXS-97 and SHELXL-97, FORTRAN Programs for Crystal Structure Solution and Refinement, University of Gottingen, 1997.

[11] (a) F. Basuli, A.K. Das, M. Golam, S.M. Peng, S. Bhattacharya, Polyhedron 19 (2000) 1663;
(b) M. Menon, A. Pramanik, S. Chattopadhyay, N. Bag, A. Chakravorty, Inorg. Chem. 34 (1995) 1361;
(c) M.C. Barral, R.J. Aparicio, E.C. Royer, M.J. Saucedo, F.A. Urbanos, E.G. Puebla, C.R. Valero, J. Chem. Soc., Dalton Trans. (1991) 1609.

[12] (a) C. Mealli, D.M. Proserpio, J. Chem. Educ. 67 (1990) 399;
(b) C. Mealli, D.M. Proserpio, CACAO Version 4.0, Italy, 1994.

[13] L.P. Hammett, Physical Organic Chemistry, 2nd edn., McGraw Hill, New York, 1970.

[14] R.N. Mukherjee, O.A. Rajan, A. Chakravorty, Inorg. Chem. 21 (1982) 785.

step-by-step synthesis allowed us for the first time to generate oligophosphazenes having up to five different types of side groups [23]. Unexpectedly, in contrast with results previously reported [6,7], the X-ray diffraction study of the structure of a compound possessing one P=N—P=S linkage gave identical values for the P=N and P–N bond lengths (1.5806(15) and 1.5734(14) Å, respectively) [23].

In order to determine the influence of substituents on the reaction process and on the properties, we report here the synthesis and characterization of new oligophosphazenes bearing different types of end groups. The X-ray diffraction structure of three new compounds including one possessing a P=N—P=S linkage is also reported.

2. Results and discussion

As indicated in the introduction, the step-by-step synthesis of oligophosphazenes through Staudinger reactions necessitates the use of $N_3P(S)(R')_2$ derivatives which must be first synthesized. As previously shown [9], $P(S)Cl_3$ is a suitable precursor, which reacts easily with two equivalents of phenols **1** in basic conditions, to afford $ClP(S)(OAr)_2$ derivatives **2**. In order to avoid the presence of two azides on the same phosphorus atom (potentially explosive), the presence of $Cl_2P(S)(OAr)$ derivatives must be avoided, thus a slight excess of phenol is used, and a small amount of trisubstituted derivative of type **3** is also obtained. In the case of the **a** series, the trisubstituted compound **3a** is isolated by crystallization in ethylacetate/pentane (1:3), and its structure determined by X-ray diffraction. The ORTEP drawing of compound **3a** is shown in Fig. 1 and the X-ray data are gathered in Table 1 (see Scheme 1).

The next step to obtain the thiophosphorylazide consists of the reaction of the remaining Cl in compounds **2** with sodium azide, to afford compounds **4**, which are isolated by column chromatography. These compounds, as well as all the other compounds reported in this paper, are characterized by multinucleus NMR (^{31}P, ^{1}H, and ^{13}C) and elemental analyses. Few compounds possessing a λ^4,σ^5-phosphorus azide linkage were previously characterized by X-ray diffraction [14,24–29], thus single crystals of **4b** are grown from ether/pentane (1:4). The crystal contains two isomeric forms of compound **4b** (forms a and b, 50% each) which are shown in Fig. 2. The difference between both isomers concerns the N3(a,b)N2(a,b)N1(a,b)—P=S linkage, which is disordered. All these atoms are in a plane in both cases, but N3a and S are in s-*cis* position relative to the P–N1a bond in form a, whereas N3b and S are in s-*trans* position relative to the P–N1b bond in form b.

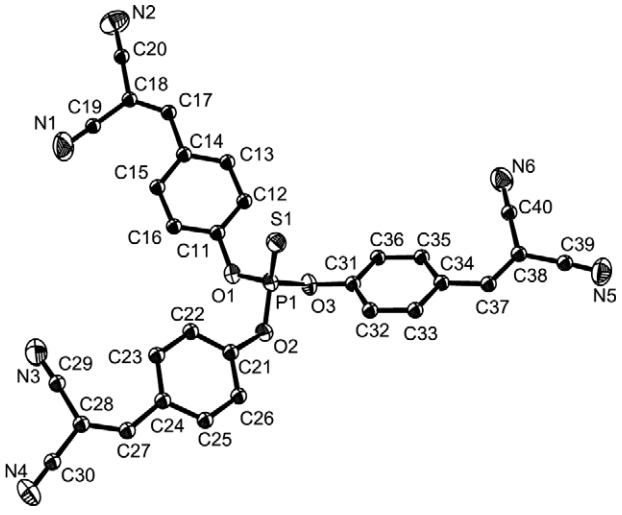


Fig. 1. Structure of compound **3a** (ORTEP drawing, hydrogen atoms are omitted for clarity). Selected bond lengths (Å) and angles (°): P1–S1 1.9000(7); C–N 1.137–1.152(3); O1–P1–O2 101.52(8); O1–P1–O3 99.83(8); O2–P1–O3 100.44(8); O1–P1–S1 117.07(6); O2–P1–S1 117.36(6); O3–P1–S1 117.55(6).

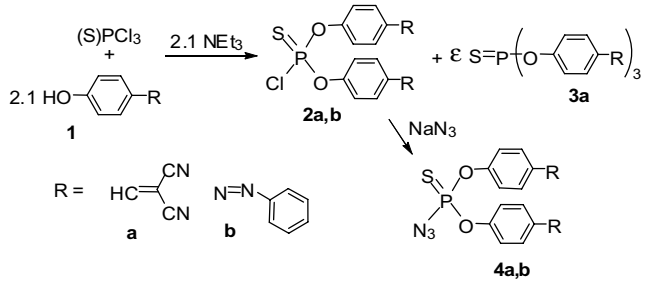
Azides **4a** and **4b** as well as **4c** and **4d** [14] are reacted with Ph_3P to create the phosphazene linkage. The Staudinger reaction occurs easily and quantitatively to afford compounds **5a–d**, each of them possessing one P=N—P=S linkage (Scheme 2). The reaction is easily monitored by ^{31}P NMR, which displays the appearance of two doublets at ca. 14 ppm for P=N and ca. 50 ppm for P=S. The structure of compound **5d** is confirmed by X-ray diffraction (Fig. 3). The bond lengths and angles for the P=N—P fragment are slightly different from the data previously obtained for compound **5c** [23] (P=N 1.5686(18) for **5d**, 1.5806(15) Å for **5c**; P–N 1.5733(18) for **5d**, 1.5734(14) Å for **5c**; P=N—P 141.46(13) for **5d**, 134.67(10)° for **5c**), however the lack of bond length alternation is observed in both cases for the P=N—P linkage. The P1···P2 distance is 2.9659(11) Å, a value typically found for cyclotriphosphazenes.

The next step to continue the synthesis is the reaction with methyltriflate to alkylate the P=S group. This reaction is attempted with compounds **5a,c,d**, but not with **5b**, due to the propensity of the azo group to isomerize spontaneously (*trans* → *cis*) with ambiant light, which complicates the work-up. The reaction with **5d** fails, due to a partial alkylation of the NMe_2 groups, whereas the cationic derivatives **6a** and **6c** are isolated (Scheme 3). The alkylation of sulfur induces a dramatic shielding of the signal corresponding to the PS group in ^{31}P NMR from ca. 50 ppm for **5a,c** to ca. 23 ppm for **6a,c**. A deshielding of the signal corresponding to the phosphazene is also observed from ca. 15 ppm to ca. 23 ppm. Two doublets are observed for **6a,c** as expected, but their attribution is ambiguous because both signals corresponding to P=N—P resonate at ca. 23 ppm.

The desulfurization of both compounds is attempted using the nucleophilic phosphine $P(NMe_2)_3$ to transfer the S–Me group from the phosphazene to $P(NMe_2)_3$ (Scheme 3). The reaction works nicely with **6c** to afford **7c** in quantitative yield [23]. Unexpectedly, the same reaction fails with compound **6a**, as shown by ^{31}P NMR, with the appearance of numerous signals. The second phosphazene linkage is thus obtainable only from **7c**, illustrating the sensitivity of this reaction process to the type of substituents.

Table 1
Crystal data and structure refinement for **3a**, **4b**, and **5d**

Compound	**3a**	**4b**	**5d**
Formula	$C_{30}H_{15}N_6O_3PS$	$C_{12}H_9N_5OP_{0.5}S$	$C_{34}H_{35}N_3O_2P_2S$
Formula weight	570.51	286.79	611.65
T (K)	160(2)	180(2)	160(2)
Crystal system	monoclinic	orthorhombic	monoclinic
Space group	$P2(1)/c$	$Pmn2(1)$	$P2(1)/c$
a (Å)	11.3933(10)	26.843(3)	18.809(4)
b (Å)	13.8191(9)	7.7751(8)	9.376(2)
c (Å)	18.0696(14)	5.6201(4)	18.612(4)
β (°)	105.786(10)	90	107.24(3)
V (Å^3)	2737.7(4)	1172.94(19)	3134.8(12)
Z	4	4	4
D_{calc} (g cm^{-3})	1.384	1.296	1.296
Absorption coefficient (mm^{-1})	0.221	0.345	0.241
$F(000)$	1168	590	1288
Crystal size (mm)	$0.43 \times 0.13 \times 0.10$	$0.50 \times 0.38 \times 0.13$	$0.37 \times 0.26 \times 0.12$
θ Range for data collection (°)	2.34–26.07	2.62–26.17	4.12–26.37
Index ranges	$-14 \leqslant h \leqslant 13$, $-17 \leqslant k \leqslant 17$, $-22 \leqslant l \leqslant 22$	$-32 \leqslant h \leqslant 33$, $-9 \leqslant k \leqslant 9$, $-6 \leqslant l \leqslant 6$	$-23 \leqslant h \leqslant 22$, $-11 \leqslant k \leqslant 11$, $-18 \leqslant l \leqslant 23$
Reflections collected	20977	7983	13194
Independent reflections [R_{int}]	5311 [0.0458]	2287 [0.0469]	5441 [0.0784]
Completeness to	$\theta = 26.07°$: 98.4%	$\theta = 26.17°$: 97.6%	$\theta = 26.37°$: 84.9%
Maximum/minimum transmission	0.9783/0.9110	0.9565/0.8465	0.9717/0.9161
Data/restraints/parameters	5311/0/370	2287/42/191	5441/0/384
Goodness-of-fit on F^2	1.011	1.171	1.098
Final R indices [$I > 2\sigma(I)$]	$R_1 = 0.0391$, $wR_2 = 0.0925$	$R_1 = 0.1038$, $wR_2 = 0.2604$	$R_1 = 0.0593$, $wR_2 = 0.1385$
R indices (all data)	$R_1 = 0.0627$, $wR_2 = 0.1009$	$R_1 = 0.1174$, $wR_2 = 0.2762$	$R_1 = 0.0720$, $wR_2 = 0.1462$



Scheme 1.

The reaction of the azides **4a** and **4d** with **7c** affords the diphosphazene **8ca** and **8cd**, respectively, which possess two types of functional groups (Scheme 3). In both cases, the central phosphorus atom (labeled P_1) is coupled with its two neighbors with two very different coupling constants (ca. 24 Hz for $^2J_{P0P1}$ with PPh_3 and ca. 58 Hz for $^2J_{P1P2}$ with P(S)) giving a doublet of doublets in the ^{31}P NMR spectra. The chemical shift value (ca. −15 ppm) compares well with that found for polyphosphazenes substituted by phenols [30].

The behavior of compounds **8ca** and **8cd** toward alkylation is comparable to that of **5a** and **5d**, respectively. Indeed, alkylation of some NMe_2 groups occurs in the case of **8cd**, hampering the formation of **9cd**, whereas the alkylation of **8ca** occurs only on the PS group as expected, leading to the cationic derivative **9ca** (Scheme 3). A charge

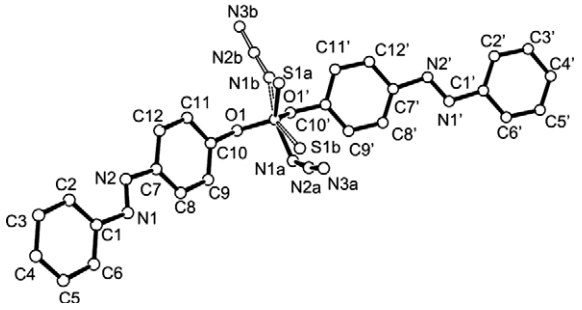
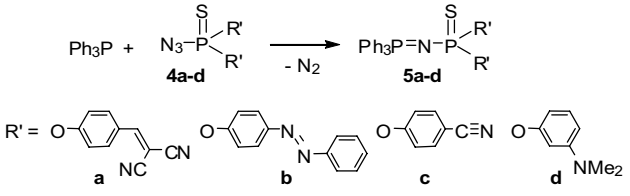


Fig. 2. Forms a (50%) and b (50%) of compound **4b** (hydrogen atoms are omitted for clarity). Selected bond lengths (Å) and angles (°): P–N1a 1.724(14), P–N1b 1.721(14); P–S1a 1.851(4), P–S1b 1.861(15); N1a–N2a 1.262(11), N1b–N2b 1.255(11); N2a–N3a 1.255 (11), N2b–N3b 1.256(12); N1–N2 1.250(7) (a and b); N2a–N1a–P 122.1(18), N2b–N1b–P 127.0(14); N3a–N2a–N1a 164(2), N1b–N2b–N3b 177(2); N1a–P–S1a 119.8(7), N1b–P–S1b 109.8(6). The diedral angle S–P–N1–N2 is 82.76° for form a, and 179.98° for form b.



Scheme 2.

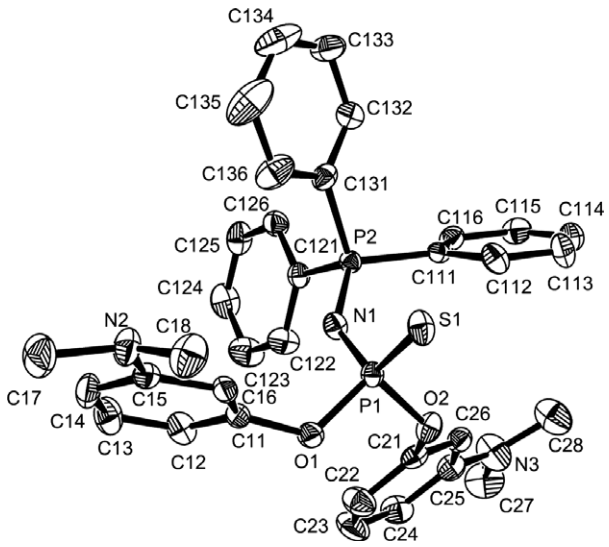
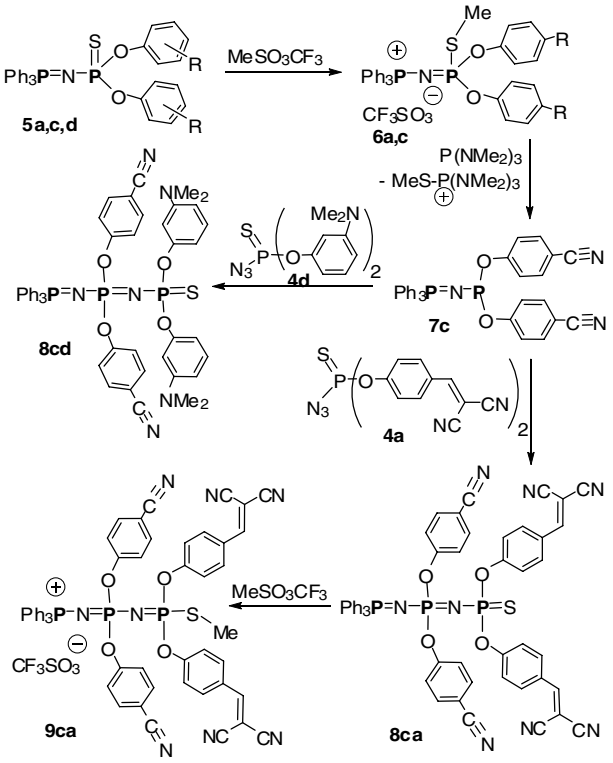


Fig. 3. Structure of compound **5d** (ORTEP drawing, hydrogen atoms are omitted for clarity). Selected bond lengths (Å) and angles (°): P1–S1 1.9375(10); P1–N1 1.5733(18); P2–N1 1.5686(18); N1–P1–S1 120.36(8); P2–N1–P1 141.46(13).



Scheme 3.

transfer through the whole PNPNPS linkage is observed, as shown by ^{31}P NMR. Indeed, the signal corresponding to the PS group (labeled P_2) is shielded from 45.1 to 23.8 ppm, whereas the signal corresponding to Ph_3P (labeled P_0) is deshielded from 16.5 to 23.7 ppm. The attribution of the signals for **9ca** is non ambiguous (contrarily to what was observed for **6a** and **6c**) because the $^2J_{PP}$ coupling constants with the central phosphorus (P_1) are very different ($^2J_{P0P1} = 25.8$ Hz for **8ca** and 26.2 Hz for **9ca**; $^2J_{P1P2} = 58.4$ Hz for **8ca** and 53.2 Hz for **9ca**). On the contrary, the chemical shift value for P_1 does not change on going from **8ca** to **9ca** ($\Delta\delta = 0.6$ ppm) (Fig. 4). Thus, the positive charge is delocalized along the phosphazene linkage of **9ca**, up to the PPh_3 group.

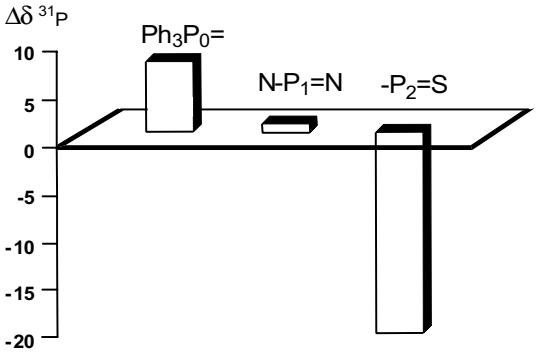


Fig. 4. Variation of the ^{31}P NMR chemical shifts on going from **8ca** to **9ca** for each individual phosphorus of the chain $Ph_3P_0{=}N{-}P_1{=}N{-}P_2{=}S$.

As could be expected from the reaction of $P(NMe_2)_3$ with **6a**, its reaction with **9ca** affords numerous signals in ^{31}P NMR, and the product of desulfurization cannot be isolated.

In conclusion, we have reported the synthesis and the characterization of a new series of compounds possessing phosphazene linkages, obtained by Staudinger reactions. The X-ray diffraction structure of a compound of type $R_3P{=}N{-}PR'_2(S)$ give an identical length for both PN bonds in accordance with the observation we previously reported [23], but contrarily to what was reported for $Cl_3P{=}N{-}PCl_2(O)$ [5], emphasizing the role of the substituents. The synthetic process used for lengthening the oligophosphazene chain is also highly dependant on the substituents, and two new compounds of type $R_3P{=}N{-}PR'_2{=}PR''_2(S)$ possessing three different substituents have been isolated and characterized. Alkylation of sulfur allows to demonstrate the delocalization of the charge up to the other side of the inorganic phosphazene chain (the R_3P group) using ^{31}P NMR, and contributes to a better understanding of the phosphazene bond.

3. Experimental section

All reactions were carried out in the absence of air using standard Schlenk techniques and vacuum-line manipulations. Commercial samples were used as received. All solvents were dried before use (THF and ether over sodium/benzophenone, pentane and dichloromethane over phosphorus pentoxide). ^{1}H, ^{13}C, ^{19}F, ^{31}P NMR measurements were performed on Bruker AC 200, AM 250, ARX 250, or DPX 300. References for NMR chemical shifts are 85% H_3PO_4 for ^{31}P NMR, $SiMe_4$ for ^{1}H and ^{13}C NMR, CF_3CO_2H for ^{19}F NMR. The attribution of ^{13}C NMR signals has been done using J_{mod}, two dimensional HMBC,

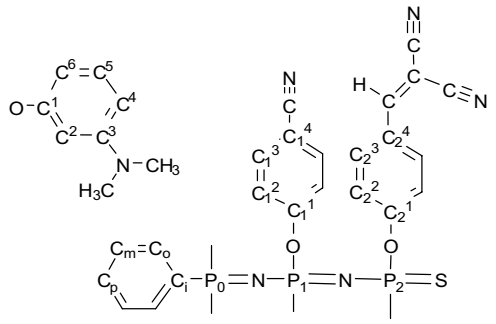


Fig. 5. Numbering used for NMR assignments. The lower script number of substituents refers to the phosphorus to which they are connected.

and HMQC, Broad Band or CW ^{31}P decoupling experiments when necessary. The numbering used for NMR assignments is depicted in Fig. 5. Syntheses of compounds **4c** and **4d** [14], as well as compounds **5c**, **6c** and **7c** [23] were already published.

3.1. Synthesis of compounds *3a, 4a and 4b*

A solution of phenol derivative (for **4a**: 0.35 g, 2.07 mmol of 4-hydroxybenzylidenemalononitrile; for **4b**: 0.275 mL, 1.97 mmol of 4-hydroxyazobenzene) and triethylamine (for **4a**: 0.300 mL, 2.15 mmol; for **4b**: 0.275 mL, 1.97 mmol) in THF (20 mL), was added dropwise at −100 °C under stirring to a solution of trichlorophosphine sulphide (0.1 mL, 0.985 mmol) in THF (10 mL). The temperature was slowly allowed to rise to room temperature at the end of the addition. The resulting mixture was stirred for 12 h, then the precipitate of triethylamine hydrochloride was removed by filtration, and the solution was evaporated to dryness. The resulting oil mainly consisted of compound **2a** or **2b**; it was solubilized in acetone (20 mL), then sodium azide was added (0.064 g, 0.985 mmol). Acetone was evaporated after 24 h at room temperature, then THF (20 mL) was added. Sodium chloride and excess azide were eliminated by centrifugation. THF was evaporated to afford a viscous liquid (yellow for **4a**, orange for **4b**), which contained derivatives **4** contaminated by a small amount of derivatives **3**. Compounds **4** were purified by column chromatography on silica (eluent: AcOEt/Pentane: 1/3 for **4a**; AcOEt/Hexane: 3/7 for **4b**). In the case of **4a**, chromatography also allowed to isolate **3a**, obtained as a side-product. Slow evaporation of this fraction afforded single crystals of **3a** suitable for X-ray diffraction.

3a: Yellow crystals. ^{31}P $\{^1H\}$ NMR ($CDCl_3$): $\delta = 49.2$ (s). ^1H NMR ($CDCl_3$): $\delta = 7.41$ (dd, $^3J_{HH} = 8.8$ Hz, $^4J_{HP} = 1.6$ Hz, 6H, H–C^2), 7.77 (s, 3H, H–C^5), 7.99 (d, $^3J_{HH} = 8.8$ Hz, 6H, H–C^3). ^{13}C $\{^1H\}$ NMR ($CDCl_3$): $\delta = 112.5$ (s, C–CN), 113.7 (s, CN), 121.8 (d, $^3J_{CP} = 7$ Hz, C^2), 129.0 (s, C^4), 129.8 (s, C^3), 154.0 (d, $^2J_{CP} = 9$ Hz, C^1), 158.3 (s, C^5). IR (KBr): 2230 (ν-CN) cm^{-1}. *Anal.* Calc. for $C_{30}H_{15}N_6O_3PS$ (570.5): C, 63.16; H, 2.65; N, 14.73. Found: C, 63.18; H, 2.68; N, 14.70%.

4a: Yellow powder isolated in 35% yield. ^{31}P $\{^1H\}$ NMR ($CDCl_3$): $\delta = 57.5$ (s). ^1H NMR ($CDCl_3$): $\delta = 7.41$ (dd, $^3J_{HH} = 8.7$ Hz, $^4J_{HP} = 1.7$ Hz, 4H, H–C^2), 7.78 (s, 2H, H–C^5), 7.98 (d, $^3J_{HH} = 8.8$ Hz, 4H, H–C^3). ^{13}C $\{^1H\}$ NMR ($CDCl_3$): $\delta = 112.7$ (s, C–CN), 113.8 (s, CN), 121.9 (d, $^3J_{CP} = 5.3$ Hz, C^2), 129.4 (d, $^5J_{CP} = 2.1$ Hz, C^4), 133.2 (d, $^4J_{CP} = 1.6$ Hz, C^3), 154.2 (d, $^2J_{CP} = 8.1$ Hz, C^1), 158.5 (d, $^6J_{CP} = 1.3$ Hz, C^5). IR (KBr): 2230 (ν-CN), 2172 (ν-N_3) cm^{-1}. Mass (CI, NH_3) m/z: $[M]^+ = 443$, $[M+NH_4]^+ = 461$. *Anal.* Calc. for $C_{20}H_{10}N_7O_2PS$ (443.4): C, 54.18; H, 2.27; N, 22.11. Found: C, 54.25; H, 2.31; N, 22.06%.

4b: Single crystals suitable for X-ray diffraction were grown at −20 °C in Ether/Pentane (1:4).

3.2. Synthesis of compounds *5a, 5b and 5d*

A solution of triphenylphosphine (for **5a**: 0.051 g, 0.195 mmol; for **5b**: 0.061 g, 0.23 mmol; for **5d**: 0.233 g, 0.888 mmol) in THF (3 mL for **5a**) or CH_2Cl_2 (3 mL for **5b** or **5d**) was added at room temperature to a solution of azide (**4a**: 0.085 g, 0.19 mmol; **4b**: 0.110 g, 0.22 mmol; **4d**: 0.319 g, 0.845 mmol) in degazed THF (3 mL for **5a**) or CH_2Cl_2 (3 mL for **5b** or **5d**), and stirred for 12 h. Then, the solution was evaporated to dryness, and the resulting powder was washed three times with THF/Pentane (1/20), to afford compounds **5**.

5a: Yellow powder, 99% yield. ^{31}P $\{^1H\}$ NMR (THF): $\delta = 14.1$ (d, $^2J_{PP} = 32.0$ Hz, P_0=N), 49.5 (d, $^2J_{PP} = 32.0$ Hz, P_1=S). ^1H NMR ([D_8] THF): $\delta = 7.46$ (dd, $^3J_{HH} = 8.7$ Hz, $^4J_{HP} = 1.3$ Hz, 4H, H–C_1^2), 7.50–7.73 (m, 9H, H–C^m, H–C^p), 7.81 (ddd, $^3J_{HH} = 8.4$ Hz, $^4J_{HH} = 1.6$ Hz, $^3J_{HP} = 13.2$ Hz, 6H, H–C^0), 8.00 (d, $^3J_{HH} = 8.7$ Hz, 4H, H–C_1^3), 8.19 (s, 2H, H–C_1^5). ^{13}C $\{^1H\}$ NMR ([D_8] THF): $\delta = 114.2$ (s, C_1^6), 115.2 (s, CN), 123.6 (d, $^3J_{CP} = 5.5$ Hz, C_1^2), 128.8 (s, C_1^4), 129.8 (dd, $^1J_{CP} = 105.0$ Hz, $^3J_{CP} = 4.3$ Hz, C^i), 129.8 (d, $^3J_{CP} = 13.0$ Hz, C^m), 133.4 (s, C^p), 133.9 (s, C_1^3), 134.0 (d, $^2J_{CP} = 11.2$ Hz, C^0), 158.0 (d, $^2J_{CP} = 8.8$ Hz, C_1^1), 160.3 (s, C_1^5). IR (KBr): 2227 (ν-CN) cm^{-1}. M.P.: 69–71 °C. *Anal.* Calc. for $C_{38}H_{25}N_5O_2P_2S$ (677.7): C, 67.35; H, 3.72; N, 10.34. Found: C, 67.48; H, 3.77; N, 10.24%.

5b: Red oil, 99% yield. ^{31}P $\{^1H\}$ NMR (CH_2Cl_2): $\delta = 13.9$ (d, $^2J_{PP} = 29.7$ Hz, P_0=N), 50.8 (d, $^2J_{PP} = 29.7$ Hz, P_1=S). ^1H NMR ([D_8] THF): $\delta = 7.45$ (dd, $^3J_{HH} = 8.8$ Hz, $^4J_{HP} = 1.5$ Hz, 4H, H–C_1^2), 7.50–7.60 (m, 12H, H–C^m, H–C_1^7, H–C_1^8), 7.68 (ttd, $^3J_{HH} = 8.8$ Hz, $^4J_{HH} = 1.5$ Hz, $^5J_{HP} = 1.9$ Hz, 3H, H–C^p), 7.81 (ddd, $^3J_{HH} = 8.4$ Hz, $^4J_{HH} = 1.5$ Hz, $^3J_{HP} = 13.1$ Hz, 6H, H–C^0), 7.92–8.02 (m, 8H, H–C_1^3, H–C_1^6). ^{13}C $\{^1H\}$ NMR ([D_8] THF): $\delta = 127.4$ (d, $^3J_{CP} = 6.0$ Hz, C_1^2), 128.0 (s, C_1^6), 129.1 (s, C_1^3), 133.9 (s, C_1^7), 134.2 (d, $^3J_{CP} = 19.8$ Hz, C^m), 134.5 (dd, $^1J_{CP} = 106.4$ Hz, $^3J_{CP} = 3.8$ Hz, C^i), 136.1 (s, C_1^8), 137.9 (s, C^p), 138.4 (d, $^2J_{CP} = 9.8$ Hz, C^0), 154.6 (s, C_1^4), 158.2 (s, C_1^5), 160.4 (d, $^2J_{CP} = 10.2$ Hz, C_1^1). *Anal.* Calc. for $C_{42}H_{33}N_5O_2P_2S$ (733.8): C, 68.75; H, 4.53; N, 9.54. Found: C, 68.84; H, 4.62; N, 9.32%.

5d: White powder, 99% yield. Single crystals suitable for X-ray diffraction were obtained by slow evaporation at room temperature of a solution in THF/pentane (1/20). ^{31}P $\{^1H\}$ NMR ($CDCl_3$): $\delta = 12.4$ (d, $^2J_{PP} = 28.8$ Hz, P_0═N), 51.2 (d, $^2J_{PP} = 28.8$ Hz, P_1═S). ^1H NMR ($CDCl_3$): $\delta = 2.78$ (s, 12H, NMe_2), 6.46 (d, $^3J_{HH} = 8.2$ Hz, 2H, H–C_1^6), 6.59 (d, $^4J_{HP} = 1.8$ Hz, 2H, H–C_1^2), 6.66 (d, $^3J_{HH} = 8.1$ Hz, 2H, H–C_1^4), 7.07 (“t”, $^3J_{HH} = 8.1$ Hz, 2H, H–C_1^5), 7.37 (“td”, $^3J_{HH} = 7.7$ Hz, $^4J_{HP} = 3.2$ Hz, 6H, H–C^m), 7.49 (ttd, $^3J_{HH} = 7.5$ Hz, $^4J_{HH} = 1.4$ Hz, $^5J_{HP} = 1.8$ Hz, 3H, H–C^p), 7.63 (ddd, $^3J_{HH} = 7.6$ Hz, $^4J_{HH} = 1.4$ Hz, $^3J_{HP} = 13.1$ Hz, 6H, H–C^0). ^{13}C $\{^1H\}$ NMR ($CDCl_3$): $\delta = 40.4$ (s, NMe_2), 106.2 (d, $^3J_{CP} = 5.6$ Hz, C_1^2), 108.3 (s, C_1^4), 109.7 (d, $^3J_{CP} = 4.7$ Hz, C_1^6), 128.4 (d, $^3J_{CP} = 12.9$ Hz, C^m), 129.0 (dd, $^1J_{CP} = 107.2$ Hz, $^3J_{CP} = 4.0$ Hz, C^i), 129.1 (s, C_1^5), 132.3 (sl, C_p), 132.7 (d, $^2J_{CP} = 11.1$ Hz, C_0), 151.4 (s, C_1^3), 153.2 (d, $^2J_{CP} = 10.1$ Hz, C_1^1). *Anal.* Calc. for $C_{34}H_{35}N_3O_2P_2S$ (611.7): C, 66.76; H, 5.77; N, 6.87. Found: C, 66.83; H, 5.81; N, 6.80%.

3.3. Synthesis of compound *6a*

Methyltriflate (40 μL, 0.35 mmol) was added dropwise at room temperature to a solution of **5a** (0.338 g, 0.35 mmol). The resulting solution was stired for 20 min then evaporated to dryness. The residue was washed thrice with THF/pentane (1:20) to give compound **6a** as a pale green powder in 96% yield.

6a: ^{31}P $\{^1H\}$ NMR ($CDCl_3$): $\delta = 23.5$ and 23.8 (2d, $^2J_{PP} = 22.1$ Hz, P_0 and P_1). ^1H NMR ($CDCl_3$): $\delta = 2.58$ (d, $^3J_{HP} = 18.0$ Hz, 3H, SCH_3), 7.25 (d, $^3J_{HH} = 9.0$ Hz, 4H, H–C_1^2), 7.44 (dd, $^3J_{HH} = 8.1$ Hz, $^3J_{HP} = 14.0$ Hz, 3H, H–C^0), 7.56 (“td”, $^3J_{HH} = 7.7$ Hz, $^4J_{HP} = 4.0$ Hz, 6H, H–C^m), 7.75 (t, $^3J_{HH} = 7.7$ Hz, 3H, H–C^p), 7.95 (s, 2H, H–C_1^2), 7.97 (d, $^3J_{HH} = 9.0$ Hz, 4H, H–C_1^3). ^{13}C $\{^1H\}$ NMR ($CDCl_3$): $\delta = 13.8$ (d, $^2J_{CP} = 5.0$ Hz, S–CH_3), 113.2 (s, C_1^6), 113.8 (s, CN), 121.9 (d, $^3J_{CP} = 5.3$ Hz, C_1^2), 124.3 (d, $^1J_{CP} = 110.0$ Hz, C^i), 129.8 (d, $^3J_{CP} = 12.0$ Hz, C^m), 129.9 (s, C_1^4), 132.1 (d, $^2J_{CP} = 11.1$ Hz, C^0), 134.6 (br s, C^p), 134.8 (s, C_1^3), 153.5 (d, $^2J_{CP} = 10.1$ Hz, C_1^1), 158.7 (s, C_1^5). ^{19}F $\{^1H\}$ NMR ($CDCl_3$): $\delta = -1.5$ (s, CF_3). IR (KBr): 2227 (ν-CN) cm^{-1}. *Anal.* Calc. for $C_{40}H_{28}F_3N_5O_5P_2S_2$ (841.76): C, 57.08; H, 3.35; N, 8.32. Found: C, 57.20; H, 3.39; N, 8.25%.

3.4. Synthesis of compounds *8ca* and *8cd*

A solution of **4a** (0.300 g, 0.68 mmol) or **4d** (0.061 g, 1.61 mmol) in THF (5 mL) was added to a solution of **7c** (for **8ca**: 0.350 g, 0.64 mmol; for **8cd**: 0.088 g, 1.61 mmol) in THF (5 mL) at room temperature. The resulting solution was stirred for 12 h, then evaporated to dryness, to afford a powder, which was purified by column chromatography on silica (eluent: AcOEt/Pentane 1/1 for **8ca**, 1/2 for **8cd**).

8ca was obtained as a pale green powder in 85% yield. ^{31}P $\{^1H\}$ NMR ($CDCl_3$): $\delta = -14.6$ (dd, $^2J_{P1P2} = 58.4$ Hz, $^2J_{P0P1} = 25.8$ Hz, P_1), 16.5 (d, $^2J_{P0P1} = 25.8$ Hz, P_0), 45.1 (d, $^2J_{P1P2} = 58.4$ Hz, P_2). ^1H NMR ($CDCl_3$): $\delta = 7.10$ (dd, $^3J_{HH} = 8.7$ Hz, $^4J_{HP} = 1.1$ Hz, 4H, H–C_1^2), 7.13 (dd, $^3J_{HH} = 8.8$ Hz, $^4J_{HP} = 1.0$ Hz, 4H, H–C_2^2), 7.46 (tl, $^3J_{HH} = 7.6$ Hz, 6H, H–C^m), 7.46 (d, $^3J_{HH} = 8.7$ Hz, 4H, H–C_1^3), 7.56 (ddd, $^3J_{HH} = 8.4$ Hz, $^4J_{HH} = 1.3$ Hz, $^3J_{HP} = 13.3$ Hz, 6H, H–C^0), 7.64 (ttd, $^3J_{HH} = 7.4$ Hz, $^4J_{HH} = 1.3$ Hz, $^5J_{HP} = 1.8$ Hz, 3H, H–C^P), 7.69 (s, 2H, H–C_2^5), 7.74 (d, $^3J_{HH} = 8.8$ Hz, 4H, H–C_2^3). ^{13}C $\{^1H\}$ NMR ($CDCl_3$): $\delta = 109.2$ (d, $^5J_{CP} = 1.2$ Hz, C_1^4), 113.6 (s, C_2^6), 114.3 (s, $CN^{(2)}$), 118.6 (s, $CN^{(1)}$), 122.3 (d, $^3J_{CP} = 5.4$ Hz, C_2^2), 122.6 (d, $^3J_{CP} = 5.9$ Hz, C_1^2), 127.4 (d, $^5J_{CP} = 1.0$ Hz, C_2^4), 127.8 (dd, $^1J_{CP} = 107.7$ Hz, $^3J_{CP} = 4.2$ Hz, C^i), 129.6 (d, $^3J_{CP} = 13.2$ Hz, C^m), 132.8 (s, C_1^3), 132.9 (d, $^2J_{CP} = 11.6$ Hz, C^0), 133.9 (d, $^4J_{CP} = 3.0$ Hz, C^p), 134.2 (s, C_2^3), 154.8 (d, $^2J_{CP} = 9.2$ Hz, C_2^1), 157.0 (d, $^2J_{CP} = 8.5$ Hz, C_1^1), 159.2 (s, C_2^5). IR (KBr): 2228 (ν-CN) cm^{-1}. *Anal.* Calc. for $C_{52}H_{33}N_8O_4P_3S$ (959): C, 65.14; H, 3.47, N, 11.69. Found: C, 65.28; H, 3.52; N, 11.51%.

8cd was obtained as a pale green powder in 95% yield. ^{31}P $\{^1H\}$ NMR ($CDCl_3$): $\delta = -14.9$ (dd, $^2J_{P1P2} = 59.0$ Hz, $^2J_{P0P1} = 22.6$ Hz, P_1), 14.6 (d, $^2J_{P0P1} = 22.6$ Hz, P_0), 47.6 (d, $^2J_{P1P2} = 59.0$ Hz, P_2). ^1H NMR ($CDCl_3$): $\delta = 2.79$ (s, 12H, NMe_2), 6.35–6.55 (m, 6H, H–C_2^2, H–C_2^4, H–C_2^6), 7.01 (“t”, $^3J_{HH} = 8.0$ Hz, 2H, H–C_2^5), 7.04 (dd, $^4J_{HP} = 1.1$ Hz, $^3J_{HH} = 8.7$ Hz, 4H, H–C_1^2), 7.40 (d, $^3J_{HH} = 8.7$ Hz, 4H, H–C_1^3), 7.47 (”td”, $^4J_{HP} = 3.4$ Hz, $^3J_{HH} = 7.7$ Hz, 6H, H–C^m), 7.55–7.70 (m, 9H, H–C^0, H–C^p). ^{13}C $\{^1H\}$ NMR ($CDCl_3$): $\delta = 40.4$ (s, NMe_2), 105.9 (d, $^3J_{CP} = 5.8$ Hz, C_2^2), 107.9 (s, C_1^4), 108.2 (s, C_2^4), 109.4 (d, $^3J_{CP} = 4.9$ Hz, C_2^6), 118.5 (s, CN), 121.8 (d, $^3J_{CP} = 5.7$ Hz, C_1^2), 127.8 (dd, $^1J_{CP} = 107.8$ Hz, $^3J_{CP} = 3.7$ Hz C^i), 128.9 (d, $^3J_{CP} = 13.2$ Hz, C^m), 129.1 (s, C_2^5), 132.6 (d, $^2J_{CP} = 11.7$ Hz, C^0), 133.0 (d, $^4J_{CP} = 2.9$ Hz, C^p), 133.4 (s, C_1^3), 151.4 (s, C_2^3), 153.1 (d, $^2J_{CP} = 9.2$ Hz, C_2^1), 154.6 (d, $^2J_{CP} = 8.8$ Hz, C_1^1). IR (KBr): 2230 (ν-CN) cm^{-1}. *Anal.* Calc. for $C_{48}H_{43}N_6O_4P_3S$ (892.9): C, 64.57; H, 4.85; N, 9.41. Found: C, 64.62; H, 4.89; N, 9.28%.

3.5. Synthesis of compound *9ca*

Methyl triflate (26 μl, 0.22 mmol) was added dropwise at room temperature to a solution of **8ca** (0.200 g, 0.21 mmol) in CH_2Cl_2 (2 mL). After stirring for 20 min. the solution was evaporated to dryness to afford a powder, which was washed three times with THF/Pentane (1/20). Compound **9ca** was isolated as a pale green powder in 95% yield.

9ca: ^{31}P $\{^1H\}$ NMR ($CDCl_3$): $\delta = -14.0$ (dd, $^2J_{P1P2} = 53.2$ Hz, $^2J_{P0P1} = 26.2$ Hz, P_1), 23.7 (d, $^2J_{P0P1} = 26.2$ Hz, P_0), 23.8 (d, $^2J_{P1P2} = 53.2$ Hz, P_2). ^1H NMR ($CDCl_3$): $\delta = 2.60$ (d, $^3J_{HP} = 18.5$ Hz, 3H, S-CH_3), 7.03 (dd, $^3J_{HH} = 8.9$ Hz, $^4J_{HP} = 1.5$ Hz, 4H, H–C_1^2), 7.26 (dd, $^3J_{HH} = 9.0$ Hz, $^4J_{HP} = 1.5$ Hz, 4H, H–C_2^2), 7.45 (ddd, $^3J_{HH} = 8.5$ Hz, $^4J_{HH} = 1.3$ Hz, $^3J_{HP} = 13.6$ Hz, 6H,

H–C^0), 7.58 (''td'', $^3J_{HH} = 7.7$ Hz, $^4J_{HP} =$ Hz, 6H, H–C^m), 7.62 (d, $^3J_{HH} = 8.9$ Hz, 4H, H–$C_1{}^3$), 7.77 (ttd, $^3J_{HH} = 7.5$ Hz, $^4J_{HH} = 1.3$ Hz, $^5J_{HP} = 1.9$ Hz, 3H, H–C^P), 7.96 (s, 2H, H–$C_2{}^5$), 7.97 (d, $^3J_{HH} = 9.0$ Hz, 4H, H–$C_2{}^3$). ^{13}C {^1H} NMR ($CDCl_3$): $\delta = 14.0$ (d, $^2J_{CP} = 5.3$ Hz, S–CH_3), 110.7 (d, $^5J_{CP} = 1.2$ Hz, $C_1{}^4$), 113.0 (s, $C_2{}^6$), 113.7 (s, $CN^{(2)}$), 118.0 (s, $CN^{(1)}$), 121.7 (d, $^3J_{CP} = 5.4$ Hz, $C_2{}^2$), 121.8 (d, $^3J_{CP} = 5.3$ Hz, $C_1{}^2$), 126.0 (dd, $^1J_{CP} = 108.0$ Hz, $^3J_{CP} = 4.2$ Hz, C^i), 130.0 (d, $^3J_{CP} = 13.5$ Hz, C^m), 130.1 (s, $C_2{}^4$), 132.6 (d, $^2J_{CP} = 11.4$ Hz, C^0), 133.5 (s, $C_1{}^3$), 134.7 (d, $^4J_{CP} = 2.9$ Hz, C^p), 134.9 (s, $C_2{}^3$), 153.1 (d, $^2J_{CP} = 10.9$ Hz, $C_2{}^1$), 153.2 (d, $^2J_{CP} = 9.9$ Hz, $C_1{}^1$), 158.6 (s, $C_2{}^5$). ^{19}F {^1H} NMR ($CDCl_3$): $\delta = -0.8$ (s, CF_3). IR (KBr): 2228 (ν-CN) cm^{-1}. M.P.: 106–108 °C. *Anal.* Calc. for $C_{54}H_{36}F_3N_8O_7P_3S_2$ (1123): C, 57.76; H, 3.23; N, 9.98. Found: C, 57.83; H, 3.27; N, 9.85%.

3.6. X-ray structure determination for compounds **3a**, **4b**, and **5d**

Measurement were carried out on a one circle IPDS STOE X-ray diffractometer system (Mo-radiation, $\lambda = 0.71073$ Å, 50 KV/30 mA power). All compounds were collected at low temperature, at $T = 160(2)$ K for **3a** and **5d**, and 180(2) K for **4b**. Frames were integrated with the aid of STOE, X-RED, data reduction for STADI4 and IPDS, Revision 1.08, Stoe software [31].

In all cases a hemisphere of reflections was collected. Structures were solved by using direct methods, with the aid of SIR92 [32] and refined by least-squares procedures on F^2, using SHELXL-97 included in the WINGX programs version 1.64 04[1]. Direct methods of phase determination followed by subsequent Fourier cycles of refinement led to an electron density map, from which most of the non-hydrogen atoms were identified for all compounds. All of the non-hydrogen atoms were identified with subsequent isotropic refinement. Atomic coordinates, isotropic and anisotropic displacement parameters of all the non-hydrogen atoms were refined by means of a full matrix least-squares procedure on F^2. The hydrogen atoms were included in the refinement in calculated positions, riding on the carbon atoms to which they were attached. Drawings of molecules were realized with the aid of ORTEP32 [33]. Atomic scattering factors were taken from International tables for X-ray crystallography [34]. Due to the presence of a strong disorder on the N_3 groups for compound **4b**, restraints put on interatomic distances, angles and on ADP's were necessary to use in order to get a chemically reasonable model, some residuals electronics densities very close to N_3 groups are also still visible on the difference Fourier maps but all attempts to try to fit them failed.

[1] SHELX97 [Includes SHELXS97, SHELXL97, CIFTAB] – programs for crystal structure analysis (Release 97-2). G. M. Sheldrick, Institüt für Anorganische Chemie der Universität, Tammanstrasse 4, D-3400 Göttingen, Germany, 1998.

Acknowledgement

We thank the CNRS for financial support, and the European Community for a grant to G. Spataro (Fond Social Européen).

Appendix A. Supplementary material

CCDC 633330, 633331, and 633332 contain the supplementary crystallographic data for **3a**, **4b** and **5d**. These data can be obtained free of charge via http://www.ccdc.cam.ac.uk/conts/retrieving.html, or from the Cambridge Crystallographic Data Centre, 12 Union Road, Cambridge CB2 1EZ, UK; fax: (+44) 1223-336-033; or e-mail: deposit @ccdc.cam.ac.uk. Supplementary data associated with this article can be found, in the online version, at doi:10.1016/j.poly.2007.04.011.

References

[1] H.R. Allcock, Chemistry and Applications of Polyphosphazenes, Wiley–Interscience, Hoboken, New Jersey, 2002.
[2] M. Gleria, R. de Jaeger, Top. Curr. Chem. 250 (2005) 165.
[3] M. Gleria, R. de Jaeger, Phosphazenes, A Worldwide Insight, Nova, Hauppage, 2004.
[4] A.B. Chaplin, J.A. Harrison, P.J. Dyson, Inorg. Chem. 44 (2005) 8407.
[5] H.R. Allcock, N.M. Toffelson, R.A. Arcus, R.R. Whittle, J. Am. Chem. Soc. 107 (1985) 5166.
[6] (a) Y. Chatani, K. Yatsuyanagi, Macromolecules 20 (1987) 1042;
(b) H. Sun, J. Am. Chem. Soc. 119 (1997) 3611;
(c) R. Caminiti, M. Gleria, K.B. Lipkowitz, G.M. Lombardo, G.C. Pappalardo, J. Am. Chem. Soc. 119 (1997) 2196;
(d) B. Chaplin, J.A. Harrison, P.J. Dyson, Inorg. Chem. 44 (2005) 8407.
[7] (a) Y.G. Gololobov, L.F. Kasukhin, Tetrahedron 48 (1992) 1353;
(b) F. Lopez Ortiz, Current. Org. Synth. 3 (2006) 187.
[8] A.M. Caminade, J.P. Majoral, Chem. Rev. 94 (1994) 1183.
[9] J. Mitjaville, A.M. Caminade, J.C. Daran, B. Donnadieu, J.P. Majoral, J. Am. Chem. Soc. 117 (1995) 1712.
[10] C. Galliot, D. Prévoté, A.M. Caminade, J.P. Majoral, J. Am. Chem. Soc. 117 (1995) 5470.
[11] L. Brauge, G. Magro, A.M. Caminade, J.P. Majoral, J. Am. Chem. Soc. 123 (2001) 6698.
[12] V. Maraval, A.M. Caminade, J.P. Majoral, J.C. Blais, Angew. Chem., Int. Ed. 42 (2003) 1822.
[13] V. Maraval, J. Pyzowski, A.M. Caminade, J.P. Majoral, J. Org. Chem. 68 (2003) 6043.
[14] V. Maraval, R. Laurent, B. Donnadieu, M. Mauzac, A.M. Caminade, J.P. Majoral, J. Am. Chem. Soc. 122 (2000) 2499.
[15] S. Merino, L. Brauge, A.M. Caminade, J.P. Majoral, D. Taton, Y. Gnanou, Chem. Eur. J. 7 (2001) 3095.
[16] C. Larré, A.M. Caminade, J.P. Majoral, Angew. Chem., Int. Ed. Engl. 36 (1997) 596.
[17] C. Larré, B. Donnadieu, A.M. Caminade, J.P. Majoral, J. Am. Chem. Soc. 120 (1998) 4029.
[18] J. Omelanczuk, J. Chem. Soc. Chem. Commun. (1992) 1718.
[19] C. Galliot, C. Larré, A.M. Caminade, J.P. Majoral, Science 277 (1997) 1981.
[20] C. Larré, D. Bressolles, C. Turrin, B. Donnadieu, A.M. Caminade, J.P. Majoral, J. Am. Chem. Soc. 120 (1998) 13070.
[21] V. Cadierno, A. Igau, B. Donnadieu, A.M. Caminade, J.P. Majoral, Organometallics 18 (1999) 1580.
[22] L. Brauge, A.M. Caminade, J.P. Majoral, S. Slomkowski, M. Wolszczak, Macromolecules 34 (2001) 5599.

[23] G. Magro, B. Donnadieu, A.M. Caminade, J.P. Majoral, Chem. Eur. J. 9 (2003) 2151.
[24] U. Müller, Chem. Ber. 110 (1977) 788.
[25] H.W. Roesky, M. Noltemeyer, G.M. Sheldrick, Z. Naturforsch. B 41B (1986) 803.
[26] R.J. Wehmschulte, M.A. Khan, S.I. Hossain, Inorg. Chem. 40 (2001) 2756.
[27] S. Kumaraswamy, P. Kommana, N.S. Kumar, K.C.K. Swamy, Chem. Commun. (2002) 40.
[28] A. Maraval, G. Magro, V. Maraval, L. Vendier, A.M. Caminade, J.P. Majoral, J. Organomet. Chem. 691 (2006) 1333.
[29] M. Gökel, K. Karaghiosoff, T.M. Klapöte, Angew. Chem., Int. Ed. 45 (2006) 6037.
[30] A.K. Adrianov, A. Marin, J. Chen, Biomacromolecules 7 (2006) 394.
[31] STOE, X-RED, Data Reduction for STADI4 and IPDS, Revision 1.08.
[32] A. Altomare, G. Cascarano, G. Giacovazzo, A. Guagliardi, M.C. Burla, G. Polidori, M. Camalli, J. Appl. Cryst. 27 (1994) 435.
[33] J. Farrugia, Appl. Cryst. 32 (1999) 837.
[34] International tables for X-ray crystallography, vol. IV, 1974, Kynoch Press, Birmingham, England.

simultaneously coordinating two or more metal centers also provide the bridge for the magnetic interaction; especially when the metal ions are relatively far from each other. In this category, $X_2C_2Y_2$ bridge, where X and Y atoms bound to different metal ions may be O, N, or S, has been used efficiently to propagate the magnetic interactions between two and in very few cases three metal centers. The examples include highly symmetrical bridge oxalato, $O_2C_2O_2^{2-}$ [21–23], oxamido, $N_2C_2O_2^{2-}$ [24–27], and dithiooxamido, $N_2C_2S_2^{2-}$ [28–30]. In particular, the oxamido ligand provide two planar NCO bridge between the metal centres and the result is a very strong antiferromagnetic coupling [24–27].

In this paper, we describe the design and synthesis of two amide-based ligands and their copper coordination chemistry. The ligands coordinate the copper ion via deprotonated $N_{amidate}$ and neutral N_{amine} donors. Interestingly, in one case, flipping of the amide containing arm take place to afford a linear copper trinuclear complex. This is a rare example, where deprotonated amide group coordinate via both ends, $N_{amidate}$ as well as $O_{amidate}$ [31,32]. The second complex also shows sharing of the amide group between copper centres affording a one-dimensional zig-zag chain. The bridging ligand present between the copper(II) ions is NCO, thus we have chopped off one unit (one NCO fragment) of the oxamido ligand. The result of this alteration on the structure and magnetic properties of the copper complexes is presented.

2. Experimental

2.1. Materials

All reagents were obtained from the commercial sources and used as received. *N*,*N*-dimethyl formamide (DMF) was dried and distilled from 4 Å molecular sieves and was stored over sieves. Acetonitrile (MeCN) was dried by distillation from anhydrous CaH_2. Diethyl ether and petroleum ether (boiling range 60–80 °C) were dried by refluxing over sodium metal under inert atmosphere. Tetrahydrofuran (THF) was dried by refluxing and distilling from sodium metal and benzophenone. Ethyl alcohol (C_2H_5OH) and methyl alcohol (CH_3OH) were distilled from magnesium ethoxide and magnesium methoxide, respectively. Chloroform ($CHCl_3$) and dichloromethane (CH_2Cl_2) were purified by washing with 5% sodium carbonate solution followed by water and finally dried over anhydrous $CaCl_2$, before a final reflux and distillation. *N*,*N*′-bis(chloroacetyl)ethylenediamine and *N*,*N*′-bis(chloroacetyl)-*o*-phenylenediamine were synthesized according to a reported procedure [33,34].

2.2. Physical measurements

The conductivity measurements were done in organic solvents using the digital conductivity bridge from Popular Traders, India (model number: PT-825). The elemental analysis data were obtained from Elementar Analysensysteme GmbH Vario EL-III instrument. The NMR measurements were done using an Avance Bruker (300 MHz) instrument. The infra-red spectra (either as KBr pellet or as a mull in mineral oil) were recorded using the Perkin–Elmer FTIR 2000 spectrometer. The absorption spectra were recorded using the Perkin–Elmer Lambda-25 spectrophotometer. The mass spectra were obtained on a Jeol SX102/DA-6000 instrument. The thermal analyses were performed with a Shimadzu DTG-60 instrument in the temperature range of 25–800 °C. EPR spectra of the polycrystalline samples were recorded at X-band (9.4 GHz) frequencies with a Bruker ESP-300E spectrometer, from room temperature to 4 K at the Servei de Magnetoquimica of the Universitat de Barcelona. Room temperature solution EPR spectra were recorded with a Jeol JES-3XG spectrometer.

2.3. Crystallography

Single crystals suitable for X-ray diffraction studies were grown by the vapour diffusion of diethyl ether to a DMF solution of complex **1** and slow evaporation of a saturated MeOH solution of **2**. The suitable crystals of **1** and **2** were mounted lengthways with the largest dimension in a sealed capillary. The intensity data for **1** were collected at 295 K on a Siemens P4 X-ray diffractometer by using scanning mode with graphite monochromatized Mo Kα radiation. A total of 15503 reflections were measured of which 10999 reflections ($I > 2\sigma(I)$) were used in the structure refinement. The data were corrected for Lorentz and polarization effects and a psi-scan absorption correction was also applied. The structure was solved by direct methods and refined by full-matrix least-squares refinement techniques on F^2. There are two crystallographically independent molecules of the complex and the solvent DMF in the unit cell. All calculations were performed using SHELXTL-PC. One of the DMF molecules showed rotational disorder which has been treated by refining all five non-hydrogen atoms of this molecule (C60, C61, C62, N20, O12) being split at two sites with total site occupancy of 1.00 for each one of them. This DMF molecule was refined isotropically with similar U_{iso} values assigned to two atoms of the pair. The molecule was refined with restraints on the bond distances of this disordered molecule being C(sp^3)–N 1.440(3), C(sp^2)–N 1.350(3), C=O 1.226(3) Å and non-bonding distances being 2.20(3) Å. All non-hydrogen atoms except for one DMF molecule were refined anisotropically. All hydrogen atoms were attached geometrically except for those belonging to the water molecules which were determined from the difference Fourier map. For **2**, the intensity data were collected on a BRUKER AXS SMART-APEX CCD diffractometer equipped with a molybdenum sealed tube (Mo Kα = 0.71073 Å) and a highly orientated graphite monochromator [35]. Frames were collected at $T = 293$ K by ω, ϕ and 2θ-rotation at 10 s per frame with SMART [35]. The measured intensities were reduced to F^2 and corrected for absorption with

SADABS [36]. The structure of **2** was solved by SIR 92 expanded by Fourier difference syntheses and refined with the SHELXL 97 package incorporated in WINGX 1.64 crystallographic collective package [37–39]. The positions of the hydrogen atoms were calculated by assuming ideal geometries but not refined. All non-hydrogen atoms were refined with anisotropic thermal parameters by full-matrix least-squares procedures on F^2. Details of the crystallographic data are given in Table 1.

2.4. Magnetic measurements

Magnetic susceptibility measurements for crushed crystalline samples of **1** and **2** were carried out at the Servei de Magnetoquimica of the Universitat de Barcelona with a Quantum Design SQUID MPMS-XL susceptometer. The magnetic susceptibility data were recorded in the 2–300 K temperature range under magnetic fields of 500 G (2–30 K) and 10 000 G (2–300 K). Diamagnetic corrections were estimated from Pascal Tables. The fits were performed minimizing the function $R = \Sigma(\chi_M T_{exp} - \chi_M T_{cal})^2/\Sigma(\chi_M T_{exp})^2$. Magnetic fields ranging from 0 to 50 000 G were used for magnetization measurements at 2 K.

2.5. Ligand Syntheses

2.5.1. Synthesis of H_2L^1

To a solution of diethylamine (1.37 g, 18.76 mmol) in MeCN (30 cm^3), K_2CO_3 (39 g, 282 mmol) and *N*,*N*′-bis(chloroacetyl)ethylenediamine (2 g, 9.38 mmol) were added and the mixture was refluxed for 24 h. The mixture was cooled, filtered and the solvent was removed under reduced pressure to afford an off-white solid. The crude product was recrystallized by layering the $CHCl_3$ solution with the petroleum ether (boiling range 60–80 °C). Yield: 2.24 g, 83%. Microanal. Calc. for H_2L^1, $C_{14}H_{30}N_4O_2$: C, 58.74; H, 10.57; N, 19.58. Found: C, 58.28; H, 10.96; N, 19.52%. M.p. 80 °C. Selected IR bands (FT-IR, KBr) ν (cm^{-1}): 3301s (NH), 2965m, 2933m, 2873w, 2814w (CH), 1649s (C=O). ^1H NMR spectrum ($CDCl_3$): δ 1.023 (t, $J = 6.8$ Hz, 12H, ethyl CH_3), 2.54 (quartet, $J = 6.7$ Hz, 8H, ethyl CH_2), 3.01 (s, 4H, CH_2CO), 3.42 (s, 4H, ethylene CH_2), 7.65 (br s, 2H, amidic NH). ESI mass spectrum (CH_3CN): $m/z = 287.24$ [M+H^+].

2.5.2. Synthesis of H_2L^2

To a solution of *N*,*N*′-bis(chloroacetyl)-*o*-phenylenediamine (2 g, 7.6 mmol) in ethanol (25 cm^3), 40% aqueous solution of dimethylamine (5.2 g, 46 mmol) was added and the mixture was refluxed for 24 h. The mixture was cooled and the solvent was removed under reduced pressure. The resultant oil was washed with a saturated solution of $NaHCO_3$ (10 cm^3) and the ligand was then extracted with dichloromethane (3×10 cm^3). The combined extracts were dried over Na_2SO_4 and evaporated under reduced pressure to leave a pale yellow solid. The crude product was then recrystallized by layering the $CHCl_3$ solution with the petroleum ether (boiling range 60–80 °C). Yield: 1.8 g, 85%. Microanal. Calc. for H_2L^2, $C_{14}H_{22}N_4O_2$: C, 60.31; H, 7.8; N, 20.10. Found: C, 59.59; H, 7.6; N, 19.86%. M.p. 82 °C. Selected IR bands (FT-IR, KBr) ν (cm^{-1}): 3231m (NH), 2952w, 2826m, 2780m (CH), 1693s (C=O), 1601m (C=C). ^1H NMR spectrum ($CDCl_3$): δ 2.30 (s, 12H, methyl CH_3), 3.03 (s, 4H, CH_2CO), 7.10 (m, 2H, benzyl CH) 7.56 (m, 2H, benzyl CH), 9.17 (br s, 2H, amidic NH). ESI mass spectrum (CH_3CN): $m/z = 279.4$ [M+H^+].

Table 1
Crystallographic data for complexes, $[Cu_3(L^1)_2(Cl)_2(H_2O)] \cdot DMF$ (**1**) and $[Cu(L^2)]_n$ (**2**)

	1 · DMF	**2**
Formula	$C_{31}H_{65}N_9O_6Cl_2Cu_3$	$C_{14}H_{20}N_4O_2Cu$
M_r	921.47	339.88
Crystal system	triclinic	orthorhombic
Space group	$P\bar{1}$ (#2)	$Pn21a$ (#33)
a (Å)	13.078(5)	16.560(5)
b (Å)	17.696(5)	8.427(5)
c (Å)	21.210(5)	11.203(5)
α (°)	102.420(5)	90.0
β (°)	93.680(5)	90.0
γ (°)	110.500(5)	90.0
V (Å^3)	4438(2)	1563.4(13)
Z	4	4
T (K)	295(2)	293(2)
Colour, shape	blue, prism	blue, block
Crystal size (mm)	$0.18 \times 0.15 \times 0.13$	$0.3 \times 0.2 \times 0.2$
D_{calc} (g cm^{-3})	1.379	1.444
$F(000)$	1932	708
R[a]	0.0598	0.0450
wR[b]	0.1683	0.1171
Goodness of fit on F^2	1.031	0.831
$\Delta\rho_{max,min}$ (e Å^{-3})	0.710, −1.184	0.351, −0.560

[a] $R = \sum ||F_o| - |F_c|| / \sum |F_o|$.
[b] $wR = \{[\sum(|F_o|^2 |F_c|^2)^2]\}^{1/2}$.

2.6. Syntheses of the copper complexes

2.6.1. $[Cu_3(L^1)_2(Cl)_2(H_2O)] \cdot 2H_2O$ (**1**)

To a stirred solution of H_2L^1 (0.200 g, 0.699 mmol) in DMF (10 cm^3), solid NaH (0.033 g, 1.398 mmol) was added under dinitrogen atmosphere. The resulting mixture was stirred until H_2 evolution ceased. To this $CuCl_2$ (0.141 g, 1.048 mmol) was added as solid followed by the addition of few drops of water. The resulting green-blue solution was stirred at room temperature for 2 h. During this time the colour changed to dark blue. The solution was passed through a celite pad in a medium porosity frit. The resultant solution was layered with diethyl ether and stored at 4 °C. This afforded dark blue microcrystalline product within a day. Yield: 0.18 g, 61%. Microanal. Calc. for **1**, $C_{28}H_{58}N_8O_5Cl_2Cu_3 \cdot 2H_2O$: C, 38.03; H, 7.01; N, 12.68. Found: C, 38.36; H, 7.20; N, 12.56%. Selected IR bands (FT-IR, KBr) ν (cm^{-1}): 3367m br. (OH), 2967m, 2930m, 2874m (CH), 1610s, 1572s (C=O). UV–Vis

spectrum (MeCN: λ_{max} (nm) [ε_{max}] (M^{-1} cm^{-1})): 625 [390], 515sh [280], 350sh [4230], 317sh [7700], 264 [14050]. UV–Vis spectrum (MeOH: λ_{max} (nm) [ε_{max}] (M^{-1} cm^{-1})): 625 [370], 260 [15200], 215 [27800]. Conductivity (CH_3CN, ~1 mM solution, 298 K): $\Lambda_M = 12\ \Omega^{-1}\ cm^2\ mol^{-1}$. ESI mass spectrum ($CH_3OH$) $m/z = 852.5$ ($[Cu_3(L^1)_2(CH_3OH)(OCH_3)_2]+H^+$).

2.6.2. $[Cu(L^2)]_n$ (2)

To a stirred solution of H_2L^2 (0.200 g, 0.719 mmol) in DMF (10 cm^3), solid NaH (0.034 g, 1.438 mmol) was added under dinitrogen atmosphere. The resulting solution was stirred until H_2 evolution ceased. Solid $CuCl_2$ (0.097 g, 0.719 mmol) was added to the above mixture. The resulting indigo-blue solution was stirred at room temperature for 2 h. The DMF was then removed under reduced pressure and the residue was redissolved in CH_3OH (50 cm^3). The solution was passed through the celite pad in a medium porosity frit and allowed to evaporate for a day to afford dark blue microcrystalline product. The product was filtered and dried under vacuum. Yield: 0.20 g, 82%. Microanal. Calc. for **2**, $C_{14}H_{20}N_4O_2Cu$: C, 49.33; H, 5.89; N, 16.49. Found: C, 49.33; H, 6.03; N, 16.33%. Selected IR bands (FT-IR, KBr) ν (cm^{-1}): 3060w, 2893w, 2793w (CH), 1616s, 1598s (C=O), 1564s, 1478m, 1454w (C=C). UV–Vis spectrum (MeOH: λ_{max} (nm) [ε_{max}] (M^{-1} cm^{-1})): 550 [410], 413sh [180], 311sh [12270], 302sh [18600], 270 [47050], 250sh [52500], 240 [62050]. UV–Vis spectrum (MeCN: λ_{max} (nm) [ε_{max}] (M^{-1} cm^{-1})): 530 [360], 405sh [175], 311sh [11050], 280 [31000], 242 [50400], 214 [28000]. conductivity (CH_3OH, ~1 mM solution, 298 K): $\Lambda_M = 16\ \Omega^{-1}\ cm^2\ mol^{-1}$. ESI mass spectrum ($CH_3OH$) $m/z = 362.18$ ($[Cu(L^2)]+Na^+$).

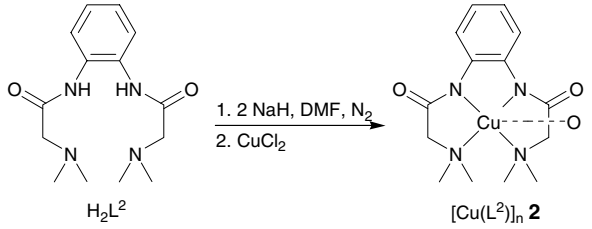
3. Results and discussion

3.1. Ligand design and synthesis

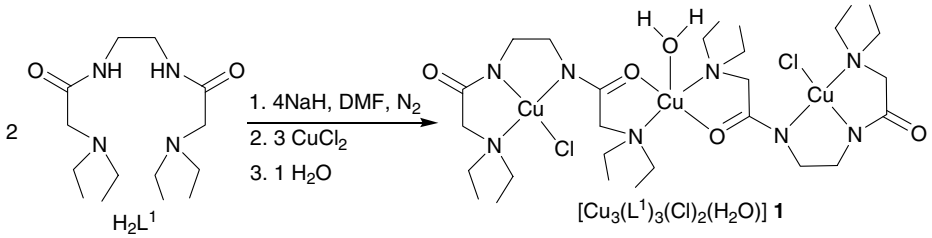
The ligands H_2L^1 and H_2L^2 are designed to simultaneously provide two amide and two amine coordinations to the metal centre while maintaining an identical primary coordination environment around it. While the ligand H_2L^1 has a flexible ethylenediamine backbone, the ligand H_2L^2 incorporates a rigid *o*-phenylenediamine backbone. These ligands are synthesized in two steps starting from the corresponding primary diamines. In the first step, the diamine is converted to the respective bis(chloroamide) by treating with 2 equiv. of chloroacetyl chloride [33,34]. In the second step, the bis(chloroamide) was subsequently treated with diethyl- or dimethyl-amine to afford the ligands, H_2L^1 and H_2L^2, respectively. Excess Me_2NH (6 equiv.) was used for the synthesis of H_2L^2, where it also functioned as a base in the reaction. Both ligands were characterized thoroughly and gave satisfactory microanalyses results.

3.2. Synthesis and characterization of copper complexes

Complex **1** was synthesized by the initial reaction of 2 equiv. of deprotonated ligands with 3 equiv. of $CuCl_2$. The reaction mixture was then treated with few drops of water to afford the final compound (Scheme 1). The complex **2** was also synthesized in an analogous fashion by treating deprotonated ligand, $[L^2]^{2-}$, with $CuCl_2$ (Scheme 2). In the FTIR spectra, the absence of ν(N–H) stretching frequency confirms the deprotonated nature of the amide ligands. Moreover, a *red* shift was observed for the amidate C=O group compared to the free ligand, thus indicating coordination through anionic amidate-N center. The complex **1** also shows the ν(OH) stretches in the region of ~3370 cm^{-1} for the coordinated as well as lattice water [40]. Solution conductivity data [41] confirms the non-electrolytic nature of both copper complexes, whereas elemental analyses results authenticate the purity of the bulk samples. In the electrospray mass spectrum for complex **1** in CH_3CN, the molecular ion peak was observed at 887.35 that matches well with the following composition, $[Cu_3(L^1)_2(Cl)_2(H_2O)] + H_2O + Na^+$ (calculated $m/z = 887.64$). This is to be noted, however, when recorded in CH_3OH, a new molecular ion peak was observed at 852.5 which fits well with the following composition,



Scheme 2. Synthesis of complex **2**.



Scheme 1. Synthesis of complex **1**.

$[Cu_3(L^1)_2(OCH_3)_2(CH_3OH)] + H^+$ (calculated $m/z = 852.3$). Interestingly, while recording the spectrum in CH_3OH, two chloride ions were replaced by methoxide ions while the coordinated water got exchanged with methanol. Complex **2**, on the other hand, shows the molecular ion peak at 362.18 that matches well with $[Cu(L^2)] + Na^+$ (calculated $m/z = 362.25$).

3.3. Solid state structures

3.3.1. Structure of complex *1*

The molecular structure of **1** contains two slightly different independent trinuclear motifs of $[Cu_3(L^1)_2(Cl)_2(H_2O)]$, hereafter referred as molecule A and molecule B. The thermal ellipsoidal representation of molecules A and B are shown in Fig. 1 while important structural parameters are presented in Table 2. Each trinuclear assembly is composed of two $[L^1]^{2-}$ ligands, three copper ions, two chloride ions, and a water molecule. The terminal copper ions (Cu1 and Cu3 in molecule A; and Cu4 and Cu6 in molecule B) are coordinated by two amidate-N centres, one amine-N centre, and a chloride ion completing a distorted square-planar geometry. The central copper ion (Cu2 and Cu5 in molecules A and B, respectively) is coordinated by two amine-N centres, two amidate-O centres, and an apical water molecule. The geometry around the central copper(II) ion is distorted square-pyramidal. The τ value [42], which is an indication of the distortion of the 5-coordinate geometry towards square-pyramidal ($\tau = 0$) or trigonal bipyramidal ($\tau = 1$), is 0.14 and 0.04, for central copper ion in molecules A and B, respectively. It is clear from the value of τ that the central Cu(II) ion has much more distorted geometry in molecule A. The displacement from the basal plane (defined by two amide-N, one amine-N, and a Cl^-) for the terminal copper centres (Cu1, Cu3, Cu4, and Cu6) is quite small, 0.028–0.087 Å. On the other hand, the central coppers are significantly displaced out of basal plane (defined by two amide-Os and two amine-Ns) towards the apical water molecule; displacement for Cu2 and Cu5 is 0.210 and 0.171 Å, respectively. These values again indicate that the copper ion in molecule A has much more distorted geometry than in B. The bond length difference for the coordination of two amidate-N centres to the terminal Cu(II) ions (for example, between Cu1–N2 and Cu1–N3 for molecule A) is quite significant, ~0.1 Å. This difference may be attributed due to the presence of a delocalized structure of one of the amide group which is involved in the bonding with the central Cu(II) ion. This

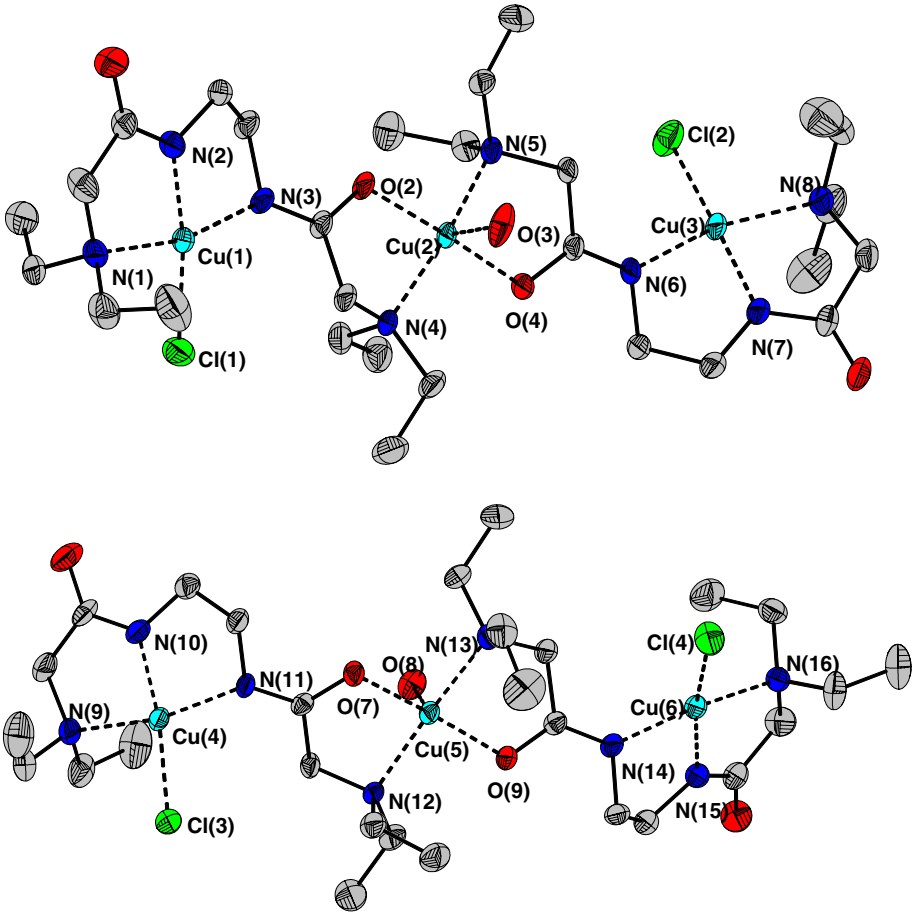


Fig. 1. Thermal ellipsoidal representation (30% probability level with partial numbering) of complex **1** (molecule **A** (top) and molecule **B** (bottom) Hydrogen atoms and solvent molecules are omitted for clarity.

Table 2
Selected bond distances (Å) and angles (°) for molecules A and B in complex $[Cu_3(L^1)_2(Cl)_2(H_2O)]$ (**1**)

Molecule A		Molecule B	
Bond distances			
Cu1–N1	2.105(4)	Cu4–N9	2.083(4)
Cu1–N2	1.898(4)	Cu4–N10	1.891(4)
Cu1–N3	2.007(4)	Cu4–N11	1.993(4)
Cu1–Cl1	2.2226(19)	Cu4–Cl3	2.2393(17)
Cu2–N4	2.051(4)	Cu5–N12	2.057(4)
Cu2–N5	2.045(4)	Cu5–N13	2.043(4)
Cu2–O2	1.938(3)	Cu5–O7	1.938(3)
Cu2–O3	2.192(4)	Cu5–O8	2.271(4)
Cu2–O4	1.942(3)	Cu5–O9	1.923(3)
Cu3–N6	1.981(4)	Cu6–N14	2.001(4)
Cu3–N7	1.894(4)	Cu6–N15	1.894(4)
Cu3–N8	2.109(4)	Cu6–N16	2.117(4)
Cu3–Cl2	2.2332(19)	Cu6–Cl4	2.2251(18)
Bond angles			
N2–Cu1–N3	83.04(17)	N10–Cu4–N11	83.00(19)
N2–Cu1–N1	81.98(18)	N10–Cu4–N9	83.4(2)
N3–Cu1–N1	164.89(18)	N11–Cu4–N9	161.3(2)
N2–Cu1–Cl1	171.24(15)	N10–Cu4–Cl3	166.18(17)
N3–Cu1–Cl1	102.56(14)	N11–Cu4–Cl3	102.02(13)
N1–Cu1–Cl1	92.10(14)	N9–Cu4–Cl3	94.16(15)
O4–Cu2–O2	172.18(17)	O9–Cu5–O7	168.71(17)
O4–Cu2–N5	83.30(15)	O9–Cu5–N13	84.75(16)
O2–Cu2–N5	96.03(15)	O7–Cu5–N13	95.75(16)
O4–Cu2–N4	95.42(15)	O9–Cu5–N12	94.02(15)
O2–Cu2–N4	83.07(15)	O7–Cu5–N12	83.69(15)
N5–Cu2–N4	164.00(18)	N13–Cu5–N12	170.85(19)
O4–Cu2–O3	94.08(16)	O9–Cu5–O8	93.97(16)
O2–Cu2–O3	93.73(16)	O7–Cu5–O8	97.26(16)
N5–Cu2–O3	97.54(19)	N13–Cu5–O8	93.18(18)
N4–Cu2–O3	98.5(2)	N12–Cu5–O8	95.95(17)
N7–Cu3–N6	82.35(18)	N15–Cu6–N14	82.76(19)
N7–Cu3–N8	82.55(18)	N15–Cu6–N16	81.80(18)
N6–Cu3–N8	164.07(19)	N14–Cu6–N16	162.59(19)
N7–Cu3–Cl2	166.77(16)	N15–Cu6–Cl4	167.67(16)
N6–Cu3–Cl2	100.61(14)	N14–Cu6–Cl4	100.66(14)
N8–Cu3–Cl2	95.24(14)	N16–Cu6–Cl4	96.12(14)
Cu1–Cu2–Cu3	176.61(11)	Cu4–Cu5–Cu6	170.139(12)

delocalization of the electron density has contributed in inducing a partial negative charge on the amidate-O atom that eventually coordinate to the central copper ion to afford the linear trinuclear complex. The implication of this delocalized resonance structure is the lengthening of the C=O bond involved in the bonding than the un-coordinated one. The C=O bond length increased from a average value of ~1.23(2) Å (uncoordinated one) to ~1.28(2) Å (coordinated one). This lengthening is lower for molecule B (0.03–0.04 Å) than for molecule A (0.05–0.06 Å). The $Cu–O_{amide}$ distances for the central metal ion, are in the range of 1.923(3)–1.942(3) Å for molecules A and B. These distances are on the lower side than the examples reported in the literature and indicate a stronger bond to the copper ion [31,32]. The $Cu–OH_2$ bond distances are also on the lower side compared to the similar distance in other structurally characterized complexes [43–47]. The Cu–Cl distances are comparable to other structurally characterized complexes [48–50]. The average distance between the neighbouring copper centres is ~5.74(3) Å, while the terminal copper ions are separated by ~11.5(3) Å. The coordinated water molecule forms hydrogen bonds with the carbonyl oxygen atoms from the neighbouring complexes, the distance are within the range of ~2.62(3)–2.68(4) Å.

There are strong H-bonding interactions involving the amide oxygens, water molecules and the DMF molecule resulting in an interesting crystal structure of the molecule. The water molecule O3 of molecule A shows strong intermolecular O···O bonding with amide oxygens O1 and O5 of its centrosymmetrically related molecules (Table S1). This gives rise to polymeric, pleated ribbon like chains running along the *c* axis in the *bc* plane (Fig. S1) constituting lattice I. The DMF molecule close to this is not involved in any O···O bonding but is merely being held in space by weak C···O H-bonding interactions. On the other hand second DMF molecule is acting as H-bond acceptor to water molecule O8 of molecule B, which is also behaving as a H-bond donor to amide oxygen O10. These interactions give rise to a H-bonded 2B:2DMF tetrameric synthon as shown in Fig. S2, constituting lattice II. There are only some weak C···O H-bonding interactions between these synthons. Thus involvement of DMF in H-bonding interactions with the trinuclear coordination compound destroys the polymeric nature of molecule B. Taken together the crystal structure may be looked at as two interpenetrating lattices I and II (Fig. S3).

The alignment of the basal plane containing metal centers plays a very important role in the magnetic exchange interactions in any multimetallic system [51,52]. If these planes are coplanar with each other, a strong antiferromagnetism results and deviation from this planarity results in the alteration of the extent of orbital overlapping. The angle between the basal planes containing copper ion is within the range of 20–40°. For example, in molecule B, the angle between the planes containing Cu(4) and Cu(5) is 39.61°. These numbers suggest a moderate to weak antiferromagnetic interaction between the magnetic orbitals emerging from the planes containing copper ions (cf. magnetic properties).

3.3.2. Structure of complex **2**

The molecular structure of this complex is shown in Fig. 2 and the selected bonding parameters are presented in Table 3. The complex **2** exists as a one-dimensional (1D) chain of infinite length. The copper(II) ion is coordinated by the ligand $[L^1]^{2-}$, in a tetradentate fashion via two deprotonated amidate-N and two amine-N centers. The 5th coordination comes from the oxygen atom of the amide group of the neighbouring complex, with the distance of 2.354(2) Å. This additional interaction leads to the generation of an infinite length chain in the solid state. The geometry around the Cu(II) ion is almost perfect square – pyramidal with a very small τ value [42] of 0.01. The average $Cu–N_{amide}$ distance at 1.935(2) Å is shorter by 0.14 Å than the average $Cu–N_{amine}$ bond lengths of 2.075(3) Å, thus indicating a tight chelation from the

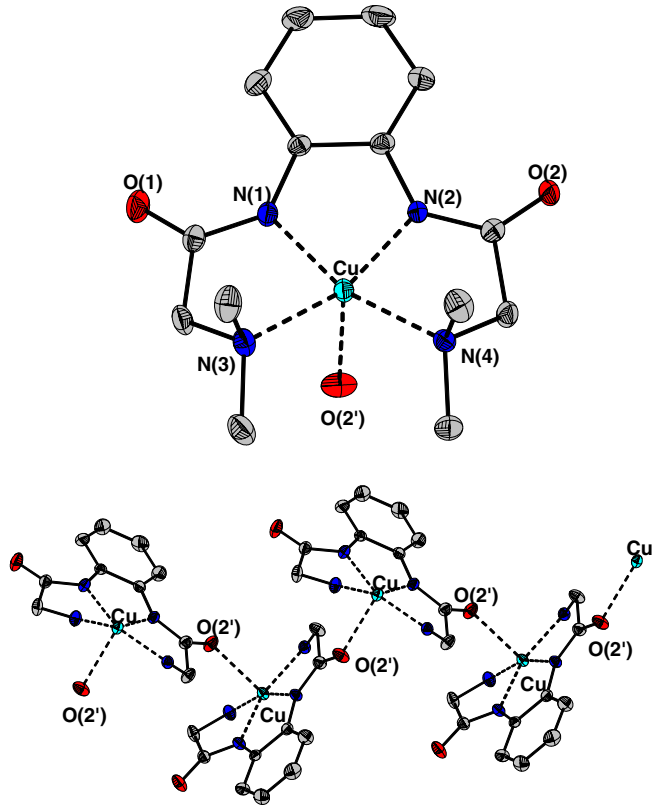


Fig. 2. Thermal ellipsoidal representation (30% probability level with partial numbering, hydrogen atoms are omitted for clarity) of complex **2**. Top: monomeric unit; bottom: zig-zag chain formation (methyl substituents are removed for clarity).

Table 3
Selected bond distances (Å) and angles (°) for complex $[Cu(L^2)]_n$ (**2**)

Bond distances			
Cu–N1	1.930(2)	C14–O1	1.232(4)
Cu–N2	1.939(2)	C7–O2	1.238(4)
Cu–N3	2.060(3)	N1–C14	1.321(4)
Cu–N4	2.090(3)	N2–C7	1.316(4)
Cu–O2′	2.354(2)		
Bond angles			
N1–Cu–N2	82.47(10)	N1–Cu–O2′	101.98(11)
N1–Cu–N3	162.19(11)	N2–Cu–O2′	104.48(10)
N2–Cu–N3	82.61(11)	N3–Cu–O2′	91.14(10)
N1–Cu–N4	82.29(11)	N4–Cu–O2′	88.91(11)
N2–Cu–N4	161.50(10)		
N3–Cu–N4	110.27(10)		

anionic amidate donors. The lateral 5-membered chelate rings are making an angle of ~13° with each other, while they make an angle of 8–10° with the central 5-membered chelate ring. The copper(II) ion is 0.202 Å out of the least square basal plane (defined by N1, N2, N3, and N4) towards the apical amide oxygen atom from the neighbouring molecule. Any of the two copper ions in the chain are separated by ~6 Å. The two neighbouring molecular planes containing copper ions make an angle of ~74(1)° with each other. This significant number suggests that any of the two monomeric units in the 1D chain are almost orthogonal to each other and gave us a clue about their expected magnetic behaviour (cf. magnetic properties).

Vagg and co-workers [53] have reported a copper(II) complex with a pyridine-amide based ligand (*N*,*N*′-bis-(6′-methylpyridine-2′-carboxamide)-1,2-benzene) where oxygen atoms of the neighbouring molecules coordinate to form a chain. However, this is to be noted that here two O-atoms from two neighbouring molecules coordinate to complete an octahedral geometry around the copper ion. The two $Cu–O_{amide}$ bond distances are 2.693(6) and 2.798(6) Å, respectively, and are quite longer than that of **2**. The average $Cu–N_{amide}$ and $Cu–N_{pyridine}$ distances are 1.934(7) and 2.079(7) Å, respectively, and are quite similar to that of complex **2**. Interestingly, when the authors used the un-substituted pyridine-amide ligand (*N*,*N*′-bis(2′-pyridinecarboxamide)-1,2-benzene), only one water molecule coordinate axially to afford a square-pyramidal copper complex [54]. The authors have reasoned that the presence of methyl substituents on the pyridine ring in the former case caused the distortion around the metal centre and resulted in the twisting of the basal plane. The implication of this twisting is the availability of the coordination sites both from top and bottom of the basal plane, thus O_{amide} coordinate to the copper ion affording the octahedral geometry in the former case. Despite an interesting chain structure of the Cu(II) complex of Vagg and co-workers, magnetic properties have not been carried out.

3.4. Magnetic properties

The magnetic properties of **1** and **2** in the form of $\chi_M T$ versus T plot are shown in Figs. 3 and 4. For **1**, the value of $\chi_M T$, at room temperature is 1.13 $cm^3\ mol^{-1}$ K, close to the expected value for three uncoupled Cu(II) ions. The $\chi_M T$ product decreases upon cooling, reaching a plateau at 23 K, with $\chi_M T$ value equal to 0.4 $cm^3\ mol^{-1}$. This value is close to the expected value for a spin state $S = 1/2$. This behaviour is characteristic of an antiferromagnetic

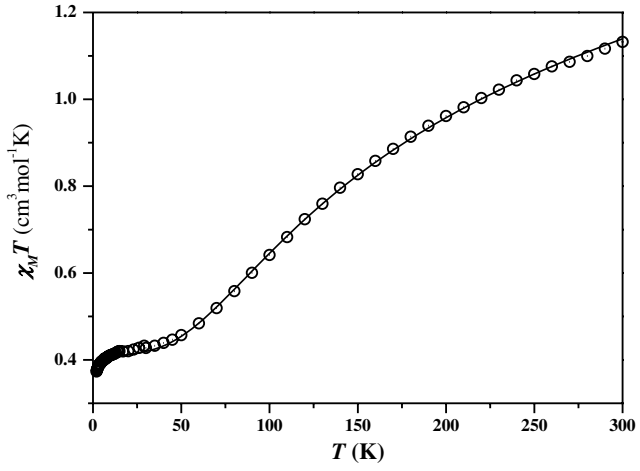


Fig. 3. $\chi_M T$ vs. T plot for compound **1**. The solid line was calculated with the parameters reported in the text.

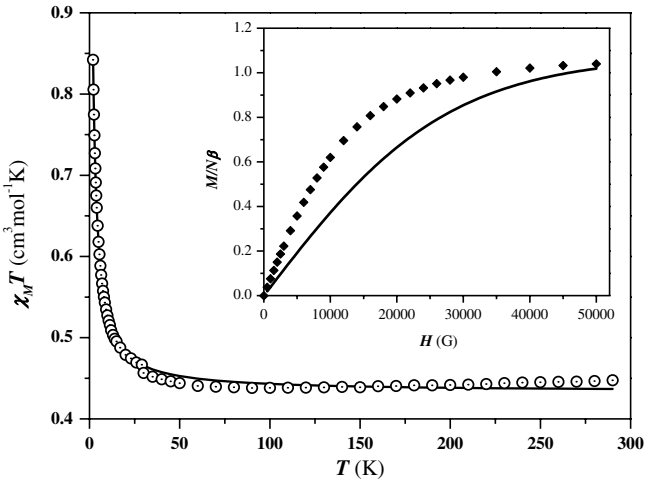


Fig. 4. $\chi_M T$ vs. T plot for compound **2**. The solid line was calculated with the parameters reported in the text. In the inset, experimental $M/N\beta$ vs. H plot (♦) and calculated from the brillouin equation for a $S = 1/2$ (solid line).

coupling. Below 4 K, $\chi_M T$ product decreases again, indicating that an intermolecular antiferromagnetic interaction also occur in this compound.

The experimental data were fitted using the theoretical expression deduced from the following Heisenberg Hamiltonian $H = -J(S_1 \cdot S_2 + S_2 \cdot S_3) - J'(S_1 \cdot S_3)$. Taking into account the geometry of this compound (the terminal copper centres are separated by the distance in the range of 11.4–11.5 Å), the interaction between the two terminal Cu(II) ions was assumed to be nil ($J' = 0$). The best fit was obtained for $J = -110.34\ \text{cm}^{-1}$ and $g = 2.06$ ($R = 1.8 \times 10^{-4}$).

For **2**, the $\chi_M T$ value at room temperature is $0.45\ \text{cm}^3\ \text{mol}^{-1}$ K, which is as expected for one magnetically quasi-isolated Cu(II) ion ($g > 2.0$). On cooling, the $\chi_M T$ values smoothly increases up to $0.84\ \text{cm}^3\ \text{mol}^{-1}$ K at 2 K. The shape of this curve clearly indicates weak ferromagnetic coupling among the Cu(II) ions. The mathematical formula derived by Baker et al. [55] for ferromagnetic 1D systems with $S = 1/2$ is valid only at relatively high temperatures. Thus, when the ferromagnetic coupling is weak, this formula is not very accurate. For this reason, the fit of the experimental data was performed in the numerical form from a full-matrix diagonalization of the Hamiltonian corresponding to a ring of 12 local $S = 1/2$ centers with the adequate J coupling parameter using the CLUMAG program [56]. With this program, the use of 12 cycled centers give a good approximation for the system, which is actually infinite. The best fit parameters of the data are $J = +3.08\ \text{cm}^{-1}$ and $g = 2.15\ \text{cm}^{-1}$ ($R = 8.6 \times 10^{-5}$). The reduced molar magnetization ($M/N\beta$) per Cu entity tends to be 1 $N\beta$ (electron) (Fig. 4 inset) but the shape of the experimental curve is clearly above the theoretical ones for the Brillouin law. These features agree with the global ferromagnetic coupling between the copper(II) ions.

Compounds **1** and **2** show the same bridging motif, NCO, between the Cu(II) ions, nevertheless the magnetic behaviour is very different. For the trinuclear complex (compound **1**) strong antiferromagnetic coupling is observed, while the one-dimensional system (compound **2**) shows a ferromagnetic interaction.

In the trinuclear compound, the coordination around the two terminal ions is square planar, while for the central ion is a square pyramidal, and its basal plane is quite coplanar with the coordination planes of the terminal ions. For the three copper(II) ions, the single electron is in the $x^2 - y^2$ orbital, and taking into consideration that these orbitals are almost coplanars, a good overlap through the bridging motif NCO could be attended (Fig. 5). In the one-dimensional system, the coordination polyhedra of the Cu(II) ion is a square pyramidal, but, in this case, the basal planes between neighbours ions are almost perpendicular (in the crystal structure, two planes make an angle of 74° with each other), and as a result of this, the $x^2 - y^2$ orbital are orthogonal, and a very small overlap through the bridge must be attended (Fig. 6). So, the different magnetic behaviour observed for compounds **1** and **2**, could be explained by the different disposition of the magnetic orbitals.

Several trinuclear compounds with oxamide bridging ligands have been reported in the literature [24–30]. These trinuclear compounds show significant antiferromagnetic coupling with the J value ranging between −80 and

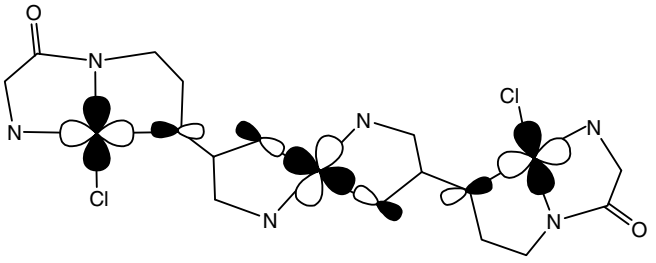


Fig. 5. Schematic drawing of the disposition of the $x^2 - y^2$ orbital in the trinuclear compound **1**.

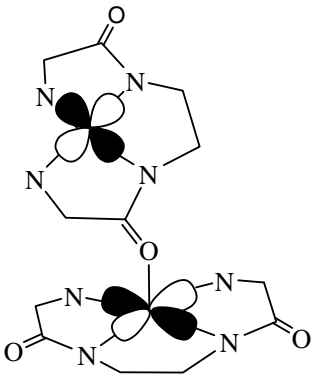


Fig. 6. Schematic drawing of the disposition of the $x^2 - y^2$ orbital in the one-dimensional system **2**.

$-600\ cm^{-1}$ [51,52]. The extent of coupling (J value) has been found to be very sensitive to the geometry around the terminal Cu(II) ions with respect to the central copper(II) ion. For the square-planar, 4-coordinate, or square-based geometries (such as (4 + 1)- or (4 + 2)-coordinate), the magnetic orbitals are predominantly $d_{x^2-y^2}$ in nature. These terminal metal-based magnetic orbitals are approximately coplanar with that of the central ion and have $x^2 - y^2$ symmetry. Thus, the magnetic coupling is well described by the antibonding combination of the $d_{x^2-y^2}$ metallic orbitals with the symmetry-adapted molecular orbitals of the oxamido bridge. However, in case of trigonal bipyramidal geometry for the terminal copper ions, the magnetic orbitals are predominantly d_{z^2} in character; this reduces the effective overlap and the magnitude of the interaction is smaller (lower value of $-J$) [25–27]. Basically, when the magnetic orbitals of the three Cu(II) ions are not coplanar with respect to each other, the J value decreases. The oxamido ligand provides two coplanars NCO bridging motifs, while for compound **1**, only one NCO group bridge the two Cu(II) ions. Therefore, in compound **1**, with only one way for the magnetic exchange, the antiferromagnetic coupling must be smaller than in the oxamide complexes. This agrees nicely with the smaller J value found for **1** ($-110\ cm^{-1}$) compared to the oxamido bridged complexes.

The solution state magnetic moment were also determined for both complexes using Evans' method [57]. The room temperature magnetic moment (μ_{eff}) for complex **2** in $(CH_3)_2SO$, was found to be 1.85 μ_B which matches very well with the solid state value of 1.90 μ_B. The similarity between the results from the solid and the solution state indicate a similar structure. However, taking into account that at room temperature if the magnetic coupling is small, the values are close to the uncoupled ions; it is, therefore, not possible to be sure if the 1D structure is maintained or if it is a mononuclear structure in the solution. For trinuclear complex **1**, however, a value of 2.68 μ_B/trimer was obtained at room temperature in $(CH_3)_2SO$ or DMF. This value is lower by ~0.3 μ_B/trimer than the solid state value. The difference in the magnetic moment is indicative of some changes in the geometry of the trinuclear complex and indicate that the copper centres are better antiferromagnetically coupled in the solution state at room temperature. This could happen due to a more relaxed geometry around the copper ions allowing better overlap of the metal based magnetic orbitals through ligand based magnetic orbitals.

3.5. EPR spectra

Powder electron paramagnetic resonance spectra (EPR) were recorded at 298, 77 and 4 K for compounds **1** and **2** (Figs. 7, S4 and S5). The trinuclear complex **1**, with an appreciable antiferromagnetic coupling ($J = -110.34\ cm^{-1}$), shows a ground state of $S = 1/2$, and a narrow signal ($\Delta H_{p-p} = 62$ G) centered at $g = 2.08$ was observed in the EPR spectrum at 4 K. The experimentally observed g value of 2.08 in EPR measurement matches very well with the g value (=2.06) obtained after fitting the magnetic data. For one-dimensional compound, **2**, the EPR spectrum at 4 K, shows two superimposed bands at 2.11 and 2.06, with a $\Delta H_{p-p} = 145$ G (Fig. 7). The two different g values clearly indicate the anisotropy [58] around the copper centre caused due to the coordination of the O-atom of the neighbour molecule, as observed structurally (cf. crystal structure of **2**). The effect of the temperature in the peak-to-peak gap is opposite in both compounds. For compound **1**, a narrowing of the band was observed on cooling, from 190 to 62 G. However, for **2**, a little broadening of the band was observed, from 130 to 145 G. The observed temperature-dependent behaviour for both complexes clearly indicates that they significantly differ with each other and support their opposite magnetic properties (cf. magnetic measurements).

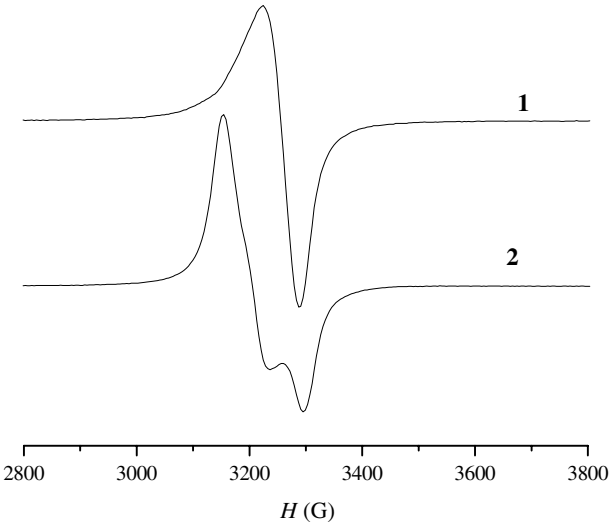


Fig. 7. Powder EPR spectra for compounds **1** and **2** at 4 K.

The EPR spectra were also recorded in the solution state to understand the solution-based geometry and the effect of solvent (CH_3OH and pyridine). For **1**, a broad feature, with the g_{iso} at 2.107 and 2.097 was observed in methanol and pyridine, respectively. In solution, at room temperature there is only one isotropic g value. For complex **2**, a four lines signal was observed in methanol or pyridine at room temperature. This feature is characteristic of the hyperfine coupling with the nuclear spin of the Cu ($I = 3/2$) and typically observed for a tetragonal copper ion in solution [58]. The g_{iso} was observed at ~2.12 with the $A(Cu)_{iso}$ value of 106 G.

3.6. Absorption spectra

The electronic spectra of both complexes were recorded in the solid state (dispersed in mineral oil) as well as in solutions (CH_3OH, CH_3CN, and pyridine) to gain insight into the coordination geometry around the copper ion (Figs. S6

and S7). The solid state spectrum of **1** displays a broad band in the visible region at 655 with a low energy shoulder at ~850 nm, suggestive of a square-pyramidal geometry [59,60]. A less clear feature was also observed at ~515 nm which we assign due to the square-planar Cu(II) ion. This corroborate the findings from the crystal structure of **1** that clearly show that terminal copper ions are square-planar while the central ion is square-pyramidal. In CH_3OH or CH_3CN, a main peak was observed at 625 nm while a less intense peak at ~515 nm was also noticed. We tentatively assign the former from the square-pyramidal ion (central copper) while the later due to the square-planar ion (terminal coppers). For **2**, a broad band at 590 nm with a weak shoulder at ~760 nm was displayed in the solid state spectrum. These features clearly support a 5-coordinate geometry around the Cu(II) ion [59,60] as seen in the crystal structure of **2**. However, a shift in the λ_{max} was noticed when the spectra were recorded in various solvents; the λ_{max} changed from 530 in CH_3CN to 548 in MeOH to 555 nm in pyridine. This experiment strongly suggests that the axial position(s) occupied by the O_{amide} in the solid state (as seen in the crystal structure) are displaced by the solvent molecule(s) when the spectrum is recorded in the solution state.

4. Conclusions

The present work show interesting coordination behaviour of the amide-based ligands towards copper(II) ion. The backbone flexibility of the ligand $[L^1]^{2-}$, resulted in the flipping of one of the arm to accommodate the second copper ion; this generates the trinuclear complex, $[Cu_3(L^1)_2(Cl)_2(H_2O)]$ **1**. This trinuclear complex belongs to a rare group of complexes where both amidate-N and amidate-O participate in the coordination [31,32]. The ligand $[L^2]^{2-}$, incorporating the rigid *o*-phenylene backbone affords a simple mononuclear complex. The substituted methyl groups restricted the coordination of any additional axial ligand. However, the molecular basal plane tilt in a unique way to allow the coordination of the neighbouring amidate-O to the Cu(II) centre [53,54]. This generates a zig-zag one-dimensional chain, $[Cu(L^2)]_n$ **2**. Both complexes, **1** and **2** have *NCO* bridge between the copper ions and show interesting but contrast magnetic properties. The **1** shows moderately strong antiferromagnetic coupling ($J = \sim -110\ cm^{-1}$). The moderate nature of antiferromagnetic coupling in **1** is due to the availability of only one magnetic exchange pathway (*NCO* bridge) between the copper ions compared to two in the oxamido-bridged systems. Whereas **2** shows a weak ferromagnetic interaction ($J = \sim +3\ cm^{-1}$) due to the accidental orthogonality of the magnetic orbitals from two copper containing basal planes.

Acknowledgements

R.G. thanks University Grant Commission (UGC), Delhi, and Department of Science & Technology (DST), New Delhi for the generous financial support, and DST funded single crystal facility at IIT – Delhi for the data collection of complex **2**. M.C. thanks Ministerio de Educacion y Ciencia for financial support (CTQ2006 – 01759/BQU). J.S. thanks CSIR – UGC for the JRF fellowship.

Appendix A. Supplementary material

CCDC 634199 and 634200 contain the supplementary crystallographic data for **1** and **2**. These data can be obtained free of charge via http://www.ccdc.cam.ac.uk/conts/retrieving.html, or from the Cambridge Crystallographic Data Centre, 12 Union Road, Cambridge CB2 1EZ, UK; fax: (+44) 1223-336-033; or e-mail: deposit@ccdc.cam.ac.uk. Supplementary data associated with this article can be found, in the online version, at doi:10.1016/j.poly.2007.04.021.

References

[1] P.V. Rao, R.H. Holm, Chem. Rev. 104 (2004) 527.
[2] E.I. Solomon, R.K. Szilagyi, S.D. George, L. Basumallick, Chem. Rev. 104 (2004) 419.
[3] M.L. Alvarez, J.Y. Ai, W. Zumft, J. Sanders-Loehr, D.M. Dooley, J. Am. Chem. Soc. 123 (2001) 576.
[4] S. Suzuki, K. Kataoka, K. Yamaguchi, Acc. Chem. Res. 33 (2000) 728.
[5] R.L. Lieberman, D.B. Shrestha, P.E. Doan, B.M. Hoffman, T.L. Stammler, A.C. Rosenzweig, Proc. Natl. Acad. Sci. USA 100 (2003) 3820.
[6] K. Brown, K. Djinovic-Carugo, T. Haltia, I. Cabrito, M. Saraste, J.J.G. Moura, I. Moura, M. Tegoni, C. Cambillau, J. Biol. Chem. 275 (2000) 41133.
[7] K. Brown, M. Tegoni, M. Prudencio, A.S. Pereira, S. Besson, J.J.G. Moura, I. Moura, C. Cambillau, Nat. Struct. Biol. 7 (2000) 191.
[8] B.T. Rasmussen, B.C. Berks, J. Sanders-Loehr, D.M. Dooley, W.G. Zumft, A.J. Thomson, Biochemistry 39 (2000) 12753.
[9] P. Chen, I. Cabrito, J.J.G. Moura, I. Moura, E.I. Solomon, J. Am. Chem. Soc. 124 (2002) 10497.
[10] R.L. Lieberman, A.C. Rosenzweig, Nature 434 (2005) 177.
[11] R.L. Lieberman, K.C. Kondapalli, D.P. Shrestha, A.S. Hakemian, S.M. Smith, J. Telser, J. Kuzelka, R. Gupta, A.S. Borovik, S.J. Lippard, B.M. Hoffman, A.C. Rosenzweig, T.L. Stemmler, Inorg. Chem. 45 (2006) 8372.
[12] M. Melnik, Coord. Chem. Rev. 42 (1982) 259.
[13] D.J. Hodgson, in: S.J. Lippard (Ed.), Progress in Inorganic Chemistry, vol. 19, Wiley, New York, 1975, p. 173.
[14] M. Kato, Y. Muto, Coord. Chem. Rev. 92 (1988) 45.
[15] L. Merz, W. Haase, J. Chem. Soc., Dalton Trans. (1980) 875.
[16] M. Handa, N. Koga, S. Kida, Bull. Chem. Soc. Jpn. 61 (1988) 3853.
[17] R. Gupta, R. Hotchandani, R. Mukherjee, Polyhedron 19 (2000) 1429.
[18] R. Gupta, S. Mukherjee, R. Mukherjee, J. Chem. Soc., Dalton Trans. (1999) 4025.
[19] L.K. Thompson, S.K. Mandal, S.S. Tandon, J.N. Bridson, M.K. Park, Inorg. Chem. 35 (1996) 3117.
[20] S.S. Tandon, L.K. Thompson, J.N. Bridson, V. McKee, A.J. Downard, Inorg. Chem. 31 (1992) 4635.
[21] K. Nonoyama, H. Ojima, K. Ohki, N. Nonoyama, Inorg. Chim. Acta 41 (1980) 155.
[22] N.F. Curtis, I.R.N. McCormick, T.N. Waters, J. Chem. Soc., Dalton Trans. (1973) 1537.
[23] D.M. Duggan, D.N. Hendrickson, Inorg. Chem. 12 (1973) 2422.
[24] Y. Journaux, J. Sletten, O. Kahn, Inorg. Chem. 25 (1986) 439.

[25] A. Garcia, R. Costa, J. Ribas, Inorg. Chim. Acta 168 (1990) 249.
[26] R. Costa, A. Garcia, J. Ribas, T. Mallah, Y. Journaux, J. Sletten, X. Solans, V. Rodriguez, Inorg. Chem. 32 (1993) 3733.
[27] R. Costa, A. Garcia, R. Sanchez, J. Ribas, X. Solans, V. Rodriguez, Polyhedron 12 (1993) 2697.
[28] R. Veit, J.-J. Girerd, O. Kahn, F. Robert, Y. Jeannin, Inorg. Chem. 25 (1986) 4175.
[29] J.-J. Girerd, S. Jeannin, Y. Jeannin, O. Kahn, Inorg. Chem. 17 (1978) 3034.
[30] R. Veit, J.-J. Girerd, O. Kahn, F. Robert, Y. Jeannin, N. El Murr, Inorg. Chem. 23 (1984) 4448.
[31] U.P. Chaudhuri, L.R. Whiteaker, L. Yang, R.P. Houser, Dalton Trans. (2006) 1902.
[32] A. Mondal, Y. Li, M.A. Khan, J.H. Ross Jr., R.P. Houser, Inorg. Chem. 43 (2004) 7075.
[33] A. Davison, A.G. Jones, C. Orvig, M. Sohn, Inorg. Chem. 20 (1981) 1629.
[34] H.-J. Krugar, G. Peng, R.H. Holm, Inorg. Chem. 30 (1991) 734.
[35] Bruker Analytical X-ray System, SMART: Bruker Molecular Analysis Research Tool, Version 5.0 618, 2000.
[36] Bruker Analytical X-ray System, SAINT-NT, Version 6.10, 2000.
[37] G. Cascarano, L. Favia, C. Giacovazzo, J. Appl. Crystallogr. 25 (1992) 310.
[38] G.M. Sheldrick, SHELXL-97: Program for Crystal Structure Refinement, University of Göttingen, Göttingen, Germany, 1997.
[39] L.J. Farrugia, WINGX Version 1.64, An Integrated System of Windows Programs for the Solution, Refinement and Analysis of Single-Crystal X-ray Diffraction Data, Department of Chemistry, University of Glasgow, Glasgow, UK, 2003.
[40] K. Nakamoto, Infrared and Raman Spectra of Inorganic and Coordination Compounds, Wiley, 1986.
[41] W.J. Geary, Coord. Chem. Rev. 7 (1971) 81.
[42] A.W. Addition, T.N. Rao, J. Reedijk, J. van Rijn, G.C. Verschoor, J. Chem. Soc., Dalton Trans. (1984) 1349.
[43] F.S. Stephens, R.S. Vagg, Inorg. Chim. Acta 88 (1984) 7.
[44] F.S. Stephens, R.S. Vagg, Inorg. Chim. Acta 57 (1982) 43.
[45] M. Mulqi, F.S. Stephens, R.S. Vagg, Inorg. Chim. Acta 52 (1981) 177.
[46] F.S. Stephens, R.S. Vagg, Inorg. Chim. Acta 51 (1981) 149.
[47] M. Mulqi, F.S. Stephens, R.S. Vagg, Inorg. Chim. Acta 51 (1981) 9.
[48] J.M. Rowland, M.M. Olmstead, P.K. Mascharak, Inorg. Chem. 39 (2000) 5326.
[49] A. Mondal, E.L. Klein, M.A. Khan, R.P. Houser, Inorg. Chem. 42 (2003) 5462.
[50] M.C.B. de Oliveira, M. Scarpellini, A. Neves, H. Terenzi, A.J. Bortoluzzi, B. Szpoganics, A. Greatti, A.S. Mangrich, E.M. de Souza, P.M. Fernandez, M.R. Soares, Inorg. Chem. 44 (2005) 921.
[51] O. Kahn, Angew. Chem., Int. Ed. Engl. 24 (1985) 834, and references therein.
[52] O. Kahn, Inorg. Chim. Acta 62 (1982) 3, and references therein.
[53] R.L. Chapman, F.S. Stephens, R.S. Vagg, Inorg. Chim. Acta 52 (1981) 169.
[54] R.L. Chapman, F.S. Stephens, R.S. Vagg, Inorg. Chim. Acta 43 (1980) 29.
[55] G.A. Baker, G.S. Rushbreoke, H.E. Gilbert, Phys. Rev. A. 135 (1964) 1272.
[56] D. Gatteschi, L. Pardi, Gazz. Chim. Ital. 123 (1993) 231.
[57] D.F. Evans, J. Chem. Soc. (1959) 2003.
[58] B.J. Hathaway, in: G. Wilkinson, R.D. Gillard, J.A. McCleverty (Eds.), Comprehensive Coordination Chemistry, vol. 5, Pergamon Press, Oxford, 1987, p. 533.
[59] T.K. Lal, R. Gupta, S. Mahapatra, R. Mukherjee, Polyhedron 18 (1999) 1743.
[60] R. Gupta, R. Mukherjee, Polyhedron 19 (2000) 719.

dures. The dimethyl calixarene derivative **1** [16], [Pd(COD)Cl_2] [17] and chlorophosphazane $Ph_2PN(^iPr)$-PPhCl [18] were prepared by following the literature procedures. The NMR spectra were recorded on Bruker Avance-400 MHz spectrometer using standard pulse sequences; $CDCl_3$ was used as solvent throughout. For the NOESY experiments, the mixing time was chosen as 300 ms.

2.2. Synthesis of the calix[4]arene diphosphazane ligand $Ph_2PN(CHMe_2)P(Ph)$\{1,3-dimethoxycalix[4]arene\} (2)

A suspension of 25,27-dihydroxy-26,28-dimethoxy-*p*-*tert*-butyl-calix[4]arene (**1**) (2.703 g, 0.004 mol) and NaH (60% dispersion in oil) (0.322 g, 0.0084 mol) in THF (100 mL) was heated under reflux for 12 h. $Ph_2PN(CHMe_2)P(Ph)Cl$ (0.01 mol) in THF (50 mL) was added at 0 °C and the reaction mixture stirred for 2 h at 25 °C. The reaction was followed by TLC [$R_f = 0.5$ (ligand **2**); silicagel; EtOAc/petrol(bp 60–80 °C) 3/97-v/v]. Solvent was evaporated under reduced pressure and the residue was subjected to column chromatography [SiO_2, EtOAc/petrol 3/97-v/v] to obtain the title compound **2** as a colorless solid. Yield: 1.1 g (26.8%). Mp 185–190 °C. *Anal.* Calc. for $C_{67}H_{81}NO_4P_2$ (mol wt.: 1025.26): C, 78.4; H, 7.9; N, 1.4. Found: C, 78.0; H, 7.7; N, 1.5%. $^{31}P\{^1H\}$ NMR ($CDCl_3$, 162 MHz): δ 34.1 (PPh_2, d, $^2J_{P-P} = 23.0$ Hz), 36.0 (PPh_2, d, $^2J_{P-P} = 25.1$ Hz), 37.7 (PPh_2, d, $^2J_{P-P} = 25.3$ Hz), 124.3 (PPhO, d, $^2J_{P-P} = 32.1$ Hz), 126.8 and 127.1 (PPhO, two doublets overlapping) (three conformers). ^1H NMR ($CDCl_3$, 400 MHz): δ 2.80 and 3.28 (2s, 3H each, OMe), 3.57 and 3.73 (2s, 3H each, OMe), 3.85 and 3.96 (2s, 3H each, OMe) [other peaks were not resolved].

2.3. Synthesis of [$Cl_2Pd(2)$] (3)

A mixture of 95 mg (8.84×10^{-5} mol) of ligand **2** and 25 mg (8.84×10^{-5} mol) of [Pd(COD)Cl_2] was dissolved in 20 mL of benzene. The solution was stirred for 1 h at 25 °C. The reaction mixture was washed with hot petrol and the residue crystallized from petrol–chloroform solution (5:1 ratio v/v) to which a few drops of acetone were added, to obtain the title compound **3** as light green crystals. Yield: 0.055 g (40%). Mp 168–172 °C (dec.). *Anal.* Calc. for $C_{67}H_{81}NO_4P_2PdCl_2$ (mol wt.: 1202.4): C, 66.9; H, 6.7; N, 1.2. Found: C, 66.5; H, 6.8; N, 1.0%. $^{31}P\{^1H\}$ NMR ($CDCl_3$, 162 MHz): δ 36.9 (d, PPh_2, $^2J_{P-P} =$ 18.3 Hz), 64.3 (d, POPh, $^2J_{P-P} = 18.3$ Hz). ^1H NMR ($CDCl_3$, 400 MHz): δ −0.05 (d, 6H, Me_2CH–), 0.81, 1.01 (2s, 9H each, –$C(CH_3)_3$), 1.29 (s, 18H, –$C(CH_3)_3$), 3.07 and 3.72 (2s, 3H each, –OCH_3); 3.20, 3.28, 3.45, 3.59, 3.67, 4.58, 4.81, 5.00 (8d, 1H each, $ArCH_2Ar$, four AB systems); 4.48 (m, 1H, Me_2CH–); 6.6–9.2 (m, ArH).

2.4. X-ray crystallographic studies

The X-ray diffraction data were collected on a Bruker SMART APEX CCD diffractometer (graphite-monochromated Mo Kα radiation, $\lambda = 0.71073$ Å). The SMART [19] software was used for cell refinement and data acquisition and the SAINT [20] software was used for data reduction. An absorption correction was made on the intensity data using the SADABS [21] programme. The structures were solved using SHELXTL [22] and the WinGX graphical user interface [23]. Least square refinements were performed by the full-matrix method with SHELXL-97 [24]. All non-hydrogen atoms were refined anisotropically and hydrogen atoms were refined isotropically. Details of data collection and refinement are summarized in Table 1.

3. Results and discussion

3.1. Synthesis and NMR analysis of conformationally flexible diphosphazane 2

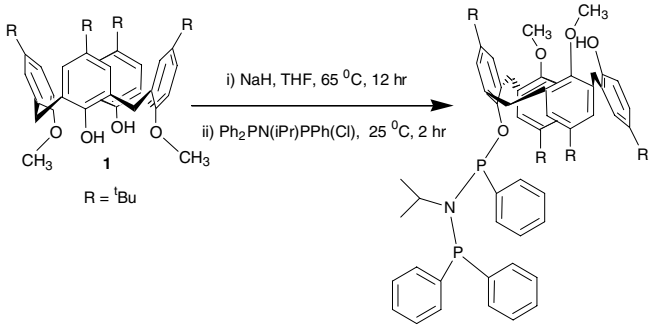
When a suspension of 1,3-dimethoxy *p*-*tert*-butylcalix[4]arene (**1**) in toluene is treated with $Ph_2PN(CHMe_2)PPh(Cl)$ in the presence of NaH, the diphosphazane derivative (**2**) of calix[4]arene is obtained in 26.8% yield (Scheme 1). The main reason for the low yield is the loss of material during the chromatographic separation step (see Section 2). Crystallization of the crude product from petrol (bp 60–

Table 1
Crystal data for **2** and **3**

Empirical formula	$C_{67}H_{81}NO_4P_2$ (**2**)	$C_{70}H_{87}Cl_2NO_5P_2Pd$ (**3**)
Formula weight	1025.26	1261.65
Temperature (K)	293(2)	293(2)
Wavelength (Å)	0.71073	0.71073
Crystal system	monoclinic	orthorhombic
Space group	$P2_1/n$	$P2_12_12_1$
Unit cell dimensions		
a (Å)	13.4435(18)	13.879(4)
b (Å)	24.601(3)	21.261(6)
c (Å)	18.831(3)	22.722(6)
α (°)	90	90
β (°)	107.168(3)	90
γ (°)	90	90
Volume (Å^3)	5950.3(14)	6705(3)
Z	4	4
D_{calc} (Mg/m^3)	1.144	1.250
Absorption coefficient (mm^{-1})	0.120	0.452
$F(000)$	2204	2656
Crystal size (mm)	$0.22 \times 0.07 \times 0.02$	$0.45 \times 0.43 \times 0.23$
θ Range for data collection (°)	1.40–24.71	1.75–28.07
Reflections collected	41 888	58 968
Independent reflections [R_{int}]	10 135 [0.1380]	15 979 [0.0513]
Completeness to theta (%)	100.0	99.1
Maximum and minimum transmission	0.9976 and 0.9740	0.9032 and 0.8224
Data/restraints/parameters	10 135/0/646	15 979/0/1066
Goodness-of-fit on F^2	1.021	1.053
Final R indices [$I > 2\sigma(I)$]	$R_1 = 0.1406$, $wR_2 = 0.3267$	$R_1 = 0.0477$ $wR_2 = 0.0895$
R indices (all data)	$R_1 = 0.2332$, $wR_2 = 0.3797$	$R_1 = 0.0628$, $wR_2 = 0.0950$
Largest difference in peak and hole (e Å^{-3})	1.028 and −0.495	0.956 and −0.357

80 °C) gave single crystals of the partial-cone conformer (B) of **2**. The structure of the partial cone conformer (B) has been established by X-ray crystallography. When a solid sample of conformer (B) was dissolved in $CDCl_3$, the solution showed the presence of three conformers (A)–(C) as revealed by three pairs of doublets in the ^{31}P NMR spectrum in the region of δ 30–40 and δ 120–130 for the PPh_2 and OPPh phosphorus nuclei, respectively. The ratio of the conformers A–C is 3.2:2.6:1 as shown by the relative intensities of the corresponding ^{31}P NMR signals. The observed $^2J_{P-P}$ values (23–25 Hz) indicate a *trans*-type of ligand conformation [18,25,26] in which the lone pairs on the two phosphorus atoms are far apart from each other. Assignment of the methylene protons to the respective conformers was not possible because of the overlapping of the resonances. A pair of singlets at δ 2.78 [$-OCH_3(1)$] and 3.26 [$-OCH_3(2)$] may be assigned to the conformer A; another pair of singlets at δ 3.55 [$-OCH_3(3)$] and 3.71 [$-OCH_3(4)$] may be assigned to the methoxy protons of the other conformer (B). The intensity ratio of the signals arising from A and B is 1:1.2. The ^1H–^1H NOESY experiment shows the presence of several cross peaks with the same phase as that of the diagonal indicating exchange among the conformers (see Electronic supplementary information (ESI)). The ^{31}P–^{31}P NOESY experiment shows clear cross peaks among the three different phosphorus atoms in the $-PPh_2$ region (Fig. 1) and confirms that all the three conformers undergo exchange among each other. Careful analysis of the ^1H–^1H NOESY spectrum (see ESI) reveals that the major conformer has an 1,2-alternate conformation (A in Fig. 2) and the minor conformer adopts a partial cone conformation (B in Fig. 2) in which the calix[4]arene aryl ring containing the P–N–P moiety is in inverted (anti) orientation. The same partial cone structure is observed in the solid state as established by X-ray crystallography. The solution structure of the remaining conformer (C) could not be determined owing to its low abundance and hence low intensity of the peaks in the ^1H NMR spectrum.

A variable temperature NMR study ($CDCl_3$, 400 MHz) of ligand **2** has been carried out between −50 °C and +50 °C. The ^{31}P NMR spectra do not show any significant change but the ^1H NMR spectra show considerable changes. The resonances of the hydroxyl protons show



Scheme 1. Synthesis of calix-diphosphazane ligand (**2**).

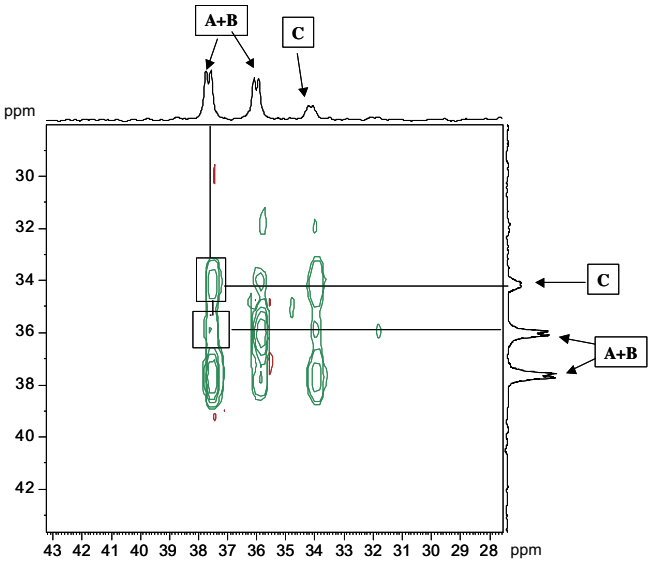


Fig. 1. The ^{31}P–^{31}P NOESY spectrum of the calix[4]arene diphosphazane ligand **2**.

appreciable up-field shift with an increase in temperature, indicating the breaking of hydrogen bonds (see later) and consequently facile movement of the corresponding phenolic rings towards the calix[4]arene cavity. Broadening of almost all ^1H resonances upon increasing the temperature suggests the existence of dynamic exchange processes among the conformers A–C.

3.2. Synthesis and NMR analysis of palladium dichloride complex of ligand 2

Reaction of ligand **2** with $[Pd(COD)Cl_2]$ yields the dichloride complex **3** in which the calixarene is frozen in the cone conformation. Crystallization of the crude prod-

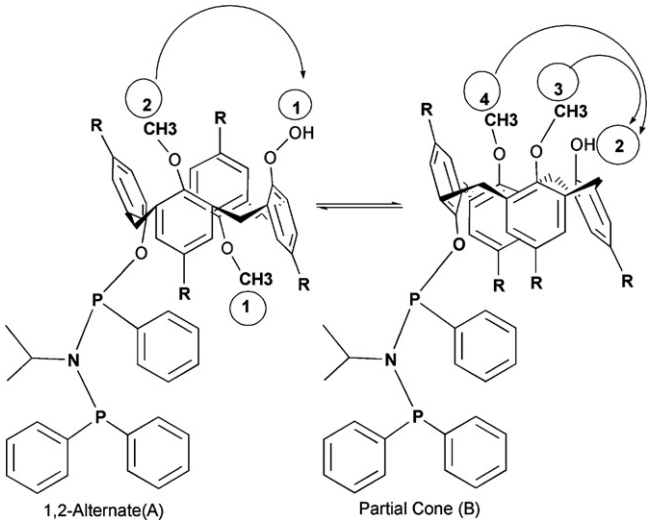


Fig. 2. Two major conformers of ligand **2** in solution; arrows represent the protons showing "through-space" interaction in the NOESY spectrum.

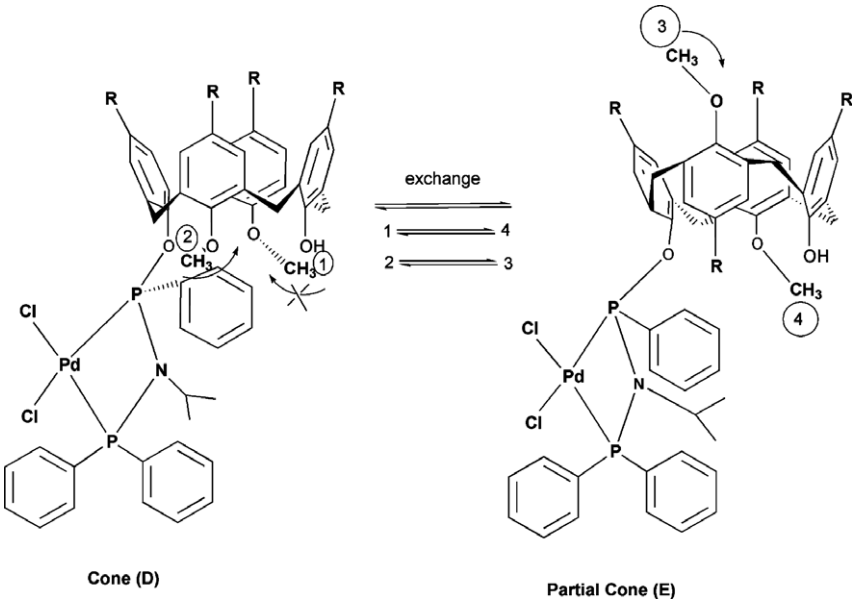


Fig. 3. A schematic representation of exchange process between the conformers of complex **3** in solution (arrows represents movement of aryl rings).

uct from chloroform–petrol gave single crystals of cone conformer (D) (Fig. 3). The cone conformation of calixarene framework in the solid-state has been confirmed by single crystal X-ray analysis. When the solid sample of conformer (D) is dissolved in $CDCl_3$, the solution shows the presence of two conformers (D) and (E) as revealed by the ^1H and ^{31}P NMR spectra (see ESI, Fig. S3). The ^{31}P NMR spectrum of the product shows two doublets at δ 36.9 and 64.3 for the major conformer and two doublets at δ 38.2 and 57.0 for the minor conformer. The ratio of the major to minor conformer in the reaction mixture is 15:1. The ^1H NMR spectrum of complex **3** shows four AX patterns for the eight methylene bridge protons and two singlets at δ 3.07 [–OCH_3(1)] and 3.72 [–OCH_3(2)] for the protons of two methoxy groups. This NMR pattern suggests that the major isomer of **3** does not contain any element of symmetry. The singlet in the comparatively shielded region (δ 3.07) may be assigned to the protons of the methoxy group which is near to the aryl ring of the OP(Ph) fragment. The 2D COSY and NOESY experiments show that the major isomer in solution adopts the cone conformation (see ESI, Fig. S4) which is also the conformation observed in the solid state as revealed by X-ray crystallography. Two singlets at δ 1.88 [–OCH_3(3)] and 3.70 [–OCH_3(4)] arising from the protons of two nonequivalent methoxy groups of the minor conformer could be identified. Two-dimensional ^1H–^1H NOESY experiment (see ESI, Fig. S5) indicates the movement of one of the aryl rings through the calix[4]arene cavity (Fig. 3). The possible rotation of a single aryl ring is also supported by the molecular structure of the complex which is shown in Fig. 5. The perspective view along an axis which passes through the center of the calix[4]arene cavity shows that the aryl ring of OP(Ph) fragment resides at a corner of the cavity and thus prevents the movement of the three of the aryl rings. Only the remaining aryl ring can rotate through the cavity to give rise to the partial cone conformer in solution as the minor isomer.

3.3. Solid state structures of the calix "P–N–P" ligand, $Ph_2PN(CHMe_2)P(Ph)$\{1,3-dimethoxycalix[4]arene\} (2) and its palladium dichloride complex (3)

The structures of the *p-tert*-butyl-calix[4]arene diphosphazane ligand (**2**) and the corresponding palladium dichloride complex (**3**) have been determined by X-ray crystallography and are shown in Figs. 4 and 5, respectively. Selected bond lengths and bond angles for both the compounds are listed in Tables 2 and 3, respectively. The calix[4]arene framework in ligand **2** adopts the partial

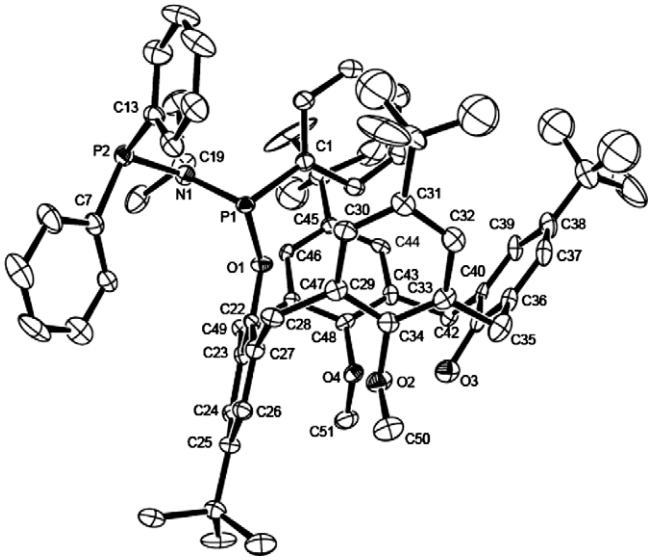


Fig. 4. ORTEP picture of ligand **2** showing the atom labeling scheme.

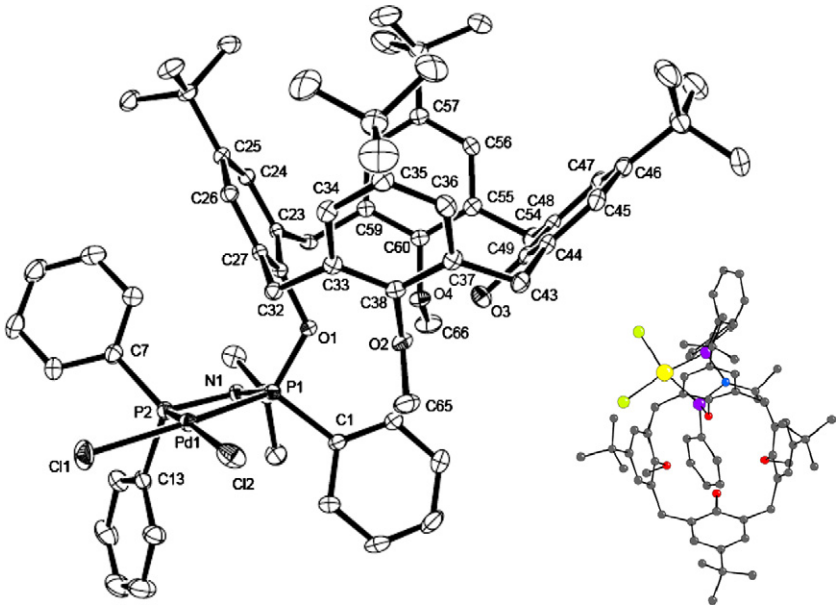


Fig. 5. ORTEP picture of complex **3** showing the atom labeling scheme (inset: view through the axis passing through the calix[4]arene cavity and perpendicular to the plane of the $-CH_2-$ carbon atoms).

cone conformation; in contrast, in the palladium dichloride complex **3**, the calixarene framework adopts the cone conformation. The two Pd–P bond lengths are different; Pd1–P1 bond is 0.02 A° longer than the Pd1–P2 bond. This difference may be attributed to the greater π-acceptor ability of P1 phosphorus atom owing to its attachment to the electronegative oxygen atom. This trend is also reflected in the Pd–Cl bonds; the Pd1–Cl1 (*trans* to the phosphorus atom which is bonded to oxygen) is shorter than Pd1–Cl2 bond.

The dihedral angles of the aryl rings, directly attached to the phosphorus atoms with respect to the P1–N1–P2 plane in **2** and **3** indicate a considerable change in the relative orientation of the aryl rings with respect to the P–N–P plane upon complexation. The P–N bond distances fall within the range of values reported for P–N–P ligands and their complexes. There is a considerable decrease (∼20°) in the P1–N1–P2 angle of the ligand upon chelate formation. The central nitrogen atom in both the ligand and the complex shows a trigonal planar geometry as observed for numerous other diphosphazanes and their complexes [1a,4,5,27].

The conformations of the calixarene framework in **2** and **3** can be defined by torsion angles or dihedral angles. The torsion angles are listed in Tables 4 and 5 for **2** and **3**, respectively. An examination of torsion angles shows the sequence of signs for ϕ and χ to be $+-$, $++$, $--$, $+-$ and $-+$, $-+$, $-+$, $-+$ for **2** and **3**, respectively, as expected for partial cone and cone conformations, respectively. For ligand **2**, four of the eight torsion angles differ significantly from the ideal cone torsion angles [$\phi = 90°$ and $\chi = 90°$]. These values indicate that one of the aryl rings of the calix[4]arene framework is oriented in the inverted direction in the molecule. A low value (40.8°) of the dihedral angle between the plane of the aryl ring (D) (which contains the OH group in the lower rim) and the methylene bridge plane (*X*) observed for complex (**3**) (Table 6) indicates considerable flattening of the ideal cone conformation and as a result, the conformation is intermediate between that of an ideal cone and a pinched cone [28].

Complex **3** crystallizes with a solvent (acetone) molecule trapped inside the cavity of the calix[4]arene framework.

Table 2
Selected bond distances (Å) for **2** and **3**

Distance	Ligand (**2**)	Complex (**3**)
O(1)–P(1)	1.665(5)	1.604(2)
P(1)–N(1)	1.704(7)	1.684(2)
P(2)–N(1)	1.705(7)	1.705(2)
P(1)–Pd(1)		2.225(1)
P(2)–Pd(1)		2.206(1)
Cl(1)–Pd(1)		2.343(1)
Cl(2)–Pd(1)		2.354(1)

Table 3
Selected bond angles (°) for **2** and **3**

Angle	Ligand (**2**)	Complex (**3**)
P(1)–N(1)–P(2)	119.1(4)	100.3(1)
O(1)–P(1)–N(1)	105.9(3)	108.6(1)
O(1)–P(1)–C(1)	93.4(3)	98.5(1)
N(1)–P(2)–C(7)	107.3(4)	111.0(1)
N(1)–P(2)–C(13)	104.5(4)	110.0(1)

Table 4
Torsion angles to define the conformation of calix[4]arene diphosphazane ligand (**2**)

Torsion angle	ϕ (°)	Torsion angle	χ (°)
C37–C36–C35–C33	90 (1)	C36–C35–C33–C32	−77 (1)
C30–C29–C28–C27	137.8 (8)	C29–C28–C27–C26	116.8 (8)
C24–C23–C49–C47	−119.3 (8)	C23–C49–C47–C46	−139.1 (7)
C44–C43–C42–C40	89.9 (9)	C43–C42–C40–C39	−94.4 (1)

Table 5
Torsion angles to define the conformation of palladium dichloride complex (**3**)

Torsion angle	ϕ (°)	Torsion angle	χ (°)
C58–C59–C70–C23	−74.5(4)	C59–C70–C23–C24	77.4(3)
C26–C27–C32–C33	−77.1(3)	C27–C32–C33–C34	83.3(4)
C36–C37–C43–C44	−83.1(4)	C37–C43–C44–C45	105.2(4)
C47–C48–C54–C55	−103.2(4)	C48–C54–C55–C56	73.1(4)

Table 6
Dihedral angles between the planes[a] of the aryl rings of the calixarene framework and the mean plane (*X*) defined by methylene carbon atoms

Planes	Dihedral angles (°) [ligand (**2**)]	Dihedral angles (°) [complex (**3**)]
A–*X*	64.9(2)	62.5(1)
B–*X*	78.4(2)	65.7(1)
C–*X*	60.0(2)	72.0(1)
D–*X*	52.9(2)	40.8(1)

[a] *A*–*D* are the planes of aromatic rings defined by C29–C34, C22–C27, C43–C48 and C36–C41, respectively for **2** and C33–C38, C22–C27, C55–C60 and C44–C49, respectively for **3**.

The unit cell of complex **3** contains four molecules. The molecules are held together by C–H–O and C–H–Cl hydrogen bonds (see ESI, Fig. S6, Tables S2 and S3). The acetone molecule plays an important role in holding the molecules together.

3.4. Application of palladium dichloride complex (3) in catalytic Heck reaction

In recent years, Pd(II) complexes bearing multidentate ligands that contain significantly different types of hard (N, O) and soft (P) donor functions have been studied in catalytic Heck reaction [29,30]. In contrast, application of Pd(II) complexes of P–N–P ligands in Heck coupling reactions has not been studied. Palladium catalyzed Heck coupling reaction between styrene and aryl halides (X = Br, I) is investigated using the Pd(II) complex (**3**). Although the results show that complex **3** is able to catalyze the Heck reaction, the yield of the product (*trans* stilbene) is considerably less compared to most of the other Pd(II) catalysts known in literature [31,32] (see ESI for details of the catalytic studies).

3.5. Reactions with other palladium precursors

Reactivity of ligand **2** with other Pd(0) e.g. $[Pd(dba)_2]$ and Pd(II) e.g. $[Pd(\eta^3\text{-allyl})Cl]_2$ precursors has been investigated. The ^{31}P NMR spectra show definite evidence for the formation of complexes but none of the complexes could be isolated in a pure form (see ESI).

4. Conclusions

A "P–N–P" ligand containing a calix[4]arene backbone (which could be a forerunner to a new series of "calixphosphine" ligands) and its Pd dichloride complex have been synthesized. The partial cone conformation of the calixarene framework in the ligand changes to the cone conformation upon complexation to palladium as shown by X-ray crystallographic studies. Movement of the aryl rings of calix[4]arene fragment to generate different conformers in solution has been demonstrated by a two-dimensional NMR study. Preliminary investigations on the application of palladium dichloride complex in Heck coupling reaction have been carried out. In spite of the presence of bulky calix[4]arene framework, this diphosphazane ligand shows a tendency to form complexes when treated with Pd(II) and Pd(0) precursors. It would be interesting to investigate the coordination chemistry of this type of calix-diphosphazane ligands with various transition metals including catalytic applications of the complexes.

Acknowledgements

We thank the Department of Science and Technology (DST), New Delhi, India, for financial support and Dr. P. Munshi for help in X-ray crystallographic studies. SSK thanks the Indian National Science Academy, New Delhi, for the position of a Senior Scientist.

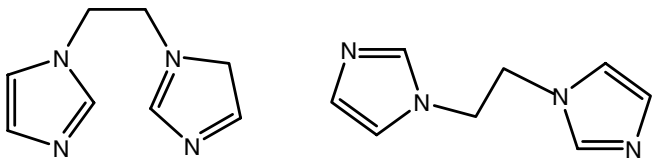
Appendix A. Supplementary material

CCDC 630525 and 630526 contain the supplementary crystallographic data for **2** and **3**. These data can be obtained free of charge via http://www.ccdc.cam.ac.uk/conts/retrieving.html, or from the Cambridge Crystallographic Data Centre, 12 Union Road, Cambridge CB2 1EZ, UK; fax: (+44) 1223-336-033; or e-mail: deposit@ccdc.cam.ac.uk. Supplementary data associated with this article can be found, in the online version, at doi:10.1016/j.poly.2007.04.019.

References

[1] (a) M.S. Balakrishna, V.S. Reddy, S.S. Krishnamurthy, J.F. Nixon, J.C.T.R. Burckett, St. Laurent, Coord. Chem. Rev. 129 (1994) 1;
(b) K. Raghuraman, S.K. Mandal, T.S. Venkatakrishnan, S.S. Krishnamurthy, M. Nethaji, Proc. Indian Acad. Sci. (Chem. Sci.) 114 (2002) 233.
[2] M. Witt, H.W. Roesky, Chem. Rev. 94 (1994) 1163.
[3] P. Bhattacharya, J.D. Woollins, Polyhedron 14 (1995) 3367.
[4] (a) A. Xia, P.R. Sharp, Polyhedron 21 (2002) 1305;
(b) A.F. Heyduk, D.G. Nocera, J. Am. Chem. Soc. 122 (2000) 9415;
(c) H. Krishna, S.S. Krishnamurthy, M. Nethaji, Polyhedron 25 (2006) 3189.
[5] G. Prabusankar, N. Palanisami, R. Murugavel, R.J. Butcher, Dalton Trans. (2006) 2140.
[6] (a) C.D. Gutsche, Calixarenes, Royel Society of Chemistry, Cambridge, 1989;
(b) C.D. Gutsche, Calixarenes Revisited, Royal Society of Chemistry, Cambridge, 1998;
(c) L. Mandolini, R. Ungaro, Calixarenes in Action, Imperial College Press, London, 2000.
[7] V. Boehmer, Angew. Chem., Int. Ed. 34 (1995) 713.

[8] (a) E. Ghidhini, F. Ugozzoli, R. Ungaro, S. Harkema, A.A. El-Fadl, D.N. Reinhoudt, J. Am. Chem. Soc. 112 (1990) 6979;
(b) T. Harade, J.M. Rudziriski, S. Shinkai, J. Chem. Soc., Perkin Trans. 2 (1992) 2109;
(c) J. Blixt, C. Detellier, J. Am. Chem. Soc. 116 (1994) 11960.
[9] D.M. Roundhill, Prog. Inorg. Chem. 43 (1995) 533.
[10] I. Neda, T. Kaukorat, R. Schmutzler, Main Group Chem. News 6 (1998) 4.
[11] (a) C. Jeunesse, D. Armspach, D. Matt, Chem. Commun. 45 (2005) 5603;
(b) C. Jeunesse, C.B. Dieleman, D. Matt, Coord. Chem. Rev. 165 (1997) 93.
[12] (a) R. Paciello, L. Siggal, M. Roeper, Angew. Chem., Int. Ed. 38 (1999) 1920;
(b) L. Mahalakshmi, S.S. Krishnamurthy, M. Nethaji, Curr. Sci. 83 (2002) 870.
[13] F.J. Parlevliet, C. Kiener, J. Franje, K. Goubitz, M. Lutz, A.N. Spek, P.C.J. Kamer, P.W.N.M. van Leeuwen, J. Chem. Soc., Dalton Trans. (2000) 1113.
[14] (a) C.J. Cobley, D.D. Ellis, A.G. Orpen, P.G. Pringle, J. Chem. Soc., Dalton Trans. (2000) 1101;
(b) C.J. Cobley, D.D. Ellis, A.G. Orpen, P.G. Pringle, J. Chem. Soc., Dalton Trans. (2000) 1109.
[15] O. Aleksiuk, F. Grynszpan, S.E. Biali, J. Incl. Phenom. Mol. Recog. 19 (1994) 237.
[16] P.J. Dijkstra, J.A.J. Brunink, K.E. Bugge, D.N. Reinhoudt, S. Harkema, R. Ungaro, F. Ugozzoli, E. Ghidini, J. Am. Chem. Soc. 111 (1989) 7567.
[17] D. Drew, J.R. Doyle, Inorg. Synth. 13 (1972) 52.
[18] R.J. Cross, T.H. Green, R. Keat, J. Chem. Soc., Dalton Trans. (1976) 1424.
[19] Bruker SMART, V. 6.028, Bruker AXS Inc., Madison Wisconsin, USA, 1998.
[20] Bruker SAINT, V. 6.02, Bruker AXS Inc., Madison Wisconsin, USA, 1998.
[21] G.M. Sheldrick, SADABS, University of Göttingen, Germany, 1997.
[22] Bruker SHELXTL, NT V. 5.10, Bruker AXS Inc., Madison Wisconsin, USA, 1998.
[23] L.J. Farrugia, J. Appl. Crystallogr. 32 (1999) 837.
[24] G.M. Sheldrick, SHELXL-97, Programme for Refinement of Crystal Structures, University of Göttingen, Germany, 1997.
[25] R. Keat, L. Manojlovic-Muir, K.W. Muir, D.S. Rycroft, J. Chem. Soc., Dalton Trans. (1981) 2192.
[26] I.J. Colquhoun, W. McFarlane, J. Chem. Soc., Dalton Trans. (1977) 1674.
[27] (a) S.K. Mandal, G.A.N. Gowda, S.S. Krishnamurthy, T. Stey, D. Stalke, J. Organomet. Chem. 690 (2005) 742;
(b) S.K. Mandal, T.S. Venkatakrishnan, A. Sarkar, S.S. Krishnamurthy, J. Organomet. Chem. 691 (2006) 2969.
[28] F. Ugozzoli, G.D. Andreetti, J. Incl. Phenom. Mol. Recog. 13 (1992) 337.
[29] U. Christmann, R. Vilar, Angew. Chem., Int. Ed. 44 (2005) 366.
[30] D. Prim, J.M. Campagne, D. Joseph, B. Andrioletti, Tetrahedron 58 (2002) 2041.
[31] M. Feuerstein, H. Doucer, M. Santelli, Tetrahedron Lett. 43 (2002) 2191.
[32] M. Nowotny, U. Hanefeld, H. van Koningsveld, T. Maschmeyer, Chem. Commun. (2000) 1877.



Scheme 1. Two different conformations of 1,2-bis(imidazol-1′-yl)ethane.

which two different conformations (*gauche* and *anti*) were included [14]. However, the control of different conformation of flexible ligands in the synthetic reactions is still a tremendous challenge to chemists owing to the influence of many subtle factors, such as solvent, pH value, metal ions and additional ligands.

1,2-Bis(imidazol-1′-yl)ethane (bime), an analogue to well-investigated 1,2-bis(4-pyridyl)ethane, also possesses *gauche* and *anti* conformations (Scheme 1) as a consequence of the free rotation of the ethyl group. However, the effect of its isomerism and manifestation on structures and properties remains to be less explored. To our knowledge, only one copper–bime complex was prepared, in which both of its isomers (*gauche*:*anti* = 1:1.5) were observed [15]. As a part of our ongoing research about the effect of neutral, electron-donating and electron-withdrawing groups in dicarboxylate ligands on structures and properties of metal–organic compounds [16], herein, we wish to report the syntheses, crystal structures and characterizations of four-coordination polymers $\{[Zn(gauche\text{-bime})(bdc)]\cdot 0.5H_2O\}_n$ (**1**), $\{[Zn(anti\text{-bime})(HO\text{-bdc})]\cdot 2.5H_2O\}_n$ (**2**), $[Cu(gauche\text{-bime})_{0.5}(anti\text{-bime})_{0.5}(O_2N\text{-bdc})]_n$ (**4**) and $[Ni_2(gauche\text{-bime})(anti\text{-bime})(O_2N\text{-bdc})_2(H_2O)_2]_n$ (**5**) (H_2bdc = *m*-isophthalic acid, HO-H_2bdc = 5-hydroxyisophthalic acid, O_2N-H_2bdc = 5-nitroisophthalic acid), in which the conformational isomerisms of bime are heavily influenced by the coexistent groups of dicarboxylate ligands and used metal ions. At the same time, previously reported $\{[Zn(anti\text{-bime})(O_2N\text{-bdc})]\cdot H_2O\}_n$ (**3**) [17] as a comparable substance in the research system was also mentioned.

2. Experimental

2.1. Materials and general methods

All the reagents were commercially available and used as purchased except that 1,2-bis(imidazol-1′-yl)ethane was synthesized by the literature method [15]. Thermogravimetric experiments were performed using a TGA/SDTA851 instrument (heating rate of 10 °C/min, air stream). IR spectra as KBr pellets were recorded on a Magna 750 FT-IR spectrophotometer. Elemental analyses of C, H, and N were determined using a Perkin–Elmer 240C elemental analyzer. X-ray powder diffraction measurements were recorded on RIGAKU DMAX2500PC diffractometer using Cu Kα radiation.

2.2. Synthesis of $\{[Zn(gauche\text{-bime})(bdc)]\cdot 0.5H_2O\}_n$ (*1*)

A mixture of $Zn(NO_3)_2\cdot 6H_2O$ (0.074 g, 0.25 mmol), 1,2-bis(imidazol-1′-yl)ethane (0.040 g, 0.25 mmol), H_2bdc (0.042 g, 0.25 mmol) and KOH (0.028 g, 0.50 mmol) was dissolved in CH_3OH (8 mL) and H_2O (10 mL). The mixture was transferred to a 25 mL stainless-steel reactor with Teflon liner and heated to 160 °C automatically. The temperature was kept at 160 °C for 4 days and cooled to room temperature during 24 h. Colorless block crystals of **1** were obtained (yield: 0.042 g, 42%, based on Zn). Elemental *Anal*. Calc. for $C_{16}H_{15}ZnN_4O_{4.5}$ (400.69): C, 47.96; H, 3.77; N, 13.98. Found: C, 47.91; H, 3.65; N, 14.02%. IR (KBr, cm^{-1}): 3427 (bs), 1622 (vs), 1347 (vs), 1236 (m), 1104 (m), 1227 (w), 835 (m), 746 (s), 652 (m), 567 (w).

2.3. Synthesis of $\{[Zn(anti\text{-bime})(HO\text{-bdc})]\cdot 2.5H_2O\}_n$ (*2*)

The process was similar to the synthesis of **1** except that H_2bdc was replaced by HO-H_2bdc (0.045 g, 0.25 mmol). Colorless block crystals of **2** were obtained (yield: 0.041 mg, 36% based on Zn). Elemental *Anal*. Calc. for $C_{16}H_{19}ZnN_4O_{7.5}$ (452.72): C, 42.45; H, 4.23; N, 12.38. Found: C, 42.39; H, 4.17; N, 12.42%. IR (KBr, cm^{-1}): 3462 (bs), 1622 (vs), 1349 (vs), 1244 (m), 1100 (m), 956 (w), 777 (s), 726 (s), 652 (m), 629 (w).

2.4. Synthesis of $[Cu(gauche\text{-bime})_{0.5}(anti\text{-bime})_{0.5}(O_2N\text{-bdc})]_n$ (*4*)

The process was similar to the synthesis of **1** except that H_2bdc and $Zn(NO_3)_2\cdot 6H_2O$ were replaced by O_2N-H_2bdc (0.053 g, 0.25 mmol) and $Cu(NO_3)_2\cdot 3H_2O$ (0.060 g, 0.25 mmol), respectively. Blue prism crystals of **4** were obtained (yield: 0.031 g, 29% based on Cu). Elemental *Anal*. Calc. for $C_{16}H_{13}CuN_5O_6$ (434.85): C, 44.19; H, 3.01; N, 16.10. Found: C, 44.21; H, 3.05; N, 16.08%. IR (KBr, cm^{-1}): 1614 (vs), 1594 (s), 1344 (vs), 1276 (m), 1100 (m), 843 (w), 726 (s), 703 (s), 653 (m), 551 (w).

2.5. Synthesis of $[Ni_2(gauche\text{-bime})(anti\text{-bime})(O_2N\text{-bdc})_2(H_2O)_2]_n$ (*5*)

The process was similar to the synthesis of **1** except that H_2bdc and $Zn(NO_3)_2\cdot 6H_2O$ were replaced by O_2N-H_2bdc (0.053 g, 0.25 mmol) and $Ni(NO_3)_2\cdot 6H_2O$ (0.075 g, 0.25 mmol), respectively. Green prism crystals of **5** were obtained (yield: 0.037 g, 33% based on Ni). Elemental *Anal*. Calc. for $C_{32}H_{30}Ni_2N_{10}O_{14}$ (896.08): C, 42.89; H, 3.37; N, 15.63. Found: C, 42.92; H, 3.25; N, 15.66%. IR (KBr, cm^{-1}): 3412 (bs), 1614 (vs), 1528 (vs), 1376 (vs), 1341 (vs), 1287 (w), 1084 (m), 995 (w), 777 (s), 723 (s), 653 (m), 524 (w).

2.6. Crystal structure determinations

Measurements of **1**, **4** and **5** were conducted on a Rigaku Mercury CCD diffractometer with graphite-monochromated Mo Kα radiation ($\lambda = 0.71073$ Å) at low temperature (−100 °C) [18]. Intensity data for **2** were measured on a Siemens Smart CCD diffractometer with graphite-monochromated Mo Kα radiation ($\lambda = 0.71073$ Å) at room temperature, the empirical absorption corrections were applied by using the SADABS program [19]. All of the four structures were solved by direct methods with the SHELX-97 programs [20] and refined on F^2 by full-matrix least-squares using the SHELXL-97 program package [21]. The positions of H atoms were generated geometrically (C–H bond fixed at 0.96 Å), assigned isotropic thermal parameters, and allowed to ride on their parent carbon atoms before the final cycle of refinement. Crystal data and structure determination summaries for **1**, **2**, **4** and **5** are listed in Table 1. The selected bond lengths and angles for the four complexes are listed in Table 2.

3. Results and discussion

3.1. Syntheses

Similar to neutral N-donor dipyridyl ligands, bime is a promising ligand towards the syntheses of extended structural frameworks owing to its simple bridging mode and strong coordination ability to transition metal ions. Usually, assembly of this ligand with metal ions requires the presence of counterions to balance the charge [22]. Deprotonated di- or polycarboxylate ligands are another excellent candidates for the preparation of coordination networks owing to the rich coordination modes of carboxylate groups [23], they can serve as anions and balance charge by themselves. The combination of the foregoing two types of ligands not only can simplify the effect of counterions on the final products, but also can produce compounds with intriguing structures and useful properties.

Our research aims at synthesizing desired coordination polymers *via* combining bime, isophthalic acid or its derivatives (Scheme 2) and metal ions, and at further studying the influence of coexistent groups of carboxylate group and different metal ions on the isomerisms of bime. The presence of the electron-donating (–OH, –Me) and electron-withdrawing (–NO_2) uncoordination groups in dicarboxylate ligands changes their electronic property and steric hindrance, which can generate complexes different from those from the common dicarboxylate ligands [24]. The solvothermal reaction of bime and H_2bdc with $Zn(NO_3)_2 \cdot 6H_2O$ gave rise to **1**, in which only *gauche*-bime was observed. While H_2bdc replaced by HO-H_2bdc bearing electron-donating group and O_2N-H_2bdc bearing

Table 1
Crystal data and structure determination summaries for **1**, **2**, **4** and **5**

Compound	**1**	**2**	**4**	**5**
Formula	$C_{16}H_{15}ZnN_4O_{4.5}$	$C_{16}H_{19}ZnN_4O_{7.5}$	$C_{16}H_{13}CuN_5O_6$	$C_{32}H_{30}Ni_2N_{10}O_{14}$
Formula weight	400.69	452.72	434.85	896.08
Crystal size (mm)	0.38 × 0.35 × 0.30	0.42 × 0.22 × 0.20	0.20 × 0.15 × 0.03	0.25 × 0.20 × 0.15
Crystal system	monoclinic	monoclinic	orthorhombic	orthorhombic
Space group	$P2_1/c$	$P2_1/c$	*Pnna*	$Pna2_1$
a (Å)	9.6110(7)	10.2458(3)	16.4217(17)	16.4362(9)
b (Å)	17.5803(14)	21.9840(3)	19.8241(15)	10.1770(6)
c (Å)	10.2386(8)	9.0406(2)	10.233	22.0839(14)
α (°)	90	90	90	90
β (°)	99.192(3)	103.010(1)	90	90
γ (°)	90	90	90	90
V (Å^3)	1707.7(2)	1984.07(8)	3331.3(4)	3694.0(4)
Z	4	4	8	4
D_{calc} (g cm^{-3})	1.558	1.516	1.734	1.611
μ (mm^{-1})	1.470	1.286	1.360	1.102
F(000)	820	932	1768	1840
T (K)	173(2)	293(2)	293(2)	173(2)
λ(Mo Kα) (Å)	0.71073	0.71073	0.71073	0.71073
Reflections collected	12994	6330	25949	27412
Unique reflections	3924	3467	4137	7135
R_{int}	0.0262	0.0296	0.0399	0.0431
Parameters	227	262	253	531
Goodness-of-fit (S) on F^2	1.089	1.686	1.097	0.929
R_1 [$I > 2\sigma(I)$][a]	0.0434	0.0756	0.0411	0.0431
wR_2 [$I > 2\sigma(I)$][b]	0.1366	0.2122	0.1367	0.1235
R_1 (all data)	0.0508	0.0945	0.0466	0.0492
wR_2 (all data)[b]	0.1446	0.2277	0.1409	0.1290
$\Delta\rho_{max}$ and $\Delta\rho_{min}$ (e/Å^3)	0.781 and −0.465	1.665 and −1.036	0.473 and −0.417	0.466 and −0.337

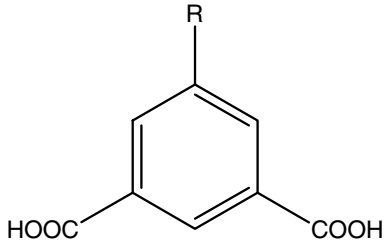
[a] $R = \sum\|F_o| - |F_c\|/\sum|F_o|$.
[b] $wR_2 = [\sum w(F_o^2 - F_c^2)^2/\sum w(F_o^2)^2]^{1/2}$.

Table 2
Selected bond lengths (Å) and angles (°) for **1**, **2**, **4**, and **5**

*Compound **1***			
Zn–O4A	1.9431(18)	Zn–N4B	1.998(2)
Zn–O2	1.9766(19)	Zn–N1	2.008(2)
O4A–Zn–O2	118.26(8)	O4A–Zn–N(1)	115.01(9)
O4A–Zn–N4B	107.64(9)	O2–Zn–N1	98.41(9)
O2–Zn–N4B	101.78(9)	N4B–Zn–N1	115.15(9)
*Compound **2***			
Zn–O(1)	1.987(4)	Zn–N(1)	1.993(5)
Zn–N4B	1.992(4)	Zn–O4A	2.007(4)
O1–Zn–N4B	102.96(18)	O1–Zn–O4A	101.85(16)
O1–Zn–N1	105.51(19)	N4B–Zn–O4A	110.66(17)
N4B–Zn–N1	124.3(2)	N1–Zn–O4A	108.9(2)
*Compound **4***			
Cu–O4B	1.9651(17)	Cu–O2	2.029(2)
Cu–N3	1.976(2)	Cu–O3A	2.3317(19)
Cu–N1	1.9880(19)		
O4B–Cu–N3	89.25(8)	N1–Cu–O2	88.65(7)
O4B–Cu–N1	88.87(8)	O4B–Cu–O3A	106.29(7)
N3–Cu–N1	173.26(9)	N3–Cu–O3A	93.48(7)
O4B–Cu–O2	161.06(7)	N1–Cu–O3A	93.26(7)
N3–Cu–O2	91.04(7)	O2–Cu–O3A	92.59(6)
*Compound **5***			
Ni1–N1	2.053(4)	Ni1–OW1	2.106(3)
Ni1–O1	2.064(3)	Ni1–O4A	2.145(3)
Ni1–N5	2.071(4)	Ni1–O3A	2.175(3)
Ni2–N8	2.050(4)	Ni2–OW2	2.077(3)
Ni2–O7	2.051(3)	Ni2–O10A	2.119(3)
Ni2–N4B	2.070(4)	Ni2–O9A	2.195(3)
N1–Ni1–O1	90.75(13)	N5–Ni1–O4A	90.68(14)
N1–Ni1–N5	176.66(16)	OW1–Ni1–O4A	164.38(12)
O1–Ni1–N5	88.38(13)	N1–Ni1–O3A	88.74(12)
N1–Ni1–OW1	90.17(15)	O1–Ni1–O3A	158.17(12)
O1–Ni1–OW1	98.33(12)	N5–Ni1–O3A	93.27(12)
N5–Ni1–OW1	86.76(15)	OW1–Ni1–O3A	103.49(12)
N1–Ni1–O4A	92.64(14)	O4A–Ni1–O3A	61.24(11)
O1–Ni1–O4A	97.00(12)		
N8–Ni2–O7	92.29(14)	N4B–Ni2–O10A	93.11(14)
N8–Ni2–N4B	172.40(16)	OW2–Ni2–O10A	166.16(12)
O7–Ni2–N4B	94.65(14)	N8–Ni2–O9A	86.26(13)
N8–Ni2–OW2	85.71(15)	O7–Ni2–O9A	158.37(13)
O7–Ni2–OW2	95.70(13)	N4B–Ni2–O9A	88.43(13)
N4B–Ni2–OW2	90.49(16)	OW2–Ni2–O9A	105.69(13)
N8–Ni2–O10A	89.09(14)	O10A–Ni2–O9A	61.10(11)
O7–Ni2–O10A	97.32(12)		

Symmetry codes for **1**: A $x-1$, y, z; B $-x+2$, $-y$, $-z+1$. For **2**: A $x-1$, y, z; B $-x$, $y-1/2$, $-z+1/2$. For **4**: A x, $-y+1/2$, $-z-1/2$, B x, y, $z+1$; **5** A x, $y+1$, z, B $-x-1/2$, $y+1/2$, $z-1/2$.

electron-withdrawing group, respectively, **2** and **3** were generated, in which only *anti*-bime were exhibited. As compared with **3**, when using $Cu(NO_3)_2\cdot 3H_2O$ and $Ni(NO_3)_2\cdot 6H_2O$ instead of $Zn(NO_3)_2\cdot 6H_2O$, **4** and **5** were generated, respectively, where both *gauche*- and *anti*-conformations (1:1) of bime were displayed. This may indicate that the coordination geometries of different metal ions are also critical factors in the control of different conformation of bime ligand.



R = H, *m*-isophthalic acid

R = -OH, 5-hydroxylisophthalic acid

R = -NO_2, 5-nitroisophthalic acid

Scheme 2.

3.2. Description of crystal structures

3.2.1. $\{[Zn(gauche\text{-}bime)(bdc)]\cdot 0.5H_2O\}_n$ (**1**)

Single-crystal X-ray diffraction analysis reveals that **1** is a 1D linear coordination polymer containing only *gauche* isomer of bime. As shown in Fig. 1, each Zn^{II} center is coordinated by two oxygen atoms and two nitrogen atoms from different bdc and bime ligands, respectively, in a distorted tetrahedral geometry. The bond angles range from 98.41(9)° to 118.26(8)°, and the average bond lengths of Zn–O and Zn–N are 1.9596(19) and 2.003(2) Å, respectively. The deprotonated bdc serves as [a] bridge through its bis-monodentate carboxylate groups. The bime ligand adopts *gauche*-conformation to connect two zinc(II) centers, and the dihedral angle between two imidazolyl rings is 50.5°. Therefore, two bime link two zinc(II) centers to generate a –Zn–bime–Zn–bime– closed circuit, and the bis-monodentate bdc further extend the closed circuits into a 1D bamboo-like chain, in which the distances of adjoining zinc(II) centers separated by bime and bdc are 6.244 and 9.611 Å, respectively (Fig. 2). The crystal packing

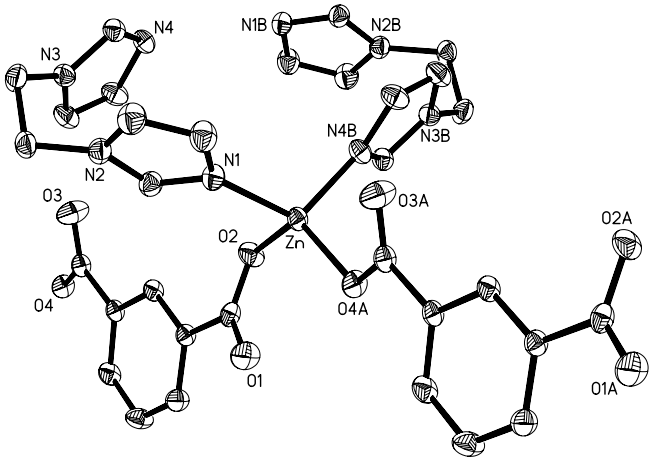


Fig. 1. The coordination geometry of Zn^{II} in **1** with the thermal ellipsoids at 30% probability level, free water molecule and hydrogen atoms were omitted for clarity.

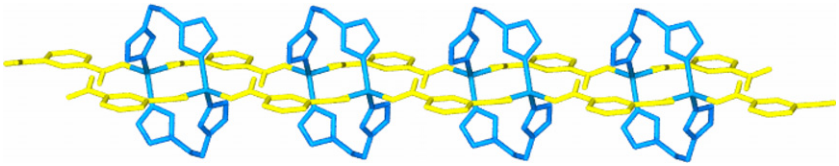


Fig. 2. View of the 1D bamboo-like chain, in which the –Zn–bime–Zn–bime– closed circuits are exhibited.

diagram for **1** is shown in Fig. 3, which reveals that there are free water molecules situated in the crystal lattice.

*3.2.2. $\{[Zn(anti\text{-}bime)(HO\text{-}bdc)]\cdot 2.5H_2O\}_n$ (**2**)*

When HO-H_2bdc replaced H_2bdc under the same condition, **2** was successfully isolated. Different from the 1D linear structure of **1**, **2** is a 3D supramolecular architecture in which only *anti* isomer of bime is included. The asymmetric unit consists of one Zn^{II}, one HO-bdc, one bime and two and half free water molecules (Fig. 4). Similar to that in **1**, each Zn^{II} center is in a distorted tetrahedral geometry, determined by two oxygen atoms and two nitrogen atoms from the carboxylate groups of different HO-bdc and bime ligands with the average bond lengths of Zn–O and Zn–N being 1.997(4) and 1.992(5) Å, respectively. Each HO-bdc ligand bridges two Zn^{II} centers through its bis-monodentate carboxylate groups, the hydroxyl group (–OH) is involved in hydrogen bonding interactions with another adjacent hydroxyl group [O5–H···O5A^{i} 2.840 Å, (i) $-x+1, -y, -z+2$], although it does not take part in coordination. Different from that found in **1**, bime adopts only *anti*-conformation to coordinate to two zinc centers. The two imidazolyl rings are almost coplanar with the dihedral angle between them being 163.0°. Thereby, the bis-monodentated HO-bdc and the *anti*-conformational bime connect Zn^{II} centers into a 2D (4,4) network with cavities of 10.246×11.358 Å^2 determined by adjoining Zn···Zn distances separated by HO-bdc and bime, respectively (Fig. 5). In order to minimize the void cavities and stabilize the whole framework, the crystal packing adopts ABAB mode, and the abundant hydrogen bonding interactions between free water molecules and carboxylate groups, free water molecules and free water molecules as well as the above-mentioned the hydroxyl groups and the hydroxyl groups, connect the 2D layer into a 3D supramolecular architecture [OW1–H···O2^{ii} 2.798 Å; OW2–H···O3^{iii} 2.790 Å; OW1–H···OW3 2.699 Å; OW2–H···OW3

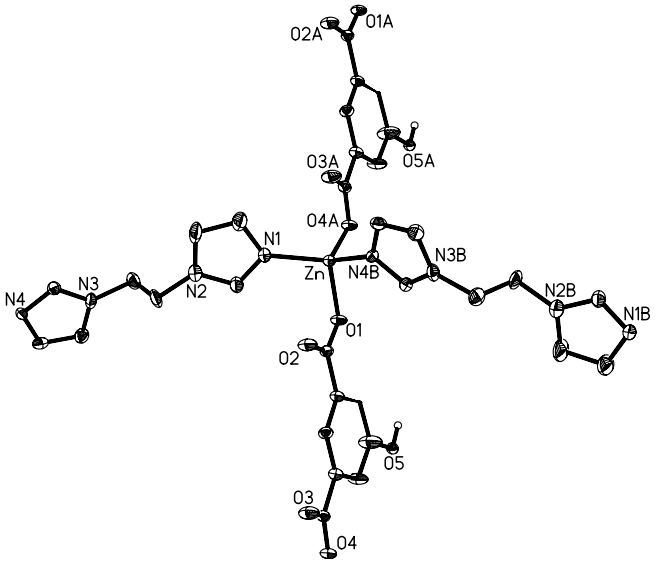


Fig. 4. The coordination geometry of Zn^{II} in **2** with the thermal ellipsoids at 30% probability level, free water molecules and hydrogen atoms were omitted for clarity.

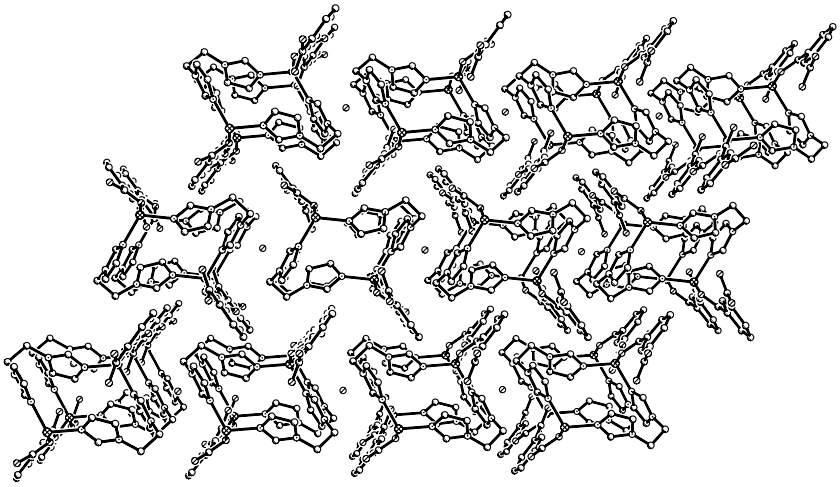


Fig. 3. View of the packing diagram of **1** along *c*-axis.

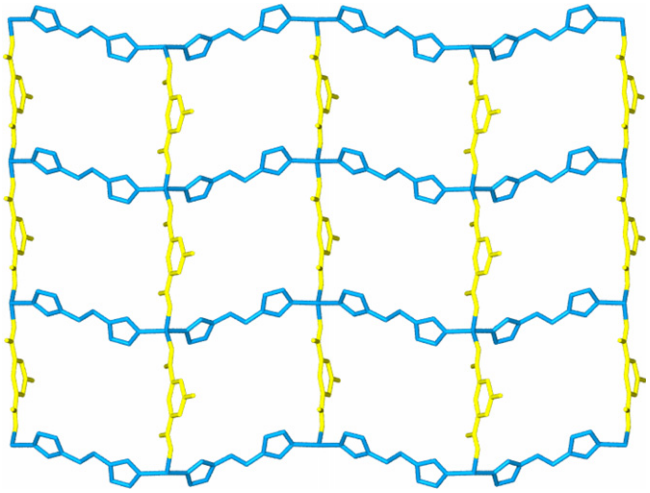


Fig. 5. View of the 2D (4,4) network.

2.690 Å; symmetry codes: (ii) $x, -y + 1/2, -z + 1$; (iii) $x, y, z + 1$] (Fig. 6). Compared to **1**, it is notable that the electron-donating hydroxyl group in the dicardoxylate ligand plays an important role in the change of the conformational isomerism of bime in **2**.

3.2.3. $\{[Zn(bime)(O_2N\text{-}bdc)] \cdot H_2O\}_n$ (**3**)

When selected bime, O_2N-H_2bdc and $Zn(NO_3)_2 \cdot 6H_2O$ as starting materials, **3** was generated. As previously reported, **3** is a tetrahedrally four-connected $6.6.6.6.6_2.8_3$ topological network. Similar to that in **2**, the Zn^{II} center is in a distorted tetrahedral geometry and the bime ligand also behaves in *anti*-conformation to link zinc^{II} centers (see Fig. S1). The Zn···Zn distance across bime is 11.762 Å, slightly longer than that in **2**. Based on **3**, different metal ions possessing different coordination geometries were induced into the reaction system in order to further study the conformation preference of bime. Therefore, the following **4** and **5** were generated from the solvothermal reactions of bime and O_2N-H_2bdc with $Cu(NO_3)_2 \cdot 3H_2O$ and $Ni(NO_3)_2 \cdot 6H_2O$, respectively, in which both *gauche*- and *anti*-conformations (1:1) of bime were exhibited.

3.2.4. $[Cu(gauche\text{-}bime)_{0.5}(anti\text{-}bime)_{0.5}(O_2N\text{-}bdc)]_n$ (**4**)

Compound **4** is a 2D wave-like layer consisting of dinuclear units, in which both *gauche*- and *anti*-conformations of bime are observed. There is only one unique Cu^{II} center in **4**, its coordination environment is shown in Fig. 7. Cu^{II} is surrounded by five atoms in a distorted trigonal bipyramidal coordination geometry. The equatorial plane is determined by three carboxylate oxygen atoms from different O_2N-bdc with the bond angles ranging from 92.59(6)° to 161.06(7)°, while the axial positions are occupied by two nitrogen atoms from different bime with the N1–Cu–N3 bond angle and the average Cu–N bond length being 173.26(9)° and 1.982 (2) Å, respectively. Each O_2N-bdc

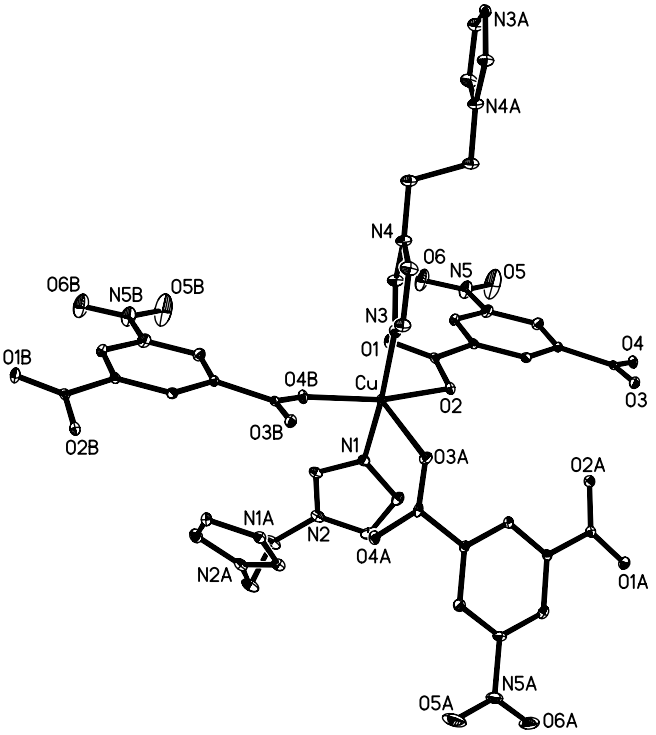


Fig. 7. The coordination geometry of Cu^{II} in **4** with the thermal ellipsoids at 30% probability level, hydrogen atoms were omitted for clarity.

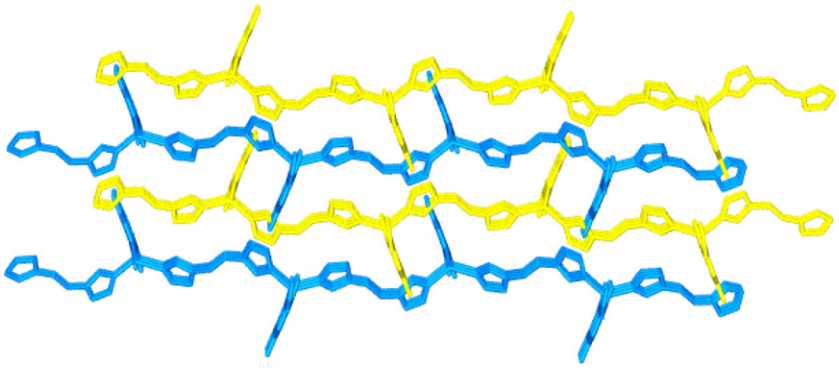


Fig. 6. View of the 3D supramolecular architecture of **2** along *a*-axis.

behaves as a μ_3-bridge linking three Cu^{II} centers through one monodentate carboxylate and one μ_2,η^2-carboxylate groups into a 1D double-chain, in which dinuclear units are exhibited (Fig. 8), the nitro group ($-NO_2$) neither takes part in coordination nor involves in hydrogen bonding interaction. Interestingly, there are two kinds of bime: one adopts *gauche*-conformation and acts as a bridge between two Cu^{II} centers in the dinuclear unit; while the other adopts *anti*-conformation to extend the 1D double-chain into a 2D wave-like layer (Fig. 9). The ratio of bime conformation is 1:1, which is different from that found in another copper–bime complex [7]. With respect to the *gauche*-bime, the dihedral angle between two imidazolyl rings is 30.9°, smaller than that in **1**, and the Cu···Cu distance across it is 4.445 Å. The two imidazolyl rings in *anti*-bime are almost coplanar with the dihedral angle between them being 180.0°, and the adjoining Cu···Cu distance separated by it is 11.543 Å. The packing diagram displays that no guest molecules and weak interactions are included between layers, although there are large void spaces in the wave-like layer (Fig. S2).

3.2.5. $[Ni_2(gauche\text{-}bime)(anti\text{-}bime)(O_2N\text{-}bdc)_2(H_2O)_2]_n$ (**5**)

Compound **5** is also a 2D wave-like layer including both *gauche*- and *anti*-conformations of bime, but the bridging fashion of O_2N-bdc and coordination environments of metal centers are different from those in **4**. The coordination environments of Ni^{II} centers are shown in Fig. 10. Both Ni^{II} ions adopt distorted octahedral coordination geometries, in which two nitrogen atoms from different bime stand at the apical positions, and three carboxylate oxygen atoms and one water molecule consist of the equatorial plane. Firstly, the O_2N-bdc acts as a bridge linking adjoining Ni^{II} centers to give rise to a 1D chain through its monodentate and chelating carboxylate groups, the nitro group ($-NO_2$) neither participates in coordination nor involves in hydrogen bonding interaction (Fig. 11). Secondly, the 1D chain is extended by two kinds of bridging bime to generate a 2D wave-like layer, in which the intramolecular hydrogen bonding interaction between coordinated water molecule and carboxylate group further stabilize the framework (Fig. 12 and Fig. S3). Similar to

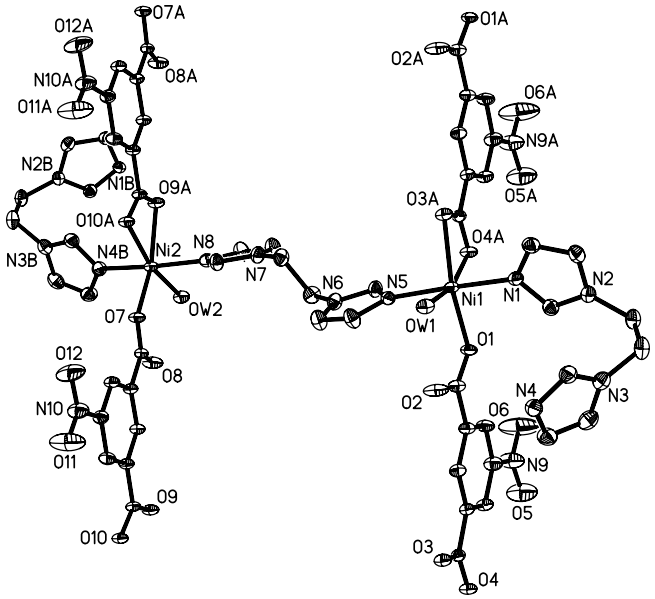


Fig. 10. The coordination geometries of Ni^{II} ions in **5** with the thermal ellipsoids at 30% probability level, hydrogen atoms were omitted for clarity.

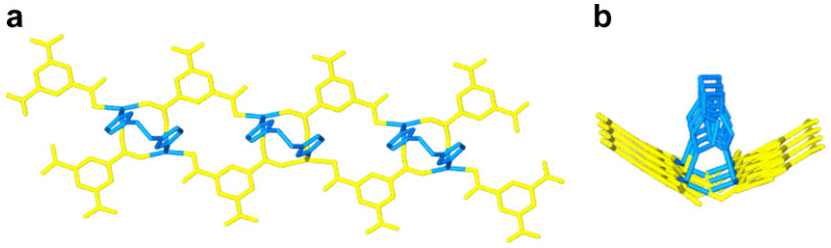


Fig. 8. View of the 1D double chain along different directions, (a) for *a*-axis, (b) for *c*-axis, in which the dinuclear units are exhibited.

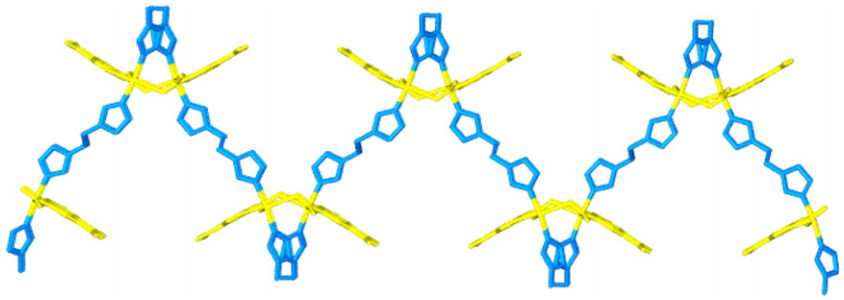


Fig. 9. View of the 2D wave-like layer.

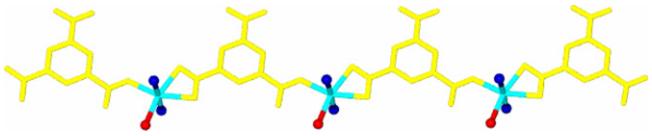


Fig. 11. View of the 1D chain.

those found in **4**, both *gauche*- and *anti*-isomers of bime are observed in **5**, and the ratio of the different conformations is also 1:1. The dihedral angle between two imidazolyl rings in *gauche*-bime is 50.6°, almost equivalent to that in **1** but larger than that in **4**, while the two imidazolyl rings in *anti*-bime is approximately coplanar with the dihedral angle being 166.3°. The neighboring Ni···Ni distances separated by *gauche*- and *anti*-bime are 5.873 and 11.715 Å, respectively.

3.3. Infrared spectroscopy

The IR spectrum of **1** shows a strong and broad peak at 3427 cm^{-1}, which indicates the presence of water molecules. The strong peaks at 1622 cm^{-1} and 1347 cm^{-1} are attributed to the asymmetric and symmetric vibrations of carboxylate groups, respectively. For **2**, similar to that in **1**, the strong and broad peak at 3462 cm^{-1} suggests the existence of water molecules, the characteristic bands of carboxylate groups are shown at 1622 cm^{-1} for asymmetric stretching vibration and 1349 cm^{-1} for symmetric stretching vibration. The similar splitting of **1** and **2** reveals the similar bis-monodentate coordination fashion of dicarboxylate ligands. For **4**, the characteristic bands of asymmetric and symmetric stretching vibrations of carboxylate groups are shown at 1614 cm^{-1}, 1594 cm^{-1} and 1344 cm^{-1}, respectively. For **5**, the strong and broad peak at 3412 cm^{-1} suggests the presence of hydrogen bonding interactions. The strong peaks at 1614 cm^{-1}, 1528 cm^{-1} and 1376 cm^{-1}, 1341 cm^{-1} are attributed to the asymmetric and symmetric stretching vibrations of carboxylate groups, respectively.

3.4. Thermogravimetric analyses

The thermal stability of the four complexes was determined by thermogravimetric analysis (TGA) on polycrystalline samples in an air atmosphere (Figs. S4–S7). For **1**, the first weight loss of 1.98% from 45 to 130 °C is equivalent to the loss of half free water molecule [$0.5H_2O$/[Zn(*gauche*-bime)(bdc)] · $0.5H_2O$, calculated: 2.25%]. The second weight loss of 77.18% from 386 to 582 °C, corresponds to the decomposition of **1**. The residual weight of 20.40% is ascribed to ZnO (ZnO/[Zn(*gauche*-bime)(bdc)] · $0.5(H_2O)$, calculated 20.31%). Similar to **1**, the TGA curve of **2** also shows two significant weight losses: 9.76% between 49 and 120 °C, and 71.98% between 365 and 552 °C. The former can be ascribed to the loss of two and half free water molecules ($2.5H_2O$/[Zn(*anti*-bime)(HO-bdc)] · $2.5H_2O$, calculated 9.94%), while the latter suggests the chemical decomposition of **2**. The residue composition is attributed to ZnO (ZnO/[Zn(*anti*-bime)(HO-bdc)] · $2.5H_2O$, calculated 17.97%, found 18.26%). For **4**, the TGA curve exhibits only one weight loss (80.91% from 281 to 520 °C), which indicates the decomposition of **4**. The residual weight of 19.09% corresponds to CuO (CuO/Cu(*gauche*-bime)$_{0.5}$(*anti*-bime)$_{0.5}$-(O_2N-bdc), calculated 18.29%). For **5**, the TGA curve displays two weight losses: one (3.96% from 124 to 162 °C) corresponds to the loss of coordinated water molecule ($2H_2O$/Ni_2(*gauche*-bime)(*anti*-bime)(O_2N-bdc)$_2$(H_2O)$_2$, calculated 4.02%); the other (78.96% from 396 to 538 °C) indicates the decomposition of **5**. The residue is attributed to NiO (2NiO/Ni_2(*gauche*-bime)(*anti*-bime)(O_2N-bdc)$_2$-(H_2O)$_2$, calculated 16.67%, found 17.08%).

3.5. X-ray powder diffraction

The original samples of the four complexes were also characterized by X-ray powder diffraction (XRPD) at room temperature (Figs. S8–S11). The experimental patterns are in good agreement with the theoretical ones generated from the single-crystal X-ray data of the complexes, which clearly indicate the good purity of the four complexes.

4. Conclusions

The solvothermal reactions of *m*-isophthalic acid or its derivatives bearing electron-donating and electron-withdrawing coexistent groups, bime and different metal ions generated five novel coordination polymers, in which bime adopt *gauche* (**1**), *anti* (**2** and **3**) and mixed conformations of *gauche* and *anti* (1:1) (**4** and **5**), respectively. This

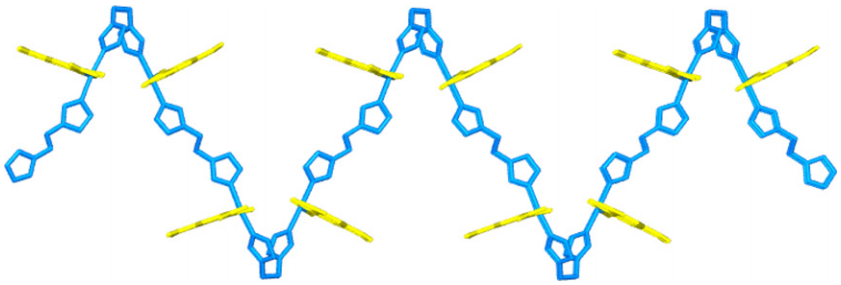


Fig. 12. View of the 2D wave-like layer.

research reveals that (i) the electron-donating and electron-withdrawing coexistent groups in dicarboxylate ligands are not involved in coordination, but they have important effect on the conformational preference of bime; (ii) the coordination geometries of different metal ions also play critical roles on the conformational preference of bime; and (iii) the conformational isomerisms of bime make it a good candidate to the construction of supramolecular networks.

Acknowledgments

This work was supported by the National Natural Science Foundation of China (Nos. 90206040, 20325106, and 20333070), Natural Science Foundation of Fujian Province and "One Hundred Talent Project" from CAS.

Appendix A. Supplementary material

CCDC 615191, 615192, 615193 and 615194 contain the supplementary crystallographic data for **1**, **2**, **4** and **5**. These data can be obtained free of charge via http://www.ccdc.cam.ac.uk/conts/retrieving.html, or from the Cambridge Crystallographic Data Centre, 12 Union Road, Cambridge CB2 1EZ, UK; fax: (+44) 1223-336-033; or e-mail: deposit@ccdc.cam.ac.uk. Supplementary data associated with this article can be found, in the online version, at doi:10.1016/j.poly.2007.04.043.

References

[1] (a) H.J. Choi, T.S. Lee, M.P. Suh, Angew. Chem., Int. Ed. 38 (1999) 1405;
(b) P.J. Hagrman, D. Hagrman, J. Zubieta, Angew. Chem., Int. Ed. 38 (1999) 2638.
[2] (a) O.R. Evans, W. Lin, Acc. Chem. Res. 35 (2002) 511;
(b) S. Horike, R. Matsuda, D. Tanaka, M. Mizuno, K. Endo, S. Kitagawa, J. Am. Chem. Soc. 128 (2006) 4222;
(c) J.L.C. Rowsell, O.M. Yaghi, Microporous Mesoporous Mater. 73 (2004) 3.
[3] (a) K.A. Hirsch, S.R. Wilson, J.S. Moore, Chem. Commun. (1998) 13;
(b) D.M. Shin, I.S. Lee, Y.K. Chung, M.S. Lah, Inorg. Chem. 42 (2003) 5459;
(c) L. Carlucci, G. Ciani, D.M. Proserpio, F. Porta, CrystEngComm 7 (2005) 78.
[4] (a) S.L. Zheng, M.L. Tong, H.L. Zhu, Y. Fang, X.M. Chen, J. Chem. Soc., Dalton Trans. (2001) 2049;
(b) A.J. Blake, N.R. Champness, A.N. Khlobystov, S. Parsons, M. Schröder, Angew. Chem., Int. Ed. 39 (2000) 2317.
[5] (a) D.A. Beauchamp, S.J. Loeb, Chem. Commun. (2002) 2484;
(b) M. Du, S.T. Chen, X.H. Bu, Cryst. Growth Des. 2 (2002) 625.
[6] (a) M. Fujita, K. Umemoto, M. Yoshizawa, N. Fujita, T. Kusukawa, K. Biradha, Chem. Commun. (2001) 509;
(b) H.K. Fun, S. Shanmuga Sundara Raj, R.G. Xiong, J.L. Zuo, Z. Yu, X.L. Zhu, X.Z. You, J. Chem. Soc., Dalton Trans. (1999) 1711.
[7] (a) S.Y. Yu, Z.X. Zhang, E.C.C. Cheng, Y.Z. Li, V.W.W. Yam, H.P. Huang, R. Zhang, J. Am. Chem. Soc. 127 (2005) 17994;
(b) N. Fatin-Rouge, É. Tóth, D. Perret, R.H. Backer, A.E. Merbach, J.G. Bünzli, J. Am. Chem. Soc. 122 (2000) 10810;
(c) Y. Kim, D.Y. Jung, Inorg. Chem. 39 (2000) 1470.
[8] (a) F.M. Tabellion, S. Russell Seidal, A.M. Arif, P.J. Stang, Angew. Chem., Int. Ed. 40 (2001) 1529;
(b) K.I. Nättinen, K. Rissanen, Inorg. Chem. 42 (2003) 5126;
(c) L. Carlucci, G. Ciani, D.M. Proserpio, Chem. Commun. (2004) 380.
[9] (a) X.H. Bu, W. Chen, S.L. Lu, R.H. Zhang, D.Z. Liao, W.M. Bu, M. Shionova, F. Brisse, J. Ribas, Angew. Chem., Int. Ed. 40 (2001) 3201;
(b) K. Kasai, M. Aoyagi, M. Fujita, J. Am. Chem. Soc. 122 (2000) 2140;
(c) R.H. Wang, M.C. Hong, J.H. Luo, R. Cao, J.B. Weng, Chem. Commun. (2003) 1018.
[10] (a) L. Pan, K.M. Adams, H.E. Hernandez, X. Wang, C. Zheng, Y. Hattori, K. Kaneko, J. Am. Chem. Soc. 125 (2003) 3062;
(b) Y. Qi, Y. Wang, C. Hu, M. Cao, L. Mao, E. Wang, Inorg. Chem. 42 (2003) 8519.
[11] (a) L. Carlucci, G. Ciani, M. Moret, D.M. Proserpio, S. Rizzato, Angew. Chem., Int. Ed. 39 (2000) 1506;
(b) H.F. Zhu, L. Li, T. Okamura, W. Zhao, W.Y. Sun, N. Ueyama, Bull. Chem. Soc. Jpn. 76 (2003) 761.
[12] (a) M.L. Hernández, M. Karmele Urtiaga, M. Gotzone Barandika, R. Cortés, L. Lezama, N. de la Pinta, M. Isabel Arriortua, T. Rojo, J. Chem. Soc., Dalton Trans. (2001) 3010;
(b) L. Carlucci, G. Ciani, D.M. Proserpio, S. Rizzato, Chem. Commun. (2000) 1319;
(c) M. Du, C.P. Li, X.J. Zhao, CrystEngComm 8 (2006) 552.
[13] (a) M.L. Hernández, M. Gotzone Barandika, M. Karmele Urtiaga, R. Cortés, L. Lezama, M. Isabel Arriortua, T. Rojo, J. Chem. Soc., Dalton Trans. (1999) 1401;
(b) Q.M. Wang, G.C. Guo, T.C.W. Mak, Chem. Commun. (1999) 1849;
(c) F.A. Almeida, J. Klinowski, Inorg. Chem. 43 (2004) 3948.
[14] T.L. Hennigar, D.C. MacQuarrie, P. Losier, R.D. Rogers, M.J. Zaworotko, Angew. Chem., Int. Ed. Engl. 36 (1997) 972.
[15] L.P. Wu, Y. Yamagiwa, T. Kuroda-Sowa, T. Kamikawa, M. Munakata, Inorg. Chim. Acta 256 (1997) 155.
[16] (a) X.J. Li, R. Cao, W.H. Bi, Y.Q. Wang, Y.L. Wang, X. Li, Z.G. Guo, Cryst. Growth Des. 5 (2005) 1651;
(b) X.J. Li, R. Cao, D.F. Sun, W.H. Bi, Y.Q. Wang, X. Li, M.C. Hong, Cryst. Growth Des. 4 (2004) 775.
[17] X.J. Li, R. Cao, Z.G. Guo, W.H. Bi, D.Q. Yuan, Inorg. Chem. Commun. 9 (2006) 551.
[18] CRYSTALCLEAR, Version 1.36, Molecular Structure Corporation Rigaku, MSC/SSI, 491, South Orem Boulevard, Orem, UT 84058, 2001.
[19] G.M. Sheldrick, SADABS: Program for Empirical Absorption Correction of Area Detector Data, University of Göttingen, Göttingen, Germany, 1996.
[20] G.M. Sheldrick, SHELXS-97: Program for Crystal Structure Solution, University of Göttingen, Göttingen, Germany, 1997.
[21] G.M. Sheldrick, SHELXS-97: Program for Crystal Structure Refinement, University of Göttingen, Göttingen, Germany, 1997.
[22] J.F. Ma, J.F. Liu, Y. Xing, H.Q. Jia, Y. H Lin, J. Chem. Soc., Dalton Trans. (2000) 2403.
[23] (a) Y. Liu, V.C. Kravtsov, D.A. Beauchamp, J.F. Eubank, M. Eddaoudi, J. Am. Chem. Soc. 127 (2005) 7266;
(b) Z. Ni, A. Yassar, T. Antoun, O.M. Yaghi, J. Am. Chem. Soc. 127 (2005) 12752.
[24] (a) H. Abourahma, B. Moulton, V. Kravtsov, M.J. Zaworotko, J. Am. Chem. Soc. 124 (2002) 9990;
(b) M. John Plater, M.R.S.J. Foreman, R. Alan Howie, J.M.S. Skakle, S.A. McWilliam, E. Coronado, C.J. Gómez-Garcäa, Polyhedron 20 (2001) 2293.

dithiocarbonato ligand [14]. Treatment of the latter complexes with phosphine or phosphite ligands gave the mixed carbonyl-phosphine or phosphite complexes Cp′Fe(CO)-(L)(κ*S*-S_2COEt) (L = PBu_3, PPh_3, $P(OEt)_3$, $P(OPh)_3$) [14].

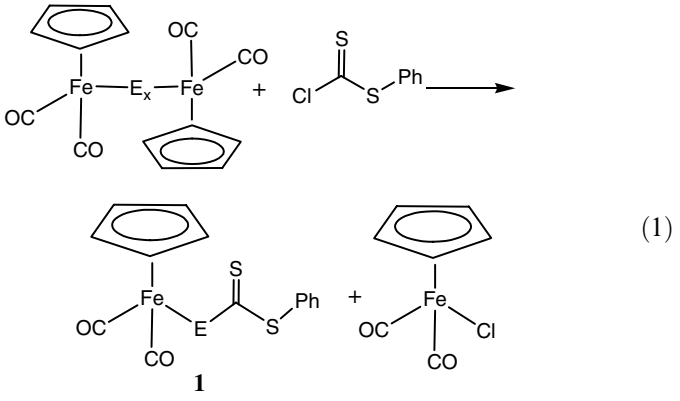
The trithiocarbonato complexes $CpFe(CO)_2$(κ*S*-SCS_2R) have been made by substitution of the iodide ligand of $CpFe(CO)_2I$ by the trithiocarbonate anions $RSCS_2^-$ (R = Me, Et, Ph) [15]. The chelated forms, CpFe(CO)-(κ^2*S*,*S*-S_2CSR) were obtained by photolysis of the dicarbonyl analogs [15].

In continuation of our work on the area of organoiron complexes containing thio- and selocarbonate ligands, this paper describes the syntheses and X-ray structures of iron trithiocarbonate and selenodithiocarbonate complexes.

2. Results and discussion

2.1. Synthesis and characterization

The trithio- and the dithioselenocarbonate complexes are obtained in good yields by the reactions of the iron chalcogenide complexes (μ-E_x)[$CpFe(CO)_2]_2$ (E = S; *x* = 2, 3. E = Se; *x* = 1) with PhSC(S)Cl, as shown in Eq. (1).

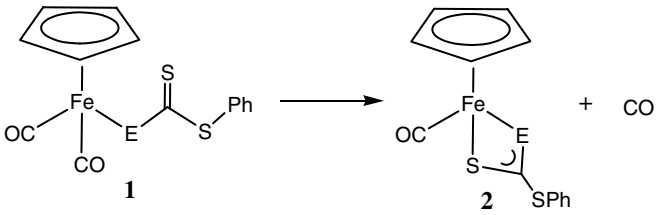


(1)

E= S (**a**), Se (**b**).

The orange complex **1a** and the brown complex **1b** are air stable as solids and in solution. They are soluble in common polar organic solvents but insoluble in hydrocarbons. The identities of **1** and **2** have been confirmed by IR, ^{1}H NMR spectroscopy, elemental analysis and crystal structure determination. The ^{1}H NMR spectra of **1** reveal one singlet in the range of 5.06–5.11 ppm for the Cp-proton resonances. These chemical shifts fall within the typical range reported for analogous thiocarbonato and selenocarbonato complexes of iron [8–11]. The protons of the phenyl group appear as two multiplets in the ratio of 3:2, as expected. The bands at 2050 and 2002 cm^{-1} in the IR spectrum of **1a** are due to *ν*(CO) of the two terminal carbonyl groups. For **1b**, these bands are found at lower wavenumbers (2040, 1990 cm^{-1}) due to stronger *σ*-donor and/or weaker π-acceptor properties of the selenodithiocarbonate ligand compared to the trithiocarbonate ligand. A similar shift for simple thiocarboxylato versus selenocarboxylato complexes has been reported [2–5].

Photolyzing THF solutions of complexes **1** in the absence of added ligand produces the chelate complexes CpFe(CO)(κ^2*E*,*S*-ECS_2Ph) (**2**) as shown in Eq. (2). The trithiocarbonate ligand of **2a** is bonded to the metal through the two sulfur atoms. In a similar fashion, the dithioselenocarbonate ligand of **2b** is bonded through the selenium and sulfur atoms. These dark red complexes are soluble in most organic solvents, including hydrocarbons.



E= S (**a**), Se (**b**).

(2)

Complexes **2** have been characterized by IR, ^{1}H NMR, as well as elemental analysis. The IR spectra of **2** in CH_2Cl_2 show the characteristic *ν*CO absorption in the range of 1947–1954 cm^{-1}. This absorption is similar to those of CpFe(CO)(κ^2*S*,*E*-EC(S)OR) (1941–1957 cm^{-1}) [10,11] and are lower than those of the starting complexes **1**. The latter difference might be attributed to the weak π-acid character of the chelate trithio- or selenodithio-carbonate ligand compared to that of carbonyl ligand. Complexes **2** exhibit ^{1}H NMR spectra showing a singlet in the range of 4.65–4.66 ppm for the Cp-protons. This chemical shift range is lower than that for the corresponding Cp resonances in complexes **1** and is similar to the analogous range reported for CpFe(CO)(κ^{2}S,E-EC(S)OR) complexes (4.63–4.69 ppm) [10,11].

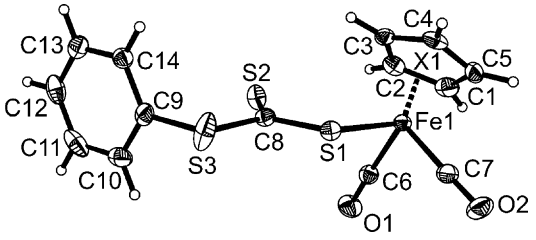


Fig. 1. An ORTEP representation of the structure of $CpFe(CO)_2$-(κ*S*-SCS_2Ph) (**1a**). The thermal ellipsoids are drawn at the 50% probability level.

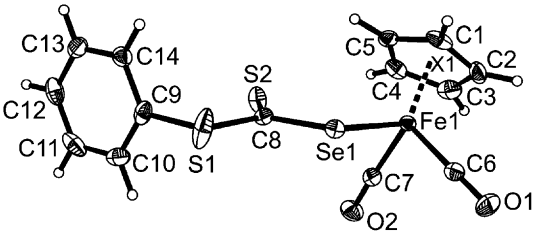


Fig. 2. An ORTEP representation of the structure of $CpFe(CO)_2$(κ*Se*-$SeCS_2$Ph) (**1b**). The thermal ellipsoids are drawn at the 50% probability level.

Table 1
Selected bond lengths (Å) and bond angles (°) in $CpFe(CO)_2(\kappa S\text{-}SCS_2Ph)$ (**1a**), $CpFe(CO)_2(\kappa Se\text{-}SeCS_2Ph)$ (**1b**) and $CpFe(CO)(\kappa^2 Se,S\text{-}SeCS_2Ph)$ (**2b**)

1a		**1b**		**2b**	
Fe–C1	2.0871(17)	Fe–C1	2.0928(17)	Fe–C8	2.070(11)
Fe–C2	2.1035(16)	Fe–C2	2.0830(19)	Fe–C9	2.063(12)
Fe–C3	2.1111(16)	Fe–C3	2.0840(18)	Fe–C10	2.095(14)
Fe–C4	2.0960(16)	Fe–C4	2.0985(17)	Fe–C11	2.045(14)
Fe–C5	2.0871(172)	Fe–C5	2.1072(17)	Fe–C12	2.051(14)
Fe–C6	1.7879(16)	Fe–C6	1.7783(18)	Fe–C13	1.732(14)
Fe–C7	1.7831(17)	Fe–C7	1.7834(17)	Fe–Se1	2.3872(18)
Fe–S1	2.2706(4)	Fe–Se1	2.3844(3)	Fe–S1	2.310(2)
S1–C8	1.7232(16)	Se1–C8	1.8908(3)	Se1–C1	1.800(9)
S2–C8	1.6379(16)	S2–C8	1.6293(16)	S1–C1	1.734(9)
S3–C9	1.7675(18)	S1–C8	1.7568(17)	S2–C1	1.736(8)
S3–C8	1.7733(16)	S1–C9	1.7692(14)	S2–C2	1.792(10)
C6–O1	1.134(2)	C6–O1	1.137(2)	C13–O1	1.129(16)
C7–O2	1.134(2)	C7–O2	1.133(2)		
C6–Fe–C7	94.16(8)	C6–Fe–C7	94.21(8)	C13–Fe–Se1	95.8(4)
C7–Fe–S1	89.86(6)	C7–Fe–Se1	89.26(6)	C13–Fe–S1	92.8(4)
C6–Fe–S1	89.93(5)	C6–Fe–Se1	88.95(6)	Se1–Fe–S	77.63(7)
C8–S1–Fe	110.37(7)	C8–Se1–Fe	106.98(5)	Se1–C1–S1	112.8(5)
C9–S3–C8	103.73(7)	C8–S1–C9	104.03(8)	Se1–C1–S2	121.8(5)
S2–C8–S1	128.91(9)	S2–C8–Se1	128.14(10)	S1–C1–S2	125.4(5)
S2–C8–S3	123.37(10)	S2–C8–S1	124.59(10)	C1–S2–C2	102.2(4)
S1–C8–S3	107.72(8)	S1–C8–Se1	107.26(8)		

2.2. Crystal structures

The structures of complexes **1a** and **1b** are shown in Figs. 1 and 2, respectively. Selected bond distances and angles for these complexes are collected in Table 1. These complexes display a three-legged piano-stool configuration at Fe. The Fe–C(Cp) and Fe–C(CO) bond lengths in **1a** and **1b** are similar to those found in $CpFe(CO)_2$-containing complexes [5,8–10]. The Fe–S bond distance of 2.2677(4) Å in **1a** is comparable to that found in $CpFe(CO)_2SX$ complexes [$X = SO_2CCl_3$ (2.2803(13) Å), CO_2Et (2.2675(10) Å), CO-2-$C_6H_4NO_2$ (2.266(1) Å), C(S)O–C_6H_4Cl (2.2765(5) Å)] [5,8,16,17]. The Fe–Se bond distance in **1b** of 2.3839(4) Å is also comparable to that found in $CpFe(CO)_2SeY$ complexes [$Y = SO_2Ph$ (2.394(3) Å), CO_2Et (2.3829(8) Å), C(S)O-4-C_6H_4Cl (2.3985(2) Å)] [7,10,18].

The crystal structure of **2b** is presented in Fig. 3. Selected bond distances and angles of **2b** are listed in Table 1. The Fe–Se bond distance in **2b** is 2.3872(18) Å, which is similar to that of **1b.** The Fe–S bond length in **2b** of 2.310(2) Å is longer than that of **1a**. The Fe–CO bond length of **2b** (1.732(14) Å) is shorter than the corresponding lengths observed for **1a** and **1b** in line with higher π-back donation from the Fe-*d* orbitals to the empty π*-orbital of CO in **2b** compared to those of **1a** and **1b**.

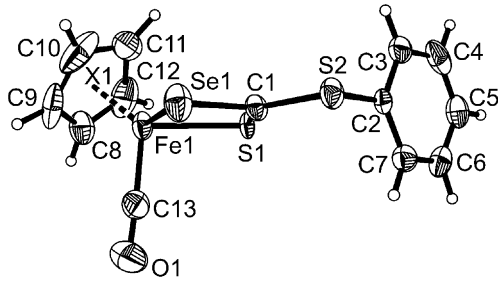


Fig. 3. An ORTEP representation of the structure of $CpFe(CO)(\kappa^2 Se,S\text{-}SeCS_2Ph)$ (**2b**). The thermal ellipsoids are drawn at the 30% probability level.

3. Experimental

3.1. General

All manipulations were performed using standard Schlenk and inert-atmosphere techniques under an argon atmosphere. Diethyl ether, hexane, and benzene were dried over sodium and benzophenone, and were freshly-distilled under nitrogen prior to use. Dichloromethane was heated under reflux over P_2O_5, and was freshly-distilled under nitrogen prior to use. The compounds $(\mu\text{-}S_x)[CpFe(CO)_2]_2$ [1] and $(\mu\text{-Se})[CpFe(CO)_2]_2$ [2] were prepared by previously published procedures. The iron dimer $[CpFe(CO)_2]_2$, the PhSC(S)Cl precursor, selenium, and sulfur were purchased from Aldrich and were used as received.

Nuclear magnetic resonance (NMR) spectra were recorded on a Bruker 400 MHz spectrometer. Chemical shifts are given in ppm relative to TMS at 0 ppm. Infrared (IR) spectra were recorded on a Nicolat-Impact 410 FT-IR spectrometer. Elemental analyses of C, H and S were performed in the Institute of Organic Chemistry, Vienna University, Austria. Melting points were reported on an electrothermal melting point apparatus and are uncorrected. The photolytic reactions were carried out using a conventional tungsten lamp (100 W).

3.2. General procedure for the preparation of $CpFe(CO)_2(\kappa E\text{-}ECS_2Ph)$ (**1**)

A solution of PhSC(S)Cl (1.20 mmol) in 10.0 mL of diethyl ether was dropwise added to a solution of the iron chalcogenides $(\mu\text{-}E_x)[CpFe(CO)_2]_2$ (1.00 mmol) in 50.0 mL of diethyl ether. The deep red solution was stirred for 2 h under protection of light. The solution was stripped to dryness and the resulting solid was redissolved in a minimum amount of dichloromethane and introduced to a silica gel column made up in hexane. Elution with hexane removes the unreacted PhSC(S)Cl. A red band of the product was eluted with diethyl ether:hexane solution (1:1 v:v ratio), followed by another red band which was also collected and identified as $CpFe(CO)_2Cl$. The products $CpFe(CO)_2(\kappa E\text{-}ECS_2Ph)$ were recrystallized from dichloromethane/hexane.

3.2.1. $CpFe(CO)_2(\kappa S\text{-}SCS_2Ph)$ (**1a**)

Yield: 85%. m.p. = 57–59 °C. IR (CH_2Cl_2, cm^{-1}): 2044(s), 1999(s) ($\nu_{C\equiv O}$). ^1H NMR ($CDCl_3$): δ 5.11 (s, 5H, C_5H_5); 7.45 (m, 3H, C_6H_5); 7.55 (m, 2H, C_6H_5). *Anal.* Calc. for $C_{14}H_{10}FeO_2S_3$: C, 46.42; H, 2.78; S, 26.55. Found: C, 46.31; H, 2.62; S, 26.80%.

3.2.2. $CpFe(CO)_2(\kappa Se\text{-}SeCS_2Ph)$ (**1b**)

Yield: 83%. m.p. = 130–131 °C. IR (CH_2Cl_2, cm^{-1}): 2038(s), 1993(s) ($\nu_{C\equiv O}$). ^1H NMR ($CDCl_3$): δ 5.14 (s, 5H, C_5H_5); 7.48 (m, 3H, C_6H_5); 7.56 (m, 2H, C_6H_5). *Anal.* Calc. for $C_{14}H_{10}FeO_2S_2Se$: C, 41.10; H, 2.46; S, 15.67. Found: C, 41.00; H, 2.36; S, 15.71%.

3.3. General procedure for the preparation of $CpFe(CO)(\kappa^2 E,S\text{-}ECS_2Ph)$ (**2**)

A THF solution (30 mL) of $CpFe(CO)_2(\kappa E\text{-}ECS_2Ph)$ (0.25 mmol) was irradiated under a stream of N_2 for 15 min. The colour of the reaction mixture turned from orange to dark red. The volatile components were removed by vacuum and the resulting solids were purified by column chromatography using silica gel columns. The columns were eluted with (1:5 v:v ratio) of CH_2Cl_2/hexane to separate the products, which were subsequently recrystallized by slow evaporation of hexane solutions.

3.3.1. $CpFe(CO)(\kappa^2 S,S\text{-}SCS_2Ph)$ (**2a**)

Yield: 75%. m.p. = 121–122 °C. IR (CH_2Cl_2, cm^{-1}): 1955(s) ($\nu_{C\equiv O}$). ^1H NMR ($CDCl_3$): δ 4.64 (s, 5H, C_5H_5); 7.30 (m, 3H, C_6H_5); 7.51 (m, 2H, C_6H_5). *Anal.* Calc. for $C_{13}H_{10}FeOS_3$: C, 46.71; H, 3.02; S, 28.78. Found: C, 46.31; H, 3.09; S, 27.80%.

3.3.2. $CpFe(CO)(\kappa^2 S,Se\text{-}SeCS_2Ph)$ (**2b**)

Yield: 78%. m.p. = 98–99 °C. IR (CH_2Cl_2, cm^{-1}): 2049(s) ($\nu_{C\equiv O}$). ^1H NMR ($CDCl_3$): δ 4.61 (s, 5 H, C_5H_5); 7.48 (m, 3H, C_6H_5). *Anal.* Calc. for $C_{13}H_{10}FeOS_2Se$: C, 40.96; H, 2.64; S, 16.83. Found: C, 41.25; H, 2.62; S, 15.21%.

Table 2
Crystallographic data and refinement details for $CpFe(CO)_2(\kappa S\text{-}SCS_2Ph)$ (**1a**), $CpFe(CO)_2(\kappa Se\text{-}SeCS_2Ph)$ (**1b**), and $CpFe(CO)(\kappa^2 Se,S\text{-}SeCS_2Ph)$ (**2b**)

Compound	**1a**	**1b**	**2b**
Empirical formula	$C_{14}H_{10}FeO_2S_3$	$C_{14}H_{10}FeO_2S_2Se$	$C_{13}H_{10}FeOS_2Se$
Formula weight	362.25	409.15	381.14
Crystal size (mm)	$0.60\times0.40\times0.40$	$0.40\times0.30\times0.28$	$0.30\times0.14\times0.12$
Crystal system	monoclinic	monoclinic	monoclinic
Space group	$P2_1/c$	$P2_1/c$	$P2_1/c$
Volume ($Å^3$)	1464.56(7)	1488.16(9)	1423.32(11)
Z	4	4	4
Unit cell dimensions			
a (Å)	10.3722(3)	10.3802(4)	14.6540(6)
b (Å)	12.0814(4)	12.0808(4)	8.1790(4)
c (Å)	11.7589(3)	11.9470(4)	12.8734(5)
β (°)	96.320(1)	96.626(2)	112.710(2)
Index ranges	$-14\leqslant h\leqslant 14$, $-17\leqslant k\leqslant 17$, $-16\leqslant l\leqslant 16$	$-14\leqslant h\leqslant 14$, $-17\leqslant k\leqslant 17$, $-16\leqslant l\leqslant 16$	$-17\leqslant h\leqslant 17$, $-9\leqslant k\leqslant 9$, $-15\leqslant l\leqslant 15$
Data/parameters	4302/181	4348/181	2504/163
$F(000)$	736	808	752
D_{calc} (g/cm^3)	1.643	1.826	1.779
μ (mm^{-1})	1.453	3.735	3.893
λ (Å)	0.71073	0.71073	0.71073
R_1^a	0.0267	0.0218	0.0817
wR_2^b	0.0796	0.0551	0.2780
Goodness-of-fit[c]	1.036	1.016	1.057

[a] $R_1 = \sum\|F_o| - |F_c\|/\sum|F_o|$.
[b] $wR_2 = \{\sum[w(F_o^2 - F_c^2)^2]/\sum[w(F_o^2)^2]\}^{1/2}$.
[c] Goodness-of-fit $= \{\sum[w(F_o^2 - F_c^2)^2]/(n-p)\}^{1/2}$, where n is the number of reflections and p is the total number of parameters refined.

3.4. X-ray crystal structure analysis

Details of data collections and structure refinement for complexes **1a**, **1b** and **2b** are collected in Table 2. Single crystals suitable for X-ray structure determination were obtained by re-crystallization of **1a** and **1b** from THF/hexane mixtures, and from hexane for **2b**. X-ray diffraction measurements were performed on X8APEXII CCD diffractometer with graphite monochromated Mo Kα radiation, $\lambda = 0.71073$ Å at 100, 100 and 296 K for **1a**, **1b** and **2b**, correspondingly. Single crystals were positioned at 40 mm from the detector and 3099, 1936 and 1487 frames were measured, each for 5, 5 and 40 s over 1° scan width. The data were processed using SAINT software while absorption corrections were performed using the program SADABS [16]. The structures were solved by direct methods and refined by full-matrix least-squares techniques. Non-hydrogen atoms were refined with anisotropic displacement parameters. H atoms were placed in geometrically-calculated positions and were refined as riding atoms in subsequent least-squares model refinements. The isotropic thermal parameters were estimated to be 1.2 times the values of the equivalent isotropic thermal parameters of the atoms to which hydrogens were bonded. The following computer programs were used: structure solution, SHELXS-97 [17]; refinement, SHELXL-97 [18]; molecular diagrams, ORTEP [19]. Scattering factors were taken from the literature [20].

4. Supplementary material

CCDC 632056, 632055 and 632057 contain the supplementary crystallographic data for **1a**, **1b** and **2b**. These data can be obtained free of charge via http://www.ccdc.ac.uk/conts/retrieving.html, or from the Cambridge Crystallographic Data Centre, 12 Union Road, Cambridge CB2 1EZ, UK; fax: (+44) 1223-336-033; or e-mail: deposit@ccdc.cam.ac.uk.

Acknowledgements

M.E. thanks the Jordan University of Science and Technology for financial support and the Alexander von Humboldt Foundation for a scholarship. We thank Prof. V. Arion for his help in the crystallographic analysis.

References

[1] M.A. El-Hinnawi, A. Ajlouni, J. Organomet. Chem. 332 (1987) 321.
[2] M.A. El-Hinnawi, A. Ajlouni, J. Abu-Nasser, K. Powell, H. Vahrenkamp, J. Organomet. Chem. 359 (1989) 79.
[3] M.A. El-Hinnawi, M. El-khateeb, I. Jibril, S.T. Abu-Orabi, Synth. Reac. Inorg. Met.-Org. Chem. 19 (1989) 809.
[4] I. Jibril, O. Abu Nimreh, Synth. React. Inorg. Met.-Org. Chem. 26 (1996) 1409.
[5] M. El-khateeb, H. Goerls, W. Weigand, Inorg. Chim. Acta 360 (2007) 705.
[6] M. El-khateeb, A. Shaver, A.-M. Lebuis, J. Organomet. Chem. 622 (2001) 293.
[7] M. El-khateeb, T. Obidate, Polyhedron 20 (2001) 2393.
[8] M. El-khateeb, K.J. Asali, A. Lataifeh, Polyhedron 22 (2003) 3105.
[9] M. El-khateeb, Inorg. Chim. Acta 357 (2004) 4341.
[10] M. El-khateeb, K.J. Asali, A. Lataifeh, Polyhedron 25 (2006) 1695.
[11] M. El-khateeb, Polyhedron 25 (2006) 1387.
[12] M. Moran, I. Cuadrado, J.R. Masaguer, J. Losada, C. Foces-Foces, F.H. Cano, Inorg. Chim. Acta 143 (1988) 59.
[13] M. Moran, I. Cuadrado, C. Munoz-Reja, J.R. Masaguer, J. Losada, J. Chem. Soc., Dalton Trans. (1988) 149.
[14] M. Moran, I. Cuadrado, J.R. Masaguer, J. Losada, J. Organomet. Chem. 352 (1987) 255.
[15] R. Bruce, G. Knox, J. Organomet. Chem. 6 (1966) 67.
[16] Bruker Programs, SAINT-NT, version 6.0; SAINT, version 7.12A; SADABS, version 2.10; XPREP, version 5.1, Bruker AXS Inc., Madison, WI, USA, 2003.
[17] G.M. Sheldrick, SHELXS97: Program for Crystal Structure Solution, University of Göttingen, Germany, 1997.
[18] G.M. Sheldrick, SHELXL97: Program for Crystal Structure Refinement, University of Göttingen, Germany, 1997.
[19] C.K. Johnson, Report ORNL-5138, OAK Ridge National Laboratory, OAK Ridge, TN, 1976.
[20] International Tables for X-ray Crystallography; vol. C. Kluwer Academic Press, Dodrecht, The Netherlands, 1992. Tables 4.2.6.8 and 6.1.1.4.

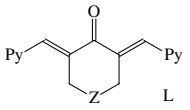


Chart 1.

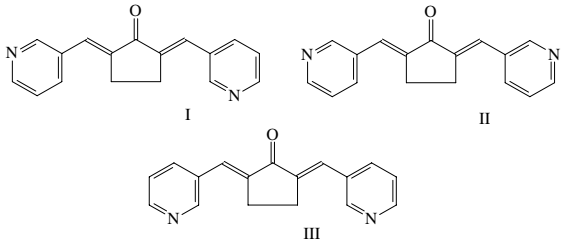


Fig. 1. Possible conformations of L.

symmetry of the donating units L and the geometries of the vacant metal coordination sites [5]. Recently, we focused our attention to ligands which feature conjugated π-systems with aromatic and heteroaromatic linker units because such species accept a planar conformation [6]. As a consequence thereof, any M_2L_2 square can approve such a structure, which would allow efficient stacking of the metallomacrocycles in the solid state. Furthermore, we are currently working on the exploitation of novel π-conjugated *exo*-polydentate molecules, *i.e.* heterocyclic dienones and derivatives of cyclic ketones (Chart 1). Their use as multidentate ligands in coordination chemistry is being developed as well [7]. The reaction behavior, and hence coordination ability, of the latter type of ligands relates to the nature of their central linking unit Z and the size of the central ring (Chart 1). These parameters together with the pyridine isomers 2-, 3-, or 4-py allow the control of the orientation of the donating vector of the respective pyridyl ligands ($Z = (CH_2)_n$, NR) (Chart 1 and Fig. 1).

Recently, it was shown that in the reaction of 3-pyridyl cyclohexanones with silver salts, such as [$AgNO_3$], coordination polymers are formed, which preferably possess conformation I in the solid state (Fig. 1) [7]. We report herein the straightforward synthesis of a discrete 26-membered disilver macrocyclic molecule by treatment of 2,5-bis[(*E*)-(3-pyridyl)methylene]cyclopentanone with [$AgClO_4$] as well as our attempts on the synthesis of analogous compounds with [AgOTf] and [$AgNO_3$].

2. Experimental

Safety notes! Silver perchlorate should be handled with appropriate precaution because perchlorates are known for their potential hazardous behavior.

2,5-Bis[(*E*)-(3-pyridyl)methylene]cyclopentanone (**2**) was synthesized according to reference [8]. All other chemicals were purchased from commercial suppliers and were used without further purification.

2.1. Synthesis

2.1.1. $[Ag(C_{17}H_{14}N_2O)(CH_3CN)]_2(ClO_4)_2$

An acetonitrile solution (3 mL) containing [$AgClO_4$] (**1**) (26 mg, 0.125 mmol) was layered with a chloroform solution containing **2** (33 mg, 0.125 mmol) (3 mL) at room temperature. The flask was protected from sunlight by aluminum foil. After 3 days yellow crystals suitable for single X-ray diffraction studies could be isolated by decanting the supernatant solution. Mp = 240–242 °C. ^{1}H NMR (300 MHz, DMSO-d_6, 27 °C, δ, ppm, J, Hz): 2.07 (3H, s), 3.15 (4H, br s), 7.50 (2H, s), 7.54 (2H, dd, $J = 4.8$, $J = 7.9$), 8.13 (2H, br d, $J = 7.9$), 8.60 (2H, dd, $J = 1.4$, $J = 4.8$), 8.90 (2H, br d, $J = 1.4$). Microanalysis: Calc. for $C_{19}H_{17}AgClN_3O_5$: C, 44.69; H, 3.36; N, 8.23. Found: C, 44.68; H, 3.38; N, 8.21%. IR (KBr disc) ν/cm^{-1}: 2253 (CN), 1684 (C=O), 1627 (C=C), 1601, 1585, 1563 (py); 1145, 1090 (ClO_4). ESI-TOF (MeCN): m/z 147.9/149.9 $[AgMeCN]^+$, 189.0/191.0 $[Ag(MeCN)_2]^+$, 263.0 $[HL]^+$, 410.0/412.0 $[AgLMeCN]^+$, 631.1/633.1 $[AgL_2]^+$, 369.0/371.0 $[Ag_2L_2]^{2+}$, 839.0/841.0 $[Ag_2L_2ClO_4]^+$.

2.2. X-ray single-crystal analysis

$C_{19}H_{17}AgClN_3O_5$ 510.68 g/mol, triclinic, $P\bar{1}$, $a = 9.8310(5)$ Å, $b = 10.0617(5)$ Å, $c = 10.3599(5)$ Å, $\alpha = 92.9340\ (10)°$, $\beta = 102.4490(10)°$, $\gamma = 101.3510(10)°$, $V = 976.40(8)$ Å^3, $Z = 2$, $D_{calc} = 1.737$ g/cm^3, μ(Mo Kα) = 1.206 mm^{-1}. 11 233 reflections collected, 4006 unique, $R_{int} = 0.0241$, 301 parameters and 156 restraints. Final R indices: R_1 ($I > 2\sigma(I)$) = 0.0299, wR_2 ($I > 2\sigma(I)$) = 0.0819 and R_1 (all data) = 0.0336, wR_2 (all data) = 0.0844. Largest difference in peak and hole: 0.673 and −0.486 e Å^{-3}. Data were collected on a Bruker Smart 1k CCD diffractometer at $T = 298(2)$ K using Mo Kα radiation ($\lambda = 0.71073$ Å). Reflections were collected in the θ scan modus in 0.4° steps and an exposion time of 20 s per frame. The structure was solved by direct methods using SHELXS-97 [9]. The structure was refined by full-matrix least-squares procedures on F^2 using SHELXL-97 [9]. All non-hydrogen atoms were refined anisotropically. All hydrogen atom positions were refined using a riding model. All hydrogen atom positions have been selected from the difference Fourier map and refined freely.

3. Results and discussion

Layering an acetonitrile solution containing [$AgClO_4$] (**1**) with 2,5-bis[(*E*)-(3-pyridyl)methylene]cyclopentanone (L) (**2**) dissolved in chloroform produced yellow crystals of [$Ag(MeC{\equiv}N)(OClO_3)(\mu\text{-}L)]_2$ (**3**) at room temperature after three days. Applying the same procedure to [AgOTf] and [$AgNO_3$] led to a yellow powder for the former salt (product **4**) and to a mixture of pale yellow and colorless powders for the later one. From the crystals of **3** a single-crystal X-ray structure determination was performed. The molecular view of **3** is shown in Fig. 2. Selected bond

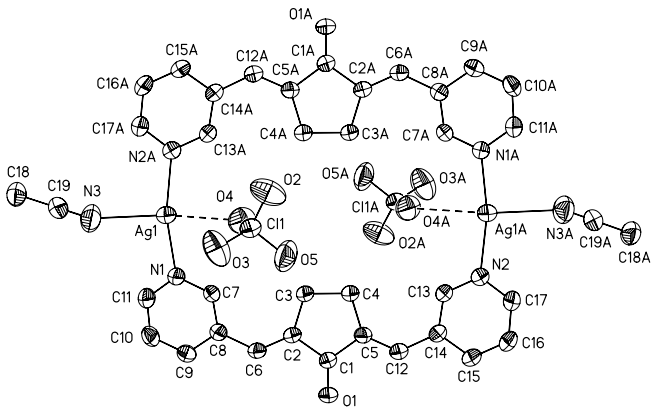


Fig. 2. ORTEP plot (50% probability level) of **3** with the atom numbering scheme (the hydrogen atoms and one position of the disordered $OClO_3^-$ anion are omitted for clarity). Selected bond distances (Å) and angles (°): Ag1–N2A 2.199(2), Ag1–N1 2.208(2), Ag1–N3 2.573(3), C2–C6 1.334(3), C5–C12 1.342(3), C6–C8 1.469(3), C12–C14 1.466(3) N2–Ag1A 2.199(2), Ag1–O4 2.829(14) N1–Ag1–N2A 163.87(8), N2A–Ag1–N3 98.38(10), N1–Ag1–N3 93.98(10), Ag1–N3–C19 153.9(3).

distances (Å) and angles (°) are given in the legend of Fig. 2.

Complex **3** forms a 26-membered disilver macrocycle in the solid state, with the asymmetric unit containing half of the ring (Fig. 2). The other half of the metallomacrocycle is generated by an inversion center positioned halfway between the two silver(I) centers, Ag1 and Ag1A. The perchlorate anion was refined on two disordered positions with occupation factors of 0.369 and 0.631 (Cl1–O5).

In **3** the silver(I) ions possess coordination number 4, showing a distorted tetrahedral environment from two *trans*-oriented pyridyl units of neighboring ligand molecules, a coordinated acetonitrile molecule and a weakly-coordinated perchlorate counter-anion (Fig. 2). The M_2L_2 fragment of **3** is almost planar (r.m.s. deviation 0.142 Å). The vectors of the donating nitrogen lone-pair of electrons are not parallel oriented, the deviation angles from the normal is 16.16°. Thus, the distances between the nitrogen centers N1–N2A and N2–N1H is 10.35 Å, which is shorter than the distance between Ag1 and Ag1A within the dimer (10.85 Å). The Ag1–O4 separation is 2.829(14) Å, indicating that the perchlorate group is weakly coordinated by O4 to the silver(I) center (Fig. 2). This structural motif is common for silver(I) perchlorate molecules with coordinated nitrogen ligands [10].

In the solid state the dimeric **3** forms infinite 2D layers in which distinct molecules are linked to each other via a system of short C–H···O contacts (Fig. 3). These contacts mainly consist of interactions between the perchlorate oxygen atoms and the hydrogen atoms of pyridines (range of distances 2.42–2.59 Å) as well as acetonitrile methyl groups (2.65 Å). Short contacts also exist between the carbonyl oxygen atoms and the hydrogen atoms in the gamma position of the pyridine rings (2.52 Å).

The shortest interlayer distances (2.38 Å) are those between the carbonyl atom O1 and the hydrogen atom

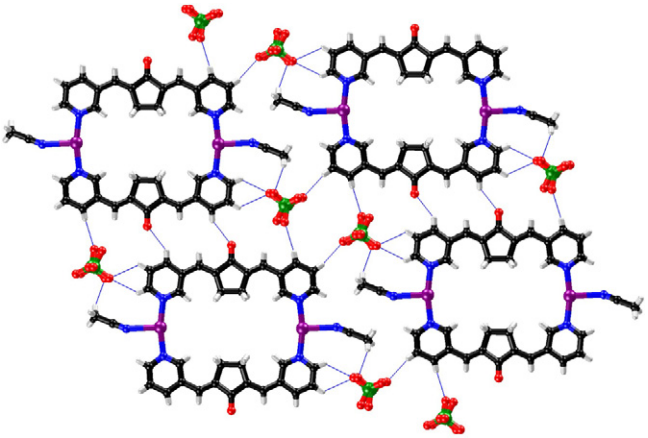


Fig. 3. C–H···O contacts within the layer formed by dimers of **3** in the crystal.

H16 of an adjacent acetonitrile molecule. The neighboring layers stack with such an offset so as to allow accommodation of perchlorate anions, which additionally interact with dimers of **3** via C–H···O contacts (2.39–2.65 Å, Fig. 4). An interlayer contact exists between the silver atom Ag1 and the methyne hydrogen atom H10 (3.25 Å), the appropriate Ag1···C10 distance is 3.28 Å. As a result thereof, infinite narrow channels filled with perchlorate anions run through the crystal along the crystallographic *c* axis (Fig. 5).

To define the geometrical conditions for the solid state [2+2] photochemical transformations, one has to analyze the distance in between and the mutual orientation of the reactive double bonds. If these data are in accord with the so-called principle of "minimal atomic and molecular movements" (parallel double bonds with the distance between carbon atoms <4.2 Å [11a]), there is a possibility for topochemical reactions. Although this approach was criticized recently [11b], we did analyze the relevant data from the X-ray study of **3**. Due to the interlayer offset in

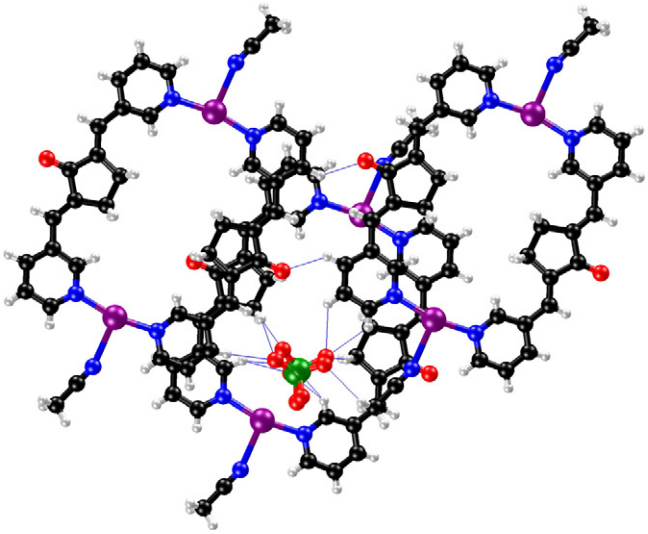


Fig. 4. C–H···O contacts within adjacent layers in **3**.

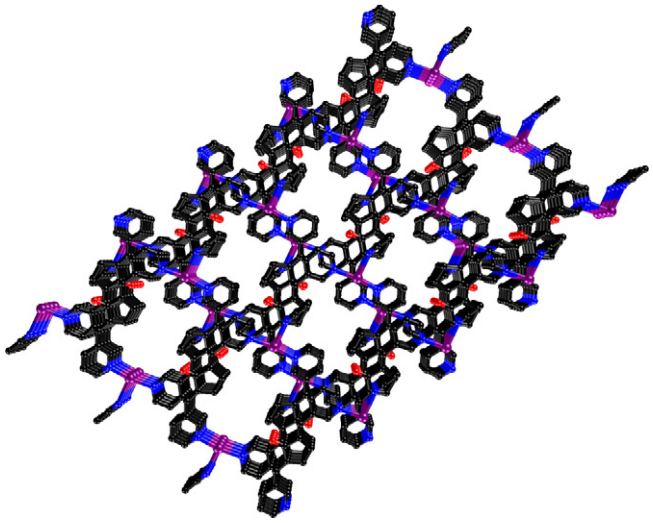


Fig. 5. A view of the structure of **3** along the crystallographic *c* axis (perchlorate anions and hydrogen atoms are omitted).

crystals of **3**, the closest dimethylencyclopentanone units lie in a head-to-tail orientation with the carbonyl carbon C1 superimposed on the tertial olefinic carbon C2 (C1···C2B 3.55 Å, symmetry transformations $-x+1$; $-y+2$; $-z+1$). The distances between possible cycloaddition partner double bonds are 3.95 Å (C2···C5) and 3.99 (C6···C12); the angle between the bonds is 48.3°. According to Schmidts' rules [11a], the solid state topochemical [2+2]-cycloaddition reaction is prohibited, but if it did occur, the only product would be cyclobutane with C_2 symmetry (Fig. 6, structure b).

During the study of the photostability of *crystals* of **3**, we did not find any significant changes in the NMR spectra after 6 months of exposure to direct sunlight. At the same time, *solutions* of **3** in DMSO undergo rapid photochemical changes upon exposure to ambient light (*vide infra*). Due to the insolubility of **3** in common deuterated chlorinated organic solvents, the ^{1}H NMR spectra of the title compound were recorded in DMSO-d_6. It was found that the spectrum of **3** is identical concerning the chemical shifts and signal patterns with that of pure L, indicating that **3**

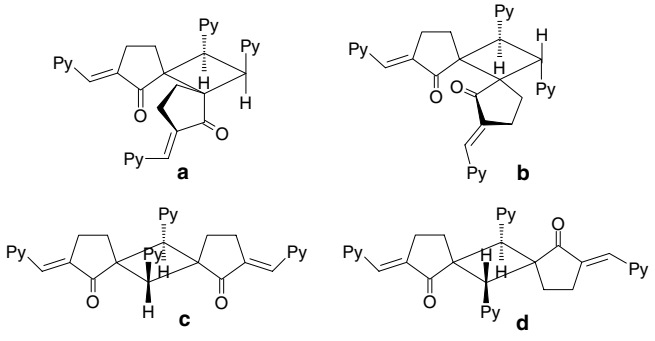


Fig. 6. Possible isomers which could be derived from [2+2]-cycloaddition reactions of **2**.

dissociates from its dimeric form (found in the solid state) into its starting components upon dissolution in DMSO. Alternatively, a fast equilibrium between free L, solvated metal ions $[Ag(N{\equiv}CMe)_n]^+$ and **3** (and several intermediate complexes) is possible [12].

ESI-TOF mass-spectrometric studies were carried out with **3** in acetonitrile solutions. Ion peaks at *m*/*z* 147.9/149.9 (100%), 189.0/191.0, 263.0 (53%), 410.0/412.0, 631.1/633.1, 369.0/371.0 and 839.0/841.0 are typical for the fragments $[AgMeCN]^+$, $[Ag(MeCN)_2]^+$, $[HL]^+$, $[AgLMeCN]^+$, $[AgL_2]^+$, $[Ag_2L_2]^{2+}$ and $[Ag_2L_2ClO_4]^+$, respectively, (L = 2,5-bis[(*E*)-(3-pyridyl)methylene]cyclopentanone). Obviously, in coordinating solvents such as acetonitrile complex **3** dissociates forming more stable silver–acetonitrile fragments, indicating that in **3** labile silver–nitrogen(pyridyl) bonds exist [12c,13].

During the ^{1}H NMR studies we observed spontaneous changes in spectra of those samples which were exposed to sunlight. The samples protected from light remained unchanged. Careful examination of the spectral changes allowed us to conclude that we are dealing with *trans*/*cis*-isomerization and [2+2] cycloaddition reactions of L in solution, because the same behavior was observed for the pure ligand L earlier [8]. The [2+2] cycloaddition process yields the only a cyclobutane product which possesses C_2 symmetry (Fig. 6, structure b). These findings prove again the dissociative nature of complex **3** in coordinating solvents.

Attempts to form products by the reaction of L and silver(I) triflate furnished the yellow powder **4**, whose composition, according to elemental analysis, was closer to $[Ag_2L_4(OTf)_2CHCl_3CH_3CN]$ rather than $[Ag_2L_2(OTzf)_2(CH_3CN)_2]$, as in **3**. NMR spectroscopy was of little use as no changes compared to the spectra of L and **3** were detected. However, in the NMR spectra of **4** we did not observe the peaks of chloroform or acetonitrile molecules; this would indicate that the experimental composition does not correspond to the compounds with the composition shown above, but rather to some products which do not contain both chloroform and acetonitrile. In ESI-TOF mass-spectra of **4** (DMSO) peaks corresponding to $[AgL_2]^+$ and $[Ag_2L_2ClO_4]^+$ were found. This indicates the possible presence of dimeric structural units within the whole structure of **4**. The coexistence of different products cannot be ruled out at this stage.

In conclusion, we found the cisoid conformation III (Fig. 1) in **2** clearly favors the formation of the bimetallic macrocycle **3** rather than polymers in the solid state by a self-assembly process. It has been demonstrated by ^{1}H NMR spectroscopy and ESI-TOF mass-spectrometry that complex **3** dissociates to the starting components **1** and **2** in coordinating solvents. Light-driven reactivity of the rectangular metallocycle **3** in polar solvent solution has been investigated by ^{1}H NMR studies: on exposure to sunlight the organic component of the solution undergoes *trans*/*cis* isomerization and [2+2]-cycloaddition reactions.

4. Supplementary material

CCDC 623859 contains the supplementary crystallographic data for this paper. These data can be obtained free of charge via http://www.ccdc.cam.ac.uk/conts/retrieving.html, or from the Cambridge Crystallographic Data Centre, 12 Union Road, Cambridge CB2 1EZ, UK; fax: (+44) 1223-336-033; or e-mail: deposit@ccdc.cam.ac.uk.

Acknowledgement

A.A.M. Aly gratefully thanks the Alexander von Humboldt foundation for a generous fellowship. S.Z.V. and A.V.C. thank the RFBR for support (Grant #06-03-33077). H.L. is grateful to the Fonds der Chemischen Industrie for financial support.

References

[1] (a) D.L. Caulder, K.N. Raymond, Acc. Chem. Res. 32 (1999) 975;
(b) J.A.R. Navarro, B. Lippert, Coord. Chem. Rev. 222 (2001) 219;
(c) B.J. Holliday, C.A. Mirkin, Angew. Chem., Int. Ed. 40 (2001) 2022;
(d) M. Albrecht, Chem. Rev. 101 (2001) 3457;
(e) S.R. Seidel, P.J. Stang, Acc. Chem. Res. 35 (2002) 972;
(f) G.F. Swiegers, T.J. Malefetse, Coord. Chem. Rev. 225 (2002) 91;
(g) F. Würthner, C.-C. You, C.R. Saha-Moeller, Chem. Soc. Rev. 33 (2004) 133;
(h) O. Waldmann, M. Ruben, U. Ziener, P. Muller, J.M. Lehn, Inorg. Chem. 45 (2006) 6535.
[2] M. Fujita, Acc. Chem. Res. 32 (1999) 53.
[3] S. Leininger, B. Olenyuk, P.J. Stang, Chem. Rev. 100 (2000) 853.
[4] (a) C. Piguet, G. Bernardinelli, G. Hopfgartner, Chem. Rev. 97 (1997) 2005;
(b) A.N. Khlobystov, M.T. Brett, A.J. Blake, N.R. Champness, P.M.W. Gill, D.P. O'Neill, S.J. Teat, C. Wilson, M. Schroder, J. Am. Chem. Soc. 125 (2003) 6753.
[5] (a) B. Chatterjee, J.C. Noveron, M.J.E. Resendiz, J. Liu, T. Yamamoto, D. Parker, M. Cinke, C.V. Nguyen, A.M. Arif, P.J. Stang, J. Am. Chem. Soc. 126 (2004) 10645;
(b) N.L.S. Yue, M.C. Jennings, R.J. Puddephatt, Inorg. Chem. 44 (2005) 1125;
(c) M. Oh, C.L. Stern, C.A. Mirkin, Inorg. Chem. 44 (2005) 2647.
[6] (a) S.Z. Vatsadze, V.N. Nuriev, A.V. Chernikov, N.V. Zyk, Russ. Chem. Bull. 51 (2002) 1957;
(b) M.C. Aragoni, M. Arca, N.R. Champness, A.V. Chernikov, F.A. Devillanova, F. Isaia, V. Lippolis, N.S. Oxtoby, G. Verani, S.Z. Vatsadze, C. Wilson, Eur. J. Inorg. Chem. (2004) 2008;
(c) M. Al-Anber, T. Stein, S.Z. Vatsadze, H. Lang, Inorg. Chim. Acta 358 (2005) 50;
(d) M. Al-Anber, S.Z. Vatsadze, R. Holze, H. Lang, W.R. Thiel, J. Chem. Soc., Dalton Trans. (2005) 3632.
[7] S.Z. Vatsadze, M.A. Kovalkina, N.V. Sviridenkova, N.V. Zyk, A.V. Churakov, L.G. Kuz'mina, J.A.K. Howard, CrystEngComm. 6 (2004) 112.
[8] S.Z. Vatsadze, M.A. Manaenkova, N.V. Sviridenkova, N.V. Zyk, D.P. Krut'ko, A.V. Churakov, M.Yu. Antipin, J.A.K. Howard, H. Lang, Russ. Chem. Bull. Int. Ed. 55 (2006) 1184.
[9] G.M. Sheldrick, SHELXL-97, University of Göttingen, Germany, 1997.
[10] (a) K. Tani, T. Mihana, T.M. Yamagata, T. Saito, Chem. Lett. (1991) 2047;
(b) Y. Suenaga, T. Komiya, T. Kuroda-Sowa, M. Maekawa, M. Murakata, Inorg. Chim. Acta 308 (2000) 17.
[11] (a) G.M.J. Schmidt, Pure Appl. Chem. 27 (1971) 647;
(b) G. Kaupp, Cryst. Eng. Comm. 5 (2003) 117.
[12] (a) A.N. Khlobystov, N.R. Champness, C.J. Roberts, S.J. Tendler, C. Thompson, M. Schröder, CrystEngComm. 4 (2002) 426;
(b) C.-Y. Su, Y.-P. Cai, C.-L. Chen, M.D. Smith, W. Kaim, H.-C. zur Loye, J. Am. Chem. Soc. 125 (2003) 8595;
(c) C.-L. Chen, H.-Y. Tan, J.-H. Yao, Y.-Q. Wan, C.-Y. Su, Inorg. Chem. 44 (2005) 8510.
[13] A.N. Khlobystov, A.J. Blake, N.R. Champness, D.A. Lemenovskii, A.G. Majouga, N.V. Zyk, M. Schröder, Coord. Chem. Rev. 222 (2001) 155.

2. Experimental

2.1. General comments

All starting materials were obtained from Aldrich chemical company, and with the exception of 2-ethyl-4-methyl-imidazole which was vacuum distilled before use, all chemicals were used as received. Oleum was rated at 26–33% SO_3. NMR spectra of sulfonated imidazoles and their derivatives were recorded in D_2O on a 300 MHz Bruker instrument and referenced to DSS. Trimethylsilyl derivatives and other air sensitive materials were handled in the Dri-Lab or on the vacuum line, and their NMR spectra were obtained in a C_6D_6 solution referenced to TMS using the carbons or the residual protons of the solvent. Ethylene glycol ditosylate was prepared from ethylene glycol and tosyl chloride using pyridine as a base according to standard methods. Water was triple distilled. Potassium amide was prepared by a reaction of K with anhydrous NH_3 (l) in a Hoke SS316 cylinder. Fluorescence spectra in the visible region were obtained with an Ocean Optics spectrometer using a standard 4 W longwave UV lamp as an excitation source. Elemental analysis was done by Complete Analysis Laboratories, Parsippany, NJ.

2.2. Crystal structures

Single crystals of **1** through **5** were chosen and glued to the end of a thin glass fiber and transferred to a Bruker SMART 1K CCD diffractometer equipped with Mo Kα radiation and a graphite monochromator. Cell dimensions and other relevant crystal data were collected by standard methods [7] and are listed in Table 1. A semi-empirical absorption correction was obtained from equivalents in all cases.

2.3. 2-Methylimidazole-5-sulfonic acid (*1*)

2-Methylimidazole (1.529 g, 18.6 mmol) added to 10 mL oleum, with stirring, for 30 h. The mixture is neutralized with $BaCl_2$, forming a precipitate. After the sulfuric acid is fully precipitated out as $BaSO_4$, mixture is filtered, and the volume of the filtrate is reduced by vacuum evaporation. Crystals form overnight, and the supernatant is decanted and the crystals of $\mathbf{1}\cdot H_2O$ (1.15 g, 34%) dried under vacuum at room temperature. NMR: ^{1}H 2.67 (s, Me), 4.83 (N–H, exch), 7.64 (C–H); ^{13}C, 13.5 (Me), 121.2 (C–H), 136.2, 149.0.

2.4. 2-Ethyl-4-methylimidazole-5-sulfonic acid (*2*)

Oleum (59 mL, ~350 mmol SO_3) was slowly added to an Erlenmeyer flask containing 2-ethyl-4-methyl-imidazole (36 g, 327 mmol), while stirring on a hotplate. The temperature reached 110 °C from the exotherm, and was maintained at 125 °C for 1 h. NMR of an aliquot shows that the reaction is complete. The product was poured into H_2O in a large beaker, and brought to a boil. Barium carbonate (227 g) was slowly added until the mixture was alkaline to pH paper. The $BaCO_3$ must be added very slowly near the endpoint since the mixture has a tendency to froth over as the last acid is neutralized. After filtration

Table 1
Crystal data for **1**–**5**

	$\mathbf{1}\cdot H_2O$	**2**	$\mathbf{3}\cdot H_2O$	**4**	**5**
Formula	$C_4H_8N_2O_4S$	$C_6H_{10}N_2O_3S$	$C_6H_{11}LiN_2O_4S$	$C_6H_9AgN_2O_3S$	$C_{12}H_{26}N_2O_3SSi_2$
Formula weight	180.18	190.22	214.17	297.08	334.59
Space group	$P2_1/c$	$P2_1/n$	$P2_1/c$	$P\bar{1}$	$Pca2_1$
a (Å)	6.3958(4)	7.8613(8)	8.192(2)	9.361(3)	16.6758(19)
b (Å)	15.8472(11)	8.9819(9)	7.8227(19)	10.899(3)	8.8083(10)
c (Å)	7.6399(5)	12.0690(12)	14.474(4)	11.172(3)	12.2010(14)
α (°)	90	90	90	62.203(5)	90
β (°)	108.3560(10)	104.133(2)	95.374(4)	68.015(5)	90
γ (°)	90	90	90	66.857(5)	90
V (Å^3)	734.95(8)	826.39(14)	923.5(4)	901.2(4)	1792.1(4)
Z	4	4	4	4	4
Crystal color, habit	cls. prism	cls. prism	cls. needle	cls. plate	cls. chunk
ρ_{calc} (g cm^{-3})	1.628	1.529	1.540	2.190	1.240
μ (Mo Kα) (mm^{-1})	0.409	0.360	0.338	2.443	0.322
Temperature (K)	93(2)	93(2)	93(2)	93(2)	103(2)
Reflections collected	5647	6188	7077	9719	18906
Independent reflections [R_{int}]	1780 [0.0311]	1988 [0.0238]	2230 [0.0361]	3954 [N/A][a]	4977 [0.0209]
T_{min}/T_{max}	0.828/1.00	0.673/1.00	0.789/1.00	0.693/1.00	0.8352/0.8793
R (F) (%)	3.20	3.02	3.87	4.49	2.43
R (wF^2) (%)	9.10	8.13	9.15	11.5	6.23
Goodness-of-Fit on F^2	1.061	1.043	1.099	1.078	1.039
Largest difference in peak and hole (e Å^{-3})	0.491 and −0.437	0.414 and −0.333	0.504 and −0.480	1.827 and −1.762	0.334 and −0.215

cls. = colorless.

[a] This crystal was twinned so the data could not be averaged due to overlap of reflections.

and washing with H_2O, the filtrate was reacidified with H_2SO_4 until no more $BaCO_3$ precipitated, and then filtered again. After rotary evaporation, the filtrate was recrystallized from MeOH with H_2O added to increase solubility by allowing a hot concentrated solution to cool to room temperature, and crystals (41.77 g, 67%) were dried at 100 °C under vacuum. *Anal.* Calc. for $C_6H_{10}N_2SO_3$: C, 37.89; H, 5.30; N, 14.73. Found: C, 38.36; H, 5.25; N, 14.65%. NMR: ^{1}H 1.24 (t), 2.32 (s), 2.87 (q), 4.76 (N–H, exch) ; ^{13}C 11.6, 13.2 (Me), 21.5 (CH_2), 131.2, 131.9, 151.1 (C_3N_2 ring).

2.5. Lithium 2-ethyl-4-methylimidazole-5-sulfonate (*3*)

Lithium carbonate (1.13 g, 15.3 mmol) and **2** (2.89 g, 15.2 mmol) were combined in 25 mL H_2O and heated to boiling on a hotplate. Mixture was decanted hot from 0.49 g (recovered) undissolved Li_2CO_3, and vacuum evaporated to dryness, redissolved in cold H_2O, filtered, and the solvent removed affording 2.98 g **3** (100%), which was identified by its NMR spectrum. Lithium hydroxide was prepared by slow addition of Li powder (0.232 g, 33.4 mmol) to water under inert atmosphere and added to **2** (3.16 g, 16.6 mmol). A portion was crystallized by slow evaporation under N_2 affording crystals of $\mathbf{3 \cdot H_2O}$ that were used for the X-ray structure. NMR: ^{1}H 4.84 (N–H, exch), 2.63 (q), 2.34 (s), 1.20 (t); ^{13}C 152.2, 136.8, 131.2 (C_3N_2 ring), 23.5 (CH_2), 14.5 (Me), 12.2.

2.6. Silver 2-ethyl-4-methylimidazole-5-sulfonate (*4*)

The free acid **2** (21.70 g, 114 mmol) was dissolved in H_2O (250 mL) and Ag_2O (13.02 g, 56.2 mmol) was added with stirring. The mixture was mildly heated with a heat gun and five drops of NH_4OH were added to help dissolve the Ag_2O. The next day, 1 g (4.3 mmol) more Ag_2O was added and the mixture was heated to reflux for 3 h and filtered while hot. On cooling, a white solid crystallized and was isolated by filtration and dried under vacuum. Isolated yield, 28.70 g (85%). *Anal.* Calc. for $C_6H_9N_2SO_3Ag$: C, 24.26; H, 3.05; N, 9.43; Ag, 36.31. Found: C, 24.80; H, 2.92; N, 10.18; Ag, 37.86%. NMR: ^{1}H, 1.29 (t), 2.40 (s, Me), 2.81 (q, Et), 4.77 (N–H, exch); ^{13}C, 12.4 (br), 14.7, 24.6, 131.3 (br), 136.3 (br), 153.1.

3. Attempts to make dialkali metal salts

(a) In a 10 mL flask **2** (3.00 g, 15.7 mmol) was dissolved in a minimum amount of water and KOH (1.7 g, 30.3 mmol) was added. After rotary evaporation, the material was recrystallized from hot water/MeOH containing several grams of excess KOH, affording clear crystals (1.64 g). A crystal from this batch was used for the poor crystal structure that is in the supplementary material. (b) Reaction of **2** with NaOMe. Sodium spheres (0.75 g, 32.6 mmol) were loaded onto one side of an H-tube and **2** (3.00 g, 15.8 mmol) loaded onto the other side under vacuum. Dry MeOH condensed into both sides. Once the Na dissolved, the MeONa solution was added to the free acid. Initially a soluble salt was formed then a thick white solid precipitated. The solid would not dissolve in the MeOH even when hot. Mixture was filtered and the white solid removed and heated under dynamic vacuum to 100 °C affording an isolated yield of 2.93 g. *Anal.* Calc. for $C_6H_{8.5}N_2SO_3Na_{1.5}$: C, 32.29; H, 3.84; N, 12.55; Na, 15.45. Found: C, 31.25; H, 3.68; N, 11.63; Na 15.92%. *Anal.* Calc. for $C_6H_{8.45}N_2SO_3Na_{1.55}$: C, 32.13; H, 3.80; N, 12.49; Na, 15.89. Found: C, 31.25; H, 3.68; N, 11.63; Na 15.92%.

3.1. Bis(trimethylsilyl)-2-ethyl-4-methylimidazole-5-sulfonate (*5*)

In an H-tube, anhydrous ammonia (~100 mL) was condensed (at −78 °C) on the free acid **2** (8.92 g, 46.9 mmol) and potassium amide (5.20 g, 94.3 mmol) which causes a substantial volume expansion of the solid. After standing at −78 °C for an hour, it was allowed to warm up naturally. The mixture did not stir, but was agitated a bit by shaking. The NH_3 was allowed to slowly boil off over several hours through a bubbler attached to the vacuum line, and the remaining NH_3 was removed under dynamic vacuum by heating to 110 °C. THF (50 mL) and Me_3SiCl (13.5 mL) were added and the mixture was heated with stirring at 110 °C for 16 h. The mixture was filtered and the solids washed several times with recondensed solvent. A crude liquid product of 5.5 g was distilled under dynamic vacuum in an all-glass H-tube/still at a pot temperature of 140 °C, and the distillate was recrystallized from heptane twice and pumped dry, affording 2.71 g of a product that contains both mono and disilylated product (by NMR). Vacuum sublimation of the material to an ice-cooled cold finger from a flask heated in a 100 °C oil bath afforded 2.07 g (13%) **5**. NMR: (C_6D_6) 1H, −0.12, 0.40 (Me_3Si), 1.29 (t, Et), 2.29 (q, Et), 2.35 (s, Me); ^{13}C, 0.67, 1.55 (Me_3Si), 12.48, 12.65 (CH_3), 24.17 (CH_2), 135.09, 137.06, 153.68 (C_3N_2 ring).

3.1.1. Reaction of *4* with 1,4-dibromobutane

Reaction was conducted in both NMP and tetraglyme. (a) 1,4-dibromobutane (0.26 g, 1.2 mmol) and **4** (0.74 g, 2.5 mmol) were combined in 2 mL NMP under inert atmosphere and stirred for 3 d in a 120 °C oil bath. The NMP was removed under dynamic vacuum and the crude product mixed with water, filtered and the filtrate was vacuum evaporated to dryness. The crude product was mixed with hot ethanol, filtered, and the filter residue was dried under vacuum. A total of 0.14 g (27%) 6 isolated. NMR: (D_2O) ^{1}H, 4.76 (NH, exch), 4.29, 4.10* (br, CH_2–N), 2.92 (q, CH_2 on Et), 2.45*, 2.38 (s, Me), 1.88 (br, CH_2), 1.30 (t, CH_3) (* = minor isomer); ^{13}C, 151.48, 133.24, 131.93 (C_3N_2 ring), 48.17 (CH_2–N), 28.79 (CH_2), 20.99 (CH_2 on Et), 12.59, 12.54 (CH_3) (b) 1,4-dibromobutane (3.34 g, 15.5 mmol) and **4** (9.11 g, 30.7 mmol) were combined in

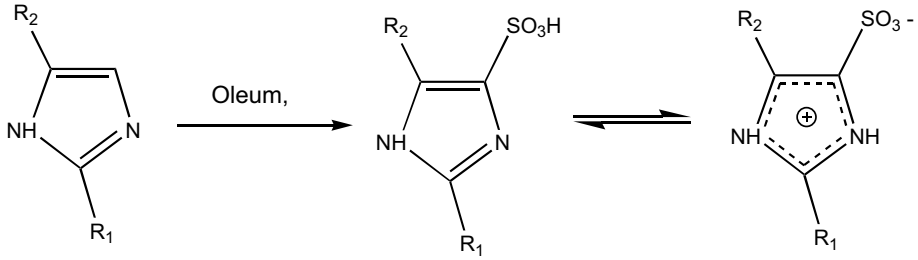
15 mL tetraglyme in a bulb with a Kontes valve under inert atmosphere and heated at 130 °C for 6 d. Water and HCl (to neutralize unreacted **4**) added, and the mixture filtered. The filtrate was vacuum evaporated and recrystallized from hot isopropanol. The solid was heated under vacuum to remove most of the solvent residue, but a small amount of tetraglyme remains. Yield 1.18 g (17%) *Anal.* Calc. for $C_{16}H_{26}N_4S_2O_6$: C, 44.23, H, 6.03, N, 12.89. Found: C, 44.91, H, 6.52, N, 11.63%.

4. Results and discussion

4.1. Synthesis

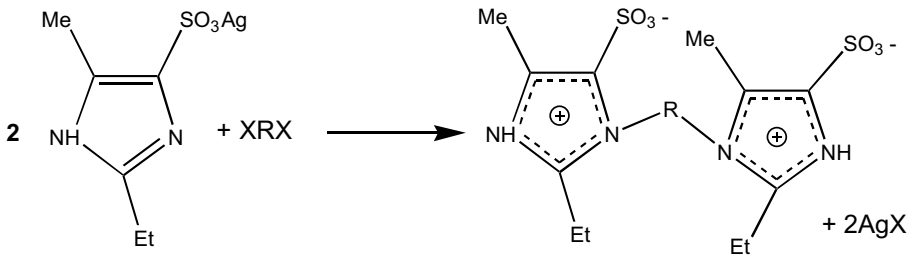
Both 2-methylimidazole and 2-ethyl-4-methyl imidazole are readily sulfonated with fuming sulfuric acid (oleum). The 2-methylimidazole appears to sulfonate in both the 4- and 5-positions according to NMR data, but the disulfonate readily decomposes to 2-methylimidazole-5-sulfonic acid (**1**) during isolation. The synthesis of **1**, but not its NMR or crystal structure, was reported previously [6e]. The imidazole sulfonic acids are readily isolated from the concentrated acid by formation of the barium salt, which is water soluble, and easily separated from the insoluble $BaSO_4$ by filtration, which is then reacidified to liberate the free acid [6]. The remainder of this work concentrates on the 2-ethyl-4-methyl substitution so as to avoid any complications from multiple sulfonation of the imidazole ring (see Scheme 1).

However, 2-ethyl-4-methylimidaziole-5-sulfonic acid (**2**) does not act as a nucleophile toward either $Br(CH_2)_4Br$ or $TosCH_2CH_2Tos$. Since these sulfonic acids actually exist as zwitterionic compounds (see crystal structures) this is not too surprising. One might expect a metal salt of these acids to react with an alkyl halide much more readily. The mono Li salt (**3**) and the Ag salt (**4**) of **2** are easily prepared in H_2O from the acid and Li_2CO_3 or Ag_2O, respectively. However, reaction between **4** and $Br(CH_2)_4Br$ or $TosCH_2CH_2Tos$ in H_2O or protic solvents such as dry MeOH result in the formation of **2** and AgBr. Substitution does take place very slowly at elevated temperatures in dry non-protic solvents in which **3** or **4** have some solubility, such as NMP or tetraglyme. The inability of sulfonated imidazoles to partake in many standard reactions of sulfonic acids (esterification, etc.) was noted previously [6e], but not explained, and is probably due to hydrolytic instability of the products or intermediates. Presumably, the attachment of an alkyl group onto a nitrogen atom by reaction of a sulfonate salt with an alkyl halide goes through an organosulfate intermediate, which apparently hydrolyzes in protic solvents before a nucleophillic substitution on an N atom can take place. By doing the substitution in NMP or tetraglyme, a linked dimer **6** can be prepared from a 2:1 reaction of **4** with a dihalide (Scheme 2). Naturally, three different isomers are formed since the $CH_2CH_2CH_2CH_2$ moiety can be bonded to either N1 or N3 on each imidazole ring. The isolated yields are relatively low. The reaction in NMP resulted in primarily the most symmetrical isomer (based on NMR) while doing the reaction in tetraglyme produced larger amounts of the other isomers. The reaction seemed to work better in NMP, possibly due to the much greater solubility of **4** in that solvent.



R_1 = Me, R_2 = H (**1**)
R_1 = Et, R_2 = Me (**2**)

Scheme 1.



R = $(CH_2)_4$ (**6**)

Scheme 2.

Multiple deprotonation of **2** also takes place, and is readily apparent in the NMR spectra of **2** combined with various amounts of base. Fig. 1 shows the ^{13}C chemical shifts of the aromatic carbons in **2** as different amounts of NaOH are added to its solution in D_2O, and the chemical shifts stabilize around 3 equiv. of base. The NMR spectra of all the monoalkali metal salts (Li, Na, K) in D_2O are virtually identical as is expected for an ionic compound. A titration with NaOH using a pH meter as indicator (supplementary material) shows an ordinary neutralization at 1 equiv. NaOH and a small, barely perceptible change at 1.5 equiv., but the pH meter may not have the range to observe a second neutralization. Products with full removal of both protons did not crystallize in water with an excess of KOH or LiOH or in methanol with NaOMe. In all cases, the maximum amount of deprotonation observed in the solid products is 3/2 as determined by a poor crystal structure of a $K_{3/2}$ salt (not shown, supplementary material), elemental analysis of an Na derivative, and the chemical shifts of the solid products in D_2O solution, which matched either the mono or the 3/2 equiv. shifts (supplementary material). Also, the product from reaction of Me_3SiCl with the solid product of **2** + 2 equiv. KOH, NMR clearly shows both a mono and disilylated product are present. The evidence seems to indicate that fully deprotonated species are present in strongly basic aqueous solutions, but do not crystallize from water. However a fully deprotonated product does appear to precipitate in liquid anhydrous NH_3 using 2 equiv. KNH_2 as the base, and K_2 salt prepared by this method was used to prepare the pure bis(trimethylsilyl) derivative (**5**). However, the yield is low, possibly due to low solubility of the intermediate K_2 salt in THF.

These materials all exhibit fluorescence under irradiation with a UV lamp. Fig. 2 shows the change in the emission spectrum of the 2-ethyl-4-methyl-imidazole ligand upon sulfonation. The emission spectra of the Ag salt **4** and the monopotassium salt have the same emission peaks as the free acid, with some changes in relative intensity. Although some Ag complexes are highly luminescent, all emissions from **4** can be attributed to ligand emission bands. Luminescent Ag complexes tend to have Ag···Ag bonding [8], which is not present in **4**.

4.2. Crystal structures

Crystal structures were obtained for **2**, **4**, and **5** and the monohydrates of **1** and **3**, the crystal data are listed in Table 1, and selected lengths and bond angles are listed in Tables 2 and 3. By convention, the imidazole atoms are numbered consecutively from N1 to C5, the carbon between the nitrogens is C2, and the sulfonate group in **1**–**5** always attached to C5. There is little variation in the C-S distances which range from 1.737(1) to 1.757(1) Å. By comparison, a sulfonamide attached to an imidaz-

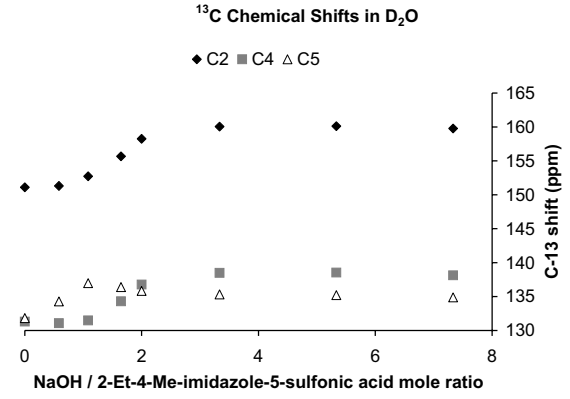


Fig. 1. ^{13}C chemical shifts of the aromatic carbons in **2** (in D_2O) with varying amounts of NaOH added.

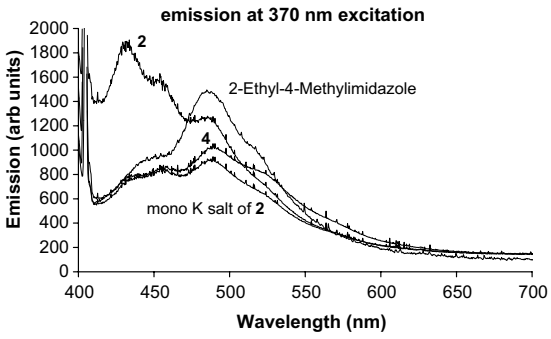


Fig. 2. Emission spectra of 2-ethyl-4-methyl-imidazole and several of its sulfonated derivatives. The absolute intensity is meaningless as all spectra were not obtained with the same instrument and conditions. The peak at 404 nm is from the light source (longwave UV lamp).

Table 2
Selected bond lengths (Å) for the sulfonated imidazole skeleton in **1**–**5**

	1 · H_2O	**2**	**3** · H_2O	**4**	**5**
N1–C2	1.3293(19)	1.3282(18)	1.319(2)	1.332(7), 1.331(8)	1.3886(16)
C2–N3	1.3310(18)	1.3281(17)	1.362(2)	1.344(8), 1.352(8)	1.3109(16)
N3–C4	1.3814(18)	1.3897(16)	1.374(2)	1.382(8), 1.375(9)	1.3786(15)
C4–C5	1.3583(19)	1.3641(18)	1.368(3)	1.374(7), 1.374(8)	1.3711(17)
C5–N1	1.376(2)	1.3834(17)	1.390(2)	1.380(7), 1.381(7)	1.3960(15)
C5–S1	1.7562(14)	1.7570(13)	1.7534(18)	1.753(6), 1.748(6)	1.7367(12)
C2–C	1.483(2)	1.4903(19)	1.494(3)	1.488(8), 1.481(9)	1.4996(17)
C4–C		1.4880(18)	1.484(3)	1.477(8), 1.485(9)	1.4898(17)

Table 3
Selected bond lengths (Å) and angles (°) around M–O and M–N bonds in **3**–**5**

3 · H_2O
Li–O1 2.011(4)
Li#1–O(2) 1.922(3)
Li–O2#2 1.922(3)
Li–O1w 1.917(4)
Li–N1 2.050(4)
O1w–Li–O2#2 107.90(17)
O1w–Li–O1 116.87(17)
O2#2–Li–O1 108.47(16)
O1w–Li–N1 116.81(17)
O2#2–Li–N1 119.74 O1–Li–N1 85.58(14)
4
Ag1–N1A 2.097(5)
Ag1–N1B 2.106(5)
Ag2–O1A 2.359(5)
Ag2–O1B 2.398(4)
Ag2–O2B#3 2.401(4)
Ag2–O3A#4 2.473(4)
N1A–Ag1–N1B 168.36(19)
O1A–Ag2–O1B 98.51(16)
O1A–Ag2–O2B#3 131.87(16)
O1B–Ag2–O2B#3 112.41(16)
O1A–Ag2–O3A#4 128.18(15)
O1B–Ag2–O3A#4 102.84(16)
O2B#3–Ag2–O3A#4 80.77(15)
5
Si1–N3 1.8179(11)
Si2–O1 1.7174(10)
S1–O1 1.5470(9)
S1–O2 1.4298(12)
S1–O3 1.4332(10)

#1 $-x+1$, $y-1/2$, $-z+3/2$; #2 $-x+1$, $y+1/2$, $-z+3/2$. #3 $-x+1$, $-y$, $-z$; #4 $-x+2$, $-y$, $-z$.

ole ring in the 5-position has a C–S distance of 1.726(5) Å [9]. Several structures are known of imidazoles sulfonated at the 2-position, and the C–S distances in those compounds are slightly longer at 1.76(2), 1.788(4), and 1.822(2) Å [10].

Fig. 3 shows the asymmetric units of all compounds, except for the Ag complex **4** which is pictured in Fig. 5. The nearly equal C2–N bond distances show the positive charge to be equally delocalized over both N atoms in **1 · H_2O**, **2**, and **4** [10b]. In **3 · H_2O** the distance to N3 is significantly longer, possibly indicating that the positive charge is concentrated on N1, the nitrogen coordinated to the Li cation. In the bis(trimethylsilyl) derivative **5**, one silicon is bonded to N3 and the other one is attached to O1 of the sulfonate, and **5** is the only derivative that has no hydrogen or coordinate bonding between imidazole units. As the S1–O1 bond distance of 1.5470(9) Å shows that oxygen to be only singly bonded to the sulfur, and the N1–C2 bond distance is much less than the C2–N3 distance, **5** is really a trimethylsilyl ester and not a sulfonate. The Si–O and Si–N distances in **5** are normal for single bonds. In **1 · H_2O**–**4** the S–O bond lengths are nearly equal (range 1.4394(4)–1.471(5), average 1.455 Å) and similar to those in other zwitterionic sulfonates [10b], which shows that the negative charge is equally distributed over the O atoms (see Table 4).

In **1 · H_2O**–**4**, hydrogen bonding and metal coordination link the sulfonated imidazoles into extended networks. The imidazole sulfonate moieties are clearly directed by hydrogen bonding into puckered sheets and ribbons that have some similar features to BEDT-TTF fluorosulfonates [11] and several series of guanidinium sulfonates [12]. The high favorability of hydrogen bonding in these compounds may offer a partial explanation as to why the doubly deprotonated imidazole sulfonic acids are not crystallized from water, as such compounds would lack N–H bonds. In the hydrate of **1**, strong H bonds between the water and the sulfonates and the N–H groups link the lattice tightly in all 3 dimensions (Fig. 4). In contrast, **2**, which has more steric bulk and no coordinated water, has pleated two-dimensional sheets that are formed from by the strong NH···O–S hydrogen bonds. There are also short CH···O–S approaches (weak H-bonds) between these layers, that are considerably less than 2.62 Å, the H···O vdW contact value. Hydrogen bonds between CH and OS are present in **1 · H_2O** also. A fair amount of precedent exists for H-bonding between C–H moieties and sulfonates, as for example in 1-butylimidazolium-3-*n*-butanesulfonate which has seven weak H-bonds between the ring hydrogens and the sulfonate oxygens with O···H–C distances of 3.067(3)–3.515(3) Å [13]. In the monolithium salt (**3 · H_2O**), coordination of the Li cation to N1 and a O1 creates an asymmetric unit consisting of two fused 5-membered rings. These units form a puckered chain (Fig. 4) by linkage of the nearly tetrahedrally coordinated Li atoms to a neighboring sulfonate O2A and the water oxygen, and by H-bonding between a water hydrogen and O3. Additional H-bonding between O3 and another water hydrogen, and between O1 and a N–H on a neighboring asymmetric unit, link these chains in all three dimensions.

The Ag salt **4** (Fig. 5) has the most interesting structure of these compounds. Its asymmetric unit is a dimer, with a nearly linear Ag1 linking both N1 nitrogens, and Ag2 linking both sulfonate O1s resulting in a 10-membered ring. The Ag–N bond distances of 2.097(5) and 2.106(5) and nearly linear geometry are very similar to those reported (2.05(1)–2.12(1) Å, 167.6(1)–178.2(1)°) for a series of Ag(I) imidazolates where a negatively charged imidazole ion links Ag(I) ions into chains [14]. Since compounds where Ag^+ ions are coordinated to neutral organic nitrogen ligands can have a very similar geometry [15], one can not conclude much more than **4** displays the normal coordination mode for 2-coordinate silver. These dimers are additionally linked together through Ag2 and sulfonate oxygens O2B and O3A into 8-membered $(Ag–O–S–O)_2$ rings, which are joined through the Ag2 atoms into an infinite chain. The geometry around Ag2 is a highly distorted tetrahedron, with the angles ranging from 80.77(15) to 131.87(16)°. These

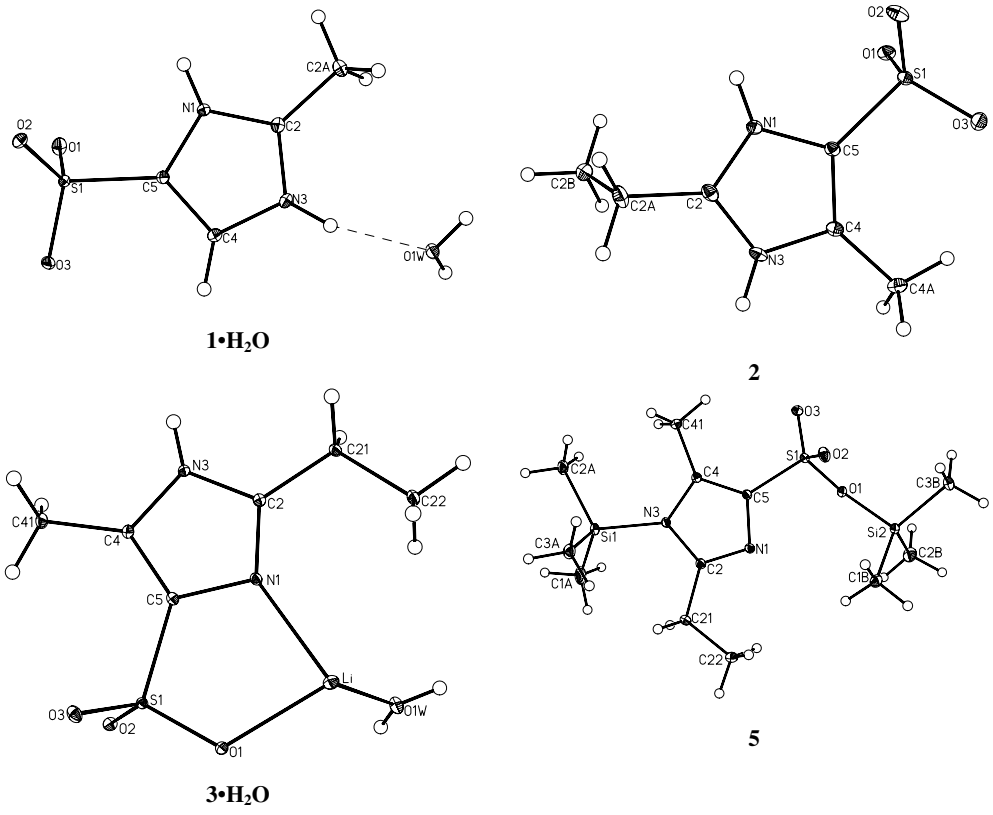


Fig. 3. Asymmetric units in $\mathbf{1 \cdot H_2O}$, **2**, $\mathbf{3 \cdot H_2O}$, and **5** with all ellipsoids drawn at the 50% level.

Table 4
Hydrogen bond geometry in **1**–**4**

D–H···A	d(D–H)	d(H···A)	d(D···A)	<(DHA)
1 · H$_2$O				
N1–H1A···O2#3	0.88	1.96	2.8104(16)	161.4
N1–H1A···O1w#4	0.88	2.58	3.0417(17)	113.4
N3–H3A···O1w	0.88	1.88	2.7327(16)	162.1
C4–H4A···O1#5	0.95	2.39	3.1338(18)	134.6
O1w–H1w1···O3#1	0.825(15)	1.983(15)	2.8075(15)	177(2)
O1w–H1w1···O3#2	0.814(15)	1.976(15)	2.7878(15)	174(2)
2				
N1–H1A···O1#1a	0.88	1.87	2.7451(15)	170.8
N3–H3A···O3#2a	0.88	1.98	2.7736(15)	149.2
C2B–H2BB···O1#2a	0.98	2.53	3.4251(19)	152.2
3 · H$_2$O				
O1w–H1w2···O3#3b	0.823(16)	2.157(16)	2.954(2)	163(2)
O1w–H1w1···O3#1b	0.817(16)	2.040(16)	2.857(2)	178(3)
N3–H3A···O1#4b	0.88	2.02	2.878(2)	165.9
4				
N3A–H3AA···O2B#3c	0.88	1.93	2.797(7)	167.0
N3B–H3BA···O2A#4c	0.88	2.00	2.815(6)	152.4

Symmetry transformations used to generate equivalent atoms: #1 $-x+1$, $y+1/2$, $-z+3/2$; #2 $-x+1$, $-y+1$, $-z+1$; #3 $-x$, $-y+1$, $-z+2$; #4 $x-1$, y, z; #5 $x+1$, y, z; #1a $-x$, $-y+1$, $-z+1$; #2a $x+1/2$, $-y+1/2$, $z+1/2$; #1b $-x+1$, $y-1/2$, $-z+3/2$; #2b $-x+1$, $y+1/2$, $-z+3/2$; #3 $x+1$, y, z; #4 x, $-y+1/2$, $z-1/2$; #3c $-x+1$, $-y$, $-z+1$; #4c $-x+1$, $-y+1$, $-z$.

chains are hydrogen bonded together by the H atoms on the N3s to the O2s of both sulfonates into a 3-dimensional network.

Silver sulfonate networks have received increased attention within the last decade [15,16]. Part of this is due to the observation that silver is an exception to the general rule that sulfonate is a weakly coordinating anion to transition metals, and partly a result of a search for new materials that reversibly intercalate various substances including alcohols and amines. As d^{10} ions have a lot of coordinative flexibility, a wide variety of structural motifs can be obtained with Ag. Eight-membered $(Ag–O–S–O)_2$ rings have been observed in a series of pyrazine complexes of Ag sulfonates [16d], and appear in Ag complexes of sulfosalicylic acid as well [16a]. Chains of linked eight-membered rings similar to those in **4** appear in the Ag salt of 4-pyridinesulfonic acid, which like **4**, also has 2-coordinate linear Ag atoms bonded to the ligand nitrogens [16b]. Most of the previously reported Ag sulfonate structures are layered, and their ability to intercalate alcohols and/or amines have been studied [16b,16e,16g]. A zwitterionic imidazolium propanesulfonate complex with silver salts is also linked into an extended network by bonding between the sulfonate and the Ag ions, and has been explored as an ion exchange membrane [17].

5. Conclusions

Contrary to previous belief, imidazoles sulfonated in the 4/5 position can engage in substitution reactions that make sulfonic esters or *N*-alkyl substituted products. However, the use of non-protic solvents and the rigorous

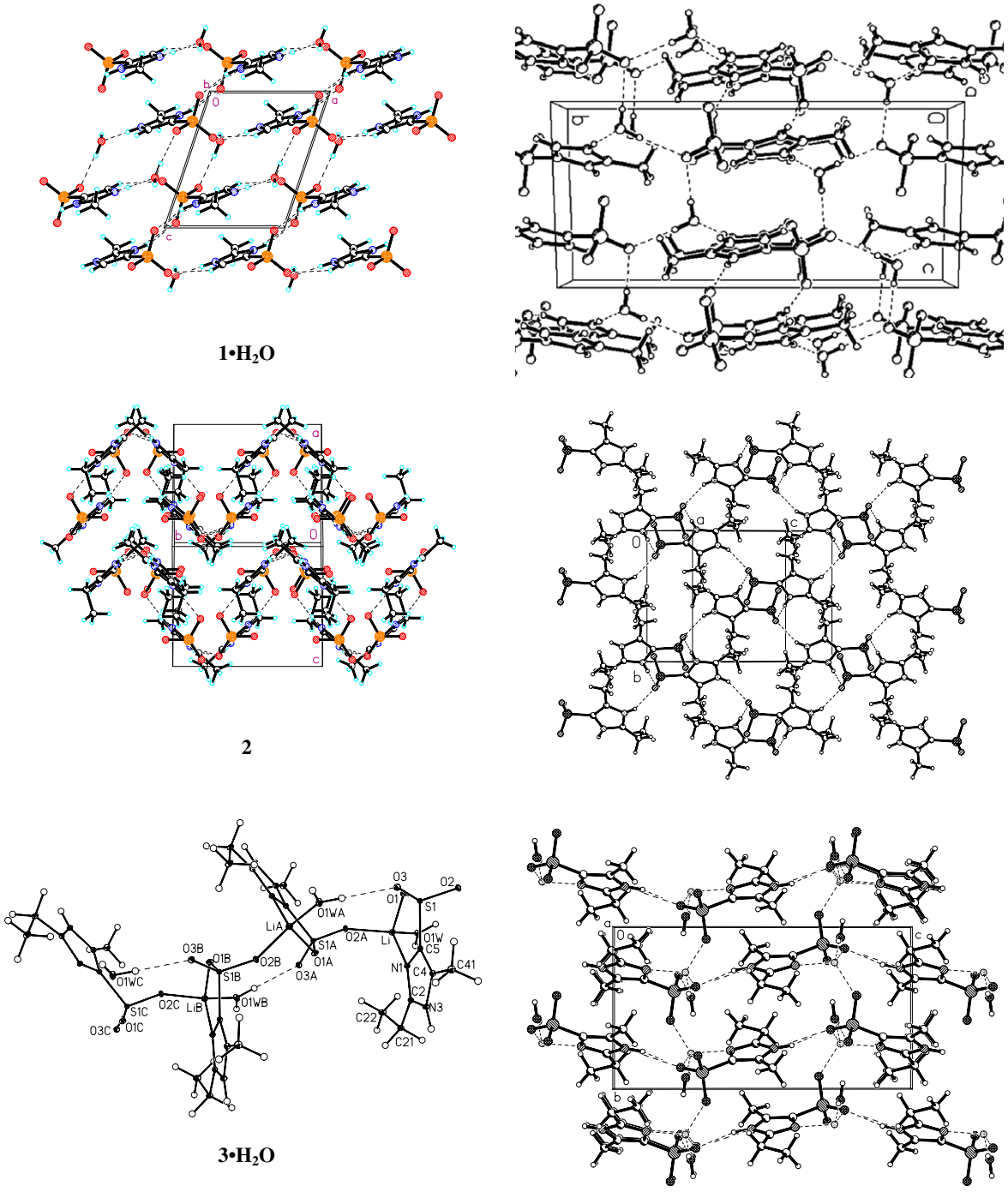


Fig. 4. Top: A view down the b axis of the packing in the crystal of **1** · H_2O (left), and a view down the *a* axis (right). Each water accepts and donates twice to form four strong hydrogen bonds which link the crystal in all three dimensions. Middle: A view of the packing in the crystal of **2** down a direction perpendicular to the 103 plane (left). A view down the 101 plane is shown on right. Bottom: Li cations quasi-tetrahedrally coordinated to two sulfonate O's, a ring N atom, and water. A view down a is shown on the right.

exclusion of water is necessary, and the substitution reactions are slow. Sulfonated imidazoles and their salts form hydrogen bonded networks in the solid state. The silver salt of 2-ethyl-4-methylimidazolesulfonic acid crystallizes in an elaborate 3-dimensional network structure, and shows that it may be possible to use sulfonated imidazoles as a building block for new metal-ligand frameworks.

Acknowledgements

We thank the ONR for financial support.

Appendix A. Supplementary material

CCDC 631530, 631531, 631532, 631533, 631534 and 642622 contain the supplementary crystallographic data

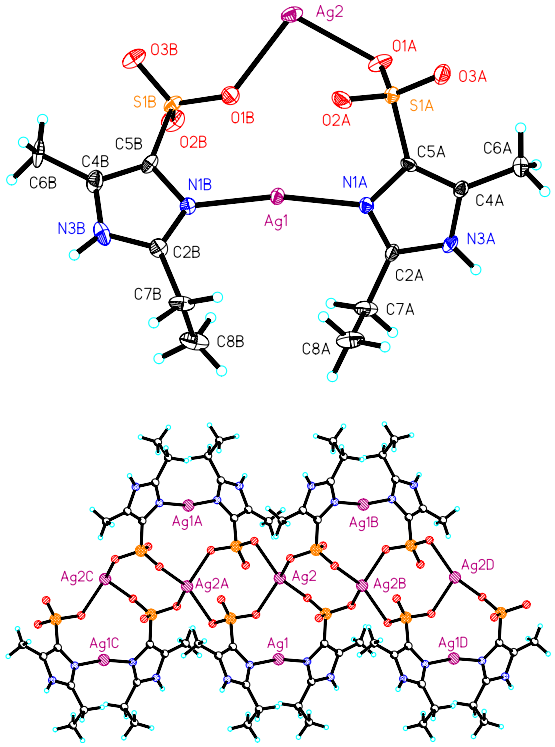


Fig. 5. Top: Asymmetric unit of crystal of **4**. One silver, Ag1, is quasi-linear, the other, Ag2, is quasi-tetrahedral in coordination. Bottom: The 4-coordinate silver atoms link through sulfonate groups to other 4-coordinate silver atoms, forming an infinite chain of eight-membered rings. Four such rings are shown above, forming part of a horizontal chain.

for **1** · H_2O, **2**, **3** · H_2O, **4**, **5** and potassium 3/2 salt. These data can be obtained free of charge via http://www.ccdc.cam.ac.uk/conts/retrieving.html, or from the Cambridge Crystallographic Data Centre, 12 Union Road, Cambridge CB2 1EZ, UK; fax: (+44) 1223-336-033; or e-mail: deposit @ccdc.cam.ac.uk. The cif files and other supplementary data can be obtained in the online version of this article, at doi:10.1016/j.poly.2007.04.024.

References

[1] Z. Zhu, A.G. Einset, C. Yang, W. Chen, G.E. Wnek, Macromolecules 27 (1994) 4076–4079.

[2] J. Cardoso, R. Manrique, M. Albores-Velasco, A. Huanosta, J. Poly. Sci. B Polym. Phys. 35 (1997) 479–488.

[3] Bartnikar, Eichorn (Eds.), Engineering Dielectrics, Volume IIA, ASTM special technical publication, 1983, p. 783.

[4] D.F. Mayers, E.T. Kaiser, J. Am. Chem. Soc. 90 (1968) 6192.

[5] L.L. Bennett, H.T. Baker, J. Am. Chem. Soc. 79 (1957) 2188.

[6] (a) R. Graeve, I. Okyayuz-Baklouti, D. Seiffge, US Patent 5, 232, 922, 1993;
(b) M.H. Fisher, W.H. Nicholson, R.S. Stuart, Can. J. Chem. 39 (1961) 1336;
(c) G.R. Barnes, F.L. Pyman, J. Chem. Soc. 130 (1927) 2711;
(d) I.E. Balaban, H. King, J. Chem. Soc. (1927) 1858;
(e) R. Forsyth, J. Moore, F.L. Pyman, J. Chem. Soc. 121 (1924) 919;
(f) F.L. Pyman, L.A. Ravald, J. Chem. Soc. 117 (1920) 1429;
(g) L. Light, F.L. Pyman, J. Chem. Soc. 121 (1922) 2626;
(h) A.P. Purdy, J. Luther, R. Gilardi, Abstracts of the 230th National Meeting of the American Chemical Society, August 28 (2005), ORGN 130.

[7] R.J. Butcher, J.C. Bottaro, R.D. Gilardi, Acta Crystallogr. E59 (2003) o1780–o1782.

[8] X. Liu, G.C. Guo, M.L. Fu, X.H. Liu, M.S. Wang, J.S. Huang, Inorg. Chem. 45 (2006) 3679.

[9] L.J. Guggenberger, Acta Crystallogr. B31 (1975) 13.

[10] (a) N. Kuhn, K. Eichele, M.Z. Walker, Anorg. Allg. Chem. 627 (2001) 2565;
(b) S. Chidambaram, G. Aravamudan, M. Seshasayee, Acta Crystallogr. C44 (1988) 898;
(c) N. Kuhn, K. Eichele, M. Walker, T. Berends, R. Minkwitz, Z. Anorg. Allg. Chem. 628 (2002) 2026.

[11] U. Geiser, J.A. Schlueter, A.M. Kini, H.H. Wang, B.H. Ward, M.A. Whited, J. Mohtasham, G.L. Gard, Synth. Met. 133–134 (2003) 401.

[12] (a) V.A. Russel, M.D. Ward, J. Mater. Chem. 7 (1997) 1123;
(b) V.A. Russel, M.D. Ward, New J. Chem. (1998) 149;
(c) J.A. Swift, A.M. Pivovar, A.M. Reynolds, M.D. Ward, J. Am. Chem. Soc. 120 (1998) 5887;
(d) V.A. Russel, M. Ward, Acta Crystallogr. B52 (1996) 209;
(e) V.A. Russel, M.C. Etter, M.D. Ward, Chem. Mater. 6 (1994) 1206.

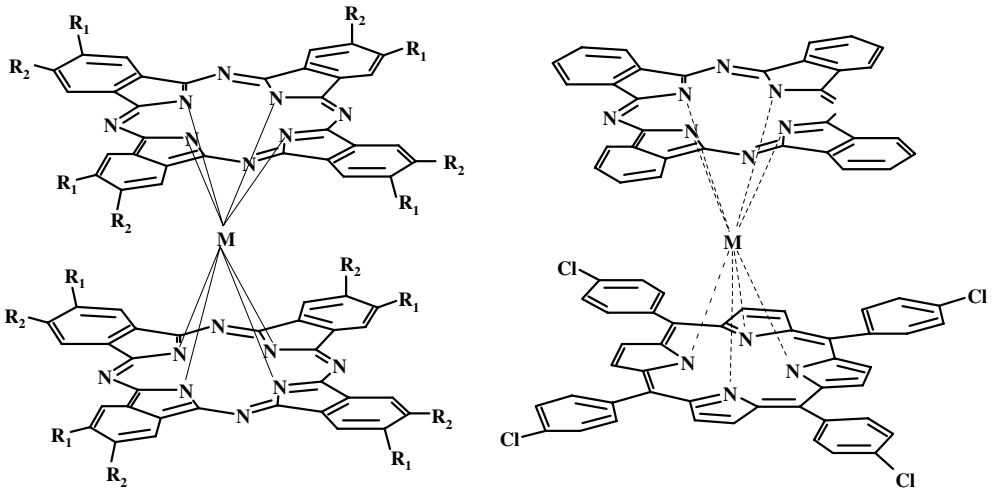
[13] J.M. Pringle, C.M. Forsyth, M. Forsyth, D.R. MacFarlane, Acta Crystallogr. E59 (2003) o1759.

[14] X. Huang, J. Zhang, X. Chen, Cryst. Growth Des. 6 (2006) 1194.

[15] F. Li, J. Ma, S. Song, J. Yang, H. Jia, N. Hu, Cryst. Growth Des. 6 (2006) 209–215.

[16] (a) J.-F. Ma, J. Yang, S.-L. Li, S.-Y. Song, H.-J. Zhang, H.-S. Wang, K.-Y. Yang, Cryst. Growth Des. 5 (2005) 807;
(b) L.M. May, G.K.H. Shimizu, Chem. Mater. 17 (2005) 217;
(c) N.J. Melcer, G.D. Enright, J.A. Ripmeester, G.K.H. Shimizu, Inorg. Chem. 40 (2001) 4641;
(d) F.-F. Li, J.-F. Ma, S.-Y. Song, J. Yang, Y.-Y. Liu, Z.-M. Su, Inorg. Chem. 44 (2005) 9374;
(e) A.P. Cote, M.J. Ferguson, K.A. Khan, G.D. Enright, A.D. Kulynych, S.A. Dalrymple, G.K.H. Shimizu, Inorg. Chem. 41 (2002) 287;
(f) A.P. Cote, G.K.H. Shimizu, Inorg. Chem. 43 (2004) 6663;
(g) G.K.H. Shimizu, G.D. Enright, C.I. Ratcliffe, G.S. Rego, J.L. Reid, J.A. Ripmeester, Chem. Mater. 10 (1998) 3282;
(h) F.-F. Li, J.-F. Ma, S.-Y. Song, J. Yang, H.-Q. Jia, N.H. Hu, Cryst. Growth Des. 6 (2006) 209.

[17] H. Lee, D.B. Kim, S.H. Kim, H.K. Kim, S.J. Kim, D.K. Choi, Y.S. Kang, J. Won, Angew. Chem., Int. Ed. Engl. 43 (2004) 3053.



Scheme 1. Schematic diagrams of bis(phthalocyaninato) rare earth complexes (a) $R_1 = R_2 = H$, $M(Pc)_2$, (b) $R_1 = R_2 = OC_6H_4OCH_3$, $M[Pc(MeOPhO)_8]_2$, (c) $R_1 \neq R_2 = H$, *tert*-C_4H_9, $M(TBPc)_2$ and mixed [tetrakis(4-chlorophenyl)porphyrinato](phthalocyaninato) rare earth complexes M(TClPP)(Pc).

the electronic absorption properties for bis(phthalocyaninato) rare earth compounds $M(Pc)_2$, $M(TBPc)_2$, $M[Pc(MeOPhO)_8]_2$ (M = Y, La...Lu except for Pm) and mixed [tetrakis(4-chlorophenyl)porphyrinato](phthalocyaninato) complexes M(TClPP)(Pc) (M = Y, La...Lu except for Pm), as shown in Scheme 1. The influence of the symmetry of bis(phthalocyaninato) rare earth molecules, the effects of ionic radius of the rare earth metal and the influence of substituent species (*tert*-butyl and 4-methoxyphenoxy groups) onto the peripheral benzene rings on the electronic absorption characteristics of sandwich-type compounds have also been tentatively studied.

2. Experimental

The bis(phthalocyaninato) rare earth double-decker complexes were prepared according to published procedures [6,7]. The mixed [tetrakis(4-chlorophenyl)porphyrinato](phthalocyaninato) rare earth complexes M(TClPP)(Pc) were prepared by means of phthalonitrile tetramerization method using M(TClPP)(acac) as template [8]. Their sandwich nature has been well established through a series of spectroscopic methods including IR, ^{1}H NMR, MCD, ESR, and in particularly the X-ray single crystal molecular structure analysis result [4,7–9]. High resolution mass spectroscopic and NMR characterization for these complexes confirm the purity of these materials. The UV–Vis and near-IR spectra were obtained on HP 8543 and Hitachi U-4100 Spectrophotometer.

3. Results and discussion

3.1. UV–Vis characteristics of bis(phthalocyaninato) rare earth complexes $M(Pc)_2$ (M = Y, La...Lu except Pm)

The electronic absorption spectral data of the unsubstituted phthalocyaninato double-deckers $M(Pc)_2$ in $CHCl_3$ are collected in Table S1. Due to the similar molecular structure among the whole series of bis(phthalocyaninato) lanthanide compounds, all these compounds (except Ce) show similar UV–Vis characteristics. Fig. 1 shows the UV–Vis spectra of La, Ce, Dy, and Lu double-deckers. It can be seen from Fig. 1 and Table S1 that all these homoleptic tervalent double-deckers (except La, Ce and Pr) exhibit a weak split Soret band with maxima around 320–327 and 334–343 nm, an intense Q band at 661–691 nm and a π-radical band at 454–491 nm [9,10]. Along with the decrease of rare earth ionic size from La to Lu, all the corresponding absorptions are systematically blue-shifted as shown in Table S1, clearly revealing the rare earth size effect. As for the unsubstituted bis(phthalocyaninato) complexes, a linear correlation exists between the energy of the Soret/Q bands and the M^{III} ionic radii as shown in Fig. 2. All these observations indicate that the interaction between the two rings becomes stronger as the ring-ring separation

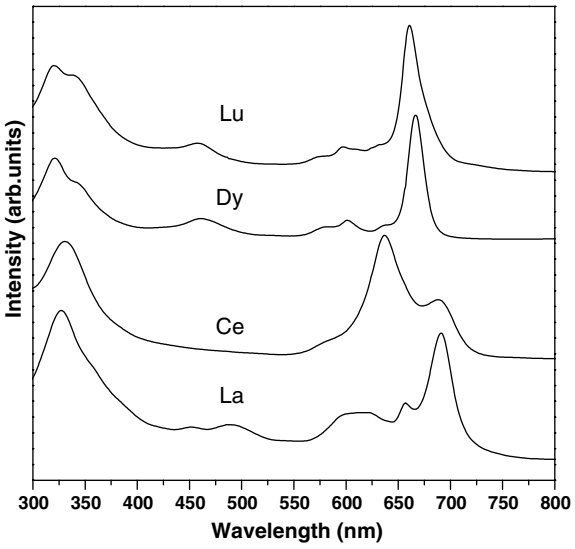


Fig. 1. Electronic absorption spectra of $M(Pc)_2$ (M = La, Ce, Dy and Lu) in $CHCl_3$.

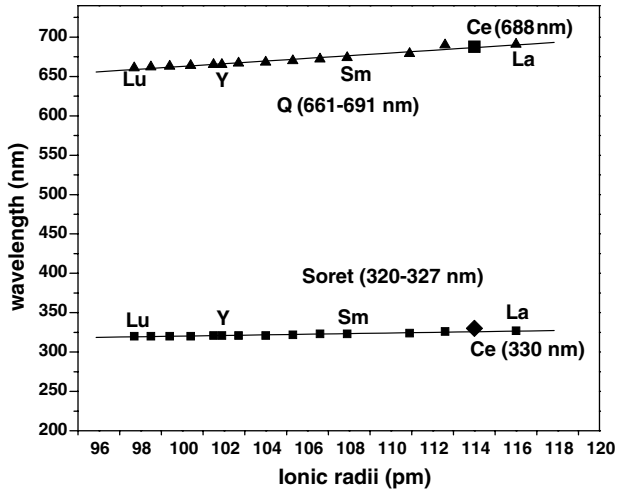


Fig. 2. Plot of wavelengths of the Soret and Q band absorptions of $M(Pc)_2$ as a function of the ionic radius of M^{III}/Ce^{IV}.

decreases because of the contraction of the radius of the rare earth metal ion [4]. Moreover, the extent of splitting of the Soret bands also undergoes a systematic change with this parameter.

Among the whole series of unsubstituted bis(phthalocyaninato) rare earth complexes, the cerium double-decker is particularly interesting. As indicated from the Raman and IR spectra [11,12], both the phthalocyanine rings exist as dianions in bis(phthalocyaninato) cerium $Ce(Pc^{2-})_2$ despite of the intermediate valence state between III and IV of the cerium, which differs from other analogues in the rare earth series in the form of $M^{III}(Pc^{2-})(Pc^{\cdot-})$ as shown in Fig. 1. The UV–Vis spectrum of $Ce(Pc^{2-})_2$ is very much resembling those of the reduced double-deckers of tervalent rare earths $[RE(Pc)_2]^-$ and $HRE(Pc)_2$ [9b,13], which in reverse demonstrates the dianion nature of the phthalocyanine rings in $Ce(Pc)_2$. The absence of the phthalocyanine π-radical anion around 454–491 nm clearly indicates the absence of a phthalocyanine radical anion in this double-decker. $Ce(Pc)_2$ shows strong band at 330 nm, which is attributed to the Soret band absorption of this complex. It is worth noting that $Ce(Pc)_2$ showed obvious Q-band splitting around 637 and 688 nm compared with those of tetravalent metal $M^{III}(Pc)_2$ (M = La...Lu, except Pm).

3.2. Electronic absorption spectra characteristics of bis[2,3,9,10,16,17,23,24-octakis(4-methoxyphenoxy)-phthalocyaninato] rare earth complexes M[Pc(MeO-PhO)$_8$]$_2$ (M = Y, La...Lu except Pm)

The electronic absorption spectra $M[Pc(MeOPhO)_8]_2$ were recorded in $CHCl_3$ and the data are summarized in Table S2. The spectral features resembled those of unsubstituted bis(phthalocyaninato) rare earth complexes [4,7], except that all the absorption bands were significantly red-shifted due to larger aromatic substituents.

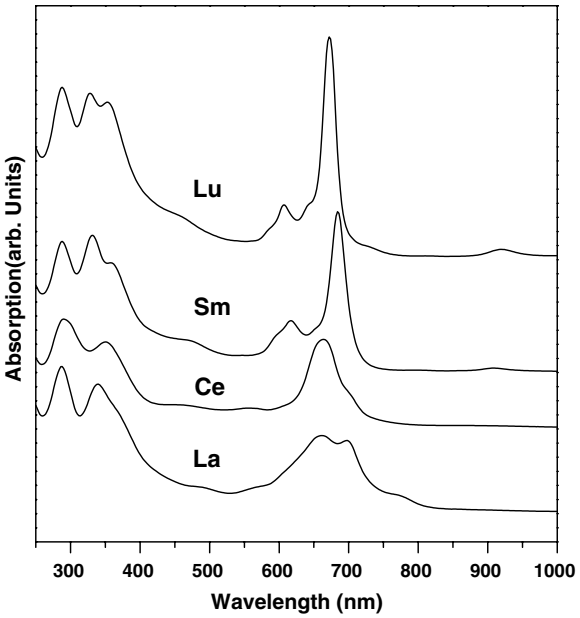


Fig. 3. Electronic absorption spectra of $M^{III}[Pc(MeOPhO)_8]$ (M = La, Ce, Sm and Lu) in $CHCl_3$.

Fig. 3 gives the electronic absorption spectra of La, Ce, Sm, and Lu sandwich complexes. It can be seen from Fig. 3 and Table S2 that all these homoleptic double-deckers (M = Y, La...Lu except Ce and Pm) exhibit split Soret band with maxima around 328–340 and 352–359 nm, which are analogous to those of related counterparts $M(Pc)_2$. Particularly, the introduction of electron-donating groups onto the Pc macrocycles induces a redshift for all the corresponding absorption bands compared with their unsubstituted analogs, indicating that the ring-ring interaction does not change significantly by introduction of these substituents onto the Pc macrocycle [4]. Both the Q band at 672–698 (M = Y, La...Lu except Ce and Pm) nm as the

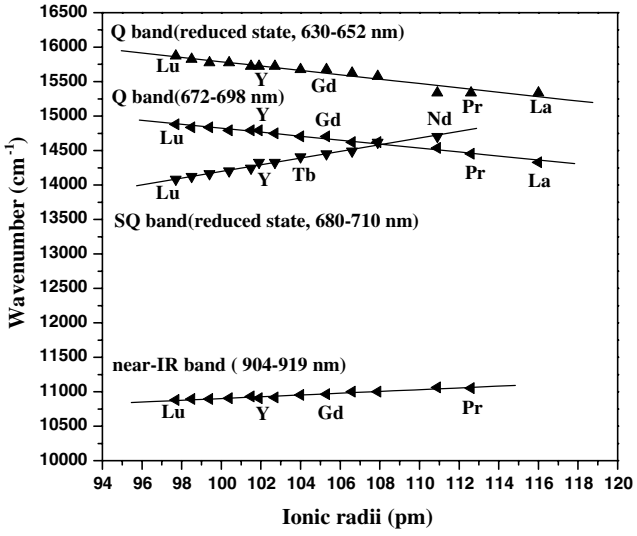


Fig. 4. Plot of wavenumbers of the three Q and one near-IR bands of $M^{III}[Pc(MeOPhO)_8]$ and $\{RE[Pc(MeOPhO)_8]_2\}^-$ as a function of the ionic radius of M^{III}.

most intense absorption band and the π-radical anion band at 455–485 nm as the very weak absorption band are shifted to the blue as the ionic radius of the tervalent metal cation decreases form La to Lu, as shown in Fig. 4. A similar trend was also observed for the broad near-IR band at 1542–2132 nm, which is characteristic of sandwich-type complexes with one unpaired electron in one of the rings [7,8], as shown in Fig. 5. Similar to the Pc and Por analogs [3,7,8], a linear correlation could be established between the wavenumbers of these absorptions and the rare earth ionic radii as shown in Fig. 4. All these observations indicate that the interaction between the two rings becomes stronger as the ring-ring separation decreases because of the contraction of the radius of the rare earth metal ion. Moreover, a weak near-IR absorption in the region of 904–919 nm from Pr to Lu also has a plot of the wavenumber against the ionic radius of M^{III} (except La and Ce), as illustrated in Fig. 4. It might be attributed to the electron transition from the semi-occupied HOMO orbital to the first unoccupied LUMO orbital [7]. It should be pointed out that the origins of the Near-IR absorptions at ca. 1257–1262 and 1419–1443 nm are not very clear. On the other hand, the compound of La[Pc(MeOPhO)$_8$]$_2$ shows a split Q band at 662 and 698 nm (Fig. 3), which is different from those of other complexes due to its unique electronic structure($4f^0 5d^1 6s^2$) [7].

Upon addition of hydrazine hydrate to solutions of the whole series (except Ce) in $CHCl_3/CH_3OH$ (5:1), the absorption spectra were remarkably changed and the resulting spectra could be attributed to the monoanions $\{M[Pc(MeOPhO)_8]_2\}^-$, in which both macrocycles are dianionic [7,8]. The spectral data for these anions are summarized in Table S3, and the spectra for La, Sm, and Lu double-deckers after being treated with hydrazine hydrate by comparison with Ce are shown in Fig. 6.

It is worth noting that no splitting of the Soret band was observed at about 350 nm for $\{M[Pc(MeOPhO)_8]_2\}^-$, which is unshifted upon reduction. These facts seem to suggest that the splitting of Soret band is due to the presence of $\{Pc[(MeOPhO)_8]\}^{\cdot -}$. The π-radical anion band was not exhibited and the Q band is splitted for these anions giving an intense and blue-shifted main band at 630–652 nm from Pr to Lu together with a weak and red-shifted satellite Q band (SQ) at 680–710 nm from Nd to Lu, as shown in Fig. 4. Fig. 4 shows plot of the wavenumbers of the two Q band components for these reduced bis(phthalocyaninato) rare earth compounds against the radii of the rare earth ions. It can be seen from Table S3 and Fig. 4 that the intense Q band (630–652 nm) of $\{M[Pc(MeOPhO)_8]_2\}^-$ undergoes a linear blue-shift with the decrease of the radius of the sandwiched metal ion, while conversely the satellite Q band at 680–710 nm shifts linearly to the red. Along with the lanthanide contraction, the satellite band shifts to lower energy (Table S3) and the intensity increases gradually, becoming a distinguishable band for Lu as shown in Fig. 6. So the energy gap between these two Q bands is enhanced by the decrease of ionic radius from La to Lu.

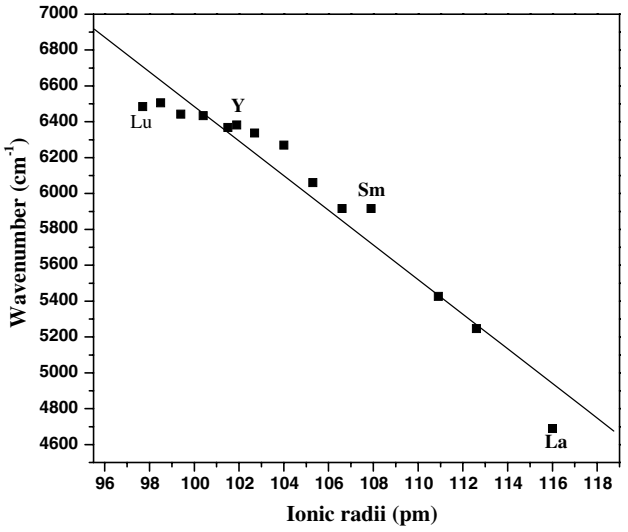


Fig. 5. Plot of wavenumber of the near-infrared band at 1542–2132 nm of $M^{III}[Pc(MeOPhO)_8]$ as a function of the ionic radius of M^{III}.

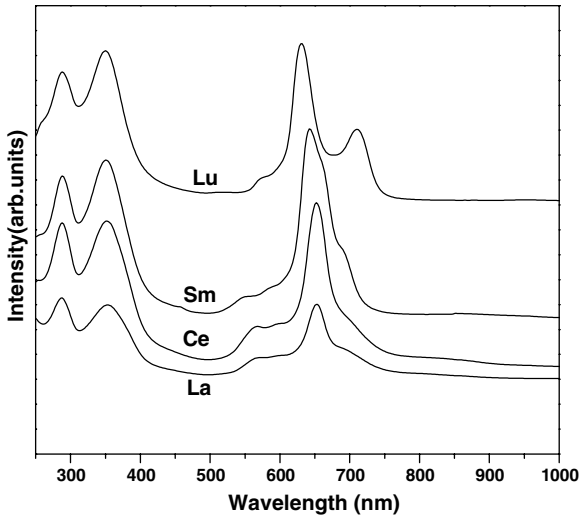


Fig. 6. Electronic absorption spectra of $\{M[Pc(MeOPhO)_8]_2\}^-$ (M = La, Ce, Sm and Lu) in $CHCl_3$/MeOH by addition of hydrazine hydrate.

As expected, the characteristic Near-IR band was not seen for these anions, showing that the single-hole species (except for M = Ce) underwent a one-electron ring-reduction. However, the extent of their Q-band splitting is different for different ionic size of the sandwiched metal. The light rare earths from La to Nd almost exhibited no distinguishable Q-band splitting in the electronic absorption spectra of their reduced sandwich-type bis(phthalocyaninato) compounds. Conversely, the middle and heavy rare earths after Nd usually showed obvious Q-band splitting in their electronic spectra, which was enhanced with the decrease of ionic size of the sandwiched metal. The enhanced splitting of the Q-bands obviously reflects the extent of π–π interaction of two Pc rings in the double-deckers.

As in $Ce(Pc)_2$, cerium in Ce[Pc(MeOPhO)$_8$]$_2$ also employs an intermediate valence state between III and IV [11,12] while both the substituted phthalocyanine rings

exist as dianions. $Ce[Pc(MeOPhO)_8]_2$ shows clear Soret band splitting at 290 and 350 nm, however, the Q band does not show obvious splitting compared with unsubstituted $Ce(Pc)_2$, as shown in Fig. 3. This observation is not consistent with that found in the double-decker $Ce(Pc)_2$. It might be attributed to the introduction of huge electron-donating substituents according to scattered reports [1,5,7].

3.3. UV–Vis characteristics of bis[3(4),12(13),21(22),30(31)-tetra(tert-butyl)-phthalocyaninato] rare earth complexes $M(TBPc)_2$ (M = Y, La...Lu except Pm)

The electronic absorption spectra of the whole series of sandwich double-decker compounds were measured in $CHCl_3$ and the data are collected in Table S4. The spectral characteristics resembled those of unsubstituted bis(phthalocyaninato) rare earth complexes [4]. However, it is noteworthy that the intensity of phthalocyanine π-radical anion band at 470–501 nm and the band at 603–621 nm and the extent of their Soret band splitting increase by comparison with those of $M(Pc)_2$, showing obvious molecular symmetry effect (Table S4). The possible reason is that the presence of *tert*-butyl substituents on the phthalocyanine rings multiplies the intensity of certain UV–Vis absorptions due to the lower symmetry and probably distortions in the macrocycle rings. As might be noticed from Fig. 7 and Table S4, the complexity in the number of the UV–Vis spectra of $M(TBPc)_2$ compared with those of unsubstituted and octa(4-methoxyphenoxy)-substituted bis(phthalocyaninato) rare earth complexes indeed reminds us of the decreased molecular symmetry of these compounds.

Fig. 7 shows the UV–Vis spectra of four compounds $M^{III}(TBPc)_2$ (M = La, Ce, Sm and Lu), typical for the light, middle, and heavy rare earths, respectively. Due to the similar molecular structure among the whole series of

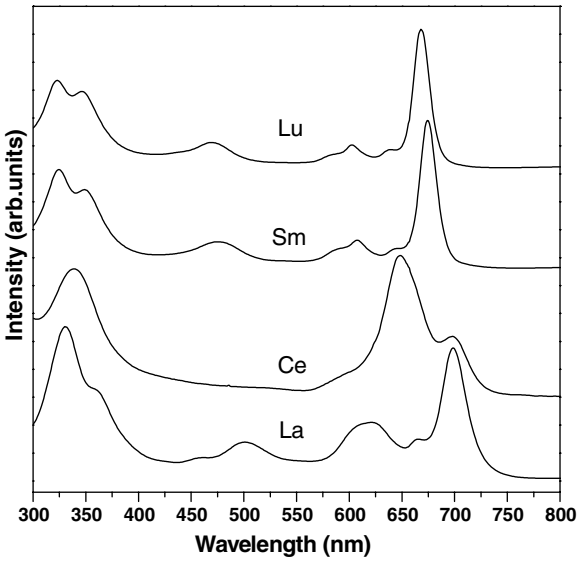


Fig. 7. Electronic absorption spectra of $M(TBPc)_2$ (M = La, Ce, Dy and Lu) in $CHCl_3$.

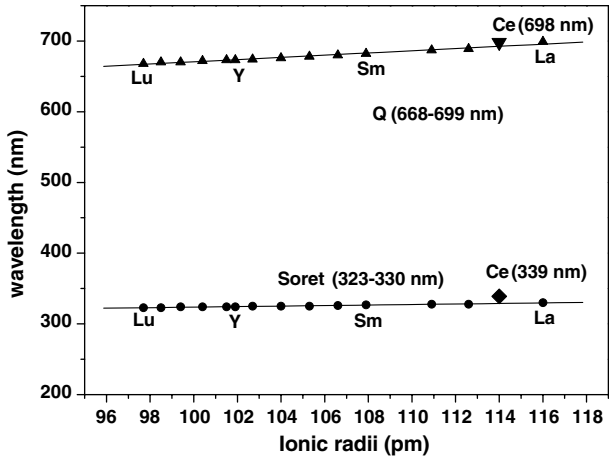


Fig. 8. Plot of wavelengths of the Soret and Q band absorptions of $M(TBPc)_2$ as a function of the ionic radius of M^{III}.

bis(phthalocyaninato) lanthanide compounds, all these compounds show similar UV–Vis characteristics [1–4]. As can be clearly seen from Table S4 that $M^{III}(TBPc)_2$ (except Ce) exhibit a obvious split Soret band with maxima around 323–330 and 335–351 nm, an intense Q band at 668–699 nm and a π-radical band at 470–501 nm. Because of the introduction of *tert*-butyl substituents and the contraction of the lanthanides, the number of the UV–Vis absorption bands increases and all the corresponding absorption wavelengths are systematically red-shifted compared with those unsubstituted $M^{III}(Pc)_2$, clearly showing molecular symmetry effect and substituent effect. Meanwhile, all the corresponding absorptions are systematically blue-shifted along with the decrease of rare earth ionic size from La to Lu as shown in Fig. 8, displaying evident the rare earth ionic size effect.

We now move to the cerium compound, whose UV–Vis spectroscopic data are different from those of the rest of the whole series, but resembles those of $[RE(Pc)_2]^-$ and $HRE(Pc)_2$ due to their similar electronic structures [9,13,14], as shown in Fig. 7. As indicated by the IR absorption and ^1H NMR spectra [15], the two phthalocyanine rings exist as dianions in $Ce(TBPc^{2-})(TBPc^{2-})$ despite the XANES results that suggest a valence state intermediate between III and IV for the cerium [1–4]. This makes the complex differ from other analogues that have the form $M(TBPc^{2-})$-$(TBPc^{\bullet-})$. This is supported by the fact that the UV–Vis absorption of characteristic π-radical band at 470–501 nm was not observed (Table S4). However, the Q band shows obvious splitting at 648 and 698 nm. This observation is well consistent with that found in the double-decker $Ce(Pc)_2$.

3.4. Electronic absorption spectra characteristics of mixed [tetrakis(4-chlorophenyl)porphyrinato](phthalocyaninato) rare earth double-decker complexes M(TClPP)(Pc) (M = Y, La...Lu except Pm)

The electronic absorption spectra of the series of sandwich double-decker compounds were measured in $CHCl_3$

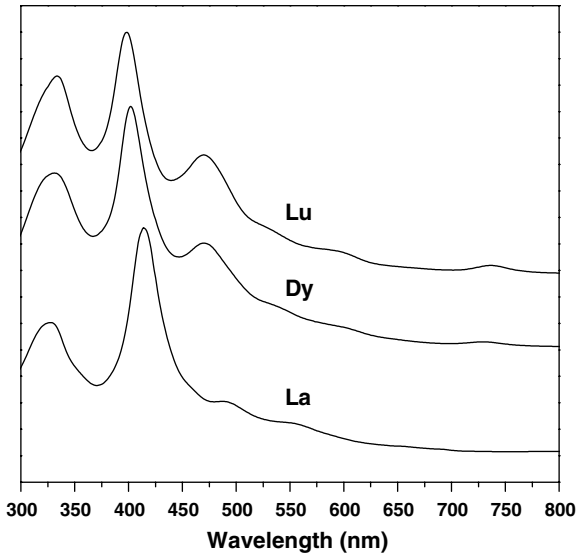


Fig. 9. Electronic absorption spectra of M(TClPP)(Pc) (M = La, Dy and Lu) in $CHCl_3$.

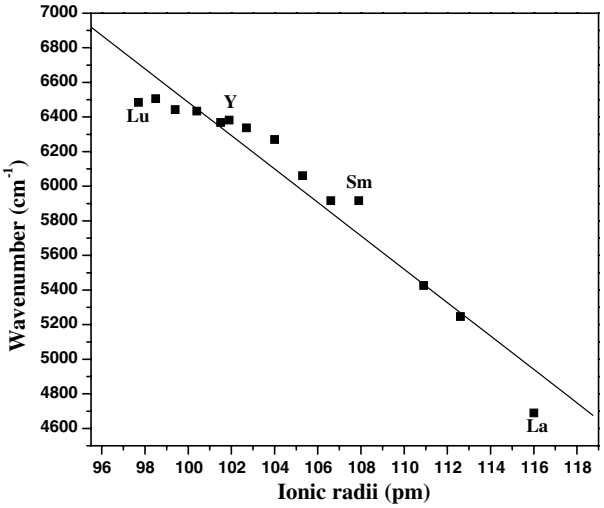


Fig. 10. Plot of wavenumber of ring-to-ring charge transfer transition from the second HOMO to the first semi-occupied HOMO of M^{III}(TClPP)(Pc) at ca. 1148–1418 nm as a function of the ionic radius of M^{III}.

and the data are compiled in Table S5. The dependence of the spectral features of the double-deckers on the metals is illustrated with electronic absorption spectra of M(TClPP)(Pc) for M = La, Dy, Lu as shown in Fig. 9, which are analogous to those reported for related counterparts M(Por)(Pc) (Por = TPP, TBPP, TMPP, TPyP) [16–19]. M(TClPP)(Pc) show strong Pc and TClPP Soret bands at 328–334 and 398–414 nm, respectively. The absorptions at 469–492 and 923–1089 nm for the various rare earth complexes are attributed to the electron transition related to the hole localized on the Pc ring. Similar to the Soret bands of Pc and TClPP, the absorption positions of these two bands are also sensitive to the ionic radii of the metal center. When the metal center becomes smaller, the longer-wavelength near-IR band (923–1089 nm) shifts gradually to the red, while the former one is blue-shifted (Table S5). Furthermore, for the whole series of tervalent rare earth double-deckers M(TClPP)(Pc), an additional near IR band at 1148–1418 nm with a shoulder at 1587–1693 nm can also be observed (Table S5). This band, which is highly characteristic for the single-hole homoleptic double-decker tetrapyrrole compounds $M^{III}(Pc')_2$ (Pc′ = Pc [20], OOPc [21]) and $M^{III}(Por)_2$ (Por = OEP, TPP) [22], can be similarly attributed to an electron transition from the second HOMO which contains primarily TClPP character to the first semi-occupied HOMO with mainly Pc character [23]. Meanwhile, the frequency of this charge-transfer transition is also dependent on the rare earth ionic size, shifting linearly to the higher energy along with the decrease of rare earth radius as shown in Fig. 10, making the separation between the two near-IR band at 923–1089 and 1148–1418 nm get smaller along with the same order (Table S5). As shown in Fig. 11, the two near-IR bands for Lu(TClPP)(Pc) almost coalesce to form a broad signal. This result is in line with that observed for

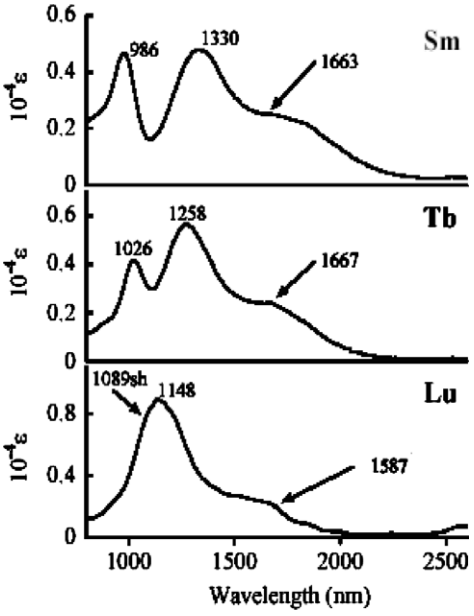


Fig. 11. Near-IR regional electronic absorption spectra of M(TClPP)(Pc) for M = Sm, Tb, and Lu in $CHCl_3$.

M(OEP)(Nc) [24]. It is likely that this absorption was overlapped by the one in the region of 1025–1146 nm for all the rare earth complexes in their spectra [25]. Interestingly, a weak absorption in the region of 689–738 nm, which is ignored for analogous compounds in the previous work [16–19], was observed for the series of tervalent rare earth mixed ring double-deckers. Both the intensity and the wavelength of this band are sensitive to the rare earth metal. Along with the lanthanide contraction, this band gradually gets some intensity, becoming an obviously distinguishable band for Lu(TClPP)(Pc), as shown in Fig. 9, and shifts to the lower energy (Table S5). This absorption

is mainly contributed from the Q absorptions of phthalocyanine ligand together with some contribution also from the Q absorptions of Porphyrin ring [8].

In mixed double-deckers M(TClPP)(Pc), the close proximity of the TClPP and Pc conjugated π-systems, in a face-to-face configuration induces the splitting of the monomer (one TClPP and one Pc) molecular orbital due to the interactions between the rings, resulting in two doubly degenerate (e_g) lowest unoccupied molecular orbital (the LUMO and second LUMO) and two non-degenerate (a_{1u}) highest occupied molecular orbital (the HOMO and second HOMO), as shown in Fig. 12 [8,26]. Due to the intrinsic difference between the molecular composition and electronic structure of TClPP and Pc, the a_{1u} orbital of Pc is higher in energy than that of TClPP while the e_g orbitals are lower than those of TClPP. Therefore both the HOMO and LUMO of M(TClPP)(Pc) are mainly contributed from the phthalocyanine ligand whereas the second HOMO and second LUMO with more TClPP character. However, the Pc-dominated HOMO level of the mixed (porphyrinato)(phthalocyaninato) double-deckers is semi-occupied, making for some unique spectral features. In the spectra of M(TClPP)(Pc), the absorption band at 923–1089 nm, which shifts slightly to the red with decreasing the metal ionic radius, is proposed to be due to the electronic transition from the semi-occupied HOMO to the degenerate LUMO [8,26]. Meanwhile, the absorption of even lower energy at 1148–1418 nm is due to the transition from the second HOMO to the semi-occupied HOMO [8]. The energy of the latter transition reflects the extent of electronic coupling between the macrocycles, which increases as the size of the metal center decreases. As mentioned above, the absorption positions of the band at 470–492 nm are also dependent on the central rare earth metal. This absorption is attributed to the electron transition from a deeply-occupied molecular orbital with both TClPP and Pc character to the semi-occupied HOMO [8].

When the Pc macrocycle in the homoleptic phthalocyaninato rare earth double-deckers are replaced by the porphyrin ring, which possesses a nearly extended π-system, a very similar electronic absorption spectrum is observed [4,8]. To summarize, it is obvious that there are many common features and correlations between the homoleptic and the mixed sandwiches. The characteristics of electronic spectra for the mixed porphyrinato and phthalocyaninato metal double-deckers could be easily understood and explained by analogy with their homoleptic counterparts, not clearly showing macrocycle effect due to similar extended π-system between the porphyrin and phthalocyanine rings. For instance, a linear correlation between the energies of near-IR absorptions and the sandwiched rare earth metal radii also exists in the double-decker M(TClPP)(Pc) [8]. Moreover, both the Soret and Q bands in the absorption spectra of mixed (porphyrinato)(naphthalocyaninato) rare earth complexes undergo evident redshift compared with those in mixed (porphyrinato)(phthalocyaninato) derivatives, as expected because of the introduction of naphthalocyanine chromophores, showing obvious macrocycle ring effect [27].

The absorption spectra of Ce(TClPP)(Pc) resembles those of [M^{IV}(TPP)(Pc)] (M = Zr, Hf, Th and U) [28], Li[M^{III}(TPyP)(Pc)] (M = Eu and Gd) [19], in which both of the rings are regarded as dianionic. For instance, the spectrum of Ce(TClPP)(Pc) shows strong Pc and TClPP Soret bands at 332 and 400 nm, respectively, and the Q bands at 562, 626, and 826 nm as shown in Fig. 13. The spectrum also shows the shoulder at 468 nm, which can be attributed to transitions from delocalized orbital involving both macrocycles [28]. The spectrum of Ce(TClPP)(Pc) is very different from those of [M^{III}(Por)(Pc)] [19,29]. Particularly, the characteristic near-IR absorption due to π-radical anion was not detected, as shown in Fig. 13. These data strongly suggest that the cerium center in Ce(TClPP)(Pc) is predominantly tetravalent.

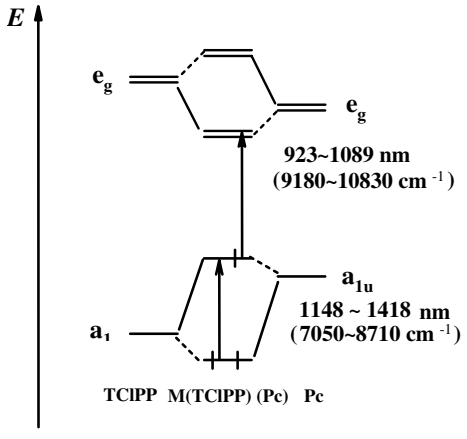


Fig. 12. Diagram of HOMO and LUMO of M^{III}(TClPP)(Pc) drawn based on their electrochemical results.

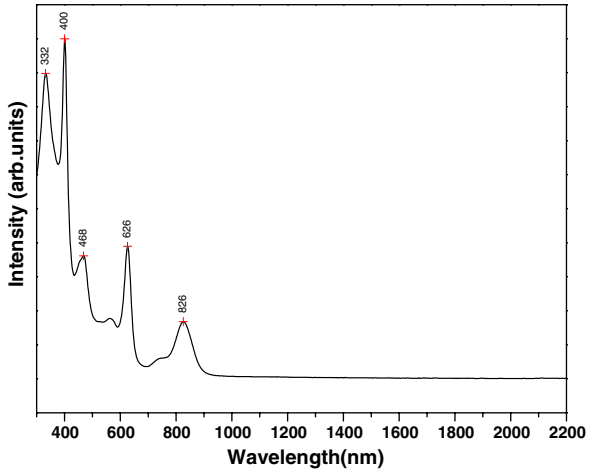


Fig. 13. Electronic absorption spectra of Ce(TClPP)(Pc) in $CHCl_3$.

4. Conclusions

According to the electronic absorption spectra investigation, all the corresponding absorptions are systematically blue-shifted, clearly revealing the rare earth size effect. In conclusion, the influence of the symmetry of macrocycle rare earth molecules, the effects of ionic radius of the rare earth metal and the influence of substituent species (*tert*-butyl and 4-methoxyphenoxy groups) onto the peripheral benzene rings on the electronic absorption characteristics of sandwich-type compounds have also been detailed studied by means of comparative research over the electronic absorption spectra of unsubstituted, substituted bis(phthalocyaninato) and mixed [tetrakis(4-chlorophenyl)porphyrinato](phthalocyaninato) rare earth complexes of the whole lanthanide series, namely $M(Pc)_2$, $M[Pc(MeOPhO)_8]_2$, $M(TBPc)_2$, and M(TClPP)(Pc).

Acknowledgement

The author thanks the Young Teacher Foundation of Tianjin University (5110108) for financial support.

Appendix A. Supplementary data

Supplementary data associated with this article can be found, in the online version, at doi:10.1016/j.poly.2007.04.017.

References

[1] C.C. Leznoff, A.B.P. Lever (Eds.), Phthalocyanines – Properties and Applications, vols. 1–4, VCH, New York, 1989–1996.
[2] N.B. McKeown, Phthalocyanine Materials – Synthesis, Structure and Function, Cambridge University Press, New York, 1998.
[3] K.M. Kadish, K.M. Smith, R. Guilard (Eds.), The Porphyrin Handbook, vols. 1–10, Academic Press, San Diego, 2000.
[4] J. Jiang, K. Kasuga, D.P. Arnold, in: H.S. Nalwa (Ed.), Supramolecular Photo-sensitive and Electro-active Materials, Academic Press, New York, 2001, pp. 113–210.
[5] D.K.P. Ng, J. Jiang, Chem. Soc. Rev. 26 (1997) 433.
[6] (a) J. Jiang, J. Xie, M.T.M. Choi, D.K.P. Ng, J. Porphyr. Phthalocyan. 3 (1999) 322;
(b) J. Jiang, J. Xie, D.K.P. Ng, Y. Yan, Mol. Cryst. Liq. Cryst. 337 (1999) 385.
[7] F. Lu, L. Zhang, H. Liu, J. Cui, X. Yan, Chin. J. Inorg. Chem. 21 (2005) 1131.
[8] F. Lu, X. Sun, R. Li, D. Liang, P. Zhu, C.F. Choi, D.K.P. Ng, T. Fukuda, N. Kobayashi, J. Jiang, New J. Chem. 28 (2004) 1116.
[9] (a) I.S. Kirin, P.N. Moskalev, Russ. J. Phys. Chem. 41 (1967) 251;
(b) C. Clarisse, M.T. Riou, Inorg. Chim. Acta 130 (1987) 139;
(c) D. Battisti, L. Tomilova, R. Acoca, Chem. Mater. 4 (1992) 1323.
[10] (a) J.S. Shirk, J.R. Lindle, F.J. Bartoli, M.E. Boyle, J. Phys. Chem. 96 (1992) 323;
(b) G. Ostendorp, H. Homborg, Z. Anorg. Allg. Chem. 622 (1996) 1222.
[11] F. Lu, M. Bao, C. Ma, X. Zhang, D.P. Arnold, J. Jiang, Spectrochim. Acta – Part A 59 (2003) 3273.
[12] J. Jiang, M. Bao, L. Rintoul, D.P. Arnold, Coord. Chem. Rev. 250 (2006) 424.
[13] (a) M.S. Haghighi, A. Franken, H. Homborg, Z. Naturforsch. 49b (1994) 812;
(b) M.S. Haghighi, H. Homborg, Z. Anorg. Allg. Chem. 620 (1994) 1278;
(c) G. Ostendorp, H. Homborg, Z. Anorg. Allg. Chem. 622 (1996) 1415;
(d) G. Ricciardi, S. Belviso, F. Leli, S. Ristori, J. Porphyr. Phthalocyan. 2 (1998) 177;
(e) M.S. Haghighi, C.L. Teske, H. Homborg, Z. Anorg. Allg. Chem. 73 (1992) 608;
(f) G. Ostendorp, H.W. Rotter, H. Homborg, Z. Naturforsch. 51b (1995) 567.
[14] L.G. Tomilova, K.M. Dyumaev, Mendeleev Commun. (1995) 109.
[15] (a) A. Aroca, E. Johnson, Langmuir 8 (1992) 3137;
(b) R.E. Clavijo, D. Battisti, R. Aroca, G.J. Kovacs, C.A. Jennings, Langmuir 8 (1992) 113;
(c) J. Souto, L. Tomilova, R. Aroca, Langmuir 8 (1992) 942;
(d) M.L.R. Mendez, R. Aroca, Chem. Mater. 5 (1993) 933;
(e) J. Souto, R. Aroca, J. Raman Spectrosc. 22 (1991) 349.
[16] T.H. Tran-Thi, T. Mattioli, D. Chabach, A. De Cian, R. Weiss, J. Phys. Chem. 98 (1994) 8279.
[17] F. Lu, J. Cui, Q. Yang, Inorg. Chim. Acta 360 (2007) 2751.
[18] J. Jiang, M.T.M. Choi, J. Chen, D.K.P. Ng, Polyhedron 17 (1998) 3903.
[19] J. Jiang, T.C.W. Mak, D.K.P. Ng, Chem. Ber. 129 (1996) 933.
[20] (a) A. De Cian, M. Moussavi, J. Fischer, R. Weiss, Inorg. Chem. 24 (1985) 3162;
(b) N. Ishikawa, O. Ohno, Y. Kaizu, Chem. Phys. Lett. 180 (1991) 51.
[21] W. Liu, J. Jiang, D. Du, D.P. Arnold, Aust. J. Chem. 53 (2000) 131.
[22] (a) J.W. Buchler, B. Scharbert, J. Am. Chem. Soc. 110 (1988) 4272;
(b) J.W. Buchler, P. Hammerschmitt, I. Kaufeld, J. Loffler, Chem. Ber. 124 (1991) 2151.
[23] P. Zhu, F. Lu, N. Pan, D.P. Arnold, S. Zhang, J. Jiang, Eur. J. Inorg. Chem. 3 (2004) 510.
[24] J. Jiang, Y. Bian, F. Furuya, W. Liu, M.T.M. Choi, H.W. Li, N. Kobayashi, Q. Yang, T.C.W. Mak, D.K.P. Ng, Chem. Eur. J. 7 (2001) 5059.
[25] J. Jiang, W. Liu, K.-L. Cheng, K.-W. Poon, D.K.P. Ng, Eur. J. Inorg. Chem. (2001) 413.
[26] N. Ishikawa, J. Porphyr. Phthalocyan. 5 (2001) 87.
[27] (a) F. Guyon, A. Pondaven, P. Guenot, M. L'Her, Inorg. Chem. 33 (1994) 4748;
(b) F. Guyon, A. Pondaven, M. L'Her, Chem. Commun. (1994) 1125.
[28] (a) K.M. Kadish, G. Moninot, Y. Hu, D. Dubois, A. Ibnlfassi, J.-M. Barbe, R. Guilard, J. Am. Chem. Soc. 115 (1993) 8153;
(b) R. Guilard, J.-M. Barbe, A. Ibnlfassi, A. Zrineh, V.A. Adamian, K.M. Kadish, Inorg. Chem. 34 (1995) 1472.
[29] D. Chabach, M. Tahiri, A. De Cian, J. Fischer, R. Weiss, M. El Malouli Bibout, J. Am. Chem. Soc. 117 (1995) 8548.

solution [21–24] and other methods [24–26]. It remains a challenge to find a novel and simple synthetic route for one-dimensional nanosized materials. The use of single-source molecular precursors for nanoparticles, was initially reported by Trindade and O'Brien [27,28] and such methods have provided efficient routes to high quality crystalline monodispersed nanoparticles of semi-conducting material. This method has been used with alkylthiourea complexes to prepare metal sulfide nanoparticles [7,29]. The cadmium(II) complexes of thiourea and *N*-alkylthioureas (where alkyl groups = methyl, ethyl, isopropyl and cyclohexyl) have been reported as precursors for the preparation of TOPO-capped CdS nanoparticles [7,30].

In this paper we report on the use of *N*,*N*′-diisopropylthiourea and *N*,*N*′-dicyclohexylthiourea cadmium(II) complexes as single-source precursors for the synthesis of the HDA-capped CdS nanoparticles. These alkyl substituted thiourea cadmium complexes are very easy to prepare, air-stable for very long periods and the HDA provides a more stable capping environment on the surface of nanoparticles. The crystal structures of the two complexes are also discussed.

2. Experimental

2.1. General

HDA (hexadecylamine) and TOP (tri^{n}octylphosphine) were purchased from Aldrich. Toluene and methanol were obtained from BDH. Toluene was stored over molecular sieves (40 Å, BDH) before use. Cadmium acetate, *N*,*N*′-diisopropylthiourea, *N*,*N*′-dicyclohexylthiourea and ethanol (analytical grade) obtained from Aldrich, were used as purchased to prepare the precursors.

2.2. Optical characterization

A Perkin–Elmer Lambda 20 UV–Vis Spectrophotometer was used to carryout the optical measurements and the samples were placed in silica cuvettes (1 cm, path length), using toluene as a reference solvent. A Jobinyvon-spex-Fluorolog-3-Spectrofluorimeter with a xenon lamp (150 W) and a 152 P photo multiplier tube as a detector was used to measure the photoluminescence of the particles. The samples were placed in quartz cuvettes (1 cm path length).

2.3. Electron microscopy

The TEM and HRTEM images were obtained using a Philips CM 200 compustage electron microscope operated at 200 kV with a EDS analyzer. The samples were prepared by placing a drop of a dilute solution of sample in toluene on a copper grid (400 mesh, agar). The samples were allowed to dry completely at room temperature.

2.4. X-ray diffraction

X-ray diffraction patterns on powdered samples were measured on Phillips X'Pert materials research diffractometer using secondary graphite monochromated Cu Kα radiation ($\lambda = 1.54060$ Å) at 40 kV/50 mA. Samples were supported on glass slides. Measurements were taken using a glancing angle of incidence detector at an angle of 2°, for 2θ values over 20–60° in steps of 0.05° with a scan speed of $0.01°2\theta\ s^{-1}$.

2.5. Microanalysis

Microanalysis was performed on a CARLO ERBA elemental analyzer for C, H, N, S.

2.6. X-ray crystallography

X-ray data were collected on a Bruker APEX CCD [31] diffractometer with Mo Kα radiation ($\lambda = 0.71069$ Å) using ϕ and ω scans. The crystals were mounted using a drop of fomblin (perfluoropolymethylisopropyl ether) oil in a Hamilton Cryoloop and sample cooling was achieved using a nitrogen gas stream from an Oxford Cryosystems 700 Series Cryostream Cooler. The data were processed using SAINT [32] and empirical absorption corrections were applied using SADABS [31]. Because the crystals of compound **I**, $[Cd(CH_3COO)_2(SC(NHC_6H_{11})_2)_2]$ diffracted very weakly, the data were cut at 0.95 Å resolution for this sample. The structures were solved by direct methods using SHELXS97 [33] and refined anisotropically (non-hydrogen atoms) by full-matrix least-squares on F^2 using SHELXL-97 [33]. The H atoms were calculated geometrically and refined with a riding model. In compound **II**, $Cd(CH_3COO)_2(SC(NHC_3H_7)_2)_2]$ atoms O1 and O2 were disordered over two sites whose occupancies were constrained to sum to 1.0, with the highest fraction refining to an occupancy of 0.579(9). The SHELXTL package [31] was used for all the calculations and preparation of the plots for publication.

2.7. NMR and FT-IR spectroscopy

Infrared spectra were recorded on FT-IR Perkin–Elmer paragon 1000 spectrophotometer using Nujol mull. NMR spectra were recorded on a Varian Associates Inova spectrometer (400 and 300 MHz).

2.8. Synthesis of precursors

2.8.1. $[Cd(CH_3COO)_2(SC(NHC_6H_{11})_2)_2]$ (**I**)

A hot solution of *N*,*N*′-dicyclohexylthiourea (1.00 g, 4.17 mmol) in ethanol (20 mL) was added into a heated solution of cadmium acetate (0.48 g, 2.08 mmol) in ethanol (25 mL). The mixture was stirred while hot for 1 h and allowed to cool to room temperature. The solution was filtered and left in a covered beaker at room temperature to

give yellow crystalline product after 24 h. The product was filtered, washed twice with ethanol and dried under vacuum. Yield 1.26 g, 87.9%; m.p. 138.5–142.7 °C. *Anal.* Calc. for $C_{30}H_{54}N_4O_4S_2Cd$: C, 50.68; H, 7.60; N, 7.80; S, 9.01. Found: C, 49.73; H 7.47; N 7.46; S 8.51%. IR (Nujol mull)/cm^{-1}: 3240(m), 2931(s), 2854(m), 1543(vs), 1419(vs), 1342(sh), 1234(w), 1157(vw), 1095(vw), 987(vw), 894(w), 756(m). ^1H NMR (δ, $CDCl_3$) ppm: 2.21 (s, 3H, CH_3COO); 2.10 (br, s, 1H), 1.78 (br, s, 4H), 1.64 (br, d, 4H) and 1.25 (m, 2H, $-C_6H_{11}$). $^{13}C\{^1H\}$ NMR (δ, $CDCl_3$) ppm: 53.51(s, CH_3–CH_3COO), 32.79, 31.21, 25.59 and 25.02 (s, C_6H_{11}).

2.8.2. *[Cd(CH$_3$COO)$_2$(SC(NHC$_3$H$_7$)$_2$)$_2$] (**II**)*

A hot solution of *N*,*N*′-diisopropylthiourea (1.00 g, 6.25 mmol) in ethanol (20 mL) was added into a heated solution of cadmium acetate (0.72 g, 3.13 mmol) in ethanol (20 mL). The mixture was stirred and refluxed for 1 h. The yellow solution was filtered hot to remove any traces of unreacted materials and was left in an open beaker at room temperature. Yellow crystalline product was obtained after 24 h. The product was filtered, washed twice with ethanol and dried under vacuum. Yield 1.44 g, 83.5%; m.p. 148.5–152.7 °C. *Anal.* Calc. for $C_{18}H_{38}N_4O_4S_2Cd$: C, 39.54; H, 6.90; N, 10.71; S, 11.83. Found: C, 40.34; H 7.37; N 11.02; S 12.51%. IR (Nujol mull)/cm^{-1}: 3255(m), 2878(s), 1558(vs), 1404(vs), 1280(s), 1156(s), 1002(m), 941(w), 848(vw). ^1H NMR (δ, $CDCl_3$) ppm: 2.19 (s, 3H, CH_3COO); 2.07 (s, 1H, $CH(CH_3)_2$); 1.24 (d, 6H, $CH(CH_3)_2$). ^{13}C $\{^1H\}$ NMR (δ, $CDCl_3$) ppm: 207.35 (s, COO), 179.38 (s, CS); 46.52 (s, CH_3, CH_3COO), 31.19 (s, CH) and 22.58 (s, CH_3–CH_3COO).

2.8.3. *Method for the preparation of CdS nanoparticles*

In a typical experiment, $[Cd(CH_3COO)_2(SC(NHC_6H_{11})_2)_2]$ (1.0 g, 2.12 mmol) was dissolved in TOP (10–20 mL). This solution was then injected into 6.25 g (25.9 mmol) of hot HDA at 180 or 240 °C, a decrease in temperature of 20–30 °C was observed. The solution was allowed to stabilize at 180 °C and heated for 60 min at this temperature. The solution was then allowed to cool to about 70 °C, and methanol was added to remove excess HDA. A flocculent precipitate formed and this solid product was separated by centrifugation and redispersed in toluene. Toluene was removed by evaporation under reduced pressure to give yellow HDA-capped CdS nanoparticles. The particles were washed three times with methanol and redispersed in toluene.

3. Results and discussion

3.1. Description of structures of complexes

Both complexes were subjected to single crystal X-ray structural analysis after recrystallization from ethanol or methanol by slow evaporation at room temperature which gave transparent cubic crystals. These were stable to air and moisture with melting points in the range between 138 and 152 °C and reasonably good yields. The formulae of the resulting complexes were consistent with the molecular structures and other forms of analyses such as microanalysis, infrared and NMR spectroscopy. Details of the crystal data and structure refinements are provided in Table 1. ORTEP diagrams of complexes **I** and **II** with the non-hydrogen atomic labelling scheme are shown in Figs. 1 and 2, respectively. Selected bond lengths and angles are given in Tables 2 and 3.

The structure of complex $[Cd(CH_3COO)_2(SC(NHC_6H_{11})_2)_2]$ (**I**) (Fig. 1) comprises a six coordinate Cd(II) ion in a distorted octahedron with two S atoms and four O atoms from the acetate ligands. The Cd–S bond distances are slightly longer than for the corresponding chloro complex, dichlorobis(*S*-thiourea)cadmium(II) (Cd–S; 2.517(1) Å) [34] and are 2.588(4) Å for Cd(1)–S(1) and 2.568(4) Å for Cd(1)–S(2). The first acetate ligand has unequal bond distances to Cd of 2.279(8) Å for Cd(1)–O(1) and 2.612(10) Å for Cd(1)–O(2) indicating that it is verging on being monodentate. The second acetate ligand has nearly equal bond distances to Cd of 2.425(12) Å for Cd(1)–O(3) and 2.382(14) Å for Cd(1)–O(4). The C–S

Table 1
Crystal data and detailed structure refinement for complexes **I** and **II**

Complex	**I**	**II**
Empirical formula	$C_{30}H_{54}CdN_4O_4S_2$	$C_{18}H_{38}CdN_4O_4S_2$
Formula weight	711.29	551.04
Temperature (K)	100(2)	230(2)
Wavelength (Å)	0.71073	0.71073
Crystal system	monoclinic	monoclinic
Space group	$P2_1/n$	$P2_1/n$
Unit cell dimensions		
a (Å)	14.115(6)	11.791(2)
b (Å)	17.044(7)	16.948(3)
c (Å)	15.800(7)	13.731(3)
β (°)	108.70(7)	105.078
Volume (Å^3)	3600(3)	2649.4(9)
Z	4	4
D_{calc} (Mg/m^3)	1.312	1.382
Absorption coefficient (mm^{-1})	0.759	1.009
F(000)	1496	1144
Crystal size (mm)	$0.30 \times 0.20 \times 0.03$	$0.40 \times 0.40 \times 0.20$
θ Range for data collection (°)	1.69–21.97	1.95–25.03
Index ranges	$-14 \leqslant h \leqslant 14$, $-17 \leqslant k \leqslant 17$, $-16 \leqslant l \leqslant 16$	$-13 \leqslant h \leqslant 14$, $-20 \leqslant k \leqslant 20$ $-16 \leqslant l \leqslant 16$
Reflections collected	18 733	18 793
Independent reflections (R_{int})	4392 (0.1161)	4680 (0.0451)
Completeness to θ (%)	100.0 ($\theta = 21.97°$)	99.9 ($\theta = 24.98°$)
Maximum and minimum transmission	0.9776 and 0.8043	0.8237 and 0.6884
Goodness-of-fit on F^2	1.051	1.055
Final R indices	$R_1 = 0.099$, $wR_2 = 0.2236$	$R_1 = 0.0283$, $wR_2 = 0.0703$
R indices (all data)	$R_1 = 0.1438$, $wR_2 = 0.2458$	$R_1 = 0.0316$, $wR_2 = 0.0723$

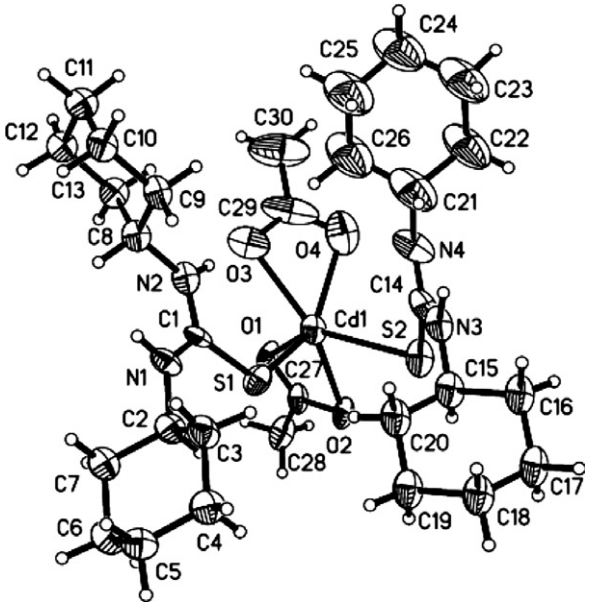


Fig. 1. Molecular structure of complex **I**, $[Cd(CH_3COO)_2(SC(NHC_6H11)_2)_2]$ with thermal ellipsoids drawn at the 50% probability level.

and C–N bonds in alkylthiourea ligands show intermediate character between a single and a double bond length. These bond distances are in good agreement with those of thiourea molecules reported in the Cambridge Structural database (CSD by Allen et al. [35] in 1991) i.e. 1.726 (C–S) and 1.322 Å (C–N). The additional C–N bond due to the hexyl carbon atoms attached to the nitrogen atoms are of a single bond character with an average bond distance of 1.455 Å. The C–O bond distances average at 1.28 Å, is intermediate between a single and double bond length for the bidentate acetate ligands. The bond angles around the O–Cd–O in each acetate ligand gave an average of 54.1°. This also confirms the chelating effect of the acetate ligand. The bond angle between the alkylthiourea ligands, S(2)–Cd(1)–S(1) is 92.6(1)°, whereas those angles between the oxygen atoms and sulfur atoms of the ligands vary from 78.0(2)° (S(2)–Cd(1)–O(2)) to 137.3(3)° (O(3)–Cd(1)–S(2)). All the bond angles show a large degree of distorted octahedral geometry (Table 2).

The structure of complex **II**, $[Cd(CH_3COO)_2(SC(NHC_3H_7)_2)_2]$ (Fig. 2) has as a four/five coordinate cadmium with two diisopropylthiourea ligands and two/three oxygen atoms of the acetate ligands, one of which has disordered oxygen atoms. The Cd–S bond distances are similar to those in complex **I**, $[Cd(CH_3COO)_2(SC(NHC_6H_{11})_2)_2]$, (Tables 2 and 3) One of the acetate groups is monodentate, whilst the oxygen atoms of the other are disordered over two sites each, with the higher occupancy fraction monodentate and the lower occupancy fraction bidentate. The monodentate components of the two acetate ligands have bond distances to Cd(1) which are shorter than those for complex **I**, 2.212(5) Å for Cd(1)–O(2) and 2.240(2) Å for Cd(1)–O(3). The bidentate component has Cd–O bond distances of 2.338(6) Å (Cd(1)–O(1B)) and 2.395(6) Å (Cd(1)–O(2B)). The C–O distances average at 1.25 Å. The co-ordination around

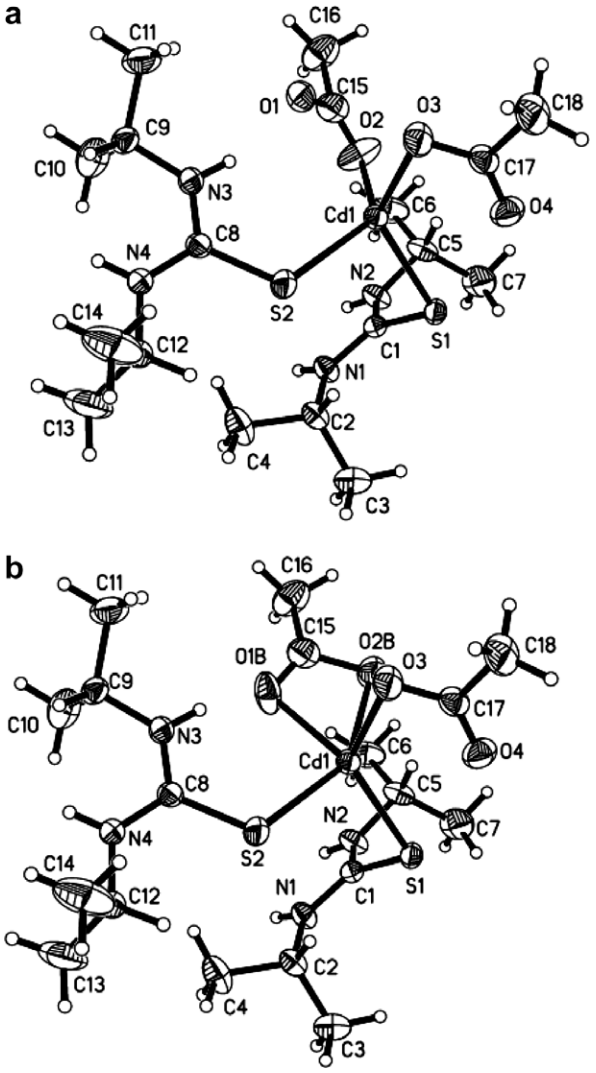


Fig. 2. Molecular structure of complex **II**, $[Cd(CH_3COO)_2(SC(NHC_3H_7)_2)_2]$ with thermal ellipsoids drawn at the 30% probability level showing similar views of the two disordered components (a) the higher occupancy disordered component, with two monodentate acetate ligands; (b) the lower occupancy disordered component with one bidentate and one monodentate acetate ligands.

Table 2
Selected bond distances (Å) and bond angles (°) for complex **I**

Bond distances (Å)		Bond angles (°)	
Cd(1)–O(1)	2.279(8)	O(1)–Cd(1)–O(4)	98.7(4)
Cd(1)–O(2)	2.612(10)	O(4)–Cd(1)–O(2)	116.1(4)
Cd(1)–O(3)	2.425(12)	O(1)–Cd(1)–O(3)	86.7(4)
Cd(1)–O(4)	2.382(14)	O(1)–Cd(1)–O(2)	53.3(3)
Cd(1)–S(1)	2.588(4)	O(1)–Cd(1)–S(2)	130.4(3)
Cd(1)–S(2)	2.568(4)	O(3)–Cd(1)–S(1)	93.4(3)
		O(3)–Cd(1)–S(2)	137.3(3)
		O(1)–Cd(1)–S(1)	109.2(3)
		S(2)–Cd(1)–O(2)	78.0(2)
		S(1)–Cd(1)–O(2)	107.4(2)
		S(2)–Cd(1)–S(1)	92.63(14)

Table 3
Selected bond distances (Å) and bond angles (°) for complex **II**

Bond distances (Å)		Bond angles (°)	
Cd(1)–O(1B)	2.338(6)	O(2)–Cd(1)–O(3)	104.24(19)
Cd(1)–O(2)	2.212(5)	O(2)–Cd(1)–O(1B)	36.9(2)
Cd(1)–O(3)	2.240(2)	O(1B)–Cd(1)–O(2B)	53.6(2)
Cd(1)–S(1)	2.5362(7)	O(3)–Cd(1)–S(1)	130.12(5)
Cd(1)–S(2)	2.5803(8)	O(3)–Cd(1)–S(2)	97.54(7)
Cd(1)–O(2B)	2.395(6)	O(1B)–Cd(1)–S(1)	122.4(2)
		O(2B)–Cd(1)–S(1)	98.09(19)
		S(2)–Cd(1)–S(1)	103.45(3)
		O(3)–Cd(1)–O(1B)	99.3(3)
		O(3)–Cd(1)–O(2B)	84.7(3)

the Cd(II) ion is a distorted tetrahedral geometry for the disordered component with the monodentate acetate and distorted square pyramidal for the component with the bidentate acetate. The O–Cd–O bond angle between the two monodentate acetate ligands is 104.2(2)° (O(2)–Cd(1)–O(3)). The bond angle between the alkylthiourea ligands, S(2)–Cd(1)–S(1) is 103.45(3)°, which is larger than for complex **I** (92.6(1)°). Other geometric parameters are shown in Table 3.

3.2. Synthesis of HDA-capped CdS nanoparticles

The precursors **I** and **II** were subjected to thermolysis in HDA at the temperatures of 180 °C and 240 °C and also varying the concentration of reactants. The amount of HDA used were 3.13 g, 6.25 g, 12.50 g and 25.00 g in each case with 1.00 g of precursor. The nanoparticles were synthesized at different precursor concentration using between 1.25 g and 12.50 g of HDA. Previous reports suggest that high concentrations favour anisotropic growth whereas lower concentrations favour isotropic growth [36]. Particles showed some degree of dependence on concentration of their shapes with higher concentration giving rod-shaped material and lower temperatures one with spherical shapes. It is evident that thermolysis of these precursors produced CdS nanoparticles with a variety of properties which are not directly influenced by the alkyl groups on the thiourea ligands but by other factors such as temperature, time and concentration. Cadmium complexes of thiosemicarbazide have been reported to produce CdS nanorods, in which their morphology is thought to affect their optical properties [28]. It was also observed by Li et al. [21] that temperature in combination of other conditions such as concentration greatly influences the morphology of nanoparticles from spherical to rod-shaped.

3.3. Optical properties of CdS nanoparticles

3.3.1. Effect of concentration on CdS nanoparticles

Macrocrystalline hexagonal CdS particles have an optical band gap of 2.41 eV (515 nm) at room temperature. The band-edges for CdS samples prepared in this study are blue-shifted in relation to the bulk material. This effect is associated with the CdS nanoparticles being smaller than the exciton radius of bulk CdS. During preparation there is generally an increase of particle size of the nanoparticles with time, which is consistent with an Ostwald ripening process. After injection of the precursor there is a critical size dependence on the concentration of the precursor. The depletion of the precursor causes the size distribution to broaden because smaller, less stable particles aggregate to form larger particles.

Figs. 3 and 4 shows absorption and photoluminescence spectra of CdS nanoparticles prepared from complex **I**, respectively, those for complex **II** are shown in Figs. 5 and 6. The optical band-edge showed a blue-shift in relation to bulk of 515 nm indicative of the decrease in particle size. As the concentration is decreased, from a 1:1 ratio to 1:8, there was a decrease in absorption band-edge, relating to a decrease in particle sizes. The sizes can be approximated to 5.96 nm (1:8) to 6.2 nm (1:1), for precursor **I**, and 5.7 nm (1:8) to 6.3 nm (1:1) for precursor **II** using Brus equation [37,38]. The photoluminescence spectra in Fig. 4 were all red-shifted from the absorption edges. They also

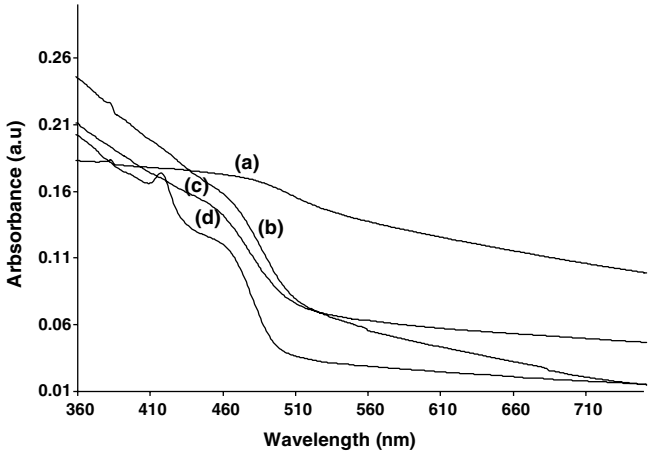


Fig. 3. Absorption spectra of HDA-capped CdS nanoparticles from complex **I** synthesized at 180 °C by varying the concentration, (a) 1:1 (b) 1:2 (c) 1:4 and (d) 1:8.

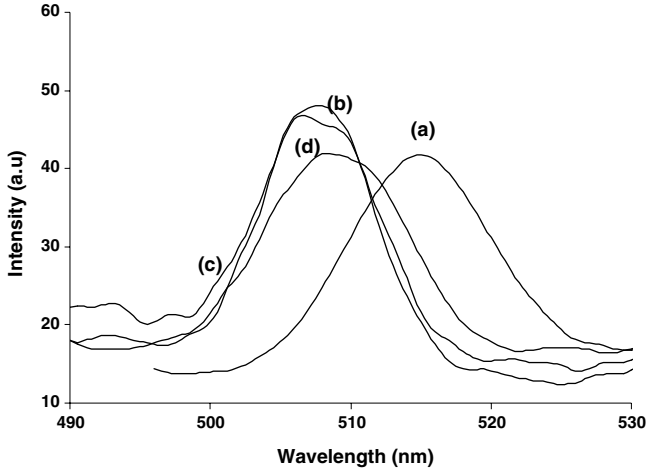


Fig. 4. Photoluminescence spectra of HDA-capped CdS nanoparticles from complex **I** synthesized at 180 °C by varying the concentration, (a) 1:1 (b) 1:2 (c) 1:4 and (d) 1:8.

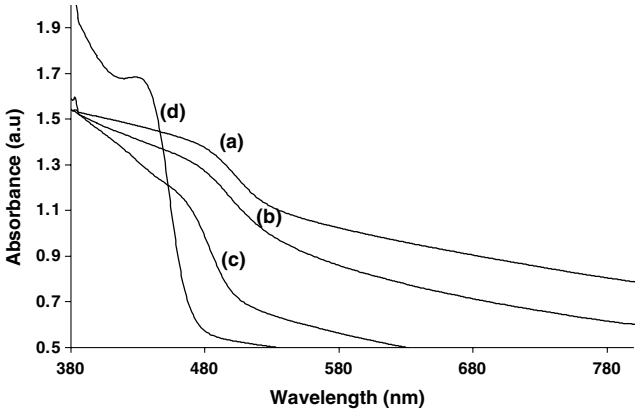


Fig. 5. Absorption spectra of HDA-CdS nanoparticles from complex **II** synthesized at 180 °C by varying the concentration, (a) 1:1 (b) 1:2 (c) 1:4 and (d) 1:8.

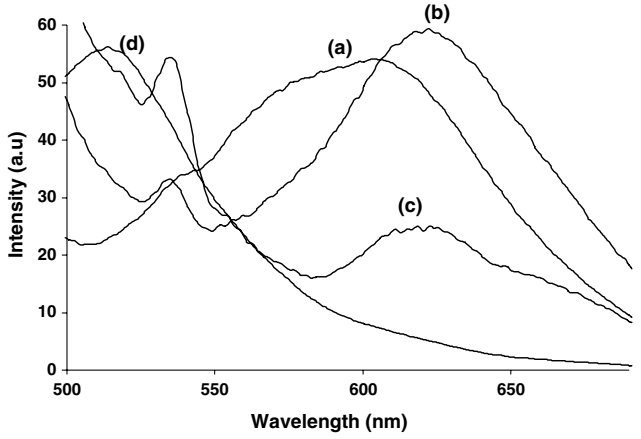


Fig. 6. Photoluminescence spectra of HDA-capped CdS nanoparticles from complex **II** synthesized at 180 °C by varying the concentration, (a) 1:1 (b) 1:2 (c) 1:4 and (d) 1:8.

showed good particle size distribution due to the relatively narrow peaks as well as good surface passivation evident from single smooth peaks being obtained. At higher concentration (1:1 ratio) the absorption band-edge for complex **I** indicate tailing which is usually associated with wide size distribution of particles but in this case caused by the formation of rod-shaped particles. It was observed by Cheon and co-workers [36] that the formation of rod shape particles changes the optical properties. The lower concentration shows a well-defined excitonic peak characteristic of spherical CdS nanoparticles. The CdS particles showed the largest emission maxima (with the large red-shift) for the concentration ratio 1:2 obtained from complex **II** at the same excitation and temperature in relation to other concentration ratios (Fig. 6). In contrast the concentration ratio 1:8 gave the lowest emission maximum (515 nm). The second emerging peaks at lower wavelength for the emission spectra of complex **II** could be associated with the surface defects. This is in comparison to the well passivated CdS nanoparticles prepared from complex **I** (Fig. 4).

3.3.2. Effect of temperature on CdS nanoparticles

Temperature has been proven to have a major effect on size, generally with particle sizes increasing with increasing temperatures [28,29]. The CdS nanoparticles were prepared using 1:2 molecular ratio of precursor in HDA at temperatures 180–240 °C. The absorption spectra in Fig. 7 have band-edges (491, 508 nm) blue-shifted from bulk. The sample prepared at a higher temperature had a well-defined excitonic peak with a sharp band-edge, an indication of monodispersity. The difference in the quality of the samples is further substantiated by their photoluminescence spectra (Fig. 8). The samples prepared at a lower temperature have a narrow PL peak with an emission maximum at 521 nm, red-shift in relation to the band-edge. The higher temperature sample shows a slightly broader peak with the maximum at 539 nm.

3.4. Structural properties of CdS nanoparticles

CdS nanoparticles can exist either as the cubic, orthorhombic or hexagonal phase and the existence of a mixture

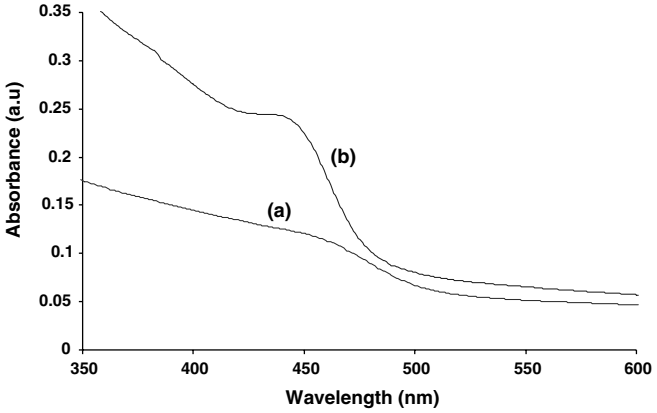


Fig. 7. Absorption spectra of CdS nanoparticles prepared from dicyclohexylthiourea (**I**) at (a) 180 °C and (b) 240 °C.

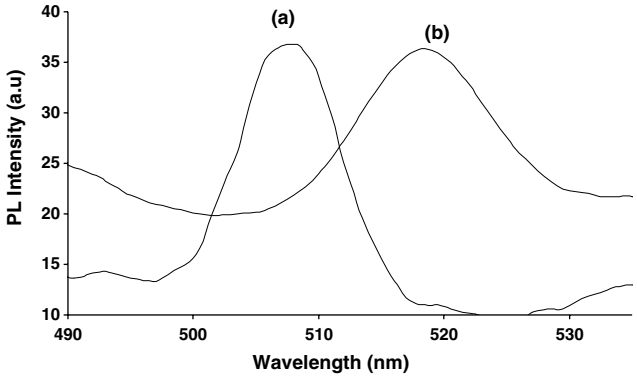


Fig. 8. Photoluminescence spectra of CdS nanoparticles prepared from dicyclohexylthiourea (**I**) at (a) 180 °C and (b) 240 °C.

of cubic and hexagonal phase with the predominance of one over the other was reported by Bawendi et al. [39] for CdSe. The powder X-ray diffraction patterns of CdS nanoparticles synthesized from the alkylthiourea complexes at 180 °C using a ratio of 1 mol of the precursor: 2 mol HDA, are shown in Fig. 9. Both patterns can be

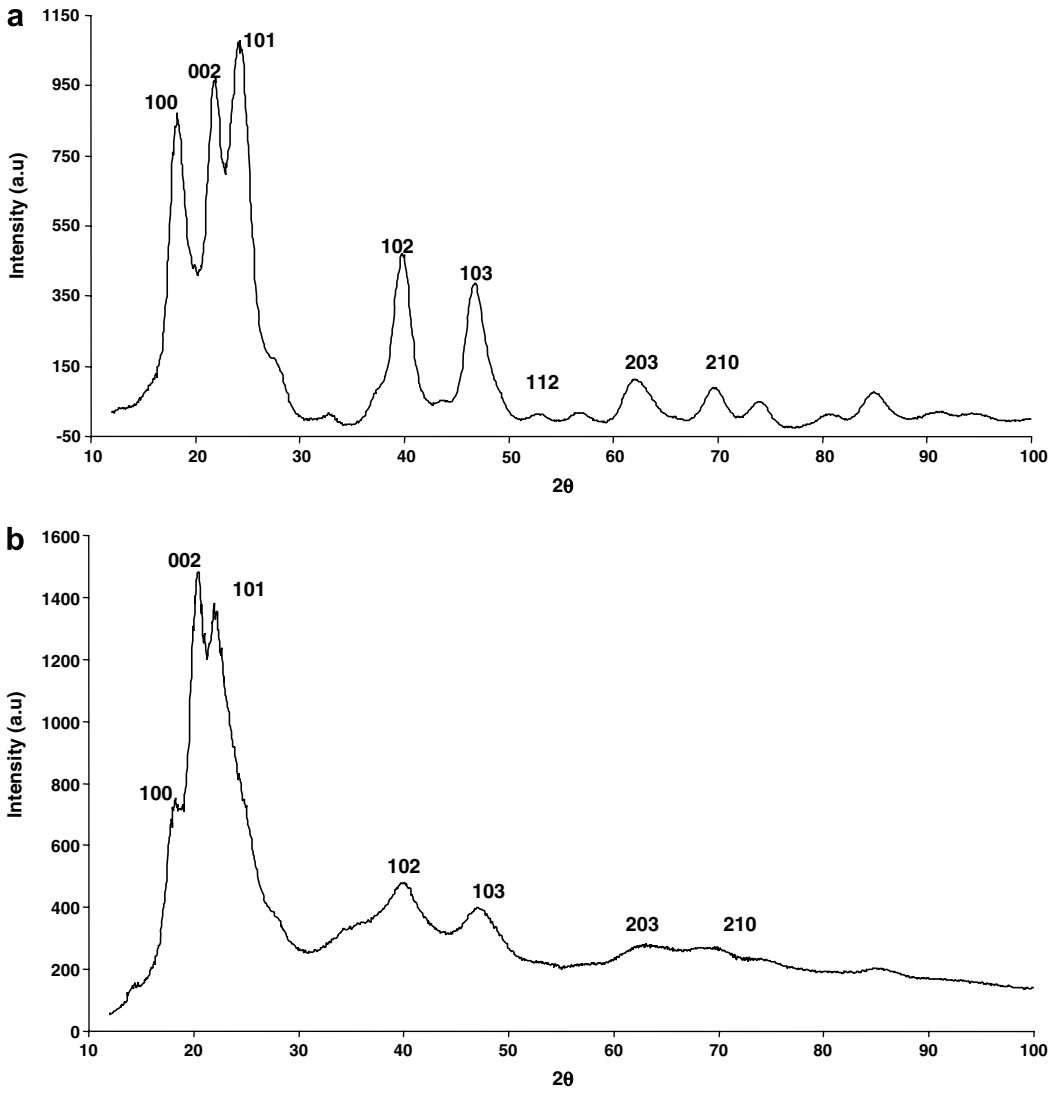


Fig. 9. X-ray diffraction pattern of CdS nanoparticles (1.00 g: 6.25 g) synthesized at 180 °C from (a) dicyclohexylthiourea complex (**I**) and (b) diisopropylthiourea complex (**II**).

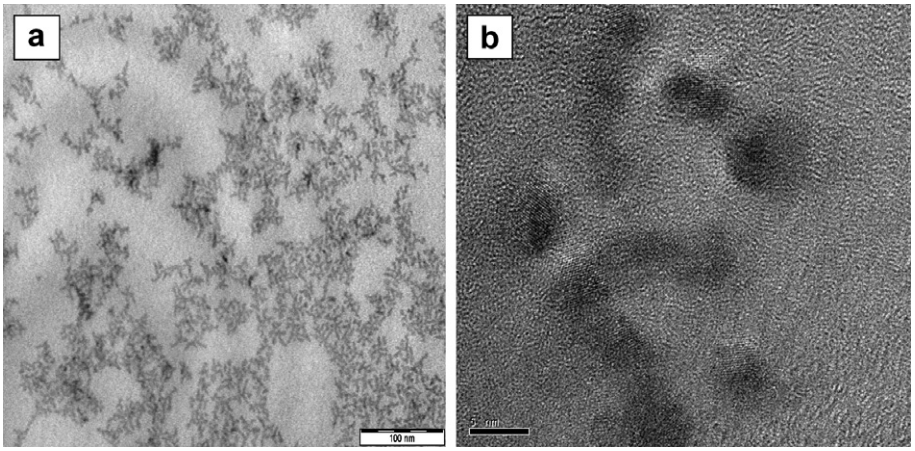


Fig. 10. (a) TEM and (b) HRTEM image of CdS nanoparticles (1.00 g: 6.25 g) synthesized at 180 °C from dicyclohexylthiourea complex (**I**).

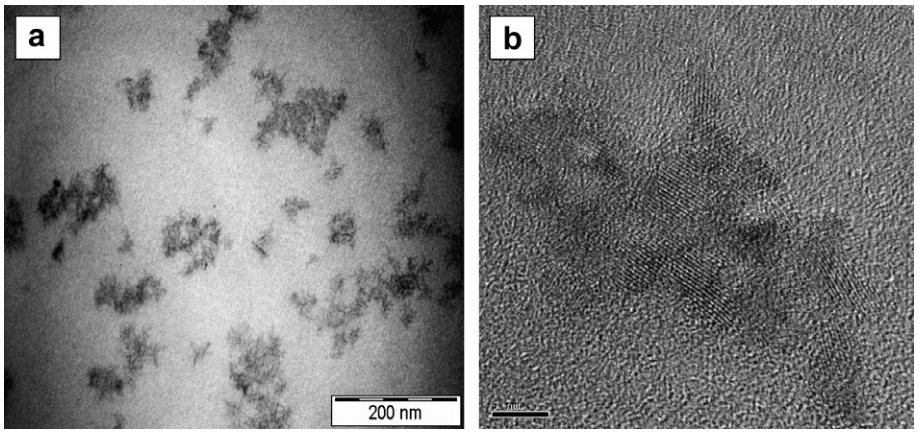


Fig. 11. (a) TEM and (b) HRTEM image of CdS nanoparticles (1.00 g: 6.25 g) synthesized at 180 °C from diisopropylthiourea complex (**II**).

Table 4
Absorption and PL spectral data of HDA-capped nanoparticles at different concentrations (at 180 °C) and different temperatures for precursors **I** and **II**

I			**II**			Mole ratio at 180 °C
Band-edge (nm)	Particle size (nm)	Emission maxima (nm)	Band-edge (nm)	Particle size (nm)	Emission maxima (nm)	
502	6.2	517	508	6.3	539	1:1
494	6.1	509	503	6.2	620	1:2
491	6.0	508	494	6.0	535	1:4
487	5.9	508	472	5.7	515	1:8
						Temperature (°C)
491		521	478		536	180
508		539	509		543	240

indexed to the hexagonal phase. The three predominant peaks between 10° and 30° can be indexed to 100, 002 and 101 planes and the rest of the peaks (40° = 102, 47° = 103, 54° = 112, 63° = 203 and 70° = 210) are further confirming the hexagonal phase. Both the patterns have broadened peaks, which is a good indication of both the crystallinity as well as the small size of the particles.

The TEM image of the CdS synthesized from complex **I** at 180 °C using a 1:2 ratio shows particles with well-defined 1D 'rod-shaped' which are *ca.* 5 nm in length and 2 nm in width (Fig. 10a). At similar reaction conditions, the TEM image (Fig. 11a) of CdS from complex **II** show particles with an oblate shape. These particles are approximately 3–5 nm in size, which is in agreement with the estimated sizes from the absorption band-edges (Table 4). Previous reports using similar precursors thermolysed in TOPO yielded hexagonal QD particles [30]. Therefore it is evident that the capping agent has a marked influence on the morphology of the particles. The morphology and the size of the nanoparticles synthesized from the thiourea precursors are consistent with their optical properties. The small blue-shift in absorption band-edge of the CdS nanoparticles could have been influenced by the relative lengths of the nanorods, thus making the overall particle size large, with diameter well within the range of typical nanoparticles. The HRTEM images in Fig. 10b and 11b show CdS nanocrystals from diisopropyl and dicyohexylthiourea respectively with crystal lattice planes.

4. Conclusions

The cadmium complexes of diisopropyl and dicyclohexylthioureas were easy to prepare, highly stable and proved to be good precursors for the synthesis of CdS nanoparticles. The variation of the amounts of HDA and temperature of thermolysis are factors influencing the optical properties and morphology of particles. The particles are rod-shaped irrespective of the type of precursor with hexagonal phase from their XRD patterns.

5. Supplementary material

CCDC 628913 and 628914 contain the supplementary crystallographic data for $[Cd(CH_3COO)_2(SC(NHC_6H_{11})_2)_2]$ and $[Cd(CH_3COO)_2(SC(NHC_3H_7)_2)_2]$. These data can be obtained free of charge via http://www.ccdc.cam.ac.uk/conts/retrieving.html, or from the Cambridge Crystallographic Data Centre, 12 Union Road, Cambridge CB2 1EZ, UK; fax: (+44) 1223-336-033; or e-mail: deposit@ccdc.cam.ac.uk.

Acknowledgements

This work was supported by the National Research Foundation (South Africa) and Royal Society (United Kingdom).

References

[1] S. Bourne, K.R. Koch, J. Chem. Soc., Dalton Trans. (1993) 2071.
[2] K.S. Kumar, S.K. Singh, S.N. Pandeya, Bolletino Chimico Farmaceutico 140 (4) (2001) 238.
[3] I. Küçükgüzel, S.G. Küçükgüzel, S. Rollas, M. Kiras, Bioorg. Med. Chem. Lett. 11 (2001) 1703.
[4] T.K. Venkatachalam, E.A. Sudbeck, F.M. Uckun, Tetrahedron Lett. 42 (2001) 6629.
[5] G. Vasilev, I. Tafrdzhiiski, N.P. Masher, Dokl. Bolg. Akad. Nauk 27 (8) (1974) 1121.
[6] R. Campo, J.J. Criado, E. Garcia, M.R. Hermosa, A. Jimenez-Sanchez, J.L. Manzano, E. Monte, E. Rodriguez-Fernandez, F. Sanz, J. Inorg. Biochem. 289 (1–2) (2002) 74.
[7] M.J. Moloto, N. Revaprasadu, P. O'Brien, M.A. Malik, J. Mat. Sci.: Mat. Electron. 15 (5) (2004) 313.
[8] G. Schmid, Nanoparticles: From Theory to Application, Wiley-VCH, Weinheim, Germany, 2004.
[9] J.Z. Zhang, Z.-L. Wang, J. Liu, S. Chen, G.-Y. Liu, Self-Assembled Nanostructures, Kluwer Academic/Plenum Publishers, New York, 2003.
[10] C.B. Murray, D.J. Norris, M.G. Bawendi, J. Am. Chem. Soc. 115 (1993) 8706.
[11] Z.A. Peng, X. Peng, J. Am. Chem. Soc. 124 (2002) 3343.
[12] D.J. Milliron, S.M. Hughes, Y. Cui, L. Manna, J. Li, L.-W. Wang, A.P. Alivisatos, Nature 430 (2004) 190.
[13] M. Achermann, M.A. Petruska, S. Kos, D.L. Smith, D.D. Koleske, V.I. Klimov, Nature 429 (2004) 642.
[14] A.P. Alivisatos, Nat. Biotechnol. 22 (2004) 47.
[15] Y. Jun, Y. Jung, J. Cheon, J. Am. Chem. Soc. 124 (2002) 615.
[16] A. Ghezelbash, M.B. Sigman Jr., B.A. Korgel, Nano Lett. 4 (2004) 537.
[17] J.R. Heath, P.J. Kuekes, G. Synder, R.S. Williams, Science 280 (1998) 717.
[18] A. Thess, R. Lee, P. Nikolave, H. Dai, P. Petit, J. Robert, C.H. Xu, Y.H. Lee, S.G. Kim, A.G. Rinzler, D.T. Colbert, G.E. Scuseria, D. Tomanek, J.E. Fisher, R.E. Smalley, Science 271 (1999) 483.
[19] C.R. Martin, Science 266 (1994) 1961.
[20] B.R. Martin, D.J. Dermody, B.D. Reiss, M.M. Fang, L.A. Lyon, M.J. Natan, T.E. Mallouk, Adv. Mater. 11 (1999) 1021.
[21] T.J. Trentler, K.M. Hickman, S.C. Goel, A.M. Viano, P.C. Gibbons, W.E. Buhro, Science 270 (1995) 1971.
[22] Y. Li, Y. Ding, Z. Wang, Adv. Mater. 11 (1999) 847.
[23] J.D. Hopwood, S. Mann, Chem. Mater 9 (1997) 1819.
[24] Z.W. Pan, Z.R. Dai, Z.L. Wang, Science 291 (2001) 1947.
[25] Z.G. Bai, D.P. Yu, H.Z. Zhang, Y. Ding, Y.P. Wang, X.Z. Gai, Q.L. Hang, G.C. Xiong, S.Q. Feng, Chem. Phys. Lett. 303 (1999) 311.
[26] P. Yang, C.M. Lieber, Science 273 (1996) 1836.
[27] T. Tridade, P. O'Brien, Adv. Mater. 8 (1996) 161.
[28] T. Tridade, P. O'Brien, Chem. Mater. 9 (1997) 523.
[29] P.S. Nair, N. Revaprasadu, T. Radhakrishnan, G.A. Kolawole, J. Mater. Chem. 11 (2001) 1555.
[30] P.Sreekumari Nair, M.M. Chili, T. Radhakrishnan, N. Revaprasadu, P. Christian, P. O'Brien, S. Afr. J. Sci. 101 (2005) 466.
[31] Bruker, SMART (Version 5.625), SADABS (Version 2.03a) and SHELXTL (Version 6.12). Bruker AXS Inc., Madison, Wisconsin, USA, 2001.
[32] Bruker, SAINT. Version 6.36a. Bruker AXS Inc., Madison, Wisconsin, USA, 2002.
[33] G.M. Sheldrick, SHELX97. Programs for Crystal Structure Analysis (Release 97-2), University of Gottingen, Germany, 1997.
[34] C. Marcos, J.M. Alia, V. Adovasio, M. Prieto, S. Garcia-Granda, Acta Crystallogr., Sect. C 54 (9) (1998) 1225.
[35] F.H. Allen, O. Kennard, D.G. Watson, L. Brammer, A.G. Orpen, R. Taylor, in: A.J.C. Wilson (Ed.), International Tables of Crystallography, Vol. C, Kluwer Publishers, Dordrecht, 1991, p. 685.
[36] Y. Jun, J. Choi, J. Cheon, Angew. Chem., Int. Ed 45 (2006) 3414.
[37] L.E. Brus, J. Chem. Phys. 80 (1984) 4403.
[38] L.E. Brus, J. Chem. Phys. 79 (1983) 5566.
[39] M.G. Bawendi, M.L. Steigerwald, L.E. Brus, Annu. Rev. Phys. Chem. 41 (1990) 477.

UV–Vis spectrophotometry for functional group characterization [11–13]. On the other hand, nuclear magnetic resonance in the form of the solid state was found to provide valuable information about the modified physisorbed or chemisorbed silica via measurements of ^{1}H, ^{13}C, ^{15}N, ^{29}Si and ^{31}P by magic-angle spinning techniques [14–18]. However, hydration processes of chemisorbed or physisorbed silica gel phases can affect the chemical environments and functional groups in these phases as previously reported [18]. The mass spectrometric technique is well known for characterization of organic as well as inorganic species [19,20]. However, direct use of mass spectrometry, especially electron impact mode of ionization, for characterization of surface modification of chemisorbed or physisorbed silica phases is limited to only few reports due to the consideration of the high thermal stability of these modified silica gel phases [21,22].

Chemical or physical modification of silica with nitrogen and oxygen containing chelating compounds for the sake of applications as chelating sorbents were reported [23]. Among these are silica-modified-diethylenetriamine, with naphthaldehyde and salicylaldehyde [24]. Formylsalicylic acid derivatives on the surface of an amino group containing silica were previously reported [25,26]. Octadecyl-bonded silica membrane disks modified with a synthesized Schiff's base 2,2′–[1,2-ethanediyl-bis- (nitriloethylidyne)]-bis-(1-naphthalene) was also reported [27]. Silica impregnated with a mixture of Aliquat 336 and Titan Yellow was investigated [28]. Immobilization of mixed-donor (O, N) crown ether macrocycles to a silica matrix was described [29]. A number of methods for the immobilization of 8-hydroxyquinoline (8HQ) onto silica substrates were proposed, characterized and optimized [30–34].

2,5-Dioxypiperazine (DOPZ) is an example of a nitrogen and oxygen containing compound, known for its high biological activity [35,36] and is an important part of many reports concerned with the synthesis of a variety of biologically important compounds including peptides [37–39]. 2,5-Dioxypiperazine is also identified to have certain chelating characters via these two donor atoms. Chemical or physical binding of 2,5-dioxypiperazine to the surface of silica matrix has not been previously reported. Therefore, the aim of this work is to synthesize chemisorbed and physisorbed silica-immobilized-DOPZ for the sake of metal chelation applications. In addition, characterization and differentiation between newly chemisorbed and physisorbed silicas were also targeted by the aid of the direct insertion probe-mass spectrometric technique via the electron impact ionization mode.

2. Experimental

2.1. Apparatus

The electron impact mass spectra (EI-MS) of silica and the metal complexes were carried out using a Varion MAT 212 mass spectrometer equipped with a direct insertion probe (DIP) and the elemental analysis was performed by a GmbH Vario EL (III) system in the Institute for Inorganic and Analytical Chemistry, Muenster University, Germany. Differential scanning calorimetry (DSC) was conducted in an inert atmosphere (flowing nitrogen at a rate of 50 ml/min) on a Metter TA 3000 system (sample mass 20 mg, heating rate 20 K/min). Infrared spectra were performed using a Perkin–Elmer spectrophotometer model 1430, covering the frequency range 200–4000 cm^{-1}. Flame atomic absorption spectrophotometric measurements of metal ions were determined by a Perkin–Elmer 2380 atomic absorption spectrophotometer in the microanalytical laboratory of Faculty of Science, Alexandria, Egypt.

2.2. Chemicals and materials

3-Chloropropyltrimethoxysilane was received from Aldrich Chemical Company, USA. Silica (70–230 mesh, 60 Å pore diameter) was purchased from Riedel de Haën, Hannover, Germany. 2,5-Dioxypiperazine (DOPZ), also known as piperazine-2,5-dione or glycine anhydride, was purchased from Aldrich Chemical Company, USA. Metal salts were all of analytical reagent grade and were purchased from BDH Chemical Company, Poole, UK and Fluka Chemie AG, Switzerland. All chemicals were used as received and organic solvents were dried according to conventional methods. Metallic ion solutions were prepared from doubly distilled water (DDW).

2.3. Synthesis of modified silica and their metal complexes

Si–Cl, a silica-chemically immobilized-chloropropyl derivative, was prepared by the reaction of active silica with 3-chloropropyltrimethoxysilane as previously reported [6,7]. [Si–$(CH_2)_3$–DOPZ] was synthesized by the reaction of Si–Cl with DOPZ according to this method. Five millimol (~0.60 g) of 2,5-dioxypiperazine was completely dissolved in 50 ml methanol/50 ml toluene. Si–Cl, 5.0 g, was then suspended in this solution and the reaction mixture was stirred under reflux for four hours. [Si–$(CH_2)_3$–DOPZ] was filtered, washed with toluene, methanol and diethyl ether and dried in an oven at 70 °C for 6 h. Silica-physically adsorbed-DOPZ, [Si–DOPZ], was synthesized by the direct reaction of 5.0 g-active silica with 0.60 g-DOPZ already dissolved in 50 ml methanol/50 ml toluene. This reaction mixture was stirred at room temperature for 4 h. [Si–DOPZ] was filtered, washed with toluene, methanol and diethyl ether and dried in an oven at 70 °C for 6 h.

Cadmium(II), lead(II), mercury(II) and copper(II) complexes of [Si–$(CH_2)_3$–DOPZ] were synthesized by the reaction of 0.300 g-[Si–$(CH_2)_3$–DOPZ] with 60 ml of 0.1 mol/L of the selected metal ion in buffer solution, pH 6. This reaction mixture was automatically shaken for 1 h. The products [Si–$(CH_2)_3$–DOPZ]–Cd(II), [Si–$(CH_2)_3$–DOPZ]–Pb(II), [Si–$(CH_2)_3$–DOPZ]–Cu(II) and [Si–$(CH_2)_3$–

DOPZ]–Hg(II) were filtered, washed with DW and dried in an oven at 70 °C for 6 h.

2.4. Determination of the metal chelating values of [Si–$(CH_2)_3$–DOPZ]

1.0 ml of 0.1 mol/L–metal ion {Mg(II), Ca(II), Mn(II), Cr(III), Fe(III), Co(II), Ni(II), Cu(II), Zn(II), Cd(II), Hg(II) and Pb(II)} and 9.0 ml of selected acidic and buffer solutions pH 1–6 were mixed, and to this mixture 50.0 ± 0.1 mg of [Si–$(CH_2)_3$–DOPZ] was added. This mixture was shaken by an automatic shaker for 30 min at room temperature. The unextracted metal ion by solid phase in the reaction solution was filtered, washed with 50 ml of DDW and subjected to complexometric titration or atomic absorption analysis.

2.5. Distribution coefficient and separation factor values

Standard solutions, 1.0 mg/L each, of these metal ions in buffer solution with pH 6 as the optimized solution were prepared to determine the distribution coefficient values of Mg(II), Ca(II), Mn(II), Cr(III), Co(II), Ni(II), Cu(II), Zn(II), Cd(II), Hg(II) and Pb(II). Fe(III) was prepared in a buffer solution with pH 4. In a 25 ml measuring flask, 100 mg ± 1 mg of the modified silica [Si–$(CH_2)_3$–DOPZ] was weighed. Ten milliliters of 1.0 mg/L metal ion was then added and shaken by an automatic shaker for 1 h. This mixture was filtered and washed with 10 ml DDW. The volume of metal ion was completed to 50 ml by 5% nitric acid solution. Standard and blank solutions of the metal ions were also prepared. The concentration of metal ions in the sample, standard and blank solutions were determined by atomic absorption analysis.

3. Results and discussion

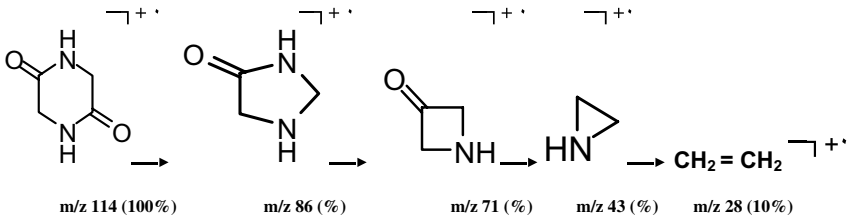
3.1. Surface characterization of chemisorbed [Si–$(CH_2)_3$–DOPZ] and physisorbed [Si–DOPZ]

The 70-eV EI-MS of the organic modifier, DOPZ, silica-chemically immobilized-DOPZ, [Si–$(CH_2)_3$–DOPZ], and silica gel-physically adsorbed-DOPZ, [Si–DOPZ] were studied and evaluated. It was found that DOPZ exhibited a characteristic molecular ion peak at m/z 114 (100%) as the base peak. Several other fragment ion peaks located at m/z 86 (8%), 71 (44%), 43 (18%), 30 (36%) and 28 (20%) were found to be correlated to the successive losses of CO, NH, CO and either CH or NH ions from the molecular ion. Scheme 1 represents the suggested fragmentation pathways for DOPZ by 70-eV EI-MS.

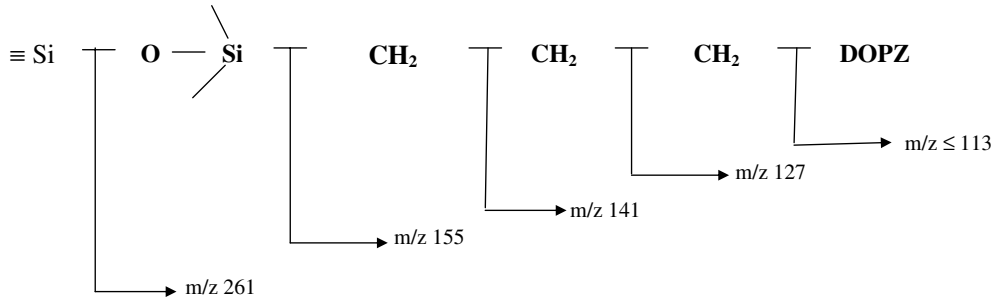
The use of a direct insertion probe (DIP) is a common method for the introduction of volatile and low melting point samples into the mass spectrometer and ionization chamber by direct heating of the sample either in the solid or liquid state. A temperature range of 400–500 °C is always used as the maximum heating temperature of the probe. This temperature range is sufficient to volatilize the analyte of interest and deliver it to the ion source in the gas phase. According to this procedure silica, either chemically or physically modified, is considered to be thermally non-volatile. However, heating these silica matrices to the maximum temperature of the DIP can lead to a desorption process of the organic modifier as DOPZ or other similar compounds. The desorbed or volatilized species from the modified silica can then be detected by the mass spectrometer, and the EI-MS spectrum can be further used to confirm the direct binding of the organic modifier to the surface of thermally stable silica matrix.

The 70-eV EI-MS of chemically modified silica [Si–$(CH_2)_3$–DOPZ] was found to show no evidence for the existence of the ion peak at m/z 114, but only a peak at m/z 113 with a relative abundance of 12%. The presence of this fragment ion clearly proves the suggested chemical binding of DOPZ to the surface of Si–Cl phase via the elimination of a HCl molecule and formation of a covalent bond between the two reacting species [7]. This trend can be also confirmed by the absence of the major fragment ions shown in Scheme 1. Only other fragment ions at m/z 85 (8%), and 70 (12%) were found to exist in the EI-MS of [Si–$(CH_2)_3$–DOPZ]. Other evidences for the chemical binding of DOPZ to the surface of Si–Cl can be concluded and outlined from the presence of other higher mass ion peaks at m/z 127 (7%), 141 (3%), 155 (3%) and 261 (13%). Mass assignment of these fragment ion peaks is given in Scheme 2.

The 70-eV EI-MS of physically adsorbed silica, [Si–DOPZ] was found to exhibit interesting results which can be outlined as follows. First are the identical mass spectra of both DOPZ and [Si–DOPZ]. Second is the identification of the same fragment ion peaks at m/z 114 (100%) as the base peak, 86 (5%), 71 (31%), 43 (13%), 30 (31%), 29 (10%) and 28 (13%). Third is the absence of direct evidence for the existence of any type of chemical binding of DOPZ to the surface of active silica.



Scheme 1. 70-eV EI-MS fragmentation pathways of DOPZ.



Scheme 2. Mass assignment of [Si–$(CH_2)_3$–DOPIZ].

Table 1
Thermal data of DOPZ, [Si–$(CH_2)_3$–DOPZ] and [Si–DOPZ]

Compound	Step	T_{max} (K)	Thermal effect	n	Ea (kJ mol^{-1})	ΔS^* (J mol^{-1} K^{-1})	ΔH^* (kJ mol^{-1})
DOPZ	1	610.6	exothermic	0.58	377.02	−0.223	−136.33
[Si–$(CH_2)_3$–DOPZ]	1	568.6	exothermic	1.7	367.72	−0.222	−126.32
[Si–DOPZ]	1	576.4	exothermic	1.16	212.28	−0.227	−128.89

Thus, 70-eV EI-MS studies by the application of the DIP technique was found to provide good information about silica modification with the DOPZ moiety on the basis of fragment ion peaks generated with the mass spectrometric technique. In addition, this technique was confirmed to give good and valuable information about the thermal desorption process of the loaded organic compound on the surface of the modified silica gel phase. Moreover, EI-MS fragment ion peaks to account and differentiate between the chemical binding or physical adsorption of the organic modifier DPOZ is considered as another dimension in such an investigation.

The infrared studies of [Si–$(CH_2)_3$–DOPZ] and [Si–DOPZ] were also used to confirm the possible binding of DOPZ to the surface of the silica gel phase via some characteristic peaks. Several characteristic IR peaks were detected in the infrared spectrum of DOPZ and these are centered at 1682, 2987 and 3330 cm −1 due to the presence of υC=O, υC–H aliphatic and υN–H, respectively. No evidence was observed for the existence of υO–H in the infrared spectrum of DOPZ and this trend can be used to report the existence of DOPZ in the keto form, not the enol form. The appearance and intensity of these peaks in [Si–$(CH_2)_3$–DOPZ] and [Si–DOPZ] are very low compared to their intensity in the infrared spectrum of DOPZ. This is mainly due to the low percentage value of DOPZ that was found to be bound on the surface of silica gel. In addition, the infrared spectra of [Si–$(CH_2)_3$–DOPZ] and [Si–DOPZ] were characterized by the presence of a strong and broad peak at <1400 cm $^{-1}$ due to the presence of the silica gel matrix. Based on the infrared and EI-MS results, chemical binding of the silica gel matrix is confirmed to occur on either one of the two N–H groups of DOPZ due to their positional similarities.

Differential scanning calorimetry (DSC) was also applied to DOPZ as well as the chemically modified silica gel phase [Si–$(CH_2)_3$–DOPZ] and physically adsorbed silica gel phase [Si–DOPZ] in order to compare and evaluate their thermal and kinetic characteristics. DOPZ was found to exihibt an exothermal peak at a T_{max} value of 610.6 K. The same exothermal peak was also detected for the two newly modified silica gel phases at 568.6 and 576.4 K for [Si–(CH_2)–DOPZ] and [Si–DOPZ], respectively. The calculated order of the thermal decomposition steps indicated that those thermal steps are not kinetically simple. Table 1 compiles the different thermal parameters.

3.2. Surface coverage and metal chelation properties of [Si–$(CH_2)_3$–DOPZ] and [Si–DOPZ]

The surface coverage values of [Si–$(CH_2)_3$–DOPZ] in mmol g^{-1} were determined on the basis of elemental analysis of nitrogen content [6] as well as by the metal probe testing method by considering the highest metal chelating capacity of the tested metal ions as a direct indicative and representative value of surface coverage [8,9]. These values were found to correspond to 0.179 and 0.160 for [Si–$(CH_2)_3$–DOPZ] by elemental analysis of nitrogen content and the cadmium (II) probe testing method, respectively. The determined mmol g^{-1} value of [Si–DOPZ] was only determined by nitrogen analysis and was found to be 0.251. The stability of the newly chelating silica [Si–$(CH_2)_3$–DOPZ] and [Si–DOPZ] in various acidic and buffer solutions (pH 1–7) [8] was also studied to evaluate their performance and leaching process. Chemically modified silica [Si–$(CH_2)_3$–DOPZ] was found to be highly stable in these acidic buffer solutions, with a maximum leaching percentage of $\leqslant$5.5% in acidic solutions of pH 1 and 2. In higher acidic buffer solutions, pH > 2, [Si–$(CH_2)_3$–DOPZ] displayed good chemical stability behavior. On the other hand, the degree of leaching of the organic modifier from the surface of [Si–DOPZ] was found to be higher than

the chemically modified one. The maximum leaching percentage of DOPZ in [Si–DOPZ] was found to be in the range of 17–39% in acidic solutions with pH 1–3. Thus, one can conclude a higher chemical stability of [Si–$(CH_2)_3$–DOPZ] in buffer solutions compared to [Si–DOPZ] and this trend can be attributed to the covalent binding of DOPZ. The metal chelating properties of chemically modified silica [Si–$(CH_2)_3$–DOPZ] toward various metal ions was only studied and evaluated due to its high chemical stability compared to the silica-physically adsorbed-DOPZ phase. Table 2 compiles the data in μmol g^{-1} for a series of metal ions, as well as the distribution coefficient values.

Evaluation of the metal chelation properties of newly modified silica [Si–$(CH_2)_3$–DOPZ] is considered more convenient by the metal capacity values expressed in either mmol g^{-1} or μmol g^{-1} or by the distribution coefficient (K_d) when the concentrations of the tested metal ions are very low, especially in the range of part per million (mg/L) or part per billion (μg/L). Therefore, both methods were used and applied in this study for better evaluation and comparison. The listed metal capacity values are the optimum ones based on determination in various acidic and buffer solutions (pH 1–6). The reported metal capacity and distribution coefficient values for this series of metal ions refer to high similarities in the behavior of newly modified silica gel phases for chelation or binding with the tested metal ions as listed in Table 2. The low metal chelating capacity values given in Table 2 can be related to the low surface coverage values identified for these phases. The same trends for the high selective chelating characters of [Si–$(CH_2)_3$–DOPZ] towards Cd(II), Pb(II), Cu(II) and Hg(II) compared to other metal ions are also observed in Table 2. This behavior is mainly attributed to the presence of donor atoms as N and O on the surface of the newly modified silica via the immobilization of (DOPZ) [23].

The possible separation efficiency and selective chelating character incorporated into chemically or physically adsorbed silica with organic chelating compounds towards various metal ions can be evaluated on the basis of the separation factor (α) expression [21,22]. In order for the silica gel-modified-chelating compound to accomplish any separation of two ions, it is necessary that one of these cations is extracted by the silica gel phase in a distinct preference to the other. This can be calculated from the distribution coefficient values of the two metal ions as given by the following equation:

$$\alpha_{A/IMI} = \frac{K_d(A)}{K_d(IMI)}$$

where $\alpha_{A/IMI}$ is the separation factor for the analyte (A) versus the interfering metal ion (IMI), K_d (A) is the distribution coefficient value of the analyte (A) and K_d (IMI) is the distribution coefficient value of the interfering metal ion (IMI). The values of the distribution coefficient were calculated according to the following equation.

$$K_d, \text{ml g}^{-1} = \frac{C_{i,\,ex}(\mu g g^{-1})}{C_{i,\,sol}(\mu g\ \text{ml}^{-1})}$$

where as $C_{i,ex}$ and $C_{i,\,sol}$ are the concentration values of surface-bound metal ion and solution-free metal ion, respectively.

Table 3 lists the separation factors for Cd(II), Pb(II), Hg(II) and Cu(II) versus other interfering metal ions as determined by [Si–$(CH_2)_3$–DOPZ]. Based on the listed values, one can conclude that the metal ions Cd(II), Pb(II), Hg(II) and Cu(II) are individually separated from the interfering ions Mg(II), Ca(II), Mn(II), Co(II), Ni(II), Cr(III), Fe(III) and Zn(II) by the use of [Si–$(CH_2)_3$–DOPZ]. On the other hand, possible interference of Pb(II), Hg(II) and Cu(II) in selective extraction of Cd(II) is expected due to the low separation factor of these three metal ions ($\alpha_{Cd(II)/\,IMI} = 1.1$–$1.3$). The outlined order of the metal ions chelating selective property by [Si–$(CH_2)_3$–DOPZ] based on the values of the distribution coefficient and separation factor can be listed as: Cd(II) > Pb(II) > Hg(II) > Cu(II) >>> Zn(II) > Fe(III) > Cr(III) > Ni(II) > Co(II) > Mn(II) > Ca(II) > Mg(II).

3.3. Stoichiometric properties of metal ions with [Si–$(CH_2)_3$–DOPZ]

Cd(II), Pb(II), Hg(II) and Cu(II) were selected to study the stoichiometric properties of metal binding with chemi-

Table 2
Metal capacity (μmol g^{-1}) and distribution coefficient K_d

Metal ion	μmol g^{-1} (buffer range)	K_d (buffer solution)
Mg(II)	0–10 (pH 3–6)	212 (pH 6)
Ca(II)	0–10 (pH 3–6)	240 (pH 6)
Mn(II)	5–20 (pH 3–4)	450 (pH 6)
Cr(III)	20–30 (pH 3–6)	820 (pH 6)
Fe(III)	30–50 (pH 3–4)	1125 (pH 4)
Co(II)	5–20 (pH 4–6)	560 (pH 6)
Ni(II)	5–20 (pH 3–6)	590 (pH 6)
Cu(II)	30–80 (pH 4–6)	32 620 (pH 6)
Zn(II)	20–30 (pH 4–6)	5230 (pH 6)
Cd(II)	70–160 (pH 3–6)	41 560 (pH 6)
Hg(II)	40–70 (pH 3–6)	33 485 (pH 6)
Pb(II)	50–90 (pH 3–6)	37 500 (pH 6)

Table 3
Separation factor ($\alpha_{A/IMI}$) of some metal ions by [Si–$(CH_2)_3$–DOPZ]

Interfering metal ion	($\alpha_{Cd(II)/IMI}$)	($\alpha_{Pb(II)/IMI}$)	($\alpha_{Hg(II)/IMI}$)	($\alpha_{Cu(II)/IMI}$)
Mg(II)	196.0	176.9	157.9	153.9
Ca(II)	173.2	156.3	139.5	135.9
Mn(II)	92.4	83.3	74.4	72.5
Co(II)	74.2	67.0	59.8	58.3
Ni(II)	70.4	63.6	56.8	55.3
Cr(III)	50.7	45.7	40.8	39.8
Fe(III)	36.9	33.3	29.8	29.0
Zn(II)	7.9	7.2	6.4	6.2
Cu(II)	1.3	1.1	1.0	
Hg(II)	1.2	1.1		
Pb(II)	1.1			
Cd(II)				

cally modified silica [Si–$(CH_2)_3$–DOPZ] due to their high affinity and selectivity characteristics compared to the other tested metal ions and based on the determined and calculated distribution and separation factors. According to the elemental analysis of nitrogen and metal contents, these metal ions were proved to give surface coverage values of 0.097–0.105, 0.093–0.110, 0.082–0.992 and 0.079–0.996 mmol g^{-1} for [Si–$(CH_2)_3$–DOPZ]–Cd(II), [Si–$(CH_2)_3$–DOPZ]–Pb(II), [Si–$(CH_2)_3$–DOPZ]–Hg(II) and [Si–$(CH_2)_3$–DOPZ]–Cu(II), respectively. Simple comparison of these values with the surface coverage of [Si–$(CH_2)_3$–DOPZ], 0.160–179 mmol g^{-1}, confirms the possible binding of all the tested metal ions, Cd(II), Pb(II) and Hg (II) and Cu(II), with [Si–$(CH_2)_3$–DOPZ] according to a molar stoichiometric ratio of 1:2.

The EI-MS via 70-eV was also used and applied to confirm the binding of the tested metal ions to the surface of [Si–$(CH_2)_3$–DOPZ]. The EI-MS of [Si–$(CH_2)_3$–DOPZ]–metal complexes were found to exhibit several characteristic fragment ion peaks that can be classified into three main groups. The first is mainly related to DOPZ, the second is referred to [Si–$(CH_2)_3$–DOPZ] and the third group due to [Si–$(CH_2)_3$–DOPZ]–metal complex. In the case of [Si–$(CH_2)_3$–DOPZ]–Cd(II), the first identified fragment ions group in the EI-MS was found to correspond to DOPZ at *m*/*z* 113 (4%), 112 (7%), 111 (4%), 85 (7%), 84 (4%), 71 (10%), 70 (7%), 69 (6%), 42 (8%), 41 (8%), 29 (4%) and 28 (3%) and the second group of identified fragment ions contains *m*/*z* 261(5%), 233 (25%), 155 (2%), 141 (3%) and 127 (3%), and these are related to [Si–$(CH_2)_3$–DOPZ]. The third group of ions attributed to fragmentation of [Si–(CH_2)–DOPZ]–Cd(II) were found at *m*/*z* 224 (2%), 210 (2%), 196 (2%) and 168 (7%). Table 4 compiles the major fragment ion peaks, their mass assignments and origin of these ions identified in the case of [Si–$(CH_2)_3$–DOPZ]–Cd(II). The same three groups of fragment ions were also characterized from the EI-MS of [Si–$(CH_2)_3$–DOPZ]–Pb(II) and these are listed as first, *m*/*z* 113 (8%), 112 (8%), 111 (19%), 85 (18%), 84 (10%), 71 (22%), 70 (13%), 69 (25%), 42 (8%), 41 (21%), 29 (8%) and 28 (73%). The second group of ions contains *m*/*z* 261(8%), 155 (5%), 141 (5%) and 127 (4%). The fragment ions at *m*/*z* 320 (4%), 252 (23%), 208 (15%) and 207 (6%) represents the third group. The identified three fragment ions groups in the EI-MS of [Si–$(CH_2)_3$–DOPZ]–Hg(II) were identified as first, *m*/*z* 113 (13%), 112 (13%), 111 (12%), 85 (26%), 84 (10%), 71 (32%), 70 (13%), 69 (16%), 42 (3%), 41 (14%), 29 (7%) and 28 (27%), second, at *m*/*z* 261(6%), 155 (8%), 141 (7%) and 127 (11%) and third group of fragment ions is located at *m*/*z* 341 (4%), 327 (4%) and 313 (2%). In the case of [Si–$(CH_2)_3$–DOPZ]–Cu(II) the identified fragment ions were found at *m*/*z* 113 (13%), 112 (10%), 111 (14%), 85 (28%), 84 (7%), 70 (12%), 69 (16%), 42 (27%), 41 (14%) and 29 (8%) as the first group of ions. The second group of fragment ions were found at *m*/*z* 127 (12%), 141 (9%) and 155 (8%) and there was no evidence for the formation of fragment ions that are related to [Si–$(CH_2)_3$–DOPZ]–Cu(II). This may be due to the high thermal stability of [Si–$(CH_2)_3$–DOPZ]–Cu(II) compared to the other metal complexes.

Table 4
EI-MS assignment of the major fragment ions of [Si–$(CH_2)_3$–DOPZ]–Cd(II)

Ion (Relative abundance, %)	Ion assignment	Origin of ions
113 (4)	M−H	DOPZ
112 (7)	M−2H	
111 (4)	M−3H	
85 (7)	M−[H + CO]	
84 (4)	M−[2H + CO]	
71 (10)	M−[H + CO + NH]	
70 (7)	M−[2H + CO + NH]	
69 (6)	M−[3H + CO + NH]	
42 (8)	C_2H_4N	
41 (8)	C_2H_3N	
29 (4)	C_2H_5	
28 (3)	C_2H_4	
261 (5)	M+$C_3H_6SiO_3(CH_3)_2$–[H]	[Si–$(CH_2)_3$–
233 (25)	M+$C_3H_6SiO_3(CH_3)_2$−[H + CO]	DOPZ]
155 (2)	M+C_3H_6−[H]	
141 (3)	M+C_2H_4–[H]	
127 (3)	M+CH_2–[H]	
224 (2)	DOPZ + Cd–[H_2]	[Si–$(CH_2)_3$–
210 (2)	DOPZ + Cd–[H_2+N]	DOPZ]–Cd(II)
196 (2)	DOPZ + Cd–[H_2+CO]	
168 (2%)	DOPZ + Cd–[H_2+2CO]	

Differential scanning calorimetry (DSC) was also used to study and evaluate the thermal characteristics of the same four metal complexes with chemically modified silica. The thermal analysis data are calculated as previously reported [40,41] and compiled in Table 5. These species

Table 5
Thermal data of the [Si–$(CH_2)_3$–DOPZ]–metal complex

Compound	Step	T_{max} (K)	Thermal effect	*n*	Ea (kJ mol^{-1})	ΔS^* (J mol^{-1} K^{-1})	ΔH^* (kJ mol^{-1})
Cd-complex	1	572.2	exothermic	2.19	629.69	−0.212	−124.90
	2	637.9	exothermic	1.88	664.73	−0.218	−139.09
Pb-complex	1	568.7	exothermic	0.66	144.28	−0.231	−131.162
Cu-complex	1	719.6	exothermic	0.613	70.56	−0.241	−178.28
Hg-complex	1	572.6	exothermic	1.92	766.50	−0.215	−123.09
	2	688	exothermic	1.21	91.986	−0.237	−136.60

were found to exhibit exothermic peaks at 572.2, 568.7, 572.6 and 719.6 K for [Si–$(CH_2)_3$–DOPZ]–Cd(II), [Si–$(CH_2)_3$–DOPZ]–Pb(II), [Si–$(CH_2)_3$–DOPZ–Hg(II) and [Si–$(CH_2)_3$–DOPZ]–Cu(II), respectively. However, the cadmium and mercury complexes were found to give an extra exothermic peak at 637.9 and 688 K, respectively. A remarkable feature was observed and detected in the DSC of [Si–$(CH_2)_3$–DOPZ]–Cu(II) and this corresponds to the pronounced high stability character due to formation of only one exothermic peak at the highest identified temperature, 719.6 K, compared to the other metal complexes. This observation is also confirmed and found to be consistent with the 70-eV EI-MS of [Si–$(CH_2)_3$–DOPZ]–Cu(II). The activation energy changes of the decomposition processes (first step) for the metal complexes were found to follow this order: [Si–$(CH_2)_3$–DOPZ]–Cu(II) < [Si–$(CH_2)_3$–DOPZ]–Pb(II) < [Si–$(CH_2)_3$–DOPZ]–Cd(II) < [Si–$(CH_2)_3$–DOPZ]–Hg(II). In addition, the fractions appeared in the calculated order of the thermal decomposition steps, indicating that those thermal steps are not kinetically simple. The narrow range of the entropy changes (−0.212 to −0.241) given in Table 5 illustrate the similarity of the thermal behavior. The negative sign indicates that the transition state of the thermal reaction is more ordered.

4. Conclusion

Surface modification of silica gel with DOPS via covalent binding was proved to change the chelating character of the silica matrix. The strong affinity of [Si–$(CH_2)_3$–DOPZ] to chelate toxic heavy metals such as Cd(II), Hg(II) and Pb(II) compared to other tested metals can add another dimension to this work and direct more interest towards the potential application of this new chelating sorbent for extraction, removal, separation and preconcentration of these metals from their environments in a pure state and without interference of other metal ions.

References

[1] M. Zougagh, J.M.C. Pavon, T.A. Garcia, Anal. Bioanal. Chem. 38 (2005) 1103.
[2] A. Goswami, A.K. Singh, Talanta 58 (2002) 669.
[3] J.A.A. Sales, F.P. Faria, A.G.S. Prado, C. Airoldi, Polyhedron 23 (2004) 719.
[4] N.L.D. Fihlo, Polyhedron 18 (1999) 2241.
[5] H. Mizuguchi, E. Kaneko, T. Yosuyanagi, Analyst 125 (2000) 1667.
[6] T. Seshadri, G. Dietz, H.-J. Haupt, Fresenius Z. Anal. Chem. 319 (1984) 403.
[7] P.K. Jal, S. Patel, B.K. Mishra, Talanta 62 (2004) 1005.
[8] M.E. Mahmoud, M.M. Osman, M.E. Amer, Anal. Chim. Acta 415 (2000) 33.
[9] M.E. Mahmoud, M.S.M. Al Saadi, Anal. Chim. Acta 450 (2001) 239.
[10] M.E. Mahmoud, G.A. Gohar, Talanta 51 (2000) 77.
[11] D.E. Lyden, D.S. Kendall, L.W. Burggarf, F.J. Pern, M. deBello, Anal. Chem. 54 (1982) 101.
[12] I. Shimizu, H. Okabayashi, K. Taga, C.J. O'Connor, Colloid. Polym. Sci. 275 (1997) 555.
[13] H. Okabayashi, I. Shimizu, E. Nisho, C.J. O'Connor, Colloid. Polym. Sci. 275 (1997) 744.
[14] M.J. Wirth, M.D. Ludes, D.J. Swinton, Anal. Chem. 71 (1999) 3911.
[15] T. Bernstein, P. Fink, V.M. Mastikhin, A.A. Shubin, J. Chem. Soc, Faraday Trans. 1 (1986) 1879.
[16] K. Hegger, G. Marx, E. Brendler, B. Thomas, Fresenius J. Anal. Chem. 358 (1997) 240.
[17] P. Sutra, F. Fajula, D. Brunel, P. Lenz, G. Daelen, J.B. Nagy, Colliod. Surf. A: Physicochem. Eng. Aspects 158 (1999) 21.
[18] G.S. Caravajal, D.E. Lyden, G.R. Quinting, G.E. Maciel, Anal. Chem. 60 (1988) 1776.
[19] A.W. Ehlers, C.G. de Koster, R.J. Meier, K. Lammertsrna, J. Phys. Chem. 105 (2001) 8691.
[20] G. A Nurgalieva, Y.S. Nekrasov, D.V. Zagrorevskii, D.N. Kursanov, J. Organomet. Chem. 202 (1980) 77.
[21] M.E. Mahmoud, M.M. El-Essawi, S.A. Kholeif, E.I. Fathallah, Anal. Chim. Acta. 525 (2004) 123.
[22] M.E. Mahmoud, M.M. El-Essawi, E.I. Fathallah, J. Liq. Chrom. Rel. Technol. 27 (2004) 1.
[23] M.E. Mahmoud, Encyclopedia of Chromatograhy, Taylor & Francis, 2006 (on-line).
[24] E.M. Soliman, M.E. Mahmoud, S.A. Ahmed, Talanta 54 (2001) 243.
[25] M.E. Mahmoud, E.M. Soliman, Talanta 44 (1997) 15.
[26] M.E. Mahmoud, E.M. Soliman, Talanta 44 (1997) 1063.
[27] M. Shamsipur, A.R. Ghiasvand, H. Sharghi, N. Naeimi, Anal. Chim. Acta 408 (2000) 271.
[28] R. Kocjan, S. Przeszlakowski, Talanta 39 (1992) 63.
[29] V. Dudler, L.F. Lindoy, D. Sallin, C.W. Sclaaepfer, Aust. J. Chem. 40 (1987) 1557.
[30] T. Honjo, H. Kitayama, K. Terada, T. Kiba, Fresenius Z. Anal. Chem. 330 (1988) 159.
[31] B.J. Daih, H.J. Huang, Anal. Chim. Acta 258 (1992) 245.
[32] S. Nakashima, R.E. Stugeon, S.N. Willie, S.S. Berman, Fresenius Z. Anal. Chem. 330 (1988) 592.
[33] C.H. Risner, J.R. Jezorek, Anal. Chim. Acta 186 (1986) 233.
[34] U. Pyell, G. Stork, Fresenius J. Anal. Chem. 343 (1992) 576.
[35] C.E. Frantz, H. Smith, D.M. Eadas, A.J. Grosovsky, D.A. Eastmond, Cancer Lett. 120 (1997) 135.
[36] R.M. Snapka, S.H. Woo, A.V. Blokhin, D.T. Witiak, Biochem. Pharmacol. 52 (1996) 543.
[37] M. Belohradsky, I. Ciaslova, P. Holy, J. Pastor, J. Zavada, Tetrahedron 58 (2002) 8811.
[38] I.L. Rodionov, L.N. Rodionova, L.K. Baidakova, A.M. Romashko, T.A. Balashova, V.T. Ivanov, Tetrahedron 58 (2002) 8515.
[39] C.J. Dinsmore, D.C. Beshore, Tetrahedron 58 (2002) 3297.
[40] H.J. Borchardt, F.J. Daniels, J. Am. Chem. Soc. 79 (1975) 41.
[41] K.K. Aravindakshan, K. Muralcedharan, Thermochim. Acta 159 (1990) 101.

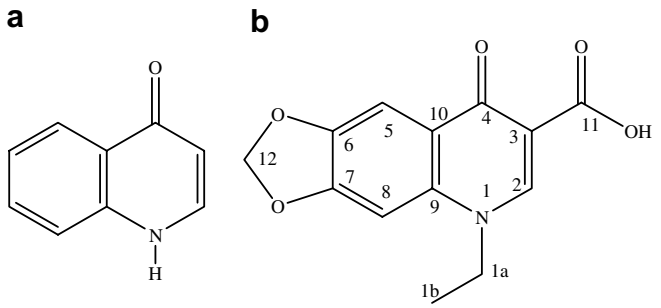


Fig. 1. (a) The 4-oxo-1,4-dihydroquinoline skeleton. (b) Oxolinic acid (Hoxo = 5,8-dihydro-5-ethyl-8-oxo-1,3-dioxolo[4,5-g]quinoline-7-carboxylic acid) and atom labeling.

to examine the mode of binding and possible synergetic effects. The resultant mononuclear complexes have been characterized with elemental analysis and various spectroscopic techniques (IR, UV–Vis and NMR spectroscopy). Molecular modeling techniques have been employed to assess the lowest energy model structure of the complexes $VO(oxo)_2(H_2O)$, $Mn(oxo)_2(H_2O)_2$ and $Fe(oxo)_3$. The interaction of all the complexes with calf-thymus (CT) DNA has been studied with UV and circular dichroism (CD) spectroscopy.

2. Experimental

2.1. Materials

Oxolinic acid and CT DNA were purchased from Sigma, $VOSO_4 \cdot 5H_2O$, $MnCl_2 \cdot 4H_2O$, $FeCl_3 \cdot 3H_2O$, $CoCl_2 \cdot 6H_2O$, $NiCl_2 \cdot 6H_2O$, $ZnCl_2$, $CdCl_2 \cdot 2.5H_2O$, KOH and all the solvents were purchased from Aldrich Co, NaCl was purchased from Merck and trisodium citrate was purchased from Riedel–de Haen. All the chemicals were reagent grade and were used as purchased. Dimethylformamide (dmf) was distilled from calcium hydride (CaH_2) and CH_3OH from magnesium (Mg) and were stored over 3 Å molecular sieves. Diethyl ether, anhydrous grade and absolute ethanol were used without any further purification.

DNA stock solutions (5 mM) were prepared by dilution of CT DNA to the 5 mM buffer (containing 150 mM NaCl and 15 mM trisodium citrate at pH 7.0) followed by exhaustive stirring at 4 °C for three days [31], and kept at 4 °C for no longer than a week. The nucleotide concentrations were determined by their absorption at 260 nm using $\varepsilon = 6600\ M^{-1}\ cm^{-1}$ (expressed as phosphate).

2.2. Synthesis of the complexes

2.2.1. $VO(oxo)_2(H_2O)$ (1)

A methanolic solution (15 mL) of oxolinic acid (0.4 mmol, 105 mg), deprotonated with KOH (0.4 mmol, 22 mg), was added to a methanolic solution (10 mL) of $VOSO_4 \cdot 5H_2O$ (0.2 mmol, 51 mg) and the reaction mixture was refluxed for 2 h. The solution was filtered and left for slow evaporation. After a few days a green microcrystalline product was deposited, collected with filtration, washed with methanol and dried. Yield: 96 mg, ~80%. *Anal.* Calc. for $VO(oxo)_2(H_2O)$ ($C_{26}H_{22}N_2O_{12}V$) (MW = 605.41): C, 51.58, H, 3.66, N, 4.63. Found: C, 51.15; H, 3.53; N, 5.02%. The complex is soluble in dmso, dmf and H_2O and is non-electrolyte.

Complexes **2**–**7** were prepared in a similar way with the use of the corresponding metal salt. All the resultant complexes are non-electrolytes.

2.2.2. $Mn(oxo)_2(H_2O)_2$ (2)

$MnCl_2 \cdot 4H_2O$ (0.2 mmol, 40 mg) was used. A yellow microcrystalline product was collected. Yield: 90 mg, ~75%. *Anal.* Calc. for $Mn(oxo)_2(H_2O)_2$ ($C_{26}H_{24}N_2O_{12}Mn$) (MW = 611.42): C, 51.07; H, 3.96; N, 4.58. Found: C, 50.82; H, 4.15; N, 3.89%. The complex is soluble in dmso.

2.2.3. $Fe(oxo)_3$ (3)

$FeCl_3 \cdot 3H_2O$ (0.2 mmol, 44 mg) and oxolinic acid (0.6 mmol, 158 mg) were used. An orange microcrystalline product was collected. Yield: 130 mg, ~80%. *Anal.* Calc. for $Fe(oxo)_3$ ($C_{39}H_{30}N_3O_{15}Fe$) (MW = 836.53): C, 56.00; H, 3.62; N, 5.02. Found: C, 55.93; H, 3.91; N, 5.21%. The complex is soluble in dmso, dmf and H_2O.

2.2.4. $Co(oxo)_2(H_2O)_2$ (4)

$CoCl_2 \cdot 6H_2O$ (0.2 mmol, 48 mg) was used. A pink microcrystalline product was collected. Yield: 86 mg, ~70%. *Anal.* Calc. for $Co(oxo)_2(H_2O)_2$ ($C_{26}H_{24}N_2O_{12}Co$) (MW = 615.42): C, 50.74; H, 3.93; N, 4.55. Found: C, 50.84; H, 4.07; N, 4.65%. The complex is soluble in dmso and dmf.

2.2.5. $Ni(oxo)_2(H_2O)_2$ (5)

$NiCl_2 \cdot 6H_2O$ (0.2 mmol, 48 mg) was used. A light green microcrystalline product was collected. Yield: 98 mg, ~80%. *Anal.* Calc. for $Ni(oxo)_2(H_2O)_2$ ($C_{26}H_{24}N_2O_{12}Ni$) (MW = 615.19): C, 50.76; H, 3.93; N, 4.55. Found: C, 50.41; H, 4.01; N, 4.27%. The complex is soluble in dmso.

2.2.6. $Zn(oxo)_2(H_2O)_2$ (6)

$ZnCl_2$ (0.2 mmol, 28 mg) was used. A pale yellow microcrystalline product was collected. Yield: 95 mg, ~75%. *Anal.* Calc. for $Zn(oxo)_2(H_2O)_2$ ($C_{26}H_{24}N_2O_{12}Zn$) (MW = 621.86): C, 50.22; H, 3.89; N, 4.51. Found: C, 50.41; H, 3.83; N, 4.33%. The complex is soluble in dmso and dmf.

2.2.7. $Cd(oxo)_2(H_2O)_2$ (7)

$CdCl_2 \cdot 2.5H_2O$ (0.2 mmol, 46 mg) was used. A pale yellow microcrystalline product was collected. Yield: 95 mg, ~70%. *Anal.* Calc. for $Cd(oxo)_2(H_2O)_2$ ($C_{26}H_{24}N_2O_{12}Cd$) (MW = 668.89): C, 46.69; H, 3.62; N, 4.19. Found: C, 46.51; H, 3.85; N, 4.25%. The complex is soluble in dmso and dmf.

2.3. Instrumentation

Infrared (IR) spectra (400–4000 cm^{-1}) were recorded on a Nicolet Magna-IR 550 with samples prepared as KBr pellets. UV–visible (UV–Vis) spectra were recorded as nujol mulls and in solution at concentrations in the range 10^{-5}–10^{-3} M on a Thermo Electron Corporation Helios α dual beam spectrophotometer. C, H and N elemental analysis were performed on a Perkin–Elmer 240B elemental analyzer. Electric conductance measurements were carried out with a WTW model LF 530 conductivity outfit and a type C cell, which had a cell constant of 0.996. Nuclear magnetic resonance (NMR) spectra were recorded with a Bruker Avance 500 MHz instrument and were processed by X-WIN NMR 2.6 (Bruker Analytik GmbH).

The interaction of the complexes with CT DNA has been investigated with UV and CD spectroscopies. In both techniques, the spectra of CT DNA in the presence of each complex have been recorded for a constant CT DNA concentration ($3.125x10^{-4}$ M) in diverse complex:CT DNA mixing ratios (r). All the UV and CD spectra were recorded after incubation of the complex with CT DNA for 24 h at 37 °C.

The CD spectra were recorded on a Jasco J-700 spectropolarimeter using a 1.0 cm path quartz cell and the following acquisition parameters: $\lambda = 190$–400 nm, scan speed 50 nm min^{-1}, resolution step 0.2 nm, sensitivity 50 mdeg, response 1 s, bandwidth 1.0 nm, accumulations 10. In some cases, the spectra were averaged over an appropriate number of scans.

2.4. Molecular modeling

Although diverse crystallization techniques were employed, we did not manage to obtain a crystal suitable for the structure determination with X-ray crystallography. With the aim to present a molecular model for each new complex that is unbiased by the starting structure, we have used Langevin dynamics with a simulated annealing protocol. Using this method, the mean total energy of an ensemble of structures guides the selection of the most favorable configuration for each complex. Starting structures were constructed using the program HyperChem and the MM^+ force field that is based on the Allinger's MM2 force field [32]. For all the metal ions we used a default parameter set with $R^* = 2.20$ Å and $e^* = 0.02$ kcal mol^{-1}, since their van der Waals interactions are not expected to play a major role in such bonded representations as in octahedral complexes. Metal–ligand bond lengths were corrected in the final models using harmonic restraints with equilibrium values that were extracted from crystallographic data of similar compounds [33–52] (Tables S1, S3, S5). Nonbonded interactions were calculated in vacuo with no cutoff and the electrostatic energy term was treated using bond dipoles. Initial energy minimizations were carried out by a conjugate gradient method with rms gradient <0.01 as convergence criterion.

Each model (Schemes S1, S2, S3) was subjected to 20 individual rounds of simulated annealing setting different value to the seed for the assignment of the starting velocities. To integrate the Langevin equation [53] the step size was set to 1 fs and the collision frequency to 1 ps^{-1}. The annealing calculation comprised three phases: (i) raising the temperature of the system from 10 to 1000 K over 2 ps, (ii) keeping the system at 1000 K for 3 ps and (iii) cooling the system down to 0 K over 15 ps. A tight coupling of the system with temperature (0.1 ps) was used for the heating and equilibration phases. During the cooling phase the bath relaxation time was gradually decreased from 5.0 ps (7000 steps), 2.0 ps (3000 steps), 1.0 ps (2000 steps), 0.5 ps (2000 steps) to 0.05 ps (1000 steps). At the final step all structures had rms gradient <0.01 and their total energy was recorded (Tables S2, S4, S6). The models presented herein were selected among the lowest energy structures that were generated for each starting geometry. A final minimization of their energy was performed as above, but having applied the metal–ligand distance restraints.

3. Results and discussion

3.1. Synthesis of the complexes

All the complexes have been prepared at high yield (70–80%) via the addition of a methanolic solution of deprotonated oxolinic acid to a methanolic solution of the metal ion at a ratio 3:1 for Fe^{3+} and 2:1 for the remaining divalent metal ions according to the reaction:

$$M^{n+} + n\,\text{oxo} \rightarrow M(\text{oxo})_n(H_2O)_x$$

where $M^{n+} = Fe^{3+}$ ($n = 3$, $x = 0$), VO^{2+} ($n = 2$, $x = 1$), and Mn^{2+}, Co^{2+}, Ni^{2+}, Zn^{2+} and Cd^{2+} ($n = 2$, $x = 2$). The resultant complexes **1**–**7** are mainly soluble in dmso and dmf and are non-electrolytes.

3.2. IR spectroscopy

In Table 1 the characteristic absorptions of the IR spectra of all the complexes are listed. In the IR spectra of the

Table 1
Characteristic absorptions (in cm^{-1}) of IR spectra of the complexes

	ν(O–H)	ν(C=O)$_p$	$\nu(CO_2)_{asym}$	$\nu(CO_2)_{sym}$	Δ[a]	ν(M=O)
Hoxo		1633	1712[b]			
$VO(oxo)_2(H_2O)$	3410	1645	1602	1376	226	930
$Mn(oxo)_2(H_2O)_2$	3405	1636	1606	1385	221	
$Fe(oxo)_3$		1640	1605	1380	225	
$Co(oxo)_2(H_2O)_2$	3410	1639	1599	1395	204	
$Ni(oxo)_2(H_2O)_2$	3400	1637	1592	1390	202	
$Zn(oxo)_2(H_2O)_2$	3405	1638	1601	1393	208	
$Cd(oxo)_2(H_2O)_2$	3410	1636	1604	1395	209	
$Cu(oxo)_2(H_2O)$, [24]	3410	1639	1599	1388	211	

[a] $\Delta = \nu(CO_2)_{asym} - \nu(CO_2)_{sym}$.
[b] as ν(COOH).

complexes **1**–**7**, the absorption at 1712 cm^{-1} in the spectrum of oxolinic acid attributed to the absorption of the $\nu(C{=}O)_{carb}$ has disappeared. Two very strong characteristic bands are present in the range of 1592–1606 cm^{-1} and 1375–1395 cm^{-1} that could be assigned as ν(O–C–O) asymmetric, $\nu_{asym}(CO_2)$, and symmetric, $\nu_{sym}(CO_2)$, stretching vibrations, respectively, whereas $\nu(C{=}O)_p$ is slightly shifted from 1633 to 1636–1645 cm^{-1} upon bonding. The difference $\Delta = \nu_{asym}(CO_2) - \nu_{sym}(CO_2)$ is a useful characteristic for determining the coordination mode of the carboxylato ligands. The Δ values fall in the range 202–226 cm^{-1} indicating a monodentate coordination mode of the carboxylato group of oxolinato ligands [54,55]. These changes of the IR spectra suggest that the oxolinato ligand is coordinated to the metal via the pyridone oxygen and one carboxylato oxygen [4,24].

The existence and the number of the $\nu(V{=}O)$ absorptions is a useful diagnostic tool of the vanadyl complexes characterization. The appearance of the V=O stretching frequency in complex **1** at ~930 cm^{-1} implies that a monoanionic ligand lies in *trans* position to the vanadyl oxygen (O_v) [56]. This acceptance is indicative of the arrangement of one O_c or O_p atom in the axial position of the octahedron around V atom and excludes the O_w atom.

The band at ~3400–3410 cm^{-1} in the IR spectra of the complexes **1**, **2** and **4**–**7** can be attributed to ν(O–H) vibration of one or two coordinated water molecules [30,54].

3.3. Electronic spectroscopy

The UV–Vis spectra of all the complexes have been recorded as nujol mulls and in dmso solution. Practically, the spectra in dmso solution are identical with those in nujol with the exception of a few nm shifts in some cases. The UV–Vis spectral data of all the complexes in dmso solution are given in Table 2.

The UV spectra of the complexes are practically identical with that of the oxolinic acid but slightly shifted, indicative of coordination through the pyridone oxygen and one carboxylate oxygen.

In the visible spectra, there are characteristic bands attributed to d–d transitions only for VO^{2+}, Fe^{3+}, Co^{2+} and Ni^{2+} complexes. In the visible spectrum of $VO(oxo)_2(H_2O)$, three low-intensity bands at 790 (band I), 600 (band II) and 498 (band III) nm attributed to d–d transitions are observed. Band I at $\lambda = 790$ nm ($\varepsilon = 10\ M^{-1}\ cm^{-1}$) can be attributed to a $b_2(d_{xy}) \rightarrow e_\pi^*(d_{xz}, d_{yz})$ transition of the $V^{IV}O^{2+}$ and band II at $\lambda = 600$ nm ($\varepsilon = 20\ M^{-1}\ cm^{-1}$) to a $b_2(d_{xy}) \rightarrow b_1^*(d_{x^2-y^2})$ transition [57]. Band III at $\lambda = 498$ nm ($\varepsilon = 28\ M^{-1}\ cm^{-1}$) is also observed and can be attributed to a $d_{xy} \rightarrow d_{z^2}$ transition although it usually lies under the much stronger ligand-to-metal charge-transfer transition (LMCT) at $\lambda = 433$ nm ($\varepsilon = 150\ M^{-1}\ cm^{-1}$) and can be difficulty distinguished [58,59]. These bands are typical for distorted octahedral VO^{2+} complexes [38,39,41,56].

The spectrum of $Fe(oxo)_3$ exhibits two bands that can be attributed to d–d transitions: one weak band I at $\lambda = 605$ nm ($\varepsilon = 35\ M^{-1}\ cm^{-1}$) which can be assigned as a $^6A_{1g} \rightarrow {}^5T_{1g}$ transition and an intense one, band II, at $\lambda = 510$ nm ($\varepsilon = 80\ M^{-1}\ cm^{-1}$) assigned as a $^6A_{1g} \rightarrow T_{2g}$ (G) transition [60,61]. These bands are typical for distorted octahedral Fe^{3+} [33–37] complexes.

In the spectra of $Co(oxo)_2(H_2O)_2$ and $Ni(oxo)_2(H_2O)_2$ one band at $\lambda = 560$ nm ($\varepsilon = 40\ M^{-1}\ cm^{-1}$) for **4** and at $\lambda = 650$ nm ($\varepsilon = 35\ M^{-1}\ cm^{-1}$) for **5** attributed to d–d transition has been found as it is expected for octahedral high-spin Co^{2+} [62,63] and Ni^{2+} [64,65] complexes, respectively. Similar behavior has been observed for the octahedral high-spin Co^{2+} [66] and Ni^{2+} [67] cinoxacin complexes.

All the complexes also exhibit an absorption band (as a shoulder) in the range $\lambda = 429$–438 nm ($\varepsilon \sim 140$–

Table 2
Characteristic bands [λ_{max}, in nm (ε, in $M^{-1}\ cm^{-1}$)] in UV–Vis spectra of the complexes in dmso solution

	IL bands			Band CT	d–d Bands		
Hoxo	285	315	345 (sh)				
	(6400)	(7600)	(2400)				
$VO(oxo)_2(H_2O)$	286	323	350	433(sh)[a]	498	600	790
	(7600)	(4200)	(3350)	(150)	(28)	(20)	(10)
$Mn(oxo)_2(H_2O)_2$	289	323	346	429(sh)			
	(7820)	(4250)	(3230)	(145)			
$Fe(oxo)_3$	287	325	345	438(sh)	510	605	
	(7850)	(4260)	(2950)	(170)	(80)	(35)	
$Co(oxo)_2(H_2O)_2$	285	325	346	432(sh)	560		
	(7420)	(3150)	(2430)	(140)	(40)		
$Ni(oxo)_2(H_2O)_2$	287	325	345	432 (sh)		650	
	(7250)	(4600)	(3680)	(160)		(35)	
$Zn(oxo)_2(H_2O)_2$	289	325	342	433(sh)			
	(7500)	(5200)	(3360)	(150)			
$Cd(oxo)_2(H_2O)_2$	287	324	345	430(sh)			
	(7550)	(5450)	(3480)	(155)			

[a] (sh) = shoulder.

Table 3
Chemical shifts (δ, in ppm) in ^{1}H NMR spectra of Hoxo, $Zn(oxo)_2(H_2O)_2$ and $Cd(oxo)_2(H_2O)_2$ in d_6-dmso

	Hoxo	$Zn(oxo)_2(H_2O)_2$	$Cd(oxo)_2(H_2O)_2$
H1a	4.49	4.58	4.55
H1b	1.35	1.40	1.42
H2	8.86	9.13	9.16
H5	7.60	8.38	8.41
H8	7.60	7.67	7.68
H12	6.26	6.32	6.34

200 M^{-1} cm^{-1}) which can be assigned to the LMCT transition for the quinolone ligand [24–30].

3.4. NMR spectroscopy

^{1}H NMR spectra of Hoxo, $Zn(oxo)_2(H_2O)_2$ and $Cd(oxo)_2(H_2O)_2$ were recorded in d_6-dmso. Full assignment of every signal in the ^{1}H NMR spectrum of complexes **6** and **7** was achieved by comparing the spectrum of each complex with the spectrum of the ligand and those reported in the literature [28,30,68]. The results are shown in Table 3.

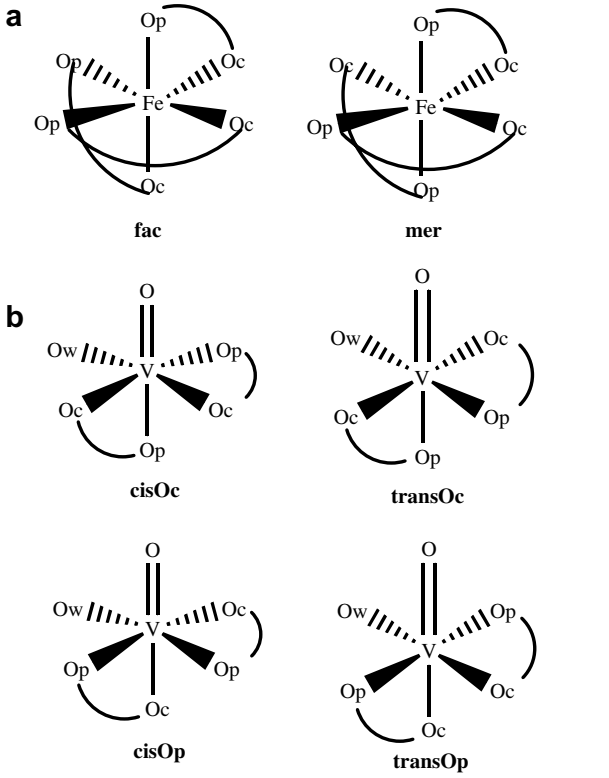
Comparison of the ^{1}H NMR spectra of $Zn(oxo)_2(H_2O)_2$ and $Cd(oxo)_2(H_2O)_2$ with that of Hoxo shows a significant perturbation of the chemical shifts of the aromatic protons H2 (up to 0.3 ppm) and H5 (up to 0.8 ppm) indicating that H2 and H5 are close to the coordination site of the ligand. The signals for the aliphatic protons H1a and H1b as well as those of H8 and H12 (perturbations of the chemical shifts up to 0.1 ppm) are practically unchanged since they lie further than H2 and H5 from the binding site. The overall changes of the NMR spectra of the complexes are indicative of coordination of oxolinato ligand to the metal via the pyridone oxygen and one carboxylate oxygen [28,30].

3.5. Molecular dynamics

Diverse crystallization techniques were employed in order to obtain a crystal suitable for the structure determination with X-ray crystallography. Nevertheless, all the complexes were collected as microcrystalline product. In order to propose a possible structure for the complexes, the lowest energy model structures of $Fe(oxo)_3$, $VO(oxo)_2(H_2O)$ and $Mn(oxo)_2(H_2O)_2$ have been determined with molecular modeling calculations.

3.5.1. $Fe(oxo)_3$

We have constructed the two *fac* and the two *mer* $Fe(oxo)_3$ enantiomers (Scheme S1) in order to present a model for the complex $Fe(oxo)_3$. The average energy of each set of enantiomers is almost equal (Table S2), as it is expected from such molecular mechanics calculations [69]. However, the final structures of *mer*-[$Fe(oxo)_3$] isomers (Scheme 1a) exhibit lower energies by more than 1.7 kcal mol^{-1} in comparison to the energies of the *fac* isomers. For the *mer* isomers we have applied a set of harmonic restraints at the metal–ligand bonds [33–37] during an additional minimization phase (Table S1). Based on these results we present the lowest energy model of one *mer*-[$Fe(oxo)_3$] enantiomer as the favorable configuration of the complex (Figure S1). However, we can neither exclude the formation of any of the other isomers, nor unambiguously distinguish between the favorable enantiomers.



Scheme 1. The isomers of (a) $Fe(oxo)_3$ and (b) $VO(oxo)_2(H_2O)$ employed in the simulated annealing calculations. Oc and Op are the carboxylate and the pyridone oxygen atoms, respectively, of oxolinic acid.

3.5.2. $VO(oxo)_2(H_2O)$

Using the same approach as above, we have constructed eight diastereoisomers of $VO(oxo)_2(H_2O)$ complex (Scheme S2). In all these models, the water molecule occupies a *cis* position with respect to the V=O, in accordance with the experimental results and just as in similar vanadyl complexes [15,38–41,69]. The resultant models of all $VO(oxo)_2(H_2O)$ isomers exhibit comparable average total energy with the two *transOc* and the two *cisOc* enantiomers (as are arbitrarily designated in Scheme S2) being more stable than the other four isomers by ~1 kcal mol^{-1} (Table S4). The difference between the average total energy of *transOc* and *cisOc* isomers is ~0.3 kcal $mol^{-1}$with the two *transOc* enantiomers exhibiting the lower value. Applying the distance restraints to M–L bonds (Table S3) and making corrections of the geometry by minimizing the energy of the complex, the structure of the predicted most stable isomer (a *transOc* isomer) has been obtained (Fig. 2). However, we can neither distinguish between *transOc* or *cisOc* isomers (Scheme 1b), nor unambiguously choose between the favorable enantiomers.

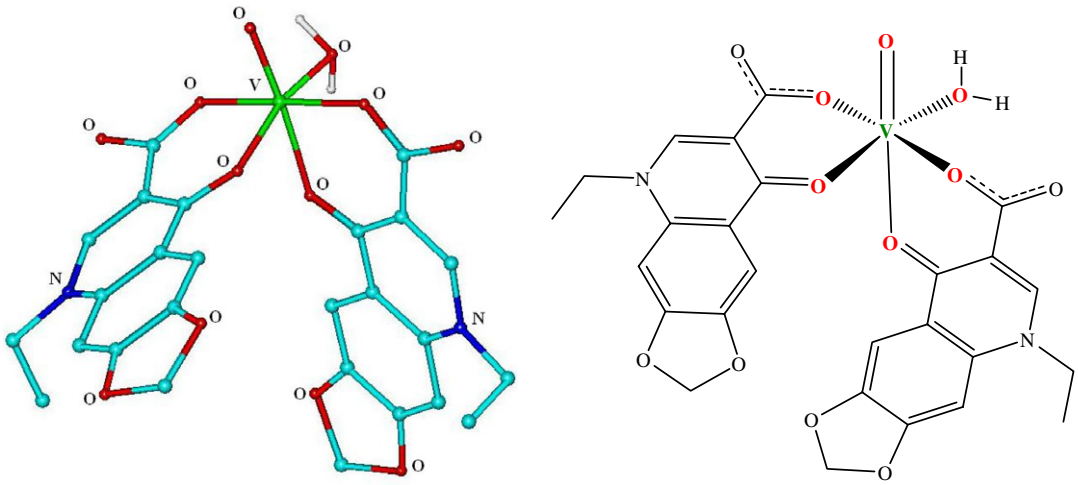
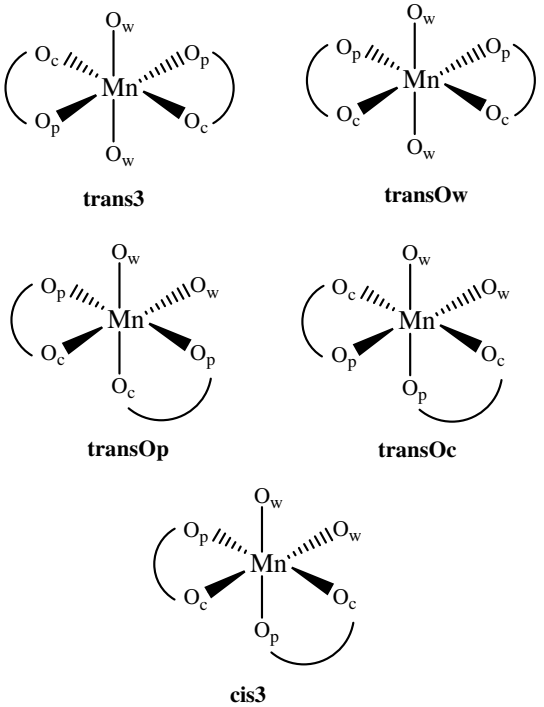


Fig. 2. Lowest energy model of $VO(oxo)_2(H_2O)$.

3.5.3. $Mn(oxo)_2(H_2O)_2$

We have constructed ten diastereoisomers as starting models of $Mn(oxo)_2(H_2O)_2$ (Scheme S3). The total number of all the possible diastereoisomers could not be limited since, according to similar Mn(II) complexes reported in the literature, the two Ow atoms can lie either at *trans* [43–47] or at *cis* [48–52] positions. After the Langevin dynamics simulated annealing calculations, we obtained the total energy results of 20 different conformations for each starting model (Table S6). The average energy of each set of enantiomers is almost equal, as it is expected from such molecular mechanics calculations [69]. However, the final structures of the isomers with Ow and Op at *cis* positions (*cis3* and *transOc* isomers, Scheme 2) exhibit lower average energies by more than 1.6 kcal mol^{-1} than the other isomers (*trans3*, *transOp* and *transOw*, Scheme 2).

The difference between the average total energy of *transOc* and *cis3* isomers is ~0.48 kcal $mol^{-1}$with the two *transOc* enantiomers being more stable since they exhibit the lower energy. Applying the distance restraints (Table S5) to M–L bonds [42–52] for the *transOc* model with the lowest energy and making corrections of the geometry by minimizing the energy of the complex once again, the structure of the predicted most stable isomer (a *transOc* isomer) has been obtained (Fig. 3). However, we cannot exclude the formation of any of the other isomers.



Scheme 2. The isomers of $Mn(oxo)_2(H_2O)_2$ employed in the simulated annealing calculations. Oc and Op are the carboxylate and the pyridone oxygen atoms, respectively, of oxolinic acid.

3.6. Interaction of the complexes with CT DNA

DNA can provide three distinctive binding sites for the quinolone metal complexes; namely, groove binding, binding to phosphate group and intercalation [70]. This behavior is of great importance with regard to the relevant biological role of quinolone antibiotics in the body [71].

3.6.1. UV spectroscopy

The absorption spectra of the interaction of the complexes **1**–**7** with CT DNA have been recorded for a constant CT DNA concentration (3.125×10^{-4} M) in different complex:CT DNA mixing ratios (r). Representative UV spectra of complexes **1**, **3** and **6** with CT DNA are shown in Fig. 4. The changes (mainly the increase of the intensity at $\lambda_{max} = 258$ nm) observed in the UV spectra of all the complexes (the UV spectra of complex **3** with CT DNA at diverse r values are shown in Fig. 5) after mixing

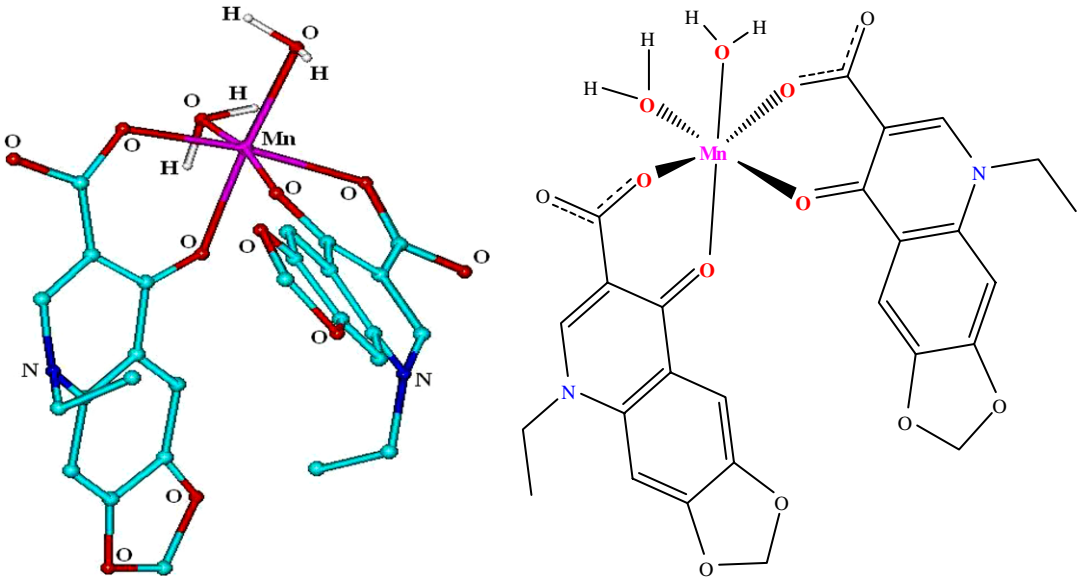


Fig. 3. Lowest energy model of $Mn(oxo)_2(H_2O)_2$.

with CT DNA indicate that the interaction of each complexes **1**–**7** with CT DNA takes place by a direct formation of a new complex with double-helical CT DNA [72].

3.6.2. CD spectroscopy

CD spectroscopy is useful in diagnosing changes in DNA morphology during drug–DNA interactions, as the positive band due to base stacking (275 nm) and the negative one due to right-handed helicity (248 nm) are quite sensitive to the mode of DNA interactions with small molecules [73,74]. The changes in the CD signals of CT DNA observed on interaction with drugs may often be assigned to the corresponding changes in CT DNA structure [75]. Thus, simple groove binding and electrostatic interaction of small molecules show less or no perturbation on the base-stacking and helicity bands, while intercalation enhances the intensities of both the bands stabilizing the right-handed B conformation of CT DNA as observed for the classical intercalator methylene blue [76].

The CD spectra of each complex with double-stranded CT DNA for different *r* values can provide us with useful information concerning the complex–nucleotide interaction. The CD spectra of the interaction of the free oxolinic acid with CT DNA do not show any shifts of the maxima or increase of the intensity because there is not any asymmetry or chirality in the molecule of the ligand [24,72]. The CD spectrum of free CT DNA is conservative and consists of a negative band at 246 nm and a positive one at 274 nm, characteristic of the B-form of DNA [77].

The CD spectra of CT DNA in the presence of complex $VO(oxo)_2(H_2O)$ (**1**) are shown in Fig. 6. They consist of a strong negative band I at 246 nm and two discrete positive

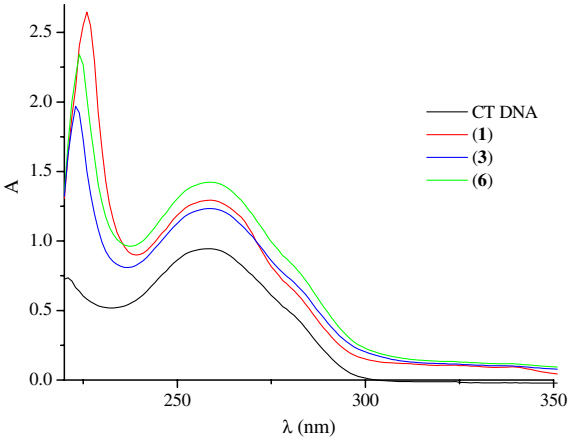


Fig. 4. Absorption spectra of complexes **1**, **3** and **6** in the presence of CT DNA. The *r* value is 1:200. The spectra were recorded at 25 °C after complexes had been incubated with CT DNA for 24 h at 37 °C.

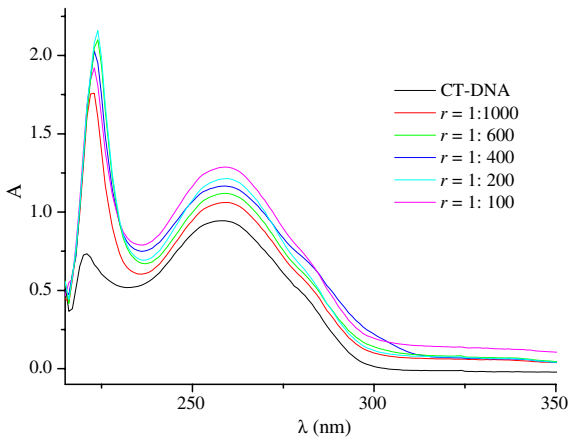


Fig. 5. UV spectra of complex **3** in the presence of CT DNA in different *r* values. The spectra were recorded at 25 °C after complex had been incubated with CT DNA for 24 h at 37 °C.

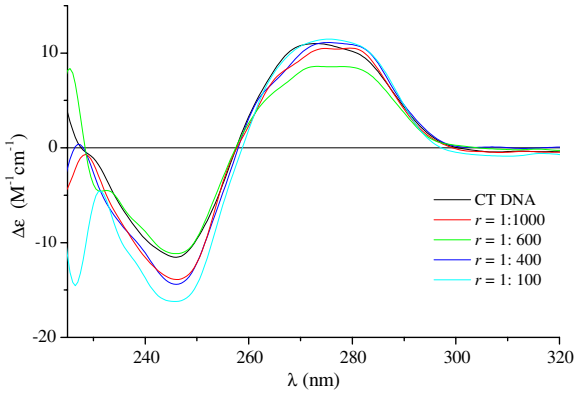


Fig. 6. CD spectra of CT DNA in 5 mM buffer (containing 150 mM NaCl and 15 mM trisodium citrate at pH 7.0) in the presence of complex **1** $VO(oxo)_2(H_2O)$ in different r values. The spectra were recorded at 25 °C after complex had been incubated with CT DNA for 24 h at 37 °C.

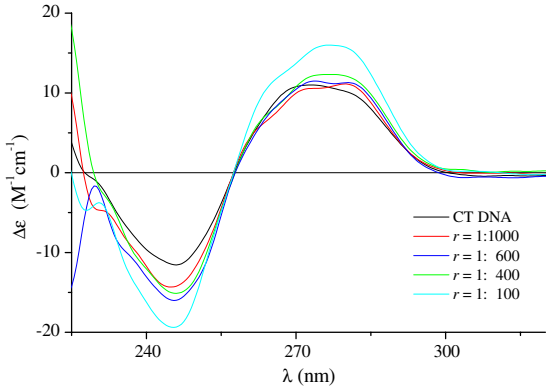


Fig. 7. CD spectra of CT DNA in 5 mM buffer (containing 150 mM NaCl and 15 mM trisodium citrate at pH 7.0) in the presence of complex **3** $Fe(oxo)_3$ in different r values. The spectra were recorded at 25 °C after complex had been incubated with CT DNA for 24 h at 37 °C.

bands II at 273 nm and III at 281 nm. More specifically, for r values up to 1:400, each CD spectrum consists of one negative band I at 246 nm and two positive bands II at 273 nm and III at 281 nm. Upon increase of the r value, the λ_{max} of these three bands remain, in general, unchanged while the intensity of helicity band I is increased and the intensity of bands II and III is decreased. Nevertheless, the exact mode of binding cannot be safely concluded. When r increases further (up to 1:50), the two positive bands II and III cannot be distinguished resulting to a unique broad band at $\lambda_{max} = 276$ nm while the intensity increases marginally. On the other hand, the negative band I at $\lambda_{max} = 246$ nm of remains unchanged in all the spectra, although an slight increase of the intensity is observed. The dominating spectral feature for this series of spectra is the slight increase of the intensities of both the bands of CT DNA. Taking into account all the changes observed, the exact mode of binding of **1** to CT DNA cannot be safely concluded.

Similar behavior is observed in the CD spectra of CT DNA in the presence of complexes $Mn(oxo)_2(H_2O)_2$, $Co(oxo)_2(H_2O)_2$ and $Ni(oxo)_2(H_2O)_2$.

The CD spectra of CT DNA in the presence of complex $Fe(oxo)_3$ (**3**) are shown in Fig. 7. They consist of a strong negative band I at 246 nm and two discrete positive bands II at 273 nm and III at 281 nm. When **3** is incubated with CT DNA at diverse r values, the CD spectrum of CT DNA undergoes changes in both the positive and negative bands. Taking into account all the changes observed in the CD spectra of Fig. 6 for diverse r values, the interaction of complex **3** with CT DNA could be summarized into the following points:

(a) For r values up to 1:400, each spectrum consists of one negative band I at 246 nm and two positive bands II at 273 nm and III at 281 nm. Upon increase of the r value, the λ_{max} of these three bands remain practically unchanged while the intensity of helicity band I is increased and the intensity of bands II and III is decreased. Nevertheless, the exact mode of binding cannot be safely concluded.

(b) When r increases further (up to 1:50), the two positive bands II and III cannot be distinguished resulting to a unique broad band at λ_{max} of 276 nm while the intensity increases. On the other hand, the λ_{max} at 246 nm of negative band I remains unchanged in all the spectra, although an increase of the intensity is observed. The dominating spectral feature for this series of spectra is the increase of the intensities of both the bands of CT DNA. Although the exact mode of binding cannot be safely concluded, the binding of complex **3** to CT DNA by the intercalative mode that enhances the intensities and possibly stabilizes the right-handed B-conformation of CT DNA cannot be ruled out [73,76].

The CD spectra of CT DNA in the presence of complex $Zn(oxo)_2(H_2O)_2$ (**6**) are shown in Fig. 8. They consist of a strong negative band I at 246 nm and two discrete positive

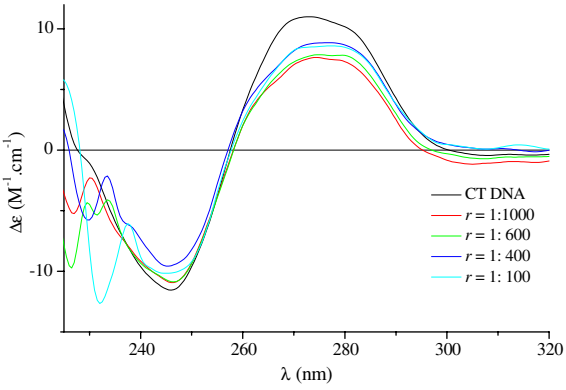


Fig. 8. CD spectra of CT DNA in 5 mM buffer (containing 150 mM NaCl and 15 mM trisodium citrate at pH 7.0) in the presence of complex **6** $Zn(oxo)_2(H_2O)_2$ in different r values. The spectra were recorded at 25 °C after complex had been incubated with CT DNA for 24 h at 37 °C.

bands II at 273 nm and III at 280 nm. More specifically, for r values up to 1:400, each spectrum consists of one negative band I at 246 nm and two positive bands II at 274 nm and III at 280 nm. Upon increase of the r value, the λ_{max} of these three bands remain practically unchanged while the intensities of all the bands are marginally decreased. In these spectra, the exact mode of binding cannot be safely concluded. For further increase of r (up to 1:50), the two positive bands II and III are consolidated and cannot be distinguished resulting to a unique broad band at $\lambda_{max} = 276$ nm while the intensity remains practically unchanged. On the other hand, the λ_{max} of the negative band I at 246 nm remains unchanged in all the spectra. The dominating spectral feature for this series of spectra is the lack of any perturbation on both the bands of CT DNA and shows the possible existence of simple groove binding or electrostatic interaction [76].

Quite similar behavior is observed in the CD spectra of CT DNA in the presence of complex $Cd(oxo)_2(H_2O)_2$.

In conclusion, the behavior of CT DNA in the presence of complexes **1**–**7** is interesting. All the complexes can bind to CT DNA and, at low r values, the exact mode of binding cannot be safely concluded. At high r values, especially for complex **3** the dominating spectral feature is indicative of binding by the intercalative mode and for complexes **6** and **7** the dominating spectral feature shows possible simple groove binding or electrostatic interactions.

4. Conclusions

The synthesis and characterization of seven new oxolinato complexes with VO^{2+}, Mn^{2+}, Fe^{3+}, Co^{2+}, Ni^{2+}, Zn^{2+}, and Cd^{2+} has been realized with physicochemical and spectroscopic methods. In all the complexes, oxolinic acid is on deprotonated mode and acts as a bidentate ligand coordinated to the metal ion through the pyridone oxygen and one carboxylate oxygen.

Each metal is six-coordinate and the environment around each metal could be described as distorted octahedron. With the use of molecular modeling, the lowest energy model structures of $Fe(oxo)_3$, $VO(oxo)_2(H_2O)$ and $Mn(oxo)_2(H_2O)_2$ have been determined revealing the possible arrangement of the ligands around the metal.

The interaction of complexes **1**–**7** with CT DNA has been investigated with diverse spectroscopic techniques. It has been found that all the complexes can bind to CT DNA and the exact mode of binding cannot be safely concluded. Nevertheless, at high r values, the intercalative binding mode for complex **3** and the simple groove binding or electrostatic interactions for complexes **6** and **7** cannot be ruled out.

Acknowledgments

The work was partially supported by the ''Excellence in the Research Institutes'' Program, Action 3.3.1 co-funded by the Greek Ministry of Development and E.U. We thank Dr. A. Papakyriakou, Institute of Physical Chemistry, NCSR ''Demokritos'', Greece, for the supply of the molecular modeling routine.

Appendix A. Supplementary material

IR and UV–Vis spectral data for Hoxo and complexes **1**–**7** and ^{1}H NMR chemical shifts for Hoxo, $Zn(oxo)_2(H_2O)_2$ and $Cd(oxo)_2(H_2O)_2$ in d_6–dmso. Three schemes (Schemes S1, S2 and S3) for the diastereoisomers of $Fe(oxo)_3$, $VO(oxo)_2(H_2O)$ and $Mn(oxo)_2(H_2O)_2$ employed in the simulated annealing calculations. Three tables (Tables S1, S3, S5) for the metal–ligand distance restraints applied during the energy minimization phase in order to adjust the geometry of $Fe(oxo)_3$, $VO(oxo)_2(H_2O)$ and $Mn(oxo)_2(H_2O)_2$ models. Three tables (Tables S2, S4, S6) for the energy statistics from the simulated annealing results of $Fe(oxo)_3$, $VO(oxo)_2(H_2O)$ and $Mn(oxo)_2(H_2O)_2$ diastereoisomers, respectively. Three figures (Figures S1, S2, S3) for the lowest energy models of the $Fe(oxo)_3$, $VO(oxo)_2(H_2O)$ and $Mn(oxo)_2(H_2O)_2$ enantiomers. Supplementary data associated with this article can be found, in the online version, at doi:10.1016/j.poly.2007.04.031.

References

[1] A. Albert, The Physico-Chemical Basis of Therapy: Selective Toxicity, sixth ed., Chapman & Hall, London, 1979.
[2] M.N. Hughes, The Inorganic Chemistry of Biological Processes, second ed., Wiley, New York, 1981.
[3] S.J. Lippard, J.M. Berg, Principles of Bioinorganic Chemistry, University Science Books, Mill Valley, CA, USA, 1994.
[4] I. Turel, Coord. Chem. Rev. 232 (2002) 27, and references therein.
[5] D.C. Hooper, E. Rubinstein (Eds.), Quinolone Antimicrobial Agents, third ed., ASM Press, Washington, DC, 2003.
[6] V.T. Andriole (Ed.), The Quinolones, third ed., Academic Press, San Diego, 2000.
[7] D. Beermann, J. Kuhlmann, A. Dalhoff, H.J. Zeiler (Eds.), Quinolone Antibacterials, Springer-Verlag Telos, 1998.
[8] D.E. King, R. Malone, S.H. Lilley, Am. Fam. Physician 61 (2000) 2741.
[9] K. Sandstrom, S. Warmlander, M. Leijon, A. Graslund, Biochem. Biophys. Res. Commun. 304 (2003) 55.
[10] E. Canton, J. Peman, M.T. Jimenez, M.S. Ramon, M. Gobernado, Antimicrob. Agents Chemother. 36 (1992) 558.
[11] J.A. Wiles, Q. Wang, E. Lucien, A. Hashimoto, Y. Song, J. Cheng, C.W. Marlor, Y. Ou, S.D. Podos, J.A. Thanassi, C. Thoma, M. Deshpande, M.J. Pucci, B.J. Bradbury, Bioorg. Med. Chem. Lett. 16 (2006) 1272.
[12] E.S. Pfeiffer, H. Hiasa, Antimicrob. Agents Chemother. 48 (2004) 608.
[13] Y. Xia, Z.-Y. Yang, P. Xia, K.F. Bastow, Y. Tachibana, S.-C. Kuo, E. Hamel, T. Hackl, K.-H. Lee, J. Med. Chem. 41 (1998) 1155.
[14] D.K. Saha, U. Sandbhor, K. Shirisha, S. Padhye, D. Deobagkar, C.E. Anson, A.K. Powell, Bioorg. Med. Chem. Lett. 14 (2004) 3027.
[15] I. Turel, A. Golobic, A. Klavzar, B. Pihlar, P. Buglyo, E. Tolis, D. Rehder, K. Sepcic, J. Inorg. Biochem. 95 (2003) 199.
[16] M.P. Lopez-Gresa, R. Ortiz, L. Perello, J. Latorre, M. Liu-Gonzalez, S. Garcia-Granda, M. Perez-Priede, E. Canton, J. Inorg. Biochem. 92 (2002) 65.
[17] N. Jimenez-Garrido, L. Perello, R. Ortiz, G. Alzuet, M. Gonzalez-Alvarez, E. Canton, M. Liu-Gonzalez, S. Garcia-Granda, M. Perez-Priede, J. Inorg. Biochem. 99 (2005) 677.

[18] P. Drevensek, I. Turel, N. Poklar Ulrih, J. Inorg. Biochem. 96 (2003) 407.
[19] R. Piccolomini, G. Ravagnan, Chemioterapia 5 (1986) 249.
[20] M.S. Sabbour, M.A. El Bokl, L.M. Osman, Infection 12 (1984) 377.
[21] S. Kalowski, P. Kincaid-Smith, R. Pavillard, Med. J. Aust. 1 (1979) 345.
[22] Y. de Rautlin de la Roy, V. Toma, B. Bobin, Curr. Med. Res. Opin. 5 (1978) 743.
[23] D.J. D'Alessio, V.M. Olexy, G.G. Jackson, Antimicrob. Agents Chemother. 7 (1967) 490.
[24] G. Psomas, A. Tarushi, E.K. Efthimiadou, Y. Sanakis, C.P. Raptopoulou, N. Katsaros, J. Inorg. Biochem. 100 (2006) 1764.
[25] E.K. Efthimiadou, M. Katsarou, Y. Sanakis, C.P. Raptopoulou, A. Karaliota, N. Katsaros, G. Psomas, J. Inorg. Biochem. 100 (2006) 1378.
[26] E.K. Efthimiadou, Y. Sanakis, C.P. Raptopoulou, A. Karaliota, N. Katsaros, G. Psomas, Bioorg. Med. Chem. Lett. 16 (2006) 3864.
[27] E.K. Efthimiadou, H. Thomadaki, Y. Sanakis, C.P. Raptopoulou, N. Katsaros, A. Scorilas, A. Karaliota, G. Psomas, J. Inorg. Biochem. 101 (2007) 64.
[28] E.K. Efthimiadou, G. Psomas, Y. Sanakis, N. Katsaros, A. Karaliota, J. Inorg. Biochem. 101 (2007) 525.
[29] E.K. Efthimiadou, N. Katsaros, A. Karaliota, G. Psomas, Bioorg. Med. Chem. Lett. 17 (2007) 1238.
[30] E.K. Efthimiadou, Y. Sanakis, N. Katsaros, A. Karaliota, G. Psomas, Polyhedron 26 (2007) 1148.
[31] E. Tselepi-Kalouli, N. Katsaros, J. Inorg. Biochem. 37 (1989) 271.
[32] N.L. Allinger, J. Am. Chem. Soc. 99 (1977) 8127.
[33] M.V. Twigg, J. Burgess, in: J.A. McCleverty, T.J. Meyer (Eds.), Comprehensive Coordination Chemistry II, vol. 5, Elsevier, 2003, pp. 403–553, and references therein.
[34] M. Scarpellini, A. Neves, A.J. Bortoluzzi, I. Vencato, V. Drago, W.A. Ortiz, C. Zucco, J. Chem. Soc., Dalton Trans. (2001) 2616.
[35] L. Westerheide, F.K. Muller, R. Than, B. Krebs, J. Dietrich, S. Schindler, Inorg. Chem. 40 (2001) 1951.
[36] J.M. Rowland, M. Olmstead, P.K. Mascharak, Inorg. Chem. 40 (2001) 2810.
[37] K. Matsumoto, T. Ozawa, K. Jitsukawa, H. Einaga, H. Masuda, Inorg. Chem. 40 (2001) 190.
[38] D.C. Crans, J.J. Smee, in: J.A. McCleverty, T.J. Meyer (Eds.), Comprehensive Coordination Chemistry II, vol. 4, Elsevier, 2003, pp. 175–239, and references therein.
[39] I. Correia, J. Costa Pessoa, M.T. Duarte, R.T. Henriques, M.F.M. Piedade, L.F. Veiros, T. Jakusch, T. Kiss, A. Dornyei, M.M.C.A. Castro, C.F.G.C. Geraldes, F. Avecilla, Chem. Eur. J. 10 (2004) 2301.
[40] S.S. Amin, K. Cryer, B. Zhang, S.K. Dutta, S.S. Eaton, O.P. Anderson, S.M. Miller, B.A. Reul, S.M. Brichard, D.C. Crans, Inorg. Chem. 39 (2000) 406.
[41] J. Costa Pessoa, I. Cavaco, I. Correia, I. Tomaz, T. Duarte, P.M. Matias, J. Inorg. Biochem. 80 (2000) 35.
[42] D.C. Weatherburn, S. Mandal, S. Mukhopadhyay, S. Bhaduri, L.F. Lindoy, in: J.A. McCleverty, T.J. Meyer (Eds.), Comprehensive Coordination Chemistry II, vol. 5, Elsevier, 2003, pp. 1–125, and references therein.
[43] V. Tangoulis, G. Psomas, C. Dendrinou-Samara, C.P. Raptopoulou, A. Terzis, D.P. Kessissoglou, Inorg. Chem. 35 (1996) 7655, and references therein.
[44] D. Huang, W. Wang, X. Zhang, C. Chen, F. Chen, Q. Liu, D. Liao, L. Li, L. Sun, Eur. J. Inorg. Chem. (2004) 1454.
[45] J. Zhu, Y. Zhao, M. Hong, D. Sun, Q. Shi, R. Cao, Chem. Lett. (2002) 484.
[46] C.H.L. Kennard, S.W. Stewart, E.J. O'Reilly, G. Smith, A.H. White, Polyhedron 4 (1985) 697.
[47] T. Lis, Acta Crystallogr., Sect. B 33 (1977) 2964.
[48] R. Koferstein, C. Robl, Z. Anorg. Allg. Chem. 630 (2004) 185.
[49] D. Armentano, G. de Munno, F. Guerra, J. Faus, F. Lloret, M. Julve, Dalton Trans. (2003) 4626.
[50] R. Carballo, B. Covelo, E. Garcia-Martinez, E.M. Vazquez-Lopez, A. Castineiras, J. Niclos, Polyhedron 22 (2003) 1051.
[51] M. McCann, M.T. Casey, M. Devereux, M. Curran, V. McKee, Polyhedron 16 (1997) 2741, and references therein.
[52] A. Karipides, A.T. Reed, Inorg. Chem. 15 (1976) 44.
[53] M.P. Allen, D.J. Tildesley (Eds.), Computer Simulation of Liquids, Oxford University Press, 1989.
[54] K. Nakamoto, Infrared and Raman Spectra of Inorganic and Coordination Compounds, fourth ed., Wiley, New York, 1986.
[55] G.B. Deacon, R.J. Phillips, Coord. Chem. Rev. 33 (1980) 227.
[56] E.J. Tolis, V.I. Teberekidis, C.P. Raptopoulou, A. Terzis, M.P. Sigalas, Y. Deligiannakis, T.A. Kabanos, Chem. Eur. J. 7 (2001) 2698.
[57] E. Garribba, G. Micera, A. Panzanelli, D. Sanna, Inorg. Chem. 42 (2003) 3981.
[58] H. Kelm, H.-J. Kruger, Inorg. Chem. 35 (1996) 3533.
[59] M. Nakai, M. Obata, F. Sekiguchi, M. Kato, M. Shiro, A. Ichimura, I. Kinoshita, M. Mikuriya, T. Inohara, K. Kawabe, H. Sakurai, C. Orvig, S. Yano, J. Inorg. Biochem. 98 (2004) 105.
[60] W.O. Koch, V. Schunemann, M. Gerdan, A.X. Trautwein, H.-J. Kruger, Chem. Eur. J. 4 (1998) 1255.
[61] H. Chun, C.N. Verani, P. Chaudhuri, E. Bothe, E. Bill, T. Weyhermuller, K. Wieghardt, Inorg. Chem. 40 (2001) 4157.
[62] D.A. Buckingham, C.R. Clark, in: G. Wilkinson (Ed.), Comprehensive Coordination Chemistry, vol. 4, Pergamon Press, Oxford, 1989, pp. 635–900.
[63] P.V. Bernhardt, G.A. Lawrance, in: J.A. McCleverty, T.J. Meyer (Eds.), Comprehensive Coordination Chemistry II, vol. 6, Elsevier, 2003, pp. 1–145, and references therein.
[64] L. Sacconi, F. Mani, A. Bencini, in: G. Wilkinson (Ed.), Comprehensive Coordination Chemistry, vol. 5, Pergamon Press, Oxford, 1989, pp. 1–347.
[65] F. Meyer, H. Kozlowski, in: J.A. McCleverty, T.J. Meyer (Eds.), Comprehensive Coordination Chemistry II, vol. 6, Elsevier, 2003, pp. 247–554, and references therein.
[66] M. Ruiz, R. Ortiz, L. Perello, J. Latorre, J. Server-Carrio, J. Inorg. Biochem. 65 (1997) 87.
[67] M. Ruiz, R. Ortiz, L. Perello, A. Castineiras, M. Quiros, Inorg. Chim. Acta 211 (1993) 133.
[68] M. Sakai, A. Hara, S. Anjo, M. Nakamura, J. Pharm. Biomed. Anal. 18 (1999) 1057.
[69] P. Christofis, M. Katsarou, A. Papakyriakou, Y. Sanakis, N. Katsaros, G. Psomas, J. Inorg. Biochem. 99 (2005) 2197, and references therein.
[70] A. Rodger, B. Norden (Eds.), Circular Dichroism and Linear Dichroism, Oxford University Press, Oxford–New York–Tokyo, 1997.
[71] T.C. Jenkins in K.R. Fox (Ed.), Drug–DNA Interaction Protocols, Humana Press Inc., Totowa, NJ, 1997, pp. 195–218.
[72] G.S. Son, J.-A. Yeo, M.-S. Kim, S.K. Kim, A. Holmen, B. Akerman, B. Norden, J. Am. Chem. Soc. 120 (1998) 6451.
[73] P. Uma Maheswari, M. Palaniandavar, J. Inorg. Biochem. 98 (2004) 219.
[74] V.I. Ivanov, L.E. Minchenkova, A.K. Schyolkina, A.I. Poletayev, Biopolymers 12 (1973) 89.
[75] P. Lincoln, E. Tuite, B. Norden, J. Am. Chem. Soc. 119 (1997) 1454.
[76] B. Norden, F. Tjerneld, Biopolymers 21 (1982) 1713.
[77] W. Curtis-Johnson, in: K. Nakanishi, N. Berova, R.W. Woody (Eds.), CD of Nucleic Acids in Circular Dichroism, Principles and Applications, VHS, New York, 1994, pp. 523–540.

$MoO_2[S_2CNR_2]_2$ (R = Et [18], *n*-Pr [19]) have been reported but none with *O*-alkyl dithiocarbonates or *O*,*O*′-dialkyl(alkylene) dithiophosphates. However, several structures have been reported of binuclear oxomolybdenum(V) complexes with *N*,*N*′-dialkyl dithiocarbamates, $Mo_2O_3[S_2CNEt_2]_4$ [20], and $Mo_2O_3[S_2CN(n\text{-}Pr)_2]_4$ [19], *O*-alkyl dithiocarbonates, $Mo_2O_3[S_2COEt]_4$ [21] and $Mo_2O_3[S_2CO\textit{i}\text{-}Pr]_4$ [22] and *O*,*O*′-dialkyl dithiophosphates, $Mo_2O_3[S_2P(OR)_2]_4$ (R = Me [16], Et [23,24], *n*-Pr[25], Ph [26]). We report the synthesis and characterization of several new binuclear oxomolybdenum(V) complexes involving dithiophosphate ligands and dioxomolybdenum(VI) complexes with *O*,*O*′-ditolyl dithiophosphates, along with the crystal structures of $Mo_2O_3[S_2P(OC_6H_4Me\text{-}o)_2]_4$, $Mo_2O_3[S_2P(OC_6H_4Me\text{-}m)_2]_4$ and $MoO_2[S_2P(OC_6H_4Me\text{-}p)_2]_2$.

2. Experimental

Sodium molybdate dihydrate, phosphorus pentasulfide, *o*-cresol, *m*-cresol, *p*-cresol and benzyl alcohol were purchased from E. Merck. All solvents (ether and benzene) were dried by standard methods before use. Stringent precautions were taken to exclude moisture during experimental manipulations. Literature methods were used for the preparation of the ammonium salt of *O*,*O*-ditolyl dithiophosphoric acids [27,28].

2.1. Synthesis of $Mo_2O_3[S_2P(OC_6H_4Me\text{-}o)_2]_4$ (1), $Mo_2O_3[S_2P(OC_6H_4Me\text{-}m)_2]_4$ (2), $Mo_2O_3[S_2P(OC_6H_4Me\text{-}p)_2]_4$ (3)

An aqueous solution (15 mL) of the ammonium salt of *O*,*O*-di(2-tolyl)dithiophosphoric acid (1.87 g, 5.71 mmol) was added drop wise to an aqueous solution (10 mL) of sodium molybdate (0.69 g, 2.86 mmol) with constant stirring. A purple precipitate was obtained immediately which was filtered and washed with ether and dried over P_2O_5. Purple crystals were obtained on recrystallization from benzene:diethyl ether (1:2). $Mo_2O_3[S_2P(OC_6H_4Me\text{-}o)_2]_4$ (**1**). Purple crystalline solid. Yield: 4.01 g, 95%; m.p. 112 °C. *Anal.* Calc. for $C_{56}H_{56}O_{11}P_4S_8Mo_2$: Mo, 12.99; S, 17.36. Found: Mo, 13.29; S, 17.51%.

Method as above gave $Mo_2O_3[S_2P(OC_6H_4Me\text{-}m)_2]_4$ (**2**). Purple crystalline solid. Yield: 90%; m.p. 118 °C. *Anal.* Calc. for $C_{56}H_{56}O_{11}P_4S_8Mo_2$: Mo, 12.99; S, 17.36. Found: Mo, 12.72; S, 17.66%.

Method as above gave $Mo_2O_3[S_2P(OC_6H_4Me\text{-}p)_2]_4$ (**3**). Purple crystalline solid. Yield: 90%; m.p. 120 °C. *Anal.* Calc. for $C_{56}H_{56}O_{11}P_4S_8Mo_2$: Mo, 12.99; S, 17.36. Found: Mo, 12.86; S, 17.52%.

2.2. Synthesis of $MoO_2[S_2P(OC_6H_4Me\text{-}o)_2]_2$ (4), $MoO_2[S_2P(OC_6H_4Me\text{-}m)_2]_2$ (5), $MoO_2[S_2P(OC_6H_4Me\text{-}p)_2]_2$ (6) and $MoO_2[S_2P(OCH_2C_6H_5)_2]_2$ (7)

$Mo_2O_3[S_2P(OC_6H_4Me\text{-}o)_2]_4$ (0.22 g, 0.15 mmol) was dissolved in benzene (25 mL) and a benzene solution of triphenylphosphine oxide was added (0.05 g, 0.18 mmol) with constant stirring. The colour of the solution changed from purple to yellow after 30 min. The volume of the solvent was reduced to 2–3 mL by pumping and then n-hexane (10 mL) was added. Yellow crystals were obtained on keeping the solution in the refrigerator overnight. $MoO_2[S_2P(OC_6H_4Me\text{-}o)_2]_2$ (**1**): Yellow solid. Yield: 0.18 g, 82%; m.p. 118 °C. *Anal.* Calc. for $C_{28}H_{28}O_6P_2S_4Mo$: Mo, 12.85; S, 17.18. Found: Mo, 12.66; S, 17.43%.

Method as above gave $MoO_2[S_2P(OC_6H_4Me\text{-}m)_2]_2$ (**5**). Yellow solid. Yield: 85%; m.p. 114 °C. *Anal.* Calc. for $C_{28}H_{28}O_6P_2S_4Mo$: Mo, 12.85; S, 17.18. Found: Mo, 13.21; S, 17.56%.

Method as above gave $MoO_2[S_2P(OC_6H_4Me\text{-}p)_2]_4$ (**6**). Yellow solid. Yield: 80%; m.p. 124 °C. *Anal.* Calc. for $C_{28}H_{28}O_6P_2S_4Mo$: Mo, 12.85; S, 17.18. Found: Mo, 12.86; S, 17.23%.

Method as above gave $MoO_2[S_2P(OCH_2C_6H_5)_2]_4$ (**7**). Yellow solid. Yield: 80%; m.p. 124 °C. *Anal.* Calc. for $C_{28}H_{28}O_6P_2S_4Mo$: Mo, 12.85; S, 17.18. Found: Mo, 12.86; S, 17.23%.

2.3. Physical measurements

Molybdenum was estimated by precipitation as molybdenum oxinate, $MoO_2(C_9H_6ON)_2$ and sulfur as barium sulfate [Messenger's method]. IR spectra were recorded in the range 4000–200 cm^{-1}on a Perkin–Elmer 983G spectrophotometer (Nujol mull). ^1H NMR and ^{31}P NMR spectra were recorded on a Bruker DRX-300 Spectrometer in $CDCl_3$ using TMS as an internal and 85% H_3PO_4 as an external reference, respectively.

2.4. X-ray diffraction analysis

The data for **1** and **6** were collected on an Enraf Nonius Kappa CCD area detector diffractometer, with Φ and ω scans chosen to give a complete asymmetric unit, and for **2** on a Siemens SMART System CCD diffractometer with the collection of a hemisphere of data. Cell refinements [29] corresponded to monoclinic cells for **1** and **6** and triclinic for **2**. Dimensions are given in Table 3 along with other experimental parameters. Absorption corrections were applied [30]. The structures were solved by direct methods [31] and were refined using the WinGX version [32] of SHELX-97 [33]. All of the non-hydrogen atoms were treated anisotropically. Hydrogen atoms were included in idealized positions with isotropic thermal parameters set at 1.2 times that of the carbon atom to which they were attached. The final cycle of full-matrix least-squares refinement was based on 7211 (**1**), 5792 (**2**) and 5450 (**6**), observed reflections and 5894 (**1**), 2633 (**2**), and (4103 (**6**) for $F^2 > 4s(F^2)$) and 368 (**1**), 365 (**2**), and 374 (**6**) variable parameters and converged (largest parameter shift was 0.001 times its esd). Distances and bond angles are given

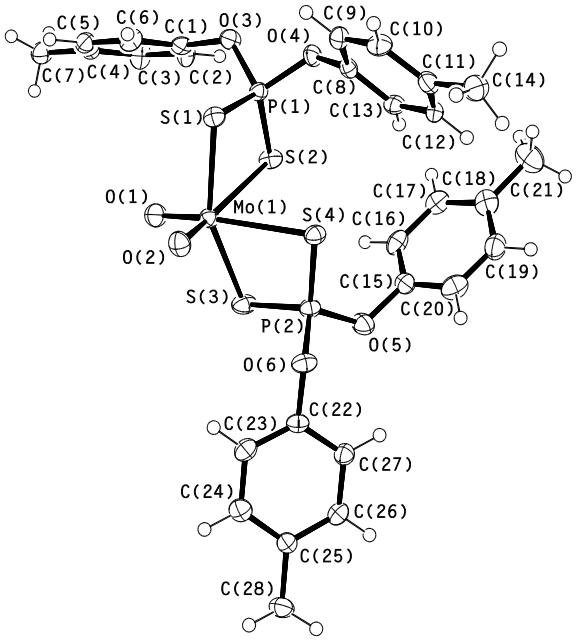


Fig. 1. ORTEP plot of $MoO_2[S_2P(OC_6H_4CH_3\text{-}p)_2]_2$. The non-hydrogen atoms are drawn with 50% probability ellipsoids.

in Table 4 for molecules **1**, **2** and **6**, respectively and ORTEP diagrams are displayed in Figs. 1–3.

3. Results and discussion

Binuclear oxomolybdenum(V) *O*,*O*-ditolyl dithiophosphate complexes, $Mo_2O_3[S_2P(OR)_2]_4$ were synthesized by the drop wise addition of aqueous solution of the ammonium salt of *O*,*O*-ditolyl dithiophosphoric acid into an acidic solution of sodium molybdate with constant stirring to yield purple solids:

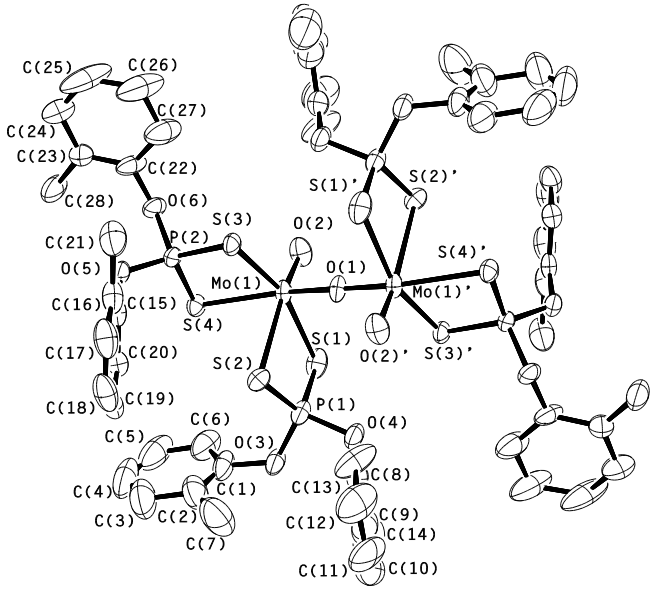


Fig. 2. ORTEP plot of the molecule $Mo_2O_3[S_2P(OC_6H_4Me\text{-}o)_2]_4$. The non-hydrogen atoms are drawn with 50% probability ellipsoids. Hydrogen atoms omitted for clarity.

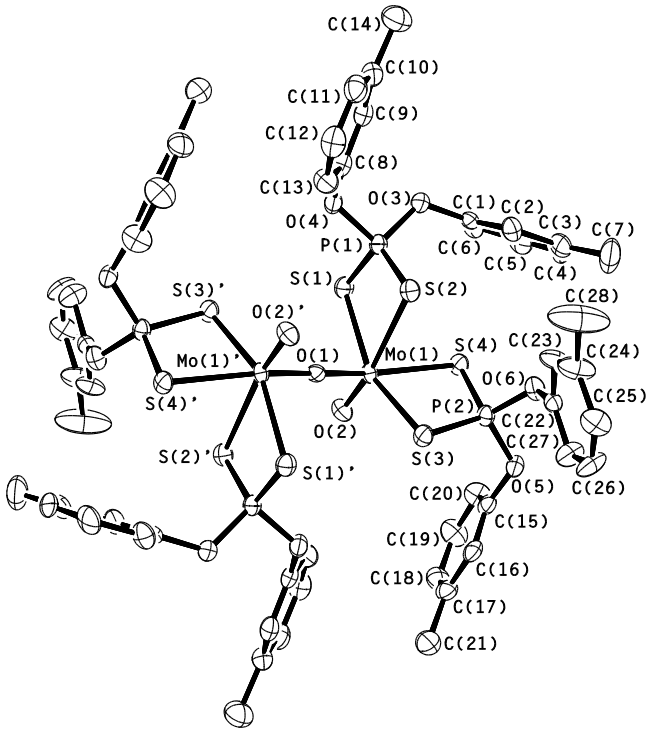


Fig. 3. ORTEP plot of $Mo_2O_3[S_2P(OC_6H_4Me\text{-}p)_2]_2$. The atoms are drawn with 50% probability ellipsoids. Hydrogen atoms are omitted for clarity.

$$Na_2MoO_4\cdot 2H_2O + 2NH_4S_2P(OR)_2 \rightarrow 0.5Mo_2O_3[S_2P(OR)_2]_4$$
(R = *o*-, *m*- and *p*-C_6H_4Me)

Dioxomolybdenum(VI) *O*,*O*-ditolyl dithiophosphates were prepared by oxygen atom transfer reactions of binuclear oxomolybdenum(V) *O*,*O*-ditolyl dithiophosphate complexes with triphenylphosphine oxide in benzene.

$$Na_2MoO_4\cdot 2H_2O + 2NH_4S_2P(OR)_2 \rightarrow MoO_2[S_2P(OR)_2]_2$$
(R = *o*-, *m*-, *p*-C_6H_4Me and $CH_2C_6H_5$)

These dioxomolybdenum(VI) complexes are yellow powdery solids that are soluble in common organic solvents viz. benzene, chloroform and dichloromethane etc. and were characterized by elemental analysis, IR, ^1H and ^{31}P NMR spectroscopy.

3.1. IR spectra

The assignments of the IR bands for binuclear oxomolybdenum(V) *O*,*O*-ditolyl dithiophosphate and dioxomolybdenum(VI) *O*,*O*-ditolyl dithiophosphate complexes (Table 1) were made by comparison with the spectra of the precursors of the complexes; the ammonium salts of *O*,*O*-ditolyl dithiophosphates [27,28]. The bands due to *ν*[(P)–O–C] and *ν*[P–O–(C)] which occur in the regions 1139–1102 and 833–792 cm^{-1}, respectively, in the parent ammonium salts, are unalterred in the molybdenum complexes. The band due to *ν*(P═S) present at 694–670 cm^{-1} in the ammonium salts shows a small but notable shift

Table 1
IR spectral data (cm^{-1}) for the binuclear oxomolybdenum(V) and dioxomolybdenum(VI) *O,O*-ditolyl dithiophosphate complexes[a]

S. no.	Compound	ν[(P)–O–C]	$\nu(Mo{=}O)_{asym}$	$\nu(Mo{=}O)_{sym}/\nu(Mo{-}O{-}Mo)$	ν[P–O–(C)]	$\nu(P{-}S)_{asym}$	$\nu(P{-}S)_{sym}$	ν(Mo–S)
1	$Mo_2O_3[S_2P(OC_6H_4Me\text{-}o)_2]_4$	1105,m	970,m	771,m	803,s	658,s	555,m	335,w
2	$Mo_2O_3[S_2P(OC_6H_4Me\text{-}m)_2]_4$	1134,m	993,m	778,m	778,s	685,s	550,m	330,w
3	$Mo_2O_3[S_2P(OC_6H_4Me\text{-}p)_2]_4$	1101,m	953,m	758,s	819,s	688,s	529,m	327,w
4	$MoO_2[S_2P(OC_6H_4Me\text{-}o)_2]_2$	1120,s	963,s	918,s	830,m	687,s	540,s	340,w
5	$MoO_2[S_2P(OC_6H_4Me\text{-}m)_2]_2$	1121,s	964,m	918,s	835,s	690,s	540,s	333,w
6	$MoO_2[S_2P(OC_6H_4Me\text{-}p)_2]_2$	1103,m	945,s	927,s	821,s	648,s	503,m	341,w
7	$MoO_2[S_2P(OCH_2C_6H_5)_2]_2$	1072,s	997,m	968,s	827,s	688,s	541,s	338,w

[a] Key: s = strong; m = medium; w = weak.

($\nu = 22$–$25\ cm^{-1}$) to lower wave-number in the molybdenum complexes indicating attachment of the ligand to the metal atom. New peaks of medium to strong intensity that are present at 993–953 and 778–758 cm^{-1} in the binuclear oxomolybdenum(V) complexes **1**–**3** are assigned to ν(Mo=O) and ν(Mo–O–Mo), respectively. Two strong bands in the dioxomolybdenum(VI) complexes **4**–**7**, due to ν(Mo=O), are found in the region 997–918 cm^{-1}. Similarly, additional peaks for ν(Mo–S) stretching bands of weak intensity are observed in the region 341–327 cm^{-1}.

3.2. ^1H NMR spectra

The chemical shifts and integrated intensity ratios of the protons in the binuclear oxomolybdenum(V) *O,O*-ditolyl dithiophosphate and dioxomolybdenum(VI) *O,O*-ditolyl dithiophosphate complexes are presented in Table 2. These spectra were recorded in $CDCl_3$ solutions at room temperature. The ^1H NMR data of complexes **1**–**7**, are remarkably similar to those of the salts of *O,O*-ditolyl dithiophosphates [27,28] probably due to the large separation between the molybdenum and the protons.

3.3. ^{31}P NMR spectra

The ^{31}P NMR spectra were recorded in $CDCl_3$ solutions (Table 2) and show a singlet in the region δ, 96.57–85.90 ppm, indicating the equivalent nature of the phosphorus nuclei as well as the symmetric nature of the species in solution. The ^{31}P NMR chemical shifts for the binuclear oxomolybdenum(V) complexes **1**–**3** and dioxomolybdenum(VI) complexes **4**–**7**, are shifted ~20 and ~10 ppm upfield, respectively, from those of the corresponding salts of dithiophosphoric acids indicating the bidentate and anisobidentate nature [34] of the dithiophosphate moieties in Mo(V) and Mo(VI) complexes, respectively.

3.4. Molecular structures of $Mo_2O_3[S_2P(OC_6H_4Me\text{-}o)_2]_4$ (**1**), $Mo_2O_3[S_2P(OC_6H_4Me\text{-}m)_2]_4$ (**2**) and $MoO_2[S_2P(OC_6H_4Me\text{-}p)_2]_2$ (**6**)

The molecular structure of $MoO_2[S_2P(OC_6H_4Me\text{-}p)_2]_2$ (**6**) is the first of this type reported with dithiophosphate ligands. Fig. 1 and the selected bond distances and angles in Table 4 show that Mo has a distorted octahedral environment in which cis oxo groups are typical of dioxomolybdenum(VI) species. The M=O distances of 1.694(3) and 1.700(3) Å and the O=Mo=O angle of 104.7(2)° are similar to those reported for $MoO_2[S_2CNEt_2]_2$ [18], $MoO_2[S_2CN(n\text{-}Pr)_2]_2$ [19], $MoO_2[S_2CNC_4H_8]_2$ [35] (ave 1.701(2) Å and 106.1(7)°). The dithiophosphate ligands in (**6**) are anisobidentate with one short (ave 2.467(10)) and one long (ave 2.74(2) Å) Mo–S bond. The longer bond is trans, S–Mo=O angle (ave 163.3(4)°), to a Mo=O bond. The trans influence was also evident in the three related dithiocarbamate derivatives $MoO_2[S_2NCR_2]_2$, (R = Et, *n*-Pr) and $MoO_2[S_2CNC_4H_8]_2$ [18,19,35] where the shorter (ave 2.452(7)) and longer Mo–S bonds (ave 2.645(26) Å) were both slightly shorter than those in **6**, and the trans S–Mo=O angles ranged from 155.8(6) to 157.56(9)°. The S–Mo–S bite angles in $MoO_2[S_2P(OC_6H_4Me\text{-}p)_2]_2$ (**6**) (76.32(4) and 76.90(4)^o) are, as is to be expected, larger than those in the three dithiocarbamates (ave 68.8(3)°) [18,19,35]. Further, in **6** the longer Mo–S bond is associ-

Table 2
^1H and ^{31}P NMR Chemical shifts for the binuclear oxomolybdenum(V) *O,O*-ditolyl dithiophosphate and dioxomolybdenum(VI) *O,O*-ditolyl dithiophosphate complexes[a,b]

S. no.	Compound	CH_3/OCH_2	C_6H_4	^{31}P
1	$Mo_2O_3[S_2P(OC_6H_4Me\text{-}o)_2]_4$	2.20 (24H, s)	6.72–7.12 (32H, m)	85.90
2	$Mo_2O_3[S_2P(OC_6H_4Me\text{-}m)_2]_4$	2.20 (24H, s)	6.75–7.16 (32H, m)	86.61
3	$Mo_2O_3[S_2P(OC_6H_4Me\text{-}p)_2]_4$	2.24 (24H, s)	6.94–7.12 (32H, m)	86.35
4	$MoO_2[S_2P(OC_6H_4Me\text{-}o)_2]_2$	2.22 (12H, s)	6.70–7.15 (16H, m)	96.57
5	$MoO_2[S_2P(OC_6H_4Me\text{-}m)_2]_2$	2.24 (12H, s)	6.64–7.08 (16H, m)	95.56
6	$MoO_2[S_2P(OC_6H_4Me\text{-}p)_2]_2$	2.20 (12H, s)	6.70–7.06 (16H, m)	96.03
7	$MoO_2[S_2P(OCH_2C_6H_5)_2]_2$	4.90 (8H, s, $J = 10$ Hz)	6.70–7.06 (20H, m)	95.56

[a] The spectra were recorded in $CDCl_3$ and reported in δ ppm from MeSi for ^1H and from H_3PO_4 for ^{31}P.
[b] Number of protons and multiplicities are in parentheses (s = singlet; m = multiplet).

Table 3
Crystal data and structure refinement for $Mo_2O_3[S_2P(OC_6H_4Me\text{-}o)_2]_4$ (**1**) and $Mo_2O_3[S_2P(OC_6H_4Me\text{-}m)_2]_4$ (**2**) and $MoO_2[S_2P(OC_6H_4Me\text{-}p)_2]_2$ (**6**)

Compound	**1**	**2**	**6**
Empirical formula	$C_{56}H_{56}O_{11}P_4S_8Mo_2$	$C_{56}H_{56}O_{11}P_4S_8Mo_2$	$C_{28}H_{28}O_6P_2S_4Mo$
Formula weight	1477.25	1477.25	746.62
Temperature (K)	120(2)	298(2)	120(2)
Wavelength (Å)	0.71073	0.71073	0.71073
Crystal system	monoclinic	triclinic	monoclinic
Space group	$P2_1/n$	$P\bar{1}$	$P2_1/c$
a (Å)	11.0684(6)	10.760(2)	9.936(1)
b (Å)	13.606(1)	12.478(3)	36.906(5)
c (Å)	21.134(2)	14.125(3)	9.502(1)
α (°)		114.162(3)	
β (°)	98.976(5)	102.701(3)	116.02(1)
γ (°)		95.975(3)	
Volume (Å^3)	3143.6(4)	1647.3(6)	3131.3(6)
Z	2	1	4
D_{calc} (calculated) (g/cm^3)	1.561	1.489	1.584
Absorption coefficient (mm^{-1})	0.823	0.785	0.828
$F(000)$	1504	752	1520
Crystal size (mm)	$0.12 \times 0.06 \times 0.05$	$0.25 \times 0.25 \times 0.20$	$0.08 \times 0.06 \times 0.04$
θ Range for data collection (°)	2.99–27.51	1.65–25.00	2.90–27.44
Index ranges	$-12 \leqslant h \leqslant 14$, $-17 \leqslant k17$, $-27 \leqslant l \leqslant 27$	$12 \leqslant h \leqslant 12$, $-14 \leqslant k14$, $-16 \leqslant l \leqslant 16$	$-12 \leqslant h \leqslant 12$, $-47 \leqslant k \leqslant 47$, $-12 \leqslant l \leqslant 12$
Reflections collected	50 816	15 968	9481
Independent reflections [R_{int}]	7211 [0.0523]	5792 [0.1407]	5450 [0.0415]
Maximum and minimum transmission	0.9600 and 0.9077	0.8588 and 0.8279	0.9676 and 0.9367
Refinement method	full-matrix least-squares on F^2	full-matrix least-squares on F^2	full-matrix least-squares on F^2
Data/restraints/parameters	7211/1/368	5792/0/365	5450/0/374
Goodness-of-fit on F^2	1.023	0.960	1.035
Final R indices [$F^2 > 4\sigma(F^2)$]	$R_1 = 0.0549$, $wR_2 = 0.1274$	$R_1 = 0.0719$, $wR_2 = 0.0963$	$R_1 = 0.0516$, $wR_2 = 0.1040$
R indices (all data)	$R_1 = 0.0706$, $wR_2 = 0.1383$	$R_1 = 0.1828$, $wR_2 = 0.1276$	$R_1 = 0.0798$, $wR_2 = 0.1144$
Extinction coefficient	0.0021(4)		
Largest difference peak and hole (e Å^{-3})	1.590 and −0.746	0.490 and −0.445	0.659 and −0.704

ated with the shorter P–S bond and vice versa, with S(2)–P(1) and S(4)–P(2) (ave 1.955 (2) Å) and S(1)–P(1) and S(3)–P(2) (ave 2.024 (4) Å) as was observed in the three dithiocarbamate derivatives with shorter (ave 1.702(9) Å) and longer (1.737(4) Å) C–S bonds.

The molecular structures of $Mo_2O_3[S_2P(OC_6H_4Me\text{-}o)_2]_4$ (**1**) and $Mo_2O_3[S_2P(OC_6H_4Me\text{-}m)_2]_4$ (**2**) in Figs. 2 and 3 show the distorted octahedral geometry of the MoO_2S_4 cores. The terminal Mo=O bonds are mutually in the syn conformation and cis to the Mo–O bonds of the linear Mo–O–Mo bridge in **1** and **2**, as is to be expected on the basis of the structures of the related compounds, $Mo_2O_3[S_2P(OPh)_2]_4$ [26], $Mo_2O_3[S_2P(OMe)_2]_4$ [16], $Mo_2O_3[S_2P(OEt)_2]_4$ [23] and $Mo_2O_3[S_2P(O\{n\text{-}Pr\})_2]_4$ [25]. The Mo–O(bridge) bonds (1.8540(3) and 1.8578 (8) Å in **1** and **2**, respectively) are considerably longer than the Mo=O(terminal) bonds (1.669(3) and 1.668(5) Å in **1** and **2**, respectively). The two bond distances are essentially the same as in the dithiophosphate analogues $Mo_2O_3[S_2P(OPh)_2]_4$ (1.8567(5) and 1.66(1) Å) [26], and $Mo_2O_3[S_2P(OR)_2]_4$, where R = Me, Et or *n*-Pr, (ave 1.86(2) and 1.65(2) Å) [16,23,25], as well as in the related dithiocarbonate $Mo_2O_3[S_2COEt]_4$ and $Mo_2O_3[S_2CO\text{-}i\text{-}Pr]_4$ (ave 1.87(1) and 1.68(2) Å) [21,22] and dithiocarbamate derivatives $Mo_2O_3[S_2CNEt_2]_4$, $Mo_2O_3[S_2CN(n\text{-}Pr)_2]_4$, and $Mo_2O_3[S_2CN(CH_2Ph)_2]_4$, (ave 1.869(9) and 1.682(6) Å) [20,19,22].

In contrast with **6**, in both **1** and **2** one of the dithiophosphate ligands is bidentate and only one is anisobidentate with the Mo–S bond that is trans to the Mo=O(terminal) bond being considerably longer (2.800(1) and 2.815(2) Å in **1** and **2**, respectively) than the other three Mo–S bonds (ave 2.50(4) Å). This pattern is identical to those in the $Mo_2O_3[S_2P(OR)_2]_4$ analogues (ave 2.81(2) for the long Mo–S bond and 2.50(3) Å for the rest) as well as in the dithiocarbonate $Mo_2O_3[S_2COR]_4$, R = Et and *i*-Pr (ave 2.72(2) for the long Mo–S bond and 2.51(4) Å for the rest) [21,22] and dithiocarbamate derivatives $Mo_2O_3[S_2CNR_2]_4$, R = Et, *n*-Pr and $[(CH_2Ph)_2]_4$, (ave 2.692(2) for the long Mo–S bond and 2.48(4) Å for the rest) [20,19,22], although the longer bond is shorter than in the dithiophosphates suggesting a slightly weaker trans influence. The additional restraint of the smaller bite angles (67–71°) in the dithiocarbonate and -carbamate ligands compared to 75.33(4)–80.23(7)° for **1** and **2** results in the S–Mo=O(terminal) angle being further from 180° ranging from 156.0(2) to 161(1) in $Mo_2O_3[S_2COR]_4$, [21,22] and 154.7(1)–159(1)° in $Mo_2O_3[S_2CNR_2]_4$ [20,19,22], compared to 166.8(1) in **1**

Table 4
Selected bond lengths (Å) and angles (°) for $Mo_2O_3[S_2P(OC_6H_4Me\text{-}o)_2]_4$ (**1**), $Mo_2O_3[S_2P(OC_6H_4Me\text{-}m)_2]_4$ (**2**) and $MoO_2[S_2P(OC_6H_4Me\text{-}p)_2]_2$ (**6**)

Compound	1	2	6
Mo(1)–O(1)	1.8540(3)	1.8578(8)	1.700(3)
Mo(1)–O(2)	1.669(3)	1.668(5)	1.694(3)
Mo(1)–S(1)	2.501(1)	2.511(2)	2.472(1)
Mo(1)–S(2)	2.800(1)	2.845(2)	2.727(1)
Mo(1)–S(3)	2.453(1)	2.446(2)	2.462(1)
Mo(1)–S(4)	2.539(1)	2.530(2)	2.753(1)
S(1)–P(1)	2.005(2)	2.001(3)	2.021(2)
S(2)–P(1)	1.957(2)	1.949(3)	1.956(2)
S(3)–P(2)	2.007(1)	1.993(3)	2.026(2)
S(4)–P(2)	1.976(2)	1.975(3)	1.954(2)
P(1)–O(3)	1.592(3)	1.600(5)	1.585(3)
P(1)–O(4)	1.586(3)	1.581(5)	1.587(3)
P(2)–O(5)	1.582(3)	1.585(5)	1.593(4)
P(2)–O(6)	1.583(3)	1.575(5)	1.578(4)
O(1)–Mo(1)′	1.8540(3)	1.8578(8)	
O(3)–C(1)	1.404(6)	1.427(9)	1.415(6)
O(4)–C(8)	1.459(7)	1.426(9)	1.414(6)
O(5)–C(15)	1.414(5)	1.419(9)	1.413(6)
O(6)–C(22)	1.414(6)	1.405(7)	1.419(5)
O(1)–Mo(1)–O(2)	102.4(1)	102.4(2)	104.7(2)
S(1)–Mo(1)–S(2)	75.33(4)	74.95(7)	76.32(4)
S(3)–Mo(1)–S(4)	79.87(3)	80.23(7)	76.90(4)
S(2)–Mo(1)–O(2)	166.8(1)	168.8(2)	163.0(1)
S(4)–Mo(1)–O(1)	160.54(3)	160.71(6)	163.5(1)
S(1)–Mo(1)–S(3)	159.28(4)	157.11(8)	156.11(5)
S(1)–Mo(1)–S(4)	91.74(4)	87.80(7)	85.29(4)
S(2)–Mo(1)–S(3)	84.81(3)	84.46(7)	85.21(4)
S(2)–Mo(1)–S(4)	83.07(3)	84.43(7)	81.09(4)
O(2)–Mo(1)–S(3)	107.8(1)	106.7(2)	105.1(1)
O(1)–Mo(1)–S(1)	95.78(3)	96.92(6)	104.9(1)
O(2)–Mo(1)–S(4)	95.3(1)	95.9(2)	88.0(1)
O(2)–Mo(1)–S(1)	91.7(1)	93.8(2)	89.9(1)
O(1)–Mo(1)–S(3)	86.94(3)	88.64(6)	89.5(1)
O(1)–Mo(1)–S(2)	81.53(3)	78.82(5)	88.7(1)
Mo(1)–S(1)–P(1)	90.39(5)	90.8(1)	90.68(6)
Mo(1)–S(2)–P(1)	83.05(5)	82.5(1)	84.87(6)
Mo(1)–S(3)–P(2)	86.67(5)	86.9(1)	89.11(6)
Mo(1)–S(4)–P(2)	84.98(5)	85.0(1)	82.62(6)
S(1)–P(1)–S(2)	110.11(7)	111.8(1)	108.03(8)
S(1)–P(1)–O(3)	110.7(2)	110.7(2)	112.1(1)
S(1)–P(1)–O(4)	105.4(2)	105.3(2)	111.0(2)
S(2)–P(1)–O(3)	113.4(1)	113.3(2)	114.9(1)
S(2)–P(1)–O(4)	117.2(1)	116.0(2)	116.2(1)
O(3)–P(1)–O(4)	99.4(2)	98.9(3)	94.4(2)
S(3)–P(2)–S(4)	107.22(6)	107.9(1)	109.53(8)
S(3)–P(2)–O(5)	112.2(1)	112.8(2)	108.0(2)
S(3)–P(2)–O(6)	113.4(1)	113.4(2)	110.3(2)
S(4)–P(2)–O(5)	115.1(1)	114.6(2)	116.2(2)
S(4)–P(2)–O(6)	108.5(1)	108.2(2)	109.3(1)
O(5)–P(2)–O(6)	100.4(2)	99.8(3)	103.4(2)
Mo(1)–O(1)–Mo(1)′	180	180	
C(1)–O(3)–P(1)	122.5(3)	121.2(5)	122.8(3)
C(8)–O(4)–P(1)	120.5(3)	120.4(5)	124.6(3)
C(15)–O(5)–P(2)	122.9(2)	122.0(5)	121.7(3)
C(22)–O(6)–P(2)	123.0(3)	124.7(4)	126.5(3)

and 168.2(2)° in **2**. By comparison, the two S–Mo=O(terminal) angles in **6** are slightly smaller 163.0(1) and 163.5(1)°. In **1** and **2**, the S–Mo–O(bridge) angle (160.54(3) and 160.71(6)°, respectively) is similar to the S–Mo–S angle (159.28(4) and 157.11(8)°, respectively); both of these angles being slightly larger than the S–Mo–S angle of 156.11(5)° in **6**. The O=Mo–O(bridge) angle (ave 104.4(2)° in **1** and **2**) also only differs slightly from the O=Mo=O angle in **6** (102.4)°. Table 4 shows the similarities, along with the slight differences, of the overall environment around the Mo atoms in the structures of both the monomeric and dimeric complexes.

4. Concluding comments

We have successfully prepared and characterized the binuclear oxomolybdenum(V) *O*,*O*′-ditolyl dithiophosphate complexes, $Mo_2O_3[S_2P(OR)_2]_4$ (R = *o*-, *m*-, *p*-C_6H_4Me) and dioxomolybdenum(VI) *O*,*O*′-ditolyl dithiophosphate complexes, $MoO_2[S_2P(OR)_2]_2$ (R = *o*-, *m*-, *p*-C_6H_4Me and $CH_2C_6H_5$). The IR, ^1H and ^{31}P NMR spectra of all of these oxomolybdenum complexes and the molecular structures of $Mo_2O_3[S_2P(OC_6H_4Me\text{-}o)_2]_4$ (**1**), $Mo_2O_3[S_2P(OC_6H_4Me\text{-}m)_2]_4$ (**2**) and $MoO_2[S_2P(OC_6H_4Me\text{-}p)_2]_2$ (**6**) were determined. The geometry of the MoO_2S_4 core in all of these molecules, whether in the dimeric $Mo_2O_3[S_2P(OR)_2]_4$ Mo(V) species **1** and **2** or the monomeric Mo(VI) species **6**, is that of a distorted octahedron, with the Mo–O bonds *cis* to one another. Apart from the bond length differences of Mo=O(terminal) and Mo–O(bridge) bonds, the clearest difference in the molybdenum surroundings is the presence of one long Mo–S bond in **1** and **2** compared to two such bonds in **6**. This is consistent with the larger *trans* influence of Mo=O.

Acknowledgements

Three of us (L.A., R.K. and R.R.) are grateful to UGC, New Delhi and K.S. is thankful to DST, New Delhi for financial support. M.B.H. thanks the EPSRC, UK for support of the X-ray facilities at Southampton University. J.E.D. wishes to thank the University of Windsor for financial support. We also thank Dr. Guancai Bai for X-ray data collection at the University of Windsor.

Appendix A. Supplementary material

CCDC 633736, 633737 and 633738 contain the supplementary crystallographic data for **1**, **2** and **6**. These data can be obtained free of charge via http://www.ccdc.ac.uk/conts/retrieving.html, or from the Cambridge Crystallographic Data Centre, 12 Union Road, Cambridge CB2 1EZ, UK; fax: (+44) 1223-336-033; or e-mail: deposit@ccdc.cam.ac.uk. Supplementary data associated with this article can be found, in the online version, at doi:10.1016/j.poly.2007.04.034.

References

[1] R. Colton, Coord. Chem. Rev. 90 (1988) 29.
[2] D. Collison, C.D. Garner, J.A. Joule, Chem. Soc. Rev. (1996) 25.
[3] R. Hille, Chem. Rev. 96 (1996) 2757.

[4] E.I. Stiefel, J. Chem. Soc. Dalton Trans. (1997) 3915.
[5] R. Ratnani, P. Nag, B.S. Joshi, R. Bohra, Advances in Metallo-Organic Chemistry, in: R. Bohra (Ed.), RBSA. Publishers, Jaipur, 1999, p. 253.
[6] A. Thapper, R.J. Deeth, E. Nordlander, Inorg. Chem 38 (1999) 1015.
[7] B.J. Hamstra, B. Cheng, M.K. Ellison, W.R. Schiedt, Inorg. Chem. 38 (1999) 3554.
[8] A. Thapper, J.P. Conathue, K.B. Musgrave, M.W. Willer, E. Nordlunder, B. Hedman, K.O. Hodgson, R.H. Holm, Inorg. Chem. 38 (1999) 4104.
[9] M.L. Mader, M.D. Carducci, J.H. Enemark, Inorg. Chem. 39 (2000) 525.
[10] L.S. Villata, M.R. Feliz, A.L. Capparelli, Coord. Chem. Rev. 196 (2000) 65.
[11] J.M. Tunney, J. McMaster, C.D. Garner, Comprehensive Coordination Chemistry II, in: J.A. McCleverty, T.J. Meyer, (Eds.), vol. 8, Elsevier, Amsterdam, 2003, pp. 459.
[12] R.H. Holm, Chem. Rev. 87 (1987) 1401.
[13] F.E. Kuhn, M. Groarke, E. Bencze, E. Herdtweck, A. Prazeres, A.M. Santos, M.J. Calhorda, C.C. Romao, I.S. Goncalves, A.D. Lopes, M. Pillinger, Eur. J. Chem. 8 (2002) 2370.
[14] F.W. Moore, M.L. Larson, Inorg. Chem. 6 (1967) 998.
[15] R.N. Jowitt, P.C.H. Mitchell, J. Chem. Soc 21 (1970) 1702.
[16] R.L. Thompson, S.J. Geib, N.J. Copper, Inorg. Chem. 32 (1993) 6076.
[17] G.J.J. Chen, J.W. McDonald, W.E. Newton, Inorg. Nucl. Chem. Lett. 12 (1976) 697.
[18] J.M. Berg, K.O. Hodgson, Inorg. Chem. 19 (1980) 2180.
[19] L. Ricard, J. Estienne, P. Karagiannidis, P. Toledano, A. Mitchell, R. Weiss, J. Coord. Chem. 3 (1974) 277.
[20] C.D. Garner, N.C. Howlader, F.E. Mabbs, A.T. McPhail, K.D. Oman, J. Chem. Soc. Dalton (1979) 962.
[21] A.B. Blake, F.A. Cotton, J.S. Wood, J. Am. Chem. Soc. 86 (1964) 3024.
[22] R.L. Thompson, S. Lee, S.J. Geib, N.J. Cooper, Inorg. Chem. 32 (1993) 6067.
[23] D. Wu, J. Huang, J. Huang, Jieqou Huaxue 3 (1984) 109.
[24] J.R. Knox, C.K. Prout, Acta Crystallogr. 25B (1969) 2281.
[25] R. Ratnani, R. Bohra, G. Srivistava, R.C. Mehrotra, J. Crystallogr. Spectrosc. Res. 20 (1990) 541.
[26] R. Ratnani, A.G. Mislankar, J.E. Drake, Inorg. Chem. 35 (1996) 2665.
[27] R. Ratnani, J.E. Drake, C.L.B. Macdonald, A. Kumar, S.K. Pandey, J. Chem. Crystallogr 35 (6) (2005) 447.
[28] A.L. Bingham, J.E. Drake, C. Gurnani, M.B. Hursthouse, M.E. Light, M. Nirwan, R. Ratnani, J. Chem. Crystallogr 36 (10) (2006) 627.
[29] A.J.M. Duisenberg, J. Appl. Crystallogr. 25 (1992) 92.
[30] G.M. Sheldrick, SADABS V2.10, 2003.
[31] G.M. Sheldrick, Acta Crystallogr. A 46 (1990) 467.
[32] L.J. Farrugia, J. Appl. Crystallogr. 32 (1999) 837.
[33] G.M. Sheldrick, SHELXL97, University of Gottingen, Germany, 1997.
[34] C. Glidewell, Inorg. Chim. Acta 25 (1977) 159.
[35] H. Teruel, Y.C. Gorrin, L.R. Falvello, Inorg. Chim. Acta 316 (2001) 1.

ical properties of compounds such as $[Ru(bpy)_3]^{2+}$ (bpy = 2,2′-bipyridine) have been studied in great detail and these studies have led to a better general understanding of photochemical processes in inorganic compounds [3]. The properties of the excited state, such as the temperature dependence of the luminescence lifetime and quantum yield of emission have been investigated as a function of the electronic properties of the coordinated ligands [4,5]. Especially, ruthenium(II) complexes containing symmetrical bipyridine-like ligands, such as substituted bipyridines, phenanthrolines and biquinolines, have been investigated in detail [6,7]. However, less attention has been paid to ruthenium(II) complexes containing asymmetric bidentate diimine ligands with two chemically different coordinating sites, although complexes with the following asymmetric ligands, pyridylpyrazoles, pyridylbenzimidazoles, pyridyltriazines, pyridyltriazoles, pyridylthiazoles and pyridylpyrimidine, have been reported [5,8–11]. So we became interested in synthesising and studying the properties of mixed-ligand ruthenium(II) complexes containing the asymmetric ligand 3-(pyridin-2-yl)-5,6-diphenyl-1,2,4-triazine (dppt, Scheme 1). Our choice of this ligand was because it is used as a sensitive reagent in the quantitative determination of Ru(II) and Fe(II) [12]. Further, it would be interesting to determine whether the coordination of the ambidentate triazine ring of dppt occurs through N2 or the sterically hindered N4 donor atom. In fact, we have shown that N2 is coordinated to Cu(II) in $[Cu(dppt)_2(H_2O)_2](ClO_4)_2$ [13]. It is obvious that the mode of coordination will have a critical role on the electronic properties of the complexes, e.g. its π-acceptor properties, because of the localised nature of the double bonds in 1,2,4-triazine [11]. The ligand is also of interest as it has rather low energy LUMO levels, as revealed by Resonance Raman spectral measurements [11] and electrochemical data [11]. The triazine nitrogen has a weak σ-donor but strong π-acceptor property [11], the two coordinating nitrogen atoms therefore will confer quite different electronic properties on the Ru(II) complexes.

We have already shown that mixed-ligand complexes [14] of the symmetrical ligands bpy and 1,10-phenanthroline (phen) can be isolated by the facile ring cleavage reaction of di-μ-chloro dimers $[Ru(pdto)Cl]_2(ClO_4)_2$ and $[Ru(bbdo)Cl]_2(ClO_4)_2$, where pdto is 1,8-bis(pyrid-2-yl)-3,6-dithiaoctane and bbdo is 1,8-bis(benzimidazol-2-yl)-3,6-dithiaoctane (Scheme 1), with bidentate ligands. In the present work we have reacted the di-μ-chloro dimers with the asymmetric ligand dppt to obtain new mononuclear Ru(II) complexes, which are of interest for the following reasons: (i) as they are mixed-ligand complexes, their electronic, emission and electrochemical properties can be easily tuned and illustrated in comparison with the corresponding symmetric bpy and phen mixed-ligand complexes; (ii) they constitute a family of mononuclear complexes containing *cis* coordinated thioether sulfur donors and an asymmetric ligand and provide an opportunity to evaluate the effect of thioether sulfur coordination on the metal to ligand charge-transfer (MLCT) involving the dppt ligand; (iii) the σ-donor properties of dppt are weaker than those of bpy, which would lead to higher Ru(II)/Ru(III) oxidation potentials. The effect of the asymmetric dppt on the electronic and redox properties of the complexes involving thioether sulfur ligands will be investigated. In this paper we report the synthesis, characterisation, electronic and electrochemical properties of the mixed-ligand complexes.

2. Results and discussion

2.1. Synthesis and characterisation

The mixed-ligand complexes $[Ru(pdto)(dppt)]^{2+}$ (**1**) and $[Ru(bbdo)(dppt)]^{2+}$ (**2**) have been prepared using the facile bridge cleavage reaction employed for isolating the bpy analogues [14]. The di-μ-chloro dimers $[Ru(pdto)Cl]_2^{2+}$ and $[Ru(bbdo)Cl]_2^{2+}$ were treated with stoichiometric amounts of the dppt ligand in aqueous ethanol (Scheme 2). To the reaction mixture was added a saturated aqueous solution of $NaClO_4$ to isolate the complexes as their perchlorates in good yields. Purification was effected by chromatography on alumina with ethanol as the eluent, followed by crystallisation of the complexes from a water–acetonitrile (2:1 v/v) mixture.

pdto bbdo

dppt

Scheme 1.

Scheme 2.

The complexes are soluble in water and other polar solvents. Their microanalytical data are in good agreement with the mixed-ligand composition of the chelates [Ru(pdto)(dppt)]$(ClO_4)_2$ (**1**) and [Ru(bbdo)(dppt)]$(ClO_4)_2$ (**2**). The conductivity of the complexes in acetonitrile solution (Λ_M: **1**, 284; **2**, 288 Ω^{-1} cm^2 mol^{-1}) show that they behave as 1:2 electrolytes and both the dications are essentially diamagnetic. A very strong and broad IR band near 1100 cm^{-1} and a strong and sharp band near 630 cm^{-1}, characteristic of ionic perchlorate, [15] are observed for both the complexes. Because of the presence of bis(pyrid-2-yl)- and bis(benzimidazol-2-yl)-dithioether ligands, neither the electronic nor electrochemical properties of the compounds can be used to identify unambiguously the way in which the ligand is bound to ruthenium. It is expected that NMR, in particular, will yield sufficient information.

2.2. ^1H NMR spectra

The chemical shifts of the free and coordinated ligands are provided in Section 4, along with the coordination-induced shifts (c.i.s. $= \delta_{complex} - \delta_{ligand}$). The assignment of ^1H and ^{13}C spectra of the complexes was made by comparison with those of the free ligands (Fig. 1) and the corresponding bpy complexes $[Ru(pdto)(bpy)]^{2+}$ (**3**) and $[Ru(bbdo)(bpy)]^{2+}$ (**4**) [14]. Also, ^1H–^1H COSY experiments [10] were carried out to unambiguously assign the spectra of the complexes.

On coordination to ruthenium, the five- and six-membered chelate rings involving the –S–CH_2–CH_2–S– and –S–CH_2–CH_2-py/bzim bridges in **1** and **2** are expected to exist in the envelope (Fig. 2a) and boat [33] (Fig. 2b–e) conformations, respectively, as in the X-ray crystal structures [14] of the related complexes **3** and **4**. Thus the two protons of each of the six methylene groups in both **1** and **2** become

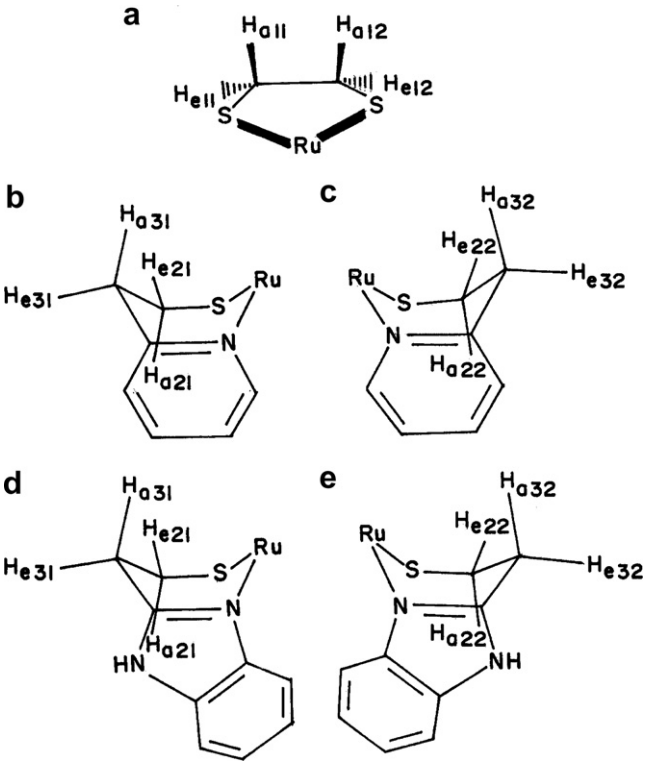


Fig. 2. Schematic view of chelation-imposed conformations of [Ru(L)(dppt)]$(ClO_4)_2$.

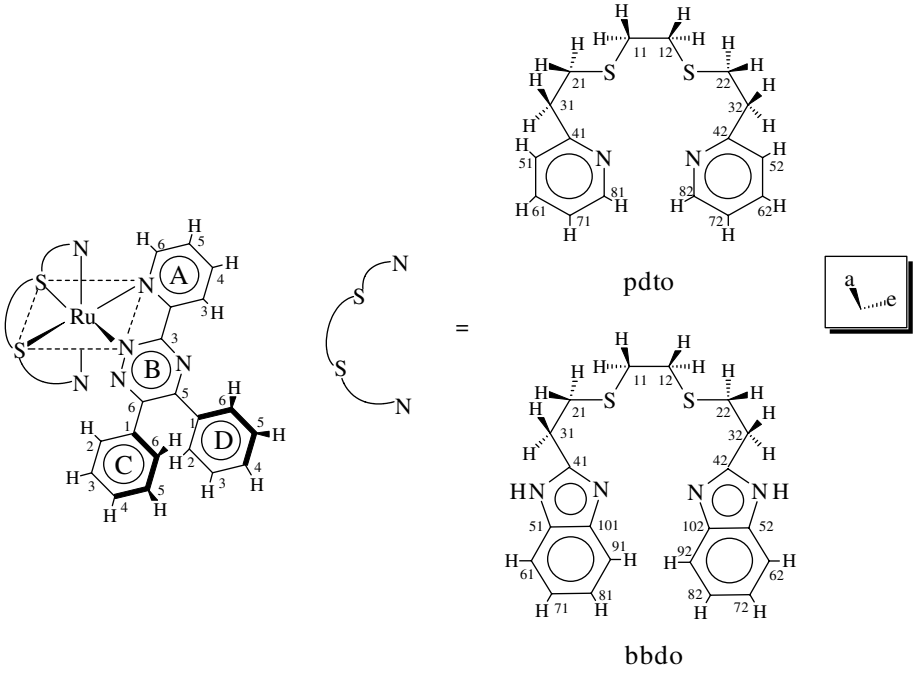


Fig. 1. Ligand orientation and proton numbering pattern for [Ru(N_2S_2)(dppt)]$(ClO_4)_2$ complexes (N_2S_2 = pdto or bbdo).

diastereotopic, axial (a) and equatorial (e), and give rise to, interestingly, 12 individual resonances. It is interesting to note that in **3** and **4** only six individual resonances have been observed, illustrating the effect of coordination of the asymmetric dppt ligand. For both **1** and **2**, the observed c.i.s. values for H_{a11} and H_{a12} are negative whereas those for H_{e11} and H_{e12} are positive. It is likely that the H_{a11} and H_{a12} protons are in close proximity to the metal, experiencing metal electron density in the envelope conformation imposed by the five-membered chelate ring (Fig. 2a). The negative c.i.s. values observed for the H_{a21} and H_{a22} protons are undoubtedly due to intraligand through-space ring-current anisotropy effects since on complexation the protons involved all lie over the shielding plane of the aromatic rings (Fig. 2b–e). The c.i.s. values for the H_{e21}, H_{e22}, H_{a31}, H_{e31}, H_{a32} and H_{e32} protons are all positive on account of chelation-imposed conformational changes.

For **1** and **2** totally four different types of aromatic rings are expected (Fig. 1): two non-equivalent py (**1**, H_{51}–H_{81} and H_{52}–H_{82}) or bzim (**2**, H_{61}–H_{91} and H_{62}–H_{92}) rings in axial positions and one py (**A**, H_{A3}–H_{A6}) and one triazine (tra, **B**) ring of dppt ligand occupying the two equatorial positions. This is in contrast to the observation of only two types of aromatic rings for **3** and **4**. Thus the magnetic non-equivalence of py (**1**) or bzim (**2**) ring protons may originate from the steric clashes of these rings with the asymmetric dppt ligand to different extents, which are expected to be more pronounced in **2** than in **1** due to the bulky bzim moieties in the former. This leads to the appearance of H_{71} (and H_{72}) and H_{81} (and H_{82}) protons of **1** as a triplet (7.735 ppm) and a doublet (7.352 ppm), respectively. Interestingly, the two bzim N–H protons in **2**, which experience lesser repulsion than the py ring protons, become magnetically equivalent and appear as a singlet (13.188 ppm). An examination of the c.i.s. values for the aromatic ring protons reveal that the chemical shifts of H_{61}, H_{62} and H_{81} (and H_{82}) (**1**) and H_{72} and H_{81} (**2**) show upfield shifts, while H_{51}, H_{52} and H_{71} (and H_{72}) (**1**) and H_{82}, H_{71}, H_{92}, H_{91}, H_{62} and H_{61} (**2**) protons exhibit downfield shifts due to ligand-to-metal σ-donation. A similar positive shift is expected for the H_{61} and H_{62} (**1**) and H_{72} and H_{81} (**2**) protons, but interestingly, only negative shifts are exhibited. In fact, these protons show downfield shifts in the corresponding bpy complexes **3** and **4**. The upfield shifts for the protons H_{61} and H_{62} (**1**) and H_{72} and H_{81} (**2**) are interesting and anomalous, as similar shifts have not been observed previously [16,17] for the Ru(II) complexes of py and bzim ligands. As coordination forces the py and tra rings of dppt to be coplanar, the py/bzim rings in pdto/bbdo are obliged to rotate away from dppt in order to minimise the steric interactions with dppt, and hence the H_{61} and H_{62} (**1**) and H_{72} and H_{81} (**2**) protons are exposed to the shielding magnetic anisotropy due to the ring currents of the py and tra rings of dppt. This reveals an unusual effect of the coordination by the aromatic ring nitrogens of the pdto or bbdo ligand wherein steric interactions are relieved by lengthening the $Ru–N_{py}$ or $Ru–N_{bzim}$ bond and by rotation of the py and bzim rings about the bond between the aromatic ring and the adjacent aliphatic carbon atom. The large negative c.i.s. values observed for the H_{81} (and H_{82}) proton of **1** may be due to metal-to-ligand π-back donation, which would increase the electron density at these sites adjacent to the py nitrogens of pdto.

The ^{1}H NMR spectra of **1** and **2** consist of four sets of signals for the **A** ring protons of dppt (Figs 3 and 4) and they should be significantly different from other resonances as the ring experiences a *trans* effect of the thioether ligand. The H_{A3} signal of **1** (10.116 ppm) and **2** (10.634 ppm) appear at fields lower than that of $[Ru(dppt)_3]^{2+}$ (9.110 ppm) [11]. This is expected as the thioether sulfur atom should cause a *trans* effect higher than that of the aromatic nitrogen atom. The dppt ligand is expected to coordinate through N2 of the tra ring and *via* the py nitrogen atom, as observed for $[Ru(dppt)_3]^{2+}$, as it would involve a much smaller steric interaction between the phenyl rings and aromatic rings of pdto or bbdo. In fact, the crystal structures [13,18] of $[Cu(dppt)_2(H_2O)_2](ClO_4)_2$ and $[Ru(tpy)(dppht)](ClO_4)_2$ [dppht = 3-(1,10-phenanthroline-2-yl)-5,6-diphenyl-*as*-triazine] reveal the coordination of N2 to Cu(II) and Ru(II), respectively. A negative c.i.s. value observed for the H_{A6} proton, adjacent to the coordinating nitrogen in both the complexes, would result from interligand through-space ring-current anisotropy effects and there is a lesser influence on the H_{A4} and H_{A5} protons, as expected. The large positive c.i.s. value for the H_{A3} proton of dppt suggests that the ligand-to-metal σ-donation is more important (as this will decrease the electron density at this site leading to a positive c.i.s. value) than the metal-to-ligand π-back donation in the ground state of these complexes. The chemical shifts of the protons of the phenyl rings **C** and **D** are not affected so much (free dppt, 7.423–7.656 ppm; **1** and **2**, 7.425–7.800 ppm) upon coordination, indicating that the effect of steric hindrance is not appreciable.

For **1** the c.i.s values of the primary ligand are less positive than those for **2** suggesting that the bbdo ligand is a better σ-donor for ruthenium(II) than the pdto ligand. Interestingly, the py (**1**) protons are shifted upfield, in contrast to the bzim (**2**) protons, which are shifted downfield. This illustrates that the ring-current-induced fields depend upon the aromaticity and π-polarisability of the heterocycles, which differ significantly for different types of heterocycles [19]. This is expected as the py nitrogen is a weaker σ-donor [20] than the bzim nitrogen, given the higher ligand basicity of the bzim ring system and probably the lower geometric constraints on the chelate bite of the bzim ring. Thus the sign and magnitude of the c.i.s. values throw light on the nature of the metal–ligand bonding and changes in conformations of the chelate rings as well.

As shown in Scheme 3, there are two sets of potentially possible diastereoisomers, depending upon whether the N_2S_2 donors of pdto or bbdo occupy positions "*cis*-α" (**A** and **B**) or "*cis*-β" (**C** and **D**) to each other. If they are coordinated in a "*cis*-α" fashion (**A** and **B**), a plane of

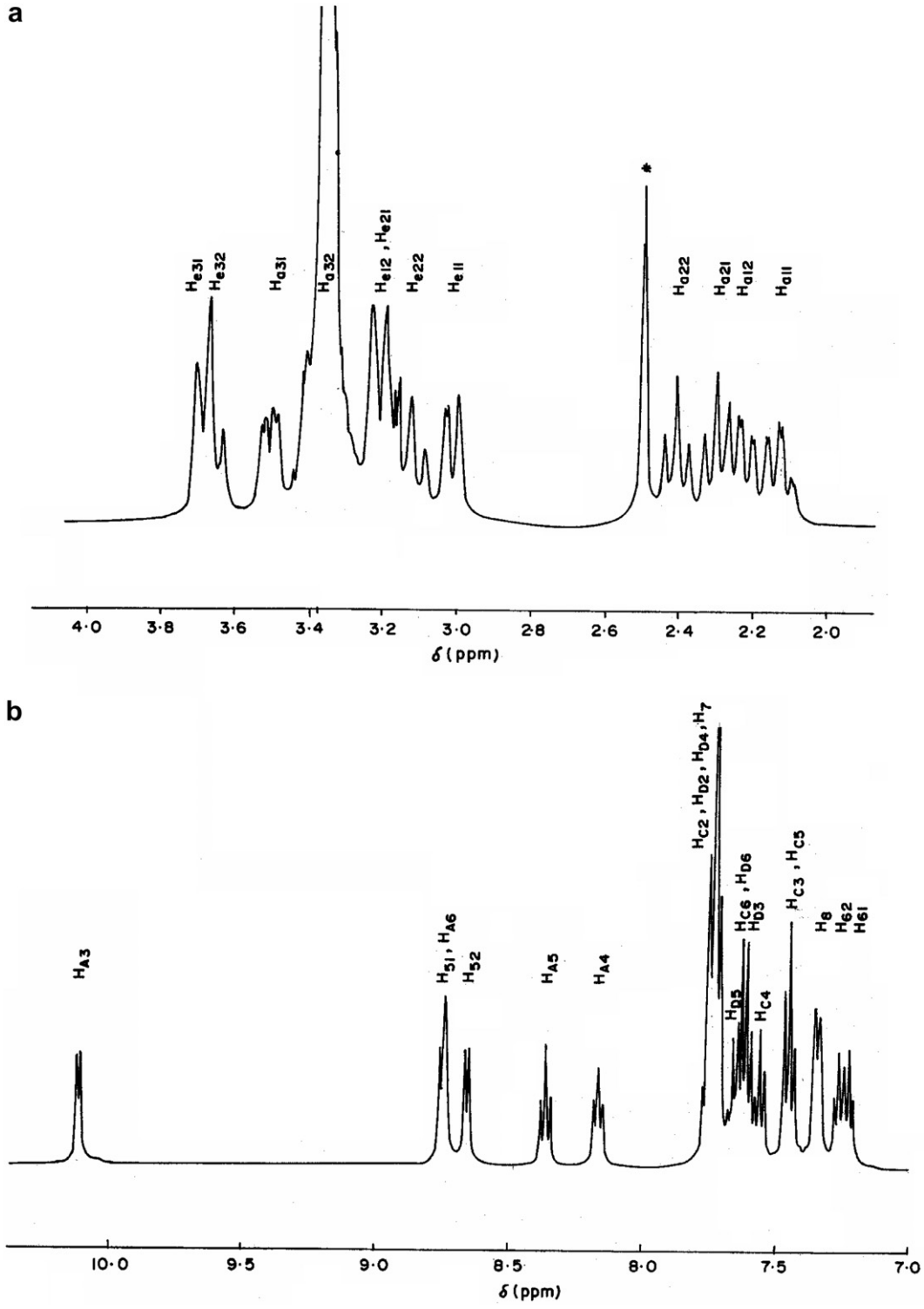


Fig. 3. ^{1}H NMR spectrum of [Ru(pdto)(dppt)]$(ClO_4)_2$ (**1**) in $(CD_3)_2SO$.

symmetry (ignoring the two nitrogens of dppt) that would contain the ruthenium atom and the two sulfur atoms would transform both the aromatic rings of the N_2S_2 ligand. The RuN_2S_2 core would also have an inversion center that would transform the aromatic rings of the N_2S_2 ligand. As a result both the aromatic rings would end up being equivalent and therefore only one set of aromatic resonances are expected to be observed in the NMR spectra. On the other hand, the coordination of two aromatic nitrogens of the N_2S_2 ligand in a "*cis*-β" fashion (**C** and **D**), would leave the aromatic rings magnetically non-equivalent since a plane of symmetry and a center of inversion would be absent, leading to the observation of two sets of aromatic resonances. Actually, both the complexes **1**

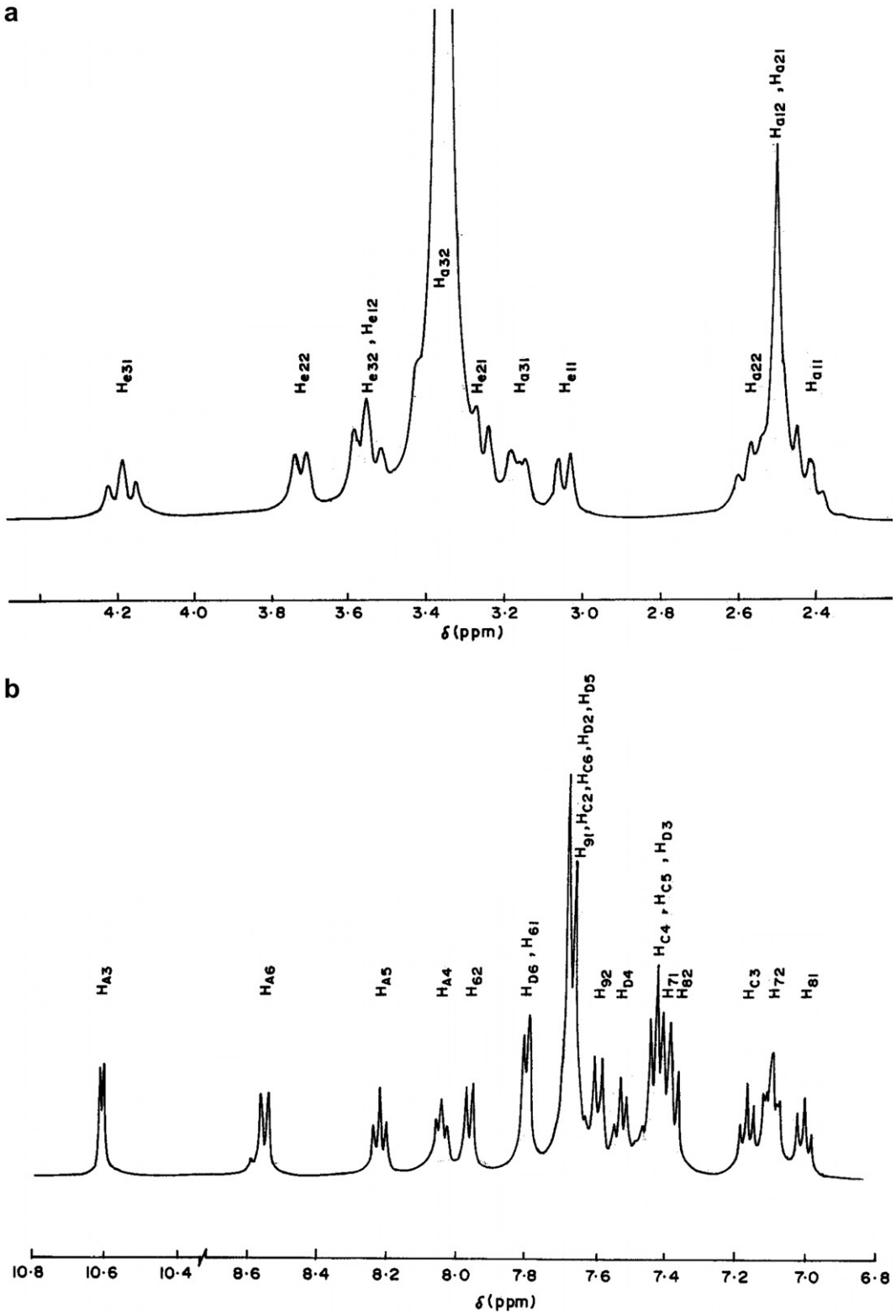
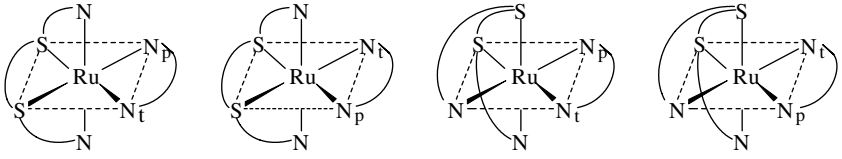


Fig. 4. ^{1}H NMR spectrum of [Ru(bbdo)(dppt)](ClO$_4$)$_2$ (**2**) in (CD$_3$)$_2$SO.

and **2** display two sets of aromatic signals (Figs. 3 and 4) corresponding to the two aromatic rings of the N_2S_2 ligand; however, H_{71} and H_{72} (7.735 ppm) and H_{81} and H_{82} (7.352 ppm) protons of **1** and the two bzim-NH (13.188 ppm) protons of **2** resonate at the same field, revealing that the two aromatic rings are magnetically equivalent and hence the possibility of a "*cis*-α" configuration (**A** and **B**) for the present complexes. The magnetic non-equivalence of the other protons in the two aromatic rings of the N_2S_2 ligand arise from the incorporation of



Scheme 3.

the asymmetric dppt ligand. Further, the ^{1}H NMR spectra of **1** and **2** show only single resonances for all the aromatic protons, substantiating the possibility of the presence of only one set of diastereoisomers. Thus the enantiomers **A** and **B** are formed in equal proportions and therefore a racemic mixture of **1** and **2** is obtained. Even though the formation of two sets of diasteroisomers ("*cis*-α" and "*cis*-β") is expected for ruthenium complexes [21], it is not observed. The "*cis*-β" enantiomers **C** and **D** are not formed, possibly due to the strong steric interaction between the aromatic rings of the N_2S_2 ligand and dppt. Single crystal X-ray structures are needed to confirm the *cis*-α configuration, but attempts to grow good single crystals of **1** and **2** were fruitless.

2.3. ^{13}C NMR spectra

The ^{13}C NMR chemical shifts of the free ligands and complexes are provided in Section 4 along with c.i.s. values. The asymmetry introduced by the dppt ligand in both complexes render all the six aliphatic carbons non-equivalent, leading to the observation of peaks for each of the carbon atoms. In contrast, the analogous bpy (**3**, **4**) complexes exhibit three aliphatic carbon signals due to the identical environment introduced by coordination of the symmetrical bpy ligand. The ^{13}C NMR c.i.s. values do not correlate in sign or magnitude with those for the ^{1}H NMR spectra because the relative contribution of the through-space ring-current anisotropy should be less important in ^{13}C than in ^{1}H NMR [19]. All the aliphatic carbons, except C_{21} and C_{22}, exhibit the largest negative c.i.s. values for **1**, suggesting that the C_{21} and C_{22} carbons are more sensitive to σ-donation effects. As the aliphatic carbons are not sensitive to π-back donation, their ^{13}C NMR shifts are more shielded in **2** than in **1**. These results support the suggestion [22] that ^{13}C NMR shifts of aliphatic carbons are susceptible to upfield shifts due to steric-compression effects, since the aliphatic carbons of both pdto and bbdo undergo changes in conformation upon complexation due to 'folding' of the flexible N_2S_2 ligand in the presence of the asymmetric dppt ligand. However, the effect is weaker in the presence of the symmetric bpy ligand.

Like the aliphatic carbons, the py (**1**) and bzim (**2**) ring carbons are non-equivalent resulting in the observation of up to 10 and 14 resonances, respectively. Interestingly, the analogous bpy complexes show only five (**3**) and seven (**4**) resonances for the symmetrical bpy ligand. The high positive c.i.s. values (+2.15 to +7.85 ppm) observed for the py (**1**) ring carbons are consistent with the presence of predominant ligand-to-metal σ-donation. The highly negative c.i.s. values observed for the C_{91} and C_{92} carbons of the bzim (**2**) ring are attributed to upfield steric-compression effects [23]. The c.i.s. values of the C_{61}, C_{62}, C_{81} and C_{82} bzim (**2**) ring carbons are lower than these carbons indicating a smaller steric-compression effect for these carbons. It is noteworthy that the C_{71} and C_{72} carbons in the bzim ring show significant positive c.i.s. values suggesting an effective dπ–π metal–ligand interaction involving these carbon sites [19].

The main contributor to the ^{13}C NMR c.i.s. values appears to be ligand-to-metal σ-donation, which generally leads to positive c.i.s. values for the **A** and **B** ring carbons (+1.27 to +4.64 ppm), except the C_{A3} (**1**) and C_{B6} (**2**) carbons of dppt in both complexes. The relatively large negative c.i.s. values for the phenyl carbons C_{C1}, C_{C2}, C_{C4}, C_{C6} and C_{D1} indicate that the metal-to-ligand π-back donation is predominant; however, the other carbons show positive c.i.s. values mainly due to ligand-to-metal σ-donation. Interestingly, the c.i.s. value (−3.29 ppm) of the C_{A3} carbon of dppt ligand in **1** is quite different from that (+4.4 ppm) of C_3 of bpy in **3**, which is systematically shifted upfield. This carbon is probably very much affected by the change in conformation of the free ligand on complexation and may experience an upfield shift due to steric-compression [22] from the lone pair of electrons on N4 of triazine. In contrast, the C_{A3} (+1.27 ppm) carbon in **2** is shifted downfield, which is quite similar to the C_3 carbon of bpy in **4**. The py carbon C_{A4} (**1**, +2.65; **2**, 2.16 ppm), *para* to the coordinated nitrogen atom of dppt (**1** and **2**), and C_{61} (+2.15 ppm) and C_{62} (+2.30) of pdto (**1**) are shifted upfield compared to the other py carbon atoms of dppt and pdto (**1**). This reveals that the coordinated nitrogen reflects the degree of π-back bonding [22,24] on the *para* carbon. However, this result has been contested on the basis of π-electron density calculations [25].

2.4. Electronic absorption and emission spectra

Complex **1** exhibits an intense band around 470 nm while **2** shows a band at 515 nm with a shoulder around 450 nm (Table 1, Fig. 5), with the absorptivity of the former being higher. These spectra are similar to the bpy (**3** and **4**) analogues and are assigned to the $d\pi(Ru^{II}) \rightarrow \pi^{*}$(dppt) metal-to-ligand charge-transfer (MLCT) transition [11]. The higher energy bands (235–325 nm) for the

Table 1
Electronic,[a] emission[b] and redox[e,f,g] properties of ruthenium(II) complexes

Compound	λ_{max} (nm) (ε[c], $M^{-1}\,cm^{-1}$)	λ_{em} nm[d]	E_{pc} V	E_{pa} V	ΔE_p mV	$E^h_{1/2}$ V	$E^i_{1/2}$ V	i_{pc}/i_{pa}	$D\times10^6$ $cm^2\,s^{-1}$	$\Delta E^j_{1/2}$ V	$E_{1/2}^{3+/2+*k}$ V	$E_{1/2}^{2+*/+1}$ V
$[Ru(pdto)(dppt)](ClO_4)_2$ (**1**)	470 (10990) 320 sh (20770) 285 (25210) 240 (18770)	650	1.144	1.222	78	1.183 −0.966 −1.090	1.185	0.88	7.2	2.45	−0.43	0.64
$[Ru(bbdo)(dppt)](ClO_4)_2$ (**2**)	515 (6720) 450 sh (3740) 320 sh (11560) 285 (19920) 270 (20260)	650	0.862	0.938	76	0.900 −1.058 −1.418	0.897	0.91	4.7	2.26	−0.70	0.60

[a] In acetonitrile solution.
[b] In N_2-purged CH_3CN at 298 K.
[c] ε obtained from solutions with concentrations of $3.0–8.9\times10^{-5}$ M.
[d] Excitation wavelength: **1**, 510 and **2**, 550 nm.
[e] Measured vs. non-aqueous Ag/Ag^+ reference electrode; scan rate, 50 mV s^{-1}; supporting electrolyte, $[(C_4H_9)_4N](ClO_4)$ (0.1 M).
[f] Complexes **1** and **2** in acetonitrile.
[g] Negative values are ligand reduction potentials.
[h] One redox potential corresponds to the Ru^{II}/Ru^{III} couple.
[i] Differential pulse voltammetry, scan rate, 1 mV s^{-1}; pulse height, 50 mV.
[j] $\Delta E_{1/2} = E_{ox} - E_{red}$.
[k] Calculated by using Eq. (3) in text.
[l] Value calculated using Eq. (4) in text.

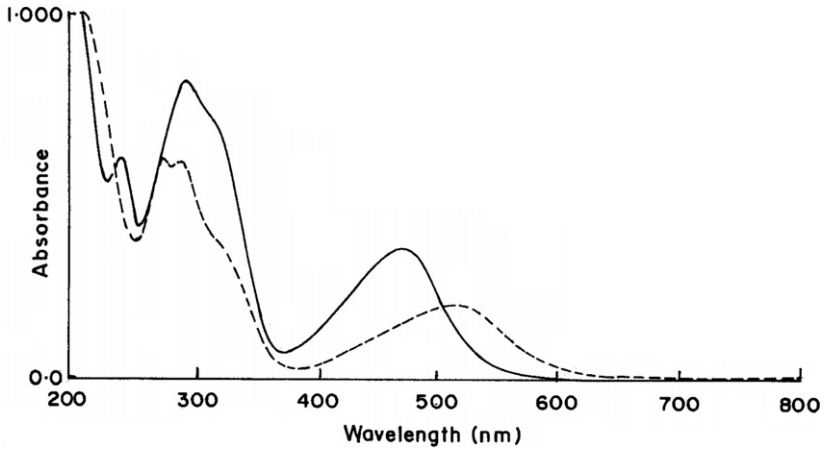


Fig. 5. Electronic spectra of the complexes $[Ru(pdto)(dppt)](ClO_4)_2$ (**1**) (—) and $[Ru(bbdo)(dppt)](ClO_4)_2$ (**2**) (----) in acetonitrile solution.

complexes **1** and **2** observed in solution arise from intraligand π–π* type transitions [26]. These bands are slightly lower in energy and higher in absorptivity than the analogous bpy complexes [**3**, 430 nm (3710 $M^{-1}\,cm^{-1}$); **4**, 450 nm (2720 $M^{-1}\,cm^{-1}$)]. This is because the LUMO levels [11] of dppt are lower in energy than the symmetric bidentate diimine ligand bpy, with the MLCT transition being affected by the enhanced π-acceptor and decreased σ-donor properties of the dppt ligand compared to bpy. The negative charge built on Ru(II) by the strongly σ-donating bzim moieties in **2** would be expected to destabilise the metal dπ orbital and hence lower the $d\pi(Ru^{II}) \rightarrow \pi^*$ MLCT band energy (~45 nm) from 470 nm in **1** to 515 nm in **2**. The different electronic transitions originating from different metal d orbitals [27], as observed in $[Ru(dppt)_3]^{2+}$, may contribute to the higher intensities of these absorption bands, which renders it difficult to discern the $Ru(d\pi) \rightarrow S(\pi^*)$ MLCT bands and hence evaluate the effects of the Ru–S bond on the electronic properties.

When **1** and **2** are excited at 510 and 550 nm, respectively, at room temperature in CH_3CN solution a strong luminescence is observed for both the complexes (**1**, **2**, 650 nm; Fig. 6). The emission spectral band is suggested to be MLCT in origin, which is supported by the excitation spectra of the corresponding solutions of the complexes. The emission bands are rather narrow (half-width, 1430–1520 cm^{-1}), which is typical of a ^{3}MLCT emission, as observed for $[Ru(dppt)_3]^{2+}$ and certain other Ru(II)-polypyridine complexes [11,28]. This is further substantiated by the energy differences between the intense absorption and emission bands for **1** (5400 cm^{-1}) and **2** (4000 cm^{-1}), [4a] which are lower than those for the corresponding binu-

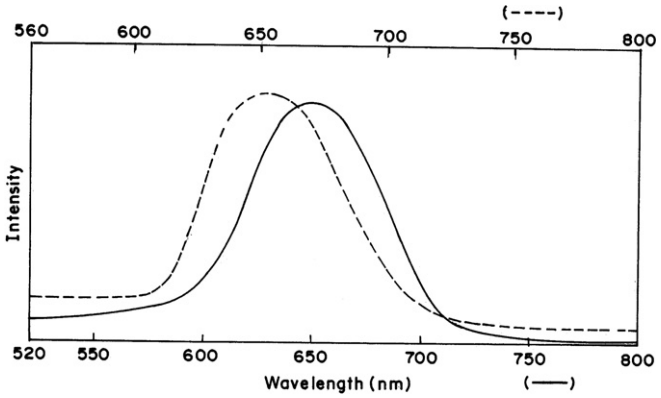


Fig. 6. Emission spectra of the complexes $[Ru(pdto)(dppt)](ClO_4)_2$ (**1**) (—) and $[Ru(bbdo)(dppt)](ClO_4)_2$ (**2**) (----) in acetonitrile solution at room temperature.

clear complexes $[Ru(pdto)Cl]_2^{2+}$ and $[Ru(bbdo)Cl]_2^{2+}$ exhibiting ^3MC emission [14].

2.5. Electrochemical behaviour

The electrochemical properties of both **1** and **2** have been studied by cyclic voltammetry (CV) and differential pulse voltammetry (DPV) on a Pt working electrode in acetonitrile solution in the potential range ± 2 V at 25.0 ± 0.2 °C. Both the complexes exhibit a redox wave ($E_{1/2}$, **1**, 1.18; **2**, 0.90 V versus Ag/Ag^+, Table 1, Fig. 7) assignable to the Ru(II)/Ru(III) couple based on the magnitude of the diffusion coefficients (D, $4.7–7.2 \times 10^6$ $cm^2\ s^{-1}$) calculated from the CV responses at different scan rates (30–500 mV). The linearity of the i_{pa} versus $v^{1/2}$ plots [29], which pass through the origin, indicates that the redox processes occurring at the electrode are diffusion controlled. The peak potential separations ΔE_p (74–90 mV) are generally larger than the ideal Nernstian value of 59 mV for a one-electron transfer, but commonly observed for complexes of this type apparently due to uncompensated solution resistance [30].

The Ru(II) → Ru(III) oxidation of the bzim based complex **2** is more facile than the py-based complex **1**, which is consistent with the higher MLCT band energy of the former (see above). Obviously, the σ-bonding ability of the bzim nitrogen is higher than that of the py nitrogen leading to stabilisation of the Ru(III) oxidation state. The Ru(II)/Ru(III) redox potentials in chelates containing thioether donors are attributed to the π-acceptor ability of thioether donors in stabilising the lower oxidation state. Further, the $E_{1/2}$ values of the present complexes are higher than the analogous bpy complexes **3** and **4** ($E_{1/2}$, **3**: 1.14; **4**: 0.85 V), which may be attributed to the weak σ-bonding ability of the N2 nitrogen of the dppt ligand, conferred by the strongly electron withdrawing phenyl groups. Also, Huckel calculations have shown that the LUMO of pyridyltriazine in dppt with phenyl substituents is lower than that of bpy [11], leading to the weaker σ-donor but stronger π-acceptor property of dppt. Therefore, it is evident that coordination of the strongly π-accepting dppt ligand tends to stabilise the lower Ru(II) oxidation state better than that of the analogous bpy complexes **3** and **4**.

Both the complexes display two ligand based reduction waves (**1**, −0.97, −1.09; **2**, −1.06, −1.42 V, Table 1), the one-electron nature of which is established by the magnitude of the peak currents. Since the free pdto or bbdo ligand does not exhibit any ligand reduction within the potential range used for the complexes, the observed reduction waves are assigned to two successive reductions of the coordinated dppt ligand, involving triazine (tra) and pyridine (py) moieties (Eqs. (1) and (2)). Further, the ligand reduction potential of **1** is more positive than **2** indicating that the extent of π-delocalisation of the

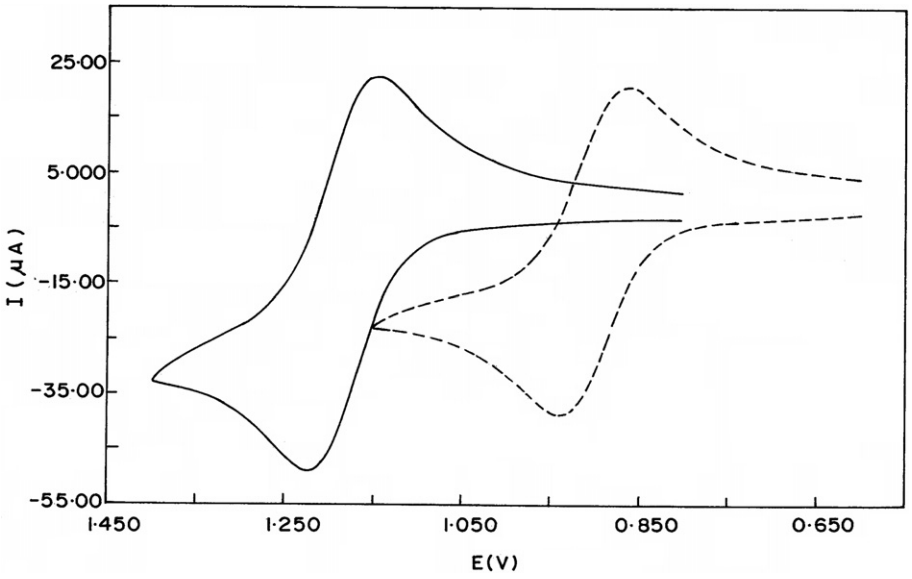


Fig. 7. Cyclic voltammograms of 0.001 M complexes $[Ru(pdto)(dppt)](ClO_4)_2$ (**1**) (—) and $[Ru(bbdo)(dppt)](ClO_4)_2$ (**2**) (----) in CH_3CN at 25 °C at 0.05 V s^{-1} scan rate.

$$[Ru^{II}(L)(py\text{-}tra)]^{2+} + e^- \rightleftharpoons [Ru^{II}(L)(py\text{-}tra^{\cdot-})]^{+} \quad (1)$$

$$[Ru^{II}(L)(py\text{-}tra^{\cdot-})]^{+} + e^- \rightleftharpoons [Ru^{II}(L)(py^{-}\text{-}tra^{\cdot-})] \quad (2)$$

asymmetric dppt ligand is stronger in pdto than in bbdo. Interestingly, the first ligand reduction potential of the present complexes is approximately the same as that of $[Ru(dppt)_3]^{2+}$ (tra-based reduction) [11], while the second ligand reduction potential is the same as that of the first ligand reduction potential of $[Ru(bpy)_3]^{2+}$ (py-based reduction) [31], thus substantiating that two chemically different imine fragments of dppt ligand are reduced at different potentials.

The excited-state redox potentials ${E_{1/2}}^{3+/2+*}$ and ${E_{1/2}}^{2+*/+}$ of the complexes were calculated by Eqs. (3) and (4), respectively, [32], where $E_{1/2}(Ru^{III/II})$ is the observed

$$E_{1/2}^{3+/2+*} = E_{1/2}(Ru^{III/II}) - E_{em} \quad (3)$$

$$E_{1/2}^{2+*/+} = E_{1/2}(L') + E_{em} \quad (4)$$

reduction potential for the Ru(III/II) couple, $E_{1/2}(L')$ is the first ligand reduction potential and E_{em} is the excited-state luminescent energy in electron volts (approximate value estimated from the luminescence maximum observed at room temperature rather than for a frozen solution). The calculated excited-state redox potentials of **1** and **2** indicate that the complexes would behave as both photooxidants and photoreductants. As photoreductants, the driving force for the py-based complex is higher than that for the bzim based complex (${E_{1/2}}^{3+/2+*}$, **1**, −0.43; **2**, −0.70 V versus SCE); however, as photooxidants, the potentials (${E_{1/2}}^{2+*/+}$, **1**, 0.64; **2**, 0.60 V versus SCE) show only a little variation.

Lever [33] introduced a ligand electrochemical parameter, $E_L(L)$, based upon the observed Ru(II)/Ru(III) redox potential (E_{obs}) as an electrochemical standard. He also proposed a relationship (Eq. (5)) between $E_L(L)$ and E_{obs} for a series of complexes $[Ru(bpy)_nL_{6-2n}]^{m+}$ ($n = 0$–3; L may be a mono-, di-, tri- and polydentate ligands). Using Eq. (5) and the data from the ligand electrochemical series proposed by Lever

$$E_{obs}(Ru^{II}/Ru^{III}) = 2n \times 0.255 + (6 - 2n)E_L(L) \quad (5)$$

[33,34], the $E_L(L)$ values for pdto, bbdo, dppt and related pyridyltriazines were calculated[1] and then used to calculate the Ru(II)/Ru(III) potentials for compounds containing substituted pyridyltriazine ligands (Table 2). The calculated values are plotted against experimental values in Fig. 8 to obtain, interestingly, a straight line. Further, the value of $E_L(L)$ for pdto is higher than that of bbdo, revealing that the role of the coordinated pdto and bbdo ligands is to raise the redox potentials of the Ru(II)/Ru(III) couple.

[1] Thus $E_L(L)$ value of dppt was calculated from the observed [11] $E_{1/2}$ of $[Ru(dppt)_3]^{2+}$ (1.790 V) and $[Ru(bpy)_2(dppt)]^{2+}$ (1.640 V) by assuming $n = 0$ and 2, respectively. Similarly those of tpt [3,5,6-tris(pyridin-2-yl)-1,2,4-triazine] and dmpt [5,6-dimethyl-3-(pyridin-2-yl)-1,2,4-triazine] were calculated from the literature $E_{1/2}$ values of $[Ru(bpy)_2(tpt)]^{2+}$ (1.710 V) [11] and $[Ru(bpy)_2dmpt]^{2+}$ (1.600 V) [11] by assuming $n = 2$. For pdto and bbdo, the $E_L(L)$ values were calculated from $[Ru(pdto)(bpy)]^{2+}$ (1.682 V) [14] and $[Ru(pdto)(bpy)]^{2+}$ (1.682 V) [14] by assuming $n = 1$.

Table 2
Electrochemical potential of ligands and calculated/experimental Ru(II)/Ru(III) redox potentials of the ruthenium(II) complexes

Ligand (L)	$E_L(L)$[a] (V vs. NHE)	Compound[b]	Ru(II)/Ru(III)	
			E^c_{calc}	E^c_{expt}
dppt	0.304	**1**[d]	1.780	1.727
tpt	0.345	**2**[d]	1.496	1.444
dmpt	0.291	**3**	1.824	1.790
pdto	0.293	**4**	1.644	1.640
bbdo	0.222	**5**	1.544	1.520
bpy[e]	0.259	**6**	1.726	1.710
		7	1.618	1.600

[a] $E_L(L)$ values calculated using Eq. (5).
[b] Compounds **1**–**7** are $[Ru(pdto)(dppt)]^{2+}$ (**1**), $[Ru(bbdo)(dppt)]^{2+}$ (**2**), $[Ru(dppt)_3]^{2+}$ (**3**), $[Ru(bpy)_2(dppt)]^{2+}$ (**4**), $[Ru(bpy)_3]^{2+}$ (**5**), $[Ru(bpy)_2(tpt)]^{2+}$ (**6**), $[Ru(bpy)_2(dmpt)]^{2+}$ (**7**).
[c] Values are expressed in V vs. NHE.
[d] Present work.
[e] From Ref. [33].

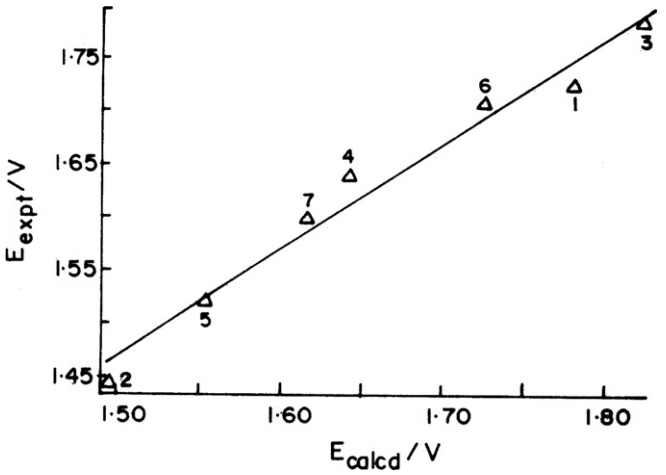


Fig. 8. Correlation between the calculated (E_{calc}) and experimental (E_{expt}) potentials of $Ru^{III/II}$ (with reference to NHE). Points **1**–**7** are for $[Ru(pdto)(dppt)]^{2+}$ (**1**), $[Ru(bbdo)(dppt)]^{2+}$ (**2**), $[Ru(dppt)_3]^{2+}$ (**3**), $[Ru(bpy)_2(dppt)]^{2+}$ (**4**), $[Ru(bpy)_3]^{2+}$ (**5**), $[Ru(bpy)_2(tpt)]^{2+}$ (**6**) and $[Ru(bpy)_2(dmpt)]^{2+}$ (**7**).

2.6. Correlation between electronic and electrochemical data

When the absorption or emission maxima (in eV) of Ru(II) complexes are plotted against the difference in the oxidation and reduction potentials of the Ru(II) complex and ligand, respectively, a linear correlation (Fig. 9) is obtained for the new mixed-ligand ruthenium complexes of dppt, including $[Ru(dppt)_3]^{2+}$, $[Ru(bpy)_2(dppt)]^{2+}$ [11], $[Ru(bpy)_3]^{2+}$ [31] and Ru(II) complexes of pyridyltriazoles [9]. A similar correlation has been reported previously for other Ru(II) systems. The linearity illustrates that the same type of orbitals are involved in the absorption and emission processes as well as the metal oxidation and ligand

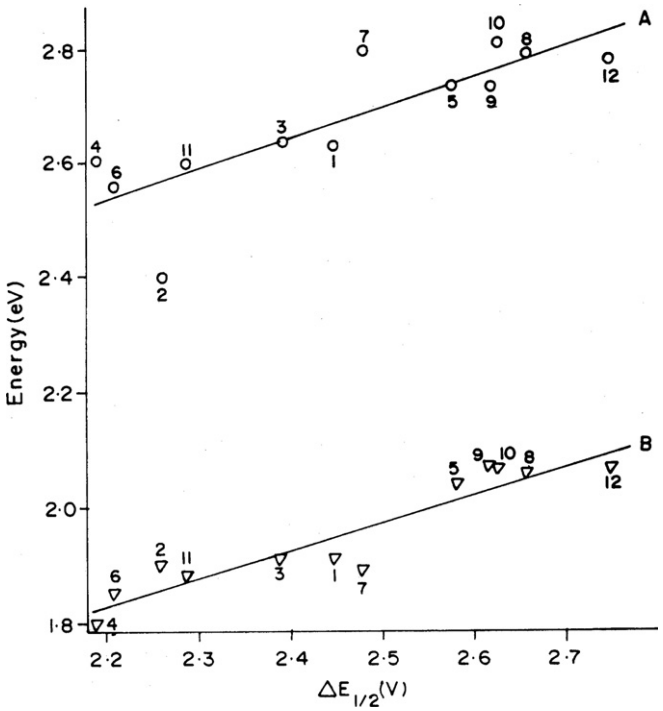


Fig. 9. Correlation between $\Delta E_{1/2}$ and the energy of absorption (A) and emission (B) maxima as measured in acetonitrile at room temperature. Points **1** and **2** refer to the compounds presented in Table 1, while points **3**–**12** are for $[Ru(dppt)_3]^{2+}$ (**3**), $[Ru(bpy)_2(dppt)]^{2+}$ (**4**), $[Ru(bpy)_3]^{2+}$ (**5**), $[Ru(bpy)_2(tpt)]^{2+}$ (**6**), $[Ru(bpy)_2(dmpt)]^{2+}$ (**7**), $[Ru(bpz)_3]^{2+}$ (**8**), $[Ru(bpy)_2(1Mptr)]^{2+}$ (**9**), $[Ru(bpy)_2(4Mptr)]^{2+}$ (**10**), $[Ru(bpy)_2(5Mptr)]^{+}$ (**11**) and $[Ru(bpy)_2(5MHptr)]^{2+}$ (**12**), taken from Refs. [25,29,38].

reduction processes of the complexes [7,9,35]. In an MLCT absorption process, an electron is removed from the filled metal orbital (dπ) to an empty orbital of the ligand (π*). Also, an electron removed from the d orbitals on electrochemical oxidation is excited to the LUMO of the complex revealing that similar processes are involved in the MLCT emission also [36]. The electrochemical and emission spectral results indicate that the lowest π* orbital of the present complexes is dppt-based, as in $[Ru(dppt)_3]^{2+}$ [11] and related complexes [37]. Hückel calculations reveal that all these pyridyltriazine ligands exhibit stronger π-acceptor properties (lower π* orbitals) but weaker σ-donor properties, which would lead to destabilisation of Ru(III) and hence higher Ru(II)/Ru(III) oxidation potentials.

3. Conclusions

Two new mixed-ligand Ru(II) complexes of the type $[Ru(L)(dppt)]^{2+}$, where L represents the bis(pyrid-2-yl)-dithioether (pdto) and bis(benzimidazol-2-yl)-dithioether (bbdo) ligands, each with a N_2S_2 donor set, and dppt is 3-(pyridin-2-yl)-5,6-diphenyl-1,2,4-triazine, have been isolated and characterised. The ^1H and ^{13}C NMR spectral studies on the complexes reveal the exclusive formation of an isomer in which the N_2S_2 ligands are *cis*-α coordinated to ruthenium and with the involvement in coordination of both triazine N2 and pyridine nitrogen atom of dppt. The observed c.i.s. values provide useful information about the structure and bonding, which reinforce the data obtained from electronic and electrochemical studies. The complexes show ^{3}MLCT luminescence at room temperature, which is mainly due to the involvement of the low-lying LUMO level of dppt in the charge transfer. Further, the weak σ-donor property of dppt as well as the *cis* coordination of 'soft' sulfur atoms appear to be responsible for the higher Ru(II)/Ru(III) redox potentials and lower energies of the MLCT absorption and ^{3}MLCT emission bands of the complexes in comparison with the corresponding symmetric bpy complexes. The Ru(II) to Ru(III) oxidation in the bzim complex is more facile than in the py analogue, which is reflected in the energies of the MLCT bands and the NMR chemical shifts. Interestingly, the difference between the oxidation and reduction potentials of the complexes correlates linearly with the energy of the absorption or emission spectral band, illustrating that the orbitals involved in the redox and absorption and emission processes are the same. Electrochemical parameterisation of the Ru(II)/Ru(III) redox potentials has been carried out using Lever's method to illustrate the contribution of the ligand donors to the Ru(II)/Ru(III) redox potentials of the present complexes.

4. Experimental

4.1. Materials

Ruthenium(III) chloride trihydrate (Arora-Matthey Limited) and 3-(pyridin-2-yl)-5,6-diphenyl-1,2,4-triazine (dppt, Aldrich) were used without further purification. *Tetra*-butylammonium perchlorate was prepared from *tetra*-butylammonium bromide (G.F. Smith, USA) by a standard procedure [38]. The product was recrystallised twice from water, dried at 110 °C for 24 h and was tested for the absence of bromide. All the common chemicals were of reagent grade and were used as received. Reagent grade solvents were dried and distilled by usual methods and the solvents were stored over molecular sieves (4 Å). The ligands 1,8-bis(pyrid-2-yl)-3,6-dithiaoctane (pdto) and 1,8-bis(benzimidazol-2-yl)-3,6-dithiaoctane (bbdo) were prepared as reported in the literature [39,40].

4.2. Synthesis of the complexes

The di-μ-chloro dimers $[Ru(pdto)Cl]_2(ClO_4)_2$ and $[Ru(bbdo)Cl]_2(ClO_4)_2$ were synthesised by the procedure described elsewhere [14]. The mononuclear mixed-ligand complexes $[Ru(pdto)(dppt)](ClO_4)_2$ (**1**) and $[Ru(bbdo)(dppt)](ClO_4)_2$ (**2**) were prepared by using the following general procedure. A sample of $[Ru(pdto)Cl]_2(ClO_4)_2$ (0.27 g, 0.25 mmol) or $[Ru(bbdo)Cl]_2(ClO_4)_2$ (0.31 g, 0.25 mmol) was refluxed with dppt (0.16 g, 0.5 mmol) for 5 h in 60 mL of ethanol–water (1:1 v/v) mixture. After evaporation to dryness, the remaining solid was dissolved in 15 mL of methanol and then gradually added to an

excess of aqueous $NaClO_4$ solution (5 mmol in 3 mL of water). The precipitate, which was filtered off and dissolved in 3 mL of acetone, was purified by using column chromatography (neutral alumina; ethanol as eluent). The compound was finally crystallised from water–acetonitrile (2:1 v/v) mixture. The resulting red orange (**1**) or pinkish violet (**2**) precipitate was isolated by slow evaporation at 10 °C, filtered off and dried in *vacuo*. Yield: **1**, 0.30 g, 65%; **2**, 0.34 g, 68%. *Anal.* Calc. for $C_{36}H_{34}Cl_2O_8N_6S_2Ru$ (**1**): C, 47.27; H, 3.75; N, 9.19. Found: C, 47.50; H, 4.08; N, 8.96%. ^{1}H NMR (DMSO-d_6, 400 MHz): δ (multiplicity, integration, assignment, coordination-induced shifts: c.i.s., $\delta_{complex} - \delta_{ligand}$), ppm 2.124 (t, 1H, H_{a11}, −0.798), 3.013 (d, 1H, H_{e11}, 0.091), 2.236 (t, 1H, H_{a12}, −0.686), 3.194 (d, 1H, H_{e12}, 0.272), 2.299 (t, 1H, H_{a21}, −0.675), 3.194 (d, 1H, H_{e21}, 0.220), 2.406 (t, 1H, H_{a22}, −0.568), 3.102 (t, 1H, H_{e22}, 0.128), 3.501 (d, 1H, H_{a31}, 0.134), 3.671 (t, 1H, H_{e31}, 0.304), 3.371 (t, 1H, H_{a32}, 0.004), 3.671 (t, 1H, H_{e32}, 0.304), 8.750 (d, 1H, H_{51}, 1.449), 8.661 (d, 1H, H_{52}, 1.360), 7.231 (t, 1H, H_{61}, −0.456), 7.268 (t, 1H, H_{62}, −0.419), 7.735 (t, 2H, H_{71} and H_{72}, 0.526), 7.352 (d, 2H, H_{81} and H_{82}, −1.135), 10.116 (d, 1H, H_{A3}, 1.542), 8.168 (t, 1H, H_{A4}, 0.076), 8.367 (t, 1H, H_{A5}, 0.763), 8.750 (d, 1H, H_{A6}, −0.121), 7.747 (d, 1H, H_{C2}, 0.091), 7.453 (t, 1H, H_{C3}, −0.040), 7.562 (t, 1H, H_{C4}, 0.116), 7.453 (t, 1H, H_{C5}, −0.040), 7.623 (d, 1H, H_{C6}, −0.005), 7.747 (d, 1H, H_{D2}, 0.103), 7.615 (t, 1H, H_{D3}, 0.151), 7.535 (t, 1H, H_{D4}, 0.112), 7.648 (t, 1H, H_{D5}, 0.184), 7.623 (d, 1H, H_{D6}, 0.035). ^{13}C NMR (DMSO-d_6, 400 MHz): δ (assignment, coordination-induced shifts: c.i.s., $\delta_{complex} - \delta_{ligand}$), ppm 26.26 ($C_{11}$, −4.24), 26.63 ($C_{12}$, −3.87), 31.27 ($C_{21}$, 0.05), 32.01 ($C_{22}$, 0.79), 32.99 ($C_{31}$, −4.62), 33.99 ($C_{32}$, −3.62), 163.20 ($C_{41}$, 3.64), 163.36 ($C_{42}$, 3.80), 127.22 ($C_{51}$, 5.79), 127.38 ($C_{52}$, 5.95), 138.44 ($C_{61}$, 2.15), 138.59 ($C_{62}$, 2.30), 130.77 ($C_{71}$, 7.74), 130.88 ($C_{72}$, 7.85), 152.94 ($C_{81}$, 4.02), 153.12 ($C_{82}$, 4.20), 156.54 ($C_{A2}$, 4.04), 126.44 ($C_{A3}$, −3.29), 140.07 ($C_{A4}$, 2.65), 132.05 ($C_{A5}$, 1.43), 154.15 ($C_{A6}$, 4.00), 165.10 ($C_{B3}$, 4.64), 158.57 ($C_{B5}$, 2.64), 157.53 ($C_{B6}$, 1.18), 133.86 ($C_{C1}$, −1.61), 129.52 ($C_{C2}$, −1.10), 128.53 ($C_{C3}$, 0.04), 123.56 ($C_{C4}$, −2.18), 128.53 ($C_{C5}$, 0.04), 129.52 ($C_{C6}$, −1.10), 133.98 ($C_{D1}$, −1.35), 130.35 ($C_{D2}$, 0.75), 129.00 ($C_{D3}$, 0.60), 124.06 ($C_{D4}$, 0.13), 129.00 ($C_{D5}$, 0.60), 130.35 ($C_{D6}$, 0.95). IR (KBr): $\nu(ClO_4^-)$, cm^{-1} 1101vs, 631s. *Anal.* Calc. for $C_{40}H_{36}Cl_2O_8N_8S_2Ru$ (**2**): C, 48.39; H, 3.65; N, 11.29. Found: C, 48.45; H, 3.76; N, 11.61%. ^{1}H NMR (DMSO-d_6, 400 MHz): δ (multiplicity, integration, assignment, coordination-induced shifts: c.i.s., $\delta_{complex} - \delta_{ligand}$), ppm 2.434 (t, 1H, H_{a11}, −0.315), 3.046 (d, 1H, H_{e11}, 0.297), 2.501 (t, 1H, H_{a12}, −0.248), 3.550 (d, 1H, H_{e12}, 0.801), 2.501 (t, 1H, H_{a21}, −0.502), 3.239 (d, 1H, H_{e21}, 0.236), 2.568 (t, 1H, H_{a22}, −0.435), 3.725 (d, 1H, H_{e22}, 0.722), 3.185 (d, 1H, H_{a31}, 0.099), 4.184 (t, 1H, H_{e31}, 1.098), 3.355 (d, 1H, H_{a32}, 0.269), 3.550 (t, 1H, H_{e32}, 0.464), 7.800 (d, 1H, H_{61}, 1.449), 7.963 (d, 1H, H_{62}, 0.491), 7.405 (t, 1H, H_{71}, 0.290), 7.096 (t, 1H, H_{72}, −0.019), 7.004 (t, 1H, H_{81}, −0.111), 7.385 (t, 1H, H_{82}, 0.270), 7.597 (d, 1H, H_{91}, 0.125), 7.575 (d, 1H, H_{92}, 0.103), 13.188 (b, 2H, NH), 10.634 (d, 1H, H_{A3}, 2.060), 8.042 (t, 1H, H_{A4}, −0.050), 8.217 (t, 1H, H_{A5}, 0.613), 8.551 (d, 1H, H_{A6}, −0.320), 7.675 (d, 1H, H_{C2}, 0.019), 7.165 (t, 1H, H_{C3}, −0.328), 7.425 (t, 1H, H_{C4}, −0.021), 7.425 (t, 1H, H_{C5}, −0.068), 7.675 (d, 1H, H_{C6}, 0.057), 7.675 (d, 1H, H_{D2}, 0.031), 7.425 (t, 1H, H_{D3}, −0.039), 7.528 (t, 1H, H_{D4}, 0.105), 7.675 (t, 1H, H_{D5}, 0.211), 7.800 (d, 1H, H_{D6}, 0.212). ^{13}C NMR (DMSO-d_6, 400 MHz): δ (assignment, coordination-induced shifts: c.i.s., $\delta_{complex} - \delta_{ligand}$), ppm 24.25 ($C_{11}$, −9.19), 25.20 ($C_{12}$, −8.24), 25.68 ($C_{21}$, −8.05), 26.21 ($C_{22}$, −7.52), 31.85 ($C_{31}$, −3.59), 32.38 ($C_{32}$, −3.06), 156.36 ($C_{41}$, −1.37), 156.76 ($C_{42}$, −0.97), 143.41 ($C_{51}$, 0.51), 143.83 ($C_{52}$, 0.93), 117.18 ($C_{61}$, −1.61), 117.33 ($C_{62}$, −1.46), 128.53 ($C_{71}$, 2.95), 129.52 ($C_{72}$, 3.94), 122.99 ($C_{81}$, −2.59), 123.22 ($C_{82}$, −2.36), 112.27 ($C_{91}$, −6.52), 112.66 ($C_{92}$, −6.13), 133.46 ($C_{101}$, −9.44), 133.76 ($C_{102}$, −9.14), 154.24 ($C_{A2}$, 1.74), 131.00 ($C_{A3}$, 1.27), 139.58 ($C_{A4}$, 2.16), 131.89 ($C_{A5}$, 1.27), 152.81 ($C_{A6}$, 2.66), 162.70 ($C_{B3}$, 2.24), 158.94 ($C_{B5}$, 2.97), 155.36 ($C_{B6}$, −0.99), 132.57 ($C_{C1}$, −2.90), 129.52 ($C_{C2}$, −1.20), 128.53 ($C_{C3}$, 0.04), 121.84 ($C_{C4}$, −3.90), 128.53 ($C_{C5}$, 0.04), 129.52 ($C_{C6}$, −1.10), 132.70 ($C_{D1}$, −2.63), 129.82 ($C_{D2}$, 0.22), 129.10 ($C_{D3}$, 0.70), 126.39 ($C_{D4}$, 2.46), 129.10 ($C_{D5}$, 0.70), 129.82 ($C_{D6}$, 0.42). IR (KBr): $\nu(ClO_4^-)$, cm^{-1} 1098vs, 629s.

Caution. All the complexes described in this paper contain the perchlorate anion. Perchlorate salts of metal complexes with organic ligands are potentially explosive! Only a small quantities of material were prepared and they were handled with great caution.

4.3. Physical measurements

The elemental analyses were performed at the Central Drug Research Institute, Lucknow. The solution electrical conductivity was obtained using a Systronic 305 conductivity bridge. The IR spectra of the complexes were measured on a Shimadzu IR 435 spectrophotometer. The electronic spectra were recorded using an Hitachi U3410 double beam UV–Vis–NIR spectrophotometer. The solution emission properties were obtained using a Jasco FP 6500 spectrofluorometer. The NMR spectra were obtained at room temperature using a Bruker 400 MHz spectrometer. The chemical shift values in DMSO-d_6 are reported with respect to tetramethylsilane as an internal standard and the values are reported as: δ-values (multiplicity, integration, assignment). Cyclic voltammetry and differential pulse voltammetry on a platinum sphere electrode were performed at 25 ± 0.2 °C. The temperature of the electrochemical cell was maintained by a cryocirculator (HAAKE D8-G). Voltammograms were generated with the use of an EG&G PAR Model 273 potentiostat. An IBM PS-2 computer along with EG&G M270 software was employed to control the experiments and acquire data. An EPSON FX-850 printer and HP plotter (DMP-40) were used to print and plot out the cyclic voltammograms, respectively. A three-electrode system consisting of a platinum sphere

(0.2866 cm^2), a platinum auxiliary electrode and a reference electrode was used. The reference electrode for non-aqueous solution was $Ag(s)/Ag^+$ which consists of an Ag wire immersed in a solution of $AgNO_3$ (0.01 M) and *tetra-N*-hexylammonium perchlorate (0.1 M) in acetonitrile placed in a tube fitted with a vycor plug using a sleeve [41]. The $E_{1/2}$ and ΔE_p values observed under identical conditions for the Fc/Fc^+ couple in acetonitrile were 0.100 V and 76 mV, respectively, with respect to the Ag/Ag^+ reference electrode. The cyclic voltammograms (CV) and differential pulse voltammograms (DPV) of **1** and **2** were obtained in CH_3CN solutions with 0.1 M $[(C_4H_9)_4N]ClO_4$ as the supporting electrolyte at ambient temperatures under N_2. Redox potentials were measured relative to the Ag/Ag^+ reference electrode.

Acknowledgements

We thank the Department of Science and Technology, India (Grant No. SP/S1/F-10/92 and SP/S1/F-20/2001) for financial support. M.M. thanks Council of Scientific and Industrial research, New Delhi for a Senior Research Fellowship. We thank Dr. R. Ramaraj, School of Chemistry, Madurai Kamaraj University, Madurai for providing the emission spectral facility. Sophisticated Instrumentation Facility, Indian Institute of Science, Bangalore is acknowledged for NMR spectra.

References

[1] (a) K.R. Seddon, Coord. Chem. Rev. 41 (1982) 79;
(b) K. Kalyanasundaram, Coord. Chem. Rev. 46 (1982) 159.
[2] (a) G.J. Samuels, T.J. Meyer, J. Am. Chem. Soc. 103 (1981) 307;
(b) L. Roecker, W. Kutner, A. Gilbert, M. Simmons, R.W. Murray, T.J. Meyer, Inorg. Chem. 24 (1985) 3784.
[3] (a) W.M. Wacholtz, R.A. Auerbach, R.H. Schmell, M. Ollino, W.R. Cherry, Inorg. Chem. 24 (1985) 1785;
(b) W.J. Vining, J.V. Caspar, T.J. Meyer, J. Phys. Chem. 89 (1985) 1095.
[4] (a) A. Juris, F. Barigelleti, V. Balzani, P. Belser, A. von Zelewsky, Inorg. Chem. 24 (1985) 202;
(b) D.V. Pinnick, B. Durham, Inorg. Chem. 23 (1984) 3841;
(c) J.M. Kelly, C. Long, C.M. O'Connell, J.G. Vos, A.H.A. Tinnemans, Inorg. Chem. 22 (1983) 2818.
[5] M.-A. Haga, Inorg. Chim. Acta 75 (1983) 29.
[6] R.A. Krause, Structure and Bonding, 67, Springer Verlag, Berlin, 1987, p. 1.
[7] A. Juris, V. Balzani, F. Barigelletti, P. Belser, A. von Zelewsky, Coord. Chem. Rev. 84 (1988) 85.
[8] (a) C. Marzin, F. Budde, P.J. Steel, D. Lerner, Nouv. J. Chim. 11 (1987) 33;
(b) R. Hage, J.G. Haasnoot, J. Reedijk, J.G. Vos, Inorg. Chim. Acta 118 (1986) 73;
(c) C.R. Leidner, B.P. Sullivan, R.A. Reed, B.A. White, M.T. Crimmins, R.W. Murray, T.J. Meyer, Inorg. Chem. 26 (1987) 882.
[9] R. Hage, R. Prins, J.G. Haasnoot, J. Reedijk, J.G. Vos, J. Chem. Soc., Dalton Trans. (1987) 1389.
[10] R. Hage, A.H.J. Dijkhuis, J.G. Haasnoot, R. Prins, J. Reedijk, B.E. Buchanan, J.G. Vos, Inorg. Chem. 27 (1988) 2185.
[11] R. Hage, J.H. van Diemen, G. Ehrlich, J.G. Haasnoot, D.J. Stufkens, T.L. Snoeck, J.G. Vos, J. Reedijk, Inorg. Chem. 29 (1990) 988.
[12] (a) L.C. Kamra, G.H. Ayres, Anal. Chim. Acta 78 (1975) 423;
(b) C.D. Chriswell, A.A. Schilt, Anal. Chem. 46 (1974) 992.
[13] R. Uma, M. Palaniandavar, R.J. Butcher, J. Chem. Soc., Dalton Trans. (1996) 2061.
[14] M. Murali, M. Palaniandavar, Dalton Trans. (2006) 730.
[15] D. Bhattacharyya, S. Chakraborty, P. Munshi, G.K. Lahiri, Polyhedron 18 (1999) 2951.
[16] C. Brevard, P. Granger, Inorg. Chem. 22 (1983) 532.
[17] X. Xiaoming, M.-A. Haga, T.M. Inoue, Y. Ru, A.W. Addison, K. Kano, J. Chem. Soc., Dalton Trans. (1993) 2477.
[18] H. Chao, G. Yang, G.-Q. Xue, H. Li, H. Zang, I.D. Williams, L.-N. Ji, X.-M. Chen, X.-Y. Li, J. Chem. Soc., Dalton Trans. (2001) 1326.
[19] P.J. Steel, E.C. Constable, J. Chem. Soc., Dalton Trans. (1990) 1389.
[20] (a) T. Kojima, T. Amano, Y. Ishii, M. Ohba, Y. Okaue, Y. Matsuda, Inorg. Chem. 37 (1998) 4076;
(b) T. Kojima, Chem. Lett. (1996) 121.
[21] G. Orellana, C.A. Ibarra, J. Santoro, Inorg. Chem. 27 (1988) 1025.
[22] P.J. Steel, F. Lahousse, D. Lerner, C. Marzin, Inorg. Chem. 22 (1983) 1488.
[23] J.B. Stothers, Carbon-13 NMR Spectroscopy, Academic Press, New York, 1972.
[24] (a) J.L. Templeton, J. Am. Chem. Soc. 101 (1979) 4906;
(b) D.K. Lavallee, M.D. Baughman, M.P. Phillips, J. Am. Chem. Soc. 99 (1977) 718.
[25] H.V. Dam, G. Booxhoorn, D.J. Stufkens, A. Oskam, Inorg. Chim. Acta 53 (1981) L235.
[26] (a) P.C. Fantucci, V. Valenti, F. Cariati, Inorg. Chim. Acta (1971) 425;
(b) H.B. Gray, N.A. Beach, J. Am. Chem. Soc. 85 (1963) 2922.
[27] (a) H. Yersin, E. Gallhuber, G. Hensler, Chem. Phys. Lett. 134 (1987) 497;
(b) G. Hensler, E. Gallhuber, H. Yersin, Inorg. Chem. 26 (1987) 1641;
(c) H. Yersin, G. Hensler, E. Gallhuber, Inorg. Chim. Acta 140 (1987) 157.
[28] L.M. Vogler, K.J. Brewer, Inorg. Chem. 35 (1996) 818.
[29] (a) R.S. Nicholson, I. Shain, Anal. Chem. 36 (1964) 706;
(b) T. Pandiyan, M. Palaniandavar, M. Lakshminarayanan, H. Manohar, J. Chem. Soc., Dalton Trans. (1992) 3377.
[30] (a) B.P. Sullivan, D.J. Salmon, T.J. Meyer, Inorg. Chem. 17 (1978) 3334;
(b) R.W. Callahan, F.R. Keene, T.J. Meyer, D.J. Salmon, J. Am. Chem. Soc. 99 (1977) 1064.
[31] D.P. Rillema, D.S. Jones, C. Woods, H.A. Levy, Inorg. Chem. 31 (1992) 2935.
[32] W.-M. Xue, W.J. Perez, D.P. Rillema, Inorg. Chim. Acta 296 (1999) 114.
[33] A.B.P. Lever, Inorg. Chem. 29 (1990) 1271.
[34] H. Masui, A.B.P. Lever, Inorg. Chem. 32 (1993) 2199.
[35] (a) R.J. P. Williams, J. Chem. Soc. (1955) 137;
(b) J.V. Casper, T.J. Meyer, Inorg. Chem. 22 (1983) 2444;
(c) F. Barigelletti, A. Juris, V. Balzani, P. Belser, A. von Zelewsky, Inorg. Chem. 26 (1987) 4115.
[36] S. Ernst, W. Kaim, Inorg. Chem. 28 (1989) 1520.
[37] (a) W. Kaim, J. Am. Chem. Soc. 104 (1982) 3833;
(b) D.P. Rillema, G. Allen, T.J. Meyer, D. Conrad, Inorg. Chem. 22 (1983) 1617;
(c) D.P. Rillema, K.B. Mack, Inorg. Chem. 21 (1982) 3849;
(d) D.P. Rillema, R.W. Callahan, K.B. Mark, Inorg. Chem. 21 (1982) 2589;
(e) R.J. Crutchley, A.B.P. Lever, Inorg. Chem. 21 (1982) 2276.
[38] M.J. Root, E. Deutsch, Inorg. Chem. 24 (1985) 1464.
[39] H.A. Goodwin, F. Lions, J. Am. Chem. Soc. 82 (1960) 5013.
[40] M. Vaidyanathan, U. Sivagnanam, M. Palaniandavar, J. Chem. Soc., Dalton Trans. (2001) 3498.
[41] V.D. Parker, in: A.J. Bard (Ed.), Electroanalytical Chemistry, vol. 14, Marcel Dekker, New York, 1986, p. 18.

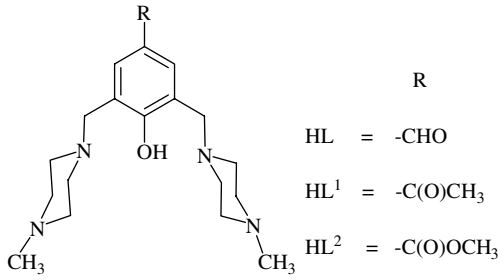


Chart 1.

metallobiosites. However, the complexes derived with macrocyclic and side-off ligands have some limitations when used as models for metallobiosites because such systems are so rigid with restricted coordination geometries. Also they do not favour the formation of exogenous bridges due to the small distance between the bimetal centres when compared to the biosites [22]. Phenol based end-off ligands having two chelating arms attached to the *ortho* positions of the phenolic –OH provide phenolato endogenous bridging units such as acetato, hydroxo, azido, cyanato, chloro, bromo, etc. They have better coordination environments with an ideal distance between the donor sites and the endogenous bridges [23–25].

Protein binuclear copper sites effect remarkable reactions with dioxygen, including reversible binding (haemocyanin), activation (tyrosinase) and reduction (laccase) [5,26]. Non-redox-active metals such as Ni(II) and Zn(II) are potentially of interest as hydrolytic cleaving agents and their reactivity in model systems may lead to functional DNA cleaving molecules [27].

Complexes of end-off ligands with various *p*-substituents on the phenolic ring and their comparative study of spectral, magnetic, electrochemical and kinetic studies are sparse. We have already reported a group of end-off complexes having CHO as the *p*-substituent on the phenolic ring [28]. Thus, in the present work, we have synthesized two new end-off ligands that contain N and O donor atoms, by varying the *p*-substituents ($COCH_3$ and $C(O)OCH_3$) of the phenolic ring, and their mono and binuclear copper(II), nickel(II) and zinc(II) complexes. A comparative study of spectral, magnetic, electrochemical and kinetic studies was carried out on the basis of the varying electron withdrawing nature of the *p*-substituents of the phenolic ring. The chemical structure of the ligand [HL] has already been reported [28], and it is shown alongside the target ligands, HL^1 and HL^2 in Chart 1.

2. Experimental

2.1. Physical measurements

Elemental analyses of the complexes were obtained using a Haereus C, H, N; rapid analyzer. ^1H NMR spectra were recorded using a JEOL GSX 400 MHZ NMR spectrometer. Electronic spectral studies were carried out on a Hitachi 320 spectrophotometer in the range 200–850 nm. IR spectra were recorded on a Shimadzu FT-IR 8300 series spectrophotometer on KBr disks in the range 4000–400 cm^{-1}. Mass spectra were obtained on a JEOL DX-303 Mass spectrometer. Molar conductivity was measured by using an Elico digital conductivity bridge model CM-88 using a freshly prepared solution of the complexes in dimethyl formamide. Cyclic voltammograms were obtained on CHI-600A electrochemical analyzer. The measurements were carried out under oxygen free conditions using a three-electrode cell in which a glassy carbon electrode was the working electrode, a saturated Ag/AgCl electrode was the reference electrode and platinum wire was used as the auxiliary electrode. A ferrocene/ferrocenium (1+) couple was used as an internal standard and $E_{1/2}$ of the ferrocene/ferrocenium (Fc/Fc^+) couple under the experimental conditions is 470 mV. Tetra (*n*-butyl)ammonium perchlorate (TBAP) was used as the supporting electrolyte. The room temperature magnetic moment was measured on a PAR vibrating sample magnetometer Model-155. Variable temperature magnetic moments were measured on an EG&G Princeton applied research VSM model 4500. X-band ESR spectra were recorded at 25 °C on a Varian EPR-E 112 spectrometer using diphenylpicrylhydrazine (DPPH) as the reference. The atomic absorption spectral data were recorded using a Varian spectra AA-200 model atomic absorption spectrophotometer. The catalytic oxidation of catechol to *o*-quinone by the copper complexes and the hydrolysis of 4-nitrophenylphosphate by the copper, nickel and zinc complexes were studied in a 10^{-3} M dimethylformamide solutions. The reaction was followed spectrophotometrically by choosing the strongest absorbance of *o*-quinone at 390 nm and monitoring the increase in the absorbance, and the hydrolysis of *p*-nitrophenyl phosphate was monitored by following the UV absorbance change at 420 nm (assigned to the 4-nitrophenolate anion) as a function of time. A plot of $\log(A_\infty/A_\alpha - A_t)$ versus time was made for each complex and the rate constant for the catalytic oxidation and the hydrolysis of 4-nitrophenyl phosphate was calculated.

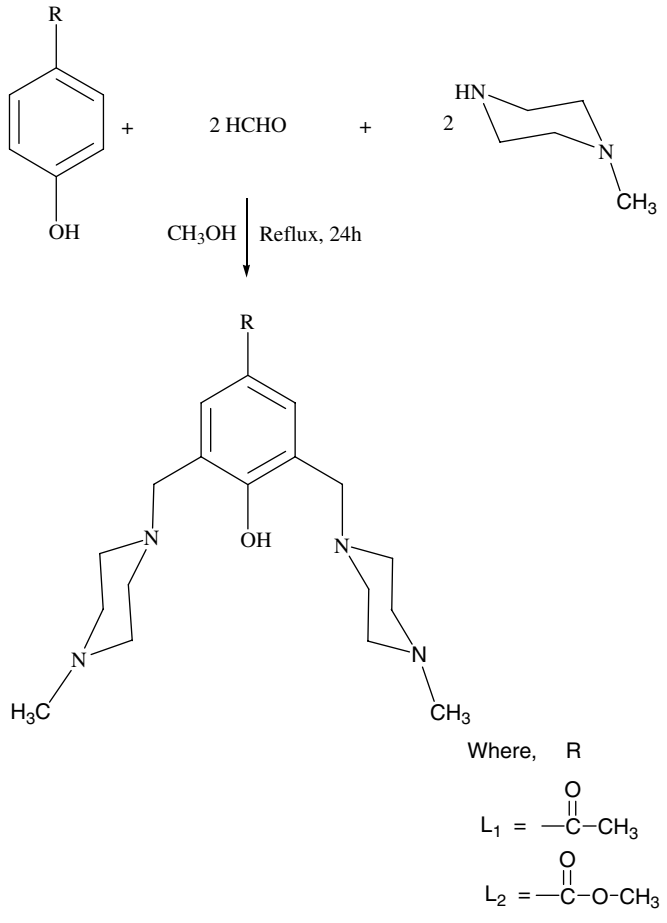
2.2. Materials and safety note

Formaldehyde solution, *N*-methyl piperazine, *p*-hydroxy acetophenone and *p*-hydroxy methylbenzoate were purchased from Qualigens and used as such. Methanol, acetonitrile and dimethyl formamide were purchased from Qualigens and distilled before the usage. TBAP, used as a supporting electrolyte in the electrochemical measurements, was purchased from Fluka and recrystallised from hot methanol. (*Caution!* TBAP is potentially explosive; hence care should be taken in handling the compound.) All other chemicals and solvents were of analytical grade and were used as received without any further purification.

2.3. Synthesis of ligands

2.3.1. Synthesis of 2,6-bis(4-methyl piperazin-1-yl-methyl)-4-acetyl phenol (HL^1)

The ligand HL^1 was synthesized by taking *p*-hydroxy acetophenone (4.76 g, 0.035 mol) in methanol (100 ml) mixed with *N*-methyl piperazine (7.76 ml, 0.07 mol) and the solution was refluxed for 1 h. Then a formaldehyde solution (37%) (5.28 ml, 0.07 mol) was added slowly with stirring and the mixture was kept at this temperature for 24 h. Two 5 ml portions of formaldehyde were added at approximately 8 h intervals. After that time, methanol was evaporated under vacuum and the resulting oil was extracted with chloroform (Scheme 1). A light brown oily compound was obtained. Yield: 7.56 g (60%) Mass (EI) *m*/*z*: 361.46. *Anal*. Calc. for $C_{20}H_{32}N_4O_2$: C, 66.64; H, 8.95; N, 15.54. Found: C, 66.56; H, 8.89; N, 15.57%. Selected IR data (KBr disc, ν/cm^{-1}): 1685 (C=O) s, 3395 (OH) br, 1453 (N-CH_3) br. ^1H NMR (δ ppm in $CDCl_3$) ~2.28 (s, 3H, –C(O)CH_3), ~2.30 (s, 6H, N-CH_3), ~2.52 (br s, 16H, methylene protons), ~3.68 (s, 4H, benzylic protons), ~7.71 (s, 2H, Ar-H). UV–Vis [λ_{max}/nm ($\varepsilon/M^{-1}\,cm^{-1}$)] in MeOH: 288 (21 300).



Scheme 1.

2.3.2. Synthesis of 2,6-bis[(4-methyl piperazin-1-yl-methyl)]-(4-methylcarboxy) phenol (HL^2)

The ligand HL^2 was synthesized by taking *p*-hydroxy methylbenzoate (5.32 g, 0.035 mol) in methanol (100 ml) mixed with *N*-methyl piperazine (7.76 ml, 0.07 mol) and the solution was refluxed for 1 h. Then formaldehyde solution (37%) (5.28 ml, 0.07 mol) was added slowly with stirring and it was kept at this temperature for 24 h. Two 5 ml portions of formaldehyde were added at approximately 8 h intervals. After that time, methanol was evaporated under vacuum and the resulting oil was extracted with chloroform and recrystallised with diethylether (Scheme 1). A colourless compound was obtained. Yield: 8.29 g (63%), m.p.: 72 °C. Mass (EI) *m*/*z*: 376.24. *Anal*. Calc. for $C_{20}H_{32}N_4O_3$: C, 63.80; H, 8.57; N, 14.88. Found: C, 63.75; H, 8.63; N, 14.83%. Selected IR data (KBr disc, ν/cm^{-1}): 1720 (C=O) s, 3397 (OH) br, 1455 (N-CH_3) br. ^1H NMR (δ ppm in $CDCl_3$) ~2.27 (s, 6H, N-CH_3), ~2.47 (br s, 16H, methylene protons), ~3.63 (s, 4H, benzylic protons), ~3.83 (s, 3H, –OCH_3 protons), ~7.72 (s, 2H, Ar-H). UV–Vis [λ_{max}/nm ($\varepsilon/M^{-1}\,cm^{-1}$)] in MeOH: 290 (20 900).

2.4. Synthesis of mono and binuclear complexes

2.4.1. Synthesis of mononuclear complexes of HL^1

2.4.1.1. Synthesis of the $[CuL^1(OAc)]\cdot H_2O$ complex. To a 40 ml methanol solution of the ligand HL^1 (1.081 g, 0.003 mol) was added $Cu(OAc)_2\cdot H_2O$ (0.598 g, 0.003 mol) dissolved in 20 ml of methanol and the resulting solution was refluxed for 4 h. After the reaction was over, the solution was filtered when hot and allowed to stand at room temperature. After slow evaporation of the solvent at 25 °C, a dark green compound was obtained. The compound was recrystallised from acetonitrile. Yield: 1.05 g (70%). *Anal*. Calc. for $[C_{22}H_{34}N_4O_4Cu]\cdot H_2O$: C, 52.84; H, 7.26; N, 11.20; Cu, 12.71. Found: C, 52.76; H, 7.31; N, 11.13; Cu, 12.63%. Selected IR data (KBr disc, ν/cm^{-1}): 3447, 1683, 1449. UV–Vis [λ_{max}/nm ($\varepsilon/M^{-1}\,cm^{-1}$)] in MeOH: 597 (132), 358 (17 900), 294 (24 100), $g_{\|} = 2.25$, $g_{\perp} = 2.07$ and $A_{\|} = 183$. $\mu_{eff} = 1.73$ BM.

2.4.1.2. Synthesis of the $[NiL^1(OAc)]\cdot H_2O$ complex. The Ni(II) complex was prepared by following the above procedure using the ligand HL^1 (1.081 g, 0.003 mol) and $Ni(OAc)_2\cdot 4H_2O$ (0.746 g, 0.003 mol). A pale green compound was obtained on recrystallisation from acetonitrile. Yield: 1.01 g (68%) *Anal*. Calc. for $[C_{22}H_{34}N_4O_4Ni]\cdot H_2O$: C, 53.36; H, 7.33; N, 11.31; Ni, 11.85. Found: C, 53.28; H, 7.28; N, 11.25; Ni, 11.89%. Selected IR data (KBr disc, ν/cm^{-1}): 3454, 1679, 1454. UV–Vis [λ_{max}/nm ($\varepsilon/M^{-1}\,cm^{-1}$)] in MeOH: 579 (151), 362 (16 900), 293 (22 800).

2.4.1.3. Synthesis of the $[ZnL^1(OAc)(H_2O)_2]$ complex. The Zn(II) complex was prepared by following the above procedure using the ligand HL^1 (1.081 g, 0.003 mol) and $Zn(OAc)_2\cdot 2H_2O$ (0.658 g, 0.003 mol). A colourless

compound was obtained on recrystallisation from acetonitrile. Yield: 1.04 g (67%) *Anal.* Calc. for $[C_{22}H_{34}N_4O_4Zn(H_2O)_2]$: C, 50.82; H, 7.37; N, 10.78; Zn, 12.58. Found: C, 50.89; H, 7.27; N, 10.72; Zn, 12.55%. Selected IR data (KBr disc, ν/cm^{-1}): 3456, 1683, 1456. UV–Vis [λ_{max}/nm ($\varepsilon/M^{-1}\,cm^{-1}$)] in MeOH: 289 (21 900).

2.4.2. Synthesis of binuclear complexes of HL^1

2.4.2.1. Synthesis of the $[Cu_2L^1(OAc)_2](ClO_4)\cdot H_2O$ complex. A solution of the ligand HL^1 (0.721 g, 0.002 mol) in MeOH (40 ml) was added to $Cu(OAc)_2\cdot H_2O$ (0.798 g, 0.004 mol) in MeOH (20 ml) and the resulting solution was refluxed for 7 h. The mixture was then reacted with one equivalent of $NaClO_4$ dissolved in 10 ml of methanol and refluxed for a further hour. A dark green precipitate was collected on evaporation of the resulting solution to half the volume and then allowing the solution to cool by standing at room temperature (25 °C). A dark green coloured compound was obtained on recrystallisation from acetonitrile. Yield: 1.02 g (71%). *Anal.* Calc. for $[C_{24}H_{37}N_4O_6Cu_2](ClO_4)\cdot H_2O$: C, 39.92; H, 5.44; N, 7.76; Cu, 17.60. Found: C, 39.87; H, 5.41; N, 7.68; Cu, 17.54%. Selected IR data (KBr disc, ν/cm^{-1}): 3445, 1682, 1482, 1107, 651. Conductance ($\Lambda_m/S\,cm^2\,mol^{-1}$) in DMF 86. UV–Vis [$\lambda_{max}$/nm ($\varepsilon/M^{-1}\,cm^{-1}$)] in MeOH: 667 (126), 367 (16 400), 290 (25 100). $g = 2.1$. $\mu_{eff} = 1.56$ BM.

2.4.2.2. Synthesis of the $[Ni_2L^1(OAc)_2(H_2O)_2](ClO_4)$ complex. The Ni(II) complex was prepared by following the above procedure by using the ligand HL^1 (0.721 g, 0.002 mol) and $Ni(OAc)_2\cdot 4H_2O$ (0.995 g, 0.004 mol). A green compound was obtained on recrystallisation from acetonitrile. Yield: 1.08 g (74%). *Anal.* Calc. for $[C_{24}H_{37}N_4O_6Ni_2(H_2O)_2](ClO_4)$: C, 39.46; H, 5.66; N, 7.67; Ni, 16.07. Found: C, 39.49; H, 5.61; N, 7.72; Ni, 16.11%. Selected IR data (KBr disc, ν/cm^{-1}): 3450, 1681, 1465, 1106, 650. Conductance ($\Lambda_m/S\,cm^2\,mol^{-1}$) in DMF 81. UV–Vis [$\lambda_{max}$/nm ($\varepsilon/M^{-1}\,cm^{-1}$)] in MeOH: 803 (114), 622 (138), 564 (221), 370 (17 900), 291 (23 800).

2.4.2.3. Synthesis of the $[Zn_2L^1(OAc)_2(H_2O)_2](ClO_4)$ complex. The Zn(II) complex was prepared by following the above procedure using the ligand HL^1 (0.721 g, 0.002 mol) and $Zn(OAc)_2\cdot 2H_2O$ (0.878 g, 0.004 mol). A colourless compound was obtained on recrystallisation from acetonitrile. Yield: 0.98 g (66%) *Anal.* Calc. for $[C_{24}H_{37}N_4O_6Zn_2(H_2O)_2](ClO_4)$: C, 38.75; H, 5.56; N, 7.53; Zn, 17.58. Found: C, 38.67; H, 5.51; N, 7.58; Zn, 17.51%. Selected IR data (KBr disc, ν/cm^{-1}): 3449, 1679, 1469, 1112, 652. Conductance ($\Lambda_m/S\,cm^2\,mol^{-1}$) in DMF 88. UV–Vis [$\lambda_{max}$/nm ($\varepsilon/M^{-1}\,cm^{-1}$)] in MeOH: 290 (23 900).

2.4.3. Synthesis of mononuclear complexes of HL^2

2.4.3.1. Synthesis of the $[CuL^2(OAc)]\cdot H_2O$ complex. To a 40 ml methanol solution of the ligand HL^2 (1.129 g, 0.003 mol) was added $Cu(OAc)_2\cdot H_2O$ (0.598 g, 0.003 mol) dissolved in 20 ml of methanol and the resulting solution was refluxed for 4 h. After the reaction was over, the solution was filtered when hot and allowed to stand at room temperature. After slow evaporation of the solvent at 25 °C, a dark green compound was obtained. The compound was recrystallised from acetonitrile. Yield: 1.10 g (71%). *Anal.* Calc. for $[C_{22}H_{34}N_4O_5Cu]\cdot H_2O$: C, 51.20; H, 7.03; N, 10.86; Cu, 12.31. Found: C, 51.17; H, 7.01; N, 10.79; Cu, 12.37%. Selected IR data (KBr disc, ν/cm^{-1}): 3451, 1723, 1451. UV–Vis [λ_{max}/nm ($\varepsilon/M^{-1}\,cm^{-1}$)] in MeOH: 600 (141), 362 (18 200), 297 (24 300), $g_{\|} = 2.26$, $g_{\perp} = 2.09$ and $A_{\|} = 185$. $\mu_{eff} = 1.73$ BM.

2.4.3.2. Synthesis of the $[NiL^2(OAc)]\cdot H_2O$ complex. The Ni(II) complex was prepared by following the above procedure using the ligand HL^2 (1.129 g, 0.003 mol) and $Ni(OAc)_2\cdot 4H_2O$ (0.746 g, 0.003 mol). A pale green compound was obtained on recrystallisation from acetonitrile. Yield: 1.12 g (73%) *Anal.* Calc. for $[C_{22}H_{34}N_4O_5Ni]\cdot H_2O$: C, 51.69; H, 7.10; N, 10.96; Ni, 11.48. Found: C, 51.61; H, 7.15; N, 10.89; Ni, 11.41%. Selected IR data (KBr disc, ν/cm^{-1}): 3453, 1726, 1450. UV–Vis [λ_{max}/nm ($\varepsilon/M^{-1}\,cm^{-1}$)] in MeOH: 583 (153), 366 (17 400), 297 (22 900).

2.4.3.3. Synthesis of the $[ZnL^2(OAc)(H_2O)_2]$ complex. The Zn(II) complex was prepared by following the above procedure using the ligand HL^2 (1.129 g, 0.003 mol) and $Zn(OAc)_2\cdot 2H_2O$ (0.658 g, 0.003 mol). A colourless compound was obtained on recrystallisation from acetonitrile. Yield: 1.04 g (65%) *Anal.* Calc. for $[C_{22}H_{34}N_4O_5Zn(H_2O)_2]$: C, 49.30; H, 7.15; N, 10.45; Zn, 12.20. Found: C, 49.23; H, 7.18; N, 10.36; Zn, 12.17%. Selected IR data (KBr disc, ν/cm^{-1}): 3457, 1721, 1456. UV–Vis [λ_{max}/nm ($\varepsilon/M^{-1}\,cm^{-1}$)] in MeOH: 290 (22 200).

2.4.4. Synthesis of binuclear complexes of HL^2

2.4.4.1. Synthesis of the $[Cu_2L^2(OAc)_2](ClO_4)\cdot 2H_2O$ complex. A solution of the ligand HL^2 (0.753 g, 0.002 mol) in MeOH (40 ml) was added to $Cu(OAc)_2\cdot H_2O$ (0.798 g, 0.004 mol) in MeOH (20 ml) and the resulting solution was refluxed for 7 h. The mixture was then reacted with one equivalent of $NaClO_4$ dissolved in 10 ml of methanol and refluxed for a further hour. A dark green precipitate was collected on evaporation of the resulting solution to half the volume and then allowing the solution to cool by standing at room temperature (25 °C). A dark green coloured compound was obtained on recrystallisation from acetonitrile. Yield: 1.12 g (74%). *Anal.* Calc. for $[C_{24}H_{37}N_4O_7Cu_2](ClO_4)\cdot 2H_2O$: C, 38.12; H, 5.47; N, 7.41; Cu, 16.81. Found: C, 38.15; H, 5.42; N, 7.36; Cu, 16.73%. Selected IR data (KBr disc, ν/cm^{-1}): 3454, 1725, 1481, 1112, 650. Conductance ($\Lambda_m/S\,cm^2\,mol^{-1}$) in DMF 89. UV–Vis [$\lambda_{max}$/nm ($\varepsilon/M^{-1}\,cm^{-1}$)] in MeOH: 671 (138), 373 (16 800), 293 (25 500). $g = 2.1$. $\mu_{eff} =$ 1.55 BM.

2.4.4.2. Synthesis of the $[Ni_2L^2(OAc)_2(H_2O)_2](ClO_4)$ complex. The Ni(II) complex was prepared by following the above procedure by using the ligand HL^2 (0.753 g, 0.002 mol) and $Ni(OAc)_2 \cdot 4H_2O$ (0.995 g, 0.004 mol). A green compound was obtained on recrystallisation from acetonitrile. Yield: 1.07 g (72%). *Anal.* Calc. for $[C_{24}H_{37}N_4O_7Ni_2(H_2O)_2](ClO_4)$: C, 38.62; H, 5.54; N, 7.51; Ni, 15.73. Found: C, 38.52; H, 5.46; N, 7.54; Ni, 15.67%. Selected IR data (KBr disc, ν/cm^{-1}): 3453, 1726, 1477, 1109, 654. Conductance ($\Lambda_m/S\,cm^2\,mol^{-1}$) in DMF 82. UV–Vis [$\lambda_{max}/nm$ ($\varepsilon/M^{-1}\,cm^{-1}$)] in MeOH: 804 (121), 624 (143), 565 (219), 376 (18600), 294 (24400).

2.4.4.3. Synthesis of the $[Zn_2L^2(OAc)_2(H_2O)_2](ClO_4)$ complex. The Zn(II) complex was prepared by following the above procedure using the ligand HL^2 (0.753 g, 0.002 mol) and $Zn(OAc)_2 \cdot 2H_2O$ (0.878 g, 0.004 mol). A colourless compound was obtained on recrystallisation from acetonitrile. Yield: 1.05 g (69%) *Anal.* Calc. for $[C_{24}H_{37}N_4O_7Zn_2(H_2O)_2](ClO_4)$: C, 37.94; H, 5.44; N, 7.37; Zn, 17.21. Found: C, 37.83; H, 5.38; N, 7.32; Zn, 17.24%. Selected IR data (KBr disc, ν/cm^{-1}): 3446, 1627, 1468, 1114, 652. Conductance ($\Lambda_m/S\,cm^2\,mol^{-1}$) in DMF 85. UV–Vis [$\lambda_{max}/nm$ ($\varepsilon/M^{-1}\,cm^{-1}$)] in MeOH: 292 (25300).

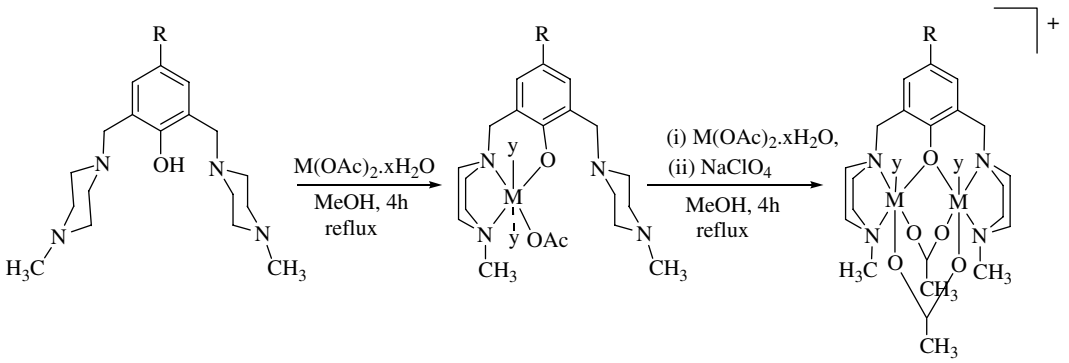
3. Results and discussion

We have synthesized an end-off ligand and its mono and binuclear Cu(II), Ni(II) and Zn(II) complexes having CHO as a *p*-substituent on the phenolic ring, and reported it earlier [28] (Chart 1). Two new end-off ligands having $C(O)CH_3(HL^1)$ and $C(O)OCH_3(HL^2)$ as *p*-substituents on the phenolic ring have been synthesized by means of the Mannich reaction (Scheme 1) and characterized. The electron withdrawing nature of the *p*-substituents is in the order CHO [28] > $C(O)CH_3$ > $C(O)OCH_3$. Using these two end-off ligands, mono and binuclear Cu(II), Ni(II) and Zn(II) complexes were prepared as shown in Scheme 2. Their spectral, magnetic, electrochemical and catalytic behaviours are discussed and compared on the basis of the nature of the *p*-substituent of the phenolic ring.

3.1. Spectral studies

The IR spectra of the ligands show a broad band around 3395 cm^{-1} due to the presence of the phenolic OH group. The sharp band around 1680 cm^{-1} for HL^1 and 1720 cm^{-1} for HL^2 shows the presence of an aromatic carbonyl in the ligands and it remains unchanged in all the complexes, indicating that the carbonyl group is undisturbed on complexation. The absence of a peak around 3395 cm^{-1} in all the complexes indicates the absence of ν(OH) due to deprotonation followed by complexation [29]. The strong $\nu(CO_2)$ bands at around 1450 cm^{-1} in the mononuclear complexes indicates the presence of acetate linkage. The biacetato bridged binuclear complexes showed strong $\nu(CO_2)$ bands at 1460–1490 cm^{-1} [30]. A broad band in the region around 3450 cm^{-1} indicates the presence of ν(OH) of water molecules for all the complexes. The presence of uncoordinated perchlorate anions in all of the binuclear complexes are inferred from a single broad band around 1100 cm^{-1} (ν_3-antisymmetric stretching) which are not split and a band around 650 cm^{-1} (ν_4-antisymmetric bending). The band around 930 cm^{-1} (ν_2-symmetric stretching) due to coordinated perchlorate is not observed and this indicates that no perchlorate ions are coordinated in the complexes [31,32].

The absorption spectra of the complexes exhibit three main features: one or two intense peaks below 300 nm assigned to an intraligand charge transfer transition [33], a peak or shoulder in the range 350–380 nm due to



Where, R

L_1 = $-C(=O)-CH_3$

L_2 = $-C(=O)-O-CH_3$

Complexes	M	x	y
1	Cu	1	-
2	Ni	4	-
3	Zn	2	H_2O

Complexes	M	x	y
4	Cu	1	-
5	Ni	4	H_2O
6	Zn	2	H_2O

Scheme 2.

phenolate to copper charge transfer transitions [34,35] and a band around λ_{max} at 600 nm for the mononuclear Cu(II) complexes due to the d–d transition, characteristic of a square planar geometry, and the d–d transition for the binuclear Cu(II) complexes observed around 670 nm, which is indicative of a distorted square-pyramidal geometry [36,37]. The mononuclear Ni(II) complexes show a single weak d–d band observed around 580 nm due to an $^1A_{1g} \rightarrow {}^1A_{2g}$ transition and this indicates that the complexes have a square planar geometry [38,39]. The binuclear Ni(II) complexes show three d–d transitions around 800, 620 and 560 nm assigned to $^3A_{2g} \rightarrow {}^3T_{2g}$, $^3A_{2g} \rightarrow {}^3T_{1g}$, $^3A_{2g} \rightarrow {}^3T_{1g}(P)$ spin allowed electronic transitions, which are characteristic of Ni^{2+} in an octahedral site [40,41]. The mono and binuclear Zn(II) complexes display only ligand centred charge transfer transitions in the UV region [42].

The position of the phenolato-to-copper LMCT charge-transfer band is sensitive to the electron density on the central copper atom [43,44]. There is a slight decrease in wavelength for the complexes having *p*-substituents in the order: $-C(O)OCH_3$ (362–376 nm) > $-C(O)CH_3$ (358–370 nm) > –CHO (352–363 nm) [28]. The *para* position of the phenolic ring substituted by the higher electron withdrawing nature of –CHO [28], when compared to other two groups, increases the Lewis acidity of the copper centre, thus shifting the phenolato-to-copper LMCT band to higher energy, and lower wavelength [45], whereas for the complexes of HL^1 and HL^2, the less electron withdrawing nature of $-C(O)CH_3$, and $-C(O)OCH_3$ at the *para* position of the phenolic ring, decreases the Lewis acidity of the copper and hence causes a red shift in the LMCT band, i.e., a shift to the lower energy region.

3.2. ESR spectra

The solid state ESR spectra of the copper(II) complexes were recorded in the X-band region at room temperature. The ESR spectra of mononuclear copper(II) complex **1** and binuclear copper(II) complex **4** are shown in Fig. 1. The ESR spectra of the mononuclear copper(II) complexes **1** and **7** show four lines [46] with a nuclear hyperfine spin 3/2, having $g_\parallel$ values of 2.25 and 2.26, $g_\perp$ values of 2.07 and 2.09, and $A_\parallel$ values of 183 and 185 cm^{-1}, respectively. A broad spectrum [47] with no hyperfine splitting was obtained for both the dicopper complexes **4** and **10** with $g = 2.1$ centred at 3200 G, indicating the presence of an antiferromagnetic interaction between the two copper ions. Owing to the favourable relative orientation of the magnetic orbitals and in spite of the Cu–Cu separation, an antiferromagnetic interaction is observed. All the nickel(II) complexes are diamagnetic in nature.

3.3. Magnetic studies

The measured magnetic moment of both the mononuclear copper(II) complexes $[CuL^1(OAc)] \cdot H_2O$ and

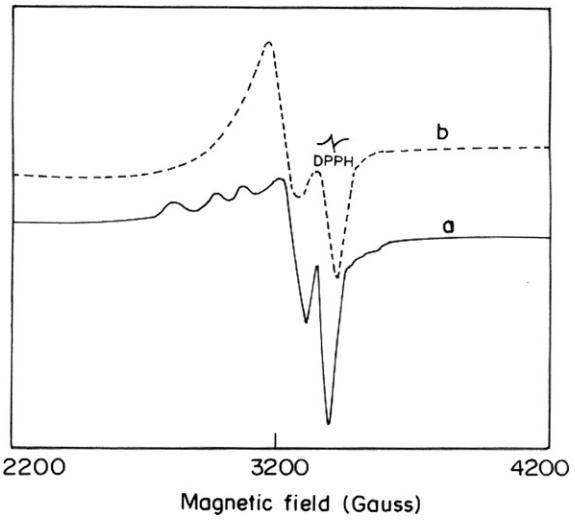


Fig. 1. ESR spectra of: (a) mononuclear $[CuL^1(OAc)] \cdot H_2O$ (**1**) and (b) binuclear $[Cu_2L^1(OAc)_2](ClO_4) \cdot H_2O$ (**4**) complexes.

$[CuL^2(OAc)] \cdot H_2O$ is 1.73 BM and that is equal to the spin only value. Room temperature magnetic moment of the binuclear copper(II) complexes $[Cu_2L^1(OAc)_2](ClO_4) \cdot 2H_2O$ and $[Cu_2L^2(OAc)_2](ClO_4) \cdot 2H_2O$ are 1.56 and 1.55 BM which are lower than the spin only value. In order to find out the magnetic exchange interaction, the magnetic moment of the complexes **2** and **8** were measured in the temperature range 77–300 K. The variable temperature magnetic study of the binuclear copper complex of HL^1 is shown in Fig. 2. The temperature dependence of the magnetic property of the complex was interpreted using the modified Bleany–Bowers equation [48]

$$\chi_m = (Ng^2\beta^2/3kT)[3 + \exp(-2J/kT)]^{-1}(1 - P) + (0.45P/T) + N_\alpha,$$

where χ_m is the paramagnetic susceptibility per metal atom after the correction for diamagnetism, N is Avogadro's number, g is the average gyromagnetic ratio, β is the Boltz-

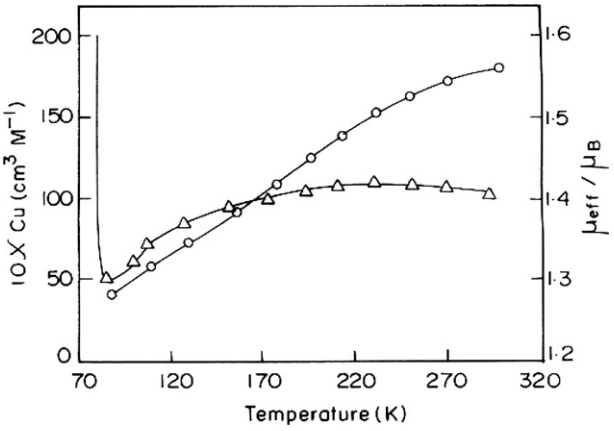


Fig. 2. Temperature-dependence magnetic properties for complex $[Cu_2L^1(OAc)_2](ClO_4) \cdot H_2O$ (**4**) where ○ is μ_{eff}/μ_B, △ is χ.

man constant, P is the fraction of monomeric copper(II) impurities, $-2J$ is the singlet–triplet energy separation, N_α is the temperature independent fraction, usually assumed to be 120×10^{-6} cgs units for copper(II) compounds. The values of the exchange integral $-2J$ for the binuclear copper complexes are 149 and 158 cm^{-1}, indicative of weak antiferromagnetic coupling between the copper(II) ions. This higher value shows formation of additional bridges between the copper(II) centres apart from the phenolate bridge.

The antiferromagnetic exchange interaction $-2J$ values observed for the binuclear copper complexes **4** and **10** are comparable to that of the analogous end-off complex reported by Narayanan and co-workers [28]. A higher $-2J$ value is observed for complex **8** than complex **6** and the complex of the parallel component with –CHO as a *p*-substituent [28]. This higher $-2J$ value may be due to the geometry around the Cu(II) ions and also due to the substitution effect in the ligand. Complexes **4** and **10** show λ_{max} around 667 and 671 nm, respectively. This small difference does not have much influence on the structure of the complexes, which may have the same geometry. So the change in the magnetic exchange interaction is mainly influenced by the *p*-substituent of the phenolic ring. The electron withdrawing group in the *para* position of the phenolic ring decreases the electron density on the copper centres [34,43], and so the antiferromagnetically coupling. Reduction in the electron density weakens the Cu–O bond and reduces the spin exchange interaction [49–51]. The electron withdrawing nature is decreasing in the order $CHO > C(O)CH_3 > C(O)OCH_3$. Hence, the $-2J$ values of the complexes having the *p*-substituent increase in the order CHO [28] $< C(O)CH_3 < C(O)OCH_3$ (134 [28], 149 and 158 cm^{-1}, respectively). The mononuclear Ni(II) complexes **2** and **8** have a square planar geometry and are diamagnetic [52]. The binuclear Ni(II) complexes **5** and **11** have a magnetic moment value of 2.96 and 2.95 BM, respectively, which is characteristic of Ni^{2+} in an octahedral site [41,53].

3.4. Electrochemical studies

The conductance measurement of all the complexes was carried out in DMF. For the mononuclear complexes, the conductance value was found to be in the range 10–15 (Λ_m/S cm^2 mol^{-1}) indicating that the complexes are neutral. Conductance values of the binuclear complexes are in the range 80–90 (Λ_m/S cm^2 mol^{-1}) indicating that they are of the 1:1 electrolyte type [54].

3.4.1. Reduction process at negative potential

The electrochemical properties of the complexes were studied by cyclic voltammetry in the potential range 0 to −1.7 V in DMF containing 0.1 M TBAP as the supporting electrolyte, and the data are summarized in Table 1. The electronegativity and hard nature of the phenoxide ligands influence the electrochemical properties of the complexes

Table 1
Electrochemical data[a] for the complexes (reduction at cathodic potential)

No.	Complexes	E_{pc}^1 (V)	E_{pc}^2 (V)
1	$[CuL^1(OAc)] \cdot H_2O$	−0.78	
2	$[NiL^1(OAc)] \cdot H_2O$	−0.87	
3	$[ZnL^1(OAc)(H_2O)_2]$	−0.90	
4	$[Cu_2L^1(OAc)_2](ClO_4) \cdot H_2O$	−0.77	−1.25
5	$[Ni_2L^1(OAc)_2(H_2O)_2](ClO_4)$	−0.76	−1.40
6	$[Zn_2L^1(OAc)_2(H_2O)_2](ClO_4)$	−0.79	−1.76
7	$[CuL^2(OAc)] \cdot H_2O$	−0.80	
8	$[NiL^2(OAc)] \cdot H_2O$	−0.89	
9	$[ZnL^2(OAc)(H_2O)_2]$	−0.93	
10	$[Cu_2L^2(OAc)_2](ClO_4) \cdot 2H_2O$	−0.79	−1.27
11	$[Ni_2L^2(OAc)_2(H_2O)_2](ClO_4)$	−0.78	−1.43
12	$[Zn_2L^2(OAc)_2(H_2O)_2](ClO_4)$	−0.82	−1.89

[a] Measured by CV at 50 mV s^{-1}. *E* vs. Ag/AgCl conditions: GC working and Ag/AgCl reference electrodes; supporting electrolyte TBAP; concentration of complex 1×10^{-3} M, concentration of TBAP 1×10^{-1} M.

[55–57]. In general, this type of end-off complexes shows irreversible reduction waves at the cathodic potential region [36]. The cyclic voltammograms for the binuclear copper(II) and nickel(II) complexes are depicted in Figs. 3 and 4, respectively. Cyclic voltammograms with different scan rates show no corresponding anodic peak in the cathodic direction, which indicates that the electrode process is irreversible in nature. The mononuclear copper(II), nickel(II) and zinc(II) complexes **1**–**3** and **7**–**9** show an irreversible one-electron transfer reduction in the cathodic region. The binuclear copper(II), nickel(II) and zinc(II) complexes **4**–**6** and **10**–**12** show two step irreversible one-electron transfer reductions. Controlled potential electrolysis was also carried out for the complexes at 100 mV s^{-1} more negative to the cathodic peak, and these consumed one electron per molecule ($n = 0.95$), which indicates that each wave corresponds to a one-electron transfer process. So, the two reduction processes are assigned generally as follows:

$$M^{II}M^{II} \rightarrow M^{II}M^{I} \rightarrow M^{I}M^{I}$$

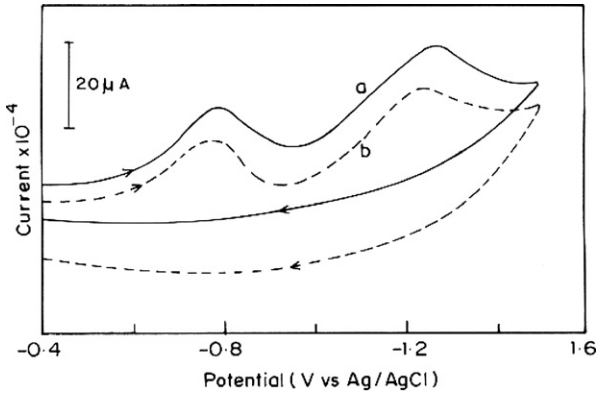


Fig. 3. Cyclic voltammograms of the binuclear copper(II) complexes: (a) $[Cu_2L^2(OAc)_2](ClO_4) \cdot H_2O$ (**10**) and (b) $[Cu_2L^1(OAc)_2](ClO_4) \cdot 2H_2O$ (**4**) (reduction process).

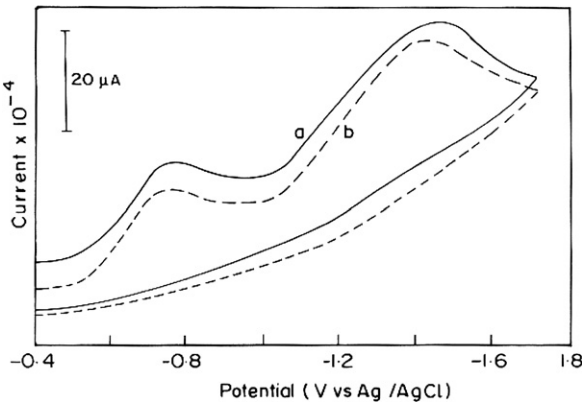


Fig. 4. Cyclic voltammograms of the binuclear nickel(II) complexes: (a) $[Ni_2L^2(OAc)_2(H_2O)_2](ClO_4)$ (**11**) and (b) $[Ni_2L^1(OAc)_2(H_2O)_2](ClO_4)$ (**5**) (reduction process).

The reduction potentials for all the mononuclear complexes of HL^1 are slightly lower than those of the mononuclear complexes of HL^2. In the same way, the reduction potentials of the binuclear complexes of HL^1 are also slightly lower than those of the binuclear complexes of HL^2. This is because the reduction potential is affected by the substituents at the *para* position of the phenoxide of the phenyl ring. The electron withdrawing nature of the *p*-substituents decreases the electron density around the metal ion and favours easy reduction [43,50]. When the electron withdrawing nature of the *p*-substituents increases, the reduction potential decreases, i.e., it favours an anodic shift, and it is in the order CHO [28] < $C(O)CH_3$ < $C(O)OCH_3$ (−0.74 [28], −0.78 and −0.80 V, respectively, for mono nuclear copper complexes – all the other complexes also have the same trend).

3.4.2. Oxidation process at anodic potential

The cyclic voltammogram of the binuclear nickel(II) complexes **5** and **11** in the anodic potential region is given in Fig. 5. The mononuclear Ni(II) complexes **2** and **8** show an irreversible oxidation wave in positive potential at +0.74 V and +0.73 V. The binuclear Ni(II) complexes **5** and **11** show two-step one-electron transfer processes in the potential range from +0.79 V to +1.35 V and from +0.75 V to +1.30 V. The mono and binuclear Ni(II) complexes are all found to be irreversible in nature. The two oxidation processes for the binuclear Ni(II) complexes are assigned generally as follows:

$$M^{II}M^{II} \rightarrow M^{III}M^{II} \rightarrow M^{III}M^{III}$$

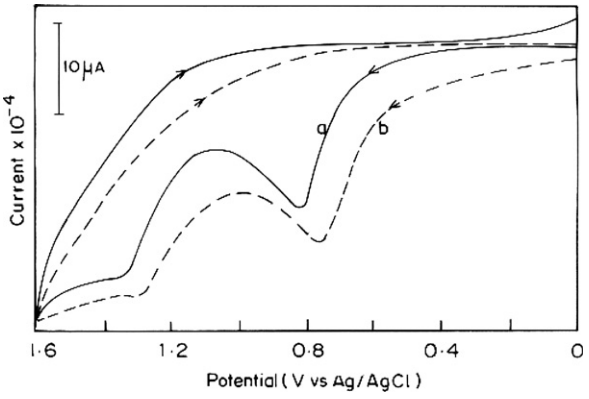


Fig. 5. Cyclic voltammograms of the binuclear nickel(II) complexes: (a) $[Ni_2L^1(OAc)_2(H_2O)_2](ClO_4)$ (**5**) and (b) $[Ni_2L^2(OAc)_2(H_2O)_2](ClO_4)$ (**11**) (oxidation process).

3.5. Kinetic studies

3.5.1. Oxidation of pyrocatechol (catecholase activity)

Efforts have also been made to investigate the catecholase activity of both mono and binuclear copper(II) complexes using pyrocatechol as a convenient model substrate for the identification of functional models for the metalloenzymes [58,59]. All the mono and binuclear copper(II) complexes synthesized were subjected for catecholase activity. The course of the reaction was followed spectrophotometrically at 390 nm nearly for 45 min at regular time intervals of 5 min. The slope was determined by the method of initial rates by monitoring the growth of the 390 nm band of the product *o*-quinone. A linear relationship for initial rate and the complex concentration obtained for all the complexes shows a first-order dependence on the complex concentration for the systems. It was found that under anerobic conditions little product was formed, so the solvent was saturated with O_2 before the kinetic experiments. Oxygen must participate directly in the catalytic cycle of the oxidation reaction, acting as a thermodynamic driving force by reoxidizing any generated copper(I) species back to the active copper(II) species.

A plot of $\log(A_\alpha/A_\alpha - A_t)$ versus time for catecholase activity of the mono and binuclear copper complexes of HL^1 and HL^2 were obtained and their observed initial rate constant values are given in Table 2. The catecholase activities of the copper complexes of HL^1 are shown in Fig. 6. It is found that the binuclear copper(II) complex shows a higher reactivity than the mononuclear complex. This is due to the fact that the oxidation of pyrocatechol to *o*-quinone requires two metal ions in close proximity [60]; hence the rate constant for the binuclear copper complex is high. Copper(II) complexes of HL^2 show higher catecholase activities than those of HL^1. This may be due to the easier reduction of the Cu(II) ions on increasing the electron withdrawing nature of the *p*-substituent [43,50] ($C(O)CH_3 > C(O)OCH_3$) of the phenolic ring.

3.5.2. Kinetic studies of hydrolysis of 4-nitro phenyl phosphate

The kinetics of hydrolysis of 4-nitro phenyl phosphate by the mono and binuclear copper(II), nickel(II) and zinc(II) complexes was determined spectrophotometrically by monitoring the increase of the 4-nitrophenolate anion characteristic absorption at 420 nm over time in DMF at 25 °C. For this purpose, 10^{-3} mol dm^{-3} solutions of the

Table 2
Hydrolysis of 4-nitrophenylphosphate[a] and catecholase activity[a]

No.	Complexes	Rate constant (k) ($\times 10^{-3}$ min^{-1})	
		NPP	Catecholase
1	$[CuL^1(OAc)] \cdot H_2O$	4.80	6.70
2	$[NiL^1(OAc)] \cdot H_2O$	5.10	
3	$[ZnL^1(OAc)(H_2O)_2]$	4.50	
4	$[Cu_2L^1(OAc)_2](ClO_4) \cdot H_2O$	11.40	13.10
5	$[Ni_2L^1(OAc)_2(H_2O)_2](ClO_4)$	12.80	
6	$[Zn_2L^1(OAc)_2(H_2O)_2](ClO_4)$	9.80	
7	$[CuL^2(OAc)] \cdot H_2O$	4.90	6.90
8	$[NiL^2(OAc)] \cdot H_2O$	5.50	
9	$[ZnL^2(OAc)(H_2O)_2]$	4.70	
10	$[Cu_2L^2(OAc)_2](ClO_4) \cdot 2H_2O$	11.60	13.40
11	$[Ni_2L^2(OAc)_2(H_2O)_2](ClO_4)$	13.10	
12	$[Zn_2L^2(OAc)_2(H_2O)_2](ClO_4)$	10.10	

Concentration of the complexes: 1×10^{-3} M.
Concentration of 4-nitrophenylphosphate: 1×10^{-1} M.
Concentration of pyrocatechol: 1×10^{-1} M.
[a] Measured spectrophotometrically in DMF.

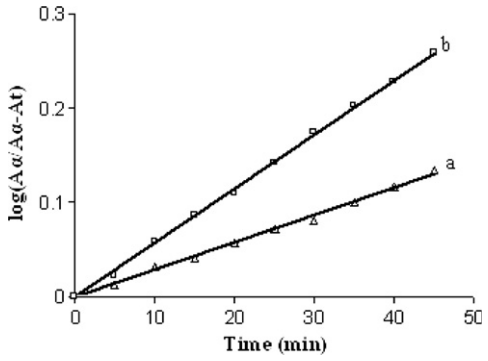


Fig. 6. Catecholase activity of the copper(II) complexes: (a) $[CuL^1(OAc)] \cdot H_2O$ (**1**) and (b) $[Cu_2L^1(OAc)_2](ClO_4) \cdot H_2O$ (**4**).

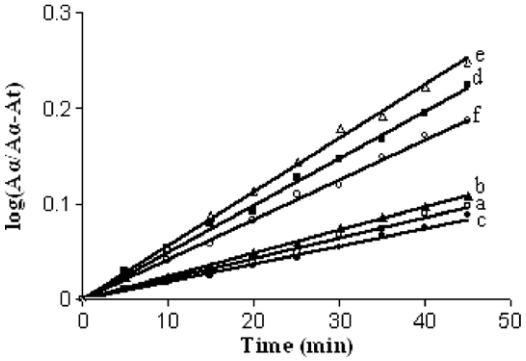


Fig. 7. Hydrolysis of 4-nitrophenylphosphate by the copper(II), nickel(II) and zinc(II) complexes: (a) $[CuL^1(OAc)] \cdot H_2O$ (**1**); (b) $[NiL^1(OAc)] \cdot H_2O$ (**2**); (c) $[ZnL^1(OAc)(H_2O)_2]$ (**3**); (d) $[Cu_2L^1(OAc)_2](ClO_4) \cdot H_2O$ (**4**); (e) $[Ni_2L^1(OAc)_2(H_2O)_2](ClO_4)$ (**5**); and (f) $[Zn_2L^1(OAc)_2(H_2O)_2](ClO_4)$ (**6**).

complexes in dimethyl formamide and a 2.5×10^{-3} M solution of tetramethylammonium hydroxide were treated with 100 equivalents of nitrophenyl phosphate in the presence of air.

The course of the reaction was followed at 420 nm for nearly 45 min at regular time intervals. The slope was determined by the method of initial rates by monitoring the growth of the 420 nm band of the product, the 4-nitro phenolate anion. A linear relationship for all the complexes shows a first-order dependence on the complex concentration for the systems. Plots of $\log(A_\alpha/A_\alpha - A_t)$ versus time for the hydrolysis of 4-nitro phenyl phosphate activity of the complexes are obtained and are shown in Fig. 7. The observed initial rate constant values for the mononuclear and binuclear copper(II) complexes are given in Table 2. It is found that the binuclear complexes show higher reactivity than their corresponding mononuclear complexes due to the fact that this kind of mechanism requires two metal ions in close proximity. The mechanism of action has already been explained with the help of model complexes [61].

On the comparison of hydrolysis of 4-nitrophenylphosphate by the Cu(II), Ni(II) and Zn(II) complexes, the Ni(II) complexes have a higher rate constant value than those of the Cu(II) and Zn(II) complexes, which is similar to our earlier report [28]. From the results, it is found that the catalytic activity of the Cu(II) complexes towards oxidation of pyrocatechol is more than that of the phosphate hydrolysis.

4. Summary

Two new phenol based "end-off" acetate bridged binuclear Cu(II), Ni(II) and Zn(II) complexes have been prepared and characterized. Both the variable temperature magnetic and ESR spectral studies of the binuclear Cu(II) complexes show the presence of a magnetic exchange interaction between the two copper atoms. The complexes show a significant change in their characteristics by varying the nature of the *p*-substituent of the phenolic ring. On lowering electron withdrawing nature of the *p*-substituent of the phenolic ring, (a) there is a red shift in LMCT-charge transfer band in electronic spectra of the complexes and (b) there is an increase in the antiferromagnetic interaction between the two copper(II) centres. Increasing the electron

withdrawing nature of the *p*-substituent of the phenolic ring, (a) causes an anodic shift in the reduction potential of the metal complexes and (b) causes a decrease in the catecholase activity of the copper complexes.

Acknowledgement

Financial support from University Grants Commission, New Delhi is gratefully acknowledged.

References

[1] M.A. Halcrow, G. Christou, Chem. Rev. 94 (1994) 2421.
[2] J.D. Crane, D.E. Fenton, J.M. Lartour, A. Smith, J. Chem. Soc., Dalton Trans. (1991) 2979.
[3] (a) K. Wieghardt, Angew. Chem., Int. Ed. Engl. 28 (1989) 1153;
(b) Roland Krämer, I.O. Fritsky, H. Pritzkow, L.A. Kovbasyuk, J. Chem. Soc., Dalton Trans. (2002) 1307;
(c) S.L. Jain, P. Bhattacharyya, H.L. Milton, A.M.Z. Slawin, J.A. Crayston, J.D. Woollins, J. Chem. Soc., Dalton Trans. (2004) 862.
[4] (a) T. Chattopadhyay, K.S. Banu, A. Banerjee, J. Ribas, A. Majee, M. Nethaji, Debasis Das, J. Mol. Struct. 833 (2007) 13;
(b) M.H. Klingele, B. Moubaraki, J.D. Cashion, K.S. Murray, S. Brooker, Chem. Commun. (2005) 987;
(c) B.A. Leita, B. Moubaraki, K.S. Murray, J.P. Smith, J.D. Cashion, Chem. Commun. (2004) 156;
(d) K. Nakano, S. Kawata, Ko. Yoneda, A. Fuyuhiro, T. Yagi, S. Nasu, S. Morimoto, S. Kaizaki, Chem. Commun. (2004) 2892;
(e) Y. Journaux, V. Lozan, J. Klingele, B. Kersting, Chem. Commun. (2006) 83.
[5] (a) R.R. Gagne, R.P. Kreh, J.A. Dodge, J. Am. Chem. Soc. 101 (1979) 6917;
(b) S. Brooker, Coord. Chem. Rev. 222 (2001) 33.
[6] J.-M. Lehn, Supramolecular Chemistry, VCH, Weinheim, 1995.
[7] B. Linton, A.D. Hamilton, Chem. Rev. 97 (1997) 1669.
[8] M.A. Holmes, I. Le Trong, S. Turley, L.C. Sleker, R.E. Stenkamp, J. Mol. Biol. 218 (1991) 583.
[9] E. Jabri, M.B. Carr, R.P. Hausinger, P.A. Karplus, Science 268 (1995) 998.
[10] P. Chaudhuri, C. Stocheim, K. Wieghardt, R. Gregorzik, H. Vahrenkamp, B.NuberandJ. Weiss, Inorg. Chem. 31 (1992) 1451.
[11] S. Uhlenbrock, B. Krebs, Angew. Chem. Int. Ed. Engl. 31 (1992) 1647.
[12] D.E. Wilcox, Chem. Rev. 96 (1996) 1647.
[13] N. Strater, W.N. Lipscomb, T. Klabunde, B. Krebs, Angew. Chem., Int. Ed. Engl. 35 (1996) 2024.
[14] T. Gadja, R. Kramer, A. Jancso, Eur. J. Inorg. Chem. (2000) 1635.
[15] S.O. Kang, M. Kim, J. Am. Chem. Soc. 125 (2003) 4684.
[16] H. Sakiyama, H. Okawa, R. Isobe, J. Chem. Soc., Chem. Commun. (1993) 882.
[17] C. Higuchi, H. Sakiyama, H. Okawa, D.E. Fenton, J. Chem. Soc., Dalton Trans. (1995) 4015.
[18] K. Abe, J. Izumi, M. Ohba, T. Yokoyama, H. Okawa, Bull. Chem. Soc. Jpn. 74 (2001) 85.
[19] M. Suzuki, H. Furutachi, H. Okawa, Coord. Chem. Rev. 200 (2000) 105.
[20] T. Koga, H. Furutachi, H. Nakamura, N. Fukita, M. Ohba, K. Takahashi, H. Okawa, Inorg. Chem. 37 (1998) 989.
[21] S. Uozumi, H. Furutachi, M. Ohba, H. Okawa, D.E. Fenton, K. Shindo, S. Murata, D.J. Kitko, Inorg. Chem. 37 (1998) 6281.
[22] D.E. Fenton, S.E. Gayada, J. Chem. Soc., Dalton Trans. (1977) 2109.
[23] E.E. Eduok, C.J.O. Connor, Inorg. Chim. Acta 85 (1984) 229.
[24] T. Mallah, M.L. Boillot, O. Kahn, J. Gouteron, S. Jeannin, R. Jeannin, Inorg. Chem. 25 (1986) 3058.
[25] T.N. Sorrell, C.J.O. Connor, O.P. Anderson, J.H. Reibenspies, J. Am. Chem. Soc. 107 (1985) 4199.
[26] (a) H.S. Mason, Annu. Rev. Biochem. 35 (1965) 595;
(b) S.M. Annigeri, M.P. Sathisha, V.K. Revankar, Transition Met. Chem. 32 (2007) 81;
(c) M. Bera, P.K. Nanda, U. Mukhopadhyay, Debashis Ray, J. Chem. Sci. 116 (2004) 151.
[27] M.A. De Rosch, W.C. Trogler, Inorg. Chem. 29 (1990) 2409.
[28] K. Shanmuga Bharathi, A. Kalilur Rahiman, K. Rajesh, S. Sreedaran, P.G. Aravindan, D. Velmurugan, V. Narayanan, Polyhedron 25 (2006) 2859.
[29] D. Saravanakumar, N. Sengottuvelan, G. Priyadarshni, M. Kandaswamy, H. Okawa, Polyhedron 23 (2004) 665.
[30] G.B. Deacon, R. Phillips, J. Coord. Chem. Rev. 33 (1980) 227.
[31] K. Nakamoto, Infrared and Raman Spectra of Inorganic and Coordination Compounds, Wiley–Interscience, New York, 1978.
[32] M. Lachkar, R. Guilard, A. Atmani, A. DeCian, J. Fischer, R. Weiss, Inorg. Chem. 37 (1998) 1575.
[33] J. Manonmani, M. Kandaswamy, V. Narayanan, R. Thirumurugan, S. Shanmuga Sundara Raj, G. Shanmugam, M.N. Ponnuswamy, H.K. Fun, Polyhedron 20 (2001) 3039.
[34] E.V. Rybak-Akimova, D.H. Bush, P.K. Kahol, N. Pinto, N.W. Alcock, H.J. Clase, Inorg. Chem. 36 (1997) 510.
[35] Ty. Garber, S.V. Wallendael, D.P. Rillema, M. Kirk, W.E. Hatfield, J.H. Welch, P. Singh, Inorg. Chem. 29 (1990) 1863.
[36] K. Bertoncello, G.D. Fallon, J.H. Hodgkin, K.S. Murray, Inorg. Chem. 27 (1988) 4750.
[37] D. Reinen, C. Friebel, Inorg. Chem. 23 (1984) 791.
[38] A.B.P. Lever, Inorganic Electronic Spectroscopy, 2nd ed., Elsevier, Amsterdam, 1984.
[39] S. Bhattacharyya, T.J.R. Weakley, M. Chaudhury, Inorg. Chem. 38 (1999) 633.
[40] M.F. Cabral, B. Murphy, J. Nelson, Inorg. Chim. Acta 90 (1984) 169.
[41] T.C. Higgs, C.J. Carrano, Inorg. Chem. 36 (1997) 298.
[42] F. Yilmaz, V.T. Yilmaz, S. Topcu, N. Menek, J. Coord. Chem. 56 (2003) 903.
[43] R. Mahalakshmy, R. Venkatesan, P.S. Sambasiva Rao, R. Kannappan, T.M. Rajendiran, Transition Met. Chem. 29 (2004) 623.
[44] E.W. Ainscough, A.G. Bingham, A.M. Brodie, J. Husbands, J.E.J. Plowman, J. Chem. Soc., Dalton Trans. 1701 (1981).
[45] R.C. Holz, J.M. Brink, F.T. Gobena, C.J. O'Conner, Inorg. Chem. 33 (1994) 6086.
[46] S. Zhu, F. Kon, H. Lin, C. Lin, M. Lin, Y. Chen, Inorg. Chem. 35 (1997) 3851.
[47] R.C. Agarwal, N.K. Singh, R.P. Singh, Inorg. Chem. 20 (1981) 2794.
[48] B. Bleaney, K.D. Bowers, Proc. R. Soc. Lond. Ser. A 214 (1952) 451.
[49] L.K. Thompson, S.K. Mandal, S.S. Tandon, J.N. Bridson, M.K. Park, Inorg. Chem. 35 (1996) 3117.
[50] M.J. Mac Lachlan, M.K. Park, L.K. Thompson, Inorg. Chem. 35 (1996) 5492.
[51] R.J. Butcher, J.W. Overman, E. Sinn, J. Am. Chem. Soc. 102 (1980) 3276.
[52] A. Bottcher, H. Elias, E. Jager, H. Lanffelderova, M. Mazur, L. Mullor, H. Paulas, P. Pelikan, M. Rudolph, M. Valko, Inorg. Chem. 32 (1993) 4131.
[53] M.P. Suh, B.Y. Shim, T.S. Yoon, Inorg. Chem. 33 (1994) 5509.
[54] W.J. Geary, Coord. Chem. Rev. 7 (1971) 81.
[55] G.S. Patterson, R.W. Holm, Bioinorg. Chem. 4 (1975) 257.
[56] K.D. Karlin, Y. Guitnech, Inorg. Chem. 35 (1987) 219.
[57] F. Azevedo, C.T. Carrondo, B. Caseto, M. Convery, D. Domingues, C. Freire, T. Durate, K. Neilson, C. Santos, Inorg. Chim. Acta 219 (1994) 43.
[58] A. Neves, L.M. Rossi, A. Horn, I. Vencato, A.J. Bortoluzzi, C. Zucco, A.S. Mangrich, Inorg. Chem. Commun. 8 (1999) 334.
[59] A. Neves, L.M. Rossi, I. Vencato, V. Drago, W. Hasse, R. Werner, Inorg. Chim. Acta 281 (1998) 111.
[60] A. Neves, L.M. Rossi, A.J. Bortoluzzi, B.S. Szpoganicz, C. Wiezbicki, E. Schwingel, W. Haase, S. Ostrovsky, Inorg. Chem. 41 (2002) 1788.
[61] R.G. Clewley, H. Slebocka-Tilk, R.S. Brown, Inorg. Chim. Acta 157 (1989) 233.

hexacoordinate ferrous TPA starting compound, possible coordination of a solvent molecule or weak anionic ligands to the Fe^{IV}=O center was suggested [10]. For example, $[TMCFe^{IV}=O(MeCN)]^{2+}$ was prepared from the oxidation of $TMCFe(OTf)_2$ with PhIO or H_2O_2, and the hexacoordinate ferrous center did not change its coordination geometry through the reaction [6a]. Herein, we report the structure and physical properties of the pentacoordinated $[TPAFeCl]^+$ complex, which suggests the possible formation of the pentacoordinated $[TPAFe^{IV}=O]^{2+}$ or dinuclear $[TPA_2Fe^{IV}_2(\mu\text{-}O)_2]^{4+}$ complex in the presence of non-coordinating solvents. The $[TPAFeCl]^+$ complex has been characterized by physical methods to elucidate its ground spin-state. Additionally, free energy values of the possible ground spin-states were obtained with semi-empirical ZINDO/S calculations.

2. Experimental

2.1. General

All experiments and reactions were carried out under a dinitrogen atmosphere using standard Schlenk line techniques or in an inert atmosphere glove box. All solvents were distilled under dinitrogen and nitrogen gas was bubbled through before each use in the glove box. $FeCl_2$, PEt_3 and P^nPr_3 were purchased from Aldrich and were used without further purification. $H_3TPA(ClO_4)_3$ was prepared from the published method [11]. $Fe(PEt_3)_2Cl_2$ and $Fe(P^nPr_3)_2Cl_2$ were prepared from a 1:2 molar ratio of $FeCl_2$ and P^nPr_3 in THF [12].

^1H NMR spectra were recorded on a Bruker 400 MHz NMR spectrometer in DMSO-d_6, using non-deuteriated solvent as the internal standard. FT-IR spectra were collected on a Nicolet DX V. 4.56 FT-IR spectrometer in KBr pellets and the spectra were corrected for background effects. UV–Vis spectra were obtained on a Shimadzu UV-1601 UV–VIS spectrometer in the range 200–1000 nm. Elemental analyses were performed in the Microanalytical Laboratory at the University of Michigan and the data were corrected using acetanilide as a standard. ESI-Mass spectra were obtained on a Finnigan LCQ-DECA mass spectrometer by direct injection. Cyclic voltammetry was performed on a BAS-voltammograph. Three electrodes consisting of a glassy carbon working electrode, Pt auxiliary electrode and a saturated calomel electrode (SCE) as a reference electrode were used for the measurements. The complexes were dissolved in 1,2-dichloroethane together with 0.1 M tetrabutylammonium hexafluorophosphate as a supporting electrolyte, and the scanning rate was 100 mV/s. Under the same condition, 0.1 M of ferrocene showed an oxidation wave at 650 mV. The magnetic susceptibility of $[TPAFeCl]_2(FeCl_4)(MeCN)_2$ was measured in the temperature ranges 20–300 K with a Quantum Design MPMS SQUID. The magnetic field of the measurements was 5000 G for the temperature-dependent experiments. The crystalline sample was put into a cellophane capsule under a dinitrogen atmosphere. The magnetic susceptibility of the holder was determined separately and diamagnetic corrections were estimated from Pascal's constants [13].

The energy and molecular orbital calculations were carried out with ZINDO/S Hamiltonian using the unrestricted Hartree–Fock (UHF) method [14]. The geometries of the $[TPAFeCl]^+$, $TPAFeCl_2$ and $[TPAFe(MeCN)_2]^{2+}$ complexes were obtained from the X-ray crystallographic structures [15,16]. The same optimized geometry with different spin-states was used as an input of ZINDO/S UHF single point calculation to obtain the energies of $S = 1$, $S = 3$ and $S = 5$ spin-states.

2.2. $[TPAFeCl]_2(FeCl_4)(MeCN)_2$

$(H_3TPA)(ClO_4)_3$ (296 mg, 0.5 mmol) and $FeCl_2(P^nPr_3)_2$ (224 mg, 0.5 mmol) were dissolved in 10 mL of MeCN

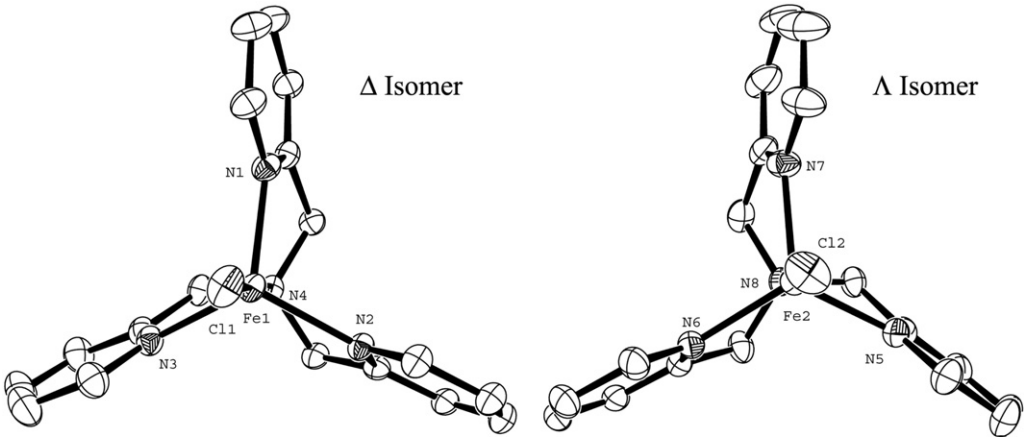


Fig. 1. Single crystal X-ray crystallographic structure of the Δ and Λ isomers of $[TPAFeCl]^+$ in the unit cell. Selected bond lengths (Å) and angles (°): Fe(1)–Cl(1), 2.3087(6); Fe(1)–N(1), 2.1214(18); Fe(1)–N(2), 2.0897(16); Fe(1)–N(3), 2.1218(18); Fe(1)–N(4), 2.2502(16); Fe(2)–Cl(2), 2.3091(6); Fe(2)–N(5), 2.1074(18); Fe(2)–N(6), 2.0954(17); Fe(2)–N(7), 2.1104(18); and N(2)–Fe(1)–Cl(1), 103.93(5); N(1)–Fe(1)–Cl(1), 103.50(5); N(3)–Fe(1)–Cl(1), 101.67(5); N(4)–Fe(1)–Cl(1), 178.61(4); N(6)–Fe(2)–Cl(2), 105.03(5); N(5)–Fe(2)–Cl(2), 105.13(5); N(7)–Fe(2)–Cl(2), 99.51(5); N(8)–Fe(2)–Cl(2), 176.38(5).

and stirred for 12 h in the glove box. The reaction mixture was filtered off and 40 mL of diethyl ether was layered over the filtrate. After a day, about 200 mg of greenish yellow crystals (0.38 mmol, 76% isolation yield) were formed on the bottom of flask. $[TPAFeCl]_2(FeCl_4)(MeCN)_2$ *Anal.* Calc. for $C_{40}H_{42}Cl_6Fe_3N_{10}$ (MW: 1043.09): C, 46.06; H, 4.06; N, 13.43. Found: C, 46.12; H, 4.03; N, 13.44%. FT-IR (KBr, cm^{-1}) 3096(w), 3064(m), 3043(w), 3022(w), 2248(w), 2246(m), 1607(vs), 1480(s), 1441(s), 774(s). ^1H NMR (400 MHz, DMSO) 142 (α, 3H), 53.5 (β, 3H), 47.5 (β′, 3H), 26.0 (γ, 3H), −0.05 (CH_2, 6H) UV(CH_3CN, nm) 257, 325, 402. Cyclic voltammetry (0.1 M $^nBu_4NPF_6$ in 1,2-dichloroethane, versus SCE, V) 0.30(rev), 0.62(rev). Magnetic susceptibility (solid, for $[TPAFeCl]_2(FeCl_4)(MeCN)_2$): μ_{eff} (20 K) 7.40 μ_B, μ_{eff} (300 K) 5.48 μ_B.

2.3. X-ray crystallography

Greenish yellow needle-shaped crystals of $[TPAFeCl]_2(FeCl_4)(MeCN)_2$ were obtained from the mother liquor. The diffraction data were collected at 123(2) K, using a Bruker SMART area diffractometer equipped with a monochromator in the Mo Kα ($\lambda = 0.71073$ Å) incident beam. The CCD data were integrated and scaled using the BRUKER-SAINT software package [17], and the structure was solved and refined using SHEXTL V5.10 (Fig. 1) [18]. The crystal data and structural parameters are shown in Tables 1 and 2. The structure for $[TPAFeCl]_2(FeCl_4)(MeCN)_2$ was solved by direct methods to locate heavy atoms, and the non-hydrogen atoms were located through subsequent difference Fourier syntheses. Structural refinement was carried out by full-matrix least squares on F^2. All non-hydrogen atoms were refined with anisotropic thermal parameters. Hydrogen atoms were placed in calculated positions, allowed to ride on their corresponding atoms and refined isotropically.

Table 1
Crystal data and structure refinement for $[TPAFeCl]_2(FeCl_4)(MeCN)_2$

Formula	$C_{40}H_{42}Cl_6Fe_3N_{10}$
Formula weight	1043.09
Temperature (K)	123(2)
Wavelength (Å)	0.71073
Crystal system	monoclinic
Space group	*Cc*
a (Å)	12.019(2)
b (Å)	27.550(5)
c (Å)	14.138(2)
β (°)	94.168(3)
Volume (Å^3)	4668.9(13)
Z	4
D_{calc} (Mg/m^3)	1.484
Absorption coefficient (mm^{-1})	1.304
F(000)	2128
Crystal size (mm)	0.40 × 0.30 × 0.24
θ Range for data collection (°)	1.85–28.47
Limiting indices	$-16 \leqslant h \leqslant 16$, $-36 \leqslant k \leqslant 36$, $-18 \leqslant l \leqslant 18$
Reflections collected/unique [R_{int}]	52 747/11 600 [0.0377]
Data/restraints/parameters	11 600/2/534
Goodness-of-fit on F^2	1.032
Final *R* indices [$I > 2\sigma(I)$]	$R_1 = 0.0246$, $wR_2 = 0.0602$
R indices (all data)	$R_1 = 0.0287$, $wR_2 = 0.0623$

Table 2
Selected bond lengths (Å) and angles (°) for $[TPAFeCl]_2(FeCl_4)(MeCN)_2$

Fe(1)–Cl(1)	2.3087(6)	N(2)–Fe(1)–N(4)	77.34(6)
Fe(1)–N(1)	2.1214(18)	N(1)–Fe(1)–N(4)	76.49(6)
Fe(1)–N(2)	2.0897(16)	N(3)–Fe(1)–N(4)	77.13(6)
Fe(1)–N(3)	2.1218(18)	N(1)–Fe(1)–Cl(1)	103.50(5)
Fe(1)–N(4)	2.2502(16)	N(2)–Fe(1)–Cl(1)	103.93(5)
Fe(2)–Cl(2)	2.3091(6)	N(3)–Fe(1)–Cl(1)	101.67(5)
Fe(2)–N(5)	2.1074(18)	N(4)–Fe(1)–Cl(1)	178.61(4)
Fe(2)–N(6)	2.0954(17)	N(5)–Fe(2)–N(6)	116.52(7)
Fe(2)–N(7)	2.1104(18)	N(5)–Fe(2)–N(7)	114.16(7)
Fe(2)–N(8)	2.2463(16)	N(6)–Fe(2)–N(7)	113.99(7)
Fe(3)–Cl(3)	2.3099(6)	N(5)–Fe(2)–N(8)	76.69(6)
Fe(3)–Cl(4)	2.3245(7)	N(6)–Fe(2)–N(8)	76.62(6)
Fe(3)–Cl(5)	2.3110(6)	N(7)–Fe(2)–N(8)	76.87(7)
Fe(3)–Cl(6)	2.3049(6)	N(5)–Fe(2)–Cl(2)	105.13(5)
N(1)–Fe(1)–N(2)	110.23(6)	N(6)–Fe(2)–Cl(2)	105.03(5)
N(1)–Fe(1)–N(3)	115.32(7)	N(7)–Fe(2)–Cl(2)	99.51(5)
N(2)–Fe(1)–N(3)	119.66(6)	N(8)–Fe(2)–Cl(2)	176.38(5)

3. Results and discussion

From the equimolar reaction between $(H_3TPA)(ClO_4)_3$ and $Fe(P^nPr_3)_2Cl_2$ in MeCN, $[TPAFeCl]_2(FeCl_4)(MeCN)_2$ was isolated as greenish yellow crystals. The same reaction with $Fe(PEt_3)_2Cl_2$ also produced same product in a similar yield (Eq. (1)). On the contrary, the reaction of $(H_3TPA)(ClO_4)_3$ in the presence of triethylamine produced the mononuclear $TPAFeCl_2$ or dinuclear $[TPA_2Fe_2(\mu\text{-}Cl)_2](ClO_4)_2$ complex [19] (Eqs. (2) and (3)). The $TPAFeCl_2$ complex appears to dimerize under certain conditions with the formation of $[TPA_2Fe_2(\mu\text{-}Cl)_2]^{2+}$ and $(HNEt_3)Cl$, but the conditions that lead to the dimerization are not clear yet. Thus, although trialkylphosphine is not found from the product, the product formation seems to require presence of PR_3. Trialkylphosphine appears to have a role in preventing the pentacoordinated mononuclear $[TPAFeCl]^+$ complex from being dimerized to the dinuclear $[TPA_2Fe_2(\mu\text{-}Cl)_2]^{2+}$ complex, but we could not find any related examples of reaction product control by trialkylphosphine.

$$2(H_3TPA)(ClO_4)_3 + 3Fe(PR_3)_2Cl_2(R = Et,{}^nPr) \rightarrow [TPAFeCl]_2(FeCl_4) + 6(HPR_3)(ClO_4) \quad (1)$$

$$2(H_3TPA)(ClO_4)_3 + 2FeCl_2 + 6NEt_3 \rightarrow [TPA_2Fe_2(\mu\text{-}Cl)_2](ClO_4)_2 + 4(HNEt_3)(ClO_4) + 2(HNEt_3)Cl \quad (2)$$

$$(H_3TPA)(ClO_4)_3 + FeCl_2 + 3NEt_3 \rightarrow TPAFeCl_2 + 3(HNEt_3)(ClO_4) \quad (3)$$

From Eq. (1), formation of the five-coordinated $[TPAFeCl]^+$ complex seemed to be achieved by de-chlorination of the six-coordinated $TPAFeCl_2$ in the presence of excess $FeCl_2$, due to the thermodynamic stability of $FeCl_4^{2-}$

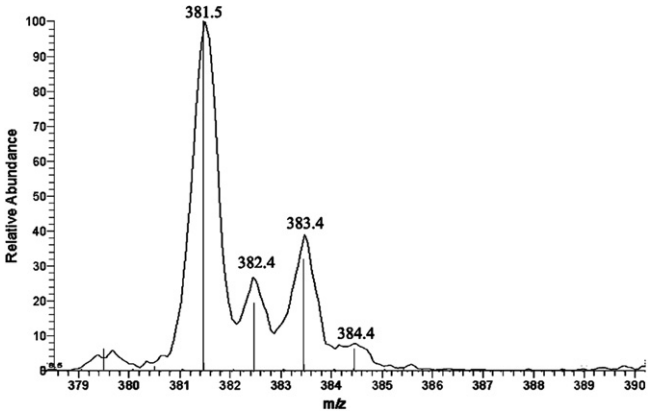


Fig. 2. ESI-MS spectrum of $[TPAFeCl]^+$. The bars represent theoretical isotope distributions of the $[TPAFeCl]^+$ ion peak.

under the reaction conditions. When the reaction proceeds in the presence of NEt_3, the synthesis of $TPAFeCl_2$ could be achieved with the formation of $(HNEt_3)(ClO_4)$. The ESI-MS spectrum of $[TPAFeCl]^+$ in MeCN showed only the peak corresponding to mononuclear complex at 381.5 *m/z* with the expected isotope distribution (Fig. 2).

Since the pyridyl groups of TPA are not parallel to the axial axis of Cl–Fe–N_{amino}, two different absolute configurations are possible from the crystallographic structure of the trigonal bipyramidal $[TPAFeCl]^+$ complex (Fig. 1). The configuration of the five-membered ring formed by the Fe, N_{pyr}, C_{pyr}, $C_{methylenyl}$ and N_{amino} atoms around the Cl–Fe–N_{amino} axial axis was used to determine the Δ and Λ stereoisomers. Formation of an enantiomeric mixture in the solid state seems to be due to the low transition state energy. Simple out-of-plane bending of the methylenyl groups is required for the transformation between the isomers. The average Fe–Cl bond distance is 2.3089(6) Å, which is slightly shorter than the average Fe–Cl distance of 2.3126(41) Å in the $[FeCl_4]^{2-}$ anion.[3] Two different Fe–Cl distances of 2.370(2) and 2.582(2) Å are reported for the dinuclear $[TPA_2Fe_2(\mu\text{-}Cl)_2]^{2+}$ complex and the octahedral $TPAFeCl_2$ complex also shows two significantly different Fe–Cl bond distances of 2.337(3) and 2.463(2) Å [15]. The Fe–Cl bond distances increase in the order $[TPAFeCl]^+ < TPAFeCl_2 < [TPA_2Fe_2(\mu\text{-}Cl)_2]^{2+}$.

It has been known that ferrous TPA complexes can have two different spin states depending on the terminal ligand. When two MeCN solvent molecules are coordinated $[TPAFe(MeCN)_2]^{2+}$ forms a low spin complex, but $TPAFe(OTf)_2$ and $TPAFeCl_2$ complexes form high spin complexes [16]. Fe–N distances and chemical shifts of ^1H NMR spectra have been used as characteristic parameters to determine the spin state [20]. The average bond distances of Fe–N_{pyr} and Fe–N_{amino} in $[TPAFeCl]^+$ are 2.1077(54) and 2.2483(20) Å, respectively. The average bond distances of Fe–N_{pyr} and Fe–N_{amino} in $TPAFeCl_2$ are 2.206(11) and 2.270(4) Å, respectively, and this complex was reported as a high spin complex. These are much longer than the Fe–N distances between 1.934(3) and 1.978(3) Å in the low spin $[TPAFe(MeCN)_2]^{2+}$ complex [16]. The corresponding Fe–N distances in the $[TPA_2Fe_2(\mu\text{-}Cl)_2]^{2+}$ complex are 2.165(5) and 2.231(3) Å, respectively. Hence, the Fe–N distances in the pentacoordinated $[TPAFeCl]^+$ complex are close in value to those of a high spin complex, and the Fe–Cl and Fe–N bond distances in $[TPAFeCl]^+$ are generally shorter than those of the dinuclear $[TPA_2Fe_2(\mu\text{-}Cl)_2]^{2+}$ complex. The ^1H NMR spectrum of the $[TPAFeCl]^+$ complex shows chemicals shifts between 145 ppm and −1 ppm, which is another evidence for a high spin complex. It is unlikely that the Δ and Λ stereoisomers show different NMR signals due to a low transition energy. The high spin $TPAFeCl_2$ complex is reported to show similar chemical shifts in the ^1H NMR spectrum [15], while the low spin $[TPAFe(MeCN)_2]^{2+}$ complex showed a narrow chemical shift distribution between 12 ppm and 8 ppm [16].

The trigonal bipyramidal coordination geometries between the two Δ and Λ isomers are a little different. The angles of N(1)–Fe(1)–Cl(1), N(2)–Fe(1)–Cl(1), N(3)–Fe(1)–Cl(1) and N(4)–Fe(1)–Cl(1) in the Δ isomer are found to be 103.50(5)°, 103.93(5)°, 101.67(5)° and 178.61(4)°, respectively. The Fe center is about 13° above the N_{pyr} trigonal plane and the Δ isomer is an axially distorted trigonal bipyramidal complex. On the contrary, Cl(2) in the Λ isomer is more bent towards the N(7) atom and the N(5)–Fe(2)–Cl(2), N(6)–Fe(2)–Cl(2), N(7)–Fe(2)–Cl(2) and N(8)–Fe(2)–Cl(2) angles are found to be 105.13(5)°, 105.03(5)°, 99.51(5)° and 176.38(5)°, respectively. Such a distortion is due to the van der Waals interaction between Cl(2) and H6B, a methylenyl proton of the Δ isomer, with a distance of 2.801 Å.

Cyclic voltammetric measurements of $[TPAFeCl]_2(FeCl_4)$ showed two quasireversible oxidation waves at 0.30 and 0.62 V, which can be assigned to the oxidation of the $FeCl_4^{2-}$ counter anion and $[TPAFeCl]^+$, respectively. In fact, the first oxidation of $FeCl_4^{2-}$ in 1,2-dichloroethane occurs at $E^{0'} = +0.30$ V versus SCE (or, −0.35 V versus Fc/Fc^+). In confirmation, the oxidation of $(^nBu_4N)_2FeCl_4$ in DMF was reported to be localized at −0.41 V (versus Fc/Fc+) [21] and the reduction of $FeCl_4^{2-}$ in MeCN was reported at −0.37 V (versus Fc/Fc^+) [22]. The oxidation of $[TPAFeCl]^+$ at 0.62 V (Fe^{II}/Fe^{III}) was much higher than that of $TPAFeCl_2$, which showed two reversible oxidation waves at 0.22 V and 0.40 V under the same conditions (Fig. 3). The reduction potential of $[TPAFeCl_2]^+$ was reported at −0.014 V [23]. Oxidation of the $[TPAFeCl]^+$ complex requires a higher oxidation potential and it seems the trigonal bipyramidal $[TPAFeCl]^+$ complex with one less chloride ligand is more stable to oxidation, compared to the octahedral $TPAFeCl_2$ complex. The oxidation potential difference between the $[TPAFeCl]^+$ and $TPAFeCl_2$ complexes is probably due to the more covalent

[3] The number in the parenthesis of average bond distances represents the larger of the individual standard deviations or the standard deviation from the mean, $\sigma = \mathrm{SQRT}[\Sigma_{i=1}{}^{n}(x_i - x)^2/n(n-1)]$, where x_i is an individual standard deviation, x is the average of individual standard deviations.

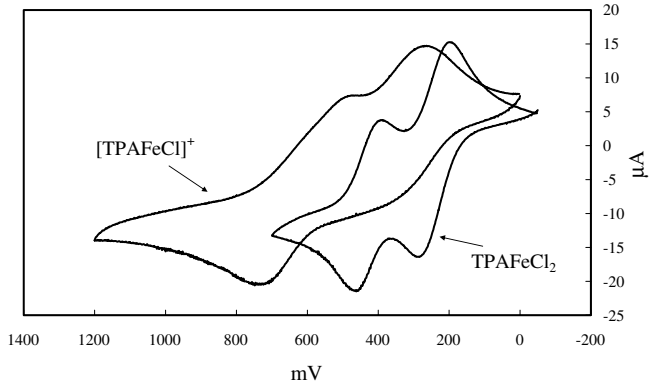


Fig. 3. Cyclic voltammograms of $[TPAFeCl]^+$ and $TPAFeCl_2$ in CH_2ClCH_2Cl at a scan rate of 100 mV/s. Supporting electrolyte: 0.1 M $^nBu_4NPF_6$.

Table 3
Relative UHF energies (in kcal/mol) for the spin-states projected from different UHF wavefunctions for the Δ and Λ isomers of the $[TPAFeCl]^+$, $[TPAFeCl_2]$ and $[TPAFe(MeCN)_2]^{2+}$ complexes

Spin-state	Δ $[TPAFeCl]^+$	Λ $[TPAFeCl]^+$	$TPAFeCl_2$	$[TPAFe(MeCN)_2]^{2+}$
$S=0$	44.89	46.14	33.79	0.00 (256.67)
$S=1$	18.03	19.11	25.34	31.41
$S=2$	0.00 (233.29)	0.00 (233.49)	0.00 (205.45)	36.38

The lowest spin states are denoted as of zero energy. The numbers in the parentheses show the energy differences of the one-electron oxidized complexes.

bond characteristics of the Fe–Cl bond of the $[TPAFeCl]^+$ complex and the coulombic effect of the charged $[TPAFeCl]^+$ complex [24].

The energies of $[TPAFeCl]^+$, $TPAFeCl_2$ and $[TPAFe(MeCN)_2]^{2+}$ at different ground spin states were obtained with the ZINDO/S Hamiltonian (Table 3). From the results, $TPAFeCl_2$ has the lowest energy at $S=2$ ground spin-state, while $[TPAFe(MeCN)_2]^{2+}$ has lowest energy at $S=0$ ground spin-state. Because the $TPAFeCl_2$ and $[TPAFe(MeCN)_2]^{2+}$ complexes have been reported as a high spin and a low spin complex, respectively, the ZINDO/S UHF calculation is considered valid for ground spin-state assignment of the $[TPAFeCl]^+$ complex. The energy of $[TPAFeCl]^+$ at $S=2$ is lower than the next accessible spin-state of $S=1$ by 19.11 kcal/mol. Besides spectroscopic and magnetic measurements, the results obtained from the calculations also suggest $S=2$ ground spin-state of the $[TPAFeCl]^+$ complex. The net charges of the Fe centers were found to be +0.184 and +0.144 for ground state $[TPAFeCl]^+$ and $TPAFeCl_2$, respectively. Thus, oxidation of the $[TPAFeCl]^+$ complex would requires a higher potential. The first oxidation potential waves for $[TPAFeCl]^+$ and $TPAFeCl_2$ are found at 0.62 V and 0.22 V, respectively. The energy differences between the ferrous and ferric complex were 233.39 kcal/mol and 205.45 kcal/mol for $[TPAFeCl]^+$ and $TPAFeCl_2$, respectively (Table 3). The oxidation potential of $[TPAFe(MeCN)_2]^{2+}$ in MeCN was reported at 0.62 V versus SCE [20]. The energy difference between $[TPAFe(MeCN)_2]^{2+}$ and $[TPAFe(MeCN)_2]^{2+}$ was the largest and was found at 256.67 kcal/mol from the calculations.

In summary, we have successfully synthesized and characterized the pentacoordinated trigonal bipyramidal $[TPAFeCl]^+$ complex. The $[TPAFeCl]^+$ complex is expected to produce high valent reactive species of pentacoordinated $[TPAFe^{IV}{=}O]^{2+}$ or dinuclear $[TPA_2Fe^{IV}_2(\mu\text{-}O)_2]^{4+}$ and the catalytic properties of the reactive species will be of a great interest.

Acknowledgement

This work was supported by the Korean Research Foundation Grant (KRF-2006-331-F00015) funded by the Korean Government (MOEHRD).

Appendix A. Supplementary material

CCDC 619185 contains the supplementary crystallographic data for $[TPAFeCl]_2(FeCl_4)(MeCN)_2$. These data can be obtained free of charge via http://www.ccdc.cam.ac.uk/conts/retrieving.html, or from the Cambridge Crystallographic Data Centre, 12 Union Road, Cambridge CB2 1EZ, UK; fax: (+44) 1223-336-033; or e-mail: deposit@ccdc.cam.ac.uk. Supplementary data associated with this article can be found, in the online version, at doi:10.1016/j.poly.2007.04.041.

References

[1] E. Wigner, E.E. Witmer, Z. Physik 51 (1928) 859.
[2] (a) J. Han, S.-Y. Kim, J. Jung, Y. Lim, J.-H. Ahn, S.-I. Kim, H.-G. Hur, Appl. Environ. Microbiol. 71 (2005) 5354;
(b) J.T. Groves, J. Inorg. Biochem. 100 (2006) 434;
(c) L. Que Jr., R.Y.N. Ho, Chem. Rev. 96 (1996) 2607.
[3] (a) S.O. Kim, C.V. Sastri, M.S. Seo, J. Kim, W. Nam, J. Am. Chem. Soc. 127 (2005) 4178;
(b) C.V. Sastri, M.S. Seo, M.J. Park, K.M. Kim, W. Nam, Chem. Commun. (2005) 1405;
(c) N.Y. Oh, Y. Suh, M.J. Park, M.S. Seo, J. Kim, W. Nam, Angew. Chem., Int. Ed. 44 (2005) 4235;
(d) J.-U. Rohde, S. Torelli, X. Shan, M.H. Lim, E.J. Klinker, J. Kaizer, K. Chen, W. Nam, L. Que Jr., J. Am. Chem. Soc. 126 (2004) 16750;
(e) A. Decker, J.-U. Rohde, L. Que Jr., E.I. Solomon, J. Am. Chem. Soc. 126 (2004) 5378;
(f) J. Kaizer, E.J. Klinker, N.Y. Oh, J.-U. Rohde, W.J. Song, A. Stubna, J. Kim, E. Münck, W. Nam, L. Que Jr., J. Am. Chem. Soc. 126 (2004) 472.
[4] M. Costas, M.P. Mehn, M.P. Jensen, L. Que Jr., Chem. Rev. 104 (2004) 939.
[5] (a) X. Shan, L. Que Jr., J. Inorg. Biochem. 100 (2006) 421;
(b) M.R. Bukowski, K.D. Koehntop, A. Stubna, E.L. Bominaar, J.A. Halfen, E. Münck, W. Nam, L. Que Jr., Science 310 (2005) 1000.
[6] (a) J.-U. Rohde, J.-H. In, M.H. Lim, W.W. Brennessel, M.R. Bukowski, A. Stubna, E. Münck, W. Nam, L. Que Jr., Science 299 (2003) 1037;
(b) E.J. Klinker, J. Kaizer, W.W. Brennessel, N.L. Woodrum, C.J. Cramer, L. Que Jr., Angew. Chem., Int. Ed. 44 (2005) 3690.

[7] (a) R. Mas-Balleste, M. Fujita, C. Hemmila, L. Que Jr., J. Mol. Cat., A. 251 (2006) 49;
(b) M.P. Jensen, S.J. Lange, M.P. Mehn, E.L. Que, L. Que Jr., J. Am. Chem. Soc. 125 (2003) 2113;
(c) K. Chen, K.M. Costas, J.H. Kim, A.K. Tipton, L. Que Jr., J. Am. Chem. Soc. 124 (2002) 3026.
[8] M.H. Lim, J.-U. Rohde, A. Stubna, M.R. Bukowski, M. Costas, R.Y.N. Ho, E. Münck, W. Nam, L. Que Jr., Proc. Natl. Acad. Sci. USA 100 (2003) 3665.
[9] N.Y. Oh, M.S. Seo, M.H. Lim, M.B. Consugar, M.J. Park, J.-U. Rohde, J. Han, K.M. Kim, J. Kim, L. Que Jr., W. Nam, Chem. Commun. (2005) 5644.
[10] J.-U. Rohde, A. Stubna, E.L. Bominaar, E. Münck, W. Nam, L. Que Jr., Inorg. Chem. 45 (2006) 6435.
[11] J.B. Mandel, C. Maricondi, B.E. Douglas, Inorg. Chem. 27 (1988) 2990.
[12] (a) J. Han, W. Nam, Bull. Kor. Chem. Soc. 25 (2004) 910;
(b) J. Han, M. Koutmos, S. Al-Ahmad, D. Coucouvanis, Inorg. Chem. 40 (2001) 5985.
[13] L.N. Mulay, E.A. Boudreaux (Eds.), Theory and Applications of Molecular Diamagnetism, Wiley-Interscience, New York, 1976.
[14] HYPERCHEM v. 7, Hypercube Inc., Gainesville, FL.
[15] D. Mandon, A. Machkour, S. Goetz, R. Welter, Inorg. Chem. 41 (2002) 5364.
[16] A. Diebold, K.S. Hagen, Inorg. Chem. 37 (1988) 215.
[17] Bruker, SMART and SAINT, Bruker AXS Inc, Madison, WI, USA, 1997.
[18] Bruker, SHELXTL. Version 5.10, Bruker AXS Inc., Madison, WI, USA, 1998.
[19] Y. Zang, H.G. Jang, Y.-M. Chiou, M.P. Hendrich, L. Que Jr., Inorg. Chim. Acta 213 (1993) 41.
[20] Y. Zang, J. Kim, Y. Dong, E.C. Wilkinson, E.H. Appelman, L. Que Jr., J. Am. Chem. Soc. 119 (1997) 4197.
[21] W. van den Berg, J.G.M. van der Linden, B.A. van Rieseen, B. de Bruin, W.P. Bosman, J.M.M. Smits, P.T. Beurskens, Inorg. Chem. 32 (1993) 3637.
[22] M.D. Vaira, F. Mani, P. Stoppioni, J. Chem. Soc., Dalton Trans. (1997) 1375.
[23] T. Kojima, R.A. Leising, S. Yan, L. Que Jr., J. Am. Chem. Soc. 115 (1993) 11328.
[24] G. Stupka, L. Gremaud, A.F. Williams, Helv. Chim. Acta 88 (2005) 487.

A considerable number of Schiff-base complexes have potential biological interest, being used as more or less successful models of biological compounds [8]. Transition metal complexes of Schiff-bases containing tetradentate ligands have also showed antimicrobial activity [9]. It has been reported that transition metal complexes with redox active ligands bearing sterically hindered salicylaldimines undergo one or two electron transfers [10]. Redox-active transition metal complexes that stabilize various oxidation states of the metal centers are of considerable interest, because of their potential significance as models of redox metalloenzymes [11,12] and as effective redox reactants or catalysts [13]. Furthermore, a recently emerged field of research concerns the use of redox-active metal complexes, for instance, copper(II) complexes with salen and related Schiff-bases, as synthetic chemical nucleases or DNA damaging agents [14]. For a specific metal ion, the main factors that determine the redox properties include the nature and the arrangement of the donor atoms around the metal bonding site and the nature and the position of the substituents. Among the various ligands, many Schiff-bases derived from salicylaldehyde and related aromatic aldehydes have been found to stabilize copper(I), with respect to the Cu(II/I) potential [15]. Although the redox behavior of a number of metal complexes containing Schiff-base ligands have been reported, the electrochemical properties of such complexes are not completely clear [16–18]. Several researches have proposed that the redox potential of macrocyclic and Schiff-base complexes is directly related to many of the biologically relevant chemical characteristics of the entire complex, e.g. dioxygen binding ability and nucleophilicity [19]. Thus, there has been a strong interest in determining thermodynamically meaningful redox potentials of copper Schiff-base complexes and in understanding the relationship between these potentials and the detailed structure of the Schiff-base ligand [20].

In the present paper we report the synthesis and characterization of two new Schiff- base ligands (L^1 and L^2, where L^1 = *N*-*N*′-bis(3,5-di-*tert*-butylsalicylaldimine)-1,4-cyclohexane bis(methylamine) and L^2 = *N*-*N*′-bis(3,5-di-*tert*-butylsalicylaldimine)-1,8-diamino-3,6-dioxaoctane) involving N_2O_2 and N_2O_4 donor sites, and their copper(II) and cobalt(II) complexes. It is known that the combination of electrochemical and spectroelectrochemical methods provides a power tool to reveal the complementary nature of the molecular structure and electrochemical information of the electroactive molecules [21–26]. Very little work has been done on spectroelectrochemical characterization of Schiff-base metal complexes [27,28]. The aim of this study is to establish a comparative electro-spectrochemical study on the new Schiff-base copper and cobalt complexes based on the different molecular structures with N_2O_2 and N_2O_4 donor sites. In this study, the different binding modes of the new Schiff-base ligands for complexing with some transition metals such as copper and cobalt were confirmed by electrochemical and thin-layer spectroelectrochemical techniques, in addition to other spectroscopic methods such as IR, magnetic susceptibility, ^1H and ^{13}C NMR.

2. Experimental

2.1. Material and methods

Unless otherwise stated, all chemicals were of analytical reagent-grade and were purchased from Sigma, Merck and Across Organics. 3,5-Di-*tert*-butyl-2-hidroxybenzaldehyde (3,5-DTB) was synthesized according to the literature procedure [29a]. *N*-*N*′-Bis(3,5-di-*tert*-butylsalicylaldimine)-1,4-cyclohexane bis(methylamine) (L^1) and *N*-*N*′-bis(3,5-di-*tert*-butylsalicylaldimine)-1,8-diamino-3,6-dioxaoctane (L^2) were prepared here for the first time. The elemental analyses and ^1H NMR and ^{13}C NMR spectra were carried out in the laboratory of Tubitak (Scientific and Technical Research Council of Turkey), IR spectra were recorded on a Perkin Elmer Spectrum RXI FT-IR Spectrometer as KBr pellets, Magnetic Susceptibilities were determined on a Sherwood Scientific Magnetic Susceptibility Balance (Model MK1) at room temperature (20 °C) using $Hg[Co(SCN)_4]$ as a calibrant; diamagnetic corrections were calculated from Pascal's constants [29b]. Thermogravimetric (TGA) studies were recorded on a Seteram Labsys TG-16 thermobalance. UV–Vis spectra were recorded on an Agillent Model 8453 diode array spectrophotometer. Cyclic voltammograms (CV) were carried out using CV measurements with a Princeton Applied Research Model 2263 potentiostat controlled by an external PC. A three electrode system (BAS model solid cell stand) was used for CV measurements in DMSO and consisted of a 2 mm sized platinum disc electrode as the working electrode, a platinum wire counter electrode and an Ag/AgCl reference electrode. The reference electrode was separated from the bulk solution by a fritted-glass bridge filled with the solvent/supporting electrolyte mixture. The ferrocene/ferrocenium couple (Fc/Fc^+) was used as an internal standard, but all potentials in the paper are referenced to the Ag/AgCl reference electrode. Solutions containing the complexes were deoxygenated by a stream of high purity nitrogen for at least 5 min before running the experiment, and the solution was protected from air by a blanket of nitrogen during the experiment. Controlled potential electrolysis (CPE) was performed with a Princeton Applied Research Model 2263 potentiostat/galvanostat. A BAS model electrolysis cell with a fritted glass to separate the cathodic and anodic portions of the cell was used for bulk electrolysis. The sample and solvent were placed into the electrolysis cell under nitrogen. UV–Vis spectroelectrochemical experiments were performed with a home-built thin-layer cell that utilized a light transparent platinum gauze working electrode [30]. Potentials were applied and monitored with a Princeton Applied Research Model 2263 potentiostat. Time-resolved UV–Vis spectra were recorded on an Agillent Model 8453 diode array spectrophotometer.

2.2. Synthesis of the ligands L^1 and L^2

The ligands *N*-*N*′-bis(3,5-di-*tert*-butylsalicylaldimine)-1,4-cyclohexane bis(methylamine) (L^1) and *N*-*N*′-bis(3,5-di-*tert*-butylsalicylaldimine)-1,8-diamino-3,6-dioxaoctane (L^2) were synthesized by the reaction of 6 mmol 3,5-di-*tert*-butyl-2-hidroxybenzaldehyde in 20 ml absolute ethanol with 3 mmol 1,4-cyclohexane bis(methylamine) and 3 mmol 1,8-diamino-3,6-dioxaoctane in 10 ml ethanol, respectively. Also, 3–4 drops of acetic acid were added. The mixtures were refluxed for 3 h, followed by cooling to room temperature. The crystals were filtered in vacuum, then the products were recrystallized from ethanol. The products are soluble in common solvents such as $CHCl_3$, DMF and DMSO.

For ligand L^1: Color: yellow; mp: 194 °C; yield (%): 78; *Anal*. Calc. for $C_{38}H_{58}N_2O_2$: C, 79.44; H, 10.10; N, 4.88. Found: C, 79.31; H, 10.15; N, 4.74%. ^{1}H NMR ($CDCl_3$, TMS, δ ppm): 13.78 [(O*H*), s, 2H], 8.30 and 8.33 [(C*H*=N), d, 2H, ($J = 14.8$ Hz)], 1.32 [(C–CH_3), s, 18H], 1.45 [(C–CH_3), s, 18H], 7.05 [(Ar-*H*), s, 2H], 7.35 [(Ar-*H*), s, 2H], 3.46 and 3.57 [(N–CH_2), d, 4H, ($J = 5.6$ Hz and 6.8 Hz)], 1.56–1.91 [(Cyc-CH_2), m, 8H], 1.08–1.13 [(Cyc-C*H*–), m, 2H]. ^{13}C NMR ($CDCl_3$, TMS, δ ppm): $C_{1,7}$ (29.73), $C_{2,6}$ (31.82 and 31.00), C_3 (126.78), C_4 (136.86), C_5 (125.91 and 125.89), C_8 (158.43), C_9 (118.06 and 118.04), C_{10} (139.95 and 139.91), C_{11} (166.00 and 166.03), C_{12} (66.63 and 63.79), C_{13} (39.34 and 36.70), C_{14} (35.28 and 34.35). IR (KBr pellets, cm^{-1}): 3410 *v*(OH), 2957, 2865 *v*(Aliph-H), 1633 *v*(C=N), 1175 *v*(C–O). UV–Vis [in C_2H_5OH λ_{max}/nm ($\log\varepsilon$), (*: shoulder peak)]: 262 (3.82), 331 (3.15), 419* (2.32).

For ligand L^2: Color: yellow; mp: 106 °C; yield (%): 71; *Anal*. Calc. for $C_{36}H_{56}N_2O_4$: C, 74.48; H, 9.65; N, 4.82. Found: C, 73.76; H, 10.03; N, 4.46%. ^{1}H NMR ($CDCl_3$, TMS, δ ppm): 13.66 [(O*H*), s, 2H], 8.35 [(C*H*=N), s, 2H], 7.02 [(Ar-*H*), s, 2H], 7.36 [(Ar-*H*), s, 2H], 3.71 and 3.74 [(Ar-*H*), d, 8H], 3.63 [(N–CH_2), s, 4H], 1.31 [(C–CH_3), s, 18H], 1.45 [(C–CH_3), s, 18H]. IR (KBr pellets, cm^{-1}): 3413 *v*(OH), 2960, 2876 *v*(Aliph-H), 1633 *v*(C=N), 1173 *v*(C–O), 1139 *v*(C–O–C). UV–Vis [in C_2H_5OH λ_{max}/nm ($\log\varepsilon$), (*: shoulder peak)]: 251* (4.19), 262 (5.02), 329 (4.02), 414* (2.54).

2.3. Synthesis of the metal complexes

2 mmol of the ligands L^1 and L^2 were dissolved in 40 ml absolute methanol and 2 mmol $Cu(Ac)_2 \cdot 2H_2O$ and $Co(Ac)_2 \cdot 4H_2O$ in 20 ml methanol were mixed. The mixtures were heated at 50 °C with constant stirring until they were concentrated. The mixtures were evaporated to a volume of 15–20 ml in vacuum and left to cool to room temperature. The compounds were precipitated after adding 5 ml ethanol. The products were filtered in vacuum and washed with a small amount of methanol and water. The products were recrystallized from methanol. All the complexes are stable at room temperature and soluble in solvents such as $CHCl_3$, DMF and DMSO.

[Co(L^1)]: Color: dark yellow; mp: 214 °C; yield (%): 67; Λ_M: 1.2 Ω^{-1} cm^2 mol^{-1}; $\mu_{eff} = 3.61$ BM. *Anal*. Calc. for $C_{38}H_{56}N_2O_2Co$: C, 72.26; H, 9.19; N, 4.44. Found: C, 72.58; H, 8.94; N, 4.38%. IR (KBr pellets, cm^{-1}): 2957, 2866 *v*(Aliph-H), 1619 *v*(C=N), 1167 *v*(C–O), 488 (M–O), 544 (M–N). UV–Vis [in $CHCl_3$ λ_{max}/nm ($\log\varepsilon$), (*: shoulder peak)]: 227* (3.70), 263 (4.56), 330* (4.11).

[Cu(L^1)]: Color: brown; mp: 232 °C; yield (%): 70; Λ_M: 3.5 Ω^{-1} cm^2 mol^{-1}; $\mu_{eff} = 1.89$ BM. *Anal*. Calc. for $C_{38}H_{56}N_2O_2Cu$: C, 71.75; H, 8.81; N, 4.40. Found: C, 71.98; H, 8.65; N, 4.32%. IR (KBr pellets, cm^{-1}): 2956, 2861 *v*(Aliph-H), 1618 *v*(C=N), 1170 *v*(C–O), 493 (M–O), 537 (M–N). UV–Vis [in $CHCl_3$ λ_{max}/nm ($\log\varepsilon$)]: 286 (4.25), 328 (4.23), 380 (4.17).

[Co(L^2)]: Color: dark yellow; mp: 123 °C; yield (%): 65; Λ_M: 1.8 Ω^{-1} cm^2 mol^{-1}; $\mu_{eff} = 3.76$ BM. *Anal*. Calc. for $C_{36}H_{54}N_2O_4Co$: C, 67.76; H, 8.47; N, 4.39. Found: C, 67.13; H, 8.82; N, 4.01%. IR (KBr pellets, cm^{-1}): 2955, 2866 *v*(Aliph-H), 1615 *v*(C=N), 1171 *v*(C–O), 1124 *v*(C–O–C), 487 and 465 (M–O), 546 (M–N). UV–Vis [in $CHCl_3$ λ_{max}/nm ($\log\varepsilon$), (*: shoulder peak)]: 233* (5.32), 248 (4.81), 375* (4.24), 876* (1.66).

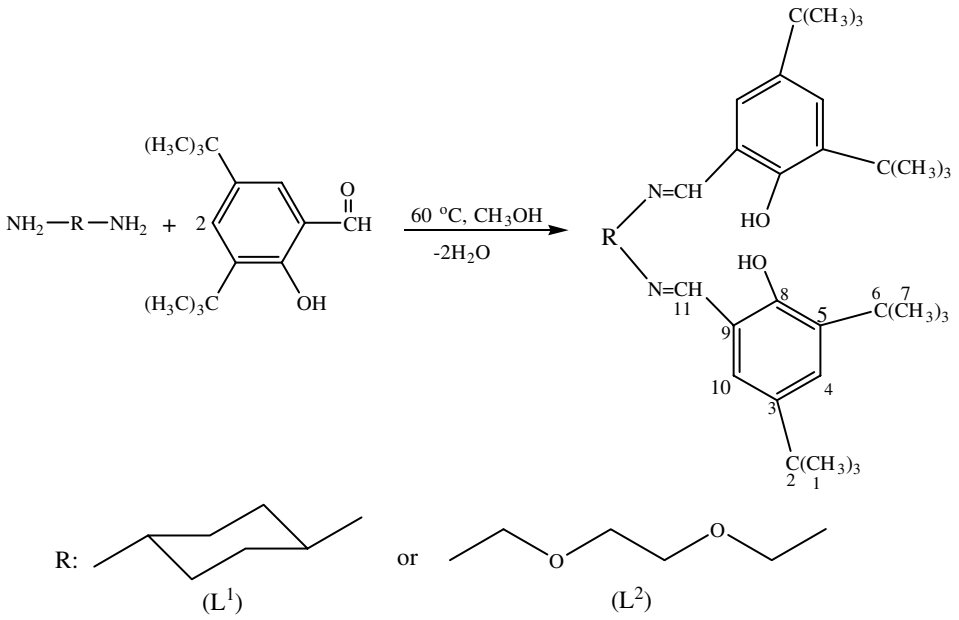
[Cu(L^2)]: Color: black; mp: 195 °C; yield (%): 68; Λ_M: 3.9 Ω^{-1} cm^2 mol^{-1}; $\mu_{eff} = 1.95$ BM. *Anal*. Calc. for $C_{36}H_{54}N_2O_4Cu$: C, 67.34; H, 8.41; N, 4.36. Found: C, 68.02; H, 8.76; N, 4.12%. IR (KBr pellets, cm^{-1}): 2953, 2865 *v*(Aliph-H), 1625 *v*(C=N), 1173 *v*(C–O), 1112 *v*(C–O–C), 490 and 466 (M–O), 534 (M–N). UV–Vis [in $CHCl_3$ λ_{max}/nm ($\log\varepsilon$), (*: shoulder peak)]: 276* (5.24), 321 (4.87), 364* (2.27), 443* (2.29), 665 (2.28)

3. Results and discussion

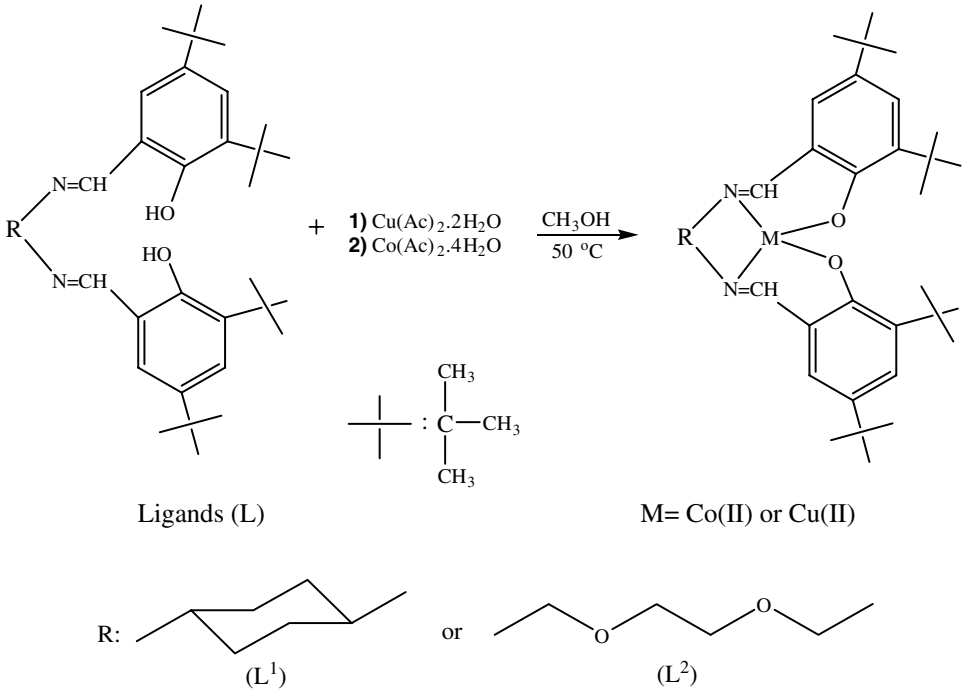
3.1. Synthesis

The reaction for the synthesis of the ligands is given in Scheme 1. The first step is the synthesis of *N*-*N*′-bis(3,5-di-*tert*-butylsalicylaldimine)-1,4-cyclohexane bis(methylamine) (L^1) and *N*-*N*′-bis(3,5-di-*tert*-butylsalicylaldimine)-1,8-diamino-3,6-dioxaoctane (L^2) from the reaction of 3,5-di-*tert*-butyl-2-hidroxybenzaldehyde with 1,4-cyclohexane bis(methylamine) and 1,8-diamino-3,6-dioxaoctane, respectively. The second step is the synthesis of [CuL^1], [CuL^2] and [CoL^1], [CoL^2] complexes from the reaction of *N*-*N*′-bis(3,5-di-*tert*-butylsalicylaldimine)-1,4-cyclohexane bis(methylamine) (L^1) and *N*-*N*′-bis(3,5-di-*tert*-butylsalicylaldimine)-1,8-diamino-3,6-dioxaoctane (L^2) with the corresponding metal salts (Scheme 2).

The metal to ligand ratios of the Co(II) and Cu(II) complexes were found to be 1:1. Infrared spectra of ligands and their complexes were recorded in KBr pellets from 4000 to 400 cm^{-1}. The IR spectra of the ligands are characterized by the appearance of a band at 3410 cm^{-1} for L^1 and 3413 cm^{-1} for L^2 due to the *v*(O–H) groups [31]. In the spectra of the Cu(II) and Co(II) complexes, these bands disappear. The vibrations of the azomethine groups of the free ligands are observed at 1633 cm^{-1}. In the case of



Scheme 1. Synthetic route to the ligands.



Scheme 2. Synthetic route to the complexes.

the complexes, these bands are shifted to the lower frequencies, indicating that the nitrogen atom of the azomethine groups is coordinated to the metal ion, as expected [32]. The bands at 1175 cm^{-1} for L^1 and 1173 cm^{-1} for L^2 are ascribed to the phenolic C–O stretching vibrations. These bands are shifted to lower frequencies due to O-metal coordination [33]. Additionally, a peak observed at 1139 cm^{-1} in the free ligand (L^2) has been assigned to the etheric C–O–C stretching. On complexation, this band is shifted to a lower frequency range 1124–1112 cm^{-1}, indicating coordination through the etheric oxygen. The coordination of the azomethine nitrogen is confirmed with the presence of a new band between 534 and 546 cm^{-1}, assignable to ν(M–N) for the Co(II) and Cu(II) complexes [34]. The coordination of the azomethine oxygen group is confirmed with the presence of a new band at between 465 and 493 cm^{-1}, assignable to ν(M–O) for the Co(II) and Cu(II) complexes.

The ^1H NMR and ^{13}C NMR spectra of the ligands L^1 and L^2 were recorded in $CDCl_3$ solution at 400 MHz. The ^1H NMR spectrum of L^2 and the ^{13}C NMR spectrum of L^1 are given in Fig. 1. The ^1H NMR spectra of the ligands L^1 and L^2 showed one singlet peak at $\delta = 13.78$ ppm and $\delta = 13.66$ ppm due to –OH protons, respectively. Also, the L^1 and L^2 ligands indicate the presence of two equivalent azomethine groups. Due to the equivalent chemical environments, two signals for L^1 at 8.30 and 8.33 ppm (d, 2H) and one signal for L^2 at 8.35 ppm (s, 2H) are recorded for the azomethine protons [35]. However, the protons of the *tert*-butyl groups of the ligands exhibit two sharp singlet peaks between 1.31 and 1.45 ppm, indicating that the *tert*-butyl protons of these compounds are magnetically non-equivalent [36,37]. On the other hand, the ^1H and ^{13}C NMR spectra of the ligand L^1 showed signals at 166.07 and 166.03 ppm belonging to C_{11}, 66.63 and 63.79 ppm belonging to C_{12}, CH=N (8.30 and 8.33 ppm) and N–CH_2 (3.53–3.57 and 3.45–3.46 ppm). These carbon and proton resonances have a double resonance indicating that ligand (L^1) has *cis–trans* isomerism [38]. The isomer ratio was found to be 60% *cis*-isomer and 40% *trans*-isomer from the ^1H and ^{13}C NMR data. The NMR data of the ligands and their complexes are given in Section 2. Since the Co(II) and Cu(II) complexes are paramagnetic nature, their NMR spectra could not be obtained.

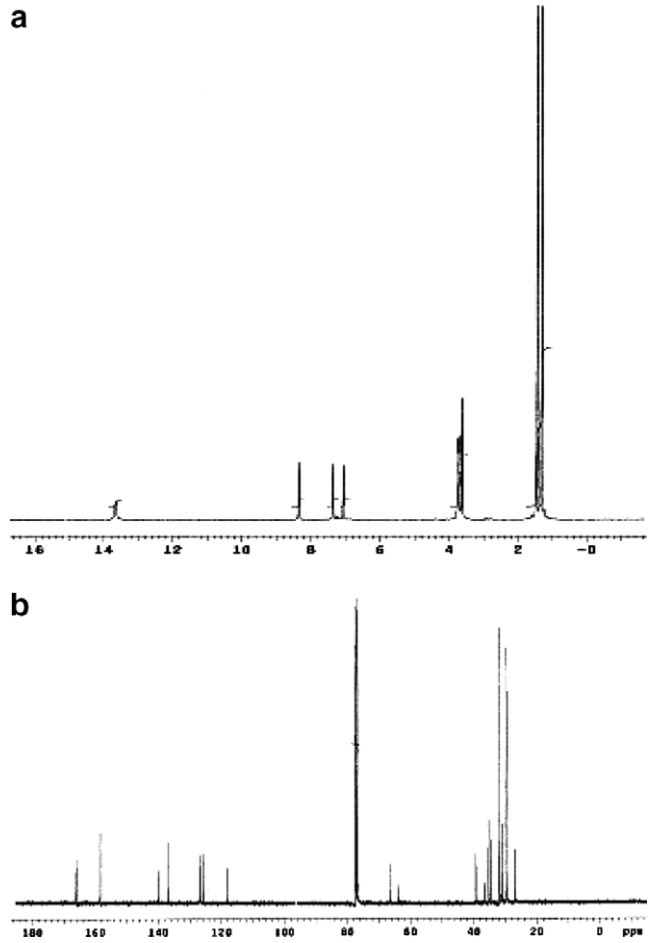


Fig. 1. The ^1H NMR spectrum of L^2 (a); the ^{13}C NMR spectrum of L^1 (b).

The electronic spectra of the ligands and their metal complexes were recorded in C_2H_5OH for the ligands and in $CHCl_3$ for the complexes. The bands below 331 nm are attributable to intramolecular $\pi \rightarrow \pi^*$ and $n \rightarrow \pi^*$ transitions. The very intense bands at low wavelengths have been assigned to charge transfer transitions [39,40], for metal complexes with aromatic bridges these bands occur at longer wavelengths, as expected from the higher aromaticity of the ligands which eases delocalization of electron density.

3.2. Magnetic measurements

Room temperature magnetic moments of the Cu(II) complexes are between 1.89 and 1.95 BM, which is typical for mononuclear compounds of Cu(II) with a $S = 1/2$ spin-state and does not indicate antiferromagnetic coupling of the spins at this temperature. The room temperature magnetic moment of between 3.61 and 3.76 BM determined for the Co(II) complexes are close to the spin-only magnetic moments ($\mu = 3.87$ BM) for three unpaired electrons.

3.3. Thermal analysis

The thermal stability of the ligands and the Co(II) and Cu(II) metal complexes was investigated by TGA. The TGA curves were obtained at a heating rate of 5 and 10 °C min^{-1} under a nitrogen atmosphere over the 20–900 °C range, and they show that L^1 and L^2 and the Cu(II) and Co(II) complexes are thermally stable up to 198 for L^1, 164 for L^2, 240 for [Cu(L^1)], 214 for [Co(L^1)], 174 for [Cu(L^2)] and 189 for [Co(L^2)] °C. As a results of the thermal analysis, the most thermally stable complex is [Cu(L^1)], whereas the least stable complex is [Cu(L^2)] [35c].

3.4. Molar conductivity

The molar conductivities (Λ_M) of the Cu(II) and Co(II) metal complexes in DMF (dimethyl formamide) at 10^{-3} M were found to be in the range 1.2–3.9 Ω^{-1} cm^2 mol^{-1}. These low values indicate that all of the metal complexes are non-electrolytes due to no counter ions in the proposed structures of the Cu(II) and Co(II) metal complexes (Scheme 2) [35b,35c]. The difference in the number of protons in the Cu(II) and Co(II) metal complexes probably points to the difference in size of the +2 oxidation state of these metal ions, with the different polarizing ability due to the different sizes. Thus, the electrical conductivities of the Cu(II) complexes are higher than the Co(II) metal complexes [41,42].

3.5. Electrochemistry

The electrochemical behavior of [Cu(L^1)], [Cu(L^2)] and [Co(L^1)], [Co(L^2)] was investigated using the cyclic

Table 1
The electrochemical potentials of the copper and cobalt complexes

Complexes	Electrolyte	Solvent	M(II)/M(I) E_{pc}^{b}	ΔE^{a} (V)	M(II)/M(III) E_{pa}^{b}	ΔE^{a} (V)
[Cu(L$_1$)]	TBAP	CH_2Cl_2			1.40	
[Cu(L$_2$)]	TBAP	CH_2Cl_2	−1.07	358	1.09	
[Co(L$_1$)]	TBAP	CH_2Cl_2			0.859	
[Co(L$_2$)]	TBAP	CH_2Cl_2			0.348	248

[a] $\Delta E_p = (E_{pa} - E_{pc})$.
[b] Anodic peak potential and cathodic peak potential for the irreversible process.

voltammetric (CV) technique in CH_2Cl_2 solution containing 0.1 M TBAP. The data obtained in this work are listed in Table 1. Fig. 2 shows the CVs of [Cu(L^1)] and [Cu(L^2)] at 0.100 V s^{-1} scan rate. As can be seen from Fig. 2a, [Cu(L^1)] displayed one oxidation wave in CH_2Cl_2 containing the Ag/AgCl electrode system. The anodic peak potential for the oxidation process displayed at $E_{pa} = 1.40$ V versus Ag/AgCl. The oxidation process has a large value for the cathodic to anodic peak separation, and deviates from unity for the peak cathodic and peak anodic current ratios, i_{pc}/i_{pa}, at 0.100 V s^{-1} scan rate. The results show that the redox process is irreversible in the scan range of 0.025–0.250 V s^{-1} in CH_2Cl_2 solution, and can be indicative of a decomposition reaction occurring under the CV conditions. As can be seen from Fig. 2b, [Cu(L^2)] exhibited a totally irreversible oxidation process without a corresponding anodic wave at 0.100 V s^{-1} scan rate, and its anodic potential displayed at $E_{pa} = 1.09$ V versus Ag/AgCl. On reverse scan, a cathodic wave (II′) appeared at 0.200 V following the oxidation potential (II), which was assigned to an EC process. [Cu(L^2)] also showed one reduction process (I_c) at $E_{pc} = -1.07$ V. This reduction wave is an irreversible process because of the large value of the cathodic to the anodic peak separation ($\Delta E = 358$ V at 0.100 V s^{-1} scan rate), even if it has the corresponding anodic wave (I_a). The results reveal that the [Cu(L^1)] and [Cu(L^2)] complexes exhibit different electrochemical behavior under the same experimental conditions. It is well known from the literature [43] that redox potentials of Schiff-base complexes are markedly dependent on the ligand, solvent and geometry of the complexes. Electron-withdrawing substituents on the ligands shift the redox potential positively, whereas electron-donating groups have the opposite effect. On the other hand, the oxidation potentials are also dependent on the imine bridge of the Schiff-base, with the more positive potentials observed for complexes with aromatic bridges. Two possible explanations can be invoked to explain this behavior. (i) An increase in unsaturation that would ease electron-density delocalization from the metal to the ligand, and (ii) higher rigidity of the ligand, imparted by the aromatic bridge, that would hinder a contraction of the hole cavity. Moreover, the redox potentials show a cathodic shift with an increase in the donor capacity of the solvent. For example, oxidation of square-planar metal(II) complexes to metal(III) takes place with a concomitant increase in coordination number, as these latter complexes are normally six-coordinate. The cathodic shift in the redox potentials ongoing from DMF to DMSO is attributed to the stronger axial bonds that are established between the metal(III) center and the molecules of the better donor, and that help to stabilize the high oxidation state of the metal [43a]. The size of the coordination cavity in the complexes, and the geometric requirements and the size of the metal ions in different oxidation states also affect the redox potential [44]. For example, a tetrahedral structure of the Schiff-base complex enhances the ease of reduction of Cu(II) to Cu(I) compared to a planar coordination about the copper atom [43e]. In our case, the experiments

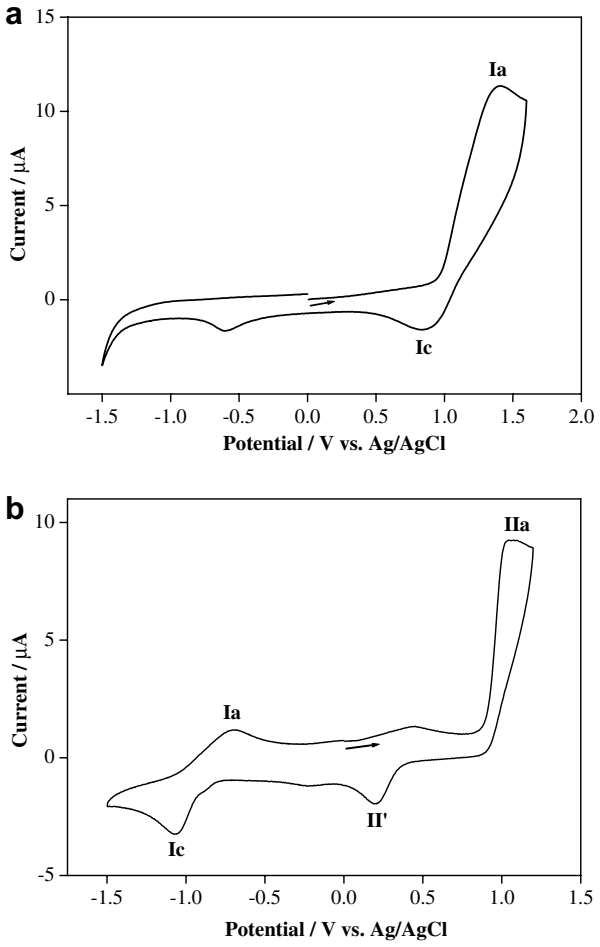


Fig. 2. Cyclic voltammograms of [Cu(L^1)] (a); [Cu(L^2)] (b) in CH_2Cl_2 solution containing 0.1 M TBAP. Scan rates = 0.100 V s^{-1}.

were carried out in CH_2Cl_2 solution so any solvent effect can be eliminated on comparing the electrochemical behavior. Taking into account substituent effects for the two copper Schiff-base complexes, both cyclohexane and dioxaoctane bridged on the imine group of the Schiff-base can be considered as weak electron-donating groups, thus a large potential shift could not be expected for these copper complexes. However, the structural differences of the [Cu(L^1)] and [Cu(L^2)] complexes should be taken into account for the different electrochemical behavior of the complexes under the same experimental conditions. Because the CV of [Cu(L^2)] showed a lower oxidation potential compared to [Cu(L^1)], it was seen that the oxidation wave (II) of [Cu(L^2)] was accompanied by an EC process (II′), which was not observed for [Cu(L^1)]. Also, [Cu(L^2)] gave a reduction process but [Cu(L^1)] did not. If the anodic scan was limited to the potential $E = 0.6$ V, the EC process was not observed. These results indicate that the Cu(II) ion in [Cu(L^2)] is coordinated by N_2O_4 donor sites where two complementary lone pairs come from dioxaoctane binding on the imine group of the Schiff-base responsible for this binding mode of the ligand. On the other hand, [Cu(L^1)] presents a square-planar structure with four donor atoms, as observed for several Schiff-base complexes with N_2O_2 donor groups. In the case of [Cu(L^2)], the oxidation of Cu(II) (d^9) to Cu(III) (d^8) involves a drastic decrease in the metal radius and a conformation change from octahedral to square-planar. This structural reorganization of the oxidized complex resulted in the observation of the EC process. This process (II′), following the oxidation wave (II) in the CV of the complex, exhibited re-reduction of the oxidized copper ion (Cu(III) → Cu(II)) where the complex changed into its original form. The reduction process was observed for octahedral [Cu(L^2)] complex but not for the square-planar [Cu(L^1)] complex. The reduction of Cu(II) (d^9) to Cu(I) (d^{10}) involves a drastic increase in the metal radius, so [Cu(L^2)] favors its original geometry. Therefore, no EC process was observed following the reduction process (Ic). The fact that [Cu(L^2)] exhibits a reduction process can be attributed to the different geometry of the complex compared to [Cu(L^1)].

The electrochemical behavior of the [Co(L^1)] and [Co(L^2)] complexes is presented in Fig. 3. On the positive scan, [Co(L^1)] gave one oxidation wave without a corresponding cathodic wave (Ia) (Fig. 2a). The process is totally irreversible and its anodic peak potential is at $E_{pa} = 0.859$ V versus Ag/AgCl. On the other hand, [Co(L^2)] exhibited one oxidation wave with a corresponding cathodic wave. This oxidation process is diffusion controlled with the anodic current function ($I_{pa}/v^{1/2}$) independent of the scan rate (v) over the scan range 0.025–0.250 V s^{-1}. The peak potentials separation is $\Delta E_p = 248$ mV and the ratio of cathodic to anodic peak current deviates from unity. So the oxidation process is irreversible at all sweep rates in the range 0.025–0.250 V s^{-1}. Both oxidation processes for [Co(L^1)] and

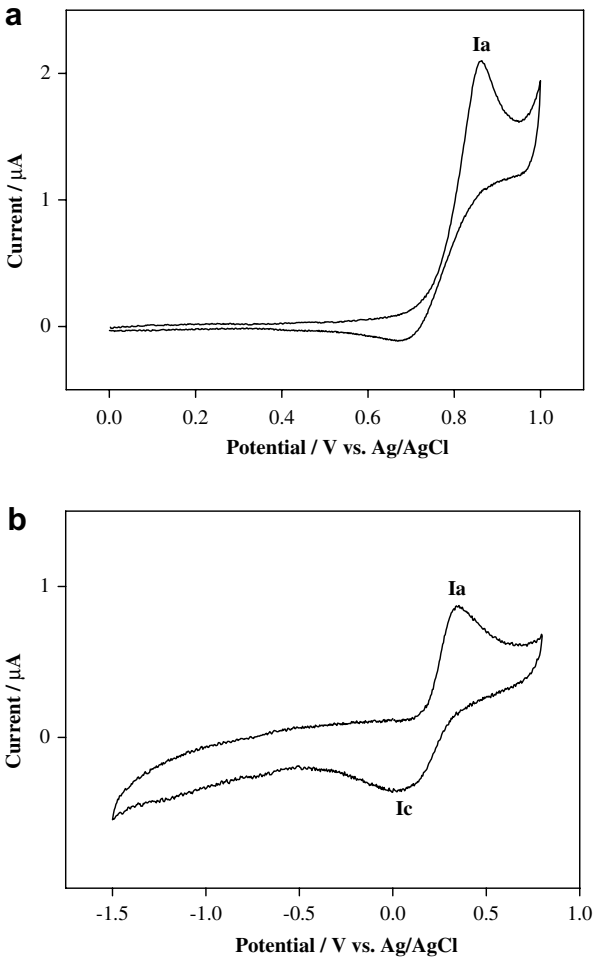


Fig. 3. Cyclic voltammograms of [Co(L^1)] (a); [Co(L^2)] (b) in CH_2Cl_2 solution containing 0.1 M TBAP. Scan rates = 0.100 V s^{-1}.

[Co(L^2)] are based on the cobalt center and are assign to the Co(II) → Co(III) process. The electrochemical behavior of [Co(L^2)] differs from that of [Co(L^1)] under the same experimental conditions due to their different structures, as observed for the copper complexes. The oxidation potential of [Co(L^2)] cathodically shifts compared with that of [Co(L_1)]. An EC process following the oxidation wave (II) in the CV of the [Co(L_2)] was not observed, probably due to favoring an octahedral structure in the case of Co(III) (d^6), which indicates no structural change during the oxidation process.

3.6. UV–Vis spectra of the electro-oxidized and electro-reduced complexes

The spectroelectrochemical behavior of the copper and cobalt complexes was investigated using an *in situ* spectroelectrochemical technique including chronoamperometry and UV–Vis spectroscopy in CH_2Cl_2 solution containing 0.2 M TBAP. The UV–Vis spectral changes for the reduced and oxidized species of the corresponding complexes were obtained in a thin-layer cell with the applied potentials.

The absorption spectra of the neutral complexes and their electrochemically generated species are given in Figs. 4–6. The convenient applied potentials values for the *in situ* spectroelectrochemical experiment were determined for each process by taking CVs of the complexes in the thin-layer cell.

Fig. 4a shows the changes of the electronic spectrum of [Cu(L^1)] that is accompanied by the oxidation process in the thin-layer cell. Well-defined isosbestic points are observed at $\lambda = 321$ and 328 nm, confirming that the electrode reaction proceeds in a quantitative fashion and therefore the absence of any coupled chemistry. The band at 327 nm, assigned to the Cu(II) $d_{x^2-y^2}$-to-phenolate (π) LMCT transition for the neutral copper complex [Cu(L^1)], changed into two new bands. The first, with higher intensity, shifted to a lower energy ($\lambda = 362$ nm) and the second, also with higher intensity, appeared at a higher energy (293 nm) as a result of removing one electron from the copper(II) ion in the complex. The one electron oxidation results in a Cu(II) (d^9) → Cu(III) (d^8) process

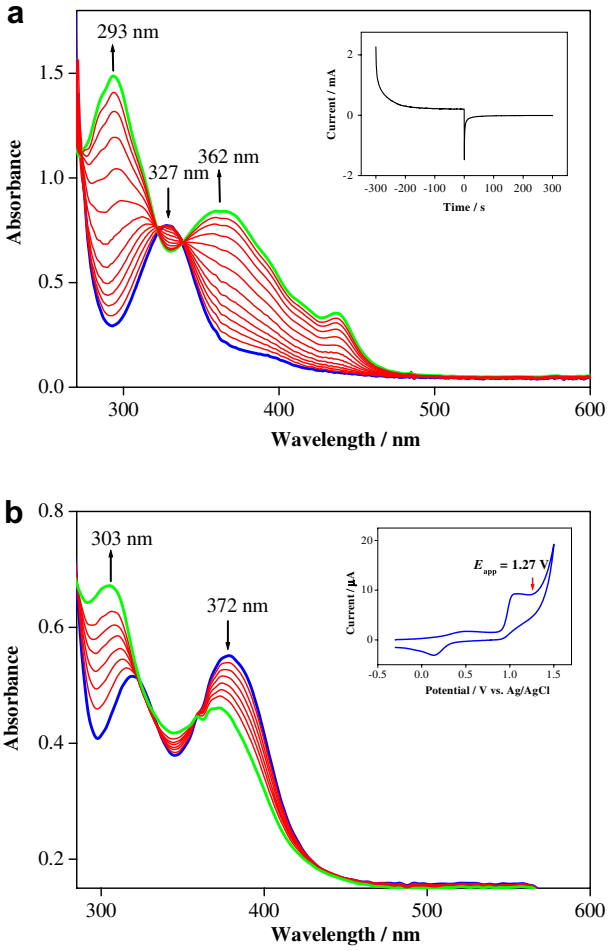


Fig. 4. Time-resolved UV–Vis spectral changes of [Cu(L^1)] (a); [Cu(L^2)] (b) during the oxidation at $E_{app} = 1.27$ V in CH_2Cl_2 solution containing 0.2 M TBAP. For (a), the inset figure shows chronoamperometry of [Cu(L^1)]. For (b), the inset figure shows the thin-layer CV of [Cu(L^2)] under the same experimental conditions.

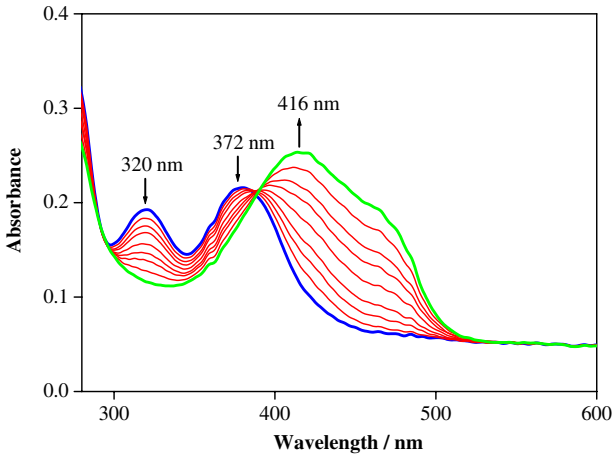


Fig. 5. Time-resolved UV–Vis spectral changes of [Cu(L^2)] during the reduction at $E_{app} = -1.52$ V in CH_2Cl_2 solution containing 0.2 M TBAP.

which makes the electron transition from the ligand to the metal easier, as expected. So the LMCT was observed at a lower energy compared with that of the neutral com-

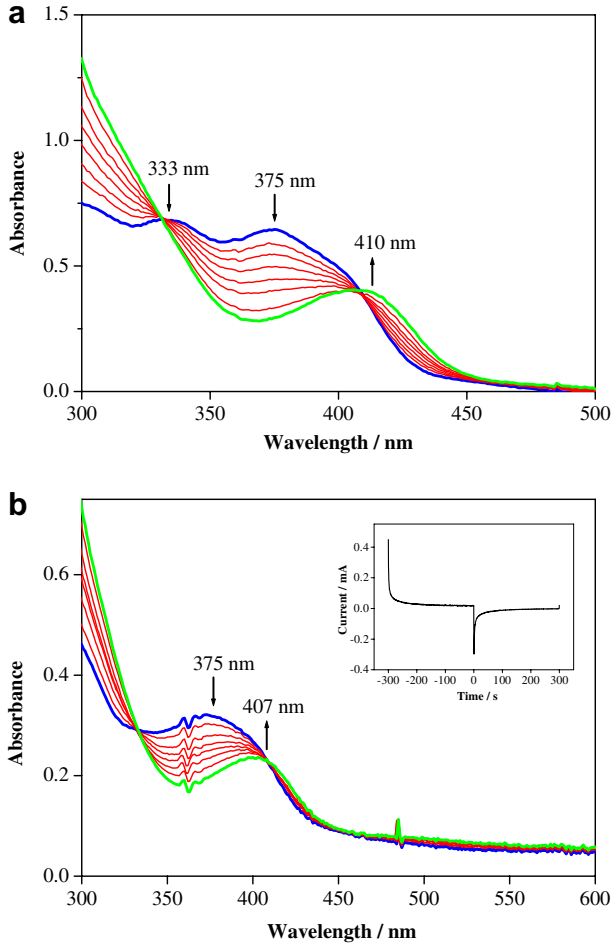


Fig. 6. Time-resolved UV–Vis spectral changes of [Co(L^1)] (a); [Co(L^2)] (b) during oxidation at $E_{app} = 1.00$ V for the first and $E_{app} = 0.75$ V for the latter in CH_2Cl_2 solution containing 0.2 M TBAP. For (b), the inset figure shows chronoamperometry of [Co(L^2)].

plex. The second band, observed at 293 nm and corresponds to an intramolecular $\pi \rightarrow \pi^*$ transition, dominated when the LMCT transition shifted to lower energy. As seen from Fig. 4a and b, the final spectra (green solid lines[1]) of the oxidized species for the [Cu(L^1)] and [Cu(L^2)] complexes exhibited similar features. The corresponding main bands of the oxidized species of [Cu(L^1)] and [Cu(L^2)] appeared at 293 and 362 nm, and 303 and 372 nm, respectively. Comparing the main bands, a small red shift for the oxidized [Cu(L^2)] complex is seen, probably due to its different environment. However, one can also observe an absorption band at about 450 nm in the final spectrum of the oxidized [Cu(L^1)], but, as seen Fig. 4a, this band appears with a very low intensity compared the main bands, which is probably due to the result of the different solubility degree of the resultant products in the thin layer cell. It is evident that the bands of [Cu(L^2)] are seen with a lower intensity compared with those of [Cu(L^1)] under the same experimental conditions. Hence, this weak band could not be attributed to structural changes for the oxidized product of [Cu(L^1)]. These spectral changes are similar to those previously observed for some copper Schiff-base complexes [28]. Although the oxidation process was observed to be electrochemically irreversible from the CV of [Cu(L^1)], the original spectrum of the complex was obtained upon re-reduction during the spectroelectrochemical measurements. The controlled potential coulometric (CPC) study indicated that the number of electrons transferred for the forward and reverse electrochemical reactions of the complex was one for both the oxidation and re-reduction processes, based on the Cu(II)/Cu(III) couples. Thus, the oxidized [Cu(L^1)] complex remained chemically stable throughout the experiment indicating the oxidized [Cu(L^1)] complex remains in its original geometry.

The UV–Vis spectral changes upon oxidation of [Cu(L^2)] are shown in Fig. 4b where the inset figure exhibits the CV of [Cu(L^2)] in a CH_2Cl_2 solution in the thin-layer cell, containing 0.2 M TBAP. The neutral complex showed two intense bands at 320 and 372 nm, which can be attributed to an intramolecular $\pi \rightarrow \pi^*$ transition and Cu(II) $d_{x^2-y^2}$-to-phenolate (π) LMCT transition, respectively [45]. The LMCT transition of [Cu(L^2)] is shifted to a lower energy compared with that of [Cu(L^1)] as a result of the different binding mode of the ligand of [Cu(L^2)] where two additional oxygen lone pairs coming from dioxaoctane coordinate to the copper ion. As can be seen from Fig. 4b, the isosbestic points of the UV–Vis spectral changes were found at 329 nm and 359 nm, which clearly verify the formation of the mono-oxidized species of [Cu(L^2)]. The band intensity corresponding to the 372 nm peak decreased, but a shift to a lower energy was not observed. The final spectrum of the oxidized species of [Cu(L^2)] is similar to that of [Cu(L^1)] with the only difference being that the absorption bands of the oxidized [Cu(L^2)] are shifted to a lower energy compared with those of [Cu(L^1)] because of their different coordination environment. Finally, the oxidized species of the two copper complexes present a square-planar structure. The original spectrum of the neutral complex [Cu(L^2)] was not recovered upon re-reduction at the applied potential $E_{app} = 0.6$ V, but could be recovered upon re-reduction at the applied potential $E_{app} = -0.3$ V. These result indicate that the geometry of [Cu(L^2)] changed into square-planar after the complex was totally oxidized and the neutral complex was only recovered following the EC process observed in the CV of [Cu(L^2)].

The well-defined UV–Vis spectral changes observed during the reduction of [Cu(L^2)] are shown in Fig. 5. After the reduction process, one electron was included in the metal system, thus a Cu(II) (d^9) → Cu(I) (d^{10}) process took place. As expected, the ligand to metal charge transfer (LMCT) at 372 nm decreases and a relatively strong peak at 416 nm develops. The absorption maximum at 416 nm is attributed to an MLCT transition in the Cu(I) complexes. These changes are in agreement with the expected results for a metal-centered reduction, Cu(II) → Cu(I) [27,28].

The UV–Vis spectral changes upon oxidation of [Co(L^1)] and [Co(L^2)] are shown in Fig. 6. The electronic spectra of the Co(II) complexes showed intense absorption bands at 330 and 375 nm that are assigned to a $\pi \rightarrow \pi^*$ transition associated with the imine linkage. For the two cobalt complexes, the bands corresponding to the $\pi \rightarrow \pi^*$ transition disappeared and new bands with small red shifts and of lower intensity were observed during the oxidation process. These new bands are attributed to the LMCT transition. Isosbestic points are observed at 330 and 408 nm for [Co(L^1)] and 330 and 408 nm for [Co(L^2)]. The final spectra of the oxidized species of the cobalt complexes are similar to each other and to those previously reported for the oxidations of Schiff base cobalt complexes [28]. Re-reduction at a negative potential of the oxidized species of [Co(L^2)] generates the neutral complex [Co(L^2)] indicating that the oxidized species is chemically stable throughout the spectroelectrochemical timescale, probably due to the six coordination of the [Co(L^2)] complex, which is able to stabilize the oxidized species compared to the tetrahedral [Co(L^1)] complex for which the original spectrum could not be recovered upon re-reduction [43a].

4. Conclusion

New Schiff-base copper and cobalt complexes, [Cu(L^1)], [Cu(L^2)], and [Co(L^1)], [Co(L^2)] (where L^1 = *N*-*N*′-bis(3,5-di-*tert*-butylsalicylaldimine)-1,4-cyclohexane bis(methylamine) and L^2 = *N*-*N*′-bis(3,5-di-*tert*-butylsalicylaldimine)-1,8-diamino-3,6-dioxaoctane), were synthesized and their electro-spectrochemical properties were investigated using cyclic voltammetric and thin-layer spectroelectrochemical techniques in a dichloromethane solution (CH_2Cl_2). The combination of the electrochemical and

[1] For interpretation of color in Fig. 4, the reader is referred to the web version of this article.

spectroelectrochemical methods provided a powerful tool to reveal the complementary nature of the molecular structure and electron-transfer reactions of the oxidized and reduced species of the new electroactive Schiff-base complexes. The comparative electro-spectrochemical studies revealed that the [Cu(L^1)] and [Co(L^1)] complexes showed four coordination with the ligand (L^1), having two N and two O donor sites, while the [Cu(L^2)] and [Co(L^2)] complexes resulted in six coordination with the ligand (L^2) carrying two N and four O donor sites. The electro-oxidized species of the [Cu(L^1)] and [Co(L^2)] complexes remained stable on the spectroelectrochemical timescale, although the complexes exhibited an irreversible oxidation processes in their CV measurements. Finally, the CVs and the well-defined spectral changes observed with the applied potentials in the thin-layer cell spectral data support the corresponding structures of the copper and cobalt Schiff-base complexes.

Acknowledgements

This work has been supported, in part, by the Research Fund of Harran University (Sanliurfa, Turkey). The support of the State Planning Organization (DPT, Project No. 90177) is gratefully acknowledged. This work has also been supported, in part, by the Turkish Academy of Sciences in the framework of the Young Scientist Award Program (TÜBA-GEBİP).

References

[1] S. Yamada, Coord. Chem. Rev. 192 (1999) 537.
[2] R.H. Holm, J. Am. Chem. Soc. 82 (1960) 5632.
[3] E.C. Niederhoffer, J.H. Timmons, A.E. Martell, Chem. Rev. 84 (1984) 137.
[4] K. Srinivasan, P. Michaud, J.K. Kochi, J. Am. Chem. Soc. 108 (1986) 2309.
[5] W. Zhang, J.L. Loebach, S.R. Wilson, E.N. Jacobsen, J. Am. Chem. Soc. 112 (1990) 2801.
[6] J. Tisato, F. Refosco, F. Bandoli, Coord. Chem. Rev. 135 (1994) 325.
[7] E. Gallo, C. Floriani, H. Miyasaka, N. Matsumoto, Inorg. Chem. 35 (1996) 5964.
[8] K.S. Suslick, T.J. Reinert, J. Chem. Educ. 62 (1988) 974.
[9] N. Raman, A. Kulandaisamy, C. Thangaraja, K. Jeyasubramanian, Trans. Met. Chem. 28 (2003) 29.
[10] J.F. Larrow, E.N. Jacobsen, Y. Gao, Y. Hong, X. Nie, C.M. Zepp, J. Org. Chem. 59 (1994) 1939.
[11] R.H. Holm, P. Kennepohl, E. I Solomon, Chem. Rev. 96 (1996) 2239.
[12] M. Vaidyanathan, R. Visvanathan, M. Palaniandavar, T. Balasubramanian, P. Prabhaharan, T.P. Muthiah, Inorg. Chem. 37 (1998) 6418.
[13] W. Adam, R.T. Fell, V.R. Stegmann, C.R. Saha-Möller, J. Am. Chem. Soc. 120 (1998) 708.
[14] C.J. Burrows, J.G. Muller, Chem. Rev. 98 (1998) 1109.
[15] J. Costamagana, J. Vargas, R. Latorre, A. Alvarado, G. Mena, Coord. Chem. Rev. 119 (1992) 67.
[16] V.T. Kasumov, Spectrochim. Acta 57A (2001) 2337.
[17] G. Karthikeyan, P. Pitchaimani, Trans. Met. Chem. 28 (2003) 482.
[18] V.T. Kasumov, Trans. Met. Chem. 27 (2002) 228.
[19] M.J. Carter, D.P. Rillema, F. Basolo, J. Am. Chem. Soc. 96 (1974) 392.
[20] D.F. Averill, R.F. Bromann, Inorg. Chem. 17 (1978) 3389.
[21] I. Yilmaz, A.G. Gurek, V. Ahsen, Polyhedron 24 (2005) 791.
[22] I. Yilmaz, M. Kocak, Polyhedron 23 (2004) 1279.
[23] K.M. Kadish, T. Nakanishi, V. Ahsen, I. Yilmaz, J. Phys. Chem. B 105 (2001) 9817.
[24] I. Yilmaz, T. Nakanishi, A. Gürek, K.M. Kadish, J. Porphyrins Phthalocyanines 7 (2003) 227.
[25] T. Nakanishi, I. Yilmaz, N. Nakashima, K.M. Kadish, J. Phys. Chem. B 107 (2003) 12789.
[26] (a) S. Arslan, I. Yilmaz, Polyhedron, doi:10.1016/j.poly.2006.11.047;
(b) S. Arslan, I. Yilmaz, Trans. Met. Chem. 32 (2007) 292;
(c) S. Arslan, I. Yilmaz, Inorg. Chem. Commun. 10 (2007) 385.
[27] J. Losata, I. Del Peso, L. Beyer, Inorg. Chim. Acta 321 (2001) 107.
[28] D.F. Rohrbach, W.R. Heineman, E. Deutsch, Inorg. Chem. 18 (1979) 2536.
[29] (a) J.F. Larrow, E.N. Jacobsen, Y. Gao, Y. Hong, X. Nie, C.M. Zepp, J. Org. Chem. 59 (1994) 1939;
(b) A. Earnshaw, Introduction to Magnetochemistry, Academic Press, London, 1968, p. 4.
[30] X.Q. Lin, K.M. Kadish, Anal. Chem. 57 (1985) 1498.
[31] R.C. Felicio, G.A. Silva, L.F. Ceridorio, E.R. Dockal, Synth. React. Inorg. Met. Org. Chem. 29 (2) (1999) 171.
[32] P. Sousa, J.A.G. Vazguez, J.A. Masaquer, Trans. Met. Chem. 9 (1984) 318.
[33] E. Tas, M. Aslanoglu, M. Ulusoy, H. Temel, J. Coord. Chem. 57 (2004) 677.
[34] (a) S.K. Agrawal, D.R. Tuflani, R. Gupta, S.K. Hajcla, Inorg. Chim. Acta 129 (1987) 257;
(b) N. Saha, S. Sinha, Ind. J. Chem. 29A (1990) 292.
[35] (a) S. Pal, G. Mukherjee, S.N. Poddar, J. Indian Chem. Soc. 69 (1992) 461;
(b) W. Geary, J. Chem. Rev. 7 (1971) 81;
(c) E. Tas, M. Aslanoglu, A. Kilic, O. Kaplan, H. Temel, J. Chem. Res. (S) 4 (2006) 242.
[36] B.S. Garg, D.N. Kumar, Spectrochim. Acta Part A 59 (2003) 229.
[37] E. Tas, M. Aslanoglu, M. Ulusoy, H. Temel, J. Coord. Chem. 8 (2004) 677.
[38] E. Tas, M. Aslanoglu, A. Kilic, Z. Kara, Trans. Met. Chem. 30 (2005) 758.
[39] A.B.P. Lever, Inorganic Electronic Spectroscopy, second ed., Elsevier, New York, 1984.
[40] A.H. Maki, J. Chem. Phys. 28 (1958) 651.
[41] H. Temel, S. İlhan, M. Sekerci, R. Ziyadanogulları, Spectrosc. Lett. 35 (2002) 219.
[42] A. Kilic, E. Tas, B. Gumgum, I. Yilmaz, Polish J. Chem. 80 (2006) 1967.
[43] (a) C. Freire, B. de Castro, J. Chem. Soc., Dalton Trans. (1998) 1491;
(b) J.A. Streeky, D.G. Pillsbury, D.H. Busch, Inorg. Chem. 19 (1980) 3148;
(c) K.M. Kadish, Prog. Inorg. Chem. 34 (1986) 435;
(d) B. DE Castro, C. Freire, Inorg. Chem. 29 (1990) 5113;
(e) R.C. Elder, M.C. Hill, Inorg. Chem. 18 (1979) 729.
[44] E.-Q. Gao, W.-M. Bu, G.-M. Yang, D.-Z. Liao, Z.-H. Jiang, S.-P. Yan, G.-L. Wang, J. Chem. Soc., Dalton Trans. (2000) 1431.
[45] A.R. Amudsen, J. Whelan, J. Bosnich, J. Am. Chem. Soc. 99 (1977) 6730.

$Pr[Co(CN)_6]\cdot 5H_2O$ belongs to $P6_3/m$ just as for other pentahydrates reported before. In the present study, we have reinvestigated the crystal structures of $Pr[M(CN)_6]\cdot 5H_2O$ (M = Cr, Fe, Co) and established a reassignment of the space group to $P6_3/mmc$ (no. 194). The spectral characteristics of these compounds have been interpreted and a clear spectral distinction is made between the tetrahydrate and pentahydrate series.

2. Experimental

$PrCl_3\cdot xH_2O$ was prepared from Pr_6O_{11} (Strem, 99.9%) by repeated evaporation with concentrated HCl (AR grade, Reidel-de-Haen). $K_3M(CN)_6$ (M = Cr, Fe, Co) was purchased from Strem Chemicals.

2.1. Syntheses

$Pr^{III}[M^{III}(CN)_6]\cdot 5H_2O$ (M = Cr, Fe, Co) were prepared by slow evaporation of aqueous solutions of $PrCl_3\cdot xH_2O$ and $K_3M(CN)_6$ containing stoichiometric amounts of M:Pr. The crystals were dried by tissue and used immediately.

2.2. Spectral measurements

The UV–Visible absorption spectra of aqueous solutions of the complexes were recorded using a HP UV-8453 spectrophotometer to measure the range between 200 and 1100 nm in H_2O at 298 K. Room temperature and 10 K luminescence spectra were excited by the 355 nm line of a Continuum Nd-YAG laser. The emission was dispersed through an Acton 0.5 m monochromator with an 1800 $g\,mm^{-1}$ grating blazed at 250 nm and detected by a back-illuminated SpectruMM CCD detector. The sample was housed in an Oxford Instruments closed cycle cryostat, with a base temperature of 10 K. The emission from $Pr[Co(CN)_6]\cdot 5H_2O$ was very weak with two broad features at 16257, 16361 cm^{-1} due to Pr^{3+} emission, and a lower energy band at 14488 cm^{-1}. Infrared absorption spectra were recorded at 295 K using KBr discs. A Perkin–Elmer 2000 FTIR spectrometer was employed with resolution 2 cm^{-1}.

2.3. X-ray crystallography

The X-ray intensity data of the three isomorphous complexes were collected on a Bruker SMART 1000 CCD diffractometer with graphite-monochromatized Mo Kα radiation ($\lambda = 0.71073$ Å) at 293 K. In each hkl file, reflections $(hh\bar{2}hl)$ with $l = 2n + 1$ are systematically absent, indicating that the space group is $P6_3/mmc$. In the scenario that such reflections all happen to be too weak to be observed, space group $P6_3/m$ is also possible though unlikely. The structure was solved by direct methods and refined by full-matrix least squares based on F^2 using the SHELXTL program package. All the non-hydrogen atoms were subjected to anisotropic refinement. The aqua ligand O1W and lattice water molecule O2W respectively occupy sites of symmetry m and 3 in space group $P6_3/m$, and mm and $3m$ in space group $P6_3/mmc$. The hydrogen atoms, which are necessarily disordered when the oxygen atoms occupy the latter three sites, cannot be reliably located in the structure refinement.

3. Results and discussion

3.1. Crystal structures

Table 1 presents experimental and statistical summaries for compounds $Pr[M(CN)_6]\cdot 5H_2O$ (M = Co, Cr, Fe) refined in space groups $P6_3/m$and $P6_3/mmc$. The structural parameters refined in both space groups show insignificant differences, and consequently the space group of higher symmetry, namely $P6_3/mmc$, should be assigned according to convention. Interestingly, Pretsch et al. [7] reported that when orthorhombic $Cmcm$ $Er[Co(CN)_6]\cdot 4H_2O$ loses all its bound and unbound water molecules, it is transformed to hexagonal $Er[Co(CN)_6]$ which belongs to space group $P6_3/mmc$.

The crystal and molecular structure of $Pr[M(CN)_6]\cdot 5H_2O$ herein are almost identical to those reported for $La[Co(CN)_6]\cdot 5H_2O$ [19] and $La[Fe(CN)_6]\cdot 5H_2O$ [8]. The structural characteristics of $Pr[Cr(CN)_6]\cdot 5H_2O$ are specified by listing their Wyckoff positions and site symmetries: Pr(1) in 2(*c*), $\bar{6}m2$; Cr(1) in 2(*a*), $\bar{3}m$; C(1) in 12(*k*), *m*; N(1) in 12(*k*), *m*; O(1 W) in 6(*h*), *mm*; and O(2 W) in 4(*f*), 3*m* (see Fig. 1 for the atom labeling). The Pr^{3+} ion is nine-coordinated in the form of a $PrN_6(H_2O)_3$ group; the Cr^{3+} ion is six-coordinated in the form of an octahedral CrC_6 group; and cyanide linkages between $PrN_6(H_2O)_3$ and CoC_6 groups build an infinite polymeric array (see Fig. 2). Two uncoordinated water molecules occupy zeolitic holes on a 6-fold rotatory-inversion axis above and below the Pr^{3+} ion. The Pr^{3+} ion is coordinated to three aqua ligands in the mirror plane and to the N atoms of six cyanides, with three on each side of the mirror plane. The coordination geometry of Pr^{3+} is thus approximately D_{6h}. The uncoordinated water molecule O(2W) is linked to the coordinated water molecule O(1W) through a weak hydrogen bond, as in $Pr[Co(CN)_6]\cdot 5H_2O$ [21], $La[Co(CN)_6]\cdot 5H_2O$ [19] and $La[Fe(CN)_6]\cdot 5H_2O$ [8].

The bond lengths and angles in $Pr[M(CN)_6]\cdot 5H_2O$ are reported in Table 2. The C≡N bond distances do not differ from standard values [22]. The M–C bond distance is 8.5% shorter for the low-spin $3d^6$ ion compared with low-spin $3d^3$, and the trend with atomic number exhibits the linear relation shown in Fig. 3. A similar linear regression, but with a 7% more negative slope, is found for the M–C bond distances in $K_3M(CN)_6$ (M = Cr, Mn, Fe, Co [22]) where there is no cyanide bridging. The involvement of covalency in the M–C bond in $Pr[M(CN)_6]\cdot 5H_2O$ is exhibited by its strict directional character with the angle N–C–M being linear.

Table 1
Experimental and statistical summaries for $Pr[M(CN)_6]\cdot 5H_2O$

	$Pr[Co(CN)_6]\cdot 5H_2O$		$Pr[Cr(CN)_6]\cdot 5H_2O$		$Pr[Fe(CN)_6]\cdot 5H_2O$	
	$P6_3/m$	$P6_3/mmc$	$P6_3/m$	$P6_3/mmc$	$P6_3/m$	$P6_3/mmc$
Empirical formula	$C_6H_{10}CoN_6O_5Pr$	$C_6H_{10}CoN_6O_5Pr$	$C_6H_{10}CrN_6O_5Pr$	$C_6H_{10}CrN_6O_5Pr$	$C_6H_{10}FeN_6O_5Pr$	$C_6H_{10}FeN_6O_5Pr$
Formula weight	446.04	446.04	439.11	439.11	442.96	442.96
Crystal system	hexagonal	hexagonal	hexagonal	hexagonal	hexagonal	hexagonal
Space group	$P6_3/m$ (no.176)	$P6_3/mmc$ (no.194)	$P6_3/m$ (no.176)	$P6_3/mmc$ (no.194)	$P6_3/m$ (no.176)	$P6_3/mmc$ (no.194)
a (Å)	7.4748 (6)	7.4748 (6)	7.6734(5)	7.6734(5)	7.524(1)	7.524(1)
b (Å)	7.4748(6)	7.4748(6)	7.6734(5)	7.6734(5)	7.524(1)	7.524(1)
c (Å)	14.220(3)	14.220(3)	14.674(2)	14.674(2)	14.351(3)	14.351(3)
α (°)	90	90	90	90	90	90
β (°)	90	90	90	90	90	90
γ (°)	120	120	120	120	120	120
V (Å^3)	688.1(1)	688.1(1)	748.2(1)	748.2(1)	703.5(2)	703.5(2)
Z	2	2	2	2	2	2
T (K)	293(2)	293(2)	293(2)	293(2)	293(2)	293(2)
D (mg m^{-3})	2.153	2.153	1.949	1.949	2.091	2.091
μ (mm^{-1})	4.728	4.728	3.965	3.965	4.476	4.476
Total data	1953	1849	2018	1900	2298	272
Unique data	699	425	759	458	242	240
Goodness-of-fit	1.083	1.104	1.134	1.173	1.102	1.061
R_1 $[I > 2\sigma(I)]$[a]	0.0244	0.0234	0.0212	0.0183	0.0352	0.0419
wR_2 $[I > 2\sigma(I)]$ [b]	0.0619	0.0618	0.0528	0.0445	0.0972	0.1178
R_1 (all data)	0.0276	0.0241	0.0293	0.0213	0.0465	0.0492
wR_2 (all data)	0.0634	0.0620	0.0557	0.0456	0.1042	0.1235

[a] $R_1 = \sum\|F_o| - |F_c\|/\sum|F_o|$.
[b] $wR_2 = [\sum[w(F_o^2 - F_c^2)^2]/\sum[w(F_o^2)^2]^{1/2}$.

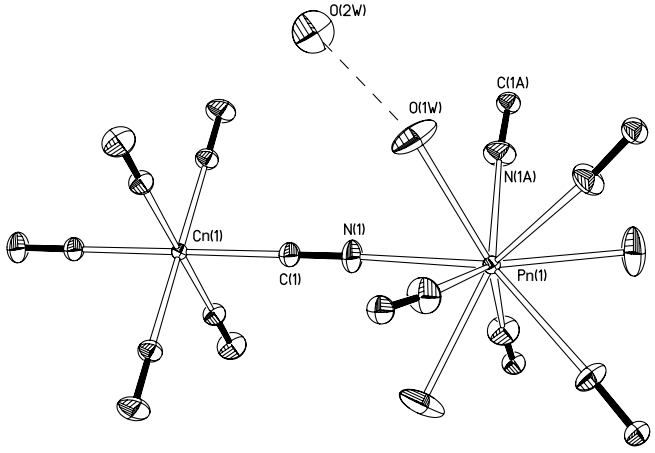


Fig. 1. Coordination environment of the metal atoms in $Pr[Cr(CN)_6]\cdot 5H_2O$ (50% thermal ellipsoids) with atom labeling.

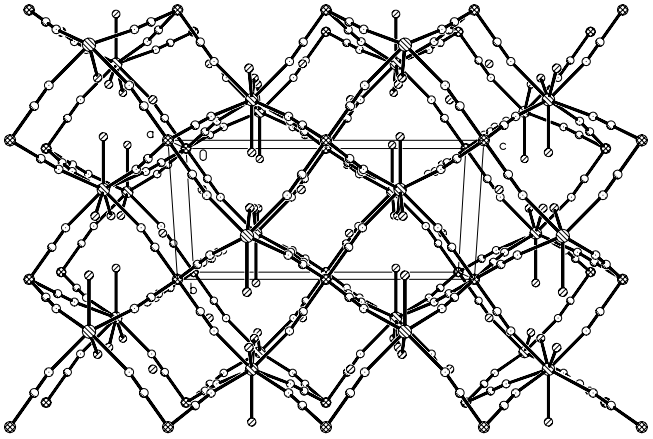


Fig. 2. Three-dimensional coordination network of $Pr[Cr(CN)_6]\cdot 5H_2O$ bridged by cyanide groups viewed along the a-axis. Uncoordinated water molecules are omitted for clarity.

In contrast, the C–N–Pr angle is bent, and the Pr-O distance is longer whereas the Pr–N distance is shorter for M = Cr than for M = Co. However, these changes are minor (<1.5%) and of similar magnitudes to measurement errors. The La–O and La–N bond distances in $La[M(CN)_6]\cdot 5H_2O$ (M = Fe, Co) [8,19]; refined in space group $P6_3/m$) are slightly longer (~2–3%) than those in the corresponding $Pr[M(CN)_6]\cdot 5H_2O$ compounds.

3.2. Infrared spectra

The vibrational mode of predominantly CN stretching character in octahedral $M(CN)_6^{3-}$ ions in the solid state

Table 2
Bond lengths (Å) and angles (°) for $Pr[M(CN)_6]\cdot 5H_2O$

	M = Cr	M = Fe	M = Co
Pr(1)–O(1W)	2.563(4)	2.54 (1)	2.536(6)
Pr(1)–N(1)	2.563(3)	2.58 (1)	2.577(4)
M(1)–C(1)	2.061(3)	1.96 (1)	1.889(4)
C(1)–N(1)	1.144(4)	1.12 (2)	1.145(6)
O(1W)–Pr(1)–N(1)	69.13(3)	69.1 (1)	69.13(4)
N(1)–C(1)–M(1)	179.1(3)	179(1)	180.0(5)
C(1)–N(1)–Pr(1)	171.7(3)	171(1)	170.6(4)

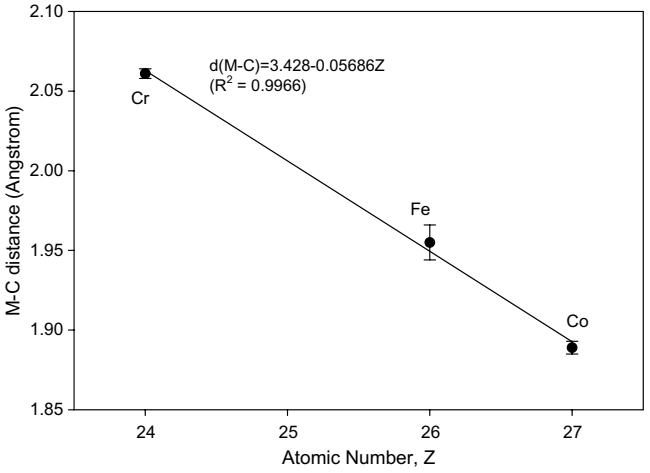


Fig. 3. Plot of M–C bond distance versus atomic number of M for $Pr[M(CN)_6] \cdot 5H_2O$.

is observed at 2142 cm^{-1} (M = Co) and at 2138 cm^{-1} (M = Cr) [22]. For $Ln[M(CN)_6] \cdot nH_2O$, members of the $n = 5$ series easily transform at room temperature into $n = 4$, but the two series are readily distinguished by the characteristic water and CN stretching peaks in the IR spectra, as shown for $Pr[Cr(CN)_6] \cdot 5H_2O$ and $Pr[Fe(CN)_6] \cdot 4H_2O$ in Fig. 4, where the appropriate structures are also drawn. The inset in the figure shows the spectral region of $Pr[Cr(CN)_6] \cdot 5H_2O$ between 2100 and 2200 cm^{-1} in detail. Note that only one strong CN stretch band is observed (corresponding to $^{12}C^{14}N$ at 2156 cm^{-1}) for the pentahydrate. From their positions and relative intensities, the weak features at 2112, 2125 cm^{-1} in the inset correspond to $^{13}C^{14}N$ and $^{12}C^{15}N$ stretching bands, respectively. By contrast, two prominent CN stretching bands are observed for the tetrahydrate system $Pr[Fe(CN)_6] \cdot 4H_2O$. Furthermore, the water bending mode region (~1610 cm^{-1}) shows one broad band for the pentahydrate but two prominent sharper bands for the tetrahydrate. The large breadth of this band in $Pr[Cr(CN)_6] \cdot 5H_2O$ (Fig. 4) illustrates the large thermal amplitude of the coordinated aquo ligand. The water stretching region (3000–3610 cm^{-1}) is complex for both the tetrahydrate and pentahydrate systems because bands due to both coordinated and hydrogen-bonded water appear together with vibrational overtones. The lowest energy band in Fig. 4 for the spectrum of $Pr[Cr(CN)_6] \cdot 5H_2O$ is the Cr–C stretch at 435 cm^{-1}.

3.3. UV–Vis spectra of aqueous solutions of $Pr[M(CN)_6]$

The UV–Vis absorption spectra of aqueous solutions of $Pr[M(CN)_6] \cdot 5H_2O$ are compared with $K_3[Co(CN)_6]$(aq) in Fig. 5 and serve to show the presence of free $M(CN)_6^{3-}$ ions in solution. The sharp, weak features between 443 nm and 485 nm are due to $4f^2$–f^2 intra-configurational transitions of Pr^{3+}. Although the lowest energy band (485 nm) clearly corresponds to the $^3P_0 \leftarrow {}^3H_4$ transition, the higher energy features are not clearly resolved and too broad to permit specific assignments. The bands at 306, 379 nm for M = Cr occur at similar wavelengths (308, 375 nm) to corresponding features in the room temperature absorption spectrum of crystalline $Cs_2KCr(CN)_6$ [23]. These features have been assigned to spin-allowed ligand field transitions corresponding to $^4T_{1g}$, $^4T_{2g} \leftarrow {}^4A_{2g}$, respectively [23]. The much stronger bands at 262 and ~200–220 nm correspond to charge-transfer transitions. The features at ~257 and 307 nm in the spectrum of aqueous $Pr[Co(CN)_6]$ are at similar wavelengths to the spectrum of aqueous $K_3Co(CN)_6$ and correspond to $^1T_{2g}$, $^1T_{1g} \leftarrow {}^1A_{1g}$ transitions, respectively [22]. The sharp increase in absorbance at ~200 nm corresponds to a charge transfer transition. This band is at higher energy than in $Cr(CN)_6^{3-}$ due to the greater cation polarizing power and shorter M–C bond distance.

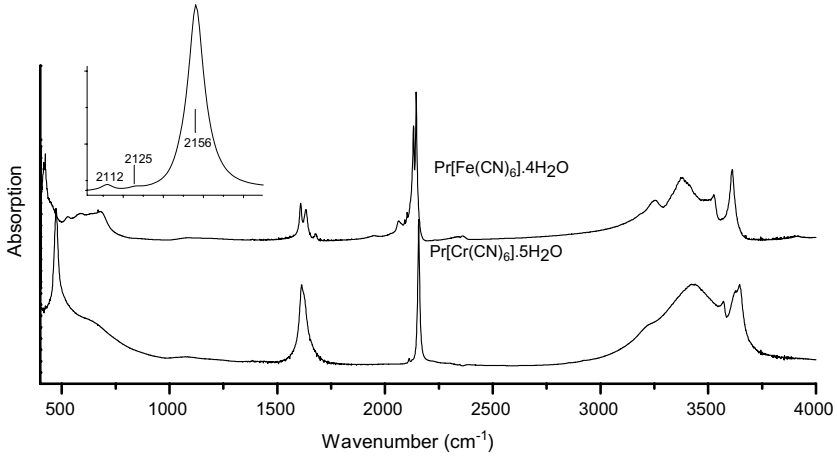


Fig. 4. FTIR spectra of $Pr[Fe(CN)_6] \cdot 4H_2O$ and $Pr[Cr(CN)_6] \cdot 5H_2O$. The inset shows the expanded CN stretch region of the latter.

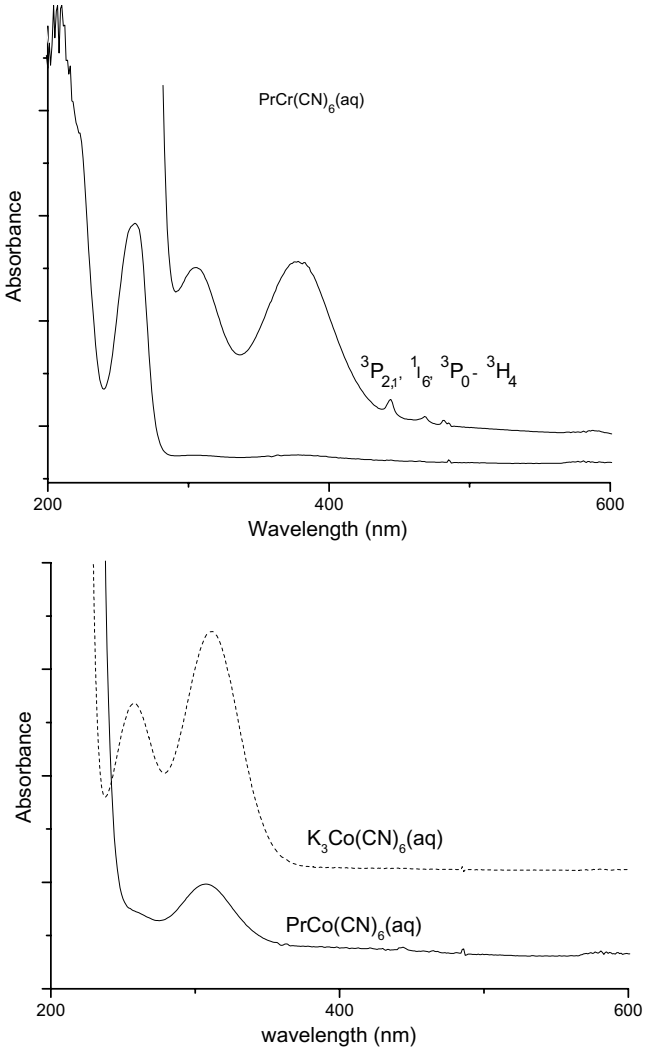


Fig. 5. UV–visible absorption spectra between 200 and 600 nm of aqueous solutions of $Pr[M(CN)_6]$ (M = Cr, Co) and comparison with $K_3Co(CN)_6$(aq). The scale expansion is shown in the top figure.

4. Conclusions

The space group $P6_3/m$ previously reported for the crystal structure of $Pr[Co(CN)_6]\cdot 5H_2O$ [21] has been revised herein to $P6_3/mmc$, which also holds for the isomorphous Cr and Fe compounds. The distinction between the $Ln[M(CN)_6]\cdot nH_2O$ tetrahydrate ($n = 4$) and pentahydrate ($n = 5$) series has been demonstrated on the basis of IR spectral assignments. Our spectra for the pentahydrates are in essential agreement with that reported for $La[Co(CN)_6]\cdot 5H_2O$ [19], but show differences from the spectra reported for $Ln[Fe(CN)_6]\cdot 5H_2O$ (Ln = La, Pr, Nd) where some decomposition to the tetrahydrates may have occurred [18]. Our IR spectrum of $Pr[Fe(CN)_6]\cdot 4H_2O$ is similar to that reported for $Nd[Fe(CN)_6]\cdot 4H_2O$ [24].

Acknowledgements

We thank Dr. S.K. Mak for technical help in the early part of this study and the Hong Kong University Grants Council for support under CERG Grant CityU 1115/02P.

Appendix A. Supplementary material

CCDC 637207, 637208 and 645301 contain the supplementary crystallographic data for this paper. These data can be obtained free of charge via http://www.ccdc.cam.ac.uk/conts/retrieving.html, or from the Cambridge Crystallographic Data Centre, 12 Union Road, Cambridge CB2 1EZ, UK; fax: (+44) 1223-336-033; or e-mail: deposit@ccdc.cam.ac.uk. Supplementary data associated with this article can be found, in the online version, at doi:10.1016/j.poly.2007.05.002.

References

[1] S. Nakayama, M. Sakamoto, K. Matsuki, Y. Okimura, R. Ohsumi, Y. Nakayama, Y. Sadaoka, Chem. Lett. 11 (1992) 2145.
[2] Y. Matuura, S. Matsushima, M. Sakamoto, Y. Sadaoka, J. Mater. Chem. 3 (1993) 1329.
[3] Y. Sadaoka, K. Watanabe, Y. Sakai, M. Sakamoto, J. Alloys Comp. 224 (1995) 194.
[4] N. Kondo, H. Itoh, M. Kurihara, M. Sakamoto, H. Aono, Y. Sadaoka, J. Alloys Comp. 408–412 (2006) 1026.
[5] C. James, P.S. Willand, J. Am. Chem. Soc. 38 (1916) 1497.
[6] Y. Masuda, K. Nagaoka, H. Ogawa, O. Nakazato, Y. Yukawa, H. Miyamoto, J. Alloys Compd. 235 (1996) 23.
[7] T. Pretsch, K.W. Chapman, G.J. Halder, C.J. Kepert, Chem. Commun. (2006) 1857.
[8] W.E. Bailey, R.J. Williams, W.O. Milligan, Acta Crystallogr., Sect. B 29 (1973) 1365.
[9] H. Kietaibl, W. Petter, Helv. Phys. Acta 47 (1974) 425.
[10] M.C. Bonnet, Bull. Soc. Chim. France (1975) 1062.
[11] M.C. Bonnet, Bull. Soc. Chim. France (1975) 1067.
[12] F. Hulliger, M. Landolt, H. Vetsch, J. Solid State Chem. 18 (1976) 238.
[13] F. Hulliger, M. Landolt, H. Vetsch, J. Solid State Chem. 18 (1976) 307.
[14] D.F. Mullica, H.O. Perkins, E.L. Sappenfield, D.A. Grossie, J. Solid State Chem. 74 (1988) 9.
[15] D.F. Mullica, H.O. Perkins, E.L. Sappenfield, D. Leschnitzer, Acta Crystallogr., Sect. C 45 (1989) 330.
[16] W. Petter, V. Gramlich, F.J. Hulliger, J. Solid State Chem. 82 (1989) 6.
[17] D.F. Mullica, E.L. Sappenfield, J. Solid State Chem. 82 (1989) 161.
[18] X.Y. Wang, Y. Yukawa, Y. Masuda, J. Alloys Comp. 290 (1999) 85.
[19] D.F. Mullica, W.O. Milligan, W.T. Kouba, J. Inorg. Nucl. Chem. 41 (1979) 967.
[20] D.F. Mullica, W.O. Milligan, Acta Crystallogr., Sect. B 36 (1980) 2561.
[21] Y. Yukawa, S. Igarashi, T. Kawaura, H. Miyamoto, Inorg. Chem. 35 (1996) 7399.
[22] A.G. Sharpe, The Chemistry of the Cyano Complexes of the Transition Metals, Academic Press, London, 1976.
[23] J. Hanuza, K. Hermanowicz, B. Jezowska-Trzebiatowska, A. Pietraszko, S.P. Feofilov, T.J. Maksimova, S.A. Basun, Bull. Pol. Acad. Sci. Chem. 39 (1991) 331.
[24] M.C. Navarro, E.V. Pannunzio-Miner, S. Pagola, M.I. Gomez, R.E. Carbonio, J. Solid State Chem. 178 (2005) 847.

higher-dimensional metal–organic frameworks easily [7b,9]. In the present work, we chose H_2psa as a bridging ligand to link Cu(II) ions. Auxiliary ligands, phen, 2bpy, 4bpy, and N_3^-, were introduced to the Cu(II)/$[psa]^{2-}$ system under solvothermal conditions, five new complexes $[Cu(psa)(phen)]\cdot 3H_2O$ (**1**), $[Cu(psa)(2bpy)]\cdot 0.5H_2O$ (**2**), $[Cu(psa)(2bpy)(H_2O)]\cdot 3H_2O$ (**3**), $[Cu(psa)(4bpy)]\cdot H_2O$ (**4**), and $[Cu(psa)_{0.5}(N_3)(2bpy)]$ (**5**) were obtained. The details of their synthesis, structure, and thermal stability are reported.

2. Experimental

2.1. Materials and characterization

All reagents were used as received without further purification. The C, H, N microanalyses were carried out with a Vario EL elemental analyzer. Thermogravimetric analyses were conducted on a ZRY-2P thermal analyzer using a heating rate of 10 °C/min from room temperature to 1000 °C under nitrogen. The IR spectra were recorded with a Nicolet Avatar 360 FT-IR spectrometer using the KBr pellet technique.

2.2. Synthesis

2.2.1. Synthesis of $[Cu(psa)(phen)]\cdot 3H_2O$ (*1*)

A mixture of H_2psa (0.019 g, 0.1 mmol), phen (0.020 g, 0.1 mmol), $Cu(Ac)_2\cdot H_2O$ (0.019 g, 0.1 mmol), NaOH aqueous solution (0.15 ml, 0.65 mol/L), 10 ml distilled water and 1 ml ethanol was placed in a 25 ml Teflon-lined stainless steel autoclave, and the vessel was sealed and heated to 140 °C for 72 h, then cooled at 10 °C h^{-1} to 100 °C, followed by slowly cooling to room temperature. The resulting blue wedge shape crystals of complex **1** were obtained. Yield: 0.032 g (64.2%). *Anal.* Calc. for $C_{22}H_{22}CuN_2O_7$: C, 53.87; H, 4.52; N, 5.71. Found: C, 53.93; H, 4.85; N, 5.33%. IR data (KBr pellet, cm^{-1}): 3450s, 1592s, 1519w, 1494w, 1429m, 1397m, 1313w, 850m, 720m.

2.2.2. Synthesis of $[Cu(psa)(2bpy)]\cdot 0.5H_2O$ (*2*) and $[Cu(psa)(2bpy)(H_2O)]\cdot 3H_2O$ (*3*)

The synthesis of complex **2** was similar to that of complex **1** expect that 2bpy (0.016 g, 0.1 mmol) was used instead of phen. The blue square flake crystals of complex **2** were obtained. Yield: 0.004 g (9.5%). We left the mother solution at room temperature for two days and obtained the light green crystal of complex **3**. Yield: 0.018 g (37.2%). *Anal.* Calc. for $C_{20}H_{17}CuN_2O_{4.5}$ (**2**): C, 57.01; H, 4.07; N, 6.65. Found: C, 57.38; H, 4.68; N, 6.82%. IR data (KBr pellet, cm^{-1}): 3442s, 1587s, 1568s, 1495w, 1473w, 1447m, 1410s, 1395s, 1381s, 1273w, 773s, 715m. *Anal.* Calc. for $C_{20}H_{24}CuN_2O_8$ (**3**): C, 49.63; H, 4.99; N, 5.79. Found: C, 49.39; H, 5.77; N, 6.07%. IR data (KBr pellet, cm^{-1}): 3447s, 1569s, 1494w, 1468w, 1446m, 1412s, 1385s, 775m, 744w, 731w, 701w.

2.2.3. Synthesis of $[Cu(psa)(4bpy)]\cdot H_2O$ (*4*)

The synthesis of complex **4** was similar to that of complex **1** expect that 4bpy (0.018 g, 0.1 mmol) was used instead of phen. Dark blue column crystals of complex **4** were obtained. Yield: 0.030 g (69.9%). *Anal.* Calc. for $C_{20}H_{18}CuN_2O_5$: C, 55.87; H, 4.22; N, 6.52. Found: C, 56.24; H, 4.23; N, 6.38%. IR data (KBr pellet, cm^{-1}): 3441s, 1610s, 1575s, 1487w, 1411m, 1375m, 1320w, 1215w, 1065m, 826m, 734m, 701m, 627m.

2.2.4. Synthesis of $[Cu(psa)_{0.5}(N_3)(2bpy)]$ (*5*)

A mixture of H_2psa (0.019 g, 0.1 mmol), 2pby (0.016 g, 0.1 mmol), $Cu(Ac)_2\cdot H_2O$ (0.019 g, 0.1 mmol), NaN_3 (0.007 g, 0.1 mmol), 10 ml distilled water and 3 ml ethanol was placed in a 25 ml Teflon-lined stainless steel autoclave, and the vessel was sealed and heated to 140 °C for 72 h, then cooled at 10 °C h^{-1} to 100 °C, followed by slowly cooling to room temperature. Dark green block crystals of complex **5** were obtained. Yield: 0.029 g (80.9%). *Anal.* Calc. for $C_{15}H_{12}CuN_5O_2$: C, 50.34; H, 3.38; N, 19.57. Found: C, 50.12; H, 3.90, N, 19.39%. IR data (KBr pellet, cm^{-1}): 3441br, 2048s, 1607s, 1567m, 1493m, 1472m, 1447m, 1361m, 1158w, 1029w, 772m, 732m.

2.3. X-ray structure determination

The single-crystal X-ray data collections for the five complexes were performed with a Bruker SMART 1000 CCD diffractometer, using graphite-monochromatized Mo Kα radiation ($\lambda = 0.71073$ Å). Semi-empirical absorption corrections were applied using the SADABS program [10]. The structures were solved by direct methods [11] and refined by full-matrix least squares method on F^2 using SHELXS97 and SHELXL97 programs, respectively [11,12]. All non-hydrogen atoms were refined anisotropically. The hydrogen atoms were generated geometrically and treated by a mixture of independent and constrained refinement. The crystallographic data for complexes **1**–**5** are listed in Table 1, selected bond lengths (Å) and angles (°) are listed in Table 2, the details of the hydrogen bonds for complexes **1** and **3** are listed in Table 3.

3. Results and discussion

3.1. Structure description of $[Cu(psa)(phen)]\cdot 3H_2O$ (*1*)

In the asymmetric unit of complex **1**, there are one Cu(II) ion, one $[psa]^{2-}$ ligand, one chelating phen ligand and three lattice water molecules. As shown in Fig. 1, the Cu(II) ion is four-coordinated by two nitrogen atoms (N1, N2) from one phen ligand, two oxygen atoms (O1, O4A) of the carboxylate groups from two $[psa]^{2-}$ ligands. The average Cu–N bond length is slightly longer than that of Cu–O distance. In complex **1**, $[psa]^{2-}$ ligand displays cis-configuration and adopts bis(monodentate) mode (see Scheme 1a). Cu(II) ions are bridged by $[psa]^{2-}$ ligands into 1D chains (see Fig. 1). The phen ligands are arranged at

Table 1
Crystallographic data of complexes **1**–**5**

	1	**2**	**3**	**4**	**5**
Empirical formula	$C_{22}H_{22}CuN_2O_7$	$C_{20}H_{17}CuN_2O_{4.5}$	$C_{20}H_{24}CuN_2O_8$	$C_{20}H_{18}CuN_2O_5$	$C_{30}H_{24}Cu_2N_{10}O_4$
M (g mol^{-1})	489.96	420.90	483.95	429.90	715.67
Crystal system	monoclinic	monoclinic	orthorhombic	monoclinic	monoclinic
Space group	*P*2(1)	*C*2/*c*	*Pca*2(1)	*Pc*	*C*2/*c*
a (Å)	6.9209(19)	30.474	19.329(4)	5.710(2)	13.768(3)
b (Å)	17.591(5)	7.585	6.3717(14)	9.622(4)	16.752(3)
c (Å)	9.088(2)	17.188	16.976(4)	17.509(7)	13.330(4)
α (°)	90	90	90	90	90
β (°)	101.81	116.81	90	102.686(12)	105.192(6)
γ (°)	90	90	90	90	90
V (Å^3)	1083.0(5)	3546(3)	2090.7(8)	938.5(6)	2967.0(12)
Z	2	8	4	2	4
D_{calc} (g cm^{-1})	1.503	1.577	1.538	1.521	1.602
μ (mm^{-1})	1.055	1.265	1.095	1.198	1.489
F(000)	506	1728	1004	442	1456
Reflections collected	5317	3104	10723	4906	8067
Reflections unique	3750	3104	4032	2620	3057
Date/restraints/parameters	3750/10/289	3104/3/257	4032/10/280	2620/23/254	3057/39/232
Final R indices [$I > 2\sigma(I)$]	$R_1 = 0.0467$, $wR_2 = 0.0837$	$R_1 = 0.0694$, $wR_2 = 0.1930$	$R_1 = 0.0503$, $wR_2 = 0.0853$	$R_1 = 0.0563$, $wR_2 = 0.1004$	$R_1 = 0.0550$, $wR_2 = 0.1189$
R indices (all data)	$R_1 = 0.0741$, $wR_2 = 0.0965$	$R_1 = 0.1015$, $wR_2 = 0.2168$	$R_1 = 0.1279$, $wR_2 = 0.1112$	$R_1 = 0.1275$, $wR_2 = 0.1238$	$R_1 = 0.1390$, $wR_2 = 0.1479$
Flack parameter	0.03(2)		0.06(3)	0.0(5)	
Goodness-of-fit on F^2	1.068	1.097	1.078	1.019	0.999
Largest difference peak and hole (e Å^{-3})	0.472 and −0.515	1.321 and −1.748	0.828 and −1.182	0.714 and 0.449	0.519 and −0.469

one side of the chains, while the benzene rings of the $[psa]^{2-}$ ligands locate at the other side of the chains, which may be contributed to the steric effect from both the phen and H_2psa ligands. The similar coordination geometry and structure can be observed in the complex of Cu(II) with 1,4-phenylenediacetic acid (H_2pda) [13] which is an isomer of H_2psa. In this $[pda]^{2-}$ complex, the auxiliary ligand phen has π–π stacking interactions, while in complex **1**, the π–π interactions could not be found.

In complex **1**, three lattice water molecules form a trimer through hydrogen bonds (O5–H5B···O7, O6–H6A···O5), which acts as bridges between adjacent chains forming a 2D supramolecular network in *ab* plane by three kinds of hydrogen bonds, as shown in Fig. 2. The details of hydrogen bonds are listed in Table 3. Undoubtedly, the hydrogen bonds play an important role in the formation of the 2D supramolecular network.

3.2. Structure description of $[Cu(psa)(2bpy)] \cdot 0.5H_2O$ (**2**)

The asymmetric unit of complex **2** contains one Cu(II) ion, one $[psa]^{2-}$ ligand, one 2bpy ligand and one half of an non-coordinated water molecule. Similar to complex **1**, in complex **2**, $[psa]^{2-}$ is also cis-configuration (see Scheme 1a) and bis(monodentate) coordination mode, the Cu(II) ion is four-coordinated by two N atoms from a chelating 2bpy ligand and two oxygen atoms of two $[psa]^{2-}$ ligands, and Cu(II) ions are linked by $[psa]^{2-}$ ligands into 1D chains too, as shown in Fig. 3. However, in complex **2**, the approximately parallel 2bpy ligands allow pairing of two related single chains to generate double zipper-like chain, in which aromatic π–π stacking interactions exist between 2bpy pairs. The face-to-face distance between the paired 2bpy rings is 3.258 Å, and the centroid–centroid distance is 3.466 Å [14], indicating moderately strong aromatic π–π stacking interactions. The disordered water molecules exist between the zippers and the hydrogen bonds (O(5)–H(5A)···O(3), O···O distance 2.987 Å) between water molecules and the uncoordinated carboxyl oxygen atoms connect parallel zippers to give a 2D supramolecular structure, as shown in Fig. 4.

3.3. Structure description of $[Cu(psa)(2bpy)(H_2O)] \cdot 3H_2O$ (**3**)

In the symmetric unit of complex **3**, there are one Cu(II) ion, one $[psa]^{2-}$ ligand, one 2bpy ligand, one coordinated water molecule and three lattice water molecules. In complex **3**, the Cu(II) ion is five-coordinated with two nitrogen atoms (N1, N2) from 2bpy ligand, two oxygen atoms (O1, O3A) of two $[psa]^{2-}$ ligands, and one oxygen atoms(O5) from one coordinated water molecule forming a distorted tetragonal pyramid geometry, as shown in Fig. 5. The Cu–O5(W) bond length (2.245 Å) is much longer than the mean Cu–O(carboxyl) distance (1.978 Å) indicating that the O5 coordinates to the Cu(II) ion weakly.

In complex **3**, the $[psa]^{2-}$ ligand shows cis-configuration (see Scheme 1a) and adopts bis(monodentate) coordination mode, the Cu(II) ions are bridged by $[psa]^{2-}$ into 1D chains, and the 2bpy ligands locate at the same side of the chains. In complex **3**, the lattice water molecules constitute trimers as in complex **1**. And an interesting feature of

Table 2
Selected bond distances (Å) and angles (°) for complexes **1**–**5**

Complex **1**			
Cu(1)–O(1)	1.926(3)	Cu(1)–N(1)	2.010(4)
Cu(1)–O(4)#1	1.976(4)	Cu(1)–N(2)	1.999(4)
O(1)–Cu(1)–O(4)#1	90.7(2)	N(1)–Cu(1)–O(4)#1	172.5(2)
O(1)–Cu(1)–N(1)	93.3(2)	N(1)–Cu(1)–N(2)	81.8(2)
O(1)–Cu(1)–N(2)	174.6(3)	N(2)–Cu(1)–O(4)#1	94.4(2)
Symmetry transformations used to generate equivalent atoms: #1 $x-1$, y, z			
Complex **2**			
Cu(1)–O(1)	1.962(5)	Cu(1)–N(1)	1.973(6)
Cu(1)–O(4)#1	1.923(5)	Cu(1)–N(2)	1.988(7)
O(1)–Cu(1)–O(4)#1	94.6(2)	N(1)–Cu(1)–O(4)#1	160.1(3)
O(1)–Cu(1)–N(1)	94.3(2)	N(1)–Cu(1)–N(2)	81.0(3)
O(1)–Cu(1)–N(2)	164.4(2)	N(2)–Cu(1)–O(4)#1	94.7(3)
Symmetry transformations used to generate equivalent atoms: #1 x, $y+1$, z			
Complex **3**			
Cu(1)–O(1)	1.969(5)	Cu(1)–N(1)	1.988(5)
Cu(1)–O(5)	2.245(5)	Cu(1)–N(2)	1.985(6)
Cu(1)–O(3)#1	1.939(5)		
O(1)–Cu(1)–O(5)	87.8 (2)	O(5)–Cu(1)–N(1)	124.5(2)
O(1)–Cu(1)–N(1)	146.8(2)	O(5)–Cu(1)–N(2)	88.6(2)
O(1)–Cu(1)–N(2)	93.9(2)	N(1)–Cu(1)–O(3)#1	92.3(2)
O(1)–Cu(1)–O(3)#1	92.8(2)	N(1)–Cu(1)–N(2)	80.9(2)
O(5)– Cu(1)–O(3)#1	93.7(2)	N(2)–Cu(1)–O(3)#1	173.0(2)
Symmetry transformations used to generate equivalent atoms: #1 x, $y+1$, z			
Complex **4**			
Cu(1)–O(1)	1.930(8)	Cu(1)–N(1)	2.051(8)
Cu(1)–O(4)#1	1.928(9)	Cu(1)–N(2)#2	2.047(8)
O(1)–Cu(1)–O(4)#1	178.2(5)	O(4)#1–Cu(1)–N(2)#2	89.8(4)
O(1)–Cu(1)–N(1)	90.3(3)	N(1)–Cu(1)–O(4)#1	89.3(4)
O(1)–Cu(1)–N(2)#2	90.5(4)	N(1)–Cu(1)–N(2)#2	179.2(5)
Symmetry transformations used to generate equivalent atoms: #1 x, $-y+2$, $z+1/2$; #2 $x+1$, $y+1$, z			
Complex **5**			
Cu(1)–O(1)	1.918(3)	Cu(1)–N(2)	2.015(3)
Cu(1)–N(1)	2.013(3)	Cu(1)–N(3)	1.987(3)
O(1)–Cu(1)–N(1)	171.7(1)	N(1)–Cu(1)–N(2)	80.0(1)
O(1)–Cu(1)–N(2)	93.1(1)	N(1)–Cu(1)–N(3)	92.8(1)

complex **3** is that the water trimer, the coordinated water molecule and the uncoordinated carboxyl oxygen atom (O4) form hydrogen bonds ring in a graph set $R_5^5(10)$ [15] which link the neighbor chains by hydrogen bond between H8A(W) and uncoordinated carboxyl oxygen atom(O2), resulting in a 2D supramolecular structure (see Fig. 6). The details of hydrogen bonds are listed in Table 3.

3.4. Structure description of $[Cu(psa)(4bpy)]\cdot H_2O$ (**4**)

X-ray diffraction analysis reveals that complex **4** possesses a 3D porous metal–organic framework with twofold interpenetration. The asymmetric unit of **4** consists of one Cu(II) ion, one $[psa]^{2-}$ ligand, one 4bpy ligand, and one lattice molecule. Cu(II) ion is also four-coordinated by two oxygen atoms (O1, O4A) of two $[psa]^{2-}$ ligands and two nitrogen atoms (N1, N2A) from two independent 4bpy, the geometry can be described as a slightly distorted square (see Fig. 7).

In complex **4**, the $[psa]^{2-}$ ligand shows trans-configuration (see Scheme 1b) and also adopts bis(monodentate) coordination mode. 4bpy ligands link the Cu(II) ions into

Table 3
Parameters (Å, °) for hydrogen bonds of complexes **1** and **3**

D–H···A	*d*(D–H)	*d*(H···A)	*d*(D···A)	∠DHA	Symmetry code
Complex **1**					
O(5)–H(5A)···O(3)	0.86	1.99	2.787	155	$-1+x$, y, z
O(5)–H(5B)···O(7)	0.86	2.16	2.721	123	x, y, z
O(6)–H(6A)···O(5)	0.89	1.90	2.767	165	x, y, z
O(6)–H(6B)···O(2)	0.85	1.99	2.821	164	$1-x$, $-1/2+y$, $1-z$
O(7)–H(7A)···O(4)	0.96	2.07	2.897	144	$2-x$, $-1/2+y$, $1-z$
Complex **3**					
O(5)–H(5A)···O(6)	0.85	2.20	2.698	117	x, y, z
O(5)–H(5B)···O(4)	0.85	1.96	2.594	130	x, $1+y$, z
O(6)–H(6A)···O(5)	0.86	1.85	2.698	169	x, y, z
O(6)–H(6B)···O(8)	0.86	2.00	2.766	148	x, y, z
O(7)–H(7A)···O(8)	0.88	2.48	2.836	105	x, y, z
O(7)–H(7B)···O(4)	0.86	2.43	2.802	107	x, $1+y$, z
O(8)–H(8A)···O(2)	0.85	2.01	2.768	148	$1/2-x$, $1+y$, $-1/2+z$

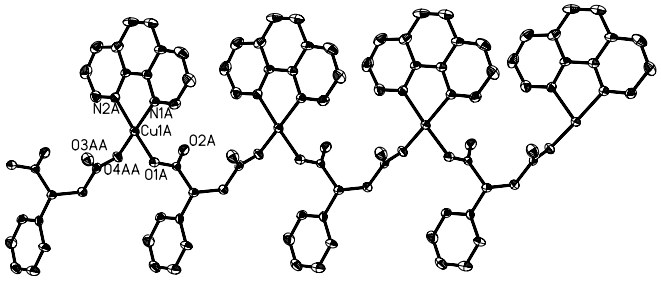
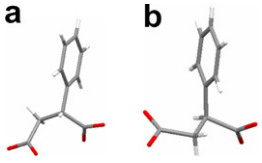


Fig. 1. The 1D chain structure of complex **1**.



Scheme 1. The configurations of $[psa]^{2-}$ ligand in complexes **1**–**5**. (a) cis-form (in complexes **1**–**3**); (b) trans-form (in complexes **4** and **5**).

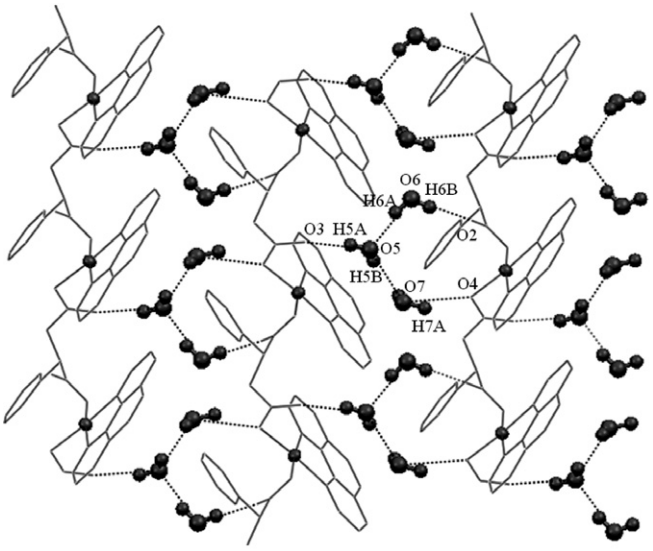


Fig. 2. The 2D supramolecular network of complex **1** formed by hydrogen bonds in *ab* plane.

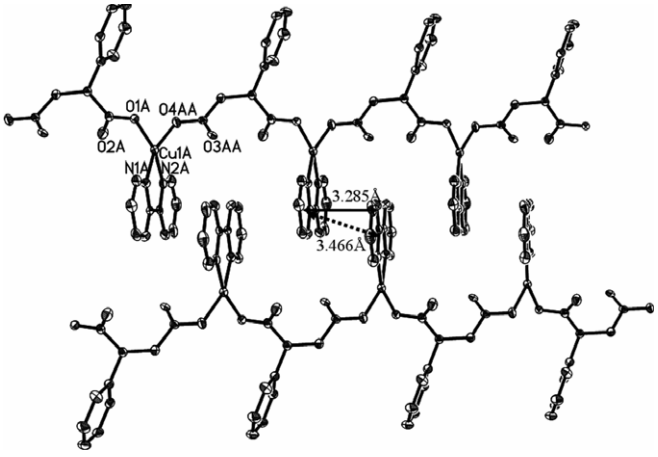


Fig. 3. The zipper structure of complex **2**.

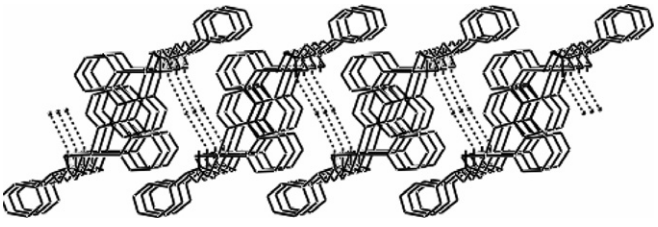


Fig. 4. The 2D supramolecular network formed by hydrogen bonds and π–π packing in complex **2** viewed along *b*-axis.

1D chains along two different directions, and the two sets of the chains (angle 33.5°) are bridged by $[psa]^{2-}$ ligand into a 3D $CdSO_4$-like structure with large 1D channels along the [1 1 0] direction, as shown in Fig. 8. The distances between the Cu(II) ions at the corners of the rectangular channels are 17.509 and 11.189 Å, respectively. Without the existence of large inclusion ions or molecules in such

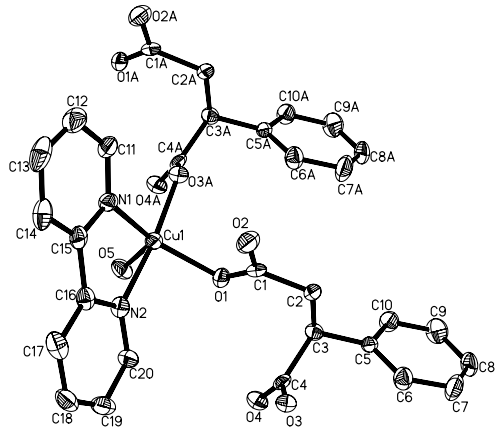


Fig. 5. The coordination environment of Cu(II) ion in complex **3**.

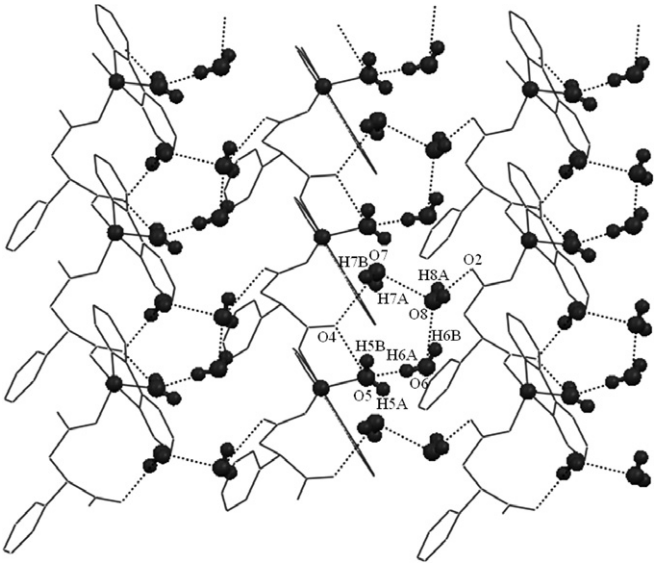


Fig. 6. The 2D network of complex **3** formed by hydrogen bonds in *ab* plane.

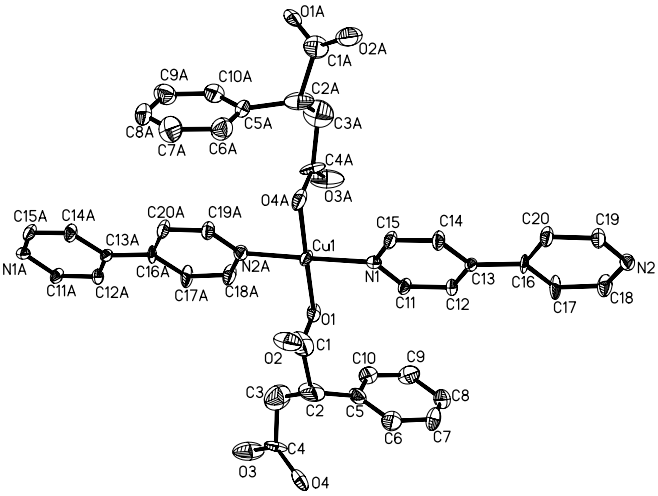


Fig. 7. The coordination environment of Cu(II) ion in complex **4**.

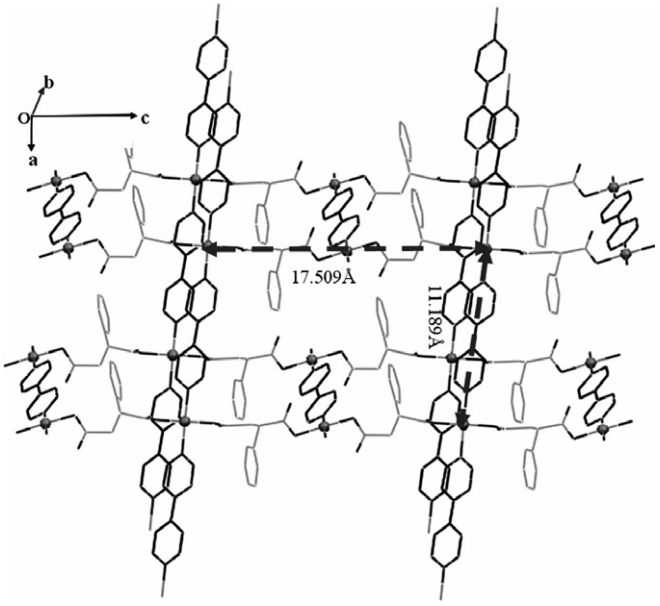


Fig. 8. The $CdSO_4$-like structure of complex **4**.

network, twofold interpenetration happens (see Fig. 9). And thus the volume of the effective void calculated using PLATON [16] is 5.3% of the unit-cell volume in the self-inclusion structure which is occupied by the non-coordinated water molecules. Hydrogen bonds (O5–H5B···O2, O···O distance 2.781 Å) can be found between the non-coordinated water molecules and the 3D metal–organic framework.

3.5. Structure description of $[Cu(psa)_{0.5}(N_3)(2bpy)]$ (5)

Complex **5** is a dinuclear compound, and in the asymmetric of complex **5**, there are one Cu(II) ion, one half of $[psa]^{2-}$ ligand, one N_3^- ligand and one 2bpy ligand. In complex **5**, each Cu(II) ion is four-coordinated by two nitrogen atoms (N1, N2) from one chelating ligand 2bpy, one nitrogen atoms (N3) of one N_3^- ligand, and one oxygen atom (O1) from $[psa]^{2-}$ ligand (see Fig. 10). Thus Cu(II) ion is in a slightly distorted square geometry. The mean Cu–N bond length is longer than the Cu–O distance.

In complex **5**, the $[psa]^{2-}$ ligand adopts bis(monodentate) coordination mode and is also trans-configuration (see Scheme 1b) bridging two Cu(II) ions. While the terminal ligands 2bpy and monodentate N_3^- hinder the extension of the structure, forming a dinuclear structure. The dinuclear structures are interlinked by hydrogen bonds (C–H···O) and cooperated with π–π interactions (face to face distance 3.243 Å) to form 3D brick-wall supramolecular structure viewed along *b*-axis (Fig. 11).

Comparing complexes **1**, **2**, and **4**, their synthetic conditions are very similar, and the main difference among them is the employment of different auxiliary ligands. However, the differences in the auxiliary ligands have a significant effect on the structure of the complexes. In complexes **1**, **2**, and **4**, Cu(II) ions are all four-coordinated, while the $[psa]^{2-}$ ligands are transformed from cis-configuration in complexes **1** and **2** by the introduction of phen and 2bpy ligands to trans-configuration in complex **4** because of the application of the bridging 4bpy ligand. And chelating ligands phen and 2bpy tend to forming low-dimensional structure, while the linear ligand 4bpy is able to construct 3D metal–organic framework. Complexes **2** and **3** were

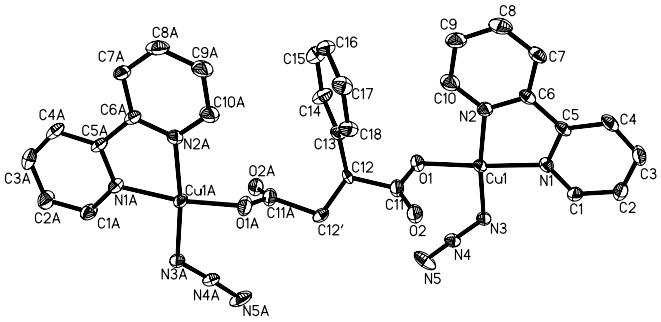


Fig. 10. The coordination environment of Cu(II) ion in complex **5**.

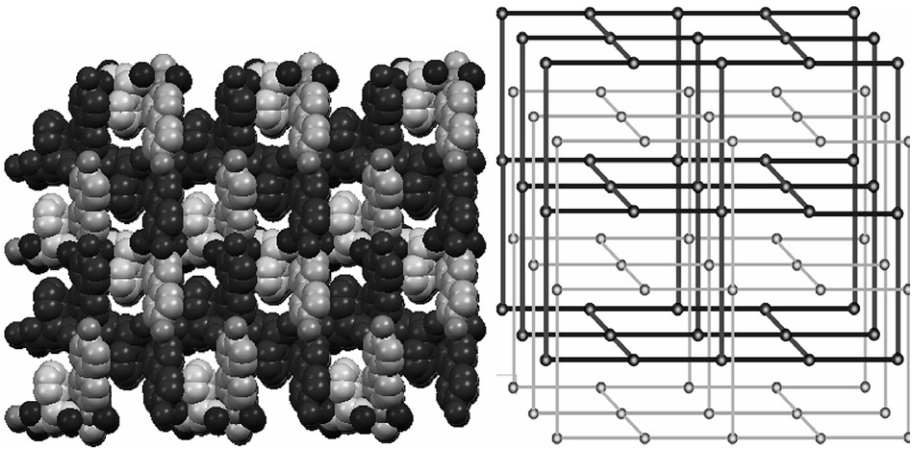


Fig. 9. The twofold interpenetrated spacefilling diagram of complex **4**, the water molecules occupied the channels are omitted (left). The simplified representation structure of complex **4** viewed along [1 1 0] (right).

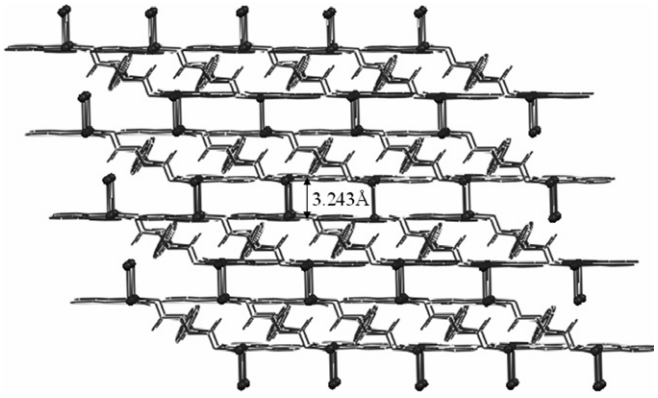


Fig. 11. 3D supramolecular structure of complex **5** viewed along *b*-axis.

formed in one-pot reaction. Complex **3** was obtained by leaving the mother solution of complex **2** at room temperature. Probably with the decrease of temperature, the water molecules attack the axial site of the square and coordinated to the Cu(II) ions leading to formation of complex **3**. And the coordinated water molecules result in different stacking patterns for 1D chains and thus the final network. With addition of N_3^- to system **2**, the half of $[psa]^{2-}$ ligands are replaced by the N_3^- ligands, complex **5** is formed. In complex **5**, two Cu(II) ions are bridged by one $[psa]^{2-}$ ligand. While both 2pby and N_3^- ligands as terminal ligands hinder the extending of the structure, forming a dinuclear structure. The results show the importance of the selection of auxiliary ligands in assembly of complexes.

3.6. Thermal analyses of complexes *1*, *3*–*5*

Complexes **1**–**5** are very stable in air at ambient temperature and almost insoluble in common solvents such as water, alcohol, acetonitrile, chloroform, methanol, and acetone. In order to examine their thermal stability, we carried out thermal gravimetric analyses (TGA) of the five complexes expect complex **2** because of the lower yield. The result shows that complex **1** is stable up to 75 °C. A total weight loss of 10.5% occurred in the temperature range 75–126 °C, corresponding to the loss of the three lattice water molecules in the complex (Calc. 11.0%), the further decomposition occurred at 205 °C, and the final pyrolysis was completed at 670 °C, giving the powder of CuO. For complex **3**, the TG curve exhibits that complex **3** is stable up to 73 °C with the first weight loss of 13.4% from 73 °C to 107 °C, which corresponds to the loss of four water molecules (Calc. 13.2%), and unknown decomposition reactions took place over 200 °C. The thermal decomposition behavior of complex **4** shows that complex **4** began complicated decomposition up to 207 °C, and the structure collapsed with the loss of the guest water molecule since no flateau in TG curve was observed during the decomposition of complex **4**. The TG curve shows that complex **5** is stable up to 213 °C, and decomposes rapidly in the temperature range 213–229 °C. The residue CuO powder in 23.3% was obtained at 580 °C (Calc. 22.3%).

4. Conclusions

In summary, using solvothermal reaction conditions, we obtained five new Cu(II) complexes **1**–**5** with $[psa]^{2-}$ ligand and different auxiliary ligands phen, 2bpy, 4bpy, and N_3^-. Complexes **1**–**3** are composed of 1D chains, extending into 2D supramolecular structure by hydrogen bonds (complexes **1** and **3**) or hydrogen bonds and π–π stacking interactions (complex **2**), in which $[psa]^{2-}$ ligand shows cis-configuration and adopts bis(monodentate) coordination mode. Interestingly, complexes **2** and **3** were obtained by one-pot reaction, showing that different complexes can be obtained by controlling the reaction condition in the same system. Complex **4** is of a 3D $CdSO_4$-like metal–organic framework formed by bridging ligands $[psa]^{2-}$ and 4bpy linking Cu(II) ion, and $[psa]^{2-}$ is in trans-configuration. The different structures of complexes **1**–**5** show that the auxiliary ligands have a significant effect on the formation and the construction of the complexes **1**–**5**.

Acknowledgement

The authors thank the financial support of National Nature Science Foundation of China (20331010, 20501003).

Appendix A. Supplementary material

CCDC 634194, 634195, 634196, 634197, and 634198 contain the supplementary crystallographic data for **1**, **2**, **3**, **4**, and **5**. The data can be obtained free of charge via http://www.ccdc.cam.ac.uk/conts/retrieving.html, or from the Cambridge Crystallographic Data Centre, 12 Union Road, Cambridge CB2 1EZ, UK; fax: (+44) 1223-336-033; or e-mail: deposit@ccdc.cam.ac.uk. Supplementary data associated with this article can be found, in the online version, at doi:10.1016/j.poly.2007.04.016.

References

[1] (a) R.J. Hill, D.L. Long, N.R. Champness, P. Hubberstey, M. Schröder, Acc. Chem. Res. 38 (2005) 335;
(b) M. Oh, G.B. Carpenter, D.A. Sweigart, Acc. Chem. Res. 37 (2004) 1;
(c) O.M. Yaghi, M. O'Keeffe, N.W. Ockwig, H.K. Chae, M. Eddaoudi, J. Kim, Nature 423 (2003) 705.
[2] (a) C. Janiak, Dalton Trans. (2003) 2781;
(b) D. Fiedler, D.H. Leung, R.G. Bergman, K.N. Raymond, Acc. Chem. Res. 38 (2005) 349;
(c) S. Kitagawa, R. Kitaura, S. Noro, Angew. Chem., Int. Ed. 43 (2004) 2334.
[3] (a) S. Kitagawa, R. Kitaura, S. Noro, Angew. Chem., Int. Ed. 43 (2004) 2334;
(b) R. Eberhardt, M. Allmendiger, M. Zintl, C. Troll, G.A. Luinstra, B. Rieger, Macromol. Chem. Phys. 205 (2004) 42;

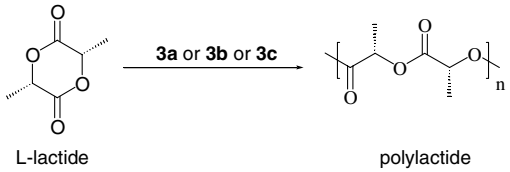
(c) W. Mori, T. Sato, T. Ohmura, C.N. Kato, T. Takei, J. Solid State Chem. 178 (2005) 2555.
[4] (a) D.N. Dybtsev, H. Chun, S.h. Yoon, D. Kim, K. Kim, J. Am. Chem. Soc. 126 (2004) 32;
(b) K.S. Min, M.P. Suh, Chem. Eur. J. 7 (2001) 303.
[5] (a) F. Mori, T. Nyui, T. Ishida, T. Nogami, K. Ychoi, H. Nojiri, J. Am. Chem. Soc. 128 (2006) 1440;
(b) S.C. Manna, E. Zangrando, Michael G.B. Drew, J. Ribas, N.R. Chaudhuri, Eur. J. Inorg. Chem. (2006) 481.
[6] (a) J. Lefebvre, R.J. Batchelor, D.B. Leznoff, J. Am. Chem. Soc. 126 (2004) 16117;
(b) S.I. Noro, S. Horike, D. Tanaka, S. Kitagawa, T. Akutagawa, T. Nakamura, Inorg. Chem. 45 (2006) 9290;
(c) M.D. Stephenson, M.J. Hardie, Dalton Trans. (2006) 3407;
(d) D.K. Kumar, A. Das, P. Dastidar, New J. Chem. 30 (2006) 1267;
(e) W. Oueuette, A.V. Prosvirin, V. Chieffo, K.R. Dunbar, B. Hudson, J. Zubieta, Inorg. Chem. 45 (2006) 9346;
(f) M.A. Halcrow, Dalton Trans. (2003) 4375.
[7] (a) M. Kurmoo, H. Kumagai, K.W. Chapman, C.J. Kepert, Chem.Commun. (2005) 3012;
(b) Z.H. Zhou, J.M. Yang, H.L. Wan, Crystal Growth Des. 5 (2005) 1825;
(c) S.C. Manna, E. Zangrando, A. Bencini, C. Benelli, N.R. Chaudhuri, Inorg. Chem. 45 (2006) 9114;
(d) T.A. Bowden, H.L. Milton, A.M. Z. Slawin, P. Lightfoot, Dalton Trans. (2003) 936;
(e) H.Y. Mao, C.Z. Zhang, G. Li, H.Y. Zhang, H.W. Hou, L.K. Li, Q.A. Wu, Y. Zhu, E.B. Wang, Dalton Trans. (2004) 3918;
(f) J. Perles, M. Iglesias, C.R. Valero, N. Snejko, Chem. Commun. (2003) 346.
[8] (a) B. Covelo, R. Carballo, E.M. Vazquez-Lopez, E. Garcia-Martinez, A. Castineiras, S. Balboa, J. Niclos, CrystEngComm 8 (2006) 167;
(b) R. Carballo, B. Covelo, C. Loderior, E.M. Vazquez-Lopez, CrystEng Comm. 7 (2005) 294;
(c) R. Carballo, J.S. Casas, E. Garcia-Martinez, G. Pereiras-Gabian, A. Sanchez, U. Abram, E.M. Azquez-Lopez, CrystEngComm 7 (2005) 113.
[9] (a) R. Matsuda, R. Kitaura, S. Kitagawa, Y. Kubota, T.C. Kobayashi, S. Horike, M. Takata, J. Am. Chem. Soc. 126 (2004) 14063;
(b) S.I. Noro, R. Kitaura, M. Dondo, S. Kitagawa, T. Ishii, H. Matsuzaka, M. Yamashita, J. Am. Chem. Soc. 124 (2002) 2568.
[10] G.M. Sheldrick, SADABS, Program for Empirical Absorption Correction of Area Detector Data, University of Göttingen, Göttingen, Germanny, 1997.
[11] G.M. Sheldrick, SHELXS97, Program for Crystal Structure Solution, University of Göttingen, Germany, 1997.
[12] G.M. Sheldrick, SHELXL97, Program for Crystal Structure Refinement, University of Göttingen, Germany, 1997.
[13] J. Zhou, C.Y. Sun, L.P. Jin, J. Mol. Struct. 832 (2007) 55.
[14] C. Janiak, J. Chem. Soc., Dalton Trans. (2000) 3885.
[15] M.C. Etter, Acc. Chem. Res. 23 (1990) 120.
[16] A.L. Spek, J. Appl. Crystallogr. 36 (2003) 7.

of which have contributed significantly to the development of the respective fields. The successes of phenoxy-imines are presumably due to the availability of scope for suitable tuning of the sterics and the electronics of the ligand ancillary and also due to their easy synthetic accessibility, as the phenoxy-imines are often prepared by Schiff base condensation reactions. Interestingly enough, despite extensive utility of phenoxy-imines in many important chemical transformations, their application in ring-opening polymerization (ROP) of L-lactide largely remains unexplored [20].

Our interest in the ring-opening polymerization (ROP) of L-lactide arises mainly because of its eco-friendly nature as the polylactide polymer (PLA) is biodegradable and also because the lactide monomer can be generated from renewable resources like the corn fermentation process or from agricultural starch wastes [21,22]. The PLAs are biocompatible and exhibit good mechanical properties and, hence, are long known for their use in medical and pharmaceutical related applications [23,24]. One of our core programs is centered around designing novel initiators for the bulk ring-opening polymerization of L-lactide, and in this regard we have recently reported Ag(I) [25] and Au(I) [26] complexes of N-heterocyclic carbenes (NHC) as initiators for the bulk polymerization of L-lactide under solvent-free melt conditions. It is noteworthy that the PLAs can be synthesized by both solution polymerization [27] and bulk polymerization [28], however, the solution polymerization suffers from certain disadvantages like being susceptible to the impurity levels and to various unwanted reactions namely racemization, transesterifications, etc. The bulk polymerization, which does not suffer from such limitations, is thus, often preferred for the large-scale production of PLAs [29].

With regard to designing new initiators for our ROP program we observed that the phenoxy-imine ligands, despite their proven successes in chemical catalysis, remain to be tried for ring-opening polymerization (ROP) of L-lactide [20] and so we became interested in exploring the scope of phenoxy-imine based transition metal complexes as catalysts for bulk polymerization of L-lactide. Furthermore, phenoxy-imine metal complexes, bearing a metal–alkoxide bond, are natural candidates for the catalysis, as the well accepted catalysts for the ring-opening polymerization (ROP) of L-lactide are often the metal–alkoxide complexes [21,30–33] (see Fig. 1).

Here in this contribution, we report the synthesis, structural characterizations and catalysis studies of a series of nickel (**2a** and **2b**) and copper (**3a**, **3b** and **3c**) complexes of phenoxy-ketimine ligands with varying steric demands, namely 2-[1-(2,6-diethylphenylimino)ethyl]phenol (**1a**), 2-[1-(2,6-dimethylphenylimino)ethyl]phenol (**1b**) and 2-[1-(2-methylphenylimino)ethyl]phenol (**1c**). Furthermore, we disclose that while the copper complexes (**3a**, **3b** and **3c**) were found to be efficient initiators for ring-opening polymerization of L-lactide at elevated temperatures under solvent-free melt conditions, producing polylactide polymers



Equation 1. Polymerization of L-lactide by **3a**, **3b** and **3c**.

of moderate molecular weights with narrow molecular weight distributions (Eq. (1)), the nickel complexes (**2a** and **2b**) failed to yield a polylactide polymer.

2. Results and discussion

A series of monoanionic phenoxy-ketimine ligands, namely 2-[1-(2,6-diethylphenylimino)ethyl]phenol (**1a**), 2-[1-(2,6-dimethylphenylimino)ethyl]phenol (**1b**) and 2-[1-(2-methylphenylimino)ethyl]phenol (**1c**) were synthesized by a modification of a $TiCl_4$ catalyzed procedure reported in the literature for the condensation of α-haloketones with amines [34]. Specifically, the condensation reaction of *o*-hydroxyacetophenone with the respective anilines in presence of a catalytic amount of $TiCl_4$ gave the phenoxy-

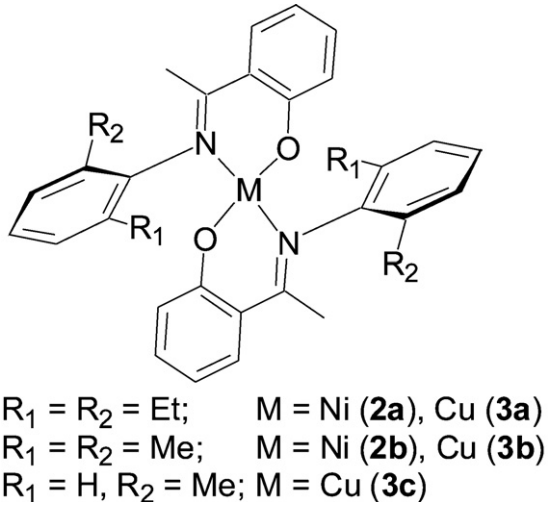
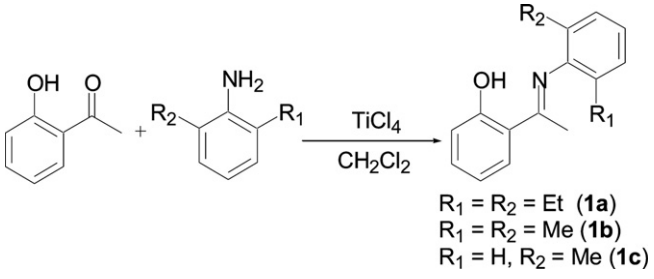


Fig. 1. Ni(II) and Cu(II) complexes of a series of phenoxy-ketimine ligands with controlled variation of sterics.



Scheme 1. Synthesis of phenoxy-ketimine ligands **1a**, **1b** and **1c**.

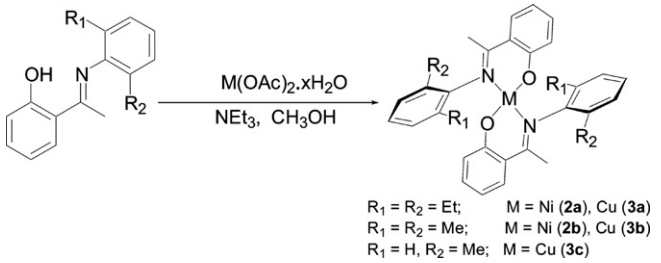
ketimine ligands, **1a**, **1b** and **1c** [35], in ca. 21–23% yield (Scheme 1). It is interesting to note that the ketimine ligands are often synthesized by two different methods, namely: (i) Schiff base condensation of ketones with amines in the presence of a catalytic amount of an acid like HCO_2H [36] or *p*-toluenesulfonic acid [16] and (ii) Friedel-Crafts acylation of the imidoyl chloride with the *ortho*-unsubstituted phenol [37]. The compounds **1a**, **1b** and **1c** have been characterized by ^{1}H NMR, ^{13}C NMR, IR, UV–Vis and mass spectrometry. The ^{1}H NMR spectra of **1a**, **1b** and **1c** showed the ketimine methyl (*Me*C=N) resonances as singlets at 2.09–2.17 ppm, while the phenolic –O*H* protons appeared as broad peaks at 14.7–14.8 ppm. The substantially high downfield shifts of the phenolic –O*H* protons in **1a**, **1b** and **1c** are attributed to an intramolecular hydrogen bonding interaction, [phenolic –OH···N=C (imine N)]. A similar downfield shift of the phenolic –O*H* proton (16.8 ppm) due to an intramolecular hydrogen bonding interaction has been reported for the Schiff base ligand 1-(2-hydroxy-3,5-dichlorophenyl)-2,5-diaza-6-methylnona-1,6-diene-8-one [38]. Furthermore, the ketimine moieties (MeC=N) appeared at 171.1–171.9 ppm (Me*C*=N) in the ^{13}C NMR spectra and at 1609–1614 cm^{-1} ($\nu_{C=N\ str}$) in the infrared spectra. The electronic spectra of the phenoxy-ketimine ligands **1a**, **1b** and **1c** in $CHCl_3$ exhibited two distinct absorption bands in the UV region which have been identified as high energy π–π^* and low energy n–π^* transitions, based on the assignment made for a series of related phenoxy-imine ligands, namely 2-[1-(R)methyl]phenol (where R = –CH_3, –C_6H_{11} and –C_5H_4N) [39]. The high energy bands due to the π–π^* transitions showed absorptions at 256 nm for **1a** ($\varepsilon = 17263$ L mol^{-1} cm^{-1}), 256 nm for **1b** ($\varepsilon = 17933$ L mol^{-1} cm^{-1}) and 257 nm for **1c** ($\varepsilon = 21873$ L mol^{-1} cm^{-1}), while the low energy n–π^* transition appeared at 323 nm for **1a** ($\varepsilon = 5945$ L mol^{-1} cm^{-1}), 322 nm for **1b** ($\varepsilon = 5919$ L mol^{-1} cm^{-1}) and 324 nm for **1c** ($\varepsilon = 8776$ L mol^{-1} cm^{-1}). Electrospray mass analysis gave peaks at $m/z = 268$ (**1a**), 240 (**1b**) and 226 (**1c**), corresponding to the respective M+1 ions in 100% abundances.

The nickel (**2a** and **2b**) and copper (**3a**, **3b** and **3c**) complexes were synthesized by the reaction of the ligands with $M(OAc)_2 \cdot xH_2O$ (M = Ni, Cu) in the presence of NEt_3 in methanol in 71–75% and 70–87% yields, respectively (see Scheme 2). Both of the nickel complexes, **2a** and **2b**, were diamagnetic in nature, consistent with a square planar geometry of the Ni(II) d^8 configuration. The ketimine methyl moieties (MeC=N) in **2a** and **2b** appeared as singlets at 1.87–1.94 ppm (*Me*C=N) in the ^{1}H NMR spectra and at 168.6–168.9 ppm (Me*C*=N) and 19.7–20.6 ppm (*Me*C=N) in the ^{13}C{^{1}H} NMR spectra. Comparison of infrared spectra for the $\nu_{C=N}$ stretching frequencies for **2a** (1574 cm^{-1}) and **2b** (1571 cm^{-1}) showed red shifts of ca. 35–43 cm^{-1} relative to the respective parent ligands **1a** (1609 cm^{-1}) and **1b** (1614 cm^{-1}). The $\nu_{C=N}$ stretching frequency values observed for **2a** and **2b** are similar to that of a related complex, {2-[1-(2,6-diisopropylphenylimino)-methyl]phenoxy}$_2$Ni(II) [36] (1602 cm^{-1}).

The paramagnetic copper complexes **3a**, **3b** and **3c** were characterized by IR, electronic spectroscopy, ESR, elemental analysis and X-ray diffraction studies. The $\nu_{C=N}$ stretching frequencies in the copper complexes, **3a** (1599 cm^{-1}), **3b** (1601 cm^{-1}) and **3c** (1599 cm^{-1}), are comparable to the closely related complex, {2-[1-(2-methoxyphenylimino)-methyl]phenoxy}$_2$Cu(II) [40], (1600 cm^{-1}) and, as was observed in the case of the nickel complexes **2a** and **2b**, the $\nu_{C=N}$ stretching frequencies are all red shifted by ca. 10–13 cm^{-1} relative to the ligands, **1a** (1609 cm^{-1}), **1b** (1614 cm^{-1}) and **1c** (1611 cm^{-1}).

The electronic spectra of the nickel complexes, **2a** and **2b**, in $CHCl_3$ showed absorption bands due to d–d transitions at 601 nm ($\varepsilon = 118$ L mol^{-1} cm^{-1}) and 592 nm ($\varepsilon = 102$ L mol^{-1} cm^{-1}), respectively, which are comparable to those reported for other square planar Ni(II) complexes. For example, square planar Ni(II) complexes of a series of [N_2O_2] chelating salen type ligands with varying spacer lengths showed similar low intensity absorbances due to d–d transitions at 532–550 nm ($\varepsilon = 240$–260 L mol^{-1} cm^{-1}) [41]. The Cu complexes, **3a**, **3b** and **3c**, on the other hand showed the d–d transitions at 696 nm ($\varepsilon = 89.4$ L mol^{-1} cm^{-1}), 670 nm ($\varepsilon = 130$ L mol^{-1} cm^{-1}) and 630 nm ($\varepsilon = 125$ L mol^{-1} cm^{-1}), respectively, which are also similar to other square planar copper complexes, like *bis*-[(N2-(2-pyridylmethyl)-3-thenyl-carboxamido)copper(II)]perchlorate [42] (675 nm). Similar comparisons of the d–d transitions in **3a**, **3b** and **3c** can also be drawn with another set of Schiff base copper complexes, {3-methoxy-2-[1-(2-pyridylmethylimino)methyl]phenoxy}Cu(II)X [43] (X = Cl, Br), based on a phenolato-pyridine ligand, which showed weak broad bands in the 600–700 nm region which were attributed to d–d transitions. The differences in the absorption bands amongst the copper complexes **3a**, **3b** and **3c** is notable, showing marked shifts of ca. 30 nm with the decrease in steric bulk of the 2,6-*di*-substituted phenyl ring on going from **3a** to **3b** to **3c**. In contrast, the Ni complexes did not show any appreciable difference in the d–d transitions on going from **2a** to **2b**.

The EPR spectra of the copper complexes **3a**, **3b** and **3c**, recorded in the frozen state in CH_2Cl_2 at 77 K (Table 1), showed a commonly observed axial pattern consisting of two well resolved peaks and two overlapping peaks of low intensities in the low field region ($g_{\|}$) due to hyperfine



Scheme 2. Synthesis of the metal complexes.

Table 1
EPR parameters of **3a**, **3b** and **3c** in CH_2Cl_2 at 77 K

Complex	$A_{\parallel}$	$A_{\perp}^{a}$	$g_{\parallel}$	$g_{\perp}$
3a	143	NR	2.2517	2.0399
3b	140	NR	2.2517	2.0463
3c	140	NR	2.2447	2.0465

[a] NR, not resolved.

splitting by the copper nucleus ($I = 3/2$) along with a high intensity peak in the high field region ($g_{\perp}$). In this context, it is worth mentioning that in square planar copper complexes, an unpaired electron when residing in the $d_{x^2-y^2}$ orbital ($^2B_{1g}$ ground state) exhibits $g_{\parallel} > g_{\perp}$ whereas the same when present in the other axial d_{z^2} orbital ($^2A_{1g}$ ground state) displays $g_{\perp} > g_{\parallel}$ [44–46]. Quite notably, in all the three copper complexes **3a**, **3b** and **3c**, the observed $g_{\parallel} > g_{\perp}$ is consistent with a square planar geometry at the metal center with the unpaired electron placed in the $d_{x^2-y^2}$ orbital [44–46]. Furthermore, the observed g and A values of **3a**, **3b** and **3c** are comparable to those of other reported copper complexes. For example, the average g and A values recorded at 77 K for the square planar complex {2-[1-(*N*,*N*-diethylethyleneimino)methyl]phenol)}$_2$Cu-$(ClO_4)_2$ [47] are $g_{\parallel}$ (2.225), $g_{\perp}$ (2.070) and $A_{\parallel}$ (179.7) and that of {4-[1-(4-methoxyphenylimino)-pent-2-ene-2-oxy]}$_2$-Cu(II) [45] are $g_{\parallel}$ (2.328), $g_{\perp}$ (2.067) and $A_{\parallel}$ (140).

The molecular structures of the nickel (**2a** and **2b**) (Figs. 2 and 3) and copper complexes (**3a**, **3b** and **3c**) (Figs. 4–6) have been determined by X-ray diffraction studies, which revealed the formation of metal complexes having 2:1 ligand to metal stoichiometries. The metal ions in these complexes reside at the center of a *trans*-N_2O_2 core which is perfectly square planar in case of the nickel (**2a** and **2b**) and two of the copper complexes (**3a** and **3c**), whereas it is distorted square planar in the other copper complex **3b**.

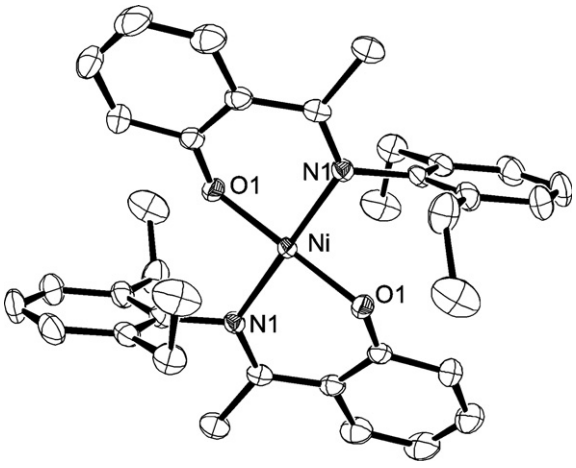


Fig. 2. ORTEP of **2a**. Thermal motion ellipsoids are drawn at the 50% probability level for the non-hydrogen atoms. Selected bond lengths (Å) and angles (°): Ni1–N1 1.9085(14), Ni1–N1 1.9085(14), Ni1–O1 1.8258(11), Ni1–O1 1.8258(11), N1–Ni1–N1 180.00(13), O1–Ni1–O1 180.00(9), N1–Ni1–O1 91.10(6), N1–Ni1–O1 88.90(6).

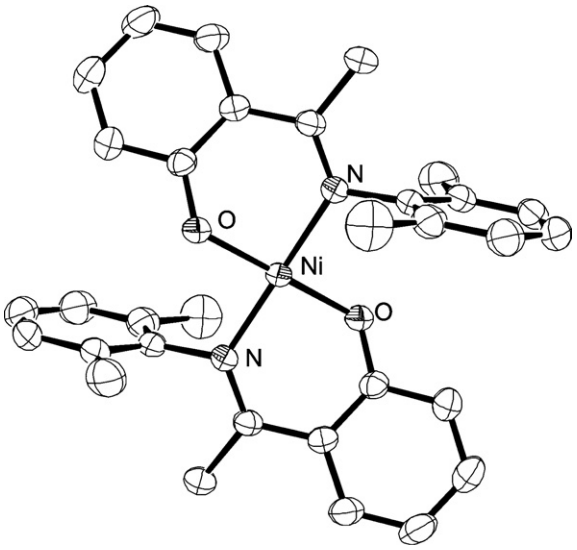


Fig. 3. ORTEP of **2b**. Thermal motion ellipsoids are drawn at the 50% probability level for the non-hydrogen atoms. Selected bond lengths (Å) and angles (°): Ni–N 1.9199(11), Ni–N 1.9199(11), Ni–O 1.8248(10), Ni–O 1.8248(10), N–Ni–N 180.00(4), O–Ni–O 180.00(5), N–Ni–O 90.93(5), N–Ni–O 89.07(5).

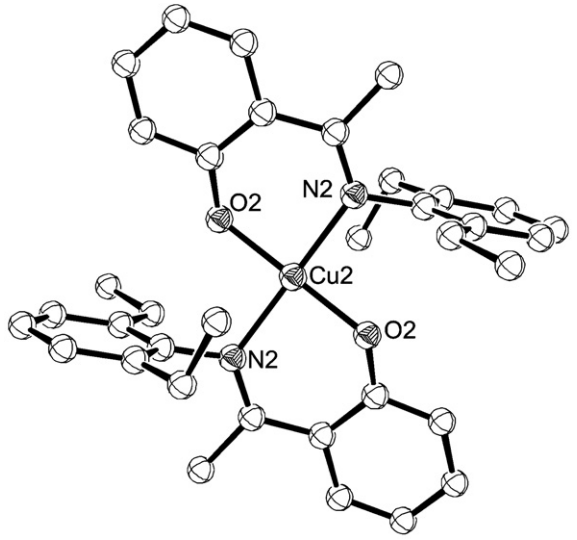


Fig. 4. ORTEP of **3a**. Thermal motion ellipsoids are drawn at the 50% probability level for the non-hydrogen atoms. Selected bond lengths (Å) and angles (°): Cu2–N2 2.0161(14), Cu2–N2 2.0161(14), Cu2–O2 1.8631(11), Cu2–O2 1.8630(11), N2–Cu2–N2 180.00(12), O2–Cu2–O2 180.00(7), O2–Cu2–N2 90.50(5), O2–Cu2–N2 89.50(5).

Consistent with a square planar geometry, the Ni(II) centers in **2a** and **2b** are surrounded by two equidistant Ni–N [**2a**: 1.9085(14) Å (Fig. 2); **2b**: 1.9199(11) Å (Fig. 3)] and two equidistant Ni–O [**2a**: 1.8258(11) Å (Fig. 2); **2b**: 1.8248(10) Å (Fig. 3)] bond distances. The Ni–N and the Ni–O bond distances in **2a** and **2b** are, however, somewhat longer than the sum of the individual covalent radii of the respective atoms (Ni–N = 1.854 Å, Ni–O = 1.814 Å) [48]. Quite expectedly, the complementary ∠O–Ni–N and ∠N–Ni–O angles at the nickel centers in **2a** [91.10(6),

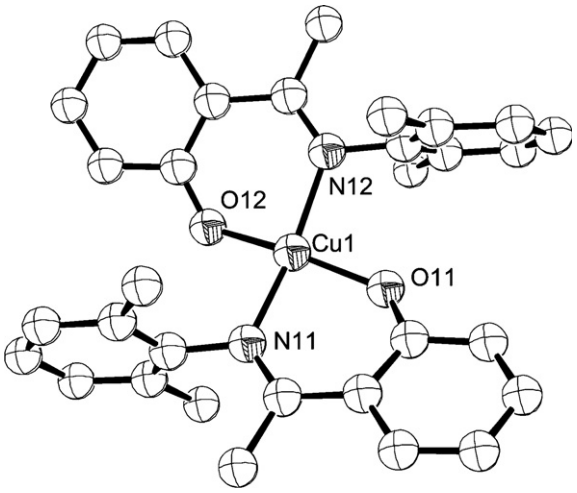


Fig. 5. ORTEP of **3b**. Thermal motion ellipsoids are drawn at the 50% probability level for the non-hydrogen atoms. Selected bond lengths (Å) and angles (°): Cu1–N11 2.007(5), Cu1–N12 2.006(4), Cu1–O11 1.858(4), Cu1–O12 1.856(4), N11–Cu1–N12 161.58(19), O11–Cu1–O12 159.8(2), O12–Cu1–N12 89.36(17), O11–Cu1–N12 91.96(18).

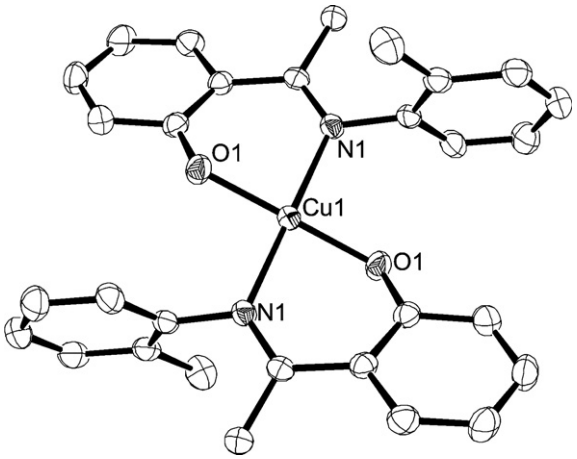


Fig. 6. ORTEP of **3c**. Thermal motion ellipsoids are drawn at the 50% probability level for the non-hydrogen atoms. Selected bond lengths (Å) and angles (°): Cu1–N1 2.001(2), Cu1–N1 2.001(2), Cu1–O1 1.872(2), Cu1–O1 1.872(2), N1–Cu–N1 180.00(16), O1–Cu1–O1 180.00(12), O1–Cu1–N1 89.16(9), N1–Cu1–O1 90.84(9).

88.90(6)°] and **2b** [89.07(5), 90.93(5)°] are equal to ca. 90°. The *trans* disposition of the phenyl rings of the 2,6-disubstituted-phenyl moieties in both complexes **2a** and **2b** is a consequence of the reduction of steric strain.

The comparison of the molecular structures of **2a** and **2b** with the other reported nickel phenoxy-ketimine and phenoxy-aldimine complexes is important. For example, the Ni–O and Ni–N bond distances in the phenoxy-ketimine complex, {2-[1-(2,6-diisopropylphenylimino)ethyl]phenoxy}$_2$Ni(II) [36] [Ni–O = 1.8081(10) Å; Ni–N = 1.9262 (11) Å], and in the phenoxy-aldimine nickel complex, {3-*t*-butyl-5-methyl-2-[1-(ethylimino)methyl]phenoxy}$_2$Ni(II) [49], [Ni–O = 1.861(2), 1.852(2) Å; Ni–N = 1.905(2), 1.893(2) Å] are in good agreement with those in the complexes **2a** and **2b**.

The copper complexes **3a**, **3b** and **3c** are isostructural with their nickel counterparts, **2a** and **2b**, though certain variations were observed. The *di*-ethyl derivative **3a** and the *mono*-methyl derivative **3c** exhibit square planar geometries like the nickel complexes **2a** and **2b**, whilst a slightly distorted square planar geometry was observed in case of the *di*-methyl derivative **3b**. Thus, unlike the square planar nickel (**2a** and **2b**) and copper (**3a** and **3c**) complexes, in which two sets of equidistant M–O and M–N (M = Ni, Cu) bond lengths were observed, the Cu–N and Cu–O bond lengths of the *trans*-N_2O_2 core in **3b** are all marginally unequal, a consequence of the slight distortion of the square planar geometry around the copper center. For example, in **3b** the Cu1–N11 and Cu1–N12 bond lengths are 2.007(5) Å and 2.006(4) Å, while the Cu1–O11 and Cu1–O12 distances are 1.858(4) Å and 1.856(4) Å, respectively (Fig. 5). Owing to the presence of the distortion, the four ∠N–Cu–O bond angles at the copper center in **3b** are also marginally different from the ideal value of 90° [∠N12–Cu1–O12 = 89.36(17)° and ∠N12–Cu1–O11 = 91.96(18)°], while the diagonal angles [∠N11–Cu1–N12 = 161.58(19)° and ∠O11–Cu1–O12 = 159.8(2)°] at the copper in **3b** are significantly deviated from the expected value of 180°. The extent of the distortion of the square planar structure in **3b** becomes apparent upon comparison with the perfectly square planar nickel analog **2b** (Fig. 7b). It is interesting to note that although significant square planar distortion (as reflected in the angles, θ and ϕ, in Fig. 7b) is observed in the *di*-methyl derivative **3b** (θ = 21.4°, ϕ = 17.7°) relative to the square planar nickel counterpart **2b**, no such distortion was visible in case of the *di*-ethyl copper complex **3a** (θ = 1.0°, ϕ = 1.8°) relative to the nickel analog **2a** (Fig. 7a). The *mono*-methyl copper complex **3c** also showed no distortion and closely resembled the square planar copper complex **3a**.

The Cu–O and Cu–N bond distances in **3a**, **3b** and **3c** are comparable to those observed in other analogous copper phenoxy-ketimine complexes, {2-[1-(2-phenylethylimino)ethyl]phenoxy}$_2$Cu(II) [50] [Cu–O = 1.865(2) Å, Cu–N = 1.977(2) Å] and {2-[1-(2-methylpropylimino)ethyl]-phenoxy}$_2$Cu(II) [51] [Cu–O = 1.891(2) Å, Cu–N = 2.003(2) Å], as well as in the related copper phenoxy-aldimine complexes, {5-bromo-2-[1-(3-methylphenylimino)methyl]-phenoxy}$_2$Cu(II) [52] [Cu–O = 1.884(8) Å, Cu–N = 2.005(7) Å] and {2-[1-(phenylimino)methyl]phenoxy}$_2$-Cu(II) [53] [Cu–O = 1.878(3) Å, Cu–N = 1.993(4) Å].

3. Polymerization studies

Quite significantly, the copper complexes **3a**, **3b** and **3c** efficiently catalyzed the ring-opening polymerization (ROP) of L-lactide at elevated temperatures under solvent-free melt conditions [28]. In stark contrast to the

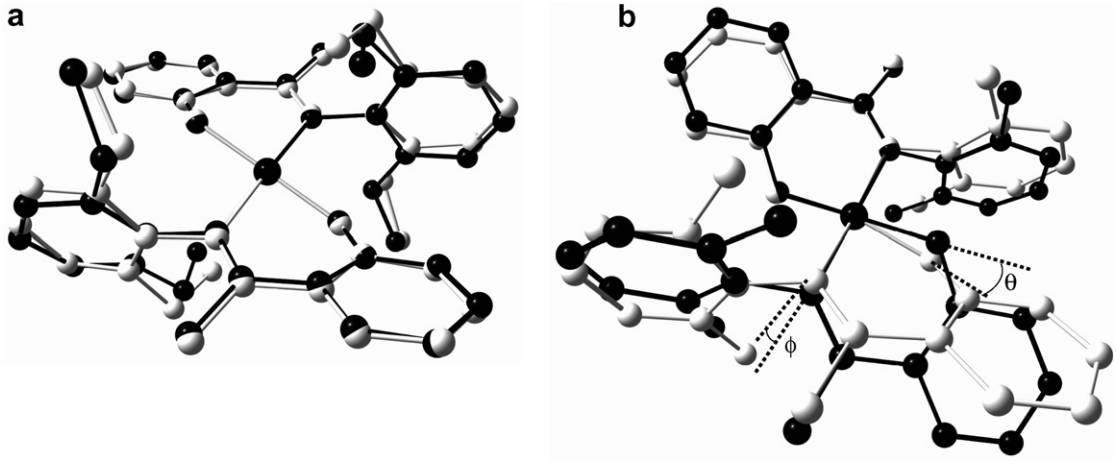


Fig. 7. (a). Overlaid structures of Ni (**2a**) (black) and Cu (**3a**) (grey) complexes. (b). Overlaid structures of Ni (**2b**) (black) and Cu (**3b**) (grey) complexes.

Table 2
X-ray crystallographic data for **2a**, **2b**, **3a**, **3b** and **3c**

Compound	**2a**	**2b**	**3a**	**3b**	**3c**
Lattice	triclinic	monoclinic	monoclinic	orthorhombic	monoclinic
Formula	$C_{36}H_{40}NiN_2O_2$	$C_{32}H_{32}NiN_2O_2$	$C_{36}H_{40}CuN_2O_2$	$C_{32}H_{32}CuN_2O_2$	$C_{30}H_{28}CuN_2O_2$
Formula weight	591.41	535.31	596.24	540.14	512.08
Space group	$P\bar{1}$	$P2_1/n$	$P2_1/a$	$P2_12_12_1$	$P2_1/n$
a (Å)	7.5871(9)	9.3513(6)	8.8749(18)	12.0618(8)	6.010 (3)
b (Å)	9.878(3)	7.8591(5)	20.702(5)	12.0625(7)	14.886 (3)
c (Å)	11.720(3)	18.2914(12)	16.6067(11)	37.054(3)	13.368 (3)
α (°)	64.95(3)	90.00	90.00	90.00	90.00
β (°)	74.013(15)	93.3590(10)	97.281(10)	90.00	91.90 (3)
γ (°)	87.642(15)	90.00	90.00	90.00	90.00
V (Å^3)	762.1(3)	1341.98(15)	3026.6(10)	5391.2(6)	1195.2 (6)
Z	1	2	4	8	2
Temperature (K)	150(2)	243(2)	293(2)	243(2)	150 (2)
Radiation (λ, Å)	0.71073	0.71073	0.71073	0.71073	0.71073
ρ(calcd.) (g cm^{-3})	1.289	1.325	1.309	1.331	1.423
μ(Mo Kα) (mm^{-1})	0.671	0.754	0.756	0.842	0.945
θ max (°)	32.1953	28.32	32.1670	27.893	29.9988
Number of data	2674	2452	10077	9875	2095
Number of parameters	190	172	379	681	162
R_1	0.0273	0.0266	0.0396	0.0651	0.0388
wR_2	0.0619	0.0737	0.0989	0.1231	0.0971
Goodness-of-fit	1.099	1.058	0.924	1.123	0.930

copper complexes **3a**, **3b** and **3c**, the nickel complexes **2a** and **2b**, however, failed to yield the polylactide polymer.

Specifically, a typical polymerization experiment involved heating L-lactide with any of the copper initiators **3a** or **3b** or **3c**, taken in the desired ratio, in a sealed vessel under vacuum at designated temperatures for stipulated periods of time. Under these conditions the reaction mixture would form a monomer melt in which the polymerization would occur. A study of the variation of monomer to initiator ratio [M]:[I] ratio (M = monomer, I = initiator) at 160 °C showed that the maximum molecular weights for **3a** ($M_w = 18.5 \times 10^3$ entry 1, Table 3), **3b** ($M_w = 10.4 \times 10^3$ entry 1, Table 4) and **3c** ($M_w = 15.9 \times 10^3$ entry 1, Table 5) were obtained at ratios of 50:1 in each case. The observed polydispersity indices (PDIs) were in the range 1.05–1.46 (**3a**), 1.08–1.43 (**3b**) and 1.10–1.58 (**3c**). An interesting correlation between the initiator structure and the polymer molecular weight that emerges is the structurally similar square planar complexes **3a** and **3c**, which differ significantly from the distorted square planar complex **3b**, also exhibit a similar resemblance in their polymer molecular weights [**3a** ($M_w = 18.5 \times 10^3$ entry 1, Table 3); **3c** ($M_w = 15.9 \times 10^3$ entry 1, Table 5)] that are significantly greater than that observed in the case of **3b** ($M_w = 10.4 \times 10^3$ entry 1, Table 4) obtained at the 50:1 [M]:[I] ratio. Consistent with the observed molecular weight distributions, no correlation of the polymer molecular weight with time was seen in the time dependency studies (**3a**: entries 1 and 9–12, Table 3, **3b**: entries 1 and 9–12, Table 4, **3c**: entries 1 and 9–12, Table 5). The temper-

Table 3
Melt polymerization of L-lactide by **3a**

Entry	L-Lactide/(**3a**) ratio	Temperature (°C)	Time (h)	M_w	M_w/M_n	Conversion (%)
1	50	160	4	18.5×10^3	1.28	66
2	100	160	4	6.2×10^3	1.08	51
3	150	160	4	3.2×10^3	1.09	54
4	200	160	4	2.2×10^3	1.09	58
5	250	160	4	2.3×10^3	1.08	52
6	50	120	4	9.9×10^3	1.07	27
7	50	140	4	16.5×10^3	1.27	62
8	50	180	4	26.3×10^3	1.46	57
9	50	160	1	7.6×10^3	1.05	71
10	50	160	2	9.8×10^3	1.18	67
11	50	160	3	11.3×10^3	1.1	80
12	50	160	6	14.6×10^3	1.3	86

Table 4
Melt polymerization of L-lactide by **3b**

Entry	L-Lactide/(**3b**) ratio	Temperature (°C)	Time (h)	M_w	M_w/M_n	Conversion (%)
1	50	160	4	10.4×10^3	1.32	70
2	100	160	4	8.2×10^3	1.17	72
3	150	160	4	4.7×10^3	1.3	74
4	200	160	4	4.5×10^3	1.43	76
5	250	160	4	4.5×10^3	1.08	33
6	50	120	4	5.3×10^3	1.22	39
7	50	140	4	8.2×10^3	1.21	54
8	50	180	4	12.0×10^3	1.23	64
9	50	160	1	7.1×10^3	1.19	53
10	50	160	2	8.5×10^3	1.21	59
11	50	160	3	8.5×10^3	1.2	58
12	50	160	6	11.2×10^3	1.24	72

Table 5
Melt polymerization of L-lactide by **3c**

Entry	L-Lactide/(**3c**) ratio	Temperature (°C)	Time (h)	M_w	M_w/M_n	Conversion (%)
1	50	160	4	15.9×10^3	1.36	55
2	100	160	4	14.1×10^3	1.14	25
3	150	160	4	6.4×10^3	1.58	33
4	200	160	4	6.5×10^3	1.29	28
5	250	160	4	2.9×10^3	1.1	20
6	50	120	4	8.6×10^3	1.18	54
7	50	140	4	11.1×10^3	1.11	60
8	50	180	4	13.8×10^3	1.21	61.5
9	50	160	1	8.0×10^3	1.16	45.2
10	50	160	2	8.1×10^3	1.16	48
11	50	160	3	13.4×10^3	1.31	48
12	50	160	6	10.2×10^3	1.24	72

ature dependence study carried out at the 50:1 [M]:[I] ratio in the range (100–180 °C)[1] showed that the molecular weight of the polymer increased with temperature for the initiators **3a** (Table 3: M_w: 9.9×10^3, 16.5×10^3, 18.5×10^3, 26.3×10^3) and **3b** (Table 4: M_w: 5.3×10^3, 8.2×10^3, 10.4×10^3, 12.0×10^3) whereas a slight decrease in molecular weight was observed in the case of **3c** at higher temperatures (Table 5: M_w: 8.6×10^3, 11.1×10^3, 15.9×10^3 and 13.8×10^3) at 120, 140, 160 and 180 °C, respectively.

Worth comparing are the copper initiators **3a**, **3b** and **3c** with other known catalysts for the ring-opening polymerization of L-lactide under solvent-free melt conditions, particularly the copper ones. Interestingly enough, even though very many metals like Mg [54,27a,31c], Ti [55], Zn [56,20a,33b,30a,30b,30d,32a], Al [57,20b,20d], Sn [58,30c], etc. have been reported for lactide polymerization, we are aware of only a single report of lactide polymerization by a Cu catalyst, K[LCu(II)].nH_2O (H_3L = L-aspartic acid–salicylidene Schiff base) [20c]. The viscosity average molecular weight ($M_v = 4.86\times10^3$) obtained at a 200:1 [M]:[I] ratio after 24 h at 130 °C for K[LCu(II)]$\cdot n H_2O$ (H_3L = L-aspartic acid–salicylidene Schiff base [20c] is slightly smaller than that observed for **3a** (M_w: 18.5×10^3), **3b** (M_w: 10.4×10^3), **3c** (M_w: 15.9×10^3) obtained at a 50:1 [M]:[I] ratio after 4 h at 160 °C. Similar comparisons of **3a**, **3b** and **3c** can also be extended to other metal catalysts. For example, the polymer molecular weights and the polydispersity indices observed at a 50:1 [M]:[I] ratio for **3a** (M_w: 18.5×10^3, PDI = 1.28), **3b** (M_w: 10.4×10^3, PDI = 1.32), **3c** (M_w: 15.9×10^3, PDI = 1.36), obtained after 4 h at 160 °C, are also comparable to several other melt polymerization catalysts, such as [3-mesityl-1-picolylimidazol-2-ylidene]Zn(Et)I [30a] (M_w: 29.4×10^3, PDI = 2.45, 100:1 [M]:[I] ratio, 140 °C, 5 min), {[3-mesityl-1-picolylimidazol-2-ylidene]$_2$ZnI}I [30a] (M_w: 15.3×10^3, PDI = 2.51, 50:1 [M]:[I] ratio, 140 °C, 5 min), [(1-*i*-propyl-3-{*N*-phenylacetamido}imidazol-2-ylidene)$_2$Ag]$^+$Cl$^-$ [25] (M_w: 12.2×10^3, PDI = 1.40, 100:1 [M]:[I] ratio, 160 °C, 4 h), [1-(2-hydroxy-cyclohexyl)-3-(*N*-*t*-butylacetamido)imidazol-2-ylidene]AgCl [26] (M_w: 6.27×10^3, PDI = 1.23, 100:1 [M]:[I] ratio, 160 °C, 4 h) and [1-(2-hydroxy-cyclohexyl)-3-(*N*-*t*-butylacetamido)imidazol-2-ylidene]AuCl [26] (M_w: 6.31×10^3, PDI = 1.17, 100:1 [M]:[I] ratio, 160 °C, 4 h). Furthermore, comparable viscosity-average molecular weights (M_v) were also reported for a series of late-transition metal based initiators of the type K[LM(II)]$\cdot n H_2O$ (H_3L = L-aspartic acid–salicylidene Schiff base) [20c] where M = Co (5.15×10^3), Ni (11.1×10^3) and Zn (5.23×10^3), obtained at a 200:1 [M]:[I] ratio after 24 h at 130 °C. However, several other initiators have also been reported, which produced higher molecular weight polymers, e.g., anhydrous Fe(OAc)$_2$ [59] (M_w: 65.9×10^3, PDI = 5.25, 0.24 weight % of catalyst, 170 °C, 10 h), iron isobutyrate [59] (M_w: 148×10^3, PDI = 1.60, 0.12 weight % of catalyst, 190 °C, 2 h) and [L]TiO(2,6-*i*-Pr$_2$C$_6$H$_3$) [28c] (H_3L = triethanolamine) (M_w: 66.1×10^3, PDI = 1.97, 300:1 [M]:[I] ratio, 130 °C, 24 h). Thus, the detailed comparison with other known catalysts revealed that the copper initiators **3a**, **3b** and **3c** are moderately active for lactide polymerization.

[1] The bulk polymerization temperatures were chosen higher than the melting point of the lactide monomer (96 °C).

4. Experimental

4.1. General procedures

All manipulations were carried out using a combination of a glovebox and standard Schlenk techniques. Solvents were purified and degassed by standard procedures. 2,6-Dimethylaniline and 2,6-diethylaniline were purchased from Sigma–Aldrich, Germany and o-hydroxyacetophenone was purchased from SD-fine Chemicals (India), and they were used without any further purification. ^{1}H and $^{13}C\{^{1}H\}$ NMR spectra were recorded on a Varian 400 MHz NMR spectrometer. ^{1}H NMR peaks are labelled as singlet (s), doublet (d), triplet (t) and multiplet (m). Infrared spectra were recorded on a Perkin Elmer Spectrum One FT-IR spectrometer. The electronic spectra were recorded in chloroform by using a Perkin–Elmer Lamda 35 UV-Visible spectrophotometer and JASCO V-570 UV/Vis/NIR spectrophotometer. Mass spectrometry measurements were done on a Micromass Q-Tof spectrometer. The EPR measurements were made with a Varian model 109C E-line X-band spectrometer fitted with a quartz Dewar for measurements at 77 K. The spectra were calibrated by using tetracyanoethylene (tcne) ($g = 2.0037$). The polymer molecular weights were determined using a Waters GPC (Waters 2414 RI Detector) with PL-gel, 5μ Mixed-D (2×300 mm) Column, with polystyrene standards in chloroform, covering molecular weight ranging from l40 to 4×10^5.

4.2. Synthesis of the ligands

4.2.1. Synthesis of 2-[1-(2,6-diethylphenylimino)ethyl]-phe- nol (*1a*)

o-Hydroxyacetophenone (4.31 g, 31.7 mmol) and 2,6-diethylaniline (14.3 g, 96.0 mmol) were taken in CH_2Cl_2 (ca. 75 mL) maintained at 0 °C and a solution of $TiCl_4$ (3 mL, 27.3 mmol) in CH_2Cl_2 (ca. 10 mL) was added. The reaction mixture was stirred in an ice bath for 1 h, after which it was allowed to warm up to room temperature over a period of 3 h. An aqueous NaOH solution (20 mL, 2 M) was added to the reaction mixture and washed thoroughly. The organic layer was separated, dried over anhydrous $MgSO_4$ and the solvent removed under vacuum to get the crude product as a yellow oil. The crude compound was purified by the removal of excess 2,6-diethylaniline and *o*-hydroxyacetophenone by vacuum distillation (180 °C, 0.2 mbar) to obtain the product as a yellow solid (1.83 g, 22%). ^{1}H NMR ($CDCl_3$, 400 MHz, 25 °C) δ 14.8 (s, 1H, O*H*), 7.64 (d, 1H, $^{3}J_{HH} = 8$ Hz, *o*-C_6H_4(OH)), 7.40 (t, 1H, $^{3}J_{HH} = 8$ Hz, *p*-C_6H_4(OH)), 7.16–7.11 (m, 3H, *m*/*p*-$C_6H_3(CH_2CH_3)_2$), 7.04 (d, 1H, $^{3}J_{HH} = 8$ Hz, *m*-C_6H_4(OH)), 6.91 (t, 1H, $^{3}J_{HH} = 8$ Hz, *m*-C_6H_4(OH)), 2.48–2.32 (m, 4H, CH_2CH_3), 2.17 (s, 3H, CH_3(C=N)), 1.13 (t, 6H, $^{3}J_{HH} = 8$ Hz, CH_2CH_3). ^{13}C NMR ($CDCl_3$, 100 MHz, 25 °C) δ 171.9 (*C*=N), 162.4 (C_6H_4(OH), 143.8 (*ipso*-$C_6H_3(CH_2CH_3)_2$), 133.0 (*o*-C_6H_4(OH)), 133.1 (*o*-$C_6H_3(CH_2CH_3)_2$), 128.9 (*p*-C_6H_4(OH)), 126.1 (*m*-$C_6H_3(CH_2CH_3)_2$), 124.8 (*p*-$C_6H_3(CH_2CH_3)_2$), 119.1 (*ipso*-C_6H_4(OH)), 118.3 (*m*-C_6H_4(OH)), 118.0 (*m*-(C_6H_4-(OH)), 24.7 ($C_6H_3(CH_2CH_3)_2$), 17.3 ((C=N)CH_3), 14.0 ($C_6H_3(CH_2CH_3)_2$). LRMS (ES): *m*/*z* 268 $(M+H)^+$ 100%. HRMS (ES): calcd. for $[M+H]^+$ 268.1701, found *m*/*z* 268.1696. IR data cm^{-1} KBr pellet: 1609 (s) ($\nu_{C=N}$). λ_{max} (ε) $CHCl_3$: 256 nm ($\varepsilon = 17263$ L mol^{-1} cm^{-1}), 323 nm ($\varepsilon = 5945$ L mol^{-1} cm^{-1}).

4.2.2. Synthesis of 2-[1-(2,6-dimethylphenylimino)ethyl]-phenol (*1b*)

o-Hydroxyacetophenone (8.51 g, 62.5 mmol) and 2,6-dimethylaniline (12.4 g, 102 mmol) were taken in CH_2Cl_2 (ca. 75 mL) maintained at 0 °C and a solution of $TiCl_4$ (2 mL, 18.2 mmol) in CH_2Cl_2 (ca. 10 mL) was added. The reaction mixture was stirred in an ice bath for 1 h, after which it was allowed to warm up to room temperature over a period of 3 h. An aqueous NaOH solution (20 mL, 2 M) was added to the reaction mixture and washed thoroughly. The organic layer was separated, dried over anhydrous $MgSO_4$ and the solvent removed under vacuum to get the crude product as a yellow oil. The crude compound was purified by column chromatography (4% EtOAc–hexane mixture) followed by the removal of excess 2,6-dimethylaniline by vacuum distillation (180 °C, 0.2 mbar) to obtain the product as a yellow solid (3.09 g, 21%). ^{1}H NMR ($CDCl_3$, 400 MHz, 25 °C) δ 14.7 (s, 1H, O*H*), 7.57 (d, 1H, $^{3}J_{HH} = 8$ Hz, *o*-C_6H_4(OH)), 7.32 (t, 1H, $^{3}J_{HH} = 8$ Hz, *p*-C_6H_4(OH)), 7.03 (d, 2H, $^{3}J_{HH} = 8$ Hz, *m*-$C_6H_3(CH_3)_2$), 6.98–6.92 (m, 2H, *p*-$C_6H_3(CH_3)_2$and *m*-C_6H_4(OH) overlapped), 6.83 (t, 1H, $^{3}J_{HH} = 8$ Hz, *m*-C_6H_4(OH)), 2.09 (s, 3H, CH_3(C=N)), 1.99 (s, 6H, $C_6H_3(CH_3)_2$). ^{13}C NMR ($CDCl_3$, 100 MHz, 25 °C) δ 171.7 (*C*=N), 162.2 (C_6H_4-(OH), 145.0 (*ipso*-$C_6H_3(CH_3)_2$), 132.9 (*o*-C_6H_4(OH)), 128.8 (*p*-C_6H_4(OH)), 127.9 (*m*-$C_6H_3(CH_3)_2$), 127.5 (*p*-$C_6H_3(CH_3)_2$), 124.3 (*ipso*-C_6H_4(OH), 119.1 (*m*-C_6H_4-(OH)), 118.1 (*m*-C_6H_4(OH)), 117.9 (*o*-$C_6H_3(CH_3)_2$), 18.1 (CH_3(C=N)), 16.8 ($C_6H_3(CH_3)_2$). LRMS (ES): *m*/*z* 240 $(M+H)^+$ 100%. HRMS (ES): calcd. for $[M+H]^+$ 240.1388, found *m*/*z* 240.1380. IR data cm^{-1} KBr pellet: 1614 (s) ($\nu_{C=N}$). λ_{max} (ε) $CHCl_3$: 256 nm ($\varepsilon = 17933$ L mol^{-1} cm^{-1}), 322 nm ($\varepsilon = 5919$ L mol^{-1} cm^{-1}).

4.2.3. Synthesis of 2-[1-(2-methylphenylimino)ethyl]phenol (*1c*)

o-Hydroxyacetophenone (7.25 g, 53.2 mmol) and 2-methylaniline (8.62 g, 80.5 mmol) were taken in CH_2Cl_2 (ca. 60 mL) maintained at 0 °C and a solution of $TiCl_4$ (2 mL, 18.2 mmol) in CH_2Cl_2 (ca. 10 mL) was added. The reaction mixture was stirred in an ice bath for 2 h, after which it was allowed to warm up to room temperature over a period of 3 h. An aqueous NaOH solution (40 mL, 2 M) was added to the reaction mixture and washed thoroughly. The organic layer was separated, dried over anhydrous $MgSO_4$ and the solvent removed under vacuum to get the crude product as a yellow oil. The crude

compound was purified by the removal of excess 2-methylaniline and *o*-hydroxyacetophenone by vacuum distillation (180 °C, 0.2 mbar) to obtain the product as a yellow oil (2.72 g, 23%). ^{1}H NMR ($CDCl_3$, 400 MHz, 25 °C) δ 14.7 (s, 1H, O*H*), 7.63 (d, 1H, $^3J_{HH} = 7$ Hz, *o*-C_6H_4(OH)), 7.37 (t, 1H, $^3J_{HH} = 9$ Hz, *p*-C_6H_4(OH)), 7.25 (d, 1H, $^3J_{HH} = 8$ Hz, *m*-$C_6H_4(CH_3)$), 7.21 (t, 1H, $^3J_{HH} = 8$ Hz, *m*-$C_6H_4(CH_3)$), 7.10 (t, 1H, $^3J_{HH} = 8$ Hz, *m*-C_6H_4(OH)), 7.02 (d, 1H, $^3J_{HH} = 8$ Hz, *m*-C_6H_4(OH)), 6.89 (t, 1H, $^3J_{HH} = 8$ Hz, *p*-$C_6H_4(CH_3)$), 6.76 (d, 1H, *o*-$C_6H_4(CH_3)$), 2.26 (s, 3H, $C_6H_4(CH_3)$), 2.15 (s, 3H, CH_3(C=N)). ^{13}C NMR ($CDCl_3$, 100 MHz, 25 °C) δ 171.1 (*C*=N), 162.0 (C_6H_4(OH), 145.8 (*ipso*-$C_6H_4(CH_3)$), 133.0 (*o*-C_6H_4(OH)), 130.5 (*o*-$C_6H_4(CH_3)$), 128.8 (*p*-C_6H_4(OH)), 126.4 (*m*-$C_6H_4(CH_3)$), 124.8 (*p*-$C_6H_4(CH_3)$), 120.5 (*o*-$C_6H_4(CH_3)$), 119.5 (*ipso*-C_6H_4(OH), 118.1 (*m*-C_6H_4(OH)), 118.0 (*m*-(C_6H_4(OH)), 17.9 ((C=N)CH_3), 17.0 ($C_6H_4(CH_3)$). LRMS (ES): *m*/*z* 226 $(M+H)^+$ 100%. HRMS (ES): calcd. for $[M+H]^+$ 226.1232, found *m*/*z* 226.1234. IR data cm^{-1} KBr pellet: 1611 (s) ($\nu_{C=N}$). λ_{max} (ε) $CHCl_3$: 257 nm ($\varepsilon = 21873$ L mol^{-1} cm^{-1}), 324 nm ($\varepsilon = 8776$ L mol^{-1} cm^{-1}).

4.3. Synthesis of the Ni complexes

4.3.1. Synthesis of {2-[1-(2,6-diethylphenylimino)ethyl]-phenoxy}$_2$Ni(II) (**2a**)

$Ni(OAc)_2 \cdot 4H_2O$ (0.449 g, 1.81 mmol) and 2-[1-(2,6-diethylphenylimino)ethyl]phenol (**1a**) (0.478 g, 1.79 mmol) were taken in methanol (ca. 30 mL) and stirred at room temperature until a clear solution was obtained. To the solution was added NEt_3 (0.274 g, 2.70 mmol) with constant stirring. The reaction mixture was refluxed for 12 h and then allowed to cool to room temperature, when the product precipitated out as a green solid and was isolated by filtration and air dried (0.493 g, 71%). Crystals suitable for X-ray structure determination were obtained by slow evaporation from a saturated methanol solution. ^{1}H NMR ($CDCl_3$, 400 MHz, 25 °C) δ 7.31 (d, 1 H, $^3J_{HH} = 8$ Hz, *o*-C_6H_4(OH)), 7.21 (t, 1H, *p*-C_6H_4(OH)), 7.11 (d, 2H, $^3J_{HH} = 8$ Hz, *m*-$C_6H_3(CH_2CH_3)_2$), 6.84 (t, 1H, $^3J_{HH} = 8$ Hz, *p*-$C_6H_3(CH_2CH_3)_2$), 6.38 (t, 1H, $^3J_{HH} = 8$ Hz, *m*-C_6H_4(OH)), 5.50 (d, 1H, $^3J_{HH} = 8$ Hz, *m*-C_6H_4(OH)), 3.29–3.19 (m, 2H, CH_2CH_3), 2.90–2.80 (m, 2H, CH_2CH_3), 1.94 (s, 3H, CH_3(C=N)), 1.45 (t, 6H, $^3J_{HH} = 8$ Hz, CH_2CH_3). ^{13}C NMR ($CDCl_3$, 100 MHz, 25 °C) δ 168.9 (*C*=N), 163.6 (C_6H_4(OH), 145.8 (*ipso*-$C_6H_3(CH_2CH_3)_2$)), 136.1 (*o*-C_6H_4(OH)), 132.2 (*p*-C_6H_4(OH)), 129.0 (*p*-$C_6H_3(CH_2CH_3)_2$), 125.0 (*m*-$C_6H_3(CH_2CH_3)_2$ and *ipso*-(C_6H_4(OH)), 123.2 (*m*-C_6H_4-(OH), 122.1 (*o*-$C_6H_3(CH_2CH_3)_2$), 113.9 (*m*-C_6H_4(OH)), 24.6 ($C_6H_3(CH_2CH_3)_2$), 20.6 (CH_3(C=N)), 13.7 ($C_6H_3(CH_2CH_3)_2$). IR data cm^{-1} KBr pellet: 1574 (s) ($\nu_{C=N}$). λ_{max} (ε) $CHCl_3$: 601 nm ($\varepsilon = 118$ L mol^{-1} cm^{-1}). *Anal.* Calc. for $C_{36}H_{40}NiO_2N_2$: C, 73.11; H, 6.82; N, 4.74. Found: C, 72.78; H, 7.06; N, 3.87%.

4.3.2. Synthesis of {2-[1-(2,6-dimethylphenylimino)ethyl]-phenoxy}$_2$Ni(II) (**2b**)

$Ni(OAc)_2 \cdot 4H_2O$ (0.543 g, 2.19 mmol) and 2-[1-(2,6-dimethylphenylimino)ethyl]phenol (**1b**) (0.508 g, 2.12 mmol) were taken in methanol (ca. 30 mL) and stirred at room temperature until a clear solution was obtained. To the solution was added NEt_3 (0.324 g, 3.20 mmol) with constant stirring. The reaction mixture was stirred at room temperature for another 6 h when the product precipitated out as a green solid and was isolated by filtration and air dried (0.459 g, 75%). Crystals suitable for X-ray structure determination were obtained by slow evaporation from a saturated benzene solution. ^{1}H NMR ($CDCl_3$, 400 MHz, 25 °C) δ 7.26 (d, 1H, $^3J_{HH} = 8$ Hz, *o*-C_6H_4(OH)), 7.19 (br, 1H, *p*-C_6H_4(OH)), 7.02 (br, 2H, *m*-$C_6H_3(CH_3)_2$), 6.83 (t, 1H, $^3J_{HH} = 8$ Hz, *p*-$C_6H_3(CH_3)_2$), 6.35 (t, 1H, $^3J_{HH} = 8$ Hz, *m*-C_6H_4(OH)), 5.66 (d, 1H, $^3J_{HH} = 8$ Hz, *m*-C_6H_4(OH)), 2.53 (s, 6H, $C_6H_3(CH_3)_2$), 1.87 (s, 3H, CH_3(C=N)). ^{13}C NMR ($CDCl_3$, 100 MHz, 25 °C) δ 168.6 (*C*=N), 163.7 (C_6H_4(OH), 146.4 (*ipso*-$C_6H_3(CH_3)_2$)), 132.3 (*o*-C_6H_4(OH)), 130.9 (*p*-C_6H_4(OH)), 129.0 (*p*-$C_6H_3(CH_3)_2$), 127.6 (*m*-$C_6H_3(CH_3)_2$), 124.9 (*ipso*-C_6H_4(OH), 122.0 (*m*-C_6H_4(OH)), 118.2 (*m*-(C_6H_4(OH)), 114.1 (*o*-$C_6H_3(CH_3)_2$), 19.7 (CH_3(C=N)), 19.2 (C_6H_3-$(CH_3)_2$). IR data cm^{-1} KBr pellet: 1571 (s) ($\nu_{C=N}$). λ_{max} (ε) $CHCl_3$: 592 nm ($\varepsilon = 102$ L mol^{-1} cm^{-1}). *Anal.* Calc. for $C_{32}H_{32}NiO_2N_2$: C, 71.80; H, 6.03; N, 5.23. Found: C, 71.14; H, 6.21; N, 4.88%.

4.4. Synthesis of the Cu complexes

4.4.1. Synthesis of {2-[1-(2,6-diethylphenylimino)ethyl]-phenoxy}$_2$Cu(II) (**3a**)

$Cu(OAc)_2 \cdot H_2O$ (0.266 g, 1.33 mmol) and 2-[1-(2,6-diethylphenylimino)ethyl]phenol (**1a**) (0.709 g, 2.62 mmol) were taken in methanol (ca. 40 mL) and stirred at room temperature until a clear solution was obtained. To the solution was added NEt_3 (0.298 g, 2.94 mmol) with constant stirring. The reaction mixture was stirred at reflux for 24 h and then allowed to cool to room temperature when the product was obtained as dark brown crystals which were isolated by filtration and vacuum dried (0.542 g, 70%). Crystals suitable for X-ray structure determination were obtained by slow evaporation from a saturated benzene solution. IR data cm^{-1} KBr pellet: 1599 (s) ($\nu_{C=N}$). λ_{max} (ε) $CHCl_3$: 696 nm ($\varepsilon = 89.4$ L mol^{-1} cm^{-1}). *Anal.* Calc. for $C_{36}H_{40}CuO_2N_2$: C, 72.52; H, 6.76; N, 4.70. Found: C, 72.07; H, 7.06; N, 4.39%.

4.4.2. Synthesis of {2-[1-(2,6-dimethylphenylimino)-ethyl]phenoxy}$_2$Cu(II) (**3b**)

$Cu(OAc)_2 \cdot H_2O$ (0.418 g, 2.14 mmol) and 2-[1-(2,6-dimethylphenylimino)ethyl]phenol (**1b**) (0.512 g, 2.14 mmol) were taken in methanol (ca. 30 mL) and stirred at room temperature until a clear solution was obtained. To the solution was added NEt_3 (0.282 g, 2.78 mmol) with constant stirring. The reaction mixture was stirred at room

temperature for another 6 h when the product precipitated out as a dark brown solid and was isolated by filtration and vacuum dried (0.505 g, 87%). Crystals suitable for X-ray structure determination were obtained by slow evaporation from a saturated benzene solution. IR data cm^{-1} KBr pellet: 1601 (s) ($\nu_{C=N}$). λ_{max} (ε) $CHCl_3$: 670 nm ($\varepsilon = 130$ L mol^{-1} cm^{-1}). *Anal.* Calc. for $C_{32}H_{32}CuO_2N_2$: C, 71.15; H, 5.97; N, 5.19. Found: C, 71.18; H, 6.41; N, 5.34%.

4.4.3. Synthesis of {2-[1-(2-methylphenylimino)ethyl]-phenoxy}$_2$Cu(II) (3c)

$Cu(OAc)_2 \cdot H_2O$ (0.582 g, 2.92 mmol) and 2-[1-(2-methylphenylimino)ethyl]phenol (**1c**) (0.677 g, 3.00 mmol) were taken in methanol (ca. 40 mL) and stirred at room temperature until a clear solution was obtained. To the solution was added NEt_3 (0.314 g, 3.10 mmol) with constant stirring. The reaction mixture was stirred at reflux for 12 h and then allowed to cool to room temperature when the product was obtained as reddish-brown solid which was isolated by filtration and vacuum dried (0.573 g, 75%). Crystals suitable for X-ray structure determination were obtained by slow evaporation from a saturated benzene solution. IR data cm^{-1} KBr pellet: 1599 (s) ($\nu_{C=N}$). λ_{max} (ε) $CHCl_3$: 630 nm ($\varepsilon = 125$ L mol^{-1} cm^{-1}). *Anal.* Calc. for $C_{30}H_{28}CuO_2N_2$: C, 70.36; H, 5.51; N, 5.47. Found: C, 69.84; H, 5.55; N, 5.40%.

4.5. Polymerization experiments

Typical polymerization experiments: L-lactide (1.000 g, 6.94 mmol) and **3a**, **3b** and **3c**, in a stipulated molar ratio, were charged in an ampoule inside a glove box. The ampoule was taken out and put under vacuum at 50 °C for 30 min, after which the ampoule was sealed under vacuum and heated at 160 °C for 4 h. Under these conditions the reaction mixture turned into a monomer melt in which polymerization occurred. Subsequently, the molten reactive polymer mixture was cooled by immersing the sealed ampoule in liquid nitrogen to stop the polymerization. Conversion of L-lactide monomer was determined using the size exclusion chromatography method. The analyses were performed on the crude reaction mixture and no precipitation was executed to avoid fractionation of the sample in order to not influence the results.

4.6. X-ray analyses

X-ray diffraction data were collected either on a Bruker P4 diffractometer equipped with a SMART CCD detector or on an Oxford Diffraction XCalibur-S, and crystal data collection and refinement parameters are summarized in Table 2. The structures were solved using direct methods and standard difference map techniques, and were refined by full-matrix least-squares procedures on F^2 with SHELXTL (Version 6.10).

5. Conclusion

In summary, a series of new nickel (**2a**, **2b**) and copper (**3a**, **3b**, **3c**) complexes, bearing a 2:1 ligand:metal stoichiometry, has been synthesized from the respective ligands, 2-[1-(2,6-diethylphenylimino)ethyl]phenol (**1a**), 2-[1-(2,6-dimethylphenylimino)ethyl]phenol (**1b**) and 2-[1-(2-methylphenylimino)ethyl]phenol (**1c**), by the reactions with the corresponding $M(OAc)_2 \cdot xH_2O$ (M = Ni, Cu) in the presence of NEt_3 as a base in moderate to high yields. The complexes **2a**, **2b**, **3a**, **3b** and **3c** have been structurally characterized by X-ray diffraction studies, which revealed that the geometry around the metal center is square planar in the nickel (**2a**, **2b**) and copper (**3a**, **3c**) complexes whilst it is distorted square planar in the copper **3b** complex. The catalysis studies revealed that while the copper complexes **3a**, **3b** and **3c**, efficiently catalyzed the ring-opening polymerization of L-lactide under solvent-free melt conditions, producing polylactide polymers of moderate molecular weights and having narrow molecular weight distributions, the nickel counterparts **2a** and **2b** failed to yield any polylactide polymer.

Acknowledgements

We thank Council of Scientific and Industrial Research (CSIR), New Delhi, for financial support of this research. We are grateful to the National Single Crystal X-ray Diffraction Facility at IIT Bombay as well as to Professor Gerard Parkin, Columbia University for the crystallographic results. PG thanks Professor Goutam Kumar Lahiri, IIT Bombay, for valuable discussion and Professor M. Ravikanth, IIT Bombay, for help with the electronic studies. AJ thanks CSIR, New Delhi for a research fellowship.

Appendix A. Supplementary material

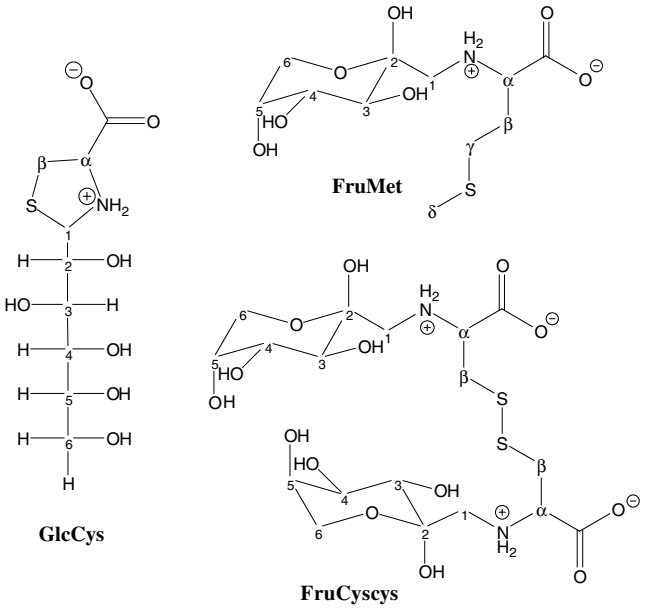
CCDC 609004, 605462, 607766, 605461 and 609526 contain the supplementary crystallographic data for **2a**, **2b**, **3a**, **3b** and **3c**. These data can be obtained free of charge via http://www.ccdc.cam.ac.uk/conts/retrieving.html, or from the Cambridge Crystallographic Data Centre, 12 Union Road, Cambridge CB2 1EZ, UK; fax: (+44) 1223-336-033; or e-mail: deposit@ccdc.cam.ac.uk. Supplementary data associated with this article can be found, in the online version, at doi:10.1016/j.poly.2007.04.039.

References

[1] (a) P.K. Mascharak, Coord. Chem. Rev. 225 (2002) 201;
(b) J.G. Muller, L.A. Kayser, S.J. Paikoff, V. Duarte, N. Tang, R.J. Perez, S.E. Rokita, C.J. Burrows, Coord. Chem. Rev. 185–186 (1999) 761;
(c) D.P. Kessissoglou, Coord. Chem. Rev. 185–186 (1999) 837;
(d) V.E. Kaasjager, L. Puglisi, E. Bouwman, W.L. Driessen, J. Reedjik, Inorg. Chim. Acta 310 (2000) 183.
[2] See the following review and the references therein, Y. Sunatsuki, Y. Motoda, N. Matsumoto, Coord. Chem. Rev. 226 (2002) 199.

[3] (a) P.G. Cozzi, Chem. Soc. Rev. 33 (2004) 410;
(b) C.-M. Che, J.-S. Huang, Coord. Chem. Rev. 242 (2003) 97.
[4] R.I. Kureshy, N.H. Khan, S.H.R. Abdi, S.T. Patel, R.V. Jasra, Tetrahedron Lett. 42 (2001) 2915.
[5] Z.-Y. Wu, D.-J. Xu, Z.-X. Feng, Polyhedron 20 (2001) 281.
[6] A. Pui, I. Berdan, I. Morgenstern-Badrau, A. Gref, M. Perree-Fauvet, Inorg. Chim. Acta 320 (2001) 167.
[7] (a) J. Saito, Y. Tohi, N. Matsukawa, M. Mitani, T. Fujita, Macromolecules 38 (2005) 4955;
(b) Y. Nakayama, H. Bando, Y. Sonobe, T. Fujita, J. Mol. Catal. A: Chem. 213 (2004) 141.
[8] (a) R. Ziessel, Coord. Chem. Rev. 216–217 (2001) 195;
(b) R. Paschke, S. Liebsch, C. Tschierke, M.A. Oakle, E. Sinn, Inorg. Chem. 42 (2003) 8230.
[9] P.G. Lacroix, F. Averseng, I. Malfant, K. Nakatani, Inorg. Chim. Acta 357 (2004) 3825.
[10] (a) A.F. Mason, G.W. Coates, J. Am. Chem. Soc. 126 (2004) 16326;
(b) J. Tian, P.D. Hustad, G.W. Coates, J. Am. Chem. Soc. 123 (2001) 5134;
(c) J. Tian, G.W. Coates, Angew. Chem. Int. Ed. 39 (2000) 3626.
[11] (a) H. Makio, T. Fujita, Bull. Chem. Soc. Jpn. 78 (2005) 52;
(b) N. Matsukawa, S. Ishii, R. Furuyama, J. Saito, M. Mitani, H. Makio, H. Tanaka, T. Fujita, e-Polymers 021 (2003) 1.
[12] (a) T.R. Younkin, E.F. Connor, J.I. Henderson, S.K. Fredrich, R.H. Grubbs, D.A. Bansleben, Science 287 (2000) 460;
(b) C. Wang, S. Friedrich, T.R. Younkin, R.T. Li, R.H. Grubbs, D.A. Bansleben, M.W. Day, Organometallics 17 (1998) 3149.
[13] C. Carlini, S. Giaiacopi, F. Marchetti, C. Pinzino, A.M.R. Galletti, G. Sbrana, Organometallics 25 (2006) 3659.
[14] E.M. McGarrigle, D.G. Gilheany, Chem. Rev. 105 (2005) 1563.
[15] R.I. Kureshy, N.H. Khan, S.H.R. Abdi, S.T. Patel, R.V. Jasra, Tetrahedron: Assymetry 12 (2001) 433.
[16] Y.-C. Lai, H.-Y. Chen, W.-C. Hung, C.-C. Lin, F.-E. Hong, Tetrahedron 61 (2005) 9484.
[17] A.A. Khandar, K. Nejati, Z. Rezvani, Molecules 10 (2005) 302.
[18] (a) M. Mitani, T. Nakano, T. Fujita, Chem. Eur. J. 9 (2003) 2396;
(b) M. Mitani, R. Furuyama, J. Mohiri, J. Saito, S. Ishii, H. Terao, T. Nakano, H. Tanaka, T. Fujita, J. Am. Chem. Soc. 125 (2003) 4293;
(c) M. Mitani, J. Mohri, Y. Yoshida, J. Saito, S. Ishii, K. Tsuru, S. Matsui, R. Furuyama, T. Nakano, H. Tanaka, S. Kojoh, T. Matsugi, N. Kashiwa, T. Fujita, J. Am. Chem. Soc. 124 (2002) 3327;
(d) S. Ishii, J. Saito, M. Mitani, J. Mohri, N. Matsukawa, Y. Tohi, S. Matsui, N. Kashiwa, T. Fujita, J. Mol. Catal. A: Chem. 179 (2002) 11;
(e) M. Mitani, R. Furuyama, J. Mohiri, J. Saito, S. Ishii, H. Terao, N. Kashiwa, T. Fujita, J. Am. Chem. Soc. 124 (2002) 7888;
(f) J. Saito, M. Mitani, J. Mohri, Y. Yoshida, S. Matsui, S. Ishii, S. Kojoh, N. Kashiwa, T. Fujita, Angew. Chem. Int. Ed. 40 (2001) 2918.
[19] (a) M. Palucki, G.J. McCormick, E.N. Jacobsen, Tetrahedon Lett. 36 (1995) 5457;
(b) S. Chang, R.M. Heid, E.N. Jacobsen, Tetrahedron Lett. 35 (1994) 669.
[20] We are aware of only a handful of reports of the usage of phenoxy-imine catalysts for ring-opening polymerization (ROP) of lactide see
(a) J.-C. Wu, B.-H. Huang, M.-L. Hsueh, S.-L. Lai, C.-C. Lin, Polymer 46 (2005) 9784;
(b) M.H. Chisholm, N.J. Patmore, Z. Zhou, Chem. Commun. (2005) 127;
(c) J. Sun, W. Shi, D. Chen, C. Liang, J. Appl. Polym. Sci. 86 (2002) 3312;
(d) T.M. Ovitt, G.W. Coates, J. Am. Chem. Soc. 124 (2002) 1316;
(e) T.M. Ovitt, G.W. Coates, J. Am. Chem. Soc. 121 (1999) 4072.
[21] (a) O. Dechy-Cabaret, B. Martin-Vaca, D. Bourissou, Chem. Rev. 104 (2004) 6147;
(b) B.J. O'Keefe, M.A. Hillmyer, W.B. Tolman, J. Chem. Soc., Dalton Trans. (2001) 2215.
[22] (a) K.A.M. Thakur, R.T. Kean, E.S. Hall, J.J. Kolstad, E.J. Munson, Macromolecules 31 (1998) 1487;
(b) K.A.M. Thakur, R.T. Kean, E.S. Hall, J.J. Kolstad, T.A. Lindgren, M.A. Doscotch, J.I. Siepmann, E.J. Munson, Macromolecules 30 (1997) 2422.
[23] A.-C. Albertsson, I.K. Varma, Biomacromolecules 4 (2003) 1466.
[24] (a) M. Okada, Prog. Polym. Sci. 27 (2002) 87;
(b) H.R. Kriecheldorf, Chemosphere 43 (2001) 49.
[25] M.K. Samantaray, V. Katiyar, D. Roy, K. Pang, H. Nanavati, R. Stephen, R.B. Sunoj, P. Ghosh, Eur. J. Inorg. Chem. (2006) 2975.
[26] L. Ray, V. Katiyar, M.J. Raihan, H. Nanavati, M.M. Shaikh, P. Ghosh, Eur. J. Inorg. Chem. (2006) 3724.
[27] (a) J. Ejfler, M. Kobylka, L.B. Jerzykiewicz, P. Sobota, Dalton Trans. (2005) 2047;
(b) M.H. Chisholm, J. Gallucci, K. Phomphrai, Chem. Commun. (2003) 48;
(c) M. Myers, E.F. Connor, T. Glauser, A. Möck, G. Nyce, J.L. Hedrick, J. Polym. Sci. Part A: Polym. Chem. 40 (2002) 844;
(d) P. Dubios, N. Ropson, R. Jérôme, P. Teyssié, Macromolecules 29 (1996) 1965.
[28] (a) X. Wang, K. Liao, D. Quan, Q. Wu, Macromolecules 38 (2005) 4611;
(b) H. Li, C. Wang, F. Bai, J. Yue, H.-G. Woo, Organometallics 23 (2004) 1411;
(c) Y. Kim, J.G. Verkade, Organometallics 21 (2002) 2395;
(d) A.J. Nijenhuis, D.W. Grijpma, A.J. Pennings, Macromolecules 25 (1992) 6419.
[29] D. Garlotta, J. Polym. Environ. 9 (2001) 63.
[30] (a) T.R. Jensen, C.P. Schaller, M.A. Hillmyer, W.B. Tolman, J. Organomet. Chem. 690 (2005) 5881;
(b) C.K. Williams, L.E. Breyfogle, S.K. Choi, W. Nam, V.G. Young Jr., M.A. Hillmyer, W.B. Tolman, J. Am. Chem. Soc. 125 (2003) 11350;
(c) K.B. Aubrecht, M.A. Hillmyer, W.B. Tolman, Macromolecules 35 (2002) 644;
(d) C.K. Williams, N.R. Brooks, M.A. Hillmyer, W.B. Tolman, Chem. Commun. (2002) 2132;
(e) B.J. O'Keefe, S.M. Monnier, M.A. Hillmyer, W.B. Tolman, J. Am. Chem. Soc. 123 (2001) 339;
(f) B.M. Chamberlain, B.A. Jazdzewski, M. Pink, M.A. Hillmyer, W.B. Tolman, Macromolecules 33 (2000) 3970.
[31] (a) M.-L. Hsueh, B.-H. Huang, J. Wu, C.-C. Lin, Macromolecules 38 (2005) 9482;
(b) H.-Y. Chen, B.-H. Huang, C.-C. Lin, Macromolecules 38 (2005) 5400;
(c) T.-L. Yu, C.-C. Wu, C.-C. Chen, B.-H. Huang, J. Wu, C.-C. Lin, Polymer 46 (2005) 5909.
[32] (a) M.H. Chisholm, J.C. Gallucci, K. Phomphrai, Inorg. Chem. 44 (2005) 8004;
(b) M.H. Chisholm, J.C. Gallucci, H. Yin, H. Zhen, Inorg. Chem. 44 (2005) 4777;
(c) M.H. Chisholm, J.C. Gallucci, K. Phomphrai, Inorg. Chem. 43 (2004) 6717.
[33] (a) M.S. Hill, P.B. Hitchcock, J. Chem. Soc., Dalton Trans. (2002) 4694;
(b) B.M. Chamberlain, M. Cheng, D.R. Moore, T.M. Ovitt, E.B. Lobkovsky, G.W. Coates, J. Am. Chem. Soc. 123 (2001) 3229.
[34] N.D. Kimpe, R. Verhe, L.D. Buyck, L. Moens, N. Schamp, Synthesis (1982) 43.
[35] 2-[1-(2-Methylphenylimino)ethyl]phenol (**1c**) has been reported previously by a different method using anhydrous $ZnCl_2$. See, S. Mal, J.L. Norula, M.S.M. Rawat, Ind. J. Chem. 21B (1982) 120.
[36] M. Kettunen, A.S. Abu-Sarrah, H.M. Abdel-Halim, T. Repo, M. Leskela, M. Laine, I. Mutikainen, M. Ahlgren, Polyhedron 23 (2004) 1649.
[37] S. Reinartz, A.F. Mason, E.B. Lobkovsky, G.W. Coates, Organometallics 22 (2003) 2542.
[38] X.R. Bu, C.R. Jackson, D. van Derveer, X.Z. You, Q.J. Meng, R.X. Wang, Polyhedron 16 (1997) 2991.
[39] R. Ramesh, S. Maheswaran, J. Inorg. Biochem. 96 (2003) 457.

[40] P.A.N. Reddy, M. Nethaji, A.R. Chakravarty, Inorg. Chem. Commun. 6 (2003) 698.
[41] A. Anthonysamy, S. Balasubramanian, Inorg. Chem. Commun. 8 (2005) 908.
[42] S.J. Howell, C.S. Day, R.E. Noftle, Inorg. Chim. Acta 358 (2005) 3711.
[43] R. Kannappan, S. Tanase, I. Mutikainen, U. Turpeinen, J. Reedjik, Inorg. Chim. Acta 358 (2005) 383.
[44] N. Raman, Y.P. Raja, A. Kulandaisamy, Proc. Indian Acad. Sci. (Chem. Sci.) 113 (2001) 183.
[45] N. Raman, V. Muthuraj, S. Ravichandran, A. Kulandaisamy, Proc. Indian Acad. Sci. (Chem. Sci.) 115 (2003) 161.
[46] C. Jubert, A. Mohamadou, J. Marrot, J.-P. Barbier, J. Chem. Soc., Dalton Trans. (2001) 1230.
[47] P.S. Subramanian, E. Suresh, D. Srinivas, Inorg. Chem. 39 (2000) 2053.
[48] L. Pauling, The Nature of The Chemical Bond, 3rd ed., Cornell University Press, Ithaca, NY, 1960, pp. 224–228, 256–258.
[49] R. Knoch, H. Elias, H. Paulus, Inorg. Chem. 34 (1995) 4032.
[50] R.M. Kirchner, G.D. Andreetti, D. Barnhart, F.D. Thomas II, D. Welsh, E.C. Lingafelter, Inorg. Chim. Acta 7 (1973) 17.
[51] C.A. Ghilardi, E.C. Lingafelter, Acta Cryst. B26 (1970) 1807.
[52] J. Costamanga, F. Caruso, J. Vargas, V. Manriquez, Inorg. Chim. Acta 267 (1998) 151.
[53] L. Wei, R.M. Stogsdill, E.C. Lingafelter, Acta Cryst. 17 (1964) 1058.
[54] L.F. Sánchez-Barbara, D.L. Hughes, S.M. Humphrey, M. Bochmann, Organometallics 25 (2006) 1012.
[55] (a) D. Patel, S.T. Liddle, S.A. Mungur, M. Rodden, A.J. Blake, P.L. Arnold, Chem Commun. (2006) 1124;
(b) C.K.A. Gregson, I.J. Blackmore, V.C. Gibson, N.J. Long, E.L. Marshall, A.J.P. White, Dalton Trans. (2006) 3134;
(c) S.K. Russell, C.L. Gamble, K.J. Gibbins, K.C.S. Juhl, W.S. Mitchell III, A.J. Tumas, G.E. Hofmeister, Macromolecules 38 (2005) 10336;
(d) Y. Takashima, Y. Nakayama, T. Hirao, H. Yasuda, A. Harada, J. Organomet. Chem. 689 (2004) 612;
(e) Y. Kim, G.K. Jnaneshwara, J.G. Verkade, Inorg. Chem. 42 (2003) 1437;
(f) Y. Takashima, Y. Nakayama, K. Watanabe, T. Itono, N. Ueyama, A. Nakamura, H. Yasuda, A. Harada, J. Okuda, Macromolecules 35 (2002) 7538.
[56] H.Y. Chen, H.Y. Tang, C.C. Lin, Macromolecules 39 (2006) 3745.
[57] (a) H. Ma, G. Melillo, L. Oliva, T.P. Spaniol, U. Englert, J. Okuda, Dalton Trans. (2005) 721;
(b) N. Nomura, R. Ishii, M. Akakura, K. Aoi, J. Am. Chem. Soc. 124 (2002) 5938.
[58] (a) M. Lahcini, P.M. Castro, M. Kalmi, M. Leskela, T. Repo, Organometallics 23 (2004) 4547;
(b) A.P. Dove, V.C. Gibson, E.L. Marshall, A.J.P. White, D.J. Williams, Chem. Commun. (2001) 283.
[59] M. Stolt, A. Södergård, Macromolecules 32 (1999) 6412.



Scheme 1.

geometry is an important parameter in anti-tumor activity and added other criteria, stating that: (i) a pair of good leaving groups is necessary but not sufficient, anyway the presence of ligands with intermediate leaving ability is preferred to reduce systemic toxicity; (ii) the complex should be uncharged; (iii) the maximum activity is observed with maximum solubility, since diffusion is the principal way of penetration through cell membranes. In order to satisfy all these requirements we have now synthesized glycosylated adducts of cystine, cysteine and methionine and here, we report a study on Pt(II) coordination properties of the ligands listed in Scheme 1. The presence of carbohydrate moiety may provide enhanced water solubility, cell penetration, and drug–receptor interaction of the complexes.

NMR is a powerful technique that gives useful information about Pt(II) coordination, although literature reports only few examples of 2D ^{1}H–^{195}Pt heterocorrelated experiments on Pt(II)–aminoacids systems [13]. Here, we report a complete NMR study on Pt(II)-Amadori compounds based on 1D and 2D ^{1}H, ^{13}C and ^{195}Pt homo and heteronuclear techniques.

2. Experimental

2.1. NMR measurements

NMR spectra were registered with a Bruker FT-NMR Avance 400 spectrometer (Broad Band 5 mm probe, inverse detection). Nominal frequencies are 400.13 MHz for ^{1}H, 100.61 MHz for ^{13}C and 86.02 MHz for ^{195}Pt. An internal lock on the deuterium of D_2O was used for all spectra. The chemical shift references, at 300 K, were as follows: ^{1}H and ^{13}C, TSP; ^{195}Pt (external) at −1614 ppm (referred to $[PtCl_6]^{2-}$) [14], 1 M K_2PtCl_4 containing 1 M NaCl in D_2O. The negative sign of ^{195}Pt chemical shifts indicates a lower frequency (higher field) with respect to the reference.

^{1}H NMR conditions were as follows: 30° pulses (2.03 μs); 8–16 k data points; 0.5–1 s relaxation delay; collection of 32–128 transients; for 2D H,H-Homonuclear Correlated Spectroscopy (COSY [15]) and nuclear Overhauser effect spectroscopy (NOESY [16]) typical parameters were used. For the latter, a mixing time ranging from 800 to 300 ms was used. For 1D ^{13}C NMR spectra acquisition conditions were as follows: 90° pulses (14.9 μs); 16–32 k data points; 0.5–1 s relaxation delay; collection of 32 k transients. ^{195}Pt NMR spectra were typically the result of 90° pulses (20 μs), 16–32 k data points, 0.1–1 s relaxation delay; 1–4 k transients. It was not possible to scan the whole ^{195}Pt spectral region (13 000 ppm) in a single experiment, since maximum instrumental frequency width is 1000 ppm. For 2D H,X-Hetero Correlated Spectroscopy HMBC [17] and HMQC [18] opportune parameters were used (50–90° pulses; 32 k data points; 1-s relaxation delay; 8–64 k transients; $^{1}J_{H-C}$ 125–145 Hz; $^{3}J_{H-C}$ 5–15 Hz; $^{2}J_{H-Pt}$ 50–250 Hz). H_2O resonance was suppressed with a presaturation pulse [19].

The temperature was increased from 300 K to 330 K and maintained within ±0.1 K using the variable-temperature controller BVT3200.

2.2. General procedure for the synthesis of Amadori compounds [20]

A suspension of 0.010 mol of anhydrous β-D-glucose and 0.2 g of sodium bisulfite in a mixture of 6 mL of methanol and 3 mL of glycerol was refluxed for 30 min, followed by the addition of 0.007 mol of aminoacid (methionine or cystine) and 1 mL of acetic acid. The solution was refluxed until almost all the aminoacid had reacted, as evidenced by TLC. TLC was performed on silica gel $60F_{254}$ glass plates and employing the mixture *n*-butanol–acetic acid–water 4:1:1 as moving phase. For detection of aminoacid derivatives as well as sugars the plates were sprayed with a 0.2% ninhydrin in ethanol solution and heated at 120 °C. The solvent (methanol) was removed in vacuum at 35 °C, the resulting brown syrup was diluted with 1 vol. of water and placed on a 2×45 cm column filled with DOWEX 50WX8-200 (H^+) ion-exchange resin conditionated with water. The column was eluted with water followed by 0.075 M ammonia solution. Early water fractions contained glucose, glycerol, pigments and glucose-derived degradation products. The Amadori compound was eluted at the beginning of the ammonium hydroxide wash, followed by unreacted amino acid. Fractions containing only Amadori compound were evaporated in vacuum at 35 °C. A solution methanol–ethanol 50/50 V/V was added to the resulting syrup, and the mixture was stirred at room temperature for a night. The light brown solid was filtered off and washed with ethanol and dried in vacuum over calcium chloride. *N*-(1-deoxy-β-fructos-1-yl)-L-methionine [FruMet]: *Anal.*

Calc. for $C_{11}H_{21}NO_7S$: C, 42.43; H, 6.80; N, 4.50; S, 10.30. Found: C, 42.45; H, 6.77; N, 4.58; S, 10.26% (Yield: 35%); *N*,*N*′-di-(1-deoxy-β-fructos-1-yl)-L-cystine [FruCyscys]: *Anal*. Calc. for $C_9H_{16}NO_7S$: C, 38.29; H, 5.71; N, 4.96; S, 11.36. Found: C, 38.26; H, 5.72; N, 4.93; S, 11.30% (Yield: 20%).

2.3. Synthesis of 2-(1,2,3,4,5-pentahydroxypentyl)-1,3-thiazolidine-4-carboxylic acid [GlcCys] [21]

A methanol suspension of anhydrous β-D-glucose and L-cysteine in equimolar ratio was refluxed for 2 h. The reaction was filtered off and the product was recrystallized from a water–methanol 1:1 V:V solution. *Anal*. Calc. for $C_9H_{17}NO_7S$: C, 38.16; H, 6.05; N, 4.94; S, 11.32. Found: C, 38.09; H, 6.08; N, 5.00; S, 11.26% (Yield: 80%).

2.4. Synthesis of Pt(II) complexes

A solution of 2×10^{-4} mol of FruMet in 10 ml of water was added dropwise, under stirring, to a solution of 1×10^{-4} mol of K_2PtCl_4 in 5 ml of water. The solution was kept in the dark and under stirring at 50 °C for 5 h to avoid metallic Pt formation. The reaction was filtered and concentrated to 2 mL, in order to favour precipitation 4 mL of ethanol were added. The product [Pt(FruMet-*N*,*S*)$_2$Cl$_2$] was recrystallized from ethanol. *Anal*. Calc. for $C_{22}H_{42}Cl_2N_2O_{14}PtS_2$: C, 29.73; H, 4.76; N, 3.15; S, 7.22. Found: C, 29.64; H, 4.63; N, 3.07; S, 7.16% (Yield: 60%). The same procedure using 1×10^{-4} mol of FruMet and 1×10^{-4} mol of K_2PtCl_4 separates a Pt/L 1:1 complex [Pt(FruMet-*N*,*S*)Cl$_2$]. *Anal*. Calc. for $C_{11}H_{21}Cl_2NO_7PtS$: C, 22.93; H, 3.50; N, 2.43; S, 5.56. Found: C, 23.01; H, 3.55; N, 2.39; S, 5.48% (Yield: 70%). The same procedure was used to obtain the Pt(II) complex of FruCyscys: [Pt$_2$FruCyscysCl$_4$]. *Anal*. Calc. for $C_9H_{16}Cl_2NO_7PtS$: C, 19.72; H, 2.94; N, 2.55; S, 5.85. Found: C, 19.78; H, 2.90; N, 2.62; S, 5.83% (Yield: 50%).

2.5. Partition coefficient

The shake-flask method is performed: 2 mL of the ligand stock solution (10^{-4} M) at pH 4 and 7.4 are mixed in a vessel with a known volume of high purity analytical grade *n*-octanol (0.5–2 mL) and shaken at 37 °C for 4 h. The two phases are then separated and the concentration of the ligand is determined in the aqueous solution by spectrophotometric method using a Perkin–Elmer Lambda 20 spectrophotometer.

2.6. Cytotoxicity study

The 2008 cell line, established from a patient with serious cystadenocarcinoma of the ovary and the cDDP-resistant C13* subline, generated as previously described [22] were grown as monolayers in RPMI 1640 medium (BioWhittaker Europe) containing 10% heat-inactivated fetal bovine serum (BioWhittaker Europe) and 50 μg/ml gentamycin sulfate. Cultures were equilibrated with humidified 5% CO_2 in air at 37 °C. Cells were treated for three days with different concentrations of [Pt(FruMet-*N*,*S*)Cl$_2$] (0–600 μM). All studies were performed in Mycoplasma negative cells, as routinely determined with the Mycotest detection kit (Euroclone, Switzerland). Cell growth was determined by a modification of the crystal violet dye assay [23]. On selected days, after removal of the tissue culture medium, the cell monolayer was fixed with methanol prior to staining with 0.25% crystal violet solution in 80% absolute ethanol for at least 30 min. After washing several times with distilled water to remove the dye excess, the cells were let to dry. The incorporated dye was solubilized in acidic isopropanol (1 N HCl: 2-propanol, 1:10). After appropriate dilution, dye was determined spectrophotometrically at 540 nm. The extracted dye was proportional to cell number. Percentage of cytotoxicity was calculated by comparing the absorbance of exposed to non-exposed (control) cultures.

3. Results and discussion

3.1. [FruMet]

^{1}H and ^{13}C FruMet NMR spectra were registered in D_2O and H_2O/D_2O (95/5) in order to completely characterize the ligand, chemical shifts are reported in Table 1. The addition of K_2PtCl_4 to a solution of FruMet in 1:2 M/L molar ratio, at room temperature and in acid conditions (pH 3), brings slowly to the formation of different complex species, as shown by the presence of many peaks in ^{195}Pt NMR spectrum (Fig. 1), and to a line broadening of proton signals close to the coordination site. Even if it is difficult to define the nature and stoichiometry of the formed complexes, ^{1}H NMR spectra suggest an *N*,*S* metal coordination, since significant downfield shifts are observed mainly for H-1, H-α and H-δ and slightly for H-β and H-γ (Scheme 1). The carboxylic group is in the protonated form. On increasing pH from 3 to 7 a downfield shift is observed for carboxylic carbon (from 172.5 ppm to 176 ppm) as a consequence of the deprotonation reaction. The same coordination mode is reported for analogous sulphur containing aminoacid complexes of Pt(II) [24].

To better investigate the 1:2 Pt/FruMet system, the solid complex [Pt(FruMet-*N*,*S*)$_2$]Cl$_2$ was synthesized in acid condition (pH ∼ 1.9) and studied in solution at physiological pH.

^{195}Pt NMR spectrum of [Pt(FruMet-*N*,*S*)$_2$]Cl$_2$ (Fig. 2) shows two main peaks at −3438(2) and −3445(2) ppm, attributed to two different isomers. Each platinum signal correlates with a different set of protons. The main cross peaks are due to platinum scalar coupling with aminic hydrogen (∼7 ppm) and δ-methyl group (∼2.7 ppm), suggesting an *N*,*S* coordination mode, which is furthermore supported by long-range couplings of platinum with H-α and H-γ. Methylenic H-β protons, that are almost chemical

Table 1
^{1}H and ^{13}C NMR data of FruMet and [Pt(FruMet-*N*,*S*)$_2$]Cl$_2$ registered at 300 K (*D_2O, **H_2O/ D_2O 95/5 V/V; "*A*" and "*B*" stand for the two isomers present in solution: *R*,*R* and *S*,*S*)

		H-1	H-3	H-4	H-5	H-6	H-6′	H-α	H-β	H-γ	H-δ	NH
FruMet*		3.28 3.25	3.70	3.82	3.94	3.96	3.70	3.78	2.13	2.58	2.07	
FruMet**		3.39	3.91	3.96	4.08	4.10	3.84	3.93	2.27	2.72	2.21	9.11
[Pt(FruMet-*N*,*S*)$_2$]Cl$_2$*	A	3.69	3.96	4.00	4.09	4.10	3.86	4.03	2.58 2.88	3.06 3.36	2.68	
	B	3.94							2.65 2.84	3.08 3.20	2.62	
[Pt(FruMet-*N*,*S*)$_2$]Cl$_2$**	A	3.68	3.96	4.00	4.10	4.10	3.86	3.99	2.59 2.86	3.04 3.35	2.67	6.90
	B	3.97							2.65 2.83	3.06 3.19	2.61	6.97
		C-1	C-2	C-3	C-4	C-5	C-6	C-α	C-β	C-γ	C-δ	COO
FruMet*		52.6	95.0	69.8	69.3	68.9	63.9	62.4	28.8	29.0	14.0	173.0
FruMet**		53.4	96.0	70.6	70.1	69.6	64.5	63.1	29.4	29.7	14.7	173.5
[Pt(FruMet-*N*,*S*)$_2$]Cl$_2$*	A	63.4	95.6	70.6	70.1	69.8	64.8	59.8	28.3	31.8	21.4	172.5
	B								27.4	33.9	19.3	

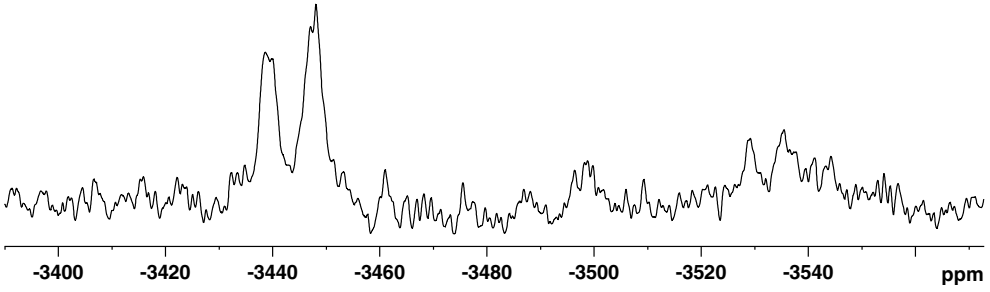


Fig. 1. ^{195}Pt NMR spectrum of Pt/FruMet 1:2 molar ratio D_2O solution in acid condition (pH 3) at 300 K.

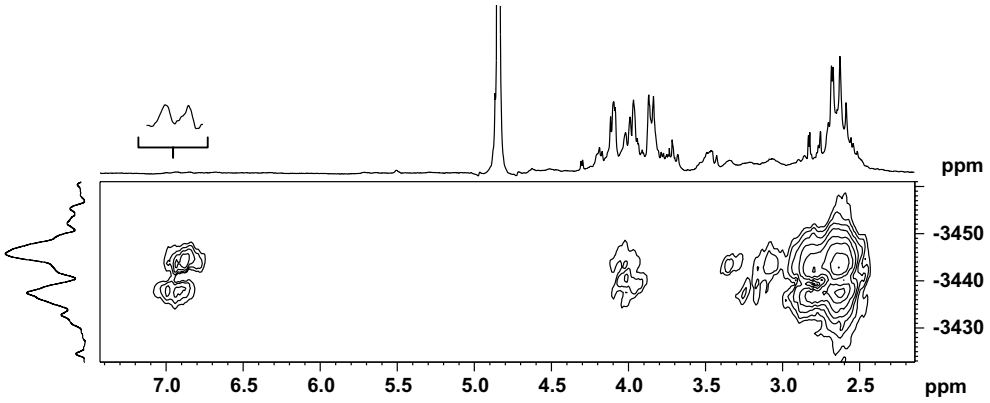


Fig. 2. [^{1}H, ^{195}Pt] HMBC spectrum in H_2O/D_2O 95/5 V/V at 300 K of [Pt(FruMet-*N*,*S*)$_2$]Cl$_2$. Cross peaks between metal ion and aminic hydrogen confirm an *N*,*S* coordination mode.

shift equivalent in the pure ligand, result strongly splitted since their free rotation is removed in the chelate ring formation. A same behaviour is observed for H-γ protons.

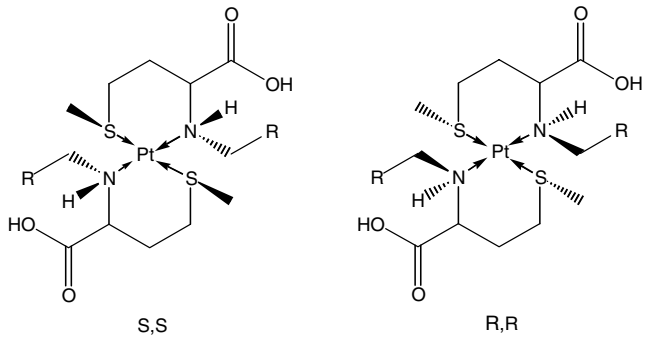
A correlation between ^{195}Pt chemical shift (δ) and the coordination geometry of platinum ion is reported [14]. For PtX_2L_2 species the *cis* isomer is usually upfield shifted with respect to *trans*; the shift is as big as the difference in the hard-soft nature of the ligands is increased [14]. As previously reported [25] the difference in δ ($\Delta\delta$) between *cis* and *trans* isomers in PtS_2N_2 type is around 200 ppm; in our system $\Delta\delta$ is around 10 ppm, therefore the same geometry for the two species is suggested: both *cis* or both *trans*. The *trans* isomer is here proposed because δ values are similar to those found for *trans* platinum–methionine complexes [25]. In order to substantiate this assumption a NOESY experiment was performed; the spectrum shows the presence of cross peaks relating *S*-CH_3 group with aminic proton and glycosidic moiety. This spatial proximity of

S-CH_3 and aminic group is consistent with a *trans* configuration that favours a reduction of the steric hindrance of the bulky nitrogen atoms and enhances a strong *trans* effect of sulphur atom [10]. Taking into account [^{1}H, ^{195}Pt] HMBC data (Fig. 2), each Pt atom correlates with a unique type of nitrogen atom therefore both *N* atoms coordinated to the same Pt ion must have the same *R* or *S* configuration, the same is observed for sulphur atom. As a consequence sulphur and nitrogen possible combinations of configurations are: *R*,*R*; *R*,*S*; *S*,*R* and *S*,*S*. According to NMR data only two of these combinations are present in solution, so we propose their attribution to *R*,*R* and *S*,*S* configurations on the basis of steric hindrance as shown in Scheme 2. On increasing temperature until 330 K all the peaks show a shift but no ^{195}Pt signals coalescence is observed, anyway epimerization at the chiral sulphur atom cannot be excluded at lower temperature, as previously observed in methionine containing Pt(II) complexes [11]. Although numerous examples exist in literature of possible N inversion in Pt(II) complexes [26], the presence in ^{1}H NMR spectrum of two different signals for aminic proton suggests no reversible configuration on N atom, probably due to the steric hindrance of the bulky nitrogen substituents.

Typically $^3J_{Pt-S-CH}$ is 50 Hz [27] and $^2J_{Pt-NH}$ is 85 Hz [24], anyway a value of 250 Hz was modulated in [^{1}H, ^{195}Pt] HMBC experiments in order to decrease evolution time and not to lose signals because of fast relaxation.

By addition of K_2PtCl_4 to a FruMet solution up to 1:1 M/L molar ratio a broad ^{195}Pt peak around −2790 ppm immediately appears, suggesting the formation of polymeric species. By standing the solution at 50 °C for few hours three quite sharp main peaks appear, at the same time a decrease of the broad signal (−2790 ppm) is registered, hinting the rearrangement of the polymeric species to form more ordinate complexes. Two kinds of 1:1 Pt/FruMet systems can be proposed. In a series of closely related chloride complexes, platinum signal moves to high field in the order P > S > N > Cl^- > O [14]. Thus the signals at upper field (−2918 and −2924 ppm) (Fig. 3) are attributed to the species [Pt(FruMet-*N*,*S*)Cl_2], in which platinum is coordinated by an hexatomic *N*,*S*-chelate ring, as also suggested by Norman et al. for similar platinum–methionine complexes [25]. The chelate complexes show two different signals related to the possible *R* or *S* configurations of the sulphur centre, the chirality of nitrogen atom does not influence platinum spectrum. The same behaviour is observed dissolving the solid [Pt(FruMet-*N*,*S*)Cl_2] in water.

The signal at lower field (−2841 ppm) is ascribed to the species [Pt(FruMet-*S*)Cl_3]$^-$ in which only the sulphur atom is involved in metal coordination, as a consequence no ring closure is observed (Scheme 3). The equilibrium between the two complexes slowly moves towards the formation of the thermodynamic more stable chelate species, which is totally formed in three days.



Scheme 2.

3.2. [GlcCys]

The condensation reaction of β-D-glucose and L-cysteine leads to the formation of the thiazolidine ring, NMR data (Fig. 4a, Table 2) confirm the presence of two configurational isomers as regards C-1. We found some discrepancies with what previously reported in literature, according to which thiazolidine rings are stable and do not open under mild conditions [21]. In our experiments GlcCys is

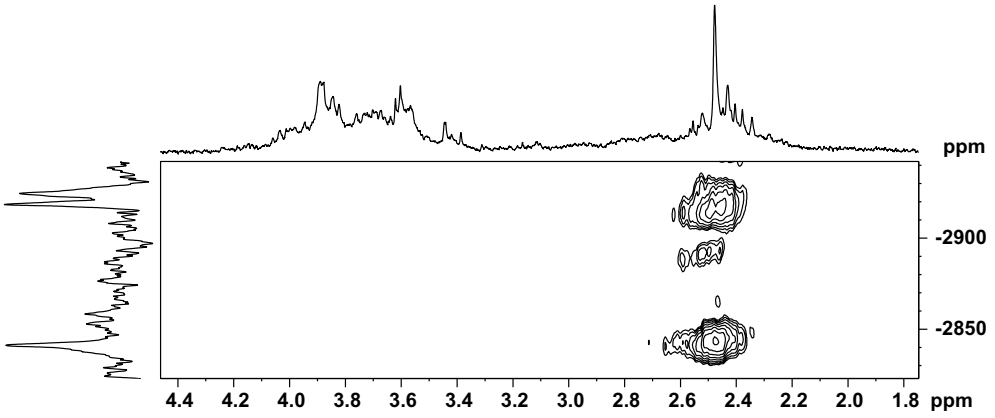
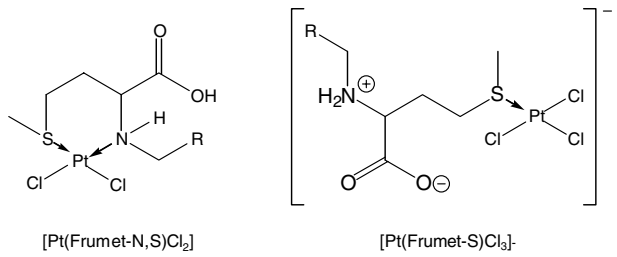


Fig. 3. [^{1}H, ^{195}Pt] HMBC spectrum of a mixture of [Pt(FruMet-*S*)Cl_3]$^-$ and [Pt(FruMet-*N*,*S*)Cl_2] in D_2O at 300 K.



Scheme 3.

very unstable, regardless solvent, pH, temperature and ionic strength. Thiazolidine ring break goes through the equilibria reported in Scheme 4.

^{1}H NMR spectrum of a freshly prepared D_2O GlcCys solution at 300 K in acid conditions (pH 2.7) shows only one species, the thiazolidinic one (Fig. 4a). After 24 h the presence of free β-D-glucose and L-cysteine tests the breakage of the thiazolidinic ring. This process is made faster as pH is increased (>7.0) or decreased (<1.0), as well as temperature is raised (from 300 K to 330 K). The great stability of [Pt(Cys-*N*,*S*)$_2$] and its low solubility in aqueous media make it suddenly precipitate when K_2PtCl_4 reacts with GlcCys solution with the immediate breaking of thiazolidine ring, so it is not possible to obtain Pt(II)-GlcCys complexes. The formation of [Pt(Cys-*N*,*S*)$_2$] is confirmed by elemental analysis of the separated solid compound (*Anal*. Calc. for $C_6H_{12}N_2PtS_2$: C, 16.55; H, 2.78; N, 6.43; S, 14.73. Found C, 16.53; H, 2.75; N, 6.44; S, 14.75%) and by NMR spectrum that shows an increase in free glucose signals as far as Pt(II) is added (Fig. 4).

3.3. [FruCyscys]

Maillard reaction between β-D-glucose and L-cystine, and the following Amadori rearrangement give rise to only one symmetric species, confirming that both aminic nitrogens are involved in the condensation process. In order to verify the stability of disulfide bridge polarographic measurements (cyclic voltammetry) were made, but the results were not useful since the solvents implied (MeOH, EtOH, and acetonitrile) discharged before Amadori's compound.

FruCyscys IR spectrum shows a weak band at 520 cm^{-1} typical of S–S stretching, furthermore the absence of a strong signal around 2550 cm^{-1} due to S–H stretching supports the hypothesis that disulfide bridge is enough stable in our reaction conditions.

Pt-FruCyscys system behaves very differently from the previously reported Pt/FruMet. The reaction with Pt(II), independently on the M/L ratio (1:1 or 2:1), separates the yellow solid [Pt_2FruCyscysCl_4], where the ligand bridges two Pt(II) ions. The stoichiometry of the complex was suggested on the basis of elemental analysis. The retaining in the IR spectrum of S–S stretching band confirm the stability of the S–S bond also in the complex. The NMR study is made difficult by the extreme line broadening of proton signals. Many measurements, varying spectral range and relaxation delay, were performed in order to improve spectral resolution, some results were obtained for proton while for platinum spectrum all kind of efforts failed and no signal was observed. The presence of disulfide bridge in which

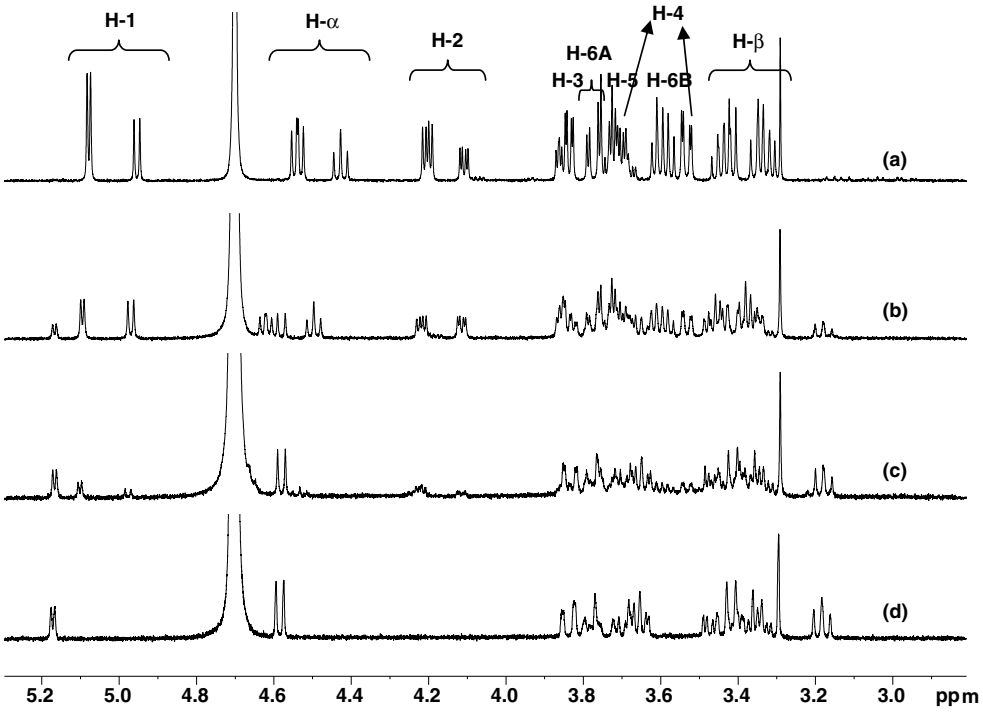
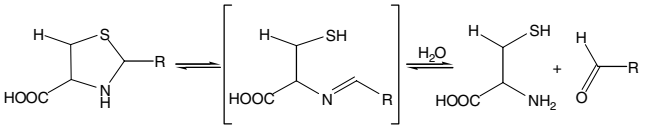


Fig. 4. ^{1}H NMR titration of a GlcCys D_2O solution with increasing addition of K_2PtCl_4 in acid condition (pH 2.7) at 300 K. The free ligand (a) shows the two sets of resonances corresponding to C-1 isomers; as platinum is added (b,c) [Pt(Cys-*N*,*S*)$_2$] separates, and when M/L 1:2 molar ratio is reached (d) only α and β-glucose species are present in solution.

Table 2
^{1}H and ^{13}C NMR data of GlcCys (D_2O) and FruCyscys (H_2O/D_2O 95/5 V/V) at 300 K

		H-1	H-2	H-3	H-4	H-5	H-6	H-6′	H-α	H-β
GlcCys	A	5.08	4.20	3.84	3.53	3.73	3.75	3.59	4.53	3.33
	B	4.95	4.11	3.86	3.69				4.42	3.43
FruCyscys		3.22		3.69	3.81	3.93	3.69	3.94	3.70	1.43
		C-1	C-2	C-3	C-4	C-5	C-6	C-α	C-β	COO
GlcCys	A	66.1	70.7	71.3	70.3	72.2	62.6	64.5	33.1	
	B	67.0	71.7	70.4	71.0	71.0		64.9		
FruCyscys		51.8	95.5	70.0	69.6	69.1	63.9	58.6	14.9	174.4

"A" and "B" stand for the two C-1 configurational isomers present in solution.



Scheme 4.

the formal oxidation state of sulphur atom (−1) is higher than in FruMet (−2), is responsible for an evident decrease in electronic charge density and an increased polarizability. These factors favour the "soft" Lewis base character of sulphur atom, which is able to strongly interact with Pt(II) ion with the formation of an almost covalent bond.

This strong ligand interaction with two different metal ions is responsible for the very fast relaxation observed in NMR spectra.

In order to better explain this behaviour, the analogous Pt(II)–cystine system was analysed. Neither in this system signals' assignment was possible, because of extreme line broadening due to fast relaxation; anyway, taking into account that even in deficit of metal ion the only separated solid species is [Pt_2cystineCl_4], we can suggest the same stoichiometry for both cystine and FruCyscys. H-α, H-β and H-1 undergo the greatest line-broadening and shifts, therefore we suppose that both cystine and FruCyscys bind Pt(II) with the formation of an *N*,*S* five membered chelate ring and that the sugar moiety is not involved in the complex formation. The extremely fast relaxation in ^{1}H NMR spectra of these dinuclear platinum(II) complexes with respect to the NMR time scale may be due to the spatial proximity of the two metal ions that enhances the positive charge density on the ligand and probably favour dipolar phenomena [28]. In addition, dynamic effects due to fluxional rearrangement of the disulphide bridge may contribute to line broadening, as previously observed in Pt(IV)–disulphide complexes [29].

3.4. Biological study

[Pt(FruMet-*N*,*S*)Cl_2] compound apparently sums different properties of potential anticancer drug. It is uncharged and could penetrate cell membranes mainly through diffusion processes. It is commonly assumed that for cisplatin like compounds the interaction with DNA occurs after chloride ligands are lost through aquation so to yield positively charged monoaqua and diaqua species [30]. Differently from cisplatin, this compound is characterized by only one amine group and, as second carrier ligand, a sulphur atom, which has a stronger *trans* effect than nitrogen and so can better promote chloride lost. Furthermore, steric hindrance of fructose moiety inhibits access to platinum by bulky molecules. To better investigate the biological activity of this complex we have also tested its cytotoxicity.

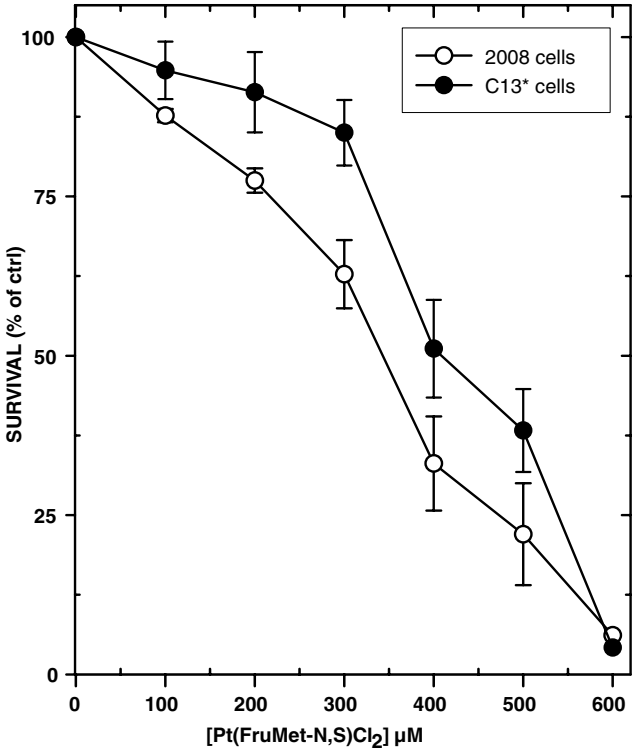


Fig. 5. Survival of colonies of 2008 cells and C13* cells following treatment with [Pt(FruMet-*N*,*S*)Cl_2]. Each point represents mean values ± SE of three separate experiments, each conducted with triplicate plates.

As shown in Fig. 5, the C13* human ovarian carcinoma cisplatin-resistant cells are as sensitive to [Pt(FruMet-*N*,*S*)Cl_2] as their parental 2008 cells. The IC_{50} values are about 340 μM and about 400 μM for 2008 and C13* cells,

respectively. Unfortunately, the cytotoxic activity of [Pt(FruMet-*N*,*S*)Cl_2] is much lower than cisplatin (0.04 μM) [31,32]. The maximal difference in cytotoxicity is achieved at 300 μM, while at higher concentrations the sensitivity of the two cell lines becomes similar.

We have also compared lipophilicity of our complex with that of cisplatin. Lipophilicity is commonly assessed by measuring partition coefficient between two phases, typically *n*-octanol and water [33]. The measured log *P* (−2.04) for [Pt(FruMet-*N*,*S*)Cl_2] is consistent with the presence of a sugar moiety that enhances water solubility and it is close to the value of cisplatin (log *P* −2.35) [34].

This low lipophilicity does not exclude that in vivo metabolic processes may allow good biodisponibility since we cannot reject a possible role of sugar moiety in mediated transport by specific receptors.

Acknowledgements

We are grateful to the "Centro Interdipartimentale Grandi Strumenti – C.I.G.S." of the University of Modena and Reggio Emilia and to the "Fondazione Cassa di Risparmio di Modena" for supplying NMR spectrometer.

References

[1] C.J. Ziegler, A.P. Silverman, S.J. Lippard, J. Biol. Inorg. Chem. 5 (2000) 774.
[2] K.R. Barnes, S.J. Lippard, J. Stephen, Metal Ions Biol. Syst. 42 (2004) 143.
[3] J. Reedijk, Chem. Rev. 99 (1999) 2499.
[4] B.A.J. Jansen, J. Brower, J. Reedijk, J. Inorg. Biochem. 89 (2002) 197.
[5] E. Eastman, Pharmac. Ther. 34 (1987) 155.
[6] S.J. Berners-Price, P.W. Kuchel, J. Inorg. Biochem. 38 (1990) 305.
[7] E.F. Bernstein, H.A. Pass, J.R. Glass, A.M. De Luca, S. Cook, J. Fisher, J.A. Cook, Int. J. Oncol. 7 (1995) 353.
[8] J. Sastre, E. Diaz-Rubio, J. Blanco, L. Cifuentes, Oncol. Rep. 3 (1996) 1149.
[9] R.T. Dorr, Platinum and other Metal Coordination Compounds in Cancer Chemotherapy, vol. 2, Plenum Press, New York, 1996.
[10] T.G. Appleton, Coord. Chem. Rev. 166 (1997) 313.
[11] C. Rothenburger, M. Galanski, V.B. Arion, H. Görls, W. Weigand, B.K. Keppler, Eur. J. Inorg. Chem. (2006) 746.
[12] T.W. Hambley, Coord. Chem. Rev. 166 (1997) 181.
[13] D. Gudat, A. Dogan, W. Kaim, A. Klein, Magn. Res. Chem. 42 (2004) 781.
[14] P.S. Pregosin, Coord. Chem. Rev. 44 (1982) 247.
[15] K. Nagayama, A. Kumar, K. Wuethrich, R.R. Ernst, J. Magn. Reson. 40 (1980) 321.
[16] G. Wagner, K. Wűthrich, J. Mol. Biol. 155 (1982) 347.
[17] A. Bax, M.F. Summers, J. Am. Chem. Soc. 108 (1986) 2093.
[18] A. Bax, R.H. Griffey, B.L. Hawkins, J. Magn. Reson. 55 (1983) 301.
[19] A. Bax, D.G. Davis, J. Magn. Reson. 65 (1985) 355.
[20] V.V. Mossine, G.V. Glinsky, M.S. Feather, Carbohydr. Res. 262 (1994) 257.
[21] T. Gajda, L. Nagy, K. Burger, J. Chem. Soc., Dalton. Trans. (1990) 3155.
[22] P.A. Andrews, K.D. Albright, Cancer Res. 52 (1992) 1895.
[23] W. Kueng, E. Siber, U. Eppenberger, Anal. Biochem. 182 (1989) 16.
[24] L.E. Erickson, P.D. Bailey, T.L. Kimball, B.J. Morgan, Inorg. Chim. Acta 346 (2003) 169.
[25] R.E. Norman, J.D. Ranford, P.J. Sadler, Inorg. Chem. 31 (1992) 877.
[26] F.P. Fanizzi, L. Maresca, G. Natile, M. Lanfranchi, A.M. Manotti-Lanfredi, A. Tiripicchio, Inorg. Chem. 27 (1988) 2422.
[27] T.G. Appleton, J.W. Connor, J.R. Hall, Inorg. Chem. 27 (1988) 130.
[28] M. Liu, J.C. Lindon, Concept Magnetic Res. 8 (1996) 161–173.
[29] E.W. Abel, A.R. Khan, K. Kite, K.G. Orrell, V. ŠiK, J. Chem. Soc. Dalton (1980) 2220.
[30] D.B. Bancroft, C.A. Lepre, S.J. Lippard, J. Am. Chem. Soc. 112 (1990) 6860.
[31] G. Marverti, G. Piccinini, S. Ghiaroni, D. Barbieri, D. Quaglino, M.S. Moruzzi, Int. J. Cancer 78 (1998) 33.
[32] G. Marverti, P.A. Andrews, G. Piccinini, S. Ghiaroni, D. Barbieri, M.S. Moruzzi, Eur. J. Cancer 33 (1997) 669.
[33] M.D. Habgood, Z.D. Liu, L.S. Dehkordi, H.H. Khodr, J. Abbot, R.C. Hider, Biochem. Pharmacol. 57 (1999) 1305.
[34] L. Feng, A. De Dille, V.J. Jameson, L. Smith, W.S. Dernell, M.C. Manning, Cancer Chemother. Pharmacol. 54 (2004) 441.

the organic one) and the metal ion, scientists aim to tune the physical properties and, thus, realize various applications of coordination polymers in catalysis, electrical conductivity, luminescence, magnetism, non-linear optics, molecular electronics, sensing and zeolitic behaviour [2,4]. Coordination polymers are also significant from a structural chemistry perspective with new, intriguing molecular topologies being discovered, as well as providing numerous examples of interesting phenomena such as the interpenetration of networks [5]. Some structures of minerals, such as diamond [6], quartz [7], rutile [8], perovskite [9], PtS [10], zeolite [11] and feldspar [12] have been artificially produced by "replacing" monoatomic anions (O^{2-}, S^{2-}) with polyatomic organic ligands as linkers and utilizing metal centers (with well-defined coordination geometries) as nodes.

An interesting family of coordination polymers consists of complexes that *simultaneously* contain a bridging, *anionic* organic ligand and a bridging, *anionic* inorganic ligand [2,4]. Their simplest general formula is $MLX_n^{0,a+ora-}$. The pyridine *mono*carboxylate 3-pyridinecarboxylate (nicotinate) and 4-pyridinecarboxylate (isonicotinate) ligands have been shown to act as connecting units in metal coordination networks [2,4,13] with a variety of topologies. In contrast to the obtained large body of knowledge, the isomeric 2-pyridinecarboxylate (picolinate) ligand has been less employed, mainly because of its inherent tendency to form a chelating ring which favours the formation of mononuclear or polynuclear complexes. The most frequently used bridging inorganic ligands are *mono* anionic, e.g. Cl^-, Br^-, CN^-, N_3^-, SCN^- etc. [2,4,13]. In contrast, the use of *di*- or *trianions*, e.g. SO_4^{2-}, PO_4^{3-}, VO_4^{3-}, etc., for the construction of coordination polymer is rather restricted [2,4,13].

With the above information in mind, we set forth in 2005 to systematically use the picolinate(−)/sulfate(−2) ligand "blend" in the construction of coordination polymers of 3d- and 4f-metal ions. The picolinate ion (pic^-) contains two carboxylate oxygen atoms and one pyridyl nitrogen atom as potential donor sites, exhibiting a variety of ligation modes. The up-to-now crystallographically established coordination modes of pic^- and the Harris notation [14] that describes these modes are conveniently presented in Fig. 1. Beyond its terminal behaviour (monodentate, chelating), the pic^- ligand can bridge up to four metal ions. A great number of picolinate metal complexes have been reported in the last two decades, but only few of them have a polymeric structure [15]. On the other hand, the sulfate ion is currently an inorganic ligand of great interest [16,17]. The great coordinative flexibility and versatility of the pic^- ligand, as well as the μ_2, μ_3, μ_4, $\mu_5$or μ_6 potential of SO_4^{2-} (Fig. 2) [16], prompted us to combine the pic^- ligand with the SO_4^{2-} anion for the *first time in coordination chemistry* to aim for new types of coordination

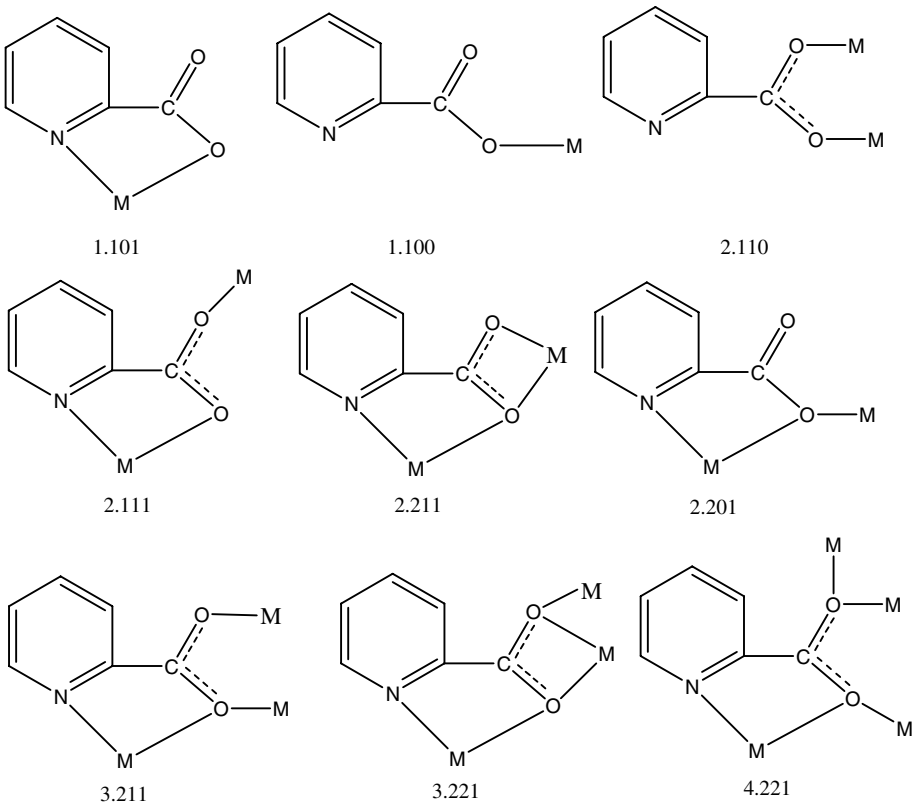


Fig. 1. The up-to-now crystallographically established coordination modes of the picolinate ligand and the Harris notation [14] that describes these modes.

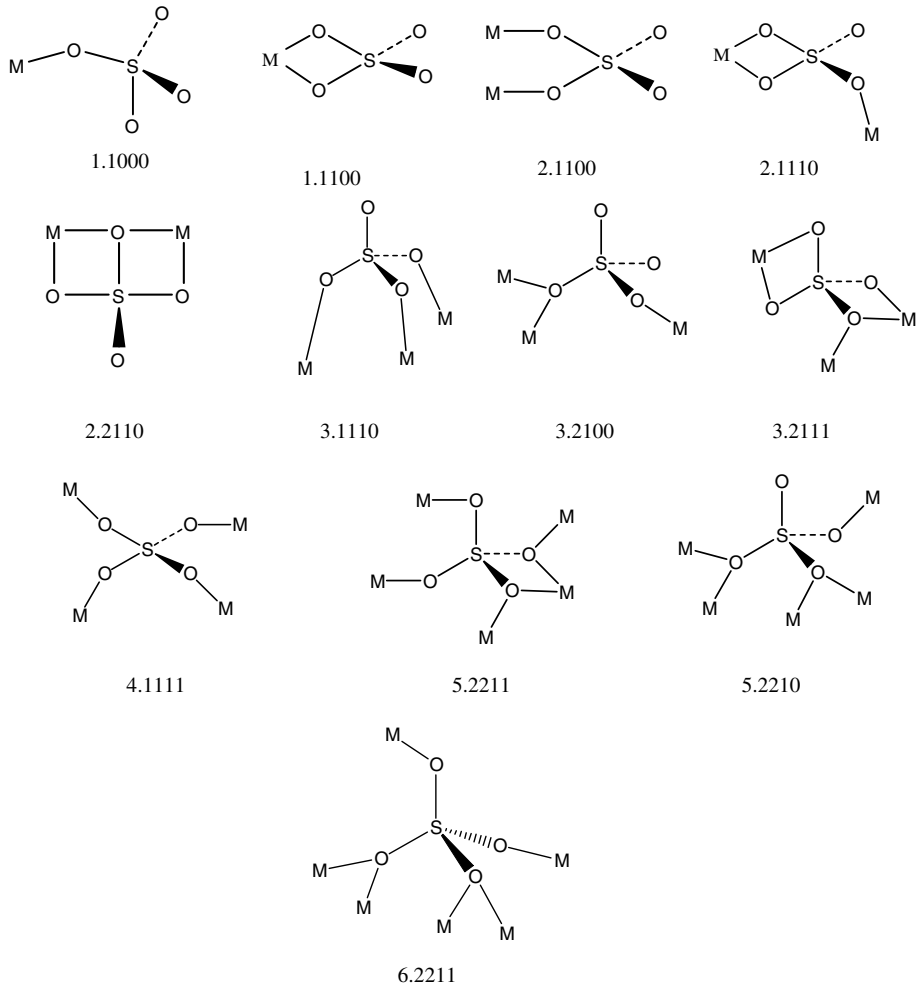


Fig. 2. The hitherto crystallographically established coordination modes of the sulfato ligand and the Harris [14] notation that describes these modes.

polymers. Our belief was that the simultaneous employment of the two ligand systems in transition metal chemistry would give structural flexibility in the pic^-/SO_4^{2-} "blend". The possible advantages of using SO_4^{2-} instead of *mono* anionic inorganic ligands include (i) the possibility of triggering aggregation of preformed smaller species containing only pic^- into new, polymeric products, and (ii) the possible diversion of known reaction systems developed using inorganic *mono*anions to new polymeric species as a result of the higher charge and higher density/bridging capability of SO_4^{2-}.

We illustrate herein how the pic^-/SO_4^{2-} ligand combination leads to two interesting coordination polymers of Zn(II) and Cd(II). The two complexes have the same metal: SO_4^{2-}: pic^- ratio, but different structures. The initial choice of Zn^{II} and Cd^{II} for our study is due to the fact that these d^{10} metal ions are particularly suited for the construction of coordination networks [13,18]. The spherical d^{10} configuration is associated with a flexible coordination environment so that geometries for each metal ion can vary; thus, severe distortions of the ideal polyhedra occur easily. Further, due to their general lability, the formation of coordination bonds is reversible, and this enables Zn^{II} or Cd^{II} and ligands to rearrange during the polymerization process to give highly ordered network structures [13]. Consequently, these metal ions can accommodate all kinds of architectures. The present work can be considered as continuation of our research efforts on 3d- and 4f-metal coordination polymers [19,20].

2. Experimental

2.1. General and physical measurements

All manipulations were performed under aerobic conditions using materials (reagent grade) and solvents as received. Microanalyses (C, H, N) were performed by the University of Ioannina (Greece) Microanalytical Laboratory using an EA 1108 Carlo Erba analyzer.

IR spectra (4000–400 cm^{-1}) were recorded on a Perkin–Elmer 16 PC FT-spectrometer with samples prepared as KBr pellets. Thermogravimetric (TG), differential thermogravimetric (DTG) and differential thermal analysis (DTA) experiments were performed on the SDT-2960

module from TA-instruments under a dinitrogen gas flow; sample weights of 5–15 mg and heating rates of 1 and 5 °C min^{-1} were used. The Raman spectrum of the Cd(II) complex was measured in the micro-Raman backscattering geometry. The spectra were excited with the 441.6 nm line of an air-cooled HeCd laser of Kimmon Electric Co. (Dual, 325/442 nm, UV/blue, 20/80 mW, IK5651R-G model laser). A narrow-bandpass interference filter was used for the elimination of the laser plasma lines. The excitation beam was directed to the sample compartment of a confocal open microscope attachment for punctual analysis. The microscope was used for the delivery of the excitation laser beam on the sample. The focusing objective was a Long Working distance (8 mm) 50×/0.55 Olympus lens. The spectrum was obtained using a ~5 mW laser power on the specimen for a total integration time of 5 s. The Raman scattered radiation was focused on a confocal entrance slit (of 100 μm width) of an achromatic flat field spectrograph of 800 nm focal length. The integrated laser Raman system employed was the UV–Vis Labram HR of the Jobin Yvon-Horiba group. The dispersion and the detection of the Raman photons were done by an 1800-grooves/mm grating on a 2D CCD detector (operating at 140 K), respectively. The spectral slit width was approximately 3 cm^{-1}.

2.2. Compound preparation

2.2.1. $[Zn_2(SO_4)(pic)_2(H_2O)_3]_n$ (1)

A colourless aqueous solution (5 ml) of picH (0.037 g, 0.30 mmol) was added to a solution of $ZnSO_4 \cdot 7H_2O$ (0.086 g, 0.30 mmol) in H_2O (5 ml). The reaction solution was stirred for about 1 h and layered with Me_2CO (20 ml). Slow mixing gave well-formed, X-ray quality colourless prismatic crystals, which were collected by filtration, washed with Me_2CO (24 × 3 ml) and dried in air. Typical yields were in the 50–60% range. IR (KBr pellet): ν = 3336sb, 1624s, 1594s, 1568s, 1478m, 1448m, 1406s, 1374s, 1294m, 1260w, 1144s, 1110s, 1068s, 1022m, 984m, 836m, 794s, 702s, 646s, 612m, 568m, 460m, 455s. *Anal.* Calc. for $C_{12}H_{14}O_{11}N_2SZn_2$ (525.05): C, 27.46; H, 2.69; N, 5.34. Found: C, 28.19; H, 2.60; N, 5.46%.

2.2.2. $[Cd_2(SO_4)(pic)_2(H_2O)_3]_n \cdot nH_2O$ ($2 \cdot nH_2O$)

A colourless aqueous solution (5 ml) of picH (0.049 g, 0.40 mmol) was added to a solution of $3CdSO_4 \cdot 8H_2O$ (0.103 g, 0.13 mmol) in H_2O (5 ml). The reaction solution was stirred for about 1 h and layered with Me_2CO (20 ml). Slow mixing gave well-formed, X-ray quality colourless needles of the product, which were collected by filtration, washed with Me_2CO (2 × 3 ml) and dried in air. Typical yields were in the 55–65% range. IR (KBr pellet): ν = 3374 mb, 1621s, 1590s, 1562m, 1476m, 1445m, 1379s, 1290m, 1237w, 1160sh, 1116s, 1014m, 961w, 850m, 762m, 702m, 617s, 560sh, 455m. *Anal.* Calc. for $C_{12}H_{16}O_{12}N_2SCd_2$ (637.13): C, 22.62; H, 2.54; N, 4.40. Found: C, 23.01; H, 2.28; N, 4.52%.

2.3. Single-crystal X-ray crystallography

Crystals of **1** and $\mathbf{2} \cdot nH_2O$ were mounted in air and covered with epoxy glue. The X-ray data set for **1** was collected with a $P2_1$ Nicolet diffractometer upgraded by Crystal Logic using graphite-monochromated Cu radiation. Diffraction measurements for $\mathbf{2} \cdot nH_2O$ were made on a Crystal Logic Dual Goniometer diffractometer using graphite-monochromated Mo radiation. Complete crystal data and parameters for data collection and processing are listed in Table 1. Unit cell dimensions were determined and refined by using the angular settings of 25 automatically centred reflections in the ranges $22° < 2\theta < 54°$ (for **1**) and $11° < 2\theta < 23°$ (for $\mathbf{2} \cdot nH_2O$). Intensity data were recorded using the θ–2θ scan method. Three standard reflections monitored every 97 reflections showed less than 3% variation and no decay. Lorentz, polarization and Ψ-scan absorption were applied using the Crystal Logic software package.

The structures were solved by direct methods using SHELXS-86 [21] and refined by full-matrix least-squares techniques on F^2 with SHELXL-97 [22]. For the structure of **1**, all hydrogen atoms were located by difference maps and

Table 1
Summary of crystal data, data collection and structure refinement for the X-ray diffraction study of complexes **1** and $\mathbf{2} \cdot nH_2O$

Complex	**1**	$\mathbf{2} \cdot nH_2O$
Empirical formula	$C_{12}H_{14}N_2O_{11}SZn_2$	$C_{12}H_{16}N_2O_{12}SCd_2$
Formula weight	525.05	637.13
Crystal size (mm)	0.07 × 0.15 × 0.30	0.07 × 0.20 × 0.50
Colour, habit	colourless prisms	colourless needles
Crystal system	monoclinic	monoclinic
Space group	$P2_1/n$	$P2_1/n$
a (Å)	18.640(9)	11.200(5)
b (Å)	8.506(4)	13.231(6)
c (Å)	11.768(5)	13.650(6)
β (°)	108.84(2)	110.360(10)
V (Å^3)	1765.9(14)	1896.4(15)
Z	4	4
ρ_{calc} (g cm^{-3})	1.975	2.232
Radiation, λ (Å)	Cu Kα, 1.54180	Mo Kα, 0.71073
μ (mm^{-1})	5.058	2.419
F(000)	1056	1240
Temperature (K)	298	298
$2\theta_{max}$ (°)	118	50
hkl Ranges	−20 → 0, 0 → 9, −12 → 13	−13 → 12, −15 → 0, 0 → 16
Measured reflections	2612	3430
Unique reflections [R_{int}]	2525 [0.0164]	3280 [0.0238]
Reflections used ($I > 2\sigma(I)$)	2430	3103
Parameters refined	307	285
Goodness-of-fit (on F^2)	1.094	1.047
R_1^a ($I > 2\sigma(I)$)	0.0293	0.0593
WR_2^b ($I > 2\sigma(I)$)	0.0800	0.1705
$(\Delta\rho)_{max}/(\Delta\rho)_{min}$ (e Å^{-3})	0.423/−0.482	0.918/−0.844

[a] $R_1 = \sum(|F_o| - |F_c|)/\sum(|F_o|)$.
[b] $wR_2 = \{\sum[w(F_o^2 - F_c^2)^2]/\sum[w(F_o^2)^2]\}^{1/2}$.

refined isotropically. In the case of $\mathbf{2}\cdot n\mathrm{H_2O}$, the hydrogen atoms of the water molecules were located by difference maps and refined isotropically, while the rest were introduced at calculated positions as riding on bonded atoms. For both structures, all non-hydrogen atoms were refined using anisotropic thermal parameters.

3. Results and discussion

3.1. Brief synthetic comments

Reaction of $\mathrm{MSO_4}\cdot x\mathrm{H_2O}$ (M = Zn, $x = 6$; M = Cd, $x = 8/3$) with one equivalent of picH in $\mathrm{H_2O}$ and conventional workup leads to the isolation of the polymeric complexes $[\mathrm{Zn_2(SO_4)(pic)_2(H_2O)_3}]_n$ (**1**) and $[\mathrm{Cd_2(SO_4)(pic)_2(H_2O)_3}]_n\cdot n\mathrm{H_2O}$ ($\mathbf{2}\cdot n\mathrm{H_2O}$) according to the balanced equations (1) and (2), respectively:

$$2n\mathrm{ZnSO_4}\cdot 7\mathrm{H_2O} + 2n\mathrm{picH} \xrightarrow{\mathrm{H_2O}} \underset{\mathbf{1}}{[\mathrm{Zn_2(SO_4)(pic)_2(H_2O)_3}]_n} + n\mathrm{H_2SO_4} + 11n\mathrm{H_2O} \quad (1)$$

$$2n\mathrm{CdSO_4}\cdot 8/3\mathrm{H_2O} + 2n\mathrm{picH} \xrightarrow{\mathrm{H_2O}} \underset{\mathbf{2}\cdot n\mathrm{H_2O}}{[\mathrm{Cd_2(SO_4)(pic)_2(H_2O)_3}]_n\cdot n\mathrm{H_2O}} + n\mathrm{H_2SO_4} + 4n/3\mathrm{H_2O} \quad (2)$$

In both complexes the picolinate ligands are deprotonated as it is expected from the value of pK_a of the carboxylic group (5.25).

Few features of the reactions represented by chemical equations (1) and (2) deserve comments: First, the appearance of $\mathrm{H_2SO_4}$ in the products might imply that complexes **1** and $\mathbf{2}\cdot n\mathrm{H_2O}$ (which contain deprotonated organic ligands) decompose under "acidic" conditions. We did not have such evidence probably due to high dilution. A second point of synthetic interest is the absence of a base from the reaction mixtures that lead to **1** and $\mathbf{2}\cdot n\mathrm{H_2O}$. The employment of base in the $\mathrm{ZnSO_4}\cdot 7\mathrm{H_2O}$/picH reaction system in $\mathrm{H_2O}$ leads to the precipitation of a colourless, microcrystalline solid. Microanalyses indicated the formula $\mathrm{Zn(pic)_2}\cdot 4\mathrm{H_2O}$, while there are no bands in the IR spectrum attributable to sulfate ions/ligands. Thus, this solid appears to be complex *trans*-$[\mathrm{Zn(pic)_2(H_2O)_2}]\cdot 2\mathrm{H_2O}$, which has been structurally characterized in two polymorphic forms [23,24]. Similarly, the 1:2:2 $\mathrm{CdSO_4}\cdot 8/3\mathrm{H_2O}$/picH/$\mathrm{OH^-}$ reaction mixture in $\mathrm{H_2O}$ gives the known complex $[\mathrm{Cd_2(pic)_4}]_n$ [15g]. And third, complexes **1** and $\mathbf{2}\cdot n\mathrm{H_2O}$ seem to be the only products from the general reaction system $\mathrm{M^{II}/SO_4^{2-}}$/picH (M = Zn, Cd) in $\mathrm{H_2O}$. The metal to ligand reaction ratio, the presence of counterions (e.g. $\mathrm{NBu_4^n}$ or $\mathrm{ClO_4^-}$ for the possible isolation of anionic or cationic compounds) and the precipitation/crystallization (the products can also be precipitated by slow evaporation of $\mathrm{H_2O}$ at room temperature over a period of 1–2 weeks) method have no influence on the identity of the products.

From the use of $\mathrm{H_2O}$ viewpoint, the preparation of the two polymeric complexes may be considered as a "green" procedure [25]. The use of environmentally benign solvents (and solventless systems) has been one of the most active areas of green chemistry over the past 10 years [25].

3.2. Description of structures

The structure of **1** is based on 1D helical chains, which interact to each other through hydrogen bonding and stacking interactions. The asymmetric unit of the architecture is presented in Fig. 3, and selected interatomic distances and angles are listed in Table 2.

The asymmetric unit of **1** contains pairs of $\mathrm{Zn^{II}}$ atoms and bridging picolinato ligands, one bridging sulfato ligand and three terminally coordinated water molecules. One of the $\mathrm{Zn^{II}}$ atoms [Zn(1)] is five-coordinate in a distorted trigonal bipyramidal environment, while the other [Zn(2)] is in an octahedral coordination environment. Both metal ions are bonded to the $\mathrm{NC_2O}$ chelating part of different

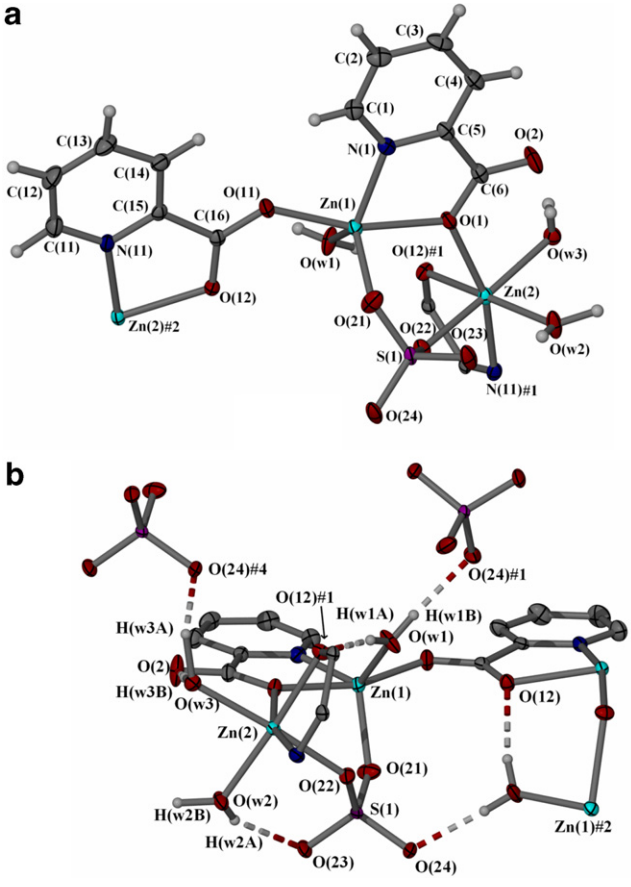


Fig. 3. (a) A thermal ellipsoid (40%) plot of the asymmetric unit of **1**, extended to show the coordination spheres of the metal ions and the coordination modes of the ligands. Symmetry operations to generate equivalent atoms: #1 $-x+3/2$, $y-1/2$, $-z-1/2$; #2 $-x+3/2$, $y+1/2$, $-z-1/2$. (b) The intra-helix H-bonds present in the 1D polymer **1**. Symmetry operations to generate equivalent atoms: #1 $-x+3/2$, $y-1/2$, $-z-1/2$; #2 $-x+3/2$, $y+1/2$, $-z-1/2$; #4 x, $y-1$, z.

Table 2
Selected bond distances (Å) and angles (°) for complex **1**

Bond distances			
Zn(1)–O(1)	2.169(2)	Zn(1)–O(21)	1.967(2)
Zn(1)–O(11)	2.048(2)	Zn(2)–O(1)	2.138(2)
Zn(1)–O(w1)	1.974(2)	Zn(2)–O(12)#1	2.150(2)
Zn(2)–N(11)#1	2.110(3)	Zn(2)–O(w2)	2.050(2)
Zn(2)–O(22)	2.100(2)	Zn(1)···Zn(2)	3.706(3)
Zn(2)–O(w3)	2.103(2)	Zn(1)···Zn(2)#2	5.480(3)
Zn(1)–N(1)	2.068(3)	Zn(2)···Zn(2)#2	8.050(4)
Bond angles			
O(21)–Zn(1)–OW1	117.22(11)	O(21)–Zn(1)–O(11)	99.58(10)
O(w1)–Zn(1)–O(11)	93.90(10)	O(21)–Zn(1)–N(1)	112.97(11)
O(w1)–Zn(1)–N(1)	128.14(11)	O(11)–Zn(1)–N(1)	89.96(10)
O(21)–Zn(1)–O(1)	94.50(9)	O(w1)–Zn(1)–O(1)	86.30(10)
O(11)–Zn(1)–O(1)	164.01(9)	N(1)–Zn(1)–O(1)	77.51(9)
O(w2)–Zn(2)–O(22)	88.68(10)	O(w2)–Zn(2)–O(w3)	85.98(10)
O(22)–Zn(2)–O(w3)	170.69(8)	O(w2)–Zn(2)–N(11)#1	95.35(11)
O(22)–Zn(2)–N(11)#1	88.15(9)	O(w3)–Zn(2)–N(11)#1	99.93(9)
O(w2)–Zn(2)–O(1)	99.35(10)	O(22)–Zn(2)–O(1)	83.92(8)
O(w3)–Zn(2)–O(1)	89.42(8)	N(11)#1–Zn(2)–O(1)	163.10(9)
O(w2)–Zn(2)–O(12)#1	169.80(10)	O(22)–Zn(2)–O(12)#1	97.62(8)
O(w3)–Zn(2)–O(12)#1	88.77(8)	N(11)#1–Zn(2)–O(12)#1	76.94(9)
O(1)–Zn(2)–O(12)#1	89.32(80)		

Hydrogen bonds

Donor–H···Acceptor	D–H	H···A	D···A	D–H···A
O(w1)–H(w1A)···O(12)#1	0.84(5)	1.89(5)	2.723(4)	169(4)
O(w1)–H(w1B)···O(24)#1	0.79(4)	1.89(4)	2.679(3)	172(4)
O(w2)–H(w2A)···O(23)	0.68(5)	2.19(5)	2.821(4)	156(5)
O(w2)–H(w2B)···O(23)#3	0.97(5)	1.77(5)	2.732(4)	172(5)
O(w3)–H(w3A)···O(24)#4	1.19	1.56	2.725(3)	165
O(w3)–H(w3B)···O(2)	0.71	1.96	2.661(4)	169

Symmetry operations used to generate equivalent atoms: #1 $-x+3/2$, $y-1/2$, $-z-1/2$; #2 $-x+3/2$, $y+1/2$, $-z-1/2$; #3 $-x+3/2$, $y-1/2$, $-z+1/2$; #4 x, $y-1$, z.

ligands and to an oxygen atom belonging to an adjacent bridging picolinate [Zn(1)–O(11), 2.048(2); Zn(2)–O(1), 2.138(2) Å]. The coordination polyhedra are completed by one and two aqua ligands for Zn(1) and Zn(2), respectively. The two Zn^{II} atoms of the asymmetric unit are bridged by the 2.1100 [14] sulfato ligand and one of the picolinates which utilizes only one of the carboxylate oxygen atoms [O(1)] for the bridge; thus, this pic^- ion behaves as a 2.201 ligand (Fig. 1) [14]. The C(6)–O(2) bond distance [1.237(4) Å] involving the "free" picolinate oxygen atom is shorter than the C(6)–O(1) bond length [1.286(4) Å] involving the bridging picolinate oxygen atom, as expected. The second picolinato ligand is 2.111 [14] and bridges two asymmetric units through its syn, anti carboxylate group leading to the formation of an infinite helical chain. The planes defined by the different organic ligands in the asymmetric unit are almost parallel [the angle between them is 7.61(8)°], and responsible for the formation of the helix is the angle between the planes of the 2.111 pic^- ligand with a symmetry related $(-x+3/2,\ y+1/2,\ -z-1/2)$ 2.201 pic^- ligand. The helices run along the b axis with a pitch of 8.51 Å. The one-dimensional structure is stabilized by an extended array of H-bonds (five per asymmetric unit) (see Table 2 and Fig. 3b).

The ranges of the Zn(1)–(O,N) and Zn(2)–(O,N) bond lengths are typical for five- [19c,19d,26] and six-coordinate [23,24,26a,26b,27] zinc(II) complexes, respectively. The Zn(1)–O(11), Zn(1)–O(21), Zn–O(w1) and Zn(1)–N(1) distances are shorter than the corresponding Zn(2)–O(12) $[-x+3/2,\ y-1/2,\ -z-1/2]$, Zn(2)–O(22), Zn(2)–O(w2,w3) and Zn(2)-N(11) $[-x+3/2,\ y-1/2,\ -z-1/2]$ distances, respectively. The decreased bond lengths for Zn(1) may be a consequence of the lower coordination number of this metal ion compared to that for Zn(2) (five versus six). However, an analogous trend does not hold true for the Zn(1,2)–O(1) bond distances involving the bridging oxygen of the 2.201 pic^- ligand; the Zn(1)–O(1) bond distance [2.169(2) Å] is longer than the Zn(2)–O(1) bond distance [2.138(2) Å].

As depicted in Fig. 4, homochiral right-handed *P*-chains interact through two, symmetry related, H-bonds per asymmetric unit giving rise to the formation of a 2D layer parallel to the *bc* plane. The water molecule w2 acts as a donor to a symmetry related sulfate [O(w2)–H(w2B)···O(23)$(-x+3/2, y-1/2, -z+1/2)$] connecting two different helices. The same interaction occurs from the other site of the helix with the sulfate's O(23) being the acceptor. A stacking interaction between the aromatic rings of one pic^- ligand proceeds parallel to the [1 0 1] direction of the unit cell, alternately connecting *P*- and *M*-helical chains, resulting in the supramolecular structure shown in Fig. 5. The characteristics of the stacking interaction are: centroid distance = 3.57 Å, least square planes distance = 3.48 Å, offset = 0.82 Å. The architecture is racemic due to the existence of equal amount of *P*- and *M*-helices.

Taking into account the above mentioned interactions and considering the asymmetric unit as a node (i.e. the centroid of the two metal ions) a 3D 5-connected network is formed as shown in Fig. 6. The topological type is sqp and the total Schlafli symbol is $[4^4.6^6]$. To our knowledge this topological type is rather scarce in MOFs' chemistry [28].

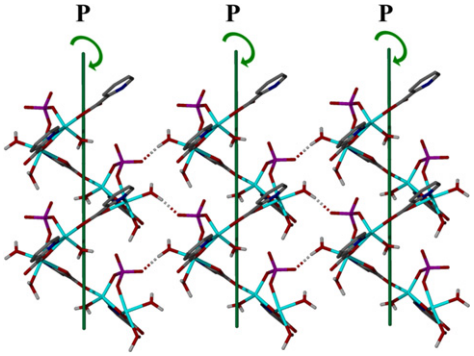


Fig. 4. A view of the inter-helix H-bonding interaction of the 1D *P*-helical chains in the *bc* plane of complex **1**. Organic protons and intra-helix H-bonds have been omitted for clarity. The rods represent the helical axes.

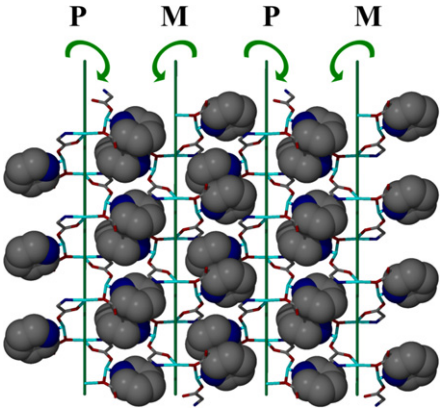


Fig. 5. A view of the alternate arrangement of the *P*- and *M*- helices, showing the stacking interactions that lead to the 3D supramolecular architecture in **1**. The water molecules, the non-stacked aromatic rings and the aromatic protons have been omitted for clarity. The rods represent the helical axes.

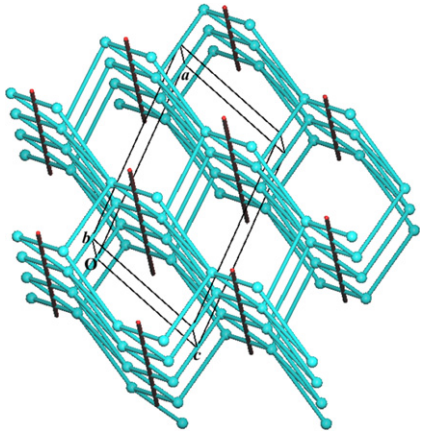


Fig. 6. The 5-connected sqp network formed in **1**, when intra-chain H-bonds and stacking interactions are taken into account. Spheres represent the centroids of the two metal ions in the asymmetric unit. The rods are the helical axes.

The structure of $\mathbf{2}\cdot n\mathrm{H_2O}$ is based on a 2D 4-connected network. The asymmetric unit of the polymer is presented in Fig. 7, and selected interatomic distances and angles are listed in Table 3.

The asymmetric unit consists of two Cd^{II} atoms, two picolinato ligands, one bridging sulfate anion, three coordinated (two terminal and one bridging) and one lattice water molecules. The coordination geometry of Cd(1) can be better described as distorted pentagonal bipyramidal. The equatorial plane is occupied by one oxygen and one nitrogen atom belonging to one 2.201 picolinato ligand [Cd(1)–O(1), 2.338(8); Cd(1)–N(1), 2.343(9) Å], two oxygen atoms belonging to the chelating/bridging carboxylate of the 2.211 pic^- [Cd(1)–O(11)#1, 2.497(8); Cd(1)–O(12)#1, 2.378(9) Å; #1: $-x+1$, $y-1/2$, $-z+1/2$] and one bridging H_2O molecule [Cd(1)–O(w1), 2.490(9) Å], while the axial positions are held by two terminal H_2O molecules

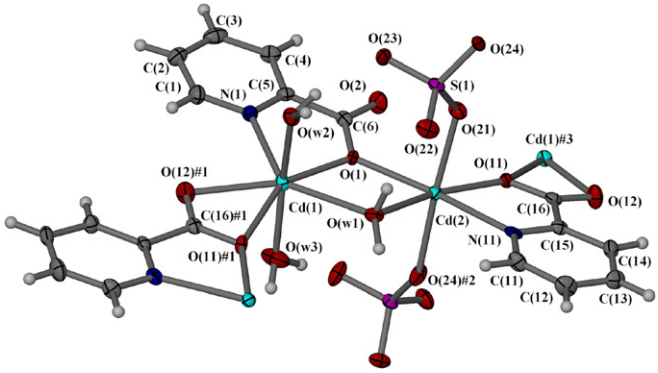


Fig. 7. A thermal ellipsoid (40%) plot of the asymmetric unit of $\mathbf{2}\cdot n\mathrm{H_2O}$, extended to show the coordination spheres of the metal ions and the coordination modes of the ligands. The lattice water molecule has been omitted for clarity. Symmetry operations to generate equivalent atoms: #1 $-x+1$, $y-1/2$, $-z+1/2$; #2 x, $-y+1/2$, $z-1/2$; #3, $-x+1$, $y+1/2$, $-z+1/2$.

Table 3
Selected interatomic distances (Å) and angles (°) for complex $\mathbf{2}\cdot n\mathrm{H_2O}$

Bond distances			
Cd(1)–O(1)	2.338(8)	Cd(1)–O(w3)	2.198(10)
Cd(1)–O(11)#1	2.497(8)	Cd(1)–O(w2)	2.282(8)
Cd(1)–O(w1)	2.490(9)	Cd(2)–O(1)	2.189(8)
Cd(1)–O(12)#1	2.378(9)	Cd(2)–O(w1)	2.517(9)
Cd(2)–O(24)#2	2.238(8)	Cd(2)–O(21)	2.289(8)
Cd(2)–O(11)	2.240(8)	Cd(1)···Cd(2)	3.820(8)
Cd(2)–N(11)	2.324(10)	Cd(1)···Cd(2)#1	4.598(8)
Cd(1)–N(1)	2.343(9)	Cd(2)···Cd(2)#2	6.846(8)
Bond angles			
O(w3)–Cd(1)–O(w2)	167.8(4)	O(w3)–Cd(1)–O(1)	84.7(3)
O(w2)–Cd(1)–O(1)	102.8(3)	O(w3)–Cd(1)–N(1)	102.2(4)
O(w2)–Cd(1)–N(1)	89.6(3)	O(1)–Cd(1)–N(1)	69.6(3)
O(w3)–Cd(1)–O(12)#1	87.4(4)	O(w2)–Cd(1)–O(12)#1	90.7(3)
O(1)–Cd(1)–O(12)#1	149.5(3)	N(1)–Cd(1)–O(12)#1	83.4(3)
O(w3)–Cd(1)–O(w1)	90.4(4)	O(w2)–Cd(1)–O(w1)	83.0(3)
O(1)–Cd(1)–O(w1)	71.3(3)	N(1)–Cd(1)–O(w1)	137.4(3)
O(12)#1–Cd(1)–O(w1)	138.3(3)	O(w3)–Cd(1)–O(11)#1	82.4(3)
O(w2)–Cd(1)–O(11)#1	86.7(3)	O(1)–Cd(1)–O(11)#1	152.6(2)
N(1)–Cd(1)–O(11)#1	136.9(3)	O(12)#1–Cd(1)–O(11)#1	53.7(3)
O(w1)–Cd(1)–O(11)#1	84.7(3)	N(11)–Cd(2)–O(w1)	92.6(3)
O(1)–Cd(2)–O(24)#2	95.6(3)	O(1)–Cd(2)–O(11)	121.0(3)
O(24)#2–Cd(2)–O(11)	89.0(3)	O(1)–Cd(2)–O(21)	87.8(3)
O(24)#2–Cd(2)–O(21)	176.7(3)	O(11)–Cd(2)–O(21)	89.3(3)
O(1)–Cd(2)–N(11)	165.4(3)	O(24)#2–Cd(2)–N(11)	88.0(3)
O(11)–Cd(2)–N(11)	73.1(3)	O(21)–Cd(2)–N(11)	88.7(3)
O(1)–Cd(2)–O(w1)	73.1(3)	O(24)#2–Cd(2)–O(w1)	92.8(3)
O(11)–Cd(2)–O(w1)	165.6(3)	O(21)–Cd(2)–O(w1)	88.2(3)

Hydrogen bonds

Donor–H···Acceptor	D–H	H···A	D···A	D–H···A
O(w1)–H(w1A)···O(22)	0.83(14)	1.92(14)	2.744(13)	170(4)
O(w1)–H(w1B)···O(2)#1	1.11(19)	1.72(19)	2.758(13)	154(13)
O(w2)–H(w2A)···O(23)	0.89	1.89	2.733(13)	156
O(w2)–H(w2B)···O(22)#4	1.23	1.60	2.733(12)	151
O(w3)–H(w3A)···O(23)#2	0.99	1.74	2.723(15)	171
O(w3)–H(w3B)···O(w4)#5	0.92	2.02	2.734(15)	133
O(w4)–H(w4A)···O(2)#1	0.95	2.59	2.934(16)	102
O(w4)–H(w4B)···O(21)#4	1.11	1.77	2.848(14)	161

Symmetry operations used to generate equivalent atoms: #1 $-x+1$, $y-1/2$, $-z+1/2$; #2 x, $-y+1/2$, $z-1/2$; #4 $-x+1$, $-y$, $-z+1$; #5 $-x+1$, $-y$, $-z$.

[Cd(1)–O(w2), 2.282(8); Cd(1)–O(w3), 2.198(10) Å]. Cd(2) is sited in the centre of a rather distorted octahedron, bonded to the bridging aquo ligand [Cd(2)–O(w1), 2.517(9) Å], to one oxygen atom belonging to the 2.201 picolinato ligand [Cd(2)–O(1), 2.189(8) Å], and to the 2.211 picolinato residue through N(11) and O(11) [Cd(2)–N(11), 2.324(10); Cd(2)–O(11), 2.240(8) Å] in the equatorial plane, while the axial positions are occupied by two oxygen atoms belonging to two symmetry related (#2: x, $-y+1/2$, $z-1/2$) bridging sulfates [Cd(2)–O(21), 2.289(8); Cd(2)–O(24)#2, 2.239(8) Å].

Each picolinate anion bridges two metal ions through the carboxylate moiety; one forms a monoatomic bridge, O(1), and behaves as a 2.201 ligand [14], while the other uses its carboxylate group as chelating/bridging acting as a 2.211 [14] ligand.

The ranges of the Cd(1)–(O,N) and Cd(2)–(O,N) bond lengths are typical for seven- [20e,29] and six-coordinate [11,18b,30] cadmium(II) complexes, respectively. The Cd(1)–O bond distance for the bridging H_2O molecule [Cd(1)–O(w1), 2.490(9) Å] is longer than the Cd(1)–O distances exhibited by the terminal H_2O ligands [2.282(8) and 2.198(10) Å]. The Cd(1)–O(carboxylate) distances are longer than the Cd(2)–O(carboxylate) distances, probably due to the higher coordination number of the former metal ion (seven versus six). The Cd(1)–O(11) [$-x+1$, $y-1/2$, $-z+1/2$] bond distance for the bridging carboxylate oxygen atom is longer than the distance exhibited by the terminal oxygen atom, O(12) [$-x+1$, $y-1/2$, $-z+1/2$], to the same Cd^{II} atom [2.497(8) versus 2.378(9) Å]. The increase in bond length upon bridging relative to terminal ligation has been observed previously [31] in many complexes containing carboxylate ligands with one bridging oxygen atom. Based on theoretical and experimental studies which have indicated that the *syn* lone pairs of the carboxylate groups are more basic than the *anti* lone pairs [32], one might expect that the Cd(1)–O(11) [$-x+1$, $y-1/2$, $-z+1/2$] distance to be shorter or approximately equal (to compensate for the change in coordination number) to the Cd–O(11) distance; however, the reverse relation holds for $\mathbf{2}\cdot n\mathrm{H_2O}$ (see Table 3). This result, which is in accordance with results obtained for many cadmium(II) carboxylate complexes [31], suggests that the Cd–O bond distances involving $\eta^1{:}\eta^2{:}\mu_2$ (2.21) RCO_2^- groups are mainly influenced by geometrical factors rather than the electronic properties of the carboxylate group.

From the first point of view the topological description of the 2D polymer looks relatively difficult. This is due to the two different Cd^{II} atoms; only one of them [Cd(2)] can be considered as a node, while the other [Cd(1)] is part of a linker formulated as $\{Cd(pic)_2(\mu\text{-}H_2O)(H_2O)_2\}$. Eventually these moieties form a ribbon (Fig. 8) that propagates parallel to b axis, and this is additionally stabilized by an intra-chain hydrogen bond between the bridged H_2O ligand and the non-coordinated carboxylate oxygen O(2). The ribbons are crosslinked by the bridging sulfato ligands which are bound only to Cd(2) [Cd(2)–O(21), 2.289(8); Cd(2)–O(24)#2, 2.238(8) Å; #2 : x, $-y+1/2$, $z-1/2$]. This way undulating 2D thick layers (the approximate width is 14 Å) representing a 4-connected net with Schläfli symbol [$4^4.6^2$] are formed (see Fig. 9).

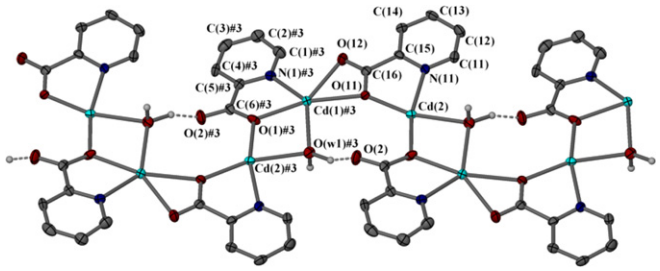


Fig. 8. The cadmium(II) ribbon formed in $\mathbf{2}\cdot n\mathrm{H_2O}$ viewed down to c. The organic protons, the terminal water molecules and the sulfato ligands have been omitted for clarity. Symmetry operation to generate equivalent atoms: #3 $-x+1$, $y+1/2$, $-z+1/2$.

There are extensive H-bonding interactions within the layer which assist the stabilization of the net (Table 3). All the water molecules and the sulfate anions are involved in those interactions leading to the formation of infinite H-bonded chains, proliferating parallel to b, between the Cd^{II} ribbons (see Fig. 10).

Besides the coordination bonds and the H-bonds within the layers, which propagate parallel to the bc plane, stacking interactions play their role for the stabilization of the 3D supramolecular architecture present in the crystal of

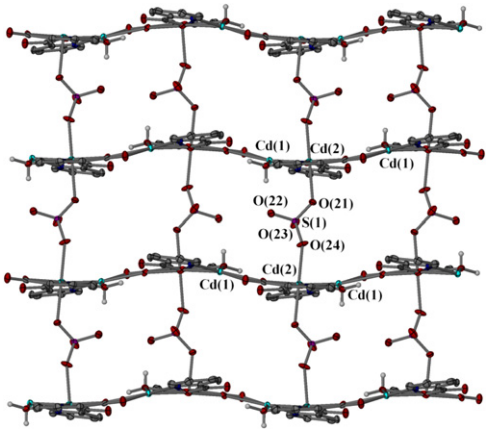


Fig. 9. A part of the grid-like 2D network formed in $\mathbf{2}\cdot n\mathrm{H_2O}$ viewed on the bc plane. Organic hydrogen atoms, terminal and lattice water molecules are omitted for clarity.

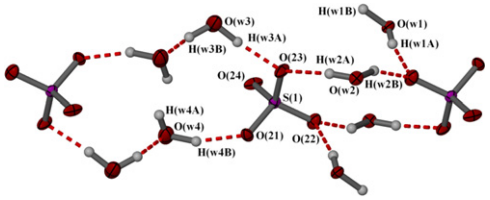


Fig. 10. A part of the water–sulfate chain formed in $\mathbf{2}\cdot n\mathrm{H_2O}$ showing the hydrogen bonding motif present.

2 · nH$_2$O. The 2D layers are arranged parallel in a way that the pyridine rings of one layer are situated in the void spaces between the pyridine rings of an adjacent layer. The pyridine moieties of different layers are involved in π–π stacking. Though the least square planes are not strictly parallel (the corresponding dihedral angles are 7.42 and 9.23°), the average distance of the defining atoms is ca. 3.4 Å, indicating strong interactions [2,33] (see Fig. 11).

Complexes **1** and **2** · nH$_2$O join a small group of structurally characterized, non-organometallic zinc(II) [15o,23,24,34] and cadmium(II) [15c,15f,15g,15o,35] picolinate complexes, some of which are polymeric [15c,15f,15g,15o]. These complexes are also new members of the still growing family of metal picolinate coordination polymers which are gathered in Table 4 (this table lists complexes in which at least one pic$^-$ ligand is bridging). Inspection of Table 4 reveals that (i) **1** and **2** · nH$_2$O are the first metal coordination polymers which have the pic$^-$/SO$_4^{2-}$ ligand combination, (ii) compound **1** is the second, structurally characterized zinc(II) picolinato coordination polymer, and (iii) the 2.201 and 2.211 coordination modes for the pic$^-$ ligand are observed simultaneously for the first time in **2** · nH$_2$O. Complexes **1** and **2** · nH$_2$O are new additions to the family of zinc(II) and cadmium(II) sulfato complexes [16–18b,26b,29a,29b,36].

3.3. Vibrational spectra

The IR spectrum of freshly prepared crystals of complex **2** · nH$_2$O is shown in Fig. 12. The prepared complexes exhibit a medium to strong intensity IR band at ~3350 cm^{-1}, assignable to ν(OH) vibrations of the coordinated (in both complexes) and lattice H$_2$O (in **2** · nH$_2$O). The broadness and relatively low frequency of this band are both indicative of hydrogen bonding.

The IR spectrum of the free, i.e. ionic, sulfate (the ion belongs to the T_d point group) consists of two bands at ~1105 and ~615 cm^{-1}, assigned to the $\nu_3(F_2)$ stretching [ν_d(SO)] and $\nu_4(F_2)$ bending [δ_d(OSO)] modes, respectively [16,17f,37]. The coordination of SO$_4^{2-}$ to metal ions decreases the symmetry of the group and the ν_3 and ν_4 modes are split [16,37]. Furthermore, the Raman-active $\nu_1(A_1)$ stretching [ν_d(SO)] and ν_2(E) bending [δ_d(OSO)] modes of the free SO$_4^{2-}$ become IR-active upon coordination, i.e. once the symmetry is lowered [37]. In the case the

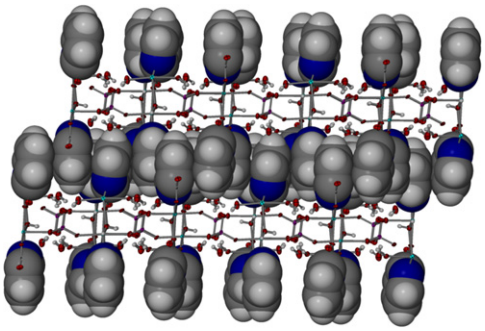


Fig. 11. A packing diagram of **2** · nH$_2$O viewed down to b axis. The pyridine rings of the picolinato ligands are drawn in space filling mode to emphasize the stacking interactions between the 2D layers.

Table 4
Formulae and coordination modes of the picolinate ligand for the structurally characterized metal picolinato coordination polymers

Complex[a]	Coordination mode of pic$^-$[b]	Ref.
$[Mn_2(pic)_2(N_3)_2(H_2O)_2]_n$	3.211	[15b]
$[Mn(pic)(N_3)(H_2O)]_n$	2.201	[15b]
$[Mn(pic)_2]_n$	2.201, 2.111	[15d]
$[MnCl(pic)(H_2O)_2]_n$	2.111	[15d]
$[MnCl(pic)]_n$	2.211	[15d]
$[Mn(O_2CPh)(pic)(paOH)]_n$[c]	2.111	[15p]
$[Na_2Mn_4(sal)_4(pic)_4(MeOH_2)]_n$[d]	3.211	[15e]
$[NaCu(pic)(N_3)_2]_n$	4.221	[15a]
$[KCu(pic)(N_3)_2]_n$	4.221	[15a]
$[NaCu(pic)_2(N_3)(H_2O)_2]_n$	1.101, 3.221	[15m]
$[CuCl(pic)]_n$	2.211	[15n]
$[Zn(pic)(4\text{-pc})]_n$[e]	2.111	[15o]
$[Zn_2(SO_4)(pic)_2(H_2O)_3]_n$	2.201, 2.111	this work
$[Cd(pic)(N_3)]_n$	3.211	[15c]
$[Cd(pic)(NCS)]_n$	2.211	[15c]
$[Cd(pic)Cl]_n$	2.111	[15f]
$[Cd_2(pic)_4]_n$	2.201, 2.111	[15g]
$[Cd(pic)(4\text{-pc})(H_2O)]_n$[e]	2.211	[15o]
$[Cd_2(SO_4)(pic)_2(H_2O)_3]_n$	2.201, 2.211	this work
$[Hg(pic)_2]_n$	2.111	[15l]
$[SmNi(pic)_3(H_2O)_5]_n^{2+}$	2.211, 2.111	[15h]
$[Tb(pic)_4]_n^-$	2.111, 1.101	[15k]
$[LnNa(pic)_4(H_2O)]_n$[f]	3.211, 2.201	[15k]
$[Ho_2(pic)_8]_n^{2-}$	1.101, 2.111	[15j]
$[Nd_2(pic)_8]_n^{2-}$	1.101, 2.111	[15q]
$[Cu_2Ln(pic)_4(H_2O)_6]_n^{3+g}$	2.111, 1.101	[15i]
$[Cu_5Ln_2(pic)_{10}(H_2O)_8]_n^{6+h}$	2.111, 1.101	[15i]
$[CuNd(pic)_2(H_2O)_3(DMF)_4]_n^{3+}$	2.111	[15i]

[a] Counterions and lattice solvent molecules have been omitted.
[b] Using Harris notation [14].
[c] paOH = 2-Pyridine aldoxime.
[d] sal = Salicylate(2−).
[e] 4-py = 4-Pyridine carboxylate.
[f] Ln = Tb, Eu, Gd, Ho.
[g] Ln = Pr, Nd, Sm.
[h] Ln = Sm, Nd, Gd, Dy, Eu, Pr, Yb.

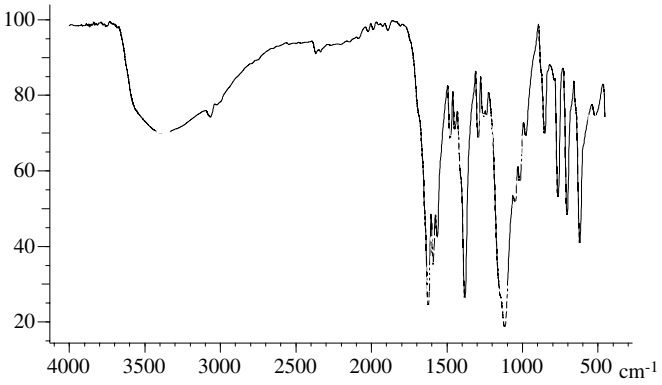


Fig. 12. The IR (KBr pellet) spectrum of the crystalline complex **2** · nH$_2$O.

SO_4^{2-}-site symmetry is lowered from T_d to C_{3v} (monodentate coordination), both ν_1 and ν_2 appear in the IR spectrum with weak to medium intensity, while ν_3 and ν_4 each splits into two bands in both IR and Raman spectra [37]. In the case the SO_4^{2-}-site symmetry is lowered from T_d to C_{2v} (bidentate chelating or bridging coordination), again both ν_1 and ν_2 appear in the IR spectrum (ν_2 splits into two Raman modes), while ν_3 and ν_4 each splits into three IR-active and Raman-active vibrations [37].

Both complexes have C_{2v} symmetry at the sulfato ligand, and the IR bands at ~1020, ~1115 and ~1150 cm^{-1} are therefore attributable [37] to the ν_3 modes. The bands/shoulders at ~565, ~615 and ~700 cm^{-1} are assigned [37] to the ν_4 modes, with the higher wavenumber band being superimposed by a ligand vibration. The band at 970 cm^{-1} and the shoulder at ~455 cm^{-1} are assigned to the ν_1 and ν_2 modes, respectively [17f,37]. The Raman sulfato lines (Fig. 13) of $\mathbf{2}\cdot n\mathrm{H_2O}$ appear at 1178 (ν_3), 1069 (ν_3), 1027 (ν_3), 994 (ν_1), 695 (ν_4), 635 (ν_4), 627(ν_4), 477 (ν_2) and 452 (ν_2) cm^{-1}. Thus, the number and wavenumbers of the IR and Raman bands are both in agreement [37] with the crystallographically established coordination mode of the sulfato ligand in $\mathbf{2}\cdot n\mathrm{H_2O}$.

Several bands (six in $\mathbf{2}\cdot n\mathrm{H_2O}$, seven in **1**) appear in the 1625–1370 cm^{-1} region. Contributions from picolinate $\nu_{as}(CO_2)$ and $\nu_s(CO_2)$ modes would be expected in this region, but overlap with the stretching vibrations of the aromatic ring and δ(HOH) renders assignments difficult [15p]. The bands at ~1620, ~1590 and ~1450, ~1380 are assigned to $\nu_{as}(CO_2)$ and $\nu_s(CO_2)$, respectively [15c,34b]. The appearance of two bands for each vibrational modes may be due to the presence of two different types of carboxylate groups in **1** and $\mathbf{2}\cdot n\mathrm{H_2O}$ [20e]. The difference Δ [$\Delta = \nu_{as}(CO_2) - \nu_{as}(CO_2)$] for any $\nu_{as}(CO_2)/\nu_s(CO_2)$ pair is less than the Δ value of Napic (263 cm^{-1}) [34b], as expected for the bridging modes of carboxylation ligation for the pic^- ligands in the two complexes [38]. In the Raman spectrum of the cadmium(II) complexes, two $\nu_s(CO_2)$ lines appear at wavenumbers higher than 1400 cm^{-1}, while the $\nu_{as}(CO_2)$ vibrations appear weak (as expected [39]) and are masked under the aromatic stretch at 1610 cm^{-1}. The Raman lines at 180–240 cm^{-1} are assigned to ν(Cd–N) vibrations [15c].

3.4. Thermal decomposition studies of complex $2\cdot n\mathrm{H_2O}$

The thermal decomposition of complex $\mathbf{2}\cdot n\mathrm{H_2O}$ was studied using thermogravimetric (TG), differential thermogravimetric (DTG) and differential thermal analysis (DTA) techniques under nitrogen. TG and DTG data are shown in Fig. 14.

Complex $\mathbf{2}\cdot n\mathrm{H_2O}$ decomposes via an anhydrous stable intermediate. Between room temperature and ~140 °C an initial, endothermic mass loss of 8.8% is observed that corresponds satisfactorily to the release of the lattice H_2O molecules and two aqua ligands (Calc. 8.9%). Between 150 °C and 210 °C there is a second endothermic mass loss of 3.0% that corresponds to the release of the stronger bonded third coordinated H_2O molecule (Calc. 2.8%). A clear plateau is reached at about 215 °C up to ~310 °C, suggesting that the anhydrous species with the empirical formula "$Cd_2(SO_4)(pic)_2$" is thermally stable. The formation of this intermediate is summarized by Eq. (3). The IR spectrum of the completely anhydrous product (obtained after a TG experiment up to 220 °C by keeping the heating rate at 1 °C min^{-1}) is different in the sulfate and carboxylate bands' regions compared to that of the original complex $\mathbf{2}\cdot n\mathrm{H_2O}$. This may indicate formation of an anhydrous coordination polymer through bridging sulfato and picolinato ligands with higher (than in $\mathbf{2}\cdot n\mathrm{H_2O}$) density levels. Unfortunately, attempts for the preparation (and subsequent crystallization) of compound "$Cd_2(SO_4)(pic)_2$" from solution have been unsuccessful.

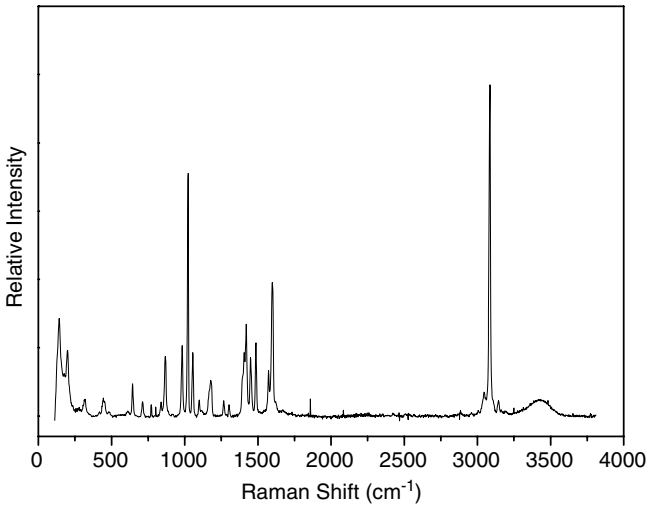


Fig. 13. The Raman spectrum of the crystalline complex $\mathbf{2}\cdot n\mathrm{H_2O}$.

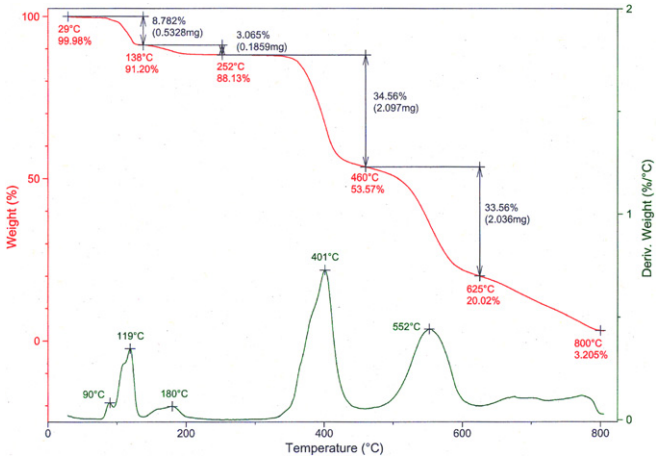


Fig. 14. Thermogravimetric (up) and differential thermogravimetric (down) data for complex $\mathbf{2}\cdot n\mathrm{H_2O}$.

$$\underset{\mathbf{2}\cdot n\mathrm{H_2O}}{[\mathrm{Cd_2(SO_4)(pic)_2(H_2O)_3}]_n\cdot n\mathrm{H_2O}} \xrightarrow[30\text{–}215\ ^\circ\mathrm{C,2\ steps}]{\mathrm{N_2}} n[\mathrm{Cd_2(SO_4)(pic)_2}] + 4n\mathrm{H_2O} \quad (3)$$

The anhydrous intermediate decomposes above 310 °C with a complicated degradation mechanism, as revealed by the appearance of five DTG maxima and without the formation of new thermally stable intermediates. The very low residue at 800 °C (~3%) clearly indicates that sublimation has occurred.

4. Concluding comments and perspectives

The initial use of the pic^-/SO_4^{2-} "ligand blend" in Zn(II) and Cd(II) chemistry has provided access to two new neutral coordination polymers with interesting structures and topologies, namely $[Zn_2(SO_4)(pic)_2(H_2O)_3]_n$ (**1**) and $[Cd_2(SO_4)(pic)_2(H_2O)_3]_n\cdot nH_2O$ ($\mathbf{2}\cdot nH_2O$). In both complexes, the organic ligand is coordinated to the metal centres in two different ligation modes (2.111 and 2.201 in **1**; 2.211 and 2.201 in $\mathbf{2}\cdot nH_2O$), while the sulfate ion acts as a bidentate bridging ligand. **1** and $\mathbf{2}\cdot nH_2O$ join a rather small family of structurally characterized picolinato coordination polymers and they are the first complexes of any metal in which picolinato and sulfato ligands coexist.

Complexes of other 3d-metal ions with the pic^-/SO_4^{2-} ligand combination are not known to date, and it is currently not evident whether the structure of such compounds is dependent on the particular nature of the metal ion. We are studying this matter. Synthetic efforts are also in progress to "activate" higher bridging capabilities, e.g. μ_3 or μ_4, of the pic^- and SO_4^{2-} ligands as a means to get access to 3D coordination polymers.

Acknowledgements

S.P.P. and C.P. thank the European Social Fund (ESF), the Operational Program for Educational and Vocational Training II (EPEAEK II) and particularly the Program PYTHAGORAS (Grant b. 365.037) for funding the above work. We are also grateful to Dr. G.A. Voyatzis (Applied Molecular Spectroscopy group of FORTH/ICE-HT, Patras, Greece) for recording the Raman spectrum of the cadmium(II) coordination polymer.

Appendix A. Supplementary material

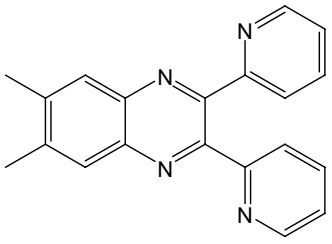
CCDC 642386 and 642387 contain the supplementary crystallographic data for (**1**) and ($\mathbf{2}\cdot nH_2O$) in CIF format. These data can be obtained free of charge via http://www.ccdc.cam.ac.uk/conts/retrieving.html, or from the Cambridge Crystallographic Data Centre, 12 Union Road, Cambridge CB2 1EZ, UK; fax: (+44) 1223-336-033; or e-mail: deposit@ccdc.cam.ac.uk. Supplementary data associated with this article can be found, in the online version, at doi:10.1016/j.poly.2007.05.022.

References

[1] M.H. Chisholm, Acc. Chem. Res. 33 (2000) 53.
[2] For an excellent review, see: C. Janiak, Dalton Trans. (2003) 2781, Dalton Perspective.
[3] (a) The first use of the term "coordination polymer" may be found in: J.C. Bailar Jr., in: W.L. Jolly (Ed.), Preparative Inorganic Chemistry, vol. 1, Interscience, New York, 1964, pp. 1–25;
(b) O.M. Yaghi, M. O'Keeffe, N.W. Ockwig, H.K. Chae, M. Eddaoudi, J. Kim, Nature 423 (2003) 705.
[4] (a) For interesting reviews see: A.Y. Robin, K.M. Fromm, Coord. Chem. Rev. 250 (2006) 2127;
(b) Y. Zhou, M. Hong, X. Wu, Chem. Commun. (2006) 135 (feature article);
(c) S.R. Batten, Curr. Opin. Solid State Mater. Sci. 5 (2001) 107;
(d) M. Munakata, L.P. Wu, T. Kuroda-Sowa, Adv. Inorg. Chem. 46 (1999) 173;
(e) S. Kitagawa, S. Noro, in: J.A. McCleverty, T.J. Meyer (Eds.), Comprehensive Coordination Chemistry III, vol. 7, Elsevier, Amsterdam, 2004, pp. 231–261.
[5] (a) V.A. Blatov, L. Carlucci, G. Ciani, D.M. Proserpio, CryEngCom 6 (2004) 377;
(b) S.R. Batten, R. Robson, Angew. Chem., Int. Ed. Engl. 37 (1998) 1460.
[6] B.F. Hoskins, R. Robson, J. Am. Chem. Soc. 112 (1990) 1546.
[7] J.Y. Sun, L.H. Weng, Y.M. Zhou, J.X. Chen, Z.X. Chen, Z.C. Liu, D.Y. Zhao, Angew. Chem., Int. Ed. 41 (2002) 4471.
[8] S.R. Batten, B.F. Hoskins, R. Robson, J. Chem. Soc., Chem. Commun. (1991) 445.
[9] L. Carlucci, G. Cianni, D.M. Proserpio, A. Sironi, Angew. Chem., Int. Ed. Engl. 34 (1995) 1895.
[10] B. Chen, M. Eddaoui, T.M. Reineke, J.W. Kampf, M. O' Keeffe, O.M. Yaghi, J. Am. Chem. Soc. 122 (2000) 11599.
[11] Q.-R. Fang, G.-S. Zhu, M. Xue, J.-Y. Sun, S.-L. Qiu, Dalton Trans. (2006) 2399.
[12] S.W. Keller, Angew. Chem., Int. Ed. Engl. 36 (1997) 247.
[13] A. Erxleben, Coord. Chem. Rev. 246 (2003) 203.
[14] R.A. Coxall, S.G. Harris, D.K. Henderson, S. Parsons, P.A. Tasker, R.E.P. Winpenny, J. Chem. Soc., Dalton Trans. (2000) 2349.
[15] (a) M.A.S. Goher, F.A. Mautner, Polyhedron 14 (1995) 1439;
(b) M.A.S. Goher, M.A.M. Abu-Youssef, F.A. Mautner, A. Popitsch, Polyhedron 11 (1992) 2137;
(c) M.A.S. Goher, M.A.M. Abu-Youssef, F.A. Mautner, Polyhedron 16 (1997) 235;
(d) D. Huang, W. Wang, X. Zhang, C. Chen, F. Chen, Q. Liu, D. Liao, L. Li, L. Sun, Eur. J. Inorg. Chem. (2004) 1454;
(e) X.S. Tan, Z.S. Ma, N.C. Shi, D.G. Fu, J. Chen, W.X. Tang, J. Chem. Soc., Dalton Trans. (1996) 2735;
(f) Y. Kang, J. Zhang, Z.-J. Li, Y.-Y. Qin, Y.-G. Yao, Inorg. Chem. Commun. 8 (2005) 722;
(g) J.-P. Deloume, H. Loiseleur, Acta Crystallogr. 30 (1974) 607;
(h) A.Q. Wu, G.-H. Guo, F.-K. Zheng, M.-S. Wang, Y. Li, G.-C. Guo, J.-S. Huang, Inorg. Chem. Commun. 8 (2005) 1078;
(i) A.Q. Wu, G.-H. Guo, C. Yang, F.-K. Zheng, X. Liu, G.-C. Guo, J.-S. Huang, Z.-C. Dong, Y. Yakano, Eur. J. Inorg. Chem. (2005) 1947;
(j) P. Starynowicz, Acta Crystallogr., Sect. C 49 (1993) 1895;
(k) D. Sendor, M. Hilder, T. Juestel, P.C. Junk, U.H. Kinast, New J. Chem. 27 (2003) 1070;
(l) A. Alvarez-Larena, J.F. Piniella, J. Pons, R. March, J. Casbo, Z. Kristallogr. 209 (1994) 695;
(m) M.A.S. Goher, F.A. Mautner, Polyhedron 13 (1994) 2149;
(n) M.A.S. Goher, A.K. Hafez, M.A.M. Abu-Youssef, A. Popitsch, H.P. Fritzer, F.A. Mautner, Monatsch. Chem. 125 (1994) 833;
(o) Y.-T. Wang, H.-H. Fan, H.-Z. Wang, X.-M. Chen, Inorg. Chem. 44 (2005) 4148;

(p) C.J. Milios, E. Kefalloniti, C.P. Raptopoulou, A. Terzis, A. Escuer, R. Vicente, S.P. Perlepes, Polyhedron 23 (2004) 83;
(q) P. Starynowics, Acta Crystallogr., Sect. C 47 (1991) 294.
[16] G. Tamasi, R. Cini, Dalton Trans. (2003) 2928, and references therein.
[17] (a) M.I. Khan, S. Cevik, R.J. Doedens, Chem. Commun. (2001) 1930;
(b) J. Moriyama, H. Nishiguchi, T. Ishihara, Y. Takita, Ind. Eng. Chem. Res. 41 (2002) 32;
(c) S.-Y. Wan, Y.-Z. Li, T.-A. Okamura, J. Fian, W.-Y. Sun, N. Ueyama, Eur. J. Inorg. Chem. (2003) 3783;
(d) T.C. Ullrich, M. Blaesse, R. Huber, EMBO J. 20 (2001) 316;
(e) J. Reedijk, Inorg. Chim. Acta 198–200 (1992) 873;
(f) C. Papatriantafyllopoulou, C.G. Efthymiou, C.P. Raptopoulou, R. Vicente, E. Manessi-Zoupa, V. Psycharis, A. Escuer, S.P. Perlepes, J. Mol. Struct. 829 (2007) 176;
(g) C. Papatriantafyllopoulou, G. Aromi, A.J. Tasiopoulos, V. Nastopoulos, C.P. Raptopoulou, S.J. Teat, A. Escuer, S.P. Perlepes, Eur. J. Inorg. Chem. 2007 (2007) 2761.
[18] (a) B. Ding, L. Li, Y. Wang, P. Cheng, D.-Z. Liao, S.-P. Yan, Z.-H. Jiang, H.-B. Song, H.-G. Wan, Dalton Trans. (2006) 665;
(b) X. Meng, Y. Song, H. Hou, H. Han, B. Xiao, Y. Fan, Y. Zhu, Inorg. Chem. 43 (2004) 3528.
[19] (a) A. Michaelides, C.D. Papadimitriou, J.C. Plakatouras, S. Skoulika, P.G. Veltsistas, Polyhedron 23 (2004) 2587;
(b) G.E. Kostakis, L. Casella, N. Hadjiliadis, E. Monzani, N. Kourkoumelis, J.C. Plakatouras, Chem. Commun. (2005) 3859;
(c) I. Vlahou, N. Kourkoumelis, A. Michaelides, S. Skoulika, J.C. Plakatouras, Inorg. Chim. Acta 359 (2006) 3540;
(d) G.E. Kostakis, E. Nordlander, N. Hadjiliadis, M. Haukka, J.C. Plakatouras, Inorg. Chem. Commun. 9 (2006) 915.
[20] (a) C.J. Milios, G.S. Papaefstathiou, C.P. Raptopoulou, A. Terzis, S.P. Perlepes, Bioinorg. Chem. Appl., in press;
(b) A. Messimeri, V. Nastopoulos, A. Terzis, C.P. Raptopoulou, C. Papadimitriou, S.P. Perlepes, Inorg. Chem. Commun. 8 (2005) 578;
(c) K. Skorda, Th.C. Stamatatos, A.P. Vafiadis, A.T. Lithoxoidou, A. Terzis, S.P. Perlepes, J. Mrozinski, C.P. Raptopoulou, J.C. Plakatouras, E.G. Bakalbassis, Inorg. Chim. Acta 358 (2005) 565;
(d) I. Chadjistamatis, A. Terzis, C.P. Raptopoulou, S.P. Perlepes, Inorg. Chem. Commun. 6 (2003) 1365;
(e) Th.C. Stamatatos, E. Katsoulakou, V. Nastopoulos, C.P. Raptopoulou, E. Manessi-Zoupa, S.P. Perlepes, Z. Naturforsch. b 58 (2003) 1045;
(f) G.S. Papaefstathiou, R. Vicente, C.P. Raptopoulou, A. Terzis, A. Escuer, S.P. Perlepes, Eur. J. Inorg. Chem. (2002) 2488;
(g) G.S. Papaefstathiou, S.P. Perlepes, A. Escuer, R. Vicente, A. Gantis, C.P. Raptopoulou, A. Tsohos, V. Psycharis, A. Terzis, E.G. Bakalbassis, J. Solid State Chem. 159 (2001) 371;
(h) K. Skorda, G.S. Papaefstathiou, A. Vafiadis, A. Lithoxoidou, C.P. Raptopoulou, A. Terzis, V. Psycharis, E.G. Bakalbassis, V. Tangoulis, S.P. Perlepes, Inorg. Chim. Acta 326 (2001) 53;
(i) G.S. Papaefstathiou, A. Tsohos, C.P. Raptopoulou, A. Terzis, V. Psycharis, D. Gatteschi, S.P. Perlepes, Cryst. Growth Des. 1 (2001) 191;
(j) V. Tangoulis, C.P. Raptopoulou, V. Psycharis, A. Terzis, K. Skorda, S.P. Perlepes, O. Cador, O. Kahn, Inorg. Chem. 39 (2000) 2522.
[21] G.M. Sheldrick, SHELXS-86, Structure Solving Program, University of Göttingen, Germany, 1986.
[22] G.M. Sheldrick, SHELXL-97, Program for the Refinement of Crystal Structures from Diffraction Data, University of Göttingen, Germany, 1997.
[23] (a) Y. Yoshikawa, E. Ueda, K. Kawabe, H. Miyake, T. Takino, H. Sakurai, Y. Kojima, J. Biol. Inorg. Chem. 7 (2002) 68;
(b) A.H. Yunuskhodzhaev, U.A. Mukarramova, Z. Karimov, Kristallografiya 43 (1998) 42.
[24] (a) P. Lumme, G. Lundgren, W. Mark, Acta Chem. Scand. 23 (1969) 3011;
(b) A. Takenaka, H. Utsumi, N. Ishihara, A. Furusaki, I. Nitta, J. Chem. Soc. Jpn., Pure Chem. 91 (1970) 921;
(c) R. Uggla, S. Lundell, J. Patrikka, Suom. Kemistil. B 42 (1969) 270.
[25] P.T. Anastas, M.M. Kirchoff, Acc. Chem. Res. 35 (2002) 686.
[26] (a) M. Alexiou, E. Katsoulakou, C. Dendrinou-Samara, C.P. Raptopoulou, V. Psycharis, E. Manessi-Zoupa, S.P. Perlepes, D.P. Kessissoglou, Eur. J. Inorg. Chem. (2005) 1964;
(b) E. Katsoulakou, N. Lalioti, C.P. Raptopoulou, A. Terzis, E. Manessi-Zoupa, S.P. Perlepes, Inorg. Chem. Commun. 5 (2002) 719;
(c) X.-L. Wang, C. Qin, E.-B. Wang, Z.-M. Su, Chem. Eur. J. 12 (2006) 2680.
[27] M. Tiliakos, P. Cordopatis, A. Terzis, C.P. Raptopoulou, S.P. Perlepes, E. Manessi-Zoupa, Polyhedron 20 (2001) 2203.
[28] N.W. Ockwig, O. Delgado-Friedrichs, M. O'Keeffe, O.M. Yaghi, Acc. Chem. Res. 38 (2005) 176.
[29] (a) M.L. Post, J. Troter, J. Chem. Soc., Dalton Trans. (1974) 1922;
(b) W. Harrison, J. Troter, J. Chem. Soc., Dalton Trans. (1972) 956.
[30] (a) Y. Xu, W.-h. Bi, X. Li, D.-f. Sun, R. Cao, M.-c. Hong, Inorg. Chem. Commun. 6 (2003) 495;
(b) S.D. Huang, R.-G. Xiong, J. Han, B.R. Weiner, Inorg. Chim. Acta 294 (1999) 95.
[31] S.-L. Li, T.C.W. Mak, Inorg. Chim. Acta 258 (1997) 17, and references therein..
[32] (a) R.L. Rardin, W.B. Tolman, S.J. Lippard, New J. Chem. 15 (1991) 417;
(b) M.R. Peterson, I.G. Csizmadia, J. Am. Chem. Soc. 101 (1979) 1076;
(c) K.B. Wiberg, K.E. Laidig, J. Am. Chem. Soc. 109 (1987) 5935.
[33] V. Russell, M. Scudder, I. Dance, J. Chem. Soc., Dalton Trans. (2001) 789.
[34] (a) N.V. Kaminskaia, B. Spingler, S.J. Lippard, J. Am. Chem. Soc. 123 (2001) 6555;
(b) M.A.S. Goher, M.A.M. Abu-Youssef, F.A. Mautner, Polyhedron 15 (1996) 453.
[35] M. Odoko, N. Isomoto, N. Okabe, Acta Crystallogr., Sect. E 57 (2001) m371.
[36] C. Liu, Y. Yin, X. Shi, D. Zhang, M. Hu, Inorg. Chem. Commun. 10 (2007) 37.
[37] K. Nakamoto, Infrared and Raman Spectra of Inorganic and Coordination Compounds, fourth ed., Wiley, New York, 1986, pp. 248–251.
[38] G.B. Deacon, R.J. Phillips, Coord. Chem. Rev. 33 (1980) 227.
[39] H.O. Desseyn, in: S. Patai (Ed.), The Chemistry of Acid Derivatives, vol. 2, Wiley, New York, 1992, pp. 271–303.

various dinuclear arene ruthenium and osmium complexes containing 2,2′-bipyrimidine as bridging chelate ligand have shown that the two chloro ligands can be found in both *cis* and *trans* orientations [6]. Therefore, in order to determine if the increase in the catalytic activity is correlated to the *cis–trans* conformations, we prepared a series of exclusively *trans* oriented dinuclear arene ruthenium complexes with the sterically hindered chelate ligand, 6,7-dimethyl-2,3-di(pyridine-2-yl)quinoxaline ($dpqMe_2$). The catalytic activity of the dinuclear complexes and of their corresponding mononuclear congeners for the transfer hydrogenation of aromatic ketones to give the corresponding secondary alcohol with sodium formate as the hydrogen donor in aqueous solution is reported. We also present the single-crystal X-ray structure analysis of some representatives.

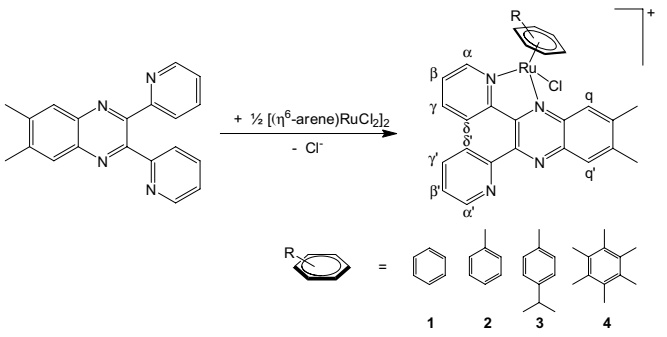


$dpqMe_2$

2. Results and discussion

2.1. Synthesis of the mononuclear complexes 1–4 as hexafluorophosphate salts

The arene ruthenium complexes $[(\eta^6\text{-arene})Ru(\mu\text{-}Cl)Cl]_2$ (arene = C_6H_6, C_6H_5Me, $p\text{-}Pr^iC_6H_4Me$, C_6Me_6) react with 2 equiv. of 6,7-dimethyl-2,3-di(pyridine-2-yl)quinoxaline ($dpqMe_2$) in methanol at 50 °C in the presence of KPF_6 to form the cationic arene ruthenium complexes $[(\eta^6\text{-}C_6H_6)RuCl(dpqMe_2)]^+$ (**1**), $[(\eta^6\text{-}C_6H_5Me)RuCl(dpqMe_2)]^+$ (**2**), $[(\eta^6\text{-}p\text{-}Pr^iC_6H_4Me)RuCl(dpqMe_2)]^+$ (**3**) and $[(\eta^6\text{-}C_6Me_6)RuCl(dpqMe_2)]^+$ (**4**), which are isolated as their hexafluorophosphate salts (Scheme 1). The hexafluorophosphate salts of complexes **1**–**4** are red-purple, non-hygroscopic, air-stable, crystalline solids. They are sparingly soluble in methanol and chloroform, but well soluble in dichloromethane, acetone and acetonitrile. All compounds have been characterised on the basis of elemental analysis, ^1H NMR, IR, UV–Vis and mass spectroscopy.



Scheme 1. Synthesis of cations **1**–**4**.

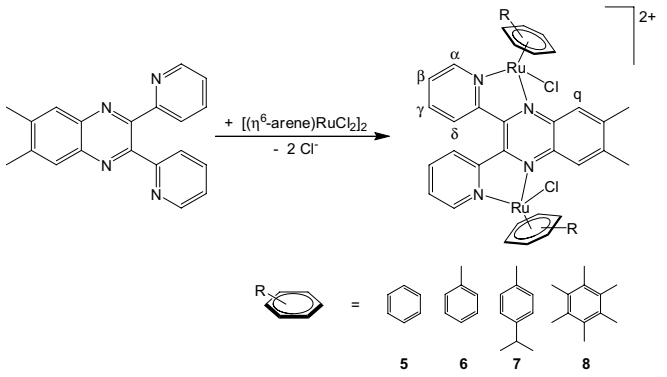
In the mass spectra they give rise to the corresponding $[M]^+$ molecular peaks m/z at 527, 541, 583 and 611, respectively. The ^1H NMR spectra of **1**–**4** exhibit, other than the signals corresponding to the aromatic ligand, a characteristic set of 12 independent signals for the diastereotopic protons of the $dpqMe_2$ ligand. The ruthenium atom is stereogenic due to the coordination of four different ligator atoms. Upon coordination to the ruthenium atom, the aromatic protons of the $dpqMe_2$ ligand are shifted downfield, especially the H_α of the coordinated pyridyl group which is observed at $\delta \sim 9.4$ ppm, while the $H_{\alpha'}$ of the non-coordinated pyridyl group is observed at only 8.65 ppm. Accordingly, the aromatic protons of the quinoxaline moiety are observed at $\delta \sim 8.6$ (H_q) and 8.1 ($H_{q'}$), respectively. The ^1H NMR spectrum of **3** exhibits two doublets for the diastereotopic methyl protons of the isopropyl group. Likewise, the diastereotopic CH protons of the *p*-cymene ligand give rise to four doublets observed between $\delta = 5.7$–6.1 ppm. A septet at $\delta = 2.51$ ppm is observed for the CH proton of the isopropyl group. Similarly, the aromatic protons of the toluene ligand in **2** give rise to five multiplets observed between $\delta = 5.7$–6.2 ppm and a singlet at $\delta = 2.36$ ppm for the methyl group.

The UV–Vis data of complexes **1**–**4** have been recorded in acetonitrile. The electronic spectra display a medium intensity band in the visible region at ~385 nm and an intense band at ~280 nm. The low intensity band at ~385 nm is assigned to the metal-to-ligand charge transfer transition (MLCT), while the high-energy band at ~280 nm is assigned to intra-ligand π–π^* transitions [7].

2.2. Synthesis of the dinuclear complexes 5–8 as hexafluorophosphate salts

The reaction of the dimeric chloro complexes $[(\eta^6\text{-arene})Ru(\mu\text{-}Cl)Cl]_2$ (arene = C_6H_6, C_6H_5Me, $p\text{-}Pr^iC_6H_4Me$, C_6Me_6) with 1 equiv. of 6,7-dimethyl-2,3-di(pyridine-2-yl)quinoxaline ($dpqMe_2$) in refluxing methanol in the presence of KPF_6 results in the formation of the red-purple coloured, air-stable dinuclear complex dications $[\{(\eta^6\text{-}C_6H_6)RuCl\}_2(\mu\text{-}dpqMe_2)]^{2+}$ (**5**), $[\{(\eta^6\text{-}C_6H_5Me)RuCl\}_2(\mu\text{-}dpqMe_2)]^{2+}$ (**6**), $[\{(\eta^6\text{-}p\text{-}Pr^iC_6H_4Me)RuCl\}_2(\mu\text{-}dpqMe_2)]^{2+}$ (**7**) and $[\{(\eta^6\text{-}C_6Me_6)RuCl\}_2(\mu\text{-}dpqMe_2)]^{2+}$ (**8**), which can be isolated as their hexafluorophosphate salts (Scheme 2).

Complexes **5**–**8** have been characterised by mass, UV–Vis, ^1H NMR spectroscopy and elemental analysis. In the mass spectra the hexafluorophosphate salts give rise to two main peaks; a minor peak with an approximately 50% intensity attributed to $[M^{2+}+PF_6^-]^+$ at m/z 887, 915, 999 and 1055, respectively, and a major peak which corresponds after decomplexation of an $[(arene)RuCl]^+$



Scheme 2. Synthesis of the dications **5**–**8**.

fragment to the mononuclear cations **1**–**4** at $m/z = 527$, 541, 583 and 611, respectively. The UV–Vis data of complexes **5**–**8** in acetonitrile show that the position of the MLCT transitions of the dinuclear complexes **5**–**8** is significantly red shifted (~490 nm) as compared to their mononuclear congeners.

The ^{1}H NMR spectra of **5**–**8** exhibit, other than the signals corresponding to the aromatic ligand, a characteristic set of six signals for the protons of the dpqMe$_2$ ligand. Despite the fact that the two ruthenium atoms are stereogenic and therefore should generate a mixture of *rac* and *meso* diastereoisomers, only the *rac* isomer is observed. The sterically hindered dpqMe$_2$ ligand forces the chloro ligands to adopt exclusively a *trans* orientation, thus giving rise to only the (*R*,*R*) and (*S*,*S*) enantiomers and consequently six signals for the dpqMe$_2$ bridging ligand. As observed in **1**–**4**, the aromatic protons of the dpqMe$_2$ ligand are shifted downfield, especially the H$_\alpha$ of the pyridyl groups which are observed at $\delta \sim 9.4$ ppm, while the aromatic protons of the quinoxaline moiety are observed at $\delta \sim 8.7$ ppm.

2.3. Crystal structure analysis of [(η^6-C$_6$H$_6$)RuCl(dpqMe$_2$)][PF$_6$] ([**1**][PF$_6$]), [(η^6-*p*-Pr^{i}C$_6$H$_4$Me)RuCl(dpqMe$_2$)][PF$_6$] ([**3**][PF$_6$]) and [(η^6-C$_6$H$_5$Me)RuCl(μ-dpqMe$_2$)][PF$_6$]$_2$ ([**6**][PF$_6$]$_2$)

The molecular structures of [(η^6-C$_6$H$_6$)RuCl(dpqMe$_2$)]$^+$ (**1**) and [(η^6-*p*-Pr^{i}C$_6$H$_4$Me)RuCl(dpqMe$_2$)]$^+$ (**3**) have been established by single-crystal X-ray structure analysis of their hexafluorophosphate salts. Both complexes show a typical piano-stool geometry with the metal centres coordinated by the arene ligand, a terminal chloride and the chelating dpqMe$_2$ ligand. The molecular structures of [**1**][PF$_6$] and [**3**][PF$_6$] are presented in Figs. 1 and 2, respectively, while selected geometrical parameters are presented in Table 1.

In the mononuclear complexes **1** and **3**, the metal centre is stereogenic. However, since none of the ligand contains a chiral information, **1** and **3** are obtained as racemic mixtures and crystallised in the centrosymmetric space group *C*2/*c* and *P*2$_1$/*n*, respectively.

The Ru–N bond distances ranging from 2.057(3) to 2.118(2) Å in **1** and **3** are comparable to those in [(η^6-*p*-Pr^{i}C$_6$H$_4$Me)RuCl(2,3-bis(2-pyridyl)pyrazine)][BF$_4$] [8] and [(η^6-*p*-Pr^{i}C$_6$H$_4$Me)RuCl(2,3-bis(α-pyridyl)quinoxaline)][PF$_6$] [9a]. Accordingly, there is no significant difference in the Ru–Cl bond length in **1** or **3** [2.389(1) and 2.3878(9) Å] and reported values [9–11]. The N(1)–Ru(1)–N(2) bond angle in complexes **1** [76.04(15)°] and **3** [76.33(10)°] are similar to those of complexes [(η^6-*p*-Pr^{i}C$_6$H$_4$Me)RuCl(2,3-bis(2-pyridyl)pyrazine)]$^+$ [N(1)–Ru(1)–N(2) = 76.5(2)°] [8] and [(η^6-*p*-Pr^{i}C$_6$H$_4$Me)RuCl(2,3-bis(α-pyridyl)quinoxaline)]$^+$ [N(1)–Ru(1)–N(2) = 76.2(2)°] [9a].

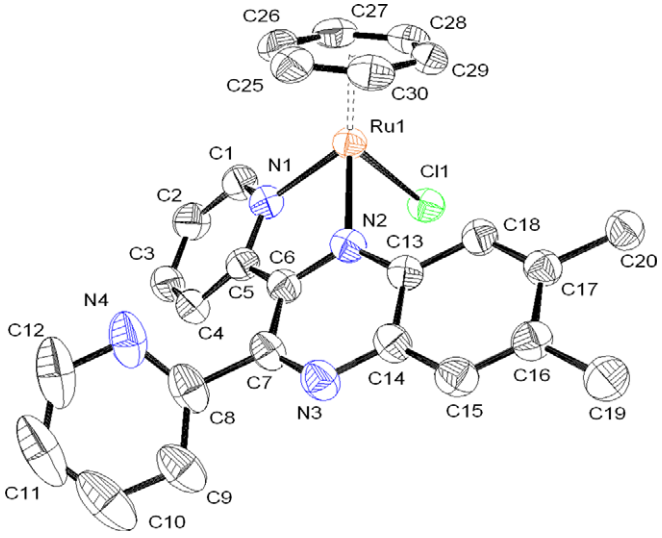


Fig. 1. Molecular structure of **1** at 50% probability level with hydrogen atoms, acetonitrile molecules and hexafluorophosphate anion being omitted for clarity.

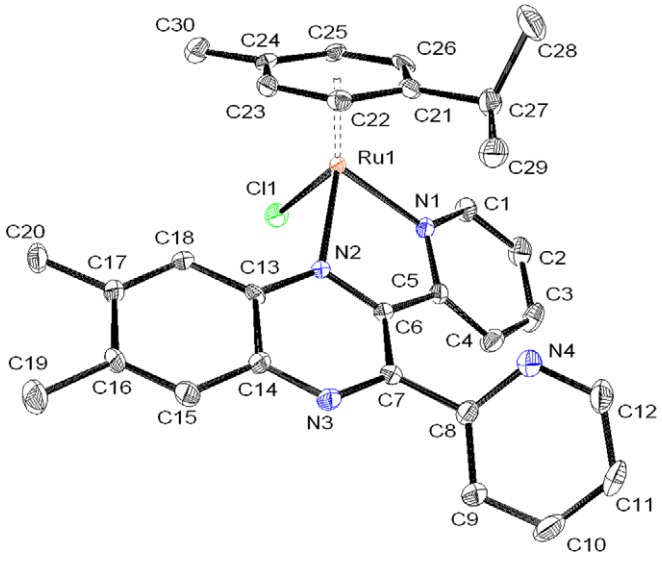


Fig. 2. Molecular structure of **3** at 50% probability level with hydrogen atoms, acetonitrile molecule and hexafluorophosphate anion being omitted for clarity.

Table 1
Selected bond lengths (Å) and angles (°) for [**1**][PF_6], [**3**][PF_6] and [**6**][PF_6]$_2$

	[**1**][PF_6]	[**3**][PF_6]	[**6**][PF_6]$_2$	
			Ru1	Ru2
Interatomic distances				
Ru1–N1 (Ru2–N3)	2.067(4)	2.057(3)	2.083(6)	2.109(5)
Ru1–N2 (Ru2–N4)	2.108(4)	2.118(2)	2.115(6)	2.063(6)
Ru1–Cl1 (Ru2–Cl2)	2.389(1)	2.3878(9)	2.393(2)	2.384(2)
Ru–centroid (arene)	1.692	1.694	1.698	1.695
C5–C6	1.472(6)	1.466(4)	1.482(9)	
C7–C8	1.509(7)	1.467(5)	1.473(10)	
Angles and torsion angles				
N1–Ru1–N2 (N3–Ru2–N4)	76.04(15)	76.33(10)	76.3(2)	76.4(2)
N1–Ru1–Cl1 (N3–Ru2–Cl2)	85.93(11)	86.08(7)	85.51(19)	88.48(17)
N2–Ru1–Cl1 (N4–Ru2–Cl2)	85.55(10)	88.27(7)	88.47(18)	86.29(19)
N1–C5–C6–N2	−11.2(6)	14.7(4)	16.5(9)	
N3–C7–C8–N4	131.8(5)	−131.2(3)	12.5(10)	
C5–C6–C7–C8	−23.1(8)	18.3(4)	32.9(12)	

In the crystal packing of [**1**][PF_6] · $2CH_3CN$, two molecules of **1** form a dimer through π-stacking interactions, see Fig. 3. The centroid–centroid separations are 3.73 and 4.32 Å. The distance observed between the π–π interacting systems is in accordance with the theoretical value calculated for this stacking mode [10].

Cation **6** crystallises in the space group P-1 with both enantiomers *R*,*R*-**6** and *S*,*S*-**6** being present in the crystal. As mentioned earlier, the sterically hindered $dpqMe_2$ ligand forces the chloro atoms to adopt a *trans* orientation, thus generating only the *rac* isomers. An ORTEP drawing with the atom labelling scheme for **6** is shown in Fig. 4 and the selected geometrical parameters are presented in Table 1. As expected, cation **6** contains two metal centres bonded to η^6-C_6H_5Me and chloro ligands and bridged by a $dpqMe_2$ ligand through its nitrogen atoms. The distance between the ruthenium atoms is 6.96 Å, which is in accordance with the metal–metal distances observed in the homo-bimetallic complex [(η^6-*p*-$Pr^iC_6H_4Me$)$_2$$Ru_2Cl_2$-(μ-2,3-di(pyridine-2-yl)pyrazine)][PF_6]$_2$ (Ru–Ru distance = 6.84 Å) [9b] and in the hetero-bimetallic $dpqMe_2$ complex [(bipy)$_2$Ru(μ-$dpqMe_2$)Cu(PPh_3)$_2$][BF_4]$_3$ (bipy = 2,2′-bipyridine) (Ru–Cu distance = 6.82 Å) [11].

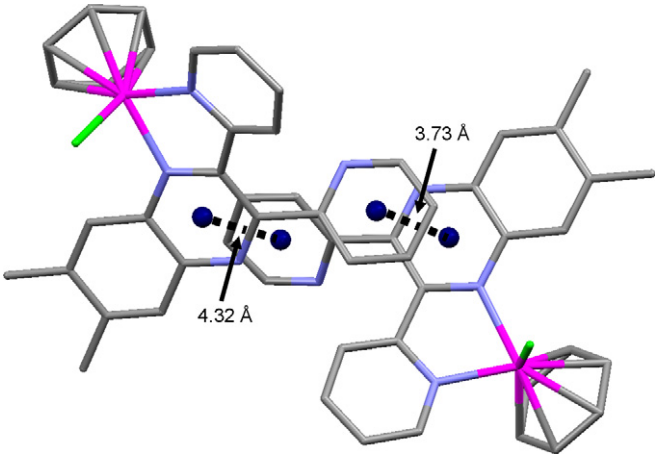


Fig. 3. Dimeric structure of **1** showing the intermolecular π-stacking interactions.

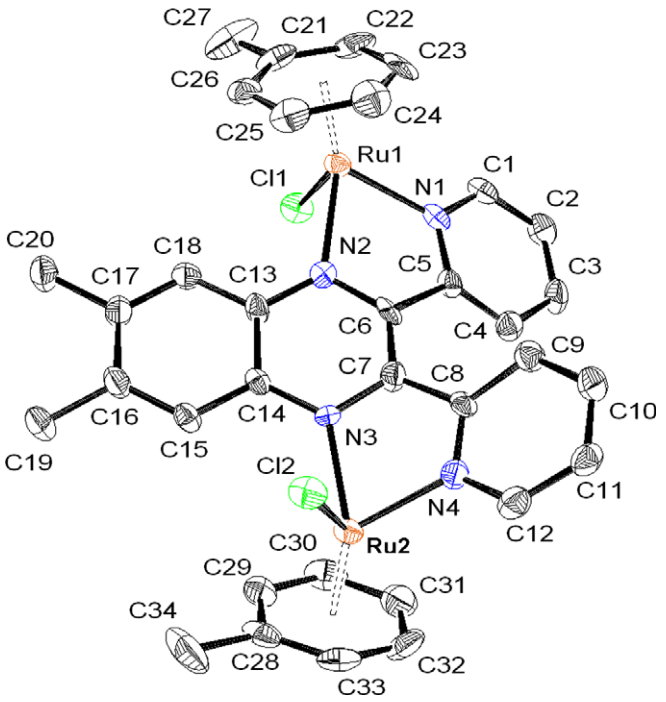


Fig. 4. Molecular structure of **6** at 50% probability level with hydrogen atoms, acetonitrile molecules and hexafluorophosphate anions being omitted for clarity.

Upon formation of mono or dinuclear complexes, the bond lengths between the connecting carbon atoms between the pyridyl and the quinoxaline moieties of the $dpqMe_2$ ligand are slightly reduced. Indeed, as compared to the free 6,7-dimethyl-2,3-di(pyridine-2-yl)quinoxaline in which the C–C distances (C5–C6 and C7–C8) are both at 1.493 Å [12], the corresponding C–C distances in the mononuclear complexes **1** and **3** are 1.472(6) and 1.466(4) Å, respectively, while in the dinuclear complex **6** the distances are 1.473(10) and 1.482(9) Å. These bond length changes are in agreement with a back-donation from the metallic fragments to the $dpqMe_2$ system, thus increasing the inter-ring bond order [6,13].

The major distortion imposed on the $dpqMe_2$ structure upon coordination is encountered by the pyridyl groups, see Fig. 5. In the free ligand the two pyridyl groups are twisted by 39.6° relative to the plane of the quinoxaline moiety. However, in **1** and **3** the twist of the coordinated pyridyl unit is 26.0(2) and 28.1(1)°, respectively, while the non-coordinated pyridyl unit remains at 41.7(1) and 41.1(1)°, respectively. Finally, the twist imposed on the pyridyl rings is raised to a maximum at 28.8(3) and 29.4(3)° in **6**.

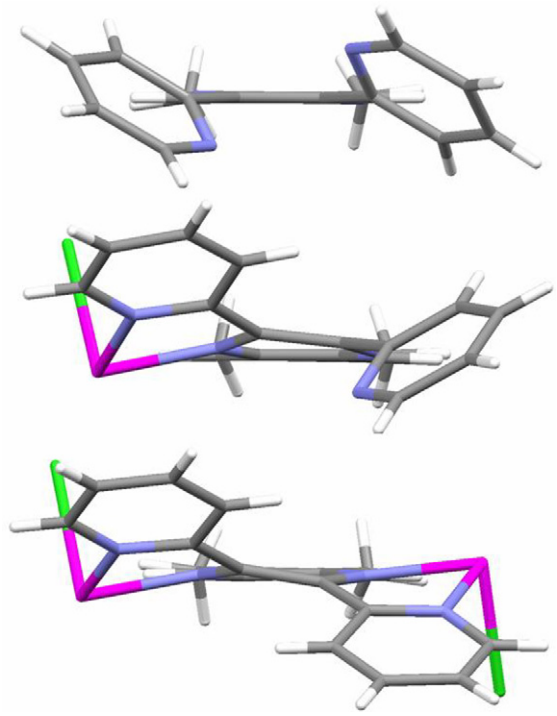
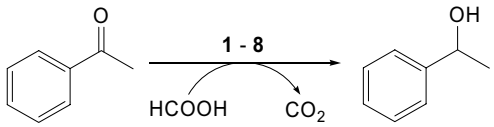


Fig. 5. Axial views of the free $dpqMe_2$ ligand (top), the mononuclear cation **3** (middle) and the dinuclear dication **6** (bottom). The quinoxaline moiety points away and the arene ligands are omitted for clarity.

2.4. Catalytic evaluation of *1–8* for the transfer hydrogenation of acetophenone in aqueous solution

Based on the pioneering study of Ogo et al. on the use of 2,2′-bipyridine complexes $[(\eta^6\text{-}C_6Me_6)Ru(bipy)(OH_2)]^+$ [14] and $[(\eta^5\text{-}C_5Me_5)Ir(bipy)(OH_2)]^+$ [15] and on our previously reported results on arene ruthenium phenanthroline (phen) complexes $[(\eta^6\text{-arene})Ru(phen)(OH_2)]^+$ (arene = C_6H_6, *p*-Pr^{i}C$_6$H$_4$Me, C_6Me_6)[16], the catalytic potential of the 6,7-dimethyl-2,3-di(pyridine-2-yl)quinoxaline complexes **1**–**8** was evaluated for the transfer hydrogenation of acetophenone in water using formic acid as hydrogen source (Table 2).



All complexes were found to poorly catalyse the transfer hydrogenation of acetophenone to give phenylethanol in aqueous solution at pH 4, which corresponds to the pK_a of the formic acid (3.77). In the best cases (complexes **6** and **7**, entries 6 and 7) the conversion of acetophenone does not exceed 6% within 16 h. This means that, in comparison to the corresponding 2,2′-bipyrimidine complexes [5], the introduction of a sterically hindered ligand system which forces the dinuclear complexes to adopt a *trans* configuration causes a pronounced drop in the catalytic activity.

Table 2
Catalytic transfer hydrogenation of acetophenone using the mononuclear $[(\eta^6\text{-arene})RuCl(dpqMe_2)]^+$ (**1**–**4**) and dinuclear complexes $[\{(\eta^6\text{-arene})RuCl\}_2(\mu\text{-}dpqMe_2)]^{2+}$ (**5**–**8**) as catalysts and formate as hydrogen donor in water[a]

Entry	Catalyst	$(\eta^6$-arene)Ru	Conversion % (h)[b]	TOF (h^{-1})[c]
1	**1**	$(C_6H_6)Ru$	<1 (15)	
2	**2**	$(C_6H_5Me)Ru$	<1 (15)	
3	**3**	(*p*-Pr^{i}C$_6$H$_4$Me)Ru	<1 (15)	
4	**4**	$(C_6Me_6)Ru$	<1 (15)	
5	**5**	$\{(C_6H_6)Ru\}_2$	2 (15)	0.1
6	**6**	$\{(C_6H_5Me)Ru\}_2$	5 (15)	0.3
7	**7**	$\{(p\text{-}Pr^iC_6H_4Me)Ru\}_2$	6 (16)	0.4
8	**8**	$\{(C_6Me_6)Ru\}_2$	1 (15)	0.1

[a] Conditions: Reactions carried out at 50 °C, at pH = 4, in 5 mL of water, acetophenone (0.64 mmol), the ratio catalyst/substrate/formate being 1:100:500.
[b] Determined by gas chromatography.
[c] TOF: turnover frequencies are expressed in mol of product/(mol of Ru · h).

3. Experimental

3.1. General

6,7-Dimethyl-2,3-di(pyridine-2-yl)quinoxaline ($dpqMe_2$) and KPF_6 were purchased from Aldrich and used as received. $[Ru(\eta^6\text{-arene})(\mu\text{-}Cl)Cl]_2$ (arene = C_6H_6, C_6H_5Me, *p*-Pr^{i}C$_6$H$_4$Me, C_6Me_6) were prepared according to published methods [17]. The NMR spectra were recorded on a Varian Gemini 200 MHz spectrometer using the residual protonated solvent as internal standard. Infrared spectra were recorded as KBr pellets on a Perkin–Elmer FTIR 1720-X spectrometer. UV–Vis absorption spectra were recorded on an Uvikon 930 spectrophotometer. Microanalyses were performed by the Laboratory of Pharmaceutical Chemistry, University of Geneva (Switzerland). Electrospray mass spectra were obtained in positive-ion mode with an LCQ Finnigan mass spectrometer.

3.2. Preparation of the mononuclear complexes *1–4*

3.2.1. $[(\eta^6\text{-}C_6H_6)RuCl(dpqMe_2)][PF_6]$ ($[\mathbf{1}][PF_6]$)

In a typical experiment, $[(\eta^6\text{-}C_6H_6)Ru(\mu\text{-}Cl)Cl]_2$ (100 mg, 0.20 mmol) is dissolved in methanol (50 mL). The resulting solution is added dropwise to a two-necked flask equipped with a reflux condenser and containing a methanol solution (50 mL) of $dpqMe_2$ (125 mg, 0.40 mmol) and KPF_6 (73.6 mg, 0.40 mmol). The mixture is heated to 50 °C and stirred for 24 h. After cooling to room temperature, the volume is reduced and the product is precipitated by addition of diethylether. The yellow-orange solid is filtered, washed with *n*-pentane and dried under vacuum to give $[(\eta^6\text{-}C_6H_6)RuCl(dpqMe_2)][PF_6]$ (80 mg, 0.12 mmol, yield 30%). ^{1}H NMR (400 MHz, CD_3CN): δ (ppm) =

9.40 (d, 1H, $^3J = 7.8$ Hz, H_{pyr}), 8.65 (d, 1H, $^3J = 7.5$ Hz, H_{pyr}), 8.63 (s, 1H, H_{qnox}), 8.11 (m, 2H, H_{pyr}), 8.08 (s, 1H, H_{qnox}), 7.77 (dd, 1H, H_{pyr}), 7.62 (m, 2H, H_{pyr}), 7.06 (d, 1H, $^3J = 7.1$ Hz, H_{pyr}), 6.13 (s, 6H, H_{ar}), 2.74 (s, 3H, Me_{qnox}), 2.65 (s, 3H, Me_{qnox}); IR (KBr, cm^{-1}): 840 s ν(P–F); 558 m. UV–Vis (1.19×10^{-5} M, CH_3CN): λ_{max} 386 nm ($\varepsilon = 2.07 \times 10^4$ M^{-1} cm^{-1}), 274 nm ($\varepsilon = 3.78 \times 10^4$ M^{-1} cm^{-1}). ESI-MS (*m/z*): 527 [M^+]; *Anal.* Calc. for $C_{26}H_{22}N_4ClF_6PRu$: C, 46.47; H, 3.30; N, 8.34. Found: C, 46.12; H, 3.69; N, 7.77%.

3.2.2. [(η^6-C_6H_5Me)RuCl(dpqMe$_2$)][PF_6] ([**2**][PF_6])

The compound is prepared by the same procedure as described above for [**1**][PF_6] using [(η^6-C_6H_5Me)Ru(μ-Cl)Cl]$_2$ (100 mg, 0.19 mmol), dpqMe$_2$ (118.2 mg, 0.38 mmol) and KPF_6 (69.7 mg, 0.38 mmol) and affording [(η^6-C_6H_5Me)RuCl(dpqMe$_2$)][PF_6] (140 mg, 0.20 mmol, yield 54%). ^{1}H NMR (400 MHz, CD_3CN): δ (ppm) = 9.32 (d, 1H, $^3J = 7.1$ Hz, H_{pyr}), 8.66 (d, 1H, $^3J = 7.4$ Hz, H_{pyr}), 8.55 (s, 1H, H_{qnox}), 8.13 (m, 2H, H_{pyr}), 8.08 (s, 1H, H_{qnox}), 7.77 (dd, 1H, $^3J = 8.3$ Hz, H_{pyr}), 7.61 (m, 2H, H_{pyr}), 7.07 (d, 1H, $^3J = 9.5$ Hz, H_{pyr}), 6.16 (dd, 1H, H_{ar}), 5.99 (dd, 1H, $^3J = 5.9$ Hz, H_{ar}), 5.92 (d, 1H, $^3J = 6.1$ Hz, H_{ar}), 5.74 (d, 1 H, H_{ar}), 5.68 (dd, 1H, $^3J = 5.8$ Hz, H_{ar}), 2.73 (s, 3H, Me_{qnox}), 2.65 (s, 3H, Me_{qnox}), 2.36 (s, 3H, Me_{ar}); IR (KBr, cm^{-1}): 840s ν(P–F); 558 m. UV–Vis (1.16×10^{-5} M, CH_3CN): λ_{max} 385 nm ($\varepsilon = 4.46 \times 10^4$ M^{-1} cm^{-1}), 278 nm ($\varepsilon = 8.82 \times 10^4$ M^{-1} cm^{-1}). ESI-MS (*m/z*): 541 [M^+]; *Anal.* Calc. for $C_{27}H_{24}N_4ClF_6PRu$: C, 47.27; H, 3.53; N, 8.17. Found: C, 47.00; H, 3.70; N, 8.19%.

3.2.3. [(η^6-*p*-Pr^iC_6H_4Me)RuCl(dpqMe$_2$)][PF_6] ([**3**][PF_6])

The compound is prepared by the same procedure as described above for [**1**][PF_6] using [(η^6-*p*-Pr^iC_6H_4-Me)Ru(μ-Cl)Cl]$_2$ (100 mg, 0.16 mmol), dpqMe$_2$ (102.0 mg, 0.32 mmol) and KPF_6 (60.1 mg, 0.32 mmol) and affording [(η^6-*p*-Pr^iC_6H_4Me)RuCl(dpqMe$_2$)][PF_6] (150 mg, 0.20 mmol, yield 63%). ^{1}H NMR (400 MHz, CD_3CN): δ (ppm) = 9.37 (d, 1H, $^3J = 7.1$ Hz, H_{pyr}), 8.69 (d, 1 H, $^3J = 6.5$ Hz, H_{pyr}), 8.52 (s, 1H, H_{qnox}), 8.09 (m, 2H, H_{pyr}), 8.06 (s, 1H, H_{qnox}), 7.70 (m, 2H, H_{pyr}), 7.60 (dd, 1H, H_{pyr}), 7.00 (d, 1H, H_{pyr}), 6.09 (d, 1H, $^3J = 6.9$ Hz, H_{ar}), 5.85 (m, 2H, H_{ar}), 5.72 (d, 1H, $^3J = 6.6$ Hz, H_{ar}), 2.73 (s, 3H, Me_{qnox}), 2.64 (s, 3H, Me_{qnox}), 2.51 (sept, 1H, $^3J = 6.9$ Hz, C$H_{ar}$$Me_2$), 2.36 (s, 3H, Me_{ar}), 1.11 (d, 3H, CH$_{ar}$$Me_2$), 1.04 (d, 3H, CH$_{ar}$$Me_2$); IR (KBr, cm^{-1}): 840 s ν(P–F); 557 m. UV–Vis (5.50×10^{-6} M, CH_3CN): λ_{max} 436 nm ($\varepsilon = 19\,695.82$ M^{-1} cm^{-1}), 387 nm ($\varepsilon = 8.53 \times 10^4$ M^{-1} cm^{-1}), 278 nm ($\varepsilon = 17.55 \times 10^4$ M^{-1} cm^{-1}). ESI-MS (*m/z*): 583 [M^+]; *Anal.* Calc. for $C_{30}H_{30}N_4ClF_6PRu$: C, 49.49; H, 4.15; N, 7.70. Found: C, 49.17; H, 4.66; N, 7.47%.

3.2.4. [(η^6-C_6Me_6)RuCl(dpqMe$_2$)][PF_6] ([**4**][PF_6])

The compound is prepared by the same procedure as described above for [**1**][PF_6] using [(η^6-C_6Me_6)Ru(μ-Cl)Cl]$_2$ (100 mg, 0.15 mmol), dpqMe$_2$ (93.4 mg, 0.30 mmol) and KPF_6 (55.1 mg, 0.30 mmol) and affording [(η^6-C_6Me_6)RuCl(dpqMe$_2$)][PF_6] (145 mg, 0.20 mmol, yield 64%). ^{1}H NMR (400 MHz, CD_3CN): δ (ppm) = 8.77 (d, 1H, $^3J = 7.7$ Hz, H_{pyr}), 8.65 (d, 1 H, $^3J = 7.4$ Hz, H_{pyr}), 8.29 (s, 1H, H_{qnox}), 8.17 (m, 2H, H_{pyr}), 8.05 (s, 1H, H_{qnox}), 7.75 (dd, 1H, H_{pyr}), 7.60 (m, 2H, H_{pyr}), 7.07 (d, 1H, $^3J = 7.5$ Hz, H_{pyr}), 2.67 (s, 3H, Me_{qnox}), 2.62 (s, 3H, Me_{qnox}), 2.20 (s, 18H, Me_{ar}); IR (KBr, cm^{-1}): 843 s ν(P–F); 558 m. UV–Vis (1.06×10^{-5} M, CH_3CN): λ_{max} 377 nm ($\varepsilon = 3.15 \times 10^4$ M^{-1} cm^{-1}), 281 nm ($\varepsilon = 7.89 \times 10^4$ M^{-1} cm^{-1}). ESI-MS (*m/z*): 611 [M^+]; *Anal.* Calc. for $C_{32}H_{34}N_4ClF_6PRu$: C, 50.83; H, 4.53; N, 7.41. Found: C, 50.94; H, 4.62; N, 7.42%.

3.3. Preparation of the dinuclear complexes **5**–**8**

3.3.1. [{(η^6-C_6H_6)RuCl}$_2$(μ-dpqMe$_2$)][PF_6]$_2$ ([**5**][PF_6]$_2$)

In a typical experiment, [(η^6-C_6H_6)Ru(μ-Cl)Cl]$_2$ (150 mg, 0.30 mmol), dpqMe$_2$ (93.6 mg, 0.30 mmol) and KPF_6 (110.0 mg, 0.60 mmol) are dissolved in methanol (30 mL). The resulting solution is heated to 60 °C and stirred for 4 h. After cooling to room temperature, the volume is reduced and the product is precipitated by addition of diethylether. The red solid is filtered, washed with *n*-pentane and dried under vacuum to give [{(η^6-C_6H_6)-RuCl}$_2$(μ- dpqMe$_2$)][PF_6]$_2$ (150 mg, 0.14 mmol, yield 48%). ^{1}H NMR (400 MHz, CD_3CN): δ (ppm) = 9.43 (d, 2H, $^3J = 6.4$ Hz, H_{pyr}), 8.69 (s, 2H, H_{qnox}), 8.56 (d, 2H, $^3J = 8.2$ Hz, H_{pyr}), 8.08 (dd, 2H, $^3J = 7.8$ Hz, H_{pyr}), 7.81 (dd, 2H, $^3J = 6.9$ Hz, H_{pyr}), 6.15 (s, 12H, H_{ar}), 2.80 (s, 6H, Me_{qnox}); IR (KBr, cm^{-1}): 840 s ν(P–F); 559 m. UV–Vis (6.20×10^{-5} M, CH_3CN): λ_{max} 486 nm ($\varepsilon = 0.53 \times 10^4$ M^{-1} cm^{-1}), 330 nm ($\varepsilon = 2.25 \times 10^4$ M^{-1} cm^{-1}). ESI-MS (*m/z*): 887 [M+PF_6]$^+$; 527 [M−{(η^6-C_6H_6)RuCl}]$^+$; *Anal.* Calc. for $C_{32}H_{28}N_4Cl_2F_{12}P_2Ru_2$: C, 37.26; H, 2.74; N, 5.43. Found: C, 36.98; H, 3.23; N, 5.51%.

3.3.2. [{(η^6-C_6H_5Me)RuCl}$_2$(μ-dpqMe$_2$)][PF_6]$_2$ ([**6**][PF_6]$_2$)

The compound is prepared by the same procedure as described above for [**5**][PF_6]$_2$ using [(η^6-C_6H_5Me)Ru(μ-Cl)Cl]$_2$ (530 mg, 0.1 mol), dpqMe$_2$ (312 mg, 0.1 mol) and KPF_6 (368 mg, 0.2 mol) and affording [{(η^6-C_6H_5Me)R-uCl}$_2$(μ- dpqMe$_2$)][PF_6]$_2$ (990 mg, 0.09 mol, yield 94%). ^{1}H NMR (400 MHz, CD_3CN): δ (ppm) = 9.34 (d, 2H, $^3J = 5.5$ Hz, H_{pyr}), 8.57 (s, 2H, H_{qnox}), 8.52 (d, 2H, $^3J = 8.1$ Hz, H_{pyr}), 8.07 (dd, 2H, $^3J = 6.6$ Hz, H_{pyr}), 7.80 (dd, 2H, $^3J = 6.6$ Hz, H_{pyr}), 6.20 (dd, 2H, $^3J = 5.9$ Hz, H_{ar}), 5.94 (m, 4H, H_{ar}), 5.77 (d, 2H, $^3J = 5.9$ Hz, H_{ar}), 5.67 (dd, 2H, H_{ar}), 2.76 (s, 6H, Me_{qnox}), 2.45 (s, 6H, H_{ar}); IR (KBr, cm^{-1}): 843 s ν(P–F); 558 m. UV–Vis (3.77×10^{-6} M, CH_3CN): λ_{max} 492 nm ($\varepsilon = 0.95 \times 10^4$ M^{-1} cm^{-1}), 327 nm ($\varepsilon = 4.43 \times 10^4$ M^{-1} cm^{-1}). ESI-MS (*m/z*): 915 [M+PF_6]$^+$; 541 [M−{(η^6-C_6H_6)RuCl}]$^+$; *Anal.* Calc. for $C_{34}H_{32}N_4Cl_2F_{12}P_2Ru_2$: C, 38.54; H, 3.04; N, 5.29. Found: C, 38.21; H, 2.94; N, 5.11%.

3.3.3. [{(η⁶-p-Pr^{i}C$_6$H$_4$Me)RuCl}$_2$(μ-dpqMe$_2$)][PF$_6$]$_2$ ([7][PF$_6$]$_2$)

The compound is prepared by the same procedure as described above for [**5**][PF$_6$]$_2$ using [(η⁶-*p*-Pr^{i}C$_6$H$_4$-Me)Ru(μ-Cl)Cl]$_2$ (200 mg, 0.33 mmol), dpqMe$_2$ (76.5 mg, 0.33 mmol) and KPF$_6$ (90.2 mg, 0.66 mmol) and affording [{(η⁶-*p*-Pr^{i}C$_6$H$_4$Me)RuCl}$_2$(μ-dpqMe$_2$)][PF$_6$]$_2$ (270 mg, 0.24 mmol, yield 72%). ^{1}H NMR (400 MHz, CD$_3$CN): δ (ppm) = 9.38 (d, 2H, ^3J = 7.7 Hz, H$_{pyr}$), 8.59 (s, 2H, H$_{qnox}$), 8.39 (d, 2H, ^3J = 8.1 Hz, H$_{pyr}$), 8.10 (dd, 2H, ^3J = 7.7 Hz, H$_{pyr}$), 7.84 (dd, 2H, ^3J = 6.9 Hz, H$_{pyr}$), 6.10 (d, 4H, H$_{ar}$), 5.81 (d, 4H, ^3J = 6.3 Hz, H$_{ar}$), 2.78 (s, 6H, Me$_{qnox}$), 2.73 (sept, 2H, ^3J = 6.9 Hz, C*H*$_{ar}$Me$_2$), 1.41 (s, 6H, Me$_{ar}$), 1.13 (d, 6H, CH$_{ar}$*Me*$_2$), 0.87 (d, 6H, CH$_{ar}$*Me*$_2$); IR (KBr, cm^{-1}): 842 s *ν*(P–F); 558 m. UV–Vis (7.35×10^{-5} M, CH$_3$CN): λ_{max} 508 nm ($\varepsilon = 0.43 \times 10^4$ M^{-1} cm^{-1}), 327 nm ($\varepsilon = 1.68 \times 10^4$ M^{-1} cm^{-1}). ESI-MS (*m*/*z*): 999 [M+PF$_6$]$^+$; 583 [M−{(η⁶-*p*-Pr^{i}C$_6$H$_4$Me)RuCl}]$^+$; *Anal.* Calc. for C$_{40}$H$_{44}$N$_4$Cl$_2$F$_{12}$P$_2$Ru$_2$: C, 42.00; H, 3.88; N, 4.90. Found: C, 39.95; H, 3.79; N, 4.60%.

3.3.4. [{(η⁶-C$_6$Me$_6$)RuCl}$_2$(μ-dpqMe$_2$)][PF$_6$]$_2$ ([8][PF$_6$]$_2$)

The compound is prepared by the same procedure as described above for [**5**][PF$_6$]$_2$ using [(η⁶-C$_6$Me$_6$)Ru(μ-Cl)Cl]$_2$ (200 mg, 0.30 mmol), dpqMe$_2$ (93.4 mg, 0.30 mmol) and KPF$_6$ (110 mg, 0.60 mmol) and affording [{(η⁶-C$_6$Me$_6$)RuCl}$_2$(μ-dpqMe$_2$)][PF$_6$]$_2$ (145 mg, 0.12 mmol, yield 40%). ^{1}H NMR (400 MHz, CD$_3$CN): δ (ppm) = 8.77 (d, 2H, ^3J = 7.9 Hz, H$_{pyr}$), 8.65 (d, 2H, ^3J = 7.5 Hz, H$_{pyr}$), 8.05 (s, 2H, H$_{qnox}$), 7.75 (dd, 2H, ^3J = 8.3 Hz, H$_{pyr}$), 7.64 (dd, 2H, ^3J = 7.6 Hz, H$_{pyr}$), 3.29 (s, 6H, Me$_{qnox}$), 2.63 (s, 18H, Me$_{ar}$); IR (KBr, cm^{-1}): 844 s *ν*(P–F); 558 m. UV–Vis (5.30×10^{-5} M, CH$_3$CN): λ_{max} 551 nm ($\varepsilon = 0.58 \times 10^4$ M^{-1} cm^{-1}), 403 nm ($\varepsilon = 1.49 \times 10^4$ M^{-1} cm^{-1}), 328 nm ($\varepsilon = 2.45 \times 10^4$ M^{-1} cm^{-1}). ESI-MS (*m*/*z*): 1055 [M+PF$_6$]$^+$; 611 [M−{(η⁶-*p*-Pr^{i}C$_6$H$_4$Me)RuCl}]$^+$; *Anal.* Calc. for C$_{44}$H$_{52}$N$_4$Cl$_2$F$_{12}$P$_2$Ru$_2$: C, 44.04; H, 4.37; N, 4.67. Found: C, 42.29; H, 4.60; N, 4.26%.

3.4. Single-crystal X-ray structure analyses

Crystals of complexes [**1**][PF$_6$]·2CH$_3$CN, [**3**][PF$_6$]·CH$_3$CN and [**6**][PF$_6$]$_2$·2CH$_3$CN were mounted on a Stoe Image Plate Diffraction system equipped with a φ circle goniometer, using Mo Kα graphite monochromated radiation (λ = 0.71073 Å) with φ range 0–200°. The structures were solved by direct methods using the program SHELXS-97 [18]. Refinement and all further calculations were carried out using SHELXL-97 [18]. The H-atoms were included in calculated positions and treated as riding atoms using the SHELXL default parameters. The non-H atoms were refined anisotropically, using weighted full-matrix least-squares on F^2. Crystallographic details are summarised in Table 3. Figs. 1, 2 and 4 were drawn with ORTEP [19] and Figs. 3 and 5 with the software MERCURY [20].

Table 3
Crystallographic and selected experimental data for [**1**][PF$_6$]·2CH$_3$CN, [**3**][PF$_6$]·CH$_3$CN and [**6**][PF$_6$]$_2$·2CH$_3$CN

	[**1**][PF$_6$]·2CH$_3$CN	[**3**][PF$_6$]·CH$_3$CN	[**6**][PF$_6$]$_2$·2CH$_3$CN
Chemical formula	C$_{30}$H$_{28}$ClF$_6$N$_6$PRu	C$_{32}$H$_{33}$ClF$_6$N$_5$PRu	C$_{38}$H$_{38}$Cl$_2$F$_{12}$N$_6$P$_2$Ru$_2$
Formula weight	754.07	769.12	1141.72
Crystal system	monoclinic	monoclinic	triclinic
Space group	*C*2/*c* (no. 15)	*P*2$_1$/*n* (no. 14)	*P*$\bar{1}$ (no. 2)
Crystal colour and shape	red rod	red block	red block
Crystal size	0.2 × 0.2 × 0.1	0.3 × 0.3 × 0.15	0.4 × 0.4 × 0.2
a (Å)	34.208(4)	14.450(3)	13.003(1)
b (Å)	7.4461(5)	8.370(2)	13.340(1)
c (Å)	29.870(3)	27.320(5)	14.516(2)
α (°)			111.43(1)
β (°)	124.652(6)	97.16(3)	106.64(1)
γ (°)			100.00(1)
V (Å^3)	6258.9(10)	3278.5(12)	2133.8(4)
Z	8	4	2
T (K)	173(2)	173(2)	173(2)
D_{calc} (g cm^{-3})	1.601	1.558	1.777
μ (mm^{-1})	0.705	0.674	0.998
Scan range (°)	1.45 < θ < 25.17	2.55 < 2θ < 26.15	2.42 < 2θ < 25.97
Unique reflections	5558	6176	7760
Observed reflections [$I > 2\sigma(I)$]	4125	4407	4876
R_{int}	0.0985	0.0358	0.1736
Final *R* indices [$I > 2\sigma(I)$][a]	0.0549, wR_2 0.1427	0.0341, wR_2 0.0776	0.0603, wR_2 0.1597
R indices (all data)	0.0690, wR_2 0.1477	0.0532, wR_2 0.0822	0.0976, wR_2 0.2007
Goodness-of-fit	0.948	0.897	1.022
Maximum, minimum Δρ (e Å^{-3})	1.465, −1.279	0.473, −1.484	1.315, −1.755

[a] Structures were refined on F_o^2: $wR_2 = [\sum[w(F_o^2 - F_c^2)^2]/\sum w(F_o^2)^2]^{1/2}$, where $w^{-1} = [\sum(F_o^2) + (aP)^2 + bP]$ and $P = [\max(F_o^2, 0) + 2F_c^2]/3$.

3.5. Transfer hydrogenation catalysis

The transfer hydrogenation reactions of acetophenone (0.64 mmol) using **1**–**8** as their hexafluorophosphate salts (6.4 μmol) with formate (3.2 mmol) are carried out in water (5 mL) using a buffer of HCOOH/HCOONa at pH 4 under inert atmosphere. The reaction is quenched by cooling the mixture to 0 °C. The products are extracted by Et_2O and identified (and turnover determined) by gas chromatography. The pH is monitored using a pH meter (Mettler Toledo InLab® 413).

Acknowledgements

Financial support of this work by the Swiss National Science Foundation and a generous loan of ruthenium(III) chloride hydrate from the Johnson Matthey Research Centre are gratefully acknowledged.

Appendix A. Supplementary material

CCDC 641057, 641058 and 641059 contain the supplementary crystallographic data for $[\mathbf{1}][PF_6]\cdot 2CH_3CN$, $[\mathbf{3}][PF_6]\cdot CH_3CN$ and $[\mathbf{6}][PF_6]_2\cdot 2CH_3CN$. These data can be obtained free of charge via http://www.ccdc.cam.ac.uk/conts/retrieving.html, or from the Cambridge Crystallographic Data Centre, 12 Union Road, Cambridge CB2 1EZ, UK; fax: (+44) 1223-336-033; or e-mail: deposit@ccdc.cam.ac.uk. Supplementary data associated with this article can be found, in the online version, at doi:10.1016/j.poly.2007.05.005.

References

[1] (a) G. Di Marco, A. Bartolotta, V. Ricevuto, S. Campagna, G. Denti, L. Sabatino, G. De Rosa, Inorg. Chem. 30 (1991) 270;
(b) V. Balzani, A. Juris, M. Venturi, S. Campagna, S. Serroni, Chem. Rev. 96 (1996) 759;
(c) J.F. Endicott, H.B. Schlegel, Md. J. Uddin, D.S. Seniveratne, Coord. Chem. Rev. 229 (2002) 95;
(d) W.R. Browne, R. Hage, J.G. Vos, Coord. Chem. Rev. 250 (2006) 1653.

[2] (a) T. Ohta, S. Nakahara, Y. Shigemura, K. Hattori, I. Furukawa, Appl. Organometal. Chem. 15 (2001) 699;
(b) S. Ogo, K. Uehara, T. Abura, Y. Watanabe, S. Fukuzumi, Organometallics 23 (2004) 3047;
(c) C.A. Sandoval, T. Ohkuma, N. Utsumi, K. Tsutsumi, K. Murata, R. Noyori, Chem. Asian J. 1–2 (2006) 102.

[3] (a) J.-P. Sauvage, J.-P. Collin, J.-C. Chambron, S. Guillerez, C. Coudret, V. Balzani, F. Barigelletti, L. De Cola, L. Flamigni, Chem. Rev. 94 (1994) 993;
(b) Z. Shirin, R. Mukherjee, J.F. Richardson, R.M. Buchanan, J. Chem. Soc., Dalton Trans. (1994) 465;
(c) W. Kaim, R. Reinhardt, J. Fiedler, Angew. Chem., Int. Ed. Engl. 36 (1997) 2493;
(d) S. Chellamma, M. Lieberman, Inorg. Chem. 40 (2001) 3177;
(e) T.J. Meyer, M.H.V. Huynh, Inorg. Chem. 42 (2003) 8140;
(f) M. Newell, J.A. Thomas, Dalton Trans. (2006) 705.

[4] (a) S.L. Darling, C.C. Mak, N. Bampos, N. Feeder, S.J. Teat, J.K.M. Sanders, New J. Chem. 23 (1999) 359;
(b) H. Miyasaka, C.S. Campos-Fernández, R. Clérac, K.R. Dunbar, Angew. Chem., Int. Ed. 39 (2000) 3831;
(c) L. Böttcher, A. Scholz, D. Walther, N. Weisbach, H. Görls, Z. Anorg. Allg. Chem. 629 (2003) 2103;
(d) K. Severin, Chem. Commun. (2006) 3859;
(e) P. Govindaswamy, D. Linder, J. Lacour, G. Süss-Fink, B. Therrien, Chem. Commun. (2006) 4691;
(f) J.G. Vos, J.M. Kelly, Dalton Trans. (2006) 4869;
(g) P. Govindaswamy, G. Süss-Fink, B. Therrien, Organometallics 26 (2007) 915.

[5] P. Govindaswamy, J. Canivet, B. Therrien, G. Süss-Fink, P. Štěpnička, J. Ludvík, J. Organomet. Chem., doi:10.1016/j.organchem.2007.04.048.

[6] F. Baumann, A. Stange, W. Kaim, Inorg. Chem. Commun. 1 (1998) 305.

[7] C.S. Araújo, M.G.B. Drew, V. Félix, L. Jack, J. Madureira, M. Newell, S. Roche, T.M. Santos, J.A. Thomas, L. Yellowlees, Inorg. Chem. 41 (2002) 2250.

[8] A. Singh, N. Singh, D.S. Pandey, J. Organomet. Chem. 642 (2002) 48.

[9] (a) R. Lalrempuia, M.R. Kollipara, Polyhedron 22 (2003) 3155;
(b) A. Singh, S.K. Singh, M. Trivedi, D.S. Pandey, J. Organomet. Chem. 690 (2005) 4243.

[10] S. Tsuzuki, K. Honda, T. Uchimura, M. Mikami, K. Tanabe, J, Am. Chem. Soc. 124 (2004) 104.

[11] S.M. Scott, K.C. Gordon, A.K. Burrell, J. Chem. Soc., Dalton Trans. (1999) 2669.

[12] K. Wozniak, T.M. Krygowski, E. Grech, W. Kolodziejski, J. Klinowski, J. Phys. Chem. 97 (1993) 1862.

[13] D.J. Berg, J.M. Boncella, R.A. Andersen, Organometallics 21 (2002) 4622.

[14] S. Ogo, T. Abura, Y. Watanabe, Organometallics 21 (2002) 2964.

[15] S. Ogo, N. Makihara, Y. Kaneko, Y. Watanabe, Organometallics 20 (2001) 4903.

[16] (a) J. Canivet, L. Karmazin-Brelot, G. Süss-Fink, J. Organomet. Chem. 690 (2005) 3202;
(b) P. Štěpnička, J. Ludvík, J. Canivet, G. Süss-Fink, Inorg. Chim. Acta 359 (2006) 2369.

[17] (a) R.A. Zelonka, M.C. Baird, Can. J. Chem. 50 (1972) 3063;
(b) M.A. Bennett, A.K. Smith, J. Chem. Soc., Dalton Trans. (1974) 233;
(c) M.A. Bennett, T.-N. Huang, T.W. Matheson, A.K. Smith, Inorg. Synth. 21 (1982) 74.

[18] G.M. Sheldrick, SHELX suite of programs for crystal structure solution and refinement, University of Göttingen, Göttingen, Germany, 1997.

[19] L.J. Farrugia, J. Appl. Cryst. 30 (1997) 565.

[20] I.J. Bruno, J.C. Cole, P.R. Edgington, M. Kessler, C.F. Macrae, P. McCabe, J. Pearson, R. Taylor, Acta Crystallogr., Sect. B 58 (2002) 389.

the level of ROS produced during normal cellular metabolism and the amount of endogenous antioxidants (such as ROS scavengers and enzymes) present in the cells which protect tissues from oxidative damage. If this balance is disrupted a condition referred to as oxidative stress develops which is implicated in numerous pathophysiological processes such as rheumatoid arthritis, aging, inflammation and carcinogenesis [1]. Recently, it has been found that ROS such as the superoxide radical ($O_2^{\cdot-}$) or hydrogen peroxide (H_2O_2) are important regulators of cell death [2]. Particularly, H_2O_2 is implicated as a mediator of apoptosis in cells [3]. The cellular damage caused by H_2O_2 is likely produced in part through $OH^{\cdot}$ radical production formed when H_2O_2 reacts with Fe^{2+} or Cu^{2+} [4]. Enzymatic antioxidants regulate superoxide concentration by dismutation of $O_2^{\cdot-}$ to hydrogen peroxide (SOD activity) which is then converted to water (peroxidase activity) or dismutated to water and dioxygen (catalase activity).

Many tumour cells have increased rates of metabolism compared with normal cells, which would typically lead to increased numbers of ROS [5]. Manganese SOD (MnSOD) is found in the matrix of mitochondria and has been shown to be depleted in most cancers when compared to normal tissue [6]. The activity of cytoplasmic SOD (CuZnSOD) has also been shown to vary in cancer cells [6]. This suggests that a large amount of intracellular $O_2^{\cdot-}$ is found in such cancerous cells and that in the absence of significant SOD activity this $O_2^{\cdot-}$ can further metabolise to peroxynitrite ($OONO^-$) and the perhydroxyl radical ($HO_2^{\cdot}$) which play a role in the tumour formation [7]. It has been demonstrated that returning MnSOD and CuZnSOD enzyme activity to levels close to those found in non-malignant cells has resulted in conversion of the excess $O_2^{\cdot-}$ to H_2O_2 which leads to decreased tumour cell growth in a number of model systems [8–10].

The use of SOD enzymes as pharmaceutical agents is limited by cost and because of instability and low membrane permeability resulting from their high molecular weight. Low molecular weight copper SOD mimetic complexes can dismutate excess intracellular $O_2^{\cdot-}$ to H_2O_2 and O_2, suggesting that they may increase the concentration of H_2O_2 in cancer cells thus inducing cell death by apotosis. Furthermore, compared to manganese systems copper complexes are less likely to act as catalase mimics and catalytically disproportionate the H_2O_2 to water and molecular oxygen but rather react with it to form the desirable cytotoxic hydroxyl radical (Fenton chemistry). However, a small number of copper carboxylate complexes have recently been reported in the literature that show significant catalase mimetic functionality [11,12].

Recently, we have been studying the anticancer activities of a range of simple copper complexes incorporating different types of nitrogen donor ligands [13–17]. We have found that the bis- or tris-chelate copper complexes incorporating 1,10-phenanthroline and 1,10-phenanthroline-5,6-dione (which possess N_4 or N_6 ligation) are potent anticancer agents in vitro and that they appear to have a mechanism of action significantly different to that of the clinically used drug cisplatin [16,17]. Furthermore, a number of these copper complexes are excellent SOD mimics [14,18] and have been shown to induce apoptosis in cultured mammalian cells [19].

In an effort to throw some light on the structure–activity-relationship of this class of simple copper complexes we have studied systems in which only two nitrogen atoms (either as chelates or monodentate ligands) are bound to the copper centre. Herein, we detail the preparation, catalase and SOD mimetic activities and the chemotherapeutic potentials of copper acetate, salicylate and benzoate complexes incorporating phen, bipy and simple benzimidazole ligands. The X-ray crystal structures of $[CuBZA_2(bipy)(H_2O)]$, $[Cu(salH)_2(BZDH)_2]$ and $[Cu(CH_3CO_2)_2(5,6\text{-DMBZDH})_2]$ are also reported.

2. Results and discussion

2.1. Synthesis and characterisation of the complexes

$[Cu_2(CH_3COO)_4(H_2O)_2]$ (**1**) was obtained commercially and was not further purified. $[Cu(salH)_2(H_2O)_2]$ (**2**) ($salH_2$ = salicylic acid) was generated using a method previously published [20]. $\{Cu(BZA)_2(H_2O)\}_n$ (**3**) was the major product from a reaction between copper(II) hydroxide and benzoic acid. Reaction of **1** with 1,10-phenanthroline (phen) in ethanol gave $[Cu(CH_3COO)_2(phen)]$ (**4**) in good yield and a similar reaction between **2** and phen resulted in the generation of [Cu(sal)(phen)] (**5**). $[Cu(BZA)_2(bipy)(H_2O)]$ (**6**) was obtained in good yield when **1** reacted with 2,2′-bipyridine (bipy) in the presence of benzoic acid. $[Cu(CH_3COO)_2(5,6\text{-DMBZDH})_2]$ (**7**), $[Cu(salH)_2(BZDH)_2]$ (**8**) and $[Cu(BZA)_2(BZDH)_2]$ (**9**) were easily produced when **1**, **2** and **3** were treated with the relevant benzimidazoles in refluxing ethanol (where 5,6-DMBZDH = 5,6-dimethylbenzimidazole and BZDH = benzimidazole, respectively).

The physico-chemical properties for **2** are the same as a compound that was previously reported for which the crystal structure revealed a square planar geometry with the salicylate ligands *trans* to one another and bound through the carboxylate groups in a monodentate fashion [21]. In the IR spectrum of **3**, the asymmetric and symmetric OCO bands of the benzoate ligands are split [$\nu(OCO)_{assym}$: 1597 cm^{-1} and 1556 cm^{-1}; $\nu(OCO)_{sym}$: 1408 cm^{-1} and 1376 cm^{-1}] and thus two modes of interaction are likely for the carboxylate ligands with the copper centres. The microanalysis and the magnetic moment of **3** are similar to those of an anhydrous copper benzoate complex previously reported which had an empirical formula of $Cu(BZA)_2$ [22]. The magnetic moment (1.56 BM) for **3** is slightly lower than that expected for simple copper(II) species (i.e. those lacking Cu–Cu interactions) [23]. Thus, it is likely that at least one of the benzoate ligands is in some type of bridging mode as reported recently for several copper(II) complexes of substituted benzoates [24–26]. The

crystal structure of copper benzoate trihydrate has been reported and the complex incorporates both coordinated and uncoordinated benzoate anions [27]. The structure comprises linear chains of $\{Cu(BZA)(\mu\text{-}H_2O)_2\}_n$ with uncoordinated H_2O molecules and BZA^- anions intervening between them. The room temperature magnetic moment for the trihydrate was reported as being unusual for a (μ-H_2O)(μ-BZA) bridged complex (1.87 BM) and therefore it seems that the structure of **3** is not quite the same as this trihydrate. Indeed it is significant that three magnetically different modifications of anhydrous copper(II) benzoate have been previously reported [28].

When compared to those of **1**, **2** and **3** the spectra of **4**, **5** an **6** are far more complex and contain new absorption bands which are characteristic of the presence of chelating phen {723 and 851 cm^{-1} (**4**); 721 and 847 cm^{-1} (**5**)} [29] and bipy {775 cm^{-1} and 729 cm^{-1} (**6**)} [30]. As well as the bands that have been assigned to the chelating phen and bipy ligands the spectra of **4**–**6** also contain bands that are characteristic of carboxylate anions with $\nu(OCO)_{asym}$ {1631 cm^{-1} (**4**), 1598 cm^{-1} (**5**) and 1599 cm^{-1} (**6**)} and $\nu(OCO)_{sym}$ {1431 cm^{-1} (**4**), 1360 cm^{-1} (**5**) and 1379 cm^{-1}(**6**)} values. The calculated Δ_{OCO} of 200 cm^{-1} (**4**), 238 cm^{-1} (**5**) and 220 cm^{-1} (**6**) are quite similar and in the region expected for monodentate carboxylate ligands [30]. Complex **4** has very similar physico-chemical properties to those of the copper complex [Cu(*N*-baa)$_2$(phen)] (*N*-baaH = *N*-benzoylanthanilic acid) [12]. The X-ray crystal structure of [Cu(*N*-baa)$_2$(phen)] has revealed it to have a mononuclear structure with two asymmetrical bidentate chelating carboxylates which both have one very long Cu–O bond (2.626 Å). The overall geometry around what is effectively a four-coordinate copper ion is described as a distorted tetragonal motif which contains a *trans*-$N_2O_2 + O_2$ chromophore. It is likely that **4** has a similar structure to this complex. Complex **5** clearly contains a doubly deprotonated chelating sal^{2-} ligand and its physico-chemical data fit for a square planar geometry similar to that of the structurally characterized bipy analogue [Cu(sal)(bipy)] · EtOH · H_2O [20]. A peak at 844 cm^{-1} in the spectrum of **6**, which does not appear in the spectra of either **4** or **5** is characteristic of the presence of a coordinated water molecule supporting its inclusion in the formulation of **6** (also observed in the crystal structure) [31].

Complexes **7**–**9** formulate as having the same metal:benzimidazole:carboxylate ratio of 1:2:2 and their IR spectra are very similar suggesting that the three complexes share a common structure. The N–H stretching and bending bands in the spectra of the BZDH and 5,6-DMBZDH free ligands also appear (although shifted slightly) in the spectra of the three complexes indicative of the fact that the ligands are present in their neutral state. Furthermore, the bands associated with the imidazolic υ(C=N) in the free ligands (1587 cm^{-1} and 1553 cm^{-1}, respectively) have shifted significantly in the spectra of **7**, **8** and **9** (1499 cm^{-1}, 1581 cm^{-1} and 1615 cm^{-1}, respectively) indicating that the benzimidazoles are bound to the metals through the nitrogen atom. For all three complexes the $\nu(OCO)_{asym}$ and $\nu(OCO)_{sym}$ bands are not split and are in similar positions. The Δ(OCO) values of 161 cm^{-1}, 173 cm^{-1} and 177 cm^{-1} for **7**–**9**, respectively, are all lower than the values expected for monodentate carboxylate ligands (>200 cm^{-1}) but the relative reduction in the Δ(OCO) values are typical where such carboxylate groups are involved in hydrogen bonding [32].

The room temperature magnetic susceptibility values for **4**–**9** (1.65–2.11 BM) are in the range expected for the observed or proposed mononuclear structures in which there are no significant Cu–Cu interactions [23]. Furthermore, the electronic spectra of the complexes obtained in the solid state as Nujol mulls all exhibit broad bands in the region 531–662 nm due to d–d transitions and are in the range expected for mononuclear copper(II) complexes that contain either a CuN_2O_2 or a CuN_2O_3 chromophore and have square planar or related geometries [33]. When the electronic spectra are recorded in DMSO solution these bands all shift to higher energy indicative of changes in geometry as a possible consequence of DMSO solvation. The molar conductivities of complexes **2**–**9** in DMSO were found to be in the range 0.9 and 7.9 S cm^2 mol^{-1} indicating that they are essentially non-electrolytes and thus do not dissociate in that solvent.

2.2. Crystal structures of 6, 7 and 8

The X-ray crystal structures of [Cu(BZA)$_2$(bipy)(H_2O)] (**6**), [Cu(CH_3COO)$_2$ (5,6-DMBZDH)$_2$] (**7**) and [Cu(salH)$_2$-(BZDH)$_2$] (**8**) are shown in Figs. 1–6 and selected bond lengths and angles are listed in Table 1.

The crystal structure determination of **6** showed that the square pyramidal copper centre has an axially coordinated water molecule. An aqua H forms an intramolecular hydrogen bond with unbound carboxylate oxygen O_2 (Fig. 1 and Table 2). Consequently, this carboxylate group

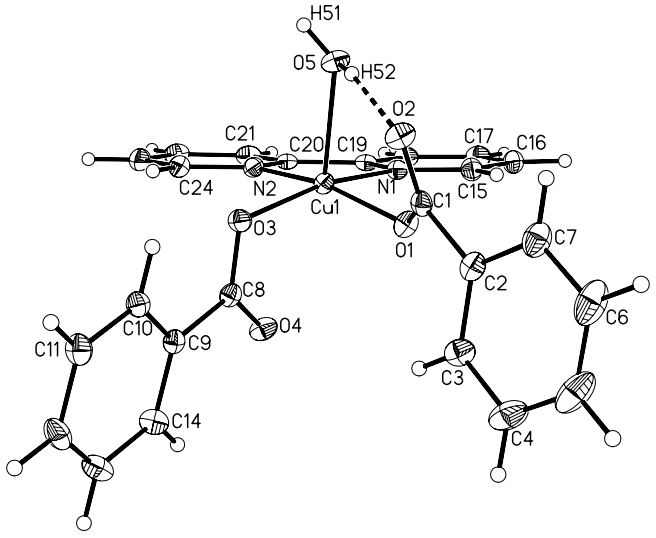


Fig. 1. The structure of [Cu(BZA)$_2$(bipy)(H_2O)] (**6**).

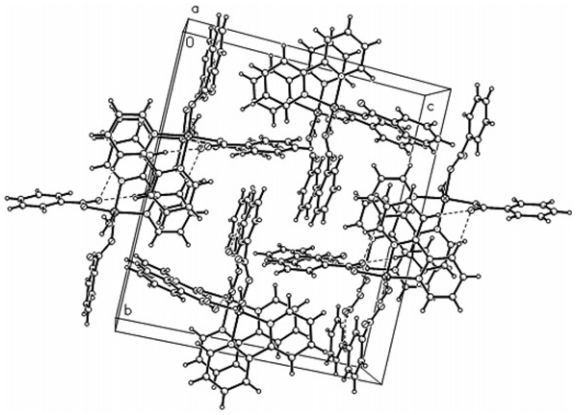


Fig. 2. The packing diagram for $[Cu(BZA)_2(bipy)(H_2O)]$ (**6**) showing stacking and hydrogen bonding.

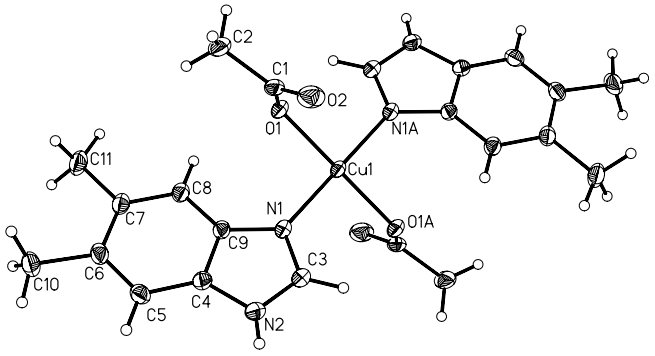


Fig. 3. The structure of $[Cu(CH_3COO)_2$ (5,6-DMBZDH)$_2]$ (**7**).

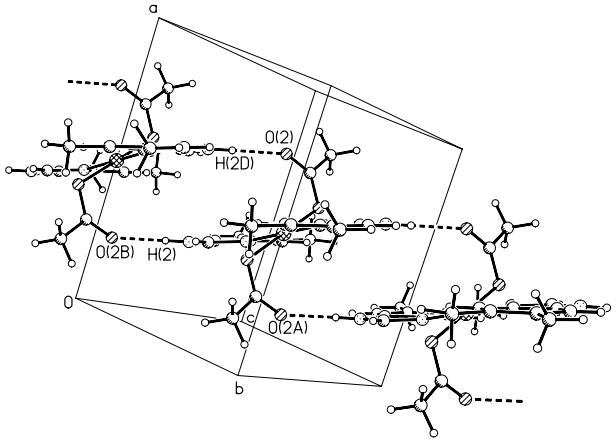


Fig. 4. The packing diagram for $[Cu(CH_3COO)_2$(5,6-DMBZDH)$_2]$ (**7**) showing the hydrogen bonding where suffixes on labels correspond to the symmetry operations A: $x+1, -y+2, -z$; B $-x+1, -y+1, -z$.

is significantly twisted, by 36.31(9)°, with respect to the phenyl ring. This is in contrast to the other chemically identical benzoate which takes part in intermolecular hydrogen bonding with water bound to another molecule. In this case the phenyl-carboxylate twist angle is 6.56(9)°. Thus, this hydrogen bonding motif generates a chain parallel to the *a*-axis. The bipyridyl ligand is inclined at 85.18(7)° to phenyl C2–C7 (bound to the intramolecular hydrogen bonding carboxylate) and 77.04(6)° to the other phenyl group (C9–C14). There are no close π-stacking interactions (Fig. 2) but several close H…H distances, the shortest being 2.43 Å between H4A and H7A in neighbouring molecules.

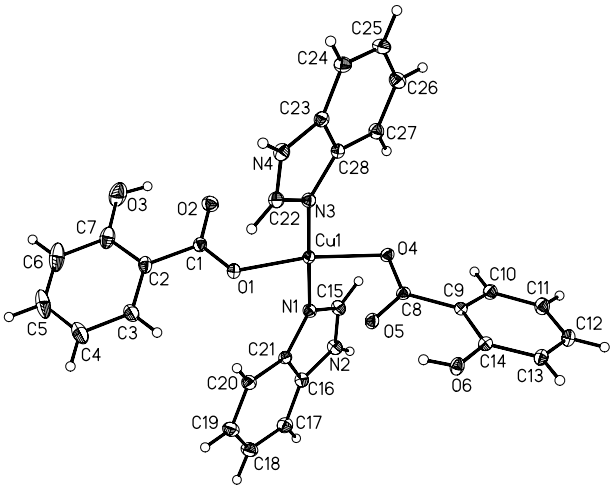


Fig. 5. The structure of $[Cu(salH)_2(BZDH)_2]$ (**8**).

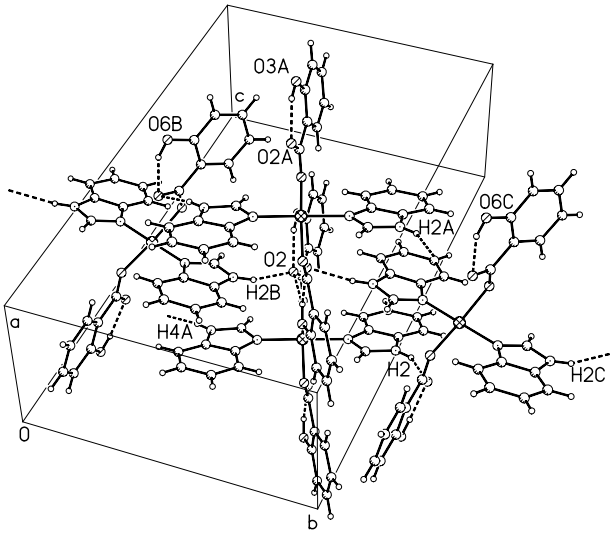


Fig. 6. The packing diagram for $[Cu(salH)_2(BZDH)_2]$ (**8**) where suffixes on labels correspond to the symmetry operations A: $1+x, y, z$; B: $-x+3/2, y+1/2, -z+1/2$; C: $-x+3/2, y+3/2, -z+1/2$.

In contrast both **7** and **8** have square planar copper centres (Figs. 3 and 5, respectively) which contain two *trans* benzimidazole and two acetate (**7**) or two salicylate (**8**) ligands. Whereas the copper atom is situated on an inversion centre in **7**, it is not so in **8** where the hydrogen bonding motif differs between the two carboxylate groups. The protonated benzimidazole N is capable of hydrogen bonding and makes intermolecular hydrogen bonds with carboxylate O atoms in both cases (Fig. 4; Table 3 and Fig. 5; Table 4, respectively) thus forming a double linked chain which is propagated along the shortest axis (*b*) in **7** so that the hydrogen bonding pattern is similar to **6** apart

Table 1
Selected bond lengths (Å) and angles (°) around the copper centres for $[Cu(BZA)_2(bipy)(H_2O)]$ (**6**), $[Cu(CH_3COO)_2(5,6\text{-DMBZDH})_2]$ (**7**) and $[Cu(salH)_2(BZDH)_2]$ (**8**)

6		**7**		**8**	
Cu(1)–O(1)	1.9551(12)	Cu(1)–O(1)	1.9477(8)	Cu(1)–O(1)	1.9601(9)
Cu(1)–O(3)	1.9633(11)	Cu(1)–O(1a)	1.9477(8)	Cu(1)–O(4)	2.0115(9)
$Cu(1)–O(5)_r$	2.2272(12)	Cu(1)–N(1A)	1.9805(10)	Cu(1)–N(1)	1.9951(10)
Cu(1)–N(1)	2.0111(13)			Cu(1)–N(3)	1.9827(10)
Cu(1)–N(2)	2.0064(14)				
N(1)–Cu(1)–N(2)	80.53(5)	O(1)–Cu(1)–O(1A)	180.00(3)	N(1)–Cu(1)–N(3)	179.47(4)
O(1)–Cu(1)–O(3)	90.22(5)	O(1)–Cu(1)–N(1)	90.82(4)	O(1)–Cu(1)–O(4)	169.42(3)
O(5)–Cu(1)–N(1)	96.43(5)	O(1A)–Cu(1)–N(1)	89.18(4)	O(1)–Cu(1)–N(1)	89.86(4)
O(5)–Cu(1)–N(2)	101.96(5)	O(1)–Cu(1)–N(1A)	90.82(4)	O(1)–Cu(1)–N(3)	90.52(4)
O(5)–Cu(1)–O(1)	91.53(5)			O(4)–Cu(1)–N(1)	87.90(4)
O(5)–Cu(1)–O(3)	96.81(5)			O(4)–Cu(1)–N(3)	91.65(4)

The suffix A denotes the symmetry operation $x+1, -y+2, -z$ applied to generate equivalent atoms.

Table 2
Hydrogen bonds for $[Cu(BZA)_2(bipy)(H_2O)]$ (**6**) (Å) and (°)

D–H...A	*d*(D–H)	*d*(H...A)	*d*(D...A)	∠(DHA)
O(5)–H(52)...O(2)	0.823(16)	1.879(17)	2.6720(17)	161(2)
O(5)–H(51)...O(4A)	0.808(16)	1.925(17)	2.7237(17)	170(3)

The suffix A denotes the symmetry operation: $x+1, y, z$ applied to generate equivalent atoms.

Table 3
Hydrogen bonds for $[Cu(CH_3COO)_2(5,6\text{–}DMBZDH)_2]$ (**7**) (Å) and (°)

D–H...A	*d*(D–H)	*d*(H...A)	*d*(D...A)	∠(DHA)
N(2)–H(2)...O(2A)	0.81(2)	1.92(2)	2.7169(14)	168.3(19)

The suffix A denotes the symmetry operation: A: $-x+1, -y+1, -z$ applied to generate equivalent.

Table 4
Hydrogen bonds for $[Cu(salH)_2(BZDH)_2]$ (**8**) (Å) and (°)

D–H...A	*d*(D–H)	*d*(H...A)	*d*(D...A)	∠(DHA)
O(3)–H(3O)...O(2)	0.82	1.85	2.5681(15)	146.3
O(6)–H(6O)...O(5)	0.82	1.88	2.5974(13)	145.2
O(6)–H(6O)...O(2A)	0.82	2.28	2.8682(13)	129.5
N(2)–H(2)...O(2B)	0.86	2.04	2.8220(14)	150.9
N(4)–H(4A)...O(5C)	0.86	2.11	2.9627(13)	168.7
N(4)–H(4A)...O(6C)	0.86	2.85	3.4523(14)	128.8

Symmetry transformations used to generate equivalent atoms:
A: $x-1, y, z$ B: $-x+3/2, y+1/2, -z+1/2$ C: $-x+1/2, y-1/2, -z+1/2$.

from two NH···O hydrogen bonds forming the link rather than the single OH...O seen in **6**. In **8**, the *ortho* hydroxy group makes hydrogen bonds to one carboxylate O atom and so would be expected to keep the carboxylate co-planar with the phenyl ring which is the case for the carboxylate containing O1, O2. However, for the other benzoate ligand the carboxylate is twisted by 18.33(6)° with respect to the plane made by the phenyl ring and O6. In this case, the hydroxyl O makes intermolecular hydrogen bonds to a carboxyl O and a longer NH...O link (Table 4). In contrast O3 makes just an intramolecular hydrogen bond to O2. As seen in **6** and **7**, **8** forms hydrogen bonded chains parallel to the shortest axis, although there is an extra NH...O bond in **7** and **8**. However, in **8** these chains interdigitate such that the benzimidazoles form a stack and the distance between the imidazole centroids in these stacks alternates between 3.6622(7) and 3.8424(7) Å, albeit rather too long for significant p–p stacking interactions. In the structure of **7** neighbouring molecules are link by significant π–π stacking involving the benzimidazole ligands (Fig. 4). Despite these differences, the major hydrogen bonding motif, a chain propagated by OH...O (**6**, **8**) or NH...O (**7**) bonds along the shortest axis, is common to all three crystal structures.

2.3. Catalase activity

The catalytic activity of complexes **1**–**9** towards the disproportionation of hydrogen peroxide was investigated by measuring the volume of evolved oxygen during the course of the reaction. None of the nine complexes exhibited catalytic activity on their own. We have previously shown that the catalase mimetic activity of manganese complexes is significantly improved in the presence of the base imidazole [29,34,35], a phenomenon also observed by others [36]. Consequently, we examined the catalase mimetic properties of complexes **1**–**9** in the presence of this base. The results from these reactions are summarised in Tables 5 and 6. The catalytic activity of the complexes is relatively poor when compared to the double salt $[\{Mn_2(oda)(phen)_4(H_2O)_2][Mn_2(oda)_3(phen)_4\}]$ ($odaH_2$ = octanedioic acid) which had been shown to be the best manganese catalase mimic previously produced in this laboratory [29,37]. Table 5 shows the rate of evolution of oxygen from the respective reactions for the complexes over the first 20 min. Examination of Table 6 shows that over the first minute of reaction **5** appears to be the most efficient catalyst with 1012 molecules of peroxide disproportionated by one molecule of the complex. Complex **8** appears to be the least efficient catalyst over the first minute with one molecule of the compound knocking down just 216 molecules of the peroxide.

Table 5
Time course of oxygen evolution in H_2O_2 disproportionation by complexes **1**–**9** and {$[Mn_2(oda)(phen)_4(H_2O)_2][Mn_2(oda)_3(phen)_4]$} ($odaH_2$ = octanedioic acid) [29,37] with added imidazole (50 mg) at 25 °C

Time (min)	Imidazole	**1**	**2**	**3**	**4**	**5**	**6**	**7**	**8**	**9**	{$[Mn_2(oda)(phen)_4(H_2O)_2]$ $[Mn_2(oda)_3(phen)_4]$}
1	18	123	106	94	87	295	186	93	41	84	800
2	22	136	117	105	145	346	261	102	72	107	900
3	26		119	108	271	369	281	104	88	117	930
4	27			109	297	376	295	105	98	120	970
5	30			110	305	379	303		104	122	991
6	33				312	381	308		108		1021
7	45				317		314		112		1070
8	52				319		316		114		1082
9	55						320		115		1099
10	59						323		116		1110
15							334		121		1122
20							341		122		1141

Table 6
Molecules of H_2O_2 disproportionated by the complexes (in the presence of added imidazole) at STP conditions

Complex	Total number of molecules of H_2O_2 disproportionated by one molecule of complex	Number of molecules of H_2O_2 disproportionated during first min by one molecule of the complex
1	486	440
2	409	364
3	317	270
4	1017	278
5	1308	1012
6	1450	790
7	446	396
8	640	216
9	606	416
{$[Mn_2(oda)(phen)_4(H_2O)_2][Mn_2(oda)_3(phen)_4]$}	24 570	19 500

It should be noted that imidazole itself causes only a very slight disproportionation of the peroxide (Table 5).

2.4. Superoxide dismutase activity

The SOD mimetic activities of the complexes **1**–**9** were examined with an indirect method in which the xanthine/xanthine-oxidase system served as the source for superoxide radicals [38]. The activities of the complexes were compared to that of $[Cu_2(indo)_4(H_2O)_2]$ {indoH = indomethacin [1-(4-chlorobenzoyl)-5-methoxy-2-methyl-1H-indole-3-acetic acid]} which is considered to be an excellent SOD mimetic [39] and which is used therapeutically as an oral anti-inflammatory drug in veterinary medicine [40,41]. The results are given in Table 7 as concentrations equivalent to one unit of SOD activity (IC_{50} values).

Significant activities were seen for all compounds tested with one unit of SOD activity arising from the range of 0.63–1.98 μM aqueous solutions. Interestingly, the complexes all have activities comparable with that (1.31 μM in this study) of $[Cu_2(indo)_4L_2]$ (L = DMSO or DMF) for which the IC_{50} values vary significantly in the literature and appear to be solvent dependent (the reported value in DMSO is 2 μM [39]). It is interesting that the SOD activity of the copper(II) acetate complexes decreases in the order $[Cu_2(CH_3COO)_4(H_2O)_2]$ (**1**) > $[Cu(CH_3COO)_2$ (5,6-DMBZDH)$_2]$ (**7**) > $[Cu(CH_3COO)_2(phen)]$ (**4**) where it appears that the inclusion of the nitrogen donor ligands reduce the SOD activity. Whereas **4** and **7** are monomeric complexes **1** is dimeric and has a similar "paddle wheel" structure to that of $[Cu_2(indo)_4(DMF)_2]$ [42]. The copper(II) complexes $[Cu_2(valp)_4(H_2O)_2]$ and $[Cu(valp)_2(phen)]$ [valpH = valproic acid {$(CH_3CH_2CH_2)_2CHCOOH$}] were recently reported and are iso-structural to **1** and **4**, respectively [43]. Their SOD mimetic activities were much lower relative to **1** and **4** (10.4 and 4.5 μM) with the phen derivative being the superior catalyst. Clearly there is no correlation between solid state nuclearity (monomeric versus dimeric structures) and SOD mimetic activity but the type of carboxylate present appears to be important. The three monomeric copper(II) salicylates exhibit SOD activity in the order $[Cu(salH)_2(BZDH)_2]$ (**8**) > [Cu(sal)(phen)] (**5**) > $[Cu(salH)_2(H_2O)_2]$ (**2**) where the activity increases upon inclusion of the nitrogen bases in the inner sphere of the complexes. The activities of complexes **2** and **5** fall in the lower end of the range (0.17–29 μM) previously reported for copper(II) salicylate derivatives, a number of which are used therapeutically as anti-inflammatory agents in human and veterinary medicine [40,44]. The benzoate complex $\{Cu(BZA)_2(H_2O)\}_n$ (**3**) displays potent SOD activity (0.9 μM) and is approximately twice as active as its bipy derivative $[Cu(BZA)_2(bipy)(H_2O)]$ (**6**).

Table 7
Superoxide dismutase (SOD) activities of complexes **1**–**8**, $[Cu_2(indo)_4(H_2O)_2]$ [39], $CuSO_4$ and native CuZnSOD as assessed by the NBT assay

Complex	Concentration (μM) equivalent to 1 U SOD (IC_{50})
$[Cu_2(CH_3COO)_4(H_2O)_2]$ (**1**)	0.63
$[Cu(salH_2)(H_2O)_2]\cdot 0.5H_2O$ (**2**)	1.23
$\{Cu(BZA)_2(H_2O)\}_n$ (**3**)	0.90
$[Cu(CH_3COO)_2(phen)]$ (**4**)	1.18
[Cu(sal)(phen)] (**5**)	1.01
$[Cu(BZA)_2(bipy)(H_2O)]$ (**6**)	1.98
$[Cu(CH_3COO)_2(5,6\text{-DMBZDH})_2]$ (**7**)	0.91
$[Cu(salH)_2(BZDH)_2]$ (**8**)	0.74
$[Cu_2(indo)_4(H_2O)_2]$ [39,40]	1.31
$CuSO_4$ [41]	30
Native CuZnSOD [39]	0.04

Where $salH_2$ = salicylic acid; BZAH = benzoic acid; phen = 1,10-phenanthroline; bipy = 2,2′-bipyridine; 5,6-DMBZDH = 5,6-dimethylbenzimidazole; BZDH = benzimidazole; indoH = indomethacin {1-(4-Chlorobenzoyl)-5-methoxy-2-methyl-1H-indole-3-acetic acid}.

$[Cu(BZA)_2(BZDH)_2]$ (**9**) was insoluble in DMSO and its SOD activity could not be determined. Attempts to dissolve **9** in hot DMSO caused an immediate precipitation of the known red polymeric Copper(II) complex $\{Cu(BZD)_2\}_n$ [45]. All of the other complexes were stable in hot DMSO (no change in their UV spectra) again demonstrating how changing the type of carboxylate ligand may influence the reactivity of this class of simple copper(II) complexes.

2.5. Cytotoxicity studies

To evaluate their cancer chemotherapeutic potential the ability of the DMSO soluble copper complexes **1**–**8** to kill human derived cancer cells was investigated using the hepatocellular carcinoma (Hep-G_2), kidney adenocarcinoma (A-498) and lung cancer (A-549) cell lines and was determined by calculation of IC_{50} (the drug concentration causing a 50% reduction in cellular viability). Cells were continuously exposed to test agent for 96 h, and their effects on cellular viability was evaluated. It was intended that the results from these studies would allow the identification of those derivatives with cancer chemotherapeutic potential. Therefore, profiles of cell viability against complex concentration were established and used to calculate the IC_{50} values for each derivative (Table 8). Comparison of IC_{50} values, allowed the relative potency of each of the test compounds to be determined and ranked.

With the exception of phen all of the free ligands are essentially inactive. A number of the compounds screened displayed a concentration-dependent cytotoxic profile across the three cell lines studied here. The most sensitive cell line was the A-549 lung cancer with seven of the compounds showing significant improvements in activity when compared to the uncoordinated free ligands. The overall order of the observed cytotoxicity was seen as (**4**) > (**5**) > (**6**) > (**7**) > (**8**) > (**1**) > (**2**) ⋙ (**3**) with (**4**) appearing as the most potent and (**3**) as the least potent effectively displaying no activity. The results presented in Table 8 also illustrates that the $CuSO_4$ (free Cu^{2+}) was incapable of eliciting a cytotoxic response. The inclusion of the *N*,*N*-donor ligands 1,10-phenanthroline (phen) and 2,2′-bipyridine (bipy) in the simple Cu(II) complexes of the acetic, salicylic and benzoic acids significantly increased the potency of the system. However, it is also noteworthy that the metal free phenanthroline is itself significantly cytotoxic and that the best copper complex containing it (**4**) is approximately 2, 6 and 2 times more potent for the respective cell lines. Complexes **4** and **5** were capable of killing all three cancer

Table 8
The anti-cancer activity of the free ligands, complexes **1**–**8** and cisplatin against human hepatic (Hep-G_2), renal (A-498) and lung (A-549) cancer cell lines expressed as IC_{50} (μM)[a]

Test compound	Toxicities (IC_{50} μM)		
	Hep-G_2 Mean ± SD	A-498 Mean ± SD	A-549 Mean ± SD
$salH_2$	>500	>500	>500
BZAH	>500	>500	>500
Phen	4.1 ± 0.5	5.8 ± 0.3	2.94 ± 0.1
Bipy	>500	>500	>500
BZDH	>500	>500	>500
5,6-DMBZDH	>500	>500	>500
$CuSO_4$	>500	>500	>500
$[Cu_2(CH_3COO)_4(H_2O)_2]$ (**1**)	320 ± 2.5	134 ± 2.2	>500
$[Cu(salH)_2(H_2O)_2]\cdot 0.5H_2O$ (**2**)	350 ± 2.8	142 ± 1.8	59.81 ± 13.7
$\{Cu(BZA)_2(H_2O)\}_n$ (**3**)	>500	>500	>500
$[Cu(CH_3COO)_2(phen)]$ (**4**)	1.8 ± 0.3	1.0 ± 0.2	1.19 ± 0.2
[Cu(sal)(phen)] (**5**)	2.5 ± 0.5	1.6 ± 0.3	1.42 ± 0.3
$[Cu(BZA)_2(bipy)(H_2O)]$ (**6**)	26 ± 6.1	16 ± 6.7	82.99 ± 7.8
$[Cu(CH_3COO)_2(5,6\text{-DMBZDH})_2]$ (**7**)	105 ± 2.6	58 ± 1.9	23.44 ± 4.9
$[Cu(salH)_2(BZDH)_2]$ (**8**)	138 ± 2.5	65 ± 1.4	58.15 ±
Cisplatin	15 ± 2.7	14 ± 1	11.0 ± 4.7

[a] IC_{50} (μM), indicates the compound concentration that inhibits the proliferation rate of tumour cells by 50% as compared to the control untreated cells. The values are means ± S.D. of 9 independent experiments.

derived cell lines at very low concentrations (IC_{50} values: 1.8, 1.0 and 1.55 μM for **4** and 2.5, 1.6 and 1.44 μM for **5** for the liver, kidney and lung cell lines, respectively). The activities of **4** and **5** fall well within the accepted activity parameters adopted for in vitro screening of potential chemotherapeutic drugs [46]. Furthermore, the IC_{50} values for them are superior to those of the clinically used drug *cis*-platin [47]. Significantly, no correlation was found between the potencies of SOD mimic capabilities and cell growth inhibitory activity for the eight complexes. However, with the exception of **3** all of the complexes do show significant activity against the renal and lung cell lines. It is of course possible that the complexes act on the cancer cells through mechanism other than (or in conjunction with) SOD activity. Indeed the bis-1,10-phenanthroline copper(II) complex $[Cu(phen)_2]^{2+}$ is known as a potent nuclease agent which causes oxidative cleavage of DNA in the presence of reducing agents [48].

3. Conclusion

The carboxylate complexes **1**–**8** exhibit potent SOD mimicking activity and are inactive as catalase mimics in the absence of added imidazole. Upon addition of the base they display only poor catalytic potential for the disproportionation of hydrogen peroxide. Complexes **4**–**8** exhibit significant cytotoxicity with the mono-phen derivatives **4** and **5** being the most potent displaying activity approximately seven times that of the clinical anticancer drug cisplatin. Significantly, **4** and **5** are relatively soluble compared to the other six complexes and they have cytotoxicity comparable with the copper(II) bis-phenanthroline complexes previously studied in this laboratory [17] but are one quarter as active as the copper(II) tris-phenanthroline-diones [16]. The lack of correlation between the SOD and cytotoxicity IC_{50} values supports the notion that mechanisms other than SOD mimicking may also be responsible for the anticancer properties of these complexes. Indeed complexes **4** and **5** are structurally related to the novel anticancer agent casiopeina II {[Cu(1,4-dimethyl-1,10-phenanthroline)-(glycine)]NO_3} which has been shown to have a very complex in vivo cytotoxicity [49]. An interesting compound is the benzoate complex **3** which is an excellent SOD mimic but has little or no cytotoxicity. Such a non-toxic compound might have potential use as a therapeutic agent for treatment of other disorders where SOD activity is pathologically reduced.

4. Experimental

4.1. Chemistry

Chemicals were purchased from commercial sources and used without further purification. IR spectra were recorded in the region 4000–400 cm^{-1} on a Nicolet-400 Impact spectrometer. UV spectra were recorded in the region of 400–1000 nm on a Specord 200 spectrophotometer. Magnetic susceptibility measurements were made using a Johnson Matthey Magnetic Susceptibility balance. $[HgCo(SCN)_4]$ was used as a reference. Conductivity readings were obtained using an Orion model 150 plus conductivity meter. Satisfactory microanalytical data for the complexes were reported by the Microanalytical Laboratory, University College Cork, Ireland. $[Cu_2(indo)_4(H_2O)_2]$ (indoH = indomethacin) was synthesised and characterised using the method previously published [39].

4.1.1. $[Cu_2(CH_3COO)_4(H_2O)_2]$ (1)

$[Cu_2(CH_3COO)_4(H_2O)_2]$ was obtained commercially from the Aldrich Chemical Company and used without further purification.

4.1.2. $[Cu(salH)_2(H_2O)_2]$ (2)

$[Cu(salH)_2(H_2O)_2]$ (**2**) was synthesised using a method previously published [20] as follows: $Cu(OH)_2$(0.97 g, 9.94 mmol) and salicylic acid ($salH_2$) (2.76 g, 19.98 mmol) were refluxed in ethanol (50 cm^3) for 4 h giving a brown suspension. On cooling to room temperature the brown product was filtered off, washed with two portions of water and ethanol, and then air-dried. Yield: 1.42 g, 56%. *Anal.* Calc. C, 40.3; H, 2.4. Found: C, 41.09; H, 2.3%. IR (KBr): 3438, 1603, 1568, 1529, 1485, 1455, 1410, 1303, 1232, 1149, 1099, 1037, 891, 838, 808, 775, 763, 711, 673, 621, 595, 512, 451, 428, 415, 406 cm^{-1}. μ_{eff}: 1.81 BM. Solubility: insoluble in water, ethanol, methanol, acetone, trichloromethane. Soluble in DMSO. λ_{max} (Nujol Mull): $\lambda_{d-d} = 742$ nm. λ_{max} (DMSO): $\lambda_{d-d} = 754$ nm, $\varepsilon = 169.5\ M^{-1}\ cm^{-1}$. Λ_M (DMSO): 4.2 S $cm^2\ mol^{-1}$.

4.1.3. $\{Cu(BZA)_2(H_2O)\}_n$ (3)

To a solution of freshly prepared $Cu(OH)_2$ (1.0 g, 10.25 mmol) in ethanol (50 cm^3) was added an ethanolic solution (25 cm^3) of benzoic acid (2.5 g, 20.5 mmol) and the resulting suspension was refluxed for 3 h. The blue-green powder that deposited was filtered off, washed with a small volume of ethanol, and then air-dried. Yield: 1.6 g, 49%. *Anal.* Calc. C, 51.93; H, 3.73. Found: C, 53.3; H, 3.3%. IR (KBr): 3061, 2970, 1597, 1561, 1520, 1509, 1445, 1402, 1309, 1179, 1146, 1071, 1026, 929, 845, 718, 685, 510, 481 cm^{-1} μ_{eff}: 1.57 BM. Solubility: insoluble in water, ethanol, methanol, acetone, and trichloromethane. Soluble in DMSO. λ_{d-d} (Nujol Mull) = 686 nm. λ_{d-d} (DMSO) = 734 nm, $\varepsilon = 125\ M^{-1}\ cm^{-1}$. Λ_M (DMSO) = 1.17 S $cm^2\ mol^{-1}$.

4.1.4. $[Cu(CH_3COO)_2(phen)]$ (4)

To a solution of phen (1 g, 5.6 mmol) in EtOH (50 cm^3) was added $[Cu_2(CH_3COO)_4(H_2O)_2]$ (**1**) (0.5 g, 1.25 mmol) and the resulting blue solution refluxed for 1 h. The solution was reduced by rotary evaporation to 5 cm^3 and acetone (20 cm^3) then added. This solution was further reduced to 10 cm^3. The resulting blue powder which deposited was filtered off washed with two por-

tions of water and ethanol, and then air-dried. Yield: 0.28 g, 62%. *Anal*. Calc. C, 50.6; H, 4.3; N, 7.4. Found: C, 51.0; H, 4.1, N, 7.9%. IR (KBr): 3442, 3012, 2925, 2854, 1632, 1608, 1587, 1544, 1524, 1448, 1431, 1401, 1341, 1255, 1220, 1143, 1107, 1054, 1020, 962, 942, 875, 851, 785, 723, 683, 648, 627, 482, 432 cm^{-1}. μ_{eff}: 1.89 BM. Solubility: soluble in water, EtOH, MeOH and DMSO. λ_{max} (Nujol Mull): $\lambda_{d-d} = 630$ nm. λ_{max} (DMSO): $\lambda_{d-d} = 682$ nm, $\varepsilon = 51.6\ M^{-1}\ cm^{-1}$. Λ_M (DMSO): 7.9 S $cm^2\ mol^{-1}$.

4.1.5. [Cu(sal)(phen)] (5)

[Cu(sal)(phen)] (**5**) was synthesised using a method previously published [20] as follows: $[Cu(salH)_2(H_2O)_2]$ (**2**) (0.4 g, 1.92 mmol) and 1,10-phenanthroline (0.427 g, 2.37 mmol) were refluxed in EtOH (50 cm^3) for 2 h giving a green suspension. On cooling to room temperature the green product was filtered, washed with two portions of water and ethanol, and then air-dried. Yield: 0.73 g, 72%. *Anal*. Calc. C, 60.1; H, 3.2; N, 7.4. Found: C, 58.9; H, 3.3, N, 7.0%. IR (KBr): 3416, 3089, 3059, 2360, 2342, 1629, 1599, 1574, 1543, 1519, 1492, 1461, 1450, 1429, 1360, 1342, 1320, 1243, 1223, 1136, 1107, 1032, 911.884, 874, 847, 809, 772, 741, 721, 710, 667, 651, 628, 585, 543, 432 cm^{-1}. μ_{eff}: 2.11. Solubility: insoluble in water acetone and trichloromethane. Soluble in EtOH, MeOH and DMSO. λ_{max} (Nujol Mull): $\lambda_{d-d} = 589$ nm. λ_{max} (DMSO): $\lambda_{d-d} = 635$ nm, $\varepsilon = 134.3\ M^{-1}\ cm^{-1}$. Λ_M (DMSO): 1.8 S $cm^2\ mol^{-1}$.

4.1.6. [Cu(BZA)$_2$(bipy)(H$_2$O)] (6)

To a heated solution of $[Cu_2(CH_3COO)_4(H_2O)_2]$ (**1**) (0.5 g, 1.25 mmol) and benzoic acid (0.31 g, 2.5 mmol) in ethanol (50 cm^3) was added 2,2-bipyridine (0.39 g, 2.5 mmol). The resulting dark blue solution was stirred for 30 min and allowed to cool and stand. After 48 h blue needle-like crystals formed that were suitable for X-ray crystallography. Yield: 0.37 g, 61.67%. *Anal*. Calc. C, 60.0 ; H, 4.2; N, 5.83. Found: C, 59.40; H, 4.18; N, 5.66%. IR (KBr): 3357.11, 3111.63, 3081.23, 3030.09, 1599.59, 1555.06, 1493.96, 1473.36, 1445.49, 1397.01, 1379.35, 1313.09, 1285.66, 1260.50, 1254.75, 1170.95, 1156.30, 1142.41, 1105.07, 1070.15, 1054.39, 1031.28, 1019.61, 977.99, 930.12, 913.08, 846.41, 820.11, 775.38, 729.24, 678.25, 665.38, 650.65, 639.83, 548.40, 455.46, 432.92, 416.63 cm^{-1}. μ_{eff}: 1.87 BM. Solubility: insoluble in water, ethanol, methanol, acetone, and trichloromethane. Soluble in DMSO. λ_{max} (Nujol): $\lambda_{d-d} = 662$ nm. λ_{max} (DMSO): $\lambda_{d-d} = 677$ nm, $\varepsilon = 117.77\ dm^3\ mol^{-1}\ cm^{-1}$. Λ_M (DMSO): 7.2 S $cm^2\ mol^{-1}$.

4.1.7. [Cu(CH$_3$COO)$_2$ (5,6-DMBZDH)$_2$] (7)

To a solution of $Cu_2(CH_3COO)_4(H_2O)_2]$ (**1**) (0.5 g, 1.25 mmol) in ethanol (100 cm^3) was added 5,6-dimethylbenzimidazole (0.73 g, 5 mmol) and the resulting dark green solution refluxed for 4 h. A quantity of blue crystals suitable for X-ray structural analysis, were obtained from the solution upon standing for one week. Yield: 0.25 g, 42%. *Anal*. Calc. C, 55.7; H, 5.5; N, 11.8. Found: C, 55.9; H, 5.6; N, 11.4%. IR (KBr): 3432, 3102, 3062, 2966, 2934, 2879, 2815, 2656, 1772, 1706, 1559, 1500, 1474, 1448, 1408, 1337, 1307, 1271, 1251, 1212, 1191, 1159, 1087, 1047, 1006, 968, 931, 882, 856, 841, 823, 784, 732, 675, 647, 618, 575, 486, 452, 435 cm^{-1}. μ_{eff}: 1.65 BM. Solubility: insoluble in water, ethanol, methanol, acetone, trichloromethane. Soluble in DMSO. λ_{max} (Nujol Mull): $\lambda_{d-d} = 531$ nm. λ_{max} (DMSO): $\lambda_{d-d} = 726$ nm, $\varepsilon = 123.4\ M^{-1}\ cm^{-1}$. Λ_M (DMSO): 0.9 S $cm^2\ mol^{-1}$.

4.1.8. [Cu(salH)$_2$(BZDH)$_2$] (8)

$[Cu(salH)_2(H_2O)_2]$ (**2**) (0.5 g, 2.39 mmol) and benzimidazole (0.846 g, 7.17 mmol) were refluxed in ethanol (100 cm^3) for 3 h giving a red suspension. On cooling to room temperature a small amount of red powder ($\{Cu(bzd)_2\}_n$) was filtered off, and the blue filtrate allowed to stand for several days where a quantity of blue crystals of **8** which were suitable for X-ray structural analysis deposited. Yield: 0.51 g, 37%. *Anal*. Calc. C, 58.6; H, 3.9; N, 9.8%. Found: C, 58.9; H, 3.8; N, 9.8%. IR (KBr): 3238, 3145, 3112, 3064, 2990, 2916, 2839, 1760, 1741, 1619, 1595, 1582, 1568, 1509, 1497, 1479, 1454, 1395, 1355, 1323, 1305, 1272, 1224, 1195, 1141, 1113, 1086, 1031, 1010, 977, 971, 925, 864, 849, 832, 817, 777, 756, 733, 716, 705, 669, 634, 606, 560, 548, 536, 443, 420 cm^{-1}. μ_{eff}: 1.83 BM. Solubility: insoluble in water, ethanol, methanol, acetone, trichloromethane. Soluble in DMSO. λ_{max} (Nujol Mull): $\lambda_{d-d} = 579$ nm. λ_{max} (DMSO): $\lambda_{d-d} = 738$ nm, $\varepsilon = 84.1\ M^{-1}\ cm^{-1}$. Λ_M (DMSO): 13.2 S $cm^2\ mol^{-1}$.

4.1.9. [Cu(BZA)$_2$(BZDH)$_2$] (9)

To a solution of $\{Cu(BZA)_2(H_2O)\}_n$ (**3**) (1.0 g, 3.0 mmol) in ethanol/water (100 cm^3, 1:1) was added benzimidazole (1.25 g, 10.0 mmol) and the resulting suspension was stirred for 24 h. The purple powder that deposited was filtered off, washed with a small volume of ethanol and water, and then air-dried. Yield: 1.53 g, 94.09%. *Anal*. Calc. C, 62.04; H, 4.09; N, 10.33. Found: C, 61.33; H, 4.03; N, 10.05%. IR (KBr): 3326.11, 3139.56, 3056.98, 2985.24, 2915.51, 2887.72, 2845.62, 2754.33, 1964.64, 1911.00, 1783.54, 1615.42, 1597.55, 1557.91, 1487.96, 1464.43, 1446.28, 1428.34, 1405.57, 1381.42, 1361.48, 1315.83, 1302.93, 1270.64, 1252.56, 1176.14, 1150.84, 1125.03, 1107.73, 1068.13, 1024.20, 1010.63, 973.86, 933.40, 906.24, 886.97, 846.44, 840.40, 827.51, 788.77, 776.50, 764.82, 742.46, 714.43, 685.37, 631.93, 613.62, 577.07, 548.59, 447.32, 425.24 cm^{-1}. μ_{eff}: 1.86 BM. Solubility: insoluble in all common solvents. λ_{max} (Nujol): $\lambda_{d-d} =$ 593 nm.

4.2. X-ray crystallography

Intensity data were collected in single crystals of **6**, **7** and **8** at 100 K on a Bruker Nonius X8 Apex2 diffractometer with monochromatic Mo Kα radiation. Solution and

refinement were performed using the BRUKER suite of programs [50]. All H atom positions were calculated (except N-bound H2 in 7) and all H atom displacement parameters were treated as riding on the bound atom. Further details are given in Table 9.

4.3. Catalase activity

The ability of the complexes to disproportionate hydrogen peroxide was assayed using a method previously published by this laboratory [29] as follows: To a solid sample (ca. 10 mg) of the copper complex was added aqueous H_2O_2 (35% w/w, 10 cm^3, 114 mmol). The mixture was stirred and thermostated at 25 °C and the evolved O_2 was measured volumetrically (volume ± 0.10 cm^3). In cases where imidazole (50 mg) was added, this was introduced into the reaction vessel before the addition of H_2O_2.

4.4. Superoxide dismutase (SOD) activity

The $O_2^{\cdot-}$ dismutase activities of the metal complexes were assessed using a modified Nitro-Blue-Tetrazolium (NBT) assay with xanthine–xanthine oxidase system as the source of $O_2^{\cdot-}$ [38]. The quantitative reduction of NBT to blue Formazan by the $O_2^{\cdot-}$ was followed spectrophotometrically at 550 nm. All reagents were obtained from Sigma–Aldrich Chemical Co. Ltd. and assays were run in 3 ml of solution. Results are graphed as the % inhibition of NBT reduction for three concentrations. Tabulated results were derived from linear regression analyses and are given as the concentration (μM) equivalent to 1 U of bovine erythrocyte SOD activity. A unit SOD activity is the concentration of the complex or enzyme which causes 50% inhibition in the reduction of NBT (referred to as the IC_{50} value).

4.5. Cytotoxicity testing

Dimethyl sulphoxide (DMSO) and all cell culture reagents and media were purchased from Signa–Aldrich Ireland, Ltd., unless otherwise stated. Cytotoxicity assays were performed using three human malignant model cell lines in order to assess the cancer chemotherapeutic potential of the Cu complexes. Hepatocellular carcinoma (Hep-G2), kidney adenocarcinoma (A-496) and lung cancer (A-549) cell lines were purchased from the ATCC.

The hepatocellular carcinoma (Hep-G2) and kidney adenocarcinoma (A-496) cell lines were grown as monolayers in Eagle's minimum essential medium, supplemented with 2 mM L-glutamine and Earle's balanced salt solution, containing 1.5 g dm^{-3} sodium bicarbonate, 0.1 mM non-essential amino acids, 1.0 mM sodium pyruvate, 100 U cm^{-3} penicillin and 100 μg cm^{-3} streptomycin supplemented to contain 10% (v/v) foetal bovine serum (Flow Laboratories, Herts, UK). All cells were grown at 37 °C in a humidified atmosphere, in the presence of 5% CO_2 and were in the exponential phase of growth at the time of assay. Cytotoxicity was assessed using MTT assay. Each of the two cell lines (100 μl) were seeded at a density of 5×10^4 cells cm^{-3} into sterile 96 well flat-bottomed plates (Falcon Plastics, Becton Dickinson) and grown in 5% CO_2 at 37 °C. Test compounds were dissolved in DMSO and diluted with culture media. The maximum percentage of DMSO present in all wells was 0.2% (v/v). Each drug solution (100 μl) was added to replicate wells in the concentration range of 0.1–1000 μM and incubated for 96 h A miniaturised viability assay using 3-(4,5-dimethylthiazol-2-yl)-2,5-diphenyl tetrazolium bromide (MTT) was carried

Table 9
Crystal data and structure refinement for complexes **6**, **7** and **8**

Compound	**6**	**7**	**8**
Empirical formula	$C_{24}H_{20}CuN_2O_5$	$C_{22}H_{26}N_4O_4Cu$	$C_{28}H_{22}N_4O_6Cu$
Formula weight	479.96	474.01	574.04
Temperature (K)	100(2)	100(2)	100(2)
Crystal system	monoclinic	monoclinic	monoclinic
Space group	$P2_1/c$	$P2_1/n$	$P2_1/n$
a (Å)	6.8631(4)	10.6616(6)	7.2216(6)
b (Å)	18.7829(12)	.0458(5)	13.9991(11)
c (Å)	16.8774(9)	14.8903(9)	23.9378(18)
α (°)	90	90	90
β (°)	97.573(4)	100.950(3)	91.502(4)
γ (°)	90	90	90
V (Å^3)	2156.7(2)	1098.19(12)	2419.2(3)
Z	4	2	4
D_{calc} (Mg/m^3)	1.478	1.433	1.576
Absorption coefficient (mm^{-1})	1.052	1.030	0.957
$F(000)$	988	494	1180
Crystal size (mm^3)	$0.22 \times 0.18 \times 0.08$	$0.42 \times 0.40 \times 0.22$	$0.5 \times 0.20 \times 0.15$
Crystal description	blue needle	blue block	blue blocks
θ Range (°)	2.17–30.64	2.60–30.45	1.67–28.52
Reflections collected	32564	13637	35163
Independent reflections [R_{int}]	6522 [0.0505]	3214 [0.0183]	10562 [0.0309]
Completeness to θ (°)	(25.00) 99.2%	(25.00) 98.3%	(25.00) 99.4%
Maximum and minimum transmission	0.919 and 0.715	0.8051 and 0.6715	0.866 and 0.654
Data/restraints/parameters	6522/2/297	3214/0/194	10562/0/354
Goodness-of-fit on F^2	0.996	1.041	0.850
Final R indices [$I > 2\sigma(I)$]	$R_1 = 0.0334$ $wR_2 = 0.0733$	$R_1 = 0.0254$ $wR_2 = 0.0687$	$R_1 = 0.0366$ $wR_2 = 0.1070$
R indices (all data)	$R_1 = 0.0510$ $wR_2 = 0.0800$	$R_1 = 0.0303$ $wR_2 = 0.0719$	$R_1 = 0.0582$ $wR_2 = 0.1219$
Largest difference peak and hole (e Å^{-3})	0.438 and −0.400	0.418 and −0.236	0.952 and −0.939

out according to the method described by Mosman [51]. The IC_{50} value, defined as the drug concentration causing a 50% reduction in cellular viability, was calculated for each drug. Each assay was carried out using five replicates and repeated on at least three separate occasions. Viability was calculated as a percentage of solvent-treated control cells, and expressed as a % of the control. The significance of any reduction in cellular viability was determined using one-way ANOVA (analysis of variance). A probability of 0.05 or less was deemed statistically significant.

The lung (A-549) cells were cultured in Kaighn's medium (F12K) with 2 mM L-glutamine supplemented with 10% foetal calf serum (FCS) and 45 IU ml^{-1} penicillin and 45 μg ml^{-1} streptomycin at 37 °C in 5% CO_2 humidified incubator. For subcultivation, the cells were detached using a Versene/trypsin solution (1 mM EDTA/0.25% trypsin) in Ca^{2+}- and Mg^{2+}-free Hanks Balanced Salts Solution (HBSS). For cytotoxicity assays cells were seeded in 96-well microplates (Sarstedt) at a density of 2×10^4 cells/ml. This density was found to be optimal to achieve the desired confluence at the end of the exposure period. After 24 h of cell attachment, plates were washed with 100 μl/well phosphate buffered saline (PBS) and cells treated with each compound for 96 h. Six replicate wells were used for each control, and test concentration per microplate. Cytotoxicity was assessed using the MTT assay. Following 96 h of exposure, control or test exposures were removed, cells rinsed with PBS and 100 μl of fresh media (without phenol-red sodium salt, FCS or supplements) was added to each well. Ten microlitres of MTT (5 mg/ml) prepared in PBS was then added to each well and plates incubated for 3 h at 37 °C in a 5% CO_2 humidified incubator. After this incubation period the medium was discarded, cells washed with 100 μl of PBS and 100 μl of DMSO was added to each well to extract the dye. The plate was shaken at 240 rpm for 10 min and absorbance measured at 570 nm. Experiments were conducted in triplicate (three independent experiments). Raw data from cell cytotoxicity assays were collated and analysed using Microsoft Excel® (Microsoft Corporation, Redmond, WA). Cytotoxicity is expressed as mean percentage survival relative to the unexposed control ±standard error of the mean (SEM). Control values were set at 100%. Coefficient of variation (CV) for the controls of each test was calculated to ascertain reproducibility. Cytotoxicity data were fitted to a sigmoidal curve and a four parameter logistic model used to calculate IC_{50} values. This analysis was performed using XLFIT3™ a curve fitting add-in for Microsoft® Excel (ID Business Solutions, UK).

5. Supplementary material

CCDC 634440, 634441 and 634442 contain the supplementary crystallographic data for **6**, **7** and **8**. These data can be obtained free of charge via http://www.ccdc.cam.ac.uk/conts/retrieving.html, or from the Cambridge Crystallographic Data Centre, 12 Union Road, Cambridge CB2 1EZ, UK; fax: (+44) 1223-336-033; or e-mail: deposit@ccdc.cam.ac.uk.

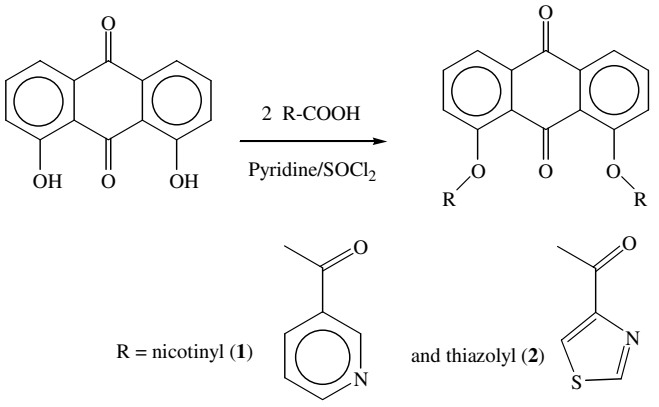
Acknowledgements

M.O.C. acknowledges Irish Technological Sector Research Strand I programme 2002 (Project No. PT03147). The authors also acknowledge funding received through the Irish Technological Sector Research Strand III programme 2002 (Project No. CRS02-TA01) and DIT Team Research Scheme (TERS) funding for Interdisciplinary Cancer Research. This work has been carried out (in part) within the structures of the Facility for Optical Characterisation and Spectroscopy (now the FOCAS Institute, DIT), funded under The Irish National Development Plan 2000–2006 with assistance from the European Regional Development Fund.

References

[1] J.D. Scandalis (Ed.), Oxidative Stress and the Molecular Biology of Antioxidant Defenses, Cold Spring Harbor Laboratory Press, Raleigh, USA, 1997.
[2] S.M. Cardoso, C. Pereira, C.R. Oliveira, Biochem. Biophys. Res. Commun. 246 (1998) 83.
[3] M. Mates, Toxicology 153 (2000) 83.
[4] D.M. Miller, G.R. Buettner, S.D. Aust, Free, Radic. Biol. Med. 8 (1990) 95.
[5] P. Huang, L. Feng, E.A. Oldam, M.J. Keating, W. Plunkett, Nature 407 (2000) 390.
[6] L.W. Oberley, Antioxid. Redox Signal. 3 (2001).
[7] C. Muscoli, S. Cuzzocrea, D. Riley, J.L. Zweier, C. Thiemerman-Salvemini, Br. J. Pharmacol. 140 (2003) 445.
[8] C.J. Darby Weydert, B.B. Smith, L. Xu, K.C. Kregel, J.M. Ritchie, C.S. Davis, L.W. Oberley, Free Radic. Biol. Med. 34 (2003) 316.
[9] E.W.N. Lam, H.M. Hammand, R. Zwacka, C.J. Darby, K.R. Baumgardner, B.L. Davidson, T.D. Oberley, J.F. Engelhardt, L.W. Oberley, Cancer Res. 57 (1997) 5550.
[10] C.J. Weydert, T.A. Waugh, J.M. Ritchie, K.S. Iyer, J.L. Smith, L. Li, D.R. Spitz, L.W. Oberley, Free Radic. Biol. Med. 41 (2006) 226.
[11] J. Kaiser, R. Csonka, G. Speier, M. Giorgi, M. Reglier, J. Mol. Catal. A: Chem. 236 (2005) 12.
[12] J. Kaiser, T. Csay, G. Speier, M. Reglier, M. Giorgi, Inorg. Chem. Commun. 9 (2006) 1037.
[13] M. Devereux, M. McCann, D. O Shea, R. Kelly, D. Egan, C. Deegan, V. McKee, J. Inorg. Biochem. 98 (2004) 1023.
[14] M. Devereux, M. McCann, D.O Shea, M.O Connor, E. Kiely, V. McKee, D. Naughton, A. Fisher, A. Kellett, M. Walsh, D. Egan, C. Deegan, Bioinorg. Chem. Appl. 2006, Article ID: 80283.
[15] B. Thati, A. Noble, B.S. Creavan, M. Walsh, M. McCann, K. Kavanagh, M. Devereux, D.A. Egan, Cancer Lett. in press, 2006, doi:10.1016/j.canlet.2006.08.009.
[16] C. Deegan, M. McCann, M. Devereux, B. Coyle, D. Egan. Chemico-Biol. Interact., in press, 2006, doi:10.1016/j.cbi.2006.08.025.
[17] C. Deegan, M. McCann, M. Devereux, B. Coyle, D. Egan, Cancer Lett., in press, 2006, doi:10.1016/j.canlet.2006.04.006.
[18] A. Kellett, Ph.D. thesis, The Institute of Technology, Tallaght Dublin, Ireland, 2006.
[19] B. Coyle, P. Kinsella, M. McCann, M. Devereux, R. O'Connor, M. Clynes, K. Kavanagh, Toxicol. In Vitro 18 (2004) 63.
[20] M. Geraghty, V. Sheridan, M. McCann, M. Devereux, V. McKee, Polyhedron 18 (1999) 2931.
[21] V.F. Hanic, J. Michalov, Acta Crystallogr. 13 (1960) 299.

[22] R. Whyman, W.E. Hatfield, C.S. Fountain, Inorg. Chim. Acta 1 (1964) 429.
[23] F.A. Cotton, G. Wilkinson (Eds.), Advanced Inorganic Chemistry, 6th edn., Wiley, New York, 1999, p. 867.
[24] U. Schatzschneider, T. Weyhermüller, E. Rentschler, Inorg. Chim. Acta 337 (2002) 122.
[25] S. Takamizawa, E. Nakata, H. Yokoyama, Inorg. Chem. Comm. 6 (2003) 763.
[26] K. Deka, R.J. Sarma, J.B. Baruah, Inorg. Chem. Commun. 9 (2006) 931.
[27] H. Koizumi, K. Osaki, T. Watanabé, J. Phys. Soc. Jpn. 18 (1963) 117.
[28] M. Inoue, M. Kishita, M. Kubo, Inorg. Chem. 3 (1964) 239.
[29] M.T. Casey, M. McCann, M. Devereux, M. Curran, C. Cardin, M. Convery, V. Quillet, C. Harding, J. Chem. Soc., Chem. Commun. (1994) 2643.
[30] K. Nakamoto, Infrared and Raman Spectra of Inorganic and Coordination Compounds, 5th ed., John Wiley and Sons, 1997.
[31] M.S. Refat, I.M. El-Deen, H.K. Ibrahim, S. El-Ghool, Spectrochimica Acta, Part A 65 (2006) 1191.
[32] G.B. Deacon, R.J. Philips, Coord. Chem. Rev. 33 (1980) 227.
[33] B.N. Figgis, Introduction to Ligand Fields, Interscience, New York, 1966.
[34] M. Devereux, M. McCann, V. Leon, V. McKee, R.J. Ball, Polyhedron 21 (2002) 1063.
[35] M. Devereux, M. McCann, M.T. Casey, M. Curran, International Patent (1994) IPA No. S940892.
[36] Y. Naruta, K. Maruyama, J. Chem. Soc., Chem. Commun. (1994) 2667.
[37] M. Curan, Ph.D. Thesis, National University of Ireland, 1996.
[38] S. Goldstein, G. Czapski, in: Free Radicals – A Practical Approach, Oxford University Press, UK, 1996, p. 52.
[39] U. Weser, K.H. Sellenger, E. Lengfelder, W. Werner, J. Strähle, Biochim. Biophys. Acta 631 (1980) 232.
[40] J.F. Weder, C.T. Dillon, T.W. Hambley, B.J. Kennedy, P.A. Lay, J.R. Biffin, H.L. Regtop, N.M. Davies, Coord. Chem. Rev. 232 (2002) 95.
[41] IVS Annual; MIMS Publishing, Crows Nest, NSW, Sydney, 1997, p. 145, 276.
[42] J.E. Weder, T.W. Hambley, B.J. Kennedy, P.A. Lay, D. Maclachlan, R. Brambley, C.D. Delfs, K.S. Murray, B. Moubaraki, B. Warick, J.R. Biffin, H.L. Regtop, Inorg. Chem. 38 (1999) 1736.
[43] A.L. Abuhijleb, J. Inorg. Biochem. 68 (1997) 167.
[44] A.L. Abuhijleh, C. Woods, Inorg. Chem. Commun. 5 (2002) 269.
[45] M. Goodman, L.I.B. Haing, J. Chem. Soc., A (1966) 174.
[46] R.S. So, A.A. Adjei, J. Clin. Oncol. 17 (1999) 409.
[47] B. Rosenberg, Metal Ions Biol. Syst. 11 (1980) 127.
[48] T. Hirohama, Y. Kuranuki, E. Ebina, T. Sugizaki, H. Arii, M. Chikira, P.T. Selvi, M. Palaniandavar, J. Inorg. Biochem. 99 (2005) 1205.
[49] A. Rivero-Müller, A. De Vizcaya-Ruiz, N. Plant, L. Ruiz, M. Dobrota, Chemico-Biol. Interact., 2006 doi:10.1016/j.cbi.2006.12.002.
[50] Bruker AXS. APEX2 and SHELXTL, Bruker AXS Inc., Madison, WI, USA, 2004.
[51] T. Mosmann, J. Immunol. 65 (1983) 55.



Scheme 1.

voltammograms were recorded using a CH Instruments 660 electrochemical workstation. 200 MHz ^{1}H and 50 MHz ^{13}C NMR spectra were obtained at room temperature in $CDCl_3$ using a Varian 200.

Caution: Although we have experienced no difficulties with the perchlorate salts, these should be regarded as potentially explosive and handled with care.

2.2. Synthesis of 1,8-bis(nicotinyloxy)-9,10-anthracenedione (1)

2.00 g (16.3 mmol) of nicotinic acid was stirred in 15 mL thionyl chloride with formation of a white precipitate. Pyridine was added (~20 mL) to yield a clear solution and excess thionyl chloride was removed using a stream of air. 1.95 g (8.12 mmol) of 1,8-dihydroxyanthraquinone in 30 mL of pyridine was added and the solution stirred for 10 min. This mixture was poured into cold water and the resulting precipitate filtered, washed with water and air dried. Yield: 3.6 g (~96%). Melting point = 228–31 °C. ^{1}H NMR: 7.19 (d, 2H, 5-pyridine rings); 7.51 (d, 2H, 2,7-anthraquinone); 7.81 (t, 2H, 3,6-anthraquinone); 8.20 (d, 2H, 4-pyridine rings); 8.27 (d, 2H, 4,5-anthraquinone); 8.69 (d, 2H, 6-pyridine rings); 9.16 (d, 2H, 2-pyridine rings). ^{13}C NMR: δ 123.2, 125.4, 125.8, 130.2, 134.4, 134.94, 137.4, 149.8, 151.2, 153.6, 163.7. Elemental *Anal.* Calc. for $C_{26}H_{14}N_2O_6$: C, 69.33; H, 3.13, N, 6.22. Found: C, 69.17; H, 3.24; N, 6.10%.

2.3. Synthesis of 1,8-bis(thiazolyloxy)-9,10-anthracenedione (2)

Thiazole-4-carboxylic acid was purchased from Aldrich and reacted with 1,8-dihydroxyanthraquinone in a procedure identical to **1**, yielding a yellow solid in 98% yield. Melting point = 260–262 °C. ^{1}H NMR: 7.59 (d, 2H, 2,7-anthraquinone), 7.81 (t, 2H, 3,6-anthraquinone), 8.25 (d, 2H, 4,5-anthraquinone), 8.31 (d, 2H, 5-thiazole rings), 8.83 (d, 2H, 2-thiazole ring). Elemental *Anal.* Calc. for $C_{22}H_{10}N_2O_6S_2$: C, 57.14; H, 2.18; N, 6.06. Found: C, 56.63; H, 2.04; N, 5.97%.

2.4. Synthesis of [1,8-bis(nicotinyloxy)-9,10-anthracenedione · 2H](ClO$_4$)$_2$ (3)

Crystals of **3** are obtained by dissolving **1** in acetonitrile in the presence of a drop of concentrated perchloric acid. Lemon yellow colored crystals were obtained upon slow evaporation of the solvent. Elemental analyses confirm that the diprotonated form is produced. Melting point = 148–150 °C. Elemental *Anal.* Calc. for $C_{26}H_{16}N_2Cl_2O_{14}$: C, 47.95; H, 2.48; N, 4.30. Found: C, 48.09; H, 2.39; N, 4.53%. ESI-MS calculated for $[\mathbf{1}\cdot H]^+ = 451.4$; found 451.07 *m*/*z*.

2.5. Synthesis of [(1,8-bis(nicotinyloxy)-9,10-anthracenedione)$_2$ · Cd · (CH$_3$CN)$_2$](ClO$_4$)$_2$ (4)

0.040 g (0.088 mmol) of **1** was dissolved in 25 mL of CH_2Cl_2 and 0.014 g (0.044 mmol) of $Cd(ClO_4)_2\cdot H_2O$ in 10 mL CH_3CN was added to the ligand solution drop wise. The mixture was stirred for 3 h. A pale yellow colored solid was obtained, filtered and washed with diethyl ether. The solid was recrystallized in warm CH_3CN and yellow crystals were obtained. Melting point = 278–81 °C. ^{1}H NMR: 7.59 (d, 2H, 5-from pyridine); 7.81 (d, 2H, 2,7-anthraquinone); 8.12 (t, 2H, 3,6-anthraquinone); 8.53–8.57 (m, 4H, 4-pyridine rings + 4, 5-anthraquinone), 8.95 (d, 2H, 6-pyridine); 9.39 (s, 2H, 2-pyridine rings). ^{13}C NMR: δ 125.7, 127.7, 132.1, 136.3, 137.0, 140.2, 145.6, 151.6, 152.4, 154.9, 165.6. Elemental *Anal.* Calc. for $[Cd(\mathbf{1})_2(CH_3CN)_2](ClO_4)_2$; $C_{56}H_{34}N_6O_{20}Cl_2Cd$: C, 51.96; H, 2.65; N, 6.49. Found: C, 51.52; H, 2.46; N, 6.51%. ESI-MS calculated for $[Cd(\mathbf{1}_2)(ClO_4)]^+ = 1112.7$; found 1112.68 *m*/*z*.

2.6. Synthesis of [{1,8-bis(thiazolyloxy)-9,10-anthracenedione}Pb](ClO$_4$)$_2$ (5)

0.150 g (0.324 mmol) of ligand **2** was dissolved completely in 25 mL of a $CHCl_3/CH_3OH$ mixture (2:1 ratio). 0.149 g (0.324 mmol) of $Pb(ClO_4)_2\cdot 3H_2O$ was dissolved in 10 mL of CH_3OH and added to the ligand solution dropwise. The solution turns orange-brown and the mixture was stirred for 3 h and the solvent removed. The dried product was dissolved in CH_3CN and crystallized by vapor diffusion using diethyl ether. Elemental *Anal.* Calc. for $[Pb(\mathbf{2})](ClO_4)_2$; $C_{22}H_{10}Cl_2N_2O_{14}PbS_2$: C, 30.42; H, 1.16; N, 3.22. Found: C, 30.69; H, 1.42; N, 3.25%.

2.7. Synthesis of RuCl$_2$(1,8-bis(nicotinyloxy)-9,10-anthracenedione)(DMSO)$_2$ (6)

cis-$RuCl_2(DMSO)_4$ [19] (0.248 g, 0.51 mmol) and **1** (0.231 g, 0.51 mmol) were mixed in 40 mL of benzene and refluxed for 5 h. The mixture was cooled to room temperature and all solvent removed under reduced pressure. The residue was dissolved in 10 mL of methylene chloride and mixed with hexane. A yellow colored solid was

obtained, filtered and air dried. The product was dissolved in 20 mL of chloroform–methanol (8:2) mixture and diffused with hexane. Fine orange-colored blocks were obtained. Yield: 0.3 g (75%) and the melting point = 240–245 °C (dec.). ^{1}H NMR: δ 3.32 (s, 12H, coordinated DMSO); 7.45 (t, 2H, 5-pyridine); 7.60 (d, 2H, 2,7-anthraquinone); 7.86 (t, 2H, 3, 6 from anthraquinone); 8.24 (d, 2H, 4-pyridine); 8.39 (d, 2H, 4,5-anthraquinone); 9.95 (d, 2H, 6-pyridine) and 10.49 (s, 2H, 2-pyridine). ^{13}C NMR ($CDCl_3$, 25 °C): δ 45.2 (S-coordinated DMSO); 124.1, 125.9, 125.8, 127.0, 130.6, 134.5, 134.8, 139.2, 149.1, 154.5, 157.9, 163.5, 180.5, 181.6. Elemental *Anal*. Calc. for [Ru(**1**)Cl_2(DMSO)$_2$]; $C_{30}H_{26}Cl_2N_2O_8S_2Ru$: C, 46.28; H, 3.37; N, 3.60; S, 8.23. Found: C, 45.86; H, 3.81; N, 3.59; S, 7.67%. ESI-MS calculated for [Ru(**1**)Cl_2(DMSO)$_2$]: 778.7; found 779.00 *m*/*z*.

2.8. Synthesis of [Ru(1,8-bis(nicotinyloxy)-9,10-anthracenedione)(bpy)$_2$Cl]ClO$_4$ (7)

cis-$RuCl_2(bpy)_2 \cdot 2H_2O$ [20] (0.2311 g, 0.44 mmol) and ligand **1** (0.29 g, 0.44 mmol) were mixed together in 30 mL of 95% ethyl alcohol. This mixture was refluxed for 8 h under nitrogen atmosphere with constant stirring. The solution was cooled to room temperature and the solvents were evaporated under reduced pressure. The residue was dissolved in 10 mL of methanol and mixed with an excess of lithium perchlorate in water. A brick red colored precipitate was obtained. The solid was filtered, washed with a small amount of water, diethyl ether and dried under vacuum. The crude product was recrystallized from hot ethanol–ethyl acetate (2:1). Melting point is >200 °C (dec.). ^{1}H NMR (CD_3CN-d_6): 7.39 (d, 2H, bipyridine); 7.62–8.84 (m, 26H, anthraquinone + bipyridine); 9.78 (s, 2H, 2-pyridine rings). Elemental *Anal*. Calc. for [Ru(**1**)-(bpy)$_2$Cl]ClO_4; $C_{46}H_{30}N_6O_{10}RuCl_2$: C, 55.33; H, 3.00; N, 8.41. Found: C, 55.12; H, 3.05; N, 8.31%. ESI-MS calculated for $[RuCl(bpy)_2(\mathbf{1})]^+ = 899.3$; found 899.17 *m*/*z*.

2.9. X-ray crystallography

Crystallographic data for **3** and **4** were collected at 293(2) K using Mo Kα radiation on a Nonius CAD4 serial diffractometer. Cell constants were calculated from 25 reflections. Psi-scan data were used for absorption corrections. Date reduction and refinement were completed using the WinGX suite of crystallographic software [21,22]. Structures were solved using SIR-97 [23]. All hydrogen

Table 1
Crystallographic and refinement data for 1,8-bis(thiazolyl)anthraquinone (**2**); [1,8-bis(nicotinyloxy)anthraquinone · 2H](ClO$_4$) (**3**); [{1,8-bis(nicotinyloxy)anthra-quinone}$_2$Cd · (CH$_3$CN)$_2$](ClO$_4$)$_2$ · H$_2$O · CH$_3$CN (**4**); and [(1,8-bis(thiazolyloxy)anthra-quinone)Pb · CH$_3$CN · H$_2$O](ClO$_4$)$_2$ (**5**)

Compound	**2**	**3**	**4**	**5**
Empirical formula	$C_{22}H_{10}N_2O_4S_2$	$C_{26}H_{16}Cl_2N_2O_{14}$	$C_{58}H_{39}CdCl_2N_7O_{21}$	$C_{24}H_{15}Cl_2N_3O_{15}PbS_2$
Formula weight	462.44	1302.62	1353.26	927.60
System	Bruker CCD	Nonius CAD4	Nonius CAD4	Bruker CCD
Temperature (K)	173(2)	293(2)	293(2)	173(2)
Crystal system	orthorhombic	triclinic	triclinic	monoclinic
Space group	*Fd2d*	$P\bar{1}$	$P\bar{1}$	$P2_1/c$
a (Å)	5.1086(3)	7.980(5)	10.284(3)	8.2738(10)
b (Å)	24.6716(17)	18.083(15)	14.466(2)	18.497(2)
c (Å)	29.944(2)	20.064(17)	19.851(5)	19.150(2)
α (°)		65.35(7)	89.987(20)	
β (°)		78.70(7)	98.350(29)	96.184(2)
γ (°)		81.89(6)	101.915(16)	
Volume (Å^3)	3774.1(4)	2574.6	2857.6	2913.8(6)
Z	8	2	2	4
D_{calc} (g cm^{-3})	1.628	1.680	1.573	2.115
Absorption coefficient (mm^{-1})	0.330	0.335	0.563	6.198
F(000)	1888	1328	1372	1792
θ Range (°)	2.14–25.05	1.13–24.97	1.04–25.17	1.5–27.5
Index ranges	$-6 \leqslant h \leqslant 5$, $-28 \leqslant k \leqslant 28$, $-35 \leqslant l \leqslant 35$	$0 \leqslant h \leqslant 9$, $-20 \leqslant k \leqslant 21$, $-22 \leqslant l \leqslant 23$	$0 \leqslant h \leqslant 12$, $-17 \leqslant k \leqslant 16$, $-23 \leqslant l \leqslant 23$	$-9 \leqslant h \leqslant 10$, $24 \leqslant k \leqslant 24$, $-22 \leqslant k \leqslant 24$
Independent reflections	7359	9061	10269	6640
Observed reflections	1658	7159	6136	5615
Maximum/minimum transmission	1.0/0.89	0.90/0.825	0.89/0.87	0.64/0.16
Data/restraints/parameters	7359/1/147	9061/0/810	10269/0/837	6640/0/425
Goodness-of-fit	1.22	1.177	1.024	1.027
Final *R* indices [$I > 2\sigma(I)$]	0.0393	0.0854	0.0530	0.0566
R indices (all data)	0.0766	0.1099	0.1310	0.1562
Peak/hole (e Å^{-3})	0.22/−0.23	1.10/−0.45	0.71/−0.65	4.1/−2.8

atoms were placed in ideal positions and refined as riding atoms with relative isotropic displacement parameters. Table 1 lists additional crystallographic and refinement information. Compound **3** has one perchlorate, Cl(4), disordered over two positions in a 84:16 ratio. Crystals of compound **4** have one perchlorate rotationally disordered around the O(15)–Cl(1) bond in a 70:30 ratio, and a second perchlorate is also rotationally disordered around the O(17)–Cl(2) bond in a 77:23 ratio. Crystallographic data for **2** and **5** were collected at 173(2) K using Mo Kα radiation on a Bruker CCD diffractometer. Final cell constants were calculated from the *xyz* centroids of typically more than 3000 reflections from the data collection after integration [24]. Structures were solved by direct methods using SIR-97 [12] and refined using SHELXL-97 [25]. The high residual electron density in **5** is centered around the lead and is due to an absorption correction error. Attempts to correct for the error were unsuccessful.

3. Results

3.1. Synthesis and crystallography

Two new anthraquinone ligands containing nicotinyl (**1**) and thiazolyl (**2**) chelating elements have been synthesized beginning from common, inexpensive starting materials in high yield. Using a simple, one-step synthetic pathway, 1,8-dihydroxyanthraquinone and the corresponding carboxylic acids are condensed in a 1:2 molar ratio via the acid chloride (Scheme 1). Yields are almost quantitative and characterization is complete by NMR, elemental analyses, and X-ray crystallography.

The X-ray crystal structure of **3**, grown by evaporation of **1** in acetonitrile/perchloric acid, confirms the chelating potential of the bipodand and shows that both nicotinyl nitrogens have been protonated (Fig. 1). Hydrogen bonds exist between the protonated nitrogens and the perchlorate anions, N(1)–O(23) = 2.840(8) and N(2)–O(32) = 2.864 (8) Å. The two nicotinyl pyridine rings are parallel to each other with the two pyridine nitrogen atoms facing in opposite directions. The bond distances for the two nicotinyl carbonyls, C(15)–O(4) and C(21)–O(6), are 1.183(8) and 1.186(8) Å, respectively, and they also face in opposite directions. The quinone carbonyl bond distances, C(13)–O(1) and C(14)–O(2), equal 1.212(8) and 1.205(8) Å.

The crystal structure of the anthraquinone ligand (**2**) also confirms that two thiazolyl groups add to form the bis-substituted product (Fig. 2). Each side of the molecule is identical by symmetry and the thiazolyl rings are rotated 66.9° out of the plane of the anthraquinone. Thiazolyl carbonyl oxygen, nitrogen and sulfur atoms face in opposite directions and the anthraquinone is itself virtually planar producing π–π stacks with 3.6–3.7 Å separations. Because thiazole contains both basic nitrogen and sulfur Lewis sites, either heteroatom could potentially chelate with metal ions. Rotation of one of the thiazolyl ligands by 180°, orientates the nitrogens face-up towards the anthraquinone; while the sulfurs could also potentially orientate in a traditional chelating fashion with the opposite conformation of the thiazolyls.

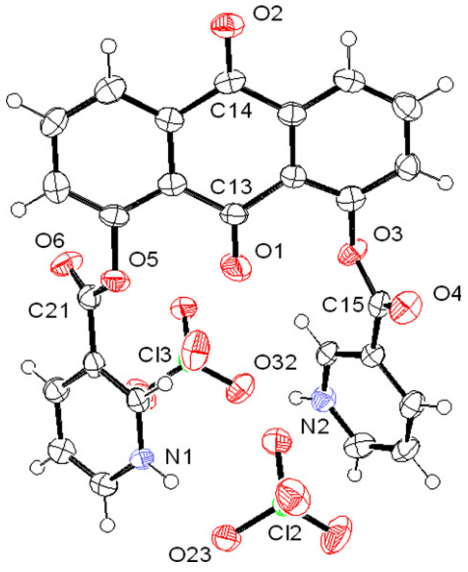


Fig. 1. Thermal ellipsoid diagram (50%) of [1,8-bis(nicotinyl)anthraquinone · 2H](ClO$_4$)$_2$ (**3**). Only one of the protonated 1,8-bis(nicotinyl)-anthraquinone adducts in the asymmetric unit is shown.

Preliminary exploration of the complexation chemistry of these ligands has been conducted using perchlorate salts of transition and main group metal ions and confirms that both **1** and **2** can act as chelating, polydentate ligands. Addition of two equivalents of **1** and one equivalent of cadmium perchlorate yields the bis-chelate complex **4**. Crystals grown from acetonitrile confirm that two bis-nicotinyl anthraquinone ligands chelate the cadmium metal center in an equatorial arrangement, which is capped axially by

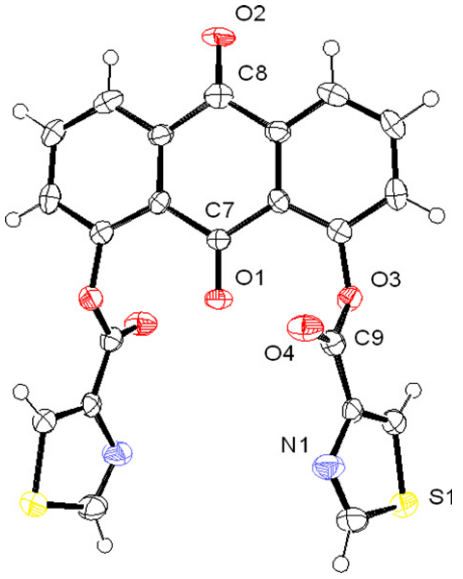


Fig. 2. Thermal ellipsoid diagram (50%) of 1,8-bis(thiazolyl)anthraquinone (**2**).

two acetonitrile ligands in a near perfect octahedral geometry (Fig. 3). Two nearly identical cadmium–nicotinic complexes comprise the asymmetric unit. The bond distances between the nicotinyl nitrogens and the cadmium average 2.36 Å, and the average bond distance between the cadmium and the acetonitrile nitrogen is approximately the same, 2.38 Å. In order to adopt a chelate structure, the nicotinyl carbonyl groups and the pyridine nitrogens orientate '*cis*' with respect to the anthraquinone plane, and the nicotinyl rings are rotated $51 \pm 4°$ out of the plane of the anthraquinone. The plane of the anthraquinone rings are slightly bent (8° and 10°, respectively, for the two complexes found in the asymmetric unit), and packing within the unit cell shows π–π stacking interactions between the anthraquinones (~3.5–3.6 Å separation). All the carbonyl carbon-oxygen bond distances in the structure are 1.20 ± 0.01 Å. Combination of cadmium perchlorate with three equivalents of **1** yields only the bis-substituted complex **4**, which may indicate a steric limitation to the number of bis-substituted anthraquinone ligands that can coordinate to metal centers.

In the case of the dithiolyl ligand **2**, a 1:1 complex forms between Pb^{2+} and **2** when combined together in equal amounts (Fig. 4). Crystals were grown from acetonitrile and show both thiazolyl units bind to the lead ion as a chelating bidentate ligand. A seven-coordinate Pb^{2+} complex forms where the coordination sphere is completed by one acetonitrile solvate, Pb(1)–N(3) = 2.653(9) Å, one H_2O molecule, Pb(1)–O(7) = 2.532(8) Å, and an additional oxygen from a nearby perchlorate anion, Pb(1)–O(8) = 2.837 (10) Å. The sulfur atoms do not participate in bonding in this structure. For the dithiazolyl ligand, bond distances between the thiazolyl nitrogens, N(1) and N(2), and the lead ion are identical, 2.624(8) Å and 2.625(8) Å. Bond distances from the metal to the carbonyl oxygens are unequal, however, Pb(1)–O(5) = 2.556(7) and Pb(1)–O(6) = 2.740(7) Å. To form the chelate, the carbonyl groups of the thiazolyl rings are located on the same side of the anthraquinone plane and the thiazolyls are rotated 53.7° and 61.1° out of the anthraquinone plane. The coordinated carbonyl bond distances are normal, C(15)–O(5) = 1.213(11) and C(19)–O(6) = 1.205(12) Å, and the anthraquinone carbonyl carbon-oxygen bond distances are very similar, C(6)–O(1) = 1.229(11) and C(13)–O(2) = 1.220(12) Å. A carbonyl oxygen, O(2), from a neighboring anthraquinone is the other closest coordinating atom with a bond distance of 3.27 Å from the lead. Hydrogen bonds also form between the water and the two perchlorate anions, O(7)–H···O(11) = 2.846(12) and O(7)–H···O(13) = 2.905(15). The anthraquinone plane is bent by 8.0°, and anthraquinones within the unit cell exhibit π–π stacking (3.7–3.8 Å separations).

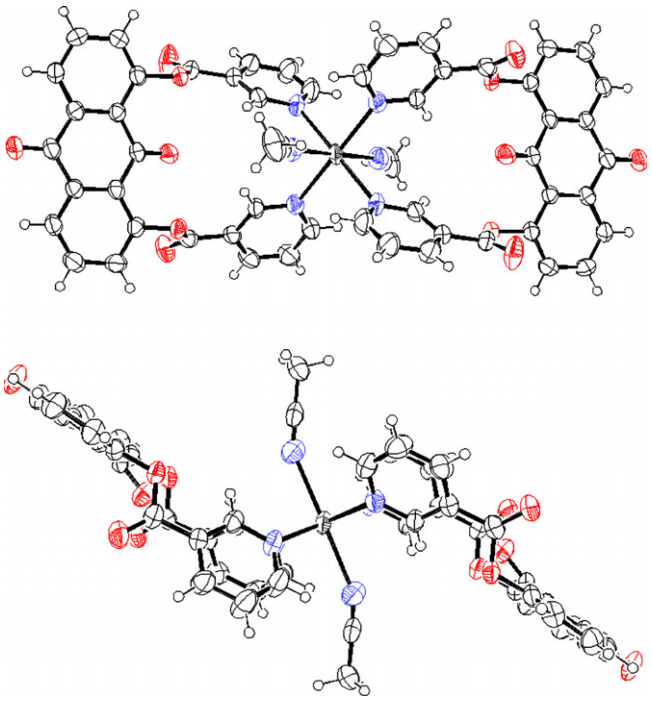


Fig. 3. Thermal ellipsoid diagrams (50%) of $[\{1,8\text{-bis(nicotinyl)anthraquinone}\}_2 \cdot Cd \cdot (CH_3CN)_2](ClO_4)_2 \cdot H_2O \cdot CH_3CN$ (**4**). The solvates and perchlorate anions have been removed for clarity. There are two nearly identical cadmium complexes within the asymmetric unit. Only one is shown.

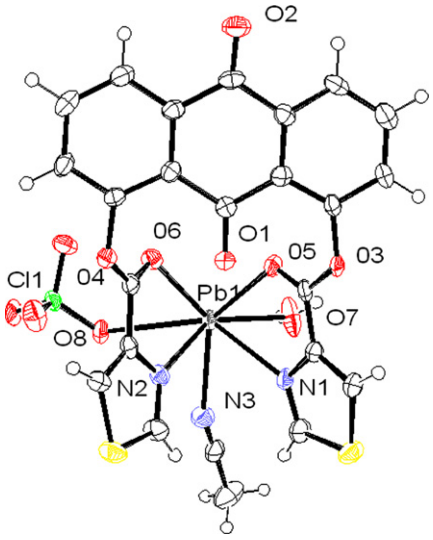


Fig. 4. Thermal ellipsoid diagram (50%) of $[(1,8\text{-bis(thiazolyl)anthraquinone})Pb \cdot CH_3CN \cdot H_2O](ClO_4)_2$ (**5**). One perchlorate anion has been removed for clarity.

3.2. Electrochemistry

$E_{1/2}$ values for free and complexed ligands were obtained by cyclic voltammetry in 0.1 M TBAH in either CH_2Cl_2 or DMF versus Ag/AgCl and are listed in Table 2. In all cases, the first, reversible one-electron reduction of the anthraquinone to the radical anion was observed at approximately −0.70 V in DMF and −0.90 V in CH_2Cl_2. The second one-electron anthraquinone reductions were within −1.03 to −1.14 V. Reduction of com-

Table 2
Electrochemical data at 22 ± 2 °C

Compound	Solvent	$E^{a}_{1/2}$				
		$AQ^{0/-1}$	$AQ^{-1/-2}$	$M^{0/II}$	$Ru^{III/II}$	$Bpy^{0/-1}$
1	CH_2Cl_2	−0.90	−1.14			
	DMF	−0.70	−1.13			
2	CH_2Cl_2	−0.90	−1.12			
	DMF	−0.75	−1.16			
4	DMF	−0.61[b]	−1.03	−0.61[b]		
$[Cd(bpy)_3](PF_6)_2$	DMF			−0.75[c]		
5	DMF		[e]	−0.72[d]		
$[Pb(bpy)_2](PF_6)_2$	DMF			−0.95[d]		
6	CH_2Cl_2	−0.80	−1.13		1.09	
7	CH_2Cl_2	−0.84	−1.14		0.85	−1.58

[a] Referenced vs. Ag/AgCl, glassy carbon, 1 mM, 0.1 M TBAH.
[b] The first one-electron quinone reduction and the cadmium$^{0/II}$ reduction are overlapping, $i_{pc}/i_{pa} = 1.6$, $\Delta E_p = 75$ mV.
[c] Quasi-reversible ($i_{pc}/i_{pa} = 1.5$, $\Delta E_p = 420$ mV).
[d] Irreversible.
[e] Not observed.

pound **4** and **5** were conducted in DMF due to poor solubility in CH_2Cl_2 and is complicated by the reduction of M(II) at the same potential as the first one-electron anthraquinone reduction. This is confirmed by reduction of $[Cd(bpy)_3]^{2+}$ and $[Pb(bpy)_2]^{2+}$ under the same conditions which exhibit either quasi-reversible or irreversible reductions at the same potential [26–28].[1] Similar to **4**, $[Cd(bpy)_3]^{2+}$ has an inner coordination sphere that includes six nitrogen atoms.

Towards the goal of constructing complexes with potential electron transfer properties, ruthenium-containing anthraquinone compounds **6** and **7** were synthesized. Addition of equal molar ratios of **1** and *cis*-$RuCl_2(DMSO)_4$ results in substitution of two of the DMSO ligands by the chelating nicotinyl ligand to form $[RuCl_2(DMSO)_2(\mathbf{1})]$ (**6**). Elemental analyses, mass spectrometry and cyclic voltammetry confirm the formula and the presence of the anthraquinone in the complex. Two one-electron anthraquinone reductions are observed at almost the same potentials as the free ligand with the addition of the ruthenium III/II couple centered at $E_{1/2} = 1.09$ V (Fig. 5a). Reaction of compound **6** with 2,2′-bipyridine did not produce further substitution of the chloride or DMSO ligands, however, even using high boiling solvents such as ethylene glycol. Addition of Ag salts to **6** did not displace chloride, and reactions with an excess of **1** (up to three equivalents) with *cis*-$RuCl_2(DMSO)_4$ produced only compound **6**.

As an alternate route to synthesizing a ruthenium complex containing both an anthraquinone and a complete pyridyl coordination sphere, substitution of the chlorides in *cis*-$RuCl_2(bpy)_2$ by **1** was also attempted. Characterization data show that the resulting product does contain one molecule of **1**; however, only one of the nicotinic nitrogens is complexed to the ruthenium which forms $[RuCl(bpy)_2(\mathbf{1})]^{+}$ (**7**). Both elemental analyses and mass spec data (parent ion) indicate a chloride remains coordinated to the ruthenium and that **1** does not bridge two ruthenium metal centers to form a dimer. Reduction peaks for the anthraquinone as well as the bipyridine ligand are

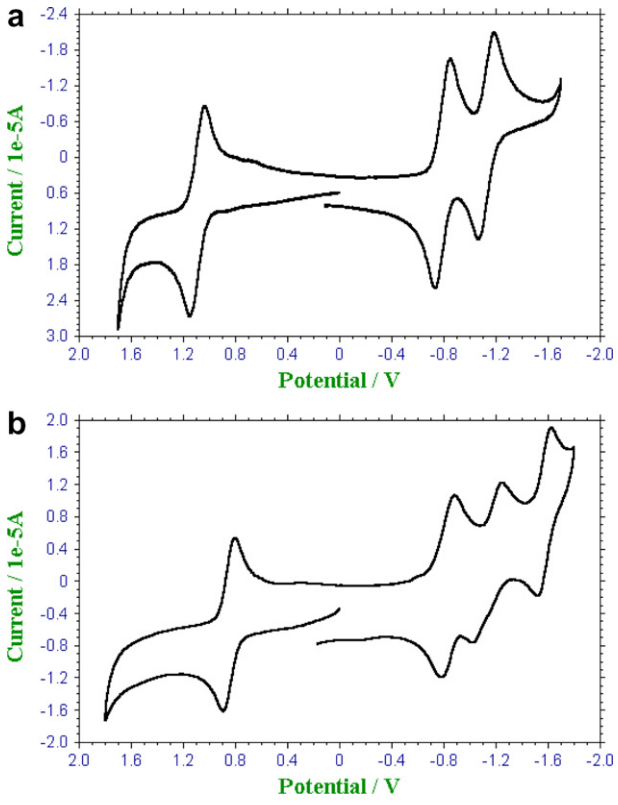


Fig. 5. Cyclic voltammograms of (a) 1.0 mM $[RuCl_2(DMSO)_2(\mathbf{1})]$ (**6**) and (b) 1.0 mM $[RuCl(bpy)_2(\mathbf{1})](ClO_4)$ (**7**) in CH_2Cl_2/0.1 M TBAH vs. Ag/AgCl on glassy carbon.

[1] We have determined that the addition of three equivalents of 2,2′-bipyridine to $Pb(ClO_4)_2$ results in the formation of the bis(bipyridine)lead(II) perchlorate complex. This is consistent with the X-ray structure of this complex reported in Ref. [28]. The X-ray crystal data for the hexafluorophosphate metathesis product, $[Pb(bpy)_2](PF_6)_2$, will be reported elsewhere.

well resolved in addition to the $Ru^{III/II}$ oxidation wave (Fig. 5b).

4. Discussion

Both cadmium(II) and lead(II) complexes of nicotinic acid have been previously synthesized. Often the nitrogen atom on the pyridine ring acts as a Lewis base and forms a number of monodentate ligand metal complexes [29–31]. Bidentate nicotinic cadmium complexes (binding through both the pyridine and carboxylate functionalities) have also been produced resulting in three-dimensional supramolecular structures [30]. Numerous 4,4′-bithiazole and thiazolylbenzimidazole complexes that contain the thiazolyl group have been reported in the literature; however, no metal complexes using thiazolyl itself have been reported; although the same type of bidentate chelating ability as **2** has been previously observed between lead(II) and *ortho*-substituted carboxylato-pyridine ligands [32]. Picolinic acid (containing a pyridine nitrogen located *ortho* to the carboxylic acid group) has the same arrangement of chelating nitrogen and oxygen atoms as thiazolyl and may be expected to exhibit the same type of coordination chemistry as **2**. However, we have been unsuccessful in synthesizing the disubstituted, picolinic–anthraquinone derivative, when substituting picolinic acid for nicotinic acid under the same reaction conditions as in the preparation of **1**.

On two occasions steric limitations in the coordination of these new ligands to metal centers have been observed. In the first case, only the bis-substituted complex **4** (Fig. 3) can be produced, even when an excess of **1** is employed in the synthesis, and the two chelating anthraquinone ligands remain decidedly *trans* to one another. In the second case, substitution of *cis*-$RuCl_2(bpy)_2$ with **1** does not produce a chelate complex, rather the anthraquinone ligand remains monodentate, even after extended treatment in higher boiling solvents.

The work by Hambley and co-workers [1] and Meyer and co-workers [18] report anthraquinones that are pendent to either cyclam or bipyridine groups coordinated to metal cations. The anthraquinones attached to these ligands are connected via short alkane or amide linkages. Crystallographic studies in the case of Hambley's anthraquinone–cyclam structure [1] show a metal–quinone carbonyl oxygen interatomic distance of 6.2 Å. Crystallographic data for Meyer's $[(AQbpy)Ru(bpy)_2]^{2+}$ complex is not available; however, molecular modeling studies indicate a metal–quinone oxygen interatomic distance ranging from 9 to 13 Å, depending upon the conformation of the connecting chain. In comparison, the interatomic, through-space distances between the metal centers and the intraannular anthraquinone carbonyl oxygen in **4** and **5** are much shorter than previously observed. In **4** this distance equals 5.6 Å, while the interatomic distance between the lead and the carbonyl oxygen in **5** is much shorter due to coordination of the thiazolyl carbonyl oxygen and is equal to 4.4 Å. However, electrochemical evidence suggests that no electrostatic communication between the metal centers and the quinones are established. Although the first one-electron reduction in **4** is obscured by the overlapping $cadmium^{0/II}$ reduction, the second one-electron reduction is still observed at approximately the same reduction potential as the free ligand. The close proximity of the electropositive metal center near the intraannular quinone oxygen would produce an anodic shift in reduction potential, which does not seem to occur for **4**. For **5** where the anthraquinone carbonyl is much closer to the metal center (4.4 Å), the second one-electron reduction is unfortunately not observed likely due to passivation of the electrode surface by the $Pb^{0/II}$ reduction at -0.72 V making any metal–quinone interaction unobservable. The first one-electron reductions in the ruthenium complexes **6** and **7** are observed at slightly more anodic potentials than the free ligands, but this can be attributed to an electronic inductive effect due to the greater charge-to-size ratio of the ruthenium metal center. The potentials of the second one-electron reductions in **6** and **7** remain unchanged.

5. Conclusion

Two new chelating anthraquinone ligands have been made and the complexation chemistry with transition and main group metals has been explored. Nicotinyl and thiazolyl ligands, pendent to the anthraquinone, are free to rotate as observed by the '*trans*' conformations in the protonated and free ligands (structures **2** and **3**) versus the '*cis*' conformations of the metal complexes **4** and **5**. These new ligands represent a new architecture that involves a chelating approach rather than singly-attached pendant anthraquinones as has been demonstrated in the past and should be amenable to incorporation into a wide variety of different metal complexes and applications. Two different chelating geometries have been demonstrated: (a) using the bidentate chelating anthraquinone–nicotinyl ligand **1**, and (b) using the tetradentate chelating anthraquinone-thiazolyl ligand **2**, which has not previously been demonstrated. Quinone reduction chemistry is complicated by overlapping metal-centered reductions, but initial results indicate that electrostatic interaction between the metal center and the intraannular carbonyl does not take place. We are currently exploring the synthesis of other bis and possibly tris-substituted anthraquinone complexes using ligands of this type. We are also pursuing the coordination chemistry of the 1,8-bis(isonicotinyl)anthraquinone derivative, where the pyridine nitrogens are located in the *para* positions and has the potential to form new bridging anthraquinone metal complexes.

Acknowledgments

The authors thank the National Science Foundation (0082978) and the South Dakota 2010 Initiative for finan-

cial support. We also thank the University of South Dakota and NSF-EPSCOR (9720642 and 0091948) for the purchase and upgrade of a Nonius CAD4 X-ray diffractometer, and Benjamin Kucera and the University of Minnesota X-ray Diffraction Laboratory for help with structure determinations. The elemental analyzer was purchased using NSF-URC funding (CHE-0532242).

Appendix A. Supplementary material

CCDC 637400, 637397, 637398 and 637399 contain the supplementary crystallographic data for **2**, **3**, **4** and **5**. These data can be obtained free of charge via http://www.ccdc.cam.ac.uk/conts/retrieving.html, or from the Cambridge Crystallographic Data Centre, 12 Union Road, Cambridge CB2 1EZ, UK; fax: (+44) 1223-336-033; or e-mail: deposit@ccdc.cam.ac.uk. Supplementary data associated with this article can be found, in the online version, at doi:10.1016/j.poly.2007.05.012.

References

[1] L.T. Ellis, D.F. Perkins, P. Turner, T.W. Hambley, Dalton Trans. (2003) 2728.
[2] E. Boseggia, M. Gatos, L. Lucatello, F. Mancin, S. Moro, M. Palumbo, C. Sissi, P. Tecilla, U. Tonellato, G. Zagotto, J. Am. Chem. Soc. 126 (2004) 4543.
[3] I.R. Butler, A.G. Callabero, G.A. Kelly, J.R. Amey, T. Kraemer, D.A. Thomas, M.E. Light, T. Gelbrich, S.J. Coles, Tetrahedron Lett. 45 (2004) 467.
[4] E.M. McGale, B.H. Robinson, Simpson, J. Organomet. 22 (2003) 931.
[5] M. Murata, M. Yamada, T. Fujita, K. Kojima, M. Kurihara, K. Kubo, Y. Kobayashi, H. Nishihara, J. Am. Chem. Soc. 133 (2001) 12903.
[6] H.M. Ali, S. Nadiah, A. Halim, S. Koushik, S.W. Ng, Acta Crystallogr., Sect. E 61 (2005) ml431.
[7] H.M. Ali, S. Nadiah, A. Halim, S. Koushik, N.H. Lajis, W.J. Basirun, S.W. Ng, Acta Crystallogr., Sect. E 61 (2005) m691.
[8] T. Moriuchi, T. Watanabe, I. Ikeda, A. Ogawa, T. Hirao, Eur. J. Inorg. Chem. (2001) 277.
[9] M.J. Maroney, R.O. Day, T. Psyris, L.M. Fleury, J.P. Whitehead, Inorg. Chem. 28 (1989) 173.
[10] M. Kadarkaraisamy, A.G. Sykes, Polyhedron 26 (2007) 1323.
[11] Z. Liu, A.G. Sykes, J. Chem. Crystallogr. 36 (2006) 875.
[12] M. Kadarkaraisamy, A.G. Sykes, Inorg. Chem. 45 (2006) 779.
[13] M. Kadarkaraisamy, E. Dufek, D. Lone Elk, A.G. Sykes, Tetrahedron 61 (2005) 479.
[14] B. Kampmann, Y. Lian, K. Klinkel, P.A. Vecchi, H.L. Quiring, C.C. Soh, A.G. Sykes, J. Org. Chem. 67 (2002) 3878.
[15] V. Young Jr., A.G. Sykes, Inorg. Chem. 37 (1998) 376.
[16] V.G. Young, H.L. Quiring, A.G. Sykes, J. Am. Chem. Soc. 119 (1997) 12477.
[17] W. Nakanishi, S. Hayashi, N. Itoh, J. Org. Chem. 69 (2004) 1676.
[18] K.A. Opperman, S.L. Mecklenburg, T. Meyer, J. Inorg. Chem. 33 (1994) 5295.
[19] P. Evans, A. Spencers, G. Wilkinson, J. Chem. Soc., Dalton Trans. (1973) 204.
[20] B.P. Sullivan, D.J. Salmon, T. Meyer, J. Inorg. Chem. 17 (1978) 3334.
[21] L.J. Farrugia WinGX: An Integrated System of Windows Programs for the Solution, Refinement, and Analysis of Single Crystal X-ray Diffraction Data, Ver. 1.70, J. Appl. Crystallogr. 32 (1999) 837.
[22] G.M. Sheldrick, SHELX-97: Programs for Crystal Structure Analysis (Release 97-2), Institüt für Anorganische Chemie der Universität, Tammanstrasse 4, D-3400, Göttingen, Germany, 1998.
[23] A. Altomare, M.C. Burla, M. Camalli, G.L. Cascarano, C. Giacovazzo, A. Guagliardi, A.G.G. Moliterni, G. Polidori, R. Spagna, J. Appl. Crystallogr. 32 (1999) 115.
[24] SAINT V6.1, Bruker Analytical X-ray Systems, Madison, WI, 1999.
[25] SHELXTL-Plus V5.10, Bruker Analytical X-ray Systems, Madison, WI, 1998.
[26] J.B. Chlistunoff, A. Bard, J. Inorg. Chem. 32 (1993) 3521.
[27] N. Kunda, D. Mandal, M. Chaudhury, E.R. Tiekink, Appl. Organomet. Chem. 19 (2005) 1268.
[28] L.M. Engelhardt, J.M. Harrowfield, H. Miyanae, J.M. Patrick, B.M. Skelton, A.A. Soudi, A.H. White, Aust. J. Chem. 49 (1996) 1111.
[29] Z.Y. Fu, X.T. Wu, J.C. Dai, L.M. Wu, C.P. Cui, S.M. Hu, Chem. Commun. (2001) 1856.
[30] G. Yang, H.G. Zhu, B.H. Liang, X.M. Chen, J. Chem. Soc., Dalton Trans. (2001) 580.
[31] Y. Zhou, W. Bi, X. Li, J. Chen, R. Cao, M. Hong, Acta Crystallogr., Sect. E 59 (2003) m356.
[32] K.A. Beveridge, G.W. Bushnell, Can. J. Chem. 57 (1979) 2498.

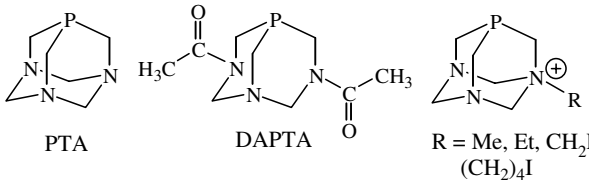


Fig. 1. 1,3,5-Triaza-7-phosphaadamantane (PTA) and some of its derivatives.

has recently been extensively studied [9]. While the water-solubility of PTA is approximately 1.5 M [10], the solubility of its complexes is variable and is sometimes extremely low [11]. This is problematic in that its ultimate utility is as a ligand for aqueous catalysis. In fact, PTA complexes have recently been shown to catalyze many hydrogenations reactions [12] and the intramolecular hydroamination of alkynylamines [11a,13] in water (see Fig. 1).

In an effort to enhance the water-solubility of the phosphine and its metal complexes, PTA has been derivatized by reacting it with acetic anhydride [10], MeI [8] or MeO-SO_2CF_3 [14], EtI [15], $I(CH_2)_4I$ [16], and $PhCH_2Cl$ [17] to respectively form the di-*N*-acylated compound 3,7-diacetyl-1,3,7-triaza-5-phosphabicyclo[3.3.1]nonane (DAPTA), and the *N*-alkylated compounds [PTA(R)]X (R = Me, Et, $(CH_2)_4I$, and CH_2Ph). A library of water-soluble ligands, such as this, is important in that it allows for the preparation of a series of metal complexes that differs by only the phosphine, and this may permit the electronic properties of the compounds to be tuned. For example, it was recently shown that the oxidation potentials of $[CpRuL_2X]$ (L = PTA, $PTA(Me)^+$; X = I, Cl) complexes could be raised by over 300 mV by switching from PTA to $[PTA(Me)]^+$ [18].

To further add to the existing library of water-soluble phosphines, the di-*N*-formylated analog of DAPTA, 3,7-diformyl-1,3,7-triaza-5-phosphabicyclo[3.3.1]nonane (**1**, DFPTA), and the *N*-methylpyridyl derivative of PTA, 1-pyridylmethyl-3,5-diaza-1-azonia-7-phosphatricyclo[3.3.1.1]decane bromide (**2**, [pymePTA]Br) were prepared, fully characterized, and their solubilities explored. Compound **1** is only the second acyl derivative of PTA to be prepared while **2** is only the second derivative of PTA reported that contains an aromatic appendage. The findings of this study are presented herein.

2. Experimental

2.1. Methods, measurements, and materials

All manipulations were carried out under a purified N_2 atmosphere with use of standard Schlenk techniques unless otherwise noted. This airless procedure was used even though the final compounds were air stable. Elemental analyses were carried out by Galbraith Laboratories, Inc., Knoxville, TN. Fast atom bombardment mass spectrometric (FAB-MS) experiments were carried out at Michigan State University with the use of a JEOL HX-110 double-focusing mass spectrometer. Infrared spectra were measured in KBr pellets on a Jasco 460 Plus spectrometer. ^1H and $^{13}C\{^1H\}$ NMR spectra were recorded at 300 MHz and 75.5 MHz respectively, with use of a Bruker ARX 300 MHz spectrometer. $^{31}P\{^1H\}$ NMR spectra were recorded at 121.5 MHz on a Varian Mercury 300 MHz spectrometer. The ^{13}C and ^{31}P spectra were run with proton decoupling and ^{31}P spectra are reported in ppm relative to an external H_3PO_4 standard, with positive shifts down field. ^{13}C NMR spectra are reported in ppm relative to external tetramethylsilane (TMS), with positive shifts downfield. The solvents were distilled and dried prior to use. Formic acid, 1,3-dicyclohexylcarbodiimide (DCC), and 2-bromomethylpyridine hydrobromide were obtained from Aldrich and used without further purification. 1,3,5-Triaza-7-phosphaadamantane (PTA) was prepared as described in the literature [8].

2.2. Synthesis of compounds

2.2.1. 3,7-Diformyl-1,3,7-triaza-5-phosphabicyclo[3.3.1]heptane (*1*, DFPTA)

A 100 mL Schlenk flask was charged with a 6.56 g (31.8 mmol) sample of 1,3-dicyclohexylcarbodiimide (DCC) and 25 mL diethyl ether and put into a −5 °C KCl-ice bath. A separate 100 mL Schlenk flask was charged with 2.50 mL formic acid (66.3 mmol) and 25 mL diethyl ether and put into a −5 °C KCl-ice bath. The DCC solution was added to the formic acid under N_2 over a 10 min period to form a colorless solution of formic anhydride and solid 1,3-dicyclohexylurea. A 250 mL round-bottom flask equipped with a jacketed frit, gas inlet, and rubber septum was charged with 1.01 g PTA (6.43 mmol) and 20 mL H_2O. The jacketed frit and round-bottom flask were then cooled to −5 °C. After stirring for 90 min at −5 °C, the formic anhydride/1,3-dicyclohexylurea slurry was transferred under N_2 to the jacketed frit. This mixture was filtered over a 10-min period into the 250 mL round-bottom flask to remove the 1,3-dicyclohexylurea. After stirring for 15 min at −5 °C, vacuum was applied to the reaction for 30 min to remove the diethyl ether. After this time, the solution was stirred at 0 °C for an additional 30 min. The cloudy solution was cold filtered in the air into a 100 mL round bottom flask that was previously cooled to 0 °C. Over a 10 min period, 6.85 mL of cold $NHEt_2$ (66.2 mmol) was added dropwise to deprotonate any remaining formic acid. The solution was transferred to the rotary evaporator and vacuum was applied at 5 °C. Under vacuum, the solution was allowed to gradually warm to 20 °C and ultimately to 35 °C. The solvents were removed in vacuo to form a white residue. 10 mL of 95% EtOH was added to the flask to dissolve any ammonium salts that may have formed during the workup. The slurry was stirred for 15 min and filtered on a medium frit. The resulting white solid was washed with EtOH (2 × 5 mL), DMSO to remove unreacted PTA

(2×3 mL), and Et_2O (3×5 mL), and dried in vacuo (yield: 655 mg, 3.25 mmol: 50.5% calculated for PTA). Compound **1** was recrystallized by two methods. Needles that were not suitable for X-ray analysis were grown by layering a CH_2Cl_2 solution of **1** with Et_2O. X-ray quality crystals of **1** were prepared by the slow evaporation of solvent from a CH_2Cl_2 solution. Data for **1** were as follows. Elemental *Anal*. Calc. for $PO_2N_3C_7H_{12}$ (mol. wt. 201.17): C, 41.79; H, 6.01; N, 20.89. Found: C, 41.42; H, 6.01; N, 20.37%. IR (KBr): ν(C=O) 1670 (br) cm^{-1}; ν(C(O)–H) 2785, 2801 (br) cm^{-1}. ^1H NMR ($CDCl_3$, 20 °C): δ 3.39 (m, $J_{H^AH^B} = 2.6$ Hz, $J_{PH} = 15.4$ Hz, 1H, PCH^AH^BN); δ 3.75 (d, $J_{PH} = 11.7$ Hz, 2H, PCH_2N); δ3.85 (d of d, $J_{H^AH^B} = 2.6$Hz, $J_{PH} = 15.4$ Hz, 1H, PCH^AH^BN); δ 4.09 (d, $J_{H^AH^B} = 14.3$ Hz, 1H, NCH^AH^BN); δ 4.16 (d, $J_{H^AH^B} = 14.3$ Hz, 1H, NCH^AH^BN); δ 4.64 (m, $J_{H^AH^B} = 5.4$ Hz, $J_{PH} = 10.5$ Hz, 2H, PCH^AH^BN); δ 4.99 (d, $J_{HH} = 14.4$ Hz, 1H, NCH^AH^BN); δ 5.52 (d, $J_{HH} = 14.4$ Hz, 1H, NCH^AH^BN); δ7.90 (s, 1H, C(O)H); δ7.95 (s, 1H, C(O)H). $^{13}C\{^1H\}$ NMR ($CDCl_3$, 20 °C): δ36.37 (d, $J_{PC} = 27.6$ Hz, PCH_2N); δ 42.51 (d, $J_{PC} = 27.6$ Hz, PCH_2N); δ 48.40 (d, $J_{PC} = 18.4$ Hz, PCH_2N); δ 60.40 (s, NCH_2N); δ 67.25 (s, NCH_2N); δ 161.43 (d, $J_{PC} = 11.6$ Hz C(O)H); δ162.33 (d, $J_{PC} = 10.5$ Hz, C(O)H). $^{31}P\{1H\}$ NMR ($CDCl_3$, 20 °C): $\delta -74.2$ ppm. FABMS (*m*-nitrobenzyl alcohol matrix): observed *m*/*z* 202.2 {calc. 202.2 for $PO_2N_3C_7H_{13} = MH^+$}.

2.2.2. 1-Pyridylmethyl-3,5-diaza-1-azonia-7-phosphatricyclo[3.3.1.1]decane bromide (*2*, *[pymePTA]Br*)

A 1.65 g sample of $Na_2CO_3 \cdot H_2O$ (13.3 mmol)was dissolved in 5 mL of H_2O in the air. A 0.169 g sample of 2-bromomethylpyridine hydrobromide (0.668 mmol) was dissolved in 1 mL H_2O in the air. In the absence of light, the pyridinium salt was added to the base over a 10 min period to form a red solution. After 60 min, the organic product was extracted with Et_2O (3×10 mL). The ethereal solution was dried over magnesium sulfate, transferred to a 100 mL Schlenk flask and degassed. A 100 mL, 3-necked, round-bottom flask equipped with a reflux condenser, gas inlet, and rubber septa was charged with 0.100 g PTA (0.636 mmol) and 25 mL acetone. The solution of 2-bromomethylpyridine was added to the 3-necked flask via cannula, and the ether was removed in vacuo. The resulting clear, colorless solution was heated to reflux in the absence of light. Within 2 min, a white solid formed. After refluxing for 30 min, the mixture was cooled to room temperature. The white precipitate was collected on a frit, washed with acetone (2×5 mL) and Et_2O (3×5 mL), and dried in vacuo (yield: 139 mg, 0.422 mmol: 66.5% calculated for PTA). Compound **2** was recrystallized by layering a wet MeOH solution with Et_2O. Data for **2** were as follows: Elemental *Anal*. Calc. for crystalline $PBrN_4C_{12}H_{18} \cdot H_2O$ (mol. wt. 347.19): C, 41.51; H, 5.81; N, 16.14. Found: C, 41.79; H, 5.72; N, 15.98%. ^1H NMR (d_6-DMSO, 20 °C): δ 3.84, 3.89 (m, $J_{H^AH^B} = 14.7$ Hz, $J_{PH^A} = 13.8$ Hz, $J_{PH^B} = 9.9$ Hz, 4H, PCH^AH^BN); δ4.24 (s, 2H, CCH_2N^+); δ 4.36 (d, $J_{PH} = 6.3$ Hz, 2H, PCH_2N^+);δ 4.41 (d, $J_{H^AH^B} = 13.2$ Hz, 1H, NCH^AH^BN); δ 4.55 (d, $J_{H^AH^B} = 13.2$ Hz, 1H, NCH^AH^BN); δ 5.05 (d, $J_{H^AH^B} = 11.4$ Hz, 2H, $NCH^AH^BN^+$); 5.18 (d, $J_{H^AH^B} = 11.4$ Hz, 2H, $NCH^AH^BN^+$); δ7.56 (m, 1H, H_{py}); δ 7.66 (d, $J_{HH} = 7.8$ Hz, 1H, H_{py}); δ 7.98 (t, $J_{HH} = 7.8$ Hz, 1H, H_{py}); δ8.74 (d, $J_{HH} = 4.5$ Hz, 1H, H_{py}). $^{13}C\{^1H\}$ NMR (d_6-DMSO, 20 °C): δ 46.17 (d, $J_{PC} = 20.4$ Hz, PCH_2N); δ 53.01 (d, $J_{PC} = 32.4$ Hz, PCH_2N^+); δ 66.24 (s, $pyCH_2N^+$); δ79.98 (s, NCH_2N); δ 79.98 (s, NCH_2N^+); δ 125.64 (s, C_{py}); δ128.72 (s, C_{py}); δ138.46 (s, C_{py}); δ148.39 (s, C_{py}); δ150.95 (s, C_{py}). $^{31}P\{1H\}$ NMR (d_6-DMSO, 20 °C): δ −82.8 ppm. FABMS (*m*-nitrobenzyl alcohol matrix): observed *m*/*z* 249.2 {calc. 249.3 for $PN_4C_{12}H_{18} = M^+$}.

2.3. X-ray structure determination of 3,7-diformyl-1,3,7-triaza-5-phosphabicyclo[3.3.1]heptane (*1*, *DFPTA*) and 1-pyridylmethyl-3,5-diaza-1-azonia-7-phosphatricyclo[3.3.1.1]decane bromide (*2*, *[pymePTA]Br*)

2.3.1. Collection and reduction of data

A summary of crystallographic data for **1** and **2** are presented in Table 1 and as Supplementary Material. An X-ray quality crystal of **1** was prepared by the slow evaporation of solvent from a CH_2Cl_2 solution. An appropriate crystal of **2** was prepared by layering a methanol solution with Et_2O. Compound **1** was mounted on a thin glass fiber while **2** was mounted in a glass capillary. Both samples were transferred to a Bruker/Nonius MACH3S diffractometer equipped with graphite-monochromated Mo Kα radiation ($\lambda = 0.71073$ Å). Relevant crystallographic information is given in Table 1. Unit cell constants were determined from a least squares refinement of the setting angles of 25 machine-centered reflections in the range $8.63° < \theta < 16.21°$ for **1** and 24 reflections in the range $5.34° < 2\theta < 34.24°$ for **2**. Intensity data was collected using the $\omega/2\theta$ scan technique to a 2θ maximum value of 53.90° for **1** and 43.9° for **2**. The sample of **2** had very limited intensity beyond 22°θ. An absorption correction was not applied for **1** as the calculated maximum and minimum transmission factors differed by less than 5%. An absorption correction, based on azimuthal scans of three reflections, was applied for **2** which resulted in transmission factors ranging from 0.49 to 1.00. A correction for crystal decay was not required for either sample. The intensity data of **1** were corrected for Lorentz and polarization effects and converted to structure factors using the program XCAD4 [19].

2.3.2. Solution and refinement of structure

Systematic absences, packing considerations, and a statistical analysis of intensity distribution allowed the space groups of **1** and **2** to be determined as $C2/c$ and $R\bar{3}$, respectively. Successful direct-methods solutions were calculated which provided the positions of most of the non-hydrogen

Table 1
Crystallographic data for 3,7-diformyl-1,3,7-triaza-5-phosphabicyclo[3.3.1]heptane (**1**, DFPTA) and 1-pyridylmethyl-3,5-diaza-1-azonia-7-phosphatricyclo[3.3.1.1]decane bromide (**2**, [pymePTA]Br)

	1	**2**(**Br**)
Empirical formula	$PO_2N_3C_7H_{12}$	$PBrN_4C_{12}H_{18}$
Formula weight (amu)	201.17	329.18
Crystal color, habit	colorless, block	colorless, plate
Crystal dimensions (mm)	$0.42 \times 0.36 \times 0.18$	$0.45 \times 0.30 \times 0.04$
Crystal system	monoclinic	trigonal
Space group	$C2/c$	$R\bar{3}$
Cell parameters at T (K)	293	293
a (Å)	21.018(3)	12.510(2)
b (Å)	6.0220(8)	
c (Å)	14.570(1)	47.513(4)
β (°)	90.38(1)	
V (Å^3)	1844.1(4)	6439.6(16)
Z	8	18
D_{calc} (Mg m^{-3})	1.449	1.528
$F(000)$	848	3024
Absorption correction	not applied	Lorentz-polarization
θ Range for collection (°)	2.80–26.95	2.54–21.94
Number of reflections collected	2055	2048
Number of independent reflections	2003	2043
Observed reflections $[I > X\sigma(I)]$	$X = 2$ 1537	$X = 3$ 1746
Refinement method	full matrix least squares on F^2	full matrix least squares on F^2
Final R indices $[I > X\sigma(I)]$	$X = 2$ $R_1 = 0.0414$ $wR_2 = 0.1024$	$X = 3$ $R_1 = 0.065$ $wR_2 = 0.188$
Goodness-of-fit on F^2	1.025	1.100

atoms of **1**. The remaining non-hydrogen atoms were located after several cycles of structure expansion and full-matrix least squares refinement. The structure of **2** was solved by direct methods and expanded using Fourier techniques. All non-hydrogen atoms of **1** and **2** were refined with anisotropic displacement parameters. The hydrogen atoms of **1** were added geometrically unless otherwise noted. Carbon-bound hydrogen atoms of **1** were refined as riding atoms with group isotropic displacement parameters fixed at $1.2 \times U_{eq}$ of the host carbon atom. The hydrogen atoms of **2** were included but not refined. The final difference map of **1** was featureless, with the largest residual peak (0.34 e$^-$ Å^{-3}) located 0.91 Å from C1. The maximum and minimum peaks on the final difference Fourier map of **2** corresponded to 1.42 and −0.81 e$^-$ Å^{-3}, respectively. The final structure of **2** had three independent bromide ions, each residing on a special position with 1/3rd occupancy.

2.4. Water solubility of *1* and *2*

The water-solubility of compounds **1** and **2** were quantified by the slow addition of water via 100 μL syringe to a 100 mg sample of the respective phosphine. The process was repeated several times. In a typical trial, a 450 μL aliquot of water was required to dissolve 100 mg of **1** and a 125 μL aliquot was required for **2**.

3. Results

3.1. Synthesis and spectroscopic characterization of *3,7-diformyl-1,3,7-triaza-5-phosphabicyclo[3.3.1]heptane (1, DFPTA) and 1-pyridylmethyl-3,5-diaza-1-azonia-7-phosphatricyclo[3.3.1.1]decane bromide (2, [pymePTA]Br)*

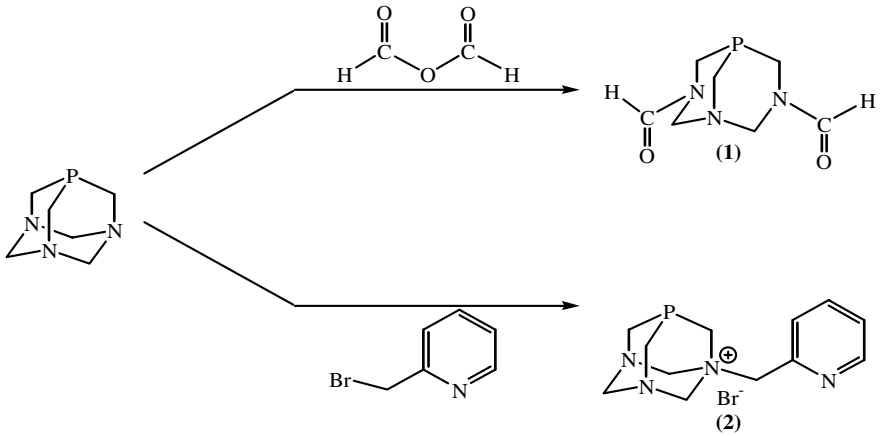
Characterization data for compounds **1** and **2** are included in Section 2 and, when appropriate, discussed below.

DAPTA is quite water-soluble (7.4 M), but its neutral metal complexes often have very limited water-solubility [10]. It was hypothesized that this problem could be alleviated by preparing a related ligand that contained less carbon. To probe this theory, the di-*N*-formylated analog of DAPTA, 3,7-diformyl-1,3,7-triaza-5-phosphabicyclo [3.3.1]- nonane (**1**, DFPTA) was synthesized by producing formic anhydride in situ [20] and reacting it with an aqueous solution of 1,3,5-triaza-7-phosphaadamantane (PTA) at −5 °C. Upon low temperature removal of the solvent and work-up in ethanol, **1** was produced in good yield. Once isolated, compound **1** was found to be air and thermally stable.

To further add to the existing library of water-soluble phosphines, the *N*-pyridylmethyl derivative of PTA, 1-pyridylmethyl-3,5-diaza-1-azonia-7-phosphatricyclo[3.3.1.1] decane bromide (**2**, pymePTA), was prepared. This was accomplished by deprotonating 2-bromomethylpyridine hydrobromide [21] and refluxing the resulting amine in an acetone solution of PTA. After 30 min, **2** precipitated in good yield as an air stable, white solid (see Scheme 1).

Fast atom bombardment–mass spectrometry and elemental analysis data were employed to confirm the empirical formulae of compounds **1** and **2** as $PO_2N_3C_7H_{12}$ and $PBrN_4C_{12}H_{18}$, respectively. The IR spectrum of **1** possessed an intense band at 1670 cm^{-1} (br) and two smaller signals at 2785 and 2801 cm^{-1} (br) that were collectively indicative of a formamide functionality. The C=O stretch is 30 cm^{-1} higher than that of the acetyl analog ($\nu_{co} = 1640$ cm^{-1}) [10]. A shift of this magnitude is common when comparing formamides and acetamides. For example, the C=O stretch of DMF appears at 1675 cm^{-1} and the corresponding resonance of *N*,*N*-dimethylacetamide is at 1646 cm^{-1}.

The most striking features of the ^{1}H NMR spectrum of **1** were the sharp singlets at 7.90 and 7.95 ppm, the expected region for formamide protons. The presence of two formamide signals indicated that the C=O moieties were in an *anti*conformation [10]. This hypothesis was confirmed by the presence of two doublets at 4.99 and 5.52 ppm that possessed identical $^2J_{H-H}$ values of 14.4 Hz. These signals were due to the geminal protons of one of the N–CH_2–N moieties (Fig. 2). The axial proton (H_A) appeared further down field than its equatorial counterpart because it was more shielded by the C=O group on the adjacent N than was the equatorial proton (H_B).



Scheme 1. The synthetic reactions which formed DFPTA (**1**) and [pymePTA]Br (**2**).

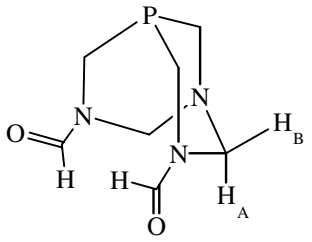


Fig. 2. The *anti* confirmation of DFPTA (**1**).

The fact that each doublet integrated as only 1 proton indicated that the hydrogens of the other N–CH_2–N group must not encountering this shielding, and hence that the adjacent C=O group must be in a different confirmation.

The presence of two inequivalent formamide groups was further confirmed by the ^{13}C NMR spectrum. Two doublets were observed at 161.4 and 162.3 ppm ($^3J_{P-C}$ = 11.6 Hz and 10.5 Hz), and these corresponded to the C atoms of the N*C*(O)H moieties. It is interesting to note that the ^{31}P coupling encountered by these C atoms was not observed with the C atoms of the N–C–N groups even though they were also 3 bond lengths away from the P. These C atoms were simply observed as singlets at 60.40 and 67.25 ppm. The P–C–N carbons were observed as doublets at 36.37, 42.51, and 48.40 ppm with $^1J_{P-C}$ coupling constants of 27.6, 27.6, and 18.4 Hz, respectively.

As is often the case with *N*-alkyl derivatives of PTA [22], the ^1H NMR spectrum of [pymePTA]Br (**2**) was more complicated than that of its precursor. The reduction of molecular symmetry from that of PTA caused the methylene protons of **2** to become inequivalent, and in some cases, to be diastereotopic. As a result, these hydrogens were observed as doublets with either phosphorous-proton or proton–proton coupling. For example, the N–CH_2–N protons appeared as two separate doublets at 4.41 ppm and 4.55 ppm with identical $^2J_{H-H}$ coupling constants of 13.2 Hz. A similar set of doublets ($^2J_{H-H}$ = 11.4 Hz) was observed further downfield at 5.05 and 5.18 ppm. These corresponded to the geminal N–CH_2–N^+ protons. The ^1H spectrum of **2** also showed the presence of a pyridyl moiety. The methylene group that linked the PTA moiety to the aromatic ring appeared as a sharp singlet at 4.24 ppm, and the four protons of the ring produced a multiplet, a doublet, a triplet, and another doublet at 7.56, 7.66, 7.98, and 8.74 ppm with $^3J_{HH}$ coupling constants on the order of 4.5 or 7.8 Hz. The presence of a pyridine ring was further proven by the 5 singlets of the ^{13}C spectrum at 125.64, 128.72, 138.46, 148.39, and 150.95 ppm. The carbon atoms of the $pyCH_2N^+$, NCH_2N, and NCH_2N^+ moieties also appeared as singlets at 66.24, 69.98, and 79.98 ppm, respectively. Due to P–C coupling, the PCH_2N and PCH_2N^+ carbons appeared as doublets at 46.17 and 53.01 ppm with $^1J_{P-C}$ values of 20.4 and 32.4 Hz, respectively. This is similar to the ^{13}C spectrum of the benzyl analog [23]. As expected, the $^{31}P\{^1H\}$ spectra of **1** and **2** were very simple. Each contained only a singlet at −74.2 ppm and −82.8 ppm, respectively.

*3.2. Crystallographic characterization of 3,7-diformyl-1,3,7-triaza-5-phosphabicyclo[3.3.1]heptane (**1**, DFPTA) and 1-pyridylmethyl-3,5-diaza-1-azonia-7-phosphatricyclo[3.3.1.1]decane bromide (**2**, [pymePTA]Br)*

*3.2.1. Solid-state structure of 3,7-diformyl-1,3,7-triaza-5-phosphabicyclo[3.3.1]nonane (**1**, DFPTA)*

An X-ray quality, colorless block crystal of compound **1** was formed by the slow evaporation of a CH_2Cl_2 solution, and it was found to form in the *C*2/*c* space group. Table 1 contains the collection parameters and crystallographic data of the experiment. The structure of the phosphine is shown in Fig. 3. Selected interatomic distances and angles are given in Table 2. Additional crystallographic data are provided as Supplementary Material.

The geometry about the P was compressed pyramidal as evidenced by the small C–P–C bond angle average of 98.36(10)°. N(3) also possessed a distorted pyramidal

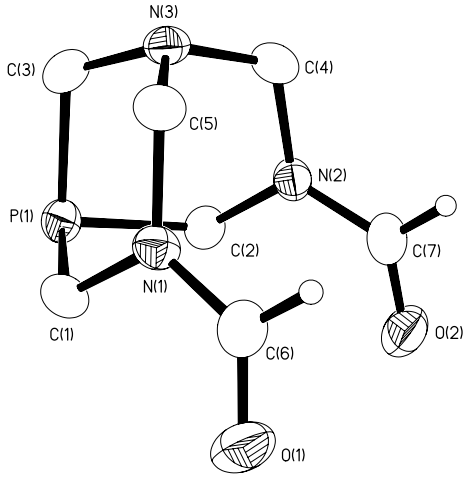


Fig. 3. Thermal ellipsoid representation of 3,7-diformyl-1,3,7-triaza-5-phosphabicyclo[3.3.1]nonane (**1**, DFPTA). Thermal ellipsoids are drawn at the 50% probability level.

Table 2
Selected bond distances (Å) and bond angles (°) with estimated standard deviations of 3,7-diformyl-1,3,7-triaza-5-phosphabicyclo[3.3.1]nonane (**1**, DFPTA)

Bond distances			
P1–C1	1.847 (2)	C6–O1	1.218 (3)
N1–C1	1.456 (3)	C7–O2	1.223 (3)
N1–C6	1.339 (3)		
Bond angles			
C1–P1–C2	102.89 (10)	C4–N3–C5	115.13 (18)
C1–P1–C3	95.72 (10)	C1–N1–C6	120.48 (19)
C2–P1–C3	96.47 (11)	C1–N1–C5	117.69 (17)
C3–N3–C4	111.92 (18)	C5–N1–C6	121.82 (19)
C3–N3–C5	112.22 (17)	N1–C6–O1	125.0 (2)

geometry but deviated less from ideality as shown by an average C–N–C bond angle of 113.09(18)°. The average C–N–C bond angles around N(1) and N(2) were 120.00(19)° and 119.92(19)°, respectively thus illustrating that the geometry around each of these atoms was trigonal planar, and hence, that they were involved in forming a Schiff base (N=C) double bond. This was supported by the observation that the N(1)–C(6) and N(2)–C(7) bond lengths (each 1.339(3) Å) were shorter than the other N–C bond lengths within the molecule (1.444(3)–1.467(3) Å). Darensbourg reported a similar finding with the acetyl analog, DAPTA [10], and it is believed that this character caused the phosphine to exhibit remarkable water-solubility. The solid-state structures of **1** and DAPTA differ in two important ways. First, the average P–C bond distance in **1** (1.849(3) Å) was substantially longer than the corresponding average (1.728(14) Å) of DAPTA [10]. The average P–C length of **1** was instead similar to that of PTA (1.857(3) Å) [24]. Second, the C(O)R (R = H, CH_3) moieties were *syn* to each other in **1** but *anti* to each other in DAPTA. The *anti* confirmation of **1** was observed, but only in solution (vide supra).

*3.2.2. Solid-state structure of 1-pyridylmethyl-3,5-diaza-1-azonia-7-phosphatricyclo[3.3.1.1]decane bromide (**2**, [pymePTA]Br)*

X-ray quality crystals of **2** were grown by slow diffusion of Et_2O into a MeOH solution of [pymePTA]Br. Complex **2** was found to crystallize in an R-centered trigonal cell (laue class: −3). Experimental data are presented in Table 1. A thermal ellipsoid representation of **2** is shown in Fig. 4. Selected interatomic distances and angles are given in Table 3 while complete crystallographic data are provided as supplementary material.

The small average C–P–C bond angle (96.6(5)°) illustrated that the geometry about the P of **2** was compressed pyramidal. This is more compact that the average C–P–C bond angle of **1** and comparable to the corresponding angle of PTA (96.1(1)°) [17]. The geometries around N(2) and N(3) were also distorted pyramidal but deviated less from ideality as shown by average C–N–C bond angles of 110.8(8)° and 111.1(9)°, respectively. A nearly ideal, tetrahedral geometry was observed around the quaternary nitrogen, N(1), as evidenced by its average C–N–C bond angle of 109.8(7)°. The average N–C bond distance involving this nitrogen (1.53(1) Å) was slightly longer than that around N(2) (1.45(1) Å) and N(3) (1.46(2) Å). A similar

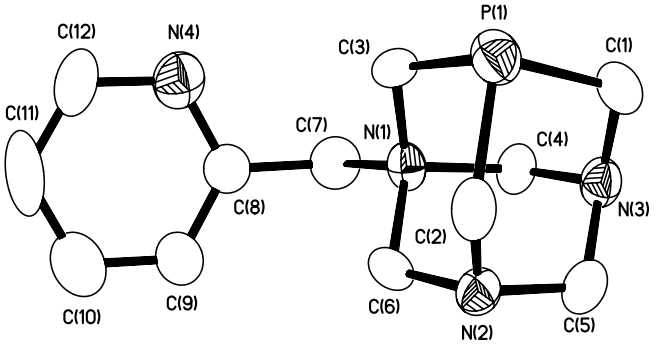


Fig. 4. Thermal ellipsoid representation of 1-pyridylmethyl-3,5-diaza-1-azonia-7-phosphatricyclo[3.3.1.1]decane bromide (**2**, [pymePTA]Br). Thermal ellipsoids are drawn at the 50% probability level.

Table 3
Selected bond distances (Å) and bond angles (°) with estimated standard deviations for 1-pyridylmethyl-3,5-diaza-1-azonia-7-phosphatricyclo[3.3.1.1]-decane bromide (**2**, [pymePTA]Br)

Bond distances			
P1–C1	1.85 (1)	N4–C8	1.35 (2)
N1–C3	1.51 (2)	N4–C12	1.35 (2)
N1–C7	1.52 (1)	C7–C8	1.48 (1)
N2–C2	1.47 (2)	C8–C9	1.36 (1)
N2–C6	1.42 (1)	C9–C10	1.34 (2)
Bond angles			
C1–P1–C2	97.0 (5)	C3–N1–C7	111.3 (7)
C1–P1–C3	96.2 (5)	C2–N2–C6	110.1 (8)
C2–P1–C3	96.5 (6)	C8–N4–C12	117 (1)
C3–N1–C4	109.2 (8)	C8–C7–N1	114.7 (7)

result has previously been observed with the *N*-butyl iodide analog of PTA, [PTA-$(CH_2)_4$ I]I [16]. In this species, the average N–C bond length about the quaternary N was 1.53 Å while the average N–C bond length around the remaining N atoms was 1.44 Å. The N–C(alkyl) bond lengths of **2** and [PTA-$(CH_2)_4$I]I were comparable as the N(1)–C(7) distance of **2** was 1.52(1) Å and the N–C span of the *N*-butyl iodide analog was 1.53 Å [16].

*3.3. Solubility studies of 3,7-diformyl-1,3,7-triaza-5-phosphabicyclo[3.3.1]heptane (**1**, DFPTA) and 1-pyridylmethyl-3,5-diaza-1-azonia-7-phosphatricyclo[3.3.1.1]decane bromide (**2**, [pymePTA]Br)*

The primary purpose of this study was to prepare phosphines that could possibly function as water-soluble ligands. Therefore, the solubilities of **1** and **2** in aqueous and organic media were examined.

Compound **1** was found to be insoluble in DMSO and only sparingly soluble in halogenated hydrocarbons and alcohols. This is in marked contrast from its acetyl analog, DAPTA, which was reported to be soluble in many common organic solvents and water [10]. In fact, the water-solubility of DAPTA was reportedly quite high (7.4 M). Unfortunately, in this study, only 1.1 M aqueous solutions of **1** could be prepared. This is quite striking in light of the fact that both DFPTA (**1**) and DAPTA form Schiff bases, and it is believed that this characteristic gives DAPTA its remarkable water solubility [10].

The solubility of compound **2** in the previously mentioned organic solvents was found to be better than that of **1**. The improved solubility in halogenated hydrocarbons is surprising in light of the fact that **2** is an ionic compound while **1** is neutral. Not surprisingly, this characteristic caused **2** to be much more water-soluble than **1**. In fact, the water-solubility of **2** was found to be 2.4 M. This solubility is greater than that of PTA (1.5 M) [10] and even the trisulfonated derivative of triphenylphosphine, TPPTS (1.9 M) [24].

4. Conclusion

Through this study, two new phosphines have been added to the library of water-soluble ligands. The second acyl derivative of PTA, 3,7-diformyl-1,3,7-triaza-5-phosphabicyclo[3.3.1]heptane (**1**, DFPTA), and the second derivative of PTA containing an aromatic appendage, 1-pyridylmethyl-3,5-diaza-1-azonia-7-phosphatricyclo[3.3.1.1]decane bromide (**2**, [pymePTA]Br), have been prepared and fully characterized. The solubility of **1** in all solvents, including water, was far less than that of its acetyl analog, DAPTA. This was surprising in light of the fact that both species were believed to from Schiff bases. Phosphine **2** was found to be more soluble than **1** in water and common organic solvents, including halogenated hydrocarbons. We are presently expanding this work to further derivatize PTA with hopes of increasing the water-solubility of the ligand and its transition metal complexes.

Acknowledgements

The authors thank the Concordia College Alumni Chemistry Research Fund, the Concordia College Centennial Scholars Program and to the Donors of The Petroleum Research Fund, administered by the American Chemical Society, for partial support (Grant 33818-GB3 to D.A.K. and Grant 33450-GB3 to J.A.H.) of this research.

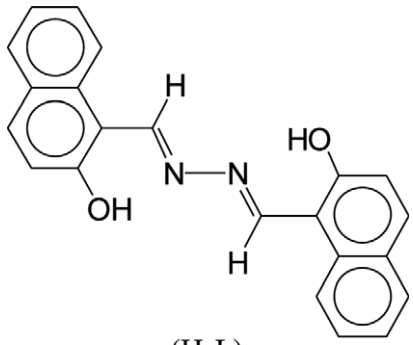
Appendix A. Supplementary material

CCDC 641687 and 641688 contain the supplementary crystallographic data for **1** and **2**. These data can be obtained free of charge via http://www.ccdc.cam.ac.uk/conts/retrieving.html, or from the Cambridge Crystallographic Data Centre, 12 Union Road, Cambridge CB2 1EZ, UK; fax: (+44) 1223-336-033; or e-mail: deposit @ccdc.cam.ac.uk. Supplementary data associated with this article can be found, in the online version, at doi:10.1016/j.poly.2007.05.003.

References

[1] B. Cornils, E. Wiebus, in: B. Cornils (Ed.), Multiphase Homogeneous Catalysis, Wiley-VCH Verlag, Weinheim, 2005, p. 143.
[2] C.J. Li, L. Chen, Chem. Soc. Rev. 35 (2006) 68.
[3] (a) R. Breslow, U. Maitra, Tetrahedron Lett. 25 (1984) 1239;
(b) R. Breslow, U. Maitra, Tetrahedron Lett. 24 (1983) 1901;
(c) D.C. Rideout, R. Breslow, J. Am. Chem. Soc. 102 (1980) 7816.
[4] (a) J. Fraga-Dubreuil, M. Poliakoff, Pure Appl. Chem. 78 (2006) 1971;
(b) C.J. Li, Chem. Rev. 105 (2005) 3095;
(c) J.M.W. Scott, Can. J. Chem. 83 (2005) 1667.
[5] T.J. Geldbach, G. Laurenczy, R. Scopelliti, P.J. Dyson, Organometallics 25 (2006) 733.
[6] W.A. Herrmann, C.W. Kohlpainter, Angew. Chem., Int. Ed. Engl. 32 (1993) 1524.
[7] O. Stelzer, S. Rossenbach, D. Hoff, in: B. Cornils, W.A. Herrmann (Eds.), Aqueous-Phase Organometallic Catalysis, 2nd ed., Wiley-VCH Verlag, Weinheim, 2004, p. 100.
[8] D.J. Daigle, Inorg. Synth. 32 (1998) 40.
[9] (a) B. Korthals, I. Gottker-Schnetmann, S. Mecking, Organometallics 26 (2007);
(b) B.J. Frost, C.M. Bautista, R. Huang, J. Shearer, Inorg. Chem. 45 (2006) 3481;
(c) J. Ruiz, N. Cutillas, F. Lopez, G. Lopez, D. Bautista, Organometallics 25 (2006) 5768;
(d) F. Mohr, S. Sanz, E.R. Tiekink, M. Laguna, Organometallics 25 (2006) 3084;
(e) A.D. Phillips, L. Gonsalvi, A. Romerosa, F. Vizza, M. Peruzzini, Coord. Chem. Rev. 248 (2004) 955.
[10] D.J. Darensbourg, C.G. Ortiz, J.W. Kamplain, Organometallics 23 (2004) 1747.
[11] (a) D.A. Krogstad, S.B. Owens, J.A. Halfen, V.G. Young Jr., Inorg. Chem. Comm. 8 (2005) 65;
(b) E.C. Alyea, G. Ferguson, S. Kannan, Polyhedron 17 (1998) 2727.
[12] (a) C.A. Mebi, R.P. Nair, B.J. Frost, Organometallics 26 (2007) 429;
(b) C.A. Mebi, B.J. Frost, Organometallics 24 (2005) 2339;
(c) S. Bolano, L. Gonsalvi, F. Zanobini, F. Vizza, V. Bertolasi, A. Romerosa, M. Peruzzini, J. Mol. Cat. A. 224 (2004) 61.

[13] (a) D.A. Krogstad, A.J. DeBoer, W.J. Ortmeier, J.W. Rudolf, J.A. Halfen, Inorg. Chem. Commun. 8 (2005) 1141;
(b) D.A. Krogstad, J. Cho, A.J. DeBoer, J.A. Klitzke, W.R. Sanow, H.A. Williams, J.A. Halfen, Inorg. Chim. Acta 359 (2006) 136.
[14] A. Romerosa, T. Campos-Malpartida, C. Lidrissi, M. Saoud, M. Serrano-Ruiz, M. Peruzzini, J.A. Garrido-Cardenas, F. Garcia-Maroto, Inorg. Chem. 45 (2006) 1289.
[15] J.M. Forward, R.J. Staples, C.W. Liu, J.P. Fackler Jr., Acta Crystllogr., Sect. C 53 (1997) 195.
[16] J.M. Forward, R.J. Staples, J.P. Fackler Jr., Z. Kristallogr. 211 (1996) 129.
[17] E. Fluck, J.E. Forster, J. Weidlein, E. Hadicke, Z. Naturforsch. 32B (1977) 499.
[18] V. Gutkin, J. Gun, P.V. Prikhodchenko, O. Lev, L. Gonsalvi, M. Peruzzini, A. Romerosa, T. Campos-Malpartida, C. Lidrissi, J. Electrochem. Soc. 154 (2007) F7.
[19] K. Harms, University of Marburg, 1996.
[20] I. Muramatsu, M. Itoi, M. Tsuji, A. Hagitani, Bull. Chem. Soc. Jpn. 37 (1964) 756.
[21] The deprotonation step was performed by using the methodology of Grundemann et al. as described in the following reference: S. Grundemann, A. Kovacevic, M. Albrecht, J.W. Faller, R.H. Crabtree, J. Am. Chem. Soc. 124 (2002) 10473.
[22] F.P. Pruchnik, P. Smolenski, Appl. Organomet. Chem. 13 (1999) 829.
[23] K.J. Fisher, E.C. Alyea, N. Shahnazarian, Phosphorous, Sulfur, and Silicon 48 (1990) 37.
[24] E.G. Kuntz, Chemtech 17 (1987) 570.



(H_2L)

In the present work, we have used the Schiff base H_2L which is analogous to H_2salhn to look at the efficacy of a sterically bulky N_2O_2-donor diazine system (L^{2-}) in providing dinuclear triple helical structures. Three dinuclear complexes of manganese(III), iron(III) and cobalt(III) are synthesized. In the following account, the characterization and the physical properties of $[Mn_2(\mu\text{-}L)_3]$ (**1**), $[Fe_2(\mu\text{-}L)_3]$ (**2**) and $[Co_2(\mu\text{-}L)_3]$ (**3**) are described. The triple helical structures of **2** and **3** are confirmed by X-ray crystallography.

2. Experimental

2.1. Materials

The Schiff base H_2L was prepared in ~90% yield by reacting one mole equivalent of hydrazine with two mole equivalents of 2-hydroxy-1-naphthaldehyde in methanol [32,35–38]. All other chemicals and solvents used in this work were of analytical grade available commercially and were used without further purification.

2.2. Physical measurements

Microanalytical (C, H, N) data were obtained with a Thermo Finnigon Flash EA1112 series elemental analyzer. Infrared spectra were collected by using KBr pellets on a Jasco-5300 FT-IR spectrophotometer. Solution electrical conductivities were measured with a Digisun DI-909 conductivity meter. A Shimadzu 3101-PC UV/vis/NIR spectrophotometer was used to record the electronic spectra. The proton NMR spectrum of $[Co_2(\mu\text{-}L)_3]$ (**3**) was recorded with the help of a Bruker 400 MHz NMR spectrometer. The variable temperature (18–300 K) magnetic susceptibility measurements with powdered samples were performed using the Faraday technique with a set-up comprising a George Associates Lewis coil force magnetometer, a CAHN microbalance and an Air Products cryostat. $Hg[Co(NCS)_4]$ was used as the standard. Diamagnetic corrections calculated from Pascal's constants [39] were used to obtain the molar paramagnetic susceptibilities.

2.3. Syntheses of complexes

2.3.1. $[Mn_2(\mu\text{-}L)_3]$ (1)

H_2L (100 mg, 0.3 mmol) and KOH (34 mg, 0.6 mmol) were taken in a mixture of methanol (20 ml) and acetonitrile (10 ml). The mixture was heated until a clear orange solution was obtained. Solid $MnCl_2 \cdot 4H_2O$ (40 mg, 0.2 mmol) was added to this solution and the mixture was stirred for 2 h at room temperature followed by slow evaporation in air. The brown solid separated was collected by filtration, washed with water and cold methanol and finally dried in air. Yield, 70 mg (62%). *Anal*. Calc. for $Mn_2C_{66}H_{42}N_6O_6$: C, 70.47; H, 3.76; N, 7.47. Found: C, 70.18; H, 3.61; N, 7.24%. Electronic spectral data in CH_2Cl_2 (λ_{max} (nm) (ε ($M^{-1}\,cm^{-1}$))): 480sh (9,300), 430 (26,700), 410 (29,900), 390sh (23,400), 333 (23,200), 263 (55,600).

2.3.2. $[Fe_2(\mu\text{-}L)_3]$ (2) and $[Co_2(\mu\text{-}L)_3]$ (3)

Complexes **2** and **3** were synthesized in comparable yields by following procedures very similar to that described above using $FeCl_3$ and $CoCl_2 \cdot 6H_2O$, respectively, as the metal ion source.

Anal. Calc. for $Fe_2C_{66}H_{42}N_6O_6$ (**2**): C, 70.35; H, 3.76; N, 7.46. Found: C, 70.23; H, 3.59; N, 7.32%. Electronic spectral data in CH_2Cl_2 (λ_{max} (nm) (ε ($M^{-1}\,cm^{-1}$))): 585 (9,300), 485sh (11,000), 430sh (21,900), 390 (30,500), 320 (44,000).

Anal. Calc. for $Co_2C_{66}H_{42}N_6O_6$ (**3**): C, 69.97; H, 3.74; N, 7.42. Found: C, 69.65; H, 3.52; N, 7.17%. Electronic spectral data in CH_2Cl_2 (λ_{max} (nm) (ε ($M^{-1}\,cm^{-1}$))): 476 (15,100), 430sh (12,700), 367sh (24,500), 355 (28,400), 267 (92,100).

2.4. X-ray crystallography

Single crystals of **2** were grown by slow evaporation of a dichloromethane–acetonitrile (1:1) solution of the complex. On the other hand, single crystals of **3** were obtained directly from the reaction mixture. In each case, unit cell parameters and the intensity data were obtained on a Bruker-Nonius SMART APEX CCD single crystal diffractometer, equipped with a graphite monochromator and a Mo Kα fine-focus sealed tube ($\lambda = 0.71073$ Å) operated at 2.0 kW. The detector was placed at a distance of 6.0 cm from the crystal. Data were collected at 298 K with a scan width of 0.3° in ω and an exposure time of 15 s/frame. The SMART software was used for data acquisition and the SAINT-PLUS software was used for data extraction [40]. The absorption corrections were performed with the help of SADABS program [41]. The complexes crystallize as **2**·$2CH_2Cl_2$ and **3**·$2CH_3CN$ in the space groups $P\bar{1}$ and $Pna2_1$, respectively. The structures were solved by direct methods and refined on F^2 by block-matrix and full-matrix least-squares procedures for **2**·$2CH_2Cl_2$ and **3**·$2CH_3CN$, respectively. The asymmetric unit of **2**·$2CH_2Cl_2$ contains two molecules of **2** and four molecules of CH_2Cl_2. Among the four CH_2Cl_2 molecules, three are of full occupancy,

whereas the last one is found at two different sites with half occupancy for each. The chlorine atoms of one of the full occupancy CH_2Cl_2 molecule are disordered and were located at four different sites. In this context, it may be noted that structure of a solvatomorph of **2** was reported before. This species (**2**·3HC(=O)N$(CH_3)_2$) also crystallizes in the space group $P\bar{1}$ [42]. In **2**·2CH_2Cl_2, the non-hydrogen atoms of the CH_2Cl_2 molecules having partial occupancies were refined isotropically. All other non-hydrogen atoms in both structures were refined using anisotropic thermal parameters. The hydrogen atoms were included in the structure factor calculation at idealized positions by using a riding model. The SHELX-97 programs [43] of the WINGX package [44] were used for structure solution and refinement. The ORTEX6a [45] and PLATON [46] packages were used for molecular graphics. Selected crystallographic data are listed in Table 1.

3. Results and discussion

3.1. Synthesis and characterization

The complexes were synthesized in moderate yields by reacting metal chlorides, H_2L and KOH (2:3:6 mole ratio) in methanol–acetonitrile media. The elemental analysis data for all the complexes are in good agreement with the general molecular formula $[M_2L_3]$ (M = Mn (**1**), Fe (**2**) and Co (**3**)). Complexes **1** and **2** are paramagnetic, while complex **3** is diamagnetic. The diamagnetic character of **3** and the room temperature (300 K) magnetic moments of **1** and **2** (*vide infra*) indicate that both metal ions are trivalent in each complex. All the three complexes are soluble in non-polar solvents such as dichloromethane and chloroform and they are electrically non-conducting in solutions. During the synthesis of **2**, $FeCl_3$ was used as the metal ion source. However, hydrated chloride salts of manganese(II) and cobalt(II) were used as the starting materials for the synthesis of **1** and **3**, respectively. As the synthetic reactions were performed under aerobic conditions the oxygen in air is the most likely oxidant for the oxidation of the metal ions during the synthesis of **1** and **3**.

Table 1
Crystallographic data for $[Fe_2(\mu\text{-}L)_3]$·2CH_2Cl_2 (**2**·2CH_2Cl_2) and $[Co_2(\mu\text{-}L)_3]$·2CH_3CN (**3**·2CH_3CN)

	2·2CH_2Cl_2	**3**·2CH_3CN
Empirical formula	$Fe_2C_{68}H_{46}N_6O_6Cl_4$	$Co_2C_{70}H_{48}N_8O_6$
Formula weight	1296.61	1215.02
Crystal size (mm)	0.45 × 0.32 × 0.24	0.47 × 0.27 × 0.22
Crystal system	triclinic	orthorhombic
Space group	$P\bar{1}$	$Pna2_1$
a (Å)	14.1302(9)	22.5393(11)
b (Å)	19.6413(12)	13.7949(6)
c (Å)	23.0268(14)	19.0982(9)
α (°)	104.078(1)	90
β (°)	102.802(1)	90
γ (°)	95.452(1)	90
V (Å^3)	5969.3(6)	5938.2(5)
Z	4	4
ρ_{calc} (g/cm^3)	1.443	1.359
μ (mm^{-1})	0.725	0.620
Reflections collected	57684	55250
Unique reflections	20928	10449
Observed reflections ($I \geqslant 2\sigma(I)$)	14043	9531
Data/restraints/parameters	20928/12/1544	10449/1/775
Goodness-of-fit on F^2	1.036	1.103
R_1, wR_2 ($I \geqslant 2\sigma(I)$)	0.0779, 0.2131	0.0481, 0.1336
R_1, wR_2 (all data)	0.1135, 0.2398	0.0530, 0.1379
Largest peak and hole (e/Å^3)	1.457, −0.912	1.145, − 0.326

3.2. Spectroscopic characteristics

Absence of any band assignable to the phenolic OH group in the infrared spectra of the complexes suggests that the ligands are dianionic in each complex. The strong band observed at ~1616 cm^{-1} is most likely due to the C=N stretch [32,35]. The infrared spectra of **1**, **2** and **3** are essentially identical except for some insignificant shifts of frequencies. The similarity of all the three spectra indicates similar molecular structures of **1**, **2** and **3**.

The electronic spectra of the complexes in dichloromethane solutions display several strong absorptions in the visible as well as ultra-violet region. The absorptions in the visible region are attributed to the ligand-to-metal charge transfer transitions [32,35]. The higher energy bands are likely to be due to ligand based transitions.

A $CDCl_3$ solution of the diamagnetic dicobalt(III) complex (**3**) was used to record the proton NMR spectrum. For an ideal triple helical D_3 symmetric structure of **3**, the six halves of the three twisted ligands (L^{2-}) are expected to be essentially equivalent. It may be expected that H6 and H9 protons of the naphthalene moiety will have similar chemical shifts. Likewise H7 and H8 protons should also have similar chemical shifts. Slightly different chemical shifts can be anticipated for H3 and H4 protons. The signal for the azomethine proton in twisted L^{2-} may display high-field shift due to its proximity to the naphthalene rings of the same ligand or other ligands. The spectrum of **3** displays closely spaced signals centred at δ 7.75, 7.56, 7.19 and 6.50 ppm in the ratio 2:2:2:1. The resonances at δ 7.75, 7.56 and 7.19 are ascribable to the three pairs of protons (H6, H9), (H7, H8) and (H3, H4), respectively. The one at δ 6.50 ppm has been assigned to the azomethine proton. The observation of this pattern suggests a nearly ideal triple helical structure of **3** in solution.

3.3. Magnetic properties

The magnetic susceptibilities of **1**, **2** and **3** were measured with powdered samples of the complexes. The dicobalt(III) complex (**3**) is diamagnetic. The magnetic susceptibilities of the paramagnetic dimanganese(III) and the diiron(III) complexes (**1** and **2**) were measured in the temperature range 17–300 K at a constant magnetic field of 5 kG. For both **1** and **2** the effective magnetic moment (μ_{eff}) decreases gradually with the decrease of temperature indicating antiferromagnetic interaction between the two

metal ions (Fig. 1). At 300 K the μ_{eff} value (6.58 μ_B) of **1** is slightly smaller than the spin-only moment (6.93 μ_B) expected for a dimer containing two metal ions with $S = 2$ spin states. The moment of **1** decreases to 4.89 μ_B at 17 K. In the case of **2**, the μ_{eff} value (8.39 μ_B) at 300 K is essentially identical with the spin-only moment (8.37 μ_B) expected for a diiron(III) complex where both the metal ions are high spin ($S = 5/2$). At 17 K the μ_{eff} value decreases to 6.30 μ_B. The data were fitted using the expressions for χ_M versus T derived from the isotropic spin-exchange Hamiltonian $H = -2JS_1 \cdot S_2$, where $S_1 = S_2 = 2$ (for **1**) and $S_1 = S_2 = 5/2$ (for **2**) [47]. The best least-squares fits [48] were obtained with $J = -1.57(1)$ cm^{-1} and $g = 1.927(4)$ for **1** and $J = -1.13(1)$ cm^{-1} and $g = 2.035(1)$ for **2**. The extent of intramolecular antiferromagnetic coupling in dicopper(II) species having one or two =N–N= bridges is largely determined by the twisting of the dinucleating ligand along the N–N single bond [23–27]. It is reported that the effective orthogonality between the magnetic orbitals of the Cu(II) centers and that between the nitrogen p-orbitals involved in the spin-exchange process is attained when the twist angle (dihedral angle between the two chelating sites) is ~70° [24–26]. Magnetic properties of very few dinuclear complexes of 3d metal ions other than copper(II) having the diazine bridge are reported. These are the diiron(III) complexes of salhn^{2-} and its derivative [32,35] and some dimetal(II) (M = Ni, Co and Mn) complexes with *N*,*N*′-bis(picolinylidene)hydrazine or its derivatives [20,21,26]. In all these complexes, the metal ions are connected by three =N–N= bridges and they exhibit no spin-exchange or very weak spin-exchange. In the two structurally characterized diiron(III) complexes, the average twist angles between the two chelate rings along the N–N single bonds are 42.6 and 63.5° [32,35]. On the other hand, the average twist angles are very similar in the dimanganese(II) (~68°) and the dinickel(II) complexes (~70°) [26]. Except for one diiron(III) complex, these twist angles are essentially identical or very close to the twist angle found as the orthogo-

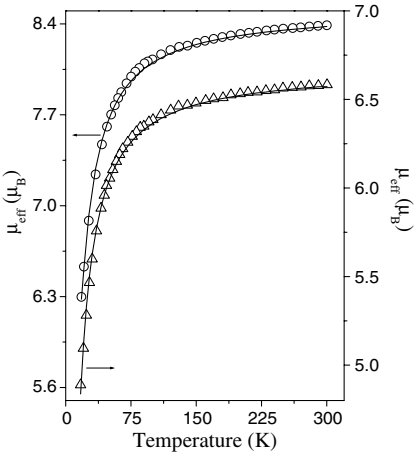


Fig. 1. The effective magnetic moments of $[Mn_2(\mu\text{-}L)_3]$ (△) and $[Fe_2(\mu\text{-}L)_3]$ (○) as a function of temperature. The continuous lines were generated from the best least-squares fit parameters given in the text.

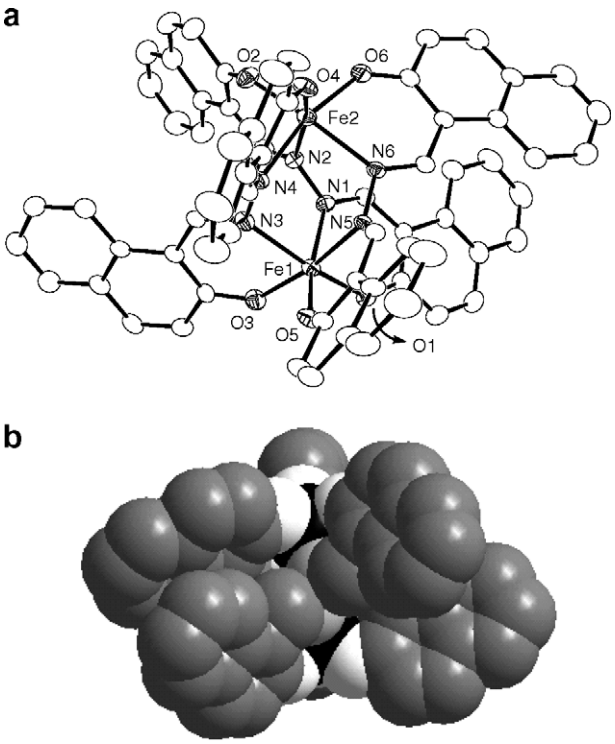


Fig. 2. Molecular structure of $[Fe_2(\mu\text{-}L)_3]$. Out of two molecules present in the asymmetric unit one is shown. Hydrogen atoms are omitted for clarity. (a) ORTEP diagram depicting the 30% probability thermal ellipsoids. (b) Space filling representation of the triple helical structure.

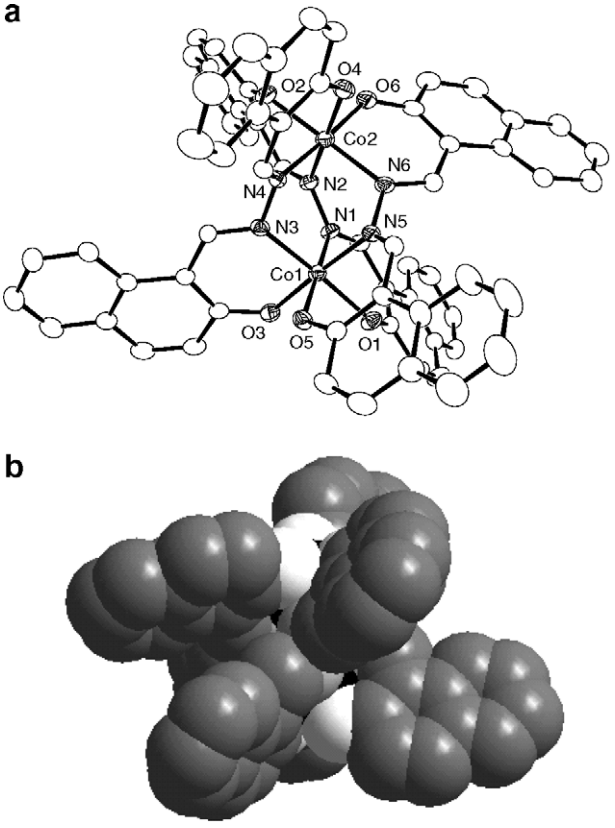


Fig. 3. Molecular structure of $[Co_2(\mu\text{-}L)_3]$. Hydrogen atoms are omitted for clarity. (a) ORTEP diagram depicting the 30% probability thermal ellipsoids. (b) Space filling representation of the triple helical structure.

nal limit for the dicopper(II) complexes with similar ligands. Although the X-ray structure of **1** could not be determined due to the lack of single crystals but for **2** the twist angles (73.1(1)–87.08(6)°) (*vide infra*) are not far off from the above orthogonal limit.

3.4. X-ray structures of 2 and 3

The molecular structures of **2** and **3** are shown in Figs. 2 and 3, respectively. The bond parameters associated with the metal centres in **2** and **3** are listed in Tables 2 and 3, respectively. The asymmetric unit of **2** contains two complex molecules. The bond parameters (Table 2) indicate that both molecules are essentially identical. In both complex molecules, each of the three dinucleating ligands coordinates the two metal ions via the two phenolate-O and the two imine-N atoms. As a result the metal ions are in facial O_3N_3 coordination spheres and connected by three diaza (=N–N=) bridges. The M–O(phenolate) and M–N(imine) bond lengths (Tables 2 and 3) in the diiron complex (**2**) as well as in the dicobalt complex (**3**) are consistent with the +3 oxidation state of the metal ions [32–35,42]. The Fe···Fe distances (3.920(1) and 3.896(1) Å) observed in the two molecules of **2** are significantly longer than the Co···Co distance (3.4156(7) Å) observed in **3**. In each complex, all the three ligands are twisted along the N–N single bonds to accommodate the two metal ions and consequently the triple helical structure is generated (Figs. 2 and 3). The average twisting of the three ligands is larger in **2** compared to that in **3**. For **2**, the dihedral angles between the two bidentate chelating sites of the three ligands are 79.36(7)°, 87.08(6)° and 78.26(7)° in molecule 1 and 81.30(7)°, 86.71(7)° and 73.05(10)° in molecule 2. These dihedral angles are 30.60(8)°, 50.93(6)° and 54.91(8)° in **3**. The values of these dihedral angles indicate that the helical twist of L^{2-} in **2** is significantly larger than the helical twist of L^{2-} in **3**. Perhaps this difference is responsible for the longer Fe···Fe distance in **2** compared to the Co···Co distance in **3**.

Table 2
Selected bond lengths (Å) and angles (°) for $[Fe_2(\mu\text{-}L)_3]\cdot 2CH_2Cl_2$ ($\mathbf{2}\cdot 2CH_2Cl_2$)

Molecule 1		Molecule 2	
Fe(1)–O(1)	1.921(3)	Fe(3)–O(7)	1.929(3)
Fe(1)–O(3)	1.929(4)	Fe(3)–O(9)	1.921(4)
Fe(1)–O(5)	1.928(4)	Fe(3)–O(11)	1.918(4)
Fe(1)–N(1)	2.158(4)	Fe(3)–N(7)	2.144(4)
Fe(1)–N(3)	2.146(4)	Fe(3)–N(9)	2.151(4)
Fe(1)–N(5)	2.206(4)	Fe(3)–N(11)	2.192(4)
Fe(2)–O(2)	1.910(4)	Fe(4)–O(8)	1.938(4)
Fe(2)–O(4)	1.935(3)	Fe(4)–O(10)	1.923(4)
Fe(2)–O(6)	1.923(4)	Fe(4)–O(12)	1.922(4)
Fe(2)–N(2)	2.172(4)	Fe(4)–N(8)	2.162(4)
Fe(2)–N(4)	2.143(4)	Fe(4)–N(10)	2.154(4)
Fe(2)–N(6)	2.171(4)	Fe(4)–N(12)	2.168(4)
O(1)–Fe(1)–O(3)	94.61(15)	O(7)–Fe(3)–O(9)	94.83(15)
O(1)–Fe(1)–O(5)	99.16(16)	O(7)–Fe(3)–O(11)	97.55(16)
O(1)–Fe(1)–N(1)	82.74(15)	O(7)–Fe(3)–N(7)	82.55(15)
O(1)–Fe(1)–N(3)	165.52(15)	O(7)–Fe(3)–N(9)	96.83(16)
O(1)–Fe(1)–N(5)	98.22(15)	O(7)–Fe(3)–N(11)	168.68(15)
O(3)–Fe(1)–O(5)	95.71(16)	O(9)–Fe(3)–O(11)	99.36(17)
O(3)–Fe(1)–N(1)	99.56(16)	O(9)–Fe(3)–N(7)	166.90(16)
O(3)–Fe(1)–N(3)	81.86(15)	O(9)–Fe(3)–N(9)	82.66(15)
O(3)–Fe(1)–N(5)	167.14(15)	O(9)–Fe(3)–N(11)	96.44(16)
O(5)–Fe(1)–N(1)	164.42(15)	O(11)–Fe(3)–N(7)	93.71(17)
O(5)–Fe(1)–N(3)	95.17(17)	O(11)–Fe(3)–N(9)	165.26(15)
O(5)–Fe(1)–N(5)	81.49(14)	O(11)–Fe(3)–N(11)	81.71(15)
N(1)–Fe(1)–N(3)	84.00(15)	N(7)–Fe(3)–N(9)	84.91(15)
N(1)–Fe(1)–N(5)	82.94(14)	N(7)–Fe(3)–N(11)	86.22(15)
N(3)–Fe(1)–N(5)	85.88(15)	N(9)–Fe(3)–N(11)	83.56(15)
O(2)–Fe(2)–O(4)	96.75(16)	O(8)–Fe(4)–O(10)	94.74(16)
O(2)–Fe(2)–O(6)	95.19(16)	O(8)–Fe(4)–O(12)	97.77(16)
O(2)–Fe(2)–N(2)	82.26(15)	O(8)–Fe(4)–N(8)	82.55(15)
O(2)–Fe(2)–N(4)	97.95(17)	O(8)–Fe(4)–N(10)	166.20(15)
O(2)–Fe(2)–N(6)	165.54(15)	O(8)–Fe(4)–N(12)	97.46(16)
O(4)–Fe(2)–O(6)	99.28(16)	O(10)–Fe(4)–O(12)	95.97(17)
O(4)–Fe(2)–N(2)	166.61(15)	O(10)–Fe(4)–N(8)	96.85(16)
O(4)–Fe(2)–N(4)	81.99(14)	O(10)–Fe(4)–N(10)	82.68(15)
O(4)–Fe(2)–N(6)	97.68(16)	O(10)–Fe(4)–N(12)	167.80(15)
O(6)–Fe(2)–N(2)	94.10(16)	O(12)–Fe(4)–N(8)	167.11(16)
O(6)–Fe(2)–N(4)	166.56(15)	O(12)–Fe(4)–N(10)	95.98(16)
O(6)–Fe(2)–N(6)	81.61(15)	O(12)–Fe(4)–N(12)	82.26(15)
N(2)–Fe(2)–N(4)	84.92(15)	N(8)–Fe(4)–N(10)	84.30(15)
N(2)–Fe(2)–N(6)	83.91(15)	N(8)–Fe(4)–N(12)	84.92(15)
N(4)–Fe(2)–N(6)	84.96(15)	N(10)–Fe(4)–N(12)	85.50(15)

Table 3
Selected bond lengths (Å) and angles (°) for $[Co_2(\mu\text{-}L)_3]\cdot 2CH_3CN$ ($\mathbf{3}\cdot 2CH_3CN$)

Co(1)–O(1)	1.882(3)	Co(2)–O(2)	1.898(3)
Co(1)–O(3)	1.891(3)	Co(2)–O(4)	1.895(3)
Co(1)–O(5)	1.891(3)	Co(2)–O(6)	1.896(3)
Co(1)–N(1)	1.917(3)	Co(2)–N(2)	1.920(3)
Co(1)–N(3)	1.894(3)	Co(2)–N(4)	1.906(3)
Co(1)–N(5)	1.927(3)	Co(2)–N(6)	1.909(3)
O(1)–Co(1)–O(3)	87.49(12)	O(2)–Co(2)–O(4)	86.91(14)
O(1)–Co(1)–O(5)	86.20(12)	O(2)–Co(2)–O(6)	88.74(13)
O(1)–Co(1)–N(1)	92.94(12)	O(2)–Co(2)–N(2)	91.66(14)
O(1)–Co(1)–N(3)	175.96(13)	O(2)–Co(2)–N(4)	88.08(13)
O(1)–Co(1)–N(5)	89.27(13)	O(2)–Co(2)–N(6)	178.30(13)
O(3)–Co(1)–O(5)	89.18(13)	O(4)–Co(2)–O(6)	88.25(13)
O(3)–Co(1)–N(1)	88.74(13)	O(4)–Co(2)–N(2)	175.18(14)
O(3)–Co(1)–N(3)	91.84(13)	O(4)–Co(2)–N(4)	92.07(13)
O(3)–Co(1)–N(5)	176.75(13)	O(4)–Co(2)–N(6)	92.37(14)
O(5)–Co(1)–N(1)	177.78(13)	O(6)–Co(2)–N(2)	87.12(14)
O(5)–Co(1)–N(3)	89.81(13)	O(6)–Co(2)–N(4)	176.78(14)
O(5)–Co(1)–N(5)	90.99(13)	O(6)–Co(2)–N(6)	92.78(13)
N(1)–Co(1)–N(3)	91.03(14)	N(2)–Co(2)–N(4)	92.48(14)
N(1)–Co(1)–N(5)	91.05(14)	N(2)–Co(2)–N(6)	89.18(14)
N(3)–Co(1)–N(5)	91.41(13)	N(4)–Co(2)–N(6)	90.41(14)

4. Conclusion

Three dinuclear triple helical complexes having the general formula $[M_2(\mu\text{-}L)_3]$ (M = Mn(III), Fe(III) and Co(III)) with a tetradentate diazine ligand (L^{2-}) are reported. The complexes are characterized with the help of elemental analysis, solution electrical conductivity, various spectroscopic and cryomagnetic measurements. Dicobalt(III) complex is diamagnetic while the temperature dependent magnetic susceptibility data of the dimanganese(III) and

the diiron(III) complexes indicate a weak intramolecular antiferromagnetic spin-exchange between the metal ions. The molecular structures of the diiron(III) and the dicobalt(III) complexes are determined by X-ray crystallography. The dinucleating tetradentate ligand (L^{2-}) coordinates the metal ions via the two phenolate-O and the two imine-N atoms. In each complex, both metal ions are in facial N_3O_3 coordination spheres. The triple helical structure of $[M_2(\mu\text{-}L)_3]$ is generated due to the twisting of the two N,O-donor chelating sites of each L^{2-} along the N–N single bond enforced by the two pseudo-octahedral metal ions.

Supplementary material

CCDC 642656 and 642657 contain the supplementary crystallographic data for $\mathbf{2}\cdot 2CH_2Cl_2$ and $\mathbf{3}\cdot 2CH_3CN$. These data can be obtained free of charge via http://www.ccdc.cam.ac.uk/conts/retrieving.html, or from the Cambridge Crystallographic Data Centre, 12 Union Road, Cambridge CB2 1EZ, UK; fax: (+44) 1223-336-033; or e-mail: deposit@ccdc.cam.ac.uk.

Acknowledgements

Financial support for this work was provided by the Council of Scientific and Industrial Research, New Delhi (Grant No. 01(1880)/03/EMR-II). We thank the University Grants Commission, New Delhi for the facilities provided under the UPE and CAS programs. Our sincere thanks are due to Prof. A. R. Chakravarty for providing the cryomagnetic data. X-ray crystal structures were determined at the National Single Crystal Diffractometer Facility, School of Chemistry, University of Hyderabad (established by the Department of Science and Technology, New Delhi).

References

[1] J.-M. Lehn, Supramolecular Chemistry, VCH, Weinheim, 1995.
[2] C. Piguet, G. Bernardinelli, G. Hopfgartner, Chem. Rev. 97 (1997) 2005.
[3] A. Williams, Chem.-Eur. J. 3 (1997) 15.
[4] M. Albrecht, Chem. Rev. 101 (2001) 3457.
[5] M.J. Hannon, L.J. Childs, Supramol. Chem. 16 (2004) 7.
[6] O. Kahn, Molecular Magnetism, VCH, Weinheim, 1993.
[7] C.-T. Chen, K.S. Suslick, Coord. Chem. Rev. 128 (1993) 293.
[8] M. Eddaoudi, D.B. Moler, H. Li, B. Chen, T.M. Reineke, M. O'Keeffe, O.M. Yaghi, Acc. Chem. Res. 34 (2001) 319.
[9] B. Kesanli, W. Lin, Coord. Chem. Rev. 246 (2003) 305.
[10] B. Schoentjes, J.-M. Lehn, Helv. Chim. Acta 78 (1995) 1.
[11] I. Meistermann, V. Moreno, M.J. Prieto, E. Molderheim, E. Sletten, S. Khalid, M. Rodger, J. Perberdy, C.J. Isaac, A. Rodger, M.J. Hannon, Proc. Natl. Acad. Sci. USA 99 (2002) 5069.
[12] M.H.V. Huynh, D.M. Dattelbaum, T.J. Meyer, Coord. Chem. Rev. 249 (2005) 457.
[13] J.-M. Lehn, J. Siegel, J. Harrowfield, B. Chevrier, D. Moras, Proc. Natl. Acad. Sci. USA 84 (1987) 2565.
[14] E.C. Constable, Tetrahedron 48 (1992) 10013.
[15] R. Krämer, J.-M. Lehn, A. Marquis-Rigault, Proc. Natl. Acad. Sci. USA 90 (1993) 5394.
[16] M.A. Houghton, A. Bilyk, M.M. Harding, P. Turner, T.W. Hambley, J. Chem. Soc., Dalton Trans. (1997) 2725.
[17] W.J. Stratton, D.H. Busch, J. Am. Chem. Soc. 80 (1958) 1286.
[18] W.J. Stratton, D.H. Busch, J. Am. Chem. Soc. 80 (1958) 3191.
[19] W.J. Stratton, D.H. Busch, J. Am. Chem. Soc. 82 (1960) 4834.
[20] P.W. Ball, A.B. Blake, J. Chem. Soc. A (1969) 1415.
[21] W.J. Stratton, Inorg. Chem. 9 (1970) 517.
[22] P.D.W. Boyd, M. Gerloch, G.M. Sheldrick, J. Chem. Soc., Dalton Trans. (1974) 1097.
[23] C.J. O'Connor, R.J. Romananch, D.M. Robertson, E.E. Eduok, F.R. Fronezek, Inorg. Chem. 22 (1983) 449.
[24] Z. Xu, L.K. Thompson, D.O. Miller, Inorg. Chem. 36 (1997) 3985.
[25] L.K. Thompson, Z. Xu, A.E. Goeta, J.A.K. Howard, H.J. Clase, D.O. Miller, Inorg. Chem. 37 (1998) 3217.
[26] Z. Xu, L.K. Thompson, D.O. Miller, H.J. Clase, J.A.K. Howard, A.E. Goeta, Inorg. Chem. 37 (1998) 3620.
[27] Z. Xu, L.K. Thompson, C.J. Matthews, D.O. Miller, A.E. Goeta, C. Wilson, J.A.K. Howard, M. Ohba, H. Okawa, J. Chem. Soc., Dalton Trans. (2000) 69.
[28] G. Dong, D. Chun-ying, F. Chen-jie, M. Qing-jin, J. Chem. Soc., Dalton Trans. (2002) 834.
[29] J. Hamblin, A. Jackson, N.W. Alcock, M.J. Hannon, J. Chem. Soc., Dalton Trans. (2002) 1635.
[30] G. Dong, P. Ke-liang, D. Chin-ying, H. Cheng, M. Qing-jin, Inorg. Chem. 41 (2002) 5978.
[31] P.V. Bernhardt, P. Chin, D.R. Richardson, J. Chem. Soc., Dalton Trans. (2004) 3342.
[32] J. Saroja, V. Manivannan, P. Chakraborty, S. Pal, Inorg. Chem. 34 (1995) 3099.
[33] M. Hong, G. Dong, D. Chun-ying, L. Yu-ting, M. Qing-jin, J. Chem. Soc., Dalton Trans. (2002) 3422.
[34] M. Hong, F. Chen-jie, D. Chun-ying, L. Yu-ting, M. Qing-jin, J. Chem. Soc., Dalton Trans. (2003) 1229.
[35] S.G. Sreerama, S. Pal, Inorg. Chem. 44 (2005) 6299.
[36] F. Umland, E. Hohaus, K. Brodtke, Chem. Ber. 106 (1973) 2427.
[37] E. Hohaus, Z. Anorg. Allg. Chem. 506 (1983) 185.
[38] H. Höpfl, N. Farfán, Can. J. Chem. 76 (1998) 1853.
[39] W.E. Hatfield, in: E.A. Boudreaux, L.N. Mulay (Eds.), Theory and Applications of Molecular Paramagnetism, Wiley, New York, 1976, p. 491.
[40] SMART Version 5.630 and SAINT-PLUS Version 6.45, Bruker-Nonius Analytical X-ray Systems Inc., Madison, WI, USA, 2003.
[41] G.M. Sheldrick, SADABS, Empirical Absorption Correction Program, University of Göttingen, Göttingen, Germany, 1997.
[42] D. Guo, J.-H. Li, J.-J. Xie, C.-Y. Duan, Q.-J. Meng, Chin. J. Inorg. Chem. 18 (2002) 1215.
[43] G.M. Sheldrick, SHELX-97, Structure Determination Software, University of Göttingen, Göttingen, Germany, 1997.
[44] L.J. Farrugia, J. Appl. Crystallogr. 32 (1999) 837.
[45] P. McArdle, J. Appl. Crystallogr. 28 (1995) 65.
[46] A.L. Spek, PLATON, A Multipurpose Crystallographic Tool, Utrecht University, Utrecht, The Netherlands, 2002.
[47] C.J. O'Connor, Prog. Inorg. Chem. 29 (1982) 203.
[48] G.V.R. Chandramouli, C. Balagopalakrishna, M.V. Rajasekharan, P.T. Manoharan, Comput. Chem. 20 (1996) 353.

[18]. Here we report the synthesis and characterization of five new Zn(II) complexes of a recently reported salicylaldehyde 3-hexamethyleneiminyl thiosemicarbazone [19] with different coligands, pyridine, 2,2′-bipyridine, 1,10-phenanthroline and γ-picoline.

2. Experimental

2.1. Materials

All the solvents used for the synthesis of the thiosemicarbazone ligands and their complexes were purified by distillation. Pyridine, γ-picoline, 1,10-phenanthroline and 2,2′-bipyridine were used as received. The synthesis of the ligand H_2L is reported elsewhere [19].

2.2. Synthesis of complexes

Complex **1** was synthesized by refluxing an ethanolic solution of H_2L^1 (2 mmol, 0.554 g) with an ethanolic solution of $Zn(OAc)_2 \cdot 2H_2O$ (1 mmol, 0.219 g) for 4 h. The complex formed was filtered, washed with ethanol, then ether and dried over P_4O_{10} *in vacuo*. All the other complexes were prepared by refluxing an ethanolic solution of the ligand H_2L^1 (1 mmol, 0.277 g) and heterocyclic bases like pyridine, bipyridine, 1,10-phenanthroline and γ-picoline (1 mmol) with an ethanolic solution of $Zn(OAc)_2 \cdot 2H_2O$ (1 mmol, 0.219 g) 1:1:1 molar ratio for 4 h. The complexes that separated were filtered, washed with ethanol and finally with ether and dried over P_4O_{10} *in vacuo*. Crystals suitable for X-ray analysis for compound **1** were obtained by slow evaporation of a solution of the compound from an ethanol solution in eight days.

2.3. Physical measurements

Elemental analyses were carried out using a Vario EL III CHN analyzer at SAIF, Kochi, India. Infrared spectra were recorded on a Thermo Nicolet, AVATAR 370 DTGS model FTIR spectrophotometer as KBr pellets at SAIF, Kochi, India. Electronic spectra were recorded on a UVD 3500 UV–Vis-Double beam spectrophotometer from solutions in DMF. ^{1}H NMR spectra were recorded on a Brucker AMX 400 in $CDCl_3$ with TMS as an internal standard.

2.4. X-ray crystallography

The molecular structure of compound **1** was determined by single crystal X-ray diffraction method. Intensity data and cell parameters were recorded at room temperature (293 K) on a Nonius, MACH3 diffractometer equipped with graphite monochromated Mo Kα ($\lambda = 0.71073$ Å) radiation. Crystallographic and experimental details for the structure are summarized in Table 1. Maxus (Nonius software) was used for data reduction [20]. Two atoms, C11 and C12 in the ring containing N(3), are disordered as the two carbons split over two sets of positions. Restraints were applied to assist the geometry of the disordered atoms. The ratio of major to minor disorder component is 56.8:43.2. The trial structure was solved using SHELXS-97 [21] and refinement was carried out by full- matrix least squares on F^2 (SHELXL-97) [22]. The non-hydrogen atoms were refined with anisotropic thermal parameters. All hydrogen atoms were geometrically fixed and refined using a riding model. The intensity data were collected by the ω-scan mode within $1.59° < \theta < 24.99°$ for *hkl* ($-12 \leqslant h \leqslant 12$, $-13 \leqslant k \leqslant 13$, $-15 \leqslant l \leqslant 0$) on a triclinic system. The molecular graphics employed were ORTEP [23] and PLATON [24].

Table 1
Crystal refinement parameters of compound (**1**)

Empirical formula	$C_{28}H_{36}N_6O_2S_2Zn$
Formula weight	618.12
Temperature (K)	293(2)
Wavelength (Å)	0.71073
Crystal system, space group	triclinic, $P\bar{1}$
Unit cell dimensions	
a (Å)	10.3390(8)
b (Å)	11.0940(10)
c (Å)	13.0270(14)
α (°)	82.641(8)
β (°)	82.662(7)
γ (°)	79.174(7)
Volume (Å^3)	1447.3(2)
Z, calculated density (Mg/m^3)	2, 1.418
Absorption coefficient (mm^{-1})	1.030
F(000)	648
Crystal size (mm)	$0.30 \times 0.15 \times 0.15$
θ Range for data collection (°)	1.59–24.99
Index ranges	$-12 \leqslant h \leqslant 12$, $-13 \leqslant k \leqslant 13$, $-15 \leqslant l \leqslant 0$
Reflections collected/unique (R_{int})	5298/5053 (0.0260)
Completeness to 2θ	24.99 99.2%
Absorption correction	ψ-scan
Maximum and minimum transmission	0.8609 and 0.7476
Refinement method	full-matrix least-squares on F^2
Data/restraints/parameters	5053/0/371
Goodness-of-fit on F^2	1.012
Final R indices [$I > 2\sigma(I)$]	$R_1 = 0.0417$, $wR_2 = 0.0891$
R indices (all data)	$R_1 = 0.1122$, $wR_2 = 0.1049$
Largest difference in peak and hole (e Å^{-3})	0.425 and −0.509

3. Results and discussion

The colors and partial elemental analysis data of all the complexes are listed in Table 2. All the complexes except **1** were assigned the general formula MLB, where B represents heterocyclic bases, pyridine, 2,2′-bipyridine, 1,10-phenanthroline and γ-picoline. The complexes **3** and **4** contain uncoordinated water molecules also. From the structural, elemental and spectral studies, compounds **1**–**5** were assigned the empirical formulae $[Zn(HL)_2]$, [Zn(L)py], $[Zn(L)bipy] \cdot 3.5H_2O$, $[Zn(L)phen] \cdot H_2O$ and [Zn(L)γ-pic] respectively.

Table 2
Stoichiometries, colors and partial elemental analyses of the complexes

Compound	Stoichiometries	Color	*Anal.* Found (Calc.) %		
			C	H	N
H_2L	$C_{14}C_{19}N_3OS$	pale yellow	60.25(60.62)	7.37(6.9)	15.09(15.15)
$[Zn(HL)]_2$ (**1**)	$C_{28}H_{36}N_6O_2SZn$	yellow	54.27(54.4)	5.98(5.87)	13.60(13.60)
[ZnLpy] (**2**)	$C_{19}H_{22}N_4OSZn$	yellow	54.23(54.35)	5.30(5.28)	13.26(13.34)
[ZnLbipy3.5H_2O] (**3**)	$C_{24}H_{32}N_5O_4SZn$	yellow	51.67(51.47)	5.77(5.76)	12.54(12.51)
[ZnLphenH_2O] (**4**)	$C_{26}H_{27}N_5O_2SZn$	orange	57.87(57.94)	5.27(5.05)	13.43(12.99)
[ZnLγ-pic] (**5**)	$C_{20}H_{24}N_4OSZn$	yellow	54.86(55.36)	5.76(5.58)	12.81(12.91)

3.1. Crystal structure of $[Zn(HL)_2]$ (1)

The molecular structure of compound **1**, along with the atom numbering scheme, is given in Fig. 1 and selected bond lengths and bond angles are summarized in Table 3. The ligands coordinate to the Zn(II) ion through the azomethine nitrogen and thiolate sulfur to form a highly distorted tetrahedral geometry. The phenolic group of the ligand is retained as such and is placed away from the metal center. This is because of the change of conformation of the ligand from the *E* form to the *Z* form about the azomethine bond. The free ligand H_2L in its solid form is in a position to bond the metal in a tridentate ONS manner [19]. The conformation change of a ligand from a bidentate to a tridentate manner on coordination is known, but this reverse case is seen for the first time for thiosemicarbazone ligands of Zn(II) complexes. However a CSD search shows a similar conformation in Zn(II) hydrazones [25–27].

The NS chelation results in two five membered planar rings, Zn1, N1, N2, C8, S1 having a maximum deviation of −0.053(4) Å for C8 and Zn1, S2, N4, N5, C22 with a maximum deviation of 0.002(3) Å for N4. The dihedral angle between these planar rings is 89.28(9)°. The smaller angles around Zn(II) are 86.29(9)° for N4–Zn1–S2 and 86.57(10)° for N1–Zn1–S1. These factors clearly point out the rigidity of the core thiosemicarbazone moiety, even after coordination, and the highly distorted tetrahedral coordination. The other angles around zinc are between 110.90(12)° and 134.39(5)°. The Zn–N distances in the complex are smaller compared to $[Zn(Acehexim)_2]$ (Zn–N12 2.044(9) and Zn–N22 2.068(10) Å) [28]; $[Zn(PzAm4M)_2]\cdot 2CH_3CN$ (Zn1–N12 2.072(2) and Zn1–N22 2.071(2) Å) [29]; $[ZnL^1_2MeOH]$ (Zn–N3 2.114(2) and Zn–N13 2.108(2) Å) [30], $[Zn(Am4m)(OAc)_2]_2$ (Zn1–N2 2.050(2) Zn1–N2 2.227(2) Å) [31] and $[Zn(HAm4E)I_2]$ (Zn–N12 2.120(7) Å) [32]. This indicates stronger coordination of the azomethine nitrogen in compound **1**. The

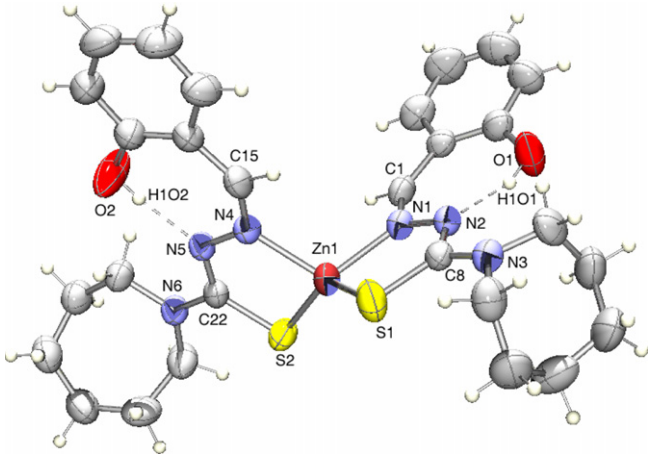


Fig. 1. ORTEP diagram for compound **1** with 50% probability ellipsoids. Minor disorder components at C11/C12 are removed for clarity.

Table 3
Comparison of bond lengths (Å) and bond angles (°) of H_2L and $[Zn(HL)_2]$ (**1**)

	H_2L[a]	$[Zn(HL)_2]$
Bond lengths (Å)		
Zn1–N1		2.026(3)
Zn1–N4		2.040(3)
Zn1–S1		2.2597(13)
Zn1–S2		2.2462(12)
C1–N1	1.269(3)	1.293(5)
C15–N4		1.296(5)
N1–N2	1.356(3)	1.385(4)
N4–N5		1.383(4)
N2–C8	1.362(3)	1.332(5)
N5–C22		1.329(4)
C8–S1	1.684(3)	1.744(4)
C22–S2		1.749(4)
C3–O1	1.344(3)	1.336(4)
O2–C17		1.334(5)
Bond angles (°)		
N1–Zn1–N4		110.90(12)
N1–Zn1–S2		123.53(10)
N4–Zn1–S2		86.29(9)
N1–Zn1–S1		86.57(10)
N4–Zn1–S1		116.40(10)
S2–Zn1–S1		134.39(5)
C15–N4–N5		119.6(3)
C15–N4–Zn1		121.9(3)
N5–N4–Zn1		118.5(2)
C1–N1–N2	120.0(2)	119.5(3)
C1–N1–Zn1		122.2(3)
N2–N1–Zn1		118.1(2)
N2–C8–N3	115.4(2)	117.2(3)
N2–C8–S1	119.5(2)	125.8(3)
N3–C8–S1	125.0(2)	117.0(3)
N5–C22–N6		115.9(3)
N5–C22–S2		126.3(3)
N6–C22–S2		117.8(3)

[a] Ref. [19].

Zn–S bond distance is found to be smaller than that for the other zinc compounds, $[Zn(Am4M)(OAc)]_2$ (Zn1–S1 2.370(1) Å) [31] $[Zn(Am4E)(OAc)]_2$ (Zn1–S1 2.431(6) Å) [32] and $[Zn(HAm4E)I_2]$ (Zn–S1 2.502(3) Å) [32] and $[ZnL_2^4]\cdot 0.5H_2O$ (Zn1–S1 2.3731(10) Å) [33]. This may be due to the bulkiness of the thiosemicarbazone moiety. The coordination results in the changes of bond lengths and angles of the thiosemicarbazone moiety, as expected. The C–S bond length increases from 1.684(3) Å to 1.744(4) and 1.749(4) Å. Similarly C8–N2 (and C22–N5) suffers a significant decrease from 1.362(3) Å seen in the free ligand. These changes indicate the coordination of the deprotonated sulfur after enolization. The other bond lengths and angles also suffer some changes, but not significantly. The chair conformation of the hexamethyleneiminyl ring is retained in the complex. The intramolecular hydrogen bond $O–H\cdots N_{azomethine}$ seen in the free ligand is retained in compound **1**, but the O–H···S bond disappears. Relevant hydrogen bonding interactions are given in Table 4. However no significant π–π or C–H···π interactions are found in the packing. In the unit cell, the molecules are packed in a 'face-to-face' manner along the *a* axis and the weak intermolecular hydrogen bonds, C18–H18···O1, link the molecules into one-dimensional sheets along the *c* axis (Fig. 2).

3.2. Infrared spectra

The IR spectral bands most useful for the determination of the mode of coordination are given in Table 5. The bands corresponding to *ν*(N–H) appear at 3315 cm^{-1} for H_2L, but disappear in the spectra of all the complexes. The band at 1612 due to *ν*(C=N) of the thiosemicarbazone moiety shifts to ~1590 cm^{-1} upon coordination [32]. This confirms the coordination *via* the azomethine nitrogen. Coordination of the azomethine nitrogen is also consistent with the presence of a band in the range 405–420 cm^{-1}, assignable to *ν*(Zn–N), for these complexes [32]. A small shift in the absorption bands due to the *ν*(N–N) stretching vibrations from 1037 to a higher region is due to the increase in the double bond character off-setting the loss of electron density *via* donation to the metal and is a confirmation of the coordination of the ligand through the azomethine nitrogen atom [3]. Coordination *via* the thiolate sulfur is indicated by a decrease in the frequency of the thioamide band *ν*(C=S), found at 1324 and 861 cm^{-1} in the uncomplexed thiosemicarbazone, by 20–100 cm^{-1} in the complexes [34,35]. This decrease in stretching frequency of thiolate sulfur in the complexes is indicated by

Table 4
H-bonding interactions in compound **1**

D–H···A	D···H (Å)	H···A (Å)	D···A (Å)	D–H···A (°)
O1–H1O1···N2^{i}	0.79(5)	1.77(5)	2.556(5)	174(5)
O2–H1O2···N5^{i}	0.85(6)	1.73(6)	2.568(5)	172(6)

D = donor, A = acceptor, equivalent position code: i = *x*, *y*, *z*.

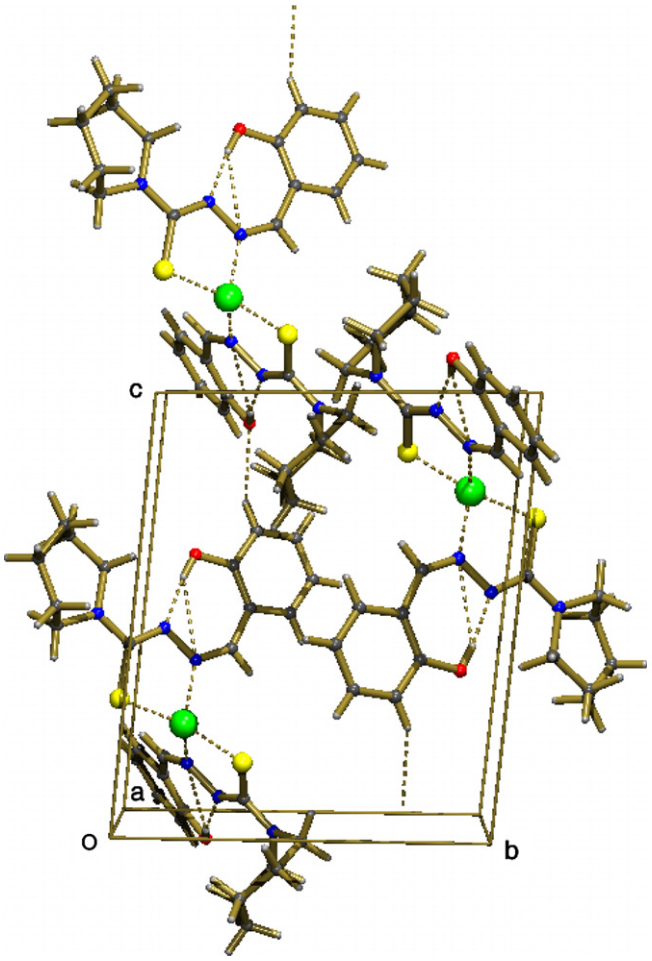


Fig. 2. Unit cell packing of the compound **1** along the *a* axis.

Campbell [36]. Another strong band is found in the region of 1535–1545 cm^{-1} and is due to the newly formed *ν*(N=C) bond in the spectra for these complexes. The bands at 325–380 cm^{-1}, assignable to *ν*(Zn–S) in the complexes, are consistent with sulfur coordination [1,37]. The new peaks observed in the range 520–570 cm^{-1} are due to the Zn–$O_{(phenolic)}$ bond [38]. Except in complex **1**, coordination via the phenolic oxygen is indicated by a decrease in the frequency of *ν*(CO), found at 1271 cm^{-1} in the uncomplexed thiosemicarbazone, by 60–80 cm^{-1} in the spectra of the complexes. In complex **1**, *ν*(CO) does not shift to a much lower frequency, indicating that coordination does not occur through the phenolic oxygen.

3.3. ^1H NMR spectra

The numbering schemes used in the ^1H NMR spectra of the ligand and its complexes are shown in Fig. 3. The ^1H NMR spectrum of H_2L shows a sharp singlet, integrating as one hydrogen, at $\delta = 11.31$ (s, 1H) ppm which is assigned to the proton attached to the oxygen atom. The downfield shift of this proton is assigned to its intra and intermolecular hydrogen bonding interactions. The hydrogen bonding decreases the electron density around the pro-

Table 5
IR Spectroscopic assignments for H_2L and its zinc complexes

Compound	ν(CN)	ν(NN)	ν(CO)	ν(CS)	ν(ZnN)	ν(ZnS)	ν(ZnO)	Bands due to heterocyclic bases
H_2L	1612	1037	1271	1324,764				
$[Zn(HL)_2]$ (**1**)	1583	1097	1261	1285,754	404	360		
[ZnLpy] (**2**)	1592	1091	1190	1276,753	417	325	547	1421, 632, 453
$[ZnLbipy]\cdot 3.5H_2O$ (**3**)	1584	1083	1202	1285,755	415	380	525	1434, 664, 452
$[ZnLphen]\cdot H_2O$ (**4**)	1590	1099	1200	1287,755	420	330	528	1425, 640, 449
[ZnLγ-pic] (**5**)	1589	1099	1188	1298,755	416	325	545	1420, 664, 447

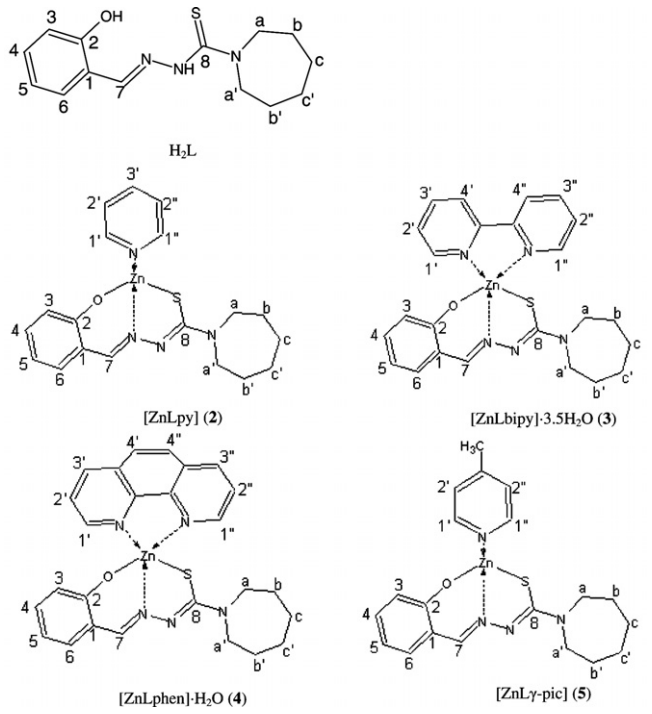


Fig. 3. The structures of the ligand and complexes are given along with their atom labelling.

ton and thus moves the proton absorption to a lower field [39]. Absence of any coupling interactions by ^{2}NH due to the unavailability of protons on neighboring atoms render a singlet peak for the imine proton at $\delta = 8.89$ (s, 1H). A sharp singlet at $\delta = 7.99$ (s, 1H) ppm corresponds to the ^{7}CH = proton. The downfield shift of this proton is due to the presence of the aromatic ring present in the thiosemicarbazone moiety. Aromatic protons ^{4}CH, ^{6}CH, ^{3}CH, ^{5}CH appear in the range 6.68–7.14 ppm. Aliphatic protons of the hexamethyleneiminyl ring were observed as three signals *viz* 3.36 (s, 4H), 1.66 (s, 4H) and 1.42 (s, 4H), assigned to positions a, b and c respectively. ^{1}H NMR assignments are in agreement with values already reported [2,3,40,41].

^{1}H NMR assignments for the Zn(II) complexes are included in Table 6. The signals for the phenolic OH (except in **1**) and ^{2}NH are absent from the spectra of the complexes, as expected because of their loss on complex formation, which is evidence for the coordination of the ligand as a doubly deprotonated anion. This confirms the coordination through the phenolic oxygen and also *via* the thiolate sulfur atom in those complexes. Complex **1** shows a peak at $\delta = 13.36$ ppm due to the presence of the uncoordinated hydroxyl group. The more downfield shift of the OH protons compared to the uncomplexed thiosemicarbazone is due to overall loss of electron density and intra and intermolecular hydrogen bonding interactions. This is confirmed from the crystal structure. There is considerable downfield shifting of the signals for the ring protons in the spectra of complexes compared to the uncomplexed thiosemicarbazone. This is due to the loss of electron density *via* coordination of the ligand to the metal center. Protons due to the heterocyclic bases appear in the region 8.49–7.15 ppm. The downfield shift of the proton peaks corresponding to ^{6}H Ph, H^1 of the heterocyclic bases are the result of the withdrawal of electron density from the thiosemicarbazone moiety and the

Table 6
($CDCl_3$) assignments of ligand H_2L and its Zn(II) complexes (δ in ppm)

Compound	Aromatic protons								
	OH	H^6 Ph	H^4 Ph	H^3 Ph	H^5 Ph	^{8}CH=	^{a}CH$_2$	^{b}CH$_2$	^{c}CH$_2$
H_2L	11.3	7.09	6.97	6.80	6.67	7.99	3.63	1.66	1.42
$[Zn(HL)_2]$ (**1**)	13.36	7.16	7.14	6.91	6.81	8.20	3.89	1.88	1.59
[ZnLpy] (**2**)		7.18	7.05	6.68	6.68	8.63	3.83	1.78	1.54
$[ZnLbipy]\cdot 3.5H_2O$ (**3**)		7.25	7.17	6.91	6.82	8.4	3.85	1.88	1.62
$[ZnLphen]\cdot H_2O$ (**4**)		7.20	7.05	6.81	6.81	8.48	3.65	1.71	1.49
[ZnLγ-Pic] (**5**)		7.18	7.06	6.81	6.68	8.52	3.76	1.74	1.52

[ZnLpy] (**2**)			$[ZnLbipy]\cdot 3.5H_2O$ (**3**)				$[ZnLphen]\cdot H_2O$ (**4**)				[ZnLγ-Pic] (**5**)	
H$^{1'}$	H$^{3'}$	H$^{2'}$	H$^{1'}$	H$^{4'}$	H$^{3'}$	H$^{2'}$	H$^{1'}$	H$^{3'}$	H$^{4'}$	H$^{2'}$	H$^{1'}$	H$^{2'}$
8.41	7.76	7.31	8.12	7.98	7.70	7.35	8.49	8.29	7.75	7.65	7.27	7.20
s, 2H	t, 2H	s, 2H	d, 2H	d, 2H	t, 2H	t, 2H	d, 2H	d, 2H	s, 2H	dd, 2H	s, 2H	d, 2H

heterocyclic base due to coordination with the metal atom [42]. A small downfield shift occurs for the aliphatic protons in the complexes due to the overall loss of electron density.

3.4. Electronic spectra

The electronic spectrum of the ligand H_2L recorded in DMF shows bands at 280 and 321 nm assignable to $\pi\rightarrow\pi^*$ transitions of the phenyl ring [3,41,43] and $n\rightarrow\pi^*$ transitions of the azomethine and thioamide functions respectively. A second $n\rightarrow\pi^*$ band is found at 339 nm [44,45]. These intraligand bands are slightly shifted on complexation. In the spectra of the complexes these bands are found in the region of 280–290 nm and 325–340 nm respectively. The shift of the $\pi\rightarrow\pi^*$ bands to a longer wavelength region in the complexes is the result of the C–S bond being weakened and the conjugation system enhanced on complexation [46,47].

A moderately intense broad band for the complex in the region 370–400 nm is assigned to Zn(II) → S transitions. MLCT maxima of the phenolate complex shows line broadening with a tail running into the visible part of the spectrum. This may result from a phenolate to Zn(II) LMCT band being superimposed on the low energy side of Zn(II) → S transitions [1]. No appreciable absorptions occurred above 500 nm in DMF solution, indicating the absence of d–d bands which is in accordance with the d^{10} configuration of the Zn(II) ion.

Acknowledgements

L. Latheef thanks the Council of Scientific and Industrial Research, New Delhi, India and E. Manoj thanks the University Grant Commission, New Delhi, India for financial support in the form of fellowships. M.R.P. Kurup is thankful to the DST, New Delhi, India for financial support. The authors also thank the National Single Crystal X-ray diffraction Facility, IIT, Bombay for X-ray data collection.

Appendix A. Supplementary material

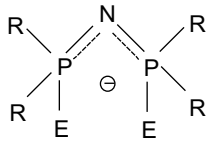
CCDC 279327 contains the supplementary crystallographic data for **1**. These data can be obtained free of charge via http://www.ccdc.cam.ac.uk/conts/retrieving.html, or from the Cambridge Crystallographic Data Centre, 12 Union Road, Cambridge CB2 1EZ, UK; fax: (+44) 1223-336-033; or e-mail: deposit@ccdc.cam.ac.uk. Supplementary data associated with this article can be found, in the online version, at doi:10.1016/j.poly. 2007.05.023.

References

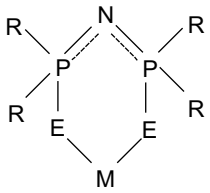
[1] A. Sreekanth, S. Sivakumar, M.R.P. Kurup, J. Mol. Struct. 655 (2003) 47.
[2] P. Bindu, M.R.P. Kurup, T.R. Satyakeerthy, Polyhedron 18 (1998) 321.
[3] R.P. John, A. Sreekanth, M.R.P. Kurup, A. Usman, I.A. Razak, H.K. Fun, Spectrochim. Acta, Part A 59 (2003) 1349.
[4] A. Sreekanth, R.P. John, M.R.P. Kurup, in: XXXXVth International Conference on Coordination Chemistry (ICCC 35) P4.005, Heidelberg, Germany, July, 21–26, 2002, p. 543.
[5] C.K. Alphonsa, M.R.P. Kurup, Synth. React. Inorg. Met.-Org. Chem. 29 (1999) 805.
[6] D.X. West, S.B. Padhye, P.B. Sonawane, R.C. Chikate, Asian J. Chem. Rev. 1 (1990) 125.
[7] D.L. Klayman, J.F. Bartosevich, T.S. Griffin, C.J. Manson, J.P. Scovill, J. Med. Chem. 22 (1979) 885.
[8] D.K. Demertzi, A. Domopoulou, M.A. Demertzis, G. Valle, A.J. Papageorgiou, J. Inorg. Biochem. 68 (1997) 147.
[9] D.L. Klayman, J.P. Scovill, J.F. Bartosevich, J. Bruce, J. Med. Chem. 26 (1983) 35.
[10] I. Garcia-Santos, U. Abram, R. Alberto, E.V. Lopez, A. Sanchez, Inorg. Chem. 43 (2004) 1836.
[11] B. Singh, U. Srivastava, Synth. React. Inorg. Met.-Org. Chem. 19 (1989) 279.
[12] Z. Lu, A.C. Whyte, A.L. Rheingold, R.H. Crabtree, Inorg. Chem. 32 (1993) 3991.
[13] D.X. West, M.M. Salberg, G.A. Bain, A.E. Liberta, J.V. Martinez, S.H. Ortega, Transition Met. Chem. 21 (1996) 206.
[14] M. Chatterjee, S. Ghosh, Transition Met. Chem. 23 (1998) 355.
[15] M.B. Ferrari, G.G. Fava, C. Pelizzic, P. Tarasconi, J. Chem. Soc., Dalton Trans. (1992) 2153.
[16] D. Solaiman, L. Saryan, D.H. Petering, J. Inorg. Biochem. 10 (1979) 135.
[17] M.K. Saxena, R. Singh, B.K. Sinha, J.P. Srivastava, Asian J. Chem. 7 (1995) 266.
[18] W.L. Kwik, K.P. Ang, H.S.O. Chan, V. Chebolu, S.A. Koch, J. Chem. Soc., Dalton Trans. (1986) 2519.
[19] L. Latheef, E. Manoj, M.R.P. Kurup, Acta Crystallogr., Sect C 62 (2006) 16.
[20] Nonius, MACH3 software, B.V. Nonius, Delft, The Netherlands, 1997.
[21] G.M. Sheldrick, Acta Crystallogr., Sect. A 46 (1990) 467.
[22] G.M. Sheldrick, SHELXL-97 and SHELXS-97 Program for the solution of Crystal Structures, University of Gottingen, Germany, 1997.
[23] L.J. Farrugia, J. Appl. Cryst. 30 (1997) 565.
[24] A.L. Spek, J. Appl. Cryst. 36 (2003) 7.
[25] A. Lyubchova, N. Jouini, A. Massat, J.P. Doucet, K. Boubekeur, A. Cosse-Barbi, Z. Kristallogr. 216 (2001) 556.
[26] H. Ali, N.A. Khamis, W.J. Basirun, B.M. Yamin, Acta Crystallogr., Sect. E 60 (2004) m873.
[27] H. Ali, N.A. Khamis, B.M. Yamin, Acta Crystallogr., Sect. E 60 (2004) m1311.
[28] A. Castineiras, D.X. West, J. Mol. Struct. 604 (2002) 113.
[29] E. Labisbal, A. Sousa-Pedrares, A. Castineiras, J.K. Swearingen, D.X. West, Polyhedron 21 (2002) 1553.
[30] J.S. Casas, M.V. Castano, M.S. Garcia-Tasende, A. Sanchez, J. Sordo, A. Touceda, Polyhedron 24 (2005) 3057.
[31] I. Garcia, E. Bermejo, A.K. El Sawaf, A. Castineiras, D.X. West, Polyhedron 21 (2002) 729.
[32] E. Bermejo, A. Castineiras, L.M. Fostiak, I.G. Santos, J.K. Swearingen, D.X. West, Polyhedron 23 (2004) 2303.
[33] J.S. Casas, M.V. Castano, M.S. Garcia-Tasende, E.R. Castellon, A. Sanchez, L.N. Sanjuan, J. Sordo, J. Chem. Soc., Dalton Trans. (2004) 2019.
[34] R.P. John, A. Sreekanth, V. Rajakannan, T.A. Ajith, M.R.P. Kurup, Polyhedron 23 (2004) 2549.
[35] A. Sreekanth, M. Joseph, H.-K. Fun, M.R.P. Kurup, Polyhedron 25 (2006) 1408.
[36] M.J.M. Campbell, Coord. Chem. Rev. 15 (1975) 279.
[37] E. Bermejo, A. Casterineiras, I. Garcia-Santos, D.X. West, Z. Anorg. Allg. Chem. 30 (2004) 1097.
[38] G.C. Percy, D.A. Thornton, J. Inorg. Nuclear Chem. 34 (1972) 3351.

[39] R.M. Silverstein, G.C. Bassler, T.C. Morril, Spectrometric Identification of Organic Compounds, fourth ed., John Wiley & Sons, New York, 1981.
[40] S. Jayasree, K.K. Aravindakshan, Transition Met. Chem. 18 (1993) 85.
[41] M. Nazimuddin, M.A. Ali, F.E. Smith, Polyhedron 10 (1991) 327.
[42] D.X. West, Y. Yang, T.L. Klein, K.I. Goldberg, A.E. Liberta, J.V. Martinez, R.A. Toscano, Polyhedron 14 (1995) 1681.
[43] E. Bermejo, R. Carballo, A. Castineiras, R. Dominguez, A.E. Liberta, C. Maichle-Mossmer, D.X. West, Z. Naturforsch. 54 (1999) 777.
[44] A. Castineiras, E. Bermejo, D.X. West, L.J. Ackerman, J.V. Martinez, S.H. Ortega, Polyhedron 18 (1999) 1469.
[45] A.D. Naik, V.K. Revankar, Proc. Indian Acad. Sci. (Chem. Sci.) 113 (2001) 285.
[46] V. Philip, V. Suni, M.R.P. Kurup, Polyhedron 25 (2006) 1931.
[47] I.-X. Li, H.A. Tang, Yi-Zhi Li, M. Wang, L.-F. Wang, C.-G. Xia, J. Inorg. Biochem. 78 (2000) 167.

prepared by metathesis reactions between $MnCl_2 \cdot 4H_2O$ and the alkaline salt of the corresponding ligand by Szekely et al. [14].



1



2

In this study, we are reporting the preparation of cationic palladium(II) complexes containing $[Ph_2P(S)NP(S)Ph_2]^-$ [disulfideimidodiphosphinato] of the type $[Pd(L\text{-}L)(dppaS_2\text{-}H)]ClO_4$ [L-L = dppm (**1**), dppe (**2**), dppp (**3**)]. Complex **2** was also synthesized **2a** by using of $Pd(dppe)Cl_2$ and $K[N(PSPh_2)_2]$ as starting materials. All of these complexes have been characterized $^{31}P\{^1H\}$ NMR, IR and elemental analyses. Complex **2** was recrystallized from acetone/hexane, complex **3** was recrystallized from acetone/diethyl ether and complex **2a** was recrystallized from dichloromethane/diethyl ether for X-ray crystallography.

2. Results and discussion

Previous works have demonstrated that the iminobis(phosphinechalcogenide) ligands can be deprotonated to afford coordinated dichalcogenoimidodiphosphinato anions by the reaction of metal–halides or starting complexes containing metal–halide bonds [15]. The starting complexes, $Pd(L\text{-}L)Cl_2$ (L-L = dppm, dppe, dppp) and $K[N(PP_2S)_2]$ were synthesized according to the literature (see Section 2). $^{31}P\{^1H\}$ NMR spectra of these compounds only a singlet δP values are −51.17, 67.67, 13.64 and 36.70 ppm, respectively. $[Pd(L\text{-}L)(dppaS_2\text{-}H)]ClO_4$ complexes (**1**, **2**, **3**) were prepared by the mixing of solution of $Pd(L\text{-}L)Cl_2$ complexes in CH_2Cl_2 and $dppaS_2$ ligand and $NaClO_4 \cdot H_2O$ salt in $(CH_3)_2CO$. Another method was used to prepared $[Pd(dppe)(dppaS_2\text{-}H)]ClO_4$ (**2a**). In this method, the solution of $K[N(PP_2S)_2]$ salt in CH_3OH was added solution of $Pd(dppe)Cl_2$ in CH_2Cl_2 as a molar ratio 1:1 in the presence of $NaClO_4 \cdot H_2O$ salt.

Solid state IR spectra of the complexes (**1**–**3**) showed the characteristic absorption of P=S group at 570.0, 573.0 and 570.0 cm^{-1}. These absorptions are shifted to the lower frequencies according to the free ligand, $dppaS_2$, absorption which is at 612.9 cm^{-1}. This shows that the ligand is coordinating to Pd(II) center via S donor atoms in the complexes. ClO_4^- group vibrations give rise to two bonds in 1100 and 620 cm^{-1} region. IR spectra of free acid, $dppaS_2$, exhibits absorption of medium intensity at 2630.8 cm^{-1} and very strong absorption at 922.0 cm^{-1} which were assigned to υ(N–H) stretching vibration and $\upsilon_{as}(P_2NH)$ stretching vibration, respectively. In IR spectra of complexes **1**, **2**, **3**, presence of strong absorptions in the regions 1150–1170 cm^{-1}, assigned to the $\upsilon_{as}(P_2NH)$ stretching vibrations, indicate that the $dppaS_2$ ligand is coordinated to the palladium center in the deprotonated form [6]. In $K[N(PP_2S)_2]$ salt, which is prepared to obtain $[Pd(dppe)(dppaS_2\text{-}H)]ClO_4$ **2a** by different method, $\upsilon_{as}(P_2N)$ vibration is at 1171.2 cm^{-1}. This absorption is at 1146.7 cm^{-1} in complex **2a**. Analytical data of four complexes are in accordance with the proposed formulation.

In complexes **1**, **2**, **3** and **2a**, the resonance due to the diphosphines (dppm, dppe, dppp) phosphorus atoms appear at –42.25, 72.06, 11.35 and 69.55 ppm, respectively. It has been seen that the signals of chelate dppm and dppe ligands are shifted to the downfield related to the starting complexes $[Pd(L\text{-}L)Cl_2]$ (L-L = dppm, dppe), but dppp ligand is shifted to the upfield on relative to the starting complex, $Pd(dppp)Cl_2$. Phosphorus chemical shifts of $dppaS_2$-H are 36.16, 38.67 and 37.63 ppm in complexes **1, 2** and **3**, respectively.

In $^{31}P\{^1H\}$ NMR of pottassium salt, $K[N(PP_2S)_2]$, there is a shifted at 38.69 ppm. This resonance is at 38.65 ppm in complex **2a** and is suitable with value of the complex **2**.

Solid state structures of complexes **2**, **2a,** and **3** were determined by single crystal X-ray diffraction. Complex **2** was recrystallized from acetone/hexane and includes one molecule acetone, complex **2a** was recrystallized from CH_2Cl_2/diethyl ether and has one molecule CH_2Cl_2. Complex **3** was recrystallized from acetone/diethyl ether and includes one molecule acetone. The perspective view of complexes **2**, **2a** and **3** are given in Figs. 1–3, respectively. The selected bond distances and angles are listed in Table. 1. Complexes **2** and **2a** are monoclinic and complex **3** is triclinic crystal systems. The solvent $(CH_3)_2CO$ and CH_2Cl_2 lie in the lattice on non-bonded molecules in the complexes **2** and **3**, respectively. All of the data for complex **2** and **2a** are similar. Palladium atoms in every complex are distorted square planar environments with from P(3)Pd(1)S(1) and P(4)Pd(1)S(2) are 168.90(4)° and 169.99(4)° for complex **2**, 170.66(3)° and 170.92(3)° for complex **2a** and 171.57(2)° and 173.96(2)° for complex **3**. The bite angles of iminobis(diphenylphosphine sulfide) in complexes **2** and **2a** [102.94(3)° and 102.69(3)°) are different from complex **3** (98.82(2)°]. This difference can be explained by diphosphine bite angle [P(4)Pd(1)P(3); 84.85(4)° for complex **2** and 84.61(3)° for complex **2a** and 91.62(2)° for complex **3**]. These values are comparable with the complexes $[Pd(dppaS_2\text{-}H)_2]$ [5].

Pd–S bond lengths are slightly different from each other. Pd(1)–S(1) and Pd(1)–S(2) are 2.3933(10) and 2.4114(10) Å for complex **2**; 2.3853(9) and 2.4110(9) Å for complex **2a**; 2.4017(6) and 2.3674(6) Å for complex **3**. These are comparable with the literature values [16].

In complex **3**, six membered dppp chelate ring has chair conformation with Pd(1)P(3)C(13)C(14) and Pd(1)P(4)-C(15)C(14) torsion angles of −44.4(3)° and 60.2(2)°, respectively, and with Pd(1) and C(14) atoms are located at −0.6932(21) Å below and 0.7342(45) Å above the plane defined by the atoms P(3)–P(4)–C(13)–C(15).

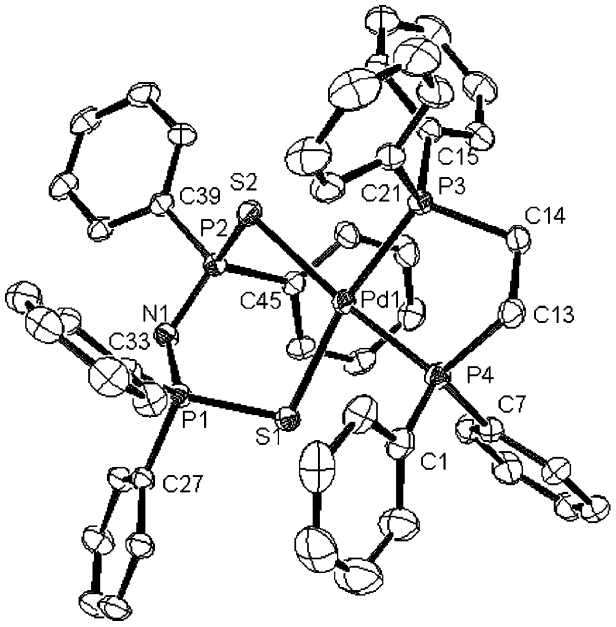


Fig. 1. The perspective view of **2** (20% thermal probability). Hydrogen atoms, anions and solvent molecule are omitted for clarity.

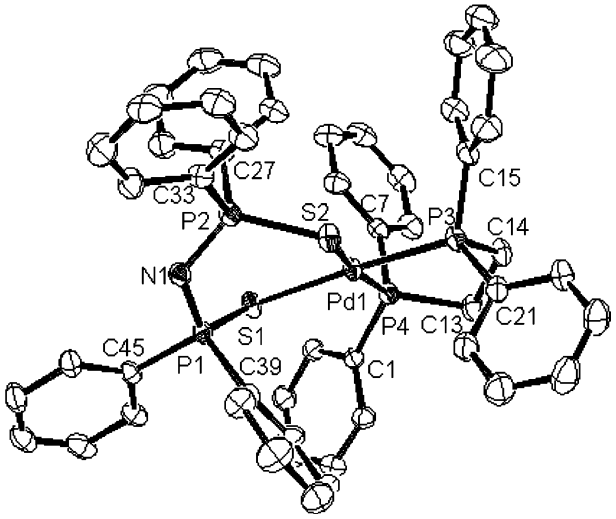


Fig. 2. The perspective view of **2a** (20% thermal probability). Hydrogen atoms, anions and solvent molecule are omitted for clarity.

Six membered dppaS_2-H rings are twist boat conformations in three complexes and are very similar to that observed related platinum analogue [Pt(PEt_3)$_2${Ph_2P(S)-NHP(S)Ph_2}]PF_6 in the literature [17].

PNP bond angles are 122.41(19)°, 120.74(17)° and 121.47(13)°, respectively. These angles show the sp^2 character at the nitrogen atoms [5].

P–S bond lengths are 2.0184(14) and 2.0170(15) Å for complex **2**; 2.0165(11) and 2.0239(12) Å for complex **2a** and 2.0304(9) and 2.0152(9) Å for complex **3**. P–S bond distances, as expected, are longer than the analogous P=S distances in the sulfur compounds and are suitable with the similar compounds in the literature [6,7,14].

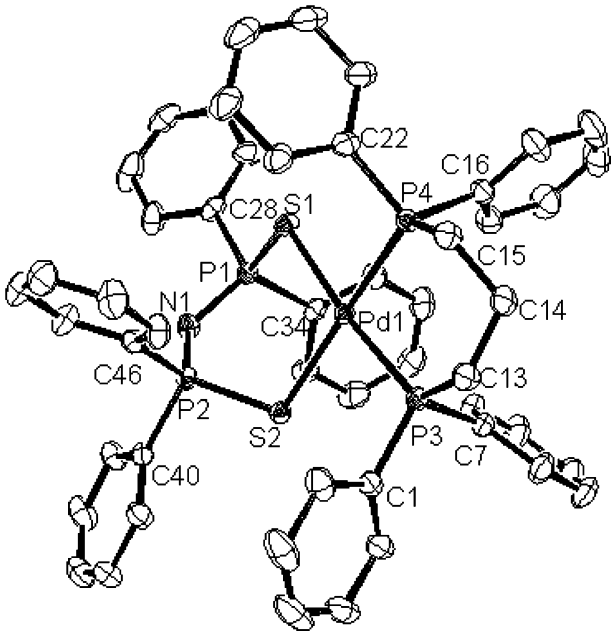


Fig. 3. The perspective view of **3** (20% thermal probability). Hydrogen atoms, anions and solvent molecule are omitted for clarity.

Table 1
Selected bond angles (°) and distances (Å) for [Pd(dppe)(dppaS_2-H)]-(ClO_4) · $(CH_3)_2CO$ (**2**), [Pd(dppe)(dppaS_2-H)](ClO_4) · CH_2Cl_2 (**2a**) and [Pd(dppp)(dppaS_2-H)](ClO_4) · $(CH_3)_2CO$ (**3**)

	2	**2a**	**3**
Bond distances			
Pd(1)–S(1)	2.3933(10)	2.3853(9)	2.4017(6)
Pd(1)–S(2)	2.4114(10)	2.4110(9)	2.3674(6)
P(1)–S(1)	2.0184(14)	2.0165(11)	2.0304(9)
P(2)–S(2)	2.0170(15)	2.0239(12)	2.0152(9)
Pd(1)–P(3)	2.2667(10)	2.2616(9)	2.2915(6)
Pd(1)–P(4)	2.2622(11)	2.2614(9)	2.2819(6)
Bond angles			
S(1)–Pd(1)–S(2)	102.69(3)	102.94(3)	98.82(2)
P(4)–Pd(1)–S(2)	169.99(4)	170.92(3)	173.96(2)
P(3)–Pd(1)–P(4)	84.85(4)	84.61(3)	91.62(2)
P(3)–Pd(1)–S(1)	168.90(4)	170.66(3)	171.57(2)
P(3)–Pd(1)–S(2)	88.13(3)	86.39(3)	84.50(2)
P(4)–Pd(1)–S(1)	84.72(4)	86.06(3)	85.66(2)

As a result, three new complexes have been synthesized. Two different synthetic route was used for one of them and their structures were determined by spectroscopic methods.

3. Experimental

Solvents were dried according to the methods given in the literature and were purified under inert conditions [18]. All synthesis were carried using standard Schlenk tube techniques under inert atmosphere.

dppm, dppe, dppp, $NaClO_4 \cdot H_2O$ and acetone were purchased from Merck Chemical; dichloromethane, toluene, methanol, hexane and diethylether were purchased from Lab-Scan. The starting complexes, [$PdCl_2$(COD)] (COD = 1,5-cyclooctadiene) [19], which is used for prepar-

ing the [$PdCl_2$(L-L)] complexes [L-L = dppm ($Ph_2PCH_2PPh_2$), dppe ($Ph_2PCH_2CH_2PPh_2$), dppp ($Ph_2PCH_2CH_2CH_2PPh_2$)] [20], dppa ($Ph_2PNHPPh_2$) and $dppaS_2$ ($Ph_2P(S)NHP(S)Ph_2$) were synthesized according to the method given in the literature [21].

$^{31}P\{^1H\}$ NMR spectra were recorded on Varian AS 400+Mercury instruments, chemical shifts, in ppm, related to external 85% H_3PO_4. Coupling constants are in Hz. IR spectra were recorded from 4000 to 400 cm^{-1} with a Perkin–Elmer 100 FT-IR instrument. Melting points were determined by Electrothermal melting point detection apparatus. Elemental analyses were performed by the TÜBİTAK-Ankara Test and Analyse Laboratories. There is potential explosion hazard arising from the use of perchlorates in the presence of organic material, so quantities should be kept small and heating (especially to dryness) avoided.

3.1. Method I

3.1.1. [Pd(dppm)(dppaS$_2$-H)](ClO$_4$) (1)

$PdCl_2$(dppm) (0.18 mmol, 0.10 g) and $dppaS_2$ (0.18 mmol, 0.08 g) were placed in 30 mL $CH_2Cl_2$and stirred. The solution of $NaClO_4 \cdot H_2O$ (0.71 mmol, 0.10 g) in 20 mL acetone was added dropwise to the stirring solution. Stirring was continued for 24 h at room temperature. After that, the solution was removed in vacuo. Yellow solid was dissolved in CH_2CI_2 and then it was filtered through celite in order to separate NaCI. The solution was removed in vacuo again. Complex **1** was recrystallized from acetone/diethyl ether (1:3 v/v) to give yellow crystals. Yield 0.08 g, 41.9%. Data for **1**: $^{31}P\{^1H\}$ NMR (DMSO): −42.30 ppm (s), 36.18 ppm (s). Selected IR data (KBr): *v*(PS) 570.0 cm^{-1}, 1098.5 (s) and 622.7 (m) cm^{-1} (ClO_4^-). *Anal.* Calc. for $C_{49}H_{42}NClO_4P_4PdS_2$: C, 56.65; H, 4.04; S, 6.17; N, 1.34. Found: C, 56.12; H, 4.16; S, 5.80; N, 1.65%.

3.1.2. [Pd(dppe)(dppaS$_2$-H)](ClO$_4$)$_2$ (2)

[$PdCl_2$(dppe)] (0.17 mmol, 0.10 g), $dppaS_2$ (0.17 mmol, 0.08 g) were placed together in 30 mL CH_2CI_2 and stirred. The solution of $NaClO_4 \cdot H_2O$ (0.71 mmol, 0.10 g) in 20 mL acetone was added dropwise to the stirring solution. After 24 h, the solution was removed in vacuo. The solid was dissolved in CH_2CI_2 and then it was filtered through celite to separate NaCI. After the resulting solution was removed in vacuo this complex was obtained as a cream solid and it was recrystallized from acetone/hexane. (1:3 v/v). Yield 0.07 g, 40%. Data for **2:** $^{31}P\{^1H\}$ NMR (DMSO): 72.13 ppm (s), 38.76 ppm (s). Selected IR data (KBr): *v*(PS) 573.0 cm^{-1}, 1098.5 (s) and 622.7 (m) cm^{-1} (ClO_4^-). *Anal.* Calc. for $C_{50}H_{44}NClO_4P_4PdS_2$: C, 57.04; H, 4.21; S, 6.09; N, 1.33. Found: C, 56.44; H, 4.15; S, 5.53; N, 1.76%.

3.1.3. [Pd(dppp)(dppaS$_2$-H)](ClO$_4$)$_2$ (3)

This complex was obtained as a yellow solid, in a manner similar to **1** and **2** from [$PdCl_2$(dppp)] (0.17 mmol, 0.10 g), $dppaS_2$ (0.17 mmol, 0.08 g) and $NaClO_4 \cdot H_2O$ (0.71 mmol, 0.10 g). Yellow crystals, suitable for X-ray analysis, were obtained by slow diffusion

Table 2
Crystal data, data collection and structure-refinement parameters for complex **2**, **2a** and **3**

Empirical formula	**2**	**2a**	**3**
	$C_{50}H_{44}NClO_4P_4PdS_2 \cdot (CH_3)_2CO$	$C_{50}H_{44}NClO_4P_4PdS_2 \cdot CH_2Cl_2$	$C_{51}H_{46}NClO_4P_4PdS_2 \cdot (CH_3)_2CO$
Color	light yellow	colorless	yellow
Crystal size (mm)	0.750 × 0.333 × 0.070	0.560 × 0.353 × 0.190	0.640 × 0.440 × 0.330
Crystal system	monoclinic	monoclinic	triclinic
Space group	*P*21/*c*	*P*21/*c*	$P\bar{1}$
Unit cell dimensions			
a (Å)	17.2474(8)	13.2643(6)	11.0367(5)
b (Å)	11.1817(4)	27.6872(8)	13.1618(6)
c (Å)	27.3800(12)	15.3404(7)	20.6186(9)
α (°)	90.00	90.00	73.135(3)
β (°)	98.217(4)	111.568(3)	77.898(4)
γ (°)	90.00	90.00	68.038(3)
Volume (Å^3)	5226.2(4)	5239.3(4)	2641.0(2)
Z	4	4	2
D_{calc} (Mg m^{-3})	1.412	1.442	1.414
Formula weight	1110.79	1137.64	1124.82
Absorption coefficient (mm^{-1})	0.656	0.753	0.650
F (000)	2280	2320	1156
Index ranges	$-20 \leqslant h \leqslant 20$, $-13 \leqslant k \leqslant 13$, $-32 \leqslant l \leqslant 32$	$-15 \leqslant h \leqslant 15$, $-32 \leqslant k \leqslant 32$, $-18 \leqslant l \leqslant 18$	$-12 \leqslant h \leqslant 13$, $-16 \leqslant k \leqslant 16$, $-25 \leqslant l \leqslant 25$
θ Range (°)	1.50–25.03	1.47–25.04	1.72–26.00
Number of data measured	9164	9190	10 375
Number of data with [$I > 2\sigma(I)$]	5612	7266	8827
R_1 [$I > 2\sigma(I)$]	0.0413	0.0397	0.0339
WR_2 [$I > 2\sigma(I)$]	0.0714	0.1117	0.0933

of diethylether into a acetone solution of **3**. (1:3 v/v). Yield 0.09 g, 50.5%. Data for **3:** $^{31}P\{^1H\}$ NMR (DMSO): 11.39 ppm (s), 37.67 ppm (s). Selected IR data (KBr): ν(PS) 570.0 cm^{-1}, 1098.5 (s) and 622.7 (m) cm^{-1} (ClO_4^-). *Anal.* Calc. for $C_{51}H_{46}NClO_4P_4PdS_2$: C, 57.42; H, 4.31 ; S, 6.01; N, 1.31. Found: C, 56.25; H, 4.41; S, 5.20; N, 1.50%.

3.2. Method II

3.2.1. *[Pd(dppe)(dppaS$_2$-H)](ClO$_4$)$_2$ (**2a**)*

$dppaS_2$ (0.45 mmol, 0.2 g) and $KOBu^t$ (0.45 mmol, 0.05 g) were stirred in diethyl ether and $K[N(SPPh_2)_2]$ synthesized.

$K[N(SPPh_2)_2]$ (0.17 mmol, 0.085 g) in 5 mL methanol and $NaClO_4 \cdot H_2O$ (0.71 mmol, 0.10 g) in 2 mL methanol was added to $PdCl_2$dppe (0.17 mmol, 0.1 g) in 15 mL CH_2Cl_2. After 24 h, the solvent was removed in vacuo. Complex **2a** was recrystallized from CH_2Cl_2/diethyl ether (1:3 v/v). Yield 0.11 g, 58.08%. Data for **2a**: $^{31}P\{^1H\}$ NMR ($CDCl_3$): 69.5 ppm (s), 38.6 ppm (s). Selected IR data (KBr): ν(PS) 576.0 cm^{-1}, 1093.7 (s) and 623.1 (m) cm^{-1} (ClO_4^-). *Anal.* Calc. for $C_{50}H_{44}NClO_4P_4PdS_2$: C, 57.04; H, 4.21; S, 6.09; N, 1.33. Found: C, 56.09; H, 4.38; S, 5.5; N, 1.65%.

3.2.2. *X-ray crystallographic study of **2**, **2a** and **3***

The intensity data of the complexes **2**, **2a** and **3** were collected using a STOE IPDS 2 diffractometer with graphite-monochromated Mo Kα radiation ($\lambda = 0.71073$) at 296 K. Details of crystal data, data collection, structure solution and refinement are given in Table 2. Data collection: Stoe X-AREA [22]. Cell refinement: Stoe X-AREA [22]. Data reduction: Stoe X-RED [22]. The structure was solved by direct-methods using SHELXS-97 [23] and anisotropic displacement parameters were applied to non-hydrogen atoms in a full-matrix least-squares refinement based on F^2 using SHELXL-97 [24]. All hydrogen atoms were included using a riding model. Molecular drawings were obtained using ORTEP-III [25].

4. Supplementary material

CCDC 622361, 622362 and 622363 contains the supplementary crystallographic data for $C_{50}H_{44}NClO_4P_4PdS_2 \cdot (CH_3)_2CO$, $C_{50}H_{44}NClO_4P_4PdS_2 \cdot CH_2Cl_2$ and $C_{51}H_{46}NClO_4P_4PdS_2 \cdot (CH_3)_2CO$ respectively. These data can be obtained free of charge via http://www.ccdc.ac.uk/conts/retrieving.html, or from the Cambridge Crystallographic Data Centre, 12 Union Road, Cambridge CB2 1EZ, UK; fax: (+44) 1223-336-033; or e-mail: deposit@ccdc.cam.ac.uk.

Acknowledgements

The authors acknowledge the Faculty of Arts and Sciences, Ondokuz Mayis University, Turkey, for the use of the STOE IPDS II diffractometer (purchased under Grant F.279 of the University Research Fund).

References

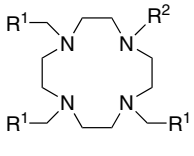
[1] K.K. Hii, Thornton-Pett, A. Jutand, R.P. Tooze, Organometallics 18 (1999) 1887.
[2] G.R. Newkome, Chem. Rev. 93 (1993) 2067.
[3] A. Bader, E. Lindner, Coord. Chem. Rev. 108 (1991) 27.
[4] N.J. Hovestad, E.B. Eggeling, H.J. Heidbüchel, J.T.B.H. Jastrzebski, U. Kragl, W. Keim, D. Vogt, G. van Koten, Angew. Chem. Int. Ed. Engl. 38 (1999) 1655.
[5] P. Bhattacharyya, J. Novasad, J. Phillips, A.M.Z. Slawin, D.J. Williams, J.D. Woollins, J. Chem. Soc. Dalton Trans. (1995) 1607.
[6] J. Novasad, M. Necas, J. Marek, P. Veltsistas, C. Papadimitriou, I. Haiduc, M. Watanabe, J.D. Woollins, Inorg. Chim. Acta 290 (1999) 256.
[7] G. Balazs, J.E. Drake, C. Silvestru, I. Haiduc, Inorg. Chim. Acta 287 (1999) 61.
[8] M.B. Smith, A.M.Z. Slawin, Inorg. Chim. Acta 299 (2000) 172.
[9] P. Bhattacharyya, A.M.Z. Slawin, M.B. Smith, J.D. Woollins, Inorg. Chem. 35 (1996) 3675.
[10] M.B. Smith, A.M.Z. Slawin, J.D. Woollins, Polyhedron 15 (1996) 1579.
[11] P. Bhattacharyya, A.M.Z. Slawin, M.B. Smith, J. Chem. Soc., Dalton Trans. (1998) 2467.
[12] A.M.Z. Slawin, M.B. Smith, J.D. Woollins, J. Chem. Soc., Dalton Trans. (1998) 1537.
[13] A.M.Z. Slawin, M.B. Smith, J.D. Woollins, J. Chem. Soc., Dalton Trans. (1996) 3659.
[14] I. Szekely, C. Silvestru, J.E. Drake, G. Balazs, S.I. Farcas, I. Haiduc, Inorg. Chim. Acta 299 (2000) 247.
[15] T.Q. Ly, J.D. Woollins, Coord. Chem. Rev. 176 (1998) 451.
[16] S. İrişli, S. Yanar, Polyhedron 25 (2006) 1333.
[17] J.R. Phillips, A.M.Z. Slawin, A.J.P. White, D.J. Williams, J.D. Woollins, Dalton Trans. (1995) 2467.
[18] W.L. Jolly, The Synthesis and Characterization of Inorganic Compounds, Prentice-Hall, Englewood Cliffs, 1970, p. 116.
[19] J. Chat, L.M. Vallarino, L.M. Venanzi, J. Chem. Soc. (1957) 3413.
[20] W.L. Steffen, G.J. Palenik, Inorg. Chem. 15 (10) (1976) 2432.
[21] F.T. Wang, J. Najdzionek, K.L. Leneker, H. Wasserman, D.M. Braitsch, Synth. React. Inorg. Met.-Org. Chem. 8 (1978) 119.
[22] Stoe & Cie, X-area (version 1.18) and X-red32 (version 1.04), Stoe & Cie, Darmstadt, Germany, 2002.
[23] G.M. Sheldrick, Acta Cryst. A46 (1990) 467.
[24] G.M. Sheldrick, SHELXL-97, University of Göttingen, Germany, 1997.
[25] M.N. Burnett, C.K. Johnson, OrtepIII. Report ORNL-6895. OAK Ridge National Laboratory, Tennessee, USA, 1996.

are strongly influenced by the type of derivatization of the ligand skeleton, as has been demonstrated on the H_4dota derivatives with phosphorus acid pendant arms [11]. These macrocyclic ligands have some similarities to the acetic parent compound due to the acid character of the groups, but the other properties (bulkiness, basicity, hydrogen bond formation ability) are different [11]. Generally, they form more stable complexes with lanthanide(III) ions than do the respective macrocyclic dota-like ligands [11,12].

The thermodynamic and kinetic properties of europium(III) complexes with macrocyclic ligands (see Scheme 1) were studied for H_2do2a [13], H_3do3a [14], H_4dota [15–19], H_5do3ap [12] and H_8dotp [20,21] with the application of various experimental techniques; mostly pH glass-electrode potentiometry [13,15,18–20], molecular absorption spectroscopy in the UV/VIS region [14–21] and luminescence spectroscopy [14,16,17,21]. Also, the thermodynamic and kinetic studies of other lanthanides (mostly gadolinium(III)) complexes were performed, *e.g.* Gd(III)-H_3do3a [22,23], Gd(III)-H_4dota [24] and Gd(III)-H_8dotp [25]. In addition, the analogous system Y(III)-H_4dota was studied from theoretical [26,27] and experimental [28] points of view. In this contribution, the kinetic properties of europium(III) complexes of cyclen derivatives containing acetic and phosphonic/phosphinic acid pendant groups were investigated (Scheme 1) by means of UV/VIS molecular absorption spectroscopy. Time-resolved laser-induced fluorescence spectroscopy (TRLIFS) was applied for determination of the hydration numbers of the europium(III) ion during the course of complex formation and dissociation in order to elucidate the intimate reaction mechanism.

2. Experimental

A stock solution of europium(III) perchlorate/chloride (0.05 mol l^{-1}) was obtained by dissolving Eu_2O_3 (spectroscopically pure, prepared at the Department of Rare Earths, Faculty of Chemistry, Adam Mickiewicz University, Poznań or from Alfa, Darmstadt, Germany) in a perchloric/hydrochloric acid solution (Analar grade, Fluka). The H_3do3a · H_2SO_4 was a kind gift of Bracco SpA (Italy). The other ligands were prepared according to previously described procedures: H_4dota [29], H_5do3ap [30] and H_5do3ap^{PrA} [28]. Stock solutions of the ligands were prepared by dissolving a weighed amount in bidistilled water. All other chemicals of the highest available purity were used as received.



R^1	R^2	Ligand
CO_2H	H	H_3do3a
CO_2H	CH_2CO_2H	H_4dota
CO_2H	$CH_2PO_3H_2$	H_5do3ap
CO_2H	$CH_2P(O)(OH)(CH_2)_2CO_2H$	H_5do3ap^{PrA}
PO_3H_2	$CH_2PO_3H_2$	H_8dotp

Scheme 1.

The experimental methodology for the kinetic study of the europium(III) complexation and decomplexation was the same as for other lanthanide(III) complexes with H_5do3ap, and details are given elsewhere [12].

All spectrophotometric kinetic measurements were carried out on a diode array spectrophotometer HP-8453 A (Hewlett–Packard, USA) at the temperature of 25.0 ± 0.1 °C. The formation kinetics of the $[Eu(H_2O)(do3ap)]^{2-}$ complex was followed under pseudo-first order conditions ($c_{Eu} = (0.8–4.0) \times 10^{-3}$ mol l^{-1}, $c_{do3ap} = 8 \times 10^{-5}$ mol l^{-1}, $I = 0.1$ mol l^{-1} KCl) in the pH range 4.0–5.5 and in the wavelength region 290–340 nm. Dissociation kinetics of the europium(III) complexes were measured in the proton concentration range 0.10–3.00 mol l^{-1} and ionic strength $I = 3.00$ mol l^{-1} (Na,H)ClO_4 ($c_{EuL} \sim 5 \times 10^{-3}$ mol l^{-1}). The decomplexation of the europium(III) complexes was followed by a decrease of its CT band [15,21]. Data from kinetic experiments were processed by non-linear regression using EXCEL, HP and/or PROK-II [31] software, giving identical results. The measured values of absorbances were corrected for background analytical signals.

The luminescence lifetime measurements at room temperature were carried out using a detection system consisting of a nitrogen laser and a tunable dye laser ($\lambda_{exc} = 394$ nm), as described earlier [32,33]. The kinetics of the formation reaction of the europium(III) complexes were studied in 1-cm sample cells where the ligand excess over europium(III) was ensured: $c_{Eu} = 0.005$ mol l^{-1}, $c_L = 0.01$ mol l^{-1}, $c_{MES} = 0.3$ mol l^{-1} (pH 5.6). The formation kinetics experiments were initiated by the addition of the Eu(III) stock solution to the cell containing the ligand and a buffer. After mixing of all the reagents, the first decay curve was usually measured between the 10th and the 15th second (reaction dead time). The experiments were stopped when the luminescence decay became constant. The kinetics of the dissociation reaction of the europium(III) complexes ($c_{EuL} \sim 0.01$ mol l^{-1}) was followed in acidic media (perchloric, hydrochloric acids) with acid concentrations between 0.3 and 3.0 mol l^{-1}. The reaction was initiated by the addition of the complex solution to the cell containing an acid. The first measurement was usually done between the 30th and the 60th second after the reaction was started (reaction dead time). Experiments were stopped when the measured lifetime of the luminescent decay was equal to the lifetime of the "free" Eu(III) hydrated ion (~110 μs). All lifetime experiments were repeated at least three times in order to get average values, and they were corrected for the dead time in the kinetic treatment. The experimental luminescence decay data were fitted by one-term, two-term or three-term exponential equations as follows:

$$I_{tot} = I_1 \times e^{-\frac{t}{\tau_1}} + I_2 \times e^{-\frac{t}{\tau_2}} + (I_3 \times e^{-\frac{t}{\tau_3}}) \quad (1)$$

where I_{tot} is measured intensity of fluorescence as a function of time (μs), I_n are the fluorescence intensities and τ_n are the lifetimes of the luminescence decay of the individual species. Monoexponential decay was observed only for the

formation (H_3do3a, H_5do3ap, H_5do3ap^{PrA}) and dissociation kinetic studies (H_3do3a) whilst a two-exponential decay was found for the study of the dissociation of the europium(III) complexes of the H_4dota, H_5do3ap and H_5do3ap^{PrA}. In agreement with the literature [19], tri-exponential decay was observed for the formation of the europium(III) complex with H_4dota. The luminescence decay measurements were used for the estimation of the number of water molecules as discussed earlier [10,33–35]. In this work, the hydration numbers, q, of the complexes were determined by means of the equation below [33,36]

$$q_B = 1.05 \times \tau^{-1} - 0.7 \quad (2)$$

which is a simplified modification of Horrock's equation [33,35,37,38], demonstrated in our previous work. Results based on both equations are in a good agreement [33]. The calculated parameters for the luminescent decay as functions of time were used for the calculation of rate constants.

3. Results and discussion

3.1. Thermodynamic stability of europium(III) complexes of the macrocyclic ligands

The europium(III) ion forms stable complexes [11–20] of EuL stochiometry with the H_4dota-like ligands (see Table 1). The solid-state structure of the sodium salt of the $[Eu(H_2O)(dota)]^-$ complex was determined by X-ray crystallography [42]. The eight coordination sites of the europium(III) ion are occupied by four nitrogens atoms of the cyclen ring and four oxygen donor atoms from each of the four carboxylate arms of the ligand. The coordination sphere is completed by a water molecule, leading to a distorted capped square antiprismatic arrangement [42] which is crystallographically isostructural with sodium salts of the $[Y(H_2O)(dota)]^-$ and $[Gd(H_2O)(dota)]^-$ complexes [43]. The water molecule in the first coordination sphere of the complex is also present in solution [33].

The presence of the phosphonic acid pendant arm in H_5do3ap leads to an increase in the stability of the $[Eu(H_2O)(do3ap)]^{2-}$ complex in comparison to those of the europium(III) complexes of H_3do3a and H_4dota (Table 1) [12]. Attachment of other functional groups to the phosphorus atom, as in the bifunctional chelator (BFC) H_5do3ap^{PrA}, caused a slight decrease in the stability of its europium(III) complex compared with that of H_4dota [28]. Since the europium(III) complexes of H_5do3ap and H_5do3ap^{PrA} bind one water molecule in the first coordination sphere [33] all pendant arms have to be coordinated to europium(III) ions, similarly to other lanthanide(III) complexes of H_5do3ap [30], its monoethyl ester [44] and its aminobenzylphosphinic acid analogs [45] in solution.

Table 1
The summary of dissociation constants of the macrocyclic ligands and their stability constants with the europium(III) ion ($T = 298.2$ K, $I = 0.1$ mol l^{-1})

Ligand	H_3do3a	H_4dota	H_5do3ap[g]	H_5do3ap^{PrA}[h]	H_8dotp[i]
pK_1	12.46[a]	11.9[b]	13.83	12.32	14.65
pK_2	9.49[a]	9.72[b]	10.35	9.20	12.40
pK_3	4.26[a]	4.60[b]	6.54	4.91	9.28
pK_4	3.51[a]	4.13[b]	4.34	4.19	8.09
pK_5	1.97[a]	2.36[b]	3.09	2.93	6.12
pK_6			1.63	1.8	5.22
pK_7			1.07		
log β(EuL)	20.7[c]	23.4[d] 26.2[e] 26.5[f]	27.8	25.3	29.5

[a] Ref. [39] TMACl.
[b] Ref. [40] TMANO_3/Cl.
[c] Ref. [14] KCl.
[d] Ref. [17] KCl.
[e] Ref. [13] NaCl.
[f] Ref. [19] TMACl.
[g] Ref. [12] TMACl.
[h] Ref. [28] TMACl.
[i] Ref. [41] TMACl.

3.2. Formation kinetics

The formation of the europium(III) complex with H_5do3ap was studied by molecular absorption spectroscopy and a monotonic increase of absorbance in the 270–300 nm region was observed. The same phenomena was described for the europium(III)-H_4dota system [15].

Pseudo-first order reaction conditions were employed (10–50 molar excess of europium(III) ion over ligand), and the resulting data follow a rate law for complex formation given by Eq. (3) (the charges of the complexes are omitted for the sake of clarity).

$$\frac{d[EuL]}{dt} = {}^{Eu}k_{f,obs} \times [L]_{tot} \quad (3)$$

The model frequently used to describe the complexation reaction assumes fast formation of a reaction intermediate characterized by the conditional stability constant ${}^{Eu}K^{**}$ (Eq. (4))

$${}^{Eu}K_n^{**} = \frac{[Eu(H_nL)]}{[Eu^{3+}] \times [L]_{tot}} \quad (4)$$

This reaction step is followed by a slow rate-determining step, leading to the final product which is defined by rate constant ${}^{Eu}k_f$.

$${}^{Eu}k_{f,obs} = \frac{{}^{Eu}k_f \times {}^{Eu}K_n^{**} \times [Eu^{3+}]_{tot}}{1 + {}^{Eu}K_n^{**} \times [Eu^{3+}]_{tot}} \quad (5)$$

As a consequence of this fact, the conditional pseudo-first order rate constant ${}^{Eu}k_{f,obs}$ is dependent on the total (analytical) concentration of europium(III) (Eq. (5)). The pseudo-first order rate constant ${}^{Eu}k_{f,obs}$ (for $c(Eu^{3+}) \geqslant 10\ c(H_5do3ap)$) was observed to be practically independent on total europium(III) concentration in the pH regions 4.0–5.5. The same effect was observed for the cerium(III)-H_5do3ap system (metal ion or ligand excess with respect to the other reactant [12]). This means that the formation

of the reaction intermediate is quantitative ($^{Eu}K^{**} \times [Eu^{3+}]_{tot} \gg 1$ in the denominator of Eq. (5)), and the relationship can be simplified as $^{Eu}k_{f,obs} \approx {}^{Eu}k_f$.

The measured conditional equilibrium constant $^{Eu}K^{**}$ is dependent on the pH of the solution [13,15], while other protonated species of ligand are presented in solution (Eq. (6), $K_{p,n}$ are stepwise ligand protonation constants),

$$^{Eu}K_3^{**} = \frac{[Eu(H_3L)]}{[Eu^{3+}] \times [H_3L] \times (1 + K_{p,4} \times [H^+] + K_{p,4} \times K_{p,5} \times [H^+]^2)} = \frac{^{Eu}K_3^*}{\alpha_{H_3L(H)}} \quad (6)$$

and therefore the equilibrium constant $^{Eu}K^*$ is defined by the following equation:

$$^{Eu}K_3^* = \frac{[Eu(H_3L)]}{[Eu^{3+}] \times [H_3L]} \quad (7)$$

The equilibrium constant $^{Eu}K_3{}^{**}$ is a pH-dependent parameter, and it can be calculated from the absorbance values extrapolated to zero time ($A_{t=0}$) [12,15]. The conditional equilibrium constant $^{Eu}K_3{}^{**}$ is corrected according to Eq. (7) in order to calculate $^{Eu}K_3{}^*$, and the value $\log {}^{Eu}K_3{}^* = 3.01 \pm 0.03$ was estimated. This value should be constant for the intermediate species prevailing in solution under the given experimental conditions. However, this requirement was not fulfilled for the $[Eu(H_2do3ap)]^*$ species. The value of $^{Eu}K_3{}^*$ of the $[Eu(H_3do3ap)]^{*+}$ species differs from that $\log {}^{Eu}K_2{}^*$ of the $[Eu(H_2dota)]^{*+}$ species obtained by UV molecular absorption spectroscopy (4.4 ± 0.1) or potentiometry (4.32 ± 0.05) [15]. However, different values for the same $[Eu(H_2dota)]^{*+}$ intermediate species (5.88 and 6.26) were obtained by means of TRLIFS [16,17]. The hypothesis is confirmed by the fact that the most abundant protonated species of the monophosphonate ligand in the pH region of the study is H_3do3ap^{2-} [12]. In order to determine the composition of the most probable reaction intermediate, knowledge about the kinetics of the other lanthanide(III) systems with H_5do3ap (Ce^{3+} and Gd^{3+} [12]) or other europium(III)-macrocyclic ligand systems (H_2do2a [13], H_3do3a [14] and H_4dota [15,17–19]) should be taken into account. Thus, the $[Eu(H_3do3ap)]^{*+}$ reaction intermediate should be considered as the most abundant species in the studied pH region. The $[Eu(H_2do3ap)]^*$ and the $[Eu(Hdo3ap)]^{*-}$ species are minor ones and all the species are in a fast protonation equilibrium (Scheme 2); the $[Eu(Hdo3ap)]^{*-}$ species, present in only a trace concentration, is probably kinetically the most reactive species.

The rate-limiting step of the formation reaction is the deprotonation of the nitrogen atoms in the intermediate species, catalyzed by hydroxide ions and simultaneous translocation of the metal ion inside the ligand cavity (Eq. (8), Scheme 2, Fig. 1)

$$^{Eu}k_f = {}^{Eu}k_{f,obs} = {}^{Eu}k_{OH} \times [OH^-] + {}^{Eu}k_0 \quad (8)$$

The rate constant $^{Eu}k_{OH} = (2.7 \pm 0.2) \times 10^6\ M^{-1}\ s^{-1}$ is given by the slope of the linear dependence, and $k_0 = (0.9 \pm 0.5) \times 10^{-3}\ s^{-1}$ is its intercept (Fig. 1). The water-assisted (proton-transfer) pathway characterized by k_0 was neglected in the description of the formation reaction of europium(III) ion with some macrocyclic ligands (Table 2). Both hydroxide- and solvent-assisted reaction pathways were also observed for the formation of the gadolinium(III) complex with H_5do3ap [12]. The rate constant $^{Eu}k_{OH}$ for H_5do3ap is slightly lower than the respective rate constant for H_4dota (see Table 2) and comparable with the value $^{Eu}k_{OH} = (4.8 \pm 0.07) \times 10^6\ M^{-1}\ s^{-1}$ ($I = 1.0$ M KCl, $T = 298.2$ K) for the do3a-butriol derivate [13].

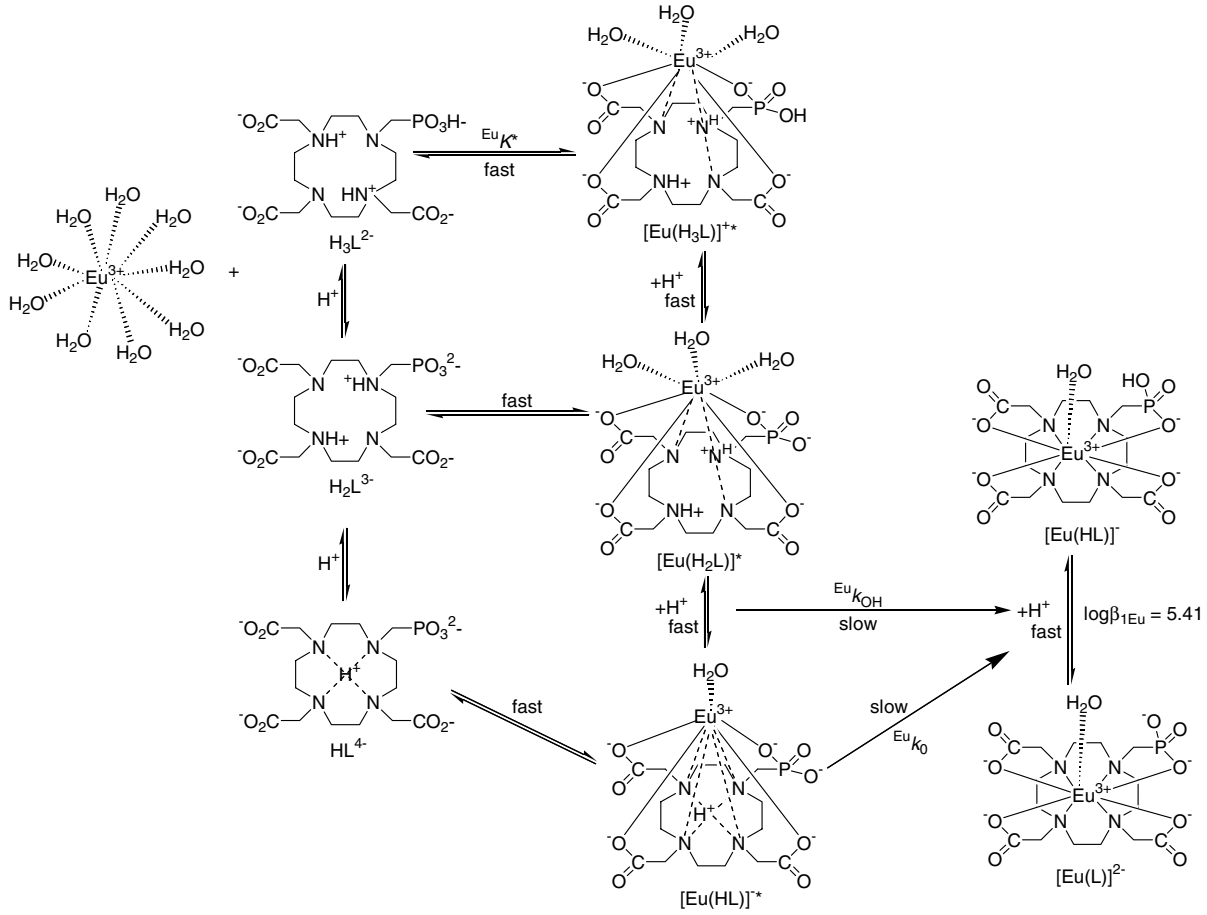
The formation kinetics in the europium(III)-H_5do3ap system was also followed by means of TRFLIS under similar experimental conditions as studied by molecular absorption spectroscopy in the UV region (see Fig. 2). In addition, to determine the kinetic parameters the technique provides information about the nature of the reaction intermediates. The luminescent decays recorded at different reaction times were monoexponential (see Eq. (1)), and the number of water molecules obtained from the lifetimes of luminescent decay decreased during the reaction time. The mechanism of europium(III) complex formation discussed above can be briefly written as (the charges of complexes and protons bound to the ligand are omitted for the sake of clarity)

$$Eu(H_2O)_n^{3+} + L \underset{+(m-n)H_2O}{\overset{K^{**}}{\rightleftarrows}} EuL(H_2O)_m^* \overset{^{Eu}k_f}{\rightarrow} EuL(H_2O)_p \quad (A)$$

The reaction intermediate is formed in a fast equilibrium, and its transformation to the final product proceeds *via* a slower rate-determining step characterized by the first-order rate constant $^{Eu}k_f$. If there is a ligand excess with respect to the europium(III) ion, as in our experiment, only the reaction intermediate and the final product (see reaction (A)) are present in solution. Both species differ in the number of coordinated water molecules and their normalized concentrations can be followed by TRFLIS with assumptions that the average number of water molecules consists of contributions from both species and that the number of water molecules is independent of species concentration. Thus, the average number of water molecules as function of time is defined as

$$q_t = q_t(EuL^*) + q_t(EuL) \quad (9)$$

The change in the number of water molecules is driven by the first-order kinetics:



Scheme 2. The proposed reaction mechanism for complexation of europium(III) with H_5do3ap (sites of the protonations are tentative). The thermodynamic dissociation constant of $[Eu(H_2O)(Hdo3ap)]^-$ is taken from [12].

$$q_t(\mathrm{EuL}^*) = q_{t=0}(\mathrm{EuL}^*) \times e^{-{}^{Eu}k_f \times t} \quad (10)$$

$$q_t(\mathrm{EuL}) = q_{t=\infty}(\mathrm{EuL}) \times (1 - e^{-{}^{Eu}k_f \times t}) \quad (11)$$

The combination of Eq. (9) with Eqs. (10) and (11) leads to relationship (12)

$$q_t = q_{t=0}(\mathrm{EuL}^*) \times e^{-{}^{Eu}kf \times t} + q_{t=\infty}(\mathrm{EuL}) \times (1 - e^{-{}^{Eu}k_f \times t})$$
$$= e^{-{}^{Eu}k_f \times t}(q_{t=0}(\mathrm{EuL}^*) - q_{t=\infty}(\mathrm{EuL})) + q_{t=\infty}(\mathrm{EuL}) \quad (12)$$

After rearrangement, the final relationship (13) is obtained:

$$\ln(q_t - q_{t=\infty}(\mathrm{EuL})) = \ln(q_{t=0}(\mathrm{EuL}^*) - q_{t=\infty}(\mathrm{EuL})) - {}^{Eu}k_f \times t \quad (13)$$

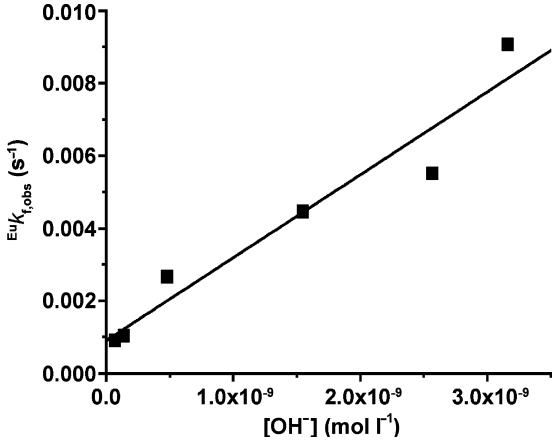


Fig. 1. Dependence of the observed pseudo-first order rate constants $^{Eu}k_{f,obs}$ on $[OH^-]$ for the formation of the $[Eu(H_2O)(do3ap)]^{2-}$ complex (UV–Vis measurements).

The linearized relationship (13) or relationship (12) combined with a non-linear least-square procedure, can be used for determination of the rate constant $^{Eu}k_f$ and the number of water molecules in the final product and in the reaction intermediate at the beginning of the reaction, *i.e.* immediately after mixing of the reactants. The results of the non-linear fit for the reactions of europium(III) with the three macrocyclic ligands (H_3do3a, H_5do3ap and H_5do3ap^{PrA}) are given in Table 3. Also the number of water molecules determined from equilibrium and the kinetic measurements are in fair agreement (see Table 3, [33]). A special case is the europium(III) complexation by H_4dota. It was shown that two reaction intermediates ($[EuH_n(dota)(H_2O)_5]^{(n-1)**}$ (intermediate **1**) and $[EuH_n(dota)(H_2O)_3]^{(n-1)*}$ (intermediate **2**)) and the final product ($[Eu(dota)(H_2O)]^-$ (**3**)) are formed at pH ≈ 2.5–

Table 2
The overview of the rate constants for the formation/dissociation reactions of europium(III) complexes of cyclen derivatives ($T = 298.2$ K)

Ligand	Eu^{3+}	
	Formation	Dissociation[e,f]
H_4dota	$k_{OH} = 1.1 \times 10^7\ M^{-1}\ s^{-1}$ $\log K_2^* = 4.4$ (4.32) (Ref. [15]) [a]	$k_{H1} = 1.4. \times 10^{-5}\ M^{-1}\ s^{-1}$ $k_{H2} = 1.0 \times 10^{-3}\ M^{-2}\ s^{-1}$ $k_{d,1} = 1 \times 10^{-6}\ s^{-1}$ $k_{d,2} = 6.2 \times 10^{-4}\ s^{-1}$ $K_1 = 14\ M^{-1}$
	$k_{OH} = 7.2 \times 10^6\ M^{-1}\ s^{-1}$ $\log K_2^* = 5.88$ (6.22) (Ref. [16])[b]	$K_2 = 0.12\ M^{-1}$ Ref. [15][c]
H_8dotp		$k_{H1} = 1.3 \times 10^{-3}\ M^{-1}\ s^{-1}$ $k_{d,2} = 6.2 \times 10^{-4}\ M^{-1}\ s^{-1}$ $^{H}K_5 = 2.0\ M^{-1}$ Ref. [21]
H_5do3ap[d]	$k_{OH} = 2.7 \times 10^6\ M^{-1}\ s^{-1}$ $k_0 = 0.9 \times 10^{-3}\ s^{-1}$ $\log K_3^* = 3.01$	$k_{H1} = 9.8 \times 10^{-5}\ M^{-1}\ s^{-1}$ $k_{d,2} = 4.6 \times 10^{-4}\ M^{-1}\ s^{-1}$ $^{H}K_3 = 0.21\ M^{-1}$
H_5do3ap^{PrA}[d]		$k_{H1} = 1.03 \times 10^{-4}\ M^{-1}\ s^{-1}$ $k_{d,2} = 5.3 \times 10^{-4}\ M^{-1}\ s^{-1}$ $^{H}K_3 = 0.20\ M^{-1}$

The parameters are defined in the article or otherwise are given under table.
[a] $I = 1.0$ mol l^{-1} NaCl.
[b] $I = 0.1$ mol l^{-1} KCl.
[c] $I = 3.0$ mol l^{-1} $NaClO_4$.
[d] This work: formation $I = 0.1$ mol l^{-1} KCl, dissociation $I = 3.0$ mol l^{-1} (H,Na)ClO_4; determined by UV–Vis spectroscopy.
[e] $k_{d,obs} = k_{H1} \times [H^+] + k_{H2} \times [H^+]^2$.
[f] $k_{d,obs} = \frac{k_{d,2} \times {}^{H}K_n \times [H^+]}{1 + {}^{H}K_n \times [H^+]}$ ($n = 3$ for H_5do3ap, $n = 5$ for H_8dotp).

Table 3
The summary of the results obtained from the TRFLIS study of the formation of Eu^{3+}-complexes with H_4dota-like ligands

Species	pH	τ (H_2O)[e] (ms)	Final product		Reaction intermediate[f]	
			q[e]	q[f]	q	$k_{f,obs}$ (s^{-1})
Eu^{3+}	2.2[a]	0.1082	9.0			
[Eu(do3a)]	5.6[b]	0.375[c]	2.1	2.2	4.6[c]	$(9.5_6 \pm 0.8_7) \times 10^{-3}$[c]
	5.6[b]	0.371[d]	2.1			
$[Eu(dota)]^-$	5.6[b]	0.6765	0.9		see text	see text
$[Eu(do3ap)]^{2-}$	5.6[b]	0.692	0.8	0.7	3.0[c]	$(4.6_9 \pm 0.3_0) \times 10^{-3}$c
$[Eu(do3ap^{PrA})]^{2-}$	5.8[b]	0.674	0.9	0.7	3.9[c]	$(5.7_1 \pm 0.4_7) \times 10^{-3}$c

[a] No buffer used.
[b] MES used as buffer.
[c] $c(Eu) = 0.005$ mol l^{-1}, $c(L) = 0.006$ mol l^{-1}.
[d] $c(Eu) = 0.005$ mol l^{-1}, $c(L) = 0.010$ mol l^{-1}.
[e] Thermodynamic study [33].
[f] This work; kinetic study.

3.0 [19]. The intermediates are stable for several days and were characterized by EXAFS and luminescence spectroscopy; they differ in the number of coordinated water molecules (5 and 3) [19]. By analyzing NMR spectra recorded immediately after mixing of europium(III) and H_4dota at pD ≈ 4.3–4.6, it was shown that the intermediate(s) demonstrate the rigidity of the tetraaza macrocycle ring [24]. The measured luminescence decay traces measured here were deconvoluted with published lifetimes (taken from [19]: $\tau_1 = 0.6427$ ms, $\tau_2 = 0.2851$ ms and $\tau_3 = 0.2013$ ms; see Eq. (1)), and the intensities calculated for the intermediate species (after normalization) are presented in Fig. 3. As it can be seen, a decrease in solution acidity (a pH rise from 2.5–3.0 in [19] to 5.5 here) accelerates the rate of complex formation from days to minutes, and the same effect was observed in the studies with the pH range 2.5–4.6 [15,19].

On the basis of these observations, a reaction mechanism for formation of the $[Eu(H_2O)(do3ap)]^{2-}$ complex can be postulated. In the first fast step, the reaction intermediate $[Eu(H_2O)_3(H_3do3ap)]^{*+}$, having three water molecules in the first coordination sphere, is formed. Analogously, the $[Ce(H_3do3ap)]^{*+}$ species was also found in the cerium(III)-H_5do3ap system in weakly acidic medium [12], and this species is probably rather stable towards further deprotonation under those conditions. The same phenomena was

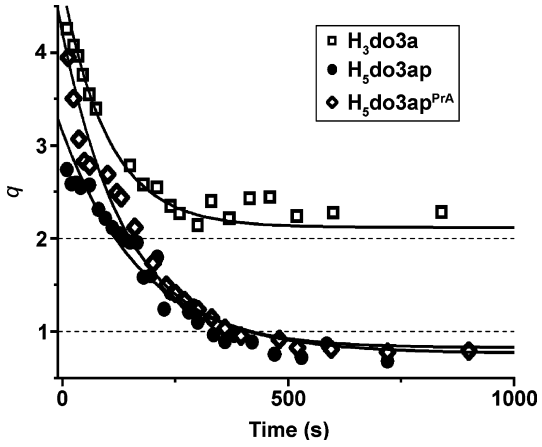


Fig. 2. Time dependence of change in the number of bound water molecules (q) during formation of the europium(III) complexes with given macrocyclic ligands ($c_{Eu} = 0.005$ mol l^{-1}, $c_L = 0.006$ mol l^{-1}, pH 5.6).

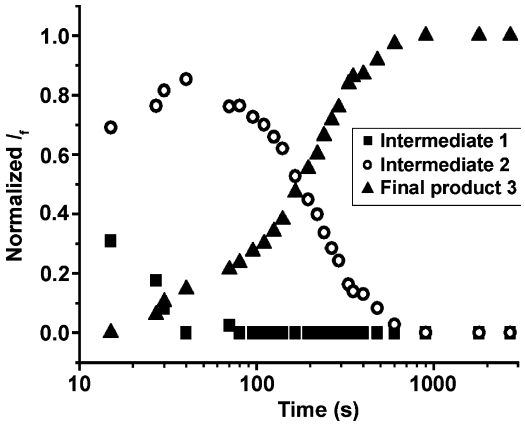


Fig. 3. Time dependence of abundance of the kinetic species during formation of the $[Eu(H_2O)(dota)]^-$ complex ($c_{Eu} = 0.005$ mol l^{-1}, $c_L = 0.006$ mol l^{-1}, pH 5.6).

observed in the case of the europium(III)-H_4dota system [15,18] where the presence of the corresponding double-protonated species $[Eu(H_2dota)]^{*+}$ is crucial. The structure of the reaction intermediates for both ligands (H_5do3ap and H_4dota) is probably similar under the assumption that two nitrogen atoms of the cyclen ring are protonated. In the $[Eu(H_2O)_3(H_3do3ap)]^{*+}$ species, the third proton is probably attached to the phosphonate moiety coordinated to the lanthanide(III) ion. Recently, such double nitrogen protonation was observed in the solid-state structure of the $[Er(H_2O)_2(H_2do3ap^{Ph})]_2Cl_2$ dimeric complex crystallized from acid solutions (pH < 4.5; H_4do3ap^{Ph} is the phenylphosphinic acid analog of H_5do3ap) [46] as well as in the gadolinium(III) complex of the diprotonated form of dotam (dotam is the tetraamide of H_4dota) in the solid state where four water molecules are bound to the central metal ion [47]. On the other hand, a different structure (protonated on one nitrogen atom) was predicted for an intermediate in complexation in the yttrium(III)-H_4dota system by quantum chemical calculations [26]. Such a monoprotonated species $[Eu(HL)]^*$ is supposed to be a crucial intermediate for the transformation of the reaction intermediate(s) to the final product having one water molecule. This scenario, with participation of the monoprotonated species, is very probable because of the increase in values of the rate constant k_f with increasing ionic strength for yttrium(III) complexation by the same H_4dota-like ligands [28]. This supports the hypothesis that the reaction takes place between reactants of the same charge (i.e. here $[Eu(HL)]^-$ vs. OH^- for the phosphorus acid derivatives) [28].

The proposed reaction mechanism can be also assumed for complexation of europium(III) ion by the other macrocyclic ligands (H_3do3a, H_5do3ap^{PrA}) as was proved for the yttrium(III) complex formation [28]. The reaction intermediates formed differ in the number of bound water molecules and in the number of protons (see Scheme 2), but their structure should be similar. In the case of H_4dota, the reaction mechanism proposed in the literature [19] was verified in the present study.

3.3. Dissociation kinetics

Acid-assisted decomplexation was investigated in order to determine the kinetic inertness of the europium(III) complexes with the macrocyclic ligands under study since the rate of complex dissociation is slow in slightly acidic media [48]. The kinetic inertness of the europium(III) complexes with H_4dota-like ligands is attributed to the rigid structure of the coordinated cyclen ring. The proton-assisted dissociation kinetics is usually studied in the presence of strong mineral acids ($c = 0.1$–1.0 mol l^{-1}) since the europium(III) complexes are thermodynamically unstable under these experimental conditions. In the literature, the mechanism for dissociation of the europium(III) complex with the H_4dota has been established [15,48]. Assuming the $[Eu(H_nL)]^*$ species as the active ones in the dissociation process with respective protonation constants

$$ {}^{H}K_n = \frac{[Eu(H_nL)]}{[Eu(L)] \times [H^+]^n} \tag{14} $$

then generally, the rate of dissociation of the europium(III) complexes is defined as

$$ -\frac{d[EuL]}{dt} = {}^{Eu}k_{d,obs} \times [EuL]_{tot} = \sum_{i=1}^{n} k_{d,i} \times [Eu(H_iL)] \tag{15} $$

taking into account the mass-balance equation (Eq. (16))

$$ [EuL]_{tot} = \sum_{i=0}^{n} [Eu(H_iL)] \tag{16} $$

Combining Eqs. (14)–(16), the following relationship (17) can be written as

$$ {}^{Eu}k_{d,obs} = \frac{k_{d,1} \times {}^{H}K_1 \times [H^+] + k_{d,2} \times {}^{H}K_1 \times {}^{H}K_2 \times [H^+]^2}{1 + {}^{H}K_1 \times [H^+] + {}^{H}K_1 \times {}^{H}K_2 \times [H^+]^2} \tag{17} $$

In weakly acidic medium ($[H^+] < 0.0001$–0.001 mol l^{-1}), the simplified Eq. (18) was described for the acid-assisted dissociation of lanthanide(III) complexes with H_3do3a or H_4dota [15,16,48]:

$$ {}^{Eu}k_{d,obs} = k_{d,1} \times {}^{H}K_1 \times [H^+] \tag{18} $$

An additional term k_0, that characterizes the spontaneous dissociation of the complex, can be determined, but with large errors [12,15,21].

For H_5do3ap and the H_5do3ap^{PrA}, one extra proton is attached to the phosphonate group or the carboxyl group of the phosphinate side chain, and therefore, in the acidity region employed for complex dissociation, there is no $[Ln(H_2O)(do3ap)]^{2-}$ species present in the solution and our systems are formally shifted by one proton (Scheme 3a) compared to the complexes with H_3do3a or H_4dota, and the dependence of ${}^{Eu}k_{d,obs}$ on the proton concentration can be reformulated as follows:

$$ {}^{Eu}k_{d,obs} = \frac{k_{d,1} \times {}^{H}K_2 \times [H^+] + k_{d,2} \times {}^{H}K_2 \times {}^{H}K_3 \times [H^+]^2}{1 + {}^{H}K_2 \times [H^+] + {}^{H}K_2 \times {}^{H}K_3 \times [H^+]^2} \tag{19} $$

From Scheme 3a, one can suggest that $k_{d,1} \ll k_{d,2}$. Furthermore, $1 \ll {}^{H}K_2 \times [H^+] + {}^{H}K_2 \times {}^{H}K_3 \times [H^+]^2$ (compare data in Table 2) and therefore Eq. (22) can be simplified in the following way:

$$ {}^{Eu}k_{d,obs} \approx \frac{k_{d,2} \times {}^{H}K_3 \times [H^+]}{1 + {}^{H}K_3 \times [H^+]} \tag{20} $$

For a low value of ${}^{H}K_3$ or low acidity of the solution ($1 \gg {}^{H}K_3 \times [H^+]$), this equation can be rewritten as Eq. (21):

$$ {}^{Eu}k_{d,obs} \approx k_{d,2} \times {}^{H}K_3 \times [H^+] = k_{H,1} \times [H^+] \tag{21} $$

The kinetics of the proton-assisted decomplexation of the europium(III) complexes with the phosphorus acid ligands H_5do3ap and H_5do3ap^{PrA} were studied in the region 0.50–3.00 mol l^{-1} $HClO_4$. The dependence of the pseudo-first order rate constants ${}^{Eu}k_{d,obs}$ on the proton

concentration for both complexes is presented in Fig. 4. As it can be seen, the experimental points for both europium(III) complexes fall together. Eq. (20) was used to fit the experimental points, and the following parameters were estimated: $k_{d,2} = (4.6_2 \pm 0.9_8) \times 10^{-4}\ s^{-1}$, $^{H}K_3 = 0.21_2 \pm 0.04_6\ M^{-1}$, $k_{H1} = 0.977 \times 10^{-5}\ M^{-1}\ s^{-1}$ (H_5do3ap); $k_{d,2} = (5.2_5 \pm 0.9_1) \times 10^{-4}\ s^{-1}$, $^{H}K_3 = 0.19_6 \pm 0.03_5\ M^{-1}$, $k_{H1} = 1.027 \times 10^{-4}\ M^{-1}\ s^{-1}$ (H_5do3ap^{PrA}). The estimated parameters are almost identical, however they are uncertain because of the simplifying assumptions made in deriving the relationship used for the fitting. Therefore, the parameters k_{H1} were calculated in order to compare them with the parameters of dissociation for other lanthanide(III) complexes with H_5do3ap, see Refs. [12,28]: $k_{H1} = 1.22 \times 10^{-3}\ M^{-1}\ s^{-1}$ (Ce^{3+}); $k_{d,2} = 7.0 \times 10^{-3}\ s^{-1}$, $^{H}K_3 = 0.2\ M^{-1}$, $k_{H1} = 1.09 \times 10^{-3}\ M^{-1}\ s^{-1}$ (Y^{3+}), $k_{d,2} = 5.8 \times 10^{-2}\ s^{-1}$, $^{H}K_3 = 0.048\ M^{-1}$, $k_{H1} = 2.78 \times 10^{-3}\ M^{-1}\ s^{-1}$ (Gd^{3+}); and the similar kinetic inertness of the $[Y(H_2O)(do3ap^{PrA})]^{2-}$ complex ($k_{d,2} = 3.4 \times 10^{-3}\ s^{-1}$, $^{H}K_3 = 1.3\ M^{-1}$, $k_{H1} = 4.4 \times 10^{-3}\ M^{-1}\ s^{-1}$ [28]). The results are in agreement with the kinetic behaviour of both europium(III) complexes demonstrated above.

The rate of the $[Eu(H_2O)(do3ap)]^{2-}$ complex dissociation is about 10 times slower than that of the other lanthanide(III) complexes, and it seems that the europium(III) complex is the most inert among the studied lanthanide(III) complexes of H_5do3ap. A similar exceptional behaviour was described for acid-assisted dissociation of lanthanide(III) complexes of a triacetate derivative of the pyridine-containing cyclen analog [49] or the H_4edta ligand [50]. It can be possibly explained by a different hydration of the "free" ions. It is known that the europium(III) aqua ion

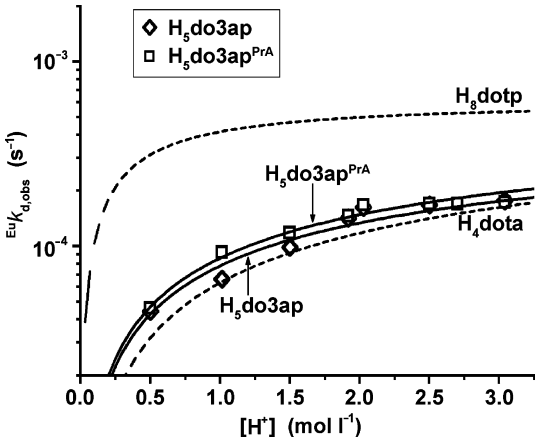
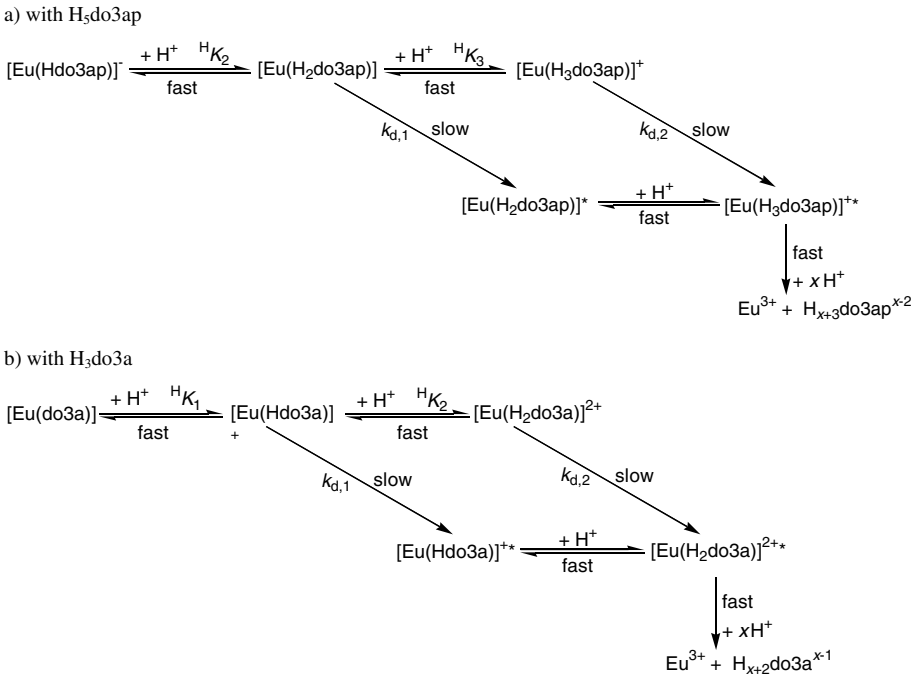


Fig. 4. Dependence of the pseudo-first rate constants $^{Eu}k_{d,obs}$ on the solution acidity for the dissociation of europium(III) complexes with phosphorus-containing macrocyclic ligands ($c_{EuL} = 0.015\ mol\ l^{-1}$, $I = 3.00\ mol\ l^{-1}$ (Na/H)ClO_4, UV–Vis measurements). The dashed lines were calculated according to Eq. (22) using the parameters given in Table 2.

varies its hydration number between 8 and 9, lying just on the borderline between lighter (hydration number 9) and heavier (hydration number 8) lanthanide(III) ions [34]. An equilibrium was observed between the differently hydrated europium(III) complex species with H_2do2a and H_3do3a, and the squaric acid derivative of H_3do3a, deviating by one water molecule in the first coordination sphere of the complex [51–53]; the corresponding constants and thermodynamic parameters describing the equilibrium were determined. The formation of the species with higher coordination and hydration numbers (more abundant at



Scheme 3. The proposed reaction mechanism for the dissociation of the europium(III) complex: (a) with H_5do3ap and (b) with H_3do3a.

room temperature) is preferred at lower temperature in comparison with the species with lower coordination and hydration numbers [18,51–53], which would be probably more kinetically inert species. It can be assumed that the nine-coordinated complexes of lighter lanthanides(III) ions would be less kinetically inert than the eight-coordinated complexes of heavier lanthanides(III) ions. Another effect, having an influence on the kinetic inertness, can be a difference in protonation constants of the complexes (*e.g.* Eu(III) vs. Gd(III) complex in Table 2 and Ref. [12] or Ref. [49]).

In order to elucidate the intimate reaction mechanism of the complex dissociation, TRFLIS was again employed. The decay traces of the europium(III) complexes with the macrocyclic ligands were recorded at different time points during the course of the dissociation reaction (see example in Fig. 5). The europium(III) complexes can be divided into two groups according to their behavior in the presence of an acid.

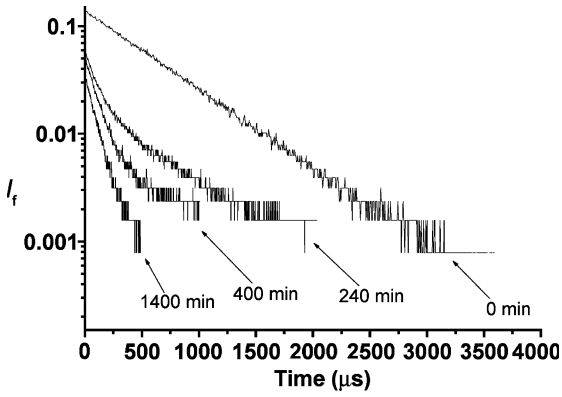


Fig. 5. Examples of TRFLS traces during decomplexation of the $[Eu(H_2O)(do3ap)]^{2-}$ complex recorded at different times ($[HClO_4] = 3.00$ mol l^{-1}, $c_{complex} = 0.01$ mol l^{-1}).

For the first group, involving europium(III) complexes of H_4dota and H_5do3ap, their luminescence decay traces recorded at the beginning and the end of the dissociation reaction can be deconvoluted monoexponentially (see Eq. (1) and Fig. S1 in the supplementary material) and the decay lifetimes τ are related to the number of coordinated water molecules in the complex and the free europium(III)-aqua ion, respectively (see Table 3). Thus, the luminescent decays recorded during the dissociation reaction have to be deconvoluted with two exponentials giving lifetimes (see Eq. (1)) corresponding to the starting monoaqua europium(III) complex and the final free nona-aqua europium(III) ion, while no other intermediate luminescence-active europium(III) species were detected in these systems. The decreasesing intensity of the luminescence signal of the monoaqua europium(III) complex species determined by luminescent decay deconvolutions (see Eq. (1)) for different time points recorded during the dissociation reaction (see Fig. S1) can be used for the determination of rate constants (see Table 4). In the case of H_4dota (Fig. S1A) and H_5do3ap (see Fig. S1B), the pseudo-first rate constants in perchloric and hydrochloric acids calculated from the TRFLIS experimental data are almost identical (see Table 4). The agreement between the results obtained from TRFLIS and UV spectroscopy is also satisfactory taking into account the precision of the measurements, and the slight difference between the values can be ascribed to the different experimental techniques and conditions employed in these studies. In addition, the dissociation of the europium(III) complexes of H_4dota and H_5do3ap is similar (see Fig. 4), and the process is not dependent on the nature of the anion (perchlorate vs. chloride) as was described for the luminescence behavior of the europium(III)-aqua ion [54–58]. Our results presented above confirm that the inner coordination sphere of the europium(III) ion in the $[Eu(H_2O)(dota)]^-$ complex is not affected by protonation in strongly acidic medium [15,18].

Table 4
The summary of the results obtained for the dissociation of Eu^{3+} complexes with H_4dota-like ligands (the ionic strength was not adjusted)

Species	Method	Acidity	Rate constant $k_{d,obs}$ (s^{-1})	Hydration number q of the intermediate
[Eu(do3a)]	TRFLIS (q)	0.3 mol l^{-1} $HClO_4$	$k_{d,1} = (8.2_0 \pm 0.4_7) \times 10^{-4}$	5.6
			$k_{d,2} = (1.80 \pm 0.04) \times 10^{-3}$	2.8
	TRFLIS (q)	1.0 mol l^{-1} $HClO_4$	$(6.1_2 \pm 0.2_0) \times 10^{-3}$	2.1
	TRFLIS (q)	3.0 mol l^{-1} $HClO_4$	$(1.22 \pm 0.08) \times 10^{-2}$	3.1
$[Eu(dotp)]^{5-}$[a]	TRFLIS (q)	3.0 mol l^{-1} $HClO_4$	$(1.53 \pm 0.08) \times 10^{-4}$[a]	0.4[a]
$Eu(dota)^-$]	TRFLIS (intensity)	3.0 mol l^{-1} $HClO_4$	$(2.95 \pm 0.08) \times 10^{-4}$	
	TRFLIS (intensity)	3.0 mol l^{-1} HCl	$(3.1_4 \pm 0.1_7) \times 10^{-4}$	
	UV spectroscopy	3.0 mol l^{-1} $HClO_4$	$(1.6_2 \pm 0.3_3) \times 10^{-4}$[b]	
$[Eu(do3ap)]^{2-}$	TRFLIS (intensity)	3.0 mol l^{-1} $HClO_4$	$(2.1_6 \pm 0.6_1) \times 10^{-4}$	
	TRFLIS (intensity)	3.0 mol l^{-1} HCl	$(2.9_1 \pm 0.1_1) \times 10^{-4}$	
	UV spectroscopy	3.0 mol l^{-1} $HClO_4$	$(1.8_0 \pm 0.5_5) \times 10^{-4}$[c]	
$[Eu(do3ap^{PrA})]^{2-}$	UV spectroscopy	3.0 mol l^{-1} $HClO_4$	$(1.9_4 \pm 0.4_8) \times 10^{-4}$[c]	

[a] Ref. [21]; for $q_{t=\infty} = 4.1$.
[b] Recalculated from Ref. [15].
[c] Recalculated from parameters in Table 2 and Fig. 4.

On the contrary, for the second group of europium(III) complexes, of H_3do3a (this work) and H_8dotp [21], the lumininiscence-decay traces are always deconvoluted monoexponentially (see Eq. (1)). The lifetime decay τ was used for the determination of the average number of bound water molecules in the europium(III) complex (see Eq. (2)) as a function of the time of the dissociation reaction (Fig. 6a). The average number of water molecules (q) is a weighted value defined analogously as in the section on the formation kinetics

$$q_t = q_{t=0}(\mathrm{EuL}^*) \times \mathrm{e}^{-{}^{\mathrm{Eu}}k_d \times t} + q_{t=\infty}(\mathrm{Eu}) \times (1 - \mathrm{e}^{-{}^{\mathrm{Eu}}k_d \times t}) = \mathrm{e}^{-{}^{\mathrm{Eu}}k_d \times t}(q_{t=0}(\mathrm{EuL}^*) - q_{t=\infty}(\mathrm{Eu})) + q_{t=\infty}(\mathrm{Eu}) \quad (22)$$

The final relationship (23) is obtained after rearrangement:

$$\ln(q_{t=\infty}(\mathrm{Eu}) - q_t) = \ln(q_{t=\infty}(\mathrm{Eu}) - q_{t=0}(\mathrm{EuL}^*)) - {}^{\mathrm{Eu}}k_{\mathrm{d}} \times t \quad (23)$$

For H_3do3a, Eq. (23) was used for treatment of the experimental data. The rate of dissociation was not dependent on the nature of the anion (perchlorate vs. chloride).

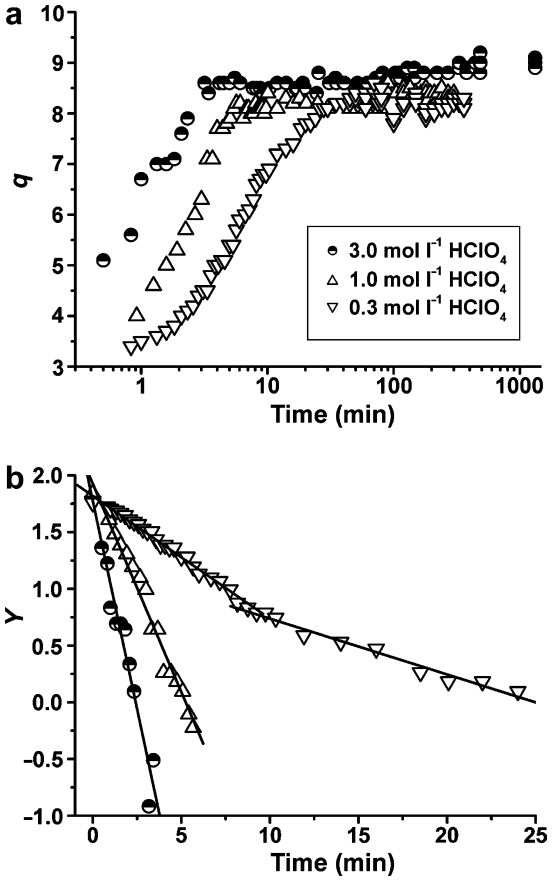


Fig. 6. (a) Time course of change in the number of coordinated water molecules (q) during dissociation of the [Eu(H_2O)$_2$(do3a)] complex ($c_{\mathrm{EuL}} = 0.01$ mol l^{-1}); (b) the linearized transformation ($Y = \ln(9 - q_{\mathrm{ML}})$) of the change in the number of coordinated water molecules for the Eu(III)-H_3do3a system measured at different solution acidities. The ionic strength of the solutions was not kept constant; it is identical with the acid concentration.

Two steps were observed at lower acidity while only one step was identified at higher acidities (Fig. 6b). The analysis gives the values of the rate constants with estimates of the number of water molecules in the reaction intermediates (the precision of the measurement is ±0.5) and the values are given in Table 4. The number of water molecules in the starting [Eu(H_2O)$_2$(do3a)] complex is equal to two, as it was determined formerly (see Chapter Formation Kinetics or Refs. [33,52]), while the reaction intermediate has three water molecules in its coordination sphere. The value of the first protonation constant of the [Eu(H_2O)(dota)]$^-$ complex was estimated to be $\log K \approx 1$ [15,18] and this value can also be taken as an approximation for the corresponding constant of the [Eu(H_2O)$_2$(do3a)] complex. This means that the [Eu(Hdo3a)(H_2O)$_3$]$^+$ species should be considered as a reactive intermediate at the beginning of the dissociation reaction. Taking into account the reaction mechanism proposed for the dissociation of the [Eu(H_2O)(dota)]$^-$ complex [15], an identical reaction mechanism can be adopted for the [Eu(H_2O)$_2$(do3a)] complex (see Scheme 3b). The reaction step, represented by the rate constant $k_{\mathrm{d},1}$ can be detected only at lower acidities while the pathway with the $k_{\mathrm{d},2}$ rate constant is fully dominating at higher acidities (see Eq. (19)) [15,18]. The same reaction mechanism (see Scheme 3b) has been proposed for the acid-catalysed dissociation of the [Eu(dotp)]$^{5-}$ complex, when the final product for the given reaction timescale has four (for perchlorate) or five (for chloride) coordinated water molecules (see Table 4, [21]); this means that the phosphonic acid pendant arms can coordinate the europium(III) ion even in strongly acidic media. The same effect was observed for lanthanide(III) complexation by diphosphonate ligands [59] and it can be an explanation of the differences in the apparent kinetic inertness among europium(III) complexes of H_8dotp and the other H_4dota-like ligands (see Fig. 4, Tables 2 and 4).

It is interesting to note that the kinetic inertness seems to be related to the spectroscopic properties. It was postulated recently [60,61] that the luminescence band intensity ratio ($\Delta J = 2/\Delta J = 1$) related to the $^5D_0$–$^7F_2$ (619 nm) and $^5D_0$–$^7F_1$ (594 nm) transitions of europium(III) in complexes is a sensitive and useful parameter for evaluation of changes in the ion coordination environment. The first group of europium(III) complexes (H_4dota, H_5do3ap, H_5do3ap$^{\mathrm{PrA}}$) shows a luminescence intensity ratio ($\Delta J = 2/\Delta J = 1$) of about 0.65–0.75, while the ratio ($\Delta J = 2/\Delta J = 1$) is equal to 1.60–1.70 for the second group (H_3do3a, H_8dotp) [33]. It was shown for H_4dota-like ligands that this ratio is a relative measure of the thermodynamic stability of ternary europium(III) complexes (having the third ligand in the axial position) and the free energy describing the formation of the complex is an expression of the strength of the interaction between the europium(III) ion and the donor atom of the axial ligand [61]. This effect was correlated with structural information obtained by NMR spectroscopy [61]. Here, it can be suggested that this parameter can be used for a prediction of

the kinetic behaviour. However, more europium(III) complexes should be investigated.

4. Conclusions

Formation kinetics of the $[Eu(H_2O)(do3ap)]^{2-}$ complex was studied and the results show that the reactivity is similar to that observed in the europium(III)-H_4dota system. TRLIFS, as a new experimental tool for the study of such chemical reactions, seems to be suitable for kinetic investigations. It can be used for the detailed study of the reaction mechanism of complex formation, also in cases when this process is a multistep one. This methodology has some limitations for the study of the reaction mechanism of complex dissociation as this method gives reliable results in the case where the number of coordinated water molecules changes during the course of the reaction. Kinetic constants obtained by UV–Vis spectroscopy and TRLIFS are comparable. The bifunctional phosphinate ligand H_5do3ap^{PrA} shows similar chemical properties towards europium(III) as do H_4dota and H_5do3ap.

Acknowledgements

This work was supported by Ministry of Education, Youth and Sports (9/2006/CZ, Czech-Polish KONTAKT Bilateral Program) and was performed in frame of the EU COST D38 Action.

Appendix A. Supplementary material

Supplementary data associated with this article can be found, in the online version, at doi:10.1016/j.poly.2007.05.014.

References

[1] A.E. Merbach, É. Tóth (Eds.), The Chemistry of Contrast Agents in Medical Magnetic Resonance Imaging, Wiley, Chichester, 2001.
[2] P. Caravan, J.J. Ellison, T.J. McMurry, R.B. Lauffer, Chem. Rev. 99 (1999) 2293.
[3] J.C.G. Bünzli, G.R. Choppin (Eds.), Lanthanide Probes in Life, Chemical and Earth Sciences. Theory and Practice, Elsevier, Amsterdam, 1989.
[4] P.R. Selvin, Ann. Rev. Biophys. Biomol. Struct. 31 (2002) 275.
[5] D. Parker, Coord. Chem. Rev. 205 (2000) 109.
[6] D. Parker, R.S. Dickins, H. Puschmann, C. Crossland, J.A.K. Howard, Chem. Rev. 102 (2002) 1977.
[7] S. Faulkner, J.L. Matthews, Fluorescent complexes for biomedical applications, in: J.A. McCleverty, T.J. Meyer (Eds.), Comprehensive Coordination Chemistry II, vol. 9, Elsevier, Amsterdam, 2004, pp. 913–944.
[8] G.R. Motson, J.S. Fleming, S. Brooker, Adv. Inorg. Chem. 55 (2004) 361.
[9] S. Liu, D.S. Edwards, Bioconjugate Chem. 12 (2001) 7.
[10] S. Lis, J. Alloys Compd. 341 (2002) 45.
[11] I. Lukeš, J. Kotek, P. Vojtíšek, P. Hermann, Coord. Chem. Rev. 216–217 (2001) 287.
[12] P. Táborský, P. Lubal, J. Havel, J. Kotek, J. Rudovský, P. Hermann, I. Lukeš, Collect. Czech. Chem. Commun. 70 (2005) 1909.
[13] E. Szilágyi, E. Tóth, Z. Kovács, J. Platzek, B. Radüchel, E. Brücher, Inorg. Chim. Acta 298 (2000) 226.
[14] S.-L. Wu, W.DeW. Horrocks, Anal. Chem. 68 (1996) 394.
[15] E. Tóth, E. Brücher, I. Lázár, I. Tóth, Inorg. Chem. 33 (1994) 4070.
[16] S.-L. Wu, W.DeW. Horrocks, Inorg. Chem. 34 (1995) 3724.
[17] S.-L. Wu, W.DeW. Horrocks, J. Chem. Soc., Dalton Trans. (1997) 1497.
[18] E. Szilágyi, E. Tóth, E. Brücher, A.E. Merbach, J. Chem. Soc., Dalton Trans. (1999) 2481.
[19] J. Moreau, E. Guillon, J.-C. Pierrard, J. Rimbault, M. Port, M. Aplincourt, Chem. Eur. J. 10 (2004) 5218.
[20] A.D. Sherry, J. Ren, J. Huskens, E. Brücher, É. Tóth, C.F.G.C. Geraldes, M.M.C.A. Castro, W.P. Cacheris, Inorg. Chem. 35 (1996) 4604.
[21] Z. Piskula, I. Svobodová, P. Lubal, Z. Hnatejko, S. Lis, P. Hermann, Inorg. Chim. Acta, in press, doi:10.1016/j.ica.2007.05.009.
[22] H.-Z. Cai, T.A. Kaden, Helv. Chim. Acta 77 (1994) 383.
[23] K. Kumar, C.A. Chang, M.F. Tweedle, Inorg. Chem. 32 (1993) 587.
[24] X. Wang, J. Tianzhu, V. Comblin, A.L. Mut, E. Merciny, J.F. Desreux, Inorg. Chem. 31 (1992) 1095.
[25] L. Burai, R. Király, I. Lázár, E. Brücher, Eur. J. Inorg. Chem. (2001) 813.
[26] Y.-H. Jang, M. Blanco, S. Dasgupta, D.A. Keire, J.E. Shively, W.A. Goddard, J. Am. Chem. Soc. 121 (1999) 6142.
[27] E.Y. Lau, F.C. Lightstone, M.E. Colvin, Inorg. Chem. 45 (2006) 9225.
[28] M. Försterová, I. Svobodová, P. Lubal, P. Táborský, J. Kotek, P. Hermann, I. Lukeš, Dalton Trans. (2007) 535.
[29] J.F. Desreux, Inorg. Chem. 19 (1980) 1319.
[30] J. Rudovský, P. Cígler, J. Kotek, P. Hermann, P. Vojtíšek, I. Lukeš, J.A. Peters, L.V. Elst, R.N. Muller, Chem. Eur. J. 11 (2005) 2373.
[31] M. Maeder, Y.-M. Neuhold, G. Puxty, P. King, Phys. Chem. Chem. Phys. 5 (2003) 2836.
[32] S. Lis, Z. Hnatejko, Z. Stryłła, Opt. Appl. 31 (2001) 643.
[33] P. Táborský, I. Svobodová, Z. Hnatejko, P. Lubal, S. Lis, M. Försterová, P. Hermann, I. Lukeš, J. Havel, J. Fluoresc. 15 (2005) 507.
[34] E.N. Rizkalla, G.R. Choppin, Hydration and hydrolysis of lanthanides, in: K.A. GschneidnerJr., L. Eyring (Eds.), Handbook on the Physics and Chemistry of Rare Earth, vol. 15, Elsevier, Amsterdam, 1991, pp. 393–402 (Chapter 103).
[35] I. Billard, Lanthanide and actinide solution chemistry as studied by time-resolved emission spectroscopy, in: K.A. GschneidnerJr., J.-C.G. Bünzli, V.K. Pekharsky (Eds.), Handbook on the Physics and Chemistry of Rare Earth, vol. 33, Elsevier, Amsterdam, 2003, pp. 465–514 (Chapter 216).
[36] P. Barthelemy, G.R. Choppin, Inorg. Chem. 28 (1989) 3354.
[37] W.DeW. Horrocks, D.R. Sudnick, J. Am. Chem. Soc. 101 (1979) 334.
[38] W.DeW. Horrocks, D.R. Sudnick, Acc. Chem. Res. 14 (1981) 384.
[39] A. Bianchi, L. Calabi, C. Giorgi, P. Losi, P. Mariani, P. Paoli, P. Rossi, B. Voltancoli, M. Virtuani, J. Chem. Soc., Dalton Trans. (2000) 697.
[40] G. Anderegg, F. Arnaud-Neu, R. Delgado, J. Felcman, K. Popov, Pure Appl. Chem. 77 (2005) 1445.
[41] F. Marques, L. Gano, M.P. Campello, S. Lacerda, I. Santos, L.M.P. Lima, J. Costa, P. Antunes, R. Delgado, J. Inorg. Biochem. 100 (2006) 270.
[42] M.R. Spirlet, J. Rebinzat, J.F. Desreux, M.F. Loncin, Inorg. Chem. 23 (1984) 359.
[43] C.A. Chang, L.C. Franncesconi, M.F. Malley, K. Kumar, J.Z. Gougoutas, M.F. Tweedle, Inorg. Chem. 32 (1993) 3501.
[44] P. Lebdušková, P. Hermann, L. Helm, É. Tóth, J. Kotek, K. Binnemans, J. Rudovský, I. Lukeš, A.E. Merbach, Dalton Trans. (2007) 493.
[45] J. Rudovský, J. Kotek, P. Hermann, I. Lukeš, V. Mainero, S. Aime, Org. Biomol. Chem. 3 (2005) 112.
[46] P. Vojtíšek, J. Rohovec, Collect. Czech. Chem. Commun. 71 (2006) 264.

[47] P.A. Stenson, A.L. Thompson, D. Parker, Dalton Trans. (2006) 3291.
[48] E. Brücher, Top. Curr. Chem. 221 (2002) 103.
[49] G. Tircsó, Z. Kovács, A.D. Sherry, Inorg. Chem. 45 (2006) 9269.
[50] T. Ryhl, Acta Chem. Scand. 27 (1973) 303.
[51] F. Yerly, F.A. Dunand, E. Tóth, A. Figueirinha, Z. Kovács, A.D. Sherry, C.F.G.C. Geraldes, A.E. Merbach, Eur. J. Inorg. Chem. (2000) 1001.
[52] E. Tóth, O.M.N. Dhubhghaill, G. Besson, L. Helm, A.E. Merbach, Magn. Reson. Chem. 37 (1999) 701.
[53] F.A. Dunand, S. Aime, S.G. Crich, G.B. Giovenzana, A.E. Merbach, Magn. Reson. Chem. 40 (2002) 87.
[54] P.J. Breen, W.DeW. Horrocks, Inorg. Chem. 22 (1983) 536.
[55] S. Lis, G.R. Choppin, Mater. Chem. Phys. 31 (1992) 159.
[56] T. Kimura, Y. Kato, J. Alloys Compd. 278 (1998) 92.
[57] P.G. Allen, J.J. Bucher, D.K. Shuh, N.M. Edelstein, I. Craig, Inorg. Chem. 39 (2000) 595.
[58] A. Nehlig, M. Elhabiri, I. Billard, A.-M. Albrecht-Gary, K. Lutzenkirchen, Radiochim. Acta 91 (2003) 37.
[59] K.L. Nash, J. Alloys Compd. 249 (1998) 33.
[60] R.S. Dickins, D. Parker, Signalling reversible anion binding in aqueous media, in: K. Gloe (Ed.), Macrocyclic Chemistry. Current Trends and Future Perspectives, Springer, Dordrecht, 2005.
[61] R.S. Dickins, D. Parker, J.I. Bruce, D.J. Trozer, Dalton Trans. (2003) 1264.

study in representative cases. The photoluminescence properties of the complexes are also examined.

2. Experimental

2.1. Materials

The metal salts $Zn(NO_3)_2 \cdot 6H_2O$, $ZnCl_2$, $Zn(OAc)_2 \cdot 2H_2O$, $Cd(NO_3)_2 \cdot 4H_2O$, $CdCl_2 \cdot 2H_2O$, $Cd(OAc)_2 \cdot 2H_2O$, $Hg(NO_3)_2$, $HgCl_2$ and $Hg(OAc)_2$, and NaN_3 and NH_4SCN were purchased from Loba Chemi, Bombay. $Zn(ClO_4)_2 \cdot 6H_2O$, $Cd(ClO_4)_2 \cdot 6H_2O$ and $Hg(ClO_4)_2 \cdot 6H_2O$ were prepared by adding the corresponding MCO_3 [M = Zn(II), Cd(II), Hg(II)] to a warm 1:1 $HClO_4$ solution followed by slow evaporation in a fused $CaCl_2$ desiccator. 8-Aminoquinoline was purchased from Aldrich. All other chemicals and solvents were used after drying [17].

2.2. Physical measurements

Microanalyses (C, H, N) were performed using a Perkin–Elmer 2400 CHN/O elemental analyzer. Spectroscopic measurements were carried out using the following instruments: UV–Vis spectra, Perkin–Elmer, model Lambda 25; FT-IR spectra (KBr disk, 4000–200 cm^{-1}), Perkin–Elmer FT-IR Spectrophotometers. Molar conductances (Λ_M) were measured in a Systronics conductivity meter 304 model using *ca.* 10^{-3} M solutions in DMF. ^1H NMR spectra were recorded using a Brucker 300 MHz FT NMR in DMSO-d_6. The luminescence properties were measured using a LS-55 Perkin–Elmer fluorescence spectrophotometer at room temperature (298 K) in DMF solution with a 1 cm path length quartz cell.

The fluorescence quantum yield of 8-aq and its complexes were determined using carbazole laser dye as a reference with a known ϕ_R of 0.42. The complex and the reference dye were excited at 330 nm, maintaining nearly equal absorbance (~0.1), and the emission spectra were recorded from 350 to 700 nm in DMF (because of insolubility or sparing solubility in common organic solvents. $CHCl_3$ is used additionally to check for a solvent effect for 8-aq). The area of the emission spectrum was integrated using the software available in the instrument and the quantum yield is calculated according to the following equation:

$$\phi_S/\phi_R = [A_S/A_R] \times [(Abs)_R/(Abs)_S] \times [\eta^2{}_S/\eta^2_R]$$

Here, ϕ_S and ϕ_R are the fluorescence quantum yield of the sample and reference, respectively. A_S and A_R are the area under the fluorescence spectra of the sample and the reference, respectively $(Abs)_S$ and $(Abs)_R$ are the respective optical densities of the sample and the reference solution at the wavelength of excitation, and η_S and η_R are the values of the refractive index for the respective solvent used for the sample and reference.

CAUTION! Azide and ClO_4^- complexes of transition metal ions containing organic ligands are potentially explosive. Only a small amount of materials should be prepared, and it should be handled with care.

2.3. Synthesis of the complexes

2.3.1. Di-aquo-bis-(8-aminoquinoline)zinc(II) nitrate, $[Zn(8\text{-}aq)_2(H_2O)_2]\ (NO_3)_2$, 1

49 mg (0.34 mmol) 8-aminoquinoline (8-aq) in 20 ml MeOH was added to a clear solution of 50 mg (0.17 mmol) $Zn(NO_3)_2 \cdot 6H_2O$ in 20 ml MeOH and stirring was continued for 1 h; the colour changed to light yellow. The volume of the solution was reduced to 10 ml, filtered and kept for crystallization after addition of 2 drops of 2-methoxy ethanol. Yellowish crystals were obtained by slow evaporation of the solvent. Yield was 58.9 mg, (67.20%).

The other complexes were prepared following an identical procedure and the yields of products varied in the range 65–75%. Microanalytical data: Anal. Cal. $C_{18}H_{20}N_6O_8Zn$ (**1**): C, 42.11; H, 3.92; N, 16.37. Found: C, 42.26; H, 3.83; N, 16.50%. $C_{18}H_{20}N_4\ Cl_2O_{10}Zn$ (**2**): C, 36.73; H, 3.40; N, 9.52. Found: C, 36.67; H, 3.37; N, 9.65%. $C_9H_8N_2Cl_2Zn$ (**3**): C, 38.57; H, 2.86; N, 10.00. Found: C, 38.45; H, 2.80; N, 9.92%. $C_{18}H_{20}N_6O_8Cd$ (**6**): C, 38.57; H, 3.57; N, 15.00. Found: C 38.66; H, 3.48; N, 15.13%. $C_{18}H_{20}N_4Cl_2O_{10}Cd$ (**7**): C, 34.01; H, 3.17; N, 8.82. Found: C, 34.19; H, 3.15; N, 8.73%. $C_9H_8N_2Cl_2Cd$ (**8**): C, 33.03; H, 2.46; N, 8.56. Found: C, 33.12; H, 2.54; N, 8.75%. $C_{18}H_{20}N_6O_8Hg$ (**11**): C, 33.30; H, 3.10; N, 12.95. Found: C, 33.19; H, 2.93; N, 13.04%. $C_{18}H_{20}N_4Cl_2O_{10}Hg$ (**12**): C, 29.88; H, 2.78; N, 7.75. Found: C, 30.00; H, 2.85; N, 7.86%. $C_9H_8N_2Cl_2Hg$ (**13**): C, 25.99; H, 1.94; N, 6.74. Found: C, 25.86; H, 2.03; N, 6.85%.

2.3.2. Bis-azido-(8-aminoquinoline)zinc(II), $[Zn(8\text{-}aq)(N_3)_2]n$, 4

65 mg (0.45 mmol) 8-aminoquinoline (8-aq) in 5 ml MeOH was added to a clear solution of 100 mg (0.46 mmol) $Zn(OAc)_2 \cdot 2\ H_2O$ in 20 ml MeOH and stirring was continued for 1 h. To this solution 30 mg (0.47 mmol) NaN_3 in MeOH (5 ml) was added and stirred for another 5 min; the colour changed to light yellow. The volume of the solution was reduced to 15 ml, filtered and kept for crystallization after addition of 2 drops of 2-methoxy ethanol. Yellowish crystals were obtained by slow evaporation of the solvent. Yield was 81 mg (61%).

The other azido and thiocyanato derivative complexes were synthesized following an identical procedure. Microanalytical data: Anal. Calcd. for $C_9H_8N_8Zn$ (**4**): C, 36.86; H, 2.75; N, 38.22; found: C, 36.95; H, 2.82; N, 38.14%. $C_{11}H_8N_4S_2Zn$ (**5**): C, 40.62; H, 2.48; N, 17.23. Found: C, 40.74; H, 2.41; N, 17.33%. $C_9H_8N_8Cd$ (**9**): C, 31.76; H, 2.37; N, 32.94; Found: C, 31.70; H, 2.32; N, 33.02%. $C_{11}H_8N_4S_2Cd$ (**10**): C, 35.48; H, 2.17; N, 15.05. Found: C, 35.55; H, 2.08; N, 15.00%. $C_9H_8N_8Hg$ (**14**): C, 25.20; H, 1.88; N, 26.13. Found: C, 25.13; H, 1.94; N, 26.00%. $C_{11}H_8N_4S_2Hg$ (**15**): C, 28.66; H, 1.75; N, 12.16. found: C, 28.51; H, 1.83; N, 12.24%.

2.4. X-ray crystal structure analysis of $[Zn(8\text{-aq})_2(H_2O)_2](NO_3)_2$ (1) and $[Cd(8\text{-aq})(N_3)_2]_n$ (9)

The crystals were grown by slow evaporation of the reaction mixture over a week. Data were collected with a Bruker CCD area detector diffractometer using fine-focus sealed graphite-monochromatized Mo Kα radiation ($\lambda = 0.71073$ Å) at 295(2) K for **1** (with crystal dimensions $0.20 \times 0.20 \times 0.05$ mm) and a CAD4 single crystal X-ray diffractometer for **9** (with crystal dimensions $0.26 \times 0.24 \times 0.18$ mm) by the ω-scan method. Diffractions were recorded with 2θ in the range $2.90 \leqslant 2\theta \leqslant 56.58°$ for **1** and $3.22 \leqslant 2\theta \leqslant 49.94°$ for **9**. A summary of the crystallographic data and structure refinement parameters are given in Table 1. Reflection data were recorded using the ψ and ω scan techniques. Data were corrected for Lp and an empirical absorption correction in the $h\ k\ l$ range: $-11 \leqslant h \leqslant 11$; $-11 \leqslant k \leqslant 9$; $-18 \leqslant l \leqslant 19$ for **1** and $0 \leqslant h \leqslant 7$; $0 \leqslant k \leqslant 26$; $-18 \leqslant l \leqslant 18$ for **9**. Data reduction was carried out using the SAINT program. The structures were solved by the direct method using SHELXS-97 [18] and successive difference Fourier syntheses. All non-hydrogen atoms were refined anisotropically. The hydrogen atoms were fixed geometrically and refined using the riding model. The molecular graphics were carried out using the ORTEP-3 for Windows [19] and PLATON-99 [20] programs. The residual electron density was in the range 0.316 and −0.260 for **1** and +1.020 to −0.768 e Å^{-3} for **9**.

Table 1
Summarised crystallography data for $[Zn(8\text{-aq})_2(H_2O)_2](NO_3)_2$ (**1**) and $[Cd(8\text{-aq})(N_3)_2]_n$ (**9**)

Crystal parameters	(**1**)	(**9**)
Empirical formula	$C_{18}H_{20}N_4\ Cl_2O_{10}Zn$	$C_9H_8N_8Cd$
Formula weight	513.77	340.64
Crystal system	Monoclinic	Monoclinic
Space	$P2_1$	$P2_1/n$
a (Å)	8.8296(10)	6.682(3)
b (Å)	8.4969(9)	21.981(6)
c (Å)	14.3027(16)	15.509(8)
β (°)	101.675	92.08(12)
V(Å^3)	1050.8(2)	2276.4
λ (Å)	0.71073	0.71073
ρ_{calcd} (Mg m^{-3})	1.624	1.988
Z	2	4
T (K)	295(2)	293(2)
μ (M_o–K_α) mm^{-1})	1.229	1.914
Total data	7123	4346
Unique data	2901	3991
Refined parameters	330	325
R	0.0341	0.0401
wR_2	0.0685	0.1329
GOF	0.846	1.407

[a] $R = \|\|F_o\|-\|F_c\|\|/\Sigma|F_o|$.
[b] $wR_2 = [\Sigma(w|F_o|^2-|F_c|^2)^2/\Sigma w(|F_o|)]^{1/2} w = 1/[\sigma^2(F_o^2) + (0.0299P)^2]$ for **1** and $1/[\sigma^2(F_o^2) + (0.0516P)^2 + 1.8227P]$ for **9**, $P = (F_o^2 + 2F_c^2)/3$.
[c] GOF (Goodness of Fit) is defined as $[w(F_o-F_c)/(n_o-n_v)]^{1/2}$ where n_o and n_v denote the number of data and variables, respectively.

3. Results and discussion

3.1. Synthesis and formulation

The complexes were synthesized by reacting a methanolic solution of the requisite number of moles of 8-aminoquinoline (8-aq) and Group 12 metal salts for mononuclear complexes, $[M(8\text{-aq})_2(H_2O)_2]\,(X)_2$ (X = NO_3 or ClO_4) and $M(8\text{-aq})Cl_2$. Addition of 2 equivalents of NaN_3 or NH_4CNS to the mixture of $M(CH_3COO)_2$ and 8-aq (1:1 mole ratio) in MeOH has synthesized bridged polymeric complexes, $[M(8\text{-aq})(Y)_2]_n$ (Y = N_3 or CNS). Microanalytical data suggest complexes of following composition: $[M(8\text{-aq})_2(H_2O)_2]\,(X)_2$ (X = NO_3 (**1**, **6**, **11**) or ClO_4 (**2**, **7**, **12**) where M = Zn(II) (**1**, **2**); Cd(II) (**6, 7**), Hg(II) (**11, 12**); $[M(8\text{-aq})Cl_2]$ (M = Zn(II), **3**; Cd(II), **8**; Hg(II), **13**) and $[M(8\text{-aq})(Y)_2]$n (Y = N_3 (**4**, **9**, **14**) or NCS (**5**, **10**, **15**) where M = Zn(II), (**4**, **5**); Cd(II), (**9**, **10**); Hg(II), (**14, 15**)). We have carried out experiments with different metal:-ligand ratios (1:1, 1:2; 2:3), but in all the experiments we ended up with the complexes of the noted composition. Molar conductance data show that the complexes $[M(8\text{-aq})_2(H_2O)_2]\,(X)_2$ are 1:2 electrolytes in nature while the others are non-conducting. Spectral and single crystal structure determination in some cases support the composition. Because of the explosive nature of NO_3^-, ClO_4^-, N_3^- we did not perform thermal studies of the complexes.

3.2. Spectral studies

The FT-IR bands were assigned by comparing with the free ligand values. All the complexes show a moderately sharp absorption at 3100–3200 cm^{-1} which is assigned to the asymmetric stretching of coordinated $-NH_2$ (the free ligand shows $\nu(NH_2)$ at 3448 and 3348 cm^{-1}). Besides, complexes **1**, **2**, **6**, **7**, **11** and **12** show medium intense broad band(s) centred at 3390–3410 cm^{-1} which is assigned to a coordinated H_2O band. The complexes $[M(8\text{-aq})_2(H_2O)_2]\,(NO_3)_2$ (**1**, **6**, **11**) show an intense sharp absorption at 1380–1390 cm^{-1} which is assigned to non-coordinated $\nu(NO_3)$ (this is supported by conductance data and single crystal X-ray data) [21], while $\nu(ClO_4)$ in $[M(8\text{-aq})_2(H_2O)_2](ClO_4)_2$ appears as a sharp absorption at 1090–1105 cm^{-1} and a weak shoulder at 625–630 cm^{-1} for the uncoordinated ClO_4 anion [21]. It is assumed that infrared active M–Cl stretchings appear at 258–280 cm^{-1} in the complexes, $M(8\text{-aq})Cl_2$ [22–24]. The azide complexes show a sharp peak at 2070–2080 cm^{-1} whereas the Cd- and Hg-azide show a sharp absorption at 2040–2048 cm^{-1}; this spectral feature supports azido bridging structures, $[M(8\text{-aq})(N_3)_2]_n$. Similarly the thiocyanato complexes also exhibit ν(NCS) at 2083–2109 cm^{-1} and support the composition $[M(8\text{-aq})(NCS)_2]_n$. One of the structures has been supported by single crystal X-ray structure data.

Table 2
UV–Vis and emission spectroscopic data in DMF

Compounds	λ/nm (ε/M^{-1} cm^{-1})	λ_{ex}	λ_{em}	Φ
8-aq*	354 (3893), 267 (7219)	354	481	0.046
$[Zn(8\text{-aq})_2(H_2O)_2](NO_3)_2$ (**1**)	455 (22.5), 352(7883), 272 (7650)	352	478	0.037
$[Zn(8\text{-aq})_2(H_2O)_2](ClO_4)_2$ (**2**)	451 (24.2), 354 (8159), 270 (8086)	354	479	0.030
$[Zn(8\text{-aq})Cl_2]$ (**3**)	444 (31.0), 352 (3112), 270 (3669)	352	481	0.035
$[Zn(8\text{-aq})(N_3)_2]n$ (**4**)	485 (26.3), 357 (4142), 268 (6501)	357	480	0.015
$[Zn(8\text{-aq})(SCN)_2]n$ (**5**)	488 (43.13), 356 (6158), 269 (8222)	356	480	0.011
$[Cd(8\text{-aq})_2(H_2O)_2](NO_3)_2$ (**6**)	467 (21.7), 354 (6516), 270 (6032)	354	480	0.039
$[Cd(8\text{-aq})_2(H_2O)_2](ClO_4)_2$ (**7**)	458 (33.5), 353 (8150), 270 (10810)	353	479	0.034
$[Cd(8\text{-aq})Cl_2]$ (**8**)	462 (14.5), 352 (4148), 270 (4500)	352	480	0.030
$[Cd(8\text{-aq})(N_3)_2]n$ (**9**)	483 (10.6), 355 (4304), 269 (5469)	355	480	0.021
$[Cd(8\text{-aq})(SCN)_2]n$ (**10**)	497 (27.8), 356 (6214), 268 (7994)	356	481	0.015
$[Hg(8\text{-aq})_2(H_2O)_2](NO_3)_2$ (**11**)	480 (19.4), 336 (5224), 271 (8842)	336	480	0.024
$[Hg(8\text{-aq})_2(H_2O)_2](ClO_4)_2$ (**12**)	486 (21.2), 354 (3625), 269 (5212)	354	480	0.027
$[Hg(8\text{-aq})Cl_2]$ (**13**)	478 (24.5), 353 (2431), 269 (5197)	353	484	0.022
$[Hg(8\text{-aq})(N_3)_2]n$ (**14**)	Insoluble			
$[Hg(8\text{-aq})(SCN)_2]n$ (**15**)	Insoluble			

* In $CHCl_3$: 340 (2464), 260 (9079); $\lambda_{ex} = 340$ nm; $\lambda_{em} = 451$ nm; $\Phi = 0.048$.

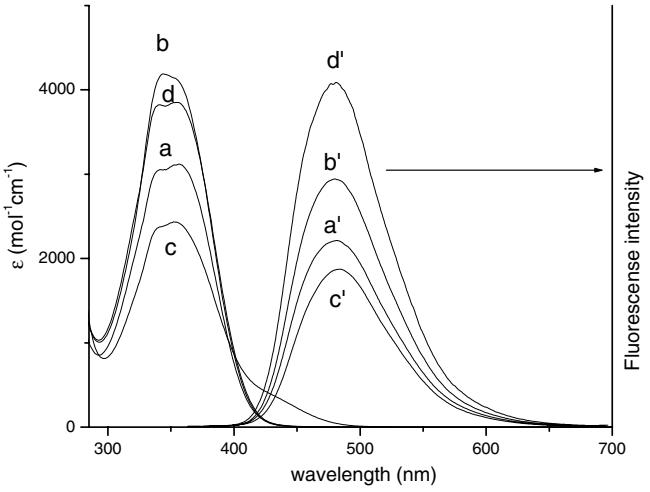


Fig. 1. UV–Vis spectra of (a) $Zn(8\text{-aq})Cl_2$, (b) $Cd(8\text{-aq})Cl_2$, (c) $Hg(8\text{-aq})Cl_2$ and (d) 8-aq. Fluorescence spectra of (a′) $Zn(8\text{-aq})Cl_2$, (b′) $Cd(8\text{-aq})Cl_2$, (c′) $Hg(8\text{-aq})Cl_2$, (d′) 8-aq in DMF.

The solution electronic spectra of the complexes were recorded in DMF solution in the range 250–550 nm. The data are listed in Table 2. All the complexes exhibit an intense band in the 350–400 nm range. These transitions are presumably due to intra-ligand π–π^*/and n–π^* transitions (Fig. 1). A red shift of the band in the UV–Vis spectra of <10 nm from the free ligand values for the metal complexes has been observed. A weak transition in the visible region (440–500 nm) is assigned to a MLCT band.

From a close inspection of the ^{1}H NMR data (Table 3), a small shift in the δ values of the C–H signals and the NH_2 proton indicate bonding with the d^{10} metal (Zn(II), Cd(II), Hg(II)) system. The C–H protons appear at a slightly lower δ value due to weak back-bonding from M(II) to 8-aminoquinoline. On the other hand, a higher δ value of the NH_2 proton (5.89–5.97 ppm) is observed because of the lowering of electron density during complexation.

Table 3
^{1}H NMR spectra* in DMSO-d_6

Compounds	2H[d]	3H[t]	4H[d]	5H[d]	6H[m]	7H[d]	NH_2
8-aq[a]	8.77 (4.4)	7.37 (8.0)	8.14 (8.2)	6.94 (7.6)	7.42	7.16 (8.1)	4.21
(**1**)	8.70 (3.6)	7.28 (7.8)	8.15 (8.2)	6.85 (8.2)	7.46	7.04 (7.5)	5.89
(**2**)	8.71 (3.6)	7.25 (7.8)	8.15 (8.3)	6.86 (8.2)	7.45	7.09 (7.5)	5.89
(**3**)	8.70 (3.5)	7.24 (7.8)	8.39 (8.3)	6.86 (8.2)	7.46	7.05 (7.5)	5.86
(**4**)	8.71 (4.2)	7.06 (9.0)	8.19 (9.0)	6.88 (6.0)	7.46	7.05 (6.0)	5.88
(**5**)	8.71 (4.2)	7.06 (9.0)	8.18 (9.0)	6.87 (6.0)	7.46	7.06 (6.0)	5.89
(**6**)	8.71 (4.0)	7.20 (7.8)	8.15 (8.2)	6.86 (7.6)	7.44	7.02 (7.8)	5.89
(**7**)	8.70 (4.1)	7.20 (7.8)	8.15 (8.2)	6.86 (7.6)	7.44	7.03 (7.8)	5.89
(**8**)	8.70 (4.0)	7.25 (7.8)	8.14 (8.2)	6.86 (7.6)	7.45	7.05 (7.8)	5.88
(**9**)	8.71 (4.0)	7.31 (7.5)	8.19 (9.0)	6.86 (6.0)	7.45	7.05 (6.0)	5.88
(**10**)	8.71 (4.0)	7.30 (7.5)	8.17 (9.0)	6.86 (6.0)	7.45	7.05 (6.0)	5.89
(**11**)	8.71 (3.9)	7.30 (7.7)	8.17 (8.2)	6.88 (7.9)	7.47	7.07 (8.1)	5.97
(**12**)	8.71 (3.9)	7.30 (7.8)	8.17 (8.2)	6.88 (8.0)	7.47	7.07 (8.0)	5.97
(**13**)	8.71 (3.9)	7.30 (7.7)	8.17 (8.2)	6.88 (8.0)	7.47	7.10 (8.1)	5.96

[a] In $CDCl_3$.
[d] Doublet.
[m] Multiplet.
[t] Triplet.
* $[Hg(8\text{-aq})_2(N_3)_2]_n$ and $[Hg(8\text{-aq})_2(SCN)_2]_n$ complexes are insoluble in common organic solvents.

3.3. Crystal structures

3.3.1. [Zn(8-aq)(H_2O)$_2$](NO_3)(1)

The ORTEP view of the structure of **1** is shown in Fig. 2. The octahedral molecule bears N_{amine}–Zn–$N_{quinoline}$ chelate bite angles of 80.26 and 80.95°, all the N–Zn–O bond angles vary from 85.70 to 90.47° and the O(1)–Zn–O(2) bond angle is 179.03°, which is in agreement with the octahedral geometry. Two chelate planes Zn–N(3)–C(18)–C(17)–N(4) and Zn–N(1)–C(9)–C(8)–N(2) make a dihedral angle of 7.85°; every chelate plane is almost planar with the corresponding 8-aminoquinoline ring (the dihedral angle varies from 1.42 to 2.18°), which supports that the two ligands are almost planar to each other.

The molecule shows a C–H – π and π–π interaction with the 8-aminoquinoline ring of an adjacent molecule (Fig. 3). The molecule shows a H-bonding network through the oxygen atom of the nitrate anion and a hydrogen atom of a water molecule (coordinated with Zn), and also through the oxygen atom of the nitrate anion and the hydrogen atom of C-19 and C-20 of the 8-aminoquinoline ring. The bond parameters are given in Table 4.

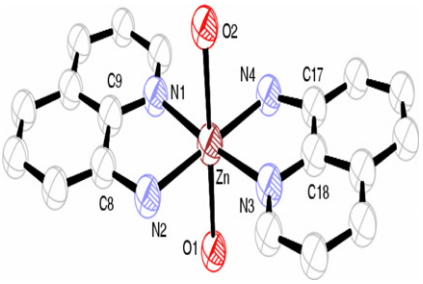


Fig. 2. ORTEP structure of **1**, hydrogen atoms and NO_3^- have been removed for clarity.

3.3.2. [Cd(8-aq)(N_3)$_2$]n, (9)

The ORTEP view of **9** is shown in Fig. 4 and selected bond parameters are listed in Table 5. The cadmium atom is in a distorted octahedral environment with CdN_6 coordination. 8-aq acts as an unsymmetric N,N′ chelating ligand (quinoline-N refers to N and NH_2 refers to N′). The azido (N_3) groups act as end-on (μ−1,1 EO) double bridging agents with two neighboring cadmium atoms. The bridging Cd_2N_4 unit constitutes a quadrilateral unit with bond lengths Cd(1)–N(5) 2.503(7), Cd(1)–N(8) 2.280(8), Cd(2)–N(5) 2.320(7), Cd(2)–N(8) 2.398(8) Å and bond angles Cd(1)–N(8)–Cd(2) 107.5(3), Cd(1)–N(5)-Cd(2) 103.7(3), N(5)–Cd(1)–N(8) 73.9(3)°, N(5)–Cd(2)–N(8) 75.2(3)°. The small chelate angle (∠N(1)–Cd(1)–N(2), 72.5(3)°) may cause the structural distortion. The bridge angles (103–107°) lie in the reported angular range [25]. A 1D neutral chain runs along the a-direction due to a repeating Cd_2N_4 unit. The distortion in the CdN_6 coordination is supported by six unequal Cd–N bond distances. One of the bridging azido–N bonds shows the longest distance in the series of Cd–N distances (Cd(1)–N(5) 2.503(7), Cd(2)–N(11) 2.516(7)). The Cd–N(amine) distance is expectedly longer (by 0.01–0.04 Å) than that of the Cd–

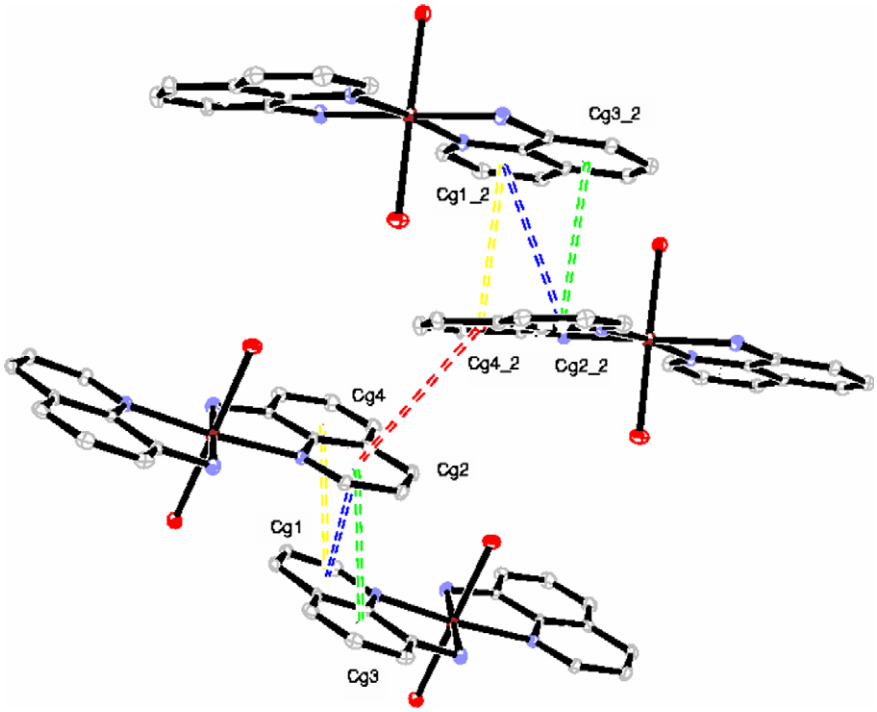


Fig. 3. π–π interaction.

N(quinoline) distances. The azide N–N distances are within the reported range [26].

The 1D chains are self-assembled to form a molecular sheet *via* C–/N–H–N(azido) and π–π interactions between aromatic rings, and are described in Figs. 5 and 6. The π–π interaction with the aromatic rings (Fig. 5) ((Cg(7)–Cg(8) 3.816 Å (symmetry $3/2-x$, $-1/2+y$, $3/2-z$), Cg(8)–Cg(7) 3.832 Å (symmetry $5/2-x$, $1/2+y$, $3/2-z$), Cg(9)–Cg(6) 3.776 Å (symmetry $3/2-x$, $-1/2+y$, $3/2-z$) and Cg(9)–Cg(6) 3.764 Å (symmetry, $5/2-x$, $-1/2+y$, $3/2-z$), where Cg(6): N(1), C(1), C(2), C(3), C(4), C(9); Cg(7), N(4), C(17), C(16), C(15), C(14), C(18); Cg(8): C(4), C(5), C(6), C(7), C(8), C(9); Cg(9): C(10), C(11), C(12), C(13), C(14), C(18)). The robustness of the supramolecular geometry has been enhanced through intermolecular hydrogen bondings (Fig. 6). It is observed that the $-NH_2$ protons and some of the aromatic C–H protons act as H-donors and the bridged azido–N (both coordinated and free N) act as H-acceptors. The acceptable hydrogen bonds are: N(2)–H(2A)–N(16): N(2)–H(2A) 0.90, H(2A)–N(16) 2.409(2), N(2)–N(16) 3.222(12) Å, ∠N(2)–H(2A)–N(16) 150.36° and symmetry $1/2+x$, $1/2-y$, $-1/2+z$. N(2)–H(2B)–N(7): N(2)–H(2B) 0.90, H(2B)–N(7) 2.2251, N(2)–N(7) 3.103(12) Å ∠N(2)–H(2B)–N(7) 164.82° and symmetry $-1+x, y, z$. N(3)–H(3A)–N(13): N(3)–H(3A) 0.90, H(3A)–N(13) 2.2218, N(3)–N(13) 3.106(11) Å, ∠N(3)–H(3A)–N(13) 167.28°. N(3)–H(3B)–N(13): N(3)–H(3B) 0.90, H(3B)–N(13) 2.3144, N(3)–N(13) 3.121(10) Å, ∠N(3)–H(3B)–N(13) 149.07° and symmetry $2-x$, $-y$, $1-z$. C(3)–H(3)–N(13): C(3)–H(3) 0.93, H(3)–N(13) 2.4970, C(3)–N(13) 3.393(14) Å, ∠C(3)–H(3)–N(13) 161.80° and symmetry $3/2-x$, $-1/2+y$, $3/2-z$. C(6)–H(6)–N(10): C(6)–H(6) 0.93, H(6)–N(10) 2.6248, C(6)–N(10) 3.455(16) Å and

Table 4
Selected bond distances (Å) and angles (°) for $[Zn(8\text{-aq})_2(H_2O)_2](NO_3)_2$ (**1**) along with their esd in parentheses

	Distances (Å)		Angles (°)
Zn–N(1)	2.133(3)	N(1)–Zn–N(2)	80.96(13)
Zn–N(2)	2.095(3)	N(3)–Zn–N(4)	80.26(13)
N(1)–C(9)	1.372(4)	O(1)–Zn–O(2)	179.05(16)
N(2)–C(8)	1.444(5)	N(1)–Zn–O(1)	90.45(11)
Zn–O(1)	2.225(3)	N(1)–Zn–O(2)	89.09(13)
Zn–O(2)	2.268(3)	N(1)–Zn–N(3)	174.70(12)
Zn–N(3)	2.145(3)	N(1)–Zn–N(4)	98.92(13)
Zn–N(4)	2.097(3)	N(2)–Zn–N(4)	179.86(18)
N(3)–C(18)	1.354(4)	N(2)–Zn–N(3)	99.86(13)
N(4)–C(17)	1.445(5)	N(2)–Zn–O(1)	89.65(13)
		N(2)–Zn–O(2)	89.46(16)
		N(3)–Zn–O(1)	94.78(11)
		N(3)–Zn–O(2)	85.96(12)
		N(4)–Zn–O(1)	90.29(14)
		N(4)–Zn–O(2)	90.60(15)

π–π interactions

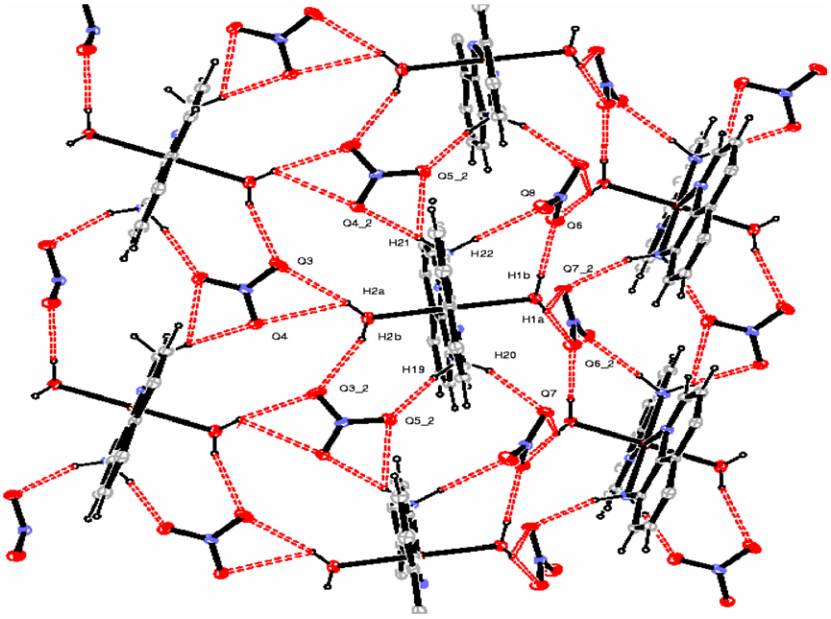
Interaction members	Kind of π–π interaction	Distance between ring centroids (Å)
Cg(1)–Cg(2) (#1.1)	face to face	3.8394
Cg(1)–Cg(4) (#1.1)	face to face	3.8686
Cg(2)–Cg(3)(#1.2)	face to face	3.7679
Cg(2)–Cg(4) (#2.1)	face to face	4.3978

Hydrogen Bonds (for detail of symbols see below)

Donor–H...Acceptor	D–H (Å)	H...A(Å)	D...A(Å)	Angel of D–H–A (°)
O(1)–H(1A)...O(6)[a]	0.80	2.09	2.8817	177
O(1)–H(1A)...O(7)[a]	0.80	2.60	3.1510	128
O(1)–H(1B)...O(6)	0.81	2.06	2.8689	173
O(2)–H(2A)...O(3)[b]	0.79	2.24	3.0157	172
O(2)–H(2A)...O(4)[b]	0.79	2.50	2.9625	119
O(2)–H(2B)...O(3)[c]	0.78	2.25	2.9824	157
N(2)–H(19)...O(5)[c]	0.93	1.95	2.8752	172
N(2)–H(20)...O(7)[d]	0.89	2.23	3.0372	152
N(4)–H(21)...O(4)[e]	0.90	2.11	3.0066	173
N(4)–H(21)...O(5)[e]	0.90	2.45	3.0846	127
N(4)–H(22)...O(8)	0.93	2.08	3.0001	168

Cg(1): N1–C1–C2–C3–C4–C9; Cg(2): N3–C10–C11–C12–C13–C18; Cg(3): C4–C5–C6–C7–C8–C9; Cg(4): C13–C14–C15–C16–C17–C18(#1.1) = $-1+x$, y, z; (#1.2) = $1+x$, y, z; (#2.1) = $1-x$, $-1/2+y$, $1-z$.

Table 4 (*continued*)



[a] $-x, -1/2+y, -z$.
[b] $-1+x, y, z$.
[c] $1-x, -1/2+y, 1-z$.
[d] $x, -1+y, z$.
[e] $1-x, 1/2+y, 1-z$.

∠C(6)–H(6)–N(10), 149.01° and symmetry $3/2-x, 1/2+y, 3/2-z$. C(12)–H(12)–N(16): C(12–H(12) 0.9296, H(12)–N(16) 2.5125, C(12)–N(16) 3.414(13) Å, ∠C(12)–H(12)–N(16), 163.44° and symmetry: $3/2-x, -1/2+y, 3/2-z$ (see Scheme 1).

3.4. Photoluminescence properties

The photoluminescence properties of 8-aq and its complexes were studied at room temperature (298 K) (Fig. 1) in DMF solution. Because of the very low solubility of the complexes we have been forced to study the spectral and emission measurements in DMF solution. Since, the ligand, 8-aq, is soluble in several organic solvents we have carried out emission measurements in DMF and $CHCl_3$ to make a comparison when using polar and non-polar solvents. Data are collected in Table 2. The spectrum shows two intense transitions in DMF corresponding to 267 nm, π–π^* and 354 nm, n–π^* transitions. They are shifted to higher energy positions when the spectrum is recorded in

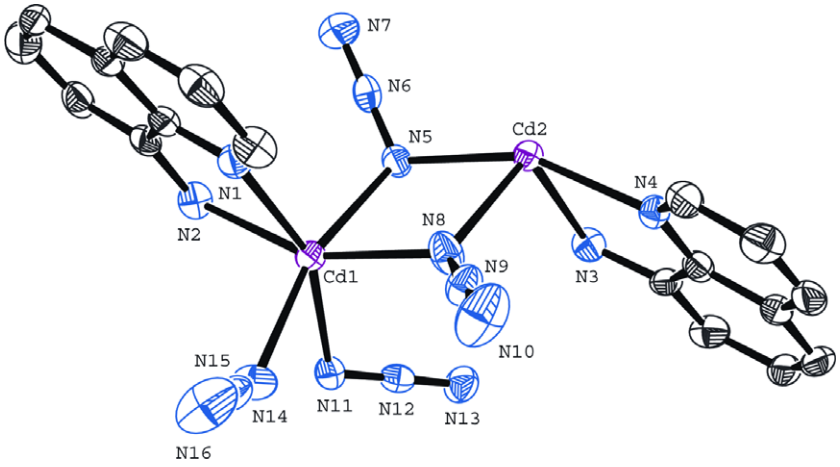


Fig. 4. ORTEP diagram representing the asymmetric unit of the complex $[Cd(8\text{-aq})(N_3)_2]_n$ (**9**). Hydrogen atoms are not shown for clarity.

Table 5
Selected bond distances (Å) angles (°) for $[Cd(8\text{-aq})(N_3)_2]_n$ (**9**)

	Distances (Å)		Angles (°)
Cd(1)–N(1)	2.317(8)	N(1)–Cd(1)–N(2)	72.5(3)
Cd(1)–N(2)	2.358(7)	N(1)–Cd(1)–N(5)	104.6(3)
Cd(1)–N(5)	2.503(7)	N(1)–Cd(1)–N(8)	99.7(3)
Cd(1)–N(8)	2.280(8)	N(1)–Cd(1)–N(11)	156.7(3)
Cd(1)–N(11)	2.336(8)	N(1)–Cd(1)–N(14)	88.4(3)
Cd(1)–N(14)	2.441(8)	N(2)–Cd(1)–N(5)	85.6(2)
Cd(2)–N(3)	2.348(7)	N(2)–Cd(1)–N(8)	155.6(3)
Cd(2)–N(4)	2.338(7)	N(2)–Cd(1)–N(11)	96.7(3)
Cd(2)–N(5)	2.320(7)	N(2)–Cd(1)–N(14)	106.7(3)
Cd(2)–N(8)	2.398(8)	N(5)–Cd(1)–N(11)	94.9(3)
Cd(2)–N(11)[a]	2.516(7)	N(5)–Cd(1)–N(8)	73.9(3)
Cd(2)–N(14)[b]	2.290(8)	N(5)–Cd(1)–N(14)	164.5(3)
N(5)–N(6)	1.215(10)	N(5)–Cd(1)–N(11)	94.9(3)
N(6)–N(7)	1.156(11)	N(8)–Cd(1)–N(14)	95.9(3)
N(8)–N(9)	1.183(10)	N(1)–Cd(1)–N(8)	99.7(3)
N(9)–N(10)	1.126(11)	N(8)–Cd(1)–N(11)	98.0(3)
		N(11)–Cd(1)–N(14)	74.7(3)
		Cd(1)–N(1)–Cd(2)[a]	103.7(3)
		Cd(1)–N(14)–Cd(2)[a]	107.5(3)
		N(5)–N(6)–N(7)	178.7(10)
		N(8)–N(9)–N(10)	178.4(13)
		N(11)–N(12)–N(13)	179.1(10)
		N(14)–N(15)–N(16)	178.6(12)
		N(5)–Cd(2)–N(14)[b]	100.5(3)
		N(4)–Cd(2)–N(14)[b]	98.1(3)
		N(5)–Cd(2)–N(4)	156.2(3)
		N(11)–Cd(2)–N(14)[b]	74.1(3)
		N(5)–Cd(2)–N(11)[b]	93.4(3)
		N(4)–Cd(2)–N(11)[b]	106.0(2)
		N(3)–Cd(2)–N(11)[b]	85.7(2)
		N(8)–Cd(2)–N(11)	166.0(3)
		N(3)–Cd(2)–N(14)[b]	154.8(3)
		N(5)–Cd(2)–N(3)	95.5(3)
		N(4)–Cd(2)–N(3)	72.8(3)
		N(8)–Cd(2)–N(14)[b]	99.6(3)
		N(5)–Cd(2)–N(8)	75.2(3)
		N(4)–Cd(2)–N(8)	87.1(3)
		N(3)–Cd(2)–N(8)	103.3(3)
		Cd(2)–N(5)–Cd(1)	103.1(3)

Symmetry codes: [a] $-1+x, y, z$; [b] $1+x, y, z$.

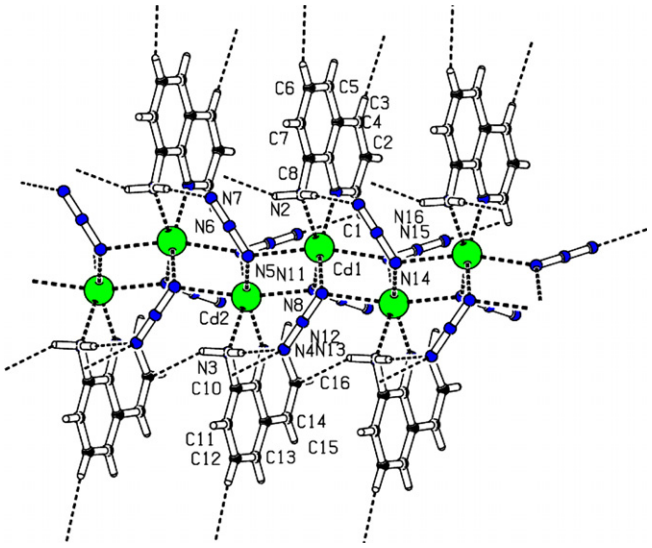


Fig. 6. Hydrogen bonded 1D chain of the azido bridged $[Cd(8\text{-aq})(N_3)_2]_n$.

$CHCl_3$. 8-aq exhibits photoluminescence with an emission at 481 nm upon excitation at 354 nm in DMF, while the emission appears at 451 nm upon excitation at 340 nm in $CHCl_3$. The complexes show strong fluorescence with a high quantum yield in DMF solvent (shown in Table 2), excitation of the molecule at 330–350 nm gives an emission at 478–486 nm. No emissions originating from metal-centered excited states are expected for the Zn(II), Cd(II) and Hg(II) complexes, since they are difficult to oxidize or reduce due to their d^{10} configuration. Thus, the emission observed in the complexes is assigned to the $(\pi - \pi^*)$ intraligand fluorescence and these are red shifted by >120 nm. The intensity of the emission is found to be higher than that of the free ligand. It has been reported that metal ions can enhance or quench the fluorescence emission of pyridine containing compounds [27,28]. In the absence of metal ions the fluorescence of the ligand is probably quenched by

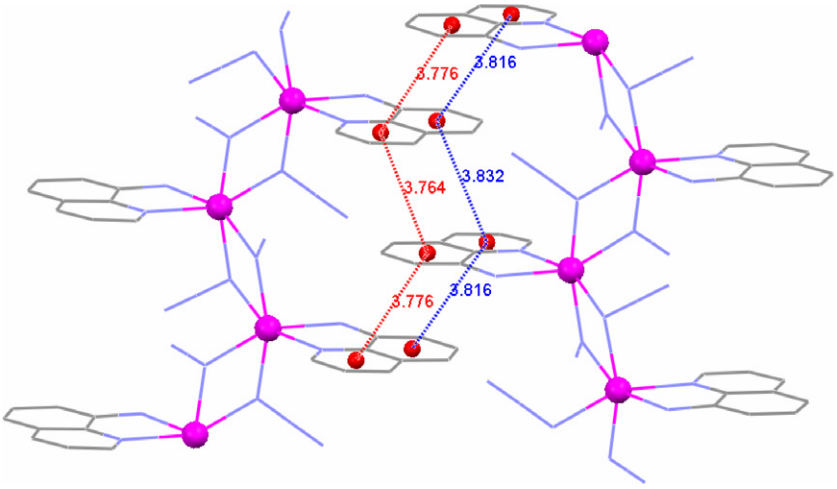
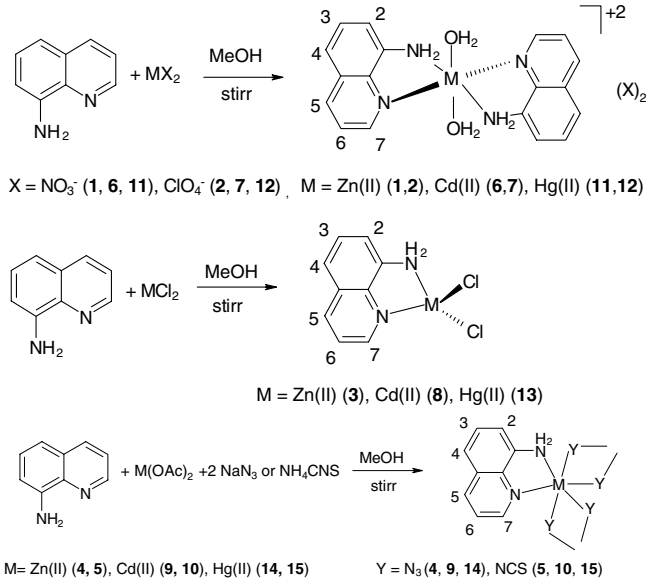


Fig. 5. The zig–zag π–π complementary interactions in the packing of $[Cd(8\text{-aq})(N_3)_2]_n$ (**9**).



Scheme 1.

the occurrence of a photoinduced electron transfer (PET) process due to the presence of a lone pair of the nitrogen atoms. Such a PET process is prevented by complexation of the ligand with metal ions; thus the fluorescence intensity may be greatly enhanced by coordination to M(II), which is defined as chelation enhanced fluorescence intensity. The chelation of the ligands increases the rigidity and reduces the loss of energy by thermal vibrational decay. The quantum yields are estimated with reference to carbazole (Table 2) and appear at 0.01 to 0.04. Because of the insolubility of $[Hg(8\text{-aq})(N_3)_2]_n$ and $[Hg(8\text{-aq})(NCS)_2]$ we could not perform luminescence measurements.

4. Conclusion

This paper describes mononuclear MX_2 complexes (M = Zn, Cd, Hg; X = Cl, NO_3, ClO_4) of 8-aminoquinoline. The complexes are characterized by different physicochemical methods. The single crystal X-ray structure determination of $[Zn(8\text{-aq})_2(H_2O)_2](NO_3)_2$ shows an octahedral ZnN_4O_2 coordination arrangement. The azido complexes are end-on bridging polymers and in one case, $[Cd(8\text{-aq})(N_3)_2]$, the structure determination shows a supramolecular structure of an azido bridged 1D chain *via* hydrogen bonding and π–π interactions. The complexes show ligand centered potential photoluminescence properties.

5. Supplementary material

Crystallographic data for the structures have been deposited with the Cambridge Crystallographic data center, CCDC No. 639302 for $[Zn(8\text{-aq})_2(H_2O)_2](NO_3)_2$ (**1**) and 639303 for $[Cd(8\text{-aq})(N_3)_2]_n$ (**9**). Copies of this information may be obtained free of charge from the Director, CCDC, 12 Union Road, Cambridge CB2 1EZ, UK (e-mail: deposit @ccdc.cam.ac.uk or www:http://www.ccdc.cam.ac.uk).

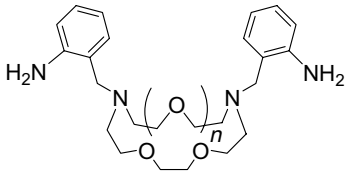
Acknowledgement

Financial support from the University Grants Commission and the All India Council for Technical Education, New Delhi, are gratefully acknowledged. One of us, MP, thanks CSIR for a fellowship. Our sincere thanks to Prof. Debasis Ray, Department of Chemistry, Indian Institute of Technology, Kharagpur, Paschim Medinipur, West Bengal, India for his help in the structure solution of $[Cd(8\text{-aq})(N_3)_2]$.

References

[1] F. Blau, Ber. Dtsch. Chem. Ges. 27 (1888) 1077.
[2] G. Wilkinson, R.D. Gillard, J. McCleverty (Eds.), Comprehensive Coordination Chemistry, Vol. 1–7, Pergamon Press, Oxford, 1987.
[3] F.A. Cotton, G. Wilkinson, Advanced Inorganic Chemistry, 5th ed., John Wiley and Sons, New York, 1988.
[4] M. Cais, Progress in Coordination Chemistry, American Elsevier, New York, 1968.
[5] D.H. Bush, Chem. Rev. 93 (1993) 847.
[6] B.L. Tekwami, L.A. Walker, Curr. Opin. Infect. Dis. 19 (2006) 623.
[7] J.M. Fritsch, K.A. Thoreson, K. McNeill, J. Chem. Soc. Dalton Trans. (2006) 4814.
[8] J.L. Nowicki, K.S. Johnson, K.H. Coale, V.A. Elord, S.H. Lieberman, Anal. Chem. 66 (1994) 2732.
[9] B. Macias, I. Garcia, M.V. Villa, J. Borras, A. Casiineiras, F. Sanz, Z. Anorg. Alleg. Chemie 629 (2003) 255.
[10] X.-G. Li, Y.-M. Hua, M.R. Huang, Chem. Eur J. 11 (2005) 4247.
[11] M.H. Lim, B.A. Wong, W.H. Pitcock Jr., D. Mokshagundam, M.-A. Baik, S.J. Lippard, J. Am. Chem. Soc. 128 (2006) 14364.
[12] Y.-H. Kim, J.S. Youk, S.Y. Moon, J.-I. Choe, S.-K. Chang, Chem. Lett. 33 (2004) 702.
[13] D. Banerjee, B.C. Mondal, A.K. Das, J. Indian Chem. Soc. 81 (2004) 50.
[14] M. Ray, S. Bhattacharya, P. Bannerjee, J. Indian Chem. Soc. 76 (1999) 121.
[15] M. Mortoluzzi, G. Paolucci, B. Pitteri, A. Vavasori, Inorg. Chem. Commun. 9 (2006) 1301.
[16] (a) O. Kahn, Molecular Magnetism, VCH, New York, 1993;
(b) J.S. Miller, M. Drillon (Eds.), Magnetism: Molecules to Materials, Wiley-VCH, Weinheim, Germany, 2002;
(c) J.D. Woodward, R.V. Backov, K.A. Abboud, D. Dai, H.-J. Koo, M.-H. Whangbo, M.W. Meisel, D.R. Talham, Inorg. Chem. 44 (2005) 63.
[17] A.I. Vogel, A Text Book of Practical Organic Chemistry, 2nd ed., Longman, London, 1959.
[18] G.M. Sheldrick, SHELXL 97 Program for the Solution of Crystal Structure, University of Gottingen, Germany, 1997.
[19] L.J. Farrugia, ORTEP-3 for Windows J. Appl. Cryst. 30 (1997) 565.
[20] A.L. Spek, PLATON Molecular Geometry Program, University of Utrecht, The Netherlands, 1999.
[21] U. Casellato, P.A. Vigato, Coord. Chem. Rev. 36 (1981) 183.
[22] B.G. Chand, G. Mostafa, T.-H. Lu, L.R. Falvello, C. Sinha, Polyhedron 22 (2003) 3161.
[23] B.G. Chand, U.S. Ray, J. Cheng, T.-H. Lu, C. Sinha, Polyhedron 22 (2003) 1213.
[24] B.G. Chand, U.S. Ray, P.K. Santra, G. Mostafa, T.-H. Lu, C. Sinha, Polyhedron 22 (2003) 1205.

[25] B.G. Chand, U.S. Ray, G. Mostafa, T.-H. Lu, C. Sinha, Polyhedron 23 (2004) 1669.
[26] U.S. Ray, B.K. Ghosh, M. Monfort, J. Ribas, G. Mostafa, T.-H. Lu, C. Sinha, Eur. J. Inorg. Chem. (2004) 250.
[27] H.F. Zhu, L. Li, T. Okamura, W. Zhao, W.Y. Skn, N. Ueyama, Bull. Chem. Soc. Jpn. 76 (2003) 761.
[28] X.H. Be, H. Liu, M. Du, K.M.C. Wong, V.W.W.W. Yam, Inorg. Chim. Acta 333 (2002) 32.



L^1: $n = 1$
L^2: $n = 2$

Scheme 1.

mimetic showed antitumor [15], anti-inflammatory [16] and pain-relieving [17] activities. Therefore, the investigation of seven-coordinate Mn(II) metal complexes can provide useful information for the understanding of these metalloenzymes and therapeutic agents.

Herein, we describe the synthesis and structure of Mn(II) complexes with the heptadentate and octadentate receptors *N*,*N*′-bis(2-aminobenzyl)-1,10-diaza-15-crown-5 ($\mathbf{L}^1$) and *N*,*N*′-bis(2-aminobenzyl)-1,10-diaza-18-crown-6 ($\mathbf{L}^2$), derived from azacrowns (Scheme 1). These receptors are structurally related and $\mathbf{L}^2$ may be seen as being derived from $\mathbf{L}^1$ by incorporation of a $-CH_2-O-CH_2-$ fragment into the ligand backbone. $\mathbf{L}^1$ has been revealed as an excellent receptor to impose seven-coordination on divalent first-row transition metal ions [18,19], whereas $\mathbf{L}^2$ is a versatile receptor able to adapt to the coordinative preferences of the particular metal cation guest. It has been reported that $\mathbf{L}^2$ forms binuclear complexes with first-row transition metal ions such as Co(II), Ni(II) and Cu(II) [18,21], and mononuclear complexes with main group cations such as Pb(II) and alkaline earth metal ions, as well as with Cd(II) and Zn(II) [20,22–24].

2. Experimental

2.1. Reagents

N,*N*′-Bis(2-aminobenzyl)-1,10-diaza-15-crown-5 ($\mathbf{L}^1$) [25] and *N*,*N*′-bis(2-aminobenzyl)-1,10-diaza-18-crown-6 ($\mathbf{L}^2$) [18] were prepared as previously reported by us. All other chemicals were purchased from commercial sources and were used without further purification. The solvents were of reagent grade, and were purified by the usual methods.

Caution! Although we have experienced no difficulties with the perchlorate salts, these salts combined with organic ligands are potentially explosive and should be handled in small quantities and with the necessary precautions [26].

2.2. Synthesis

2.2.1. $[Mn(L^1)](ClO_4)_2$ (**1**)

A mixture of $\mathbf{L}^1$ (0.051 g, 0.119 mmol) and $Mn(ClO_4)_2 \cdot 6H_2O$ (0.043 g, 0.119 mmol) in acetonitrile (15 mL) was stirred and heated to reflux over a period of 6 h. Slow evaporation of the resultant solution gave rise to colourless single crystals suitable for X-ray diffraction. Yield 0.039 g (48%). *Anal.* Calc. for $C_{24}H_{36}Cl_2MnN_4O_{11}$: C, 42.24; H, 5.32; N, 8.21. Found: C, 42.40; H, 5.26; N, 8.17%. FAB-MS: *m*/*z* (%BPI) = 582 (70) $[Mn(L^1)(ClO_4)]^+$, 482 (99) $[Mn(L^1-H)]^+$. IR (KBr discs): 3310, 3277 ($\nu(NH_2)$), 1618 (δ (NH_2)), 1092 ν_{as} (Cl–O), 620 δ_{as} (O–Cl–O) cm^{-1}. Λ_M (acetonitrile $\sim 10^{-3}$ M, 20 °C): 336 $cm^2\,\Omega^{-1}\,mol^{-1}$ (2:1 electrolyte).

2.2.2. $[Mn(L^2)](ClO_4)_2$ (**2**)

A solution of $Mn(ClO_4)_2 \cdot 6H_2O$ (0.080 g, 0.221 mmol) in absolute ethanol (8 mL) was added dropwise to a solution of $\mathbf{L}^2$ (0.099 g, 0.209 mmol) also in absolute ethanol (12 mL). After the addition was complete, a white precipitate appeared. The reaction mixture was stirred and heated to reflux over a period of 6 h. The precipitate was collected by filtration and air-dried. Yield 0.128 g (84%). *Anal.* Calc. for $C_{26}H_{40}MnCl_2N_4O_{12}$: C, 42.99; H, 5.55; N, 7.71. Found: C, 43.39; H, 5.49; N, 7.77%. FAB-MS: *m*/*z* (%BPI) = 626 (61) $[Mn(L^2)(ClO_4)]^+$, 526 (41) $[Mn(L^2-H)]^+$. IR (KBr discs): 3402, 3310, 3277 ($\nu(NH_2)$), 1620 (δ (NH_2)), 1096 ν_{as} (Cl–O), 624 δ_{as} (O–Cl–O) cm^{-1}. Λ_M (acetonitrile $\sim 10^{-3}$ M, 20 °C): 288 $cm^2\,\Omega^{-1}\,mol^{-1}$ (2:1 electrolyte).

2.2.3. $[Mn(L^2)](NO_3)_2$ (**3**)

A solution of $Mn(NO_3)_2 \cdot 4H_2O$ (0.059 g, 0.235 mmol) in absolute ethanol (15 mL) was added dropwise to a solution of $\mathbf{L}^2$ (0.100 g, 0.211 mmol) also in absolute ethanol (8 mL). The reaction mixture was stirred and heated to reflux over a period of 6 h. After the reaction was complete, the black solid formed was filtered off. Slow diffusion of diethyl ether into the resultant solution gave rise to a few colourless single crystals suitable for X-ray diffraction. Yield 0.017 g (12%). *Anal.* Calc. for $C_{26}H_{40}MnN_6O_{10}$: C, 47.93; H, 6.19; N, 12.90. Found: C, 48.37; H, 6.37; N, 12.42%. M.p.: 138.7 °C. FAB-MS: *m*/*z* (%BPI) = 590 (8) $[Mn(L^2)(NO_3)]^+$, 526 (9) $[Mn(L^2-H)]^+$. IR (solid sample): 3471, 3281 ($\nu(NH_2)$), 1617 (δ (NH_2)), 1320 $\nu(NO_3)$ cm^{-1}. Λ_M (acetonitrile $\sim 10^{-3}$ M, 20 °C): 245 $cm^2\Omega^{-1}$ mol^{-1} (2:1 electrolyte).

2.3. Measurements

Elemental analyses were carried out on a Carlo Erba 1180 elemental analyser. FAB mass spectra were recorded on a Fisons Quatro mass spectrometer with a Cs ion gun using 3-nitrobenzyl alcohol as the matrix. IR spectra were recorded using a Bruker Vector 22 spectrophotometer. Conductivity measurements were carried out at 20 °C with a Crison Micro CM 2201 conductivimeter using *ca.* 10^{-3} M solutions of the complexes in acetonitrile. UV–Vis spectra were recorded on a Perkin–Elmer Lambda 900 spectrophotometer, with quartz cells (path length: 1 cm). The cell holder was thermostated at 25 °C, through circulating water. Spectrophotometric titrations were performed at 25 °C on 10^{-5} M solutions of $\mathbf{L}^1$ or $\mathbf{L}^2$ in MeCN

(polarographic grade). Typically, aliquots of a fresh $Mn(ClO_4)_2 \cdot 6H_2O$ standard solution were added and the UV–Vis spectra of the samples were recorded. All spectrophotometric titration curves were fitted with the HYPERQUAD program [27].

Table 1
Crystal data and structure refinement for **1** and **3**

	1	**3**
Formula	$C_{24}H_{36}Cl_2MnN_4O_{11}$	$C_{26}H_{40}MnN_6O_{10}$
Molecular weight	682.41	651.58
T (K)	298(2)	150(2)
Crystal system	monoclinic	triclinic
Space group	$P2_1/c$	$P\bar{1}$
a (Å)	18.2415(10)	8.203(2)
b (Å)	12.5882(7)	9.691(3)
c (Å)	12.6042(7)	10.586(3)
α (°)	90	89.886(4)
β (°)	92.0070(10)	72.557(4)
γ (°)	90	80.282(5)
V (Å^3)	2892.5(3)	790.2
$F(000)$	1420	343
Z	4	1
D_{calc} (g cm^{-3})	1.567	1.369
μ (mm^{-1})	0.707	0.479
θ (°)	1.97–28.33	2.02–27.53
R_{int}	0.0294	0.0314
Reflections measured	18342	5180
Reflections observed	4869	2457
Goodness-of-fit on F^2	1.023	1.106
R_1 [$I > 2\sigma(I)$][a]	0.0452	0.0607
wR_2 (all data)[b]	0.1235	0.1627
Largest differences peak and hole (e Å^{-3})	−0.448 and 1.288	−0.461 and 0.437

[a] $R_1 = \sum||F_o| - |F_c||/\sum|F_o|$.
[b] $wR_2 = \{\sum[w(|F_o|^2 - |F_c|^2)^2]]/\sum[w(F_o^4)]\}^{1/2}$.

2.4. X-ray crystallography

Three-dimensional X-ray data for compounds **1** and **3** were collected on a Bruker Smart 1000 CCD. Data were corrected for Lorentz and polarisation effects and for absorption by semi-empirical methods. Complex scattering factors were taken from the program package SHELXTL [28], as implemented on a Pentium computer. The structure was solved by direct methods and refined by full-matrix least-squares on F^2. Hydrogen atoms were included in calculated positions and refined in the riding mode, except the hydrogen atoms H(3A), H(3B), H(4A) and H(4B) for **1**, and H(1N) and H(2N) for **3**, which were left to refine freely. Refinement converged with anisotropic displacement parameters for all non-hydrogen atoms. Crystal data and details of data collection and refinement are summarised in Table 1.

3. Results and discussion

The UV–Vis spectrum of *N*,*N*′-bis(2-aminobenzyl)-1,10-diaza-18-crown-6 ($\mathbf{L}^2$) shows two bands at 250 and 290 nm (E_2 and B bands of the aromatic rings), resulting from the $\pi \rightarrow \pi^*$ and $n \rightarrow \pi^*$ transitions on the aromatic subunits of the ligand [19]. Upon addition of Mn(II) perchlorate both absorption bands shift towards shorter wavelengths while their intensity decreases. Fig. 1 shows the spectral changes observed during the formation of the Mn(II) complex with $\mathbf{L}^2$. The titration profile indicates a 1:1 reaction stoichiometry, since the data display a single inflection point when the M:Ligand molar ratio is close to 1, with no evidence for the formation of binuclear species. The steep curvature of the titration profiles corresponds to an especially high

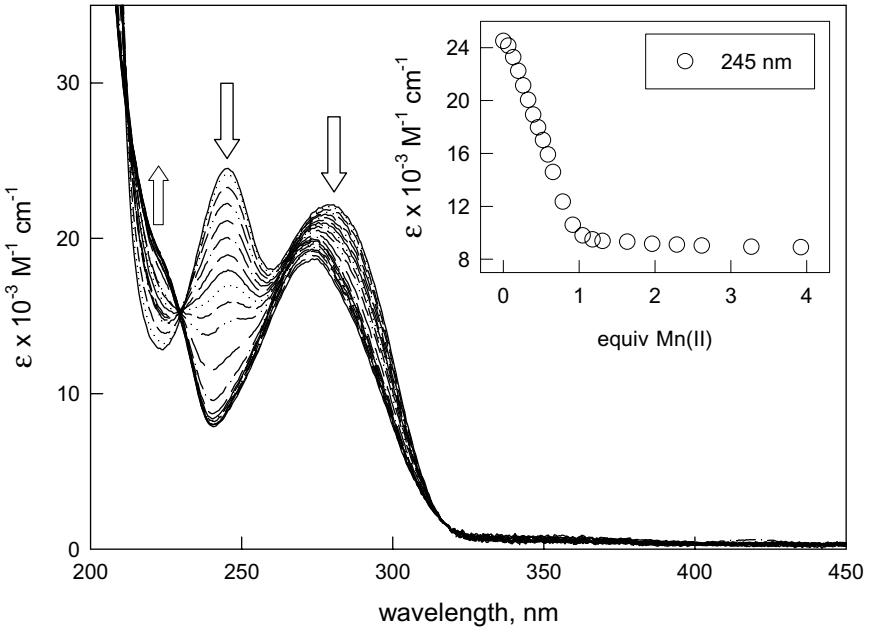


Fig. 1. UV–Visible spectrum of $\mathbf{L}^2$ in acetonitrile solution and spectral changes upon addition of aliquots of a solution of $Mn(ClO_4)_2 \cdot 6H_2O$ in the same solvent.

equilibrium constant ($\log K > 7$). In particular, the p parameter (p = [concentration of complex]/[maximum possible concentration of complex]) was found to be higher than 0.8, a condition which does not permit the determination of a reliable equilibrium constant [29]. Similar behaviour was previously observed for the Mn complex of $\mathbf{L}^1$ [19]. These results indicate that both $\mathbf{L}^1$ and $\mathbf{L}^2$ only form mononuclear complexes with Mn(II) in acetonitrile solution.

Reaction of stoichiometric amounts of $\mathbf{L}^1$ or $\mathbf{L}^2$ with Mn(II) salts (perchlorates or nitrates) in acetonitrile or ethanol solution gives compounds of formula $[Mn(L^1)](ClO_4)_2$ (**1**), $[Mn(L^2)](ClO_4)_2$ (**2**) and $[Mn(L^2)](NO_3)_2$ (**3**). The FAB-mass spectrum of each compound displays very intense peaks corresponding to the $[Mn(L–H)]^+$ and $[Mn(L)(X)]^+$ fragments ($L = \mathbf{L}^1$ or $\mathbf{L}^2$, $X = ClO_4^-$ or NO_3^-), thereby confirming the formation of the complexes. In the region 3500–3300 cm^{-1} the infrared spectra show bands corresponding to both $\nu_{as}(NH_2)$ and $\nu_s(NH_2)$ stretching frequencies of the coordinated amine groups. Likewise, the IR spectra (KBr discs) of the perchlorate complexes **1** and **2** also show bands corresponding to the ν_{as}(Cl–O) stretching and δ_{as}(O–Cl–O) bending modes of the perchlorate groups at *ca.* 1090 and 620 cm^{-1} [30], whereas the spectrum of the nitrate complex **3** exhibits an intense band centred at 1320 cm^{-1} due to uncoordinated nitrate [30]. The low yield of compound **3** (12%) is probably due to a dismutation processes, as evidenced by the formation of a black powdery solid during the reaction, which was rejected.

The solid state structures of compounds **1** and **3** were determined by single-crystal X-ray diffraction analyses. Crystals of **1** contain the $[Mn(L^1)]^{2+}$ cation and two crystallographically independent perchlorate anions, both involved in hydrogen-bonding interactions with the aniline groups [N(3)···H(3A) 0.86(3), H(3A)···O(10) 2.19(3), N(3)···O(10) 3.0193(3)Å, N(3)–H(3A)–O(10) 166(3)°; N(4)···H(4A) 0.93(3), H(4A)···O(6) 2.17(3)Å, N(4)–H(4A)–O(6) 178(3)°]. The structure of the cation is shown in Fig. 2, while selected bond lengths and angles are given in Table 2. The cation $[Mn(L^1)]^{2+}$ contains a MnN_4O_3 core with the seven heteroatoms of $\mathbf{L}^1$ coordinated to the Mn(II) ion, showing a slightly distorted C_2 symmetry. The metal ion resides in the macrocyclic cavity bound to the three ether oxygen atoms and the two pivotal nitrogen atoms of the azacrown moiety, while the donor atoms of the pendant arms coordinate apically. The receptor adopts an *anti* conformation, with both pendant arms pointing to opposite sides of the crown moiety, and the coordination sphere of the manganese ion can be described as a distorted pentagonal bipyramid whose equatorial plane is defined by the three oxygen atoms and the two pivotal nitrogen atoms. The mean deviation from planarity of the plane containing the five equatorial donor atoms and the metal ion amounts to 0.211 Å. The N(3)–Mn(1)–N(4) angle is 174.06(10)°, whereas the angles O(1)–Mn(1)–O(2), N(2)–Mn(1)–O(2), O(3)–Mn(1)–N(2), O(3)–Mn(1)–N(1) and N(1)–Mn(1)–O(1) take values close to 72° (Table 2). Likewise, the vectors

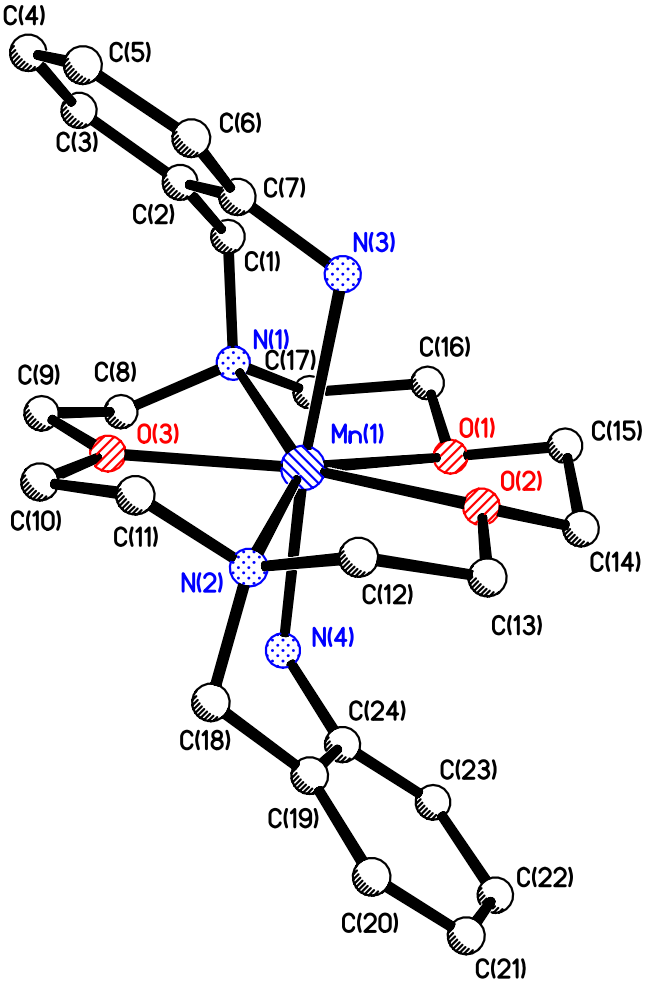


Fig. 2. X-ray crystal structure of the cationic complex $[Mn(L^1)]^{2+}$ present in **1**. Hydrogen atoms are omitted for the sake of clarity.

Table 2
Selected bond lengths (Å) and angles (°) for **1**

Mn(1)–O(3)	2.202(2)	Mn(1)–N(4)	2.311(2)
Mn(1)–O(2)	2.252(2)	Mn(1)–N(2)	2.320(2)
Mn(1)–O(1)	2.289(2)	Mn(1)–N(1)	2.369(2)
Mn(1)–N(3)	2.303(2)		
O(3)–Mn(1)–O(2)	145.13(7)	O(2)–Mn(1)–N(2)	74.10(7)
O(3)–Mn(1)–O(1)	144.69(7)	O(1)–Mn(1)–N(2)	140.31(7)
O(2)–Mn(1)–O(1)	70.17(7)	N(3)–Mn(1)–N(2)	100.21(9)
O(3)–Mn(1)–N(3)	94.89(8)	N(4)–Mn(1)–N(2)	84.01(8)
O(2)–Mn(1)–N(3)	81.52(7)	O(3)–Mn(1)–N(1)	72.16(7)
O(1)–Mn(1)–N(3)	91.19(8)	O(2)–Mn(1)–N(1)	139.95(7)
O(3)–Mn(1)–N(4)	90.37(9)	O(1)–Mn(1)–N(1)	74.57(8)
O(2)–Mn(1)–N(4)	95.73(8)	N(3)–Mn(1)–N(1)	80.82(8)
O(1)–Mn(1)–N(4)	82.91(9)	N(4)–Mn(1)–N(1)	98.21(8)
N(3)–Mn(1)–N(4)	174.06(10)	N(2)–Mn(1)–N(1)	144.56(8)
O(3)–Mn(1)–N(2)	72.46(7)		

defined by the metal ion and the axial donors [N(3) and N(4)] form angles close to 90° with the vectors containing the metal ion and the equatorial donor atoms, as expected for a pentagonal bipyramidal coordination environment. On the other hand, the Mn-crown ether oxygen bonds are

in line with those observed for a seven coordinate Mn(II) complex of 15-crown-5, which shows average Mn–O distances of 2.23 Å [31]. Although the Mn-donor distances found for **1** are close to those found in the $[Mn(L^1)](NO_3)\cdot 2CH_3CN$ analogue [19] (with the most important difference occurring for the Mn–O(1) distance, which is *ca.* 0.06 Å longer in **1**), the structure of the $[Mn(L^1)]^{2+}$ cation found in the nitrate salt [19] is somewhat more symmetrical than the one found in the perchlorate salt described here. Inspection of the X-ray crystal data reveals that compound **1** crystallises in the $P2_1/c$ monoclinic space group, as previously found for the $[M(L^1)](ClO_4)_2$ (M = Ni, Cu, Zn) analogues [18–20], whereas the corresponding nitrate salts, $[M(L^1)](NO_3)_2$ (M = Mn, Co, Zn) [19,20], crystallise in the $C2/c$ group. It has been also found that the corresponding $[M(L^1)]^{2+}$ cations (M = Co, Zn) present in the nitrate salts are more symmetrical than those found in the perchlorate salts. These results show that even when the anions (nitrate or perchlorate) remain uncoordinated in this family of complexes, the nature of the anion present in the crystal appears to have a certain influence on the structure of the cation in the solid state due to crystal packing effects [32].

Crystals of **3** consist of the $[Mn(L^2)]^{2+}$ cation (Fig. 3) and nitrate anions involved in hydrogen-bonding interactions with the aniline groups [N(1)···H(2N) 0.81(4), H(2N)···O(1S) 2.29(4), N(1)···O(1S) 3.065(4) Å, N(1)–H(2N)–O(1S) 160(4)°; N(1)···H(1N), 0.82(4), (1N)···O(1S), 2.40(4), N(1)···O(1SB) 3.192(4) Å, N(1)–H(1N)–O(1SB) 163(3)°]. The crystal presents a disorder

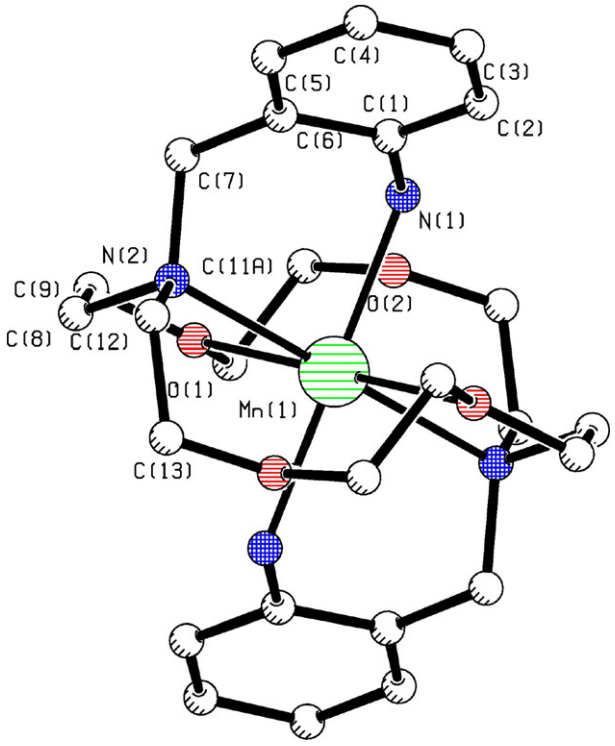


Fig. 3. X-ray crystal structure of the cationic complex $[Mn(L^2)]^{2+}$ present in **3**. Hydrogen atoms are omitted for the sake of clarity.

Table 3
Selected bond lengths (Å) and angles (°) for **3**[a]

Mn(1)–N(1)	2.271(3)	Mn(1)–N(2A)	2.491(3)
Mn(1)–N(1A)	2.271(3)	Mn(1)–O(1)	2.328(2)
Mn(1)–N(2)	2.491(3)	Mn(1)–O(1A)	2.328(2)
N(1)–Mn(1)–N(1A)	180.0(1)	O(1A)–Mn(1)–N(2)	109.0(1)
N(1A)–Mn(1)–O(1A)	99.7(1)	O(1)–Mn(1)–N(2)	71.0(1)
N(1)–Mn(1)–O(1A)	80.4(1)	N(1A)–Mn(1)–N(2A)	80.7(1)
N(1A)–Mn(1)–O(1)	80.4(1)	N(1)–Mn(1)–N(2A)	99.3(1)
N(1)–Mn(1)–O(1)	99.7(1)	O(1A)–Mn(1)–N(2A)	71.0(1)
O(1A)–Mn(1)–O(1)	180.0(1)	O(1)–Mn(1)–N(2A)	109.0(1)
N(1A)–Mn(1)–N(2)	99.3(1)	N(2)–Mn(1)–N(2A)	180.0(1)
N(1)–Mn(1)–N(2)	80.7(1)		

[a] Symmetry transformations used to generate equivalent atoms: A $1-x, -y+2, -z+2$.

on two carbon atoms of the crown moiety that has been solved, so that for each carbon atom two atomic sites have been observed [site occupancy factors C(10A) 0.500, C(11A) 0.500]. As observed for $[Mn(L^1)]^{2+}$, the Mn(II) ion in $[Mn(L^2)]^{2+}$ is placed in the crown hole, with the organic receptor also adopting an *anti* conformation. However, due to the larger cavity of the crown receptor, only six of its eight available donor atoms form part of the Mn(II) coordination sphere in $[Mn(L^2)]^{2+}$ (see Fig. 3 and Table 3). The Mn(II) ion is only bound to two of the four oxygen donor atoms [O(1) and O(1A)], as well as to both aniline nitrogen atoms [N(2) and N(2A)] and to both pivotal nitrogen atoms [N(1) and N(1A)]. The distances between the Mn(II) ion and the other two oxygen atoms [O(2) and O(2A)] is 2.791(3) Å, considerably longer than an unequivocal Mn–O bond. The Mn–$N_{aniline}$ distances are slightly shorter than those found in $[Mn(L^1)]$, whereas the Mn–O and Mn–N_{pivot} distances are 0.1–0.15 Å longer. The coordination polyhedron can be best described as a distorted octahedron. The structure of $[Mn(L^2)]^{2+}$ resembles the Pb(II) analogue $[Pb(L^2)]^{2+}$ [24], in which the Pb(II) ion is also symmetrically placed in the crown hole, with the organic receptor in an *anti* conformation. However, in the lead complex the Pb(II) guest ion fits very well in the crown hole, so that the eight donor atoms of the macrocyclic receptor are bound to the metal ion, which results in a very different coordination polyhedron around the Pb(II) ion that is described as a slightly distorted cube [24]. The distances between the two aniline nitrogen atoms and between the two pivotal nitrogen atoms are shorter in the Mn(II) complex [N(1)···N(1A) = 4.543(6), N(2)···N(2A) = 4.982(6) Å] than in the Pb(II) analogue [N(1)···N(1A) = 5.367, N(2)···N(2A) = 5.590 Å]. This shows that the receptor $\mathbf{L}^2$ possesses a certain degree of flexibility to adapt its conformation to the coordinative and sterical preferences of the metal ion guest.

4. Concluding remarks

Receptors *N*,*N*′-bis(2-aminobenzyl)-1,10-diaza-15-crown-5 ($\mathbf{L}^1$) and *N*,*N*′-bis(2-aminobenzyl)-1,10-diaza-18-crown-6

($\mathbf{L}^2$) form stable mononuclear Mn(II) complexes, and no evidence for the formation of binuclear complexes was obtained. In $[Mn(L^1)](ClO_4)_2$, the Mn(II) ion is deeply buried in the receptor cavity, and the good fit between the macrocyclic cavity of $\mathbf{L}^1$ and the ionic radius of the metal ion gives a seven-coordinate Mn(II) complex where the perchlorate anions are forced to remain outside the metal coordination sphere. The particular architecture of this receptor allows it to impose a relatively unusual pentagonal bipyramidal geometry on the Mn(II) guest. On the other hand, in spite of the higher denticity of $\mathbf{L}^2$ this receptor is unable to form the expected Mn(II) binuclear complexes, while previous studies have shown the formation of binuclear complexes with other first-row transition metal ions [Co(II), Ni(II) and Cu(II)]. In fact, $\mathbf{L}^2$ only gives mononuclear complexes with this metal ion, as observed with main group cations such as Pb(II), alkaline earth ions, Cd(II) and Zn(II). The fact that the Mn(II) and Zn(II) complexes of $\mathbf{L}^2$ show a different nuclearity with respect to the corresponding Co(II), Ni(II) and Cu(II) complexes is probably related to the high-spin d^5 and d^{10} configurations of the former metals, which provide no crystal-field stabilisation energy. The X-ray crystal structure of $[Mn(L^2)]^{2+}$ present in $[Mn(L^2)](NO_3)_2$ shows the Mn(II) ion also placed in the crown hole but now the large crown cavity of this receptor provokes that only six of its eight available donor atoms form part of the coordination sphere, with the Mn(II) ion found in a distorted octahedral environment.

Acknowledgement

Authors thank Universidade da Coruña for financial support.

Appendix A. Supplementary material

CCDC 640567 and 640568 and contain the supplementary crystallographic data for **1** and **3**. These data can be obtained free of charge via http://www.ccdc.cam.ac.uk/conts/retrieving.html, or from the Cambridge Crystallographic Data Centre, 12 Union Road, Cambridge CB2 1EZ, UK; fax: (+44) 1223-336-033; or e-mail: deposit@ccdc.cam.ac.uk.

References

[1] G. Christou, Acc. Chem. Res. 22 (1989) 328.
[2] V.L. Pecoraro, M.J. Baldwin, A. Velasco, Chem. Rev. 94 (1994) 807.
[3] D.P. Riley, Chem. Rev. 99 (1999) 2573.
[4] L. Que, A.E. True, Prog. Inorg. Chem. 38 (1990) 97.
[5] V.L. Pecoraro (Ed.), Manganese Redox Enzymes, VCH, New York, 1992.
[6] C.F. Yokum, V.L. Pecoraro, Curr. Opin. Chem. Biol. 3 (1999) 182.
[7] S. Mukhopadhyay, S.K. Mandal, S. Bhaduri, W.H. Armstrong, Chem. Rev. 104 (2004) 3981.
[8] (a) L.S. Hurley, E. Wooten, G.J. Everson, C.W. Asling, J. Nutr. 71 (1960) 15;
(b) T.E. Tuormaa, J. Orthomol. Med. 11 (1996) 69;
(c) M.N. Hughes, in: The Inorganic Chemistry of Biological Processes, Springer, 1988, pp. 297–298.
[9] A.B. Blake, F.A. Cotton, Inorg. Chem. 3 (1964) 5.
[10] W.C. Stallings, K.A. Pattridge, R.A. Strong, M.L. Ludwig, J. Biol. Chem. (1985) 1524.
[11] H.S. Gill, D. Eisenberg, Biochemistry 40 (2001) 1903.
[12] K.A. Johnson, L. Chen, H. Yang, M.F. Roberts, B. Stec, Biochemistry 40 (2001) 618.
[13] D. Salvemini, Z.-Q. Wang, J.L. Zweier, A. Samouilov, H. McArthur, T.P. Misko, M.G. Currie, S. Cuzzocrea, J.A. Sikorski, D.P. Riley, Science 286 (1999) 304.
[14] D.P. Riley, S.L. Henke, P.J. Lennon, R.H. Weiss, W.L. Neumann, W.J. Rivers Jr., K.W. Aston, K.R. Sample, H. Rahman, C.-S. Ling, J.-J. Shieh, D.H. Busch, W. Szulbinksi, Inorg. Chem. 35 (1996) 5213.
[15] W.E. Samlowski, R. Petersen, S. Cuzzocrea, H. McArthur, D. Burton, J.R. McGregor, D. Salvemini, Nat. Med. 9 (2003) 750.
[16] (a) D. Salvemini, C. Muscoli, D.P. Riley, S. Cuzzocrea, Pulm. Pharmacol. Ther. 15 (2002) 439;
(b) R. Di Paola, E. Mazzon, F. Rotondo, F. Dattola, D. Britti, M. De Majo, T. Genovese, S. Cuzzocrea, Eur. J. Pharm. 516 (2005) 151.
[17] (a) S. De Bono, Trends Biochem. Sci. 26 (2001) 283;
(b) C. Muscoli, V. Mollace, J. Wheatley, E. Masini, M. Ndengele, Z.-Q. Wang, D. Salvemini, Pain 111 (2004) 96.
[18] C. Rodríguez-Infante, D. Esteban, F. Avecilla, A. de Blas, T. Rodríguez-Blas, J. Mahía, A.L. Macedo, C.F.G.C. Geraldes, Inorg. Chim. Acta 317 (2001) 190.
[19] C. Platas-Iglesias, L. Vaiana, D. Esteban-Gómez, F. Avecilla, J.A. Real, A. De Blas, T. Rodríguez-Blas, Inorg. Chem. 44 (2005) 9704.
[20] L. Vaiana, C. Platas-Iglesias, D. Esteban-Gómez, F. Avecilla, A. De Blas, T. Rodríguez-Blas, Eur. J. Inorg. Chem. (2007) 1874.
[21] L. Vaiana, C. Platas-Iglesias, D. Esteban-Gómez, F. Avecilla, J.M. Clemente-Juan, J.A. Real, A. De Blas, T. Rodríguez-Blas, J. Chem. Soc., Dalton Trans. (2005) 2031.
[22] D. Esteban, D. Bañobre, R. Bastida, A. de Blas, A. Macías, A. Rodríguez, T. Rodríguez-Blas, D.E. Fenton, H. Adams, J. Mahía, Inorg. Chem. 38 (1999) 1937.
[23] C. Platas-Iglesias, D. Esteban, V. Ojea, F. Avecilla, A. de Blas, T. Rodríguez-Blas, Inorg. Chem. 42 (2003) 4299.
[24] D. Esteban, F. Avecilla, C. Platas-Iglesias, J. Mahía, A. de Blas, T. Rodríguez-Blas, Inorg. Chem. 41 (2002) 4337.
[25] D. Esteban, D. Bañobre, A. de Blas, T. Rodríguez-Blas, R. Bastida, A. Macías, A. Rodríguez, D.E. Fenton, H. Adams, J. Mahía, Eur. J. Inorg. Chem. (2000) 1445.
[26] W.C. Wolsey, J. Chem. Educ. 50 (1973) A335.
[27] P. Gans, A. Sabatini, A. Vacca, Talanta 43 (1996) 1739.
[28] G.M. Sheldrick, SHELXTL Bruker Analytical X-ray System, release 5.1, Madison, WI, 1997.
[29] C.S. Wilcox, in: Frontiers in Supramolecular Chemistry and Photochemistry, VCH, Weinheim, 1991, pp. 123–143.
[30] K. Nakamoto, Infrared and Raman Spectra of Inorganic and Coordination Compounds, 5th ed., J. Wiley & Sons, Inc., New York, Chichester, Weinheim, Brisbane, Singapore and Toronto, 1997.
[31] J.L. Atwood, P.C. Junk, Polyhedron 19 (2000) 85.
[32] U. Ziener, E. Breuning, J.-M. Lehn, E. Wegelius, K. Rissanen, G. Baum, D. Fenske, G. Vaughan, Chem. Eur. J. 6 (2000) 4132.

Table 1
Selected bond lengths (Å) and angles (°) for [$GaCl_3(Me_3PO)$]

Ga1–O1	1.828(6)	Ga1–Cl1	2.162(2)
Ga1–Cl2	2.161(2)	Ga1–Cl3	2.159(2)
P1–O1	1.518(7)		
O1–Ga1–Cl3	108.9(3)	O1–Ga1–Cl2	106.5(2)
Cl3–Ga1–Cl2	109.60(11)	O1–Ga1–Cl1	109.9(2)
Cl3–Ga1–Cl1	111.28(10)	Cl2–Ga1–Cl1	110.52(12)
P1–O1–Ga1	147.9(4)		

solvents. Crystals of [$GaCl_3(Me_3PO)$] were obtained from CH_2Cl_2–hexane and showed the expected pseudo-tetrahedral structure (Table 1, Fig. 1). The *d*(P–O) (1.518(7) Å) is lengthened from the value in Me_3PO itself (1.489(6) Å) [31] and *d*(Ga–O) 1.828(6) Å is similar to the value in [$GaCl_3(Ph_3PO)$] (1.818(10) Å) [28], although in the latter the phosphine oxide coordination is linear by symmetry (although adp ellipsoids suggest some disorder [28]), compared to the significantly bent geometry in the present complex (angle Ga–O–P = 148°). The three [$GaX_3(Me_3PO)$] complexes show strong *ν*(P=O) stretches in the IR spectra at ~1100 cm^{-1}, lowered from 1166 cm^{-1} in Me_3PO, and *ν*(GaX) are typical of tetrahedral Ga(III) (Table 2, Section 6). In chlorocarbon solvents the ^1H NMR spectra show sharp doublets for the Me resonances, and the $^{31}P\{^1H\}$ NMR spectra are sharp singlets with substantial high frequency coordination shifts from Me_3PO ($\delta = 38$). The chemical shifts fall with halogen: $\delta = 73.5$ (Cl), 72.0 (Br), 70.5 (I), suggesting the Lewis acidity of the GaX_3 also falls in this order. All exhibit relatively sharp singlets in the ^{71}Ga NMR spectra[1] at ambient temperatures (Table 2), which will be discussed further below. Although the spectroscopic data on [$GaI_3(Me_3PO)$] showed only the neutral species present, a solution in CH_2Cl_2–hexane produced a small number of colourless crystals which were shown to be the ionic product, [$GaI_2(Me_3PO)_2$][GaI_4]. The structure is shown in Fig. 2 (Table 3) and contains a tetrahedral $[GaI_4]^-$ anion (d(Ga–I) = 2.548(2) Å) and a pseudo-tetrahedral cation with *d*(Ga–O) = 1.854(8), 1.848(8) Å and *d*(Ga–I) = 2.488(2), 2.500(2) Å, with Ga–O–P angles of 136.8(6) and 140.6(6)°. The Ga–I distances are somewhat shorter in the cation than the anion as expected, but the notable difference is the longer *d*(Ga–O) (1.851 (av) Å), compared to the neutral [$GaCl_3(Me_3PO)$] (1.828 Å) (above). In spite of the crystallographic evidence for $[GaI_2(Me_3PO)_2]^+$, $[GaCl_2(Me_3PO)_2]^+$ could not be prepared from [$GaCl_3(Me_3PO)$], Me_3PO and either $FeCl_3$ or $SbCl_5$ (as chloride abstractors).

The structure of [$(GaBr_3)_2\{\mu$-*o*-$C_6H_4(CH_2P(O)Ph_2)_2\}$] (Table 4, Fig. 3) shows a bridging diphosphine dioxide coordinated to two pseudo-tetrahedral gallium moieties, which are staggered to minimise steric crowding. The Ga–O distances 1.892(4) and 1.858(4) Å are surprisingly

[1] ^{71}Ga, $I = 3/2$, 39.9%, $\Xi = 30.49$ MHz, $Q = 0.112 \times 10^{-28}$ m^2; ^{69}Ga, $I = 3/2$, 60.1%, $\Xi = 24.00$ MHz, $Q = 0.178 \times 10^{-28}$ m^2 [32].

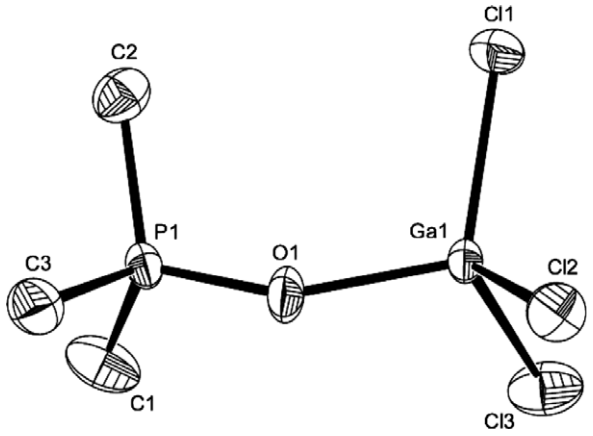


Fig. 1. View of the structure of [$GaCl_3(Me_3PO)$] with atom numbering scheme adopted. Ellipsoids are drawn at the 50% probability level and H atoms are omitted for clarity.

different, but the other parameters seem unexceptional, including the non-linear Ga–O–P angles of 148° and 153°. Spectroscopically the three [$(GaX_3)_2\{\mu$-*o*-C_6H_4-$(CH_2P(O)Ph_2)_2\}$] complexes show similar trends to those with Me_3PO described above, notably the significant fall in *ν*(PO) on coordination and the high frequency coordination shifts in $\delta(^{31}P)$ which vary with halogen Cl > Br > I (Table 2). Curiously, we were unable to observe a ^{71}Ga NMR resonance for any of the diphosphine dioxide complexes over the temperature range 295–180 K, presumably due to the line broadening resulting from fast relaxation of the quadrupolar gallium nucleus in these large and asymmetric molecules.

2.2. Gallium phosphine and arsine complexes

As indicated in Section 1, it is of interest to compare the spectroscopic and structural consequences of changing the hard R_3PO donor for a soft R_3P or R_3As ligand. Initially [$GaX_3(Me_3P)$] were prepared, but were found to be very poorly soluble in solvents suitable for spectroscopic studies (cf. Ref. [19]), and we have therefore used [$GaX_3(Ph_3P)$] and [$GaX_3(Ph_3As)$] as comparator complexes (the R group is expected to have a minimal effect on the trends). These complexes have been reported previously and some data presented [20–23,26]. The complexes were obtained in high yield by reaction of the appropriate GaX_3 and Ph_3E in anhydrous diethyl ether. X-ray crystal structures were determined for [$GaX_3(Ph_3P)$] (X = Cl or Br) (Table 5, Figs. 4 and 5). There are two reports [20,21,26] of the crystal structure of [$GaI_3(Ph_3P)$] both in the trigonal space group $R\bar{3}$, but with one using hexagonal and the other rhombohedral basis vectors. The Ga–P (2.416(5), 2.413(4) Å) and Ga–I (2.5212(9), 2.518(2) Å) are in excellent agreement, as are the I–Ga–I (*ca.* 113.8°) and I–Ga–P (*ca.* 104.6°) angles. [$GaCl_3(Ph_3P)$] and [$GaBr_3(Ph_3P)$] show the expected pseudo-tetrahedral monomer geometry. The Ga–P distances increase along the series Cl (2.372(2)) → Br (2.385(1)) → I (2.416(5) Å) consistent with reduced Lewis

Table 2
Selected spectroscopic data

Complex	ν(P=O)/ cm^{-1}	$\delta(^{31}P)$[a]	$\delta(^{71}Ga)$[b]
$[GaCl_3(Me_3PO)]$	1100	73.5	230
$[GaBr_3(Me_3PO)]$	1095	72.0	106
$[GaI_3(Me_3PO)]$	1102	70.5	−242
$[GaCl_3(Ph_3PO)]$[c]	1144	45.9	230
$[(GaCl_3)_2\{\mu\text{-}o\text{-}C_6H_4(CH_2P(O)Ph_2)_2\}]$	1088, 1070	52.5	n.o.
$[(GaBr_3)_2\{\mu\text{-}o\text{-}C_6H_4(CH_2P(O)Ph_2)_2\}]$	1091, 1080	52.0	n.o.
$[(GaI_3)_2\{\mu\text{-}o\text{-}C_6H_4(CH_2P(O)Ph_2)_2\}]$	1086, 1076	51.4	n.o.
$[GaCl_3(Ph_3P)]$		−5.5(m)	264 (d, $J = 721$ Hz)
$[GaBr_3(Ph_3P)]$		−10.7(m)	152 (d, $J = 693$ Hz)
$[GaI_3(Ph_3P)]$		−29.7(m)	−151 (d, $J = 466$ Hz)
$[GaCl_3(Ph_3As)]$			264
$[GaBr_3(Ph_3As)]$			132
$[GaI_3(Ph_3As)]$			−203

[a] Relative to external 85% H_3PO_4, ligand shifts are Me_3PO $\delta = 38$, $o\text{-}C_6H_4(CH_2P(O)Ph_2)_2$ $\delta = 30.8$, PPh_3 $\delta = -6$.
[b] Relative to $[Ga(H_2O)_6]^{3+}$ in water at pH = 0, $[GaCl_4]^-$ $\delta = 251$, $[GaBr_4]^-$ $\delta = 64$, $[GaI_4]^-$ $\delta = -455$.
[c] Data from Ref. [28].

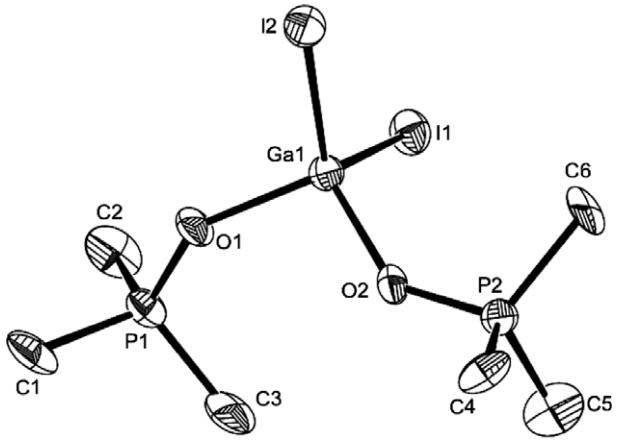


Fig. 2. View of the structure of the cation in $[GaI_2(Me_3PO)_2][GaI_4]$ with atom numbering scheme adopted. Ellipsoids are drawn at the 50% probability level and H atoms are omitted for clarity.

Table 3
Selected bond lengths (Å) and angles (°) for $[GaI_2(Me_3PO)_2][GaI_4]$

Ga1–O1	1.854(8)	Ga1–O2	1.846(8)
Ga1–I1	2.4997(17)	Ga1–I2	2.4875(16)
Ga2–I3	2.5472(16)	Ga2–I4	2.5482(15)
Ga2–I5	2.5461(15)	Ga2–I6	2.5258(16)
P1–O1	1.523(9)	P2–O2	1.525(8)
O2–Ga1–O1	101.3(4)	O2–Ga1–I2	111.8(3)
O1–Ga1–I2	106.7(3)	O2–Ga1–I1	109.8(3)
O1–Ga1–I1	109.2(3)	I2–Ga1–I1	116.89(6)
Ga1–O1–P1	136.8(6)	Ga1–O2–P2	140.6(6)

acidity of the gallium as the halide becomes less electronegative, whilst the changes in Ga–X follow the changes in covalent radii of X. The literature structure of $[GaI_3(Ph_3As)]$ [20,21] is isomorphous with the Ph_3P analogue ($R\bar{3}$) with a slightly shorter Ga–I (2.509(1) Å) and with Ga–As = 2.490(1) Å. We note that in the series containing the silyl phosphine, $[GaX_3\{P(SiMe_3)_3\}]$ (X = Cl, Br, I), [17] the Ga–P distances decrease Cl → Br → I, which is the reverse of that observed in organophosphine complexes.

The $^{31}P\{^1H\}$ NMR spectra of $[GaX_3(Ph_3P)]$ are notable in showing resolved ^{31}P–$^{69/71}Ga$ couplings. $[GaCl_3(Ph_3P)]$ in CH_2Cl_2 solution shows no $^{31}P\{^1H\}$ NMR resonance at room temperature, but a broad feature appears on cooling the solution to 273 K, and at 183 K this has resolved into a broad multiplet which approximates to two overlapping quartets due to coupling to the $I = 3/2$ ^{69}Ga and ^{71}Ga. For $[GaBr_3(Ph_3P)]$ the room temperature $^{31}P\{^1H\}$ NMR resonance is an ill-defined multiplet, becomes a quartet at 273 K (although the lines are too broad to show resolved couplings to the separate gallium isotopes). For $[GaI_3(Ph_3P)]$ two superimposed quartet couplings are

Table 4
Selected bond lengths (Å) and angles (°) for $[(GaBr_3)_2\{\mu\text{-}o\text{-}C_6H_4(CH_2P(O)Ph_2)_2\}]$

Ga1–O1	1.892(4)	Ga1–Br1	2.2669(9)
Ga1–Br3	2.2952(8)	Ga1–Br2	2.3133(8)
Ga2–O2	1.858(4)	Ga2–Br5	2.2853(9)
Ga2–Br4	2.2983(8)	Ga2–Br6	2.2990(8)
P2–O2	1.520(4)	P1–O1	1.525(4)
O1–Ga1–Br1	109.11(11)	O1–Ga1–Br3	106.88(10)
Br1–Ga1–Br3	112.50(3)	O1–Ga1–Br2	101.93(11)
Br1–Ga1–Br2	113.99(3)	Br3–Ga1–Br2	111.62(3)
O2–Ga2–Br5	105.55(13)	O2–Ga2–Br4	102.32(11)
Br5–Ga2–Br4	113.41(3)	O2–Ga2–Br6	107.24(12)
Br5–Ga2–Br6	114.01(3)	Br4–Ga2–Br6	113.10(3)
P1–O1–Ga1	148.3(2)	P2–O2–Ga2	153.9(2)

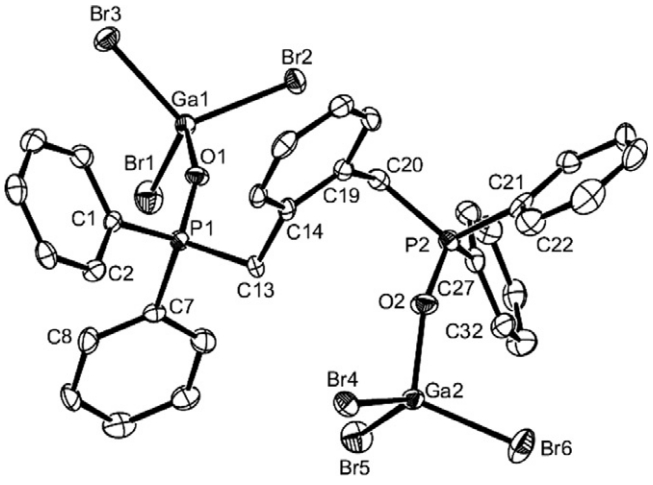


Fig. 3. View of the structure of $[(GaBr_3)_2\{o\text{-}C_6H_4(CH_2P(O)Ph_2)_2\}]$ with the atom numbering scheme adopted. Ellipsoids are shown at the 50% probability level and H atoms are omitted for clarity.

Table 5
Selected bond lengths (Å) and angles (°) for $[GaX_3(Ph_3P)]$

	X = Cl	X = Br (Ga1)	X = Br (Ga2)[a]
Ga1–P1	2.3717(16)	2.3848(13)	2.3879(13)
Ga1–X1	2.1677(15)	2.3134(7)	2.3133(7)
Ga1–X2	2.1679(16)	2.3048(7)	2.3212(7)
Ga1–X3	2.1696(15)	2.3225(7)	2.3082(8)
X1–Ga1–P1	104.17(6)	105.83(4)	106.71(4)
X2–Ga1–P1	104.08(6)	107.45(4)	106.88(4)
X3–Ga1–P1	111.46(6)	107.50(4)	105.93(4)
X1–Ga1–X2	112.98(6)	111.79(3)	111.68(3)
X1–Ga1–X3	112.40(6)	114.27(3)	112.39(3)
X2–Ga1–X3	111.24(6)	109.63(3)	112.73(3)

For comparison $[GaI_3(Ph_3P)]$ has Ga–I = 2.5212(9) or 2.518(2) Å (Refs. [26,20] respectively), Ga–P = 2.416(5) or 2.413(4) Å and $[GaI_3(Ph_3As)]$ has Ga–I = 2.509(1) Å and Ga–As = 2.490(1) Å (Ref. [21]).

[a] For the second molecule the data are for Ga2, P2, X4, X5 and X6.

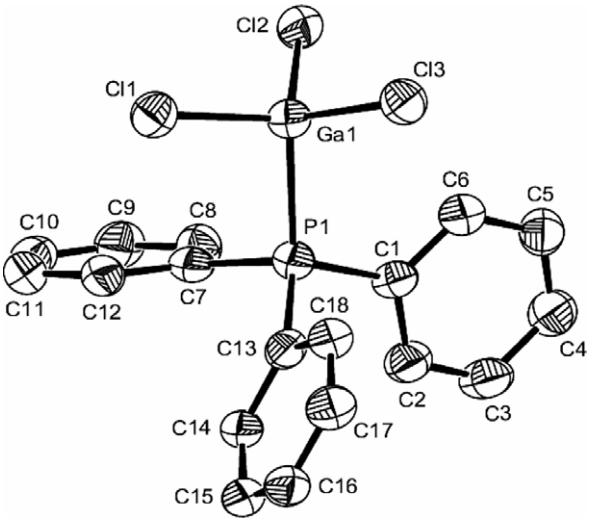


Fig. 4. View of the structure of $[GaCl_3(Ph_3P)]$ showing the atom numbering scheme adopted. Ellipsoids are drawn at the 50% probability level and H atoms are omitted for clarity.

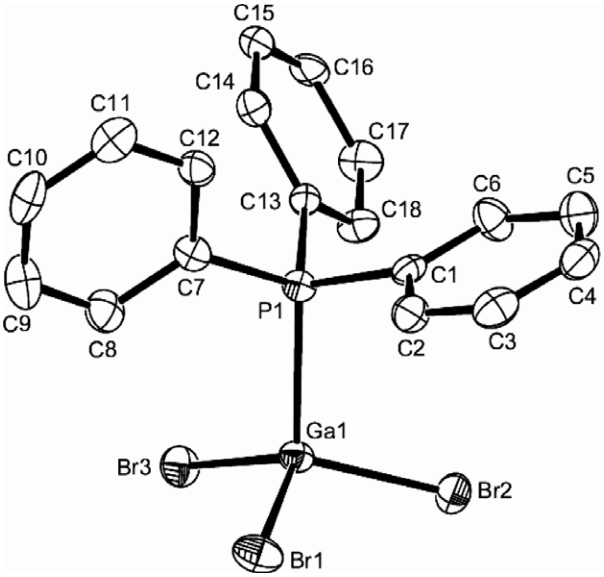


Fig. 5. View of the structure of $[GaBr_3(Ph_3P)]$ showing the atom numbering scheme adopted. Ellipsoids are drawn at the 50% probability level and H atoms are omitted for clarity. The other molecule in the asymmetric unit is very similar.

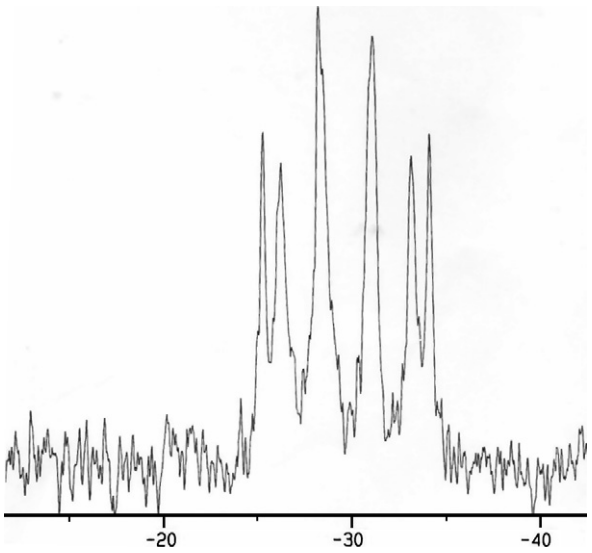


Fig. 6. $^{31}P\{^1H\}$ NMR of $[GaI_3(Ph_3P)]$ in CH_2Cl_2 at 273 K.

clearly resolved at ambient temperatures; the lines sharpen on cooling to 273 K (Fig. 6) and then broaden on further cooling. The changes with halide and temperature reflect the different electric field gradients in the three compounds and how these affect the quadrupolar relaxation rates of the gallium nuclei over this temperature range. The ^{71}Ga NMR spectra of all three compounds show clear doublet couplings to ^{31}P (Table 2) with $^1J(^{31}P\text{-}^{71}Ga)$ falling from Cl → Br → I.

The *o*-xylyl diphosphine *o*-$C_6H_4(CH_2PPh_2)_2$ is somewhat pre-organised for chelation by the central *o*-phenylene backbone, and functions as a chelate to many late transition metals, despite forming a seven-membered ring in the process [33]. However, on reaction with GaX_3 it behaves as a bridging bidentate, forming $[(GaX_3)_2\text{-}\{o\text{-}C_6H_4(CH_2PPh_2)_2\}]$ as confirmed by the crystal structure of the iodo-complex (Table 6, Fig. 7). The molecule has approximate twofold symmetry and the ligand conformation places the two GaI_3 groups '*anti*' to minimise steric interactions (Ga1–P1···P2–Ga2 = 161°). Spectroscopically these complexes (Table 2) are similar to those of Ph_3P, but provide a useful comparison with the diphosphine dioxide compounds described above.

3. Some comparisons of the effect of donor types on gallium(III)

The spectroscopic and structural data set out in previous sections clearly support the expected conclusion that Lewis acidity decreases in the gallium(III) halides Cl > Br > I,

Table 6
Selected bond lengths (Å) and angles (°) for $[(GaI_3)_2\{\mu\text{-}o\text{-}C_6H_4(CH_2PPh_2)_2\}]$

Ga1–P1	2.3891(9)	Ga2–P2	2.3872(9)
Ga1–I1	2.5312(4)	Ga2–I4	2.5143(4)
Ga1–I2	2.5286(4)	Ga2–I5	2.5211(4)
Ga1–I3	2.5194(4)	Ga2–I6	2.5516(5)
P1–Ga1–I1	111.78(2)	P2–Ga2–I4	109.57(2)
P1–Ga1–I2	102.22(2)	P2–Ga2–I5	109.66(2)
P1–Ga1–I3	105.87(2)	P2–Ga2–I6	99.97(2)
I1–Ga1–I2	112.752(15)	I4–Ga2–I5	111.195(15)
I1–Ga1–I3	111.335(15)	I4–Ga2–I6	115.297(15)
I2–Ga1–I3	112.337(16)	I5–Ga2–I6	110.526(14)

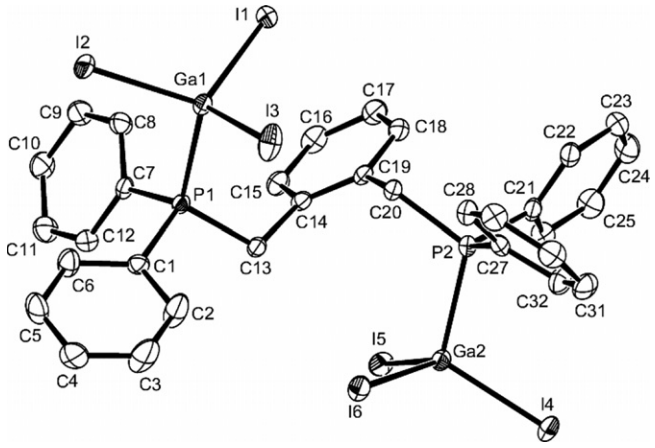


Fig. 7. View of the structure of $[(GaI_3)_2\{o\text{-}C_6H_4(CH_2PPh_2)_2\}]$ showing the atom numbering scheme adopted. Ellipsoids are drawn at the 50% probability level and H atoms are omitted for clarity.

towards both hard and soft donor ligands. The second point to note is the trends in bond lengths about the gallium centre with Ga–Cl (~2.15 Å), Ga–Br (~2.3 Å), Ga–I (~2.5 Å), Ga–O (~1.85 Å), Ga–P (~2.4 Å) and Ga–As (~2.5 Å). It is clear that the Ga–X and the Ga–O bond lengths are *ca.* 0.1 Å shorter than the sum of the covalent radii, [34] whilst the Ga–P(As) are rather longer than expected, suggesting that the softer donors are more weakly bound. Support for this came from *in situ* $^{31}P\{^1H\}$ NMR measurements (CH_2Cl_2 solution) which showed that Me_3PO displaced Ph_3P or Ph_3As (L) from their $[GaCl_3L]$ complexes, but that $[GaCl_3(Me_3PO)]$ was unaffected by the presence of excess L.

The ^{71}Ga NMR spectra show progressive low frequency shifts with halide Cl → Br → I, but the trends with neutral donor are more variable, giving evidence that several competing factors are involved.

4. Studies on oxidation and hydrolysis of gallium phosphines

In the presence of dioxygen, tin(IV) halides readily convert phosphines to phosphine oxides [8,10,29] and similar behaviour, although less thoroughly explored, is observed with Bi and Sb halides [11,30]. In order to explore whether $[GaX_3(Ph_3P)]$ forms Ph_3PO in chlorocarbon solvents, solutions of all three complexes in anhydrous CH_2Cl_2 were placed in 10 mm o.d. NMR tubes, the tubes filled with dry O_2 and the $^{31}P\{^1H\}$ NMR spectra monitored at regular intervals over a three week period. The spectra showed no evidence for phosphine oxide formation (although some $[R_3PH][GaX_4]$ were evident due to trace hydrolysis). We conclude that, in marked contrast to the Group 15 MX_3 and especially the Sn(IV) systems, gallium halides do not promote phosphine oxidation under these conditions.

In rigorously anhydrous chlorocarbons (CH_2Cl_2 or $CHCl_3$ and their deuterated analogues), gallium(III) halide phosphine and diphosphine complexes exhibit $^{31}P\{^1H\}$ NMR spectra consistent with the presence of a single species in each. In favourable cases with the (C_{3v}) $GaPX_3$ donor sets, ^{71}Ga NMR spectra lead to the same conclusions. However, even brief exposure of the solutions of $[GaX_3(R_3P)]$ to air resulted in the appearance of new resonances. In the $^{31}P\{^1H\}$ NMR spectra the new features were broad with ill-defined structure and typically to high frequency of that of the gallium complex, and were assigned to the corresponding phosphonium cations $[R_3PH]^+$ both by comparison of their chemical shifts with literature values [35], and from the ^1H-coupled ^{31}P NMR spectra which showed doublets due to $^1J_{PH}$ (300–700 Hz).[2] The ^{71}Ga spectra also showed resonances due to the corresponding $[GaX_4]^-$ anion at X = Cl: $\delta = 251$; X = Br: $\delta = 64$; X = I: $\delta = -455$ [32]. All of the complexes we examined showed a tendency to form phosphonium salts, although it is particularly evident with alkyl phosphines, probably because these are the strongest proton bases [36].

Addition of small amounts of water to the solutions resulted in immediate and complete loss of the resonances due to $[GaX_3(R_3P)]$ and the only species evident in the ^{71}Ga NMR spectra were the $[GaX_4]^-$ anions. The formation of phosphonium salts was also observed in the gallium–diphosphine complexes, and we note that Sigl et al. [37] identified the hydrolysis product of $[GaCl_2\{o\text{-}C_6H_4(PPh_2)_2\}][GaCl_4]$ as $[o\text{-}C_6H_4(PPh_2)(PPh_2H)][GaCl_4]$ by an X-ray crystal structure.

Final confirmation of the identity of the hydrolysis products comes from the crystal structure of $[Me_2PhPH][GaCl_4]$ (Fig. 8). Colourless crystals of which were obtained from a solution shown by NMR spectroscopy to contain mainly $[GaCl_3(Me_2PhP)]$, showing the ionic species crystallise preferentially. $[GaCl_3(Ph_3P)]$ is quantitatively converted into $[Ph_3PH][GaCl_4]$ by treatment with HCl gas in CH_2Cl_2 solution, which provides the most convenient synthesis for these phosphonium species.

[2] The broad lines arise from incomplete decoupling of the P–H proton under normal broad band decoupling settings.

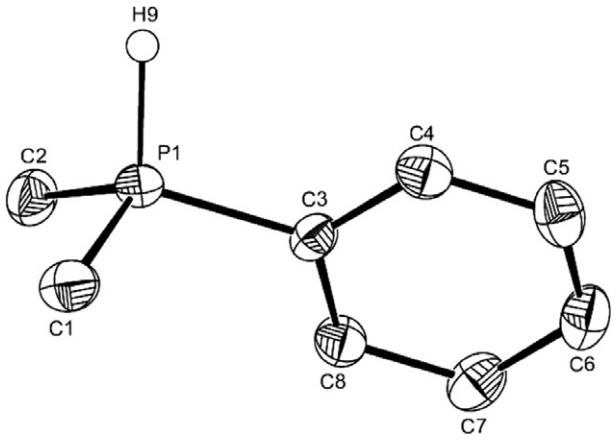


Fig. 8. View of the structure of the cation in $[Me_2PhPH][GaCl_4]$ with numbering scheme adopted. Ellipsoids are drawn at the 50% probability level and H atoms (except that on P1) are omitted for clarity. Selected bond lengths (Å) and angles (°): P1–C1 1.788(4); P1–C2 1.784(3); P1–C3 1.788(3); C–P1–C 110.08(16)–111.50(17); Ga1–Cl 2.1657(11)–2.1770(11).

5. Conclusions

These results show that the Lewis acidity of GaX_3 decreases as the halide becomes heavier and that the maximum coordination number at the gallium in these species is four. With only one exception, all the complexes were neutral with X_3O or X_3E (X = Cl, Br or I; E = P or As) donor sets. Competitive NMR studies on the $GaCl_3$ systems show that R_3PO are preferred to R_3E suggesting that $GaCl_3$ is quite a hard Lewis acid.

6. Experimental

All the reactions and manipulations were performed in an inert atmosphere (N_2) glovebox or using Schlenk techniques. Diethyl ether and hexane were dried by distillation over sodium/benzophenone and dichloromethane was dried by distillation from CaH_2. Infrared spectra were measured as Nujol mulls between CsI plates on a Perkin–Elmer PE983 spectrometer. ^1H NMR spectra were recorded in $CDCl_3$ solution on a Bruker AV300, $^{31}P\{^1H\}$ and ^{71}Ga NMR spectra on a Bruker DPX400 and referenced to 85% H_3PO_4 and $[Ga(H_2O)_6]^{3+}$ respectively. Me_3PO (Aldrich) was freshly sublimed prior to use. *o*-$C_6H_4(CH_2P(O)Ph_2)_2$ was obtained as a white solid by stirring a CH_2Cl_2 solution of *o*-C_6H_4-$(CH_2PPh_2)_2$ in dry air with a catalytic amount of SnI_4 [29] followed by hydrolysis, extraction with CH_2Cl_2 and drying ($MgSO_4$). ^1H NMR ($CDCl_3$): $\delta = 3.90$ (d, [4H], CH_2, $^2J_{PH} = 13.0$ Hz), 6.68 (m, [2H], *o*-C_6H_4), 6.78 (m, [2H], *o*-C_6H_4), 7.30–7.67 (m, [20H], Ph). $^{13}C\{^1H\}$ NMR ($CDCl_3$): $\delta = 35.9$ (d, CH_2, $^1J_{PC} = 66.4$ Hz), 126.6–133.3 (aromatic C). $^{31}P\{^1H\}$ NMR ($CDCl_3$): 30.8. IR (Nujol): $\nu = 1181$ br s (P=O) cm^{-1}.

6.1. [$GaCl_3(Me_3PO)$]

$GaCl_3$ (0.19 g, 1.09 mmol) in CH_2Cl_2 (5 mL) was combined with a CH_2Cl_2 solution (10 mL) of Me_3PO (0.10 g, 1.09 mmol) and the reaction mixture was stirred under N_2 for *ca.* 2 h. The volatiles were then removed *in vacuo* and the white solid rinsed with hexane and dried *in vacuo*. Yield 0.26 g, 88%. *Anal.* Calc. for $C_3H_9Cl_3GaOP$: C, 13.4; H, 3.4. Found: C, 13.7; H, 3.4%. ^1H NMR ($CDCl_3$, 298 K): $\delta = 1.83$ (d, Me, $^2J_{PH} = 12.8$ Hz). $^{13}C\{^1H\}$ NMR ($CDCl_3$): $\delta = 17.1$ (d, Me, $^1J_{PC} = 70.6$ Hz). $^{31}P\{^1H\}$ NMR ($CDCl_3$): $\delta = 73.5$. ^{71}Ga NMR ($CDCl_3$): $\delta = 230$. IR (Nujol): $\nu = 1100$ br s (P=O), 387, 358 (Ga–Cl) cm^{-1}.

6.2. [$GaBr_3(Me_3PO)$]

Method as above, but using $GaBr_3$. White solid (62%). *Anal.* Calc. for $C_3H_9Br_3GaOP$: C, 9.0; H, 2.6. Found: C, 9.1; H, 2.0%. ^1H NMR ($CDCl_3$, 298 K): $\delta = 1.85$ (d, Me, $^2J_{PH} = 13.0$ Hz). $^{13}C\{^1H\}$ NMR ($CDCl_3$): $\delta = 17.3$ (d, Me, $^1J_{PC} = 70.2$ Hz). $^{31}P\{^1H\}$ NMR ($CDCl_3$): $\delta = 72.0$. ^{71}Ga NMR ($CDCl_3$): $\delta = 106$. IR (Nujol): $\nu = 1095$ br s (P=O), 283, 244 (Ga–Br) cm^{-1}.

6.3. [$GaI_3(Me_3PO)$]

Method as above, but using GaI_3. White solid (65%). *Anal.* Calc. for $C_3H_9GaI_3OP \cdot CH_2Cl_2$: C, 7.6; H, 1.8. Found: C, 7.4; H, 1.8%. ^1H NMR ($CDCl_3$, 298 K): $\delta = 1.85$ (d, Me, $^2J_{PH} = 13.0$ Hz). $^{13}C\{^1H\}$ NMR ($CDCl_3$): $\delta = 17.0$ (d, Me, $^1J_{PC} = 70.5$ Hz). $^{31}P\{^1H\}$ NMR ($CDCl_3$): $\delta = 70.5$. ^{71}Ga NMR ($CDCl_3$): $\delta = -242$. IR (Nujol): $\nu = 1102$ (P=O), 250 (Ga–I) cm^{-1}.

6.4. [$(GaCl_3)_2\{\mu$-*o*-$C_6H_4(CH_2P(O)Ph_2)_2\}$]

Method as above, but using a 2:1 $GaCl_3$:diphosphine ratio. White solid (89%). *Anal.* Calc. for $C_{32}H_{28}Cl_6Ga_2O_2P_2 \cdot 0.25CH_2Cl_2$: C, 44.0; H, 3.3. Found: C, 44.1; H, 2.6%. ^1H NMR ($CDCl_3$, 298 K): $\delta = 4.08$ (d, CH_2, 4H, $^2J_{PH} = 12.4$ Hz), 6.51 (m, *o*-C_6H_4, 2H), 6.98 (m, *o*-C_6H_4, 2H), 7.50–7.78 (m, Ph, 20H). $^{13}C\{^1H\}$ NMR ($CDCl_3$): $\delta = 33.7$ (d, CH_2, $^1J_{PC} = 68.1$ Hz), 124.3–135.4 (aromatic C). $^{31}P\{^1H\}$ NMR ($CDCl_3$): $\delta = 52.5$. ^{71}Ga NMR ($CDCl_3$): not observed. IR (Nujol): $\nu = 1088$ br s, 1070 sh (P=O), 397, 356 (Ga–Cl) cm^{-1}.

6.5. [$(GaBr_3)_2\{\mu$-*o*-$C_6H_4(CH_2P(O)Ph_2)_2\}$]

Method as above, but using a 2:1 $GaBr_3$:diphosphine ratio. White solid (94%). *Anal.* Calc. for $C_{32}H_{28}Br_6Ga_2O_2P_2 \cdot CH_2Cl_2$: C, 32.8; H, 2.5. Found: C, 32.4; H, 2.1%. ^1H NMR ($CDCl_3$, 298 K): $\delta = 4.11$ (d, CH_2, 4H, $^2J_{PH} = 12.3$ Hz), 6.50 (m, *o*-C_6H_4, 2H), 6.95 (m, *o*-C_6H_4, 2H), 7.50–7.77 (m, Ph, 20H). $^{13}C\{^1H\}$ NMR ($CDCl_3$): $\delta = 34.1$ (d, CH_2, $^1J_{PC} = 68.0$ Hz), 124.2–135.4 (aromatic C). $^{31}P\{^1H\}$ NMR ($CDCl_3$): $\delta = 52.0$. ^{71}Ga NMR ($CDCl_3$): not observed. IR (Nujol): $\nu = 1091$ s, 1080 s (P=O), 296, 230 (Ga–Br) cm^{-1}.

6.6. [(GaI$_3$)$_2${μ-o-C$_6$H$_4$(CH$_2$P(O)Ph$_2$)$_2$}]

Method as above, but using a 2:1 GaI$_3$:diphosphine ratio. White solid (65%). *Anal.* Calc. for $C_{32}H_{28}Ga_2I_6O_2P_2$: C, 27.3; H, 2.0. Found: C, 27.4; H, 1.7%. ^{1}H NMR ($CDCl_3$, 298 K): $\delta = 4.15$ (d, CH_2, 4H, $^2J_{PH} = 12.6$ Hz), 6.50 (m, *o*-C_6H_4, 2H), 6.95 (m, *o*-C_6H_4, 2H), 7.50–7.80 (m, Ph, 20H). ^{13}C{^{1}H} NMR ($CDCl_3$): $\delta = 33.6$ (d, CH_2, $^1J_{PC} = 68.1$ Hz), 124.1–135.3 (aromatic C). ^{31}P{^{1}H} NMR ($CDCl_3$): $\delta = 51.4$. ^{71}Ga NMR ($CDCl_3$): not observed. IR (Nujol): $\nu = 1086$ s, 1076 s (P=O), 240 (Ga–I) cm^{-1}.

6.7. [GaCl$_3$(Ph$_3$P)]

A solution of Ph_3P (0.300 g, 1.14 mmol) in diethyl ether (5 mL) was added dropwise to a stirred solution of $GaCl_3$ (0.201 g, 1.14 mmol) in diethyl ether (4 mL). After stirring at room temperature for 15 h, the resultant white precipitate was filtered off, washed with diethyl ether (2 mL) and dried *in vacuo*. Yield 0.32 g, 65%. *Anal.* Calc. for $C_{18}H_{15}Cl_3GaP$: C, 49.3; H, 3.5. Found: C, 48.7; H, 3.8%. ^{1}H NMR ($CDCl_3$, 295 K): δ 7.69–7.41 (m, Ph). ^{31}P{^{1}H} NMR ($CDCl_3$): 295 K not observed; 273 K $\delta = -5.4$ (m). ^{71}Ga NMR ($CDCl_3$): $\delta = 264$ (br d, $J = 721$ Hz). IR (Nujol): $\nu = 387$ s, 347 m (Ga–Cl) cm^{-1}.

6.8. [GaBr$_3$(Ph$_3$P)]

Made similarly to the chloro compound. White solid (64%). *Anal.* Calc. for $C_{18}H_{15}Br_3GaP$: C, 37.8; H, 2.9. Found: C, 38.1; H, 2.8%. ^{1}H NMR ($CDCl_3$, 295 K): δ 7.81–7.38 (m, Ph). ^{31}P{^{1}H} NMR ($CDCl_3$): $\delta = -10.7$. ^{71}Ga NMR ($CDCl_3$): $\delta = 152$ (d, $J = 693$ Hz). IR (Nujol): $\nu = 289$ s, 234 m (Ga–Br) cm^{-1}.

6.9. [GaI$_3$(Ph$_3$P)]

Made similarly to the chloro compound. White solid (66%). *Anal.* Calc. for $C_{18}H_{15}GaI_3P$: C, 30.3; H, 2.1. Found: C, 30.5; H, 2.0%. ^{1}H NMR ($CDCl_3$, 295 K): δ 7.81–7.38 (m, Ph). ^{31}P{^{1}H} NMR ($CDCl_3$): $\delta = -29.7$. ^{71}Ga NMR ($CDCl_3$): $\delta = -151$ (d, $J = 466$ Hz). IR (Nujol): $\nu = 241$ m (Ga–I) cm^{-1}.

6.10. [(GaBr$_3$)$_2${o-C$_6$H$_4$(CH$_2$PPh$_2$)$_2$}]

Made similarly using a 2:1 Ga:ligand mol. ratio. White solid (76%). *Anal.* Calc. for $C_{32}H_{28}Br_6Ga_2P_2$: C, 35.2; H, 2.6. Found: C, 35.5; H, 2.5%. ^{1}H NMR ($CDCl_3$): 3.72 (d, 4H, CH_2), 6.53–6.97 (m), 7.45–7.75 (m, aromatic H). ^{31}P{^{1}H} NMR ($CDCl_3$): $\delta = -14.2$ (s). ^{71}Ga NMR ($CDCl_3$): $\delta = 156$ (br). IR (Nujol): $\nu = 281$ s, 227 m (Ga–Br) cm^{-1}.

6.11. [(GaI$_3$)$_2${o-C$_6$H$_4$(CH$_2$PPh$_2$)$_2$}]

Prepared similarly to the previous compound. White solid (75%). *Anal.* Calc. for $C_{32}H_{28}Ga_2I_6P_2$: C, 27.9; H, 2.1. Found: C, 28.2; H, 1.9%. ^{1}H NMR ($CDCl_3$): 3.60 (d, 4H, CH_2), 6.97–6.69 (m), 7.63–7.40 (m, aromatic H). ^{31}P{^{1}H} NMR ($CDCl_3$): $\delta = -33.7$ (s). ^{71}Ga NMR ($CDCl_3$): $\delta = -146$ (s). IR (Nujol): $\nu = 234$ m (Ga–I) cm^{-1}.

6.12. [GaCl$_3$(Ph$_3$As)]

A solution of Ph_3As (0.220 g, 0.718 mmol) in diethyl ether (10 mL) was added dropwise to a stirred solution of $GaCl_3$ (0.126 g, 0.718 mmol) in diethyl ether (5 mL). After stirring at room temperature for 4 h, removal of Et_2O gave a white solid, which was dried *in vacuo*. (Yield 0.32 g, 92%). ^{71}Ga NMR ($CDCl_3$): $\delta = 264$ (s, $W_{1/2} = 4000$ Hz). IR (Nujol): $\nu = 392$ s, 365 m (Ga–Cl) cm^{-1}.

6.13. [GaBr$_3$(Ph$_3$As)]

Prepared similarly to the chloro compound. White solid (93%). ^{71}Ga NMR ($CDCl_3$): $\delta = 132$ (s, $W_{1/2} = 3000$ Hz). IR (Nujol): $\nu = 285$ br s, 219 m (Ga–Br) cm^{-1}.

6.14. [GaI$_3$(Ph$_3$As)]

Prepared similarly to the chloro compound. White solid (90%). ^{71}Ga NMR ($CDCl_3$): $\delta = -203$ (s, $W_{1/2} = 2500$ Hz). IR (Nujol): $\nu = 244$ m (Ga–I) cm^{-1}.

6.15. [Me$_2$PhPH][GaCl$_4$]

Crystals of [$PPhMe_2H$][$GaCl_4$] were isolated from solutions of the corresponding [$GaCl_3$(Me_2PhP)] in CH_2Cl_2 solution by vapour diffusion of *n*-hexane under nitrogen. ^{1}H-coupled ^{31}P NMR ($CDCl_3$): δ −0.47 (d, $^1J = 511$ Hz). ^{71}Ga NMR: $\delta = +251$ (s).

6.16. X-ray experimental

Crystallographic parameters are given in Table 7. All the crystals were grown from CH_2Cl_2 solutions of the complexes by vapour diffusion of *n*-hexane under dinitrogen. Data collections were carried out with a Bruker-Nonius Kappa CCD diffractometer with graphite-monochromated Mo Kα radiation ($\lambda = 0.71073$ Å) and with the crystals held at 120 K in a nitrogen gas stream. The structure solutions were straightforward [38–40] except as indicated below with the hydrogen atoms being introduced into the models in calculated positions with default C–H distances. The phosphonium H atom had P–H fixed at 1.40 Å. [$GaCl_3$(Me_3PO)] is reported in the space group *Cc* although the 'checkcif' software raised the possibility of missed symmetry. The *Cc*-*C*2/*c* problem is well known [41,42], but with *Z* of 4 a *C*2/*c* solution would require the molecule to have symmetry (or to be disordered). Attempts to find a *C*2/*c* solution failed. [$GaI_2(Me_3PO)_2$][GaI_4] belongs to one of the 11 pairs of enantiomorphous space groups and the fit to the data was slightly improved by the inclusion of a TWIN command. The data for

Table 7
Crystallographic data[a]

Complex	$[GaCl_3(Me_3PO)]$	$[GaI_2(Me_3PO)_2][GaI_4]$	$[(GaBr_3)_2\{o\text{-}C_6H_4(CH_2P(O)Ph_2)_2\}]$	$[(GaI_3)_2\{o\text{-}C_6H_4\text{-}(CH_2PPh_2)_2\}]$	$[Me_2PhPH][GaCl_4]$	$[GaCl_3(Ph_3P)]$	$[GaBr_3\text{-}(Ph_3P)]$
Formula	$C_3H_9Cl_3GaOP$	$C_6H_{18}Ga_2I_6O_2P_2$	$C_{32}H_{28}Br_6Ga_2O_2P_2$	$C_{32}H_{28}Ga_2I_6P_2$	$C_8H_{12}Cl_4GaP$	$C_{18}H_{15}Cl_3GaP$	$C_{18}H_{15}Br_3GaP$
Formula weight	268.14	1084.98	1125.38	1375.32	350.67	438.34	571.72
Crystal system	monoclinic	tetragonal	triclinic	monoclinic	monoclinic	monoclinic	monoclinic
Space group	*Cc* (#9)	$P4_32_12$ (#96)	$P\bar{1}$ (#2)	$P2_1/c$ (#14)	$P2_1/c$ (#14)	$C2/c$ (#15)	$P2_1/c$ (#14)
a (Å)	8.144(2)	12.259(2)	8.8772(15)	25.401(2)	6.705(2)	16.155(2)	16.193(2)
b (Å)	10.216(3)	12.259(2)	13.6809(15)	8.1399(5)	12.499(4)	14.567(2)	14.3938(12)
c (Å)	12.418(4)	32.976(9)	16.2405(15)	20.094(2)	16.848(4)	15.924(2)	17.779(2)
α (°)	90	90	67.503(7)	90	90	90	90
β (°)	105.577(15)	90	87.495(8)	106.943(5)	99.352(16)	98.249(8)	109.652(4)
γ (°)	90	90	87.788(7)	90	90	90	90
U (Å^3)	995.3(5)	4956.2(18)	1820.0(4)	3974.4(6)	1393.3(6)	3708.6(8)	3902.5(7)
Z	4	8	2	4	4	8	8
μ(Mo Kα) (mm^{-1})	3.664	9.773	8.183	6.118	2.820	1.998	7.631
R_{int}	0.0604	0.0801	0.0730	0.042	0.0525	0.163	0.088
Total number of reflections	4208	37005	36009	46651	16050	53745	43220
Unique reflections	2047	5707	8378	9147	3184	4269	8934
Number of parameters/ restraints	86/2	164/13	397/0	379/0	129/0	208/0	415/0
R_1^b [$I_o > 2\sigma(I_o)$]	0.054	0.054	0.047	0.024	0.042	0.060	0.042
R_1 [all data]	0.073	0.065	0.075	0.028	0.060	0.155	0.108
wR_2^b [$I_o > 2\sigma(I_o)$]	0.110	0.113	0.090	0.050	0.082	0.130	0.069
wR_2 [all data]	0.121	0.121	0.099	0.052	0.088	0.167	0.086

[a] Common items: temperature = 120 K; wavelength (Mo Kα) = 0.71073 Å; θ(max) = 27.5°.
[b] $R_1 = \sum||F_o| - |F_c||/\sum|F_o|$. $wR_2 = [\sum w(F_o^2 - F_c^2)^2/\sum wF_o^4]^{1/2}$.

$[GaCl_3(Ph_3P)]$ was collected in the triclinic system and yielded a solution with $Z = 4$ in the space group $P\bar{1}$. Inspection of the data and the cell dimensions showed the data could be transformed to a $C2/c$ monoclinic system with $Z = 8$ with one molecule in the asymmetric unit and this is the solution reported.

Acknowledgement

We thank RCUK for support (EP/C006763/1).

Appendix A. Supplementary material

Crystallographic data in cif format have been deposited with the Cambridge Crystallographic Data Centre (CCDC) and given numbers 640911 (Cl/O), 640912 (I/O), 640913 (Br/O), 640914 (Cl/P), 640915 (Br/P), 640916 (I/P), 640917 (Cl). The atoms in parentheses denote the atom types bonded to Ga; the final one is the phosphonium salt. These data can be obtained free of charge via http://www.ccdc.cam.ac.uk/conts/retrieving.html, or from the Cambridge Crystallographic Data Centre, 12 Union Road, Cambridge CB2 1EZ, UK; fax: (+44) 1223-336-033; or e-mail: deposit@ccdc.cam.ac.uk. Supplementary data associated with this article can be found, in the online version, at doi:10.1016/j.poly.2007.05.008.

References

[1] F.A. Cotton, G. Wilkinson, M. Bochmann, C.A. Murillo, Advanced Inorganic Chemistry, sixth ed., Wiley, NY, 1998.
[2] J.A. McCleverty, T.J. Meyer (Eds.), Comprehensive Coordination Chemistry II, vol. 3, Elsevier, Oxford, 2004 (Chapters 4–7).
[3] N.C. Norman, Chemistry of Arsenic Antimony and Bismuth, Blackie, London, 1998 (Chapter 1).
[4] P. Pyykkö, Chem. Rev. 97 (1997) 597.
[5] G.A. Landrum, R. Hoffmann, Angew. Chem., Int. Ed. Engl. 37 (1998) 1887.
[6] S.E. Dann, A.R.J. Genge, W. Levason, G. Reid, J. Chem. Soc., Dalton Trans. (1996) 4471.
[7] S.E. Dann, A.R.J. Genge, W. Levason, G. Reid, J. Chem. Soc., Dalton Trans. (1997) 2207.
[8] A.R.J. Genge, W. Levason, G. Reid, Inorg. Chim. Acta 288 (1999) 142.
[9] M.F. Davis, W. Levason, G. Reid, M. Webster, Polyhedron 25 (2006) 930.
[10] M.F. Davis, M. Clarke, W. Levason, G. Reid, M. Webster, Eur. J. Inorg. Chem. (2006) 2773.
[11] A.R.J. Genge, N.J. Hill, W. Levason, G. Reid, J. Chem. Soc., Dalton Trans. (2001) 1007.
[12] A.J. Barton, A.R.J. Genge, W. Levason, G. Reid, J. Chem. Soc., Dalton Trans. (2000) 2163.
[13] A.J. Barton, A.R.J. Genge, W. Levason, G. Reid, J. Chem. Soc., Dalton Trans. (2000) 859.
[14] N.J. Hill, W. Levason, M.E. Light, G. Reid, Chem. Commun. (2003) 110.
[15] A.J. Barton, N.J. Hill, W. Levason, B. Patel, G. Reid, Chem. Commun. (2001) 95.

[16] A.J. Barton, N.J. Hill, W. Levason, G. Reid, J. Chem. Soc., Dalton Trans. (2001) 1621.
[17] J.F. Janik, R.A. Baldwin, R.L. Wells, W.T. Pennington, G.L. Schimek, A.L. Rheingold, L.M. Liable-Sands, Organometallics 15 (1996) 5385.
[18] S. Nogai, H. Schmidbaur, Inorg. Chem. 41 (2002) 4770.
[19] J.C. Carter, G. Jugie, R. Enjalbert, J. Galy, Inorg. Chem. 17 (1978) 1248.
[20] L.-J. Baker, L.A. Kloo, C.E.F. Rickard, M.J. Taylor, J. Organometal. Chem. 545–546 (1997) 249.
[21] L.-J. Baker, C.E.F. Rickard, M.J. Taylor, J. Organometal. Chem. 464 (1994) C4.
[22] A.J. Carty, Can. J. Chem. 45 (1967) 345.
[23] A.J. Carty, Can. J. Chem. 45 (1967) 3187.
[24] N. Burford, T.S. Cameron, D.J. LeBlanc, P. Losier, S. Sereda, G. Wu, Organometallics 16 (1997) 4712.
[25] C. Perchard, J. Angenault, J.-C. Couturier, Spectrochim. Acta A 33 (1977) 793.
[26] M.A. Brown, J.A. Castro, D.G. Tuck, Can. J. Chem. 75 (1997) 333.
[27] M. Sigl, A. Schier, H. Schmidbaur, Eur. J. Inorg. Chem. (1998) 203.
[28] N. Burford, B.W. Royan, R.E.v.H. Spence, T.S. Cameron, A. Linden, R.D. Rogers, J. Chem. Soc., Dalton Trans. (1990) 1521.
[29] W. Levason, R. Patel, G. Reid, J. Organomet. Chem. 688 (2003) 280.
[30] G.R. Willey, M.D. Rudd, C.J. Samuel, M.G.B. Drew, J. Chem. Soc., Dalton Trans. (1995) 759.
[31] L.M. Engelhardt, C.L. Raston, C.R. Whitaker, A.H. White, Aust. J. Chem. 39 (1986) 2151.
[32] J. Mason, Multinuclear NMR, Plenum, NY, 1987.
[33] M.D. Brown, W. Levason, G. Reid, R. Watts, Polyhedron 24 (2005) 75.
[34] J. Emsley, The Elements, OUP, Oxford, 1989.
[35] J.G. Verkade, L.D. Quin, Phosphorus-31 NMR Spectroscopy in Stereochemical Analysis, VCH, Deerfield Beach, FL, 1987.
[36] H.R. Hudson, in: F.R. Hartley (Ed.), The Chemistry of Organophosphorus Compounds, vol. 1, Wiley, NY, 1990, p. 474.
[37] M. Sigl, A. Schier, H. Schmidbaur, Z. Naturforsch., Teil B 53 (1998) 1313.
[38] G.M. Sheldrick, SHELXS 97, Program for Crystal Structure Solution, University of Göttingen, Germany, 1997.
[39] G.M. Sheldrick, SHELXL 97, Program for Crystal Structure Refinement, University of Göttingen, Germany, 1997.
[40] H.D. Flack, Acta Crystallogr., Sect. A 39 (1983) 876.
[41] W.H. Baur, D. Kassner, Acta Crystallogr., Sect. B 48 (1992) 356.
[42] R.E. Marsh, Acta Crystallogr., Sect. B 53 (1997) 317.

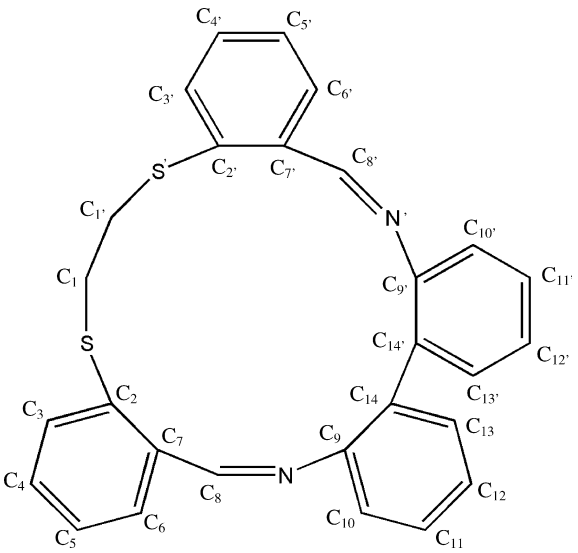


Fig. 1. Atom notation in the bite ligand.

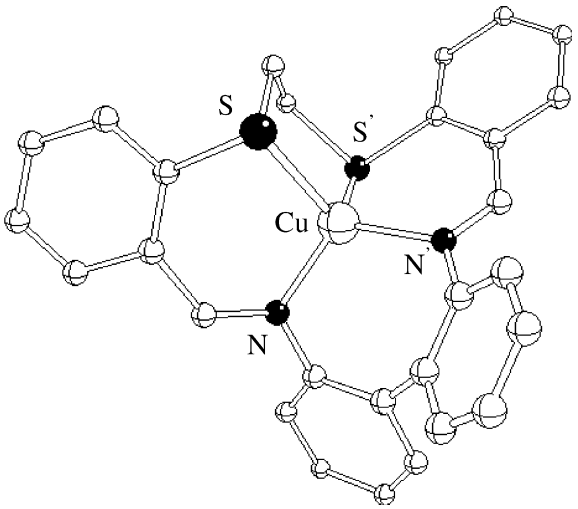


Fig. 2. The structure of quasi-tetrahedral Cu(bite)$^{+}$ (H atoms omitted).

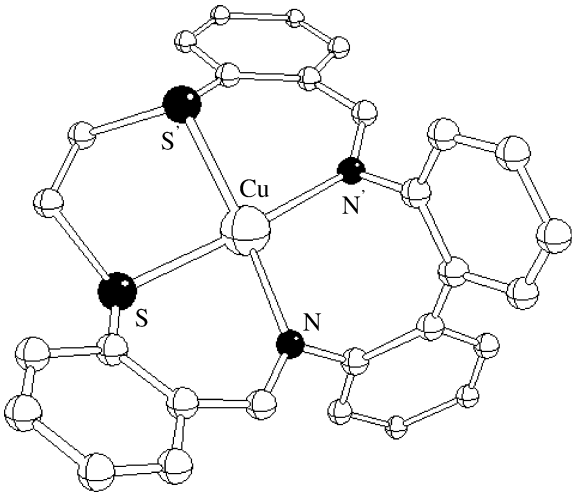


Fig. 3. The structure of quasi-square planar Cu(bite)$^{2+}$ (H atoms omitted).

ESR experiments [4] confirmed the presence of two different $[Cu^{II}(bite)]^{2+}$ forms (tetrahedral and square-planar) in frozen acetonitrile solution at 77 K.

Many experts denote the macrocyclic compounds as very poor model systems of blue copper proteins (blue copper proteins cannot be modelled by strained complexes, their electronic structure is quite different, their electron transfer rate is very low, etc.). Nevertheless, DFT quantum-chemical calculations [6] indicate that the reorganization and strain energy values of Cu(bite)$^{+/2+}$ complexes are comparable with analogous DFT/MM data for tetracoordinate copper complexes with monodentate imidazole and thiolate ligands that are generally used as model systems for blue copper proteins. Thus these complexes are worth of further experimental as well as theoretical investigation as blue protein model systems. The aim of this study is AIM (atoms-in-molecule) topological analysis of the electron density of Cu(bite)$^{+/2+}$ complexes as well as of the bite ligands in both the above mentioned conformers.

2. Method

Ab initio MP2 calculations were performed using the standard Gaussian98 program package [7] with standard 6-31G basis sets [8]. For comparison, the 6-311G basis set [9] has been used for the sulfur atoms. The optimal geometries of all the systems under study have been obtained by the DFT method in the previous part of this study [4,5]. AIM topological analysis of electron density [10] has been elaborated using the AIM2000 program package [11] and the results have been evaluated in terms of atomic volumes, and AIM atomic charges that have been obtained using the electron density integrated over atomic basins (up to 0.001 e/bohr^3 level) as well as in terms of electron density ρ, density Laplacian L

$$L = \lambda_1 + \lambda_2 + \lambda_3 \quad (1)$$

and bond ellipticity ε

$$\varepsilon = \lambda_1/\lambda_2 - 1 \quad (2)$$

at bond critical points (BCP) where $\lambda_1 < \lambda_2 < 0 < \lambda_3$ are the eigenvalues of the Hessian of the BCP electron density. Alternatively, the electronic structures of the compounds under study have been evaluated in terms of natural bond orbital (NBO) analysis [7,12] (natural atomic charges, overlap weighted NBO bond orders).

3. Results and discussion

The results of AIM topological analysis of the electron density of Cu(bite)$^{+}$, Cu(bite)$^{2+}$ and bite with tetrahedral and square-planar geometries of the S_2N_2 polyhedron are collected in Tables 1–5, and the analogous NBO data in Tables 6 and 7. The results of MP2 calculations with the 6-311G basis on the sulfur atoms in the tetrahedral Cu(bite)$^{+}$ system (if different from the 6-31G ones) are in parentheses. It is evident that the differences are not significant

Table 1
Atomic volumes [a.u.] (for atom notation see Fig. 1)

Compound	Tetrahedral geometry			Square-planar geometry		
	$Cu(bite)^+$	$Cu(bite)^{2+}$	$bite^0$	$Cu(bite)^+$	$Cu(bite)^{2+}$	$bite^0$
Cu	91 (90)[a]	81	–	101	87	–
S	165 (163)[a]	157	173	166	157	173
N	88	95	94	87	92	99
C_1	64	65	64	64	64	63
C_2	75	77	73	75	76	74
C_3	79	81	79	80	82	80
C_4	82	82	83	82	82	82
C_5	82	84	83	82	84	83
C_6	81	80	81	81	80	81
C_7	71	74	70	70	74	70
C_8	67	60	68	67	59	68
C_9	65	66	62	64	65	62
C_{10}	81	83	83	82	83	82
C_{11}	82	83	83	82	84	82
C_{12}	83	83	84	83	84	84
C_{13}	80	82	82	81	83	81
C_{14}	68	68	65	68	68	68

[a] With 6-311G basis on sulfur.

Table 2
AIM atomic charges (for atom notation see Fig. 1)

Compound	Tetrahedral geometry			Square-planar geometry		
	$Cu(bite)^+$	$Cu(bite)^{2+}$	$bite^0$	$Cu(bite)^+$	$Cu(bite)^{2+}$	$bite^0$
Cu	0.60	1.08	–	0.69	1.12	–
S	0.23 (0.22)[a]	0.23	0.27	0.21	0.22	0.29
N	−0.99	−1.18	−0.90	−0.98	−1.20	−0.90
C_1	−0.11	−0.10	−0.10	−0.11	−0.11	−0.11
C_2	−0.20	−0.22	−0.19	−0.20	−0.22	−0.19
C_3	0.01	0.02	0.00	0.01	0.01	0.00
C_4	0.02	0.05	−0.01	0.02	0.05	−0.01
C_5	0.02	0.03	0.00	0.02	0.03	0.00
C_6	0.00	0.02	−0.02	0.00	0.03	0.00
C_7	0.01	−0.02	0.01	0.00	−0.03	0.01
C_8	0.55	0.65	0.55	0.55	0.67	0.56
C_9	0.25	0.23	0.30	0.23	0.22	0.28
C_{10}	−0.02	−0.03	−0.03	0.00	−0.03	−0.02
C_{11}	0.02	0.02	0.00	0.01	0.01	0.00
C_{12}	0.01	0.01	−0.01	0.00	0.00	−0.02
C_{13}	−0.01	0.00	−0.02	−0.01	−0.01	−0.02
C_{14}	0.00	−0.02	0.01	−0.01	−0.02	0.00

[a] With 6-311 G basis on sulfur.

and are restricted to Cu and S atoms only. Thus it may be concluded that the basis set extension should not lead to any significant changes in the electronic structure parameters of our systems.

It may be seen (Table 1) that the S atoms have the largest atomic volumes, those of Cu and N atoms are significantly lower. The C_1 atoms have the lowest atomic volume. The lower values of this parameter for the C_2, C_7, C_8, C_9 and C_{14} atoms in comparison with the remaining aromatic carbon atoms may be ascribed to their non-aromatic character (C_2, C_8) or to their partial non-aromatic bonding. Atomic volumes of the Cu, S and C_8 atoms decrease with oxidation whereas the N and C_7 atoms exhibit the reverse trend. The copper atoms in a tetrahedral coordination have larger volumes than in a square-planar geometry, whereas the reverse relation holds for N atoms. As expected, the S and N atoms volumes in a free bite ligand are larger than in its Cu complexes.

Table 3
Electron density at bond critical points, ρ_{BCP} [a.u.] (for atom notation see Fig. 1)

Compound	Tetrahedral geometry			Square-planar geometry		
	$Cu(bite)^+$	$Cu(bite)^{2+}$	$bite^0$	$Cu(bite)^+$	$Cu(bite)^{2+}$	$bite^0$
Cu–S	0.07/0.06	0.07	–	0.05	0.06	–
Cu–N	0.10	0.09	–	0.08	0.08	–
S–C_1	0.15	0.14	0.15	0.15	0.15	0.15
C_1–$C_{1'}$	0.23	0.23	0.23	0.22	0.23	0.22
S–C_2	0.16 (0.15)[a]	0.16	0.16	0.16	0.16	0.17
C_2–C_7	0.27	0.27	0.28	0.27	0.28	0.27
C_2–C_3	0.29	0.29	0.29	0.28	0.28	0.28
C_3–C_4	0.29	0.29	0.29	0.29	0.29	0.29
C_4–C_5	0.29	0.29	0.29	0.29	0.29	0.29
C_5–C_6	0.29	0.30	0.29	0.29	0.30	0.29
C_6–C_7	0.28	0.28	0.28	0.28	0.28	0.28
C_7–C_8	0.26	0.26	0.25	0.26	0.26	0.25
C_8–N	0.34	0.35	0.35	0.34	0.35	0.35
N–C_9	0.26	0.26	0.28	0.26	0.26	0.28
C_9–C_{14}	0.28	0.28	0.28	0.28	0.28	0.28
C_9–C_{10}	0.29	0.29	0.28	0.29	0.29	0.28
C_{10}–C_{11}	0.29	0.29	0.29	0.29	0.29	0.29
C_{11}–C_{12}	0.29	0.29	0.29	0.29	0.29	0.29
C_{12}–C_{13}	0.29	0.29	0.28	0.28	0.28	0.28
C_{13}–C_{14}	0.29	0.29	0.29	0.28	0.29	0.28
C_{14}–$C_{14'}$	0.23	0.24	0.25	0.24	0.24	0.24

[a] With 6-311G basis on sulfur.

Table 4
Laplacian of electron density at bond critical points, $\nabla^2\rho_{BCP}$ [a.u.] (for atom notation see Fig. 1)

Compound	Tetrahedral geometry			Square-planar geometry		
	$Cu(bite)^+$	$Cu(bite)^{2+}$	$bite^0$	$Cu(bite)^+$	$Cu(bite)^{2+}$	$bite^0$
Cu–S	0.18/0.17 (0.18/0.16)[a]	0.16	–	0.15	0.13	–
Cu–N	0.43	0.37	–	0.33	0.31	–
S–C_1	−0.13 (−0.11)[a]	−0.12	−0.14	−0.13	−0.12	−0.14
C_1–$C_{1'}$	−0.39	−0.40	−0.38	−0.38	−0.39	−0.39
S–C_2	−0.17 (−0.15)[a]	−0.18	−0.18	−0.18	−0.18	−0.18
C_2–C_7	−0.56	−0.55	−0.57	−0.56	−0.56	−0.56
C_2–C_3	−0.63	−0.62	−0.64	−0.60	−0.61	−0.58
C_3–C_4	−0.66	−0.67	−0.65	−0.66	−0.66	−0.65
C_4–C_5	−0.66	−0.68	−0.64	−0.66	−0.68	−0.65
C_5–C_6	−0.68	−0.69	−0.67	−0.68	−0.69	−0.67
C_6–C_7	−0.60	−0.60	−0.60	−0.61	−0.60	−0.62
C_7–C_8	−0.52	−0.55	−0.50	−0.53	−0.57	−0.51
C_8–N	−0.82	−1.07	−0.94	−0.85	−1.10	−0.91
N–C_9	−0.62	−0.63	−0.72	−0.62	−0.62	−0.70
C_9–C_{14}	−0.59	−0.59	−0.59	−0.59	−0.61	−0.58
C_9–C_{10}	−0.62	−0.61	−0.62	−0.63	−0.63	−0.62
C_{10}–C_{11}	−0.67	−0.67	−0.65	−0.66	−0.67	−0.66
C_{11}–C_{12}	−0.66	−0.66	−0.65	−0.66	−0.66	−0.65
C_{12}–C_{13}	−0.66	−0.66	−0.59	−0.61	−0.60	−0.61
C_{13}–C_{14}	−0.62	−0.61	−0.64	−0.62	−0.64	−0.62
C_{14}–$C_{14'}$	−0.43	−0.47	−0.48	−0.46	−0.47	−0.46

[a] With 6-311G basis on sulfur.

Table 5
Bond ellipticity at bond critical points, ε_{BCP} (for atom notation see Fig. 1)

Compound	Tetrahedral geometry			Square-planar geometry		
	$Cu(bite)^+$	$Cu(bite)^{2+}$	$bite^0$	$Cu(bite)^+$	$Cu(bite)^{2+}$	$bite^0$
Cu–S	0.07 (0.05)[a]	0.10	–	0.07	0.04	–
Cu–N	0.06/0.08	0.08/0.09	–	0.01	0.09	–
$S–C_1$	0.09	0.06	0.13	0.11	0.10	0.13
$C_1–C_{1'}$	0.02	0.03	0.02	0.02	0.02	0.02
$S–C_2$	0.10	0.09	0.17	0.14	0.11	0.21
$C_2–C_7$	0.14	0.19	0.13	0.15	0.20	0.14
$C_2–C_3$	0.14	0.18	0.14	0.15	0.18	0.14
$C_3–C_4$	0.13	0.11	0.14	0.13	0.11	0.14
$C_4–C_5$	0.12	0.10	0.13	0.12	0.11	0.13
$C_5–C_6$	0.13	0.11	0.14	0.13	0.11	0.14
$C_6–C_7$	0.13	0.15	0.13	0.13	0.16	0.14
$C_7–C_8$	0.06	0.02	0.06	0.06	0.02	0.06
$C_8–N$	0.09	0.04	0.11	0.08	0.05	0.10
$N–C_9$	0.03	0.04	0.01	0.03	0.05	0.01
$C_9–C_{14}$	0.16	0.21	0.15	0.17	0.20	0.15
$C_9–C_{10}$	0.16	0.20	0.15	0.16	0.21	0.15
$C_{10}–C_{11}$	0.13	0.14	0.14	0.13	0.13	0.14
$C_{11}–C_{12}$	0.13	0.12	0.14	0.13	0.13	0.14
$C_{12}–C_{13}$	0.13	0.12	0.13	0.13	0.13	0.14
$C_{13}–C_{14}$	0.14	0.16	0.15	0.15	0.16	0.15
$C_{14}–C_{14'}$	0.02	0.02	0.01	0.03	0.04	0.03

[a] With 6-311G basis on sulfur.

Table 6
Natural atomic charges (for atom notation see Fig. 1)

Compound	Tetrahedral geometry			Square-planar geometry		
	$Cu(bite)^+$	$Cu(bite)^{2+}$	$bite^0$	$Cu(bite)^+$	$Cu(bite)^{2+}$	$bite^0$
d Electron population						
Cu	9.54 (9.56)[a]	9.04	–	9.63	9.09	–
Atomic charges						
Cu	1.01 (0.98)[a]	1.53	–	0.95	1.50	–
S	0.20 (0.19)[a]	0.25	0.30	0.22	0.26	0.34
N	−0.56	−0.83	−0.37	−0.55	−0.85	−0.36
C_1	−0.61	−0.62	−0.61	−0.61	−0.61	−0.62
C_2	−0.19	−0.22	−0.18	−0.18	−0.19	−0.17
C_3	−0.22	−0.24	−0.23	−0.23	−0.26	−0.24
C_4	−0.20	−0.13	−0.22	−0.20	−0.12	−0.22
C_5	−0.20	−0.21	−0.23	−0.21	−0.22	−0.23
C_6	−0.19	−0.13	−0.20	−0.19	−0.12	−0.20
C_7	−0.11	−0.20	−0.09	−0.12	−0.23	−0.10
C_8	0.11	0.33	0.08	0.12	0.38	0.09
C_9	0.12	0.08	0.15	0.12	0.09	0.14
C_{10}	−0.24	−0.27	−0.24	−0.24	−0.27	−0.25
C_{11}	−0.21	−0.21	−0.23	−0.22	−0.21	−0.23
C_{12}	−0.21	−0.19	−0.23	−0.22	−0.20	−0.24
C_{13}	−0.21	−0.20	−0.22	−0.21	−0.20	−0.22
C_{14}	−0.05	−0.08	−0.03	−0.07	−0.08	−0.06

[a] With 6-311G basis on sulfur.

The most positive AIM charges are at the Cu atoms (Table 2). Positive charges at C_8 atoms are higher than the nearly equal C_9 and S positive charges. The most negative charges are at the N atoms, and the C_2 atoms have more negative charge than the C_1 atoms. The charges at the remaining carbon atoms are minimal. The electron density at the Cu and C_8 atoms decreases with oxidation whereas the N atoms exhibit the reverse trend (lower electron density corresponds to lower atomic volume – compare to Table 1). On the other hand, the Cu electron density is higher in tetrahedral compared to square-planar coordination. A larger atomic volume with lower electron density indicates increasing mechanical strain at the square-planar coordinated Cu atom [10]. Lower electron density at S and N in the free bite ligand than in its copper complexes may be ascribed to the missing Cu atom. The same trend at C_9 and the reverse trend at C_8 with nearly constant atomic volumes indicates the important role of mechanical strain at these sites.

Table 7
Overlap weighted NBO bond order (for atom notation see Fig. 1)

Compound	Tetrahedral geometry			Square-planar geometry		
	$Cu(bite)^+$	$Cu(bite)^{2+}$	$bite^0$	$Cu(bite)^+$	$Cu(bite)^{2+}$	$bite^0$
Cu–S	0.23/0.20 (0.24/0.21)[a]	0.25	–	0.16	0.23	–
Cu–N	0.15	0.18	–	0.12	0.16	–
$S–C_1$	0.68	0.66	0.69	0.66	0.65	0.67
$C_1–C_{1'}$	0.82	0.83	0.81	0.82	0.82	0.81
$S–C_2$	0.73	0.74	0.76	0.75	0.74	0.79
$C_2–C_7$	1.07	1.11	1.06	1.06	1.12	1.05
$C_2–C_3$	1.11	1.18	1.10	1.09	1.18	1.08
$C_3–C_4$	1.09	1.13	1.09	1.09	1.14	1.10
$C_4–C_5$	1.08	1.14	1.08	1.08	1.16	1.08
$C_5–C_6$	1.10	1.16	1.10	1.10	1.16	1.10
$C_6–C_7$	1.05	1.11	1.06	1.06	1.12	1.07
$C_7–C_8$	0.93	0.93	0.91	0.92	0.91	0.90
$C_8–N$	1.15	1.24	1.20	1.16	1.26	1.21
$N–C_9$	0.84	0.83	0.89	0.83	0.83	0.87
$C_9–C_{14}$	1.07	1.14	1.04	1.07	1.14	1.05
$C_9–C_{10}$	1.09	1.16	1.09	1.09	1.18	1.08
$C_{10}–C_{11}$	1.09	1.17	1.09	1.09	1.15	1.09
$C_{11}–C_{12}$	1.09	1.15	1.10	1.09	1.17	1.09
$C_{12}–C_{13}$	1.09	1.16	1.07	1.08	1.15	1.08
$C_{13}–C_{14}$	1.08	1.15	1.10	1.08	1.18	1.09
$C_{14}–C_{14'}$	0.86	0.88	0.86	0.87	0.86	0.86

[a] With 6-311G basis on sulfur.

According to ρ_{BCP} data (Table 3) the bond strengths increase in the order:

$$Cu–S < Cu–N < S–C_1 < S–C_2 < C_{14}–C'_{14}$$

The remaining aromatic bonds are stronger; the C_8–N bond is the strongest one. The Cu–S and Cu–N bonds are stronger in a tetrahedral than in a square-planar conformation. The N–C_9 bond in the free bite ligand is stronger than in its copper complexes.

Positive L_{BCP} values of Cu–S and especially Cu–N bonds are in agreement with their ionic ('non-sharing' [10]) character (Table 4). The 'sharing' or covalent character ($L_{BCP} < 0$) of the other bonds increases in the sequence:

$$S–C_1 < S–C_2 < C_1–C'_1 < C_{14}–C'_{14}$$

The remaining bonds are of more "sharing" character (more negative L_{BCP}), the most negative L_{BCP} corresponds

to the N–C_8 bond. The L_{BCP} values of Cu–S, Cu–N, C_7–C_8 and N–C_8 bonds decreases with oxidation whereas the S–C_1 one increases. The ionic character of the Cu–S and Cu–N bonds is higher in a tetrahedral than in a square-planar conformation. The covalent character of the C_7–C_8 and N–C_9 bonds is stronger in the free bite ligand than in its copper complexes.

The highest ellipticity ε_{BCP} and thus the π bonding character may be ascribed to the C_9–C_{14} and C_9–C_{10} bonds (Table 5) whereas the lowest ones belong to the C_{14}–$C_{14'}$, N–C_9 and C_1–$C_{1'}$ bonds, with the lowest π bond contributions. Increasing ellipticities of the Cu–N, C_9–C_{14} and C_9–C_{10} bonds with oxidation as well as the reverse trend of the N–C_8 and C_6–C_7 ones in connection with their nearly constant bond strengths (see Table 3) indicate the significant role of mechanical strain rather than the changes in their π bonding character. On the other hand, higher S–C_1 and S–C_2 bond ellipticities in the free bite ligand than in its copper complexes are explainable by increasing π bonding only.

The trends in natural atomic charges (Table 6) are only in partial agreement with the AIM ones (Table 2). In both cases the most positive charges are at the Cu atoms, electron density at the Cu and C_8 atoms decreases with oxidation whereas the N atoms exhibit the reverse trend and the electron density at S and N in the free bite ligand is lower than in its copper complexes. On the other hand, the most negative charges at the N atoms is in the oxidized systems only. The most negative charges at the C_1 atoms in the remaining systems do not seem realistic. Unlike AIM data, all the carbon atoms except C_8 and C_9 have negative charges. Moreover, the natural electron density at the S atom increases with oxidation whereas the C_4, C_6 and C_7 ones exhibit the reverse trend. Unlike AIM, the natural electron density at the Cu and C_8 atoms is lower in a tetrahedral than in a square-planar coordination and the C_9 value is lower in the free ligand, unlike that of C_8. Additional information represents a Cu^{II} d electron population of ca. 9.0 and the Cu^{I} one of ca. 9.6.

It is surprising that unlike the above differences in atomic charges, the overlap weighted NBO bond orders (Table 7) exhibit the same trends like the analogous AIM data with only one exception related to the reverse order of Cu–N and Cu–S bond strengths. In this connection the question of the reliability of both types of electronic structure parameters arises. According to the authors' opinion, the AIM treatment should be preferred.

Finally it may be concluded that AIM topological analysis of electron density of the compounds under study grants valuable information on their electron structure as well as on mechanical strain and thus on their reactivity. Energy considerations [6] point out the role of mechanical strain but say nothing on its localization. Our results indicate the highest mechanical strain at the central copper atom and at the carbons bonded to nitrogen atom. Future model studies on the redox properties of $Cu(bite)^{+/2+}$ should be related preferentially to these sites.

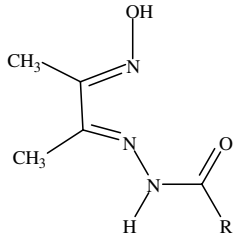
Acknowledgements

This work has been supported by Slovak Research and Development Agency (Contract No. APVV-20-0045/04), National Science Foundation of USA (Project No. NSF-CHE9981864), Slovak Grant Agency VEGA (Project Nos. 1/2449/05 and 1/3566/06) and the Project HPC-EUROPA (RII3-CT-2003-506079), with the support of the European Community – Research Infrastructure Action under the FP6 "Structuring the European Research Area" Program. We thank Prof. P. Coppens (SUNY at Buffalo, USA) for helpful discussions and valuable suggestions.

References

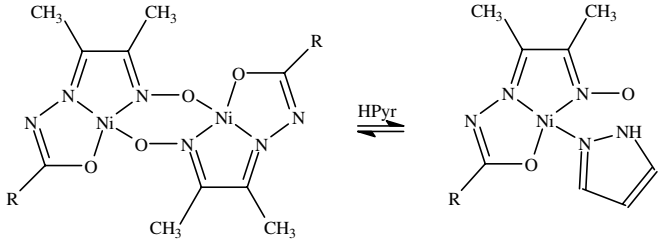
[1] (a) B.C. Dunn, L.A. Ochrymowycz, D.B. Rorabacher, Inorg. Chem. 36 (1997) 3253;
(b) N.M. Villeneuve, R.R. Schroeder, L.A. Ochrymowycz, D.B. Rorabacher, Inorg. Chem. 36 (1997) 4475;
(c) B.C. Dunn, P. Wijetunge, J.R. Vyvyan, T.A. Howard, A.J. Grall, L.A. Ochrymowycz, D.B. Rorabacher, Inorg. Chem. 36 (1997) 4484;
(d) E.A. Ambundo, M.-V. Deydier, A.J. Grall, N. Aguera-Vega, L.T. Dressel, T.H. Cooper, M.J. Heeg, L.A. Ochrymowycz, D.B. Rorabacher, Inorg. Chem. 38 (1999) 4233;
(e) K. Krylova, Ch.P. Kulatilleke, M.J. Heeg, C.A. Salhi, L.A. Ochrymowycz, D.B. Rorabacher, Inorg. Chem. 38 (1999) 4322;
(f) P. Wijetunge, Ch.P. Kulatilleke, L.T. Dressel, M.J. Heeg, L.A. Ochrymowycz, D.B. Rorabacher, Inorg. Chem. 39 (2000) 2897;
(g) Q. Yu, C.A. Salhi, E.A. Ambundo, M.J. Heeg, L.A. Ochrymowycz, D.B. Rorabacher, J. Am. Chem. Soc. 123 (2001) 5720.
[2] S. Flanagan, J. Dong, K. Haller, S. Wang, W.R. Scheidt, R.A. Scott, T.R. Webb, D.M. Stanbury, L.J. Wilson, J. Am. Chem. Soc. 119 (1997) 8857.
[3] B. Xie, L.J. Wilson, D.M. Stanbury, Inorg. Chem. 40 (2001) 3606.
[4] P. Rapta, J. Kožíšek, M. Breza, M. Gembický, L. Dunsch, J. Electroanal. Chem. 566 (2004) 123.
[5] M. Breza, J. Kožíšek, J. Mol. Struct. (Theochem) 718 (2005) 175.
[6] M. Breza, J. Kožíšek, Polyhedron 25 (2006) 2559.
[7] M.J. Frisch, G.W. Trucks, H.B. Schlegel, G.E. Scuseria, M.A. Robb, J.R. Cheeseman, V.G. Zakrzewski, J.A. Montgomery Jr., R.E. Stratmann, J.C. Burant, S. Dapprich, J.M. Millam, A.D. Daniels, K.N. Kudin, M.C. Strain, O. Farkas, J. Tomasi, V. Barone, M. Cossi, R. Cammi, B. Mennucci, C. Pomelli, C. Adamo, S. Clifford, J. Ochterski, G.A. Petersson, P.Y. Ayala, Q. Cui, K. Morokuma, D.K. Malick, A.D. Rabuck, K. Raghavachari, J.B. Foresman, J. Cioslowski, J.V. Ortiz, A.G. Baboul, B.B. Stefanov, G. Liu, A. Liashenko, P. Piskorz, I. Komaromi, R. Gomperts, R.L. Martin, D.J. Fox, T. Keith, M.A. Al-Laham, C.Y. Peng, A. Nanayakkara, M. Challacombe, P.M.W. Gill, B. Johnson, W. Chen, M.W. Wong, J.L. Andres, C. Gonzalez, M. Head-Gordon, E.S. Replogle, J.A. Pople, Gaussian 98 Revision A.9, Gaussian, Inc., Pittsburgh, PA, 1998.
[8] (a) A.J.H. Wachters, J. Chem. Phys. 52 (1970) 1033;
(b) P.C. Hariharan, J.A. Pople, Theoret. Chim. Acta 28 (1973) 213.
[9] A.D. McLean, G.S. Chandler, J. Chem. Phys. 72 (1980) 5639.
[10] R.F.W. Bader, Atoms in Molecules: A Quantum Theory, Clarendon Press, Oxford, 1990.
[11] (a) F. Biegler-König, J. Schönbohm, D. Bayles, J. Comput. Chem. 22 (2001) 545;
(b) <http://www.aim2000.de/>.
[12] (a) J.E. Carpenter, F. Weinhold, J. Mol. Struct. (Theochem) 169 (1988) 41;
(b) A.E. Reed, R.B. Weinstock, F. Weinhold, J. Chem. Phys. 83 (1985) 735;
(c) A.E. Reed, L.A. Curtiss, F. Weinhold, Chem. Rev. 88 (1988) 899.

substituents in $[\{Cu(HL\text{-}R)\}_2]\cdot 2NO_3\cdot nH_2O$ and $[\{Cu(L\text{-}R)\}_2]\cdot nH_2O$ has been also studied [18]. In the present work, we report the synthesis and characterization of some nickel(II) complexes of the type $[\{Ni(L\text{-}R)\}_2]$ and $[Ni(HL\text{-}R)_2]$ obtained from the reaction of substituted aroylhydrazoneoximes (**I**) with nickel(II) acetate.



R	Abbreviated as
C_6H_5	H_2L-H
p-$CH_3C_6H_4$	H_2L-CH_3
p-$CH_3OC_6H_4$	H_2L-CH_3O
p-ClC_6H_4	H_2L-Cl
p-$NO_2C_6H_4$	H_2L-NO_2

I



II III

In metal complexes having pyrazole as coligand, the N–H of the coordinated pyrazole is usually involved in hydrogen bond formation with available hydrogen donor or hydrogen acceptor sites giving rise to supramolecular assemblies [3,19–24]. In this context, nickel (II) complexes with dinegative tridentate aroylhydrazoneoximes having pyrazole (HPyr) as coligand have been also prepared and characterized. The X-ray molecular and supramolecular structures of [Ni(L-H);HPyr], [Ni(L-OCH_3)HPyr] and [Ni(L-Cl)HPyr] will also be discussed.

2. Experimental

2.1. Materials

Diacetylmonoxime was obtained from Sigma and used without further purification. Aroylhydrazoneoximes (**I**, R = C_6H_5, p-$CH_3C_6H_4$, p-$CH_3OC_6H_4$, p-ClC_6H_4 and p-$NO_2C_6H_4$) were prepared as previously described [18]. Pyrazole was obtained from Aldrich and was used without further purification.

2.2. Synthesis of nickel(II) complexes

2.2.1. Synthesis of $[\{Ni(L\text{-}R)\}_2]\cdot nH_2O$ (**II**, R = C_6H_5, p-$CH_3C_6H_4$, p-$CH_3OC_6H_4$, p-ClC_6H_4 and p-$NO_2C_6H_4$) (**1–5**)

A solution of nickel(II) acetate tetrahydrate (0.01 mole) in ethanol (30 cm^3) was added to a suspension of the appropriate aroylhydrazoneoxime (**I**, R = C_6H_5, p-$CH_3C_6H_4$, p-$CH_3OC_6H_4$, p-ClC_6H_4 and p-$NO_2C_6H_4$) (0.01 mole) in ethanol (50 cm^3). The resulting mixture was treated with a solution of KOH (0.02 mole) in ethanol (20 cm^3). The mixture was then refluxed, with constant stirring, for 3 h. The isolated complex was then filtered off, washed several times with ethanol then dried in vacuo.

2.2.2. Synthesis of $[Ni(HL\text{-}R)_2]\cdot nH_2O$ (**6–10**)

A solution of nickel(II) acetate tetrahydrate (0.01 mole) in ethanol (30 cm^3) was added drop wise, with constant

Table 1
Elemental analyses of the prepared nickel(II) complexes

Compound number	Complex		Yield (%)	Found (Calc.) (%)		
	R	*n*		C	H	N
(i) $[\{Ni(L\text{-}R)\}_2]\cdot nH_2O$						
1	H	1	70	46.65 (46.37)	4.32 (4.24)	14.20 (14.75)
2	CH_3	2	66	46.77 (46.80)	4.76 (4.91)	13.37 (13.64)
3	CH_3O	1	65	45.91 (45.76)	4.46 (4.48)	13.31 (13.34)
4	Cl	4	69	38.29 (38.14)	3.54 (4.07)	11.38 (12.13)
5	NO_2	3	70	37.95 (37.97)	3.54 (3.77)	15.44 (16.10)
(ii) $[Ni(HL\text{-}R)_2]$						
6	H		64	53.72 (53.36)	4.48 (4.89)	16.88 (16.97)
7	CH_3		63	54.78 (55.09)	5.54 (5.39)	15.62 (16.06)
8	CH_3O		63	51.81 (51.92)	5.15 (5.08)	14.93 (15.14)
9	Cl		58	47.59 (46.85)	4.11 (3.93)	14.48 (14.90)
10	NO_2		57	44.45 (44.47)	3.91 (3.90)	18.62 (18.86)
(iii) [Ni(L-R)HPyz]						
11	H		51	48.82 (48.88)	4.42 (4.39)	20.13 (20.36)
12	CH_3		50	50.06 (50.32)	4.76 (4.97)	19.47 (19.56)
13	CH_3O		63	48.30 (48.17)	4.60 (4.58)	18.80 (18.72)
14	Cl		65	44.24 (44.43)	3.99 (3.73)	18.61 (18.51)
15	NO_2		65	43.16 (43.23)	3.68 (3.64)	21.29 (21.60)

stirring, to a suspension of the aroylhydrazoneoxime (0.02 mole) in ethanol (50 cm^3). The reaction mixture was then refluxed with constant stirring for 3 h. The isolated complex was filtered off, washed several times with ethanol and then dried in vacuo.

2.2.3. Synthesis of [Ni(L-R)(HPyr)] (*III*, R = C_6H_5, *p*-$CH_3C_6H_4$, *p*-$CH_3OC_6H_4$, *p*-ClC_6H_4 and *p*-$NO_2C_6H_4$) (*11–15*)

To a suspension of the $[\{Ni(L\text{-}R)\}_2]\cdot nH_2O$ complex (**II**, R = C_6H_5, *p*-$CH_3C_6H_4$, *p*-$CH_3OC_6H_4$, *p*-ClC_6H_4 and *p*-$NO_2C_6H_4$) (0.01 mole) in ethanol (40 cm^3), a sufficient amount of solid pyrazole (0.05 mole) was added and the reaction mixture was heated under reflux until complete dissolution. The resulted solution was filtered and the filterate solution was further heated for ca. 1/2 h. On cooling the imidazole-nickel complex which was precipitated was isolated by filtration then washed with diethyl ether and dried in vacuo.

The prepared nickel(II) complexes (**1–15**) together with their elemental analyses are listed in Table 1.

2.3. Physical measurements

The infrared spectra were recorded on a Perkin–Elmer 1430 Data system and/or a Perkin–Elmer (FT-IR) Paragon 1000 PC spectrophotometer. Solid samples were examined as KBr discs. The ultraviolet and visible absorption spectra were recorded on double beam ratio recording Lambada 4B Perkin–Elmer spectrophotometers. Electrospray ionization mass spectra (ESI MS) were recorded on Esquire-LC from Bruker with Daltonic Nebulizer 10 psi (dry gas 8 L/min, dry temp. 250 °C). Theoretical isotopic distribution patterns for ionic species were generated using ISOFORM program and/or Sheffield University Chemputer software [25]. ^{1}H NMR spectra were recorded on Brucker WM 300 using tetramethylsilane (TMS) as an internal standard. Magnetic susceptibilities of powdered dried samples were recorded on a Faraday-type magnetometer using a sensitive computer controlled D-200 Cahn RG microbalance. The magnetic field applied was ~1.5 T. Experimental susceptibility data were corrected for the underlying diamagnetism using Pascal's constants [26].

3. Results and discussion

3.1. Synthesis and characterization

In methanol, the reaction of 3-hydroxyimino-2-butanone aroylhydrazones (H_2L-R) (**I**, R = C_6H_5, *p*-$CH_3C_6H_4$, *p*-$CH_3OC_6H_4$, *p*-ClC_6H_4, *p*-$NO_2C_6H_4$) with nickel(II) acetate tetrahydrate, using (1:1) molar ratio, in presence of KOH afforded the neutral complexes of stoichiometric composition $Ni(L\text{-}R)\cdot nH_2O$. Similar to the corresponding copper(II) complexes [17,18], nickel(II) and copper(II) complexes with tridentate 3-hydroxyimino-2-butanone thiosemicarbazones [27,28] and other copper(II) complexes of tridentate 3-hydroxyimino-2-butanone Schiff bases [29–31], a dimeric structure $[\{Ni(L\text{-}R)\}_2]$ (**II**, R = C_6H_5, *p*-$CH_3C_6H_4$, *p*-CH_3 OC_6H_4, *p*-ClC_6H_4, *p*-$NO_2C_6H_4$) can be proposed for the prepared solid nickel(II) complexes where the oximate group functions as a bridge between two nickel(II) ions. Elemental analyses of the prepared $[\{Ni(L\text{-}R)\}_2]\cdot nH_2O$ complexes, Table 1, are in a good agreement with the proposed formulation. The actual structure of these complexes must remain in doubt until complete X-ray molecular structures are available. Attempts to isolate single crystals suitable for X-ray structural analysis were unsuccessful.

The IR spectra of $[\{Ni(L\text{-}R)\}_2]$ (**I**, R = C_6H_5, *p*-$CH_3C_6H_4$, *p*-$CH_3OC_6H_4$, *p*-ClC_6H_4 and *p*-$NO_2C_6H_4$) lack absorptions attributable to oxime *ν*(O–H), hydrazide

Table 2
Solution electronic absorption spectra of nickel(II) complexes

Complex R	Sovent	λ_{max} (nm) (log ε)		
		L–L*	LMCT/d–d	MLCT
(i) $[\{Ni(L\text{-}R)\}_2]\cdot nH_2O$				
H	DMF	280, 360	400 sh, 465 sh	530 sh
CH_3	DMF	280, 360	400 sh, 465 sh	535 sh, 600 sh
CH_3O	DMF	280, 365	400 sh, 460 sh,	512 sh, 600 sh
Cl	DMF	280, 365	400 sh, 470 sh,	530 sh, 570 sh
(ii) $[Ni(HL\text{-}R)_2]$				
H	DMF	280 sh, 380 (4.30)	650 (1.20), 665 sh, 855 (0.80)	
CH_3	DMF	280 sh, 380 (4.28)	585 sh, 650 (1.20), 670 sh, 850 (0.90)	
CH_3O	DMF	285 sh, 380 (4.18)	585 sh, 650 (1.30), 665 sh, 850 (0.80)	
Cl	DMF	290 sh, 375 (4.28)	585 sh, 652 (1.60), 685 sh, 845 (0.85)	
NO_2	DMF	302 sh, 395 (4.30)	580 sh, 655 (1.55), 668 sh, 840 (1.40)	
(iii) [Ni(L-R)HPyr]				
H	$CHCl_3$	285 (4.32), 360 (4.00)	435 sh	480 sh, 520 (3.00), 575 sh
CH_3	$CHCl_3$	295 (4.31), 368 (4.00)	430 sh	490 sh, 515 (3.10)
CH_3O	$CHCl_3$	290 (4.40), 362 (4.00)	440 sh	485 sh, 515 (3.10), 575 sh
Cl	$CHCl_3$	290 (4.38), 362 (4.03)	440 sh	490 sh 525 (3.10), 585 sh
NO_2	$CHCl_3$	295 (4.30), 368 (4.00)		490 sh, 540 (3.00), 600 sh

ν(N–H), amide I [ν(C=O)], and amide II [δ(N–H)] bands, implying the deprotonation of both oxime and aroylhydrazone residues. The spectra, however, show intense band at ca. 1600 cm^{-1} due to the ν(C=N–N=C). Both oxime ν(C=N) (1520–1480 cm^{-1}) and ν(N–O) (1125–1135 cm^{-1}) appear at lower frequencies while the amide III band [ν(C–N)] (1300–1320 cm^{-1}) is shifted to higher frequencies as compared to the corresponding metal free aroylhydrazoneoxime. Both elemental analyses and IR spectral data suggest that the aroylhydrazoneoxime in [{Ni(L-R)}$_2$] complexes acts as a dinegative NNO tridentate ligand and is coordinated to the central Ni(II) via deprotonated oximate oxygen, hydrazone imine nitrogen and deprotonated enolimine oxygen. The two nickel(II) centers in [{Ni(L-R)}$_2$] complexes are bridged by the deprotonated oximate function forming six membered rings (**I**, R = C_6H_5, *p*-$CH_3C_6H_4$, *p*-$CH_3OC_6H_4$, *p*-ClC_6H_4, *p*-$NO_2C_6H_4$) [17,18,27–31].

At room temperature (298 K), the dimeric neutral Ni(II) complexes [{Ni(L-R)}$_2$] (**I**, R = C_6H_5, *p*-$CH_3C_6H_4$, *p*-$CH_3OC_6H_4$, *p*-ClC_6H_4, *p*-$NO_2C_6H_4$) are diamagnetic, indicating square planar arrangement with $^1A_{1g}$ ground state. The solution electronic absorption spectra of these complexes, in DMF, Table 2, are in agreement with this assignment. The high energy bands at ca. 280 and 360 nm are assigned to (L–L*) interligand transitions. The shoulder at 400 nm is assigned to LMCT transition while absorption at 460 ± 5 nm may originate from d–d transitions ($^1A_g \rightarrow {}^1B_{1g}$, $^1B_{3g}$). The two absorptions at ca. 510–535 and 570–600 nm can be related to the different d(π^*) → L(π^*) (MLCT) transitions [32,33].

For solubility reasons, the ^{1}H NMR spectra of diamagnetic [{Ni(L-R)}$_2$] complexes in deuterated chloroform could not be recorded. However, in deuterated DMSO, the spectra suggest the formation of paramagnetic solvated species as evident from the broadening of ^{1}H NMR signals.

Reaction of nickel(II) acetate tetrahydrate with 2 equiv. of aroylhydrazoneoxime **I** (R = H, *p*-CH_3, *p*-CH_3O, *p*-Cl, *p*-NO_2) in methanol afforded the bisligand complexes [Ni(HL-R)$_2$]. The aroylhydrazoneoxime in [Ni(HL-R)$_2$] complexes acts as mononegative NNO tridentate ligand. The IR spectra lack absorptions due to hydrazone ν(N–H), amide I [ν(C=O)] and amide II [δ(N–H)] bands, but show intense absorptions attributed to oxime ν(O–H) (3440 cm^{-1}), ν(C=N–N=C) (1601–1610 cm^{-1}), oxime ν(C=N) (1520– 1510 cm^{-1}) and amide III [ν(C–N)] (1330–1320 cm^{-1}) indicating the deprotonation of the aroylhydrazone residue while the oxime residue remains protonated.

Solid bisligand nickel(II) complexes are paramagnetic with magnetic moments being within the range 3.20–3.33 μ_β (298 K) suggesting octahedral structure. Deprotonation of the paramagnetic green bisligand complexes with KOH in methanol gave the diamagnetic brown dinuclear complexes [{Ni(L-R)}$_2$]. The electronic absorption spectra of bisligand complexes [Ni(HL-R)$_2$] display a series of bands at ca. 585, 650, 670 and 845 nm which can be, respectively, assigned to d–d transitions from $^3B_{1g}$ to $^3A_{2g}$, ^3E_g, $^3A_{2g}$ and $^3B_{2g}$ characteristic of distorted octahedral Ni(II) complexes in D_{4h} symmetry [34]. Both $^3B_{1g} \rightarrow {}^3E_g$ and LMCT transitions are most probably hidden under the intense L–L* absorption band at ca. 370 nm.

Reaction of **I** (R = C_6H_5, *p*-$CH_3C_6H_4$, *p*-$CH_3OC_6H_4$, *p*-ClC_6H_4, *p*-$NO_2C_6H_4$) with excess pyrazole in methanol proceeds by the rupture of the oximate bridges and eventually gives the corresponding monomeric complexes [Ni(L-R)HPyr] (**III**, R = C_6H_5, *p*-$CH_3C_6H_4$, *p*-$CH_3OC_6H_4$, *p*-ClC_6H_4, *p*-$NO_2C_6H_4$) with pyrazole as coligand. The IR

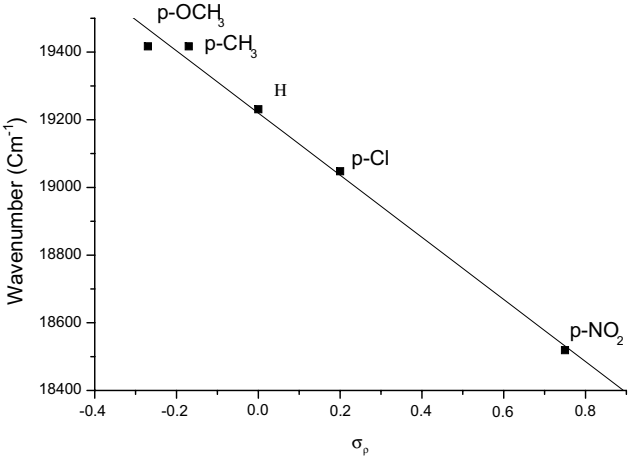


Fig. 1. Plot of MLCT band energies (Cm^{-1}) for [Ni(L-R)HPyr] complexes against Hammett's σ_p.

Table 3
^{1}Hnm spectra of nickel(II) complexes containing pyrazole as coligands in d^6-DMSO

Compound	δ ppm (No. of protons)				
	CH_3–C=N–N	CH_3–C=N–O	Aromatic (C–H)	HPyr (C–H)/(N–H)	Others
[Ni(L-H)HPyr]	1.907 (3)	2.107 (3)	7.169 (2) 7.490 (1) 7.913 (2)	6.50 b 10.20 (1)	
[Ni(L-CH_3)HPyr]	1.829 (3)	1.965 (3)	7.176 (2) 7.729 (2)	6.60 b	CH_3, 2.146 (3)
[Ni(L-CH_3O)HPyr]	1.994 (3)	2.154 (3)	6.856 (2) 7.913 (2)	6.40 b	CH_3O, 3.843 (3)
[Ni(L-NO_2)HPyr]	1.907 (6)		7.368 (2) 8.136 (1) 8.261 (1)	8.706 (1) 11.91 (1)	

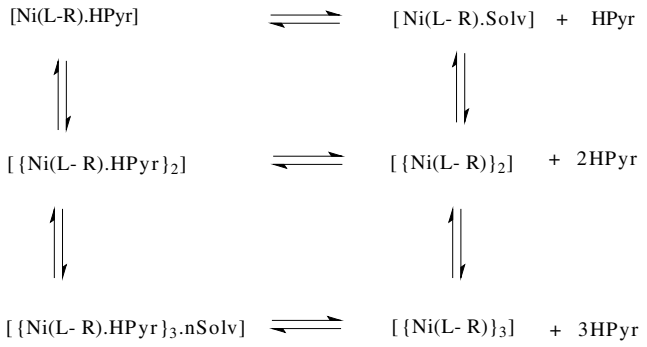
spectra of [Ni(L-R)HPyr] display the pyrazole ν(N–H) at ca. 3140 ± 20 cm^{-1} besides a series of intense bands within the range 3100–2850 cm^{-1} attributed to [ν(N–H) + ν(C–H)] coupled vibrations. The spectra of the pyrazole complexes indicate the deprotonation of both aroylhydrazone and oxime residues similar to that recorded for [{Ni(L-R)}$_2$] complexes. The pyrazole complexes are diamagnetic and their electronic absorption spectra in DMF, Table 2, are

Table 4
Positive mode ESI mass spectra of nickel(II) complexes derived from aroylhydrazonemonoximes

Complex	Solvent	m/z Found (Calc.)	RA	Assignment
[{Ni(L-H)}$_2$] · H$_2$O	CHCl$_3$/MeOH	277.1 (276.9247)	22	[{Ni(L-H)}$_2$ + 2H]$^{2+}$
		308.2 (308.9668)	35	[Ni(L-H) + MeOH + H]$^{1+}$
		496.1 (496.1673)	42	[{Ni(L-H)}$_2$ + H]$^{1+}$
		552.1 (552.8412)	100	[Ni(HL-H)$_2$ + H]$^{1+}$
		828.2 (828.7582)	10	[{Ni(L-H)}$_3$ + H]$^{1+}$
[{Ni(L-CH$_3$)}$_2$] · H$_2$O	CHCl$_3$/MeOH	290.1 (290.9515)	38	[{Ni(L-CH$_3$)}$_2$ + 2H]$^{2+}$
		308.1 (308.9668)	43	[Ni(L-CH$_3$) H$_2$O + H]$^{1+}$
		407.1 (407.5861)	18	[Ni$_2$(HL-CH$_3$)$_3$ + H]$^{2+}$
		423.1 (423.6072)	65	[Ni$_2$(HL-CH$_3$)$_3$ (MeOH) + H]$^{2+}$
		523.2 (524.2210)	40	[Ni(HL-CH$_3$)$_2$ + H]$^{1+}$
		580.2 (580.8952)	100	[{Ni(L-CH$_3$)}$_2$ + H]$^{1+}$
[{Ni(L-CH$_3$O)}$_2$] · H$_2$O	CHCl$_3$/MeOH	307.1 (306.9509)	18	[{Ni(L-CH$_3$O)}$_2$ + 2H]$^{2+}$
		338.1 (338.9929)	32	[Ni(L-CH$_3$O) + MeOH + H]$^{1+}$
		431.1 (431.5853)	25	[Ni$_2$(HL-CH$_3$O)$_3$ + H]$^{2+}$
		556.1 (556.2198)	20	[Ni(HL-CH$_3$O)$_2$ + H]$^{1+}$
		612.2 (612.8940)	100	[{Ni(L-CH$_3$O)}$_2$ + H]$^{1+}$
[{Ni(L-Cl)}$_2$] · H$_2$O	CHCl$_3$/MeOH	343.1 (343.4118)	22	[Ni(L-Cl) + MeOH + H]$^{1+}$
		466.1 (466..5508)	14	[{Ni(L-Cl)}$_3$ + 2H]$^{2+}$
		475.1 (475..5584)	100	[{Ni(L-Cl)}$_3$ + H$_2$O + 2H]$^{2+}$
		621.1 (621.7318)	12	[{Ni(L-Cl)}$_2$ + H]$^{1+}$
		643.1 (643.7136)	37	[{Ni(L-Cl)}$_2$ + Na]$^{1+}$
[{Ni(L-NO$_2$)}$_3$] · H$_2$O	DMF/MeOH	396.1 (395.0167)	53	[Ni(L-NO$_2$) · DMF + H]$^{1+}$
		454.1 (454.0425)	43	[Ni$_2$(HL-NO$_2$)$_3$ + H]$^{2+}$
		468.0 (468.1111)	19	[Ni(L-NO$_2$)(DMF)$_2$ + H]
		482.1 (482.3796)	100	[{Ni(L-NO$_2$)}$_3$ + 2H]$^{2+}$
		642.2 (642.8367)	14	[{Ni(L-NO$_2$)}$_2$ + H]$^{1+}$
[Ni(L-H)HPyr]	CHCl$_3$/MeOH	345.0 (345.0027)	100	[Ni(L-H)HPyr + H]$^{1+}$
		552.1 (552.8416)	52	[{Ni(L-H)}$_2$ + H]$^{1+}$
		829.0 (828.7582)	6	[{Ni(L-H)}$_3$ + H]$^{1+}$
[Ni(L-CH$_3$)HPyr]	CHCl$_3$/MeOH	359.1 (359.0296)	100	[Ni(L-CH$_3$)HPyr + H]$^{1+}$
		451.1 (451.9443)	8	[{Ni(L-CH$_3$)}$_3$ + MeOH + 2H]$^{2+}$
		483.1 (483.9863)	30	[{Ni(L-CH$_3$)MeOH}$_3$ + 2H]$^{2+}$
		580.1 (580.8952)	43	[{Ni(L-CH$_3$)}$_2$ + H]$^{1+}$
		601.1 (602.8771)	17	[{Ni(L-CH$_3$)}$_2$ + Na]$^{1+}$
		771.1 (771.0751)	20	[{Ni(L-CH$_3$)HPyr}$_2$+ MeOH + Na]$^{1+}$
		870.2 (870.8387)	11	[{Ni(L-CH$_3$)]$_3$ + [H]$^{1+}$
[Ni(L-CH$_3$O)HPyr]	CHCl$_3$/MeOH	375.0 (375.0288)	100	[Ni(L-CH$_3$O)HPyr + H]$^{1+}$
		385.0 (385.7096)	49	[{Ni(L-CH$_3$O)HPyr}$_3$ + MeOH + 3H]$^{3+}$
		555.2 (554.2039)	39	[Ni(L-CH$_3$O)$_2$ + H]$^{1+}$
		577.3 (576.1859)	9	[Ni(L-CH$_3$O)$_2$ + Na]$^{1+}$
		611.1 (612.8940)	33	[{Ni(L-CH$_3$O)}$_2$ + H]$^{1+}$
		633.1 (634.8758)	6	[{Ni(L-CH$_3$O)}$_2$ + Na]$^{1+}$
[Ni(L-Cl)HPyr]	CHCl$_3$/MeOH	378.1 (379.4478)	79	[Ni(L-Cl)HPyr + H]$^{1+}$
		390.1 (390.1285)	93	[{Ni(L-Cl)]$_3$ + MeOH + 3[H]$^{3+}$
		466.0 (466.5508)	27	[{Ni(L-Cl)}$_3$ + 2H]$^{2+}$
		514.0 (514.6138)	100	[{Ni(L-Cl)MeOH}$_3$ + 2H]$^{2+}$
		584.2 (548.5887)	22	[{Ni(L-Cl)HPyr}$_3$ + MeOH + 2H]$^{2+}$
		621.2 (621.7318)	20	[{Ni(L-Cl)}$_2$ + H]$^{1+}$
		812.0 (811..9117)	41	[{Ni(L-Cl)HPyr}$_2$ + MeOH + Na]$^{1+}$
[Ni(L-NO$_2$)HPyr]	CHCl$_3$/MeOH	389.1 (390.0003)	100	[Ni(L-NO$_2$)HPyr + H]$^{1+}$
		513.1 (514.4215)	12	[{Ni(L-NO$_2$)}$_3$ + 2MeOH + 2H]$^{2+}$
		531.0 (530.4426)	3	[{Ni(L-NO$_2$)MeOH}$_3$ + 2H]$^{2+}$
		584.1 (584.4965)	11	[{Ni(L-NO$_2$)HPyr}$_3$ + 2H]$^{2+}$

typical for square planar nickel(II) complexes [32]. The shoulder(s) at lower energy side (430–455 nm) of the ligand intense absorption band can be assigned to $^1A_{1g} \rightarrow {}^1A_{2g}$ transition, however the contribution of LMCT transitions to this absorption cannot be ruled out. The spectra also show a series of absorption bands in the 460–600 nm range which can be attributed to different MLCT transitions. The well resolved absorption band in the 525–585 nm range is attributed to $d(\pi^*) \rightarrow L(\pi^*)$ MLCT transition and suffers a blue shift on introducing electron releasing substituents (**III**, R = *p*-$CH_3C_6H_4$ and *p*-$CH_3OC_6H_4$) while electron withdrawing substituents (**III**, R = *p*-ClC_6H_4 and *p*-$NO_2C_6H_5$) cause a red shift relative to that of the unsubstituted complexes. The energy of this MLCT band, measured in wavenumber (cm^{-1}) can be correlated with Hammett's σ_p constants and plots of wavenumbers recorded for pyrazole complexes against σ_p, Fig. 1, gave straight line with a negative slope, in agreement with the MLCT nature of this transition.

The ^1H NMR spectra of [Ni(L-R)HPyr] complexes in DMSO, Table 3, reveal that the two methyl groups of the diimine residue are magnetically nonequivalent. The methyl group adjacent to the hydrazone residue (Me–C=N–N–) is more shielded and appears in the 1.82–2.00 ppm range while the methyl group adjacent to the oxime residue appears at 1.96–2.15 ppm. The aroyl protons appear as two multiplets centered at (6.90–7.20 ppm) and (7.60–8.2 ppm) depending on the substituent R. The C–H and N–H protons of the pyrazole ring appear as very broad signals (6.60–7.7 ppm), most probably due to rapid exchange between coordinated and free uncoordinated pyr-



Scheme 1.

Table 5
Crystallographic data and structure refinement parameter for **11**, **13** and **14**

	11	**13**	**14**
Empirical formula	$C_{14}H_{15}N_5NiO_2$	$C_{15}H_{17}N_5NiO_3$	$C_{14}H_{14}ClN_5NiO_2$
Formula weight	344.02	374.08	378.46
Temperature (K)	299(2)	293(2)	299(2)
Wavelength (Å)	0.71073	1.54180	0.71073
Crystal system	orthorhombic	monoclinic	monoclinic
Space group	*P*212121	*P*21	*P*21/*n*
Unit cell dimensions			
a (Å)	5.658(5)	8.719(2)	7.4384(8)
b (Å)	8.464(5)	5.4124(5)	19.985(2)
c (Å)	31.416(17)	17.268(3)	21.295(2)
α (°)	90	90	90
β (°)	90	97.20(1)	96.045(7)
γ (°)	90	90	90
Volume ($Å^3$)	1504.5(18)	808.5(2)	3148.0(5)
Z	4	2	8
D_{calc} ($Mg\ m^{-3}$)	1.519	1.537	1.597
Absorption coefficient (mm^{-1})	1.304	1.953	1.418
F(000)	712	388	1552
Crystal size (mm)	0.80 × 0.06 × 0.04	0.50 × 0.03 × 0.01	0. 24 × 0.12 × 0.06
θ Range for data collection (°)	4.09–24.71	2.58–66.92	4.08–24.71
Limiting indices	$-4 \leqslant h \leqslant 6$, $-9 \leqslant k \leqslant 9$, $-36 \leqslant l \leqslant 36$	$-10 \leqslant h \leqslant 1$, $-6 \leqslant k \leqslant 0$, $-20 \leqslant l \leqslant 20$	$-8 \leqslant h \leqslant 5$, $-23 \leqslant k \leqslant 23$, $-25 \leqslant l \leqslant 25$
Reflections collected	7942	1733	18013
Independent reflections [R_{int}]	2485 [0.1951]	1615 [0.0800]	5348 [0.0864]
Completeness to θ	24.71	99.0%	66.92
Absorption correction	analytical	psi-scan	analytical
Maximum and minimum transmission	0.975 and 0.767	0.9980 and 0.8249	0.998 and 0.559
Refinement method	full-matrix least-squares on F^2	full-matrix least-squares on F^2	full-matrix least-squares on F^2
Data/restraints/parameters	2485/6/174	1615/1/217	5348/0/415
Goodness-of-fit on F^2	0.879	0.994	1.299
Final *R* indices ($I > 2\sigma(I)$)	$R_1 = 0.0779$, $wR_2 = 0.1172$	$R_1 = 0.0540$, $wR_2 = 0.1119$	$R_1 = 0.1061$, $wR_2 = 0.1810$
R indices (all data)	$R_1 = 0.2121$, $wR_2 = 0.1559$	$R_1 = 0.1361$, $wR_2 = 0.1352$	$R_1 = 0.1371$, $wR_2 = 0.1946$
Largest difference in peak and hole (e $Å^{-3}$)	0.352 and −0.553	0.370 and −0.350	0.366 and −0.431

azole. In deuterated chloroform, however, the ^{1}H NMR spectra of [Ni(L-R)HPyr] show broad signals, most probably due to equilibrium between diamagnetic planar ($S = 0$) and tetrahedral ($S = 1$) species.

4. Electrospray ionization mass spectra (ESI MS)

The positive ion ESI MS of [{Ni(L-R)}$_2$] complexes (**I**, R = C_6H_5, *p*-$CH_3C_6H_4$ and *p*-$CH_3OC_6H_4$) in $CHCl_3$/

Table 6
Selected bond distances (Å) and bond angles (°) for [Ni(L-H)(HPyr)](**11**) , [Ni(L-CH_3O)(HPyr)] (**13**) and [Ni(L-Cl)(HPyr)] (**14**)

	11	**13**	**14**			
			Ni1 Molecular unit		Ni2 Molecular unit	
Ni–O1	1.907(8)	1.891(5)	Ni1–O1	1.867(5)	Ni2–O3	1.871(5)
Ni–N1	1.851(10)	1.803(8)	Ni1–N1	1.793(6)	Ni2–N6	1.813(7)
Ni–N3	1.953(9)	1.887(7)	Ni1–N3	1.884(7)	Ni2–N8	1.881(7)
Ni–N4	1.934(12)	1.881(8)	Ni1–N4	1.870(7)	Ni2–N9	1.870(7)
O2–N3	1.287(12)	1.306(9)	O2–N3	1.312(8)	O4–N8	1.313(8)
C9–N3	1.329(15)	1.325(13)	C2–N3	1.321(10)	C16–N8	1.316(10)
C8–C9	1.414(18)	1.449(12)	C2–C1	1.467(11)	C16–C15	1.434(11)
C8–N1	1.250(16)	1.270(11)	C1–N1	1.281(10)	C15–N6	1.289(9)
N1–N2	1.410(13)	1.392(9)	N1–N2	1.389(8)	N6–N7	1.391(8)
C1–N2	1.365(16)	1.313(12)	C3–N2	1.327(10)	C17–N7	1.326(9)
C1–O1	1.313(15)	1.313(12)	C3–O1	1.288(9)	C17–O3	1.304(9)
C1–C2	1.505(16)	1.483(12)	C3–C4	1.479(10)	C17–C18	1.466(10)
N1–Ni–O1	84.0(5)	83.8(3)	N1–Ni1–O1	83.3(3)	N6–Ni2–O3	83.2(3)
N1–Ni–N3	82.6(6)	82.7(3)	N1–Ni1–N3	83.6(3)	N6–Ni2–N8	83.4(3)
N3–Ni–N4	98.9(6)	100.1(3)	N3–Ni1–N4	99.0(3)	N8–Ni2–N9	98.7(3)
O1–Ni–N4	94.5(5)	93.5(3)	O1–Ni1–N4	94.1(3)	O3–Ni2–N9	94.7(3)
N3–Ni–O1	166.6(5)	166.4(4)	N3–Ni1–O1	166.9(3)	N8–Ni2–O3	166.5(3)
N1–Ni–N4	177.0(5)	176.2(3)	N1–Ni1–N4	177.0(3)	N6–Ni2–N9	177.1(3)
O2–N3–C9	125.2(11)	120.3(7)	O2–N3–C2	120.0(7)	O4–N8–C16	120.5(7)
N3–C9–C8	115.7(14)	112.1(8)	N3–C2–C1	112.9(7)	N8–C16–C15	113.3(7)
N1–C8–C9	114.6(15)	112.7(9)	N1–C1–C2	111.5(8)	N6–C15–C16	112.9(7)
C8–N1–N2	125.8(13)	123.8(9)	C1–N1–N2	122.8(7)	C15–N6–N7	125.7(7)
C1–N2–N1	105.4(11)	106.2(8)	C3–N2–N1	104.3(6)	C17–N7–N6	106.5(6)
N2–C1–O1	125.3(12)	124.8(9)	N2–C3–O1	125.3(7)	N7–C17–O3	123.1(7)
N2–C1–C2	116.1(14)	119.5(9)	N2–C3–C4	116.2(7)	N7–C17–C18	118.6(7)
O1–C1–C2	118.5(13)	115.7(9)	O1–C3–C4	118.4(7)	O3–C17–C18	118.2(7)

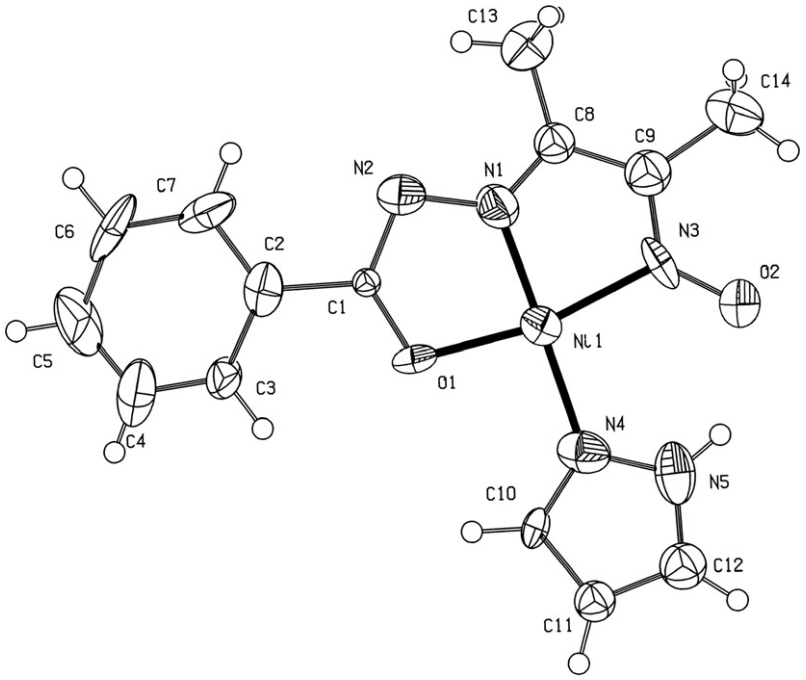


Fig. 2. ORTEP representation of [Ni(L-H)HPyr] (**11**) with labeling of atoms.

MeOH (50v:50v) as solvent, Table 4, are dominated by the parent dinickel(II) species $[\{Ni(L\text{-}R)\}_2 + H]^{1+}$. The spectra also show peaks of lower relative intensities corresponding to the dipositive dinuclear cation $[\{Ni(L\text{-}R)\}_2 + 2H]^{2+}$ and monopositive trinuclear cation $[\{Ni(L\text{-}R)\}_3 + H]^{1+}$. Different from the positive ion ESI MS of **I** with electron releasing substituents ($R = C_6H_5$, p-$CH_3C_6H_4$ and p-$CH_3OC_6H_4$), the spectra of **I** with electron withdrawing substituents ($R = p$-ClC_6H_4 and p-$NO_2C_6H_4$) are dominated by the dipositive trinuclear cation $[\{Ni(L\text{-}R)\}_3 + 2H]^{2+}$. It seems that the presence of electron withdrawing substituents in the aroyhydrazone residue results in an increase of the positive formal charge of the central nickel(II), thus favouring the preferential formation of the trinuclear rather than the dinuclear species. The positive ion ESI MS of **I** complexes with both electron releasing and withdrawing substituents ($R = C_6H_5$, p-$CH_3C_6H_4$, p-$CH_3OC_6H_4$ and p-ClC_6H_4 p-$NO_2C_6H_4$) display a set of

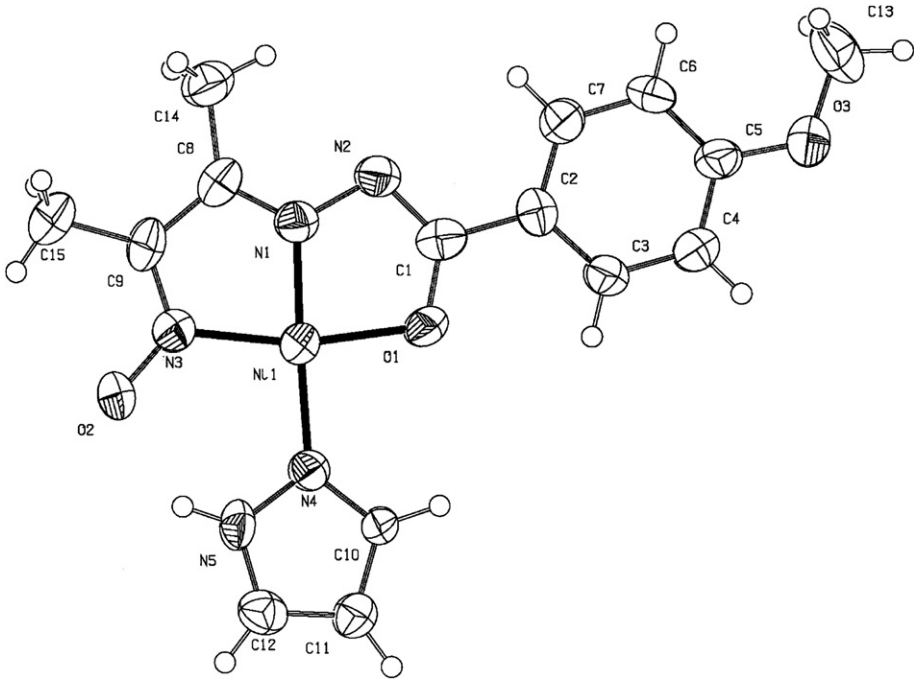


Fig. 3. ORTEP representation of [Ni(L-CH_3O)HPyr] (**13**) with labeling atoms.

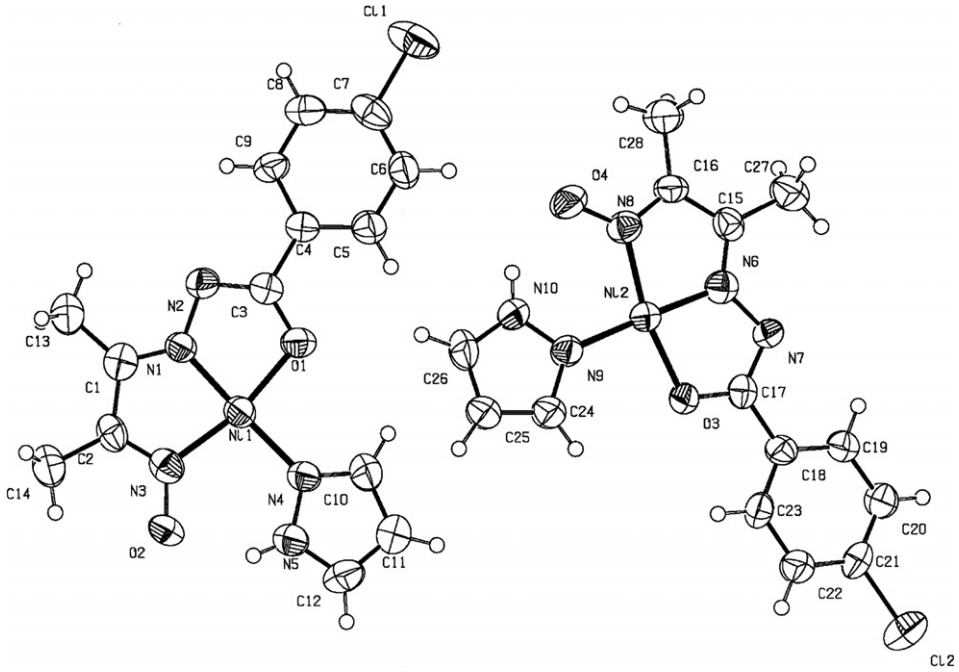


Fig. 4. ORTEP representation of [Ni(L-Cl)HPyr] (**14**) with labeling atoms.

peaks corresponding to the solvated mononuclear species $[Ni(HL\text{-}R)Solv]^{1+}$ (Solv. = MeOH, H_2O or DMF), besides peaks corresponding to the $[Ni(HL\text{-}R)_2 + H]^{1+}$ and $[Ni_2(HLR)_3 + H]^{2+}$ cations. These cations apparently arise from the parent intact dinuclear cation $[\{Ni(L\text{-}R)\}_2 + H]^{1+}$ via the protonation of the oximate oxygens followed by the rupture of the oximate bridges to give the mononuclear solvated cations $[Ni(HL\text{-}R)(Solv)]^{1+}$. This cation may undergo a series of disproportionation reactions and eventually gives $[Ni(HL\text{-}R)_2 + H]^{1+}$ and $[Ni_2(HL\text{-}R)_3 + H]^{2+}$ cations.

The positive ESI MS of [Ni(L-R)HPyr] complexes in CH_3Cl/MeOH, Table 4, show intense peaks corresponding to protonated monomeric species $[Ni(L\text{-}R)HPyr + H]^{1+}$, besides the dipositive solvated trimeric cations $[\{Ni(L\text{-}R)HPyr\}_3 + n\text{MeOH} + 2H]^{2+}$ ($n = 0$–3). The spectra also display peaks corresponding to dimeric $[\{Ni(L\text{-}R)\}_2 + H]^{1+}$ and trimeric $[\{Ni(L\text{-}R)\}_3 + H]^{1+}$cations. The positive mode ESI MS data of [Ni(L-R)HPyr] suggest the following equilibria (Scheme 1).

5. X-ray molecular and supramolecular structures

The crystal data and structure refinement parameters for [Ni(L-H)HPyr] (**11**), $[Ni(L\text{-}CH_3O)HPyr]$ (**13**) and [Ni(L-Cl)HPyr] (**14**) are given in Table 5. Selected bond distances and angles for **11**, **13** and **14** are collected in Table 6. The molecular structures of both **11** and **13** consist of one type of discrete molecular units, while the crystal structure of **14** consists of two types of molecular units, namely Ni1 and Ni2 molecular units, which are crystallographically independent but chemically similar. The structure of **11**, **13** and **14** together with the atomic numbering scheme are, respectively shown in Figs. 2–4. These nickel(II) complexes

Table 7
Noncovalent bond interactions of **11**, **13** and **14** complexes

D–H···A	Symmetry	*d*(D–H) Å	*d*(H–A) Å	*d*(D–A) Å	∠(DHA)°
[Ni(L-H)HPyr]					
Intrachain noncovalent bond interactions					
N5H···O2 (intra)	x, y, z	0.861	1.922	2.633	138.95
N5H···O2 (inter)	$-1/2 + x, 1.5 - y, -z$	0.861	2.840	3.283	113.8
CH12···O2	$-1/2 + x, 1.5 - y, -z$	0.932	2.595	3.178	121.1
CH14C···Cg2	$1/2 - x, -y, 1/2 + z$	0.959	3.470	4.384	160.1
CgC···Cg2	$1/2 - x, 1/2 - y, -z$	CgC–Cg3 = 3.358 Å, ∠N4–Cg3–CgC = 95.8°			
[Ni(L-CH_3O)HPyr]					
Intrachain noncovalent bond interactions					
NH5···O2 (intra)	x, y, z	0.860	1.903	2.615	139.3
NH5···O2 (inter)	$-x, -1/2 + y, 2 - z$	0.860	2.789	3.257	115.8
CH12···O2	$-x, -1/2 + y, 2 - z$	0.932	2.601	3.183	121.0
CgC–Cg2	$-x, 1/2 + y, -z$	CgC–Cg3 = 3.352 Å, ∠N4–Cg3–CgC = 93.8°			
Interchain noncovalent bond interactions					
CH13C···Cg1	$-x, 1/2 + y, 1 - z$	0.960	3.485	4.212	134.3
CH14C···Cg1	$-x, 1/2 + y, -z$	0.961	2.895	3.825	163.3
[Ni(L-Cl)HPyr]					
Intramolecular hydrogen bonds					
N5H···O2	x, y, z	0.861	1.887	2.600	139.1
N10H···O4	x, y, z	0.860	1.865	2.581	139.7
Intermolecular noncovalent bond interactions between Ni1 molecular units					
Dimer formation (Ni molecular units)					
CH12···O2	$-x, -y, -z$	0.930	2.521	3.185	128.6
O2···H12C	$-x, -y, -z$	0.930	2.513	3.179	128.8
Interdimer noncovalent bond interactions					
CH11···Cl1	$-1/2 + x, 1/2 - y, -1/2 + z$	0.93	2.847	3.613	140.5
Intermolecular noncovalent bond interactions between Ni2 molecular units					
CH20···O4	$-1/2 + x, 1/2 + y, 1/2 - z$	0.930	2.543	3.221	130.0
CH27A···C26	$-1/2 - x, 1/2 + y, 1/2 - z$	0.961	2.885	3.767	153.0
Intermolecular noncovalent bond interactions between Ni1 and Ni2 molecular units					
CH13B···Cg2	$1/2 - x, 1/2 + y, 1/2 - z$	0.960	2.925	3.879	173.0
CH14B···C20	$1/2 - x, -1/2 + y, 1/2 - z$	0.960	2.879	3.816	165.5
CH24···Cl1	$1 - x, -y, 1 - z$	0.930	2.926	3.598	130.3

Cg1 (*p*-methoxyphenyl ring centriod); Cg2 (Pyrazole ring centriod) and CgC (diimine chelate ring centroid).

have square planar geometry, where the Ni(II) is coordinated to the oximate nitrogen (N3), hydrazone nitrogen (N1), deprotonated enolimine oxygen (O1) of the dinegative NNO tridentate aroylhydrazoneoxime anion. The fourth coordination site is occupied by the pyrazole nitrogen (N4). In **11**, **13** complexes the angles between the pyrazole plane and the Ni(II) mean coordination plane (Ni, O1, N1, N3, N4) are 3.03° and 4.81°, respectively, while the corresponding angles in Ni1 and Ni2 molecular units of **14** are 9.92° and 10.82°, respectively. The phenyl planes in **11** (C2–C7) and **13** (C2–C7) are, respectively, deviated from the Ni(II) mean coordination plane by 6.58°and 4.98° angles while the deviation of the phenyl planes (C4–C9) and (C18–C23) from the Ni(II) mean coordination planes in Ni1 and Ni2 molecular units of **14** are 9.46° and 6.70° respectively. The diimine (N1–Ni–N3) and the aroylhydrazone (N1–Ni–O1) bite angles in **11**, **13**, **14**, Table 6, are more or less similar with a mean value of 82.8° and 83.4°, respectively. In these complexes, the Ni–N3 (oxime) bond lengths [1.882–1.964 Å] are within the range reported for other Ni(II) oximate complexes [27,28,35–41], but longer than the Ni–N1 (hydrazone) bond distances [1.794–1.828 Å] as shown in Table 6. The elongation of Ni–N3 relative to Ni–N1 can be attributed to the presence of the more electronegative oximate oxygen (O1) which decreases the electron density on the oximate nitrogen (N3), thus decreasing bond strength of the Ni–N3 relative to that of Ni–N1 bond. Both Ni–N1 (1.794–1.828 Å) and Ni–O1 (1.868–1.912 Å) bond distances are within the range reported for other Ni(II) complexes with dinegative tridentate aroylhydrazones [21,42–44]. The Ni–N4 bond distances (1.872–1.929 Å) are within the normal range reported for square planar Ni(II) complexes with dinegative tridentate ligands having pyrazole as coligand [21]. The N3–O2 bond lengths (1.294–1.317 Å) reveal appreciable double bond character and are comparable to those reported for nonbridged oximate N–O bonds [37].

The bond distances between the central Ni(II) and the donor atoms (O1, N1, N3 and N4) in these complexes, are affected by the nature of substituents in the aroylhydrazone residue. The presence of both electron releasing (**III**, R = *p*-$CH_3OC_6H_4$) or electron withdrawing (**III**, R = *p*-ClC_6H_4) substituent in the aroylhydrazone residue resulted in a pronounced decrease in Ni–O1, Ni–N1, Ni–N3 and Ni–N4 bond distances relative to that of the unsubstituted complex (**III**, R = C_6H_5). This behaviour may suggest that both σ- and π-back donation are operative. Electron releasing substituent will favour σ-donation while electron withdrawing substituent will enhance π-back donation, in both cases a decrease in bond distances is expected.

The oximate O2 oxygen of **11**, **13** and **14** is involved in intramolecular hydrogen bond with the pyrazole N5–H proton (Table 7). This hydrogen bond motif of graph set descriptor **S(6)** [45,46] forms a six-membered ring which is almost coplanar with the two five-membered chelate rings as well as the pyrazole ring. The molecular units of both **11** and **13** are linked together by two reciprocal intermolecular hydrogen bonds between oximate O2 and pyrazole N5H proton of the adjacent molecular units. This hydrogen bond of graph set descriptor **C(6)**, forms a rectangular helical chain propagating, respectively, along *a*- and *b*-axis as shown in Fig. 5. No such intermolecular hydrogen bonding was observed in the structure of **14**. In both **11** and **13**, the molecular units of the helical chains are arranged parallel to each other on both sides of a backbone of intra- and intermolecular hydrogen bonds. The Ni mean coordination planes of the molecular units on one side make, respectively, angles of 72.1° (for **11**) and 77.2° (for**13**) with the corresponding coordination plane on the other side. In the crystal lattice of **11** and **13**, the parallel arrangement of the molecular units on both sides of the helical chains are stabilized by $\pi\cdots\pi$ interactions between the delocalized diimine chelate ring, which acts as an aromatic ring [47,48], and the aromatic heterocyclic pyrazole rings of the adjacent molecular units [48,49]. The mean plane of the diimine chelate ring is almost parallel to that of the pyrazole plane and the dihedral angles between these planes are 4.10° and 5.58°, respectively. The perpendicular molecular units are also stabilized by CH···O [50,51] intrachain interactions between pyrazole C12H protons and the oximate oxygens (O2) of the neighboring molecular units. In **11** the perpendicular arrangement is further stabilized by an additional CH14···π (pyrazole) intrachain interaction [52,53]. The intrachain noncovalent interactions of both **11** and **13** are listed in Table 7.

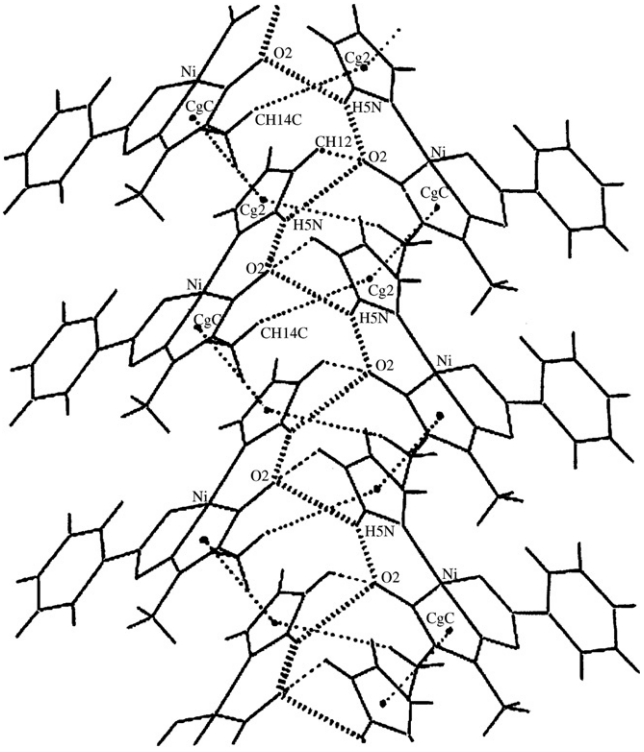


Fig. 5. Diagrammatic representation of inter and intramolecular noncovalent bond interactions in the helical chain of [Ni(L-H)HPyr] (**11**).

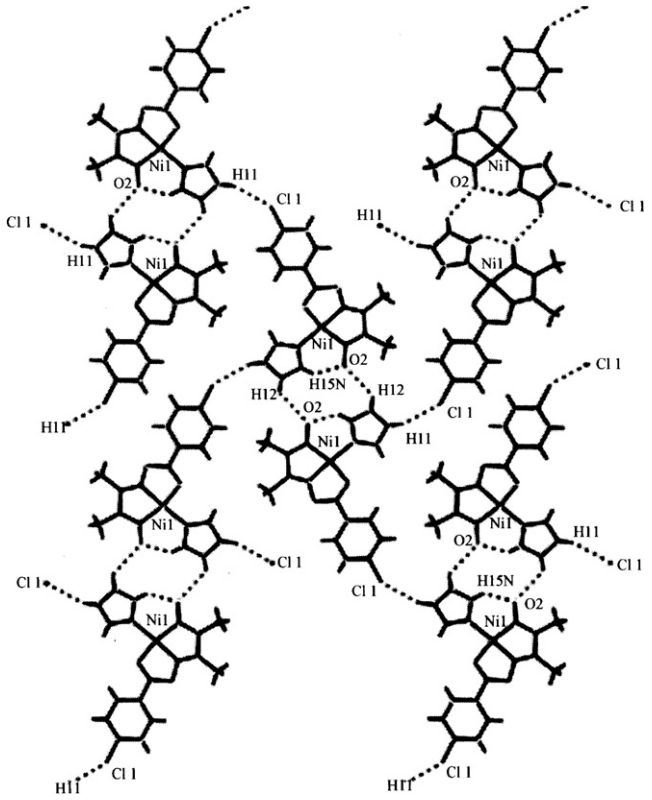


Fig. 6. Diagrammatic representation of noncovalent bond interactions between Ni1 molecular units of [Ni(L-Cl)HPyr] (**14**).

The helical chains in **11** are linked together by Van der Waals forces and no other interchain interactions were observed. However, in **13**, the helical chains are jointed together by reciprocal CH···π interchain interactions between CH13C protons of the methoxy groups of one chain and the π system of the *p*-methoxy phenyl ring (C2–C7) of the adjacent chain , forming a two dimensional array of helical chains propagating parallel to the ac plane. The CH14C protons of the methyl group adjacent to the hydrazone imine in one chain are also involved in CH···π interactions with the aromatic rings (C2–C7) of the neighboring chains forming three dimensional arrays of helical chains.

In addition to intramolecular N5H···O2 hydrogen bond, the oxime O2 in **14** is also involved in weak hydrogen bond with the pyrazole CH12 proton of the adjacent Ni1 molecular unit giving rise to a dimeric structure as shown in Fig. 6. Each dimer is connected to four neighboring dimeric units via two pairs of reciprocal weak hydrogen bonds between the pyrazole CH11 proton and the Cl1, Table 7, thus forming a ^{2}D wavy sheet. The Ni1 molecular units in this sheet are arranged in rows. In each row the Ni1 coordination planes are arranged parallel to each other, but make an angle of 17.28° with the corresponding planes in the next neighboring row. Similarly, the Ni2 molecular units are joined together by CH···O hydrogen bonds between the oximate O4 and phenyl CH20 proton, as well as a weak noncovalent interaction between the CH27A proton of the methyl group adjacent to the hydrazone residue and the pyrazole C26 forming a chain of Ni2 molecular units propagating along the *b*-axis. In this chain, the Ni2 coordination plane makes an angle of 23.36° with the next coordination plane. Each Ni1 molecular unit in Ni1 sheet is connected to three Ni2 molecular units of different Ni2 chains by three noncovalent interactions namely: (i) CH13B···π (pyrazole) and (ii) CH14B···C20 and Cl1···H24, respectively. These interactions gives rise to multidimensional arrays of Ni2 chains enclosed between sheets of Ni molecular units.

Acknowledgement

Thanks are due to BMBF/Forschungszentrm, Jüelich, ÖA-IB/Wo WTZ for supporting this bilateral project.

Appendix A. Supplementary material

CCDC 640560, 640561, and 640562 contain the supplementary crystallographic data for [Ni(L-H)HPyr], [Ni(L-CH_3O)HPyr], and [Ni(L-Cl)HPyr]. These data can be obtained free of charge via http://www.ccdc.cam.ac.uk/conts/retrieving.html, or from the Cambridge Crystallographic Data Centre, 12 Union Road, Cambridge CB2 1EZ, UK; fax: (+44) 1223-336-033; or e-mail: deposit @ccdc.cam.ac.uk. Supplementary data associated with this article can be found, in the online version, at doi:10.1016/j.poly.2007.05.010.

References

[1] M.F. Iskander, L. El-Sayed, N.M.H. Salem, W. Haase, H.J. Lindner, S. Foro, Polyhedron 23 (2004) 23.
[2] M.F. Iskander, T.E. Khalil, W. Haase, R. Werner, I. Svoboda, H. Fuess, Polyhedron 20 (2001) 2787.
[3] M.F. Iskander, T.E. Khalil, R. Werner, W. Haase, I. Svoboda, H. Fuess, Polyhedron 19 (2000) 181.
[4] M.F. Iskander, T.E. Khalil, R. Werner, W. Haase, I. Svoboda, H. Fuess, Polyhedron 19 (2000) 949.
[5] E.W. Ainscough, A.M. Brodie, W.A. Denny, G.J. Finlay, S.A. Gothe, J.D. Ranford, J. Inorg. Biochem. 77 (1999) 125.
[6] L.L. Koh, O.L. Kon, K.W. Loh, Y.C. Long, J.D. Ranford, A.L.C. Tan, Y.Y. Tjan, J. Inorg. Biochem. 72 (1998) 155.
[7] E.W. Ainscough, A.M. Brodie, A.J. Dobbs, J.D. Ranford, J.M. Waters, Inorg. Chim. Acta 267 (1998) 27.
[8] T.B. Chaston, D.R. Richardson, J. Biol. Inorg. Chem. 8 (2003) 427.
[9] C.M. Armstrong, P.V. Bernhardt, P. Chin, D. Richardson, Eur. J. Inorg. Chem. (2001) 1145.
[10] P.V. Bernhardt, P. Chin, D. Richardson, J. Boil. Inorg. Chem. 6 (2001) 801.
[11] N.R. Sangeetha, S. Pal, S. Pal, Polyhedron 19 (2000) 2713.
[12] S. Pal, J. Pushparaju, N.R. Sengeetha, S. Pal, Trans. Met. Chem. 25 (2000) 529.
[13] N.R. Sengeetha, S. Pal, S. Pal, Polyhedron 19 (2000) 2713.
[14] N.R. Sengeetha, S. Pal, Polyhedron 19 (2000) 593.
[15] M.M. Mostafa, K.M. Ibrahim, M.N.H. Moussa, Trans. Met. Chem. 9 (1984) 243.
[16] S. Ghosh, T.K. Bandyopadhyay, Trans. Met. Chem. 10 (1985) 57.
[17] M.F. Iskander, L. El-Sayed, N.M.H. Salem, R. Werner, W. Haase, J. Coord. Chem. 56 (2003) 1075.
[18] N.M.H. Salem, L. El-Sayed, W. Haase, M.F. Iskander, J. Coord. Chem. 58 (2005) 1327.

[19] B. Barszcz, T. Glowiak, J. Jezierska, A. Tomkiewicz, Polyhedron 23 (2004) 1309.
[20] S. Das, S. Pal, J. Mol. Struct. 741 (2005) 183.
[21] A. Mukhopadhay, G. Padmaja, S. Pal, S. Pal, Inorg. Chem. Commun. 6 (2003) 381.
[22] S.A. Warda, C. Friebel, J. Sivy, G. Plesch, M. Blahova, Acta Crystallogr. C53 (1997) 50.
[23] S.A. Warda, C. Frieble, J. Sivy, G. Plesch, O. Svajlenova, Acta Crystallogr C52 (1996) 2763.
[24] V. Kettmann, E. Fresova, M. Blahova, J. Kratsmar-Smogrovic, Acta Crystallogr C49 (1993) 1932.
[25] Sheffield Chemputer, Isotope pattern. Available online at w.w.w.shef.ac.uk/chemistry/isotopes.html.
[26] A. Weiss, H. Witte, Magnetochemie, Verlag Chemie, Weinheim, 1973.
[27] W. Kaminsky, J.P. Jasinski, R. Woudenberg, K.I. Goldberg, D.X. West, J. Mol. Struct. 608 (2002) 135.
[28] E. Bermejo, A. Castineiras, D.X. West, Z. Naturforsch. B 56 (2001) 369.
[29] M. Maekawa, S. Kitagawa, Y. Nakao, S. Sakamoto, A. Yatani, W. Mori, S. Kashino, M. Munakata, Inorg. Chim. Acta 293 (1999) 20.
[30] R.J. Butcher, C.J. O'Connor, E. Sinn, Inorg. Chem. 18 (1979) 1913.
[31] Y. Song, X.-T. Chen, C.-G. Zheng, D.-R. Zhu, X.-Z. You, Trans. Met. Chem. 26 (2001) 247.
[32] A.B.P. Lever, Inorganic Electronic Spectroscopy, 2nd ed., Elsevier, Amsterdam, 1984.
[33] H.B. Gray, Electronic structures of square planar metal complexes, in: R.L. Carlin (Ed.), Transition Metal Chemistry, vol. 1, Marcel Dekker Inc., New York, 1965.
[34] L. Sacconi, Electronic structure and stereochemistry of nickel(II), in: R.L. Carlin (Ed.), Transition Metal Chemistry, vol. 4, Marcel Dekker Inc., New York, 1968.
[35] J.D. Martin, K.A. Abboud, K.-H. Dahmen, Inorg. Chem. 37 (1998) 5811.
[36] I.O. Fritsky, H. Kozlowski, E.V. Prisyazhnaya, Z. Rzaczynska, A. Karaczyn, T.Y. Sliva, T. Glowiak, J. Chem. Soc., Dalton Trans. (1998) 3629.
[37] T.Y. Sliva, A.M. Duda, T. Glowiak, I.O. Fritsky, V.M. Amirkhanov, A.A. Mokhir, H. Kozlowski, J. Chem. Soc., Dalton Trans. (1997) 273.
[38] M.J. Lacey, C.G. Macdonald, Chem. Commun. (1971) 1206.
[39] S. Seth, S. Chakraboty, Acta Crystallogr. C40 (1984) 1530.
[40] L.-H. Huo, Z.-Z. Lu, S. Gao, H. Zhao, Acta Crystallogr. E60 (2004) m1450.
[41] S. Gao, L.-H. Huo, H. Zhao, S.W. Ng, Acta Crystallogr. E60 (2004) m1750.
[42] S. Gao, L.-H. Huo, Z.-P. Deng, H. Zhao, Acta Crystallogr. E60 (2005) m152.
[43] G.V. Karunakar, N.R. Sangeetha, V. Susila, S. Pal, J. Coord. Chem. 50 (2000) 51.
[44] P. Domiano, A. Musatti, M. Nardelli, C. Pelizzi, J. Chem. Soc. Dalton (1975) 295.
[45] M.C. Etter, Acc. Chem. Res. 23 (1990) 120.
[46] C.B. Aakeroy, K.S. Seddon, Chem. Soc. Rev. 93 (1993) 397.
[47] Z.D. Tomic, S.B. Novakovic, S.D. Zaric, Eur. J. Inorg. Chem. (2004) 2215.
[48] Z.D. Tomic, V.M. Leovac, S.V. Pokorni, D. Zobel, S.D. Zaric, Eur. J. Inorg. Chem. (2003) 1222.
[49] C. Janiak, J. Chem. Soc., Dalton Trans. (2000) 3885.
[50] G.R. Desiraju, Acc. Chem. Res. 29 (1996) 441.
[51] G.R. Desiraju, Acc. Chem. Res. 24 (1991) 290.
[52] G.R. Desiraju, T. Steiner, The Weak Hydrogen Bonds in Structural Chemistry and Biology, Oxford University Press, 1999.
[53] M. Nishio, M. Hirota, Y. Umezawa, The CH/π Interaction, Evidence, Nature and Consequences, John Wiley and Sons Inc., New York, 1998.

2. Experimental

2.1. General

All procedures were performed under an atmosphere of dry, purified nitrogen using standard Schlenk techniques. Solvents were distilled and dried by standard methods [15]. Thiophene and 1-bromo-3-chloropropane were purchased from Across. *n*-Butyllithium (1.55 M solution in hexane) was purchased from Aldrich. Potassium diphenylphosphide (0.5 M solution in THF) and palladium(II) chloride were purchased from Fluka. Benzonitrile was purchased from Wardle Chemicals. $[PdCl_2(PhCN)_2]$ [16], and 2-(3-chloropropyl)thiophene [17,18] were prepared as reported. The IR Spectra were recorded, as KBr discs, on Nicolet Impact-400 FT-IR spectrometer. The NMR spectra were recorded on a Bruker DPX 300 MHz spectrometer using TMS as internal reference. The chemical shifts for the ^{31}P NMR spectra are relative to external H_3PO_4. Melting points were determined with Philip-Harris melting point apparatus and are uncorrected. Elemental analyses were performed by the Microanalytical Laboratories of AL al-Bayt University, Jordan.

2.2. Syntheses

2.2.1. Preparation of 2-[3-(diphenylphosphino)propyl]-thiophene (*P-S3*)

The compound was prepared following literature procedure [17,18] with modifications. A solution of 2-(3-chloropropyl)thiophene (8.0 g, 0.05 mol) in dry THF (50 mL) was introduced into a 250-mL three-necked round bottomed flask equipped with a nitrogen inlet, dropping funnel, and a condenser that is connected to an oil bubbler. A solution of potassium diphenylphosphide (100 mL of 0.5 M, 0.05 mol) was then slowly added at −45 °C. After the addition was complete, the cooling bath was removed and the reaction mixture was stirred for 2 h at room temperature. Solvent was completely removed under reduced pressure. The residue was dissolved in diethyl ether (100 mL), and the ether solution was washed with distilled water (2 × 100 mL). The ether layer was dried over anhydrous sodium sulfate over night. After filtration, ether was removed under reduced pressure, and the thick yellow residue was dissolved in methanol (50 mL). When the solution was stored at 0 °C a white precipitate was formed. The precipitate was filtered, washed three times with cold methanol, and dried under vacuum at room temperature. Yield: 14.3 g (92%). White powder; m.p. 65–67 °C. Selected IR bands (KBr pellet, cm^{-1}): 3071 (m), 3050 (m), 2931 (m), 2856 (m), 1120 (s) (P–Ph). ^1H NMR (300 MHz, $CDCl_3$): $\delta = 1.81$ (m, 2H, $-CH_2C\boldsymbol{H}_2CH_2P-$), 2.09 (m, 2H, $-C\boldsymbol{H}_2P-$), 2.94 (t, $J = 13.5$ Hz, 2H, $-C\boldsymbol{H}_2CH_2CH_2P-$), 6.75 (d, $J = 3.1$ Hz, $1H_{thiophene}$), 6.89 (t, $J = 4.2$ Hz, $1H_{thiophene}$), 7.10 (d, $J = 5.0$ Hz, $1H_{thiophene}$), 7.31–7.76 (m, 10H, H_{phenyl}). ^{13}C NMR (75 MHz, $CDCl_3$): δ: ($C_{aliphatic}$) 27.3 (d, $^2J_{C-P} = 11.5$ Hz, 1C), 28.0 (d, $^1J_{C-P} = 17.0$ Hz, 1C), 31.2 (d, $^3J_{C-P} = 13.5$ Hz, 1C); δ: ($C_{thiophene}$) 123.2 (s, 1C), 124.5 (s, 1C), 126.8 (s, 1C), 144.6 (s, 1C); δ: (C_{phenyl}) 128.5 (d, $^3J_{C-P} = 6.6$ Hz, 4C), 128.6 (s, 2C), 132.8 (d, $^2J_{C-P} = 18.3$ Hz, 4C), 138.6 (d, $^1J_{C-P} = 12.5$ Hz, 2C). $^{31}P\{^1H\}$ NMR (121 MHz, $CDCl_3$): $\delta = -12.25$.

2.2.2. Preparation of trans-[Pd(μ-Cl)Cl(P-S3)]$_2$ (*I*)

A sample of **P-S3** (0.31 g, 1.0 mmol) in dry benzene (20 mL) was slowly added to a filtered solution of $[PdCl_2(PhCN)_2]$ (0.40 g, 1.0 mmol) in dry benzene (30 mL). The solution was stirred for 1 h at room temperature. During that time, the solution changed color gradually from dark brown to orange. Solvent was removed under reduced pressure till a volume of about 10 mL. Upon addition of pet. ether (boiling range of 40–60 °C), an orange precipitate was separated, the product was recrystallized from CH_2Cl_2/pet. ether, washed with pet. ether and dried under vacuum at 50 °C. Yield: 0.48 g (92%). Orange solid; m.p. 225–227 (dec). Selected IR bands (KBr pellet, cm^{-1}): 3056 (m), 2936 (m), 2896 (m), 1102 (s) (P–Ph). ^1H NMR (300 MHz, $CDCl_3$): $\delta = 1.89$ (m, 4H, $-CH_2C\boldsymbol{H}_2CH_2P-$), 2.50 (m, 4H, $-C\boldsymbol{H}_2P-$), 2.87 (t, $J = 7.2$ Hz, 4H, $-C\boldsymbol{H}_2CH_2CH_2P-$), 6.69 (d, $J = 2.8$ Hz, $2H_{thiophene}$), 6.87 (dd, $J = 3.4$, 5.1 Hz, $2H_{thiophene}$), 7.07 (d, $J = 5.1$ Hz, $2H_{thiophene}$), 7.22–7.68 (m, 20H, H_{phenyl}). ^{13}C NMR (75 MHz, $CDCl_3$): δ: ($C_{aliphatic}$) 25.9 (s, 2C), 26.5 (d, $^1J_{C-P} = 35.9$ Hz, 2C), 30.5 (d, $^3J_{C-P} = 17.5$ Hz, 2C); δ: ($C_{thiophene}$) 123.5 (s, 2C), 124.9 (s, 2C), 126.9 (s, 2C), 143.1 (s, 2C); δ: (C_{phenyl}) 127.7 (s, 4C), 128.8 (d, $^3J_{C-P} = 11.9$ Hz, 8C), 131.4 (s, 4C), 133.3 (d, $^2J_{C-P} = 10.2$ Hz, 8C). $^{31}P\{^1H\}$ NMR (121 MHz, $CDCl_3$): $\delta = 31.81$. *Anal.* Calc. for $[C_{38}H_{38}Cl_4P_2Pd_2S_2]$ (975.34): C, 46.79; H, 3.93; S, 6.57. Found: C, 46.23; H, 3.66; S, 5.51%.

2.2.3. Preparation of trans-[PdCl$_2$(P-S3)$_2$] (*II*)

A filtered solution of $[PdCl_2(PhCN)_2]$ (0.40 g, 1.0 mmol) in dry benzene (30 mL) was slowly added to a sample of **P-S3** (0.78 g, 2.5 mmol) in dry benzene (20 mL). The solution was stirred for 1 h at room temperature. Solvent was removed under reduced pressure till a volume of about 10 mL. Upon addition of pet. ether (boiling range of 40–60 °C), a yellow precipitate was formed. The product was collected, recrystallized from CH_2Cl_2/pet. ether washed with pet. ether and dried under vacuum at 50 °C. Yield: 0.50 g (60%). Yellow solid; m.p. 143–144 °C. Selected IR bands (KBr pellet, cm^{-1}): 3081 (m), 3051 (m), 2919 (m), 1431 (s), 1105 (s) (P–Ph). ^1H NMR (300 MHz, $CDCl_3$): $\delta = 1.88$ (m, 4H, $-CH_2C\boldsymbol{H}_2CH_2P-$), 2.50 (m, 4H, $-C\boldsymbol{H}_2P-$), 2.87 (t, $J = 7.2$ Hz, 4H, $-C\boldsymbol{H}_2CH_2CH_2P-$), 6.68 (d, $J = 2.7$ Hz, $2H_{thiophene}$), 6.86 (dd, $J = 3.4$, 5.1 Hz, $2H_{thiophene}$), 7.07 (dd, $J = 1.1$, 5.1 Hz, $2H_{thiophene}$), 7.34–7.73 (m, 20H, H_{phenyl}). $^{13}P\{^1H\}$ NMR (121 MHz, $CDCl_3$): $\delta = 17.53$. *Anal.* Calc. for $[C_{38}H_{38}Cl_2P_2PdS_2]$ (798.04): C, 57.19; H, 4.80; S, 8.04. Found: C, 57.21; H, 4.79; S, 8.08%.

2.3. Reaction of compound *I* with *P-S3*

To an orange solution of **I** (0.40 g, 0.41 mmol) in dry $CHCl_3$ (30 mL) was slowly added a solution of **P-S3** (0.31 g, 1.0 mmol) in dry $CHCl_3$ (20 mL). The solution was stirred for 2 h at room temperature. During that time, the solution changed color gradually from orange to yellow. Solvent was removed under reduced pressure till a volume of about 10 mL. Upon addition of pet. ether (boiling range of 40–60 °C), a precipitate was separated, washed with pet. ether and dried under vacuum at 50 °C. The product was characterized by its melting point and ^{1}H NMR and found to be identical to compound **II**.

2.4. Crystal structure determination of *trans*-[Pd(μ-Cl)Cl(P-S3)]$_2$ (*I*)

A suitable single crystal (yellow platelets) of compound **I** was selected for collecting X-ray data. All measurements were made at 293(2) K using a Bruker/Siemens SMART APEX instrument (Mo Kα radiation, $\lambda = 0.71073$ Å) equipped with a Cryocool NeverIce low temperature device. Data were measured using omega scans of 0.3° per frame for 5 s, and a full sphere of data was collected. A total of 2400 frames were collected with a final resolution of 0.83 Å. Cell parameters were retrieved using SMART [19] software and refined using SAINTPLUS [20] on all observed reflections. Data reduction and correction for Lp and decay were performed using the SAINTPLUS software. Absorption corrections were applied using SADABS [21]. The structure was solved by direct methods and refined by least squares method on F^2 using the SHELXTL program package [22]. The structure was solved in the space group $P\bar{1}$ (#2) by analysis of systematic absences. All non-hydrogen atoms were refined anisotropically. The thiophene group was rotationally disordered and refined in two positions with refined occupancies of 49:51%. Bond lengths and thermal parameters were loosely restrained. No decomposition was observed during data collection. Details of the data collection and refinement are given in Table 1. Further details are provided in the Supporting Information. Hydrogen atoms were placed geometrically and refined with a riding model, with U_{iso} constrained to be $1.2U_{eq}$ of the carrier atom.

2.5. Crystal structure determination of *trans*-[PdCl$_2$(P-S3)$_2$] (*II*)

A suitable crystal (yellow parallelopiped) of compound **II** was selected, attached to a glass fiber and data were collected at 293(2) K using a syntax diffractometer "upgraded to Bruker's P4 specifications" instrument (Mo Kα radiation, $\lambda = 0.71073$ Å) equipped with a Cryocool NeverIce low temperature device. Collection and treatment of data were done similar to compound **I** with the exception that cell parameters were retrieved and refined using XSCANS [23] software on all observed reflections. Data reduction and correction for Lp and decay were performed using the SHELXTL [22] software. Absorption corrections were applied using psi scans. Details of the data collection and refinement are given in Table 1. Further details are provided in the Supporting Information.

Table 1
Crystal data for complexes *trans*-[Pd(μ-Cl)Cl(P-S3)]$_2$ (**I**) and *trans*-[PdCl$_2$(P-S3)$_2$] (**II**)

Parameter	[Pd(μ-Cl)Cl(P-S3)]$_2$ (**I**)	[PdCl$_2$(P-S3)$_2$] (**II**)
Chemical formula	$C_{38}H_{38}Cl_4P_2Pd_2S_2$	$C_{38}H_{38}Cl_2P_2PdS_2$
Formula weight	975.34	798.04
Temperature (K)	293(2)	293(2)
Wavelength (Å)	0.71073	0.71073
Crystal system	triclinic	triclinic
Space group	$P\bar{1}$	$P\bar{1}$
Unit cell dimensions		
a (Å)	9.3962(19)	7.9828(10)
b (Å)	9.954(2)	10.699(2)
c (Å)	11.100(2)	10.9374(19)
α (°)	84.62(3)	91.761(17)
β (°)	77.96(3)	105.217(5)
γ (°)	73.51(3)	96.463(14)
V (Å^3)	972.9(4)	893.9(3)
Z	1	1
D_{calc} (Mg/m^3)	1.665	1.483
Absorption coefficient (mm^{-1})	1.416	0.902
F(000)	488	408
Crystal dimensions (mm)	0.40 × 0.20 × 0.05	0.40 × 0.30 × 0.15
θ Range for data collection (°)	1.88–25.25	1.92–25.50
Index ranges	$-11 \leqslant h \leqslant 11$, $-11 \leqslant k \leqslant 11$, $-3 \leqslant l \leqslant 13$	$-9 \leqslant h \leqslant 1$, $-12 \leqslant k \leqslant 12$, $-13 \leqslant l \leqslant 13$
Reflections collected	14 345	4081
Independent reflections [R_{int}]	3527 [0.0250]	3293 [0.0000]
Data/restraints/parameters	3527/10/224	3318/0/205
Goodness-of-fit on F^2	1.046	1.068
Final R indices [$I > 2\sigma(I)$]	$R_1^a = 0.0268$, $wR_2^b = 0.0676$	$R_1 = 0.0337$, $wR_2 = 0.0878$
R indices (all data)	$R_1 = 0.0301$, $wR_2 = 0.0699$	$R_1 = 0.0393$, $wR_2 = 0.0915$
Largest difference in peak and hole (e Å^{-3})	0.543 and −0.468	0.709 and −0.475

[a] $R_1 = \sum\{|F_o| - |F_c|\}/\sum|F_o|$.
[b] $wR_2 = \{\sum[w(F_o^2 - F_c^2)^2]/\sum[w(F_o^2)^2]\}^{0.5}$.

3. Results and discussion

3.1. Syntheses

The phosphorus–sulfur ligand, 2-[3-(diphenylphosphino)propyl]thiophene (**P-S3**), was prepared *via* reaction of 2-(3-chloropropyl)thiophene [17,18] with potassium diphenylphosphide in dry THF. The product was collected and recrystallized several times from methanol. It was fully characterized by its IR, ^{1}H, ^{13}C and ^{31}P NMR spectroscopy. The ^{1}H NMR spectrum of **P-S3** shows, in addition

to the signals due to phenyl protons, two multiplets centered at $\delta = 1.81$ (–$CH_2C\boldsymbol{H}_2CH_2P$–) and 2.09 (–$C\boldsymbol{H}_2P$–), and a triplet centered at $\delta = 2.94$ (–$C\boldsymbol{H}_2CH_2CH_2P$–). The three protons of thiophene appear as two doublets centered at $\delta = 6.75$, 7.10 and a triplet centered at $\delta = 6.89$. The ^{13}C NMR spectrum of **P-S3** shows, δ: ($C_{aliphatic}$) at 27.3 (d, $^2J_{C-P} = 11.5$ Hz, 1C), 28.0 (d, $^1J_{C-P} = 17.0$ Hz, 1C), and 31.2 (d, $^3J_{C-P} = 13.5$ Hz, 1C); δ: ($C_{thiophene}$) at 123.2 (s, 1C), 124.5 (s, 1C), 126.8 (s, 1C), and 144.6 (s, 1C); δ: (C_{phenyl}) at 128.5 (d, $^3J_{C-P} = 6.6$ Hz, 4C), 128.6 (s, 2C), 132.8 (d, $^2J_{C-P} = 18.3$ Hz, 4C), and 138.6 (d, $^1J_{C-P} = 12.5$ Hz, 2C). The above ^{13}C NMR assignment was confirmed by running Dept-135 experiment that shows, disappearance of the two quaternary carbons at $\delta = 138.6$, and 144.6. The ^{31}P NMR spectrum shows one signal at $\delta = -12.25$.

Reaction of **P-S3** with equimolar amount of $[PdCl_2(PhCN)_2]$ afforded the binuclear complex *trans*-$[Pd(\mu\text{-}Cl)Cl(P\text{-}S3)]_2$ (**I**). Complex **I** is soluble in acetone, chloroform, and dichloromethane, and insoluble in diethyl ether, dioxane, and hexane. Elemental analysis of **I** for C, H, and S is consistent with the above formulation. The ^1H NMR spectrum of **I** shows, in addition to the phenyl proton signals, two multiplets centered at $\delta = 1.89$ (–$CH_2C\boldsymbol{H}_2CH_2P$–) and 2.50 (–$C\boldsymbol{H}_2P$–), and a triplet centered at $\delta = 2.87$ (–$C\boldsymbol{H}_2CH_2CH_2P$–). The signals of the thiophene protons appear as doublets centered at $\delta = 6.69$, and $\delta = 7.07$, and a doublet of doublet centered at $\delta = 6.87$. Compared with the free ligand, the ^{31}P NMR signal of complex **I** is downfield shifted to $\delta = 31.81$. The ^{13}C NMR spectrum of **I** shows, δ: ($C_{aliphatic}$) at 25.9 (s, 2C), 26.5 (d, $^1J_{C-P} = 35.9$ Hz, 2C), and 30.5 (d, $^3J_{C-P} = 17.5$ Hz, 2C); δ: ($C_{thiophene}$) at 123.5 (s, 2C), 124.9 (s, 2C), 126.9 (s, 2C), and 143.1 (s, 2C); δ: (C_{phenyl}) at 127.7 (s, 4C), 128.8 (d, $^3J_{C-P} = 11.9$ Hz, 8C), 131.4 (s, 4C), and 133.3 (d, $^2J_{C-P} = 10.2$ Hz, 8C). Comparing the ^{13}C NMR spectrum of **I** with that for the **P-S3** ligand shows no difference on the chemical shift of the thiophene ring carbons, which is consistent with the ligand being coordinated through the phosphorus atom only. The ^{13}C NMR signal for $\boldsymbol{C}_{phenyl}$–P was shifted upfield upon coordination with the palladium metal to 127.7 ppm and appeared as a singlet. Similarly, the signal for $\boldsymbol{C}H_2$–P was shifted upfield upon coordination with the palladium metal to 26.5 ppm with an increase in J value ($J = 35.9$ Hz). The bidentate mode of bonding for **P-S3** seems to be unfavorable with respect to the formation of the 7-membered chelate ring and the poor donor ability of thiophene sulfur. In view of the above data the complex is believed to have a dimeric structure which was confirmed by single X-ray structure analysis (Fig. 1).

As expected, reaction of the chlorobridged palladium complex **I** with triphenylphosphine in a 1:2 molar ratio afforded the monomeric complex, $[PdCl_2(P\text{-}S3)(PPh_3)]$. This complex was characterized by its ^1H NMR spectrum which shows two multiplets centered at $\delta = 1.89$ (–$CH_2C\boldsymbol{H}_2CH_2P$–), 2.52 (–$C\boldsymbol{H}_2P$–) and a triplet centered at $\delta = 2.85$ (–$C\boldsymbol{H}_2CH_2CH_2P$–). The thiophene protons show

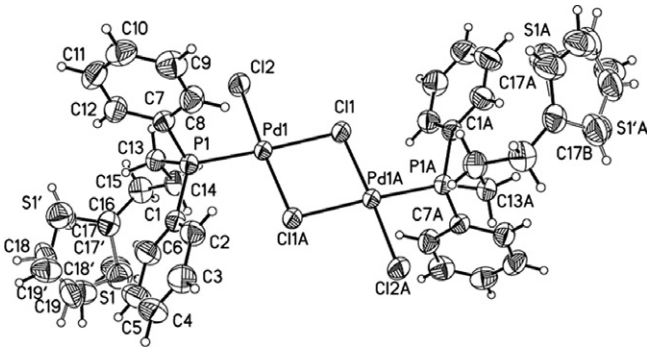


Fig. 1. ORTEP plot of the molecular structure of compound **I**. Showing the rotationally disordered of thiophene group. Thermal ellipsoids are drawn at 50% probability level.

two doublets centered at $\delta = 6.67$, 7.06 and a triplet centered at $\delta = 6.85$. The phenyl protons appear as a multiplet at $\delta = 7.57$–7.73. Comparing the ^1H NMR spectra of **I** and $[PdCl_2(P\text{-}S3)(PPh_3)]$ shows no appreciable differences on the chemical shift of aliphatic and thiophene protons.

In a similar way, reaction of complex **I** with **P-S3** in a 1:2 molar ratio afforded the monomeric complex, $[PdCl_2(P\text{-}S3)_2]$ (**II**), which is characterized by elemental analysis and NMR spectroscopy. The ^1H NMR spectrum of **II** shows, in addition to the phenyl proton signals, a multiplet centered at $\delta = 1.88$ (–$CH_2C\boldsymbol{H}_2CH_2P$–), $\delta = 2.50$ (–$C\boldsymbol{H}_2P$–), and a triplet centered at $\delta = 2.87$ (–$C\boldsymbol{H}_2CH_2CH_2P$–). The signals of the thiophene protons appear as a doublet centered at $\delta = 6.68$ and two (doublet of doublet) centered at $\delta = 6.86$ ($J = 3.4$, 5.1 Hz) and $\delta = 7.07$ ($J = 1.1$, 5.1 Hz). Comparing the ^1H NMR spectrum of **I** and **II** shows no appreciable differences in both spectra, indicating similar mode of bonding for the ligand in both complexes. The ^{31}P NMR spectrum of **II** shows one signal at $\delta = 17.53$. The greater downfield shift of the ^{31}P peak in complex **I** relative to complex **II** is attributed to the increase in Pd–P bond strength, that is *trans* to bridging Cl ligand.

Complex **II** was also prepared by the direct reaction of $[PdCl_2(PhCN)_2]$ with **P-S3** in a 1:2.5 molar ratio. The isolated yellow compound was characterized by ^1H and ^{13}C NMR and found to be identical with an authentic sample of complex **II** that has been prepared previously by the reaction of complex **I** with **P-S3**.

3.2. The molecular structure of $[Pd(\mu\text{-}Cl)Cl(P\text{-}S3)]_2$ (**I**)

Yellow platelet-like crystals of **I** were grown from double layer system of CH_2Cl_2/pet. ether. The solid state structure was established by X-ray crystallography (Fig. 1). Selected bond lengths and angles are collected in Table 2. The two **P-S3** ligands bind to the Pd metal through the phosphorus atoms in a *trans* position. The two chlorobridged ligands form with the palladium atoms a four-membered ring with Cl–Pd–Cl angles of 85.24(3)°, and Pd–Cl–Pd angles of 94.76(3)°. The Pd–Cl bond dis-

Table 2
Selected bond distances (Å) and angles (°) for *trans*-[Pd(μ-Cl)Cl (P-S3)]$_2$

Bond distances (Å)		Bond angles (°)	
Pd(1)–P(1)	2.2239(11)	P(1)–Pd(1)–Cl(2)	86.21(4)
Pd(1)–Cl(2)	2.2747(11)	P(1)–Pd(1)–Cl(1A)	96.89(3)
Pd(1)–Cl(1A)	2.3081(11)	Cl(2)–Pd(1)–Cl(1A)	176.89(3)
Pd(1)–Cl(1)	2.4156(12)	P(1)–Pd(1)–Cl(1)	177.44(2)
Cl(1)–Pd(1A)	2.3080(11)	Cl(2)–Pd(1)–Cl(1)	91.67(4)
P(1)–C(7)	1.812(3)	Cl(1A)–Pd(1)–Cl(1)	85.24(3)
P(1)–C(1)	1.818(3)	Pd(1A)–Cl(1)–Pd(1)	94.76(3)
P(1)–C(13)	1.823(3)	C(7)–P(1)–C(1)	104.28(12)

tance of the terminal chloride is shorter than that of the bridging chloride. It is interesting to note that, the two Pd^1–Cl_{bridge} (Fig. 1) bond distances are different; the Pd^1–Cl_{bridge} *trans* to terminal chloride is shorter than the one *trans* to the P-atom. This is consistent with the higher *trans* influence of phosphine ligand compared with Cl. The thiophene ring was rotationally disordered and refined in two positions with refined occupancies of 50% (Fig. 2).

3.3. The molecular structure of [$PdCl_2$(P-S3)$_2$] (**II**)

Yellow crystals of complex **II** were grown by slow evaporation of CH_2Cl_2/pet. ether solution at room temperature. The solid state structure of **II** is shown in Fig. 3, and selected bond length and angles are collected in Table 3. As indicated in Fig. 3, the two **P-S3** ligands bind to the Pd metal atom through their phosphorus atoms in *trans* positions. The palladium atom is in the center of the symmetry and it displays square planar stereochemistry. The Pd–P distance in **II** is longer than that in **I**, which is consistent with the competition for π-bonding between the *trans* phosphorus atoms in **II**.

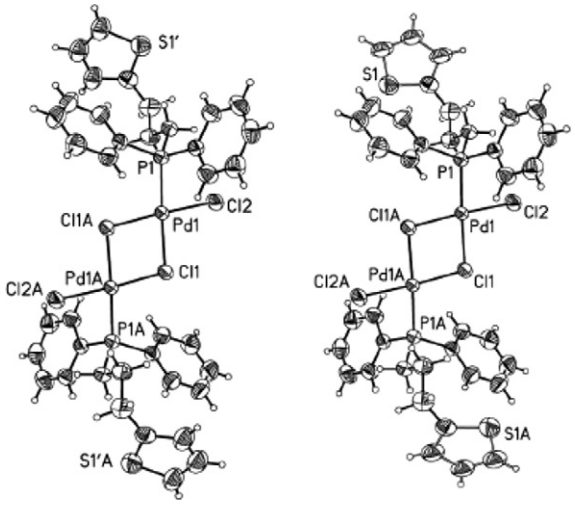


Fig. 2. X-ray crystal structure of the complex **I** showing the rotational disorder of the thiophene ring.

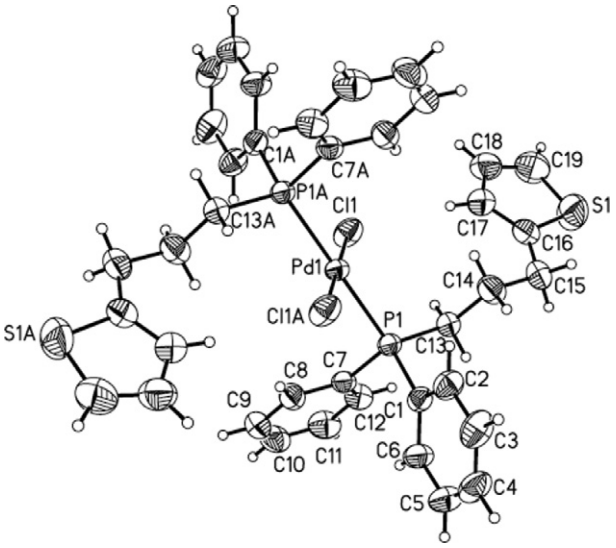


Fig. 3. ORTEP plot of the molecular structure of compound **II** showing the atom labeling scheme. Thermal ellipsoids are drawn at the 50% probability level.

Table 3
Selected bond distances (Å) and angles (°) for the complex *trans*-[$PdCl_2$(P-S3)$_2$] (**II**)

Bond distances (Å)		Bond angles (°)	
P(1)–Pd(1)	2.3356(8)	Cl(1A)–Pd(1)–Cl(1)	180.00(4)
Cl(1)–Pd(1)	2.2952(9)	Cl(1)–Pd(1)–P(1)	86.58(3)
C(1)–P(1)	1.826(3)	Cl(1A)–Pd(1)–P(1)	93.42(3)
C(7)–P(1)	1.819(3)	C(1)–P(1)–Pd(1)	120.76(9)
C(13)–P(1)	1.836(3)	C(7)–P(1)–Pd(1)	106.54(9)
		C(13)–P(1)–Pd(1)	115.07(10)
		C(1)–P(1)–C(7)	104.14(13)
		C(1)–P(1)–C(13)	102.36(14)
		C(7)–P(1)–C(13)	106.79(13)

Acknowledgements

We thank Prof. B. Twamley, University of Idaho for the X-ray structural analysis. We also thank Mr. M.H. Al-Huniti, University of Jordan for obtaining the ^{31}P NMR spectra.

Appendix A. Supplementary material

CCDC 611542 and 632706 contain the supplementary crystallographic data for **I** and **II**. These data can be obtained free of charge via http://www.ccdc.cam.ac.uk/conts/retrieving.html, or from the Cambridge Crystallographic Data Centre, 12 Union Road, Cambridge CB2 1EZ, UK; fax: (+44) 1223-336-033; or e-mail: deposit @ccdc.cam.ac.uk. Supplementary data associated with this article can be found, in the online version, at doi:10.1016/j.poly.2007.05.011.

References

[1] P. Braunstein, F. Naud, Angew. Chem. Int. Ed. 40 (2001) 680.
[2] J.R. Puddephatt, Chem. Soc. Rev. (1983) 99.

[3] J. Holz, R. Kadyrov, S. Borns, D. Heller, A. Borner, J. Organomet. Chem. 603 (2000) 61.
[4] E. Lindner, M. Schmid, P. Wegner, C. Nachtigal, M. Steimann, R. Fawzi, Inorg. Chim. Acta 296 (1999) 103.
[5] E. Lindner, S. Pautz, R. Fawzi, M. Steimann, Organometallics 17 (1998) 3006.
[6] A.M. Saleem, H.A. Hodali, Inorg. Chim. Acta 174 (1990) 223.
[7] D.A. Evans, K.R. Campos, J.S. Tedraw, F.E. Michael, M.R. Gagne, J. Am. Chem. Soc. 122 (2000) 7905.
[8] J.R. Dilworth, N. Wheatley, Coord. Chem. Rev. 199 (2000) 89.
[9] G.K. Anderson, R. Kumar, J. Organomet. Chem. 342 (1988) 263.
[10] A.R. Sanger, Can. J. Chem. 61 (1983) 2214.
[11] E.M. Alshami, A.S. Abu-Surrah, M. Klinga, H.A. Hodali, Z. Anorg. Allg. Chem. 628 (2002) 1433.
[12] A.S. Abu-Surrah, K. Lappalainen, T. Repo, M. Klinga, M. Leskelä, H.A. Hodali, Polyhedron 19 (2000) 1601.
[13] A.S. Abu-Surrah, K. Lappalainen, M. Klinga, M. Leskelä, H.A. Hodali, B. Rieger, Acta Crystallogr. C55 (1999) 188.
[14] A.S. Abu-Surrah, K. Lappalainen, M. Kettunen, T. Repo, M. Leskelä, H.A. Hodali, B. Rieger, Macromol. Chem. Phys. 202 (2001) 599.
[15] D.D. Perrin, W. Armarego, D.R. Perrin, Purification of Laboratory Chemicals, 2nd ed., Pergamon Press, Oxford, 1981, p. 74.
[16] G.K. Anderson, M. Lin, Inorg. Synth. 28 (1990) 60.
[17] M. Alvarez, N. Lugan, B. Donnadieu, R. Mathieu, Organometallics 14 (1995) 365.
[18] K.A. Salmeia, H.A. Hodali, Synth. React. Inorg. Met-Org.Nano-Met. Chem. 36 (2006) 535.
[19] SMART, v.5.630, Madison, WI, 2001.
[20] SAINTPLUS, v. 7.23a, Data Reduction and Correction Program, Madison, WI, 2004.
[21] SADABS, v. 2004/1, An Empirical Absorption Correction Program, Madison, WI, 2004.
[22] G.M. Sheldrick, SHELXTL: (XCIF, XL, XP, XPREP, XS) v. 6.14, Structure Determination Software Suite, Madison, WI, 2004.
[23] XSCANS, Version 2.00, Madison, WI, 1993.

In particular, it was shown that 4-picoline (4-Mepy) formed isostructural complexes with iron and cobalt phthalocyanines, in which the central M is biaxially ligated by 4-Mepy, and the compounds crystallized with the composition $[MPc(4\text{-}Mepy)_2]\cdot 2(4\text{-}Mepy)$ [18]. For these reasons, we expected that the beryllium, magnesium and zinc phthalocyanines, when recrystallized in 4-Mepy, will show significant individuality in features of the eventually formed crystalline complexes, in particular for the coordination geometry of the central metal. Additionally, all of the new metallophthalocyanine complexes are potentially interesting colorants and materials for modern industry [19].

2. Experimental

2.1. Synthesis

Firstly, it should be stressed here that an attempt was made to perform the reactions of BePc as well as MgPc and ZnPc with 4-Mepy in water-free conditions.

The BePc sample used in the synthesis was obtained as described elsewhere [3]. The magnesium phthalocyanine (90% dye content) and zinc phthalocyanine (97% dye content) as well as 4-picoline (bp 145 °C) were purchased from Sigma–Aldrich Co. Before use, the magnesium and zinc phthalocyanines were zone refined. The transformative recrystallization processes of the BePc, MgPc and ZnPc samples with 4-picoline were performed as follows. A sample of one of the selected M(II)Pc's was pressed into a pellet, about 0.5 g in mass. The pellet was inserted in a glass ampoule and covered with c.a. 8 mL 4-picoline. The sample was then degassed and sealed off. Next, the suspension was thermally processed over the several days to ensure the completeness of the transformative process as well as effective crystallization. Next the crystalline product was immediately filtered after opening the ampoule. The best single crystals of the respective compounds, [BePc(4-Mepy)]-(4-Mepy) – (**I**), $MgPc(4\text{-}Mepy)_2$ – (**II**) and ZnPc(4-Mepy) – (**III**), were obtained by prolonged heating of the suspension of the beryllium phthalocyanine at 80 °C, the magnesium phthalocyanine at 120 °C and the zinc phthalocyanine at 160 °C. Routinely the crystalline products (**I**, **II** and **III**) were checked by X-ray powder diffraction and energy dispersive spectroscopy for their uniformity and composition. Elemental *Anal.* Calc. for $C_{44}H_{30}N_{10}Be$ (**I**): Be, 1.27; C, 74.67; N, 19.79, H, 4.27. Found: Be, 1.25; C, 74.72; N, 19.73; H, 4.30%. Elemental *Anal.* Calc. for $C_{44}H_{30}N_{10}Mg$ (**II**): Mg, 3.36; C, 73.09; N, 19.37; H, 4.18. Found: Mg, 3.30; C, 73.27; N, 19.29; H, 4.09%. Elemental *Anal.* Calc. for $C_{38}H_{23}N_9Zn$ (**III**): Zn, 9.74; C, 68.02; N, 18.79; H, 3.46. Found: Zn, 9.60; C, 68.12; N, 18.87; H, 3.40%.

2.2. X-ray single crystal diffraction

Single crystals of **I**, **II** and **III** were used for data collection on a four-circle KUMA KM4 diffractometer equipped with a two dimensional CCD area detector. Graphite monochromatized Mo Kα radiation ($\lambda = 0.71073$ Å) and the ω-scan technique ($\Delta\omega = 1°$) were used for data collection. Data collection and reduction along with absorption correction were performed using the CRYSALIS software package [20].

The structures were solved by direct methods using SHELXS-97, revealing positions of almost all the non-hydrogen atoms. The remaining atoms were located from subsequent difference Fourier syntheses. The structures were refined using SHELXL-97 [21] with anisotropic thermal displacement parameters. Hydrogen atoms were located from the difference Fourier maps, but in the final refinement the positions of all hydrogen atoms were constrained. Details of the data collection parameters, crystallographic data and final agreement parameters are collected in Table 1. Selected geometrical parameters are listed in Table 2.

2.3. Thermal measurements

The thermogravimetric measurements (TG) and differential thermal analyses (DTA) were carried out on a Linseis L-81 thermobalance with Pt crucibles. The initial sample masses were about 15 mg. Powder Al_2O_3 was used as a reference. The measurements of the sample were performed under static air and recorded at the heating rate of 5 °C min^{-1}. Upper temperature limits were introduced to prevent eventual contamination of the apparatus, as indicated by our previous experiences. The observed weight loss is ~26.5%, 25.5% and 13.9% for compounds **I**, **II** and **III**, respectively. The respective values calculated for these compounds are 26.30%, 25.74% and 13.87%.

2.4. X-ray powder diffraction measurement

The rest of the sample left after thermogravimetric analyses was measured on a STOE powder diffractometer equipped with a linear PSD detector [22] using Cu Kα1 radiation ($\lambda = 1.54060$ Å) at room temperature.

3. Results and discussion

3.1. Synthesis: equilibrium in solution

The procedure described in Section 2.1 gave for each complex (**I**, **II** and **III**) well developed crystals suitable for X-ray analysis, showing the typical red-violet colour for the phthalocyanines. However, we want here to add some observation registered during the thermal processing of the ampoule with the beryllium phthalocyanine in 4-picoline suspension. Namely, it occurs that by heating the ampoule resting in the oven, the liquid seen over the sedimented solid species is practically non-transparent, as could be expected, but it was so only till up ca. 100 °C. With further temperature increase, being however still

Table 1
Crystallographic data for **I**, **II** and **III**

Formula	$C_{44}H_{30}N_{10}Be$	$C_{44}H_{30}N_{10}Mg$	$C_{38}H_{23}N_9Zn$
Molecular weight	707.79	723.09	671.02
Temperature (K)	295(2)	295(2)	295(2)
Crystal system	triclinic	monoclinic	triclinic
Space group	$P\bar{1}$ (no. 2)	$P2_1/c$ (no. 14)	$P\bar{1}$ (no. 2)
a (Å)	12.387(2)	11.736(2)	9.626(2)
b (Å)	14.205(3)	18.249(3)	13.167(2)
c (Å)	23.347(4)	8.693(2)	13.966(3)
α (°)	106.64(2)		105.67(1)
β (°)	96.79(2)	105.04(2)	105.87(1)
γ (°)	102.94(2)		109.64(1)
V (Å^3)	3762.2(13)	1798.0(6)	1470.0(5)
Z	4	2	2
D_{obs} (Mg m^{-3})	1.25	1.33	1.51
D_{calc} (Mg m^{-3})	1.250	1.336	1.516
μ (mm^{-1})	0.077	0.099	0.883
Crystal size (mm^3)	$0.24 \times 0.22 \times 0.18$	$0.22 \times 0.15 \times 0.11$	$0.28 \times 0.22 \times 0.21$
Total/unique/observed reflections [R_{int}]	32671/14758/7432 [0.0872]	9223/4096/2788 [0.0385]	15939/6979/5817 [0.0190]
$R[F^2 > 2\sigma(F^2)]$[a]	0.0785	0.0657	0.0311
$wR[F^2$ all reflections][b]	0.1294	0.1459	0.0804
S	1.001	1.012	1.001
Residual electron density, $\Delta\rho_{max}$, $\Delta\rho_{min}$ (e Å^{-3})	+0.282, −0.200	+0.214, −0.372	+0.302, −0.467

[a] $R = \sum ||F_o| - |F_c|| / \sum F_o$.
[b] $wR = \{\sum[w(F_o^2 - F_c^2)^2] / \sum wF_o^4\}^{1/2}$; $w^{-1} = \sigma^2(F_o^2) + (aP)^2$ where $P = (F_o^2 + 2F_c^2)/3$. The a parameter is 0.015 for **I**, 0.064 for **II**, 0.0488 for **III**.

below the boiling point of the 4-picoline, it becomes markedly brilliant and eye transparent. This phenomenon is fully reversible if subsequently the temperature is lowered, and is undoubtedly connected with the releasing and, respectively, binding of the 4-picoline molecules by beryllium ions of the BePc molecules. The observed strong light absorption changes are evidently correlated with the appropriate TG plot as shown in Fig. 1. The crystals of all compounds have been obtained in water-free conditions, since, especially for Be and Mg complexes, the crystals in the 4-Mepy solution under conditions of moist atmosphere transform into a polycrystalline form after several days. During this process the crystals of BePc-(4-Mepy) · 4-Mepy (**I**), as well as the crystals of MgPc-(4-Mepy)$_2$ (**II**), interact with water molecules and convert into aqua(phthalocyaninato) complexes according to the equation illustrated in Scheme 1. The speed of the conversion takes place several times quicker in a solution of non-purified 4-Mepy.

Studies of the aqua complexes formed during the transformations of complexes **I** and **II** in the 4-Mepy/H_2O solution are still under investigation.

Table 2
Selected bond lengths (Å) and angles (°)

BePc(4-Mepy) · 4-Mepy (**I**)	
Be1–N1a	1.878(5)
Be1–N3a	1.899(5)
Be1–N5a	1.935(5)
Be1–N7a	1.943(5)
Be1–N9a	1.839(4)
N1a–Be1–N3a	89.8(2)
N3a–Be1–N5a	89.4(2)
N5a–Be1–N7a	89.1(2)
N7a–Be1–N1a	89.0(2)
N1a–Be1–N9a	99.8(2)
N3a–Be1–N9a	100.1(2)
N5a–Be1–N9a	98.5(2)
N7a–Be1–N9a	97.9(2)
Be2–N1b	1.839(4)
Be2–N3b	1.891(5)
Be2–N5b	1.915(5)
Be2–N7b	1.925(5)
Be2–N9b	1.830(4)
N1b–Be1–N3b	89.4(2)
N3b–Be1–N5b	88.1(2)
N5b–Be1–N7b	87.9(2)
N7b–Be1–N1b	88.2(2)
N1b–Be1–N9b	98.5(2)
N3b–Be1–N9b	100.2(2)
N5b–Be1–N9b	100.7(2)
N7b–Be1–N9b	99.1(2)
MgPc(4-Mepy)$_2$ (**II**)	
Mg–N1	2.009(2)
Mg–N3	2.005(2)
Mg–N5	2.412(2)
N1–Mg–N3	89.57(8)
N1–Mg–N5	90.07(8)
N1–Mg–N3^i	90.43(8)
Symmetry code: (i) $1-x, -y, 1-z$	
ZnPc(4-Mepy) (**III**)	
Zn–N1	2.020(2)
Zn–N3	2.021(2)
Zn–N5	2.006(2)
Zn–N7	2.034(2)
Zn–N9	2.166(2)
N1–Zn–N3	89.32(6)
N1–Zn–N7	87.13(5)
N3–Zn–N5	87.32(5)
N5–Zn–N7	89.28(5)
N1–Zn–N9	100.02(5)
N3–Zn–N9	106.84(6)
N5–Zn–N9	99.84(5)
N7–Zn–N9	93.259(6)

3.2. Thermal measurements and analysis

The thermogravimetric analyses (TG) together with the differential thermal analyses (DTA) of the solid state samples of compounds **I**, **II** and **III** are shown in Fig. 1a, b and c, respectively. For a better comparison, the most characteristic data resulting from the TG and DTA plots and XRD powder measurements of the residues left are collected in Table 3.

As can be seen from Fig. 1a, compound **I** losses the solvated as well as coordinated 4-Mepy molecules at the same

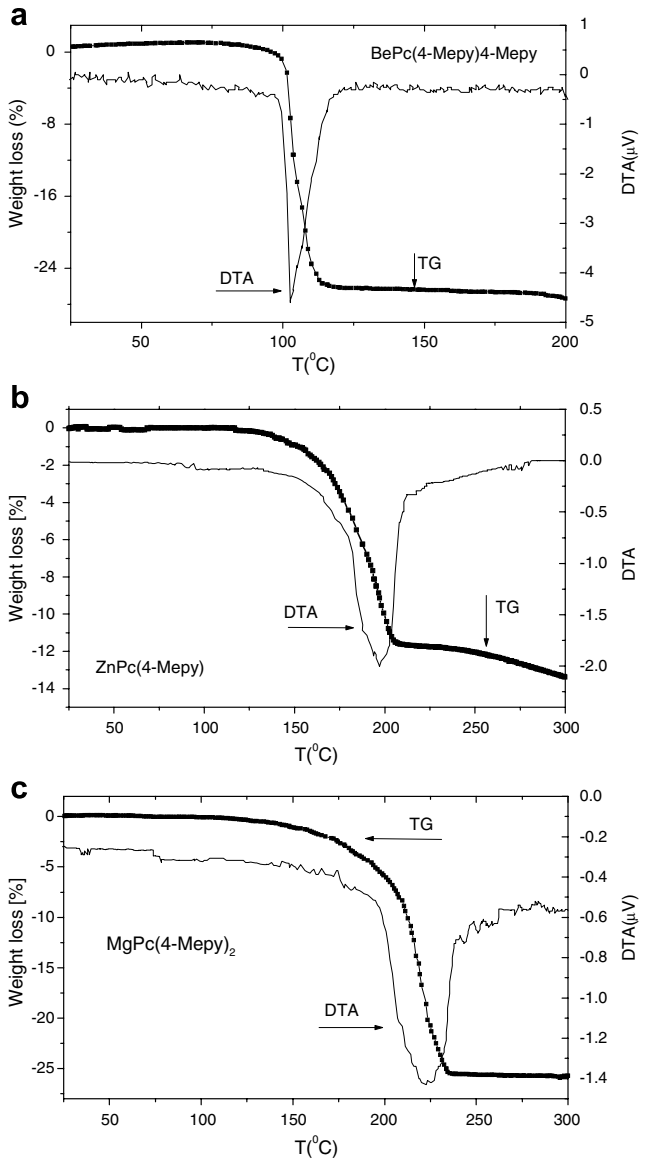


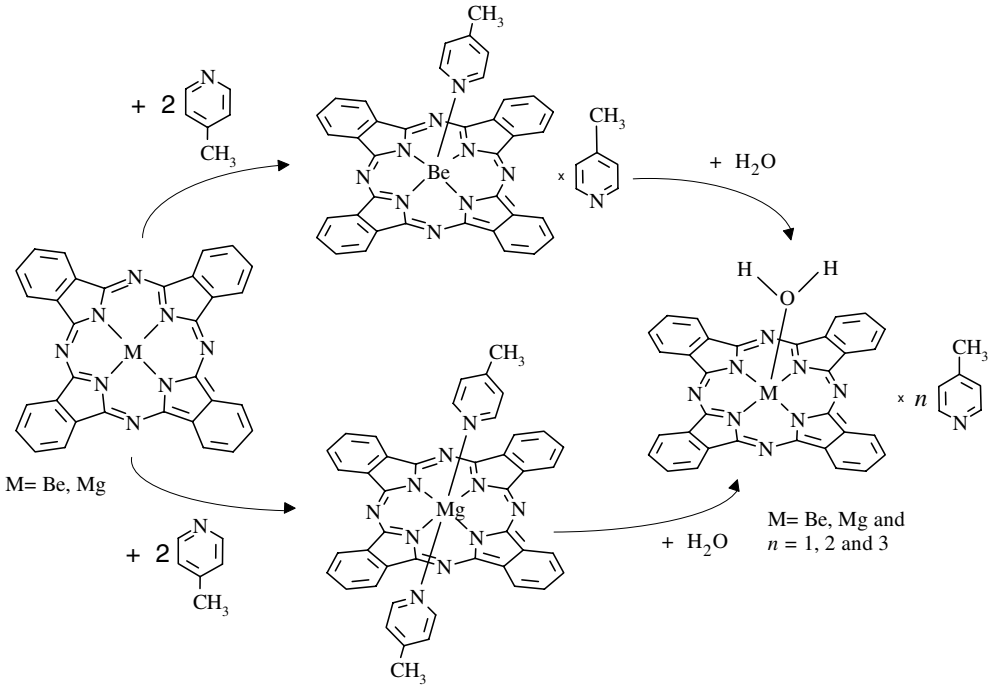
Fig. 1. Thermograms for the solid state samples of **I** (a), **II** (b) and **III** (c).

temperature (~100 °C), although in the crystal of **I** there are two crystallographically independent units (BePc-(4-Mepy) · 4-Mepy) and different 4-Mepy molecules. One of them is the 4-Mepy molecule coordinated to Be(II) of the BePc molecule and the other one is solvated. As seen in the TG analysis of **I** (the weight loss of ~26.5%), both solvated and coordinated 4-Mepy molecules are released simultaneously. This can be understood, if we take into account the arrangement of the (BePc(4-Mepy) · 4-Mepy) units and solvated 4-Mepy molecules in the crystalline network. The ligated and solvated 4-Mepy molecules are located in channels formed by the BePc molecules that are aligned almost parallel to the [100] direction in the crystal. The high thermal vibration of solvated 4-Mepy molecules at $T \sim 100$ °C accounts for the breaking of the Be–N bond of the coordinated 4-Mepy molecule in the solid sample of **I**, and as a result we have in the TG only one slope down (Fig. 1a). We suppose that in the case of compound **I**, besides the molecular arrangement, the exclusively narrow temperature range for the loss of the ligand molecules results from the extremely small radius of the beryllium ion [6,7], which in relation to the Mg and Zn ions in **II** and **III**, respectively, is over two times smaller. Therefore, as the temperature only reaches the value of the $Be(N_{iso})_4$–N(4-Mepy) bonding energy, the 4-Mepy molecule is released and the beryllium ion comes back to its equilibrium position in the BePc center, where the beryllium ion is no longer able to attract the ligand molecules. This is because it sits between the four N_{iso} atoms as in a square well, as described in [3]. In consequence, only the repulsion forces between the basal N_{iso} atoms and apical N(4-Mepy) atom become effective and at these conditions the ligand can readily be liberated.

The compounds **II** and **III** liberate the coordinated 4-Mepy molecules at significantly higher temperatures and also with wider temperature ranges. The slightly different decomposition temperature of **II** and **III**, corresponding to the release of the 4-Mepy molecules (see Fig. 1b and c), is connected not only with the strength of the axial M(II)–N bonds joining the 4-Mepy molecules, but also with the molecular arrangement. In **II**, both axial Mg–N bonds break simultaneously, releasing the 4-Mepy molecules. In all samples, the thermal process leading to the loss of 4-Mepy molecules and conversion of the remaining samples into the respective M(II)Pc's in the β-form was verified by powder X-ray diffraction. For these three compounds, the process of releasing of 4-Mepy molecules is endothermic.

3.3. Stereochemistry and crystal structures

All three structures are built up of independent moieties of **I**, **II** and **III** arranged in a different fashion. The crystalline network of the beryllium compound (**I**) consists of BePc and 4-Mepy molecular units in the proportion 1:2. One of the two 4-Mepy molecules is axially coordinated to Be of the BePc unit and the another one is a solvated molecule. Thus the Be(II) ion has a 4 + 1 coordination. In the crystal, there are two independent BePc-(4-Mepy) · 4-Mepy units (Fig. 2a). However, in the two independent units we have not observed any geometrical differences greater than 3 e.s.d's, but they show a different orientation of the ligated 4-Mepy in relation to BePc. Additionally, the geometries of the ligated and solvated 4-Mepy molecules are also very similar. The BePc(4-Mepy) molecule is not planar. The planar BePc molecule adopts a saucer-shape form due to the axial ligation by 4-Mepy. Interaction between the N atom of 4-Mepy, with a lone-pair of electrons, and the positively charged Be(II) ion of the BePc molecule leads to the deviation of Be by 0.302(3) and 0.320(3) Å from the plane defined by the four *N*-isoindole atoms of Pc in both crystallographically independent BePc(4-Mepy) units. The orientation of the 4-Mepy molecule in one of the two crystallographically independent BePc(4-Mepy) molecules is stabilized by a



Scheme 1.

Table 3
Comparison of the TG, DTA and XRD data for the complexes **I**, **II** and **III**

Compound	TG, 4-Mepy loss	DTA, 4-Mepy releasing guide	XRD identified residue
I	at 100 °C, sharp steep	endothermal	β-form
II	at 180–220 °C range, gradual diffused	endothermal	β-form
III	at 190 °C, diffused	endothermal	β-form

C–H···N(azamethine) interaction between the H atom in the ortho- position of 4-Mepy and the azamethine N atoms of the Pc ring (the N1a–Be1–N9a–C37a torsion angle is equal to −46.8°). In the second independent BePc(4-Mepy) molecule, the interaction in the crystalline network with the neighbouring molecule makes the respective torsion angle (N1b–Be2–N9b–C37b) equal to −29.3°. Two pairs of symmetrically equivalent BePc(4-Mepy) molecules related by an inversion center are π–π stacked in a back-to-back fashion as dimers with an interplanar distance of ∼3.4 Å (see Fig. 3), indicating the interaction between the π-clouds of the phthalocyaninato(2-) macrorings, since the distance is comparable to the typical distance between aromatic rings in systems with such an interaction [23]. This mutual arrangement of BePc(4-Mepy) molecules forms channels in which the solvated 4-Mepy molecules are located. The solvated 4-Mepy molecules possess relatively higher thermal ellipsoids in comparison with the BePc(4-Mepy) molecules, since they are taking more than the necessary space in the structure at room temperature. The voids in the solvent region have been found by the SQUEEZE procedure of the PLATON software package [24,25], but no significant residual electron density was observed. So, the thermal displacement of solvated 4-Mepy is considered as the effect of the high temperature crystallization process of compound **I** (at ∼80 °C), in which these molecules possess quite high kinetic energy. Therefore, they require more space in the crystal structure, in comparison with the room temperature at which the X-ray measurement was performed.

The crystalline network of the magnesium compound (**II**) consists of MgPc and 4-Mepy molecular units, similar to **I**, in the proportion 1:2. However, in the magnesium compound two 4-Mepy units are biaxially coordinated to the central Mg(II) atom of the MgPc molecule (Fig. 2b). The central Mg(II) cation, lying on the inversion center and in the plane defined by the four isoindole nitrogen atoms of the Pc macroring, coordinates all four nitrogen atoms of the Pc macroring and two nitrogen atoms of the 4-Mepy molecules in a distorted tetragonal bi-pyramid (4 + 2 coordination). The axial Mg–N bonds are longer by ∼0.4 Å than the four equatorial Mg–N_{iso} bonds (see Table 2). The axial M–N(4-Mepy) bonds are slightly weaker (2.412(2) Å) than the corresponding axial Mg–N(py) bonds (2.376(2) Å) in the biaxially ligated complex of $MgPc(py)_2$ [26]. The phthalocyaninato macroring in the $MgPc(4\text{-}Mepy)_2$ molecule is almost planar. The 4-Mepy molecules, ligated on both sides of the MgPc molecular plane, are not perpendicular to it. The dihedral angle between the N_4–isoindole plane and the 4-Mepy molecular plane is equal to 83.2(2)° and the torsion N1–Mg–N5–C21 describing the orientation of the coordinated 4-Mepy molecule in relation to the Pc ring is equal to −19.1(2)°. This inclination is similar to that in $CoPc(4\text{-}Mepy)_2$ and is slightly greater than that in $FePc(4\text{-}Mepy)_2$ [18]. This incli-

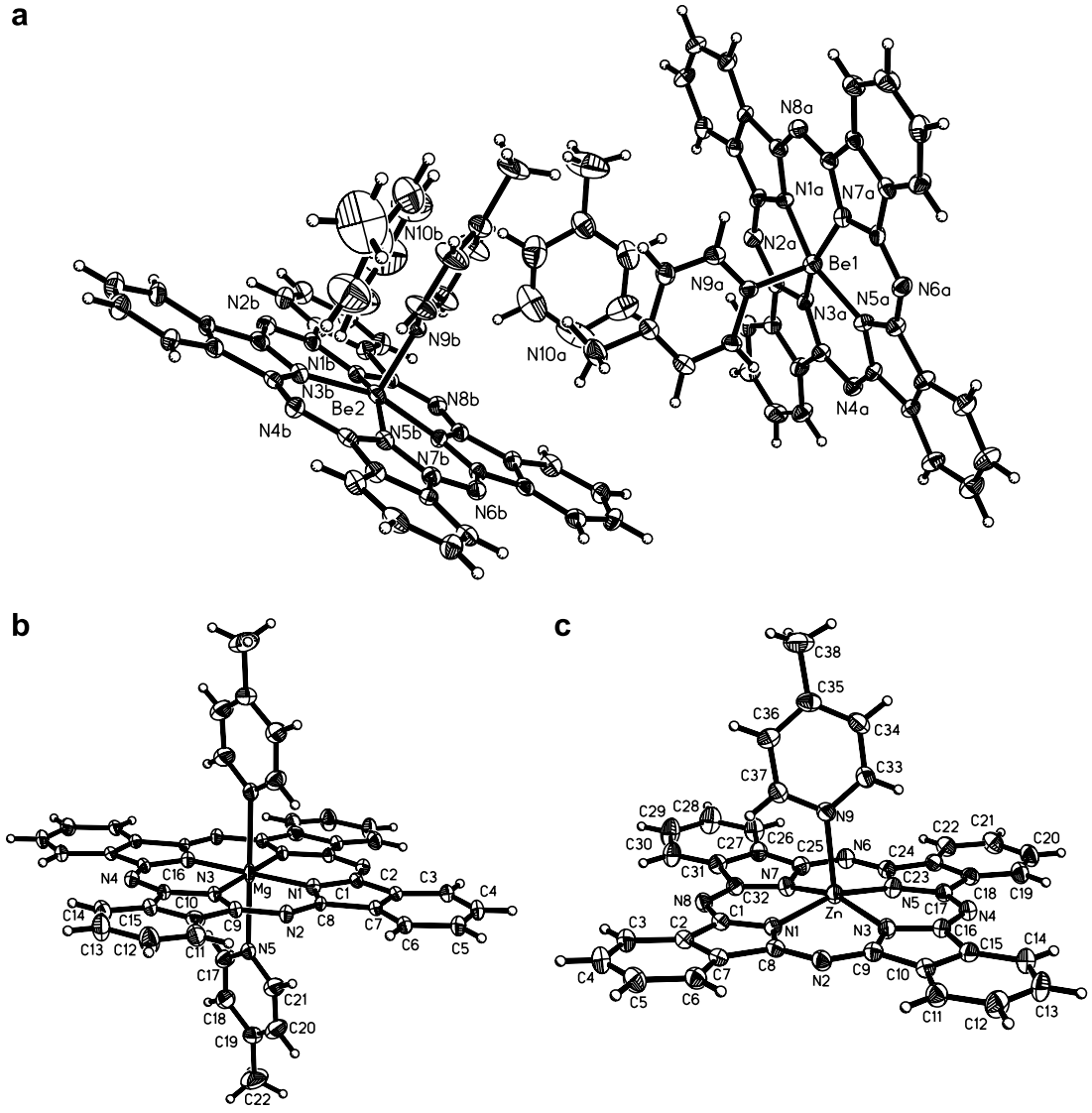


Fig. 2. Molecular structure of independent parts of **I** (a), **II** (b) and **III** (c).

nation correlates well with the molecular arrangement in the crystal, where one $MgPc(4\text{-}Mepy)_2$ molecule is oriented by the coordinated 4-Mepy molecules close to the phenyl ring of the Pc ring of a neighbouring $MgPc(4\text{-}Mepy)_2$ molecule, forcing the non-perpendicular coordination. Additionally, this interaction causes the rotation of the ligated 4-Mepy molecules in relation to the Pc ring from 45°, for the most stable conformation, to 19.1(2)° (N1–Mg–N5–C21). In the biaxially coordinated $MgPc(py)_2$ analogue [26] and in the other $CoPc(py)_2$, $FePc(py)_2$ and $MnPc(py)_2$ complexes, the corresponding angles are close to 90° [27,28]. The arrangement of $MgPc(4\text{-}Mepy)_2$ molecules in the crystal is shown in Fig. 4. The $MgPc(4\text{-}Mepy)_2$ molecules are arranged in a herring-bone fashion and form alternating sheets parallel to the *ac*-plane. The MgPc planes are parallel within one sheet (and separated by ~3.26 Å), whereas they make an angle of ~72° in relation to the neighbouring sheets.

The crystal structure of **III** consists of mono-axially coordinated ZnPc(4-Mepy) molecules (Fig. 2c). The planar ZnPc molecule, upon ligation by the 4-Mepy molecule, adopts the saucer-shape form, due to the interaction of the positively charged Zn(II) central atom of ZnPc with the ring N atom of the 4-Mepy molecule. This interaction leads to a deviation of Zn(II) from the centre cavity of the Pc macroring toward the coordinated 4-Mepy molecule, making the four equatorial $Zn–N_{iso}$ bonds longer by 0.04 Å in relation to ZnPc [5]. The deviation of the Zn atom from the plane defined by the four isoindole nitrogen atoms is equal to 0.352(2) Å toward the coordinated 4-Mepy molecule, thus the Zn atom has a 4 + 1 coordination environment. The displacement of Zn(II) from the N_4–isoindole plane in **III** is smaller than that in ZnPc(*n*-hexylamine), ~0.48 Å [29] and ZnPcCl, ~0.59 Å [30] and is comparable to $ZnPc(H_2O)\cdot 2DMF$, ~0.38 Å [31]. The molecular plane of the ligated 4-Mepy is not perpendicular

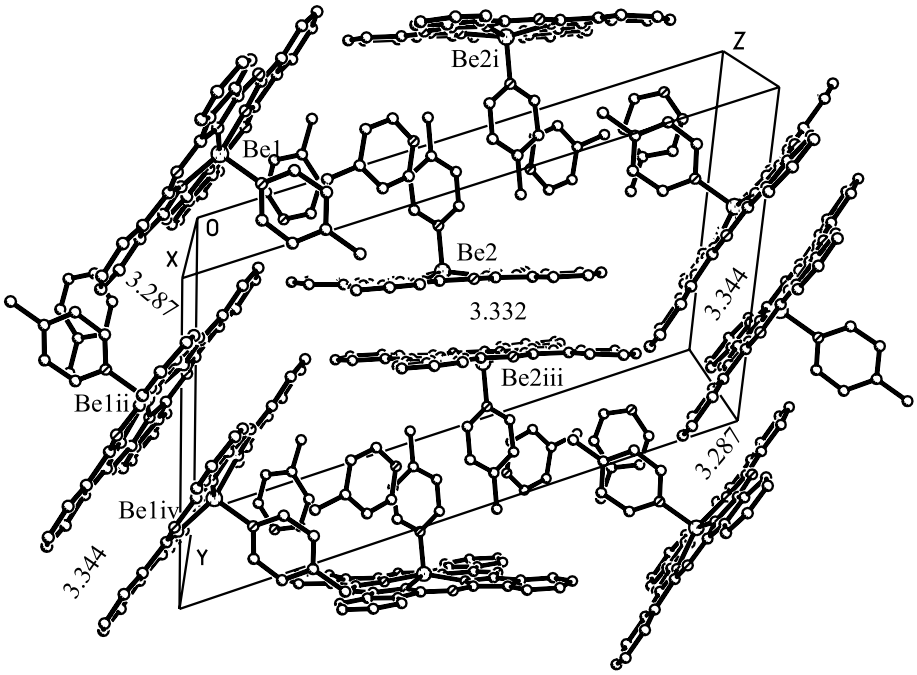


Fig. 3. View of the molecular arrangement of **I** showing the channels of the 4-Mepy solvent along the [001] direction and the π–π interacting stacked back-to-back dimers. H atoms are omitted for clarity. Symmetry code: (i) $1-x, -y, -z$; (ii) $2-x, -y, -z$; (iii) $1-x, 1-y, 1-z$ and (iv) $x,1-y, z$.

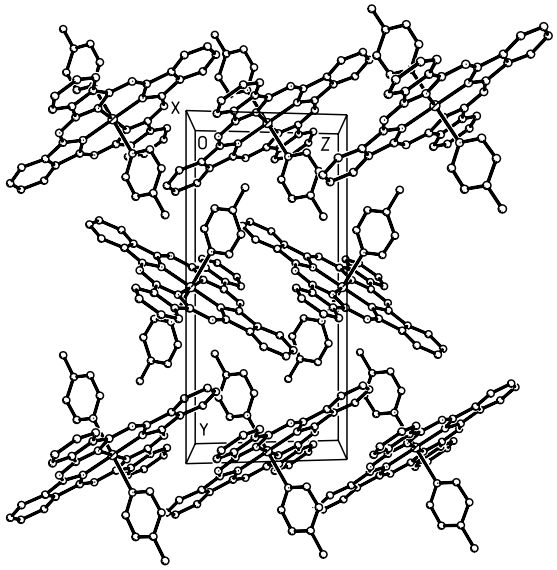


Fig. 4. Arrangement of the $MgPc(4\text{-}Mepy)_2$ molecules in the unit cell. H atoms are omitted for clarity.

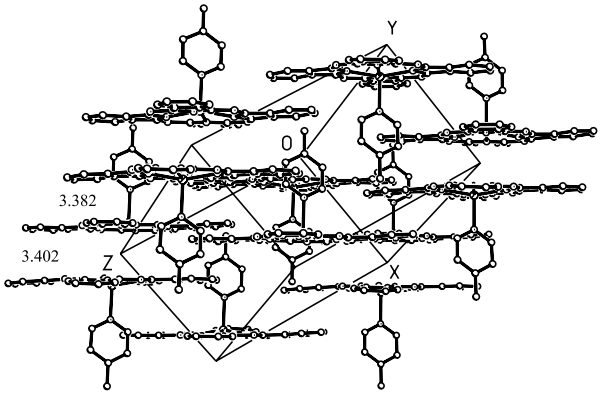


Fig. 5. Arrangement of the ZnPc(4-Mepy) molecules in the unit cell showing the π–π interacting stacked back-to-back molecules. H atoms are omitted for clarity.

to the N_4–isoindole plane of the Pc ring, but is inclined. The dihedral angle between the N_4-plane and the plane of the coordinated 4-Mepy molecule is equal to 77.8(1)°. The inclination of the 4-Mepy to ZnPc plane results from the mutual interaction of the ligated 4-Mepy with the Pc ring of a neighbouring ZnPc(4-Mepy) in the crystal. The ZnPc(4-Mepy) molecules related by an inversion center are stacked in a back-to-back fashion as dimers with an interplanar distance of ~3.4 Å between the N_4–isoindole planes (see Fig. 5).

In these three compounds, the chemically equivalent C–N and C–C bonds of the Pc(2-) macroring and 4-Mepy molecules are similar and very typical, and corresponding well with $MPc(4\text{-}Mepy)_2$ (M = Fe, Co) [18]. The main stereo chemical data for the metal atoms in the complexes **I**, **II** and **III** are collected in Table 4. For completeness, the data of the Fe and Co analogue compounds [18] are also included. As can be seen from the table, only in the case of the beryllium compound is the axial M–N(4-Mepy) distance smaller than the four equatorial M–N distances. It is noteworthy that also in the case of the BePc complex with an O-donor ligand such an exclusive correlation between the axial and equatorial bonds is observed [3]. It may be, however, easier understood if we recognize that for the

Table 4
Comparison of the coordination of the central M(II) atom in mono- and biaxially coordinated by 4-Mepy complexes

Compound	Average equatorial M–N distance (Å)	Axial M–N distance (Å)	Deviation of M from the N_4 plane	Coordination geometry of M
BePc(4-Mepy) · 4-Mepy	1.914(6) (Be1)	1.839(4)	0.320(3)	square pyramid
	1.892(6) (Be2)	1.830(4)	0.302(3)	
$MgPc(4\text{-}Mepy)_2$	2.007(2)	2.412(2)	0	elongated octahedral
ZnPc(4-Mepy)	2.020(2)	2.166(2)	0.352(2)	square pyramid
$FePc(4\text{-}Mepy)_2 \cdot 2(4\text{-}Mepy)$	1.935(3)	2.040(3)	0	elongated octahedral
$CoPc(4\text{-}Mepy)_2 \cdot 2(4\text{-}Mepy)$	1.930(4)	2.322(5)	0	

beryllium ion the central hole of the essentially planar and rigid Pc moiety is far too big. For comparison in the case of a compound in which the beryllium ion is, as is normal for it, tetrahedrally coordinated, the relative two Be–N(py) bonds are only 1.753 (Å) long and another two Be–N(thiocyanate) bonds completing the tetrahedra are yet shorter by 0.1 Å [32].

4. Conclusions

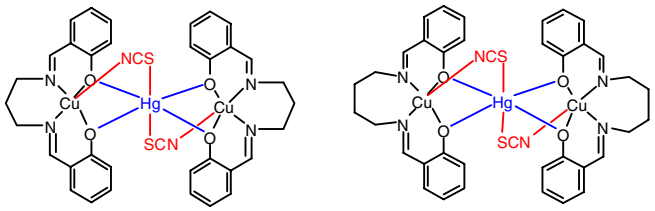
In the compounds studied here, the central M(II) ion of BePc and ZnPc is mono-axially ligated by the ring nitrogen atom of the 4-Mepy molecule, while in MgPc biaxial ligation has been observed. These complexes differ significantly in the axial M(II)–N(4-Mepy) bond strength and the ligand releasing temperature increases in the order Be < Zn < Mg. The BePc(4-Mepy) and $MgPc(4\text{-}Mepy)_2$ complexes transform into the aqua complexes $M(II)PcH_2O \cdot n(4\text{-}Mepy)$ in a solution of 4-Mepy/H_2O(M(II) = Be, Mg and $n = 1$, 2 and 3).

Appendix A. Supplementary material

CCDC 639016, 639017 and 639018 contain the supplementary crystallographic data for **I**, **II** and **III**. These data can be obtained free of charge via http://www.ccdc.cam.ac.uk/conts/retrieving.html, or from the Cambridge Crystallographic Data Centre, 12 Union Road, Cambridge CB2 1EZ, UK, fax: (+44) 1223-336-033, or e-mail: deposit@ccdc.cam.ac.uk. Supplementary data associated with this article can be found, in the online version, at doi:10.1016/j.poly.2007.05.018.

References

[1] R.P. Linstead, J.M. Robertson, J. Chem. Soc. (1936) 1736.
[2] J.M. Robertson, J. Chem. Soc. (1936) 1135.
[3] R. Kubiak, A. Waśkowska, M. Śledź, A. Jezierski, Inorg. Chim. Acta 359 (2006) 1344.
[4] J. Janczak, R. Kubiak, Polyhedron 20 (2001) 2901.
[5] W.R. Scheidt, W. Dow, J. Am. Chem. Soc. 99 (1977) 1101.
[6] I.D. Brown, Acta Crystallogr. B 44 (1988) 545.
[7] R.D. Shannon, Acta Crystallogr. A 32 (1994) 751.
[8] J. Janczak, Y.M. Idemori, Polyhedron 22 (2003) 1167.
[9] J. Mizuguchi, Z. Kristallogr, NCS 217 (2002) 251.
[10] R. Kubiak, J. Janczak, K. Ejsmont, Chem. Phys. Lett. 245 (1995) 249.
[11] P. Day, R.J.P. Williams, J. Chem. Phys. 37 (1962) 567.
[12] R. Kubiak, A. Waśkowska, J. Mol. Struct. 649 (2003) 55.
[13] V. Kinzhybalo, J. Janczak, Acta Crystallogr. C 63 (2007) m105.
[14] J. Janczak, R. Kubiak, Polyhedron, (2007) 2997.
[15] V. Kinzhybalo, J. Janczak, J. Mol. Struct., in press, doi:10.1016/j.molstruc.2006.10.064.
[16] K.M. Kadish, K.M. Smith, R. Guilard (Eds.), The Porphiryn Handbook, Phthalocyanines: Properties and Materials, vol. 17, Academic Press, Elsevier, 2003.
[17] F. Cariati, F. Morazzoni, M. Zocchi, J. Chem. Soc., Dalton Trans. (1975) 556.
[18] F. Cariati, F. Morazzoni, M. Zocchi, J. Chem. Soc., Dalton Trans. (1978) 1018.
[19] K.M. Kadish, K.M. Smith, R. Guilard (Eds.), The Porphryn Handbook, Application of Phthalocyanines, vol. 19, Academic Press, Elsevier, 2003.
[20] CRYSALIS CCD and CRYSALIS RED Program Package. Oxford Diffraction Poland, Wrocław, Poland, 2005.
[21] G.M. Sheldrick, SHELXS-97, SHELXL-97. Programs for Crystal Structure Solution and Refinement, University of Göttingen, Göttingen, Germany, 1997.
[22] WinXPow Software Manual, STOE & CIE GmbH, Darmstadt, Germany, 2003.
[23] L. Pauling, The Nature of the Chemical Bond, third ed., Cornell University Press, Ithaca, New York, 1960.
[24] P. Sluis, A.L. Spek, Acta Crystallogr. A 46 (1990) 194.
[25] A.L. Spek, J. Appl. Crystallogr. 36 (2003) 7.
[26] J. Janczak, R. Kubiak, Polyhedron 21 (2002) 265.
[27] J. Janczak, R. Kubiak, Inorg. Chim. Acta 342 (2003) 64.
[28] J. Janczak, R. Kubiak, M. Śledź, H. Borman, Yu. Grin, Polyhedron 22 (2003) 2685.
[29] T. Kobayashi, T. Ashida, N. Uyeda, E. Suito, M. Kakudo, Bull. Chem. Soc. Jpn. 44 (1971) 2095.
[30] M.M. Deneux, D. Benlian, M. Pierrot, A. Fournel, J.P. Sorbiel, Inorg. Chem. 24 (1985) 1878.
[31] L.Y. Cui, J. Yang, Q. Fu, B.Z. Zhao, L. Tian, H.L. Yu, J. Mol. Struct. 827 (2007) 149.
[32] H. Rohland, W. Hang, M. Noltenmeyer, A. Meller, H.G. Schmidt, Fersenius J. Anal. Chem. 361 (1998) 725.



$[(CuL^1)_2Hg(SCN)_2]$ (**1**) $[(CuL^2)_2Hg(SCN)_2]$ (**2**)

Scheme 1. Chemical diagram of the heterotrinuclear complexes.

in contrast to this expectation the thiocyanate ligands bound the copper atoms in the synthesized complexes.

Here, as a part of our ongoing research on homo-[11] and heteropolynuclear complexes with pseudohalide ligands, the synthesis and structures of two novel heterotrinuclear copper(II)–mercury(II)–copper(II) complexes, bridged by phenolate oxygen atoms of the Schiff bases L^1H_2 and L^2H_2, and thiocyanate anions are presented. The biological activities of these Schiff bases, their mononuclear and heterotrinuclear complexes are comparatively reported. Scheme 1 shows the chemical diagram of the complexes, $[(CuL^1)_2Hg(SCN)_2]$ and $[(CuL^2)_2Hg(SCN)_2]$.

2. Experimental

2.1. Materials and measurements

All reagents and solvents were purchased from Merck, Aldrich or Carlo Erba and were used without further purification. The elemental analysis for the ligands and the complexes were carried out at on a Eurovector 3018 CHNS analyzer. Melting points were measured using a Gallenkamp melting point apparatus. A Hitachi 8200 atomic absorption spectrometer was used for copper analyses. IR spectra were obtained by using IR grade KBr disks on a Perkin–Elmer 1600 Series FTIR spectrophotometer in the range 4000–250 cm^{-1}. Electronic spectra were obtained using a Cary |1E| UV–Visible Spectrophotometer (Varian).

2.2. Synthesis

2.2.1. Synthesis of the ligands (LH_2)

L^1H_2 [12] and L^2H_2 [13] were obtained by the condensation reaction of salicylaldehyde and the relevant diamino compounds, 1,3-diaminopropane and 1,4-diamino butane, respectively, in ethanolic solution.

2.2.2. Synthesis of the copper(II) precursors, CuL^1 and CuL^2

CuL^1 [14] and CuL^2 [15] were prepared by reacting an alkaline ethanolic solution of L^1H_2 and L^2H_2 with $CuCl_2 \cdot 2H_2O$, as described previously in the literature.

2.2.3. Synthesis of $[(CuL^1)_2Hg(SCN)_2]$ (**1**)

$Hg(SCN)_2$ (1 mmol) was dissolved in ethanol (25 mL) and added to a DMF (50 mL) solution of CuL^1 (2 mmol). The mixture was stirred for 5 min. and then the solution was left to stand in atmospheric conditions for 3 to 4 days. The dark green crystalline precipitate that formed was filtered off and dried in the open air. Yield: 59%. *Anal.* Calc. for $Hg[Cu(C_{17}H_{16}N_2O_2)SCN]_2$: C, 43.04; H, 3.18; N, 8.36; S, 6.38. Found: C, 42.84; H, 3.08; N, 8.24; S, 6.31%. The crystals were suitable for X-ray diffraction study.

2.2.4. Synthesis of $[(CuL^2)_2Hg(SCN)_2]$ (**2**)

This compound was obtained following the same procedure as in the case of compound **1**. Yield: 48%. *Anal.* Calc. for $Hg[Cu(C_{18}H_{18}N_2O_2)SCN]_2$: C, 44.20; H, 3.49; N, 8.13; S, 6.21. Found: C, 44.08; H, 3.32; N, 7.98; S, 6.12%. The crystals were suitable for X-ray diffraction study.

2.3. X-ray diffraction structure analyses

To determine the crystal structures of compounds **1** and **2**, X-ray diffraction data were collected at room temperature with graphite-monochromated Mo Kα radiation on an Enraf-Nonius CAD4 diffractometer [16], operating in $\omega/2\theta$ scan mode. Cell refinement was carried out using CAD-4 EXPRESS. During the data collection, three standard reflections were periodically measured every 120 min, both of the compounds showed no significant intensity variation. Data reduction was carried out using SHELXL97 [17].

The structures were solved by direct methods using the program SHELXS97 [17] in the WINGX package [18]. A full-matrix least-squares refinement on F^2 was done. For all non-hydrogen atoms anisotropic displacement parameters were refined. All hydrogen atoms of the compounds were placed geometrically and a riding model was used with $U_{iso}(H) = 1.2\,U_{eq}(C)$. The ORTEP drawings [19] of the molecules for **1** and **2** are shown in Figs. 1 and 2, respectively.

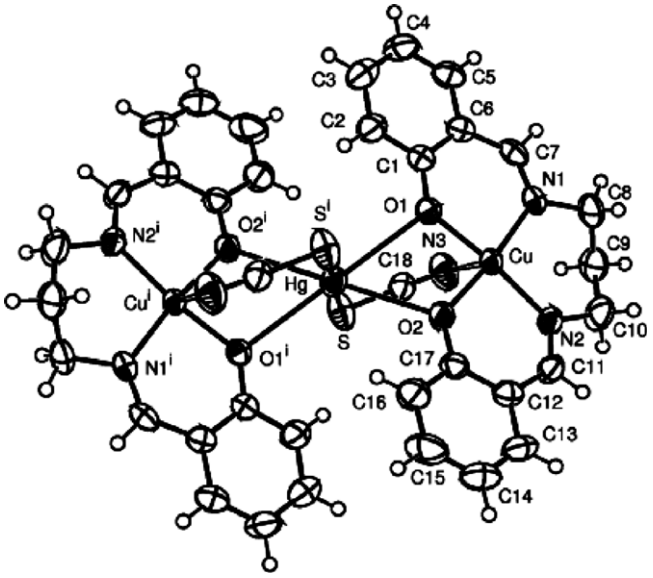


Fig. 1. ORTEP diagram for the complex $[(CuL^1)_2Hg(SCN)_2]$ showing the atom labelling scheme. Displacement ellipsoids are drawn at the 50% probability level and H atoms are shown as small circles of arbitrary radii.

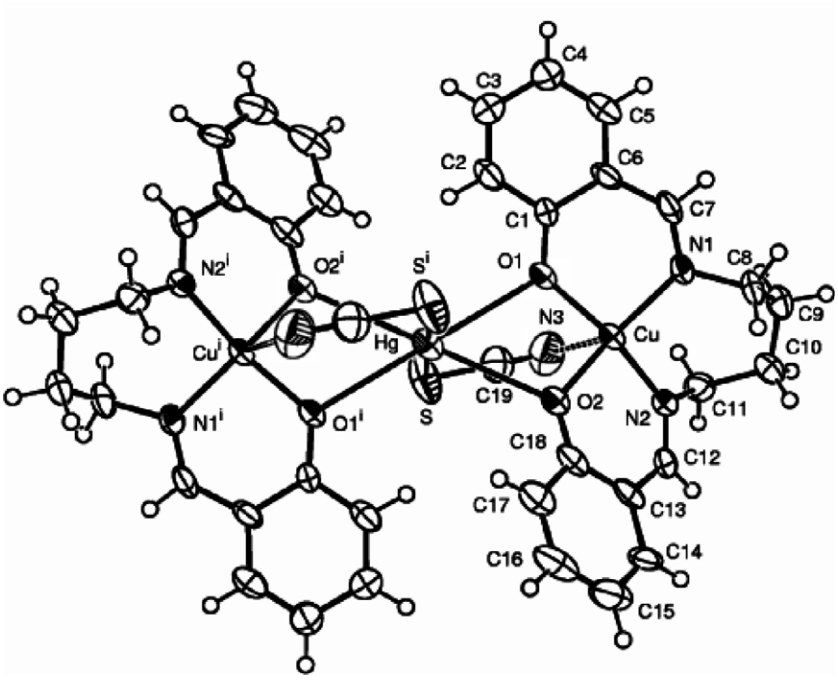


Fig. 2. ORTEP diagram for the complex $[(CuL^2)_2Hg(SCN)_2]$ showing the atom labelling scheme. Displacement ellipsoids are drawn at the 50% probability level and H atoms are shown as small circles of arbitrary radii.

Crystal and experimental data are given in Table 1, selected bond lengths and angles are given in Table 2.

2.4. Biological activity of the complexes

The agar disc diffusion method, microdilution broth susceptibility assay [20,21] and spore culture technique (for filamentous fungi) [22] were employed for the determination of antimicrobial activities. The MIC of the complexes and the free ligands against the test microorganisms were employed to the microdilution broth susceptibility assay. All tests were performed in duplicate to check the results. The screening effects of the investigated compounds in vitro were tested against the bacteria *Escherichia coli*

Table 1
Crystal data and experimental details of the title compounds

	(1)	(2)
Empirical formula	$Hg[Cu(C_{17}H_{16}N_2O_2)SCN]_2$	$Hg[Cu(C_{18}H_{18}N_2O_2)SCN]_2$
Formula weight (g/mol)	1004.51	1032.56
Crystal system, space group	triclinic, $P\bar{1}$	monoclinic, $P2_1/c$
a, b, c (Å)	9.2494(18), 10.032(2), 10.552(2)	9.918(3), 19.235(2), 10.441(2)
α, β, γ (°)	72.14(3), 87.81(2), 71.32(3)	90, 111.43(2), 90
Volume (Å^3)	880.1(4)	1854.1(7)
Z	1	2
Calculated density (g cm^{-3})	1.895	1.849
Absorption coefficient [Mo Kα] (mm^{-1})	5.716	5.429
$F(000)$	492	1016
Crystal colour and shape	black, plate	dark green, plate
Crystal size (mm)	$0.40 \times 0.10 \times 0.10$	$0.40 \times 0.35 \times 0.05$
Temperature (K)	293(2)	293(2)
Radiation (Å)	Mo Kα 0.71073	Mo Kα 0.71073
Unit cell determination: Number of reflections used, theta range (°)	15, 10.05–11.38	25, 9.98–18.04
Theta minimum–maximum (°)	2.26–26.62	3.06–26.99
Dataset	$-11 \leqslant h \leqslant 11$, $0 \leqslant k \leqslant 12$, $-12 \leqslant l \leqslant 13$	$-11 \leqslant h \leqslant 12$, $-24 \leqslant k \leqslant 0$, $-13 \leqslant l \leqslant 0$
Absorption correction (Psi-scan)	$T_{min} = 0.509$, $T_{max} = 0.565$	$T_{min} = 0.131$, $T_{max} = 0.162$
Total, unique data, R(int)	3731, 3520, 0.013	4079, 3863, 0.050
Number of reflections refined	3520	3863
Number of parameters refined	232	242
R $[F^2 > 2\sigma(F^2)]$, $wR(F^2)$, S	0.024, 0.064, 1.06	0.064, 0.177, 0.96
Refine weighting details where $P = (F_o^2 + 2F_c^2)/3$	$w = 1/[\sigma^2(F_o^2) + (0.0337P)^2 + 0.1081P]$	$w = 1/[\sigma^2 (F_o^2) + (0.1032P)^2]$
Minimum and maximum residual density (e Å^{-3})	−0.81, 0.51	−3.29, 2.68
Extinction correction and coefficient	None	SHELXL, 0.0002(5)

Table 2
Selected bond lengths and bond angles (Å, °)

$[(CuL^1)_2Hg(SCN)_2]$		$[(CuL^2)_2Hg(SCN)_2]$	
Hg···Cu	3.7623(9)	Hg···Cu	3.7778(17)
Hg–S	2.3926(13)	Hg–S	2.363(4)
Hg–O1	2.775(3)	Hg–O1	2.736(6)
Hg–O2	2.680(3)	Hg–O2	2.846(7)
Cu–O1	1.943(2)	Cu–O1	1.885(7)
Cu–O2	1.919(2)	Cu–O2	1.921(7)
Cu–N1	1.973(3)	Cu–N1	1.974(8)
Cu–N2	1.996(3)	Cu–N2	1.951(8)
S–C18	1.659(4)	S–C19	1.623(14)
C18–N3	1.151(5)	C19–N3	1.164(16)
Cu–N3	2.843(4)	Cu···N3[i]	3.037(13)
Hg–O1	97.58(7)	S–Hg–O1	96.24(18)
S–Hg–O1[i]	82.42(7)	S–Hg–O1[i]	83.76(18)
S–Hg–O2	90.54(7)	S–Hg–O2	92.84(17)
S–Hg–O2[i]	89.46(7)	S–Hg–O2[i]	87.16(17)
O1–Hg–O2	54.70(7)	O1–Hg–O2	56.1(2)
O1–Cu–O2	80.96(10)	O1–Cu–O2	87.3(3)
O1–Cu–N1	91.85(11)	O1–Cu–N1	94.6(3)
O2–Cu–N2	90.95(12)	O2–Cu–N2	92.7(3)
N1–Cu–N2	96.15(12)	N1–Cu–N2	95.4(3)
O2–Cu–N1	172.66(11)	O2–Cu–N1	158.2(3)
O1–Cu–N2	171.41(11)	O1–Cu–N2	152.2(4)
Cu–O1–Hg	104.38(10)	Cu–O1–Hg	108.3(3)
Cu–O2–Hg	108.64(10)	Cu–O2–Hg	103.1(3)
C18–S–Hg	100.69(14)	C19–S–Hg	100.3(4)
N3–C18–S	177.4(4)	N3–C19–S	176.4(12)
O1–Cu–N3	87.21(12)	O1–Cu–N3	80.3(3)
O2–Cu–N3	96.78(12)	O2–Cu–N3	92.0(3)
N1–Cu–N3	84.25(12)	N1–Cu–N3	115.6(4)
N2–Cu–N3	96.67(12)	N2–Cu–N3	77.8(3)
Cu–N3–C18	95.2(3)	Cu–N3–C19	95.2(10)

[i] $-x, -y, -z$.

ATCC 25292, *Staphylococcus aureus* ATCC 6538, *Pseudomonas aeruginosa* ATCC 27853, *Enterobacter aerogenes* NRRL 3567, *Proteus vulgaris* NRLL B 123, *Listeria monocytogenes* ATCC 7644 and *Serratia marcescens* (Clinic isolate) using the disc diffusion and microtitter well plate techniques with an incubation period of 24 h at 37 °C. The test solutions were prepared in DMF.

2.4.1. Antimicrobial screening

The agar disc diffusion method was employed for the determination of antimicrobial capacities of the free ligands and their metal complexes. A suspension of the tested microorganisms (10^8 CFU/μl) was spread on the solid media plates. Each test solution was prepared in DMF. Filter paper discs (6 mm in diameter) were soaked with 20 μl of the stock solutions and placed on the inoculated plates. After keeping the plates at 2 °C for 2 h, they were incubated at 37 °C for 24 h for bacteria and *Candida albicans*. The diameter of the inhibition zones were measured in millimeters (Table 3).

2.4.2. Determination of minimum inhibitory concentration (MIC)

For the determination of MICs, the microdilution broth susceptibility assay was used. Stock solutions of the compounds were prepared in DMF. Serial dilutions of the compounds were prepared in sterile distilled water in 96-well microtitter plates. A freshly grown bacterial suspension in double strength Mueller Hinton Broth and a yeast suspension of *Candida albican*s in Saboroud Dextrose Broth were standardized 10^8 CFU/ml (McFarland No: 0.5). Sterile distilled water served as the grown control. 100μl of each tested compound were then added to each well. The last row containing only the serial dilutions of the title compounds without microorganisms was used as a negative control. After incubation at 37 °C for 24 h, the first well without turbidity was determined as the minimal inhibitory concentration (Table 4).

2.4.3. Antifungal studies

In order to obtain conidia, the fungi were cultured on Czapex Dox Agar and Malt Extract Agar medium in 9 cm Petri dishes at 25 °C, for 10 days. Harvesting was carried out by suspending the conidia in a 1% (w/v) sodium chloride solution contain 5% (w/v) DMSO. The spore suspension was then filtered and transferred into tubes and stored at −20 °C, accordingly Hadecek and Greger [23].

Screening for antifungal activities of the stock solutions of the metal complexes and the free ligands was performed qualitatively using the disc diffusion method (Table 5) against saprophytic fungi, namely *Aspergillus flavus*, *Aspergillus niger*, *Penicillium expansum*, and *Alternaria brassicola* cultured on Malt Extract and Czapex Dox Agar medium.

Table 3
Antimicrobial screening of the ligands and their complexes (mm)

Microorganisms	Source	Stock solution						
		Diameter of inhibition zone (mm)						
		L^1	CuL^1	$(CuL^1)_2Hg(SCN)_2$	L^2	CuL^2	$(CuL^2)_2Hg(SCN)_2$	Standard
Escherichia coli	ATCC 25292	10	10	13	11	11	12	22[a]
Staphylococcus aureus	ATCC 6538	10	10	13	11	11	12	22[a]
Pseudomonas aeruginosa	ATCC 27853	9	10	12	9	11	12	23[a]
Enterobacter aerogenes	NRRL 3567	9	10	12	10	11	12	22[a]
Proteus vulgaris	NRRL 123	9	9	11	9	11	11	24[a]
Serratia marcescens	Klinik izolat	9	9	11	9	10	11	24[a]
Listeria monocytogenes	ATCC 7644	9	10	13	10	10	13	24[a]
Candida albicans	Klinik izolat	9	10	12	10	10	12	27[b]

[a] Chloramphenicol.
[b] Ketoconazol.

Table 4
Antimicrobial activity of the ligands and their complexes (μg/ml)

Microorganisms	Source	L^1	CuL^1	$(CuL^1)_2Hg(SCN)_2$	L^2	CuL^2	$(CuL^2)_2Hg(SCN)_2$	Standard
Escherichia coli	ATCC 25292	62.5	62.5	31.25	62.5	62.5	31.25	–[a]
Staphylococcus aureus	ATCC 6538	62.5	62.5	31.25	62.5	62.5	31.25	–[a]
Pseudomonas aeruginosa	ATCC 27853	125	62.5	31.25	125	62.5	31.25	–[a]
Enterobacter aerogenes	NRRL 3567	125	62.5	31.25	125	62.5	31.25	–[a]
Proteus vulgaris	NRRL 123	125	125	62.5	125	62.5	62.5	–[a]
Serratia marcescens	Klinik izolat	125	125	62.5	125	125	62.5	–[a]
Listeria monocytogenes	ATCC 7644	125	125	31.25	125	125	31.25	–[a]
Candida albicans	Klinik izolat	125	125	62.5	125	125	62.5	–[b]

– : No turbidity.
[a] Chloramphenicol.
[b] Ketoconazol.

Table 5
Antifungal activity data for the tested complexes and the free ligands

Microfungi	L^1			CuL^1			$(CuL^1)_2Hg(SCN)_2$			L^2			CuL^2			$(CuL^2)_2Hg(SCN)_2$			Standard		
	T	C	Inh (%)	T	C	Inh (%)	T	C	Inh (%)	T	C	Inh (%)	T	C	Inh (%)	T	C	Inh (%)	T	C	Inh (%)
Aspergillus flavus	50	55	9	48	55	12		55	100	47	55	13.5	45	55	17.3		55	100	11	55	80
Aspergillus niger	40	50	20	31.5	50	36.9		50	100	41	50	17.7	30	50	38.5		50	100	9	50	82
Penicillium expansum	18	20	10	17	20	15.1		20	100	17	20	15	14	20	27.2		20	100	18	20	10
Alternaria brassicola	30	50	40	24	50	52		50	100	26	50	48	22	50	54		50	100	7	50	86

C: Diameter of fungal growth on the control.
T: Diameter of fungal growth on the test plate.
Inh.: Inhibition.

One loop drop of the spore suspension was applied onto the centre of the Petri dishes. Twenty microliters of each complex and the free ligands were applied onto sterile paper discs (6 mm in diameter) and placed in the Petri dishes and incubated at 25 °C for 3 days. The test solution was prepared in DMF. The inhibition of fungal growths expressed in percentage terms was determined on the growth in test plates compared to the respective control plates, given as % inhibition [24].

$$\%\text{Inhibition} = 100(C - T)/C$$

C is the diameter of fungal growth on the control and T is the diameter of fungal growth on the test plate.

The activities of the complexes have been compared with the activity of the standard antifungicide Ketoconazole.

3. Results and discussion

3.1. General characterizations

3.1.1. Crystal and molecular structure

In this work, two similar Cu–Hg–Cu Schiff base complexes were prepared and characterized by X-ray crystallography. The complexes, bis{[μ-*N*,*N*′-bis(salicylidene)-1,3-propanediaminato-copper(II)](μ-thiocyanato)mercury(II)}, $Hg[Cu(C_{17}H_{16}N_2O_2)SCN]_2$, compound **1** and bis{[μ-*N*,*N*′-bis(salicylidene)-1,4-butanediamine-*N*,*N*′,*O*,*O*′-copper(II)]-(μ-thiocyanato)mercury(II)}, $Hg[Cu(C_{18}H_{18}N_2O_2)SCN]_2$, compound **2** are heterotrinuclear complexes, with inversion centres of triclinic (**1**) and monoclinic (**2**) unit cells, respectively.

The central Hg atom of each complex, which is located on the inversion centre, has a distorted octahedral coordination geometry. In compound **1**, the equatorial plane consists of four bridging O atoms from two *N*,*N*′-bis(salicylidene)-1,3-propanediaminate ligands [Hg–O1 2.775(3), Hg–O2 2.680(3) Å]. In compound **2**, the equatorial plane consists of four bridging O atoms from two *N*,*N*′-bis(salicylidene)-1,4-butanediamine ligands [Hg–O1 2.736(6), Hg–O2 2.846(7) Å]. In both compounds, the S atoms of the bridging thiocyanate (SCN) group occupy the axial positions of the octahedron [Hg–S 2.3926(13) Å (**1**), 2.363(4) Å (**2**)]. The greatest deviation of bond angles from the ideal octahedral angles is found for O1–Hg–O2 [54.70(7)° (**1**) and 56.1(2)° (**2**)]. The distortion from an ideal octahedral geometry is a consequence of the limited opening of the tetradentate ligands, which reduces the bridging O1–Hg–O2 angle. All other bond angles are close to the ideal values.

The inversion-related terminal Cu atoms of compounds **1** and **2** are coordinated by two O and two N atoms from the *N*,*N*′-bis(salicylidene)-1,3-propanediaminate and *N*,*N*′-bis(salicylidene)-1,4-butanediamine ligands in the equatorial plane, respectively. The Cu atom is located

0.040(2) Å (**1**) and 0.051(1) Å (**2**) from the basal plane. The planes through the atoms N1–Cu–N2 and O1–Cu–O2 have a dihedral angle of 178.6(2)° (**1**) and 145.3(3)° (**2**). The basal plane around the Cu atom is almost planar in compound **1**, but in compound **2** these two planes are twisted by nearly 35° (Fig. 2). In both compounds, there is a long range interaction between the Cu and N3 atoms of the bridging SCN group at the axial position. The observed distances of Cu–N3 2.843(4) Å in complex **1** and 3.037(13) Å complex **2** are smaller than the sum of the van der Waals radii of these two atoms (3.84 Å). In complex **1** the interactive force between Cu and N3 is bigger than in complex **2** because the steric effect of the N1···N2 bridge in the propane case is larger than the steric effect of the N1···N2 bridge in the butane case. To define the five coordination shape, the index (τ) [25] is defined in terms of the two largest bond angles (α and β) around the central atom as [$\tau = (\beta - \alpha)/60$]. If τ is equal to 0, the coordination is an ideal square pyramid and if τ is equal to 1, the coordination is an ideal trigonal bipyramid. The observed τ values for the Cu coordination sphere are $\tau = 0.02$ (**1**) and $\tau = 0.10$ (**2**). These values show that in both compounds, the Cu atoms have a slightly distorted square-pyramidal coordination geometry. As shown in Fig. 3, the distortion from an ideal square pyramidal geometry in compound **2** is more than in compound **1**. The Cu–Hg pairs are bonded by the O atoms of the Schiff base ligands and by the SCN groups. The Cu···Hg distances are 3.7623(9) Å in complex **1** and 3.7778(17) Å in complex **2**. The bridging plane is not flat, the dihedral angle between O1–Cu–O2 and O1–Hg–O2 are 149.6(1)° and 158.8(3)° for complex **1** and **2**, respectively.

The conformations of the rings were analysed using PLATON [26]. The Cremer-Pople puckering parameters [27] given below for the Hg–SCN–Cu–O1 ring and Hg–SCN–Cu–O2 ring show that these rings are in half-chair forms. The dihedral angle between the least square planes defined by the atoms of these rings is 3.33(3)° (**1**) and 2.84(9)° (**2**). In the complex (**2**), a maximum and minimum residual electron densities of 2.68 and 3.29 e/Å^3 was observed at a distance of 0.98 and 0.94 Å, respectively from Hg atom.

Ring	**1**	**2**
Hg–SCN–Cu–O1	$Q = 1.039(3)$ Å, $\theta = 129.0(2)°$, $\phi = 86.6(2)°$	$Q = 1.023(6)$ Å, $\theta = 132.7(6)°$, $\phi = 91.2(7)°$
Hg–SCN–Cu–O2	$Q = 0.984(2)$ Å, $\theta = 44.8(2)°$, $\phi = 330.4(2)°$	Q=1.070(5) Å, $\theta = 44.2(7)°$, $\phi = 317.5(5)°$

3.2. Infrared spectra

The interest in the IR spectra of the titled complexes lies mainly in the bands due to the thiocyanate and azomethine groups. The IR spectra of the complexes show strong typical absorptions at 1615 cm^{-1} (**1**) and 1619 cm^{-1} (**2**) related to the C=N stretching vibration of the Schiff base imino group. The strong band at 1619–1631 cm^{-1} attributed to the C=N stretching vibration in the ligands is shifted to the region 1615–1619 cm^{-1} in the complexes, indicating the coordination of the azomethine nitrogen. In the free ligands, strong bands at 1570–1577 cm^{-1}, assigned to uncoordinated phenolic O–H stretching vibrations, shift to higher energy by 5–10 cm^{-1} in the complexes, indicating the coordination of the phenolic oxygen atom to the metal ion. The FTIR spectra of the thiocyanate anion for complexes **1** and **2** show characteristic strong absorption bands (ν_{as}.(CN)) at 2123 and 2132 cm^{-1}, due to the presence of the bridging thiocyanato ligands, and several weak bands (ν_{sym}.(CN)) at 758 and 769 cm^{-1}, respectively. These data are consistent with literature values [28].

3.3. Absorption spectra

The absorption spectra of the ligands L^1H_2 and L^2H_2, and the complexes $[(CuL^1)_2Hg(SCN)_2]$ and $[(CuL^2)_2Hg(SCN)_2]$, were recorded in 10^{-4} M DMF, as the complexes

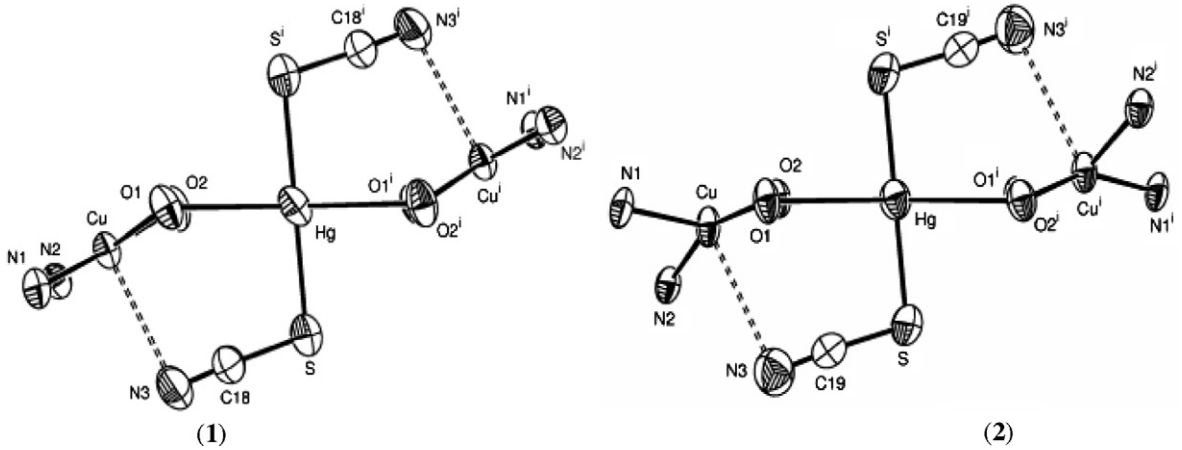


Fig. 3. Coordination geometry of the Hg and Cu metal ions in the compounds.

only show good solublity in DMF. The spectra of the ligands exhibit two quite similar absorption bands in the regions 265 and 315 nm attributable to the $\pi \rightarrow \pi^*$ transitions associated with the azomethine chromophore and n–π^* .transitions of the phenolic oxygen respectively. In the case of the complexes, the azomethine transitions shifted from 265 to 275 nm. The n-π^* transitions were shifted to a much greater extent, from 315 to 380 nm, as the phenolic oxygen had lost a hydrogen.

3.4. Biological activity

Preliminary screening for antimicrobial activities of the stock solutions of the Schiff bases and the metal complexes were performed qualitatively using the disc diffusion method (Table 3). In addition to the complex and ligands mentioned above, the biological activity of the copper complex of the ligands has also been investigated. The metal complexes and their free ligands yielded clear inhibition zones around the disc. If the inhibition zone measures 2–3 mm, then the complex has a good antimicrobial action. If the inhibition zone is more than 3 mm across, then it is considered very effective, but if there is no inhibition zone then the complex has no activity on the bacterium, and will not be retained for treatment [29].

The complexes showed more activity than the free ligands against all the tested microorganisms. The MIC values of the compounds that showed positive results in the screening process were determined as a quantitative measurement of antibacterial activity (Table 4). The results revealed $(CuL^1)_2Hg(SCN)_2$ and $(CuL^2)_2Hg(SCN)_2$ are most effective against *E. coli* ATCC 25292, *S. aureus* ATCC 6538, *P. aeruginosa* ATCC 27853, *E. aerogenes* NRRL 3567 and *L. monocytogenes* ATCC 7644 with a MIC value of 31.25 μg/ml, while CuL^1 and CuL^2 proved to be the best against the same bacteria and CuL^2 was also effective against *P. vulgaris* NRRL 123 at the same concentration (62.5 μg/ml). Also, $(CuL^1)_2Hg(SCN)_2$ and $(CuL^2)_2Hg(SCN)_2$ are effective against *C. albicans* (125 μg/ml). From a comparative study of the results in Tables 3 and 4, it was concluded that the antibacterial activity of the ligands are enhanced when it is chelated with metal ions. The growth inhibition capacity of the chelates and ligands follow the order against the tested bacteria: $(CuL^1)_2Hg(SCN)_2 > CuL^1 > L^1$; $(CuL^2)_2Hg(SCN)_2 > CuL^2 > L^2$.

At the same time these compounds were screened in order to evaluate their antifungal activity against the flamentous fungi *A. flavus*, *A. niger*, *P. expansum* and *A. brassicola* (Table 5).

The results showed that *A. brassicola* was much more sensitive against all the tested compounds compared with other filamentous fungi. On the other hand, $(CuL^1)_2Hg(SCN)_2$ and $(CuL^2)_2Hg(SCN)_2$ show more toxicity compared with other tested compounds and the standard antifungal drug, chloramphenicol, against all filamentous fungi under identical experimental conditions.

The results of antimicrobial activity show that the metal-complexes exhibit antimicrobial properties and it is important to note that they show enhanced inhibitory activity compared to their parent ligands. It may be suggested that these complexes and their ligands deactivate various cellular enzymes, which play a vital role in various metabolic pathways of these microorganisms [24]. It has also been proposed that the ultimate action of the toxicant is the denaturation of one or more proteins of the cell, which as a result, impairs normal cellular processes. Therefore, these compounds have good chemotherapeutic potential for use as antimicrobial agents against these microorganisms.

4. Conclusion

The synthetic strategy for homo- and heteropolynuclear complexes can be described in two stages: Firstly metal complexes could contain potential donor atoms for another metal ion or metal complex with an empty coordination site. Secondly, to link complexes to each other one can use bridging ligands, for example pseudohalide ligands, acting as ligands toward a second metal ion or use complexes as ligands. By this approach, we have synthesized two new heterotrinuclear complexes using Schiff bases and the thiocyanate anion. Both of the structures have been characterized by means of X-ray diffraction, elemental analyses, IR and electronic spectra. The biological activities of the characterized complexes and the ligands used were also studied. The complexes showed more activity than the free ligands against all tested microorganisms. Studies along these lines are currently in progress in our laboratory.

5. Supplementary data

CCDC 623505 and 623506 contain the supplementary crystallographic data for this paper. These data can be obtained free of charge via http://www.ccdc.cam.ac.uk/conts/retrieving.html, or from the Cambridge Crystallographic Data Centre, 12 Union Road, Cambridge CB2 1EZ, UK; fax: (+44) 1223-336-033; or e-mail: deposit@ccdc.cam.ac.uk.

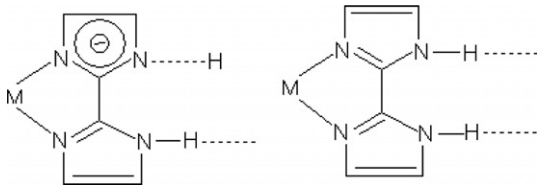
Acknowledgements

The financial support from the Scientific and Technical Research Council of Turkey (TÜBİTAK-TBAG-2452 (104T064), Balikesir University (2004-03) and Hacettepe University Syntific Research Department (Project number: 04A602004) is gratefully acknowledged.

References

[1] O. Atakol, R. Bõca, I. Ercan, F. Ercan, H. Fuess, W. Haase, R. Herchel, Chem. Phys. Lett. 423 (2006) 192.
[2] W. Liu, Y. Zou, C. Ni, Y. Li, Q. Meng, J. Mol. Struct. 751 (2005) 1.
[3] R. Tao, C. Mei, S. Zang, Q. Wang, J. Niu, D. Liao, Inorg. Chim. Acta 357 (2004) 1985.

[4] N. Dharmaraj, P. Viswanathamurthi, K. Natarajan, Trans. Metal Chem. 26 (2001) 105.
[5] P. Bühlmann, L. Yahya, R. Enderes, Electroanalysis 16 (2004) 973.
[6] C. Che, H. Kwong, W. Chu, K. Cheng, W. Lee, H. Yu, C. Yeung, K. Cheung, Eur. J. Inorg. Chem. (2002) 1456.
[7] A. Skorupa, B. Korybut-Daszkiewicz, J. Mroziński, Inorg. Chim. Acta 324 (2001) 286.
[8] R. Kurtaran, L.T. Yildirim, A.D. Azaz, H. Namli, O. Atakol, J Inorg. Biochem. 99 (2005) 1937.
[9] D.L. Reger, T.D. Wright, M.D. Smith, A.L. Rheingold, S. Kassel, T. Concolino, B. Rhagitan, Polyhedron 21 (2002) 1795.
[10] S. Banerjee, M.G.B. Drew, C. Lu, J. Tercero, C. Diaz, A. Ghosh, Eur. J. Inorg. Chem. (2005) 2376.
[11] R. Kurtaran, K.C. Emregul, C. Arici, F. Ercan, V.J. Catalano, O. Atakol, Synth. React. Inorg. Met. Org. Chem. 33 (2003) 281.
[12] O. Atakol, H. Nazir, C. Arici, S. Durmus, I. Svoboda, H. Fuess, Inorg. Chim. Acta 342 (2003) 295.
[13] H. Yao, J. Lo, B. Chen, T. Lu, Acta Cryst. C53 (1997) 1012.
[14] M.G.B. Prasad, R.N. Sharma, R.P. Acta Cryst., C41 (1985) 1755.
[15] H. Yao, J. Lo, B. Chen, T. Lu, Acta Cryst. C53 (1997) 1012.
[16] Enraf-Nonius, CAD-4 Express Software. Version 1.1. Enraf-Nonius, Delft, Netherlands, 1993.
[17] G.M. Sheldrick, SHELXS97 and SHELXL97. Program for Crystal Structure Solution and Refinement, University of Gottingen, Germany, 1997.
[18] L.J. Farrugia, J. Appl. Cryst. 32 (1999) 837.
[19] L.J. Farrugia, J. Appl. Cryst. 30 (1997) 565.
[20] NCCLS (National Committee for Clinical Laboratory Standards). Performance Standards for Antimicrobial Disc Susceptibility Test, sixth ed., Approved Standard, M2-A6. NCCLS, Wayne, PA.,(1997).
[21] E.W. Koneman, S.D. Allen, W.M. Janda, P.C. Screckenberger, W.C. Winn, Colour Atlas and Textbook of Diagnostic Microbiology, Lippincott-raven Publ., Philadelphia, 1997, 785–856.
[22] Hasenekoğlu, Laboratory Techniques for Microfungi, Atatürk University, (1990) 66, Erzurum, Turkey.
[23] F. Hadecek, H. Greger, Phytochem. Anal. 11 (2000) 137.
[24] N. Dharmaraj, P. Viswanathamurthi, K. Natarajan, Trans. Metal Chem. 26 (2001) 105.
[25] A.W. Addison, T.N. Rao, J. Reedijk, J. Vanrijn, G.C. Verchoor, J. Chem. Soc., Dalton Trans. (1984) 1349.
[26] A.L. Spek, PLATON2000, University of Utrecht, The Netherlands, 2000;
A.L. Spek, J. Appl. Cryst. 36 (2003) 7.
[27] D. Cremer, J.A. Pople, J. Amer. Chem. Soc. 97 (1975) 1354.
[28] S. Banerjee, M.G.B. Drew, C. Lu, J. Tercero, C. Diaz, A. Ghosh, Eur. J. Inorg. Chem. (2005) 2376.
[29] D. Baudoux, Antiviral and Antimicrobial Properties of Essential Oils, 12 December 2006. Available from: <www.aromabar.com/articles/baud55.htm>.



Scheme 1.

engineering, [8] in the present paper we wish to report the synthesis and X-ray crystal structure and thermal study of two Cu(II) complexes, namely $\{[Cu(H_2biim)(H_2O)(suc)](H_2O)\}_n$ (**1**) and $\{[Cu(H_2biim)_2(H_2O)][Cu(H_2biim)_2(glut)](glutH)(NO_3)\cdot 2.5H_2O\}_n$ (**2**).

2. Experimental

2.1. Materials

2,2′-Biimidazole was synthesized following a slightly modified procedure [11a] of that reported by Fieselmann et al. [11b]. All other chemicals were of AR grade and were used as received.

2.2. Physical measurements

Elemental analyses (carbon, hydrogen and nitrogen) were performed using a Perkin–Elmer 240C elemental analyzer. IR spectra were measured from KBr pellets on a Nicolet 520 FTIR spectrometer. Thermogravimetric analyses were carried out on a Mettler Toledo Star system.

2.3. Synthesis

2.3.1. $\{[Cu(H_2biim)(H_2O)(suc)](H_2O)\}_n$ (1)

An aqueous solution (5 mL) of copper nitrate trihydrate (1 mmol, 0.242 g) was poured slowly dropwise into a hot methanolic solution (10 mL) of biimidazole (2 mmol, 0.268 g). Disodium succinate (1 mmol, 0.162 g), dissolved in water (5 mL), was added to this mixture. The resultant mixture was refluxed for ~12 h. and then allowed to cool to ambient temperature. This was filtered and the filtrate was kept in a $CaCl_2$ containing desiccator. Green colored single crystals suitable for X-ray analysis were obtained from the filtrate after a few weeks. Yield 78%. *Anal.* Calc. for $C_{10}H_{14}CuN_4O_6$: C, 34.31; H, 4.00; N, 16.01. Found: C, 33.79; H, 3.89; N, 15.58%.

2.3.2. $\{[Cu(H_2biim)_2(H_2O)][Cu(H_2biim)_2(glut)](glutH)(NO_3)\cdot 2.5H_2O\}_n$ (2)

An aqueous solution (5 mL) of copper nitrate trihydrate (1 mmol, 0.242 g) was poured slowly dropwise into a hot methanolic solution (10 mL) of biimidazole (2 mmol, 0.268 g). Disodium glutarate (1 mmol, 0.176 g), dissolved in water (5 mL), was added to this mixture. The resultant mixture was refluxed for ~12 h. and then allowed to cool to ambient temperature. This was filtered and the filtrate was kept in a $CaCl_2$ containing desiccator. Green colored single crystals suitable for X-ray analysis were obtained from the filtrate after two weeks. Yield 78%. *Anal.* Calc. for $C_{34}H_{44}Cu_2N_{17}O_{14.5}$: C, 38.86; H, 4.19; N, 22.67. Found: C, 38.53; H, 4.07; N, 22.06%.

Table 1
Crystal data and structure refinements for complexes **1** and **2**

	Complex **1**	Complex **2**
Chemical formula	$C_{10}H_{14}CuN_4O_6$	$C_{34}H_{44}Cu_2N_{17}O_{14.5}$
Formula weight	349.79	1049.94
Temperature (K)	293	293
Crystal system	monoclinic	triclinic
Space group	$P2_1/n$	$P\bar{1}$
a (Å)	6.896(3)	13.871(3)
b (Å)	9.014(3)	13.995(3)
c (Å)	21.774(4)	14.133(4)
α (°)	90.0	109.94(3)
β (°)	98.01(2)	107.92(2)
γ (°)	90.0	107.91(3)
V (Å^3)	1340.3(8)	2177.3(9)
Z	4	2
D_{Calc} (g cm^{-3})	1.734	1.601
Absorption coefficient (mm^{-1})	1.664	1.064
$F(000)$	716	1082
Crystal size	$0.15\times0.15\times0.40$	
Reflections collected	17532	28672
Unique reflections [$R_{(int)}$]	4088 [0.0405]	11943 [0.0332]
Observed [$I>2\sigma(I)$]	3437	8347
Θ range	3.3–31.1	3.0–30.4
Limiting indices	$-9\leqslant h\leqslant 9$, $-12\leqslant k\leqslant 13$, $-31\leqslant l\leqslant 31$	$-19\leqslant h\leqslant 19$, $-12\leqslant k\leqslant 19$, $-18\leqslant l\leqslant 20$
Refined parameters	202	619
Goodness-of-fit (F^2)	1.017	0.988
R_1^a [$I>2\sigma(I)$]	0.0347	0.0515
wR_2^b	0.0977	0.1519
Residuals (e/Å^3)	0.479, −0.272	0.852, −0.422

[a] $R_1=\Sigma\|F_o|-|F_c\|/\Sigma|F_o|$.
[b] $wR_2=[\Sigma w(F_o^2-F_c^2)^2/\Sigma w(F_o^2)^2]^{1/2}$.

2.4. Crystal structure determination

Diffraction data for the structures reported (Table 1) were recorded at room temperature on a Nonius DIP-1030H system (Mo Kα, $\lambda=0.71073$ Å). Cell refinement, indexing and scaling of the data sets were carried out using Denzo and Scalepack [12]. Both the structures were solved by Patterson and subsequent Fourier analyses and refined by the full-matrix least-squares method based on F^2 with all observed reflections [13]. In complex **2** the difference Fourier map evidenced two disordered nitrate anions (site occupancy of 0.5 each, isotropically refined) and the electroneutrality of the compound requires a glutarate anion to be present as a monoprotonated species. Beside the coordinated aquo ligand, the ΔFourier map showed some residuals interpreted as 2.5 lattice water molecules (per asymmetric unit). The contribution of the H atoms of the water molecules O3w and O4w (0.5 occupancy, isotropically refined) was not included in the final cycles of refine-

ment. All the calculations were performed using the WINGX System, Ver 1.70.01 [14].

3. Results and discussion

3.1. IR spectra of the complexes

The complexes exhibit strong peaks at 1387, 1540 and 1593 cm^{-1} for **1**; 1384, 1526 and 1577 cm^{-1} for **2**, which are assigned to C–O stretching vibrations of the dicarboxylate. Moreover, broad peaks are present in the range 2931–3084 cm^{-1} and 2934–3124 cm^{-1} for complexes **1** and **2**, respectively, assigned to C–H stretching vibrations of the dicarboxylate [15]. Both the complexes show peaks in the region 3167–3426 cm^{-1}, assigned to O–H stretching vibrations of water molecules [15]. For complex **2**, peaks at 1128, 1347 and 1434 cm^{-1} correspond to N–O stretching vibrations of the NO_3^- anions [15]. Additional peaks for both the complexes appear in the range 681–851 cm^{-1}, indicating the presence of a N-donor ligand.

3.2. Crystal structure of the complexes

3.2.1. Complex *1*

The structure of complex **1** consists of a 1D zigzag coordination polymer extended along the crystallographic *b*-axis, built up by $Cu(H_2biim)(H_2O)$ units connected by the succinate anion acting as a μ-bidentate ligand through the carboxyl oxygens. The complex represents a rare example of a copper coordination polymer with H_2biim, since bidentate nitrogen donors preclude chain formation and only two examples of polymeric structures containing $Cu(H_2biim)$ units have been reported to date. A 2D network is formed by using the dicyanamide anions, $Cu(H_2\text{-biim})(dca)_2$, [16a] while chlorides give rise to a 1D polymer, $[Cu_{1.5}(H_2biim)_2Cl_2]$ [16b].

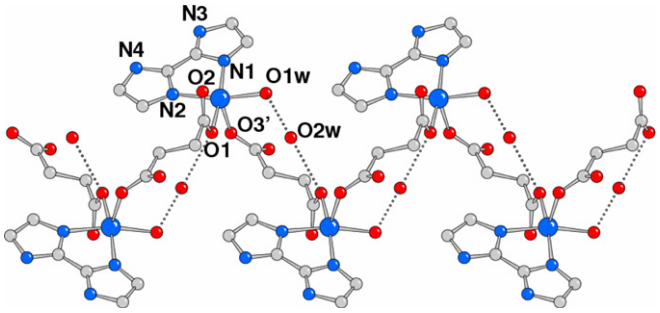


Fig. 1. Coordination polymer of complex **1** with intrachain H-bonds indicated by dotted lines. Selected bond lengths (Å): Cu–N(1) 2.017(1), Cu–N(2) 2.019(2), Cu–O(1) 1.944(1), Cu–O(1w) 2.004(1), Cu–O(3′) 2.266(2).

In the chain of **1**, the metals are separated by 7.391(1) Å along the dicarboxylate direction, with a Cu–Cu–Cu angle of 75.15(2)°. The copper has a distorted square pyramidal coordination environment with a chelating H_2biim ligand (mean Cu–N distance = 2.018(2) Å), an aquo (Cu–O(1w) = 2.004(1) Å) and succinate oxygen in the basal plane (Cu–O(1) = 1.944(1) Å). Another oxygen of a symmetry related dicarboxylate anion occupies the apical position at a longer distance (Cu–O(3′) = 2.266(2) Å). The metal is slightly displaced, by 0.138(1) Å, from the basal mean plane towards the apical oxygen donor. The polymer is reinforced by an intrachain H-bond from the lattice water molecule O(2w) bridging O(1w) and O(1) (Fig. 1, Table 2). This lattice water molecule plays a crucial role in the crystal packing since it acts also as a H-bond donor towards a symmetry related O(2) of a close polymer. The packing of complex **1** shows interdigitation of adjacent

Table 2
Hydrogen bonding interactions (Å) and angles (°) for complexes **1** and **2**

D–H	d(D–H)	d(H...A)	∠DHA	d(D...A)	A	Symmetry
1						
O1w–H11	0.858	1.867	170.55	2.718	O4	$[-x+5/2, y-1/2, -z+3/2]$
O1w–H12	0.830	1.876	167.66	2.693	O2w	
N3–H3	0.860	2.005	146.02	2.761	O3	$[x-1/2, -y+3/2, z-1/2]$
N4–H4	0.860	1.924	166.21	2.767	O4	$[x-1/2, -y+3/2, z-1/2]$
O2w–H21	0.742	2.100	168.62	2.831	O1	$[-x+3/2, y-1/2, -z+3/2]$
O2w–H22	0.899	1.928	159.32	2.787	O2	$[-x+5/2, y-1/2, -z+3/2]$
2						
N3–H3	0.860	2.073	142.83	2.807	O8	$[x-1, y-1, z]$
N4–H4	0.860	1.945	147.74	2.712	O8	$[x-1, y-1, z]$
N7–H7	0.860	2.075	148.26	2.842	O2	$[-x+1, -y+1, -z+1]$
N8–H8	0.860	2.050	148.62	2.820	O2	$[-x+1, -y+1, -z+1]$
N11–H11	0.860	1.782	177.46	2.641	O6	$[x-1, y-1, z-1]$
N12–H12	0.860	1.790	171.49	2.644	O5	$[x-1, y-1, z-1]$
N15–H15	0.860	1.790	176.91	2.649	O3	$[-x, -y+1, -z+1]$
N16–H16	0.860	1.832	176.20	2.691	O4	$[-x, -y+1, -z+1]$
O7–H7B	1.055	1.514	150.77	2.489	O1	$[-x+1, -y+1, -z]$
O1w–H1w	0.839	1.981	170.35	2.811	O2w	
O1w–H2w	0.853	1.959	170.32	2.804	O5	$[-x+1, -y+1, -z+1]$
O2w–H3w	0.857	2.146	128.72	2.764	O31	$[-x+1, -y+1, -z+2]$
O2w–H4w	0.875	1.996	171.16	2.864	O4	$[-x, -y+1, -z+1]$

chains with imidazole rings engaged in face-to-face π–π interactions (with a distance between the centroids of ca. 3.6 Å) (Fig. 2). This arrangement favors both oxygen atoms of a succinate carboxylate group attached to the H_2biim N–H donors (NH–O distances 2.76 Å) via a charge assisted hydrogen bond, allowing the formation of a "robust" 3D architecture. The flexible succinate dianions (the torsion angle of the carbon skeleton is 176.35(14)° and the dihedral angle between the carboxylate groups is 60.5(1)°) assist the described crystal packing.

3.2.2. Complex **2**

The structure of **2** is built up of bischelated $[Cu(II)(H_2biim)_2]^{2+}$ complexes, glutarate and nitrate anions, and water molecules, held together with extensive H-bonding. To assure the electroneutrality of the complex, a glutarate anion is present as a monoprotonated species at O(7) (see Section 2), according to the C–O distance and H-bond connection. Both the independent copper ions show a distorted square pyramidal coordination environment with chelating H_2biim ligands in the basal plane and with Cu–N bond distances ranging from 1.992(3) to 2.061(2) Å. The apical position of the Cu(1) and Cu(2) coordination environment is occupied by an aquo and a glutarate oxygen, respectively. The Cu(1)–O(1w) and Cu(2)–O(2) bond lengths are 2.261(2) and 2.600(2) Å and Cu(1) is displaced by 0.2 Å from the N_4 donor mean plane towards the aquo ligand, while Cu(2) is located in the basal plane. The planarity observed for the H_2biim ligands is indicative of π-electron delocalization in the imidazole rings. It is worth noting the H-bonding scheme occurring between the H_2biim ligands and glutarate anions. The NH groups of $Cu(1)(H_2biim)_2$ are bridged by a single carboxylate oxygen while those at Cu(2) interact with both glutarate carboxylate oxygens, likewise to that observed in complex **1** (Figs. 3 and 4). Correspondingly the former H-bonding interactions appear weaker (NH–O distances between 2.712 and 2.842 Å) with respect to the other, falling in the range

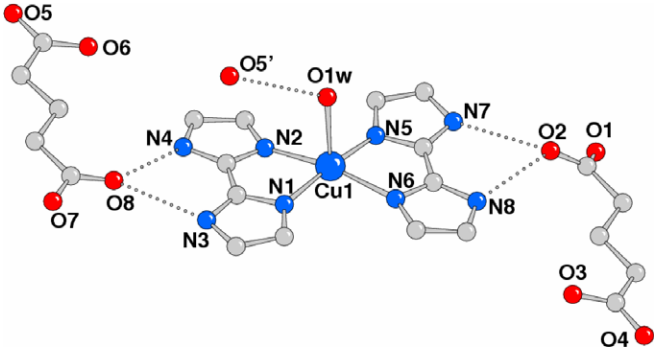


Fig. 3. Details of the crystal packing of complex **2** with indication of the metal coordination sphere about Cu(1) and H-bonds. Selected bond lengths (Å): Cu(1)–N(5) 1.992(3), Cu(1)–N(1) 1.995(3), Cu(1)–N(2) 2.049(2), Cu(1)–N(6) 2.061(2), Cu(1)–O(1w) 2.261(2).

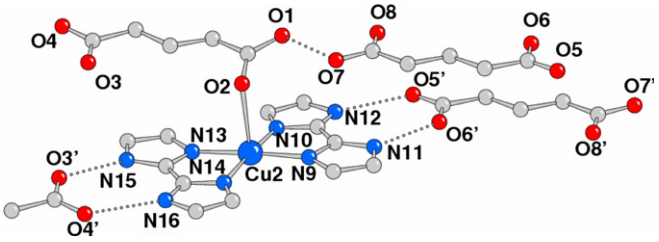


Fig. 4. The metal coordination sphere about Cu(2) of complex **2** with H-bonds indicated. O(7) represents the protonated glutarate oxygen. Selected bond lengths (Å): Cu(2)–N(9) 2.007(2), Cu(2)–N(13) 2.012(2), Cu(2)–N(14) 2.017(3), Cu(2)–N(10) 2.017(3), Cu(2)–O(2) 2.600(2).

2.641–2.691 Å (Table 2). These connections, together with the H-bonds taking place between the coordinated water (O1w) and dicarboxylate anions, give origin to a double-layered structure. The resulting crystalline architecture is enhanced to a 3D structure through weak hydrogen bonds involving the lattice water molecule O(2w). Fig. 5 shows a view of the net down the *b*-axis, evidencing channels filled by lattice water molecules and disordered nitrate anions. The results for complex **2** confirm the strong tendency of the H_2biim ligands to form bischelated species (specially

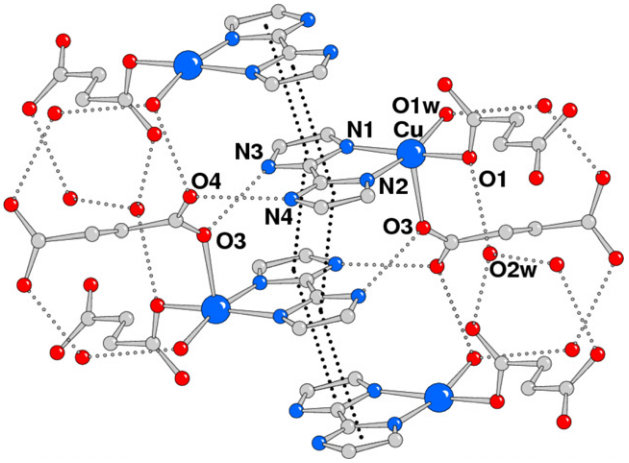


Fig. 2. 3D structure of complex **1** with π–π interactions between biim rings and H-bonds (dotted lines) occurring between NH of 2,2′-biimidazole ligands and carboxylate groups.

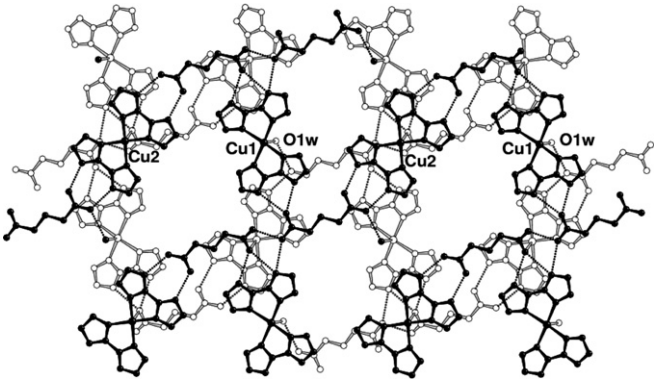


Fig. 5. Double layered net built up by $Cu(H_2biim)_2$ units and glutarate anions in complex **2** forming channels . The lattice water molecules and disordered nitrate anions filling the voids are not shown.

for square planar and octahedral complexes, [17] as for example when M = Cu^{2+} [2b], Co^{2+} [3a], Ni^{2+} [3a], Fe^{2+} [3b] and Zn^{2+} [3c]) and the dimensionality is extended through the formation of a hydrogen-bonding network. As a matter of fact, the crystal of $[Cu_{1.5}(H_2biim)_2Cl_2]$ [16b], also contains cationic species $[Cu_{1.5}(H_2biim)_2]^{2+}$ beside the 1D polymer mentioned above. Consequently the 2,2′-biimidazole-dicarboxylate hydrogen bond link appears to be a suitable motif in crystal engineering to form supramolecular networks.

3.3. Thermal analysis

Complex **1** is thermally stable up to 45 °C and on further heating it starts to lose water molecules and becomes deaquated at ~150 °C in two steps. The first step (50–80 °C) corresponds to the loss of half a lattice water molecule, whereas the second step (100–150 °C) indicates the loss of half lattice and one coordinated water molecule (Fig. S1). The elimination of the lattice water molecule in two steps is probably due to the different strengths of the H-bond (2.787 Å and 2.831 Å) (Fig. 1, Table 2) involved with the lattice water. The deaquated species does not revert on exposure to humid atmosphere, reflecting the attainment of a pentacoordinated geometry, even after dehydration, which is possible if the pendent O-atom of succinate takes part in coordination.We could not verify this as isolation of the pure species was not possible as it starts to collapse slowly upon further heating. Thermogravimetric analysis of complex **2** reveals that it loses lattice water molecules at ~100 °C in two overlapping steps (Fig. S2). Here also elimination of lattice water molecules occuring into two steps is due to the difference in strength of the H-bonds (2.764 Å and 2.864 Å) (Table 2). The structure collapses at the threshold of the deaquation.

4. Conclusion

Two Cu(II) complexes, synthesized by combining neutral H_2biim ligands and dicarboxylate anions, show that succinate in **1** acts as coordination ligand while the glutarate anion in **2** functions as a good acceptor of H-bonds, leading to supramolecular architectures. 1D zigzag coordination polymers are obtained in **1** via μ-bidentate succinate anions, and the dimensionality is extended to a ''robust'' 3D architecture through H-bonding between NH donors of H_2biim and succinate anions and through π–π interactions of interdigitated imidazole rings. In complex **2** bischelated $[Cu(II)(H_2biim)_2]^{2+}$ units, glutarate, nitrate anions and water molecules are held together through extensive H-bonding contacts, resulting in a 3D supramolecular network.

Acknowledgement

The authors acknowledge CSIR (India) for financial support.

Appendix A. Supplementary material

CCDC 634321 and 634322 contain the supplementary crystallographic data for **1** and **2**. These data can be obtained free of charge via http://www.ccdc.cam.ac.uk/conts/retrieving.html, or from the Cambridge Crystallographic Data Centre, 12 Union Road, Cambridge CB2 1EZ, UK; fax: (+44) 1223-336-033; or e-mail: deposit@ccdc.cam.ac.uk. Supplementary data associated with this article can be found, in the online version, at doi:10.1016/j.poly.2007.05.042.

References

[1] (a) T.G. Spiro (Ed.), Copper Proteins, John Wiley, New York, 1981;
(b) K.D. Karlin, J. Zubieta (Eds.), Copper Coordination Chemistry: Biochemistry & Inorganic Perspectives, Adenine Press, Guilderland, NY, 1983;
K.D. Karlin, J. Zubieta, Biological and Inorganic Copper Chemistry, vols. I and II, Adenine Press, Guilderland, NY, 1986;
(c) B.J. Hathaway, in: G. Wilkinson, R.D. Gillard, J.A. McCleverty (Eds.), Comprehensive Coordination Chemistry, vol. 5, Pergamon Press, Oxford, 1987, p. 594.

[2] (a) S.M. Roberts (Ed.), Molecular Recognition: Chemical and Biochemical Problems, RSC, Special Publication, vol. 78, 1990;
(b) A.K. Ghosh, A.D. Jana, D. Ghoshal, G. Mostafa, N. Ray Chaudhuri, Cryst. Growth Des. 6 (2006) 701.

[3] (a) R. Atencio, M. Chacón, T. Gonzalez, A. Briceño, G. Agrifoglio, A. Sierraalta, J. Chem. Soc., Dalton Trans. (2004) 505;
(b) M.A.M. Lorente, F. Dahan, Y. Sanakis, V. Petrouleas, A. Bousseksou, J.P. Tuchagues, Inorg. Chem. 34 (1995) 5346;
(c) B.H. Ye, F. Xue, G.Q. Xue, L.N. Ji, T.C.W. Mak, Polyhedron 18 (1999) 1785.

[4] (a) M. Tadokoro, K. Nakasuji, Coord. Chem. Rev. 198 (2000) 205;
(b) M. Tadokoro, K. Isobe, H. Uekusa, Y. Ohashi, J. Toyoda, K. Tashiro, K. Nakasuji, Angew Chem., Int. Ed. Engl. 38 (1999) 95;
(c) A. Mayboroda, P. Comba, H. Pritzkow, G. Rheinwald, H. Lang, G. van Koten, Eur. J. Inorg. Chem. (2003) 1703;
(d) K. Larsson, L. Öhrström, CrystEngComm 6 (2004) 354.

[5] (a) Y. Morita, T. Murata, K. Fukui, M. Tadokoro, K. Sato, D. Shiomi, T. Takui, K. Nakasuji, Chem. Lett. 33 (2004) 188;
(b) G. Aromi, P. Gamez, H. Kooijman, A.L. Spek, W.L. Driessen, J. Reedijk, Eur. J. Inorg. Chem. (2003) 1394.

[6] (a) C. Hornick, P. Rabu, M. Drillon, Polyhedron 19 (2000) 259;
(b) T.A. Bowden, H.L. Milton, A.M.Z. Slawin, P. Lightfoot, J. Chem. Soc., Dalton. Trans. (2003) 936;
(c) M. Frisch, C.L. Cahill, Dalton Trans. (2005) 1518.

[7] (a) D. Ghoshal, T.K. Maji, G. Mostafa, S. Sain, T.-H. Lu, J. Ribas, E. Zangrando, N. Ray Chaudhuri, Dalton Trans. (2004) 1687;
(b) C. Bazzicalupi, A. Bencini, A. Bianchi, V. Fusi, E.G. España, C. Giorgi, J.M. Llinares, J.A. Ramirez, B. Valtancoli, Inorg. Chem. 38 (1999) 620.

[8] (a) B. Rather, M.J. Zaworotko, Chem. Commun. (2003) 830;
(b) E.W. Lee, Y.J. Kim, D.-Y. Jung, Inorg. Chem. 41 (2002) 501;
(c) Y.J. Kim, Y.J. Park, D.-Y. Jung, Dalton Trans. (2005) 2603.

[9] (a) N. Guillou, C. Livage, M. Drillon, G. Férey, Angew Chem., Int. Ed. Engl. 42 (2003) 5314;
(b) R. Vaidhyanathan, S. Natarajan, C.N.R. Rao, J. Solid State Chem. 177 (2004) 1444.

[10] (a) J.-S. Kim, H. Kim, M. Ree, Chem. Mater. 16 (2004) 2981;
(b) F. Serpaggi, G. Férey, J. Mol. Struct. 656 (2003) 201.

[11] (a) K. Ramírez, J.A. Reyes, A. Briceño, R. Atencio, CrystEngComm 4 (2002) 208;
(b) B.F. Fieselmann, D.N. Hendrickson, G.D. Stucky, Inorg. Chem. 17 (1978) 2078.

[12] Z. Otwinowski, W. Minor, Processing of X-ray Diffraction Data Collected in Oscillation Mode, in: C.W. Carter Jr., R.M. Sweet, eds., Methods in Enzymology, vol. 276. Academic Press, New York, 1997, pp. 307–326.
[13] G.M. Sheldrick, SHELX97 Programs for Crystal Structure Analysis (Release 97-2), University of Göttingen, Germany, 1998.
[14] L.J. Farrugia, J. Appl. Crystallogr. 32 (1999) 837.
[15] K. Nakamoto, Infrared and Raman Spectra of Inorganic and Coordination Compounds, fourth ed., Wiley-Interscience, New York, 1986.
[16] (a) A. Mohamadou, G.A. van Albada, H. Kooijman, B. Wieczorek, A.L. Spek, J. Reedijk, New J. Chem. 27 (2003) 983;
(b) A. Bencini, F. Mani, Inorg. Chim. Acta 154 (1988) 215.
[17] Data retrieved from the Cambridge Crystallographic Data Centre F.H. Allen, O. Kennard, R. Taylor, Acc. Chem. Res. 16 (1983) 146.

compounds containing 8-hydroxyquinoline and transition metals has recently increased [38–41]. The title compound joins the benefits of ruthenium coordination compounds and complexes containing 8-hydroxyquinoline and carbonyl groups, thus its synthesis and determination of its properties were undertaken.

In this paper we present the synthesis, crystal, molecular and electronic structure, and luminescence and spectroscopic characterization of a new ruthenium(II) carbonyl complex with the 8-hydroxyquinoline ligand.

2. Experimental

All reagents used in the synthesis of the complex are commercially available and were used without further purification. The $[RuHCl(CO)(PPh_3)_3]$ complex was synthesized by a published procedure [42].

2.1. Physical measurements

Infrared spectra were recorded on a Nicolet Magna 560 spectrophotometer in the spectral range 4000–400 cm^{-1} with the sample in the form of a KBr pellet. Electronic spectra were measured on a spectrophotometer Lab Alliance UV–Vis 8500 in the range 800–200 nm in dichloromethane solution. Elemental analyses (C, H, N) were performed on a Perkin–Elemer CHN–2400 analyzer. The ^1H NMR spectrum was obtained at room temperature in $CDCl_3$ using an INOVA 300 spectrometer. Luminescence measurements were made on a Jobin-Yvon (SPEX) FLUOROLOG-3.12 spectrofluorometer at room temperature.

2.2. DFT calculations

The GAUSSIAN-03 program [43] was used in the calculations. The geometry optimization was carried out with the DFT method with the use of B3LYP functional [44,45]. The electronic transitions were calculated with the PCM model [46] with dichloromethane as the solvent. The calculation was performed using the DZVP basis set [47] with f functions with exponents 1.94722036 and 0.748930908 on the ruthenium atom, and polarization functions for all other atoms: 6-31g(2d,p) – chlorine, 6-31g** – carbon, nitrogen, oxygen and 6-31g(d,p) on hydrogen atoms. Natural bond orbital (NBO) calculations were performed with the NBO code [48] included in GAUSSIAN-03.

2.3. Synthesis of $[RuCl(CO)(PPh_3)_2(C_9H_6NO)]$

A suspension of $[RuHCl(CO)(PPh_3)_3]$ (0.95 g; 1×10^{-3} mol) and 8-hydroxyquinoline (0.36 g; 2×10^{-3} mol) in dimethoxyethane (100 cm^{-3}) was refluxed until the solid dissolved, then the solution was cooled and filtered. Yellow crystals suitable for X-ray crystal analysis were obtained by slow evaporation of the reaction mixture. Yield: 81%.

Anal. Calc. for $C_{46}H_{36}ClNO_2P_2Ru$: C, 66.31; H, 4.35; Cl, 4.25; N, 1.68; O, 3.84; P, 7.43; Ru, 12.13. Found: C, 66.30; H, 4.33; N, 1.66%.

IR (KBr): 3056 ν_{CH}; 2987 $\nu_{CH-phenyl}$; 1938 $\nu_{C\equiv O}$; 1569 ν_{CN}; 1462 $\delta_{(C-CH\ in\ the\ plane)}$; 1434 $\nu_{Ph(P-Ph)}$; 1373 ($\nu_{ring} + \nu_{CH}$); 1324 (δ_{CH}); 1094 $\delta_{(C-CH\ in\ the\ plane)} + \nu_{CO}$; 742 $\delta_{(C-C\ out\ of\ the\ plane)}$; 693 $\delta_{(C-C\ in\ the\ plane)}$; 604 ν_{P-Ph}.

^{31}P NMR (δ, $CDCl_3$): (s, PPh_3) 31.41.

UV–Vis (nm) in CH_2Cl_2 ($\log\varepsilon$): 417.4 (4.54); 328.2 (4.90); 259.6 (5.11); 221.2 (4.92).

2.4. Crystal structure determination and refinement

A yellow prism of the studied complex was mounted on a KM-4-CCD automatic diffractometer equipped with a CCD detector, and used for data collection. X-ray intensity data were collected with graphite-monochromated Mo Kα radiation ($\lambda = 0.71073$ Å) at the temperature 291.0(3) K, with the ω scan mode. The full Ewald sphere reflections were collected up to $2\theta = 50.24°$. The unit cell parameters were determined from least-squares refinement of the setting angles of 9369 strongest reflections for the complex. Details concerning crystal data and refinement are given in Table 1. Monitoring of 173 reflection intensities on reference frames measured every 40 frames show 7.32% decay of intensity. During the data reduction the above decay correction coefficient was taken into account. Lorentz, polarization, and numerical absorption [49] cor-

Table 1
Crystal data and structure refinement details of $[RuCl(CO)(PPh_3)_2(C_9H_6NO)]$

Empirical formula	$C_{46}H_{36}ClNO_2P_2Ru$
Formula weight	833.22
Temperature (K)	291.0(3)
Crystal system	monoclinic
Space group	$P2_1/c$
Unit cell dimensions	
a (Å)	15.6122(7)
b (Å)	20.6761(11)
c (Å)	24.8752(12)
α (°)	90.00
β (°)	101.676(4)
γ (°)	90.00
Volume (Å^3)	7863.5(7)
Z	8
D_{calc} (Mg/m^3)	1.408
Absorption coefficient (mm^{-1})	0.587
$F(000)$	3408
Crystal dimensions (mm)	$0.403 \times 0.258 \times 0.169$
θ Range for data collection (°)	2.69–25.12
Index ranges	$-18 \leqslant h \leqslant 18$, $-21 \leqslant k \leqslant 24$, $-29 \leqslant l \leqslant 29$
Reflections collected	14011
Independent reflections (R_{int})	9005 (0.0988)
Data/restraints/parameters	9005/0/955
Goodness-of-fit on F^2	1.103
Final R indices [$I > 2\sigma(I)$]	$R_1 = 0.1288$, $wR_2 = 0.1455$
R indices (all data)	$R_1 = 0.0633$, $wR_2 = 0.1202$
Largest difference in peak and hole (e Å^{-3})	0.631 and −0.553

rections were applied. The structure was solved by the Patterson method combined with a partial structure expansion procedure. All the non-hydrogen atoms were refined anisotropically using the full-matrix least-squares technique on F^2. The hydrogen atoms were found from difference Fourier synthesis after four cycles of anisotropic refinement, and refined as ''riding'' on the adjacent atom with individual isotropic temperature factors equal to 1.2 times the value of the equivalent temperature factor of the parent atom, with geometry idealization after each cycle. SHELXS-97 [50], SHELXL-97 [51] and SHELXTL [52] programs were used for all the calculations. Atomic scattering factors were those incorporated in the computer programs.

3. Results and discussion

The reaction of the complex $[RuHCl(CO)(PPh_3)_3]$ with 8-hydroxyquinoline has been performed. Refluxing a ruthenium carbonyl hydrido complex with an excess of 8–hydroxyquinoline in dimethoxyethane leads to the complex $[RuCl(CO)(PPh_3)_2(C_9H_6NO)]$ in good yield. The elemental analysis of the complex is in good agreement with its formulation. The IR spectrum of the complex is consistent with its molecular structure. The bands of C≡O and C=N stretching modes are observed at 1938 and 1569 cm^{-1}, respectively. The $\nu_{Ph(P-Ph)}$ absorption band at 1434 cm^{-1} indicates the presence of triphenylphosphine ligands. The singlet at 31.41 ppm in the ^{31}P NMR spectrum indicates both triphenylphosphoine ligands in the studied complex are equivalent and are mutually *trans* disposed.

3.1. Crystal structure

The $[RuCl(CO)(PPh_3)_2(C_9H_6NO)]$ complex crystallises in the monoclinic $P2_1/c$ group and the crystal structure is built up of two independent molecules in the asymmetric unit. Both molecules have the same conformation (the root mean square deviation of superimposed molecules atoms is 0.133 Å and the most distant O(2) atoms are separated by 0.335 Å). The relative orientation of the molecules is depicted in Fig. 1, which also shows the displacement ellipsoids of the non-hydrogen atoms. These two molecules are twisted with respect to one another by 62.81(4)°, which prevents the existence of higher crystallographic symmetry. The structural drawing is presented in Fig. 2. The most important angles and bond lengths for the complex are reported in Table 2. The weak intra- and intermolecular hydrogen bonds [53,54] are presented in Table 3.

The ruthenium atom in the complex $[RuCl(CO)(PPh_3)_2(C_9H_6NO)]$ is in a distorted octahedral environment with *trans* triphenylphosphine ligands (average P–Ru–P

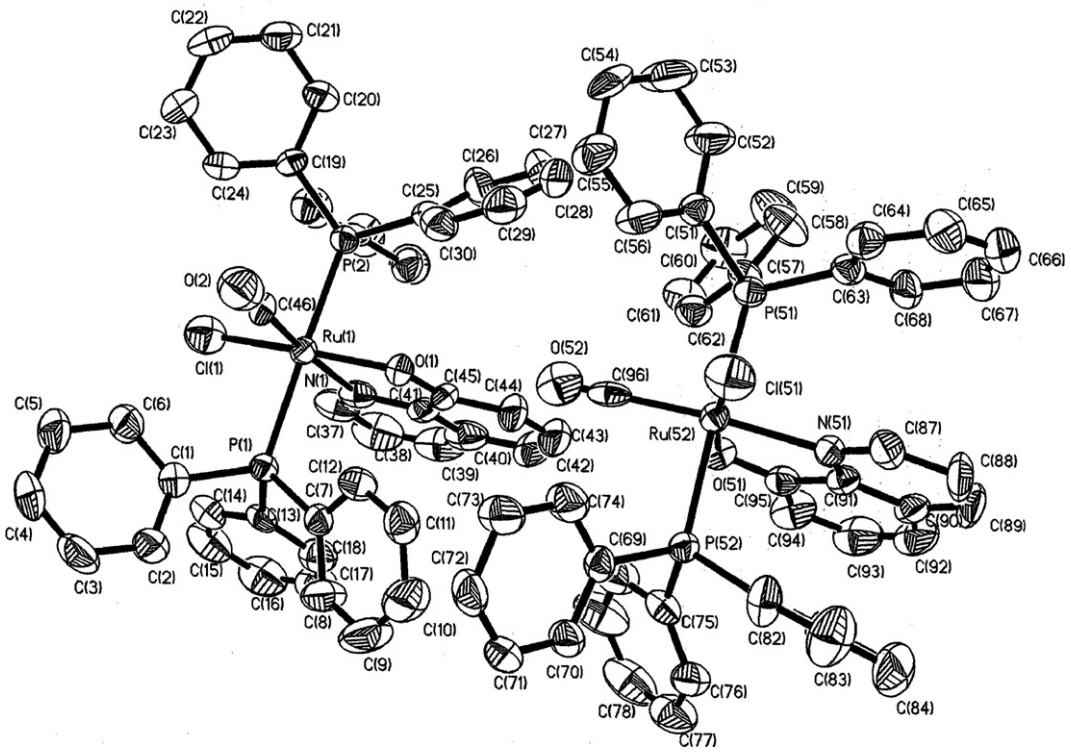


Fig. 1. Relative orientation of two molecules of the $[RuHCl(CO)(PPh_3)_2(C_9H_6NO)]$ complex in the asymmetric unit. The displacement ellipsoids are drawn with 50% probability.

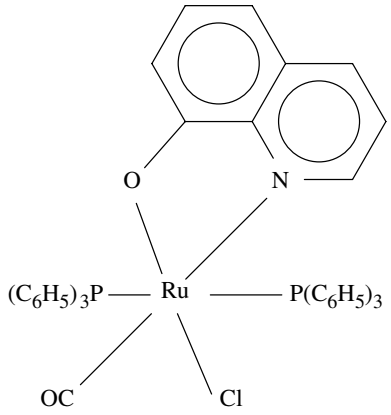


Fig. 2. Structural drawing of $[RuHCl(CO)(PPh_3)_2(C_9H_6NO)]$.

angle 177.62(5)°). The carbonyl ligand is in *trans* position to the hydroxyquinoline N donor atom (average C–Ru–N angle 170.8(3)°) and the chloride ion lies *trans* to the hydroxyquinoline oxygen atom with an average angle of 171.07(11)°. All Ru–ligand distances, such as Ru–Cl 2.4183(18), Ru–P 2.4105(14), 2.4106(14), Ru–N 2.1270(4), Ru–C 1.9585(7) and Ru–O 2.0770(3) Å, are normal and are comparable with distances in other ruthenium complexes containing heterocyclic ligands [55–58]. The C(46)–O(2) bond shows some shortening in comparison with typical distances in CO substituents, but similar distances can be found in several compounds [59–76].

The conformation of the molecule is stabilized by five weak intramolecular hydrogen bonds, three between the phenyl CH and the Cl ligand (D···A distance varies from 3.334(7) to 3.492(6) Å and D–H···A angle varies from 122.5° to 146.8°) and two linking the phosphine phenyl C–H and O (D···A distance 2.885(6) and 2.884(6) Å and D–H···A angle 117.0° and 100.1°). One intermolecular hydrogen bond is observed, C(89)–H(89)···O(52)(#1 $-x+1,\ y-1/2,\ -z+1/2$) (D···A distance 3.470(9) Å; D–H···A angle 171.1°).

3.2. Geometry optimization

The geometry of the studied complex was optimized by the DFT method with the B3LYP functional. The optimized geometry parameters for the $[RuCl(CO)(PPh_3)_2(C_9H_6NO)]$ complex are gathered in Table 2. In general, the predicted bond lengths and angles are in agreement with the values based upon the X-ray crystal structure data, and the general trends observed in the experimental data are reproduced in the calculations. The calculated bond lengths and angles for $[RuCl(CO)(PPh_3)_2(C_9H_6NO)]$ agree with the experimental results; the largest difference is found for the C(43)–O(2) bond (~0.25 Å). The maximum difference between the calculated and experimental angles are visible for N(1)–Ru(1)–P(1) and C(46)–Ru(1)–O(1) and are close to 2.1° and 2.0°, respectively.

3.3. Electronic structure and NBO analysis

In the studied complex, the occupied d_{xy} and d_{xz} ruthenium orbitals participate in backdonation from the central metal ion to the carbonyl ligand. The largest contribution of the π_{Ru-CO} bonding interaction is visible in the H−1 and H−3 orbitals. The π^*_{Ru-CO} orbitals are also distributed

Table 2
Selected bond lengths (Å) and angles (°) for $[RuCl(CO)(PPh_3)_2(C_9H_6NO)]$

Experimental				Calculated
Bond lengths (Å)				
Ru(1)–C(46)	1.975(7)	Ru(52)–C(96)	1.942(7)	1.876
Ru(1)–O(1)	2.076(3)	Ru(52)–O(51)	2.078(3)	2.106
Ru(1)–N(1)	2.127(4)	Ru(52)–N(51)	2.127(4)	2.182
Ru(1)–P(1)	2.4128(14)	Ru(52)–P(51)	2.4081(14)	2.466
Ru(1)–P(2)	2.4089(14)	Ru(52)–P(52)	2.4123(14)	2.467
Ru(1)–Cl(1)	2.4097(18)	Ru(52)–Cl(51)	2.4270(16)	2.482
C(46)–O(2)	0.884(7)	C(96)–O(52)	0.932(6)	1.159
Bond angles (°)				
C(46)–Ru(1)–O(1)	92.2(3)	C(96)–Ru(52)–O(51)	90.1(2)	93.18
C(46)–Ru(1)–N(1)	171.6(3)	C(96)–Ru(52)–N(51)	170.0(2)	171.22
O(1)–Ru(1)–N(1)	79.32(16)	O(51)–Ru(52)–N(51)	79.89(15)	78.04
C(46)–Ru(1)–P(2)	90.6(2)	C(96)–Ru(52)–P(52)	90.27(18)	88.96
O(1)–Ru(1)–P(2)	88.76(10)	O(51)–Ru(52)–P(52)	88.78(10)	91.09
N(1)–Ru(1)–P(2)	88.84(11)	N(51)–Ru(52)–P(52)	88.48(11)	91.20
C(46)–Ru(1)–Cl(1)	96.8(2)	C(96)–Ru(52)–Cl(51)	98.57(19)	97.72
O(1)–Ru(1)–Cl(1)	170.84(11)	O(51)–Ru(52)–Cl(51)	171.29(11)	169.10
N(1)–Ru(1)–Cl(1)	91.59(13)	N(51)–Ru(52)–Cl(51)	91.41(12)	91.06
P(2)–Ru(1)–Cl(1)	89.94(5)	P(52)–Ru(52)–Cl(51)	90.59(5)	89.09
C(46)–Ru(1)–P(1)	91.7(2)	C(96)–Ru(52)–P(51)	92.04(18)	88.97
O(1)–Ru(1)–P(1)	90.48(10)	O(51)–Ru(52)–P(51)	91.67(10)	91.08
P(2)–Ru(1)–P(1)	177.58(5)	P(51)–Ru(52)–P(52)	177.65(5)	177.08
Cl(1)–Ru(1)–P(1)	90.44(5)	P(51)–Ru(52)–Cl(51)	88.62(5)	89.15
N(1)–Ru(1)–P(1)	88.76(11)	N(51)–Ru(52)–P(51)	89.33(11)	91.16

Table 3
Hydrogen bonds for $[RuCl(CO)(PPh_3)_2(C_9H_6NO)]$ (Å and °)

D–H···A	d(D–H)	d(H···A)	d(D···A)	∠(DHA)
C(6)–H(6)···Cl(1)	0.93	2.70	3.452(6)	138.9
C(12)–H(12)···O(1)	0.93	2.34	2.885(6)	117.0
C(24)–H(24)···Cl(1)	0.93	2.68	3.492(6)	146.8
C(30)–H(30)···O(1)	0.93	2.57	2.884(6)	100.1
C(37)–H(37)···Cl(1)	0.93	2.74	3.334(7)	122.5
C(56)–H(56)···Cl(51)	0.93	2.79	3.455(6)	129.6
C(62)–H(62)···O(51)	0.93	2.40	2.972(6)	119.4
C(74)–H(74)···Cl(51)	0.93	2.69	3.452(6)	139.8
C(87)–H(87)···Cl(51)	0.93	2.77	3.360(6)	122.3
C(89)–H(89)···O(52)#1	0.93	2.55	3.470(9)	171.1

Symmetry transformations used to generate equivalent atoms: #1 $-x+1$, $y-1/2$, $-z+1/2$.

among several unoccupied molecular orbitals. Their contribution is visible in L+14, L+15. The HOMO orbital of the $[RuCl(CO)(PPh_3)_2(C_9H_6NO)]$ complex is composed of the d_{xz} metal orbital and the hydroxyquinoline oxygen π orbital in an anti-bonding arrangement. The LUMO orbital is localized on the hydroxyquinoline ring. The d_{z^2} orbital of the Ru atom makes the largest contribution to L+2 and, whereas L+4, L+14 and L+15 have $d_{x^2-y^2}$ character.

In some of the lowest unoccupied molecular orbitals of $[RuCl(CO)(PPh_3)_2(C_9H_6NO)]$, the contribution of the phosphorous orbitals is visible (L+1, L+2, L+3). In classical concepts empty phosphorous 3d orbitals are used in the π-back bonding between the metal center and the phosphine ligand. Now it is generally recognized that d orbitals have very high energy and play only a minor role in the π_{M-PR3} bond formation [77]. In the π-back bonding between the metal center and the phosphine ligand, the σ*(P–C) orbitals are involved. The HOMO–LUMO gap is 3.24 eV. The energy and character of the selected frontier molecular orbitals are given in Table 4.

The natural bond orbital (NBO) σ_{AB} can be written in terms of two directed valence hybrids (HHOs) h_A and h_B on atoms A and B:

$$\sigma_{AB} = c_A h_A + c_B h_B$$

where c_A and c_B are polarization coefficients. Each valence bonding NBO must in turn be paired with a corresponding valence *anti*-bonding NBO:

$$\sigma^*_{AB} = c_B h_A - c_A h_B$$

to complete the span of the valence space. The Lewis-type (donor) NBOs are thereby complemented by the non-Lewis-type (acceptor) NBOs that are formally empty in an idealized Lewis picture. The interactions between "filled" Lewis-type NBOs and "empty" non-Lewis NBOs lead to loss of occupancy from the localized NBOs of the idealized Lewis structure into the empty non-Lewis orbitals, and they are referred to as "delocalization" corrections to the zeroth-order natural Lewis structure.

For the carbonyl group of the investigated complex, three natural bond orbitals were detected for the C–O bond, and one for the Ru–C bond. The Ru–C bond orbitals are polarized towards the carbon atom, and the C–O bond orbitals are polarized towards the oxygen end. The oxygen atom of the carbonyl ligand has one lone pair (LP) orbital. The occupancies and hybridization of the CO and Ru–C bonds are gathered in Table 5 (*anti*-bonding NBOs are given in round brackets).

Not detected in NBO analysis, the $Ru–N_{(hq)}$ and $Ru–O_{(hq)}$ bonds have a character consisting of predominantly Coulomb-type interactions between the central ion and the 8-hydroxyquinoline ligand [78].

The calculated charge on the ruthenium atom in the complex $[RuCl(CO)(PPh_3)_2(C_9H_6NO)]$ is considerable lower than the formal charge of +2, and is close to 0.21.

Table 4
The energy and character of selected occupied and virtual MOs for $[RuCl(CO)(PPh_3)_2(C_9H_6NO)]$

MO	Energy	Character
H−15	−6.797	π_{PPh_3}
H−14	−6.776	π_{PPh_3}
H−13	−6.723	π_{PPh_3}
H−12	−6.651	π_{PPh_3}
H−11	−6.614	π_{PPh_3}
H−10	−6.596	π_{PPh_3}
H−9	−6.581	π_{PPh_3}
H−8	−6.514	$\pi_{PPh_3} + \pi_{Cl}$
H−7	−6.486	$\pi_{PPh_3} + \pi_{hq}$
H−6	−6.404	$\pi_{PPh_3} + \pi_{Cl}$
H−5	−6.365	$\pi_{PPh_3} + \pi_{hq}$
H−4	−6.019	$d_{Ru} + n_P$
H−3	−5.748	$d_{Ru} + \pi^*_{CO}$
H−2	−5.095	$d_{Ru} + \pi^*_{Cl}$
H−1	−4.788	$d_{Ru} + \pi^*_{Cl} + \pi^*_{CO}$
H	−4.272	$d_{Ru} + \pi^*_{O}$
L	−1.034	π^*_{hq}
L+1	−0.563	$\pi^*_{PPh_3} + n_P$
L+2	−0.487	$d_{Ru} + \pi^*_{PPh_3} + n_P$
L+3	−0.408	$\pi^*_{PPh_3} + n_P$
L+4	−0.249	$d_{Ru} + \pi^*_{PPh_3}$
L+5	−0.134	$\pi^*_{PPh_3}$
L+6	−0.027	$\pi_{PPh_3} + \pi^*_{hq}$
L+7	0.052	$\pi^*_{PPh_3}$
L+8	0.106	$\pi^*_{PPh_3}$
L+9	0.180	$\pi^*_{PPh_3}$
L+10	0.207	$\pi^*_{PPh_3}$
L+11	0.268	$\pi^*_{PPh_3}$
L+12	0.301	$\pi^*_{PPh_3}$
L+13	0.312	$\pi^*_{PPh_3}$
L+14	0.537	$d_{Ru} + \pi^*_{CO}$
L+15	1.140	$d_{Ru} + \pi^*_{CO}$

H denotes HOMO; L denotes LUMO.

Table 5
The occupancies and hybridization of the calculated Ru–C and C–O natural bond orbitals (NBOs) of $[RuCl(CO)(PPh_3)_2(C_9H_6NO)]$

BD (2-center bond)	Occupancy	Hybridization of NBO
Ru(1)–C(46)	1.955 (0.309)	$0.513(sd^{3.75})_{Ru} + 0.859(sp^{0.47})_C$
C(46)–O(2)	1.998 (0.080)	$0.533(sp^{61.70}d^{0.20})_C + 0.846(sp^{34.32}d^{0.23})_O$
	1.997 (0.091)	$0.532(sp)_C + 0.847(p)_O$
	1.995 (0.018)	$0.546(sp^{2.26})_C + 0.838(sp^{0.39})_O$

The charge on the carbon atom of the carbonyl ligand is positive (+0.59), whereas the oxygen atom is negatively charged (−0.30).

The charges on the P atoms are positive and close to 1.15; the charge on the chloride ligand is smaller than −1 (−0.62), the charge on the hydroxyquinoline ligand is close to −0.53. The occupancies of the ruthenium d orbitals, obtained from NBO analysis, are as follows: d_{xy} −1.84; d_{xz} −1.89; d_{yz} −0.86; $d_{x^2-y^2}$ −1.25; d_{z^2} −1.60.

3.4. Electronic spectrum

The experimental and calculated electronic spectra of $[RuCl(CO)(PPh_3)_2(C_9H_6NO)]$ are presented in Fig. 3. The contour of calculated spectrum was broadening by the Lorentzian function, calculated by the formula:

$$I = \frac{I_0}{1 + \left(\frac{\nu - \nu_0}{\gamma}\right)^2};$$

where $\gamma = 1/2$ spectral width on 1/2 height.

Ninety electronic transitions were calculated using the TDDFT method and they do not comprise all the experimental absorption bands. The UV–Vis spectrum was calculated up to ~225 nm, so the shortest wavelength experimental bands cannot be assigned to the calculated transitions. However, considering that the solution spectra of PPh_3 and 8-hydroxyquinoline exhibit intense absorption bands in the 260–200 nm region, some additional intraligand and interligand transitions are expected to be found at higher energies in the calculations.

The assignments of the calculated transitions to the experimental bands are based on the criterion of the energy and oscillator strength of the calculated transitions. In the description of the electronic transitions only the main components of the molecular orbitals are taken into consideration.

The longest wavelength experimental unsymmetrical broad band, with a maximum at 417.4 nm, is assigned to the transitions from the HOMO to LUMO and LUMO + 2 orbitals. As the LUMO orbital is composed of the π^* orbitals of the 8-hydroxyquinoline ring, the transition is of the *Metal–Ligand Charge Transfer* type with a d → d (Ligand Field) contribution.

The next band, with maximum at 328.2 nm, is ascribed to the metal–ligand charge transfer transitions $d \rightarrow \pi^*_{PPh_3}$ and $d \rightarrow \pi^*_{hq}$. In this region the transitions between HOMO and HOMO − 2 MOs were calculated.

The last calculated transition, attributed to experimental one at 259.6 nm, proceeds mainly from the d ruthenium

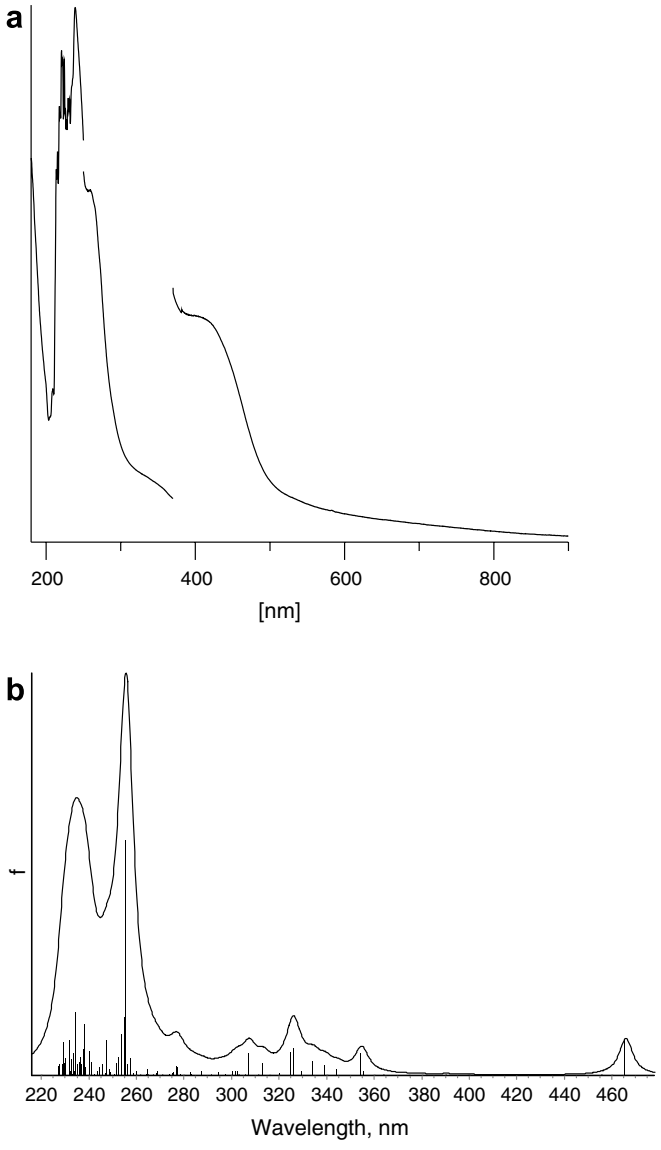


Fig. 3. The UV–Vis spectra of $[RuCl(CO)(PPh_3)_2(C_9H_6NO)]$: (a) experimental and (b) calculated.

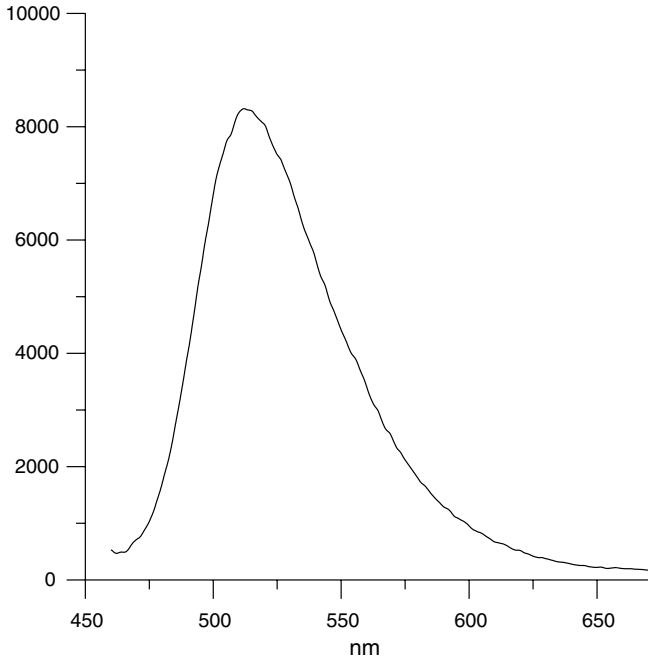


Fig. 4. The emission spectrum of $[RuCl(CO)(PPh_3)_2(C_9H_6NO)]$.

orbitals with an admixture of π chloride and π carbonyl orbitals to π^*_{Ph} and π^*_{hq}, with an admixture of *Ligand–Ligand Charge Transfer* transitions ($\pi_{PPh_3} \rightarrow \pi^*_{hq}$; HOMO − 5/6 → LUMO + 1).

The intraligand transition $\pi_{PPh_3} \rightarrow \pi^*_{PPh_3}$ was calculated at 229.9 nm and it can be assumed that the experimental band at 221.2 nm (not assigned on the basis of the calculated transitions) is composed of the transitions in the PPh_3 ligands and from $\pi \rightarrow \pi^*$ excitations in the hydroxyquinoline ligand. As it was pointed out in the literature, the TDDFT method gives such transitions at too small energies [79–87] and we may expect also that this is the case in our calculations.

The emission property of the studied complex has been examined in dichloromethane solution at room temperature. The luminescence spectrum is presented in Fig. 4. On excitation at 417 nm, an emission peak was observed at 513 nm and it was independent of the concentration of the solution. The emission originates from the lowest energy metal to ligand charge transfer (MLCT) state, derived from the excitation involving a $d_\pi \rightarrow \pi_{hq}$ transition (similar MLCT transitions are observed in ruthenium(II) bipyridyl complexes [88,89]).

4. Supplementary material

CCDC 635757 contains the supplementary crystallographic data for this paper. These data can be obtained free of charge via http://www.ccdc.cam.ac.uk/conts/retrieving.html, or from the Cambridge Crystallographic Data Centre, 12 Union Road, Cambridge CB2 1EZ, UK; fax: (+44) 1223-336-033; or e-mail: deposit@ccdc.cam.ac.uk.

Acknowledgements

The crystallographic part was financed by funds allocated by the Ministry of Science and Higher Education to the X-ray Crystallography and Crystal Chemistry Group, Institute of General and Ecological Chemistry, Technical University of Łódź. The GAUSSIAN-03 calculations were carried out in the Wrocław Centre for Networking and Supercomputing, WCSS, Wrocław, Poland under calculational Grant No 51/96.

This work was partially supported by The State Committee for Scientific Research, Project No. 3 T09A 147 29.

References

[1] J. Reedijk, in: G. Wilkinson, R.D. Gillard, J.A. McCleverty (Eds.), Comprehensive Coordination Chemistry, vol. 2, Pergamon Press, Oxford, 1987, p. 73 .
[2] K. Kalyansundaram, M. Gratzel, Coord. Chem. Rev. 177 (1998) 347.
[3] M.D. Ward, Chem. Soc. Rev. 24 (1995) 121.
[4] W.T. Wong, Coord. Chem. Rev. 131 (1994) 45.
[5] V. Balzani, A. Credi, F. Scandola, in: L. Fabbrizzi, A. Poggi (Eds.), Transition Metals in Supramolecular Chemistry, Kulwer, Dordrecht, The Netherlands, 1994, p. 1.
[6] P.A. Anderson, R.F. Anderson, M. Furue, P.C. Junk, R.F. Keene, B.T. Patterson, B.D. Yeomens, Inorg. Chem. 39 (2000) 2721.
[7] A.H. Velders, A.G. Quiroga, J.G. Haasnoot, J. Reedijk, Eur. Inorg. Chem. (2003) 713, and references therein.
[8] J.-M. Lehn, Supramolecular Chemistry, VCH, Weinheim, 1995.
[9] E. Amouyal, Sol. Energy Matter. Sol. Cells 38 (1995) 249.
[10] V. Balzani, P. Ceroni, A. Juris, M. Venturi, F. Puntari-ero, S. Campagna, S. Serroni, Coord. Chem. Rev. 545 (2001) 219.
[11] A. Beyeler, P. Belser, Coord. Chem. Rev. 230 (2002) 29.
[12] S. Campagna, P.D. Pietro, F. Loiseau, B. Maubert, N. McClenaghan, R. Passalacqua, F. Puntoriero, V. Ricevuto, S. J. Organomet. Chem. 689 (2004) 4375.
[13] K.D. Demadis, C.M. Hartshorn, T.J. Meyer, Chem. Rev. 101 (2001) 2655.
[14] B.S. Brunschwig, C. Creutz, N. Sutin, Chem. Soc. Rev. 31 (2002) 68.
[15] N.H. Dam-Rauer, G. Cerullo, A. Yeh, T.R. Boussie, C.V. Shank, J.K. McCusker, Science 275 (1997) 54.
[16] F.L. Carter, R.E. Siatkowski, in: H. Wohltjn (Ed.), Molecular Electronics Devices, North Holland, Amsterdam, The Netherlands, 1998.
[17] F. Bargiletti, L. Flamigni, Chem. Soc. Rev. 29 (2000) 1.
[18] S.S. Sun, A.J. Lees, Inorg. Chem. 41 (2001) 3154.
[19] K. Chichak, U. Jacquremard, N.R. Branda, Eur. J. Inorg. Chem. (2002) 357.
[20] T. Steiner, Angew. Chem., Int. Ed. 41 (2002) 48, and references therein.
[21] N. Gupta, N. Grover, G.A. Neyhart, P. Singh, H.H. Thorp, Inorg. Chem. 32 (1993) 310.
[22] K.E. Erkkila, D.T. Odom, J.K. Barton, Chem. Rev. 29 (1999) 2777.
[23] J. Kelly, A. Tossi, D. McConnel, C. Ohuigin, Nucleic Acids Res. 13 (1985) 6017.
[24] A. Ambroise, B.G. Maiya, Inorg. Chem. 39 (2000) 4264.
[25] S.W. Keller, S.A. Johnson, E.S. Brigham, E.T. Yonemoto, T.E. Mallouk, J. Am. Chem. Soc. 117 (1995) 12879.
[26] B.E. Buchanan, R. Wang, G.V. Johannes, R. Hage, J.G. Hassnoot, J. Reedijk, Inorg. Chem. 34 (1995) 3358.
[27] E. Brauns, W. Sumner, J.A. Clark, S.M. Molnar, Y. Kawanishi, K.J. Brewer, Inorg. Chem. 36 (1997) 2861.
[28] J.-D. Lee, L.M. Vrana, E.R. Bullock, K.J. Brewer, Inorg. Chem. 37 (1998) 3575.
[29] C. Ceroni, F. Paolucci, S. Roffia, S. Serroni, S. Campagna, A.J. Bard, Inorg. Chem. 37 (1998) 2829.
[30] D.J. Chesnut, A. Kusnet-zow, R.R. Birgeard, J. Zubieta, Inorg. Chem. 38 (1999) 2663.
[31] G. Albano, P. Belser, C. Dual, Inorg. Chem. 40 (2001) 1408.
[32] C. Metcalfe, S. Spey, H. Adams, J.A. Thomas, J. Chem. Soc., Dalton Trans. (2002) 4732.
[33] M.N. Collomb-Dunnand-Sauthier, A. Deronzier, R. Ziessel, J. Chem. Soc., Chem. Commun. (1994) 189.
[34] D. Ooyama, M. Sato, Appl. Organomet. Chem. 18 (2004) 380.
[35] J.-F. Moulin, M. Brinkmann, A. Thierry, J.-C. Wittmann, Adv. Mater. 14 (2002) 436.
[36] L.S. Sapochak, F.E. Benincasa, R.S. Schofield, J.L. Baker, K.K.C. Riccio, D. Fogarty, H. Kohlmann, K.F. Ferris, P. Burrows, J. Am. Chem. Soc. 124 (2002) 6119.
[37] G. Svehila, Vogels Qualitative Inorganic Analysis, Longmans, London, 1998.
[38] G.K. Lahiri, S. Bhattacharya, B.K. Ghosh, A. Chakravorty, Inorg. Chem. 26 (1987) 4324.
[39] S. Bhattacharya, Polyhedron 12 (1993) 235.
[40] M. Menon, A. Pramanik, N. Bag, A. Chakravorty, J. Chem. Soc., Dalton Trans. (1995) 1417.
[41] N.C. Pramanik, S. Bhattacharya, J. Chem. Res. (1997) 98.
[42] N. Ahmad, J.J. Levinson, S.D. Robinson, M.F. Uttely, Inorg. Synth. 15 (1974) 48.
[43] M.J. Frisch, G.W. Trucks, H.B. Schlegel, G.E. Scuseria, M.A. Robb, J.R. Cheeseman, J.A. Montgomery Jr., T. Vreven, K.N. Kudin, J.C. Burant, J.M. Millam, S.S. Iyengar, J. Tomasi, V. Barone,

Mennucci, M. Cossi, G. Scalmani, N. Rega, G.A. Petersson, H. Nakatsuji, M. Hada, M. Ehara, K. Toyota, R. Fukuda, J. Hasegawa, M. Ishida, T. Nakajima, Y. Honda, O. Kitao, H. Nakai, M. Klene, X. Li, J.E. Knox, H.P. Hratchian, J.B. Cross, C. Adamo, J. Jaramillo, R. Gomperts, R.E. Stratmann, O. Yazyev, A.J. Austin, R. Cammi, C. Pomelli, J.W. Ochterski, P.Y. Ayala, K. Morokuma, G.A. Voth, P. Salvador, J.J. Dannenberg, V.G. Zakrzewski, S. Dapprich, A.D. Daniels, M.C. Strain, O. Farkas, D.K. Malick, A.D. Rabuck, K. Raghavachari, J.B. Foresman, J.V. Ortiz, Q. Cui, A.G. Baboul, S. Clifford, J. Cioslowski, B.B. Stefanov, G. Liu, A. Liashenko, P. Piskorz, I. Komaromi, R.L. Martin, D.J. Fox, T. Keith, M.A. Al-Laham, C.Y. Peng, A. Nanayakkara, M. Challacombe, P.M.W. Gill, B. Johnson, W. Chen, M.W. Wong, C. Gonzalez, J.A. Pople, GAUSSIAN-03, Revision B.03, Gaussian, Inc., Pittsburgh, PA, 2003.
[44] A.D. Becke, J. Chem. Phys. 98 (1993) 5648.
[45] C. Lee, W. Yang, R.G. Parr, Phys. Rev. B 37 (1988) 785.
[46] B. Mennucci, J. Tomasi, J. Chem. Phys. 106 (1997) 5151.
[47] K. Eichkorn, F. Weigend, O. Treutler, R. Ahlrichs, Theor. Chim. Acta 97 (1997) 119.
[48] E.D. Glendening, A.E. Reed, J.E. Carpenter, F. Weinhold, NBO (version 3.1).
[49] A.D. Becke, J. Chem. Phys. 98 (1993) 5648.
[50] G.M. Sheldrick, Acta Crystallogr., Sect. A 46 (1990) 467.
[51] G.M. Sheldrick, SHELXL-97: Program for the Solution and Refinement of Crystal Structures, University of Göttingen, Göttingen, Germany, 1997.
[52] G.M. Sheldrick, SHELXTL Release 4.1 for Siemens Crystallographic Research Systems, 1990.
[53] G.A. Jeffrey, W. Saenger, Hydrogen Bonding in Biological Structures, Springer, Berlin, 1994.
[54] G.R. Desiraju, T. Steiner, The Weak Hydrogen Bond in Structural Chemistry and Biology, Oxford University Press, Oxford, 1999.
[55] R. Mukherjee, Coord. Chem. Rev. 203 (2000) 151.
[56] I.D. Brown, Acta Crystallogr., Sect. B 53 (1997) 381.
[57] T. Hirano, M. Kuroda, N. Takeda, M. Hayashi, M. Mukaida, T. Oi, H. Nagao, J. Chem. Soc., Dalton Trans. (2002).
[58] F. Basuli, Shie-Ming Peng, S. Bhattacharya, Inorg. Chem. 40 (2001) 1126.
[59] C.J. Adams, M.I. Bruce, P.A. Humphrey, B.W. Skelton, A.H. White, Aust. J. Chem. 54 (2001) 325.
[60] M.F. McGuiggan, L.H. Pignolet, Cryst. Struct. Commun. 7 (1978) 583.
[61] W. Baratta, P. Da Ros, A. Del Zotto, A. Sechi, E. Zangrando, P. Rigo, Angew. Chem., Int. Ed. 43 (2004) 3584.
[62] D. Duraczynska, J.H. Nelson, J. Chem. Soc., Dalton Trans. (2005) 92.
[63] S. Merlino, G. Montagnoli, Atti Soc. Tosc. Sci. Nat. Pisa 76 (1969) 335.
[64] S. Gopinathan, I.R. Unni, C. Gopinathan, V.G. Puranik, S.S. Tavale, T.N.G. Row, Polyhedron 6 (1987) 1859.
[65] S.S.D. Brown, I.D. Salter, L. Toupet, J. Chem. Soc., Dalton Trans. (1988) 757.
[66] D. Sellmann, F. Knoch, C. Wronna, Angew. Chem., Int. Ed. 27 (1988) 691.
[67] D.A. Weinberger, T.B. Higgins, C.A. Mirkin, C.L. Stern, L.M. Liable-Sands, A.L. Rheingold, J. Am. Chem. Soc. 123 (2001) 2503.
[68] T.E. Bitterwolf, M.B. Leonard, P.A. Horine, J.E. Shade, A.L. Rheingold, D.J. Staley, G.P.A. Yap, J. Organomet. Chem. 512 (1996) 11.
[69] E. Ngai-Man Ho, Wing-Tak Wong, J. Organomet. Chem. 626 (2001) 125.
[70] Y. Matsuo, E. Nakamura, Organometallics 22 (2003) 2554.
[71] S.B. Colbran, D.C. Craig, W.M. Harrison, A.E. Grimley, J. Organomet. Chem. 408 (1991) C33.
[72] H. Werner, M.A. Tena, N. Mahr, K. Peters, H.-G. von Schnering, Chem. Ber. 128 (1995) 41.
[73] M. Haukka, J. Kiviaho, M. Ahlgren, T.A. Pakkanen, Organometallics 14 (1995) 825.
[74] K. Severin, D. Koch, K. Polborn, W. Beck, Z. Anorg. Allg. Chem. 622 (1996) 562.
[75] T. Adatia, I.D. Salter, Polyhedron 15 (1996) 597.
[76] S.D. Drouin, S. Monfette, D. Amoroso, G.P.A. Yap, D.E. Fogg, Organometallics 24 (2005) 4721.
[77] A. Vogler, H. Kunkely, Coord. Chem. Rev. 230 (2002) 243.
[78] L. Kuznestov, A.J.L. Pombeiro, J. Chem. Soc., Dalton Trans. (2003) 738.
[79] A. Rosa, E.J. Baerends, S.J.A. van Gisbergen, E. van Lenthe, J.A. Groeneveld, J.G. Snijders, J. Am. Chem. Soc. 121 (1999) 10356.
[80] J.-F. Guillemoles, V. Barone, L. Joubert, C. Adamo, J. Phys. Chem. A 106 (2002) 11354.
[81] J.E. Monat, J.H. Rodriguez, J.K. McCusker, J. Phys. Chem. A 106 (2002) 7399.
[82] S. Fantacci, F. De Angelis, A. Selloni, J. Am. Chem. Soc. 125 (2003) 4381.
[83] A. Dreuw, M. Head-Gordon, J. Am. Chem. Soc. 126 (2004) 4007.
[84] A. Dreuw, J.L. Weisman, M. Head-Gordon, J. Chem. Phys. 119 (2003) 2943.
[85] O. Gritsenko, E.J. Baerends, J. Chem. Phys. 121 (2004) 655.
[86] S. Za'lis-, N. Ben Amor, C. Daniel, Inorg. Chem. 43 (2004) 7978.
[87] R.S. da Silva, S.I. Gorelsky, E.S. Dodsworth, E. Tfouni, A.B.P. Lever, J. Chem. Soc., Dalton Trans. (2000) 4078.
[88] V.W.W. Yam, B.W.K. Chu, C.C. Ko, K.K. Cheung, J. Chem. Soc., Dalton Trans. (2001) 1911.
[89] B.K. Panda, K.G. Ghosh, S. Chattoppadhyay, A. Chkravoty, J. Organomet. Chem. 674 (2003) 107.

isolated in good yields whatever the ratio between the trinuclear 2/1 Cu/Ca complex and the lanthanide ion. An explanation for the failure of the template effect has been put forward.

2. Experimental

2.1. Materials

The metal aldimine complexes, $L^1Cu \cdot H_2O$ [9], $L^2Cu \cdot 2H_2O$ [10] (L^1H_2: *N*,*N*′-ethylenedi(3-methoxysalicylideneimine); L^2H_2: *N*,*N*′-2,2-dimethylpropylenedi(3-methoxysalicylideneimine)), were prepared as previously described. $Ca(NO_3)_2 \cdot 4H_2O$, $Ca(OH)_2$, $Ba(OH)_2 \cdot 8H_2O$, $Sr(OH)_2 \cdot 8H_2O$, 2,2,6,6-tetramethyl-3,5-heptanedione (Aldrich) were used as purchased. High-grade solvents were used for the syntheses of complexes.

2.2. Syntheses

2.2.1. Complexes

*2.2.1.1. $L^1CuCa(thd)_2 \cdot MeOH$ (**1**).* A mixture of $L^1Cu \cdot H_2O$ (0.41 g, 1×10^{-3} mol) and $Ca(OH)_2$ (0.15 g, 2×10^{-3} mol) in methanol (20 mL) was stirred for 15 min and then filtered off. Addition of tetramethylheptanedione (0.38 g, 2×10^{-3} mol) under stirring yielded a red precipitate that was filtered off 30 min later and dried. Yield: 0.3 g (36%). *Anal.* Calc. for $C_{41}H_{60}CaCuN_2O_9$: C, 59.4; H, 7.3; N, 3.4. Found: C, 59.4; H, 7.2; N, 3.4%. Characteristic IR absorptions (KBr): 3434, 2957, 1634, 1604, 1558, 1548, 1475, 1449, 1419, 1309, 1242, 1223, 1081, 987, 974, 961, 856, 741, 643, 609 cm^{-1}. Mass spectrum (FAB^+, 3-nitrobenzyl alcohol matrix): $m/z = 612$ (100), $[L^1CuCa(thd)]^+$. Crystals suitable for a X-ray study were obtained from a dichloromethane/methanol solution. They contain a dichloromethane molecule.

Use of $Sr(OH)_2 \cdot 8H_2O$ or $Ba(OH)_2 \cdot 8H_2O$ in place of $Ca(OH)_2$ with the same experimental process and the same amount of the copper complex precursor yielded the corresponding complexes.

*2.2.1.2. $L^1CuSr(thd)_2$ (**2**).* Yield: 0.36 g (43%). *Anal.* Calc. for $C_{40}H_{56}CuN_2O_8Sr$: C, 56.9; H, 6.7; N, 3.3. Found: C, 56.3; H, 6.6; N, 3.2%. Characteristic IR absorptions (KBr): 2941, 1644, 1603, 1546, 1475, 1446, 1322, 1242, 1219, 1087, 987, 978, 968, 856, 743, 724, 646, 607 cm^{-1}. Mass spectrum (FAB^+, 3-nitrobenzyl alcohol matrix): $m/z = 660$ (100), $[L^1CuSr(thd)]^+$.

*2.2.1.3. L^1 $CuBa(thd)_2$ (**3**).* Yield: 0.5 g (56%). *Anal.* Calc. for $C_{40}H_{56}BaCuN_2O_8$: C, 53.8; H, 6.3; N, 3.1. Found: C, 53.5; H, 6.3; N, 3.1%. Characteristic IR absorptions (KBr): 2937, 1634, 1604, 1547, 1475, 1446, 1314, 1246, 1224, 1083, 988, 968, 855, 736, 644, 608 cm^{-1}. Mass spectrum (FAB^+, 3-nitrobenzyl alcohol matrix): $m/z = 710$ (100), $[L^1CuBa(thd)]^+$.

*2.2.1.4. $(L^1Cu)_2Ca(NO_3)_2 \cdot 2H_2O$ (**4**).* A mixture of $L^1Cu \cdot H_2O$ (0.41 g, 1×10^{-3} mol) and $Ca(NO_3)_2$ (0.24 g, 1×10^{-3} mol) in methanol (15 mL) was stirred for three hours. The precipitate which appeared was filtered off and dried. Yield: 0.31 g (65%). *Anal.* Calc. for $C_{36}H_{40}CaCu_2N_6O_{16}$: C, 46.0; H, 4.1; N, 8.6. Found: C, 45.6; H, 3.9; N, 8.4%. Characteristic IR absorptions (KBr): 3459, 1642, 1626, 1606, 1450, 1412, 1384, 1314, 1247, 1224, 1083, 979, 962, 857, 752, 740, 648, 609 cm^{-1}. Mass spectrum (FAB^+, 3-nitrobenzyl alcohol matrix): $m/z = 880$ (2.5), $[(L^1Cu)_2Ca(NO_3)]^+$, 818 (3.6), $[(L^1Cu)_2Ca]^+$, 491 (100), $[(L^1Cu)Ca(NO_3)]^+$.

The following complexes were prepared similarly with use of the corresponding salts.

*2.2.1.5. $(L^1Cu)_2Ba(NO_3)_2 \cdot 2H_2O$ (**5**).* Yield: 0.38 g (70%). *Anal.* Calc. for $C_{36}H_{40}BaCu_2N_6O_{16}$: C, 40.1; H, 3.7; N, 7.8. Found: C, 39.7; H, 3.6; N, 7.7. Characteristic IR absorptions (KBr): 3434, 1631, 1603, 1449, 1474, 1450, 1384, 1301, 1243, 1226, 1080, 986, 966, 853, 740, 646, 609 cm^{-1}. Mass spectrum (FAB^+, 3-nitrobenzyl alcohol matrix): $m/z = 978$ (32.0), $[(L^1Cu)_2Ba(NO_3)]^+$, 916 (19.3), $[(L^1Cu)_2Ba]^+$, 589 (100), $[(L^1Cu)Ba(NO_3)]^+$.

*2.2.1.6. $(L^1Cu)_2Ba(ClO_4)_2$ (**6**). Caution*: Due to their explosive character, perchlorate salts should be handled with care and in very low amounts. Acetone was used as solvent. Yield: 0.4 g (74%). *Anal.* Calc. for $C_{36}H_{36}BaCl_2Cu_2N_4O_{16}$: C, 38.7; H, 3.2; N, 5.0. Found: C, 39.6; H, 3.2; N, 4.9%. Characteristic IR absorptions (KBr): 1647, 1666, 1604, 1550, 1472, 1443, 1392, 1301, 1243, 1222, 1120, 1081, 1055, 1046, 981, 977, 966, 854, 737, 641, 628, 620 cm^{-1}. Mass spectrum (FAB^+, 3-nitrobenzyl alcohol matrix): $m/z = 1017$ (48.6), $[(L^1Cu)_2Ba(ClO_4)]^+$, 916 (34.2), $[(L^1Cu)_2Ba]^+$, 626 (100), $[(L^1Cu)Ba(ClO_4)]^+$.

*2.2.1.7. $L^1CuMg(H_2O)(NO_3)_2$ (**7**).* Yield: 0.5 g (90%). *Anal.* Calc. for $C_{18}H_{20}CuMgN_4O_{11}$: C, 38.9; H, 3.6; N, 10.1. Found: C, 39.0; H, 3.6; N, 9.9%. Characteristic IR absorptions (KBr): 3401, 1638, 1601, 1556, 1474, 1440, 1384, 1316, 1243, 1221, 1082, 977, 964, 858, 742, 642, 611 cm^{-1}. Mass spectrum (FAB^+, 3-nitrobenzyl alcohol matrix): $m/z = 475$ (100), $[(L^1Cu)Mg(NO_3)]^+$.

*2.2.1.8. $(L^2Cu)_2Ca(NO_3)_2 \cdot H_2O$ (**8**).* Yield: 0.34 g (65%). *Anal.* Calc. for $C_{42}H_{50}CaCu_2N_6O_{15}$: C, 48.2; H, 4.8; N, 8.0. Found: C, 47.9; H, 4.6; N, 7.8%. Characteristic IR absorptions (KBr): 3419, 1617, 1558, 1472, 1384, 1312, 1229, 1170, 1082, 1067, 983, 855, 742, 646, 623 cm^{-1}. Mass spectrum (FAB^+, 3-nitrobenzyl alcohol matrix): $m/z = 966$ (28.5), $[(L^2Cu)_2Ca(NO_3)]^+$, 902 (20.2), $[(L^2Cu)_2Ca]^+$, 533 (100), $[(L^2Cu)Ca(NO_3)]^+$.

2.3. Physical measurements

Elemental analyses were carried out at the Laboratoire de Chimie de Coordination Microanalytical Laboratory

in Toulouse, France, for C, H, and N. IR spectra were recorded on a GX system 2000 Perkin–Elmer spectrophotometer; samples were run as KBr pellets. Mass spectra (FAB^+) were recorded in dmf as solvent and 3-nitrobenzyl alcohol matrix with a Nermag R10-10 spectrometer. Magnetic data were obtained with a Quantum Design MPMS SQUID susceptometer. All samples were 3 mm diameter pellets molded from ground crystalline samples. Magnetic susceptibility measurements were performed in the 2–300 K temperature range in a 0.1 T applied magnetic field, and diamagnetic corrections were applied by using Pascal's constants [11]. The magnetic susceptibilities have been computed by exact calculations of the energy levels associated to the spin Hamiltonian through diagonalization of the full matrix with a general program for axial symmetry,[12] and with the MAGPACK program package [13,14]. Least-squares fittings were accomplished with an adapted version of the function-minimization program MINUIT [15].

2.4. Crystallographic data collection and structure determination for $[L^1Cu(CH_3OH)Ca(thd)_2]$ (1) and $[(L^2Cu)_2Ca(NO_3)_2]$ (8)

Crystals suitable for X-ray analyses were obtained by slow evaporation of the corresponding methanol solutions. Data were collected at 160 K for **1** on a IPDS STOE diffractometer and at 180 K for **8** on an Xcalibur Oxford Diffraction diffractometer using graphite-monochromated Mo Kα radiation sources ($\lambda = 0.71073$ Å) and equipped with Oxford Cryosystems Cryostream Cooler Devices. 46391 reflections were collected for **1**, 43468 for **8**, of which 9047 independent ($R_{int} = 0.08$) for **1** and 6185 ($R_{int} = 0.13$) for **8**. Multiscan absorption corrections were applied ($T_{min-max} = 0.76$–0.89 for **1**, 0.82–0.94 for **8**). The structures were solved by direct methods using SIR92 [16], and refined by means of least-squares procedures on F using the programs of the PC version of CRYSTALS [17]. Atomic scattering factors were taken from the International tables for X-ray crystallography [18]. All non-NO_3 groups and non-hydrogen atoms were refined anisotropically. The maximum and minimum peaks on the final difference Fourier maps were 0.62 and -0.63 e A^{-3} for **1**, 1.79 and -1.13 e A^{-3} for **8**. Drawings of the molecule were performed with the program CAMERON [19]. Crystal data collection and refinement parameters are given in Table 1, and selected bond distances and angles are gathered in Table 2.

Table 1
Summary of crystal data and refinement details for **1** and **8**

Empirical formula	$C_{42}H_{62}CaCl_2CuN_2O_9$	$C_{42}H_{50}CaCu_2N_6O_{15}$
M	913.49	1046.06
Temperature (K)	160	180
Wavelength (Å)	0.71073	0.71073
Crystal system	monoclinic	orthorhombic
Space group	$P2_1/n$	$Pccn$
a (Å)	12.594(1)	20.948(3)
b (Å)	14.661(1)	10.579(1)
c (Å)	25.276(3)	20.858(2)
β (°)	95.14(1)	
V (Å^3)	4648.2(7)	4622.5(10)
Z	4	4
$\rho_{(calc)}$	1.31	1.50
μ_{Mo} (mm^{-1})	0.747	1.10
Crystal size (mm)	$0.15 \times 0.30 \times 0.50$	$0.06 \times 0.10 \times 0.18$
θ Range (°)	2.14–25.98	3.36–29.07
Reflections collected/ unique	46391/9047	43468/6185
Reflection parameters	506	287
Maximum and minimum transmission	0.89 and 0.76	0.94 and 0.82
R^a	0.058 ($I \geqslant 1.2\sigma(I)$)	0.083 ($I \geqslant 3\sigma(I)$)
wR^b	0.070 ($I \geqslant 1.2\sigma(I)$)	0.081 ($I \geqslant 3\sigma(I)$)
$\Delta\rho_{max}$ and $\Delta\rho_{min}$ (e Å^3)	0.62 and -0.63	1.79 and -1.13

[a] $R = \sum ||F_o| - |F_c|| / \sum |F_o|$.
[b] $wR = [\sum w|F_o^2| - |F_c^2|^2 / \sum w|F_o^2|^2]^{1/2}$.

Table 2
Selected bond lengths and angles for **1** and **8**

Complex ***1***			
Cu–O2	1.892(3)	Ca–O3	2.444(3)
Cu–O3	1.895(3)	Ca–O4	2.724(3)
Cu–N2	1.916(5)	Ca–O5	2.365(3)
Cu–N1	1.922(5)	Ca–O6	2.310(3)
Cu–O9	2.416(3)	Ca–O7	2.336(3)
Ca–O1	2.666(3)	Ca–O8	2.369(3)
Ca–O2	2.488(3)		
O2–Cu–O3	83.8(1)	O2–Ca–O3	61.7(1)
Cu–O2–Ca	103.5(1)	Cu–O3–Ca	105.1(1)
Complex ***8***			
Cu–O2	1.949(4)	Ca–O1	2.446(4)
Cu–O3	1.942(4)	Ca–O2	2.379(4)
Cu–N2	1.972(4)	Ca–O3	2.415(4)
Cu–N1	1.958(5)	Ca–O4	2.479(4)
Cu–O5	2.854(5)	Ca–O1′	2.446(4)
Ca–O2′	2.379(4)	Ca–O3′	2.415(4)
Ca–O4′	2.479(4)		
O2–Cu–O3	79.8(2)	O2–Ca–O3	62.8(1)
Cu–O2–Ca	109.2(2)	Cu–O3–Ca	108.1(1)
O1–Ca–O1′	86.8(2)	O4–Ca–O4′	89.0(2)

Sym op: ′, $-x + 1/2$, $-y + 5/2$, z.

3. Results

3.1. Syntheses

Reaction of the *N*,*N*′-ethylenedi(3-methoxysalicylideneiminato) copper complex with calcium, strontium and barium hydroxide in the presence of 2,2,6,6-tetramethyl-3,5-heptanedione (thd) yielded a series of complexes formulated $L^1CuCa(thd)_2$ (**1**), $L^1CuSr(thd)_2$ (**2**) and $L^1CuBa(thd)_2$ (**3**), which are characterized by a 1/1 copper/alkaline-earth ratio. At variance, using alkaline-earth nitrate or perchlorate yielded complexes characterized by the 2/1 copper/alkaline-earth ratio, $(L^1Cu)_2Ca(NO_3)_2 \cdot 2H_2O$ (**4**), $(L^1Cu)_2Ba(NO_3)_2 \cdot 2H_2O$ (**5**), $(L^1Cu)_2Ba(ClO_4)_2$ (**6**). The copper complex involving the more flexible *N*,*N*′-2,2-dimethylpropylenedi(3-methoxysalicylideneiminate) L^2 ligand yielded a

similar entity $(L^2Cu)_2Ca(NO_3)_2 \cdot H_2O$ (**8**), with again a 2/1 ratio. The only exception to this 2/1 ratio occurred with magnesium ions that yielded the $L^1CuMg(NO_3)_2 \cdot H_2O$ complex (**7**). The different ionic radius of magnesium is most probably responsible for the change in Cu/alkaline-earth ratio.

3.2. Spectroscopic data

The infrared spectra of the structurally determined complexes **1** and **8** are of prime interest for the study of the remaining entities. The ν_{CN} bands of the coordinated ligands are observed at 1604 and 1617 cm^{-1} for **1** and **8**, respectively. A strong band at 1384 cm^{-1} is attributable to the monodentate NO_3 anion in **8** [20], while a strong band at 1634 cm^{-1} may be assigned to the coordinated keto functions of the thd ligands in **1** [21].

Mass spectra also yield interesting information. The three $L^1CuM(thd)_2$ complexes display very similar mass spectra (FAB^+). In all mass spectra we observe peaks corresponding to the $[L^1CuM(thd)]^+$ ions. They appear at $m/z = 612$ for **1** (M = Ca), 660 for **2** (M = Sr), and 710 for **3** (M = Ba). A different spectral pattern characterizes complex **8** with peaks at $m/z = 964$, 902 and 533, attributable to $[(L^2Cu)_2Ca(NO_3)]^+$, $[(L^2Cu)_2Ca]^+$ and $[L^2CuCa(NO_3)]^+$, respectively. If the peaks at 964 and 533 u are expected, the peak at 902 u is more surprising for it suggests a change in the oxidation state of the metal ions. Such an observation has been previously made [22]. Complexes **4** and **5** show similar peaks at 1017, 916 and 626, and 978, 916 and 589 u, respectively. For these three complexes, although it should be underlined that the most intense peak corresponds to the $[L^1CuM(NO_3)]^+$ ion, the presence of peaks at 1017 (**4**) 978 (**5**) and 964 (**8**) μm confirms their trinuclear character. Complex **7**, $L^1CuMg(NO_3)_2(H_2O)$, where $[L^1CuMg(NO_3)]^+$ is the only cationic species observed, is an exception.

3.3. Structural determinations

The molecular structure of **1** is built from isolated dinuclear complex molecules $[L^1Cu(CH_3OH)Ca(thd)_2]$. A perspective view of this dinuclear molecule with the corresponding labeling scheme is depicted in Fig. 1 while significant bond lengths and angles appear in Table 2. In each bimetallic unit, the Cu^{II} and Ca^{II} cations occupy the inner N_2O_2 and outer O_2O_2 sites, respectively. The two ions are doubly bridged to each other by phenoxo oxygen atoms, with a Cu···Ca distance of 3.460(1) Å. The copper is surrounded by five donor atoms. The equatorial N_2O_2 donors afforded by L^1 are nearly coplanar and the axial position is occupied by the methanol oxygen atom at 2.416(3) Å from the copper ion. While the copper ion is located in the N_2O_2 mean plane, the calcium ion is located 0.741(2) Å out of this plane. The five-membered ring formed by the diimine moiety chelating the copper ion is in a δ conformation. The Cu–O bond lengths do not differ significantly from the values reported for similar complexes

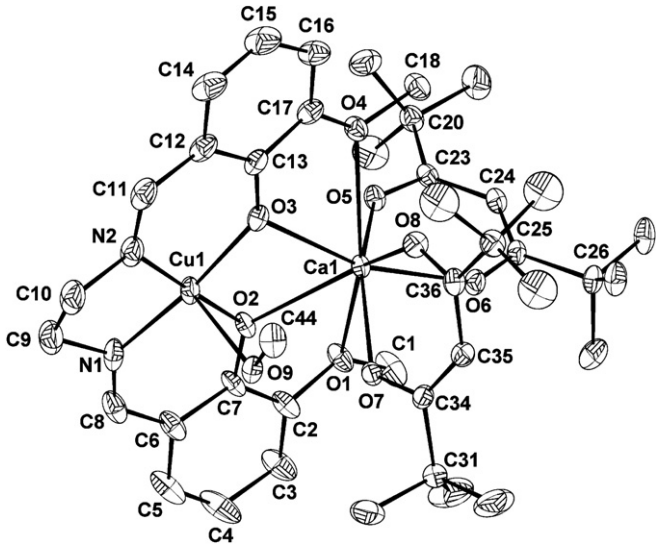


Fig. 1. Molecular structure of $[L^1Cu(CH_3OH)Ca(thd)_2]$ (**1**). The thermal ellipsoids are drawn at the 30% probability level.

[3,4]. The eight-coordinate Ca cation is surrounded by four oxygen atoms belonging to the Schiff base and by four oxygen atoms brought by two tetramethylheptanedionato anions acting as bidentate η^2 chelating auxiliary ligands. The two longer Ca–O bonds involve the OMe side arms (2.666(3) and 2.724(3) Å) while the shorter ones concern the keto oxygen atoms from the thd ligands (from 2.310(3) to 2.369(3) Å); the Ca–O bonds involving the phenoxo oxygen atoms are comprised in between these values (2.444(3) and 2.488(3) Å). π–π stacking interactions established between the aromatic cycles located around the copper coordination spheres are responsible for the presence of short intermolecular Cu(1)···Cu(1)′ (3.819(1) Å) and large Ca(1)···Ca(1)′ (8.951(2) Å) distances.

The molecular structure of complex **8**, along with the atom labeling scheme, is depicted in Fig. 2, while the rele-

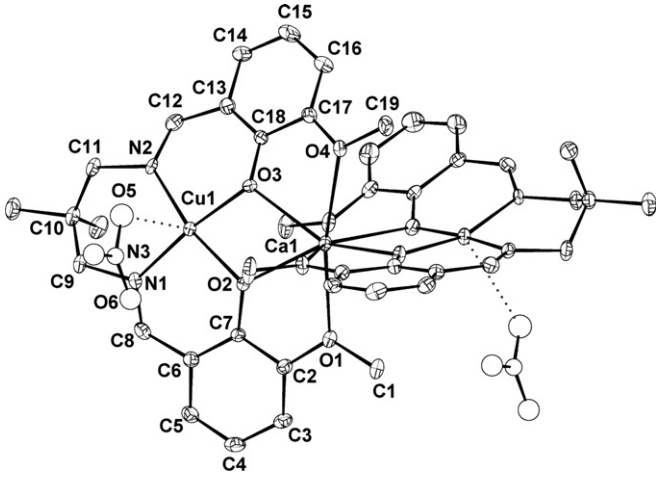


Fig. 2. Molecular structure of $(L^2Cu)_2Ca(NO_3)_2 \cdot H_2O$ (**8**). The thermal ellipsoids are drawn at the 30% probability level.

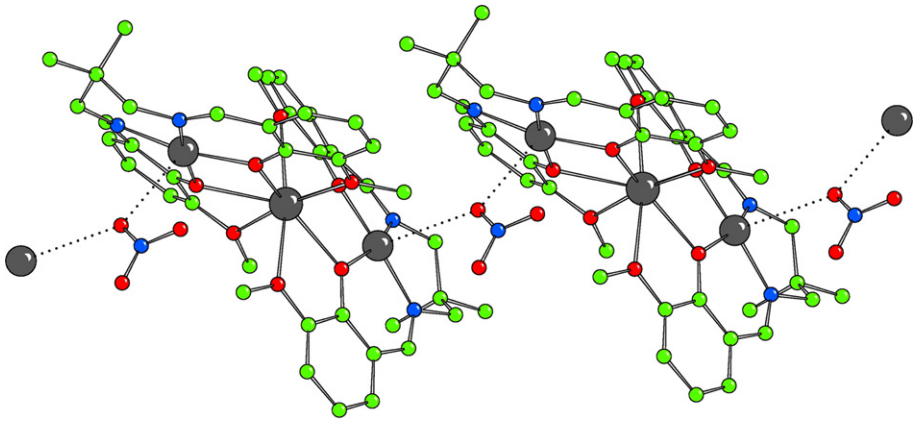


Fig. 3. Fragment of the 1D chain resulting from the η^1:μ nitrato bridging for **8**.

vant interatomic bonds lengths are collated in Table 2. The N_2O_2 donor set of $(L^2)^{2-}$ is at the basal plane of the pentacoordinate copper cation, to which an oxygen atom of the nitrato anion is axially bonded. Cu(1) is displaced from the mean equatorial N_2O_2 plane by 0.128(2) Å toward the axially coordinated nitrato oxygen atom. The two Cu(OO)Ca cores including the two bridging phenoxo oxygen atoms are essentially planar and roughly orthogonal, with a related Cu(1)···Ca(1) separation of 3.5375(6) Å yielding an intramolecular Cu(1)···Cu(1)′ separation of 7.044(3) Å through (Ca(1) (′:, $-x+1/2$, $-y+5/2$, z)). The Ca^{II} cation is eight-coordinate through two sets of four oxygen atoms from each L^2Cu building unit, and linked to each copper ion by two phenoxo bridges. The shortest intermolecular Cu(1)···Cu(1) distance is equal to 5.212(1) Å for the nitrato ion bridges two copper ions through the same oxygen atom, thus forming a 1D chain of trinuclear units (Fig. 3). As a consequence, the intermolecular Cu(1)···Cu(1)′ (9.127(1) Å) and Ca(1)···Ca(1) (10.429(3) Å) distances are large. This η^1:μ nitrato bridging mode is not common [20].

3.4. Magnetic properties

The dinuclear complexes **1**, **2**, **3**, **7**, in which the copper ion is in presence of diamagnetic centres, behave as paramagnetic entities devoid of any intermolecular interactions. The intermolecular contacts established by π–π stacking in **1** are not able to transmit a magnetic interaction. The temperature dependence of the magnetic susceptibility for **8** in the 2–300 K temperature range is shown in Fig. 4 as the $\chi_M T$ versus T variation. The $\chi_M T$ product remains constant and equal to 0.77 $cm^3\ mol^{-1}$ K in the whole temperature range. Identical results have been obtained for the complexes **4** and **5**. These results confirm that the copper ions are well isolated from each other by the alkaline-earth cations and that the bridging nitrato anions are not active. In complex **6**, the decrease of the $\chi_M T$ product is due to weak antiferromagnetic interactions operating at low temperature. These interactions must be intermolecular for the previous complexes **4**, **5** and **8** demonstrate clearly that there is

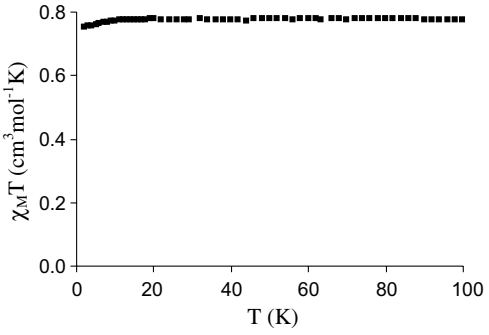


Fig. 4. Thermal dependence of the $\chi_M T$ product for $(L^2Cu)_2$-$Ca(NO_3)_2 \cdot H_2O$ (**8**).

no significant intramolecular magnetic interaction through the alkaline-earth cations. They originate from the presence of perchlorate ions that are not able to bind copper at the axial coordination site: as the copper cations are thus in a square planar environment, intermolecular Cu···Cu interactions through the phenoxo oxygen atoms must be responsible for such a weak interaction. Fitting the magnetic susceptibility data of **6** to the Bleaney–Bowers [23] equation for an exchange coupled pair of $S = 1/2$ spins with a 2J singlet–triplet energy gap yields an estimate of the intermolecular interaction equal to $-0.75\ cm^{-1}$ with $g = 2.05$ and an agreement factor R ($\sum[(\chi_M T)_{obs} - (\chi_M T)_{calc}]^2/\sum[(\chi_M T)_{obs}]^2$) equal to 1×10^{-4} (see Fig. 4).

4. Discussion

We have previously shown that compartmental Schiff base ligands resulting from the reaction of 3-methoxysalicylaldehyde with different diamines may yield discrete heterodinuclear 3d/4f complexes [5,10] with the 3d ion coordinated in the N_2O_2 site and the 4f ion in the O_2O_2 site. Very similar 3d/alkali-metal complexes have also been isolated, with the alkali-metal in the outer O_2O_2 coordination site [3,4]. The isolated complexes are formulated LMM′X or $LMLnX_3$, L standing for the ligand, M for the 3d ion (most often Ni^{2+} and Cu^{2+}), M′ for Na^+, Li^+, K^+, Ln

for the 4f ion and X for the anionic species (most often NO_3^- or ClO_4^-). The presence of methoxy groups in the 3,3′ positions of the Cu–salicylaldimine precursor complexes implies that these building units are potential ligands able to chelate metal ions in the plane of the donor atoms or to sandwich them between two sets of such Cu–salicylaldimine ligands, depending on the size of the M′ or Ln cation. These O_2O_2 compartments can be preformed or can result from self-assembling of the 3d precursor complex in the presence of alkaline or lanthanide ions [4,10]. Another factor that affects the complexing ability is the number of carbon atoms involved in the imine bridge. With a 1,3-propylene bridge, metal ions linked to the outer O_2O_2 site are located in the plane of the four donor atoms while there is a lesser adaptability with a 1,2-ethylene bridge [3]. The third factor influencing the complexation stoichiometry originates from the anions present in the reaction medium. Indeed, these anions can compete with the precursor ligand-complex, depending on their affinity with the introduced metal ion. Concerning the outer O_2O_2 coordination site, it may be considered as a polyether in which a carbon atom spacer ($O–CH_2–CH_2–O$) has been replaced by a metal ion (O–M–O), as in metallacrowns [24]. In addition, the oxygen atoms linked to the metal ion are deprotonated and capable of better bonding than the ether-type oxygen atoms. Because calcium(II) ions have a chemistry closely related to that of lighter lanthanide ions, and are thus easily replaced by lanthanide ions [25], we have studied their reaction with the 3d precursor complexes. The analytical results and the structural determinations demonstrate that the isolated complexes may be formulated as $[(L^2Cu)_2Ca(NO_3)_2]$, with a 2/1 3d/alkaline-earth ratio. This observation is really surprising for the previously studied 3d/alkaline or 3d/lanthanide complexes were characterized by a 1/1 ratio. This result is puzzling if we remember that the ionic radii of sodium, calcium and gadolinium ions span the same range of values, depending on their coordination number [25]. It is also worth noting that the flexibility of the L^2 ligand used in the present case, with its three carbon atoms chain in the diimino fragment [3], is not a factor able to introduce a change in the Cu/Ca ratio. On the contrary, the magnesium ions, with their smaller ionic radius, yield a 1/1 Cu/Mg ratio even with the more rigid L^1 ligand, while the barium ions, with their larger ionic radius, yield a 2/1 ratio in all cases. These data indicate that the ionic radius cannot be considered as the only factor responsible for the stoichiometry of the isolated complexes. In the present case, the results may be explained by the higher affinity of the alkaline-earth for the outer coordination site of the Cu–salicylaldimine precursor complex, a factor which prevails over the chelating power of the nitrato anions, thus yielding 2/1 entities which are not observed under similar experimental conditions in the case of lanthanide ions. In the latter case, the chelating effect of the nitrato anions toward the Ln ions is the most important factor, explaining why the observed 1/1 3d–4f ratio in the presence of nitrato anions is always obtained.

Increasing the number of oxygen atoms involved in the outer coordination site by introducing polyether-like chains does not modify the 3d/alkaline earth ratio, as reported earlier [7]. The only way to change this ratio is to introduce auxiliary ligands with a strong chelating ability, such as diketones. Then discrete species with a 1/1 3d/alkaline earth ratio may be isolated, as demonstrated by the structural determination of the $L^1Cu(MeOH)Ca(thd)_2$ complex **1**. Again the calcium ion is eight-coordinate, with two auxiliary thd ligands substituting one Cu–salicylaldimine building unit. Mass spectra data (FAB^+) confirm the presence of these entities in solution. Peaks corresponding to the $[L^1CuM(thd)]^+$ ions appear at $m/z = 612$ (M = Ca), 660 (M = Sr) and 710 (M = Ba), thus demonstrating that the corresponding complexes are also obtained with larger alkaline-earth ions. Again, the only exception was observed for magnesium which failed to yield such a 1/1 complex.

The magnetic data indicate that the copper ions are magnetically well isolated in the dinuclear (**1**, **2**, **3**, **7**) and trinuclear (**4**, **5**, **8**) entities. The presence of a nitrato anion or a solvent molecule at the apical position of the copper coordination sphere prevents intermolecular interactions. Furthermore, the lack of magnetic interactions through the diamagnetic alkaline-earth cations of the trinuclear species is clearly evidenced by these results. Complex **6** behaves differently. From the magnetic results and UV–Vis data, we can conclude that the copper ions are in a square planar environment, the perchlorate anion being unable to enter the coordination sphere at an axial site, thus favouring intermolecular contacts which are responsible for the slight $\chi_M T$ decrease at low temperature corresponding to weak antiferromagnetic interactions (see Fig. 5).

Up to now, we have not been able to obtain 3d–4f complexes in a 2/1 ratio with symmetrical Schiff base ligands, in presence of nitrato anions. As the 2/1 3d-alkaline-earth complexes are easily obtained, we have tried to use the template effect of the calcium ions to prepare the corresponding 2/1 3d-Ln complexes. It is known for a long time that such a replacement is possible [25]. Unfortunately all our experiments failed to yield the expected 3d–4f complexes, our attempts leading to the isolation of 1/1 3d–4f com-

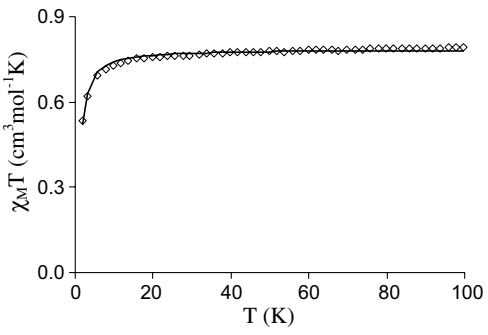


Fig. 5. Thermal dependence of the $\chi_M T$ product for $(L^1Cu)_2Ba(ClO_4)_2$ (**6**). The solid line is the best fit to the Bleaney–Bowers equation, see text.

plexes equivalent to those previously characterized. This result confirms the ready replacement of calcium by lanthanide ions. Unfortunately, the template effect of the calcium ion is not able to give the expected trinuclear 3d–4f–3d entities.

5. Conclusion

It is well known that the lanthanide ionic radii depend on their coordination number and that they span the values of the calcium ionic radii. Furthermore, the Ln ions, which are the chameleons of coordination chemistry, replace with much ease the Ca ions in coordination compounds [25]. The present work demonstrates that this replacement is in fact easy but that it yields complexes with stoichiometries different from those of the starting 3d/Ca compounds. This behaviour is explained by the different affinities of the Ln and Ca ions for the anionic species present in the reaction medium: the tetradentate donor ligand and the nitrato anions. The alkaline-earth affinity for the outer coordination site of the metal–salicylaldimine complex prevails over the chelating power of the nitrato anions while the reverse is true for the lanthanide ions. Using auxiliary ligands such as diketones, which have a strong chelating power, allows to vary the 3d-alkaline earth ratio from 2/1 to 1/1. Playing with these different factors yields a large and rich palette to the synthetic chemist. This work demonstrates that synthesis of a desired complex is not always straightforward. Eventually, the possible variation of the 3d/alkaline-earth ratio gives a supplementary interest to these complexes as single-source precursors for the MOCVD deposition of heterometallic materials.

Acknowledgements

We thank Dr. A. Mari for his contribution to the magnetic measurements. F.Z.C.F. acknowledges the Algerian Ministry for Education and Research for an abroad doctoral grant.

Appendix A. Supplementary material

CCDC 638955 and 638956 contain the supplementary crystallographic data for **1** and **8**. These data can be obtained free of charge via http://www.ccdc.cam.ac.uk/conts/retrieving.html, or from the Cambridge Crystallographic Data Centre, 12 Union Road, Cambridge CB2 1EZ, UK; fax: (+44) 1223-336-033; or e-mail: deposit@ccdc.cam.ac.uk. Supplementary data associated with this article can be found, in the online version, at doi:10.1016/j.poly.2007.05.019.

References

[1] A. Schepartz, J.P. McDevitt, J. Am. Chem. Soc. 111 (1989) 5976.
[2] O.F. Schall, K. Robinson, J.L. Atwood, G.W. Gokel, J. Am. Chem. Soc. 113 (1991) 7434.
[3] D. Cunningham, P. McArdle, M. Mitchell, N. Ni Chonchubhair, M. O'Gara, F. Franceschi, C. Floriani, Inorg. Chem. 39 (2000) 1639.
[4] J.P. Costes, F. Dahan, J.P. Laurent, Inorg. Chem. 33 (1994) 2738.
[5] J.P. Costes, F. Dahan, A. Dupuis, Inorg. Chem. 39 (2000) 165.
[6] J.P. Costes, F. Dahan, W. Wernsdorfer, Inorg. Chem. 45 (2006) 5.
[7] J.P. Costes, J.P. Laurent, P. Chabert, G. Commenges, F. Dahan, Inorg. Chem. 36 (1997) 656.
[8] A.N. Gleizes, F. Senocq, M. Julve, J.L. Sanz, N. Kuzmina, S. Troyanov, I. Malkerova, A. Alikhanyan, M. Ryazanov, A. Rogachev, E. Dedlovskaya, J. Phys. IV France 9 (1999) 943.
[9] R.H. Holm, M.J. O'Connor, Progr. Inorg. Chem. 14 (1971) 241.
[10] J.P. Costes, F. Dahan, A. Dupuis, J.P. Laurent, Inorg. Chem. 36 (1997) 3429.
[11] P. Pascal, Ann. Chim. Phys. 19 (1910) 5.
[12] J.M. Clemente-Juan, C. Mackiewicz, M. Verelst, F. Dahan, A. Bousseksou, Y. Sanakis, J.-P. Tuchagues, Inorg. Chem. 41 (2002) 1478.
[13] J.J. Borrás-Almenar, J.M. Clemente-Juan, E. Coronado, B.S. Tsukerblat, Inorg. Chem. 38 (1999) 6081.
[14] J.J. Borrás-Almenar, J.M. Clemente-Juan, E. Coronado, B.S. Tsukerblat, J. Comput. Chem. 22 (2001) 985.
[15] F. James, M. Roos, Comput. Phys. Commun. 10 (1975) 345.
[16] A. Altomare, G. Cascarano, G. Giacovazzo, A. Guagliardi, M.C. Burla, G. Polidori, M. Camalli, J. Appl. Cryst. 27 (1994) 435.
[17] P.W. Betteridge, J.R. Carruthers, R.I. Cooper, C.K. Prout, D.J. Watkin, J. Appl. Cryst. 36 (2003) 1487.
[18] International Tables for Crystallography, vol. C, Kluwer Academic Publishers, Dordrecht, The Netherlands, 1992.
[19] D.J. Watkin, C.K. Prout, L.J. Pearce, CAMERON, Chemical Crystallography Laboratory, Oxford, UK, 1996.
[20] L.W. Yang, S. Liu, S.J. Rettig, C. Orvig, Inorg. Chem. 34 (1995) 4921.
[21] K. Nakamoto, Infrared and Raman Spectra of Inorganic and Coordination Compounds, fifth ed., Wiley, New York, 1997.
[22] J.M. Miller, K. Balasanmugan, J. Nye, G.B. Deacon, N.C. Thomas, Inorg. Chem. 26 (1987) 560.
[23] B. Bleaney, K.D. Bowers, Proc. R. Soc. London, Ser. A 214 (1952) 451.
[24] M.S. Lah, V.L. Pecoraro, J. Am. Chem. Soc. 111 (1989) 7258.
[25] J.C.-G. Bünzli, in: R.S. Puche, P. Caro (Eds.), Rare Earths, Editorial Complutense, Madrid, 1998.

developed, and the products have potential applications in many diverse areas, including medicine, agents for the extraction of metal ions, supramolecular chemistry and as ligands for metals [20,21]. In view of the situation of the above two types of clusters, it would be very significant to incorporate them into one compound, both for the study of carborane chemistry and Mo(W)–S cluster chemistry. As a part of our study, we turned our interest to the diphosphine carborane-1,2-$(PPh_2)_2$-1,2-$C_2B_{10}H_{10}$, which is a typical bidentate ligand and has been widely used in transition metal chemistry [22]. Recently, we have successfully introduced this ligand into Mo–Cu–S clusters [23]. In this paper further studies on these types of reactions have been made and five heterobimetallic trinuclear clusters with two different metal skeleton cores which contain the *closo* carborane diphosphine 1,2-$(PPh_2)_2$-1,2-$C_2B_{10}H_{10}$, including their spectroscopy study and crystal structure, are reported.

2. Experimental

2.1. Materials and measurement

All the reactions were carried out under the protection of dry oxygen-free dinitrogen at room temperature. Solvents were dried with appropriate drying agents, distilled under dinitrogen and deoxygenated prior to use. $(NH_4)_2Mo(W)S_4$ and $(NH_4)_2Mo(W)OS_3$ were synthesized according to the literature procedures [24]. 1,2-$(PPh_2)_2$-1,2-$C_2B_{10}H_{10}$ was prepared as described in the literature [25]. All chemicals were purchased and used as received. UV/Visible electronic spectra were recorded on an HP-8453 UV/Visible Spectrophotometer and infrared spectra were recorded in the range 400–4000 cm^{-1} from KBr pellets on a Nicolet-460 FT-IR spectrophotometer. Elemental analysis (C, H) was carried out with a Perkin–Elmer 2400 II elemental analyzer. The ^1H and ^{13}C NMR were recorded on a Varian Mercury 400 spectrometer in $CDCl_3$ solution with tetramethylsilane (TMS) as an internal standard at 400.15 and 100.63 MHz, respectively. The ^{13}C spectra are broadband proton decoupled. The chemical shifts are reported in parts per million with respect to the references and are stated relative to external TMS for ^1H and ^{13}C NMR.

2.2. Synthesis procedures

2.2.1. Synthesis of $Cu_2MS_4[1,2\text{-}(PPh_2)_2\text{-}1,2\text{-}C_2B_{10}H_{10}]_2$ (M = Mo(1), W(3))

To a solution of 1,2-$(PPh_2)_2$-1,2-$C_2B_{10}H_{10}$ (102.4 mg, 0.20 mmol) in 10 ml of CH_2Cl_2 was added CuSCN (12.2 mg, 0.10 mmol) and $(NH_4)_2MoS_4$ (13.0 mg, 0.050 mmol) or $(NH_4)_2WS_4$ (17.4 mg, 0.050 mmol). After the mixture was stirred for 10 h at room temperature under the protection of the dry N_2, the suspension was filtered to remove any insoluble inorganic material. Concentration of the filtrate to 5 ml and followed by addition 20 ml *n*-hexane caused clusters **1** and **3** to precipitate as red solids. Single crystals suitable for X-ray diffraction were grown from a dichloromethane solution layered with *n*-hexane. **1**: 46.8 mg, 68.01%. M.p. 232–233 °C; FT-IR ν_{KBr} (cm^{-1}): 2960s, 2574m, 1636s, 1434m, 1090m, 741m, 472m. ^1H NMR (400.15 MHz, $CDCl_3$, ppm): 7.21–8.11 (phenyl-H); ^{13}C NMR (100.63 MHz, $CDCl_3$, ppm): 128–135 (48C), 77.1 (4C). *Anal.* Calc. for $C_{52}H_{60}B_{20}P_4Cu_2MoS_4$: C, 45.38; H, 4.39. Found: C, 45.30; H, 4.41%. **3**: 33.4 mg, 45.62%. M.p. 265–266 °C, FT-IR ν_{KBr} (cm^{-1}): 2968s, 2564m, 1640s, 1430m, 1095m, 731m, 465m. ^1H NMR (400.15 MHz, $CDCl_3$, ppm): 7.29–8.17 (phenyl-H); ^{13}C NMR (100.63 MHz, $CDCl_3$, ppm): 127–135 (48C), 77.2 (4C). *Anal.* Calc. for $C_{52}H_{60}B_{20}P_4Cu_2WS_4$: C, 42.65; H, 4.13. Found: C, 42.58; H, 4.11%.

2.2.2. Synthesis of $Cu_2MoS_4[1,2\text{-}(PPh_2)_2\text{-}1,2\text{-}C_2B_{10}H_{10}]_2 \cdot CH_2Cl_2$ (2)

A suspension of CuSCN (12.2 mg, 0.10 mmol), $(NH_4)_2MoS_4$ (13.0 mg, 0.050 mmol) and 1,2-$(PPh_2)_2$-1,2-$C_2B_{10}H_{10}$ (102.4 mg, 0.20 mmol) in 10 ml CH_2Cl_2 were refluxed for 5 h under the protection of dry N_2. After being filtered, the filtrate was concentrated to 5 ml, and 20 ml ether was added to precipitate a red solid. Yield: 44.8 mg, 61.32%. FT-IR ν_{KBr} (cm^{-1}): 2975s, 2573m, 1641s, 1433m, 1097m, 739m, 472m. ^1H NMR (400.15 MHz, $CDCl_3$, ppm): 7.24–8.13 (phenyl-H); ^{13}C NMR (100.63 MHz, $CDCl_3$, ppm): 128–135 (48C), 77.1 (4C). *Anal.* Calc. for $C_{53}H_{62}B_{20}P_4Cl_2Cu_2MoS_4$: C, 43.56; H, 4.28. Found: C, 43.51; H, 4.23%.

2.2.3. Synthesis of $Cu_2MOS_3[1,2\text{-}(PPh_2)_2\text{-}1,2\text{-}C_2B_{10}H_{10}]_2$ (M = Mo(4), W(5))

The procedures are similar to those for clusters **1** and **3**, except that $(NH_4)_2MS_4$ was replaced by $(NH_4)_2MoOS_3$ (12.2 mg, 0.050 mmol) or $(NH_4)_2WOS_3$ (16.6 mg, 0.050 mmol). Yields: 26.9 mg, 39.6% and 29.8 mg, 41.2% for clusters **4** and **5**, respectively. M.p. 220–221 °C for **4** and 203–204 °C for **5**. Single crystals for X-ray diffraction were grown from a dichloromethane–ether solution. Cluster **4**: FT-IR ν_{KBr} (cm^{-1}): 2920s, 2568m, 1638s, 1437m, 1107m, 920m, 746m, 470m. ^1H NMR (400.15 MHz, $CDCl_3$, ppm): 7.26–8.19 (phenyl-H); ^{13}C NMR (100.63 MHz, $CDCl_3$, ppm): 127–135 (48C), 77.0 (4C). *Anal.* Calc. for $C_{52}H_{60}B_{20}P_4Cu_2MoOS_3$: C, 45.91; H, 4.45. Found: C, 45.80; H, 4.48%. Cluster **5**: FT-IR ν_{KBr} (cm^{-1}): 2990s, 2569m, 1636s, 1435m, 1090m, 927m, 744m, 459m. ^1H NMR (400.15 MHz, $CDCl_3$, ppm): 7.20–8.23 (phenyl-H); ^{13}C NMR (100.63 MHz, $CDCl_3$, ppm): 128–135 (48C), 77.3 (4C). *Anal.* Calc. for $C_{52}H_{60}B_{20}P_4Cu_2WOS_3$: C, 43.12; H, 4.18. Found: C, 42.89; H, 4.23%.

2.3. X-ray structure determination

The collection of crystallographic data for all the clusters was carried out on a Bruker Smart-1000 CCD diffractometer, using graphite-monochromatized Mo Kα (λ = 0.71073 Å) at 298(2) K. The structures were solved by

direct methods and expanded using Fourier difference techniques with the SHELXTL-97 program package [26]. The non-hydrogen atoms were refined anisotropically by full-matrix least-squares calculations on F^2. All the H atoms were located in a difference Fourier map and thereafter refined isotropically. Details of the crystal parameters, data collection and refinement are summarized in Table 1.

3. Results and discussion

3.1. Synthesis

Clusters constructed from thiomolybdates and thiotungstates with other transition metal ions have been extensively studied not only because of the possible relevance to the Mo–Cu biological antagonism, but also for their potential applications as materials with non-linear physical properties [27]. Many these types clusters with various nuclearity and different skeleton cores have been synthesized either by reactions carried out in solution or by solid-state reactions under comparable low temperatures [13,28]. Some terminal ligands in these Mo(W)–Cu–S clusters, such as Cl^-, Br^-, I^- and SCN^-, are only loosely bound. By substitution of these weak ligands with strong ones, such as PhS^- and neutral PPh_3 [29], many new clusters can be afforded. The *closo* carborane diphosphine 1,2-$(PPh_2)_2$-1,2-$C_2B_{10}H_{10}$, which can form a five-member chelating ring between the ligand and a metal, is a good bidentate ligand and has an outstanding chelating ability to the metal. With these two points in mind, we tentatively introduced this moiety into Mo(W)–Cu–S clusters.

To start with, we carried out the reaction with a reactant ratio of Cu(I) to 1,2-$(PPh_2)_2$-1,2-$C_2B_{10}H_{10}$ of 1:1 (according to the stoichiometric proportion from the clusters obtained by using PPh_3 to substitute the terminal ligand), but no SCN^- was found to be substituted by the *closo* carborane diphosphine ligand. Then, we tentatively changed the reactant ratio. Under the protection of dry N_2, on reaction of CuSCN, $(NH_4)_2MoS_4$ and the *closo* diphosphine 1,2-$(PPh_2)_2$-1,2-$C_2B_{10}H_{10}$, with a ratio of 2:1:4 in CH_2Cl_2

Table 1
Details of the crystal parameters, data collection and refinement for clusters **1**–**5**

Crystallographic crystal data	**1**	**2**	**3**	**4**	**5**
Empirical formula	$C_{52}H_{60}B_{20}P_4Cu_2MoS_4$	$C_{53}H_{62}B_{20}P_4Cl_2Cu_2MoS_4$	$C_{52}H_{60}B_{20}P_4Cu_2WS_4$	$C_{52}H_{60}B_{20}P_4Cu_2MoOS_3$	$C_{52}H_{60}B_{20}P_4Cu_2WOS_3$
Formula weight	1376.34	1461.27	1464.25	1360.28	1448.19
Temperature (K)	298(2)	298(2)	298(2)	298(2)	298(2)
Wavelength (Å)	0.71073	0.71073	0.71073	0.71073	0.71073
Crystal system	monoclinic	triclinic	monoclinic	monoclinic	monoclinic
Space group	$C2/c$	$P\bar{1}$	$C2/c$	$P2(1)/c$	$P2(1)/c$
a (Å)	41.77(7)	11.142(2)	42.313(17)	12.773(10)	13.046(13)
b (Å)	18.82(2)	17.494(4)	18.990(8)	19.289(15)	19.75(2)
c (Å)	20.48(3)	20.324(4)	20.653(8)	30.14(2)	30.74(3)
α (°)	90	67.593(3)	90	90	90
β (°)	116.60(4)	89.576(3)	116.751(6)	93.786(14)	93.045(16)
γ (°)	90	79.962(3)	90	90	90
V (Å^3)	14391(35)	3599.0(13)	14819(10)	7411(10)	7910(14)
Z	8	2	8	4	4
Absorption coefficient (mm^{-1})	0.995	1.071	2.348	0.939	2.174
D (Mg m^{-3})	1.270	1.348	1.313	1.219	1.216
F(000)	5568	1476	5824	1476	2880
Crystal size (mm)	0.50 × 0.39 × 0.12	0.50 × 0.42 × 0.39	0.43 × 0.25 × 0.19	0.55 × 0.39 × 0.23	0.48 × 0.25 × 0.17
Θrange (°)	1.96–25.01	1.86–25.01	1.84–25.01	2.22–25.01	2.17–25.01
Limiting indices	$-44 \leqslant h \leqslant 49$, $-21 \leqslant k \leqslant 21$, $-22 \leqslant l \leqslant 24$	$-13 \leqslant h \leqslant 12$, $-19 \leqslant k \leqslant 20$, $-24 \leqslant l \leqslant 24$	$-45 \leqslant h \leqslant 50$, $-21 \leqslant k \leqslant 22$, $-24 \leqslant l \leqslant 14$	$-15 \leqslant h \leqslant 15$, $-22 \leqslant k \leqslant 22$, $-35 \leqslant l \leqslant 24$	$-10 \leqslant h \leqslant 15$, $-22 \leqslant k \leqslant 23$, $-36 \leqslant l \leqslant 36$
Independent reflection	12346	12526	12713	12424	13571
Maximum and minimum transmission	0.8899 and 0.6361	0.6802 and 0.6166	0.6639 and 0.4317	0.8130 and 0.6262	0.7088 and 0.4217
Goodness-of-fit on F^2	1.018	1.008	1.042	0.997	1.014
R [$I > 2\sigma(I)$]	$R_1 = 0.0781$ $wR_2 = 0.1990$	$R_1 = 0.0593$ $wR_2 = 0.1864$	$R_1 = 0.0801$ $wR_2 = 0.2020$	$R_1 = 0.0896$ $wR_2 = 0.1684$	$R_1 = 0.0846$ $wR_2 = 0.1721$
R (all data)	$R_1 = 0.1642$ $wR_2 = 0.2680$	$R_1 = 0.0958$ $wR_2 = 0.2176$	$R_1 = 0.1492$ $wR_2 = 0.2763$	$R_1 = 0.2237$ $wR_2 = 0.2258$	$R_1 = 0.1999$ $wR_2 = 0.2121$
Largest difference in peak and hole (×10^2 e Å^{-3})	3.220 and −1.038	2.309 and −0.657	3.682 and −1.646	1.131 and −0.721	2.266 and −2.474

under stirring conditions at room temperature, we obtained a heterobimetallic cluster containing the Cu_2Mo core, in which the three metal atoms were almost in a linear conformation and the diphosphine ligand was introduced into the cluster. This result indicated that to substitute the terminal SCN^- anion with the neutral diphosphine ligand, the ligand must be in excess. Subsequently, a similar experiment was carried out and cluster **3** was afforded. To investigate if the result of the reaction could be affected by the temperature, we carried out the reaction of CuSCN, $(NH_4)_2MoS_4$ and the ligand in CH_2Cl_2 with the ratio 2:1:4 under refluxing conditions. A cluster with a similar structure to cluster **1** was obtained. According to the crystal data listed in Table 1, the structures of these two clusters are not isostructural because of the different crystal system, space group and the solvent molecule in cluster **2**. The reactions are given in Scheme 1.

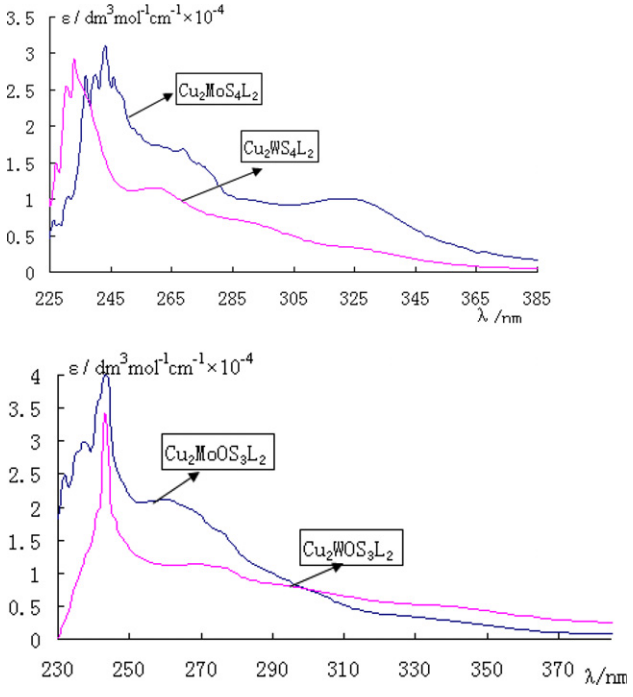
Accordingly, further experiments were carried out under the same conditions. After stirring the mixture of CuSCN, $(NH_4)_2MoOS_3$ or $(NH_4)_2WOS_3$ and 1,2-$(PPh_2)_2$-1,2-$C_2B_{10}H_{10}$ for 8–10 h, clusters **4** and **5** were obtained. These two clusters also contain a heterobimetallic $Cu_2Mo(W)$ core, but the difference between them and the above three clusters is that the skeleton of these two clusters is a butterfly-shaped conformation rather than a linear one. These two reactions are shown in Scheme 2.

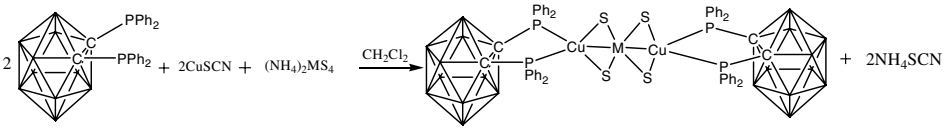
3.2. Spectral characterization

All these clusters were characterized by FT-IR, UV/Visible, ^1H and ^{13}C NMR spectroscopy. The IR spectra of these clusters have many similarity to each other and exhibit absorptions characteristic of terminal B–H vibrations from 2574 to 2564 cm^{-1}, which are in the normal range of B–H vibrations from 2625 to 2450 cm^{-1} [30]. The absorption at ca. 2970 cm^{-1} may be attributed to the ν_{C-H} stretching vibration of the benzene rings. The peaks at 470 and 920 cm^{-1} are the vibrations of M–S and Mo=O, respectively. The ^1H NMR spectra (400.15 MHz) of these clusters displayed a cluster pattern of resonances at about 7.2–8.2 ppm that can be attributed to phenyl-H of the PPh_2 groups. In the ^{13}C NMR spectra (100.63 MHz), the resonance at ca. $\delta = 127$–135 ppm can be assigned to the benzene ring C atoms, and that at ca. $\delta = 77.0$ can be assigned to the carbon atom of the carborane cage [31].

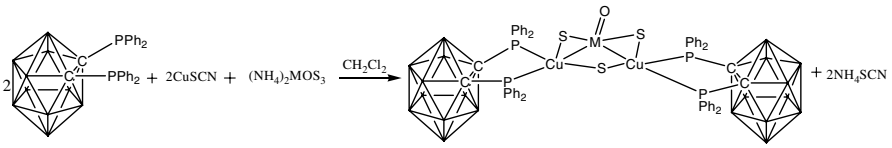
3.3. Electronic spectra

Fig. 1 depicts the UV/Visible absorption spectra of the four clusters. Comparable to the three intense bands in the 210–700 nm region exhibited by free MoS_4^{2-} or WS_4^{2-} [13], the formation of the trinuclear clusters from MoS_4^{2-} or WS_4^{2-} cause some changes in the intensity and location of the bands. These changes of the absorption bands of MoS_4^{2-} or WS_4^{2-} upon formation of these clusters probably arises from the interaction between the tetrathiometallate and the [Cu(1,2-$(PPh_2)_2$-1,2-$C_2B_{10}H_{10}$)] moieties (such interactions should disturb the molecular orbitals of the tetrathiometallates). For $Cu_2MS_4L_2$ (L = 1,2-$(PPh_2)_2$-1,2-$C_2B_{10}H_{10}$), their electronic spectra retain the three bands of the free tetrathiometallates, but obvious changes in the intensities and locations have been taken place. These absorptions are at about 242, 270, 325 nm, which are different from the location of 242, 317, 467 nm for MoS_4^{2-} and 216,277, 392 nm for WS_4^{2-} [13], especially for the ν_3 band. We also noticed that these two clusters exhibit several poorly resolved shoulders, which could be assigned to p(P) →d(Mo) transitions [32]. For $Cu_2MOS_3L_2$, their electronic spectra are very similar to each other, in which only two typical absorption bands could be found. The locations for the two absorption bands in the two clusters (ca. 240 and 270 nm) are basically consistent with the two bands for the free MOS_3^{2-}. However, on comparison to the absorption of the free trithiometallates, the other two bands at about 460, 390 nm for $MoOS_3^{2-}$ and 330, 370 nm for WOS_3^{2-} disappeared.





Scheme 1. The reaction for the preparation of clusters **1**–**3** (M = Mo (**1**, **2**); M = W (**3**)).



Scheme 2. The reactions for the preparation of the clusters **4** and **5** (M = Mo (**4**); M = W (**5**)).

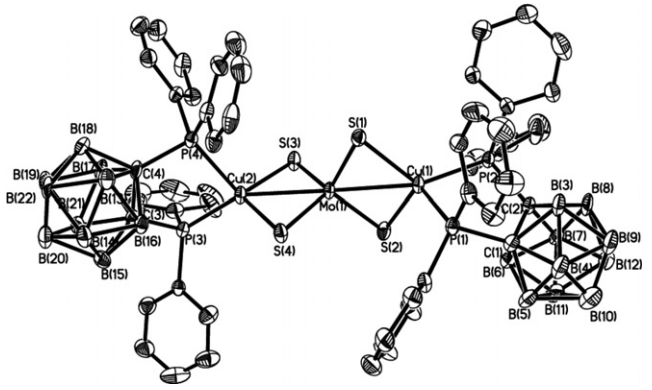


Fig. 1. The molecular structure of cluster **1**. The H atoms are omitted for clarity.

4. Crystal structure

The molecular structures of clusters **1** and **2** are shown in Figs. 1 and 2, respectively. Selected bond lengths and angles for clusters **1**–**3** are given in Table 2. The clusters **1** and **3** crystallize in the monoclinic space group $C2/c$, while cluster **2** crystallizes in the triclinic space group $P\bar{1}$. In clusters **1** and **3**, MS_4^{2-} (M = Mo, W), as a tetradentate ligand, is coordinated to two Cu atoms at the same time, in which an almost linear arrangement between the three metal atoms is formed with Cu–M–Cu–Cu (M = Mo, W) angles of 172.10(5)° and 172.06(5)°, respectively. The geometry at the central M atom is a distorted tetrahedron formed by two pairs of bridged-S atoms, in which the dihedral angle between the two MSSCu planes is about 90°.

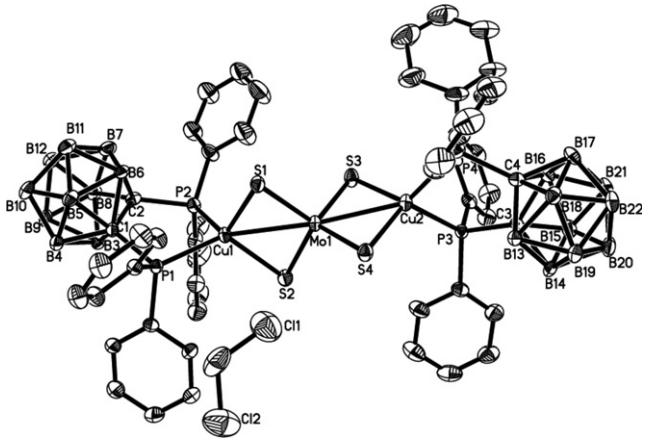


Fig. 2. The asymmetric unit consisting of a trinuclear cluster and a solvate molecule of cluster **2**. The H atoms are omitted for clarity.

The average distances of Mo–Cu and W–Cu are 2.708 and 2.7422 Å, respectively, which are in agreement with the corresponding bond lengths of 2.687 Å in $[^nBu_4N]_4[Mo_4Cu_{10}S_{16}O_3]\cdot H_2O$ and 2.748 Å in $[Et_4N]_4[Cu_4W_4S_{12}O_4]$ [33,34]. The M–S bond lengths listed in Table 2 are also consistent with the corresponding distances in other linear M–Cu–S clusters [35,36]. For each Cu atom, the coordination sphere is a distorted tetrahedron with angles varying between 89.80(9)° and 124.32(11)° in cluster **1**, 90.30(11)° and 124.65(12)° in cluster **3**, in which two positions result from two bridged-S atoms, and the other two are occupied by the *closo* carborane diphosphine 1,2-$(PPh_2)_2$-1,2-$C_2B_{10}H_{10}$. A similar coordination mode can also be found in Cu complexes containing other diphosphinocarborane ligands [37]. The P–Cu bond lengths, as listed in Table 2, are comparable to the average distance of 2.265 Å in $[Cu(PPh_3)\{7,8\text{-}(PPh_2)_2\text{-}7,8\text{-}C_2B_9H_{10}\}]\cdot Me_2CO$ [38] and 2.254 Å in $[Cu_2(\mu\text{-}Cl)_2(1,2\text{-}(PPh2)2\text{-}1,2\text{-}C_2B_{10}H_{10})_2]\cdot 2CH_2Cl_2$ [39], and this is also the case for the P–Cu–P angle, with the value being very close to 90°. On comparison of other parameters of the 1,2-$(PPh_2)_2$-1,2-$C_2B_{10}H_{10}$ moiety in these clusters and the free ligand [40], such as the P–Cc (Cc is the carbon atom of the carborane), Cc–Cc and the P–Cc–Cc angles, no noticeable differences have been found.

Fig. 3 shows the crystal structure of cluster **4**, and selective bond lengths and angles for clusters **4** and **5** are also listed in the Table 2. These two clusters crystallized in the monoclinic space group $P2(1)/c$, and have similar structures which could be characterized as a butterfly-shaped conformation. This structural conformation may also be regarded as defective cubane-like with two corners missing. Within the structures of the two clusters there is an approximate molecular mirror plane passing through the O(1), M(1) and S(1) atoms. The coordination sphere of the M atom is a distorted tetrahedron formed by three bridging S atoms and one terminal O atom. The distances between the terminal O atom and the M atom are 1.671(7) and 1.765(9) Å, respectively, The corresponding distances are 1.715(7) Å in $[MoCu_3OS_3(PPh_3)_3(CH_3COO)]$ and 1.693(8) Å in $[Cu_3WOS_3CN(py)_4]_n$ [41,42]. The three M–(μ-S) bond lengths are not equivalent, with the common feature that the M–S(1) bond length is slightly longer than the other two M–S bond lengths. The average Cu–Mo bond length of 2.722 Å in cluster **4** is almost equal to that of 2.710 Å in $[MoCu_3OS_3(PPh_3)_3(CH_3COO)]$, while the average Cu–W bond length of 2.7985 Å in **5** is slightly longer than that of 2.719 Å in $[Cu_3WOS_3CN(py)_4]_n$. The Cu–Mo–Cu angle of 91.80(6)° is obviously bigger than that of 81.56(4)° in

Table 2
Selected bond lengths (Å) and angles (°) for clusters **1**–**5**

	1 (M = Mo)	**2** (M = Mo)	**3** (M = W)		**4** (M = Mo)	**5** (M = W)
M(1)–S(1)	2.175(4)	2.1950(18)	2.203(3)	M(1)–S(1)	2.242(3)	2.280(4)
M(1)–S(2)	2.177(4)	2.1961(18)	2.207(3)	M(1)–S(2)	2.176(3)	2.224(4)
M(1)–S(3)	2.182(3)	2.1963(18)	2.204(3)	M(1)–S(3)	2.197(3)	2.229(5)
M(1)–S(4)	2.188(4)	2.2089(18)	2.211(3)	M(1)–O(1)	1.671(7)	1.765(9)
M(1)–Cu(1)	2.713(4)	2.7169(10)	2.7332(16)	M(1)–Cu(1)	2.689(2)	2.828(3)
M(1)–Cu(2)	2.695(4)	2.7128(10)	2.7512(16)	M(1)–Cu(2)	2.755(2)	2.769(2)
Cu(1)–S(1)	2.274(4)	2.2822(18)	2.297(3)	Cu(1)–S(1)	2.293(3)	2.335(4)
Cu(1)–S(2)	2.280(3)	2.2932(19)	2.294(3)	Cu(1)–S(3)	2.286(3)	2.378(4)
Cu(2)–S(3)	2.264(4)	2.2831(19)	2.312(3)	Cu(2)–S(2)	2.306(3)	2.332(4)
Cu(2)–S(4)	2.265(4)	2.2797(19)	2.289(3)	Cu(2)–S(1)	2.272(3)	2.369(5)
Cu(1)–P(1)	2.342(4)	2.2727(18)	2.342(3)	Cu(1)–P(1)	2.226(3)	2.354(4)
Cu(1)–P(2)	2.271(4)	2.3431(18)	2.277(3)	Cu(1)–P(2)	2.352(3)	2.304(5)
Cu(2)–P(3)	2.250(4)	2.2977(19)	2.367(3)	Cu(2)–P(3)	2.308(3)	2.397(4)
Cu(2)–P(4)	2.334(4)	2.3066(19)	2.299(3)	Cu(2)–P(4)	2.272(3)	2.279(4)
P(1)–C(1)	1.864(9)	1.883(6)	1.872(11)	P(1)–C(1)	1.871(12)	1.935(15)
P(2)–C(2)	1.849(9)	1.881(7)	1.881(10)	P(2)–C(2)	1.881(10)	1.857(14)
P(3)–C(3)	1.871(9)	1.867(6)	1.882(11)	P(3)–C(3)	1.849(12)	1.895(14)
P(4)–C(4)	1.845(10)	1.877(7)	1.873(11)	P(4)–C(4)	1.843(11)	1.869(15)
S(3)–M(1)–S(4)	107.94(12)	108.21(7)	107.52(11)	S(1)–M(1)–S(3)	106.07(11)	106.08(15)
S(1)–M(1)–S(2)	107.82(15)	107.97(7)	107.85(11)	S(1)–M(1)–S(2)	106.15(11)	106.53(15)
Cu(2)–M(1)–Cu(1)	172.10(5)	171.58(3)	172.06(5)	Cu(2)–M(1)–Cu(1)	91.80(6)	92.46(8)
P(2)–Cu(1)–P(1)	89.80(9)	92.20(6)	90.30(11)	P(2)–Cu(1)–P(1)	90.29(11)	90.59(15)
P(3)–Cu(2)–P(4)	90.07(12)	92.22(6)	89.83(10)	P(3)–Cu(2)–P(4)	90.32(10)	90.53(14)
M(1)–S(1)–Cu(1)	74.99(14)	74.69(6)	74.76(10)	M(1)–S(3)–Cu(1)	73.71(9)	74.72(13)
M(1)–S(2)–Cu(1)	74.75(14)	74.45(6)	74.76(10)	M(1)–S(2)–Cu(2)	75.78(10)	75.76(11)
M(1)–S(3)–Cu(2)	74.72(11)	74.52(6)	75.02(10)	S(3)–M(1)–S(2)	110.73(12)	111.54(14)
M(1)–S(4)–Cu(2)	74.68(12)	74.35(6)	75.36(10)	Cu(2)–S(1)–Cu(1)	117.81(12)	118.46(15)
C(1)–C(2)–P(2)	116.1(6)	114.9(4)	115.3(6)	C(1)–C(2)–P(2)	113.4(6)	117.5(10)
C(2)–C(1)–P(1)	112.9(6)	115.1(4)	112.7(6)	C(2)–C(1)–P(1)	115.5(6)	112.4(8)

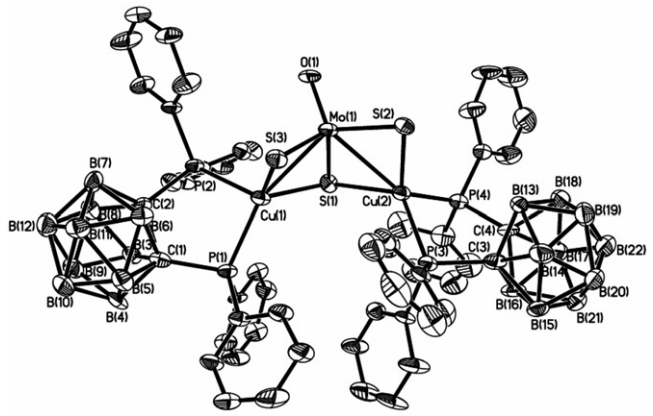


Fig. 3. The molecular structure of cluster **4**. The H atoms are omitted for clarity.

$[MoCu_3OS_3(PPh_3)_3(CH_3COO)]$, characterized as cube-like, while the value of the Cu–W–Cu angle of 92.46(8)° agrees well with the average value of 91.76° in the above W–Cu–S cluster polymer. The ranges of Cu–S bond lengths are 2.272(3) to 2.306(3) Å for **4** and 2.332(4) to 2.378(4) for **5**, which are consistent with the corresponding ranges in the above two clusters. Similar to that in clusters **1** and **3**; the coordination geometry of the two Cu atoms should also be described as distorted tetrahedral. The Cu–P distances are in the narrow range 2.226(3) to 2.397(4) Å, which is comparable to the corresponding distance 2.255 Å in $[Cu_2(\mu\text{-}Cl)_2(1,2\text{-}(PPh_2)_2\text{-}1,2\text{-}C_2B_{10}H_{10})_2]\cdot 2CH_2Cl_2$. The two P–Cu–P angles in the two clusters are 90.29(11)° and 90.59(15)°, respectively, and in the above complex it is 93.63(8)°.

5. Conclusion

In summary, we have studied the reactions of the *closo* carboranylphosphine $1,2\text{-}(PPh_2)_2\text{-}1,2\text{-}C_2B_{10}H_{10}$, MS_4^{2-} (MOS_3^{2-}) and the d^{10} metal ion Cu(I). The carborane skeleton was connected to the Mo(W)–Cu–S clusters through its two phosphorus atoms, and five heterobimetallic trinuclear clusters containing the above ligand were obtained, in which the metal skeleton could be classified into two types. With MS_4^{2-} as a starting material, the metal skeleton is in a linear conformation, while with MOS_3^{2-} it is butterfly-shaped.

6. Supplementary material

CCDC 607841, 607836, 607842, 607838 and 607837 contain the supplementary crystallographic data for **1**, **2**, **3**, **4** and **5**. These data can be obtained free of charge via http://www.ccdc.cam.ac.uk/conts/retrieving.html, or from the Cambridge Crystallographic Data Centre, 12 Union Road, Cambridge CB2 1EZ, UK; fax: (+44) 1223-336-033; or e-mail: deposit@ccdc.cam.ac.uk.

Acknowledgements

This work was supported by the National Natural Science Foundation of P.R. China (project no. 20371025) and the Open Research Fund Program of the Key Laboratory of Marine Drugs (Ocean University of China), Ministry of Education (Project No. KLMD (OUC) 2004).

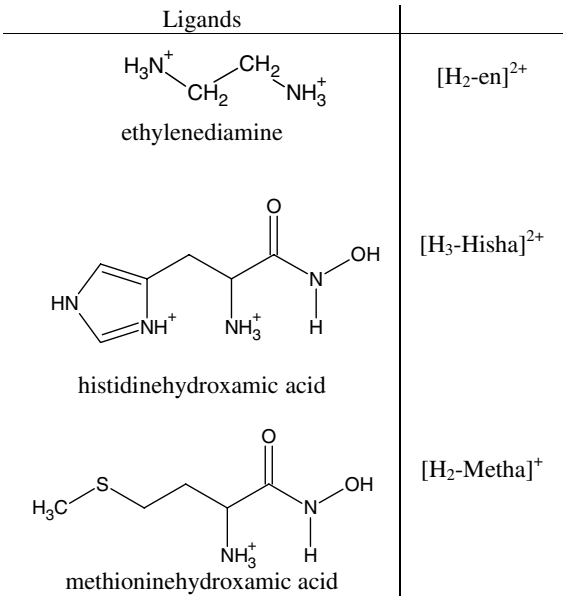
References

[1] S.C. Lee, R.H. Holm, Chem. Rev. 104 (2004) 1135.
[2] A.M. Macintosh, M.H. Chisholm, Chem. Rev. 105 (2005) 2949.
[3] R.A. Henderson, Chem. Rev. 105 (2005) 2365.
[4] E. Burkholder, V. Golub, C.J. O'Connor, J. Zubieta, Inorg. Chem. 43 (2004) 7014.
[5] W. Christen, U. Even, Phys. Chem. A 102 (1998) 9420.
[6] S. Keki, L.S. Szilagyi, J. Torok, G. Deak, M. Zsuga, J. Phys. Chem. B 107 (2003) 4818.
[7] I.V.G. Graf, J.W. Bacon, M.B. Consugar, M.E. Curley, L.N. Ito, L.H. Pignolet, Inorg. Chem. 35 (1996) 689.
[8] K.D. Demadis, S.M. Malinak, D. Coucouvanis, Inorg. Chem. 35 (1996) 4038.
[9] J.N. Agar, C. Krebs, J. Frazzon, B.H. Huynh, D.R. Dean, M.K. Johnson, Biochemistry 39 (2000) 7856.
[10] Y. Naruta, M. Sasayama, T. Sasaki, Angew. Chem. Int. Ed. Engl. 33 (1994) 1839.
[11] J.A. Jackson, M.D. Newsham, C. Worsham, D.G. Nocera, Chem. Mater. 8 (1996) 558.
[12] A. Muller, E. Diemann, R. Jostes, H. Bogge, Angew. Chem. Int. Ed. Engl. 93 (1981) 957.
[13] H.W. Hou, X.Q. Xin, S. Shi, Coord. Chem. Rev. 153 (1996) 25.
[14] (a) J.L. Zhou, Y.L. Song, Y.Z. Li, H.G. Zheng, X.Q. Xin, Z. Anorg. Alleg. Chem. 630 (2004) 609;
(b) H.G. Zheng, W. Ji, M.L.K. Low, G. Sakane, T. Shibahara, X.Q. Xin, J. Chem. Soc., Dalton Trans. (1997) 2357;
(c) M.L.K. Low, H.W. Hou, H.G. zheng, W.T. Wong, G.X. Jin, W. Ji, Chem. Commun. (1998) 505.
[15] (a) A.S. Larsen, J.D. Holbrey, F.S. Tham, C.A. Reed, J. Am. Chem. Soc. 122 (2000) 7264;
(b) G.J. Pindado, S.J. Lancaster, M. Thornton-Pett, M. Bochmann, J. Am. Chem. Soc. 120 (1998) 6816;
(c) C.A. Reed, Acc. Chem. Res. 31 (1998) 133;
(d) M.A. Curtis, M.G. Finn, R.N. Grimes, J. Organomet. Chem. 550 (1998) 469.
[16] M.F. Hawthorne, A. Maderna, Chem. Rev. 99 (1999) 3421.
[17] J. Plesek, Chem. Rev. 92 (1992) 269.
[18] (a) M. Westerhausen, C. Guckel, S. Schneiderbauer, H. Noth, N.S. Hosmane, Angew. Chem. Int. Ed. Engl. 40 (2001) 1902;
(b) A. Herzog, C.B. Knobler, M.F. Hawthorne, A. Maderna, W. Siebert, J. Org. Chem. 64 (1999) 1045;
(c) T. Peymann, A. Herzog, C.B. Knobler, M.F. Hawthorne, Angew. Chem. Int. Ed. Engl. 38 (1999) 1061;
(d) F. Teixidor, S. Gomez, M. Lamrani, C. Viñas, R. Sillanpaeae, R. Kivekäs, Organometallics 16 (1997) 1278.
[19] V.I. Bregadze, Chem. Rev. 92 (1992) 209.
[20] (a) M.F. Hawthorne, A. Maderna, Chem. Rev. 99 (1999) 3421;
(b) P.C. Andrews, C.L. Raston, J. Organomet. Chem. 600 (2000) 174;
(c) R.N. Grimes, Coord. Chem. Rev. 200 (2000) 773.
[21] G.X. Jin, Coord. Chem. Rev. 248 (2004) 587.
[22] (a) S. Paavola, R. Kivekäs, F. Teixidor, C. Viñas, J. Organomet. Chem. 606 (2000) 183;
(b) S. Paavola, F. Teixidor, C. Viñas, R. Kivekäs, J. Organomet. Chem. 645 (2002) 39;
(c) S. Paavola, F. Teixidor, C. Viñas, R. Kivekäs, J. Organomet. Chem. 657 (2002) 187;
(d) E. Bembenek, O. Crespo, M.C. Gimeno, P.G. Jones, A. Laguna, Chem. Ber. 127 (1994) 835;
(e) O. Crespo, M.C. Gimeno, P.G. Jones, A. Laguna, Inorg. Chem. 33 (1994) 6128;
(f) O. Crespo, M.C. Gimeno, A. Laguna, P.G. Jones, J. Chem. Soc., Dalton Trans. (1992) 1601;
(g) O. Crespo, M.C. Gimeno, P.G. Jones, A. Laguna, J. Chem. Soc., Chem. Commun. (1993) 1696;
(h) Y. Sun, H.S. Chan, P.H. Dixneuf, Z.W. Xie, Organometallics 23 (2004) 5864.
[23] J.M. Dou, D.P. Zhang, D.C. Li, D.Q. Wang, Inorg. Chem. Commun. 9 (2006) 1099.
[24] J.W. Mcdonald, G.D. Friesen, L.D. Rosenhein, W.E. Newton, Inorg. Chim. Acta 72 (1983) 205.
[25] R.P. Alexander, H. Schroeder, Inorg. Chem. 2 (1963) 1107.
[26] G.M. Sheldrick, SHELXTL 5.10 for Windows NT: Structure Determination Software Programs, Bruker Analytical X-ray Systems, Madison, WI, 1997.
[27] W.H. Zhang, J.X. Chen, H.X. Li, B. Wu, X.Y. Tang, Z.G. Ren, Y. Zhang, J.P. Lang, Z.R. Sun, J. Organomet. Chem. 690 (2005) 394.
[28] J.P. Lang, K. Tatsumi, Inorg. Chem. 37 (1998) 6308.
[29] (a) Y. Jeannin, F. Secheresse, S. Bernes, F. Robert, Inorg. Chim. Acta 198-200 (1992) 493;
(b) S.F. Gheller, T.W. Hambley, J.R. Rodgers, R.T.C. Brownlee, M.J. O'Connor, M.R. Snow, A.G. Wedd, Inorg. Chem. 23 (1984) 2519.
[30] J.E. Crook, N.N. Greenwood, J.D. Kennedy, J. Chem. Soc., Dalton. Trans. (1972) 171.
[31] V.P. Balema, M. Pink, J. Sieler, E. Hey-Hawkins, L. Hennig, Polyhedron 17 (1998) 2087.
[32] C.M. Che, B.H. Xia, J.S. Huang, C.K. Chan, Z.Y. Zhou, K.K. Cheung, Chem. Eur. J. 7 (2001) 3998.
[33] J. Guo, X.T. Wu, W.J. Zhang, T.L. Sheng, Q. Huang, P. Lin, Q.M. Wang, J.X. Lu, Angew. Chem. Int. Ed. Engl. 36 (1997) 2464.
[34] Q. Huang, X.T. Wu, Q.M. Wang, T.L. Sheng, J.X. Lu, Inorg. Chem. 35 (1996) 893.
[35] S.B. Qiao, C.M. Jiao, Y. Chen, J.X. Chen, Q.F. Xu, J.G. Cheng, J.P. Lang, Chem. Res. Appl. 16 (2004) 781 (in Chinese).
[36] G.H. Zheng, J.L. Zhou, Michael F. Lappert, Y.L. Song, Y.Z. Li, X.Q. Xin, Eur. J. Inorg. Chem. (2004) 2754.
[37] (a) A. Sterzik, E. Rys, S. Blaurock, E. Hey-Hawkins, Polyhedron 20 (2001) 3007;
(b) R. Kivekäs, F. Teixidor, C. Viñas, M.M. Abad, Acta Chem. Scand. 50 (1996) 499.
[38] F. Teixidor, C. Viñas, M.M. Abad, M. Lopez, J. Casabó, Organometallics 12 (1993) 3766.
[39] D.P. Zhang, J.M. Dou, D.C. Li, D.Q. Wang, Appl. Organomet. Chem. 20 (2006) 632.
[40] D.P. Zhang, J.M. Dou, D.C. Li, D.Q. Wang, Acta Crystallogr., Sect. E 62 (2006) 418.
[41] D.X. Zeng, W. Li, W.T. Wong, W.Y. Wong, X.Q. Xin, Inorg. Chim. Acta 279 (1998) 172.
[42] H.W. Hou, H.G. Zheng, H.G. Ang, Y.T. Fan, Michael K.M. Low, Y. Zhu, W.L. Wang, X.Q. Xin, W. Ji, W.T. Wong, J. Chem. Soc., Dalton Trans. (1999) 2953.

purchased from Sigma-Aldrich Chemical Co. All ligands were used without further purification and their purity was greater than 99%. The exact concentrations of the ligand solutions used for potentiometric measurements were determined by the Gran method [7]. Copper(II) chloride solution was purchased from Merck as a Titrisol concentrate for the preparation of standard solutions. The concentration of metal ion stock solution was standardized by complexometric ethylenediaminetetraacetate (EDTA) titration. Carbonate-free potassium hydroxide solution (the titrant) was prepared and standardized against a standard potassium hydrogen phthalate solution. All solutions were prepared with deionized water. The formulae of the fully protonated form of the ligands used in this study are shown in Scheme 1.

2.2. Potentiometric measurements

The stability constants of the proton and copper(II) complexes were determined by pH-metric titration of 5 cm^3 samples in aqueous solutions. All the measurements were carried out at 0.2 mol dm^{-3} ionic strength (KCl) and 25.0 ± 0.1 °C using a constant-temperature water-bath. The titrations were performed with carbonate-free KOH solution of known concentration (ca. 0.2 mol dm^{-3}) under argon atmosphere over the pH range 2.0–11.0. The data for the Cu^{2+}-en, Cu^{2+}-Metha and Cu^{2+}-Hisha binary system were reported previously [1,3]. For the ternary systems the ratios of copper(II):en:Metha/Hisha were 1:1:1, 1:1:2, 1:2:1 and 1:2:2. Titrations were made on samples containing the copper(II) ion at 4×10^{-3} mol dm^{-3}. Number of titration curves per copper(II)-en-Metha/Hisha systems was 6–8.



Scheme 1. Ligands ethylenediamine $[H_2\text{-en}]^{2+}$ histidinehydroxamic acid $[H_3\text{-Hisha}]^{2+}$methioninehydroxamic acid $[H_2\text{-Metha}]^{+}$.

The pH-metric titrations were performed with a Radelkis Op-208/1 instrument equipped with a combination pH electrode (SINGLE PORE, Hamilton) using an ABU-80 autoburette (Radiometer).The electrode system was calibrated by periodic titrations of HCl solution (1×10^{-2} mol dm^{-3} in KCl) against standard KOH solution. The resulting titration data were used to calculate the standard electrode potentials, E^0, and the dissociation constant for water ($pK_w = 13.73$). These values were then used to calculate the hydrogen ion concentration $[H^+]$ from emf readings [8]. The pH-metric results were used to establish the stoichiometry of the species and to calculate the stability constants of the species formed $\beta_{pqrs} = [M_p(en)_qL_rH_s]/[M]^p[en]^q[L]^r[H]^s$ in the ternary systems. Calculations were performed with the aid of the HYPERQUAD 2006 computer program [9]. The reported standard deviations were calculated by assuming random errors.

The charges of the complexes have been omitted in the text and tables. However, for clarity, it should be mentioned here that the fully deprotonated form of aminohydroxamic acids (Metha and Hisha) is L^- while the amine (en) is neutral.

3. UV/Vis spectroscopy

The electronic absorption spectra in the visible range were obtained on a BECKMAN DU68 spectrophotometer using 2-cm quartz cells at room temperature. The spectra were recorded digitally (0.5 nm step) over the range 400–900 nm. The metal ion concentration was 4×10^{-3} mol dm^{-3}. For the systems copper(II):en:Metha/Hisha the concentration ratio was 1:1:2.

Even at the pH value where the distribution of the species has a maximum, the other complexes coexist in a greater or a smaller extent. Therefore, in the absorption spectra measured at this pH the contributions from the other species should be included to extract the net ligand-field absorption band of each mixed-ligand species. Hence, the spectrum measured at a pH value where each of these species exhibits maximal contribution was resolved into the components corresponding to the individual species existing at that pH (as described in Ref.[2]). The molar absorptivity for the individual species was then calculated taking into account their distribution.

4. EPR spectroscopy

Electron paramagnetic resonance (EPR) spectra were performed on a Bruker 300E X-band spectrophotometer equipped with a Bruker NMR gaussmeter ER 035 M and a Hewlett-Packard frequency counter HP 5350B at 77 K in water/ethylene glycol (4:1 v/v) solution. The EPR parameters were calculated by computer simulation of the experimental spectra using Bruker's WIN-EPR SIMFONIA Software Version 1.25. The metal ion concentration was 4×10^{-3} mol dm^{-3} and the metal ion to ligands molar ratios was 1:2:2.

5. Results and discussion

The values of the protonation constants for ethylenediamine are $\log \beta_1^H = 9.95(1)$, $\log \beta_2^H = 17.13(1)$. The respective values for Metha and Hisha were determined previously [3]. The detailed discussion about the acid–base properties of these ligands can be found in our early paper [3].

The equilibrium models for the studied ternary systems and corresponding stability constants giving the best fits of the pH-metric titration curves are presented in Table 1. It can be seen that, mixed-ligand complexes with stoichiometry $[Cu(en)L]^+$ are formed in both ternary systems.

Different methods are known to estimate the formation of mixed-ligand complexes. It is possible to calculate the log X_{MAB} values for all systems (the constant due to the equilibrium $[MA_2] + [MB_2] \rightleftharpoons 2[MAB]$, Table 1, row 5). These values are higher than that expected on a statistical basis (0.6) [10], indicating that the formation of mixed complexes is favoured in these systems.

In most cases the relative stability of the mixed-ligand species [MAB] is expressed in terms of $\Delta \log K$ parameter (the constant due to the equilibrium $[MA] + [MB] \rightleftharpoons [MAB] + M$). The statistical value of $\Delta \log K$ depends on the geometry of the complex and for the distorted octahedral coordination sphere of Cu^{2+} with two different bidentate ligands was deduced as -0.9 [11,12]. It can be seen that, the $\Delta \log K$ value for the $[Cu(en)Metha]^+$ species is -1.16. For the $[Cu(en)Hisha]^+$ mixed-ligand species the $\Delta \log K$ value cannot be calculated, since the complex with 1:1 ratio is not formed in the Cu^{2+}-Hisha binary system [3].

Concentration distribution curves for the Cu^{2+}-en-Metha and Cu^{2+}-en-Hisha system are shown in Figs. 1 and 2, respectively.

Evaluation of the experimental pH-metric data on Cu^{2+}-en-Metha/Hisha systems demonstrate that the formation of mixed-ligand species is preceded mainly by the appearance of simple and polynuclear complexes with

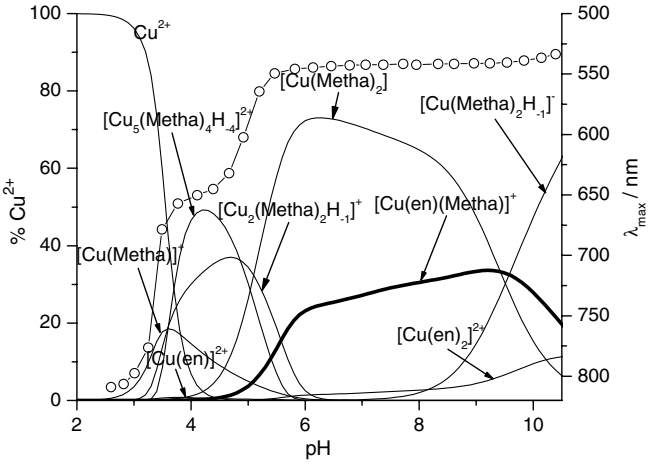


Fig. 1. Species distribution curves as a function of pH and variations of visible absorption maximum wavelength (circle) for Cu^{2+}–en-Metha ternary system at 1:1:2 molar ratio; $c_{Cu^{2+}} = 4 \times 10^{-3}$ mol dm^{-3}.

Metha or Hisha ligand (Figs. 1 and 2). In the Cu^{2+}-en-Metha system with 1:1:2 molar ratio the only mixed-ligand complex $(Cu(en)[Metha])^+$ is seen above pH 5 and reaches maximum concentration of ca. 35% in pH range 8.5–9.5, whereas in the Cu^{2+}-en-Hisha system the analogous mixed ligand species is formed just above pH 6 and has the maximum concentration in the pH range 9–9.5 (~32%). Additional information on the structure of the simple and mixed-ligand complexes may be gained from the analysis of their spectroscopic data. The formation of the mixed-ligand complexes $[Cu(en)(Metha)]^+$ and $[Cu(en)(Hisha)]^+$ does not generate significant changes in the absorption spectra if compared with the spectra of the binary systems.

The distribution-corrected absorption spectra for the mixed-ligand species exhibit a band with a maximum at 547 nm ($\varepsilon \sim 93.5$ dm^3 mol^{-1} cm^{-1}) and 552 nm ($\varepsilon \sim 87$ dm^3 mol^{-1} cm^{-1}) for $[Cu(en)(Metha)]^+$ and $[Cu(en)(Hisha)]^+$, respectively. The energy of this d–d transition

Table 1
Cumulative formation constants (log β), derived equilibrium constants (log K) and characteristic parameters for the stability of complexes formed in the ternary systems Cu^{2+}–ethylenediamine (en)–L (L = aminohydroxamic acids (Metha and Hisha)) – at 25 °C and $I = 0.2$ mol dm^{-3} (KCl)

No.	Assignments	System	
		Cu^{2+}- en-Metha	Cu^{2+}-en-Hisha
1	log β[Cu(en)L]	19.81 (1)	20.32 (2)
2	log K[Cu(en)L]; [Cu(en)] + L = [Cu(en)L][a]	9.25	9.76
3	log K[Cu(en)L]–log β[H_2L]	−6.50	−6.41
4	$\Delta \log K$	−1.16	
5	log X	0.68	0.90
6	χ^2	12.63	11.82
7	σ	11.75	11.43
8	Total number of titration points	295	235

Charges are omitted for simplicity.
[a] $\log K_{Cu(en)L} = \log \beta_{Cu(en)\ L} - \log \beta_{Cu(en)}$.

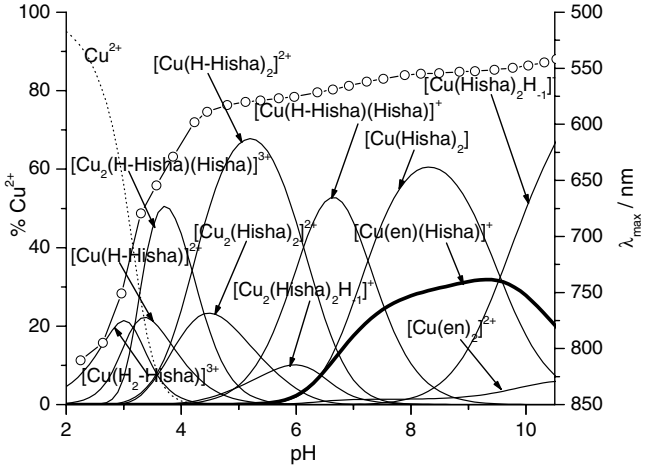


Fig. 2. Species distribution curves as a function of pH and variations of visible absorption maximum wavelength (circle) for Cu^{2+}–en-Hisha ternary system at 1:1:2 molar ratio; $c_{Cu^{2+}} = 4 \times 10^{-3}$ mol dm^{-3}.

is similar to the energies of the d–d transitions of $[Cu(en)_2]^{2+}$ ($\lambda_{max} = 549$ nm), $[Cu(Metha)_2]^{+}$ ($\lambda_{max} = 543$ nm) and $[Cu(Hisha)_2]^{+}$ ($\lambda_{max} = 553$ nm) species with four nitrogen donor atoms in the equatorial position of the metal site [3].

The EPR parameters of the spectra observed in pH range 3.0–6.0 for the ternary Cu^{2+}-en-Hisha system are almost identical with those observed for the binary Cu^{2+}-Hisha, i.e. in this pH range the same species are formed (Fig. 1, Table 2). However, the spectra at pH between 8.4 and 10.0 for liquid and frozen solution show a small but detectable change in g_{iso} and A_{iso} as well as g_z and A_z parameters, in general a little increase in relation to those observed for the Cu^{2+}-Hisha system. These parameters differ significantly from those observed for the Cu^{2+}-en system at pH 9.2. These EPR results support the formation of mixed-ligand species in basic solution with 4N coordination in the copper(II) equatorial plane ($g_z = 2.200$ and $A_z = 204 \times 10^{-4}$ cm^{-1}, Table 2). So, it can be concluded on the basis of the EPR and the absorption spectra studies that the coordination in the mixed-ligand species formed in the studied ternary system is probably realised by amine nitrogens of en (NH_2, NH_2) and both amine and hydroxamic nitrogens of Hisha (NH_2,N_{ha}) in the equatorial plane with two five-membered chelate rings. Similarly, the comparison of the EPR spectra for the binary and ternary system with Metha allow to detect the formation process of the $[Cu(en)(Metha)]^{+}$ species above pH 5.5 with 4N coordination around copper(II).

It is interesting to compare the above mentioned results with those studied previously for the ternary system of Cu^{2+}-diethylenetriamine (dien) – Metha/Hisha [3]. It was reported that the presence of dien suppresses the formation of parent polynuclear species in the ternary systems and leads to the formation of protonated mixed-ligand species apart from $[Cu(dien)(Metha)]^{+}$ and $[Cu(dien)(Hisha)]^{+}$. In the studied Cu^{2+}–en-Metha/Hisha ternary systems parent polynuclear species still exist up to pH 6.

Furthermore, the formation of mixed-ligand species in the ternary system with tridentate dien, instead of en, is accompanied by a distinct spectral change. The red shift of the d–d absorption band going from the simple to mixed-ligand species was assigned to the transition from a six to a five-co-ordination geometry [3].

Table 2
EPR parameters of the complexes formed in the binary and ternary systems

Systems	pH	g_{iso}	A_{iso}	g_z	g_x	g_y	A_z	A_x	A_y
Cu-en	4.87	2.138	68	2.283	2.060	2.060	183	14	14
				(2.210)	(2.040)	(2.040)	(196)	(15)	(15)
	5.37	2.100	83	2.283	2.060	2.060	185	14	14
				2.207	2.040	2.040	198	15	15
	9.22	2.100	86	2.207	2.040	2.040	198	20	20
Cu-Metha	4.0–5.0								
	5.5–10.0	2.097	86	2.188	2.045	2.045	209	14	14
	11.1	2.092	90	2.179	2.040	2.040	209	19	19
Cu-Hisha	3.1	2.148	60	2.420	2.075	2.075	129	10	10
				2.320	2.060	2.060	168	10	10
	3.5	2.113	83	2.320	2.06	2.06	168	10	10
				2.250	2.06	2.06	187	10	10
	3.8–4.3	2.113	83	2.245	2.060	2.060	189	14	14
	5.3	2.110	83	2.210	2.053	2.053	201	14	14
	6.7	2.106	83	2.207	2.045	2.045	202	14	14
	8.4–9.6	2.100	82	2.196	2.043	2.043	202	14	14
	11.1	2.090	88	2.186	2.035	2.035	203	14	29
Cu-en-Hisha	2.95	2.146	57	2.410	2.080	2.080	133	10	10
	3.3	2.148	60	2.320	2.060	2.060	168	10	10
				2.250	2.060	2.060	190	10	10
	3.7–4.1	2.114	85	2.250	2.060	2.060	191	14	14
	5.2–6.1	2.111	85	2.210	2.050	2.050	201	14	14
	6.6	2.107	85	2.208	2.045	2.045	205	19	19
	8.35–9.5	2.103	87	2.200	2.043	2.043	204	19	19
	10.2	2.101	87	2.200	2.043	2.043	203	19	19
	11.5	2.098	88	2.194	2.043	2.043	204	19	19
Cu-en-Metha	3.75–4.3								
	5.5–9.3	2.098	85	2.193	2.045	2.045	205	19	19
	10.2–11.5	2.097	85	2.191	2.045	2.045	206	19	19

The anisotropic and isotropic parameters are estimated on the basis of computer simulation of the experimental spectra measured at 77 K and 295 K, respectively. Parameters A are given in [10^{-4} cm^{-1}]. The parameters in the parentheses correspond to the species existing in an apparently smaller contribution.

It is worthwhile to compare the values of basicity-adjusted stability constants, $\log K_{Cu(en)L} - pK_{NH_3^+} - pK_{CONHOH}$, which take into account the difference in basicity of the coordinating donor groups of ligand L (L = Metha/Hisha/α-Alaha). The resulting values −6.50, −6.41 and −6.86 [13] for $[Cu(en)(Metha)]^+$, $[Cu(en)(Hisha)]^+$ and $[Cu(en)(\alpha\text{-Alaha})]^+$, respectively (Table 1) show that the relative stabilities of complexes with Metha or Hisha are about 0.4 order of magnitude higher than with α-Alaha. This stabilizing effect may derive from weak interactions between thioether sulfur of Metha or imidazole ring of Hisha and metal ion.

6. Conclusion

In the copper(II)-en-Metha or Hisha systems, the potentiometric, VIS and EPR results suggest the formation of mixed-ligand species in basic solution with 4N coordination – both amine and hydroxamic nitrogens of Metha or Hisha (NH_2, N_{ha}) and two amine nitrogens of en ($2 \times NH_2$) in the equatorial plane. The relative stabilities of complex with Metha or Hisha reveal weak interactions between thioether sulfur of Metha or imidazole ring of Hisha and copper(II) ion.

References

[1] B. Kurzak, D. Kroczewska, J. Coord. Chem. 34 (1995) 67.
[2] B. Kurzak, D. Kroczewska, J. Jezierska, Polyhedron 17 (11–12) (1998) 1831.
[3] B. Kurzak, K. Bogusz, D. Kroczewska, J. Jezierska, Polyhedron 20 (2001) 2627.
[4] D. Kroczewska, K. Bogusz, B. Kurzak, J. Jezierska, Polyhedron 21 (2002) 295.
[5] D. Kroczewska, B. Kurzak, J. Jezierska, Polyhedron 25 (2006) 678.
[6] H.M. Marafie, M. Makbyoun, N. Al-Salem, M.S. El-Ezaby, Electroanalysis 4 (1992) 661.
[7] G. Gran, Acta Chem. Skand. 4 (1950) 559.
[8] M. Molina, C. Melios, J.O. Tognolli, L.C. Luchiari, M. Jafelicci Jr., J. Electroanal. Chem. 105 (1979) 237.
[9] P. Gans, A. Sabatini, A. Vacca, Talanta 43 (1996) 1739.
[10] H. Sigel, Metal Ions in Biological Systems, vol. 2, Marcel Dekker, Inc., New York, 1973.
[11] H. Sigel, Angew. Chem. 87 (1975) 391.
[12] H. Sigel, Angew. Chem., Int. Ed. Engl. 14 (1975) 394.
[13] B. Kurzak, K. Bogusz, unpublished data.

symmetrical spatial distribution of ligand-metal bonds. The greater length of Pb–donor distances on the SALP side of hemidirected Pb(II) centres, which is usually attributed to repulsion between the SALP and the electron pairs of the donor atoms, is sometimes so marked that the existence of a real bonding interaction is questionable [7].

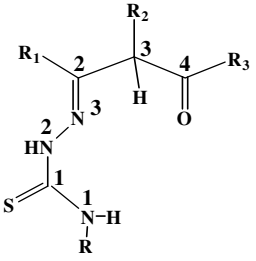
An interesting aspect of lead(II) SALPs is the possibility of their enabling the metal centre to act as a Lewis base, as tin(II) does in some of its complexes [8]. Interactions of this kind could be considered as non-conventional bonds [9]. Their existence has been hypothesized in the case of some short Pb···H [10], Pb···aromatic ring [11] and Pb···Pb [12] contacts, but the evidence has mostly been inconclusive.

New light is thrown on the above issues by the structures of certain complexes of Pb(II) with 5-pyrazolones resulting from metal-induced cyclization of thiosemicarbazones [13]. In this paper we report the synthesis of these and other Pb(II) complexes, with ligands derived from β-keto esters and β-keto amides (Scheme 1).

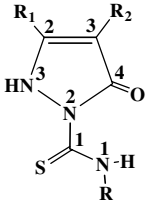
2. Experimental

2.1. Physical measurements

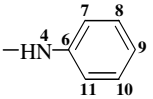
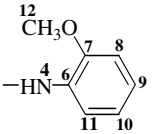
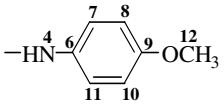
Elemental analyses were performed on a Fisons Instruments EA1108CHNS-O microanalyser. Melting points (mp) were determined with a Büchi apparatus. The electrospray mass spectra of the complexes were recorded on a Hewlett–Packard model LC-MSD 1100 instrument (positive ion mode, 98:2 MeOH/HCOOH as mobile phase, 20–100 V). IR spectra were recorded from KBr discs on a Bruker IFS66V FT-IR spectrometer and are reported in cm^{-1}. The ^{1}H and ^{13}C NMR spectra of DMSO solutions were recorded on Bruker WM-250, AMX-300 or AMX-500 instruments; chemical shifts are expressed on the δ



I (HTSC^{n})



II (HL^{n})

I/II	R	R_1	R_2	R_3
HTSC^{1}/HL^{1}	-H	-$\overset{5}{C}H_3$	-H	-O$\overset{6}{C}H_3$
HTSC^{2}/HL^{2}	-H		-H	-O$\overset{11}{C}H_2\overset{12}{C}H_3$
HTSC^{3}/HL^{3}	-H	-$\overset{5}{C}H_2O\overset{6}{C}H_3$	-H	-O$\overset{7}{C}H_3$
HTSC^{4}/HL^{4}	-H	-$\overset{5}{C}H_2\overset{6}{C}H_3$	-H	-O$\overset{7}{C}H_3$
HTSC^{5}/HL^{5}	-H	-$\overset{5}{C}H_3$	-$\overset{6}{C}H_3$	-O$\overset{7}{C}H_2\overset{8}{C}H_3$
HTSC^{6}/HL^{6}	-H	-$\overset{5}{C}H_3$	-$\overset{6}{C}H_2\overset{7}{C}H_3$	-O$\overset{8}{C}H_2\overset{9}{C}H_3$
HTSC^{7}/HL^{7}	-$\overset{5}{C}H_2\overset{6}{C}H_3$	-$\overset{7}{C}H_3$	-H	-O$\overset{8}{C}H_3$
HTSC^{8}/HL^{1}	-H	-$\overset{5}{C}H_3$	-H	
HTSC^{9}	-H	-$\overset{5}{C}H_3$	-H	
HTSC^{10}	-H	-$\overset{5}{C}H_3$	-H	

Scheme 1.

scale (downfield shifts positive) relative to tetramethylsilane. All physical measurements were carried out in the RIAIDT services of the University of Santiago de Compostela.

2.2. Materials

Thiosemicarbazide (Merck), N^1-ethylthiosemicarbazide (Merck), methyl acetoacetate (Aldrich), ethyl benzoylacetate (Aldrich), methyl 4-methoxyacetoacetate (Aldrich), methyl propionoylacetate (Aldrich), ethyl 2-methylacetoacetate (Aldrich), ethyl 2-ethylacetoacetate (Aldrich), acetoacetanilide (Merck), *o*-acetoacetanisidide (Aldrich), *p*-acetoacetanisidide (Aldrich) and lead(II) acetate trihydrate (Probus) were used as received.

2.3. Synthesis of ligands

The thiosemicarbazones derived from β-ketoesters and β-ketoamides (HTSC^n, $n = 1$–10; see Scheme 1) were prepared as per Jayasree and Aravindakshan [14]. Their physical and analytical properties, and those of the pyrazolonates HL^n that were derived from them by cyclization, have been reported elsewhere [13]. Crystals of HTSC^6, HTSC^7, HL^6 and HL^7 that were suitable for X-ray studies were obtained from the mother liquors.

2.4. Syntheses of complexes

General procedure. A solution of $Pb(OAc)_2$ in methanol was mixed in 1:2 or 1:1 mole ratio with a solution or suspension of the thiosemicarbazone ligand in the same solvent. The mixture was stirred for 6 h at room temperature or under reflux. The experimental conditions and the complexes obtained are summarized in Table 1. All these reactions are described in detail in the supporting information.

Analytical, physical and spectroscopic data of the complexes isolated are as follows.

[Pb(L^1)$_2$]. Colour yellow. Yield: 80 mg (64%). M.p.: 171 °C. *Anal.* Calc. for $C_{10}H_{12}N_6O_2S_2Pb$ (519.56): C, 23.12; H, 2.33; N, 16.18; S, 12.34%. Found: C, 22.98; H, 2.38; N, 17.08; S, 11.83%. MS (ESI$^+$): *m/z* 332 [M−{(L^1)+CH$_3$+NH$_3$}], 304 [M−{(L^1)+(C(S)NH$_2$)}]. IR (KBr, cm^{-1}): 3425 m br, 3110 w *ν*(N–H); 1636 s *ν*(C=O); 1597 s *ν*(ring); 748 m *ν*(C=S). ^{1}H NMR (300 MHz, DMSO-d_6, *δ* in ppm) 11.76, 9.69 (s, 2H, N$_{(1)}$H$_2$), 4.67 (s, 1H, C$_{(3)}$H), 1.97 (s, 3H, C$_{(5)}$H$_3$); ^{13}C NMR (75.48 MHz, DMSO-d_6, *δ* in ppm) 175.9 (C$_{(1)}$); 168.1 (C$_{(4)}$); 158.8 (C$_{(2)}$); 85.4 (C$_{(3)}$), 15.2 (C$_{(5)}$).

[Pb(OAc)(L^1)]. Colour yellow. Yield: 88 mg (40%). M.p.: 165 °C. *Anal.* Calc. for $C_7H_9N_3O_3SPb$ (422.43): C, 19.90; H, 2.15; N, 9.95; S, 7.59. Found: C, 19.98; H, 2.78; N, 10.09; S, 7.95%. MS (ESI$^+$): *m/z* 332 [M−{(OAc)+NH$_3$+CH$_3$}], 304 [M−{(OAc)+(C(S)NH$_2$)}]. IR (KBr, cm^{-1}): 3420, m br, 3126, s br, *ν*(N–H); 1613 s *ν*(C=O); 1550 s, 1379 s *ν*(CH$_3$COO); 1598 sh m *ν*(ring); 742 m *ν*(C=S). ^{1}H NMR (300 MHz, DMSO-d_6, *δ* in ppm) 11.80, 9.70 (2H, s, N$_{(1)}$H$_2$), 4.71 (s, 2H, C$_{(3)}$H), 2.10 (s, 3H, CH$_3$COO), 1.78 (s, 3H, C$_{(5)}$H$_3$); ^{13}C NMR (75.48 MHz, DMSO-d_6, *δ* in ppm) 178.2 (CH$_3$*C*OO), 176.1 (C$_{(1)}$), 168.1 (C$_{(4)}$), 158.9 (C$_{(2)}$), 85.4 (C$_{(3)}$), 27.0 (*C*H$_3$COO), 15.2 (C$_{(5)}$).

[Pb(L^2)$_2$]. Colour beige. Yield: 52 mg (58%). M.p.: 193 °C (d). *Anal.* Calc. for $C_{20}H_{16}N_6O_2S_2Pb$ (643.71): C, 37.32; H, 2.51; N, 13.06; S, 9.96. Found: C, 36.95; H, 2.45; N, 12.67; S, 9.41%. MS (ESI$^+$): *m/z* 645 [M+H], 426 [M+H−(L^2)], 331 [M−{(L^2) + Ph + NH$_3$}]. IR (KBr, cm^{-1}): 3358 m br, 3300 m br *ν*(N–H); 1598 s *ν*(C=O); 1592 s *ν*(ring); 742 m *ν*(C=S). ^{1}H NMR (300 MHz, DMSO-d_6, *δ* in ppm) 11.82, 9.79 (s, 2H, N$_{(1)}$H$_2$), 5.08 (s, 1H, C$_{(3)}$H), 7.53 (m, 2H, C$_{(6,10)}$H), 7.28 (m, 3H, C$_{(7–9)}$H); ^{13}C NMR (75.48 MHz, DMSO-d_6, *δ* in ppm) 175.9 (C$_{(1)}$), 167.7 (C$_{(4)}$), 58.4 (C$_{(2)}$), 32.9 (C$_{(5)}$), 129.0 (C$_{(6,10)}$), 128.6 (C$_{(7,9)}$), 126.0 (C$_{(8)}$), 82.8 (C$_{(3)}$).

[Pb(OAc)(L^2)]. Colour beige. Yield: 126 mg (53%). M.p.: 205 °C (d). *Anal.* Calc. for $C_{12}H_{11}N_3O_3SPb$ (484.50): C, 29.75; H, 2.29; N, 8.67; S, 6.62. Found: C, 29.77; H, 2.01; N, 10.18; S 6.46%. MS (ESI$^+$): *m/z* 425 [M−(OAc)], 67 [M+H−{(C(S)NH$_2$)+(OAc)}]. IR (KBr, cm^{-1}): 3409, 3358, 3300 m br *ν*(N–H); 1599 s br *ν*(C=O); 1573 s, 1400 sh *ν*(CH$_3$COO); 742 m *ν*(C=S). ^{1}H NMR

Table 1
Reactions of $Pb(OAc)_2$ with HTSCs in MeOH: conditions and complexes obtained

Ligand	M:L (mol ratio)	*T*	Complex
HTSC^1	1:2	r.t.	[Pb(L^1)$_2$][a]
HTSC^1	1:1	r.t.	[Pb(OAc)(L^1)][a]
HTSC^2	1:2	r.t.	[Pb(L^2)$_2$)][b]
HTSC^2	1:1	r.t.	[Pb(OAc)(L^2)]
HTSC^3	1:2	r.t.	[Pb(L^3)$_2$][b]
HTSC^3	1:1	r.t.	[Pb(OAc)(L^3)]
HTSC^4	1:2	r.t.	[Pb(L^4)$_2$][a]
HTSC^4	1:1	r.t.	[Pb(OAc)(L^4)] · H$_2$O[a]
HTSC^5	1:2	r.t.	[Pb(OAc)(L^5)][c]
HTSC^6[d]	1:2	r.t.	1st fraction, [Pb(OAc)(L^6)][e] 2nd fraction, [Pb(L^6)$_2$] · 0.5H$_2$O · 0.3MeOH
HTSC^7	1:2	r.t.	1st fraction, Pb(OAc)(L^7)][f] 2nd fraction, [Pb(L^7)$_2$][g]
HTSC^8	1:2	r.t.	[Pb(L^1)$_2$][a]
HTSC^8	1:1	r.t.	[Pb(OAc)(L^1)][a]
HTSC^9[h]	1:1	r.t.	[Pb(TSC^9)$_2$]
HTSC^{10}	1:2	r.t.	[Pb(TSC^{10})$_2$][c]

[a] Also obtained when the reaction mixture was refluxed for 6 h.
[b] Also obtained when the reaction mixture was refluxed for 6 h, for both 1:1 and 1:2 M:L ratios.
[c] Obtained under all M:L and temperature conditions.
[d] The same results were obtained refluxing a 1:1 M:L mixture for 6 h.
[e] Also obtained with a 1:1 M:L ratio at room temperature and a 1:2 ratio under reflux.
[f] Also obtained with a 1:1 M:L ratio, both at room temperature and under reflux.
[g] Also obtained with a 1:2 M:L ratio under reflux.
[h] With a 1:1 M:L ratio under reflux, and with a 1:2 M:L ratio under reflux or at r.t., unidentified products were obtained.

(300 MHz, DMSO-d_6, δ in ppm) 11.84, 9.87 (s, 2H, $N_{(1)}H_2$), 7.53 (m, 2H, $C_{(6,10)}H$), 7.28 (m, 3H, $C_{(7-9)}H$), 5.08 (s, 1H, $C_{(3)}H$), 1.69 (s, 3H, CH_3COO); ^{13}C NMR (75.48 MHz, DMSO-d_6, δ in ppm) 177.6 (CH_3COO), 176.3 ($C_{(1)}$), 167.5 ($C_{(4)}$), 158.4 ($C_{(2)}$), 133.1 ($C_{(5)}$), 128.7 ($C_{(6,10)}$), 128.5 ($C_{(7)}$), 125.9 ($C_{(9)}$), 124.5 ($C_{(8)}$), 82.4 ($C_{(3)}$), 26.8 (CH_3COO).

[Pb(L^3)$_2$]. Colour beige. Yield: 72 mg (54%). M.p.: 192 °C (d). *Anal.* Calc. for $C_{12}H_{16}N_6O_4S_2Pb$ (579.62): C, 24.87; H, 2.78; N, 14.50; S, 11.06. Found: C, 24.52; H, 2.98; N, 13.73; S, 10.70%. MS (ESI^+): *m/z* 394 [M+H−(L^3)], 303 [M−{(L^3)+(C(S)NH_2)+(CH_3O)}]. IR (KBr, cm^{-1}): 3423 m br, 3281 m *v*(N–H); 1606 s br *v*(C=O); 1606 s br *v*(ring); 747 m *v*(C=S). ^1H NMR (300 MHz, DMSO-d_6, δ in ppm) 11.61, 9.64 (s, 2H, $N_{(1)}H_2$), 4.59 (s, 1H, $C_{(3)}H$), 3.16 (s, 2H, $C_{(5)}H_2$), 4.39 (s, 3H, $C_{(6)}H_3$); ^{13}C NMR (75.48 MHz, DMSO-d_6, δ in ppm) 177.2 ($C_{(1)}$), 168.5 ($C_{(4)}$), 158.5 ($C_{(2)}$), 82.5 ($C_{(3)}$), 69.2 ($C_{(5)}$) and 59.3 ($C_{(6)}$).

[Pb(OAc)(L^3)]. Colour beige. Yield: 92 mg (44%). M.p.: 153 °C (d). *Anal.* Calc. for $C_8H_{12}N_3O_4SPb$ (453.46): C, 21.19; H, 2.67; N, 9.27; S, 7.07. Found: C, 20.55; H, 2.44; N, 8.91; S, 7.00%. MS (ESI^+): *m/z* 394 [M−(OAc)], 331 [M−{(OAc)+(CH_3OCH_2)+NH_2+H}]. IR (KBr, cm^{-1}): 3390 m br, 3123 m *v*(N–H); 1608 s *v*(C=O); 1576 s, 1400 s *v*(CH_3COO); 759 m *v*(C=S). ^1H NMR (300 MHz, DMSO-d_6, δ in ppm) 11.61, 9.73 (s, 2H, $N_{(1)}H_2$), 4.60 (s, 1H, $C_{(3)}H$), 4.40 (s, 3H, $C_{(6)}H_3$), 3.21 (s, 2H, $C_{(5)}H_2$), 1.68 (s, 3H, CH_3COO); ^{13}C NMR (75.48 MHz, DMSO-d_6, δ in ppm) 178.0 (CH_3COO), 176.3 ($C_{(1)}$), 167.8 ($C_{(4)}$), 158.4 ($C_{(2)}$), 82.3 ($C_{(3)}$), 68.0 ($C_{(5)}$), 58.8 ($C_{(6)}$), 27.0 (CH_3COO).

[Pb(L^4)$_2$]. Colour light yellow. Yield: 40 mg (31%). M.p.: 178 °C (d). *Anal.* Calc. for $C_{12}H_{16}N_6O_2S_2Pb$ (547.62): C, 26.32; H, 2.94; N, 15.35; S, 11.71. Found: C, 26.00; H, 2.81; N, 14.87; S, 11.61%. MS (ESI^+): *m/z* 548 [M], 532 [M−(CH_3+H)], 448 [M−(NCNC(S)NH_2)], 378 [M−(L^4)], 331 [M−{(L^4)+(CH_3CH_2)+NH_2+H}], 287 [M−{(L^4)+(C(S)NH_2)+(CH_3CH_2)+H}]. IR (KBr, cm^{-1}): 3426 m br, 3278 , 3132 w *v*(N–H); 1624 s *v*(C=O); 1598 sh m *v*(ring).^1H NMR (300 MHz, DMSO-d_6, δ in ppm) 11.71, 9.63 (s, 2H, $N_{(1)}H_2$), 4.60 (s, 1H, ($C_{(3)}H$), 2.40 (c, 2H, $C_{(5)}H_2$), 1.08 (t, 3H, $C_{(6)}H_3$); ^{13}C NMR (75.48 MHz, DMSO-d_6, δ in ppm) 174.9 ($C_{(1)}$), 167.4 ($C_{(4)}$), 163.6 ($C_{(2)}$), 82.7 ($C_{(3)}$), 22.0 ($C_{(5)}$), 12.7 ($C_{(6)}$).

[Pb(OAc)(L^4)]·H_2O. Colour beige. Yield: 87 mg (41%). M.p.: 173 °C (d). *Anal.* Calc. for $C_8H_{14}N_3O_4SPb$ (455.48): C, 21.10; H, 3.10; N, 9.23; S, 7.04. Found: C, 21.50; H, 2.51; N, 8.74; S, 6.88%. MS (ESI^+): *m/z* 378 [M−(OAc)] (M = [Pb(OAc)(L^4)]), 331 [M−{(OAc)+(CH_3CH_2)+NH_2+H}], 287 [M−{(OAc)+(C(S)NH_2)}]. IR (KBr, cm^{-1}): 3453 m *v*(OH); 3400 sh, 3260 m br, 3121 w *v*(N–H); 1606 s *v*(C=O); 1552 s, 1400 sh *v*(CH_3COO); 1597 sh m *v*(ring); 757 m *v*(C=S). ^1H NMR (300 MHz, DMSO-d_6, δ in ppm) 11.72, 9.65 (s, 2H, $N_{(1)}H_2$), 4.58 (s, 1H, $C_{(3)}H$), 2.42 (c, 2H, $C_{(5)}H_2$), 1.69 (s, 3H, CH_3COO), 1.08 (t, 3H, $C_{(6)}H_3$). ^{13}C NMR (75.48 MHz, DMSO-d_6, δ in ppm) 177.5 (CH_3COO), 175.5 ($C_{(1)}$), 167.8 ($C_{(4)}$), 164.3 ($C_{(2)}$), 83.3 ($C_{(3)}$), 26.3 (CH_3COO), 22.4 ($C_{(5)}$), 13.1 ($C_{(6)}$).

[Pb(OAc)(L^5)]. Colour yellow. Yield: 78 mg (78%). M.p.: 182 °C (d). *Anal.* Calc. for $C_8H_{12}N_3O_3SPb$ (437.46): C, 21.96; H, 2.78; N, 9.61; S, 7.33. Found: C, 21.60; H, 2.59; N, 9.36; S, 7.17%. MS (ESI^+): *m/z* 378 [M+H−(C(S)NH_2)], 319 [M+H−{(OAc)+(C(S)NH_2)}]. IR (KBr, cm^{-1}): 3386, 3127 m *v*(N–H); 1623 s *v*(C=O); 1542, 1388 s *v*(CH_3COO); 747 m *v*(C=S). ^1H NMR (300 MHz, DMSO-d_6, δ in ppm) 11.82, 9.61 (s, 2H, $N_{(1)}H_2$), 2.07 (s, 3H, CH_3COO), 1.67 (s, 2H, $C_{(5)}H_2$), 1.16 (s, 3H, $C_{(6)}H_3$); ^{13}C NMR (75.48 MHz, DMSO-d_6, δ in ppm) 177.7 (CH_3COO); 175.3 ($C_{(1)}$), 165.9 ($C_{(4)}$), 157.4 ($C_{(2)}$), 90.9 ($C_{(3)}$), 26.5 (CH_3COO), 13.1 ($C_{(5)}$), 6.4 ($C_{(6)}$).

[Pb(L^6)$_2$]·0.5H_2O·0.3MeOH. Colour yellow. M.p.: 146 °C (d). *Anal.* Calc. for $C_{14.6}H_{22.2}N_6O_{2.8}S_2Pb$ (594.35): C, 28.90; H, 3.73; N, 14.15; S, 10.78. Found: C, 28.87; H, 3.81; N, 14.34; S, 10.93%. MS (ESI^+): *m/z* 392 [M−(L^6)] (M = [Pb(L^6)$_2$]), 331 [M+H−{(L^6)+(C(S)NH_2)}]. IR (KBr, cm^{-1}): 3405, 3240 m br *v*(N–H); 1613 s *v*(C=O); 1598 sh *v*(ring); 745 m *v*(C=S). ^1H NMR (300 MHz, DMSO-d_6, δ in ppm) 11.67, 9.46 (s, 2H, $N_{(1)}H_2$), 2.07 (c, 2H, $C_{(6)}H_2$), 2.03 (s, 3H, $C_{(5)}H_3$), 0.84 (t, 3H, $C_{(7)}H_3$); ^{13}C NMR (75.48 MHz, DMSO-d_6, δ in ppm) 175.0 ($C_{(1)}$), 165.4 ($C_{(4)}$), 156.4 ($C_{(2)}$), 97.8 ($C_{(3)}$), 14.9 ($C_{(6)}$), 14.7 ($C_{(7)}$), 13.1 ($C_{(5)}$).

[Pb(OAc)(L^6)]. Colour yellow. Yield: 64 mg (68%). M.p.: 185 °C (d). *Anal.* Calc. for $C_9H_{13}N_3O_3SPb$ (450.48): C, 24.00; H, 2.91; N, 9.33; S, 7.12%. Found: C, 23.98; H, 2.74; N, 9.21; S, 7.33%. MS (ESI^+): *m/z* 392 [M−(OAc)], 331 [M−{(OAc)+(C(S)NH_2)+H}], 287 [M−{(OAc)+(C(S)NH_2)+(CH_3)+(CH_2CH_3)}]. IR (KBr, cm^{-1}): 3418 s br *v*(N–H); 1614 s *v*(C=O); 1597 sh m *v*(ring); 1553 s, 1394 m *v*(CH_3COO); 745 m *v*(C=S). ^1H NMR (300 MHz, DMSO-d_6, δ in ppm) 11.82, 9.62 (s, 2H, $N_{(1)}H_2$), 2.08 (c, 2H, $C_{(6)}H_2$), 2.07 (s, 3H, $C_{(5)}H_3$), 1.86 (s, 3H, CH_3COO), 0.93 (t, 3H, $C_{(7)}H_3$); ^{13}C NMR (75.48 MHz, DMSO-d_6, δ in ppm) 177.7 (CH_3COO), 175.3 ($C_{(1)}$), 165.7 ($C_{(4)}$), 156.9 ($C_{(2)}$), 97.8 ($C_{(3)}$), 26.5 (CH_3COO), 14.8 ($C_{(6)}$), 14.7 ($C_{(7)}$), 13.0 ($C_{(5)}$).

[Pb(L^7)$_2$]. Colour white. M.p.: 232 °C (d). *Anal.* Calc. for $C_{14}H_{20}N_6O_2S_2Pb$ (575.67): C, 29.21; H, 3.50; N, 14.60; S, 11.14. Found: C, 29.16; H, 3.33; N, 14.30; S, 11.33%. MS (ESI^+): *m/z* 378 [M+H−{(L^7)+(CH_3)}]. IR (KBr, cm^{-1}): 3118 m *v*(N–H); 1619 s *v*(C=O); 1568 m br *v*(ring); 751 m *v*(C=S). ^1H NMR (300 MHz, DMSO-d_6, δ in ppm) 12.85 (s, 1H, $N_{(1)}H$), 4.57 (s, 1H, $C_{(3)}H$), 3.54 (m, 2H, $C_{(5)}H_2$), 2.05 (t, 3H, $C_{(6)}H_3$), 1.17 (s, 3H, $C_{(7)}H_3$); ^{13}C NMR (75.48 MHz, DMSO-d_6, δ in ppm) 175.0 ($C_{(1)}$), 167.3 ($C_{(4)}$), 156.8 ($C_{(2)}$), 85.3 ($C_{(3)}$), 79.1 ($C_{(5)}$), 14.8 ($C_{(6)}$), 13.8 ($C_{(7)}$).

[Pb(OAc)(L^7)]. Colour pale yellow. Yield: 40 mg (44%). M.p.: 217 °C (d). *Anal.* Calc. for $C_9H_{13}N_3O_3SPb$ (450.48): C, 24.00; H, 2.91; N, 9.33; S, 7.13. Found: C, 24.76; H, 2.97; N, 10.06; S, 7.69%. MS (ESI^+): *m/z* 392 [M−(OAc)], 331 [M−{(OAc)+($NHCH_2CH_3$)+H+CH_3}], 305 [M−{(OAc)+(C(S)$NHCH_2CH_3$)}]. IR (KBr, cm^{-1}):

3120 m ν(N–H); 1612s ν(C=O); 1568 s br ν(ring); 1568 s, 1400 m ν(CH_3COO); 748 m ν(C=S). ^{1}H NMR (300 MHz, DMSO-d_6, δ in ppm) 12.85 (s, 1H, $N_{(1)}H$), 4.56 (s, 1H, $C_{(3)}H$), 3.56 (m, 2H, $C_{(5)}H_2$), 2.08 (t, 3H, $C_{(6)}H_3$), 1.66 (s, 3H, CH_3COO), 1.18 (s, 3H, $C_{(7)}H_3$); ^{13}C NMR (75.48 MHz, DMSO-d_6, δ in ppm) 177.8 (CH_3COO), 175.1 ($C_{(1)}$), 167.3 ($C_{(4)}$), 157.0 ($C_{(2)}$), 85.2 ($C_{(3)}$), 79.1 ($C_{(5)}$), 26.9 (CH_3COO), 14.7 ($C_{(6)}$), 13.9 ($C_{(7)}$).

[Pb(TSC^9)$_2$]. Colour white. Yield: 40 mg (41%). M.p.: 190 °C (d). *Anal.* Calc. for $C_{24}H_{30}N_8O_4S_2Pb$ (765.87): C, 37.64; H, 3.95; N, 14.63; S, 8.37. Found: C, 37.57; H, 3.92; N, 14.40; S, 8.00%. MS (ESI$^+$): *m/z* 767 [M+H], 487 [M−(TSC^9)], 429 [M+H−{(HTSC^9)+(C(S)NH_2)}], 303 [HTSC^9+Na]. IR (KBr, cm^{-1}): 3462 s, 3347 s ν(N–H); 1677 s ν(C=O); 1609 s ν(C=N); 1544 s, 1249 m ν(NH–Ph); 1435 w δ(OCH_3); 789 w ν(C=S).

[Pb(TSC^{10})$_2$]. Colour pale pink. Yield: 60 mg (44%). M.p.: 184 °C (d). *Anal.* Calc. for $C_{24}H_{30}N_8O_4S_2Pb$ (765.87): C, 37.64; H, 3.95; N, 14.63; S, 8.37. Found: C, 36.58; H, 3.86; N, 14.16; S, 8.10%. MS (ESI$^+$): *m/z* 767 [M+H], 525 [M+H−{2(C(S)NH_2)+($NPhOCH_3$)}], 487 [M−(TSC^{10})], 429 [M+H−{(HTSC^{10})+(C(S)NH_2)}], 364 [M−{(TSC^{10})+(OCH_3Ph)+(CH_3)}], 303 [HTSC^{10}+Na]. IR (KBr, cm^{-1}): 3456, 3330 s ν(N–H); 1656 s ν(C=O); 1609 s ν(C=N); 1244 m ν(NH–Ph); 1448 w δ(OCH_3); 825, 791 m ν(C=S). ^{1}H NMR (300 MHz, DMSO-d_6; δ in ppm) 10.11, 10.08, 9.99, 9.86 (s, 1H, $N_{(2)}H$), 7.48 (d, 2H, $C_{(7,11)}H$), 6.87 (d, 2H, $C_{(8,10)}H$), 6.68, 6.48 (s, 2H, $N_{(1)}H_2$), 3.71 (s, 3H, $C_{(12)}H_3$), 3.57, 3.51, 3.24 (s, 2H, $C_{(3)}H_2$), 2.15, 2.08, 1.96, 1.93 (s, 3H, $C_{(5)}H_3$); ^{13}C NMR (75.48 MHz, DMSO-d_6, δ in ppm) 165.8 ($C_{(4)}$), 155.1 ($C_{(2)}$), 132.1–113.7 ($C_{(Ph)}$), 55.1 ($C_{(12)}$), 46.5 ($C_{(3)}$), 25.0 ($C_{(5)}$), $C_{(1)}$ is not observed.

The compounds for which crystals suitable for X-ray diffractometry were obtained were $[Pb(L^6)_2]\cdot 0.5H_2O\cdot 0.3MeOH$, isolated as the second harvest of crystals from the mother liquor of the reaction of $Pb(OAc)_2$ with HTSC^6 in 1:1 mole ratio under reflux; and $[Pb(L^7)_2]$, obtained as a second crystal harvest from the mother liquor of the reaction of $Pb(OAc)_2$ with HTSC^7 in 1:2 mole ratio at room temperature.

2.5. X-ray crystallography

Crystal data were collected at room temperature (HL^6) or low temperature (all others) on an Enraf–Nonius CAD-4 (RIAIDT, University of Santiago de Compostela) or an Enraf–Nonius Kappa CCD (Sao Carlos Institute of Physics, University of Sao Paulo). The data were corrected for absorption by multi-scan [15] or psi-scan [16]. Structures were solved using direct methods for the ligands and the Patterson method for the complexes, followed by normal difference Fourier techniques. All hydrogen atoms were included at ideal geometrical positions. The program used was SHELX97 [17]. Molecular graphics were obtained with ORTEP [18], PLATON [19] and MERCURY [20]. Crystal and refinement data are listed in Table 2. Selected bond lengths and angles are listed in Table 3 (for HTSC^6, HTSC^7, HL^{6}and HL^7) and Table 4 (for $[Pb(L^6)_2]\cdot 0.5H_2O\cdot 0.3MeOH$ and $[Pb(L^7)_2]$). Hydrogen bond lengths and angles are listed in Table S1.

Table 2
Crystallographic data for ligands and complexes

	HTSC^6	HTSC^7	HL^6	HL^7	$[Pb(L^6)_2]\cdot 0.5H_2O\cdot 0.3MeOH$	$[Pb(L^7)_2]$
Empirical formula	$C_{18}H_{34}N_6O_4S_2$	$C_8H_{15}N_3O_2S$	$C_7H_{11}N_3OS$	$C_7H_{11}N_3OS$	$C_{14.3}H_{22.2}N_6O_{2.8}PbS_2$	$C_{14}H_{20}N_6O_2S_2Pb$
Molecular weight	462.63	217.29	185.25	185.25	594.29	575.67
T (K)	120(2)	120(2)	140(2)	140(2)	120(2)	120(2)
λ (Å)	0.71073	0.71073	1.54184	0.71073	0.71073	0.71073
Crystal system	triclinic	monoclinic	monoclinic	monoclinic	monoclinic	tetragonal
Space group	$P\bar{1}$	$P2_1/n$	$P2_1/c$	$P2_1/c$	$C2/c$	$I4_1/a$
a (Å)	9.2260(3)	6.45400(10)	11.9461(10)	6.7805(2)	27.9900(5)	14.5213(3)
b (Å)	11.5870(3)	21.6896(4)	6.7921(3)	6.1803(2)	7.2980(2)	14.5213(3)
c (Å)	13.3900(5)	7.7124(2)	12.0336(8)	21.0593(8)	37.8920(8)	17.7219(5)
α (°)	65.106(2)	90	90	90	90	90
β (°)	80.0350(10)	95.1340(10)	111.140(5)	90.3242(13)	90.2560(10)	90
γ (°)	72.359(2)	90	90	90	90	90
V (Å^3)	1235.65(7)	1075.29(4)	910.69(11)	882.49(5)	7740.2(3)	3736.99(15)
Z	2	4	4	4	16	8
$D_{calc.}$ (Mg/m^3)	1.243	1.348	1.351	1.394	2.040	2.046
μ (mm^{-1})	0.249	0.282	2.824	0.322	8.961	9.274
Measured reflections	20213	6430	3655	5239	16846	10697
Unique reflections	4337	1884	1822	1545	8406	2135
$R_{(int)}$	0.1258	0.0349	0.0262	0.0436	0.1056	0.0399
R_1 ($I > 2\sigma I$)	0.0437	0.0332	0.0318	0.0364	0.0580	0.0259
wR_2 ($I > 2\sigma I$)	0.1070	0.1082	0.0886	0.0882	0.1036	0.0579
Goodness-of-fit	1.037	1.122	1.071	1.069	1.084	1.083

Table 3
Bond lengths (Å) and angles (°) in thiosemicarbazone and pyrazolone ligands

	HTSC[6]		HTSC[7]	HL[6]	HL[7]
S(1)–C(1)	1.688(2)	1.6951(19)	1.6863(17)	1.6701(15)	1.673(2)
O(1)–C(4)	1.206(2)	1.215(2)	1.212(2)	1.2493(18)	1.251(2)
N(1)–C(1)	1.322(3)	1.318(3)	1.329(2)	1.317(2)	1.323(3)
N(2)–C(1)	1.356(3)	1.358(3)	1.367(2)	1.390(2)	1.398(3)
N(2)–N(3)	1.398(2)	1.402(2)	1.386(2)	1.3725(17)	1.379(2)
N(3)–C(2)	1.285(3)	1.288(2)	1.277(2)	1.342(2)	1.338(3)
N(2)–C(4)				1.4151(17)	1.414(2)
C(1)–N(2)–N(3)	116.97(17)	117.10(16)	118.32(14)	121.51(11)	121.61(15)
C(2)–N(3)–N(2)	116.37(18)	116.72(17)	117.72(14)	108.60(11)	108.69(16)
N(1)–C(1)–N(2)	116.57(18)	117.33(17)	116.10(15)	113.95(13)	113.31(16)
N(1)–C(1)–S(1)	123.83(16)	122.83(15)	125.04(13)	124.94(13)	126.02(15)
N(2)–C(1)–S(1)	119.57(16)	119.83(15)	118.83(12)	121.10(11)	120.67(14)
N(3)–C(2)–C(3)	114.54(19)	115.26(18)	115.69(14)	110.23(13)	109.61(17)
C(2)–C(3)–C(4)	111.45(18)	110.62(17)	113.05(14)	107.17(13)	108.15(18)
O(1)–C(4)–C(3)	125.1(2)	124.18(19)	125.11(15)	132.39(14)	133.23(18)
N(3)–N(2)–C(4)				108.11(12)	108.44(15)
C(1)–N(2)–C(4)				129.62(12)	129.79(16)
O(1)–C(4)–N(2)				121.71(14)	121.74(18)
N(2)–C(4)–C(3)				105.89(12)	105.03(16)

Table 4
Selected bond lengths (Å) and angles (°) in pyrazolonate complexes

Molecule 1		Molecule 2		Molecule 3	
[Pb(L^6)$_2$] · 0.5H$_2$O · 0.3MeOH[a]					
Pb(1)–N(13)	2.555(8)	Pb(2)–N(23)	2.599(9)	Pb(3)–N(33)	2.637(9)
Pb(1)–N(16)	2.691(9)	Pb(2)–S(21)	2.905(3)	Pb(3)–S(31)	2.922(3)
Pb(1)–S(12)	2.838(3)	Pb(2)–N(33)	3.092(9)	Pb(3)–N(23)^{v}	3.002(8)
Pb(1)–S(11)	2.920(3)	Pb(2)–S(31)	3.274(3)	Pb(3)–S(21)^{v}	3.201(3)
Pb(1)–N(16)^{i}	3.003(8)	Pb(2)···Pb(3)^{iii}	3.6096(8)	Pb(3)···Pb(2)^{vi}	3.6096(8)
Pb(1)–S(11)^{ii}	3.180(3)	Pb(2)···Pb(3)	3.6884(8)	Pb(3)···Pb(2)	3.6884(8)
Pb(1)–S(12)^{i}	3.317(3)	S(21)–C(21)	1.708(11)	S(31)–C(31)	1.723(11)
Pb(1)–N(13)^{ii}	3.371(8)	O(21)–C(24)	1.250(14)	O(31)–C(34)	1.289(12)
Pb(1)···Pb(1)^{i}	3.6234(8)				
Pb(1)···Pb(1)^{ii}	3.7562(8)				
S(11)–C(11)	1.718(11)				
S(12)–C(18)	1.736(11)				
O(11)–C(14)	1.239(14)				
O(12)–C(111)	1.264(11)				
N(13)–Pb(1)–N(16)	90.6(3)	N(23)–Pb(2)–N(23)^{iv}	109.9(4)	N(33)^{iv}–Pb(3)–N(33)	111.1(4)
N(13)–Pb(1)–S(12)	82.6(2)	N(23)–Pb(2)–S(21)^{iv}	78.0(2)	N(33)^{iv}–Pb(3)–S(31)	79.26(17)
N(16)–Pb(1)–S(12)	66.6(2)	N(23)–Pb(2)–S(21)	66.0(2)	N(33)–Pb(3)–S(31)	65.62(17)
N(13)–Pb(1)–S(11)	66.5(2)	S(21)^{iv}–Pb(2)–S(21)	115.31(12)	S(31)–Pb(3)–S(31)^{iv}	116.00(11)
N(16)–Pb(1)–S(11)	142.6(2)				
S(12)–Pb(1)–S(11)	80.93(9)				
[Pb(L^7)$_2$][b]					
Pb–N(3)	2.532(3)	N(3)^{i}–Pb–N(3)	140.15(16)	O^{ii}–Pb–O^{iii}	126.73(13)
Pb–O^{ii}	2.727(3)	N(3)–Pb–O^{ii}	96.28(10)	O^{ii}–Pb–S	75.52(7)
Pb–S	2.8142(11)	N(3)–Pb–O^{iii}	101.32(10)	O^{iii}–Pb–S	157.26(7)
S–C(1)	1.691(4)	N(3)^{i}–Pb–S	81.96(8)	S^{i}–Pb–S	82.87(5)
O–C(4)	1.261(5)	N(3)–Pb–S	68.21(8)		

[a] *i: −x + 1/2, −y + 1/2, −z + 2; ii: −x + 1/2, −y − 1/2, −z + 2; iii: x, y − 1, z; iv: −x + 1, y, −z + 1/2; v: −x + 1, y + 1, −z + 1/2; vi: x, y + 1,z.*
[b] *i: −x + 1, −y + 1/2, z; ii: y + 1/4, −x + 1/4, z + 1/4; iii: −y + 3/4, x + 1/4, z + 1/4.*

2.6. Computational details

Single-point density functional theory (DFT) calculations were performed using the Gaussian 03 package [21] on three structures modelling fragments of [Pb(L^6)$_2$] · 0.5H$_2$O · 0.3MeOH. Structure A consisted of three type 1 molecules arranged as depicted in Fig. 4a; structure B of one type 2 molecule sandwiched between two type 3

molecules; and structure C of one type 3 molecule between two type 2 molecules, as shown in Fig. 4b. All the geometries were taken from the crystallographic data. The exchange/correlation functional was B3LYP, which combines Becke's three-parameter nonlocal hybrid exchange potential [22] with the nonlocal correlation functional of Lee, Yang, and Parr [23]. The standard 6-31+G(d,p) basis set was employed for all atoms except Pb, for which the LanL2DZ effective core potential basis function [24] was used. In addition, the program AIMPAC [25] was used to analyse the DFT electron densities by means of quantum theory of atoms in molecules (QTAIM) [26] in order to assess the strength of Pb–N, Pb–S and possible Pb–Pb bonds. QTAIM identifies the critical point of minimum electron density on the bond path between mutually bonded atoms. The use of effective core potentials instead of all-electron basis sets for this purpose has been reported to afford acceptable results [27].

3. Results and discussion

3.1. Synthesis and physical properties of the complexes

All the ligands reacted with lead(II) acetate in methanol, the products being in some cases thiosemicarbazonates and in others complexes with a deprotonated pyrazolone derivative formed *in situ* by cyclization of the starting ligand. Also, the acetate was in some cases fully displaced from the coordination sphere of the metal, and in others only partially. Usually, but not always, complete displacement occurred in reactions with 1:2 M:L mole ratio, which sometimes allowed sequential isolation of both heteroleptic and homoleptic complexes (see Table 1). Thus the stoichiometry of the complexes isolated was influenced not only by the metal:ligand mole ratio used in the synthesis, but also by some more elusive factor, possibly solubility differences between the complexes.

HTSCs derived from β-ketoesters afforded hetero- or homoleptic pyrazolonates, both at room temperature and under reflux (Scheme 2). By contrast, two of the HTSCs derived from β-ketoamides, HTSC[9] and HTSC[10], gave thiosemicarbazonates, suggesting that this kind of thiosemicarbazone is less prone to cyclization.

Most of the complexes obtained in this work are coloured solids that are stable in air and decompose at temperatures of 146–232 °C. The $[Pb(L^n)_2]$ and $[Pb(OAc)(L^n)]$ complexes are soluble in methanol, ethanol, acetone, DMSO and DMF, but insoluble in water. $[Pb(TSC^{10})_2]$ is soluble in DMSO and DMF but only poorly soluble in the other solvents, and $[Pb(TSC^9)_2]$ is insoluble in all the above solvents, among others.



Scheme 2.

3.2. X-ray studies

3.2.1. Ligands

Fig. 1 shows the molecular structures of HTSC[6] and HTSC[7] together with the numbering schemes used. The asymmetric unit of HTSC[6] comprises two independent molecules, 1 and 2. Both ligands adopt *E* configuration around the C(2)–N(3) bond and place the sulphur atom *trans* to N(3), so allowing the formation of the intramolecular hydrogen bond N(1)–H(1)···N(3) (see Table S1, and Figures S1 and S2). Bond lengths and angles (Table 3) are similar to those previously found in other thiosemicarbazones [28]. Both ligands are basically arranged so as to form two planes at dihedral angles of 71.57(0.07)° [HTSC[6], molecule 1: C(11)S(1)N(11)N(12)N(13)C(12), rms = 0.0803° and C(14)O(11)O(12)C(13)C(16)C(17)C(18), rms = 0.0934], 87.31(0.06)° [HTSC[6], molecule 2: C(21)S(2)N(21)N(22)N(23)C(22)C(23)C(25), rms = 0.1403 and C(23)C(24)O(21)O(22)C(28), rms = 0.0103] and 63.51(0.05)° [HTSC[7], SC(1)N(1)N(2)N(3)C(2)C(3)C(5)C(7), rms = 0.0663 and C(3)C(4)O(1)O(2)C(8), rms = 0.0108].

In HTSC[6] each molecule of type 1 interacts with a second *via* an N(11)–H(11B)···O(11)^{i} hydrogen bond, giving rise to infinite chains parallel to the *a*-axis, and N(12)–H(12)···S(1)^{ii} hydrogen bonds connect these chains in pairs (see Table S1 and Figure S1). Type 2 molecules are con-

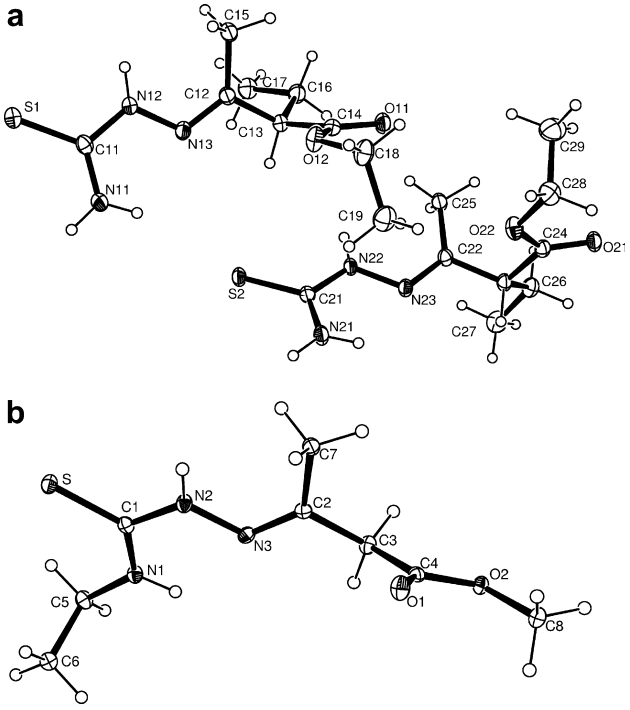


Fig. 1. Molecular structures and numbering schemes of the ligands HTSC[6] (a) and HTSC[7] (b).

nected by similar interactions, and also by an N(21)–H(21A)···O(21)[iii] hydrogen bond, resulting in a two-dimensional network parallel to the *ab*-plane (Table S1 and Figure S1).

The ethyl group on N(1) in HTSC[7] makes it less capable of hydrogen bond formation than HTSC[6]. In fact, its only intermolecular bond is N(2)–H(2)···O(1)[i], which associates the molecules in dimers (Table S1 and Figure S2).

The molecular structures of HL[6] and HL[7] are shown in Fig. 2, together with the numbering schemes used. Both ligands have bond lengths and angles (Table 3) comparable to those found in the previously studied similar molecules HL[1] [13a], HL[2] [13c], HL[4] [13c], and HL[5] [29]. In the solid state, both adopt the ketothione form and can be considered as almost planar if the terminal methyls of ethyl substituents are ignored (rms 0.063 and 0.030, respectively). Both have two intramolecular hydrogen bonds [N(1)–H(1A)···O and N(3)–H(3)···S (see Table S1, and Figures S3 and S4)] and an intermolecular bond [N(3)–H(3)···O[x]] that associates the molecules in chains. In HL[6], an additional hydrogen bond [N(1)–H(1B)···S[i]] links the chains in sheets parallel to the *bc*-plane.

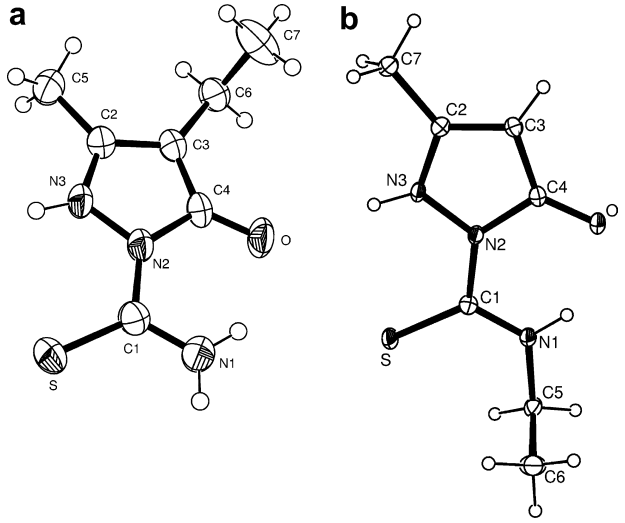


Fig. 2. Molecular structures and numbering schemes of the ligands HL[6] (a) and HL[7] (b).

3.2.2. Complexes

Crystals of $[Pb(L^6)_2]\cdot 0.5H_2O\cdot 0.3MeOH$ contain $[Pb(L^6)_2]$ molecules with the three crystallographically independent geometries shown, together with the numbering scheme used, in Fig. 3. Selected bond lengths and angles are listed in Table 4. The asymmetric unit comprises one complete molecule of type 1, half a molecule of type 2, half a molecule of type 3, a water molecule, and 0.6 molecules of MeOH. In all the ligands, the usual evolution to the thiol form upon coordination [13] is reflected in the lengthening of the C–S bond from 1.6703(15) Å in the free ligand (Table 3) to 1.708(11)–1.736(11) Å in molecules 1–3 (Table 4).

In all three independent molecules the metal forms four strong primary bonds with two N,S-dentate pyrazolonates. In molecule 1 both the two Pb–N distances and the two Pb–S distances differ, and the fact that all these bonds lie on one side of the metal atom suggests the existence of a SALP on the other side, which would make the coordination polyhedron a distorted trigonal bipyramid with the hypothesized SALP in one of the equatorial positions. Molecules 2 and 3, in both of which the two ligands are mutually symmetrical, resemble each other quite closely, although the Pb–N and Pb–S bonds are a little shorter in 2 than in 3; in both 2 and 3, as in 1, there seems likely to be a SALP on one side of the metal atom, but in these cases the coordination polyhedron is a slightly distorted square pyramid in which the hypothesized SALP occupies the apex and the donor atoms come close to defining a perfect plane (rms = 0.0308 in 2, 0.0286 in 3). In all three molecules the chelate rings are bent around the line S–N so that the two ligands are almost parallel, but whereas in molecules 2 and 3 this results in the ligands also being quasi-coplanar, in molecule 1 they are bent the other way so that they face each other (Fig. 4).

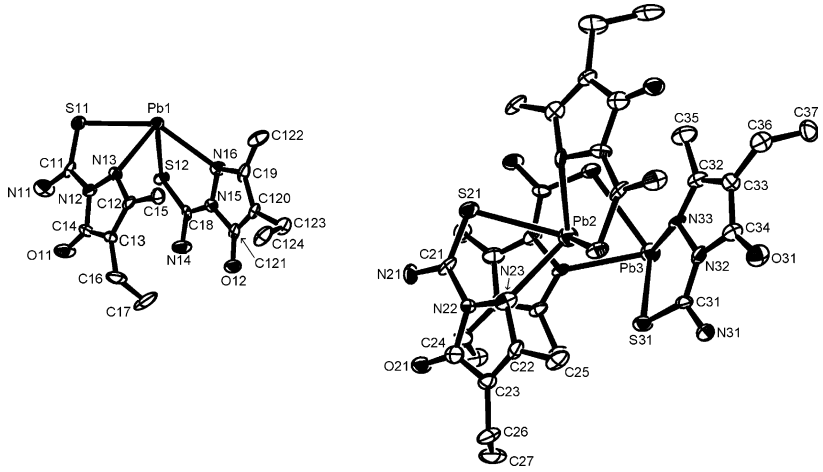


Fig. 3. Molecular structures of the three independent molecules of $[Pb(L^6)_2]$ in $[Pb(L^6)_2]\cdot 0.5H_2O\cdot 0.3MeOH$.

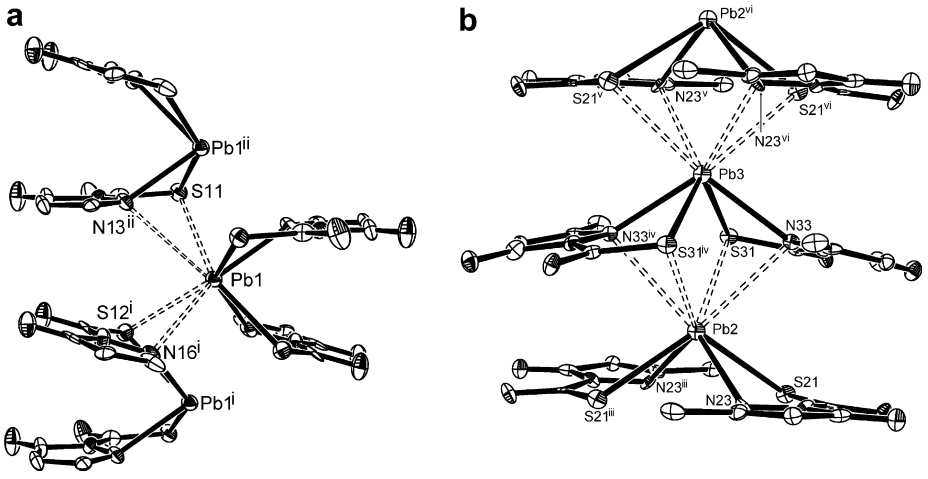


Fig. 4. Primary and secondary interactions of Pb(1) (a) and Pb(2) and Pb(3) (b) in $[Pb(L^6)_2]\cdot 0.5H_2O\cdot 0.3MeOH$.

The structural differences between molecule 1 and molecules 2 and 3 regarding their primary coordination spheres and the arrangement of their ligands are accompanied by significant differences in their intermolecular interactions, notably as regards the weak secondary bonds that, as is usual in Pb(II) complexes with hemidirected coordination [3c], appear to border the volume presumably occupied by the SALP (Fig. 4). Comparison with the sums of van der Waals radii (3.55 Å for Pb···N, 3.80 Å for Pb···S) suggests that Pb(1) has secondary bonds with the chelating N and S atoms of the nearest ligands of two neighbouring type 1 molecules [Pb(1)–N(16)^{i} = 3.003(8) Å, Pb(1)–S(12)^{i} = 3.317(3) Å, Pb(1)–N(13)^{ii} = 3.371(8) Å, Pb(1)–S(11)^{ii} = 3.180(3) Å; (i): $-x+1/2$, $-y+1/2$, $-z+2$; (ii): $-x+1/2$, $-y-1/2$, $-z+2$]. These bonds, which link the type 1 molecules in slightly zig-zag chains along the *b*-axis (Pb–Pb–Pb = 163°; see Fig. 4), are similar to those observed in other Pb(II) complexes with Pb···N and Pb···S secondary interactions [30,31]. In molecules 2 and 3, which alternate in stacks (likewise along the *b*-axis), the Pb atoms have secondary bonds with all four primary donor atoms of one of their type 3 or type 2 neighbours (see Fig. 4 and Table 4 for bond lengths). The existence of all these secondary bonds is supported by the detection of the corresponding critical points by the QTAIM calculations, which among both primary and secondary bonds showed the expected negative correlation between bond length and charge density at the critical point (Table 5).

In both the chains of molecules 1 and the stacks of type 2/3 units, the Pb···Pb distances [3.6096(8)–3.7562(8) Å] (see Fig. 5) are shorter than in $[Pb^{II}(XS_2)_2]$ complexes, where $(XS_2)^-$ is a monoanionic didentate ligand [12], and are close to the upper limit for Pb–Pb bonds in diplumbene dimers, 3.527 Å [32]. As in the case of bis(pyrrolidinecarbodithioato)lead(II), the molecules of which are stacked with a Pb···Pb distance of 3.886(1) Å [12], the possibility of weak SALP-mediated Pb–Pb bonds therefore arises. However, our QTAIM calculations failed to detect critical points of electron density supporting the existence of such bonds, so the short Pb···Pb distances in the present complex seem likely to be due simply to the secondary Pb–L^6 donor bonds.

Table 5
Electron charge densities (ρ_c, in atomic units) at the critical points of bonds with Pb(1), Pb(2) and Pb(3) in the model compounds A, B and C[a], together with the corresponding bonds lengths (Å)

	Bond length	ρ_c
Pb(1)–N(13)	2.556(8)	0.0326
Pb(1)–N(16)	2.691(9)	0.0275
Pb(1)–S(12)	2.838(3)	0.0317
Pb(1)–S(11)	2.920(3)	0.0281
Pb(1)–N(16)^{i}	3.003(8)	0.0178
Pb(1)–N(13)^{ii}	3.371(8)	0.0102
Pb(1)–S(12)^{ii}	3.180(3)	0.0196
Pb(1)–S(12)^{i}	3.317(3)	0.0161
Pb(2)–N(23)	2.599(9)	0.0311
Pb(2)–S(21)	2.905(3)	0.0295
Pb(2)–N(33)	3.092(9)	0.0160
Pb(2)–S(31)	3.274(3)	0.0169
Pb(3)–N(33)	2.637(9)	0.0293
Pb(3)–S(31)	2.922(3)	0.0285
Pb(3)–N(23)^{v}	3.002(8)	0.0183
Pb(3)–S(21)^{v}	3.201(3)	0.0185

i: $-x+1/2$, $-y+1/2$, $-z+2$; ii: $-x+1/2$, $-y-1/2$, $-z+2$; v: $-x+1$, $y+1$, $-z+1/2$.
[a] See Section 2.

Each type 1 molecule is linked to molecule 3 of its nearest type 2/3 unit by a direct N(11)–H(11B)···O(31)^{ix} bond, and to molecule 2 by a chain of hydrogen bonds that starts at N(14) and proceeds via the methanol and water molecules to N(21) (see Table S1, and Figs. S6 and S7, for these and other hydrogen bonds).

In $[Pb(L^7)_2]$, in which the two L^- ligands are mutually symmetrical (Fig. 6), the presence of the four primary bonds within quite a small solid angle suggests that, like the preceding complex, it has a SALP (see Table 4 for bond lengths and angles). In fact, it seems that it may be only steric hindrance between their N(1) ethyl groups that prevents the two ligands from drawing even closer together (which may be why the primary coordination polyhedron is not

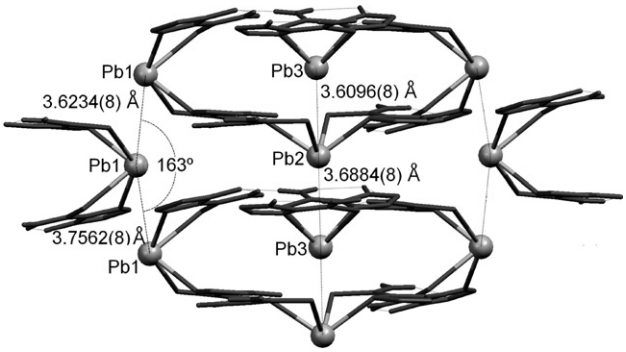


Fig. 5. Assembly of the chains of molecules 1 and the stacks of molecules 2 and 3, together with Pb···Pb distances (view perpendicular to the *b*-axis).

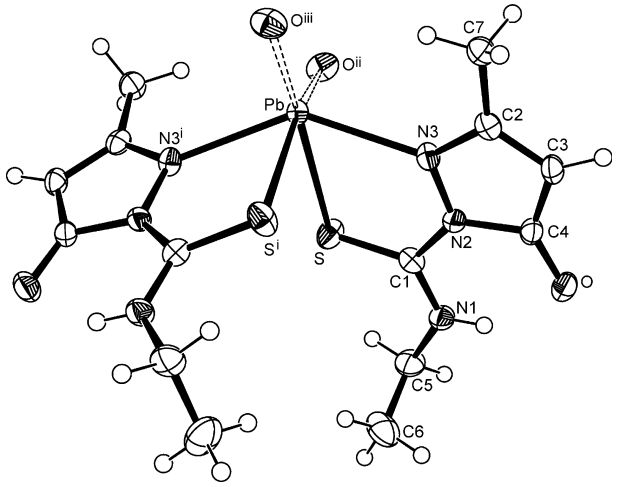


Fig. 6. Molecular structure of $[Pb(L^7)_2]$.

a square pyramid but a trigonal bipyramid with the hypothesized SALP equatorial and the N atoms apical). However, this complex has just a single type of molecule, and the chelate rings are, as usual, flat (and almost coplanar with the corresponding pyrazolonate ring), with a dihedral angle of about 70° between them. It is perhaps this, with the concomitant orientation of the C(2) methyl groups, that prevents secondary bonding to the N and S atoms of neighbouring molecules. The secondary bonds that do exist, with the O atoms of two neighbouring molecules [Pb···O^{ii} = 2.727(3) Å, O^{ii}–Pb–O^{iii} = 126.7°], link the molecules in a three-dimensional network (Figs. S8–S10). Thus in this complex the molecular and packing geometry appears to be determined largely by steric effects; because of the partial substitution of N(1) and the absence of solvent molecules, hydrogen bonding is limited to the intramolecular N(1)–H···O bond (Table S1).

3.3. IR spectroscopy

Whether or not the thiosemicarbazone ligands had undergone cyclization upon coordination was easily detected by examination of the main IR bands of the complexes (see Section 2), since the spectra of pyrazolones differ clearly from those of thiosemicarbazones [13].

In the spectra of the $[Pb(L^n)_2]$ compounds the ν(ring) band shifts to higher frequencies upon metallation while the ν(C=S) band shifts to lower frequencies or becomes weaker, which is in keeping with the observation of N,S-coordination in the L^6 and L^7 derivatives and in previously studied pyrazolonates [13].

To judge by the positions of ν(ring) and ν(C=S), the L^- ligand of the $[Pb(OAc)(L^n)]$ complexes is also N,S-coordinated. The value of $\Delta\nu = \nu_{as}(COO^-) - \nu_{sym}(COO^-)$ ranges from 151 to 173 cm^{-1}, which suggests that the carboxylate group acts as a bismonodentate bridging ligand [33].

Upon coordination, the spectra of the thiosemicarbazone ligands $HTSC^9$ and $HTSC^{10}$ undergo significant modification in the 3000–3500 cm^{-1} region due to deprotonation of N(2) and concomitant alteration of the hydrogen bond network. By contrast, the position of the strong ν(C=O) band at 1650–1670 cm^{-1} is unchanged, suggesting that this group is not involved in coordination. The slight shift of ν(C=N), the weakening, and slight shift to lower wavenumbers, of the ν(C=S) band at 800 cm^{-1}, and the vanishing of the ν(C=S) band at 1100 cm^{-1}, are all suggestive of N,S-coordination [13b].

3.4. ^1H and ^{13}C NMR spectroscopy

For assignments of the ^1H and ^{13}C NMR signals of all the complexes except $[Pb(TSC^9)_2]$ (which is insoluble in DMSO-d_6), see Section 2.

In the proton spectra of $[Pb(L^n)_2]$ and $[Pb(OAc)(L^n)]$, the non-appearance of the $HTSC^n$ signals corresponding to the R_3 group and one C(3) proton is in keeping with the release of HR_3 (methanol, ethanol or an aniline) during cyclization. Similarly, the R_3 signals are missing from the ^{13}C NMR spectra of the complexes, and C(3) is deshielded ca. 40 ppm with respect to $HTSC^n$.

The differences between the spectra of the complexes and those of the free HL^n ligands are similar to those found for the pyrazolonate derivatives of Zn(II) [13], Cd(II)[13] and Re(I) [13], and can be summarized as follows: (i) absence of the N(3)H signal due to deprotonation; (ii) deshielding of the protons on N(1); and (iii) deshielding of C(2) and C(4) by 5–13 ppm and 3–5 ppm, respectively, and shielding of C(3) by 5–8 ppm. These modifications suggest that the solid state coordination mode of $[Pb(L^6)_2]$ and $[Pb(L^7)_2]$ (see crystallographic results) persists in DMSO and is probably that of all the complexes of this type.

In the ^1H NMR spectrum of $[Pb(TSC^{10})_2]$ the signals assigned to N(2)H disappear, confirming deprotonation, and those belonging to N(4)H are split into four. The signals corresponding to the two $N(1)H_2$ groups are shifted upfield and lie closer to each other than in the free ligands, probably due to deprotonation and coordination *via* the S atom. In the ^{13}C spectrum, there is no C(1) signal and C(2) is deshielded ca. 6 ppm, suggesting the involvement of N(3) in coordination to the metal.

Acknowledgements

We thank the Secretariat General for Research and Development of the Xunta de Galicia (Spain) and the Spanish Ministry of Science and Technology for financial support under Projects PGIDIT03PXIC20306PN and CTQ2006-11805-BQU.

Appendix A. Supplementary material

CCDC 622367, 622368, 622369, 622370, 622371 and 622372 contain the supplementary crystallographic data for HTSC^6, HTSC^7, HL^6, HL^7, $[Pb(L^6)_2]\cdot 0.5H_2O\cdot 0.3$-MeOH and $[Pb(L^7)_2]$. These data can be obtained free of charge via http://www.ccdc.cam.ac.uk/conts/retrieving.html, or from the Cambridge Crystallographic Data Centre, 12 Union Road, Cambridge CB2 1EZ, UK; fax: (+44) 1223-336-033; or e-mail: deposit@ccdc.cam.ac.uk. Supplementary data associated with this article can be found, in the online version, at doi:10.1016/j.poly.2007.05.016.

References

[1] C.D. Toscano, T.R. Guilarte, Brain Res. Rev 49 (2005) 529.
[2] J.S. Magyar, T.C. Weng, C.M. Stern, D.F. Dye, B.W. Rous, J.C. Payne, B.M. Bridgewater, A. Mijovilovich, G. Parkin, J.M. Zaleski, J.E. Penner-Hahn, H.A. Godwin, J. Am. Chem. Soc. 127 (2005) 9495.
[3] (a) R.D. Hancock, in: A.F. Williams, C. Floriani, A.E. Merbach (Eds.), Perspectives in Coordination Chemistry, VCHA:VCH, Basel, 1992, p. 129;
(b) C.E. Holloway, M. Melnik, Main Group. Met. Chem. 20 (1997) 399;
(c) L. Shimoni-Livny, J.P. Gluske, C.W. Bock, Inorg. Chem. 37 (1998) 1853;
(d) E.S. Claudio, H.A. Godwin, J.S. Magyar, Prog. Inorg. Chem. 51 (2003) 1;
(e) J.S. Casas, J. Sordo, M.J. Vidarte, in: J.S. Casas, J. Sordo (Eds.), Lead: Chemistry, Analytical aspects, Environmental Impact and Health Effects, Elsevier, Amsterdam, 2006.
[4] J. Emsley, in: The Elements, Oxford Univ. Press, NY, 1998.
[5] J.E. Huheey, E.A. Keiter, R.L. Keiter, in: Inorganic Chemistry, 4th ed., HarperCollins College Publishers, New York, 1993.
[6] S. Hino, M. Brynda, A.D. Phillips, P.P. Power, Angew. Chem. Int. Ed. 43 (2004) 2655.
[7] J. Harrowfield, Helv. Chim. Acta 88 (2005) 2430.
[8] P.J. Smith (Ed.), Chemistry of Tin, 2nd ed., Blackie Academic & Professional, London, 1998.
[9] J.S. Miller, J.J. Novoa, Acc. Chem. Res. 40 (2007) 189.
[10] R.D. Hancock, J.H. Reibenspies, H. Maumela, Inorg. Chem. 43 (2004) 2981.
[11] J.M. Harrowfield, S. Maghaminia, A.A. Soudi, Inorg. Chem. 43 (2004) 1810.
[12] F. Caruso, M.L. Chan, M. Rossi, Inorg. Chem. 36 (1997) 3609.
[13] (a) J.S. Casas, M.V. Castaño, E.E. Castellano, M.S. García-Tasende, A. Sánchez, M.L. Sanjuán, J. Sordo, Eur. J. Inorg. Chem. (2000) 83;
(b) J.S. Casas, M.V. Castaño, E.E. Castellano, J. Ellena, M.S. García-Tasende, A. Gato, A. Sánchez, L.M. Sanjuán, J. Sordo, Inorg. Chem. 41 (2002) 1550;
(c) J.S. Casas, M.V. Castaño, M.S. García-Tasende, E. Rodríguez Castellón, A. Sánchez, L.M. Sanjuán, J. Sordo, Dalton Trans. (2004) 2019;
(d) J.S. Casas, M.V. Castaño, M.S. García-Tasende, A. Sánchez, J. Sordo, A. Touceda, Polyhedron 24 (2005) 3057;
(e) R. Carballo, J.S. Casas, E. García-Martínez, G. Pereiras-Gabián, A. Sánchez, J. Sordo, E.M. Vázquez-López, Inorg. Chem. 42 (2003) 6395.
[14] S. Jayasree, K.K. Aravindakshan, Polyhedron 12 (1993) 1187.
[15] R.H. Blessing, Acta Crystallogr. A 51 (1995) 33.
[16] A.C.T. North, D.C. Phillips, F.S. Mathews, Acta Crystallogr. Sect. A 24 (1968) 351.
[17] G.M. Sheldrick, in: SHELX-97, An Integrated System for Solving and Refining Crystal Structures from Diffraction Data, University of Göttingen, Göttingen, Germany, 1997.
[18] L.J. Farrugia, J. Appl. Crystallogr. 30 (1997) 565.
[19] A.L. Spek, PLATON 99, A Multipurpose Crystallographic Tool, University of Utrecht, Utrecht, The Netherlands, 1999.
[20] I.J. Bruno, J.C. Cole, P.R. Edgington, M.K. Kessler, C.F. Macrae, P. McCabe, J. Pearson, R. Taylor, Acta Crystallogr. B58 (2002) 389.
[21] M.J. Frisch et al., GAUSSIAN 03, Revision A.1, Gaussian Inc., Pittsburgh, PA, 2003.
[22] (a) A.D. Becke, J. Chem. Phys. 98 (1993) 5648;
(b) A.D. Becke, J. Chem. Phys. 96 (1992) 2155.
[23] C. Lee, W. Yang, R.G. Parr, Phys. Rev. B 37 (1988) 785.
[24] W.R. Wadt, P.J. Hay, J. Chem. Phys. 82 (1985) 284.
[25] R.F.W. Bader, in: AIMPAC, A Suite of Programs for the Theory of Atoms in Molecules, McMaster University, Hamilton, Ontario, Canada, 1994.
[26] (a) R.F.W. Bader, Chem. Rev. 91 (1991) 893;
(b) R.F.W. Bader, in: Atoms in Molecules-A Quantum Theory, Oxford University Press, Oxford, UK, 1990.
[27] A. Sierraalta, F. Ruette, Int. J. Quantum Chem. 60 (1996) 1015.
[28] J.S. Casas, M.S. García-Tasende, J. Sordo, Coord. Chem. Rev. 209 (2000) 197.
[29] R. Carballo, S. Casas, E. García-Martínez, G. Pereiras-Gabián, A. Sánchez, J. Sordo, E.M. Vázquez-López, Acta Crystallogr. E 58 (2002) o787.
[30] S. Hino, M. Olmstead, A.D. Phillips, R.J. Wright, P.P. Power, Inorg. Chem. 43 (2004) 7346.
[31] Y.Z. Yuan, J. Zhou, X. Liu, L.H. Liu, K.B. Yu, Inorg. Chem. Commun. 10 (2007) 475.
[32] A. Morsali, A.R. Mahjoub, Solid State Sci. 7 (2005) 1429.
[33] K. Nakamoto, in: Infrared and Raman Spectra of Inorganic and Coordination Compounds, 5th ed., John Wiley & Sons, Inc., NY, 1997.

larger and more complicated organic molecules such as phthalocyanines (Pcs). This led us to undertake this investigation.

Pcs and their symmetrically substituted derivatives have received extensive interest in recent decades since their special properties such as electrical conductivity [10], electrochromism [11], mesophase formation [12] and photosensitivity [13] makes them interesting substrates for novel materials [14]. The synthesis and study of binuclear or oligonuclear and sandwich type Pcs containing two metal centers are among the priorities of modern phthalocyanine (Pc) chemistry [15–21]. These complexes show a wide range of interactions between the Pc ring, mainly depending on the metal center, bridging links and the presence or absence of axial ligands. The species having flexible bridging units usually do not exhibit any measurable interaction while rigid systems such as the anthracene and naphthalene bridged species do exhibit strong interactions. Many Pc dimers and multimers, having various kinds of linkage, have been reported to date. These dimers and multimers, especially those with rigid cofacial configurations, usually show spectroscopic, electrochemical and electrical properties which differ significantly from the parent monomers. The synthesis and properties of binuclear Pcs with great numbers of cross-links have rarely been reported in the literature. Recently, a binuclear ball-type ZnPc containing phenylidene bridges has been reported [15,16]. Introducing electron donor and acceptor groups into the Pc ring also strongly affects the electrical properties of the molecule. From the viewpoint of organic semiconductors, it is known that substitution of electron donor and acceptor groups leads to p-type and n-type characteristics of the Pc ring, respectively [22,23].

We have reported on the synthesis and characterisation of novel *s*-triazines bearing three oxygen-linked metallo Pcs and lutetium bisphthalocyanine sandwich complexes [21,24]. The synthesis, characterization, conduction and gas sensing properties of novel multinuclear metallo Pcs with alkylthio substituents were also reported in the literature [25]. We achieved for the first time the synthesis of a novel ball-type four *t*-butylcalix[4]arene bridged binuclear zinc(II)Pc, namely compound **2** [26]. It was synthesized by the tetramerization of compound **1** with $Zn(OAc)_2 \cdot 2H_2O$ in dry DMF. This novel compound exhibited mixed-valence behaviour and non-Arrhenius type dependence of conductivity [26]. We have also reported *t*-butylcalix[4]arene bridged bis double-decker lutetium (III) phthalocyanine [27]. In addition to compound **2**, we report here in detail the synthesis, characterization and electrochemical properties of compounds **3** and **4**. The metal-free Pc of ball type **3** was synthesized by the condensation of compound **1** in the presence of lithium metal in dry amyl alcohol. The binuclear Pc of clamshell type **4** was obtained by the reaction of compound **1** with 4,5-bis(hexylthio)phthalonitrile and $Zn(OAc)_2 \cdot 2H_2O$.

2. Experimental

2.1. Synthesis and characterization

All reagents and solvents were of reagent grade quality, obtained from commercial suppliers. The solvents were stored over molecular sieves (4 Å). The progress of the reactions was monitored by TLC. 4-Nitrophthalonitrile [28] and 4,5-bis(hexylthio)phthalonitrile [29] were prepared by the literature methods.

Routine IR spectra were recorded on a Shimadzu IR-470 Infrared spectrometer as KBr pellets, electronic spectra on a Unicam UV 500 UV–Vis spectrometer. Elemental analysis was performed by a LECO CHNS 932 in the Instrumental Analysis Laboratory of TUBITAK Ankara Research Center. ^{1}H NMR spectra were recorded on a Bruker Avance DPX-400 spectrometer. Mass spectra were acquired on a Voyager-DE™ PRO MALDI-TOF mass spectrometer (Applied Biosystems, USA) equipped with a nitrogen UV-laser operating at 337 nm. Spectra were recorded both in linear and reflectron modes with an average of 50 shots. A 3,5-dinitrobenzoic acid (DNB) MALDI matrix was used and prepared in chloroform ($CHCl_3$) at a concentration of 20 mg/mL for the binuclear Zn(II)Pc **2**, and 3-indole acyrylic acid was prepared in methanol for the binuclear metal-free Pc **3** and in $CHCl_3$ for the binuclear Zn(II)Pc of clamshell type **4**, at a concentration of 20 mg/mL. MALDI samples were prepared by mixing sample solutions (4 mg/mL) with the matrix solution (1:10 v/v) in a 0.5 mL eppendorf® micro tube. Finally 1 μL of this mixture was deposited on the sample plate, dried at room temperature and then analyzed.

2.1.1. Preparation of 1,3-bis(3,4-dicyanophenoxy)-4-tert-butylcalix[4]arene (1)

1,3-Dimethoxy-4-*tert*-butylcalix[4]arene (1.9 g, 2.8 mmol) and 4-nitrophthalonitrile (0.972 g, 5.6 mmol) were added successively with stirring to dry dimethylsulfoxide (DMSO) (60 ml). After they were dissolved, anhydrous K_2CO_3 (1.16 g, 8.4 mmol) was added and the reaction mixture was stirred at 85 °C for 76 h. Reaction was monitored by TLC. Then, the reaction mixture was poured into 200 ml of cold water, acetic acid (2 ml) was added and it was stirred for 15 min. The precipitate was filtered off, flushed several times with cold water until the filtrate was neutral and dried in air, then at 70 °C. This compound was readily soluble in the majority of organic solvents such as ethanol, methanol, $CHCl_3$, THF, acetone, diethyl ether, DMF and DMSO. Yield: 2.26 g (87%). M.p. 165–168 °C; ^{1}H NMR ($CDCl_3$): δ, ppm 7.78–6.31 (m, 14H, arom.), 3.73–3.23 (m, 6H, OCH_3), 2.66 (s, 8H, Ar–CH_2), 1.63–1.12 (m, 36H, tBu CH_3). IR (KBr): ν, cm^{-1} 3046 (CH arom.), 2959–2869 (CH aliph.), 2822, 2357, 2323, 2229 (C≡N), 1734, 1596 (Ar C=C), 1476, 1359, 1290, 1245 (Ar–O–Ar), 1193, 1117, 1017, 949, 873, 834, 523. *Anal.* Calc. for $C_{62}H_{64}N_4O_4$ (928): C, 80.17; H, 6.89; N, 6.03. Found: C, 79.83; H, 6.68; N, 5.94%.

*2.1.2. Synthesis of binuclear zinc(II) phthalocyanine of ball type **2***

A mixture of compound **1** (0.40 g, 0.437 mmol) and $Zn(OAc)_2 \cdot 2H_2O$ (0.047 g, 0.218 mmol) was heated in a sealed glass tube for 24 h under stirring and N_2 in dry DMF (2.7 ml) at 190 °C. After cooling to room temperature, 5 ml of distilled water was added to the blue-green mixture to precipitate the product. The precipitate was suction filtered, multiply washed at first with hot water and then with hot ethanol in order to eliminate the unreacted starting materials, and dried in vacuo. Then, the crude product was repeatedly flushed with $CHCl_3$. After the filtrate had been evaporated to dryness, it was washed with ethanol until the filtrate was colorless and dried in vacuo. This compound is soluble in ethyl acetate, acetic acid, hot DMSO and $CHCl_3$. Yield: 0.071 g, 17%. M.p. > 300 °C. UV–Vis λ_{max} ($CHCl_3$, 51.98 μM) ($\log \varepsilon/dm^{-3}\,mol^{-1}\,cm^{-1}$): 350 (4.575), 620 (4.117), 688 (4.706) nm. ^1H NMR ($CDCl_3$): δ, ppm 8.57–7.11 (m, 56H, arom.), 3.23–3.18 (t, 24H, OCH_3), 2.85 (d, 32H, Ar–CH_2), 1.68–1.57 (t, 144H, tBuCH_3). MS (MALDI-TOF): *m/z* 3849.6 $[M+H]^+$, 3704.6 $[M^+-(C_{10}H_9O)]$, 3559.6 $[M^+-2(C_{10}H_9O)]$. IR (KBr): *v*, cm^{-1} 3057 (CH arom.), 2956–2866 (CH aliph.), 2330, 1730, 1658, 1605, (Ar C=C), 1472, 1359, 1285 (Ar–O–Ar), 1193, 1118, 1021, 942, 871, 757, 675, 621. *Anal.* Calc. for $C_{248}H_{256}N_{16}O_{16}Zn_2$ (3847.608): C, 77.41; H, 6.70; N, 5.82. Found: C, 77.14; H, 6.74; N, 6.18%.

*2.1.3. Synthesis of binuclear metal-free phthalocyanine of ball type **3***

A suspension of **1** (0.200 g, 0.215 mmol) in 1.8 ml of dry amyl alcohol was heated in a sealed tube at 80 °C under N_2. After addition of elemental lithium (0.035 g, 5.043 mmol) to the reaction mixture, a blue-green colour appeared in 15 min. The reaction mixture was stirred at 170 °C for 18 h. After cooling to room temperature, EtOH (20 ml) was added to the mixture and it was filtered. After the filtrate had been evaporated to dryness, the residue was washed successively with water then with diethyl ether (3 × 30 ml), $CHCl_3$ (3 × 30 ml), CH_2Cl_2 (3 × 30 ml), ethyl acetate (3 × 30 ml), THF (3 × 30 ml) and acetone (3 × 30 ml) prior to drying in vacuo (70 °C) to give the pure product **3**. The blue-green coloured product is soluble in methanol, acetic acid, DMF, hot ethanol and hot DMSO. Yield: 0.110 g, 55%. M.p. > 200 °C. UV–Vis λ_{max} (MeOH, 107.5 μM) ($\log \varepsilon/dm^{-3}\,mol^{-1}\,cm^{-1}$): 336 (3.924), 626 (3.303), 674 (3.968), 710 (4.042) nm. ^1H NMR (DMSO): δ, ppm 8.21–6.97 (m, 56H, arom.), 3.27 (s, 24H, OCH_3), 2.94 (s, 32H, Ar–CH_2), 1.63 (t, 144H, tBu CH_3). IR (KBr): *v*, cm^{-1} 3410, 3057 (CH arom.), 2952–2860 (CH aliph.), 2332, 1731, 1658, 1607, (Ar C=C), 1470, 1357, 1285 (Ar–O–Ar), 1191, 1118, 1019, 945, 871, 755, 620. *Anal.* Calc. for $C_{248}H_{260}N_{16}O_{16}$ (3716): C, 80.08; H, 6.99; N, 6.02. Found: C, 79.84; H, 6.85; N 6.24%.

*2.1.4. Synthesis of binuclear zinc(II) phthalocyanine of clamshell type **4***

A mixture of compound **1** (0.140 g, 0.15 mmol), 4,5-bis(hexylthio)phthalonitrile (0.331 g, 0.92 mmol), $Zn(OAc)_2 \cdot 2H_2O$ (0.071 g, 0.32 mmol) and dry quinoline (2 ml) was heated and stirred in a sealed glass tube at 190 °C under N_2 for 24 h. After cooling to room temperature, the dark green mixture was diluted with ethanol (10 ml) to precipitate the product, and then it was filtered. After having been washed successively with hot water, hot ethanol (3 × 20 ml), hot DMSO (3 × 20 ml) (60 °C) and methanol (3 × 20 ml) to remove the unreacted organic materials, the dark green product was dissolved in $CHCl_3$ (40 ml), the solution was filtered and the filtrate evaporated to a smaller volume (ca. 10 ml) from which a dark green precipitate was obtained by addition of ethyl acetate/diethyl ether (20 ml/15 ml). It was filtered off, washed successively with hot ethyl acetate (3 × 20 ml), acetone (3 × 20 ml) and diethyl ether (3 × 20 ml) prior to drying in vacuo to give pure product **4**. The dark green product was soluble in $CHCl_3$, CH_2Cl_2, benzene and DMF. Yield: 0.058 g, 12%. M.p. > 200 °C. UV–Vis λ_{max} ($CHCl_3$, 62.15 μM) ($\log \varepsilon/dm^{-3}\,mol^{-1}\,cm^{-1}$): 360 (4.675), 694 (4.650) nm ^1H NMR ($CDCl_3$): δ, ppm 7.64–6.45 (m, 26 H, arom.), 3.23–3.16 (t, 6H, OCH_3), 2.91 (d, 8H, Ar–CH_2), 1.93 (br s, 24H, SCH_2), 1.67–1.62 (t, 36H, tBu CH_3), 1.23 (d, 96 H, –CCH_2C–), 0.83 (d, 36H, –CH_3). IR (KBr): *v*, cm^{-1} 3040 (CH arom.), 2910–2845 (CH aliph.), 2356, 2217, 1590 (Ar C=C), 1542, 1508, 1454, 1403, 1285 (Ar–O–Ar), 1195, 1065, 1020, 939, 755, 692, 540. *Anal.* Calc. for $C_{182}H_{232}N_{16}O_4\,S_{12}Zn_2$ (3218): C, 67.86; H, 7.20; N, 6.96; S, 11.93. Found: C, 67.46; H, 7.04; N, 6.64; S, 11.48%.

2.2. Electrochemistry

Electrochemical measurements were carried out with a PAR Model VersoStat II potentiostat/galvanostat controlled by an external PC, and utilizing a three electrode configuration at 25 °C. Tetrabutyammonium perchlorate (TBAP) (Electrochemical grade, Fluka Chemical Co.) was used as the supporting electrolyte in extra pure DCM and DMSO (Fluka Chemical Co). A saturated calomel electrode (SCE) was employed as the reference electrode and separated from the bulk of the solution by a fritted glass bridge filled with the solvent/supporting electrolyte mixture. The ferrocene/ferrocenium couple (Fc/Fc^+) was used as an internal standard, but potentials were reported with respect to SCE. The working electrode was platinum in the measurements. The surface of the platinum working electrode was polished with a H_2O suspension of Al_2O_3 before each run. The last polishing was done with a particle size of 50 nm. A platinum spiral wire was used as the auxillary electrode. Solutions containing **2**–**4** were deoxygenated by a stream of high-purity nitrogen for at least 20 min prior to running the experiment, and the solution was protected from air by a blanket of nitrogen during

the experiment. For the controlled-potential coulometry (CPC) studies, a platinum gauze working electrode, a platinum wire counter electrode separated with a bridge, a SCE as reference electrode and a model 377/12 synchronous stirrer were used.

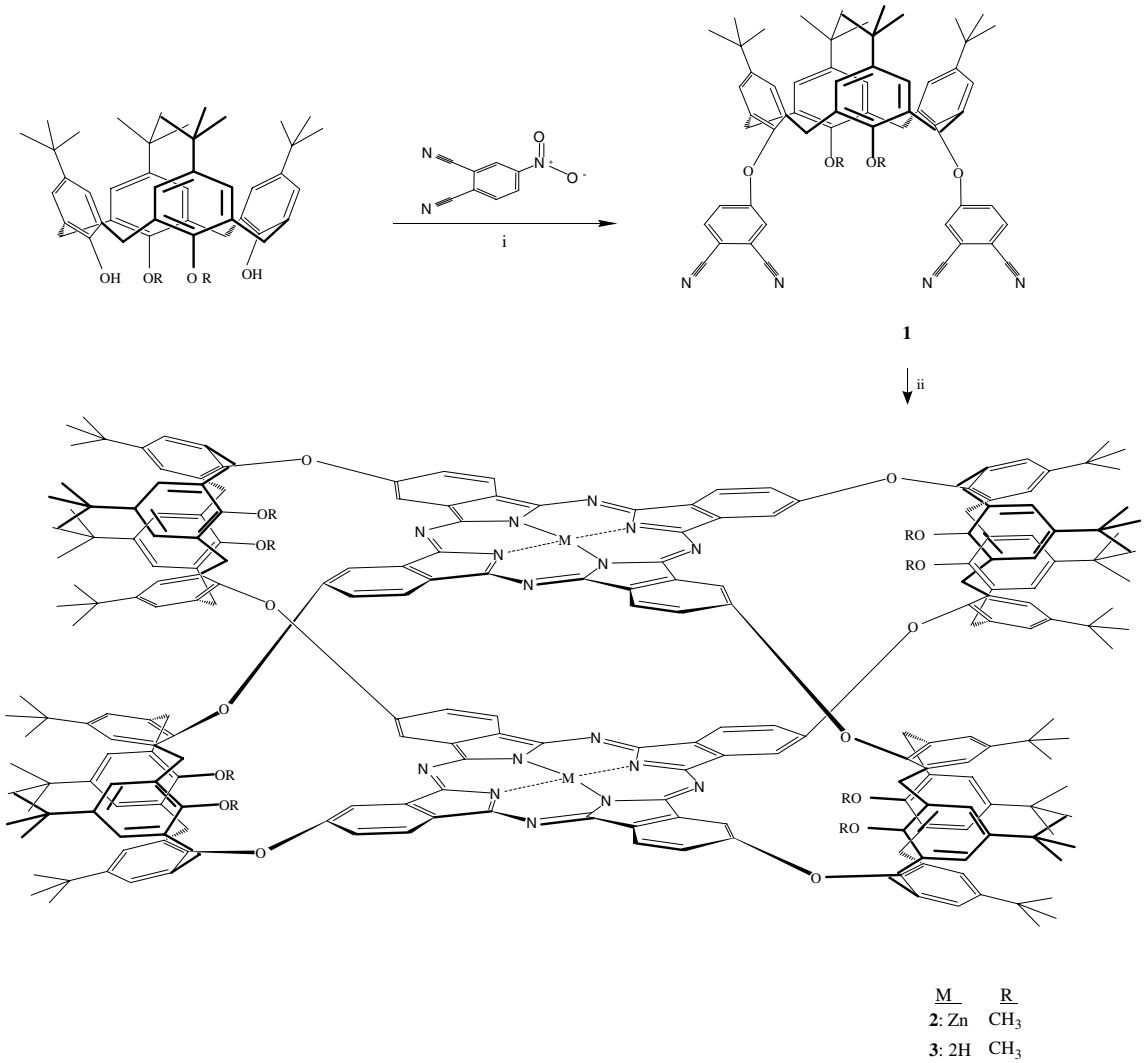
3. Results and discussion

3.1. Synthesis and characterization

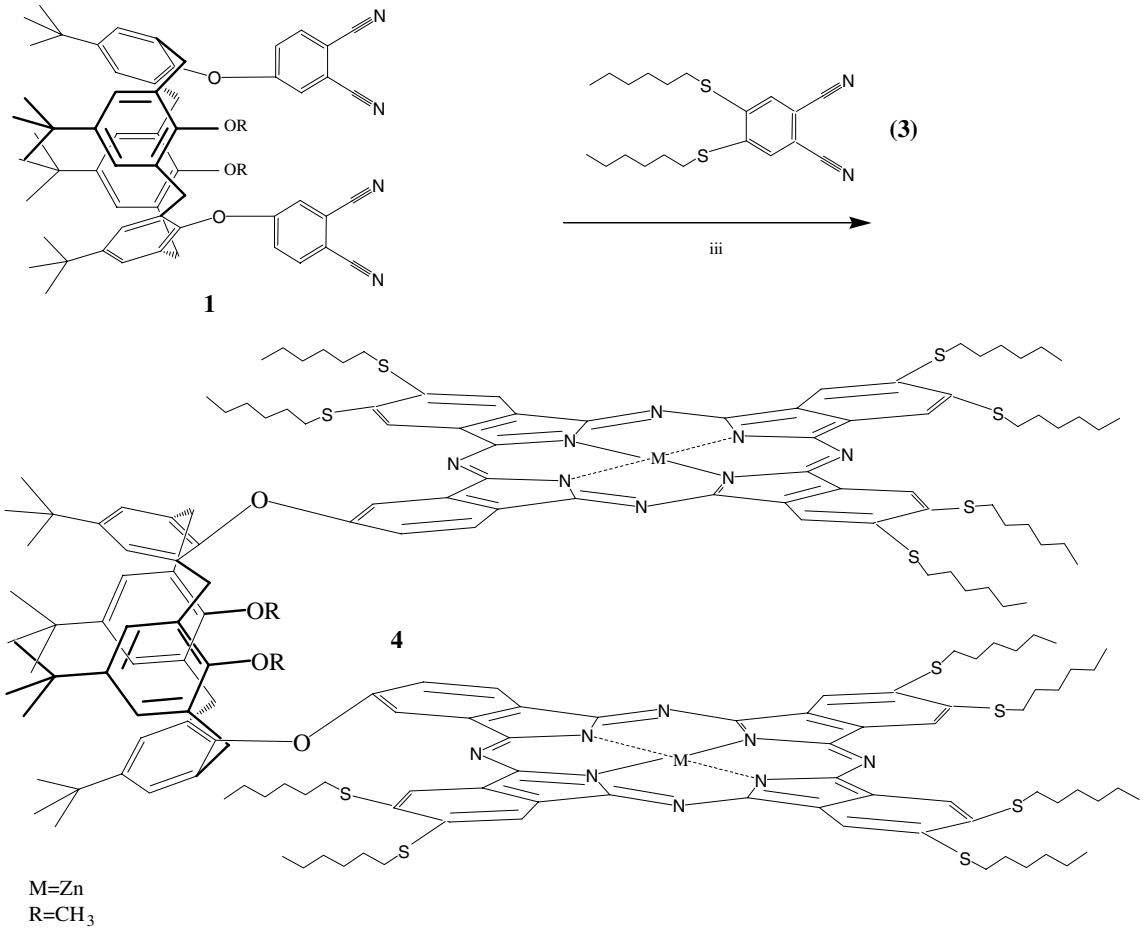
Scheme 1 shows the synthesis of the target Pcs **2** and **3**. Our key starting material is compound **1** which can be obtained via a single step reaction of 1,3-dimethoxy-4-*t*-butyl calix[4]arene with 4-nitrophthalonitrile in dry DMSO as the solvent, in the presence of the base K_2CO_3 in a yield of 87%. A new binuclear zinc(II)Pc of ball type **2** was prepared by the reaction of compound **1** and $Zn(OAc)_2$ $2H_2O$. Compound **1** was also readily condensed to a novel metal-free Pc of ball type **3** in the presence of elemental lithium. The elegance of the synthesis arises from the fact that the cone conformation of the *t*-butylcalix[4]arene directs the tetramerization of the four nitriles to a Pc of the ball-type structure.

We have previously shown that bisphthalonitrile derivative **1** is a precursor to binuclear Pc **2**, but the yield of the expected product was low (6.5%). Refluxing a solution of bisphthalodinitrile derivative **1** in dry DMF, containing a stoichiometric amount of $Zn(OAc)_2 \cdot 2H_2O$ in a nitrogen atmosphere for 23 h, leads to binuclear Pc **2** formation in a yield of 6.5% [14]. When a mixture of the starting compounds were heated in a sealed glass tube under the same reaction conditions, the yield of **2** was increased to 17%.

The binuclear Pc of clamshell type **4** was also obtained by the reaction of compound **1** with 4,5-bis(hexylthio)phthalonitrile by the method of statistically mixed condensation (Scheme 2). The high boiling solvents of choice for these reactions were DMF for **2**, amyl alcohol for **3** and quinoline for **4**.



Scheme 1. Reagents and conditions: (i) K_2CO_3, DMSO, 76 h, 85 °C; (ii) for compound **2**: DMF, $Zn(OAc)_2 \cdot 2\,H_2O$, 24 h, 190 °C; for compound **3**: Lithium metal, amyl alcohol, 18 h, 170 °C.



Scheme 2. Reagents and conditions: iii: quinoline, $Zn(OAc)_2 \cdot 2H_2O$, 24 h, at 190 °C.

Characterisation of the new products involved a combination of methods including elemental analysis, IR, UV–Vis (Table 1), MS and ^1H NMR spectroscopic techniques. The spectroscopic data of the new compounds were in accordance with the structures. The IR spectra, taken as KBr pellets, showed a –CH aliph. peak at 2959–2869 cm^{-1} and an intense absorption attributable to C≡N at 2229 cm^{-1}, Ar C=C peak at 1596 cm^{-1} and an aromatic CH peak at 3046 cm^{-1} for compound **1**.

A diagnostic feature of Pc formation from the phthalodinitrile derivative **1** is the disappearance of the sharp C≡N vibration at 2229 cm^{-1} of the reactant. The remaining spectrum is very similar to that of compound **1** for **2**–**4**. The IR spectra of **2**–**4** showed Ar–O–Ar peaks at 1285 cm^{-1}, Ar C=C peaks at around 1590–1607 cm^{-1} and aromatic CH peaks at around 3040–3057 cm^{-1}. In addition, the stretching vibrations at 2956–2866, 2952–2860 and 2910–2845 cm^{-1} indicated the presence of –CH and $–CH_3$ groups for **2**–**4**, respectively. The weak band around 3410 cm^{-1} for **3** can be attributed to the N-H stretching frequency of the inner core of the metal-free Pc.

Table 1
UV–Vis data for the phthalocyanines **2**–**4**

Compound	λ/nm (log ε/dm^3 mol^{-1} cm^{-1})
2[a]	688 (4.706), 620 (4.117), 350 (4.575)
3[b]	710 (4.042), 674 (3.968), 626 (3.303), 336 (3.924)
4[a]	694 (4.650), 632 (4.406), 360 (4.675)

[a] In $CHCl_3$.
[b] In methanol.

The ^1H NMR spectra were also in good correlation with the structures of the synthesized compounds. In the ^1H NMR spectrum of **1**, which was taken in $CHCl_3$, the aromatic protons appeared at 7.78–6.31 ppm as multiplets and the $ArCH_2$ protons at 2.66 ppm. The peaks at 3.73–3.23 and 1.63–1.12 ppm indicated the presence of a $–OCH_3$ group and a *tert*-butyl CH_3 group in the structure, respectively. In the ^1H NMR spectrum of pc **2**, which was taken in $CHCl_3$, the aromatic protons appeared at 8.57–7.11 ppm, $ArCH_2$ protons at 2.85 ppm, OCH_3 protons at 3.23–3.18 ppm and *tert*-butyl CH_3 protons at 1.68–1.57 ppm. The ^1H NMR spectrum of **3**, which was taken in DMSO, was similar to that of **2**. In the spectra of **3**, the aromatic protons appeared at 8.21–6.97 ppm, $ArCH_2$ protons at 2.94 ppm, OCH_3 protons at 3.27 ppm and *tert*-butyl CH_3 protons at 1.63 ppm. NH protons could not be observed, probably due to the broad nature of these

peaks in the presence of the intense resonances of the Pc ring [30]. In the ^{1}H NMR spectrum of **4**, which was taken in $CHCl_3$, the aromatic protons appeared at 7.64–6.45 ppm, the peaks at 3.23–3.16, 2.91 and 1.67–1.62 ppm indicated the presence of $–OCH_3$, $–CH_2$ and *tert*-butyl CH_3 groups of 1,3 dimethoxy-4-*tert*-butylcalix[4]arene, respectively, in the structure. The $–CH_3$ protons at the end of the chain appeared at 0.83 ppm, $–CCH_2C–$ protons at 1.23 ppm, and the $–SCH_2$ group neighboring an aromatic ring at 1.93 ppm.

A close investigation of the mass spectra of **2**–**4** confirmed the proposed structures. For **2**, the protonated molecular ion peak was observed at 3849.6 Da, and that exactly overlapped with the mass of **2** calculated theoretically from the elemental composition of the molecule (Fig. 1). Beside the protonated molecular ion peak of the molecule, two other peaks were observed at 3704.6 and 3559.6 in the high mass range. These two peak masses indicated a fragmentation occurred from the protonated molecular ion of **2** with 145 Da mass losses from both sides of the molecule. This fragment pointed out that the leaving group could be $C_{10}H_9O$ which exists as an end group of the molecular structure. All the MALDI-MS results showed that compound **2** was successfully synthesized and the MALDI-MS spectrum of this molecule was obtained only in 3,5-dinitrobenzoic acid matrix with a high protonated molecular ion peak intensity.

The positive ion MALDI-MS spectrum of **3** is given in Fig. 2. Many different MALDI matrices were tried to find an intense molecular ion peak and low fragmentation under the MALDI-MS conditions for this compound. Only 3-indole acrylic acid yielded a good MALDI-MS spectrum, as seen in Fig. 2. The protonated molecular

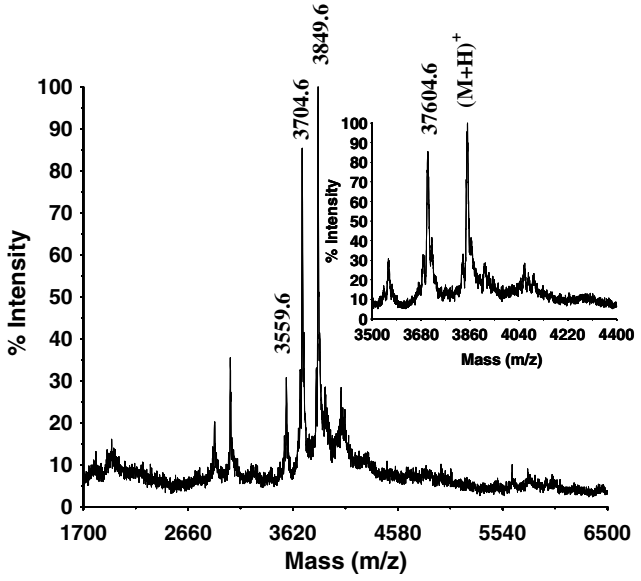


Fig. 1. Positive ion and linear mode MALDI-TOF mass spectrum of **2**, obtained in 3,5-dinitrobenzoic acid MALDI matrix using nitrogen laser accumulating 50 laser shots. Inset spectrum shows the expanded molecular mass region of the complex.

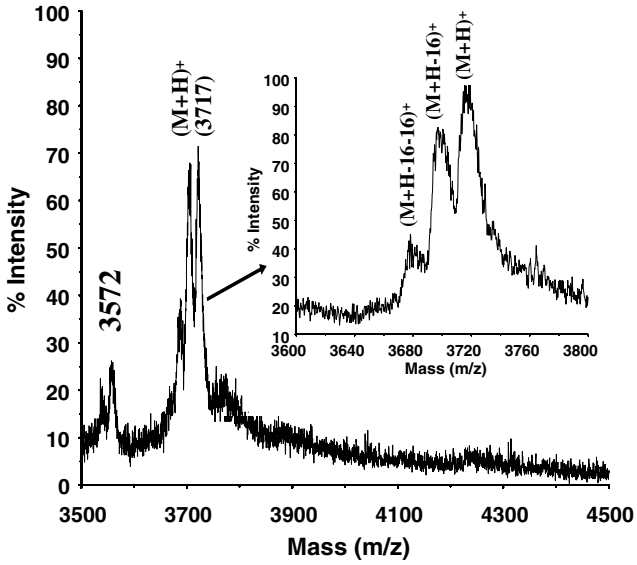


Fig. 2. Positive ion and linear mode MALDI-TOF mass spectrum of **3**, obtained in 3-indole acrylic acid MALDI matrix using nitrogen laser accumulating 50 laser shots. Inset spectrum shows the expanded molecular mass region of the complex.

ion peak of the ligand was observed at 3717 Da, with two fragment ion peaks. The mass difference between these peaks corresponds to 16 Da mass, resulting from methane elimination from the ligand at the side etheric groups. The low intensity for the protonated molecular ion peak shows the low stability of the ligand under the laser firing and mass spectrometric conditions compared to the mass spectrum of **2**, which is given in Fig. 1. In the MALDI-MS spectrum of **3**, beside methane elimination, one fragment ion was observed at 3572 Da mass, resulting from the leaving group having 145 Da mass, being lost from the molecular ion peak from one side chain. This fragment indicates that the leaving group could be $C_{10}H_9O$ which exists as an end group of the molecule.

The MALDI-MS spectrum of **4** was obtained in the best form only in a 3-indole acrylic acid MALDI matrix, though many other different matrices were tried. The positive ion MALDI-MS spectrum of this complex is given in Fig. 3. The protonated molecular ion peak intensity of this complex is dramatically lower than **2** and **3**. Also fragmentation of **4** yielded many different forms in the MALDI-MS spectrum of this complex. This is because of the less stable side alkyl chain connected to the main core of the complex, with a weak C–S linkage. The protonated molecular ion peak of this complex was observed at 3219 Da with low intensity. The following fragment peaks represented two and four cyclohexane leaving groups, from both sides of the complex. When the number of leaving groups increased, the remaining part of the complex was more stable and yielded two intense fragment peaks that appeared at 2843 and 2621 Da masses.

High resolution MALDI-MS spectra for **2**–**4** in reflectron mode could not be obtained as clear, intense spectra.

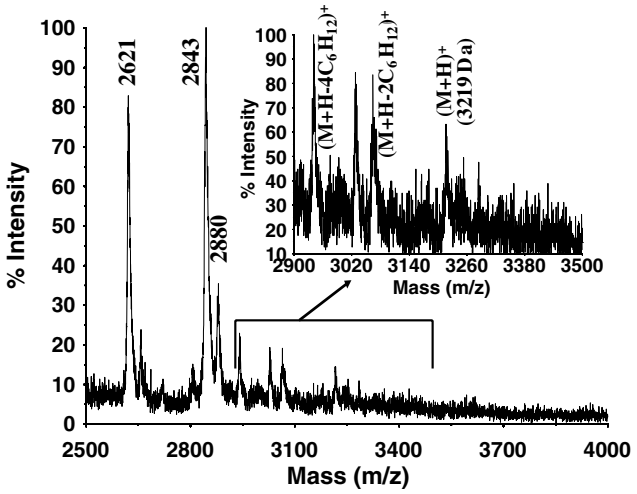


Fig. 3. Positive ion and linear mode MALDI-TOF mass spectrum of **4**, obtained in 3-indole acrylic acid MALDI matrix using nitrogen laser accumulating 50 laser shots. Inset spectrum shows the expanded molecular mass region of the complex.

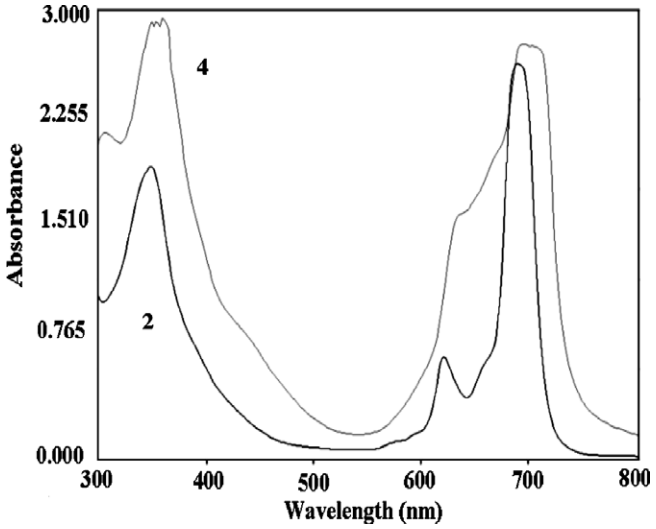


Fig. 4. UV–Vis spectra for phthalocyanines **2** and **4** in $CHCl_3$.

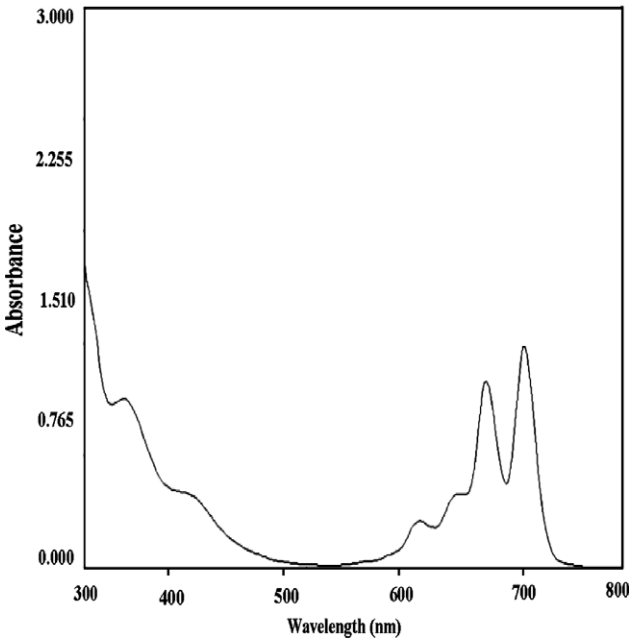


Fig. 5. UV–Vis spectrum for **3** in methanol.

This shows that the stability and also the lifetime of the ions are very low and short in the reflectron mode in MALDI-MS. When negative ion mode MALDI-MS spectra were recorded for these three different complexes no meaningful or intense spectra were obtained (data not shown).

The UV–Vis absorption spectra of the Pc system exhibited characteristic Q and B bands. Pcs **2**–**4** showed typical electronic spectra with two strong absorption regions, one in the visible region at about 600–700 nm (Q-band), which is attributed to the $\pi \rightarrow \pi^*$ transition from the highest occupied molecular orbital (HOMO) to the lowest unoccupied molecular orbital (LUMO) of the Pc(−2) ring, and the other in the UV region at about 300–400 nm (B-band), arising from the deeper π-levels → LUMO transition [31,32].

In the electronic spectra of **2** in chloroform at room temperature, an intense Q absorption band was observed at 688 nm and another in the UV region at 350 nm (B-band) arose from the deeper π-levels → LUMO transition. It shows an additional weak vibrational satellite band at ca. 68 nm to the blue of the normal Q-band as a result of exciton coupling between the Pc units [17] (Fig. 4). Although the Q-band in the spectrum of **2** is not a split, a well-defined absorption at 620 nm might also be interpreted in terms of intramolecular interactions between the Pc rings. The energies and relative intensities, and broadening of the bands observed are in accordance with the pattern that would be anticipated on the basis of the excitation coupling theory for the Pc complexes. The electronic absorption spectrum of **3** in methanol at room temperature is shown in Fig. 5. The Q-band is split, as expected, and there are two strong bands in the visible region. The split Q-band, which is characteristic for metal-free Pcs, is observed at λ_{max} 710 and 674 nm, indicating a monomeric species; the monomeric species with D_{2h} symmetry shows two intense absorptions at around 700 nm [29,33–36]. On the other hand, such split Q-band absorptions are due to $\pi \rightarrow \pi^*$ transitions of these fully-conjugated 18π electron systems. In addition, a third band at 626 nm to the blue side of the double Q-band of the metal-free complex was observed. This band, in addition to the broadness of the spectrum, is indicative of strong intramolecular interactions between the Pc rings, probably due to the ball-type cofacial structure.

The electronic spectrum of **4** shows the characteristic Q-band absorption as a single peak at 694 nm, attributed to the $\pi \rightarrow \pi^*$ transition from the HOMO to the LUMO of the Pc(−2) ring (Fig. 5). Usually aggregation of Pcs results in a spectral effect that extends from band broadening to

blue shifts of the Q and B bands. The shoulder at 632 nm indicates aggregation of **4**. Aggregation occurs readily at low concentrations, making the spectral data more difficult to interpret for many peripherally substituted Pc complexes. It is also known that aggregation is enhanced by solvent polarity and the presence of aliphatic side chains [12,37–39]. The other bands in the UV region at 336 and 360 nm (B-band) for **3** and **4**, respectively, arise from the deeper π-levels → LUMO transition.

3.2. Electrochemistry

The voltammetric measurements were carried out on platinum in DMSO for **2**, **3** and in DCM for **4**. The relevant data are given in Table 2. Compound **4** displays two reductions at $E_{1/2} = -0.90$ V and $E_{1/2} = -1.18$ V versus SCE, and a single oxidation at $E_{1/2} = 0.64$ V versus SCE. The CPC studies showed that each redox process involves the transfer of two electrons. A typical steady state cyclic voltammogram (CV) recorded after several scans for **4** at 0.100 V s^{-1} is shown in Fig. 6. The transfer of two electrons in each redox step suggests that there is not any considerable interaction between the two Pc rings in **4**, and that the two rings are reduced and oxidized at the same potentials. The overall splitting of the molecular orbitals to a high degree on going from the monomeric to dimeric, trimeric or oligomeric Pcs, depending on the intermolecular interactions between the rings, is expected to occur only in the case where the rings are positioned in a face to face orientation, as in the sandwich-type Pcs. Thus, it can be predicted that the two Pc rings are approximately planar in nature. The half-peak potential

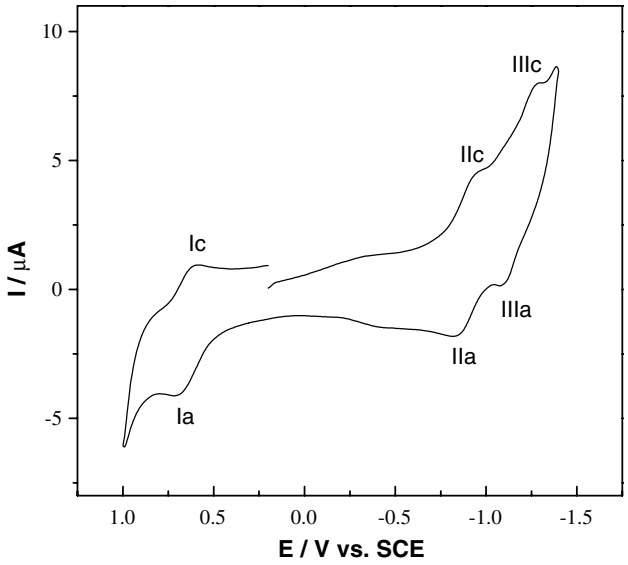


Fig. 6. Cyclic voltammogram of **4** (1.50×10^{-4} M) at 0.100 V s^{-1} on Pt in DCM/TBAP.

difference between the first ring oxidation and the first ring reduction, $\Delta E_{1/2}$ also provides additional support for the absence of or very weak interactions between two Pc rings. $\Delta E_{1/2}$ values ranging from 1.36 to 1.70 V have been reported for monomeric Pc compounds [40–44]. The separation between the first ring oxidation and the first ring reduction for **4** was found to be 1.54 V. In the case where there is a strong interaction between two Pcs in a dimer, this separation is expected to decrease as a result of the splitting of the molecular orbitals [18,19].

Table 2
Half-peak potentials for **2**–**4**, and mixed-valence splitting energies, ΔE_s, and comproportionation constants of mixed-valence species, K_c, for **2** and **3**

Compound	Redox couple	$E^a_{1/2}$ (V vs. SCE)	ΔE^b_s V	K^c_c
4	$[Pc(-1)]_2/[Pc(-2)]_2$ (I)	0.64		
	$[Pc(-2)]_2/[Pc(-3)]_2$ (II)	−0.90		
	$[Pc(-3)]_2/[Pc(-4)]_2$ (III)	−1.18		
2	$[Pc(-1)]_2/Pc(-1)Pc(-2)$ (I)	0.30	0.69[d]	7.29×10^{11}[e]
	$Pc(-1)Pc(-2)/[Pc(-2)]_2$ (II)	−0.39		
	$[Pc(-2)]_2/Pc(-2)Pc(-3)$ (III)	−0.95	0.44[f]	[g]
	$Pc(-2)Pc(-3)/[Pc(-3)]_2$ (IV)	−1.50[h]		
3	$[Pc(-1)]_2/Pc(-1)Pc(-2)$ (I)	0.66	0.62[d]	4.56×10^{10}[i]
	$Pc(-1)Pc(-2)/[Pc(-2)]_2$ (II)	0.04		
	$[Pc(-2)]_2/Pc(-2)Pc(-3)$ (III)	−0.91	0.55[j]	2.86×10^{9}[k]
	$Pc(-2)Pc(-3)/[Pc(-3)]_2$(IV)	−1.46		

[a] $E_{1/2} = (E_{pa} + E_{pc})/2$ at 0.100 V s^{-1}.
[b] The mixed-valence splitting energies.
[c] Equilibrium (comproportionation) constants for mixed-valenced species. $\ln K_c = \Delta E_s nF/RT$.
[d] The $E_{1/2}$ difference between couples I and II.
[e] It corresponds to the equilibrium, $[ZnPc(-1)]_2^{2+} + [ZnPc(-2)]_2 \rightleftarrows 2[ZnPc(-1)ZnPc(-2)]^+$.
[f] The difference between the cathodic peak potentials of III and IV.
[g] The process IV for **2** is irreversible.
[h] The cathodic peak potential of the irreversible process.
[i] It corresponds to the equilibrium, $[H_2Pc(-1)]_2^{2+} + [H_2Pc(-2)]_2 \rightleftarrows 2[H_2Pc(-1)H_2Pc(-2)]^+$.
[j] The $E_{1/2}$ difference between couples III and IV.
[k] It corresponds to the equilibrium, $[H_2Pc(-3)]_2^{2-} + [H_2Pc(-2)]_2 \rightleftarrows 2[H_2Pc(-3)H_2\ Pc(-2)]^-$.

The voltammetric behaviour of ball-type Pcs **2** and **3** are considerably different from that of **4**. These compounds show four one-electron redox processes. Typical voltammograms for these compounds are presented in Figs. 7 and 8. The transfer of one electron in each step indicates that the splitting of the molecular orbitals occurs as a result of the strong interaction between the two Pc rings in **2** and **3**, and thus each Pc ring reacts at a potential. The strong interaction between the HOMO and LUMO molecular orbitals of two Pcs in a dimer causes remarkable changes in the redox potentials, compared with the corresponding mono Pcs and non-interacting planar dimers. Generally, the oxidation potentials shift to less positive potentials while the reduction potentials shift to less negative potentials, the shift in oxidation potentials being more remarkable. Taking this observed behaviour into consideration, it can be concluded from a comparison of the voltammetric behaviour of **2** and **3** with the behaviour of **4** that the one-electron redox processes, I and II of each dimer **2** and **3** should correspond to the oxidation of two Pcs rings in each dimer while the processes III and IV are their reduction. High splitting of the Pc(−1)/Pc(−2) and Pc(−2)/Pc(−3) redox processes, i.e. mixed-valence behaviour, is observed, and thus each Pc ring in **2** and **3** is reduced and oxidized at highly different potentials as a result of the expected strong interactions between the cofacial Pc rings. The electrode reactions are schematically illustrated in Chart 1 for **2** and **3**, where the oxidations are labelled as I and II, and the reductions as III and IV.

The high splitting of the redox processes was detected with mixed-valence splitting, ΔE_s, values of 0.44 V for the first reduction, Pc(−2)/Pc(−3) and 0.69 V for the first oxidation, Pc(−1)/Pc(−2), for **2**, and 0.55 V for first reduction and 0.62 V for first oxidation for **3**. The splitting of a redox process, i.e. Pc(−1)/Pc(−2), for **2**, due to formation of a stable mixed-valence intermediate, $[ZnPc(-1)ZnPc(-2)]^+$,

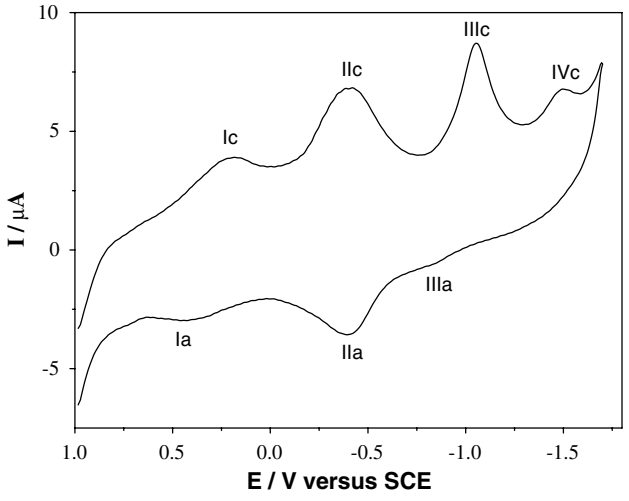


Fig. 7. Cyclic voltammogram of **2** (1.50×10^{-4} M) at 0.100 V s^{-1} on Pt in DMSO/TBAP.

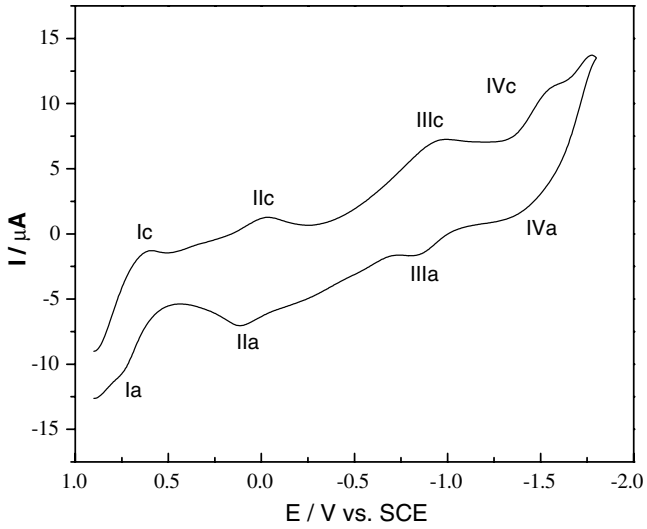


Fig. 8. Cyclic voltammogram of **3** (1.50×10^{-4} M) at 0.100 V s^{-1} on Pt in DMSO/TBAP.

is a measure of the equilibrium (comproportionation) constant, K_c, for a reaction such as [40]:

$$[ZnPc(-1)]_2^{2+} + [ZnPc(-2)]_2^{2} \rightleftarrows [ZnPc(-1)ZnPc(-2)]^+$$

where the mixed-valence splitting ΔE_s is related to K_c via:

$$\Delta E_s = (RT/nF)\ln(K_c) \quad (1)$$

The values of K_c so obtained for the other mixed-valence species, $[ZnPc(-3)ZnPc(-2)]^-$, $[H_2Pc(-1)H_2Pc(-2)]^+$ and $[H_2Pc(-2)H_2Pc(-3)]^-$, are collected in Table 2. The high mixed-valence splitting values give evidence of the delocalization of charge among the cofacial Pc rings in each ball-type Pc, **2** and **3**, and thus the formation of electrochemically stable oxidized and reduced mixed-valence species.

Some binuclear and tetranuclear Pcs [45–50] show metal-centered type or ring-centered type mixed-valence behaviour, but some of them do not. The difference is attributed mainly to the presence or absence of axial ligands, respectively inhibiting or facilitating the close approach of the rings, and to other steric factors. The least strongly coupled systems include some zinc complexes of binuclear Pcs with flexible bridging links [46–48]. However, the splitting of the first reduction and first oxidation processes of the Pc rings for **2** and **3**, and thus the comproportionation constants are considerably higher (Table 2), as compared with those observed previously in the literature for a series of mixed-valence Pc complexes of zinc, aluminum and copper, involving a redox-inactive metal center [40,46–48,50]. The comproportionation constants for these compounds are in the range from 24 to 6.0×10^6, thereby showing a wide range of stability. The results obtained in this study are compatible with the rigid structure of ball-type Pcs, **2** and **3**. The calixarene bridges in these compounds probably facilitate the close approach of the Pc rings. Moreover, mixed-valence ring reduction, Pc(−2)·Pc(−3), was observed previously only in strongly coupled silicon species [50], but not unequivocally observed with

$$[MPc(-1)]_2^{2+} \underset{I}{\overset{e^-}{\rightleftarrows}} [MPc(-1)MPc(-2)]^{+} \underset{II}{\overset{e^-}{\rightleftarrows}} [MPc(-2)]_2 \underset{III}{\overset{e^-}{\rightleftarrows}} [MPc(-3)MPc(-2)]^{-} \underset{IV^a}{\overset{e^-}{\rightleftarrows}} [MPc(-3)]_2^{2-}$$

Chart 1. Electrode reactions for **2** and **3**. M: Zn(II) for **2** and M: 2H for **3**. [a]irreversible for $[ZnPc(-2)]_2$.

the other bridged binuclear species. The presence of an extra π-electron repels the π-electron density in the other ring and therefore inhibits formation of these species unless they are constrained to lie close together. The large K_c values (2.7×10^8 for mixed valence ring oxidation and 6.0×10^6 for mixed valence ring reduction) for the silicon species was attributed to the shorter Pc···Pc contacts than in the bridged systems. As expected, a large K_c value (2.86×10^9) for mixed valence ring reduction was obtained for **3** in this study (Table 2). It could not be determined for **2** since the equation is not appropriate due to the irreversibility of couple IV (Fig. 7 and Table 2). However, the large mixed-valence splitting energy for the mixed-valence reduction of **2** (0.44 V, taking the difference between the cathodic peak potentials of processes III and IV into consideration) reflects strong interactions between the two Pc rings.

4. Conclusion

We have reported on the preparation of a phthalodinitrile derivative of a new type. This compound is used as a base for the preparation of a novel binuclear metal-free Pc of the ball type and zinc(II) Pcs of ball and clamshell types. The preparations of the new products are supported by elemental analysis, IR, UV-Vis, ^{1}H NMR and by mass spectra. It can be concluded from the voltammetric studies that the ball-type complexes **2** and **3** show ring-centered type mixed-valence behaviour as a result of the strong interaction between the two Pc rings, while there is no considerable interaction between the two Pc rings in **4**. The mixed-valence splitting energies and the comproportionation constants for **2** and **3** suggest that the mixed valence species are highly stable.

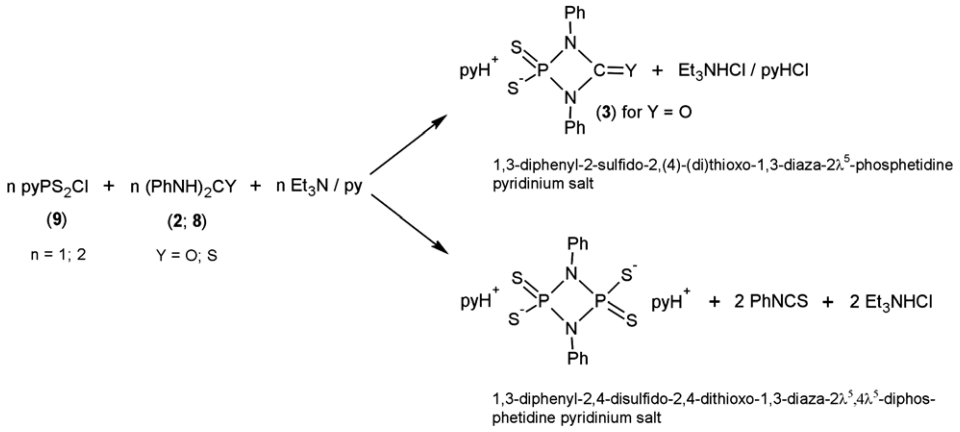
Acknowledgements

Financial assistance from The Research Fund of Gülhane Medical Academy of Ankara and in part from Turkish Academy of Sciences (TUBA) and The Research Fund of Marmara University (Project No. Science-107/020603) are gratefully acknowledged. We also thank Mr. Mesut Akyol, computer expert, Gülhane Medical Academy of Ankara for his valuable help.

References

[1] V. Böhmer, Angew Chem., Int. Ed. Engl. 34 (1995) 713.
[2] D. Diamond, M.A. McKervey, Chem. Soc. Rev. 25 (1996) 15.
[3] Z. Asfari, J. Weiss, J. Vicens, Syn. Lett. (1993) 719.
[4] I. Higler, P. Timmerman, W. Verboom, D.N. Reinhoudt, Eur. J. Org. Chem. (1998) 2689.
[5] P.R.A. Webber, G.Z. Chen, M.G.B. Drew, P.D. Beer, Angew Chem., Int. Ed. Engl. 40 (2001) 2265.
[6] A. Siepen, A. Zett, F. Vögtle, Liebigs Ann. (1996) 757.
[7] D.M. Rudkevich, W. Verboom, D.N. Reinhoudt, J. Org. Chem. 60 (1995) 6585.
[8] J. Rebek Jr., Chem. Commun. (2000) 637.
[9] For a review of CH–π interactions, see: M. Nishio, M. Hirota, Tetrahedron 45 (1989) 7201.
[10] M. Hanack, S. Deger, A. Lange, Coord. Chem. Rev. 83 (1988) 115.
[11] M. Bardin, E. Bertounesque, V. Plichon, J. Simon, V. Ahsen, Ö. Bekaroğlu, J. Electroanal. Chem. 271 (1989) 173.
[12] C. Piechocki, J. Simon, New. J. Chem. 9 (1985) 159.
[13] E. Ben-Hur, I. Rosenthal, Photochem. Photobiol. 43 (1986) 615.
[14] C.C. Leznoff, A.B.P. Lever (Eds.), Phthalocyanines – Properties and Applications, VCH Publishers, New York, 1987.
[15] A.Y. Tolbin, A.V. Ivanov, L.G. Tomilova, N.S. Zefirov, Mendelev Commun. (2002) 96.
[16] A.Y. Tolbin, A.V. Ivanov, L.G. Tomilova, N.S. Zefirov, J. Porphyr. Phthalocya. 7 (2003) 162.
[17] D.W. De Wulf, J.K. Leland, B.L. Wheeler, A.J. Bard, D.A. Batzel, D.R. Dininny, M.E. Kenney, Inorg. Chem. 26 (1987) 266.
[18] S. Abdurrahmanoglu, A. Altindal, A.R. Ozkaya, M. Bulut, Ö. Bekaroglu, Chem. Commun. (2004) 2096.
[19] S. Abdurrahmanoglu, A.R. Ozkaya, M. Bulut, Ö. Bekaroglu, J. Chem. Soc., Dalton Trans. (2004) 4022.
[20] A. Altindal, Ş. Abdurrahmanoglu, M. Bulut, Ö. Bekaroglu, Synth. Met. 150 (2005) 181.
[21] T. Ceyhan, M. Korkmaz, T. Kutluay, Ö. Bekaroğlu, J. Porphyr. Phthalocya. 8 (2004) 1383.
[22] H. Yanagi, N. Tamura, S. Taira, H. Furuto, S. Douko, G. Schnurpfeil, D. Wohrle, Mol. Cryst. Liq. Cryst. 267 (1995) 435.
[23] T. Manaka, M. Iwamoto, Thin Solid Films 438–439 (2003) 157.
[24] T. Ceyhan, M. Korkmaz, M.K. Erbil, Ö. Bekaroğlu, J. Porphyr. Phthalocya. 9 (2005) 423.
[25] T. Ceyhan, A. Altındal, M.K. Erbil, Ö. Bekaroğlu, Polyhedron 25 (2006) 737.
[26] T. Ceyhan, A. Altındal, A.R. Özkaya, B. Salih, Ö. Bekaroğlu, Chem. Commun. (2006) 320.
[27] T. Ceyhan, A. Altındal, A.R. Özkaya, M.K. Erbil, Ö. Bekaroglu, Polyhedron 26 (2007) 73.
[28] J.G. Young, W. Onyebuagu, J. Org. Chem. 55 (1990) 2155.
[29] A.G. Gürek, Ö. Bekaroğlu, J. Chem. Soc., Dalton Trans. (1994) 1419.
[30] P. Matlaba, T. Nyokong, Polyhedron 21 (2002) 2463.
[31] V. Ahsen, E. Yılmazer, M. Ertaş, Ö. Bekaroğlu, J. Chem. Soc., Dalton Trans. (1988) 401.
[32] M.J. Stilmann, T. Nykong, in: C.C. Leznoff, A.B.P. Lever (Eds.), Phthalocyanines: Properties and Applications, vol. 1, VCH, Weinheim, 1989.
[33] M. Hanack, H. Heckmann, R. Polley, Methods of Organic Chemistry, Georg Thieme Verlag, Stuttgard, 1998 (Additional Supplementary Volume, p. 776).
[34] C.F. van Nostrum, S.J. Picken, A.J. Schouten, R.J.M. Nolte, J. Am. Chem. Soc. 117 (1995) 9957.
[35] C. Wang, M.R. Bryce, A.S. Batsanow, C.F. Stanley, A. Beeby, J.A.K. Howard, J. Chem. Soc., Perkin Trans. 2 (1997) 1671.
[36] M.T.M. Choi, P.P.S. Li, D.K.P. Ng, Tetrahedron 56 (2000) 3881.
[37] A.R. Koray, V. Ahsen, Ö. Bekaroğlu, J. Chem. Soc., Chem. Commun. (1986) 932.
[38] N. Kobayashi, A.B.P. Lever, J. Am. Chem. Soc 109 (1987) 7433.

[39] Z. Gasyna, N. Kobayashi, M.J. Stillman, J. Chem. Soc., Dalton Trans. 1 (1989) 2397.
[40] A.B.P. Lever, E.R. Milaeva, G. Speier, in: C.C. Leznoff, A.B.P. Lever (Eds.), Phthalocyanines: Properties and Applications, vol. 3, VCH, Weinheim, 1993, p. 1.
[41] A.R. Özkaya, A.G. Gürek, A. Gül, O. Bekaroğlu, Polyhedron 16 (1997) 1877.
[42] A.R. Özkaya, I. Yılmaz, O. Bekaroğlu, J. Porphyr. Phthalocya. 2 (1998) 483.
[43] A.R. Özkaya, E. Hamuryudan, Z.A. Bayır, O. Bekaroğlu, J. Porphyr. Phthalocya. 4 (2000) 689.
[44] M. Kandaz, A.R. Özkaya, O. Bekaroğlu, Monatsh. Chem. 132 (2001) 1013.
[45] W.A. Nevin, W. Liu, S. Greenberg, M.R. Hempstead, S.M. Marcuccio, M. Melnik, C.C. Leznoff, A.B.P. Lever, Inorg. Chem. 26 (1987) 891.
[46] V. Manivannan, W.A. Nevin, C.C. Leznoff, A.B.P. Lever, J. Coord. Chem. 19 (1988) 139.
[47] C.C. Leznoff, H. Lam, W.A. Nevin, N. Kobayashi, P. Janda, A.B.P. Lever, Angew. Chem. Int. Ed. 26 (1987) 1021.
[48] N. Kobayashi, H. Lam, W.A. Nevin, P. Janda, C.C. Leznoff, A.B.P. Lever, Inorg. Chem. 29 (1990) 3415.
[49] C.C. Leznoff, H. Lam, S.M. Marcuccio, W.A. Nevin, P. Janda, N. Kobayashi, A.B.P. Lever, J. Chem. Soc. Chem. Commun. (1987) 699.
[50] D.W. DeWulf, J.K. Lelend, B.L. Wheeler, A.J. Bard, D.A. Batzel, D.R. Dininny, M.E. Kenney, Inorg. Chem. 26 (1987) 266.



Scheme 1.

P–N–P–N cycle was formed, whereas the pyridinium salt of 1,3,4-triaza-2λ^5-phospholane with a five-membered P–N–N–C–S cycle was prepared in the absence of a HCl acceptor.

The reaction of **9** with urea leads to the formation of the cyclic ammonium salt of 4,6-dioxo-2-sulfido-2-thioxo-1,3,5-triaza-2λ^5-phosphinane [7]. The reaction of **9** with *N*,*N*′-diphenylthiourea, $(PhNH)_2CS$ (**8**), yields, in the presence of triethylamine and depending on the reaction temperature, two different heterocyclic compounds containing P–N–C–N and P–N–P–N cycles [8] (see Scheme 1).

The reaction of $pyPS_2Cl$ (**9**) with $(PhNH)_2CO$ (**2**), as well as reactions of phosphorus pentasulfide (**1**) with **2** and **8** had not been studied as yet. Therefore they became the subject of our investigation in this work.

2. Results and discussion

2.1. Reaction of P_4S_{10} (*1*) with *N,N′*-diphenylurea (*2*)

The course of the reactions between **1** and nucleophilic reagents has commonly the character of nucleophilic reduction in which, depending on the reaction conditions, a wide variety of compounds arise [11,12].

The reaction of **1** with **2** was carried out in acetonitrile and in the presence of pyridine in the molar ratio 1:4:4. A number of reaction products arose in the course of the reaction. The composition of the reaction mixture was followed by ^{31}P NMR spectroscopy. The integral rates of all resonance signals presented in the ^{31}P NMR spectrum are shown in Table 1. Compound **13**, containing unexpectedly an oxygen atom in the molecule, is probably the product of partial hydrolysis of sulfur containing precursors. Yellow needle crystals were also formed at the same time and they were assigned to the previously undescribed compound **7**.

2.2. Reaction of P_4S_{10} (*1*) with *N,N′*-diphenylthiourea (*8*)

This reaction was carried out in a similar way to that described above. Yellow crystals were formed after 15 min heating. The resonance signals, which were found in the ^{31}P NMR spectrum of the reaction mixture, are mentioned in Table 1. After cooling the reaction mixture, the solvent was partially evaporated in vacuum at ambient temperature, the solid was filtered off and rinsed with acetonitrile. The ^{31}P NMR spectrum of this solid, dissolved in acetonitrile, proved that the solution contained only compound **4**.

2.3. Reaction of $pyPS_2Cl$ (*9*) with *N,N′*-diphenylurea (*2*)

The reaction between **9** and **2** (1:1) was carried out in acetonitrile solution in the presence of pyridine as a HCl acceptor. At first, the reaction mixture was refluxed for

Table 1
Identified ^{31}P NMR signals in the studied reaction mixtures

Compound	δ (ppm)	Reaction partners			
		$P_4S_{10} + (PhNH)_2CO$		$P_4S_{10} + (PhNH)_2CS$	$pyPS_2Cl + (PhNH)_2CO$
		Reflux (2 h) (%)	After standing 3 months (20 °C) (%)	Reflux (20 min) (%)	Reflux (1.5 h) (%)
3	88.1	89	83		9
4	109.1	4	1	94	4
5 [16]	120.3	7	1		1
6 [16]	130.4		7	4	
10 [18]	84.0				25
12 [17]	87.4		1	2	
13 [16]	32.1		7		

1.5 h. Greenish crystals precipitated in the course of the reaction and the ^{31}P NMR chemical shift (88.1 ppm) corresponds to compound **3**. The composition of the remaining reaction mixture is given in Table 1.

Further standing of the filtrate led to the crystallization of another brown solid. Its resonance signal at 120.3 ppm was found in the ^{31}P NMR spectrum, and corresponds to the resonance of compound **5**. The final solid, which was isolated from the filtrate after several weeks of standing, was elemental sulfur, as identified by MS spectrometry.

2.4. Identification and properties of the prepared compounds

2.4.1. Identification of *3*

Two independent spin systems in the regions $\delta = 7.8$–8.5 ppm and $\delta = 8.7$–9.6 ppm, and not linked together by cross peaks, were identified in the 2D ^{1}H–^{1}H COSY NMR spectrum of **3** (Fig. 1). These regions are sufficiently apart from each other to enable their resolution without difficulties. The integral rate of the first spin system is approximately twice the integral rate of the second one, which is in agreement with integral values in the 1D ^{1}H NMR spectrum. From this and from comparison with the ^{1}H NMR spectra of **9** and **2** it follows that the molecule of **3** contains one aromatic group coming from **9** (pyridine) [19] and two aromatic phenyl groups coming from **2** [20].

The molecular peak at $m/z = 306$ in the MS spectrum of **3** corresponds to the mass of the anionic part (exact mass 304.997219). The thermal behavior of **3** was followed by thermal analysis. There are two minima on the DTA curve. The first endothermic minimum at 174 °C corresponds to the melting point of **3**, and the second one at 184 °C belongs to the beginning of the thermal decomposition, accompanied by a continuous mass loss. In the region 310–400 °C, a few undistinguished minima were observed, which can be ascribed to gradual decomposition of the compound. At 424 °C, the weight loss reached 72.9%, which corresponds to the formation of $POSN_2$ (theoretical weight loss 72.2%). At 632 °C further weight loss of up to 88.0% of the starting mass of the sample was observed. This stage of decomposition corresponds to the expected end-product of the composition PN (theoretical weight loss 88.3%). X-ray diffraction analysis of **3** confirmed that this substance is the pyridinium salt of 1,3-diphenyl-2-sulfido-2-thioxo-1,3-diaza-2λ^5-phosphetidine.

2.4.2. Identification of *4*

The formation of compound **4** was detected in all the studied reaction systems (**1** with **2** or **8**; **9** with **2**). The resonance signal of **4** was found at $\delta = 109.1$ ppm (s). This chemical shift is characteristic for phosphorus (V) compounds containing the PS_2 group. The substance **4** was also studied by ^{1}H NMR spectroscopy. Resonance signals in the aromatic region ($\delta = 7.18$–7.59 ppm) belong to a phenyl group, and signals in the region 7.99–8.68 ppm are characteristic of the pyridinium cation [19]. Another resonance signal at $\delta = 8.47$ ppm in the ^{1}H NMR spectrum can be assigned to the acid hydrogen bonded to pyridine. MS spectrometry of **4** identified the molecular peak at $m/z = 436$. This mass corresponds to a compound of the composition $C_{12}H_{10}N_2P_2S_6$ (exact mass 435.864356). Therefore it was concluded that substance **4** is the pyridi-

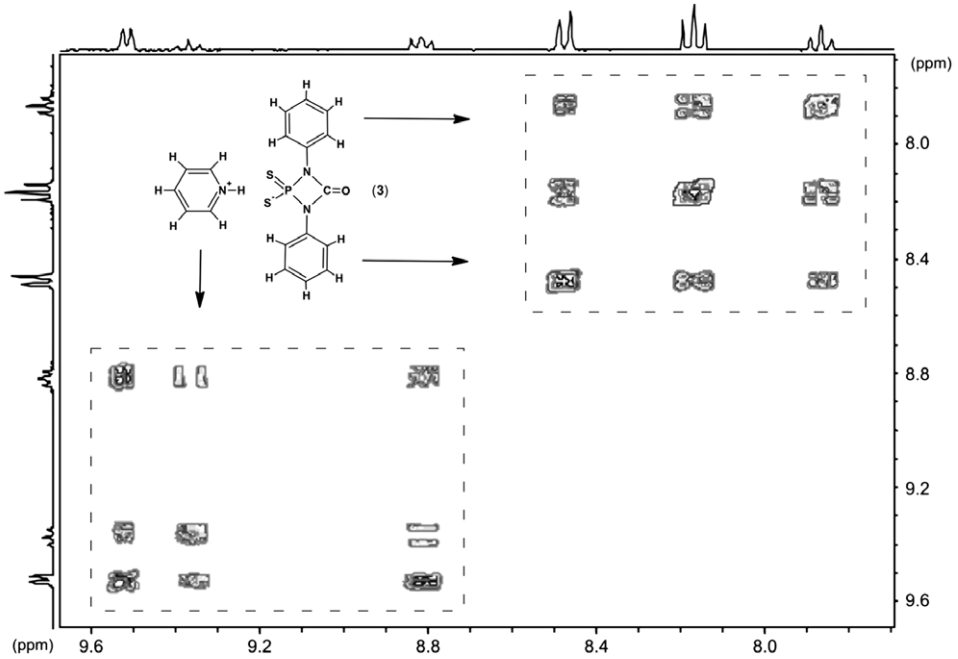
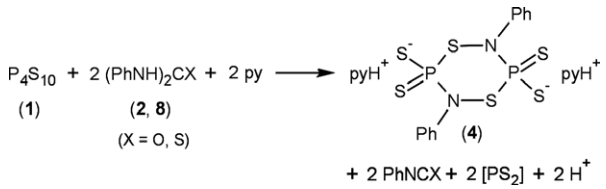


Fig. 1. 2D ^{1}H–^{1}H COSY NMR spectrum of compound **3**.

nium salt of 1,4-diphenyl-2,5-disulfido-2,5-dithioxo-1,4-dithiadiaza-2λ^5, 5λ^5-diphosphinane. Its possible formation is shown in the following equations:



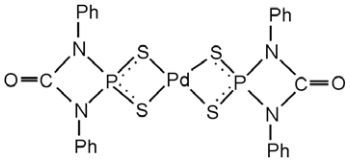
(1)

$$2\ \underset{(9)}{\mathrm{pyPS_2Cl}} + 2\ \underset{(2)}{(\mathrm{PhNH})_2\mathrm{CO}} + 1/4\ \mathrm{S_8} \rightarrow (4) + 2\ \mathrm{PhNCO} + 2\ \mathrm{H^+} + 2\ \mathrm{Cl^-} \quad (2)$$

$$2\ \underset{(10)}{[\mathrm{pyH}][\mathrm{PS_2Cl_2}]} + 2\ \underset{(2)}{(\mathrm{PhNH})_2\mathrm{CO}} + 1/4\ \mathrm{S_8} \rightarrow (4) + 2\ \mathrm{PhNCO} + 4\ \mathrm{H^+} + 4\ \mathrm{Cl^-} \quad (3)$$

2.4.3. The complex properties of 3

The presence of two sulfur atoms in the PS_2 group of **3** indicates that this substance can have an affinity to metal ions such as Ni [21], Pd [22] and Pt [23]. Therefore we allowed compound **3** to react with $Pd(CH_3COO)_2$ with the aim of preparing the Pd complex (**11**). The reaction was carried out in acetonitrile, with the starting compounds in a molar ratio of 2:1. Immediately, a brown precipitate appeared. Mass spectrometry gave a molecular peak at *m*/*z* 717, which corresponds to the mass of the expected compound $C_{26}H_{20}N_4O_2P_2PdS_4$ (exact mass 715.897915).



Compound **11** is sparingly soluble in common solvents such as CH_3CN, CH_2Cl_2 or pyridine, and is insoluble in CH_3OH. It is poorly soluble in dimethylformamide, in which it decomposes within a few hours.

The thermal behavior of **11** was followed by thermal analysis. The compound did not melt and only slow decomposition was observed with increasing temperature. The first endothermic effect occurs on DTA curve at 140.9 °C and corresponds to the beginning of the decomposition of **11**. The sample was further heated up to 1000 °C. The weight loss was 82.0% at the temperature 999 °C, which corresponds to the formation of PdO (theoretical weight loss 82.9%).

2.4.4. The formation of [pyH][PS$_2$Cl$_2$] (10)

The formation of pyridinium dichlorodithiophosphate, $[pyH][PS_2Cl_2]$ (**10**) in the reaction between **2** and **9**, can be explained as proceeding via two routes. The first one is that HCl, evolved in the first step of the substitution reaction between **2** and **9**, reacts with compound **9** with the formation of $[pyH][PS_2Cl_2]$ (**10**) [18]. The second route is based on the assumed reaction between the heterocyclic compound **3** and evolved HCl. This mechanism was proved by carrying out the direct reaction of **3** with HCl, and $(PhNH)_2CO$ (**2**) was found in the reaction mixture. The presence of both compounds was confirmed by ^{1}H NMR (**2**) [20] and ^{31}P NMR (**10**) spectroscopy.

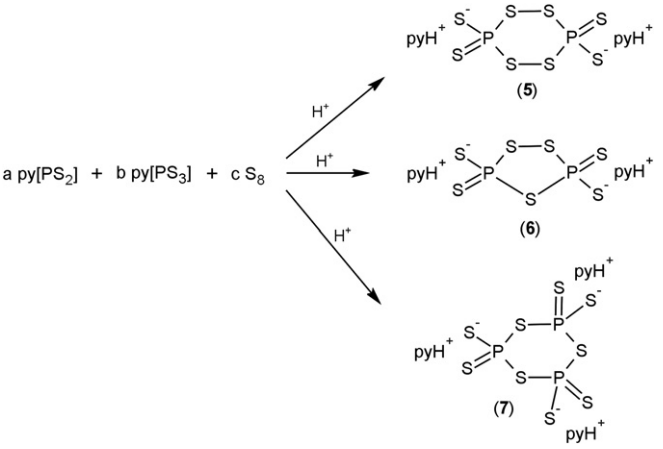
2.4.5. The formation of cyclic thiophosphates 5, 6 and 7

Cyclic phoshpates have been known for a long time. A mixture of the anions $[P_2S_8]^{2-}$ (present in **5**) and $[P_3S_9]^{3-}$ (in **7**) is formed as a result of disproportionation $[P_2S_7]^{2-}$ (in **6**) [16]. The anion $[P_3S_9]^{3-}$ is known as $[NH_4]_3[P_3S_9]$ [24] and was obtained in the reaction of P_4S_{10} and P_4S_9 in liquid ammonia below −33 °C. It was also prepared, together with $[P_2S_7]^{2-}$ and $[P_2S_8]^{2-}$, as the triethylammonium salts in the reaction mixture of triethylamine, white phosphorus and sulfur [16]. We also prepared $[pyH]_3[P_3S_9]$ (**7**) in the reaction of **9** with benzamide in a yield 67% (with respect to **1**). The anion of compound **5** was identified (as a salt with the cation $[py_2H]^+$) amongst the products of the reaction of **1** and pyridine [25], and also in the reaction mixture of **9** with 4-*iso*-propylthiosemicarbazide [10].

The formation of bis(pyridinium)-bis(μ-disulfido)-tetrathio-*cyclo*-diphosphate, $[pyH]_2[P_2S_8]$ (**5**), bis(pyridinium)-μ-disulfido-pentathio-*cyclo*-diphosphate, $[pyH]_2[P_2S_7]$ (**6**) and tris(pyridinium)-nonathio-*cyclo*-triphosphate, $[pyH]_3[P_3S_9]$ (**7**) can be explained in our reaction systems on the basis of the formation of $[PS_2]$ and $[PS_3]$ units and S_8 (Scheme 2).

2.4.6. Crystal structures of 3 and 7

Crystals of compound **3** are monoclinic and were grown from acetonitrile solution. The molecular structure (Fig. 2) has certain common features. The structure is formed by a



Scheme 2.

four-membered approximately planar heterocycle containing P–N–C–N atoms. Each of the two *N*-phenyl ring planes is tilted with respect to the plane of the P–N–C–N heterocycle [6.83(5)° or 3.34(6)°]. The plane formed by the S–P–S bonds is oriented almost perpendicularly (88.94(6)°) to the plane of the heterocycle. The values of these angles are in agreement with the expected sp^3 hybridization of the P-atom. The π-electron density of the proposed P═S bond is delocalized over the exocyclic PS_2 group, which was confirmed by the almost equal P–S bond lengths (1.94–1.96 Å). These values are comparable to those in similar substances, $[pyH][PS_2(NPh)_2CS]$ and $[pyH][PS_2NPh]_2$ [8]. Compound **3** can be considered as an almost ionic substance. In fact, the pyridinium cation is bonded to the S atoms of the PS_2 group (H3A···S1 and H3A···S2) through a van der Waals interaction; the distances between the atoms are 2.671(5) and 2.580(4) Å. This type of interaction can also be observed in similar substances, such as $[pyH][PS_2(NPh)_2CS]$ (2.42(4) Å) and $[pyH][PS_2NPh]_2$ (3,3145(3) Å) [8]. Compound **3** does not contain any other relevant H-bridges. A comparison of the corresponding bond lengths with the literature data [8] shows that there is no significant difference either in the four-membered ring, or in the exocyclic bonds. Only isolated molecules of **3** can be found in the crystal structure. Selected crystallographic data are given in Table 2.

The structure and composition of solid **7** were determined by X-ray diffraction to be tris(pyridinium)-nonathio-*cyclo*-triphosphate, $[pyH]_3[P_3S_9]$, and the structure is shown in Fig. 3. The molecular structure of the $[P_3S_9]^{3-}$ anion was previously determined by Falius et al. Compound $[pyH]_3[P_3S_9]$ was prepared in the reaction between elemental phosphorus and alkylammonium polysulfides [16]. The anion is packed together with triethylammonium cations, and the P_3S_3 ring adopts a nearly perfect chair conformation. In our compound **7**, the six-membered ring takes on a skew-boat arrangement. The bond distances and angles are comparable between $[Et_3NH]_3[P_3S_9]$ and **7**. The intracyclic P–S bond lengths range within 2.122(1) and 2.147(1) Å, while the terminal P═S bonds are shorter, reflecting their increased π-character [1.966(1)–1.986(1) Å].

Table 2
Selected crystallographic data of compounds **3** and **7**

Compound	**3**	**7**
Chemical formula	$C_{18}H_{16}N_3OPS_2$	$C_{20}H_{24}ClN_4P_3S_9$
Formula weight	385.43	737.33
Crystal size (mm)	0.20 × 0.20 × 0.30	0.30 × 0.30 × 0.25
T (K)	120	120
Crystal system	monoclinic	orthorhombic
Space group	$P2(1)/c$	$Pcca$
Unit cell dimensions		
a (Å)	13.634(3)	17.897(3)
b (Å)	10.205(2)	10.399(2)
c (Å)	13.323(3)	16.919(5)
β (°)	95.22(3)	90
Volume (Å^3)	1846.0(6)	3148.8(13)
Z	4	4
ρ_{calc} (g cm^{-3})	1.387	1.555
λ (Å)	0.71069	0.71069
μ (mm^{-1})	0.386	0.892
R_1	0.0373	0.0427
wR_2	0.0937	0.1220

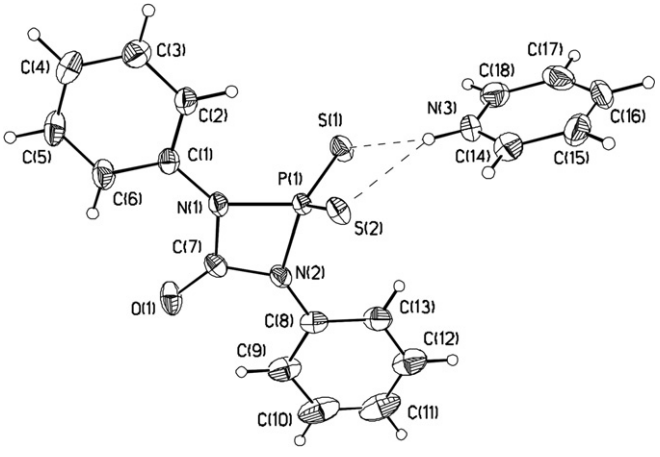


Fig. 2. The molecular structure of **3**.

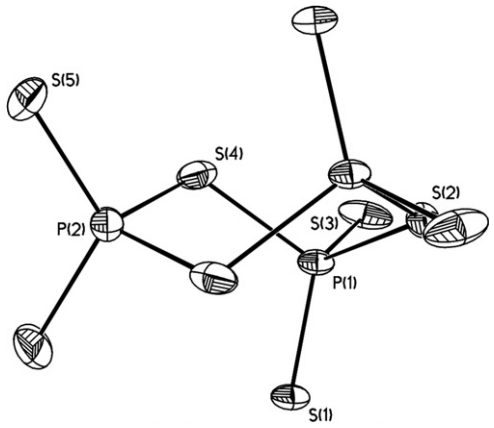


Fig. 3. The molecular structure of **7**.

3. Experimental

3.1. Physical measurements

^{1}H, ^{13}C and ^{31}P NMR spectra were recorded on 300 and 500 MHz Bruker DRX Avance NMR spectrometers. Chemical shifts are given in ppm (δ scale) relative to tetramethylsilane (for ^{1}H and ^{13}C nuclei), or 85% H_3PO_4 for ^{31}P. All samples were measured at 303 K in dimethylsulfoxide or acetonitrile in a coaxial cuvette system (an inner 4 mm cuvette with the sample placed in a 5 mm cuvette containing a small amount of D_2O). Compound **7** (dissolved in D_2O) was measured directly in the 5 mm cuvette. ^{13}C NMR spectra were measured with ^{1}H decoupling. The

2D ^1H–^1H COSY NMR spectrum was measured with two 90° pulses.

Mass spectra were measured using a multifunctional quadrupole spectrometer TRIO 1000 Series II, Finnigan MAT, Fisons Instruments. The ionization energy was 70 eV. The sample was inserted into the spectrometer by the Direct Insert Probe.

FT-IR spectra were measured in Nujol using an Equinox 55/S/NIR FT-IR Bruker spectrometer. Vibration frequencies were compared with the literature data [26,27].

Elemental analyses (C, H, N, S) were performed on a Fisons Instruments EA-1108 elemental analyzer. Phosphorus was determined gravimetrically as chinolinium molybdatophosphate.

Thermal analysis up to 1000 °C was carried out using a Derivatograph C, MOM, in a ceramic pot in static air atmosphere. The heating rate was 5 K min^{-1}.

Crystal structure determinations were performed using a four-circle diffractometer KUMA KM-4 with Mo Kα radiation ($\lambda = 0.71069$ Å), and the software packages Xcalibur CCD system for the data collection/reduction [28] and SHELXTL for the structure solution, refinement and drawing preparation [29]. The structures were solved by direct methods. Non-hydrogen atoms were refined anisotropically while hydrogen atoms were inserted in calculated positions and isotropically refined assuming a ''ride-on'' model. Selected crystallographic data of compounds **3** and **7** are shown in Table 2.

3.2. Procedures

All reactions and subsequent manipulations were carried out in an atmosphere of dry nitrogen. $pyPS_2Cl$ (**9**) was prepared according to a known procedure [30]. P_4S_{10} (**1**) was purchased from Merck, diphenylurea (**2**) and diphenylthiourea (**8**) (Fluka) and $Pd(CH_3COO)_2$ (Sigma–Aldrich) were used without further purification. Acetonitrile and pyridine were purified according to known procedures [31] and distilled before use.

3.2.1. Synthesis of the pyridinium salt of 1,3-diphenyl-2-sulfido-2-thioxo-1,3-diaza-2λ^5-phosphetidine $[pyH][PS_2(NPh)_2CO]$ (**3**)

2.786 g (13.29 mmol) of **9** and 2.800 g (13.19 mmol) of **2** in 40 ml CH_3CN were placed into a Schlenk vessel and 1.026 g (12.97 mmol) of pyridine was added to the suspension. The reaction mixture was refluxed for 1.5 h. Compound **2** gradually dissolved and the reaction mixture turned yellow. After cooling, the first portion of greenish crystals appeared. The supernatant solution was partially evaporated and greenish crystals of **3** were filtered off. The yield after recrystallization from acetonitrile was 73% (with respect to **9**).

Anal. Calc. for $C_{18}H_{16}N_3OPS_2$: N, 10.90; P, 8.04; S, 16.64. Found: N, 11.17; P, 7.91; S, 16.05%. M.p. 174.2 °C. IR (Nujol): $\nu(pyH^+)$: 1634 (m), 1611 (sh), 1525 (m), 1496 (vs); $\nu_{CH}(pyH^+)$: 3196 (vw), 3125 (w), 3082 (m), 3060 (m); $\delta(C_{arom}–H)$: 1283 (sh), 1265 (sh), 1195 (m), 1168 (w), 1103 (w), 1058 (vw), 1047 (vw), 1023 (w), 1003 (m), 987 (w), 893 (w); PS: 756 (vs), 739 (vs), 693 (vs), 674 (s), 646 (vs).

3.2.2. Synthesis of the pyridinium salt of 1,4-diphenyl-2,5-disulfido-2,5-dithioxo-1,4-dithiadiaza-2λ^5,5λ^5-diphosphinane $[pyH]_2[PS_2(SNPh)]_2$ (**4**)

A suspension of **1** (0.226 g, 0.51 mmol) and 0.458 g (2.01 mmol) of **8** in 25 ml of acetonitrile and 0.33 ml pyridine (4.1 mmol) was refluxed for 20 min. Yellow crystals of compound **4** formed after 15 min heating. The solvent was partially evaporated after cooling of the reaction mixture. The crystals that formed were filtered off and rinsed with acetonitrile. Compound **4** was obtained in 48% yield (with respect to **1**).

Anal. Calc. for $C_{22}H_{22}N_4P_2S_6$: N, 9.39; P, 10.38; S, 32.24. Found: N, 10.44; P, 11.78; S, 32.03%. M.p. 169.8–172.5 °C. IR (Nujol): $\nu_{CH}(pyH^+)$: 3121 (vw), 3085 (sh), 3051 (vw); $\nu(pyH^+)$: 1629 (w), 1606 (sh), 1595 (m), 1537 (sh), 1481 (s); 1530 (sh), 1496 (sh), 1328 (w); $\delta(C_{arom}–H)$: 1279 (m), 1261 (w), 1237 (w), 1195 (w), 1159 (w), 944 (sh), 937 (sh), 900 (m), 876 (m), 865 (sh); PS: 755 (w), 743 (sh), 740 (w), 696 (m), 670 (sh), 666 (sh), 661 (s), 606 (w), 540 (s).

3.2.3. Synthesis of tris(pyridinium)-nonathio-cyclo-triphosphate $[pyH]_3[P_3S_9]$ (**7**)

A solution of **1** (0.313 g, 0.70 mmol) and **2** (0.610 g, 2.87 mmol) in 15 ml of acetonitrile and 0.46 ml (5.64 mmol) of pyridine was refluxed for 2 h. Compound **2** dissolved gradually during heating and the reaction mixture turned yellow. The reaction mixture was kept at ambient temperature for 3 months and yellow needle crystals of **7**, soluble only in H_2O, were formed in 15% yield (with respect to **1**).

Anal. Calc. for $C_{15}H_{18}N_3P_3S_9$: C, 28.97; H, 2.92; N, 6.76; P, 14.94; S, 46.41. Found: C, 27.62; H, 2.81; N, 6.80; P, 14.92; S, 46.38%. M.p. 138.7–139.1 °C. IR (Nujol): δ(C–H): 3041 (sh), 3062 (sh); $\nu(pyH^+)$: 1628 (m), 1610 (m), 1540 (m), 1485 (sh); 1517 (s), 1476 (s), 1377 (m), 750 (s); ν(PS): 667 (s), 676 (s), 609 (w), 649 (sh); ν(P–S–P): 485 (s), 496 (s), 549 (s), 559 (s).

3.2.4. Synthesis of bis(2,2-disulfido-4-oxo-1,3-diphenyl-1,3-diaza-2λ^5-phosphetidino)palladium(II) $[Pd(Ph_2N_2COPS_2)_2]$ (**11**)

0.341 g (0.88 mmol) of **3** and 0.099 g (0.44 mmol) of $Pd(CH_3COO)_2$ was stirred in acetonitrile at ambient temperature for 12 h. The reaction product (**11**), a brown powder, was filtered off. Yield: 57% (with respect to **3**).

Anal. Calc. for $C_{26}H_{20}N_4O_2P_2PdS_4$: C, 43.55; H, 2.81; N, 7.81; P, 8.64; S, 17.89. Found: C, 42.66; H, 2.66; N, 7.84; P, 8.63; S, 15.28%. Temperature 140.9 °C (dec.). IR (Nujol): $\nu(C_{arom}–H)$: 1593 (s); $\delta(C_{arom}–H)$: 1548 (m), 1486 (s), 1312 (s), 1287 (sh), 1112 (m), 1006 (s), 992 (sh), 898

(w);PS: 752 (m), 719 (m), 692 (w), 689 (m), 680 (sh), 651 (m), 637 (w), 608 (w).

4. Conclusion

New heterocyclic compounds with exocyclic PS_2 and P–N atoms in the cycle (pyridinium salts of 1,3-diphenyl-2-sulfido-2-thioxo-1,3-diaza-2λ^5-phosphetidine, [pyH][$PS_2(NPh)_2CO$] (**3**) and 1,4-diphenyl-2,5-disulfido-2,5-dithioxo-1,4-dithiadiaza-2λ^5,5λ^5-diphosphinane, $[pyH]_2[PS_2(SNPh)]_2$ (**4**)) were prepared from two P–S precursors – P_4S_{10} (**1**) and $pyPS_2Cl$ (**9**). In the reactions cyclic thiophosphates were formed. We proved the formation of bis(μ-disulfido)-tetrathio-*cyclo*-diphosphate, $[pyH]_2[P_2S_8]$ (**5**), bis(pyridinium)-μ-disulfido-pentathio-*cyclo*-diphosphate, $[pyH]_2[P_2S_7]$ (**6**) and tris(pyridinium)-nonathio-*cyclo*-triphosphate, $[pyH]_3[P_3S_9]$ (**7**). A Pd-complex, bis(2,2-disulfido-4-oxo-1,3-diphenyl-1,3-dia- za-2λ^5-phosphetidino)palladium(II), [$Pd(Ph_2N_2COPS_2)_2$] (**11**) was also prepared.

Acknowledgements

We thank our colleagues from the Faculty of Science, Palacky University, Olomouc, Czech Republic for carrying out the elemental analyses.

Appendix A. Supplementary material

CCDC 638838 and 638971 contain the supplementary crystallographic data for **3** and **7**. These data can be obtained free of charge via http://www.ccdc.cam.ac.uk/conts/retrieving.html, or from the Cambridge Crystallographic Data Centre, 12 Union Road, Cambridge CB2 1EZ, UK; fax: (+44) 1223-336-033; or e-mail: deposit@ccdc.cam.ac.uk. Supplementary data associated with this article can be found, in the online version, at doi:10.1016/j.poly.2007.05.032.

References

[1] F. Hemmelmayr, S.B. Math.-Naturw. (1905) KL. CXIV. Bd. Abt. IIb, 335.
[2] B. Aurivillius, C. Stalhandske, Acta Chem. Scand. A 29 (1975) 717.
[3] L. Andrews, G.G. Reynolds, Z. Mielke, M. McCluskey, Inorg. Chem. 29 (1990) 5222.
[4] A. Dimitrov, I. Hartwich, B. Ziemer, et al., Z. Anorg. Allg. Chem. 631 (2005) 2439.
[5] R. Ševčík, J. Příhoda, M. Nečas, Polyhedron 24 (2005) 1855.
[6] M. Janča, M. Nečas, Z. Žák, et al., Polyhedron 20 (2001) 2823.
[7] J. Neels, K.H. Jost, M. Meisel, Z. Anorg. Allg. Chem. 541 (1986) 307.
[8] V. Novoměstská, J. Marek, J. Příhoda, Polyhedron 18 (1999) 2723.
[9] J. Marek, J. Příhoda, Z. Kristallogr. 212 (1997) 399.
[10] M. Janča, The reactions of chlorodithiophosphoric acid pyridiniumbetaine with polyfunctional nucleophiles (Reakce pyridiniumbetainu kyseliny chlorodithiofosforečné s vícefunkčními nukleofily), Thesis, Masaryk University, Brno, Czech Republic, 2002.
[11] M. Meisel, Beiträge zur Chemie von Phosphorsäure- und Thiophosphorsäurebetainen, Dissertation, ZIAC der AdW der DDR, Berlin, 1986.
[12] E. Fluck, H. Binder, Z. Anorg. Allg. Chem. 359 (1968) 102.
[13] J. Příhoda, J. Marek, Z. Krist.-New Cryst. Struct. 212 (1997) 399.
[14] M. Janča, M. Nečas, J. Příhoda, Acta Crystallogr., Sect. E 58 (2002) 772.
[15] G. Ohms, J. Zessin, Z. Žák, Phosphorus Sulfur Silicon 76 (1993) 99.
[16] H. Falius, A. Schliephake, D. Schomburg, Z. Anorg. Allg. Chem. 611 (1992) 141.
[17] K. Moedritzer, L. Maier, L.C.D. Groenweghe, J. Chem. Eng. Data 7 (1962) 307.
[18] M. Meisel, Ch. Donath, Z. Anorg. Allg. Chem. 500 (1983) 73.
[19] Ch.J. Pouchert, J. Behnke, The Aldrich Library of ^{13}C and ^{1}H FT NMR Spectra, Aldrich Chemical Company, Inc., Milwaukee, 1993.
[20] S.H. Lee, H. Matsushita, B. Clapham, K.D. Janda, Tetrahedron 60 (2004) 3439.
[21] L.A. Kushch, V.V. Gritsenko, L.I. Buravov, A.G. Khomenko, G.V. Shilov, O.A. Dyachenko, V.A. Merzhanov, E.B. Yagubskii, R. Rousseau, E. Canadell, J. Mater. Chem. 5 (1995) 1633.
[22] J.P. Fackler Jr., L.D. Thompson Jr., Inorg. Chim. Acta 48 (1981) 45.
[23] F. Bigoli, P. Deplano, M.L. Mercuri, M.A. Pellinghelli, L. Pilia, G. Pintus, A. Serpe, E.F. Trogu, Inorg. Chem. 41 (2002) 5241.
[24] G.U. Wolf, M. Meisel, Z. Anorg. Allg. Chem. 494 (1982) 49.
[25] P.C. Minshall, G.M. Sheldrick, Acta Crystallogr., Sect. B 43 (1978) 1378.
[26] M. Horák, D. Papoušek, Infrared Spectroscopy and Molecular Structure (Infračervená spektra a struktura molekul), Academia, Praha, 1976.
[27] S.K. Wang, C.S.P. Sung, Macromolecules 35 (2002) 877.
[28] Oxford Diffraction Ltd., Xcalibur CCD System, CrysAlis Software System, Version 1.171, Oxford, UK, 2004.
[29] SHELXTL, Version 5.10, Bruker AXS Inc., Madison, WI, 1997.
[30] M. Meisel, H. Grunze, Z. Anorg. Allg. Chem. 360 (1968) 277.
[31] D.D. Perrin, W.L.F. Armarego, Purification of Laboratory Chemicals, Pergamon Press, Oxford, 1988.

CD_3OD and $CDCl_3$. Melting points are uncorrected and were obtained by a Kofler Heizbank Rechart type 7841 melting point apparatus.

2.2. Synthesis of [Fe(bipy)Cl4][bipy·H] (1)

2,2′-Bipyridine (0.31 g, 2 mmol) in 20 ml HCl 0.1 M was added to a solution of $FeCl_3 \cdot 6H_2O$ (0.27 g, 1 mmol) in water (15 ml). The resulting red solution was stirred at 55–60 °C for 3 h. The yellow coloured precipitated product that was obtained was recrystallized from CH_3CN. After three days, yellow prismatic crystals of **1** were isolated (yield 0.39 g, 76.3%, m.p 216 °C). IR (KBr, cm^{-1}): 3060m (υCH), 1615m, 1599s, 1583s, 1529s, 1494w, 1473m, 1456m, 1443s, 1433m, 1384w, 1367w, 1320m, 1311s, 1270m, 1248w, 1229w, 1174m, 1158m, 110w, 1102w, 1088w, 1068w, 1058w, 1020m, 1010m, 993 sh, 929m, 908w, 881m, 808w, 764s, 733m, 724m, 652m, 630m, 610m, 524w, 425w, 441w, 418m, 400w, 393w, 362w, 333w, 308s (υFe–Cl), 290s (υFe–Cl), 255s (υFe–N). *Anal.* Calc. C, 46.96; H, 3.33; N, 10.95. Found: C, 46.58; H, 3.51; N, 10.76%.

2.3. Synthesis of [Fe(dmbipy)2Cl2][FeCl4] (2)

5,5′-Dimethyl-2,2′-bipyridine (0.2 g, 1.08 mmol) in 10.8 ml HCl 0.1 M was added to a solution of $FeCl_3 \cdot 6H_2O$ (0.147 g, 0.54 mmol) in water (10 ml), and the resulting red solution was stirred at 50–55 °C for 3 h. The orange colored precipitated product that was obtained was recrystallized from H_2O:CH_3OH (1:4). After two weeks, orange prismatic crystals of $[Fe(dmbipy)_2Cl_2][FeCl_4]$ were isolated (yield 0.14 g, 74.83%, decompose <260 °C). IR (KBr, cm^{-1}): 3053w, 1599m, 1573m, 1478s, 1504m, 1447m, 1386s, 1315s, 1285w, 1253s, 1142m, 1049s, 991w, 854w, 837s, 819m, 762w, 727s, 692m, 654m, 539w, 495w, 480w, 418m, 381s (υFe–Cl), 331s (υFe–Cl), 258s (υFe–N). *Anal.* Calc. C, 41.56; H, 3.46; N, 8.08. Found: C, 41.23; H, 3.52; N, 7.91%.

2.4. Crystal structure determination and refinement

The X-ray diffraction measurements were made on a STOE IPDS-II diffractometer with graphite monochromated Mo-Kα radiation. For $[Fe(bipy)Cl_4][bipy{\cdot}H]$, **1**, a yellow prismatic crystal with dimensions of $0.50 \times 0.25 \times 0.25$ mm and for $[Fe(dmbipy)_2Cl_2][FeCl_4]$, **2**, an orange prismatic crystal with dimensions of $0.30 \times 0.25 \times 0.13$ mm were mounted on a glass fiber and used for data collection. Cell constants and an orientation matrix for data collection were obtained by least-squares refinement of the diffraction data from 4272 unique reflections for **1** and 12577 for **2**. Data were collected at a temperature of 293(2) K to a maximum 2θ value of 53.36° for **1** and 53.66° for **2** and in a series of ω scans in 1° oscillations, and were integrated using the Stoe X-AREA [14] software package. The numerical absorption coefficients, μ, for Mo-Kα radiation are 1.212 mm^{-1} for **1** and 1.524 mm^{-1} for **2**. A numerical absorption correction was applied using X-RED [15] and X-SHAPE [16] software. The data were corrected for Lorentz and Polarizing effects. The structures were solved by direct methods [17] and subsequent difference Fourier maps and then refined on F^2 by a full-matrix least-squares procedure using anisotropic displacement parameters [18]. All the hydrogen atoms were located in a difference Fourier map and then refined isotropically. Subsequent refinement then converged with R factors and parameter errors significantly better than for all attempts to model the solvent disorder. Atomic factors are from International Tables for X-ray Crystallography [19]. All refinements were performed using the X-STEP32 crystallographic software package [20]. A summary of the crystal data, experimental details and refinement results is given in Table 1.

3. Results and discussion

3.1. Synthesis of [Fe(bipy)Cl4][bipy·H] (1) and [Fe(dmbipy)2Cl2][FeCl4] (2)

Compound **1** was obtained from the reaction of 1 equiv of $FeCl_3 \cdot 6H_2O$ with 2 equiv of 2,2′-bipyridine in a 0.1 M

Table 1
Crystallographic and structure refinement data for complexes **1** and **2**

	Complex **1**	Complex **2**
Formula	$C_{20}H_{17}Cl_4FeN_4$	$C_{24}H_{24}Cl_6Fe_2N_4$
Formula weight	511.03	692.87
Temperature (K)	293(2)	293(2)
Wavelength, λ (Å)	0.71073	0.71073
Crystal system	orthorhombic	triclinic
Space group	$Pna2_1$	$P\bar{1}$
Crystal size (mm)	$0.50 \times 0.25 \times 0.25$	$0.30 \times 0.25 \times 0.13$
a (Å)	15.938(2)	8.6072(13)
b (Å)	9.3068(15)	18.008(3)
c (Å)	14.513(3)	20.311(3)
α (°)	90	103.652(13)
β (°)	90	95.421(12)
γ (°)	90	98.724(13)
Volume ($Å^3$)	2152.7(6)	2996.0(8)
Z	4	4
$D_{calc.}$ (g cm^{-1})	1.577	1.536
θ Ranges for data collection	2.53–26.68	1.36–26.83
$F(000)$	1036	1400
Absorption coefficient	1.212	1.524
Index ranges	$-20 \leqslant h \leqslant 20$, $-10 \leqslant k \leqslant 11$, $-15 \leqslant l \leqslant 18$	$-10 \leqslant h \leqslant 9$, $-21 \leqslant k \leqslant 22$, $25 \leqslant l \leqslant 25$
Data collected	8794	27,011
Unique data (R_{int})	4272 (0.0425)	12,577 (0.0326)
Parameters, restrains	267, 1	649, 0
Final R_1, wR_2^a (Observed data)	0.0406, 0.1035	0.0634, 0.1794
Final R_1, wR_2^a (All data)	0.0414, 0.1041	0.1143, 0.2125
Goodness of fit on F^2 (S)	1.141	1.056
Extinction coefficient	0.0019(9)	0
Largest difference peak and hole (e $Å^3$)	0.430, −0.689	1.738, −1.256

[a] $R_1 = \Sigma||F_o| - |F_c||/\Sigma|F_o|, wR_2 = [\Sigma(w(F_o^2 - F_c^2)_2)/\Sigma w(F_o^2)^2]^{1/2}$.

aqueous solution of HCl at around 55 °C for 3 h, with 76% yield, Eq. (1):

$$FeCl_3 \cdot 6H_2O + 2bipy \xrightarrow[H_2O,\ HCl\ 0.1\ M]{(55\text{–}60)\ ^\circ C,\ 3\ h} [Fe(bipy)Cl_4][bipy \cdot H] \quad (1)$$

Coordination of iron(II) with 2,2′-bipyridine ligands, L, generally leads to the highly stable tris-bipy complex and to a lesser extent to $[FeL_2X_2]$, $X = CN^-$, SCN^- and Cl^- [3]. However, the presence of Fe(III) and HCl in the solution caused the formation of complex **1**. Almost the same reaction conditions as for the formation of complex **1** was employed with methanol as the solvent and with the absence of HCl, and the result was the formation of $[Fe_2L_2Cl_4]$, in which two chlorides are terminal and two are bridged to make a bimetallic iron complex [4]. Here, it seems that the presence of an aqueous HCl solution is a driving force for the formation of the bipy complex in its monomeric form with only one bipy coordinated to the iron (in spite of that stoichiometry of the metal to ligand ratio is 1:2). Note, the formation of $[Fe^{III}(bipy)_2Cl_2]$-$[Fe^{III}Cl_4]$ has even been reported with a stoichiometric amount of $FeCl_3$ and bipy in the absence of HCl [21]. Treatment of $FeCl_3 \cdot 6H_2O$ with 5,5′-dimethyl-2,2′-bipyridine, Me_2L, under exactly the same reaction conditions to those for complex **1**, produces complex **2** in 74.83% yield, Eq. (2):

$$2FeCl_3 \cdot 6H_2O + 4dmbipy \xrightarrow[H_2O,\ HCl\ 0.1\ M]{(55\text{–}60)\ ^\circ C,\ 3\ h} [Fe(dmbipy)_2Cl_2][FeCl_4] + 2dmbipy \cdot HCl \quad (2)$$

To our surprise, the formation yields of complexes **1** and **2** are similar and Eq. (2) illustrates that a slight increase in the basic ability of Me_2L compared to that of L results in the formation of the $[Fe(Me_2L)_2Cl_2]^+$ complex. Complexes **1** and **2** are stable in the solid state. They dissolve in basic solvents such as alcohol, H_2O and DMSO. However, complex **1** readily gives a ligand substitution reaction in donor solvents such as water and DMSO, whereas complex **2** is fairly stable in these solvents.

3.2. Spectroscopic characterizations of *[Fe(bipy)Cl4][bipy·H]* (*1*) and *[Fe(dmbipy)2Cl2][FeCl4]* (*2*)

IR spectra of iron bipyridine complexes have been extensively studied in the literature and their vibrations are well established [22–25]. They contain several bands in the regions 1400–1600 and 700–900 cm^{-1}, which are related to the ring modes [υ(C–C) and υ(C–N)] and the ring deformation vibrations, respectively [25]. For instance, the bands observed in the IR spectrum of the free bpy ligand at 1414, 1452, 1456 and 1578 cm^{-1} are shifted to higher frequencies upon coordination and are observed at 1433, 1456, 1583 and 1599 cm^{-1} in the spectrum of **1**. The peaks connected with the ring deformation of the aromatic N-donor heterocycles are observed in the IR spectra of all the complexes at ca. 630, 724, 764, 808 and 881 cm^{-1} [26]. The bands observed near 3060 cm^{-1}can be assigned to $\upsilon(C_{aromatic}–H)$ vibrations. Two strong bands in complex **1** at 308 and 290 cm^{-1} were assigned to Fe–Cl and the band at 255 cm^{-1} to Fe–N, based on literature reports [24,27]. The IR spectrum of compound **2** is distinguished from that of **1**, mainly by bands at 3423 and 1386 cm^{-1}, which are due to absorptions of the methyl groups. The Fe–N stretching vibration for complex **2** is seen at 258 cm^{-1}, and that for Fe–Cl is seen at 381 cm^{-1} in the anion and at 331 cm^{-1} in the cation species. The stretching vibrations of Fe–N in complex **1** and **2** are consistent with the high spin character of these complexes. Low spin frequencies for Fe–N appear around 50–70 cm^{-1} higher frequency to that of high spin compounds containing bipy [28].

The ^1H NMR data for complexes of **1** and **2** at room temperature show a multiplet in the 7–8.7 ppm region for the bipyridine protons. Protons of the methyl groups in **2** are too broad and were placed at 10–12 ppm. Solvents such as water and methanol did not affect the ^1H NMR data of complex **2**. However, complex **1** is highly sensitive to the coordinating solvent and its spectrum readily changed in polar solvents. We were able to observe its ^1H NMR in $CDCl_3$ even though its solubility is low. Details of NMR investigation and the reactivity of this compound is under investigation. In addition, magnetic susceptibility

Table 2
Selected bond lengths (Å) and angles (°) of **1** and **2**

1			
Fe(1)–N(1)	2.189(3)	N(2)–Fe(1)–Cl(2)	167.08(9)
Fe(1)–N(2)	2.197(3)	Cl(1)–Fe(1)–Cl(2)	98.15(5)
Fe(1)–Cl(1)	2.2905(1)	N(1)–Fe(1)–Cl(4)	83.48(8)
Fe(1)–Cl(2)	2.3078(1)	N(2)–Fe(1)–Cl(4)	88.93(9)
Fe(1)–Cl(4)	2.3812(1)	Cl(1)–Fe(1)–Cl(4)	94.87(5)
Fe(1)–Cl(3)	2.4037(1)	Cl(2)–Fe(1)–Cl(4)	94.76(4)
N(1)–Fe(1)–N(2)	73.91(1)	N(1)–Fe(1)–Cl(3)	86.40(8)
N(1)–Fe(1)–Cl(1)	167.66(9)	N(2)–Fe(1)–Cl(3)	82.27(9)
N(2)–Fe(1)–Cl(1)	93.86(9)	Cl(1)–Fe(1)–Cl(3)	93.68(5)
N(1)–Fe(1)–Cl(2)	94.17(9)	Cl(2)–Fe(1)–Cl(3)	92.19(5)
		Cl(4)–Fe(1)–Cl(3)	168.11(4)
2			
Fe(1)–N(1)	2.139(5)	N(1)–Fe(1)–N(4)	160.1(2)
Fe(1)–N(4)	2.146(5)	N(1)–Fe(1)–N(2)	75.2(2)
Fe(1)–N(2)	2.193(5)	N(4)–Fe(1)–N(2)	89.3(2)
Fe(1)–N(3)	2.207(5)	N(1)–Fe(1)–N(3)	89.17(19)
Fe(1)–Cl(2)	2.2529(19)	N(1)–Fe(1)–Cl(1)	96.87(15)
Fe(1)–Cl(1)	2.2597(19)	N(4)–Fe(1)–Cl(1)	95.91(14)
Fe(2)–Cl(3)	2.183(3)	N(2)–Fe(1)–Cl(1)	166.96(16)
Fe(2)–Cl(4)	2.191(2)	N(3)–Fe(1)–Cl(1)	88.18(14)
Fe(2)–Cl(5)	2.194(3)	Cl(2)–Fe(1)–Cl(1)	100.12(8)
Fe(2)–Cl(6)	2.199(3)	Cl(3)–Fe(2)–Cl(4)	109.25(11)
N(4)–Fe(1)–N(3)	76.01(19)	Cl(3)–Fe(2)–Cl(5)	111.25(14)
N(2)–Fe(1)–N(3)	81.46(19)	Cl(4)–Fe(2)–Cl(5)	107.77(11)
N(1)–Fe(1)–Cl(2)	96.47(14)	Cl(3)–Fe(2)–Cl(6)	110.50(16)
N(4)–Fe(1)–Cl(2)	96.27(15)	Cl(4)–Fe(2)–Cl(6)	109.80(11)
N(2)–Fe(1)–Cl(2)	91.17(15)	Cl(5)–Fe(2)–Cl(6)	108.21(11)
N(3)–Fe(1)–Cl(2)	169.30(15)		

measurements for **1** and **2** by the Evans method confirms the high spin character of these complexes ($\mu_{eff} = 6$ and 6.5, respectively).

UV–Vis spectra of **1** and **2** have no spin allowed signals for d–d transitions (their color is yellow in solution) but a charge transfer band is seen around 353 nm, in accord with the high spin character of iron(III).

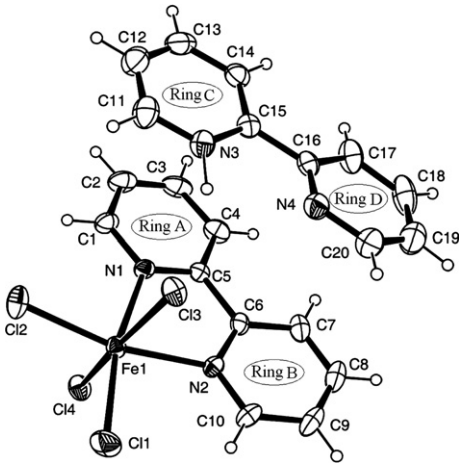


Fig. 1. The labelled diagram of [Fe(bipy)Cl_4][bipy·H] (**1**). Thermal ellipsoids are at the 30% probability level and H-atoms are shown as small spheres of arbitrary radii.

3.3. Description of the molecular structures of [Fe(bipy)Cl_4][bipy·H] (*1*) and [Fe(dmbipy)$_2Cl_2$][$FeCl_4$] (*2*)

Orange prismatic crystals of **1** were obtained by re-crystallization of micro crystals of **1** in CH_3CN. For complex **2** crystals were grown in a mixture of H_2O and CH_3OH (1:4) over two weeks. Crystallographic data for **1** and **2** are given in Table 1 and selected bond lengths and angles are presented in Table 2.

3.3.1. Structure of [Fe(bipy)Cl_4][bipy·H] (*1*)

The structure of complex **1** consists of $[Fe(bipy)Cl_4]^-$ anions and protonated bipyridine cations, Fig. 1. The iron(III) environment consists of four chloride ions and a bipyridine ligand, giving a distorted octahedral geometry. The different bond length values of the Fe(1)–Cl bonds trans to Cl and those trans to N (bipy), accompanied with the short bite angle of bipy [73.91(1)° for N(1)–Fe(1)–N(2)] are the main factors accounting for this distortion. The Fe–N (bipy) average bond distance is 2.193(3) Å and the Fe–Cl average bond distance is 2.3458(1) Å. These bond distances

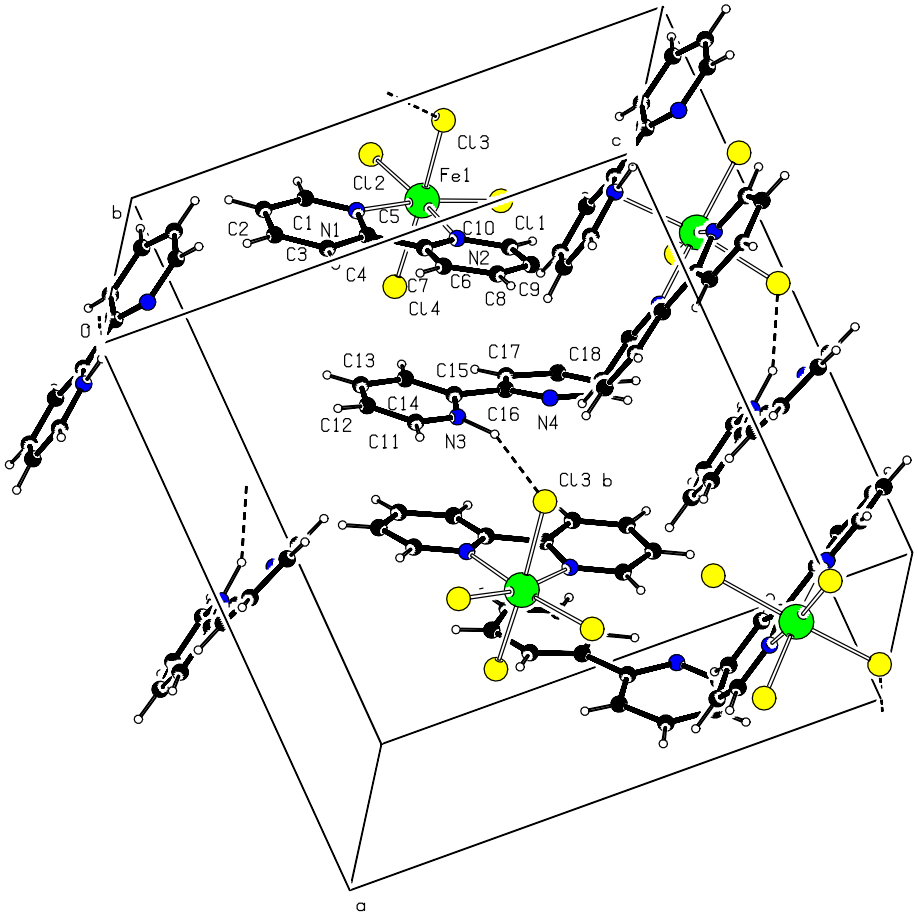


Fig. 2. Crystal packing diagram for [Fe(bipy)Cl_4][bipy·H] (**1**). Hydrogen bonds are shown as dashed lines.

are longer than those observed for similar low spin complexes [29]. The longer bond distance in complex **1** confirms that this complex is high spin with $S = 5/2$, in accord with data obtained by magnetic moment measurements. Good agreement is observed between the Fe–Cl bond distances of **1** and those reported for other chloro containing mononuclear high spin iron(III) complexes [30]. The Fe–N and Fe–Cl stretching frequencies in the infrared spectrum at 255, 308 and 290 cm^{-1} provide additional evidence for the high spin character.

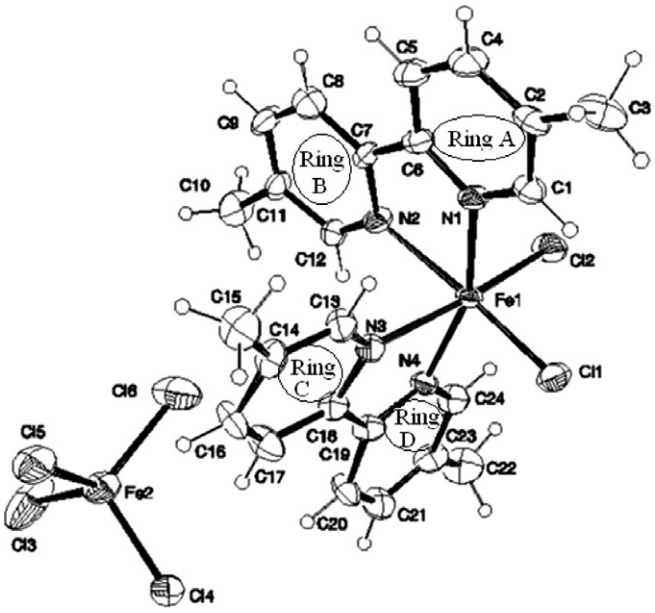


Fig. 3. The labelled diagram of cis-[Fe(dmbipy)$_2$Cl$_2$][FeCl$_4$], **2**. Thermal ellipsoids are at the 30% probability level and H-atoms are shown as small spheres of arbitrary radii.

The unit cell-packing diagram of complex **1** is presented in Fig. 2. From this packing diagram, the intermolecular bond distances and angle for N–H···Cl (H3A···Cl3 = 2.33(9), N3···Cl3 = 3.241(4) Å and N3–H3A···Cl3 = 153.47(7)°), confirms hydrogen bond formation between the counter ions. These intermolecular hydrogen bonds seem to be an effective factor in the stabilization of the crystal structure. In complex **1**, the rings A (N1/C1–C5), B (N2/C6–C10), C (N3/C11–C15) and D (N4/C16–C20) are almost planar and the dihedral angles between them are A/B = 8.90° and C/D = 11.40(3)° (A and B for pyridine rings in the coordinated bipy and C and D for bipyH$^+$ cations, Fig. 1). Further distortion of the bipyridine rings in cationic part can be related to hydrogen bondings between N–H and Cl atoms, as is shown in Fig. 2. The closest distance between the bipyridine planes in the packing is 3.7 Å and pyridine rings are not placed on the top of each other. So π–π stacking in this structure is negligible.

3.3.2. Structure of cis-[Fe^{III}(dmbipy)$_2$Cl$_2$][FeCl$_4$] (**2**)

The crystal structure of **2** is composed of cis-[Fe^{III}(dmbipy)$_2$Cl$_2$]$^+$ cations and [Fe^{III}Cl$_4$]$^-$ anions. Fig. 3 illustrates the molecular structure of complex **2** and the atom numbering scheme. The asymmetric unit of the crystal contains

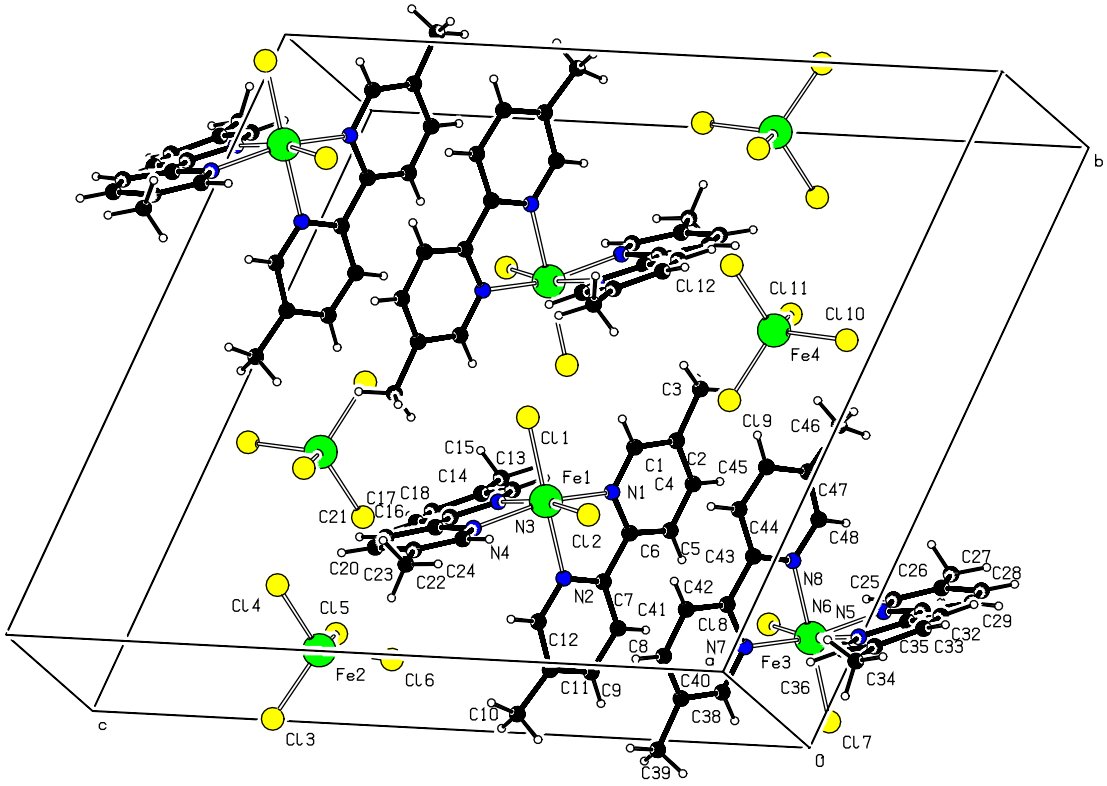


Fig. 4. Unit cell-packing diagram of cis-[Fe(dmbipy)$_2$Cl$_2$][FeCl$_4$], **2**.

two separate counter ions. Since both parts of the asymmetric unit have the same coordination behavior, here we explain only one ion pair. The Fe atom of the cation lies on a twofold axis. Two dmbipy nitrogen atoms coordinate to the iron atom in the cation with two chloride atoms coordinated to it in a cis fashion, producing a distorted octahedral geometry. The Fe atom environment in the anion is approximately tetrahedral.

The average values of the Fe–N (dmbipy) bonds in **2** is 2.171(5) Å and this distance is slightly smaller than that found in **1**, 2.193(3) Å. The average bond distance of chloride atoms for complex **2**, 2.2568(19) Å, is ≈0.1 Å smaller than that found in **1**. These values of Fe–N(dmbipy) and Fe–Cl bonds in **2** are the same as those found in the complex cis-$[Fe^{III}(bipy)_2Cl_2][FeCl_4]$ {[Fe–N(bipy) = 2.146(2) Å and Fe–Cl = 2.254(2) Å}[21]. However the Fe–N(bipy) distances in the low spin $[Fe^{III}(bipy)_2(CN)_2]$ complex are 1.972(2) and 1.973(2) Å, which are considerably smaller than the distances reported here, in accord with the high spin character of **2** [29].

The bite angle of the chelates (dmbipy) N(1)–Fe(1)–N(2) and N(3)–Fe(1)–N(4) are 75.2(2) and 76.01(19)°, close to that found for **1** (73.94° for **1**). Here also, the rings A (N1/C1–C2/C4–C6), B (N2/C7–C9/C10–C11), C (N3/C13–C14/C16–C18) and D (N4/C19–C21/C23–C24) are planar and the dihedral angles between them are A/B = 2.47(4)° and C/D = 9.82(3)°. As is shown in Fig. 4, in complex **2** there is a π–π interaction between the A–B rings in two adjacent iron complexes, whereas there is no interaction between C–D bipy rings in neighboring complexes. The close contact distance between adjacent aromatic rings is 3.41 Å. In the anion structure, $[FeCl_4]^-$, the bond angles and distances are in good agreement to that of $[FeCl_4]^-$ anions which have been found in other structures [21].

Acknowledgements

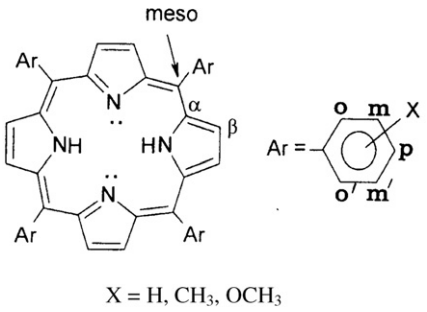
We thank the Iranian National Science Foundation and the Research and Graduate Study Councils of Shahid Beheshti University for partial financial support.

Appendix A. Supplementary material

CCDC 644042 and 644043 contain the supplementary crystallographic data for **1** and **2**. These data can be obtained free of charge via http://www.ccdc.cam.ac.uk/conts/retrieving.html, or from the Cambridge Crystallographic Data Centre, 12 Union Road, Cambridge CB2 1EZ, UK; fax: (+44) 1223 336 033; or e-mail: deposit@ccdc.cam.ac.uk. Supplementary data associated with this article can be found, in the online version, at doi:10.1016/j.poly.2007.05.050.

References

[1] A. Hazell, Polyhedron 23 (2004) 2081.
[2] M. Bakir, S. Paulson, P. Goodson, B.P. Sullivan, Inorg. Chem. 31 (1992) 1129.
[3] A.W. Cordes, B. Durham, P.N. Swepston, W.T. Pennington, S.M. Condren, R. Jensen, J.L. Walsh, J. Coord. Chem. 11 (1982) 251.
[4] S. Kasselouri, A. Garoufis, S.P. Perlepes, F. Lutz, R. Bau, S. Gourbatsis, N. Hadjiladis, Polyhedron 17 (8) (1998) 1281.
[5] K. Kalyanasundaram, Coord. Chem. Rev. 46 (1982) 159.
[6] E.C. Constable, P.J. Steel, Coord. Chem. Rev. 93 (1989) 205.
[7] P.J. Steel, Coord. Chem. Rev. 106 (1990) 227.
[8] G. Denti, S. Campagna, L. Sabatino, S. Serroni, M. Ciano, V. Balzani, Inorg. Chem. 29 (1990) 4750.
[9] J.K. Barton, Pure Appl. Chem. 61 (1989) 563.
[10] P.N. Hawker, M.V. Twigg, in: G. Wilkinson, R.D. Gillard, J.A. McCleverty (Eds.), Comprehensive Coordination Chemistry, Pergamon press, Oxford, 1987, p. 4.
[11] T.-H. Lu, H.-Y. Kao, D.I. Wu, K.C. Kong, C.H. Cheng, Acta Crystallogr. Sect. C 44 (1988) 1184.
[12] M. Nieuwenhuyzen, B. Bertram, J.F. Gallagher, J.G. Vos, Acta Crystallogr. Sect. C C54 (1998) 603.
[13] R. Claude, J.-A. Real, J. Zarembowitch, O. Kahn, L. Ouahab, D. Grandjean, K. Boukheddaden, F. Varret, A. Dworkin, Inorg. Chem. 29 (1990) 4442.
[14] R. Lescouëzec, F. Lloret, M. Julve, J. Vaissermann, M. Verdaguer, Inorg. Chem. 41 (2002) 818.
[15] Stoe & Cie, X-AREA, version 1.30: Program for the acquisition and analysis of data, Stoe & Cie GmbH, Darmatadt, Germany, 2005.
[16] Stoe & Cie, X-RED, version 1.28b: Program for data reduction and absorption correction, Stoe &Cie GmbH, Darmatadt, Germany, 2005.
[17] Stoe & Cie, X-SHAPE, version 2.05: Program for crystal optimization for numerical absorption correction, Stoe &Cie GmbH, Darmatadt, Germany, 2004.
[18] G.M. Sheldrick, SHELX97. Program for crystal structure solution and refinement, University of Göttingen, Germany, 1997.
[19] International Tables For X-ray Crystallography, vol. C, Kluwer Academic Publisher, Dordrecht, The Netherlands, 1995.
[20] Stoe & Cie, X-STEP32, Version 1.07b: Crystallographic package, Stoe &Cie GmbH, Darmstadt, Germany, 2000.
[21] N.B. Figgis, P.A. Reynolds, N. Lehner, Acta Crystallogr. Sect. B 39 (1983) 711.
[22] B. Hutchinson, J. Takemoto, K. Nakamato, J. Am. Chem. Soc. 3 (1970) 3335.
[23] J.H. Takemoto, B. Hutchinson, Inorg. Chem. 12 (3) (1973) 705.
[24] Y. Saito, J. Takemoto, B. Hutchinson, K. Nakamoto, Inorg. Chem. 11 (1972) 2003.
[25] P. Gütlich, A. Hauser, H. Spiering, Angew. Chem., Int. Ed. Engl. 33 (1994) 2024, and references cited therein.
[26] C.J. Pouchert, The Aldrich Library of Infrared Spectra, third ed., Aldrich Chemical Company, Milwaukee, WI, 1981.
[27] W.M. Reipf, B. Dockum, M.A. Weber, R.B. Frankel, Inorg. Chem. 14 (1975) 800.
[28] P. Kople, Z. Trávníček, R. Zbořil, J. Marek, Polyhedron 23 (2004) 2193.
[29] R.D. Poulsen, A. Hazell, Acta Crystallogr. Sect. E 57 (2001) m186.
[30] P. Kulkarni, S. Padhye, E. Sinn, Polyhedron 17 (1998) 2623, and references cited therein.



X = H, CH_3, OCH_3

Fig. 1. 1 *meso*-Tetraarylporphyrins (H_2t(Xp)p).

was dried over anhydrous calcium chloride for 3 days. The substituted *meso*-tetraarylporphyrins and H_2tpp were prepared by the literature methods [11], and $SbCl_3$ was obtained from Merck, and was used as received. Trifluoroacetic acid (TFA) for the diprotonation of the porphyrins was purchased from Merck and was used as received. For the quantitative analysis of the Cl ion in the $[(H_2t(Xp)p)_2Sb_2Cl_6]$ compounds, 0.05 mmol of the molecular complexes were dissolved in $CHCl_3$ (20 ml) and then decomposed by addition of double distilled water (15 ml) to the solution. $SbCl_3$ was hydrolyzed in water and the porphyrins remained in the organic solvent. Then the two phases were separated by a decanter. For the percentage of chloride ion in the molecular complex, the mercury thiocyanato method was used [12].

The NMR spectra (^1H, ^{13}C) were recorded on a Bruker 500 Ultrashield spectrometer in $CDCl_3$. To obtain good integration results (for the ^1H NMR spectra), the concentration of the molecular complexes was 0.006 M. The residual $CHCl_3$ in the conventional 99.8% atom $CDCl_3$ gives a signal at $\delta = 7.26$ ppm, which was used for calibration of the chemical shift scale. The electronic absorption spectra were recorded in chloroform solutions on an ATI UNICAM-UV\VIS Vision SOFTWARE V-2011 spectrophotometer. The cell had an optical pathlength of 1 cm. FT-IR spectra were recorded on a Magna 550 Nicolet spectrometer using KBr pellets. Far-IR spectra were recorded on a Jasco FT/IR-680 Plus spectrometer using CsI pellets in the range 200–600 cm^{-1}.

2.2. Preparation of $[(H_2tpp)_2Sb_2Cl_6]$

Equimolar quantities (0.5 mmol) of solid H_2tpp and $SbCl_3$ ground together in a pestle and mortar at ambient temperature produces the green molecular complex, $[(H_2tpp)_2Sb_2Cl_6]$, without excess of the reactants after 30 minutes. The progress of the reaction was monitored by UV–VIS spectra. The mixture had no absorption band related to the free base *meso*-tetraarylporphyrin, and the porphyrins completely change to the related molecular complex. *Anal*. Calc. for $C_{88}H_{60}N_8Sb_2Cl_6$: C, 62.7; H, 3.6; N, 6.6; Cl, 12.6. Found: C, 63.3; H, 3.7; N, 6.5; Cl, 12.3%. ^1H NMR ($CDCl_3$) δ, ppm: 0.21 (s, 2H, NH), 8.62–8.64 (d, 8H, o, o′), 8.02-8.05 (t, 8H, m, m′), 7.97–8.00 (d, 4H, p), 8.61 (s, 8H, β). IR (KBr): υ_{NH} ($\sim$3320 cm^{-1}).

2.3. Preparation of $[(H_2t(4\text{-}CH_3p)p)_2Sb_2Cl_6]$

This molecular complex is synthesized in free solvent media using the above method. *Anal*. Calc. for $C_{96}H_{76}N_8Sb_2Cl_6$: C, 64.1; H, 4.3; N, 6.2; Cl, 11.8%. Found: C, 63.8; H, 4.1; N, 6.3; Cl, 11.6%. ^1H NMR ($CDCl_3$) δ, ppm: 0.19 (s, 2H, NH), 2.8 (s, 12H, CH_3), 8.50–8.52 (d, 8H, o, o′), 7.82–7.83 (d, 8H, m, m′), 8.57 (s, 8H, β). IR (KBr): υ_{NH} ($\sim$3320 cm^{-1}).

2.4. Preparation of $[(H_2t(4\text{-}OCH_3p)p)_2Sb_2Cl_6]$

This complex is synthesized in free solvent media using the above method. *Anal*. Calc. for $C_{96}H_{76}N_8O_8Sb_2Cl_6$: C, 59.4; H, 3.9; N, 5.8; Cl, 10.9%. Found: C, 58.7; H, 4.1; N, 5.8; Cl, 11.1%. ^1H NMR ($CDCl_3$) δ, ppm: 0.57 (s, 2H, NH), 4.12 (s, 12H, OCH_3), 8.53–8.55 (d, 8H, o, o′), 7.54–7.56 (d, 8H, m, m′), 8.49 (s, 8H, β). IR (KBr): υ_{NH} ($\sim$3320 cm^{-1}).

2.5. Preparation of $[(H_2t(3\text{-}CH_3p)p)_2Sb_2Cl_6]$

Equimolar quantities (0.5 mmol) of solid H_2t(3-CH_3)pp and $SbCl_3$ ground together in a pestle and mortar at room temperature produces the green molecular complex $[(H_2t(3\text{-}CH_3p)p)_2Sb_2Cl_6]$ after 60 min. Then, hot chloroform (5 ml) was added, and the mixture was ground until complexation was complete, which was determined by the disappearance of the Soret band ($\sim$418 nm) of the porphyrin in the UV–VIS spectrum. The result of elemental analyses for the complex, which was dried in a vacuum oven for 12 h at 50 °C, was consistent with $C_{96}H_{76}N_8Sb_2Cl_6$. *Anal*. Calc. for $C_{96}H_{76}N_8Sb_2Cl_6$: C, 64.1; H, 4.3; N, 6.2; Cl, 11.8. Found: C, 63.1; H, 4.1; N, 6.4; Cl, 12.0%. ^1H NMR ($CDCl_3$) δ, ppm: 0.27 (s, 2H, NH), 2.84 (s, 12H, CH_3), 8.41–8.44 (s, 4H, o), 8.41–8.44 (d, 4H, o′), 7.89–7.92 (t, 4H, m), 7.75–7.78 (d, 4H, p), 8.64 (s, 8H, β). IR (KBr): υ_{NH} ($\sim$3320 cm^{-1}).

2.6. Preparation of $[(H_2t(3\text{-}OCH_3p)p)_2Sb_2Cl_6]$

This molecular complex was synthesized using the method used for the $[(H_2t(3\text{-}CH_3p)p)_2Sb_2Cl_6]$ complex. *Anal*. Calc. for $C_{96}H_{76}N_8O_8Sb_2Cl_6$: C, 59.4; H, 3.9; N, 5.8; Cl, 10.9. Found: C, 60.0; H, 3.8; N, 5.7; Cl, 10.7%. ^1H NMR ($CDCl_3$) δ, ppm: 0.26 (s, 2H, NH), 4.17 (s, 12H, OCH_3), 8.18 (s, 4H, o), 8.18 (d, 4H, o′), 7.90–7.93 (t, 4H, m), 7.51–7.53 (d, 4H, p), 8.64 (s, 8H, β). IR (KBr): υ_{NH} ($\sim$3320 cm^{-1}).

2.7. Preparation of $[(H_2t(2\text{-}CH_3p)p)_2Sb_2Cl_6]$

H_2t(2-CH_3p)p (0.5 mmol) and $SbCl_3$ (0.6 mmol) were ground together in a mortar for 60 min at room tempera-

ture, affording a green molecular complex. Then hot chloroform (10 ml) was added, and the mixture was ground until complexation was complete, which was determined by the disappearance of the Soret band (~418 nm) of the porphyrin in the UV–VIS spectrum. The solvent was evaporated and the excess $SbCl_3$ removed by washing the residue with dry benzene. The result of elemental analyses for the molecular complex, which was dried in a vacuum oven for 24 h at 50 °C, was consistent with $C_{96}H_{76}N_8Sb_2Cl_6$. *Anal.* Calc. for $C_{96}H_{76}N_8Sb_2Cl_6$: C, 64.1; H, 4.3; N, 6.2; Cl, 11.8. Found: C, 63.1; H, 4.1; N, 6.5; Cl, 11.5%. ^{1}H NMR ($CDCl_3$) δ, ppm: −1.02 (br, 2H, NH), 2.09 (s, 12H, CH_3), 8.33–8.38 (d, 4H, o), 7.76–7.88 (d, 4H, m), 7.76–7.88 (t, 4H, m′), 7.76–7.87 (t, 4H, p), 8.63–8.68 (s, 8H, β). IR (KBr): υ_{NH} (~3320 cm^{-1}).

2.8. Preparation of $[(H_2t(2\text{-}OCH_3p)p)_2Sb_2Cl_6]$

This complex was synthesized using the method of the $[(H_2t(2\text{-}CH_3p)p)_2Sb_2Cl_6]$ complex. *Anal.* Calc. for $C_{96}H_{76}N_8O_8Sb_2Cl_6$: C, 59.4; H, 3.9; N, 5.8; Cl, 10.9. Found: C, 58.8; H, 4.0; N, 6.0; Cl, 11.2%. ^{1}H NMR ($CDCl_3$) δ ppm: 0.30 (br, 2H, NH), 3.76 (s, 12H, OCH_3), 8.25–8.34 (d, 4H, o), 7.44-7.47 (t, 4H, m), 7.52–7.56 (t, 4H, m′), 7.79–7.92 (t, 4H, p), 8.45–8.50 (s, 8H, β). IR (KBr): υ_{NH} (~3320 cm^{-1}).

3. Results and discussion

^{1}H NMR spectra for the mixing of different equivalents of $SbCl_3$ (0.25, 0.5, 0.75, 1.0 and 2.0) with $H_2t(4\text{-}CH_3p)p$ are shown in Fig. 2. The ^{1}H NMR spectra results show that using an amount of $SbCl_3$ less than that of $H_2t(4\text{-}CH_3p)p$ leads to a superimposition of the porphyrin and the related molecular complex spectra. An excess of $SbCl_3$ to the 1:1 molar ratio causes no changes in the spectrum of the 1:1 molecular complex. Consequently, the molecular complex between $H_2t(4\text{-}CH_3p)p$ and $SbCl_3$ had a 1:1 ratio, ($SbCl_3$:$H_2t(4\text{-}CH_3p)p$). ^{1}H NMR spectra of $H_2t(4\text{-}CH_3p)p$ and the 1:1 molecular complex in $CDCl_3$ solution are shown in Fig. 2a and e, respectively. It is clearly revealed that the reaction of $SbCl_3$ with $H_2t(4\text{-}CH_3p)p$ is similar to 1:2 (donor:acceptor) complexation [1–3] and diprotonation of the *meso*-tetraarylporphyrin [10] affords an upfield shift of the β-protons (0.28 ppm) and downfield shifts of the N–H signal (2.96 ppm) and aryl ring protons, see Fig. 2. The NH and β-proton chemical shifts for the molecular complexes are listed in Table 1.

The direction of the NH and β-protons shifts of the molecular complex, $[(H_2t(4\text{-}CH_3p)p)_2Sb_2Cl_6]$, are similar to the related diprotonated porphyrin species [10]. The remarkable spectral correspondence between $[(H_2t\text{-}(4\text{-}CH_3p)p)_2Sb_2Cl_6]$ and $H_4t(4\text{-}CH_3p)p^{2+}$ suggested analogous tilted porphyrin core structures in these species, and is not related to the formation of a diprotonated porphyrin species in our reaction system. The integration of the pyrrolic NH hydrogen peak in 0.006 M $CDCl_3$ solution of

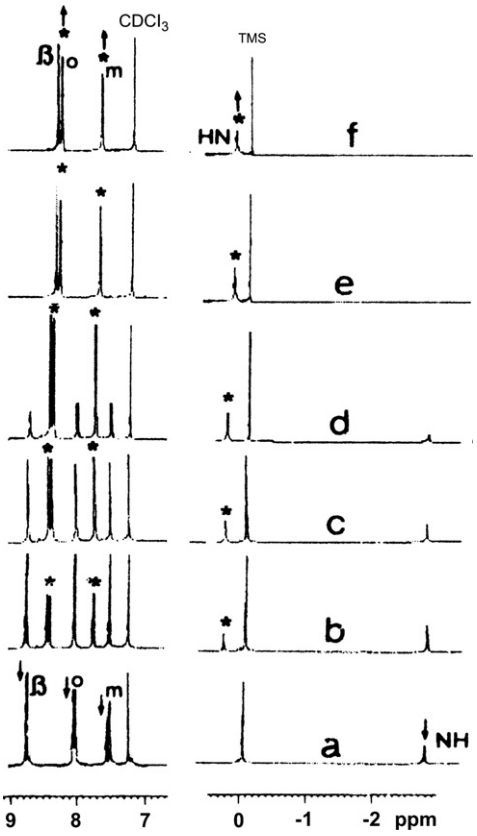


Fig. 2. ^{1}H NMR spectra for the mixing of different equivalents of $SbCl_3$ (0.25, 0.5, 0.75, 1.0 and 2.0) with $H_2t(4\text{-}CH_3p)p$ in $CDCl_3$ at 20 °C. *The peaks are related to the molecular complex $[(H_2t(4\text{-}CH_3p)p)_2Sb_2Cl_6]$.

Table 1
^{1}H NMR spectral data of different *meso*-tetraarylporphyrins, $[(H_2t(Xp)p))_2Sb_2Cl_6]$ molecular complexes and $H_4t(4\text{-}CH_3p)p^{2+}$

Compounds	N–H	H_β
$H_2t(4\text{-}CH_3p)p$	−2.77	8.85
$[(H_2t(4\text{-}CH_3p)p)_2Sb_2Cl_6]$	0.19	8.57
$\Delta\delta_1$	2.96	−0.28
$H_4t(4\text{-}CH_3p)p^{2+}$	−0.65	8.67
$\Delta\delta_2$	2.12	−0.18
$H_2t(4\text{-}OCH_3p)p$	−2.75	8.86
$[(H_2t(4\text{-}OCH_3p)p)_2Sb_2Cl_6]$	0.57	8.49
$\Delta\delta_1$	3.32	−0.37
$H_2t(3\text{-}CH_3p)p$	−2.75	8.88
$[(H_2t(3\text{-}CH_3p)p)_2Sb_2Cl_6]$	0.27	8.64
$\Delta\delta_1$	3.02	−0.26
$H_2t(3\text{-}OCH_3p)p$	−2.75	8.90
$[(H_2t(3\text{-}OCH_3p)p)_2Sb_2Cl_6]$	0.26	8.64
$\Delta\delta_1$	3.04	−0.23
$H_2t(2\text{-}CH_3p)p$	−2.64	8.67
$[(H_2t(2\text{-}CH_3p)p)_2Sb_2Cl_6]$	−1.02	8.63
$\Delta\delta_1$	1.62	−0.04
$H_2t(2\text{-}OCH_3p)p$	−2.61	8.87
$[(H_2t(2\text{-}OCH_3p)p)_2Sb_2Cl_6]$	0.30	8.50
$\Delta\delta_1$	2.91	−0.37
H_2tpp	−2.76	8.85
$[(H_2tpp)_2Sb_2Cl_6]$	0.21	8.61
$\Delta\delta_1$	2.97	−0.24

$\Delta\delta_1$: chemical shifts of the proton signals for the porphyrins upon molecular complexation. $\Delta\delta_2$: Chemical shifts of the proton signals for the $H_2t(4\text{-}CH_3p)p$ upon diprotonation with excess of TFA.

the $[(H_2t(4\text{-}CH_3p)p)_2Sb_2Cl_6]$ molecular complex was 2.1, whereas for $H_4t(4\text{-}CH_3p)p^{2+}$ it was 3.9. An excess of $SbCl_3$ had no effect on the ^1H NMR spectrum of $[(H_2t\text{-}(4\text{-}CH_3p)p)_2Sb_2Cl_6]$, but the ^1H NMR spectrum of $H_4t(4\text{-}CH_3)pp^{2+}$ was quite sensitive to the concentration of trifluoroacetic acid (TFA) [4].

The UV–VIS spectrum of $H_2t(4\text{-}CH_3p)p$ has absorption bands at 418.3 (soret), 518.4, 554.0, 593.0 and 649.0 nm [1–3,13], whereas the molecular complex shows two new absorption bands at 448.1 (soret) and 670.3 nm. Upon the addition of $SbCl_3$ to free base $H_2t(4\text{-}CH_3p)p$, the UV–VIS spectrum of the porphyrin is 21–31 nm red shifted. This is interpreted as evidence for an increased resonance interaction of the tolyl ring with the porphyrin nucleus in going from the free base to the molecular complex, which would be allowed by the tilting of the pyrroles [13b]. The results of the UV–VIS spectra for the other molecular complexes are shown in Table 2.

Table 2
UV–VIS spectral results of the different *meso*-tetraarylporphyrins, $[(H_2t(Xp)p)_2Sb_2Cl_6]$ molecular complexes and their diprotonated species in $CHCl_3$

Compounds	λ_{max}(nm)
$H_2t(4\text{-}CH_3p)p$	418.3(S), 518.4, 554.0, 593.0, 649.0
$[(H_2t(4\text{-}CH_3p)p)_2Sb_2Cl_6]$	448.1(S)670.3
$\Delta\lambda_1^a$	29.8 21.3
$H_4t(4\text{-}CH_3p)p^{2+b}$	442.2(S) 663.4
$\Delta\lambda_2^c$	23.9 14.4
$H_2t(4\text{-}OCH_3p)p$	419.5(S), 520.5, 557.1, 596.0, 653.0
$[(H_2t(4\text{-}OCH_3p)p)_2Sb_2Cl_6]$	454.3 (S)690.6
$\Delta\lambda_1^a$	34.8 37.6
$H_4t(4\text{-}OCH_3p)p^{2+b}$	450.0(S) 689.0
$\Delta\lambda_2^c$	30.5 36.0
$H_2t(3\text{-}CH_3p)p$	418.2(S), 517.5, 550.6, 590.0, 647.2
$[(H_2t(3\text{-}CH_3p)p)_2Sb_2Cl_6]$	446.2(S)661.9
$\Delta\lambda_1^a$	28.0 14.7
$H_4t(3\text{-}CH_3p)p^{2+}$	439.4(S) 657.0
$\Delta\lambda_2^c$	21.2 9.8
$H_2t(3\text{-}OCH_3p)p$	418.9(S), 517.0, 550.3, 590.3, 646.6
$[(H_2t(3\text{-}OCH_3p)p)_2Sb_2Cl_6]$	452.3(S)660.0
$\Delta\lambda_1^a$	33.4 14.4
$H_4t(3\text{-}OCH_3p)p^{2+}$	448.8(S) 657.8
$\Delta\lambda_2^c$	29.9 11.2
$H_2t(2\text{-}CH_3p)p$	418.1(S), 514.3, 550.1, 590.5, 646.5
$[(H_2t(2\text{-}CH_3p)p)_2Sb_2Cl_6]$	442.5(S)663.7
$\Delta\lambda_1^a$	24.4 17.2
$H_4t(2\text{-}CH_3p)p^{2+}$	435.5(S) 656.1
$\Delta\lambda_2^c$	17.4 9.6
$H_2t(2\text{-}OCH_3p)p$	418.3(S), 514.0, 548.2, 590.1, 647.3
$[(H_2t(2\text{-}OCH_3p)p)_2Sb_2Cl_6]$	452.1(S)653.9
$\Delta\lambda_1^a$	33.8 6.6
$H_4t(2\text{-}OCH_3p)p^{2+}$	447.8(S) 655.8
$\Delta\lambda_2^c$	29.5 8.5
H_2tpp	416.7(S), 516.8, 551.5, 592.0, 648.0
$[(H_2tpp)_2Sb_2Cl_6]$	444.1 660.5
$\Delta\lambda_1^a$	27.4 12.5
H_4tpp^{2+b}	436.1(S) 652.2
$\Delta\lambda_2^c$	19.4 4.2

(S): Soret band.
[a] $\Delta\lambda_1$: Red shifts for the bands of the porphyrins upon molecular complexation.
[b] The data are taken from Ref. [4].
[c] $\Delta\lambda_2$: Red shifts for the bands of the porphyrins upon diprotonation.

The UV–VIS spectral data of the $[(H_2t(4\text{-}CH_3p)p)_2\text{-}Sb_2Cl_6]$ molecular complex are closely related to the UV–VIS spectra of $H_4t(Xp)p^{2+}$ (Table 2). The spectrum of $H_4t(Xp)p^{2+}$ was sensitive to additional amounts of TFA[4] while an excess of $SbCl_3$ had no effect on the UV–VIS spectrum of the $[(H_2t(4\text{-}CH_3p)p)_2Sb_2Cl_6]$ molecular complex. The similarity of the spectra of $[(H_2t\text{-}(4\text{-}CH_3p)p)_2Sb_2Cl_6]$ and $H_4t(Xp)p^{2+}$ suggest an analogous porphyrin core structure in these species.

The ^{13}C NMR spectrum of $H_2t(4\text{-}CH_3p)p$ gives rise to seven sharp signals (one signal for the methyl group (19.9 ppm) and six signals for the porphine core and aryl rings (118.4, 125.7, 129.3, 132.7, 135.6, 137.7 ppm)) and a very broad signal (at 145 ppm) for the α-carbons [2,3,14]. The 1:1 interaction of $H_2t(4\text{-}CH_3p)p$ with $SbCl_3$ also leads to changes in the ^{13}C NMR spectrum of the porphyrin (it sharpens the α-carbons signal and causes small shifts in all the lines). These peaks are revealed at 22.1, 123.0, 128.4, 129.6, 137.8, 140.9, 146.5 ppm. The changes are completely similar to diprotonation [14] and 1:2 (donor:acceptor) molecular complexation of *meso*-tetra arylporphyrins with DDQ [1] or TCNE [2].

UV–VIS, ^1H and ^{13}C NMR correspondences between spectral data of 1:2 (donor:acceptor) molecular complexes of σ- or π-acceptors with *meso*-tetraarylporphyrins [1,2] or H_4tpp^{2+} [10,13,14] and $[(H_2t(Xp)p)_2Sb_2Cl_6]$ leads to the proposition of a similar structure for the porphyrin core in all of the species, with non-coplanar pyrrole rings tilted alternatively up and down. This conformation causes the lone pairs of two pyrrolenine nitrogens to act as the electron donors to one molecule of $SbCl_3$, which is located above or below the mean plane of the porphyrin, and so two hydrogen atoms of pyrroles (N-H) are located on the other side of the porphyrin plane, Fig. 3.

UV–VIS and ^1H NMR spectral shifts for the molecular complexation of various *meso*-tetraarylporphyrins with $SbCl_3$ showed that steric hindrance from ortho and meta-substituents of the aryl rings in the porphyrins is more than from the para-substituent, and causes weakening of the electron donation for ortho and meta-substituents. Further, these shifts indicate that π-resonance rather than σ-induction effects the electron donation of the porphyrins

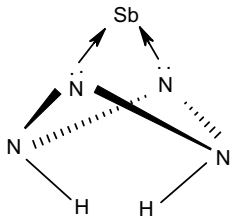


Fig. 3. In the scheme only the tetrahedrally tilted pyrrolenine nitrogens of the porphyrin core are shown. Two nitrogen atoms of pyrrolenine in one side of the porphyrin plane act as the electron donors to an antimony atom of $SbCl_3$.

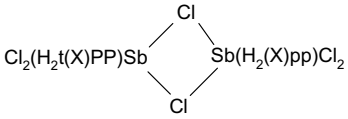


Fig. 4. Scheme for the proposed structure and bonding interactions for the $[(H_2t(Xp)p)_2Sb_2Cl_6]$ molecular complexes.

(Tables 1 and 2) [1,2,13]. The trend in electron donating ability for the substituted *meso*-tetraarylporphyrins was *para* > *meta* > *ortho*.

The mass electrospray spectrum of $[(H_2t(4\text{-}CH_3p)p)_2Sb_2Cl_6]$ (MW = 1797.8) had a peak at *m/z* 1839.1 ($[M+CH_3CN]$). The results of elemental analyses for the $[(H_2t(4\text{-}CH_3p)p)_2Sb_2Cl_6]$ molecular complex was consistent with $C_{96}H_{76}N_8Sb_2Cl_6$. *Anal*. Calc. for $C_{96}H_{76}N_8Sb_2Cl_6$: C, 64.1; H, 4.3; N, 6.2. Found: C, 63.8; H, 4.1; N, 6.3%. The far-IR spectrum (200-400 cm^{-1}) of the complex shows seven bands at 316, 299, 283, 268, 256, 240 and 224 cm^{-1}. The close correspondence between the vibration bands of Sb–Cl (268, 240, 224 cm^{-1}) in the studied complex and the complexes of $SbCl_3$ with diphosphine and diarsine ligands [15], suggests similar structures in these species. Consequently, the antimony coordination geometry was a distorted octahedron composed of the chelating $H_2t(4\text{-}CH_3p)p$, two terminal Sb–Cl's and a $(\mu\text{-}Cl)_2$bridge (Fig. 4). Two vibration bands in the 250–270 cm^{-1} region are assigned to the chloro bridge between two bismuth atoms [16]. Furthermore, the IR spectrum of free base ($H_2t(Xp)p$) shows a N–H stretching band at 3320 cm^{-1} [17], that upon the molecular complexation with $SbCl_3$ does not change. This indicates that there is no intramolecular or intermolecular hydrogen bonding for N–H of the molecular complex, to be consistent with the proposed structure.

Gunter and Rabinson [18] attributed the large downfield shift of the NH signal upon diprotonation of $H_2t(4\text{-}N(CH_3)_2p)p$ to a "decrease of ring current of the macrocyclic system". This cannot be correct as stated [10]. For the internal NH protons, the effect of the ring current in the free base is additional shielding of these protons, which is lost in the diprotonated porphyrins. Walter et al. suggested that "the downfield of the N–H signal on diprotonation could result from geometric distortion of the porphyrin ring by twisting or by rocking the four pyrrole rings to accommodate four protons and the double positive electric charge, but it is not clear how this distortion could move these protons so far as to be outside the field produced by the ring current. Alternatively, this might result from a direct decrease in ring current at the interior of the ring system which is not dependent upon geometric distortion. In either case, the evidence is that the effect of ring current on the peripheral protons is not greatly disturbed though these changes" [10].

Although for the molecular complexes a large shift for the NH signal in ^1H NMR spectra is observed, the IR spectra do not show hydrogen bonding for these complexes. This indicates that the shift of the NH signal in the ^1H NMR spectra upon molecular complexation cannot be related to intramolecular hydrogen bonding. Furthermore, the large downfield shift of the NH signal of the porphyrin in molecular complexes could not relate to distortion of the porphyrin plane, because a large out of plane deformation of the porphyrin core leads only to about 5% change in the ring current [19]. Consequently, there is one other reason for the large shift of NH. Meso-tetraarylporphyrins have 22 π-electrons in the porphyrin cores, and are aromatic systems. Upon molecular complexation of the *meso*-tetraarylporphyrin with $SbCl_3$ (donating two lone pairs electrons to one Sb atom) a double positive charge in the porphyrin core is created (the macrocycle is converted to an 18 π-electron system and the positive charges are distributed over the entire porphine core), Fig. 5. In the proposed structure, four nitrogen atoms of the pyrroles in the porphyrin are oriented to out of the resonance and are changed to 2° amines. Consequently, the unusually large downfield shifts observed for the NH signals upon molecular complexation or diprotonation of the porphyrins can related to changing of pyrrole NHs to 2° amines. This change could move these protons so far as to be outside the field produced by the ring current. For the molecular complexes, $[(H_2t(Xp)p)_2Sb_2Cl_6]$, the lone pairs of pyrrole and pyrrolenine nitrogens make no contribution to the ring current of the porphyrin molecule. Also, the observed chemical shifts for the NH signal of the molecular complexes were upfield than that of usual aliphatic 2° amines (0.5–3 ppm) [20]. This small difference may be related to the ring current effect of the porphyrin core on the internal NH protons of $H_2t(Xp)p$.

The symmetrical ^1H NMR spectra of the molecular complexes (i.e. Fig. 2e) appear to be in contrast to the presence of unsymmetrical pyrrole rings in the proposed structure. The ring inversion of the tilted core conformation of the porphyrin is probably fast on the NMR time scale. The low temperature ^1H NMR spectrum of

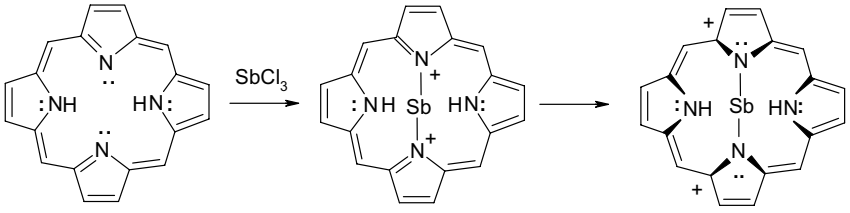


Fig. 5. Molecular complexation of *meso*-tetraarylporphyrins with $SbCl_3$ and changing of pyrrolic NHs to 2° amines.

[$(H_2t(4\text{-}CH_3p)p)_2Sb_2Cl_6$] (at −60 °C, in $CDCl_3$) was quite sharp and showed virtually no changes with respect to that at room temperature (20 °C). However, downfield (0.05 ppm) and upfield (−0.28 ppm) shifts in the β- and NH-protons signals, respectively, were observed. It may be that the lowering of temperature caused the porphyrin core to be less flexible or less planar, i.e., with greater ring currents, so the NH and β signals shifted upfield and downfield respectively [4].

4. Conclusion

Meso-tetraarylporphyrins ($H_2t(Xp)p$) with antimony(III) chloride react with the formation of dimer molecular complexes, [$(H_2t(Xp)p)_2Sb_2Cl_6$]. UV–VIS, ^1H and ^{13}C NMR spectra data show that the porphyrin core of the molecular complexes, similar to 1:2 (donor:acceptor) molecular complexes of *meso*-tetraarylporphyrins [1–4] and porphyrin diacid [10], is distorted and two nitrogen atoms of pyrrolenine are located in a side of the porphyrin plane and act as electron donors to an antimony atom of $SbCl_3$. There is no hydrogen bonding for the molecular complexes but a large downfield shift for the NH signal of the complexes is seen. The unusually large downfield shifts for the NH signals upon molecular complexation or diprotonation of the porphyrins can be related to the changing of the pyrrole NHs to 2° amines and moving the NH protons outside of the field produced by the ring current. This causes the lone pairs of the pyrrole and pyrrolenine nitrogens to make no contribution to the ring current of the porphyrin molecule.

References

[1] D. Mohajer, H. Dehghani, J. Chem. Soc., Perkin Trans. 2 (2000) 199.
[2] D. Mohajer, H. Dehghani, Bull. Chem. Soc. Jpn. 73 (2000) 1477.
[3] D. Mohajer, S. Rayati, New J. Chem. 27 (2003) 242.
[4] D. Mohajer, S. Zakavi, S. Rayati, M. Zahedi, N. Safari, H.R. Khavasi, S. Shahbazian, New J. Chem. 28 (2004) 1600.
[5] M. Asadi, A. Zabardasti, J. Ghasemi, Polyhedron 21 (2002) 683.
[6] M. Asadi, A. Zabardasti, V. Karimvand, J. Ghasemi, Polyhedron 21 (2002) 1255.
[7] M. Asadi, A. Zabardasti, J. Ghasemi, Bull. Chem. Soc. Jpn. 75 (2002) 1137.
[8] A. Zabardasti, M. Mirzaeian, Chem. Lett. 35 (2006) 1348.
[9] (a) J.S. Lindsey, R.W. Wagner, J. Org. Chem. 54 (1989) 828;
(b) E.F. Llama, A. Gradillas, C. del Campo, J.V. Sinisterra, J. Chem. Soc., Perkin Trans. 1 (1995) 2611;
(c) F.A. Walker, V.L. Balke, G.A. McDermott, Inorg. Chem. 21 (1982) 3342;
(d) R.E. Davis, M.R. Willcott, J. Am. Chem. Soc. 94 (1972) 1745;
(e) D.P. Arnold, R.D. Hartnell, G.A. Heath, L. Newby, R.D. Webester, Chem. Commun. (2002) 754;
(f) K. Kano, T. Hayakawa, S. Hashimoto, Bull. Chem. Soc. Jpn. 64 (1991) 778.
[10] E.C.A. Ojadi, H. Linschitz, M. Gouterman, R.I. Walter, J.S. Lindsey, R.W. Wagner, P.R. Droupadi, W. Wang, J. Phys. Chem. 97 (1993) 13308.
[11] (a) A.M. d'A. Rocha Gonsalves, J.M.T.B. Varejao, M.M. Pereira, J. Heterocycl. Chem. 28 (1991) 635;
(b) A.D. Adler, J. Org. Chem. 32 (1967) 476.
[12] J. Mendham, R.C. Denney, J.D. Barnes, M.J.K. Thomas, Vogel's Textbook of Quantitative Chemical Analysis, 6th ed., Wiley, New York, 2000, ch. 17, p. 672.
[13] (a) M. Meot-Ner, A.D. Adler, J. Am. Chem. Soc. 97 (1975) 5107;
(b) A. Stone, E.B. Fleischer, J. Am. Chem. Soc. 90 (1968) 2735.
[14] (a) R.J. Abraham, G.E. Hawkes, M.F. Hudson, K.M. Smith, J. Chem. Soc. Perkin 2 (1975) 204;
(b) S.S. Eaton, G.R. Eaton, Inorg. Chem. 15 (1976) 134.
[15] (a) A.R.J. Genge, N.J. Hill, W. Levason, G. Reid, J. Chem. Soc., Dalton Trans. (2001) 1007;
(b) A.J. Barton, N.J. Hill, W. Levason, G. Reid, J. Chem. Soc., Dalton Trans. (2001) 1621.
[16] (a) K. Nakamoto, Infrared and Raman Spectra of Inorganic and Coordination Compounds, 5th ed., John Wiley & Sons, Inc., New York, 1997, Part A, p. 229, 240;
(b) R.C. Burns, T.A. O'Donnell, Inorg. Chem. 18 (1979) 3081;
(c) D.A. Edwards, R.T. Ward, J. Chem. Soc. (A) (1970) 1617.
[17] H.H. Limbach, J. Henning, J. Stulz, J. Chem. Phys. 78 (1983) 5432.
[18] J. Gunter, B.C. Rabinson, Austr. J. Chem. 42 (1989) 1897.
[19] C.J. Medforth, C.M. Muzzi, K.M. Shea, K.M. Smith, R.J. Abraham, S. Jia, J.A. Shelnutt, J. Chem. Soc., Perkin Trans. 2 (1997) 839.
[20] R.M. Silverstein, G.C. Bassler, T.C. Morrill, Spectroscopic Identification of Organic Compounds, 5th ed., Wiley, New York, 1991, p. 186.

recorded with a Perkin–Elmer 883 Infrared Spectrophotometer (4000–200 cm^{-1}). Electronic spectra of the complexes in DMF solution (ca. 20 °C) were recorded with a Varian Cary 3E spectrophotometer (300–900 nm). ^1H and ^{13}C NMR spectra were recorded at 25 °C with a Varian Unity Plus 300 MHz spectrometer. For referencing, known solvent (or residual solvent) signals were used.

2.2. Crystallographic analysis

X-ray diffraction measurements were made using a Bruker SMART CCD area-detector diffractometer with Mo Kα radiation ($\lambda = 0.71073$ Å) [48]. Suitable single crystals of the complexes were mounted in glass fibers. Intensities were integrated from several series of exposures, each exposure covering 0.3° in ω, the total data set being a hemisphere [49]. Absorption corrections were applied based on multiple and symmetry-equivalent measurements [50]. The structures were solved by direct methods and refined by least squares on weighted F^2 values for all reflections [51]. All non-hydrogen atoms were assigned anisotropic displacement parameters and refined without positional constraints. Hydrogen atoms were taken into account at calculated positions and refined as riding atoms. Complex neutral-atom scattering factors were used [52].

2.3. Synthesis of the ligand S-benzyl dithiocarbazate (*HL*)

S-benzyl dithiocarbazate was prepared according to the method published by Akbar Ali et al. [46].

NMR [DMSO-d_6] δ_H: 10.86 (s, NH, thione form), 7.42–7.20 (m, 5H, C_6H_5), 4.38 (s, CH_2, thione form), 4.37 (s, CH_2, thioenol form); δ_C: 199.96 (CS_2, thione form), 186.18 (CS_2, thioenol form), 138.10, 137.83, 129.11, 128.94, 128.67, 128.43, 127.82, 127.02 (C_6H_5), 37.16 (CH_2, thione form), 36.71 (CH_2, thioenol form).

2.4. Synthesis of the ligand S-benzyl-N-isopropylidenedithiocarbazate (*HL′*)

Solid *S*-benzyl dithiocarbazate was dissolved in excess acetone and left to evaporate slowly, yielding white crystals of *S*-benzyl-*N*-isopropylidenedithiocarbazate, which was recrystallized from warm absolute ethanol (50 °C).

Melting point: 119.7 °C. *Anal.* Calc. for $C_{11}H_{14}N_2S_2$: C, 55.42; H, 5.92; N, 11.75. Found: C, 55.77; H, 5.60; N, 11.66%. NMR [$CDCl_3$] δ_H: 12.13 (s, 1H, NH), 7.40–7.23 (m, 5H, C_6H_5), 4.42 (s, 2H, CH_2), 1.98, 1.93 (s, each 3H, *gem*-$(CH_3)_2$); δ_C: 196.52 (CS_2), 157.58 (C=NN), 137.01, 129.12, 128.37, 127.15 (C_6H_5), 37.62 (CH_2), 24.93, 18.41 (*gem*-$(CH_3)_2$).

2.5. Preparation of [PdL_2] (*1*)

A solution of *S*-benzyl dithiocarbazate (0.3808 g, 1.92 mmol) in warm ethanol (20 mL) was added dropwise to a solution of K_2PdCl_4 (0.1959 g, 0.60 mmol) in water (30 mL) under magnetic stirring. A sticky brown solid was formed that was attached to the stirring bar. The beaker was positioned so that the stirring bar hit the walls and the solution was ''stirred'' in this manner overnight. The next day a beige solid had been formed. The solid was filtered, dried and dissolved in DMF. Layering of methanol yielded a golden leaf-like crystalline solid. Crystals suitable for X-ray analysis were found in this solid.

Pyrochemical detection of chloride in the golden crystalline solid was negative.

Anal. Calc. for $C_{16}H_{18}N_4PdS_4$: C, 38.36; H, 3.62; N, 11.18. Found: C, 38.25; H, 3.31; N, 11.47%. NMR [DMSO-d_6] δ_H: 8.13 (s, 2H, NH_2), 7.33–7.25 (m, 5H, C_6H_5), 4.21 (s, 2H, CH_2); δ_C: 174.11 (CS_2), 137.76, 128.93, 128.48, 127.50 (C_6H_5), 39.37 (CH_2).

2.6. Preparation of [PdL_2'] (*2*)

The same procedure as above was used, with *S*-benzyl-*N*-isopropylidenedithiocarbazate (0.4577 g, 1.92 mmol) as the ligand. The colour of the resulting solid was orange. Dissolution of the orange compound in DMF and layering of ethanol yielded orange crystals, suitable for X-ray analysis.

Pyrochemical detection of chloride in the orange crystalline solid was negative.

Anal. Calc. for $C_{22}H_{26}N_4PdS_4$: C, 45.47; H, 4.51; N, 9.64. Found: C, 45.80; H, 4.68; N, 9.77%. NMR [$CDCl_3$] δ_H: 7.40–7.27 (m, 5H, C_6H_5), 4.40, 4.32 (AB system, $^2J_{H,H} = 13.2$ Hz, 2H, CH_2), 2.42, 2.15 (s, each 3H, *gem*-$(CH_3)_2$); δ_C: 177.05 (CS_2), 172.05 (C=NN), 136.55, 128.85, 128.50, 127.30 (C_6H_5), 39.63 (CH_2), 27.41, 21.15 (*gem*-$(CH_3)_2$).

3. Results and discussion

3.1. Synthesis

We have found that the synthesis of *S*-benzyl-*N*-isopropylidenedithiocarbazate can be carried out under mild conditions, by simply dissolving *S*-benzyl dithiocarbazate in acetone. Upon standing in an open beaker, the product is formed and crystallized. In the method published by Akbar Ali et al. [47] a solution of equimolar quantities of *S*-benzyl dithiocarbazate and acetone in ethanol is refluxed for 12 h.

The preparation of complexes **1** and **2** in the mixture of solvents used (ethanol–water) is not straightforward. Initially a brown solid is formed, which sticks around the stirring bar. Upon stirring overnight, with the beaker positioned so that the stirring bar hits the walls, and thus the complexes are formed.

3.2. Electronic spectra

The electronic spectra of both complexes consist of one band overlapped with a strong band extending to the UV region, $\lambda_{max} = 440$ nm (complex **1**) and $\lambda_{max} = 456$ nm (complex **2**). These bands can be attributed to d–d transi-

tions and they indicate that *S*-benzyl dithiocarbazate is a somewhat stronger ligand than *S*-benzyl-*N*-isopropylidenedithiocarbazate.

3.3. IR spectra

S-benzyl dithiocarbazate and *S*-benzyl-*N*-isopropylidenedithiocarbazate can exhibit thione–thioenol tautomerism. In the solid state the absence of νSH at ca. 2570 cm^{-1} from the IR spectra shows that only the thione forms exist (Table 1).

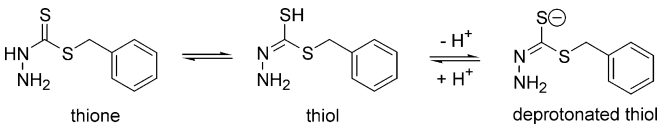
The IR spectrum of **1** exhibits νNH_2 bands at frequencies lower than those of the free ligand (Table 1), due to coordination of the NH_2 group. The νNH and νC=S bands, as well as a νSH band at ca. 2570 cm^{-1}, are missing from the IR spectra of **1** and **2** (Table 1), suggesting that the ligands exist in both complexes in their deprotonated thioenol forms. This is further supported by the positive shift of the νCN bands for both complexes with respect to the free ligands, indicating shorter C–N bond lengths, as is expected from the thioenol versus the thione forms of the ligands.

3.4. NMR spectra

In the case of *S*-benzyl dithiocarbazate, the tautomerism (Scheme 1) was certified in DMSO-d_6 solution by ^{1}H and ^{13}C NMR spectroscopy. The ^{13}C NMR spectrum reveals the existence in solution of both the thione and thioenol forms, while in the ^{1}H NMR spectrum the existence of the thioenol form is denoted by the presence of two overlapping signals for CH_2 at 4.37 and 4.38 ppm, and by the reduced intensity of the NH signal at 10.86 ppm; analysis of the CH_2 overlapping signals into Lorentzian components shows that about 30% of the molecules are in the thione form.

The ^{1}H and ^{13}C NMR spectra of *S*-benzyl-*N*-isopropylidenedithiocarbazate in $CDCl_3$ reveal the existence of only the thione form.

The ^{1}H and ^{13}C NMR spectra of the complexes suggest that the coordinated ligands are in one form. The missing NH signals suggest that this is the thioenol form, in accordance with findings from the IR spectra. Although the NH_2 signal does not appear in the ^{1}H NMR spectrum of **LH**, it appears in the spectrum of **1** at 8.13 ppm.



Scheme 1.

Coordination by the β N atom in **2** is confirmed by the shift of the CH_3 signals of the isopropylidene group from 1.93 and 1.98 ppm for the free ligand to 2.15 and 2.42 ppm.

Coordination of **LH** in **1** causes a shift of the CH_2 signal from 4.37 ppm for the free thioenol form to 4.21 ppm. Such a shift is also apparent in **2**. It is noted that while the CH_2 protons are equivalent in **1**, **LH** and **L′H**, they are diastereotopic in **2**, giving an AB pattern ($^2J_{H,H} = 13.2$ Hz).

3.5. Crystallographic analysis

For both complexes, there are two possible configurations, *cis* and *trans* (Fig. 1, Table 2).

Analysis of the crystal structure of **1** showed that the coordination geometry around Pd is square planar (Fig. 2). This complex has a *trans* configuration. In the solid state two species of **1** exist in equimolar quantities: One is highly symmetric (point group C_i); atomic coordinates for equivalent atoms are given from the transformation $(x, y, z) \rightarrow (-x, -y, -z)$. The other is slightly distorted; atomic coordinates for equivalent atoms are given from the transformation $(x, y, z) \rightarrow (-x+1, -y+1, -z+2)$.

Crystallographic analysis of **2** showed that the coordination geometry around Pd is distorted square planar (Fig. 3). This complex has a *cis* configuration. The planes of the two phenyl rings are practically vertical to the PdN_2S_2 "plane" and form a dihedral angle of ca. 130°. Such a configuration has been found elsewhere in the literature [21].

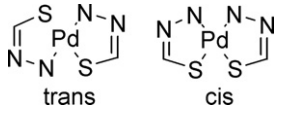


Fig. 1. Possible configurations of the complexes.

Table 1
IR spectroscopic data (ν/cm^{-1})

Compound	ν(NH)	$\nu(NH_2)$	ν(C=N)	$\delta_d(NH_2)$	ν(CN)	ν(CN)+ν(CS)	ν(C=S)	ν(CS)+ν(CN)
LH [46]	3249s	3182m 3125s		1610s	1472s	1229m	1047s	948m
1		3133m 3100m 3065m 3030m		1588m 1572m	1504s	1235m		968s
L′H	3119s		1628s		1474s	1248s	1068s	999s
2			1616m		1500s	1265w		992s

Table 2
Experimental data for crystallographic analysis

Compound	PdL_2 (**1**)	PdL_2 (**2**)
Formula	$C_{16}H_{18}N_4PdS_4$	$C_{22}H_{26}N_4PdS_4$
Formula weight	500.98	581.11
Colour	yellow	orange
Crystal size (mm)	$0.25 \times 0.20 \times 0.06$	$0.10 \times 0.20 \times 0.20$
Crystal system	triclinic	monoclinic
Space group	$P\bar{1}$	$P2_1/n$
Unit cell dimensions		
a (Å)	7.3080(14)	13.216(8)
b (Å)	9.3930(15)	11.829(7)
c (Å)	15.481(3)	16.114(9)
α (°)	82.111(4)	90
β (°)	78.754(3)	96.051(11)
γ (°)	72.365(4)	90
V (Å^3)	989.8(3)	2505(2)
Z	2	4
d_{calc} (Mg m^{-3})	1.681	1.541
Absorption coefficient (mm^{-1})	1.366	1.091
$F(000)$	504	1184
Temperature (K)	293(2)	298(2)
λ (Å)	0.71073	0.71073
θ Range for data collection (°)	2.28–23.28	1.90–23.48
Indexes ranges	$-8 \le h \le 8$, $-10 \le k \le 6$, $-17 \le l \le 17$	$-14 \le h \le 14$, $-13 \le k \le 10$, $-17 \le l \le 17$
Reflections collected	4672	11682
Independent reflections [R_{int}]	2826 [0.0216]	3668 [0.0200]
Completeness to maximum θ (%)	99.1	99.1
Goodness-of-fit on F^2	1.085	1.038
Final R indices [$I > 2\sigma(I)$]	$R_1 = 0.0245$, $wR_2 = 0.0647$	$R_1 = 0.0198$, $wR_2 = 0.0522$
R indices (all data)	$R_1 = 0.0288$, $wR_2 = 0.0691$	$R_1 = 0.0233$, $wR_2 = 0.0549$
Extinction coefficient	0.0109(9)	0.0033(2)
Largest differences in peak and hole (e Å^{-3})	0.355 and −0.453	0.230 and −0.288
Absorption correction	SADABS	none
Refinement method	full-matrix least squares on F^2	full-matrix least squares on F^2

The crystal lattice of **1** shows packing of molecules along the *b*-axis of the crystal, with an arrangement of these packings in a parallel orientation (Fig. 4). The intermolecular distance between Pd atoms of consecutive molecules in the packing is 9.39 Å. This long distance excludes the existence of any covalent intermolecular interactions.

Similarly for **2**, the complexes are packed along the *b*-axis of the crystal with an intermolecular separation between Pd atoms of 11.8 Å. However, in contrast to **1**, in **2** these packings are arranged in an antiparallel disposition (Fig. 5).

For both complexes (Tables 3 and 4), the bond lengths and angles around Pd are in the ranges found in the literature for complexes of Pd(II) with Schiff bases [21,33–35,37] and other *N*-substituted derivatives [45] of dithiocarbazates.

The Pd–N bonds in the two species of **1** (2.021(2) and 2.031(2) Å) are shorter than those in **2** (2.085(2) and 2.087(2) Å); as expected, substitution of NH_2 leads to weaker N–M bonds. In contrast, the Pd–S bonds in **1** (2.2829(8) and 2.2873(8) Å) are longer than those in **2** (2.2563(14) and 2.2625(11) Å). The N–Pd–S angles for the ligand in **1** (84.41(6) and 84.33(7)°) are bigger than those for the ligand in **2** (82.72(5) and 81.76(5)°).

In accordance with the findings from the IR spectra, the C–N bonds in **1** (1.270(4) and 1.282(4) Å) are shorter than that in the free ligand [53] (1.320(3) Å). As expected, the C–S bonds (1.748(3) and 1.745(3) Å) and N–N bonds (1.461(3) and 1.467(3) Å) are longer than those in the free ligand (1.678(3) and 1.406(3) Å, respectively).

This also applies to **2**: the C–N bonds (1.278(3) and 1.281(3) Å) are shorter than those in the free ligand [54] (1.34 Å), while the C–S bonds (1.735(3) and 1.739(3) Å) and N–N bonds (1.420(3) and 1.420(2) Å) are longer than those in the free ligand (1.65 and 1.39 Å, respectively).

The *cis* square planar **2** is monoclinic (space group $P2_1/n$), while the *cis* square planar bis(*S*-methyl-*N*-isopropylidenedithiocarbazato)palladium(II) (**3**) [37] is orthorhombic (space group $P2_12_12_1$), probably due to the effect of the phenyl rings in **2**. The Pd–S (2.2563(14) and 2.2625(11) Å) and Pd–N (2.085(2) and 2.087(2) Å) bond lengths in **2** are almost identical to those of Pd–S (2.263(6) and 2.263(5) Å) and one of the Pd–N (2.090(16) Å) bonds in **3**, while the other Pd–N bond in **3** is longer (2.135(15) Å). In general, the bond lengths and angles do not differ much between the two chelate rings of **2**, while differences arise between the chelate rings of **3**.

X-ray diffraction analysis and ^{1}H and ^{13}C NMR data show that complexes **1** and **2** exist both in the solid state and in solution in one form. The difference in the preference of the isomer formed for each complex (*cis*-**1**, *trans*-**2**) has been discussed in the past in the general context of "equilibrium between *cis* and *trans* forms of square planar d^8 metal complexes" [55–58].

The geometries of **1** and **2** are the cumulative results of the influence of many factors. In a recent paper theoretical

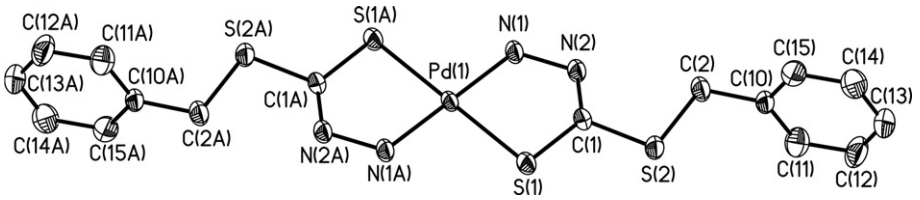


Fig. 2. Molecular structure of **1**.

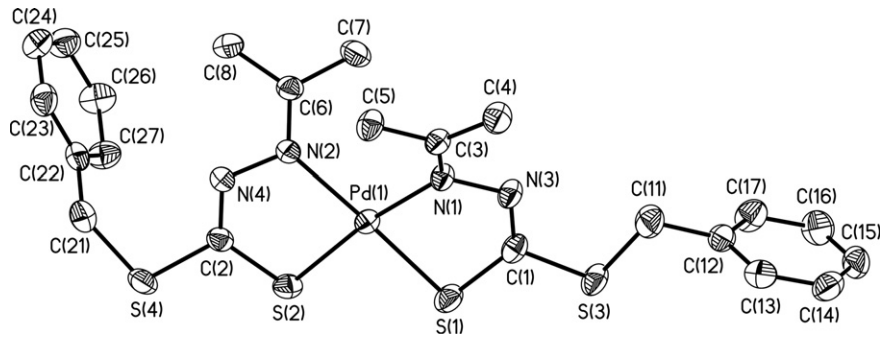


Fig. 3. Molecular structure of **2**.

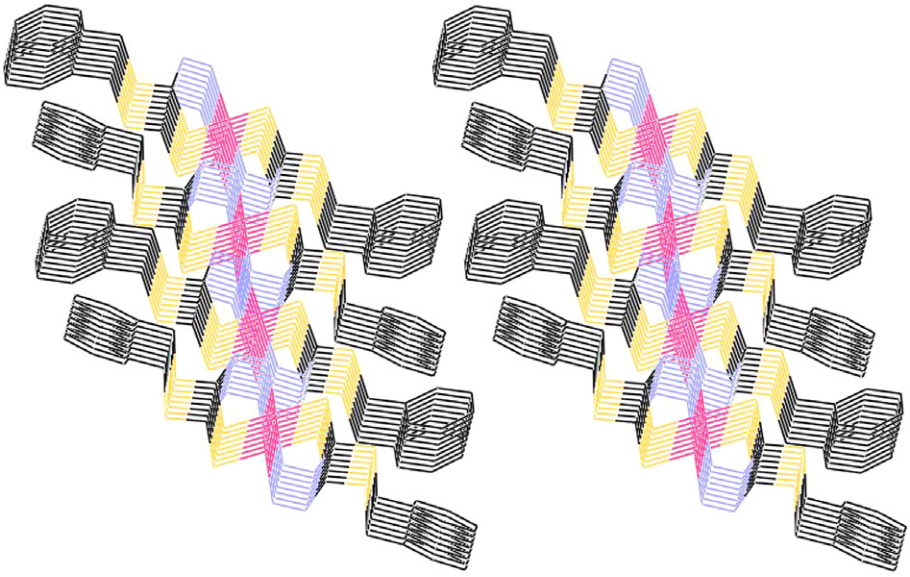


Fig. 4. Packing of molecules along the *b*-axis and arrangement of packings in the crystal lattice of **1**.

calculations have shown that electrostatic interactions stabilize the *trans* isomers [59]. On the other hand it is known that the use of polar solvents favours *cis* configurations [56].

It can also be claimed that a major contribution to the total stabilization of one configuration over the other results from the different *trans* influences of the N (NH_2 and $N{=}C(CH_3)_2$) and S "groups" of the ligands, which lead to different Pd–N and Pd–S bond energies in the *cis* and *trans* isomers.

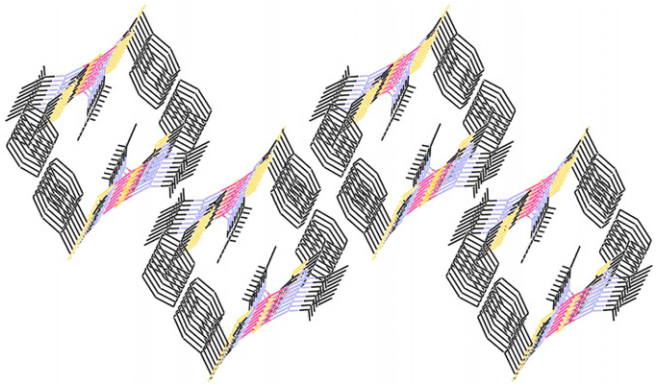


Fig. 5. Packing of molecules along the b-axis and arrangement of packings in the crystal lattice of **2**.

Table 3
Selected bond lengths (Å) and angles (°) for **1**

Bond lengths			
Pd(1)–N(1)	2.021(2)	Pd(2)–N(3)	2.031(2)
Pd(1)–N(1A)	2.021(2)	Pd(2)–N(3B)	2.031(2)
Pd(1)–S(1)	2.2829(8)	Pd(2)–S(3)	2.2873(8)
Pd(1)–S(1A)	2.2829(8)	Pd(2)–S(3B)	2.2873(8)
S(1)–C(1)	1.748(3)	S(3)–C(20)	1.745(3)
N(1)–N(2)	1.461(3)	N(3)–N(4)	1.467(3)
N(2)–C(1)	1.270(4)	N(4)–C(20)	1.282(4)
Bond angles			
N(1)–Pd(1)–N(1A)	180.0	N(3)–Pd(2)–N(3B)	180.00(13)
S(1)–Pd(1)–S(1A)	180.000(1)	S(3)–Pd(2)–S(3B)	180.00(5)
N(1)–Pd(1)–S(1)	84.41(6)	N(3)–Pd(2)–S(3)	84.33(7)
N(1A)–Pd(1)–S(1A)	84.41(6)	N(3B)–Pd(2)–S(3B)	84.33(7)
C(1)–S(1)–Pd(1)	95.64(9)	C(20)–S(3)–Pd(2)	96.07(10)
N(2)–N(1)–Pd(1)	119.68(16)	N(4)–N(3)–Pd(2)	119.51(17)
C(1)–N(2)–N(1)	112.6(2)	C(20)–N(4)–N(3)	112.7(2)
N(2)–C(1)–S(1)	127.5(2)	N(4)–C(20)–S(3)	127.2(2)

Table 4
Selected bond lengths (Å) and angles (°) for **2**

Bond lengths			
Pd(1)–N(1)	2.085(2)	Pd(1)–N(2)	2.087(2)
Pd(1)–S(1)	2.2563(14)	Pd(1)–S(2)	2.2625(11)
S(1)–C(1)	1.735(3)	S(2)–C(2)	1.739(3)
N(3)–C(1)	1.278(3)	N(4)–C(2)	1.281(3)
N(1)–C(3)	1.286(3)	N(2)–C(6)	1.282(3)
N(1)–N(3)	1.420(3)	N(2)–N(4)	1.420(2)
Bond angles			
N(1)–Pd(1)–(2)	168.98(5)	N(2)–Pd(1)–S(1)	169.71(5)
N(1)–Pd(1)–S(1)	82.72(5)	N(2)–Pd(1)–S(2)	81.76(5)
C(1)–S(1)–Pd(1)	95.36(8)	C(2)–S(2)–Pd(1)	94.55(7)
S(1)–C(1)–N(3)	127.16(18)	S(2)–C(2)–N(4)	126.79(17)
C(1)–N(3)–N(1)	112.50(19)	C(2)–N(4)–N(2)	111.69(19)
N(3)–N(1)–Pd(1)	116.51(13)	N(4)–N(2)–Pd(1)	115.65(13)
C(3)–N(1)–N(3)	113.02(18)	C(6)–N(2)–N(4)	114.48(19)
C(3)–N(1)–Pd(1)	130.09(15)	C(6)–N(2)–Pd(1)	129.15(16)

Thus the preference for the *trans* configuration in **1**, as opposed to the *cis* configuration in **2** and other square planar chelates of the form $Pd(NS)_2$ [33–35], where NS is a deprotonated Schiff base of an *S*-alkyl/aryl dithiocarbazate, can be attributed to $–NH_2$ having a larger *trans* influence than $–N{=}C(CH_3)_2$ and $–N{=}CRR'$ in general, close enough to that of $–S^-$ to unbalance the influences that would lead to the formation of the *cis* isomer.

To our best knowledge, this is the first time the crystal structure of a complex of the form $Pd(NS)_2$, where NS is an unsubstituted deprotonated *S*-alkyl/aryl dithiocarbazate, has been reported.

Acknowledgements

Financial support from the Special Account for Research Grants, University of Athens, is acknowledged. This contribution is taken in part from the Ph.D. Thesis of K.T.

Appendix A. Supplementary material

CCDC 635812 and 635813 contain the supplementary crystallographic data for **1** and **2**. These data can be obtained free of charge via http://www.ccdc.cam.ac.uk/conts/retrieving.html, or from the Cambridge Crystallographic Data Centre, 12 Union Road, Cambridge CB2 1EZ, UK; fax: (+44) 1223-336-033; or e-mail: deposit @ccdc.cam.ac.uk. Supplementary data associated with this article can be found, in the online version, at doi:10.1016/j.poly.2007.05.039.

References

[1] M. Mohan, M. Kumar, A. Kumar, P.H. Madhuranath, N.K. Jha, J. Inorg. Biochem. 33 (1988) 121.
[2] M. Das, S.E. Livingstone, Brit. J. Cancer 37 (1978) 466.
[3] K.B. Chew, M.T.H. Tarafder, K.A. Crouse, A.M. Ali, B.M. Yamin, H.K. Fun, Polyhedron 23 (2004) 1385.
[4] M.T.H. Tarafder, A. Asmadi, S.M.S. Talib, A.M. Ali, K.A. Crouse, Trans. Met. Chem. 26 (2001) 170.
[5] M.T.H. Tarafdar, M. Akbar Ali, D.J. Wee, K. Azahari, S. Silong, K.A. Crouse, Trans. Met. Chem. 25 (2000) 456.
[6] M.E. Hossain, M.N. Alam, J. Begum, M. Akbar Ali, M. Nazimuddin, F.E. Smith, R.C. Hynes, Inorg. Chim. Acta 249 (1996) 207.
[7] K.A. Crouse, K.B. Chew, M.T.H. Tarafder, A. Kasbollah, A.M. Ali, B.M. Yamin, H.K. Fun, Polyhedron 23 (2004) 161.
[8] A. Wegner, H. Kolind-Andersen, N. Jacobsen, World Int. Prop. Org. Pat. No. 8504333, 1985.
[9] S.W. Bi, G.Z. Li, Synth. React. Inorg. Met.-Org. Chem. 29 (1999) 1829.
[10] M.E. Hossain, M.N. Alam, M. Akbar Ali, M. Nazimuddin, F.E. Smith, R.C. Hynes, Polyhedron 15 (1996) 973.
[11] M. Nazimuddin, M.A. Ali, F.E. Smith, M.A. Mridha, Trans. Met. Chem. 17 (1992) 74.
[12] S.M.M.H. Majumder, M. Akbar Ali, F.E. Smith, M.A.U. Mridha, Polyhedron 7 (1988) 2183.
[13] M.R. Maurya, S. Khurana, S. Shailendra, A. Azam, W. Zhang, D. Rehder, Eur. J. Inorg. Chem. (2003) 1966.
[14] S. Shailendra, N. Bharti, F. Naqvi, A. Azam, Helv. Chim. Acta 85 (2002) 2713.
[15] N. Bharti, M.R. Maurya, F. Naqvi, A. Bhattacharya, S. Bhattacharya, A. Azam, Eur. J. Med. Chem. 35 (2000) 481.
[16] R. Hatta, I. Sumina, J. Kinugawa, B. Tamura, H. Yamamoto, S. Suzuki, British Pat. No. 963924, 1964.
[17] J. Koromogawa, B. Tamura, Japanese Pat. No. 19114, 1963.
[18] Y.P. Tian, M.L. Zhang, Z.J. Hu, H.M. Hu, J.Y. Wu, X.J. Zhang, S.Y. Zhang, X.T. Tao, M.H. Jiang, H.P. Chen, S. Chantapromma, H.K. Fun, Trans. Met. Chem. 30 (2005) 778.
[19] J.H. Zhou, Y.X. Wang, X.T. Chen, Y.L. Song, L.H. Weng, X.Z. You, Chin. J. Inorg. Chem. 18 (2002) 533.
[20] Z.M. Xue, Z.J. Zhang, Y.P. Tian, Z.Q. Liu, M.H. Jiang, Chin. J. Inorg. Chem. 18 (2002) 1009.
[21] X.H. Zhu, X.F. Chen, Y. Zhang, X.Z. You, W.L. Tan, W. Ji, J.J. Vittal, G.K. Tan, C.H.L. Kennard, New J. Chem. 24 (2000) 419.
[22] X.H. Zhu, X.F. Chen, Y. Zhang, X.Z. You, W.L. Tan, W. Ji, Chem. Lett. (1999) 1211.
[23] J.Y. Wu, Y.P. Tian, Y.H. Zhang, C.Y. Duan, F.X. Xie, S.S. Ni, Acta Chim. Sin. 57 (1999) 202.
[24] Y.P. Tian, C.Y. Duan, X.Z. You, T.C.W. Mak, Q. Luo, J.Y. Zhou, Trans. Met. Chem. 23 (1998) 17.
[25] C.Y. Duan, Y.P. Tian, Z.L. Lu, X.Z. You, T.C.W. Mac, J. Coord. Chem. 46 (1998) 59.
[26] C.Y. Duan, Y.P. Tian, X.Z. You, T.C.W. Mak, Polyhedron 16 (1997) 4097.
[27] Y.P. Tian, C.Y. Duan, Z.L. Lu, X.Z. You, H.K. Fun, B.C. Yip, Polyhedron 15 (1996) 2263.
[28] Y.P. Tian, C.Y. Duan, Z.L. Lu, X.Z. You, H.K. Fun, B.C. Yip, Trans. Met. Chem. 21 (1996) 254.
[29] S. Padhye, G.B. Kauffman, Coord. Chem. Rev. 63 (1985) 127.
[30] M.J.M. Campbell, Coord. Chem. Rev. 15 (1975) 279.
[31] M. Akbar Ali, S.E. Livingstone, Coord. Chem. Rev. 14 (1974) 101.
[32] M. Akbar Ali, S.E. Livingstone, D.J. Phillips, Inorg. Chim. Acta 5 (1971) 119.
[33] H.P. Zhou, D.M. Li, P. Wang, L.H. Cheng, Y.H. Gao, Y.M. Zhu, J.Y. Wu, Y.P. Tian, X.T. Tao, M.H. Jiang, H.K. Fun, J. Mol. Struct. 826 (2007) 205.
[34] J.Y. Wu, Y.P. Tian, F.X. Xie, S.S. Ni, Chin. Chem. Lett. 10 (1999) 251; J.Y. Wu, Y.P. Tian, F.X. Xie, S.S. Ni, Chem. Res. Chin. Univ. 15 (1999) 218.
[35] C.Y. Duan, Y.P. Tian, Z.H. Liu, X.Z. You, T.C.W. Mak, J. Organomet. Chem. 570 (1998) 155.
[36] J.Y. Wu, Y.P. Tian, F.X. Xie, S.S. Ni, Chem. Res. Chin. Univ. 15 (1999) 218.
[37] T. Glowiak, T. Ciszewska, Acta Crystallogr., Sec. B 38 (1982) 1735.
[38] M. Das, S.E. Livingstone, Inorg. Chim. Acta 19 (1976) 5.
[39] M. Akbar Ali, S.E. Livingstone, D.J. Phillips, Inorg. Chim. Acta 7 (1973) 179.
[40] M. Akbar Ali, S.E. Livingstone, D.J. Phillips, Inorg. Chim. Acta 7 (1973) 531.

[41] M. Akbar Ali, S.E. Livingstone, D.J. Phillips, Inorg. Chim. Acta 5 (1971) 493.
[42] X.Y. Wang, Z.X. Deng, B.K. Jin, Y.P. Tian, X.Q. Lin, Bull. Chem. Soc. Jpn. 75 (2002) 1269.
[43] M.A.S. Monshi, N.M. AbdelSalam, J. Chem. Soc. Pakistan 18 (1996) 155.
[44] M.A.S. Monshi, N.M. AbdelSalam, A.A. Salamah, J. Chem. Soc. Pakistan 18 (1996) 214.
[45] M. Bonamico, V. Fares, L. Petrilli, F. Tarli, G. Chiozzini, C. Riccucci, J. Chem. Soc., Dalton Trans. (1994) 3349.
[46] M. Akbar Ali, M.T.H. Tarafdar, J. Inorg. Nucl. Chem. 39 (1977) 1785.
[47] M.T.H. Tarafder, M.A. Jalil Miah, R.N. Bose, M. Akbar Ali, J. Inorg. Nucl. Chem. 43 (1981) 3151.
[48] SMART V5.051 Diffractometer Control Software, Bruker Analytical X-ray Instruments Inc., Madison, WI, 1998.
[49] SAINT V6.02 Integration Software, Bruker Analytical X-ray Instruments Inc., Madison, WI, 1999.
[50] G.M. Sheldrick, SADABS: A Program for Absorption Correction with the Siemens SMART System, University of Göttingen, Göttingen, Germany, 1996.
[51] SHELXTL Program System Version 5.1, Bruker Analytical X-ray Instruments Inc., Madison, WI, 1998.
[52] International Tables for Crystallography, vol. C, Kluwer, Dordrecht, 1992.
[53] S.S.S. Raj, B.M. Yamin, Y.A. Yussof, M.T.H. Tarafder, H.K. Fun, K.A. Grouse, Acta Crystallogr., Sec. C 56 (2000) 1236.
[54] K. Tampouris, A. Asimakopoulos, A. Rondoyanni, S. Koinis, A. Yannopoulos, 8th FIGIPAS, Book of Abstracts, PP136, 2005.
[55] G.K. Anderson, R.J. Cross, Chem. Soc. Rev. 9 (1980) 185.
[56] D.A. Redfield, J.H. Nelson, Inorg. Chem. 12 (1973) 15.
[57] J. Chatt, R.G. Wilkins, J. Chem. Soc. (1952) 273.
[58] J. Chatt, R.G. Wilkins, J. Chem. Soc. (1952) 4300.
[59] J.H. Harvey, K.M. Heslop, A.G. Orpen, P.G. Pringle, Chem. Commun. (2003) 278.

$[Pt_2(\mu\text{-}o\text{-}SC_6H_4(CF_3))_2(dppe)_2](SO_3CF_3)_2$ (**4d**) are also described.

2. Results and discussion

IR spectra of compounds **1**–**4** show the expected absorptions arising from the common dppe ligands and the corresponding thiolate moiety present in each compound. In addition, complexes **3** and **4** exhibit the characteristic bands of the $SO_3CF_3^-$ anion.

In terms of NMR, the magnetic systems corresponding to the fluorinated rings C_6F_5, p-C_6HF_4 and p-$C_6F_4(CF_3)$ can be described as AA′BB′C, AA′BB′X and AA′BB′X_3 respectively. All three systems share *ortho* (A = F) and *meta* (B = F) fluorine nuclei, bearing different *para* substituents, namely, C = F, X = H, and $X_3 = CF_3$. For the o-$C_6H_4(CF_3)$ fragment, the magnetic system can be described as ABCDX_3. ^{1}H, ^{19}F and ^{31}P NMR parameters for compounds **1** and **4**, in agreement with the descriptions above, are listed in Section 4.

^{31}P NMR spectra of compounds **1** and **3** exhibit a single absorption whereas platinum derivatives **2** and **4** show, in addition, the expected ^{195}Pt satellites. Platinum–phosphorous coupling constants show differences of up to *ca.* 150 Hz from compound **2a** to compound **2d** and increases with the fluorination degree of the ring, from 2879 Hz when Rf = o-$C_6H_4(CF_3)$ to 3033 Hz when Rf = $C_6F_4(CF_3)$, probably reflecting the *trans* influence order in this series. On the other hand palladium complexes show ^{31}P chemical shifts 7–13 ppm upfield when compared with the corresponding δ ^{31}P from the platinum analogs.

2.1. Monometallic complexes

Metathesis reactions of $[MCl_2(dppe)]$ M = Pd or Pt with the corresponding lead thiolate (Eq. (1)) render the metalloligands **1** and **2** as stable, diamagnetic yellow microcrystalline solids, soluble in acetone, dichloromethane and chloroform. Although other metallic thiolates can be used successfully to accomplish these reactions, the extremely low solubility of the resulting lead dichloride affords higher yields and cleaner products [11].

$$[MCl_2(dppe)] + Pb(SRf)_2 \rightarrow [M(SRf)_2(dppe)] + PbCl_2 \quad (1)$$

M = Pd, Rf = p-$C_6F_4(CF_3)$ **1a**, C_6F_5 **1b**, p-C_6HF_4 **1c**, o-$C_6H_4(CF_3)$ **1d**
M = Pt, Rf = p-$C_6F_4(CF_3)$ **2a**, C_6F_5 **2b**, p-C_6HF_4 **2c**, o-$C_6H_4(CF_3)$ **2d**

As expected [12], reactions with palladium compounds left over relatively long reaction times, give rise to red insoluble powders of $[\{Pd(SRf)_2\}_n]$ similar to those described earlier [13]. In order to minimize the formation of these polymeric species, relatively short reaction times were used.

Variable temperature ^{19}F NMR experiments (25 °C down to −90 °C) have been carried out for compounds **2a** to **2c** which remained as sharp signals showing no changes on their absorption spectra.

The molecular structures of $[Pd(p\text{-}SC_6HF_4)_2(dppe)]$ (**1c**), $[Pt(SC_6F_5)_2(dppe)]$ (**2b**) and $[Pt(o\text{-}SC_6H_4(CF_3))_2(dppe)]$ (**2d**) are shown in Figs. 1–3 respectively, selected bond distances and angles are shown in Table 1.

Coordination around metal centers in compounds **1c**, **2b** and **2d** are distorted square-planar (the angles around palladium and platinum add to 360.02°, 360.18° and 357.11° (molecule 1) and 360.36° (molecule 2) respectively).

The Pd–S (2.3642(7) Å) and Pd–P (2.2703(7) Å) bond lengths in **1c** are slightly longer than those found by Wei and Liu [14] in $[Pd(SC_6H_5)_2(dppe)]$ for which these bonds are Pd–S 2.3486(7) Å and Pd–P 2.2612(7) Å whereas in $[Pd(SC_6F_5)_2(dppe)]$ these distances are Pd–S 2.354(1) and 2.361(1) and Pd–P 2.268(1) and 2.258(1) [15]. The analogous nickel complex $[Ni(p\text{-}SC_6HF_4)_2(dppe)]$ has also been structurally characterized [16] showing shorter Pd–S bond distance than those found for **1c**.

The bonding angles in **1c** vary between 85.07° and 100.37° with the widest angle opposite to the P(1)–Pd–P(1)^i (symmetry code i: see Table 1) which, due to the chelating bite, is necessarily the smallest one.

For the molecular structure of compound $[Pt(o\text{-}SC_6H_4(CF_3))_2(dppe)]$ (**2d**) the asymmetric unit allocates two independent molecules of the platinum complex with significantly different conformations of the phenyl groups at the chelate ligand in the molecule. Both platinum complexes **2b** and **2d** show shorter Pt–S bond distances than

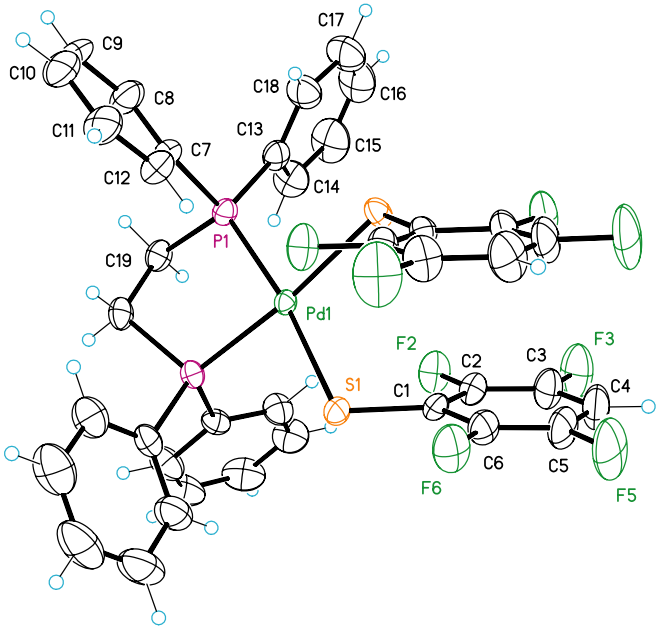


Fig. 1. ORTEP drawing and numbering scheme of $[Pd(p\text{-}SC_6HF_4)_2(dppe)]$ (**1c**). Ellipsoids are shown at the 30% probability level.

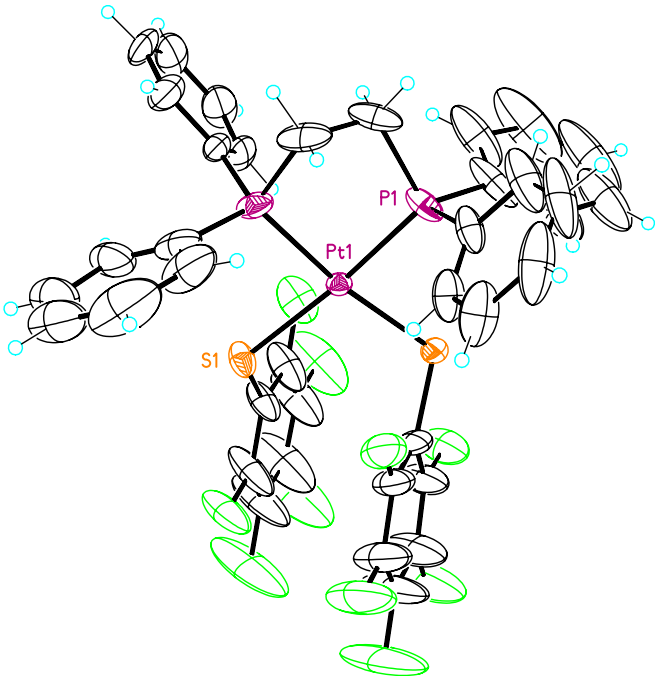


Fig. 2. ORTEP drawing and numbering scheme of [Pt(SC_6F_5)$_2$(dppe)] (**2b**). Ellipsoids are shown at the 30% probability level.

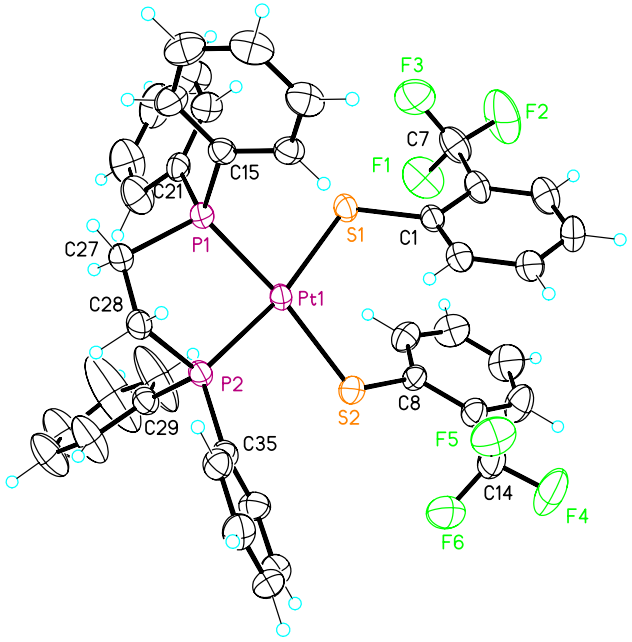


Fig. 3. ORTEP drawing and numbering scheme of [Pt(*o*-$SC_6H_4(CF_3)$)$_2$-(dppe)] (**2d**). Ellipsoids are shown at the 30% probability level.

the palladium analogues, 2.3585(17) Å for [Pt(SC_6F_5)$_2$-(dppe)] (**2b**) and 2.3481(16), 2.3604(14), 2.3636(15), 2.3685(14) Å for [Pt(*o*-$SC_6H_4(CF_3)$)$_2$(dppe)] (**2d**). The bonding angles in **2b** vary between 85.95° and 99.57° whereas in **2d** they vary between 82.21° and 102.12° for molecule 1 and between 86.13° and 97.01° for molecule 2.

Table 1
Selected bond distances (Å) and angles (°) for [Pd(*p*-SC_6HF_4)$_2$(dppe)] (**1c**), [Pt(SC_6F_5)$_2$(dppe)] (**2b**) and [Pt(*o*-$SC_6H_4(CF_3)$)$_2$(dppe)] (**2d**)

[Pd(p-SC_6HF_4)$_2$(dppe)] (**1c**)			
Pd(1)–P(1)	2.2703(7)	Pd(1)–S(1)	2.3642(7)
P(1)–Pd(1)–P(1)#1	85.07(4)	P(1)#1–Pd(1)–S(1)	87.29(3)
P(1)–Pd(1)–S(1)	172.23(3)	C(1)–S(1)–Pd(1)	109.97(9)
S(1)–Pd(1)–S(1)#1	100.37(4)		
[Pt(SC_6F_5)$_2$(dppe)] (**2b**)			
Pt(1)–P(1)	2.2447(18)	Pt(1)–S(1)	2.3585(17)
P(1)–Pt(1)–P(1)#1	85.95(13)	P(1)#1–Pt(1)–S(1)	87.33(8)
P(1)–Pt(1)–S(1)	172.44(6)	C(1)–S(1)–Pt(1)	110.4(3)
C(13)–P(1)–Pt(1)	116.5(3)	S(1)–Pt(1)–S(1)#1	99.57(2)
[Pt(o-$SC_6H_4(CF_3)$)$_2$(dppe)] (**2d**)			
Molecule 1			
Pt(1)–P(1)	2.2611(15)	Pt(1)–S(2)	2.3481(16)
Pt(1)–P(2)	2.2675(14)	Pt(1)–S(1)	2.3604(14)
P(1)–Pt(1)–P(2)	82.21(5)	P(1)–Pt(1)–S(2)	172.17(5)
P(2)–Pt(1)–S(2)	87.17(5)	P(2)–Pt(1)–S(1)	169.99(5)
P(1)–Pt(1)–S(1)	85.61(5)	S(2)–Pt(1)–S(1)	102.12(5)
C(1)–S(1)–Pt(1)	112.0(2)	C(8)–S(2)–Pt(1)	117.3(2)
Molecule 2			
Pt(2)–P(52)	2.2494(14)	Pt(2)–P(51)	2.2504(15)
Pt(2)–S(52)	2.3636(15)	Pt(2)–S(51)	2.3685(14)
P(52)–Pt(2)–P(51)	86.13(5)	S(52)–Pt(2)–S(51)	97.01(5)
P(51)–Pt(2)–S(51)	88.87(5)	P(51)–Pt(2)–S(52)	172.53(5)
P(52)–Pt(2)–S(52)	88.35(5)	P(52)–Pt(2)–S(51)	173.32(5)
C(51)–S(51)–Pt(2)	109.98(19)	C(58)–S(52)–Pt(2)	108.6(2)

Symmetry code #1 for **1c** and **2b**: $1 - x, y, 1/2 - z$.

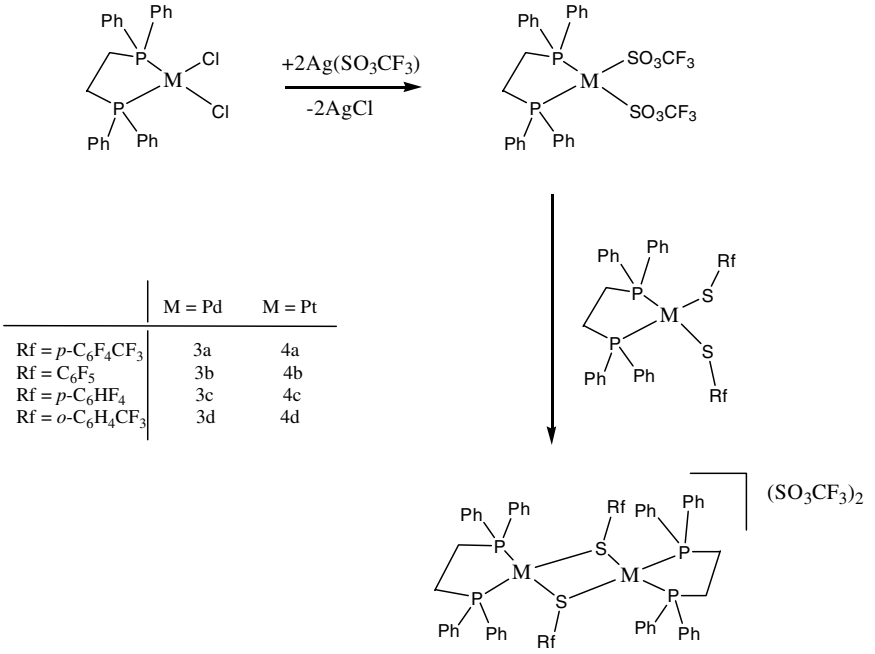
2.2. Bimetallic complexes

Dinuclear complexes **3** to **4** were prepared according to Scheme 1, where the mononuclear complexes **1** and **2** were used as metalloligands. These compounds were isolated as air stable yellow microcrystalline solids soluble in acetone, dichloromethane and chloroform.

2.3. Variable temperature NMR studies

^{1}H, ^{19}F and ^{31}P NMR spectra show the expected magnetic systems discussed above for each of the fluorinated rings. The corresponding parameters are listed in the experimental section. In addition, room temperature ^{31}P NMR for dinuclear platinum complexes **4**, exhibit single absorptions with platinum satellites. Coupling constants $^1J_{Pt-P}$ are larger in dinuclear compounds than in the mononuclear analogues, as expected if the change from terminal to bridged sulfur–metal bonds results in stronger metal–phosphorus bonds.

We have examined the variable temperature ^{1}H and ^{19}F NMR spectra of all compounds **3** and **4**. Unfortunately, at the limiting low temperature (−90 °C) all spectra of palladium containing compounds show poorly defined, very broad bands because, as has been reported before [17], the energy involved for processes on palladium complexes



Scheme 1.

is significantly smaller than that observed for platinum compounds undergoing a similar process. Therefore, the following discussion is focused on platinum compounds mainly through the ^{19}F NMR results.

The room temperature ^{19}F NMR spectra of the perfluorinated compound $[Pt_2(\mu\text{-}p\text{-}SC_6F_4(CF_3))_2(dppe)_2](SO_3CF_3)_2$ (**4a**) shows four signals: a *pseudo*triplet at −56.7 ppm (integral = 3, C–CF_3); a singlet at −77.4 ppm (integral = 3, S–CF_3); a double set of doublets at −124.0 ppm (integral = 2, *ortho*-fluorine) and a multiplet at −139.4 ppm (integral = 2, *meta*-fluorine). Increasing the temperature from ambient to 50 °C does not affect the spectra.

Decreasing the experimental temperature down to *ca.* −70 °C (see Fig. 4) broadens both the *ortho* and the *meta* fluorine signals and at −90 °C the *ortho* fluorine band is unfolded into a pair of signals with the same intensity (−122.0, −125.1, $\Delta\delta$ 3.1 ppm) although the *meta* fluorine absorption remains broad (−139.30 ppm) and unresolved at this temperature. On the other hand, the absorption arising from the *para*-CF_3 group of the thiolate ligands remains unchanged along the complete low temperature interval.

Since *ortho* and *meta* but not the *para* substituents are affected at low temperatures, the fluxional process more likely to be observed in this case is the restricted rotation of the sulfur–carbon bonds. The calculated free activation energy for this process is $\Delta G^{\neq} = 38.71 \pm 0.3$ kJ mol^{-1}, which is *ca.* 3 kJ mol^{-1} lower than the average found for bimetallic complexes of the type $[Pt_2(\mu\text{-}SR)_2(SR)_4](NBu_4)_2$ [18].

As expected, the room temperature ^{19}F NMR spectrum of $[Pt_2(\mu\text{-}SC_6F_5)_2(dppe)_2](SO_3CF_3)_2$ (**4b**), shows four signals: a singlet at −77.8 ppm (integral = 3, S–CF_3); a double set of doublets at −122.2 ppm (integral = 2, *ortho*-fluorine), a *pseudo*triplet at −148.0 ppm (integral = 2, *para*-fluorine) and a multiplet at −155.8 ppm (integral = 3, *meta*-fluorine). As before, none of these signals are modified by increasing the temperature to 50 °C.

At lower temperatures (Fig. 5) *ortho* and *meta*-fluorine absorptions become broad and in the lowest temperature limit, the *meta*-fluorine signal is split into a broad doublet (−154.5, −156.0, $\Delta\delta = 1.5$ ppm) which is also interpreted as resulting from the restricted rotation of the S–C_6F_5 bond. The calculated free activation energy for this process is $\Delta G^{\neq} = 37.39 \pm 0.4$ kJ mol^{-1}.

The fact that in **4b** the *meta*-fluorine nuclei absorption is split instead of the *ortho*-fluorine band as in **4a**, is probably due to differences in steric requirements between the thiolate rings and the phosphine benzene substituents which share a densely occupied space.

The room temperature ^{19}F NMR spectra of $[Pt_2(\mu\text{-}p\text{-}SC_6HF_4)_2(dppe)_2]^{2+}$ (**4c**) exhibits three absorptions: a singlet at −74.0 ppm (integral = 3, S–CF_3), a multiplet at −126.7 ppm (integral = 2, *ortho*-fluorine) and a multiplet at −137.6 ppm (integral = 2, *meta*-fluorine).

High temperature (Fig. 6) ^{19}F NMR experiments with compound **4c** show no changes of the absorptions up to 50 °C. As before, decreasing the temperature results in broad signals until at −90 °C the *ortho*-fluorine absorption splits into a pair of broad signals (−125.5, −126.9, $\Delta\delta = 1.4$ ppm). Unfortunately, since the experiment does not reach the point of slow exchange, the free activation energy cannot be calculated with a reliable accuracy.

Compound $[Pt_2(\mu\text{-}o\text{-}SC_6H_4(CF_3))_2(dppe)_2]^{2+}$ (**4d**), with no fluorine atoms on the *S*-phenyl rings have the less electronegative, more basic thiolate ligand, among the compounds studied here. Having an *ortho* CF_3 group, these

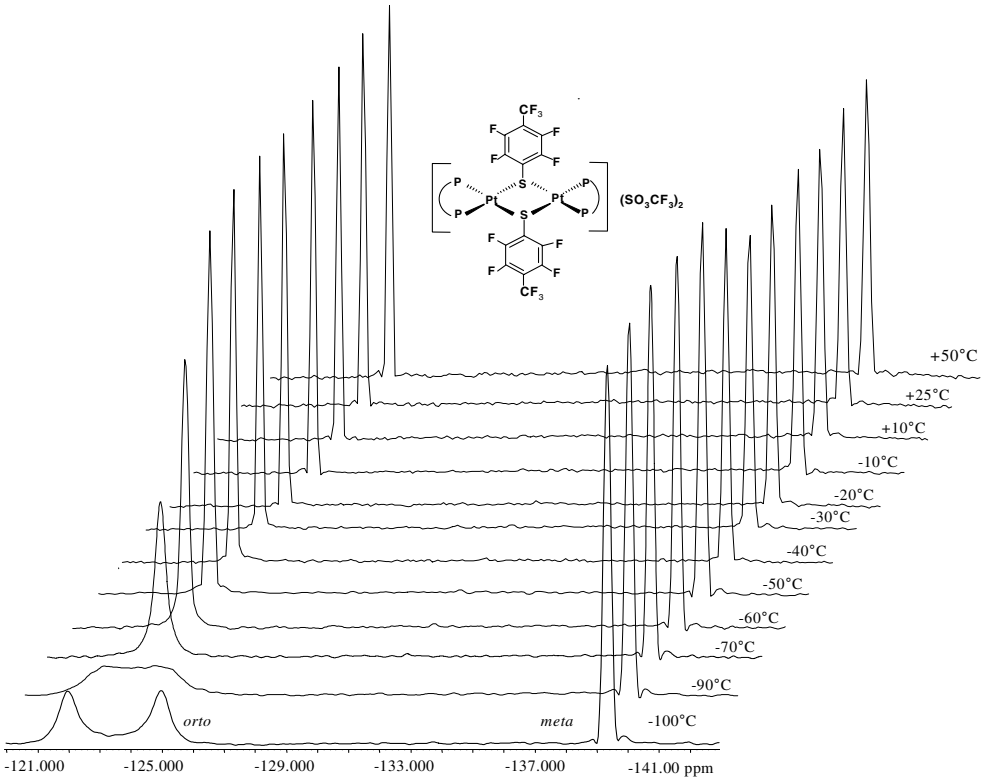


Fig. 4. Variable temperature ^{19}F NMR spectra (*ortho* and *meta* thiolate ligand signals) of $[Pt_2(\mu\text{-}p\text{-}SC_6F_4(CF_3))_2(dppe)_2](SO_3CF_3)_2$ (**4a**).

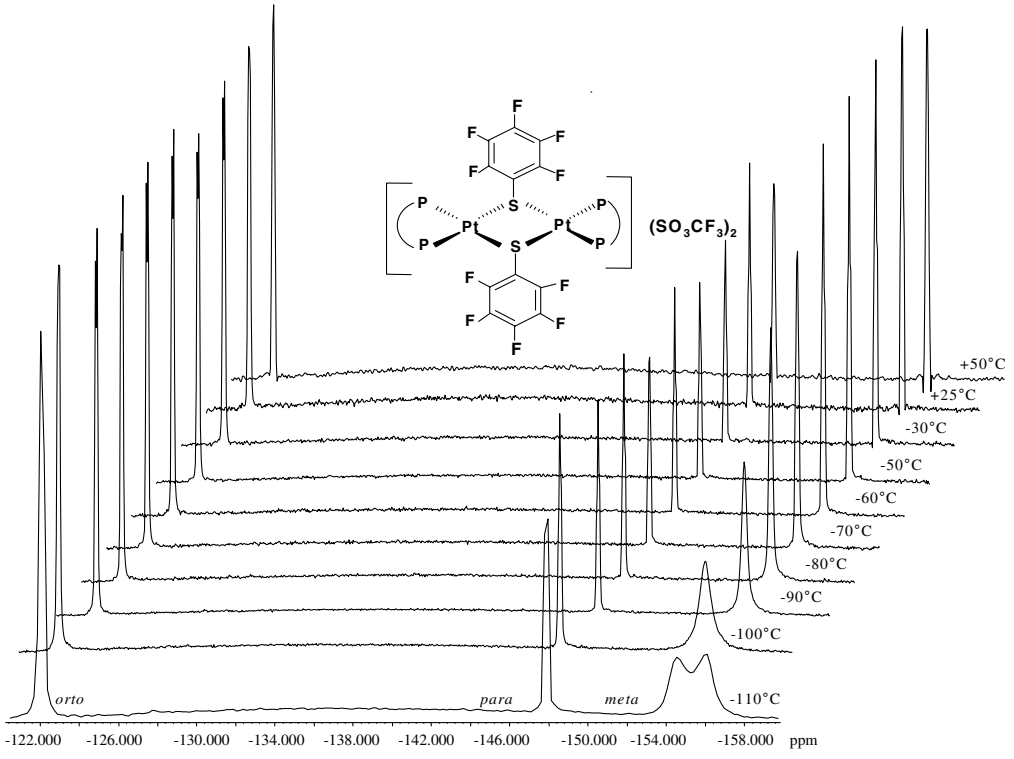


Fig. 5. Variable temperature ^{19}F NMR spectra showing the thiolate region of $[Pt_2(\mu\text{-}SC_6F_5)_2(dppe)_2](SO_3CF_3)_2$ (**4b**).

thiolate ligands are asymmetric. The orientation of these substituents relative to the Pt–S_2–Pt ring defines the isomers *cis* and *trans* as shown in Scheme 2.

At room temperature the ^{19}F NMR spectra of **4d** exhibit a pair of singlets at −57.5 ppm (integral = 1) arising from the thiolate–CF_3 and at −79.1 ppm (integral = 1) from

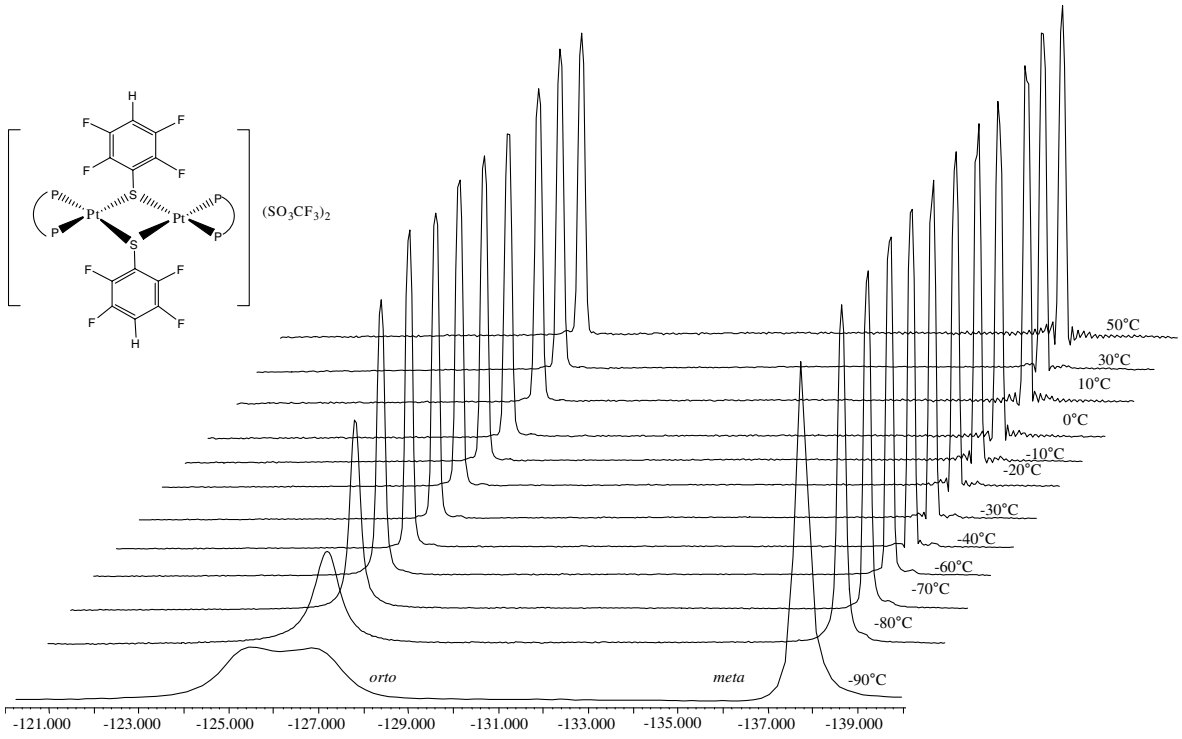
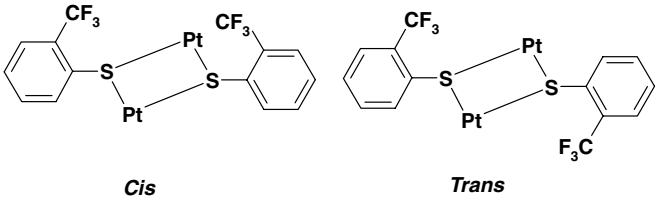


Fig. 6. Variable temperature ^{19}F NMR spectra showing the thiolate region of $[Pt_2(\mu\text{-}p\text{-}SC_6HF_4)_2(dppe)_2](SO_3CF_3)_2$ (**4c**).



Scheme 2.

the triflate–CF_3. ^1H NMR spectra are also clearly defined showing an ABB′C magnetic system for the *o*-$SC_6H_4CF_3$ substituents.

Increasing the temperature to 50 °C has no noticeable effect on the ^{19}F NMR spectra of **4d**, Fig. 7, but upon lowering the temperature, the singlet that is initially centered at δ −57.5 ppm broadens and eventually collapses at −90 °C giving rise to two broad bands centered at −58.1 and −58.6 ppm. The intensity of the downfield signal is *ca.* 11 times larger than that of the upfield absorption. Proton NMR signals undergo a similar broadening and collapsing as the temperature is lowered.

The ^{19}F NMR spectral data are consistent with the rapid interconversion of both *cis* and *trans* isomers at high temperatures and with C–S restricted rotation at low temperatures. Under these conditions the population of each isomer, in solution, is different (1:11), and it is assumed, on steric grounds, that the more intense downfield absorption corresponds to the *anti* isomer as has been found in the solid state (*vide infra*).

The calculated free activation energy for this process is $\Delta G^{\neq} = 40.1 \pm 0.6$ kJ mol^{-1}.

Although a sulfur inversion process cannot be completely discarded for this complex [19,20], it seems unlikely considering that the NMR evidence is consistent along the series studied here and that the calculated $\Delta G^{\neq}$ is nearly 17 kJ mol^{-1} lower than the energy for complexes exhibiting sulfur inversion [18].

2.4. Crystal and molecular structure

Fig. 8 shows the molecular structure of $[Pt_2(\mu\text{-}o\text{-}SC_6H_4(CF_3))_2(dppe)_2](SO_3CF_3)_2$ **4d** and main bond distances and angles are collected in Table 2. This compound has a centrosymmetric square-planar $[Pt_2(\mu\text{-}SR)_2]$ core. The crystallographic isomer stabilized in the solid state has the *anti* configuration with the substituents on the bridging thiolate ligands pointing towards opposite directions. The trifluoromethyl groups in *ortho* positions at the thiolate rings are also pointing in opposite, *trans*, directions. The thiolate $C_6H_4CF_3$ ring and two phenyl rings of neighboring phosphines are aligned in an almost coplanar fashion, allowing strong intra-cation π–π interactions, with centroid to centroid separations in the range 3.526–3.568 Å. As expected, the bridging Pt–S bond distances (2.3759(10) and 2.3749(10)) are longer than the corresponding terminal Pt–S bond distances (2.36 Å, mean) in the monometallic complex $[Pt(o\text{-}SC_6H_4(CF_3))_2(dppe)]$ (*vide supra*) and longer than the bridging Pt–SR bond lengths (2.316 Å, mean) in compounds $[Pt_2(\mu\text{-}SR)_2(SR)_4]^{2+}$, probably reflecting the different *trans* influence of the dppe ligand as compared with that of the thiolate ligand. The Pt–S bond lengths *trans* to phosphine compare with published values

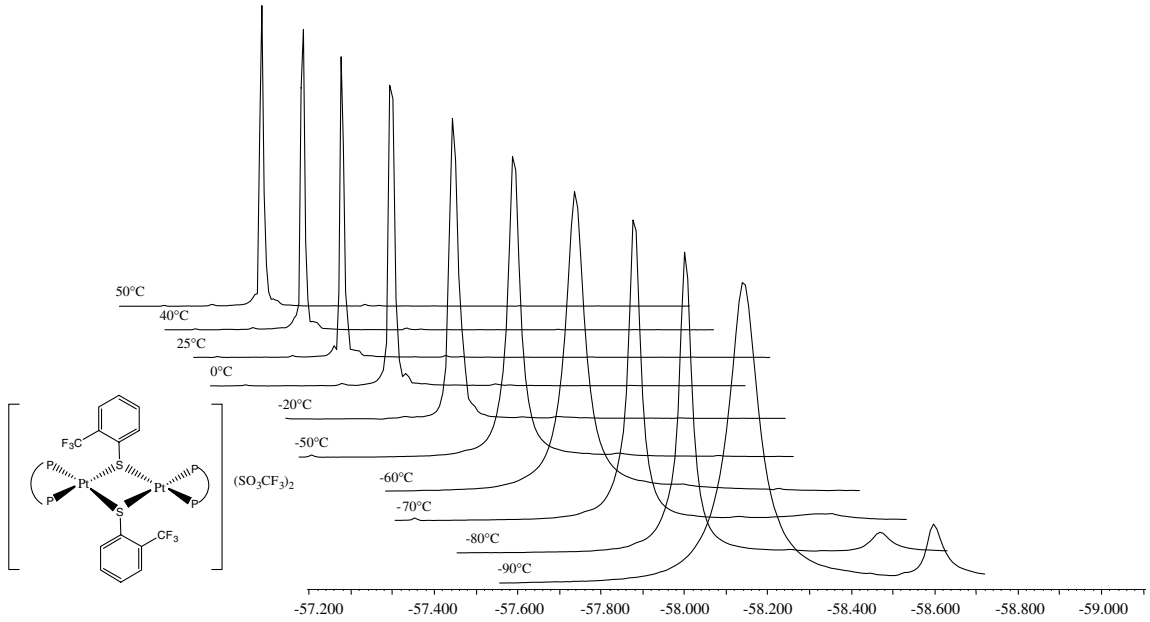


Fig. 7. Variable temperature ^{19}F NMR showing the thiolate–CF_3 region of $[Pt_2(\mu\text{-}o\text{-}SC_6H_4(CF_3))_2(dppe)_2](SO_3CF_3)_2$ (**4d**).

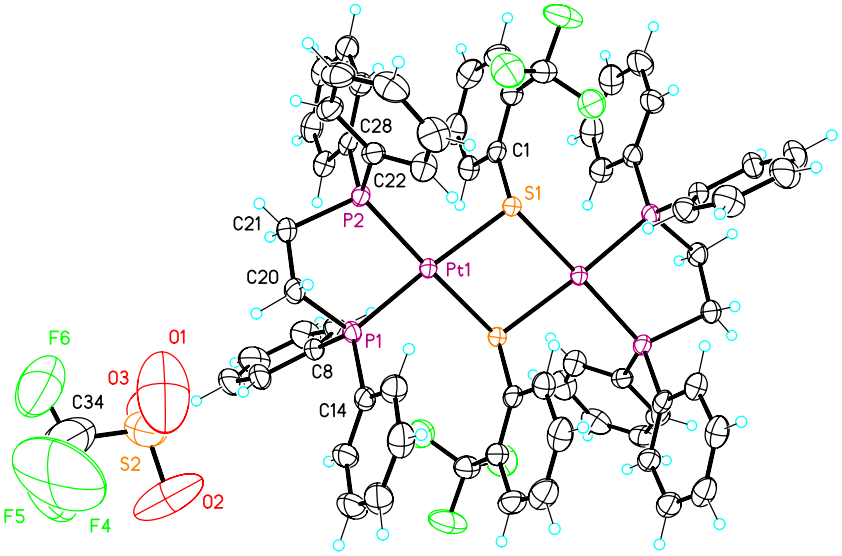


Fig. 8. ORTEP drawing and numbering scheme of $[Pt_2(\mu\text{-}o\text{-}SC_6H_4(CF_3))_2(dppe)_2](SO_3CF_3)_2$ (**4d**). Ellipsoids are shown at the 30% probability level.

Table 2
Main bond distances (Å) and angles (°) of the complex $[Pt_2(\mu\text{-}o\text{-}SC_6H_4(CF_3))_2(dppe)_2](SO_3CF_3)_2$ (**4d**)

Pt(1)–P(1)	2.2722(10)	Pt(1)–S(1)	2.3759(10)
Pt(1)–P(2)	2.2709(10)	Pt(1)–S(1)#1	2.3749(10)
P(2)–Pt(1)–P(1)	84.55(4)	Pt(1)#1–S(1)–Pt(1)	99.97(4)
P(2)–Pt(1)–S(1)#1	172.62(4)	P(1)–Pt(1)–S(1)#1	98.68(4)
S(1)#1–Pt(1)–S(1)	80.03(4)	C(1)–S(1)–Pt(1)	110.98(14)
P(2)–Pt(1)–S(1)	97.54(4)	P(1)–Pt(1)–S(1)	173.22(4)

Symmetry code #1: $2-x, -y, 1-z$.

for dinuclear compounds with thiolate ligands [21–23]. The Pt···Pt distance, 3.6386(3) Å, is rather long, and any possibility of direct magnetic interaction may be ruled out.

3. Conclusions

Homobimetalic, fluorothiolate bridged compounds of Pd and Pt, $[M_2(\mu\text{-}SRf)_2(dppe)_2]$, can conveniently be prepared by reacting the metalloligands $[M(SRf)_2(dppe)]$ with the solvato-complexes $[M(SO_3CF_3)_2(dppe)]$.

In contrast with the behavior of the monometallic compounds included in this study, all members of the bimetallic series of $[M_2(\mu\text{-}SRf)_2(dppe)_2]^{2+}$ complexes are fluxional on the NMR time scale when they are in solution. The available data suggest that the nature of the process is common to all examples. Thus the ligands $p\text{-}SC_6F_4(CF_3)$, SC_6F_5, $p\text{-}SC_6HF_4$ and $o\text{-}SC_6H_4(CF_3)$ on complexes $[M_2(\mu\text{-}SRf)_2(dppe)_2]^{2+}$, are involved in hindered C–S bond rotation

processes. Apparently, the possible rotamers experience different steric interactions, therefore, *ortho*-fluorine atoms are specially affected for *p*-$SC_6F_4(CF_3)$ and *p*-SC_6HF_4 containing compounds, *meta*-fluorine atoms are rendered distinct for the compound with SC_6F_5 bridging ligands whereas *o*-$SC_6H_4(CF_3)$, which is intrinsically asymmetric, defines *cis* and *trans* isomers.

The structure of the bimetallic complex studied bears a square-planar $[M_2(\mu\text{-SRf})_2]$ ring with sulfur substituents pointing towards opposite sites of the plane in an *anti* configuration.

4. Experimental

4.1. Materials

All reactions were carried out under a dry, oxygen-free N_2 atmosphere, using Schlenk techniques [24]. All reagents were purchased from Aldrich Chem. Co. and used as received. $[PdCl_2(dppe)]$ [25], $[PtCl_2(dppe)]$ [25], $Pb(SRf)_2$ [26], $[Pd(SC_6F_5)_2(dppe)]$ [15,27] (**1b**), $[Pd(p\text{-}SC_6HF_4)_2(dppe)]$ [16] (**1c**), $[Pt(SC_6F_5)_2(dppe)]$ [15,27] (**2b**) and $[Pt(p\text{-}SC_6HF_4)_2(dppe)]$ [16] (**2c**) were prepared by published methods.

4.2. Instruments

Microanalyses were performed using a Fisons EA1108 instrument. FT-IR spectra were recorded over the 4000–200 cm^{-1} range on a Perkin–Elmer 1600 spectrophotometer with samples prepared as CsI pellets. Data are expressed in wavenumbers (cm^{-1}) with relative intensities (vs = very strong, s = strong, m = medium, w = weak).

^1H, ^{19}F and ^{31}P NMR spectra were measured with a Varian spectrometer operating at 299.7, 282.0 and 121.5 MHz respectively. Chemical shifts are relative to TMS ($\delta = 0$ (^1H)), $CFCl_3$ ($\delta = 0$ (^{19}F)) and H_3PO_4/D_2O ($\delta = 0$ (^{31}P)). A standard variable temperature unit was used to control the probe were within ±1 °C. Complexes were dissolved in deuterated acetone. FAB mass spectra were obtained on a JEOL JMS-SX102A.

All variable temperature NMR experiments were carried out in deuterated acetone. The activation parameters for dynamic processes were calculated from simulation spectra [28] and the Eyring equation using curve fitting techniques [29–31].

4.3. *[Pd(SRf)$_2$(dppe)]* complexes **1**

A solution of 0.348 mmol of $Pb(SRf)_2$ in acetone (15 mL) was added slowly to a solution of 0.348 mmol of $[PdCl_2(dppe)]$ in acetone (10 mL). The reaction was magnetically stirred for 15 min at room temperature and the white $PbCl_2$ precipitated filtered off. The yellow product was purified by column chromatography with silica gel, using acetone/hexanes (1:2) as eluent.

4.3.1. *[Pd(p-SC$_6$F$_4$(CF$_3$))$_2$(dppe)]* (**1a**)

M.p. 192–194 °C. *Anal.* Calc. for $C_{40}H_{24}F_{14}P_2PdS_2$: C, 47.90; H, 2.41; S, 6.39. Found: C, 47.8; H, 2.5; S, 6.6%. IR (cm^{-1}): 3055w, 3029w, 1642m, 1471vs, 1436s, 1383m, 1323vs, 1167s, 1133s, 1102m, 998m, 971s, 878w, 830s, 746w, 713s, 690s, 651w, 530m, 478m. ^1H NMR (C_2D_6CO, 298 K): 7.9, 7.6 (m, 20H, phenyl from phosphine), 2.9 (m, 4H, CH_2–CH_2). ^{31}P NMR (C_2D_6CO, 298 K): 62.6. ^{19}F NMR (C_2D_6CO, 298 K): −129.1 (pd, *o*-F), −143.3 (m, *m*-F), −52.6 (t, *p*-CF_3).

4.3.2. *[Pd(o-SC$_6$H$_4$(CF$_3$))$_2$(dppe)]* (**1d**)

M.p. 212–214 °C. *Anal.* Calc. for $C_{40}H_{32}F_6P_2PdS_2$: C, 55.92; H, 3.75; S, 7.46. Found: C, 56.7; H, 4.0; S, 6.8%. IR (cm^{-1}): 3424m, 3055w, 2925w, 1676w, 1637w, 1588m, 1559w, 1483w, 1460w, 1434s, 1310vs, 1245m, 1156s, 1124vs, 1102vs, 1042s, 1029s, 999w, 876w, 817w, 751m, 702s, 689s, 646w, 597w, 529vs, 481m. ^1H NMR (C_2D_6CO, 298 K): 7.1 (m, *o*-H, thiolate), 7.6, 6.7 (m, *m*-H, thiolate), 6.7 (m, *p*-H, thiolate), 7.8, 7.5 (m, 20H, phenyl from phosphine), 2.7 (m, 4H, CH_2–CH_2). ^{31}P NMR (C_2D_6CO, 298 K): 57.1. ^{19}F NMR (C_2D_6CO, 298 K): −62.4 (pt, *o*-CF_3).

4.4. *[Pt(SRf)$_2$(dppe)]* complexes **2**

A solution of 0.211 mmol of $Pb(SRf)_2$ in acetone (10 mL) was added to a suspension of 0.211 mmol of $[PtCl_2(dppe)]$ in acetone (10 mL). The reaction was magnetically stirred for 24 h at room temperature. The $PbCl_2$ precipitated was separated by filtration through silica gel and the solution evaporated to yield a yellow powder which was recrystallized from acetone.

4.4.1. *[Pt(p-SC$_6$F$_4$(CF$_3$))$_2$(dppe)]* (**2a**)

Yield: 90.7%, m.p. 212–214 °C. *Anal.* Calc. for $C_{40}H_{24}F_{14}P_2PtS_2$: C, 44.01; H, 2.22; S, 5.87. Found: C, 44.1; H, 2.2; S, 5.6%. IR (cm^{-1}): 3433w, 3055w, 1642m, 1471vs, 1437m, 1384m, 1324vs, 1168s, 1130s, 1103m, 998w, 972vs, 880w, 750w, 713s, 690s, 653w, 532s, 483m. ^1H NMR (C_2D_6CO, 298 K): 8.0, 7.6 (m, 20H, phenyl from phosphine), 2.8 (m, 4H, CH_2-CH_2). ^{31}P NMR (C_2D_6CO, 298 K): 52.3 ($J_{Pt-P} = 3033$. Hz). ^{19}F NMR (C_2D_6CO, 298 K): −132.9 (pd, *o*-F), −147.2 (m, *m*-F), −56.9 (t, *p*-CF_3).

4.4.2. *[Pt(o-SC$_6$H$_4$(CF$_3$))$_2$(dppe)]* (**2d**)

Yield: 84.63%, m.p. 197–199 °C. *Anal.* Calc. for $C_{40}H_{32}F_6P_2PtS_2$: C, 50.69; H, 3.40; S, 6.76. Found: C, 50.8; H, 3.5; S, 6.5%. IR (cm^{-1}): 3434w, 3052w, 1710w, 1558w, 1483w, 1461m, 1435vs, 1308vs, 1246s, 1167vs, 1121vs, 1104vs, 1042s, 1029vs, 997m, 878w, 824m, 754s, 715s, 702s, 691s, 655w, 645m, 532vs, 496w, 480m, 461m, 432w, 157m. ^1H NMR (C_2D_6CO, 298 K): 7.1 (m, *o*-H, thiolate), 7.7, 6.8 (m, *m*-H, thiolate), 6.8 (m, *p*-H, thiolate), 8.0, 7.5 (m, 20H, phenyl from phosphine), 2.7 (m, 4H,

CH_2–CH_2). ^{31}P NMR (C_2D_6CO, 298 K): 50.3 (J_{Pt-P} = 2879 Hz). ^{19}F NMR (C_2D_6CO, 298 K): −68.3 (pt, *o*-CF_3).

4.5. *[Pd(μ-SRf)(dppe)]$_2$(SO_3CF_3)$_2$ complexes (**3**)*

A solution of 0.139 mmol of $AgSO_3CF_3$ in 10 mL of acetone was added to a solution of 0.07 mmol of [$PdCl_2$(dppe)] in acetone (15 mL) and stirred for 24 h at room temperature. After filtration trough Celite, 0.07 mmol of [Pd(SRf)$_2$(dppe)] in 15 mL of acetone were added and stirred for 7 h. The reaction was followed by TLC until completeness. Slow evaporation of the solvent yield a yellow powder which was recrystallized from diffusion of hexanes in acetone.

4.5.1. *[Pd(μ-p-$SC_6F_4(CF_3)$)(dppe)]$_2$(SO_3CF_3)$_2$ (**3a**)*

M.p. 168–170 °C. *Anal.* Calc. for $C_{68}H_{48}F_{20}O_6P_4Pd_2S_4$: C, 45.22; H, 2.68; S, 7.10. Found: C, 45.0; H, 2.8; S, 7.3%. IR (cm^{-1}): 3439w, 3058w, 2918w, 1643m, 1586w, 1479vs, 1437s, 1325vs, 1257vs, 1224m, 1144s, 1102m, 1029s, 997w, 978s, 942w, 881w, 825m, 749m, 714s, 690s, 656w, 637s, 531s, 480m, 437w. ^1H NMR (C_2D_6CO, 298 K): 7.7, 7.6 (m, 20H, phenyl from phosphine), 2.9 (m, 4H, CH_2–CH_2). ^{31}P NMR (C_2D_6CO, 298 K): 74.7. ^{19}F NMR (C_2D_6CO, 298 K): −122.1(pd, *o*-F), −138.4 (m, *m*-F), −54.4 (t, *p*-F), −76.4 (s, SO_3CF_3).

4.5.2. *[Pd(μ-SC_6F_5)(dppe)]$_2$(SO_3CF_3)$_2$ (**3b**)*

Yield: 70.14%. M.p. 200–201 °C and at 210 °C decomposition. *Anal.* Calc. for $C_{66}H_{48}F_{16}O_6P_4Pd_2S_4$: C, 46.48; H, 2.84; S, 7.51. Found: C, 46.0; H, 2.9; S, 7.3%. IR (cm^{-1}): 3462s, 3059w, 1639w, 1513vs, 1484vs, 1437s, 1276vs, 1258vs, 1223s, 1159s, 1102s, 1083s, 1031vs, 997m, 977s, 877w, 853m, 816m, 754m, 721s, 707m, 690s, 637vs, 573m, 531vs, 480s, 432m. ^1H NMR (C_2D_6CO, 298 K): 7.7, 7.6 (m, 20H, phenyl from phosphine), 2.8 (m, 4H, CH_2–CH_2). ^{31}P NMR (C_2D_6CO, 298 K): 68.9. ^{19}F NMR (C_2D_6CO, 298 K): −125.5 (pd, *o*-F), −160.1 (m, *m*-F), −153.5 (pt, *p*-F), −77.4 (s, SO_3CF_3).

4.5.3. *[Pd(μ-p-SC_6HF_4)(dppe)]$_2$(SO_3CF_3)$_2$ (**3c**)*

M.p. 247–29 °C. *Anal.* Calc. for $C_{66}H_{50}F_{14}O_6P_4Pd_2S_4$: C, 47.48; H, 3.02; S, 7.67. Found: C, 48.6; H, 3.2; S, 7.4%. IR (cm^{-1}): 3501w, 3056m, 2961w, 1628w, 1490vs, 1436s, 1279vs, 1223s, 1156s, 1103s, 1029vs, 915s, 878m, 817m, 753m, 721s, 708s, 668s, 637vs, 532vs, 477m. ^1H NMR (C_2D_6CO, 298 K): 7.12 (m, *p*-H, thiolate), 7.7, 7.5 (m, 20H, phenyl from phosphine), 2.8 (m, 4H, CH_2–CH_2). ^{31}P NMR (C_2D_6CO, 298 K): 67.8. ^{19}F NMR (C_2D_6CO, 298 K): −122.5 (pd, *o*-F), −134.2 (m, *m*-F), −74.0 (s, SO_3CF_3).

4.5.4. *[Pd(μ-o-$SC_6H_4(CF_3)$)(dppe)]$_2$(SO_3CF_3)$_2$ (**3d**)*

Yield: 60.57%. M.p. 227–229 °C. *Anal.* Calc. for $C_{68}H_{56}F_{12}O_6P_4Pd_2S_4$: C, 49.16; H, 3.40; S, 7.70. Found: C, 48.3; H, 3.6; S, 7.6%. IR (cm^{-1}): 3432m, 3056w, 1587w, 1483w, 1436s, 1311vs, 1259vs, 1223m, 1159vs, 1103s, 1029vs, 998m, 880w, 818w, 749m, 704m, 690s, 636vs, 572w, 530s, 482m.^1H NMR (C_2D_6CO, 298 K): 7.2 (m, *o*-H, thiolate); 8.2, 7.0 (m, *m*-H, thiolate); 7.0 (m, *p*-H, thiolate), 7.6, 7.4 (m, 20H, phenyl from phosphine), 2.6 (m, 4H, CH_2–CH_2). ^{31}P NMR (C_2D_6CO, 298 K): 65.7. ^{19}F NMR (C_2D_6CO, 298 K): −53.7 (pt, *o*-CF_3), −73.8 (s, SO_3CF_3).

4.6. *[Pt(μ-SRf)(dppe)]$_2$(SO_3CF_3)$_2$ complexes **4***

A solution of 0.1506 mmol of $AgSO_3CF_3$ in 10 mL of acetone was added to a solution of 0.0753 mmol of [$PtCl_2$(dppe)] in acetone (15 mL) and stirred for 24 h at room temperature. After filtration trough Celite, 0.0753 mmol of [Pt(SRf)$_2$(dppe)] in 15 mL of acetone were added and stirred for 7 h. The reaction was followed by TLC until completeness. Slow evaporation of the solvent yield a yellow powder which was recrystallized from diffusion of hexanes in acetone.

4.6.1. *[Pt(μ-p-$SC_6F_4(CF_3)$)(dppe)]$_2$(SO_3CF_3)$_2$ (**4a**)*

M.p. 235–237 °C. *Anal.* Calc. for $C_{68}H_{48}F_{20}O_6P_4Pt_2S_4$: C, 41.17; H, 2.44; S, 6.45. Found: C, 41.6; H, 2.5; S, 6.4%. IR (cm^{-1}): 3480w, 3058w, 1707w, 1643m, 1480vs, 1437s, 1326vs, 1257vs, 1224s, 1144vs, 1105s, 1030vs, 997m, 979vs, 823s, 750m, 714vs, 691s, 637vs, 572m, 534vs, 485s. ^1H NMR (C_2D_6CO, 298 K): 7.7, 7.6 (m, 20H, phenyl from phosphine), 2.7 (m, 4H, CH_2–CH_2). ^{31}P NMR (C_2D_6CO, 298 K): 52.8 (J_{Pt-P} = 3122 Hz). ^{19}F NMR (C_2D_6CO, 298 K): −122.8 (pd, *o*-F), −138.2 (m, *m*-F), −55.6 (t, *p*-CF_3), −77.4 (s, SO_3CF_3).

4.6.2. *[Pt(μ-SC_6F_5)(dppe)]$_2$(SO_3CF_3)$_2$ (**4b**)*

M.p. 240–242 °C. *Anal.* Calc. for $C_{66}H_{48}F_{16}O_6P_4Pt_2S_4$: C, 42.08; H, 2.57; S, 6.80. Found: C, 42.7; H, 2.7; S, 6.5%. IR (cm^{-1}): 3462m, 3057w, 1708w, 1637w, 1513s, 1488vs, 1437s, 1261vs, 1223m, 1156s, 1104s, 1087s, 1030vs, 997w, 979s, 882w, 853m, 820w, 752m, 720m, 691s, 637s, 572w, 533vs, 485m. ^1H NMR (C_2D_6CO, 298 K): 7.7, 7.6 (m, 20H, phenyl from phosphine), 2.7 (m, 4H, CH_2–CH_2). ^{31}P NMR (C_2D_6CO, 298 K): 52.3 (J_{Pt-P} = 3097 Hz). ^{19}F NMR (C_2D_6CO, 298 K): −125.5 (pd, *o*-F), −159.2 (m, *m*-F), -151.3 (pt, *p*-F), −77.3 (s, SO_3CF_3).

4.6.3. *[Pt(μ-p-SC_6HF_4)(dppe)]$_2$(SO_3CF_3)$_2$ (**4c**)*

Yield: 77.16%. M.p. 275–277 °C. *Anal.* Calc. for $C_{66}H_{50}F_{14}O_6P_4Pt_2S_4$: C, 42.90; H, 2.73; S, 6.93. Found: C, 43.2; H, 2.8; S, 6.8%. IR (cm^{-1}): 3435m, 3066w, 1629w, 1491vs, 1437s, 1377w, 1265vs, 1223m, 1155s, 1105s, 1030s, 997w, 916m, 881w, 820w, 752m, 708s, 690s, 637s, 572w, 534s, 483m. ^1H NMR (C_2D_6CO, 298 K): 7.1 (m, *p*-H, thiolate), 7.7, 7.6 (m, 20H, phenyl from phosphine), 2.68 (m, 4H, CH_2–CH_2). ^{31}P NMR (C_2D_6CO, 298 K): 52.2 (J_{Pt-P} = 3097 Hz). ^{19}F NMR (C_2D_6CO, 298 K): −122.5 (pd, *o*-F), −133.3 (m, *m*-F), −74.0 (s, SO_3CF_3).

Table 3
Crystallographic data for complexes **1c**, **2b**, **2d**, and **4d**

	1c	**2b**	**2d**	**4d**
	$C_{38}H_{26}F_8P_2PdS_2$	$C_{38}H_{24}F_{10}P_2PtS_2$	$C_{40}H_{32}F_6P_2PtS_2$	$C_{66}H_{56}F_6P_4Pt_2S_2$ ($C_2F_6O_6S_2$)
Mw	867.05	991.72	947.81	1839.43
Space group	$C2/c$	$C2/c$	$P\bar{1}$	$P\bar{1}$
a (Å)	18.7885(11)	18.6304(18)	11.9449(7)	11.4866(8)
b (Å)	12.7777(9)	12.9706(10)	15.8927(9)	12.9775(9)
c (Å)	15.8106(10)	16.1175(17)	20.4850(11)	13.3213(10)
α (°)			80.169(4)	116.085(6)
β (°)	107.295(5)	109.585(8)	88.371(5)	95.255(6)
γ (°)			77.507(4)	99.240(4)
V (Å^3)	3624.1(4)	3669.4(6)	3740.8(4)	1730.6(2)
Z	4	4	4	1
μ (mm^{-1})	0.785	4.104	4.007	4.334
ρ_{calc} (g cm^{-3})	1.589	1.795	1.683	1.765
Temperature (K)	300(2)	297(2)	299(2)	299(2)
λ (Å)	0.71073	0.71073	0.71073	0.71073
R indices ($I < 2\sigma(1)$)[a] (%)	$R_1 = 2.92$, $wR_2 = 6.67$	$R_1 = 4.01$, $wR_2 = 10.60$	$R_1 = 3.77$, $wR_2 = 7.70$	$R_1 = 3.31$, $wR_2 = 8.21$
R indices (all data)[a] (%)	$R_1 = 4.01$, $wR_2 = 7.13$	$R_1 = 6.61$, $wR_2 = 12.02$	$R_1 = 6.18$, $wR_2 = 8.52$	$R_1 = 4.06$, $wR_2 = 8.61$

[a] $R(F_o) = \sum\|F_o| - |F_c|/\sum|F_o\|$, $Rw(F_o^2) = (\sum w(|F_o| - |F_c|)^2/\sum wF_o^2)^{1/2}$.

4.6.4. *[Pt(μ-o-SC$_6$H$_4$(CF$_3$))(dppe)]$_2$(SO$_3$CF$_3$)$_2$ (**4d**)*

Yield: 54.72%. M.p. 267–269 °C. *Anal.* Calc. for $C_{68}H_{56}F_{12}O_6P_4S_4Pt_2$: C, 44.39; H, 3.07; S, 6.96. Found: C, 45.0; H, 3.1; S, 6.8%. IR (cm^{-1}): 3515w, 3054w, 2963w, 1707w, 1586w, 1572w, 1482m, 1437vs, 1309vs, 1259vs, 1222s, 1153vs, 1139vs, 1103vs, 1028vs, 997s, 887m, 828m, 753s, 713s, 687s, 660m, 636vs, 595w, 571w, 534vs, 516m, 445m. ^{1}H NMR (C_2D_6CO, 298 K): 7.0 (m, *o*-H, thiolate); 8.4, 7.3 (m, *m*-H, thiolate); 7.3 (m, *p*-H, thiolate), 7.7, 7.5 (m, 20H, phenyl from phosphine), 2.5 (m, 4H, CH_2–CH_2). ^{31}P NMR (C_2D_6CO, 298 K): 54.4 (J_{Pt-P} = 3117 Hz). ^{19}F NMR (C_2D_6CO, 298 K): −58.5 (pt, *o*-CF_3), −79.1 (s, SO_3CF_3).

4.7. X-ray diffraction data

Suitable single crystals of complexes **1c**, **2b**, **2d** and **4d** were obtained by slow evaporation of acetone solutions and were found to be stable in air. Pertinent crystal data and other crystallographic parameters are listed in Table 3. The diffraction data were collected on a Bruker P4 diffractometer [32] using graphite monochromated Mo Kα radiation ($\lambda = 0.71073$ Å) and $\theta/2\theta$ or ω scan mode with variable scan speed. Absorption corrections were applied using ψ-scans.

For all four complexes non-H atoms were refined anisotropically and H atoms were placed in idealized positions [33]. In the case of **2b**, C and F atoms were restrained so that their U_{ij} components approximate to isotropic behavior. In the case of **4d**, the triflate ion was restrained to converge to a sensible geometry, through suitable restraints on bond lengths.

Selected geometric parameters for **1c**, **2b**, **2d** and **4d** are listed in Tables 2 and 3. Complete data have been deposited as a CIF, and raw data, as structure factors, are available on request to authors.

Acknowledgements

We thank Mr. Francisco Irby for his helpful assistance. We are grateful to DGAPA-UNAM (IN119305) and CONACYT (44494) for financial support of this research.

Appendix A. Supplementary material

CCDC 626895, 626896, 626897 and 626898 contain the supplementary crystallographic data for **1c**, **2b**, **2d** and **4d**. These data can be obtained free of charge via http://www.ccdc.cam.ac.uk/conts/retrieving.html, or from the Cambridge Crystallographic Data Centre, 12 Union Road, Cambridge CB2 1EZ, UK; fax: (+44) 1223-336-033; or e-mail: deposit@ccdc.cam.ac.uk. Supplementary data associated with this article can be found, in the online version, at doi:10.1016/j.poly.2007.05.025.

References

[1] V.K. Jain, L. Jain, Coord. Chem. Rev. 249 (2005) 3075.
[2] J.P. Blower, J.R. Dilworth, Coord. Chem. Rev. 76 (1987) 121.
[3] J.J. García, A. Arévalo, V. Montiel, F. del Río, B. Quiroz, H. Adams, P.M. Maitlis, Organometallics 16 (1997) 3216.
[4] D. Sellmann, A. Hille, F.W. Heinemam, M. Moll, A. Rösler, J. Sutter, G. Brehm, M. Reiher, B.A. Hess, S. Schneider, Inorg. Chim. Acta 348 (2003) 194.
[5] B. Krebs, G. Henkel, Angew. Chem., Int. Ed. Engl. 30 (1991) 769.
[6] J.C. Bayón, C. Claver, A.M. Masdeu-Bultó, Coord. Chem. Rev. 193–195 (1999) 73.
[7] (a) H.C. Clark, V.K. Jain, G.S. Rao, J. Organomet. Chem. 279 (1985) 181;
(b) V.K. Jain, G.S. Rao, Inorg. Chim. Acta 127 (1987) 161;

(c) M.L. Clarke, Polyhedron 20 (2001) 151;
(d) G.B. Karet, N.M. Kostić, Inorg. Chem. 37 (1998) 1021.
[8] H.C. Clark, V.K. Jain, G.S. Rao, J. Organomet. Chem. 279 (1985) 181.
[9] H. Torrens, Coord. Chem. Rev. 196 (2000) 331.
[10] (a) R. Salcedo, H. Torrens, Transition Met. Chem. 5 (1980) 247;
(b) L. Villanueva, M. Arroyo, S. Bernes, H. Torrens, Chem. Commun. (2004) 1942.
[11] (a) M. Capdevila, W. Clegg, P. Gonzalez-Duarte, B. Harris, I. Mira, J. Sola, I.C. Taylor, J. Chem. Soc., Dalton Trans. (1992) 2817;
(b) A. Singhal, V.K. Jain, B. Varghese, E.R.T. Tiekink, Inorg. Chim. Acta 285 (1999) 190.
[12] D.M. Roundhill, in: G. Wilkinson (Ed.), Comprehensive Coordination Chemistry, Pergamon Press, Oxford, 1987, p. 351.
[13] W. Beck, K.M. Stetter, S. Tadros, K.E. Shwarzhaus, Chem. Ber. 100 (1967) 3944.
[14] G. Wei, H. Liu, Acta Crystallogr., Sect. C 46 (1990) 2457.
[15] A. Singhal, V.K. Jain, B. Varghese, E.R.T. Tiekink, Inorg. Chim. Acta 285 (1999) 190.
[16] M.A. Usón, J.M. Llanos, J. Organomet. Chem. 663 (2002) 98.
[17] E.W. Abel, S.K. Bhargava, K.G. Orrell, Prog. Inorg. Chem. 32 (1984) 1.
[18] G. Rivera, S. Bernès, C. Rodríguez de Barbarín, H. Torrens, Inorg. Chem. 40 (2001) 5575.
[19] S.S. Oster, W.D. Jones, Inorg. Chim. Acta 357 (2004) 1836.
[20] E.W. Abel, G.W. Farrow, K.G. Orrell, V. Sik, J. Chem. Soc., Dalton (1977) 42.
[21] E.W. Abel, D.G. Evans, J.R. Koe, M.B. Hursthouse, M. Mazid, M.F. Mahon, K.C. Molloy, J. Chem. Soc., Dalton Trans. (1990) 1697.
[22] V.K. Jain, S. Kannan, R.J. Butcher, J.P. Jasinski, J. Organomet. Chem. 468 (1994) 285.
[23] M.C. Hall, J.A. Jarvis, B.T. Kilbourn, P.G. Owston, J. Chem. Soc., Dalton Trans. (1972) 1544.
[24] (a) D.D. Perrin, W.L.F. Armarego, Purification of Laboratory Chemicals, third ed., Pergamon Press, 1988;
(b) J.A. Riddick, T.K. Sakaro, Organic Solvents: Physical properties and Methods of Purification, Techniques of Chemistry, fourth ed., vol. II, Wiley Interscience, NY, 1970.
[25] (a) T.G. Appleton, M.A. Bennett, J.B. Tomkins, J. Chem. Soc., Dalton Trans. (1976) 439;
(b) M.P. Brown, R.J. Puddephatt, M. Rashidi, K.R. Seddon, J. Chem. Soc., Dalton (1977) 951.
[26] (a) M.E. Peach, Can. J. Chem. 46 (1968) 2699;
(b) V.A. Bertrán, A.J. García, E. Martin, P. Sosa, H. Torrens, Rev. Soc. Quím. Méx. 37 (1993) 185.
[27] R. Usón, J. Forniés, M.A. Usón, S. Herrero, J. Organomet. Chem. 447 (1993) 137.
[28] P.H.M. Budzelaar, gNMR-3.6, Cherwell Scientific Publishing Limited, Oxford, UK, 1995.
[29] J. Sandström, Dynamic NMR Spectroscopy, Academic Press, New York, 1982.
[30] H. Friebolin, Basic One and Two Dimensional NMR Spectroscopy, VCH Publishers, New York, 1995.
[31] K.G. Orrell, Coord. Chem. Rev. 96 (1989) 1.
[32] J. Fait, XSCANS Users Manual, Siemens Analytical X-ray Instruments Inc., Madison, WI, 1991.
[33] G.M. Sheldrick, SHELX97 Users Manual, University of Göttingen, Göttingen, Germany, 1997.

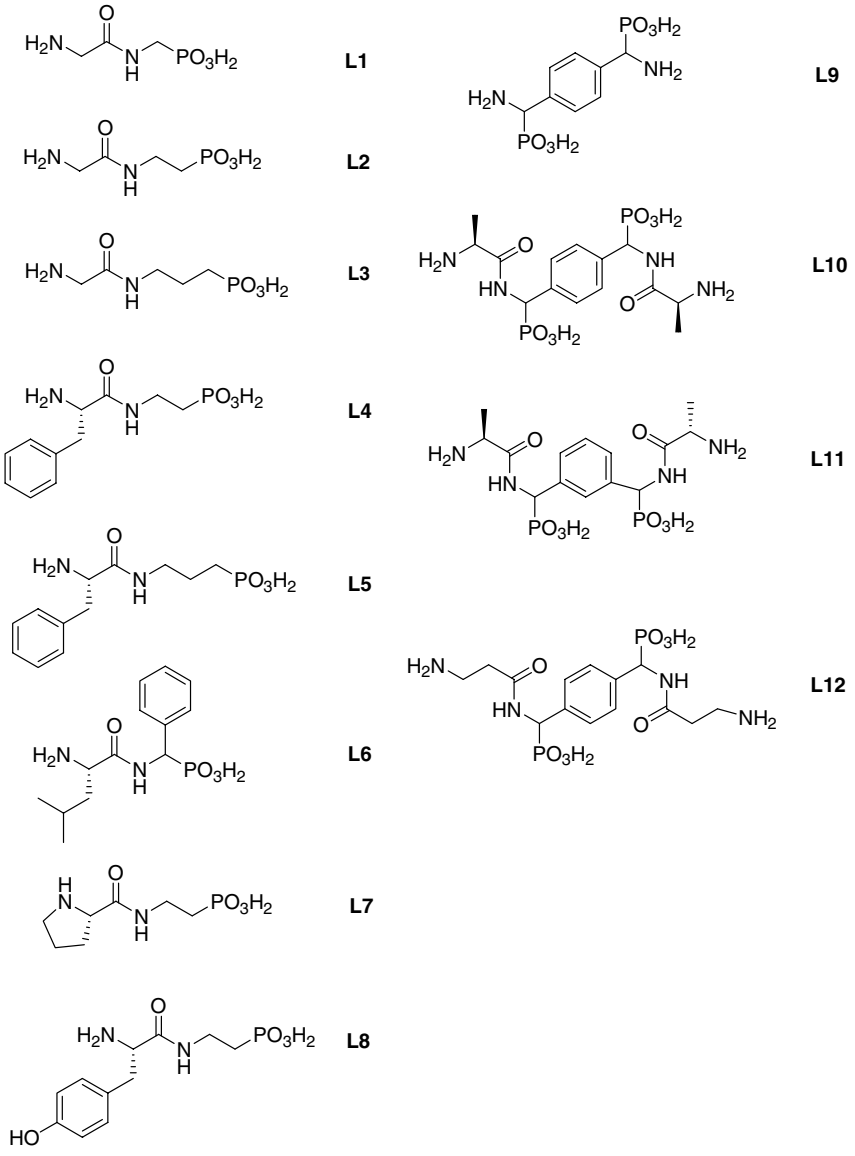


Fig. 1. Chemical structures of studied ligands.

liquids and were purified by precipitation of their oxalates from diethyl ether solutions.

Phosphono dipeptides were obtained according to previously described procedures using mixed carboxylic–carbonic acid procedure. They were purified by recrystallization from water–ethanol mixtures [10,11].

2.1.2. Diphosphonic ligands

*2.1.2.1. Synthesis of tetraethyl 1,4-phenylene-di(aminomethylphosphonate) and **L9**.* The reaction was carried out according to the procedure reported previously [12,13]. Terephthalaaldehyde (0.014 mol, 1.85 g) and benzylamine (0.028 mol, 2.98 g) were dissolved in 100 ml of methanol and stirred overnight at room temperature. The resulting crystalline Schiff base was filtered and analyzed by means of ^{1}H NMR ($CDCl_3$): δ: 4.86 (s, 2H, C**H**$_2$); 7.24–7.42 (m, 10H, benzyl protons), 7.86 (s, 4H, phenylene protons), 8.42 (s, 2H, C**H**=N), yield 80%, t.t. 102 °C. This product was of a good purity and therefore it was not purified. It was dissolved in 50 ml of toluene, and diethylphosphite (0.012 mol, 1.61 g) was added followed by refluxing the reaction mixture for 8 h. Then the volatile components of the solution were evaporated, crude product dissolved in dry diethyl ether and precipitated as oxalate upon addition of appropriate amount of anhydrous oxalic acid in ethyl ether. The formed precipitate was filtered, dried and suspended in dichloromethane (DCM). The suspension was washed with 1 M NaOH until all soil material was dissolved. After evaporation of the solvent, crude product was dissolved in 2.4 M solution of hydrogen chloride gas in methanol and hydrogenated over Pd/C catalyst at atmospheric pressure during 8 h. The progress of hydrogenation reaction was controlled by ^{31}P NMR spectroscopy. When the hydrogenation process was completed, reaction mixture was filtered through 4 cm layer of Cellite and solution was evaporated under reduced

pressure. The crude hydrochloride was purified by recrystallization from methanol/ethyl acetate mixture. In order to obtain **L9**, the tetraethyl 1,4-phenylene-di(aminomethylphosphonate) was refluxed in 36% hydrochloric acid during 8 h, then evaporated, treated with ethanol, and collected by filtration. The crude **L9** was purified by dissolving in base solution and acidification with concentrated hydrochloric acid. During this process, pure compound **L9** precipitated. For coordination studies this compound was used as dihydrochloride or tetra-sodium salt.

*2.1.2.2. Synthesis of **L10**, **L11** and **L12**.* The synthesis of these phosphono peptides **L10**, **L11** and **L12** was carried out accordingly to the general procedure described previously [14]. A solution of 0.005 mol of the Boc-L-Ala or Z-β-Ala and 0.0052 mol of triethylamine in 40 ml of dry chloroform was cooled to −5 °C and treated with (0.0055 mol) of ethyl chloroformate. After 40 min, 0.0025 mol of tetraethyl 1,4-phenylene-di(aminomethylphosphonate) (see Section 2.1.2.1) was added with stirring and the solution was left to reach room temperature, followed by slow warming up to the boiling point. The resulting solution was washed successively with water, 1 M hydrochloride acid, water, saturated solution of sodium bicarbonate and water. Finally, it was extracted with brine and dried over sodium sulphate. The solvent was distilled off and the oily residue representing crude diester of phosphono peptide was dissolved in 20 ml of 40% hydrogen bromide (for **L10**) in glacial acetic acid and left overnight. Then volatile reagents and solvents were removed under reduced pressure. The residues were dissolved in absolute ethanol and by addition of propylene oxide crude peptide precipitated. In order to hydrolyze crude diesters of **L11** and **L12** 0.041 mol (5.4 ml) of bromotrimethylsilane with each compounds were mixed during three days. Then reaction mixtures were evaporated, dissolved in methanol and stirred for 1 day. After that, the solutions were again evaporated and products precipitated by addition of ethanol. The peptides were re-crystallized from ethanol and/or ethanol–water solutions.

*2.1.3. Spectroscopic characterization of ligands: **L1**–**L12***

*2.1.3.1. N-Glycylaminomethylphosphonic acid – **L1**.* This peptide melted with decomposition at 279–284 °C. ^{1}H NMR (D_2O + NaOD) δ (ppm): 3.55 (d, 2H, $J = 13.5$ Hz, PCH_2), 4.18 (s, 2H, glycyl CH_2); ^{31}P NMR, δ: 21.52. Yield: 58%.

*2.1.3.2. N-Glycyl-2-aminoethylphosphonic acid – **L2**.* This peptide decomposed over 270 °C. ^{1}H NMR (D_2O + NaOD) δ (ppm): 1.3–2.05 (m, 2H, PCH_2CH_2), 3.05–3.85 (m, 2H, PCH_2CH_2), 3.87 (s, 2H, glycyl CH_2);^{31}P NMR, δ: 22.06. Yield: 58%.

*2.1.3.3. N-Glycyl-3-aminopropylphosphonic acid – **L3**.* M.p. 247–248 °C. ^{1}H NMR (D_2O + D_2SO_4) δ (ppm): 1.75–2.4 (m, 4H, PCH_2CH_2), 3.63 (t, 2H, $J = 6.5$ Hz, NCH_2), 4.14 (s, 2H, glycyl CH_2); ^{31}P NMR, δ: 22.75. Yield: 66%.

*2.1.3.4. N-L-Phenylalanyl-2-aminoethylphosphonic acid – **L4**.* This peptide melted with decomposition at 288–289 °C. ^{1}H NMR (D_2O + NaOD) δ (ppm): 1.25–1.90 (m, 2H, PCH_2CH_2), 2.84 (d–d, 2H, $J = 6.5$ and 7.0 Hz, CH_2Ph), 3.10–3.75 (m 3H, CH_2P and phenylalanyl α-CH), 7.08–7.50 (m, 5H, aromatic protons); ^{31}P NMR, δ: 25.61. Yield: 55%.

*2.1.3.5. N-L-Phenylalanyl-3-aminopropylphosphonic acid – **L5**.* This peptide melted with decomposition at 279–281 °C. ^{1}H NMR (D_2O + D_2SO_4) δ (ppm): 1.6–2.25 (m, 4H, PCH_2CH_2), 3.2–3.9 (m, 4H, CH_2Ph and NCH_2), 4.55 (t, 1H, $J = 7.0$ Hz, phenylalanyl α-CH), 7.68 (bs, 5H, aromatic protons); ^{31}P NMR, δ: 21.65. Yield: 93%.

*2.1.3.6. N-L-Leucyl-D,L-aminobenzylphosphonic acid – **L6**.* This peptide melted with decomposition at 266–267 °C. ^{1}H NMR (D_2O + D_2SO_4) δ (ppm): 1.24 and 1.41 (d, 3H each, $J = 7.0$ Hz, CH_3), 2.0–2.4 (m, 3H, CH_2CH), 4.70 (t, 1H, $J = 7.0$ Hz, leucyl α-CH), 5.71 (d, 1H, $J = 23.0$ Hz, CHP), 7.88 (bs, 5H, aromatic protons); ^{31}P NMR, δ: 14.89, 14.66. Yield: 55%.

*2.1.3.7. N-L-Prolyl-2-aminoethylphosphonic acid – **L7**.* This peptide melted with decomposition at 281–282 °C. ^{1}H NMR (D_2O + NaOD) δ (ppm): 1.5–2.65 (m, 6H, prolyl CH_2CH_2CH and PCH_2CH_2), 3.15–3.80 (m, 4H, PCH_2CH_2 and prolyl NCH_2), 4.35 (t, 1H, $J = 7.5$ Hz, prolyl α-CH); ^{31}P NMR, δ: 21.09. Yield: 65%.

*2.1.3.8. N-L-Tyrosyl-2-aminoethylphosphonic acid – **L8**.* This peptide melted with decomposition at 293–295 °C. ^{1}H NMR δ (ppm): 1.42–1.70 (m, 2H, PCH_2CH_2), 1.79–2.00 (m, 2H, PCH_2CH_2), 3.01 (m, 2H CH_2Ph), 3.98 (t, 1H, CHCO, $J = 6.7$ Hz), 6.81–7.10 (d, 2H each, $J = 7$ Hz aromatic protons); ^{31}P NMR, δ: 19.42. Yield: 55%.

*2.1.3.9. 1,4-Phenylene-di(aminomethylphosphonic) acid – **L9**.* Compound **L9** decomposed upon heating over 278 °C. ^{1}H NMR (D_2O + NaOD) δ: 3.55 (d, 2H, $J = 14.4$ Hz, CH), 7.10 (s, 4H, aromatic protons); ^{31}P NMR, δ: 16.26. Yield: 55%.

*2.1.3.10. 1,4-Phenylene-di(N-L-alanylaminomethylphosphonate) – **L10**.* The compound **L10** decomposed upon heating over 300 °C. ^{1}H NMR (D_2O) δ: 1.38 and 1.50 (d, 3H each, $J = 6.0$ Hz, alanyl CH_3); 4.10 (m, 2H, $J = 6.0$ Hz, alanyl α-CH), 4.99 and 4.96 (d, 1H each, $J = 19.5$ Hz, phosphonate α-CH), 7.37 (s, 4H, aromatic protons); ^{31}P NMR, δ: 14.51; 14.41. Yield: 65%.

*2.1.3.11. 1,3-Phenylene-di(N-L-alanylaminomethylphosphonate) – **L11**.* The compound **L11** decomposed upon heating over 320 °C. ^{1}H NMR (D_2O) δ: 1.40 and 1.51 (d, 3H each,

$J = 7.0$ Hz, alanyl C**H**$_3$); 4.10 (m, 2H, alanyl α-C**H**, $J = 6.0$ Hz), 4.97 and 5.00 (d, 1H each, phosphonate α-C**H**, $J = 19.0$ Hz), 7.28 (m, 4H, aromatic protons); ^{31}P NMR, δ: 14.64 (m). Yield: 23%.

*2.1.3.12. 1,3-Phenylene-di(N-β-alanylaminomethylphosphonate) – **L12**.* The compound **L12** decomposed upon heating over 320 °C. ^{1}H NMR (D_2O) δ:2.69 (m, 4H, CH_2CH_2–); 3.16 (t, 4H, CH_2CH_2, $J = 6.4$ Hz), 5.03 (d, 2H, $J = 20$ Hz, phosphonate α-C**H**), 7.29 (m, 4H, aromatic protons); ^{31}P NMR, δ: 16.1 (broad signal). Yield: 45%.

2.2. Potentiometric studies

Stability constants both for protons and complexes were determined by pH-metric titration of 1.8–2.0 cm^3 samples at 25 °C over pH range of 2.5–11. The ligand concentration in the various samples was 2×10^{-3} mol dm^{-3} and metal

Table 1
The protonation constants of **L1**–**L8** with Cu(II) at 25 °C and $I = 0.1$ mol dm^{-3} (KNO_3)

Proton complexes	L1	L2	L3	L4	L5	L6	L7	L8
$\log\beta(HL)$	8.37(1)	8.32(2)	8.51(1)	7.83(1)	7.98(1)	9.04(1)	8.05(1)	10.28(1)
$\log\beta(H_2L)$	14.48(1)	15.16(4)	15.70(1)	14.65(6)	15.08(1)	15.89(1)	14.21(1)	17.57(2)
$\log\beta(H_3L)$	~15.92(5)	~17.00(13)	~18.20(2)	~16.62(2)	~17.06(1)	~17.36(4)	~15.53(10)	23.67(2)
$\log\beta(H_5L)$								~25.26(6)
$pK_1(HL)$	8.37	8.32	8.51	7.83	7.98	9.04	8.05	10.28
$pK_2(H_2L)$	6.11	6.84	7.19	6.82	7.10	6.85	6.16	7.29
$pK_3(H_3L)$	~1.44	~1.84	~2.50	~1.97	~1.98	~1.47	~1.32	6.10
$pK_4(H_4L)$								~1.59

Table 2
The complex formation constants of **L1**–**L8** with Cu(II) at 25 °C and $I = 0.1$ mol dm^{-3} (KNO_3)

Metal complexes	L1	L2	L3	L4	L5	L6	L7	L8
$\log\beta(CuH_1L)$	12.09(4)	12.68(2)	13.41(2)		12.34(2)	13.10(8)		16.04(2)
$\log\beta(CuL)$	6.79(4)	7.38(3)	7.22(3)	7.22(2)	5.98(6)	8.33(2)	6.73(5)	10.43(2)
$\log\beta(CuH_{-1}L)$	1.63(2)	2.12(3)	0.27(10)	1.98(1)	0.14(3)	2.98(2)	1.86(2)	
$\log\beta(CuH_{-2}L)$	−8.19(7)					−7.34(7)	−7.49(3)	
$\log\beta(CuHL_2)$		19.60(15)	19.32(8)					24.81(2)
$\log\beta(CuL_2)$	12.64(6)	13.38(4)	12.70(3)	13.37(2)	11.27(4)	14.95(4)	13.08(4)	15.42(3)
$\log\beta(CuH_{-1}L_2)$	4.86(3)	5.42(3)	5.07(2)	5.99(2)	3.73(2)	6.24(4)	4.86(6)	4.66(7)
$\log\beta(CuH_{-2}L_2)$	−5.27(10)	−4.72(2)	−4.77(2)	−4.10(2)	−6.34(2)	−4.38(14)		−6.01(7)
$\log\beta(CuH_{-4}L_2)$								−28.50(14)
$pK(MHL)$	5.30	5.30	6.19		6.36	4.77		5.61
$pK(ML)$	5.16	5.26	6.95	5.24	5.84	5.35	4.87	
$pK(MH_{-1}L)$	9.82					10.32	9.35	
$pK(MH_{-2}L)$								
$pK(MHL_2)$		6.22	6.62					9.39
$pK(ML_2)$	7.78	7.96	7.63	7.38	7.54	8.71	8.22	10.76
$pK(MH_{-1}L)$	10.13	10.14	9.84	10.09	10.07	10.62		10.67

Table 3
The protonation and complex formation constants of **L9**–**L12** with Cu(II) at 25 °C and $I = 0.1$ mol dm^{-3} (KNO_3)

Proton complexes	L9	L10	L11	L12	Metal complexes	L9	L10	L11	L12
$\log\beta(HL)$	10.09(1)	8.91(1)	8.95(1)	10.48(1)	$\log\beta(CuH_2L)$	24.00(5)	22.64(4)	22.97(5)	25.94(1)
$\log\beta(H_2L)$	19.34(1)	17.13(1)	17.15(1)	20.11(1)	$\log\beta(CuH_1L)$	19.39(3)	18.18(1)	18.15(3)	18.96(3)
$\log\beta(H_3L)$	25.45(1)	23.78(1)	23.88(1)	27.14(1)	$\log\beta(CuL)$	13.31(4)	12.53(2)	12.04(4)	11.60(2)
$\log\beta(H_4L)$	30.61(1)	29.55(1)	29.58(1)	33.03(1)	$\log\beta(CuH_{-1}L)$		2.43(2)	2.16(7)	2.43(3)
$\log\beta(H_5L)$	~31.93(3)	~31.24(1)		35.26(2)	$\log\beta(CuH_{-2}L)$			−8.27(6)	
$\log\beta(H_6L)$					$\log\beta(CuHL_2)$	28.97(4)			
					$\log\beta(CuL_2)$	20.03(5)			
					$\log\beta(CuH_{-1}L_2)$	10.16(5)			
$pK_1(HL)$	10.09	8.91	8.95	10.48	$pK(MH_2L)$	4.61	4.46	4.81	6.98
$pK_2(H_2L)$	9.24	8.22	8.20	9.63	$pK(MHL)$	6.09	5.64	6.12	7.35
$pK_3(H_3L)$	6.12	6.65	6.73	7.03	$pK(ML)$		10.00	9.87	9.17
$pK_4(H_4L)$	5.15	5.77	5.70	5.89	$pK(MHL_2)$	8.94		10.43	
$pK_5(H_5L)$	~1.33	~1.69		2.23	$pK(ML_2)$	9.88			

ion to ligand ratio was set as 1:2 to 1:6. Initial solutions were titrated with NaOH (Merck) delivered by a 0.25 ml micrometer syringe previously calibrated by weight titrations of standard materials. The purities and exact concentrations of the solutions of the ligands were determined by the method of Gran [15]. The pH-metric titrations were performed involving 0.1 M KNO_3 background using a MOLSPIN automatic titration system with a Russell CMAW 711 microcombined electrode calibrated daily in hydrogen-ion concentration using HNO_3 (Aldrich) [16]. The SUPERQUAD computer program was used for calculations of stability constants [17]. Standard deviations quoted refer to random errors only. They are, however, a good indication of the importance of a particular species present in the equilibrium.

2.3. Spectroscopic studies (UV–Vis, EPR and CD)

The absorption spectra were recorded on Beckman DU 650 spectrofotometr termostated at 25 °C. Electron paramagnetic resonance (EPR) spectra were performed in ethylene glycol-water (1:2 v/v) solution at 77 K using Bruker ESP 300 spectrometer at the X-band frequency (9.3 GHz). Circular dichroizm (CD) spectra were recorded on a Jasco J-715 spectropolarimeter in the 800–235 nm range. The values of $\Delta\varepsilon$, i.e. $\varepsilon_l - \varepsilon_r$, and ε were calculated at the maximum concentration of the particular species obtained from the potentiometric data. The ligand concentration used in the spectroscopic samples was $4–6 \times 10^{-3}$ mol dm^{-3}, and metal concentration was $1–2 \times 10^{-3}$ mol dm^{-3}.

3. Results and discussion

3.1. Protonation studies

The protonation constants of the studied ligands are given in Tables 1 and 3. The dipeptides **L1**–**L7** contain three protonation sides, whereas **L8** contains one more proton located in a tyrosine side chain (pK 10.28). These are protons of the amine (pK 7.29–9.04) and phosphonic (pK 6.10–7.10) groups. One phosphonic proton is very acidic (p$K \approx 1.0$) [18,19] and it was only approximately evaluated. The ligands **L9**, **L10** and **L12** possess five protonation sides (H_5L) and **L11** peptide four (H_4L) (Table 3). The highest pK belongs to the amine groups and the remaining to the phosphonic functions.

3.2. Complexation studies

3.2.0.13. *L1–L8*

The stability constants obtained for the Cu(II) complexes are given in Tables 2 and 3. To clarify the binding modes of the complexes formed – visible, CD and EPR spectra were also measured (Tables 4 and 5). Low pH species of the CuHL type are formed for all study ligands except for **L4** and **L7**. In this species Cu(II) ion coordinates in bidentate mode *via* N-terminal amino nitrogen and peptide carbonyl group. In almost every case, CuHL is a minor species except for **L3** and **L5**, which possess longer linker between terminal phosphonic group and a peptide bond (Fig. 1). Deprotonation of CuHL results in formation of CuL, a minor species in pH range of 5–7, followed by formation of $CuH_{-1}L$. In the latter complex, the binding mode involves $\{NH_2, N^-, PO_3^{2-}\}$ donor set characteristic for dipeptides [20,21]. The binding mode in $CuH_{-1}L$ is clearly confirmed by the spectroscopic parameters with maximum of d–d transitions located at 620–650 nm and

Table 4
Spectroscopic data for Cu(II) complexes of **L1**, **L2**, **L4**–**L8**. Metal to ligand ratio = 1:3; [Cu(II)] = 0.002 M

Species	UV–Vis		CD		EPR	
	λ (nm)	ε (M^{-1} cm^{-1})	λ (nm)	$\Delta\varepsilon$ (M^{-1} cm^{-1})	$A_\parallel$ (G)	$g_\parallel$
L1						
CuL	minor				144	2.32
$CuH_{-1}L$	629	65			174	2.25
$CuH_{-2}L$	618	59			170	2.23
L2						
CuL	minor				145	2.23
$CuH_{-1}L$	650	56			177	2.26
$CuH_{-2}L_2$	638	60			175	2.24
L4						
CuL	minor				150	2.33
$CuH_{-1}L$	641	57	625	−0.192	182	2.26
			305	0.456		
$CuH_{-1}L_2$	634	59	618	−0.198	182	2.24
			304	0.478		
$CuH_{-2}L_2$	631	56	593	−0.206	182	2.23
			296	0.441		
L5						
CuL	minor				148	2.23
$CuH_{-1}L_2$	634	65	620	−0.176	195	2.32
			304	0.484		
			231	−1.680		
$CuH_{-2}L_2$	634	54	591	−0.183	191	2. 32
			698	0.021		
			294	0.487		
L6						
CuL	minor				145	2.33
$CuH_{-1}L$	643	75	610	−0.146	180	2.26
			235	−2.438		
			658	0.133		
$CuH_{-2}L$	620	67	534	−0.984		
			351	0.032		
			230	−3.130		
L7						
CuL	minor				136	2.37
$CuH_{-1}L$	621	80	631	−0.488	182	2.27
			303	0.569		
			250	−1.36		
$CuH_{-2}L$	615	74	627	−0.275	167	2.23
			296	0.650		
			284	−2.04		
L8						
CuL	646	56			164	2.27
$CuHL_2$	631	64			177	2.26
CuL_2	632	64			177	2.26

Table 5
Spectroscopic data for Cu(II) complexes of **L10**, **L11** and **L12**

Species	UV–Vis		CD		EPR	
	λ (nm)	ε ($M^{-1}\,cm^{-1}$)	λ (nm)	$\Delta\varepsilon$ ($M^{-1}\,cm^{-1}$)	$A_{\parallel}$ (G)	$g_{\parallel}$
L10						
CuH_2L	minor					
CuHL	636	75	245	−0.655	134	2.38
			291	0.445		
			590	−0.234		
			698	0.056		
CuL	628	98	258	−0.942	176	2.25
			303	0.548		
			602	−0.223		
$CuH_{-1}L$	611	93	261(sh)	−0.983	160	2.23
			297	0.440		
			587	−0.201		
L11						
CuH_2L	minor					
CuHL	645	54	298	0.331	175	2.25
			631	−0.161		
CuL	640	110	251(sh)	−1.225	176	2.25
			303	0.611		
			641	−0.138		
$CuH_{-1}L$	616	119	241(sh)	−1.016	166	2.23
			291	0.498		
			578	−0.145		
$CuH_{-2}L$	620	119	284	0.567	166	2.23
			585	−0.169		
L12						
CuH_2L	743	78				
CuHL	704	78				
CuL	632	104			171	2.26
$CuH_{-1}L$	590	109			171	2.26

Metal to ligand ratio = 1:3; [Cu(II)] = 0.002 M.

EPR parameters with $A_{\parallel}$ between 174–182 G and $g_{\parallel}$ close to 2.25 (Table 4) [18].

For first three ligands **L1**, **L2** and **L3**, the major impact on the $CuH_{-1}L$ formation has the size of the chelating ring with $\{N^-, PO_3^{2-}\}$ donor set. This size depends on the linker between two donor atoms. p*K* values of the reaction of $CuH_{-1}L$ formation which are 5.16, 5.26 and 6.95, respectively, the conclusion about five – the most favourable, six and seven-membered chelating ring can be made due to the rising p*K*.

The deprotonation of **L1**, **L6** and **L7** copper complexes in high pH leads to $CuH_{-2}L$ or $CuH_{-1}LOH$ species formation and can be assigned to hydrolysis of water molecules from the complex coordination sphere as in the simple dipeptides. Because the measurements were performed in the presence of excess of ligand, a 1:2 species were detected potentiometrically, although CuL_2 species can not be determined by spectroscopic measurements due to a overlapping with the major equimolar $CuH_{-1}L$ species. We may assume the $\{NH_2, N^-, PO_3^{2-}; NH_2, CO\}$ coordination pattern for CuL_2 form.

3.2.0.14. *L9–L12*

The interaction of Cu(II) ions with core ligand **L9** yields in the formation of CuH_2L complex (Fig. 2) in which one

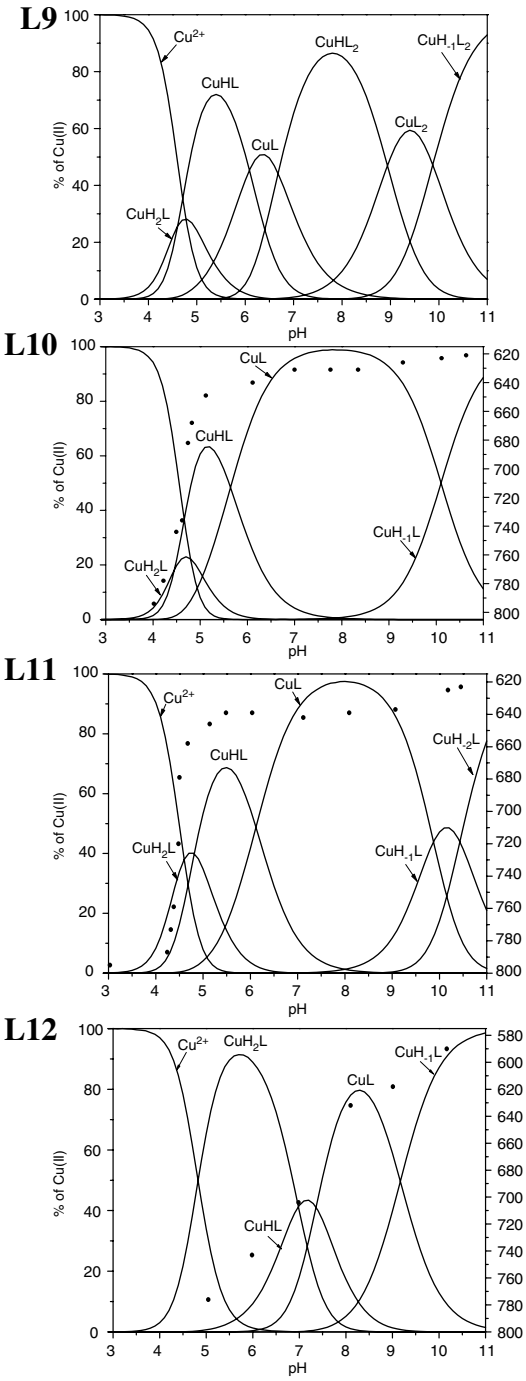


Fig. 2. Species distribution curves for the Cu(II)–**L1**, **L2**, **L3** and **L4** complexes as a function of pH. For **L10**, **L11** and **L12** overlapped with UV–Vis d–d transitions (in the same concentration conditions).

set of $\{NH_2, PO_3^{2-}\}$ donors is involved in the metal ion coordination. The formation of two other species CuHL and CuL results from the consecutive proton dissociation from amino and phosphonic functions. The coordination of Cu(II) ion causes distinct decrease of the p*K* values of the two functions located on the other side of the molecule (Table 3). The further increase of pH results in the CuL_2 complex formation with the coordination mode $\{2 \times NH_2, 2 \times PO_3^{2-}\}$. This coordination is supported by

the spectroscopic parameter, the d–d transitions centered at 637 nm. The formation of the $CuH_{-1}L_2$ species at high pH indicates the beginning of the hydrolysis process.

Two peptides **L10** and **L11** possessing two dipeptide units in *para* and *meta*-positions (Fig. 1) were found to coordinate Cu(II) ions in the same mode as X–Y–PO_3^{2-} phosphonic dipeptides. Despite different positions of attached peptide units, both ligands demonstrate similar binding properties towards Cu(II) ion, in which only one peptide moiety is involved. CuH_2L, the first formed complex, involves most likely the $\{NH_2, C{=}O, PO_3^{2-}\}$ donor set [21]. The proton dissociation in the ligand results in the formation of CuHL species. This reaction is accompanied by the significant change in the d–d transitions shifted to 628 nm in UV–Vis and to 629 nm in CD spectra. Also the EPR parameters $A_{\parallel} = 175$ and $g_{\parallel} = 2.25$ correspond to formation of the 2 N species resulting from the $\{NH_2, N^-, PO_3^{2-}\}$ binding mode [21]. The comparison of $\log K$ values of proton release from amide of these peptides and simple phosphono dipeptides due to its copper binding, showed that they are much lower. Thus, in the case of compounds **L10** and **L11**, they are 4.46 and 4.81, respectively, whereas for structurally corresponding dipeptides Ala-Leu(P) and Leu-Ala(P) they are 5.58 and 5.23 [20]. The formation of CuL and $CuH_{-1}L$ species is associated with deprotonation of phosphonic and amino groups from the unbound peptidyl fragment of the molecule.

The replacement of L-Ala residue in **L11** with β-Ala moiety leading to **L12** results in the lack of a chiral center and elongation of the peptidic chain. This change forces a little variation in the coordination properties of the ligand. The differences in stability constants derive from the different protonation constants, which for this β-Ala peptide are much higher in the case of amino group and in the change of the size of the $\{NH_2,N^-\}$ chelate ring (Table 3).

4. Conclusions

Phosphono-peptides containing simple aminophosphonic acids **L1**–**L8** exhibited a typical coordination mode which is very similar to classic dipeptides. The main species formed is the $CuH_{-1}L$ complex with $\{NH_2, N^-, PO_3^{2-}\}$ coordination mode. Phenylene-1,4-di(aminomethylphosphonic) acid **L9** coordinates Cu(II) ions using 1x or $2x\{NH_2, PO_3^{2-}\}$ donor sets deriving from aminophosphonic units located either on one or on two ligand molecules. Dipeptide derivatives of **L9** form the 1:1 complexes, in which copper ion is coordinated by only one dipeptidyl moiety. The comparison of the co-ordination abilities of **L11** and **L12** has shown that also elongation of a peptide chain does not favor the second peptidic amino nitrogen coordination.

References

[1] P. Kafarski, B. Lejczak, in: V.P. Kukhar, H.R. Hudson (Eds.), Aminophosphinic and Aminophosphonic Acids, Chemistry and Biological Activity, John Wiley & Sons Ltd, Chichester, 2000, p. 407.
[2] Yu.I. Kuznetsov, G.Yu. Kazanskaya, N.V. Tsirulnikova, Prot. Met. 39 (2003) 120.
[3] V. Kubicek, J. Rudovsky, J. Kotek, P. Hermann, L.V. Elst, R.N. Muller, Z.I. Kolar, H.T. Wolterbeek, J.A. Peters, J. Am . Soc. Chem. 122 (2005) 16477.
[4] T. Kiss, I. Lazar, in: V.P. Kukhar, H.R. Hudson (Eds.), Aminophosphinic and Aminophosphonic Acids, Chemistry and Biological Activity, John Wiley & Sons Ltd, Chichester, 2000, p. 285.
[5] R. Lipiński, L. Chruściński, P. Młynarz, B. Boduszek, H. Kozłowski, Inorg. Chim. Acta 322 (2001) 157.
[6] S. Sobek, B. Boduszek, H. Kozłowski, Inorg. Chim. Acta 355C (2003) 462.
[7] E. Gumienna-Kontecka, J. Gałęzowska, M. Drąg, R. Latajka, P. Kafarski, H. Kozłowski, Inorg. Chim. Acta 357 (2004) 1632.
[8] T. Schrader, A.D. Hamilton (Eds.), Functional Synthetic Receptors, Wiley-VCH verlag GmbH & Co., KGaA, 2005, p. 48.
[9] P. Młynarz, S. Śliwińska, A. Olbert-Majkut, G. Schroeder, B. Bańkowski, P. Kafarski, J. Mol. Struct. (in press), doi:10.1016/j.molstruc.2007.03.022.
[10] P. Kafarski, P. Mastalerz, Synthesis of dipeptides containing p-terminal 2-aminoethylphosphonic acid, Roczniki Chemii 51 (1977) 433.
[11] P. Kafarski, B. Lejczak, P. Mastalerz, J. Szewczyk, Cz. Wasielewski, Can. J. Chem. 60 (1982) 3081.
[12] J. Barycki, R. Gancarz, M. Milewska, R. Tyka, Phosphorus Sulfur Silicon 105 (1995) 117.
[13] J. Lewkowski, M. Rzezniczak, R. Skowronski, Heteroatom Chem. 11 (2000) 144.
[14] B. Lejczak, P. Kafarski, H. Sztajer, P. Mastalerz, J. Med. Chem. 29 (1987) 2212.
[15] G. Gran, Acta Chem. Scand. 29 (1950) 599.
[16] H. Irving, M.G. Miles, L.D. Pettit, Anal. Chim. Acta 38 (1967) 475.
[17] P. Gans, A. Sabatini, A. Vacca, J. Chem. Soc., Dalton Trans. (1985) 1195.
[18] A.M. Wozniak, G. Nowogrodzki, Talanta 26 (1979) 381.
[19] B.M. Wozniak, G. Nowogrodzki, Talanta 26 (1979) 1135.
[20] B. Kurzak, A. Wożna, J. Jezierska, M. Jeżowska-Bojczuk, W. Szczepanik, P. Kafarski, Polyhedron 23 (2004) 1939.
[21] J. Gałęzowska, S. Sobek, M. Drąg, A. Mucha, P. Kafarski, H. Kozłowski, Polish J. Chem. 79 (2005) 603.

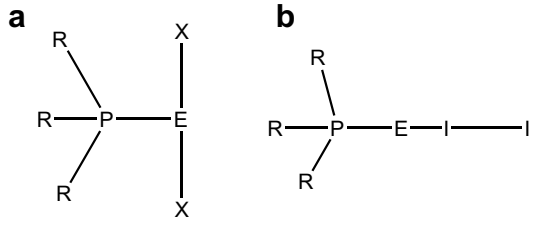


Fig. 1. Structural isomers for R_3PEX_2 (E = S, Se and Te) compounds; (a) T-shaped motif, (b) charge-transfer "molecular spoke" adduct.

formation of a stable compound, Et_3PTeCl_2 [7]. This compound has been crystallographically characterised and features a T-shaped motif at tellurium, as shown in Fig. 1a. Molecules of Et_3PTeCl_2 are linked by weak tellurium···chlorine interactions to form centrosymmetric dimers.

R_3PSeBr_2 adducts were first reported by Williams and Wynne in 1976 ($R_3 = Ph_3$, (*m*-tolyl)$_3$ and (*p*-tolyl)$_3$) [8], who assigned a T-shaped geometry to these adducts on the basis of vibrational spectroscopic data. A T-shaped geometry has subsequently been confirmed crystallographically for a series of R_3PSeBr_2 compounds, R = $(Me_2N)_3$, Cy_3 [9], $^iPr_3$, $^iPr_2{}^tBu$, $^iPr{}^tBu_2$ [10], and for a number of dibromine adducts of bidentate phosphine selenides, $dppmSe_2Br_4$ and $dppeSe_2Br_4$ [11]. These selenium(II) compounds feature a T-shaped geometry as predicted by VSEPR theory (based on a pseudo trigonal bipyramidal arrangement, taking into account the two lone pairs on selenium). Typically, in such compounds the Br–Se–Br angle should be distorted from linear as a result of repulsion from the lone pairs. These adducts do show distorted Br–Se–Br angles, but the distortion appears to be *towards* the lone pairs and away from the bulky groups on the phosphine. The distortion is more extreme where there is a higher degree of steric hindrance, e.g., in the structure of $^iPr{}^tBu_2PSeBr_2$, where Br–Se–Br: 159.16(4)° [10]. A T-shaped geometry has also been observed for the only reported R_3PTeBr_2 adduct, Et_3PTeBr_2 [7], although here the Br–Te–Br angle is distorted away from the lone pairs, possibly as a consequence of the presence of weak intermolecular tellurium···bromine interactions: similar interactions are not observed in the T-shaped selenium compounds. In contrast, the reactions of tertiary phosphine sulfides, R_3PS, with dibromine usually result in cleavage of the P–S bond and subsequent formation of R_3PBr_2 [12]. Some exceptions are known, for example, R_3PSBr_2 can be isolated when R = Cy (although this compound also undergoes P–S bond cleavage in polar solvents), and the reaction of dibromine with $(Me_2N)_3PS$ results in formation of an S_3 bridged dinuclear ionic species, $[(Me_2N)_3P–S–S–S–P(NMe_2)_3][Br_3]_2$ in moderate yield [12].

The reaction of Et_3PTe with diiodine also yields a T-shaped compound, Et_3PTeI_2 [7], but the reactions of R_3PE (E = S and Se) result in the formation of charge-transfer (CT) spoke adducts of the type shown in Fig. 1b [2,5,11–16]. These adducts consist of a 3c–4e CT system, and display I–I bonds which are lengthened with respect to diiodine in the solid state, 2.715(6) Å [17], as a consequence of donation of electron density from the chalcogen atom to the σ^* antibonding orbital of the diiodine molecule. Tertiary phosphine selenides are better donors towards diiodine than the analogous tertiary phosphine sulfides, as illustrated by a comparison of $(Me_2N)_3PSeI_2$ and $(Me_2N)_3PSI_2$. In the former, the I–I distances are 2.959(2)/2.965(2) Å [13], considerably longer than the I–I bond in the latter, 2.856(1) Å [12], and consistent with the greater donating ability of the phosphine selenide. The geometry at the chalcogen atom is bent in the CT adducts as a result of the presence of the two lone pairs at selenium. The P–E–I (E = S and Se) angles in these molecules are typically 100–108° and thus show distortion from the idealised angle for a pseudo-tetrahedral arrangement due to a combination of repulsion from the lone pairs, and retention of some double bond character in the phosphorus–chalcogen bonds, unlike the situation observed in the T-shaped R_3PSeBr_2 compounds, which feature single P–Se bonds. This phenomenon is illustrated by a comparison of the P–Se bond lengths between $(Me_2N)_3PSeBr_2$, where there is a P–Se single bond of 2.262(2) Å [9], $(Me_2N)_3PSeI_2$, where the P–Se bonds range between 2.185(7) and 2.175(8) Å [13], and $(Me_2N)_3PSe$, which has a P=Se double bond of 2.114(1) Å [18]. These observations agree with spectroscopic data *viz*. (i), a reduction in ^1J(PSe) coupling constants in the $^{31}P\{^1H\}$ NMR spectra, and (ii), a shift to lower frequencies of the ν(P–Se) band in the IR spectra upon adduct formation. Addition of excess iodine to the R_3PSeI_2 systems results in the formation of either $[R_3PSeI]^+$ or $[R_3PSe–I–SePR_3]^+$ cations linked by weak I–I interactions to polyiodide anions [19–21].

The only reported adducts of R_3PE with interhalogens are the IBr and ICl adducts of Ph_3PS, both of which display a CT spoke motif, as observed for the I_2 analogues [22]. In both cases the interhalogen is bound by the heavier iodine atom. In contrast, the Ph_3PS/I_2 system is more complex, and despite the fact that the 1:1 Ph_3PSI_2 adduct was identified in solution, it was initially believed it could not be isolated in the solid-state due to the poor donating capability of Ph_3PS [4]. The 2:3 adduct $Ph_3PSI–I–I_2–I–ISPPh_3$ was instead isolated and crystallographically characterised [23]. Later work by Kaur and Lobana showed that formation of the 1:1 adduct was solvent dependent, and could be synthesised in CH_2Cl_2, whilst the 2:3 adduct was favoured in CCl_4 [24]. The 1:1 adduct, Ph_3PSI_2, was subsequently crystallographically characterised by Bricklebank and coworkers [14], and shown to adopt the same linear E–I–I motif as Ph_3PSeI_2. A 3:1 adduct has also been reported when excess iodine is added to the system, and consists of a 1:1 Ph_3PSI_2 adduct interacting with two further molecules of diiodine in a head-to-tail fashion [25].

We now present the results obtained from the reactions of the related fluoro-substituted phosphine chalcogenides

(p-$FC_6H_4)_3PE$ (E = S and Se) with diiodine. This work has been undertaken in order to observe the effect that the presence of the electron-withdrawing fluorine atom has upon the nature of the adducts formed between these donors and diiodine.

2. Results and discussion

2.1. Synthesis and structures of phosphine chalcogenides

The reaction of (p-$FC_6H_4)_3P$ with elemental selenium powder in refluxing toluene yields the phosphine selenide (p-$FC_6H_4)_3PSe$ (**1**) in 86% yield, and the analogous reaction with sulfur yields the corresponding phosphine sulfide (p-$FC_6H_4)_3PS$ (**2**) in 77% yield, according to Scheme 1.

These reactions were followed by $^{31}P\{^1H\}$ NMR spectroscopy with the resonance of the starting phosphine, (p-$FC_6H_4)_3P$ (δ_P:–8.8) [26] being replaced in both cases by resonances at higher frequencies (δ_P: 33.6 for **1** and 42.2 for **2**). These resonances correlate well with previously reported shifts for **1** and **2** [26–28]. Additionally, the resonance for **1** displays satellites as a result of coupling to the spin active ^{77}Se nucleus ($I = 1/2$, 7.6% abundance). The magnitude of the coupling, $^1J(Se–P) = 741$ Hz, is consistent with previously reported data [26–28], and correlates with the coupling observed on the doublet resonance at −246.1 ppm in the $^{77}Se\{^1H\}$ NMR spectrum of **1**. Although compounds **1** and **2** have been previously reported [26–28], only spectroscopic data has appeared, therefore we recrystallised the materials in order to obtain structural information. Crystals of **1** and **2** were grown by slow evaporation of dichloromethane/hexane layered solutions of the compounds. The structures of **1** and **2** are shown in Figs. 2 and 3, respectively, along with selected bond lengths and angles.

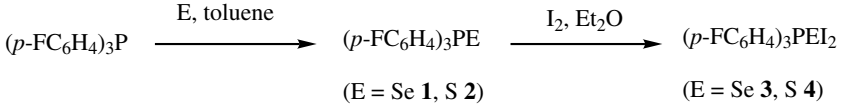
(p-$FC_6H_4)_3PSe$ (**1**) (monoclinic, $P2_1/c$), crystallises with two independent molecules in the asymmetric unit, whilst in contrast (p-$FC_6H_4)_3PS$ (**2**) (monoclinic, $P2_1/n$), crystallises with just one molecule present. The P═Se bond lengths in the two molecules of **1** are essentially identical, P(1)–Se(1): 2.1100(13) Å, Se(2)–P(2): 2.1115(12) Å. These values are consistent with other Ar_3PSe systems, for example, the P═Se bond in Ph_3PSe is 2.106(1) Å [29]. The P═Se bond lengths in **1** are also consistent with other reported phosphine selenides containing partially fluorinated aryl groups, for example, (m-$CF_3C_6H_4)_3PSe$, d(P═Se): 2.094(2) Å [30], (p-$CF_3C_6H_4)_3PSe$, d(P═Se): 2.100(1) Å, (3,5-$(CF_3)_2C_6H_3)_3PSe$, d(P═Se): 2.085(1) Å [26]. Malito and Alyea have previously described an inverse correlation whereby the P═Se in Ar_3PSe systems decreases with an increase in the ^1J(PSe) coupling [28]. Compound **1** displays a ^1J(PSe) coupling of 741 Hz (compared with a ^1J(PSe) coupling of 729 Hz for Ph_3PSe [28]), which would suggest that a decrease should be observed in the P═Se bond length for **1** compared with that of Ph_3PSe, although in fact these bond lengths are similar to each other. It should also be noted that the P═Se bond length falls over a fairly small range for all the reported Ar_3PSe structures. The P═S bond in compound **2** [P(1)–S(1): 1.9540(9) Å] is also consistent with other Ar_3PS systems, e.g., Ph_3PS, d(P═S): 1.950(3) Å [31], and (o-$CH_3C_6H_4)_3PS$, d(P═S): 1.947(4) Å [32].

One difference between the two structures is the orientation of the aryl rings. In **2** a near propeller orientation is observed, with S–P–C_i–C_o torsion angles of −49.9(2)°, −47.7(2)° and −39.9(2)°, whilst in **1** both molecules display a conformation where the rings are all twisted in the same direction, although one ring is twisted to a greater degree than the other two. The Se–P–C_i–C_o torsion angles for molecule 1 are 67.4(4)°, 16.3(4)° and 23.7(5)°, whilst for the second molecule they are −71.0(4)°, −24.8(4)° and −21.4(4)°.

2.2. Synthesis and structures of diiodine adducts

Compounds **1** and **2** were reacted in a 1:1 ratio with diiodine to form the adducts (p-$FC_6H_4)_3PSeI_2$ (**3**) and (p-$FC_6H_4)_3PSI_2$ (**4**), respectively, see Scheme 1. In both cases the $^{31}P\{^1H\}$ NMR spectra of these adducts exhibited a resonance shifted slightly to higher frequencies when compared with the starting phosphine chalcogenide, i.e., δ_P changes from 33.6 (**1**) to 44.5 (**3**), and from 42.2 (**2**) to 47.5 (**4**). Due to the poor solubility of these adducts in a variety of deuterated solvents we were unable to resolve any selenium satellites in the $^{31}P\{^1H\}$ NMR spectrum of **3**, and were also unable to obtain a $^{77}Se\{^1H\}$ NMR spectrum of this adduct. Microanalytical results showed that both **3** and **4** analyse to a 1:1 ratio of phosphine chalogenide:iodine. Formation of the 1:1 adduct is particularly surprising in the case of **4**, in view of the weak nature of the 1:1 adduct Ph_3PSI_2 [4,14,23,24]. The 1:1 adduct formed between (p-$FC_6H_4)_3PS$ and diiodine would be expected to be even weaker in view of the less basic character of (p-$FC_6H_4)_3PS$ compared with Ph_3PS. Crystals of **3** and **4** were both grown from dichloromethane:ether solutions of the compounds. The structure of **3** is shown in Fig. 4, along with selected bond lengths and angles.

The structure of (p-$FC_6H_4)_3PSeI_2$ (**3**) (orthorhombic, $Pca2_1$), contains two independent molecules within the unit cell, both of which exhibit a 1:1 CT system, with a linear



Scheme 1. Synthesis of (p-$FC_6H_4)_3PEI_2$ (E = Se and S).

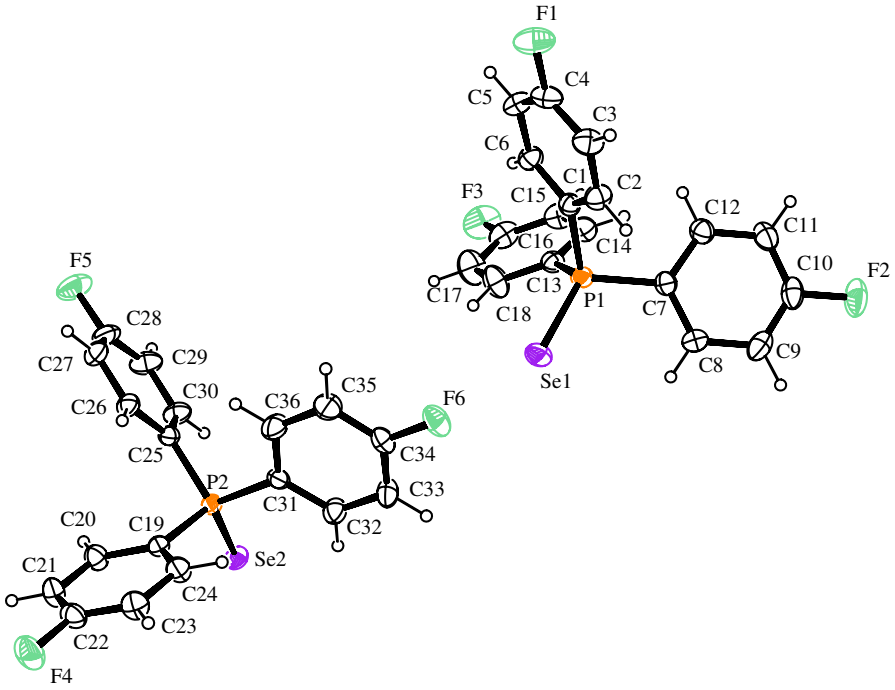


Fig. 2. The molecular structure of $(p\text{-}FC_6H_4)_3PSe$ (**1**). Thermal ellipsoids are shown at the 30% probability level. Selected bond lengths (Å) and angles (°): Se(1)–P(1): 2.1100(13), Se(2)–P(2): 2.1115(12), C(4)–F(1): 1.363(7), C(10)–F(2): 1.361(7), C(16)–F(3): 1.356(7), C(22)–F(4): 1.367(6), C(28)–F(5): 1.365(7), C(34)–F(6): 1.359(6); Se(1)–P(1)–C(1): 111.85(14), Se(1)–P(1)–C(7): 113.60(14), Se(1)–P(1)–C(13): 113.40(14), Se(2)–P(2)–C(19): 112.60(14), Se(2)–P(2)–C(25): 112.63(14), Se(2)–P(2)–C(31): 113.79(14).

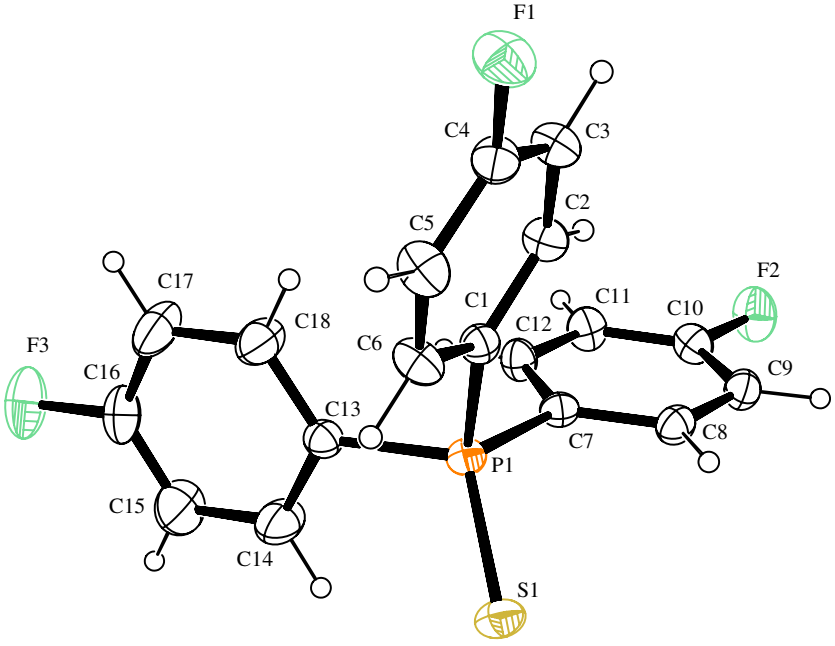


Fig. 3. The molecular structure of $(p\text{-}FC_6H_4)_3PS$ (**2**). Thermal ellipsoids are shown at the 30% probability level. Selected bond lengths (Å) and angles (°): P(1)–S(1): 1.9540(9), C(4)–F(1): 1.358(3), C(10)–F(2): 1.362(3), C(16)–F(3): 1.362(4); S(1)–P(1)–C(1): 113.29(8), S(1)–P(1)–C(7): 113.27(8), S(1)–P(1)–C(13): 113.59(8).

Se–I–I angle typical of the molecular spoke adducts. The Se–I–I angles in both molecules are close to 180°; Se(1)–I(1)–I(2): 178.17(2)°, Se(2)–I(3)–I(4): 178.02(2)°. The I–I distances display some variation between the two molecules, I(1)–I(2): 2.8888(12), I(3)–I(4): 2.8950(11) Å, as do the Se–I distances, Se(1)–I(1): 2.8153(12), Se(2)–I(3): 2.8198(12) Å, with one of the molecules [that based on Se(1)], showing both shorter I–I and Se–I bonds than the

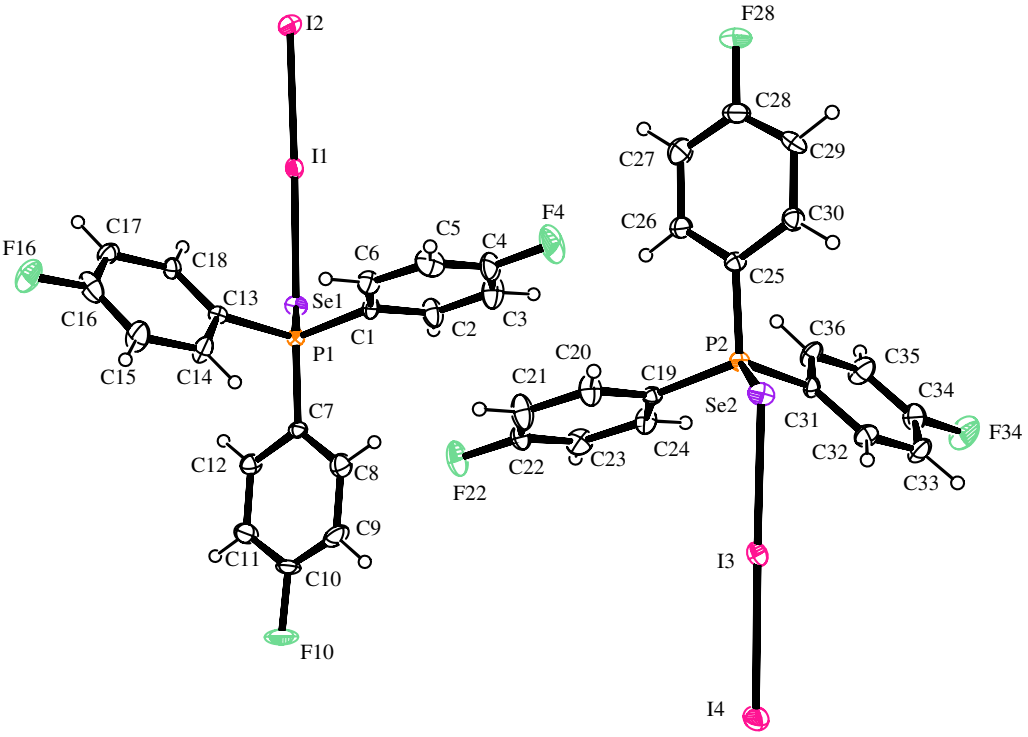


Fig. 4. The molecular structure of $(p\text{-}FC_6H_4)_3PSeI_2$ (**3**). Thermal ellipsoids are shown at the 30% probability level. Selected bond lengths (Å) and angles (°): Se(1)–I(1): 2.8153(12), Se(2)–I(3): 2.8198(12), I(1)–I(2): 2.8888(12), I(3)–I(4): 2.8950(11), P(1)–Se(1): 2.1659(18), P(2)–Se(2), 2.1673(18), C(4)–F(4): 1.374(8), C(10)–F(10): 1.378(9), C(16)–F(16): 1.323(9), C(22)–F(22): 1.361(8), C(28)–F(28): 1.376(9), C(34)–F(34): 1.385(9); Se(1)–I(1)–I(2): 178.17(2), Se(2)–I(3)–I(4): 178.02(2), P(1)–Se(1)–I(1): 100.03(5), P(2)–Se(2)–I(3): 100.66(5), Se(1)–P(1)–C(1): 112.1(2), Se(1)–P(1)–C(7): 108.9(2), Se(1)–P(1)–C(13): 113.57(18), Se(2)–P(2)–C(19): 111.8(2), Se(2)–P(2)–C(25): 107.5(2), Se(2)–P(2)–C(31): 114.23(18).

other. The Se–I and I–I distances have been compared with the small number of previously reported R_3PSeI_2 structures. The I–I distances in **3** are considerably shorter than is observed in trialkyl or tris(alkylamino) substituted R_3PSeI_2 systems, such as $(Et_2N)_3PSeI_2$, where the I–I bond is 2.985(2) Å [13]. This is expected as the weaker donor power of $(p\text{-}FC_6H_4)_3PSe$ compared to those ligands will result in a weaker Se–I bond and a stronger I–I bond. The I–I bonds in **3** would also be expected to be shorter than observed for Ph_3PSeI_2, $d(I–I) = 2.881(2)$ Å [13], as $(p\text{-}FC_6H_4)_3PSe$ is also a weaker donor than Ph_3PSe, however, contrary to expectations the I–I bonds in **3** are slightly longer than in Ph_3PSeI_2. The Se–I bonds in **3** are also slightly longer than the Se–I distance of 2.803(3) Å observed for Ph_3PSeI_2, which is consistent with the weaker donating ability of $(p\text{-}FC_6H_4)_3PSe$. The P–Se–I angles, [P(1)–Se(1)–I(1): 100.03(5)°, P(2)–Se(2)–I(3)°: 100.66(5)°] are lower than the idealised angle of 109.5° expected for a pseudo-tetrahedral arrangement around the selenium atom (taking into account the lone pairs). More significantly, the P–Se–I angles in **3** are more acute than that of 106.0(1)° observed for Ph_3PSeI_2, although P–Se–I angles of 99.6(2)° and 101.2(2)° were observed in $(Me_2N)_3PSeI_2$ [13]. We have reported that this deviation in the P–Se–I angle is probably due to a combination of repulsion from the lone pairs and the retention of partial double bond character in the P–Se bond. A comparison of the P–Se bonds in **3** [P(1)–Se(1): 2.1659(18), P(2)–Se(2), 2.1673(18) Å] with that of 2.1100(13) Å observed for **1** confirms the lengthening of the P–Se bond upon adduct formation. However, the P–Se bonds are intermediate in length between the P=Se bond of **1** and values observed for compounds which contain P–Se single bonds, for example [Cy_3PSePh]Br, where the P–Se bond is 2.2260(16) Å, [33] and P_4Se_3 which has an average P–Se bond length of 2.24(1) Å [34]. The P–Se bonds in **3** are slightly longer than that of 2.156(4) Å observed for Ph_3PSeI_2 [13].

The partial double bond character of the P–Se bonds in **3** is reflected in the shifting of the ν(P–Se) band of the IR spectra of the compound (532 cm^{-1}), compared with the ν(P–Se) band of **1** (552 cm^{-1}). The ν(P–Se) band is shifted to a value intermediate between the P=Se values observed for phosphine selenides and ν(P–Se) bands for P–Se single bond species which are typically found at lower frequencies, such as 517 cm^{-1} for Cy_3PSeBr_2 [9] and 450 cm^{-1} for [Cy_3PSePh]I [35].

Orange crystals of $(p\text{-}FC_6H_4)_3PSI_2$ (**4**) were obtained, (monoclinic, $P2_1/c$); which also feature two independent molecules in the asymmetric unit, as was observed for **3**, although the two structures are not isomorphous. The molecular structure of **4** is shown in Fig. 5, along with selected bond lengths and angles.

The structure of **4** is thus confirmed as the 1:1 diiodine adduct of $(p\text{-}FC_6H_4)_3PS$, with both of the molecules

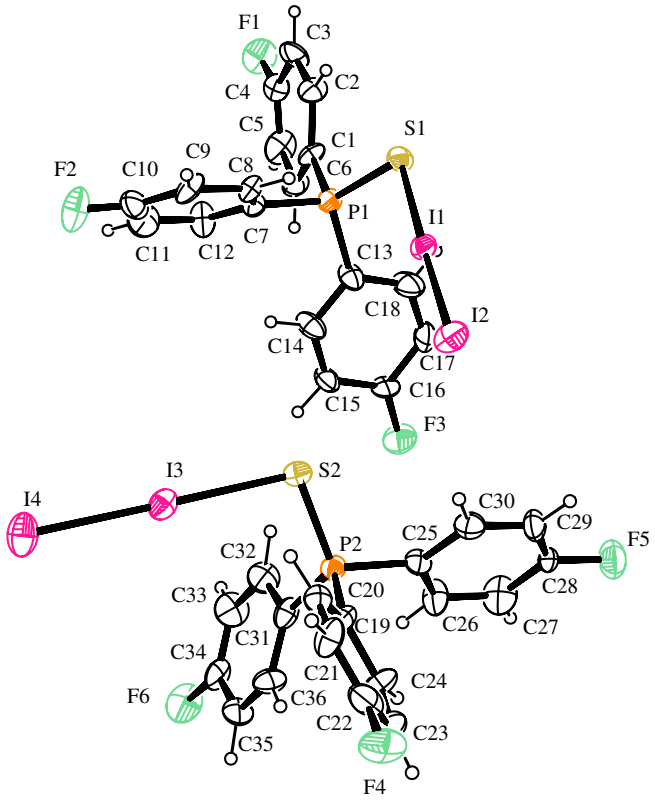


Fig. 5. The molecular structure of $(p\text{-}FC_6H_4)_3PSI_2$ (**4**). Thermal ellipsoids are shown at the 30% probability level. Selected bond lengths (Å) and angles (°): S(1)–I(1): 2.787(5), S(2)–I(3): 2.792(6), I(1)–I(2): 2.8042(17), I(3)–I(4): 2.835(2), P(1)–S(1): 1.997(6), P(2)–S(2): 1.984(5), C(4)–F(1): 1.35(2), C(10)–F(2): 1.29(3), C(16)–F(3): 1.319(19), C(22)–F(4): 1.39(2), C(28)–F(5): 1.37(2), C(34)–F(6): 1.38(2); S(1)–I(1)–I(2): 177.88(10), S(2)–I(3)–I(4): 178.94(9), P(1)–S(1)–I(1): 102.9(2), P(2)–S(2)–I(3): 100.4(3), S(1)–P(1)–C(1): 110.3(6), S(1)–P(1)–C(7): 115.0(5), S(1)–P(1)–C(13): 111.9(7), S(2)–P(2)–C(19): 112.4(5), S(2)–P(2)–C(25): 109.4(6), S(2)–P(2)–C(31): 111.6(8).

showing the expected linear S–I–I motif, S(1)–I(1)–I(2): 177.88(10)°, S(2)–I(3)–I(4): 178.94(9)°. The I–I distances in the two molecules are significantly different, I(1)–I(2): 2.8042(17) Å, I(3)–I(4): 2.835(2) Å. These values are consistent with the range of I–I distances observed for other R_3PSI_2 compounds, although the expected decrease in the I–I distances seen in **4** (compared to Ph_3PSI_2) is not consistently observed, with one of the I–I bonds in **4** being longer, and the other shorter, than was observed for Ph_3PSI_2, *d*(I–I): 2.8230(11) Å [14]. The S–I bond lengths of 2.787(5) and 2.792(6) Å in **4** are longer than that of 2.753(2) Å in Ph_3PSI_2 [14], and therefore do follow the expected trend. The P–S bonds in **4** [P(1)–S(1): 1.997(6), P(2)–S(2): 1.984(5) Å], are lengthened with respect to the free phosphine sulfide **2**, where the P–S bond was 1.9540(9) Å. These findings are consistent with the elongation observed in the analogous phosphine selenide system **3**, and once more partial retention of double bond character is observed, as the P–S bonds are shorter than observed for P–S single bonded species, such as $[Ph_3PSPh][ClO_4]$ and $[Ph_3PSCH_2C_6H_5][ClO_4]$, which have P–S bond lengths of 2.074(2) and 2.050(1) Å, respectively [36]. The reduction in the magnitude of the P–S bond is again reflected in the IR spectrum where the ν(P–S) band of **4** (571 cm^{-1}) is again shifted to lower frequency compared with the phosphine sulfide **2** (632 cm^{-1}). The P–S–I angles in the two molecules are 102.9(2)° and 100.4(3)° and are smaller than the P–S–I angle of 108.78(7)° in Ph_3PSI_2. This variation in the P–S–I angles result in the iodine atoms of one of the molecules in the asymmetric unit being held closer to the aryl ring than is the case in the other molecule. This may explain the difference in the I–I distances between the two molecules. However, the differences between the two are relatively small, and therefore lie within a range where packing effects may also be significant.

The conformation of the aryl rings are similar in both **3** and **4**, but differ slightly to that seen for **1** and **2**. The rings are in all cases twisted in the same direction, but with one of the rings twisted much less than the other two. The Se–P–C_i–C_o torsion angles for **3** are −44.0(6)°, −51.7(5)° and −13.4(6)° for molecule 1, and 51.4(6)°, 43.4(6)° and 14.1(7)° for molecule 2. The S–P–C_i–C_o torsion angles for **4** are −38.7(16)°, −9.5(13)° and −45.7(17)° for molecule 1, and 10.3(18)°, 53.4(15)° and 38.0(18)° for molecule 2. The different conformations observed for the aryl rings for compounds **1**, **2**, **3** and **4** suggest that no particular conformation is energetically preferred for the $p\text{-}FC_6H_4$ rings in these systems.

2.3. Conclusion

The introduction of fluorine in the *para*-positions in Ar_3PEI_2 (E = S and Se) systems appears to have only a minor effect on the I–I bonds in these charge-transfer adducts. Both $(p\text{-}FC_6H_4)_3PSe$ and $(p\text{-}FC_6H_4)_3PS$ react with diiodine to form 1:1 adducts, but the magnitude of the I–I bonds in these compounds are not consistently shorter than their non-fluorinated counterparts, which would be expected on the basis of the weakly basic nature of the $(p\text{-}FC_6H_4)_3PE$ donors. It is not easy to rationalise these observations on the basis of electronic arguments, but both $(p\text{-}FC_6H_4)_3PSeI_2$ and $(p\text{-}FC_6H_4)_3PSI_2$ display more acute P–E–I angles than the non-fluorinated Ph_3PEI_2 (E = S and Se) adducts. The narrowing of this angle holds the dihalogen part of the molecule closer to the aryl rings than in Ph_3PEI_2, and this may be responsible for the variation of the I–I bond lengths in the compounds reported herein. However, it should be noted that the differences in the I–I bonds are relatively small, and thus packing effects may also be responsible for these variations.

3. Experimental

3.1. Reagents and physical measurements

$(p\text{-}FC_6H_4)_3PSI_2$, and $(p\text{-}FC_6H_4)_3PSeI_2$ are moisture sensitive, therefore their synthesis was performed under anhydrous conditions. Diethyl ether and toluene (BDH) were

distilled over sodium/benzophenone ketyl before use. Tris-(*para*-fluorophenyl)phosphine, iodine, sulfur, and selenium powder were all purchased commercially (Aldrich) and used as received. ^{1}H and $^{13}C\{^{1}H\}$ NMR spectra were recorded on a Bruker DPX400 machine operating at 399.9 and 100.6 MHz, respectively. ^{19}F, $^{31}P\{^{1}H\}$ and $^{77}Se\{^{1}H\}$ NMR spectra were recorded on a Bruker DPX200 machine operating at 188.3, 81.8 and 38.2 MHz, respectively. Peak positions are quoted relative to external TMS [$^{1}H/^{13}C$], $CFCl_3$ [^{19}F], 85% H_3PO_4 [^{31}P] and Me_2Se [^{77}Se], using the high frequency positive convention throughout. All spectra were recorded at 300 K. All chemical shifts are given in ppm, and coupling constants in Hz. Infra-red spectra were recorded on a Nicolet-Nexus combined FT-IR/FT-Raman spectrometer, with samples prepared as nujol mulls held between KBr plates. Melting points were recorded on a Bibby SMP10 melting point apparatus and elemental analyses were performed by the University of Manchester School of Chemistry Microanalytical Service.

3.2. Crystallographic details

Details of the structural analyses for $(p\text{-}FC_6H_4)_3PSe$ (**1**), $(p\text{-}FC_6H_4)_3PS$ (**2**), $(p\text{-}FC_6H_4)_3PSeI_2$ (**3**) and $(p\text{-}FC_6H_4)_3PSI_2$ (**4**) are all summarised in Table 1. Diffraction data for **1**, **2** and **4** were recorded on a Nonius κ-CCD four circle diffractometer at 150(2) K. Graphite-monochromated Mo Kα radiation ($\lambda = 0.71073$ Å) was used for all three compounds. Data for compound **3** was recorded on a Bruker SMART 1K CCD diffractometer (synchrotron $\lambda = 0.69280$ Å) at 150(2) K at station 9.8 at the Daresbury SRS laboratories. The structural data for all the compounds was solved by direct methods (SHELXS97) and refined by full-matrix least squares against F^2 using all data (SHELXL97) [37], with the hydrogen atoms located in ideal positions. Absorption corrections were carried out via the multiscan method, and were applied with the SORTAV program [38]. Non-hydrogen atoms were refined with anisotropic thermal parameters. Figures were generated using ORTEP-3 for Windows [39].

3.3. Synthetic details

3.3.1. Synthesis of $(p\text{-}FC_6H_4)_3PSe$ (1)

Five grams (1.58×10^{-2} mol) of $(p\text{-}FC_6H_4)_3P$ was dissolved in 100 cm^3 of dry toluene in a 500 cm^3 flask fitted with a reflux condenser. To this flask was added 1.250 g (1.58×10^{-2} mol) of selenium powder with vigorous stirring. The solution was then refluxed under nitrogen for 3 h, after which time all the selenium powder had been consumed. The solution was allowed to cool and concentrated to half its volume. 20 cm^3 of 40:60 petroleum ether was added and the solution refrigerated overnight. The white precipitate formed was then filtered off and dried *in vacuo* for 2 h to yield **1** as a white powder, (m.p. 174–75 °C, 86.2% yield). *Anal.* Calc. for $C_{18}H_{12}F_3PSe$: C, 54.7; H, 3.0; Se, 20.0. Found: C, 54.5; H, 2.9; Se, 19.9%. ^{1}H

Table 1
Crystallographic parameters for compounds **1**–**4**

	$(p\text{-}FC_6H_4)_3PSe$ (**1**)	$(p\text{-}FC_6H_4)_3PS$ (**2**)	$(p\text{-}FC_6H_4)_3PSeI_2$ (**3**)	$(p\text{-}FC_6H_4)_3PSI_2$ (**4**)
Empirical formula	$C_{18}H_{12}F_3PSe$	$C_{18}H_{12}F_3PS$	$C_{18}H_{12}F_3I_2PSe$	$C_{18}H_{12}F_3I_2PS$
Formula weight	395.11	348.31	649.01	602.11
Colour, habit	colourless, needle	colourless, plate	orange, prism	orange, needle
Crystal system	monoclinic	monoclinic	orthorhombic	monoclinic
Space group	$P2_1/c$ (no. 14)	$P2_1/n$ (no. 14)	$Pca2_1$ (no. 29)	$P2_1/c$ (no. 14)
Crystal size (mm^3)	$0.08 \times 0.08 \times 0.22$	$0.22 \times 0.16 \times 0.07$	$0.05 \times 0.03 \times 0.03$	$0.21 \times 0.17 \times 0.10$
Unit cell dimensions				
a (Å)	18.5063(5)	10.8042(3)	14.894(4)	17.8936(6)
b (Å)	13.4703(4)	11.0077(4)	16.536(4)	16.4104(6)
c (Å)	13.2092(3)	13.6356(5)	16.422(5)	14.7853(4)
α (°)	90	90	90	90
β (°)	91.5070(10)	95.864(2)	90	114.314(2)
γ (°)	90	90	90	90
Volume ($Å^3$)	3291.72(15)	1613.19(9)	4044.5(19)	3956.5(2)
T (K)	150(2)	150(2)	150(2)	150(2)
Z	8	4	8	8
$D_{calc.}$ (mg/m^3)	1.595	1.434	2.132	2.022
λ (Å)	0.71073	0.71073	0.69280	0.71073
μ (Mo Kα) [mm^{-1}]	2.403	0.325	5.014	3.391
F(000)	1568	712	2416	2272
θ Range (°)	3.06–27.09	3.53–26.00	1.79–25.00	3.02–25.99
Number of reflections	28811 (7027 unique)	8911 (3023 unique)	16237 (6782 unique)	9368 (7589 unique)
R_1/wR_2	0.0527/0.1081	0.0425/0.0937	0.0320/0.0695	0.0680/0.1786
R_1/wR_2 (all data)	0.1078/0.1340	0.0635/0.1063	0.0353/0.0704	0.1236/0.2193
Largest differential peak and hole (e $Å^{-3}$)	0.393 and 0.381	0.252 and 0.258	2.547 and 0.477	2.233 and 1.532
Goodness-of-fit	0.982	1.025	0.989	1.057

NMR ($CDCl_3$): δ 7.18 [m, 6H, H_m], 7.73 [m, 6H, H_o]. $^{13}C\{^1H\}$ NMR ($CDCl_3$): δ 115.0 [dd, C_m, $J = 13.6$, 21.3], 126.3 [d, C_i, $^1J(PC) = 78.2$], 133.9 [dd, C_o, $J = 8.7$, 12.6], 163.9 [d, C_p, $^1J(CF) = 255.0$]. ^{19}F NMR ($CDCl_3$): $\delta -107.1$ [s]. $^{31}P\{^1H\}$ NMR ($CDCl_3$): δ 33.6 [s + satellites, $^1J(PSe) = 741$]. $^{77}Se\{^1H\}$ NMR ($CDCl_3$): $\delta -246.1$ [d, $^1J(PSe) = 741$]. IR (cm^{-1}): 552 (P–Se).

3.3.2. Synthesis of (p-FC_6H_4)$_3$PS (2)

(p-FC_6H_4)$_3$PS was synthesised by the method used for compound **1** above, using 5.00 g (1.58×10^{-2} mol) of (p-FC_6H_4)$_3$P and 0.506 g (1.58×10^{-2} mol) of sulfur. The product was isolated as above to yield **2** as a white powder, (m.p. 171–73 °C, 77.3% yield). *Anal.* Calc. for $C_{18}H_{12}F_3PS$: C, 62.1; H, 3.4; S, 9.2. Found: C, 62.0; H, 3.2; S, 9.4%. ^1H NMR ($CDCl_3$): δ 7.18 [m, 6H, H_m], 7.74 [m, 6H, H_o]. $^{13}C\{^1H\}$ NMR ($CDCl_3$): δ 115.0 [dd, C_m, $J = 13.6$, 21.3], 127.5 [dd, C_i, $^1J(PC) = 88.9$, $^4J(PF) = 2.9$], 133.6 [dd, C_o, $J = 9.7$, 12.6], 163.9 [dd, C_p, $^1J(CF) = 251.1$, $^4J(PC) = 2.9$]. ^{19}F NMR ($CDCl_3$): −107.2 [s]. $^{31}P\{^1H\}$ NMR ($CDCl_3$): δ 42.2 [s]. IR (cm^{-1}): 632 (P–S).

3.3.3. Synthesis of (p-FC_6H_4)$_3$PSeI$_2$ (3)

0.655 g (1.66×10^{-3} mol) of (p-FC_6H_4)$_3$PSe was dissolved in 50 cm^3 of anhydrous diethyl ether in a rotaflo tube against a stream of dry nitrogen. To this solution was added 0.421 g (1.66×10^{-3} mol) of diiodine. An orange solid precipitated from solution and was left to stir for 3 days. The solid was isolated using standard Schlenk techniques to yield **3** as an orange powder, (m.p. 135 °C, 74.3% yield). *Anal.* Calc. for $C_{18}H_{12}F_3I_2PSe$: C, 33.3; H, 1.8; Se, 12.2; I, 39.1. Found: C, 33.1; H, 1.8; Se, 12.0; I, 39.0%. ^1H NMR ($CDCl_3$): δ 7.20 [m, 6H, H_m], 7.67 [m, 6H, H_o]. $^{13}C\{^1H\}$ NMR ($CDCl_3$): δ 116.5 [dd, C_m, $J = 14.5$, 21.3], 125.8 [d, C_i, $^1J(PC) = 91.6$], 134.9 [dd, C_o, $J = 9.7$, 13.6], 163.6 [d, C_p, $^1J(CF) = 255.6$]. ^{19}F NMR ($CDCl_3$): $\delta -101.7$ [s, br]. $^{31}P\{^1H\}$ NMR ($CDCl_3$): δ 44.5 [s]. IR (cm^{-1}): 532 (P–Se).

3.3.4. Synthesis of (p-FC_6H_4)$_3$PSI$_2$ (4)

(p-FC_6H_4)$_3$PSI$_2$ was synthesised by the method used for compound **3** above, using 0.741 g (2.13×10^{-3} mol) of (p-FC_6H_4)$_3$PS and 0.541 g (2.13×10^{-3} mol) of diiodine. The solid was isolated using standard Schlenk techniques to yield **4** as an orange powder, (m.p. 165 °C, 61.5% yield). *Anal.* Calc. for $C_{18}H_{12}F_3I_2PS$: C, 35.9; H, 2.0; S, 5.3; I, 42.2. Found: C, 35.9; H, 2.1; S, 5.2; I, 41.9%. ^1H NMR ($CDCl_3$): δ 7.21 [m, 6H, H_m], 7.72 [m, 6H, H_o]. $^{13}C\{^1H\}$ NMR ($CDCl_3$): δ 117.0 [dd, C_m, $J = 15.5$, 20.3], 126.2 [d, C_i, $^1J(PC) = 90.8$], 135.4 [s, br, C_o], 165.7 [d, C_p, $^1J(CF) = 256.0$]. ^{19}F NMR ($CDCl_3$): $\delta -105.4$ [s, br] $^{31}P\{^1H\}$ NMR ($CDCl_3$): δ 47.5 [s]. IR (cm^{-1}): 571 (P–S).

Acknowledgements

The authors thank EPSRC for a research studentship (RTAH) and for the UMIST FT IR/Raman facility (Grant No. GR/M30135), NMR facility (Grant No. GR/L52246), and X-ray facility (Research Initiative Grant), and also the SRS Daresbury Synchrotron Laboratories for beam time.

Appendix A. Supplementary material

CCDC 645047, 645048, 645049 and 645050 contain the supplementary crystallographic data for this paper. These data can be obtained free of charge via http://www.ccdc.cam.ac.uk/conts/retrieving.html, or from the Cambridge Crystallographic Data Centre, 12 Union Road, Cambridge CB2 1EZ, UK; fax: (+44) 1223-336-033; or e-mail: deposit @ccdc.cam.ac.uk. Supplementary data associated with this article can be found, in the online version, at doi:10.1016/j.poly.2007.05.057.

References

[1] R.A. Zingaro, R.M. Hedges, J. Phys. Chem. 65 (1961) 1132.
[2] R.A. Zingaro, E.A. Meyers, Inorg. Chem. 1 (1962) 771.
[3] R.A. Zingaro, R.E. McGlothlin, E.A. Meyers, J. Phys. Chem. 66 (1962) 2579.
[4] R.A. Zingaro, Inorg. Chem. 2 (1963) 192.
[5] W. Tefteller, R.A. Zingaro, Inorg. Chem. 5 (1966) 2151.
[6] E. Krawczyk, A. Skowrońska, J. Michalski, J. Chem. Soc., Dalton Trans. (2002) 4471.
[7] J. Konu, T. Chivers, Dalton Trans. (2006) 3941.
[8] D.J. Williams, K.J. Wynne, Inorg. Chem. 15 (1976) 1449.
[9] S.M. Godfrey, S.L. Jackson, C.A. McAuliffe, R.G. Pritchard, J. Chem. Soc., Dalton Trans. (1998) 4201.
[10] C.G. Hrib, F. Ruthe, E. Seppälä, M. Bätcher, C. Druckenbrodt, C. Wismach, P.G. Jones, W-W. du Mont, V. Lippolis, F.A. Devillanova, M. Bühl, Eur. J. Inorg. Chem. (2006) 88.
[11] C.G. Hrib, P.G. Jones, W-W. du Mont, V. Lippolis, F.A. Devillanova, Eur. J. Inorg. Chem. (2006) 1294.
[12] W.I. Cross, S.M. Godfrey, S.L. Jackson, C.A. McAuliffe, R.G. Pritchard, J. Chem. Soc., Dalton Trans. (1999) 2225.
[13] S.M. Godfrey, S.L. Jackson, C.A. McAuliffe, R.G. Pritchard, J. Chem. Soc., Dalton Trans. (1997) 4499.
[14] D.C. Apperley, N. Bricklebank, S.L. Burns, D.E. Hibbs, M.B. Hursthouse, K.M. Abdul Malik, J. Chem. Soc., Dalton Trans. (1998) 1289.
[15] D.C. Apperley, N. Bricklebank, M.B. Hursthouse, M.E. Light, S.J. Coles, Polyhedron 20 (2001) 1907.
[16] N. Bricklebank, S.J. Coles, S.D. Forder, M.B. Hursthouse, A. Poulton, P.J. Skabara, J. Organomet. Chem. 690 (2005) 328.
[17] F. van Bolhuis, P.B. Koster, T. Migchelsen, Acta Crystallogr. 23 (1967) 90.
[18] C. Rømming, J. Songstad, Acta Chem. Scand. A33 (1979) 187.
[19] M.D. Rudd, S.V. Lindeman, S. Husebye, Acta Chem. Scand. 51 (1997) 689.
[20] E. Seppälä, F. Ruthe, J. Jeske, W-W. du Mont, P.G. Jones, Chem. Commun. (1999) 1471.
[21] W-W. du Mont, A. Martens-von Salzen, F. Ruthe, E. Seppälä, G. Mugesh, F.A. Devillanova, V. Lippolis, N. Kuhn, J. Organomet. Chem. 623 (2001) 14.
[22] M. Arca, F.A. Devillanova, A. Garau, F. Isaia, V. Lippolis, G. Verani, F. Demartin, Z. Anorg. Allg. Chem. 624 (1998) 745.
[23] W.W. Schweikert, E.A. Meyers, J. Phys. Chem. 72 (1968) 1561.
[24] S. Kaur, T.S. Lobana, J. Inorg. Nuc. Chem. 43 (1981) 2439.
[25] M. Arca, F. Demartin, F.A. Devillanova, A. Garau, F. Isaia, V. Lippolis, G. Verani, J. Chem. Soc., Dalton Trans. (1999) 3069.

[26] J.A.S. Howell, N. Fey, J.D. Lovatt, P.C. Yates, P. McArdle, D. Cunningham, E. Sadeh, H.E. Gottlieb, Z. Goldschmidt, M.B. Hursthouse, M.E. Light, J. Chem. Soc., Dalton Trans. (1999) 3015.
[27] R.F. de Ketelaere, G.P. van der Kelen, J. Mol. Struct. 27 (1975) 363.
[28] J. Malito, E.C. Alyea, Phosphorus, Sulfur, Silicon Relat. Elem. 54 (1990) 95.
[29] P.W. Codding, K.A. Kerr, Acta Crystallogr., Sect. B 35 (1979) 1261.
[30] D.W. Allen, L.A. March, I.W. Nowell, J. Chem. Soc., Dalton Trans. (1984) 483.
[31] P.W. Codding, K.A. Kerr, Acta Crystallogr., Sect. B 34 (1978) 3785.
[32] T.S. Cameron, B. Dahlén, J. Chem. Soc., Dalton Trans. 2 (1975) 1737.
[33] N.A. Barnes, S.M. Godfrey, R.T.A. Halton, I. Mushtaq, R.G. Pritchard, S. Sarwar, Dalton Trans. (2006) 1517.
[34] E. Keulen, A. Vos, Acta Crystallogr. 12 (1959) 323.
[35] N.A. Barnes, S.M. Godfrey, R.T.A. Halton, I. Mushtaq, R.G. Pritchard, Dalton Trans. (2006) 4795.
[36] C. Imrie, T.A. Modro, P.H. van Rooyen, C.C.P. Wagener, K. Wallace, H.R. Hudson, M. McPartlin, J.B. Nasirun, L. Powroznyk, J. Phys. Org. Chem. 8 (1995) 41.
[37] G.M. Sheldrick, SHELX-97, University of Göttingen, Göttingen, Germany, 1997.
[38] R.H. Blessing, Acta Crystallogr., Sect. A 51 (1995) 33.
[39] ORTEP-3 for Windows L.J. Farrugia, J. Appl. Crystallogr. 30 (1997) 565.

rings were situated in almost ideal axial positions, hence the coordination sphere of this complex should be described as a (4+2)-geometry. However, the position of the sixth coordination site was slightly ambiguous, therefore, we have decided to reexamine the structure of this complex by single crystal X-ray diffraction and vibrational spectroscopic methods.

Ha et al. [13] determined the crystal and molecular structure of the polymeric $[(orotato)Cu(H_2O)_2]_n$ complex. These authors have shown that Cu is also chelated by one carboxylate O atom and the deprotonated N_1 atom, while the remaining two sites of the basal plane are occupied by two water molecules. The coordination sphere at copper is extended to five by the second carboxylic oxygen atom of another complex molecule, which acts as a bridge between the copper(II) ions, forming one-dimensional polymeric chains. Icbudak et al. [15] studied the crystal and molecular structure of $[Cu(orotato)(en)(H_2O)] \cdot H_2O$, where the basal plane was formed by the O(carboxylate) and N_1 (deprotonated nitrogen) atoms, and by the two N atoms from the ethylenediamine ligand. One water molecule completed the square-pyramidal coordination around copper(II) in this complex. Wu et al. reported the crystal structure of $[Cu(orotato)(H_2O)_3] \cdot 2H_2O$, in which "the Cu(II) atom had a slightly distorted square pyramid coordination with additional three water molecules" [14], but these authors did not show the position of the lattice water molecules.

Therefore, in this study we have reinvestigated the crystal structure of *cis*-$[Cu(orotato)(NH_3)_2]$ (**1**) and can reveal some new, very important, structural features of this complex. The novel copper complex, $[Cu(orotato)(H_2O)_4] \cdot H_2O$ (**2**) has been synthesized and its structure has been determined by single crystal X-ray diffraction and vibrational spectroscopic methods.

2. Experimental

2.1. Preparation

Complex **1** was obtained similarly to the procedure used in Ref. [12]. Orotic acid (1 mmol) and $CuCl_2 \cdot 2H_2O$ (1 mmol) in a solution of concentrated ammonia (90 cm^3) and ethanol (90 cm^3) were heated at 313 K under reflux for an hour. Upon cooling, complex **1**, *cis*-$[Cu(orotato)(NH_3)_2]$, precipitated in the form of dark-purple plates. When the resulting blue solution was evaporated for several hours and then cooled, complex **2**, $[Cu(orotato)(H_2O)_4] \cdot H_2O$, precipitated in the form of blue-needles. Frequently, the two complexes co-crystallize. Suitable crystals of the two complexes were selected for single crystal X-ray analyses.

2.2. X-ray analysis

The X-ray diffraction data were collected using an automatic X-ray four-circle EXCALIBUR single crystal diffractometer with CCD area detectors (graphite monochromator, Mo Kα radiation, $\lambda = 0.071073$ nm). The intensity data were corrected for Lorentz, absorption and polarization effects. The structures were solved by direct methods using the program SHELXS-97 [17] and refined by the full-matrix least-squares method based on F^2 using SHELXL-97 [18]. All non-hydrogen atoms were refined anisotropically by unit-weighted full-matrix least square methods. Hydrogen atoms were included from the difference Fourier $\Delta\rho$ maps and refined with isotropic thermal parameters. Molecular drawings were obtained using DIAMOND [19]. The crystal data and the refinement details of **1** and **2** are given in Table 1.

Table 1
Crystal data and structure refinement for complexes $Cu[(orotato)(NH_3)_2]$ (**1**) and $[Cu(orotato)(H_2O)_4] \cdot H_2O$ (**2**)

Compound	(**1**)	(**2**)
Empirical formula	$C_5H_8N_4O_4Cu$	$C_5H_{12}N_2O_9Cu$
Formula weight	251.69	307.71
Temperature (K)	293(2)	293(2)
Wavelength (Å)	0.71073	0.71073
Crystal system	monoclinic	monoclinic
Space group	$P2_1/n$	$P2_1/n$
Unit cell dimensions		
a (Å)	7.194(1)	5.772(1)
b (Å)	7.593(1)	17.677(4)
c (Å)	15.145(3)	10.994(2)
β (°)	100.82(3)	98.56(3)
Volume (Å^3)	812.6(3)	1109.2(4)
Z (molecule/cell)	4	4
D_{calc} (Mg m^{-3})	2.057	1.843
Absorption coefficient (mm^{-1})	2.683	2.011
$F(000)$	508	628
Reflection collected/unique (R_{int})	8149/2083 (0.0581)	12960/2844 (0.0518)
Data/restraints/parameters	2083/0/160	2844/0/203
Goodness-of-fit on F^2	1.210	0.959
Final R indices [$I > 2\sigma(I)$]	$R_1 = 0.0331$, $wR_2 = 0.0762$	$R_1 = 0.0386$, $wR_2 = 0.0836$
R indices (all data])	$R_1 = 0.0408$, $wR_2 = 0.0789$	$R_1 = 0.0659$, $wR_2 = 0.0943$
Largest difference in peak and hole (e Å^{-3})	0.66 and −0.83	0.48 and −0.67

2.3. Raman and infrared spectra measurements

The FT-Raman spectra of orotic acid were recorded on a Nicolet 2000 spectrometer equipped with a Nd:YAG laser operating at 1064 nm. The spectra were measured at a resolution of 2 cm^{-1}. The FT-Raman spectra of the copper(II) complexes were recorded on a Jobin Yvon spectrometer model T6400 using a CCD camera as a detector (Princeton Instruments). Excitation was provided by an argon laser (514.5 nm line). For the FT-Raman spectral measurements, a few milligrams of each compound were placed in a capillary tube and measured directly (3000 scans were collected with a resolution of 4 cm^{-1}).

The FT-IR spectra of the compounds in KBr pellets were collected on a Bruker IFS 113 V spectrometer in the

region of 4000–400 cm^{-1} (with a resolution of 2 cm^{-1}). The far-infrared spectra (600–50 cm^{-1}) were recorded on an IFS 66/S Bruker spectrometer using the Nujoll mull technique. The accuracy of the readings was ±1 cm^{-1}.

3. Theoretical

The structures of *cis*-[Cu(orotato)$(NH_3)_2$] and [Cu(orotato)$(H_2O)_2$] were fully optimized by the density functional theory DFT(UB3LYP) [20,21]. In both complexes the copper(II) ion has one unpaired electron (d^9 electron configuration and doublet ground-state). Thus, the unrestricted UB3LYP method has been used for an open-shell electronic structure. In unrestricted methods a spin contamination of the UHF wave-function may occur, therefore the expectation value of the total spin, $\hat{S}^2$, should be examined. The final $\hat{S}^2$ value was equal to 0.7503 for **1**, and 0.7504 for **2**. Both these values are very close to 0.7500, which corresponds to the doublet ground state wave-function with no spin contamination, and confirm validity of the UB3LYP results [22]. The effective core potential (ECP) of Hay and Wadt and the concomitant LanL2DZ basis set [23] were used for the copper atom. For all the other atoms the D95V(d,p) basis set [24] was employed. The latter basis set includes d polarization functions on C, N and O atoms, and p polarization functions on hydrogen atoms. Natural bond orbital (NBO) analysis [25] has been performed to obtain the natural charges on the atoms. All computations were carried out with the GAUSSIAN 03 package [26].

4. Results and discussion

4.1. Copper(II)–π interaction in cis-[Cu(orotato)$(NH_3)_2$] (1)

The structure of the complex is shown in Fig. 1. The numbering of the atoms refers to that used for uracil and other pyrimidine bases in the literature. The primary coordination sphere around the Cu atom is square-planar with the orotate ligand chelating through the carboxylate oxygen atom O1 and the deprotonated N1 atom. Two ammonia nitrogen atoms, N4 and N5, complete the basal plane. One of the coordinated ammonia molecules is involved in an interligand hydrogen bond to the exocyclic O2 carbonyl oxygen atom of the uracil ring, with a N5···O2 distance of 2.782(2) Å and N5–H53···O2 angle of 153(2)°. The bond lengths and bond angles of **1** are listed in Table 2, together with the corresponding structural parameters reported earlier [12]. It is evident from this comparison that the structure of these complexes should be the same. However, Mutikainen and Lumme concluded that in this complex the coordination sphere is extended to the (4+2) geometry by two exocyclic carbonyl oxygen atoms, $O4^i$ and $O4^{ii}$, from neighboring uracilate rings (it should be noted that a different numbering of the oxygen atoms was used in Ref. [12]).

The stereoview of the coordination sphere of this complex is illustrated in Fig. 2. As follows from our study, the structure of **1** consists of centrosymmetric dimers, in which each copper atom is coordinated to one exocyclic carbonyl oxygen atom $O4^i$ from the neighboring molecule. The Cu–$O4^i$ distance of 2.927(3) Å is close to that reported by Mutikainen and Lumme, 2.930(4) Å [12]. However, it should be emphasized that the oxygen atom, $O4^{ii}$, from the other complex molecule is not situated at the axial position to copper. The $O4^i$–Cu–$O4^{ii}$ angle of 133.5(2)° shows significant deviation from linearity. Furthermore, the Cu–$O4^{ii}$ distance of 4.845(4) Å (Fig. 2) is too long to allow for any effective interaction between these atoms. The displacement of the Cu atom from the least-squares plane (formed by the chelating N1, O1, N4 and N5 atoms) amounts to only 0.021(1) Å. If only one axial Cu–O bond were present in the complex, the copper atom should reveal a bigger deviation from the equatorial plane. For example, in square-pyramidal *cis*-[Cu(5-nitroorotato)$(NH_3)_2$] complex, the Cu atom lies 0.120(1) Å out of the equatorial plane [27].

The coplanar location of the copper atom in **1** implies that there is another axial interaction on the other side of the basal plane, which may counteract the Cu–$O4^i$ binding

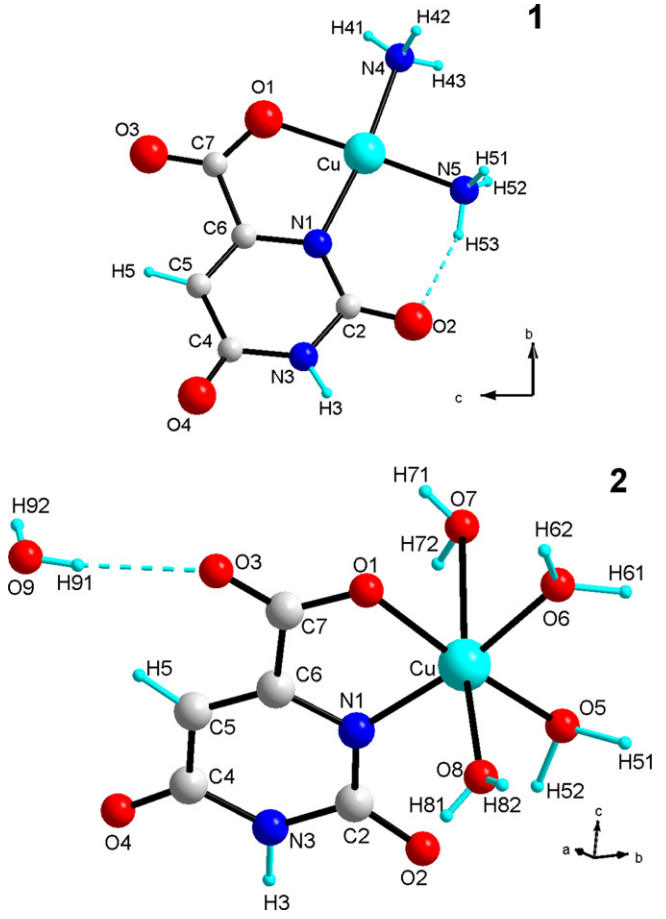


Fig. 1. The molecular structures of Cu(orotato)$(NH_3)_2$ (**1**) and [Cu(orotato)$(H_2O)_4]\cdot H_2O$ (**2**) with the labelling of the atoms. Important hydrogen bonds are indicated by dashed lines.

Table 2
Comparison of the experimental and theoretical interatomic distances (Å) and bond angles (°) of Cu[(orotato)$(NH_3)_2$] (**1**) and [Cu(orotato)$(H_2O)_4$] · H_2O (**2**)

Complex **1**	From Ref. [12]	Our data (exp.)	Calc.	Complex **2**	Exp.	Calc.
Cu–N1	2.005(3)	1.999(1)	1.977	Cu–N1	2.008(1)	1.940
Cu–O1	1.962(3)	1.959(1)	1.923	Cu–O1	1.984(1)	1.906
Cu–N4	1.996(3)	1.996(1)	2.099	Cu–O6	2.005(1)	2.060
Cu–N5	1.960(3)	1.955(1)	2.049	Cu–O5	1.992(1)	1.986
Cu–$O4^{i}$	2.930(4)	2.927(3)		Cu–O7	2.400(1)	
Cu–X^{ii}		3.293(9)		Cu–O8	2.873(2)	
N1–C2	1.372(4)	1.363(1)	1.368	N1–C2	1.355(1)	1.357
C2–N3	1.384(4)	1.377(1)	1.382	C2–N3	1.392(1)	1.373
N3–C4	1.368(4)	1.372(1)	1.414	N3–C4	1.368(1)	1.421
C4–C5	1.440(5)	1.439(1)	1.456	C4–C5	1.432(1)	1.459
C5–C6	1.358(4)	1.350(1)	1.363	C5–C6	1.354(1)	1.361
C6–N1	1.362(4)	1.365(1)	1.380	C6–N1	1.363(1)	1.378
C6–C7	1.526(4)	1.517(1)	1.523	C6–C7	1.510(1)	1.525
C7–O3	1.227(4)	1.230(1)	1.221	C7–O3	1.236(1)	1.218
C7–O1	1.285(4)	1.278(1)	1.322	C7–O1	1.275(1)	1.328
C2–O2	1.232(4)	1.233(1)	1.253	C2–O2	1.243(1)	1.263
C4–O4	1.241(4)	1.234(1)	1.228	C4–O4	1.243(1)	1.225
N5–Cu–N4	90.5(1)	90.4(1)		O6–Cu–O5	90.5(1)	97.7
O1–Cu–N4	90.3(1)	90.5(1)	81.9	O6–Cu–O1	89.1(1)	82.4
N5–Cu–N1	96.8(1)	96.6(1)		O5–Cu–N1	98.2(1)	94.9
O1–Cu–N1	82.5(1)	82.5(1)	84.0	O1–Cu–N1	81.9(1)	85.0
X^{ii}–Cu–$O4^{i}$		169.6(1)		O7–Cu–O8	174.7(1)	
C7–O1–Cu	116.5(2)	116.4(1)	116.5	C7–O1–Cu	115.8(1)	115.7
C6–N1–Cu	112.3(2)	112.1(1)	112.1	C6–N1–Cu	112.4(1)	112.6
N1–C2–N3	117.4(3)	117.6(1)	116.6	N1–C2–N3	117.9(1)	116.8
N1–C2–O2	124.4(3)	124.3(1)	123.9	N1–C2–O2	124.1(1)	122.8
C2–N3–C4	126.5(3)	126.5(1)	127.5	C2–N3–C4	126.0(1)	126.7
N3–C4–O4	120.6(3)	120.3(1)	120.0	N3–C4–O4	120.7(1)	119.7
N3–C4–C5	114.2(3)	114.0(2)	112.7	N3–C4–C5	114.4(1)	113.1
C4–C5–C6	118.2(3)	118.4(1)	119.3	C4–C5–C6	118.5(1)	119.2
C5–C6–N1	125.4(3)	125.2(1)	124.4	C5–C6–N1	125.4(1)	123.4
C6–N1–C2		117.9(1)	119.7	C6–N1–C2	117.8(1)	120.9
C5–C6–C7	120.7(3)	121.0(2)	121.6	C5–C6–C7	120.7(1)	123.2
C6–C7–O3	119.7(3)	119.6(1)	122.2	C6–C7–O3	120.6(1)	122.4
C6–C7–O1	114.6(3)	114.9(1)	113.4	C6–C7–O1	115.6(1)	113.3
O3–C7–O1		125.6(1)	124.3	O3–C7–O1	123.8(1)	124.3

The numbering of the atoms is shown in Figs. 1a and b.

force. A close inspection of the structure has revealed that the sixth coordination site is positioned at the π bond of the neighboring uracil ring (X denotes the middle of the C5═C6 bond), as illustrated in Fig. 2. The Cu–X^{ii} distance of 3.293(9) Å is close to the van der Waals contacts between the stacking bases in DNA. It should be emphasized that the $O4^{i}$–Cu–X^{ii} angle is approximately linear (169.6(1)°).

Fig. 3 shows the packing in the crystal of Cu(orotato)$(NH_3)_2$ (**1**) and displays the pseudooctahedral environment around the copper(II) ions (in each complex, the O4 atom and the middle of the π bond form the apexes on the elongated octahedron). The most important structural feature is the Cu–π axial interaction which connects the dimers into a columnar polymer along the *a*-axis (the view is down the *b*-axis). The non-covalent binding forces between the chelated copper(II) ion and the π-electron system are probably weak, nevertheless, they are very important in stabilizing the polymeric structure of complex **1**.

The stability of the columns is further enhanced by the formation of extensive intermolecular hydrogen bonds (indicated by dashed lines). Each two complex molecules are linked by a pair of Watson–Crick type hydrogen bonds, involving the O4═C4 and N3–H3 groups of each uracil ring, with a N3···$O4^{a}$ distance of 2.860(2) Å and N3–H3···$O4^{a}$ angle of 171(2)° (the symmetry codes are listed under Table 3). It is worth noting that a very similar type of intermolecular hydrogen bonding was reported for crystals of 1-methylthymine with corresponding N···O distances of 2.83 Å [28]. The remaining intermolecular hydrogen bonds in **1** involve two ammonia groups and all the oxygen atoms, as shown in Table 3.

Reedijk and coworkers [29], in their studies on copper(II) complexes with some pyrimidin-2-yl ligands, have concluded that crystal growth is driven by several synergistic intermolecular interactions: metal–ligand bonds and hydrogen bonding, as well as π–π stacking and anion–π stacking interactions. Our study of the crystal structure

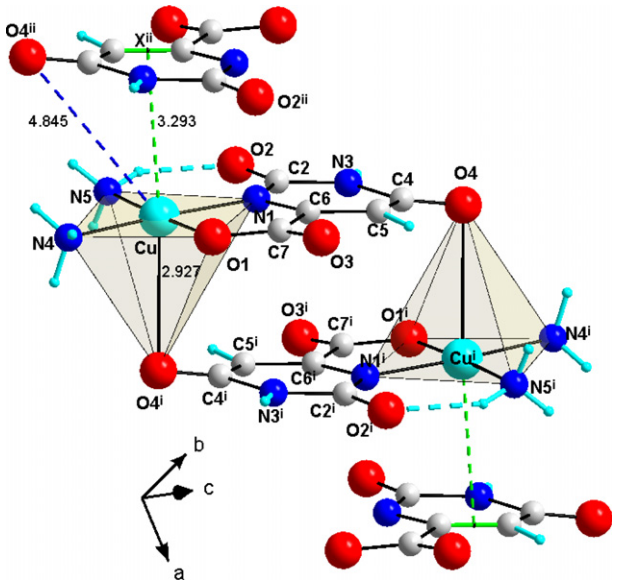


Fig. 2. The view of the dimer unit of Cu(orotato)$(NH_3)_2$ showing the axial Cu–$O4^{i}$ bonds and Cu–X^{ii} interactions (dashed lines). X^{ii} denotes the middle of the $C5^{ii}$═$C6^{ii}$ double bond of the uracilate ring. In contrast to an earlier suggestion [12], the Cu–$O4^{ii}$ distance of 4.845(3) Å is too long to allow for any effective interaction between these atoms. Symmetry codes are as follows: (i) $1.5 - x$, $-0.5 + y$, $1.5 - z$; (ii) $0.5 - x$, $-0.5 + y$, $1.5 - z$.

of **1** have revealed another type of synergistic interaction, the non-covalent binding force between the chelated copper(II) cation and the π-electrons of the uracil ring.

In the literature, there are only a few reports on a possible direct interaction between chelated copper(II) ions and an aromatic π system. The X-ray diffraction studies of Cu(II) complexes with L-tyrosine [30], glycyl-L-leucyl-L-tyrosine [31] and glycyl-L-tryptophane [32] have shown that the aromatic rings of the tyrosine or tryptophane groups are located beneath the basal plane of the copper coordination pyramid at a distances of about 3.2–3.3 Å. Thus, the Cu–π distances in all these complexes are close to the van der Waals contacts between the stacking bases in DNA.

π–π stacking interactions between uracilate rings have been observed in other Cu(II) complexes with orotic acid derivatives, the distance between partially overlapping uracilate rings varies from 3.250(3) Å in the mononuclear [Cu(5-fluoroorotato)$(NH_3)(H_2O)$] complex [16] to 3.40 Å in diammine(5-nitroorotato)copper(II) hydrate [27]. On the other hand, in the structure of the polymeric $[(orotato)Cu(H_2O)_2]_n$ complex (obtained from orotic acid methyl ester), the π–π base stacking is not retained due to some steric effects [13]. It is interesting to note that in the crystal structure of [Cu(orotato)(en)$(H_2O)] \cdot H_2O$, reported by Icbudak et al. [15], the vertical distances between the copper atom and the uracilate ring are between 3.156 and 3.274 Å (private communication).

Thus, it seems that the Cu(II)–π direct interaction can occur in copper(II) complexes containing aromatic rings, provided that some steric effects do not prevent it.

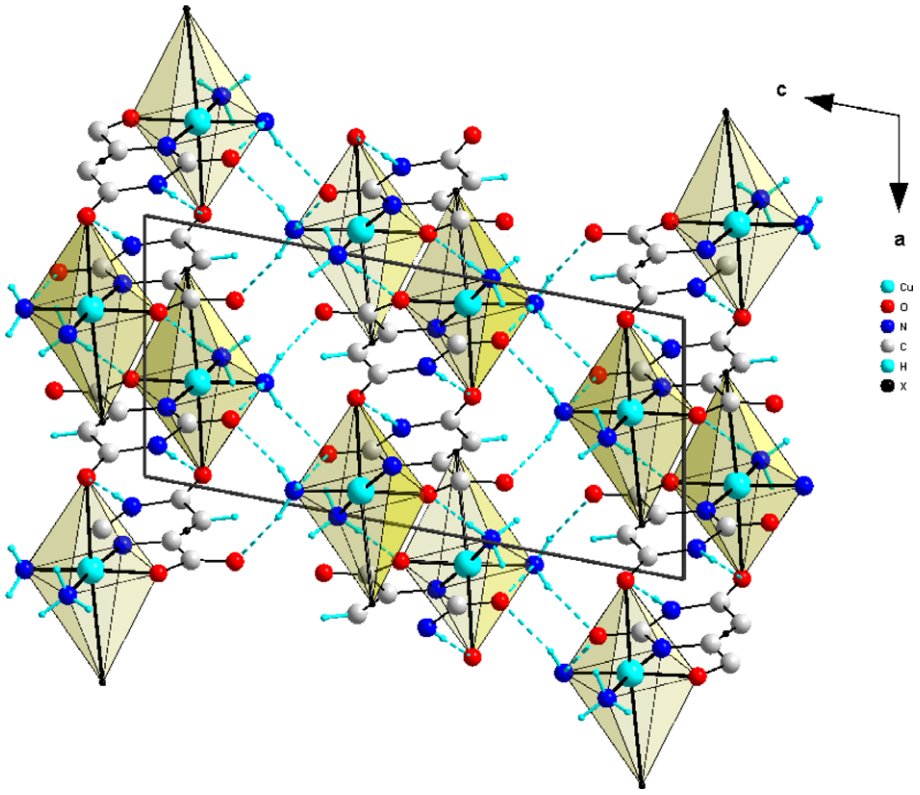


Fig. 3. A stereoscopic packing in the crystal of Cu(orotato)$(NH_3)_2$ (**1**) displaying the pseudooctahedral environment around the copper ions. Hydrogen bonds are indicated by dashed lines. Columnar polymers are along the *a* axis, the view is down the *b*-axis.

Table 3
Possible hydrogen bond distances (Å) and angles (°) for *cis*-Cu[(orotato)-$(NH_3)_2$] (**1**)

D–H···A	D–H	H···A	D···A	∠D–H···A
N5–H53···O2	0.84(2)	2.01(2)	2.782(2)	153(2)
N3–H3···O4[a]	0.85(2)	2.02(2)	2.860(2)	171(2)
N4–H41···O1[b]	0.80(2)	2.28(2)	3.039(2)	159(2)
N4–H42···O2[c]	0.92(2)	2.46(2)	3.242(2)	144(2)
N4–H43···O3[d]	0.89(2)	2.40(2)	3.246(2)	160(2)
N5–H51···O3[d]	0.84(2)	2.16(2)	2.931(2)	152(2)
N5–H52···O2[e]	0.77(2)	2.22(2)	2.975(2)	168(2)

Symmetry codes: (a) $-x+1$, $-y$, $-z+1$; (b) $-x$, $-y+2$, $-z+1$ (c) x, $y+1$, z; (d) $x-1/2$, $-y+3/2$, $z-1/2$; (e) $-x+1/2$, $y+1/2$, $-z+1/2$.

4.2. Description of the structure of $[Cu(orotato)(H_2O)_4]\cdot H_2O$ (2)

Complex **2** crystallizes in the monoclinic system (crystal data are given in Table 1). Our results (unit cell constants) are consistent with those reported by Wu et al. (refined to $wR = 0.1015$) [14], however the bond lengths and bond angles determined in this work are more accurate and the interpretation of the coordination sphere around Cu is different. The molecular structure of **2** and the numbering of atoms are shown in Fig. 1. It should be emphasized that, in contrast to the polymeric complex $[(orotato)Cu(H_2O)_2]_n$ [13], complex **2** is a mononuclear species. The copper(II) ion is chelated by the deprotonated N1 nitrogen atom and by the carboxylate O1 oxygen atom of the bidentate orotate ligand. Two water oxygen atoms (O5 and O6) complete a slightly distorted square-planar environment around Cu. The coordination sphere in **2** can be described as (4+2) geometry, where the O7 and O8 aqua ligands occupy axial coordination sites. It is worth noting that the water of crystallization (O9) acts as a proton-donor in an intermolecular hydrogen bond with the non-chelating carboxylic oxygen atom at an O9···O3 distance of 2.835(2) Å and O9–H91···O3 angle of 174(2)°.

The bond lengths and bond angles of two complexes are compared in Table 2. As follows from this comparison, the Cu–N1 atom distance in **2** is very similar to that in **1**, but the Cu–O1(carboxylate) bond length in **2** (1.984(1) Å) is slightly longer than that in **1** (1.959(1) Å). Furthermore, in the equatorial plane of **2**, the Cu–OH_2 atom distances, Cu–O5 (1.992(1) Å) and Cu–O6 (2.005(1) Å), are also slightly longer than the corresponding Cu–NH_3 distances, (1.955(1) and 1.996(1) Å), in **1**.

In complex **2**, the axial Cu–O7 bond length is equal to 2.400(1) Å. A similar Cu–O(water) atom distance of 2.480(1) Å has been found in the octahedral *trans*-$[Cu(malonamato)_2(H_2O)_2]$ complex [33]. The Cu–O8 axial bond in **2** is rather long, 2.873(2) Å, but is similar to that between the Cu and $O4^{i}$ oxygen atom found in **1** (2.927(3) Å). It should be emphasized that the O7 and O8

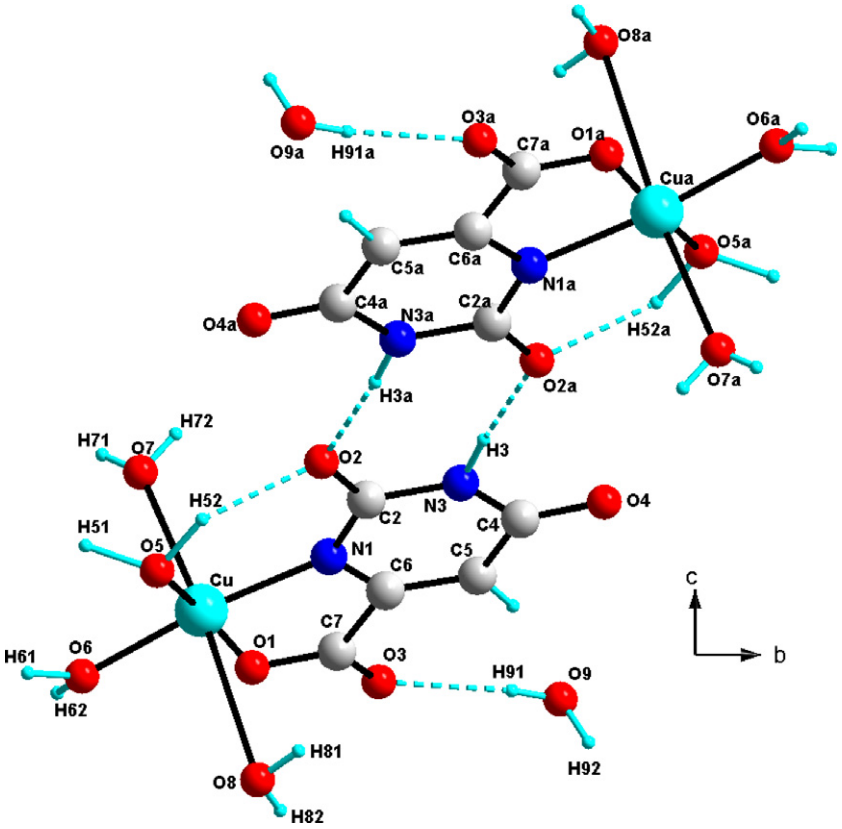


Fig. 4. The centrosymmetric dimer of $[Cu(orotato)(H_2O)_4]\cdot H_2O$ (**2**). Hydrogen bonds are indicated by dashed lines. The symmetry codes are given in Table 4.

axial ligands make an almost linear arrangement, the O7–Cu–O8 bond angle is equal to 174.7(1)°. This indicates that the O8 water molecule is weakly coordinated to the copper (II) ion, and the molecular structure of **2** can be described as an asymmetric elongated octahedron. It is worth noting that the long Cu–O distance of 2.873(2) Å in this complex can be compared with those encountered in the literature on Cu(II) complexes. Keene et al. [34] reported a Cu–O bond of 2.906(10) Å for an octahedral CuO_6 coordination sphere in the $[Cu(oxalato)_2(H_2O)]^{2-}$ dimer units. Warda [35] showed that in the Cu(II) complex with mixed ligands (*N*-ethylurea and *N*-pyruvidene-β-alanine dianion) the oxygen atom of *N*-ethylurea is weakly coordinated to the Cu(II) atom at a distance of 3.062(2) Å. He concluded on the basis of structural and spectroscopic results, that Cu(II) is near the critical point of square-pyramidal/octahedral geometry, but is still in the octahedral region, and he described the structure of this complex as an asymmetric elongated octahedron [35].

The least-squares plane through the six non-hydrogen atoms of the uracil ring in **2** reveals that the ring is approximately planar, the largest deviation being 0.021(1) Å for N1. The carboxylate group is slightly twisted, the angle between the uracil ring and the plane of the carboxylate group is 6.4(1)°. The displacement of the Cu atom from the equatorial least-squares plane (formed by the N1, O1, O5 and O6 atoms) is 0.058(1) Å.

The corresponding bond angles of the uracilate ring are similar in **1** and **2** (Table 2). Some differences are noted for the corresponding bond lengths, in particular for the exocyclic carbonyl and carboxylic C=O bonds. This effect is caused by a different pattern of intermolecular hydrogen bonding in the two title complexes.

As illustrated in Fig. 4, two molecules of complex **2** are arranged in a centrosymmetric dimer linked by two nearly linear N3–H3···O2^a hydrogen bonds between the uracil rings (the symmetry code for a is: $-x, -y, -z+1$). The intermolecular N3···O2^a distance of 2.835(2) Å is slightly shorter than the intermolecular N3···O4^a distance (2.860(2) Å) (a: $-x+1, -y, -z+1$) in the crystal of **1**. The exocyclic carbonyl O2 atom in **2** is involved in a weak H-bond contact with the water molecule (O5) coordinated to the copper(II) ion (the O5···O2 distance is 2.862(2) Å and the O5–H52···O2 angle is 140(2)°). The coordinated water molecules take part in an extensive net of intermolec-

Table 4
Possible hydrogen bond distances (Å) and angles (°) for [Cu(orotato)-$(H_2O)_4]\cdot H_2O$ (**2**)

D–H···A	D–H	H···A	D···A	∠D–H···A
O9–H91···O3	0.78(2)	2.06(2)	2.835(2)	174(2)
O5–H52···O2	1.08(2)	1.95(2)	2.862(2)	140(2)
N3–H3···O2^a	0.91(2)	1.93(2)	2.835(2)	174(2)
O7–H71···O8^b	0.70(2)	2.09(2)	2.792(2)	176(2)
O7–H72···O4^c	0.76(2)	2.00(2)	2.756(2)	169(2)
O8–H81···O3^d	0.81(2)	2.01(2)	2.800(2)	165(2)
O8–H82···O9^e	0.76(2)	2.17(2)	2.881(2)	156(2)
O6–H62···O4^f	1.13(2)	1.99(2)	3.094(2)	165(2)
O9–H92···O1^e	0.87(2)	2.37(2)	3.080(2)	140(2)

Symmetry codes: (a) $-x, -y, -z+1$; (b) $x+1/2, -y+1/2, z-1/2$; (c) $-x+1, -y, -z+1$; (d) $x-1, y, z$; (e) $-x+2, -y, -z+2$; (f) $-x+3/2, y+1/2, -z+3/2$.

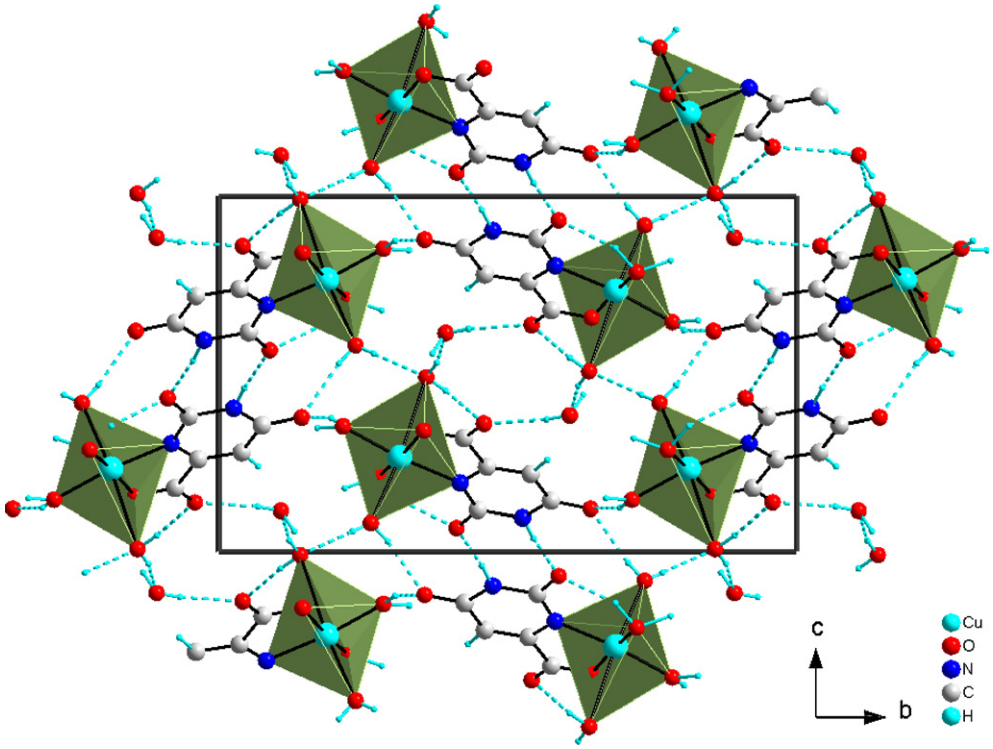


Fig. 5. The arrangement of (**2**) in the unit cell, projected down the *a*-axis hydrogen bonds are indicated by dashed lines.

ular hydrogen bonds. For example, the axial O8 atom (on a long axis), acts as the proton-donor to the O3[d] and O9[e] atoms, and simultaneously acts as a proton acceptor from the O7[b] atom of the neighboring complex molecules (Table 4). These chains of hydrogen bonds lead to an extensive three-dimensional network (Fig. 5).

5. Theoretical results

The molecular parameters predicted for Cu(orotato)$(NH_3)_2$ and Cu(orotato)$(H_2O)_2$ are in good agreement with the X-ray data. In particular, the bond lengths and angles in the uracil ring are very well predicted at this level of theory. Some discrepancies between the theoretical and experimental C=O bond lengths are attributed to intermolecular hydrogen bonding in the crystal (the calculations have been performed for an isolated molecule). It should be noted that an attempt to optimize the molecular structure of **2**, under the assumption that the (N,O)-chelated copper(II) ion is coordinated to four water molecules, has lead to dissociation of the two axial H_2O molecules. In the successive steps of the optimization process, the two axial water molecules are transferred to the basal plane and they form intermolecular hydrogen bonds with the equatorial water molecules. This result indicates that in the crystal of **2** the extensive intermolecular hydrogen bonds are very important in stabilizing the axial positions of the water molecules and the pseudooctahedral environment around the copper atom.

The calculated natural atomic charges are compared in Table 5. We have shown earlier [22] that atomic charges obtained from NBO analysis are more reliable than Mulliken charges. As shown in Table 5, the natural charges on the coordinated O1 and N1 atoms in **1** are very similar to those in **2**. The charge on the copper atom is equal to +1.237e for **1** and +1.287e for **2**. A lower positive charge on the Cu atom in **1** is due to stronger electron donation from the coordinated ammonia nitrogen atoms to Cu in **1**, as compared to the electron donation from the coordinated water oxygen atoms in **2**.

It should be emphasized that the natural charge on the copper atom in **1** is quite close to (+1e). Numerous experimental and theoretical studies [36,37] have revealed that a bare Cu^+ cation forms a stable cation–π complex with benzene. Thus, it is possible that in **1** the non-covalent Cu(II)–π binding force resembles that between the Cu^+ ion and aromatic compounds. However, the theoretical prediction of a Cu(II)–π interaction between the chelated Cu^{2+} ion and the C=C double bond in the investigated complex **1** is not an easy task. Such calculations should be performed for a large molecular model consisting of three layers of molecules: the planar *cis*-[Cu(orotato)$(NH_3)_2$] complex; the uracilate ring above the equatorial coordination plane, and some amide with the carbonyl oxygen atom coordinated to copper(II) in an axial position. Moreover, to account for the dispersion energy, which is very important in cation–π interactions, it is necessary to use the post-Hartree-Fock methods, for example, the second-order

Table 5
The calculated NBO natural charges (e) on atoms of *cis*-[Cu(orotato)$(NH_3)_2$] (**1**) and [Cu(orotato)$(H_2O)_2$] (**2**)

Atom[a]	1	2
Cu	1.237	1.287
O1	−0.857	−0.854
N1	−0.813	−0.804
N4/O6	−1.164	−1.004
N5/O5	−1.194	−1.062
C2	0.916	0.922
O2	−0.757	−0.746
N3	−0.707	−0.700
H3	0.440	0.445
C4	0.722	0.723
O4	−0.651	−0.638
C5	−0.349	−0.339
H5	0.256	0.259
C6	0.133	0.132
C7	0.871	0.870
O3	−0.633	−0.618
H41/H51	0.449	0.520
H42/H52	0.415	0.527
H43/H61	0.415	0.530
H51/H62	0.410	0.549
H52	0.410	
H53	0.451	

[a] Slash (/) separates the corresponding atoms in complexes **1** and **2**.

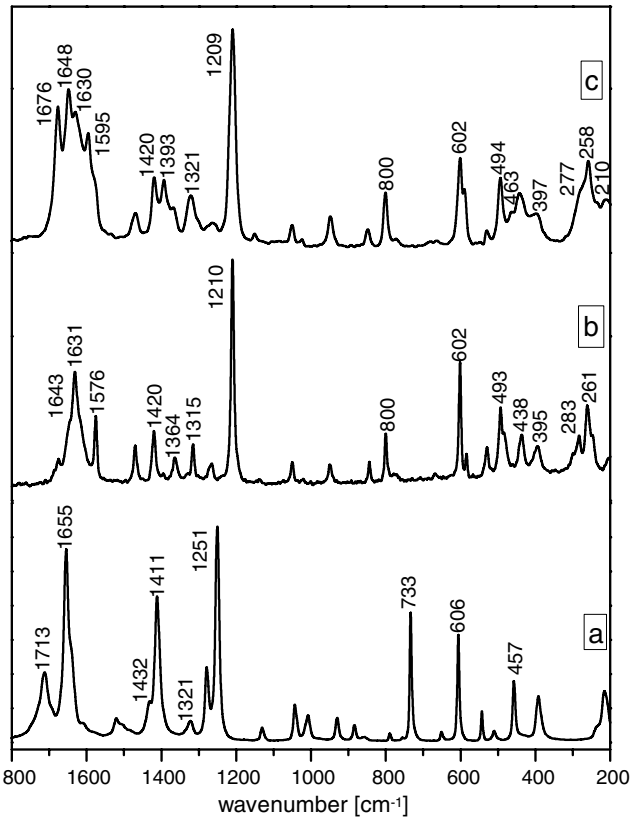


Fig. 6. The FT-Raman spectra of anhydrous orotic acid (**a**), Cu(orotato)$(NH_3)_2$ (**b**) and [Cu(orotato)$(H_2O)_4]\cdot H_2O$ (**c**), in the region 1800–200 cm^{-1}.

Möller-Plesset perturbation theory (MP2), as demonstrated in our earlier studies [38]. We hope to be able to perform such calculations, in the near future.

5.1. FT-Raman and FT-infrared spectroscopic studies

The Raman spectra of anhydrous orotic acid, Cu(orotato)$(NH_3)_2$ (**1**) and [Cu(orotato)$(H_2O)_4]\cdot H_2O$ (**2**) are illustrated in Fig. 6. The most characteristic bands are collected in Table 6. Band assignment for the ligand has been made by comparison with the results from vibrational spectroscopic studies and the calculated potential energy distributions (PEDs) for Pt(orotato)$(NH_3)_2$ [10], 1-methylthymine (1-MeT) [39] and 1-methyluracil (1-MeU) [40]. The copper–ligand stretching vibrations were assigned by comparison with the spectra of similar Cu(II) complexes [41].

The exocyclic ν(C4=O4) stretching vibration contributes to the strong band at 1661 cm^{-1} in the infrared spectrum of **1**, and at 1685 cm^{-1} in the IR spectrum of **2** (1676 cm^{-1} in the Raman spectrum). A lower frequency of the ν(C4=O4) mode in the former complex is caused by intermolecular N3–H3···O4′ hydrogen bonding in the crystal of **1**. The corresponding ν(C4=O4) vibration in 1-MeT was observed in the range 1660–1680 cm^{-1} [39]. The very strong and broad Raman bands with maxima at 1631 cm^{-1} for **1** and 1648 cm^{-1} for **2** can arise from an overlap of several transitions of similar energy. Thus, both the ν(C5=C6) and ν(C7=O3) stretching vibrations should occur in this range of frequencies. Moreover, the bending vibrations of the coordinated ammonia groups in **1**, or bending $\delta(H_2O)$ vibrations in **2**, should also be observed at about 1620–1650 cm^{-1} [41].

In the Raman spectrum of Cu(orotato)$(NH_3)_2$ we have assigned the band at 1576 cm^{-1} to the ν(C2=O2) stretching vibration. A large downward shift of this band, in comparison to the other ν(C=O) bands, is caused by the strong hydrogen bond which involves the O2 carbonyl oxygen atom and the N5 atom of the ammonia group coordinated to the copper atom.

In **2**, the Raman band at 1595 cm^{-1} can be assigned to the ν(C2=O2) stretching vibration, however, the ν(C7=O3) stretching may also contribute to this band. As revealed by the X-ray data, the non-chelating C7=O3 group in **2** is involved in intermolecular hydrogen bonding with a lattice water molecule, which may cause a shift of ν(C7=O3) to a lower frequency, in comparison to **1**. A similar band at 1593 cm^{-1} in the spectrum of Cu(glycine)$_2$ dihydrate was also assigned to a carboxylate ν(C=O) vibration [41].

The most intense bands in the FT-Raman spectra of **1** and **2** are observed at 1210 and 1209 cm^{-1}, respectively (Fig. 6). It should be noted that in the Raman spectrum of Pt(orotato)$(NH_3)_2$, the strongest band was located at 1217 cm^{-1} [10], while in the FT-Raman spectrum of [Ni(orotato)$(H_2O)_4$], a very strong band was observed at 1215 cm^{-1} [11]. On the basis of the calculated potential energy distributions (PEDs), these bands were assigned to the stretching vibration of the uracilate ring [10,11]. For anhydrous orotic acid, the corresponding very strong band occurs at 1251 cm^{-1} (Table 6). Thus, it can be concluded that the shift of the very strong Raman band from 1251 cm^{-1} (orotic acid) to the range 1209–1217 cm^{-1} (transition metal complexes) is diagnostic for N_1-deprotonation of the ligand and formation of the N_1–metal bond in these complexes.

The ν(Cu–NH_3), ν(Cu–H_2O), ν(Cu–N1) and ν(Cu–O1) stretching frequencies are of particular interest since they provide direct information about the strength of the copper–ligand bonds. In the spectra of **1**, the new bands

Table 6
Selected Raman and infrared bands (cm^{-1}) of anhydrous orotic acid ($C_5H_4N_2O_4$), *cis*-[Cu(orotato)$(NH_3)_2$] (**1**) and [Cu(orotato)$(H_2O)_4]\cdot H_2O$ (**2**)

Orotic acid		**1**		**2**		Band assignment[a]
Raman	IR	Raman	IR	Raman	IR	
1655vs	1651vs	ov	1661vs	1676s	1685vs	ν C4=O4
		1643sh	ov	1648vs	1645vs	δ NH_3 (**1**)/δ H_2O (**2**)
1713m	1704s	1631s	1639vs	1630sh	ov	ν C5=C6, ν C7=O3
		1576m		1595m		ν C2=O2, ν C7=O3 (**2**)
1432sh	1435s	1420m	1412m	1420m	1412m	ν (U ring)
1411s	1406m	1364w	1374m	1393m	1384s	δ N3–H3, ν (U ring)
1321w	1327m	1315m	1315m	1321m	1308m	ν C7–O1, ν C6–C7
1251vs		1210vs		1209vs		ν (U ring)
733m	730m	800m	803m	800m	803m	γ C7=O3
606m	602m	602m	607m	602m	609m	δ (U ring)
457m	461m	493m	492w	494m	501m	δ coor, δ (U ring)
		438m	438sh	463sh	455sh	ν Cu–NH_3 (**1**)/ν Cu–OH_2 (**2**)
		395br	406m	397m	394w	ν Cu–NH_3 (**1**)/ν Cu–OH_2 (**2**)
		283m	279m	277sh	266br	ν Cu–O1
		261m	258m	258m	ov	ν Cu–N1
			213m	210m	210m	ν Cu–N1, δ coor

[a] Abbreviations: br, broad; m, medium; ov, overlapped bands; s, strong; sh, shoulder; w, weak; v, very; ν, stretching; δ, in-plane bending; γ, out-of-plane bending; τ, torsion; coor, coordination ring; U, uracilate ring.

at 438 cm^{-1} (Raman) and 406 cm^{-1} (IR) have been assigned to the ν(Cu–NH_3) stretching vibrations. Similar bands at 426 and 420 cm^{-1} were reported for $[Cu(NH_3)_4]^{2+}$ [41]. In the spectra of **2**, the new Raman bands arising at 463 cm^{-1} (sh) and 397 cm^{-1} are due to the ν(Cu–H_2O) stretching vibrations. These frequencies are also similar to those reported for Cu–aqua complexes, at about 440 cm^{-1} [41].

It follows from this comparison that the Cu–NH_3 and Cu–H_2O bonds in **1** and **2**, respectively, have a strong covalent character.

The new Raman bands at 283 cm^{-1} for **1** and 277 cm^{-1} for **2** are assigned to the ν(Cu–O1) stretching vibrations. It should be noted that the corresponding ν(Cu–O) stretching frequency in Cu(glycine)$_2$ was reported at 337 cm^{-1} [41], which indicates that the Cu–O1 bonds in the title complexes are more ionic than the Cu–O bond in the glycine complex.

In the FT-Raman spectra (Fig. 6), new distinct bands appear at 261 cm^{-1} for **1** and 258 cm^{-1} for **2**. Both these bands can be assigned to the ν(Cu–N1) stretching vibrations in these complexes. It should be noted that the corresponding ν(Cu–N) mode in the Cu(II) complex with pyridine occurs at a very similar frequency, 268 cm^{-1} [41]. Thus, it can be concluded that the strength of the Cu–N1 bond in **1** and **2** is comparable to that in copper(II) complexes with N-aromatics. This implies that the N1-deprotonated orotate ligand displays a strong π-donating capability.

6. Conclusions

The presence of Cu^{2+}/Cu^{+} centers is mainly responsible for the oxidase activity of copper-containing enzymes and proteins, e.g. galactose oxidase (GAO) and ceruloplasmin (C_p). The experimental study on the *cis*-[Cu(orotato)(NH_3)$_2$] complex has revealed the great importance of the non-covalent Cu(II)–π binding force between the chelated Cu^{2+} ion and the uracilate ligand. The natural bond orbital analysis (NBO) indicates that the natural atomic charge on the copper(II) ion is about +1.2e in this complex. It is known that a bare Cu cation with a +1 charge is capable of interacting with simple aromatics, therefore, it is possible that the Cu(II)–π interaction can exist in aromatic systems, provided that some steric affects do not prevent it.

Thus, it is suggested that the non-covalent Cu–π interaction between the chelated Cu^{2+} ion and aromatic compounds can play a significant role in many biological processes, e.g. in binding a substrate at the active site of an enzyme. This hypothesis may shed new light on the mechanism of action of certain copper-containing enzymes.

Acknowledgements

The authors dedicate this paper to the memory of Professor Tadeusz Głowiak, a wonderful friend and great crystallographer, who first indicated the possibility of a copper(II)–π interaction in the studied complex. We gratefully acknowledge helpful discussions with Professor Jan Reedijk from Leiden University. We also thank Professor Leonard Proniewicz from the Jagiellonian University in Cracow for measuring the Raman spectra of the copper(II) complexes. The Poznań Supercomputer and Networking Center and the Wrocław Centre for Networking and Supercomputing are acknowledged for generous computer time. This work was supported by a grant from Wrocław University of Technology.

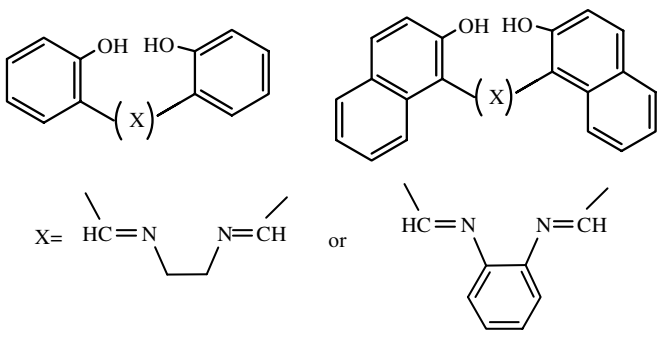
Appendix A. Supplementary material

CCDC 638205 and 638259 contain the supplementary crystallographic data for *cis*-[Cu(orotato)(NH_3)$_2$] (**1**) and [Cu(orotato)(H_2O)$_4$] · H_2O (**2**). These data can be obtained free of charge via http://www.ccdc.cam.ac.uk/conts/retrieving.html, or from the Cambridge Crystallographic Data Centre, 12 Union Road, Cambridge CB2 1EZ, UK; fax: (+44) 1223-336-033; or e-mail: deposit@ccdc.cam.ac.uk. Supplementary data associated with this article can be found, in the online version, at doi:10.1016/j.poly.2007.05.052.

References

[1] A. Lehninger, Principles of Biochemistry, Worth Publishers, New York, 1970, p. 661.
[2] J. Victor, L.B. Greenberg, D.L. Sloan, J. Biol. Chem. 254 (1979) 2647.
[3] P. Castan, E. Colacio-Rodriguez, A.L. Beauchamp, S. Cros, S. Wimmer, J. Inorg. Biochem. 38 (1990) 225.
[4] O. Kumberger, J. Riede, H. Schmidbaur, Z. Naturforsch. B 48 (1993) 961.
[5] F.L. Rosenfeldt, Cardiovasc. Drugs Ther. 12 (1998) 147.
[6] O.K. Yesilel, M.S. Soylu, H. Ölmez, O. Büyükgüngör, Polyhedron 25 (2006) 2985, and references cited therein.
[7] S.L. James, D.M.P. Mingos, X. Xu, A.J.P. White, D.J. Wiliams, J. Chem. Soc., Dalton Trans. (1998) 1335.
[8] F. Nepveu, N. Gaultier, N. Korber, J. Jaud, P. Castan, J. Chem. Soc., Dalton Trans. (1995) 4005.
[9] D.J. Darensbourg, J.D. Draper, D.L. Larkins, B.J. Frost, J.H. Reibenspies, Inorg. Chem. 37 (1998) 2538.
[10] R. Wysokiński, K. Hernik, R. Szostak, D. Michalska, Chem. Phys. 333 (2007) 37.
[11] R. Wysokiński, B. Morzyk-Ociepa, T. Głowiak, D. Michalska, J. Mol. Struct. 606 (2002) 241.
[12] I. Mutikainen, P. Lumme, Acta Crystallogr., Sect. B 36 (1980) 2233.
[13] T.T.B. Ha, A.M. Larsonneur-Galibert, P. Castan, J. Jaud, J. Chem. Crystall. 29 (1999) 565.
[14] A.Q. Wu, L.Z. Zhen, G.H. Guo, F.K. Zheng, G.C. Guo, J.G. Mao, J.S. Shun, Huang Jin-Shun, Chin. J. Inorg. Chem. 19 (2003) 879.
[15] H. Icbudak, H. Olmez, O.Z. Yesilel, F. Arslan, P. Naumov, G. Jovanovski, A.R. Ibrahim, A. Usman, H.-K. Fun, S. Chantrapromma, S.W. Ng, J. Mol. Struct. 657 (2003) 255.
[16] A.G. Schneider, H.W. Schmalle, F. Arod, E. Dubler, J. Inorg. Biochem. 89 (2002) 227.
[17] G.M. Sheldrick, SHELXS-97, Program for Crystal Structure Determination, University of Göttingen, Germany, 1997.
[18] G.M. Sheldrick, SHELXL-97, Program for the Refinement of Crystal Structures, University of Göttingen, Germany, 1993.
[19] K. Brandenburg, DIAMOND, Version 3.0. Crystal Impact GbR, Bonn, Germany, 2005.

[20] A.D. Becke, J. Chem. Phys. 104 (1996) 1040.
[21] C. Lee, W. Yang, R.G. Parr, Phys. Rev. B 37 (1988) 785.
[22] P.M. Wojciechowski, W. Zierkiewicz, D. Michalska, P. Hobza, J. Chem. Phys. 118 (2003) 10900.
[23] P.J. Hay, W.R. Wadt, J. Chem. Phys. 82 (1985) 270, and also 299.
[24] T.H. Dunning Jr., P.J. Hay, in: H.F. SchaeferIII (Ed.), Modern Theoretical Chemistry, vol. 3, Plenum Press, New York, 1976.
[25] A.E. Reed, L.A. Curtiss, F. Weinhold, Chem. Rev. 88 (1988) 899.
[26] M.J. Frisch, G.W. Trucks, H.B. Schlegel, G.E. Scuseria, M.A. Robb, J.R. Cheeseman, J.A. Montgomery Jr., T. Vreven, K.N. Kudin, J.C. Burant, J.M. Millam, S.S. Iyengar, J. Tomasi, V. Barone, B. Mennucci, M. Cossi, G. Scalmani, N. Rega, G.A. Petersson, H. Nakatsuji, M. Hada, M. Ehara, K. Toyota, R. Fukuda, J. Hasegawa, M. Ishida, T. Nakajima, Y. Honda, O. Kitao, H. Nakai, M. Klene, X. Li, J.E. Knox, H.P. Hratchian, J.B. Cross, C. Adamo, J. Jaramillo, R. Gomperts, R.E. Stratmann, O. Yazyev, A.J. Austin, R. Cammi, C. Pomelli, J.W. Ochterski, P.Y. Ayala, K. Morokuma, G.A. Voth, P. Salvador, J.J. Dannenberg, V.G. Zakrzewski, S. Dapprich, A.D. Daniels, M.C. Strain, O. Farkas, D.K. Malick, A.D. Rabuck, K. Raghavachari, J.B. Foresman, J.V. Ortiz, Q. Cui, A.G. Baboul, S. Clifford, J. Cioslowski, B.B. Stefanov, G. Liu, A. Liashenko, P. Piskorz, I. Komaromi, R.L. Martin, D.J. Fox, T. Keith, M.A. Al-Laham, C.Y. Peng, A. Nanayakkara, M. Challacombe, P.M.W. Gill, B. Johnson, W. Chen, M.W. Wong, C. Gonzalez, J.A. Pople, GAUSSIAN 03, Revision C.01, Gaussian Inc., Wallingford, CT, 2004.
[27] P. Arrizabalaga, P. Castan, F. Dahan, Inorg. Chem. 22 (1983) 2245.
[28] K. Hoogsteen, Acta Crystallogr. 16 (1963) 28.
[29] P. Gamez, G.A. van Albada, I. Mutikainen, U. Turpeinen, J. Reedijk, Inorg. Chim. Acta 358 (2005) 1975.
[30] D. Van der Helm, C.E. Tatsch, Acta Crystallogr., Sect. B 28 (1972) 2307.
[31] W.A. Franks, D. Van der Helm, Acta Crystallogr., Sect. B 27 (1971) 1299.
[32] M.B. Hursthouse, S.A.A. Jayaweera, G.H. Milburn, A. Quick, J. Chem. Soc. D (1971) 207.
[33] C. Vansant, H.O. Desseyn, V. Tangoulis, C.P. Raptopoulou, A. Terzis, S.P. Perlepes, Polyhedron 14 (1995) 2115.
[34] T.D. Keene, M.B. Hursthouse, D.J. Price, Acta Crystallgr., Sect. E 60 (2004) 378.
[35] S.A. Warda, Acta Crystallogr., Sect. C 55 (1999) 52.
[36] S.J. Klippenstein, C.-N. Yang, Int. J. Mass Spectrom. 201 (2000) 253.
[37] S.-L. Hang, L. Liu, Y. Fu, Q.-X. Guo, J. Mol. Struct. (Theochem) 757 (2005) 37.
[38] W. Zierkiewicz, D. Michalska, J. Černy, P. Hobza, Mol. Phys. 104 (2006) 2317.
[39] B. Morzyk-Ociepa, M.J. Nowak, D. Michalska, Spectrochim. Acta, Part A 60 (2004) 2113.
[40] T.P. Lewis, H.T. Miles, E.D. Becker, J. Phys. Chem. 88 (1984) 3253.
[41] K. Nakamoto, Infrared and Raman Spectra of Inorganic and Coordination Compounds, IV ed., John Wiley & Sons, 1986, p. 195, 206, 228 and 236.



H_2sal-en, **1**; H_2nap-en, **2**;

H_2sal-*o*-pndn, **3**; H_2nap-*o*-pndn, **4**

2. Experimental

2.1. Materials

All chemicals used were of Analar grade and solvents were dried following the literature procedure [26]. *cis*-$[RuCl_2(DMSO)_4]$ and the ligands (H_2sal-en, **1**; H_2nap-en, **2**; H_2sal-*o*-pndn, **3**; H_2nap-*o*-pndn, **4**) were prepared as reported earlier [27,28].

2.2. Physical methods

Infrared spectra of the ligand and the complexes have been recorded on a Nicolet Avatar model FT-IR spectrophotometer using KBr discs in the range 4000–400 cm^{-1}. Electronic spectra were recorded on a Systronics 119 UV–Vis spectrophotometer using methanol as the solvent. Elemental analyses were performed with a Vario EL III Elementar analyzer. ^1H NMR spectra were recorded on an AMX 400 instrument in DMSO solvent. Melting points were recorded with a Lab India apparatus.

2.3. X-ray crystallography

Single crystals of $[RuCl_2(DMSO)_2(o\text{-pndn})]$ suitable for X-ray diffraction studies were obtained from slow evaporation of an ethanolic solution of the complex. Diffraction data were collected on a Bruker AXS SMART APEX CCD diffractometer at 100(2) K using monochromatic Mo Kα radiation with the omega scan technique. The unit cell was determined using SMART and SAINT+ [29]. The structure was solved by direct methods and refined by full-matrix least-squares against F^2 with all reflections using SHELXTL [30]. Refinement of an extinction coefficient was found to be insignificant. All non-hydrogen atoms were refined anisotropically. All hydrogen atoms were placed in calculated positions and were refined with an isotropic displacement parameter of 1.5 (CH_3) or 1.2 (all others) times that of the adjacent carbon or nitrogen atom. The crystal data and refinement parameters are summarized in Table 1.

2.4. Synthesis of the new Ru(II) complexes

All the new mononuclear ruthenium(II) complexes were prepared by the following general procedure. An ethanolic solution of *cis*-$[RuCl_2(DMSO)_4]$ and the appropriate ligand in a 1:1 mole ratio was heated under reflux for 4 h. The solution was filtered and left for slow evaporation. The crystalline product that separated out was filtered off, washed with ethanol and dried under vacuum. The filtrate along with the ethanol washings were evaporated to dryness. The aldehyde formed was extracted with petroleum ether and then quantified. The individual syntheses are given below.

$[RuCl_2(DMSO)_2(o\text{-pndn})]$ (**5**) was prepared from *cis*-$[RuCl_2(DMSO)_4]$ (0.100 g, 0.2 mmol) and H_2sal-*o*-pndn (0.062 g, 0.2 mmol) as dark red brown crystals. Yield: 80%. *Anal.* Calc. for $RuC_{10}H_{20}N_2O_2Cl_2S_2$: C, 27.52; H, 4.60; N, 6.4; S, 14.69. Found: C, 27.44; H, 4.39; N, 6.61; S, 14.11%. IR: 3280, 3269, 1557, 1072, 1129 cm^{-1}. UV λ_{max}: 248, 289. M.p.: >200 °C (dec.).

Table 1
Crystal data and structure refinement parameters for $[RuCl_2(DMSO)_2(o\text{-pndn})]$

Empirical formula	$C_{10}H_{20}Cl_2N_2O_2RuS_2$
Formula weight	436.37
Temperature (K)	100(2)
Wavelength (Å)	0.71073
Crystal system	monoclinic
Space group	$P2_1/n$
Unit cell dimensions	
a (Å)	12.5947(8)
b (Å)	8.1650(5)
c (Å)	15.4946(9)
α (°)	90
β (°)	98.4880(10)
γ (°)	90
Volume (Å^3)	1575.95(17)
Z	4
D_{calc} (Mg/m^3)	1.839
Absorption coefficient (mm^{-1})	1.597
F(000)	880
Crystal size (mm)	$0.68 \times 0.37 \times 0.27$
θ Range for data collection (°)	1.95–28.28
Limiting indices	$-16 \leqslant h \leqslant 16$, $-10 \leqslant k \leqslant 10$, $-20 \leqslant l \leqslant 20$
Reflections collected/unique (R_{int})	15551/3899 (0.0209)
Completeness to $\theta = 28.28°$ (%)	99.8
Absorption correction	multi-scan
Maximum and minimum transmission	0.650 and 0.446
Refinement method	full-matrix least-squares on F^2
Data/restraints/parameters	3899/0/176
Goodness-of-fit on F^2	1.191
Final R indices [$I > 2\sigma(I)$]	$R_1 = 0.0211$, $wR_2 = 0.0522$
R indices (all data)	$R_1 = 0.0212$, $wR_2 = 0.0524$
Largest difference in peak and hole (e Å^{-3})	1.240 and −0.600

[$RuCl_2(DMSO)_2$(*o*-pndn)] (**5**) was also prepared from *cis*-[$RuCl_2(DMSO)_4$] (0.100 g, 0.2 mmol) and H_2nap-*o*-pndn (0.082 g, 0.2 mmol) as dark red brown crystals. Yield: 80%. *Anal*. Calc. for $RuC_{10}H_{20}N_2O_2Cl_2S_2$: C, 27.52; H, 4.60; N, 6.4; S, 14.69. Found: C, 27.03; H, 4.40; N, 6.14; S, 14.77%. IR: 3282, 3269, 1555, 1072, 1129 cm^{-1}. UV λ_{max}: 248, 289 (nm). M.p.: >200 °C (dec.).

[$RuCl_2(DMSO)_2$(en)] (**6**) was prepared from *cis*-[$RuCl_2(DMSO)_4$] (0.100 g, 0.2 mmol) and H_2sal-en (0.053 g, 0.2 mmol) as dark green crystals. Yield: 85%. *Anal*. Calc. for $RuC_6H_{20}N_2O_2Cl_2S_2$: C, 18.55; H, 5.19; N, 7.20; S, 16.51. Found: C, 18.22; H, 5.04; N, 7.21; S, 16.57%. IR: 3263, 3220, 1558, 1070, 1130 cm^{-1}. UV λ_{max}: 270, 258. M.p.: >200 °C (dec.).

[$RuCl_2(DMSO)_2$(en)] (**6**) was also prepared from *cis*-[$RuCl_2(DMSO)_4$] (0.100 g, 0.2 mmol) and H_2nap-en (0.073 g, 0.2 mmol) as dark green crystals. Yield: 85%. *Anal*. Calc. for $RuC_6H_{20}N_2O_2Cl_2S_2$: C, 18.55; H, 5.19; N, 7.20; S, 16.51. Found: C, 18.29; H, 5.08; N, 7.23; S, 16.37%. IR: 3265, 3216, 1553, 1073, 1127 cm^{-1}. UV λ_{max}: 270, 258. M.p.: >200 °C (dec.).

We were also able to synthesize compounds **5** and **6**, by refluxing an ethanolic solution of *cis*-[$RuCl_2(DMSO)_4$] and the corresponding diamine in a 1:1 mole ratio.

2.5. Antimicrobial activity

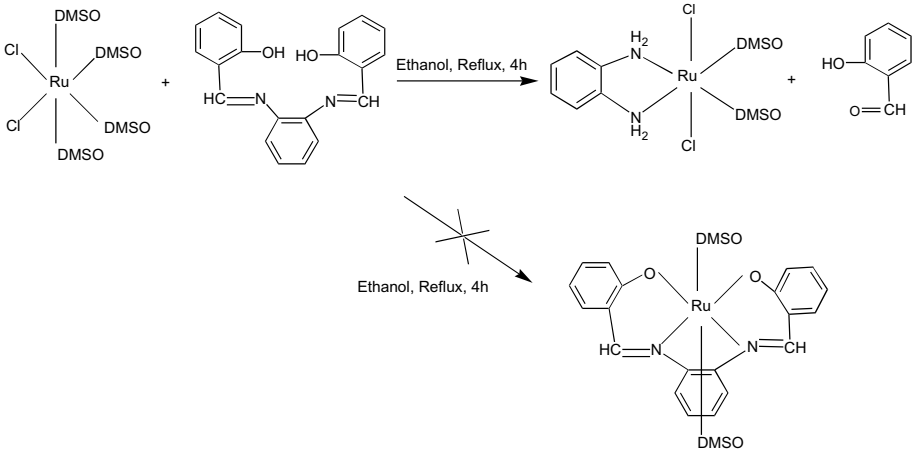
The new complexes have been tested in vitro to assess their growth inhibitory activity against the pathogenic bacteria *Aeromonas hydrophila*, *Eschericia coli*, *Salmonella typhi*, *Streptococcus faecalis*, *Klebsiella pneumonia*, *Staphylococcus aureus* and *Proteus mirabilis* by the disc diffusion method (Kirby–Bauer method) [31]. The bacteria were cultured in nutrient broth medium and used as inoculum for this study. Bacterial cells were swabbed on the surface of Mueller Hinton Agar medium [prepared from NaCl (5 g), peptone (5 g), beef extract powder (3 g), yeast extract powder (3 g) and agar (20 g) in 100 mL distilled water; pH 7.3 ± 0.2] in Petri plates. The compounds to be tested were dissolved in dimethyl sulfoxide to a final concentration of 0.25%, 0.5%, 0.75%, 1% and 1.5% and soaked in sterile discs (7 mm diameter). These discs were placed on the already seeded plates and incubated at 37 °C for 24 h. After incubation, the diameter (mm) of the inhibition zone around each disc was measured and classified as resistant (>15 mm), intermediate (13–14 mm) and sensitive (<13 mm) (Hi-media). A clear zone around the disc indicated the inhibitory activity of the compound on the organism. The data are presented in Table 4.

3. Results and discussion

New hexa-coordinated Ru(II) complexes of the type [$RuCl_2(DMSO)_2$(diamine)] (diamine = *o*-phenylenediamine and ethylenediamine) have been prepared by reacting *cis*-[$RuCl_2(DMSO)_4$] with the appropriate Schiff bases (H_2sal-en, **1**; H_2nap-en, **2**; H_2sal-*o*-pndn, **3**; H_2nap-*o*-pndn, **4**) in a 1:1 ratio. The ligands, which were expected to act as tetradentate (N_2O_2) chelates under the normal reaction conditions, were found to undergo hydrolytic cleavage to form the diamine and the corresponding aldehyde. The diamine formed reacted with [$RuCl_2(DMSO)_4$] to give complexes of the type [$RuCl_2(DMSO)_2$(diamine)], while the corresponding aldehydes were isolated in quantitative yield. The reaction scheme for one of the Schiff bases is given below and the other Schiff bases were found to follow the same route (see Scheme 1).

3.1. Elemental analysis

The analytical data obtained for the new Ru(II) complexes were entirely different from the one calculated for the expected hexa-coordinate Ru(II) complex containing the tetradentate dibasic ligand and dimethylsulfoxide. The analytical data conform to the stoichiometry of the new ruthenium complexes as [$RuCl_2(DMSO)_2$(diamine)]. The complexes obtained from H_2sal-en (**1**) and H_2nap-en (**2**) were identical and their analytical data were also



Scheme 1.

the same as that corresponding to $[RuCl_2(DMSO)_2$(ethylenediamine)]. Similarly, the complexes obtained from H_2sal-*o*-pdn (**3**) and H_2nap-*o*-pdn (**4**) were identical and their analytical data were also the same as that corresponding to $[RuCl_2(DMSO)_2$(*o*-phenylenediamine)].

3.2. Infrared spectroscopy

The IR spectra of the free ligands showed a strong band in the region 1642–1614 cm^{-1} assignable to $\nu_{-C=N}$ [32]. This band disappeared completely in the new complexes indicating the absence of any –C=N group, because if coordination of the ligand has occurred through the azomethine nitrogen then this band will undergo a bathochromic shift of 40–10 cm^{-1} [33] and not completely disappear. A new band around 1557 cm^{-1} (absent in the starting complex) appeared in the new complexes, indicating the presence of an aromatic –C=C– group [34]. Two new bands in the region 3280 and 3215 cm^{-1}, assignable to ν_{N-H}, indicate the introduction of the $-NH_2$ group (absent in the ligand and the starting complex) [35]. Two bands in the region 1120 and 1070 cm^{-1} due to $\nu_{S=O}$, characteristic of S-bonded DMSO, are present while the absence of a band around 935 cm^{-1} (due to O-bonded S=O) indicates elimination of O-bonded DMSO [27].

3.3. ^1H NMR spectroscopy

The ^{1}H NMR spectral data for complex **5** showed two signals at δ 7.2 ppm (m, 2H) and δ 7.41 ppm (t, 2H) that were assigned to the aromatic protons from *o*-phenylenediamine. A peak at δ 6.5 ppm (s, 4H) is due to the two NH_2 groups present in *o*-phenylenediamine. A sharp signal at δ 3.22 ppm (s, 12H) due to the $-CH_3$ group of S-bonded dimethylsulfoxide was also found [27]. The ^{1}H NMR spectral data for complex **6** showed no signals around δ 7 ppm indicating the absence of aromatic protons. A peak at δ 6.5 ppm (s, 4H) is due to the two NH_2 groups present in ethylenediamine. A sharp signal at δ 3.22 ppm (s, 12H) due to the $-CH_3$ group of S-bonded dimethylsulfoxide was also found.

3.4. Crystal structure of $[RuCl_2(DMSO)_2$ (*o*-pndn)]

The ORTEP diagram of $[RuCl_2(DMSO)_2$(*o*-pndn)] is shown in Fig. 1. Selected bond lengths and bond angles are given in Table 2 and details of hydrogen bonding in Table 3. The coordination environment around the ruthenium metal consists of an $N_2S_2Cl_2$ octahedron. The planar diamine ligand occupies the equatorial position along with two S-bonded dimethylsulfoxide groups, while the two chlorine atoms occupy the axial positions. The chlorine atoms, which were originally present in a *cis* position, now occupies a *trans* position, as evident from the Cl(2)–Ru(1)–Cl(1) bond angle of 170.686(15)°. Moreover the two chlorine atoms are bent away from the two dimethylsulfoxide ligands towards the diamine, as seen from the other *cis* angles, where the N–Ru–Cl angles are less (<90°) when compared to the S–Ru–Cl angles (>90°).

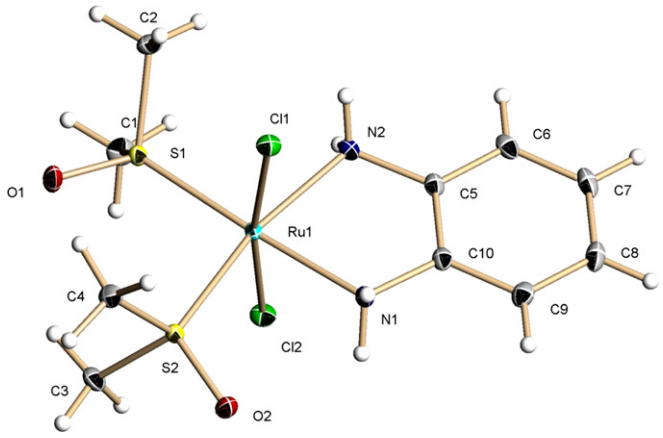


Fig. 1. ORTEP diagram of $[RuCl_2(DMSO)_2$(*o*-pndn)].

Table 2
Selected bond lengths (Å) and bond angles (°) for $[RuCl_2(DMSO)_2$(*o*-pndn)]

Bond lengths (Å)	
Ru(1)–S(1)	2.2469(4)
Ru(1)–S(2)	2.2322(4)
Ru(1)–Cl(1)	2.4102(4)
Ru(1)–Cl(2)	2.4008(4)
Ru(1)–N(1)	2.1177(14)
Ru(1)–N(2)	2.1436(14)
Bond angles (°)	
N(1)–Ru(1)–N(2)	80.98(5)
N(1)–Ru(1)–S(2)	88.22(4)
N(2)–Ru(1)–S(2)	168.91(4)
N(1)–Ru(1)–S(1)	176.95(4)
N(2)–Ru(1)–S(1)	97.45(4)
S(2)–Ru(1)–S(1)	93.450(15)
N(1)–Ru(1)–Cl(2)	87.05(4)
N(2)–Ru(1)–Cl(2)	86.49(4)
S(2)–Ru(1)–Cl(2)	90.481(15)
S(1)–Ru(1)–Cl(2)	95.483(15)
N(1)–Ru(1)–Cl(1)	85.81(4)
N(2)–Ru(1)–Cl(1)	86.50(4)
S(2)–Ru(1)–Cl(1)	95.260(15)
S(1)–Ru(1)–Cl(1)	91.495(15)
Cl(2)–Ru(1)–Cl(1)	170.686(15)

Table 3
Hydrogen bonds for $[RuCl_2(DMSO)_2$(*o*-pndn)] (Å and °)

D–H···A	*d*(D–H) (Å)	*d*(H···A) (Å)	*d*(D···A) (Å)	∠(DHA) (°)
N(1)–H(1A)···Cl(1)#1	0.92	2.86	3.7092(15)	154.5
N(2)–H(2B)···Cl(1)#2	0.92	2.50	3.3285(15)	149.6

Symmetry transformations used to generate equivalent atoms: #1: $-x+1/2$, $y-1/2$, $-z+1/2$; #2 $-x+1/2$, $y+1/2$, $-z+1/2$.

3.5. Antimicrobial activity

The antimicrobial activities of the new complexes were screened against seven pathogenic bacteria. A clear zone around the disc indicated inhibitory activity of the compound on the organism. Depending upon the diameter of the inhibition zone the new complexes were graded as sensitive (<13 mm), intermediate (14–15 mm) or resistant (>15 mm) against pathogenic bacteria. The intermediate strains were also scored as resistant. Both complexes **5** and **6** were found to exhibit good activity against the species under study. The activity was found to increase with an increase in concentration of the metal complex used. The complexes were found to exhibit moderate activity in certain cases and in a few cases, against *A. hydrophila* and *S. faecalis*, their sensitivity reached almost the values of standard Chloramphenicol and Gentamicin.

4. Mechanism for cleavage

In order to propose a cause and route for the –C=N– cleavage, a number of reactions were carried out. To start with, the ligands were refluxed in ethanol in the absence of a metal complex for various time intervals, and no cleavage was observed even after 96 h. The very fact that cleavage does not occur in the absence of metal complex indicates the involvement of the metal centre. The Schiff bases constitute a series of molecules that are susceptible both to hydrolytic cleavage and to coordination with metal ions. It is believed that the formation of bonds between the positive metal ion and nitrogen brings about a labilization of the nitrogen carbon double bonds, which are thereby rendered more susceptible to hydrolytic cleavage [36].

It is known from our previous work [37] that the same Schiff bases have acted as tetradentate ligands to form complexes with $[RuX_3(PPh_3)_3]$. Hence, we arrived at the conclusion that mere ruthenium alone is not sufficient for the cleavage. To find out if DMSO alone can cause the cleavage, the reaction was carried out with an excess of DMSO along with ethanol for various time intervals, from 1 h up to 16 h. The presence of DMSO alone was not sufficient to cause the cleavage, so the combination of ruthenium and DMSO might be the cause for the cleavage.

From this, it is evident that the Schiff base first associates itself to the $[RuCl_2(DMSO)_4]$ complex and then the cleavage occurs. Coordination to metal can cause weakening or strengthening of the –C=N– group [38] and here the former occurs resulting in hydrolytic cleavage immediately, and the intermediate could not be isolated. The cleavage is expected to be caused by trace amounts of water present in ethanol. Bravo has reported a similar type of –C=N– cleavage in platinum and palladium complexes and have found that the hydrolysis is suppressed when the reaction was handled under argon in dry solvents [39].

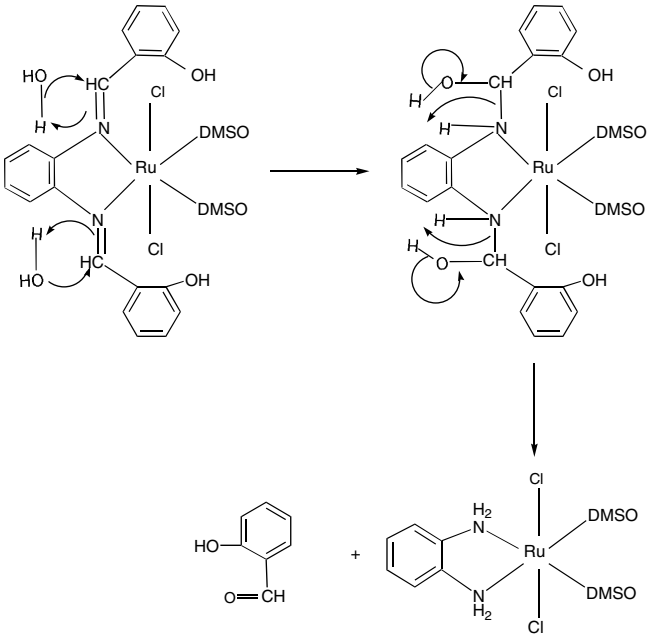
A few reports found relevant to our discussion is the hydrolysis of N-benzylimines $PhCH_2N{=}C(H)Ar$ (Ar = Ph, *p*-$MeOC_6H_4$) by trace water promoted by the ruthenium complex $[Ru_2Cl_4(dppb)_2]$ [dppb = 1,4-bis(diphenylphosphino)butane, $Ph_2P(CH_2)_4(PPh_2)$]. This reaction [40] is found to proceed through an intermediate containing a η^1-bonded imine ligand, viz., $[Ru_2Cl_4(dppb)_2(PhCH_2N{=}C(H)Ph)]$, characterized by ^1H and ^{31}P NMR spectroscopy, to yield free benzaldehyde and $[Ru_2Cl_4(dppb)_2(NH_2CH_2Ph)]$. Similarly, $CuCl_2 \cdot nH_2O$ has been found to promote the hydrolysis of semicarbazones in acetonitrile, through a mechanism involving simultaneous coordination of the lone pair of the nitrogen and the C=O bond of the semicarbazone to the metal ion [41]. A recent article [42] describes the chemo selective hydrolysis of the iminic moiety in salicylaldehyde semicarbazone promoted by $[RuCl_2(DMSO)_4]$. In concurrence with this, the following mechanism (Scheme 2) has been suggested.

The cleavage is found to occur in the presence of a metal centre, which brings about weakening of the coordinated –C=N– bond. The presence of a trace amount of water brings about cleavage. As a consequence of coordination to the metal, the C=N group is highly polarized and nucleophilic attack on the carbon atom of the C=N group may occur. Attack of water on the C=N carbon leads to an unstable amino-alcohol, which spontaneously breaks up

Table 4
Antimicrobial activity data for the new ruthenium(II) complexes

Sample	Concentration	A (mm)	B (mm)	C (mm)	D (mm)	E (mm)	F (mm)	G (mm)
5	1.50	33	27	30	22	19	25	15
	1.00	31	21	22	16	18	16	14
	0.75	29	15	22	13	15	15	14
	0.50	29	12	18	13	15	14	12
	0.25	28	12	16	13	15	12	11
6	1.50	24	20	18	25	18	22	17
	1.00	20	20	16	24	18	18	15
	0.75	20	15	16	22	18	17	12
	0.50	20	14	15	20	16	15	12
	0.25	14	14	14	14	14	15	11

A = *Aeromonas hydrophila*, B = *Eschericia coli*, C = *Salmonella typhi*, D = *Streptococcus faecalis*, E = *Klebsiella pneumonia*, F = *Staphylococcus aureus*, G = *Proteus mirabilis*.



Scheme 2.

to yield salicylaldehyde and the Ru complex containing the corresponding bound diamine. The chlorine ligands that were originally in the *cis* position in the starting complexes now occupy *trans* positions in the final complex.

In order to find out if a catalytic amount of the complex could bring out the cleavage, the reaction was carried out in 1:10 molar ratio of metal to Schiff base ligand. The Schiff base was not completely cleaved and the amount of Schiff base that cleaved depends on the ratio of the metal present. This is because the diamine formed from the initial cleavage coordinates with metal to form $[RuCl_2(DMSO)_2$-(diamine)] which could not further support cleavage. This was further confirmed by carrying out the reaction in the presence of $[RuCl_2(DMSO)_2$(diamine)] in ethanol instead of $[RuCl_2(DMSO)_4]$, where the Schiff base remained unchanged even after two days of refluxing. The reason for the disability of $[RuCl_2(DMSO)_2$(diamine)] to cause cleavage is the chelating nature of the diamine which restricts free Schiff base association with the metal centre. The effect of solvent could not be monitored due to poor solubility of $[RuCl_2(DMSO)_4]$ in non-polar solvents like benzene and acetone.

5. Conclusion

Schiff bases that were expected to act as tetradentate dibasic ligands, underwent hydrolytic cleavage at the –C=N– group to give back the aldehyde and diamine from which the Schiff base was originally formed. The diamine thus formed reacted with *cis*-$[RuCl_2(DMSO)_4]$ to give new complexes of the type $[RuCl_2(DMSO)_2$(diamine)]. The aldehyde was isolated and quantified in stoichiometric amounts.

6. Supplementary material

CCDC 622118 contains the supplementary crystallographic data for $[RuCl_2(DMSO)_2$(*o*-pndn)]. These data can be obtained free of charge via http://www.ccdc.cam.ac.uk/conts/retrieving.html, or from the Cambridge Crystallographic Data Centre, 12 Union Road, Cambridge CB2 1EZ, UK; fax: (+44) 1223-336-033; or e-mail: deposit@ccdc.cam.ac.uk.

Acknowledgements

The diffractometer was funded by NSF Grant 0087210 by the Ohio Board of Regents Grant CAP-491 and by YSU.

References

[1] S. Sarkar, K. Dey, Spectrochim. Acta A 62 (2005) 383.
[2] B.K. Panda, A. Chakravorty, J. Organomet. Chem. 690 (2005) 3169.
[3] K.R. Krishnapriya, M. Kandaswamy, Polyhedron 24 (2005) 113.
[4] K.B. Chew, M.T.H. Tarafder, K.A. Crouse, A.M. Ali, B.M. Yamin, H.K. Fun, Polyhedron 23 (2004) 1385.
[5] K.N. Kumar, R. Ramesh, Polyhedron 24 (2005) 1885.
[6] A.A. Khandar, B. Shaabani, F. Belaj, A. Bakhtiari, Polyhedron 25 (2006) 1893.
[7] A. Majumder, G.M. Rosair, A. Mallick, N. Chattopadhyay, S. Mitra, Polyhedron 25 (2006) 1753.
[8] A. Freiria, R. Bastida, L. Valencia, A. Macias, C. Lodeiro, H. Adams, Inorg. Chim. Acta 359 (2006) 2383.
[9] H. Wolfle, H. Kopacka, K. Wurst, K.H. Ongania, H.H. Gortz, P.P. Pflugl, B. Bildstein, J. Organomet. Chem. 691 (2006) 1197.
[10] K. Singh, M.S. Barwa, P. Tyagi, Eur. J. Med. Chem. 41 (2006) 147.
[11] J.M. Vila, M. Gayoso, M.T. Pereira, M.L. Torres, J.J. Fernandez, A. Fernandez, J.M. Ortigueira, J. Organomet. Chem. 506 (1996) 165.
[12] X. Chen, F.J. Femia, J.W. Babich, J. Zubieta, Inorg. Chim. Acta 308 (2000) 80.
[13] M. Mimuro, K. Hirayama, K. Uezono, H.M.S. Miyachi, Biochim. Biophy. Acta 1456 (2000) 27.
[14] S.G. Teoh, G.Y. Yeap, C.C. Loh, L.W. Foong, S.B. Teo, H.K. Fun, Polyhedron 16 (1997) 2213.
[15] X.R. Bu, C.R. Jackson, D.V. Derveer, X.Z. You, Q.J. Meng, R.X. Wang, Polyhedron 16 (1997) 2991.
[16] S. Gourbatsis, S.P. Perlepes, I.S. Butler, N. Hadjiliadis, Polyhedron 18 (1999) 2369.
[17] H. Spies, H.J. Pietzsch, Inorg. Chim. Acta 161 (1989) 151.
[18] J. Cano, A. Benito, R.M. Manez, J. Soto, J. Paya, F. Lloret, M. Julve, M.D. Marcos, E. Sinn, Inorg. Chim. Acta 231 (1995) 45.
[19] P. Govindaswamy, Y.A. Mozharivskyj, M.R. Kollipara, Polyhedron 23 (2004) 1567.
[20] R.K. Rath, M. Nethaji, A.R. Chakravarty, Polyhedron 21 (2002) 1929.
[21] R.I. Kureshy, N.H. Khan, S.H.R. Abdi, S.T. Patel, P. Iyer, J. Mol. Catal. A 150 (1999) 163.
[22] P. Munshi, R. Samanta, G.K. Lahiri, J. Organomet. Chem. 586 (1999) 176.
[23] M.G. Bhowon, H.L.K. Wah, R. Narain, Polyhedron 18 (1998) 341.
[24] D.L. Davies, J. Fawcett, R. Krafczyk, D.R. Russell, J. Organomet. Chem. 545–546 (1997) 581.
[25] Z. Shirin, R.N. Mukherjee, Polyhedron 11 (1992) 2625.
[26] A.I. Vogel, Textbook of Practical Organic Chemistry, 5th ed., Longman, London, 1989.

[27] I.P. Evans, A. Spencer, G. Wilkinson, J. Chem. Soc., Dalton Trans. (1973) 205.
[28] W.M. Coleman, R.K. Boggess, J.W. Hughes, L.T. Taylor, Inorg. Chem. 20 (1981) 700.
[29] (a) Bruker Advanced X-ray Solutions SMART for WNT/2000 (Version 5.628), Bruker AXS Inc., Madison, WI, USA, 1997–2002.;
(b) Bruker Advanced X-ray Solutions SAINT (Version 6.45), Bruker AXS Inc., Madison, WI, USA, 1997–2003.
[30] Bruker Advanced X-ray Solutions SHELXTL (Version 6.10), Bruker AXS Inc., Madison, WI, USA, 2000.
[31] A.W. Bauer, W.M.M. Kirby, J.C. Sherries, M. Truck, Am. J. Clin. Pathol. 36 (1966) 493.
[32] G. Karthikeyan, P. Pitchaimani, Transition Met. Chem. 26 (2003) 482.
[33] R. Ramesh, P.K. Sunganthy, K. Natarajan, Synth. React. Inorg. Met.-Org. Chem. 26 (1996) 47.
[34] D.M. Boghaei, S. Mohebi, J. Mol. Catal. A 179 (2002) 41.
[35] J-P. Costes, M.I.F. Garcia, Inorg. Chim. Acta 237 (1995) 57.
[36] G.L. Eichhorn, J.C. Bailar, J. Am. Chem. Soc. 20 (1953) 2905.
[37] R. Prabhakaran, R. Huang, K. Natarajan, Inorg. Chim. Acta 359 (2006) 3359.
[38] G. L Eichhorn, N.D. Archand, J. Am. Chem. Soc. 78 (1956) 2688.
[39] J. Bravo, J. Organomet. Chem. 650 (2002) 157.
[40] D.E. Fogg, B.R. James, Inorg. Chem. 34 (1995) 2557.
[41] R.N. Ram, K. Varsha, Tetrahedron Lett. 32 (1991) 5829.
[42] M. Vieites, P. Buccino, L. Otero, M. Gonzalez, O.E. Piro, R.S. Delgado, C.M.R.S. Anna, E.J. Barreiro, H. Cerecetto, D. Gambino, Inorg. Chim. Acta 358 (2005) 3065.

thiolates [13], bis(imino)pyridines [14], α-diimines [15], and phosphines [16]. These catalysts are used together with a suitable activator (co-catalyst) such as methylalumoxane (MAO), which promotes the formation of active species [17].

On the other hand, oxamide type compounds comprise a very interesting family in Coordination Chemistry [18]. These compounds may be synthesized in high yields and have a good stability as chemical ligands, which make them suitable for the formation of non-metallocenic polymerization catalysts. In particular, 1,2-bis(3,5-di-*tert*-butyl-2-hydroxiphenyl)oxamide (**L**) presents a good solubility in organic solvents and it has various potential coordination sites that would permit the formation of metal complexes [19]. As we mention before, there are catalysts with several types of ligands bearing nitrogen or oxygen atoms donors, but there are not examples of oxamides complexes used to olefins polymerization.

Thus, our work focused on the synthesis of new coordination compounds of this family and their application as catalysts for ethylene polymerization, which could open the way to a new family of non-metallocene polymerization catalysts derived from the coordination of 1,2-bis(3,5-di-*tert*-butyl-2-hydroxiphenyl)oxamide (**L**) to transition metals of the Group IV.

2. Experimental

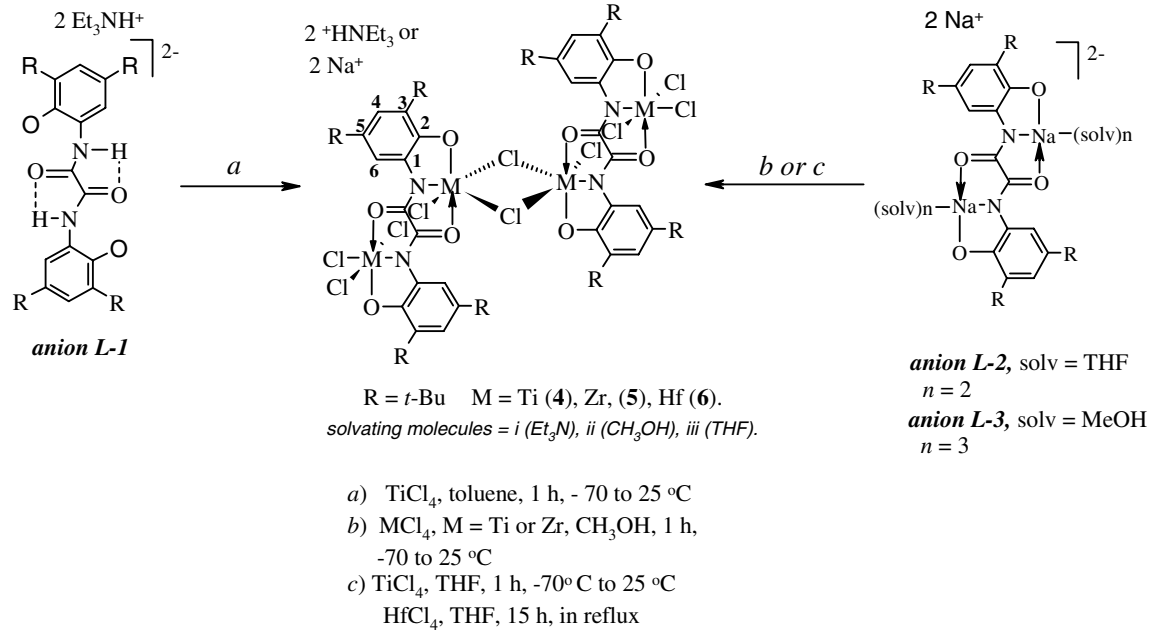
The transition metal reagents and oxamide (**L**) precursors were commercially available, thus the reactions were performed with freshly distilled solvents. The melting points were determined using a Mel-Temp II apparatus. The IR spectra in the 4000–400 cm^{-1} range were recorded on an FT-IR 1600 Perkin–Elmer spectrophotometer, using KBr pellets. The elemental analyses were performed using a Eager 300 apparatus. The fast atom bombardment mass spectra (FAB+ mass) were obtained with a JEOL SX102A instrument featured with an inverted geometry, in a matrix of 3-nitrobenzyl alcohol, in the 0–2200 *m*/*z* range. The NMR spectra were recorded at room temperature using several spectrometers: JEOL GSX-270; Jeol eclipse + 400 MHz and Bruker Advance 300 MHz. The syntheses were carried out using different bases and solvents (Et_3N/toluene, NaH/THF and NaOH/methanol) as shown in Scheme 1.

2.1. 1,2-Bis(3,5-di-tert-butyl-2-hydroxiphenyl)oxamide (*L*)

The precursor, 4,6-di-*tert*-butyl-2-amino-1-phenol, was obtained by two synthesis routes: (1) ethylenediamine and 2-propanol [19], and (2) NH_3/BH_4OH in a mixture of methanol and water [20], both involved the use of 4,6-di-*tert*-butyl-1,2-benzoquinone, which, in turn, can be synthesized from 3,5-di-*tert*-butylcathecol.

The ligand 1,2-bis(3,5-di-*tert*-butyl-2-hydroxiphenyl)-oxamide (**L**) was synthesized following some the literature procedure with slight modifications, as shown recently, using oxalyl chloride and triethylamine in ethyl ether [21]. In our case, oxalyl bromide and triethylamine in THF (yield 70%, m.p. 200 °C) were used.

The coordination complexes of Ti, Zr, Hf were finally obtained by deprotonation of the oxamide **L** using three different bases (Et_3N/toluene, NaH/THF and NaOH/methanol).



Scheme 1. Synthesis of group IV oxamide derivatives by three synthetic routes.

2.2. Anions

2.2.1. Bis(triethylamonium)-bis(4,6-di-tert-butyl-1-oxo-phenyl)oxamide, **L-1**

Compound **L** (0.5 g, 1 mmol) was dissolved in dry toluene (15 mL) and then, triethylamine (0.28 mL, 2 mmol) was added. The reaction mixture was stirred for 30 min. Removal of the solvent under reduced pressure resulted in a yellow solid. IR (KBr): ν(CO) 1647.1 s. ^{1}H NMR (CD_3OD): δ/ppm: 7.19 {s, 2H, H4}; 7.77 {s, 2H, H6}; $\Delta\delta$ (H6–H4): 0.58; 1.44 {s, 9H, H3(*t*-Bu)}; 1.32 {s, 9H, H5(*t*-Bu)}. ^{13}C{^{1}H} NMR (CD_3OD): δ/ppm: 126.9 {s, C1}; 146.0 {s, C2}; 141.7 {s, C3}; 120.6 {d, C4}; 138.9 {s, C5}; 117.0 {d, C6}; 158.2 {s, C=O}; 34.1 {s, C3(*t*-Bu)}; 35.0 {s, C5(*t*-Bu)}; 29.4 {q, C3(*t*-Bu)}; 30.9 {q, C5(*t*-Bu)}.

2.2.2. Dianion bis(4,6-di-tert-butyl-1-oxo-phenyl)oxamido-bis(sodium), **L-2**

Compound **L** (0.5 g, 1 mmol) was dissolved in dry THF (15 mL) and then, NaH (0.28 mL, 2 mmol) was added. The reaction mixture was stirred for 30 min. Removal of the solvent under reduced pressure resulted in a yellow solid. IR (KBr): ν(CO) 1646.5 s. ^{1}H NMR (CD_3OD): δ/ppm: 6.98 {s, 2H, H4}; 8.12 {s, 2H, H6}; $\Delta\delta$ (H6–H4): 1.14; 1.42 {s, 9H, H3 (*t*-Bu)}, 1.27 {s, 9H, H5(*t*-Bu)}. ^{13}C{^{1}H} NMR (CD_3OD): δ/ppm: 128.0 {s, C1}; 154.8 {s, C2}; 136.5 {s, C3}; 118.8 {d, C4}; 133.1 {s, C5}; 113.4 {d, C6}; 157.7 {s, C=O}; 33.7 {s, C3(*t*-Bu)}; 34.8 {s, C5(*t*-Bu)}; 29.4 {q, C3(*t*-Bu)}; 31.1 {q, C5(*t*-Bu)}.

2.2.3. Dianion bis(4,6-di-tert-butyl-1-oxo-phenyl)oxamido-bis(sodium), **L-3**

Compound **L** (0.5 g, 1 mmol) was dissolved in methanol (15 mL) and a 1 M solution of NaOH (2 mL, 2 mmol) was added. The reaction mixture was stirred for 30 min. Removal of the solvent under reduced pressure resulted in a yellow solid. IR (KBr): ν(CO) 1651.0 s. ^{1}H NMR (CD_3OD): δ/ppm: 8.12 {s, 2H, H6}; 6.98 {s, 2H, H4}; $\Delta\delta$ (H6–H4): 1.14; 1.44 {s, 9H, H3(*t*-Bu)}; 1.28 {s, 9H, H5(*t*-Bu)}. ^{13}C{^{1}H} NMR (CD_3OD): δ/ppm: 127.9 {s, C1}; 155.1 {s, C2}; 136.5 {s, C3}; 118.9 {d, C4}; 132.9 {s, C5}; 113.3 {d, C6}; 157.7 {s, C=O}; 33.7 {s, C3(*t*-Bu)}; 34.8 {s, C5(*t*-Bu)}; 29.3 {q, C3(*t*-Bu)}; 31.1 {q, C5(*t*-Bu)}.

2.3. General synthesis of complexes **4–6**

2.3.1. Dimeric (triethylamonium)-[(μ-Cl)-bis[(3,5-di-tert-butyl-2-oxo-phenyl)oxamido-bis(dichloride titanium (IV))] **4**

This complex was obtained following three different routes, only the counter ion is changed by Na^+ in routes b and c:

(a) A solution of 0.5 g (1 mmol) of **L** in toluene (15 mL) and triethylamine (0.28 mL, 2 mmol) was mixed with a 1 M solution of titanium chloride(IV) in methylene dichloride (2 mL, 2 mmol) at −70 °C. Upon mixing, the color instantly changed to brown-red. The solution was filtered and the solvent was evaporated for afford a brown-red solid precipitated (1.7 g, 98%), with a m.p. > 400 °C. MS-FAB$^+$ (*m*/*z*): 1573 $[C_{60}H_{83}Cl_{10}N_4O_8Ti_4+HCl]^+$. *Anal.* Calc. for $C_{60}H_{80}Cl_{10}N_4O_8Ti_4/5Et_3N$: C, 53.06; H, 7.67; N, 6.19. Found: C, 53.57; H, 8.15; N, 6.27%.

(b) A solution of 0.5 g (1 mmol) of **L** in methanol (15 mL) and a 1 M solution of NaOH (2 mL, 2 mmol) were mixed with a 1 M solution of titanium chloride(IV) in methylene dichloride (2 mL, 2 mmol). Upon mixing, the color instantly changed to brown-red. The solution was filtered and the solvent was evaporated for afford a brown-red solid precipitated (1.5 g, 98%).

(c) A solution of 0.5 g (1 mmol) of **L** in THF (15 mL) and NaH (0.48 g, 2 mmol) was mixed with 1 M solution of titanium chloride(IV) in methylene dichloride (2 mL, 2 mmol) at −70 °C. Upon mixing, the color instantly changed to brown-red. The solution was filtered and the solvent was evaporated for afford a brown-red solid precipitated (1.5 g, 98%).

2.3.2. Dimeric (sodium)-(μ-Cl)-bis[(3,5-di-tert-butyl-2-oxo-phenyl)oxamido-bis(dichloride zirconium(IV))] **5**

A solution of 0.5 g (1 mmol) of **L** in methanol (15 mL) and 1 M solution of NaOH (2 mL, 2 mmol) were mixed with zirconium chloride(IV) (0.47 g, 2 mmol) at room temperature. An orange solid (1.7 g, 98%) appeared after evaporation, with m.p. > 400 °C. MS-FAB$^+$ (*m*/*z*): 1703 $[C_{60}H_{82}Cl_{10}N_4O_8Zr_4]^+$. *Anal.* Calc. for $C_{60}H_{80}Cl_{10}N_4O_8Zr_4/CH_3OH$: C, 41.10; H, 4.75; N, 3.14. Found: C, 41.26; H, 4.80; N, 3.00%.

2.3.3. Dimeric (sodium)-(μ-Cl)-bis[(3,5-di-tert-butyl-2-oxo-phenyl)oxamido-bis(dichloride hafnium(IV))] **6**

A solution of 0.5 g (1 mmol) of **L** in THF (15 mL) and NaH (0.48 g, 2 mmol) were mixed with hafnium chloride (IV) (0.64 g, 2 mmol) and refluxed for 15 h. A green-brown solid (2.1 g, 98%) appeared after evaporation, with m.p. > 400 °C. MS-FAB$^+$ (*m*/*z*): 1888 $[C_{60}H_{81}Cl_{10}N_4O_8Hf_4Na_2\text{-}6Cl]^+$. *Anal.* Calc. for $C_{60}H_{80}Cl_{10}N_4O_8Hf_4Na_2/TH\ F,10H_2O$: C, 32.74; H, 4.46; N, 2.39. Found: C, 32.74; H, 5.11; N, 2.63%.

2.4. Polymerization

2.4.1. Materials

Toluene and heptane (J.T. Baker) were used as reaction solvents. Methylaluminoxane (WITCO) was used as a co-catalyst without purification. All the procedures were carried out under nitrogen atmosphere using the Schlenk technique.

2.4.2. Polymerization

Polymerization was carried out in a 600 mL Parr reactor equipped with mechanical agitation, a temperature control

unit and continuous measurement system for ethylene consumption. The reagents were introduced into the reactor by means of syringes, following the order: solvent + MAO + ethylene and, finally, the non-metallocene catalyst. The reaction was terminated by the addition of acidified methanol and the final product was washed with acetone.

2.4.3. Polymer characterization

The catalytic activity was evaluated from the polymer weight obtained in each polymerization, expressed as g-polymer/mmol(cat) *Pt*, where *P* is the pressure and *t* is the reaction time. A Bruker Vector 22 spectrometer was used for obtaining the FTIR spectra of the polyethylene films. The molecular weight and molecular weight distribution were determined by chromatography using trichlorobenzene in a Waters 2000 apparatus, at 135 °C. The differential scanning calorimetry (DSC) measurements were performed on a TA Instrument DSC 2920 under nitrogen atmosphere. The samples were melted at 180 °C and quenched from 180 °C to room temperature, then reheated from room temperature to 180 °C at a rate of 10 °C/min. The melting temperatures were determined from the second heating curve.

3. Results and discussion

3.1. Synthesis

Once the oxamide (**L**) was prepared, its anions were obtained with triethylamine, NaH and NaOH. The total deprotonation was effected with four equivalents of NaH and NaOH; however, when (**L**) was treated with an excess of triethylamine, only the phenolic hydrogens were deprotonated, leaving the NH function intact. ^{1}H NMR spectroscopy suggests the formation of a sodium complex when total deprotonation is achieved.

Table 1
^{1}H NMR data (in methanol-d_3)

Complexes	δ(H4)	δ(H6)	$\Delta\delta$(H6–H4)	δ(3-*t*-Bu)	δ(5-*t*-Bu)
L	7.14	7.31	0.17	1.43	1.31
Ti (**4**)	7.15	7.72	0.57	1.37	1.29
Zr (**4**)	7.14	8.11	0.97	1.44	1.35
Hf (**4**)	7.16	8.15	0.99	1.45	1.36

The difference between the chemical shifts of H3 and H5 (structure numbering in Scheme 1) in both anions amounts to 1.14 ppm. This result suggests that anions **L-2** and **L-3** reach, upon coordination, a conformational stabilization which renders the anion planar and this characteristic conformation has been observed in the well-known tin oxamide derivatives [19].

It is noticeable that the preferred conformation of the free ligand, as detected by X-ray crystal analysis [19] shows that both OH functions lie opposite to the NH group. Free rotation around the C2–N bond allows the sodium coordination of the O, N atoms to produce the planar conformation as mentioned above.

The ^{13}C NMR analysis shows that C1 and C2 are shifted to lower fields in comparison with the free ligand; this chemical shift is more evident for the anions obtained with NaH and NaOH, while carbon atoms C3 and C5 are protected.

IR Spectroscopy showed a slight displacement of the carbonyl band to lower wave numbers, the C=O bond becomes weaker due to intramolecular coordination; nevertheless, there is hardly a difference among the ν(CO) of the anions.

Later on, the transition metal group 4 compounds were prepared. A titanium derivative was obtained by means of the three synthetic routes mentioned above, in order to form the oxamide anion. For zirconium derivative, anion **L-3** was used, due to the solubility of $ZrCl_4$ in methanol. For the hafnium derivative the best result was obtained with NaH/THF under reflux for 15 h. ^{1}H and ^{13}C NMR displacements for the titanium, zirconium and hafnium complexes appear in Tables 1 and 2.

One can observe that the difference between the chemical shift, $\Delta\delta$ (H3–H5), is higher for the hafnium derivative, probably because its large size and low electronegativity; this marks a compensatory result between the inductive effect of the metal towards nitrogen and the oxygen carbonyl coordination.

For derivatives **4**–**6**, the ν(CO) shifts to lower frequencies (Table 3), with respect to the anions, because the coordination of the oxygen belonging to the carbonyl group linked to the metal is stronger. These shifts are similar to those reported in other transition metal complexes [21].

Mass spectroscopy (FAB^+) indicated formation of dimeric complexes bonded by chloride atoms as is indi-

Table 2
^{13}C NMR data (in methanol-d_3)

Complexes	δ(C1)	δ(C2)	δ(C3)	δ(C4)	δ(C5)	δ(C6)	δ(C = 0)	δ(*t*-Bu) (c)	δ(*t*-Bu) (CH_3)
L	124.0	143.3	139.8	123.2	145.8	117.7	157.3	34.4 (3) 35.4 (5)	29.9 (3) 31.5 (5)
Ti (**4**)	136.9	159.4	133.5	121.4	145.2	116.7	165.9	34.3 (3) 34.4 (5)	28.8 (3) 30.7 (5)
Zr (**5**)	136.6	158.5	134.5	121.1	140.9	116.4	168.3	34.3 (3) 34.3 (5)	28.9 (3) 31.1 (5)
Hf (**6**)	136.1	158.1	135.3	121.2	140.3	116.5	168.8	34.3 (3) 34.3 (5)	28.9 (3) 31.2 (5)

Table 3
FTIR ν(C=O) of complexes **4**–**6**

Complexes	ν(C=O) cm^{-1}
L	1658.0
Ti (**4**)	1644.5
Zr (**5**)	1622.2
Hf (**6**)	1626.2

cated in Scheme 1. Polymeric chains formation can also be possible; some similar derivatives examples with $GeCl_4$ [22], $SbCl_5$ [22], and Me_2SnCl_2 [23] and this oximade ligand have shown this behavior. On the other hand, presence of coordinated molecules (triethylamine, THF or methanol) by NMR spectroscopy is observed, Fig. 1. For that reason, they are proposed into elemental analyses.

3.2. Ethylene polymerization

The catalytic activities for gaseous monomers such as ethylene [24] are usually classified as very high (>1000), high (1000–100), moderate (100–10), low (10–1), and very low (<1) with reference to the units: g $mmol^{-1}$ h^{-1} bar^{-1}. In the present study, the highest activity was observed for zirconium catalyst (**5**) in *n*-heptane, as shown in Table 4.

The polymers obtained with this catalyst present the highest molecular weight, i.e., 98,000 Da. A change in solvent might increase both the activity as well as the molecular weight, for instance the activity of the Zr catalyst in *n*-heptane is 1.7 times greater with respect to toluene, while M_w from *n*-heptane is 1.32 times greater than the one obtained from toluene. This type of solvents effect might be explained on the basis of polarity of different solvents allowing the proximity of monomer for polymerization. In terms of T_m and crystallinity, catalyst (**5**) produces a higher density linear polyethylene (Table 4). Overall, these results suggest the exchange of the chloride atoms by the methyl groups to form cationic species as it occurs with "non-metallocene" complexes. In this way, cationic monomeric compounds are formed. The titanium atom probably generates more chloride bridges and a bigger polymeric complex with respect to the zirconium

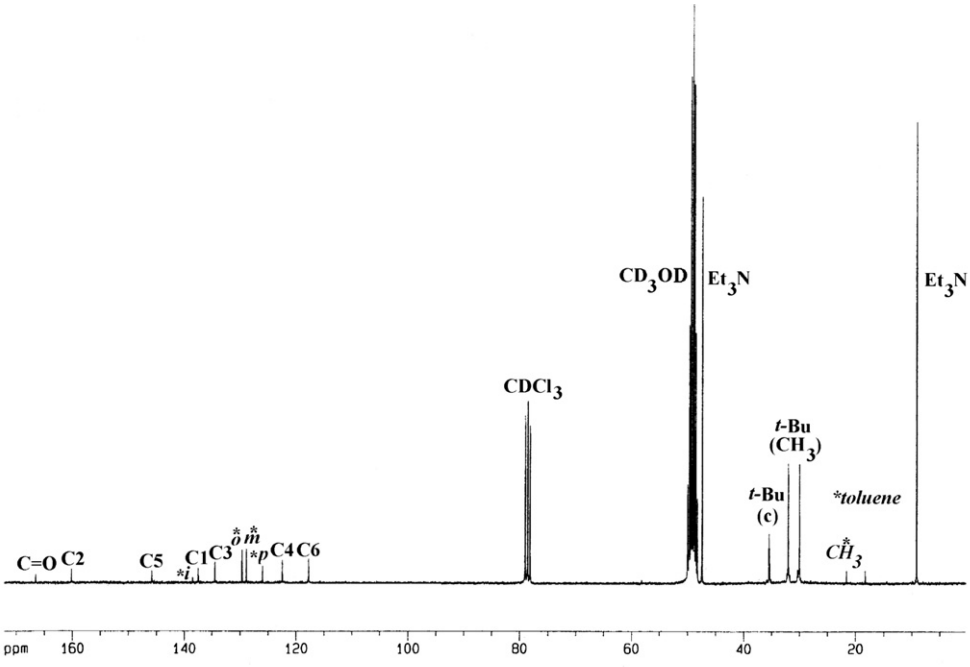


Fig. 1. ^{13}C NMR spectra of Ti (**4**) complex with triethylamine coordinated.

Table 4
Catalytic activity and polymer characterization

Catalyst in toluene	Polymer mass (g)	Activity g(polymer)/mmol(cat). h bar	M_w	M_w/M_n	T_m (°C)	Crystallinity (%)
Ti (**4**)	0.39	26.3	55,000	1.8	136	56
Zr (**5**)	1.75	118	73,700	1.8	137.4	56.5
Zr (**5**)[a]	2.75	201	98,000	2.0	136.4	57.5
Hf (**6**)	0.35	23	34,000	2.0	135.6	54

Polymerization conditions: $P = 4$ bar, time = 60 min, $T = 60$ °C, 10 mL of MAO to 10%, Al/Metal = 4000, mols cat $\sim 3.5 \times 10^{-6}$ (it is different for each one), $\Omega = 1000$ rpm. In all reactions one pre-contact with MAO was made. GPC. Universal curve, new calibration curve.

[a] In heptane.

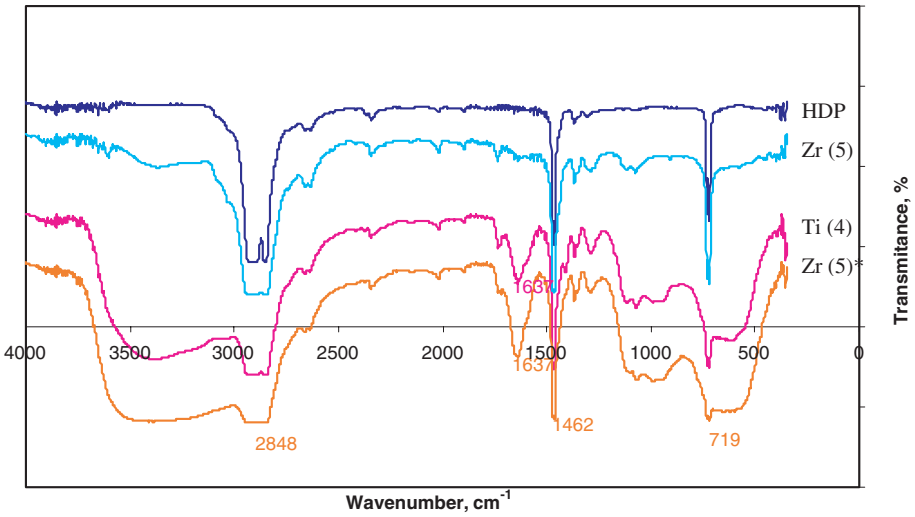


Fig. 2. FTIR spectra of polyethylene obtained with Zr (**5**), Zr (**5**)* and Ti complex **4**/MAO.

atom. The terminal chloride atoms react first with MAO, which may be the reason of higher activity of zirconium complexes. Also, it is known that hafnium, like other elements of the sixth period, exhibit lower activities due to kinetic factors (slow olefin coordination and insertion step) [2].

On the other hand, the polydispersity index M_w/M_n was determined to change from 1.8 with a solvent like toluene to about 2.0 with *n*-heptane. These values are typical for metallocene based catalysts, indicating the polymerization occurs mostly by a single-site mechanism [25].

The melting temperature (T_m) of the polymers corresponded to linear polyethylene [26]. The FTIR spectrum of Zr(**5**) displays the typical bands corresponding to high density linear polyethylene at 2930 and 2845 cm^{-1}, which can be assigned to C–H stretching of the $–CH_2$ and $–CH_3$ groups. At about 1462 cm^{-1} there is a band corresponding to the $–CH_2$ group bending, and at 719 cm^{-1} another band is verified, which corresponds to the $(–CH_2–CH_2–)_n$ rocking group, with $n > 3$ [27]. In the case of Zr (**5**)* and Ti (**4**) there is an additional signal at 1637 cm^{-1}, which can be interpreted as the one arising from double bonds originated from β-H elimination or vinyl unsaturation of the polymer chain (Fig. 2).

4. Conclusions

The 1,2-bis(3,5-di-*tert*-butyl-2-hydroxiphenyl)oxamide (**L**) was synthesized following two conventional methods. Oxamide salts were obtained by using three different bases (Et_3N/toluene, NaH/THF and NaOH/methanol); the sodium complex was formed in the last two methods. The coordinating capacity of oxamide (**L**) was corroborated by the formation of complexes with early transition metals (Ti, Zr, Hf). These complexes have a planar structure similar to the tin derivatives reported in the literature [19]. The best synthetic method for titanium and zirconium involves the use of NaOH and methanol as base and solvent, respectively. The hafnium derivative was obtained by means of NaH in THF. Finally, a study on the polymerization of ethylene showed that the oxamide series were active catalysts, with zirconium complex presenting the highest activity of the series and a marked solvent effect. Based on these results, the higher activity of Zr oxamide derivative and the promotion effects towards high density linear PE, could motivate further research for developing new catalysts with potential applications in low olefin polymerization reactions.

Acknowledgements

M.G.-R. and J.E.H.R. are grateful for the financial support from the IMP's Molecular Engineering Program; V.M.J.-P, acknowledges CONACYT for a scholarship. We thank Dr. Swadhin K. Mandal for helpful discussions and Dr. Noé Zúñiga Villarreal for writing revision. Finally, R.Q. acknowledges the financial support to CONICYT, through FONDAP Project No. 11980002.

References

[1] V.C. Gibson, S.K. Spitzmesser, Chem. Rev. 103 (2003) 283.
[2] H. Alt, A. Köppl, Chem. Rev. 100 (2000) 1205.
[3] H.H. Brintzinger, D. Fischer, R. Mulhaupt, B. Rieger, R.M. Waymouth, Angew. Chem., Int. Ed. Engl. 34 (1995) 1143.
[4] A.L. McKnight, R.M. Waymouth, Chem. Rev. 98 (1998) 2587.
[5] (a) B.L. Small, M. Brookhart, A.M.A. J. Am. Chem. Soc. 120 (1998) 4049;
(b) G.J.P. Britovsek, V.C. Gibson, B.S. Kimberley, P.J. Madox, S.J. McTavish, G.A. Solan, A.J.P. White, D.J. Williams, Chem. Commun. (1998) 849.
[6] G.W. Coates, P.D. Hustad, S. Reinartz, Angew. Chem., Int. Ed. 41 (2002) 2237.
[7] (a) M. Bochmann, S.J. Lancaster, Organometallics 12 (1993) 633;
(b) J.C. Flores, J.C.W. Chien, M.D. Rausch, Organometallics 13 (1994) 4140;

(c) S.J. Skoog, C. Mateo, G.G. Lavoide, F.J. Hollander, R.G. Bergman, Organometallics 19 (2000) 1406.
[8] (a) J.D. Scollard, D.H. McConville, J. Am. Chem. Soc. 118 (1996) 10008;
(b) S. Tsubaki, J. Jin, C.H. Ahn, T. Sano, T. Uozumi, K. Soga, Macromol. Chem. Phys. 202 (2001) 482;
(c) C.H. Lee, Y.-H. La, J.W. Park, Organometallics 19 (2000) 344.
[9] L. Bourget-Merle, M.F. Lappert, J.R. Severn, Chem. Rev. 102 (2002) 3031.
[10] (a) Y. Yoshida, S. Matsui, Y. Takagi, M. Mitani, M. Nitabaru, T. Nakano, H. Tanaka, N. Kashiwa, T. Fujita, Organometallics 20 (2001) 4793;
(b) D.M. Dawson, D.A. Walker, M. Thornton-Pett, M. Bochmann, J. Chem. Soc., Dalton Trans. (2000) 459.
[11] (a) J. Richter, F.T. Edelmann, M. Noltemeyer, H.G. Schmidt, M. Shmulinson, M.S. Eisen, J. Mol. Catal. A: Chem. 130 (1998) 149;
(b) A.P. Duncan, S.M. Mullins, J. Arnold, R.G. Bergman, Organometallics 20 (2001) 1808.
[12] (a) M. Mitani, R. Furuyama, J.I. Mohri, J. Saito, S. Ishii, H. Terao, N. Kashiwa, T. Fujita, J. Am. Chem. Soc. 124 (2002) 7888;
(b) S. Ishii, M. Mitani, J. Saito, S. Matsuura, S. Kojoh, N. Kashiwa, T. Fujita, Chem. Lett. 7 (2002) 740.
[13] (a) Y. Nakayama, K. Miyamoto, N. Ueyama, A. Nakamura, Chem. Lett. 5 (1999) 391;
(b) V.C. Gibson, N.J. Long, J. Martin, G.A. Solan, J.C. Stichbury, J. Organomet. Chem. 590 (1999) 115.
[14] B.L. Small, M. Brookhart, A.M.A. Bennett, J. Am. Chem. Soc. 120 (1998) 4049.
[15] S.D. Ittel, L.K. Johnson, M. Brookhart, Chem. Rev. 100 (2000) 1169.
[16] (a) P.W.N.M. van Leeuwen, P.C.J. Kamer, J.N.H. Reek, P. Dierkes, Chem. Rev. 100 (2000) 2741;
(b) Z. Guan, W.J. Marshall, Organometallics 21 (2002) 3580.
[17] E.Y.X. Chen, T.J. Marks, Chem. Rev. 100 (2000) 1391.
[18] R. Ruiz, J. Faus, F. Lloret, M. Julve, Y. Journaux, Coord. Chem. Rev. 193 (1999) 1069.
[19] (a) V. Jiménez, C. Camacho, M. Güizado, N. Heinrich, R. J. Organomet. Chem. 614–15 (2000) 283;
(b) R. Contreras, V.M. Jiménez-Pérez, C. Camacho-Camacho, M. Güizado-Rodríguez, B. Wrackmeyer, J. Organomet. Chem. 604 (2000) 229.
[20] V.B. Vol'eva, T.I. Prokofeva, A.I. Prokofev, I.S. Belostotskaya, N.L. Komissarova, V.V. Ershov, Russ. Chem. Bull. 44 (1995) 1720.
[21] U. Beckmann, E. Bill, T. Weyhermüller, K. Wieghardt, Eur. J. Inorg. Chem. 9 (2003) 1768.
[22] V.M. Jiménez-Pérez, Dissertation Ph. D., CINVESTAV (2005).
[23] V.M. Jiménez-Pérez, H. Nöth, A. Ariza-Castolo, A. Flores-Parra, R. Contreras, J. Organomet. Chem. 691 (2006) 1584.
[24] G.J.P. Britovsek, V.C. Gibson, D.F. Wass, Angew. Chem., Int. Ed. 38 (1999) 428.
[25] R. Quijada, J. Retuert, J.L. Guevara, R. Rojas, M. Valle, P. Saavedra, H. Palza, G. Galland, Macromol. Symp. 189 (2002) 111.
[26] M.A. Pérez, R. Quijada, F. Ortega-Jiménez, C. Alvarez-Toledano, J. Mol. Catal. A 226 (2005) 291.
[27] A.M. Domínguez, A. Zárate, R. Quijada, T. López, J. Mol. Catal. A 207 (2004) 155.

characterized by X-ray diffraction measurements. A theoretical calculation using a model optimized system is very useful in predicting the electronic structure; the electron transitions to rationalize the spectral properties and electron transfer chemical, electrochemical and photophysical properties are elegantly explained by using Density Functional calculations. We have also explained the electronic structures of the complexes by DFT and TD-DFT calculations.

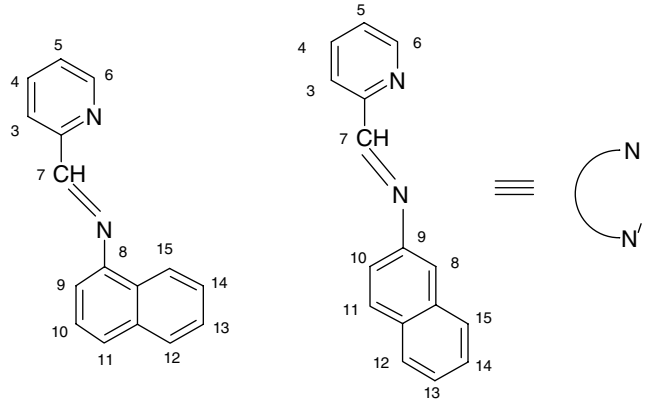
2. Results and discussion

2.1. Synthesis and infrared spectra

N-[(2-Pyridyl)methyliden]-α(and β)-aminonaphthalene (α and β-NaiPy) have been used in the present work. They were synthesized [10] by reacting pyridine-2-carboxaldehyde and α-naphthyl-amine (for α-NaiPy) and β-naphthyl-amine (for β-NaiPy) in a 1:1 mol ratio in dry ethanol solution under reflux. The compounds are recrystallised from an ethanol–chloroform mixture (Scheme 1).

The complexes were synthesized by the reaction of the ligand and $Pd(MeCN)_2Cl_2$ in a 1:1 mol ratio in MeCN solution (Eq. 1). Upon slow evaporation of the reaction mixture orange-red crystals were deposited on the wall of the beaker, and these were separated by filtration and dried over $CaCl_2$. Microanalytical data support the composition Pd(α-NaiPy)Cl_2 (**1**)/Pd(β-NaiPy)Cl_2 (**2**). The solution conductance measurement suggests a non-electrolytic nature of these complexes.

Pd(α-NaiPy)I_2 (**3**)/Pd(β-NaiPy)I_2 (**4**) were synthesized by Ag^+ assisted de-chlorination in THF, followed by addition of KI (aq) solution (Eq. (2)). Bis-chelated palladium(II) complexes have been synthesized by Ag^+ assisted de-chlorination from Pd(α-NaiPy)Cl_2 (**1**) or Pd(β-NaiPy)-Cl_2 (**2**) followed by reaction with various ligands (Eq. (3)). The reaction of $[Pd(\alpha\text{-NaiPy})(S)]^{2+}$ with α-NaiPy or $[Pd(\beta\text{-NaiPy})(S)]^{2+}$ with β-NaiPy could synthesise $[Pd(\alpha\text{-NaiPy})_2]^{2+}$ (**5**) or $[Pd(\beta\text{-NaiPy})_2]^{2+}$ (**6**), while the reaction of $[Pd(\alpha\text{-NaiPy})(S)]^{2+}$ with β-NaiPy led to the isolation of $[Pd(\alpha\text{-NaiPy})(\beta\text{-NaiPy})]^{2+}$ (**7**) as the perchlorate salt, using excess $NaClO_4$. Similarly the reaction of [Pd-



$$Pd(MeCN)_2Cl_2 + NaiPy \longrightarrow Pd(NaiPy)Cl_2 \quad \textbf{1-2} \qquad (1)$$

$$Pd(NaiPy)Cl_2 + 2KI \xrightarrow{AgNO_3\,(aq),\ THF} Pd(NaiPy)I_2 \quad \textbf{3-4} \qquad (2)$$

$$Pd(NaiPy)Cl_2 + L \xrightarrow[NaClO_4]{AgNO_3} [Pd(NaiPy)(L)](ClO_4)_2 \quad \textbf{5-13} \qquad (3)$$

Pd(α-NaiPy)Cl_2 (**1**); Pd(β-NaiPy)Cl_2 (**2**); Pd(α-NaiPy)I_2 (**3**); Pd(β-NaiPy)I_2 (**4**); $[Pd(\alpha\text{-NaiPy})_2](ClO_4)_2$ (**5**); $[Pd(\beta\text{-NaiPy})_2](ClO_4)_2$ (**6**); $[Pd(\alpha\text{-NaiPy})(\beta\text{-NaiPy})](ClO_4)_2$ (**7**); $[Pd(\alpha\text{-NaiPy})(bpy)](ClO_4)_2$ (**8**), $[Pd(\alpha\text{-NaiPy})(phen)](ClO_4)_2$ (**9**), $[Pd(\beta\text{-NaiPy})(bpy)](ClO_4)_2$ (**10**), $[Pd(\beta\text{-NaiPy})(phen)](ClO_4)_2$ (**11**), $[Pd(\alpha\text{-NaiPy})(Tai\text{-}Me)](ClO_4)_2$ (**12**) and $[Pd(\beta\text{-NaiPy})(Tai\text{-}Me)](ClO_4)_2$ (**13**).

Scheme 1. Pd(α-NaiPy)Cl_2 (**1**); Pd(β-NaiPy)Cl_2 (**2**); Pd(α-NaiPy)I_2 (**3**); Pd(β-NaiPy)I_2 (**4**); $[Pd(\alpha\text{-NaiPy})_2](ClO_4)_2$ (**5**); $[Pd(\beta\text{-NaiPy})_2](ClO_4)_2$ (**6**); $[Pd(\alpha\text{-NaiPy})(\beta\text{-NaiPy})](ClO_4)_2$ (**7**); $[Pd(\alpha\text{-NaiPy})(bpy)](ClO_4)_2$ (**8**), $[Pd(\alpha\text{-NaiPy})(phen)](ClO_4)_2$ (**9**), $[Pd(\beta\text{-NaiPy})(bpy)](ClO_4)_2$ (**10**), $[Pd(\beta\text{-NaiPy})(phen)](ClO_4)_2$ (**11**), $[Pd(\alpha\text{-NaiPy})(Tai\text{-}Me)](ClO_4)_2$ (**12**) and $[Pd(\beta\text{-NaiPy})(Tai\text{-}Me)](ClO_4)_2$ (**13**).

(α-NaiPy)(S)]$^{2+}$ or [Pd(β-NaiPy)(S)]$^{2+}$ with bpy (2,2′-bipyridine), phen (1,10-phenanthroline) or Tai-Me (1-methyl-2-(*p*-tolylazo)imidazole) yielded [Pd(α-NaiPy)(bpy)]$(ClO_4)_2$ (**8**), [Pd(α-NaiPy)(phen)]$(ClO_4)_2$ (**9**), [Pd(β-NaiPy)(bpy)]-$(ClO_4)_2$ (**10**), [Pd(β-NaiPy)(phen)]$(ClO_4)_2$ (**11**), [Pd(α-NaiPy)(Tai-Me)]$(ClO_4)_2$ (**12**) and [Pd(β-NaiPy)(Tai-Me)]-$(ClO_4)_2$ (**13**). The composition of the complexes are supported by C, H, N elemental analyses data, and the complexes exhibit 1:2 electrolytic conductivity in MeCN solution ($\Lambda_M = 130$–$160\ \Omega^{-1}\ mol^{-1}\ cm^2$).

The IR stretching frequencies of the complexes have been assigned by comparing with the free ligand data [9]. The *ν*(C=N) bands are shifted to lower frequency by 5–10 cm^{-1} compared to the free ligand value (~1600 cm^{-1}), which supports coordination of N(imine) to Pd(II). Pd(NaiPy)Cl_2 (**1**, **2**) show two *ν*(Pd–Cl) bands at *ca* 325 and 295 cm^{-1}, which support a *cis*-$PdCl_2$ configuration [13,14]. We could not confirm *ν*(Pd–I) of Pd(NaiPy)I_2 (**3**, **4**), which may appear $\leqslant$200 cm^{-1}. This is due to the non-availability of a suitable instrument in our local area. The *ν*(ClO_4) bands of **5**–**13** appear at 1082–1091 cm^{-1}, with a weak stretch at 624–627 cm^{-1}.

2.2. Molecular structure of Pd(β-NaiPy)Cl_2

An ORTEP view of Pd(β-NaiPy)Cl_2 (**2**) is shown in Fig. 1. β-NaiPy acts as a bidentate *N*,*N*′ chelator (*N*,*N*(pyridine); *N*′,*N*(imine)). Bond parameters (Table 1) show that the Pd–N(imine) and Pd–N(pyridine) distances are the same (2.037 Å). This is rarely observed in structural studies of platinum metal diimine/azoimine complexes [15–17]. Usually the M–N(pyridine) distances are shorter than the M–N(imine) distances. The Pd–Cl distances are nearly equal (Pd(1)–Cl(1), 2.2801(17); Pd(1)–Cl(2), 2.2822(17) Å). The β-NaiPy bite angle, N(2)–Pd–N(1) 80.3(2)°, is comparable with the Pd(azoheterocycle)Cl_2 system [13–17]. The pendant naphthyl group is severely distorted from the chelate plane and the dihedral angle is 56.5°. All other bond lengths and angles are comparable with reported structures [13,14].

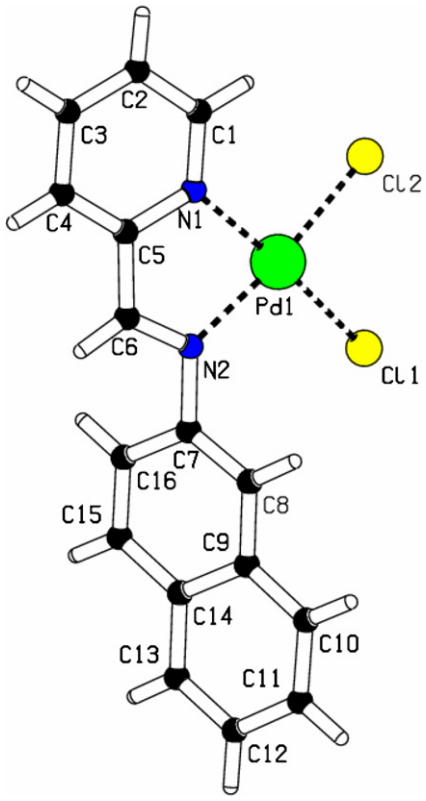


Fig. 1. ORTEP of Pd(β-NaiPy)Cl_2.

An unusual Cl–π interaction (Pd(1)–Cl(1)–Cg(2): Cl(1)–Cg(2), 3.711(4) Å and ∠Pd(1)–Cl(1)–Cg(2), 86.89 (7)°; where Cg(2) refers to N(1), C(1), C(2), C(3), C(4), C(5) and symmetry – x, $1-y$, $-z$) constitutes an intermolecular dimer which brings two Pd centres of two molecules closer to each other, with a distance of 3.679 Å (Fig. 2). Each dimer interacts weakly with a neighbouring molecule by π–π interactions between the pyridyl and naphthyl rings as evident from the long distance (the Cg(2)–Cg(3) distance is 4.245(4) Å and the perpendicular Cg(3)–Cg(3) distance is 3.929(5) Å, where Cg(3) refers to the naphthyl ring and the symmetry is $1/2 + x$, $1/2 - y$, $-z$). This interaction generates a sinusoidal sheet in the *ab* plane (Fig. 3a). The brick wall topology of the sheet is shown in Fig. 3b.

2.3. Optical absorption spectra and electronic structure calculation

The optical absorption spectra of NaiPy and the Pd(NaiPy)-complexes (**1**–**13**) in MeCN solution are reported in Fig. 4 and the data are set out in Table 2. The absorption spectra of α/β-NaiPy in MeCN illustrates the characteristics common to diimine derivatives: a structured absorption band around 330–350 nm with a molar absorption coefficient of the order of $10^4\ M^{-1}\ cm^{-1}$, and an intense high energy absorption around 250–290 nm. From the analogy with the absorption spectrum of *N*-[(2-pyridyl)methyliden]-aminobenzene, it is likely that the large absorption band around 330–350 nm corresponds to n–π* transitions, while the shorter wavelength transitions correspond to a π–π* transition. However, the bands exhibit bathochromic shifts by ~20 nm compared with *N*-[(2-pyridyl)methyliden]-aminobenzene [6].

The complexes Pd(NaiPy)Cl_2 show a weak absorption at 460–510 nm ($\varepsilon \sim 500$–$1000\ M^{-1}\ cm^{-1}$) along with intense absorptions at 400–440 nm ($\varepsilon \sim 1000$–$1500\ M^{-1}\ cm^{-1}$), and in the UV region at 350–370 nm and 265–280 nm ($\varepsilon \sim 10^4\ M^{-1}\ cm^{-1}$) (Fig. 4; Table 2). The UV-region of the spectra is comparable with the spectra of the free ligands and has been assigned to n–π* and π–π* transitions. The visible region weak transition (410–490 nm) may be due to a $d^{10}(Pd) \rightarrow \pi^*$ (ligand) state of the diimine/azoimine function.

To understand the nature of the UV–visible transitions of the ligand and [Pd(NaiPy)X_2], a series of DFT and

Table 1
Structural data of β-NaiPy, Pd(β-NaiPy)Cl_2 and Pd(β-NaiPy)I_2 obtained from the DFT calculated optimized geometry, and comparison with the X-ray structure of Pd(β-NaiPy)Cl_2 (bond lengths in Å and bond angles in °)

β-NaiPy (theoretical)	Pd(β-NaiPy)Cl_2*expt*. (*e.s.d.*) [theoretical] X = Cl	Pd(β-NaiPy)I_2 (theoritical) X = I
N(1)–C(1) 1.335	Pd(1)–X(1) 2.2801 (17) [2.364]	2.663
N(1)–C(5) 1.352	Pd(1)–X(2) 2.2822 (17) [2.371]	2.670
C(4)–C(5) 1.401	Pd(1)–N(1) 2.037 (5) [2.075]	2.134
C(5)–C(6) 1.477	Pd(1)–N(2) 2.037 (6) [2.112]	2.157
N(2)–C(6) 1.283	C(6)–N(2) 1.274 (9) [1.314]	1.310
N(2)–C(7) 1.414	X (1)–Pd(1)–X(2) 90.13 (7) [90.11]	87.96
N(1)–C(5)–C(6) 119.37	X(1)–Pd(1)–N(1) 175.39 (17) [176.08]	173.81
N(2)–C(6)–C(5) 123.50	X(1)–Pd(1)–N(2) 95.86 (16) [97.52]	98.10
C(6)–N(2)–C(7) 119.35	X(2)–Pd(1)–N(1) 93.60 (18) [92.49]	95.37
	X(2)–Pd(1)–N(2) 173.51 (16) [172.35]	173.94
	N(1)–Pd(1)–N(2) 80.3 (2) [79.86]	78.62

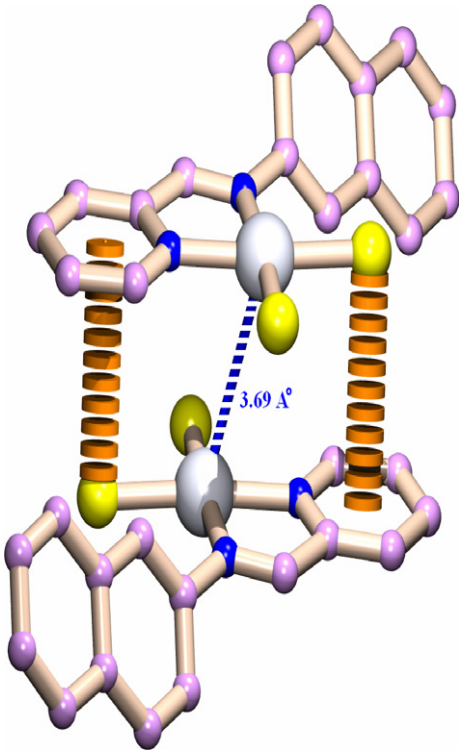


Fig. 2. Dimer unit is formed *via* the Cl–π interaction (Pd—Pd distance, 3.69 Å).

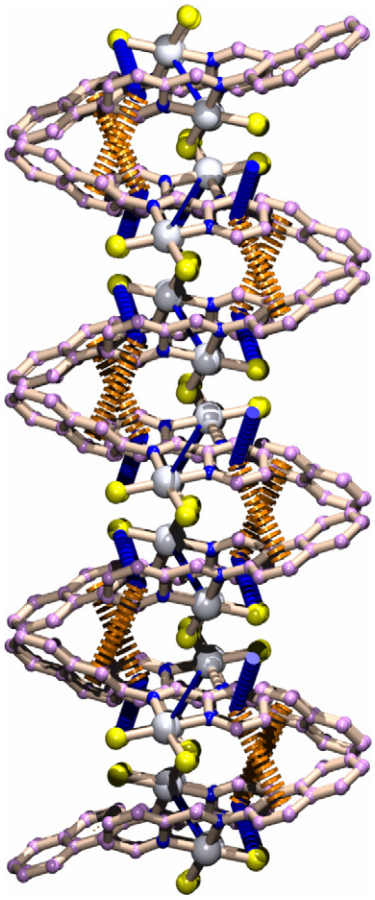


Fig. 3a. An edge-on view of the π-sheet (sinusoidal sheet) generated by π–π interactions.

TD-DFT calculations have been conducted on the optimized geometry of the compounds. To reduce the work load we have confined the calculation to β-NaiPy, Pd(β-NaiPy)Cl_2 and Pd(β-NaiPy)I_2. The structure of Pd(β-NaiPy)Cl_2 obtained from the optimized geometry calculation is comparable to the metric parameters of the X-ray determined structure (Table 1). The bond lengths are elongated by 0.04–0.1 Å in the calculated structure of the gas phase DFT study. Similarly the bond angles are also changed by 1–2°. The structural data of β-NaiPy and Pd(β-NaiPy)I_2 are also included in Table 1. In general, the iodo complex, Pd(β-NaiPy)I_2, shows longer bond parameters compared to Pd(β-NaiPy)Cl_2, which is usual because of better electron influx in I^- compared to Cl^-.

Selected electronic structures of the compounds in the gas phase and in acetonitrile solution are given in Figs. 5 and 6, while the composition of selected molecular orbitals are listed in Table 3. In β-NaiPy, the composition of the frontier orbitals are as follows: HOMO and HOMO-1 have large contributions from the naphthyl unit (Naph) (>75%)

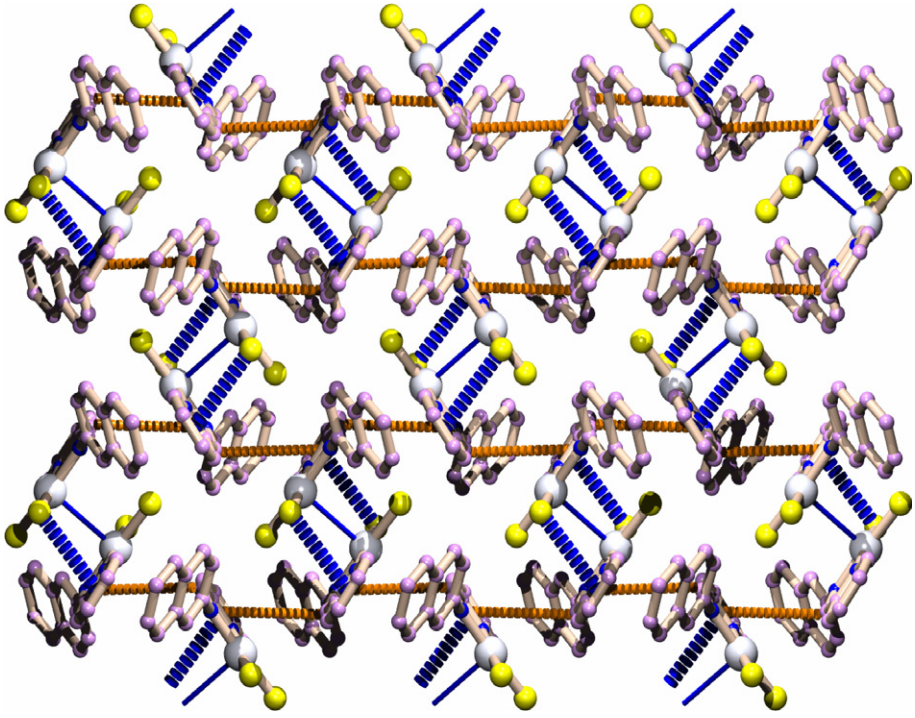


Fig. 3b. The brick wall topology of the sheet in the ab plane, a is to the right and b vertical.

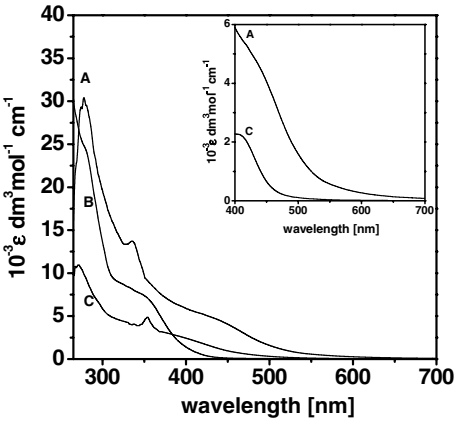


Fig. 4. Absorption spectra of A. [Pd(β-NaiPy)(phen)](ClO$_4$)$_2$, B. β-NaiPy, and C. Pd(β-NaiPy)Cl$_2$ in MeCN at room temperature.

while HOMO-2 and HOMO-3 have a larger share from the pyridyl (Py) group (>55%) (Fig. 7). Also, the energy separation between the HOMO and HOMO-1 ($\Delta E = 0.65$ eV (gas); 0.63 eV (MeCN)) is larger than HOMO-2 and HOMO-3 ($\Delta E = 0.32$ eV (gas); 0.22 eV (MeCN)). Other occupied orbitals show a substantial contribution from the Naph and Py units, and in some cases from the C=N function. Amongst the unoccupied orbitals, the LUMO has a major share from the Py group (68%) while LUMO+1 has 89% Naph character. Similarly, the composition of other orbitals are as follows: LUMO+2, 86% (Py); LUMO+3, 83% (Naph); LUMO+4, 90% (Naph), etc. Thus, the frontier molecular orbitals in the β-NaiPy ligand indicate that the most possible mechanism for the ligand–metal interaction involves the Naph and Py orbitals, and metal centered orbitals. That means in the metal–ligand σ-bonding the Naph orbitals of the ligand are used, while in the π-bonding the Py orbitals of β-NaiPy are used.

In Pd(β-NaiPy)Cl$_2$ the frontier orbitals are composed of Pd(d), ligand and Cl orbitals (Table 3). The occupied MOs HOMO, HOMO-1, HOMO-2 and HOMO-3 have a major contribution from Cl orbitals (55–75%, Fig. 8). The metal orbitals are referred to d-orbitals only. Surprisingly the HOMO has the least contribution from ligand functions while HOMO-1 has 40% ligand character. The unoccupied MOs have a very high contribution from β-NaiPy (54–98%). These results are collected from gas phase DFT calculations. However, a drastic difference is observed in the solution phase calculation using MeCN as the solvent. The HOMO, HOMO-1 and HOMO-2 are composed of 95, 42 and 60% β-NaiPy functions, respectively, while in the gas phase they have 1, 40 and 10% ligand contributions, respectively. The solvent polarity may be acting in a critical role to stabilize polar ligand functions compared to Cl dominated orbitals. The unoccupied MOs in the MeCN phase have a very large contribution from ligand functions (>90%), except LUMO+1 which has 28% ligand character and 42% Cl character. The DFT calculations of Pd(β-NaiPy)I$_2$ also support a similar conjecture (Fig. 9) with reference to gas and solution phase calculations. A correlation amongst the energy levels of the free ligand, and complexes in the gas phase and MeCN phase are given separately in Figs. 5 and 6.

The calculated transitions are listed in Table 4. They are assigned to n(Py) → π*(Py), n(Py) → π*(Naph), π(Naph)

Table 2
Absorption and fluorescence spectral data, quantum yields, lifetimes and decay constants of the compounds in MeCN

Compound	Absorption wavelength (molar extinction coefficient) λ_{abs}/nm ($10^{-3}\varepsilon$, mol^{-1} cm^{-1})	Emission spectral and life time data[a]						
		λex/nm	λem/nm	ϕ_f	τ_f (ns)	χ^2	$k_r \times 10^{-9}$ (s^{-1})	$k_{nr} \times 10^{-9}$ (s^{-1})
α-NaiPy	291 (8.41), 338 (7.56)	338	417	0.103	2.922	1.26	0.035	0.307
β-NaiPy	282 (23.48), 346 (7.61)	282	409	0.041	3.458	0.93	0.012	0.277
Pd(α-NaiPy)Cl_2 (**1**)	291 (7.51), 316 (5.71), 356 (4.45), 400 (1.44), 514 (0.60)	285	418	0.171	6.751	1.05	0.025	0.123
Pd(β-NaiPy)Cl_2 (**2**)	272 (10.89), 304 (5.45), 353 (4.82), 409 (2.31)	272	411	0.044	5.832	1.10	0.008	0.164
Pd(α-NaiPy)I_2 (**3**)	270 (8.45), 299 (4.05), 355 (1.97), 426 (1.16), 501 (0.62)	355	405	0.024	3.97	1.25	0.006	0.24
Pd(β-NaiPy)I_2 (**4**)	269 (12.29), 387 (2.39), 413 (1.91)	370	412	0.021	3.88	1.26	0.005	0.25
[Pd(α-NaiPy)$_2$] (ClO_4)$_2$ (**5**)	218 (49.85), 269 (19.79), 344 (8.69), 465 (2.87)	344	424	0.013	2.644	1.16	0.0049	0.373
[Pd(β-NaiPy)$_2$] (ClO_4)$_2$ (**6**)	221 (35.92), 271 (16.67), 382 (4.23), 415 (3.05), 513 (0.676)	221	337	0.010	1.677	1.24	0.006	0.590
[Pd(α-NaiPy)(β-NaiPy)] (ClO_4)$_2$ (**7**)	217 (2.24), 386 (2.41), 425 (4.74)	217	291	0.014	3.352	1.24	0.004	0.294
[Pd(α-NaiPy)(bpy)](ClO_4)$_2$ (**8**)	285 (7.65), 315 (5.66), 355 (2.59), 496 (0.965)	285	369	0.020	2.958	1.17	0.007	0.331
[Pd(α-NaiPy)(phen)](ClO_4)$_2$ (**9**)	275 (31.92), 291 (21.41), 314 (10.68), 356 (5.11), 462 (2.33)	314	410	0.068	1.498	1.27	0.045	0.623
[Pd(β-NaiPy)(bpy)](ClO_4)$_2$ (**10**)	276 (19.02), 319 (8.02), 366 (3.28), 412 (5.94)	276	398	0.019	3.865	1.12	0.005	0.254
[Pd(β-NaiPy) (phen)] (ClO_4)$_2$ (**11**)	278 (30.05), (34.28), 337 (13.49), 448 (4.42)	337	403	0.016	4.543	1.03	0.004	0.217
[Pd(α-NaiPy)(Tai-Me)](ClO_4)$_2$ (**12**)	217 (20.89), 377 (14.29), 475 (3.13)	217	290	0.001	4.638	1.04	0.0002	0.215
[Pd(β-NaiPy)(Tai-Me)] (ClO_4)$_2$ (**13**)	220 (19.87), 372 (13.11), 465 (2.99)	220	334	0.001	4.741	1.06	0.0002	0.211

[a] λex – excitation wavelength; λem – emission wavelength; O_f – fluorescence quantum yield, τ_f – mean fluorescence lifetime, χ^2 – goodness of fit, k_r – radiative rate constant, k_{nr} – non-radiative rate constant.

→ π*(Py), π(Naph) → π*(Naph) and π(Py) → π*(Py). On comparing with the oscillator strength (*f*), two major absorption bands in the electronic spectra may be assigned to n(Py) → π*(Py) (calculated band 340–360 nm and experimental 346 nm) and π(Naph) → π*(Py) (calculated band 270–320 nm and experimental 282 nm). The calculated transitions are grouped in three different spectral zones: 470–500 nm, 360–390 nm and 280–330 nm. The intensity of these transitions has been assessed from oscillator strengths (*f*). In fact, the observed spectrum of Pd(β-NaiPy)Cl_2 shows a similar absorption pattern whilst the transitions are shifted to a lower wavelength zone (Fig. 10, Tables 2 and 4). The basic difference between the experimental optical spectrum and theoretical one in the acetonitrile phase is that the main absorption band in the visible region in the experimental spectrum appears at a shorter λ value than that of the theoretically calculated data of acceptable oscillator strength. This may be accounted for in two ways: (i) the non-equilibrium implementation of the polarizable continuum model (PCM), which we have used during the calculation, is insufficient considering the functional constrain given by the heavy metal function of Pd and (ii) acetonitrile is a coordinating solvent and may coordinate to a square planar Pd(II) complex additionally to the solvent cage interaction with the molecular orbitals, and this has not been considered in the PCM model. The longer wavelength band at 470–500 nm may be assigned to the combination of MLCT (d_π(Pd) → π* (ligand)), ^{1}XLCT (X refers to Cl and I): n(X) → π* (ligand), π(ligand) → π* (ligand). The observed transitions appear at 508 and 409 nm. Similarly the 360–390 nm transitions correspond to d_π(Pd) → π* (ligand) and π(ligand) → π* (ligand) transitions. The experimental spectral band appears at 353 nm. The calculated UV band at 280–330 nm is assigned to d_π(Pd) → π* (ligand) and π(ligand) → π* (ligand) transitions. The observed transitions appear at 304 and 272 nm for Pd(β-NaiPy)Cl_2 (**2**) and 387 and 269 nm for Pd(β-NaiPy)I_2 (**4**).

2.4. ^{1}H NMR spectra

Table 5 summaries the ^{1}H NMR spectral data for the free ligand, NaiPy and the palladium(II) complexes. The spectra are recorded in DMSO-d_6 solution. The assignment has been made on the basis of spin–spin interaction, and on comparing with the free ligand values [10]. *N*-[(2-Pyridyl)methyliden]-α(or β)-aminonaphthalene exhibits a singlet at 8.6–8.8 ppm for –HC═N– (7H). The pyridyl protons (3-H to 6-H) appear at 7.7–8.5 ppm, with a higher δ than the naphthyl protons (8-H to 15-H) at 7.3–8.0 ppm. In the complexes the NMR signals are, in general, shifted downfield. The 6-H signal appears at 8.4–9.0 ppm as a doublet ($J = 8.0$ Hz); 3-H shows a doublet at 8.1–8.2 ppm ($J = 8.0$ Hz); 4- and 5-H appear as a triplet at 7.6–8.3 ppm ($J = 8.0$ Hz). On comparing with the NMR data of naphthylazo compounds [15,16] we have assigned the resonances to the naphthyl protons of the coordinated

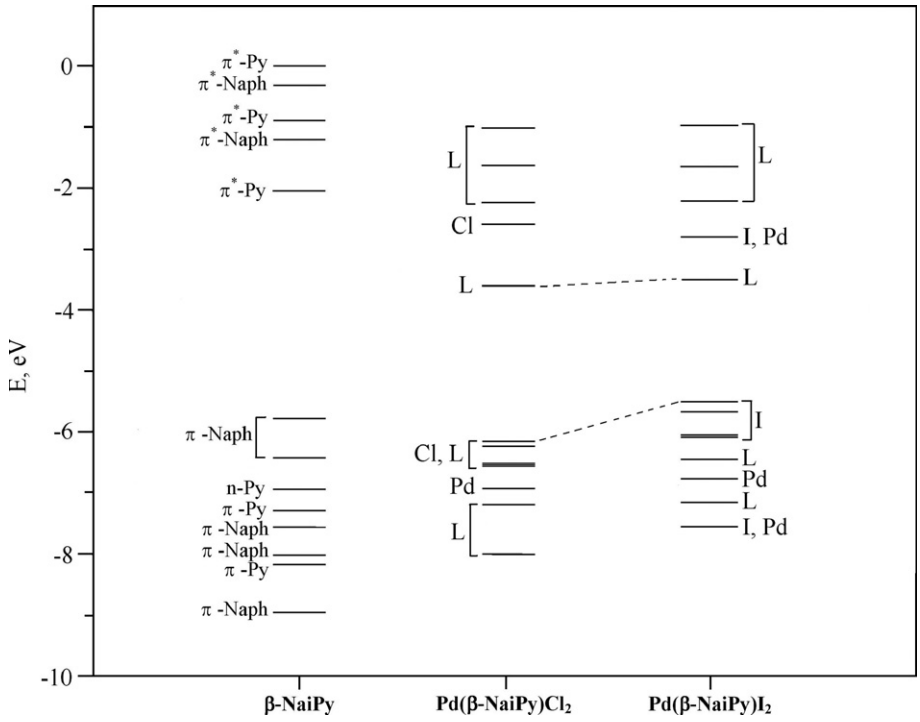


Fig. 5. Energy level correlation diagram in the gas phase.

ligand. 8-H (or 9-H) appears at higher δ because of a closer proximity of the electron withdrawing imine (–C═N–) group. 10-H to 15-H appear as a multiplet at 7.2–8.0 ppm. The bis-chelated complexes, $[Pd(\alpha\text{-}/\beta\text{-NaiPy})_2]^{2+}$ (**5** or **6**) may exist in two isomeric forms (*cis*: **I** and *trans*: **II**) but the *cis* form must not be very favoured because of steric crowding. However, the ^{1}H NMR signals are not sufficiently resolved to identify the composition.

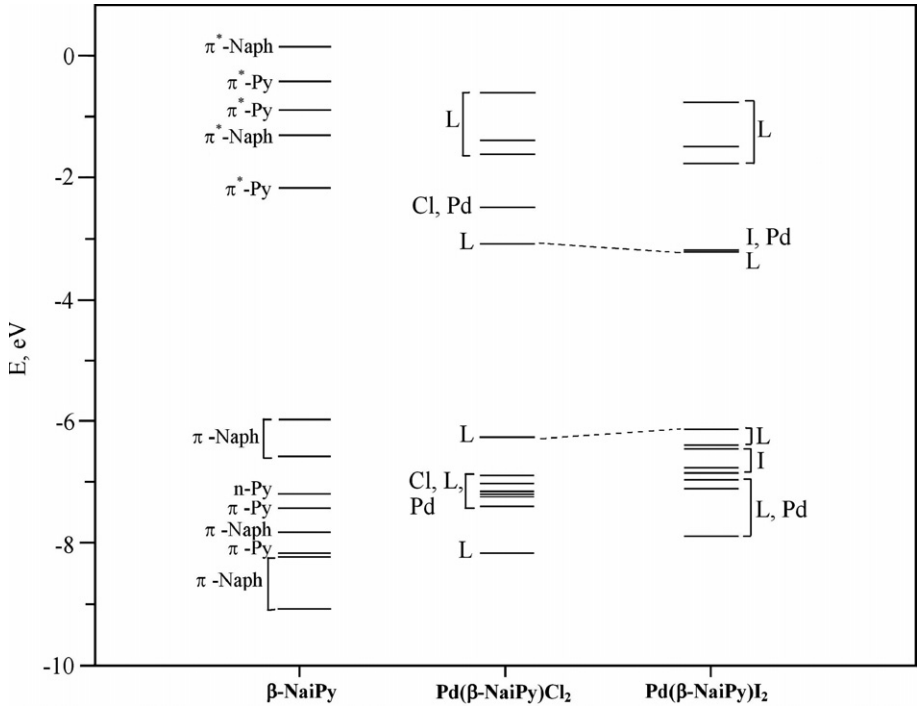


Fig. 6. Energy level correlation diagram in acetonitrile phase.

Table 3
Selected orbital energies and orbital compositions (%) for β-NaiPy, Pd(β-NaiPy)Cl_2 and Pd(β-NaiPy)I_2 in the gas phase and MeCN solution phase

(*E*, eV)	H-8 (−8.03) (π)	H-7 (−7.94) (π)	H-6 (−7.12) (π)	H-5 (−6.86) (dπ)	H-4 (−6.49) (π)	H-3 (−6.48) (n)	H-2 (−6.47) (n)	H-1 (−6.17) (n, π)	HOMO (−6.12) (n)	LUMO (−3.52) (π^*)	$L+1$ (−2.52) (π^*)	$L+2$ (−2.17) (π^*)	$L+3$ (−1.57) (π^*)	$L+4$ (−0.97) (π^*)
*Pd(β-NaiPy)Cl_2 (**2**) in gas phase*														
Pd(d)	26	36	6	77	9	19	20	6	22	7	18	20	4	2
β-NaiPy	50	50	90	10	60	20	10	40	1	89	68	54	95	98
Cl	22	12	2	11	25	58	67	55	75	2	12	24	1	–
*Pd(β-NaiPy)Cl_2 (**2**) in acetonitrile*														
(*E*, eV)	(−8.28) (π)	(−8.09) (π)	(−7.32) (n)	(−7.16) (π)	(−7.12) (dπ)	(−7.10) (n)	(−6.95) (π)	(−6.83) (n, π)	(−6.19) (π)	(−3.01) (π^*)	(−2.40) (π^*-I)	(−1.55) (π^*)	(−1.32) (π^*)	(−0.54) (π^*)
Pd(d)	3	5	30	28	51	35	28	27	1	4	27	2	2	1
β-NaiPy	90	86	2	40	8	14	60	42	95	94	28	97	98	98
Cl	7	8	66	30	38	50	12	30	3	1	42	–	–	–
*Pd(β-NaiPy)I_2 (**4**) in gas phase*														
(E, eV)	(−7.54) (dπ,π)	(−7.45) (dπ, π)	(−7.04) (π)	(−6.66) (dπ)	(−6.35) (π)	(−5.98) (π)	(−5.95) (n)	(−5.57) (n)	(−5.40) (n)	(−3.40) (π^*)	(−2.69) (π^*-I)	(−2.10) (π^*)	(−1.56) (π^*)	(−0.88) (π^*)
Pd(d)	43	30	3	80	4	14	15	14	6	3	35	1	1	1
β-NaiPy	27	14	89	3	84	6	3	–	6	94	22	98	98	99
I	28	50	4	10	8	74	78	84	87	1	43	–	–	–
*Pd(β-NaiPy)I_2 (**4**) in acetonitrile*														
(E, eV)	(−7.87) (π)	(−7.77) (π)	(−7.00) (π)	(−6.86) (π)	(−6.76) (n)	(−6.67) (n)	(−6.36) (n)	(−6.30) (π)	(−6.03) (π)	(−3.10) (π^*)	(−3.09) (π^*-I)	(−1.66) (π^*)	(−1.39) (π^*)	(−0.67) (π^*)
Pd(d)	21	35	33	26	20	21	17	2	1	9	33	2	1	–
β-NaiPy	52	54	60	66	2	4	–	66	66	86	27	98	98	99
I	24	10	6	6	72	74	83	32	32	3	40	–	–	–
β-NaiPy in gas phase														
(E, eV)	(−9.37) (n)	(−8.92) (π)	(−8.13) (π)	(−8.00) (π)	(−7.53) (π)	(−7.25) (π)	(−6.93) (n)	(−6.40) (π)	(−5.75) (π)	(−2.01) (π^*)	(−1.17) (π^*)	(−0.86) (π^*)	(−0.27) (π^*)	(0.02) (π^*)
Naph	80	54	4	70	56	12	24	82	78	14	90	6	84	1
N=C	16	22	1	8	28	20	12	8	14	18	1	5	2	1
Py	4	24	95	22	16	68	64	10	8	68	9	89	14	98
β-NaiPy in acetonitrile														
(E, eV)	(−9.45) (n)	(−9.04) (π)	(−8.19) (π)	(−8.15) (π)	(−7.79) (π)	(−7.40) (π)	(−7.18) (n)	(−6.56) (π)	(−5.93) (π)	(−2.14) (π^*)	(−1.28) (π^*)	(−0.86) (π^*)	(−0.40) (π^*)	(0.18) (π^*)
Naph	78	55	58	37	55	26	8	80	76	15	89	8	83	90
N=C	15	21	12	6	27	18	16	9	15	17	1	6	2	8
Py	7	24	30	57	18	56	76	11	9	68	10	86	15	2

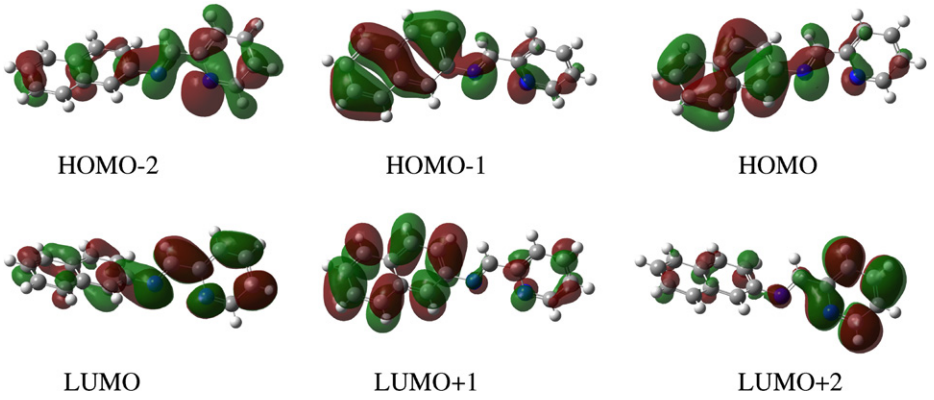


Fig. 7. Some MO pictures of β-NaiPy (gas phase DFT calculations).

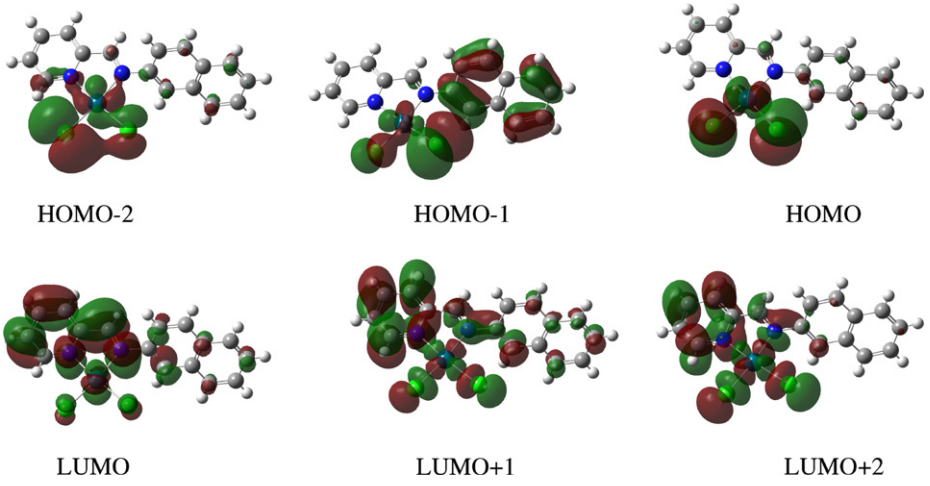


Fig. 8. Some MO pictures of Pd(β-NaiPy)Cl_2 (obtained from gas phase DFT calculations).

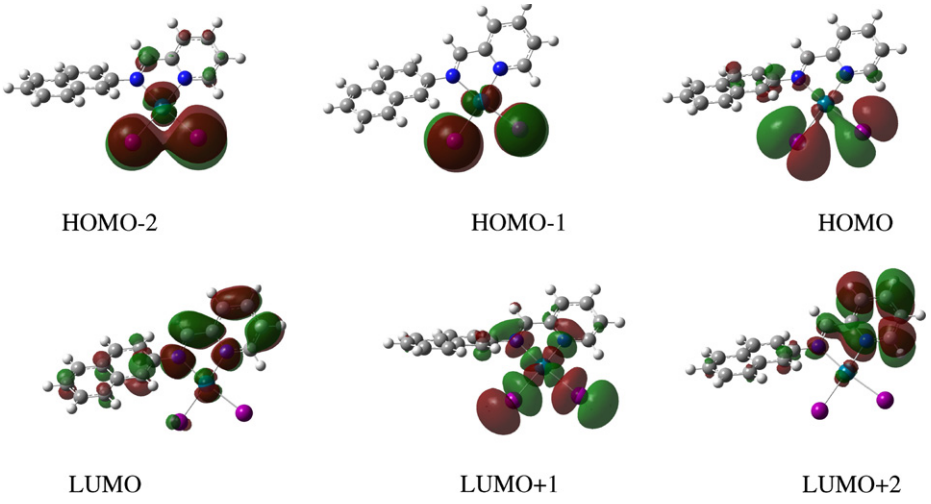


Fig. 9. Some MO pictures of Pd(β-NaiPy)I_2 (obtained from gas phase DFT calculations).

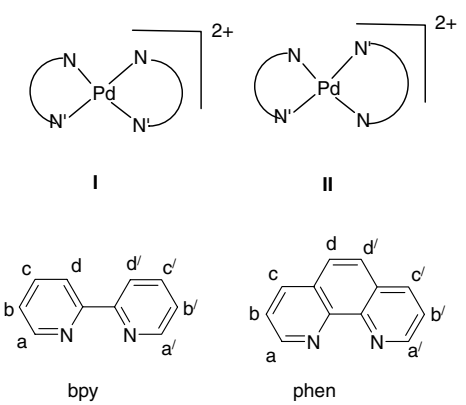
Table 4
Selected list of excited energies of β-NaiPy, Pd(β-NaiPy)Cl_2 and Pd(β-NaiPy)I_2 in the gas phase and MeCN phase

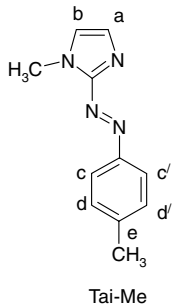
Excited state	λ, nm ($f \times 10^3$)	Major contribution
Pd(β-NaiPy)Cl_2 in gas phase		
2	602.8(9.3)	(89%)H − 1 → LUMO (XLCT, IL)
4	501.9(18.6)	(69%)H − 5 → LUMO (MLCT), (13%)H − 3 → LUMO (XLCT)
5	484.8(40.1)	(76%)H − 4 → LUMO (IL), (10%)H − 3 → LUMO (XLCT)
6	477.8(54.0)	(55%)H − 3 → LUMO (XLCT), (22%)H − 5 → LUMO (MLCT)
8	442.4(3.4)	(25%)H − 1 → L + 2 (XLCT, IL), (25%)H − 2 → L + 2 (XLCT), (17%)H − 1 → L + 1 (XLCT, IL), (16%)H − 2 → L + 1 (XLCT)
10	389.5(42.4)	(51%)H − 6 → LUMO (IL)
11	384.6(62.5)	(36%)H − 6 → LUMO (IL), (15%)H − 2 → L + 2 (XLCT), (11%)H − 1 → L + 1 (XLCT, IL), (10%)H − 1 → L + 2 (XLCT, IL)
12	381.3(3.4)	(40%)H-5 → L + 2 (MLCT), (25%)H-5() → L + 1 (MLCT)
13	361.6(40.1)	(49%)HOMO → L + 1 (XLCT), (30%)HOMO → L + 2 (XLCT)
16	331(14.4)	(42%)H-3 → L + 1 (XLCT), (28%)H-3 → L + 2 (XLCT)
17	323.5(19.5)	(27%)H-4 → L + 1 (IL), (26%)H − 4 → L + 2 (IL), (11%)H − 7 → LUMO (IL)
19	313.2(5.1)	(33%)H − 4 → L + 2 (IL), (30%)H − 4 → L + 1 (IL)
23	305(41.7)	(81%)H − 1 → L + 3 (XLCT, IL)
24	299(16.5)	(55%)H − 9 → LUMO (IL), (15%)H-8 → LUMO (IL), (13%)H − 11 → LUMO (IL)
25	289.8(52.6)	(77%)H − 10 → LUMO (IL)
28	278.4(39.5)	(70%)H − 11 → LUMO (IL)
Pd(β-NaiPy)Cl_2 in acetonitrile		
1	468.9(74.7)	(93%)HOMO → LUMO (IL)
2	433.4(2.4)	(32%)H − 1 → LUMO (XLCT, IL), (18%)H − 4 → L + 1 (MXCT), (12%)H − 1 → L + 1 (LXCT), (11%)H − 5 → L + 1 (LXCT)
4	407.6(3.1)	[(52%)H − 2 → LUMO, (16%)H − 5 → LUMO] (IL), (12%)H − 4 → LUMO (MLCT, XLCT), (10%)H − 1 → L + 1 (LXCT)
5	404.7(3.0)	(23%)H − 4 → L + 1(MXCT), (20%)H − 1 → LUMO (IL), [(19%)HOMO → L + 1, (11%)H − 5 → *L* + 1] (LXCT), (10%)H − 6 → L + 1 (XXCT)
6	398.7(4.8)	[(30%)H − 5 → L + 1, (11%)H − 2 → L + 1] (LXCT), (29%)H − 1 → LUMO (IL), (10%)H − 6 → L + 1 (XXCT), (10%)H − 4 → LUMO (MLCT)
8	378.5(18.7)	(59%)HOMO → *L* + 1 (LXCT), (14%)H − 3 → LUMO (XLCT)
9	369.2(26.6)	(50%)H − 4 → LUMO (MLCT), (32%)H − 5 → LUMO (IL)
10	360.1(63.1)	(70%)H − 3 → LUMO (XLCT), (10%)HOMO → L + 1 (LXCT)
11	358.5(177.9)	[(34%)H − 2 → LUMO, (34%)H − 5 → LUMO] (IL), (15%)H − 4 → LUMO (MLCT)
12	344.4(7.7)	(90%)H − 6 → LUMO (XLCT)
13	319.7(15.6)	(61%)H − 6 → L + 1 (XXCT), (24%)H − 5 → L + 1 (LXCT)
14	307.1(72.7)	[(42%)H − 2 → L + 1, (14%)H − 5 → L + 1, (12%)H − 1 → L + 1] (LXCT), (14%)H − 4 → L + 1 (MXCT)
15	293.8(17.4)	(95%)HOMO → L + 2 (IL)
16	278.6(175.7)	[(64%)HOMO → L + 3, (12%)H − 7 → LUMO] (IL)
17	274.2(22.1)	[(66%)H − 7 → LUMO, (10%)HOMO → L + 3] (IL)
18	269.8(33.4)	(72%)H − 1 → L + 2 (IL)
Pd(β-NaiPy)I_2 in gas phase		
2	792.5(2.2)	(94%)H − 1 → LUMO (XLCT)
6	600.5(47.9)	[(76%)H − 2 → LUMO, (12%)H − 3 → LUMO] (XLCT)
7	573(2.5)	(72%)H − 3 → L + 1 (XMCT)
9	539(11.6)	(79%)H − 5 → LUMO (MLCT), (14%)H − 4 → LUMO (IL)
10	501(91.8)	(72%)H − 4 → LUMO (IL), (16%)H − 5 → LUMO (MLCT)
13	423(5.7)	(91%)H − 1 → L + 2 (IL)
14	407(48.8)	(78%) H − 6 → LUMO (IL), (10%)H − 7 → LUMO (XLCT)
15	401(21.8)	(76%)H − 4 → L + 1 (LMCT)
16	386(8.2)	(69%)H − 8 → LUMO (MLCT), (15%)H − 7 → LUMO (XLCT)
19	374.6(7.0)	[(37%)HOMO → L + 3, (28%)H − 7 → LUMO] (XLCT)
21	371.5(78.1)	[(44%)HOMO → L + 3, (28%)H − 7 → LUMO] (XLCT)
22	355(27.3)	(50%)H − 10 → L + 1 (LMCT), (20%)H − 9 → LUMO (IL)
24	351(43.7)	(62%)H − 9 → LUMO (IL), (12%)H − 10 → L + 1 (LMCT)
25	343.8(47.8)	(72%)H − 10 → LUMO (IL)
26	327(18.4)	(57%)H − 5 → L + 2 (MLCT), (37%)H − 4 → L + 2 (IL)
27	323(35.7)	(72%)H − 6 → L + 1 (LMCT)
28	322(11.0)	(52%)H − 4 → L + 2 (IL), (37%)H − 5 → L + 2 (MLCT)
30	313(49.9)	[(41%)H − 3 → L + 3, (21%)HOMO → L + 4] (XLCT)
35	286(56.2)	[(25%)H − 11 → LUMO, (20%)H − 4 → L + 3, (14%)H − 12 → LUMO] (IL)
36	283.8(14.5)	[(24%)H − 4 → L + 3, (21%)H − 11 → LUMO] (IL)
38	278(49.3)	[(55%)H − 6 → L + 2, (18%)H − 4 → L + 3] (IL)

(*continued on next page*)

Table 4 (*continued*)

Excited state	λ, nm ($f \times 10^3$)	Major contribution
Pd(β-NaiPy)I_2 in acetonitrile		
3	556.4(2.8)	[(27%)H − 6 → L + 1, (25%)H − 5 → L + 1, (10%)H − 1 → L + 1, (10%)HOMO → L + 1] (LXCT)
4	530.6(3.2)	(66%)H − 3 → L + 1 (XXCT)
5	524.1(35.0)	(73%)HOMO → LUMO (IL)
6	512.8(6.9)	(52%)H − 4 → L + 1 (XXCT), (11%)H − 4 → LUMO (XLCT), [(10%)H − 1 → L + 1, (10%)H − 5 → L + 1] (LXCT)
7	475.2(13.1)	[(33%)H − 1 → L + 1, (10%)HOMO → L + 1] (LXCT), (35%)H − 2 → LUMO (XLCT), (14%)H − 1 → LUMO (IL)
8	474.3(2.6)	(47%)H − 2 → LUMO (XLCT), (23%)H − 1 → LUMO (IL), (10%)H − 2 → L + 1 (XXCT)
9	466.6(106.8)	(50%)H − 1 → LUMO (IL), (30%)H − 1 → L + 1 (LXCT)
10	432.2(5.5)	[(44%)H − 5 → LUMO, (26%) H − 6 → LUMO] (IL), (13%)H − 4 → LUMO (XLCT)
11	418.8(64.1)	[(76%)H − 3 → LUMO, (11%) H − 4 → LUMO] (XLCT), (10%)H − 3 → L + 1 (XXCT)
12	413.2(12.5)	(66%)H − 4 → LUMO (XLCT), (13%) H − 5 → LUMO (IL), (11%)H − 4 → L + 1 (XXCT)
13	382.7(19.6)	[(26%)H − 6 → L + 1, (25%) H − 5 → L + 1, (20%)H − 7 → L + 1] (LXCT), (10%)H − 6 → LUMO (IL)
14	377.2(169.9)	[(52%)H − 6 → LUMO, (27%) H − 5 → LUMO] (IL)
15	369.4(58.2)	[(36%)H − 7 → L + 1, (18%) H − 6 → L + 1, (17%)H − 5 → L + 1] (LXCT)
19	309.4(22.1)	[(38%)H − 13 → L + 1, (10%) H − 12 → L + 1] (LXCT), (20%)H − 8 → LUMO (IL)
20	307.9(60.0)	(61%)H − 8 → LUMO (IL), [(13%)H − 8 → L + 1, (11%)H − 13 → L + 1] (LXCT)
22	298.9(49.1)	[(40%)HOMO → L + 3, (19%)H − 1 → L + 2] (IL), (21%)H − 2 → L + 2 (XLCT)
23	298.3(55.7)	[(40%)HOMO → L + 3, (39%)H − 1 → L + 2] (IL), (11%)H − 2 → L + 2 (XLCT)
24	293.7(182.8)	[(33%)H − 10 → LUMO, (16%)H − 9 → LUMO] (IL), (14%)H − 8 → L + 1 (LXCT)
28	281.7(29.0)	[(38%)H − 1 → L + 3, (12%)HOMO → L + 4, (11%)H − 5 → L + 2] (IL), (10%)H − 3 → L + 2 (XLCT)
30	278.5(33.9)	(36%)H − 4 → L + 2 (XLCT), [(12%)H − 6 → L + 2, (12%)H − 5 → L + 2] (IL)
β-NaiPy in gas phase		
1	405(136.3)	(80%)HOMO(π-Naph) → LUMO(π*-Py)
3	317(72.8)	(52%)H − 2(*n*-Py) → LUMO(π*-Py), (12%)H − 1(π-Naph) → LUMO(π*-Py), (14%)HOMO(π-Naph) → L + 1(π*-Naph)
4	301(49.4)	(58%)HOMO(π-Naph) → L + 1(π*-Naph)
6	274(306)	(39%)H − 4(π-Naph) → LUMO(π*-Py), (25%)H − 3(π-Py) → LUMO(π*-Py), (10%)H − 2 (*n*-Py) → LUMO(π*-Py)
8	259(20.7)	(46%)H − 2(*n*-Py) → L + 2(π*-Py), (18%) H − 1(π-Naph) → L + 2(π*-Py)
9	254(542)	(32%)H − 3(π-Py) → LUMO(π*-Py), (27%)H − 4(π) → LUMO(π*-Py)
11	242(159)	(24%)H − 1(π-Naph) → L + 2(π*-Py), (19%)H − 2(*n*-Py) → L + 2(π*-Py), (13%)H − 2(*n*-Py) → L + 1(π*-Naph), (13%)H − 6(π-Py) → LUMO(π*-Py)
β-NaiPy in acetonitrile		
1	394.2(192.3)	(85%)HOMO(π-Naph) → LUMO(π*-Py)
2	334.7(14.1)	(76%)H − 1(π-Naph) → LUMO(π*-Py), (10%)H − 2(*n*-Py) → LUMO(π*-Py)
3	307.5(109.6)	(42%)H − 2(*n*-Py) → LUMO(π*-Py), (25%)HOMO(π-Naph) → L + 1(π*-Naph), (14%)H − 3(π-Py) → LUMO(π*-Py)
4	296.6(132.8)	(52%)HOMO(π-Naph) → L + 1(π*-Naph), (14%)H − 2(*n*-Py) → LUMO(π*-Py), (10%)HOMO(π-Naph) → L + 1 (π*-Naph)
5	276.8(15.5)	(56%)HOMO(π-Naph) → L + 2(π*-Py), (15%)H − 1(π-Naph) → L + 1(π*-Naph), (10%)H − 1(π-Naph) → L + 2(π*-Py)
6	271.3(340.2)	(21%)H − 3(π-Py) → LUMO(π*-Py), (18%)H − 4(π-Naph) → LUMO (π*-Py), (18%)HOMO(π-Naph) → L + 3 (π*-Naph), (14%)H − 2(*n*-Py) → LUMO(π*-Py)
7	267.4(254.5)	(32%)HOMO(π-Naph) → L + 2(π*-Py), (24%)H − 1(π-Naph) → L + 1(π*-Naph), (16%)HOMO(π-Naph) → L + 3 (π*-Naph), (10%)H − 4(π-Naph) → LUMO(π*-Py)
8	257.0(235.4)	(40%)H − 4(π-Naph) → LUMO(π*-Py), (30%)H − 3(π-Py) → LUMO(π*-Py), (10%)H − 1(π-Naph) → L + (π*-Naph)
9	245.2(15.4)	(39%)H − 2(*n*-Py) → L + 2(π*-Py), (29%)H − 1(π-Naph) → L + 2(π*-Py), (11%)H − 3(π-Py) → L + 2(π*-Py), (10%)HOMO(π-Naph) → L + 2(π*-Naph)





[Pd(α-NaiPy)(bpy)](ClO$_4$)$_2$ (**8**), [Pd(α-NaiPy)(phen)](ClO$_4$)$_2$ (**9**), [Pd(β-NaiPy)(bpy)](ClO$_4$)$_2$ (**10**) and [Pd(β-NaiPy)(phen)](ClO$_4$)$_2$ (**11**) may exist only in one isomeric form and the NMR spectra show a single set of resonances which support the existence of one isomer only. The isomers of **12** and **13** have been easily identified from the 1-Me and 9-Me signals which appear in a 4:1 intensity ratio. This may suggest the existence of two isomers in a 4:1 proportion. Because of *trans*, *trans*-*N*,*N* and *trans*, *trans*-*N*′,*N*′, isomer **II** may be in a higher yield than **I**.

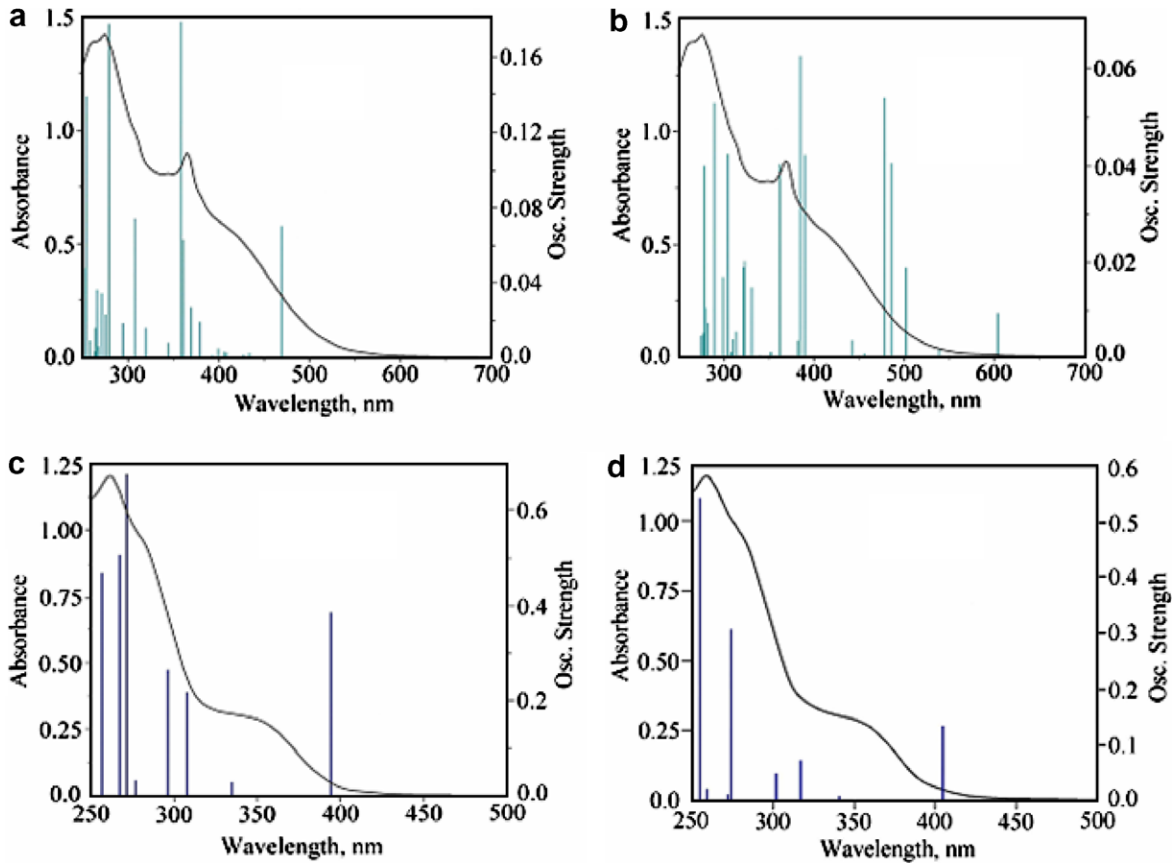


Fig. 10. Experimental optical spectra and calculated (TDDFT) transition energies of (a) Pd(β-NaiPy)Cl_2 in CH_3CN ; (b) Pd(β-NaiPy)Cl_2 in the gas phase; (c) β-NaiPy in CH_3CN and (d) β-NaiPy in the gas phase.

2.5. Luminescence studies

The photoluminescence properties of the ligands and complexes were studied at room temperature. The Schiff bases exhibit emissions at 417 and 409 nm for α-NaiPy and β-NaiPy respectively at 298 K in MeCN solution upon excitation at 338 and 282 nm, respectively. Excitation and emission wavelengths, and quantum yields are summarized in Table 2. No emissions originating from metal-centred and MLCT excited states are expected for the Pd(II) complexes, since it is difficult for the Pd(II) ion to change its electronic configuration. The main reason for Pd(II) complexes to be non-emissive is deactivation via low-lying d–d states. Thus the emission observed (Fig. 11) in the complexes is assigned to (π–π^*) fluorescence. It is interesting that the Pd(II) complexes show higher intensities than the free ligands. It has been reported that the metal ions can enhance or quench the fluorescence emission of pyridine containing compounds [18]. In the absence of metal ions the fluorescence of the ligand is probably quenched by the occurrence of a photoinduced electron transfer (PET) process due to the presence of a lone pair of nitrogen atoms. Such a PET process is prevented by the complexation of the ligand with metal ions which introduces rigidity to the organic motif; thus the fluorescence intensity may be greatly enhanced by coordination to Pd(II). Quantum yields (ϕ), in general, are higher for complexes of α-NaiPy than β-NaiPy (Table 2). The difference in photoluminescence intensity between the free ligands and the complexes is sometime interpreted in terms of free ligand impurity or free ligand produced as a result of photodissociation. This possibility is not ruled out [18d], but we have run ^{1}H NMR spectra of Pd(α-NaiPy)Cl_2 (**1**) and [Pd(α-NaiPy)(bpy)]$^{2+}$ (**8**) after irradiation for 5 min in $CDCl_3$ solution. The spectra of the non-radiated and irradiated complexes are identical in all respects. Besides, the luminescence intensity remains unchanged upon repetitive irradiation, which supports a fairly stable C=N bond.

Lifetime data of the complexes are taken in acetonitrile solution when excited at the specified wavelength (Table 2). The fluorescence decay curve was deconvoluted with respect to the lamp profile. The observed florescence decay fits nicely with a bi-exponential nature for the ligands and complexes (Fig. 12), which is supported by goodness-of-fit (χ^2) (Table 2) data in the regression analyses. Instead of placing emphasis on the magnitude of the individual decay constants in such bi-exponential decays, we have used the mean fluorescence lifetime ($\tau_f = a_1\tau_1 + a_2\tau_2$ where a_1 and a_2 are the relative amplitudes of decay processes). Radiative and non-radiative rate constants (k_r and k_{nr}) are calculated and the data show the usual higher k_{nr} than k_r value.

Table 5
^{1}H NMR spectra of the compounds in DMSO-d_6

Compound	δ ppm (J, Hz)												
	3(3′)-H[a]	4,5-(4′,5′)-H[b]	6(6′)-H[a]	7(7′)-H[c]	8(8′)-H[d]	(9′)-H[a]	10,11(10′,11′)-H[e]	12–14(12′, 14′)-H[e]	15(15′)-H[a]	a,a′-H[d]	b,b′-H[e]	c,c′-H[e]	d,d′-H[e]
α-NaiPy[f]	7.88 (8.0)	7.80 (8.0)	8.41 (8.0)	8.75		7.58 (8.4)	7.50	7.30–7.45	7.18 (7.2)				
β-NaiPy[f]	7.65 (8.0)	7.60 (8.0)	8.57 (8.0)	8.78	7.56		7.56	7.20–7.40	7.11 (9.0)				
(**1**)	8.14 (8.0)	8.23 (7.0)	8.90 (8.0)	8.67		8.00 (7.5)	7.80–7.85	7.35–7.45	7.27 (7.0)				
(**2**)	8.21 (8.0)	8.39 (7.0)	9.07 (7.0)	8.85	8.02		7.90–7.95	7.56–7.61	7.34 (7.0)				
(**3**)	8.02 (7.6)	8.11 (7.0)	8.74 (8.0)	8.55		7.92 (7.5)	7.65–7.80	7.30–7.45	7.20 (7.0)				
(**4**)	8.05 (7.5)	8.18 (7.0)	8.93 (7.0)	8.73	7.98		7.70–7.90	7.50–7.65	7.28 (7.0)				
(**5**)	8.05 (7.0)	8.18 (7.0)	8.94 (8.0)	8.74		7.95 (7.5)	7.80–7.85	7.30–7.40	7.34 (7.0)				
(**6**)	8.14 (7.0)	8.27 (7.0)	8.97 (8.0)	8.80	8.00		7.85–7.90	7.45–7.53	7.35 (7.0)				
(**7**)	8.34 (7.0)	8.20 (7.0)	8.63 (7.0)	8.64	8.05	7.94 (8.0)	7.75–7.80	7.40–7.50	7.30 (8.0)				
(**8**)	8.36 (7.6)	8.26 (7.0)	8.74 (7.0)	8.60		8.02 (8.0)	7.90–7.95	7.60–7.64	7.32 (7.5)	8.86	8.45	8.45	8.74
(**9**)	8.33 (7.6)	8.22 (7.0)	8.71 (7.0)	8.62		8.00 (7.5)	7.95–8.00	7.50–7.55	7.28 (7.0)	8.80	8.42	8.42	8.71
(**10**)	8.32 (8.0)	8.30 (7.0)	8.79 (7.6)	8.61		8.20 (8.0)	7.90–7.95	7.45–7.50	7.40 (7.0)	8.80	8.33	8.33	8.23
(**11**)	8.26 (8.0)	8.20 (7.0)	8.59 (7.0)	8.65	8.00		7.85–7.90	7.55–7.60	7.28 (7.0)	8.80	8.33	8.33	8.23
(**12**)[g,h]	8.40 (7.0)	8.28 (7.5)	8.74 (7.0)	8.61	7.38	8.00 (7.5)	7.70–7.75	7.45-7.50	7.38 (8.0)	7.14	6.97[d]	7.78[a] (8.0)	7.22[a] (7.0)
(**13**)[g,h]	8.32 (7.0)	8.12 (8.0)	8.71 (7.0)	8.60	7.38		7.75–7.80	7.50–7.55	7.22 (7.6)	7.05	6.90[d]	7.73[a] (7.0)	7.19[a] (7.0)

[a] Doublet.
[b] Triplet.
[c] Singlet.
[d] Broad.
[e] Multiplet.
[f] In DMSO-$d_6$solution.
[g] δ(N–Me): **12**, 4.25 and **13**, 4.25 ppm.
[h] δ(Ar–Me): **12**, 2.49 and **13**, 2.45 ppm.

3. Experimental

3.1. Materials

α-Naphthylamine and β-naphthylamine were purchased from Thomas Baker & Co,. Pyridine-2-carboxyaldehyde was purchased from Lancaster Ltd, England. $PdCl_2$ was purchased from Arrora Mathey, Kolkata, India. *N*-[(2-Pyridyl)methyliden]-α (and β)-aminonaphthalene (α and β-NaiPy) were synthesized by condensation of pyridine-2-carboxyaldehyde and the respective naphthylamine in ethanol [9]. All other chemicals used were of A.R. quality and were used as received from SRL, India. The solvents were used after drying [19].

UV–Vis spectra were recorded using a Lambda 25 Perkin–Elmer spectrophotometer and FT-IR spectra were obtained from Spectrum RX-1 Perkin–Elmer (KBr pellet, 4000–450 cm^{-1}) and JASCO model 420 (KBr pellet, 4000–200 cm^{-1}) spectrophotometers. Microanalyses were collected on a Perkin–Elmer 2400 CHN elemental analyser. ^1H NMR spectra were recorded on a Brucker 300 MHz FT-NMR. Solution electrical conductivity was measured by a Systronics 305 digital conductivity meter. Luminescence properties were measured using an LS-55 Perkin–Elmer fluorescence spectrophotometer at room temperature (298 K) in CH_3CN solution with a 1 cm path length quartz cell.

The fluorescence quantum yield of the Schiff bases (α/β-NaiPy) and their palladium(II) complexes (**1**–**13**) were determined using Coumarin-120 laser dye as a reference with a known ϕ_R (fluorescence quantum yield of reference) of 0.63 in MeCN. The complex and the reference dye were excited at 340 nm, maintaining nearly equal absorbance (~0.1), and the emission spectra were recorded from 350 to 600 nm. The area of the emission spectrum was integrated using the software available in the instrument and the quantum yields were calculated according to the following equation:

$$\phi_S/\phi_R = [A_S/A_R] \times [(Abs)_R/(Abs)_S] \times [\eta_S^2/\eta_R^2]$$

Here, ϕ_S and ϕ_R are the fluorescence quantum yields of the sample and the reference, respectively; A_S and A_R are the areas under the fluorescence spectra of the sample and the reference, respectively, $(Abs)_S$ and $(Abs)_R$ are the respective optical densities of the sample and the reference solution at the wavelength of excitation, and η_S and η_R are the values of refractive index for the respective solvents used for the sample and the reference. Fluorescence lifetimes were measured using a time-resolved spectrofluorometer from IBH, UK. The instrument uses a picosecond diode laser (NanoLed-07, 408 nm) as the excitation source and works on the principle of time-correlated single photon counting [20]. The instrument responses function is ~230 ps at FWHM. To eliminate depolarization effects on the fluorescence decays, measurements were done with magic angle geometry (54.7°) for the excitation and emission polarizers. The observed decays of α-NaiPy and β-NaiPy and their palladium(II) complexes fitted well with a bi-exponential function, as in Eq. (1), where the τ values are the fluorescence lifetimes and 'a' is the pre-exponential factor. For the fits, the reduced χ^2 values were within 0.9–1.3 and the distribution of the weighted residuals were random among the data channels. τ_f is the mean fluorescence lifetime (the meaning of the symbols are as usual [21]).

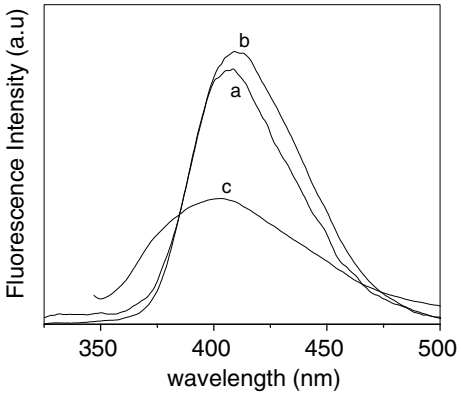


Fig. 11. Fluorescence spectra of (a) β-NaiPy, (b) $Pd(\beta\text{-NaiPy})Cl_2$, (c) $[Pd(\beta\text{-NaiPy})(Phen)](ClO_4)_2$ in CH_3CN solution at room temperature (298 K).

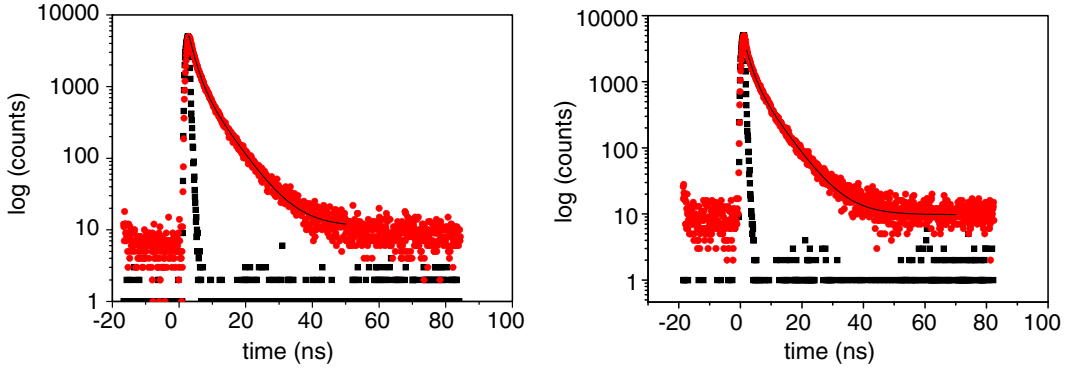


Fig. 12. Bi-exponential decay profile (•) and fitting curve (—) of (a) $[Pd(\alpha\text{-NaiPy})(bpy)](ClO_4)_2$ and (b) $[Pd(\alpha\text{-NaiPy})(\beta\text{-NaiPy})](ClO_4)_2$ in MeCN. Excitation is carried out at 370 nm.

$$I(t) = [a_1 \exp(-t/\tau_1) - a_2 \exp(-t/\tau_2)] \quad (1)$$

$$\tau_f = a_1\tau_1 + a_2\tau_2 \quad (2)$$

3.2. Preparation of the complexes

3.2.1. Synthesis of di-chloro-(N-[(2-pyridyl)methyliden]-α-aminonaphthalene)- palladium(II), Pd(α-NaiPy)Cl_2 (1)

$PdCl_2$ (0.18 g, 1.015 mmol) was taken in MeCN (15 ml) and refluxed until fully dissolved. *N*-[(2-Pyridyl)methyliden]-α-aminonaphthalene (α-NaiPy) (0.25 g, 1.08 mmol) in MeCN (10 ml) was added dropwise to above solution (10 ml) of $Pd(MeCN)_2Cl_2$ at room temperature and stirred for 2 h. The solution colour turned orange. The volume was reduced to half of its original volume by slow evaporation in air. Orange-red crystals then separated. These were filtered, washed with water and then water–MeCN (1:1, v/v). The product was then crystallized by diffusion of CH_2Cl_2 solution into hexane. The yield was 0.22 g (52%). *Anal.* Calc. for $C_{16}H_{12}N_2Cl_2Pd$ (**1**): C, 46.94; H, 2.93; N, 6.84. Found: C, 47.05; H, 2.86; N, 6.85%. [Pd(*N*-[(2-pyridyl)methyliden]-β-aminonaphthalene)$(Cl)_2$] was prepared similarly in 48% yield. *Anal.* Calc. for $C_{16}H_{12}N_2Cl_2Pd$ (**2**): C, 46.94; H, 2.93; N, 6.84. Found: C, 46.88; H, 2.85; N, 6.68%.

3.2.2. Synthesis of di-iodo-(N-[(2-pyridyl)methyliden]-α-aminonaphthalene)- palladium(II), Pd(α-NaiPy)I_2 (3)

To a THF solution (10 ml) of Pd(α-NaiPy)Cl_2 (0.1 g, 0.244 mmol) an aqueous solution of $AgNO_3$ (0.09 g, 0.53 mmol) was added with stirring. The orange brown mixture was heated to reflux for 30 min, then cooled and filtered through a G-4 Gooch funnel. To this filtrate KI (aq) solution (0.09 g, 0.54 mmol) was added and stirred for 3 h. The solution was then evaporated slowly in air. Orange-red crystals were deposited on the glass wall. They were filtered, water washed and their purity was checked by TLC. The crystals were pure and dried over P_4O_{10}. Yield, 0.07 g (48%). *Anal.* Calc. for $C_{16}H_{12}N_2I_2Pd$ (**3**): C, 32.41; H, 2.03; N, 4.73. Found: C, 32.35; H, 2.06; N, 4.85%. [Pd(*N*-[(2-pyridyl)methyliden]-β-aminonaphthalene)$(I)_2$] was prepared similarly in 44% yield. *Anal.* Calc. for $C_{16}H_{12}N_2I_2Pd$ (**4**): C, 32.41; H, 2.03; N, 4.73. Found: C, 32.48; H, 1.96; N, 4.68%.

3.2.3. Synthesis of mixed chelate palladium(II) complexes

The bis-chelated palladium(II) complexes are [Pd(α-NaiPy)$_2$]$(ClO_4)_2$ (**5**) or [Pd(β-NaiPy)$_2$]$(ClO_4)_2$ (**6**), [Pd(α-NaiPy)-(β-NaiPy)]$(ClO_4)_2$ (**7**), Pd(α-NaiPy)(bpy)]$(ClO_4)_2$ (**8**), [Pd-(α-NaiPy)(phen)]$(ClO_4)_2$ (**9**), [Pd(β-NaiPy)(bpy)]$(ClO_4)_2$-(**10**), [Pd(β-NaiPy)(phen)]$(ClO_4)_2$ (**11**), [Pd(α-NaiPy)-(Tai-Me)]$(ClO_4)_2$ (**12**) and [Pd(β-NaiPy)(Tai-Me)]$(ClO_4)_2$ (**13**).

They have been synthesized by following common procedure. Synthesis of [Pd(α-NaiPy)(bpy)]$(ClO_4)_2$ (**6**) is given in detail below.

To an acetonitrile solution (10 ml) of Pd(α-NaiPy)Cl_2 (0.1 g, 0.244 mmol) an aqueous solution of $AgNO_3$ (0.09 g, 0.53 mmol) was added with stirring. The orange brown mixture was heated to reflux for 30 min, then cooled and filtered through a G-4 Gooch. To this filtrate 2,2′-bipyridine (0.04 g, 0.26 mmol) was added and the resulting solution was stirred for 3 h. It was then filtered and aqueous $NaClO_4$ (1 g in 3 ml water) was added to it. The deep brown precipitate that fomed was filtered, washed with water and dried over P_4O_{10}. Yield, 0.1 g (59%). *Anal.* Calc. for [Pd(α-NaiPy)(bpy)]$(ClO_4)_2$ (**8**); *Anal* Calc. for $C_{26}H_{20}N_4O_8Cl_2Pd$: C, 45.02; H, 2.88; N, 8.08. Found: C, 45.15; H, 2.80; N, 7.95%.

Microanalytical data of the other complexes are as follows: [Pd(α-NaiPy)$_2$]$(ClO_4)_2$ (**5**), *Anal.* Calc. for $C_{32}H_{24}N_4O_8Cl_2Pd$: C, 49.93; H, 3.12; N, 7.28. Found: C, 50.02; H, 3.06; N, 7.35%. [Pd(β-NaiPy)$_2$]$(ClO_4)_2$ (**6**) *Anal.* Calc. for $C_{32}H_{24}N_4O_8Cl_2Pd$: C, 49.93; H, 3.12; N, 7.28. Found: C, 50.00; H, 3.00; N, 7.20%. [Pd(α-NaiPy)(β-NaiPy)]$(ClO_4)_2$ (**7**), *Anal.* Calc. for $C_{32}H_{24}N_4O_8Cl_2Pd$: C, 49.93; H, 3.12; N, 7.28. Found: C, 49.84; H, 2.96; N, 7.33%. [Pd(α-NaiPy)(phen)]$(ClO_4)_2$ (**9**) *Anal.* Calc. for $C_{28}H_{20}N_4O_8Cl_2Pd$: C, 46.86; H, 2.78; N, 7.81. Found: C, 46.95; H, 2.66; N, 7.70%. [Pd(β-NaiPy)(bpy)]$(ClO_4)_2$ (**10**), *Anal.* Calc. for $C_{26}H_{20}N_4O_8Cl_2Pd$: C, 45.02; H, 2.88; N, 8.08. Found: C, 45.10; H, 2.80; N, 8.00%. [Pd(β-NaiPy)-(phen)]$(ClO_4)_2$ (**11**) *Anal.* Calc. for $C_{28}H_{20}N_4O_8Cl_2Pd$: C, 46.86; H, 2.78; N, 7.81. Found: C, 46.90; H, 2.84; N, 7.74%. [Pd(α-NaiPy)(Tai-Me)]$(ClO_4)_2$ (**12**), *Anal.* Calc. for $C_{27}H_{24}N_6O_8Cl_2Pd$: C, 43.96; H, 3.25; N, 11.39. Found: C, 43.87; H, 3.36; N, 11.20% and [Pd(β-NaiPy)(Tai-Me)]-$(ClO_4)_2$ (**13**) *Anal.* Calc. for $C_{27}H_{24}N_6O_8Cl_2Pd$: C, 43.96; H, 3.25; N, 11.39. Found: C, 43.82; H, 3.30; N, 11.47%.

3.3. Crystallographic data collection and refinement of [Pd(β-NaiPy)Cl_2] (2)

Crystals were grown by slow diffusion of a CH_2Cl_2 solution of Pd(β-NaiPy)Cl_2 into hexane. Crystal parameters and refined data are summarized in Table 6. The crystal dimensiona are $0.34 \times 0.16 \times 0.13$ mm^3 and data were collected using a fine focus sealed tube at 173(2) K using graphite monochromated Cu-Kα radiation, ($\lambda = 1.54184$ Å). Unit cell parameters were determined from least-squares refinement of setting angles with θ in the range $3.40 \leqslant \theta \leqslant 73.28°$. Of 27224 collected data 2964 with $I > 2\sigma(I)$ were used for the structure solution. The hkl ranges are $-12 \leqslant h \leqslant 12$, $-14 \leqslant k \leqslant 14$, $-32 \leqslant l \leqslant 32$. Reflection data were recorded using the ω scan technique. Data were corrected for Lorentz polarization effects and for linear decay. Semi-empirical absorption corrections based on ψ-scans were applied. Data were computed by MacScience Xpress. Data reduction was carried out by Denzo and Scalepack. The structure was solved by a direct method using SHELXS-97 [22] and successive difference Fourier syntheses. A slightly elevated R value (0.0747) may due to inclusion of poor quality diffraction data which may arise from the X-rays generated from the Cu-Kα radiation source. All non-hydrogen atoms were refined anisotropi-

Table 6
Summarised crystallographic data for Pd(β-NaiPy)Cl_2 (**2**)

	Pd(β-NaiPy)Cl_2 (**2**)
Empirical formula	$C_{16}H_{12}Cl_2N_2Pd$
Formula weight	409.58
Temperature (K)	173(2)
Crystal system	orthorhombic
Space group	*Pbca*
Crystal size $(mm)^3$	$0.34 \times 0.16 \times 0.13$
Unit cell dimensions	
a (Å)	9.7570(2)
b (Å)	11.8910(3)
c (Å)	26.0180(6)
V $(Å)^3$	3018.62(12)
Z	8
λ (Å)	1.54184
μ (Mo-Kα) (mm^{-1})	13.111
D_{calc} $(g\ cm^{-3})$	1.802
Refine parameters	190
Reflection collected	27224
Unique data $[I > 2\sigma(I)]$	2964
R_1^a $[I > 2\sigma\ (I)]$	0.0747
wR_2^b	0.2069
Goodness of fit	1.126

[a] $R_1 = \Sigma|F_o - F_c|/\Sigma F_0$.
[b] $wR_2 = [\Sigma w(F_o^2 - F_c^2)/\Sigma wF_o^4]^{1/2}, w = 1/[\sigma^2(F^2) + (0.1461P)^2 + 9.1603P]$.

cally. The hydrogen atoms were fixed geometrically and refined using the riding model. In the final difference Fourier map the residual minima and maxima, −0.237 and 0.418 e/Å^3, were evaluated using SHELXL-97 [23]. Figures were drawn by using the molecular graphics maXus.

3.4. Computational details

All computations were performed using the GAUSSIAN03 (G03) [24] software package running under Windows. The Becke's three-parameter hybrid exchange functional and the Lee-Yang-Parr non-local correlation functional [25] (B3LYP) was used throughout. A lanL2DZ basis set [26] for Pd, 6-31G(d) for C, N, Cl, H atoms and 6-311G* for the I atom were used for all types of calculations. For Pd, N, C, Cl and H atoms we used the basis sets contained in the G03 library, while the 6-311G* basis set for I was downloaded from the EMSL basis set library [27]. Gas and solution-phase geometry optimization was carried out from the geometry obtained from the crystal structure without any symmetry constraints. In all cases, vibrational frequencies were calculated to ensure that optimised geometries represented local minima. The excitation energies were calculated by the TDDFT approach using the same basis sets used in the geometry optimization. To check the effect of salvation on the calculated optical absorption spectra, we performed TDDFT calculations of the low lying excitation at the singlet optimized geometry, including solvation effects by means of the non-equilibrium implementation of the polarizable continuum model (PCM) [28]; as in the experimental conditions, the chosen solvent was acetonitrile.

Acknowledgements

Financial support from All India Council of Technical Education (AICTE), New Delhi is gratefully acknowledged. We thank Dr. A. Mallick, Physical Chemistry Section, Department of Chemistry, Jadavpur University for lifetime measurements. Our sincere thanks are due to Mr. Atish Dipankar Jana, Department of Physics, Jadavpur University for their kind help in the X-ray crystallographic structure drawing.

Appendix A. Supplementary material

CCDC 622525 contains the supplementary crystallographic data for [Pd(β-NaiPy)Cl_2]. These data can be obtained free of charge via http://www.ccdc.cam.ac.uk/conts/retrieving.html, or from the Cambridge Crystallographic Data Centre, 12 Union Road, Cambridge CB2 1EZ, UK; fax: (+44) 1223 336 033; or e-mail: deposit@ccdc.cam.ac.uk. Supplementary data associated with this article can be found, in the online version, at doi:10.1016/j.poly.2007.05.049.

References

[1] K. Kalyansundaram, Coord. Chem. Rev. 46 (1982) 159.
[2] (a) R.-Q. Fan, D.-S. Zhu, Y. Mu, G.-H. Li, Y.-L. Yang, Q. Su, S.-H. Feng, Eur. J. Inorg. Chem. (2004) 4891;
(b) Y.L. Pui, K.K. Cheung, J. Chem. Soc., Dalton Trans. (2000) 3658.
[3] (a) Y. Wang, X.-M. Ouyang, Y.-Z. Li, W.-Y. Sun, Bull. Chem. Soc. Jpn. 76 (2003) 1403;
(b) D. Pursche, M.U. Triller, N. Reddig, A. Rompel, Z. Annorg. Allg. Chem. 629 (2003) 24.
[4] H.-F. Zhu, L. Li, T. Okamura, W. Zhao, W.-Y. Sun, N. Ueyama, Bull. Chem. Soc. Jpn. 76 (2003) 761.
[5] (a) P. Govindaswamy, Y.A. Mozharivskyj, M.R. Kollipara, Poly hedron 24 (2005) 1710;
(b) K.S. Singh, P.J. Carroll, M.R. Kollipara, Polyhedron 24 (2005) 391;
(c) T. Ederer, R.S. Herrick, W. Beck, Z. Anorg. Allg.Chem. 633 (2007) 235.
[6] (a) M. Menon, A. Pramanik, N. Bag, A. Chakravorty, Inorg. Chem. 33 (1994) 403;
(b) M. Menon, A. Pramanik, A. Chakravorty, Inorg. Chem. 34 (1995) 3310;
(c) B.K. Dirghangi, M. Menon, S. Banerjee, A. Chakravorty, Inorg. Chem. 36 (1997) 3595;
(d) D.L. Davies, J. Fawcett, R. Krafczyk, D.R. Punel, J. Organomet. Chem. 545–546 (1997) 581.
[7] (a) S. Chowdhury, A.K. Deb, S. Goswami, Polyhedron 13 (1994) 1063;
(b) A. Majumder, G.M. Rosair, A. Mallick, N. Chattopadhyay, S. Mitra, Polyhedron 25 (2006) 1753;
(c) Z.-F. Chen, Y.-Z. Tang, H. Liang, H.-K. Fun, K.-B. Yu, J. Coord. Chem. 59 (2006) 207;
G. Rajendran, G.S. Sreeletha, Asian J. Chem. 14 (2002) 1639;
(d) J.R. Nitschke, M. Hutin, G. Bernardinelli, Angew. Chem., Int. Ed. 43 (2004) 6724;
(e) D.M. Haddleton, M.C. Crossman, B.H. Dana, D.J. Dunealt, A.M. Heming, D. Kukulj, A.J. Shooter, Macromolecules 32 (1999) 2110;
(f) S.K. Dey, B. Bag, K.M. Abdul Malik, M. Salah El Fallah, J. Ribas, S. Mitra, Inorg. Chem. 42 (2003) 4029.

[8] (a) M. Sinha Ray, R. Bhattacharya, S. Chaudhuri, L. Righi, G. Bocelli, G. Mukhopadhyay, A. Ghosh, Polyhedron 22 (2003) 617;
(b) S. Chattopadhyay, M. Sinha Ray, S. Chaudhuri, G. Mukhopadhyay, G. Bocelli, A. Cantoni, A. Ghosh, Inorg. Chim Acta 359 (2006) 1367;
(c) T.K. Karmakar, B.K. Ghosh, S.K. Chandra, Indian J. Chem. 45A (2006) 1121.
[9] J.P.G. Britovsek, S. Mastroianni, G.A. Solan, S.P.D. Baugh, C. Redshaw, V.C. Gibson, A.J.P. White, D.J. Williams, M.R.J. Elsegood, Chem. Eur. J. 6 (2000) 2221.
[10] J. Dinda, C. Sinha, Transition Met. Chem. 28 (2003) 864.
[11] J. Zhang, W. Li, W. Bu, L. Wu, L. Ye, G. Yang, Inorg. Chim Acta 358 (2005) 964.
[12] (a) L.G. Nickolacheva, C.M. Vogels, R.A. Stefan, H.A. Warwish, S.J. Duffy, R.J. Ireland, A. Decken, R.H. Hudson, S.A. Westcott, Can. J. Chem. 81 (2003) 269;
(b) S.G. Telfer, T. Sato, R. Kuroda, J. Lefebvre, D.B. Leznoff, Inorg. Chem. 43 (2004) 421.
[13] J. Dinda, P.K. Santra, C. Sinha, L.R. Falvello, J. Organomet. Chem. 629 (2001) 28.
[14] (a) C.K. Pal, S. Chattopadhyay, C. Sinha, D. Bandyopadhyay, A. Chakravorty, Polyhedron 13 (1994) 999;
(b) D. Das, M.K. Nayak, C. Sinha, Trans. Met. Chem. 22 (1997) 172.
[15] (a) D.N. Neogi, P. Das, A.N. Biswas, P. Bandyopadhyay, Polyhedron 25 (2006) 2149;
(b) Z. Zhu, M. Kojima, K. Nakajima, Inorg. Chim. Acta 358 (2005) 476.
[16] (a) S. Pal, D. Das, P. Chattopadhyay, C. Sinha, K. Panneerselvam, T.-H. Lu, Polyhedron 19 (2000) 1263;
(b) J. Dinda, P.K. Santra, C. Sinha, L.R. Falvello, J. Organomet. Chem. 629 (2001) 28.
[17] C. Sinha, Ph. D. Thesis, Jadavpur University, Jadavpur, Kolkata, India, 1991.
[18] (a) H.F. Zhu, L. Li, T. Okamura, W. Zhao, W.Y. Skn, N. Ueyama, Bull. Chem. Soc. Jpn. 76 (2003) 761;
(b) X.H. Be, H. Liu, M. Du, K.M.C. Wong, V.W.W.W. Yam, Inorg. Chim. Acta 333 (2002) 32;
(c) K.Y. Yu, K.K. Cheung, C.M. Che, J. Chem. Soc., Dalton Trans. (1999) 1581;
(d) T. Tsubomura, K. Yasaku, T. Sato, M. Morita, Inorg. Chem. 31 (1992) 447.
[19] A.I. Vogel, A Text Book of Practical Organic Chemistry, second ed., Longman, London, 1959.
[20] D.V. O'Connor, D. Phillips, Time Correlated Single Photon Counting, Academic Press, New York, 1984.
[21] B. Valuer, Molecular Fluorescence: Principles and Applications, Wiley-VCH, Weinheim, 2001.
[22] G.M. Sheldrick, SHELXS 97, Program for the Solution of Crystal Structure, University of Gottingen, Germany, 1990.
[23] G.M. Sheldrick, SHELXL 97, Program for the Refinement of Crystal Structure, University of Gottingen, Germany, 1997.
[24] M.J. Frisch, G.W. Trucks, H.B. Schlegel, P.M.W. Gill, B.G. Johnson, M.A. Robb, J.R. Cheeseman, T.A. Keith, G.A. Petersson, J.A. Montgomery, K. Raghavachari, M.A. Al-Laham, V.G. Zakrzewski, J.V. Ortiz, J.B. Foresman, J. Cioslowski, B.B. Stefanov, A. Nanayakkara, M. Challacombe, C.Y. Peng, P.Y. Ayala, W. Chen, M.W. Wong, J.L. Andres, E.S. Replogle, R. Gomperts, R.L. Martin, D.J. Fox, J.S. Binkley, D.J. Defrees, J. Baker, J.P. Stewart, M. Head-Gordon, C. Gonzalez, J.A. Pople, GAUSSIAN 98; Gaussian, Inc., Pittsburgh, PA, 1998.
[25] C. Lee, W. Yang, R.G. Parr, Phys. Rev. B 37 (1988) 785.
[26] P.J. Hay, W.R. Wadt, J. Chem. Phys. 82 (1985) 270.
[27] EMSL, basis set library. http:/www.emsl.pnl.gov/forms/basisform.html.
[28] M. Cossi, V.J. Barone, Chem. Phys. 115 (2001) 4708.

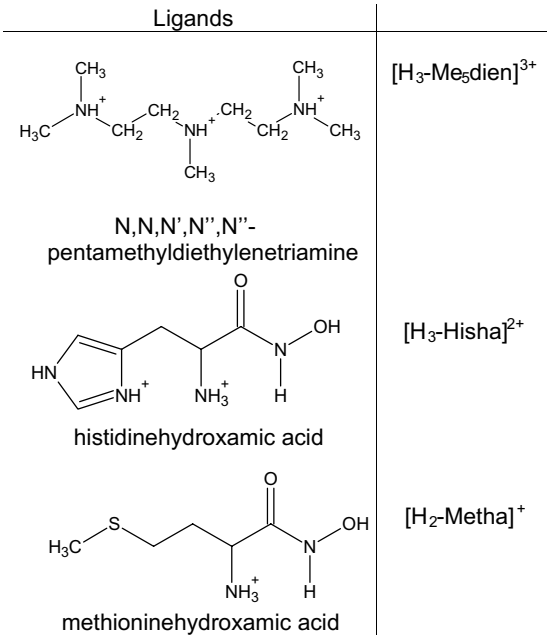
systems containing Me_5dien and aminohydroxamic acid (Metha or Hisha) using pH-metric, UV–Vis and EPR methods. The ternary system containing α-Alaha was reinvestigated as the reference which is expected to form similar chelate rings to those with participation of Metha or Hisha; the measurements were made at the same experimental conditions and the data were analyzed analogously.

2. Experimental

2.1. Materials

L-Histidinehydroxamic acid and DL-methioninehydroxamic acid were purchased from Sigma–Aldrich Chemical Co, *N*,*N*,*N*′,*N*″,*N*″-pentamethyldiethylenetriamine from Fluka, L-α-alaninehydroxamic acid was prepared via the methyl ester of α-alanine as described in Ref. [7]. All the chemicals with highest purity (greater than 99%) were used without further purification.

The exact concentrations of the ligand solutions used for potentiometric measurements were determined by the Gran method [8]. Copper(II) chloride solution was purchased from Merck as a Titrisol concentrate for the preparation of standard solutions. The concentration of metal ion stock solution was standardized by complexometric ethylenediaminetetraacetate (EDTA) titration. Carbonate-free KOH solution (the titrant) was prepared and standardized against a standard potassium hydrogen phthalate solution. All solutions were prepared with triply deionized water. The formulae of the fully protonated form of the ligands used in this study are shown in Scheme 1.



Scheme 1.

2.2. Potentiometric measurements

The stability constants of the proton and copper(II) complexes were determined by pH-metric titration of 5 cm^3 samples in aqueous solutions. All the measurements were carried out at 0.2 mol dm^{-3} ionic strength (KCl) and 25.0 ± 0.1 °C using a constant-temperature water-bath. The titrations were performed with carbonate-free KOH solution of known concentration (ca. 0.2 mol dm^{-3}) under argon atmosphere over the pH range 2.0 to ≈11.0. The data for the Cu^{2+}–Me_5dien [4,5,9] and Cu^{2+}-α-Alaha/Metha/Hisha [2,3] binary systems were reported previously but for a comparison we had to determine stability constants under identical conditions to these of ternary systems. For the binary systems the ligand concentration was 4×10^{-3} or 8×10^{-3} mol dm^{-3}. The metal ion to ligand ratios were 1:1, 1:2 or 1:4. The obtained results for Cu^{2+}–Me_5dien and Cu^{2+}–Hisha binary systems are in good agreement with earlier findings and the stability constants obtained for the complexes formed in this system are almost the same. For the Cu^{2+}–α-Alaha/Metha binary systems the only difference is observed, i.e. both dinuclear and pentanuclear species coexist in the equilibrium in the acid region of the solution in place of only the dinuclear one. Our assumption relating to the bonding modes in complexes formed in the binary systems is the same as that published previously.

For the ternary systems the ratios of copper(II):Me_5dien:α-Alaha/Metha/Hisha were 1:1:1, 1:1:2, 1:2:1 and 1:2:2. Titrations were made on samples containing the copper(II) ion at 4×10^{-3} mol dm^{-3}. The values of stability constants of the complexes formed in the binary systems were kept constant during calculating the potentiometric data of the ternary systems.

The pH-metric titrations were performed with a Radelkis Op-208/1 instrument equipped with a combination pH electrode (SINGLE PORE, Hamilton) using an ABU-80 autoburette (Radiometer). The electrode system was calibrated by periodic titrations of HCl solution (1×10^{-2} mol dm^{-3} in KCl) against standard KOH solution. The resulting titration data were used to calculate the standard electrode potentials, $E°$, and the dissociation constant for water ($pK_w = 13.73$). These values were then used to calculate the hydrogen ion concentration $[H^+]$ from emf readings [10]. The pH-metric results were used to establish the stoichiometry of the species and to calculate the stability constants of the species formed $\beta_{prs} = [M_pL_rH_s]/[M]^p[L]^r[H]^s$ and $\beta_{pqrs} = [M_p(Me_5dien)_qL_rH_s]/[M]^p[Me_5dien]^q[L]^r[H]^s$ in the binary and ternary systems, respectively. Calculations were performed with the aid of the HYPERQUAD 2006 computer program [11]. The reported standard deviations were calculated by assuming random errors.

The charges of the complexes have been omitted in the text and tables. However, for clarity, it should be mentioned here that the fully deprotonated form of aminohydroxamic acids (Metha and Hisha) is L^- while the amine (Me_5dien) is neutral.

2.3. UV/Vis spectroscopy

The electronic absorption spectra in the visible range were obtained on a BECKMAN DU68 spectrophotometer using 1-cm quartz cells at room temperature. The spectra were recorded digitally (0.5 nm step) over the range 400–900 nm. The metal ion concentration was 4×10^{-3} mol dm^{-3}. The metal ion to ligand ratios was 1:2 for the binary systems. For the ternary systems copper(II):Me_5dien: Metha/Hisha the concentration ratios were 1:2:1.

Even at the pH value where the distribution of the species has a maximum, the other complexes coexist in a greater or a smaller extent. To extract the net ligand-field absorption band of each mixed-ligand species and calculate their molar absorptivity the procedure as described in Ref. [2] was applied.

2.4. EPR spectroscopy

The measurements of electron paramagnetic resonance (EPR) spectra were performed on a Bruker 300E X-band spectrophotometer equipped with a Bruker NMR gaussmeter ER 035M and a Hewlett–Packard frequency counter HP 5350B at 77 K in water/ethyleneglycol (4:1 v/v) solution. The EPR parameters were calculated by computer simulation of the experimental spectra using Bruker's WIN-EPR SimFonia Software Version 1.25. The metal ion concentration was 4×10^{-3} mol dm^{-3} and the metal ion to ligands molar ratios were the same as those used in the absorption spectra.

3. Results and discussion

The values of the protonation constants for Metha, Hisha and Me_5dien together with the detailed discussion about the acid–base properties of these ligands can be found in our early papers [3,4]. In the wide pH range of 2–11, the fully protonated form of Me_5dien (H_3L^{3+}) is able to release three protons, Metha (H_2L^{+}) – two protons and Hisha (H_3L^{2+}) – three (the third proton from the imidazole nitrogen).

The equilibrium models for ternary systems and relevant stability constants resulting in the best fits of the pH-metric titration curves are presented in Table 1.

The four-component equilibria can be described as:

$$pM + q(Me_5dien) + r(L) + sH \rightleftharpoons M_p(Me_5dien)_q(L)_rH_s$$

where p, q, r and s are the stoichiometric coefficients corresponding to the metal ion M, Me_5dien, L (L = α-Alaha, Metha or Hisha), and H, respectively; charges are omitted.

The overall formation constants are defined as:

$$\beta_{pqrs} = [M_p(Me_5dien)_q(L)_rH_s]/[M]^p[(Me_5dien)]^q[(L)]^r[H]^s$$

The β_{1111}, β_{1110} and $\beta_{212\bar{1}}$ constants express the stability of the $[Cu(Me_5dien)(HL)]^{2+}$, $[Cu(Me_5dien)(L)]^{+}$ and $[Cu_2(Me_5dien)L_2H_{-1}]^{+}$ mixed-ligand species, respectively. Although the β_{1110} constant express the stability of the $[Cu(Me_5dien)(L)]^{+}$ mixed-ligand species, it does not represent directly the binding strength between L and copper(II) ions in the presence of Me_5dien. This effect is much better reflected by the equilibrium constant, $K_{[Cu(Me_5dien)L]^+}$

Table 1
Cumulative formation constants ($\log\beta$) and derived equilibrium constants ($\log K$) for the complexes formed in the ternary systems Cu^{2+}–*N*,*N*′,*N*″,*N*‴-pentamethyldiethylenetriamine (Me_5dien)–L (L = aminohydroxamic acids: α-Alaha, Metha or Hisha) at 25 °C and $I = 0.2$ mol dm^{-3} (KCl)

Nr	Assignments	System		
		Cu^{2+}–Me_5dien–α-Alaha	Cu^{2+}–Me_5dien–Metha	Cu^{2+}–Me_5dien–Hisha
1.	$\log\beta[Cu(H_2L)]$			20.30(14)
2.	$\log\beta[Cu(HL)]$			17.28(6)
3.	$\log\beta[CuL]$	10.96(4)	10.41(3)	
4.	$\log\beta[Cu_2L_2H]$			33.95(6)
5.	$\log\beta[Cu_2L_2]$			29.53(2)
6.	$\log\beta[Cu_2L_2H_{-1}]$	20.92(6)	20.05(5)	23.86(3)
7.	$\log\beta[Cu_5L_4H_{-4}]$	40.01(16)	38.78(10)	
8.	$\log\beta[Cu(HL)_2]$			33.52(2)
9.	$\log\beta[Cu(HL)L]$			27.33(3)
10.	$\log\beta[CuL_2]$	20.04(3)	19.36(2)	20.16(3)
11.	$\log\beta[CuL_2H_{-1}]$	10.34(4)	9.85(3)	10.35(5)
12.	$\log\beta[Cu(Me_5dien)(HL)]$			27.23(2)
13.	$\log\beta[Cu(Me_5dien)L]$	18.86(4)	18.42 (5)	18.86(9)
14.	$\log\beta[Cu_2(Me_5dien)L_2H_{-1}]$	29.78(1)	29.17 (1)	30.24(3)
15.	$pK[Cu(Me_5dien)(HL)]$			8.37
16.	$\log K[Cu(Me_5dien)L]$[a]	6.39	5.95	6.39
17.	$\log K[Cu(Me_5dien)L] - \log\beta[H_2L]$	−10.15	−9.80	−9.78
18.	$\Delta\log K$	−4.57	−4.46	
	χ^2	12.5	6.06	3.90
	σ	5.55	11.19	11.65

Charges are omitted for simplicity.

[a] $\log K_{[Cu(Me_5dien)L]} = \log\beta_{[Cu(Me_5dien)L]} - \log\beta_{[Cu(Me_5dien)]}$; $\log\beta_{[Cu(Me_5dien)]} = 12.47$, $\log\beta_{[Cu(Me_5dien)H-1]} = 3.49$ [4].

calculated according to the equation: $\log K_{[Cu(Me_5dien)L]} = \log \beta_{[Cu(Me_5dien)L]} - \log \beta_{[Cu(Me_5dien)]}$. It shows how tightly L (aminohydroxamic anion) is bound to the simple $[Cu(Me_5dien)]^{2+}$ complex.

The difference in stability between the binary and ternary complexes, $\Delta\log K$ (the constant due to the equilibrium $[MA] + [MB] = [MAB] + M$), is a way to characterize the tendency toward formation of mixed-ligand complexes. The constant for this equilibrium can be calculated from the experimentally measured stability constants according to the equation: $\Delta\log K = \log \beta_{[MAB]} - (\log \beta_{[MA]} + \log \beta_{[MB]})$. The statistical value of $\Delta\log K$ is affected by the geometry of the complex; for the distorted octahedral coordination sphere of Cu^{2+} with two different bidentate ligands was deduced as -0.9 [12,13]. It can be seen that, the $\Delta\log K$ value for the $[Cu(Me_5dien)\alpha\text{-Alaha}]^+$ and $[Cu(Me_5dien)Metha]^+$ species are low (-4.57 and -4.46, respectively). This effect of the mixed-ligand complex is due to the lower (than six) coordination number of Cu^{2+}. For the $[Cu(Me_5dien)Hisha]^+$ mixed-ligand species the $\Delta\log K$ value cannot be calculated, since the complex with 1:1 ratio is not formed in the Cu^{2+}-Hisha binary system (Table 1).

It is noteworthy that the Cu^{2+} mixed-ligand species of diethylenetriamine (dien) with α-Alaha, Metha or Hisha show lower $\log K_{[Cu(dien)L]+}$ values and $\Delta\log K$ parameter, compared with the corresponding systems with Me_5dien.

The formation constants which gave the best fit of the potentiometric data for the Cu^{2+}–Me_5dien–Metha ternary system are collected in Table 1 and the concentration distribution curves for this system are presented in Fig. 1a. It can be seen that when respective molar ratio is 1:2:1, the formation of mixed-ligand species is preceded by the appearance of simple species with Me_5dien and Metha: $[Cu(Me_5dien)]^{2+}$ and $[Cu(Metha)]^+$. The presence of Me_5-dien in the solution does not suppress the formation of the polynuclear species with Metha $[Cu_2(Metha)_2H_{-1}]^+$ and $[Cu_5(Metha)_5H_{-4}]^+$complexes in the pH range 3.5–6. The equilibrium model involves two mixed-ligand species $[Cu_2(Me_5dien)(Metha)_2H_{-1}]^+$ and the minor one – $[Cu(Me_5dien)(Metha)]^+$. Although the concentration of the mononuclear mixed-ligand species is low (~9–10% in the pH range 8.5–9.5 under these experimental conditions), the assumption of this species improves the fit between the experimental and the calculated titration data and furthermore its presence is observed in the EPR spectra (see below). The formation of $[Cu_2(Me_5dien)(Metha)_2H_{-1}]^+$ starts at pH ca. 5 and it is predominant in the solution in the wide pH range 6–11 (the concentration ca. 90%). The complexes $[Cu(Me_5dien)H_{-1}]^+$ and $[Cu(Metha)_2H_{-1}]^-$ exist above pH 10 as a minor products (ca. 5%), so their contribution is negligible (Fig. 1a). The same equilibrium model was obtained for the Cu^{2+}–Me_5-dien–α-Alaha ternary system (Table 1) but the concentration of the mononuclear mixed-ligand species is little higher (~12% in the pH range 8.5–9.5 under the same experimental conditions).

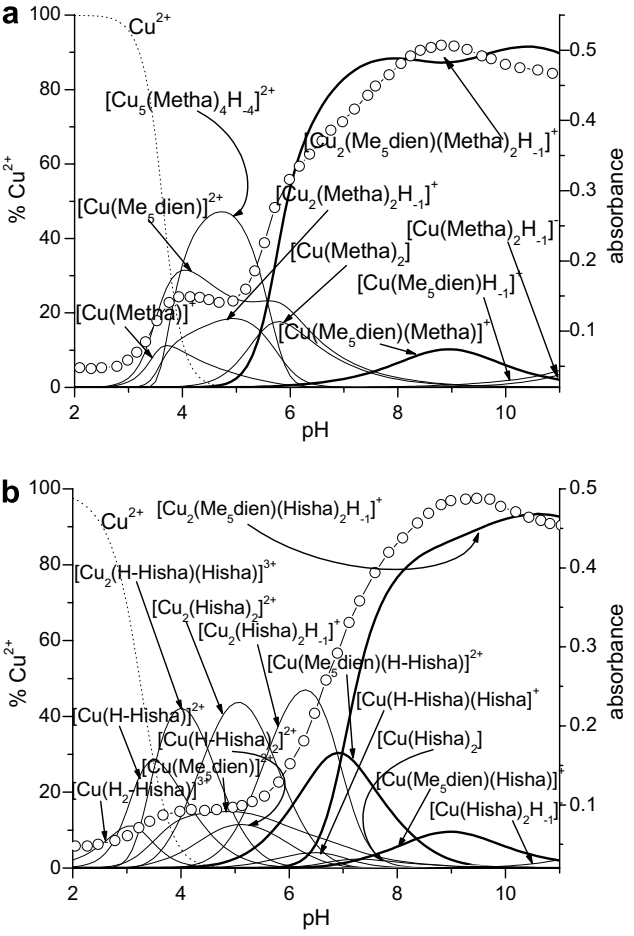


Fig. 1. Species distribution curves as a function of pH and variations of visible absorption $\lambda = 850$ nm (-o-o-) for the Cu^{2+}–Me_5dien–Metha system (a) and Cu^{2+}–Me_5dien–Hisha system (b) at 1:2:1 molar ratio; $c_{Cu^{2+}} = 4 \times 10^{-3}$ mol dm^{-3}.

In order to confirm the calculated equilibrium model and to get information about the geometry of the species formed in the Cu^{2+}–Me_5dien–Metha ternary system the measurements of the EPR spectra were performed and correlated with the species distribution curves. The analysis of the EPR spectra reveals that up to pH 5 the spectra for the Cu^{2+}–Me_5dien–Metha (1:2:1) system are the same as for Cu^{2+} complex with Me_5dien and H_2O molecules (Fig. 2). At pH between 4 and 5, the EPR parameters, $g_z = 2.240$, $g_x = 2.065$, $g_y = 2.050$ and $A_z = 183$, $A_x = 29$, $A_y = 14 \times 10^{-4}$ cm^{-1}, reflect slightly distorted geometry of $[Cu(Me_5$-$dien)]^{2+}$ complex as a result of *N*-methyl groups bulky effect. Above pH 6 the intensity of the spectral lines rapidly decreases. Because total concentration of Cu(II) ions in the solution remains unchanged this effect is most likely associated with their aggregation and with at least a weak Cu(II)–Cu(II) exchange interactions what supports the formation of $[Cu_2(Me_5dien)(Metha)_2H_{-1}]^+$ predicted by potentiometric studies. A disappearance of the EPR signals due to majority of Cu(II) species involved in the polynuclear species allows to observe the spectrum corresponding to the mononuclear $[Cu(Me_5dien)(Metha)]^+$ species which

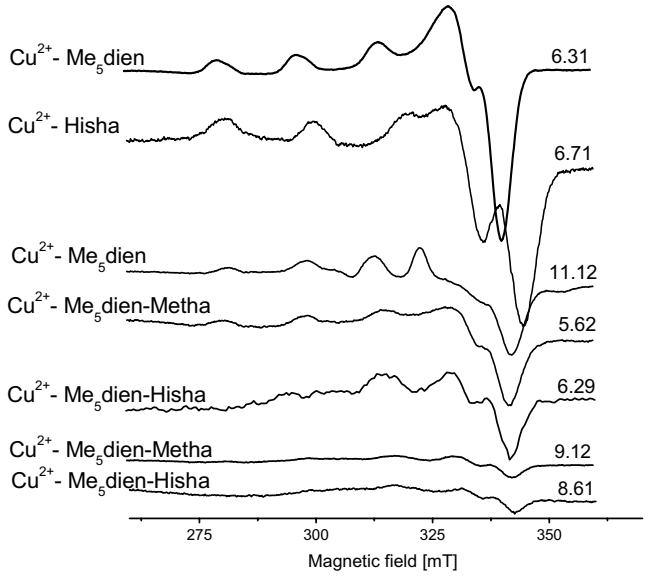


Fig. 2. EPR spectra of Cu^{2+} complexes formed in the Cu^{2+}–Me_5dien–Metha and Cu^{2+}–Me_5dien–Hisha ternary systems as a function of pH. For a comparison, the spectra for Cu^{2+}–Me_5dien and Cu^{2+}–Hisha binary systems are added.

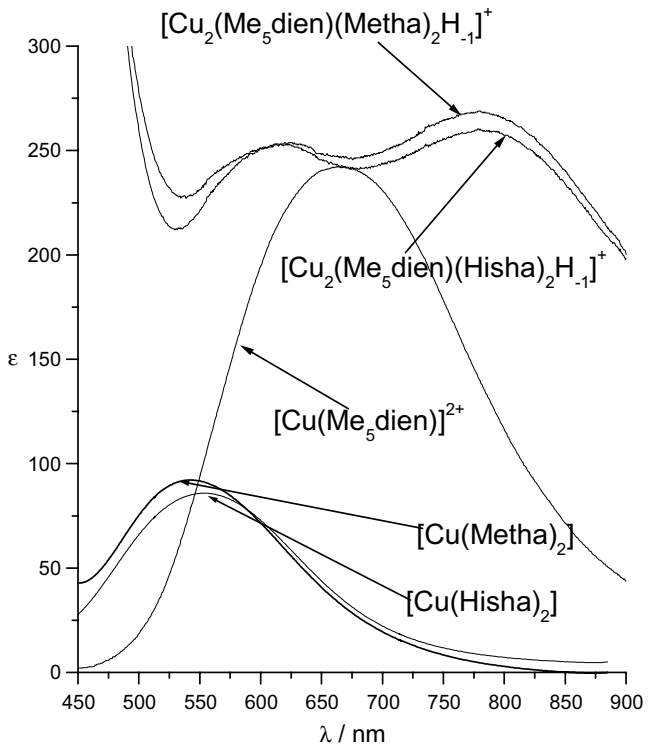
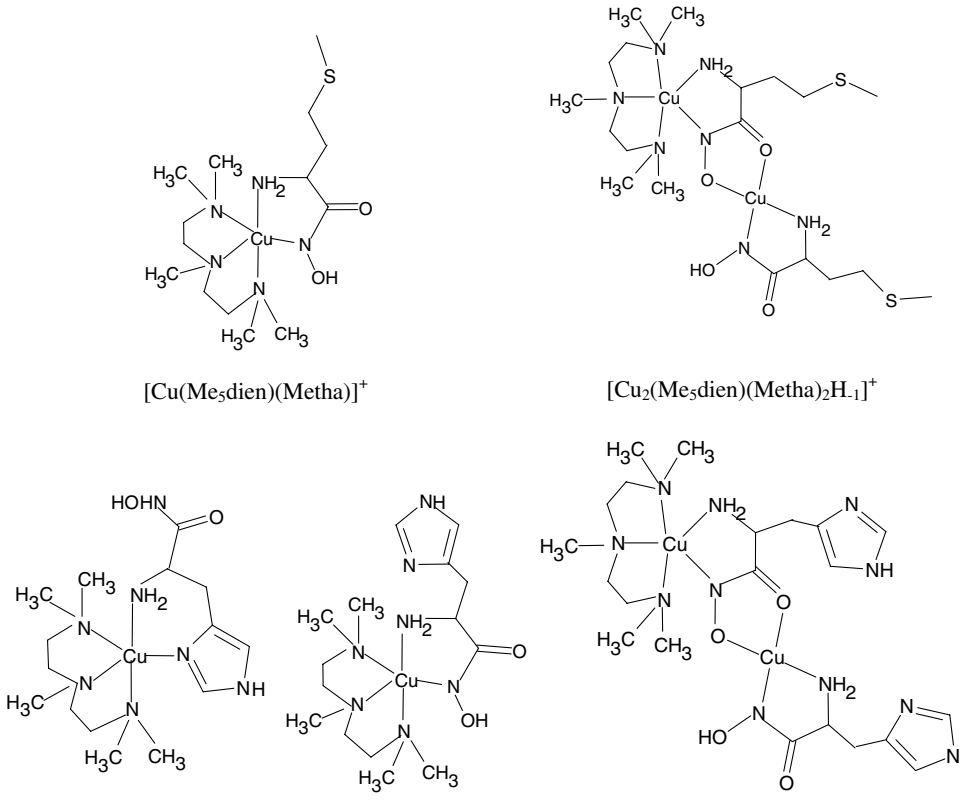


Fig. 3. Distribution-corrected absorption spectra for the $[Cu(Me_5dien)]^{2+}$, $[Cu(Metha)_2]$, $[Cu(Hisha)_2]$, $[Cu_2(Me_5dien)(Metha)_2H_{-1}]^{+}$ and $[Cu_2(Me_5dien)(Hisha)_2H_{-1}]^{+}$ species.

concentration ~10 % is anticipated by potentiometric studies in the pH range 8.5–9.5. The spectral parameters: $g_z \sim 2.23$, $g_x \sim 2.1$, $g_y \sim 2.03$ and $A_z \sim 176$, $A_x \sim 87$, $A_y \sim 17 \times 10^{-4}$ cm^{-1}, suggests that $[Cu(Me_5dien)(Metha)]^{+}$ displays a significant degree of distortion from square-pyramid to trigonal bipyramid [4,5] similarly to that observed for $[Cu(Me_5dien)(\alpha\text{-Alaha})]^{+}$ and close to that for $[Cu(Me_5dien)H_{-1}$ [4]. The spectrum with rhombic parameters is typical for the complex geometry being intermediate between square-pyramidal and trigonal-bipyramidal [4,9,14]. The coordination in the Cu^{2+} plane in this mixed-ligand complex may be realized by three nitrogen atoms of Me_5dien and N_{amino} and $N_{hydroxamate}$ donor atoms of α-Alaha or Metha. Above pH 10 a further decrease of the intensity of the EPR signals is observed and at pH 11.5 only very broad and weak line is seen supporting that the dinuclear species predominates in the solution.

The effect of the mixed-ligand species formation is observed distinctly in the electronic spectral changes (Fig. 4d). The absorption spectra exhibit the intense charge-transfer transition band in the near-UV region (at about 357 nm), which is not observed in the spectra of the $[Cu(Me_5dien)]^{2+}$ and $[Cu(Metha)_2]$ species formed at the analogous pH range of the binary systems (Fig. 3). This CT band can be reasonably assigned to the transition from hydroxamic oxygen to copper(II) (the N^{-}–$O^{-}_{(oxygen)} \rightarrow Cu^{2+}$ CT band is expected at wavelengths ca. 350 nm [15–17]). The presence of N^{-}–$O^{-}_{(oxygen)} \rightarrow Cu^{2+}$ CT band confirms the formation of dinuclear $[Cu_2(Me_5dien)(Metha)_2H_{-1}]^{+}$ species in which hydroxamic oxygens are involved in the copper(II) coordination apart from nitrogen-donor atoms (Scheme 2). The same spectral behaviour was observed in the case of the ternary system with α-Alaha [4]. For the Cu^{2+}–Me_5dien–Metha system in an acid solution the existence of a broad band in the visible region is observed. As the pH of the solution increases, the absorbance in the longer wavelength region is greatly enhanced. These spectral changes correspond well to the formation of the mixed-ligand species (Fig. 1a). From pH 8.6 to 9.7 absorption spectra are very similar, what indicates the predominance of the mixed-ligand complex in this pH range. Furthermore, the absorption spectra exhibit two noticeable maxima at pH 9 with the latter one more intense: at 624 nm ($\varepsilon = 254$ dm^3 mol^{-1} cm^{-1}) and 780 nm ($\varepsilon = 268$ dm^3 mol^{-1} cm^{-1}). This absorption pattern, two peaks with one more intense being near the IR region, suggests the structural change around the Cu^{2+} ion towards five coordinate copper(II) complexes [4,18]. A similar spectral behaviour was observed for five coordinate mixed-ligand species formed in other ternary systems with α-aminohydroxamic ligands and polyamines (dien and Me_5dien) with the involvement of all nitrogen-donor atoms in the coordination sphere [2–4]. This fact can imply that in the coordination to the metal ion in the dinuclear $[Cu_2(Me_5dien)\text{-}(Metha)_2H_{-1}]^{+}$ species formed above pH 6, in the Cu^{2+}–Me_5dien–Metha system three nitrogen atoms of polyamine and two nitrogen atoms of Metha (N_{amino}, $N_{hydroxamate}$) are involved (Scheme 2).

The stability constants obtained for the complexes formed in Cu^{2+}–Me_5dien–Hisha system are given in Table 1. The concentration distribution curves for this system



Scheme 2.

together with the variations of visible absorption at $\lambda = 850$ nm are presented in Fig. 1b. It can be seen, that in this system with 1:2:1 molar ratio, up to pH 5 mainly simple and dinuclear complexes with Hisha ligand are formed: $[Cu(H_2\text{–Hisha})]^{3+}$, $[Cu(H\text{–Hisha})]^{2+}$, $[Cu(H\text{–Hisha})_2]^{2+}$ and $[Cu_2(H\text{–Hisha})(Hisha)]^{3+}$, $[Cu_2(Hisha)_2]^{2+}$, $[Cu_2(Hisha)_2H_{-1}]^{+}$. The EPR parameters of the spectra observed in the pH range 3–3.5 for the Cu^{2+}–Me_5dien–Hisha ternary system (with 1:2:1 molar ratio) of the liquid and frozen solution are very similar to these stated for Cu^{2+}–Hisha binary system. The values of $g_{\|} = 2.250$ and $A_{\|} = 188 \times 10^{-4}$ cm^{-1} EPR parameters confirm the formation of the $[Cu(H\text{–Hisha})]^{2+}$ and $[Cu(H\text{–Hisha})_2]^{2+}$ simple species with the coordination realised through imidazole and amino nitrogens [3]. In contrast to the Cu^{2+}–dien–Hisha ternary system, the presence of Me_5dien instead of dien does not suppress the formation of parent dinclear species of Hisha [3]. In the acid solution of the Cu^{2+}–Me_5dien–Hisha ternary system the $[Cu(Me_5dien)]^{2+}$ simple species exists in the concentration less than 20% showing at pH 5 a weak EPR spectrum with parameters $g_z \sim 2.24$, $g_x \sim 2.07$, $g_y \sim 2.05$ and $A_z \sim 183$, $A_x \sim 29$, $A_y \sim 14 \times 10^{-4}$ cm^{-1}. The $[Cu(H\text{–Hisha})(Hisha)]^{+}$, $[Cu(Hisha)_2]$ and $[Cu(Hisha)_2H_{-1}]^{-}$ species are formed at very low concentration (<5%) and can be regarded as negligible (Fig. 1b).

The equilibrium model for the Cu^{2+}–Me_5dien–Hisha ternary system involves three mixed-ligand complexes: $[Cu(Me_5dien)(H\text{–Hisha})]^{2+}$, $[Cu(Me_5dien)(Hisha)]^{+}$ and dinuclear one $[Cu_2(Me_5dien)(Hisha)_2H_{-1}]^{+}$. Similarly as it was observed in the ternary system with Metha, the $[Cu(Me_5dien)(Hisha)]^{+}$ species is formed as a minor one and the maximum concentration of this species is about 9.5% at pH ~9. The first mixed-ligand species, $[Cu(Me_5dien)(H\text{–Hisha})]^{2+}$, starts to form above pH 5.5 and reaches a maximum concentration (ca. 30%) at about pH 7 (Fig. 1b). Generally, a possible mode of coordination of Hisha in the mixed-ligand species is the formation of six-membered chelate ring (N_{im}, NH_2) or five-membered chelate ring (N_{ha}, NH_2) in the plane. The $pK_{[Cu(Me_5dien)(H\text{-}Hisha)]^{2+}}$ value equal to 8.37 (Table 1), characteristic of the deprotonation step for this mixed-ligand complex is lower than the deprotonation constant of the hydroxamic group in the free ligand. Thus, it can be assigned to the deprotonation of the hydroxamic group promoted by the copper(II) binding.

The EPR spectra observed within pH range 6.7–7.4 that are ascribed to this mixed-ligand species display parameters of rhombic character reflecting a distorted geometry of $[Cu(Me_5dien)(H\text{–Hisha})]^{2+}$. A significant decrease of A_z as well as the spectrum corresponding to three different val-

ues of g and A parameters reveal the formation of the five-coordinate type of the complex ($g_z \sim 2.22$, $g_x \sim 2.08$, $g_y \sim 2.02$ and $A_z \sim 173$, $A_x \sim 50$, $A_y \sim 15 \times 10^{-4}\,cm^{-1}$) [3]. In the pH range 8–10 the weak EPR signals which may be assigned to the spectrum of mononuclear deprotonated mixed-ligand species $[Cu(Me_5dien)(Hisha)]^+$ (Fig. 2). The spectrum of $[Cu(Me_5dien)(Hisha)]^+$ with contribution about 10% may be observed because it accompanies the dinuclear species which is practically EPR not-detectable. The parameters $g_z \sim 2.22$, $g_x \sim 2.10$, $g_y \sim 2.02$ and $A_z \sim 165$, $A_x \sim 81$, $A_y \sim 19 \times 10^{-4}\,cm^{-1}$ indicate stronger rhombic distortion than for the former mixed-ligand species, $[Cu(Me_5dien)(H–Hisha)]^{2+}$. This EPR spectral difference between both mixed-ligand species may be assigned to the dissimilar chelate rings formed by Hisha ligand – a five-membered ring for deprotonated species and a six-membered ring for the protonated one (Scheme 2). The same effect was observed in the case of the mixed-ligand species of α-Alaha (five-membered chelate ring) and β-Alaha (six-membered chelate ring) with Me_5dien. In the case of the former one the stronger rhombic distortion was detected [4].

Additional evidence for the presence of mixed-ligand species provide absorption spectral data (Fig. 4a). Similarly as it was observed in the ternary system with Metha, in the Cu^{2+}–Me_5dien–Hisha system the CT transition band from hydroxamic oxygen to copper(II) is present in the near-UV region of the absorption spectra recorded at the basic solution. This corresponds to the formation of the dinuclear mixed-ligand species, $[Cu_2(Me_5dien)(Hisha)_2H_{-1}]^+$. Furthermore, a comparison between the species distribution curves (Fig. 1b) and the pH-dependent curves of the absorption (Fig. 4a) clearly indicates that the spectral changes in the visible region are attributable to the formation of the mixed-ligand species. The absorption curve at pH 9, exhibits two peaks at 625 ($\varepsilon = 250\,dm^3\,mol^{-1}\,cm^{-1}$) and 786 nm ($\varepsilon = 256\,dm^3\,mol^{-1}\,cm^{-1}$) (the latter one is more intense) as it was observed for the mixed-ligand complex in the system with Metha. This spectral characteristic strongly supports the formation of a five-coordinated mixed-ligand species with 5N in the coordination sphere in the Cu^{2+}–Me_5dien–Hisha system (Fig. 3, Scheme 2).

It is very interesting to compare the relative stabilities of the complexes formed in the ternary systems with hydroxamic acids with those of amino acids (Table 2). The order of decreasing stability ($\log K_{Cu(Me_5dien)L} - pK_{NH_3^+} - pK_{COOH}$, when L = aminoacid or $\log K_{Cu(Me_5dien)L} - pK_{NH_3^+} - pK_{CONHOH}$, when L = aminohydroxamic acid)

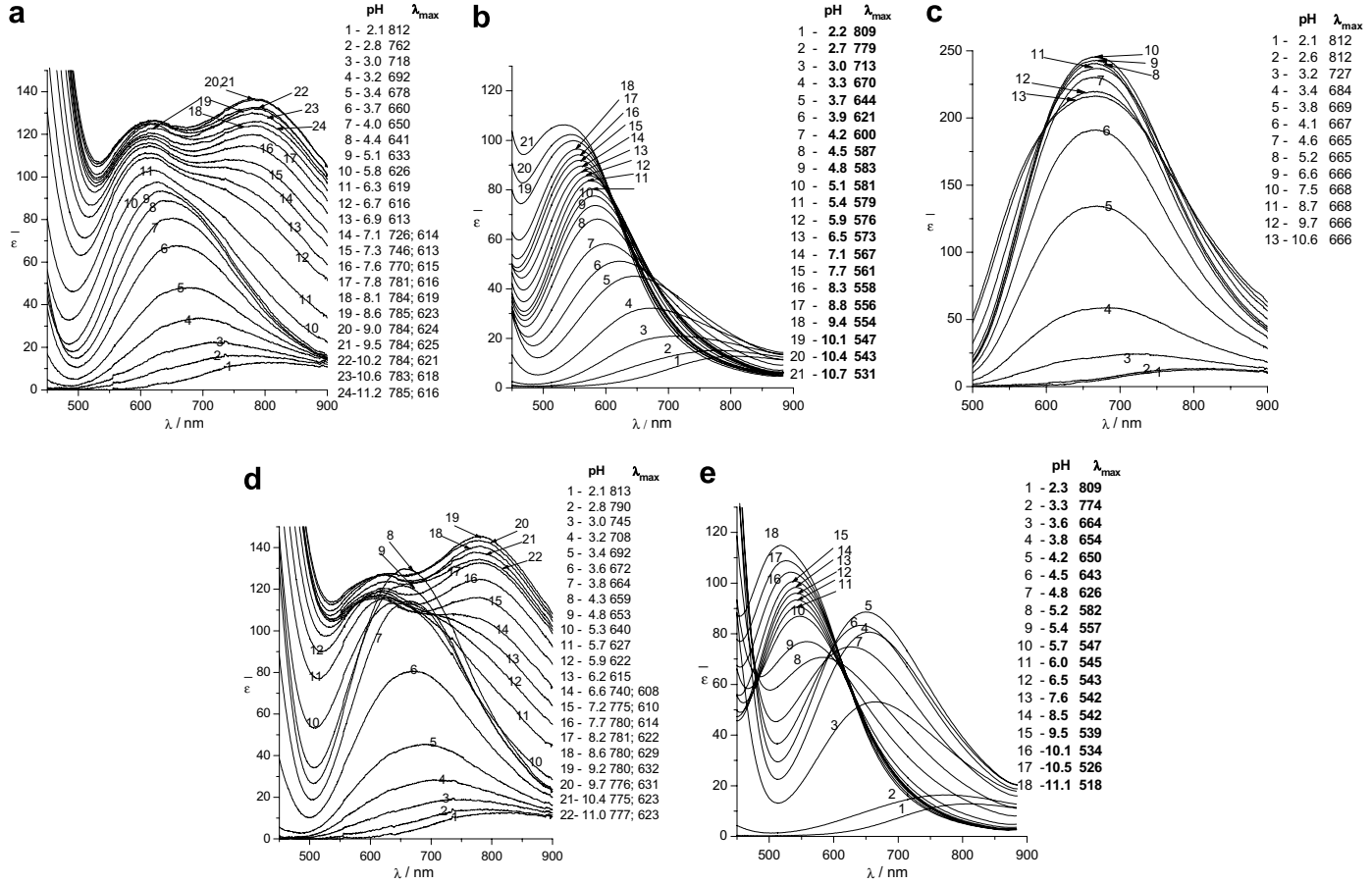


Fig. 4. pH-varied absorption spectra of the Cu^{2+}–Me_5dien–Hisha system at 1:2:1 molar ratio (a), Cu^{2+}–Hisha system at 1:2 molar ratio (b), Cu^{2+}–Me_5dien system at 1:2 molar ratio (c), Cu^{2+}–Me_5dien–Metha system at 1:2:1 molar ratio (d) and Cu^{2+}–Metha system at 1:2 molar ratio (e) ($c_{Cu^{2+}} = 4 \times 10^{-3}$ mol dm^{-3}).

Table 2
Cumulative formation constants ($\log\beta$), derived equilibrium constants ($\log K$) of mixed-ligand complexes formed in the Cu^{2+}–amine (Me_5dien, dien)–L (L = Hisha, Metha, α-Alaha, β-Alaha, His, Met, α-Ala, β-Ala) at 25 °C and $I = 0.2$ mol dm^{-3} (KCl)

	Compound L							
	Hisha	Metha	α-Alaha	β-Alaha	His	Met	α-Ala	β-Ala
	This work	This work	This work	Ref. [4]	a	a	Ref. [9]	a
$\log\beta$[Cu(Me_5dien)L]	18.86	18.42	18.86	18.91	17.09	16.79	17.33	15.44
$\log K$[Cu(Me_5dien)L]	6.39	5.95	6.39	6.44	4.67	4.37	5.13	3.02
$\log K_{[Cu(Me_5dien)L]} - pK_{NH_3^+} - pK_{CONHOH}$	−9.78	−9.80	−10.15	−11.77				
$\log K_{[Cu(Me_5dien)L]} - pK_{NH_3^+} - pK_{COOH}$						−6.86	−6.89	−10.61
$\log K_{[Cu(Me_5dien)L]} - pK_{NH_3^+} - pK_{im}$					−10.49			
	Ref. [3]	Ref. [3]	Ref. [2]	Ref. [2]	a	a	Ref. [9]	a
$\log\beta$[Cu(dien)L]	21.15	20.57	21.11	19.99	20.77	19.46	20.16	19.41
$\log K$[Cu(dien)L]	5.14	4.56	5.10	3.98	4.76	3.45	4.13	3.4
$\log K_{[Cu(dien)L]} - pK_{NH_3^+} - pK_{CONHOH}$	−10.97	−11.18	−11.44	−14.40				
$\log K_{[Cu(dien)L]} - pK_{NH_3^+} - pK_{COOH}$						−7.78	−7.89	−10.23
$\log K_{[Cu(dien)L]} - pK_{NH_3^+} - pK_{im}$					−10.4			

Charges are omitted for simplicity.
[a] B. Kurzak, K. Bogusz, unpublished data.

is: $[Cu(Me_5dien)(Met)]^+ \approx [Cu(Me_5dien)(\alpha\text{-Ala})]^+ > [Cu(Me_5dien)(\alpha\text{-Alaha})]^+ \approx [Cu(Me_5dien)(Hisha)]^+ \approx [Cu(Me_5dien)(Metha)]^+ > [Cu(Me_5dien)(\beta\text{-Ala})]^+ \approx [Cu(Me_5dien)(His)]^+ > [Cu(Me_5dien)(\beta\text{-Alaha})]^+$ which corresponds to the existence of $(N,O) \approx (N,O) > (N,N) \approx (N,N) \approx (N,N) > (N,O) \approx (N,N_{im}) > (N,N)$ chelate donors of the ligands L consequently relevant to (5) ≈ (5) > (5) ≈ (5) ≈ (5) > (6) ≈ (6) > (6) chelate rings of these ligands.

This order reflects the dependence between the type of the chelate rings formed by L and the stability of the five-coordinated mixed-ligand [Cu(Me_5dien)L] species. The stability is favoured for the complexes with L forming involving the mixed-bonding mode (N,O) and five-membered chelate rings over that for the complexes with pure type of donors (N,N) and the same type of chelate rings. Furthermore, the complexes containing only five-membered rings are favoured over systems with the five- and six-membered rings.

However, in the case of dien the mixed-bonding mode (N,O) seems to be more important factor and the complexes involving that kind of six-membered ring are even more stable than those with five-membered rings and pure type of donors.

The order of decreasing stability ($\log K_{Cu(dien)L} - pK_{NH_3^+} - pK_{COOH}$, when L = aminoacid or $\log K_{Cu(dien)L} - pK_{NH_3^+} - pK_{CONHOH}$, when L = aminohydroxamic acid) is: $[Cu(dien)(Met)]^+ \approx [Cu(dien)(\alpha\text{-Ala})]^+ > [Cu(dien)(\beta\text{-Ala})]^+ \approx [Cu(dien)(His)]^+ > [Cu(dien)(Hisha)]^+ \approx [Cu(dien)(Metha)]^+ \approx [Cu(dien)(\alpha\text{-Alaha})]^+ > [Cu(dien)(\beta\text{-Alaha})]^+$ which corresponds to the existence: $(N,O) \approx (N,O) > (N,O) \approx (N,N_{im}) > (N,N) \approx (N,N) \approx (N,N) > (N,N)$ chelate donors of the ligands L and (5) ≈ (5) > (6) ≈ (6) > (5) ≈ (5) ≈ (5) > (6) chelate rings of these ligands.

4. Conclusion

The presence of Me_5dien in the Cu^{2+}–Me_5dien–Metha/Hisha ternary systems does not suppress the formation of parent polynuclear species. Furthermore, for the first time it could be observed that in these ternary systems the dinuclear mixed-ligand species is formed as a predominant one in the basic solution. The mononuclear mixed-ligand species $[Cu(Me_5dien)L]^+$ which are usually formed in the ternary systems with aminohydroxamic acids and polyamines, in these ternary systems are formed in remarkably lower concentrations. Our spectroscopic data show that the geometry of these mixed-ligand five-coordination complexes is strongly distorted towards trigonal-bipyramid probably because of the steric effects caused by Me_5dien. The analogous five-coordinate species formed in the ternary systems with dien have a geometry in smaller degree deviated from square-pyramidal [3]. In the case of ternary systems with bidentate amine – ethylenediamine (en), in the mononuclear mixed-ligand species $[Cu(en)(Metha)]^+$ and $[Cu(en)(Hisha)]^+$ that are formed in basic solution both amine and hydroxamic nitrogens of Metha/Hisha and two amine nitrogens of en are coordinated in the copper(II) plane [4,6].

The increasing geometry distortion of the complexes formed in the Cu^{2+}–Me_5dien–L ternary system (L = aminoxydroxamic acid) in comparison to those formed in the Cu^{2+}–dien–L ternary system results in the higher relative stability of the mixed-ligand species with Me_5dien than those with dien ($\log K_{Cu(Me_5dien)L} - pK_{NH_3^+} - pK_{CONHOH} > \log K_{Cu(dien)L} - pK_{NH_3^+} - pK_{CONHOH}$). The same tendency can be observed for the ternary systems in which ligand L is replaced by an amino acid such as α-alanine and methionine, except of the systems with histidine and β-alanine.

Acknowledgments

We express our gratitude to Ms. Jadwiga Kędzierska for her technical assistance in the EPR measurements.

References

[1] B. Kurzak, D. Kroczewska, J. Coord. Chem. 34 (1995) 67.
[2] B. Kurzak, D. Kroczewska, J. Jezierska, Polyhedron 17 (11–12) (1998) 1831, 1831.
[3] B. Kurzak, K. Bogusz, D. Kroczewska, J. Jezierska, Polyhedron 20 (2001) 2627.
[4] D. Kroczewska, K. Bogusz, B. Kurzak, J. Jezierska, Polyhedron 21 (2002) 295.
[5] D. Kroczewska, B. Kurzak, J. Jezierska, Polyhedron 25 (2006) 678.
[6] B. Kurzak, K. Bogusz, A. Kamecka, J. Jezierska, Polyhedron (2007), doi:10.1016/j.poly.2007.05.024.
[7] B. Kurzak, K. Kurzak, J. Jezierska, Inorg. Chim. Acta 125 (1986) 77.
[8] G. Gran, Acta Chem. Skand. 4 (1950) 559.
[9] T. Murakami, K. Murata, Z. Ishikawa, Inorg. Chim. Acta 244 (1996) 51.
[10] M. Molina, C. Melios, J.O. Tognolli, L.C. Luchiari, M. Jafelicci Jr., J. Electroanal. Chem. 105 (1979) 237.
[11] P. Gans, A. Sabatini, A. Vacca, Talanta 43 (1996) 1739.
[12] H. Sigel, Angew. Chem. 87 (1975) 391.
[13] H. Sigel, Angew. Chem., Int. Ed. Engl. 14 (1975) 394.
[14] N. Azuma, Y. Kohno, K. Izshizu, T. Takakuwa, S. Tsuboyama, K. Tsuboyama, K. Kobayashi, T. Sakurai, Inorg. Chim. Acta 215 (1994) 109.
[15] E. Farkas, J. Szoke, T. Kiss, H. Kozłowski, W. Bal, J. Chem. Soc., Dalton Trans. (1989) 2247.
[16] B. Kurzak, L. Nakonieczna, G. Rusek, H. Kozłowski, E. Farkas, J. Coord. Chem. 28 (1993) 17.
[17] M. Carem, F. Dallavalle, M. Tegoni, I. Zagnoni, J. Inorg. Biochem. 93 (2003) 174.
[18] T. Murakami, T. Takei, Y. Ishikawa, Polyhedron 16 (1997) 89.

In the field of preparative coordination chemistry, hexacyanometallate ions are commonly employed with additional metal ions. Complex moieties are selected to obtain desirable hybrid functional Prussian Blue like complexes by self-assembling bottom-up processes. It has been shown that the reaction of $[M(SB)]^{n+}$ (SB = the salen-substituted chelating ligand) with hexacyanometallates leads to a variety of topologies depending on (i) the steric accessibility of the metal centre in $[M(SB)]^{n+}$, (ii) the total charge of the cationic precursor, (iii) the lability of the coordination sites, (iv) the steric hindrance of the Schiff base ligand and (v) the geometry of the cyanometallate tecton [4]. By introducing terminal blocking ligands, a number of heteroleptic complexes of lower symmetry have been reported. The range includes dimers [5], clusters [6], molecular squares [7], linear chains [8], ladders [9], two-dimensional honeycomb [10] and square grid [11] topologies as well as three-dimensional networks [12] exhibiting interesting electrochemical and zeolitic properties [1b,1c,12,13].

In particular, some cyano-bridged compounds exhibit spontaneous magnetism at significantly higher temperatures [1b,1c,12] and ambient temperature [1b,1c,2,14–18]. Moreover, Prussian Blue is ferromagnetic with $T_C = 5.6$ K [5]. Considering that the magnetic interactions are caused by diamagnetic $[Fe(CN)_6]^{4-}$ or $[Co(CN)_6]^{3-}$ anions, it is useful to investigate the magnetic properties of polynuclear μ-cyanido complexes derived from hexacyanoferrate(II) or hexacyanocobaltate(III). Since copper(II) is normally four-, five- or six-coordinate, it was anticipated that the coupling of a copper(II) amine to the $[Fe(CN)_6]^{4-}$ ion might lead to the formation of a novel family of magnetic compounds with potential control over the structure of the compound.

We have focused our interest on a series of polycyano copper(II) complexes that have been reported [19–28]. In this context, our group has already reported the synthesis of two new heterobimetallic cyano-bridged systems obtained from the reaction of monocationic Schiff base complexes of divalent and trivalent metal ions like Cu(II), Ca(II), Sr(II), Ba(II) and Y(III) with hexacyanometallates [29,30]. In a continuation of the earlier works, the present work is devoted to the study in some details of the crystal structure and the magnetic properties of two new trinuclear heterobimetallic compounds [(Cu L)-$[Co(CN)_6]$(CuL)]$ClO_4 \cdot 3.5H_2O$ (**1**) and [(CuL)$[Fe(CN)_6]$(CuL)] $\cdot 13H_2O$ (**2**) where [L = (3*E*,5*E*)-N^1,N^4-bis ((pyridin-2-yl)methylene) butane-1,4-diamine], using $[Co(CN)_6]^{3-}$ and $[Fe(CN)_6]^{4-}$ as template anions. The present work incorporates a study of the magneto-structural correlation for heterometallic cyano-bridged copper(II) Schiff base complexes. It is also noteworthy that the steric demand of the Schiff base ligand apparently directs the self-assembly of building blocks towards the exclusive formation of a crystallographically characterized non-racemic cyano-bridged Cu–Co mixed-metallic (two different species in the same unit) complex unlike those found in our previous investigation. The versatile nature of the metallo-salen building block to form bimetallic complexes of structural diversity has been proven in this report. Here the formation of a non-racemic Cu–Co cyano bridged complex is a function of the steric nature of the Schiff base ligand of the cation. In complex **1** the steric demand of the methyl groups of the Schiff base molecule perhaps directs the formation of the non-racemic cyano-bridged Cu–Co mixed-metallic complex, unlike in $[C_{38}H_{38}CoCu_2N_{14}O]\,[C_{22}H_{18}CoCuN_{10}] \cdot 7H_2O$.

2. Experimental

2.1. Materials

All the chemicals and solvents used for the syntheses were of analytical grade. Pyridine-2-carboxaldehyde; 1,4-diaminobutane, $K_3[Co(CN)_6]$ and $K_4[Fe(CN)_6]$ were all purchased from Aldrich Chemical Co. Inc. and were used without further purification. Copper(II) perchlorate hexahydrate, $Cu(ClO_4)_2 \cdot 6H_2O$, was prepared by treatment of basic copper(II) carbonate, $CuCO_3 \cdot Cu(OH)_2$ (E. Merck, India) with 60% perchloric acid (E. Merck, India) followed by slow evaporation. It was then filtered through a fine glass-frit and preserved in a $CaCl_2$ desiccator for further use.

2.2. Syntheses

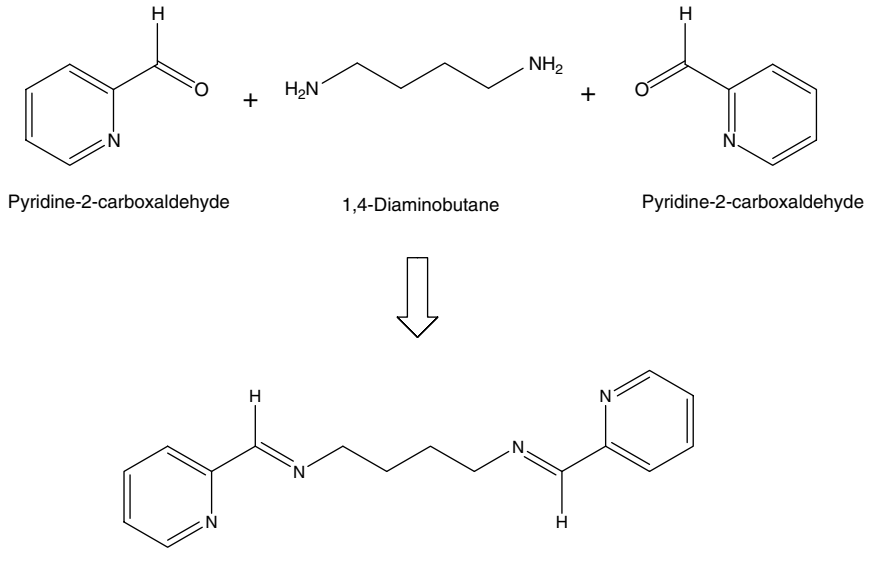
Caution! Although no problems were encountered in this work, perchlorate salts in the presence of organic ligands are potentially explosive in nature. They should be prepared in small quantities and handled with care.

2.2.1. Synthesis of the Schiff base ligand $[NC_5H_4C{=}N(CH_2)_4N{=}CNC_5H_4]$ (**L**)

The Schiff base ligand [(3*E*,5*E*)-N^1,N^4-bis((pyridin-2-yl)methylene)butane-1,4-diamine], **L** ($C_{18}H_{22}N_4$) was prepared by the condensation of a methanolic solution of pyridine-2-carboxaldehyde with 1,4-diaminobutane (2:1 mmol ratio) after refluxing for half an hour according to the literature procedure [15] (Scheme 1).

2.2.2. Synthesis of the complexes: $[(CuL)[Co(CN)_6](CuL)]ClO_4 \cdot 3.5H_2O$ (**1**) and $[(CuL)[Fe(CN)_6](CuL)] \cdot 13H_2O$ (**2**)

$Cu(ClO_4)_2 \cdot 6H_2O$ (1.05 g, 3 mmol) in 10 cm^3 methanol was added drop by drop to a vigorously stirred 20 cm^3 methanolic solution of the ligand, $[NC_5H_4CH{=}N{-}(CH_2)_4{-}N{=}CHC_5H_4N]$, (**L**) (4 mmol). A greenish precipitate appea- red. It was then dissolved on addition of methylene chloride drop by drop, avoiding excess. Hexacyanometallate compounds are very sensitive to heating and sunlight. So after filtration, the solution was cooled to 0 °C in ice bath followed by the slow addition of an aqueous solution (15 ml) of $K_3[Co(CN)_6]$ (0.33 g, 1 mmol) for complex **1** and the resulting solution was kept in a dark place. Blue plate shaped crystals for **1** suitable for X-ray analysis appeared after one day and were collected by filtration, washed with a minimum volume of ethanol and dried in air. *Anal.* Calc. for $C_{42}H_{51}ClCoCu_2N_{14}O_{7.50}$: C, 46.13; H, 4.70; N, 17.93. Found: C, 46.15; H, 4.72; N, 17.94%.



Scheme 1. Synthetic route to ligand **L**.

Green prism shaped crystals of complex **2** were prepared in the same way as that of complex **1** by using $K_4[Fe(CN)_6]$ (332 mg, 1 mmol) instead of $K_3[Co(CN)_6]$. *Anal.* Calc. for $C_{42}H_{70}Cu_2FeN_{14}O_{13}$: C, 43.41; H, 6.07; N, 16.88. Found: C, 43.42; H, 6.05; N, 16.90%.

2.3. Physical measurements

Elemental analyses (carbon, hydrogen and nitrogen) were performed on a Perkin–Elmer 2400 CHN Elemental Analyser. The Fourier Transform infrared spectra were recorded on a Perkin–Elmer RXI FT-IR spectrophotometer in the range 4000–400 cm^{-1} with a KBr disc and electronic spectra on a Perkin–Elmer Lambda-40 spectrophotometer using HPLC grade acetonitrile as the solvent at 300 K in 1 cm quartz cuvettes.

Magnetic susceptibility measurements for the compounds were carried out on polycrystalline samples at the Servei de Magnetoquímica of the Universitat de Barcelona, with a Quantum Design SQUID MPMS-XL susceptometer apparatus working in the range 2–300 K under a magnetic field of approximately 10,000 G. Diamagnetic corrections were estimated from Pascal's Tables.

2.4. X-ray crystallographic data collection and structure refinements

A good diffraction quality air stable single crystal of **1** (dimensions $0.40 \times 0.25 \times 0.03$ mm) and **2** (dimensions $0.18 \times 0.13 \times 0.08$ mm) was selected and mounted in a Nonius KappaCCD diffractometer equipped with graphite monochromated Mo-$K\alpha$ radiation ($\lambda = 0.71073$ Å). Crystal data were collected using COLLECT [31] at a temperature of 123 K. The unit cell parameters were determined from the least-squares refinement of 25 centered reflections in the range 1.75–23.15° for **1** and 1.97–25.61° for **2** using φ and ω scans. Cell refinements were carried out using DENZO-SMN for **1** and HKL SCALEPACK for **2** [32]. No significant intensity variation was observed. A total of 14,627 reflections (6524 unique reflections, $R_{int} = 0.0539$) for **1** and 13,422 reflections (4898 unique reflections, $R_{int} = 0.0310$) for **2** were collected applying the boundary condition $I \geqslant 2\sigma(I)$. Absorption correction was applied to intensity values ($T_{max} = 1.0$, $T_{min} = 0.568$ for **1** and $T_{max} = 1.0$, $T_{min} = 0.817$ for **2**) empirically using SADABS [33]. Data reduction was carried out using DENZO-SMN for **1** while HKL DENZO and SCALEPACK were used for **2**. The final structures were solved by direct methods using the program SHELXS-97 [34] and refined with full-matrix least-squares based on F^2 using SHELXL-97 [34]. The molecular graphics and crystallographic illustrations were prepared using the ORTEP-III [35] and XSEED [36] programs for **1** and **2**, respectively. For all non-hydrogen atoms, the anisotropic displacement parameters have been refined. Hydrogen atoms of the aromatic rings and the imino groups were placed geometrically and refined using the riding model taken from a difference Fourier map and refined with isotropic thermal parameters. Maximum and minimum peaks (e $Å^{-3}$) in the final difference Fourier synthesis were 1.172 and −0.665 for **1** and 0.71, −0.43 for **2**. Selected crystallographic data and structure refinement parameters are summarised in Table 1.

Table 1
Crystallographic parameters of complexes **1** and **2**

Complex	**1**	**2**
Formula	$[(Cu(C_{18}H_{22}N_4))_2Co(CN)_6]ClO_4 \cdot 3.5H_2O$	$[(Cu(C_{18}H_{22}N_4))_2Fe(CN)_6] \cdot 13H_2O$
Formula weight	1093.37	1162.05
Crystal system	triclinic	triclinic
Space group	$P\bar{1}$ (no. 2)	$P\bar{1}$ (no. 2)
a (Å)	10.0296(14)	10.8743(2)
b(Å)	12.1148(11)	11.7906(3)
c (Å)	20.7600(3)	12.0546(2)
α (°)	94.8700(3)	104.5370(2)
β (°)	98.7030(5)	102.6940(2)
γ (°)	104.1240(11)	110.2220(10)
V (Å^3)	2398.5(5)	1321.53(6)
Z	2	1
T (K)	123(2)	123(2)
λMo-Kα (Å)	0.71073	0.71073
D_c (g cm^{-3})	1.504	1.427
μ (mm^{-1})	1.341	1.141
F(000)	1126	608
Crystal dimensions (mm)	$0.40 \times 0.25 \times 0.03$	$0.18 \times 0.13 \times 0.08$
θ (°)	1.75–23.15	1.97–25.61
Total, Unique data (R_{int})	14627, 6524 (0.0539)	13422, 4898 (0.031)
Observed data ($I > 2\sigma(I)$)	4710	4271
Parameters	612	333
Goodness-of-fit on F^2	1.169	1.08
$\Delta\rho_{maximum,minimum}$ (e Å^{-3})	1.172, −0.665	0.71, −0.43

3. Results and discussion

3.1. Infrared spectra

The IR spectra of complexes **1** and **2** are consistent with the structural data presented in this paper. A broad absorption band for the ν_{str}(O–H) appears at 3400 cm^{-1} for both complexes, indicating the presence of water molecules in the crystals. The sharp bands at 1628 and 1635 cm^{-1} for complexes **1** and **2**, respectively, indicate the δ(H–O–H) mode. Again sharp bands at 418 and 421 cm^{-1} for complex **1** and **2**, respectively, may be assigned to $\rho_w(H_2O)$. The presence of $\rho_r(H_2O)$ can be correlated to the bands at 747 and 788 cm^{-1} for complex **1** and at 775 and 788 cm^{-1} for complex **2**. These results show the presence of both coordinated and lattice water molecules [26]. Two main band systems of comparable intensities are observed in the crystal lattices for the ν(C≡N) mode of $[M(CN)_6]^{3-}$. The low intensity bands at 2045 cm^{-1} for **1** and 2130 cm^{-1} for **2** are assigned to inter-metallic bridging C≡N stretching and the high intensity band that appears around 2076 cm^{-1} for **1** and 2166 cm^{-1} for **2** can be correlated to the non-bridging terminal C≡N stretching mode. In complex **1** a strong band near 1016–1104 cm^{-1} and a sharp band at 590–624 cm^{-1} indicate the presence of the uncoordinated perchlorate anion [26]. All the other peaks appear at their usual positions, except for a slight difference between the complexes due to the absence of the perchlorate anion in complex **2**.

3.2. UV/Vis spectra

Although the electronic spectra of copper complexes with multidentate Schiff base ligands are not in general good indicators of geometry, they can help to support it. The electronic spectra of complexes in acetonitrile solution show two strong absorption bands in the region 225, 276 and 235, 279 nm for **1** and **2**, respectively. They can be assigned to the high intensity charge transfer bands [25]. The bands in the region 464–337 nm can be correlated to the n–π^* transition of the azomethine group. The absorption bands observed at 380 and 388 nm for complexes **1** and **2**, respectively, can be attributed to the ligand to Cu(II) charge transfer transition (LMCT) [26,27]. The very weak low-intensity absorption bands at 670, 675 and 676 nm are assigned to Cu(II) d–d transitions [26–29] for **1** and **2**, and support the five coordinated geometry around the copper(II) ions with the CuN_5 chromophore.

3.3. Crystal structures of the complexes

The crystal structure with atom numbering scheme and important bond lengths and angles of **1** are presented in Fig. 1 and Table 2, respectively, while those of **2** are presented in Fig. 4 and Table 4, respectively.

3.3.1. $[(Cu(C_{18}H_{22}N_4))_2Co(CN)_6]ClO_4 \cdot 3.5H_2O$ (1)

The asymmetric unit of **1** contains one trinuclear Cu_2Co unit, one perchlorate counter ion and four lattice water molecules, out of which O(8) was refined at half occupancy. The trinuclear monocation (Fig. 2) contains two chemically similar but crystallographically unique $(CuL)^{2+}$ moieties bridged in a *trans*-fashion by a $Co^{III}(CN)_6^{3-}$ moiety. All the copper atoms are pentacoordinated. The coordination number five for copper(II) is very common and it possesses either a square pyramidal (SP) or a trigonal bipyramidal (TBP) geometry. Recently some complexes have been reported in which the copper(II) ion adopts a geometry intermediate between SP and TBP configurations [28,29]. In order to ascertain a more precise geometry of the metal environment, several parameters are used to quantify the distortion. One of them is the so called tetragonality, T^5, defined as the ratio between the mean in-plane Cu–L bond distance and the out of the plane Cu–L bond distance [37a]. The percentage of trigonal distortion from SP geometry is described by the structural index parameter or Addison parameter, τ, defined as $\tau = [(\theta - \Phi)/60] \times 100$, where θ and Φ are the two largest coordination angles; $\tau = 0$ for perfect square pyramidal and 100 for ideal trigonal bipyramidal geometry [37b]. For complex **1** the Cu(1) ion adopts a distorted trigonal bipyramidal arrangement, having a τ value of 59, with the three nitrogen atoms N(1), N(109) and N(122) in the equatorial plane and the other two

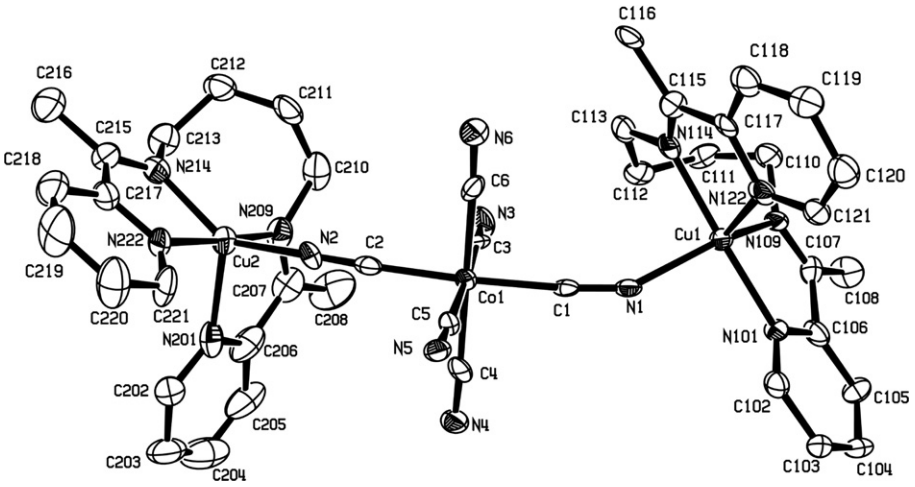


Fig. 1. The trinuclear monocation in the structure of **1** (Hydrogen atoms have been omitted for clarity; Ellipsoids are drawn at the 40% probability level.).

Table 2
Selected bond lengths and bond angles for **1**

Bond lengths	(Å)	Bond angles	(°)
Co(1)–C(1)	1.886(12)	C(2)–Co(1)–C(1)	175.4(5)
Co(1)–C(2)	1.885(13)	C(2)–Co(1)–C(3)	86.0(5)
Co(1)–C(3)	1.895(13)	C(3)–Co(1)–C(5)	177.0(5)
Co(1)–C(4)	1.913(13)	C(6)–Co(1)–C(4)	178.3(5)
Co(1)–C(5)	1.913(12)	C(5)–Co(1)–C(4)	89.9(5)
Co(1)–C(6)	1.899(12)	N(109)–Cu(1)–N(101)	80.3(4)
Cu(1)–N(1)	2.039(9)	N(109)–Cu(1)–N(114)	95.2(4)
Cu(1)–N(101)	2.006(9)	N(101)–Cu(1)–N(114)	175.5(4)
Cu(1)–N(109)	1.998(9)	N(109)–Cu(1)–N(1)	139.7(4)
Cu(1)–N(114)	2.013(9)	N(101)–Cu(1)–N(1)	94.1(3)
Cu(1)–N(122)	2.107(10)	N(114)–Cu(1)–N(1)	89.0(3)
Cu(2)–N(2)	2.008(10)	N(109)–Cu(1)–N(122)	116.3(4)
Cu(2)–N(201)	2.137(11)	N(101)–Cu(1)–N(122)	102.3(4)
Cu(2)–N(209)	1.976(10)	N(114)–Cu(1)–N(122)	80.1(4)
Cu(2)–N(214)	1.988(10)	N(1)–Cu(1)–N(122)	104.0(4)
Cu(2)–N(222)	1.984(10)	N(209)–Cu(2)–N(222)	175.4(2)

nitrogen atoms, N(101) and N(114), in the axial plane. The distortion from the ideal trigonal bipyramidal geometry is evident from the fact that the axial N(101)–Cu(1)–N(114) angle of 175.5(4)° is significantly bent from linearity and the equatorial angles vary from 104.0(4)° to 139.7(4)°. The equatorial Cu(1)–N distances fall in the range 1.998(9)–2.107(10) Å, while the mean axial Cu(1)–N distance is 2.009 Å. Similarly the Cu(2) atom, with a τ value of 54.5, can also be better described as having a distorted trigonal bipyramidal geometry with the three nitrogen atoms N(2), N(201) and N(214) in the equatorial plane and the other two nitrogen atoms, N(209) and N(222), in the axial plane.

Each hexacyanocobaltate(III) anion has the usual expected hexacoordinated octahedral geometry with slight distortions and coordinates to two adjacent $(CuL)^{2+}$ cations through two *trans*-cyano nitrogens, N(1) and N(2).

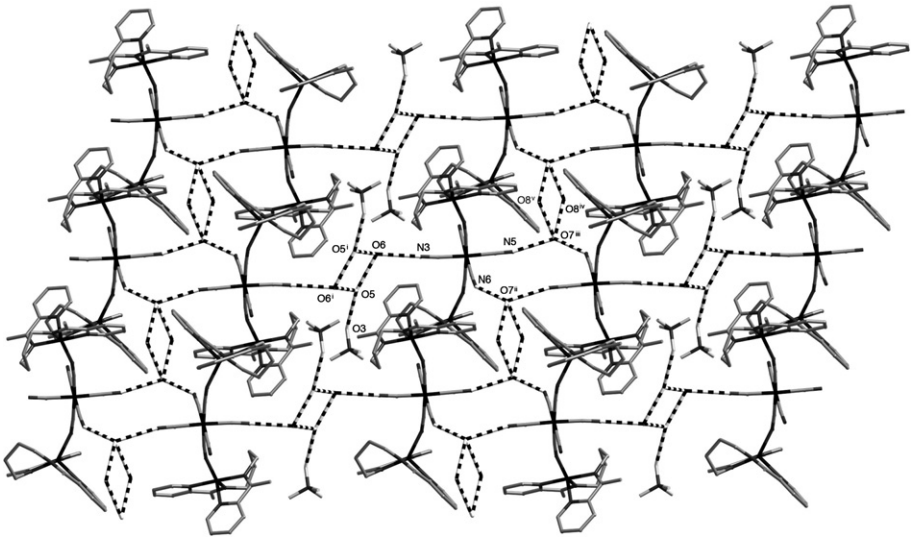


Fig. 2. The 2D hydrogen bonded layers in **1** (striped bonds represent hydrogen bonds). Symmetry operations (i) $1-x, 1-y, -z$; (ii) $x, y+1, z$; (iii) $1-x, 1-y, 1-z$; (iv) $x+1, y, z$; (v) $1-x, -y, 1-z$.

Table 3
Selected hydrogen bonding parameters for **1**

D···A	*d* (Å)
N(3)···O(6)	2.90(1)
O(3)···O(5)	2.95(2)
O(5)···O(6)	2.85(1)
O(5)···O(6)^{i}	2.70(1)
N(6)···O(7)^{ii}	2.88(1)
N(5)···O(7)^{iii}	2.92(1)
O(7)···O(8)^{iv}	2.69(2)
O(7)···O(8)^{v}	3.06(2)

Symmetry operations (i) $1-x, 1-y, -z$; (ii) $x, y+1, z$; (iii) $1-x, 1-y, 1-z$; (iv) $x+1, y, z$; (v) $1-x, -y, 1-z$.

Table 4
Selected bond lengths and bond angles for **2**

Bond lengths	(Å)	Bond angles	(°)
Cu(1)–N(1)	1.956(2)	N(1)–Cu(1)–N(4)	94.67(10)
Cu(1)–N(4)	1.993(2)	N(1)–Cu(1)–N(5)	141.65(12)
Cu(1)–N(5)	2.023(2)	N(1)–Cu(1)–N(6)	93.41(10)
Cu(1)–N(6)	2.002(2)	N(1)–Cu(1)–N(7)	111.32(12)
Cu(1)–N(7)	2.135(3)	N(4)–Cu(1)–N(5)	80.29(10)
Fe(1)–C(1)	1.901(3)	N(4)–Cu(1)–N(6)	171.86(10)
Fe(1)–C(2)	1.923(3)	N(4)–Cu(1)–N(7)	97.28(11)
Fe(1)–C(3)	1.923(3)	N(5)–Cu(1)–N(6)	93.93(9)
N(1)–C(1)	1.155(4)	N(5)–Cu(1)–N(7)	107.03(10)
N(2)–C(2)	1.157(5)	N(6)–Cu(1)–N(7)	78.84(10)
N(3)–C(3)	1.160(4)	C(1)–Fe(1)–C(2)	89.96(14)
N(4)–C(4)	1.330(5)	C(1)–Fe(1)–C(3)	91.07(14)
N(4)–C(8)	1.352(4)	C(1)–Fe(1)–C(2)*	90.04(14)
N(5)–C(9)	1.278(4)	C(1)–Fe(1)–C(3)*	88.93(14)
N(5)–C(11)	1.466(4)	C(2)–Fe(1)–C(3)	92.44(14)
N(6)–C(14)	1.469(4)	C(2)–Fe(1)–C(3)*	87.57(14)
N(6)–C(15)	1.287(4)	C(2)–Fe(1)–C(2)*	180.00
N(7)–C(17)	1.349(4)	C(1)–Fe(1)–C(1)*	180.00
N(7)–C(21)	1.334(5)	C(3)–Fe(1)–C(3)*	180.00

* Symmetry operations: $1-x, -y, -z$.

Distortion in the geometry is indicated by the variation of the *cis*-angles [86.0(5)–93.7(5)°] and *trans*-angles [175.4(5)–178.3(5)°] from the ideal values of 90° and 180°, respectively. The Co–C and C≡N distances are grouped together in narrow ranges, 1.885(13)–1.913(12) Å and 1.120(17)–1.164(15) Å, respectively. The Cu–N≡C bond angles range from 149.5(9)° to 163.9(10)°, i.e., the bridging –CN– ligands coordinate to the Cu(II) ions in a bent fashion, whereas the Co–C–N bonds are almost linear, as indicated by the angles of 174.5(11)–178.4(9)°. The shortest distances between the nearest metal centers are 4.875 Å for Co(1)···Cu(1) and 4.974 Å for Co(1)···Cu(2).

Hydrogen bonding and van der Waals cohesive forces are important in the intermolecular network of the crystal lattices of this type of compound. The molecular units in the crystal system are separated by normal van der Waals contacts. Three of the four uncoordinated nitrile nitrogen atoms from the hexacyanocobaltate moiety form hydrogen bonds to the intercalated water molecules (Table 3). The water molecules also have hydrogen bonding interactions between themselves and to the perchlorate anions, generating 2D sheets (Fig. 2). The sheets pack in an interdigitated fashion (Fig. 3), with a number of other weaker C–H···O, C–H···N interactions between the molecules.

3.3.2. *[(Cu(C$_{18}$H$_{22}$N$_4$))$_2$ Fe(CN)$_6$] · 13H$_2$O (**2**)*

The asymmetric unit of [*trans*-Fe(CN)$_4$(CNCuL)$_2$] · 3 H$_2$O contains half of a trinuclear molecule (the central Fe atom lies on an inversion centre) and seven lattice water molecules, of which O(7) is disordered over two symmetry related positions and refined at half occupancy. The trinuclear complex (Fig. 4) contains two symmetric $(CuL)^{2+}$ moieties bridged with a *trans*-$[Fe^{II}(CN)_6]^{4-}$ moiety. The local coordination of both the two copper(II) ions is the same, resembling a distorted trigonal bipyramidal geometry as indicated by the τ value of 50.5. The basal plane is formed by the N(5) and N(7) atoms of the Schiff base and the N(1) atom of the bridging cyanide, while the axial sites are occupied by the N(4) and N(6) atoms of the Schiff base [N(4)–Cu–N(6) = 171.86(10)°]. The Cu center is very slightly displaced out of the basal plane by 0.001(2) Å towards N(4). The bond distances around the copper atom are very similar to those already reported [38], the Cu–N distances ranging from 1.956(2) to 2.135(3) Å. Each cyanometallate group links the adjacent copper ions giving a one-dimensional compound. The iron(II) ion in this species is also octahedral, with Fe–C and C–N distances ranging from 1.901(3) to 1.923(3) and 1.155(4) to 1.160(4) Å, and the Cu–N(1)–C(1) bond angle is 173.0(3)°, close to values in the literature [38]. The Fe–C(1)–N(1) angle deviates slightly from linearity, 178.4(3)°.

The water molecules undergo hydrogen bonding interactions to create 2D sheets containing large windows (Table 5; Fig. 5). The complexes lie within the windows, with the uncoordinated nitrile ligands hydrogen bonded to the surrounding water molecules. The layers stack in an interdigitated fashion, as shown in Fig. 6, but there are no significant interlayer interactions.

3.4. Variable temperature magnetic susceptibility studies

Due to the diamagnetic nature of the $[Co^{III}(CN)_6]^{3-}$ and $[Fe^{II}(CN)_6]^{4-}$ anions, the paramagnetism of the prepared [Cu$_2$Co] and [Cu$_2$Fe] complexes is caused by the copper(II) atoms. The temperature dependence of $\chi_M T$ (χ_M = molar magnetic susceptibility) of complexes **1** and **2** per [Cu$_2$Co] and [Cu$_2$Fe] unit, respectively, is shown in Fig. 7. The values of $\chi_M T$ at 300 K are 0.8408 cm^3 mol^{-1} K for **1** and 0.8612 cm^3 mol^{-1} K for **2**, as expected for two isolated copper(II) ions ($S = 1/2$) with diamagnetic cobalt(III) or iron(II) ions ($S = 0$) (0.826 cm^3 mol^{-1} K per two Cu(II) with $g = 2.1$). With decreasing temperature, the $\chi_M T$ value in the two cases remains almost constant until 12 K and then it decreases sharply, giving a minimum value of 0.704 cm^3 mol^{-1} K for **1** and 0.730 cm^3 mol^{-1} K for **2** at very low temperature (2 K). We attempted to reproduce theoretically the experimental susceptibility by using the Bleaney–Bowers expression for an isotropically coupled pair of $S = 1/2$ ions, [Eq. (1)], where N is Avogadro's

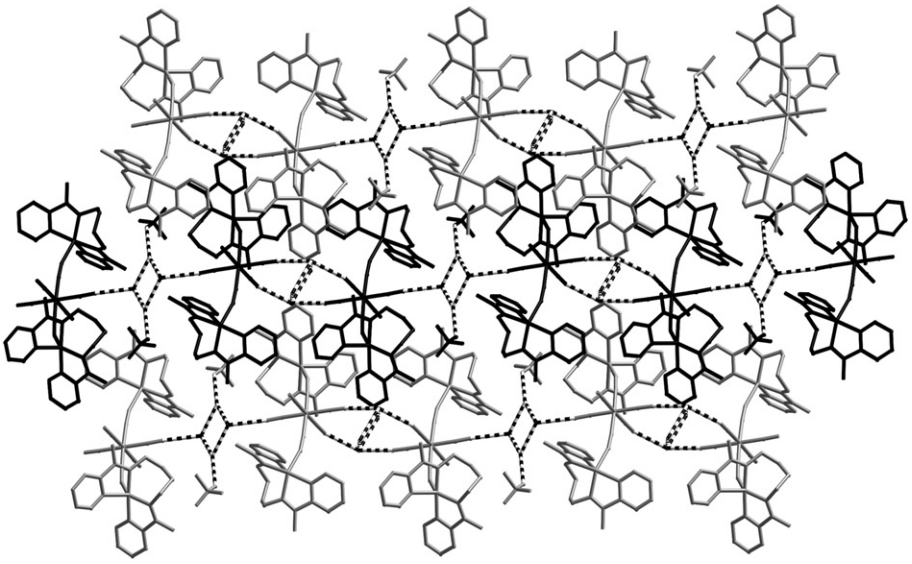


Fig. 3. The interdigitation of adjacent hydrogen bonded layers in **1**.

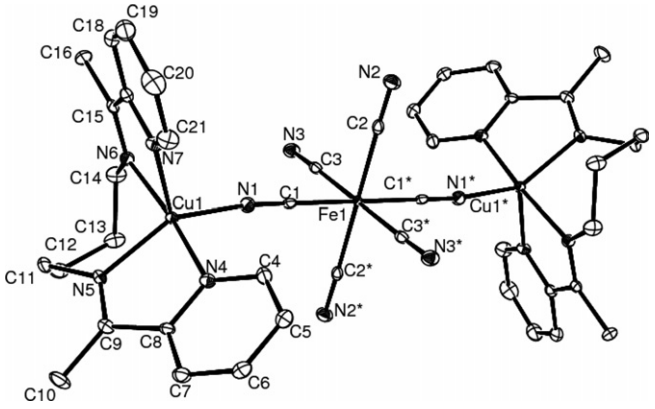


Fig. 4. Labelled ORTEP plot of **2** (Hydrogen atoms have been omitted for clarity; Ellipsoids are drawn at the 40% probability level.) Symmetry operations *: $1-x, -y, -z$.

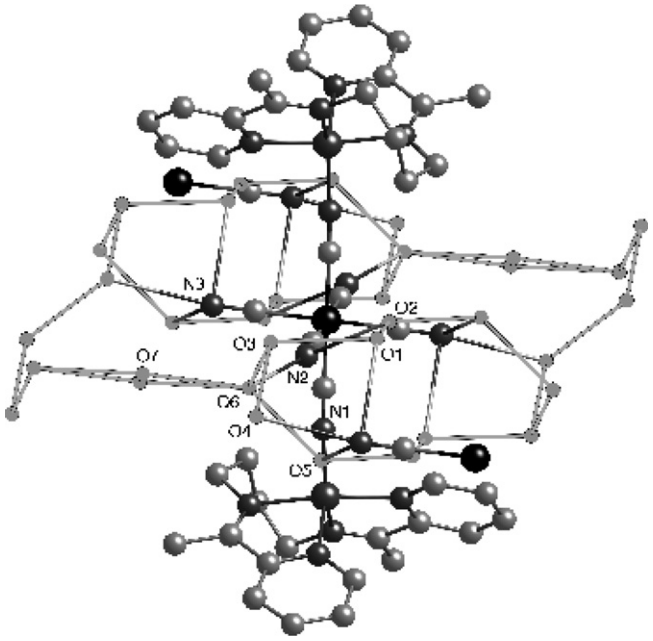


Fig. 5. Extensive hydrogen bonding network between the trinuclear complex and the intercalated water molecules in complex **2**.

Table 5
Selected hydrogen bonding parameters for **2**

D···A	*d* (Å)
O(1)···O(2)	2.750(3)
O(1)···O(3)	2.783(4)
O(1)···N(3)^{i}	3.155(4)
O(2)···N(2)	2.947(4)
O(2)···N(5)^{ii}	2.772(3)
O(3)···O(4)	2.795(3)
O(3)···O(6)	2.784(4)
O(4)···O(4)^{iii}	2.830(5)
O(5)···O(6)	2.902(4)
O(5)···N(3)^{i}	2.870(4)
O(6)···N(2)	2.819(3)
O(6)···O(7)	2.845(11)
O(6)···O(7)^{iv}	2.858(11)

Symmetry operations (i) $x-1, y, z$; (ii) $-x, -y, -z$; (iii) $-x, 1-y, 1-z$; (iv) $1-x, 1-y, 1-z$.

number, μ_B is the Bohr magneton and K is the Boltzmann constant. The best fit parameters, as shown in Fig. 7, are $J=-0.81\ \mathrm{cm}^{-1}$ and $g=2.12$ with $R=2.7\times10^{-5}$ for **1**, and $J=-0.73\ \mathrm{cm}^{-1}$ and $g=2.14$ with $R=3.3\times10^{-5}$ for **2**. $R=\Sigma_i(\chi T_{i\mathrm{calc}}-\chi\ T_{i\mathrm{exp}})^2/(\chi T_{i\mathrm{exp}})^2$

$$\chi_M=\frac{Ng^2\mu_B^2}{KT}\frac{2\exp(J/KT)}{1+3\exp(J/KT)} \quad (1)$$

The field dependence of the magnetization (0–5 T) measured at 2 K is shown in Fig. 7 (inset), in the form of $M/N\beta$ (per Cu_2Co and Cu_2Fe units) vs H. The magnetization reaches a value of 1.9 $N\beta$ for **1** and 1.99 $N\beta$ for **2** at 5 T, which

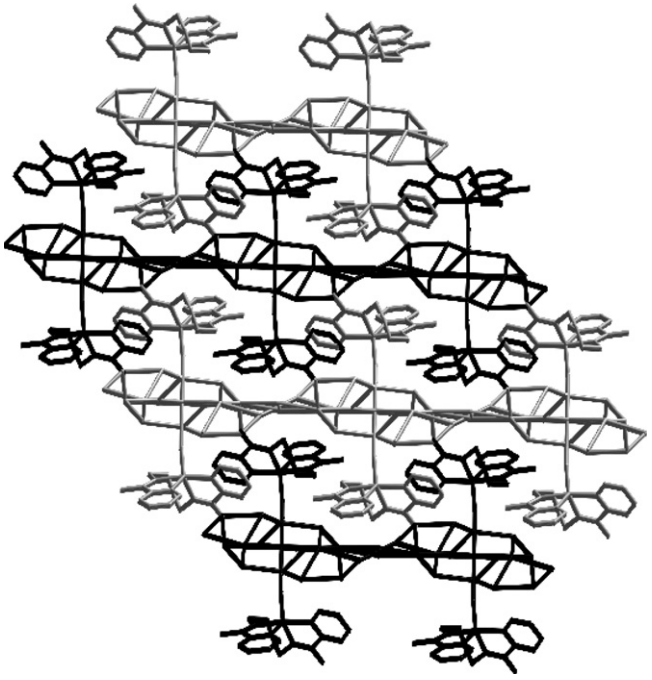


Fig. 6. The interdigitation of adjacent hydrogen bonded layers in **2**.

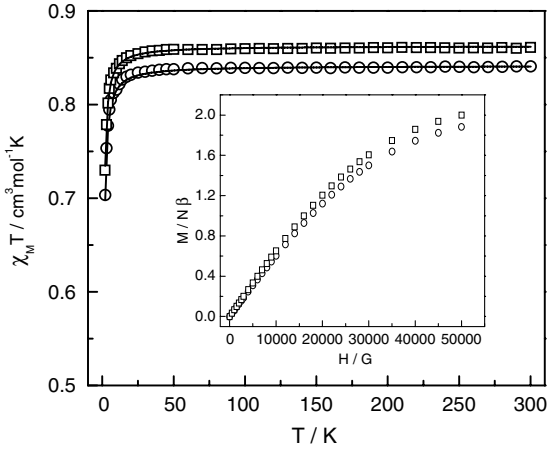


Fig. 7. Plot of observed values of $\chi_M T$ vs T and $M/N\beta$ vs H (inset) for **1** (○) and **2** (□) (The solid lines denote a theoretical fit of the data.).

is close to the expected $S = 1/2$ value of two isolated Cu(II) atoms.

The two complexes show a very weak coupling, as may be expected from the diamagnetic –NC–Co–CN– and –NC–Fe–CN– bridges. The weak magnetic exchange can be understood considering the large copper–copper distance.

4. Conclusion

We have described the synthesis, spectroscopic, structural and magnetic characterization of two trimetallic complexes containing divalent and distorted trigonal bipyramidal $[Cu(C_{18}H_{22}N_4)]^{2+}$ cation centers with slightly distorted octahedral hexacyanometallate ion. The assembly of the two components is achieved through the bridging mode of the CN^- ligand and is also due to the coordination properties of the copper ion. Interestingly, weak antiferromagnetic interactions, resulting from intermolecular interactions between the Cu(II) ions in the network, were observed for both **1** and **2** below 2 K. It can be proposed that the cooperativity arising from the network structure through hydrogen bonds plays an important role in molecular magnetization for this series of compounds.

Acknowledgements

Joy Chakraborty is thankful to the University Grants Commission, New Delhi for providing a Senior Research Fellowship to him. This work is also supported by grants given by the Ministerio de Educación y Ciencia (Programa Ramón y Cajal) and BQU2003/00539 of Spain.

Appendix A. Supplementary material

CCDC 632267 and 632268 contain the supplementary crystallographic data for **1** and **2**. These data can be obtained free of charge via http://www.ccdc.cam.ac.uk/conts/retrieving.html, or from the Cambridge Crystallographic Data Centre, 12 Union Road, Cambridge CB2 1EZ, UK; fax: (+44) 1223 336 033; or e-mail: deposit@ccdc.cam.ac.uk.

References

[1] (a) J.J. Sokol, A.G. Hee, J.R. Long, J. Am. Chem. Soc. 124 (2002) 7656;
(b) M. Verdaguer, A. Bleuzen, V. Marvaud, J. Vaissermann, M. Seuleiman, C. Desplanches, A. Scuiller, C. Train, R. Garde, G. Gelly, C. Lomenech, I. Rosenman, P. Veillet, C. Cartier, F. Villain, Coord. Chem. Rev. 190 (1999) 1023;
(c) S.M. Holmes, G.S. Girolami, J. Am. Chem. Soc. 121 (1999) 5593.
[2] W.R. Entley, G.S. Girolami, Science 268 (1995) 397.
[3] O. Kahn, Adv. Inorg. Chem. 43 (1995) 179.
[4] (a) H. Miyasaka, R. Clerac, W. Wernsdofer, L. Lecren, C. Bonhomme, K. Sugiura, M. Yamashita, Angew. Chem., Int. Ed. 43 (2004) 2801;
(b) R. Clerac, H. Miyasaka, M. Yamashita, C. Coulon, J. Am. Chem. Soc. 124 (2002) 12837.
[5] P.V. Bernhardt, B.P. Macpherson, M. Martinez, Inorg. Chem. 39 (2000) 5203.
[6] (a) J.Y. Yang, M.P. Shores, J.J. Sokol, J.R. Long, Inorg. Chem. 42 (2003) 1403;
(b) C.P. Berlinguette, J.R. Galá-Mascarós, K.R. Dunbar, Inorg. Chem. 42 (2003) 3416.
[7] H. Oshio, H. Onodera, O. Tamada, H. Mizutani, T. Hikichi, T. Ito, Chem. Eur. J. 6 (2000) 2523.
[8] (a) E. Coronado, C. Giménez-Saiz, A. Nuez, F.M. Remero, E. Rusanov, H. Stoeckli-Evans, Inorg. Chem. 41 (2002) 4615;
(b) E. Colacio, M. Ghazi, H. Stoeckli-Evans, F. Lloret, J.M. Moreno, C. Pérez, Inorg. Chem. 40 (2001) 4876.
[9] R. Lescouëzec, F. Lloret, M. Julve, J. Vaissermann, M. Verdaguer, R. Llusar, S. Uriel, Inorg. Chem. 40 (2001) 2065.
[10] E. Colacio, J.M. Domínguez-Vera, F. Lloret, J.M. Moreno Sánchez, R. Kivekäs, A. Rodriguez, R. Sillanpää, Inorg. Chem. 42 (2003) 4209.
[11] J.A. Smith, J.-R. Galán-Mascarós, R. Clérac, K.R. Dunbar, Chem. Commun. (2000) 1077.

[12] (a) S.-W. Zhang, D.-G. Fu, W.-Y. Sun, Z. Hu, K.-B. Yu, W.-X. Tang, Inorg. Chem. 39 (2000) 1142;
(b) M. Ohba, H. Ōkawa, Coord. Chem. Rev. 198 (2000) 313.
[13] S.-I. Ohkoshi, K. Hashimoto, J. Am. Chem. Soc. 121 (1999) 10591.
[14] S. Ferlay, T. Mallah, R. Ouahes, P. Veillet, M. Verdaguer, Nature 378 (1995) 701.
[15] (a) S. Wang, J.-L. Zuo, S. Gao, Y. Song, H.-C. Zhou, Y.-Z. Zhang, X.-Z. You, J. Am. Chem. Soc. 126 (2004) 8900;
(b) L.M. Toma, R. Lescouezec, F. Lloret, J. Vaissermann, M. Verdaguer, Chem. Commun. (2003) 1850;
(c) R. Lescouëzec, J. Vaissermann, C. Ruiz-Pérez, F. Lloret, R. Carrasco, M. Julve, M. Verdaguer, Y. Dromzee, D. Gatteschi, W. Wernsdorfer, Angew. Chem., Int. Ed. 42 (2003) 1483.
[16] (a) E.J. Schelter, A.V. Prosvirin, W.M. Reiff, K.R. Dunbar, Angew Chem., Int. Ed. 43 (2004) 4912;
(b) S. Wang, J.-L. Zou, H.-C. Zhou, H.J. Choi, Y. Ke, J.R. Long, X.-Z. You, Angew. Chem., Int. Ed. 43 (2004) 5940;
(c) E.J. Schelter, A.V. Prosvirin, K.R. Dunbar, J. Am. Chem. Soc. 126 (2004) 15004;
(d) A.V. Palii, S.M. Ostrovsky, S.I. Klokishner, B.S. Tsukerblat, C.P. Berlinguette, K.R. Dunbar, J.R. Galan-Mascaros, J. Am. Chem. Soc. 126 (2004) 16860;
(e) C.P. Berlinguette, D. Vaughn, C. Canada-Vilalta, J.R. Galan-Mascaros, K.R. Dunbar, Angew. Chem., Int. Ed. 42 (2003) 1523;
(f) J.J. Sokol, A.G. Hee, J.R. Long, J. Am. Chem. Soc. 124 (2002) 7656.
[17] (a) J. Larionova, M. Gross, H.A. Pilkington, H. Stoeckli-Evans, H.U. Gudel, S. Decurtins, Angew. Chem., Int. Ed. 39 (2000) 1605;
(b) Z.J. Zhong, H. Seino, Y. Mizobe, M. Hidai, A. Fujishima, S. Ohkoshi, K. Hashimoto, J. Am. Chem. Soc. 122 (2000) 2952.
[18] (a) L. Catala, C. Mathoniere, A. Gloter, O. Stephan, T. Gacoin, J.-P. Boilot, T. Mallah, Chem. Commun. (2005) 746;
(b) A. Dei, Angew Chem., Int. Ed. 44 (2005) 1160;
(c) J.M. Herrera, V. Marvaud, M. Verdaguer, J. Marrot, M. Kalisz, C. Mathoniere, Angew. Chem., Int. Ed. 43 (2004) 5468;
(d) Y. Arimoto, S. Ohkoshi, Z.J. Zhong, H. Seino, Y. Mizobe, K. Hashimoto, J. Am. Chem. Soc. 125 (2003) 9240;
(e) A. Bleuzen, C. Lomenech, V. Escax, F. Villain, F. Varret, C. Cartier dit Moulin, M. Verdaguer, J. Am. Chem. Soc. 122 (2000) 6648;
(f) C. Cartier dit Moulin, F. Villain, A. Bleuzen, M. Arrio, P. Sainctavit, C. Lomenech, V. Escax, F. Baudelet, E. Dartyge, M. Verdaguer, J. Am. Chem. Soc. 122 (2000) 6653.
[19] Z. Trávníček, Z. Smékal, A. Escuer, J. Marek, New J. Chem. 25 (2001) 655.
[20] H.Z. Kou, H.M. Wang, D.Z. Liao, P. Cheng, Z.H. Jiang, S.P. Yan, X.Y. Huang, G.L. Wang, Aust. J. Chem. 51 (1998) 661.
[21] J. Zou, X. Hu, C. Duan, Z. Xu, X. You, T.C. Mak, Transit. Met. Chem. 23 (1998) 477.
[22] H.-Z. Kou, D.-Z. Liao, P. Cheng, Z.-H. Jiang, G.-L. Wang, Transit. Met. Chem. 21 (1996) 349.
[23] R.J. Parker, D.C.R. Hockless, B. Moubaraki, K.S. Murray, L. Spiccia, Chem. Commun. (1996) 2789.
[24] H.-Z. Kou, D.-Z. Liao, P. Cheng, Z.-H. Jiang, S.-P. Yan, G.-L. Wang, X.-K. Yao, H.-G. Wang, J. Chem. Soc., Dalton Trans. (1997) 1503.
[25] E. Colacio, J.M. Domínguez-Vera, M. Gazi, R. Kivekäs, J.M. Moreno, A. Pajunen, J. Chem. Soc., Dalton Trans. (2000) 505.
[26] (a) M.J. Scott, S.C. Lee, R.H. Holm, Inorg. Chem. 33 (1994) 4561;
(b) M.T. Gardner, G. Deinum, Y. Kim, G.T. Babcock, M.J. Scott, R.H. Holm, Inorg. Chem. 35 (1996) 6878;
(c) R.T. Conley, Infrared Spectroscopy, Allyn & Bacon Inc., Boston, 1966;
(d) K. Nakamoto, Infrared and Raman Spectra of Inorganic and Coordination Compounds; Part A and B, fifth ed., Wiley, New York, 1997.
[27] N. Mondal, D.K. Dey, S. Mitra, V. Gramlich, Polyhedron 20 (2000) 607.
[28] (a) M. Ferbinteanu, S. Tanase, M. Andruh, Y. Journaux, F. Cimpoesu, I. Strenger, E. Rivière, Polyhedron 18 (1999) 3019;
(b) A.B.P. Lever, Inorganic Electronic Spectroscopy, second ed., Elsevier, Amsterdam, 1984.
[29] (a) B. Samanta, J. Chakraborty, N.K. Karan, R.K.B. Singh, G.P.A. Yap, C. Marschner, J. Baumgartner, S. Mitra, Struct. Chem. 17 (2006) 139;
(b) M.K. Saha, D.K. Dey, B. Samanta, S.K. Dey, K.M.A. Malik, S. Mitra, Z. Naturforsch. 60b (2005) 1043;
(c) N.K. Karan, B. Samanta, S. Mitra, V. Gramlich, Z. Naturforsch. 60b (2005) 640;
(d) C.R. Choudhury, S.K. Dey, S. Mitra, N. Mondal, J. Ribas, K.M.A. Malik, Bull. Chem. Soc. Jpn. 77 (2004) 959.
[30] M.K. Saha, S. Sen, P. Kundu, T. Gupta, V. Gramlich, S. Mitra, Z. Naturforsch. 53b (1998) 1281.
[31] Enraf-Nonius, COLLECT, Nonius BV, Delft (The Netherlands) 1997–2000.
[32] Z. Otwinowski (Minor), Processing of X-ray diffraction data collected in oscillation mode, Macromolecular Crystallography, Part. A. 276 (1997) 307.
[33] G.M. Sheldrick, SADABS, Programs for area detector adsorption correction, Institute for Inorganic Chemistry, University of Göttingen, Germany, 1996.
[34] G.M. Sheldrick, SHELX-97 (SHELXS and SHELXL) Program for solution and refinement of crystal structures, University of Göttingen, Göttingen, Germany, 1997.
[35] L.J. Farrugia, ORTEP-3 for windows, J. Appl. Crystallogr. 30 (1997) 565.
[36] L.J. Barbour, XSEED, A software tool for supramolecular crystallography, J. Supramol. Chem. 1 (2001) 189.
[37] (a) B.J. Hathaway, G. Wilkinson, R.D. Gillard, J.A. McCleverty (Eds.), Comprehensive Coordination Chemistry, vol. 5, Pergamon, Oxford, 1987, p. 607;
(b) A.W. Addison, T.N. Rao, J. Reedijk, J. van Rijn, G.C. Verschoor, J. Chem. Soc., Dalton Trans. (1984) 2349.
[38] (a) J. Zou, X. Hu, C. Duan, Z. Xu, X. You, T.C. Mak, Transit. Met. Chem. 23 (1998) 477;
(b) A. Yuan, J. Zou, B. Li, Z. Zha, C. Duan, Y. Liu, Z. Xu, S. Keizer, Chem. Commun. (2000) 1297.

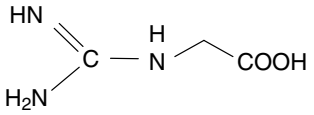


Fig. 1. Structure of guanidinoacetic acid.

extrapyramidal movements, epilepsy, as well as autistic or self-aggressive behavior in older patients [6–11].

Besides being involved in GAMT deficiency, GAA participates in a number of other biological processes. First, since it is synthesized prior to creatine and in the renal tubules, its urinary excretion rate may be used as a sensitive indicator of early-stage nephropathy [12–14]. GAA can also act as a neurotoxin and neuromodulator since it is a partial agonist of the GABA-A receptor and inhibitor of Na^+–K^+-ATPase activity [15,16]. Other GAA biological roles are related to cholesterol production [17], thyroid dysfunction [18], epileptic seizures [19], hepatic encephalopathy [20] and insulin regulation [21]. It is also well known that levels of GAA are increased in the cerebral cortex after hyperbaric oxygenation, probably due to a decrease in arginase activity, which causes an increase of both Mn and Cu, Zn-superoxide dismutase [18]. In addition, a significant decrease in the urinary excretion of GAA has been observed after cisplatin treatment in patients with urinary tract neoplasm [22].

This diversity in participation of GAA in several subject areas should be related to the pool of possible chemical reactions that it can present. We have already studied some of GAA properties by analyzing its coordination to some metal ions of biological interest. GAA complexes with Mn(II), Co(II), Ni(II), Cu(II), Zn(II), Cd(II) and Pb(II) were studied potentiometrically in aqueous solution where besides determining the stability constants of the principal species, an α-nitrogen and oxygen-carboxylate coordination to the metals was proposed [23]. From synthesized GAA powder complexes with Cr(III), Co(II), Ni(II), Cu(II) and Zn(II), the same kind of coordination, that is, through α-nitrogen and oxygen-carboxylate, was observed by infrared, ultraviolet–visible spectroscopies and electron paramagnetic resonance [24]. The involvement of α-nitrogen from GAA in the metal coordination is in agreement with the biological step of its methylation that occurs at the same site/atom.

We have also studied the guanidino-carboxylate interactions between GAA and glutamic acid or aspartic acid in the presence of Cu(II) in aqueous solution [25]. These interactions are biologically very important since they are observed in the substrate fixation of Cu, Zn-superoxide dismutase and of carboxypeptidase A besides being identified in the complex formed by a human immunodeficiency virus and the receptor on the cell wall [26,27]. From our studies we could observe that the values of stability constants of the ternary complexes involving both GAA and Glu or Asp (Cu(II):GAA:L systems, L = Glu or Asp) were higher than the expected due to the possibility of occurrence of these interactions [25].

Meanwhile, we obtained two different Cu(II) crystal complexes of GAA. One of them was a dimeric-copper(II)-bridge-carboxylate complex, tetrakis(μ-guanidinoacetic acid-κ^2O:O')bis[nitrate-κO-copper(II)], $[Cu_2(NO_3)_2(GAA)_4]$ [28]. This complex, in contrast with previous ones, presented an exclusive-oxygen coordination. The other complex, aqua[μ-(N^1-carboxylato-methylguanidino)oxidoacetato](μ-guanidinoaceticacid)di-copper(II) nitrate dehydrate, $[Cu_2(C_5H_6N_3O_5)(C_3H_7N_3O_2)\text{-}H_2O]NO_3 \cdot 2H_2O$, presented a new ligand, $C_5H_6N_3O_5$ N,N'-guandinodiacetic acid (Oag), a guanidine derivative, formed from GAA and copper(II) solution [29]. In this complex, GAA is again coordinated through both oxygen atoms of the bridged carboxylate group whereas the new ligand Oag was coordinated to two Cu(II) ions through three oxygen atoms and one nitrogen atom from the guanidino group. In order to understand the formation of we made an EPR study during different steps of the complex synthesis [30]. We proposed a mechanism of Oag formation based on a reaction between two CuH_2GAA precursor species, followed by a nucleophilic attack of the coordinated water to the α-carbon of GAA, causing its desamidination as a consequence. The fragment resultant from the latter reaction then reacts with a non-coordinated GAA and forms Oag.

Following our studies on GAA, we have investigated its complexation behavior in the presence of Cu(II) and two amino acids, glycine (Gly) and serine (Ser) separately. With Gly, the aforementioned guanidino-carboxylate interactions with GAA should not be possible if Gly were coordinated through its carboxylate group. Ser besides presenting an interesting hydroxyl group in its structure, which may involve other interactions, is present in some enzymes, specifically serine endopeptidases, which are inhibited by guanidino groups [31]. Moreover, reduced serine phosphorylation of the creatine transporter is associated with increments in myocellular creatine content after starvation [32].

Herein, we report two novel Cu(II) complexes synthesized from GAA and a copper(II) solution in the presence of Gly or Ser. Each of such complexes presents a condensed amino acid residue formed by GAA and Gly or Ser with an elongation of the carbon chain. The X-ray structures of both complexes as well as their spectroscopic characterization are herein presented. In addition, we attempt to propose a mechanism for the formation of the new ligands, serine-3-*N*-methylguanidino acetic acid and glycine-3-*N*-methylguanidino acetic acid. Another interesting point for discussion, in addition to the elongation of the carbon chain, is the methylation on the N3 atom from GAA instead of on the α-nitrogen. The synthesis of new guanidines has been intensively investigated since they play an important role in biological recognition sites and catalysis [33] and some of them are used in the design of drugs for different areas of application [34].

2. Experimental

2.1. Syntheses of the complexes O,O′,N,N′-glycine-N-3-methylguanidinoacetic acid copper(II) [CuGly-mGAA] (1) and O,O′,N,N′-serine-N-3-methylguanidinoacetic acid copper(II) [CuSer-mGAA] (2)

An aqueous solution of 3 mmol of guanidinoacetic acid (0.3513 g, Sigma-Aldrich) and 3 mmol of glycine (0.2252 g, Merck) or serine (0.3153 g, Merck) in 30 mL of deionized water was stirred at a temperature of 60 °C for 6 h until complete dissolution. A solution of 3 mmol (0.7248 g, Merck) of copper(II) nitrate in 5 mL of deionized water was then slowly added to the previous mixture, followed by stirring at a temperature of 60 °C for approximately 8 h. After that the mixture was cooled until 4 °C for 24 h. The mixture was filtered and the pH of the filtrate was adjusted to 4.3 with KOH 3 mol/L (Merck). After cooling the solution until 4 °C for 24 h, it was stocked in a glass vessel at room temperature. Slow evaporation of the solution resulted in blue needle crystals, which were washed with absolute ethanol (Merck) and dried at 50 °C for 2 h.

2.2. X-ray analyses

The crystal structures of the two complexes (CuGly-mGAA and CuSer-mGAA) were determined by X-ray diffraction. Data were collected in a Nonius KappaCCD diffractometer at $T = 293$ K. The HKL DENZO and SCALEPACK programs [35] were used for cell refinement and data reduction.

2.3. Infrared spectroscopy

The infrared spectra were recorded on a Perkin–Elmer 2000 FT-IR spectrometer. Data were collected with a 0.5 cm^{-1} interval with a resolution of 4 cm^{-1}. The scanning speed was 0.2 cm s^{-1} and 120 scans were performed. The samples were measured in the range of 4000–370 cm^{-1} as KBr pellets, and in the range of 710–30 cm^{-1} as polyethylene pellets.

2.4. DFT calculations

In order to correlate the structures obtained by X-ray diffraction with the IR spectra of the complexes we have chosen one of the complexes, complex **2**, to compare the experimental and calculated spectrum.

Vibrational assignments of the complex CuSer-mGAA (complex **2**) were carried out with the aid of density functional theory (DFT) calculations.

Ab initio optimization of the geometrical parameters, and hence structural analysis of the guanidoacetic–serinate Cu(II) complex, was carried out employing DFT levels [36–38] with B3LYP/6-31G and with B3LYP/6-311G basis sets, and the RHF/6-311G procedure.

3. Results and discussion

3.1. X-ray structure of the complexes

The equatorial coordination of copper atoms is similar for the two compounds herein described (Table 1). The ligands coordinate toward two oxygen atoms (O2 and O3) of different carboxylate groups and two nitrogen atoms (N1 and N4) to form the equatorial plane of the metal. Nitrogen N1 is positioned *trans* to oxygen O3. The equatorial planes of CuGly-mGAA and of Cu-Ser-mGAA present almost planar *cis* configurations. Similar configurations were observed in other Cu(II) amino acids complexes, $[Cu(l\text{-}Arg)_2](NO_3)_2 \cdot 3H_2O$ [39], $[Cu(l\text{-}isoleu)_2] \cdot H_2O$ [40] and $[Cu(Gly)_2] \cdot H_2O$ [41]. Bond angles in the equatorial plane of copper in CuSer-mGAA are similar to the values obtained for the Cu(II) amino acid complexes (Table 2). The O–Cu–N bond angles, inside each Cu-peptide ring, are acute (around 85°). Angles O–Cu–O and N–Cu–N, outside the Cu-peptide rings of these compounds, are obtuse. Compound Cu-Gly-mGAA, on the other hand, has all angles in the equatorial plane of copper close to 90°.

It is interesting to note the differences between N1 and N4: distances from least square planes (Table 3) show C2 and C3 closer to the least square plane towards Cu, O2, C1, N1 and O1 than C4 and C5 to the plane toward Cu, O3, C6, N4 and O4. As can be seen in Table 3, the deviation from the planes is stronger for CuSer-mGAA than for CuGly-mGAA. Atoms C2 and C3 of CuGly-mGAA are in the plane towards Cu, O2, C1, N1 and O1.

Copper axial coordination is different in the two compounds. One weak interaction between copper and the oxygen O4 (d[Cu–O4^2] = 2.380(7) Å) of a second ligand (Fig. 2) is present in CuGly-mGAA. The structure of CuSer-mGAA (Fig. 3), on the other hand, has the axial neighborhood of the metal fulfilled by two copper–water interactions. One of these is weak, with d[Cu–O7] = 2.500(4) Å; the other is very weak, with d[Cu–O6] = 2.820(4) Å. The ligands on the axial direction appear to affect the deviation of Cu from the least square planes towards its equatorial neighbor (Table 4), which is stronger in the axially less symmetric CuGly-mGAA (0.146(5) Å) than in the more symmetric CuSer-mGAA (0.084(2) Å).

The packing of Cu-Ser-mGAA (Fig. 3b) is formed by parallel layers of molecules. Molecules of neighbor layers are connected through hydrogen bonds involving the water molecules and the carboxylate oxygens (Tables 4 and 5). N–H···O hydrogen bonds also contribute to stabilize the crystal structure. The packing of Cu-Gly-mGAA (Fig. 2b), differently, is stabilized by the polymeric structure formed by molecules oriented perpendicularly to each other and linked through Cu–O4 bonds, as well as hydrogen bonds involving the water molecule and the carboxylate oxygens O4 and O1 of neighbor molecules.

Table 1
Bond lengths (Å) and angles (°) for CuSer-mGAA and CuGly-mGAA

	Cu-Ser-mGAA	Cu-Gly-mGAA
Bond lengths (Å)		
Cu(1)–O(2)	1.937(3)	1.925(7)
O(2)–C(1)	1.287(6)	1.339(13)
C(1)–O(1)	1.240(5)	1.216(11)
C(1)–C(2)	1.510(7)	1.600(17)
C(2)–N(1)	1.450(6)	1.393(10)
N(1)–Cu(1)	1.930(4)	2.024(7)
N(1)–C(3)	1.299(6)	1.374(12)
C(3)–N(2)	1.341(6)	1.408(12)
C(3)–N(3)	1.366(6)	1.315(12)
N(3)–C(4)	1.424(6)	1.414(14)
C(4)–N(4)	1.493(6)	1.388(14)
N(4)–Cu(1)	1.986(4)	1.959(9)
N(4)–C(5)	1.479(7)	1.428(12)
C(5)–C(6)	1.536(9)	1.599(14)
C(6)–O(3)	1.281(6)	1.245(11)
O(3)–Cu(1)	1.960(3)	2.037(7)
C(6)–O(4)	1.235(6)	1.287(12)
C(5)–C(7)	1.527(7)	
C(7)–O(5)	1.430(7)	
Cu(1)–O(7)	2.500(3)	
Cu(1)–O(6)	2.827(3)	
Cu(1)–O(4)[1]		2.382(7)
Bond angles (°)		
N(1)–Cu(1)–O(2)	84.97(17)	89.0(4)
N(1)–Cu(1)–O(3)	173.88(18)	165.6(3)
O(2)–Cu(1)–O(3)	94.78(14)	88.6(3)
N(1)–Cu(1)–N(4)	95.51(17)	91.4(3)
O(2)–Cu(1)–N(4)	176.18(18)	177.6(5)
O(3)–Cu(1)–N(4)	84.34(17)	90.4(3)
C(1)–O(2)–Cu(1)	114.5(3)	110.9(8)
C(6)–O(3)–Cu(1)	114.3(3)	109.5(7)
C(3)–N(1)–C(2)	119.3(4)	120.4(9)
C(3)–N(1)–Cu(1)	125.6(3)	130.1(7)
C(2)–N(1)–Cu(1)	112.0(3)	109.4(6)
C(3)–N(3)–C(4)	122.9(4)	117.4(9)
C(5)–N(4)–C(4)	115.0(4)	127.8(10)
C(5)–N(4)–Cu(1)	108.3(3)	104.9(6)
C(4)–N(4)–Cu(1)	109.2(3)	113.4(8)
O(1)–C(1)–O(2)	123.2(4)	118.1(12)
O(1)–C(1)–C(2)	119.6(4)	123.6(11)
O(2)–C(1)–C(2)	117.2(4)	118.3(10)
N(1)–C(2)–C(1)	124.3(5)	125.4(11)
N(1)–C(3)–N(2)	110.2(4)	112.4(9)
N(1)–C(3)–N(3)	119.8(4)	121.3(9)
N(2)–C(3)–N(3)	115.9(4)	113.2(9)
N(3)–C(4)–N(4)	110.7(4)	132.4(11)
N(4)–C(5)–C(6)	110.0(4)	117.5(8)
O(4)–C(6)–O(3)	123.1(5)	117.4(10)
O(3)–C(6)–C(5)	117.1(4)	117.2(10)
O(4)–C(6)–C(5)	119.7(5)	125.3(9)
O(5)–C(7)–C(5)	108.1(4)	
N(4)–C(5)–C(7)	110.6(5)	
C(7)–C(5)–C(6)	112.0(5)	
O(2)–Cu(1)–O(4)[1]		97.2(3)
N(4)–Cu(1)–O(4)[1]		85.1(4)
N(1)–Cu(1)–O(4)[1]		103.2(3)
O(3)–Cu(1)–O(4)[1]		91.3(3)
C(6)–O(4)–Cu(1)[2]		130.8(7)

Symmetry operations: 1: $X-1/2, -Y-1/2, -Z$; 2: $X+1/2, -Y-1/2, -Z$.

3.2. Infrared spectroscopy analyses

3.2.1. Infrared spectroscopy analysis of CuGly-mGAA (complex 1)

The following discussion on infrared analysis has been based on comparisons with analogous complexes. The principal infrared data of complex **1** as well as of Gly [42], GAA [24], *trans*-Cu(Gly)$_2$ [42] and *cis*-Cu(GAA)$_2$ [24] are presented in Table 6.

Several bands can be observed in the 3500–3200 cm^{-1} range. The first in 3536 cm^{-1} is relative to the stretching modes of O–H of lattice water [42]. In addition, several other bands were observed in the same range, relative to stretching N–H modes of amines, in 3332 cm^{-1}, 3422 cm^{-1} and 3199 cm^{-1}. The band in 1670 cm^{-1} attributed to νC=N of the guanidino group from GAA was shifted to 1667 cm^{-1} in *cis*-Cu(GAA)$_2$, whereas it was not observed in complex **1**, probably indicating that this group has suffered significant modifications. This makes sense since complex **1** presents a methyl group bound to the terminal nitrogen from its guanidino group.

In the 1630–1380 cm^{-1} range, the carboxylate asymmetric and symmetric stretching modes were observed probably coupled with amine deformation modes. Considering the number of carboxylate groups as well as the number of amines, the attempted assignments become very difficult.

Several new bands were observed in the 450–300 cm^{-1} range. By comparing the same spectral region observed in *trans*-Cu(Gly)$_2$ and *cis*-Cu(GAA)$_2$, the bands in 464 cm^{-1} and 409 cm^{-1} may be related approximately to ν(Cu–N) coupled with other vibrational modes while those in 361 cm^{-1} and 341 cm^{-1} to ν(Cu–O), also coupled with other framework vibrational modes. It has also been observed that the skeletal modes of GAA (436 cm^{-1} and 319 cm^{-1}) were absent, reflecting the modifications that occurred in its structure.

3.2.2. Infrared spectroscopy analysis of CuSer-mGAA (complex 2)

Table 7 presents the principal infrared bands and their assignments of complex **2**, GAA [24], Ser [43] and *cis*-Cu(GAA)$_2$ [24].

The band in 3454 cm^{-1} is relative to the stretching mode of O–H of lattice water. The other bands in the 3400–3200 cm^{-1} range are probably relative to stretching N–H modes of amines. Analogously to complex **1**, the band in 1670 cm^{-1} was not observed in **2**, for the same reasons mentioned above.

The bands in 1646 cm^{-1}, 1558 cm^{-1}, 1544 cm^{-1}, 1466 cm^{-1} and 1369 cm^{-1} are assumed to correspond to asymmetric and symmetric stretching modes of the carboxylate group, probably coupled with amine deformation modes.

Several new bands were observed in the 450–300 cm^{-1} range. The bands in 466 cm^{-1} and 429 cm^{-1} may be related to ν(Cu–N), while those in 390 and 376 cm^{-1} to ν(Cu–O).

Table 2
Geometrical parameters of the Cu coordination sphere (Å, °)

	CuGly-mGAA	CuSer-mGAA	$[Cu(l\text{-}Arg)_2](NO_3)_2 \cdot 3H_2O$	$[Cu(l\text{-}isoleu)_2] \cdot H_2O$	$[Cu(gly)_2] \cdot H_2O$
Cu–O2	1.925(7)	1.937(3)	1.930(4)	1.948	1.957(9)
Cu–O3	2.037(7)	1.960(3)	1.973(4)	1.953	1.946(9)
Cu–N1	2.024(7)	1.930(4)	1.974(5)	1.989	1.984(10)
Cu–N4	1.959(9)	1.986(4)	1.972(5)	1.995	2.021(11)
O2–Cu–O3	88.6(3)	94.78(14)	94.3(2)	91.7	92.9(4)
N1–Cu–N4	91.4(3)	95.51(17)	96.7(2)	98.6	96.6(4)
O2–Cu–N1	89.0(4)	84.97(17)	84.5(2)	84.2	85.0(4)
O3–Cu–N4	90.4(3)	84.34(17)	84.3(2)	84.5	85.4(4)

Table 3
Distances (Å) of selected atoms to selected least square planes of CuGly-mGAA and CuSer-mGAA

Plane	Atom	Cu-Gly-mGAA	Cu-Ser-mGAA
O2C1N1O1Cu	C2	0.008(12)	0.113(7)
	C3	0.057(16)	0.200(9)
O3C6N4O4Cu	C4	0.669(22)	0.797(9)
	C5	0.100(14)	0.243(7)
N1N4O3O2	Cu	0.146(5)	0.084(2)

Similarly to complex **1**, the GAA bands in 436 cm^{-1} and 319 cm^{-1}, relative to skeletal modes, were absent in **2**.

3.3. Vibrational assignments

For the discussion of vibrational assignments, we will take the DFT values corrected by a scale factor of 0.9613 as a base of comparison with the 81 experimental wave numbers of the infrared spectra joined to second derivative bands. For an accurate description of the normal modes in the metal-ligand spectral range, as we have proposed in other works [44,45], we use the percentage of deviation of geometrical parameters (PDGP) from the equilibrium position. The PDGP can be also normalized to obtain the percentage of participation of each internal vibrational coordinate that describes the framework vibrations.

3.3.1. NH and CH stretching

We expected to observe a total of four bands pertaining to the asymmetric and symmetric N–H stretching normal modes. Within a large band centered on 3333 cm^{-1}, we could identify absorption bands at 3676, 3568, 3452, 3340, 3299, 3263, 3242, 3140, 2922, 2896 and 2852 cm^{-1}. These bands can be assigned according to DFT results to the vibrational modes ν_{as}(NH), ν(OH), ν_s(NH), ν_s(NH), ν_s(NH), ν_s(NH), ν_{as}(CH) ν_{as}(CH) ν_{as}(CH) ν_{as}(CH), ν(CH)methane, ν_s(CH) and ν(CH), respectively. The second derivative spectrum shows bands at 3571, 3459, 3343, 3299, 3264, 242, 3129, 2961, 2898 and 2851 cm^{-1}, presenting good correlation with the experimental ones. When we applied the Bellamy–Williams relationship [46] for primary amines $\nu(a') = 345.5 + 0.876\nu(a'')$ to the experimental band found at 3676 cm^{-1}, we obtained the value of 3565 cm^{-1}, so we can conclude that the value calculated at 3695 cm^{-1} by the DFT method could not be considered as the ν(OH) vibrational mode. The DFT calculated bands for these NH and CH stretching vibrational modes are in good agreement with experimental ones.

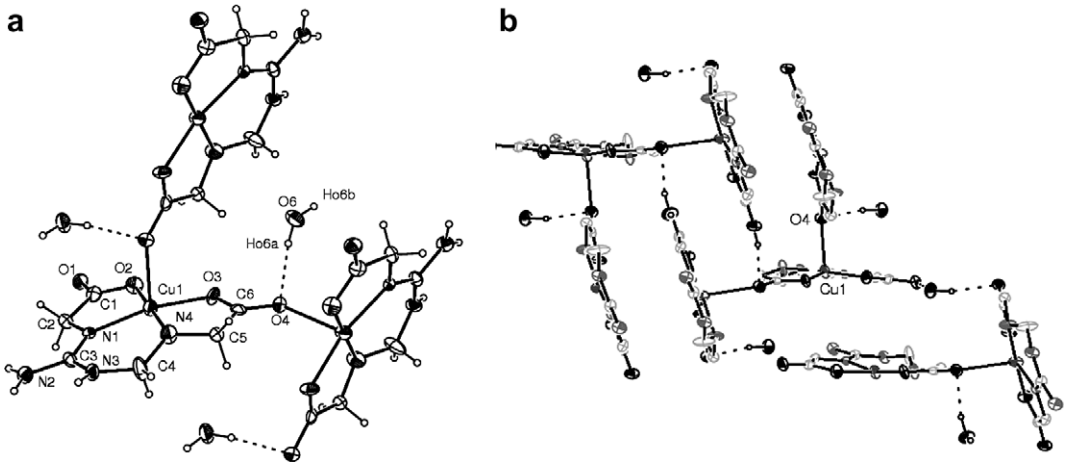


Fig. 2. ORTEP drawings of (a) the molecule of the monomer of CuGly-mGAA and its bonded neighbors, and (b) the packing of the crystal of CuGly-mGAA. Ellipsoids at 20% displacement level.

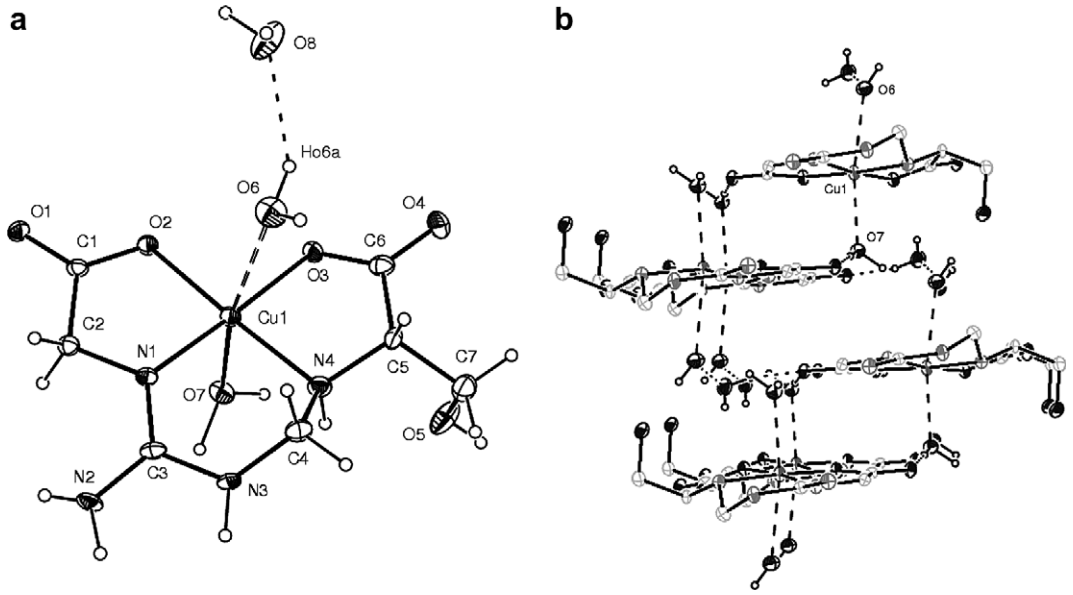


Fig. 3. ORTEP drawings of (a) the molecule of CuSer-mGAA with the water molecules that complete the asymmetric unit of the crystal, and (b) the packing of the crystal of CuSer-mGAA. Ellipsoids at 20% displacement level.

Table 4
Hydrogen bond parameters (Å, °) for CuSer-mGAA

D–H...A	D–H (Å)	H...A (Å)	D...A (Å)	D–H...A (°)
CuSer-mGAA				
O6–HO6A...O8	0.869(4)	2.063(4)	2.813(6)	144.1(3)
N4–HN4...O7	0.91	2.74	3.152(6)	108.5
O6–HO6B...O5[1]	0.861(4)	1.943(4)	2.804(5)	178.1(3)
O7–HO7A...O6[2]	0.986(3)	1.865(4)	2.813(5)	160.5(2)
O7–HO7B...O1[3]	1.104(3)	1.646(3)	2.747(4)	175.0(2)
N2–HN2B...O7[3]	0.86	2.12	2.918(5)	153.6
O8–HO8A...O1[4]	0.977(4)	1.797(3)	2.756(5)	166.1(3)
O5–HO5...O4[5]	0.82	1.91	2.707(5)	164.4
N2–HN2A...O2[6]	0.86	2.02	2.805(6)	150.9
N3–HN3...O3[7]	0.86	2.24	3.084(5)	166.6

Symmetry operations: 1: X − 1, *Y*, *Z*; 2: *X* + 1, *Y*, *Z*; 3: −*X* + 2, *Y* − 0.5, −*Z* + 1; 4 −*X* + 1, *Y* + 0.5, −*Z* + 1; 5: −*X* + 3, *Y* − 0.5, −*Z* + 2; 6: *X*, *Y* − 1, *Z*; 7: *X*, *Y* − 1, *Z*.

Table 5
Hydrogen bond parameters (Å, °) for CuGly-mGAA

D–H...A	D–H (Å)	H...A (Å)	D...A (Å)	D–H...A (°)
Cu-Gly-mGAA				
O6–HO6A...O4	0.860(7)	1.969(7)	2.818(10)	168.8(6)
O6–HO6B...O1[1]	0.869(6)	2.075(7)	2.940(9)	173.5(5)
N2–HN2A...O6[2]	0.86	2.03	2.816(11)	151.6
N3–HN3...O3[3]	0.86	2.49	3.283(12)	152.7
N3–HN3...O4[3]	0.86	2.56	3.288(12)	143.2
N4–HN4...O1[4]	0.91	2.33	3.073(13)	138.8

Symmetry operations: 1: −*X* + 1.5, −*Y* − 1, *Z* − 0.5; 2: −*X* + 1.5, −*Y*, *Z* + 0.5;3: *X*, *Y* + 1, *Z*; 4: −*X* + 1.5.

3.3.2. C=O stretching

Observing the geometrical structure of the guanidoacetic–serinate Cu(II) complex depicted in Fig. 4, we can infer only one asymmetrical and one symmetrical C=O stretching. As it is well known, the band absorption of carbonyl groups is located in the region of ~1700–1500 cm^{-1}, commonly in a higher energy region than the absorption bands pertaining to the HNH bending vibrational modes. In the infrared spectrum, we can observe two bands at 1650 cm^{-1} and at 1623 cm^{-1}. The second derivative of the spectrum and the band deconvolution analysis include values at 1650 cm^{-1} and at 1623 cm^{-1}, respectively. By means of the DFT procedure with B3LYP/6-311G and 6-311G basis sets we can assign the experimental band found at 1650 cm^{-1} (IR, second derivative) to the ν_s(C=O) vibrational mode, and the band found at 1623 cm^{-1} to the ν_{as}(C=O) vibrational mode. The match between calculated and experimental values for the ν(C=O) stretching was excellent.

3.3.3. HNH and HCH bending

In the infrared spectrum we can observe four bands at 1721, 1500 (1511 second derivative), 1470 (second derivative), 1466, 1423 (1428 second derivative), 1390, 1320 (1322 second derivative), 1283 (second derivative) 1279 and 1256 (second derivative), which can be correlated with the scaled DFT:B3LYP/6-311G values: 1642, 1518, 1487, 1483, 1427, 1388, 1317, 1295, 1283 and 1248 cm^{-1}. These bands can be assigned principally to δ(HNH)wagg, δ(HCH)wagg, δ(HCH)wagg, δ(HCH)wagg, δ(NH), δ(HCH)wagg, δ(HCH)twist, δ(HCH)twist, δ(HCH)twist and δ(HCH)twist, respectively. Rocking vibrations according to the DFT calculations can be assigned as follows: 1103 cm^{-1} to $\rho(CH)_2 + \rho(NH_2)$, 1071 cm^{-1} to ρ(OH) + $\rho(NH_2)$, 1043 cm^{-1} to $\rho(CH)_2 + \delta$(HNH)twist.

3.3.4. CN, CO, and CC stretching vibrations

A natural and considerable mixture of the internal coordinates describing isolated C–N, C–O, C–C stretching is

Table 6
Principal infrared bands (in cm^{-1}) of CuGly-mGAA (complex **1**), Gly, GAA, *trans*-Cu(Gly)$_2$ and *cis*-Cu(GAA)$_2$

Complex **1**	GAA[a]	Gly[b]	*trans*-Cu(Gly)$_2$[a]	*cis*-Cu(GAA)$_2$[b]	Approximate assignments
3535					ν(O–H) (water)
3422, 3332, 3199	3385, 3303, 3173		3320, 3260	3336, 3229	ν(N–H)
2930, 2890					ν(C–H)
2367, 2344					combination bands
	1670			1669	νC=N (guanidino)
1638, 1606, 1585, 1561, 1541, 1533, 1397, 1385				1636	ν(C=O) + δ(H–N–H)
	1626		1608	1611	δ(H–N–H)
	1582		1593	1566	ν_{as} (COO^-)
	1411		1392	1405	ν_s (COO^-)
464, 409			481	446, 410	ν(Cu–N) coupled
361, 341			333	351, 328	ν(Cu–O) coupled
	436			436	skeletal mode
	319			319	skeletal mode

[a] Ref. [24].
[b] Ref. [40].

Table 7
Principal infrared bands (in cm^{-1}) of CuSer-mGAA (complex **2**), GAA, Ser, and *cis*-Cu(GAA)$_2$

Complex **2**	GAA[a]	Ser[b]	*cis*-Cu(GAA)[a]	Attempted assignments
		3610, 3556, 3540		ν(O–H)
3676, 3568, 3542, 3340	3385, 3303, 3173	3426, 3344, 3349(R)[c], 3276(R)[c]	3336, 3229	ν(N–H)
2922, 2896		2966(R)[c], 2903(R)[c]		ν(C–H)
2362, 2342, 2332				combination bands
1650, 1622				ν (C=O)
1682	1670		1669	ν(C=N) (guanidino)
		1618(R)[c], 1592(R)[c]	1636	$\nu(COO^-) + \delta$ (NH_2)
1721, 1423	1626	1646, 1624, 1608	1611	δ (NH_2)
	1582		1566	$\nu_{as}(COO^-)$
	1411		1405	$\nu_s(COO^-)$
		1374, 1349(R)[c]		δ (OH) + ν(C–O)
596, 377, 317, 247			446, 410	ν(Cu–N) coupled mode
340,247			351, 328	ν(Cu–O) coupled mode
	436		436	skeletal mode
	319		319	skeletal mode

[a] Ref. [24].
[b] Ref. [31].
[c] Ref. [58].

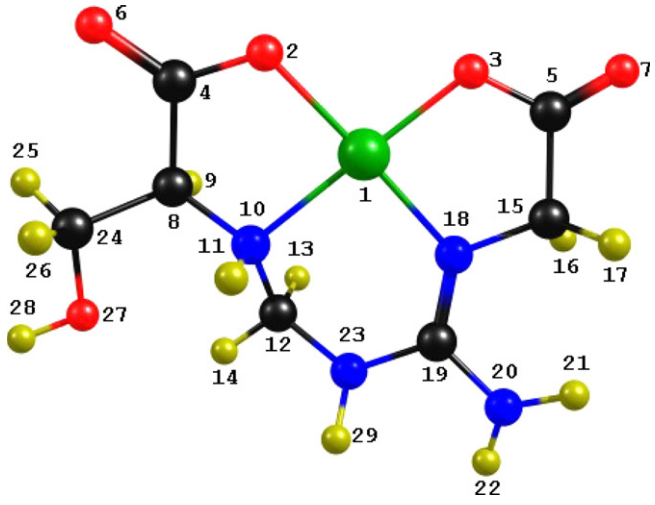


Fig. 4. Calculated DFT:B3LYP/6-311G geometrical structure of CuSer-mGAA.

found in the normal modes and is physically meaningful. For the guanidoacetic-serinate Cu(II) complex, the following infrared coupled bands can be assigned principally as 1227 (IR) cm^{-1} to ν_s(CO); 1143 cm^{-1} to ν_s(CN); 1008 cm^{-1} to ν_s(CN); 993 cm^{-1} to ν_s(CN); 956 to ν(CO) and 878 cm^{-1} to ν(CC).

3.3.5. Skeletal framework vibrations

As we have pointed out in other publications [44,45,47,48], a clear identification of the metal–ligand vibrations is not straightforward due to the higher mixture of different internal coordinates that take part in the description of the normal mode. In order to analyze the normal modes below 600 cm^{-1} we will describe the most accurate assignment we were able to deduce through the study of the distorted geometries of the normal modes described by the ab initio DFT:B3LYP/6-311G procedures. Our goal was to identify which bond lengths and

bond angle bending parameters had greater participation in the description of the normal mode.

Fig. 4 displays the distorted geometry of the normal modes for the metal–ligand vibrations obtained through the free CHEMKRAFT program [49].

3.4. Proposal of a mechanism for the formation of Gly-mGAA and Ser-mGAA

Due to the interesting formation of new amino acid derivatives, a preliminary mechanism for their synthesis is proposed here (Fig. 5). We have based this proposal on previous work on the desamidination of copper(II) complexes of GAA analyzed by epr [30] as well as on data on guanidination reactions involving amino acids, phosphates and collagen [50–57] and also on methyltransferases. Some of guanidination [50] and methyltransferases [53] reactions are mediated by zinc(II) ions or zinc(II) coordination in a similar way that we propose here for Cu(II).

Nevertheless, we omitted copper(II) complexes from this mechanism because we were not be able to analyze intermediate species. However, we do know that Cu(II) or its complexes may act both as a catalysts or template sites.

The proposed mechanism comprises two steps, both of them involving nucleophilic attack. It is interesting to note the similarity with the catalytic mechanism proposed for arginine deimination, with the difference of which carbon atom is attacked: the amidino one in the case of arginine deimination and the α-carbon in our proposed mechanism [58].

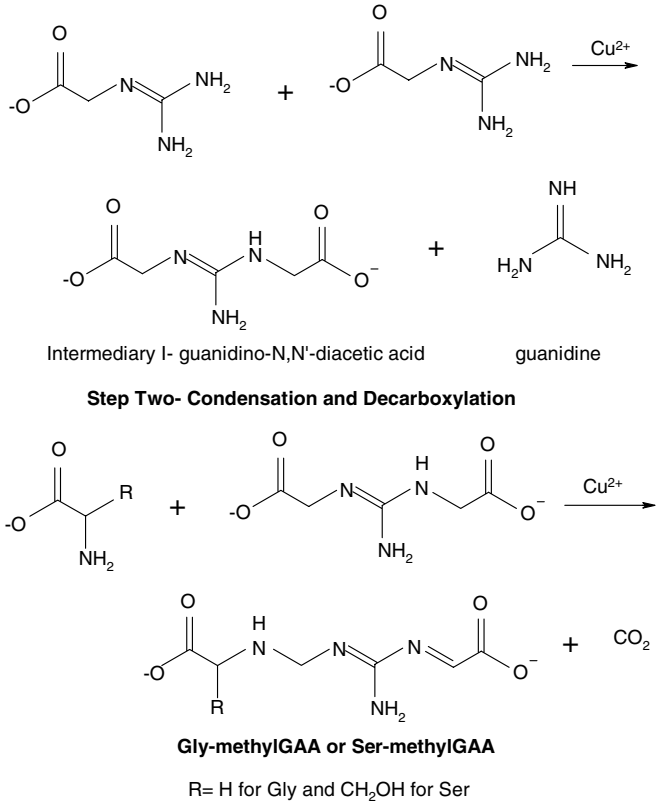


Fig. 5. Proposed mechanism for Gly-mGAA and Ser-mGAA.

Step one is based on a deguanidination reaction between two GAA species in the presence of Cu(II). Guanidination reactions are used in reactions of biological relevance such as the synthesis of L-canavanine [50], the modification of a toxic enzyme from snake venom [51], the synthesis of thrombin inhibitor [52] and also the guanidination of the phosphate linkage towards cationic phosphoramidate oligonucleotides [55]. Deguanidination modified monomeric collagen in such a way that it prevented it from polymerization and to inducing platelet aggregation [54].

In step one, the terminal amino group from GAA makes a nucleophilic attack at α-carbon from another GAA, followed by a deguanidination reaction, generating intermediate I: guanidino-*N*,*N*′-diacetic acid and guanidine (a good leaving group). A rather similar process has already been proposed between two GAA copper(II) complexes [30] by our group. Cu(II) is probably involved in the coordination through the oxygen atoms from the carboxylate group, similarly to what happens in the desamidination process [30], which favors the nucleophilic attack on the α-carbon. The proposed intermediate I, guanidino-2,4-*N*,*N*′-diacetic acid, is essential to the elongation of the carbon chain.

In step two the α-amino group from glycine or serine makes a nucleophilic attack at C-2 from intermediate I, followed by a decarboxylation process. The copper coordination is also assumed to mediate this nucleophilic attack and a Cu(II)/Cu(I) redox system may help on the decarboxylation reaction in addition to the heating experimental conditions.

As a final result, glycine-2-*N*-methyl guanidinoacetic acid or serine-2-*N*-methyl-guanidino acetic acid are formed and both of them act as a quadridentate ligand, using the oxygen atoms from the carboxylate groups and two nitrogen atoms (Fig. 4).

4. Conclusions

Two novel Cu(II) complexes were synthesized involving new condensed synthetic amino acids: one is glycine-3-*N*-methylguanidino acetic acid (Gly-mGAA), which results from the reaction between GAA and glycine, with an increase of one carbon in the chain; and the second is a similar ligand that is the product of the reaction between GAA and serine, that is, serine-3-*N*-methylguanidino acetic acid (Ser-mGAA). It is important to remark that this elongation of the carbon chain in both cases was performed in aqueous solution in the presence of Cu(II).

This can represent important mechanisms both for the synthesis of new guanidines derivates and for methylation or peptide formation with biological molecules. Modifications in the precursor of GAA, arginine, for example, can be related to changes in the immunogenicity of proteins and peptides and can create self-antigens that induce autoimmune responses [57]. If these serine or glycine GAA adducts are catalyzed by enzymes in our organisms

through an alternative biological pathway, creatine biosynthesis will be impaired, resulting in a dysfunction similar to guanidinomethyltransferase deficiency.

Deguanidination reactions instead of desamidination should also prevent GAA biosynthesis, formed by the desamidination of arginine.

In addition, an important contribution on how GAA can react with other amino acids was proposed as well as how elongation of their carbon chain can be made in aqueous solution in the presence of Cu(II).

Acknowledgements

The authors thank FAPESP (B.L.R.), CAPES (O.V.) and CNPq (J.M.R., J.F., C.A.T.S.).

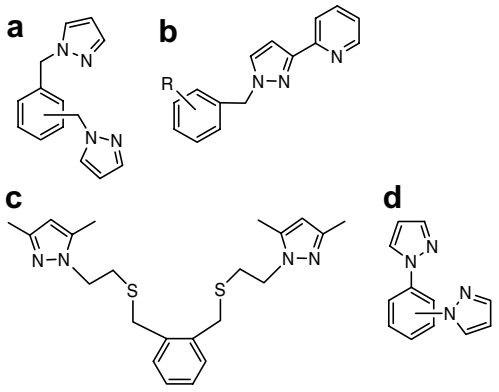
Appendix A. Supplementary material

CCDC 256924 and 256925 contain the supplementary crystallographic data for this paper. These data can be obtained free of charge via http://www.ccdc.cam.ac.uk/conts/retrieving.html, or from the Cambridge Crystallographic Data Centre, 12 Union Road, Cambridge CB2 1EZ, UK; fax: (+44) 1223-336-033; or e-mail: deposit@ccdc.cam.ac.uk. Supplementary data associated with this article can be found, in the online version, at doi:10.1016/j.poly.2007.05.029.

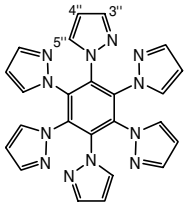
References

[1] M. Takeda, S. Nakayama, Y. Tomino, Y. Jung, H. Endou, H. Koide, in: P. P Deyn, B. Marescau, V. Stalon, I.A. Qureshi (Eds.), Guanidino Compounds in Biology and Medicine, John Libbey & Company Ltd., 1992, pp. 153–157.
[2] S. Stöckler, U. Holzbach, F. Hanefeld, I. Marquardt, G. Helms, M. Requart, W. Hanicke, J. Frahm, Pediatr. Res. 36 (1994) 409.
[3] A. Neu, H. Neuhoff, G. Trube, S. Fehr, K. Ulrich, J. Roeper, D. Isbrandt, Neurobiol. Dis. 11 (2002) 298.
[4] A.I. Zugno, F.M. Stefanello, E.L. Streck, T. Calcagnotto, C.M.D. Wannmacher, M. Wajner, A.T.S. Wyse, Int. J. Develop. Neurosci. 21 (2003) 183.
[5] M.G. Alessandri, L. Celati, R. Battini, F. Baldinotti, C. Item, V. Leuzzi, G. Cioni, Anal. Biochem. 331 (2004) 189.
[6] A. Shulze, F. Ebinger, D. Rating, E. Mayaetepek, Mol. Genet. Metab. 74 (2001) 413.
[7] V. Leuzzi, M.C. Bianchi, M. Tosetti, C. Carducci, C.A. Cerquiglini, G. Cioni, I. Antonozzi, Neurology 55 (2000) 1407.
[8] A. Schulze, T. Hess, R. Wevers, E. Mayatepek, P. Bachert, B. Marescau, M.V. Knopp, P.P. Deyn, H.J. Bremer, D. Rating, J. Pediatr. 131 (1997) 626.
[9] S. Stöckler, U. Holzbach, F. Hanefeld, I. Marquardt, G. Helms, M. Requart, et al., Pediatr. Res. 36 (3) (1994) 409.
[10] S. Stöckler, B. Marescau, P.P. De Deyn, J. Trijbels, F. Hanefeld, Metabolism 46 (10) (1997) 1189.
[11] A. Shulze, Mol. Cell Biochem. 244 (1–2) (2003) 143.
[12] M. Ishizaki, H. Kitamura, Y. Taguma, K. Aoyagi, M. Narita, in: P. Deyn, B. Marescau, V. Stalon, I.A. Qureshi (Eds.), Guanidino Compounds in Biology and Medicine, John Libbey & Company Ltd., 1992, pp. 275–280.
[13] B.D. Cohen, H. Patel, in: P.P. Deyn, B. Marescau, V. Stalon, I.A. Qureshi (Eds.), Guanidino Compounds in Biology and Medicine, John Libbey & Company Ltd., 1992, pp. 255–260.
[14] O. Levillain, B. Marescau, P.P. Deyn, in: P.P. Deyn, B. Marescau, I.A. Qureshi, A. Mori (Eds.), Guanidino Compounds in Biology and Medicine, vol. 2, John Libbey & Company Ltd., 1997, pp. 289–297.
[15] A. Neu, H. Neuhoff, G. Trube, K. Ulrich, J. Roeper, D. Isbrandt, Neurobiol. Dis. 11 (2) (2002) 298.
[16] A.I. Zugno, F.M. Stefanello, E.L. Streck, T. Calcagnotto, C.M.D. Wannmacher, M. Wajner, A.T.S. Wyse, Int. J. Develop. Neurosci. 21 (2003) 183.
[17] K. Sugyiama, A. Ohishi, H. Syiu, H. Takeuchi, J. Nutr. Sci. Vitaminol. 35 (1989) 613.
[18] J. Verhelst, J. Berwaerts, B. Marescau, R. Abs, H. Neels, C. Mahler, Metab. Clin. Exp. 46 (1997) 1063.
[19] A. Mori, M. Kohno, T. Masumizu, Y. Noda, L. Packer, Biochem. Mol. Biol. Int. 40 (1996) 135.
[20] P.P. Deyn, B. Marescau, R. D'Hooge, I. Possemiers, J. Nagler, C.H. Mahler, Neurochem. Int. 27 (1995) 227.
[21] M. Kuroda, Nephron 65 (1993) 605.
[22] M. Yasuda, K. Sugahara, J. Zhang, T. Shuin, H. Kodama, Physiol. Chem. Phys. Med NMR 32 (2000) 119.
[23] J. Felcman, J.L. Miranda, J. Braz. Chem. Soc. 8 (6) (1997) 575.
[24] J.L. Miranda, J. Felcman, Synth. React. Inorg. Met-Org Chem. 31 (5) (2001) 873.
[25] J.L. Miranda, J. Felcman, Polyhedron 22 (2003) 225.
[26] J.A. Tainer, E.D. Getzoff, J.S. Richard, D.C. Richardson, Nature 306 (1983) 284.
[27] R. Wyatt, J. Sodoroski, Science 280 (1998) 284.
[28] J.L. Miranda, J. Felcman, J.L. Wardell, J.S. Skakle, Acta Crystallogr., Sect. C 58 (2002) m471.
[29] J. Felcman, R. Alan Howie, J.L. Miranda, J.M.S. Skakle, J.L. Wardell, Acta Crystallogr., Sect. C 59 (2003) m103.
[30] J.L. Miranda, J. Felcman, O. Versiane, M.H. Herbst, Inorg. Chem. Commun. 7 (2004) 1198.
[31] Y. Yamauchi, T. Sugimoto, K. Sueyoshi, Y. Oji, K. Tanaka, Phytochemistry 58 (5) (2001) 677.
[32] C.R. Zhao, L. Shang, W. Wang, D.O. Jacobs, J. Surg. Res. 105 (1) (2002) 10.
[33] C.L. Hannon, E.V. Auslyn, in: H. Dugas, F.P. Schmidtchen (Eds.), Bioorganic Chemistry Frontiers, vol. 3, Springer, Berlin, 1993, p. 192.
[34] J.L. Grenhil, P. Lue, in: G.P. Ellis, D.K. Luscombe (Eds.), Progress in Medicinal Chemistry, vol. 30, Elsevier Science, New York, 1993 (Chapter 5).
[35] Enraf-Nonius COLLECT. Nonius BV, Delft, The Netherlands (1997–2000).
[36] R.G. Parr, W. Yang, Density-Functional Theory of Atoms and Molecules, Oxford University Press, Oxford, 1989.
[37] A.D. Becke, J. Chem. Phys. 98 (1993) 1372.
[38] M.J. Frisch, G.W. Trucks, H.B. Schlegel, G.E. Scuseria, M.A. Robb, J.R. Cheeseman, V.G. Zakrzewski Jr., J.A. Montgomery, R.E. Stratmann, J.C. Burant, S. Dapprich, J.M. Millam, A.D. Daniels, K.N. Kudin, M.C. Strain, O. Farkas, J. Tomasi, V. Barone, NM. Cossi, R. Cammi, B. Mennucci, C. ÇPomelli, C. Adamo, S. Clifford, J. Ochterski, G.A. Peterson, P.Y. Ayala, Q. Cui, K. Morokuma, D.K. Malick, A.D. Rabuck, K. Raghavachari, J.B. Foresman, J. Cioslowski, J.V. Ortiz, A.G. Baboul, B.B. Stepanov, G. Liu, A. Liashenko, P. Piskorz, I. Komaromi, R. Gomperts, R.L. Martin, D.J. Fox, T. Keith, M.A. Al-Laham, C.Y. Peng, A. Nanayakkara, C. González, M. Challacombe, P.M.W. Gill, B. Johnson, W. Chen, M.W. Wong, J.L. Andresw, C. González, M. Head-Gordon, E.S. Repogle, J.A. Pople, GAUSSIAN 98, Revision A.7, Gaussian Inc., Pittsburgh, PA, 1998.
[39] H. Masuda, A. Odani, T. Yamazaki, T. Yajima, O. Yamauchi, Inorg. Chem. 32 (1993) 1111.
[40] C.M. Weeks, A. Cooper, D.A. Norton, Acta Crystallogr., Sect. B 25 (1969) 443.
[41] H.C. Freeman, M.R. Snow, I. Nitta, K. Tomita, Acta Cryst. 17 (1964) 1463.
[42] K. Nakamoto, Infrared and Raman Spectra of Inorganic and Coordination Compounds – Part B: Applications in Coordination,

Organometallic, and Bioinorganic Chemistry, 5th ed., Wiley, 1997, pp. 53, 63, 65.
[43] B. Lambie, R. Ramaekers, G. Maes, J. Phys. Chem. 108 (2004) 10426.
[44] C.A. Téllez S, E. Hollauer, M.A. Mondragón, V.M. Castaño, Spectrochim. Acta A 60 (2004) 2171.
[45] C.A. Téllez, E. Hollauer, M.A. Mondragón, V.M. Castaño, Spectrochim. Acta A 57 (2001) 993.
[46] L.J. Bellamy, R.L. Williams, Spectrochim Acta 9 (1957) 341.
[47] J.M. Ramos, O. Versiane, J. Felcman, C.A. Téllez S, FT-IR vibrational spectrum and DFT: B3LYP/6-311G structure and vibrational analysis of bis-serinenickel (ii) complex: [Ni $(Ser)_2$], Spectrochim. Acta A 67 (3–4) (2007) 1046.
[48] J.M. Ramos, O. Versiane, J. Felcman, C.A. Téllez S, FT-IR vibrational spectrum and DFT: B3LYP/6-31G structure and vibrational analysis of guanidinoaceticserinenickel (II) complex: [Ni(GAA)(Ser)], Spectrochim. Acta A 67 (3–4) (2007) 1037.
[49] CHEMCRAFT Software <http://www.chemkraftprog.com/order.htlm>.
[50] A.J. Ozinskas, G.A. Rosenthal, Bioorg. Chem. 14 (2) (1986) 157.
[51] A.S. Babu, T.V. Gowda, Toxicon 32 (6) (1994) 749.
[52] J. Deng, Y. Hamada, T. Shioiri, Tetrahedron Lett. 37 (13) (1996) 2261.
[53] M. Machuqueiro, T. Darbre, J. Inorg. Biochem. 94 (2003) 193.
[54] Chung-Lieh Wang, T. Miyata, B. Weksler, A.L. Rubin, K.H. Stenzel, Biochim. Biophys. Acta 544 (3) (1978) 555.
[55] T. Michel, F. Debart, J-J. Vasseur, Tetrahedron Lett. 44 (35) (2003) 6579.
[56] G.A. Rosenthal, L. Harper, Insect Biochem. Mol. Biol. 26 (4) (1996) 389.
[57] M.A.M. van Boekel, W.J. Van Venrooij, Autoimmun. Rev. 2 (2003) 57.
[58] Y. Huang, J. Komoto1, K. Konishi, Y. Takata, H. Ogawa, T. Gomi, M. Fujioka, J. Mol. Biol. 298 (2000) 149.



Scheme 1.



Scheme 2.

has three bidentate positions, we have prepared complexes with one, two or three metals occupying these positions. The incorporation of three metallic centres was only possible with a small metallic fragment. As far as the fluxionality of the compounds is concerned, two types of processes were found: metallotropic shift and rotation of the uncoordinated pyrazolyl rings.

In the free ligand, each pyrazol-1-yl group can adopt two perpendicular conformations depending on the orientation of the N-2 lone pair ($u = up$, $d = down$) with regard to the benzene plane. This situation leads to several isomers. The hpzb ligand exists in the solid state in two conformations (polymorphism) – *ududud* and *udduud*. According to AM1 and SAM calculations [26], these conformations have torsion angles close to 90° with the *ududud* disposition giving the most stable conformer. NMR studies in solution have shown that, depending on the solvent and/or concentration, the *ududud* isomer is either the only one detected or is the major isomer along with the *udduud* isomer as the minor component. The fact that two isomers can be observed separately indicates that restricted rotation of the pyrazolyl rings exists in the free hpzb ligand at room temperature. The same conclusion was deduced for the monometallic derivatives, while those containing two metallic centres exhibited free rotation at room temperature of the two uncoordinated pyrazolyl rings situated *para* to one another [31].

In this work we decided to focus our attention on the study of the coordination ability of hpzb with the chiral fragment *cis*-$[Ru(bpy)_2]^{2+}$. Although complexes have been described that contain the $[Ru(bpy)_2]^{2+}$ fragment bonded to pyrazolyl-derived ligands [33–35], the coordination of hpzb to this potentially octahedral fragment has not previously been explored. It was of interest to evaluate if any selectivity existed in the coordination and also to assess the possible presence of fluxional processes.

On the other hand, ruthenium-based anticancer drugs are making significant advances as an attractive alternative to classical platinum chemotherapies. Specifically, polypyridyl–Ru complexes have been investigated as potential anticancer drug candidates, given their photoluminescence properties and both the ability of Ru to coordinate DNA nucleobases and the ability of polypyridyl ligands to intercalate DNA [36]. Because of that, we decided to explore the possible anticancer activity of the ruthenium complexes containing bpy and our ligand hpzb.

2. Results and discussion

2.1. Synthesis and characterization

The reaction of hpzb [27,28] with the system $[RuCl_2(bpy)_2]/2NH_4PF_6$ [37] was carried out (Eq. (1)) [35]. The ruthenium containing precursor has been used in anticipation that such a compound, besides providing the possibility of its substitution by two N donors, could also be exploited for its biological studies in view of earlier reports [36]. The reaction was performed in 1:1, 1:2 and 1:3 hpzb:Ru ratios. The same product, **1**, was obtained in all cases (even after prolonged reaction times of 36 h) as a dark-red solid. Elemental analysis of complex **1** shows the stoichiometry to be $[Ru(bpy)_2(hpzb)](PF_6)_2$ (see Eq. (1)) (clearly a racemic mixture would be present). The mass spectrum is also consistent with coordination of the ligand to only one metal fragment. In fact, peaks corresponding to the loss of one or two counteranions or other fragments from the proposed formula are also observed. It is worth highlighting the selectivity in the coordination of the ligand to only one metal fragment. It is possible that the ruthenium centre is sufficiently electrophilic to reduce considerably the donor ability of the uncoordinated pyrazolyl rings once the first metal centre is present. Undoubtedly, bonding of one hpzb ligand to three metal centres would involve a high level of steric hindrance:

$$[RuCl_2(bipy)_2] + hpzb + 2NH_4PF_6 \rightarrow [Ru(bipy)_2(hpzb)](PF_6)_2, 1 + 2NH_4Cl \quad (1)$$

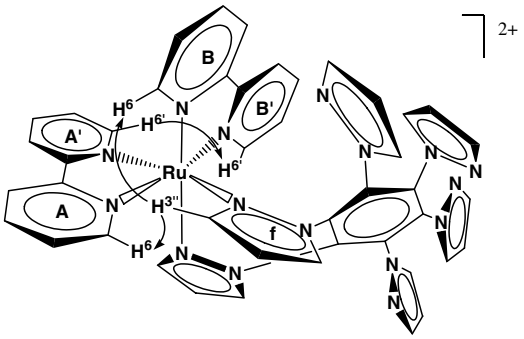
A different behaviour to that found with hpzb has been observed with the similar ligand hexakis(3,5-dimethylpyrazol-1-yl)benzene that contains substituted pyrazolyl rings. It did not react with the same ruthenium complex, possibly due to steric factors.

The ^1H NMR spectrum of compound **1** shows a very complicated pattern that consists of 34 different signals, all of which have the same integration. This observation is consistent with the presence of six different spin systems for the pyrazolyl rings and four different spin systems for

the pyridyl rings. The evidence indicates a total lack of symmetry, which can be explained as a consequence of hpzb coordination to the $[Ru(bpy)_2]^{2+}$ moiety and the boat conformation expected for the chelate ring (see Fig. 1 and Scheme 3).

COSY and NOESY experiments enabled signals corresponding to the same pyrazole ring to be grouped together. Coupling constants enabled the assignment of $H^{4''}$ and allowed us to distinguish between $H^{3''}$ and $H^{5''}$, since it is well-known that $^3J_{4-5} > {}^3J_{4-3} > {}^4J_{3-5}$. Chemical shifts can also be used to identify $H^{4''}$ protons, since all of these exhibit higher field resonances (between 6.04 and 6.34 ppm) than the other two protons in the same ring. However, the chemical shifts are not particularly useful to distinguish between $H^{5''}$ and $H^{3''}$, because both types of proton show very similar δ values and, in addition, they are strongly affected by factors such as bpy shielding. All of the pyrazolyl resonances are gathered in Table 1 and the assignments to the pyrazolyl rings labelled from **a** to **f** are given (see Table 1).

As previously stated, the bipyridine ligands give four different spin systems in the ^{1}H NMR spectrum. It was possible to identify the signals forming each spin system and to relate pairs of systems belonging to the same bpy ligand. This was achieved by means of NOESY and COSY experiments (see Figs. 2 and 3). Moreover, an additional NOE effect was detected between the two $H^{6'}$ resonances, which is reasonable given the octahedral geometry expected for the metallic centre. In fact, a second cross-peak could be expected in the NOESY spectrum between the two H^6 signals. However, these signals appear too close to one another in the 1-D spectrum. Interestingly, two cross-peaks



Scheme 3. Expected structure and some NOEs observed for complex **1**. The labelling of the bpy ligands could be opposite to that shown.

Table 1
^{1}H NMR chemical shifts (acetone-d_6) for the six pyrazolyl rings

Pz ring	$H^{3''}$	$H^{4''}$	$H^{5''}$
a	6.97	6.04	7.21
b	6.72	6.15	7.74
c	7.55	6.18	7.05
d	7.37	6.26	7.58
e	7.49	6.29	7.75
f	7.72	6.34	7.61

are observed between $H^{3''}$ of pyrazolyl ring **f** and the aforementioned H^6 resonances of the two bipyridines. This means that $H^{3''}$ of the pyrazolyl ring **f** is located in between these two H^6 protons as a consequence of the boat conformation adopted by the chelate ring. Therefore, the pyrazole labelled **f** is coordinated to the metal centre (see Scheme 3, Table 2 and Scheme 4). The free bpy ligand in solution has

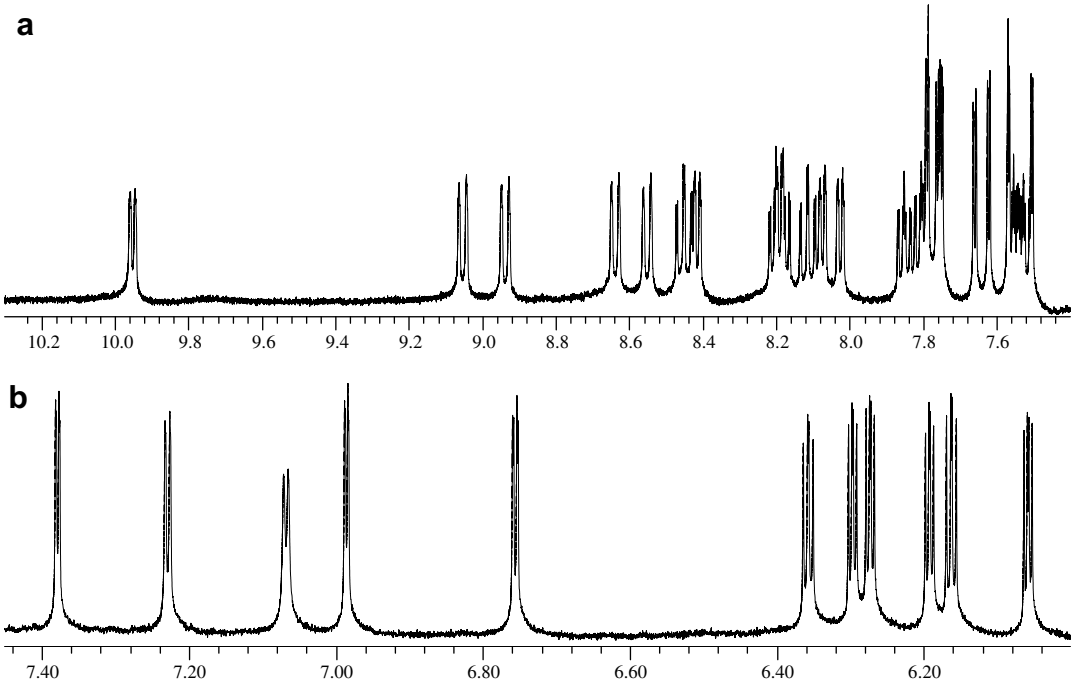


Fig. 1. ^{1}H NMR spectrum of complex **1** in the aromatic region (divided into sections a and b).

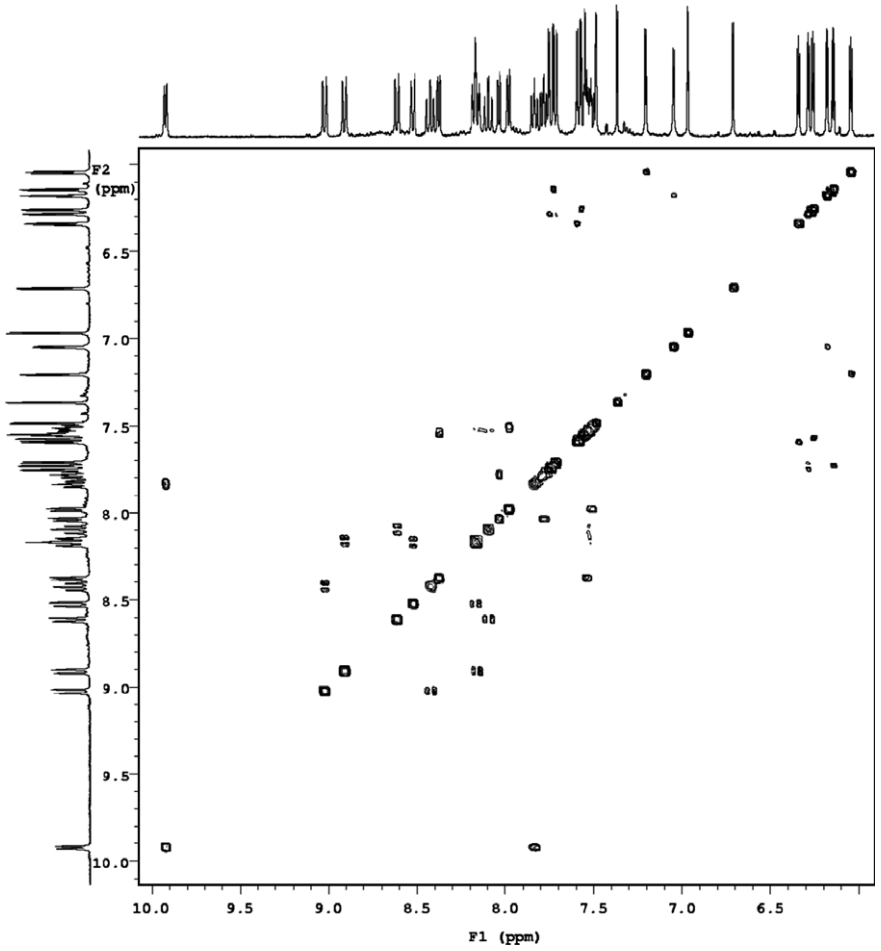


Fig. 2. 2D COSY ^{1}H–^{1}H spectrum (400 MHz) for complex **1**, in acetone-d_6 at room temperature.

a *transoid* (*trans*-coplanar) equilibrium conformation, even though the energy barrier for rotation around the interannular C–C bond is not very high. In this conformation the observed δ value can be listed from lowfield to highfield in the following order: $\delta(H^6) > \delta(H^3) > \delta(H^4) > \delta(H^5)$ [38]. However, when the ligand is coordinated to a metal centre a *cisoid* conformation is adopted and $\delta(H^3)$ moves downfield due to steric interactions between H^3 and $H^{3'}$. In contrast, some H^6 resonances may be shifted upfield because of the location of these protons directly above the π electron density of a pyridine or pyrazolyl ring in the complex (see Table 2).

Although we were able to identify all the signals in the ^{1}H NMR spectrum of **1**, we synthesized a partially deuterated bpy ligand (bpy-d_7 with H in the 4-position) and the corresponding complex [Ru(bpy-d_7)(hpzb)][PF_6)$_2$ (**1-*d***) in order to confirm the data. The ^{1}H NMR spectrum of **1-*d*** is consistent with our previous assignments. The spectrum contained all the pyrazolyl signals and the H^4 and $H^{4'}$ bpy resonances.

A $^{13}C\{^{1}H\}$ NMR spectrum of **1** was recorded and the signals were assigned by means of HMQC and HMBC experiments. The spectrum consisted of 44 singlets, as one would expect for the structure discussed above. Twenty of these signals belong to the bpy ligands, eighteen to the six non-equivalent pyrazolyl rings and six to the hpzb benzene group. The data are gathered in Section 3.

When a solution of complex **1** was heated (acetone-d_6 solution) to 50 °C, changes were not observed in the spectra. A decrease in temperature down to −90 °C did not lead to evidence of splitting of the resonances. On the basis of these data we propose that, in a similar way to the free ligand and to other mononuclear derivatives [31], in this complex there is a restricted rotation of the uncoordinated pyrazolyl rings even at room temperature. According to the number of NMR resonances only one isomer is present in solution. The possible relative pyrazolyl dispositions for a restricted rotation situation are reflected in Scheme 5 (from **I** to **X**); a black circle represents N-2 *up* and a white circle represents N-2 *down*. If the two coordinated pyrazoles were equivalent, these ten dispositions would be the ten possible conformers. However, when these two pyrazoles are not equivalent due to the asymmetry of the metallic fragment, as in this case, some of these dispositions (**I**, **II**, **IV**, **VI, VII** and **VIII**) would give rise to two different conformers: **a** and **b**. This situation occurs for the dispositions where there is not a symmetry plane on considering the local symmetry of the hpzb group. The interconversion between

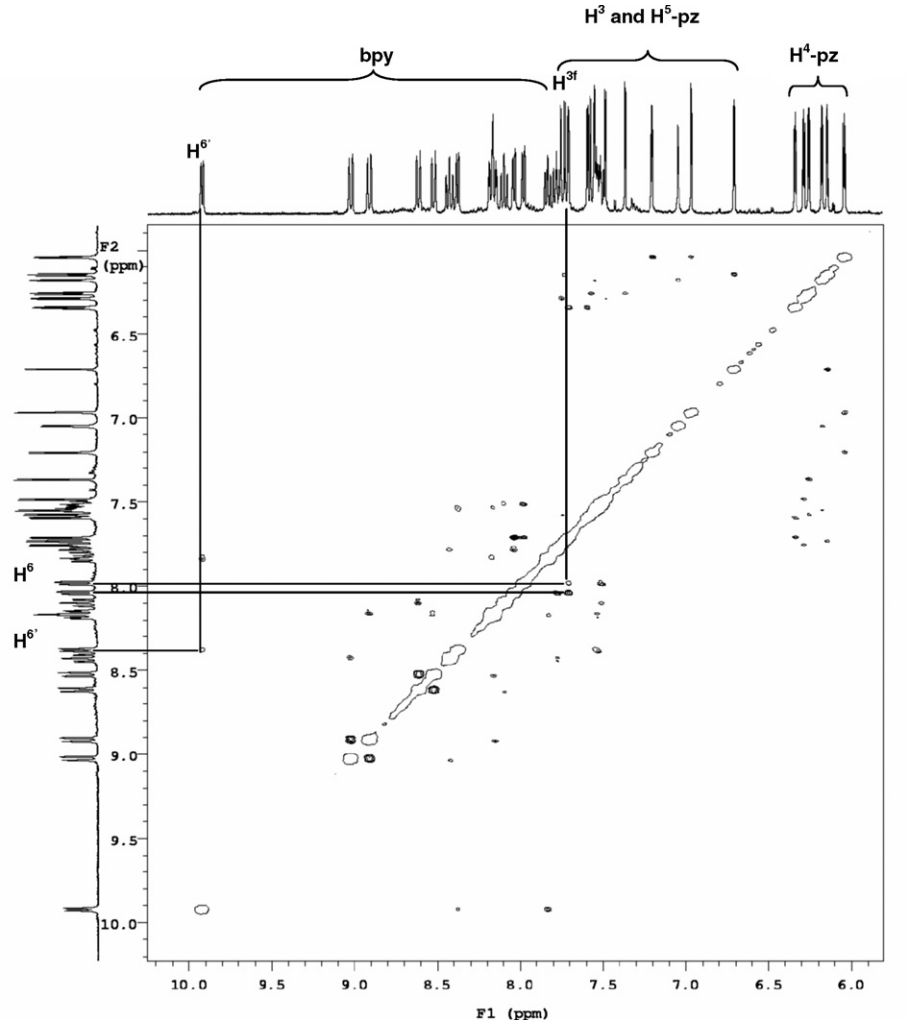
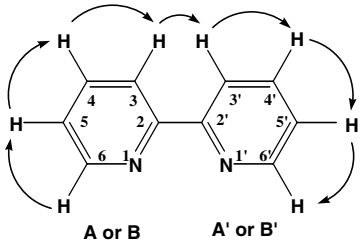


Fig. 3. 2D NOESY ^1H–^1H spectrum (400 MHz) of complex **1** in acetone-d_6 at room temperature.

Table 2
^1H NMR chemical shifts (acetone-d_6) for the two bipyridine groups, labelled with letters **AA′** and **BB′**

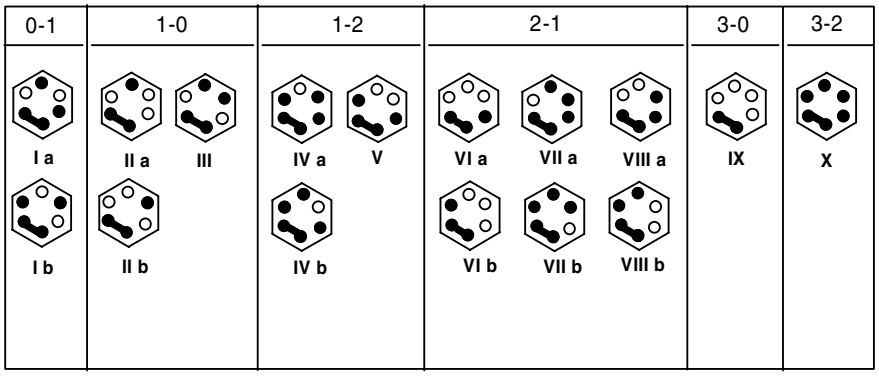
bpy ring	H^6	H^5	H^4	H^3	$H^{3'}$	$H^{4'}$	$H^{5'}$	$H^{6'}$
AA′	8.05	7.79	8.43	9.03	8.92	8.17	7.54	8.39
BB′	7.99	7.52	8.10	8.62	8.53	8.18	7.83	9.93

conformers **a** and **b** would be possible through a boat-to-boat inversion of the metallacycle – as observed in metallic bis(pyrazolyl-1-yl)methane derivatives [39]. When two contiguous pyrazoles have the same relative orientation, a repulsion between the two nitrogen electron pairs is expected (although to a lesser extent there will also be a steric interaction between two contiguous $CH^{5''}$ groups). The conformers in the Scheme are grouped according to the number of these interactions. The first number refers to the number of times where two consecutive uncoordinated pyrazoles have the same orientation and the second number refers to the same disposition but for contiguous free and coordinated pyrazolyl rings.



Scheme 4. NOE correlations and numbering scheme for the bipyridine signals.

If we assume that the free pyrazole-free pyrazole interaction (same orientation) destabilizes the molecule more than the interaction between free pyrazole and coordinated pyrazole (for a coordinated pyrazole the electron pair is involved in the coordination to the metal centre), then the most stable conformers would be **Ia** and **Ib**. We cannot conclusively establish whether complex **1** corresponds to a situation of rapid interconversion between **Ia** and **Ib** through a boat-to-boat inversion or to only one conformer that has been selectively formed.



Scheme 5.

The UV–Vis spectrum of **1** consists of three bands at 282, 334 and 449 nm. The band centred at $\lambda_{max} = 282$ nm is assigned to a $\pi \rightarrow \pi^*$ transition of the bpy ligands, that centred at $\lambda_{max} = 334$ nm to a $\pi \rightarrow \pi^*$ transition of the hpzb ligand and that at $\lambda_{max} = 449$ nm to a metal-to-ligand charge transfer (MLCT) $d \rightarrow \pi^*$ transition. A luminescence response was not observed for **1**, a situation in contrast to that found for $[Ru(bpy)_3]^{2+}$ and the majority of complexes of the type $[Ru(bpy)_2(NN)]^{2+}$ [40,41]. However, it has been reported that for $[Ru(bpy)_2Meprv]^{2+}$ luminescence is not observed either [Meprv = 1,5-dimethyl-3-(1′-methyl-3′-pyrazolyl)-6-oxoverdazyl] [34].

Electronic spectra for solutions of **1** (10^{-4} M) and HCl (10^{-4} M) and also of **1** (10^{-4} M) and HCl (5×10^{-4} M) in acetone were recorded. The spectra did not show distinct features compared to those of complex **1** in acetone. Consequently, the UV–Vis absorption spectrum is not pH dependent. The electronic spectrum of **1** is also not affected by the addition of 1 equiv. of $Zn(NO_3)_2 \cdot 6H_2O$ (10^{-4} M). Luminescence experiments were repeated in the presence of both $Zn(NO_3)_2 \cdot 6H_2O$ and HCl. No response was observed.

The molar conductivity was measured for a 10^{-3} M solution of complex **1** in acetone. The recorded value was 176 S cm^2 mol^{-1}, in agreement with a 2:1 electrolyte [42].

2.2. Electrochemistry

Cyclic voltammetry measurements were carried out in order to determine the redox behaviour of complex **1** in CH_2Cl_2. A degassed solution of $[Ru(bpy)_2(hpzb)][PF_6]_2$ (**1**) (4.08×10^{-4} M) and tetrabutylammonium hexafluorophosphate ($TBAPF_6$, 2.06×10^{-2} M), as the supporting salt, in dry CH_2Cl_2 was used. The potentiostat was equipped with a conventional three electrode cell, and the latter was purged with nitrogen gas saturated with CH_2Cl_2 during the experiment.

On the oxidation side (see Fig. 4 and Table 3), three reversible waves were recorded at $E_{1/2} = +0.21$ V, $E_{1/2} = +0.74$ V and $E_{1/2} = +1.24$ V. The first two were assigned to the oxidation of the hpzb ligand, and the third to the metal based oxidation couple (Ru^{2+}/Ru^{3+}). Several additional experiments were done to confirm this assignment. First of all, the redox behaviour of the solvent and the ligand hpzb were separately examined under the same conditions, but no oxidation processes were detected for either of them, although in both cases a dramatic increase in the intensity was observed at potentials over 1.0 V. Moreover, the starting material was also investigated and the literature Ru^{2+}/Ru^{3+} oxidation potential at $E_{1/2} = +0.4079$ was successfully confirmed. On the other hand, most of the complexes $[Ru(L–L)_3]^{2+}$, where L–L is a N-donor bidentate chelate ligand, have characteristic oxidation waves in a rather narrow range around that of the reference complex $[Ru(bpy)_3]^{2+}$, $E_{1/2}$ being between +1.27 V and +1.35 V in CH_2Cl_2 depending on the author [40,43]. Thus, these data justify our assignation of the wave at +1.24 V to the oxidation Ru^{2+}/Ru^{3+} process. Assignation of the two other waves is more speculative, though they could correspond to a two step oxidation process of the pyrazolyl groups on the coordinated ligand.

On the reduction side, the voltammogram exhibits two reversible waves at −0.85 and −1.48 V respectively, corresponding to the reduction of the bpy ligands. The reference complex $[Ru(bpy)_3]^{2+}$ shows three peaks in this region assigned to the three bpy ligands according to the literature (see Table 3).

2.3. Anticancer activity

Complex **1** has been tested in vitro, as a potential anticancer drug in two different cell lines, A2780, human ovarian carcinoma cell lines, and NCI-H460, human lung carcinoma cell lines. Unfortunately, the activity was not high enough to build the corresponding dose–response graph when tested in the second line. On the other hand, cytotoxicity was higher in the first cell line, A2780, but the maximum inhibitory effect could not be reached as a consequence of interference with the solvent DMSO. Consequently, the cytotoxicity was determined with this restriction, as both the E_{max} value (the maximum replication inhibitory effect relative to control experiments and expressed as percentage) and the IC_{50} value (the concentration that inhibits cell replication by 50%, interpolated from dose-response representations and relative to control experiments). The E_{max} value can be considered as

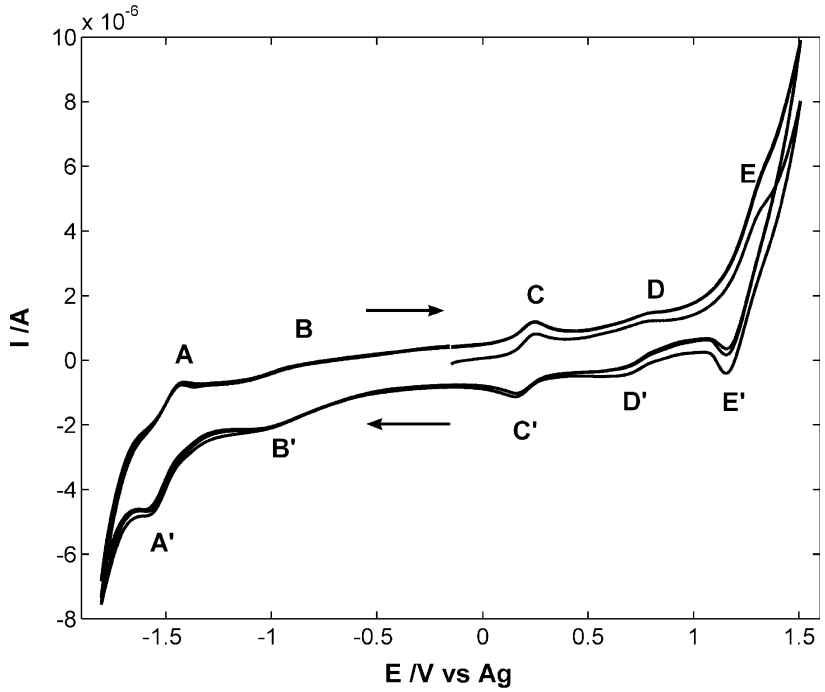


Fig. 4. Cyclic voltammogram of complex **1** (4.08×10^{-4} M) in 0.02 M of n-Bu_4NPF_6/CH_2Cl_2 at a scan rate of 100 mV/s.

Table 3
Electrochemical data, $E_{1/2}$ (ΔE_p) (V), for complex **1** (4.08×10^{-4} M) and reference $[Ru(bpy)_3]^{2+}$

100 mV	Reduction			Oxidation		
Complex		**A/A′**	**B/B′**	**C/C′**	**D/D′**	**E/E′**
1[a]		−1.48 (0.18)	−0.85 (0.16)	+0.21 (0.11)	+0.74 (0.13)	+1.24 (0.26)
$[Ru(bpy)_3]^{2+}$ [b]	−1.76 (0.07)	−1.51 (0.07)	−1.32 (0.07)			+1.35 (0.07)

[a] Recorded in CH_2Cl_2 0.02 M $TBAPF_6$ with a scan rate of 100 mV/s, using two commercial platinum disk electrodes ($d = 2$ mm) as working and counter electrode and a silver wire as the pseudo-reference electrode.
[b] Ref. [43b].

Table 4
Results of anticancer activity of complex **1** compared with cisplatin

Drug	E_{max} (% inhibition)	IC_{50} (μM)
1	64	56
Cisplatin	94	0.4

an efficiency measurement, whilst the IC_{50} value can be considered as a power measurement for a particular drug with regard to a particular cell line. The results for **1** are given in comparison to those reported for cisplatin [44] and are gathered in Table 4. The results indicate that **1** is less efficient and less powerful than cisplatin and also less powerful than analogous complexes of the type $[RuL(bipy)_2]PF_6$ [45].

3. Experimental

3.1. General methods

All manipulations were carried out under N_2 using standard Schlenk techniques. Solvents were dried and distilled under N_2 prior to use. NMR spectra were recorded at room temperature (~22 °C), unless otherwise stated, on VARIAN UNITY INOVA-400 or VARIAN UNITY INOVA-500 spectrometers. Chemical shifts (ppm) are relative to TMS (^1H, ^{13}C NMR). ^1H–^1H COSY spectrum: standard pulse sequence with an acquisition time of 0.239 s, width 4288.2 Hz, 2D width 4288.2, relaxation delay 1 s, number of repetitions 2, number of increments 200. NOESY spectrum (VARIAN INOVA-400) standard parameters: relax delay 1.000 s, mixing 0.500 s, acquisition time 0.236 s, width 4341.2 Hz, 2D width 4341.2 Hz, 64 repetitions, 2×200 increments, DATA PROCESSING Gauss apodization 0.109 s, F1 DATA PROCESSING Gauss apodization 0.042 s. HMQC standard parameters: relax delay 1.000 s, acquisition time 0.134 s, width 1906.8 Hz, 2D width 17097.7 Hz, 16 repetitions, 2×512 increments, DATA PROCESSING Gauss apodization 0.062 s, F1 DATA PROCESSING Gauss apodization 0.055 s. HMBC standard parameters: relax delay 1.000 s, acquisition time of 0.131 s, width 1947.8 Hz, 2D width 24132.7 Hz, 16 repetitions, 512 increments, DATA PROCESSING Sine bell 0.066 s, F1 DATA PROCESSING Sine bell 0.011 s. IR spectra were recorded on a Nicolet

Impact 410 spectrophotometer as KBr pellets (4000–400 cm^{-1} range) or on a Jasco FT/IR-6300 spectrophotometer (630–150 cm^{-1} range) in Nujol mulls. Elemental analyses were performed in a LECO CHNS-932 microanalyser. FAB^+ mass spectra were recorded in a Micromass AutoSpec using ionization Liquid Secondary Ion Mass Spectrometry (LSMIS+) and Cs and NBA ions as the matrix. The UV–Vis spectrum was recorded in a Hewlett-Packard 8453 spectrophotometer (±0.2 nm). The fluorescence was studied with a SHIMADZU RF-5301PC Spectrofluorophotometer. The conductivity measurements were made with a CRISON conductimeter 522. The electrochemical measurements were performed with a PGSTAT 20 (Eco Chemie B.V., The Netherlands) equipped with a conventional three electrode cell. Two commercial platinum disk electrodes ($d = 2$ mm) were used as the working electrode and counter electrode. The pseudo-reference electrode was a silver wire. The in vitro studies were performed at the Screening Unit of the Institute for Industrial Pharmacy (USEF) of the University of Santiago de Compostela (USC). The ligands hexakis(pyrazol-1-yl)benzene (hpzb) [26,28] and hexakis(3,5-dimethylpyrazol-1-yl)benzene [25] have been previously described. The derivative *cis*-$[RuCl_2(2,2'\text{-bpy})_2]$ was prepared as reported previously [37].

3.2. Synthesis of *1*

Complex **1** was synthesized using a method similar to that described in Ref. [37]: $[RuCl_2(2,2'\text{-bpy})_2]\cdot 2H_2O$ (114.6 mg, 0.22 mmol) was refluxed in an ethanol/water mixture (30 mL/10 mL) for 1 h. The ligand hpzb (104.4 mg, 0.22 mmol) was then added and heating was maintained for 24–26 h. The resulting dark-red solution was cooled to room temperature. Next, the solvent was removed from the solution obtained under vacuum and with smooth heating. The crude product was dissolved in 20 mL of distilled water and the final product was precipitated after adding NH_4PF_6 solution, drop by drop (71.7 mg, 0.44 mmol in a minimum amount of water). The product is soluble in acetone, dichloromethane, ethanol and THF but insoluble in hexane or diethyl ether. The product was recrystallized from a mixture of CH_2Cl_2/Et_2O (1:2). Yield after recrystallization: 159.8 mg (0.1357 mmol, 62%). *Anal.* Calc. for $C_{44}H_{34}N_{16}RuP_2F_{12}$: C, 44.87; H, 2.91; N, 19.03. Found: C, 45.06; H, 3.21; N, 18.69. ^1H NMR (400 MHz, CD_3COCD_3, RT, J in Hz, ppm): all resonances correspond to one proton. *Bipyridine ligands*: δ 9.93 (dm, $^3J = 5.7$, $H^{6'}$-bpy); 9.03 (dm, $^3J = 7.7$, H^3-bpy); 8.92 (dm, $^3J = 7.8$, $H^{3'}$-bpy); 8.62 (dm, $^3J = 7.9$, H^3-bpy); 8.53 (dm, $^3J = 8$, $H^{3'}$-bpy); 8.43 (ddd, $^3J = 7.6$, $^3J = 7.6$, $^4J = 1.5$, H^4-bpy); 8.39 (dm, $^3J = 5.8$, $H^{6'}$-bpy); 8.18 (ddd, $^3J = 7.6$, $^3J = 7.6$, $^4J = 1.5$, $H^{4'}$-bpy); 8.17 (ddd, $^3J = 7.6$, $^3J = 7.6$, $^4J = 1.5$, $H^{4'}$-bpy); 8.10 (ddd, $^3J = 7.7$, $^3J = 7.7$, $^4J = 1.5$, H^4-bpy); 8.05 (dm, $^3J = 5.7$, H^6-bpy); 7.99 (dm, $^3J = 5.7$, H^6-bpy); 7.83 (ddd, $^3J = 7.1$, $^3J = 5.7$, $^4J = 1.4$, $H^{5'}$-bpy); 7.79 (ddd, $^3J = 7.1$, $^3J = 5.7$, $^4J = 1.3$, H^5-bpy); 7.54 (ddd, $^3J = 7.4$, $^3J = 5.8$, $^4J = 1.4$, $H^{5'}$-bpy); 7.52 (ddd, $^3J = 7.1$, $^3J = 5.7$, $^4J = 1.4$, H^5-bpy). *Pyrazolyl rings*: 7.75 (dd, $^3J = 2.6$, $^4J = 0.5$, H^{5e}-Pz); 7.74 (dd, $^3J = 3.0$, $^4J = 0.6$, H^{5b}-Pz); 7.72 (dd, $^3J = 2.3$, $^4J = 0.7$, H^{3f}-Pz); 7.61 (dd, $^3J = 3.0$, $^4J = 0.7$, H^{5f}-Pz); 7.58 (dd, $^3J = 2.6$, $^4J = 0.5$, H^{5d}-Pz); 7.55 (dd, $^3J = 1.9$, $^4J = 0.5$, H^{3c}-Pz); 7.49 (dd, $^3J = 1.8$, $^4J = 0.5$, H^{3e}-Pz); 7.37 (dd, $^3J = 1.8$, $^4J = 0.5$, H^{3d}-Pz); 7.21 (dd, $^3J = 2.6$, $^4J = 0.5$, H^{5a}-Pz); 7.05 (dd, $^3J = 2.5$, $^4J = 0.5$, H^{5c}-Pz); 6.97 (dd, $^3J = 1.8$, $^4J = 0.5$, H^{3a}-Pz); 6.72 (dd, $^3J = 2.3$, $^4J = 0.6$, H^{3b}-Pz); 6.34 (dd, $^3J = 3.0$, $^3J = 2.3$, H^{4f}-Pz); 6.29 (dd, $^3J = 2.6$, $^3J = 1.8$, H^{4e}-Pz); 6.26 (dd, $^3J = 2.6$, $^3J = 1.8$, H^{4d}-Pz); 6.18 (dd, $^3J = 2.5$, $^3J = 1.9$, H^{4c}-Pz); 6.15 (dd, $^3J = 3.0$, $^3J = 2.3$, H^{4b}-Pz); 6.04 (dd, $^3J = 2.6$, $^3J = 1.8$, H^{4a}-Pz). $^{13}C\{^1H\}$ NMR (100.6 MHz, CD_3COCD_3, RT, ppm): all resonances correspond to one carbon and are singlets. *Bipyridine ligands*: 159.8 (C^2-bpy); 159.5 ($C^{2'}$-bpy); 158.7 ($C^{2'}$-bpy); 157.6 (C^2-bpy); 155.1 ($C^{6'}$-bpy); 153.3 (C^6-bpy); 153.1 (C^6-bpy); 152.0 ($C^{6'}$-bpy); 138.6 (C^4-bpy); 138.1 (C^4-bpy); 137.8 ($C^{4'}$-bpy); 137.5 ($C^{4'}$-bpy); 128.0 (C^5-bpy); 127.4 (C^5-bpy); 127.0 ($C^{5'}$-bpy); 127.0 ($C^{5'}$-bpy); 125.5 (C^3-bpy); 125.1 ($C^{3'}$-bpy); 124.2 ($C^{3'}$-bpy); 123.3 (C^3-bpy). *Pyrazolyl rings*: 147.9 (C^{3b}-Pz); 147.4 (C^{3f}-Pz); 142.2 (C^{3d}-Pz); 142.0 (C^{3a}-Pz); 142.0 (C^{3e}-Pz); 141.8 (C^{3c}-Pz);140.0 (C^{5b}-Pz); 139.2 (C^{5f}-Pz); 133.8 (C^{5e}-Pz); 132.9 (C^{5d}-Pz); 132.5 (C^{5c}-Pz); 132.3 (C^{5a}-Pz); 111.1 (C^{4f}-Pz); 110.4 (C^{4b}-Pz); 108.1 (C^{4d}-Pz); 107.9 (C^{4c}-Pz); 107.7 (C^{4a}-Pz); 107.4 (C^{4e}-Pz). *Benzene ring*: 140.9; 138.4; 137.2; 137.1; 135.3; 132.6. $^{31}P\{^1H\}$ NMR (161.923 MHz, CD_3COCD_3, RT, J in Hz, ppm): −143.22 (spt, $^1J_{PF} = 708.2$, 2P, PF_6^-). $^{19}F\{^1H\}$ NMR (376.308 MHz, CD_3COCD_3, RT, J in Hz, ppm): −73 (d, $^1J_{PF} = 708.2$, 12F, PF_6^-). FAB mass spectrum: m/z 1033 Da $[\{Ru(bpy)_2(hpzb)\}PF_6]^+$, $[C_{44}H_{34}N_{16}RuPF_6]^+$; m/z 888 Da $[Ru(bpy)_2(hpzb)]^+$, $[C_{44}H_{34}N_{16}Ru]^+$; m/z 732 Da $[Ru(bpy)(hpzb)]^+$, $[C_{34}H_{26}N_{14}Ru]^+$; m/z 444 Da $[Ru(bpy)_2(hpzb)]^{2+}$, $[C_{44}H_{34}N_{16}Ru]^{2+}$. IR in KBr disk ($cm^{-1}$): 3130, 3107, 2366, 2340, 1633, 1604, 1530, 1489, 1466, 1446, 1417, 1397, 1306, 1269, 1128, 1083, 1046, 956, 918, 841 (PF_6^-), 759, 670, 641, 558 (PF_6^-), 474, 447, 430. IR in Nujol mull (630-150 cm^{-1} range): 376, 359, 259, 245, 203, 194, 178. UV–Vis (λ nm, ε $dm^3\ mol^{-1}\ cm^{-1}$): 282 (2061); 334 (8303); 449 (7375).

3.3. Synthesis of *1-d*

The ligand bpy-d_7 was obtained following a similar procedure to that described in the bibliography for perdeuterated bpy [46]: 2,2′-bipyridine,1,1′-dioxide (1.88 g, 0.01 mol) was treated with 32 mL of a 1 N solution of NaOD in D_2O (0.032 mol). The mixture was heated at 150 °C for 65 h in a Fisher-Porte tube. After that time, the solution was filtered, partially evaporated and left to precipitate while cooling. The colourless needles obtained where made to react with 10 mL of PCl_3 (0.11 mol) and the solution was heated for 1.5 h at reflux. After cooling, the solution was neutralized with a solution of KOH (20%). The product was extracted

with ether (2 × 40 mL) and the solution treated with anhydrous magnesium sulfate, filtered and evaporated to dryness. The product was purified by vacuum sublimation while heating in a water bath at 60 °C. The derivative $[RuCl_2(2,2'\text{-bpy-}d_7)_2]\cdot 2H_2O$ was obtained similarly to the non-deuterated counterpart. Complex **1-*d*** is made similarly to **1**. The amounts were as follows: hpzb: 47.9 mg, 0.10 mmol; $[RuCl_2(2,2'\text{-bpy-}d_7)_2]\cdot 2H_2O$, 52.0 mg, 0.2 mmol; NH_4PF_6, 32.6 mg, 0.2 mmol. **1-*d*** obtained: 93 mg, 0.078 mmol. Yield: 78%.

3.4. Cytotoxicity: experimental procedure

3.4.1. Cell line and growth conditions

Human ovary carcinoma (A2780) cell line was purchased from ECACC and was grown in RPMI-1640 medium (Sigma-RBI, Spain) supplemented with 10% foetal bovine serum (FBS) (Sigma-RBI, Spain) and 2 mM L-glutamine (Sigma-RBI, Spain) in a humidified atmosphere of 5% CO_2 at 37 °C. Non-small cell lung cancer (NCI-H460) cell line was purchased from ATCC and was grown in RPMI-1640 medium (LGC-Promochem, Spain) supplemented with 10% foetal bovine serum (FBS) (Sigma-RBI, Spain), in a humidified atmosphere of 5% CO_2 at 37 °C. The cells were harvested using trypsin-EDTA (Sigma-RBI, Spain).

3.4.2. In vitro chemosensitivity assay on the human A2780 cell line

The cells were seeded into 96-well plates (Becton-Dickinson, Spain) in a volume of 100 μL in a number of 4000 cells/well. After attachment to the culture surface, the cells were incubated in an atmosphere containing 5% CO_2 at 37 °C for 24 h. Test drugs were dissolved in DMSO and administered maintaining the DMSO proportion at 1%. After the proper incubation time (96 h) the cells were fixed by adding 50 μL of a solution of 30% trichloroacetic acid over 60 min at 4 °C. After this time the cells were washed with H_2O and 100 μL of 0.4% sulforhodamine B in 1% acetic acid was added to the wells over 10 min at room temperature. Then cells were washed with 0.1% acetic acid and 100 μL of 10 mM Trizma were added. The plate was shaken for 15 min at room temperature and absorbance was read at a wavelength of 515 nM in a Tecan Ultra Evolution reader.

3.4.3. In vitro chemosensitivity assay on the human NCI-H460 cell line

The cells were seeded into 96-well plates (Beckton-Dickinson, Spain) in a volume of 100 μL in a number of 15000 cells/well. After attachment to the culture surface, the cells were incubated in an atmosphere containing 5% CO_2 at 37 °C for 24 h. Test drugs were dissolved in DMSO and administered maintaining the DMSO proportion at 1%.

After the proper incubation time (48 h) the growth inhibition induced by the compounds was evaluated as described before for the A2780 cell line.

3.5. Data analysis

The effects of the complex were expressed as corrected % inhibition values according to the following equation:

$$\%\ \text{inhibition}_{\text{corr}} = [1 - (T/C)] \times 100$$

where T is the mean absorbance of the treated cells and C the mean absorbance of the controls with DMSO.

$$E = \frac{E_{\max}}{1 + \left(\frac{IC_{50}}{C}\right)^n}$$

The inhibitory potency of compounds was measured by calculating concentration–% inhibition curves, these curves were adjusted to the indicated equation where E is the percentage of inhibition observed, $E_{\max}$ is the maximal effect; IC_{50} is the concentration that inhibits 50% of maximal growth, C is the concentration of compound tested and n is the slope of the semi-logarithmic dose–response curves. This non-linear fitting was performed using GraphPad Prism 2.01 Software (GraphPad Software Inc.).

For comparison purposes, the cytotoxicity of cisplatin was evaluated under the same experimental conditions.

Acknowledgements

We gratefully acknowledge financial support from the Dirección General de Investigación, Spain (Project No. CTQ2005-01430/BQU) and from the Junta de Comunidades de Castilla-La Mancha- FEDER funds (Project No. PBI-05-003). The Physical Chemistry group of the University of Burgos (UV–Vis spectra), Dr. Alvaro Colina for stimulating suggestions regarding electrochemical discussions and the SCAI service of the University of Burgos are also acknowledged.

References

[1] (a) R. Mukherjee, Coord. Chem. Rev. 203 (2000) 151;
(b) A.P. Sadimenko, Adv. Heterocycl. Chem. 80 (2001) 157.
[2] S. Trofimenko, in: Scorpionates, The Coordination Chemistry of Polypyrazolylborate Ligands, Imperial College Press, London, 1999.
[3] (a) H.L. Bigmore, S.C. Lawrence, P. Mountford, C.S. Tredget, J. Chem. Soc., Dalton Trans. (2005) 635;
(b) C. Pettinari, R. Pettinari, Coord. Chem. Rev. 249 (2005) 663.
[4] P. Cornago, C. Escolástico, M.D. Santa Maria, R. Claramunt, C. Fernández-Castaño, C. Foces-Foces, J.-P. Fayet, J. Elguero, Tetrahedron 52 (1996) 11075.
[5] (a) W.K. Chang, S.C. Sheu, G.H. Lee, Y. Wang, T.I. Ho, Y.C. Lin, J. Chem. Soc., Dalton Trans. (1993) 687;
(b) W.K. Chang, G.H. Lee, Y. Wang, T.I. Ho, Y.O. Su, Y.C. Lin, Inorg. Chim. Acta 223 (1994) 139;
(c) W.K. Chang, G.H. Lee, Y. Wang, Y.O. Su, T.I. Ho, Y.C. Lin, J. Coord. Chem. 42 (1997) 253.
[6] (a) C.M. Hartshorn, P.J. Steel, Austr. J. Chem. 48 (1995) 1587;
(b) C.M. Hartshorn, P.J. Steel, Angew. Chem., Int. Ed. 35 (1996) 2655;
(c) C.M. Hartshorn, P.J. Steel, Chem. Commun. (1997) 541;
(d) C.M. Hartshorn, P.J. Steel, Austr. J. Chem. 50 (1997) 1195;
(e) C.M. Hartshorn, P.J. Steel, Organometallics 17 (1998) 3487.
[7] J. Chen, D.M.L. Goodgame, S. Menzer, D.J. Williams, Polyhedron 16 (1997) 1679.

[8] (a) J.S. Fleming, K.L.V. Mann, C.A. Carraz, E. Psillakis, J.C. Jeffery, J.A. McCleverty, M.D. Ward, Angew. Chem., Int. Ed. 37 (1998) 1279;
Angew. Chem. 110 (1998) 1325;
(b) J.S. Fleming, K.L.V. Mann, S.M. Couchman, J.C. Jeffery, J.A. McCleverty, M.D. Ward, J. Chem. Soc., Dalton Trans. (1998) 2047.
[9] B. Therrien, T.R. Ward, Angew. Chem., Int. Ed. 38 (1999) 405.
[10] J. Chin, C. Walsdorff, B. Stranix, J. Oh, H.J. Chung, S.M. Park, K. Kim, Angew. Chem., Int. Ed. 38 (1999) 2756.
[11] N. Fatin-Rouge, E. Toth, D. Perret, R.H. Backer, A.E. Merbach, J.C.G. Bünzli, J. Am. Chem. Soc. 122 (2000) 10810.
[12] C.M. Hartshorn, P.J. Steel, Inorg. Chem. Commun. 3 (2000) 476.
[13] A.J. Canty, J. Patel, B.W. Skelton, A.H. White, J. Organomet. Chem. 607 (2000) 194.
[14] H.P. Dijkstra, M.D. Meijer, J. Patel, R. Kreiter, G.P.M. van Klink, M. Lutz, A.L. Spek, A.J. Canty, G. van Koten, Organometallics 20 (2001) 3159.
[15] (a) M.D. Ward, J.A. McCleverty, J.C. Jeffery, Coord. Chem. Rev. 222 (2001) 251;
(b) Z.R. Bell, M.D. Ward, Acta Crystallogr., Sect. E—Struct. Rep. on line 59 (2003) M787.
[16] S.P. Argent, H. Adams, L.P. Harding, T. Riis-Johannessen, J.C. Jeffery, M.D. Ward, New J. Chem. 29 (2005) 904.
[17] J. García-Antón, R. Mathieu, N. Lugan, J. Pons Picart, J. Ros, J. Organomet. Chem. 689 (2004) 1599.
[18] A.J. Canty, R.T. Honeyman, B.W. Skelton, A.H. White, J. Organomet. Chem. 389 (1990) 277.
[19] P. Cornago, C. Escolástico, M.D. Santa María, R.M. Claramunt, D. Carmona, M. Esteban, L.A. Oro, C. Foces-Foces, A.L. Llamas-Saiz, J. Elguero, J. Organomet. Chem. 467 (1994) 293.
[20] (a) T.E. Keyes, P.M. Jayaweera, J.J. McGarvey, J.G. Vos, J. Chem. Soc., Dalton Trans. (1997) 1627;
(b) T.E. Keyes, R.J. Forster, P.M. Jayaweera, C.G. Coates, J.J. McGarvey, J.G. Vos, Inorg. Chem. 37 (1998) 5925.
[21] A.M. Bond, F. Marken, C.T. Williams, D.A. Beattie, T.E. Keyes, R.J. Forster, J.G. Vos, J. Phys. Chem. B 104 (2000) 1977.
[22] M.D. Ward, J.A. McCleverty, J.C. Jeffery, Coord. Chem. Rev. 222 (2001) 251.
[23] M. Loi, M.W. Hosseini, A. Jouaiti, A. De Cian, J. Fischer, Eur. J. Inorg. Chem. (1999) 1981.
[24] A. Jouaiti, M. Loi, M.W. Hosseini, A. De Cian, Chem. Commun. (2000) 2085.
[25] C. Foces-Foces, A.L. Llamas-Saiz, R.M. Claramunt, N. Jagerovic, M.L. Jimeno, J. Elguero, J. Chem. Soc., Perkin Trans. 2 (1995) 1359.
[26] C. Foces-Foces, A.L. Llamas-Saiz, C. Escolástico, R.M. Claramunt, J. Elguero, J. Phys. Org. Chem. 9 (1996) 137.
[27] C. Foces-Foces, C. Fernández-Castaño, R.M. Claramunt, C. Escolástico, J. Elguero, J. Phys. Org. Chem. 9 (1996) 717.
[28] C. Foces-Foces, A.L. Llamas-Saiz, C. Fernández-Castaño, R.M. Claramunt, C. Escolástico, J.L. Lavandera, M.D. Santa-María, M.L. Jimeno, J. Elguero, J. Chem. Soc., Perkin Trans. 2 (1997) 2173.
[29] R.M. Claramunt, J. Elguero, C. Escolástico, C. Fernández-Castaño, C. Foces-Foces, A.L. Llamas-Sainz, M.D. Santa María, Targets Heterocycl. Chem. 1 (1997) 1.
[30] C. Foces-Foces, C. Fernández-Castaño, R.M. Claramunt, C. Escolástico, J. Elguero, J. Incl. Phenom. Macro. Chem. 33 (1999) 169.
[31] A.M. Guerrero, F.A. Jalón, B.R. Manzano, R.M. Claramunt, M.D. Santa María, C. Escolástico, J. Elguero, A.M. Rodríguez, M.A. Maestro, J. Mahía, Eur. J. Inorg. Chem. (2002) 3178.
[32] A. Caballero, A. Guerrero, F.A. Jalón, B.R. Manzano, A.M. Rodríguez, R.M. Claramunt, M.D. Santa María, C. Escolástico, J. Elguero, Inorg. Chim. Acta 347 (2003) 168.
[33] (a) S. Baitalik, U. Flörke, K. Nag, Inorg. Chem. 38 (1999) 3296;
(b) S. Baitalik, U. Flörke, K. Nag, Inorg. Chim. Acta 337 (2002) 439;
(c) S. Baitalik, P. Bag, U. Flörke, K. Nag, Inorg. Chim. Acta 357 (2004) 699;
(d) S. Baitalik, B. Dutta, K. Nag, Inorg. Chim. Acta 23 (2004) 913.
[34] J.-Z. Wu, E. Bouwman, J. Reedijk, A.M. Mills, A.L. Spek, Inorg. Chim. Acta 351 (2003) 326.
[35] P.J. Steel, E.C. Constable, J. Chem. Soc., Dalton Trans. (1990) 1389.
[36] W.H. Ang, P.J. Dyson, Eur. J. Inorg. Chem. (2006) 4003, and references herein.
[37] B.J. Sullivan, D.J. Salmon, Inorg. Chem. 24 (1978) 3334.
[38] Edwin C. Constable, Metals and Ligand Reactivity. An Introduction to the Organic Chemistry of Metal Complexes, VCH, 1996, p. 25.
[39] (a) P.K. Byers, A.J. Canty, R.T. Honeyman, Adv. Organomet. Chem. 34 (1992) 1;
(b) M.C. Carrión, A. Díaz, A. Guerrero, F.A. Jalón, B.R. Manzano, A. Rodríguez, R.L. Paul, J.C. Jeffery, J. Organomet. Chem. 650 (2002) 210;
(c) N. Arroyo, F. Gómez de la Torre, F.A. Jalón, B.R. Manzano, B. Moreno-Lara, A.M. Rodríguez, J. Organomet. Chem. 603 (2000) 174;
(d) F.A. Jalón, B.R. Manzano, A. Otero, M.C. Rodríguez-Pérez, J. Organomet. Chem. 494 (1995) 179.
[40] A. Juris, V. Balzani, F. Barigelleti, S. Campagna, P. Belser, A. von Zelewsky, Coord. Chem. Rev. 84 (1988) 85.
[41] J.N. Demas, B.A. DeGraff, Coord. Chem. Rev. 84 (1988) 85.
[42] W.J. Geary, Coord. Chem. Rev. 7 (1971) 81.
[43] (a) M. Heijden, P.M. van Vliet, J.G. Haasnoot, J. Reedijk, J. Chem. Soc., Dalton Trans. (1993) 3675;
(b) X. Liu, J. Liu, K. Jin, X. Yang, Q. Peng, L. Sun, Tetrahedron 61 (2005) 5655;
(c) M. Li, J. Liu, C. Zhao, L. Sun, J. Organomet. Chem. 691 (2006) 4189;
(d) T. Koizumi, T. Tomon, K. Tanaka, J. Organomet. Chem. 690 (2005) 1258;
(e) J. Dinda, S. Senapoti, T. Mondal, A.D. Jana, M.Y. Chiang, T.-H. Lu, C. Sinha, Polyhedron 25 (2006) 1125.
[44] S.C. Wilson, P.W. Howard, S.M. Forrow, J.A. Hartley, L.J. Adams, T.C. Jenkins, L.R. Kelland, D.E. Thurston, J. Med. Chem. 42 (1999) 4028.
[45] L. Mishra, A.K. Yadaw, S. Bhattacharya, S.K. Dubey, J. Inorg. Biochem. 99 (2005) 1113.
[46] (a) M.J. Cook, A.P. Lewis, G.S.G. McAuliffe, V. Skarda, A.J. Thomson, J.L. Glasper, D.J. Robbins, J. Chem. Soc., Perkin Trans. 2 (1984) 1293;
(b) S. Chirayil, R.P. Thummel, Inorg. Chem. 28 (1989) 813.

appreciable intermolecular forces of face-to-face π–π interactions and edge-to-face CH–π contacts are essentially pertinent to planar aromatic moieties that comprise π orbitals on the rings [5]. Such interactions are often found in systems with aromatic groups, for instance, 2,2′-bypridine and 1,10-phenanthroline as coligands, which facilitate supramolecular stacks between the flat pyridyl rings [6]. It is beneficial if ligands of interest are able to concurrently generate all the three types of intermolecular contacts in view of the resulting increment of dimensionality [7]. To this end, the tp and triazole groups mentioned above should be indeed good candidates to create complicated non-covalent bonds and subsequently build up multi-dimensional assemblies because they possess the required planar aromatic rings. Besides, triazole-bridged Cu(II) complexes have been well characterized structurally and magnetically, but examples containing Co(II) and Ni(II) ions, especially triply-bridged by triazoles, are still scarce to date [8].

Herein we report the synthesis, molecular structures and magnetic properties of two dimeric complexes $[M_2(atrz)_3(H_2O)_4(tp)_2]\cdot 11H_2O$ [M = Co(**1** · $11H_2O$), Ni(**2** · $11H_2O$); atrz = 4-aminotriazole], in which triple triazole bridges and end-capped tp ligands are present. The terminal end-on binding mode for tp is a rare example among coordination systems containing tp that function mostly as end-to-end bridges, and rarely as isolated anions [3,9]. The dinuclear entities are interconnected through multiple intermolecular forces (hydrogen bond, face-to-face π–π and edge-to-face CH–π interactions), forming 3D frameworks. Magnetic analyses reveal that antiferromagnetic intradimer couplings transmitted by triazoles and weak antiferromagnetic interdimer interactions through intermolecular contacts coexist.

2. Experimental

2.1. Preparation of $[Co_2(atrz)_3(H_2O)_4(tp)_2]\cdot 11H_2O$(**1** · $11H_2O$)

To a 10 ml aqueous solution of cobalt(II) perchlorate hexahydrate (0.25 mmol, 91 mg) was added 4-aminotriazole (0.375 mmol, 32 mg) dissolved in 10 ml water, with stirring. The pink solution was treated with potassium tp (0.25 mmol, 60 mg) dissolved in 10 ml water. The filtrate of the resulting solution was allowed to stand for several days, providing pink crystals of **1** in 50% yield. *Anal.* Calc. for $C_{22}H_{34}N_{12}O_{15}Co_2$ (**1** · $3H_2O$): C, 32.05; H, 4.16; N, 20.39. Found: C, 31.89; H, 3.83; N, 19.89%.

2.2. Preparation of $[Ni_2(atrz)_3(H_2O)_4(tp)_2]\cdot 11H_2O$ (**2** · $11H_2O$)

Compound **2** was prepared by the same synthetic procedure as **1** except for the use of nickel(II) perchlorate hexahydrate instead of the Co(II) ion. Blue crystals were separated in a yield of 61%. *Anal.* Calc. for $C_{22}H_{34}N_{12}O_{15}Ni_2$ (**2** · $3H_2O$): C, 32.07; H, 4.26; N, 20.40. Found: C, 32.00; H, 3.97; N, 20.06%.

2.3. Physical measurements

Elemental analyses for C, H and N were performed at the Elemental Analysis Service Center of Seoul Branch, Korea Basic Science Institute. Infrared spectra were obtained from KBr pellets with a Bomen MB-104 spectrometer. Magnetic susceptibilities for **1** and **2** were carried out using a Quantum Design MPMS-7 SQUID susceptometer. Diamagnetic corrections of **1** and **2** were estimated from Pascal's tables.

2.4. X-ray structural analysis

X-ray data for **1** and **2** were collected on a Bruker SMART APEXII diffractometer equipped with graphite monochromated Mo Kα radiation ($\lambda = 0.71073$ Å). The preliminary orientation matrix and cell parameters were determined from three sets of ω-scans at different starting angles. Data frames were obtained at scan intervals of 0.5° with an exposure time of 10 s per frame. The reflection data were corrected for Lorentz and polarization factors. Absorption corrections were carried out using SADABS [10]. The structures were solved by direct methods and refined by full-matrix least-squares analysis using anisotropic thermal parameters for non-hydrogen atoms with the SHELXTL program [11]. All hydrogen atoms except for hydrogens bound to water molecules and amino groups to atrz were calculated at idealized positions and refined riding on the corresponding carbon atoms with isotropic thermal parameters [$U = 1.2U(C_{methylene})$]. Crystallographic data and the details of data collection are listed in Table 1.

Table 1
Crystal data and structure refinements for **1** and **2**

	1 · $11H_2O$	**2** · $11H_2O$
Empirical formula	$C_{22}H_{50}Co_2N_{12}O_{23}$	$C_{22}H_{50}N_{12}Ni_2O_{23}$
Formula weight	968.60	968.16
Crystal system	monoclinic	monoclinic
Space group	*P*2/*c*	*P*2/*c*
a (Å)	11.7360(3)	11.6879(14)
b (Å)	12.1556(3)	12.1532(14)
c (Å)	13.9365(3)	14.0973(17)
β (°)	99.9710(10)	99.016(7)
V (Å^3)	1958.12(8)	1977.7(4)
Z	2	2
μ (mm^{-1})	0.949	1.052
ρ (g cm^{-3})	1.643	1.626
F(000)	1008	1012
Goodness-of-fit	0.951	1.002
R_1^a [$I > 2\sigma(I)$]	0.0447	0.0635
wR_2^b [$I > 2\sigma(I)$]	0.1338	0.1537

[a] $F_o > 4\sigma(F_o)$, $R_1 = \sum||F_o| - |F_c||/\sum|F_o|$.
[b] $wR_2 = [\sum w(F_o^2 - F_c^2)^2/\sum w(F_o^2)^2]^{1/2}$.

3. Results and discussion

3.1. Synthesis and characterization

A stoichiometric reaction of M^{2+} (M = Co and Ni):atrz:dipotassium tp in a ratio of 2:3:2 allowed the formation of **1** and **2**. In the IR spectra, strong and broad bands are observed at 3277 cm^{-1} (**1**) and 3275 cm^{-1} (**2**), which can be assigned to hydrogen bonds among water molecules, N–H groups of atrz ligands and carboxylate oxygens of tp. The secondary amine of atrz is detected at 3148 and 3121 cm^{-1} for **1**, and 3145 and 3130 cm^{-1} for **2**. The most particular peaks for the carboxylate groups of tp are characterized as the difference (Δ) between the antisymmetric stretching $\nu_a(CO_2^-)$ and symmetric frequency $\nu_s(CO_2^-)$ [12]. The calculated values of 193 cm^{-1} (**1**) and 189 cm^{-1} (**2**) are fairly large compared to the ionic value (=170 cm^{-1}) of dipotassium tp. This indicates that the binding mode of tp appears to be quasi-bridging, which was confirmed by the X-ray analysis.

3.2. Description of the structures

Compounds **1** and **2** crystallize in the monoclinic system with space group $P2/c$. The molecular structures are shown in Fig. 1. Selected distances and angles of both complexes are summarized in Tables 2 and 3. The M (M = Co and Ni) center adopts a distorted octahedral geometry, comprising one oxygen from tp, two water oxygens and three nitrogens from atrz ligands, with average M–N(O) distances of 2.10(2) Å for **1** and 2.08(2) Å for **2**. The two M atoms in a molecule are triply bridged by planar atrz groups and separated by 3.8228(6) Å for **1** and 3.7473(9) Å for **2**. The dihedral angles among the triazole rings of the bridging atrz ligands are 64.46(11)° (**1**), 64.03(16)° (**2**) between the N1-containing ring and N4- or N5-containing rings and 52.08(9)° (**1**), 52.60(13)° (**2**) between N4- and N5-containing rings. The dihedral angle between the carboxylate group and the benzene ring of tp is somewhat small, 5.96(18)° for **1** and 4.98(27)° for **2**, which fall in the lower range for tp-based complexes [3]. The benzene rings of the two terminal tp ligands lie almost coplanar, having dihedral angles of 3.24(7)° for **1** and 4.49(11)° for **2**. The dimeric structures are completed by two terminal tp ligands, among which one carboxylate group of a tp ligand is connected to the M atom in a monodentate mode while the other remains free. It deserves to be noted that tp serving as a terminal group in an end-on mode is a rare example because the ligand coordinates frequently as a bridge in the end-to-end mode to unsaturated metal centers or acts, very exceptionally, as an isolated counter anion [3,9]. The unbound oxygen atom (O2) of the coordinated carboxylate group is linked to the water

Table 2
Bond lengths (Å) and angles (°) for **1**[a]

Co(1)–O(1)	2.069(2)	Co(1)–N(1)	2.094(3)
Co(1)–O(5)	2.101(2)	Co(1)–O(6)	2.106(2)
Co(1)–N(5)	2.119(3)	Co(1)–N(4)	2.129(3)
O(1)–Co(1)–N(1)	89.39(10)	O(1)–Co(1)–O(5)	84.48(9)
N(1)–Co(1)–O(5)	93.46(10)	O(1)–Co(1)–O(6)	90.74(9)
N(1)–Co(1)–O(6)	178.08(9)	O(5)–Co(1)–O(6)	88.45(9)
O(1)–Co(1)–N(5)	173.88(9)	N(1)–Co(1)–N(5)	89.80(10)
O(5)–Co(1)–N(5)	89.51(10)	O(6)–Co(1)–N(5)	90.27(10)
O(1)–Co(1)–N(4)	95.08(9)	N(1)–Co(1)–N(4)	89.42(10)
O(5)–Co(1)–N(4)	177.08(10)	O(6)–Co(1)–N(4)	88.66(9)
N(5)–Co(1)–N(4)	90.98(10)	C(1)–O(1)–Co(1)	130.9(2)
C(9)–N(1)–Co(1)	127.4(2)	N(1)#1–N(1)–Co(1)	125.36(7)
C(10)–N(4)–Co(1)	128.0(2)	N(5)#1–N(4)–Co(1)	124.5(2)
C(11)–N(5)–Co(1)	127.4(2)	N(4)#1–N(5)–Co(1)	125.37(19)

[a] Symmetry transformations used to generate equivalent atoms: #1 $-x+1, y, -z+1/2$.

Table 3
Bond lengths (Å) and angles (°) for **2**[a]

Ni(1)–O(1)	2.040(3)	Ni(1)–N(1)	2.058(4)
Ni(1)–N(5)	2.078(4)	Ni(1)–N(4)	2.090(4)
Ni(1)–O(6)	2.092(3)	Ni(1)–O(5)	2.095(3)
O(1)–Ni(1)–N(1)	89.19(14)	O(1)–Ni(1)–N(5)	173.99(13)
N(1)–Ni(1)–N(5)	90.77(15)	O(1)–Ni(1)–N(4)	93.85(14)
N(1)–Ni(1)–N(4)	89.59(15)	N(5)–Ni(1)–N(4)	92.15(14)
O(1)–Ni(1)–O(6)	91.16(13)	N(1)–Ni(1)–O(6)	179.17(13)
N(5)–Ni(1)–O(6)	88.96(14)	N(4)–Ni(1)–O(6)	89.64(14)
O(1)–Ni(1)–O(5)	84.24(13)	N(1)–Ni(1)–O(5)	93.33(14)
N(5)–Ni(1)–O(5)	89.76(14)	N(4)–Ni(1)–O(5)	176.49(13)
O(6)–Ni(1)–O(5)	87.45(13)	C(1)–O(1)–Ni(1)	130.8(3)
C(9)–N(1)–Ni(1)	128.0(3)	N(1)#1–N(1)–Ni(1)	124.81(10)
C(10)–N(4)–Ni(1)	127.9(3)	N(5)#1–N(4)–Ni(1)	125.2(3)
C(11)–N(5)–Ni(1)	129.1(3)	N(4)#1–N(5)–Ni(1)	123.7(3)

[a] Symmetry transformations used to generate equivalent atoms: #1 $-x+1, y, -z+1/2$.

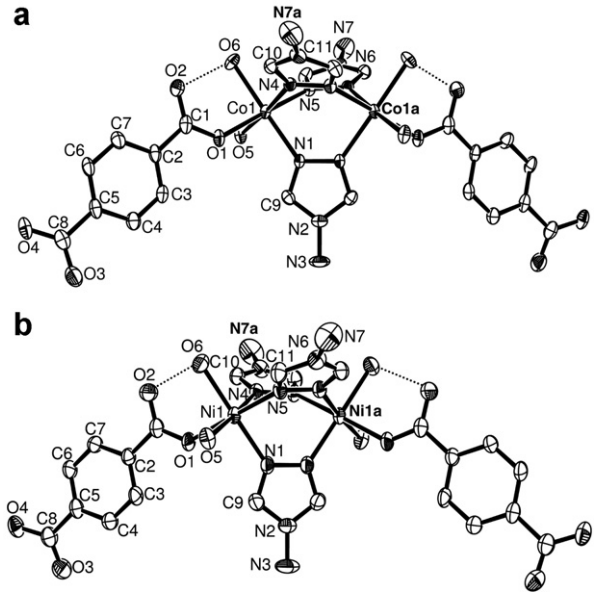


Fig. 1. ORTEP diagrams of (a) **1** and (b) **2** with the atom numbering schemes. The dotted lines represent intramolecular hydrogen bonds between coordinated water molecules and carboxylate oxygens. Symmetry code: $a = 1 - x, y, 0.5 - z$.

oxygen (O6) and one lattice water molecule (O12) via hydrogen bonds (O2···O6 = 2.630(3) Å for **1**; 2.636(5) Å for **2**). Moreover, the free carboxylate oxygens (O3 and O4) undergo multiple hydrogen bonds with lattice water molecules. Thus, the carboxylate group virtually functions as a pseudo-bridging ligator, consistent with the IR data. Hydrogen bonding is not found for the amino group (N3) of one atrz ligand while additional hydrogen bonds between the amino groups of the other two atrz ligands and lattice water molecules are observed.

Fig. 2a illustrates a 2D sheet architecture constructed by extended intermolecular face-to-face π–π interactions between the benzene rings of tp ligands operative in the crystal lattice. There exist two types of π–π contacts: for type I the planar benzene rings are stacked in the range 3.737–3.764 Å for **1** and 3.819–3.848 Å for **2** whereas type II varies in the range 3.445–4.034 Å for **1** and 3.442–4.087 Å for **2**, which are in the usual range for π–π interactions [13]. The 2D sheet is further stabilized with the assistance of edge-to-face CH–π interactions between H6-containing benzene moieties of tp ligands and N6-containing triazole rings, and the distances between H6 and the centroid of the corresponding triazole are 3.120 Å for **1** and 3.146 Å for **2** (Fig. 2b) [7]. It is thus noted that three types of intermolecular interactions are entangled in the structures and the incorporation of hydrogen bonding, π–π and CH–π contacts results in the formation of a 3D network structure. The shortest intermolecular M–M distances are 7.3562(7) Å for **1** and 7.3442(12) Å for **2**.

3.3. Magnetic properties

The magnetic susceptibility data of **1** were measured at 0.5 T from 2 to 300 K. The $\chi_m T$ value of 5.61 cm^3 K mol^{-1} at 300 K is much higher than the spin-only one (3.75 cm^3 K mol^{-1}) expected for two magnetically independent Co(II) ions, which is due to an orbital contribution from an octahedral Co(II) atom [14]. Upon cooling, $\chi_m T$ decreases slowly and then abruptly, reaching 0.127 cm^3 K mol^{-1} at 2 K. To examine the magnetic couplings between the magnetic centers, the Curie–Weiss equation was employed at $T > 80$ K yielding $C = 6.152$ cm^3 K mol^{-1} and $\theta = -28$ K. The obtained Curie constant is consistent with the normal range of 5.6–6.8 cm^3 K mol^{-1} for two hexacoordinated high-spin Co(II) centers [14,15]. The negative Weiss constant concerns a phenomenological consequence of antiferromagnetic interactions and/or spin–orbit coupling for Co(II) ions in an octahedral crystal field. In the plot of χ_m versus T (Fig. 3a), a maximum is evident at $T_{max} = 20$ K. From the ratio ($|J|/kT_{max} = 0.648$) for antiferromagnetically coupled $S = 3/2$ pairs, J was estimated to be -9.01 cm^{-1} [16].

To scrutinize the magnetic exchange coupling between Co(II) ions in the dimeric structure we modelled the present system on the basis of the spin Hamiltonian $H = -JS_{Co1} \cdot S_{Co1a}$. The fitting of the experimental data with the equation derived from the above Hamiltonian afforded a poor result (dashed line in Fig. 3a), especially around T_{max}. In

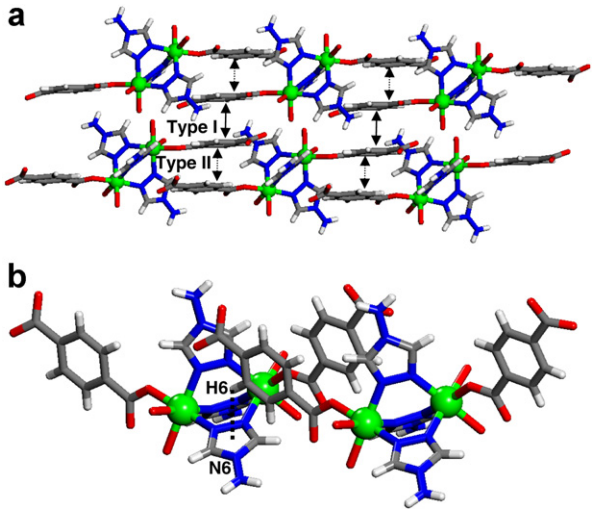


Fig. 2. (a) Extended view of **1** showing a 2D sheet formed by π–π contacts of types I and II between the benzene rings of tp ligands. (b) Additional intermolecular CH–π interaction (dashed line) between a hydrogen atom (H6) on the benzene ring and triazole rings.

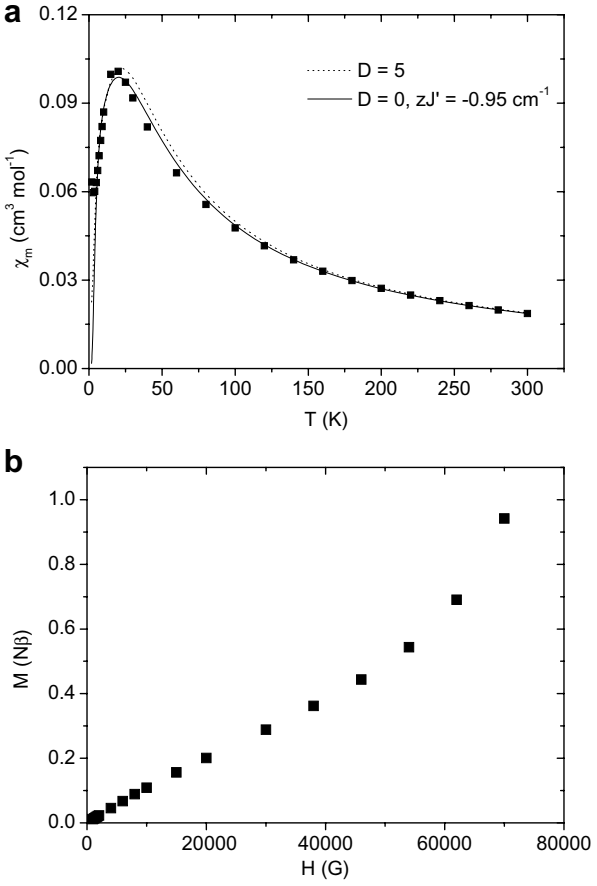


Fig. 3. Plots of: (a) χ_m vs. T and (b) M vs. H for **1**. The solid line and dotted lines represent the magnetic results with the intermolecular interaction term (zJ') and with the zero-field splitting parameter (D), respectively.

view of the presence of π–π interactions and hydrogen bonds among the dimers it is reasonable to consider an intermolecular interaction term (zJ') induced from the molecular field approximation, equated to $\chi^{corr} = \chi_m/[1 - (zJ'/Ng^2\beta^2)\chi_m]$. A better fit results and the parameters obtained with the modified formula are $g = 2.53$, $J = -9.21\ cm^{-1}$ and $zJ' = -0.95\ cm^{-1}$ (solid line in Fig. 3a). It is noticed that the J value, quite close to the estimated one from the aforementioned relation, agrees well with those of triazole-bridged Co(II) complexes [4a]. The zJ' component supports that weak interdimer antiferromagnetic interactions are mediated through the indirect linkage of the intermolecular contacts. Since the Co(II) ion is magnetically anisotropic it is necessary to include a zero-field splitting (ZFS) parameter, arising from the ZFS Hamiltonian $H_{ZFS} = D[S_z^2 - S(S+1)/3]$, in the fitting procedure. Fixing $g = 2.53$ and $J = -9.21\ cm^{-1}$, simulations with the MAGPACK program [17] to include the ZFS contribution allowed a good agreement with $D = 5\ cm^{-1}$ in the high temperature region, but significantly deviated around the peak temperature, which is due to the limit of the model adopted for explaining the magnetic properties of this dinuclear high-spin Co(II) complex. Consequently, two terms (zJ' and D) cannot be neglected to account for the observed magnetic data. It is worth mentioning that the zJ' part affects more critically the magnetic properties of **1** than D since the magnetic analysis with zJ' has a better fit than that with the D term only. The field dependence of the magnetization collected at fields from 0 to 7 T at 2 K shows a typical antiferromagnetic behavior, as depicted in Fig. 3b.

The variable temperature magnetic susceptibility data of **2** were plotted in the form of χ_m versus T (Fig. 4a). The room temperature $\chi_m T$ value of 1.97 $cm^3\ K\ mol^{-1}$ is a little lower than the expected one for two isolated Ni(II) ions. As the temperature diminishes $\chi_m T$ lessens gradually and then more rapidly, which is characteristic of antiferromagnetic interactions. The magnetic phenomenon obeys the Curie–Weiss equation at $T > 30$ K, giving $C = 2.295\ cm^3\ K\ mol^{-1}$ and $\theta = -46$ K. A cusp temperature in the $\chi_m(T)$ plot is visible at 30 K, which can be utilized to estimate the magnetic exchange coupling constant (J) from the relation $|J|/kT_{max} = 0.976$ for an antiferromagnetically coupled Ni(II) dimer, giving $J = -20.4\ cm^{-1}$ [16]. Applying the spin Hamiltonian $H = -JS_{Ni1} \cdot S_{Ni1a}$, and considering intermolecular interactions (zJ'), we obtained best-fit parameters of $g = 2.07$, $J = -21.9\ cm^{-1}$ and $zJ = -1.54\ cm^{-1}$. When zJ' is ignored and the ZFS term (D) is exclusively included in the fitting process, the resultant curves (dashed and dotted lines in Fig. 4a) are unsatisfactory, despite the unrealistic D values used. Hence, the interdimer antiferromagnetic interactions should play much more dominant role than the ZFS term in the observed magnetic behavior for **2**. The $M(H)$ data definitely suggest the presence of overall antiferromagnetic couplings (Fig. 4b).

The pair contribution J_{ij} in a simple exchange scheme between pairs of magnetic orbitals can be described on

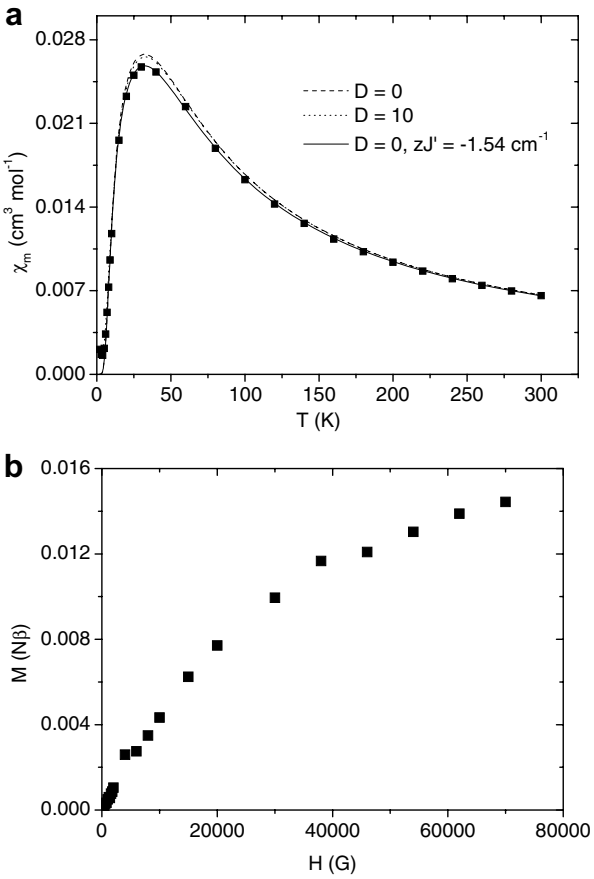


Fig. 4. Plots of: (a) χ_m vs. T and (b) M vs. H for **2**. The solid line and the other lines denote the magnetic results with the intermolecular interaction term (zJ') and with the zero-field splitting parameter (D), respectively.

the basis of coexisting ferromagnetic ($J_{ij}^F > 0$) and antiferromagnetic terms ($J_{ij}^{AF} < 0$), that is, $J = (1/n^2)\sum_{ij} J_{ij} = (1/n^2)\sum_{ij}(J_{ij}^F + J_{ij}^{AF})$ where n is the number of unpaired electrons [16]. The absolute value of n^2J, which relies on the individual contributions of the ferromagnetic (J_{ij}^F) and antiferromagnetic (J_{ij}^{AF}) interactions, corresponds to 82.9 cm^{-1} for **1** and 87.6 cm^{-1} for **2**. Moving from Ni(II) to Co(II) brings about an increase in the number of orthogonal magnetic orbitals, eventually causing an enhanced ferromagnetic contribution [18]. It is therefore manifest that the $|n^2J|$ value is reduced on going from Ni(II) to Co(II).

4. Conclusion

In summary, we have prepared two dimeric complexes constructed by triply-bridged triazole ligands and, notably, terminal end-on tp groups. An intriguing structural feature is that among dimeric molecules three types of intermolecular interactions (hydrogen bond, face-to-face π–π, and edge-to-face CH–π contacts) and intramolecular hydrogen bonds coexist, displaying a 3D architecture. Magnetic studies demonstrate that moderate intradimer antiferromagnetic interactions are evidenced together with non-negligible interdimer antiferromagnetic contributions.

Acknowledgement

This work was supported by Korea Research Foundation Grant funded by the Korea Government (MOEHRD, Basic Research Promotion Fund) (KRF-2005-070-C00068).

Appendix A. Supplementary material

CCDC 633355 and 633356 contain the supplementary crystallographic data for **1** and **2**. These data can be obtained free of charge via http://www.ccdc.cam.ac.uk/conts/retrieving.html, or from the Cambridge Crystallographic Data Centre, 12 Union Road, Cambridge CB2 1EZ, UK; fax: (+44) 1223-336-033; or e-mail: deposit@ccdc.cam.ac.uk. Supplementary data associated with this article can be found, in the online version, at doi:10.1016/j.poly.2007.05.051.

References

[1] (a) J.H. Lim, J.H. Yoon, H.C. Kim, C.S. Hong, Angew. Chem. Int. Ed. 45 (2006) 7424;
(b) J.H. Yoon, J.H. Lim, H.C. Kim, C.S. Hong, Inorg. Chem. 45 (2006) 9613.
[2] A. Dei, Angew. Chem. Int. Ed. 44 (2005) 1160.
[3] (a) L. Li, Z. Liu, S.S. Turner, D. Liao, Z. Jiang, S. Yan, Eur. J. Inorg. Chem. (2003) 62;
(b) X. Shi, G. Zhu, Q. Fang, G. Wu, G. Tian, R. Wang, D. Zhang, M. Xue, S. Qiu, Eur. J. Inorg. Chem. (2004) 185;
(c) Y. Go, X. Wang, E.V. Anokhina, A.J. Jacobson, Inorg. Chem. 44 (2005) 8265;
(d) S.S. Massoud, F.A. Mautner, R. Vicente, H.N. Sweeney, Inorg. Chim. Acta 359 (2006) 1489;
(e) D. Sun, R. Cao, Y. Liang, Q. Shi, W. Su, M. Hong, J. Chem. Soc., Dalton Trans. (2001) 2335;
(f) J. Rogan, D. Poleti, L. Karanović, G. Bogdanović, A.S. Biré, D.M. Petrović, Polyhedron 19 (2000) 1415.
[4] (a) U. Beckmann, S. Brooker, Coord. Chem. Rev. 245 (2003) 17;
(b) U. García-Couceiro, O. Castillo, A. Luque, J.P. García-Terán, G. Beobide, P. Román, Eur. J. Inorg. Chem. (2005) 4280.
[5] S. Kitagawa, R. Kitaura, S.-I. Noro, Angew. Chem. Int. Ed. 43 (2004) 2334.
[6] Y. Go, X. Wang, E.V. Anokhina, A.J. Jacobson, Inorg. Chem. 43 (2004) 5360.
[7] C.S. Hong, J.H. Yoon, J.H. Lim, H.H. Ko, Eur. J. Inorg. Chem. (2005) 4818.
[8] J.G. Haasnoot, Coord. Chem. Rev. 200–202 (2000) 131.
[9] (a) C.S. Hong, Y.S. You, Polyhedron 23 (2004) 3043;
(b) C.S. Hong, Y.S. You, Polyhedron 23 (2004) 1379;
(c) C.S. Hong, Y. Do, Inorg. Chem. 36 (1997) 5684;
(d) C.S. Hong, Y. Do, Inorg. Chem. 37 (1998) 4470.
[10] G.M. Sheldrick, SADABS, A Program for Area Detector Absorption Corrections, University of Göttingen, Germany, 1994.
[11] G.M. Sheldrick, SHELXTL, Version 5, Bruker AXS, Madison, WI, 1995.
[12] K. Nakamoto, Infrared and Raman Spectra of Inorganic and Coordination Compounds: Part B: Applications in Coordination, Organometallic, and Bioinorganic Chemistry, 5th ed., John Wiley & Sons Inc., New York, 1997.
[13] D.H. Choi, J.H. Yoon, J.H. Lim, H.C. Kim, C.S. Hong, Inorg. Chem. 45 (2006) 5947.
[14] J.M. Rueff, N. Masciocchi, P. Rabu, A. Sironi, A. Skoulios, Chem. Eur. J. 8 (2002) 1813.
[15] R. L Carlin, Magnetochemistry, Springer-Verlag, Berlin, 1986.
[16] O. Kahn, Molecular Magnetism, VCH, Weinheim, 1993.
[17] J.J. Borras-Almenar, J.M. Clemente-Juan, E. Coronado, B.S. Tsukerblat, J. Comput. Chem. 22 (2001) 985.
[18] J. Cano, G.D. Munno, J.L. Sanz, R. Ruiz, J. Faus, F. Lloret, M. Julve, A. Caneschi, J. Chem. Soc., Dalton Trans. (1997) 1915.

NMR spectra were recorded on a Bruker DPX-400 spectrometer in $CDCl_3$ with TMS as an internal standard. High-resolution mass spectra were measured on a Waters Q-Tof Micro™ spectrometer. Preparative TLC was performed on dry silica gel plates and developed with selected appropriate solvents as eluent. Solvents were dried and freshly distilled prior to usage. 2-Arylnaphthoxazole derivatives **1a**–**1c**, **3** [9,10] and $Pd(OAc)_2$ [11] were prepared according to previously reported procedures. All aryl halides were purchased and used without further treatment.

2.2. Synthesis of palladium complexes

2.2.1. General method for the synthesis of palladacycles *2a*–*2c*

A mixture of 2-arylnaphthoxazoles **1a**–**1c** (0.2 mmol) and palladium(II) acetate (0.2 mmol) in 2 mL of acetic acid was heated at 100 °C under nitrogen for 6 h. After cooling to room temperature, water was added and the mixture was extracted with dichloromethane. Then the combined organic phases were dried over $MgSO_4$, filtered and the solvent was removed under reduced pressure. The residue was purified by preparative TLC giving yellow product.

Compound **2a***:* Yield 82%. Yellow solid, m.p. 190 °C (dec.); *Anal*. Calc. for $C_{38}H_{26}N_2O_6Pd_2$: C, 55.70; H, 3.20; N, 3.42. Found: C, 55.58; H, 3.11; N, 3.35%. IR (KBr): υ_{max} 1598, 1572, 1522, 1452, 1414, 1382, 1345, 1297, 1279, 1246, 1128, 1092, 1041, 1001, 963, 884, 802, 767, 743, 724, 695 cm^{-1}; ^1H NMR (400 MHz, $CDCl_3$): δ 2.33 (s, 6H, CH_3), 5.62–5.66 (m, 2H, Ar–H), 6.25–6.28 (m, 4H, Ar–H), 6.92 (d, $J = 7.0$ Hz, 2H, Ar–H), 7.43 (d, $J = 8.9$ Hz, 2H, Ar–H), 7.50–7.58 (m, 4H, Ar–H), 7.69 (d, $J = 8.9$ Hz, 2H, Ar–H), 7.86 (d, $J = 8.4$ Hz, 2H, Ar–H), 8.85 (d, $J = 8.0$ Hz, 2H, Ar–H) ppm; ^{13}C NMR (100 MHz, $CDCl_3$): δ 25.0(CH_3), 110.4(CH), 123.1(CH), 123.7(CH), 124.1(C), 124.3(CH), 125.8(CH), 126.6(CH), 126.7(CH), 128.1(CH), 128.3(CH), 128.9(C), 129.6(CH), 131.1(C), 133.8(C), 142.8(C), 146.0(C), 168.6(C=N), 181.5(C=O) ppm.

Compound **2b***:* Yield 78%. Yellow solid, m.p. 199 °C (dec.); *Anal*. Calc. for $C_{40}H_{30}N_2O_6Pd_2$: C, 56.69; H, 3.57; N, 3.31. Found: C, 56.59; H, 3.46; N, 3.24%. IR (KBr): υ_{max} 2921, 1599, 1572, 1518, 1463, 1406, 1385, 1346, 1278, 1248, 1140, 1103, 1039, 1001, 960, 884, 803, 739, 694 cm^{-1}; ^1H NMR (400 MHz, $CDCl_3$): δ 1.09 (s, 6H, CH_3), 2.33 (s, 6H, CH_3), 6.06 (d, $J = 7.7$ Hz, 2H, Ar–H), 6.13 (s, 2H, Ar–H), 6.82 (d, $J = 7.5$ Hz, 2H, Ar–H), 7.44 (d, $J = 8.9$ Hz, 2H, Ar–H), 7.49–7.52 (m, 2H, Ar–H), 7.55–7.59 (m, 2H, Ar–H), 7.68 (d, $J = 8.9$ Hz, 2H, Ar–H), 7.86 (d, $J = 8.0$ Hz, 2H, Ar–H), 8.89 (d, $J = 8.3$ Hz, 2H, Ar–H) ppm; ^{13}C NMR (100 MHz, $CDCl_3$): δ 21.1(CH_3), 25.1(CH_3), 110.5(CH), 123.0(CH), 124.0(C), 124.3(CH), 124.5(CH), 125.8(CH), 126.1(C), 126.2(CH), 126.6(CH), 128.2(CH), 131.6(C), 131.7(CH), 133.9(C), 140.3(C), 142.7(C), 145.9(C), 168.9(C=N), 181.4(C=O) ppm.

Compound **2c***:* Yield 76%. Yellow solid, m.p. 201 °C (dec.); *Anal*. Calc. for $C_{40}H_{30}N_2O_8Pd_2$: C, 54.62; H, 3.44; N, 3.19. Found: C, 54.55; H, 3.38; N, 3.10%. IR (KBr): υ_{max} 2927, 1599, 1567, 1520, 1467, 1412, 1388, 1346, 1315, 1264, 1230, 1178, 1130, 1101, 1036, 1000, 960, 884, 800, 742, 696 cm^{-1}; ^1H NMR (400 MHz, $CDCl_3$): δ 2.31 (s, 6H, CH_3), 2.79 (s, 6H, CH_3), 5.79–5.84 (m, 4H, Ar–H), 6.86 (d, $J = 8.3$ Hz, 2H, Ar–H), 7.40 (d, $J = 8.9$ Hz, 2H, Ar–H), 7.48–7.50 (m, 2H, Ar–H), 7.52–7.54 (m, 2H, Ar–H), 7.66 (d, $J = 8.9$ Hz, 2H, Ar–H), 7.86 (d, $J = 8.0$ Hz, 2H, Ar–H), 8.85 (d, $J = 8.2$ Hz, 2H, Ar–H) ppm; ^{13}C NMR (100 MHz, $CDCl_3$): δ 25.0(CH_3), 53.8(CH_3), 110.5(CH), 111.4(CH), 114.0(CH), 121.2(C), 123.7(C), 124.1(CH), 124.4(CH), 125.5(CH), 125.8(CH), 126.4(CH), 128.2(CH), 131.5(C), 133.7(C), 145.5(C), 145.7(C), 158.7(C), 169.0(C=N), 181.3(C=O) ppm.

2.2.2. General method for the synthesis of palladium complex *4*

To a solution of Li_2PdCl_4 (0.2 mmol) in methanol (2 mL), a methanolic solution (2 mL) of corresponding 2-arylnaphthoxazole **3** (0.2 mmol) and NaOAc (0.2 mmol) was added at room temperature. Then, the solution was stirred for about 10 h and a precipitate was formed. The precipitate was filtered and washed with methanol.

Compound **4***:* Yield 94%. Red solid, m.p. >270 °C; IR (KBr): υ_{max} 1601, 1555, 1528, 1465, 1429, 1383, 1322, 1248, 1151, 1133, 1069, 1004, 976, 885, 857, 797, 747, 704 cm^{-1}; ^1H NMR (400 MHz, $CDCl_3$): δ 6.21 (d, $J = 8.5$ Hz, 2H, Ar–H), 6.58–6.62 (m, 2H, Ar–H), 6.96–6.70 (m, 2H, Ar–H), 7.57–7.61 (m, 2H, Ar–H), 7.64–7.68 (m, 2H, Ar–H), 7.71 (d, $J = 8.9$ Hz, 2H, Ar–H), 7.87 (d, $J = 8.0$ Hz, 2H, Ar–H), 7.90 (d, $J = 8.9$ Hz, 2H, Ar–H), 7.99 (d, $J = 8.0$ Hz, 2H, Ar–H), 9.46 (d, $J = 8.4$ Hz, 2H, Ar–H) ppm; HRMS (positive ESI) Calc. for $C_{34}H_{20}N_2O_4Pd$: 627.0536 $[M+H]^+$, Found: 627.0533 $[M+H]^+$.

2.3. General procedure for Heck reactions

A 5 mL round-bottom flask was charged with appropriate aryl halides (0.5 mmol), ethyl acrylate (0.75 mmol), *n*-Bu_4NBr (1.0 mmol) and base (1 mmol). The catalyst was introduced as a solvent solution (0.4 mg/mL) *via* syringe, and additional solvent was added to give a total volume of 2 mL. The reaction mixture was then placed in an oil bath and heated at 140 °C until the starting aryl halides had been completely consumed, as monitored by thin-layer chromatography. After cooling to room temperature, water was added and the mixture was extracted with dichloromethane. Then the combined organic phases were dried over $MgSO_4$, filtered and the solvent was removed under reduced pressure. The residue was purified by column chromatography on silica gel (the purified products were identified by comparison of melting points with the literature data or by ^1H NMR).

2.4. X-ray structure determination

Intensity data of the complexes **2c** and **4** were measured on a Rigaku-Raxis-IV X-ray diffractometer using graphite-monochromated Mo Kα radiation ($\lambda = 0.71073$ Å) at 291(2) K. All data were collected using $\omega - 2\theta$ scan technique and corrected for Lorebtz-polarization effects. A correction for secondary extinction was applied. The two structures were solved by direct methods [12] and expanded using Fourier techniques. The full-matrix least-squares calculations on F^2 were applied on the final refinement. Their raw data were corrected and the structures were solved using the SHELXTL-97 program [13]. Details of crystal structure determination of the complexes **2c** and **4** are summarized in Table 1.

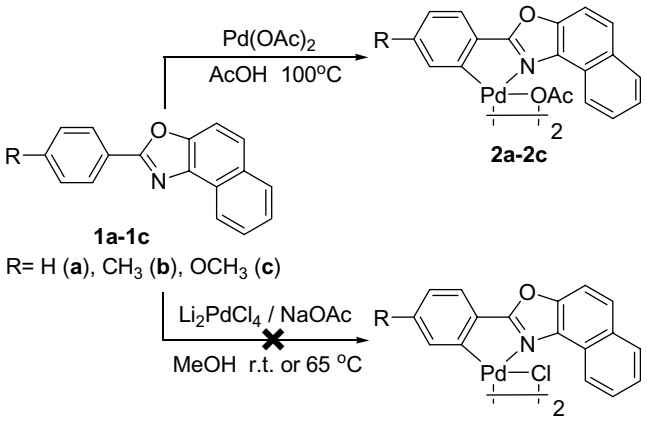
Table 1
Crystal and structure refinement data for **2c** and **4**

Compound	**2c**	**4**
Empirical formula	$C_{40}H_{30}N_2O_8Pd_2$	$C_{34}H_{20}N_2O_4Pd$
Formula weight	879.46	626.92
Crystal system	monoclinic	monoclinic
Crystal size (mm)	$0.20 \times 0.18 \times 0.17$	$0.20 \times 0.18 \times 0.18$
Space group	$P2(1)/c$	$C2/c$
a (Å)	8.3599(17)	20.202(4)
b (Å)	15.124(3)	8.4717(17)
c (Å)	27.690(6)	14.692(3)
α (°)	90	90
β (°)	98.38(3)	92.61(3)
γ (°)	90	90
V (Å^3)	3463.6(12)	2511.8(9)
Z	4	4
D_{Calc} (g cm^{-3})	1.687	1.658
μ(Mo Kα) (mm^{-1})	1.097	0.786
θ Range (°)	1.49–25.00	2.02–27.51
Data/restraints/parameters	5725/0/470	2768/0/187
Goodness-of-fit on F^2	1.082	1.047
$R(F)$ [$I > 2\sigma(I)$]	$R_1 = 0.0499$, $wR_2 = 0.1076$	$R_1 = 0.0404$, $wR_2 = 0.1010$
R indices (all data)	$R_1 = 0.0652$, $wR_2 = 0.1152$	$R_1 = 0.0475$, $wR_2 = 0.1069$

3. Results and discussion

3.1. Synthesis and characterization of palladium complexes

Cyclopalladation of 2-arylnaphthoxazole derivatives **1a**–**1c** readily occurred using $Pd(OAc)_2$ in acetic acid at 100 °C under nitrogen to give yellow cyclopalladated complexes **2a**–**2c** in moderate yields (Scheme 1). Unfortunately, the μ-Cl bridged cyclopalladated complexes were not obtained by the reaction of 2-arylnaphthoxazole derivatives **1a**–**1c** with Li_2PdCl_4 in MeOH in the presence of NaOAc as a proton scavenger at room temperature or 65 °C, respectively. Complexes **2a**–**2c** were fully characterized by elemental analysis, IR, ^{1}H and ^{13}C NMR. The IR spectra of **1a**–**1c** show a sharp band at about 1637 cm^{-1} [9,10], while for complexes **2a**–**2c**, this band shifted to 1599 cm^{-1}, indicating that the nitrogen atom was coordinated to palladium through its lone pair. The appearance of the signal at about δ 2.3 ppm in ^{1}H NMR spectra and the signal at δ 181 ppm in ^{13}C NMR spectra suggested the presence of acetate group. Finally, the structure of complex **2c** has been confirmed by X-ray diffraction study (Fig. 1).



Scheme 1.

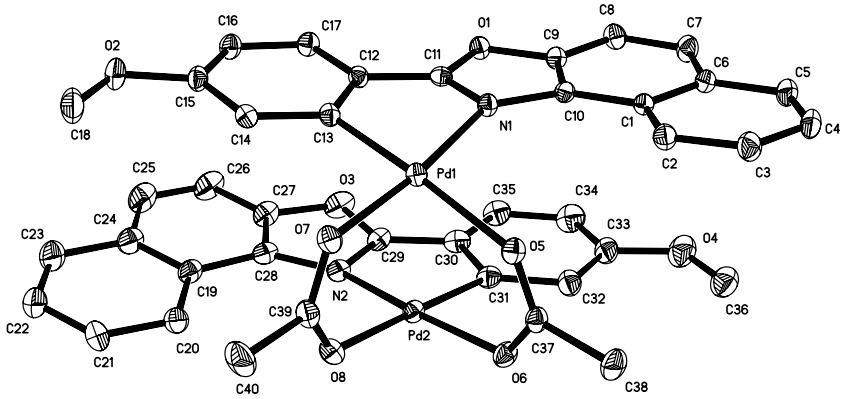
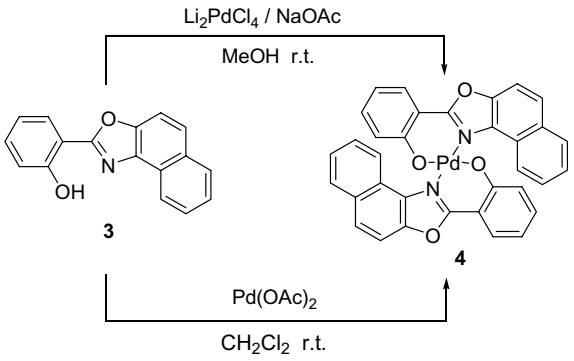


Fig. 1. Molecular structure of acetate-bridged dimer **2c**.



Scheme 2.

Table 2
Selected bond lengths (Å) and angles (°) for **2c** and **4**

2c			
Pd(1)–C(13)	1.976(6)	C(13)–Pd(1)–N(1)	81.8(2)
Pd(1)–O(7)	2.034(4)	O(7)–Pd(1)–N(1)	173.4(2)
Pd(1)–N(1)	2.071(4)	C(13)–Pd(1)–O(5)	176.0(2)
Pd(1)–O(5)	2.141(4)	O(7)–Pd(1)–O(5)	87.0(2)
Pd(2)–C(31)	1.996(7)	N(1)–Pd(1)–O(5)	99.5(2)
Pd(2)–O(6)	2.030(4)	C(31)–Pd(2)–O(6)	90.5(2)
Pd(2)–N(2)	2.091(5)	C(31)–Pd(2)–N(2)	81.3(3)
Pd(2)–O(8)	2.126(4)	O(6)–Pd(2)–N(2)	171.4(2)
C(11)–N(1)	1.314(7)	C(31)–Pd(2)–O(8)	176.5(2)
C(29)–N(2)	1.318(8)	O(6)–Pd(2)–O(8)	86.2(2)
C(13)–Pd(1)–O(7)	91.7(2)	N(2)–Pd(2)–O(8)	102.1(2)
4			
Pd(1)–O(2)	1.999(3)	O(2)–Pd(1)–O(2)#1	169.4(2)
Pd(1)–O(2)#1	1.999(3)	O(2)–Pd(1)–N(1)	89.4(1)
Pd(1)–N(1)	2.029(3)	O(2)#1–Pd(1)–N(1)	90.9(1)
Pd(1)–N(1)#1	2.029(3)	O(2)–Pd(1)–N(1)#1	90.9(1)
N(1)–C(11)	1.319(4)	O(2)#1–Pd(1)–N(1)#1	89.4(1)
N(1)–C(10)	1.398(4)	N(1)–Pd(1)–N(1)#1	177.8(2)
O(2)–C(13)	1.320(4)	C(11)–N(1)–Pd(1)	118.9(2)
C(11)–C(12)	1.437(5)	C(10)–N(1)–Pd(1)	133.5(2)
C(12)–C(13)	1.418(5)	C(13)–O(2)–Pd(1)	119.1(2)

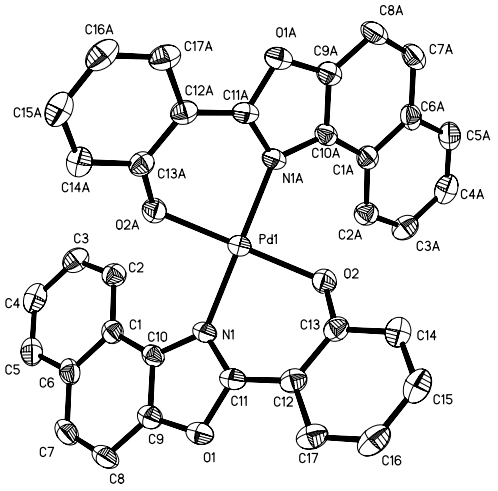


Fig. 3. Molecular structure of complex **4**.

The reaction of 2-arylnaphthoxazole derivative **3** with Li_2PdCl_4 in MeOH in the presence of NaOAc as a proton scavenger at room temperature afforded quantitatively red coordination compound **4**, but no cyclopalladated complex formed. On the other hand, when $Pd(OAc)_2$ was stirred in CH_2Cl_2 with **3** at room temperature, the same product – complex **4** was obtained (Scheme 2). Complex **4** was fully characterized by elemental analysis, IR and ^1H NMR. The $\upsilon_{C=N}$ at 1601 cm^{-1} in the IR spectrum of **4** is lower than that of **3** (1641 cm^{-1}) [9], due to the intramolecular coordination of nitrogen to palladium. Nevertheless, because of its low solubility in $CDCl_3$ and other solvents, we were unable to obtain its ^{13}C NMR spectra with high enough resolution. Fortunately, the structure of complex **4** was unequivocally confirmed by X-ray diffraction analysis (Fig. 3).

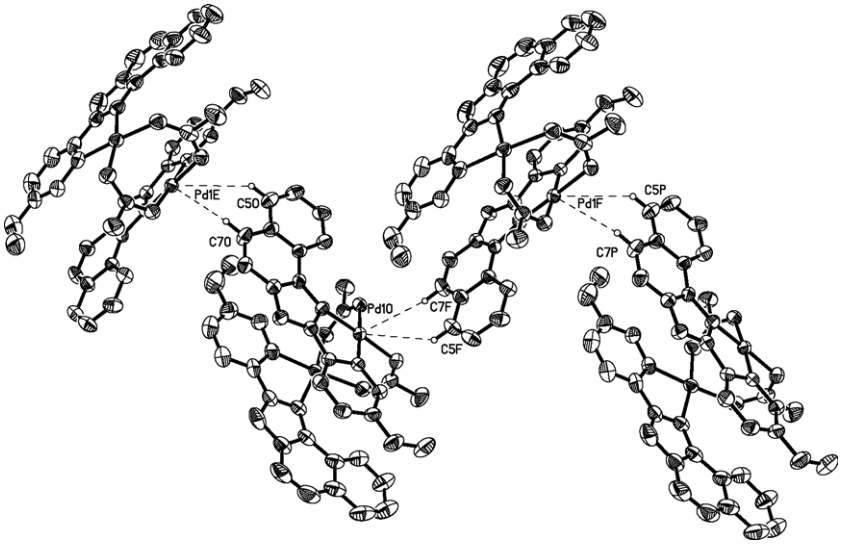


Fig. 2. One-dimensional chain structure of complex **2c**.

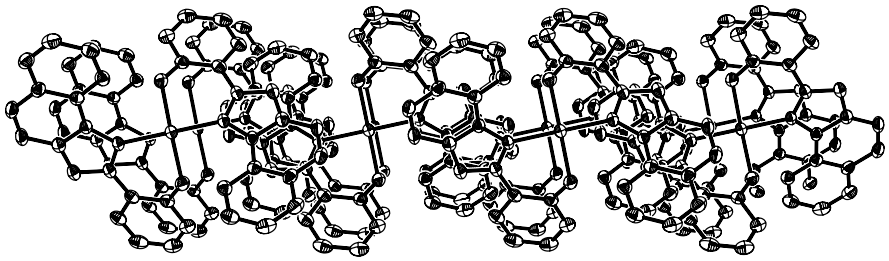


Fig. 4. The π–π interactions in complex **4**.

3.2. X-ray diffraction studies: crystal structures of palladium complexes *2c* and *4*

The crystal structures of complexes **2c** and **4** were determined, and the crystal data and refinement details for both structures are listed in Table 1. Selected bond length (Å) and angles (°) are listed in Table 2.

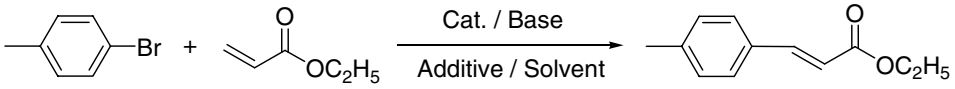
Perspective view of the molecular structure for complex **2c**, together with the corresponding atom-labeling scheme, is given in Fig. 1. The Pd atom in complex **2c** is in a square-planar environment bonded to nitrogen, carbon atoms of the naphthoxazole ligand and two oxygen atoms (one from each of the acetate ligands). The Pd–N and Pd–C bonds form the basis for five-membered chelate rings. The Pd1···Pd2 distance is 2.8735(8) Å, which is regarded as non-bonding, the covalent radius of square-planar Pd(II) has been estimated as approximately 1.31 Å [14]. The Pd1 and Pd2 are bridged by two acetate ligands and the coordination planes of the Pd atoms are not coplanar (dihedral angle is 24.0°). This leads to interligand repulsions on the "open" side of the molecule. Fig. 2 shows that in the crystal of **2c** there exist intermolecular Pd···H hydrogen bonds (Pd1F···H5P = Pd1O···H5F = 3.162 Å, Pd1F···H7P = Pd1O···H7F = 3.020 Å), which are attributed to construct the 1D chain structure of complex **2c**.

Fig. 3 shows that the Pd atom in complex **4** is in a slightly distorted square-planar environment (deviation from plane 0.1016 Å), ligand **3** coordinates to Pd(II) as a ON bidentate ligand. In contrast to complex **2c**, the Pd–N and Pd–O bonds form the basis for six-membered chelate rings in complex **4**. The Pd–N (2.029(3) Å) bond length is similar to that of the related complex (2.026(7) Å and 2.014(6) Å) [15], while it is shorter than that of complex **2c** (2.071(4) Å and 2.091(5) Å). It can be seen from Fig. 4 that the two naphthoxazole rings of neighboring molecules are almost parallel with each other with mean interplanar distance of 3.3305 Å (dihedral angle is 0.0°), indicating strong intermolecular π–π stacking interaction between the two neighboring molecules.

3.3. Catalytic activity of palladium complexes in Heck reactions

Palladacycles have been thoroughly investigated as pre-catalysts in C–C bond formation reactions. One of the

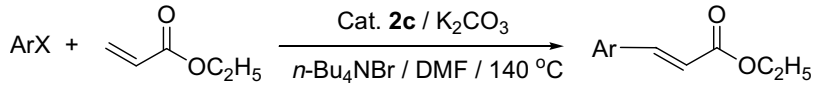
Table 3
Influence of bases, solvents and catalysts on Heck reactions of 4-bromotoluene with ethyl acrylate



Entry	Cat. (mol%)	Base	Additive	Solvents	*T* (°C)	Yield[a] (%)
1	**2a** (0.01)	K_2CO_3	none	DMF	140	38
2	**2a** (0.01)	K_2CO_3	*n*-Bu_4NBr	DMF	140	93
3	**2a** (0.01)	Et_3N	*n*-Bu_4NBr	DMF	140	52
4	**2a** (0.01)	CsF	*n*-Bu_4NBr	DMF	140	68
5	**2a** (0.01)	K_3PO_4	*n*-Bu_4NBr	DMF	140	90
6	**2a** (0.01)	Cs_2CO_3	*n*-Bu_4NBr	DMF	140	65
7	**2a** (0.01)	$KF \cdot H_2O$	*n*-Bu_4NBr	DMF	140	88
8	**2a** (0.01)	Na_2CO_3	*n*-Bu_4NBr	DMF	140	71
9	**2a** (0.01)	K_2CO_3	*n*-Bu_4NBr	dioxane	100	44
10	**2a** (0.01)	K_2CO_3	*n*-Bu_4NBr	toluene	110	60
11	**2a** (0.01)	K_2CO_3	*n*-Bu_4NBr	xylene	140	90
12	**2a** (0.01)	K_2CO_3	*n*-Bu_4NBr	DMA	140	92
13	**2b** (0.01)	K_2CO_3	*n*-Bu_4NBr	DMF	140	93
14	**2c** (0.01)	K_2CO_3	*n*-Bu_4NBr	DMF	140	95
15	**4** (0.02)	K_2CO_3	*n*-Bu_4NBr	DMF	140	90

Reaction conditions: 4-bromotoluene (0.5 mmol), ethyl acrylate (0.75 mmol), base (1.0 mmol), additive (1.0 mmol), solvent (1 mL), 24 h reaction time.
[a] Isolated yields (average of two runs) based on 4-bromotoluene.

Table 4
Heck reactions of aryl halide with ethyl acrylate catalyzed by **2c**



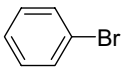
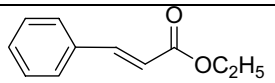
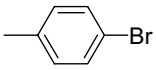
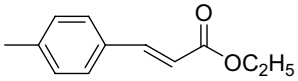
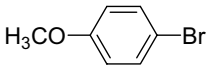
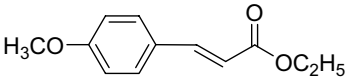
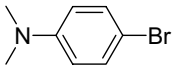
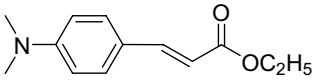
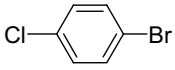
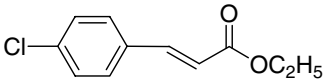
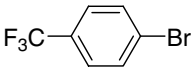
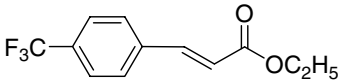
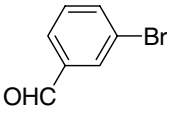
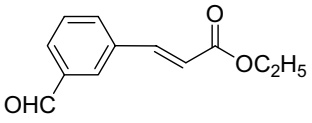
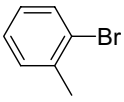
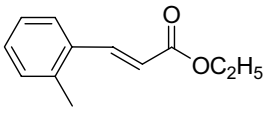
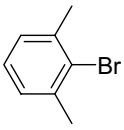
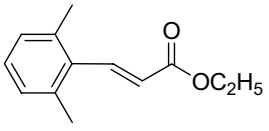
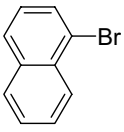
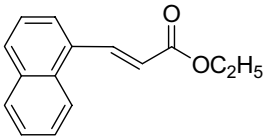
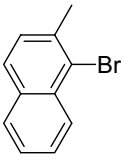
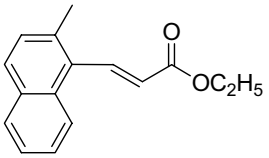
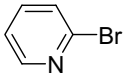
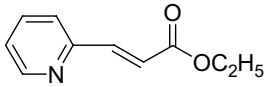
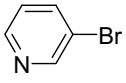
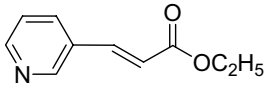
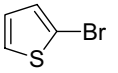
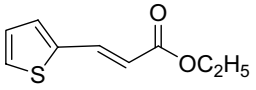
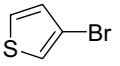
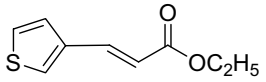
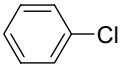
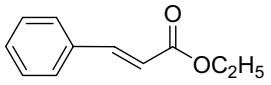
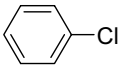
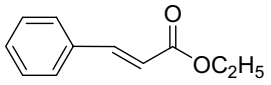
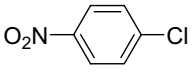
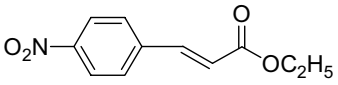
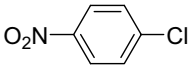
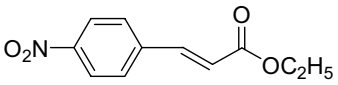
Entry	ArX	Cat. **2c** (mol%)	Time (h)	Product	Yield[a] (%)
1		**2c** (0.01)	16		96
2		**2c** (0.01)	16		93
3		**2c** (0.01)	24		93
4		**2c** (0.01)	24		88
5		**2c** (0.01)	12		95
6		**2c** (0.01)	12		96
7		**2c** (0.01)	12		96
8		**2c** (0.01)	24		89
9		**2c** (0.01)	24		72
10		**2c** (0.01)	16		95
11		**2c** (0.01)	24		90

Table 4 (*continued*)

Entry	ArX	Cat. **2c** (mol%)	Time (h)	Product	Yield[a] (%)
12		**2c** (0.01)	16		79
13		**2c** (0.01)	16		88
14		**2c** (0.01)	24		76
15		**2c** (0.01)	24		70
16		**2c** (0.01)	24		trace
17		**2c** (0.1)	24		19
18		**2c** (0.01)	24		23
19		**2c** (0.1)	24		45

Reaction conditions: ArX (0.5 mmol), ethyl acrylate (0.75 mmol), K_2CO_3 (1.0 mmol), *n*-Bu_4NBr (1.0 mmol), DMF (1 mL), 140 °C, 24 h reaction time.
[a] Isolated yields (average of two runs) based on ArX.

most popular cross-couplings is Heck reactions. A wide variety of substrates has been used to design catalyst precursors endowed with good activity in Heck reactions. So we thought it interesting to study whether the air-stable palladium(II) complexes **2a**–**2c** and **4** would be efficient catalysts for Heck reactions.

Our initial exploration of reaction conditions focused on the coupling of 4-bromotoluene with ethyl acrylate. The results are shown in Table 3. It showed that the reaction occurred smoothly in air and afforded the product in excellent yield in the presence of additive *n*-Bu_4NBr which could react as reducing agent to generate active Pd(0) species and stabilize the intermediates by coordination or formation of ion-pairs in the catalytic cycle [16] (entries 1 and 2). After screening a variety of bases, K_2CO_3 was found to give the best result (entries 2–8). Then, a quick survey of solvents indicated that DMF was superior to others (entries 2, 9–12). With the appropriate base (K_2CO_3) and solvent (DMF) in hand, the relative activities of palladium complexes **2a**–**2c** and **4** for the same model reaction were studied (entries 2, 13–15). All the complexes exhibited high activity with catalyst loadings as low as 0.01%. Among them, complex **2c** was slightly more active than others probably because of its electron-donating methoxy group (entry 14).

Under the optimized conditions (K_2CO_3, DMF, 140 °C), the substrate scope of Heck reactions was examined. As shown in Table 4, a variety of electronically and structurally diverse aryl bromides including heteroaryl bromides could be coupled efficiently with ethyl acrylate catalyzed by 0.01 mol% of complex **2c**. The coupled products were isolated in moderate to high yields for non-activated and deactivated aryl bromide substrates in this catalytic system after 16 or 24 h (entries 1–4). For activated aryl bromides, such as 4-bromochlorobenzene, and 4-bromobenzotrifluoride, it was not surprising that excellent yields were obtained (entries 5–7). When *ortho*-substituents were used, Heck reactions also could occur efficiently (entries 8–11).

Even with the very sterically hindered 1-bromo-2-methylnapthalene, the reaction gave the coupled product in 90% isolated yields (entry 11). Coupling of heteroaryl bromides with ethyl acrylate proceeded smoothly and moderate yields were obtained (entries 12–15). In contrast to corresponding aryl bromides, this catalyst system showed decreased or even no activity for the coupling of aryl chlorides (entries 1 and 16). In the case of chlorobenzene, **2c** was almost inactive under the optimized reaction conditions (entry 16). Increasing catalyst loading to 0.1% gave 19% yield (entry 17). For activated aryl chlorides, such as 4-chloronitrobenzene, the yield of the coupled product could be reached 45% by using 0.1% of **2c** (entry 19).

4. Conclusions

In summary, we have found that air- and moisture-stable new palladium complexes **2a**–**2c** and **4**, especially palladacycle **2c**, behave as efficient phosphine-free catalysts for Heck reactions of aryl bromides with ethyl acrylate. Further investigations on the catalytic activity of this kind of palladium complexes are currently underway in our laboratory.

Acknowledgements

We are grateful to the National Natural Science Foundation of China (Project 20472074) and the Innovation Fund for Outstanding Scholar of Henan Province (Project 0621001100) for the financial support given to this research.

Appendix A. Supplementary material

CCDC 620288 and 620290 contain the supplementary crystallographic data for **2c** and **4**. These data can be obtained free of charge via http://www.ccdc.cam.ac.uk/conts/retrieving.html, or from the Cambridge Crystallographic Data Centre, 12 Union Road, Cambridge CB2 1EZ, UK, fax: (+44) 1223-336-033, or e-mail: deposit@ccdc.cam.ac.uk. Supplementary data associated with this article can be found, in the online version, at doi:10.1016/j.poly.2007.05.031.

References

[1] (a) J. Tsuji, Palladium Reagents and Catalyst, Wiley, New York, 1996;
(b) F. Diederich, P.J. Stang (Eds.), Metal-catalyzed Cross-coupling Reactions, Wiley-VCH, Weinheim, 1998;
(c) E. Negishi, A. de Mejere, Handbook of Organopalladium Chemistry for Organic Synthesis, Wiley-VCH, Weinheim, 2002.

[2] (a) For some recent reviews on the Heck reactions, see P. Beletskaya, A.V. Cheprakov, Chem. Rev. 100 (2000) 3009;
(b) C. Amatore, A. Jutand, Acc. Chem. Res. 33 (2000) 314;
(c) A.B. Donnay, L.E. Overman, Chem. Rev. 103 (2003) 2945;
(d) A. de Meijere, F. Diederich (Eds.), Metal-catalyzed Cross-coupling Reactions, second ed., Wiley-VCH, Weinheim, 2004 (Chapter 5).

[3] (a) G.C. Fu, S.T. Nguyen, R.H. Grubbs, J. Am. Chem. Soc. 115 (1993) 9856;
(b) S.T. Nguyen, R.H. Grubbs, J.W. Ziller, J. Am. Chem. Soc. 115 (1993) 9858.

[4] (a) Y.C. Jung, R.K. Mishra, C.H. Yoon, K.W. Jung, Org. Lett. 5 (2003) 2231;
(b) Y. Na, S. Park, S.B. Han, H. Han, S. Ko, S. Chang, J. Am. Chem. Soc. 126 (2004) 250;
(c) A.E. Wang, J.H. Xie, L.X. Wang, Q.L. Zhou, Tetrahedron 61 (2005) 259;
(d) T. Mino, Y. Shirae, Y. Sasai, M. Sakamoto, T. Fujita, J. Org. Chem. 71 (2006) 6834;
(e) S. Li, Y.J. Lin, H.B. Xie, S.B. Zhang, J.N. Xu, Org. Lett. 8 (2006) 391;
(f) B. Altava, M.I. Burguete, E.G. Verdugo, N. Karbass, S.V. Luis, A. Puzary, V. Sans, Tetrahedron Lett. 47 (2006) 2311.

[5] (a) See for example: M. Beller, H. Fischer, W.A. Herrmann, K. Ofele, C. Brossmer, Angew. Chem., Int. Ed. Engl. 34 (1995) 1844;
(b) D.E. Bergbreiter, P.L. Osburn, Y.S. Liu, J. Am. Chem. Soc. 121 (1999) 9531;
(c) D.A. Alonso, C. Najera, M.C. Pacheco, Org. Lett. 2 (2000) 1823;
(d) D.A. Alonso, C. Nájera, M.C. Pacheco, Adv. Synth. Catal. 344 (2002) 172;
(e) M.E. van der Boom, D. Milstein, Chem. Rev. 103 (2003) 1759;
(f) D.E. Bergbreiter, P.L. Osburn, J.D. Frels, Adv. Synth. Catal. 347 (2005) 172.

[6] (a) W.A. Herrmann, V.P.W. Bohm, C.P. Reisinger, J. Organomet. Chem. 576 (1999) 23;
(b) R.B. Bedford, Chem. Commun. (2003) 1787;
(c) I.P. Beletskaya, A.V. Cheprakov, J. Organomet. Chem. 689 (2004) 4055;
(d) J. Dupont, C.S. Consorti, J. Spencer, Chem. Rev. 105 (2005) 2427.

[7] (a) M. Ohff, A. Ohff, M.E. van der Boom, D. Milstein, J. Am. Chem. Soc. 119 (1997) 11687;
(b) A.S. Gruber, D. Zim, G. Eberling, A.L. Monteiro, J. Dupont, Org. Lett. 2 (2000) 1287;
(c) E. Peris, J. Mata, J.A. Loch, R.H. Crabtree, Chem. Commun. (2001) 201;
(d) C.S. Consorti, M.L. Zanini, S. Leal, G. Ebeling, J. Dupont, Org. Lett. 5 (2003) 983.

[8] (a) M. Ohff, A. Ohff, D. Milstein, Chem. Commun. (1999) 357;
(b) P.A. Gossage, H.A. Jenkins, P.N. Yadav, Tetrahedron Lett. 45 (2004) 7689;
(c) M. Rosol, A. Moyano, J. Organomet. Chem. 690 (2005) 2291;
(d) Y. Kawashita, C. Ueba, M. Hayashi, Tetrahedron Lett. 47 (2006) 4231.

[9] V.V. Somayajulu, Proc. India Acad. Sci. Sect., A 61 (1965) 139.

[10] M.A. Abbady, Indian J. Chem. B 17 (1979) 450.

[11] T.A. Stephenson, S.M. Morehouse, A.R. Powell, J.P. Heffer, G. Wilkinson, J. Chem. Soc. (1965) 3632.

[12] SIR92: A. Altomare, M.C. Burla, M. Camalli, M. Cascarano, C. Giacovazzo, A. Guagliardi, G. Polidori, J. Appl. Cryst. 27 (1994) 435.

[13] G.M. Sheldrick, SHELXL-97, Program for Refinement of Crystal Structure, University of Göttingen, Germany, 1997.

[14] M.R. Churchill, Perspect. Struct. Chem. 3 (1970) 91.

[15] M.R. Churchill, H.J. Wasserman, G.J. Young, Inorg. Chem. 19 (1980) 762.

[16] (a) W.A. Herrmann, M. Elison, J. Fischer, C. Köcher, G.J. Artus, Angew. Chem., Int. Ed. Engl. 34 (1995) 2371;
(b) A.M. Magill, D.S. McGuinness, K.J. Cavell, G.J.P. Britovsek, V.C. Gibson, A.J.P. White, D.J. Williams, A.H. White, B.W. Skelton, J. Organomet. Chem. 617–618 (2001) 546;
(c) V. Calo, A. Nacci, A. Monopoli, M. Spinelli, Eur. J. Org. Chem. (2003) 1382.

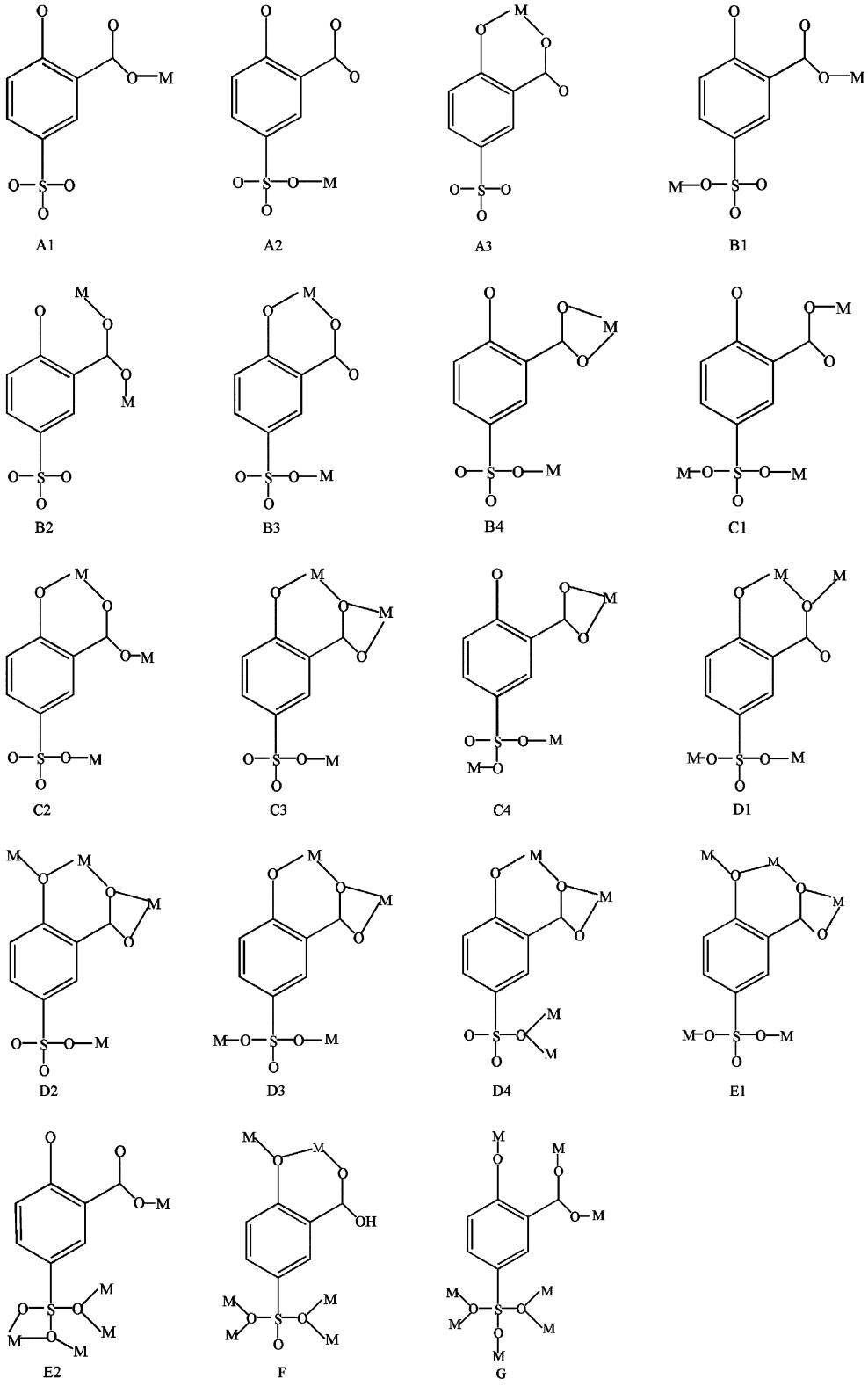


Chart 1. Coordination modes of 5-sulfosalicylates in recent reports (A, B, C, D, E, F, G denote that the 5-sulfosalicylate ligand acts as μ_1, μ_2, μ_3, μ_4, μ_5, μ_6, μ_8 connectors to link metal ions, respectively).

novel metal–organic supramolecular network through specific and directional hydrogen bonds as well as π–π stacking due to the presence of aryl rings [5–7], (2) 5-sulfosalicylic acid has been found to have biological activity and its metal complexes with Cu(II), Ni(II), Co(II), Mn(II), Fe(II), Zn(II) and VO(II) exhibit antimicrobial activity

stronger than that of the free ligand [5b,8]. In order to avoid the formation of higher dimensional coordination networks, polycyclic aromatic chelating ligands such as 2,2′-bipyridyl (2,2′-bipy) and 1,10-phenanthroline (1,10-phen) were introduced based on the following considerations: (1) chelating bipyridyl-like ligands may provide supramolecular recognition sites for π–π, C–H···π stacking and C–H···O hydrogen bonding to form interesting supramolecular structures [4b,4f,9], (2) the conjugated π systems containing (hetero) aromatic rings are currently of interests in the development of fluorescent materials [10].

In order to understand the coordination chemistry of H_3ssal and to prepare new supramolecular materials with intriguing structures and potential physical properties, we have recently focused our research on coordination complexes based on 5-sulfosalicylic acid and chelating bipyridyl-like ligands. Here, we report the syntheses and crystal structures of six new complexes, namely, $[Cu_4(OH)_2(ssal)_2(phen)_4 \cdot 7H_2O]$ (**1**), $[Cu_4(OH)_2(ssal)_2(bipy)_4 \cdot 2H_2O]$ (**2**), [Cd(Hssal)(bipy)] (**3**), $[Cd(HL)_2(phen)_2]$ (**4**), $[Cr(ssal)(bipy)(H_2O)_2 \cdot 2H_2O]$ (**5**) and $[Cr(ssal)(phen)_2]$ (**6**), together with the magnetic properties of complexes **1** and **2**. The crystal structures of complexes Mn(Hssal)$(bipy)_2(H_2O) \cdot 2H_2O$ (**7**) [6b] and Zn(Hssal)$(bipy)(H_2O)_2$ (**8**) [7d] were reported previously. The results demonstrate that the discrete or polymeric complexes may build up higher network connectivity through π–π stacking, C–H···π, O···π and hydrogen-bonding interactions including weak C–H···O contacts.

2. Experimental

2.1. Materials and physical measurements

All chemicals purchased were of reagent grade and were used without further purification. Elemental analyses (C, H, N) were performed on a Perkin–Elmer 240C elemental analyzer. IR spectra were measured on a Perkin–Elmer Spectrum One FT-IR spectrometer using KBr pellets. Magnetic measurements were obtained using an MPMS-XL magnetometer at H = 1000 Oe in the temperature range 5–300 K. The magnetic susceptibility data were corrected for the diamagnetism of the constituent atoms using Pascal's constants.

2.2. Syntheses of the complexes

2.2.1. $Cu_4(OH)_2(ssal)_2(phen)_4 \cdot 7H_2O$ (*1*)

A mixture of $CuSO_4 \cdot 5H_2O$ (0.131 g, 0.5 mmol), 5-sulfosalicylic acid (0.130 g, 0.5 mmol), phen (0.103 g, 0.5 mmol), KOH (0.062 g, 1.1 mmol) and water (15 ml) was stirred for 30 min at room temperature, transferred to and sealed in a 25 ml Teflon-lined stainless steel reactor, and then heated at 150 °C for 72 h. Upon cooling to room temperature, the dark green crystals that were obtained were filtered and washed with water. Yield: 58% based on Cu. *Anal*. Calc. for $C_{62}H_{56}N_8O_{21}Cu_4S_2$ **1**: C, 47.47; H, 3.57; N, 7.15; S, 4.08. Found: C, 47.52; H, 3.48; N, 7.13; S, 4.12%. IR (KBr, cm^{-1}): 3407vs, 1603s, 1563m, 1522w, 1472m, 1414m, 1320m, 1221m, 1167m, 1131s, 1146s, 1020s, 849s, 722vs, 604m, 479w.

2.2.2. $Cu_4(OH)_2(ssal)_2(bipy)_4 \cdot 2H_2O$ (*2*)

The hydrothermal procedure for the synthesis of complex **2** is similar to that for **1** except for the replacement of phen with 2,2-bipy (0.082 g, 0.5 mmol). Yield: 82% based on Cu. *Anal*. Calc. for $C_{54}H_{44}N_8O_{16}Cu_4S_2$ **2**: C, 46.98; H, 3.19; N, 8.12; S, 4.64. Found: C, 46.85; H, 3.02; N, 8.09; S, 4.58%. IR (KBr, cm^{-1}): 3444m, 1602s, 1562m, 1470m, 1413w, 1341w, 1253w, 1211m, 1186m, 1150m, 1030s 771m, 604m, 470w.

2.2.3. Cd(Hssal)(bipy) (*3*)

A mixture of $3CdSO_4 \cdot 8H_2O$ (0.403 g, 0.5 mmol), 5-sulfosalicylic acid (0.132 g, 0.5 mmol), 2,2′-bipy (0.081 g, 0.5 mmol), KOH (0.08 g, 1.4 mmol) and water (15 ml) was stirred for 30 min at room temperature, transferred to and sealed in a 25 ml Teflon-lined stainless steel reactor, and then heated at 150 °C for 72 h. Upon cooling to room temperature, the light red crystals that were obtained were filtered and washed with water. Yield: 58% based on Cd. *Anal.* Calc. for $C_{17}H_{12}N_2O_6CdS$ **3**: C, 42.08; H, 2.48; N, 4.95; S, 6.60. Found: C, 41.94; H, 2.52; N, 4.87; S, 6.63%. IR (KBr, cm^{-1}): 3112m, 1626w, 1596m, 1559m, 1478m, 1440m, 1254m, 1158m, 1127s, 1017s, 769m, 676m, 602m.

2.2.4. $Cd(HL)_2(phen)_2$ (*4*)

A mixture of $3CdSO_4 \cdot 8H_2O$ (0.407 g, 0.5 mmol), 5-sulfosalicylic acid (0.132 g, 0.5 mmol), phen (0.108 g, 0.5 mmol), KOH (0.071 g, 1.3 mmol) and water (15 ml) was stirred for 30 min at room temperature, transferred to and sealed in a 25 ml Teflon-lined stainless steel reactor, and then heated at 150 °C for 72 h. Upon cooling to room temperature, a colorless solution and a spot of white precipitate were obtained. The solution was filtered and the filtrate was allowed to stand at room temperature. After slow evaporation over several days, red block single crystals were obtained. Yield: 62% based on Cd. *Anal*. Calc. for $C_{36}H_{26}N_4O_8CdS_2$ **4**: C, 52.74; H, 3.17; N, 6.84; S, 7.81. Found: C, 52.67; H, 3.23; N, 6.79; S, 7.83%. IR (KBr, cm^{-1}): 3168m, 1586m, 1506m, 1424m, 1237s, 1156s, 1122s, 1031s, 844s, 728s, 566m, 451w.

2.2.5. $Cr(ssal)(bipy)_2(H_2O)_2 \cdot 2H_2O$ (*5*)

A mixture of $Cr_2(SO_4)_3 \cdot 6H_2O$ (0.255 g, 0.5 mmol), 5-sulfosalicylic acid (0.134 g, 0.5 mmol), 2,2′-bipy (0.082 g, 0.5 mmol), KOH (0.051 g, 0.9 mmol) and water (15 ml) was stirred for 30 min at room temperature, transferred to and sealed in a 25 ml Teflon-lined stainless steel reactor, and then heated at 150 °C for 72 h. Upon cooling to room temperature, the green crystals that were obtained were filtered and washed with water. Yield: 5% based on Cr. *Anal*. Calc. for $C_{17}H_{19}N_2O_{10}CrS$ **5**: C, 41.18; H, 3.84;

N, 5.65; S, 6.46. Found: C, 41.11; H, 3.90; N, 5.57%. IR (KBr, cm^{-1}): 3446s, 1608s, 1571m, 1447m, 1472m, 1150s, 1031s, 763m, 602m.

2.2.6. Cr(ssal)(phen)$_2$ (6)

A mixture of $Cr_2(SO_4)_3 \cdot 6H_2O$ (0.253 g, 0.5 mmol), 5-sulfosalicylic acid (0.136 g, 0.5 mmol), phen (0.106 g, 0.5 mmol), KOH (0.062 g, 1.1 mmol) and water (15 ml) was stirred for 30 min at room temperature, transferred to and sealed in a 25 ml Teflon-lined stainless steel reactor, and then heated at 150 °C for 72 h. Upon cooling to room temperature, a red solution was obtained, which was filtered and the filtrate was allowed to stand at room temperature. After slow evaporation over several days, red block single crystals were obtained. Yield: 35% based on Cr. *Anal*. Calc. for $C_{31}H_{19}N_4O_6CrS$ **6**: C, 59.28; H, 3.03; N, 8.92; S, 5.10. Found: C, 59.35; H, 2.84; N, 8.97; S, 5.18%. IR (KBr, cm^{-1}): 3078vw, 1608s, 1574m, 1517m, 1469s, 1426s, 1311m, 1167s, 1033s, 845m, 721m, 601m, 451m.

2.2.7. Mn(Hssal)(bipy)$_2$(H$_2$O) · 2H$_2$O (7)

The hydrothermal procedure for the synthesis of complex **7** is similar to that for **6** except for the replacement of $Cr_2(SO_4)_3 \cdot 6H_2O$ with $MnCl_2 \cdot 4H_2O$ (0.108 g, 0.5 mmol). The yellow solution was obtained, filtered, and the filtrate was allowed to stand at room temperature. After slow evaporation over several days, yellow block single crystals were obtained. Yield: 65% based on Mn. *Anal*. Calc. for $C_{27}H_{26}N_4O_9MnS$ **7**: C, 50.82; H, 4.08; N, 8.78; S, 5.02. Found: C, 50.65; H, 3.96; N, 8.97; S, 5.18%. IR (KBr, cm^{-1}): 3453s, 1592s, 1517m, 1469s, 1426m, 1311m, 1167vs, 1033s, 845m, 721s, 601m, 451m.

2.2.8. Zn(Hssal)(bipy)(H$_2$O)$_2$ (8)

The hydrothermal procedure for the synthesis of complex **8** is similar to that for **6** except for the replacement of $Cr_2(SO_4)_3 \cdot 6H_2O$ with $ZnCl_2$ (0.074 g, 0.5 mmol). A colorless solution and a spot of white deposition were obtained. The solution was filtered and the filtrate was allowed to stand at room temperature. After slow evaporation over several days, colorless block single crystals were obtained. Yield: 72% based on Zn. *Anal*. Calc. for $C_{17}H_{16}N_2O_8SZn$ **8**: C, 43.06; H, 3.38; N, 5.91; S, 6.75. Found: C, 44.12; H, 3.66; N, 5.97; S, 6.68%. IR (KBr, cm^{-1}): 3283s, 1584s, 1441s, 1153vs, 1053s, 672s, 567s.

2.3. X-ray diffraction data and crystal structure determination

The crystal structures were determined by a single-crystal X-ray diffraction experiment. The reflection data were collected on a Bruker SMART CCD area-detector diffractometer (Mo Kα radiation, graphite monochromator) at room temperature with the ω-scan mode. Empirical adsorption corrections were applied to all data using the SADABS

Table 1
The crystallographic data for complexes **1**–**6**

	1	2	3	4	5	6
Empirical formula	$C_{62}H_{56}Cu_4N_8O_{21}S_2$	$C_{54}H_{44}Cu_4N_8O_{16}S_2$	$C_{17}H_{12}CdN_2O_6S$	$C_{36}H_{26}CdN_4O_8S_2$	$C_{17}H_{19}CrN_2O_{10}S$	$C_{31}H_{19}CrN_4O_6S$
Formula weight	1567.43	1379.25	484.75	819.16	495.40	627.57
Crystal system	monoclinic	monoclinic	triclinic	monoclinic	monoclinic	monoclinic
Space group	*P*2(1)/*c*	*P*2(1)/*c*	$P\bar{1}$	*C*2/*c*	*P*2(1)/*c*	*C*2/*c*
a (Å)	10.839(2)	10.919(1)	8.553(2)	20.307(6)	10.102(2)	31.602(4)
b (Å)	14.459(3)	12.405(7)	9.809(2)	13.753(9)	14.882(4)	10.265(2)
c (Å)	19.674(4)	20.239(3)	10.562(3)	14.296(9)	14.206(3)	16.536(2)
α (°)	90	90	93.984(4)	90	90	90
β (°)	102.575(4)	104.452(2)	103.786(4)	123.917(4)	110.669(3)	105.406(2)
γ (°)	90	90	104.416(4)	90	90	90
Volume	3010.3(1)	2654.0(6)	825.7(3)	3313.1(4)	1998.3(8)	5171.8(1)
Z	2	2	2	4	4	8
ρ_{calc} (g cm^{-3})	1.730	1.726	1.950	1.642	1.647	1.612
Absorption coefficient (mm^{-1})	1.553	1.741	1.489	0.847	0.737	0.581
θ Range (°)	1.76–26.08	1.94–26.09	2.00–26.10	1.91–26.06	2.05–26.11	1.34–26.04
Reflections collected	17220	15230	4660	9111	11286	14198
Unique reflections [R_{int}]	5911 [0.0777]	5232 [0.0518]	3178 [0.0212]	3276 [0.0137]	3932 [0.0477]	5101 [0.0409]
Completeness	99.1%	99.3%	97.0%	99.7%	98.8%	99.9%
Goodness-of-fit on F^2	0.998	1.024	1.032	1.060	1.040	1.023
R indexes [$I > 2\sigma(I)$][a]	$R_1 = 0.0533$, $wR_2 = 0.1023$	$R_1 = 0.0494$, $wR_2 = 0.1084$	$R_1 = 0.0403$, $wR_2 = 0.0872$	$R_1 = 0.0423$, $wR_2 = 0.1106$	$R_1 = 0.0697$, $wR_2 = 0.1646$	$R_1 = 0.0529$, $wR_2 = 0.1175$
R (all data)[a]	$R_1 = 0.1034$, $wR_2 = 0.1202$	$R_1 = 0.0724$, $wR_2 = 0.1203$	$R_1 = 0.0512$, $wR_2 = 0.0921$	$R_1 = 0.0438$, $wR_2 = 0.1121$	$R_1 = 0.1054$, $wR_2 = 0.1841$	$R_1 = 0.0797$, $wR_2 = 0.1318$

[a] $R_1 = \sum||F_o| - |F_c||/\sum|F_o|$; $wR_2 = [\sum w(F_o^2 - F_c^2)_2/\sum w(F_o^2)^2]^{1/2}$.

Table 2
Selected bond lengths (Å) and angles (°) for complexes **1-6**

Compound **1**			
Cu(1)–O(7)	1.947(3)	O(7)–Cu(1)–N(3)	161.3(4)
Cu(1)–O(7)#1	1.947(4)	O(7)#1–Cu(1)–N(3)	99.1(4)
Cu(1)–N(4)	2.009(4)	N(4)–Cu(1)–N(3)	82.0(2)
Cu(1)–N(3)	2.012(4)	O(7)–Cu(1)–O(3)	97.8(9)
Cu(1)–O(3)	2.297(3)	O(7)#1–Cu(1)–O(3)	85.0(1)
Cu(1)–Cu(1)#1	2.939(1)	N(4)–Cu(1)–O(3)	93.1(2)
Cu(2)–O(3)	1.882(3)	N(3)–Cu(1)–O(3)	100.8(1)
Cu(2)–O(1)	1.907(3)	O(3)–Cu(2)–O(1)	93.2(3)
Cu(2)–N(1)	2.005(4)	O(3)–Cu(2)–N(1)	171.1(9)
Cu(2)–N(2)	2.021(4)	O(1)–Cu(2)–N(1)	95.5(4)
O(7)–Cu(1)–O(7)#1	82.0(7)	O(3)–Cu(2)–N(2)	90.5(4)
O(7)–Cu(1)–N(4)	97.4(3)	O(1)–Cu(2)–N(2)	165.7(1)
O(7)#1–Cu(1)–N(4)	177.9(6)	N(1)–Cu(2)–N(2)	81.2(6)
Compound **2**			
Cu(1)–O(7)#2	1.952(3)	O(7)–Cu(1)–N(4)	159.7(2)
Cu(1)–O(7)	1.966(3)	N(3)–Cu(1)–N(4)	80.6(7)
Cu(1)–N(3)	1.994(3)	O(7)#1–Cu(1)–O(6)	83.7(5)
Cu(1)–N(4)	2.012(3)	O(7)–Cu(1)–O(6)	96.0(1)
Cu(1)–O(6)	2.221(3)	N(3)–Cu(1)–O(6)	96.4(5)
Cu(1)–Cu(1)#2	2.989(1)	N(4)–Cu(1)–O(6)	104.2(5)
Cu(2)–O(6)	1.908(3)	O(6)–Cu(2)–O(5)	91.8(1)
Cu(2)–O(5)	1.916(3)	O(6)–Cu(2)–N(2)	175.0(2)
Cu(2)–N(2)	1.984(3)	O(5)–Cu(2)–N(2)	93.2(1)
Cu(2)–N(1)	2.017(4)	O(6)–Cu(2)–N(1)	93.9(6)
Cu(2)–O(7)#2	2.311(3)	O(5)–Cu(2)–N(1)	158.1(4)
O(7)#1–Cu(1)–O(7)	80.5(8)	N(2)–Cu(2)–N(1)	81.3(2)
O(7)#1–Cu(1)–N(3)	179.2(7)	O(6)–Cu(2)–O(7)#2	82.2(8)
O(7)–Cu(1)–N(3)	98.7(1)	O(5)–Cu(2)–O(7)#2	102.4(7)
O(7)#1–Cu(1)–N(4)	100.0(1)	N(2)–Cu(2)–O(7)#2	96.9(1)
		N(1)–Cu(2)–O(7)#2	99.2(3)
Compound **3**			
Cd(1)–N(2)	2.305(3)	O(2)–Cd(1)–O(1)	54.8(3)
Cd(1)–O(2)	2.305(3)	O(6)–Cd(1)–O(1)	91.9(4)
Cd(1)–O(6)	2.318(3)	N(1)–Cd(1)–O(1)	86.2(5)
Cd(1)–N(1)	2.327(4)	N(2)–Cd(1)–O(4)	86.4(1)
Cd(1)–O(1)	2.452(3)	O(2)–Cd(1)–O(4)	82.2(6)
Cd(1)–O(4)	2.584(3)	O(6)–Cd(1)–O(4)	120.0(6)
Cd(1)–O(6)#3	2.619(3)	N(1)–Cd(1)–O(4)	80.0(3)
N(2)–Cd(1)–O(2)	168.1(8)	O(1)–Cd(1)–O(4)	130.2(8)
N(2)–Cd(1)–O(6)	91.1(4)	N(2)–Cd(1)–O(6)#3	92.0(4)
O(2)–Cd(1)–O(6)	97.4(1)	O(2)–Cd(1)–O(6)#3	83.9(7)
N(2)–Cd(1)–N(1)	71.3(8)	O(6)–Cd(1)–O(6)#3	66.2(5)
O(2)–Cd(1)–N(1)	103.2(6)	N(1)–Cd(1)–O(6)#3	132.4(3)
O(6)–Cd(1)–N(1)	153.1(9)	O(1)–Cd(1)–O(6)#3	131.1(6)
N(2)–Cd(1)–O(1)	133.3(9)	O(4)–Cd(1)–O(6)#3	54.0(5)
Compound **4**			
Cd(1)–O(1)	2.236(3)	N(1)#4–Cd(1)–N(1)	163.7(5)
Cd(1)–N(1)	2.341(3)	O(1)–Cd(1)–N(2)#4	160.2(8)
Cd(1)–N(2)	2.346(3)	N(1)–Cd(1)–N(2)#4	71.4(7)
O(1)–Cd(1)–O(1)#4	88.4(3)	O(1)–Cd(1)–N(2)	92.8(9)
O(1)–Cd(1)–N(1)#4	102.6(9)	N(1)–Cd(1)–N(2)	97.0(4)
O(1)–Cd(1)–N(1)	89.0(5)	N(2)#4–Cd(1)–N(2)	92.4(8)
Compound **5**			
Cr(1)–O(3)	1.881(3)	O(2)–Cr(1)–O(4W)	91.4(2)
Cr(1)–O(2)	1.918(3)	O(3W)–Cr(1)–O(4W)	179.4(1)
Cr(1)–O(3W)	1.997(4)	O(3)–Cr(1)–N(1)	93.8(9)
Cr(1)–O(4W)	1.997(4)	O(2)–Cr(1)–N(1)	172.7(5)
Cr(1)–N(1)	2.062(4)	O(3W)–Cr(1)–N(1)	90.2(9)
Cr(1)–N(2)	2.067(4)	O(4W)–Cr(1)–N(1)	90.1(1)
O(3)–Cr(1)–O(2)	93.2(6)	O(3)–Cr(1)–N(2)	172.0(3)
O(3)–Cr(1)–O(3W)	91.4(6)	O(2)–Cr(1)–N(2)	94.7(4)
O(2)–Cr(1)–O(3W)	88.1(6)	O(3W)–Cr(1)–N(2)	89.0(9)
O(3)–Cr(1)–O(4W)	89.0(1)	O(4W)–Cr(1)–N(2)	90.5(4)
		N(1)–Cr(1)–N(2)	78.1(7)
Complex **6**			
Cr(1)–O(3)	1.886(2)	O(1)–Cr(1)–N(1)	93.8(1)
Cr(1)–O(1)	1.912(2)	N(3)–Cr(1)–N(1)	169.8(9)
Cr(1)–N(3)	2.061(3)	O(3)–Cr(1)–N(4)	87.6(3)
Cr(1)–N(1)	2.064(3)	O(1)–Cr(1)–N(4)	173.1(2)
Cr(1)–N(4)	2.077(3)	N(3)–Cr(1)–N(4)	79.7(5)
Cr(1)–N(2)	2.091(3)	N(1)–Cr(1)–N(4)	93.1(1)
O(3)–Cr(1)–O(1)	91.8(4)	O(3)–Cr(1)–N(2)	173.6(5)
O(3)–Cr(1)–N(3)	92.5(3)	O(1)–Cr(1)–N(2)	90.5(6)
O(1)–Cr(1)–N(3)	93.4(3)	N(3)–Cr(1)–N(2)	93.2(3)
O(3)–Cr(1)–N(1)	94.3(3)	N(1)–Cr(1)–N(2)	79.6(4)
		N(4)–Cr(1)–N(2)	90.7(3)

#1 $-x+1$, $-y$, $-z+2$; #2 $-x+1$, $-y$, $-z$; #3 $-x+1$, $-y$, $-z+1$; #4 $-x+1$, y, $-z+1/2$.

Table 3
Geometrical parameters of hydrogen bonds in complexes **1**–**6**

D–H···A	d(D–H)	d(H···A)	d(D···A)	∠(DHA)
Compound **1**				
O7–H9···O4(a)	0.69	2.28	2.98	176.24
O1w···O4w(b)			2.89	
O1w···O4w(c)			2.89	
O2w···O4(d)			3.13	
O2w···O3			2.79	
O3w–H3wA···O2(e)	0.85	1.96	2.76	155.82
O3w–H3wB···O4w(f)	0.85	2.10	2.90	156.84
O4w–H4wB···O1w(g)	0.85	2.25	2.89	131.71
O4w–H4wA···O6	0.85	1.99	2.79	155.77
Compound **2**				
O1w···O1(h)			2.87	
O1w···O4(i)			2.95	
O7–H20···O4(j)	0.83	2.02	2.85	172.30
Compound **3**				
C7–H12···O5(k)	0.96	2.44	3.41	174.72
C4–H1···O5(k)	0.97	2.43	3.39	175.51
Compound **4**				
O4–H13···O3(l)	0.91	1.93	2.71	141.49
Compound **5**				
O1w–H1wA···O4(m)	0.87	2.28	3.00	140.36
O1w–H1wB···O1(n)	0.85	1.95	2.80	168.89
O2w–H2wA···O1(o)	0.86	1.94	2.79	167.20
O2w–H2wB···O5(p)	0.85	1.83	2.67	176.29
O3w–H3wA···O2w(q)	0.84	1.78	2.61	172.77
O3w–H3wB···O4(r)	0.85	1.97	2.72	146.25
O4w–H4wA···O1w(s)	0.84	1.78	2.61	172.12
O4w–H4wB···O6(t)	0.82	1.88	2.67	162.98
Compound **6**				
C10–H4···O5(u)	0.95	2.30	3.11	141.26
C22–H9···O4(v)	0.94	2.35	3.07	132.46

Symmetry code: (a) $-x+1$, $y-1/2$, $-z+3/2$; (b) $1-x$, $1-y$, $1-z$; (c) $-1+x$, y, $-1+z$; (d) x, $0.5-y$, $-0.5+z$; (e) x, y, $z-1$; (f) $-x+2$, $-y+1$, $-z+1$; (g) $x+1$, y, $z+1$; (h) $-1+x$, y, z; (i) $1-x$, $1-y$, $-z$; (j) $-x+1$, $y+1/2$, $-z+3/2$; (k) $1-x$, $-y$, $-$;z; (l) x, $-y$, $z+1/2$; (m) $-x+1$, $-y+1$, $-z+1$; (n) $x+1$, $-y+1/2$, $z+1/2$; (o) $x+1$, y, z; (p) $-x+1$, $-y+1$, $-z$; (q) $-x+1$, $y-1/2$, $-z+1/2$; (r) $-x$, $y-1/2$, $-z+1/2$ (s) $-x+1$, $y-1/2$, $-z+1/2$; (t) $-x+1$, $y-1/2$, $-z+1/2$; (u) x, $2-y$, $-0.5+z$; (v) x, $1-y$, $-0.5+z$.

program. The structures were solved by direct methods and refined by full-matrix least squares on F^2 using SHELXTL97 software [11]. Non-hydrogen atoms were refined anisotropically. The hydrogen atoms were located from difference maps and refined with isotropic temperature factors in complexes **1**–**6**. All calculations were carried out using SHELXTL97 [11] and PLATON99 [12]. The crystallographic data and pertinent information are summarized in Table 1, and any additional refinement information is given below.

Complex **1** O1w showed disorder over two positions and was refined at 0.50 and 0.50 occupancy for each position. The hydrogen atoms of O1 w, O2w and O3w were not located from difference Fourier maps, and the O–H distances of O4w were refined with a DFIX restraint of 0.85 Å.

Complex **2** Hydrogen atoms of O1w were not located from difference Fourier maps.

Complex **5** O2 and O3 atoms of the sulfonate group both showed disorder over two positions and were refined at 0.50 and 0.50 occupancy, and 0.41 and 0.59 occupancy, respectively.

Selected bond lengths and angles for complexes **1**–**6** are summarized in Table 2. Geometrical parameters of the hydrogen bonds in complexes **1**–**6** are summarized in Table 3.

3. Results and discussion

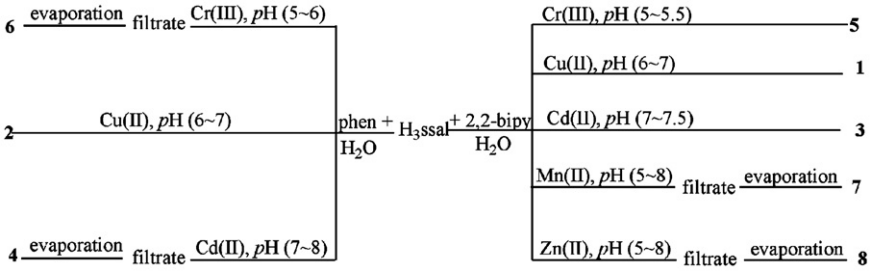
3.1. Synthesis

5-Sulfosalicylic acid and bipyridyl-like mixed ligands were reacted in aqueous medium with different metal salts ($Cr_2(SO_4)_3 \cdot 6H_2O$, $MnCl_2 \cdot 4H_2O$, $CuSO_4 \cdot 5H_2O$, $ZnCl_2$, $3CdSO_4 \cdot 8H_2O$) in a molar ratio of 1:1:1 at different pH levels ranging from 5 to10 in an attempt to investigate the reactivity. The reactions were carried out in a 25 ml Teflon-lined stainless steel reactor at 150 °C for 72 h. We obtained compounds **1**–**8** (Scheme 1) at different pH values. Coordination complexes of Cr(III), Cu(II) and Cd(II) were obtained under weakly acidic, neutral and weakly basic conditions, respectively. Complexes **7** and **8** were easily obtained for the wider pH range 5–8. It is worth noting that complexes **1**, **2**, **3** and **5** were all directly obtained through the hydrothermal method, however, complexes **4**, **6**, **7** and **8** were synthesized through evaporation of the filtrate after the hydrothermal reaction. We tried to synthesize complexes **4**, **6**, **7** and **8** at room temperature, but failed. This demonstrates that complexes **4**, **6**, **7** and **8** were synthesized under hydrothermal conditions.

3.2. Crystal structures of the complexes

3.2.1. Structure description of $Cu_4(OH)_2(ssal)_2(phen)_4 \cdot 7H_2O$ (**1**)

X-ray single crystal diffraction reveals that compound **1** possesses a centrosymmetric Cu_4O_4 core based on a stepped topology (Fig. 1) [13]. The Cu_4O_4 core is composed of two crystallographically independent Cu (II) atoms [namely, Cu1 and Cu2]. Cu1 and Cu2 both possess the configuration of a distorted square pyramid, however, there are two sets of coordination environments around the copper atoms. Cu1 is located in a plane consisting of two nitrogen atoms (N3 and N4) from a chelating phen molecule and two hydroxides (O7 and O7#1), and the axial position is occupied by the phenolato oxygen atom (O3). For Cu2, the plane is composed of two nitrogen atoms (N1 and N2) from the phen molecule, one carboxylate oxygen (O1) and one phenolato oxygen atom (O3), and the corresponding axial position is taken by one hydroxide ion (O7#1). Cu1 and Cu2 atoms, with two symmetry-related copper centres, are connected into a Cu_4O_4 core by two μ_3-hydroxo groups and two phenolato oxygen atoms. The Cu_4O_4 core consists of a stepped structure in which three Cu_2O_2 planes are formed by Cu2 Cu1 O3 O7#1 I, Cu1 Cu1#1 O7 O7#1 II and Cu2#1 Cu1#1 O3#1 O7 III. Planes I and III, with a maximum deviation of 0.1308 Å from their least-squares planes, are parallel to each other, but both have the same bihedral angle of 103° with plane II. In the Cu_4O_4 core, we observed that the four Cu atoms form a flat rhomboid with sides Cu1···Cu2 and Cu1#1···Cu2 of lengths 3.18 and 3.59 Å, respectively, a short diagonal (Cu1···Cu1#1) of 2.94 Å and a long diagonal (Cu2···Cu2#1) of 6.10 Å. Offset π–π interactions between phen molecules with a face-to-face distance of 3.43 Å and offset angle of 28.74° stabilize the tetranuclear complex. To the best of our knowledge, only one copper complex constructed from mixed organic ligands with a stepped topology has previously been reported [13a].



Scheme 1. The reactions to prepare complexes **1**–**8**.

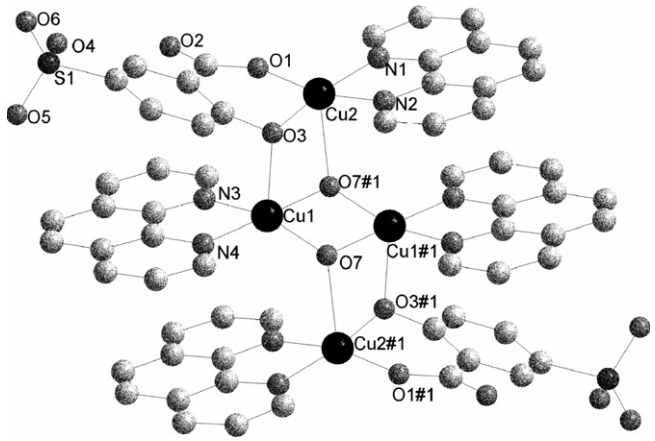


Fig. 1. The molecular structure of complex **1**.

Each $Cu_4(OH)_2(ssal)_2(phen)_4$ molecule is linked to four neighboring tetrameric units to form a 2D supramolecular layer (S-Fig. 1) of rhombic windows (with dimensions of 6.05×13.44 Å) through hydrogen bonding between μ_3-hydroxo groups (O7) and the uncoordinated sulfonate oxygen atoms (O4). The 2D layers are connected into a 3D supramolecular network by water heptamers (Fig. 2), the geometrical parameters of the hydrogen bonds are given in Table 3. In addition to hydrogen bonding, inter-layer contacts are strengthened by intermolecular π–π interactions between adjacent $Cu_4(OH)_2(ssal)_2(phen)_4$ units (offset π–π interaction between phen molecules with a face-to-face distance of 3.47 Å and offset angle 36.53°). Interestingly, the water heptamers and sulfonate anions are interconnected into a 2D supramolecular layer with very large rhombic windows (with dimensions of 12.57×17.77 Å) through hydrogen bonding (Fig. 3). The tetranuclear Cu (II) units are right inside the large rhombic windows between the 2D layers (S-Fig. 2).

3.2.2. Structure description of $Cu_4(OH)_2(ssal)_2(bipy)_4 \cdot 2H_2O$ (**2**)

Complexes **1** and **2** have the same space group, $P2_1/c$. The molecular structures of complexes **1** and **2** show some similarities as follows: (a) Both possess the centrosymmetric Cu_4O_4 (S-Fig. 3) core based on a stepped topology. (b) The central copper atoms in both complexes have the same coordination geometry, and the bond lengths and angles, as shown in Table 2, are also similar. (c) Both possess similar 2D supramolecular layers based on tetranuclear Cu (II) units. However, the replacement of phen by bipy, a chelating aromatic ligand of a smaller size, leads to some subtle differences. One difference worth noticing between the crystal structures of **1** and **2** concerns the numbers of water molecules in their asymmetric units: 3.5 water molecules for **1** and one water molecule for **2**. This results in the formation of a 3D supramolecular network (Fig. 4) for compound **2** differing from that of compound **1**. In compound **2**, the 2D layers are connected into a 3D supramolecular network through O1w with symmetry-related layers and π–π interactions between adjacent $Cu_4(OH)_2(ssal)_2(bipy)_4$ units (offset π–π interactions between 2,2′-bipy molecules with a face-to-face distance of 3.54 Å and offset angle of 24.71°).

3.2.3. Structure description of Cd(Hssal)(bipy) (**3**)

The crystal analysis of complex **3** reveals that it is a one-dimensional ladder coordination polymer containing Cd_2O_8 (2,2′-bipy)$_2$ units (Fig. 5a) with Hssal as the bridge ligands. The asymmetric unit of complex **3** consists of one Cd atom, one Hssal anion and one 2,2′-bipy ligand. The Cd center adopts a distorted capped-octahedral conformation (Fig. 5b) in which the basal plane is formed by two nitrogen atoms (N1 and N2) from a chelating 2,2′-bipy ligand, a carboxylate oxygen atom (O2) and a sulfonate oxygen atom (O6) from two different Hssal anions. The axial positions are taken by a carboxylate oxygen atom

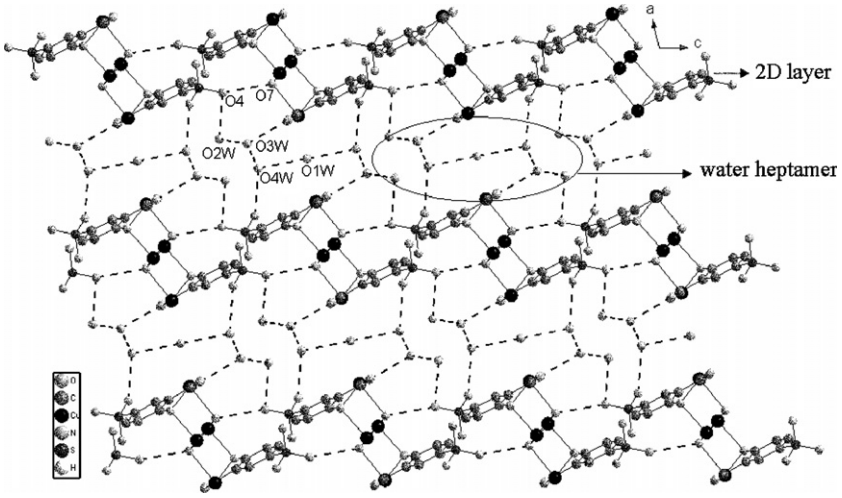


Fig. 2. Perspective view of the 3D supramolecular network of complex **1**, phen ligands and H atoms were removed for clarity.

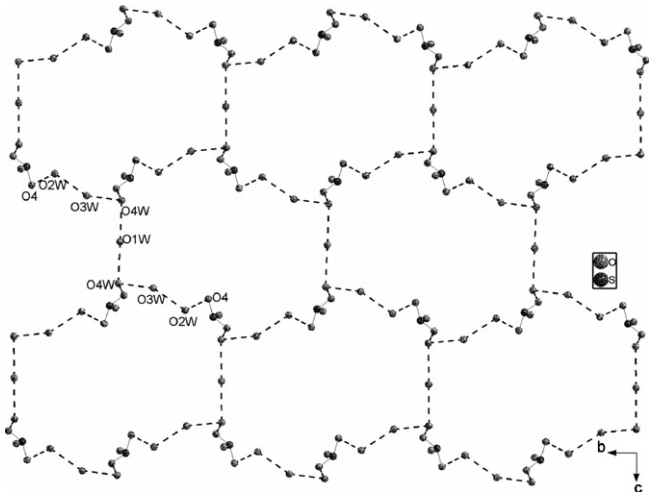


Fig. 3. 2D supramolecular layer consisting of hydrogen bonded water heptamers and sulfonate anions in complex **1**.

(O1) and a sulfonate oxygen atom (O6#3). The sulfonate oxygen atom (O4) occupies the capped position. Each pair of Cd ions is bridged by a sulfonate oxygen atom (O6) with symmetry-related partner (O6#3) to form a Cd_2O_8 (2,2′-bipy)$_2$ unit. These dimeric Cd_2 units, featuring a 1D ladder (Fig. 6a) along the crystallographic*a* axis, are interconnected by Hssal^{2-} anions. Each Hssal^{2-} anion connects three Cd (II) atoms (Fig. 6b) with the carboxylic group and sulfonate group, adopting $\mu_1 - \eta^1{:}\eta^1$-chelating and $\mu_2 - \eta^0{:}\eta^1{:}\eta^2$-bridging/chelating coordination modes [14]. As far as we know, this kind of new coordination mode of the Hssal^{2-} group has not been reported previously. The adjacent chains are further aggregated into a 2D sheet (S-Fig. 4) through π–π interactions between phen ligands, with a face-to-face distance of 3.47 Å and offset angle 36.52°, chelating C–H···O hydrogen bonding (C4···O5 = 3.39, C7···O5 = 3.41 Å) and C–H···π interactions between C8 and H5 from 2,2′-bipy ligands and Hssal^{2-} rings containing C16 (S-Fig. 5, H5···π = 2.72 and C8···π = 3.59 Å).

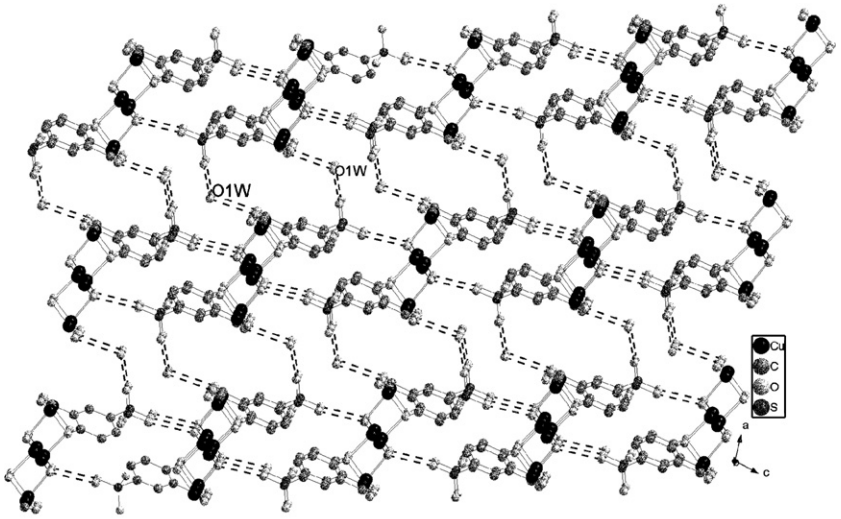


Fig. 4. Perspective view of the 3D supramolecular network of complex **2**, 2,2-bipy ligands were removed for clarity.

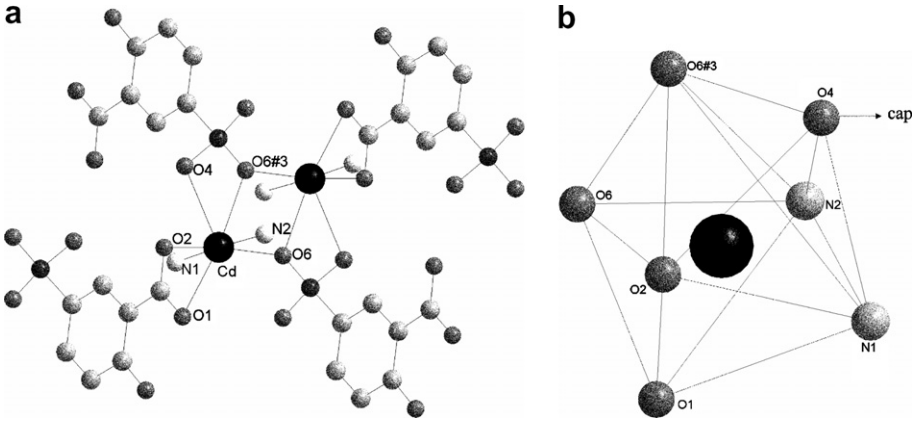


Fig. 5. (a) Perspective view of a dimeric Cd unit in complex **3**, the C atoms of 2,2′-bipy are omitted for clarity. (b) A distorted capped-octahedral conformation of the Cd (II) ion.

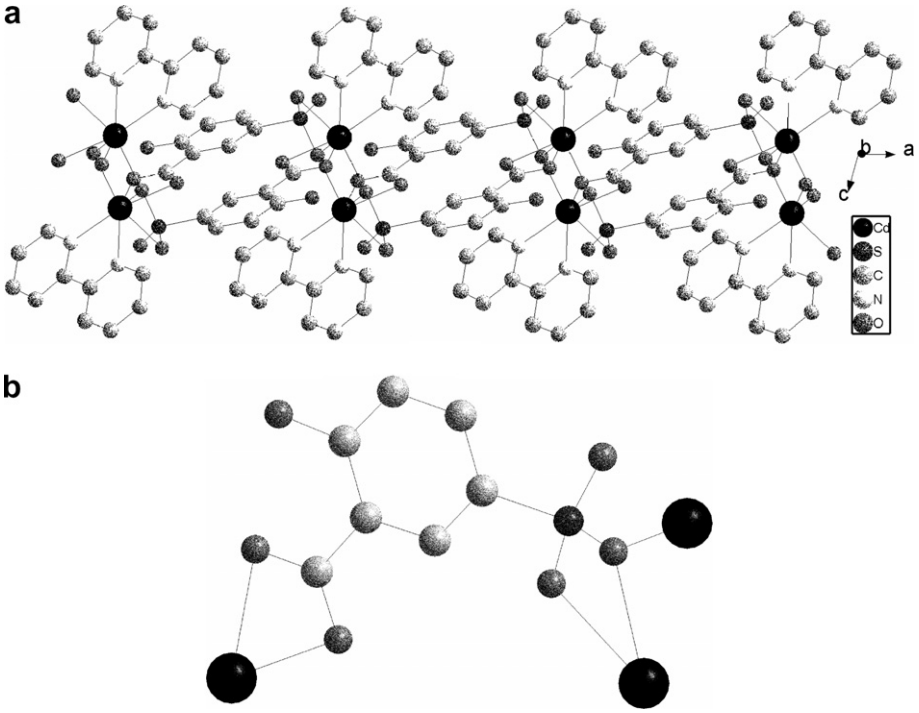


Fig. 6. (a) A 1D ladder constructed by dimeric $Cd_2O_8N_4$ units along the *a*-axis. (b) The coordination mode of the $Hssal^{2-}$ ligand in complex **3**.

3.2.4. Structure description of $Cd(HL)_2(phen)_2$ (**4**)

The crystal analysis of complex **4** reveals that it is a mononuclear complex consisting of one Cd (II) ion, two phen molecules and two *p*-hydroxybenzenesulfonic acid anions. The Cd (II) center exhibits a distorted octahedral surrounding (Fig. 7), in which the basal plane is formed by three nitrogen atoms (N1, N1#4 and N2) from two symmetry-related phen molecules and one sulfonate oxygen atom (O1#4). The axial positions are occupied by a nitrogen atom (N1#4) from a phen molecule and a sulfonate oxygen atom (O1). The π–π interactions between the aromatic rings of the different ligands are favorable to stabilize complex **4**. The closest centroid separation is 3.76 Å from the *p*-hydroxybenzenesulfonic ligand to the C_6 ring of the phen ligand, with an offset angle of 19.85°. Interestingly, the $Cd(L)_2(phen)_2$ molecules are connected into 1D supramolecular double chains (S-Fig. 6), sharing $Cd(phen)_2$ units by O–H···O hydrogen bonding (O4···O3 = 2.71 Å) along the crystallographic *c*-axis. The adjacent double chains are further aggregated into a 3D supramolecular network (Fig. 8) through π–π interactions between phen ligands (the closest centroid separation is 3.679 Å between C_6 rings with an offset angle of 16.31°) and C–H···O hydrogen bonding (C18···O2 = 3.20 Å).

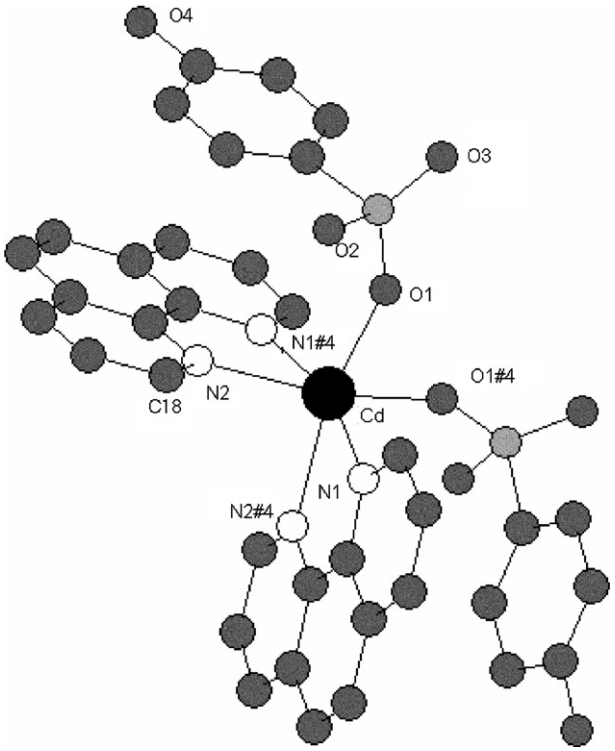


Fig. 7. The molecular structure of complex **4**.

3.2.5. Structure description of $Cr(ssal)(bipy)(H_2O)_2 \cdot 2H_2O$ (**5**)

X-ray single crystal diffraction reveals that the asymmetric unit of **5** contains one Cr(III) ion, one ssal anion, one 2,2′-bipy molecule, two coordinated water and two lattice water molecules. The Cr(III) center exhibits a distorted octahedral surrounding (Fig. 9), in which the basal plane is formed by two nitrogen atoms from a chelating 2,2′-bipy ligand (N1 and N2) and one carboxylate oxygen (O2) and one phenolic oxygen (O3) from a ssal ligand.

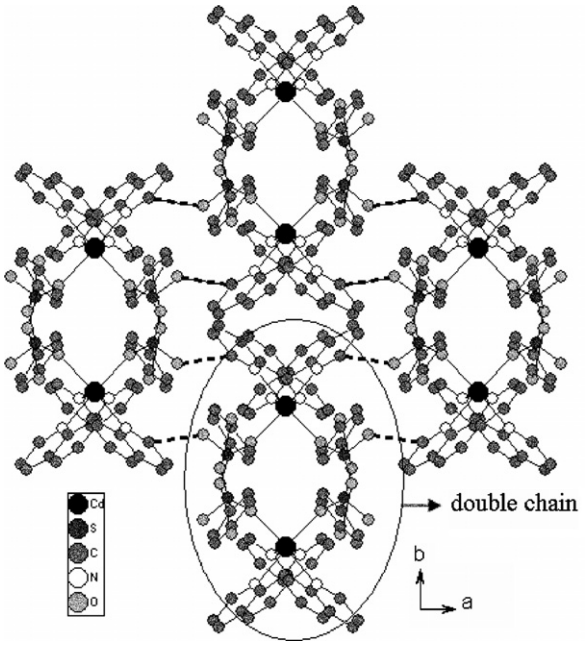


Fig. 8. The 3D supramolecular network in complex **4**.

The axial positions are occupied by O3w and O4w. Each $Cr(ssal)(bipy)_2(H_2O)_2$ unit is hydrogen bonded to two other units to form a 1D supramolecular helical chain (Fig. 9) resulting from O–H···O hydrogen bonds involving O3w, O2w, O1, O1w and O4. Within the chain, the π–π interactions between the aromatic rings of the different ligands may stabilize the polymeric supramolecular chain. The closest centroid separation is 4.01 Å from the $ssal^{3-}$ ligand to the C_5N ring (containing the N2 atom) of the 2,2′-bipy ligand with an offset angle of 26.09°. The 1D chains are further linked into a 2D layer (Fig. 10) through O–H···O hydrogen bonding (O2w···O5, O1w···O4w), the geometrical parameters of the hydrogen bonds of compound **5** are collected in Table 3. The most remarkable feature of this 2D layer is that there exist a supramolecular ring (S-Fig. 7) consisting of four coordinated water molecules (O3w and O4w), six lattice water molecules (O1w and O2w), three $ssal^{3-}$ anions and three Cr^{3+} ions, formed through covalent bonds and hydrogen bonds. Only the 2,2′-bipy molecules occupy the supramolecular rings, preventing interpenetration. Finally, the 2D layers are hydrogen bonded through O4wB-H4wB···O6 to afford a 3D supramolecular network (S-Fig. 8). Compared with some active transition metals (Zn, Cd, Cu, etc.), coordination complexes of Cr are relatively fewer due to its inertness (slow polymerization and difficulty of substitution) [15,16]. To the best of our knowledge, complex **5** is the first example of a chromium 5-sulfosalicylate complex.

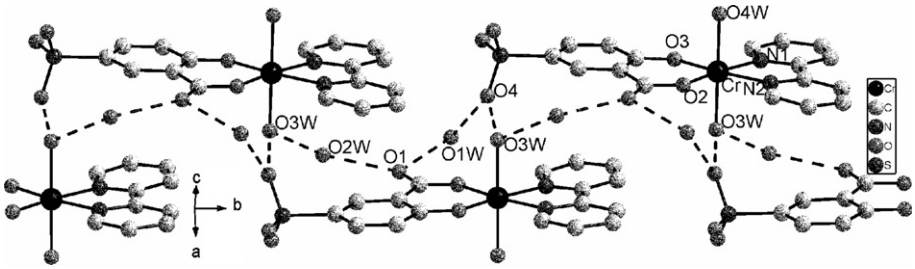


Fig. 9. 1D supramolecular helical chains consisting of $Cr(ssal)(bipy)_2(H_2O)_2$ units in complex **5**.

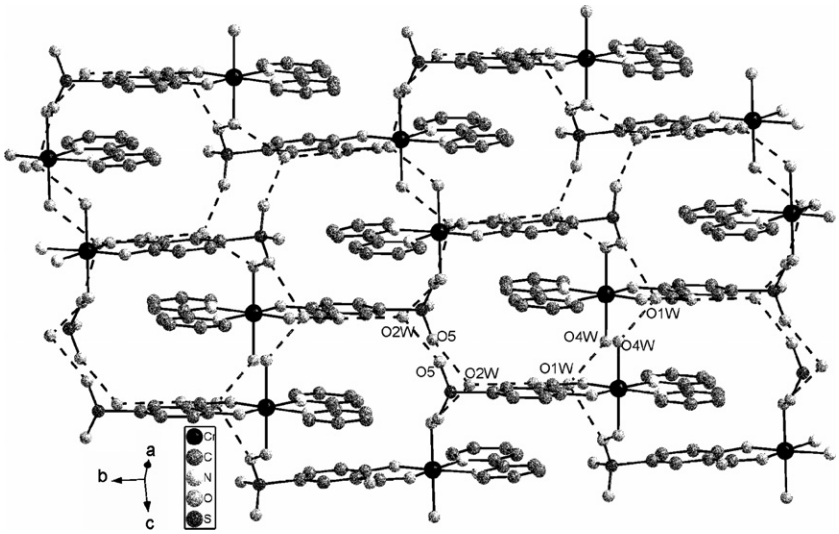


Fig. 10. Perspective view of the 2D supramolecular layer in complex **5**.

3.2.6. Structure description of Cr(ssal)(phen)$_2$ (6)

The asymmetric unit of **6** (Fig. 11) contains one Cr (III) ion, one ssal anion and two phen molecules. The Cr(III) center exhibits a distorted octahedral surrounding, in which the basal plane is formed by two nitrogen atoms from two different phen ligands (N2 and N4) and two bidentate chelating coordination oxygen atoms from one carboxylate oxygen (O1) and one phenolic oxygen (O3). The axial positions are occupied by N1 and N3 from two different phen ligands. Each Cr(ssal)(phen)$_2$ unit is hydrogen bonded to four other units to form a 2D puckered supramolecular layer (S-Fig. 9) through C–H···O (C10–H8···O5, C22–H9···O4). Moreover, O···π (S-Fig. 10, the distance of O5 to the C_5N ring containing the N3 atom is 3.10 Å) [17] and π···π interactions between the aromatic rings of different ligands (the closest centroid separation is 3.91 Å from the aryl of the ssal anion ligand to the C_6 ring of the phen ligand with an offset angle of 23.91°) stabilize the 2D puckered supramolecular layer. The 2D layers are held together into a 2D supramolecular double-layer through π···π interactions between phen ligands (the closest centroid separation is 3.79 Å between the C6 rings of phen ligands with an offset angle of 25.79°). The 2D double layers are further aggregated into a 3D supramolecular network (Fig. 12) through infinite π-stacking between the phen ligands in head-to-tail way (the closest centroid separation is 3.86 Å with an offset angle of 13.27°).

3.3. Magnetic studies of complexes 1–2

The variable temperature magnetic susceptibility of complexes **1** and **2** was measured at 1000 G in the temperature range 5–300 K. The magnetic behaviors of **1** are depicted in Fig. 13 in the forms of χ_M and μ_{eff} versus T plots (χ_M being the molar magnetic susceptibility). As the temperature is lowered, χ_M increases slowly until about 50 K, then it dramatically increases at lower temperatures. The data between 300 and 5 K can be fit to the Curie–Weiss expression, $\chi_M = C/(T-\theta)$, $[C = 0.125\, g^2 \sum S(S+1)]$, with the Curie constant $C = 1.71$ cm^3 K mol^{-1}, Weiss constant $\theta = 7.5$ K and $g = 2.14$. On the other hand, at room temperature the effective magnetic moment (μ_{eff}) equals 3.701 μ_B, which is slightly higher than the spin-only value of four

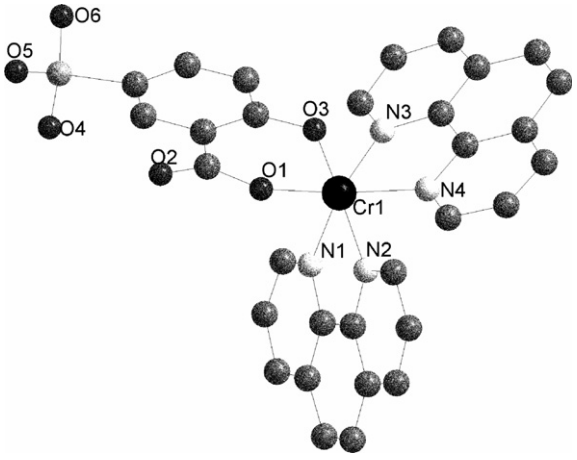


Fig. 11. The molecular structure of complex **6**. Hydrogen atoms are removed for clarity.

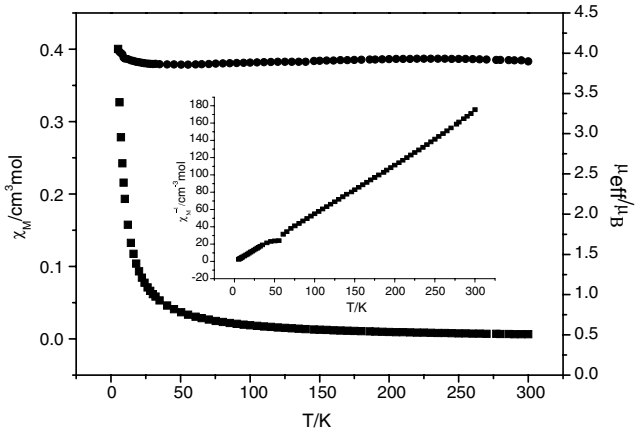


Fig. 13. Plots of χ_M and μ_{eff} vs. T for complex **1**. The inset is the plot of $1/\chi_M$ vs. T.

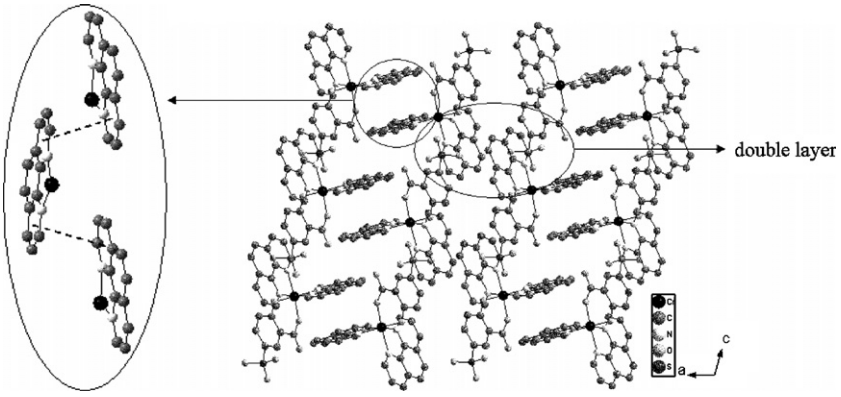


Fig. 12. The 3D representation of the packing arrangement for complex **6**. The insets show the existence of infinite π-stacking in a head-to-tail way. H atoms have been removed for clarity.

uncoupled copper (II) $S = 1/2$ ions (theoretical value for $g = 2$, $\mu_{eff} = 3.464\ \mu_B$). The μ_{eff} value increases gradually until 5 K, reaching a value of 4.037 μ_B. This feature is characteristic of the presence of significant ferromagnetic interactions between the copper (II) ions [13b,13f]. Moreover, the positive sign of the Weiss constant also indicates there exist ferromagnetic interactions between the Cu (II) centers.

The magnetic behavior of complex **2** is shown in Fig. 14 in the forms of χ_M and μ_{eff} versus T plots. As the temperature is lowered, χ_M increases slowly until about 38 K, then it dramatically increases at lower temperatures. The data between 300 and 38 K can be fit to the Curie–Weiss expression, $\chi_M = C/(T-\theta)$, $[C = 0.125\, g^2 S(S+1)]$, with the Curie constant $C = 0.784\ cm^3\ mol^{-1}$ K and Weiss constant $\theta = -0.401$ K. The effective magnetic moment (μ_{eff}) in **2** decreases slowly from 3.43 μ_B at 300 K to 3.21 μ_B at 55 K, and then falls rapidly, reaching 2.46 μ_B at 5 K. At room temperature the effective magnetic moment (μ_{eff}) equals 3.43 μ_B, which is slightly lower than the spin-only value of four uncoupled copper (II) $S = 1/2$ ions (theoretical value for $g = 2$, $\mu_{eff} = 3.46\ \mu_B$). These features indicate that there exist anti-ferromagnetic interactions amongst the Cu (II) centers [13e]. The difference in the magnetic properties of complexes **1** and **2** is possibly the result of the different intermolecular contacts.

3.4. Fluorescent properties of complexes 3–4

The solid-state fluorescent spectra of complexes **3** and **4** are depicted in Figs. 15 and 16, respectively. In order to understand the nature of the emission bands of complex **3** and **4**, we also investigated the luminescence of the free 2, 2-bipy, phen · H_2O and H_3ssal · $2H_2O$ ligands in the solid state at room temperature. The emission bands for free phen · H_2O are at 365, 381, 403 and 437 nm ($\lambda_{exc.} = 344$ nm), which may be attributed to the $\pi^* \rightarrow \pi$ transition (S-Fig. 11). Similar to free phen · H_2O, the emission bands for the free 2, 2-bipy ligand, at 390, 413 and 438 nm ($\lambda_{exc.} = 352$ nm), are also attributed to the $\pi^* \rightarrow \pi$ transition (S-Fig. 12). However, the emission bands for free H_3ssal · $2H_2O$ are mainly located at about 387 nm with a shoulder peak at 440 nm (H_3ssal · $2H_2O$: $\lambda_{exc.} = 335$ nm) and are attributed to $\pi^* \rightarrow n$ transitions (S-Fig. 13). Complex **3** exhibits intense green photoluminescence with an emission maximum at ca. 520 nm upon excitation at 347 nm (Fig. 15). Compared with the emission spectra of the free 2, 2-bipy and H_3ssal · $2H_2O$ ligands, the band at 520 nm for **3** might be assigned to the emission of a ligand-to-metal charge transfer (LMCT), similar to reported Cd complexes [18]. Complex **4** displays intense blue photoluminescence with an emission maximum at ca. 440 nm upon excitation at 329 nm (Fig. 16), compared with the emission spectra of the free phen · H_2O and H_3ssal · $2H_2O$ ligands, the band at 440 nm for **4** is neither LMCT (ligand-to-metal charge transfer) nor MLCT (metal-to-ligand charge transfer) in nature, and tentatively might be assigned to an intraligand fluorescent emission [19,20].

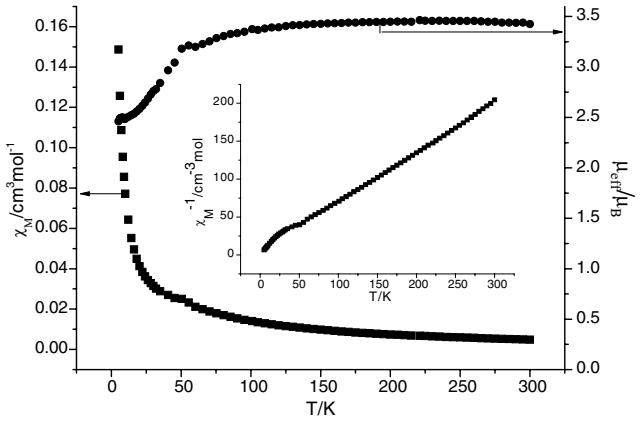


Fig. 14. plots of χ_M and μ_{eff} vs. T for complex **2**. The inset is the plot of $1/\chi_M$ vs. T.

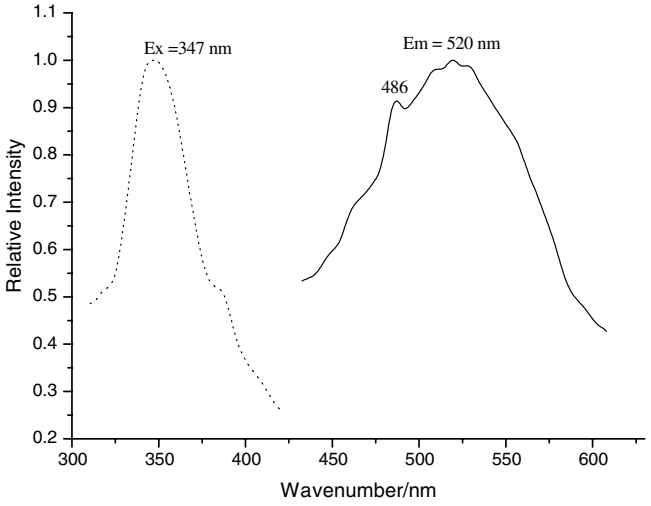


Fig. 15. Solid-state excitation fluorescent (dashed line) and emission (full line) spectra of complex **3** at room temperature.

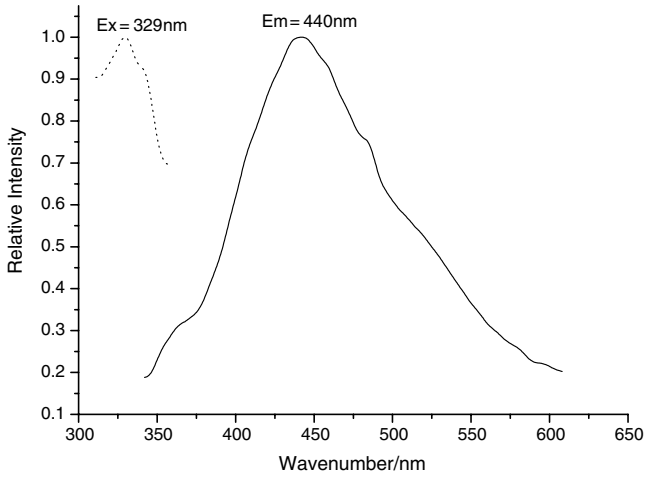
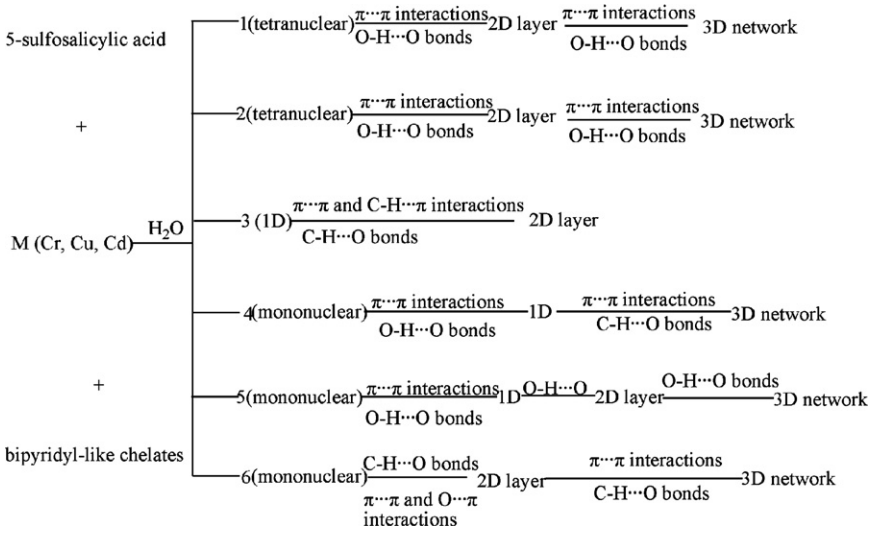


Fig. 16. Solid-state excitation fluorescent (dashed line) and emission (full line) spectra of complex **4** at room temperature.



Scheme 2.

4. Conclusion

Six new complexes constructed from 5-sulfosalicylic acid and bipyridyl-like ligands (2,2′-bipy and 1,10-phen), namely $[Cu_4(OH)_2(ssal)_2(phen)_4 \cdot 7H_2O]$ (**1**), $[Cu_4(OH)_2(ssal)_2(bipy)_4 \cdot 2H_2O]$ (**2**), [Cd(Hssal)(bipy)] (**3**), $[Cd(HL)_2(phen)_2]$ (**4**), $[Cr(ssal)(bipy)(H_2O)_2 \cdot 2H_2O]$ (**5**) and $[Cr(ssal)(phen)_2]$ (**6**), (H_3ssal = 5-sulfosalicylic acid, H_2L = *p*-hydroxybenzenesulfonic acid, bipy = 2,2′-bipy, phen = 1,10-phen) were prepared under hydrothermal conditions and their structures were determined by single-crystal X-ray diffraction. Complexes **1** and **2** are both tetranuclear copper complexes with a stepped topology. In complex **3**, a new coordination mode of the $Hssal^{2-}$ group is reported in this work. During the synthetic process of complex **4**, *in situ* decarboxylation of 5-sulfosalicylic acid into *p*-hydroxybenzenesulfonic acid is involved. Two chromium 5-sulfosalicylates (**5** and **6**) are reported for the first time. These new complexes display different supramolecular structures by O–H···O, C–H···O hydrogen bonds as well as π···π, C–H···π and O···π interactions (Scheme 2). Of the six complexes described in this work, the π-stacking interactions (O···π, C–H···π and π···π) play an important role in the observed structural stability. It is likely that studies on similar systems would be favorable for understanding the nature of the π-stacking and its role in structural stability.

Acknowledgement

This work was supported by the National Natural Science Foundation of China (Grant Nos. 20571032 and 20333070).

Appendix A. Supplementary material

CCDC 627686, 627687, 627688, 627689, 627690 and 627691 contain the supplementary crystallographic data for **1**, **2**, **3**, **4**, **5** and **6**. These data can be obtained free of charge via http://www.ccdc.cam.ac.uk/conts/retrieving.html, or from the Cambridge Crystallographic Data Centre, 12 Union Road, Cambridge CB2 1EZ, UK; fax: (+44) 1223-336-033; or e-mail: deposit@ccdc.cam.ac.uk.

X-ray crystallographic files of compounds **1**–**6** in CIF format, a perspective view of the 2D supramolecular layer for complex **1** (S-Fig. 1), the plot of the tetranuclear Cu (II) units included in large rhombic windows consisting of water heptamers and sulfonate anions (S-Fig. 2), the molecular structure of complex **2** (S-Fig. 3), the 2D packing structure of complex **3** (S-Fig. 4), chelating C–H···O hydrogen bonding and C–H···π interactions in complex **3** (S-Fig. 5), 1D supramolecular double chains for compound **4** (S-Fig. 6), the supramolecular ring of the 2D layer in complex **5** (S-Fig. 7), a plot of the 3D supramolecular network for complex **5** (S-Fig. 8), a plot of the 2D supramolecular layer in complex **6** (S-Fig. 9), the mode of O···π and π···π interactions in complex **6** (S-Fig. 10), the plots of the solid-state excitation fluorescent and emission spectra of the 2,2-bipy ligand (S-Fig. 11), phen · H_2O (S-Fig. 12) and H_3ssal · $2H_2O$ (S-Fig. 13) at room temperature. Supplementary data associated with this article can be found, in the online version, at doi:10.1016/j.poly.2007.05.037.

References

[1] G.R. Desiraju, Crystal Engineering: The Design of Organic Solids, Elsevier, Amsterdam, 1989.
[2] (a) S.R. Batten, R. Robson, Angew. Chem., Int. Ed. 37 (1998) 1460;
(b) G.F. Swiegers, J. Malefetse, Chem. Rev. 100 (2000) 3483;
(c) R. Robson, J. Chem. Soc. Dalton Trans. (2000) 3735;
(d) S.R. Batten, CrystEngCommun 3 (2001) 67;
(e) B.J. Holliday, C.A. Mirkin, Angew. Chem., Int. Ed. 40 (2001) 2022;
(f) M. Eddaoudi, D.B. Moler, J. Li, B.L. Chen, T.M. Reineke, M. O'Keeffe, O.M. Yaghi, Acc. Chem. Res. 34 (2001) 319;
(g) C. Janiak, J. Chem. Soc., Dalton Trans. (2003) 2781.

[3] (a) S. Kitagawa, R. Kitaura, S. Noro, Angew. Chem., Int. Ed. 43 (2004) 2334;
(b) L. Brammer, Chem. Soc. Rev. 33 (2004) 476;
(c) N. Malabika, R. Koner, S.E. Helen, M. Sasankasekhar, Cryst. Growth. Des. 5 (2005) 1907;
(d) S.G. Baca, I.G. Filippova, C. Ambrus, M. Gdaniec, Y.A. Simonov, N. Gerbeleu, O.A. Gherco, S. Decurtins, Eur. J. Inorg. Chem. (2005) 3118;
(e) E. Tynan, P. Jensen, A.C. Lees, B. Moubaraki, K.S. Murray, P.E. Kruger, CrystEngCommun (2005) 90;
(f) D. Sunirban, A.M. Simi, P. Satyanarayan, P. Samudranil, Cryst. Growth Des. 9 (2006) 2103.

[4] (a) O.M. Yaghi, H.L. Li, T.L. Groy, J. Am. Chem. Soc. 118 (1996) 9096;
(b) L.Y. Zhang, G.F. Liu, S.L. Zheng, B.H. Ye, X.M. Zhang, X.M. Chen, Eur. J. Inorg. Chem. (2003) 2965;
(c) Y.B. Go, X.Q. Wang, E.V. Anokhina, A.J. Jacobson, Inorg. Chem. 43 (2004) 5360;
(d) A.D. Burrows, R.W. Harrington, M.F. Mahon, S.J. Teat, CrystEngCommun (2005) 388;
(e) W.Z. Shen, X.Y. Chen, P. Cheng, S.P. Yan, B. Zhai, D.Z. Liao, Z.H. Jiang, Eur. J. Inorg. Chem. (2005) 2297;
(f) P. Mahata, S. Natarajan, Eur. J. Inorg. Chem. (2005) 2156;
(g) B. Covelo, R. Carballo, E.M. Vázquez-López, E. García-Martínez, A. Castiñeiras, S. Balboa, J. Niclós, CrystEngCommun (2006) 167;
(h) C.K. Xia, C.Z. Lu, D.Q. Yuan, Q.Z. Zhang, X.Y. Wu, S.C. Xiang, J.J. Zhang, D.M. Wu, CrystEngCommun (2006) 281.

[5] (a) H.Y. Sun, C.H. Huang, X.L. Jin, G.X. Xu, Polyhedron 14 (1995) 1201;
(b) A. Marzotto, D.A. Clemente, T. Gerola, G. Valle, Polyhedron 20 (2001) 1079;
(c) J.F. Li, Y.J. Zhao, X.H. Li, M.L. Hu, Acta Crystallogr. E60 (2004) m1210;
(d) Z.F. Chen, S.M. Shi, R.X. Hu, M. Zhang, H. Liang, Z.Y. Zhou, Chin. J. Chem. 21 (2003) 1059;
(e) E. Hecht, Acta Crystallogr. E60 (2004) m1286;
(f) W.G. Wang, J. Zhang, L.J. Song, J.F. Ju, Inorg. Chem. Commun. 7 (2004) 858;
(g) X.Q. Wang, J. Zhang, Z.J. Li, Y.H. Wen, J.K. Cheng, Y.G. Yao, Acta Crystallogr. C60 (2004) m657.

[6] (a) S.R. Fan, L.G. Zhu, Acta Crystallogr. E61 (2005) m2480;
(b) S.R. Fan, L.G. Zhu, H.P. Xiao, S.W. Ng, Acta Crystallogr. E61 (2005) m377;
(c) W.X. Ma, B.H. Qian, J. Gao, X.Y. Xu, L.D. Lu, X.J. Yang, X. Wang, H.B. Song, Chin. J. Inorg. Chem. 21 (2005) 612;
(d) J.F. Ma, J. Yang, S.L. Li, S.Y. Song, H.J. Zhang, H.S. Wang, K.Y. Yang, Cryst. Growth Des. 5 (2005) 807;
(e) S.R. Fan, L.G. Zhu, Acta Crystallogr. E61 (2005) m174;
(f) S.R. Fan, G.Q. Cai, L.G. Zhu, H.P. Xiao, Acta Crystallogr. C61 (2005) m177;
(g) S.R. Fan, L.G. Zhu, Chin. J. Inorg. Chem. 23 (2005) 1292.

[7] (a) S.R. Fan, H.P. Xiao, L.G. Zhu, Acta Crystallogr. E62 (2006) m18;
(b) B. Liu, Z.J. Wang, S.P. Huang, B.S. Yang, Acta Crystallogr. E62 (2006) m608;
(c) S.R. Fan, L.G. Zhu, Acta Crystallogr. E61 (2005) m2080;
(d) S.R. Fan, L.G. Zhu, H.P. Xiao, Acta Crystallogr. E61 (2005) m804;
(e) F.F. Li, J.F. Ma, S.Y. Song, J. Yang, Cryst. Growth Des. 1 (2006) 209;
(f) Z.D. Lu, L.L. Wen, J. Yao, Z.Z. Zhu, Q.J. Meng, CrystEngCommun (2006) 847;
(g) S.R. Fan, L.G. Zhu, Inorg. Chem. 45 (2006) 7935.

[8] P.V. Khadikar, S. Joshi, S.G. Kashkhedikar, B.D. Heda, Indian J. Pharm. Sci. 46 (1984) 209, and references therein.

[9] (a) X.L. Wang, C. Qin, E.B. Wang, L. Xu, Z.M. Su, C.W. Hu, Angew. Chem., Int. Ed. 43 (2004) 5036;
(b) B.H. Ye, M.L. Tong, X.M. Chen, Coord. Chem. Rev. 249 (2005) 545.

[10] U.W. Grummt, E. Birckner, E. Klemm, D.A.M. Egbe, B. Heise, J. Phys. Org. Chem. 13 (2000) 112.

[11] G.M. Sheldrick, SHELXS97, Program for Crystal Structure Refinement, University of Göttingen, Göttingen, Germany, 1997.

[12] A.L. Spek, PLATON, Molecular Geometry Program, University of Utrecht, The Netherlands, 1999.

[13] (a) I.I. Mathews, H. Manohar, J. Chem. Soc., Dalton Trans. (1991) 2139;
(b) G.A. van Albada, I. Mutikainen, O. Roubeau, U. Turpeinen, J. Reedijk, Inorg. Chem. Acta 331 (2002) 208;
(c) R.L. Lindtvedt, M.D. Glick, B.K. Tomolovic, D.P. Gavel, J.M. Kuszaj, Inorg. Chem. 15 (1976) 1633;
(d) I. Katharina, F. Patrick, A. Christina, B. Gérald, D. Silvio, F.W. Alan, Inorg. Chem. 44 (2005) 3896;
(e) S.H. Gou, M. Qian, Z. Yu, C.Y. Duan, X.F. Sun, W. Huang, J. Chem. Soc., Dalton Trans. (2001) 3232;
(f) Y.Q. Zheng, J.L. Lin, Z. Anorg. Allg. Chem. 628 (2002) 203.

[14] H.F. Zhu, J. Fan, T.A. Okamura, Z.H. Zhang, G.X. Liu, K.B. Yu, W.Y. Sun, N. Ueyama, Inorg. Chem. 45 (2006) 3941.

[15] C. Baes, R.E. Mesmer, The Hydrolysis of Cations, Krieger Publishing Company, Malabar, FL, 1986.

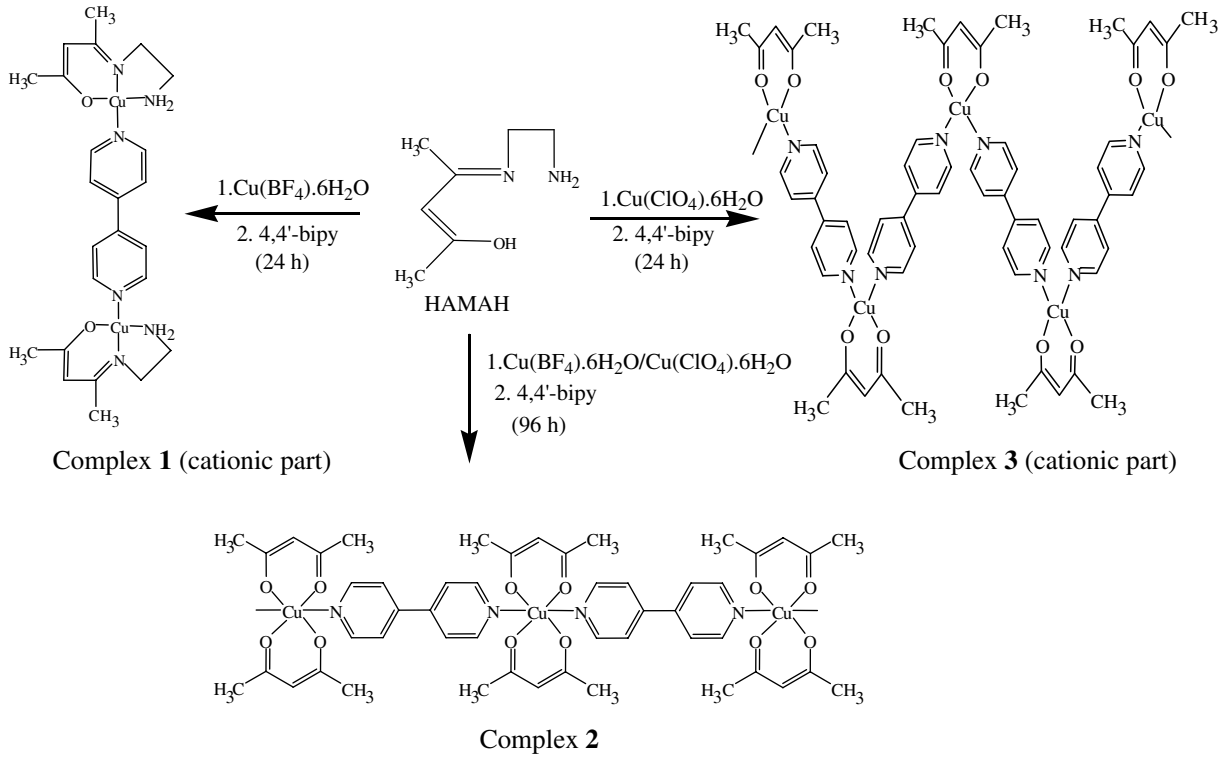
[16] J.P. Jolivet, De la Solution a L'oxyde, Intereditions/CNRS Editions, Paris, France, 1994.

[17] (a) P.U. Maheswari, B. Modec, A. Pevec, B. Kozlevčar, C. Massera, P. Gamez, J. Reedijk, Inorg. Chem. 45 (2006) 6637;
(b) I.A. Gural'skiy, P.V. Solntsev, H. Krautscheid, K.V. Domasevitch, Chem. Commun. (2006) 4808.

[18] W.G. Lu, L. Jiang, X.L. Feng, T.B. Lu, Cryst. Growth Des. 2 (2005) 564.

[19] X. Shi, G.S. Zhu, X.H. Wang, G.H. Li, Q.R. Fang, G. Wu, G. Tian, M. Xue, X.J. Zhao, R.W. Wang, S.L. Qiu, Cryst. Growth Des. 1 (2005) 207.

[20] X. Shi, G.S. Zhu, Q.R. Fang, G. Wu, G. Tian, R.W. Wang, D.L. Zhang, M. Xue, S.L. Qiu, Eur. J. Inorg. Chem (2004) 185.



Scheme 1.

with 4,4′-bipyridine for the synthesis of di- or poly-nuclear complexes.

Here, we report the synthesis and crystal structure of a di-nuclear copper(II) complex using HAMAH and 4,4′-bipyridine. During the synthesis, the Schiff base ligand undergoes hydrolysis. Hydrolysis of Schiff bases containing acetylacetone is considered as a common problem in the synthesis of their complexes and sometimes leads to the formation of different Schiff base complexes than are expected [6]. However, to our knowledge no attempt has previously been made to characterize structurally the non-Schiff base complexes that are formed as the result of hydrolysis. In the present work, we have isolated two different Cu(II) compounds containing acetylacetone and 4,4′-bipyridine in the course of hydrolytic reaction. A crystal structure determination reveals that one of the complexes, $[\{Cu(acac)(CH_3OH)(\mu\text{-}4,4'\text{-bipy})\}(ClO_4)]_n$ (**3**) possesses a zigzag chain structure although its benzoylacetone analogue is a discrete tetranuclear species [7]. In this paper, we also put forward for the first time a probable explanation for the different shape and size of the thermodynamically stable polynuclear complexes that are formed by Cu(II) and 4,4′-bipyridine.

2. Experimental

2.1. Reagents

All chemicals were commercial products of reagent grade and used without further purification.

Caution! Although no problems were encountered in this work, perchlorate salts containing organic ligands are potentially explosive. They should be prepared in small quantity and handled with great care.

2.2. Preparations

2.2.1. Synthesis of the tridentate ligand 7-amino-4-methyl-5-aza-3-hepten-2-one (HAMAH)

The ligand HAMAH was prepared as viscous oil following the literature method [5,8] using 1,2-diaminoethane and acetylacetone (acac).

2.2.2. Synthesis of $[\{Cu(AMAH)\}_2(\mu\text{-}4,4'\text{-bipy})](BF_4)_2$ (**1**) and $[Cu(acac)_2(\mu\text{-}4,4'\text{-bipy})]_n$ (**2**)

A solution of $Cu(BF_4)_2 \cdot 6H_2O$ (5 mmol, 1.726 g) in methanol (5 cm^3) was added to a solution of HAMAH (5 mmol) in methanol (10 cm^3) followed by the addition of methanol solution (10 cm^3) of 4,4′-bipyridine (2.5 mmol, 0.391 g). The mixture was stirred for about half an hour and filtered to remove a small amount of precipitate that appeared immediately. The filtrate was left at room temperature. Overnight, reddish-blue single crystals of **1**, suitable for X-ray diffraction were obtained.

After separation of the crystals of compound **1**, the filtrate was left for several days for slow evaporation of the methanol. The solution became concentrated and dark green in color. However, no more crystals of **1** appeared in this period. After about 4 days crystalline compounds

of **2** were obtained in good yield. Some of these crystals were of diffraction quality.

Complex ***1***: Yield: 0.35 g (19%). *Anal.* Calc. for $C_{24}H_{34}B_2Cu_2F_8N_6O_2$: C, 38.99; H, 4.64; N, 11.37; Cu, 17.19. Found: C, 38.78; H, 4.8; N, 11.19; Cu, 17.42%. UV–Vis spectrum, λ_{max} (nm), [ε_{max} ($dm^3\,mol^{-1}\,cm^{-1}$)] (methanol): 610 (187), 318 (11943), 274 (9329); $\mu_{eff} = 1.77$ BM (per copper ion). IR (KBr, cm^{-1}): 3349 and 3295 cm^{-1} for $\nu(NH_2)$; 1521 cm^{-1} for $\nu(C{=}N)$; 1075 cm^{-1} for $\nu(BF_4^-)$.

Complex ***2***: Yield: 0.48 g (46%). *Anal.* Calc. for $C_{20}H_{22}CuN_2O_4$: C, 57.47; H, 5.31; N, 6.7O; Cu, 15.20. Found: C, 57.25; H, 5.45; N, 6.83; Cu, 15.16%. UV–Vis spectrum, λ_{max} (nm), [ε_{max} ($dm^3\,mol^{-1}\,cm^{-1}$)] (methanol): 852 (25), 637 (98), 293 (9478); $\mu_{eff} = 1.77$ BM.

2.2.3. Synthesis of [{Cu(acac)(CH$_3$OH)(μ-4,4′-bipy)}-(ClO$_4$)]$_n$ (3)

Compound **3** was obtained in a similar way as **1**, but $Cu(ClO_4)_2 \cdot 6H_2O$ was used instead of $Cu(BF_4)_2 \cdot 6H_2O$. A solution of $Cu(ClO_4)_2 \cdot 6H_2O$ (5 mmol, 1.852 g) in methanol (5 cm^3) was added to a solution of HAMAH (5 mmol) in methanol (10 cm^3) followed by the addition of methanol solution (10 cm^3) of 4,4′-bipyridine (2.5 mmol, 0.391 g). The mixture was stirred for about half an hour and filtered to remove a small amount of precipitate that appeared immediately. Overnight, the filtrate yielded **3** as a green crystalline compound which was separated by filtration. The filtrate on being concentrated in open atmosphere yielded compound **2** in several days.

Yield: 0.54 g (48%). *Anal.* Calc. for $C_{16}H_{18}ClCuN_2O_7$: C, 42.77; H, 4.04; N, 6.23; Cu, 14.14. Found: C, 42.69; H, 4.11; N, 6.37; Cu, 14.06%. UV–Vis spectrum, λ_{max} (nm), [ε_{max} ($dm^3\,mol^{-1}\,cm^{-1}$)] (methanol): 729 (74), 303 (21234); $\mu_{eff} = 1.77$ BM. IR (KBr, cm^{-1}): 3438 cm^{-1} for ν(O–H); 1094 cm^{-1} for $\nu(ClO_4^-)$.

2.3. Physical measurements

Elemental analyses (carbon, hydrogen and nitrogen) were performed using a Perkin–Elmer 240C elemental analyzer. IR spectra in KBr (4500–500 cm^{-1}) were recorded using a Perkin–Elmer RXI FT-IR spectrophotometer. Electronic spectra in acetonitrile (1200–350 nm) were recorded in a Hitachi U-3501 spectrophotometer. The magnetic susceptibility measurements were done with an EG & PAR vibrating sample magnetometer, model 155, at room temperature and diamagnetic corrections were made using Pascal's constants. The thermal analyses (TGA–DTA) were carried out on a Mettler Toledo TGA/STDA 851 thermal analyzer in a dynamic atmosphere of dinitrogen (flow rate: 30 $cm^3\,min^{-1}$). The samples were heated in an alumina crucible at a rate of 10 °C min^{-1}.

2.4. X-ray crystallography

Crystal data and refinement details for **1** and **3** are given in Table 1. Intensity data were measured via the Oxford X-Calibur CCD System using Mo Kα radiation. The crystals were positioned at 50 mm from the CCD. 321 frames were measured with a counting time of 3 s. Data analyses were carried out with the CRYSALIS program [9]. The structures were solved using direct methods with the SHELX-97 program [10]. The non-hydrogen atoms were refined with anisotropic thermal parameters. The hydrogen atoms bonded to carbon were included in geometric positions and given thermal parameters equivalent to 1.2 times those of the atom to which they were attached. Empirical absorption corrections were carried out using the ABSPACK program [11]. The structures were refined on F^2 using SHELX-97.

Table 1
Crystal data and refinement details of complexes **1** and **3**

Compound	**1**	**3**
Formula	$C_{24}H_{34}B_2Cu_2F_8N_6O_2$	$C_{16}H_{18}ClCuN_2O_7$
Formula weight	739.28	449.31
Temperature (K)	150	150
Space group	$P2_1/n$	$P\bar{1}$
Crystal system	monoclinic	triclinic
Crystal size (mm)	$0.30 \times 0.05 \times 0.05$	$0.30 \times 0.05 \times 0.05$
a (Å)	8.345(1)	8.580(1)
b (Å)	10.178(1)	9.008(1)
c (Å)	17.519(2)	12.325(2)
α (°)	(90)	83.53(1)
β (°)	95.24(1)	75.27(1)
γ (°)	(90)	79.47(1)
V (Å^3)	1481.8(2)	903.5(2)
Z	2	2
D_{calc} (g/cm^3)	1.657	1.652
μ (mm^{-1})	1.520	1.399
F (000)	752	460
Total reflections	10080	6289
Unique reflections	4316	5013
Observed data ($[I > 2\sigma(I)]$	3130	3311
Number of parameters refined	205	244
R_{int}	0.021	0.0755
R indices (all data)	$R_1 = 0.0481$, $wR_2 = 0.1003$	$R_1 = 0.0801$, $wR_2 = 0.1830$
R indices $[I > 2\sigma(I)]$	$R_1 = 0.0324$, $wR_2 = 0.0966$	$R_1 = 0.0621$, $wR_2 = 0.1727$

3. Results and discussion

3.1. Synthesis of the complexes

It is well known that the tridentate Schiff base, HAMAH reacts readily with Cu(II) to occupy its three coordination sites whereas several anionic or neutral ligands can be coordinated to the fourth coordination site to yield different type of complexes [5]. Thus there is a possibility that the two ends of a 4,4′-bipyridine molecule can join two $[Cu(AMAH)]^+$ units and with this expectation, we added HAMAH to a methanol solution of Cu(II) perchlorate followed by 4,4′-bipyridine. On keeping the mixture overnight, a crystalline compound, $[\{Cu(acac)(CH_3OH)(\mu\text{-}4,4'\text{-bipy})\}(ClO_4)]_n$ (**3**)

resulted (Scheme 1). After separation of the compound, the filtrate was kept at open atmosphere when its color changed to deep green and finally yielded the crystalline compound $[Cu(acac)_2(\mu\text{-}4,4'\text{-bipy})]_n$ (**2**) in a few days. The reactions clearly show that the Schiff base undergoes hydrolysis in the reaction conditions. Previously, it was observed that when a proton is liberated from the Schiff base during complex formation, then this causes the hydrolysis of Schiff base ligands [6]. In the present case use of triethyl amine or any other base to neutralise the reaction mixture in an attempt to prevent the hydrolysis, however, resulted in the formation of the hydroxo-bridged trinuclear complex, $[\{Cu(AMAH)\}_3OH]^{2+}$ [5b]. To synthesize the desired 4,4′-bipyridine bridged Cu(II) containing unhydrolyzed Schiff base, we changed the counter anion of the copper salt to BF_4^- and were able to obtain the complex $[\{Cu(AMAH)\}_2(\mu\text{-}4,4'\text{-bipy})](BF_4)_2$ (**1**). Interestingly, if the crystals of **1** are not separated from mother liquor after ca. 24 h, they start to dissolve and after several days compound **2** is formed, indicating that **1** is hydrolyzed in the reaction medium. The isolation of **1** with BF_4^- counter ion but not with ClO_4^- may be due to the slight difference in the solubility of the complexes in methanol.

3.2. Crystal structures of complexes *1* and *3*

All three complexes have been characterized by single crystal X-ray analysis. However, the crystal structure of **2** has been reported previously [12]. Therefore, we report here only the structure of complexes **1** and **3**. Structural data for **2** are given in Supplementary material.

3.2.1. Complex *1*

An ORTEP view of **1** is shown in Fig. 1. Table 2 shows the selected bond lengths and angles. The structure of **1** contains discrete dimeric cations and BF_4^- anions. The centrosymmetic dimeric structure of **1** shows a planar 4,4′-bipyridine ligand bridging two copper atoms with a Cu(1)–N(21) distance of 2.026(2) Å. In addition, each copper atom is bonded to three atoms of the ligand, with the two nitrogen atoms N(15) at 1.930(2) Å and N(18) at 2.005(2) Å and an oxygen O(18) at 1.888(1) Å. The metal coordination sphere is approximately square planar with the CuN_3O equatorial plane. The sum of the four angles around the Cu atom is 363.3° indicating the slightly distorted square-planer geometry around the metal atom. The distortion may also conveniently be measured by the *trans* angles that are ideally 180° for a square-planar complex and 109.5° in a tetrahedral complex. In complex **1**, the *trans* angles are found to be 165.85(8)° (O11–Cu1–N18) and 166.14(7)° (N15–Cu1–N21). Deviations of the coordinating atoms O11, N15, N18, N21 from the least-square mean plane through them are 0.239(1), −0.247(1), 0.233(1), −0.2259(1) Å, respectively, and that of copper atom from the same plane is 0.001(1) Å. The 4,4′-bipyridine ligand intersects the equatorial plane at an angle of 34.0(1)°. The acetyl acetone ring around the metal ion is essentially planar. The Cu···Cu separation in the dimeric unit is 11.12 Å. The five-membered ring Cu(1)–N(15)–C(16)–C(17)–N(18) has an envelope conformation on C(17) with puckering parameters $Q(2) = 0.427(2)$ and $\phi(2) = 106.9(2)°$ [13]. The closest contact between the copper atom and the anion is 2.94 Å to F(13) in an axial position but this cannot be considered to be other than van der Waals interaction.

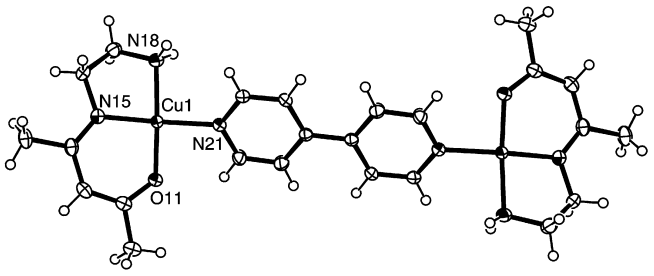


Fig. 1. The structure of the dimeric cation of **1** with ellipsoids at 25% probability.

Table 2
Selected bond lengths (Å) and bond angles (°) for complex **1**

Bond lengths (Å)	
Cu(1)–N(15)	1.930(2)
Cu(1)–O(11)	1.888(2)
Cu(1)–N(18)	2.005(2)
Cu(1)–N(21)	2.026(2)
Bond angles (°)	
O(11)–Cu(1)–N(15)	94.10(7)
O(11)–Cu(1)–N(18)	165.85(8)
N(15)–Cu(1)–N(18)	85.22(7)
O(11)–Cu(1)–N(21)	89.30(6)
N(15)–Cu(1)–N(21)	166.14(7)
N(18)–Cu(1)–N(21)	94.72(7)

In complex **1**, a 2-D hydrogen bonded sheet structure with rectangular channels along the *b*-direction is formed. The uncoordinated tetrafluoroborate anions play a significant role in the H-bonding and function as a bridge connecting two neighboring Cu(II) dimeric units. Both hydrogen atoms on the amine nitrogen (N18) form hydrogen bonds to F14 of the counter tetrafluoroborate anion (Table 3). However, while H181 is directed towards F14 at x, y, z, H182 is directed towards F14 at symmetry element $3/2 - x, -1/2 + y, 3/2 - z$) thus leading to the formation of a 1-D zigzag H-bonded structure (Fig. 2a). These 1-D zigzag H-bonded chains are further linked to each other

Table 3
Hydrogen bonding distances (Å) and angles (°) for the complex **1**

D–H···A	D–H (Å)	D···A (Å)	A···H (Å)	∠D–H···A (°)
N18–H181···F14	0.87(2)	2.13(2)	2.95(3)	157(2)
N18–H182···F14′	0.83(2)	2.21(3)	2.95(2)	148(2)

Symmetry element ′: $3/2 - x, y - 1/2, 3/2 - z$.

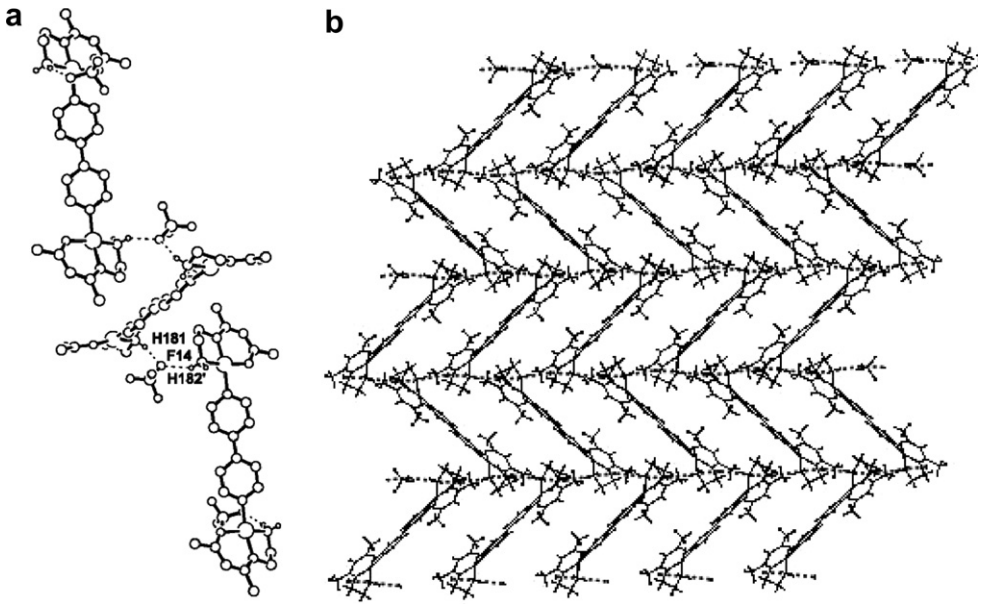


Fig. 2. Extended hydrogen-bonding network in complex **1**.

through hydrogen-bonding interactions via centrosymmetrically related fluorine and hydrogen atoms to form the final 2-D hydrogen-bonded rectangular grid network (Fig. 2b) with dimensionality of 10.178 Å × 12.208 Å.

3.2.2. Complex *3*

An ORTEP view of compound **3** together with the atom-numbering scheme is shown in Fig. 3. Selected bond lengths and angles are summarized in Table 4. The structure of **3** is a one-dimensional polymer with $[\{Cu(acac)(CH_3OH)(\mu\text{-}4,4'\text{-bipy})\}_n]^{n+}$ cations in which the metal centres are bridged via 4,4′-bipyridyl units and discrete perchlorate anions. Each copper atom has a square pyramidal five-coordinate environment with O(35) from a methanol molecule in an axial position. The equatorial plane consists of two *cis*-coordinated 4,4′-bipyridine ligands and two oxygen atoms of the acac moiety. The deviations of the equatorially coordinating four donor atoms N(11), N(21), O(31), O(315) from the least-square mean plane through them are −0.040(4), 0.044(4), −0.047(3), −0.044(3) Å, respectively. The copper atom is displaced 0.12 Å from the plane towards the epically coordinated oxygen (O35) of the methanol molecule as is usual for square-pyramid structures. Each 4,4′-bipyridine ligand links adjacent $[Cu(acac)(CH_3OH)]^+$ units, which gives rise to the 1-D zigzag chain. The two independent 4,4′-bipyridine ligands are perforce planar with the centres positioned on crystallographic centres of symmetry. The two ligands intersect the equatorial plane of the metal at angles of 17.4(2)° and 59.2(2)°, respectively. Bond lengths are within expected ranges, Cu(1)–O(31) 1.919(3) Å, Cu(1)–O(315) 1.920(3) Å, Cu(1)–N(11) 2.032(3) Å, Cu(1)–N(21) 2.038(3) Å with the axial bond Cu(1)–O(35) at 2.313(3) Å. The Cu···Cu separation is 11.16 Å. There is a slight distortion of the square pyramidal environment of copper atom towards trigonal bipyramid geometry as is evident form its Addition parameter ($\tau = 0.046$) [14].

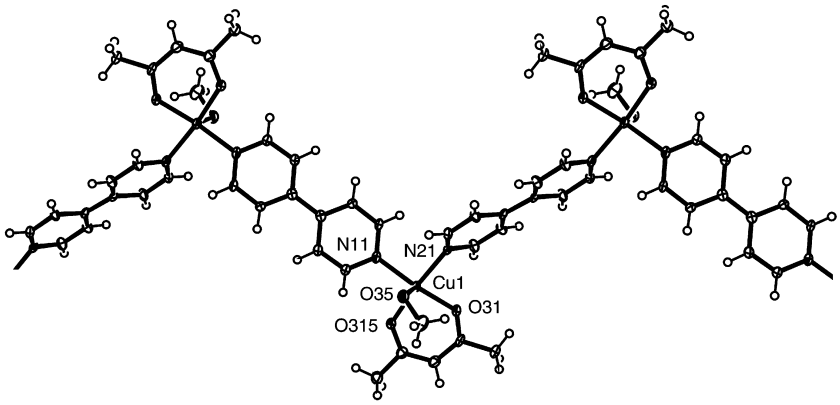


Fig. 3. The structure of **3** with ellipsoids at 25% probability.

Table 4
Selected bond lengths (Å) and bond angles (°) for complex **3**

Bond lengths (Å)	
Cu(1)–O(31)	1.919(3)
Cu(1)–O(35)	2.313(3)
Cu(1)–O(315)	1.920(3)
Cu(1)–N(11)	2.032(3)
Cu(1)–N(21)	2.038(3)
Bond angles (°)	
O(31)–Cu(1)–O(315)	91.9(1)
O(31)–Cu(1)–N(11)	169.9(1)
O(315)–Cu(1)–N(11)	91.0(1)
O(31)–Cu(1)–N(21)	81.9(1)
O(315)–Cu(1)–N(21)	172.6(1)
N(11)–Cu(1)–N(21)	94.5(1)
O(31)–Cu(1)–O(35)	100.1(1)
O(315)–Cu(1)–O(35)	91.9(1)
N(11)–Cu(1)–O(35)	89.5(1)
N(21)–Cu(1)–O(35)	93.1(1)

3.3. Discussion

The bifunctional ligand, 4,4′-bipyridine has extensively been used to link the metal ions by coordination driven self-assembly to form discrete 2-D and 3-D species with well defined shape and sizes [15]. It is well established that square planar Pt(II) and Pd(II) in which two *cis* positions are occupied by blocking ligands, act as 90° acceptor units and that a 180° donor unit, e.g. 4,4′-bipyridine on reaction with such acceptor units forms a self-assembled molecular square. First row transition metal ions, on the other hand, mostly produce dimers or one- to three-dimensional extended structures with 4,4′-bipyridine. Apparently, it seems that unlike Pt(II) and Pd(II), the shape, size and structure of such self-assembled species cannot be predicted. We attempt here to rationalize the formation of thermodynamically stable polynuclear complexes of Cu(II) containing 4,4′-bipyridine.

The reported complexes of Cu(II) containing 4,4′-bipyridine reveal that a wide variety of structures can be obtained ranging from discrete dinuclear species to 3-D polymers. Cu(II) being a d^9 system is liable to undergo Jahn–Teller distortion resulting in a (4 + 2) coordination. The strong field ligands coordinate to the four equatorial sites leaving the two axial positions to be occupied by weakly coordinating ligands (e.g. solvent molecules). Therefore, the number of coordination sites of the blocking ligands and their crystal field strength are very important for the nuclearity and shape of resulted species. 4,4′-Bipyridine being a strong field ligand prefers to occupy the equatorial position of the Cu(II). However, if the blocking ligands are stronger field than the 4,4′-bipyridine and thus occupy all four equatorial positions, it may be forced to coordinate to the axial position(s) [16]. When there is a tridentate blocking ligand in the equatorial position, then 4,4′-bipyridine usually coordinates to the remaining fourth position of two units to result in the formation of a dinuclear entity in almost all cases [17]. On the contrary, when two *cis* positions of the equatorial plane are available for its coordination, either a zigzag chain [1q,18] (as is found in compound **3**) or a molecular square as in Pt(II) and Pd(II) complexes may result [19]. Four such complexes are reported and it is found that only one is a molecular square whereas the other three are infinite chains [1q,18]. Therefore, a chain structure seems to be preferred for Cu(II) in contrast to finite supra-molecules which are preferred for 2nd or 3rd row transition metals [15]. In this context, it is worthwhile to compare the structure of **3** with that of the reported molecular square as the blocking ligand in both cases is very similar – acetylacetonate in **3** and 1-benzolyacetonate in the square [7]. The bond angles and distances of the two compounds are also very similar. The only significant difference is found in *cis*-O–Cu–N angles. In **3** the two bipy ligands intersect the equatorial plane of the metal at angles of 17.4(2)° and 59.2(2)°, respectively, which is responsible for the two very different N–Cu–O *cis* angles, 81.9(1)° and 91.0(1)°. The steric repulsion between the phenyl group and the adjacent bipyridine ligand as well as the smaller difference of the angle between the 4,4′-bipy ring and the equatorial plane in the square widens one O–Cu–N angle appreciably to 86.2(1)° which in turn decreases the other *cis*-O–Cu–N angle 88.0(1)° [7]. The angle subtended by the two donor nitrogen atoms in the two *cis*-4,4′-bipyridine moieties is 93.3(1)° in the square compared to 94.5(1)° in **3**. These small differences seem responsible for the drastic variation in the supra-molecular structure of the two compounds.

It is to be mentioned here that this rationalization is made considering the formation of only thermodynamically stable products which may well not be the case – kinetic products of lower solubility can preferentially crystallize and make the situation complicated. However, in most cases it is found that for the coordination driven self-assembly the thermodynamically controlled product is the only one that is finally formed in high yield [15,18].

3.4. Thermal analysis

The thermo-gravimetric analysis of the complex **3** shows that a weight loss of 6.8% takes place in the temperature range 35–60° corresponding to the loss of methanol molecule (calculated 7.1%). The heated species neither shows any change in color nor absorbs any water molecule on keeping in open atmosphere. In its IR spectra there is no band at ca. 3400 cm^{-1} confirming the elimination of methanol molecule.

4. Conclusions

The tridentate Schiff base ligand, HAMAH reacts with copper(II) to occupy its three equatorial positions. A 4,4′-bipyridine ligand coordinates to the fourth equatorial position of two copper units to yield the dimeric species **1**. The isolation of such dimeric species in the solid state, however, is dependent on the counter anion. As is found

in this study, the BF_4^- ion allows the separation of the complex from the reaction mixture but ClO_4^- does not although they have very similar geometry. Compound **1** is susceptible to hydrolysis in the reaction medium and the acetylacetone moiety that is one of the hydrolysis products coordinates to Cu(II) and along with 4,4′-bipyridine yields two different one-dimensional chain compounds **2** and **3**. In **2**, the two chelating acetylacetonate moieties being stronger field ligand, occupy the equatorial plane. The 4,4′-bipyridine molecule then coordinates weakly to the axial positions to form the linear chain. On the contrary, in **3** only one acetylacetonate is found and two equatorial positions are therefore blocked making it a 90° acceptor and hence a very good candidate for the formation of a molecular square with a linear donor such as 4,4′-bipyridine. However, the crystal structure of **3** shows that it is a one-dimensional chain compound although the closely related benzoylacetonate analogue with Pd(II) is a molecular square. Thus, unlike the more straightforward chemistry of Pt(II) and Pd(II) complexes, prediction of the size and shape of any supra-molecular assembly involving Cu(II) is more difficult as small changes in electronic or steric factors can lead to very different structures. Nevertheless, the rationalization of the formation of different polynuclear structures on the basis of coordination sites and crystal field strength of the blocking ligands and the Jahn–Teller effect present in Cu(II) center would be helpful to design the coordination polymers of such systems.

Acknowledgments

This work was supported by the University Grants Commission (UGC), India (Fellowship for C. Biswas, Sanction No. UGC/29/Jr. Fellow (S.C.). 2005/2006). We thank EPSRC and the University of Reading for funds for the X-Calibur system.

Appendix A. Supplementary material

CCDC 641000, 641001 and 641002 contain the supplementary crystallographic data for **1**, **2** and **3**. These data can be obtained free of charge via http://www.ccdc.cam.ac.uk/conts/retrieving.html, or from the Cambridge Crystallographic Data Centre, 12 Union Road, Cambridge CB2 1EZ, UK; fax: (+44) 1223-336-033; or e-mail: deposit @ccdc.cam.ac.uk. Supplementary data associated with this article can be found, in the online version, at doi:10.1016/j.poly.2007.05.034.

References

[1] (a) K.B. Yu, S.H. Gou, X.Z. You, Acta Crystallogr., Sect. C 47 (1991) 2653;
(b) S.H. Gou, X.Z. You, Z. Xu, Acta Crystallogr., Sect. C 47 (1991) 1303;
(c) J. Lu, G. Crisci, T. Niu, J. Jacobson, Inorg. Chem. 36 (1997) 5140;
(d) C. Chen, D. Xu, Y. Xu, C. Cheng, Acta Crystallogr., Sect. C 48 (1992) 1231;
(e) M. Fuijita, Y.J. Kwon, S. Washizu, K. Ogura, J. Am. Chem. Soc. 116 (1994) 1325;
(f) J. Lu, T. Paliwala, S.C. Lim, C. Yu, T.Y. Niu, A.J. Jacobson, Inorg. Chem. 36 (1997) 923;
(g) L.R. MacGillivray, S. Subramanian, J. Zaworatko, J. Chem. Soc., Chem. Commun. (1995) 1325;
(h) S. Subramanian, M.J. Zaworatko, Angew. Chem., Int. Ed. Engl. 34 (1995) 2127;
(i) L. Carlucci, G. Ciani, D.M. Proserpio, A. Sironi, Angew. Chem., Int. Ed. Engl. 1995 (1895) 34;
(j) R.W. Gable, B.F. Hoskins, R. Robson, J. Chem. Soc., Chem. Commun. (1990) 1677;
(k) O.M. Yaghi, H. Li, T.L. Groy, Inorg. Chem. 36 (1997) 4292;
(l) O.M. Yaghi, H.L. Li, J. Am. Chem. Soc. 118 (1996) 295;
(m) F. Robinson, M.J. Zaworotko, J. Chem. Soc., Chem. Commun. (1995) 2413;
(n) L. Carlucci, G. Ciani, D.M. Proserpio, A. Sironi, J. Chem. Soc., Chem. Commun. (1994) 2755;
(o) M. Fujita, O. Sasaki, T. Mitsuhashi, T. Fujita, J. Yazaki, K. Yamaguchi, K. Ogura, J. Chem. Soc., Chem. Commun. (1996) 1535;
(p) R.V. Slone, J.T. Up, C.L. Stern, T.E. Albercht-Schmitt, Inorg. Chem. 35 (1996) 4096;
(q) H.W. Park, S.M. Sung, K.S. Min, H. Bang, Eur. J. Inorg. Chem. (2001) 2857.
[2] (a) V. Tudor, V. Kravtsov, M. Julve, F. Lloret, Y.A. Simonov, J. Lipkowski, V. Buculie, M. Andruh, Polyhedron 20 (2001) 3033;
(b) M.L. Tong, H.K. Lee, X.M. Chen, R.B. Huang, T.C.W. Mak, J. Chem. Soc., Dalton Trans. (1999) 3657;
(c) M. Andruh, H.W. Roesky, M. Noltemeyer, H.G. Schmidt, Z. Naturforsch. B 49 (1994) 31;
(d) K. Biradha, M. Fujita, Chem. Commun. (2001) 15;
(e) Q. Wang, X. Wu, W. Zhang, T. Sheng, P. Lin, J. Li, Inorg. Chem. 38 (1999) 2223.
[3] (a) L.G. Zhu, S. Kitagawa, H. Miyasaka, H.C. Chang, Inorg. Chim. Acta 355 (2003) 121;
(b) S. Noro, R. Kitaura, M. Kondo, S. Kitagawa, T. Ishii, H. Matsuzaka, M. Yamashita, J. Am. Chem. Soc. 124 (2002) 2568;
(c) S. Noro, R. Kitaura, M. Kondo, K. Seki, Angew. Chem., Int. Ed. 39 (2000) 2081;
(d) S. Kitagana, M. Kondo, Bull. Chem. Soc. Jpn. 71 (1998) 1739;
(e) Y.B. Dong, R.C. Layland, N.G. Pschirer, M.D. Smith, U.H.F. Bunz, H.C. Loye, Chem. Mater. 11 (1999) 1413;
(f) O.M. Yaghi, H.L. Li, C. Davis, D. Richardson, T.L. Groy, Acc. Chem. Res. 31 (1998) 474.
[4] V. Tudor, V. Kravtsov, M. Julve, F. Lloret, Y.A. Simonov, J. Lipkowski, V. Buculei, M. Andruh, Polyhedron 20 (2001) 3033.
[5] (a) M.S. Ray, A. Ghosh, R. Bhattacharya, G. Mukhopadhyay, M.G.B. Drew, J. Ribas, Dalton Trans. (2004) 252;
(b) J.P. Costes, F. Dahan, J.P. Laurent, Inorg. Chem. 25 (1986) 413;
(c) J.P. Costes, J.F. Serra, F. Dahan, J.P. Laurent, Inorg. Chem. 25 (1986) 2790.
[6] S. Chattopadhyay, M.S. Ray, S. Chaudhuri, G. Mukhopadhyay, G. Bocelli, A. Cantoni, A. Ghosh, Inorg. Chim. Acta 359 (2006) 1367.
[7] S.K. Dey, B. Bag, Z. Zhou, A.S.C. Chan, S. Mitra, Inorg. Chim. Acta 357 (2004) 1991.
[8] M.S. Ray, R. Bhattacharya, L. Right, G. Bocelli, S. Chaudhuri, G. Mukhopadhyay, A. Ghosh, Polyhedron 22 (2003) 617.
[9] CRYSALIS, Oxford Diffraction Ltd., Version 1, 2005.
[10] G.M. Sheldrick, SHELX-97: Program for Crystal Structure Calculations, University of Göttingen, Göttingen, Germany, 1997.
[11] ABSPACK, Oxford Diffraction Ltd., 2005.
[12] S. Shu, X. Yuanzhi, J. Huaxue, Chin. J. Struct. Chem. 4 (1985) 38.
[13] D. Cremer, J.A. Pople, J. Am. Chem. Soc. 97 (1975) 1354.
[14] A.W. Addison, T.N. Rao, J. Reedijk, J. van Rinj, C.G. Verscholar, J. Chem. Soc., Dalton Trans. (1984) 1349.
[15] (a) D.L. Caulder, K.N. Raymond, Acc. Chem. Res. 32 (1999) 975;
(b) F.A. Cotton, C. Lin, C.A. Murillo, Acc. Chem. Res. 34 (2001) 759;

(c) M. Fujita, Chem. Soc. Rev. 6 (1998) 417;
(d) S. Leininger, B. Olenyuk, P. Stang, J. Chem. Rev. 100 (2000) 853;
(e) S.R. Seidel, P.J. Stang, Acc. Chem. Res. 35 (2002) 972;
(f) G.F. Swiegers, T.J. Malefetse, Coord. Chem. Rev. 225 (2002) 91.
[16] (a) M.G.B. Drew, J.P. Naskar, S. Chowdhury, D. Datta, Theor. Anal. Chem. 42 (2003) 2531;
(b) M.X. Li, Z. Xu, X.Z. You, C.G. Chen, Acta Crystallogr., Sect. C 50 (1994) 1699.
[17] (a) D.A. Tocher, M.G.B. Drew, S. Chowdhury, P. Purkayastha, D. Datta, Indian J. Chem. A 42 (2003) 484;
(b) X.L. Liu, R. Zhao, X.H. Liu, J.J. Yue, Y.X. Yin, Y. Sun, X. Zhang, Chin. J. Chem. 21 (2003) 1047;
(c) M. Julve, M. Verdaguer, J. Faus, F. Tinti, J. Moratal, A. Monge, E.G. Puebla, Inorg. Chem. 26 (1987) 3520;
(d) B.Y. Lou, D.Q. Yuan, B.L. Wu, M.C. Hong, Acta Crystallogr., Sect. E 60 (2004) m1976.
[18] (a) V. Tudor, G. Marin, V. Kravtsov, Y.A. Simonov, J. Lipkowski, M. Brezeanu, M. Andruh, Inorg. Chim. Acta 353 (2003) 35;
(b) M.L. Tong, H.J. Chen, X.M. Chen, Inorg. Chem. 39 (2000) 2235.
[19] (a) M. Fujita, O. Sasaki, T. Mitsuhashi, T. Fujita, J. Yazaki, K. Yamaguchi, K. Ogura, J. Chem. Soc., Chem. Commun. (1996) 1535;
(b) P.J. Stang, D.H. Cao, S. Saito, A.M. Arif, J. Am. Chem. Soc. 117 (1995) 6273;
(c) S. Belanger, J.T. Hupp, C.L. Stern, R.V. Slone, D.F. Watson, T.G. Carrell, J. Am. Chem. Soc. 121 (1999) 557;
(d) D.E. Janzen, K.N. Patel, D.G. VanDerveerb, G.J. Grant, Chem. Commun. (2006) 3540.

particles using a simple modification of the well-known Tollen's reduction in the presence of SDS. Utilization of silver nano particles as anti-microbial agent is well established though the underlying mechanism behind the activity is still ambiguous. In this paper the most important aspect of the synthesized Ag nano particles is its high efficacy as anti-microbial agent against a range of harmful microbes [*Escherichia coli* (ATCC 10536), *Vibrio cholerae* (7), *Shigella flexneri* (80903), *Salmonella typhimurium* (NCTC 74) and three varieties of *Staphylococcus aureus* (ATCC 29737, ML 276 and ML 422)] with a very low MIC value (2 μg/ml) in aqueous solution. To the best of our knowledge such a low value of MIC showed by silver nano particles is unprecedented.

2. Experimental

2.1. Reagents

All the reagents were of analytical grade. $AgNO_3$ (Aldrich) was used as received. Sodium dodecyl sulphate (SDS), *m*-hydroxy benzaldehyde, ammonia were purchased from Merck and also used as received. De-ionized water was used throughout the reaction.

2.2. Instruments

The prepared samples were characterized by FESEM and EDAX analyzer (JEOL JSM-6700 F), X-ray Powder Diffractometer (Bruker D-8 Advance) and the UV–Vis spectra of the as prepared colloidal solutions was recorded in a Perkin–Elmer UV Lambda 25 spectrophotometer.

2.3. Synthesis of Ag nano particles and study of anti-microbial activity by Agar dilution technique

Silver nitrate solution {0.02 (M)} was prepared by dissolving the required amount of $AgNO_3$ in (1:1) ammonia. Similarly, the aldehyde solution and the surfactant solution having equal concentration to that of the silver nitrate solution were prepared in dehydrated ethanol and water, respectively. Then 1 ml silver nitrate solution was taken in a well-cleaned dry beaker; 1 ml SDS solution was added to it and was mixed well for a few minutes (5 min for each set) by continuous stirring.1 ml aldehyde solution was finally added to this mixture. A light yellow color appeared at room temperature (30 °C). The solution was heated on a water-bath and the temperature was noted. When the temperature of the solution reached 80 °C, the light yellow color of the solution started turning into deep yellow. Then the color gradually changed through yellowish brown (82 °C) to reddish brown (84 °C) and finally turned into brownish black (86 °C) (Fig. 1). On further increasing the temperature of the solution, no perceptible change in color was observed. It is interesting to note that the range of reduction temperature is nearly identical to that reported by Chu et al. [33] for the case of Au. The gradual change of color in this temperature range indicated the formation of Ag nano particles of different dimensions [34]. So we have continued our study by preparing five different set solutions at the above-mentioned temperatures (i.e. at 30, 80, 82, 84 and 86 °C).

The anti-microbial study was carried out with the Ag nano particles (i.e. prepared at 86 °C) by standard agar dilution technique [36]. In short: (i) different amounts of the Ag nano particles were dispersed in phosphate buffer to get colloidal suspension; (ii) agar powder was dissolved in ultra pure water under mild heating; (iii) the molten agar solution was mixed with the prepared suspension in culture plates; (iv) the plates were cooled to turn the mixture into hydrogel; (v) diluted bacterial suspensions were transferred to the wells of an inoculum-replicating apparatus which in turn was used to transfer the inocula to the series of culture plates including a control plate without silver nano particles; and (vi) the inoculum spots were allowed to dry at room temperature and then the plates were incubated at 35 °C in air for 18 h. Finally, growth was observed and MIC values were determined in each case.

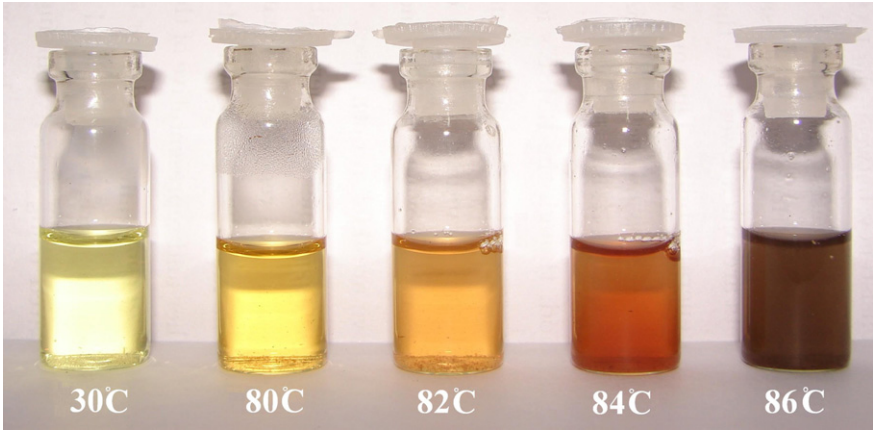


Fig. 1. The temperature-dependent color change during the progression of the reaction.

3. Results and discussion

3.1. FE-SEM analysis

Figs. 2–5 depict the SEM images of the samples obtained from the colloidal Ag solutions prepared at 80, 82, 84 and 86 °C. Fig. 2 is the SEM image of the sample prepared from the Ag colloidal solution of 80 °C that shows the existence of very few spherical nano particles. At 82 °C the SEM feature (Fig. 3A) clearly reveals the globular nano clusters in the diameter range 45–50 nm. This is the dominant morphology at this temperature, but a small number of stacked nano-disks could also be seen (Fig. 3B). Fig. 4A–D are the SEM images of the samples corresponding to 84 °C colloidal silver solution. In this temperature also the predominant morphology is the spherical nano-aggregates but the proportion of nano-disks is higher compared to the 82 °C sample. The overall morphological features are depicted in (Fig. 4A). An interesting feature of the globular nano-aggregates is its hierarchical growth nature from multiple nucleating centers leading to the 'cauliflower' like morphology of the whole spherical assembly (Fig. 4B). A minute proportion of triangular, truncated triangular nano-structures (Fig. 4C) could also be seen. In this temperature the nano-disks were ~90–120 nm long and ~54 nm in diameter. The SEM images for the sample, prepared from the colloidal solution at 86 °C are most interesting because of the equal proportion of spherical (3D) nano particles and flat nano-disks (2D) prevailing at this temperature (Fig. 5A–C). This figure that shows the overall feature of the sample at the micrometer level is a uniform distribution of disk-like structures interspersed with 'cauliflower'-like globular aggregates. The disks in the SEM image have been obtained as edge on and face on. It is to be noted that the width of individual disk is in the range 45–50 nm and they could be grown as long as a few micrometers in diameter (Fig. 5B). The spherical nano-globules have dimensions as large as 260 nm, but are composites of smaller spherical nano particles, which become as small as 15 nm (Fig. 5B and C). A 'cauliflower'-like morphology (Fig. 5C) is due to the hierarchical growth of spherical nano particles of different diameters simultaneously from different nucleating centers that are positioned very close to each other and ultimately form larger globular aggregates of different diameters. A closer look at the SEM images (Fig. 5B) also reveals that the nano-disks are not monolithic; they are composed of smaller plates which join edge on to form a disk of larger diameter.

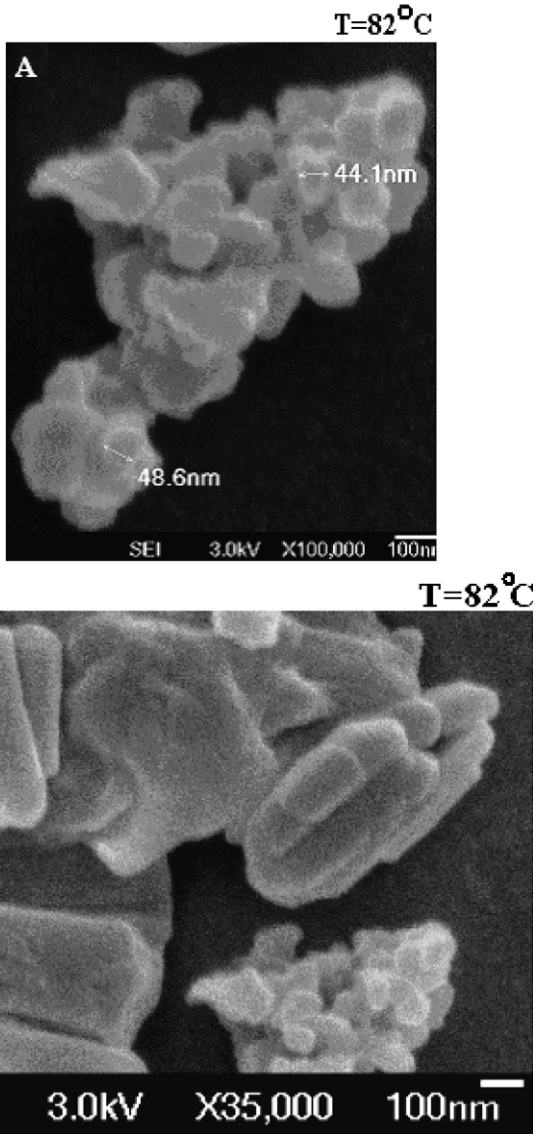


Fig. 3. Aggregated Ag nano particles (A) and Stacked nano-plates (B).

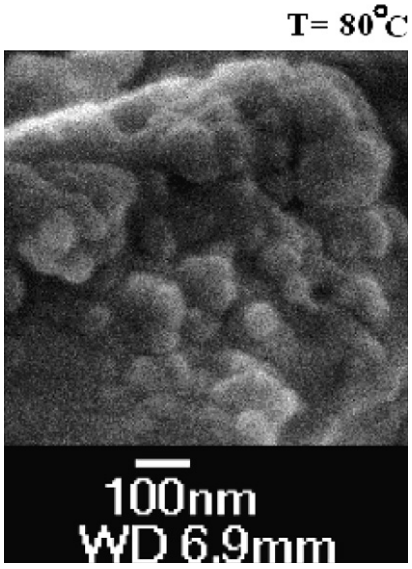


Fig. 2. Beginning of clusterization of spherical nano particles.

3.2. EDAX analysis

The purity of the prepared sample was determined by the energy dispersive X-ray analysis (EDAX). The EDAX

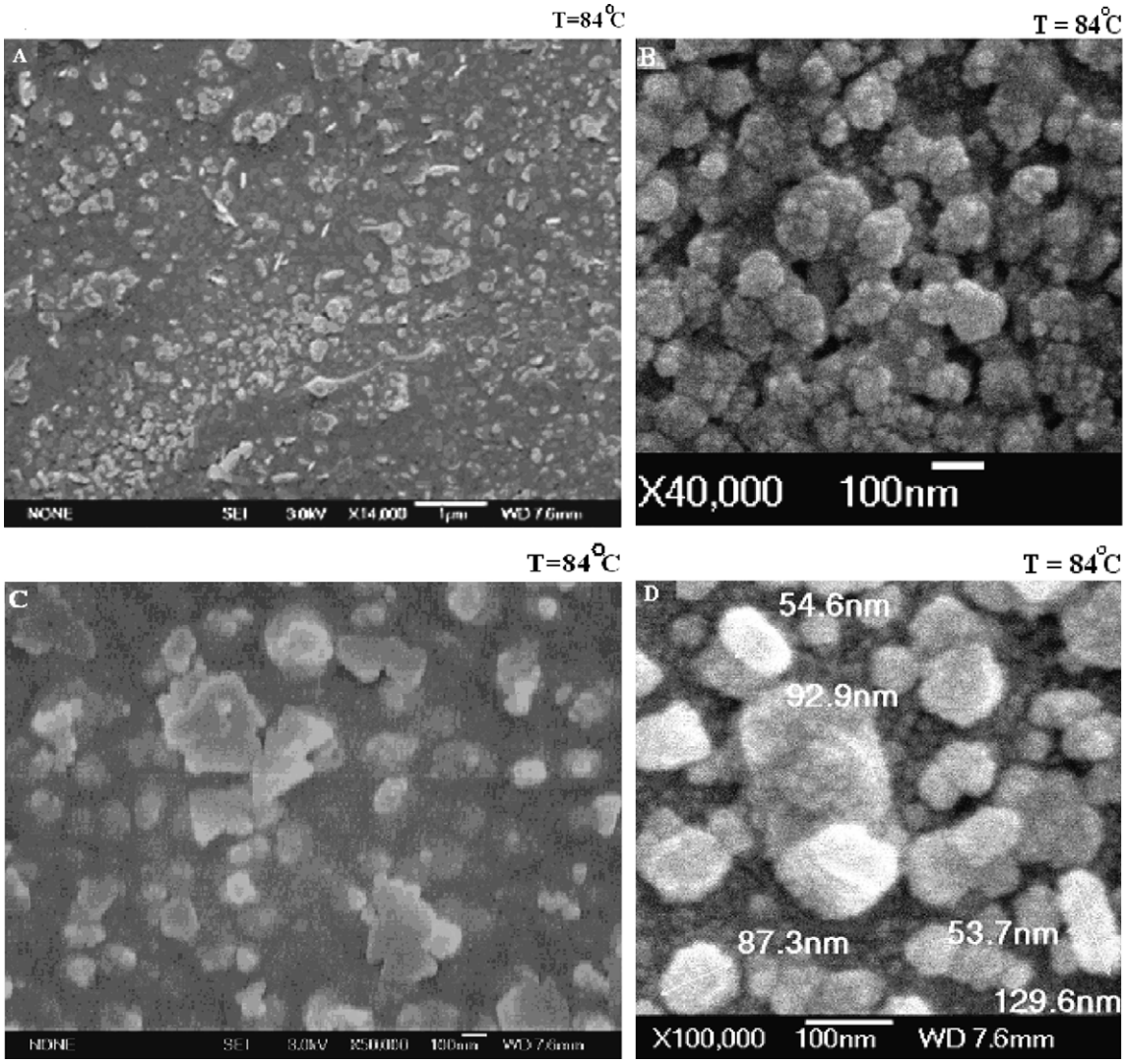


Fig. 4. Simultaneous presence of nano-plates and nano-globules (A); Cauliflower like morphology of globular nano-clusters (B); triangular and truncated triangular nano-plates (C) and dimension of nano-plates and nano-globules at 84 °C (D).

spectrum of the nano-structures prepared using SDS is shown in Fig. 6. The other peaks of Si, Mn, O, and Na appear probably due to the contribution from the borosilicate glass on which the samples were drop coated for the FESEM.

3.3. UV–Vis spectroscopic study

Fig. 7 is the UV–Vis spectrum of the sample solutions prepared at a temperature interval of 2 °C along with the solution prepared at room temperature (i.e. without aging). From the spectra it is noted that (a) there is almost no shift in the peak position and (b) the maxima are at the wavelength ~ 350 nm.This observed peak position is ascertained with the formation of silver nano-clusters $\{Ag\}_n$ made up from very low dimensional nano particles and agreed well with previous reports on silver clusters [35]. The increasing intensity demonstrates the gradual increase in surface plasmon absorption by the colloidal silver particles in solution in which the concentrations of the particles were raised due to the rise in temperature.

3.4. Powder X-ray diffraction pattern

The crystallinity of the silver nano-clusters was established by performing the Powder X-ray diffraction (Fig. 8) the data of which was collected with Cu Kα radiation, in the range 26–80° in steps of 0.02° per second. The four diffraction peaks, obtained at an angle 39.98°, 44.28°, 64.46° and 77.32°, respectively, could be completely attributed to the face-centered cubic (fcc) crystalline nature of the sample. As shown in the above figure, the highly intense diffraction peak was located at $2\theta = 39.98°$. This peak is from the (1 1 1) plane of the fcc silver. Referring to the above pattern, the lattice constant for the Ag was estimated to be $a = 4.0875$ Å which was consistent with the reported value ($a = 4.0862$ Å; JCPDS File No. 04-0783). The (2 0 0), (2 2 0) and (3 1 1) peaks are less intense. It is worth noting

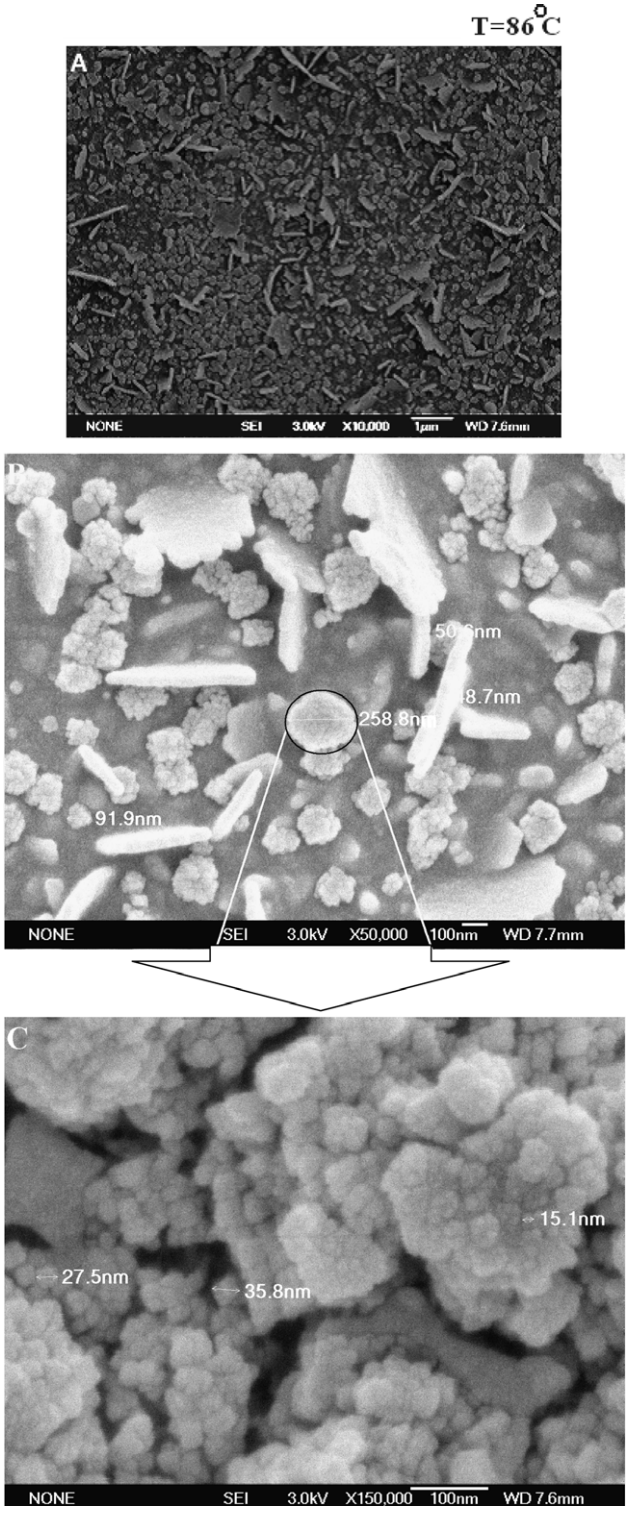


Fig. 5. Almost equally concentrated nano-disks and nano-globules (A); Nano-disks and nano-globules at high resolution (B) and "Cauliflower" like morphology of a 3D aggregate in high resolution (C).

that here the ratio of the intensities of (200) and (111) peak is lower than the conventional value (0.34 versus 0.4) and also that the ratio of (220) to (111) peak is higher than the reported one (0.32 versus 0.25), both of which clearly demonstrate the great abundance of the (111) peak. So, in this case, we might conclude that the nano-assemblies were mainly composed of (111) lattice planes. This might be the result of the lower surface free energy of that plane relative to (100) and (110) planes. This reflection is in good agreement with the previous results obtained during the structural characterization of silver nano-structures [3].

3.5. Anti-microbial activity study

The antibacterial study was carried out against seven of the most devastating bacterial strains: 1. *E. coli* (ATCC 10536); 2. *V. cholerae* (7); 3. *S. flexneri* (80903); 4. *S. aureus* (ML 422); 5. *S. typhimurium* (NCTC 74); 6. *S. aureus* (ATCC 29737) and 7. *S. aureus* (ML 276). Curiously, two strains 1 and 4 showed no growth in 2 μg/ml concentration of Ag nano particles in agar solution but they showed growth when penicillin is taken as the reference drug. None of the seven bacterial strains showed a positive growth at 4 μg/ml Ag concentration. The activity data are given in Table 1. To the best of our knowledge such a low MIC as 4 μg/ml is unprecedented.

3.6. Correlation of reaction temperature with the growth of nano particles

Hydrated silver ion, $[Ag(H_2O)x]^+$ in the presence of NH_3 form more stable silver–ammine complex ion, $[Ag(NH_3)_2]^+$. The reduction potential for the aquated and the ammoniated complex is given below:

$$[Ag(H_2O)x]^+ + e- = Ag + xH_2O \quad E^0 = 0.799\ V \qquad (I)$$

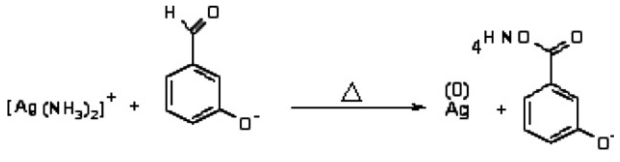
$$[Ag(NH_3)_2]^+ + e- = Ag + 2NH_3 \quad E^0 = 0.373\ V \qquad (II)$$

From the above data it is easy to understand that the ammoniated complex is more difficult to reduce than the hydrated one. But the reductant aldehyde is oxidized more easily in the presence of base (NH_3) than in its absence in aqueous medium, which is clear from the following half-cell reaction involved with this oxidation phenomenon:

$$RCHO + H_2O = RCOOH + 2H^+ + 2e^- \qquad (III)$$

Thus, from Eqs. (I) and (II) it is clear that due to the difficulty in reduction in ammoniacal medium, silver ions are slowly reduced. But this process is continuous due to the facile oxidation of the aldehyde in the same medium. This slow and steady formation of silver particles helps in effective capping by SDS.

The reduction reaction is given below:



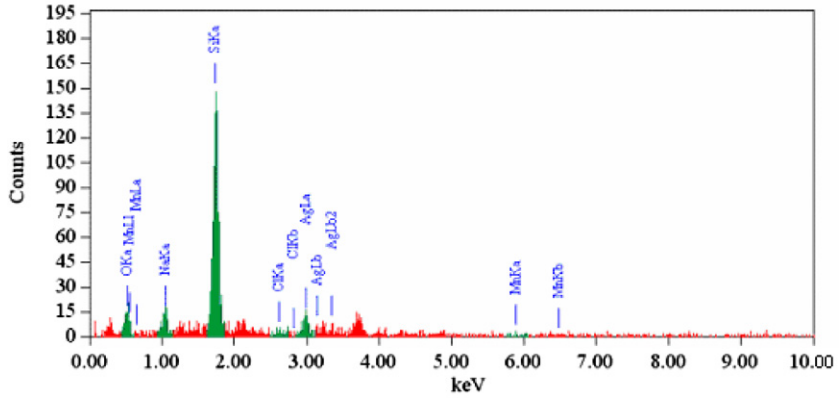


Fig. 6. EDAX spectra of the sample.

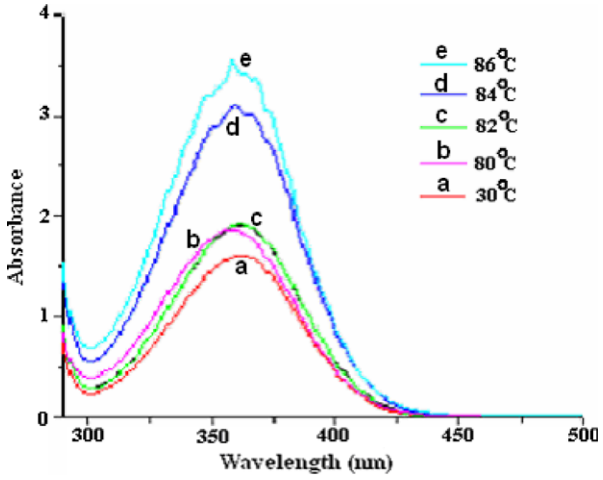


Fig. 7. The UV–Vis spectra taken for the freshly prepared colloidal solutions at the mentioned temperatures.

It is worth noting that the temperature required for the initiation of the reduction is quite low as compared to relatively higher temperatures of other reported thermally assisted solution phase nano synthesis procedures [3,37,38]. Here, the formation of the nano-aggregates could be explained on the basis of classical chemical kinetics theory [39]. The SEM images clearly demonstrate the strong dependence of the reaction on temperature. We have noticed the morphological change of the nano assemblies with the increasing temperature. The observed dimensional change was ~15 nm (80 °C) to ~45 nm (82 °C) to ~50–100 nm (84 °C) to ~120–260 nm and this change in dimensionality was qualitatively noticed through the sequential change in color of the solutions prepared at the said temperatures. With the increase of temperature, the kinetic energy of the Ag nano particles in the solution increases; as a result the collision fre-

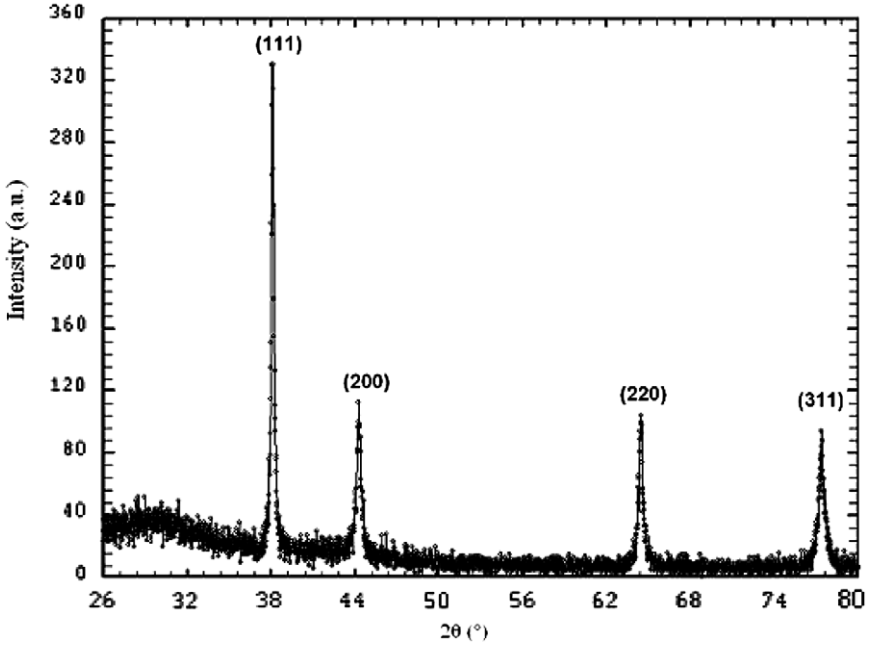


Fig. 8. Powder Diffraction Pattern of the silver nano materials.

Table 1
Activity of Ag nano particles in different concentrations against seven bacterial strains

Bacterial strains	Penicillin (Pc) concentration (2 μg/ml)	Concentration (0 μg/ml)[a]	Concentration (1 μg/ml)	Concentration (2 μg/ml)	Concentration (4 μg/ml)
Escherichia coli (ATCC 10536)	+	+	+	–	–
Vibrio cholerae (7)	–	+	+	–	–
Shigella flexneri (80903)	–	+	+	–	–
Salmonellatyphimurium (NCTC 74)	+	+	+	+	–
Staphylococcus aureus (ATCC 29737)	–	+	+	+	–
Staphylococcus aureus (ML 276)	–	+	+	+	–
Staphylococcus aureus (ML 422)	+	+	+	–	–

+, Growth.
–, No growth.
[a] Control plate without Ag nano particles.

quency between the particles also rises and this leads to the higher rate of agglomeration. The outcome of this is the formation of the higher dimensional nano-disks and nano-globules. As reported by Zukoski et al. [40], surface potential of silver particles is inversely related to temperature. With increasing temperature the gradual decrease in that potential of the particles accelerates the aggregation and thus the cluster formation, as observed in our case.

4. Conclusions

We have been able to synthesize both 2D and 3D Ag nano-structures having disk and globular morphology by carrying out the simple silver-mirror reaction in the presence of an anionic surfactant. The aldehyde-mediated reduction of silver nitrate occurred at relatively low temperatures (80–86 °C), which is easily producible, making the process facile and faster. SEM study revealed the temperature-dependent morphological variation of the nano particles. While at lower temperatures, only globular morphology was observed, at higher temperatures disk morphology proportionately increased and at 86 °C they appeared with equal proportion. Nano-disks of uniform thickness could be grown up to micron size. The antibacterial study established the hitherto highest activity of Ag nano-structures against a series of most devastating bacterial strains. It is more powerful than Penicillin for two bacteria (*E. coli* {ATCC 10536} and *S. aureus* {ML 422}).

In summary we have successfully designed a facile and faster synthesis route to produce Ag nano particles and the nano particles so produced exhibit unprecedented efficiency as anti-microbial agents. The synthesis method adopted here is very simple and can be easily implemented for any kind of scientific as well as industrial application due to its cost effective nature. An important characteristic of the Ag nano particles obtained in the present report is its homogeneous colloidal dispersion in water which is one of the essential requirements for biologically relevant nano-device applications. A detailed study is in progress towards unraveling the underlying mechanism behind the high activity of Ag nano particles as anti-microbial agents.

Acknowledgements

S. Sarkar acknowledges financial support from the Council of Scientific and Industrial Research (CSIR), New Delhi, under the JRF program (F. No. 10-2(5)/2004(ii)-E.U.II). G.M. acknowledges J.U. for research grant under the ''Nano Science and Technology Program'' under University with Potential for Excellence Scheme of UGC. We are thankful to Prof. N. Ray Chaudhuri, Department of Inorganic Chemistry, IACS, Kolkata, W.B. for helping us in obtaining FESEM images.

References

[1] E.A. Chandross, R.D. Miller, Chem. Rev. 99 (1999) 1641.
[2] R. Djalali, J. Samson, H. Matsui, J. Am. Chem. Soc. 126 (2004) 7935.
[3] Y. Sun, Y. Xia, Science 298 (2002) 2176.
[4] T. Vossmeyer, B. Guse, I. Besnard, R.E. Bauer, K. Mullen, A. Yasuda, Adv. Mater. 14 (2002) 238.
[5] (a) K. Mallik, M. Manda, N. Pradhan, T. Pal, NanoLetters 1 (2001) 319;
(b) S. Panigrahi, S. Kundu, S.K. Ghosh, S. Nath, S. Praharaj, S. Basu, T. Pal, Polyhedron 25 (2006) 1263.
[6] M. Lahav, E.A. Weiss, Q. Xu, G.M. Whitesides, NanoLetters 6 (2006) 2166.
[7] G. Schmid, L.F. Chi, Adv. Mater. 10 (1998) 515.
[8] K.L. Kelly, E. Coronado, L.L. Zhao, G.C. Schatz, J. Phys. Chem. B 107 (2003) 668.
[9] L.N. Lewis, Chem. Rev. 93 (1993) 2693.
[10] S.A. Maier et al., Adv. Mater. 13 (2001) 1501.
[11] G. Carotenuto, Appl. Organomet. Chem. 15 (2001) 344.
[12] D.M.K. Lam, B. Rossiter, Sci. Am. 80 (1991) 265.
[13] Y. Kim, R.C. Johnson, J.T. Hupp, NanoLetters 1 (2001) 165.
[14] S. Nie, S.R. Emory, Science 275 (1997) 1102.

[15] A. Melaiye, Z. Sun, K. Hindi, A. Milsted, D. Ely, D.H. Reneker, C.A. Tessier, W.J. Youngs, J. Am. Chem. Soc. 127 (2005) 2285.
[16] C. Aymonier, U. Schlotterbeck, L. Antonietti, P. Zacharias, R. Thomann, J.C. Tiller, S. Mecking, Chem. Commun. 24 (2002) 3018.
[17] L. Balogh, D.R. Swanson, D.A. Tomalia, G.L. Hagnauer, A.T. McManus, NanoLetters 1 (2001) 18.
[18] U. Samuel, J.P. Guggenbichler, Int. J. Antimicrob. Agents 23 (2004) 75.
[19] C.L. Fox Jr., W.W. Monafo Jr., V.H. Ayvazian, M.A. Skinner, S. Modak, J.C.C. Stanford, Surg. Gynecol. Obstet. 144 (1977) 668.
[20] M.A.A. Youssef, V.M. Langer, L. Öhrström, Dalton Trans. 21 (2006) 2542.
[21] F. Zeng, C. Hou, S. Wu, X. Liu, Z. Tong, S. Yu, Nanotechnology 18 (2007) 1.
[22] N.R. Jana, L. Gearheart, C.J. Murphy, Adv. Mater. 13 (2001) 1389.
[23] S. Chen, D.L. Carroll, Nano Lett. 2 (2002) 1003.
[24] M. Maillard, S. Giorgio, M.P. Pileni, Adv. Mater. 14 (2002) 1084.
[25] D.O. Yener, J. Sindel, C.A. Randall, J.H. Adair, Langmuir 18 (2002) 8692.
[26] Y. Sun, B. Mayers, T. Herricks, Y. Xia, NanoLetters 3 (2003) 7.
[27] M. Brust, M. Walker, D. Bethell, D.J. Schiffrin, R. Whyman, J. Chem. Soc., Chem. Commun. 7 (1994) 801.
[28] C.H. Kuo, M.H. Huang, Langmuir 21 (2005) 2012.
[29] S. Mandal, S.K. Arumugam, R. Pasricha, M. Sastry, Bull. Mater. Sci. 28 (2005) 503.
[30] S.K. Ghosh, S. Kundu, M. Mandal, S. Nath, T. Pal, J. Nanoparticle Res. 5 (2003) 577.
[31] N.R. Jana, L. Gearheart, C.J. Murphy, Chem. Commun. 7 (2001) 617.
[32] T.K. Sau, C.J. Murphy, J. Am. Chem. Soc. 126 (2004) 8648.
[33] H.C. Chu, C.H. Kuo, M.H. Huang, Inorg. Chem. 45 (2006) 808.
[34] J. Zhang, S. Xu, E. Kumacheva, Adv. Mater. 17 (2005) 2336.
[35] N.K. Chaki, S.G. Sudrik, H.R. Sonawaneb, K. Vijayamohanan, Chem. Commun. 1 (2002) 76.
[36] Performance standards for anti-microbial susceptibility testing National Committee for Clinical Laboratory Standards (NCCLS) Wayne PA, 1999.
[37] Y. Sun, Y. Xia, Adv. Mater. 14 (2002) 833.
[38] D. Kim, S. Jeong, J. Moon, Nanotechnology 17 (2006) 4019.
[39] S. Glasstone, D. Lewis, Elements of Physical Chemistry, second ed., D. Van Nostrand Co. Ltd., Princeton, 1960.
[40] D.L.V. Hyning, W.C. Klemperer, C.F. Zukoski, Langmuir 17 (2001) 3120.

In this report we focus on the examination of the reaction of $[ReOCl_3(PPh_3)_2]$ with 5,6-diphenyl-3-(2-pyridyl)-1,2,4-trazine (dppt). The isolated $[ReCl_3(OPPh_3)(dppt)]$ complex easily reacts with an excess of triphenylphosphine to give $[ReCl_3(PPh_3)(dppt)]$. The last one can be also prepared in the reaction of $[ReCl_3(MeCN)(PPh_3)_2]$ with 5,6-diphenyl-3-(2-pyridyl)-1,2,4-trazine. Here we present spectroscopic characterization, crystal, molecular and electronic structure of $[ReCl_3(OPPh_3)(dppt)]$ (**1**) and $[ReCl_3(PPh_3)(dppt)]$ (**2**) complexes. The molecular orbital diagrams of **1** and **2** have been calculated with the density functional theory (DFT) method. Currently density functional theory (DFT) is commonly used to examine the electronic structure of transition metal complexes. It meets with the requirements of being accurate, easy to use and fast enough to allow the study of relatively large molecules of transition metal complexes [7]. The electronic spectra of **1** and **2** have been discussed on the basis of time-dependent DFT calculations. Recent studies have supported the TD-DFT method to be applicable for open- and closed-shell of 5d-metal complexes (including rhenium complexes) giving good assignment of experimental spectra [8–10].

2. Experimental

2.1. General procedure

The reagents used to the synthesis were commercially available and were used without further purification. The $[ReOCl_3(PPh_3)_2]$ complex was prepared according to the literature method [11].

IR spectra were recorded on a Nicolet Magna 560 spectrophotometer in the spectral range 4000-400 cm^{-1} with the samples in the form of KBr pellets. Electronic spectra were measured on a spectrophotometer Lab Alliance UV–VIS 8500 in the range 1000–200 nm in chloroform solution. Elemental analyses (C, H, N) were performed on a Perkin–Elmer CHN-2400 analyzer.

2.2. Preparation of $[ReCl_3(OPPh_3)(dppt)]\cdot CH_2Cl_2$ ($\mathbf{1}\cdot CH_2Cl_2$)

To a solution of $[ReOCl_3(PPh_3)_2]$ (0.50 g, 0.6 mmol) in 30 ml dichloromethane was added 0.19 g (0.61 mmol) of 5,6-diphenyl-3-(2-pyridyl)-1,2,4-trazine (dppt). The resulting solution was magnetically stirred for 2 h at room temperature, and during this time the colour changed from light green to violet. 20 ml of CH_2Cl_2 was distilled off and 50 ml of diethyl ether was added. $[ReCl_3(OPPh_3)(dppt)]\cdot CH_2Cl_2$ was filtered off, washed with ethanol, diethyl ether and dried (yield 90%). The dark violet crystals of $\mathbf{1}\cdot CH_2Cl_2$ for X-ray investigation were obtained by recrystallization from dichloromethane.

IR (KBr; ν/cm^{-1}): 1601 (m), 1590(m) and 1504 (m) ν_{CN} and $\nu_{C=C}$; 1141(s) and 1115(s) $\nu_{P=O}$.

Anal. Calc. for $C_{39}H_{31}Cl_5N_4OPRe$: C, 48.48; H, 3.23; N, 5.80. Found: C, 48.60; H, 3.18; N, 5.85%.

2.3. Preparation of $[ReCl_3(PPh_3)(dppt)]$ (**2**)

Method A: To a solution of complex **1** (0.20 g, 0.23 mmol) in chloroform (20 ml), PPh_3 (0.24 g, 0.92 mmol) was added and the solution was refluxed for 1 h. The solvent was then removed under reduced pressure. The precipitate was washed several times with ethanol and hexane, and finally dried *in vacuo*. The crystals of **2** suitable for X-ray investigation were obtained by recrystallization from chloroform (yield 95%).

Method B: $[Re(MeCN)Cl_3(PPh_3)_2]$ (0.5 g, 0.58 mmol) and dppt (0.19 g, 0.61 mmol) in chloroform (40 cm^3) were refluxed for 4 h. The starting material gradually dissolved and the colour of the reaction solution became dark red. The volume was condensed to 10 cm^3, diethyl ether (100 cm^3) was added and dark violet microcrystalline solid was filtered. The product was washed with EtOH and cold ether, and dried *in vacuo* (yield 90%).

IR (KBr; ν/cm^{-1}): 1599(m), 1572(w) and 1507 (w) ν_{CN} and $\nu_{C=C}$.

Anal. Calc. for $C_{38}H_{29}Cl_3N_4PRe$: C, 52.75; H, 3.38; N, 6.48. Found: C, 52.62; H, 3.45; N, 6.37%.

2.4. Crystal structures determination and refinement

The X-ray intensity data of $\mathbf{1}\cdot CH_2Cl_2$ and **2** were collected on a KM-4-CCD automatic diffractometer equipped with CCD detector and graphite-monochromated Mo Kα radiation ($\lambda = 0.71073$ Å) at room temperature. Details concerning crystal data and refinement are given in Table 1. Lorentz polarization and absorption correction [12] were applied. The structures were solved by the Patterson method and subsequently completed by the difference Fourier recycling. All the non-hydrogen atoms were refined anisotropically using full-matrix, least-squares technique. The hydrogen atoms were treated as ''riding'' on their parent carbon atoms and assigned isotropic temperature factors equal 1.2 times the value of equivalent temperature factor of the parent atom. SHELXS-97 [13], SHELXL-97 [14] and SHELXTL [15] programs were used for all the calculations. Atomic scattering factors were those incorporated in the computer programs.

2.5. Computational details

GAUSSIAN-03 program [16] was used in the calculations. The geometry optimizations of **1** and **2** were carried out with the DFT method with the use of B3LYP functional [17,18]. The electronic spectra of **1** and **2** were calculated with the TD-DFT method [19]. The calculations were performed by using ECP basis set on the rhenium atom, the standard 6-31+G** basis for chlorine, oxygen, and nitrogen, 6-31G* for carbon and 6-31G for hydrogen atoms. The Xe core electrons of Re were replaced by an effective core potential and DZ quality Hay and Wadt Los Alamos ECP basis set (LANL2DZ) [20] was used for the valence electrons. Additional *d* function with exponent $\alpha = 0.3811$

Table 1
Crystal data and structure refinement for complexes **1** and **2**

Compound	**1** · CH_2Cl_2	**2**
Empirical formula	$C_{39}H_{31}Cl_5N_4OPRe$	$C_{38}H_{29}Cl_3N_4PRe$
Formula weight	966.10	865.17
Temperature (K)	291.0(3)	295(2)
Wavelength (Å)	0.71073	0.71073
Crystal system	monoclinic	monoclinic
Space group	$P2_1/c$	$P2_1/c$
Unit cell dimensions		
a (Å)	9.7664(4)	10.2122(4)
b (Å)	18.9933(8)	12.1143(3)
c (Å)	21.7652(8)	28.2982(12)
β (°)	94.151(3)	90.834(3)
Volume (Å^3)	4026.8(3)	3500.5(2)
Z	4	4
D_{calc} (Mg/m^3)	1.594	1.642
Absorption coefficient (mm^{-1})	3.425	3.780
$F(000)$	1904	1704
Crystal size (mm)	$0.13 \times 0.28 \times 0.50$	$0.03 \times 0.08 \times 0.30$
θ Range for data collection (°)	2.91–25.11	2.97–25.00
Index ranges	$-11 \leqslant h \leqslant 11$, $-22 \leqslant k \leqslant 22$, $-25 \leqslant l \leqslant 25$	$-11 \leqslant h \leqslant 6$, $-14 \leqslant k \leqslant 7$, $-26 \leqslant l \leqslant 33$
Reflections collected	42201	10927
Independent reflections (R_{int})	7169 (0.0575)	6168 (0.0374)
Completeness to 2θ (%)	99.5	99.9
Maximum and minimum transmission	0.586 and 0.260	0.888 and 0.711
Data/restraints/parameters	7169/0/460	6168/0/424
Goodness-of-fit on F^2	1.116	0.893
Final R indices [$I > 2\sigma(I)$]	$R_1 = 0.0338$, $wR_2 = 0.0788$	$R_1 = 0.0279$, $wR_2 = 0.0439$
R indices (all data)	$R_1 = 0.0389$, $wR_2 = 0.0815$	$R_1 = 0.0555$, $wR_2 = 0.0462$
Largest difference in peak and hole (e Å^{-3})	1.358 and −0.803	1.013 and −0.815

and f function with exponent $\alpha = 2.033$ on the rhenium atom were added.

2.6. Magnetic measurement

Magnetic measurements in the temperature range 1.8–300 K were performed using a Quantum Design SQUID-based MPMSXL-5-type magnetometer. The SQUID magnetometer was calibrated with the palladium rod sample (Materials Research Corporation, measured purity 99.9985%). The superconducting magnet was generally operated at a field strength ranging from 0 to 5 T. Measurements were made at a magnetic field of 0.5 T. Corrections are based on subtracting the sample – holder signal and contribution χ_D estimated from the Pascal constants [21] and equal – 425×10^{-6} cm^3 mol^{-1} for complex [$ReCl_3$(OPPh$_3$)(dppt)]. The effective magnetic moment was calculated from the equation, $\mu_{eff} = 2.83(\chi_M T)^{1/2}$ (BM).

3. Results and discussion

3.1. Preparation and infrared data

The [$ReCl_3$(dppt)(OPPh$_3$)] (**1**) complex has been prepared in good yield in the reaction of [$ReOCl_3(PPh_3)_2$] with 5,6-diphenyl-3-(2-pyridyl)-1,2,4-trazine (dppt) in dichloromethane:

$$[ReOCl_3(PPh_3)_2] + dppt \rightarrow [ReCl_3(dppt)(OPPh_3)] + PPh_3$$

It can be supposed that the [$ReOCl_3$(dppt)] oxocompound, formed in the first step reaction, is an oxidant transferring an oxygen atom to PPh$_3$. The oxygen atom transfer is believed to proceed *via* initial nucleophilic attack on the Re≡O π^* orbitals, the π acidity of the dppt ligand facilitates the attack of triphenylphosphine [22]. The produced triphenylphosphine oxide remains bonded to the reduced rhenium ion in complex **1**. Many instances of formation of phosphine oxides from $Re^{V}O$ and tertiary phosphines can be given, but examples when the phosphine oxide remain firmly bonded to the reduced metal centre are rare [22–25]. The complex **1** easily reacts with an excess of PPh$_3$ to give [$ReCl_3$(dppt)(PPh$_3$)] (**2**). The last one has been also isolated in the reaction of [$ReCl_3(MeCN)(PPh_3)_2$] with dppt.

The elemental analyses of the **1** · CH_2Cl_2 and **2** complexes are in good agreement with their formulation. The characteristic bands corresponding to the ν(CN), ν(C=C) modes of the dppt ligand appear in the range 1610-1500 cm^{-1}in the IR spectrum of **1** and **2**. The absence of the characteristic strong ν(Re=O) band at ~980 cm^{-1} is clear indication that there is no oxo-Re(V) starting material left in the samples **1** and **2**. The strong bands at 1141 and 1115 cm^{-1} in the IR spectrum of **1** confirm the presence of the coordinated OPPh$_3$ molecule [26].

3.2. Crystal structures

The complex **1** crystallises as dichloromethane solvate **1** · CH_2Cl_2, and the dichloromethane molecule is not bonded to any atom of the Re(III) complex. The structure of **2** consist of discrete and well-separated [$ReCl_3$(dppt)-(PPh$_3$)] monomers. Any intermolecular interactions with enough strength to govern crystal packing or molecule conformation were not found in the structures of **1** and **2**. Only weak intramolecular and intermolecular hydrogen bonds [25–27] were detected in crystals **1** and **2**, and they are gathered in Table 2.

The molecular structures of **1** and **2** are presented in Figs. 1 and 2, respectively, and the selected bond distances and angles are collected in Tables 3 and 4, respectively. Both complexes show distorted octahedral geometry about Re with the three chloride ions arranged in *meridional* fashion in complex **1** and in *facial* configuration in complex **2**. The coordination polyhedron least squares planes are inclined at 88.54(6)°, 82.95(11)°, and 74.58(13)° in compound **1** and at 89.05(5)°, 86.90(8)°, and 87.87(5)° in

Table 2
Hydrogen bonds for **1** and **2**

D	A	d(H···A) (Å)	d(D···A) (Å)	∠D–H···A (°)
Compound ***1***				
C(6)	Cl(3)#1	2.81	3.467(4)	129.1
C(8)	Cl(1)#2	2.80	3.655(5)	153.5
C(30)	Cl(2)#3	2.77	3.593(7)	147.5
Compound ***2***				
C(9)	Cl(3)#4	2.73	3.562(6)	149.2

Symmetry codes: #1: $1-x, -y, -z$; #2: $-x, -y, -z$; #3: $-1+x, y, z$; #4: $-x, y$-1/2, $-z+1/2$.

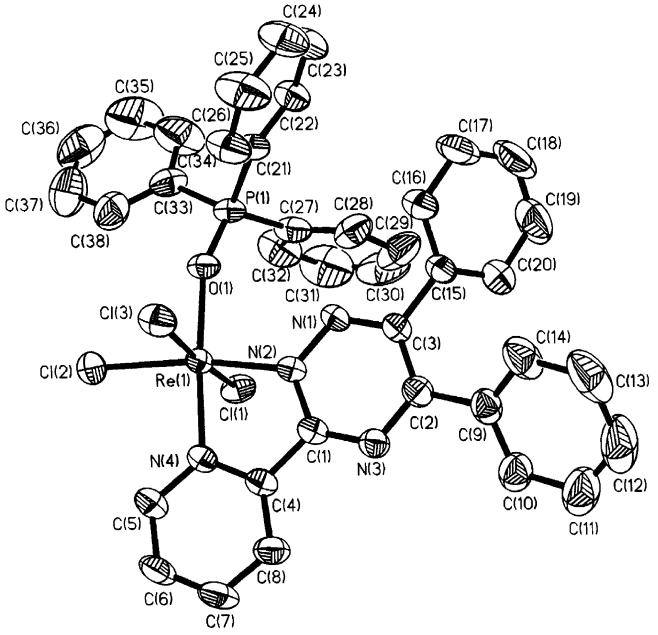


Fig. 1. The molecular structure of **1**.

compound **2** what shows that polyhedron distortion is distinctly smaller in compound **2**. The $OPPh_3$ ligand is pure donor and $PPh_3P{=}O \rightarrow Re \rightarrow \pi^*$(dppt) interaction is suited to the *meridional* configuration. In the presence of PPh_3 the electronic situation is affected by π acidity of the phosphine ligand. In complex **2**, two good π acceptor, dppt and PPh_3, are coordinated to rhenium (III) centre, and the back-bonding effect is maximized in the *facial* disposition which ensures minimum competition between the two ligands for identical metal orbitals. It is significant that the Re–N distances in **2** are longer than those in **1** where the dppt ligand alone is available for back bonding. The presence of Re–PPh_3 back-bonding diminishes the demand on π^*(dppt) orbitals. Some differences are observed between the Re–N(pyridine) and Re–N(triazine) bond lengths in **1** and **2** complexes. It indicates different π acidity strength of the two rings – the triazine ring favours π-back donation from the rhenium ion. Nevertheless, the Re–N bond lengths of both complexes are similar to those found for the other rhenium(III) polypirydyl compounds: in $[ReCl_2(bipy)_2]PF_6$ – 2.094(5) and 2.096(5) Å [27] and in the $[ReL(terpy)_2]^{2+}$ (L = Cl, OH, NCS) complexes – about 2.10 Å [28]. These values are significantly shorter than comparable distances for saturated amine complexes, where metal-to-ligand π-back bonding is not possible, for instance, the Re–NH_2 distance in the $[Re(N_2)(ampy)(tbpy)(PPh_3)]PF_6$ compound is 2.197(7) [29].

The Re–Cl(3) distance of **2** is affected by *trans* influence of triphenylphospnie and is therefore longer than the Re–Cl(1) and Re–Cl(2) bond lengths located in *trans* positions to the dppt ligand. In both compounds the 3-(2-pyridyl)-1,2,4-trazine moiety is close to planarity (maximum least squares plane atom deviation of 0.073(3) Å exists for C(2) atom in compound **1** and of 0.122(3) Å exists for N(4) atom in compound **2**). The dppt phenyl rings are

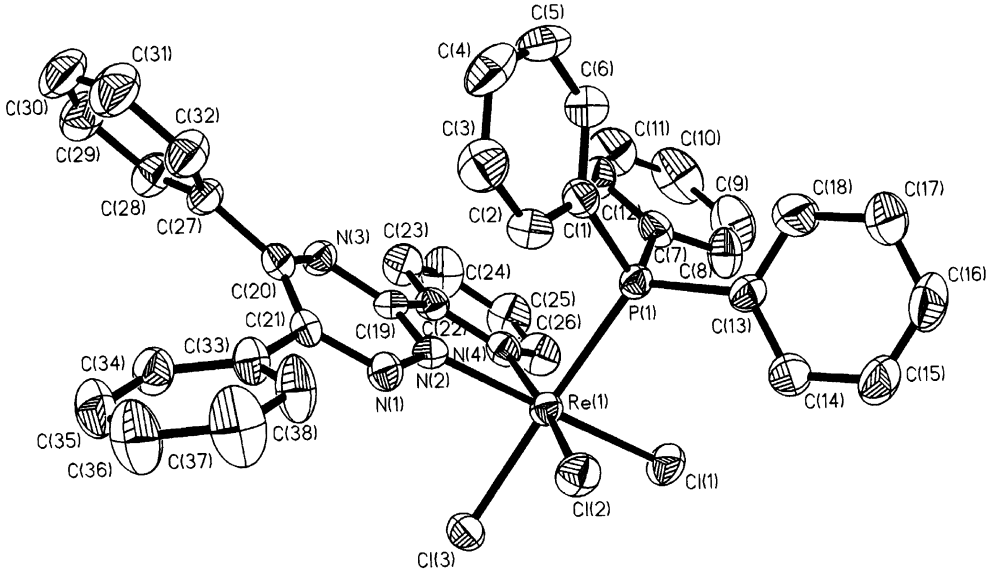


Fig. 2. The molecular structure of **2**.

Table 3
The experimental and optimized bond lengths (Å) and angles (°) for **1**

Bond lengths	Experimental	Optimized	Bond angles	Experimental	Optimized
Re(1)–O(1)	2.054(3)	2.06	N(2)–Re(1)–O(1)	98.22(12)	96.26
Re(1)–N(2)	2.016(3)	2.03	N(2)–Re(1)–N(4)	76.94(12)	77.18
Re(1)–N(4)	2.068(3)	2.08	O(1)–Re(1)–N(4)	175.15(12)	173.38
Re(1)–Cl(1)	2.3664(11)	2.42	N(2)–Re(1)–Cl(1)	90.34(9)	90.32
Re(1)–Cl(2)	2.3900(11)	2.42	O(1)–Re(1)–Cl(1)	89.31(8)	90.00
Re(1)–Cl(3)	2.3856(11)	2.43	N(4)–Re(1)–Cl(1)	90.95(9)	90.91
			N(2)–Re(1)–Cl(3)	89.54(9)	89.78
			O(1)–Re(1)–Cl(3)	86.32(8)	87.09
			N(4)–Re(1)–Cl(3)	93.34(9)	91.95
			Cl(1)–Re(1)–Cl(3)	175.57(4)	177.09
			N(2)–Re(1)–Cl(2)	171.34(9)	171.97
			O(1)–Re(1)–Cl(2)	90.43(9)	91.76
			N(4)–Re(1)–Cl(2)	94.41(10)	94.79
			Cl(1)–Re(1)–Cl(2)	89.57(4)	90.03
			Cl(3)–Re(1)–Cl(2)	91.22(4)	90.27

Table 4
The experimental and optimized bond lengths (Å) and angles (°) for **2**

Bond lengths	Experimental	Optimized	Bond angles	Experimental	Optimized
Re(1)–P(1)	2.4505(11)	2.54	N(2)–Re(1)–N(4)	75.91(15)	76.26
Re(1)–N(2)	2.044(4)	2.06	N(2)–Re(1)–Cl(2)	95.36(11)	94.28
Re(1)–N(4)	2.117(4)	2.13	N(4)–Re(1)–Cl(2)	171.27(10)	170.52
Re(1)–Cl(1)	2.3600(13)	2.43	N(2)–Re(1)–Cl(1)	168.43(11)	168.39
Re(1)–Cl(2)	2.3386(14)	2.38	N(4)–Re(1)–Cl(1)	92.73(11)	92.18
Re(1)–Cl(3)	2.4009(10)	2.42	Cl(2)–Re(1)–Cl(1)	95.98(5)	97.26
			N(2)–Re(1)–Cl(3)	87.58(9)	87.97
			N(4)–Re(1)–Cl(3)	88.48(9)	86.20
			Cl(2)–Re(1)–Cl(3)	90.85(4)	92.85
			Cl(1)–Re(1)–Cl(3)	89.95(4)	90.21
			N(2)–Re(1)–P(1)	94.53(9)	96.73
			N(4)–Re(1)–P(1)	91.24(9)	94.45
			Cl(2)–Re(1)–P(1)	89.77(4)	87.28
			Cl(1)–Re(1)–P(1)	87.82(4)	85.09
			Cl(3)–Re(1)–P(1)	177.73(4)	175.27

inclined to the 3-(2-pyridyl)-1,2,4-trazine moiety at 37.95(16)° and 50.37(16)° in compound **1** and at 32.37(13)° and 39.62(16)° in compound **2**.

3.3. Geometry optimization

The geometries of **1** and **2** were optimized in triplet and singlet states using the DFT method with the B3LYP functional. The energies of the singlet states are of 15.2 and 15.7 kcal/mol higher for **1** and **2**, respectively. The optimized geometric parameters of the triplet states are gathered in Tables 3 and 4. In general, the predicted bond lengths and angles are in agreement with the values based upon the X-ray crystal structure data, and the general trends observed in the experimental data are well reproduced in the calculations.

3.4. Molecular orbitals

The energies and characters of several highest occupied and lowest unoccupied molecular orbitals of **1** and **2** are presented in Tables 5 and 6. The selected HOMO and LUMO orbitals of **1** and **2** with α spin are depicted in Figs. 3 and 4. Among the highest occupied MOs of **1** and **2**, the largest numbers constitute π orbitals of the dppt and phenyl rings of PPh_3 or $OPPh_3$ with a contribution from the Cl and O (for **1**) atoms. For both **1** and **2**, the highest molecular orbital with α-spin can be represented as a combination of π^*_{Re-Cl}, and π^*_{dppt}, with predominant involvement of the former component. The same character have the HOMO orbitals with β-spin of **1** and **2**, but contribution of π orbitals of dppt ligand is considerable larger. The H-2 and H-1 α molecular orbitals of **1** correspond to combination of π^*_{Re-Cl} and $\pi^*_{Re-OPPh3}$ interaction, whereas the H-2 and H-1 α molecular orbitals of **2** have π^*_{Re-Cl} character. To a large extent, the L + 1 and L + 3 β orbitals of **1** and L and L + 2 β orbitals of **2** are also formed by rhenium d_π atomic orbital (d_{xz}, d_{yz} or d_{xy}). Among the lowest unoccupied MOs of **1** and **2**, the largest numbers constitute π orbitals of the dppt and phenyl rings of PPh_3 or $OPPh_3$. For both complexes the LUMO and LUMO + 1 with α-spin have π*(dppt) character. The π* phenyl ring orbitals

Table 5
The energy and character of the selected molecular orbitals with α and β spins for **1**

	MOs with α spin		MOs with β spin	
	E (eV)	Character	*E* (eV)	Character
HOMO − 2	−6.065	d_{xy}(Re), π(Cl), π(O)	−6.840	π(dppt), π(Cl)
HOMO − 1	−5.622	d_{xz}(Re), π(Cl), π(O)	−6.475	π(Cl)
HOMO	−5.399	d_{yz}(Re), π(Cl), π*(dppt)	−4.566	d_{xz}(Re), π(Cl), π*(dppt)
LUMO	−2.520	π*(dppt)	−2.754	π*(dppt), d_{xz}(Re)
LUMO + 1	−2.331	π*(dppt)	−2.556	d_{xy}(Re), π(Cl), π(O)
LUMO + 2	−1.624	$\pi^*(Ph_{OPPh3})$	−2.359	π*(dppt), d_{xz}(Re)
LUMO + 3	−1.471	$\pi^*(Ph_{OPPh3})$	−2.086	d_{yz}(Re), π*(dppt)

Table 6
The energy and character of the selected molecular orbitals with α and β spins for **2**

	MOs with α spin		MOs with β spin	
	E (eV)	Character	*E* (eV)	Character
HOMO − 2	−5.721	d_{xy}(Re), π(Cl)	−6.417	π(Cl), n(P)
HOMO − 1	−5.680	d_{xz}(Re), π(Cl)	−6.403	π(Cl), n(P), $\pi(Ph_{PPh3})$
HOMO	−5.515	d_{yz}(Re), π(Cl)	−4.851	d_{yz}(Re), π(Cl), π*(dppt)
LUMO	−2.647	π*(dppt)	−2.904	d_{xz}(Re), π*(dppt), π(Cl)
LUMO + 1	−2.411	π*(dppt)	−2.577	π*(dppt), d_{yz}
LUMO + 2	−1.448	π*(dppt)	−2.467	d_{xy}(Re), π(Cl)
LUMO + 3	−1.098	$\pi^*(Ph_{PPh3})$, d_{z^2}(Re)	−2.295	π*(dppt), d_{yz}

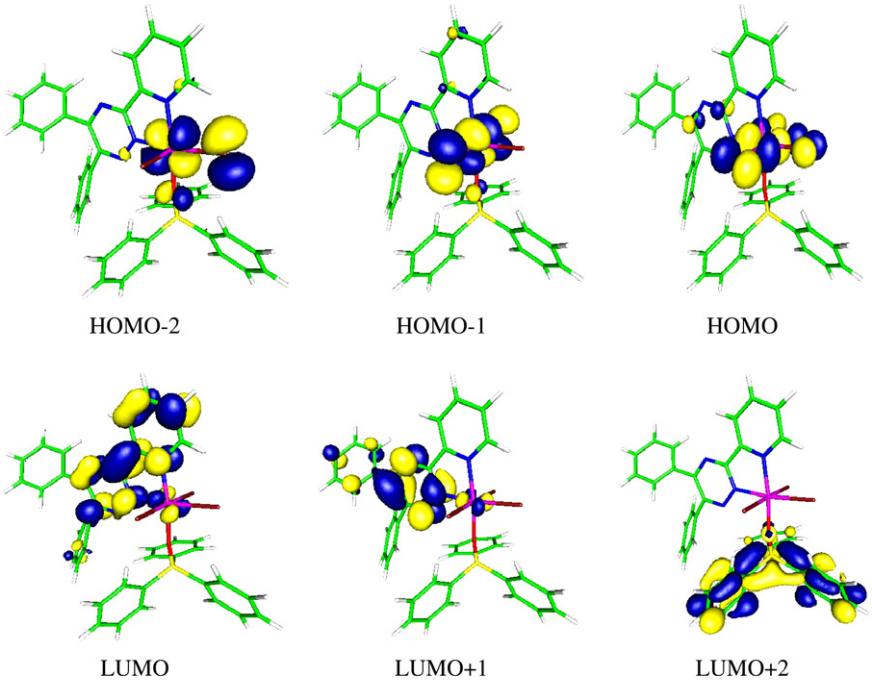


Fig. 3. The selected HOMO and LUMO orbitals with α-spin for **1**. HOMO − 2 HOMO − 1 HOMO LUMO LUMO + 1 LUMO + 2.

of the triphenylphosphine or triphenylphosphine oxide ligands participates in the higher unoccupied orbitals.

3.5. Electronic spectra

The spin-allowed triplet–triplet electronic transitions calculated with the TD-DFT method for **1** and **2** are gathered in Tables 7 and 8. For the high energy part of the spectrum, only transitions with oscillator strengths larger than 0.020 are listed in Tables 7 and 8.

The investigated complexes are of large size; the numbers of basis functions are equal to 969 and 799 for **1** and **2**, respectively. The calculated electron transitions (110 and 100 for **1** and **2**) do not comprise all the experimental absorption bands. The UV–Vis spectrum was calculated to ~290 nm for **1**, and to 300 nm for complex **2**. Thus

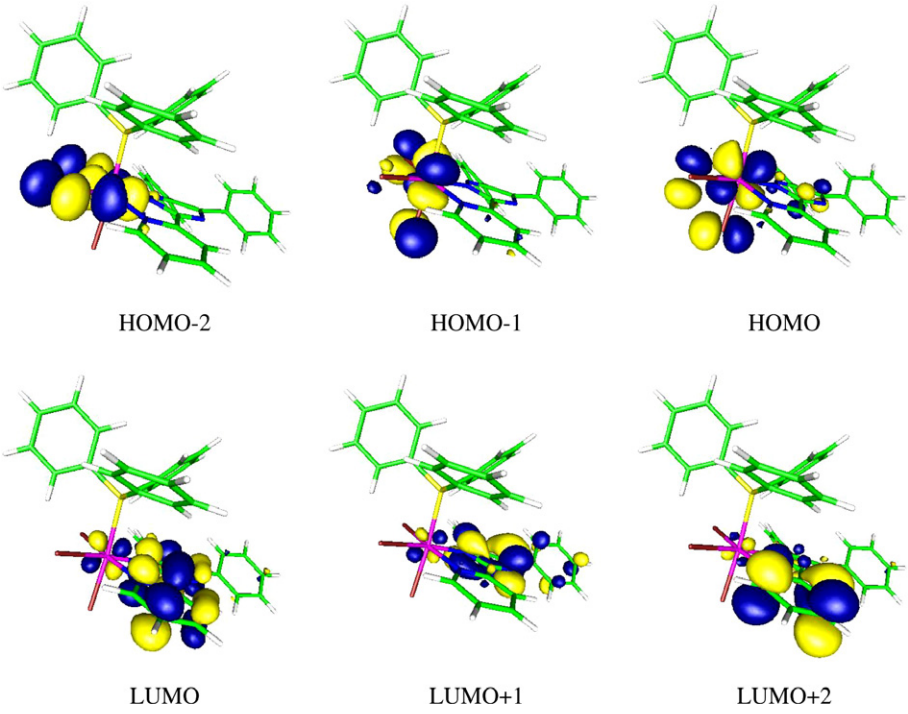


Fig. 4. The selected HOMO and LUMO orbitals with α-spin for **2**. HOMO − 2 HOMO − 1 HOMO LUMO LUMO + 1 LUMO + 2.

Table 7
The energy and molar absorption coefficients of experimental absorption bands and the electronic transitions calculated with the TD-DFT method for **1**

The most important orbital excitations	Character	λ (nm)	E (eV)	f	Experimental Λ (nm) (E (eV)) ε
H(β) → L + 3(β)	d → d/π*(dppt)	929.2	1.33	0.0242	840.0 (1.48) 450 705.9 (1.76) 1150
H(α) → L(α)	d → π*(dppt)	575.6	2.15	0.0227	
H(β) → L + 6(β)	d → d/π*(dppt)	514.6	2.41	0.0586	
H(β) → L + 4(β)	d → π*(Ph_{OPPh3})				
H(α) → L + 1(α)	d → π*(dppt)	502.1	2.47	0.0736	549.7 (2.26) 1700
H-1(α) → L + 1(α)	d → π*(dppt)	481.6	2.57	0.0926	
H(β) → L + 7(β)	d → π*(dppt)	443.3	2.80	0.0216	420.8 (2.95) 1070
H-5(β) → L(β)	π(Ph_{OPPh3})/π(Cl) → π*(dppt)	352.7	3.52	0.0247	
H-1(α) → L + 4(α)	d → (Ph_{OPPh3})				
H-1(β) → L + 3(β)	π(Cl) → d/π*(dppt)	345.8	3.59	0.0228	
H-3(α) → L + 1(α)	π(Cl) → π*(dppt)	342.9	3.62	0.0618	328.3 (3.78) 5380
H-6(β) → L + 1(β)	π(Ph_{OPPh3})/π(Cl) → d	334.0	3.71	0.0338	
H-1(β) → L + 3(β)	π(Cl) → d/π*(dppt)				
H-1(α) → L + 3(α) H(β) → L + 14(β)	d → π*(Ph_{OPPh3})	333.0	3.72	0.0315	
H-4(α) → L(α)	π(dppt)/π(Cl) → π*(dppt)	329.1	3.78	0.0243	
H(α) → L + 2(α)	d → π*(Ph_{OPPh3})				
H(β) → L + 15(β)	d → π*(Ph_{OPPh3})	321.5	3.86	0.0230	
H-1(α) → L + 7(α)	d → π*(Ph_{OPPh3})	292.9	4.23	0.0210	274.0 (4.52) 9775 226.6 (5.47) 23650

ε, molar absorption coefficient ($dm^3\ mol^{-1}\ cm^{-1}$); f, oscillator strength; H, highest occupied molecular orbital; L, lowest unoccupied molecular orbital.

the shortest wavelength experimental bands of **1** and **2** are not assigned to the calculated transitions; some additional intraligand and interligand transitions are expected to be found at higher energies in the calculations for **1** and **2**.

In the visible region (400–1000 nm), complexes **1** and **2** display multiple transitions of moderate intensity in the form of peaks and shoulders. The longest wavelength experimental band of **1** with maximum at 705.9 nm and shoulder at 840 nm is very broad. It is assigned to the transition of d → d/π*(dppt) character with relatively large oscillator strength. The calculated transition (at 929.2 nm) lies in the low energy end of the experimental band. For complex **2**, two absorption bands are observed in this range, and this arrangement is reproduced in the calculations. The experimental bands of **2** at 998.9 and 674.1 nm are attributed to the d → d/π*(dppt) transitions

Table 8
The energy and molar absorption coefficients of experimental absorption bands and the electronic transitions calculated with the TD-DFT method for **2**

The most important orbital excitations	Character	λ (nm)	E (eV)	f	Experimental Λ (nm) (E (eV)) ε
H(β) → L + 1(β)	d → d/π*(dppt)	976.3	1.27	0.0211	998.9 (1.24) 80
H(β) → L + 3(β)	d → d/π*(dppt)	806.0	1.54	0.0137	674.1 (1.84) 4400
H(α) → L(α)	d → d/π*(dppt)	562.0	2.21	0.0226	
H(α) → L + 1(α)	d → d/π*(dppt)	505.1	2.45	0.1167	520.3 (2.38) 5400
H-1(α) → L + 1(α)	d → d/π*(dppt)	486.4	2.55	0.0549	
H-5(β) → L(β)	$\pi(Cl)/\pi(Ph_{PPh3})/\pi$(dppt) → d/π*(dppt)	431.9	2.87	0.0225	432.9 (2.86) 4750
H-4(α) → L + 1(α)	π(Cl)/π(dppt) → d/π*(dppt)	370.3	3.35	0.0427	
H-3(β) → L(β)					
H-7(α) → L(α)	$\pi(Cl)/\pi(Ph_{PPh3})/\pi$(dppt) → d/π*(dppt)	356.6	3.48	0.0235	
H-5(α) → L(α)					
H-3(α) → L + 1(α)	$\pi(Cl)/n(P)/\pi(Ph_{PPh3})$ → d/π*(dppt)	354.6	3.50	0.0363	
H-3(β) → L + 1(β)	π(Cl)/π(dppt) → d/π*(dppt)				
H-4(β) → L + 1(β)	$\pi(Cl)/\pi(Ph_{PPh3})$ → d/π*(dppt)	345.2	3.59	0.0537	328.3 (3.78) 18240
H-7(α) → L(α)	$\pi(Cl)/\pi(Ph_{PPh3})/\pi$(dppt) → d/π*(dppt)	340.5	3.64	0.0474	
H-6(α) → L(α)	$\pi(Ph_{PPh3})$ → d/π*(dppt)	337.3	3.68	0.0664	
H-3(β) → L + 3(β)	π(Cl)/π(dppt) → d/π*(dppt)				
H-7(β) → L + 1(β)	π(Cl)/π(dppt) → d/π*(dppt)	317.6	3.90	0.0299	
H-8(α) → L(α)	π(dppt) → d/π*(dppt)				
H-12(β) → L + 2(β)	$\pi(Cl)/\pi(PPh_3)/\pi$(dppt) → d	316.1	3.92	0.0250	
H(α) → L + 4(α)	d → $\pi^*(Ph_{PPh3})$				
					300.0 (4.13) 23200
					258.5 (4.80) 23680
					228.2 (5.43) 38850

calculated at 976.3 and 806.0 nm. The same character [d → d/π*(dppt)] have the experimental absorption bands at 549.7 nm for complex **1** and at 520.3 nm for complex **2**. The observed shift of the d → d/π*(dppt) bands to higher energy in going from triphenylphosphine oxide (**1**) to triphenylphosphine (**2**) coordination is consistent with the stabilization of the t_{2g} shell of complex **2** *via* back-bonding.

Some differences can be noticed in the assignment of the experimental absorption bands at 420.8 nm and 432 nm for **1** and **2**, respectively. The first one is assigned to the d → d/π*(dppt) transition, whereas the absorption band of complex **2** corresponds to ligand–ligand charge transfer ($\pi(Cl)/\pi(PPh_3)/\pi$(dppt) → d/π*(dppt)) transitions.

For both complexes the absorption bands below 400 nm are attributed to metal–ligand charge transfer, ligand–metal charge transfer and ligand–ligand charge transfer and interligand (IL) transitions (Tables 7 and 8).

3.6. Magnetic properties

The magnetic properties of **1** complex under the form μ_{eff} versus T (μ_{eff} the effective magnetic moment) is shown in Fig. 5. The chloro-derivative of the rhenium(III) shows room temperature magnetic moment 2.01 BM (0.502 $cm^3\ mol^{-1}\ K$). The magnetic moment of the solid is temperature independent between 300 and 60 K. In the temperature range 55–14 K it is observed only slightly

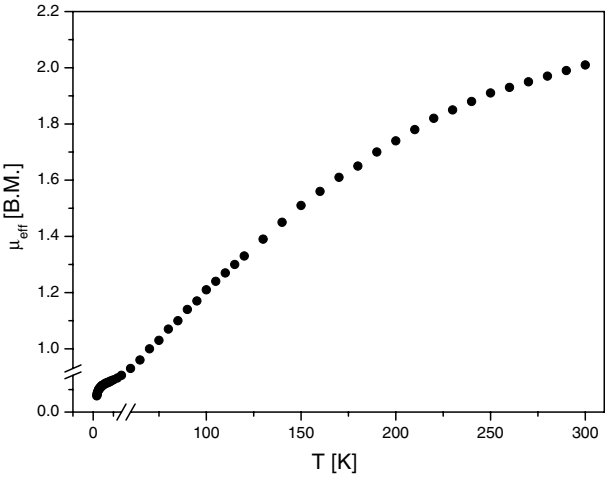


Fig. 5. Plots of the experimental effective magnetic moment μ_{eff} (●) vs. temperature for complex **1**.

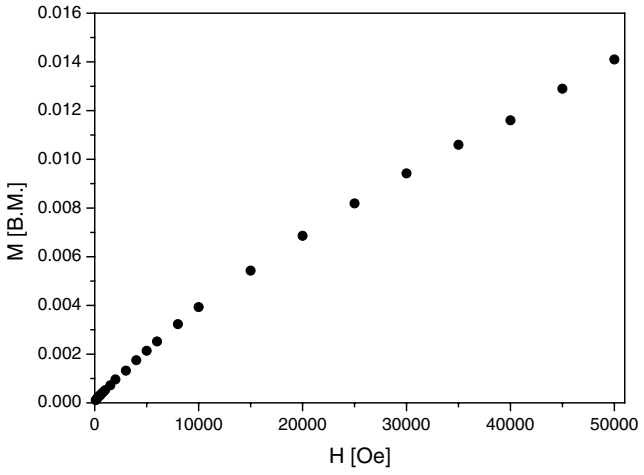


Fig. 6. Field dependence of the magnetization for complex **1** at 2 K.

magnetic anomaly and below 14 K the value of χ_M product increases with temperature lowering. This behavior is characteristic of mononuclear complexes with d^4 low-spin octahedral Re(III) complexes ($^3T_{1g}$ ground state) [30–38] and arise because of the large spin–orbit coupling ($\zeta = 2500\ cm^{-1}$ [39]), which gives diamagnetic ground state. It seems that in room temperature, in accordance Boltzmann's distribution, it is populated higher magnetic state, which is depopulated with temperature lowering and decreasing of the magnetic moment is observed.

The variation of the magnetization M versus the magnetic field H for complex **1** at 2 K is shown in Fig. 6. The M versus H curve for complex very slowly increases and indicates value of the magnetization near zero (0.014 BM) at 5 T. Magnetization of the sample confirms that the ground state is diamagnetic.

4. Supplementary material

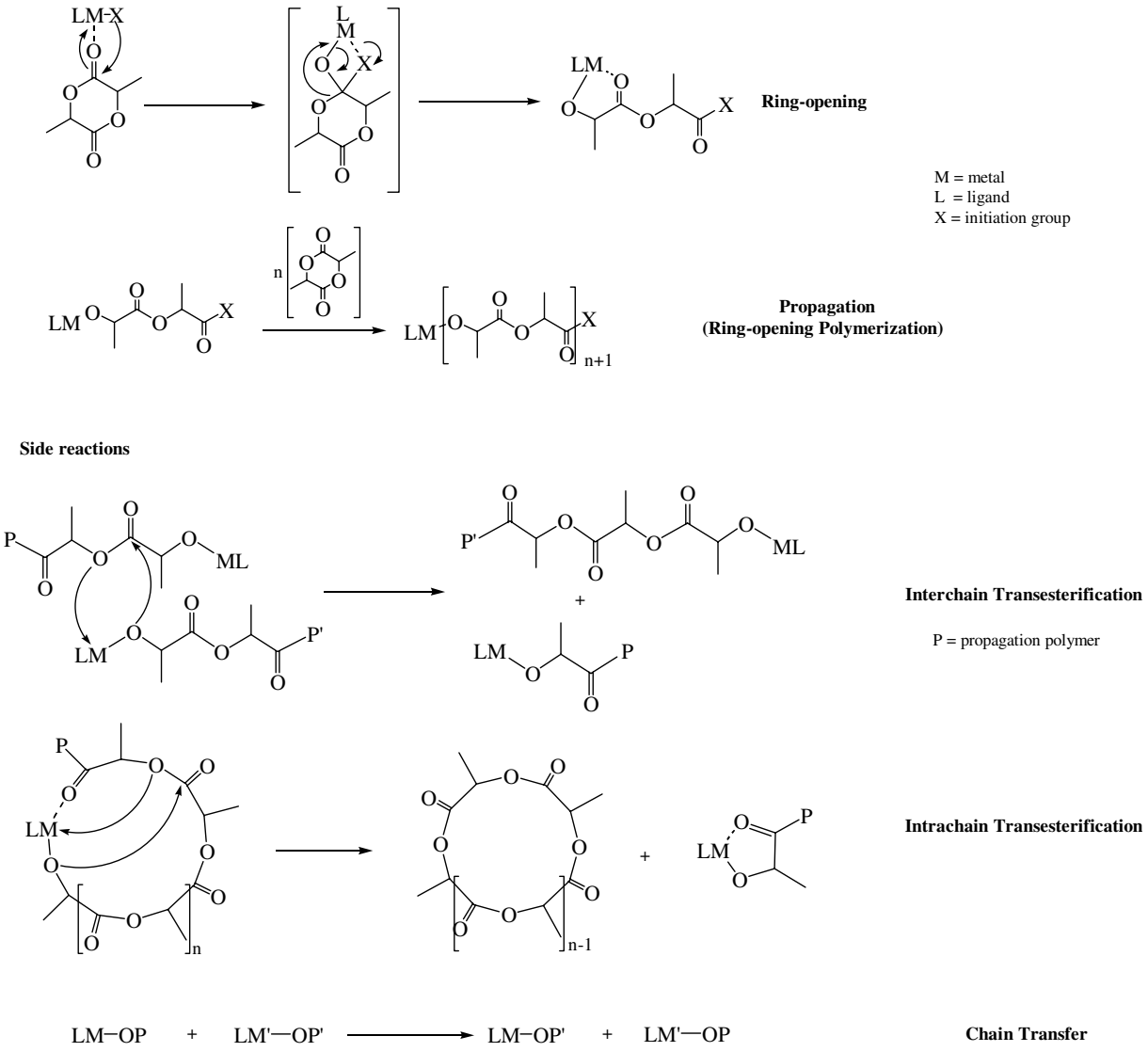
CCDC 640907 and 640908 contain the supplementary crystallographic data for $C_{39}H_{31}Cl_5N_4OPRe$ and $C_{38}H_{29}Cl_3N_4Pr$. These data can be obtained free of charge via http://www.ccdc.cam.ac.uk/conts/retrieving.html, or from the Cambridge Crystallographic Data Centre, 12 Union Road, Cambridge CB2 1EZ, UK; fax: (+44) 1223-336-033; or e-mail: deposit@ccdc.cam.ac.uk.

Acknowledgements

The GAUSSIAN-03 calculations were carried out in the Wrocław Centre for Networking and Supercomputing, WCSS, Wrocław, Poland. The work was supported by the Polish Ministry of Science and Higher Education Grant No. 1T09A12430.

References

[1] R.H. Holm, Chem. Rev. 87 (1987) 1401.
[2] C.C. Romão, F.E. Kühn, W.A. Hermann, Chem. Rev. 97 (1997) 3197.
[3] S.B. Seymore, S.N. Brown, Inorg. Chem. 39 (2000) 325.
[4] W. Volkert, W.F. Goeckeler, G.J. Ehrhardt, A.R. Ketring, J. Nucl. Med. 32 (1991) 174.
[5] E.A. Deutsch, K. Libson, J.L. Vanderheyden, Technetium and Rhenium in Chemistry and Nuclear Medicine, Raven Press, New York, 1990.
[6] B. Machura, Coord. Chem. Rev. 249 (2005) 591.
[7] H. Chermette, Coord. Chem. Rev. 178-180 (1998) 699.
[8] M.C. Aragoni, M. Arca, T. Cassano, C. Denotti, F.A. Devillanova, F. Isaia, V. Lippolis, D. Natali, L. Niti, M. Sampietro, R. Tommasi, G. Verani, Inorg. Chem. Commun. 5 (2002) 869.
[9] P. Romaniello, F. Lelj, Chem. Phys. Lett. 372 (2003) 51.
[10] P. Norman, P. Cronstrand, J. Ericsson, Chem. Phys. 285 (2002) 207.
[11] G. Rouschias, G. Wilkinson, J. Chem. Soc. A (1966) 465.
[12] (a) CrysAlis RED, Oxford Diffraction Ltd., Version 1.171.29.2.; (b) STOE & Cie, X-RED: Version 1.18, STOE & Cie GmbH, Darmstadt, Germany, 1999.
[13] G.M. Sheldrick, Acta Crystallogr., Sect. A 46 (1990) 467.
[14] G.M. Sheldrick, SHELXL-97: Program for the Refinement of Crystal Structures, University of Göttingen, Göttingen, Germany, 1997.
[15] G.M. Sheldrick, SHELXTL: release 4.1 for Siemens Crystallographic Research Systems, 1990.
[16] M.J. Frisch, G.W. Trucks, H.B. Schlegel, G.E. Scuseria, M.A. Robb, J.R. Cheeseman, J.A. Montgomery Jr., T. Vreven, K.N. Kudin, J.C. Burant, J.M. Millam, S.S. Iyengar, J. Tomasi, V. Barone, B. Mennucci, M. Cossi, G. Scalmani, N. Rega, G.A. Petersson, H. Nakatsuji, M. Hada, M. Ehara, K. Toyota, R. Fukuda, J. Hasegawa, M. Ishida, T. Nakajima, Y. Honda, O. Kitao, H. Nakai, M. Klene, X. Li, J.E. Knox, H.P. Hratchian, J.B. Cross, C. Adamo, J. Jaramillo, R. Gomperts, R.E. Stratmann, O. Yazyev, A.J. Austin, R. Cammi, C. Pomelli, J.W. Ochterski, P.Y. Ayala, K. Morokuma, G.A. Voth, P. Salvador, J.J. Dannenberg, V.G. Zakrzewski, S. Dapprich, A.D. Daniels, M.C. Strain, O. Farkas, D.K. Malick, A.D. Rabuck, K. Raghavachari, J.B. Foresman, J.V. Ortiz, Q. Cui, A.G. Baboul, S. Clifford, J. Cioslowski, B.B. Stefanov, G. Liu, A. Liashenko, P. Piskorz, I. Komaromi, R.L. Martin, D.J. Fox, T. Keith, M.A. Al-Laham, C.Y. Peng, A. Nanayakkara, M. Challacombe, P.M.W. Gill, B. Johnson, W. Chen, M.W. Wong, C. Gonzalez, J.A. Pople, GAUSSIAN-03, Revision B.03, Gaussian, Inc., Pittsburgh, PA, 2003.
[17] A.D. Becke, J. Chem. Phys. 98 (1993) 5648.
[18] C. Lee, W. Yang, R.G. Parr, Phys. Rev. B 37 (1988) 785.
[19] M.E. Casida, in: J.M. Seminario (Ed.), Recent Developments and Applications in Modern Density Functional Theory, Theoretical and Computational Chemistry, vol. 4, Elsevier, Amsterdam, 1996.
[20] P.J. Hay, W.R. Wadt, J. Chem. Phys. 82 (1985) 299.
[21] E. König, Magnetic Properties of Coordination and Organometallic Transition Metal Compounds, Springer, Berlin, 1966.
[22] I. Chakraborty, S. Bhattacharyya, S. Banerjee, B.K. Dirghangi, A. Chakravorty, J. Chem. Soc., Dalton Trans. (1999) 3747.
[23] S. Sengupta, J. Gangopadhyay, A. Chakravorty, Dalton Trans. (2003) 4635.
[24] S. Das, I. Chakraborty, A. Chakravorty, Polyhedron 22 (2003) 901.
[25] J. Gangopadhyay, S. Sengupta, S. Bhattacharyya, I. Chakraborty, A. Chakravorty, Inorg. Chem. 41 (2002) 2616.
[26] K. Nakamoto, Infrared and Raman Spectra of Inorganic and Coordination Compounds, 4th ed., Wiley–Interscience, New York, 1986.
[27] L.E. Helberg, S.D. Orth, M. Sabat, W.D. Harman, Inorg. Chem. 35 (1996) 5584.
[28] J. Rall, F. Weingart, D.M. Ho, M.J. Heeg, F. Tisato, E. Deutsch, Inorg. Chem. 33 (1994) 3442.
[29] S.D. Orth, J. Barrerra, M. Sabat, W.D. Harman, Inorg. Chem. 33 (1994) 3026.
[30] J.E. Fergusson, Coord. Chem. Rev. 1 (1966) 459.
[31] B.N. Figgis, J. Lewis, Prog. Inorg. Chem. 6 (1964) 37.
[32] B.N. Figgis, Introduction to Ligand Field, Wiley–Interscience, New York, 1966, p. 248.
[33] J. Chatt, G.J. Leigh, D.M.P. Mingos, E.W. Randall, D. Shaw, J. Chem. Soc., Chem. Commun. (1968) 419.
[34] H.P. Gunz, G.J. Leigh, J. Chem. Soc. (1971) 2229.
[35] B. Coutinho, J.R. Dilworth, P. Jobanputra, R.M. Thompson, S. Schmidt, J. Strähle, C.M. Archer, J. Chem. Soc., Dalton Trans. (1995) 1663.
[36] M. Hirsch-Kuchma, T. Nicholson, A. Davison, W.M. Davis, A.G. Jones, Inorg. Chem. 36 (1997) 3237.
[37] C.A. McConnachie, E.I. Stiefel, Inorg. Chem. 36 (1997) 6144.
[38] C. Pearson, A.L. Beauchamp, Can. J. Chem. 75 (1997) 220.
[39] A. Earnshaw, B.N. Figgis, J. Lewis, R.D. Peacok, J. Chem. Soc. (1961) 3132.



Scheme 1. Reactions involved in ring-opening polymerization employing a coordination catalyst.

One advantage of studying a slow catalytic system is that one may judge the relative importance of subtle changes at the metal center on the rate of the reaction and in this regard we were attracted to the study of organotin(IV) complexes in the ring-opening and ROP of lactide. We found previously that the rate of initial ring-opening of LA by Ph_3SnX complexes was very sensitive to the nature of the X group and followed the order $X = NMe_2 > OMe > OPr^i > OBu^t > N(SiMe_3)_2 > OPh$ which indicated the importance of both steric and electronic factors, namely the nucleophilicity of the X group [15]. In the ROP of LA by Ph_3SnX initiators it was also noted that the tin(IV) complexes were subject to ligand redistribution reactions yielding Ph_4Sn and $Ph_2Sn(OP)_2$ species and furthermore that when the initiating group $X = NMe_2$ intrachain *trans*-esterification was favored yielding cyclic-oligoesters and $Ph_2Sn(OCHMeC(O)NMe_2)_2$ [16,17]. In contrast the $Ph_2Sn(OPr^i)_2$ initiators produced a much "better behaved" catalytic system for the ROP of LA and this prompted us to evaluate the influence of various aryl substitutents *p*-XC_6H_4, where $X = CF_3$, F, H, OMe and NMe_2, on the kinetics of the ROP by bisaryltin(IV) complexes $(C_6H_4)_2Sn(OPr^i)_2$ and to compare these with the dialkyltin(IV) complex $(Bu^n)_2Sn(OPr^i)_2$. These considerations provide the basis for the work described herein.

2. Experimental

2.1. General

The manipulation of air-sensitive compounds involved standard Schlenk line and dry box techniques. All solvents were distilled under nitrogen from alkali metals and stored over 4 A molecular sieves. L-Lactide was purified by sublimation under vacuum three times. Benzene-D_6 was dried over activated molecular sieves and stored in the glove

box. The tin dichlorides of general formula (p-$XC_6H_4)_2SnCl_2$ (where X = CF_3, F, H, Me, MeO, NMe_2) were synthesized via the Kochesnikov redistribution reaction involving the tin tetrachloride with (p-$XC_6H_4)_4Sn$ and isolated by re-crystallization from toluene as described previously [18,19]. Samples of high purity were obtained by a distillation under vacuum using a Kugelrohr apparatus, except for (p-$Me_2NC_6H_4)_2SnCl_2$ which was recrystallized twice from toluene. Tin chlorides of formula (p-$XC_6H_4)_3SnCl$ (where X = CF_3, F, Me) were synthesized via the Kochesnikov redistribution reaction involving (p-$XC_6H_4)_2SnCl_2$ with (p-$XC_6H_4)_4Sn$ in the neat at 170 °C and purified by distillation under vacuum (Kugelrohr apparatus) [20]. Ph_3SnNMe_2 was synthesized by the reaction of $LiNMe_2$ with Ph_3SnCl in benzene according to the literature procedure [4]. ^1H, ^{13}C and ^{118}Sn NMR spectra were obtained from either Bruker DPX-400 or DPX-250 spectrometers using benzene-D_6 as solvent and elemental analyses were performed by the Atlantic Microlab, Inc. All kinetic data were obtained from NMR scale reactions. Standard solutions of (p-$XC_6H_4)_2Sn(O^iPr)_2$ and L-lactide were made in benzene-D_6 and stored in the dry box. Appropriate aliquots of both reagents (molar ratio = 1:50) were transferred to a J. Young NMR tube. The reaction temperatures were regulated via a thermostatically controlled oil bath. For lactide polymerizations reaction rates of polymerization were determined from ^1H NMR data (400 MHz) where the sum of the area of monomer and polymer peaks (CH and Me) was assumed to be 100% and rates of disappearance of monomer were calculated by the substraction of the polymer peaks from the monomer peaks and dividing by the concentration of monomer at $t = 0$ to give a ratio. Equilibrium monomer concentrations were determined by polymerizing L-lactide using the (p-$XC_6H_4)_2Sn(O^iPr)_2$ catalyst precursors in benzene-D_6 (1:25 O^iPr: L-lactide; $[LA]_{init} = 0.1229$ M]) at various temperatures. The natural log of the equilibrium monomer concentration was then plotted against $1/T$ to give a straight line. These data were used in the various polymerization reactions as indicated in Fig. 4. The value of k_{prop} was determined from the gradient a plot of $-\ln[(A - A_{eq})/(A_0 - A_{eq})]$ versus time (Fig. 6), where $A = [LA]$, A_{eq} = the equilibrium [LA] for a given temperature and $A_0 = [LA]$ at $t = 0$.

2.2. Synthesis

2.2.1. (p-$Me_2NC_6H_4)_2SnCl_2$

Following the procedure given in the literature [20], (p-$Me_2NC_6H_4)_4Sn$ (11.62 g, 19.4 mmol) and $SnCl_4$ (2.27 ml, 19.4 mmol) were dissolved in toluene (100 ml) and heated up to 110 °C. Cooling down slowly to room temperature gave crystals of the title compound, which were isolated by filtration. Yield 15.04 g, 90%. ^1H NMR (C_6D_6, 400 MHz): δ 7.57 (d, $^3J_{H-H} = 8.8$ Hz, m-CH aryl, 4 H), 6.43 (d, $^3J_{H-H} = 8.8$ Hz, d, o-CH aryl, 4 H), 2.35 (s, $N(CH_3)_2$, 12 H) ppm; ^{13}C NMR (C_6D_6, 100.6 MHz): δ 152.5 (C–$N(CH_3)_2$), 136.7 (m-CH), 122.5 (ipso-C–Sn), 112.7 (o-CH), 39.1 ($N(CH_3)_2$) ppm; ^{118}Sn NMR (C_6D_6, 149.2 MHz): δ −3.3 ppm.

2.3. General procedure for the synthesis of (p-$XC_6H_4)_2Sn(O^iPr)_2$ (X = CF_3, F, H, Me, MeO) and (p-$Me_2NAr)_3SnO^iPr$

Typically, a solution of (p-$XC_6H_4)_2SnCl_2$ (1 equiv) in benzene was added via a syringe to a vigorously stirred and ice cooled suspension of $LiNMe_2$ (2.2 equiv) in benzene. After stirring at room temperature for 2 days, the suspension was separated by centrifugation or filtration. All volatiles were removed under high vacuum to quantitatively leave (p-$XC_6H_4)_2Sn(NMe_2)_2$ (as shown by NMR spectroscopy) as colorless oils or solids. The compounds were redissolved in hexanes and a ten-fold excess of isopropanol was added at room temperature. After stirring for ca. 4 h all volatiles were removed under vacuum and the solid residues were recrystallized from hexanes at −40 °C to yield analytically pure samples of the title compounds.

2.3.1. (p-$CF_3C_6H_4)_2Sn(O^iPr)_2$

(p-$CF_3C_6H_4)_2SnCl_2$ (1105 mg, 2.30 mmol) and $LiNMe_2$ (260 mg, 5.10 mmol). Yield 450 mg, 37%. M.p. 83–85 °C; ^1H NMR (C_6D_6, 400 MHz): δ 7.50 (d, $^3J_{H-H} = 7.6$ Hz, o-CH aryl, 4 H), 7.37 (d, $^3J_{H-H} = 8.0$ Hz, m-CH aryl, 4 H), 4.28 (sept, $^3J_{H-H} = 6$ Hz, $OCH(CH_3)_2$, 2 H), 1.24 (d, $^3J_{H-H} = 6$ Hz, $OCH(CH_3)_2$, 12 H) ppm; ^{13}C NMR (C_6D_6, 100.6 MHz): δ 142.8 (ipso-C–Sn), 136.6 (o-CH), 132.8 (d, $^2J_{C-F} = 40.2$ Hz, C–CF_3), 125.6 (d, $^3J_{C-F} = 4.0$ Hz, m-CH), 124.5 (d, $^1J_{C-F} = 272.6$ Hz, C–CF_3), 68.2 ($OCH(CH_3)_2$), 27.6 ($OCH(CH_3)_2$) ppm; ^{118}Sn NMR (C_6D_6, 149.2 MHz): δ −173.7 ppm; *Anal.* Calc. for $C_{20}H_{22}F_6O_2Sn$ (527.088): C, 45.57; H, 4.21. Found: C, 45.43; H, 4.02%.

2.3.2. (p-$CF_3C_6H_4)_2Sn(NMe_2)_2$

^1H NMR (C_6D_6, MHz): δ 7.4–7.5 (m, CH aryl, 8 H), 2.81 (s, $N(CH_3)_2$, 12 H) ppm; ^{13}C NMR (C_6D_6, MHz): δ 142.4 (ipso-C–Sn), 137.2 (o-CH), 132.2 (d, $^2J_{C-F} = 32.2$ Hz, C–CF_3), 125.4 (d, $^3J_{C-F} = 3$ Hz, m-CH), 124.7 (d, $^1J_{C-F} = 271.6$ Hz, CF_3), 43.6 ($N(CH_3)_2$) ppm; ^{118}Sn NMR (C_6D_6, 149.2 MHz): δ −83.7 ppm.

2.3.3. (p-$FC_6H_4)_2Sn(O^iPr)_2$

(p-$FC_6H_4)_2SnCl_2$ (1270 mg, 3.38 mmol) and $LiNMe_2$ (362 mg, 7.10 mmol). Yield 910 mg, 63%. M.p. 85–87 °C; ^1H NMR (C_6D_6, 400 MHz): δ 7.43 (dd, $^3J_{H-H} = 8.4$ Hz, $^3J_{H-F} = 6$ Hz, m-CH aryl, 4 H), 6.82 (tr, $^3J_{H-H} = 8.4$ Hz, o-CH aryl, 4 H), 4.33 (sept, $^3J_{H-H} = 6$ Hz, $OCH(CH_3)_2$, 2 H), 1.28 (d, $^3J_{H-H} = 6$ Hz, $OCH(CH_3)_2$, 12 H) ppm; ^{13}C NMR (C_6D_6, 100.6 MHz): δ 164.9 (d, $^1J_{C-F} = 250.5$ Hz, C–F), 138.2 (d, $^3J_{C-F} = 7$ Hz, m-CH), 133.1 (d, $^4J_{C-F} = 4$ Hz, ipso-C–Sn), 116.6 (d, $^2J_{C-F} = 20.1$ Hz, o-CH), 67.9 ($OCH(CH_3)_2$), 27.8 ($OCH(CH_3)_2$) ppm; ^{118}Sn NMR (C_6D_6, 149.2 MHz): δ −152.6 ppm; *Anal.* Calc. for

$C_{18}H_{22}F_2O_2Sn$ (427.073): C, 50.62; H, 5.19. Found: C, 50.34; H, 5.08%.

2.3.4. $(p\text{-}FC_6H_4)_2Sn(NMe_2)_2$

^{1}H NMR (C_6D_6, 250 MHz): δ 7.35 (dd, $^3J_{H-H} = 8.5$ Hz, $^3J_{H-F} = 6.3$ Hz *m*-CH aryl, 4 H), 6.88 (dd, $^3J_{H-H} = 8.5$ Hz, $^4J_{H-F} = 8.6$ Hz *o*-CH aryl, 4 H), 2.84 (s, $N(CH_3)_2$, 12 H) ppm; ^{13}C NMR (C_6D_6, 62.9 MHz): δ 164.6 (d, $^1J_{C-F} =$ 245 Hz, C–F), 138.7 (d, $^3J_{C-F} = 7.1$ Hz, *m*-CH), 132.7 (d, $^4J_{C-F} = 4.4$ Hz, ipso-C–Sn), 116.4 (d, $^2J_{C-F} = 19.7$ Hz, *o*-CH), 43.6 ($N(CH_3)_2$) ppm.

2.3.5. $Ph_2Sn(O^iPr)_2$

Ph_2SnCl_2 (2057 mg, 5.98 mmol) and $LiNMe_2$ (670 mg, 13.14 mmol). Yield 1610 mg, 69%. M.p. 83–84 °C (dec.). The analytical data obtained were in agreement with those previously reported [4].

2.3.6. $(p\text{-}MeC_6H_4)_2Sn(O^iPr)_2$

(p-$MeC_6H_4)_2SnCl_2$ (974 mg, 2.62 mmol) and $LiNMe_2$ (280 mg, 5.49 mmol). Yield 330 mg, 30%. M.p. 77-78 °C (dec.); ^{1}H NMR (C_6D_6, 400 MHz): δ 7.64 (d, $^3J_{H-H} =$ 8 Hz, *m*-CH aryl, 4 H), 7.02 (d, $^3J_{H-H} = 8$ Hz, *o*-CH aryl, 4 H), 4.47 (sept, $^3J_{H-H} = 6$ Hz, OC*H*$(CH_3)_2$, 2 H), 2.04 (s, CH_3, 6 H), 1.35 (d, $^3J_{H-H} = 6$ Hz, OCH(C*H*$_3)_2$, 12 H) ppm; ^{13}C NMR (C_6D_6, 100.6 MHz): δ 140.6 (*C*–CH_3), 136.5 (*m*-CH), 134.7 (ipso-C–Sn), 130.1 (*o*-CH), 67.7 (O*C*H$(CH_3)_2$), 28.0 (C–*C*H_3), 21.4 (OCH(*C*$H_3)_2$) ppm; ^{118}Sn NMR (C_6D_6, 149.2 MHz): $\delta -$ 147.1 ppm; *Anal.* Calc. for $C_{20}H_{28}O_2Sn$ (419.145): C, 57.31; H, 6.73. Found: C, 57.19; H, 6.65%.

2.3.7. $(p\text{-}MeC_6H_4)_2Sn(NMe_2)_2$

^{1}H NMR (C_6D_6, 250 MHz): δ 7.60 (d, $^3J_{H-H} = 7.9$ Hz, *m*-CH aryl, 4 H), 7.07 (d, $^3J_{H-H} = 7.9$ Hz, *o*-CH aryl, 4 H), 2.99 (s, $N(CH_3)_2$, 12 H), 2.08 (s, CH_3, 6 H) ppm; ^{13}C NMR (C_6D_6, 62.9 MHz): δ 139.7 (*C*–CH_3), 137.1 (*m*-CH), 134.3 (ipso-C–Sn), 129.9 (*o*-CH), 43.9 ($N(CH_3)_2$), 21.4 (C–*C*H_3) ppm.

2.3.8. $(p\text{-}MeOC_6H_4)_2Sn(O^iPr)_2$

(p-$MeOC_6H_4)_2SnCl_2$ (1031 mg, 2.56 mmol) and $LiNMe_2$ (274 mg, 5.37 mmol). Yield 750 mg, 65%. ^{1}H NMR (C_6D_6, 250 MHz): δ 7.66 (d, $^3J_{H-H} = 8.8$ Hz, *m*-CH aryl, 4 H), 6.83 (d, $^3J_{H-H} = 8.8$ Hz, *o*-CH aryl, 4 H), 4.52 (sept, $^3J_{H-H} = 6$ Hz, OC*H*$(CH_3)_2$, 2 H), 3.21 (s, CH_3O, 6 H), 1.40 (d, $^3J_{H-H} = 6$ Hz, OCH(C*H*$_3)_2$, 12 H) ppm; ^{13}C NMR (C_6D_6, 100.6 MHz): δ 162.1 (*C*–OMe), 138.0 (*m*-CH), 128.1 (ipso-C–Sn), 115.2 (*o*-CH), 67.7 (O*C*H$(CH_3)_2$), 54.4 (CH_3O), 28.3 (OCH(*C*$H_3)_2$) ppm; ^{118}Sn NMR (C_6D_6, 149.2 MHz): δ −133.7 ppm; *Anal.* Calc. for $C_{20}H_{28}O_4Sn$ (451.144): C, 53.25; H, 6.26. Found: C, 52.98; H, 6.14%.

2.3.9. $(p\text{-}MeOC_6H_4)_2Sn(NMe_2)_2$

^{1}H NMR (C_6D_6, 400 MHz): δ 7.58 (d, $^3J_{H-H} = 8.4$ Hz, *m*-CH aryl, 4 H), 6.87 (d, $^3J_{H-H} = 8.4$ Hz, *o*-CH aryl, 4 H), 3.29 (s, OCH_3, 6 H); 3.00 (s, $N(CH_3)_2$, 12 H) ppm; ^{13}C NMR (C_6D_6, 100.6 MHz): δ 161.6 (*C*-OCH_3), 138.3 (*m*-CH), 128.3 (ipso-C–Sn), 115.1 (*o*-CH), 54.5 (C–O*C*H_3), 43.9 ($N(CH_3)_2$) ppm; ^{118}Sn NMR (C_6D_6, 149.2 MHz): δ −7.4 ppm.

2.3.10. $(p\text{-}Me_2NC_6H_4)_3SnO^iPr$

(p-$Me_2NC_6H_4)_2SnCl_2$ (858 mg, 1.99 mmol) and $LiNMe_2$ (224 mg, 4.39 mmol). Yield 170 mg, 32%. M.p. 125–126 °C (dec.); ^{1}H NMR (C_6D_6, 250 MHz): δ 7.86 (d, $^3J_{H-H} =$ 8.4 Hz, *m*-CH aryl, 6 H), 6.68 (d, $^3J_{H-H} = 8.4$ Hz, *o*-CH aryl, 6 H), 4.59 (sept, $^3J_{H-H} = 6$ Hz, OC*H*$(CH_3)_2$, 1 H), 2.48 (s, $N(CH_3)_2$, 18 H), 1.48 (d, $^3J_{H-H} = 6$ Hz, OCH(C*H*$_3)_2$, 6 H) ppm; ^{13}C NMR (C_6D_6, 100.6 MHz): δ 151.7 (*C*–NMe_2), 138.0 (*m*-CH), 125.3 (ipso-C–Sn), 113.4 (*o*-CH), 67.5 (O*C*H$(CH_3)_2$), 39.8 ($N(CH_3)_2$), 28.4 (OCH(*C*$H_3)_2$) ppm; ^{118}Sn NMR (C_6D_6, 149.2 MHz): δ −66.6 ppm; *Anal.* Calc. for $C_{27}H_{37}ON_3Sn$ (538.312): C, 60.24; H, 6.93. Found: C, 60.12; H, 6.78%.

2.3.11. $(p\text{-}Me_2NC_6H_4)_2Sn(NMe_2)_2$

(p-$Me_2NC_6H_4)_2SnCl_2$ (2094 mg, 4.87 mmol) and $LiNMe_2$ (550 mg, 10.78 mmol). Yield 1900 mg, 87%. M.p. 75–76 °C (dec.); ^{1}H NMR (C_6D_6, 400 MHz): δ 7.69 (d, $^3J_{H-H} = 8.4$ Hz, *m*-CH aryl, 4 H), 6.66 (d, $^3J_{H-H} =$ 8.4 Hz, *o*-CH aryl, 4 H), 3.11 (s, Sn–$N(CH_3)_2$, 12 H), 2.49 (s, *p*-$N(CH_3)_2$, 12 H) ppm; ^{13}C NMR (C_6D_6, 100.6 MHz): δ 151.7 (*C*–$N(CH_3)_2$), 138.0 (*m*-CH), 123.1 (ipso-C–Sn), 113.4 (*o*-CH), 44.1, (Sn–$N(CH_3)_2$), 39.7 (*p*-$N(CH_3)_2$) ppm; ^{118}Sn NMR (C_6D_6, 149.2 MHz): δ −60.8 ppm; *Anal.* Calc. for $C_{20}H_{32}N_4Sn$ (447.205): C, 53.71; H, 7.21. Found: C, 53.44; H, 7.03%.

2.4. General procedure for the synthesis of $(p\text{-}XC_6H_4)_3SnO^iPr$ ($X = CF_3$, F, Me)

Typically, a suspension of (p-$XC_6H_4)_3SnCl$ (1 equiv) and LiO^iPr (1.1 equiv) in benzene was vigorously stirred for two days at room temperature and for ca 4 h at 60 °C. After centrifugation and filtration of the mixture all volatiles were removed under vacuum and the residues were either recrystallized from hexanes at −40 °C or distilled under vacuum (Kugelrohr apparatus) to yield analytically pure samples of the title compounds.

2.4.1. $(p\text{-}MeC_6H_4)_3SnO^iPr$

(p-$MeC_6H_4)_3SnCl$ (1735 mg, 4.06 mmol) and LiO^iPr (280 mg, 4.24 mmol). Yield 1340 mg, 73%. Bp. 135 °C (4×10^{-2} mbar); ^{1}H NMR (C_6D_6, 400 MHz): δ 7.7 (d, $^3J_{H-H} = 7.6$ Hz, *m*-CH aryl, 6 H), 7.06 (d, $^3J_{H-H} =$ 7.6 Hz, *o*-CH aryl, 6 H), 4.42 (sept, $^3J_{H-H} = 6$ Hz, OC*H*$(CH_3)_2$, 1 H), 2.07 (s, CH_3, 9 H), 1.36 (d, $^3J_{H-H} =$ 6 Hz, OCH(C*H*$_3)_2$, 6 H) ppm; ^{13}C NMR (C_6D_6, 62.9 MHz): δ 139.8 (*C*–CH_3), 137.0 (*m*-CH), 135.7 (ipso-C–Sn), 129.9 (*o*-CH), 67.9 (O*C*H$(CH_3)_2$), 28.2 (C–*C*H_3), 21.4 (OCH(*C*$H_3)_2$) ppm; ^{118}Sn NMR (C_6D_6, 149.2 MHz): δ −85.9 ppm; *Anal.* Calc. for $C_{24}H_{28}OSn$ (451.189): C, 63.89; H, 6.26. Found: C, 63.67; H, 6.05%.

2.4.2. $(p\text{-}FC_6H_4)_3SnO^iPr$

(p-$FC_6H_4)_3SnCl$ (1336 mg, 3.04 mmol) and LiO^iPr (220 mg, 3.33 mmol). Yield 880 mg, 63%. M.p. 53–54 °C; ^1H NMR (C_6D_6, 400 MHz): δ 7.36 (dd, $^3J_{H-H} = 8.4$ Hz, d, $^3J_{H-F} = 6$ Hz, *m*-CH aryl, 4 H), 6.87 (tr, $^3J_{H-H} = 8.4$ Hz, *o*-CH aryl, 4 H), 4.18 (sept, $^3J_{H-H} = 6$ Hz, $OCH(CH_3)_2$, 1 H), 1.23 (d, $^3J_{H-H} = 6$ Hz, $OCH(CH_3)_2$, 6 H) ppm; ^{13}C NMR (C_6D_6, 62.9 MHz): δ 164.7 (d, $^1J_{C-F} = 249.7$ Hz, C–F), 138.5 (d, $^3J_{C-F} = 6.9$ Hz, *m*-CH), 133.5 (d, $^4J_{C-F} = 3.8$ Hz, ipso-C–Sn), 116.5 (d, $^2J = 20.1$ Hz, *o*-CH), 68.0 ($OCH(CH_3)_2$), 28.0 ($OCH(CH_3)_2$) ppm; ^{118}Sn NMR (C_6D_6, 149.2 MHz): δ −89.1 ppm; *Anal.* Calc. for $C_{21}H_{19}F_3OSn$ (463.080): C, 54.47; H, 4.14. Found: C, 54.21; H, 4.07%.

2.4.3. $(p\text{-}CF_3C_6H_4)_3SnO^iPr$

(p-$CF_3C_6H_4)_3SnCl$ (967 mg, 1.64 mmol) and LiO^iPr (120 mg, 1.82 mmol). Yield 840 mg, 84%. M.p. 92–93 °C; ^1H NMR (C_6D_6, 400 MHz): δ 7.41 (d, $^3J_{H-H} = 8$ Hz, *o*-CH aryl, 6 H), 7.37 (d, $^3J_{H-H} = 8$ Hz, *m*-CH aryl, 6 H), 4.14 (sept, $^3J_{H-H} = 6$ Hz, $OCH(CH_3)_2$, 2 H), 1.20 (d, $^3J_{H-H} = 6$ Hz, $OCH(CH_3)_2$, 12 H) ppm; ^{13}C NMR (C_6D_6, 62.9 MHz): δ 142.5 (ipso-C–Sn), 137.0 (*o*-CH), 132.6 (d, $^2J_{C-F} = 32.7$ Hz, *C*–CF_3), 125.7 (d, $^3J_{C-F} = 3.8$ Hz, *m*-CH), 124.6 (d, $^1J_{C-F} = 272.4$ Hz, C–CF_3), 68.5 ($OCH(CH_3)_2$), 27.9 ($OCH(CH_3)_2$) ppm; ^{118}Sn NMR (C_6D_6, 149.2 MHz): δ −106.0 ppm; *Anal.* Calc. for $C_{24}H_{19}F_9OSn$ (613.103): C, 47.02; H, 3.12. Found: C, 46.89; H, 2.98%.

2.5. Competitive studies on the ring-opening of lactide with $(p\text{-}X\text{-}C_6H_4)_3SnOiPr$ where X = F, Me, NMe_2

(1) 11.8 mg of (p-$FC_6H_4)_3SnOiPr$ and 11.6 mg of (p-$MeC_6H_4)_3SnOiPr$ and 3.7 mg of L-lactide (1:1:1 ratio) were dissolved in benzene-D_6 (0.5 mL) and the reaction was monitored after ca. 13 h at r.t. by ^1H NMR spectroscopy (ratio: 1.0:0.7 for X = F:Me).

(2) 6.8 mg of (p-$MeC_6H_4)_3SnOiPr$ and 8.1 mg of (p-$Me_2NC_6H_4)_3SnOiPr$ and 2.5 mg of L-lactide (1:1:1 ratio) were dissolved in benezene-D_6 (0.5 mL) and the reaction was monitored after ca. 130 min at r.t. by ^1H NMR spectroscopy (ratio: 0.9:1.0 for X = Me:NMe_2). In competitive experiments the initial loss of the triaryltin complex was monitored. At longer time the ^1H NMR spectra are complicated by other reactions including further LA insertion and *trans* esterification.

2.6. Crystallography

A summary of crystal data collection and refinement details for compounds (p-$Me_2NC_6H_4)_3SnO^iPr$, $Ph_2Sn(O^iPr)_2$ and (p-$FC_6H_4)_2Sn(O^iPr)_2$ is given in Table 1. The data collection crystals for (p-$Me_2NC_6H_4)_3SnO^iPr$ were colorless rectangular plates, $Ph_2Sn(O^iPr)_2$ was a colorless plate, and (p-$FC_6H_4)_2Sn(O^iPr)_2$ was a colorless triangular chunk. Single crystal data sets were collected on a Nonius Kappa CCD diffractometer with Mo Kα radiation at low temperature using an Oxford Cryosystems Cryostream Cooler. All sets were measured out to 2θ of 55°. Data integration was done with Denzo [18]. Scaling and merging of the data was done with Scalepack [18]. All structures were solved by the direct methods procedure or the Patterson method in SHELXS-86[19a] or SHELXS-97 [19b]. Full-matrix least-squares refinements based on F^2 were done SHELXL-97 [20], as incorporated in the WINGX package [21].

The methyl group hydrogen atoms were added at calculated positions using a riding model with U(H) = 1.5*Ueq-(bonded C atom). For each methyl group, the torsion angle, which defines its orientation about the C–C bond was refined. The other hydrogen atoms were included in

Table 1
Summary of crystallographic data

Compound	(p-$Me_2NC_6H_4)_3SnO^iPr$	$[Ph_2Sn(O^iPr)_2]_2$	$[(p\text{-}FC_6H_4)_2Sn(O^iPr)_2]_2$
Formula	$C_{27}H_{37}ON_3Sn$	$C_{36}H_{48}O_4Sn_2$	$C_{36}H_{44}F_4O_4Sn_2$
Molar mass	538.29	782.12	854.13
Crystal system	monoclinic	monoclinic	monoclinic
Space group	$P2_1/c$	$P2_1/c$	$P2_1/n$
a (Å)	10.5507(1)	10.538(1)	10.869(1)
b (Å)	23.5325(3)	15.684(2)	13.324(2)
c (Å)	11.5562(1)	11.641(1)	13.220(2)
β (°)	112.646(1)	112.089(4)	106.118(5)
V (Å^3)	2648.01(5)	1782.8(3)	1839.2(4)
Z	4	2	2
$\rho_{(calc)}$ (Mg/m^3)	1.35	1.457	1.542
Crystal size (mm)	0.04 × 0.15 × 0.38	0.15 × 0.23 × 0.27	0.31 × 0.31 × 0.35
Temperature (K)	150(2)	200(2)	150(2)
Absorption coefficient (mm^{-1})	0.987	1.435	1.413
Data/restraints/parameters	6046/0/289	4070/0/194	4213/0/212
R_1 [$I > 2\sigma$(I)]	0.030	0.020	0.021
R_1, wR_2 all data	0.064, 0.061	0.030, 0.045	0.032, 0.049
Goodness of fit	0.995	1.033	1.045
Maximum and minimum peaks in final difference map (e/Å^3)	0.772 and −0.359	0.748 and −0.373	0.569 and −0.435

the model at calculated positions using a riding model with U(H) = 1.2*Ueq(bonded C atom). Neutral atom scattering factors were used and include terms for anomalous dispersion [22].

3. Results and discussion

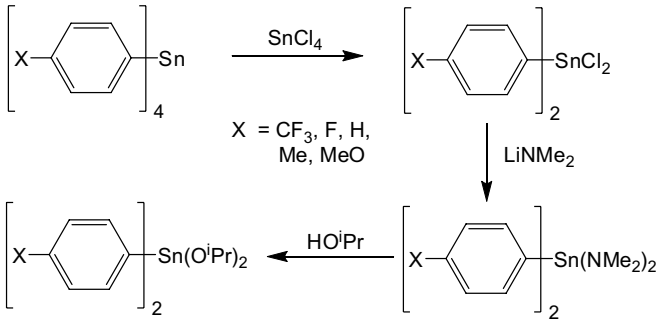
3.1. Preparations

The new compounds described in this work were prepared via the Kochesnikov redistribution reactions as shown in Schemes 2–4.

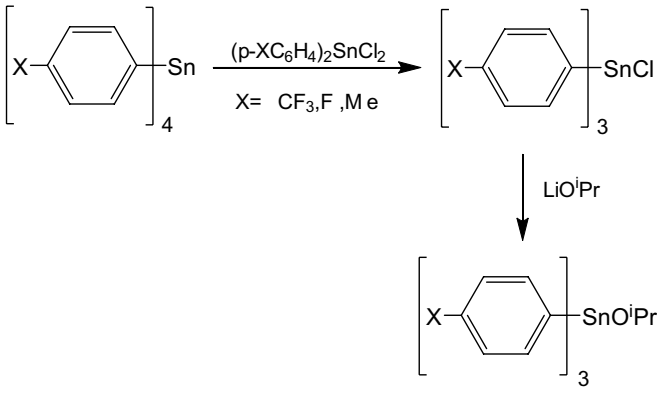
3.2. Structures

The $(p\text{-}XC_6H)_3Sn(OPr^i)$ compounds are monomeric in benzene solution and in the solid state and the molecular structure of the complex $(p\text{-}Me_2NC_6H_4)_3Sn(OPr^i)$ is shown in Fig. 1.

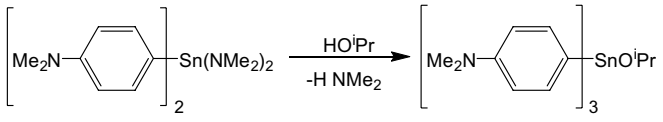
In contrast the bisaryltin(IV) isopropxides are loosely associated dimeric species in the solid state. The molecular structure of the $[(Ph)_2Sn(OPr^i)_2]_2$ dimer is shown in Fig. 2.



Scheme 2. Synthesis of $(p\text{-}XC_6H_4)_2Sn(O^iPr)_2$ (X = CF_3, F, H, Me, MeO).



Scheme 3. Synthesis of $(p\text{-}XC_6H_4)_3SnO^iPr$ (X = CF_3, F, Me).



Scheme 4. Synthesis of $(p\text{-}Me_2NAr)_3SnO^iPr$.

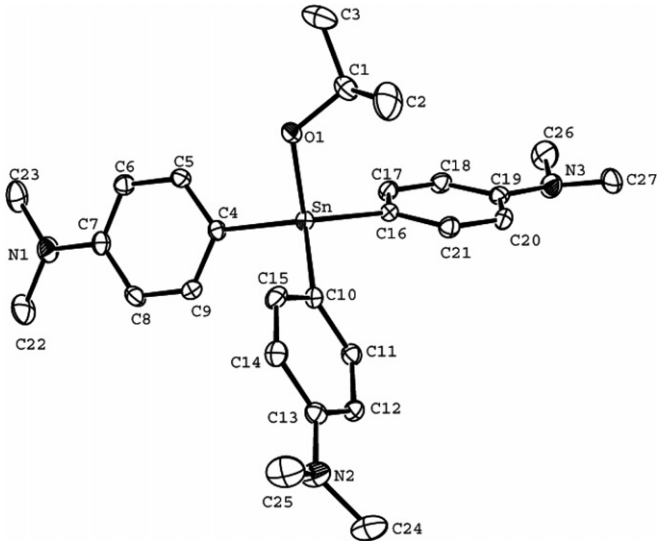


Fig. 1. Molecular structure of $(p\text{-}Me_2NC_6H_4)_3SnO^iPr$ in the crystal. The thermal ellipsoids correspond to 30% probability. Hydrogen atoms are omitted for clarity. Selected bond lengths (Å) and angles (°): Sn–O1 2.0007(15), Sn–C4 2.110(2), Sn–C10 2.121(2), Sn–C16 2.120(2), C1–O1 1.423(3), C1–C2 1.501(3), C1–C3 1.514(3), O1–C1–C2 110.2(2), O1–C1–C3 108.61(19), Sn–O1–C1 119.79(13), O1–Sn–C4 100.38(7), O1–Sn–C16 105.84(7), O1–Sn–C10 110.09(8), C4–Sn–C16 119.09(8), C4–Sn–C10 109.64(8), C16–Sn–C10 111.00(8).

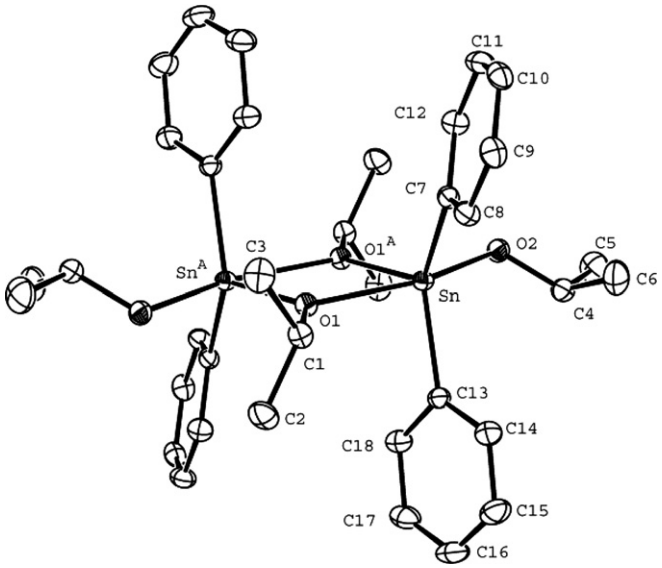
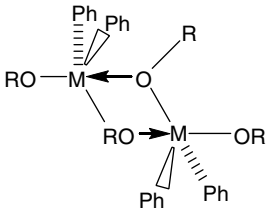


Fig. 2. Molecular structure of $[Ph_2Sn(O^iPr)_2]_2$ in the crystal. The thermal ellipsoids correspond to 30% probability. Hydrogen atoms are omitted for clarity.

The molecule has a crystallographically imposed center of inversion. The coordination geometry about the Sn(IV) center can be described as that of a highly distorted trigonal bipyramid with the terminal Sn–O2 and bridging Sn–O1 bonds being mutually *trans*, O2–Sn–O1 = 162.71(5)°. The bridging Sn–O bonds are very asymmetric with one being short, Sn–O1A = 2.020(1) and one long Sn–O1 = 2.356(1) Å. Another way to view the geometry is to consider that the structure is the result of two pseudo tetrahedral SnO_2C_2

centers weakly associating via the formation of a Sn–O dative bond as depicted below.



The molecular structure of the related complex $[(p\text{-}FC_6H_4)_2Sn(OPr^i)_2]_2$ is shown in Fig. 3 and a comparison of structural data is given in Table 2.

3.3. Solution NMR studies

In order to interrogate the nature of the bis-aryl tin alkoxides in solution we undertook NMR studies that imply that the weakly associated dimers observed in the solid state dissociated to monomers in solution. (1) Only one type of alkoxide group is seen by NMR spectroscopy, (2) the ^{119}Sn NMR signals are sharp and their chemical shifts appear in the range of other known monomeric triarylstannalkoxides and (3) the DOSY NMR spectra for these two compounds yield diffusion coefficients and estimated radii that are comparable to the known monomeric compounds Ph_2SnCl_2 and Ph_3SnCl.

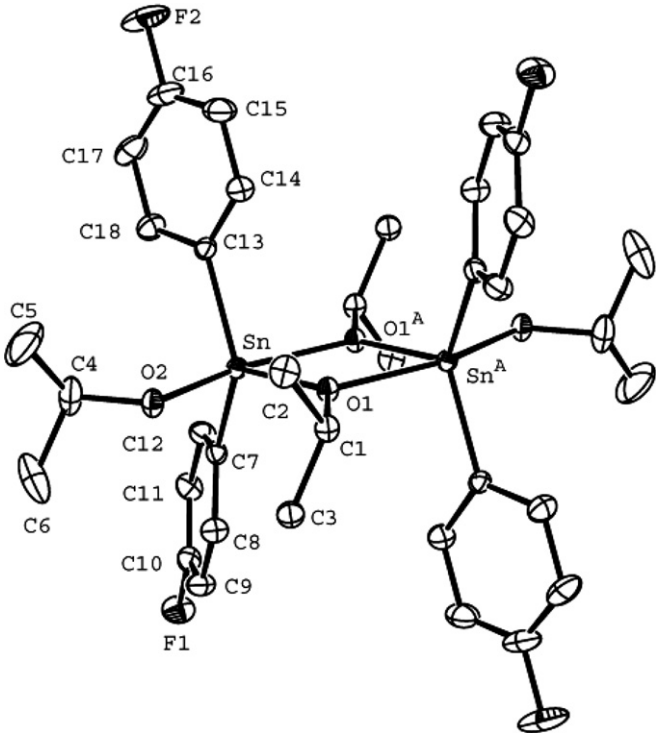


Fig. 3. Molecular structure of $[(p\text{-}FC_6H_4)_2Sn(O^iPr)_2]_2$ in the crystal. The thermal ellipsoids correspond to 30% probability. Hydrogen atoms are omitted for clarity.

Table 2
Selected distances [Å] and angles [°] of $Ph_2Sn(O^iPr)_2$ and $(p\text{-}FC_6H_4)_2Sn(O^iPr)_2$

	$Ph_2Sn(O^iPr)_2$	$(p\text{-}FC_6H_4)_2Sn(O^iPr)_2$
Sn–O1	2.356(1)	2.021(1)
Sn–O1A	2.020(1)	2.292(1)
Sn–O2	2.013(1)	2.011(1)
C1–O1	1.448(2)	1.458(2)
C4–O2	1.424(2)	1.419(2)
Sn–C7	2.131(2)	2.133(2)
Sn–C13	2.131(2)	2.126(2)
O1–Sn–O1A	68.44(5)	68.76(5)
Sn–O1–SnA	111.56(5)	111.24(5)
O1–Sn–O2	162.71(5)	91.95(5)
O2–Sn–O1A	94.31(5)	160.71(5)
Sn–O1–C1	119.35(10)	129.38(10)
Sn–O2–C4	120.85(11)	118.52(12)

3.4. Studies of kinetics

As described in the Experimental Section the reactions were monitored by ^1H NMR spectroscopy in benzene-d_6 over various temperatures with the catalyst to monomer L-LA ratio of 1:50. The conversion of monomer LA to polymer PLA was determined by integration as was the equilibrium concentration of monomer as a function of temperature. The natural log of the equilibrium monomer concentration was then plotted against $1/T$ to give a straight line. These data are shown in Fig. 4 and were used in the various polymerization reactions.

The values of k_{obs} were determined from the gradient of a plot of $-\ln\{[A]-[A]_{eq}/[A]_0-[A]_{eq}\}$ versus time as shown in Fig. 5.

The activation parameters, $\Delta H^{\neq}$ and $\Delta S^{\neq}$, were extracted from the Arrhenius plots of $-\ln k/T$ versus $1/T$ (see Fig. 6). The activation parameters are summarized in Table 3.

We also examined the order of the reaction in [Sn] under pseudo-first-order conditions where [LA]/[Sn] > 45. The plot of k_{obs} versus [Sn] for the five samples examined when [Sn] represents the concentration of $Ph_2Sn(OPr^i)_2$

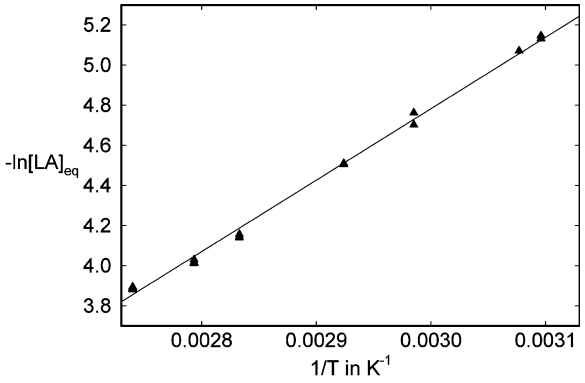


Fig. 4. Plots of $-\ln[LA]_{eq}$ vs. $1/T$ giving a straight line, which allows for the determination of the equilibrium monomer concentration of L-lactide (LA) at various temperatures.

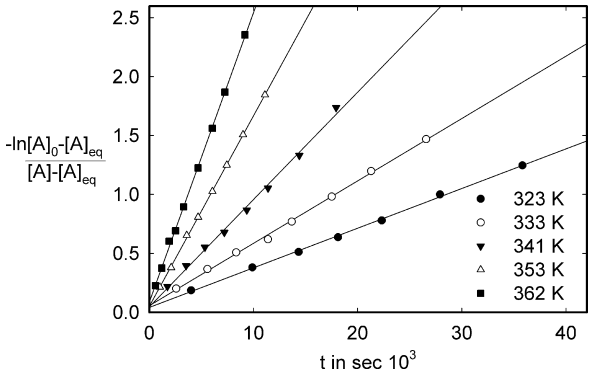


Fig. 5. Typical plot of $-\ln[[A_0] - [A_{eq}]/[A] - [A_{eq}]]$ vs. time in the ROP of L-lactide by $Ph_2Sn(O^iPr)$ at various temperatures.

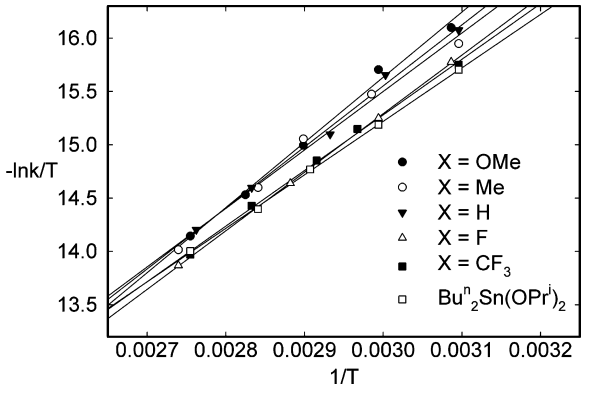


Fig. 6. Plots of $-\ln k/T$ vs. $1/T$, giving a straight line, which allows for the determination of the activation parameters ΔH^* and ΔS^*.

Table 3
Calculated activation parameters for the polymerization of lactide with (p-$XC_6H_4)_2Sn(O^iPr)_2$ and $Bu^n_2Sn(OPr^i)_2$ as catalysts

Catalysts	ΔH^*(kcal/mol)	ΔS^* (e.u.)
(p-$MeOC_6H_4)_2Sn(O^iPr)_2$	12.1(5)	−53(5)
$(Ph)_2Sn(O^iPr)_2$	11.4(5)	−50(5)
(p-$MeC_6H_4)_2Sn(O^iPr)_2$	10.9(5)	−49(5)
(p-$FC_6H_4)_2Sn(O^iPr)_2$	11.2(5)	−44(5)
(p-$CF_3C_6H_4)_2Sn(O^iPr)_2$	10.4(5)	−48(5)
(n-$Bu)_2Sn(O^iPr)_2$	10.0(5)	−47(5)

employed in the polymerization at 70 °C is shown in Fig. 7a. As can be seen the plot yields a straight line with a non-zero intercept in [Sn]. The only reasonable explanation for this is that in each case studied an equivalent amount of the catalyst is inactive and is presumably removed from the system by hydrolysis or some other reaction that leads to its inactivity. This situation is not uncommon and was specifically noted by Hillmyer et al. [23] in a related study of the polymerization of LA by a monomeric zinc alkoxide complex.

The plot of $\ln k$ versus $-\ln[Sn]$ from which the order of the reaction in tin can be deduced is shown in Fig. 7b (order in [Sn] 1.41). In constructing this plot we have assumed the correlation for the concentration of [Sn] by its intercept in Fig. 7a. From this we obtain an order in [Sn] of 0.93., which we take to imply first order reactivity. Once again this situation is similar to that described by Hillmyer [23].

As can be seen from Table 3 there is a very small range of $\Delta H^{\neq}$ values and for the p-XC_6H_4 groups it appears that the electron withdrawing substituents lower that activation enthalpy when compared with the electron donating OMe group. However, the range is very small. A plausible interpretation of this would be that the more electrophilic the metal center exhibits greater Lewis acidity toward the LA monomer thus favoring a larger K_{eq} for the reversible binding of LA. The reactivity of $(Bu^n)_2Sn(OPr^i)_2$ which is comparable to the (p-$CF_3C_6H_4)_2Sn(OPr^i)_2$ complex is an outrigger in as much as its steric factors are not the same.

Irrespective of the interpretation that may be placed on the subtle factors influencing $\Delta H^{\neq}$, one point that emerges unequivocally from this study is that the entropy of activation is large in magnitude and negative, $\Delta S^{\neq} \sim -50 \pm 5$ eu. This is quite a bit larger than typically seen for a bimolecular reaction for which $\Delta S^{\neq}$ values fall in the range of −25 to −35 eu. Values of ~ -50 eu imply a very highly ordered transition state as is sometimes found for constrained cyclic transition states. For example, 2 + 2 cycloadditions in organic chemistry generally have $\Delta S^{\neq}$ values of 35 ± 5 eu [24]. Recent computations by Gibson et al. [25,26] on the ROP of LA by Mg and Sn alkoxides would seem to sup-

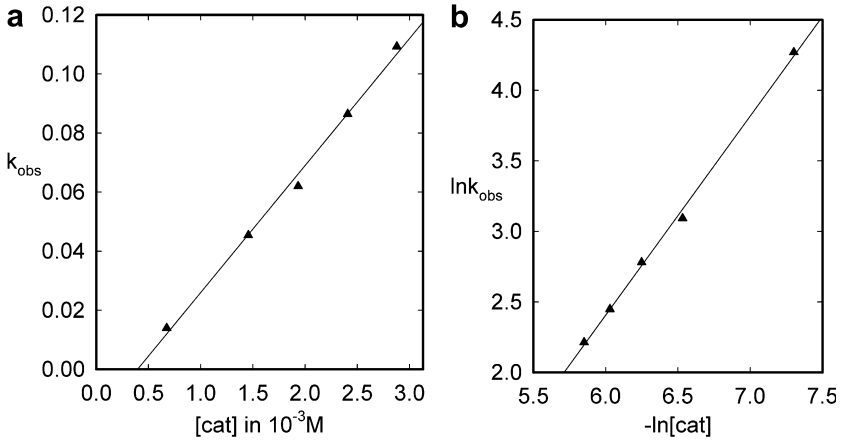


Fig. 7. Plots of k_{obs} vs. [cat] (a) and $\ln k_{obs}$ vs. $-\ln$[cat] (b) in the ROP of L-lactide by different concentrations of $Ph_2Sn(OPr^i)_2$ at 70 °C.

port this view but in our present study we have not evaluated the influence of solvent.

4. Supplementary material

CCDC 637509, 637508 and 637510 contain the supplementary crystallographic data for $(p\text{-}Me_2NC_6H_4)_3SnO^iPr$, $Ph_2Sn(O^iPr)_2$ and $(p\text{-}FC_6H_4)_2Sn(O^iPr)_2$. These data can be obtained free of charge via http://www.ccdc.cam.ac.uk/conts/retrieving.html, or from the Cambridge Crystallographic Data Centre, 12 Union Road, Cambridge CB2 1EZ, UK; fax: (+44) 1223-336-033; or e-mail: deposit@ccdc.cam.ac.uk.

Acknowledgements

We thank the Department of Energy, Office of Basic Sciences, Chemistry Division for support of this work.

References

[1] O. Dechy-Cabaret, B. Martin-Vaca, D. Bourissou, Chem. Rev. 104 (2004) 6147.
[2] F. Neederberg, E.F. Connor, T. Glausser, J.L. Hedrick, Chem. Commun. (2001) 2006.
[3] F. Neederberg, E.F. Connor, M. Moeller, T. Glauser, J.L. Hedrick, Angew. Chem., Int. Ed. 40 (2001) 2712.
[4] G.W. Nyce, T. Glauser, E.F. Connor, A. Möck, R.M. Waymouth, J.L. Hedrick, J. Am. Chem. Soc. 125 (2003) 3046.
[5] B.J. O'Keefe, M.A. Hillmyer, W.B. Tolman, J. Chem. Soc., Dalton Trans. (2001) 2215.
[6] M.H. Chisholm, Z. Zhou, in: L. Baugh, J. Canich (Eds.), Stereoselective Polymerization with Single Site Catalysts, Taylor and Francis publishers, 2007.
[7] N. Spassky, M. Wisniewski, C. Pluta, A. LeBorgne, Macromol. Chem. Phys. 197 (1996) 2627.
[8] N. Spassky, C. Pluta, V. Simic, M. Thiam, M. Wisniewski, Macromol. Symp. 128 (1998) 39.
[9] C.P. Radano, G.L. Baker, M.R. Smith III, J. Am. Chem. Soc. 122 (2000) 1552.
[10] T.M. Ovitt, G.W. Coates, J. Am. Chem. Soc. 124 (2002) 1316.
[11] P. Hormnirun, E.L. Marshall, V.C. Gibson, A.J.P. White, D. Williams, J. Am. Chem. Soc. 126 (2004) 2688.
[12] Z. Zhong, P.J. Dijkstra, J. Feijen, J. Am. Chem. Soc. 125 (2003) 11291.
[13] Z. Tang, X. Chen, X. Pang, Y. Yang, X. Zhang, X. Jing, Biomacromolecules 5 (2004) 965.
[14] M.H. Chisholm, Z. Zhou, Chem. Commun. (2005) 127.
[15] M.H. Chisholm, E.E. Delbridge, New J. Chem. 27 (2003) 1167.
[16] M.H. Chisholm, E.E. Delbridge, New J. Chem. 27 (2003) 1177.
[17] M.H. Chisholm, E.E. Delbridge, J.C. Gallucci, New J. Chem. 28 (2004) 145.
[18] DENZO: Z. Otwinowski, W. Minor, in: C.W. CarterJr., R.M. Sweet (Eds.), Methods in Enzymology, vol. 276: Macromolecular Crystallography, part A, Academic Press, 1997, pp. 307–326.
[19] (a) SHELXS-86 G.M. Sheldrick, Acta Cryst. A46 (1990) 467–473; (b) G.M. Sheldrick, SHELXS-97, Universitat Gottingen, Germany, 1997.
[20] G.M. Sheldrick, SHELXL-97, Universitat Gottingen, Germany, 1997.
[21] WINGX-Version 1.64.05 L.J. Farrugia, J. Appl. Cryst. 32 (1999) 837–838.
[22] International Tables for Crystallography, Volume C. Dordrecht: Kluwer Academic Publishers, 1992.
[23] C.K. Williams, L.E. Breyfogle, S.K. Choi, W. Nam, V.G. Young, M.A. Hillmyer, W.B. Tolman, J. Am. Chem. Soc. 125 (2003) 11350.
[24] R.B. Woodward, R. Hoffmann, The Conservation of Orbital Symmetry, Academic Press, New York, 1969.
[25] E.L. Marshall, V.C. Gibson, H.S. Rzepa, J. Am. Chem. Soc. 127 (2005) 6048.
[26] A.P. Dove, V.C. Gibson, E.L. Marshall, H.S. Rzepa, A.J.P. White, D.J. Williams, J. Am. Chem. Soc. 128 (2006) 9834.

2. Results and discussion

2.1. Ligand synthesis and structural characterization

The transformation of 2,2,6,6-tetramethylheptane-3,5-dione (Htmhd) into 2,2,6,6-tetramethyl-3-amino-4-hepten-5-one (Htmha or **1**) may be presented as Eq. (1)

$$\mathrm{Htmhd} + \mathrm{NH_3} \rightarrow \mathrm{Htmha} + \mathrm{H_2O} \quad (1)$$

This reaction is quite possible if water is removed from the reaction mixture by a physical method (distillation or binding with molecular sieves) or by chemical methods (the reaction with $TiCl_4$, $SiCl_4$, $Si(CH_3)_3Cl$, $AlCl_3$, PCl_5, etc.). We have chosen $TiCl_4$ as the water acceptor. $TiCl_4$ is supposed to react with water in the organic solvent in two stages (Eqs. (2) and (3)) [17]

$$TiCl_4 + H_2O \rightarrow TiOCl_2 + 2HCl \quad (2)$$

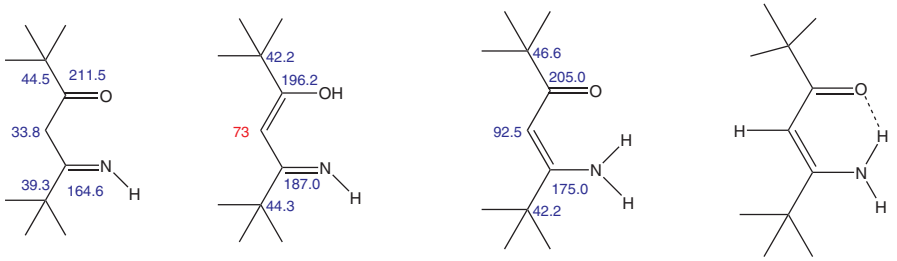
$$TiOCl_2 + H_2O \rightarrow TiO_2 + 2HCl \quad (3)$$

Our investigation shows that these two stages are suitable for the synthesis of Htmha from Htmhd under an excess of dry ammonia, but the best yield of the product was obtained for the combination of reactions (1) + (3). Therefore we added for the synthesis technique proposed an appropriate amount of water to $TiCl_4$ to produce $TiOCl_2$ before the addition of Htmhd. At the final stage of the synthesis we used an adequate amount of aqueous ammonia to hydrolyze the intermediate. Our technique allowed us to obtain only the N,O substituted product **1**, the product with a higher amination degree (N,N substituted diimine) being not isolated. Nevertheless, the formation of diimine products has been demonstrated in the literature [12,16], though it was established for compounds without bulky *tert*-butyl substituents. Hence, we cannot exclude the diimine product formation in our case, but it might have been destroyed by water. The IR spectra of the compound obtained show two bands at 3405 and 3346 cm^{-1}, assigned to ν(N–H) [18] vibrations. The chemical analysis results evidence the presence of only one imino group in the molecule. In combination, the whole data collection on the compound identification confirms the preparation of Htmha. It should be noted that our synthesis technique is easily monitored and is guided by the color change during the procedure, due to the specific colors of each titanium intermediate.

It is possible to present the synthesized 2,2,6,6-tetramethyl-3-amino-4-hepten-5-one (**1**) as three tautomeric structures with the oxygen atom in the ketone or enol form (Fig. 1a–c, numbers in Fig. 1 represent ^{13}C chemical shifts estimated with the help of ChemDraw Ultra 8.0). The observed ^{13}C NMR spectrum unambiguously reveals that the ketone form **1a** does not exist in the investigated solution, because there is a signal for the =CH– group and no signal of a $–CH_2–$ group. The unresolved triplet of the =CH– group exists in the ^1H NMR spectrum and, moreover, there are two broad signals which can be referred to protons of HNH– or –NH– and OH– groups.

The chemical shifts of 205.5 and 173.3 ppm in the ^{13}C NMR spectrum fit well to the results computed for carbons bonded to heteroatoms in structure **1c** (205 and 175 ppm respectively). This agrees with commonly accepted views that enaminoketones of all types exist predominantly in the carbonyl form [19]. However, the noticeable deviation of the computed chemical shifts for **1c** from the observed ones for γ-carbon and quaternary carbons of the $–C(CH_3)$ groups makes us assume that compound **1** exists in solution as a form close to **1d**, that arises from **1c** due to a hydrogen bond forming between one of the protons of the $–NH_2$ group and an oxygen atom. In the ^1H NMR spectrum the broad signal at 10.4 ppm corresponds to the hydrogen atom of the –HN–*H*–O– moiety, and the second broad signal at 5 ppm is assigned to another proton of the amino group, not connected with an oxygen atom.

A single-crystal X-ray diffraction study reveals that there are two crystallographically independent molecules in the crystal structure of Htmha, which are shown with atom numbering in Fig. 2. The structure and the conformation of the molecules are very close, the average lengths of the C=N and C=O bonds being 1.326 and 1.254 ($\Delta = 0.074$) Å respectively (Table 2). The length difference for the C–Cγ bonds does not exceed 0.04 Å. In the *tert*-butyl substituents the $C–CH_3$ distances are the same, 1.530 Å. In the amino group, one of the N–H bonds is elongated by ~0.1 Å to the oxygen atom of the ketone group, while the HNH···O distance is two times longer than the N–H bonds, suggesting some certain intramolecu-



1a 1b 1c 1d

Fig. 1. Possible tautomeric forms of Htmha in solution.

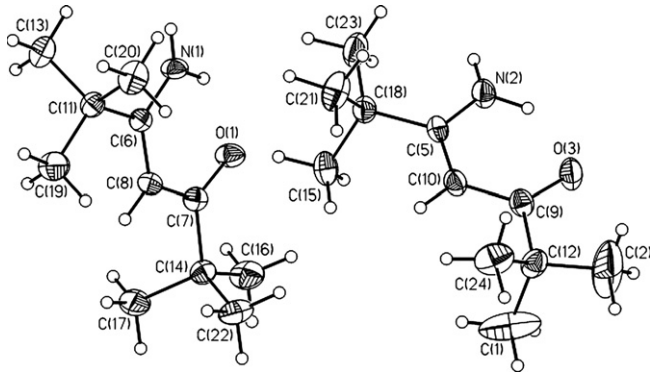


Fig. 2. ORTEP drawing of enaminoketone (**1**) molecules.

lar hydrogen bonding in the molecule (H···O 1.85 and 1.93 Å). Another hydrogen bond between the molecules occurs in the crystal with a H···O distance of 2.09 Å. A distinctive feature of the amino- group is that it is planar, and the C–NH_2 bond is much shorter than that in amines, indicating the unshared electron pair (UEP) of the nitrogen atom participates in conjugate chemical bonding. Judging from the length of the adjacent chemical bonds, a π-conjugated electron system forms at least over the N–C–C atoms in the molecule. As to the delocalization of electrons down to the ketone group, π-conjugation over the C–C–O atoms is less pronounced. Thus in the solid state, the pure ligand also appears to be rather an enaminoketone than an enol. Our data on the structure of Htmha are in good agreement with those obtained by other authors (P.-L. Franceschini, H.W. Schmalle, H. Berke, private communication, 2004, CCDC No. 249230).

2.2. Synthesis and structural characterization of $Cu[(CH_3)_3CC(NH)CHC(O)C(CH_3)_3]_2$ (**2**)

For the synthesis of the copper complex **2** we used a technique based on the reaction between the ligand and $CuCl_2 \cdot 2H_2O$ in aqueous ammonia. The reaction performance in alkaline media prevented ligand hydrolysis and raised the product yield. There is a band at 3374 cm^{-1} in the IR spectrum of **2** that indicates N–H chemical bond vibrations [18]. This data and elemental analysis results confirm the successful preparation of $Cu[(CH_3)_3CC(NH)CHC(O)C(CH_3)_3]_2$.

The crystal structure of the copper complex is molecular, built of a separate *trans*-complexes. Fig. 3 depicts the structure of compound **2**. The copper atom is located at the centre of symmetry and displays square planar coordination by two nitrogen and two oxygen atoms, giving CuO_2N_2 coordination. The difference between the Cu–O and Cu–N bond lengths is negligible, being only 0.003 Å. The distinction between C=N, C=O and symmetrical C–Cγ bonds in the chelate rings is also minimal (Table 3), i.e. the chemical bonds are leveled in the chelate ring comparing to the free ligand. For the Bu^t substituents the average C–CH_3 distance is 1.534 Å, and the C–C–C angles are close to tetrahedral within the ±5° error. The chelate rings are slightly bent along the O···N line by 1.5°. The revealed geometric parameters of this compound are in agreement with the data obtained for other copper ketoiminates [2]. Fig. 4 illustrates the package of molecules along the *x*-axis. All the intermolecular contacts are Van-der-Waals. The shortest Cu···CH_3 distance is 3.74 Å. Each molecule is surrounded by six others, and four Cu···Cu distances are

Table 1
Crystal data and structure refinement for **1**–**3**

Empirical formula	$C_{11}H_{21}NO$ (**1**)	$C_{22}H_{40}N_2O_2Cu$ (**2**)	$C_{22}H_{40}N_2O_2Ni$ (**3**)
Formula weight	183.28	428.10	423.3
Temperature (K)	150(2)	150(2)	150(2)
Wavelength (Å)	0.71073	0.71073	0.71073
Crystal system	monoclinic	monoclinic	monoclinic
Space group	$P2_1/c$	$P2_1/n$	$P2_1/n$
Unit cell dimensions			
a (Å)	12.0668(5)	9.7748(2)	9.9370(20)
b (Å)	17.6966(5)	11.9246(3)	11.8895(24)
c (Å)	11.6092(5)	11.1926(3)	11.0401(22)
β (°)	106.814(2)	110.0290(10)	110.185(30)
Volume ($Å^3$)	2373.06(16)	1225.71(5)	1224.23
Z	2	2	2
D_{calc} (g/cm^3)	1.026	1.160	1.148
Absorption coefficient (mm^{-1})	0.065	0.908	
F(000)	816	462	
θ-Range for data collection (°)	2.11–25.35	2.94–36.30	
Reflections collected	6228	14956	
Independent reflections	3500 [$R_{int} = 0.0165$]	5870 [$R_{int} = 0.0148$]	
Completeness to $\theta = 25.00°$ (%)	81.3	99.7	
Refinement method	full-matrix least-squares on F^2	full-matrix least-squares on F^2	
Data/restraints/parameters	3500/0/264	5870/0/192	
Goodness-of-fit on F^2	1.071	1.110	
Final *R* indices [$I > 2\sigma(I)$]	$R_1 = 0.0443$, $wR_2 = 0.1159$	$R_1 = 0.0353$, $wR_2 = 0.1217$	
R indices (all data)	$R_1 = 0.0589$, $wR_2 = 0.1305$	$R_1 = 0.0471$, $wR_2 = 0.1277$	

Table 2
Selected bond lengths (Å) and angles (°) for compound **1**

O(1)–C(7)	1.252(2)	O(3)–C(9)	1.255(2)
N(1)–C(6)	1.331(2)	N(2)–C(5)	1.322(2)
C(6)–C(8)	1.386(3)	C(5)–C(10)	1.386(2)
C(7)–C(8)	1.428(2)	C(9)–C(10)	1.414(3)
C(6)–C(11)	1.530(2)	C(5)–C(18)	1.529(3)
C(7)–C(14)	1.540(3)	C(9)–C(12)	1.538(3)
N(1)–C(6)–C(8)	120.53(16)	N(2)–C(5)–C(10)	120.86(17)
N(1)–C(6)–C(11)	116.35(16)	N(2)–C(5)–C(18)	118.27(16)
C(8)–C(6)–C(11)	123.11(16)	C(10)–C(5)–C(18)	120.87(16)
O(1)–C(7)–C(8)	122.61(16)	O(3)–C(9)–C(10)	122.43(17)
O(1)–C(7)–C(14)	118.35(15)	O(3)–C(9)–C(12)	118.60(16)
C(8)–C(7)–C(14)	119.03(16)	C(10)–C(9)–C(12)	118.95(16)
C(6)–C(8)–C(7)	123.83(16)	C(5)–C(10)–C(9)	124.31(17)

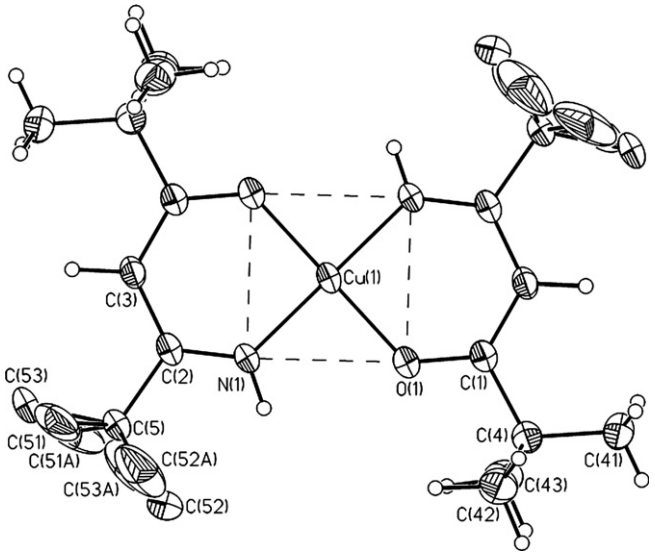


Fig. 3. ORTEP drawing of the copper(II) β-ketoiminate (**2**) molecule.

Table 3
Selected bond lengths (Å) and angles (°) for compound **2**

Cu(1)–O(1)	1.9072(10)
Cu(1)–N(1)	1.9099(9)
O(1)–C(1)	1.2884(14)
N(1)–C(2)	1.2928(13)
C(1)–C(3)#1	1.3935(16)
C(1)–C(4)	1.5325(18)
C(2)–C(3)	1.4130(17)
C(2)–C(5)	1.5395(16)
O(1)–Cu(1)–N(1)	88.19(4)
O(1)#1–Cu(1)–N(1)	91.81(4)
C(1)–O(1)–Cu(1)	127.86(8)
C(2)–N(1)–Cu(1)	128.89(8)
O(1)–C(1)–C(3)#1	124.29(11)
N(1)–C(2)–C(3)	122.47(10)
C(1)#1–C(3)–C(2)	124.64(10)

Symmetry transformations used to generate equivalent atoms: #1 $-x+2$, $-y$, $-z+2$.

8.486 Å whilst the other two are 9.775 Å. On the whole, the structure of $Cu(tmha)_2$ is close to that of $Cu(tmhd)_2$ [20]. The X-ray powder diffraction study and preliminary single-crystal experiments for $Ni[(CH_3)_3CC(NH)CHC(O)C(CH_3)_3]_2$ show that compounds **2** and **3** are isostructural.

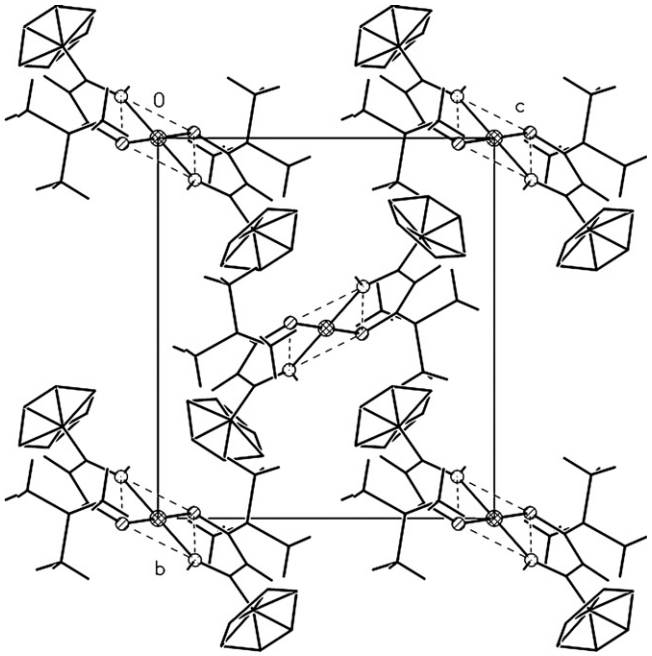


Fig. 4. Projection of the crystal packing of compound (**2**) onto the *a* plane.

2.3. Thermogravimetry study of $Cu[(CH_3)_3CC(NH)CHC(O)C(CH_3)_3]_2$ (**2**) and $Ni[(CH_3)_3CC(NH)CHC(O)C(CH_3)_3]_2$ (**3**)

A TG study, performed under a helium flow up to a final temperature of 400 °C, was carried out to compare the thermal stability of the related ketoiminate and diketonate derivatives of copper and nickel (Fig. 5). The TG curves show that the evaporation rate of **2** becomes noticeable after the melting point and is higher than that of $Cu(tmhd)_2$. The decomposition rate of compound **2** during

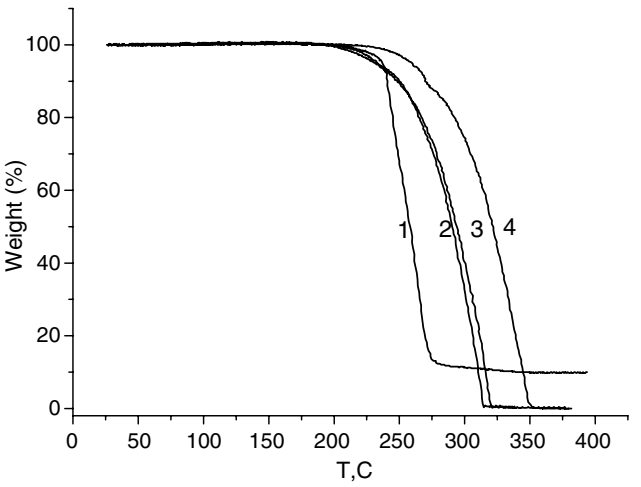


Fig. 5. TGA profiles for 1 – $Cu(tmha)_2$; 2 – $Cu(tmhd)_2$; 3 – $Ni(tmhd)_2$; 4 – $Ni(tmha)_2$.

heating also increases resulting in 9% of a solid residue. At the same time, $Cu(tmhd)_2$ evaporates slower and without decomposition at higher temperatures. Thus, compound **2** seems to be more volatile but less stable under heating than $Cu(tmhd)_2$. Surprisingly, $Ni(tmha)_2$ appeared to be less volatile than $Ni(tmhd)_2$. Even though compound **3** is less volatile than **2**, its stability to heating is obvious.

3. Concluding remarks

The ligand $(CH_3)_3CC(NH)CHC(O)C(CH_3)_3$ (**1**) was synthesized from 2,2,6,6- tetramethylheptane-3,5-dione by amination with dry ammonia in the presence of $TiCl_4$ in benzene at room temperature. The Cu(II) complex $Cu[(CH_3)_3CC(NH)CHC(O)C(CH_3)_3]_2$ (**2**) and the Ni(II) complex $Ni[(CH_3)_3CC(NH)CHC(O)C(CH_3)_3]_2$ (**3**) were synthesized in water/alcohol alkaline solutions. The compounds obtained were identified by elemental analysis, ^1H and ^{13}C NMR, IR-spectroscopy and characterized by TGA, X-ray powder diffraction and single-crystal X-ray diffraction studies. A crystallographic analysis shows that the metal complexes (**2**) and (**3**) are isostructural to each other and related β-diketonate complexes.

4. Experimental

4.1. General considerations

The solvents used in the preparation were dried and distilled from sodium benzophenone ketyl. Htmhd (2,2,6,6-tetramethylheptane-3,5-dione = dipivaloylmethane) of 99% purity (Merck) was used without pretreatment. Commercially available $TiCl_4$, $CuCl_2 \cdot 2H_2O$, $NiCl_2 \cdot 6H_2O$, NaOH, and aqueous ammonia of adequate purity were used. The synthesis of $Cu(tmhd)_2$ and $Ni(tmhd)_2$ was carried according to [21,22] respectively.

Compounds **1**, **2** ($Cu(tmha)_2$), **3** ($Ni(tmha)_2$), $Cu(tmhd)_2$ and $Ni(tmhd)_2$ were purified by vacuum sublimation in a gradient tube oven ($P \sim 10^{-3}$ Torr, $T = 50$–300 °C). The elemental analysis was performed on a Carlo-Erba 1106 device (Italy). The infrared spectra were measured in KBr pellets on a Scimitar FTS2000 spectrometer. The NMR spectra were recorded on a Bruker MSL300 spectrometer; chemical shifts were referenced to the protio impurity of the NMR solvent (^1H) or to the NMR solvent (^{13}C). The thermal analysis was performed in a He flow at the heating rate 10°/min (~150 mg samples) using a Q-1000 (F. Paulik, J. Paulik, L. Erdey) device.

The X-ray powder diffraction analysis was performed with a DRON-3M diffractometer. Ni-filtered Cu Kα radiation was used. The diffraction pattern was scanned in an angular range from 5° to 45° 2θ at room temperature.

X-ray intensity data were collected on a Bruker X8Apex CCD diffractometer at 150 K using the standard technique (ω- and φ-scans of narrow frames) and corrected for absorption effects (SADABS). The structures were solved by direct methods and refined by full-matrix least-squares on F^2 using the SHELX97 program set (Sheldrick 1998) [23]. The crystallographic data and details of single-crystal diffraction experiments for compounds **1** and **2** are given in Table 1. All non-hydrogen atoms were refined anisotropically. Hydrogen atoms of CH_3 groups were calculated by geometrical methods. In the copper complex, the Bu^t-groups from the side of the nitrogen atoms are disordered at low temperature. Selected bond lengths and angles are given in Tables 2 and 3.

4.2. Synthesis of the $(CH_3)_3CC(NH_2)CHC(O)C(CH_3)_3$ ligand (*1*)

The synthesis of $(CH_3)_3CC(NH_2)CHCOC(CH_3)_3$ (**1**) was carried out under an inert atmosphere of dry nitrogen. Htmhd (1:10 in benzene) was added dropwise to a suspension of $TiOCl_2$ ($TiCl_4 + H_2O$) in benzene under vigorous stirring in a three-neck flask. The reactants were taken in a molar ratio of 1:1 producing a red-brown mixture. A slow flow of dry nitrogen was purged above the mixture overnight. Gaseous ammonia was obtained from the reaction of NaOH with aqueous ammonia. Then NH_3, dried over NaOH, was bubbled through the mixture under stirring for a day until the reaction mixture became hazel colored. After that, a stoichiometric amount of aqueous ammonia was added by pipette under stirring over 2 h. The mixture was settled for 30 min, producing a white precipitate and a colorless solution. The solution was decanted, and the precipitate was washed with a portion of benzene and decanted again. The crude product was separated on a rotary evaporator and recrystallized from heptane after cooling in the refrigerator. The pure ligand in the form of white crystals was obtained after sublimation in a vacuum ($T = 100$ °C, $P = 10^{-3}$ Torr). Yield ~80%. *Anal.* Calc. for $C_{11}H_{21}NO$: C, 72.08; H, 11.55; N, 7.64. Found: C, 72.24; H, 11.55; N, 7.64%.

^1H and ^{13}C NMR spectra in $CDCl_3$ and $CDCl_3/CCl_4$ solutions indicate that the compound exists in the ketone form, revealing the structure with an intramolecular hydrogen bond as in Fig. 1d. ^1H NMR (300 MHz, 25 °C, ppm): 1.14 [s, $(CH_3)_3CCN$]; 1.21 [s, $(CH_3)_3CC(O)$]; 5.0 (br s, *H*NH–O); 5.32 (unresolved triplet, CH); 10.44 (br s, HN*H*–O,). ^{13}C NMR{^1H} (75.4 MHz, 25 °C, ppm): 28.5 (s, CH_3); 29.5 (s, CH_3); 36.5 (s, *C*–C=N); 42.6 (s, *C*–C=O); 87.0 (s, CH); 173.3 (s, C–N); 205.5 (s, C=O).

IR (cm^{-1}): 3405 (vs), 3347 (s), 3176 (m), 2967 (vs), 2907 (m), 2869 (m), 1633 (m), 1596 (s), 1525 (vs), 1500 (m), 1387 (m), 1363 (m), 1300 (m), 1216 (m), 1151 (vs), 1065 (vw), 1014 (m), 937 (vw), 868 (s), 798 (vw), 774 (m), 728 (w), 690 (m), 634 (m), 531 (vw), 472 (m), 406 (vw). M.p.: 131–132 °C.

4.3. Synthesis of $Cu(CH_3)_3CC(NH)CHCOC(CH_3)_3]_2$ (*2*)

0.366 g (2.0 mmol) of **1** was dissolved in 10 ml of ethanol and 2 ml of aqueous ammonia. Then a solution of 0.170 g (1.0 mmol) $CuCl_2 \cdot 2H_2O$ in 5 ml of ethanol was added

under stirring. The mixture was transferred to an evaporation dish and left for evaporation in air. 10 ml of benzene was added to the solid residue in the dish. The obtained solution was filtered and dark-violet crystals of **2** appeared after the solvent was removed. The product was purified by vacuum sublimation ($T = 180$ °C, $P = 10^{-3}$ Torr). Yield 0.3 g (70%). *Anal.* Calc. for $C_{22}H_{40}CuN_2O_2$: C, 61.72; H, 9.42; N, 6.54. Found: C, 61.95; H, 9.52; N, 6.44%.

IR (cm^{-1}): 3374 (s), 2960 (vs), 2907 (m), 2867 (m), 1579 (vs), 1524 (s), 1483 (s), 1427 (vs), 1357 (m), 1330 (s), 1237 (s), 1178 (s), 1025 (vw), 958 (w), 931 (vw), 875 (m), 777 (s), 742 (vw), 657 (vw), 627 (m), 523 (vm), 499 (m), 438 (vw), 396 (vw). M.p.: 209–210 °C.

4.4. Synthesis of $Ni(CH_3)_3CC(NH)CHCOC(CH_3)_3]_2$ (3)

0.238 g (1.0 mmol) of $NiCl_2 \cdot 6H_2O$ dissolved in 20 ml of ethanol was added under stirring to a solution of 0.366 g (2.0 mmol) of ligand **1** and 0.112 g (2.0 mmol) of KOH in 20 ml of ethanol. The mixture was heated at 60–80 °C for 1 h and then left in air until it dried. The solid residue was treated with chloroform. The extract was filtered, and red crystals of the product were isolated after the solvent evaporated. The product was purified by vacuum sublimation ($T = 190$ °C, $P = 10^{-3}$ Torr). Yield: 0.34 g (80%). *Anal.* Calc. for $C_{22}H_{40}NiN_2O_2$: C, 62.43; H, 9.53; N, 6.62. Found: C, 62.55; H, 9.41; N, 6.50.

^1H and $^{13}C\{^1H\}$ NMR spectra in $CDCl_3/CCl_4$ solution indicate that only one isomer exists in solution. It seems to us that it is the *trans*-isomer. ^1H NMR (300 MHz, 25 °C, ppm, Hz): 0.99 [s, $(CH_3)_3C$]; 1.27 [s, $(CH_3)_3C$]; 5.082 (d, CH, 2.8); 5.37 (br s, HN). $^{13}C\{^1H\}$ NMR (75.4 MHz, 25 °C, ppm): 29.0 (s, CH_3); 29.3 (s, CH_3); 38.0 (s, *C*–$C(H_3)_3$); 38.8 (s, *C*–$C(H_3)_3$); 89.0 (s, CH); 176.7 (s, C–N); 185.8 (s, C=O).

IR (cm^{-1}): 3366 (s), 3175 (vw), 2959 (vs), 2867 (s), 1587 (vs), 1497 (vs), 1431 (s), 1357 (m), 1326 (s), 1241 (m), 1222 (s), 1173 (s), 1113 (w), 1026 (w), 969 (w), 931 (vw), 880 (m), 823 (vw), 782 (vs), 701 (vw), 666 (m), 532 (w), 515 (w), 443 (vw), 408 (vw). M.p.: 267–268 °C.

5. Supplementary material

CCDC 634189 and 634188 contain the supplementary crystallographic data for **1** and **2**. These data can be obtained free of charge via http://www.ccdc.cam.ac.uk/conts/retrieving.html, or from the Cambridge Crystallographic Data Centre, 12 Union Road, Cambridge CB2 1EZ, UK; fax: (+44) 1223-336-033; or e-mail: deposit@ccdc.cam.ac.uk.

References

[1] J.A. McCleverty, T.J. Meyer (Editors-in-Chief), Comprehensive Coordination Chemistry II, vol. 1, Chapter 1.19 and vols. 3 and 4, Elsevier Ltd., 2003.
[2] P.A. Stabnikov, I.A. Baidina, S.V. Sysoev, N.S. Vanina, N.B. Morozova, I.K. Igumenov, J. Struct. Chem. 44 (2003) 1054.
[3] T.T. Kodas, M.J. Hampden-Smith, The Chemistry of Metal CVD, VCH, Weinheim, Germany, 1994.
[4] J. Rickerby, J.H.G. Steinke, Chem. Rev. 102 (2002) 1525.
[5] S.C. McGeachin, Can. J. Chem. 46 (1968) 1903.
[6] J.V. Greenhill, Chem. Soc. Rev. 6 (1977) 277.
[7] M.E.F. Braibante, H.S. Braibante, L. Missio, A. Andricopulo, Synthesis (1994) 898.
[8] D.V. Baxter, K.G. Caulton, W.-C. Chiang, M.H. Chisholm, V.F. DiStasi, S.G. Dutremez, K. Folting, Polyhedron 20 (2001) 2589.
[9] I.L. Kotlyarevskii, A.S. Zanina, S.I. Shergina, I.E. Sokolov, E.M. Shvarts, R.T. Ignash, P.N. Tel'zhenskaya, Russ. Chem. Bull. 36 (1987) 568.
[10] H.-K. Shin, M.J. Hampden-Smith, T.T. Kodas, A.L. Rheingold, J. Chem. Soc., Chem. Commun. 3 (1992) 217.
[11] V.I. Filyakova, Y.G. Ratner, N.S. Karpenko, K.I. Pashkevich, Russ. Chem. Bull. 45 (1996) 2163.
[12] H. Hamaki, N. Takeda, T. Yamasaki, T. Sasamori, N. Tokitoh, J. Organomet. Chem. 692 (2007) 44.
[13] W.S. Rees Jr., O. Just, S.L. Castro, J.S. Matthews, Inorg. Chem. 39 (2000) 3736.
[14] D.B. Studebaker, D.A. Neumayer, B.J. Hinds, C.L. Stern, T.J. Marks, Inorg. Chem. 39 (2000) 3148.
[15] N.L. Edleman, A. Wang, J.A. Belot, A.W. Metz, J.R. Babcock, A.M. Kawaoka, Jun Ni, M.V. Metz, C.J. Flaschenriem, C.L. Stern, L.M. Liable-Sands, A.L. Rheingold, P.R. Markworth, R.P.H. Chang, M.P. Chudzik, C.R. Kannewurf, T.J. Marks, Inorg. Chem. 41 (2002) 5005.
[16] T.R. Boussie, V. Murphy, K.A. Hall, C. Coutard, C. Dales, M. Petro, E. Carlson, H.W. Turner, T.S. Powers, Tetrahedron 55 (1999) 11699.
[17] Comprehensive Inorganic Chemistry, vol. 3, Pergamon Press, 1973, p. 355.
[18] A.J. Gordon, R.A. Ford, The Chemist's Companion, Handbook of Practical Data, Techniques and References, John Wiley and Sons, New York, 1972.
[19] J.V. Greenhill, Cem. Soc. Rev. 6 (1977) 277.
[20] S. Sans-Lenain, A. Gleizes, Inorg. Chem. Acta 211 (1993) 67.
[21] G.S. Hammond, D.C. Nonheckel, C.H.S. Wu, Inorg. Chem. 2 (1963) 73.
[22] F.A. Cotton, J.J. Wise, Inorg. Chem. 5 (1966) 1200.
[23] G.M. Sheldrick, SHELXS97 and SHELXL97. Programs for the Refinement of Crystal Structures, University of Göttingen, Germany, 1997.

self-assembled molecular squares of multidentate ligands [5]. Recently we have reported the first molecular square grid of a carbohydrazone ligand with Zn(II) ions [6]. Here we report magnetically coupled Ni(II) molecular squares of two carbohydrazone building blocks along with that of two thiocarbohydrazone building blocks.

2. Experimental

Quinoline-2-carbaldehyde (Aldrich), di-2-pyridyl ketone (Aldrich), 2-benzoylpyridine (Aldrich), thiocarbohydrazide (Aldrich) and carbohydrazide (Fluka) were used as received. Nickel(II) chloride hexahydrate (Merck) and ammonium hexafluorophosphate (Fluka) were used as supplied and solvents were purified by standard procedures before use.

2.1. Synthesis of ligands

The synthesis of H_2L^1 was reported [7] meagerly, without any spectral studies. The other three ligands were synthesized as already reported by us [6,8,9]. The structures of these ligands are given in Scheme 1.

2.1.1. H_2L^1

Dipyridyl ketone (0.391 g, 2.1 mmol) in 10 ml methanol was added to thiocarbohydrazide (0.011 g, 1 mmol) dissolved in hot methanol (30 ml). After adding a drop of HCl, the solution was refluxed for 1 h and on cooling a yellow mass precipitated. It was then washed with methanol and ether and dried over P_4O_{10} *in vacuo*. Yield 80%. M.p. 188 °C. Elemental *Anal.* Calc. C, 63.00; H, 4.14; N, 25.55; S, 7.31. Found: C, 62.30; H, 4.32; N, 25.19; S, 7.27%. IR (KBr pellet, cm^{-1}): 3340br (νN–H), 3049m (νC–H), 1581m, 1483s, 1456vs, 1423s (νC=N+ νC=C), 1303m, 1282m (νC–N/νheterocyclic), 1223s (νC=S), 1118s (νN–N), 872m, 802s, 741m (δC–H), 646m (δpy). UV–Vis [methanol, λ_{max} cm^{-1} (ε $M^{-1}\,cm^{-1}$)]: 43480 (12270), 36230 (11390), 28250 (18300). ^1H NMR ($CDCl_3$, δ ppm): 15.45 (1H, s), 14.56 (1H, s), 8.73 (1H, d), 8.62 (1H, d), 8.50 (1H, d), 8.21 (1H, d), 7.92 (1H, d), 7.84 (1H, t), 7.75 (3H, m), 7.55 (1H, d), 7.51 (1H, d), 7.38 (1H, t), 7.31 (1H, t), 7.25 (1H, t), 7.20 (2H, d).

2.2. Synthesis of the complexes

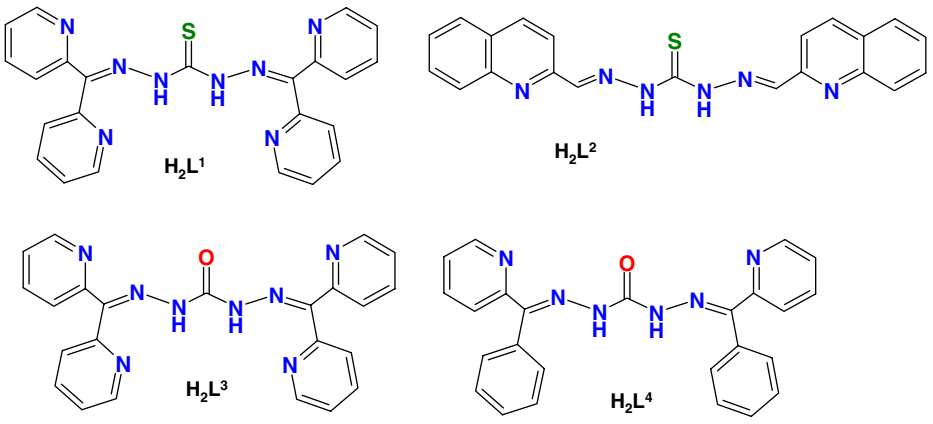
All the complexes were prepared by a general procedure. To a hot solution of the respective ligand (1 mmol) in 50 ml methanol was added an equivalent amount of nickel(II) chloride hexahydrate (0.240 g) dissolved in 10 ml hot methanol. The mixture was refluxed for an hour and NH_4PF_6 (2 mmol, 0.3326 g) was added in 20 ml methanol. The resulting solution was refluxed for 2 more hours and allowed to stand at room temperature. The compound precipitated was filtered, washed with methanol and ether and recrystallized in acetonitrile/ethanol (1:1 v/v) mixture and dried *in vacuo* over P_4O_{10}.

2.2.1. $[Ni(HL^1)]_4(PF_6)_4 \cdot 11H_2O$ (**1**)

Yield: 0.440 g (63%). Elemental *Anal.* Calc. C, 40.00; H, 3.28; N, 16.22; S, 4.64. Found: C, 39.72; H, 2.98; N, 16.76; S, 4.99%. It was found to be very difficult to get good quality single crystals for X-ray diffraction. However crystals suitable for X-ray analysis were obtained by slow evaporation of a solution of the compound in an ethanol–methanol mixture. The complex $[Ni(HL^1)]_4[PF_6]_4 \cdot 11H_2O$ (**1**) crystallized as $[Ni(HL^1)]_4(PF_6)_4 \cdot 0.5\ CH_3CH_2OH \cdot 2.8H_2O$ (**1a**) and the relatively high R-factors of **1a** are due to the bad quality of the crystal. All attempts to get better quality crystals failed. IR (KBr pellet, cm^{-1}): 3422br (νN–H), 3065m, 3012m (νC–H), 1588s, 1547s, 1493s, 1462s, 1427s, 1393s (νC=N+νC=C), 1328m, 1267s (νC–N/νheterocyclic), 1094s (νC–S), 1161m, 1116m (νN–N), 998m, 978m, 789m, 742m, 710m (δC–H), 842vs (νP–F), 352m (νNi–S), 429m (νNi–N_{azo}), 280s (νNi–N_{py}). UV–Vis [DMF, λ_{max} cm^{-1} (ε $M^{-1}\,cm^{-1}$)]: 17700 (64800), 18940 (113800), 29590 (36300).

2.2.2. $[Ni_2(HL^2)L^2]_2(PF_6)_2 \cdot 7H_2O$ (**2**)

Yield: 0.430 g (78%). Elemental *Anal.* Calc. C, 46.22; H, 3.33; N, 15.40; S, 5.88. Found: C, 46.57; H, 3.15; N, 15.09; S, 6.00%. IR (KBr pellet, cm^{-1}): 3414br, 3114w (νN–H),



Scheme 1. Structures of the ligands used.

3063m (νC–H), 1586s, 1526s, 1505s, 1411s (νC=N+ νC=C), 1350s, 1313s (νC–N/νheterocyclic), 1085vs (νC–S), 1212s, 1143s (νN–N), 989m, 782m, 747s, (δC–H), 843vs (νP–F), 353s (νNi–S), 425m (νNi–N_{azo}), 282s (νNi–N_{qu}). UV–Vis [DMF, λ_{max} cm^{-1} (ε M^{-1} cm^{-1})]: 11250 (2000), 16660sh (54600), 17850 (79200), 22730 (28300), 30120 (42100).

2.2.3. $[Ni(HL^3)]_4(PF_6)_4 \cdot 12H_2O$ (3)

Yield: 0.236 g (35%). Elemental *Anal.* Calc. C, 40.68; H, 3.41; N, 16.50. Found: C, 40.22; H, 2.76; N, 16.98%. IR (KBr pellet, cm^{-1}): 3413br, 3110m (νN–H), 3010m (νC–H), 1598m, 1580m, 1566s, 1519s, 1454s, 1422m (νC=N + νC=C), 1362m, 1297m (νC–N/νheterocyclic), 1316vs (νC–O), 1163m, 1126s, 1104s (νN–N), 909m, 794m, 743s (δC–H), 842vs (νP–F), 400m (νNi–N_{azo}), 251m (νNi–N_{py}). UV–Vis [DMF, λ_{max} cm^{-1} (ε M^{-1} cm^{-1})]: 19530 (222000), 22930 (60800), 29760 (83600).

2.2.4. $[Ni(HL^4)]_4(PF_6)_4 \cdot 9H_2O$ (4)

Yield: 0.357 g (54%). Elemental *Anal.* Calc. C, 45.24; H, 3.57; N, 12.66. Found: C, 44.77; H, 3.56; N, 13.35%. IR (KBr pellet, cm^{-1}): 3437br, 3211m (νN–H), 3049m (νC–H), 1648m, 1566m, 1528s, 1464m, 1436m (νC=N+ νC=C), 1295m, 1267m, 1212m (νC–N/νheterocyclic), 1323s (νC–O), 1154m, 1102s (νN–N), 789m, 743m, 704m (δC–H), 840vs (νP–F), 421m (νNi–N_{azo}), 250s (νNi–N_{py}). UV–Vis [DMF, λ_{max} cm^{-1} (ε M^{-1} cm^{-1})]: 11150 (500), 19080 (55900), 24210 (53300), 32050 (41500).

2.3. Physical measurements

Elemental analyses were carried out using a Vario EL III CHNS analyzer at SAIF, Kochi, India. Infrared spectra were recorded on a Thermo Nicolet, AVATAR 370 DTGS model FT-IR spectrophotometer with KBr pellets and the ATR technique at SAIF, Kochi, India. The far IR spectra were recorded using polyethylene pellets in the 500–100 cm^{-1} region on a Nicolet Magna 550 FTIR instrument at the Regional Sophisticated Instrumentation Facility, Indian Institute of Technology, Bombay, India. Electronic spectra were recorded on a Cary 5000 version 1.09 UV–vis spectrophotometer. High-resolution MALDI spectra were measured by the MS-service (Laboratorium für Organische Chemie, ETH Zürich, Switzerland) on an IonSpec HiResM-ALDI apparatus in a DCTB matrix and dichloromethane solvent. The magnetic susceptibility measurements were carried out at the Department of Physics, Boise State University, Boise, USA in the polycrystalline state on a Quantum Design PPMS superconducting magnetometer at 500 Oe field strength. The molar conductances of the complexes in DMF solutions at room temperature were measured using a direct reading conductivity meter.

2.4. X-ray crystallography

The crystallographic data and structure refinement parameters for compound **1a** are given in Table 1. The data were collected using a Bruker Apex2 CCD diffractometer equipped with graphite monochromated Mo Kα ($\lambda = 0.71073$ Å) radiation on a triclinic single crystal of dimensions $0.37 \times 0.15 \times 0.04$ mm^3 with $P\bar{1}$ symmetry at the X-ray Crystallography Unit, School of Physics, Universiti Sains Malaysia. The unit cell dimensions and intensity data were measured at 100 K. The trial structure was solved using SHELXS-97 [10] and refinement was carried out by full-matrix least squares on F^2 (SHELXTL). One of the pyridyl groups is disordered over two sites and the rings have been constrained to be regular hexagons. Hydrogen atoms were placed at calculated positions and allowed to ride on their parent atoms. The hydrogen atoms of the water molecules could not be located from the difference map, which was obtained by WINGX [11]. The molecular graphics employed were ORTEP-III [12], MERCURY [13], DIAMOND version 3.0 [14] and PLATON [15].

Table 1
Crystal data and structure refinement parameters of **1a**

Parameters	$[Ni(HL^1)]_4(PF_6)_4 \cdot 0.5CH_3CH_2OH \cdot 2.8H_2O$
Empirical formula	$C_{93}H_{76.6}F_{24}N_{32}Ni_4O_{3.3}P_4S_4$
Formula weight (M)	2638.22
Temperature, T (K)	100.0(2)
Wavelength (Mo Kα) (Å)	0.71073
Crystal system	triclinic
Space group	$P\bar{1}$
Lattice constants	
a (Å)	14.9345(8)
b (Å)	15.4023(8)
c (Å)	24.6220(13)
α (°)	98.950(3)
β (°)	96.098(3)
γ (°)	101.434(3)
Volume, V (Å^3)	5428.5(5)
Z	2
D_{calc} (ρ) (g cm^{-3})	1.614
Absorption coefficient, μ (mm^{-1})	0.926
F(000)	2674
Crystal size (mm^3)	$0.37 \times 0.15 \times 0.04$
θ Range for data collection	0.85–20.00
Limiting indices	$-14 \leqslant h \leqslant 14$, $-14 \leqslant k \leqslant 14$, $-23 \leqslant l \leqslant 23$
Reflections collected	56387
Independent reflections (R_{int})	10136 (0.1051)
Refinement method	full-matrix least-squares on F^2
Data/restraints/parameters	10136/0/1387
Goodness-of-fit on F^2	1.043
Final R indices [$I > 2\sigma(I)$]	$R_1 = 0.0849$, $wR_2 = 0.2282$
R indices (all data)	$R_1 = 0.1296$, $wR_2 = 0.2809$
Largest difference in peak and hole (e Å^{-3})	1.427 and −1.317

3. Results and discussion

Carbohydrazones and thiocarbohydrazones can exist in keto/thioketo and enol/thioenol tautomeric forms [16]. The absence of a ν(SH) band at ~2600 cm^{-1} in the IR spectra

of H_2L^1, H_2L^2, **1** and **2** is a clear indication of the absence of thiol tautomers in the free or coordinated form in these compounds. Molar conductivity measurement in a 10^{-3} M DMF solution of **2** shows it to be a 2:1 electrolyte ($147\ \Omega^{-1}\ cm^2\ mol^{-1}$) [17]. For all the other three compounds the conductance values obtained are $\sim 30\ \Omega^{-1}\ cm^2\ mol^{-1}$ in 10^{-4} M DMF solution. Complex **2** was assigned the formula $[Ni_2(HL^2)L^2]_2\ (PF_6)_2 \cdot 7H_2O$ and **1**, **3** and **4** were assigned the general formula $[Ni(HL)]_4[PF_6]_4 \cdot nH_2O$. The variable temperature magnetic studies reveal intramolecular antiferromagnetic couplings for all molecular square grids. The MALDI-MS spectra reveal the formation of tetra-nuclear molecular square structures for all the four compounds. The theoretical simulation of isotropic distribution patterns of all molecular ion peaks and their fragmentation peaks could be achieved well, confirming the proposed structural formulae. The structure of **1** has been confirmed by a single crystal X-ray study and is in good agreement with the mass structural study.

3.1. Mass spectral studies

For the unequivocal characterization of large molecules, mass spectrometry was found useful as a complementary tool. The structure and stability of coordination complexes under ionization conditions are dependent on various factors like the ligand itself, metal ions, counter ions, solvent, temperature, concentration, etc. MALDI mass spectra as a DCTB mix on the positive ion mode is found to give excellent results for stable Ni(II) square grids of both thiocarbohydrazones and carbohydrazones.

The MALDI-MS spectrum of compound **1** in dichloromethane shows the presence of three main peaks at *m*/*z* 495.0602, 991.1073 and 1981.2342. The peak centered at 1981.2342 is assigned to the molecular ion peak expected for $[Ni_4(HL^1)L^1_3]^+$ (calc. 1981), with good agreement with the simulated spectrum (Fig. 1). The base peak at *m*/*z* 495.0602 is assigned to $[Ni(HL^1)]^+$ (calc. *m*/*z* 495) and the other major peak at 991.1073 is assigned to $[Ni_2(HL^1)L^1]^+$ (calc. 991). In the case of compound **2**, two major peaks are obtained at *m*/*z* 1827.1019 and 1765.1557. Here the peak at 1765.1557 is assigned to the $[Ni_4(HL^2)L^2_3]^+$ ion (calc. 1765), with a well matching simulation (Fig. 2). The base peak at 1827.1019 is assigned to the molecular ion peak with two methanol molecules (calc. 1827). Another peak at 1323.1211 is assigned to $[Ni_3(HL^2)L^2_2]^+$ (calc. 1323).

Considering the carbohydrazone compounds, the MALDI MS spectrum of compound **3** displays only two main peaks centered at *m*/*z* 479.0873, as the base peak, and at 1917.4364, the molecular ion peak. The former peak is assigned to $[Ni(HL^3)]^+$ (calc. *m*/*z* 479) and the latter to the $[Ni_4(HL^3)L^3_3]^+$ ion (calc. 1917) (Fig. 3), agreeing well with the calculated isotropic distribution pattern of the

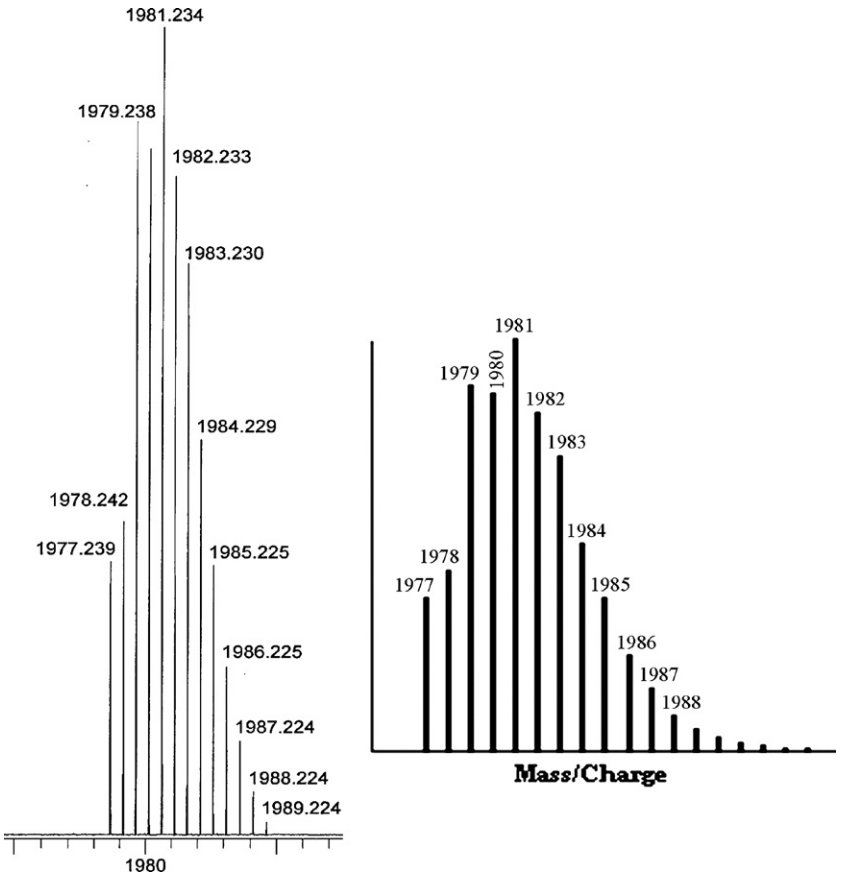


Fig. 1. The isotropic distribution pattern of the molecular ion peak $[Ni_4(HL^1)L^1_3]^+$ of **1** and its theoretical simulation on the right.

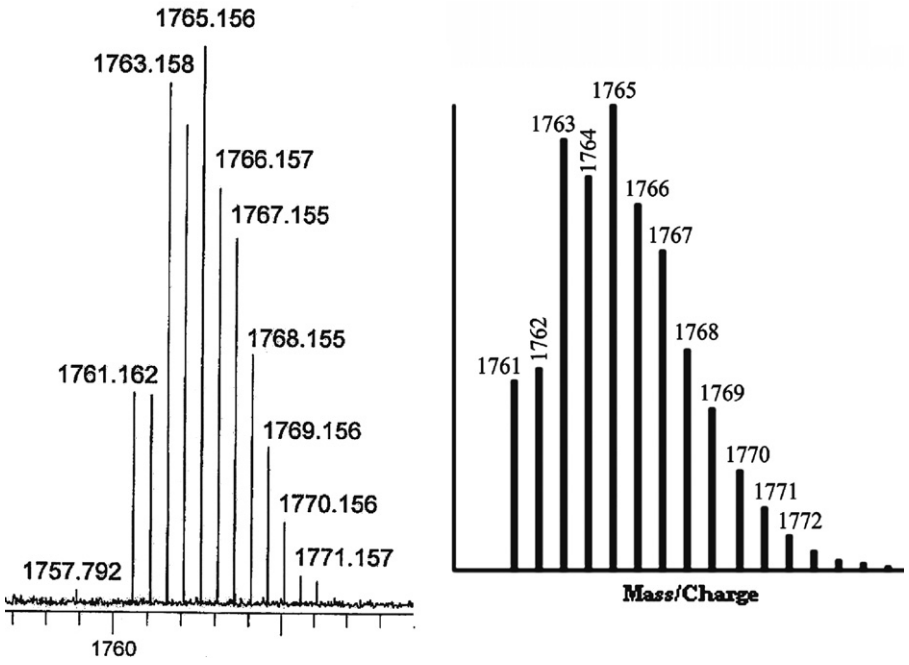


Fig. 2. The isotropic distribution pattern of peak corresponding to $[Ni_4(HL^2)L^2_3]^+$ of complex **2** and its theoretical simulation.

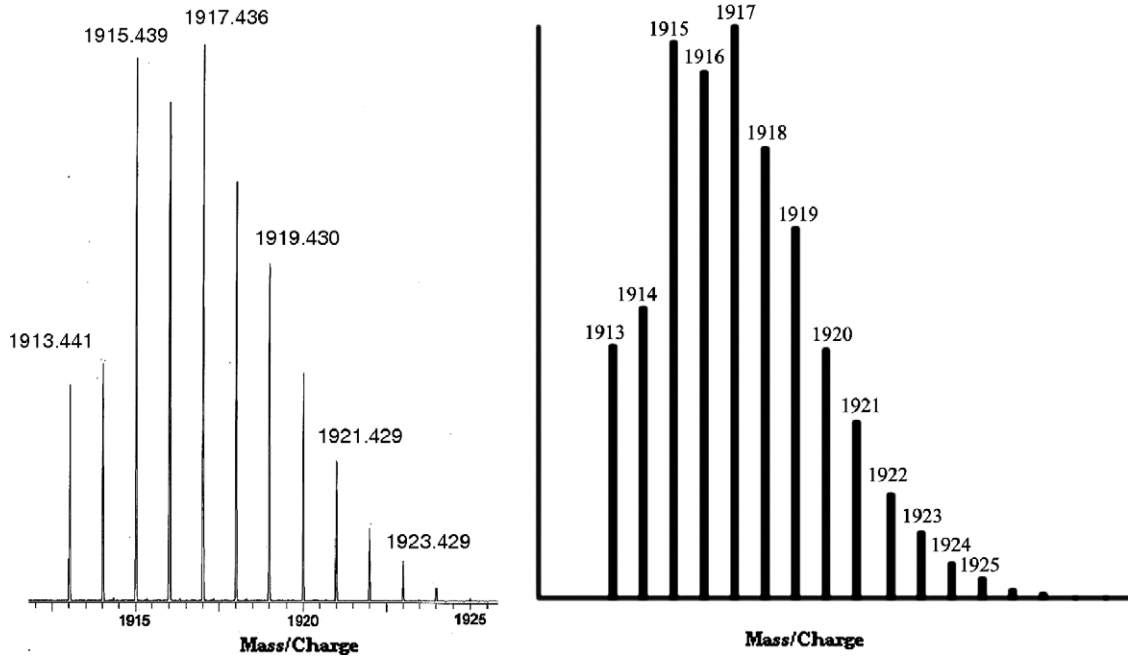


Fig. 3. The isotropic distribution pattern of $[Ni_4(HL^3)L^3_3]^+$ of complex **3** and its theoretical simulation.

molecular square structure and being characteristic results. Small peaks centered at *m*/*z* 536 and 958 are assigned as $[Ni_2(L^3)–H]^+$ (calc. 535) and $[Ni_2(HL^3)L^3]^+$ (calc. 957) respectively, also agreeing well with the calculated isotropic pattern. Complex **4**, however, exhibits many peaks centered at *m*/*z* 477.0968, 702.1126, 760.0297, 953.1987, 1011.1215, 1068.0470, 1100.0369, 1264.1392, 1487.2386, and a base peak at 1909.4594. Of these, the peaks at 477.0968 and 1909.4594 are assigned to the $[Ni(HL^4)]^+$ (calc. 477) and $[Ni_4(HL^4)L^4_3]^+$ ions (calc. 1909), with agreeing simulations. The latter peak (Fig. 4) is characteristic of a molecular square structure and the former is its monomer, usually obtained under MALDI ionization. The two other major peaks at 1011.1215 and 1487.2386, assigned to $[Ni_3(L^4)_2–H]^+$ (calc. 1011) and $[Ni_4(L^4)_3–H]^+$ (calc. 1487) respectively, also support the expected molecular square structure $[Ni(HL^4)]_4(PF_6)_4 \cdot 9H_2O$. Another peak centered at 2443.5110 is assigned to $[Ni_4(HL^4)_3L^4(PF_6)_2 \cdot 2CHCl_2 \cdot 4H_2O]^+$ (calc. 2443). However some weaker peaks at 1100.0369 and 1264.1392 are assigned to $[Ni_3(L^4)_2Cl \cdot$

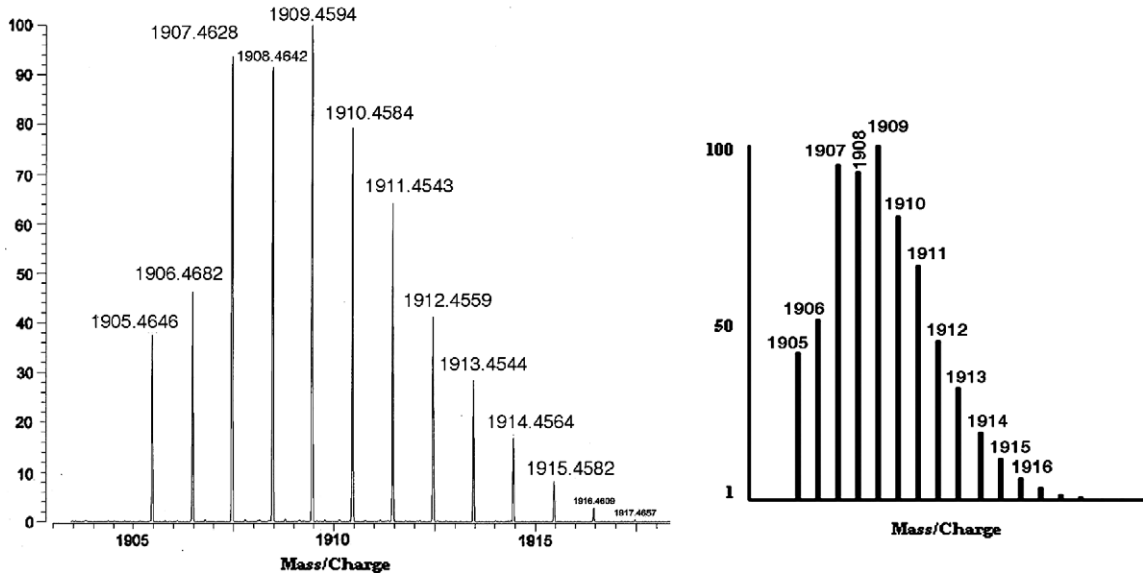


Fig. 4. The isotropic distribution patterns of $[Ni_4(HL^4)L_3^4]^+$ of complex **4** and its simulation.

$3H_2O]^+$ (calc. 1101) and $[Ni_3(L^4)_2Cl \cdot H_2O$+benzoylpyridine hydrazone$]^+$ (calc. 1262) respectively, due to the presence of the impurity of the chloride complex. These results are indicative of the stability of Ni(II) molecular squares in the solution phase.

3.2. Crystal structure of compound *1a*

The molecular structure of **1a** is given in Fig. 5 and the coordination core about the Ni(II) centers and their atom numbering scheme are given in Fig. 6. Selected bond lengths and bond angles are summarized in Table 2. The tetranuclear $[Ni(HL^1)]_4^{4+}$ cation has four Ni(II) centers, organized by four monodeprotonated ligands HL^1, as a molecular square. Each metal center is octahedrally coordinated by making use of atoms like one of the pyridyl nitrogen atoms, its nearby azomethine nitrogen and thiolate sulfur atoms of two perpendicular HL^{1-} ligands. These two HL^{1-} ligands bind to Ni(II) in the *mer* configuration, with pairs of sulfur atoms and pyridyl N atoms each bearing a *cis* relationship and the azomethine N atoms keep a *trans* configuration, as found in related octahedral Ni(II) thiocarbohydrazone [5,18] and thiosemicarbazone complexes [19,20]. As a result four fused five membered chelate

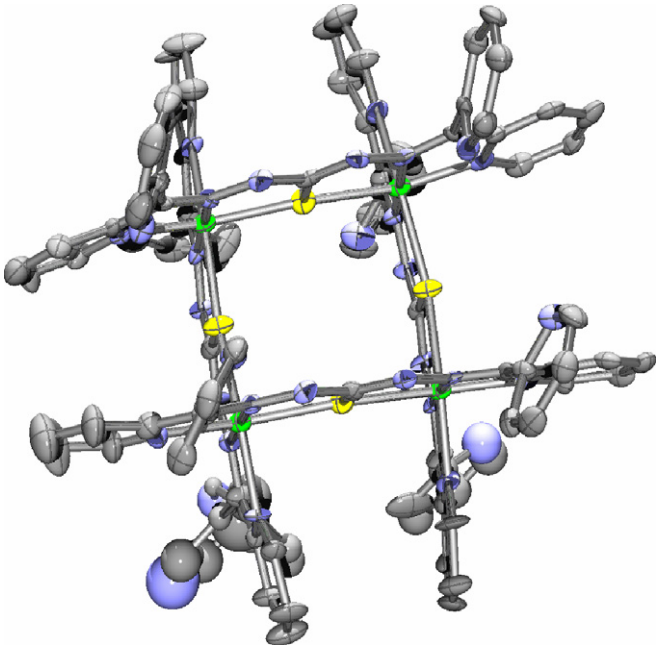


Fig. 5. ORTEP diagram for compound **1a** with 50% probability ellipsoids. Hydrogen atoms, ethanol, anions and lattice water molecules are omitted for clarity.

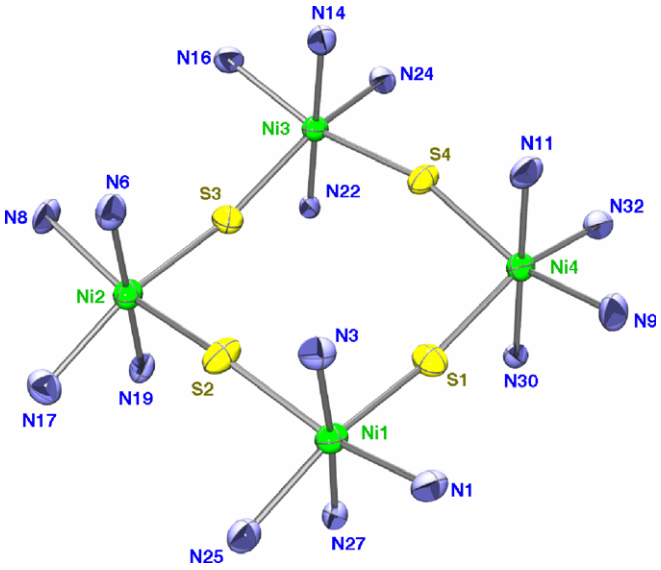


Fig. 6. The coordination core about the Ni(II) centers of **1a** with the numbering scheme showing the octahedral centers of Ni(II) are connected by sulfur bridges.

Table 2
Selected bond lengths and angles of $[Ni(HL^1)]_4(PF_6)_4 \cdot 0.5\ CH_3CH_2OH \cdot 2.8H_2O$

Bond lengths (Å)		Bond angles (°)	
Ni(1)–N(3)	2.014(10)	N(3)–Ni(1)–N(27)	175.0(4)
Ni(1)–N(27)	2.018(10)	N(3)–Ni(1)–N(1)	79.5(5)
Ni(1)–N(1)	2.055(10)	N(27)–Ni(1)–N(1)	104.7(4)
Ni(1)–N(25)	2.066(10)	N(3)–Ni(1)–N(25)	98.2(4)
Ni(1)–S(2)	2.356(4)	N(27)–Ni(1)–N(25)	79.0(4)
Ni(1)–S(1)	2.405(4)	N(1)–Ni(1)–N(25)	95.3(4)
Ni(2)–N(19)	2.022(10)	N(3)–Ni(1)–S(2)	82.4(3)
Ni(2)–N(6)	2.018(11)	N(27)–Ni(1)–S(2)	93.4(3)
Ni(2)–N(8)	2.064(10)	N(1)–Ni(1)–S(2)	161.9(3)
Ni(2)–N(17)	2.073(11)	N(25)–Ni(1)–S(2)	87.9(3)
Ni(2)-(S2)	2.356(4)	N(3)–Ni(1)–S(1)	100.5(3)
Ni(2)–S(3)	2.422(4)	N(27)–Ni(1)–S(1)	82.3(3)
Ni(3)–N(22)	2.011(10)	N(1)–Ni(1)–S(1)	89.3(3)
Ni(3)–N(14)	2.008(10)	N(25)–Ni(1)–S(1)	161.3(3)
Ni(3)–N(16)	2.048(10)	S(2)–Ni(1)–S(1)	93.30(14)
Ni(3)–N(24)	2.073(11)	N(19)–Ni(2)–N(6)	178.5(4)
Ni(3)–S(3)	2.398(4)	N(19)–Ni(2)–N(8)	98.8(4)
Ni(3)–S(4)	2.403(4)	N(6)–Ni(2)–N(8)	79.6(5)
Ni(4)–N(30)	2.023(10)	N(19)–Ni(2)–N(17)	78.6(5)
Ni(4)–N(11)	2.033(10)	N(6)–Ni(2)–N(17)	101.4(5)
Ni(4)–N(32)	2.061(11)	N(8)–Ni(2)–N(17)	93.1(4)
Ni(4)–N(9)	2.079(11)	N(19)–Ni(2)–S(2)	100.3(3)
Ni(4)–S(1)	2.382(4)	N(6)–Ni(2)–S(2)	81.2(3)
Ni(4)–S(4)	2.411(4)	N(8)–Ni(2)–S(2)	160.8(3)
S(1)–C(81)	1.748(13)	N(17)–Ni(2)–S(2)	91.4(3)
S(2)–C(12)	1.735(14)	N(19)–Ni(2)–S(3)	81.6(3)
S(3)–C(58)	1.696(13)	N(6)–Ni(2)–S(3)	98.3(3)
S(4)–C(35)	1.732(13)	N(8)–Ni(2)–S(3)	89.5(3)
N(3)–N(4)	1.374(14)	N(17)–Ni(2)–S(3)	160.2(4)
N(4)–C(12)	1.347(16)	S(2)–Ni(2)–S(3)	92.53(13)
N(5)–N(6)	1.343(14)	N(22)–Ni(3)–N(14)	177.5(4)
N(5)–C(12)	1.349(17)	N(22)–Ni(3)–N(16)	98.9(4)
N(11)–N(12)	1.340(14)	N(14)–Ni(3)–N(16)	79.9(4)
N(12)–C(35)	1.368(16)	N(22)–Ni(3)–N(24)	79.6(4)
N(13)–C(35)	1.338(16)	N(14)–Ni(3)–N(24)	98.2(4)
N(13)–N(14)	1.355(14)	N(16)–Ni(3)–N(24)	91.9(4)
N(19)–N(20)	1.338(14)	N(22)–Ni(3)–S(3)	82.1(3)
N(20)–C(58)	1.379(15)	N(14)–Ni(3)–S(3)	100.1(3)
N(21)–C(58)	1.349(15)	N(16)–Ni(3)–S(3)	89.5(3)
N(21)–N(22)	1.373(14)	N(24)–Ni(3)–S(3)	161.6(3)
N(27)–N(28)	1.355(14)	N(22)–Ni(3)–S(4)	99.9(3)
N(28)–C(81)	1.384(16)	N(14)–Ni(3)–S(4)	81.4(3)
N(29)–C(81)	1.324(16)	N(16)–Ni(3)–S(4)	161.3(3)
N(29)–N(30)	1.380(14)	N(24)–Ni(3)–S(4)	91.1(3)
		S(3)–Ni(3)–S(4)	93.51(13)
		N(30)–Ni(4)–N(11)	179.3(4)
		N(30)–Ni(4)–N(32)	78.7(5)
		N(11)–Ni(4)–N(32)	101.3(4)
		N(30)–Ni(4)–N(9)	100.5(4)
		N(11)–Ni(4)–N(9)	78.8(5)
		N(32)–Ni(4)–N(9)	91.8(4)
		N(30)–Ni(4)–S(1)	82.4(3)
		N(11)–Ni(4)–S(1)	97.6(3)
		N(32)–Ni(4)–S(1)	160.7(3)
		N(9)–Ni(4)–S(1)	88.1(3)
		N(30)–Ni(4)–S(4)	98.6(3)
		N(11)–Ni(4)–S(4)	82.1(3)
		N(32)–Ni(4)–S(4)	90.3(3)
		N(9)–Ni(4)–S(4)	160.8(3)
		S(1)–Ni(4)–S(4)	96.17(13)
		Ni(1)–S(2)–Ni(2)	166.30(18)
		Ni(3)–S(3)–Ni(2)	168.68(16)
		Ni(3)–S(4)–Ni(4)	165.30(17)
		Ni(4)–S(1)–Ni(1)	168.71(17)

rings share each metal center. The sulfur atoms share a position of adjacent Ni(II) octahedra (Fig. 6) and thus connect the centers to build a symmetrical molecular square (Fig. 7). The adjacent Ni–Ni distances are ~4.7 Å {they vary from 4.679(2) Å for Ni(1)–Ni(2) to 4.797(2) Å for Ni(2)–Ni(3)} and the angles subtended at the sulfur atoms Ni–S–Ni varies from 165.30(17)° for Ni(3)–S(4)–N(4) to 168.71(17)° for Ni(1)–S(3)–Ni(4). The Ni–Ni distances across the diagonals of the square are 6.749(2) Å for Ni(1)–Ni(3) and 6.692(2) Å for Ni(2)–Ni(4) and the Ni–Ni–Ni angles are ~90° {these vary from 88.73(4)° for Ni(2)–Ni(3)–Ni(4) to 90.82(4)° for Ni(1)–Ni(2)–Ni(3)}. The four Ni atoms are in a plane with a maximum mean plane deviation of 0.0525(17) Å for Ni(1). The sulfur atoms S(2) and S(4) are above and S(1) and S(3) are below this plane by ~0.2 Å.

The bond parameters (Table 2) show that the geometry around the Ni(II) centers are distorted significantly from perfect octahedra. For example, considering the octahedron around the Ni(1) atom, the mean plane of the bicyclic chelate ring Ni(1), N(1), C(5), C(6), N(3), N(4), C(12), S(2) {having a maximum deviation of 0.020(11) Å for the N(1) atom} makes a dihedral angle of 86.8(2)° with that of its counterpart chelate ring defined by Ni(1), N(25), C(74), C(75), N(27), N(28), C(81), S(1) {having a maximum deviation of -0.125(13) Å for the C(74) atom}. The bond lengths Ni–$N_{azomethine}$, Ni–N_{py} and Ni–S around the Ni(1) atom increase in that order, as in similar compounds [5,18] and as in mononuclear Ni(II) octahedral thiosemicarbazone complexes [19–23]. Also, the trans angles N(1)–Ni(1)–S(2), N(25)–Ni(1)–S(1) and N(3)–Ni(1)–N(27) are 161.9(3)°, 161.3(3)° and 175.0(4)° respectively. These factors suggest considerable distortion from a perfect octahedral geometry around the Ni(1) center.

The C–S bond lengths of ~1.73 Å are within the normal range of a C–S single bond. The hydrogen atoms were

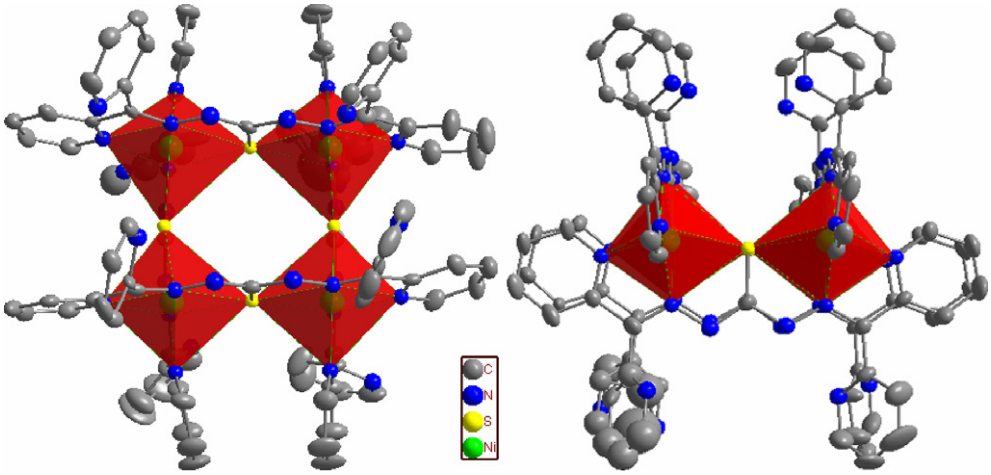


Fig. 7. Top view and side view of the cationic part of the molecule with octahedral polyhedra around the Ni(II) centers, showing the symmetrical nature of **1a**. Hydrogen atoms are removed for clarity.

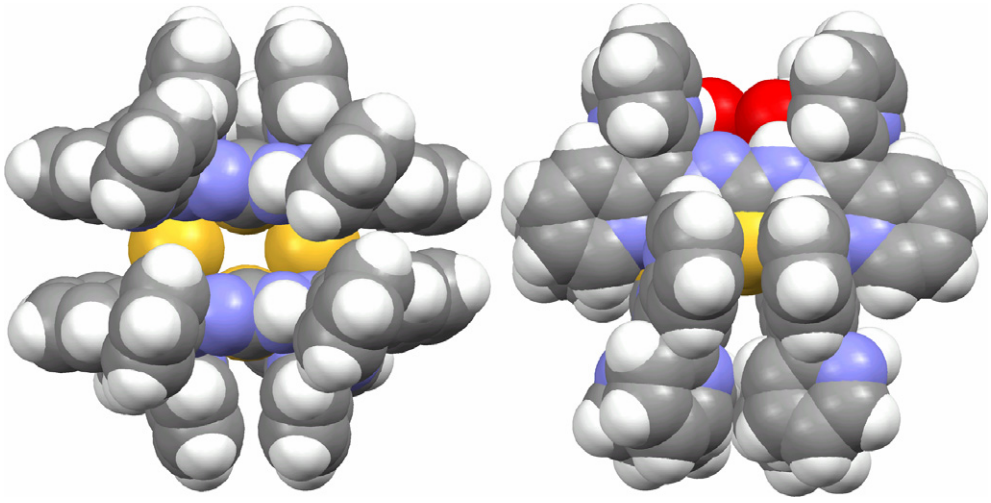


Fig. 8. Spacefill models of complex **1a**, showing the cavity inside the square grid $[Ni(HL^1)]_4^{4+}$ (left, top view) and side view showing the trapped water molecules inside the four uncoordinated pyridyl groups of it (right).

located at N(5), N(12), N(20) and N(28). The N(13)–C(35), N(21)–C(58) and N(29)–C(81) bond distances are smaller compared to their counterparts {by 0.030(23), 0.030(21) and 0.060(23) Å respectively}, confirming the deprotonation of the thiol tautomeric form to form the square grid by four monoanionic ligands. The molecules are connected by various intermolecular interactions involving water and PF_6^- anions. Two of the water molecules are trapped inside the four uncoordinated pyridyl groups (Fig. 8). Some C–H···π and very weak π···π interactions are involved in the packing of the molecules in the lattice (Fig. 9). Relevant hydrogen bonding and other interactions are summarized in Table 3.

3.3. Magnetic studies

For all four compounds, the temperature dependence of the molar magnetic susceptibility χ_m was investigated over the temperature range 5–325 K. All compounds show common features. The effective magnetic moments μ_{eff} at room temperature of **2** and **3** are found to be low compared to that expected for four independent Ni(II) ions and also decrease with decreasing temperature, suggesting antiferromagnetic interactions between the Ni(II) ions. The temperature dependence curves of **1** and **4** are similar to that of **2** and **3**, but with slightly higher μ_{eff} values at room temperature. These features indicate a dominant antiferromagnetic interaction in these compounds.

The room temperature effective magnetic moments μ_{eff} of the sulfur-bridged squares are found to be 6.05 μ_B for **1** and 4.01 μ_B for **2**. As the temperature is lowered μ_{eff} of both **1** and **2** decreases gradually and reaches a minimum of 0.51 μ_B for **2** and 0.45 μ_B for **1** at 5 K. The variable temperature magnetic behaviour of both compounds are indicative of antiferromagnetic coupling between the Ni(II) ions, and this is greater in **2**. The room temperature μ_{eff} of 4.50 μ_B shown by complex **3** is low compared to its sulfur bridged counterpart compound **1**. The thermal dependence curve of **3** implies strong antiferromagnetic interactions between the Ni(II) centers. The μ_{eff} values show a regular decrease upon decreasing the temperature and reach a minimum value of 0.66 μ_B at 5 K. The antiferromagnetic coupling in complex **4** is found to be low compared to that of **3**, as evidenced by the room temperature magnetic moment of 5.80 μ_B. On cooling, μ_{eff} decreases and reaches a minimum value of 0.83 μ_B at 5 K.

To fit and interpret the magnetic susceptibility data of the complexes, first it is necessary to find all possible magnetic

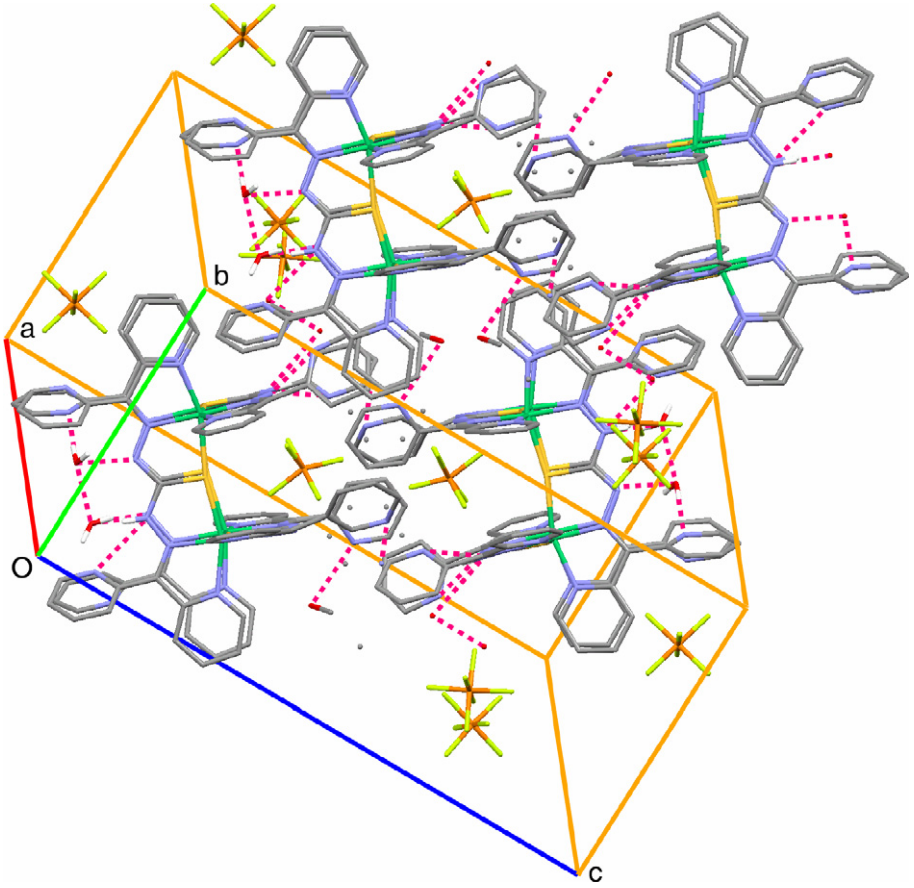


Fig. 9. A view of the packing diagram of compound **1a**, showing relevant hydrogen bonding interactions. Hydrogen atoms not involved in HB interactions are removed for clarity.

Table 3
Relevant interactions in $[Ni(HL^1)]_4(PF_6)_4 \cdot 0.5\ CH_3CH_2OH \cdot 2.8H_2O$

D–H···A	H···A (Å)	D···A (Å)	D–H···A (°)
O(2W)–H(1W2)···N(31)[a]	2.02	2.864(14)	173
O(2W)–H(1W2)···N(21)[a]	2.24	2.974(13)	144
O(3W)–H(1W3)···N(18)[a]	2.38	3.084(14)	141
C(93)–H(93B)···N(2)[b]	1.89	2.78(3)	151
C(3)–H(3A)···F(20)[a]	2.42	3.25(2)	149
C(26)–H(26A)···F(24)[a]	2.53	3.35(3)	148
C(32)–H(32A)···F(22)[c]	2.26	3.10(4)	150
C(44)–H(44A)···F(8)[d]	2.38	3.151(19)	140
C(48)–H(48A)···F(23)[d]	2.33	3.24(2)	167
C(57)–H(57A)···F(6)[e]	2.51	3.388(17)	157
C(78)–H(78A)···F(5)[e]	2.49	3.361(19)	156
C(84)–H(84A)···F(18)[f]	2.51	3.30(2)	143
C(94)–H(94B)···F(23)[a]	2.49	3.44(5)	170
N(12)–H(12A)···N(10)	2.26	2.825(19)	123
N(20)–H(20B)···N(18)	2.30	2.888(15)	125
C(66)–H(66A)···N(23)	2.52	3.103(18)	121
C(73)–H(73A)···N(26)	2.56	3.136(19)	120
D–H···π	H···Cg (Å)	D···Cg (Å)	D–H···Cg (°)
C(8)–H(8A)···Cg(23)[b]	2.75	3.38(2)	126
C(22)–H(22A)···Cg(32)[d]	2.87	3.690(16)	148
C(23)–H(23A)···Cg(6)[a]	2.96	3.254(14)	100
C(23)–H(23A)···Cg(8)[a]	2.98	3.298(15)	102
C(34)–H(34A)···Cg(18)[b]	2.94	3.71(2)	141
C(46)–H(46A)···Cg(9)[a]	2.89	3.240(14)	104
C(47)–H(47A)···Cg(5)[a]	2.96	3.316(17)	105
O(3W)–H(1W3)···Cg(30)[a]	2.96	3.132(11)	94
P(1)–F(1)···Cg(26)[g]	3.300(11)	4.668(7)	141.2(5)
P(1)–F(3)···Cg(9)[g]	3.963(10)	5.163(6)	131.0(5)
π···π *interactions*			
Cg(I)···Cg(J)	Cg–Cg (Å)	α (°)	β (°)
Cg(2)···Cg(29)[a]	3.962(7)	75.58	33.12
Cg(20)···Cg(21)[d]	3.719(9)	5.94	18.33
Cg(21)···Cg(20)[g]	3.719(9)	5.94	13.08

D = donor, A = acceptor; only hydrogen bonding of angles >140 are included, except for intramolecular interactions. Cg = Centroid, α = dihedral angles between planes I and J, β = angle Cg(I)–Cg(J). Equivalent position codes: $a = x, y, z$; $b = 1 - x, 1 - y, 1 - z$; $c = 2 - x, 1 - y, 1 - z$; $d = -1 + x, y, z$; $e = 1 - x, -y, -z$; $f = 1 - x, 1 - y, -z$; $g = 1 + x, y, z$.
Cg(2) = Ni(1), S(2), C(12), N(4), N(3); Cg(5) = Ni(2), S(2), C(12), N(5), N(6);
Cg(6) = Ni(2), S(3), C(58), N(20), N(19); Cg(8) = Ni(2), N(17), C(51), C(52), N(19);
Cg(9) = Ni(3), S(3), C(58), N(21), N(22); Cg(18) = N(2), C(7), C(11), C(10), C(9), C(8);
Cg(20) = N(8), C(19), C(20), C(21), C(22), C(23); Cg(21) = N(9), C(24), C(25), C(26), C(27), C(28);
Cg(23) = N(15), C(37), C(41), C(40), C(39), C(38); Cg(26) = N(18), C(53), C(54), C(55), C(56), C(57);
Cg(29) = N(25), C(70), C(71), C(72), C(73), C(74); Cg(30) = N(26), C(76), C(80), C(79), C(78), C(77);
Cg(32) = N(32), C(88), C(89), C(90), C(91), C(92).

pathways in the complicated but regular structures. Assuming all the four Ni(II)–X–Ni(II) couplings are equal, ie using a single coupling constant J that takes into account all the exchange pathways to be equal, is a reasonable assumption in light of the X-ray crystallographic study of **1a** which reveals a similar nature of the M–S–M angles (~167°), there is probably a super exchange mechanism through the intervening sulfur atoms. Therefore, for a square arrangement of four metal centers, a D_{4h} [2 × 2] grid, a suitable exchange Hamiltonian [24] is used.

$$\hat{H} = -2J(\hat{S}_1 \cdot \hat{S}_2 + \hat{S}_2 \cdot \hat{S}_3 + \hat{S}_3 \cdot \hat{S}_4 + \hat{S}_1 \cdot \hat{S}_4)$$

The allowed eigenvalues were then substituted in to the modified van Vleck equation,

$$\chi_M = \frac{N\beta^2 g^2}{3k(T-\Theta)} \frac{\sum S'(S'+1)(2S'+1)e^{-E(S')/kT}}{\sum (2S'+1)e^{-E(S')/kT}}(1-\rho) + \frac{N\beta^2 g^2 S(S+1)\rho}{3kT} + \mathrm{TIP}$$

where $E(S')$ refers to the energy of each spin state defined by S'. For Ni(II) molecular squares $S' = S_1 + S_2 + S_3 + S_4$. The best-fit results using the program MAGMUN4.1 [25] for **2** and **3** are given in Figs. 10 and 11 along with the fitting parameters. Relatively high J (negative) values are consistent with strong intramolecular antiferromagnetic coupling interactions in the Ni(II) complexes. TIP was assumed as 6×10^{-4} emu mol^{-1}, a typical value for Ni_4 complexes [26]. However, we could not get a reasonable fit for

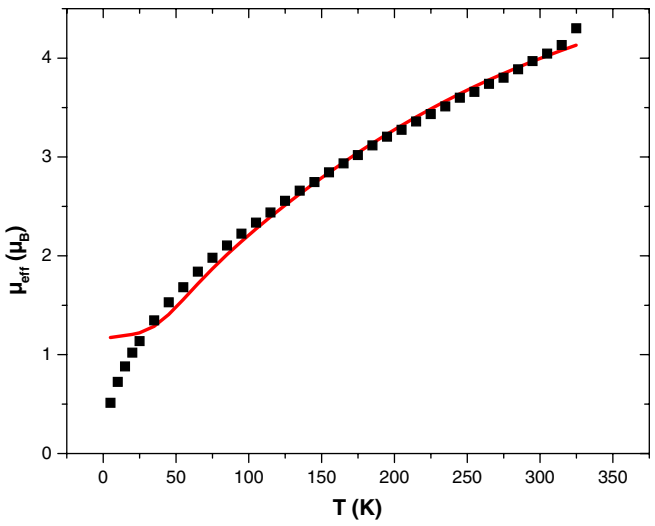


Fig. 10. Temperature dependence of the effective magnetic moment μ_{eff} (solid squares) for the thiocarbohydrazone Ni(II) square complex **2**. The solid line represents the best fit obtained with $g = 2.047 \pm 0.067$, $J = -126.24 \pm 8.88\ cm^{-1}$, $\Theta = -0.0385$ K, $\rho = 0.0405$, $R = 4.57 \times 10^{-2}$.

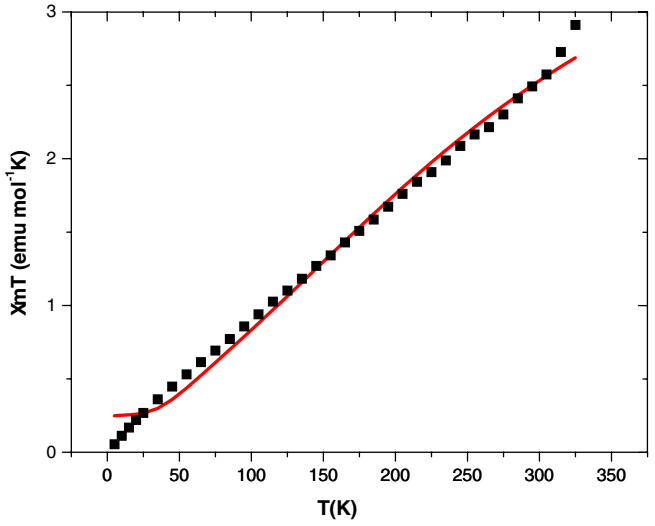


Fig. 11. $\chi_m T$ data (solid squares) as a function of temperature for the carbohydrazone Ni(II) square complex **3**. The solid line represents the best fit obtained with $g = 2.221 \pm 0.064$, $J = -113.85 \pm 7.57\ cm^{-1}$, $\Theta = -0.016$ K, $\rho = 0.05$, $R = 4.90 \times 10^{-2}$.

complexes **1** and **4**, which may be associated with zero-field splitting (D), especially at lower temperatures and/or due to slight variations in the M–X–M angles, so that more J values need to be considered. The M–O–M arrangement of 180° is known as an ideal structure for strong antiferromagnetism [27]. This linearity as the origin of strong AF coupling is in accordance with VB [28–30] and MO [31] studies. Logically, Kahn also explained this feature in his book [32].

Acknowledgements

E. Manoj thanks the University Grants Commission, New Delhi, India for financial support in the form of a fellowship. Dr. L.K. Thompson, Memorial University, St. John's, Newfoundland, Canada is gratefully acknowledged for useful discussions. H.-K. Fun is thankful to the Malaysian Government and the Universiti Sains Malaysia for the Scientific Advancement Grant Allocation (SAGA; Grant No. 304/PFIZIK/635003/A118). M.R.P. Kurup is thankful to the CSIR, New Delhi, India for financial support. The research at Boise State University was supported in part by NSF-Idaho-EPSCoR Program (EPS-0447689) and DoE-EPSCoR grant (DE-FG02-04ER46142).

Appendix A. Supplementary material

CCDC 626766 contains the supplementary crystallographic data for this paper. These data can be obtained free of charge via http://www.ccdc.cam.ac.uk/conts/retrieving.html, or from the Cambridge Crystallographic Data Centre, 12 Union Road, Cambridge CB2 1EZ, UK; fax: (+44) 1223-336-033; or e-mail: deposit@ccdc.cam.ac.uk. Supplementary data associated with this article can be found, in the online version, at doi:10.1016/j.poly. 2007.05.048.

References

[1] F. Wurthner, C.-C. You, C.R. Saha-Moller, Chem. Soc. Rev. 33 (2004) 133.
[2] M. Fujita, Chem. Soc. Rev. 27 (1998) 417.
[3] L.K. Thompson, L. Zhao, Z. Xu, D.O. Miller, W.M. Reiff, Inorg. Chem. 42 (2003) 128.
[4] P.J. Stang, B. Olenyuk, Acc. Chem. Res. 30 (1997) 502.
[5] C. He, C.-y. Duan, C.-j. Fang, Y.-j. Liu, Q.-j. Meng, J. Chem. Soc., Dalton Trans. (2000) 1207, and references cited therein.
[6] E. Manoj, M.R.P. Kurup, H.-K. Fun, Inorg. Chem. Commun. 10 (2007) 324.
[7] C.-y. Duan, Z.-h. Liu, X.-z. You, F. Xue, T.C.W. Mak, Chem. Commun. (1997) 381.
[8] E. Manoj, M.R.P. Kurup, H.-K. Fun, S. Chantrapromma, Acta.Crystallogr., E 61 (2005) o4110.
[9] E. Manoj, M.R.P. Kurup, E. Suresh, J. Chem. Cryst., submitted for publication.
[10] G.M. Sheldrick, SHELXS97 and SHELXL97, Bruker AXS Inc., Madison, Wisconsin, USA, 1997.
[11] L.J. Farrugia, J. Appl. Cryst. 32 (1999) 837.
[12] L.J. Farrugia, J. Appl. Cryst. 30 (1997) 565.
[13] C.F. Macrae, P.R. Edgington, P. McCabe, E. Pidcock, G.P. Shields, R. Taylor, M. Towler, J. van de Streek, J. Appl. Cryst. 39 (2006) 453.
[14] K. Brandenburg, H. Putz, DIAMOND version 3.0, Crystal Impact, GbR, Postfach 1251, D-53002 Bonn, Germany, 2004.
[15] A.L. Spek, J. Appl. Cryst. 36 (2003) 7.
[16] C. Bustos, O. Burckhardt, R. Schrebler, D. Carrillo, A.M. Arif, A.H. Cowley, C.M. Nunn, Inorg. Chem. 29 (1990) 3996.
[17] W.J. Geary, Coord. Chem. Rev. 7 (1971) 81.
[18] G. Han, D. Guo, C.-y. Duan, H. Mo, Q.-J. Meng, New J. Chem. 26 (2002) 1371.
[19] A. Sreekanth, S. Sivakumar, M.R.P. Kurup, J. Mol. Struct. 655 (2003) 47.
[20] V. Suni et al., Polyhedron (2007), doi:10.1016/j.poly.2007.02.015.
[21] I. Garcý'a, E. Bermejo, A.K. El Sawaf, A. Castineiras, D.X. West, Polyhedron 21 (2002) 729.
[22] K.A. Ketcham, I. Garcia, E. Bermejo, J.K. Swearingen, A.K. El Sawaf, E. Bermejo, A. Castineiras, D.X. West, Polyhedron 21 (2002) 859.
[23] N.C. Kasuga, K. Sekino, C. Koumo, N. Shimada, M. Ishikawa, K. Nomiya, J. Inorg. Biochem. 84 (2001) 55.

[24] C.J. Mathews, K. Avery, Z. Xu, L.K. Thompson, L. Zhao, D.O. Miller, K. Biradha, K. Poirier, M.J. Zaworotko, C. Wilson, A.E. Goeta, J.A.K. Howard, Inorg. Chem. 38 (1999) 5266.
[25] http://www.ucs.mun.ca/~lthomp/magmun. MAGMUN has been developed by Dr Zhiqiang Xu (Memorial University), and OW01.exe by Dr O. Waldmann.
[26] M. Fondo, N. Ocampo, A.M. Garcý'a-Deibe, R. Vicente, M. Corbella, M.R. Bermejo, J. Sanmartin, Inorg. Chem. 45 (2006) 255.
[27] Y.-B. Jiang, H.-Z. Kou, R.-J. Wang, A.-L. Cui, J. Ribas, Inorg. Chem. 44 (2005) 709.
[28] J.B. Goodenough, Phys. Rev. 100 (1955) 565.
[29] J.B. Goodenough, J. Phys. Chem. Solids 6 (1958) 287.
[30] J. Kanamori, J. Phys. Chem. Solids 10 (1959) 87.
[31] P.J. Hay, J.C. Thibeault, R. Hoffmann, J. Am. Chem. Soc. 97 (1975) 4884.
[32] O. Kahn, Molecular Magnetism, VCH Publishers, New York, 1993.

Table 1
Crystal data and structure refinement for **1**–**4**

Complex	**1**	**2**	**3**	**4**
Formula	$C_{19}H_{18}ClCuN_3O_6$	$C_{18}H_{14}CuN_2O_3$	$C_{16}H_{11}CuN_5O$	$C_{17}H_{11}CuN_3OS$
CCDC No.	CCDC-624808	CCDC-624809	CCDC-641561	CCDC-624810
Formula weight	483.35	369.85	352.84	368.89
Crystal system	monoclinic	monoclinic	monoclinic	monoclinic
Space group	*P*2(1)/*n*	*C*2/*c*	*C*2/*c*	$P2_1/n$
a (Å)	8.6220(17)	16.967(3)	17.1612(5)	11.298(2)
b (Å)	12.010(2)	9.885(2)	7.3241(3)	9.767(2)
c (Å)	19.517(4)	18.202(4)	22.9754(7)	13.588(3)
α (°)	90	90	90	90
β (°)	94.58(3)	100.20(3)	102.947(2)	100.09(3)
γ (°)	90	90	90	90
V (Å^3)	2014.5(7)	3004.6(10)	2814.37(17)	1476.3(5)
Z	4	8	8	4
μ (mm^{-1})	1.259	1.473	1.564	1.627
Collected reflections	3948	4775	3206	3866
Unique reflections	2250	3592	2381	298
R_1 [$I > 2\sigma(I)$]	0.0651	0.0335	0.0443	0.0310
wR_2	0.1695	0.0870	0.1064	0.0834

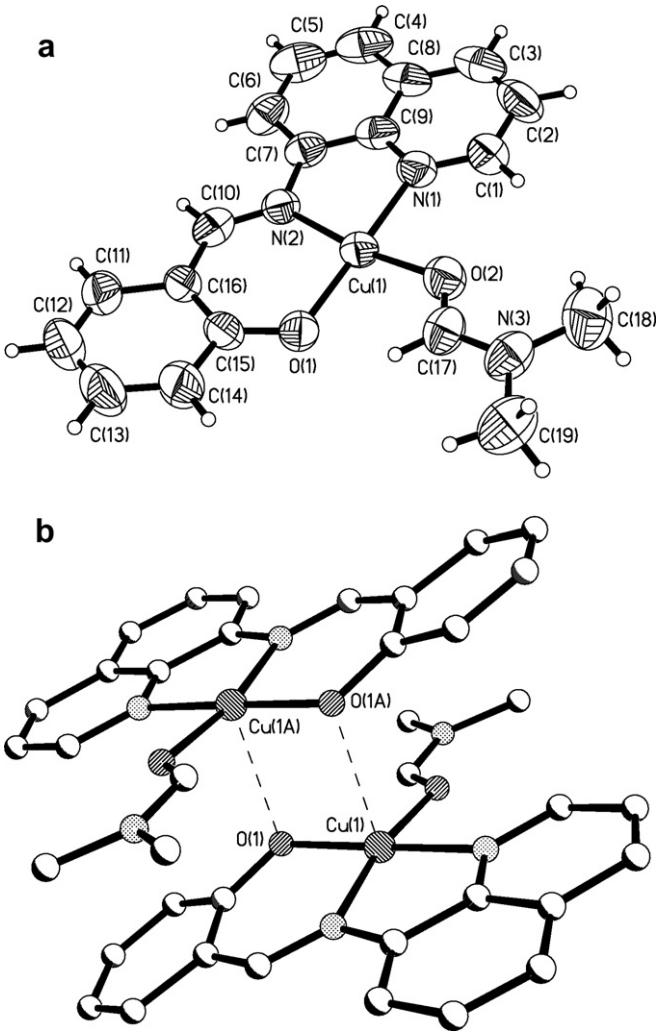


Fig. 1. (a) Molecular structure of the CuL^+ mono-cation and (b) $[(CuL)_2]^{2+}$ dimer (symmetric code $A = 1 - x, -y, -z$ and H atoms omitted for clarity) for **1**.

procedure [11], therefore, it is still necessary to design, synthesize and characterize structurally new families of transition metal complexes, investigate the self-assembly features of the specific molecular architectures, and further understand the magnetostructural relationship. Herein we reported on the syntheses and characterizations of the crystal structure for four new complexes which are based on the molecular architecture CuL^+ (L = *N*-(8-quinolyl)salicylaldimine), from dimeric entities to one-dimensional (1D) chain systems, and further investigated their magnetic behaviors.

2. Experimental

2.1. Materials and measurements

The reagents and solvents employed were commercially available and were used as received. *N*-(8-quinolyl)salicylaldimine (HL) was prepared from 8-aminoquinoline and salicylaldehyde in MeOH according to the literature [12]. C, H and N microanalyses were carried out with a Perkin–Elmer 240 elemental analyzer. IR spectra were recorded using KBr discs on a Bruker Vector 22 spectrophotometer in the range 4000–400 cm^{-1}. Magnetic susceptibilities of polycrystalline samples were measured over the range 2–350 K using a Quantum Design MPMS-5S superconducting quantum interference device (SQUID) magnetometer, and diamagnetic corrections were made using Pascal's constants. EPR spectra were recorded on a Bruker 2000-D-SRC spectrometer at 293 K and the microwave frequency is near to 9.7 GHz.

2.2. Preparation of compounds *1*–*4*

N-(8-quinolyl)salicylaldimine and $Cu(ClO_4)_2$ were mixed in a molar ratio of 1:1 in a minimum amount of

DMF, the mixture was stirred at room temperature until all the solid dissolved, and then it was filtered. The filtrate was stood in a refrigerator at ca. 4 °C for 3 days, and the formed brown crystals of CuL(DMF)(ClO_4) (**1**) were collected by filtration, washed with Me_2CO and dried in air. Yield ca. 50% based on Cu. Elemental analysis Calc. for $C_{19}H_{18}ClCuN_3O_6$: C, 47.2; H, 3.75; N, 8.70. Found: C, 46.9; H, 3.87; N, 8.64%. IR spectrum (cm^{-1}): 2934.9m (ν_{C-H} of DMF), 1644.4m ($\nu_{C=N}$ of DMF), 1086.2s (ν_{Cl-O} of ClO_4^-).

The syntheses of CuL(Ac) (**2**), CuL(N_3) (**3**) and CuL(SCN) (**4**) were similar to that of **1** except for using the corresponding anion instead of ClO_4^-. Brown crystals of **2** were obtained (yield ca. 53% based on Cu). Elemental analysis Calc. for $C_{18}H_{14}CuN_2O_3$: C, 58.5; H, 3.82; N, 7.57. Found: C, 58.2; H, 3.90; N, 7.36%. IR spectrum (cm^{-1}): 2924.6m (ν_{C-H} of CH_3COO^-), 1613.7m ($\nu_{as(C=O)}$ of CH_3COO^-). Brown crystals of **3** were obtained (yield ca. 47% based on Cu). Elemental analysis Calc. for $C_{16}H_{11}CuN_5O$: C, 54.5; H, 3.14; N, 19.9. Found: C, 54.4; H, 3.66; N, 19.7%. IR spectrum (cm^{-1}): 2048.9s ($\nu_{as}(N{=}N{\equiv}N)^-$ of N_3^-). Brown crystals of **4** were obtained (yield 49% based on Cu). Elemental analysis Calc. for $C_{17}H_{11}CuN_3OS$: C, 55.4; H, 3.01; N, 11.4. Found: C, 55.5; H, 3.24; N, 11.3%. IR spectrum (cm^{-1}): 2100.1s ($\nu_{(CN)}$ of SCN^-), 758.5m ($\nu_{(CS)}$ of SCN^-).

2.3. X-ray single crystal structures

Suitable single crystals of **1**–**4** were selected and mounted onto thin glass fibers. X-ray intensity data were measured at 293 K on a Bruker SMART APEX CCD-based diffractometer with graphite-monochromatic Mo Kα radiation ($\lambda = 0.71073$ Å). Data reductions and absorption corrections were performed with the SAINT and SADABS software packages, respectively [13]. All structures were solved by a combination of direct methods and difference Fourier syntheses and refined against F^2 by the full-matrix least-squares technique [14]. Anisotropic displacement parameters were refined for all non-hydrogen atoms except for the disordered atoms. Hydrogen atoms were added theoretically and were riding on their parent atoms. In the crystal of **1**, the ClO_4^- anion is disordered, in which three atoms, O(4), O(5) and O(6), occupy two positions and the occupancy factors for each position are fixed as 0.5 in the refinement procedure. Crystallographic

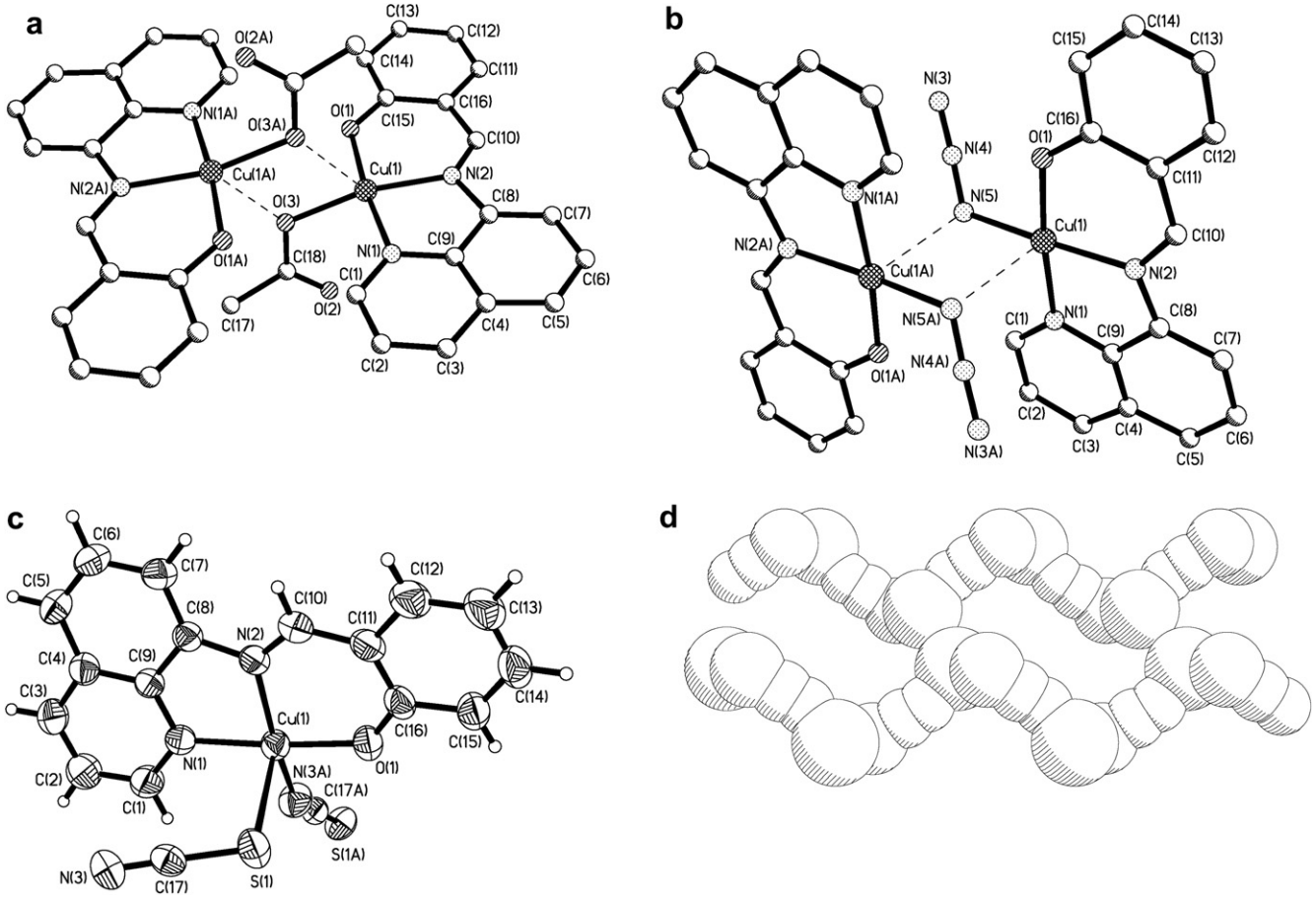


Fig. 2. Molecular structures of a dimer with H-atoms omitted for clarity (a) for **2** (symmetric code $A = -x, -y, -z$) and (b) for **3** (symmetric code $A = 0.5 - x, 1.5 - y, -z$); (c) ORTEP view of **4** with 50% thermal possibility (symmetric code $A = 1.5 - x, 0.5 + y, 0.5 - z$); (d) 1D helical chain in **4** constructed from ···SCN–Cu–SCN–Cu··· (space fill graph in which only Cu and SCN remain and other atoms are omitted for clarity).

data and other pertinent information for **1**–**4** are summarized in Table 1. Selected bond lengths and angles are listed in Table S1.

3. Results and discussion

3.1. Structure description

The asymmetric unit of **1** contains one $CuL(DMF)^+$ cation together with one ClO_4^- anion, and Fig. 1a shows a portion of the structure of $CuL(DMF)^+$. The Cu^{2+} center in **1** is chelated by one deprotonated tridentate *N*-(8-quinolyl)salicylaldimine anionic ligand and coordinated by one solvent ligand (DMF) to furnish a square-planar coordination environment. The Cu–N bond lengths are 1.952(5) and 1.980(5) Å, and the Cu–O bond lengths are 1.889(4) (from phenolate), 1.956(4) (from DMF) Å. Two neighboring $CuL(DMF)^+$ cations stack face-to-face and form a dimer via the μ_2-O atoms of the phenolate (Fig. 1b) with a Cu···O distance of 2.604 Å. Therefore, the actual coordination geometry of the Cu^{2+} center might be considered as a square-pyramid. Within a dimer the Cu···Cu separation is 3.274 Å, the O(1)–Cu(1)···O(1A) and Cu(1)–O(1)···Cu(1A) (symmetric code $A = 1 - x, -y, -z$) angles are 87.9° and 92.2°, respectively. Between neighboring dimers the Cu···Cu distance is more than 5.716 Å.

Replacement of $Cu(ClO_4)_2$ with $Cu(Ac)_2$ and $Cu(N_3)_2$ lead to compounds **2** and **3**, respectively. Both complexes are isostructural with each other, in which two CuL^+ cations form a dimer through two bridged μ_2-O from $-COO^-$ (for **2**) or μ_2-N from N_3^- (for **3**) atoms. For such two compounds, not only are the binding fashions in the coordination sphere around the Cu^{2+} ion very similar but also the packing diagrams are nearly identical to each other (cf. Figs. S2 and S3), thus just the structure of **2** is described.

As shown in Fig. 2a, in the dimeric **2**, each Cu^{2+} center is pentacoordinated and adopts a slightly distorted square-pyramidal geometry (the τ value of the Cu^{2+} center is ~0.11, and the geometry about the pentacoordinate metal ion is analyzed with the formalism in which internal angles are combined into a single parameter, τ, which ranges from 0 for square pyramidal to 1 for trigonal bipyramidal [15]) with one O and two N atoms from the tridentate ligand and one O atom from the acetate anion forming the base plane. The bond distances and angles around the Cu^{2+} center are within the normal range. The O atom from another moiety of the dimer occupies the vertex position with angles of O(3A)–Cu(1)–O(3) = 71.7°, O(3A)–Cu(1)–O(1) = 91.4°, O(3A)–Cu(1)–N(1) = 88.3° and O(3A)–Cu(1)–O(1) = 120.4°, and the O(3A)–Cu(1) distance is 2.680Å. The Cu···Cu separation is 3.788 Å within a dimer, and is more than 7.360 Å between neighboring dimers.

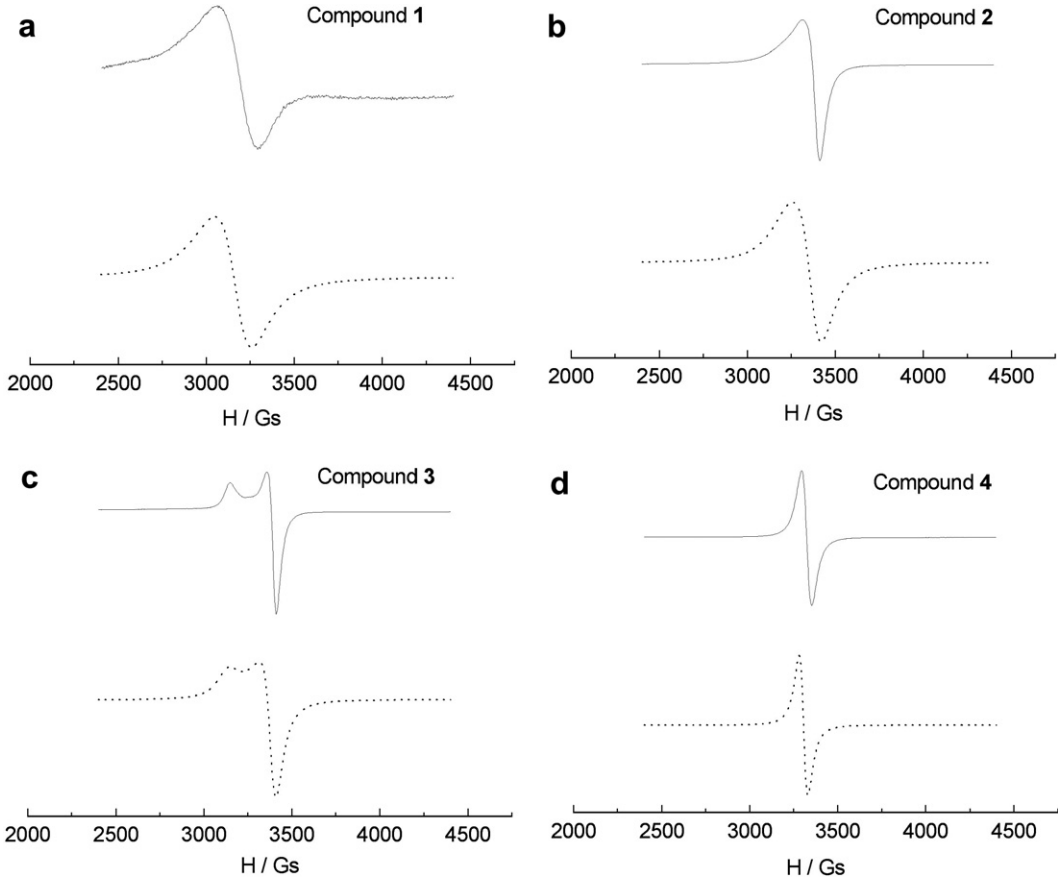


Fig. 3. EPR spectra of **1**–**4** at room temperature (solid lines: experimental data; dot lines: simulated plots).

In the crystal of **4**, the binding fashions in the coordination sphere around the Cu^{2+} ion are similar to those in **2** and **3**, namely the Cu^{2+} center in **4** is surrounded by one deprotonated tridentate ligand and two SCN^- anions to form a distorted square-pyramidal coordination environment (the τ value of the Cu^{2+} center is ~0.29), as illustrated in Fig. 2c, and the bonding parameters in the coordination sphere around the Cu^{2+} ion, summarized in Table S1, are comparable with those in **2** and **3**. However, there is a distinct difference from **2** and **3** in that the neighboring Cu^{2+} ions are bridged by SCN^- anions in a fashion ···SCN–Cu–SCN–Cu··· to extend a helix and uniform chain along the *b*-axis direction (cf. Fig. 2d). The Cu···Cu separation is 6.185 Å in the chain, and more than 4.605 Å between neighboring chains.

For **1**–**4**, in the presence of different anions under similar experimental conditions, the Cu^{2+} centers adopt a square-pyramidal geometry, but the crystal packing structures are distinct. Due to the ClO_4^- anion possessing a weak binding interaction with the metal ion, the Cu^{2+} center completes its coordination requirement via a solvent ligand (DMF) in **1**, and this is why the crystals of **1** are only facilitated from DMF solution. In crystals of both **2** and **3**, the $-COO^-$ and N_3^- anions are, respectively, bound to the Cu^{2+} ion in the manner of μ_2-O ($-COO^-$) and μ_2-N (N_3^-), even if the ligand can serve as a bifunctional ligand. The CuL^+ tectons form discrete dimers through a μ_2-bridging atom in **1**–**3**, and a 1D helical chain linked through the SCN^- anion, which serves as a bifunctional ligand, in **4**. The results reveal that the counter ion, solvent and metal ion features as well as weak intermolecular interactions cooperatively affect the formation of the supramolecular architecture, and finally control the crystal packing manner of the coordination compound.

3.2. EPR spectra and magnetic properties

Fig. 3 displays typical X-band EPR spectra of **1**–**4** that were carried out on polycrystalline samples at 293 K. From the viewpoint of the crystal structure, the coordination environments around the Cu^{2+} ion in **1**–**4** are similar to each other, however the spectral features are distinct. The EPR spectra of **1**–**3** show axial symmetrical signals and smaller linewidths, even if $g_{\parallel}$ and $g_{\perp}$ are not well resolved in the spectra of **1** and **2**, and the EPR spectrum of **4** displays an isotropic feature. If we take into consideration

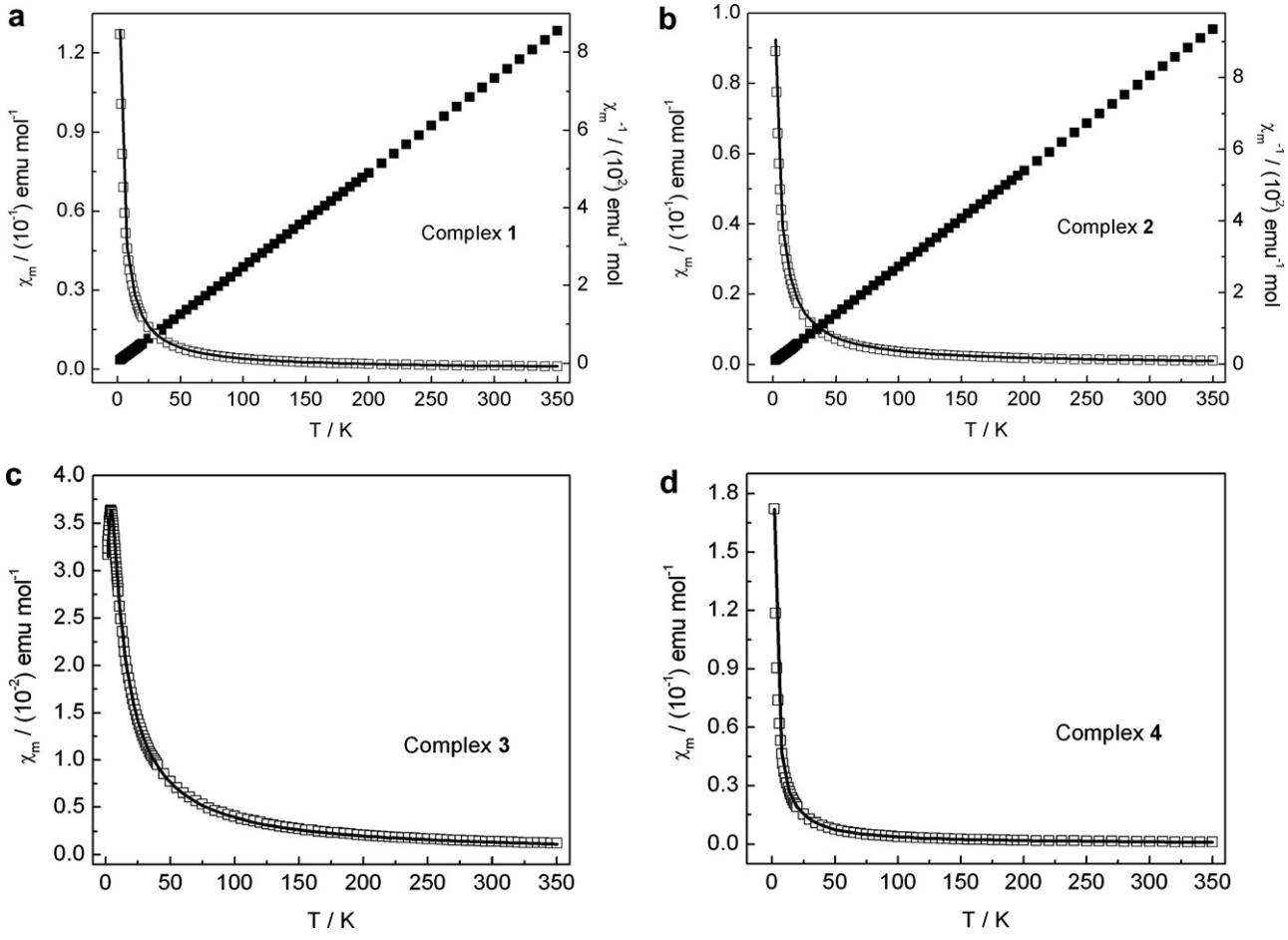


Fig. 4. Plots of χ_m (calculated per mole Cu^{2+} ion) vs. *T* for **1**–**4** (open squares: experimental data; solid lines: theoretical reproduction and details, see the text).

the field derivative of the absorption signal and Lorentzian line shape to simulate the EPR spectra of **1**–**4** and the corresponding parameters, the *g*-factor and the half-width at half-height, the best fits are given below: $g_x = g_y = 2.196$ with a half-width of 175 Gs, and $g_z = 2.285$ with a half-width of 270 Gs for **1**; $g_x = g_y = 2.071$ with a half-width of 120 Gs, and $g_z = 2.165$ with a half-width of 170 Gs for **2**; $g_x = g_y = 2.063$ with a half-width of 70 Gs, and $g_z = 2.228$ with a half-width of 90 Gs for **3**; $g_x = g_y = g_z = 2.113$ with a half-width of 50 Gs for **4**.

Temperature dependences of the magnetic susceptibilities for **1**–**4** are presented in Fig. 4. Owing to the structural findings, it is reasonable to consider **1**–**3** as isolated spin dimer systems and **4** as a uniform spin chain with $S = 1/2$. From the plots of $\chi_m - T$, it was found that the variations of magnetic susceptibility with temperature for **1**, **2** and **4** follow the simple Curie–Weiss behavior, so we fitted the magnetic susceptibility data to Eq. (1) to yield the parameters $C = 0.429(2)$ emu K mol^{-1} and $\theta = -1.33(2)$ K for **1**, $C = 0.406(4)$ emu K mol^{-1} and $\theta = -2.39(6)$ K for **2**, and $C = 0.383(0)$ emu K mol^{-1} and $\theta = -0.23(0)$ K for **4**. The *g*-factors deduced from the *C* constants are 2.14 for **1**, 2.08 for **2** and 2.02 for **4**

$$\chi_m = \frac{C}{T - \theta}. \quad (1)$$

Structurally, the magnetic behavior of **3** should obey an isolated spin dimer system with $S = 1/2$. In fact, a maximum is observed in its plot of $\chi_m - T$ which means the magnetic coupling feature within the dimer is AFM. In a dimmer, the function of magnetic susceptibility as temperature is described by Eq. (2) which is based on the spin Hamiltonian $H = -2JS_1S_2$:

$$\chi_m = \frac{Ng^2\mu_B^2}{k_BT} \cdot \frac{1}{3 + \exp(-2J/k_BT)}. \quad (2)$$

The best fit for the magnetic susceptibility of **3** in the temperature range 6–350 K gives a *g*-factor = 2.021(5) and $J/k_B = -4.32(1)$ K. The *g*-factor values for **1**–**4** obtained from the fits are comparable with the experimental values from EPR measurements.

4. Conclusion

In summary, we have synthesized four new complexes utilizing the deprotonated tridentate *N*-(8-quinolyl)salicylaldimine anionic ligand (L) by reaction with CuX_2 ($X = ClO_4^-$, Ac^-, N_3^- and SCN^-), and investigated their crystal structures and magnetic properties. Although the coordination geometries of the Cu^{2+} centers are similar to each other in the four complexes, their EPR spectra are totally different, which discloses their distinct electronic structures. The tectons of CuL^+ form discrete dimers [$(CuL(DMF))_2$ in **1** and $(CuLX)_2$ in **2** and **3**] and a 1D helical chain of $\cdots$CuL(SCN)$\cdots$ in **4**. These findings demonstrate that the binding ability and structural features of the counter anion play an important role in controlling the final packing structure of the complex. As we addressed in the Section 1, the issue of the assembly of novel supramolecular entities with desired structures and properties is still one of the great challenges in the supramolecular field.

Acknowledgment

The authors thank the Natural Science Foundation for Outstanding Scholars of Anhui Province, PR China (Grant Nos. 044-J-04011, 2004kj266 and KJ2007B092) for financial support.

Appendix A. Supplementary material

CCDC 624808, 624809, 624810 and 641561 contain the supplementary crystallographic data for **1**, **2**, **3** and **4**. These data can be obtained free of charge via http://www.ccdc.cam.ac.uk/conts/retrieving.html, or from the Cambridge Crystallographic Data Centre, 12 Union Road, Cambridge CB2 1EZ, UK; fax: (+44) 1223-336-033; or e-mail: deposit@ccdc.cam.ac.uk. Supplementary data associated with this article can be found, in the online version, at doi:10.1016/j.poly.2007.05.047.

References

[1] (a) S. Ferlay, T. Mallah, R. Ouahes, P. Veillet, M. Verdaguer, Nature 378 (1995) 701;
(b) J.M. Manriquez, G.T. Yee, R.S. McLean, A.J. Epstein, J.S. Miller, Science 252 (1991) 1415;
(c) J.S. Miller, J.C. Calabrese, H. Rommelmann, S.R. Chittipeddi, J.H. Zhang, W.M. Reiff, A.J. Epstein, J. Am. Chem. Soc. 109 (1987) 769;
(d) Y. Pei, M. Verdaguer, O. Kahn, J. Am. Chem. Soc. 108 (1986) 7428.
[2] S. Ohkoshi, Y. Tsunobuchi, H. Takahashi, T. Hozumi, M. Shiro, K. Hashimoto, J. Am. Chem. Soc. 129 (2007) 3084.
[3] M. Moragues-Canovás, C.E. Talbot-Eeckelaers, L. Catala, F. Lloret, W. Wernsdorfer, E.K. Brechin, T. Mallah, Inorg. Chem. 45 (2006) 7038.
[4] M.L. Taliaferro, M.S. Thorum, J.S. Miller, Angew Chem. Int. Ed. 45 (2006) 5326.
[5] (a) E. Coronado, J.R. Galán-Mascarós, C. Martí-Gastaldo, A. Ribera, Chem. Mater 18 (2006) 6112;
(b) E. Coronado, C.J. Gómez-García, A. Nuez, F.M. Romero, E. Rusanov, H. Stoeckli-Evans, Inorg. Chem. 41 (2002) 4615.
[6] W. Kaneko, M. Ohba, H. Okawa, S. Kitagawa, Inorg. Chem. 45 (2006) 7191.
[7] X.M. Ren, S. Nishihara, T. Akutagawa, S. Noro, T. Nakamura, W. Fujita, K. Awaga, Chem. Phys. Lett. 418 (2006) 423.
[8] (a) Y. Umezono, W. Fujita, K. Awaga, J. Am. Chem. Soc. 128 (2006) 1084;
(b) H. Tokoro, S. Ohkoshi, T. Matsuda, K. Hashimoto, Inorg. Chem. 43 (2004) 5231.
[9] (a) J.F. Létard, P. Guionneau, L. Goux-Capes, Top. Curr. Chem. 235 (2004) 221;
(b) Y. Sunatsuki, H. Ohta, M. Kojima, Y. Ikuta, Y. Goto, N. Matsumoto, S. Iijima, H. Akashi, S. Kaizaki, F. Dahan, J.-P. Tuchagues, Inorg. Chem. 43 (2004) 4154;
(c) H. Spiering, T. Kohlhaas, H. Romstedt, A. Hauser, C. Bruns-Yilmaz, J. Kusz, P. Gütlich, Coord. Chem. Rev. 190–192 (1999) 629;
(d) O. Kahn, C. Jay-Martinez, Science 279 (1998) 44;

(e) J.F. Létard, P. Guionneau, L. Goux-Capes, E. Codjovi, O. Lavastre, G. Bravic, D. Chasseau, O. Kahn, J. Am. Chem. Soc. 119 (1997) 10861;
(f) W. Vreugdenhil, J.H. Van Diemen, A.G. De Graff, J.G. Haasnoot, J. Reedijk, A.M. Van der Kraan, O. Kahn, J. Zarembowitch, Polyhedron 9 (1990) 2971;
(g) P. Gütlich, Struct. Bonding (Berlin) 44 (1981) 83.

[10] (a) S. Dorbes, L. Valade, J.A. Real, C. Faulmann, Chem. Commun. (2005) 69;
(b) E. Coronado, J.R. Galén-Mascarós, C.J. Gómez-Garcia, V. Laukhin, Nature 408 (2000) 447.

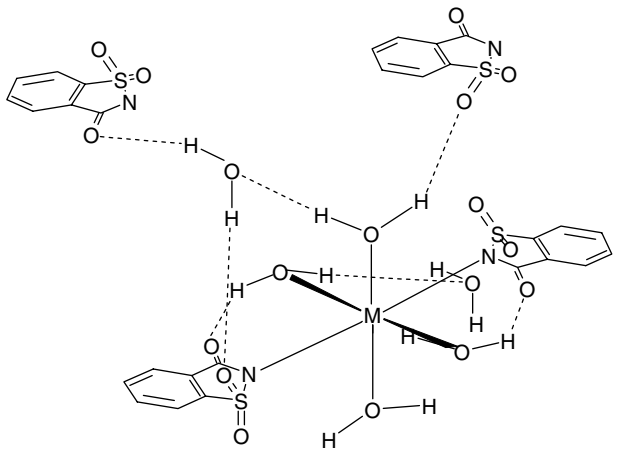
[11] E. Coronado, J.R. Galán-Mascarós, C.J. Gómez-García, C. Martí-Gastaldo, Inorg. Chem. 44 (2005) 6197.

[12] (a) R.C. Dickinson Jr., W.A. Baker, R.L. Collins, J. Inorg. Nucl. Chem. 39 (1977) 1531;
(b) H. Xu, Z.P. Ni, X.M. Ren, Q.J. Meng, J. Mol. Struct. 752 (2005) 159.

[13] Software packages SMART and SAINT, Siemens Analytical X-ray Instrument Inc., Madison,WI, 1996.

[14] SHELXTL, Version 5.1, Bruker AXS, Inc., Madison, WI, 1997.

[15] A.W. Addison, T.N. Rao, J. Reedijk, J. Vanrijn, G.C. Verschoor, J. Chem. Soc., Dalton Trans. (1984) 1349.



Scheme 1. Hydrogen bond network for $[M(sac)_2(H_2O)_4]\cdot 2H_2O$ complexes.

which is in chemical equilibrium with the dimeric compound $[Cr_2(sac)_4(py)_2]$.

Another relevant feature is that the saccharinate ion is a multifunctional ligand. This molecule has three coordination centers: the carbonyl and the sulphonyl oxygen atoms and the nitrogen atom, see Scheme 2. It can bind to a metal ion as a monodentate ligand, as is observed in the isostructural set of compounds of general formula $[M(C_7H_4NO_3S)_2(H_2O)_4]\cdot 2H_2O$, or as a bidentate ligand as in $[Cr_2(sac)_4]$, $[Cu_2(sac)_4(Himid)_4]$, (Himid = imidazole) and $[Cd_2(sac)_4(Himid)_4]$ [7–9].

This feature has attracted interest on the use of saccharinate compounds as starting materials to prepare mixed-ligand complexes, using monodentate or bidentate ligands such as pyridine [3,5,6], imidazole [10] phosphine [11], or 2,2-bipyridine [12].

The aim of this work was to study the effect of the pyrazole, (Hpz), molecule as co-ligand in mixed-ligand saccharinate complexes. Pyrazole molecule has the dual capability of to act as a monodentate or as a bridging ligand when deprotonated or using the N–H group to participated in hydrogen bond formation with available hydrogen bond acceptor and/or hydrogen donor sites [13,14]. We were successful in preparing and characterizing complexes with the formula $[M(sac)_2(Hpz)_2(H_2O)_2]$, M = Co(II), Ni(II) and Cu (II); with zinc(II) the product was $[Zn(sac)_2(Hpz)_2]$. We describe here the crystal structures, spectroscopic and thermogravimetric properties of the products obtained.

2. Experimental

2.1. Methods and materials

Solvents, methanol, ethanol, pyrazole (Hpz), nickel(II) nitrate, cobalt(II) nitrate, copper(II) nitrate, zinc(II) nitrate and sodium saccharinate were used as purchased. The transition metal saccharinates, $[M(sac)_2(H_2O)_4]\cdot 2H_2O$, where M = Ni(II), Co(II), Cu(II) and Zn(II), were prepared as described in the literature [15] and isolated as crystalline materials.

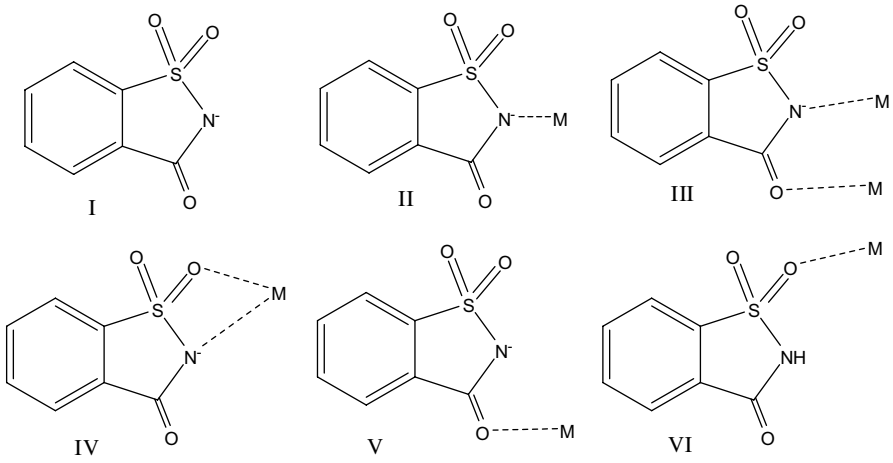
2.2. Synthesis of the complexes

2.2.1. $[Co(sac)_2(Hpz)_2(H_2O)_2]$

A sample of pyrazole, 0.27 g, (4.0 mmol) was added to a solution of 0.53 g (1.0 mmol) of cobalt(II) saccharinate in 25.0 mL of water. The reaction mixture was refluxed for 40 min. The solution was cooled to room temperature and after two days red crystals were obtained. They were filtered off and washed with cold water. Yield: 0.48 g (81%). Crystals suitable for X-ray measurements were obtained by slow evaporation of the mother liquid over a few days. *Anal.* Calc. for $C_{20}H_{20}N_6O_8S_2Co$: C, 40.3; H, 3.4; N, 14.1; Co, 9.9. Found: C, 40.9; H, 3.4; N, 13.8; Co, 9.9%. IR (KBr pellet, cm^{-1}): 3513(s), 3310 (s), 1635(vs), 1586(m), 1344(m), 1264(m), 1150(m), 1054(m), 953(m), 895(m), 754(m), 721(m), 681(m). μ_{eff} (298 K): 4.87 B.M. λ_{max} (H_2O) (ε M^{-1} cm^{-1}): 470sh, 490sh, 524(22).

2.2.2. $[Ni(sac)_2(Hpz)_2(H_2O)_2]$

Pyrazole, 0.27 g (4.0 mmol) was added to a solution of 0.53 g (1.0 mmol) of nickel saccharinate in 25.0 mL of



Scheme 2. Coordination modes of saccharinate ion I.

water. The reaction mixture was refluxed for 1 h. The hot solution was filtered, and the resulting solution was left standing overnight. A light blue microcrystalline solid was obtained. It was filtered and washed with cold water. Yield was 0.42 g (71%). Crystals suitable for X-ray measurements were obtained by slow evaporation of a water solution of the compound. *Anal.* Calc. for $C_{20}H_{20}N_6O_8S_2Ni$: C, 40.3; H, 3.3; N, 14.1; Ni, 9.8. Found: C, 40.6; H, 3.6; N, 13.7; Ni, 9.6%. IR (KBr pellet, cm^{-1}): 3519(m), 3312 (s), 3005(s), 1636(vs), 1586(vs), 1344(m), 1266(vs), 1151(vs), 1055(m), 953(s), 859(m), 754(m), 682(m). μ_{eff} (299 K): 3.2 B.M. λ_{max} (H_2O) (ε M^{-1} cm^{-1}): 380(15), 630(7) 1031(5) nm.

2.2.3. *[Cu(sac)$_2$(Hpz)$_2$(H$_2$O)$_2$]*

A sample of pyrazole, 0.27 g (4.0 mmol) was added to a solution of 0.53 g (1.0 mmol) of copper saccharinate in 75 mL of water. The reaction mixture was refluxed for 20 min while stirring. The resulting solution was cooled and allowed to evaporate slowly few days at room temperature. The resulting deep blue crystals were collected by suction filtration and dried in air. The crystals obtained in this way were suitable for X-ray analysis. Yield was 0.31 g (50%). *Anal.* Calc. for $C_{20}H_{20}N_6O_8S_2Cu$: C, 39.9; H, 3.0; N, 14.0; Cu, 10.6. Found: C, 39.9; H, 2.9; N, 13.9; Cu, 10.6%. IR (KBr pellet, cm^{-1}): 3543(m), 3334 (m), 3141(s), 3089(m), 3068(m), 1611(vs), 1579(vs), 1347(m), 1298(vs), 1263(s), 1171(s), 1158(m), 1070(m), 1059(m), 950(s), 859(m), 783(m), 754(s), 680(m), 594(m), 539(m). μ_{eff}: 1.90 B.M. UV–Vis (λ, nm (ε, M^{-1} cm^{-1})): 670(81).

2.2.4. *[Zn(sac)$_2$(Hpz)$_2$]*

Pyrazole, 0.27 g (4.0 mmol) was added to a solution of 0.53 g (1.0 mmol) of zinc saccharinate in 50.0 mL of water. The reaction mixture was refluxed for 45 min. The resulting solution was cooled and allowed to evaporate slowly over a few days at room temperature and a crop of crystals was obtained. The colorless crystals were collected by suction filtration and dried in air. The crystals obtained in this way were suitable for X-ray analysis. Yield was 0.35 g (62%). *Anal.* Calc. for $C_{20}H_{16}N_6O_6S_2Zn$: C, 42.4; H, 4.7; N, 16.6; Zn, 11.6. Found: C, 42.6; H, 4.6; N, 16.9; Zn, 11.6%. IR (KBr pellet, cm^{-1}): 3108(s), 1656(vs), 1591(vs), 1528(m), 1456(m), 1359(m), 1308(s), 1256(s), 1171(s), 1071(m), 947(s), 784(m), 751(s), 677(m), 594(m).

2.3. Physical measurements

FT-IR spectra were recorded for KBr pellets with a Perkin–Elmer Spectrum 1000. Thermal analyses were performed on a Texas Instruments Thermal Advantage

Table 1
Summary of crystallographic data collection and structure refinements of **1**–**4**

	1	**2**	**3**	**4**
Empirical formula	$C_{20}H_{20}N_6O_8S_2Co$	$C_{20}H_{20}N_6O_8S_2Ni$	$C_{20}H_{20}N_6O_8S_2Cu$	$C_{20}H_{16}N_6O_6S_2Zn$
FW	595.47	545.25	600.08	565.88
Crystal system	monoclinic	monoclinic	triclinic	monoclinic
Space group	$P2_1/n$	$P2_1/c$	$P\bar{1}$	$C2/c$
a (Å)	12.3254(18)	10.3299(15)	7.2946(4)	18.2138(12)
b (Å)	8.3149(12)	8.3317(12)	8.6074(8)	10.2481(8)
c (Å)	12.6947(18)	14.377(2)	10.5153(6)	13.0634(10)
α (°)	90	90	76.87	90
β (°)	109.231(3)	93.238(3)	69.91(1)	109.24(1)
γ (°)	90	90	67.90	90
V (Å^3)	1228.4(3)	1235.4(3)	570.85(6)	2302.2(3)
Z	2	2	1	4
Radiation used, λ (Å)	Mo Kα (0.71073)	Mo Kα (0.71073)	Mo Kα (0.71073)	Mo Kα (0.71073)
T (K)	295(2)	298(2)	100(2)	100(2)
D_{calc} (g cm^{-3})	1.610	1.600	1.746	2.302
μ(Mo Kα) (mm^{-1})	0.927	1.012	1.202	1.299
F(000)	610	612	307	1152
Crystal color	red	light blue	blue	color less
Crystal shape	block	block	block	parallelepiped
Crystal size (mm)	0.36 × 0.26 × 0.23	0.48 × 0.45 × 0.20	0.4 × 0.32 × 0.23	0.46 × 0.34 × 0.20
Diffractometer type	CCD	CCD	Siemens Smart CCD	Novius Kappa CCD
Data collection method	psi + omega-scan	psi + omega-scan	psi + omega-scan	psi + omega-scan
T_{max}/T_{min}	0.963/0.674	rel. 1.96/rel. 1.29	0.7918/0.5981	0.7812/0.5864
Total reflections/θ_{max} (°)	10054/30.52	9993/30.51	6186/33.22	15104/33.22
Unique (R_{int})	3743 (0.0322)	3741 (0.0446)	3731 (0.0283)	4235 (0.0641)
Refinement data	F^2	F^2	F^2	F^2
H-atom treatment	mixed	refined	mixed	calculated
Data/parameters	3743, 197	3741, 211	3730, 178	4235, 159
Data with [$I > 2\sigma(I)$]	2882	2555	3372	4050
Goodness-of-fit	1.017	0.999	1.057	1.067
R_1, wR_2 [$I > 2\sigma(I)$]	0.0533, 0.1362	0.0424, 0.1049	0.0294, 0.0773	0.0291, 0.0797
R_1, wR_2 (all data)	0.0694, 0.1490	0.0610, 0.1084	0.0336, 0.0802	0.0307, 0.0810
ρ_{max}/ρ_{min} (e Å^{-3})	3.343/−0.557	1.678/−1.182	0.630/−0.498	0.571/−0.821

Universal Analysis 2000, under a dynamic nitrogen atmosphere with the sample kept in aluminum crucibles (aluminum oxide a standard; constant heating rate 10 K min^{-1}). Magnetic susceptibility was measured using a Johnson Matthey MSB-1 balance at 25 °C. Electronic spectra of freshly prepared DMF solutions of the complexes were recorded on a Shimadzu spectrophotometer UV-1601 PC, using 10 mm quartz cells.

2.4. X-ray crystallography

Single-crystal X-ray diffraction data for compounds **1** and **2** were gathered at room temperature, while data for compound **3** were collected at 100 K using a Siemens SMART CCD-based diffractometer. The reflections were integrated using the commercial program SAINT, and corrected for systematic errors with the public-domain program SADABS [16–18]. Compound **4** was measured on a Nonius Kappa-CCD diffractometer equipped with a nitrogen cold stream operating at 100 K and a Mo-target rotating-anode X-ray source. Final cell constants were obtained from least squares fits of all integrated reflections. Structures were solved by direct methods [17] and refined to F^2 by full-matrix least-squares [18]. The refinements converged with the residuals given in Table 1, which summarizes the most important crystal data and refinement parameters.

3. Results and discussion

3.1. Synthesis

The aim of this work was to study the effects of a pyrazole co-ligand on the coordination mode of saccharinate in mixed-ligand complexes. Previous observations showed that a second ligand in the coordination sphere of saccharinate complexes could produce N- or O-coordination of the saccharinate ion, as observed in $[Cu_2(sac)_4(Himid)_4]$, $[V(sac)_2(py)_4]$ and $[Ni(sac)_2(py)_4]$ and recently in $[Cu(sac)_2(Hpz)_4]$ [19]. The reaction with pyrazole in water solution yields compounds of the formula $M(sac)_2(Hpz)_2(H_2O)_2$ for M = Co(II), Ni(II), Cu(II), and $Zn(sac)_2(Hpz)_2$, all with saccharinate ions N-coordinated. Their compositions were checked by analysis of their C, H and N content. The values are in good agreement with the above formulas.

3.2. Description of the crystal structures

Figs. 1–4 give the thermal ellipsoid drawings of the structures of the Ni, Co, Cu and Zn compounds, indicating the atom numbering schemes. Bond lengths and angles are given in Table 2. The complexes **1**, **2** and **3** have the general molecular formula $[M(sac)_2(HPz)_2(H_2O)_2]$ and **4** is Zn(sac)2(Hpz)$_2$. The metal atoms in **1**, **2** and **3** are located on crystallographic inversion centers and have distorted pseudo-octahedral geometry. The coordination environment of each metal center is made up of two pyrazole molecules, two water molecules and two saccharinate ligands, all in the *trans* configurations. It can be affirmed that the saccharinate and the two non-substituted water molecules of the original saccharinate complexes are retained. In the original series of saccharinate complexes, two different orientations were found for the coordinated water molecules – the so called *flat* and *pyramidal* cases [2]. In the idealized flat case, the M–O bond lies in the plane of the water molecule; all four atoms are coplanar. In the pyramidal case the M–O and two H–O bonds point roughly at three of the four vertices of a tetrahedron. In the structures considered in this work, only the pyramidal case is present; the other water molecules were substituted by a nitrogen atom

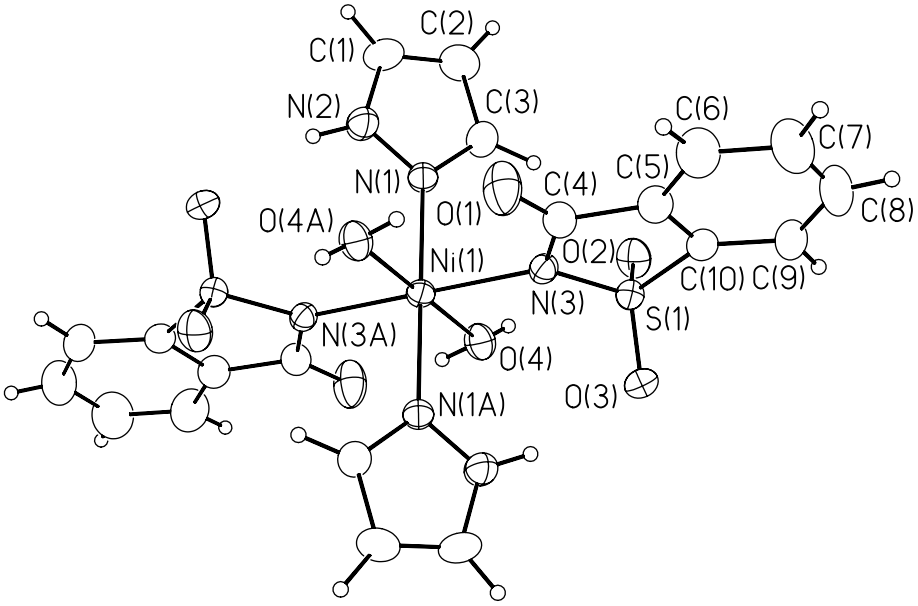


Fig. 1. Drawing of the compound **1** showing 50% probability displacement ellipsoids.

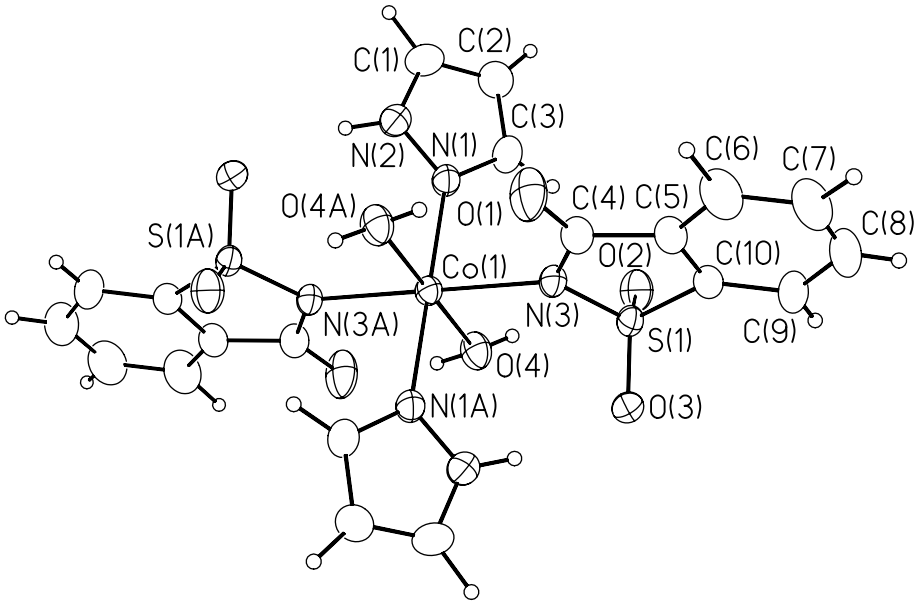


Fig. 2. Drawing of the compound **2** showing 50% probability displacement ellipsoids.

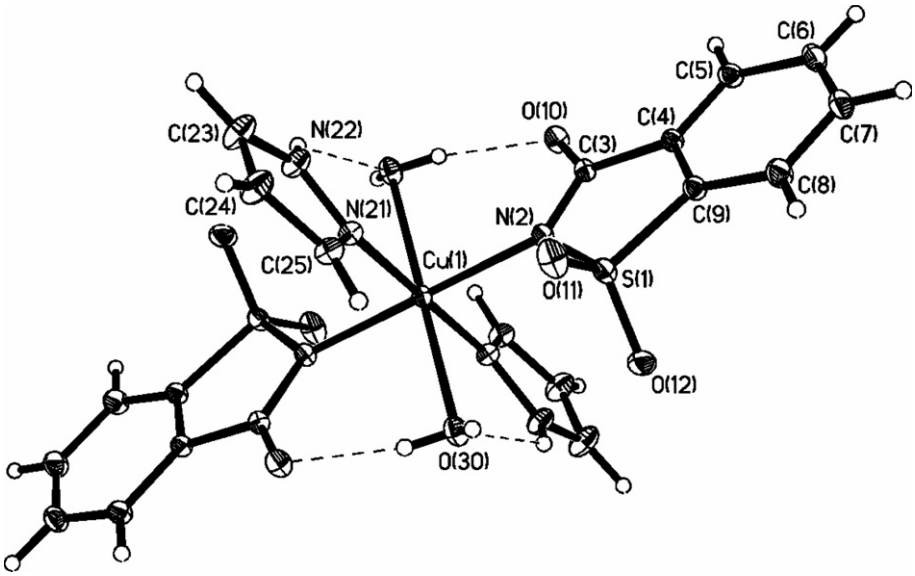


Fig. 3. Drawing of the compound **3** showing 50% probability displacement ellipsoids.

of the pyrazole ring. It is likely that the water molecules are pyramidal here in conjunction with the formation of strong intramolecular hydrogen bonds with the carbonyl oxygen of the saccharinate ligand. The N–H group forms hydrogen bonds with the saccharinate sulfonyl oxygen atoms in the cobalt and nickel complexes. In the copper complex, the hydrogen bonding is formed with the coordinate water molecule oxygen atom, see Table 3. As expected for a metal ion with a d^9 electronic configuration, the copper complex shows an elongated axis along the O–Cu–O bonds 2.4266(11) Å. In spite of the mixed ligand set (4N and 2O) there is not a rigorously, octahedral coordination sphere, and hence, no rigorous electronic degeneracy is possible. It would appear, however, that the structure comes close enough to the ideal case that the vibronic problem envisioned in the work by Jahn and Teller plays a role in the structures of this work. The distortion causes the arrangement around the metal ion to change with respect to the cobalt(II) and nickel(II) complexes, as shown in Fig. 5. In the Ni(II) and Co(II)-complexes, the saccharinate and water molecules are on the same plane but, in the copper compound they are not. The bond distances M–Nsac and M–Ow are longer than in the former saccharinate complexes [4], the M–NHpz distances are shorter than the M–Nsac for the Co(II), Ni(II) and Cu(II)-complexes. The zinc complex shows a pseudo-tetrahedral coordination around the metal ion. There is no difference between the Zn–N bonds, and the N–Zn–N angles are around 112°.

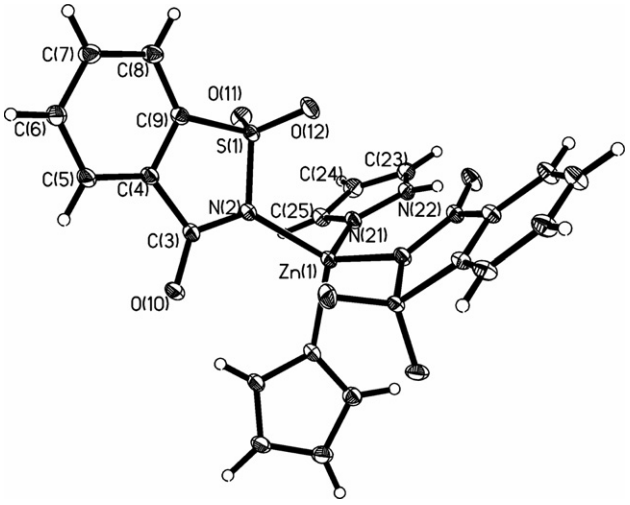


Fig. 4. Drawing of the compound **4** showing 50% probability displacement ellipsoids.

Table 3
Hydrogen bonds distances for **1**, **2** and **3**

D–H···A	*D*(D···A)
[Co(sac)$_2$(Hpz)$_2$(H$_2$O)$_2$]	
N(2)···O(3)#1	2.987(3)
N(2)···O(2)#2	3.133(3)
O(4)···O(1)#1	2.626(3)
O(4)···O(3)#3	2.941(2)
O(4)···O(2)	3.008(3)
[Ni(sac)$_2$(Hpz)$_2$(H$_2$O)$_2$]	
N(2)···O(3)#1	2.967(3)
O(4)···O(1)#1	2.610(3)
O(4)···O(3)#2	2.951(3)
[Cu(sac)$_2$(Hpz)$_2$(H$_2$O)$_2$]	
N(22)···O(30)	2.652
O(10)···O(30)	2.799
O(10)···O(30A)	2.908

The final difference-Fourier maps for **1** and **2** show, respectively, two peaks and one peak greater than 1.0 e/Å^3. The peaks can be explained in both cases by the presence of intergrowths, as detailed below.

Evidence for polymorphic intergrowths in the structures of compounds **1** and **2.** Both structures, **1** and **2**, have larger than normal residual peaks in their final difference-Fourier maps. An explanation for these peaks, in terms of polymorphic intergrowths, can be understood through an examination of the packing patterns of the two structures. The two crystal structures, which are based on almost isostructural molecules, are nevertheless quite distinct, but related crystal structure types. Beginning with the unit cell of **2**, the nickel complex, the following

Table 2
Selected bond distances (Å) and angles (°) for [Co(sac)$_2$(Hpz)$_2$(H$_2$O)$_2$] (**1**), [Ni(sac)$_2$(Hpz)$_2$(H$_2$O)$_2$] (**2**), [Cu(sac)$_2$(Hpz)$_2$(H$_2$O)$_2$] (**3**) and [Zn(sac)$_2$(Hpz)$_2$] (**4**)

	Co(sac)$_2$(Hpz)$_2$(H$_2$O)$_2$ (**1**)	Ni(sac)$_2$(Hpz)$_2$(H$_2$O)$_2$ (**2**)	[Cu(sac)$_2$(Hpz)$_2$(H$_2$O)$_2$] (**3**)	[Zn(sac)2(Hpz)2] (**4**)
Bond lengths				
M–N(1)	2.1143(18)	2.0839(19)		
M–N(3)	2.2154(18)	2.1874(18)		
M–O(4)	2.1286(18)	2.0828(19)		
Cu–N(21)#1			1.9805(11)	
Cu–N(2)#1			2.0902(11)	
Cu–O(30)#1			2.4266(11)	
Zn–N(2)				1.9974(9)
Zn–N(21)				1.9991(10)
Bond angles				
N(1)–M–O(4)	93.65(7)	93.58(8)		
N(1)–M–O(4)#1	86.35(7)	86.42(8)		
N(1)–M–N(3)	87.92(7)	88.40(7)		
N(1)–M–N(3)#1	92.08(7)	91.60(7)		
O(4)–M–N(3)	88.13(7)	87.72(7)		
O(4)–M–N(3)#1	91.87(7)	92.28(7)		
N(21)–Cu–N(21)#1			180.0	
N(21)–Cu–N(2)|			92.50(5)	
N(21)#–Cu–N(2)			87.50(5)	
N(2)–Cu–N(2)#1			180.0	
N(21)–Cu–O(30)			94.40(4)	
N(21)#1–Cu–O(30)			85.60(4)	
N(2)–Cu–O(30)			90.54(4)	
N(2)#1–Cu–O(30)			89.46(4)	
O(30)–Cu–O(30)#1			180.0	
N(2)–Zn–N(2)#1				116.17(6)
N(2)–Zn–N(21)#1				111.16(4)
N(2)–Zn–N(21)				103.11(4)
N(21)#1–Zn–N(21)				112.45(5)

Symmetry transformations for **1**, #1 $(1-x, 1-y, -z)$; for **2**, #1 $(-x, -y, -z)$.
Symmetry transformations for **3**: #1 $(-x, -y, -z)$.
Symmetry transformations for **4**: #1 $(1-x+1, -y+1, -z+1)$ #2 $(-x, -y+1, -z+1)$.

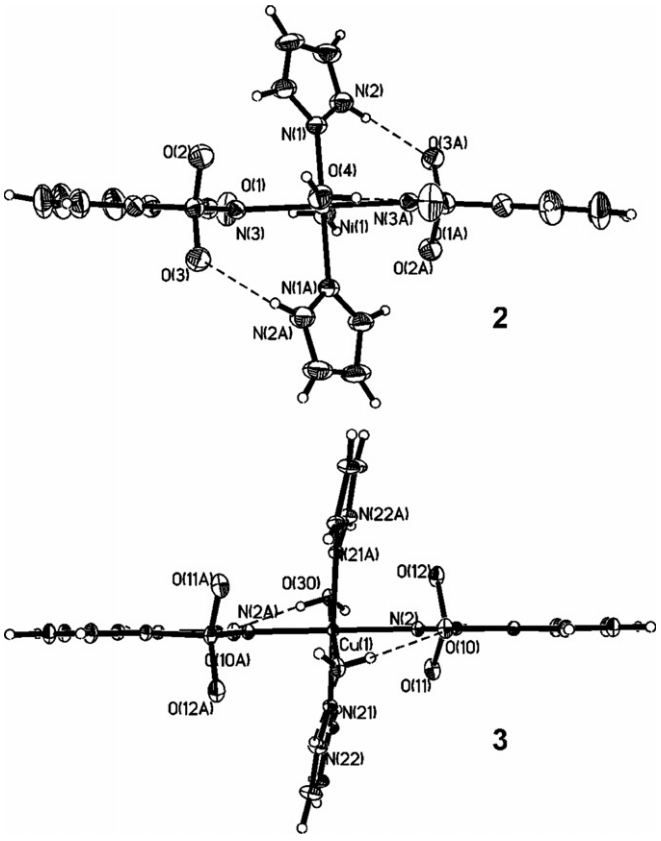


Fig. 5. Ligand orientation around the metal ion and hydrogen bonds interactions in compounds **2** and **3**.

transformation, if valid, would give a unit cell almost identical to that of the cobalt complex: $a' = a + 0.5c$; $b' = b$; $c' = -a + 0.5c$. $a' = 12.247$, $b' = 8.332$, $c' = 12.914$ Å, $\beta' = 110.36°$. These values can be compared to the cell parameters of **1**, (Table 1.) The transformation is not, in fact, valid, as it involves non-integral lattice translations that are not present in the structure of **2**. Thus, while the two cells have a geometrical relationship, the structures are not the same; detailed examination of the packing patterns indeed establishes that the structure types are different, see Fig. 6.

In the final difference-Fourier map for the nickel complex, **2**, there is a peak of 1.68 e/Å^3, located at $(0, 0.5, 0)$. Taking due account of symmetry and cell transformations, these coordinates represent the difference between the principal M–M Patterson vector in **1** and that in **2**. (It is one of several possibilities, all related by symmetry.) This difference peak could arise if a small component of a polymorph, with the same structure type as **1** was present in the sample of **2** from which the X-ray data were gathered. In a similar fashion, the final difference map for the cobalt complex, **1**, shows two residual peaks with densities greater than 1.0 e/Å^3 – one of 3.34 e/Å^3 at $(0.5, 0, 0)$ and a second, 1.85 e/Å^3 at $(0.2164, 0.8707, -0.1139)$. Again, taking appropriate account of cell transformations and symmetry, the relationship of the first peak to the cobalt atom, and of the second peak to the sulfur atom, represent the differences between the relative locations of these atoms in the two structures. Taken together with what is observed in the difference map for the nickel complex, this provides strong evidence that both of these structures are affected, albeit to different degrees, by minor intergrowths of a second polymorph with the structure of the nickel complex representing the polymorphic type for the cobalt compound and vice versa.

A more detailed analysis of this structural feature will be published elsewhere.

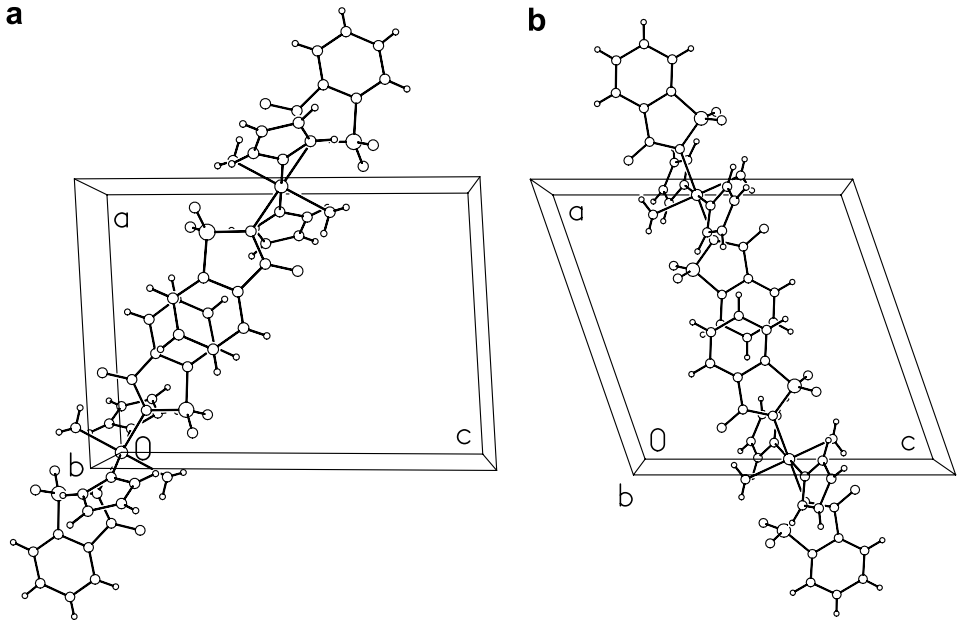


Fig. 6. Packing diagram of the compounds **1, a** and **2, b**, shown as the a-b face.

Table 4
Assignment of the most characteristic IR bands of **1**, **2**, **3** and **4**

Modes	1	2	3	4
ν(O–H) with intramolecular hydrogen bonds	3513/ 3310	3519/ 3312 f	3546/ 3337 f	
ν(N–H)	3066	3063	3141/3089/3068	3187/3108
ν(C=O)	1635	1636	1611	1656
$\nu_{as}(SO_2)$	1264	1266	1285	1298
$\nu_{s}(SO_2)$	1151	1151	1158	1171

3.3. Spectroscopic and magnetic properties

The most significant frequencies in the IR spectra of the metal complexes are given in Table 4. The IR spectra of the Ni(II), Co(II) and, Cu(II)-complexes resemble each other indicating a similar structural pattern. The strong and sharp bands in the range 3546–3310 cm^{-1} are attributed to the ν(OH) vibrations of water molecules with intramolecular hydrogen bond interactions [20]. As shown in Figs. 1 and 2, the water molecules form hydrogen bonds with the carbonyl oxygen atom and intermolecular interactions with the sulfonyl groups for **1** and **2**, and with the carbonyl group in **3**, the O···O distance being ca. 2.9 Å. The Zn(II) compound shows no O–H bands. The N–H stretching vibrations for the pyrazole moiety appear in the range 3066–3187 cm^{-1} as sharp bands. The copper compound displays three bands, with a splitting pattern that can be attributed to the hydrogen bonding interactions. The ν(CO) bands of the sac ligands appear at 1635 in **1** and **2**, 1656 in **3** and 1611 cm^{-1} in **4**. The low frequency in the latter compound could be attributed to the intra- and intermolecular hydrogen bonds; this is in agreement with the higher frequency of the carbonyl stretching vibration in the zinc(II) complex where there are no hydrogen bonds. The $\nu_{asym}(SO_2)$ sac absorptions appear as strong bands between 1264 and 1285 cm^{-1}, while $\nu_{sym}(SO_2)$ bands occur as strong bands at ca. 1150 cm^{-1}. The SO_2 vibration frequencies in these complexes are similar to those for the sodium saccharinate monohydrate; the sulfonyl groups are less susceptible to changes in the vibration frequency as a result of hydrogen bonding interactions.

The spectroscopic data are consistent with octahedral coordination geometry and indicate that the structure showed in solid state is preserved in solution. The λ_{max} values are blue-shifted, respect to tetra-hydrated sacharinate complexes, as expected for pyrazole as stronger ligand than water [21]. The effective magnetic moments at room temperature are in the range for high-spin complexes with octahedral coordination geometry, as observed in the crystal structures [22].

3.4. Thermal analysis

The thermal behavior of the compounds was investigated by means of thermogravimetric (TG) and differentia-thermal analysis (DTA) measurements in a flowing nitrogen atmosphere (temperature range 25–512 °C). Thermo-analytical data (decomposition stages, temperature ranges, peak maxima and mass losses) for the metal complexes are summarized in Table 5. The degradation of compounds **1**, **2** and **3** occurs in four or five successive TG steps. In the first two steps the mass loss corresponds to the release of two water molecules for **1** and **3**. For the case of compound **2**, two steps correspond to two water molecules and one pyrazole. It is accompanied by two endothermic DTA signals. The next step involves the loss of two pyrazole molecules, with an endothermic DTA signal. In the last step, an exothermic process takes place, which corresponds to the elimination of a saccharinate molecule.

Table 5
Thermoanalytical data for the metal complexes **1**, **2**, **3** and **4**

Compound/ Stage[a]	Temperature range, °C	DTG^{b}_{max}, °C	Removed group[a]	Mass loss (%)	
				Calculated	Found
[Co(sac)$_2$(pz)$_2$(H$_2$O)$_2$]					
1	40–148	129(−)	H_2O	3.53	3.02
2	148–197	176(−)	H_2O	3.8	3.05
3	178–374	335(+)	2Hpz	25.3	22.8
4	375–512	408(+)	Hsac	31.02	30.6
[Ni(sac)$_2$(pz)$_2$(H$_2$O)$_2$]					
1	46–198	167(−)	Hpz	10.95	11.42
2	198–260	207(−)	$2H_2O$	6.42	6.02
3	260–373	337(−)	Hpz	14.37	11.42
4	374–512	425(+)	Hsac	35.95	30.06
[Cu(sac)$_2$(pz)$_2$(H$_2$O)$_2$]					
1	79–145	110(−)	$2H_2O$	6.48	6.00
2	145–239	219(−)	Hpz	11.46	11.33
3	239–304	281(−)	Hpz	18.29	11.33
4	383–790	344(−)	Hsac	23.88	30.34
5	404–512	468(+)		20.11	
[Zn(sac)$_2$(pz)$_2$]					
1	28–225	192(−)		2.1	
2	225–375	355(−)	2Hpz	21.98	24.07
3	275–512	441	Hsac	33.51	32.2

[a] pz: pyrazole, sac: saccharinate ion.
[b] (+) and (−) donate endothermic and exothermic processes, respectively.

The degradation of the zinc complex, **4** takes place with a smoothly continuous loss of mass, with one medium endothermic DTA signal, and two small DTA signals – one endothermic and one exothermic at 355 and 441 °C, respectively. This behavior is different from the other three compounds that show clear and defined step wise degradation. Probably, the absence of hydrogen bond in the zinc compound could be the determinant factor for the observed continuous degradation.

4. Conclusion

The results of this work show how hydrogen bonds between the ligands in the complex favored the arrangement around the central ion, for the Ni, Co and Cu compounds. This can be better observed, if it is compared with reported saccharinate–imidazole complexes, which show the following formula: $[M(Himid)_4(H_2O)_2]\cdot 2sac$ for

M = Co, Ni, [23,24], $[Cu_2(sac)_4(Himid)_4]$, [8], Here, the position of the second nitrogen atom in the imidazole ring, does not favor hydrogen bonding with the water molecules in the complex. The Zn compound in both cases, has the formula $[Zn(sac)_2(am)_2]$, am = Hpz or Himid, [25]. In this case, probably as a d^{10} complex, the tetrahedral compound is kinetically favored.

Acknowledgements

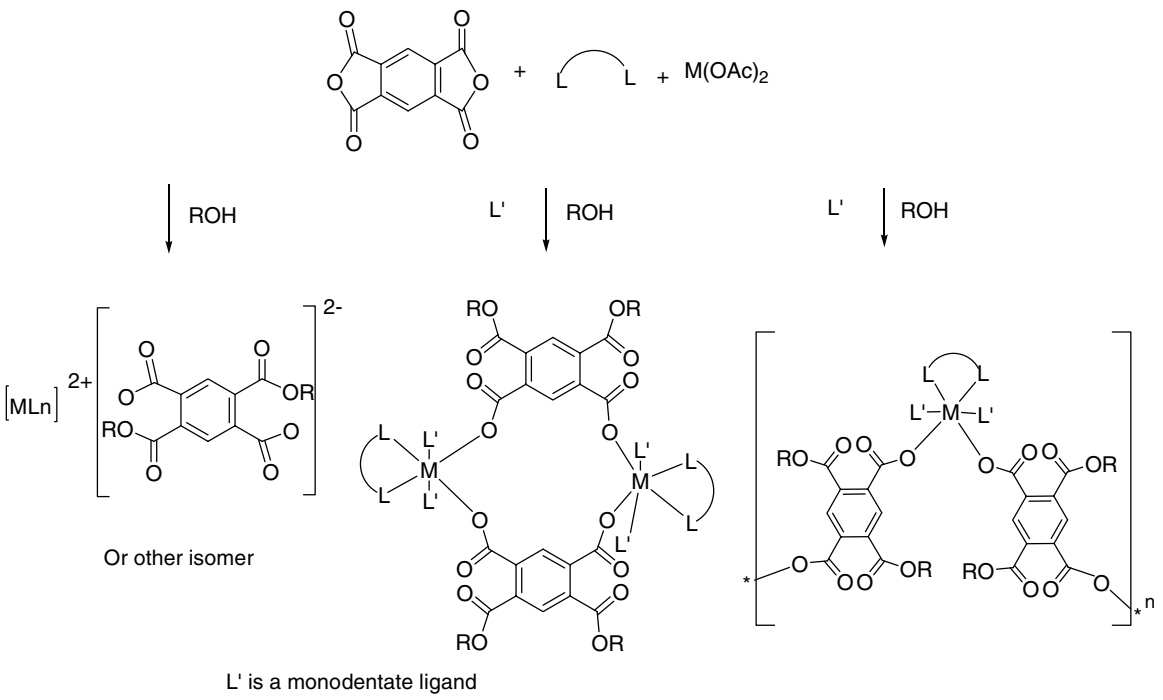
This work was supported by Vice-Rectory for Research, University of Costa Rica, grant 115-98-375. L.W. Pineda acknowledges a DAAD fellowship. We thank the Spanish Ministery of Science and Technology for financial support under Grant BQU2002-00554. We are indebted to the "Servei Central d'Instrumentació Científica (SCIC) of the University Jaume I for the use of the X-ray diffraction facilities.

Appendix A. Supplementary material

CCDC 259785, 259786, 259787 and 259788 contain the supplementary crystallographic data for this paper. These data can be obtained free of charge via http://www.ccdc.cam.ac.uk/conts/retrieving.html, or from the Cambridge Crystallographic Data Centre, 12 Union Road, Cambridge CB2 1EZ, UK; fax: (+44) 1223-336-033; or e-mail: deposit@ccdc.cam.ac.uk. Supplementary data associated with this article can be found, in the online version, at doi:10.1016/j.poly.2007.06.001.

References

[1] T. Steiner, Angew. Chem., Int. Ed. 41 (2002) 48.
[2] F.A. Cotton, G.E. Lewis, C.A. Murillo, W. Schwotzer, G. Valle, Inorg. Chem. 23 (1984) 4038.
[3] F.A. Cotton, L.R. Falvello, R. Llusar, E. Libby, C.A. Murillo, W. Schwotzer, Inorg. Chem. (1986) 4967.
[4] S.Z. Haider, K.M. Malik, K.J. Ahmed, H. Hess, R. Riffel, M.B. Hursthouse, Inorg. Chim. Acta 72 (1983) 21.
[5] O.V. Quinzani, S. Tarulli, C. Marcos, S. García Granda, E.J. Baran, Z. Anorg. Allg. Chem. 625 (1999) 1948.
[6] N.M. Alfaro, F.A. Cotton, L.M. Daniels, C.A. Murillo, Inorg. Chem. (1992) 2718.
[7] F.A. Cotton, L.R. Falvello, C.A. Murillo, G. Valle-Bourrouet, Inorg. Chim. Acta 190 (1991) 89.
[8] S. Liu, J. Huang, J. Li, W. Li, Acta Crystallogr., Sect. C C47 (1991) 41.
[9] P. Naumov, G. Jovanovski, Acta Chim. Slov. 46 (1999) 389.
[10] P. Naumov, G. Jovanovski, A. Todorovka, J. Mol. Struct. 563–564 (2001) 341.
[11] L. Falvello, J. Gómez, I. Pascual, M. Tomas, E. Urriolabeitia, A.J. Schultz, Inorg. Chem. 40 (2001) 4455.
[12] C.A. Johns, G.M.G. Hossain, K.M.A. Malik, S.Z. Haider, U.K.R. Romman, Polyhedron 20 (2001) 721.
[13] M.F. Iskander, T.E. Khalil, W. Haase, R. Werner, I. Svoboda, H. Fuess, Polyhedron 20 (2001) 2787.
[14] C.S. Hong, J.H. Yoon, Y.S. You, Inorg. Chim. Acta 358 (2005) 3341.
[15] S.Z. Haider, K.M. Malik, K.J. Ahmed, Inorg. Synth. 23 (1985) 47.
[16] (a) Data collection: SMART, Siemens Analytical X-ray instruments, Inc., Madison, WI, 1996;
(b) Integration: SAINT, Siemens Analytical X-ray Instruments, Inc., Madison, WI, 1996;
(c) Corrections G.M. Sheldrick, SADABS, Göttingen University, 1996.
[17] G.M. Sheldrick, Acta Crystallogr., Sect. A 46 (1990) 467.
[18] G.M. Sheldrick, SHELXL-97, Göttingen University, 1997.
[19] P. Naumov, G. Jovanosvski, M.G.B. Drew, S.W. Ng, Inorg. Chim. Acta 314 (2001) 154.
[20] T.R. Conley, Infrared Spectroscopy, second ed., Allyn and Bacon Inc., Boston, 1972.
[21] A.B.P. Lever, Inorganic Electronic Spectroscopy, second ed., Elsevier, Amsterdam, 1984.
[22] B.N. Figgis, J. Lewis, Prog. Inorg. Chem. 6 (1964) 37.
[23] J. Li, Y. Zhang, W. Lin, Polyhedron 11 (1992) 419.
[24] Y. Zhang, J. Li, W. Lin, S. Li, J. Huang, J. Cryst. Spec. Res. 22 (1992) 433.
[25] Valle-Bourrouet, L.W. Pineda, unpublished results.



Scheme 1. Some possibilities for metal carboxylate complex formation by ring opening reactions of pyromellitic dianhydride by alcohols.

opening, as illustrated in Scheme 1 and also to use the ring opening reactions for formation of metal complexes of first row transition metals.

2. Experimental

2.1. General

The reagents used here were purchased from commercial sources (Sigma–Aldrich or Fluka) and were used as received unless otherwise stated. The X-ray diffraction data were collected at 296 K with Mo Kα radiation ($\lambda = 0.71073$ Å) using a Bruker Nonius SMART CCD diffractometer equipped with a graphite monochromator. SMART software was used for data collection and also for indexing the reflections and determining the unit cell parameters; the collected data were integrated using SAINT software. The structures were solved by direct methods and refined by full-matrix least-squares calculations using SHELXTL software. All the non-H atoms were refined in the anisotropic approximation. The crystallographic parameters of the compounds studied are given in Table 1.

2.2. Synthetic procedures for the complexes

2.2.1. Synthesis of (2,2′-bipyridyl)dibenzoato nickel(II) [A]

Benzoic acid (733 mg, 6 mmol) and potassium hydroxide (337 mg, 6 mmol) were mixed together with nickel(II) chloride hexahydrate (710 mg, 3 mmol) in a mortar. The whole content was heated at 100 °C for 30 min. The mixture was cooled and transferred to a solution of 2,2′-bipyridine (234 mg, 3 mmol) in 10 ml of methanol. The mixture was stirred for half an hour, after which time a green colored solution was obtained and filtered. The filtrate was kept undisturbed for crystallization to give crystals of **A** (isolated yield 87%). Elemental *Anal.* Calc. for $C_{24}H_{18}N_2NiO_4$: C, 63.01; H, 3.94. Found C, 63.03; H, 3.96%. IR (KBr, cm^{-1}): 3434(b), 1593(m), 1523(s), 1426(s), 1073(w), 1026(w), 857(m), 726(m), 734(m), 685(m). Visible λ_{max}, 645 nm ($\varepsilon_{ethanol} = 9.11\ M^{-1}\ cm^{-1}$).

2.3. The ring opening reactions of pyromellitic dianhydride

The complexes with different compositions are prepared by reactions of *in situ* generated 2,5-dicarbomethoxy benzene 1,4-dicarboxylic acid or its isomer 2,4-dicarbomethoxy benzene 1,5-dicarboxylic acid (abbreviated as LH_2) with different metal salts and nitrogen containing heterocycles such 1,10-phenanthroline (phen) or 2,2′-bipyridine (bpy) as follows:

2.3.1. Synthesis of dicarboxylate complexes

$[Ni_2L_2(phen)_2(CH_3OH)_2(H_2O)_2]\cdot 2CH_3OH$ [**B**]: To a solution of pyromellitic dianhydride (218 mg, 1 mmol) in methanol (15 ml) a solution of nickel(II) acetate tetrahydrate (248 mg, 1 mmol in 5 ml methanol) was added, giving a green cloudy solution. To this solution a solution of 1,10-phenanthroline (200 mg, 1 mmol in 5 ml methanol) was added, followed by stirring at room temperature for 1 h. The solution was refluxed for 8 h and filtered, the filtrate on standing gave complex **B** (isolated yield of pure crystals 14%). Elemental *Anal.* Calc. for $C_{54}H_{60}N_4Ni_2O_{24}$: C, 51.21;

Table 1
Crystallographic parameters of compounds **A**–**H**

	A	**B**	**C**	**D**	**E**	**F**	**G**	**H**
Formulae	$C_{24}H_{18}N_2NiO_4$	$C_{54}H_{60}N_4Ni_2O_{24}$	$C_{22}H_{24}N_2Ni_1O_{12}$	$C_{24}H_{18}N_2O_{11}Zn$	$C_{32}H_{28}CoN_4O_{12}$	$C_{25}H_{26}CoN_2O_{12}$	$C_{26}H_{25}Cl_2CuN_4O_6$	$C_{84}H_{58}Cu_2N_8O_{24}$
Molecular weight	457.11	1266.48	567.12	575.79	719.51	605.41	623.94	1690.46
Crystal system	monoclinic	monoclinic	monoclinic	triclinic	monoclinic	triclinic	triclinic	triclinic
Space group	$P2_1/n$	$P2_1/c$	$P2/c$	$P\bar{1}$	$C2/c$	$P\bar{1}$	$P\bar{1}$	$P\bar{1}$
Temperature (K)	296(2)	296(2)	296(2)	296(2)	296(2)	296(2)	296(2)	296(2)
Wavelength (Å)	0.71073	0.71073	0.71073	0.71073	0.71073	0.71073	0.71073	0.71073
a (Å)	7.4322(2)	12.9793(17)	9.5081(2)	10.7940(11)	25.5622(17)	9.3313(3)	8.0962(2)	11.9018(11)
b (Å)	16.7224(4)	17.354(2)	10.3025(2)	11.2328(11)	15.8261(17)	12.6779(6)	12.9513(3)	13.2077(11)
c (Å)	17.3528(4)	14.1181(17)	14.6321(2)	11.5938(11)	19.5923(16)	13.2919(4)	13.9321(4)	15.9836(15)
α (°)	90.00	90.00	90.00	77.154(6)	90	105.996(2)	70.8500(10)	68.741(5)
β (°)	101.3810(10)	116.589(3)	120.6260(10)	76.933(6)	110.010(6)	110.445(10)	84.086(2)	78.601(6)
γ (°)	90.00	90.00	90.00	72.510(6)	90	100.325(2)	81.5520(10)	69.457(5)
V (Å^3)	2114.27(9)	2843.7(6)	1233.39(4)	1287.9(2)	7447.6(11)	1348.47(9)	1362.70(6)	2185.5(3)
Z	4	2	2	2	8	2	2	1
Density (Mg m^{-3})	1.436	1.479	1.527	1.485	1.283	1.491	1.521	1.284
Absorption coefficient (mm^{-1})	0.951	0.750	0.854	1.016	0.522	0.703	1.046	0.563
Absorption correction	none	none	none	none	none	none	none	none
F(000)	944	1320	588	588	2968	626	640	868
Total number of reflections	13,307	31,303	13,284	9359	50,847	6549	16,125	25,024
Reflections, $I > 2\sigma(I)$	5195	7073	2971	4150	9061	5485	6033	10,090
Maximum 2θ (°)	29.09	28.39	28.28	28.28	28.30	28.33	28.29	28.44
Ranges (h, k, l)	$-9 \leqslant h \leqslant 9$, $-22 \leqslant k \leqslant 19$, $-23 \leqslant l \leqslant 21$	$-17 \leqslant h <= 17$, $-21 \leqslant k \leqslant 23$, $-18 \leqslant l \leqslant 18$	$-12 \leqslant h <= 12$, $-13 \leqslant k \leqslant 13$, $-19 \leqslant l \leqslant 19$	$-14 \leqslant h <= 11$, $-14 \leqslant k \leqslant 12$, $-15 \leqslant l \leqslant 15$	$-34 \leqslant h <= 33$, $-21 \leqslant k \leqslant 18$, $-25 \leqslant l \leqslant 25$	$-34 \leqslant h <= 33$, $-21 \leqslant k \leqslant 18$, $-25 \leqslant l \leqslant 25$	$-12 \leqslant h <= 12$, $-16 \leqslant k \leqslant 16$, $-17 \leqslant l \leqslant 17$	$-15 \leqslant h <= 15$, $-16 \leqslant k \leqslant 17$, $-17 \leqslant l \leqslant 21$
Complete to 2θ (%)	91.8	99.3	96.5	69.6	98.0	97.3	89.1	91.7
Refinement method	full- matrix least-squares on F^2	full-matrix least-squares on F^2	full- matrix least-squares on F^2	full- matrix least-squares on F^2	full- matrix least-squares on F^2	full- matrix least-squares on F^2	full- matrix least-squares on F^2	full-matrix least-squares on F^2
Data/restraints/parameters	5195/0/280	7073/0/397	2971/0/169	4150/0/353	9061/0/449	6549/0/364	6033/0/373	10090/0/535
Goodness-of-fit (F^2)	1.031	1.018	1.010	1.056	1.065	1.045	1.020	1.070
R indices [$I > 2\sigma(I)$]	0.0298	0.0640	0.0374	0.0666	0.0920	0.0497	0.0425	0.1022
R indices (all data)	0.0432	0.1284	0.0424	0.1106	0.1606	0.1229	0.0866	0.1589

H, 4.74. Found C, 51.28; H, 4.87%. IR (KBr, cm^{-1}): 3421(bs), 30669(s), 2951(s), 1726(s), 1624(s), 1587(s), 1496(s), 1430(s), 1392(s), 1342(s), 1305(s), 1258(s), 1106(s), 1052(w), 963(w), 920(w), 867(m), 854(s), 797(s), 779(s), 728(s), 671(s), 643(w), 582(s), 540(s).

[Ni(bpy)(H$_2$O)$_4$]L [**C**] was prepared in an analogous manner except the reaction was carried out with 2,2′-bipyridine (reaction time 12 h at room temperature) and crystals were obtained after 15 days standing (isolated yield of pure crystals 43%). Elemental *Anal.* Calc. for $C_{22}H_{24}N_2NiO_{12}$: C, 46.55; H, 4.23. Found C, 46.48; H, 4.31%. IR (KBr, cm^{-1}): 3525(s), 3105(bs), 1716(s), 1567(s), 1493(bs), 1440(s), 1405(s), 1335(s), 1305(s), 1295(s), 1173(w), 1194(w), 1111(s), 1057(w), 1027(m), 956(m), 903(m), 804(s), 763(s), 736(s).

[{Zn(phen)(H$_2$O)L} · 3H$_2$O]$_n$ [**D**] was prepared in a similar manner to **B** but zinc(II)acetate tetrahydrate was used as the metal salt (stirred at room temperature for 1 h followed by heating at 60 °C for 8 h and allowed to crystallise, crystals obtained after about 7 days, yield of pure crystals 25%). Elemental *Anal.* Calc. for $C_{24}H_{18}N_2O_{11}Zn$: C, 50.02; H, 3.13. Found C, 50.11; H, 3.26%. IR (KBr, cm^{-1}): 3566(s), 3421(bs), 3066(bs), 1726(s), 1624(s), 1587(bs), 1430(s), 1392(s), 1342(s), 1258(s), 1106(s), 963(w), 854(s), 797(s), 728(s).

[Co(bpy)$_2$(H$_2$O)L] · 4H$_2$O [**E**]: Cobalt(II) acetate tetrahydrate (249 mg, 1 mmol) was added to a solution of pyromellitic dianhydride (218 mg, 1 mmol) in methanol (15 ml) with constant stirring. A turbid pink coloured solution appeared, and to this mixture a methanolic solution of 2,2′-bipyridine (312 mg, 2 mmol in 5 ml) was added dropwise with constant stirring. The solution turned dark yellow and stirring was continued for 2 h. On crystallization pure crystals of complex **E** could be obtained after 6 days; isolated yield of pure crystals 34%. Elemental *Anal.* Calc. for $C_{32}H_{28}CoN_4O_{12}$: C, 53.36; H, 3.89. Found C, 53.24; H, 3.96%. IR (KBr, cm^{-1}): 3402(s), 1738(s), 1717(s), 1575(s), 1493(bs), 1474(s), 1443(s), 1418(s), 1376(s), 1295(s), 1250(s), 1111(s), 1022(s), 850(s), 797(s) 772(s). Visible λ_{max}, 482 nm ($\varepsilon_{MeOH} = 5.94$ mol^{-1} dm^3 cm^{-1}). Magnetic moment 6.51 BM.

[Co(phen)(H$_2$O)$_3$L]CH$_3$OH (**F**): Cobalt(II) acetate tetrahydrate (249 mg, 1 mmol) was added to a solution of pyromellitic dianhydride (218 mg, 1 mmol) in methanol

(15 ml) with constant stirring. A turbid pink coloured solution appeared, and to this mixture a methanolic solution of 1,10-phenanthroline (200 mg, 1 mmol in 5 ml) was added dropwise with constant stirring. The solution turned dark yellow. The reaction mixture was stirred at room temperature for further 2 h. A turbidity appeared and the reaction mixture was heated at 60 °C for 6 h. On crystallization pure crystals of complex **E** could be obtained after about 12 days; isolated yield of pure crystals 30%. Elemental *Anal.* Calc. for $C_{25}H_{26}CoN_2O_{12}$: C, 49.55; H, 4.29. Found C, 49.58; H, 4.30%. IR (KBr, cm^{-1}): 3421(bs), 1726(s), 1598(s), 1518(w), 1494(bs), 1427(s), 1347(w), 1296(w), 1255(s), 1196(w), 1134(w), 1108(s), 1013(s), 868(w), 848(s). Visible λ_{max}, 487 nm ($\varepsilon_{MeOH} = 38.75\ mol^{-1}\ dm^3\ cm^{-1}$).

[Cu(bpy)$_2$Cl]Cl · LH · 2H$_2$O [**G**]: To a methanolic solution of pyromellitic dianhydride (218 mg, 1 mmol, 15 ml) cupric chloride dihydrate (171 mg, 1 mmol) was added and the mixture was stirred for 15 min at room temperature. The solution became light green. A solution of sodium acetate (82 mg, 1 mmol) in methanol (2 ml) was added. To this mixture a methanolic solution of 2,2′-bipyridine (0.312 g, 2 mmol, 10 ml) was added dropwise with constant stirring. A turbid solution of intense blue colour appeared. The mixture was refluxed for 8 h and filtered. The residue was discarded and solution was kept for crystallization. Blue crystals of **G** appeared after about 15 days; isolated yield of pure crystals, 28%. Elemental *Anal.* Calc. for $C_{26}H_{25}Cl_2CuN_4O_6$: C, 50.00; H, 4.01. Found C, 50.12; H, 4.03%. IR (KBr, cm^{-1}): 3348(s), 1732(s), 1599(s), 1493(bs), 1472(s), 1442(s), 1400(s), 1311(s), 1261(s), 1105(w), 1030(w), 1013(w), 775(s), 769(s). Visible λ_{max}, 737 nm ($\varepsilon_{MeOH} = 0.85\ mol^{-1}\ dm^3\ cm^{-1}$). Molar conductance in methanol 67.5 $ohm^{-1}\ cm^2\ mol^{-1}$.

[Cu$_2$(phen)$_4$L$_2$]L · LH [**H**]: To a solution of pyromellitic dianhydride (218 mg, 1 mmol) in methanol (15 ml) cupric acetate monohydrate (199 mg, 1 mmol) was added. A blue precipitate was formed. The mixture was stirred for 30 min. Then a methanolic solution of 1,10-phenanthroline (200 mg, 1 mmol, 10 ml) was added dropwise. The reaction mixture was further stirred overnight and filtered. The filtrate, having a light blue colour, was kept for crystallization. After five days pure crystals of **H** were obtained; isolated yield of pure crystals 19%. Elemental *Anal.* Calc. for $C_{84}H_{58}Cu_2N_8O_{24}$: C, 59.63; H, 3.43. Found C, 59.70; H, 3.51%. IR (KBr, cm^{-1}): 3421(s), 1718(s), 1591(s), 1429(s), 1396(s), 1383(s), 1248(s), 1109(s), 852(s), 812(w), 724(s).

3. Results and discussion

In order to prepare different first row transition metal carboxylates, as depicted in Scheme 1, we have tested the feasibility of a basic one-pot reaction of a nitrogen donor ligand and carboxylic acid with a first row transition metal acetate. For this purpose the reaction of benzoic acid with nickel(II) acetate in the presence of 2,2′-bipyridine was carried out in an one pot reaction. The complex (2,2′-bipyridyl)dibenzoato nickel(II) [**A**] could be easily prepared in this reaction. Alternatively the same complex also could be prepared by reaction of nickel(II) chloride with potassium benzoate followed by treatment with 2,2′-bipyridine. This complex has an IR absorption at 1593 cm^{-1} (ν_{COO^-}) corresponding to stretching of a coordinated carboxylate group; this absorption is lower in frequency than in free benzoic acid (ν_{COO^-} 1680 cm^{-1}). The synthetic procedure for complex **A** reported here is much simpler than the earlier reported procedure [6]. The complex was further characterised by determining its crystal structure. It has a distorted octahedral geometry around the nickel with benzoate groups acting as chelating ligands and one bipyridine ligand occupying the remainder of the coordination sites, as shown in Fig. 1. The carboxylate chelates are unsymmetrical, for example, the Ni1–O1 and Ni1–O2 bond distances are not equal; same is true for the Ni1–O3 and Ni1–O4 pair. Although the structure of the complex **A** is very simple, it serves as a starting point to design the synthesis for low dimensional coordination polymers or cyclic complexes.

The reaction of pyromellitic dianhydride with nickel(II) acetate tetrahydrate in methanol followed by treatment with 1,10-phenanthroline gave the metallacycle [**B**] (Scheme 2). By directly using 1,3-benzene dicarboxylic acid as a precursor, we could not prepare such cyclic complexes. However, adopting the ring opening methodology of pyromellitic dianhydride, as illustrated in Scheme 2, we could prepare novel metallacycles of nickel(II). The product has a characteristic ester frequency at 1726 cm^{-1}, showing that the pyromellitic dianhydride ring has opened to form the corresponding ester. The identity of the cyclic product has been established by crystallography (Fig. 2). In this complex each nickel(II) ion is attached to two mono-dentate

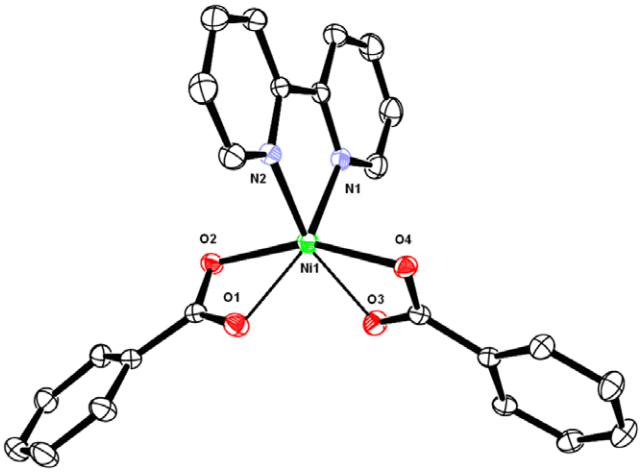
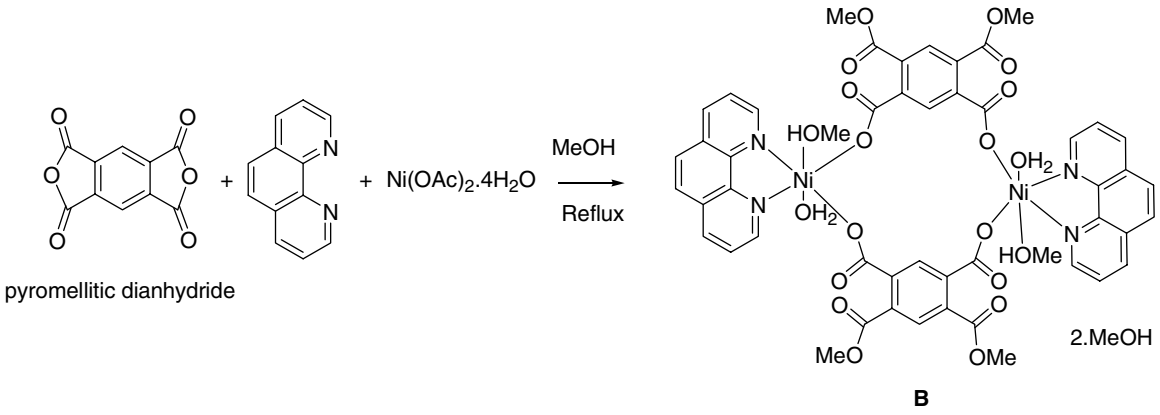


Fig. 1. The structure of (2,2′-bipyridyl)dibenzoato nickel(II) [**A**] (Drawn with 20% thermal ellipsoids; hydrogen atoms are omitted for clarity). Some bond distances (Å) and angles (°) are Ni1–N2, 2.03; Ni1–N1, 2.05; Ni1–O4, 2.05; Ni1–O2, 2.07; Ni1–O1, 2.15; Ni1–O3, 2.15; ∠N2–Ni1–N1, 79.48; ∠N2–Ni1–O4, 100.69; ∠N1–Ni–O4, 99.99; ∠N2–Ni1–O2, 96.40; ∠N1–Ni1–O2, 98.95; ∠N2–Ni1–O1, 96.26; ∠O4–Ni1–O1, 99.35; ∠N1–Ni1–O3, 97.57; ∠O1–Ni1–O3 91.91.



Scheme 2.

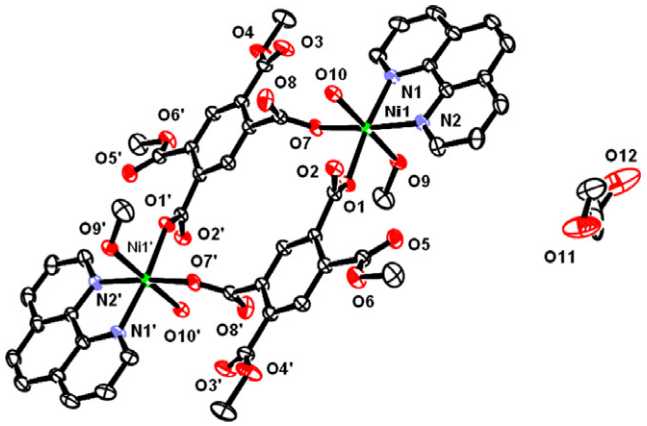


Fig. 2. The crystal structure of the cyclic nickel complex **B** (20% thermal ellipsoids; for clarity hydrogen atoms are omitted). The bond distances (Å) Ni1–N1, 2.05; Ni1–N2, 2.09; Ni1–O10, 2.09; Ni1–O1, 2.04; Ni1–O7, 2.08; Bond angles (°) ∠N1–Ni1–N2, 79.27; ∠N1–Ni1–O10, 93.77; ∠N1–Ni–O7, 93.68; ∠O1–Ni1–O9, 86.80; ∠O1–Ni1–O10, 92.04; ∠O7–Ni1–O10, 91.69; ∠O1–Ni1–O7, 89.71.

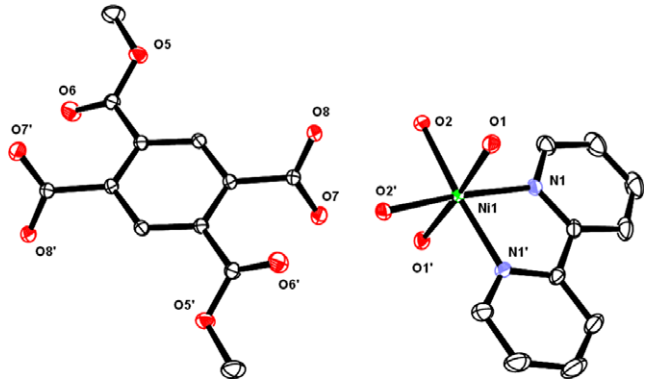
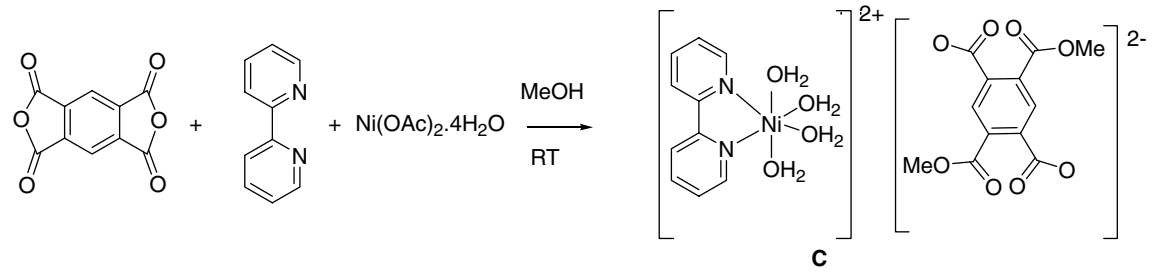


Fig. 3. The crystal structure of **C** (20% thermal ellipsoids; all hydrogen atoms are omitted for clarity). Some important bond distances (Å), Ni1–N1, 2.06; Ni1–N1′, 2.06; Ni1–O1, 2.07; Ni1–O2, 2.07; Ni1–O1′, 2.07; and bond angles (°) ∠N1–Ni1–N1′, 78.85; ∠N1–Ni1–O1, 90.86; ∠N1–Ni–O2, 94.41.

carboxylate groups from the dicarboxylic acids; these groups occupy *cis*-positions around the nickel ion. Additional to these, the six coordinations positions around the nickel(II) ion are completed by 1,10-phenanthroline, water and methanol molecules. The carboxylate groups attached at the 1,3-position of the aromatic rings facilitate the formation of the cyclic metallacarboxylato complex. The coordinated water molecules on two metals are *trans* to each other and the same is the case with the methanol molecules. Fig. 3.

In this particular case the other complex from the 1,4-dicarboxylate isomer could not be obtained and insolubility of the products has prevented further characterization of open chain compounds, if any, formed in the reaction. However, from the room temperature reaction of nickel(II) acetate tetrahydrate with pyromelletic dianhydride and 2,2′-bipyridine in methanol we could obtain the mononuclear nickel complex **C** (Scheme 3). Formation of the 1,4-dicarboxylato complex occurs due to the synthetic procedure, as we have carried out the reaction at room temperature which prefers to form thermodynamically stable products. In general such ring opening reactions of pyromellitic dianhydride by alcohol (without any other reagent being added) leads to equimolar amounts of the 1,3- and 1,4-dicarboxylic acids [5a]. Formation of **C** provides a clue that under adequate reaction conditions the 1,4-dicarboxylato anion should act as ligand by replacing the labile aqua ligand, leading to polymeric materials. The TGA of the compound **C** shows a weight loss at 129 °C due to the loss of four water molecules (experimental wt. loss 13.4%; theoretical 12.7%). When the IR spectrum of compound **C** is compared with the spectrum after heating **C** at 130 °C for 15 min, the absorption at 3525 cm^{-1} disappears and also the carboxylate frequency is shifted from 1567 cm^{-1} to 1578 cm^{-1}, showing coordination of carboxylate group/s (Fig. 4a). On heating at 130 °C compound **C** becomes very insoluble in all common solvents. The process is attributed to the dehydration of the aqua ligands. The dehydration may lead to dinuclear species as observed. However, the poor solubility of the product prevented us from further study in this direction. On prolonged heating of compound **C** at 200 °C, a profound effect on the carbonyl frequency of the ester group could



Scheme 3.

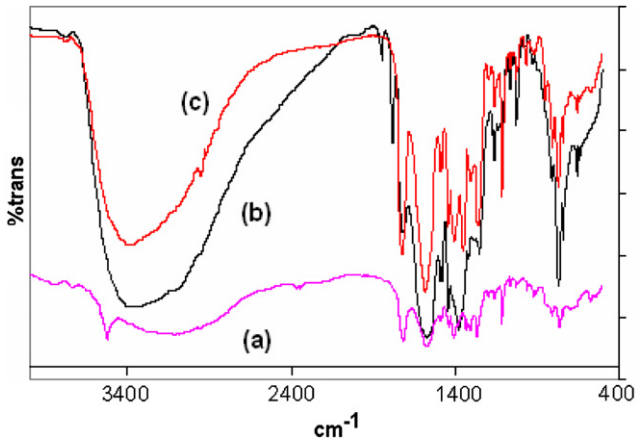


Fig. 4a. FT-IR (KBr) spectra of **C** (a) at room temperature, (b) after **C** was heated at 130 °C for 15 min, (c) after **C** was heated at 200 °C for 30 min.

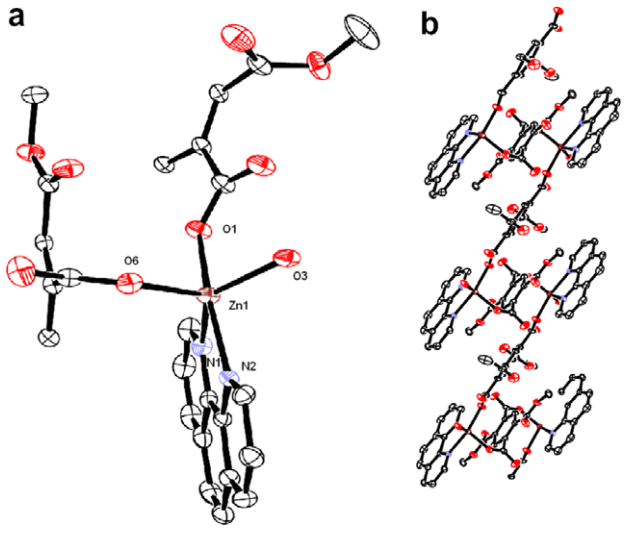
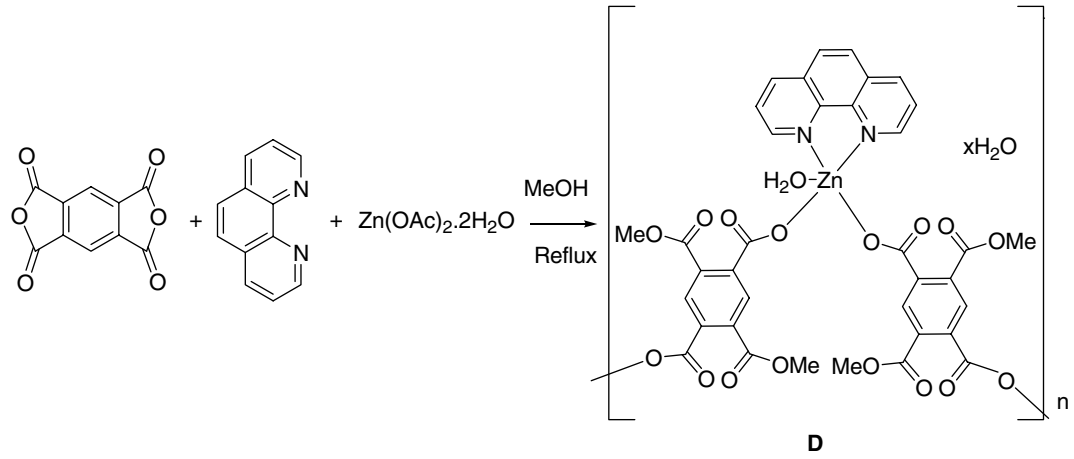


Fig. 4b. (a) The asymmetric unit of the zinc complex **D** showing the coordination environment. Some important bond distances (Å) Zn1–N1, 2.17; Zn1–N2, 2.10; Zn1–O1, 2.05; Zn1–O3, 2.00; Zn1–O6, 2.22; and bond angles (°) ∠N1–Zn1–N2, 78.13; ∠O1–Zn1–O3, 90.13; ∠O3–Zn–O6, 105.91. (b) The polymeric structure of **D** (all hydrogen atoms and water of crystallisation are omitted for clarity; drawn with 20% thermal ellipsoids).

be seen. A new absorption at 1778 cm^{-1} appeared, in addition to an absorption at 1717 cm^{-1} (Fig. 4a), and the remaining peaks became slightly broadened without much shift being observed. The OH group absorption peak at 3105 cm^{-1} of the parent compound was shifted to 3368 cm^{-1} on heating at 200 °C. This suggests that the complex formed on heating at 200 °C absorbs moisture. We have tried making the anhydrous derivative, but the attempts were not successful.

Although we could not succeed in characterising the polymeric product/s from the reactions with nickel, from a similar reaction of pyromellitic dianhydride with zinc(II) acetate and 1,10-phenanthroline in methanol, a crystalline compound **D** having a polymeric structure (Scheme 4) could be characterised. This dicarboxylate complex **D** has five coordination around the zinc ions (Fig. 4b). In the polymer, each zinc ion has a distorted square-pyramidal geometry. The five coordination positions are completed by a water molecule, 1,10-phenanthroline and two monodentate carboxylate groups. The crystals qualities of the polymer were not very good for crystallography, but the available data are good enough to describe the polymeric chain. Since all these reactions gave a low yield of polymeric product in the pure form, we looked into the other possible products in these reactions.

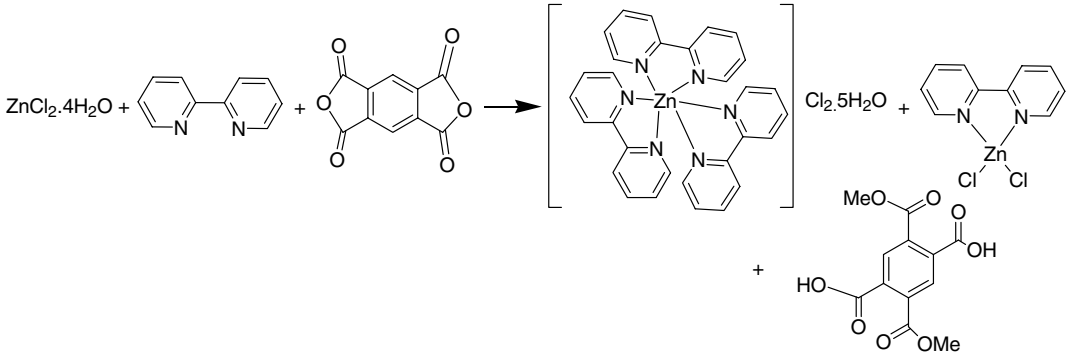
Due to limited solubility of the products we looked carefully for a reaction from which we could obtain different types of crystals. From the reaction of zinc(II) chloride with pyromellitic dianhydride in methanol with 2,2′-bipyridine (1:1:2 molar ratio); we got two crystalline compounds and a white solid. The crystal structures of the crystalline compounds were determined and they were found to be $[Zn(bpy)_3Cl_2]\cdot 5H_2O$ and $Zn(bpy)Cl_2$. The compound $[Zn(bpy)_3Cl_2]\cdot 5H_2O$ has an analogous structure to that already reported [8]. The white solid compound has characteristic features of 2,5-dicarbomethoxy benzene1,4-dicarboxylic acid as well as bipyridine, suggesting it to be a zinc complex, but lack of crystal structure and limited solubility limits our further discussion on this issue. However, it is clear that in these reactions metal bipyridine complexes are formed as side products, lowering the yield of the polymeric product, which may be attributed to such side reactions which compete with metal–oxygen bond formation by metal–nitrogen bond formation. It may also be noted



Scheme 4.

that the use of a 1:3 stoichiometric ratio of zinc to bidentate ligand, namely 2,2'-bipyridine, led to the formation of $[Zn(bpy)_3]Cl_2 \cdot 5H_2O$ along with formation of 2,5-dicarbomethoxy benzene 1,4-dicarboxylic acid (the free acid is characterised by recording its IR and ^1H NMR spectra and comparing them with those of an authentic sample). This suggests that the anhydride ring opening and the complex formation both occur in a competitive manner and the reaction can be represented by Scheme 5. This shows that the competitive reaction between the nitrogen donating ligands and carboxylic acid groups to occupy the maximum coordination sites makes the yield of the carboxylate complexes less. Nevertheless it provides a better method to obtain characterisable metal dicarboxylate complexes having optimum solubility.

Recently it has been shown that zinc complexes of phenylene diacrylic acid form clusters leading to hydrogen storage material [7]. However, complex **D** presented here has a much simpler structure with a five coordination geometry around the zinc ions. From the available data, use of a 2:1 stoichiometry of the chelating ligand with respect to the metal acetate, along with one equivalent of pyromellitic dianhydride, has not been fruitful for polymeric product formation. For example, we have observed a self-assembled structure from such a reaction with cobalt(II), in which one of the carboxylato groups remains free and participates in hydrogen bonding in the self-assembled structure. The structure of the cobalt complex **E** obtained from the reaction of cobalt(II) acetate with pyromellitic dianhydride in the presence of 2,2′-bipyridine is illustrated in Fig. 5. The complex has a distorted octahedral structure with a monodentate carboxylate group and the other carboxaylate group at the 4-position remains as the carboxylato anion. Besides the two 2,2′-bipyridine ligands, the complex has one water molecule in the coordination sphere. In addition to the one aqua ligand the complex has four water of crystallisation molecules in the lattice and has the composition $[Co(bpy)_2(H_2O)L] \cdot 4H_2O$ (where $LH_2 = 2,5$-dicarbomethoxy benzene 1,4-dicarboxylic acid). From the crystallographic study we could not locate the positions of the six hydrogen atoms around the three lattice water molecules. However, thermogravimetric analysis confirmed the loss of water molecules corresponding to the four molecules of water of crystallisation. The presence of ester group absorptions at 1738 cm^{-1} and 1717 cm^{-1} suggests that the two ester groups have slightly different environments and supports the results obtained from the crystallographic study. The complex has a visible absorption at 482 nm in methanol due to a d–d transition of the d^7-electronic configuration. It has magnetic moment of 6.51 BM corresponding to a



Scheme 5. Products from the reaction of zinc(II) chloride with pyromellitic dianhydride in methanol in the presence of 1,10-phenanthroline.

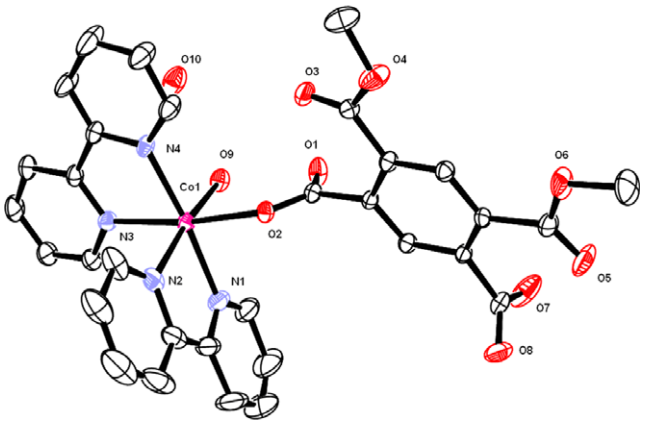


Fig. 5. The ORTEP (20% thermal ellipsoids) diagram of the cobalt(II) complex obtained from the reaction of pyromellitic dianhydride, cobalt(II) acetate and 2, 2′-bipyridine in a 1:1:2 molar ratio in methanol (hydrogen atoms are omitted for clarity). Some important bond distances (Å) Co1–O9, 2.09; Co1–N3, 2.10; Co1–N2, 2.14; Co1–N1, 2.11; Co1–O2, 2.13 and bond angles (°) ∠O1–Co1–O2, 91.75; ∠N1–Co1–N2, 76.35; ∠N2–Co2–N3, 92.34; ∠N1–Co1–O2, 86.87.

d^7-octahedral cobalt(II) complex. The reaction of pyromellitic dianhydride, cobalt(II) acetate and 1,10-phenanthroline in a 1:1:1 molar ratio in methanol gave a complex having the composition $[Co(phen)(L)(H_2O)_3]\cdot CH_3OH$, [**F**] and its crystal structure is shown in Fig. 6. This compound has a distorted octahedral geometry with one monodentate carboxylate.

The compound has a weak absorption at 487 nm corresponding to the d–d transition of an octahedral d^7 cobalt(II) system. The TGA shows that three coordinated water molecules are released on heating up to 250 °C, and they are lost in three steps.

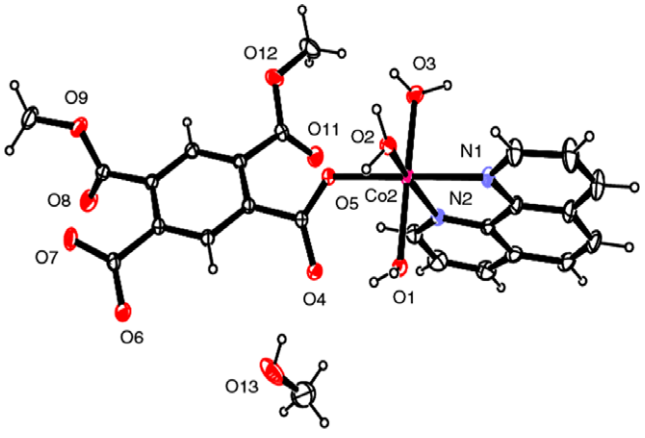


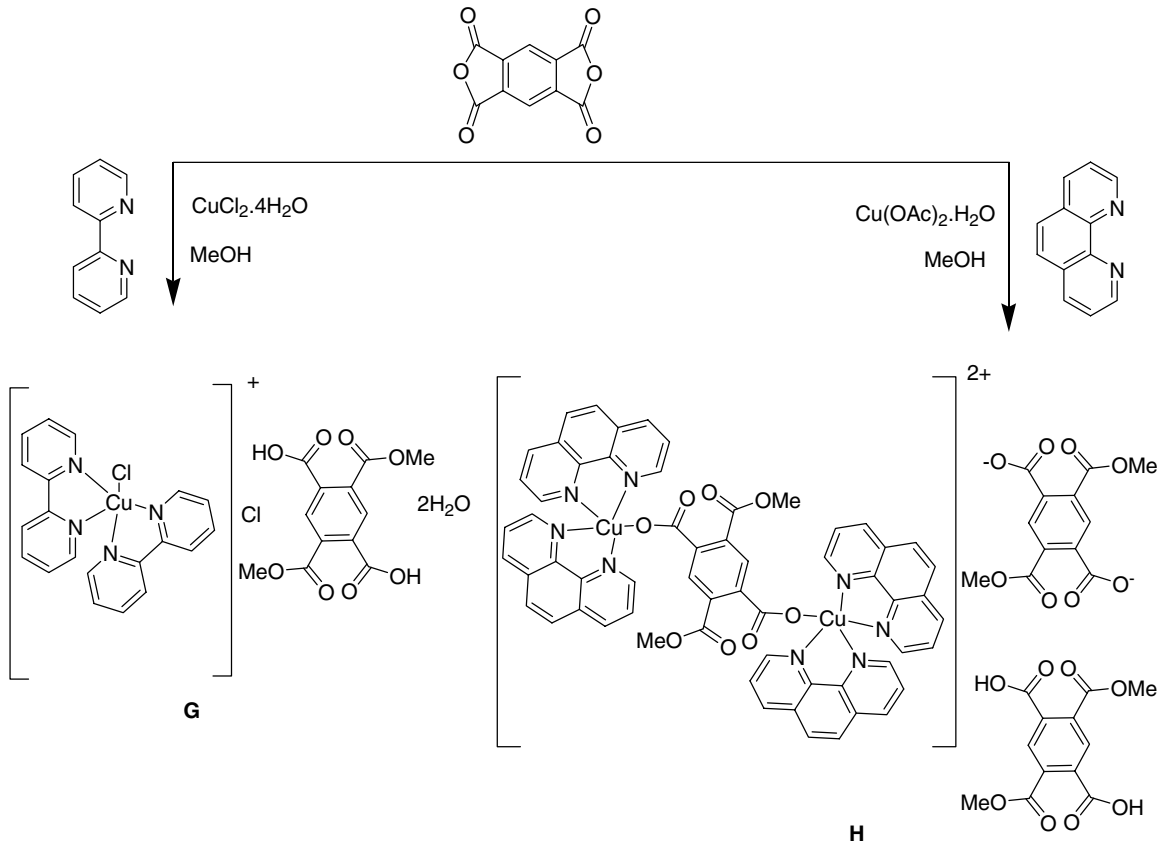
Fig. 6. The ORTEP (20% thermal ellipsoids) diagram of the cobalt(II) complex obtained from the reaction of pyromellitic dianhydride, cobalt(II) acetate and 1,10-phenathroline in a 1:1:1 molar ratio in methanol. Some important bond distances (Å) Co2–O1, 2.16; Co2–N1, 2.10; Co2–N2, 2.14; Co2–O2, 2.10; Co2–O3, 2.06; Co2–O5, 2.11 and bond angles (°) ∠O1–Co2–O2, 88.29; ∠N1–Co2–N2, 77.80; ∠N2–Co2–O1, 84.20; ∠N1–Co1–O2, 92.18.

We have also carried out independent reactions of pyromellitic dianhydride with methanol and copper(II) chloride, as well as with copper(II) acetate in the presence of bidentate aromatic heterocyclic ligands. Two different products obtained from such reactions are illustrated in Scheme 6. The reaction of copper(II) chloride with pyromellitic dianhydride in methanol with 2,2′-bipyridine led to the formation of a dinuclear complex. The complex has two 2,2′-bipyridine ligands attached to each copper and is bridged by two monodentate carboxylato groups at the 1,4-positions of 2,5-dicarbomethoxy benzene 1,4-dicarboxylic acid. The complex has the composition $[CuCl(bpy)_2]Cl\cdot 2H_2O\cdot LH_2$; where LH_2 is 2,5-dicarbomethoxy benzene 1,4-dicarboxylic acid and bpy = 2,2′-bipyridine. The ionic chloride is estimated by treatment of **G** with dilute silver nitrate and weighing the chloride as the silver chloride. An interesting feature of the complex is that in the lattice the chloride ion is hydrogen bonded to form a layered structure. The water molecules occur in pairs and each pair are hydrogen bonded to each other and are further hydrogen bonded to the chloride anion as depicted in Fig. 7c. The hydrogen bonding forms alternate four and six member rings and these rings are repeated along the crystallographic *a*-axis. The chloride ions are in T-shape three coordination environments in the hydrogen bonding scheme. Such a T-shaped hydrogen bonding environment in anion binding is important in anion recognition by amides and related compounds [9].

On the other hand, at room temperature the reaction of copper(II) acetate with pyromellitic dinahydride at room temperature followed by treatment with 1,10-phenanthroline (Scheme 6) led to a dinuclear complex having the composition $[Cu_2(phen)_4\mu\text{-}(L)]L\cdot LH_2$; (phen = 1,10-phenanthroline). In the complex two copper(II) ions are bridged by the 2,5-dicarbomethoxy benzene 1,4-dicarboxylato dianion. The charges on the metal ions are further neutralised by a dianion of an uncoordinated dicarboxylic acid. The structures of complexes **G** and **H** are shown in Fig. 7a and b. The complex has also a neutral dicarboxylic acid included as a co-crystal. In addition to the characteristic IR absorptions of 1,10-phenanthroline, the complex has the characteristic IR frequency for the ester groups at 1718 cm^{-1}.

The bond distances in the two copper(II) complexes are shown in Table 2. It clearly depicts that the compounds have five coordinated square-pyramidal geometries around the copper(II) centre. Complex **G** has a visible absorption at 737 nm due to a d–d transition. The complex shows a molar conductance of 67.5 $ohm^{-1}\,cm^2\,mol^{-1}$ in methanol which suggests it is a 1:1 electrolyte. Complex **H**, being highly insoluble in common solvents, prevented us from comparing their visible spectra in solution.

In conclusion, we have demonstrated a simple yet very useful synthetic methodology for the synthesis of first row transition metal carboxylate complexes through esterification of pyromellitic dianhydride. The ring opening



Scheme 6.

reactions of pyromellitic dianhydride with methanol can lead to either 1,4-dicarboxylic acid or 1,5-dicarboxylic acid depending on the metal salts and ancillary ligands used. Several such metal complexes are characterised by crystallography. In order to establish the selectivity in product formation, a greater understanding of the ring opening reactions by first row transition metal ions is needed. The limited solubility of the products and formation of multiple products made us take up selective cases where crystals suitable for X-ray diffraction were obtained. Present results suggest that the synergic competition between the nitrogen donor and carboxylato ligand leads to the formation of different compositions of dicarboxylate complexes. The reaction of chloride and acetate salts of copper in ring opening reactions of pyromellitic dianhydride suggested that the chloride occupies one of the coordination sites, yielding a mononuclear carboxylate complex, whereas using copper(II) acetate the product prefers coordination of the dicarboxylic acid as a bridging ligand through the two distal ends to give a dinuclear copper complex. From the

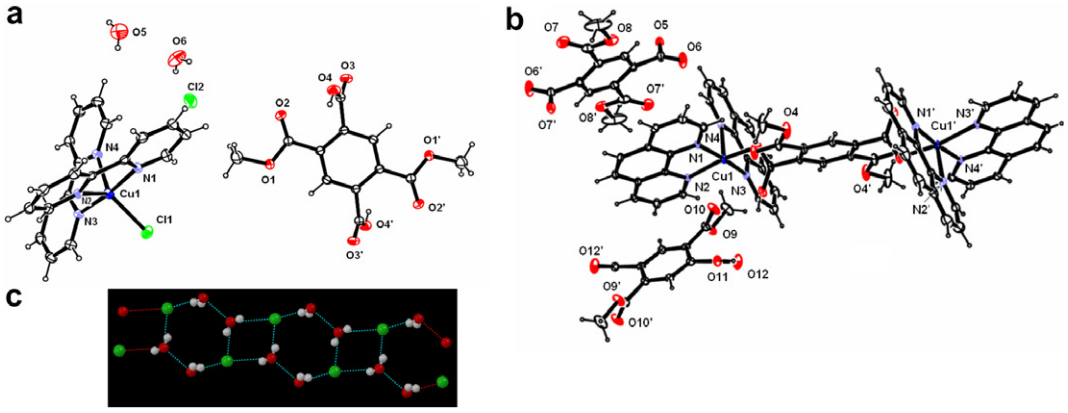


Fig. 7. The structure of (a) **G** and (b) **H** (drawn with 20% thermal ellipsoids) (c) the hydrogen bonding between the water of crystallisation and the chloride anion in the lattice of **G** (chloride, hydrogen and oxygen are represented by green, white and red balls, respectively). (For interpretation of the references to colour in this figure legend, the reader is referred to the web version of this article.)

Table 2
The selected bond parameters in **G** and **H**

Bonds	Bond distances (Å)	Angles	Bond angles (°)
For **F**			
Cu1–N1	1.98	∠N1–Cu1–Cl1	94.11
Cu1–Cl1	2.29	∠N3–Cu1–Cl1	91.78
Cu1–N3	1.99	∠N3–Cu1–N4	79.94
Cu1–N2	2.10	∠N1–Cu1–N2	79.64
Cu1–N4	2.09	∠N4–Cu1–Cl1	109.15
For **G**			
Cu1–N1	2.02	∠N1–Cu1–O1	92.57
Cu1–N2	2.18	∠N3–Cu1–O1	92.10
Cu1–N3	2.00	∠N2–Cu1–N3	101.86
Cu1–N4	2.06	∠N1–Cu1–N2	79.32
Cu1–O1	1.99	∠N4–Cu1–O1	164.35

present results it is observed that the copper complexes show 1,4-selectivity while the cobalt complexes show 1,5-selectivity on the position of the carboxylic acid groups in the ring opening reaction of pyromellitic dianhydride.

Acknowledgement

The authors thank the Department of Science and Technology, New-Delhi for financial support.

Appendix A. Supplementary material

CCDC 638667–638669, 638978, 641189, 641651, 641190 and 644270 contain the supplementary crystallographic data for for this paper. These data can be obtained free of charge via http://www.ccdc.cam.ac.uk/conts/retrieving.html, or from the Cambridge Crystallographic Data Centre, 12 Union Road, Cambridge CB2 1EZ, UK; fax: (+44) 1223 336 033; or e-mail: deposit@ccdc.cam.ac.uk. Supplementary data associated with this article can be found, in the online version, at doi:10.1016/j.poly.2007.05.054.

References

[1] (a) S.R. Batten, R. Robson, Angew. Chem., Int. Ed. 37 (1998) 1460;
(b) O.M. Yaghi, M.O. Keeffe, N/W. Ockwig, H.K. Chae, M. Eddaoudi, J. Kim, Nature 423 (2003) 705;
(c) G. Frey, C. Serre, C.M. Draznieks, F. Millange, S. Surble, J. Dutour, I. Margiolaki, Angew. Chem., Int. Ed. 43 (2004) 6296;
(d) X. Zhao, B. Xiao, A.J. Fletcher, K.M. Thomas, D. Bradshaw, M.J. Rosseinsky, Science 306 (2004) 1012;
(e) B. Moulton, M.J. Zaworotko, Chem. Rev. 101 (2001) 1629;
(f) S. Noro, S. Kitagawa, M. Kondo, K. Seki, Angew. Chem., Int. Ed. 39 (2000) 2081;
(g) P.J. Hagrman, D. Hagrman, J. Zubieta, Angew. Chem., Int. Ed. 38 (1999) 2638;
(h) J.S. Seo, D. Whang, H. Lee, S.I. Jun, J. Oh, Y.J. Jeon, K. Kim, Nature 404 (2000) 982;
(i) O.R. Evans, H.L. Ngo, W. Lin, J. Am. Chem. Soc. 123 (2001) 10395;
(j) Q.R. Fang, G.S. Zhu, M. Xue, J.Y. Sun, Y. Wei, S.L. Qiu, R.R. Xu, Angew. Chem., Int. Ed. 44 (2005) 3845;
(k) R. Xiong, X. You, B.F. Abrahams, Z. Xue, C. Che, Angew. Chem., Int. Ed. 40 (2001) 4422;
(l) J.P. Zhang, Y.Y. Lin, X.C. Huang, X.M. Chen, J. Am. Chem. Soc. 127 (2005) 5495;
(m) S.G. Baca, M.T. Reetz, R. Goddard, I.G. Fillippova, Y.A. Simonov, M. Gdaiec, N. Gerbeleu, Polyhedron 25 (2006) 1215.

[2] (a) F.A. Cotton, C. Lin, C.A. Murillo, Acc. Chem. Res. 34 (2001) 759;
(b) M. Eddaoudi, D.B. Moler, H. Li, B. Chen, T.M. Reineke, M. Keeffe, O.M. Yaghi, Acc. Chem. Res. 34 (2001) 319;
(c) S.L. James, Chem. Soc. Rev. 32 (2003) 276;
(d) R. Murugavel, M.G. Walawalkar, M. Dan, H.W. Roesky, C.N.R. Rao, Acc. Chem. Res. 37 (2004) 763;
(e) K.S. Gavrilenko, S.V. Punin, O. Cador, S. Golhen, L. Ouahab, V.V. Pavlishchuk, J. Am. Chem. Soc. 127 (2005) 12247;
(f) M. Casarin, C. Corvaja, C.D. Nicola, D. Falcomer, L. Franco, M. Monari, L. Pandolfo, C. Pettinari, F. Piccinelli, Inorg. Chem. 44 (2005) 6265;
(g) M. Eddaoudi, H. Li, O.M. Yaghi, J. Am. Chem. Soc. 127 (2005) 7110;
(h) H. Kumgai, C.J. Kepert, M. Kurmoo, Inorg. Chem. 41 (2002) 3410.

[3] (a) A. Karmakar, R.J. Sarma, J.B. Baruah, Eur. J. Inorg. Chem. (2007) 643;
(b) A. Karmakar, R.J. Sarma, J.B. Baruah, Eur. J. Inorg. Chem. (2006) 4673;
(c) N. Barooah, A. Karmakar, R.J. Sarma, J.B. Baruah, Inorg. Chem. Commun. 9 (2006) 1251;
(d) A. Karmakar, R.J. Sarma, J.B. Baruah, Inorg. Chem. Commun. 9 (2006) 1169;
(e) K. Deka, R.J. Sarma, J.B. Baruah, Inorg. Chem. Commun. 9 (2006) 931;
(f) N. Barooah, R.J. Sarma, R.J. Baruah, Eur. J. Inorg. Chem. (2006) 2942;
(g) A. Karmakar, K. Deka, R.J. Sarma, J.B. Baruah, Inorg. Chem. Commun. 9 (2006) 836;
(h) K. Deka, N. Barooah, R.J. Sarma, J.B. Baruah, J. Mol. Struct. 827 (2007) 44.

[4] (a) J. Langer, H. Goels, G. Gillies, D. Walther, Zeitschrift fuer Anorganische und Allgemeine Chemie 631 (2005) 2719;
(b) G. Braeunlich, R. Fischer, B. Nestler, D. Walther, Zeitschrift fuer Chemie 29 (1989) 417.

[5] (a) J. Otera, Esterification: Methods, Reactions and Applications, Wiley-VCH, Weinheim, 2003;
(b) Y. Chen, L. Deng, J. Am. Chem. Soc. 123 (2001) 11302;
(c) B. Rodrignez, T. Rantanen, C. Bolm, Angew. Chem., Int. Ed. Engl. 45 (2006) 6924.

[6] U. Egon, N. Bernd, Zeitschrift fuer Chemie 21 (1981) 451.

[7] Q.-R. Fang, G.-S. Zhu, M. Xue, Q.-L. Zhang, J.-Y. Sun, X.-D. Guo, S.-L. Qiu, S.-T. Xu, P. Wang, D.-J. Wang, Y. Wei, Chem. Eur. J. 12 (2006) 3754.

[8] G. Chun-hua, G. Fang, Z. Li-Tian, Z. Peng, Y. Qi, L. Qi-Tao, Liaoning Daxue Xuebao, Ziran Kexueban 30 (2003) 67.

[9] (a) M.J. Chemielewski, J. Jurczak, Chem. Eur. J. 11 (2005) 6080;
(b) C. Tamuly, R.J. Sarma, A. Batsanov, J.B. Baruah, Acta Crystallogr. Sect. C 6 (2005) o324;
(c) S.O. Kang, R.A. Begum, K. Bowman-James, Angew Chem., Int. Ed. 4 (2006) 7882.

is a well-documented phenomenon [10–12]. In our efforts to correlate structure and fluorescent properties of main group metal dithiocarbamates and their adducts, in this paper we report the synthesis and spectral characterization of six new adducts along with the single crystal X-ray structural analysis of $[Zn(4\text{-mpzdtc})_2(1,10\text{-phen})]\cdot H_2O$ (**1**).

2. Experimental

All the reagents and solvents employed were commercially available analytical grade materials and were used as supplied, without further purification. IR spectra were recorded on an ABB Bomem MB 104 spectrometer (range 4000–400 cm^{-1}) as KBr pellets. The UV–Vis spectra were recorded in CH_2Cl_2 on a HITACHI U-2001 spectrophotometer. NMR spectra were recorded on a Bruker 400 MHz spectrometer at room temperature, using $CDCl_3$ as the solvent. ^{13}C NMR spectra were recorded in the proton decoupled mode. Fluorescence spectra of the free ligands, parent complexes and adduct were recorded in $CHCl_3$. To prevent any non-linearity of the fluorescent intensity, 400 nm was chosen as the excitation wavelength.

2.1. Preparation of the complexes

2.1.1. Preparation of padtc and 4-mpzdtc

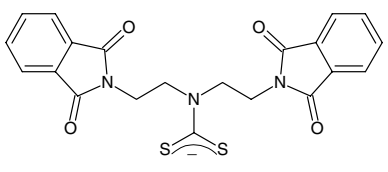
N,*N*′-(iminodiethylene)bisphthalimide 'pa' was prepared by the method reported earlier [13]. Twenty millimoles of the amines pa and mpz were converted into padtc and 4-mpzdtc (Fig. 1) by mixing with 20 mmols of carbondisulfide under ice-cold conditions.

2.1.2. Preparation of the parent complexes

The parent complexes, $[M(dtc)_2]$ [M = Zn or Cd and dtc = 4-mpzdtc or padtc], were prepared by mixing the corresponding amine (20 mmol) and carbondisulfide (20 mmol) in ethanol under ice cold conditions (5 °C). To the yellow dithiocarbamic acid solutions, aqueous solutions of the metal salts ($ZnSO_4$ or $Cd(NO_3)_2$) were added with constant stirring. Pale yellow solids separated from the solution, which were filtered, washed with water, alcohol and then dried in air.

2.1.3. Preparation of adducts ***1–6***

In general, adducts were prepared by adding a hot solution of 1,10-phenanthroline (200 mg, 1 mmol) or



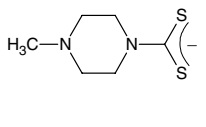


Fig. 1.

Table 1
Infrared spectral data (values in cm^{-1}) and elemental analytical values for the complexes

Compound	ν_{C-N} (thioureide)	ν_{C-S}	1,10-Phen/2,2′-bipy ring frequencies	$\nu_{C=O}$	ν_{C-N}(tertiary)	C (%)		H (%)		N (%)		Decomp. temperature (°C)
						Calculated	Experimental	Calculated	Experimental	Calculated	Experimental	
$[Zn(4\text{-mpzdtc})_2]$	1471	990										
$[Zn(4\text{-mpzdtc})_2(1,10\text{-phen})]\cdot H_2O$ (**1**)	1466	996	1620, 1510			46.9	46.7	5.3	5.1	13.7	13.5	174
$[Zn(4\text{-mpzdtc})_2(2,2'\text{-bipy})]$ (**2**)	1469	992	1596			46.2	45.8	5.3	5.0	14.7	14.4	169
$[Cd(4\text{-mpzdtc})_2]$	1459	979										
$[Cd(4\text{-mpzdtc})_2(1,10\text{-phen})]$ (**3**)	1422	992	1569, 1508			44.8	44.6	4.7	4.4	13.1	12.8	192
$[Cd(4\text{-mpzdtc})_2(2,2'\text{-bipy})]$ (**4**)	1384	973				42.7	42.4	4.9	4.5	13.6	13.4	184
$[Zn(padtc)_2]$	1462	984		1772, 1696	1399							
$[Zn(padtc)_2(1,10\text{-phen})]$ (**5**)	1420	989	1620, 1503	1768, 1709	1390	57.8	57.5	3.6	3.3	9.9	9.6	210
$[Cd(padtc)_2]$	1478	973		1772, 1717	1395							
$[Cd(padtc)_2(1,10\text{-phen})]$ (**6**)	1422	1033	1612, 1519	1771, 1711	1396	55.5	55.1	3.5	3.3	9.6	9.2	198

2,2′-bipyridine (155 mg, 1 mmol) in benzene to a hot suspension of the parent dithiocarbamate (1 mmol) in a benzene:chloroform (1:1) mixture. The resulting pale yellow solution was filtered and cooled. The yellow adduct separated out, which was filtered and recrystallised from a benzene:chloroform (1:1) solvent mixture. All the above complexes were analysed for carbon, hydrogen and nitrogen content and the results are shown in Table 1 along with the IR spectral data.

2.2. X-ray crystallography

Intensity data were collected at ambient temperature (295 K) on a Philips PW 1100 diffractometer [14] using graphite monochromated Mo Kα radiation ($\lambda = 0.71069$ Å). All the non-hydrogen atoms were refined anisotropically. The hydrogen atoms of the water molecule were located in the Fourier map and were subsequently constrained. The other remaining hydrogen atoms were fixed geometrically. The absorption correction was performed with the psi-scan technique [15]. The ORTEP diagram was drawn with the ORTEP-3 program [16].

3. Results and discussion

3.1. Infrared spectral studies

For the present set of compounds **1–6**, the ν_{C-N} (thioureide) band appears in the region 1380–1490 cm^{-1}. The reduction in ν_{C-N} (thioureide) for the adducts is attributed to the change in coordination number from 4 to 6 and the steric effect exerted by 1,10-phenanthroline or 2,2′-bipyridine. The ν_{C-S} bands are observed in the region 1000 cm^{-1} (**1–6**) without any splitting, supporting the bidentate coordination of the dithiocarbamate to the metal centre. For the padtc complexes, an intense band due to ≻C═O stretching appears in the region 1696–1772 cm^{-1}, which is due to the asymmetrical and symmetrical ≻C═O stretching modes. The carbonyl group absorption remains unaffected in the complexes indicating its non-involvement in the complexation. The characteristic bands due to 1,10-phenanthroline and 2,2′-bipyridine appear around 1600, 1510 cm^{-1} (1,10-phen) and 1595 cm^{-1} (2,2′-bipy) in the adducts **1–6** [17]. Other bands due to 1,10-phenanthroline and 2,2′-bipyridine are masked by those due to the dithiocarbamate ligands.

3.2. NMR spectral studies

NMR spectral data of all the synthesized compounds are given in Table 2 along with the splitting patterns.

3.2.1. ^1H NMR

Signals observed around 4.20 ppm for the complexes **1–4** are due to α-CH_2 protons present in the dithiocarbamate. The observed deshielding of the α-protons in all the cases [18] is attributed to the release of electrons on the nitrogen of the NR_2 groups, forcing high electron density towards the sulfur (or the metal) *via* the thioureide π-system. Although the magnitude of the deshielding decreases with the increase in distance from the metal centre or the thioureide bond, the β-CH_2 and N–CH_3 proton signals are also slightly deshielded on complexation. A change of the central metal atom [Zn/Cd] does not affect the position of the signals very much in the ^1H NMR spectra of **1–4** as the interaction is mainly electrostatic in nature. Apart from these signals, the signals observed in the downfield region of 7.36–9.21 ppm are assigned to the protons present in the nitrogenous ligands, 1,10-phenanthroline and 2,2′-bipyridine.

For complexes **5** and **6**, a triplet observed around 4.20 ppm is assigned to the α-CH_2 protons and the β-CH_2 protons appeared at around 4.06 ppm as triplets. In complexes **1–4**, the α-CH_2 protons are deshielded to a greater magnitude than the β-CH_2 protons. In complexes **5** and **6**, both α- and β-protons are deshielded to a

Table 2
^1H and ^{13}C NMR spectral data of the complexes (chemical shifts in ppm)

Compound	NMR	α-CH_2[a]	β-CH_2[a]	N–CH_3	1,10-phen/2,2′-bipy	N $^{13}CS_2$ (Thioureide)	≻C═O
1	^1H	4.18 (t)	2.44 (t)	2.28 (s)	7.66–9.21		
	^{13}C	51.4	55.0	46.0	123–150	207.6	
2	^1H	4.16 (t)	2.46 (t)	2.30 (s)	7.36–8.97		
	^{13}C	51.5	55.1	46.2	121–153	206.6	
3	^1H	4.21 (s)	2.44 (s)	2.27 (s)	7.64–9.19		
	^{13}C	52.5	54.9	46.0	123–150	207.8	
4	^1H	4.23 (s)	2.54 (s)	2.35 (s)	7.36–8.73		
	^{13}C	52.1	54.4	45.4	121–154	207.2	
5	^1H	4.21 (t)	4.04 (t)		7.62–9.19[b]		
	^{13}C	54.9	52.5		123–150[c]	207.8	168.7
6	^1H	4.23 (t)	4.06 (t)		7.35–9.05[b]		
	^{13}C	53.6	47.7		123–150[c]	207.6	168.7

[a] Chemical shift due to a, e protons.
[b] Aromatic proton signals from padtc$^-$ also merged with the 1,10-phenanthroline ring proton signals.
[c] Signals for aromatic carbons in padtc$^-$ merged with the 1,10-phenanthroline ring signals.

comparable extent because of the presence of the electron withdrawing –(O=C)$_2$–N group in the adjacent position to β-CH$_2$. The shift of electron density towards the metal centre through the thioureide bond is more pronounced than the movement of electrons towards the carbonyl groups, which leads to the very minimal deshielding of the α-CH$_2$ protons.

3.2.2. ^{13}C NMR

The signals observed around 207 ppm for complexes **1**–**6** are assigned to the thioureide carbon $\delta(N^{13}CS_2)$. A downfield shift of the α-carbon signals (to the thioureide π-system) in the case of complexes **1**–**4** is an indication of the important consequence of the complexation process, viz. a significant thioureide $N^{\delta+}\cdots C^{\cdot\delta-}$ contribution to the stability of the complexes and a resultant reduction in the electron density.

The β-CH$_2$ carbons of the complexes **1**–**4** resonate around 55 ppm and are not greatly affected on complexation, similar to the N–CH$_3$ carbon signals, which are observed around 46 ppm, because of the relative distance from the thioureide π-system and the metal centre. A small difference observed in the chemical shifts of the α- and β-carbons of **5** and **6** is mainly attributed to the presence of the electron withdrawing (O=C)$_2$N– and –NCS$_2$ π-system adjacent to the β- and α-carbons, respectively. The assignment of the deshielded signal to the α-carbon is accomplished by considering the pronounced electron withdrawing effect of the NCS$_2$ π-system and the closer proximity of the α-carbons to the metal centre.

The carbonyl carbon in complexes **5** and **6** resonates at 168.7 and 168.8 ppm, respectively. The observed small differences in chemical shifts for the 1,10-phenanthroline and 2,2′-bipyridine fragments in adducts **1**–**6** compared to the free 1,10-phenanthroline and 2,2′-bipyridine signals can be attributed to charge delocalization, which prevents the movement of electron density from the adjacent carbons. Generally, the extent of deshielding for the thioureide $N^{13}CS_2$ signal in main group metal dithiocarbamates is greater in magnitude than those of normal valence state transition metal dithiocarbamates, which is in line with the observed thioureide carbon chemical shifts of the synthesized compounds [19].

3.3. Fluorescence spectral studies

M(dtc)$_2$ (where M = Zn and Cd and dtc = general notation for the dithiocarbamate anion) complexes show less intense or no fluorescence in the visible region. It may be attributed to the absence of effective fluorophores in the parent complexes or a less effective MLCT (metal to ligand charge transfer) [20] between the metal centre and dithiocarbamate ligands. On excitation, for complexes with a MS$_4$N$_2$ chromophore (**1**–**6**), fluorescence maxima are observed in the region 440–460 nm, which may be due to a possible metal ligand charge transfer (MLCT) or the brief masking of the lone pair of electrons of nitrogen through a photoinduced electron transfer (PET) [21]. Complexes **5** and **6** show fluorescence bands with comparatively high intensity compared to the other octahedral complexes, which is attributed to the presence of the phthalimide group (where the carbonyl group is in conjugation with the aromatic π-system) along with 1,10-phenonthroline in the metal chelates.

3.4. Structural analysis

[Zn(4-mpzdtc)$_2$(1,10-phen)]·H$_2$O (**1**) is monomeric and discrete. The ORTEP diagram of **1** is shown in Fig. 2 together with the atom-numbering scheme. Four formula units are present in the unit cell. One molecule of water is co-crystallized along with the complex molecule. The molecule sits on a two fold axis. From the crystal structure of **1**, it is clear that zinc is hexacoordinated with four sulfur atoms from the dithiocarbamate ligands and two nitrogen atoms from the chelating 1,10-phenanthroline. The short thioureide C–N distance, 1.347(14) Å indicates that the π electron density is delocalized over the S$_2$CN moiety and that this bond has a strong double bond character. Because of the small bite angle [S–Zn–S = 70.26(7)°] of the dithiocarbamate and the steric influence of 1,10-phenanthroline, the central metal atom is in a highly distorted octahedral coordination environment.

The distinct asymmetry in Zn–S distances [Zn(1)–S(2) = 2.459(3) and Zn(1)–S(3) = 2.6192(16) Å] is due to the steric effect exerted by 1,10-phenanthroline, as observed for similar adducts [18]. The C–S distances [C(4)–S(3) = 1.700(9) and C(4)–S(2) = 1.712(5) Å] are symmetric, indicating that the presence of an additional neutral ligand affects the S–Zn–S bite angle and Zn–S distances. The Zn–N distance is found to be 2.195(6) Å. The C–C and C–N bond distances associated with the piperazine ring are normal. To avoid 1,3-diaxial steric interactions with the axial hydrogens, the methyl group in the terminal position (C(11) in the ORTEP diagram) is equatorially bonded to the nitrogen. The piperazine ring is in a normal chair conformation. The nitrogen, N(8) of the methyl piperazine ring shows a short contact with the hydrogen atom of the water molecule (O(1)W ··· N(8) 2.936(0.008) Å), indicating a hydrogen bonded interaction. However, the interaction involving O(1)W ··· S3 through H(2)W is less significant,

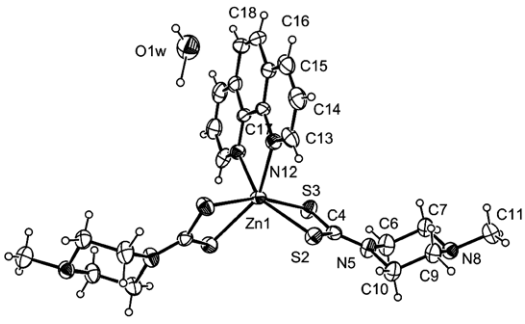


Fig. 2. ORTEP diagram of [Zn(4-mpzdtc)$_2$(1,10-phen)]·H$_2$O (**1**).

relatively (3.506(0.005) Å). The 1,10-phenanthroline ring shows normal bond parameters.

Crystal data, data collection and refinement parameters for $[Zn(4\text{-mpzdtc})_2(1,10\text{-phen})]\cdot H_2O$ (**1**): Empirical formula: $C_{24}H_{34}N_6O_2S_4Zn$; FW: 632.18; crystal dimensions (mm): $0.17 \times 0.22 \times 0.27$; colour: faint yellow; habit: needle; crystal system: orthorhombic; space group: *Pbcn*; *a*/Å: 19.588(2); *b*/Å: 14.210(2); *c*/Å: 10.373(3); $\alpha = \beta = \gamma = 90°$; *U*/Å^3: 2887.3(10); $Z = 4$; D_c/g cm^{-3}: 1.454; μ/cm^{-1}: 11.73; $F(000)$: 1320; λ/Å: Mo Kα (0.71069 Å); θ range/°: 3.20–27.97; scan type: ω–2θ; index ranges: $0 \leqslant h \leqslant 25$, $0 \leqslant k \leqslant 18$, $-13 \leqslant l \leqslant 0$; reflections collected: 1151; observed reflections ($F_0 > 4\sigma(F_0)$): 623; weighting scheme: $W = 1/[\sigma^2(F_0^2) + (0.0368P)^2 + 0.000P]$ where $P = (F_0^2 + 2F_c^2)/3$; number of parameters refined: 170; final *R*, R_w (obs. data): 0.0340, 0.0582; GOOF: 0.884. Selected bond distances (Å) and bond angles (°): Zn1–N12: 2.195(6); Zn1–S2: 2.459(3); Zn1–S3: 2.6192(16); S2–C4: 1.712(5); S3–C4: 1.700(9); C4–N5: 1.347(14); C15–C16: 1.387(16); N5–C6: 1.494(8); C6–C7: 1.50(5); C7–N8: 1.48(5); N8–C9: 1.469(8); N8–C11: 1.43(4). N12–Zn1–N12: 74.8(4); N12–Zn1–S2: 148.9(2); N12–Zn1–S2: 95.9(2); S2–Zn1–S2: 105.86(11); N12–Zn1–S3: 84.38(14); N12–Zn1–S3: 108.26(16); S2–Zn1–S3: 100.04(7); S2–Zn1–S3: 70.26(7); S3–Zn1–S3: 164.42(6); C4–S2–Zn1: 88.3(4); C4–S3–Zn1: 83.4 (2); S3–C4–S2: 118.0(6).

3.5. VBS analysis

Valence bond sum (VBS) analysis can be applied to estimate the bond lengths; vice-versa the sum of the bond lengths should give information about the valence of the central metal ion. Hence, VBS studies indirectly prove the correctness of the crystal structures determined. For complex **1**, VBS values were calculated by two procedures [22,23]. The values are 1.8098 (OK/B) and 1.8420 (B/OK), and among the two values V_i(B/OK) is closer to the expected formal oxidation state of 2. It has been already reported [17] that in the case of the parent bisdithiocabamates of Zn(II), VBS values are almost 2 and generally the values are greater than the sum for the adducts. The decrease in BVS values in the case of the adducts can be ascribed to the increase in Zn–S distances (which are longer than those observed in $Zn(dtc)_2$ complexes), due to the presence of an additional neutral ligand.

Appendix A. Supplementary material

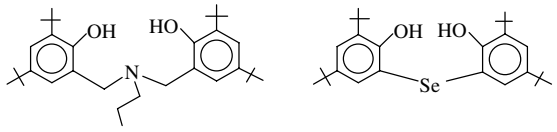
CCDC 263876 contain the supplementary crystallographic data for **1**. These data can be obtained free of charge via http://www.ccdc.cam.ac.uk/conts/retrieving.html, or from the Cambridge Crystallographic Data Centre, 12 Union Road, Cambridge CB2 1EZ, UK; fax: (+44) 1223-336-033; or e-mail: deposit@ccdc.cam.ac.uk. Supplementary data associated with this article can be found, in the online version, at doi:10.1016/j.poly.2007.06.008.

References

[1] J. Nieuwenhuizen, A.W. Ehlers, J.G. Haasnoot, S.R. Janse, J. Reedijk, J. Baerends, J. Am. Chem. Soc. 121 (1999) 163.
[2] J.A. Mc Cleverty, S. Gill, J. Chem. Soc., Dalton Trans. (1982) 493.
[3] J.S. Casas, A. Sanchez, J. Bravo, S. Garcia-Fontan, E.E. Castellano, M.M. Jones, Inorg. Chim. Acta 158 (1989) 119.
[4] M.M. Jones, S.G. Jones, Inorg. Chim. Acta 79 (1983) 288.
[5] P. Yan, Y. Xie, Y. Qian, X. Liu, Chem. Commun. (1999) 1293.
[6] D.W. Tomlin, T.M. Cooper, D.E. Zelmon, Z. Gebeyehu, J.M. Hughes, Acta Crystallogr., Sect. C 55 (1999) 717.
[7] P. O'. Brien, J.R. Walsh, I.M. Watson, M. Motevalli, L. Hendriksen, J. Chem. Soc., Dalton Trans. (1996) 2491.
[8] J. Cheon, D.S. Talaga, J.I. Zink, J. Am. Chem. Soc. 119 (1997) 163.
[9] M. Bochmann, Chem. Vap. Deposit. 2 (1996) 85.
[10] E.R.T. Tiekink, Cryst. Eng. Commun. 5 (21) (2003) 101.
[11] R.J. Magee, J.O. Hill, Rev. Anal. Chem. 8 (1985) 5.
[12] S.P. Huang, K.J. Franz, E.H. Arnold, J. Devenyi, R.H. Fish, Polyhedron 15 (1996) 4241.
[13] G.H. Searle, S.F. Lincoln, S.G. Teague, D.G. Rowe, Aust. J. Chem. 2 (1979) 519.
[14] D. Belletti, New Hardware and Software Systems for Controlling a Philips PW1100 Single Crystal Diffractometer, Parma, Italy, Internal report 1996, p. 1.
[15] A.C.T. North, D.C. Phillips, F.S. Mathews, Acta Crystallogr., Sect. A 24 (1968) 351.
[16] L.J. Faruggia, ORTEP-3 for Windows, University of Glasgow, Scotland, UK, 1999.
[17] A. Manohar, K. Ramalingam, G. Bocelli, A. Cantoni, unpublished results.
[18] M. Saravanan, K. Ramalingam, G. Bocelli, A. Cantoni, Appl. Organometal. Chem. 18 (2004) 103.
[19] H.L.M. Van Gaal, J.W. Diesveld, F.W. Pijpers, J.G.M. Van Der Lindon, Inorg. Chem. 18 (1979) 3251.
[20] F.A. Cotton, G. Wilkinson, P.L. Gaus, Basic Inorganic Chemistry, third ed., Wiley, 1994, p. 535.
[21] W. Wang, G. Springnsteen, S. Gao, B. Wang, Chem. Commun. (2000) 1283.
[22] N.E. Brese, M. O'Keeffe, Acta Crystallogr., Sect. B 47 (1991) 192.
[23] M. O' Keeffe, N.E. Brese, J. Am. Chem. Soc. 113 (1991) 3226.

oxygen species and UV/visible light [7–11]. At the same time, several studies have shown that vitamin C sometimes increases DNA damage in humans, acting as a pro-oxidant [7,12,13].

For some time we have been engaged in exploring the chemistry of bis(phenolate) ligands of transtion metal ions in a mixed ligand environment [14]. Here, we describe the synthesis, crystal structure, cyclic voltammetric and kinetic studies on the oxidation of ascorbic acid by a vanadium(V) complex, viz. $[VO(L^1)(acac)]$ ($H_2L^1 = N,N$-bis(2-hydroxy-3,5-di-*tert*-butylbenzyl)propylamine) and $[VO(L^2)(acac)]$ ($H_2L^2 = 2,2'$-selenobis(4,6-di-*tert*-butylphenol)). We hope to delineate the mechanism of the oxidation of ascorbic acid and to find relations between the kinetic parameters and pH. The results may contribute to an understanding of the behavior of vanadium complexes in human tissue and blood.



H_2L^1 H_2L^2

2. Experimental

2.1. Physical measurements

Elemental analyses were carried out using a Perkin–Elmer 240 elemental analyzer. Infrared spectra (400–4000 cm^{-1}) were recorded from KBr pellets on a Nickolet Magna IR 750 series-II FTIR spectrophotometer. Electronic spectra were recorded on an Agilent 8453 UV–Vis diode array spectrophotometer. ^1H and ^{13}C NMR spectra were recorded in $CDCl_3$ on a Bruker 300 MHz NMR spectrometer using TMS ($\delta = 0$) as an internal standard. Room temperature ^{51}V NMR spectra were obtained with a Bruker 7 tesla magnet and MSL100 pulsed NMR spectrometer. Electrochemical measurements were carried out using a computer controlled PAR model 263A VERSASTAT electrochemical instrument with a glassy carbon disk (4 mm diameter, EG&G) working electrode. Conductance measurements were carried out with a JENCONS 4010 conductivity meter.

2.2. Materials

$[VO(acac)_2]$ and the starting materials for the synthesis of ligands (H_2L^1) and (H_2L^2), namely, 2,4 di-*tert*-butylphenol, (Lancaster), formaldehyde (Merck India), *n*-butylamine (Loba Chemie, India), *n*-propylamine (Loba Chemie, India) and selenium dioxide (Loba Chemie, India) are of reagent grade and were used as received. Tetrabutyl ammonium perchlorate (TBAP) was purchased from Aldrich Chemicals. Solvents like methanol, dichloro methane, *n*-hexane and acetonitrile (Merck, India) were of reagent grade and were dried by standard methods before use. $CDCl_3$ (Aldrich) was used as received.

2.3. Synthesis

2.3.1. Synthesis of ligands

The ligands (H_2L^1 and H_2L^2) have been synthesized according to the published procedure [15] and characterized further by CHN and NMR spectroscopic analyses.

2.3.2. General methods for the synthesis of $[V^VO(L^1)(acac)]$ (**1**) and $[V^VO(L^2)(acac)]$ (**2**)

Equimolar quantities of $[VO(acac)_2]$ and the appropriate ligand were stirred in air in acetonitrile for a few hours. The resulting dark colored solution was kept at −5 °C after filtration. Diffraction quality crystals were obtained after a few days.

2.3.2.1. $[V^VO(L^1)(acac)]$ (**1**). Yield: 80%. *Anal.* Calc. for $C_{38}H_{58}NO_5V$ (659.79): C, 69.42; H, 9.26; N, 2.31. Found: C, 69.25; H, 9.20; N, 2.35%. FTIR (KBr, cm^{-1}): ν(V=O) 964. ^1H NMR ($CDCl_3$): δ 7.27 (d, 2H, Ar-H), 6.96 (d, 2H, Ar-H), 5.68 (s, 1H, acac), 3.49 (s, 4H, Ar-CH_2), 2.05 (s, 3H, –$COCH_3$), 1.7 (m, N-CH_2), 1.46 (s, 3H, CH_3), 1.57 (s, 18H), 1.29(s, 18H), 0.64 (t, 3H, CH_3); ^{13}C NMR ($CDCl_3$): δ 191.08 ($C_{carbonyl}$, acac), 188.3 ($C_{enolate}$, acac), 144.31, 136.05, 129.15, 124.97, 122.38, 103.37, 77.84 (=C, acac), 77.41 (CH_3, acac), 76.99 (CH_3, acac), 54.17 (N-CH_2), 40.56 (Ar-CH_2), 35.8 ($C(CH_3)_3$), 34.88 ($C(CH_3)_3$), 32.16 ($C(CH_3)_3$), 32.12 ($C(CH_3)_3$), 32.04 ($C(CH_3)_3$), 30.7 ($C(CH_3)_3$), 30.63 ($C(CH_3)_3$), 30.09 ($C(CH_3)_3$), 26.64($C(CH_3)_3$), 13.02 (CH_2), 12.3 (CH_3).

2.3.2.2. $[V^VO(L^2)(acac)]$ (**2**). Yield: 81%. *Anal.* Calc. for $C_{33}H_{47}O_5SeV$ (653.63): C, 60.64; H, 7.20. Found: C, 60.25; H, 7.30%. FTIR (KBr, cm^{-1}): ν(V=O) 981. ^1H NMR ($CDCl_3$): δ 7.45 (d, 2H, Ar-H), 7.28 (t, 2H, Ar-H), 5.86 (s, 1H, acac), 2.09 (s, 3H, –$COCH_3$), 1.56 (s, 3H, CH_3), 1.5 (s, 18H), 1.27(s, 18H); ^{13}C NMR ($CDCl_3$): δ 192.26 ($C_{carbonyl}$, acac), 189.2 ($C_{enolate}$, acac), 146.02, 131.01, 128.83, 125.34, 123.71, 104.33, 77.84 (=C, acac), 77.41 (CH_3, acac), 76.99 (CH_3, acac), 33.35 ($C(CH_3)_3$), 35.21 ($C(CH_3)_3$), 31.86 ($C(CH_3)_3$), 30.29 ($C(CH_3)_3$), 26.66($C(CH_3)_3$).

2.4. X-ray crystallography

Crystal data and structure refinement details for both crystals are given in Table 1. The diffraction data for both complexes were collected using Mo Kα radiation. Data for **1** were collected with a KM4CCD diffractometer with a four-circle area-detector (KUMA Diffraction, Poland), and equipped with an Oxford Cryostream Cooler (Oxford Cryosystems, UK). The ω scan technique with different κ and φ offsets for covering an independent part of the reflections in the 3.3°–25.0° θ range was performed. The cell parameters were refined from all strong reflections. Data

Table 1
Crystal data and structure refinement for complexes **1** and **2**

Parameters	1	2
Empirical formula	$C_{38}H_{58}NO_5V$	$C_{33}H_{47}O_5SeV$
Formula weight	659.79	653.63
Temperature (K)	120(2)	293(2)
Wavelength (Mo Kα) (Å)	0.71073	0.71073
Crystal system	monoclinic	monoclinic
Space group	*P*21/*c*	*P*21/*c*
Unit cell dimensions		
a (Å)	14.846(2)	8.170(9)
b (Å)	11.2114(12)	24.31(3)
c (Å)	22.190(3)	17.858(19)
β (°)	91.373(9)	100.487(10)
Volume (Å^3)	3692.3(8)	3488(7)
Z	4	4
D_{calc} (g/cm^3)	1.187	1.259
Absorption coefficient (mm^{-1})	0.309	1.363
F(000)	1424	1386
Crystal size (mm)	0.20 × 0.20 × 0.30	0.05 × 0.05 × 0.30
θ Range for data collection (°)	3.0–25.0	1.4–25.8
Index ranges	$-15 \leqslant h \leqslant 17$, $-12 \leqslant k \leqslant 13$, $-26 \leqslant l \leqslant 26$	$-9 \leqslant h \leqslant 9$, $-24 \leqslant k \leqslant 29$, $-21 \leqslant l \leqslant 21$
Reflections collected	19786	16864
Independent reflections	6495	6164
Data/restraints/parameters	6495/0/421	6164/6/405
Goodness-of-fit-on F^2	0.97	1.09
Final *R* indices [$I > 2\sigma(I)$]	$R_1 = 0.0509$, $wR_2 = 0.0825$	$R_1 = 0.0547$, $wR_2 = 0.1245$
R indices (all data)	$R_1 = 0.1060$, $wR_2 = 0.0960$	$R_1 = 0.0747$, $wR_2 = 0.1322$
Largest difference in peak and hole (e Å^{-3})	0.51 and −0.36	0.446 and −0.370

reduction was carried out using the CrysAlis RED (Oxford Diffraction, UK) program, an analytical absorption correction was applied. The structures were determined by direct methods and SHELXS-97 [16]. H atoms attached to C atoms were positioned geometrically, with C–H = 0.95–0.98 Å, and with U_{iso}(H) values of 1.2 U_{eq} (C) [1.5 U_{eq} (C) for methyl atoms].

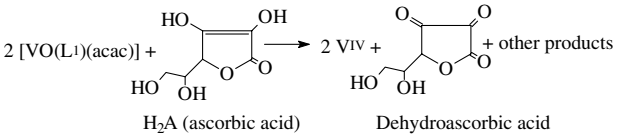
The diffraction data for complex **2** were collected using the MAR research image plate system. The structure was determined using SHELXL [16]. An empirical absorption correction was carried out using DIFABS [17]. The non-hydrogen atoms were refined anisotropically and H atoms isotropically. H atoms attached to C atoms were positioned geometrically and given thermal parameters equivalent to 1.2 times that of the atom to which they were attached. Both structures were refined to convergence on F^2 using the full matrix least-squares procedure by SHELXL-97 [18]. Data for publication were prepared by SHELXL and PARST [19], and figures by ORTEP-III [20].

2.5. Kinetic measurements

The oxidation of ascorbic acid by [VO(L^1)(acac)] (**1**) was studied in 50% MeCN–50% H_2O (v/v) at 25 °C at an ionic strength $I = 0.10$ M (KCl). The decomposition of complexes **1** and **2** in the presence of HCl was followed kinetically under identical conditions but devoid of ascorbic acid. Stock solutions were prepared freshly prior to kinetic study and saturated with dry N_2, purging for at least 15 min. All kinetic experiments were conducted under pseudo-first-order conditions with the complexes as the minor component and were followed by monitoring the disappearance of the substrate. Typical substrate concentrations were $(5.0–9.0) \times 10^{-5}$ M. The pH in self-buffered media was measured with a Systronics digital pH meter model-335 (Systronics, India), equipped with a glass electrode, and the actual pH of the solution was calculated according to Allen and Tidwell as: $pH_{actual} = pH_{observed} + 0.18$ [21]. The absorbance, over specified time intervals, was recorded for at least 5 half-lives. The absorbance-time data thus obtained were fitted with the HP-8453 system program to get the pseudo-first-order rate constants. The data for triplicate runs were found to fall within the error limit ±5%.

2.6. Stoichiometry and reaction products

To determine the stoichiometry of the reaction, a measured excess (0.003 M) of complex **1** was reacted with variable known concentrations of ascorbic acid (0.0005, 0.00075 and 0.001 M). The unreacted complex was determined spectrophotometrically in each case and a 2:1 [complex]:[ascorbic acid] stoichiometry prevailed, as depicted in Eq. (1). Parallel blank solutions were also prepared to account for the auto-decomposition of the complex.



(1)

The dehydroascorbic acid product was identified by Roe's method [22]. It was not possible to characterize or identify the reduced vanadium(IV) species due to its ready decomposition under the kinetic conditions.

3. Results and discussion

Complexes **1** and **2** were prepared by the reaction of equimolar quantities of [VO(acac)$_2$] with H_2L^1 and H_2L^2 respectively in MeCN. The conductance measurements in MeCN showed very low conductivity (3 S for **1** and 5.7 S for **2**), indicating that both the complexes are electrically neutral.

3.1. Description of the crystal structures

The unit cells consists of discrete molecules of complexes **1** and **2**, and both molecules crystallize in the P21/c (No. 14) space group. The ORTEP diagrams of the complexes, with the atom-labelling schemes, are shown in Figs. 1 and 2. Crystal data and selected inter atomic parameters are listed in Tables 1 and 2, respectively.

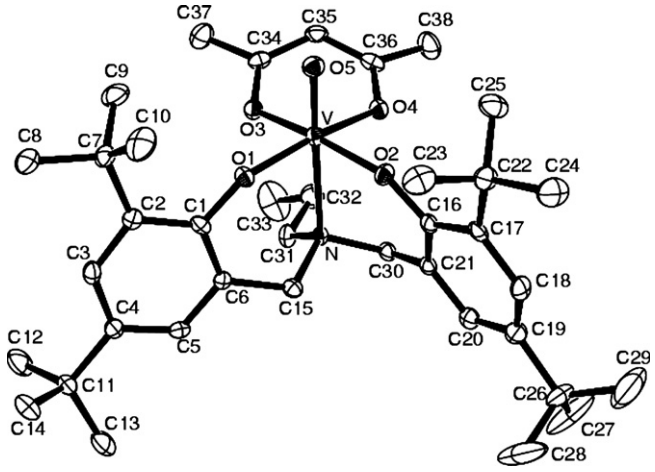


Fig. 1. ORTEP representation of $[V^{V}O(L^{1})(acac)]$ (**1**).

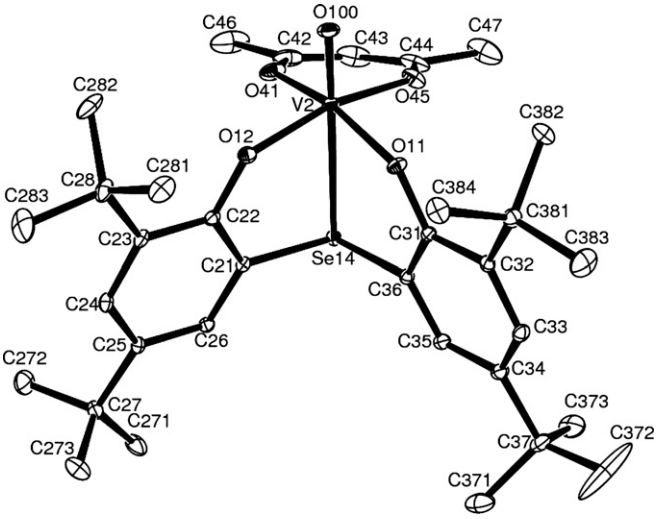


Fig. 2. ORTEP representation of $[V^{V}O(L^{2})(acac)]$ (**2**).

In complex **1** the vanadium atom in each molecule is octahedrally coordinated in an O_5N donor environment. A terminal V=O oxygen atom occupies an axial position. The ONO donor set of one ligand moiety coordinates facially with the nitrogen atom *trans* to the terminal oxygen atom. The two oxygen atoms of the bidentate acetylacetone ligand occupy the remaining two sites. The equatorial VO_4 unit is far from planar. The deviation of the vanadium atom is 0.2285(5) Å from the mean plane comprised by the two independent phenolate oxygen atoms O1, O2 and two acetylacetone oxygen atoms, O3 and O4. The two diagonal angles O1–V–O4 and O2–V–O3, 163.19(8) and 164.30(8)°, respectively, are significantly less than 180°. This deviation from the ideal geometry may be caused by the small bite angles made by two phenolate oxygen atoms and tripodal nitrogen atom with vanadium (O1–V–N = 83.34(8)° and O2–V–N = 81.19(8)°). This is again due to a remarkably longer V–N distance (2.446(2) Å) in comparison with the average length of 2.08 Å for this bond in related VNO_5 complexes reported earlier and in the

Table 2
Selected bond lengths (Å) and bond angles (°) in complexes **1** and **2**

Complex **1**		Complex **2**	
Bond lengths			
V–O1	1.837(2)	V2–O11	1.833(3)
V–O2	1.816(2)	V2–O12	1.830(3)
V–O3	1.981(2)	V2–O41	1.971(3)
V–O4	1.997(2)	V2–O45	1.966(4)
V–O5	1.588(2)	V2–O100	1.589(3)
V–N	2.446(2)	V2–Se14	2.954(2)
Bond angles			
O1–V–O2	100.34(8)	O100–V2–O12	100.5(2)
O1–V–O3	86.40(8)	O100–V2–O11	101.0(2)
O1–V–O4	163.19(8)	O12–V2–O11	93.4(2)
O1–V–O5	99.14(9)	O100–V2–O45	100.0(2)
O2–V–O3	164.30(8)	O12–V2–O45	158.9(1)
O2–V–O4	86.46(8)	O11–V2–O45	87.5(2)
O2–V–O5	99.08(9)	O100–V2–O41	100.9(2)
O3–V–O4	83.47(8)	O12–V2–O41	86.74(2)
O3–V–O5	93.77(8)	O11–V2–O41	157.74(1)
O4–V–O5	94.89(9)	O45–V2–O41	84.6(2)
O5–V–N	177.40(9)	O100–V2–Se14	176.0(1)
O1–V–N	83.34(8)	O12–V2–Se14	76.5(1)
O2–V–N	81.19(8)	O11–V2–Se14	76.54(1)
		O45–V2–Se14	83.2(1)
		O41–V2–Se14	81.8(1)

Cambridge Structural Database [14a,15]. The phenomena may be explained in terms of a *trans* labilizing effect of the oxo group, which occupies another axial position at a normal distance of 1.588 (2) Å [14a,23].

In complex **2** the geometry around the vanadium center is the same as in **1** but with a SeO_5 donor environment. The basal plane is defined by the O(11), O(12), O(41) and O(45) atoms, and the axial coordinates are occupied by the oxo group (O(100)) and sole Se(14) atom. The vanadium atom is shifted by 0.349 Å from the equatorial plane towards the apical O(100) atom, rendering a shortening in the diagonal angles O11–V2–O41 (157.74°) and O12–V2–O45 (158.9°).

The V–Se distance is 2.954(2) Å, a distance comparable to the 2.886(1) Å found by Wieghardt et al. [23b] in a dinuclear vanadium(V) complex with the same selenobis(phenolate) ligand. This could represent a weak interaction, but such an interpretation is complicated by the fact that the rigidity of the ligand forces the Se atom into occupying an octahedral position. A search of the Cambridge Crystallographic Database established 71 instances of V–Se bonds, with a mean bond length of 2.48 Å. However, these structures are from a variety of oxidation states and do not include any examples with V(V). This V–Se distance can be compared to the V–N distance of 2.446(2) Å found in **1**. This distance is also considerably higher than the norm for V–N bonds and is a reflection not only of the steric constraints of the ligand, but also of the position of the atoms *trans* to the terminal oxygen atom.

In both the complexes the two ligands H_2L^1 and H_2L^2 behave in almost a similar way. The vanadium atom is distorted more from the equatorial plane in **2** (0.349 Å) than in **1** (0.228 Å) and this may be due to the longer

V–Se coordinate bond. The axial and equatorial V–O bond distances are in rather good agreement with similar reported complexes [23]. The V–O(phenoxo) bond distances are in the range 1.96–2.00 Å. The equatorial acetylacetonate oxygen atoms shows slightly longer V–O bond distances [24]. All the aromatic rings in the two complexes retain aromaticity. The two mean planes formed by the respective aromatic rings intersect at an angle of about 64.68 and 74.59° in complexes **1** and **2**, respectively.

3.2. ^{51}V nuclear magnetic resonance (NMR) study

^{51}V NMR spectra at room temperature of complexes **1** and **2** were obtained with a Bruker MSL100 pulsed NMR spectrometer. At the calibrated magnetic field of 7.0452 Tesla, the reference frequency for ^{51}V is 78.851 MHz. The spectra of both the samples could be theoretically simulated with the consideration of anisotropic chemical shift and a lorentzian line shape. Complex **1** has a line width of about 100 kHz and chemical shift values $\sigma1 = -480$ ppm and $\sigma2 = \sigma3 = 300$ ppm. For complex **2**, the line width is about 400 kHz and $\sigma1 = -490$ ppm and $\sigma2 = \sigma3 = 380$ ppm.

In solution, the rigidity of the molecular structure breaks down due to the weakening of the bonds, giving rise to various kinds of intra-molecular motions. In NMR experiments, such mobilities are reflected in the narrowing of the resonance spectrum. Fig. 3 shows the spectra of **1** (Fig. 3a) and **2** in acetonitrile at room temperature. Complex **1** yields a narrow line at −300 ppm, indicating complete disappearance of the chemical shift anisotropy. Complex **2** (Fig. 3b) also shows a strong narrow peak in the same position, but also a peak of smaller amplitude is obtained at about 115 ppm together with a broad structure, indicating that the chemical shift anisotropy is only partially averaged out and that the structural rigidity of this compound is not entirely lost under these conditions.

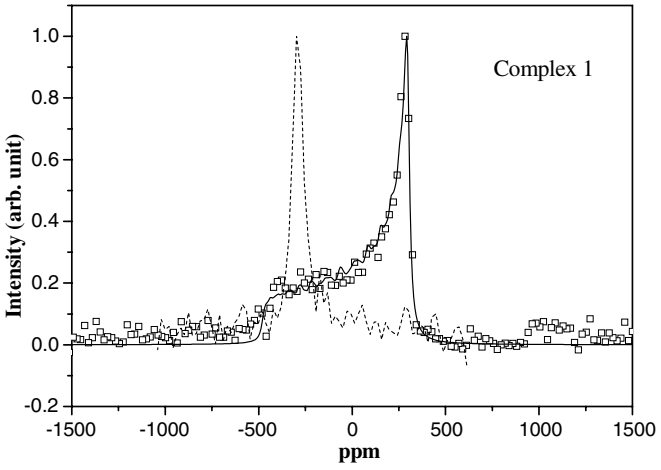


Fig. 3a. ^{51}V NMR spectra of complex **1**. The discreet points are data experimentally obtained. The solid line is a theoretical simulation, and the dashed lines represent a spectrum obtained from solution.

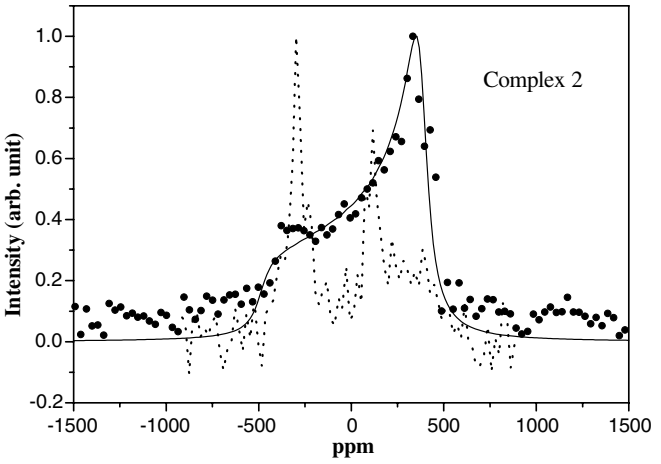


Fig. 3b. ^{51}V NMR spectra of complex **2**. The discreet points are data experimentally obtained. The solid line is a theoretical simulation, and the dashed lines represent a spectrum obtained from solution.

3.3. Electrochemical study

The electrochemical behaviors of complexes **1** and **2** were studied by cyclic voltammetric techniques in the range +1.00 to −0.6 V in acetonitrile at a glassy carbon electrode and Ag/AgC1 reference electrode using tetrabutylammonium perchlorate (TBAP) as the supporting electrolyte. Both the complexes showed reversible cyclic voltameric responses and $E_{1/2}$ appears at −0.38 and −0.10 V (−0.18 and 0.10 V versus NHE) for complexes **1** and **2**, respectively (Fig. 4). Coulometric experiments show that the waves are due to one-electron transfer processes. Since both the phenolato and acetylacetonato ligands are not reduced in the experimental potential range we propose that these potentials are metal centered and appear due to the VO^{3+}/VO^{2+} couple [25].

Complex **2** shows reduction at a less negative potential than complex **1** and indicates the nature and influence of

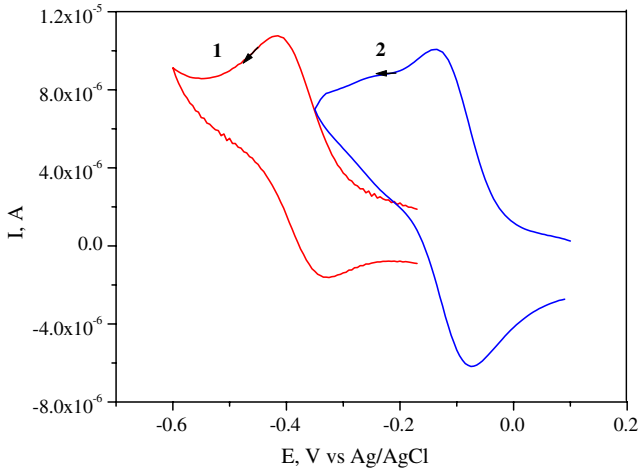


Fig. 4. Cyclic voltammograms of complexes **1** and **2** in acetonitrile solution containing 1 mM complex and 0.1 M n-Bu_4NClO_4 (scan rate = 0.1 V/s).

the bound ligands on the redox behavior of vanadium. This study strongly suggests that the stability of the VO^{3+} center is much higher in the presence of the H_2L^1 ligand than in presence of H_2L^2. A reasonable explanation comes from the hard-soft acid base principle. In complex **1**, the V(V)–N bond is a hard-hard interaction which is stable. Vanadium(V) is harder than vanadium(IV) and so reduction leads to a V(IV)–N bond, which is a soft-hard mismatch. On the other hand, the V(V)–Se bond in complex **2** is a hard-soft mismatch. Reduction to vanadium(IV) produces a V(IV)–Se bond which is a soft-soft match, making the reduction easier.

3.4. Kinetics of the oxidation of ascorbic acid

The kinetics of oxidation of ascorbic acid by complex **1** was conducted under pseudo-first-order conditions by monitoring the disappearance of the vanadium(V) species at 671 and 503 nm. The deep blue (**1**) and purple (**2**) colours of the complexes with high ε values [λ (nm) (ε, $M^{-1}\,cm^{-1}$): 330(8000), 510(5940) and 670 (8380) for **1** and 335(4400), 503(8400) and 781(4980)] for **2**] are presumably due to phenolate to vanadium(V) charge transfer transitions, and are comparable to other oxovanadium(V) complexes of phenolate derived ligands [26].

The gradual disappearance of these bands may be attributed to the fact that on reduction to vanadium(IV), complex **1** undergoes rapid decomposition in mixed aqueous solution (Fig. 5), and this is evidenced from the steady disappearance of the bands shown in the time resolved spectra for its acid catalyzed decomposition (SUP Fig. 1). The reactions were followed for more than 5 half lives and pseudo-first-order rate constants were extracted by fitting the kinetic traces to the HP-8453 system program. The kinetic conditions adopted are: $[H_2A]_t$ (where H_2A is fully protonated ascorbic acid) = 0.001–0.09 M, [Complex] ~ 1×10^{-4} M, pH 3.25–5.15, $I = 0.10$ M (KCl) and temperature 25 °C.

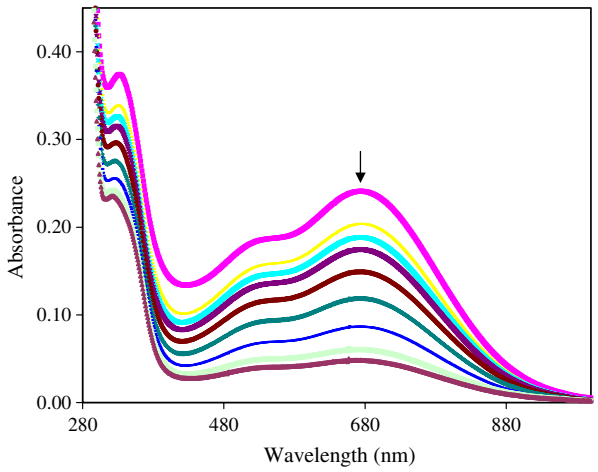


Fig. 5. Time resolved spectra for the oxidation of ascorbic acid by complex **1** at 25 °C. Conditions are: $[H_2A]$ 0.09 M, pH 4.5, $I = 0.10$ M (KCl). The first and second spectra were recorded immediately after mixing and at 200 s, respectively. Successive spectra were taken at 100 s time interval.

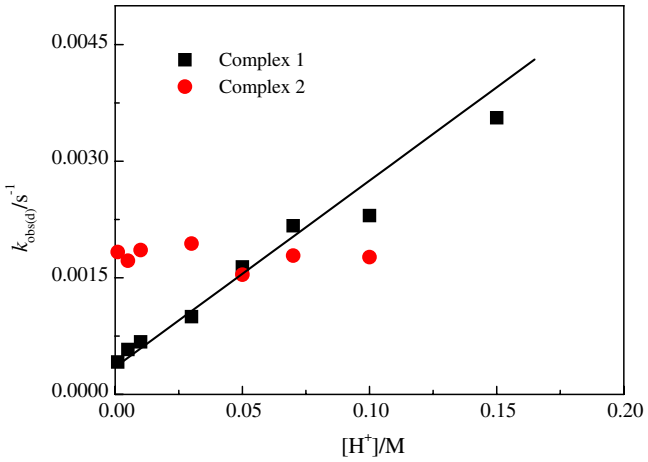


Fig. 6. Acid catalyzed decomposition of complex **1** in 50% MeCN–50% H_2O at 25 °C.

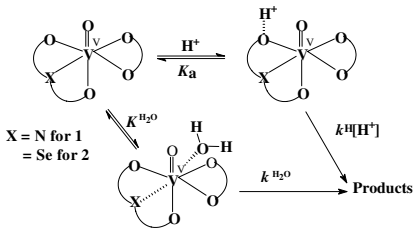
3.4.1. Decomposition of *1* and *2*

In the experimental range pH 3.25–5.15 there might be the possibility of protonation on the coordinated ligands, thereby causing the decomposition of the complexes. To explore this aspect, the acid catalyzed decomposition of the complexes was studied in the range $[H^+]$ 0.001–0.20 M in 50% MeCN–50% H_2O without ascorbic acid. For complex **1**, a plot of $k_{obs(d)}$ versus $[H^+]$ yields a straight line (Fig. 6) with a positive intercept on the rate axis, as given by Eq. (2) with k_0 as solvent mediated and k_1 as proton assisted decomposition paths, with $k_0 = (3.51 \pm 1.42) \times 10^{-4}\ s^{-1}$ and $k_1 = (2.40 \pm 0.15) \times 10^{-2}\ M^{-1}\ s^{-1}$.

$$k_{obs}(d) = k_o + k_1[H^+] \quad (2)$$

In the case of complex **2** it was surprisingly noticed that the decomposition rate is independent of $[H^+]$ and is solely mediated by the hydrolytic path with $k_0 = (4.0 \pm 0.05) \times 10^{-3}\ s^{-1}$. Based on these kinetic data a plausible overview of decomposition paths can be predicted, as shown in Scheme 1. Here, $k_0 = K^{H_2O} \cdot k^{H_2O}$ and $k_1 = K_a k^H$. Single protonation of the coordinated ligand is indicated by the first-order dependence of rate on $[H^+]$. Now the question arises whether protonation occurs on the bis-phenolate or acetylacetonate ligand. Based on pK_a values[1] it is more likely that the protonation should occur on the phenolate-oxygen atom. For the aqua-mediated decomposition path the coordination of H_2O to the metal center may take place in two ways. One is direct coordination to give a seven coordinated intermediate and another is the partial rupture of the V–X (X = N or Se) bond to facilitate the

[1] The pK_a of acetylacetone is 8.8 and that of *p*-methylphenol is 10.26 in water [27]. 2,4-Di-*tert*-butylphenol is insoluble in water but it is expected to have a higher pK_a value than alkyl-substituted phenols.



Scheme 1.

approach of H_2O towards the metal center. In the case of complex **1**, k_0 is lower than that of complex **2** and indicates the possibility of the second type of water coordination as the very weak V–Se bond facilitates this approach in the case of complex **2**. Another reason for a lower k_0 value for complex **1** may be due to the presence of the propyl group attach to the coordinated N atom of the ligand, imposing some kind of steric congestion around the metal center. As complex **2** undergoes only the hydrolytic decomposition, an attempt was taken to study the dependence of the rate on the water percentage present in the reaction medium. So, at 30%, 50%, 60% and 70% of H_2O (v/v), the decomposition rates 1.3×10^{-04}, 9.5×10^{-04}, 1.80×10^{-03}, 1.9×10^{-03} and 1.9×10^{-03}, respectively, were found, increasing with the increase in water % and becoming constant at $H_2O > 50\%$.

3.4.2. Oxidation of ascorbic acid by *1*

As the hydrolytic decomposition rate for **2** is high, probably higher than its rate of reduction by ascorbic acid; kinetics of oxidation of ascorbic acid was followed only for **1**. At pH 4.50, a variation of H_2A concentration was carried out and a plot of k'_{obs} versus $[H_2A]_t$ yielded a non-linear curve with a decreasing slope (Fig. 7) and this curve is best described by Eq. (3). As complex **1** undergoes acid catalyzed decomposition, the respective decomposition rates at the experimental pHs, $k_{obs(d)}$, were calculated with the knowledge of k_0 and k_1. Thus the pseudo-first-order rate constants (k'_{obs}) corresponding to the electron transfer process were calculated as $k'_{obs} = k_{obs(t)} - k_{obs(d)}$, where, $k_{obs(t)}$ is the total rate constant, $k_{obs(d)}$ = decomposition rate constant.

$$k'_{obs} = \frac{2kQ[H_2A]}{1+Q[H_2A]} \tag{3}$$

Here, 2 is the stoichiometric factor manifesting that ascorbic acid acts as a $2e^-$ reducing agent. Such a dependence of rate on ascorbic acid concentration indicates that the reactions proceed through a rapid pre-equilibrium formation of an intermediate (inner- or outer-sphere type) followed by slower decomposition, and can best be represented, in general, by Eq. (4).

$$A + B \overset{Q}{\rightleftharpoons} C \overset{k}{\rightarrow} \text{products} \tag{4}$$

$$k_{obs} = \frac{kQ[B]}{1+Q[B]} \tag{4a}$$

Non-linear computer fitting of the experimental data to Eq. (4a) yields $k = (1.12\pm0.04)\times10^{-3}\ M^{-1}\ s^{-1}$ and $Q = 63\pm7\ M^{-1}$ for **1**.

The oxidation of ascorbic acid has been found to depend on the pH of the medium. pH variation experiments were carried out in the range pH 3.25–5.15 at $[H_2A]_t = 0.005$ M, where a strict first-order dependence of rate on H_2A is prevailing. The pK_a of ascorbic acid (Eq. (5)) is reported to be 3.91 in H_2O at 25 °C[1] and at pH 4.5 both H_2A and HA^- species are relevant in the reaction solutions.

$$H_2A \overset{K_a}{\rightleftharpoons} HA^- + H^+ \tag{5}$$

As we did not get any saturation of decomposition rate on $[H^+]$, even at ~0.20 M, it can safely be assumed that at pH ⩾ 3.0 the protonated species of **1** would be very low in concentration at our experimental pH range. The *p*H–rate profile thus is mainly governed by Eq. (5). Plots of pH versus $\log(k')(k' = k'_{obs}/2[\ H_2A]_t)$ are S-shaped curves (Fig. 8). It is interesting to note that such a plot for complex **1** follows the normal reactivity trend, i.e., k'_{obs} increases with an increase in pH, rendering HA^- as a more reactive species than H_2A. Considering all these facts a general reaction scheme applicable for complex **1** could be framed as:

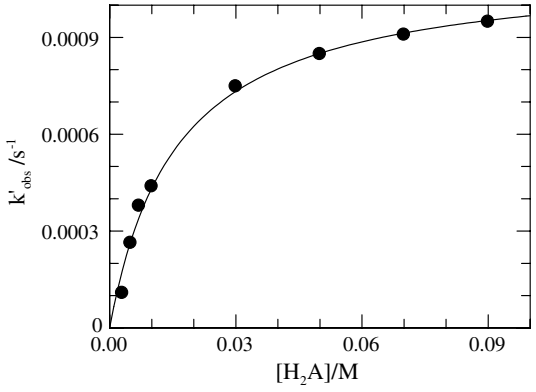


Fig. 7. Plots of k_{obs} vs. $[ascorbic\ acid]_t$ for the oxidation of ascorbic acid by complex **1** at pH 4.50 and 25 °C.

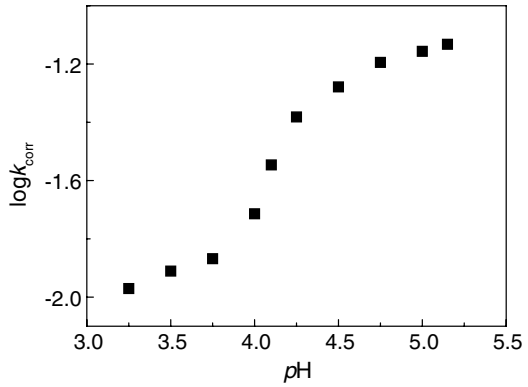


Fig. 8. Plots of $\log k_{corr}$ vs. pH for the oxidation of ascorbic acid by complex **1** at $[H_2A] = 0.005$ M.

$$[V^{V}(L^{1})(acac)] + H_2A \overset{Q_1}{\rightleftharpoons} \{[V^{V}(L^{1})(acac)], H_2A\} \overset{k_1}{\rightarrow} \{[V^{IV}(L^{1})(acac)], H_2A^{\cdot+}\} \overset{fast}{\rightarrow} HA^{\cdot} + \text{decomposition products} \quad (6)$$

$$[V^{V}(L^{1})(acac)] + H_2\ A^{-} \overset{Q_2}{\rightleftharpoons} \{[V^{V}(L^{1})(acac)], H_2A\}^{-} \overset{k_2}{\rightarrow} \{[V^{IV}(L^{1})(acac)], H_2A\} \overset{fast}{\rightarrow} HA^{\cdot} + \text{decomposition products} \quad (7)$$

$$[V^{V}(L^{1})(acac)] + HA^{\cdot} \overset{fast}{\rightarrow} \text{dehydroascorbic acid} + \text{decompostion products} \quad (8)$$

From the above reaction sequence (Eqs. (6)–(8)) the rate law (Eq. (9)) can be derived

$$k = \frac{k_1Q_1[H^+] + k_2Q_2K_{a^1}}{[H^+] + K_{a^1}} \quad (9)$$

A non-linear computer-fit program was used to fit the experimental data to Eq. (9) and the parameters thereby derived are:

$k_1Q_1 = (7.63 \pm 0.8) \times 10^{-3}$ $M^{-1}\,s^{-1}$, $k_2Q_2 = (1.02 \pm 0.03) \times 10^{-1}\,M^{-1}\,s^{-1}$ and $K_a{}^1 = (1.77 \pm 0.20) \times 10^{-5}$ M. ($pK_a{}^1 = 4.75$) for complex **1**. The pK_a value thus obtained is slightly higher than that of the reported value and this slight elevation in the pK_a value may be attributed to the H-bonding interaction of the dissociable proton with the vanadyl oxygen atom as well as with one of the phenolate oxygen atoms of the coordinated ligand. A similar elevation of the pK_a value in the ascorbic acid oxidation reactions was observed previously.

For complex **1**, the ratio $k_2Q_2/k_1Q_1 = 13.37$, which is very low compared to other reactions. In the absence of other factors like H-bonding, the $k(HA^-)/k(H_2A)$ ratio generally varies between 10^4 and 10^5 [28]. Such a low reactivity ratio implies that there is H-bonding between the OH proton of the ascorbic acid and the vanadyl oxygen atom, which provides a low energy pathway for the electron transfer process. This probability of H-bonding is more pronounced in the case of H_2A than HA^- i.e., $Q_1 > Q_2$ and thereby HA^- has a lower overall reactivity (k_2Q_2), and hence the observed reactivity trend. Similar observations were also encountered in the oxidation of ascorbic acid by several nickel(III) and nickel(IV) complexes of oxime-imine ligands [29]. One point that needs to be clarified in this study is the mechanistic route. Vanadium(IV/V) species generally react both by inner- and outer-sphere mechanisms [30]. However, no evidence for the formation of a stable intermediate was encountered during the spectral scanning of these reactions to support the inner-sphere route. Based on the higher Q values ($Q = 63$ for **1**), it can be concluded that these reactions probably proceed via an inner-sphere route, particularly through the formation of a hydrogen bonded adduct. Due to the lack of a self-exchange rate constant (k_{11}) for these complexes, it was not possible to calculate the theoretical outer-sphere rate constants by the application of the Marcus theory [31] to support or contradict this proposition.

4. Conclusion

(1) Complexes **1** and **2** were prepared by the reaction of equimolar quantities of $[VO(acac)_2]$ with H_2L^1 and H_2L^2 respectively in acetonitrile medium.
(2) The conductance measurements in acetonitrile showed very low conductivity (3 S for **1** and 5.7 S for **2**) indicating that both the complexes are electrically neutral.
(3) ^{51}V NMR both in solid and solution phases proved the presence of vanadium(V) species.
(4) Both complexes **1** and **2** showed reversible cyclic voltammeric responses with $E_{1/2} - 0.18$ and 0.10 V versus NHE, respectively.
(5) The kinetics of oxidation of ascorbic acid by complex **1** in 50% MeCN–50% H_2O (v/v) at 25 °C proceeds through pre-equilibrium formation of a H-bonded adduct and is manifested by high formation constant values ($Q = 63$), and is further supported by low k_2Q_2/k_1Q_1 ratios (13.37).

Acknowledgments

M.A. gratefully acknowledges the financial assistances from the UGC (Ref. No. F.12-22/2003(SR)) and CSIR (Ref. No. 01(1760)/02/EMR-II), New Delhi. D.M. also acknowledge UGC for the fellowship and contingent grant. M.G.B.D. thanks the EPSRC and the University of Reading for funds for the image plate system. J.M. expresses thanks to the Ministry of Education of the Czech Republic (MSMT CR MSM0021622415).

Appendix A. Supplementary material

CCDC 278612 and 627033 contain the supplementary crystallographic data for **1** and **2**. These data can be obtained free of charge via http://www.ccdc.cam.ac.uk/conts/retrieving.html, or from the Cambridge Crystallographic Data Centre, 12 Union Road, Cambridge CB2 1EZ, UK; fax: (+44) 1223-336-033; or e-mail: deposit@ccdc.cam.ac.uk. Supplementary data associated with this article can be found, in the online version, at doi:10.1016/j.poly.2007.06.010.

References

[1] N.D. Chasteen (Ed.), Vanadium in Biological System, Kluwer Academic Publishers., Dordrecht, The Netherlands, 1990.
[2] A. Butler, J.V. Walker, Chem. Rev. 93 (1993) 1937.
[3] (a) P. Barnett, W. Hemrika, H.L. Dekker, A.O. Muijsers, R. Renirie, R.J. Wever, J. Biol. Chem. 273 (1998) 23381;
(b) H. Sakurai, T. Inohara, Y. Adachi, K. Kawabe, H. Yasui, J. Takada, Biorg. Med. Chem. Lett. 14 (2004) 1093.

[4] C. Orvig, K.H. Thompson, M. Battell, J.H. McNeill, in: A. Sigel, H. Sigel (Eds.), Metal Ions in Biological Systems: Vanadium and Its Role in Life, vol. 31, Marcel Dekker, New York, 1995, p. 575.
[5] I.G. Fantus, E. Tsiani, Mol. Cell. Biochem. 182 (1998) 109.
[6] K.H. Thompson, J.H. McNeill, C. Orvig, Chem. Rev. 99 (1999) 2561.
[7] A.B. Hanck, Prog. Clin. Biol. Res. 259 (1988) 307.
[8] G. Block, Am. J. Clin. Nutr. 53 (1991) 270S.
[9] G. van Poppel, H. van den Berg, Cancer Lett. 114 (1997) 195.
[10] R.A. Jacob, Sotoudeh, Nutr. Clin. Care 5 (2002) 66.
[11] A. Carr, B. Frei, FASEB J. 13 (1999) 1007.
[12] J.F. Neault, M. Naoui, H.A. Tajmir-Riahi, J. Biomol. Struct. Dyn. 13 (1995) 387.
[13] E.A. Lutsenko, J.M. Carcamo, D.W. Golde, J. Biol. Chem. 277 (2002) 16895.
[14] (a) D. Maity, A. Ray, W.S. Sheldrick, H. Meyer-Figge, B. Bandyopadhyay, M. Ali, Inorg. Chim. Acta 359 (2006) 3197;
(b) Md. Mijanuddin, A. Ray, P.C. Mondal, J. Marek, M. Ali, J. Mol. Struct. 826 (2007) 17.
[15] (a) E.Y. Tshuva, I. Goldberg, M. Kol, Organometallics 20 (2001) 3017;
(b) T.K. Paine, T. Weyhermller, E. Bothe, K. Wieghardt, P. Chaudhuri, J. Chem. Soc., Dalton Trans. (2003) 3136.
[16] G.M. Sheldrick, Acta Crystallogr., Sect. A 46 (1990) 467.
[17] DIFABS N. Walker, D. Stuart, Acta Crystallogr., Sect. A 39 (1983) 158.
[18] G.M. Sheldrick, T.R. Schneider, Methods Enzymol. 277 (1997) 319.
[19] M. Nardelli, Comput. Chem. 7 (1983) 95.
[20] M.N. Burnett, C.K. Johnson, ORTEP-III: Oak Ridge Thermal Ellipsoid Plot Program for Crystal Structure Illustrations, Report ORNL-6895, Oak Ridge National Laboratory, Oak Ridge, TN, USA, 1996.
[21] A.D. Allen, T.T. Tidwell, J. Am. Chem. Soc. 109 (1987) 2.
[22] J.H. Roe, Methods of Biochemical Analysis, vol. 1, Interscience, New York, 1956, p. 115.
[23] (a) F. Wolff, C. Lorber, R. Choukroun, B. Donnadieu, Inorg. Chem. 42 (2003) 7839;
(b) T.K. Paine, T. Weyhermuller, L.D. Slep, F. Neese, E. Bill, E. Bothe, K. Wieghardt, P. Chaudhuri, Inorg. Chem. 43 (2004) 7324;
(c) F. Wolf, C. Lorber, R. Choukroun, B. Donnadieu, Eur. J. Inorg. Chem. (2004) 2861;
(d) P. Plitt, H. Pritzkov, R. Krämer, J. Chem. Soc., Dalton Trans. (2004) 2314;
(e) F.H. Allen, Acta Crystallogr., Sect. B 58 (2002) 380.
[24] S.X. Liu, S. Gao, Polyhedron 17 (1998) 81.
[25] T.K. Paine, T. Weyhermüller, E. Bill, E. Bothe, P. Chaudhuri, Eur. J. Inorg. Chem. (2003) 4299.
[26] (a) S.R. Cooper, Y.B. Koh, K.N. Raymond, J. Am. Chem. Soc. 104 (1982) 5092;
(b) U. Auerbach, B.S.P.C. Della Vedova, K. Wieghardt, B. Nuber, J. Weiss, J. Chem. Soc., Chem. Commun. (1990) 1004;
(c) A. Neves, A. Ceccato, I. Vencato, Y.P. Mascarenhas, C. Erasmus-Buhr, J. Chem. Soc., Chem. Commun. (1992) 652;
(d) S. Bruni, A. Caneschi, F. Cariati, C. Delfs, A. Dei, D. Gatteschi, J. Am. Chem. Soc. 116 (1994) 1388;
(e) V. Vergopoulos, S. Jantzen, D. Rodewald, D. Rehder, J. Chem. Soc., Chem. Commun. (1995) 377.
[27] A.E. Martell, R.M. Smith, Critical Stability Constants, Other Organic Ligands, vol. 3, Plenum Press, New York, 1977, pp. 181 and 244.
[28] D.H. Macartney, A. McAuely, Can. J. Chem. 59 (1981) 135.
[29] B. Saha, G. Gangopadhyay, M. Ali, P. Banerjee, J. Chem. Soc., Dalton Trans. (1995) 1083, and references therein.
[30] (a) M. Ali, S. Gangopadhyay, P. Banerjee, J. Chem. Res. (S) (1992) 316, and references therein;
(b) G.B. Shul'pin, G. Guss-Fink, J. Chem. Soc., Perkin Trans. 2 (1995) 1459;
(c) P.C. Wilkins, M.D. Johnson, A.A. Holder, D.C. Crans, Inorg. Chem. 45 (2006) 1471;
(d) K. Kustin, D.L. Toppen, Inorg. Chem. 12 (1973) 1404.
[31] R.A. Marcus, J. Phys. Chem. 72 (1968) 891.

no splitting of the v_3 mode. Johan et al. published the position of the infrared bands of tunisite at 1155 cm^{-1} (v_1), 850 cm^{-1} (v_2), 1530 cm^{-1} (v_3) [7]. No band position was given for the (v_4) mode. For these minerals the position as determined by infrared spectroscopy of the water bands was not forthcoming.

Raman spectroscopy has proven very useful for the study of minerals [10–12]. Indeed Raman spectroscopy has proven most useful for the study of diagentically related minerals as often occurs with carbonate minerals [13–17]. Some previous studies have been undertaken by the authors using Raman spectroscopy to study complex secondary minerals formed by crystallisation from concentrated sulfate solutions [18]. Very few spectroscopic studies of the hydrated double carbonates have been forthcoming and what studies that are available are not new. Few Raman studies of any note are available [19,20]. The aim of this paper is to present Raman and infrared spectra of natural hydrated double carbonates including pirssonite, gaylussite and tunisite. The paper is a part of systematic studies of vibrational spectra of minerals of secondary origin in the oxide supergene zone and their synthetic analogs.

2. Experimental

2.1. Minerals

Selected minerals were obtained from the Mineralogical Research Company and other sources including Museum Victoria. The samples were phase analysed by X-ray diffraction and for chemical composition by EDX measurements.

The origin of the minerals are as follows:

Pirssonite – Green River, Sweetwater Co., Wyoming labelled as pirssonite 1.
Pirssonite – Searles Lake, San Bernardino Co., California labelled as pirssonite 3.
The mineral pirssonite 3 is a type mineral [21] and is used as a standard or reference mineral (please go to p. 552 of Ref. [21]).
Gaylussite – Teels Marsh, Esmeralda County, Nevada. Gaylussite is listed on p. 241 of Ref. [21].
Tunisite – near Condorcet, Drome, France (p. 716 of Ref. [21]).

2.2. Raman microprobe spectroscopy

The crystals of halogenated carbonates were placed and oriented on the stage of an Olympus BHSM microscope, equipped with 10× and 50× objectives and part of a Renishaw 1000 Raman microscope system, which also includes a monochromator, a filter system and a Charge Coupled Device (CCD). Raman spectra were excited by a HeNe laser (633 nm) at a resolution of 2 cm^{-1} in the range between 100 and 4000 cm^{-1}. Repeated acquisition using the highest magnification was accumulated to improve the signal to noise ratio. Spectra were calibrated using the 520.5 cm^{-1} line of a silicon wafer. In order to ensure that the correct spectra are obtained, the incident excitation radiation was scrambled. Previous studies by the authors provide more details of the experimental technique. Details of the technique have been published by the authors [22–25].

2.2.1. Mid-IR spectroscopy

Infrared spectra were obtained using a Nicolet Nexus 870 FTIR spectrometer with a smart endurance single bounce diamond ATR cell. Spectra over the 4000–525 cm^{-1} range were obtained by the co-addition of 64 scans with a resolution of 4 cm^{-1} and a mirror velocity of 0.6329 cm/s. Spectra were co-added to improve the signal to noise ratio.

Spectral manipulation such as baseline adjustment, smoothing and normalisation were performed using the Spectracalc software package GRAMS (Galactic Industries Corporation, NH, USA). Band component analysis was undertaken using the Jandel 'PEAKFIT' software package which enabled the type of fitting function to be selected and allows specific parameters to be fixed or varied accordingly. Band fitting was done using a Lorentz–Gauss cross-product function with the minimum number of component bands used for the fitting process. The Gauss–Lorentz ratio was maintained at values greater than 0.7 and fitting was undertaken until reproducible results were obtained with squared correlations of r^2 greater than 0.995.

3. Results and discussion

The Raman spectra of two pirssonite minerals and gaylussite, shortite and quintinite in the 950–1450 cm^{-1} region are shown in Fig. 1. Adler and Kerr predicted from their infrared data that the carbonate units were crystallographically single units in the structure of pirssonite [8]. This was later confirmed by crytsallographic studies of synthetic pirssonite and gaylussite [26]. The Raman spectra of pirssonite as shown in Fig. 1a and b show a single intense band at around 1080 cm^{-1}. The position of this band is sample dependent. The band is observed at 1074 cm^{-1} for the second pirssonite mineral sample. A low intensity band at 1050 cm^{-1} is observed in the Raman spectrum and it is considered this band is a hot band. Adler and Kerr reported based on infrared spectra the position of the v_1 band as 1068 cm^{-1} [8]. The carbonate unit in galylussite is on a C_1 site and is crystallographically distinct. Thus no splitting of the carbonate bands should be observed. This is confirmed by a single Raman band for galylussite at 1078 cm^{-1}. Adler and Kerr did not report an infrared band for gaylussite in the v_1 position. In contrast the Raman spectrum of shortite (Fig. 1d) shows two Raman bands at 1070 and 1090 cm^{-1}. Adler and Kerr reported two infrared bands at 1069 and 1089 cm^{-1} in excellent agreement with the Raman data reported in this work [8].

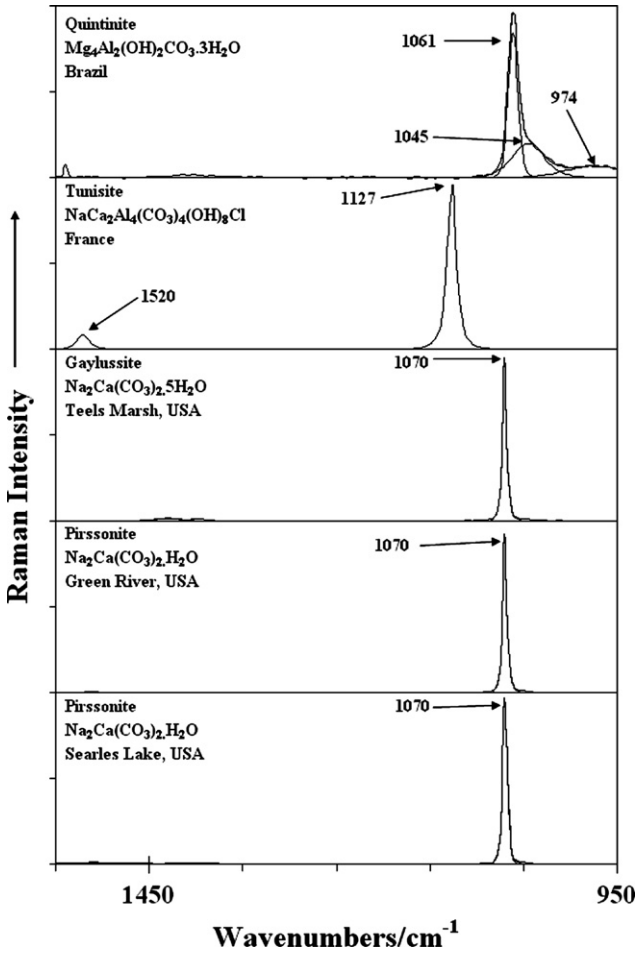


Fig. 1. Raman spectra of pirssonite (sample 1), pirssonite (sample 2), gaylussite, shortite, quintinite in the 950–1450 cm^{-1} region.

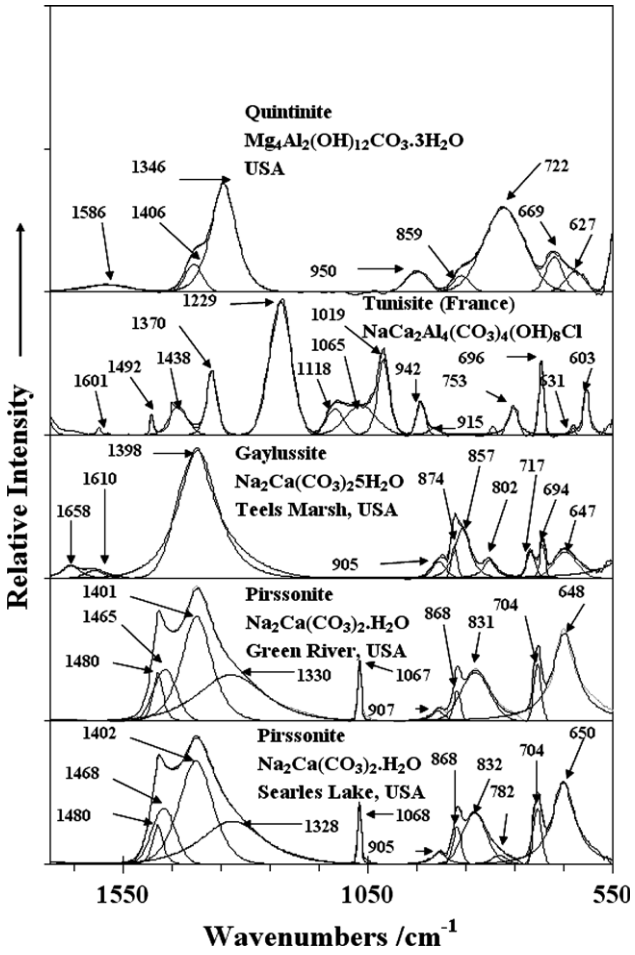


Fig. 2. Infrared spectra of pirssonite, gaylussite, tunisite, shortite and quintinite in the 550–1600 cm^{-1} region.

The Raman spectra of quintinite (a hydrotalcite) shows two bands at 1062 and 1050 cm^{-1} which may be attributed to $(CO_3)^{2-}$ symmetric stretching modes. Often the Raman spectra of carbonate in the interlayer of hydrotalcites show two or more bands for the symmetric stretching mode.

The infrared spectra of the minerals pirssonite, gaylussite, tunisite and quintite are reported in Fig. 2. The infrared spectra of pirssonite shows a low intensity band at 1067–8 cm^{-1} in close agreement with the results published by Adler and Kerr [8]. The observation of the Raman band supports the concept of distortion of the carbonate unit in pirsonite. No infrared band was observed in this position for gaylussite. In tunisite two bands are observed at 1065 and 1118 cm^{-1}. An infrared band was reported by Johan et al. for tunisite at 1155 cm^{-1} [7]. No infrared bands were observed for quintinite in this spectral region confirming the lack of distortion of the carbonate units in quintinite. This is expected since the carbonate units are held in the interlayer of the quintinite structure.

In the Raman spectrum of pirssonite three bands are observed at 1406, 1468 and 1511 cm^{-1}. These bands are assigned to the v_3 antisymmetric stretching modes. In the infrared spectra of pirssonite three bands are observed at 1402, 1465 and 1480 cm^{-1}. Adler and Kerr reported two infrared bands at 1414 and 1488 cm^{-1} [8]. Although the crystallographic data show there is only one crystallographically distinct carbonate unit in the structure of pirssonite, the observation of three antisymmetric stretching modes supports the concept that some carbonate units are distorted in the pirssonite structure. In contrast two Raman bands for gaylussite are observed for gaylussite at 1398 and 1429 cm^{-1}. In the infrared spectrum of gaylussite only a single broad band is observed at 1398 cm^{-1}. These results differ from that found by Adler and Kerr who found only a single infrared band at 1414 cm^{-1} for gaylussite. The low site symmetry of the carbonate unit in shortite results in the splitting of the v_3 antisymmetric stretching modes. Four Raman bands are observed at 1410, 1445, 1476 and 1511 cm^{-1}. Adler and Kerr found four infrared bands at 1410, 1453, 1481 and 1522 cm^{-1} [8]. For the mineral quintinite a very low intensity broad band at 1414 cm^{-1} is observed. In the infrared spectrum of quintinite three bands are observed at 1346, 1406 and 1586 cm^{-1}. The first two bands are assigned to the v_3 antisymmetric stretching modes whilst the intense band at 1346 cm^{-1} is ascribed to an OH deformation mode.

The Raman spectra of two pirssonite minerals and gaylussite, shortite and quintinite in the 100–950 cm^{-1} region are shown in Fig. 3. Further confirmation of the distortion of carbonate units in the pirssonite structure is obtained through the observation of the v_2 bending mode at around 879 cm^{-1}. Adler and Kerr reported an infrared band in this position in the infrared spectra [7]. For gaylussite a Raman band is observed at 898 cm^{-1} and is attributed to this assignment. This band for shortite is of very low intensity and is only observed through scale expansion. For quintinite low intensity bands are observed at 801 and 852 cm^{-1}. In contrast in the infrared spectra the band should show considerable intensity as may be observed in the infrared spectra of the double carbonates. The infrared spectra of pirssonite displays two bands at 832 and 868 cm^{-1}. Three bands for gaylussite are observed at 802, 857 and 874 cm^{-1}. The infrared spectrum of quintinite shows a broad band at 859 cm^{-1}.

The Raman spectrum of pirssonite shows two bands at 644 and 719 cm^{-1}. These bands are assigned to the v_4 $(CO_3)^{2-}$ bending modes. Adler and Kerr reported two infrared bands at 699 and 712 cm^{-1}. In the infrared spectra of pirssonite (Fig. 2) two bands are observed at 650 and 704 cm^{-1} in harmony with the position of the Raman results. For gaylussite three Raman bands are observed in this v_4 spectral region at 664, 699 and 719 cm^{-1}. Adler and Kerr reported only two bands in the infrared spectrum at 692 and 720 cm^{-1} [8]. Four Raman bands are observed for shortite at 695, 715, 719 and 730 cm^{-1}. Adler and Kerr reported four infrared bands at 693, 709, 719 and 730 cm^{-1} [8]. The observation of two symmetric stretching modes with different wavenumbers for shortite offers the distinction between two crystallographic different carbonate units. The low site symmetry of the carbonate unit in shortite results in the splitting of the v_4 bending modes. According to Farmer [1], the shortite structure is complex with the Ca^{2+} is 9 coordinated, one Na^{+} 8 coordinated and one Na^{+} 6 coordinated. In the structure of shortite there are two distinct $(CO_3)^{2-}$ units one on site symmetry C_{2v} and a second on a site C_s symmetry. This complexity is reflected in the Raman spectrum of shortite as shown in Fig. 1d. For the carbonate quintinite only a single low intensity band at 700 cm^{-1} is observed.

The Raman spectra of two pirssonite minerals and gaylussite, shortite and quintinite in the 3100–3800 cm^{-1} region are shown in Fig. 4. No Raman spectrum was

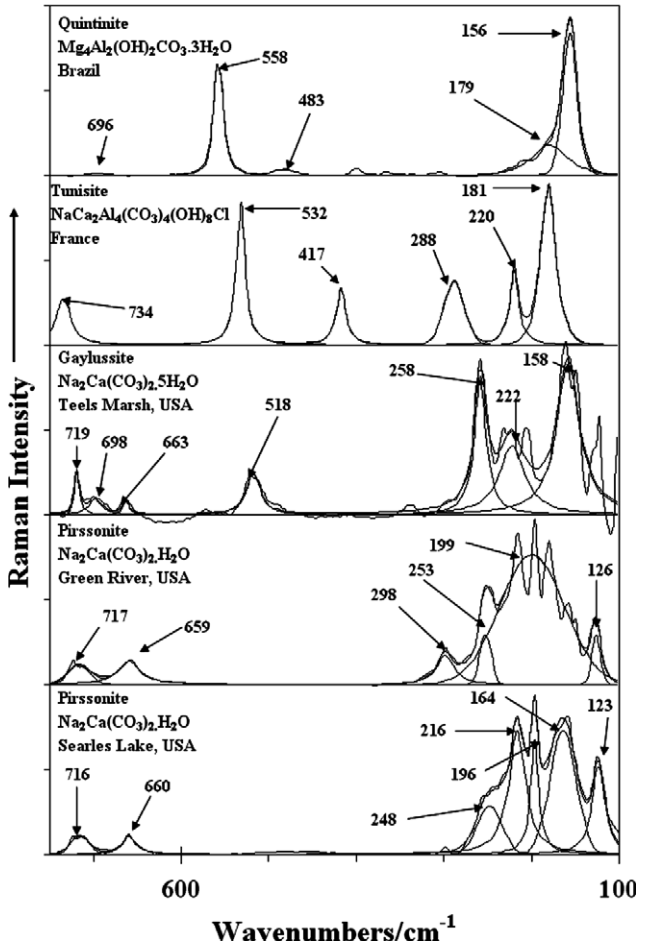


Fig. 3. Raman spectra of pirssonite (sample 1), pirssonite (sample 2), gaylussite, shortite, quintinite in the 100–950 cm^{-1} region.

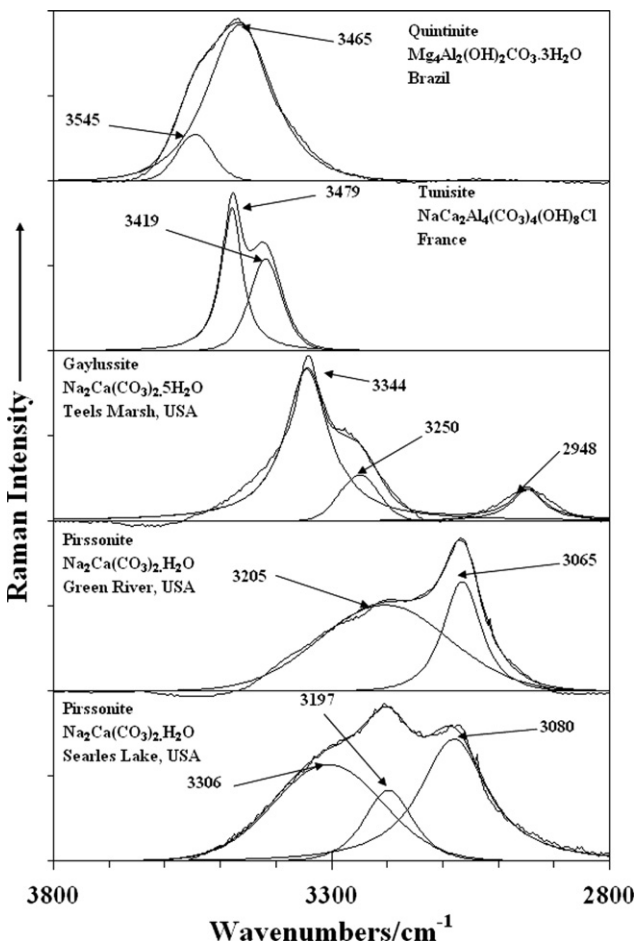


Fig. 4. Raman spectra of pirssonite (sample 1), pirssonite (sample 2), gaylussite, shortite, quintinite in the 3100–3800 cm^{-1} region.

observed for shortite in this spectral region as is expected. This confirms the shortite mineral is anhydrous. The Raman spectrum of pirssonite (sample 1) in the 2500–3700 cm^{-1} region show three bands at 3085, 3202, 3307 cm^{-1}. For the second pirssonite mineral three bands are observed at 3065, 3302 and 3284 cm^{-1}. In the infrared spectrum of pirssonite a complex system of overlapping bands is observed. This spectral region may be resolved into band components at 2954, 3058, 3188 and 3326 cm^{-1}. Adler and Kerr did not provide any information on the IR bands of the OH units for pirssonite or gaylussite in the OH stretching region. The Raman spectrum of gaylussite in the OH stretching region shows three bands at 2950, 3250 and 3347 cm^{-1}. In the infrared spectrum three bands at 2944, 3268 and 3334 cm^{-1} are observed (Fig. 5). For quintinite the Raman spectrum shows two bands at 3464 and 3546 cm^{-1}. In the infrared spectrum two bands at 3167 and 3373 cm^{-1} are observed.

Studies have shown a strong correlation between OH stretching frequencies and both O···O bond distances and H···O hydrogen bond distances [27–30]. Libowitzky (1999) showed that a regression function can be employed relating the hydroxyl stretching frequencies with regression coefficients better than 0.96 using infrared spectroscopy [31]. The function is described as: $v_1 = (3592 - 304) \times 109^{\frac{-d(O-O)}{0.1321}}$ cm^{-1}. Thus OH···O hydrogen bond distances may be calculated using the Libowitzky empirical function. Thus for pirssonite hydrogen bond distances from the infrared data of 2.639 Å (2954 cm^{-1}), 2.663 Å (3058 cm^{-1}), 2.699 Å (3188 cm^{-1}) and 2.755 Å (3326 cm^{-1}) are calculated. The Raman bands at 3085, 3202 and 3307 cm^{-1} provide values of 2.669, 2.75 and 2.746 Å. From the infrared bands of gaylussite at 2950, 3250 and 3347 cm^{-1} hydrogen bond distances of 2.639, 2.721 and 2.766 cm^{-1} are estimated. For the mineral quintinite, the IR bands at 3167 and 3373 cm^{-1} provide hydrogen bond distances of 2.693 and 2.780 Å. The Raman OH stretching band give slightly longer distances of 2.851 and 2.986 Å. The large variation hydrogen bond distances which are present in pirssonite and gaylussite can also be seen in other mixed anion minerals such as peisleyite where the distances ranging between 3.052 and 2.683 Å. Such hydrogen bond distances are typical of secondary minerals. For pirssonite and gaylussite hydrogen bond distances from 2.669 to 2.766 Å are observed. A range of hydrogen bond distances are observed from reasonably strong to weak hydrogen bonding. This range of hydrogen bonding contributes to the stability of the mineral.

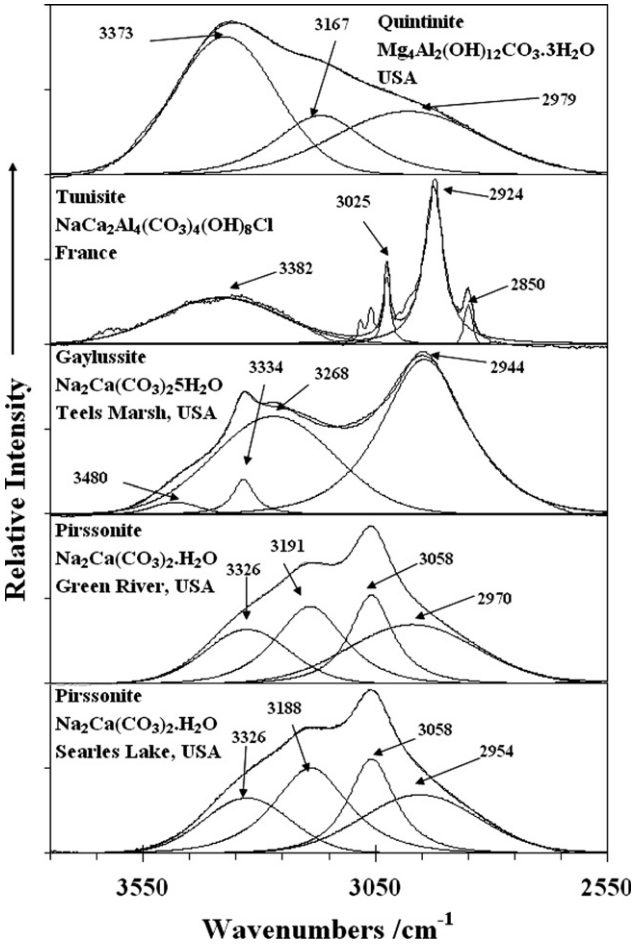


Fig. 5. Infrared spectra of pirssonite, gaylussite, tunisite and quintinite in the 2550–4000 cm^{-1} region.

4. Conclusions

The double carbonates pirssonite, gaylussite, tunisite and shortite were characterised by both Raman and infrared spectroscopy. These double carbonates are characterised by v_1 stretching bands around 1060–1080 cm^{-1}. The position of the band appears to be dependent on the symmetry of the carbonate units in the structure. For pirssonite and gaylussite only a single band is observed whilst for shortite and for comparison quintinite two bands are observed in the symmetric stretching region. This confirms the concept of more than one crystallographically distinct carbonate unit in the crystal. Multiple antisymmetric stretching modes are, however, observed for pirssonite indicating distortion of the carbonate unit in the crystal. This distortion is also observed by the number of bands in the v_4 in phase bending region where multiple bands are observed for pirssonite, gaylussite and shortite.

Acknowledgements

The financial and infra-structure support of the Queensland University of Technology, Inorganic Materials Research Program is gratefully acknowledged. The Australian Research Council (ARC) is thanked for funding the instrumentation. Mr. Dermot Henry of Museum Victoria is thanked for the loan of some of the carbonate minerals.

References

[1] V.C. Farmer, The infrared spectra of minerals, in: Mineralogical Society Monograph 4, Mineralogical Society, London, 1974.

[2] T.-J. Chi, Y.-H. Kwan, Changchun Dizhi Xueyuan Xuebao (1978) 39.
[3] E. Corazza, C. Sabelli, Acta Crystallogr. 23 (1967) 763.
[4] S. Menchetti, Atti Accad. Naz. Lin. 44 (1968) 680.
[5] E.A. Monroe, Z. Kristallogr. Krist. 124 (1967) 459.
[6] E.A. Pobedimskaya, T. Chinh Le, Vestn. Mosk. Univ. Ser. 4 (1985) 91.
[7] Z. Johan, P. Povondra, E. Slansky, Am. Mineral. 54 (1969) 1.
[8] H.H. Adler, P.F. Kerr, Am. Mineral. 48 (1963) 839.
[9] A.J. Frueh Jr., J.P. Golightly, Can. Mineral. 9 (1967) 51.
[10] R.L. Frost, S.J. Palmer, J.M. Bouzaid, B.J. Reddy, J. Raman Spectrosc. 38 (2007) 68.
[11] R.L. Frost, D.A. Henry, M.L. Weier, W. Martens, J. Raman Spectrosc. 37 (2006) 722.
[12] R.L. Frost, A.W. Musumeci, J.T. Kloprogge, M.O. Adebajo, W.N. Martens, J. Raman Spectrosc. 37 (2006) 733.
[13] R.L. Frost, J. Cejka, M. Weier, W.N. Martens, J. Raman Spectrosc. 37 (2006) 879.
[14] R.L. Frost, M.L. Weier, J. Cejka, J.T. Kloprogge, J. Raman Spectrosc. 37 (2006) 585.
[15] R.L. Frost, J. Cejka, M.L. Weier, W. Martens, J. Raman Spectrosc. 37 (2006) 538.
[16] R.L. Frost, M.L. Weier, B.J. Reddy, J. Cejka, J. Raman Spectrosc. 37 (2006) 816.
[17] R.L. Frost, M.L. Weier, W.N. Martens, J.T. Kloprogge, J. Kristof, J. Raman Spectrosc. 36 (2005) 797.
[18] R.L. Frost, R.-A. Wills, M.L. Weier, W. Martens, J. Raman Spectrosc. 36 (2005) 435.
[19] H. Fan, K. Tao, Y. Xie, K. Wang, Yanshi Xuebao 19 (2003) 169.
[20] W. Hong, S. He, S. Huang, Y. Wang, H. Hou, X. Zhu, Guangpuxue Yu Guangpu Fenxi 19 (1999) 546.
[21] J.W. Anthony, R.A. Bideaux, K.W. Bladh, M.C. Nichols, Handbook of Mineralogy, Mineral Data Publishing, Tiscon, AZ, 2003.
[22] R.L. Frost, D.A. Henry, K. Erickson, J. Raman Spectrosc. 35 (2004) 255.
[23] R.L. Frost, Spectrochim. Acta A 60A (2004) 1469.
[24] R.L. Frost, O. Carmody, K.L. Erickson, M.L. Weier, J. Cejka, J. Mol. Struct. 703 (2004) 47.
[25] R.L. Frost, O. Carmody, K.L. Erickson, M.L. Weier, D.O. Henry, J. Cejka, J. Mol. Struct. 733 (2004) 203.
[26] B. Dickens, W.E. Brown, Inorg. Chem. 8 (1969) 2093.
[27] J. Emsley, Chem. Soc. Rev. 9 (1980) 91.
[28] H. Lutz, Struct. Bond. (Berl.) 82 (1995) 85.
[29] W. Mikenda, J. Mol. Struct. 147 (1986) 1.
[30] A. Novak, Struct. Bond. (Berl.) 18 (1974) 177.
[31] E. Libowitzky, Monatsh. Chem. 130 (1999) 1047.

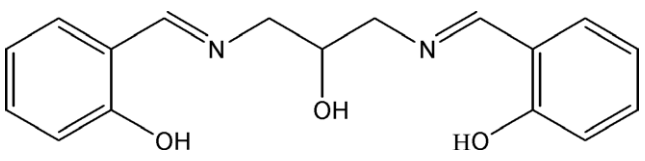
nucleases over enzymatic ones are well delineated: the former are smaller in size, rendering a fast stretching in the hindered sites of macromolecules. The redox properties of the metal and dioxygen as well are utilized for direct strand scission or base modification [33,34]. Multinuclear copper complexes seem to serve an important role [35–40].

Recently we have synthesized and characterized an octanuclear copper(II) complex of a N_2O_3-donor Schiff base which shows effective oxidative cleavage of plasmid DNA [35]. Herein, we report the synthesis, crystal structure and magnetic property of a tetranuclear copper(II) complex, $[Cu_4(L)_2(tp)(dmf)_2]$ (**1**) [H_3L = 1,3-bis(salicylideneamino)-propan-2-ol, tp = terephthalate, dmf = *N*,*N*′-dimethylformamide]. The variable temperature-dependent susceptibility measurement (2–300 K) of **1** reveals a dominant ferromagnetic coupling, $2J = 18.70\ cm^{-1}$. Complex **1** binds to double-stranded CT (calf-thymus) DNA giving a K_{app} value of $1.25 \times 10^7\ M^{-1}$ and displays efficient cleavage of supercoiled pUC19 DNA in the presence of H_2O_2 following a hydroxyl radical pathway.

2. Experimental

2.1. Materials and physical methods

All reagents and chemicals were purchased from commercial sources and were used without further purification. The ligand 1,3-bis(salicylideneamino)propan-2-ol (H_3L, Scheme 1) was prepared by a reported method [41]. The supercoiled (SC) pUC19 DNA (caesium chloride purified) was purchased from Bangalore Genie (India). The calf thymus (CT) DNA, agarose (molecular biology grade), distamycin and ethidium bromide (EB) were obtained from Sigma. Tris(hydroxymethyl)-aminomethane–HCl (Tris–HCl) buffer was prepared using deionized and sonicated triple distilled water. Solvents used for spectroscopic studies were purified and dried by standard procedures before use [42]. FT-IR spectra were obtained on a Nicolet MAGNA-IR 750 spectrometer with samples prepared as KBr pellets. Elemental analysis was carried out in a 2400 Series-II CHN Analyzer, Perkin–Elmer, USA. Variable temperature magnetic susceptibility and field dependence of magnetization measurements were performed on a Quantum Design MPMS XL-5 SQUID magnetometer. Absorption and luminescence spectra were studied on Shimadzu UV2100 UV–VIS recording spectrophotometer and Perkin–Elmer LS 55 luminescence spectrometer, respectively. Circular dichroic spectra of DNA were obtained by using JASCO J-815 automatic recording spectropolarimeter operating at 25 °C. The region between 220 and 320 nm was scanned for each sample.



Scheme 1. Schematic structure of H_3L.

CAUTION: Perchlorate salts of metal complexes with organic ligands are potentially explosive. Only a small amount of material should be prepared and handled with caution.

2.2. Synthesis of $[Cu_4(L)_2(tp)(dmf)_2]$ (1)

25 mL of a methanolic solution of $Cu(ClO_4)_2 \cdot 6H_2O$ (0.29 g, 0.8 mmol) was added to a magnetically stirred 25 mL methanolic solution of the ligand (H_3L) (0.12 g, 0.4 mmol). The mixture was stirred for 15 min with addition of NEt_3 (0.11 mL, 0.8 mmol), whereby a deep green solution was formed. The disodium salt of terephthalate acid (Na_2tp) (0.04 g, 0.2 mmol) dissolved in 5 mL of water was then added slowly to the above mixture, the green solution was stirred for another 30 min, and after that the resulting solution was refluxed for 2 h. A precipitate appeared, which was filtered. The precipitate was washed with methanol and dried at room temperature. This was dissolved in DMF and the solution was gently warmed. The solution was again filtered and the filtrate was left at room temperature. Dark green colored prismatic single crystals of **1** for X-ray crystallography were obtained on slow evaporation of the filtrate after a few days. (Yield: 65%, 0.15 g). *Anal.* Calc. for $C_{48}H_{48}Cu_4N_6O_{12}$: C, 49.87; H, 4.15; N, 7.27. Found: C, 49.65; H, 3.97; N, 7.07%. FT-IR (KBr phase) (cm^{-1}): 3432 br, 2939 br, 1665 vs, 1640 vs, 1578 vs, 1451 s, 1386 vs, 1193 w, 1149 w, 754 m, 681 w, 576 w (br, broad; w, weak; m, medium; s, strong; vs, very strong).

2.3. X-ray crystallography

Crystal data for **1**, $C_{48}H_{48}Cu_4N_6O_{12}$, $M = 1155.11$, monoclinic, space group $P2_1/c$ (No. 14), $a = 12.123(1)$, $b = 17.823(2)$, $c = 11.737(1)$ Å, $\beta = 108.82(1)°$, $V = 2400.4(4)$ Å^3, $Z = 2$, $D_c = 1.598\ g\ cm^{-3}$, $F(000) = 1180$. Reflections measured 33 793, independent 5810 with $R_{int} = 0.047$. Empirical absorption correction, SADABS ($T_{max} = 1.00$, $T_{min} = 0.755$). Final R_2 (F^2, all reflections) = 0.056, $R_{2w} = 0.084$, conventional $R_1 = 0.035$ for 334 parameters, GoF = 1.01. Bruker SMART CCD area-detector, Mo Kα radiation ($\lambda = 0.71073$ Å), $T = 150$ K, ω scan mode, $\theta_{min} = 3°$, $\theta_{max} = 28.00°$. The structure was solved by direct methods (SHELXS) and refined by full-matrix least squares with anisotropic thermal parameters for non-hydrogen atoms. Hydrogen atoms were partly refined with fixed isotropic thermal parameters, and partly placed in calculated positions. Atoms H1–H6 cannot be placed in ideal positions because carbon atoms C23 and C24 are bonded to an sp^2 nitrogen atom. Atoms H1–H6 can be placed in staggered positions in two ways, and there is no manner to predict which one is correct. Therefore, it is necessary to find them in the Fourier map and at this point there is no indication that they cannot be refined isotropi-

cally, as we have done. The program used was Personal SDP on a Pentium III PC.

2.4. DNA-binding and cleavage experiments

The concentration of CT DNA was determined from the absorption intensity at 260 nm with a known ε value of 6600 M^{-1} cm^{-1} [43]. The binding of **1** to CT DNA has been studied by the fluorescence spectral method using the emission intensity of EB. The apparent binding constant, K_{app}, for **1** was estimated by the equation: $K_{EB}[EB] = K_{app}[complex]$ where K_{EB} is 1.0×10^7 M^{-1} [44].

The DNA cleavage experiment was done by agarose gel electrophoresis. Supercoiled (SC) pUC19 DNA (2.5 μL, 0.5 μg) in Tris–HCl buffer (50 mM, pH 7.2) containing NaCl (50 mM) was treated with complex **1** in the presence or absence of additives. The DNA cleavage by **1** (10–35 μM) was studied in the presence of H_2O_2 (60–80 μM). The experimental samples were incubated first for 60 min at 37 °C and after that loading buffer (25% bromophenol, 30% glycerol (3 μL), 0.25% xylene cyanol) was added. It was finally loaded on 1% agarose gel containing 1.0 μg mL^{-1} EB. Electrophoresis was carried out at 40 V for 2.0 h in tris-acetate EDTA (TAE) buffer. The cleavage activity was measured by determining the ability of **1** in relaxing the SC DNA to its nicked circular (NC) form. Bands were visualized by UV light and photographed. The proportion of DNA in the SC and NC forms after electrophoresis was estimated quantitatively from the intensities of the bands by using a UVITEC Gel Documentation System with due correction of the low level of NC present in the original sample and the low affinity of EB binding to SC compared to NC forms of DNA [45]. Control experiments were done using different reagents such as DMSO (4 μL), distamycin (100 μM), NaN_3 (5 mM), 3-mercaptopropionic acid (MPA, 5 mM) and dithiothreitol (DTT, 5 mM) added to SC DNA prior to the addition of **1**.

3. Results and discussion

3.1. Crystal structure of *1*

Complex **1** is centrosymmetric and crystallizes from *N*,*N*-dimethylformamide in the monoclinic system, space group $P2_1/c$ (No. 14). The dinucleating pentadentate character of the ligand (H_3L) and the desired pair-of-dimers arrangement, through the incorporation of the bridging terephthalate moiety, is clearly evident and shown in Fig. 1. The copper atoms are coordinated in a slightly distorted square pyramidal arrangement within each dinucleating half of the complex and bridged mono-atomically by the secondary alkoxo oxygen of the ligand and di-atomically by the terephthalate moiety. The apical position is occupied by the oxygen atom (O(6)) of the dmf (*N*,*N*′-dimethylformamide). The dmf molecule bridges two copper atoms (Cu(1) and Cu(2)) of each dinucleating half by a μ_2-oxygen atom in an unsymmetrical manner. The distances between Cu(1)–O(6) and Cu(2)–O(6) are 2.345(2) and 2.565(2) Å, respectively. This is comparable to the Cu–O distances in some of the reported DMF coordinated complexes [46–50]. The dihedral angle between the [$CuNO_3$] moieties is 115.2(1)°, and a consequent bending of the molecule from coplanarity is evident. The intramolecular distance between Cu(1) and Cu(2) of each dinucleating half is 3.076(1) Å. This is comparable to the Cu–Cu distances in some of the terephthalate bridged complexes [51,52]. The Cu(1)–O(2)–Cu(2) bridging angle is 104.3(1)° and the angle at which the plane of the terephthalate moiety intersects the plane encompassing the Cu(1)–O(2)–Cu(2) bridge is 103.2(1)°. The pertinent across-terephthalate intramolecular copper-to-copper separations are Cu(1)–Cu(1A) 11.187(1) Å, Cu(2)–Cu(2A) 11.204(1) Å and Cu(1)–Cu(2A) 10.765(1) Å. Further important bond lengths and angles are given in Table 1.

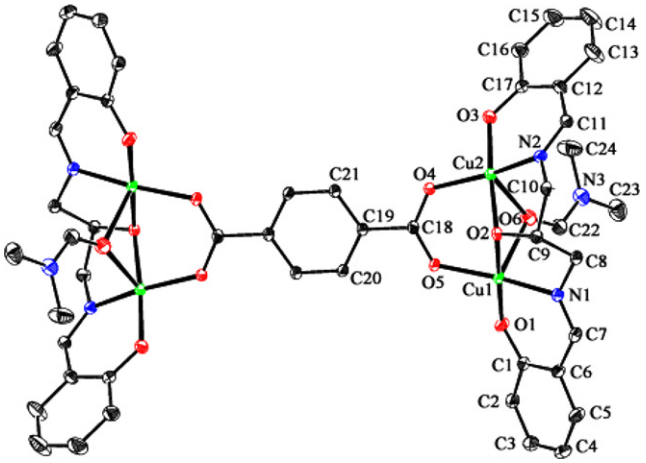


Fig. 1. ORTEP drawing and atom numbering scheme for $[Cu_4(L)_2(tp)(dmf)_2]$ (**1**), (H atoms are omitted for clarity).

The concept that C–H–O interactions exist as significant secondary interactions, and occasionally assumes the dominant interaction [53] in molecular solids is now well established [54,55]. Fig. 2 shows the molecular packing for **1** in

Table 1
Selected bond distances (Å) and bond angles (°) for $[Cu_4(L)_2(tp)(dmf)_2]$ (**1**)

Cu1–O1 1.9090(18)	Cu2–O2 1.9429(14)
Cu1–O2 1.9527(16)	Cu2–O3 1.898(2)
Cu1–O5 1.9680(12)	Cu2–O4 1.9689(13)
Cu1–O6 2.3453(16)	Cu2–O6 2.5651(18)
Cu1–N1 1.930(2)	Cu2–N2 1.916(2)
O1–Cu1–O2 174.76(6)	O2–Cu2–O4 93.22(7)
O1–Cu1–O5 90.81(6)	O2–Cu2–O6 81.62(6)
O1–Cu1–O6 96.92(6)	O2–Cu2–N2 84.89(8)
O1–Cu1–N1 92.00(7)	O3–Cu2–O4 89.74(7)
O2–Cu1–O5 91.78(6)	O3–Cu2–O6 94.46(7)
O2–Cu1–O6 87.42(6)	O3–Cu2–N2 93.34(8)
O2–Cu1–N1 84.73(7)	O4–Cu2–O6 90.41(7)
O5–Cu1–O6 94.30(7)	O4–Cu2–N2 163.83(10)
O5–Cu1–N1 170.44(9)	O6–Cu2–N2 105.15(8)
O6–Cu1–N1 94.42(9)	Cu1–O2–Cu2 104.32(6)
O2–Cu2–O3 175.10(6)	

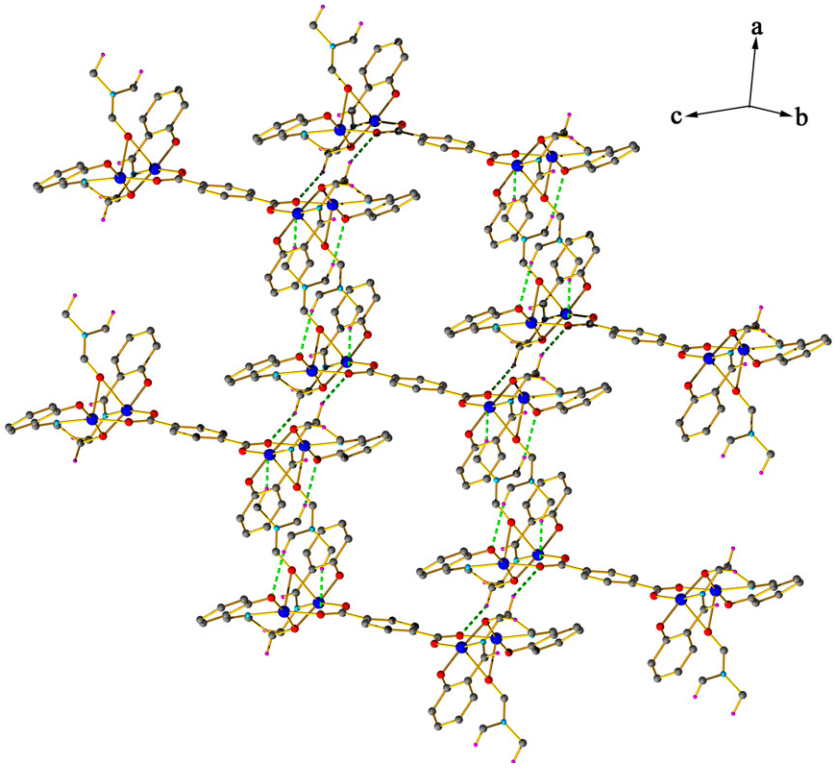


Fig. 2. The perspective view of the packing of **1** showing the intermolecular C–H–O hydrogen bonding (dotted green color) interactions between C23–H3–O5[a], C24–H6–O1[a] (a = 1 − *x*, −*y*, 1 − *z*) and C9–H14–O5[b] (b = −*x*, −*y*, 1 − *z*) along the *ac*-plane. Color codes: ■ Cu, ■ N, ■ O, ■ C, ■ H. (For interpretation of the references to color in this figure legend, the reader is referred to the web version of this article.)

which the molecules in the crystal are held together by intermolecular C–H–O hydrogen bonding interactions. Intermolecular hydrogen bonding occurs between C23–H3–O5[a], C24–H6–O1[a] (a = 1 − *x*, −*y*, 1 − *z*) and C9–H14–O5[b] (b = −*x*, −*y*, 1 − *z*) along the *ac*-plane (Fig. 2), as evident by their C–H–O distances 2.36, 2.56 and 2.54 Å (having C–H–O angles 155, 165 and 143°, respectively) being shorter than the corresponding van der Waals separation. Other intermolecular hydrogen bonds C10–H16–O3[c], C11–H17–O3[c], C11–H17–O4[c] (c = *x*, 1/2 − *y*, 1/2 + *z*) (having H–O distances 2.53, 2.40 and 2.54 Å and C–H–O angles 147, 134 and 149°, respectively) are operating along the *b*-axis (not shown in Fig. 2). These hydrogen bond distances are comparable to some of the reported systems [56,57]. Hydrogen-bond distances and bond angles are given in Table 2.

Table 2
Selected bond distances (Å) and bond angles (°) for $[Cu_4(L)_2(tp)(dmf)_2]$ (**1**)

D–H–A	D–H (Å)	H–A (Å)	D–A (Å)	D–H–A (°)
C23–H3–O5[a]	1.06	2.36	3.3572	155
C24–H6–O1[a]	0.91	2.56	3.4505	165
C9–H14–O5[b]	0.97	2.54	3.3632	143
C10–H16–O3[c]	0.97	2.53	3.3822	147
C11–H17–O3[c]	0.97	2.40	3.1541	134
C11–H17–O4[c]	0.97	2.54	3.4124	149

Symmetry codes:
a = 1 − *x*, −*y*, 1 − *z*; b = −*x*, −*y*, 1 − *z*; c = *x*, 1/2 − *y*, 1/2 + *z*.

3.2. Magnetic property

The magnetic susceptibility of complex **1** has been measured in the temperature range 300–2 K under an external field of 1000 Oe. The temperature dependence of χ_M of the $[Cu_2L]$ unit is shown in Fig. 3a. Upon cooling, χ_M increases reaching a maximum of 68.16×10^{-2} cm^3 mol^{-1} at around 2 K. The observed $\chi_M T$ product at room temperature (300 K), 1.04 cm^3 mol^{-1} K, is larger than the spin-only values of 0.75 cm^3 mol^{-1} K expected for two isolated copper(II) ions ($S = 1/2$) assuming $g = 2.00$. As the temperature is lowered, the $\chi_M T$ value continuously increases and reaches a value of 1.04 cm^3 mol^{-1} K at 2 K. Such behavior is characteristic of a dominant ferromagnetic interaction in complex **1**. This ferromagnetic interaction between the Cu^{2+} ions is probably due to the lower Cu1–O6–Cu2 angle (77.44(5)°), quite far from 90°, of the DMF bridged copper ions.

$$\chi = \frac{Ng^2\beta^2}{kT}\left[3 + \exp\left(\frac{-2J}{kT}\right)\right]^{-1}(1-P) + \frac{Ng^2\beta^2 P}{4kT} + N_\alpha \quad (1)$$

The data were first treated by applying a modified Bleaney and Bowers [58] Eq. (1), calculated for two $S = 1/2$ centers under a $-2JS_1S_2$ spin Hamiltonian, using a non-linear least-squares fitting routine which assumes that the two dinuclear moieties have no cross-ligand (H_3L) coupling, as would be expected. All the symbols in Eq. (1) have their usual meaning and P is the fraction of monomeric impu-

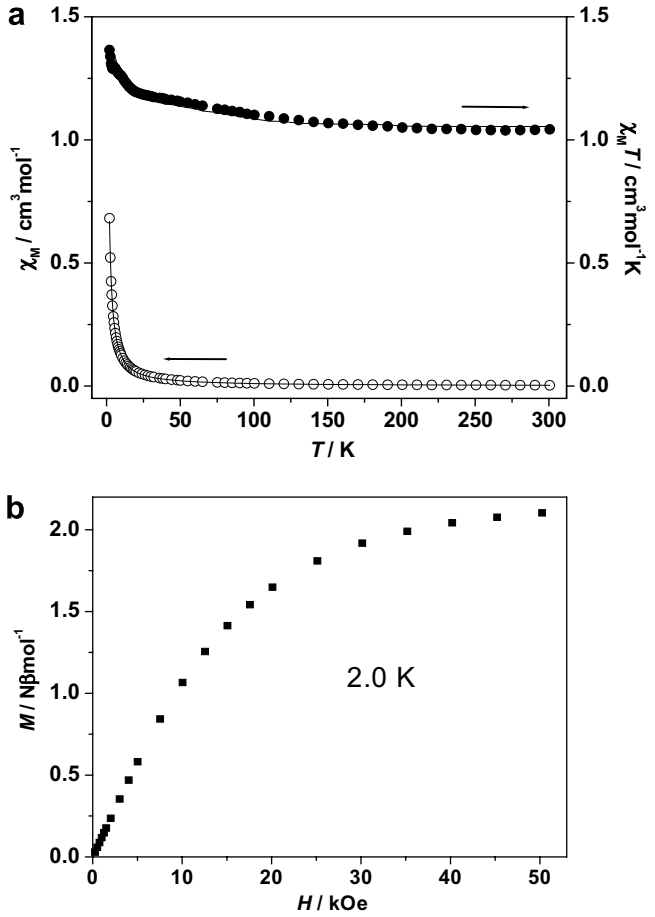


Fig. 3. (a) χ_M and $\chi_M T$ vs. T (□) under an applied magnetic field of 1000 Oe for **1** from 2 to 300 K. (b) The field dependent magnetization (■) at 2 K up to 50 KOe.

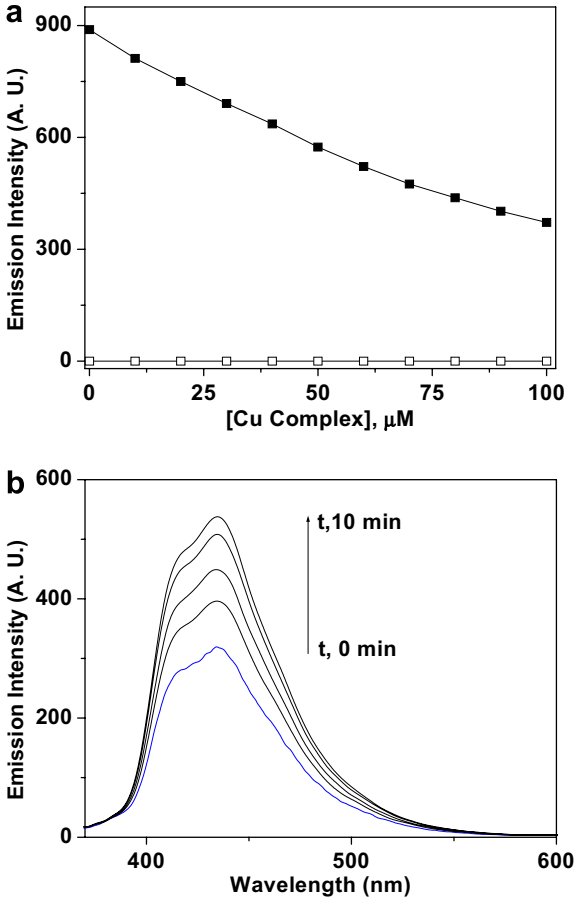


Fig. 4. (a) The effect of addition of complex **1** (■) on the emission intensity of 50 μM CT DNA-bound ethidium bromide in Tris–HCl/NaCl buffer (50 mM, pH 7.2) at 25 °C; (□) on the emission intensity of the ethidium bromide in absence of CT DNA but at different concentrations of **1**. (b) Emission spectra of complex **1** (10 μM) in the presence of CT DNA (397 μM) showing enhancement of intensity at 435 nm (excitation wavelength: 340 nm) with time in Tris–HCl/NaCl buffer (50 mM, pH 7.2). Blue line indicates the emission of **1**. (For interpretation of the references to color in this figure legend, the reader is referred to the web version of this article.)

rity. An excellent fit was obtained (Fig. 3a) using the parameter values $g = 2.24$, $2J = 18.70\ \text{cm}^{-1}$, $P = 0.012$ and $N_\alpha = 20 \times 10^{-6}\ \text{cm}^3\ \text{mol}^{-1}$. The field dependent magnetization at 2 K up to 50 KOe was also measured (Fig. 3b) with $M = 2.1\ \mu_B$ at 50 KOe, slightly larger than the $M_S = 2\ \mu_B$ for two isolated Cu^{2+} ions, confirming the dominant ferromagnetic coupling.

3.3. DNA-binding and cleavage studies

The binding of **1** to CT DNA has been studied by the fluorescence spectral method using the emission intensity of EB. EB does not show any emission in buffer medium due to fluorescence quenching by solvent molecules [59]. In the presence of CT DNA, it shows emission due to its intercalative binding to DNA. Addition of **1** results in the competitive binding to DNA, causing a reduction of the emission intensity. This is due to the displacement of EB from the DNA bound state to the free state, and the copper(II) complex from the free state to the DNA bound state. We have measured the reduction of emission intensity of EB at different concentrations of **1**, as shown in Fig. 4a. The apparent binding constant (K_{app}) has been calculated from the equation: $K_{EB}[EB] = K_{app}[complex]$, ($Kapp(EB) = 1.0 \times 10^7\ M^{-1}$) and the concentration of EB is 50 μM. The concentration of the complex is taken for observing 50% reduction of the emission intensity of EB [44]. The K_{app} value for complex **1** is estimated as $1.25 \times 10^7\ M^{-1}$ and is comparable to reported values [35,36].

Complex **1** is emissive at 435 nm (340 nm excitation) in Tris–HCl/NaCl buffer (50 mM, pH 7.2). The emission spectral changes of **1** in the presence of CT DNA have been studied. The emission intensity is found to increase with time until it reaches a constant value after *ca.* 10 min (Fig. 4b). The corresponding enhancement (at 435 nm) with longer times is due to significant intercalative binding [35].

Fig. 5 displays the CD spectra of CT DNA treated with **1** with the ratio of 0.1, 0.3, 0.5 and 0.7 (complex/DNA). Both the positive (~275 nm) and negative (~245 nm)

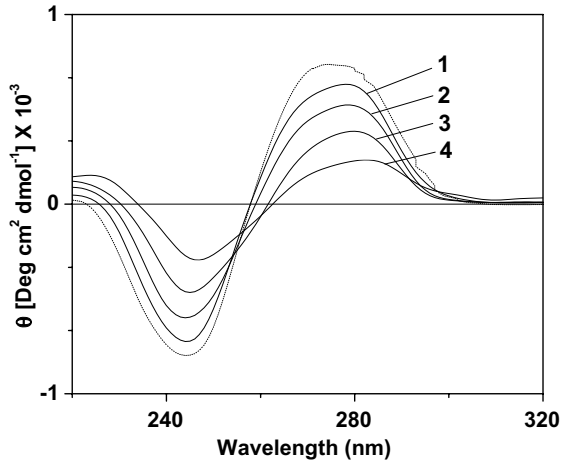


Fig. 5. CD spectra of CT DNA (100 μM) in the absence (·····) and presence (—) of complex **1** at the ratio [Cu complex]/[DNA] = 1:0.1, 2:0.3, 3:0.5 and 4:0.7.

bands decreased in intensity with the increase of the complex concentration. This suggests the Cu complex can unwind the DNA helix and lead to loss of helicity [60]. From the results of fluorescence and CD spectroscopic studies, one can conclude that **1** effectively binds to CT DNA.

A question may hang about the exact nature of the complex species involved in binding. The diffuse reflectance spectrum of **1** at 694 nm shows the characteristics of a CuO_4N core with the copper ion in a square pyramidal environment. In the working buffer medium, the electronic spectrum shows a blue shift of *ca.* 24 nm (Fig. 6). This is quite significant and indicates a modification of the coordination sphere of the metal ion during the intercalative interaction. In order to confirm that the complex remains in the solvent, the electron spray mass spectrum of **1** was obtained in water. The spectrum (Fig. 7) shows a peak at 1008.8 that can be assigned to the tetranuclear species $[Cu_4(L)_2(tp)]$ which corroborates the presence of the tetra-

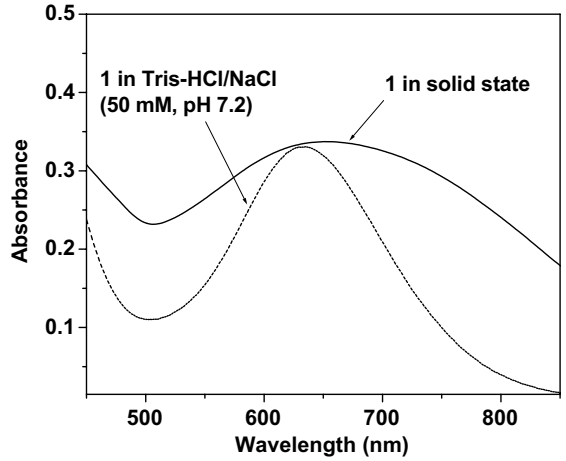


Fig. 6. Absorption spectra of **1** in the solid state and in Tris–HCl/NaCl buffer (50 mM, pH 7.2).

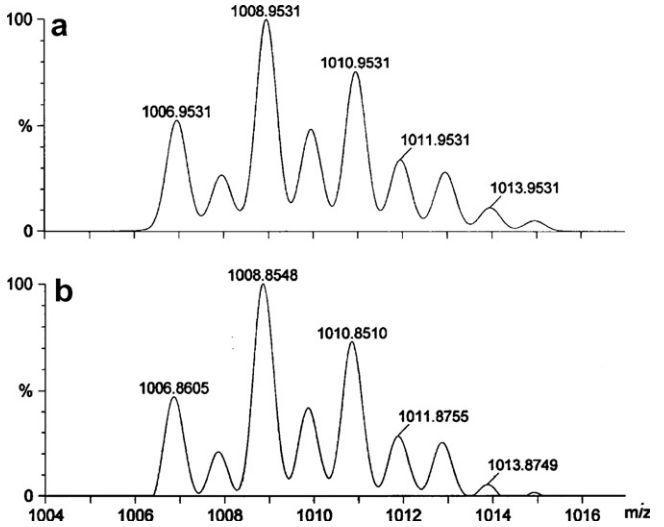


Fig. 7. Electron spray mass spectrum of **1** shows a peak at 1008.8 that can be assigned to the tetranuclear species $[Cu_4(L)_2(tp)]$. The isotopic distributions for the above molecular species in water obtained experimentally (a) correspond to the simulated patterns (b).

nuclear complex entity in solution with a modification of the coordination sphere of the metal ion. The isotopic distributions for the above molecular species in water obtained experimentally correspond to the simulated patterns (Fig. 7).

The ability of complex **1** to perform DNA cleavage has been studied by gel electrophoresis using supercoiled (SC) pUC19 DNA in Tris–HCl/NaCl buffer (50 mM, pH 7.2). The tetranuclear copper(II) complex on reaction with DNA in the presence of H_2O_2 as an oxidizing agent presents high nuclease activity (Fig. 8). In the presence of MPA (3-mercaptopropionic acid) and DTT (dithiothreitol), the compound is inactive towards any cleavage. A 35 μM solution of **1** cleaves SC DNA (0.5 μg) to the extent of ~94% on treatment with 60 μM H_2O_2. A significant cleavage (~83%) is also observed at 30 μM complex concentration using 60 μM H_2O_2. **1** could mediate the conversion of most of the supercoiled DNA to the nicked form at 35 μM, and it could not induce the conversion of SC to the

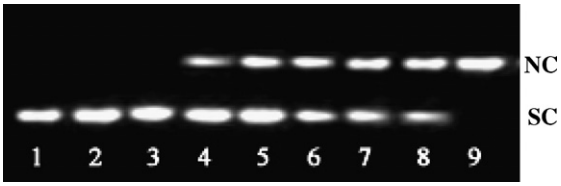


Fig. 8. Agarose gel electrophoresis diagram showing the cleavage of SC pUC19 DNA (0.5 μg) by complex **1**treated with various concentrations of H_2O_2in Tris–HCl/NaCl buffer (50 mM, pH 7.2). Incubation time: 1 h (37 °C). Lane 1: DNA control; lane 2: DNA + H_2O_2 (80 μM); lane 3: DNA + **1** (35 μM); lane 4: DNA + H_2O_2 (80 μM) + **1** (5 μM); lane 5: DNA + H_2O_2 (80 μM) + **1** (10 μM); lane 6: DNA + H_2O_2 (80 μM) + **1** (20 μM); lane 7: DNA + H_2O_2 (60 μM) + **1** (20 μM); lane 8: DNA + H_2O_2 (60 μM) + **1** (30 μM). lane 9: DNA + H_2O_2 (60 μM) + **1** (35 μM).

linear form at the tested concentrations DNA cleavage data of SC pUC19 DNA by **1** on treatment with hydrogen peroxide are given in Table 3. In fact a comparison of lanes 3 and 4 [DNA + H_2O_2 (60 μM) + $CuCl_2 \cdot 2H_2O$ (30 μM); DNA + H_2O_2 (60 μM) + $CuCl_2 \cdot 2H_2O$ (40 μM), respectively] with lane 6 [DNA + H_2O_2 (60 μM) + **1** (35 μM)] shows that **1** cleaves completely the SC DNA to NC (nicked circular) DNA while the Cu(II) salt shows only ~4–8% cleavage (Fig. 9). The control experiments, under aerobic conditions, show that H_2O_2 (80 μM) or **1** (35 μM) alone is cleavage inactive. DNA cleavage data by **1** in the presence of potential inhibitors and the copper(II) salt are given in Table 4. Control experiments also show that the addition of distamycin completely inhibits the cleavage of SC DNA which indirectly supports the minor groove binding of **1** (lane 5, Fig. 9).

Experiments with different scavenging agents were carried out to identify the intermediate reactive oxygen species (ROS) that might be formed in the DNA cleavage reaction (Fig. 10). The addition of NaN_3 to the system was found to have little effect on DNA cleavage, suggesting that singlet oxygen and H_2O_2 are not the effective ROS for the cleavage. The addition of 4 μL and 6 μL DMSO could inhibit

Table 3
DNA cleavage data[a] of SC pUC19 (0.5 μg) DNA by **1** on chemical oxidation by hydrogen peroxide

Number of chemical nuclease data	Reaction conditions	[H_2O_2] (μM)	[**1**] (μM)	DNA cleavage % NC
1	DNA control			2
2	DNA + H_2O_2	80		3
3	DNA + **1**		35	3
4	DNA + H_2O_2 + **1**	80	5	15
5	DNA + H_2O_2 + **1**	80	10	35
6	DNA + H_2O_2 + **1**	80	20	50
7	DNA + H_2O_2 + **1**	60	20	62
8	DNA + H_2O_2 + **1**	60	30	83
9	DNA + H_2O_2 + **1**	60	35	94

[a] Incubation time 1 h.

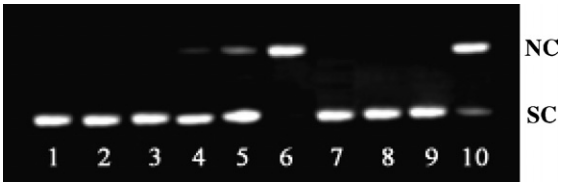


Fig. 9. Agarose gel electrophoresis diagram showing the cleavage of SC pUC19 DNA (0.5 μg) by complex **1** treated with H_2O_2 and potential inhibitors in Tris–HCl/NaCl buffer (50 mM, pH 7.2). Incubation time: 1 h (37 °C). Lane 1: DNA control; lane 2: DNA + H_2O_2 (80 μM); lane 3: DNA + H_2O_2(60 μM) + $CuCl_2 \cdot 2H_2O$ (30 μM); lane 4: DNA + H_2O_2 (60 μM) + $CuCl_2 \cdot 2H_2O$ (40 μM); lane 5: DNA + H_2O_2 (60 μM) + **1** (35 μM) + distamycin (100 μM); lane 6: DNA + H_2O_2 (60 μM) + **1** (35 μM); lane 7: DNA + dithiothreitol (DTT, 5 mM) + **1** (35 μM); lane 8: DNA + 3-mercaptopropionic acid (MPA, 5 mM) + **1** (35 μM); lane 9: DNA + H_2O_2 (60 μM) + **1** (35 μM) + DMSO (4 μL); lane 10: DNA + H_2O_2 (60 μM) + **1** (35 μM) + NaN_3 (5 mM).

Table 4
DNA cleavage data[a] of SC pUC19 (0.5 μg) DNA by **1** in the presence of potential inhibitors and copper(II) salt

Number of chemical nuclease data	Reaction conditions	[H_2O_2] (μM)	[**1**] (μM)	[Cu(II)] (μM)	DNA cleavage %NC
1	DNA control				2
2	DNA + H_2O_2	80			3
3	DNA + H_2O_2 + $CuCl_2 \cdot 2H_2O$	60		30	4
4	DNA + H_2O_2 + $CuCl_2 \cdot 2H_2O$	60		40	8
5	DNA + H_2O_2 + **1** + distamycin (100 μM)	60	35		11
6	DNA + H_2O_2 + **1**	60	35		94
7	DNA + dithiothreitol (DTT, 5 mM) + **1**		35		3
8	DNA + 3-mercaptopropionic acid (MPA, 5 mM) + **1**		35		4
9	DNA + H_2O_2 + **1** + DMSO (4 μL)	60	35		4
10	DNA + H_2O_2 + **1** + NaN_3 (5 mM)	60	35		86

[a] Incubation time 1 h.

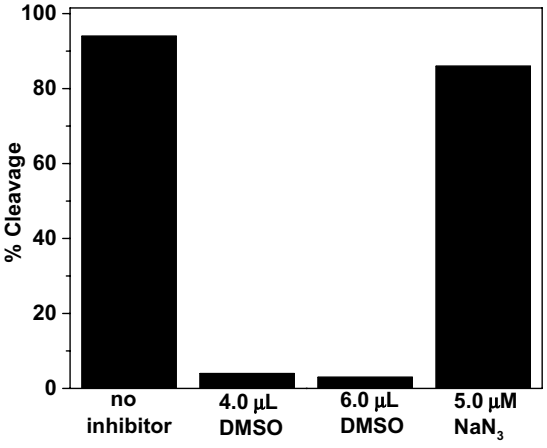


Fig. 10. Histogram representing overall strand scission (nicked form) of pUC19 plasmid DNA by **1** (35 μM) and H_2O_2 (60 μM) in the presence of standard radical scavengers.

completely the cleavage process mediated by **1**. This suggests the possible involvement of diffusible hydroxyl radicals (HO•) as the reactive species. Moreover, since the complex is not able per se to induce any effect on double-stranded DNA (Fig. 8), it appears that an oxidizing agent is required for producing the cleavage process.

To better understand the mechanism of the cleavage reaction we studied the visible spectral changes on addition of H_2O_2 to an aqueous solution of **1**. The absorption maximum ($\lambda_{max} = 635$ nm) due to the d–d transition decreased with increasing concentration of H_2O_2 (Fig. 11). This result suggests that the Cu(II) in the complex is reduced to Cu(I) by H_2O_2. For this reduction process we propose the following mechanism: [61]

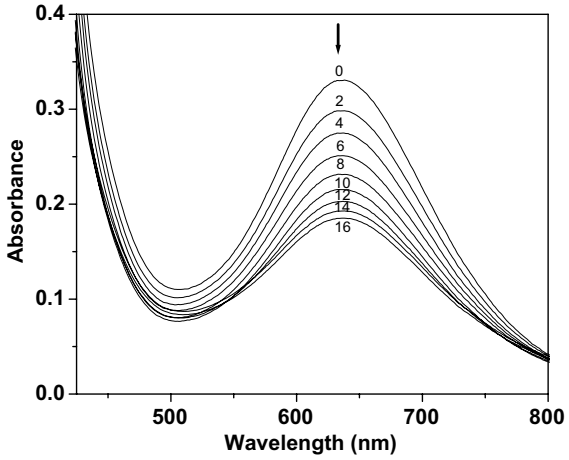


Fig. 11. Visible spectral changes of **1** (1.3 mM) in aqueous solution by addition of different amounts of H_2O_2. 2, 4, 6, 8, 10, 12, 14 and 16 μL of H_2O_2 35%.

$$Cu^{II}(L) + H_2O_2 \rightarrow Cu^{I}(L) + 2H^+ + O_2^-$$

The hydroxyl radicals involved in the cleavage process can be generated from the Cu(I) compound by a Fenton or a Haber–Weiss mechanism:

$$Cu^{I}(L) + H_2O_2 \rightarrow Cu^{II}(L) + HO^{\cdot} + OH^-$$

$$Cu^{I}(L) + O_2 \rightarrow Cu^{II}(L) + O_2^-$$

$$O_2^- + H_2O_2 \rightarrow O_2 + HO^{\cdot} + OH^-$$

On comparison of the cleavage property with some reported results [35,62,63] of Cu(II) complexes, we note that a lesser amount of oxidizing agents (here hydrogen peroxide) and complex are required in our case for maximum cleavage of DNA. The cleavage data clearly show that more than 90% cleavage occurs with a very small amount of complex concentration (35 μM).

4. Conclusions

A new terephthalate-bridged tetranuclear copper(II) metallointercalator (**1**) derived from a N_2O_3-donor Schiff base ligand H_3L has been synthesized and structurally characterized by X-ray crystallography. The copper atoms are coordinated in a slightly distorted square pyramidal arrangement within each dinucleating half of the complex, and bridged mono-atomically by the secondary alkoxo oxygen of the ligand and di-atomically by the terephthalate moiety. The apical position is occupied by the oxygen atom of dmf. The structure of **1** reveals a short intramolecular Cu–Cu separation (*ca.* 3.1 Å), in combination with long intramolecular copper separations (*ca.* 11 Å). The variable temperature-dependent susceptibility measurement (2–300 K) of **1** reveals a dominant ferromagnetic coupling, $2J = 18.70\ cm^{-1}$. Complex **1** binds to double-stranded CT (calf-thymus) DNA with a K_{app} value of $1.25 \times 10^7\ M^{-1}$ and displays efficient cleavage of supercoiled pUC19 DNA in the presence of H_2O_2 following a hydroxyl radical pathway. The results are of significance in designing a new transition metal complex based on a simple Schiff base ligand as an inorganic complex nuclease.

Acknowledgements

K.D. acknowledges the Council of Scientific and Industrial Research, New Delhi, India, for financial support. The authors appreciate the cooperation received from Professor Song Gao, College of Chemistry and Molecular Engineering, State Key Laboratory of Rare Earth Materials Chemistry and Applications, Department of Chemistry, Peking University, Beijing 100 871, PR China for his kind help in variable temperature-dependent susceptibility measurement.

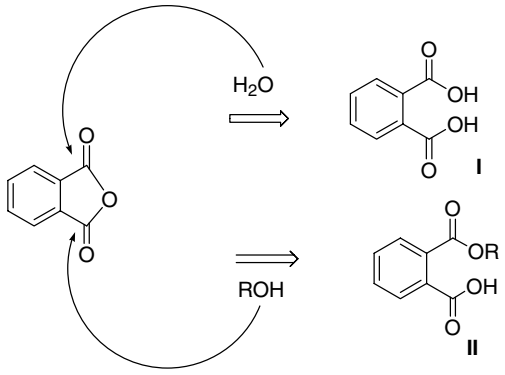
Appendix A. Supplementary material

CCDC 633735 contains the supplementary crystallographic data for **1**. These data can be obtained free of charge via http://www.ccdc.cam.ac.uk/conts/retrieving.html, or from the Cambridge Crystallographic Data Centre, 12 Union Road, Cambridge CB2 1EZ, UK; fax: (+44) 1223-336-033; or e-mail: deposit@ccdc.cam.ac.uk. Supplementary data associated with this article can be found, in the online version, at doi:10.1016/j.poly.2007.06.009.

References

[1] C. Liu, M. Wang, T. Zhang, H. Sun, Coord. Chem. Rev. 248 (2004) 147.
[2] S.J. Franklin, Curr. Opin. Chem. Biol. 5 (2001) 201.
[3] A. Sreedhara, J.A. Cowan, J. Biol. Inorg. Chem. 6 (2001) 337.
[4] J.A. Cowan, Curr. Opin. Chem. Biol. 5 (2001) 634.
[5] R. Ott, R. Krämer, Appl. Microbiol. Biotechnol. 52 (1999) 761.
[6] M. Komiyama, N. Takeda, H. Shigekawa, Chem. Commun. (1999) 1443.
[7] M. Komiyama, J. Sumaoka, Curr. Opin. Chem. Biol. 2 (1998) 751.
[8] E.L. Hegg, J.N. Burstyn, Coord. Chem. Rev. 173 (1998) 133.
[9] F. Mancin, P. Scrimin, P. Tecilla, U. Tonellato, Chem. Commun. (2005) 2540.
[10] K.E. Erkkila, D.T. Odom, J.K. Barton, Chem. Rev. 99 (1999) 2777.
[11] G. Pratviel, J. Bernadou, B. Meunier, Adv. Inorg. Chem. 45 (1998) 251.
[12] M.M. Meijler, O. Zelenko, D.S. Sigman, J. Am. Chem. Soc. 119 (1997) 1135.
[13] J.K. Bashkin, B.N. Trawick, A.T. Daniher, M. Oivanen, S. Kuusela, H. Lönnberg, D.-M. Zhou, K. Taira, R.G. Kuimelis, L.W. McLaughlin, R.T. Raines, J.A. Cowan, W.K. Pogozelski, T.D. Tullius, C.J. Burrows, J.G. Muller, R.M. Burger, B. Armitage, D.R. McMillin, K.M. McNett, S.S. David, S.D. Williams, Chem. Rev. 98 (1998) 937–1262, thematic issue (no. 3) on RNA/DNA cleavage.
[14] B.N. Trawick, A.T. Daniher, J.K. Bashkin, Chem. Rev. 98 (1998) 939.
[15] M. Dizdaroglu, Mutat. Res. 275 (1992) 331.
[16] B. Halliwell, O.I. Aruoma, FEBS Lett. 281 (1991) 9.
[17] M. Dizdaroglu, Free Radical Biol. Med. 10 (1991) 225.
[18] M. Maccabee, J.S. Evans, M.P. Glackin, Z. Hahahet, S.S. Wallace, J. Mol. Biol. 234 (1994) 514.

[19] D.I. Feig, L.C. Sowers, L.A. Loeb, Proc. Natl. Acad. Sci. USA 91 (1994) 6609.
[20] M. Moriya, C. Ou, V. Bodepudi, F. Johnson, M. Takeshita, A.P. Grollman, Mutat. Res. 254 (1991) 281.
[21] S.A. Akman, G.P. Forrest, J.H. Doroshow, M. Dizdaroglu, Mutat. Res. 261 (1991) 123.
[22] M.L. Wood, M. Dizdaroglu, E. Gajewski, J.M. Essigmann, Biochemistry 29 (1990) 7024.
[23] A.K. Basu, E.L. Loechler, S.A. Leadon, J.M. Essigmann, Proc. Natl. Acad. Sci. USA 86 (1989) 7677.
[24] C.E. Yoo, P.S. Chae, J.E. Kim, E.J. Jeong, J. Suh, J. Am. Chem. Soc. 125 (2003) 14580.
[25] A. Bencini, E. Berni, A. Bianchi, C. Giorgi, B. Valtancoli, D.K. Chand, H.-J. Schneider, J. Chem. Soc., Dalton Trans. (2003) 793.
[26] K.J. Humphreys, K.D. Karlin, S.E. Rokita, J. Am. Chem. Soc. 124 (2002) 8055.
[27] K.J. Humphreys, K.D. Karlin, S.E. Rokita, J. Am. Chem. Soc. 124 (2002) 6009.
[28] K.J. Humphreys, A.E. Johnson, K.D. Karlin, S.E. Rokita, J. Biol. Inorg. Chem. 7 (2002) 835.
[29] K.J. Humphreys, K.D. Karlin, S.E. Rokita, J. Am. Chem. Soc. 123 (2001) 5588.
[30] M.P. Suh, M.Y. Han, J.H. Lee, K.S. Min, C. Hyeon, J. Am. Chem. Soc. 120 (1998) 3819.
[31] S.T. Frey, H.H.J. Sun, N.N. Murphy, K.D. Karlin, Inorg. Chim. Acta 242 (1996) 329.
[32] K.J. Humphreys, K.D. Karlin, N. Wei, B. Jung, S. Kaderli, P. Niklaus, A.D. Zuberbühler, J. Am. Chem. Soc. 115 (1993) 9506.
[33] C.J. Burrows, J.G. Muller, Chem. Rev. 98 (1998) 1109.
[34] W.K. Pogozelski, T.D. Tullius, Chem. Rev. 98 (1998) 1089.
[35] K. Dhara, J. Ratha, M. Manassero, X.-Y. Wang, S. Gao, P. Banerjee, J. Inorg. Biochem. 101 (2007) 95.
[36] Y. Zhao, J. Zhu, W. He, Z. Yang, Y. Zhu, Y. Li, J. Zhang, Z. Guo, Chem. Eur. J. 12 (2006) 6621.
[37] M. Scarpellini, A. Neves, R. Ho1rner, A.J. Bortoluzzi, B. Szpoganics, C. Zucco, R.A. Nome Silva, V. Drago, A.S. Mangrich, W.A. Ortiz, W.A.C. Passos, M.C.B. de Oliveira, H. Terenzi, Inorg. Chem. 42 (2003) 8353.
[38] K.M. Deck, T.A. Tseng, J.N. Burstyn, Inorg. Chem. 41 (2002) 669.
[39] D.K. Chand, H.-J. Schneider, A. Bencini, A. Bianchi, C. Giorgi, S. Ciattini, B. Valtancoli, Chem. Eur. J. 6 (2000) 4001.
[40] R. Ren, P. Yang, W. Zheng, Z. Hua, Inorg. Chem. 39 (2000) 5454.
[41] P.E. Kruger, B. Moubaraki, G.D. Fallon, K.S. Murray, J. Chem. Soc., Dalton Trans. (2000) 713.
[42] D.D. Perrin, W.L.F. Armarego, D.R. Perrin, Purification of Laboratory Chemicals, Pergamon Press, Oxford, 1980.
[43] M.E. Reichmann, S.A. Rice, C.A. Thomas, P. Doty, J. Am. Chem. Soc. 76 (1954) 3047.
[44] M. Lee, A.L. Rhodes, M.D. Wyatt, S. Forrow, J.A. Hartley, Biochemistry 32 (1993) 4237.
[45] J. Bernadou, G. Pratviel, F. Bennis, M. Girardet, B. Meunier, Biochemistry 28 (1989) 7268.
[46] J. Niu, Y. Shen, J. Wang, J. Mol. Struct. 733 (2005) 19.
[47] D. Kovala-Demertzi, A. Galani, M .A. Demertzis, S. Skoulika, C. Kotoglou, J. Inorg. Biochem. 98 (2004) 358.
[48] T. Korzeniak, K. Stadnicka, M. Rams, B. Sieklucka, Inorg. Chem. 43 (2004) 4811.
[49] J. Lefebvre, R.J. Batchelor, D.B. Leznoff, J. Am. Chem. Soc. 126 (2004) 16117.
[50] M. Eddaoudi, J. Kim, D. Vodak, A. Sudik, J. Wachter, M. O'Keeffe, O.M. Yaghi, Proc. Nat. Acad. Sci. USA 99 (2002) 4900.
[51] P.S. Mukherjee, D. Ghoshal, E. Zangrando, T. Mallah, N. Ray Chaudhuri, Eur. J. Inorg. Chem. (2004) 4675.
[52] D. Sun, R. Cao, Y. Liang, Q. Shi, W. Su, M. Hong, J. Chem. Soc., Dalton Trans. (2001) 2335.
[53] Z. Berkovitch-Yellin, L. Leiserowitz, Acta Crystallogr. Sect. B 40 (1984) 159.
[54] T. Steiner, Chem. Commun. (1997) 727.
[55] G.R. Desiraju, Acc. Chem. Res. 29 (1996) 441.
[56] G.R. Desiraju, Chem. Commun. (2005) 2995.
[57] H. Matsuura, H. Yoshida, M. Hieda, S. Yamanaka, T. Harada, K. Shin-ya, K. Ohno, J. Am. Chem. Soc. 125 (2003) 13910.
[58] B. Bleaney, K.D. Bowers, Proc. R. Soc. Lond. Ser. A 214 (1952) 451.
[59] M.J. Waring, J. Mol. Biol. 13 (1965) 269.
[60] K. Karidi, A. Garoufis, N. Hadjiliadis, J. Reedijk, J. Chem. Soc., Dalton Trans. (2005) 728.
[61] T. Ozawa, A. Hanaki, K. Onodera, Polyhedron 11 (1992) 735.
[62] R. Cejudo, G. Alzuet, M. González-Álvarez, J.L. García-Gimenez, J. Borrás, M. Liu-González, J. Inorg. Biochem. 100 (2006) 70.
[63] M. González-Álvarez, G. Alzuet, J. Borrás, B. Macías, A. Castiñeiras, Inorg. Chem. 42 (2003) 2992.



Scheme 1.

3. Synthesis and spectroscopic data for compounds III–VII

The complexes of 2,3-pyridine dicarboxylic acid (LH_2) **III–V** and of pyromellitic acid (L_1H_4) were prepared by the reaction procedure given below. All the compounds **III–VII** gave satisfactory elemental analysis when analyzed in the crystalline form; however, for compounds **V–VII** in bulk, a deviation was observed probably due to solvent of crystallization.

$[Ni(LH)_2(H_2O)_2(py)_2]$ (py = pyridine) (**III**): To a solution of 2,3-pyridine dicarboxylic anhydride (0.3 g, 2 mmol) dissolved in methanol (10 ml, at 60 °C) a solution of nickel(II) acetate tetrahydrate (0.248 g, 1 mmol) in methanol (10 ml) was added. The reaction mixture was stirred at room temperature for half an hour and to this mixture pyridine (abbreviated as py) (0.16 g, 2 mmol) was added. The resulting solution on standing gave pink crystals after 4 days (yield 35%). IR (KBr, cm^{-1}): 3414(bs), 1712(m), 1599(m), 1559(s), 1480(s), 1441(s), 1418(m), 1369(s), 1275(s), 1210(s), 1152(m), 1135(m), 1101(s), 1062(m), 871(m), 847(m), 823(m), 754(s), 703(s), 665(s), 629(s), 499(s). Elemental *Anal*. Calc. for $C_{24}H_{18}N_4NiO_8$: C, 52.45; H, 3.28. Found: C, 52.46; H, 3.32%.

$[Co(LH)_2(H_2O)_2$ (**IV**): Compound **IV** was prepared in an analogous manner to **III** by the reaction of 2,3-pyridine dicarboxylic anhydride with cobalt(II)acetate tetrahydrate, but without treatment with pyridine. Yield 86%. IR (KBr, cm^{-1}): 3411(bs), 1675(s), 1562(s), 1440(s), 1373(s), 1265(m), 1178(m), 1102(s), 871(w), 758(m), 661(s), 513(m). Elemental *Anal*. Calc. for $C_{14}H_{12}CoN_2O_{10}$: C, 39.33; H, 2.81. Found: C, 39.41; H, 2.84%.

$[\{Zn_2(L)_3\}bpyH_2.3H_2O]_n$ (bpy = 4, 4′-bipyridine) (**V**): A solution of 2,3-pyridine dicarboxylic anhydride (0.3 g, 2 mmol) was prepared in methanol (10 ml, at 60 °C). To this solution a solution of zinc(II) acetate dihydrate (0.22 g, 1 mmol) in methanol (5 ml) was added. The reaction mixture was stirred at room temperature for half an hour and to this mixture 4,4′-bipyridine (abbreviated as bpy) (0.16 g, 2 mmol) was added. A white precipitate appeared. The precipitate dissolved on addition of water (10 ml) and a white crystalline zinc complex was obtained after 7 days (yield 64%). ^{1}HNMR (DMSO-d_6): 8.67 (t, 4H, $J = 12$ Hz), 8.39 (m, 1H), 8.23 (m, 2H), 8.10 (m, 1H), 7.86 (m, 1H), 7.6 (dm, 4H, $J = 12$ Hz). IR (KBr, cm^{-1}): 3375(bs), 3055(w), 1626(s), 1579(s), 1450(w), 1374(s), 1270(w), 1111(m), 964(m), 813(s), 750(w), 708(m), 678(m), 504(w).

$[Cu(phen)_2Cl]L_1H_3$ (phen = 1,10-phenathroline) (**VI**): Pyromellitic dianhydride (0.218 g, 1 mmol) was dissolved in methanol (10 ml) by stirring for 10 min. A solution of copper (II) chloride dihydrate (0.170 g, 1 mmol) in methanol (5 ml) was added to this solution and stirred further for 10 min. The solution turned green. To this a solution of 1,10-phenanthroline (0.396 g, 2 mmol) in methanol (2 ml) was added and stirred for 1 h. The solution became intense bluish green, with slight turbidity. The solution was left standing for crystallization. After three days green crystals appeared (yield 40%). IR (KBr, cm^{-1}): 3445(w), 3071(w), 1738(s), 1705(s), 1583(s), 1520(s), 1447(s), 1431(s), 1367(s), 1347(s), 1267(s), 11489(m), 1120(s), 1107(s), 995(s), 945(s), 852(s), 721(s), 632(s). UV–Vis λ_{max} (methanol): 735 nm ($\varepsilon = 155\ M^{-1}\ cm^2$) (see Table 1).

$[Cu_2(phen)_4L_1]4H_2O$ (**VII**): To a solution of pyromellitic dianhydride (0.218 g, 1 mmol) dissolved in methanol (10 ml) a solution of cupric acetate monohydrate (0.199 g, 1 mmol) in methanol (5 ml) was added and stirred for 15 min. A blue colored turbid solution appeared. To this a solution of 1,10-phenanthroline (0.396 g, 2 mmol) in methanol (2 ml) was added. The solution became slightly turbid. The solution was stirred overnight, filtered and was allowed to crystallize. After four days blue colored crystals appeared (yield 34%). IR (KBr, cm^{-1}): 3391(bs), 1738(w), 1717(s), 1590(s), 1518(m), 1427(m), 1394(m), 1360(s), 1345(s), 1251(s), 1241(s), 1107(s), 851(s), 811(m), 722(s). UV–Vis λ_{max} (methanol): 737 nm ($\varepsilon = 172.8\ M^{-1}\ cm^2$).

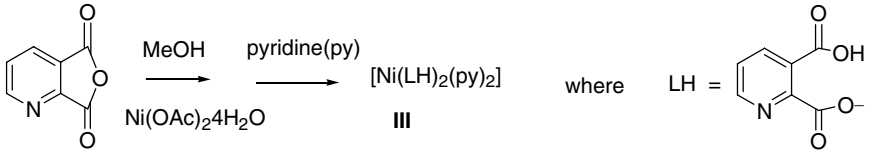
4. Results and discussions

The reaction of 2,3-pyridine dicarboxylic anhydride with first row transition metal acetates of cobalt, nickel and zinc in methanol leads to metal dicarboxylate complexes. These reactions are found to be metal dependent and in none of the cases studied here we could obtain methyl ester containing metal complexes. However, in the absence of metal salts we observed the formation of methyl ester from the reaction of methanol with 2,3-pyridine dicarboxylic anhydride. The reaction of nickel (II) acetate tetrahydrate with 2,3-pyridine dicarboxylic anhydride in methanol followed by treatment with pyridine gave the mono-nuclear nickel complex (**III**), as illustrated in Scheme 2. The structure of the complex is shown in Fig. 1. It has a six coordination environment around the nickel ion with two chelating ligands derived from the 2,3-pyridine dicarboxylato mono anion and two pyridine ligands. The pyridine molecules occupy *trans* positions in the distorted octahedral geometry.

It was observed earlier [5a] that the reaction of phthalic anhydride with nickel acetate along with pyridine in

Table 1
The crystallographic parameters for compounds **III–VI**

Compound number	**III**	**IV**	**V**	**VI**	**VII**
Formulae	$C_{24}H_{18}N_4NiO_8$	$C_{14}H_{12}CoN_2O_{10}$	$C_{34}H_{38}N_6O_{14}Zn$	$C_{34}H_{21}ClCuN_4O_8$	$C_{58}H_{44}Cu_2N_8O_{15}$
Molecular weight	549.13	427.19	820.07	712.54	1220.09
Crystal system	tetragonal	monoclinic	monoclinic	triclinic	monoclinic
Space group	*I*4(1)/*a*	*P*21/*c*	*P*2(1)/*n*	$P\bar{1}$	*C*2/*c*
Temperature (K)	296	296	296	296	296
Wavelength (Å)	0.71073	0.71073	0.71073	0.71073	0.71073
a (Å)	25.6914(3)	9.3165(9)	11.30680(10)	9.7010(3)	12.4826(3)
b (Å)	25.6914(3)	7.9357(8)	6.68510(10)	11.8680(3)	30.7692(9)
c (Å)	7.30540(10)	13.3962(11)	23.5000(3)	14.3806(6)	15.8694(4)
α (°)	90.00	90.00	90.00	102.925(2)	90.00
β (°)	90.00	128.816(5)	103.4950(10)	98.781(2)	98.391(2)
γ (°)	90.00	90.00	90.00	106.799(2)	90.00
V (Å^3)	4821.92(10)	771.699	1727.25(4)	1502.37(9)	6029.9(3)
Z	8	2	2	2	4
D_{calc} (Mg m^{-3})	1.513	1.838	1.577	1.575	1.344
Absolute coefficient (mm^{-1})	0.862	1.177	0.793	0.879	0.776
Absorption correction	none	none	none	none	none
F(000)	2256	434	852	726	2504
Total number of reflections	22883	7867	20983	15255	35509
Reflections, $I > 2\sigma(I)$	3006	1725	4270	6731	7485
Maximum 2*θ* (°)	28.33	28.43	28.32	28.30	28.28
Ranges (*h*,*k*,*l*)	$-34 \leqslant h \leqslant 24$, $-34 \leqslant k \leqslant 33$, $-9 \leqslant l \leqslant 9$	$-8 \leqslant h \leqslant 12$, $-10 \leqslant k \leqslant 9$, $-17 \leqslant l \leqslant 17$	$-15 \leqslant h \leqslant 15$, $-8 \leqslant k \leqslant 8$, $-30 \leqslant l \leqslant 31$	$-11 \leqslant h \leqslant 11$, $-15 \leqslant k \leqslant 15$, $-19 \leqslant l \leqslant 19$	$-16 \leqslant h \leqslant 16$, $-40 \leqslant k \leqslant 30$, $-20 \leqslant l \leqslant 21$
Complete to 2*θ* (%)	99.7	99.3	99.4	90.1	99.9
Refinement method	full-matrix least-squares on F^2	full-matrix least-squares on F^2	full-matrix least-squares on F^2	full-matrix least-squares on F^2	full-matrix least-squares on F^2
Data/restraints/parameters	3006/0/173	1932/0/124	4270/0/274	6731/0/437	7485/0/396
Goodness-of-fit (F^2)	1.038	1.059	1.057	1.014	1.225
R indices [$I > 2\sigma(I)$]	0.0317	0.0334	0.0505	0.0462	0.0934
R indices (all data)	0.0435	0.0759	0.0639	0.0903	0.1301



Scheme 2.

methanol gives the corresponding nickel carboxylato complex of the mono-esterified dicarboxylic acid. These results and the present observations on only the hydrolytic product formation from 2,3-pyridine dicarboxylic anhydride clearly support the coordination effect of the pyridine nitrogen atom in the reaction of nickel(II) acetate tetrahydrate with 2,3-pyridine dicarboxylic anhydride. Complex **III** shows strong intramolecular hydrogen bonding between the OH group of the neutral carboxylic acid and the carbonyl oxygen of another coordinating carboxylato group. The intramolecular hydrogen bonding parameters are d_{D-A} 2.413 Å, d_{D-H} 0.927 Å and ∠D–H···A 173.14 °.

A similar reaction of cobalt(II) acetate tetrahydrate with 2,3-pyridine dicarboxylic anhydride gave a chelated complex with the composition $[Co(LH)_2(H_2O)_2]$ (**IV**). The complex has a six coordination geometry, with the two water molecules occupying *trans*-positions with respect to each other. The structure of the complex is shown in Fig. 2. The complex has intra-molecular hydrogen bonding, O3–H···O2 (d_{D-A} 2.399 Å and ∠D–H···A 179.35°).

The reaction between zinc(II) acetate with 2,3-pyridine dicarboxylic anhydride in methanol followed by treatment with 4,4′-bipyridine gave a polymeric zinc complex (**V**) having the composition $[\{Zn_2(L)_3\}bpyH_2 \cdot 3H_2O]_n$, where L = the 2,3-pyridine dicarboxylato dianion and $bpyH_2$ = the 4,4′-bipyridinium dication, n is an integer. In this case also no methyl-ester was observed. The backbone of the polymer is shown in Fig. 3b. In this complex each zinc

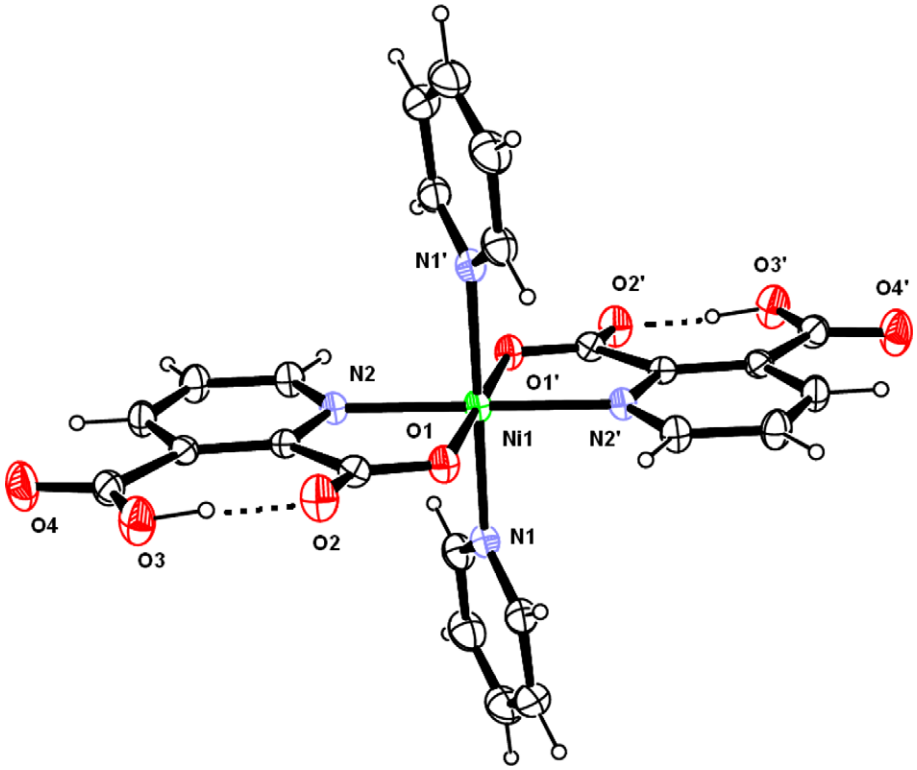


Fig. 1. Structure of complex (**III**) (Drawn with 20% thermal ellipsoids). Some selected bond distances (Å) and angles (°) are Ni1–N2, 2.05; Ni1–N1, 2.13; Ni1–O1, 2.03; ∠N1–Ni1–O1, 89.21; ∠N2–Ni1–O1, 100.89; ∠N1–Ni1–N2, 90.80.

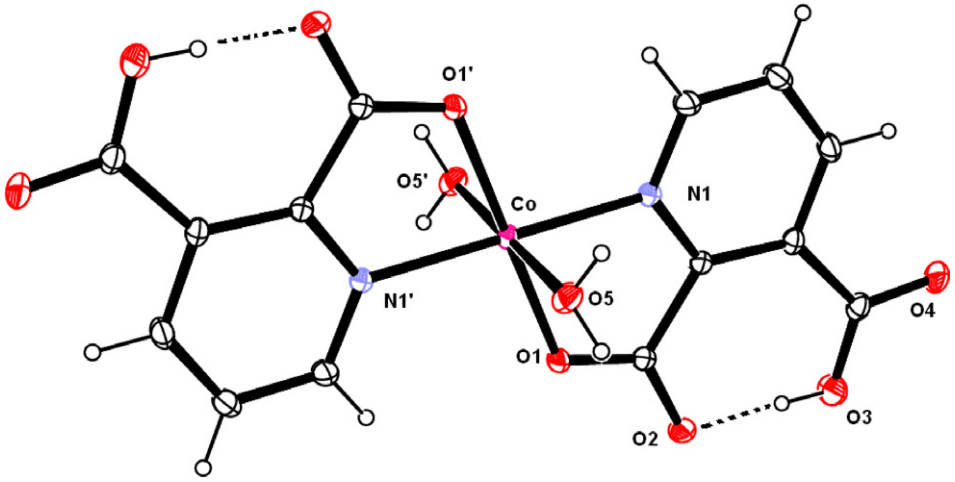


Fig. 2. The structure of $[Co(LH)_2(H_2O)_2]$ (**IV**).

ion has a six coordination number and has a N2O4 type of environment. The two Zn–O bonds along the *z*-axis are longer than the other Zn–O and Zn–N bond distances, showing distortion in the octahedral geometry. In order to compensate the negative charge on each of the zinc ions, the 4,4′-bipyridine molecules are found to be protonated and act as counter cations. In this case the polymeric chains (Fig. 3b) are formed from the coordinated carboxylato groups by opening of the anhydride rings. The coordination geometry around the zinc ions is shown in Fig. 3a. We anticipated the formation of assembled structures of dimeric units by a bridging 4,4′-bipyridine ligand, as this ligand generally acts as a bridging ligand which leads to grid like structures [7a,7b]. In contrast this ligand was found to be outside the coordination sphere, in the protonated form. In the polymeric structure of **V** each of the binuclear repeat units has three molecules of water of crystallization each and also a 4,4′-bipyridinium dication each. It may be interesting to note that in the lattice, the planarity of the bipyridine rings is lost. The two pyridine rings in the dication have a dihedral angle of 38.42° between the two rings. The protonated species of

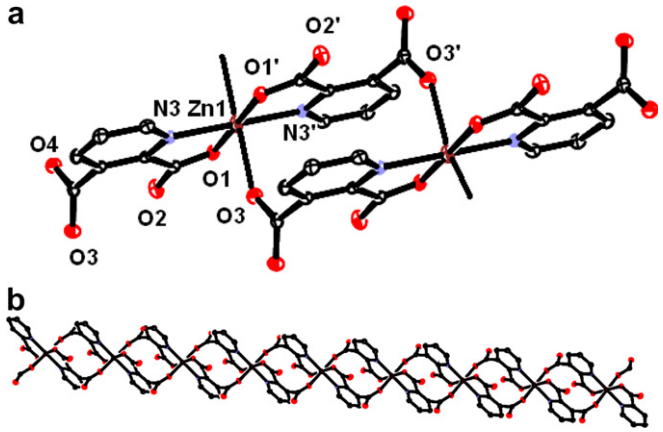


Fig. 3. (a) A part of the dimeric repeated units of (**V**) (Drawn with 20% thermal ellipsoids, hydrogen atoms are omitted for clarity). Some bond distances (Å) and angles (°) are Zn1–N3, 2.08; Zn1–O1, 2.07; Zn1–O3, 2.25; ∠N3–Zn1–O1, 79.48; ∠N3–Ni1–O3, 100.52; ∠O1–Zn1–O3, 84.09; atoms O5, O6, O7 are from water of crystallization. (b) One-dimensional chain in the coordination polymer (**V**).

analogous compounds, such as methyl-viologen, are used as cations in designing metallo-organic frameworks; where these cations assist in the inclusion of electron-rich substrates through charge transfer interactions [7c]. In these cases the planarity of the bications of methyl-viologen was also lost and a definite twisting of the pyridine rings was observed [7c]. It may be mentioned that functionalized pyromellitic diimides [8] were used for the syntheses of coordination polymers, in which dinuclear units formed by bridging ligands hold another bridging ligand, but our zinc polymer is structurally different from them. In our case the zinc centers are anionic, whereas in the earlier reported polymers the zinc centers were cationic. Moreover, the chelating nature of the ligand in the polymeric structure of **V** forces it to have repeated chain units having equal strength throughout the chain. The reaction of 2,3-pyridine dicarboxylic anhydride with zinc(II)acetate dihydrate was monitored by ^{1}H NMR spectroscopy. The 2,3-pyridine dicarboxylic anhydride has three multiplets at 7.62–7.66, 8.31–8.36 and 8.69–8.73 ppm in deuterated methanol, due to the three aromatic protons in it. On addition of zinc(II) acetate dihydrate to a solution of 2,3-pyridine dicarboxylic anhydride (1:2 molar ratio) in deuterated methanol at room temperature, besides the signals for 2,3-pyridine dicarboxylic anhydride, three additional aromatic multiplet signals with equal integration at 7.83–7.89, 8.15–8.18, 8.44–8.47 ppm appear. There is also a methyl signal at 2.0 ppm arising from liberated acetic acid. In this reaction precipitation of a white solid on addition of zinc acetate was observed. To make the solution homogeneous we added deuterated dimethylsulfoxide in order to record the ^{1}H NMR spectra. Observation of simple spectra for the reaction mixture, with only three new aromatic protons of equal integration clearly tells us there is the formation of only one type of complex in solution.

It is clear that the ester of the carboxylic acid is not formed in these reactions between the hydrated salts of cobalt, nickel and zinc acetate and 2,3-pyridine dicarboxylic anhydride in methanol. Thus, it may be imagined that the metal is allowing hydrolysis of a methyl ester formed in these reactions. Thus, we performed a control experiment between preformed methyl ester with zinc(II) chloride in methanol and observed no hydrolysis of the methyl-ester under similar conditions. From this experiment we have ruled out the possibility of hydrolysis of an ester that might have formed during the reaction. However, while carrying out reaction between copper(II) chloride and 1,10-phenanthroline with pyromellitic dianhydride, we observed that the nature of the product formed from this reaction is dependent on the reaction conditions [5b]. For example, a reaction carried out with a 1:1 ratio of cupric chloride to 1,10-phenanthroline gave methyl ester, whereas a reaction carried out with a 1:2 cupric chloride to 1,10-phenanthroline ratio gave a metal complex having the composition $[Cu(phen)_2Cl]L_1H3$ (**VI**). In this complex (**VI**), the carboxylate anion formed does not coordinate to the metal. The structure of the complex is shown in Fig. 4. The complex cation has a distorted square pyramidal geometry, in which the 1,10-phenanthroline rings do not remain in one plane but are disposed in a twisted manner. It is interesting to note that the mono-anion of 1,2,4,5-benzene tetracarboxylic acid, which neutralizes the charge, has strong intramolecular hydrogen bonding between the carboxylato and carboxylic acid groups at the 1 and 2 positions through O2–H···O3 (d_{D-A} 2.38 Å; d_{D-H} 1.22 Å; ∠D–H···A = 172.96°). The other carboxylic acids are involved in intermolecular hydrogen bonding.

The reaction of copper(II) acetate dihydrate and 1,10-phenanthroline (1:2 ratio) with pyromellitic dianhydride gave an interesting dinuclear product (**VII**) having the composition $[Cu_2(phen)_4L_1]\cdot 4H_2O$ (where L_1 = tetra-anion of 1,2,4,5-benzene tetracarboxylic acid, phen = 1,10-phenanthroline), as illustrated in Scheme 3. This reaction also did not lead to the formation of an ester complex, however changing the ratio from 1:2 between copper(II) acetate and 1,10-phenanthroline to 1:1 led to the formation of the corresponding methyl ester, namely 1,4 di-carbomethoxy 2,5-benzene dicarboxylic acid [5b]. Thus, on increase of the amount of nitrogen donor ligands (such as 1,10-phenanthroline), the esterification of pyromellitic dianhydride is inhibited. Complex **VII** has two copper ions held by two carboxylic acid groups at 1,4-positions and each copper has two 1,10-phenanthroline bidentate ligands (Fig. 5). The rest of the charge on the copper ions is balanced by the two carboxylato groups that are present on the ring as dianions. This compound has four molecules of water of crystallization. It may be mentioned that the use of polydentate ligands with dicarboxylates led to flexible structures [9] and it was also observed that the polymerization reactions leading to high molecular weight metal carboxylate polymers were inhibited by the use of bigger nitrogen donor ligands [10]. Isolation and characterization

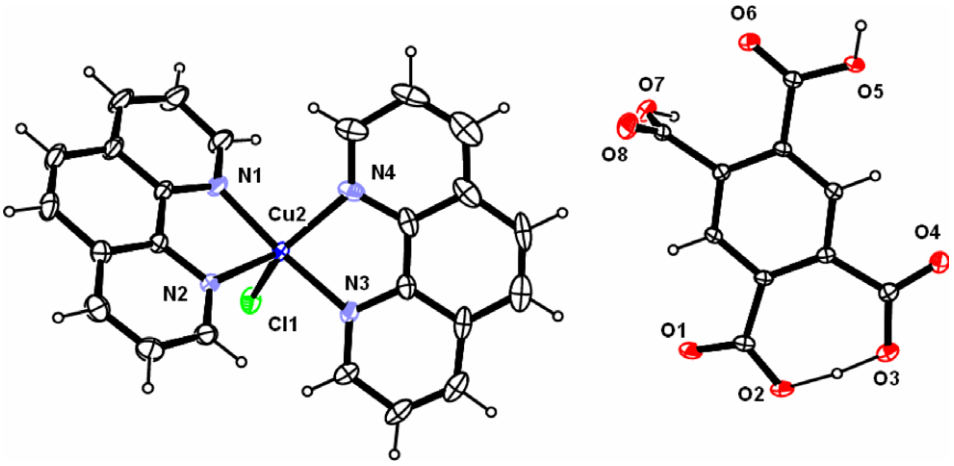
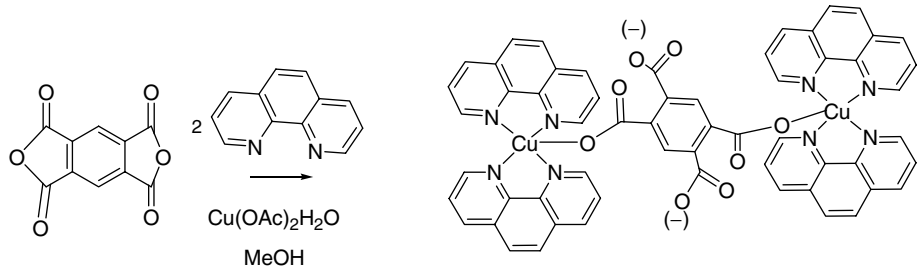


Fig. 4. Structure of (**VI**) (Drawn with 20% thermal ellipsoids). Some bond distances (Å) and angles (°) are Cu2–N1, 2.16; Cu2–N2, 1.98; Cu2–N3, 2.09; Cu2–N4, 1.99; Cu2–Cl1, 2.31; ∠N1–Cu2–N2, 80.70; ∠N1–Cu2–N4, 101.51; ∠N3–Cu2–N4, 80.29; ∠N2–Cu2–N3, 94.76; ∠N2–Cu2–Cl1, 92.58; ∠N3–Cu2–Cl1, 138.76; ∠N1–Cu2–Cl1, 103.28.



Scheme 3.

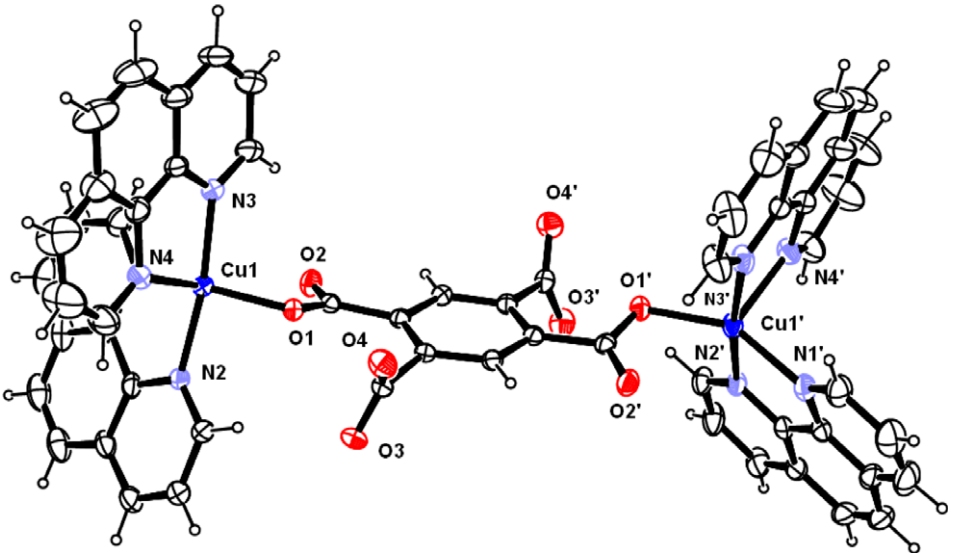


Fig. 5. Structure of (**VII**) (Drawn with 20% thermal ellipsoids). Some bond distances (Å) and angles (°) are Cu1–N1, 2.20; Cu1–N2, 2.02; Cu1–N3, 1.99; Cu1–N4, 2.07; Cu1–O1,1.98; ∠N1–Cu1–N2, 79.23; ∠N1–Cu1–N4, 101.94; ∠N3–Cu1–O1, 92.22; ∠N4–Cu1–O1, 148.54; ∠N2–Cu2–O1, 95.04; ∠N1–Cu1–O1, 109.28 (water of crystallization is omitted for clarity).

of the copper complexes **VI** and **VII** provides evidence to these facts. The complex formation with dicarboxylic acids with metal salts is generally very sensitive to the reaction conditions and type of ligand under consideration [11].

In conclusion we have demonstrated preferential hydrolysis over esterification in cyclic anhydrides by hydrated first row transition metal salts to prepare metal carboxylate complexes having diverse coordination possibilities. This study

also provides methods to synthesize dinuclear and mononuclear metal complexes by using chelating ligands. In the case of copper it is observed that the chloride ion blocks the coordination of the carboxylato group; leading to a mononuclear complex having a chloride ion in the coordination sphere. The hydrolytic cleavage of anhydride in alcoholic medium is also dependent on the reaction conditions.

Acknowledgment

The authors thank Department of Science and Technology, India for financial assistance.

Appendix A. Supplementary material

CCDC 642440, 642441, 642442, 643365 and 647898 contain the supplementary crystallographic data for **III**, **IV**, **V**, **VI**, **VII**. These data can be obtained free of charge via http://www.ccdc.cam.ac.uk/conts/retrieving.html, or from the Cambridge Crystallographic Data Centre, 12 Union Road, Cambridge CB2 1EZ, UK; fax: (+44) 1223-336-033; or e-mail: deposit@ccdc.cam.ac.uk. Supplementary data associated with this article can be found, in the online version, at doi:10.1016/j.poly.2007.06.028.

References

[1] (a) J.-Y. Wu, C.-H. Chang, T.-W. Tseng, K.-L. Lu, J. Mol. Struct. 769 (2006) 69;
(b) S. Haq, N.V. Richardson, J. Phys. Chem. B 103 (1999) 5256.
[2] (a) N. Barooah, R.J. Sarma, J.B. Baruah, CrystEngCommun 8 (2006) 608;
(b) T. Agug, T. Takeichi, J. Polym. Sci. A 38 (2000) 1467;
(c) T. Yamakata, A. Kanomata, T. Inoue, Macromol. Symp. 199 (2003) 73;
(d) H. Matsuda, J. Macromol. Sci. Chem. A 11 (1977) 431.
[3] (a) J. Otera, Esterification: Methods, Reactions and Applications, Wiley-VCH, Weinheim, 2003;
(b) Y. Chen, L. Deng, J. Am. Chem. Soc 123 (2001) 11302;
(c) B. Rodrignez, T. Rantanen, C. Bolm, Angew. Chem., Int. Ed. Engl. 45 (2006) 6924;
(d) R.A. Atiken, J.A. Hirst, J. Chem. Soc., Chem Commun (1988) 632;
(e) M.J. Petersson, C. Machal, W.A. Loughlin, I.D. Jenkin, P.C. Healy, A. Almesuker, Tetrahedron 63 (2007) 1359.
[4] (a) E. Vedej, O. Dougulis, J. Org. Chem. 61 (1996) 5702;
(b) M. Konieczny, H. Xu, R. Battaglia, S.L. Wunder, W. Volksen, Polymer 38 (1997) 2969.
[5] (a) K. Deka, N. Barooah, R.J. Sarma, J.B. Baruah, J. Mol. Struct. 827 (2007) 44;
(b) A.M. Baruah, A. Karmakar, J.B. Baruah, Polyhedron 26 (2007) 4479.
[6] (a) C.N.R. Rao, S. Natarajan, R. Vaidhyanathan, Angew Chem., Int. Ed. Engl. 43 (2004) 1466;
(b) O.M. Yaghi, M. O'Keeffe, N.W. Ockwig, H.K. Chae, M. Eddaoudi, J. Kim, Nature 423 (2003) 705;
(c) O.M. Yaghi, H. Li, C. Davis, D. Richardson, T.L. Groy, Acc. Chem Res. 31 (1998) 474;
(d) B. Moulton, M.J. Zaworotko, Chem. Rev. 101 (2001) 1629;
(e) S. Noro, S. Kitagawa, M. Kondo, K. Seki, Angew. Chem., Int. Ed. Engl. 39 (2000) 2081.
[7] (a) P.J. Steel, Acc. Chem. Res. 38 (2005) 243;
(b) M. Fujita, M. Tominaga, A. Hori, B. Therrien, Acc. Chem. Res. 38 (2005) 371;
(c) S.I. Nishikiori, Y. Sano, T. Iwamoto, Acc. Chem. Res. 38 (2005) 227.
[8] X.-Q. Lu, L. Zhang, C.-L. Chen, C.-Y. Su, B.-S. Kang, Inorg. Chim. Acta 358 (2005) 1771.
[9] P. Wang, C.N. Moorefield, M. Panzner, G.R. NewKome, Cryst. Growth Des. 6 (2006) 1563.
[10] (a) X.-L. Wang, C. Qin, E.-B. Wang, L. Xu, Z.-M. Su, C.-W. Hu, Angew Chem., Int. Ed. Engl. 43 (2004) 5036;
(b) Y. Li, N. Hao, Y. Lu, E. Wang, Z. Kang, C. Hu, Inorg. Chem. 42 (2003) 3119.
[11] (a) C. Mellot-Draznieks, G. Ferey, Prog. Solid State Chem. 33 (2005) 187;
(b) Y. Rodriguez-Martin, M. Hernandez-Molina, F.S. Delgado, J. Pasan, C. Ruiz-Perez, J. Sanchiz, F. Lloret, M. Julve, CrystEngCommun 4 (2002) 522.

strategy to produce appropriated building blocks is to use ancillary bidentate nitrogen ligands that can give rise to $[M(NN)]^{2+}$ metal corners [6].

The non-planar ligand di(2-pyridyl)sulfide (DPS) can act as an assistant ligand in coordination compounds joining two nitrogen atoms in a chelating fashion [7] or bridging two metal ions [8]. A more rare coordination mode can occur, in which nitrogen and sulphur atoms are involved [7,9]. On the other hand, the planar ligand 4,4′-dimethyl-2,2′-bipyridine (Mebpy) possesses two more basics nitrogen atoms than 2,2′-bipyridine analogous and assumes the bidentate chelating coordination mode [10]. These two nitrogen ligands can be applied in the formation of the mentioned molecular building subunits.

In this work, we report the preparation and structural characterization of four copper(II) complexes namely [μ-(ox){Cu(Mebpy)(NO_3)(H_2O)}$_2$] (**1**), [μ-(ox){Cu(Mebpy)-(ClO_4)(H_2O)}$_2$] (**2**), [μ-(ox){Cu(DPS)(H_2O)}$_2$](ClO_4)$_2$ (**3**) and [Cu(DPS)(ox)(H_2O)] · 2H_2O (**4**) that contain both oxalate dianion and the ancillary nitrogen ligands (Mebpy or DPS). These compounds can be used as novel molecular building blocks for coordination polymers construction.

2. Experimental

2.1. Materials and physical measurements

Di(2-pyridyl)sulfide (DPS) ligand was obtained according to the published method [11], however, it was purified through a chromatographic column using (hexane:ethyl acetate/7:3) solvent mixture as eluent. Yield: 5.53 g, 55%. All other reagents were purchased from Aldrich Chemical Co. and used without further purification.

Elemental analyses for C, H and N were carried out with a Perkin–Elmer 2400 analyzer. IR spectra were recorded with a Bomem Michelson 102 FTIR spectrophotometer using NaCl pellets in the wavenumber range of 4000–600 cm^{-1} with an average of 128 scans and 4 cm^{-1} of spectral resolution. Fourier-Transform Raman spectroscopy was carried out using a Bruker RFS 100 instrument, Nd^{3+}/YAG laser operating at 1064 nm in the near infrared and CCD detector cooled with liquid N_2 with an average of 500 scans and 4 cm^{-1} of spectral resolution. Thermogravimetric analysis (TG/DTG) data were collected with a TG-50 Mettler STARe using 1.0 mg packed in alumina crucible. Samples were heated at 10 °C/min from room temperature to 800 °C in a dynamic nitrogen atmosphere (flow rate = 200 mL/min). Differential scanning calorimetry (DSC) measurements were carried out with a Shimadzu DSC50, using 1.0 mg samples packed in aluminum crucible, with a heating rate of 10 °C/mim in the range of 25–480 °C. Dynamic nitrogen atmosphere (flow rate = 50 mL/mim) was used.

2.2. Synthesis of [μ-(ox){Cu(Mebpy)(NO_3)(H_2O)}$_2$] (1)

By slow diffusion, 10 mL of an aqueous solution of $Na_2C_2O_4$ (18 mg, 0.13 mmol) were added to 20 mL of methanolic solution containing Mebpy (50 mg, 0.27 mmol) and $Cu(NO_3)_2 \cdot 3H_2O$ (65 mg, 0.27 mmol) at room temperature. After few days, blue crystals suitable for X-ray analysis were obtained. Yield: 88%. *Anal*. Calc. for $C_{26}H_{28}O_{12}N_6Cu_2$: C, 41.99; H, 3.79; N, 11.30. Found: C, 41.93; H, 3.58; N, 11.37%. IR (NaCl, cm^{-1}): ν(OH), 3574 (m), 3403 (m); ν(CH), 3064 (w); $\nu(CH_3)$, 2924 (w), 2852 (w); ν_{asym}(COO), 1649 (s), 1626 (sh); ν(CC/CN), 1617 (sh), 1560 (w), 1496 (w), 1447 (w); ν_{sym}(COO, NO_3^-), 1356 (s); δ_{oop}(CH), 842 (w); δ(O–C–O), 795 (w). Raman (1064 nm, cm^{-1}): ν(CH), 3079 (m), 2928 (m); ν(CC/CN), 1617 (s), 1561 (s), 1496 (m).

2.3. Synthesis of [μ-(ox){Cu(Mebpy)(ClO_4)(H_2O)}$_2$] (2)

Caution! Perchlorate salts with organic solvents are potentially explosive. A small amount of material only should be prepared and it should be handled with care.

Complex **2** was prepared through a similar procedure used for compound **1**. 10 mL of an aqueous solution of $Na_2C_2O_4$ (18 mg, 0.13 mmol) were layered on to 20 mL of acetonitrile solution containing Mebpy (50 mg, 0.27 mmol) and $Cu(ClO_4)_2 \cdot 6H_2O$ (100 mg, 0.27 mmol) at room temperature. After 15 min, blue needle crystals suitable for X-ray analysis were obtained. Yield: 48%. *Anal*. Calc. for $C_{26}H_{28}O_{14}N_4Cl_2Cu_2$: C, 38.15; H, 3.45; N, 6.84. Found: C, 38.19; H, 3.23; N, 7.03%. IR (NaCl, cm^{-1}): ν(OH), 3574 (m), 3403 (m); ν(CH), 3082 (w), 3064 (w); $\nu(CH_3)$, 2971 (w), 2930 (w); ν_{asym}(COO), 1649 (s), 1626 (sh); ν(CC/CN), 1615 (sh), 1559 (w), 1493 (w), 1447 (w); ν_{sym}(COO), 1353 (w); $\nu(ClO_4^-)$, 1129 (sh), 1090 (s), 1078 (s), 1048 (sh), 1032 (sh); δ_{oop}(CH), 840 (w); δ(O–C–O), 794 (w). Raman (1064 nm, cm^{-1}): ν(CH), 3085 (m), 2932 (m); ν(CC/CN), 1617 (s), 1561 (s), 1497 (m).

2.4. Synthesis of [μ-(ox){Cu(DPS)(H_2O)}$_2$](ClO_4)$_2$ (3)

To 10 mL of an ethanolic solution of $Cu(ClO_4)_2 \cdot 6H_2O$ (118 mg, 0.32 mmol), 10 mL of an ethanolic solution of DPS (60 mg, 0.32 mmol) were added. A solid precipitated immediately. By slow diffusion, $Na_2C_2O_4$ (21 mg, 0.16 mmol) dissolved in 20 mL of water was added. The blue solution turned limpid and was allowed to stand. After a few days, dark blue crystals suitable for X-ray analysis were filtered. Yield: 63%. *Anal*. Calc. for $C_{22}H_{20}O_{14}N_4S_2Cu_2Cl_2$: C, 31.97; H, 2.44; N, 6.78. Found: C, 31.01; H, 2.18; N, 6.59%. IR (NaCl, cm^{-1}): ν(OH), 3541 (m), 3482 (m); ν(CH), 3095 (w), 3075 (w); ν_{asym}(COO), 1662 (s); ν(CC/CN), 1591 (m), 1568 (w), 1459 (m), 1427 (m); ν_{sym}-(COO), 1356 (w); ν (ClO_4^-), 1142 (sh), 1127 (sh), 1105 (sh), 1093 (s), 1057 (sh); δ_{oop}(CH), 782 (m); δ(O–C–O), 760 (m). Raman (1064 nm, cm^{-1}): ν(CH), 3087 (m), 3075 (m); ν(CC/CN), 1591 (w), 1568 (w), 1559 (w), 1498 (w); $\nu(ClO_4^-)$, 1094 (w).

Table 1
Crystal data and structure refinement parameters for compounds [μ-(ox){Cu(Mebpy)(NO_3)(H_2O)}$_2$] (**1**), [μ-(ox){Cu(Mebpy)(ClO_4)(H_2O)}$_2$] (**2**), [μ-(ox){Cu(DPS)(H_2O)}$_2$](ClO_4)$_2$ (**3**) and [Cu(DPS)(ox)(H_2O)] · 2H_2O (**4**)

Compound	**1**	**2**	**3**	**4**
Formula	$C_{26}H_{28}O_{12}N_6Cu_2$	$C_{26}H_{28}O_{14}N_4Cl_2Cu_2$	$C_{22}H_{20}O_{14}S_2N_4Cu_2$	$C_{12}H_{14}O_7N_2SCu$
Formula weight	743.62	818.50	826.54	393.85
Crystal system	monoclinic	monoclinic	monoclinic	orthorhombic
Space group	$P2_1/n$	$P2_1/n$	$P2_1/n$	$P2_1cn$
a (Å)	8.5605(9)	8.8898(18)	8.289(1)	7.510(2)
b (Å)	14.6675(9)	15.146(3)	15.0853(8)	11.610(5)
c (Å)	12.210(6)	12.252(3)	12.212(7)	17.850(22)
β (°)	90.286(7)	94.08(3)	102.691(7)	90.00
V/Å^3	1533.07(2)	1645.5(6)	1489.67(2)	1549.22(3)
Z	2	2	2	4
Crystal size (mm)	0.20 × 0.13 × 0.10	0.08 × 0.09 × 0.20	0.22 × 0.20 × 0.19	0.25 × 0.06 × 0.05
d_{calc} (g cm^{-3})	1.611	1.652	1.896	1.689
μ (Mo Kα) (mm^{-1})	1.459	1.527	1.826	1.582
Reflections measures/unique	20157/4365	12952/3743	30614/4951	12985/3430
Observed reflections [$F_o^2 > 2s(F_o^2)$]	3358	2796	3771	2806
Parameters	227	220	254	229
R	0.0477	0.0605	0.0415	0.0488
wR	0.0869	0.1127	0.0741	0.0764
S	1.068	1.089	1.054	1.074
RMS peak (e$^-$Å^{-3})	0.071	0.088	0.069	0.127

2.5. Synthesis of [Cu(DPS)(ox)(H_2O)] · 2H_2O (4)

DPS ligand (60 mg, 0.32 mmol) dissolved in 5 mL of ethanol was added to 5 mL of an ethanolic solution of $Cu(NO_3)_2 \cdot 3H_2O$ (77 mg, 0.32 mmol). By slow diffusion, 10 mL of an aqueous solution of $Na_2C_2O_4$ (43 mg, 0.32 mmol) were added. A blue solid precipitated and was filtered off. The mother-liquor was set aside and after three days crystals suitable for X-ray diffraction analysis were isolated. Yield: 23%. *Anal.* Calc. for $C_{12}H_{14}O_7N_2Cu$: C, 36.59; H, 3.58; N, 7.11. Found: C, 36.60; H, 3.38; N, 7.06%. IR (NaCl, cm^{-1}): ν(OH) 3509 (s), 3414 (s); ν(CH), 3099 (w), 3079 (w), 3058 (w); ν_{asym}(COO), 1708 (m), 1670 (s), 1639 (sh); ν(CC/CN),1589 (m), 1564 (w), 1458 (w), 1420 (sh); ν_{sym}(COO), 1403 (s), 1263 (m); δ_{oop}(CH), 788 (m); δ (O–C–O), 778 (m). Raman (1064 nm, cm^{-1}): ν(CH), 3144 (w), 3122 (w), 3063 (sh), 3048 (w); ν_{asym}(COO), 1709 (w), 1669 (w); ν(CC/CN), 1575 (m), 1560 (m), 1451 (w), 1420 (w); ν_{sym}(COO), 1402 (w), 1266 (w); δ_{oop}(CH), 721 (m).

2.6. X-ray diffraction measurements

Single crystal X-ray data were collected using a Bruker Kappa CCD diffractometer with Mo Kα ($\lambda = 0.71073$ Å) at room temperature. Data collection, reduction and cell refinement were performed by COLLECT, EVALCCD and DIRAX programs, respectively [12]. The structures were solved and refined using SHELXL-97 [13]. An empirical isotropic extinction parameter x was refined, according to the method described by Larson [14a]. A multiscan absorption correction was applied [14b]. The structures were drawn by ORTEP-3 for Windows [15]. Hydrogen atoms were located from Fourier difference maps. Anisotropic displacement parameters were assigned to all non-hydrogen atoms (see Table 1).

3. Results and discussion

3.1. Crystal structures of [μ-(ox){Cu(Mebpy)(NO_3)(H_2O)}$_2$] (1), [μ-(ox){Cu(Mebpy)(ClO_4)(H_2O)}$_2$] (2), [μ-(ox){Cu(DPS)(H_2O)}$_2$](ClO_4)$_2$ (3), [Cu(DPS)(ox)(H_2O)] · 2H_2O (4)

All compounds studied in this work crystallize in monoclinic systems. Figs. 1 and 2 show the ORTEP [15] views of compounds **1**, **2**, **3** and **4** molecular structures and mainly geometric parameters are displayed in Table 2.

Compounds **1** and **2** are isostructural and crystallize in $P2_1/n$ space group, forming binuclear structures, as shown in Fig. 1. Each Cu(II) center adopts a distorted octahedral geometry, in which the basal plane is formed by two nitrogen atoms of MeBpy (N1 and N2) and two oxygen atoms of oxalate ion (O1 and O2) and the axial positions are occupied by an one water molecule (O3) and oxygen atom (O4) of nitrate ion in compound (**1**) and of perchlorate ion in compound (**2**). In compound (**1**), Cu–N1, Cu–N2, Cu–O1 and Cu–O2 bond distances are 1.992(2), 1.989(2), 1.990(1) and 1.981(1) Å, respectively, while Cu–O3 and Cu–O4 bond lengths are much longer (2.410(2) and 2.472(2) Å), characterizing a tetragonally elongated octahedron (4+2 environment) due to a very pronounced Jahn–Teller effect. Similar geometry is observed in compound (**2**) where Cu–N1, Cu–N2, Cu–O1 and Cu–O2 bond distances are 1.988(3), 1.987(3), 1.990(2) and 1.986(2) Å respectively, while Cu–O3 and Cu–O4 bond lengths are also much longer (2.405(3) and 2.559(4) Å). In despite of Cu–O4 bond length is bigger in **2** than in **1**, the

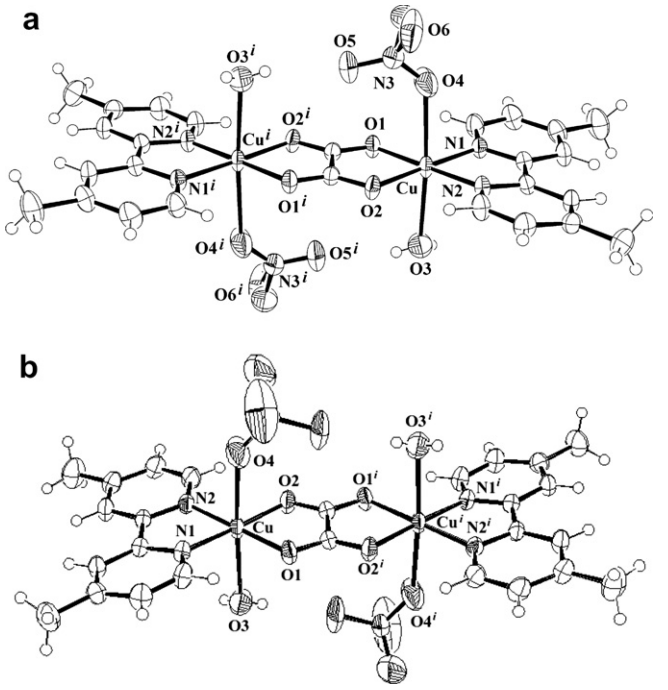


Fig. 1. Crystal structure of (a) [μ-(ox){Cu(Mebpy)(NO_3)(H_2O)}$_2$] (**1**) and (b) [μ-(ox){Cu(Mebpy)(ClO_4)(H_2O)}$_2$] (**2**). *Symmetry code:* (a) i: $-x$, $2-y$, $1-z$; (b) i: $-x$, $2-y$, $2-z$.

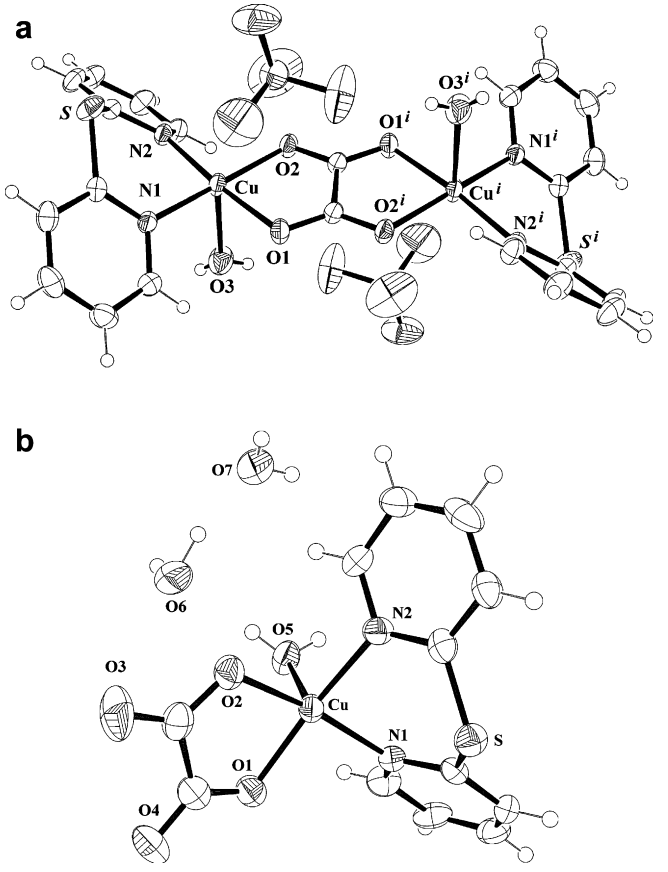


Fig. 2. Crystal structure of (a) [μ-(ox){Cu(DPS)(H_2O)}$_2$](ClO_4)$_2$ (**3**) and (b) [Cu(DPS)(ox)(H_2O)]· $2H_2O$ (**4**). *Symmetry code:* (a) i: $-x$, $2-y$, $1-z$; (b) i: $-x$, $2-y$, $-z$.

environment around Cu site is characterized in the same way (4+2). The oxalate ion acts in bis(bidentate) coordination mode bridging two Cu(II) sites with Cu···Cu distance very similar in both compounds (5.16 Å in (**1**) and 5.17 Å in **2**). There is an inversion center in the middle of oxalate C–C bond, as indicated by the analysis of IR and Raman vibrational spectra. In both compounds, the coordination water molecules of a binuclear unit are involved in medium hydrogen bonds (average distance of O···O is 2.875(4) Å) with nitrate in **1** and perchlorate in **2** anions of the adjacent unit giving rise to a one-dimensional arrangement parallel to crystallographic axis *a*, as can be seen in Fig. 3. Hydrogen bond geometric parameters of **1** are displayed in Table 3. Additionally, the pyridyl rings of neighbor molecules from two one-dimensional chains present average of centroid–centroid and interplanar distances of 3.81 and 3.70 Å, respectively, indicating the existence of π-stacking interaction, extending the dimensionality to a 2-D array, shown in Fig. 3. In compound **1** is observed a disorder in one of the oxygen atoms of nitrate anion (O6 and O6A), as can be seen in Fig. 1a. O6 and O6A are located at two different sites and the occupational distribution is not equivalent; one site presents occupational factor around 0.65.

The literature [4i] describes the crystal structure of the analogous compound [{Cu(NO_3)(H_2O)(bipy)}$_2$(ox)], which is very similar to compound **1**. In this case, the equatorial Cu–O and Cu–N distances vary from 1.96 to 1.99 Å, being in the same range to that observed in **1**. However, Cu–O distances of axial sites (2.351 and 2.755 Å) are significantly different from each other and from those observed in **1** and the authors describe the polyhedron coordination as 4+1+1 environment. Also, the crystal packing presents the same hydrogen bonds between the coordinated water molecules and nitrate groups and π-stacking interaction between pyridyl rings. Curiously, the crystal structure of the same compound, namely [Cu_2(μ-C_2O_4)(bpy)$_2$-(H_2O)$_2$(NO_3)$_2$], has been described a year later [16], but no comparison to the first description was made.

Similarly to **1** and **2**, compound **3** is also binuclear, as can be seen in Fig. 2a, and crystallizes in a monoclinic space group $P2_1/n$. In this case, however, each Cu(II) center is pentacoordinated, being surrounded by two nitrogen atoms of DPS ligand (N1 and N2), two oxygen atoms of oxalate anion (O1 and O2) and one water molecule (O3). According to the trigonality index $\tau = 0.04$ ($\tau = (\beta - \alpha)/60$, where β is the greatest basal angle and α is the second in magnitude; $\tau = 0$ and 1 for perfect square-pyramidal and trigonal-bipyramidal geometries, respectively) [17], Cu(II) ions exhibit a slightly distorted square pyramidal geometry. The basal plane is formed by N1, N2, O1 and O2 atoms and the metal ion sits at 0.078 Å above this plane. The apical positions are occupied by O3 atoms and the Jahn–Teller distortion can be observed (d(Cu–O3) = 2.294(2) Å). DPS ligands assume the bidentate chelating fashion, wherein the six-membered chelate rings adopt a boat conformation, with the angle between pyridyl

Table 2
Selected bond distances (Å) and angles (°) of compounds [μ-(ox){Cu(Mebpy)(NO_3)(H_2O)}$_2$] (**1**), [μ-(ox){Cu(Mebpy)(ClO_4)(H_2O)}$_2$] (**2**), [μ-(ox){Cu(DPS)(H_2O)}$_2$](ClO_4)$_2$ (**3**) and [Cu(DPS)(ox)(H_2O)] · 2H_2O (**4**)

	1	2	3	4
Cu–N1	1.992(2)	1.988(3)	1.992(2)	2.011(4)
Cu–N2	1.989(2)	1.987(3)	1.986(2)	2.013(4)
Cu–O1	1.990(1)	1.986(2)	1.989(2)	1.947(3)
Cu–O2	1.981(1)	1.990(2)	1.987(2)	1.966(3)
Cu–O3	2.410(2)	2.405(3)	2.294(2)	
Cu–O4	2.472(2)	2.559(4)		
Cu–O5				2.230(4)
O1–Cu–N2	179.24(6)	177.10(11)	174.74(6)	164.85(14)
O2–Cu–N1	177.46(6)	179.12(11)	172.38(6)	167.39(14)
O3–Cu–O4	175.47(8)	170.59(13)		
O1–Cu–O3	88.04(7)	85.37(10)	88.17(7)	
O2–Cu–O3	87.34(8)	93.03(10)	91.60(6)	
O1–Cu–O5				97.88(13)
O2–Cu–O5				99.62(14)
N1–Cu–O3	92.90(8)	89.21(11)	94.49(7)	
N2–Cu–O3	92.36(8)	95.10(11)	94.37(7)	
N1–Cu–O4	89.05(7)	87.79(12)		
N2–Cu–O4	91.96(7)	93.34(12)		
N1–Cu–O5				92.37(14)
N2–Cu–O5				97.07(14)

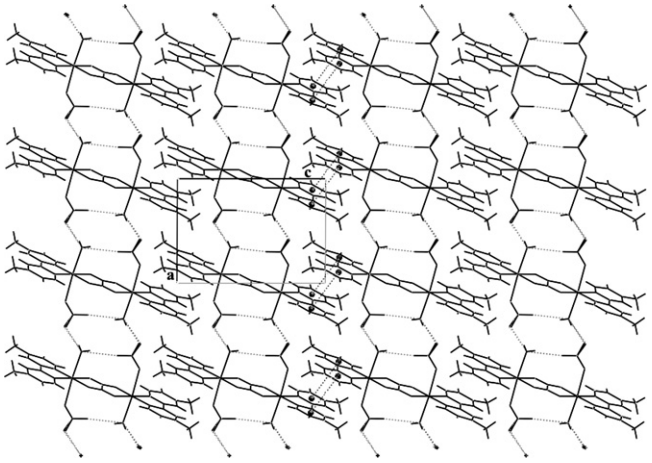


Fig. 3. Hydrogen bonding design and π-stacking interactions in **1** viewed along crystallographic *b* axis.

rings of 51.4°. As observed in compounds **1** and **2**, the binuclear structure is achieved through the bridging oxalate anion wherein the Cu···Cu distance is 5.19 Å and there is an inversion center in the middle of oxalate C–C bond, as indicated by the vibrational spectra. The complex structure is cationic and the neutral compound is formed by the presence of two perchlorate anions (Fig. 2a), which are involved in very weak interactions with the metal centers (d(O6–Cu) = 3.155(7) Å). The oxygen atoms of perchlorate anions are all disordered in two sites. They were refined in groups and the occupational factor of main group is around 0.69.

Crystal packing view along crystallographic axis *a* shows two orientations for oxalate ligands (Fig. 4) where the angle between oxalate planes is 80.5°. Perchlorate anions link binuclear units through O···S and O···O van der Waals

Table 3
Geometric parameters of hydrogen bonding system in compounds (**1**)–(**4**)

DHA	O–H (Å)	H···O (Å)	D···A (Å)	D–H···A (°)
(*1*)				
O3–H3A–O5	0.71(4)	2.25(4)	2.937(3)	163(4)
O3–H3B–O6A	0.77(3)	2.15(4)	2.910(15)	168(4)
(*2*)				
O3–H3A–O6	0.82	2.08	2.865(6)	160(3)
O3–H3B–O5	0.72	2.17	2.871(4)	163(3)
(*3*)				
O3–H3A–O5	0.73(3)	2.24(3)	2.962(5)	174(3)
O3–H3B–O4	0.62(3)	2.42(3)	2.973(6)	152(4)
(*4*)				
O5–H5A–O4	0.83(2)	2.20(3)	2.936(4)	147(4)
O5–H5B–O6	0.85(2)	1.90(3)	2.744(6)	173(6)
O6–H6A–O4	0.84(6)	2.28(6)	2.952(6)	137(5)
O6–H6B–O7	1.00(6)	1.76(6)	2.740(7)	166(5)
O7–H7A–O2	0.86(3)	2.09(5)	2.867(6)	149(6)
O7–H7B–O3	0.86(5)	2.01(5)	2.802(7)	154(5)

interactions. As can be seen in Fig. 4a, water molecules are involved in weak hydrogen bond interactions with perchlorate anions with average of O···O distance of 2.968(6) Å, forming a two-dimensional arrangement (2D). Geometric parameters of hydrogen bond in (**3**) are displayed in Table 3. The compound [Cu_2(bdpm)$_2$(H_2O)$_2$(μ-ox)](ClO_4)$_2$ · H_2O (bdpm = bis(3,5-dimethylpyrazol-1-yl)methane) described in the literature [18] presents a very similar structure in comparison to **3**. The Cu(II) centers show the same distorted square-pyramidal geometry with basal Cu–O and Cu–N and apical Cu–O (water) distances equivalent to those observed in compound (**3**).

Compound (**4**) crystallizes in a non-centrosymmetric orthorhombic space group $P2_1cn$ and, differently from

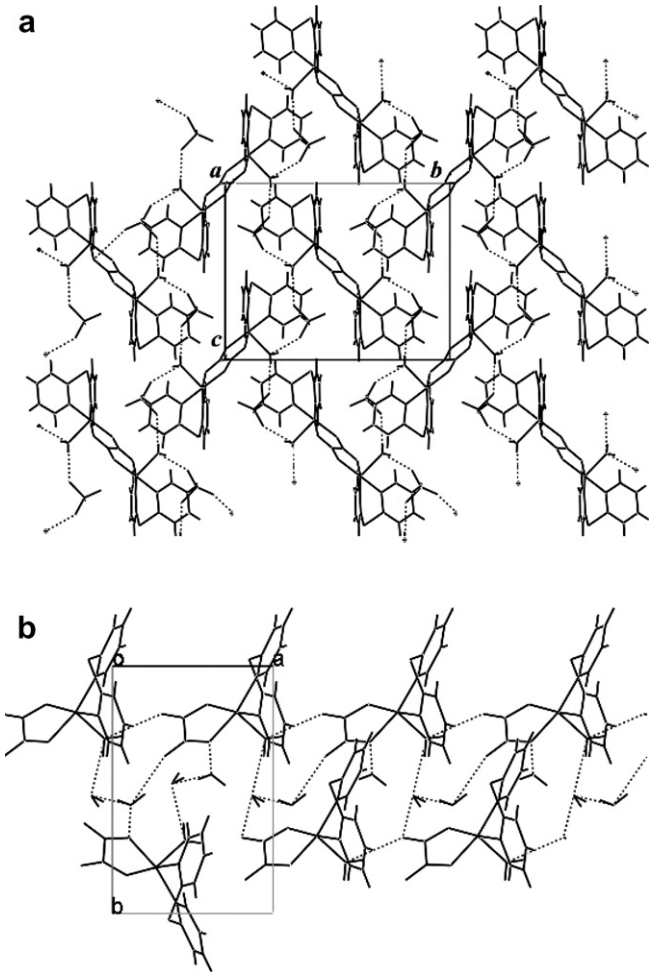


Fig. 4. (a) Crystal packing of **3** viewed along crystallographic *a* axis. (b) Hydrogen bond arrangement in **4** viewed along crystallographic *c* axis.

the others this compound is mononuclear (Fig. 2b). Cu(II) center is coordinated by two nitrogen atoms (N1 and N2) from DPS ligand in a bidentate chelating coordination mode, two oxygen atoms (O1 and O2) from oxalate dianion in a terminal bidentate chelating fashion and one oxygen atom (O5) from a water molecule, exhibiting a slightly distorted square pyramidal geometry with trigonality index $\tau = 0.04$. The metal site is located at 0.185 Å above the basal plane formed by N1, N2, O1 and O2 atoms. The angle between pyridyl rings in DPS ligand is 52.2°, similar to that observed in compound **3**. DPS pyridyl rings of adjacent complexes show average of centroid–centroid and interplanar distances of 4.42 and 3.35 Å, respectively. In despite of short interplanar distance, the centroid–centroid distance is longer than 4.0 Å, suggesting that the aromatic rings are not involved in π-stacking interaction, due to horizontal translation in crystal packing (average of 2.44 Å). In addition, two lattice water molecules are observed in crystal structure. All water molecules are involved in weak hydrogen bond to coordinated and non-coordinated oxygen atoms of oxalate ligand and medium between them in a three-dimensional arrangement (Fig. 4b). The average of O···O separation in medium and weak hydrogen bonding is 2.742(7) and 2.889(6) Å, respectively. Geometric parameters of hydrogen bond in **4** are displayed in Table 3.

There are other related compounds described in the literature, like the analogous namely $[Cu(bipy)(C_2O_4)(H_2O)]\cdot 2H_2O$ (bipy = 2,2′-bipyridine) [19a] and $[Cu(C_3H_2O_4)(C_{12}H_{12}N_2)(H_2O)]\cdot 2H_2O$ ($C_3H_2O_4$ = malonate ion and $C_{12}H_{12}N_2$ = 4,4′-dimethyl-2,2′-bipyridine) [19c]. In both cases, the metal center is five-coordinated and adopts the distorted square-pyramidal geometry in which the dicarboxylate group acts in the bidentate coordination mode and the Cu–O and Cu–N bond distances are very similar to those observed in compound **4**.

3.2. General characterization

All studied compounds were obtained by diffusion in situ of an aqueous solution of $Na_2C_2O_4$ to solutions in different solvents of respective copper(II) salts ($Cu(NO_3)_2\cdot 3H_2O$ for **1** and **4** and $Cu(ClO_4)_2\cdot 6H_2O$ for **2** and **3**) and nitrogen ligands Mebpy (for **1** and **2**) and DPS (for **3** and **4**). The analytical data indicated the formation of binuclear compounds **1**–**3** with (Cu^{2+}:Mebpy:ox/1:1:1/2) in **1** and **2** and (Cu^{2+}:DPS:ox/1:1:1/2) in **3** stoichiometric ratio, and mononuclear compound **4** in (Cu^{2+}:DPS:ox/1:1:1) proportion.

Thermogravimetric curves for compounds **1**–**4** are shown in Figure S1 in the supplementary material. For **1** and **3** it can be noticed the first weight loss in the temperature ranges of 120–180 °C and 80–160 °C, respectively, in both cases corresponding to two coordination water molecules (obsd. 4.83%, calcd. 4.83% for **1** and obsd. 4.04%, calcd. 4.36% for **3**). Differently from **1** and **3**, for compound **4** the dehydration step occurs at lower temperature range (40–60 °C) indicating the presence of two crystallization water molecules (obsd. 9.21%, calcd. 9.15%). In addition for **4**, it can be observed a second mass loss around 110 °C consistent with a coordination water molecule. Curiously, in compound **2** the dehydration temperature range is also low (40–80 °C), but in this case these two water molecules (obsd. 3.78%, calcd. 3.55%) are coordinated to the metal centers, as confirmed by X-ray diffraction analysis. In all cases, the complete thermal decomposition can be identified above 190 °C in one or two steps. The final residues at 800 °C agree with two mols of CuO for compound **1** (obsd. 22.8%, calcd. 21.3%) and one mol of CuO for compound **4** (obsd. 22.5%, calcd. 20.2%). For compounds **2** and **3**, it was not possible to calculate the final mass residue due to the presence of ClO_4^- anion that causes an explosive behavior leading to a great error in the calculations. The literature [4i] describes the thermal behavior of a compound analogous to **1**, namely $[\{Cu(NO_3)(H_2O)(bipy)\}_2(ox)]$, where bipy = 2,2′-bipyridine. In this case, the thermogravimetric curve presents the same pattern exhibited by compound **1**.

DSC curves for the four complexes are exhibited in Figure S2 in the supplementary material. In the curve of compound **1** it can be noticed two exothermic events around 264 and 306 °C, while for compounds **2** and **3** there

is only one exothermic path at 291 and 284 °C, respectively, all of them corresponding to complexes thermal decomposition. Especially for the two latter compounds, the endothermic events attributed to the dehydration process are not observable due to the high intensity of the exothermic ones mentioned above. On the other hand, for compound **4**, it is noteworthy the presence of two different endothermic events at 59 and 123 °C assigned to the lattice and coordination water molecules losses, respectively.

The infrared spectra of complexes **1**–**4** show medium to strong and broad absorption bands in the 3574–3403 cm^{-1} wavenumber range assigned to ν(OH) stretching mode indicating the presence of water molecules in all complexes, in agreement to the thermal analysis results. Pyridine rings vibrational bands shift from 1592 cm^{-1} in free Mebpy to 1617 cm^{-1} in **1** and to 1615 cm^{-1} in **2** and from 1572 cm^{-1} in free DPS to 1591 and 1589 cm^{-1} in complexes (**3**) and (**4**), respectively. In fact, the presence of ν(CC/CN) at higher wavenumbers in complexes is indicative of metal coordination to pyridine nitrogen atoms, as observed for other compounds containing pyridine derivative ligands described in the literature [7,8,20].

One of the most relevant features of IR spectra concerns the carbon–oxygen stretching frequencies of oxalate group because they can provide important information about the coordination modes of this ligand. Compounds **1**–**3** spectra display characteristics bands of the oxalate bridging ligand [4c,18] around 1650 cm^{-1} (ν_{asym}(COO)), 1356 cm^{-1} (ν_{sym}-(COO)) and 800–760 cm^{-1} (δ(O–C–O)). On the other hand, in compound **4** spectrum it can be observed a medium intensity band at 1708 cm^{-1} assigned to non-coordinated CO moiety of oxalate anion and absorptions at 1670s cm^{-1} (ν_{asym}(COO)), 1403s and 1263s cm^{-1} (ν_{sym}-(COO)) and 778m cm^{-1} (δ(O–C–O)), indicating the bidentate coordination mode, in accordance to other reported bidentate oxalate-containing copper(II) complexes [21]. Additionally, in compounds **2** and **3** spectra, strong bands at 1142–1032 cm^{-1} frequency range, confirm the presence of ClO_4^- anion.

In the Raman spectra of compounds **1**–**3** the bands related to the asymmetric and symmetric stretching modes of COO^- groups are absent due to the presence of the inversion center in the molecules structures. Differently from **1**–**3**, the Raman spectrum of compound **4** shows bands at 1709, 1669 cm^{-1} and 1402, 1266 cm^{-1} assigned to asymmetric and symmetric stretching modes of COO^- groups, respectively, reinforcing the terminal bidentate chelating coordination mode of oxalate anion toward the Cu(II) site. All the Raman spectra can be seen in Figure S3 in the supplementary materials.

4. Conclusions

In summary, this work describes the preparation, crystal structures and spectroscopic characterization of four oxalate copper(II) complexes containing the 4,4′-dimethyl-2,2′-bipyridine (Mebpy) or di(2-pyridyl)sulfide (DPS) nitrogen ligands namely [μ-(ox){Cu(Mebpy)(NO_3)(H_2O)}$_2$] (**1**), [μ-(ox){Cu(Mebpy)(ClO_4)(H_2O)}$_2$] (**2**), [μ-(ox){Cu(DPS)(H_2O)}$_2$](ClO_4)$_2$ (**3**) and [Cu(DPS)(ox)(H_2O)]·2H_2O (**4**).

X-ray diffraction measurements have shown that complexes **1**–**3** are binuclear, in which the oxalate anion bridges two Cu(II) centers, while the complex **4** is mononuclear and the oxalate anion adopts the terminal bidentate chelating coordination mode. In **1** and **2** the Cu(II) sites display a distorted octahedral geometry (4+2 environment) in which the base is formed by two oxygen atoms of oxalate anion (O1 and O2) and two nitrogen atoms of Mebpy ligand (N1 and N2). The axial positions are occupied by one *aqua* ligand and one nitrate anion in compound **1** and one perchlorate anion in coumpound **2**, both exhibiting a very pronounced Jahn–Teller distortion. For both compounds, the coordination water molecules of a binuclear unit are involved in hydrogen bonds with the anions (NO_3^- for (**1**) and ClO_4^- for **2**) of the adjacent unit giving rise to a one-dimensional arrangement parallel to crystallographic axis *a*. The dimensionality is extended to a 2-D array through π-stacking interaction between the pyridyl rings of neighbor molecules.

Differently from **1** and **2**, in compounds **3** and **4** the Cu(II) centers exhibit a slightly distorted square pyramidal geometry. In both cases, the basal plane is constituted by two oxygen atoms from oxalate anion (O1 and O2) and two nitrogen atoms from DPS ligand (N1 and N2) and, the apical position is occupied by a water molecule.

Acknowledgements

The authors are grateful to the Brazilian agencies CAPES, CNPq, FAPEMIG and FINEP for financial support and to Laboratório de Espectroscopia Molecular USP for Raman facilities.

Appendix A. Supplementary material

CCDC 617497, 626188, 617496 and 617495 contain the supplementary crystallographic data for **1**, **2**, **3** and **4**. These data can be obtained free of charge via http://www.ccdc.cam.ac.uk/conts/retrieving.html, or from the Cambridge Crystallographic Data Centre, 12 Union Road, Cambridge CB2 1EZ, UK; fax: (+44) 1223-336-033; or e-mail: deposit@ccdc.cam.ac.uk. Supplementary data associated with this article can be found, in the online version, at doi:10.1016/j.poly.2007.06.027.

References

[1] D. Venkataraman, G.B. Gardner, S. Lee, J.S. Moore, J. Am. Chem. Soc. 117 (1995) 11600.
[2] (a) J.Y. Baeg, S.W. Lee, Inorg. Chem. Commun. 6 (2003) 313;
(b) Z.Y. Fu, P. Lin, W.X. Du, L. Chen, C.P. Cui, W.J. Zhang, X.T. Wu, Polyhedron 20 (2001) 925;
(c) P. Losier, M.J. Zaworotko, Angew. Chem., Int. Ed. Engl. 35 (1996) 2779;

(d) M. Fujita, Y.J. Kwon, S. Washizu, K. Ogura, J. Am. Chem. Soc. 116 (1994) 1151.
[3] B. Moulton, M.J. Zaworotko, Curr. Opin. Solid State Mater. Sci. 6 (2002) 117.
[4] (a) S. Mukhopadhyay, P.B. Chatterjee, D. Mandal, G. Mostafa, A. Caneschi, J.v. Slageren, T.J.R. Weakley, M. Chaudhury, Inorg. Chem. 43 (2004) 3413;
(b) S. Kitagawa, T. Okubo, S. Kawata, M. Kondo, M. Katada, H. Kobayashi, Inorg. Chem. 34 (1995) 4790;
(c) M.L. Calatayud, I. Castro, J. Sletten, F. Lloret, M. Julve, Inorg. Chim. Acta 300–302 (2000) 846;
(d) O. Castillo, J. Alonso, U. Garcia-Couceiro, A. Luque, P. Román, Inorg. Chem. Commun. 6 (2003) 803;
(e) Y. Akhriff, J. Server-Carrió, A. Sancho, J. García-Lozano, E. Escrivá, J.V. Folgado, L. Soto, Inorg. Chem. 38 (1999) 1174;
(f) K.S. Min, M.P. Suh, J. Solid State Chem. 152 (2000) 183;
(g) G. De Munno, R. Ruiz, F. Lloret, J. Faus, R. Sessoli, M. Julve, Inorg. Chem. 34 (1995) 408;
(h) J.Y. Lu, M.A. Lawandy, J. Li, Inorg. Chem. 38 (1999) 2695;
(i) O. Castillo, I. Muga, A. Luque, J.M. Gutiérrez-Zorrilla, J. Sertucha, P. Vitoria, P. Román, Polyhedron 18 (1999) 1235;
(j) L. Soto, J. Garcia, E. Escriva, J.P. Legros, J.P. Tuchagues, F. Dahan, A. Fuertes, Inorg. Chem. 28 (1989) 3378.
[5] (a) S.Q. Xia, S.M. Hu, J.C. Dai, X.T. Wu, Z.Y. Fu, J.J. Zhang, W.X. Du, Polyhedron 23 (2004) 1003;
(b) S. Youngme, G.A. van Albada, N. Chaichit, P. Gunnasoot, P. Kongsaeree, I. Mutikainen, O. Roubeau, J. Reedijk, U. Turpeinen, Inorg. Chim. Acta 353 (2003) 119;
(c) K.L. Scott, K. Wieghardt, A.G. Sykes, Inorg. Chem. 12 (1973) 655.
[6] L. Carlucci, G. Ciani, A. Gramaccioli, D.M. Proserpio, S. Rizzato, CrystEngComm 29 (2000) 1.
[7] R. Scopelliti, G. Bruno, C. Donato, G. Tresoldi, Inorg. Chim. Acta 313 (2001) 43.
[8] W.M. Teles, N.G. Fernandes, A. Abras, C.A.L. Filgueiras, Trans. Met. Chem. 24 (1999) 321.
[9] P. Hannesschlager, P. Brun, G. Pèpe, Acta Crystallogr., Sect. C 54 (1998) 223.
[10] (a) A.M. Madalan, V. Ch. Kravtsov, D. Pajic, K. Zadro, Y.A. Simonov, N. Stanica, L. Ouahab, J. Lipkowski, M. Andruh, Inorg. Chim. Acta 357 (2004) 4151;
(b) A. Tovar-Tovar, L. Ruiz-Ramírez, A. Campero, A. Romerosa, R. Moreno-Esparza, M.J. Rosales-Hoz, J. Inorg. Biochem. 98 (2004) 1045.
[11] C. Chachaty, G.C. Pappalardo, G. Scarlata, J. Chem. Soc., Perkin II (1976) 1234.
[12] (a) COLLECT, Enraf-Nonius, Nonius BV, Delft, The Netherlands, 1997–2000;
(b) A.J.M. Duisenberg, J. Appl. Cryst. 25 (1992) 92;
(c) A.J.M. Duisenberg, L.M.J. Kroon-Batenburg, A.M.M. Schreurs, J. Appl. Cryst. 36 (2003) 220.
[13] G.M. Sheldrick, SHELXL-97 – A Program for Crystal Structure Refinement, 97-2, University of Goettingen, Germany, 1997.
[14] (a) A.C. Larson, Crystallogr. Comp. (1970) 291;
(b) R.H. Blessing, Acta Crystallogr., Sect. A 51 (1995) 33.
[15] L.J. Farrugia, J. Appl. Cryst. 30 (1997) 565.
[16] J. Tang, E. Gao, W. Bu, D. Liao, S. Yan, Z. Jiang, G. Wang, J. Molec. Struc. 525 (2000) 271.
[17] A.W. Addison, T.N. Rao, J. Reedijk, J. van Rijn, G.C. Verschoor, J. Chem. Soc., Dalton Trans. (1984) 1349.
[18] L. Zhang, W.-M. Bu, S.-P. Yan, Z.-H. Jiang, D.-Z. Liao, G.-L. Wang, Polyhedron 19 (2000) 1105.
[19] (a) W. Fitzgerald, J. Foley, D. McSweeney, N. Ray, D. Sheahan, S. Tyagi, B. Hathaway, P. O'Brien, J. Chem. Soc., Dalton Trans. (1982) 1117;
(b) X.-F. Chen, P. Cheng, X. Liu, B. Zhao, D.-Z. Liao, S.-P. Yan, Z.-H. Jiang, Inorg. Chem. 40 (2001) 2652;
(c) L. Gasque, R. Moreno-Esparza, E. Mollins, J.L. Briansó-Penalva, L. Ruiz-Ramírez, G. Medina-Dickinson, Acta Crystallogr., Sect. C 54 (1998) 1848.
[20] (a) G. Tresoldi, E. Rotondo, P. Piraino, M. Lanfranchi, A. Tiripichio, Inorg. Chim. Acta 194 (1992) 233;
(b) M.V. Marinho, M.I. Yoshida, K.J. Guedes, K. Krambrock, A.J. Bortoluzzi, M. Hörner, F.C. Machado, W.M. Teles, Inorg. Chem. 43 (4) (2004) 1539;
(c) W.M. Teles, M.V. Marinho, M.I. Yoshida, N.L. Speziali, K. Krambrock, C.B. Pinheiro, N.M. Pinhal, A.A. Leitão, F.C. Machado, Inorg. Chim. Acta 359 (2006) 4613.
[21] (a) O. Castillo, A. Luque, P. Román, J. Mol. Struct. 570 (2001) 181;
(b) I. Castro, J. Faus, M. Julve, A. Gleizes, J. Chem Soc., Dalton Trans. (1991) 1937, and references therein.

Table 1
Table of the pyromorphite minerals used in this work and their origin

Code	Mineral	Formula	Arsenate substitution	%PbO	$\%P_2O_5$	$\%As_2O_5$	%Cl	Origin
Pyro 1	pyromorphite	$Pb_5(PO_4)_3Cl$		82.3	16.1	0.1	2.7	Mount Isa, QLD
Pyro 2	pyromorphite	$Pb_5(PO_4)_3Cl$	AsO_4	Not measured				Brown's Prospect, Rum Jungle, NT
Pyro 3	pyromorphite	$Pb_5(PO_4)_3Cl$		82.2	14.7		2.6	Tennant Creek, NT
Pyro 4	pyromorphite	$Pb_5(PO_4)_3Cl$		82.8	15.7	trace	2.6	Broken Hill, NSW
Pyro 5	pyromorphite	$Pb_5(PO_4)_3Cl$	AsO_4	82.9	12.6	4.5	2.7	Broken Hill, NSW
Pyro 6	pyromorphite	$Pb_5(PO_4)_3Cl$		82.8	15.4	0.3	2.6	Kintore Open Cut, Broken Hill, NSW
Pyro 7	calcian pyromorphite	$(Ca,Pb)_5(PO_4)_3Cl$	Not determined					Block 14 Mine, Broken Hill, NSW
Pyro 8	arsenian pyromorphite	$Pb_5(AsO_4,PO_4)_3Cl$	AsO_4	82.9	10.6	5.5	2.8	Bunker Hill Mine, Kellogg, Idaho, USA

two minerals difficult, but usually pyromorphite is green and mimetite is yellow. Such colourations lend the minerals to NIR spectroscopy. Vanadinite is usually red. Pyromorphite's main characteristic is its unique crystal habit of stacked branching barrel-shaped crystals.

Farmer reported the vibrational spectra of minerals with a fluoroapatite structure [11]. The infrared spectra of pyromorphite showed bands at 1030 and 970 cm^{-1} attributed to phosphate v_3 antisymmetric stretching vibrations and at 572 and 542 cm^{-1} assigned to phosphate v_4 bending modes [11]. The infrared spectra of mimetite showed bands at 815, 803 and 783 cm^{-1} attributed to arsenate v_3 antisymmetric stretching vibrations and at 415 and 383 cm^{-1} assigned to arsenate v_4 bending modes [11]. The vibrational spectra of lead apatites were reported by Levitt and Condrate [12,13]. Crystal structure and factor group analysis have

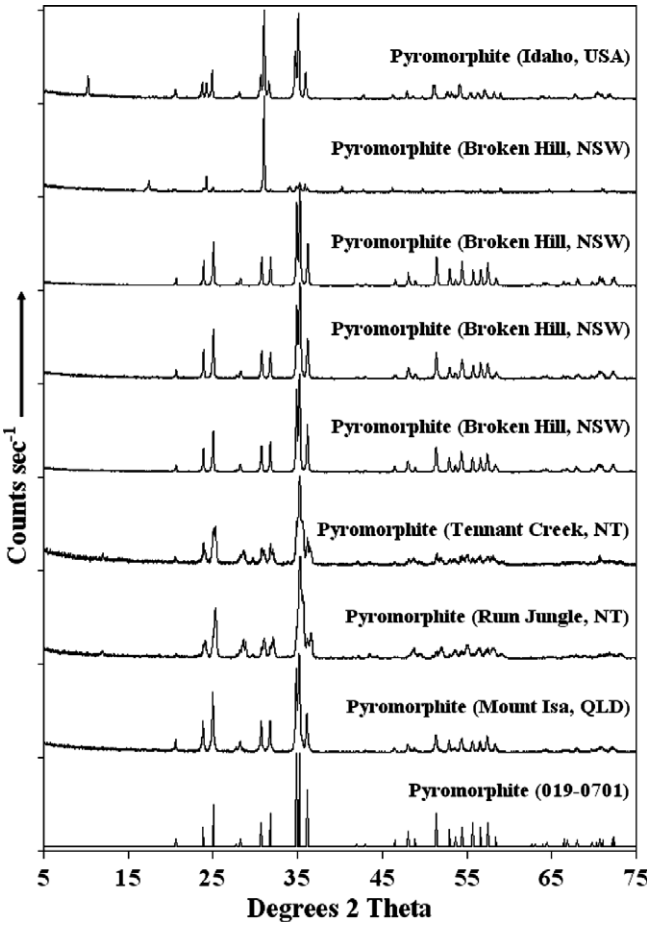


Fig. 1. XRD patterns of a selection of pyromorphite minerals.

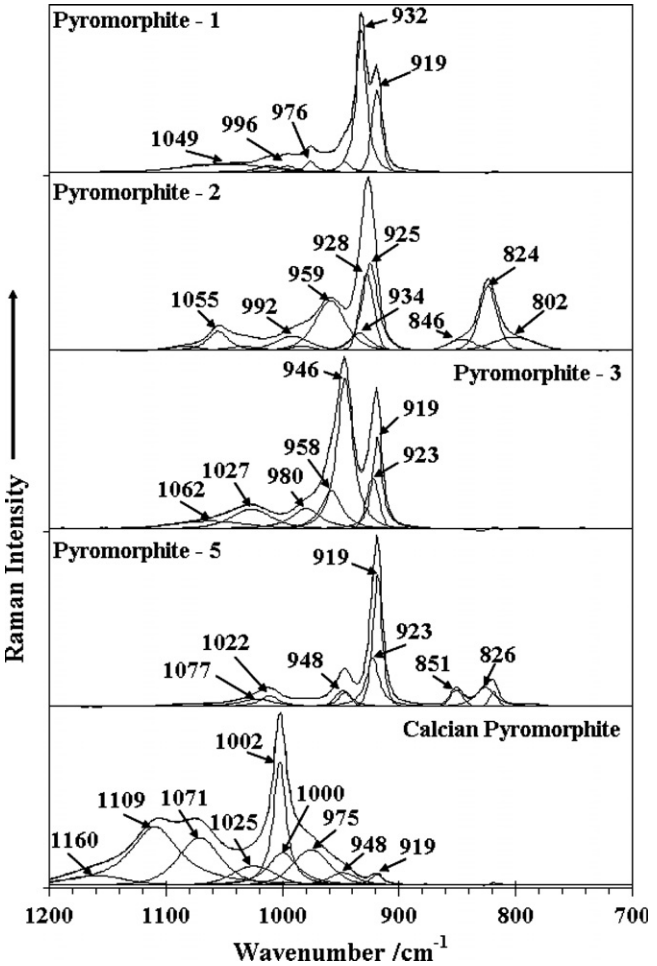


Fig. 2. Raman spectra of pyromorphite in the high wavenumber region.

been undertaken [14]. Bartholomai and Klee reported the vibrational spectra of single crystals of pyromorphite, vanadinite and mimetite [15].

Raman spectroscopy has proven very useful for the study of minerals [16–18]. Indeed Raman spectroscopy has proven most useful for the study of diagentically related minerals as often occurs with carbonate minerals [19–23]. Some previous studies have been undertaken by the authors using Raman spectroscopy to study complex secondary minerals formed by crystallisation from concentrated

Table 2
Results of the Raman spectroscopic analysis of pyromorphites (band percentage was calculated as normalised to total band areas)

Pyromorphite 1			Pyromorphite 2			Pyromorphite 3			Pyromorphite 5			Calcian pyromorphite		
Centre	FWHM	%	Centre	FWHM	%	Centre	FWHM	%	Centre	FWHM	%	Centre	FWHM	%
						3722	116	1.67	3745	101	0.62			
3642	119	3.39				3637	89	6.65	3644	121	5.70			
3508	173	4.84				3565	122	5.71	3536	161	6.43	3483	56	0.51
3395	96	18.38				3441	135	24.37	3408	124	30.85	3425	75	2.55
3341	38	5.61				3386	82	27.29	3383	72	17.06	3383	64	5.51
3304	44	3.22				3309	68	20.84	3307	69	12.75	3321	93	3.39
3262	74	3.04				3240	74	7.58	3241	61	3.82			
3195	64	1.26										1160	54	1.52
												1109	50	11.51
			1084	28	0.99				1077	53	0.44	1071	41	6.44
1049	86	5.52	1055	20	4.12	1062	71	0.29						
			1034	25	1.07									
			1031	53	4.13	1027	40	0.46	1022	34	1.09	1025	41	2.38
1011	21	1.61							1011	18	0.97	1002	12	6.34
996	16	1.05	992	33	4.57							1000	29	3.42
976	10	1.25	984	20	0.79	980	28	0.39				975	36	4.03
955	73	9.00	959	29	14.94	958	20	0.51	955	109	2.55			
947	10	1.31							948	15	0.89	948	25	1.01
932	10	14.18	934	19	3.49	946	15	1.65	946	12	0.97			
			928	13	10.04	923	12	0.36	923	12	3.20			
919	9	6.85	925	15	14.42	919	9	0.64	919	9	5.05	919	12	0.40
			846	25	2.63				851	12	0.78			
			824	17	11.20				826	18	1.64			
			802	40	5.03				819	7	0.44			
									788	19	0.22			
			606	20	0.32							624	15	1.53
595	7	1.06	592	8	0.42				583	10	0.05	592	57	4.38
591	25	0.75							581	12	0.18			
588	9	0.13	586	13	1.53				574	8	0.20	573	16	1.50
575	9	0.49	571	28	1.61	579	17	0.05	554	8	0.05	552	30	4.27
555	9	0.67	554	8	0.26	553	12	0.06	544	5	0.09			
543	8	0.18	547	14	0.53				541	6	0.07			
			451	20	0.31							450	28	6.68
437	22	0.82	430	31	3.10	436	15	0.03	432	18	0.15	440	17	4.48
429	12	1.14	424	16	1.35	419	17	0.12	420	13	0.31	422	15	2.38
418	15	1.71	402	35	2.54	416	45	0.07	418	10	0.53			
398	17	1.58	396	13	2.02	409	12	0.20	409	15	0.21			
392	11	0.53				393	9	0.12	392	14	0.45			
						390	16	0.10						
			379	15	0.19				375	9	0.15			
									366	11	0.02	361	18	0.57
			354	23	1.10				347	10	0.15	353	20	0.50
			331	21	0.92				341	9	0.03	340	24	1.59
												271	25	0.88
247	64	0.69										244	29	3.24
												230	20	4.15
									213	27	0.30	218	20	5.53
207	42	1.90	208	51	2.43	207	42	0.13				206	19	4.52
198	17	1.60	188	34	1.80	190	20	0.17						
180	19	1.21				177	15	0.14	181	50	0.65	181	25	0.85
			163	29	1.50	163	26	0.13				163	20	2.03
155	41	3.79	145	18	0.65	157	35	0.08	157	19	0.50	146	13	1.83
143	9	0.32				145	21	0.13				132	10	0.06
						114	10	0.03						
106	7	0.93				107	7	0.04	108	10	0.45			

sulphate solutions [24]. Very few recent spectroscopic studies of natural pyromorphite minerals have been forthcoming and what studies that are available are not new. Some Raman studies are available [25,26]. In this work we have obtained Raman and infrared spectra of selected pyromorphites, arsenianpyromorphite and phosphohedyphane and relate the spectra to the structure of the minerals.

2. Experimental

2.1. Minerals

The pyromorphite minerals were supplied by The Mineralogical Research Company. A selection of pyromorphite minerals were also provided by The South Australian Museum (Adelaide, Australia). Table 1 reports the pyromorphite minerals together with their origin. All of the minerals except for the arsenian pyromorphite are from Australian mineral deposits. The minerals were analysed by EDX measurements for chemical composition and by powder X-ray diffraction for phase purity. Some EDX measurements are given in Table 1. The XRD patterns of a selection of pyromorphite minerals from Australia and international origins are shown in Fig. 1. Also shown is the reference pattern for pyromorphite.

2.2. Raman spectroscopy

The crystals of pyromorphite were placed and oriented on the stage of an Olympus BHSM microscope, equipped with 10× and 50× objectives and part of a Renishaw 1000 Raman microscope system, which also includes a monochromator, a filter system and a charge coupled device (CCD). Raman spectra were excited by a HeNe laser (633 nm) at a resolution of 2 cm^{-1} in the range between 100 and 4000 cm^{-1}. Repeated acquisition using the highest magnification was accumulated to improve the signal to noise ratio. Spectra were calibrated using the 520.5 cm^{-1} line of a silicon wafer. Previous studies by the authors provide more details of the experimental technique [27–30]. Some minimal background is observed in the spectra of pyromorphites. This background is removed by using performed using the Spectracalc software package GRAMS (Galactic Industries Corporation, NH, USA) by using a multipoint fitting function (Go to Grams, select arithmetic, select baseline, select multipoint fitting, select fit points to line).

Band intensities in the Raman spectroscopy of crystals including minerals are very much dependent upon the orientation. Such studies have been undertaken by the authors [31–35]. The intensity will depend upon the orientation of the crystal relative to the incident beam. Such orientation effects were not explored in this research as it is beyond the scope of this research as the objective of the research was to study the isomorphous substitution especially looking for substitution by arsenate, hydroxyl and water in the pyromorphite structure.

2.3. Mid-IR spectroscopy

Infrared spectra of the pyromorphites were obtained using a Nicolet Nexus 870 FTIR spectrometer with a smart endurance single bounce diamond ATR cell. Spectra over the 4000–525 cm^{-1} range were obtained by the co-addition of 64 scans with a resolution of 4 cm^{-1} and a mirror velocity of 0.6329 cm/s. Spectra were co-added to improve the signal to noise ratio.

Spectral manipulation such as baseline adjustment, smoothing and normalisation were performed using the Spectracalc software package GRAMS (Galactic Industries Corporation, NH, USA). Band component analysis was undertaken using the Jandel 'Peakfit' software package which enabled the type of fitting function to be selected and allows specific parameters to be fixed or varied accordingly. Band fitting was done using a Lorentz–Gauss cross-product function with the minimum number of component bands used for the fitting process. The Gauss–Lorentz ratio was maintained at values greater than 0.7 and fitting was undertaken until reproducible results were obtained with squared correlations of r^2 greater than 0.995.

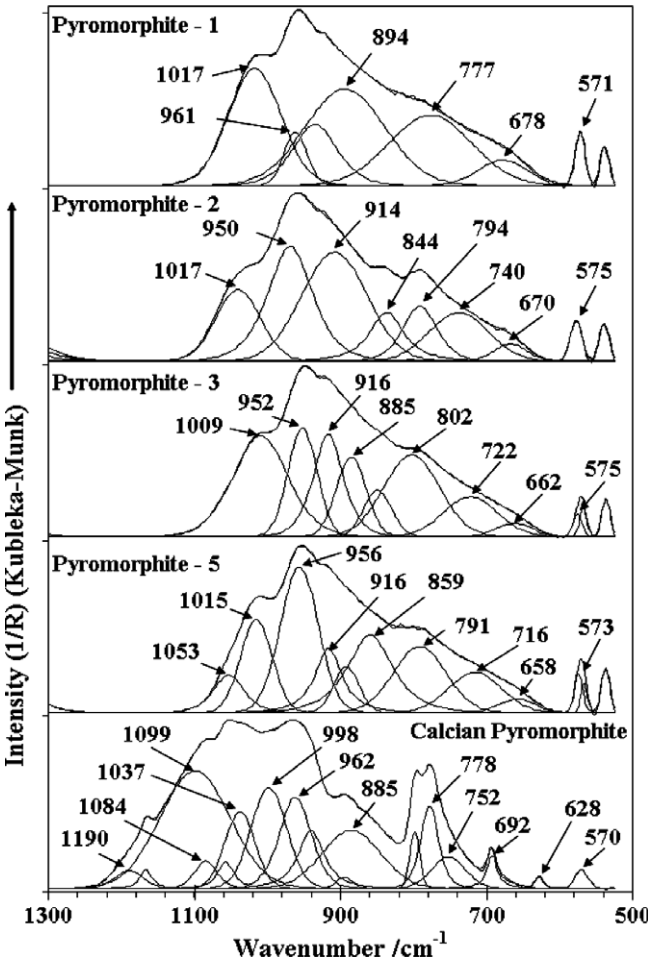


Fig. 3. Infrared spectra of pyromorphite in the high wavenumber region.

3. Results and discussion

3.1. Raman spectroscopy

The Raman spectra of selected pyromorphite minerals in the 700–1200 cm^{-1} region are shown in Fig. 2. The results of the band component analyses of the Raman spectra are reported in Table 2. The Raman spectra show intense bands in the 920–950 cm^{-1} region. Two bands are observed for pyromorphite 1 (origin Mt Isa, Queensland) at 919 and 932 cm^{-1}. A single band is observed for pyromorphite 2 (Rum Jungle, Northern Territory) at 925 cm^{-1}. This band is asymmetric and additional bands at 928 and 934 cm^{-1} may be resolved. In the spectra of pyromorphite 2, two bands are observed at 802 and 824 cm^{-1}. These bands are assigned to the $(AsO_4)^{3-}$ v_1 symmetric stretching mode. The band at 925 cm^{-1} is attributed to the $(PO_4)^{3-}$ v_1 symmetric stretching mode. Farmer based upon infrared spectra, also reported this band at 925 cm^{-1} [11]. Two bands are also observed for pyromorphite 3 (Tennant Creek, Northern territory, Australia) at 919 and 946 cm^{-1}. For pyromorphite 5 (Broken Hill, New South Wales, Australia) a single band is observed at 919 cm^{-1}. This Raman band also shows some asymmetry and an additional component at 923 cm^{-1} may be resolved. Two additional bands at 826 and 851 cm^{-1} are observed in the spectrum of pyromorphite 5. These bands are also assigned to the $(AsO_4)^{3-}$ symmetric stretching modes.

The infrared spectra are shown in Fig. 3. The results of the band component analysis of the infrared spectra are reported in Table 3. The spectra appear complex with a number of overlapping bands. An infrared band of low intensity is observed at around 916 cm^{-1}. This band is the infrared equivalent of the Raman band observed at 925 cm^{-1}. Levitt and Condrate reported the symmetric stretching mode of $(PO_4)^{3-}$ in pyromorphite at 920 cm^{-1} [12,13]. Adler and Kerr found the infrared band to occur at 926 cm^{-1} [36]. Bartholomai and Klee published the sin-

Table 3
Results of the Infrared spectroscopic analysis of pyromorphites

Pyromorphite 1			Pyromorphite 2			Pyromorphite 3			Pyromorphite 5			Calcian pyromorphite		
Centre	FWHM	%	Centre	FWHM	%	Centre	FWHM	%	Centre	FWHM	%	Centre	FWHM	%
2362	22	1.80												
2340	9	0.24												
2329	28	1.48												
												1877	77	0.49
												1790	61	0.21
												1683	117	0.38
												1608	48	0.15
			1515	31	0.43	1518	37	0.15						
			1437	73	5.64	1428	89	1.67	1432	52	1.07			
									1387	88	1.31			
			1357	108	7.89	1340	64	1.18						
			1330	39	3.37	1330	26	0.26	1312	47	1.66			
									1302	16	0.03			
												1190	45	1.70
												1166	17	0.92
												1099	112	28.43
												1084	36	2.19
									1053	49	6.74	1057	26	1.77
			1040	72	19.18							1037	48	7.98
1017	84	33.08				1009	88	27.72	1015	51	16.20	998	57	12.44
961	36	6.51	969	71	16.80	952	46	15.28	956	60	30.31	962	51	10.44
935	71	15.20										940	42	3.09
920	8	0.21	908	105	21.47	916	48	16.21	916	43	5.83			
894	129	20.55				885	48	11.51	892	40	6.34	895	24	0.58
												885	94	11.72
						849	45	6.29	859	72	10.89			
			837	55	5.99							822	174	4.92
			804	4	0.07	802	90	11.10				798	16	1.98
777	132	15.37	791	55	6.00				791	84.8	9.52	778	28	5.49
			738	95	8.60							752	53	3.63
						722	87	5.24	716	84.8	5.81			
												692	16	0.78
678	78	3.26	667	53	1.67	662	57	1.15	658	55.0	1.27			
												628	12	0.31
571	15	1.39	577	18	1.43	575	14	0.51	573	13.6	0.92	570	19	0.39
						567	11	0.97	566	10.5	1.03			
538	14	0.91	539	16	1.10	536	13	0.75	537	13.9	1.02			

gle crystal spectra of pyromorphite [15]. Two bands were observed at 920 and 919 cm^{-1} ascribed to the A_g and E_{2g} vibrational modes. The latter band was very intense and the former intense. Two bands are resolved for pyromorphite 5 at 919 and 923 cm^{-1} and these bands may be attributed to these vibrational modes.

The infrared spectra of the studied minerals are shown in Fig. 3. A series of bands for pyromorphite sample 1 were band resolved at 1049, 996 and 976 cm^{-1}. The first band may be simply part of the background. These bands are attributed to the $(PO_4)^{3-}$ antisymmetric stretching mode of pyromorphite. Typically these bands are expected to show greater intensity in the infrared spectrum as compared with the Raman spectrum. Levitt and Condrate reported three Raman bands at 1014, 980 and 947 cm^{-1} and attributed these modes to the antisymmetric stretching vibration [12]. Bartholomai and Klee assigned bands at 1025 (weak), 1011 (weak) and 949 cm^{-1} (strong) [15]. For pyromorphite 2, Raman bands are observed at 1055, 992, 959 cm^{-1} and correspond at least in part to the observations of Bartholomai and Klee. For pyromorphite 3 an intense Raman band at 946 cm^{-1} is observed which is within spectral resolution and is in agreement with the intense Raman band as published by Bartholomai and Klee. In the infrared spectra (Fig. 3) two bands are observed at around 1017 and 950 cm^{-1} and are attributed to the antisymmetric stretching modes of $(PO_4^{3-}$. Levitt and Condrate reported infrared bands for pyromorphite in similar positions [12,13].

The Raman spectra in the 500–700 cm^{-1} region for the selected pyromorphites are reported in Fig. 4. The simplest spectrum of pyromorphite 3 shows two bands at 553 and 579 cm^{-1}. Farmer based upon the work of Bhatnagar and Levitt and Condrate [13,37] reported two bands for pyromorphite at 542 and 572 cm^{-1} [11]. These bands are assigned to the v_4 phosphate bending modes. The Raman spectrum of pyromorphite 2, is more complex with a significant number of bands at 547, 554, 586 and 592 cm^{-1}. Any reduction in symmetry of the phosphate anion because of isomorphous substitution will result in the loss of degeneracy and additional bands may be observed. Such degeneracy is also observed for pyromorphite 1 where bands are observed at 543, 555, 575, 591 and 595 cm^{-1}. Unsubstituted pyromorphite 1 has one less band that substituted pyromorphite 5. This difference can be explained by crystal orientation effects.

For the calcian pyromorphite, two bands which are quite broad in comparison to the pure pyromorphites are observed at 552 and 573 cm^{-1}. These two bands, although of low intensity in the Raman spectrum, are also observed in the infrared spectra at around 540 and 575 cm^{-1} (Fig. 3).

The Raman spectra in the 100–500 cm^{-1} region of pyromorphite are displayed in Fig. 5. Bands are observed around 400–500 cm^{-1} and between 100 and 250 cm^{-1}. The first region is attributed to the v_2 bending modes of the phosphate units. For pyromorphite 3, two Raman bands are observed at 393 and 409 cm^{-1}. These bands are

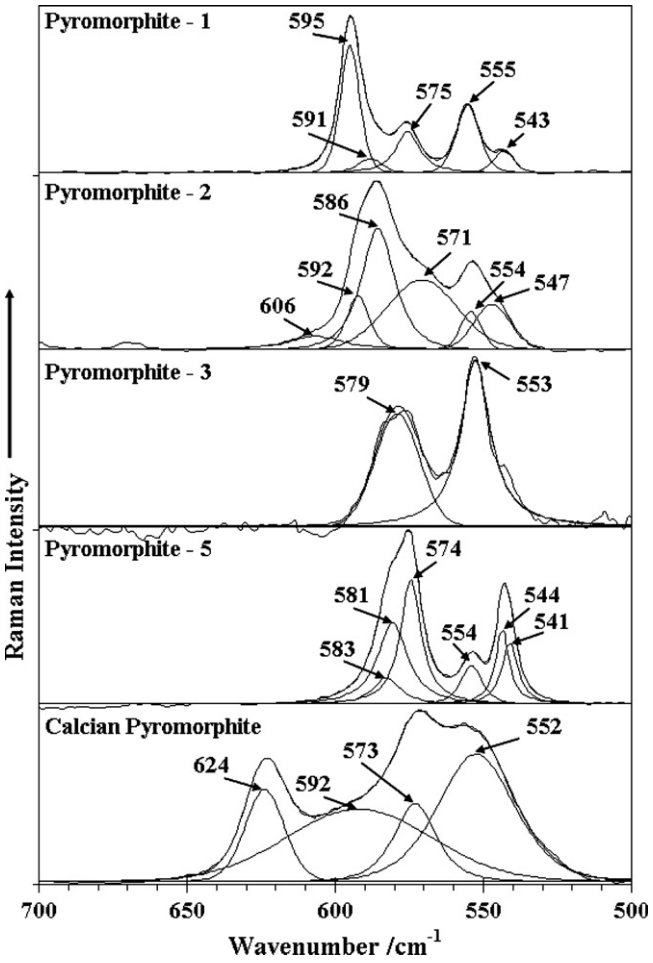


Fig. 4. Raman spectra of pyromorphite in the low wavenumber cm^{-1} region.

non-symmetric and other bands may be resolved. Additional bands are observed at 390, 419 and 436 cm^{-1}. For pyromorphite 2, Raman bands are observed at 396, 424 and 430 cm^{-1}. The additional complexity is accounted for by the reduced symmetry of phosphate anion in pyromorphite 2. In addition two bands are observed at 331 and 354 cm^{-1}. These Raman bands are attributed to the v_2 bending modes of the arsenate anion [38–45] and in effect provides evidence for some arsenate substitution of phosphate in this mineral. The Raman spectrum in pyromorphite 5 shows an even more complex profile. Two Raman bands for pyromorphite 5 at 347 and 375 cm^{-1} are attributed to the v_2 bending modes arsenate anion. Pyromorphite 2 and 5 are arsenian pyromorphite, indicated by the two additional bands. Two Raman bands at 347 and 375 cm^{-1} are attributed to the v_2 bending modes arsenate anion and the bands at 392 and 418 cm^{-1} to the v_2 bending modes of the phosphate anion. Pyromorphites 1, 2, 3 and 5 show exactly five bands after deconvolution in the range 390–451 cm^{-1}. The only difference is the additional bands 331–375 cm^{-1}, which can be accounted for arsenate substitution. It is noted that the position of these bands have not been previously reported. Farmer (page 390) simply state

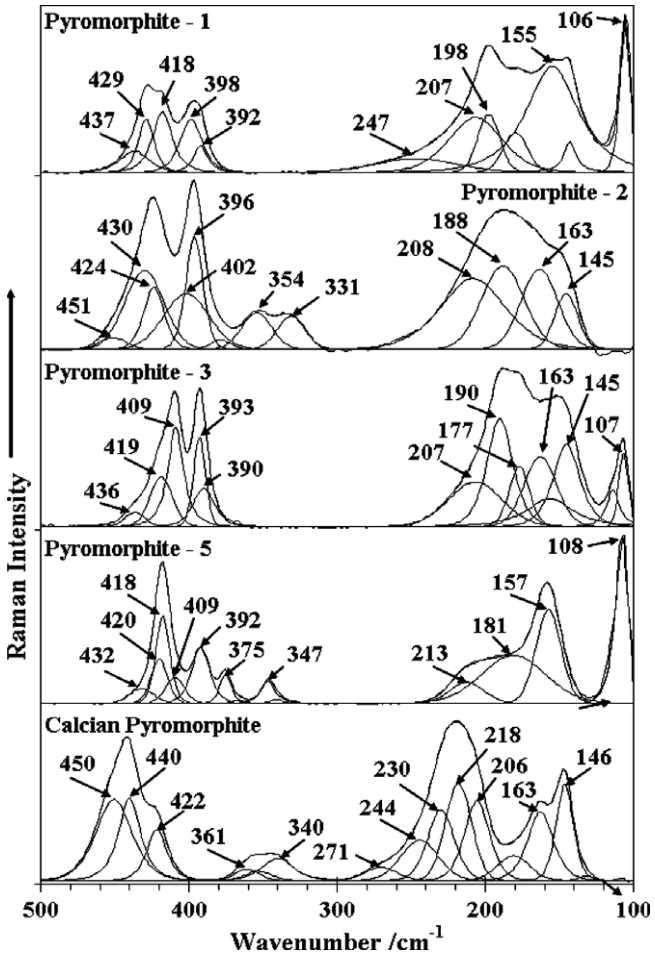


Fig. 5. Raman spectra of pyromorphite in the low wavenumber region.

that the bands occurred at <400 cm^{-1} [11]. No recent vibrational spectroscopic studies of these types of apatite minerals have been forthcoming [46–48]. Botto et al. showed that by using vibrational spectroscopic techniques the Cl in pyromorphite can be replaced by OH units [49]. These workers also showed that some carbonate anions were present in a pyromorphite mineral and replaced the phosphate in the minerals [49]. In the calcian pyromorphite, two broad low intensity Raman bands at 340 and 361 cm^{-1} are attributed to the presence of arsenate and the Raman bands at 422, 440 to the phosphate v_2 bending modes. This study has shown that several of the so called pyromorphite minerals contain arsenate as a substitute for phosphate. It is apparent that arsenate can readily replace phosphate in the structure. The study of this spectral region goes a long way to proving the solid solution formation of the mimetite–pyromorphite series [50]. A broad profile in the Raman spectra from 100 to 250 cm^{-1} is observed. It is difficult to define the attribution of bands in this spectral region other than to define the bands as lattice modes. The intense band at 107 cm^{-1} is present in pyromorphite 1, 3 and 5 spectra but is absent in the spectra of pyromorphite 2 and the calcian pyromorphite. Such a presence or absence of a band may be due to orientation effects.

The Raman spectra of selected pyromorphite minerals in the 3000–4000 cm^{-1} are shown in Fig. 6. Infrared spectra were also obtained but the quality of the spectra were lacking and were not reported. The spectra suffered from a poor signal to noise ratio and the spectrum of water vapour contributed to this noise. It is interesting that significant Raman intensity is observed in this spectral region. There are a number of possibilities for the assignment of these bands (a) OH stretching vibrations as an isomorphic substitution of OH units for Cl^- ions in the pyromorphite structure (b) the bands are due to OH vibrations of adsorbed water (c) the bands are due to OH vibrations of bonded water. The Raman spectra of pyromorphite samples 1–3 show strong similarities in the 2500–4000 cm^{-1} region. One possible interpretation is that the bands in the 3000–3450 cm^{-1} region are ascribable to water OH stretching bands; the higher wavenumber bands at for example 3508 and 3642 cm^{-1} for pyromorphite 1 may be attributed to OH stretching vibrations resulting from the OH substitution for Cl^- ions in the pyromorphite structure. The higher wavenumber bands in the OH stretching region are not observed for the calcian pyromorphite. Instead a band at 3383 cm^{-1} is found and is assigned to the OH stretching vibration of water. In other words some

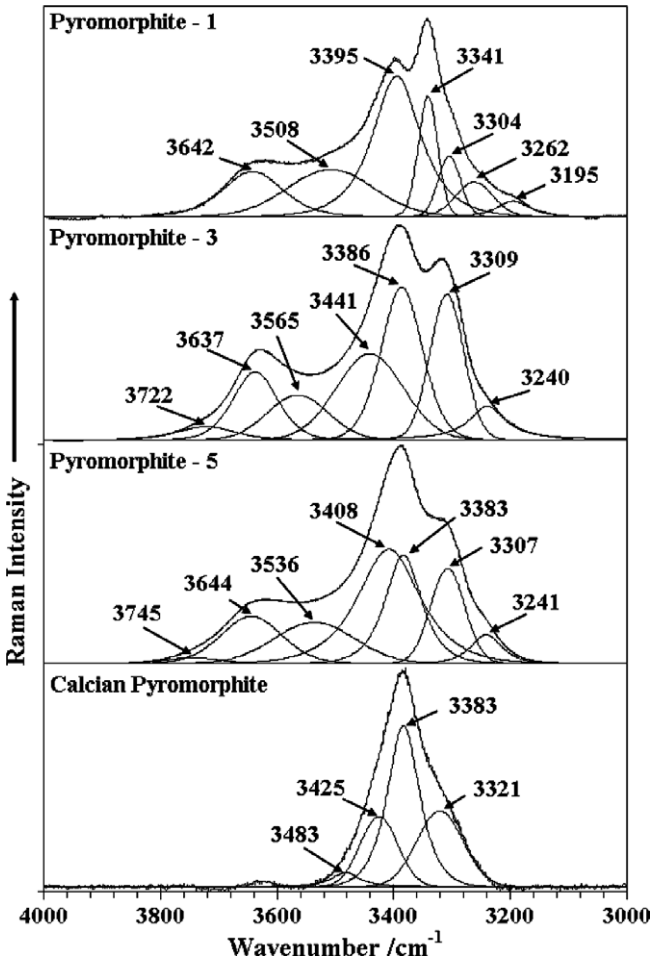


Fig. 6. Raman spectra of pyromorphite in the OH stretching region.

water is involved in the structure of natural pyromorphite. Further research would need to be undertaken to prove this concept. Botto et al. also found that Cl–OH substitution occurred for pyromorphite [49]. A previous study by the principal author on the Raman spectra of vanadinite also proved that substitution of vanadinite by phosphate and the partial replacement of chloride by hydroxyl units can occur [51].

4. Conclusions

This research has found the following results:

(a) Raman spectroscopy can be used to characterise pyromorphite and arsenian substituted pyromorphites.
(b) For most pyromorphite minerals splitting of the v_1 $(PO_4)^{3-}$ symmetric stretching mode is observed, implying the phosphate units in the structure are not equivalent.
(c) The implication is that the phosphate units are not all equivalent in the structure of pyromorphite.
(d) In selected pyromorphite minerals some replacement of phosphate by arsenate occurs as is observed in the Raman spectra.
(e) Similarly replacement of the Cl^- ion by OH^- units is confirmed by the Raman spectra in the OH stretching region.
(f) Multiple bands in both the v_4 and v_2 bending regions support the concept of the reduction in symmetry of the phosphate anion in pyromorphite.
(g) The true formula of pyromorphites in practice is significantly different from that commonly accepted. A more appropriate formula is $Pb_5(PO_4, AsO_4)_3(Cl,OH) \cdot xH_2O$. Such a formula is supported by the work of Botto et al. who showed that substitution of Pb, $(PO_4)^{3-}$, and Cl by Ca, Ba, $(CO_3)^{2-}$ and OH can readily occur [49].
(h) This research has also shown that pyromorphite contains chemically bonded water.

Acknowledgments

The financial and infra-structure support of the Queensland University of Technology, Inorganic Materials Research Program is gratefully acknowledged. The Australian Research Council (ARC) is thanked for funding the instrumentation.

References

[1] J.A. Mandarino, Fleischer's Glossary of Mineral Species, The Mineralogical Record, Tuscon, Arizona, USA, 1999.
[2] A.G. Cockbain, Mineral. Mag. J. Mineral. Soc. (1876–1968) 36 (1968) 1171.
[3] A.G. Cockbain, Mineral. Mag. J. Mineral. Soc. (1876–1968) 36 (1968) 654.
[4] W.E. Baker, Am. Mineral. 51 (1966) 1712.
[5] E. Foertsch, H. Wondratschek, Naturwissenschaften 52 (1965) 182.
[6] Y. Dai, J.M. Hughes, Can. Mineral. 27 (1989) 189.
[7] A.R. Kampf, I.M. Steele, R.A. Jenkins, Am. Mineral. 91 (2006) 1909.
[8] J.W. Anthony, R.A. Bideaux, K.W. Bladh, M.C. Nichols, Handbook of Mineralogy, Mineral Data Publishing, Tuson, Arizona, 4: Arsenates, Phosphates,Vanadates, Mineral Data Publishing, Tucson, Arizona, 2000.
[9] Y. Dai, J.M. Hughes, P.B. Moore, Can. Mineral. 29 (1991) 369.
[10] Y. Dai, Mineral. Rec. 24 (1993) 307.
[11] V.C. Farmer, The infrared spectra of minerals, in: Mineralogical Society Monograph 4, Mineralogical Society, London, 1974.
[12] S.R. Levitt, K.C. Blakeslee, R.A. Condrate, Mem. Soc. Roy. Sci. Liege, Collection in 8 Deg 20 (1970) 121.
[13] S.R. Levitt, R.A. Condrate, Am. Mineral. 55 (1970) 1562.
[14] D.M. Adams, I.R. Gardner, J. Chem. Soc., Dalton Trans.: Inorg. Chem. (1972–1999) (1974) 1505.
[15] G. Bartholomai, W.E. Klee, Spectrochim. Acta Part A: Mol. Biomol. Spectrosc. 34A (1978) 831.
[16] R.L. Frost, S.J. Palmer, J.M. Bouzaid, B.J. Reddy, J. Raman Spectrosc. 38 (2007) 68.
[17] R.L. Frost, D.A. Henry, M.L. Weier, W. Martens, J. Raman Spectrosc. 37 (2006) 722.
[18] R.L. Frost, A.W. Musumeci, J.T. Kloprogge, M.O. Adebajo, W.N. Martens, J. Raman Spectrosc. 37 (2006) 733.
[19] R.L. Frost, J. Cejka, M. Weier, W.N. Martens, J. Raman Spectrosc. 37 (2006) 879.
[20] R.L. Frost, M.L. Weier, J. Cejka, J.T. Kloprogge, J. Raman Spectrosc. 37 (2006) 585.
[21] R.L. Frost, J. Cejka, M.L. Weier, W. Martens, J. Raman Spectrosc. 37 (2006) 538.
[22] R.L. Frost, M.L. Weier, B.J. Reddy, J. Cejka, J. Raman Spectrosc. 37 (2006) 816.
[23] R.L. Frost, M.L. Weier, W.N. Martens, J.T. Kloprogge, J. Kristof, J. Raman Spectrosc. 36 (2005) 797.
[24] R.L. Frost, R.-A. Wills, M.L. Weier, W. Martens, J. Raman Spectrosc. 36 (2005) 435.
[25] H. Fan, K. Tao, Y. Xie, K. Wang, Yanshi Xuebao 19 (2003) 169.
[26] W. Hong, S. He, S. Huang, Y. Wang, H. Hou, X. Zhu, Guangpuxue Yu Guangpu Fenxi 19 (1999) 546.
[27] R.L. Frost, D.A. Henry, K. Erickson, J. Raman Spectrosc. 35 (2004) 255.
[28] R.L. Frost, Spectrochim. Acta Part A 60A (2004) 1469.
[29] R.L. Frost, O. Carmody, K.L. Erickson, M.L. Weier, J. Cejka, J. Mol. Struct. 703 (2004) 47.
[30] R.L. Frost, O. Carmody, K.L. Erickson, M.L. Weier, D.O. Henry, J. Cejka, J. Mol. Struct. 733 (2004) 203.
[31] R.L. Frost, J.T. Kloprogge, Spectrochim. Acta Part A 57 (2000) 163.
[32] R.L. Frost, J.T. Kloprogge, Spectrochim. Acta Part A 56A (2000) 931.
[33] J.T. Kloprogge, R.L. Frost, L. Rintoul, Phys. Chem. Chem. Phys. 1 (1999) 2559.
[34] R.L. Frost, W.N. Martens, L. Rintoul, E. Mahmutagic, J.T. Kloprogge, J. Raman Spectrosc. 33 (2002) 252.
[35] W.N. Martens, L. Rintoul, J.T. Kloprogge, R.L. Frost, Am. Mineral. 89 (2004) 352.
[36] H.H. Adler, Am. Mineral. 49 (1964) 1002.
[37] V.M. Bhatnagar, Can. J. Chem. 49 (1971) 662.
[38] R.L. Frost, M. Weier, W.N. Martens, Spectrochim. Acta Part A 63A (2006) 685.
[39] R.L. Frost, J.T. Kloprogge, W.N. Martens, J. Raman Spectrosc. 35 (2004) 28.
[40] W.N. Martens, J.T. Kloprogge, R.L. Frost, L. Rintoul, J. Raman Spectrosc. 35 (2004) 208.
[41] R.L. Frost, W. Martens, P.A. Williams, J.T. Kloprogge, J. Raman Spectrosc. 34 (2003) 751.
[42] W. Martens, R.L. Frost, J.T. Kloprogge, J. Raman Spectrosc. 34 (2003) 90.
[43] W. Martens, R.L. Frost, P.A. Williams, J. Raman Spectrosc. 34 (2003) 104.

[44] W.N. Martens, R.L. Frost, J.T. Kloprogge, P.A. Williams, Am. Mineral. 88 (2003) 501.
[45] R.L. Frost, W.N. Martens, P.A. Williams, J. Raman Spectrosc. 33 (2002) 475.
[46] E.E. Coleyshaw, W.P. Griffith, R.J. Bowell, Spectrochim. Acta Part A: Mol. Biomol. Spectrosc. 50A (1994) 1909.
[47] W.P. Griffith, J. Chem. Soc. [Section] A: Inorg. Phys. Theor. (1970) 286.
[48] W.P. Griffith, Nature (London, United Kingdom) 224 (1969) 264.
[49] I.L. Botto, V.L. Barone, J.L. Castiglioni, I.B. Schalamuk, J. Mater. Sci. 32 (1997) 6549.
[50] E. Foertsch, Neues Jahrbuch fuer Mineralogie, Abhandlungen 113 (1970) 219.
[51] R.L. Frost, M. Crane, P.A. Williams, J.T. Kloprogge, J. Raman Spectrosc. 34 (2003) 214.

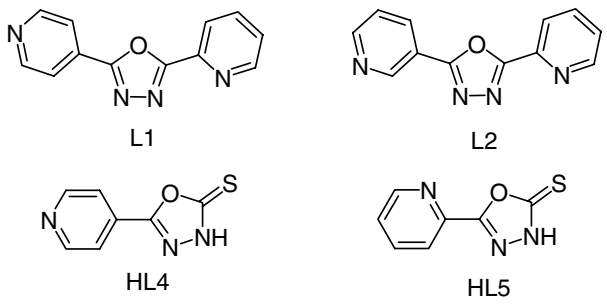


Chart 1.

discrete complexes generated from unsymmetric oxadiazole-containing organic ligands and inorganic salts. So far, a variety of products resulting from the assembly of metal salts with unsymmetric oxadiazole-bridged ligands (**L1** and **L2**, Chart 1) have been synthesized and characterized by us, which possess some specific features of tunable achiral/chiral helix and NLO-active properties [16]. Meanwhile, only few polymeric compounds containing **HL4** (Chart 1) have been reported by us and other groups [17]. Up until now, the coordination polymers or supramolecular complexes based on oxadiazole-bridged organic ligands, such as 5-(2-pyridyl)-1,3,4-oxadiazole-2-thione (**HL5**), are in general undeveloped. This encouraged us to undertake further studies on unsymmetric oxadiazole-containing ligands of this type and explore their interesting coordination chemistry. Following this approach, we now expand the coordination chemistry with **HL5**. As we all know, d^{10} transition-metal ions, such as Zn(II), Cd(II) and Hg(II), can produce a variety of complexes that not only exhibit appealing structures but also possess photoluminescence properties. In this contribution, three new divalent d^{10} transition-metal coordination polymers and discrete coordination complexes, namely, $[Zn(\mathbf{L5})_2(H_2O)_2]$ (**2**), $[Cd(\mathbf{L5})_2]_n$ (**3**) and $[Hg_2(\mathbf{L5})_4]$ (**4**), were successfully isolated, which shows the effect of metal radii on the formation of different coordination complexes. In addition, thermal stabilities, room-temperature solid state luminescent and SHG (second-harmonic generation) properties of **HL5** and **2**, **3** and **4** were investigated in detail.

2. Experimental

2.1. Materials and general methods

The reagents and solvents employed were commercially available and were used as received without further purification. Elemental analyses were performed on a Perkin–Elmer 240 elemental analyzer. The FT-IR spectra were recorded from KBr pellets in the range 400–4000 cm^{-1} on a Bruker Tensor27 spectrometer. ^1H and ^{13}C NMR spectra were recorded on a Bruker AV-400 NMR spectrometer at 400 and 100 MHz using DMSO-d_6 solution at room temperature; the DMSO-d_6 signal was used to lock the field and all chemical shifts are given relative to tetramethylsilane (TMS). Thermogravimetric analysis (TGA) data were collected with a Perkin–Elmer TGS-2 analyzer in N_2 at a heating rate of 10 °C min^{-1}. The emission/excitation spectra were recorded on an Edinburgh FLS920 spectrometer equipped with a continuous Xe900 Xenon lamp and an nF900 ns flash lamp. Kurtz powder SHG measurements were performed on ground samples of crystalline **2**–**4** with a synchroscan streak camera (Hamamatsu Model C1587, 8 ps resolution) connected to a polychromator as the detector system, and an optical parametric generator (Spectra Physics, Model:OPA-800C) pumped by a mode-locked Ti:sapphire laser oscillator–amplifier system (Spectra Physics, Model: Hurricane) as the pump source. The powder second-harmonic signals were compared to that of urea to determine the relative SHG efficiencies of **2**–**4**.

2.2. Synthesis of the ligand 5-(2-pyridyl)-1,3,4-oxadiazole-2-thione (*HL5*, *1*)

To a solution containing 95% ethanol (80 ml) and potassium hydroxide solution (1.12 g, 20 mmol) was added picolinohydrazide (2.74 g, 20 mmol). After the solution was mixed, slightly more than 1 equiv. of carbon disulfide was added and the mixture was refluxed for 4 h. After concentration of the solution to a small volume, the residue was dissolved in water. A precipitate was obtained by adding the solution to ice containing hydrochloric acid. The solid was filtered off and dried. The crude production was recrystallized from alcohol to give block pale-yellow crystals **1**. Yield 70% (2.50 g). Mp: 209–210 °C. ^1H NMR (400 MHz, DMSO-d_6) δ: 8.8 (s, 1H), 8.0 (s, 1H), 7.5 (s, 2H), 3.3 (b, 1H). IR (KBr, cm^{-1}) v: 3127 (w), 3050 (w), 2855 (m), 2664 (br), 2586 (br), 1870 (w), 1802 (br), 1727(w), 1594 (s), 1566 (m), 1522 (s), 1472 (m), 1438 (s), 1349 (m), 1315 (s), 1256 (w), 1165 (m), 1145 (m), 1072 (m), 1046 (s), 1015 (w), 1002 (s), 975 (w), 957 (m), 937 (s), 881(m), 788 (s), 739 (s), 719 (w), 692 (s), 628 (m), 561 (s), 510 (m), 486 (w). ESI-MS (ESITOF N_2): m/z 180 (M+1). *Anal.* Calc. for $C_7H_5N_3OS$: C, 46.92; H, 2.81; N, 23.45. Found: C, 46.81; H, 2.80; N, 23.54%.

2.3. Synthesis of $[Zn(L5)_2(H_2O)_2]$ (*2*)

A water solution (5 ml) containing **HL5** (0.035 g, 0.2 mmol) was placed at the bottom of a straight glass test tube of 150 mm length and 15 mm diameter. In the middle of the tube was placed a buffer layer of 1:1 methanol–water (5 ml). $ZnSO_4 \cdot 7H_2O$ (0.029 g, 0.1 mmol) in a methanol solution (4 ml) was then added above the buffer layer. After two weeks, good pale-yellow bar-shaped crystals suitable for X-ray diffraction were obtained in a yield of 75%. *Anal.* Calc. for $C_{14}H_{12}N_6O_4S_2Zn$: C, 36.73; H, 2.64; N, 18.36. Found: C, 36.63; H, 2.62; N, 18.40%. IR (KBr, cm^{-1}) v: 3239 (br, w), 3058 (w), 1616 (m), 1572 (w), 1550 (m), 1490 (m), 1442 (w), 1405 (w), 1393 (m), 1372 (s), 1301 (w), 1266 (w), 1174 (w), 1162 (m), 1102 (m), 1084 (s), 1049 (s), 1019 (m), 892 (s), 798 (s), 749 (w), 724 (m), 700 (s), 644 (m), 536 (br, m), 490 (w), 412 (m).

2.4. Synthesis of $[Cd(L5)_2]_n$ (3)

A water solution (5 ml) containing **HL5** (0.035 g, 0.2 mmol) was placed at the bottom of a straight glass test tube of 150 mm length and 15 mm diameter. In the middle of the tube was placed a buffer layer of 1:1 methanol–water (4 ml). $CdSO_4 \cdot 8/3H_2O$ (0.026 g, 0.1 mmol) in a methanol solution (5 ml) was then added above the buffer layer. After three days, pale-yellow black-shaped crystals suitable for X-ray diffraction were obtained in a yield of 65%. *Anal.* Calc. for $C_{14}H_8CdN_6O_2S_2$: C, 35.87; H, 1.72; N, 17.93. Found: C, 35.75; H, 1.70; N, 17.99%. IR (KBr, cm^{-1}) *v*: 3055 (m), 2039 (w), 1958 (w), 1606 (m), 1574 (w), 1540 (s), 1477 (s), 1418 (s), 1394 (w), 1371 (m), 1291 (w), 1266 (w), 1157 (m), 1096 (m), 1070 (s), 1035 (m), 1008 (w), 892 (s), 795 (s), 745 (m), 720 (w), 706 (m), 685 (w), 632 (m), 540 (w), 497 (w), 405 (s).

2.5. Synthesis of $[Hg_2(L5)_2]_n$ (4)

A water solution (5 ml) containing **HL5** (0.035 g, 0.2 mmol) was placed at the bottom of a straight glass test tube of 150 mm length and 15 mm diameter. In the middle of the tube was placed a buffer layer of 1:1 methanol–water (4 ml). $HgBr_2$ (0.036 g, 0.1 mmol) in a methanol solution (5 ml) was then added above the buffer layer. Well-shaped plate crystals of **4** suitable for X-ray diffraction were obtained within one week in 70% yield. *Anal.* Calc. for $C_{28}H_{16}Hg_2N_{12}O_4S_4$: C, 30.19; H, 1.45; N, 15.09. Found: C, 30.30; H, 1.44; N, 15.17%. IR (cm^{-1}) *v*: 3052 (m), 2038 (w), 1960 (w), 1607 (m), 1542 (s), 1478 (s), 1416 (s), 1370 (m), 1293 (w), 1268 (w), 1158 (m), 1094 (m), 1068 (s), 1037 (m), 1010 (w), 895 (s), 795 (s), 744 (m), 721 (w), 706 (m), 684 (w), 630 (m), 494 (w), 405 (s).

2.6. X-ray crystallography

Single-crystal X-ray diffraction measurements of **1**–**4** were carried out with a Bruker APEX II CCD diffractometer equipped with a graphite crystal monochromator situated in the incident beam for data collection at 293(2) K. The lattice parameters were obtained by least-squares refinement of the diffraction data of 567 (for **1**), 774 (for **2**), 798 (for **3**) and 668 (for **4**) reflections, and data collections were performed with Mo Kα radiation ($\lambda = 0.71073$ Å). All the measured independent reflections were used in the structural analysis, and semi-empirical absorption corrections were applied using the SADABS program. The program SAINT [18] was used for integration of the diffraction profiles. All the structures were solved by direct methods using the SHELXS program of the SHELXTL package and refined with SHELXL [19]. Metal atoms were located from the *E*-maps and other non-hydrogen atoms were located in successive difference Fourier syntheses. The final refinement was performed by full-matrix least-squares methods with anisotropic thermal parameters for

Table 1
Crystal data and structure refinement parameters for **1**–**4**

	1	**2**	**3**	**4**
Empirical formula	$C_7H_5N_3OS$	$C_{14}H_{12}N_6O_4S_2Zn$	$C_{14}H_8CdN_6O_2S_2$	$C_{28}H_{16}Hg_2N_{12}$-O_4S_4
Formula weight	179.21	457.83	468.81	1113.99
T (K)	293	293	293	293
Wavelength (Å)	0.71073	0.71073	0.71073	0.71073
Crystal system	orthorhombic	monoclinic	orthorhombic	monoclinic
Space group	*Pbca*	$P2_1/n$	*Fdd*2	$P2_1/c$
a (Å)	10.0139 (1)	6.0250(1)	16.8403(6)	19.5168(7)
b (Å)	8.6684 (1)	12.6564(2)	24.5868(8)	11.1993(4)
c (Å)	17.6270(3)	11.7183(2)	7.5603(4)	7.2642(2)
β (°)	90	102.8880(10)	90	99.610(2)
V (Å^3)	1530.10(3)	871.07(3)	3130.3(2)	1565.49(9)
Z	8	2	8	2
μ (mm^{-1})	0.370	1.685	1.685	10.121
Crystal size (mm)	$0.30 \times 0.30 \times 0.40$	$0.20 \times 0.20 \times 0.30$	$0.03 \times 0.05 \times 0.07$	$0.01 \times 0.06 \times 0.08$
ρ (g cm^{-3})	1.556	1.745	1.990	2.363
Reflections collected	8289	5070	4420	11 348
Independent reflections	1757	2456	1317	3619
reflections [$I > 2\sigma(I)$]	1595	1760	1159	2461
R_{int}	0.016	0.022	0.052	0.050
Data/restraints/parameters	1757/0/130	2456/0/148	1317/0/114	3619/0/226
θ Range	2.3, 27.5	2.4, 30.4	2.9, 27.5	1.1, 27.6
Goodness of fit on F^2	1.04	1.00	1.02	1.00
Largest peak and hole (e Å^{-3})	0.25 and −0.16	0.39 and −0.31	0.49 and −0.43	0.81 and −0.96
R_1^a [$I > 2\sigma(I)$]	0.0300	0.0347	0.0340	0.0349
wR_2^b (all data)	0.0966	0.0809	0.0677	0.1063
Flack parameter			0.48(5)	

[a] $R_1 = \sum\|F_o| - |F_c\|/\sum|F_o|$.
[b] $wR_2 = [\sum[w(F_o^2 - F_c^2)^2]/\sum[w(F_o^2)^2]]^{1/2}$.

all the non-hydrogen atoms based on F^2. All the hydrogen atoms were first found in difference electron density maps, and then placed in the calculated sites and included in the final refinement with the riding model approximation with displacement parameters derived from the parent atoms to which they were bonded. A summary of the crystallographic data and structure refinements are listed in Table 1.

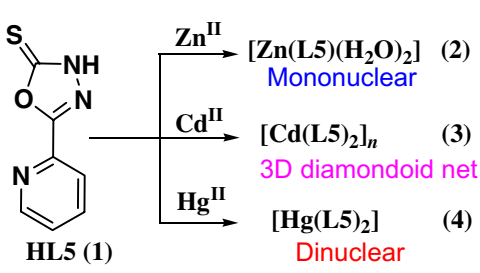
3. Results and discussion

3.1. Syntheses of complexes 2–4

All the complexes **2**–**4** were obtained as neutral complexes from a mixture of water and methanol solution by the reaction of **HL5** with three d^{10} transition-metal salts (Scheme 1). Compound **2** could also be isolated by using $Zn(NO_3)_2$ as the Zn(II) source, as confirmed by X-ray diffraction, IR spectra and elemental analyses. Similar cases were also observed for Cd(II) and Hg(II) complexes, which indicates that the final products are independent of the counter-anions in the metal salts. Furthermore, although **2**–**4** have the exact 2:1 ligand/metal compositions, our trials showed that the products do not significantly depend on the ligand-to-metal ratio (when the ligand/metal ratio is increased or decreased, complexes **2**–**4** still have 2:1 ligand/metal compositions).

3.2. Description of 1

Single X-ray analysis for compound **1** reveals that there is one molecule of **HL5** in the asymmetric unit (Fig. 1a). The pyridyl and oxadiazole plane is not co-planar (its dihedral angle is 4.47°), which is distinctively different from that of the free ligand **HL4** [17b]. It is surprisingly observed that **HL5** exists in the *cis*-conformation (Chart 2), partly because of being propitious to form hydrogen bonds. A pair of **HL5** molecules, each using the oxadiazole and pyridyl nitrogen atoms, forms one kind of hydrogen bond (N(3)–H(3A)···N(1) 2.732(2) Å) in the head-tail form. Additionally, each **HL5** molecule, using the pyridyl carbon atom and oxadiaozle sulfur atom, forms another kind of hydrogen bond (C(1)–H(1)···S(1) 3.830(1) Å) in the same head-tail form. These hydrogen bonds result in one-dimensional hydrogen-bonded chains [20]. Between the adjacent hydrogen-bonded chains, each **HL5** molecule further forms two donor-accept hydrogen bonds (C(2)–H(2)···S(1) 3.06 and 3.296 Å) with the thione sulfur of the adjacent oxadiazole ring from another pyridyl group; these chains align parallel but right about to each other, resulting in a wave-like two-dimensional hydrogen-bonded layer along the (0 1 1) plane (Fig. 1c). It is obvious that the layer structures in **HL5** are different from that in its analogue compound **HL4** [17b]. The layers are further extended into a three-dimensional supramolecular array via offset π–π aromatic stacking interactions with a face-to-face distance of ca. 3.50 Å between the oxadiazole and pyridyl rings (Fig. 1c and Figure S1). Two types of hydrogen-bonded patterns A–D, notated as



Scheme 1. Construction of a coordination polymer and discrete complexes.

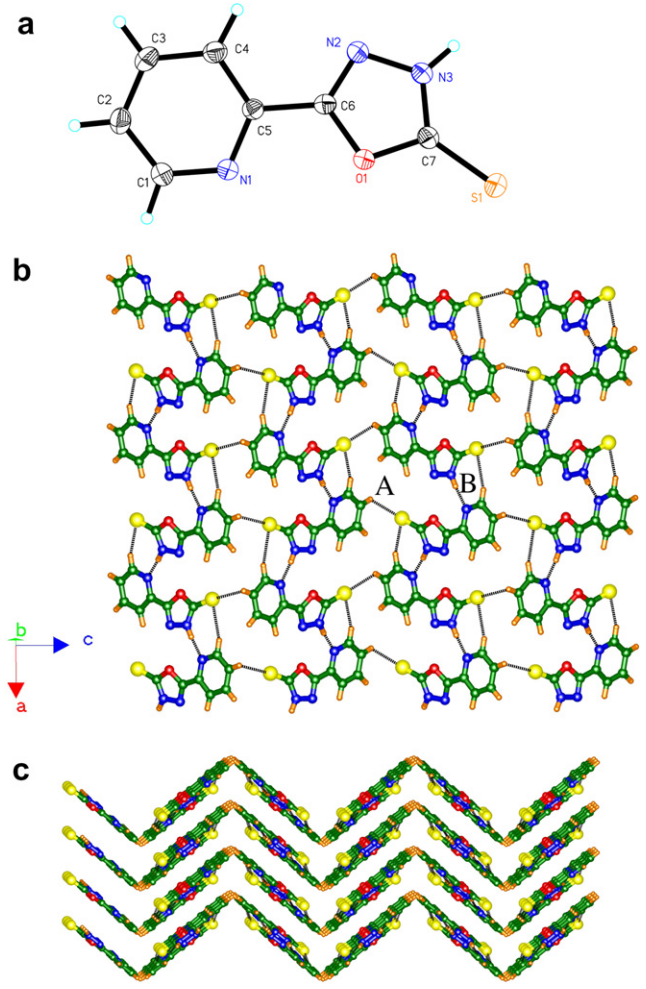


Fig. 1. (a) View of the structure of **1**. (b) 2-D supramolecular network extended by hydrogen bonds in **1**. The black dashed-lines stand for hydrogen bonds. (c) The packing diagram along the *b* axis in **1** (bottom).

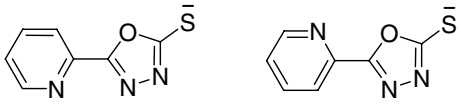


Chart 2.

$R_4^3(20)$ (Fig. 1b(A)) and $R_2^2(7)$ (Fig. 1b(B)), are interestingly observed in this 2-D array (Fig. 1b).

3.3. Description of 2

In the centrosymmetric mononuclear compound **2**, each Zn^{II} ion is located at the inversion center. Each zinc ion coordinates to two pyridyl and two oxadiazole nitrogen atoms from two distinct **L5** moieties (Zn–N distance: 2.137(2) and 2.193 (2) Å, respectively) and two distinct water molecules (Zn–O lengths: 2.111(2) Å), as shown in Fig. 2a, adopting an approximate octahedral geometry (ZnN4O2). Ligand **L5** behaves as a bidentate chelating ligand (Scheme 2a), coordinating to the Zn^{II} center with only the N_{ox} (ox = oxadiazole) and N_{py} atom, thus resulting in this mononuclear structure.

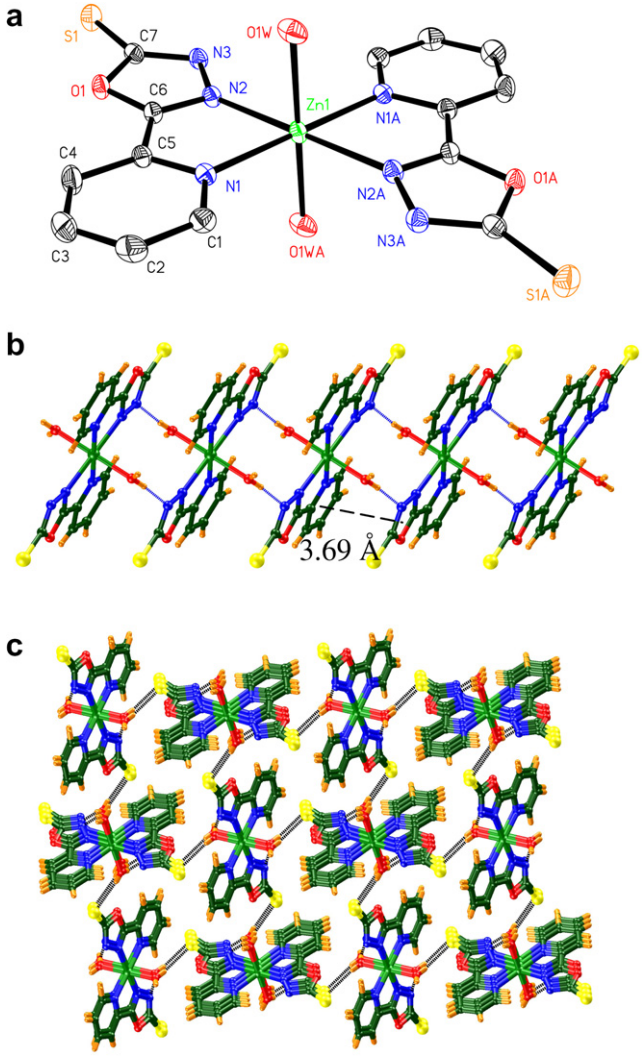
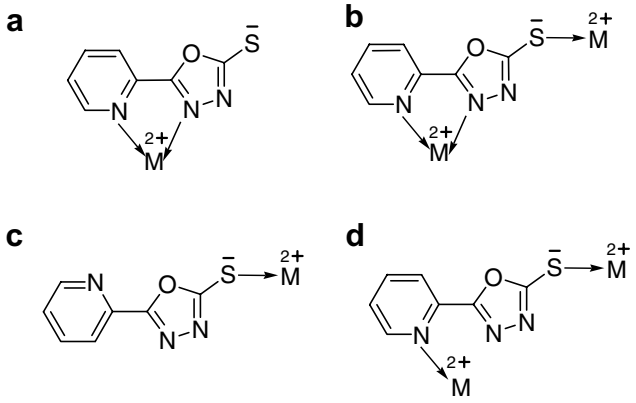


Fig. 2. (a) View of the mononuclear structure of **2** (hydrogen atoms are omitted for clarity). (b) View of the 1-D supramolecular chain along [0 1 1] plane. Thin blue lines stand for hydrogen bonds. (c) The stacking diagram of the parallel coordination sheets along the *a* axis. Thin blue lines stand for hydrogen bonds. (For interpretation of the references in color in this figure legend, the reader is referred to the web version of this article.)



Scheme 2. Coordination modes of **L5**.

Analysis of the crystal packing of **2** reveals the existence of intermolecular O–H···N hydrogen bonds, O(1w)–H(1wB)···N(3)^{i} (i = 1 + *x*, *y*, *z*), between the oxygen atom from water O(1w) ligands and the nitrogen atom from the oxadidazole group of ligand **L5** (Fig. 2b). In addition, there are intermolecular O–H···S hydrogen bonds, O(1W)–H(1WA)···S1^{ii} (ii = 1/2 + *x*, 3/2 − *y*, − 1/2 + *z*), between the sulfur atoms and one of the O(1w) water ligands from an adjacent complex molecule [20]. The O···N separation is 2.874 Å with a H···O distance of 2.09 Å, and a bond angle of 167°. Additionally, the O···S separation is 3.269 Å with a H···S distance of 2.52 Å, and a bond angle of 176°, being in the normal range of such non-covalent interactions [20].

Therefore, these mononuclear subunits are connected through these hydrogen bonds and π···π stacking interactions (3.69 Å) to form a three-dimensional supramolecular network (Fig. 2b and c).

It is very interesting that the S–C bond (the bond length is 1.674(2) Å) in **L5** is longer than that in free **HL5**, whereas the N3–C7 bond (1.319(3) Å) of **L5** anion is shorter than that of free **L5** (Table 2). These results are in agreement with its uncoordinated structural geometry. In complex **2**, the dihedral angle between the oxadiazole and pyridyl plane of **L5** (5.36°) is bigger than that of the free ligand **HL5**. It is noteworthy that the conformation of **L5** is *trans*-in complex **2**, obviously distinguished from that of the free ligand **HL5** (Chart 2 and Fig. 1a).

3.4. Description of 3

When the place of the Zn^{II} ion has been taken by the large Cd^{II} ion, a different structure is formed for **3** under similar reaction conditions. Compound **3** crystallizes in the acentric space group *Fdd2*. Each asymmetric unit of **3** contains one Cd atom and one **L5** ligand. As shown in Fig. 3a, the local coordination geometry around the Cd1 center can be described as a distorted octahedral geometry. The Cd1 center coordinates to four nitrogen atoms and two sulfur atoms from four distinct **L5** moieties (Fig. 3a).

The Cd1 center is connected to four adjacent Cd centers through the **L5** bridges resulting in a neutral 3D

Table 2
Selected bond lengths (Å) and bond angles (°) for **1**–**4**

Complex ***1***			
S1–C7	1.649(1)	N1–C5	1.344(2)
O1–C6	1.369(2)	N2–N3	1.378(2)
O1–C7	1.376(2)	N2–C6	1.282(2)
N1–C1	1.340(2)	N3–C7	1.333(2)
C6–O1–C7	105.4(1)	N2–C6–C5	125.9(1)
C1–N1–C5	117.1(1)	O1–C6–N2	113.7(1)
N3–N2–C6	103.3(1)	O1–C7–N3	105.0(1)
N2–N3–C7	112.6(1)	S1–C7–O1	125.0(1)
N1–C1–C2	123.1(1)	S1–C7–N3	123.0(1)
Complex ***2***			
Zn1–O1W	2.111(2)	Zn1–N2	2.194(2)
Zn1–N1	2.137(2)	S1–C7	1.674(2)
O1W–Zn1–N1	90.39(7)	N1–Zn1–N2	78.12(7)
O1W–Zn1–N2	87.97(7)	N1–Zn1–N2[a]	101.88(7)
Complex ***3***			
Cd1–S1	2.623(2)	Cd1–N2[b]	2.389(4)
Cd1–N1[b]	2.395(4)	S1–C7	1.700(5)
S1–Cd1–S1[a]	84.18(5)	N1[b]–Cd1–N2[b]	70.3(1)
S1–Cd1–N1[b]	163.2(1)	N1[b]–Cd1–N1[c]	103.0(2)
S1–Cd1–N2[b]	97.1(1)	N1[b]–Cd1–N2[c]	92.1(1)
S1–Cd1–N1[c]	88.1(1)	N2[b]–Cd1–N2[c]	152.0(2)
S1–Cd1–N2[c]	103.7(1)		
Complex ***4***			
Hg1–S1	2.376(2)	S1–C1	1.731(8)
Hg1–S2	2.392(2)	S2–C8	1.716(8)
Hg1–N3[a]	2.678(7)		
S1–Hg1–S2	170.64(7)	S2–Hg1–N3[a]	87.7(1)
S1–Hg1–N3[a]	98.7(1)		

Symmetry codes: for **2**, [a] $-x, 1-y, 2-z$; for **3**, [a] $-x, -y, z$; [b] $1/4-x, -1/4+y, -1/4+z$; [c] $-1/4+x, 1/4-y, -1/4+z$; for **4**, [a] $1-x, 1-y, 1-z$.

diamondoid coordination polymer (Fig. 3b) with adjacent Cd···Cd separations of 7.69(1) Å and Cd–Cd–Cd angles of 73.8–151.5°. These angles are significantly deviated from 109.45°, the expected value for an idealized diamond network [21], thus the diamondoid network in **3** is distorted (Figure S2). Although there are long Cd···Cd separations in **3**, no cavities are formed within each diamondoid net (Fig. 3b). The crystal structure of **3** is very similar to those reported previously [6c]. However, it is noted that no interpenetration was formed in the diamondoid net **3**, which is obviously different from those reported previously [6b,21], probably because of **L5** possessing a rigid structure and a short distance between the donor atoms.

Ligand **L5** acts in the bis-monodentate or chelating-tridentate mode (Scheme 2b) in **3**, which is different from that in **2**. However, it is noteworthy that **L5** in both **2** and **3** only exists in the *trans*-conformation (Chart 2).

3.5. Description of *4*

When the larger Hg^{II} ions were used instead of Zn^{II} and Cd^{II} ions, another different structure is generated, in the form of **4**, under similar reaction conditions. The structure of complex **4** is shown in Fig. 4a. The molecules of **4** exist

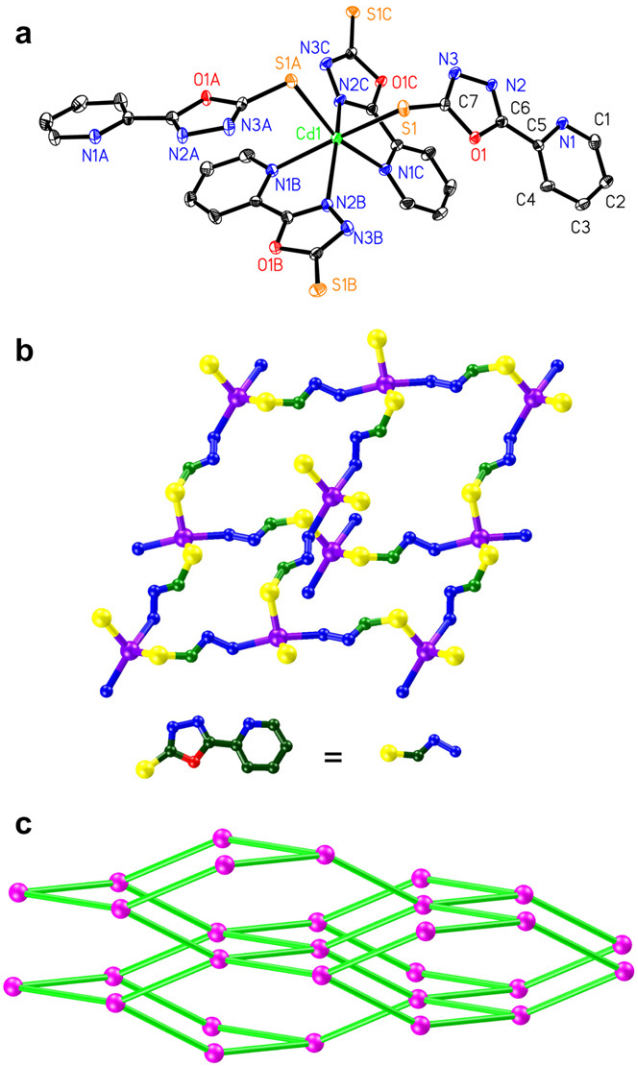


Fig. 3. (a) Coordination environment of the metal atom in **3** (hydrogen atoms are omitted for clarity). (b) The simplied presentations of the diamondoid net of **3**. (c) The schematic presentations of the uninterpenetrated diamondoid network in **3**.

as a centrosymmetric 14-membered metallacyclic ring formed by two **L5** ligands that bridge two Hg^{II} ions with the pyridine nitrogen and oxadiazole sulfur in the *trans*-form. However, the metallacyclic ring in **4** is non-planar. The dihedral angle between the pyridyl and oxadiazole rings is 6.77°. The opposite oxadiazolyl rings and pyridyl rings are parallel to each other. It is interestingly observed that intermolecular π···π stacking interactions exist between the oxadiazole rings (the distance is 3.38 Å) in the metallacycle (Fig. 4a). In this complex, the **L5** ligand has two coordination modes, a monodentate mode (Scheme 2c) and bidentate bridging mode (Scheme 2d), and each Hg^{II} center is coordinated by one pyridine nitrogen atom and two oxadizole sulfur atoms from three different **L5** ligands, showing a distorted "T" shaped geometry with a N–Hg–S average bond angle in the range 87.7(1)–170.6(1)°. The bond lengths of Hg–N of 2.39 Å and Hg–S_{av} of 2.84 Å fall within the

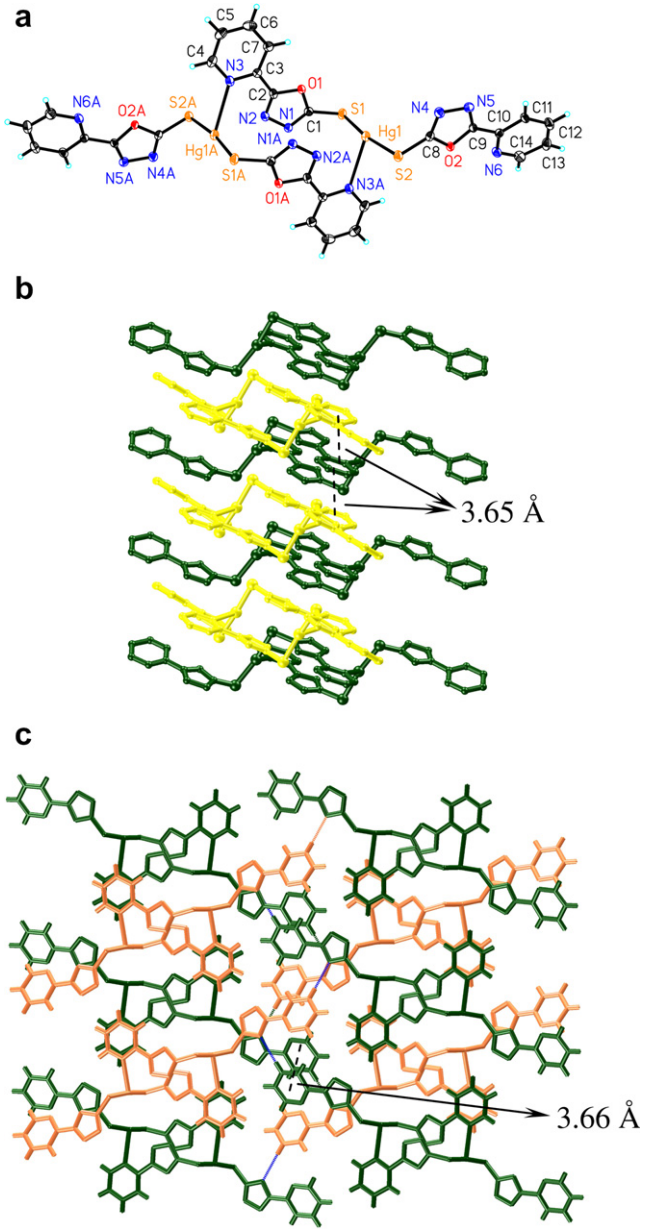


Fig. 4. (a) Coordination environment of the metal atoms in **4**. (b) View of the 1-D supramolecular chain from the side. (c) The stacking diagram of the parallel coordination sheets along the *c* axis.

range of expected values (Table 2). The binuclear structures are connected to each other through π···π stacking interactions (the distance between two macrocycles is 3.65 Å) [20] to form an infinite chain of macrocycles like a stair structure along the *c* axis (Fig. 4b and Figure S3). These 1-D chains further result in the formation of an infinite 2-D supramolecular layer along the *ab* plane through π···π stacking interactions and weak C–H···π interactions (the distance is 3.65 Å, C–H···π 2.94 Å) (Fig. 4c). These 2-D supramolecular layers are further constructed into a 3-D supramolecular structure by weak intermolecular hydrogen-bonds [C(12)–H(12A)···O1^{i} (3.33(1) Å)] ($i = -x, -1/2 + y, 1/2 - z$) and π···π stacking interactions (3.66 Å) (Fig. 4c).

It is noteworthy that **L5** in **4** exists not only in the *trans*-conformation but also in the *cis*-conformation, which is different from both **2** and **3** (Chart 2).

3.6. Thermogravimetric analysis (TGA)

To study the thermal stability of compounds **2**–**4**, thermal gravimetric analyses (TGA) were performed on the single-crystal samples. For complex **2**, the first weight loss occurred in stages starting at 155 °C and completing at 218 °C, corresponding to the loss of two coordinated water molecules. The anhydrous complex suffered serious mass loss upon heating to 275 °C, attributable to decomposition of the organic ligand. For complex **3**, there is no weight loss below 335 °C. The main structure decomposed at 405 °C, exhibiting high thermal stability. Complex **4** began to decompose at 289 °C, then there was one obvious weight-loss stage in the range 289–420 °C, corresponding to decomposition of the ligand.

3.7. Luminescent properties

Construction of coordination polymers and discrete complexes by the judicious choice of organic spacers and transition-metal ions can be an efficient method for obtaining new electroluminescent materials, due to the higher thermal stability of coordination polymers and discrete complexes, and the ability to enhance, shift and quench luminescent emission of organic ligands [4]. The luminescent spectra of free ligand **HL5** and its metal complexes **2**–**4** were investigated in the solid state at room temperature (Fig. 5). The solid state luminescent analyses show that complexes exhibit different properties. As shown in Fig. 5, the free **HL5** ligand displays weak luminescence in the solid state at room temperature; the emission for free ligand **HL5** (**1**) is at 444 nm ($\lambda_{ex} = 395$ nm), which can be assigned to the $\pi^{*}\rightarrow\pi$ transition of the oxadiazole moiety [22]. However, its complexes **2** and **3** exhibit intense greenish-blue radiative emission maxima at ca. 524 and 502 nm

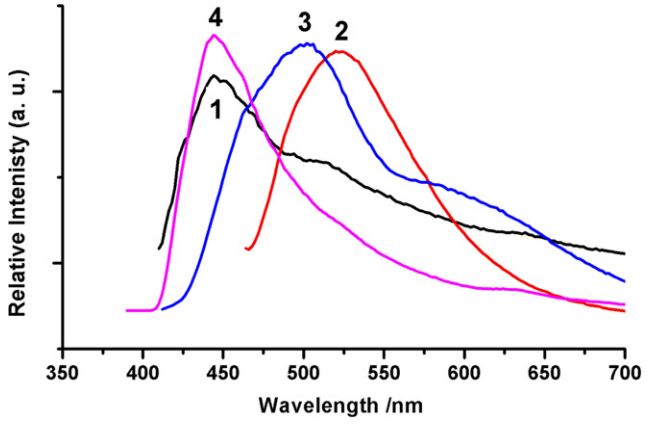


Fig. 5. Photoinduced emission spectra of free ligand **1** (**HL5**) and its complexes **2**–**4** in the solid state at room temperature.

($\lambda_{ex} = 405$ nm), which are red-shifted by 80 and 58 nm compared to the free ligand, respectively. These can be assigned tentatively to ligand-to-metal charge transfers (LMCT) [4]. However, complex **4** exhibits a strong emission at 444 nm ($\lambda_{ex} = 380$ nm), which can be tentatively assigned to the intraligand emission of the **L5** ligand. It is observed that compared to the spectra of the free ligand **HL5**, there was neither a blue-shift nor a red-shift phenomena in the spectrum of **4**. In other words, the emission color and intensity of the free ligand **HL5** is significantly affected by its incorporation into the complexes containing metal ions. Thus the difference in the intensity of emission results from the different d^{10} transition-metals, which suggests that the change of radius and coordination geometries has an important effect on the fluorescent properties.

3.8. SHG efficiency

According to the principles proposed by Kurtz and Perry [23] the strength of the second harmonic generation (SHG) efficiency of the compounds can be estimated by measuring powder samples. Only complex **3** is SHG-active (0.6 U, U = SHG intensity of urea), which confirms that it crystallizes in a polar space group and is in agreement with the structural analyses.

4. Conclusions

Three new inorganic–organic coordination polymer and discrete complexes are generated from a versatile organic ligand 5-(2-pyridyl)-1,3,4-oxadiazole-2-thione and d^{10} transition-metal salts. This work demonstrates that the rigid and unsymmetric **L5** anion adopts different coordination modes along with the variation of the metal radii, which plays a very important role in the construction and the properties of these new materials. In addition, the coordination geometry of the metal ions is very important for the formation of acentric crystal structures. We are currently extending this result by preparing other new multifunctional ligands of this type with different coordination groups. It is anticipated that this new type of organic ligands will result in a variety of coordination polymers or supramolecules with unique structural features and interesting properties.

Acknowledgements

This work was financially supported by the Starting Funding of Shandong Institute of Light Industry (to Dr. Y.-T. Wang). We also wish to thank Prof. W. T. Yu and J. D. Fan of Shandong University for collecting the data of all the crystal structures.

Appendix A. Supplementary material

CCDC 632210, 632211, 632212 and 632213 contain the supplementary crystallographic data for **1**, **2**, **3** and **4**. These data can be obtained free of charge via http://www.ccdc.cam.ac.uk/conts/retrieving.html, or from the Cambridge Crystallographic Data Centre, 12 Union Road, Cambridge CB2 1EZ, UK; fax: (+44) 1223-336-033; or e-mail: deposit@ccdc.cam.ac.uk. Supplementary data associated with this article can be found, in the online version, at doi:10.1016/j.poly.2007.06.026.

References

[1] (a) Y. Li, F.-K. Zheng, X. Liu, W.-Q. Zou, G.-C. Guo, C.-Z. Lu, J.-S. Huang, Inorg. Chem. 45 (2006) 6308;
(b) W.-G. Wang, A.-J. Zhou, W.-X. Zhang, M.-L. Tong, X.-M. Chen, M. Nakano, C.C. Beedle, D.N. Hendrickson, J. Am. Chem. Soc. 129 (2007) 1014;
(c) X.-M. Zhang, J.-J. Hou, W.-X. Zhang, X.-M. Chen, Inorg. Chem. 45 (2006) 8120;
(d) A.-L. Cheng, Na. Liu, Y.-F. Yue, Y.-W. Jiang, E.-Q. Gao, C.-H. Yan, M.-Y. He, Chem. Commun. (2007) 407;
(e) Y.-Z. Zheng, M.-L. Tong, W.-X. Zhang, X.-M. Chen, Angew. Chem., Int. Ed. 45 (2006) 6310;
(f) W. Kaneko, S. Kitagawa, M. Ohba, J. Am. Chem. Soc. 129 (2007) 248;
(g) W.-H. Zhu, Z.-M. Wang, S. Gao, Inorg. Chem. 46 (2007) 1337;
(h) D.-K. Cao, J. Xiao, J.-W. Tong, Y.-Z. Li, L.-M. Zheng, Inorg. Chem. 46 (2007) 428.

[2] (a) D.N. Dybtsev, A.L. Nuzhdin, H. Chun, K.P. Bryliakov, E.P. Talsi, V.P. Fedin, K. Kim, Angew. Chem., Int. Ed. 45 (2006) 916;
(b) C.-D. Wu, W. Lin, Angew. Chem., Int. Ed. 46 (2007) 1075;
(c) S. Hasegawa, S. Horike, R. Matsuda, S. Furukawa, K. Mochizuki, Y. Kinoshita, S. Kitagawa, J. Am. Chem. Soc. 129 (2007) 2607;
(d) J.S. Seo, D. Whang, H. Lee, S. Jun, J. Ok, Y. Jin, K. Kim, Nature 404 (2000) 982;
(e) L.-G. Qiu, A.-J. Xie, L.-D. Zhang, Adv. Mater. 17 (2005) 689;
(f) S.H. Cho, B. Ma, S.T. Nguyen, J.T. Hupp, T.E. Albrecht-Schmitt, Chem. Commun. (2006) 2563.

[3] (a) S.L. Zheng, J.P. Zhang, W.T. Wang, X.M. Chen, J. Am. Chem. Soc. 125 (2003) 6882;
(b) W.-P. Su, M.-C. Hong, J.-B. Weng, R. Cao, S.-F. Lu, Angew. Chem., Int. Ed. 39 (2000) 2911;
(c) Z.-J. Zhang, S.-C. Xiang, Y.-F. Zhang, A.-Q. Wu, L.-Z. Cai, G.-C. Guo, J.-S. Huang, Inorg. Chem. 45 (2006) 1972.

[4] (a) W.-L. Jia, R.-Y. Wang, D. Song, S.J. Ball, A.B. McLean, S.-N. Wang, Chem. – Eur. J. 11 (2005) 832;
(b) C. Seward, W.-L. Jia, R.-Y. Wang, G.D. Enright, S.-N. Wang, Angew. Chem., Int. Ed. 43 (2004) 2933;
(c) X.-Q. Lu, Y.-Q. Qiao, J.-R. He, M. Pan, B.-S. Kang, C.-Y. Su, Cryst. Growth Des. 6 (2006) 1910;
(d) X.-X. Xu, Y. Lu, E.-B. Wang, Y. Ma, X.-L. Bai, Cryst. Growth Des. 6 (2006) 2029;
(e) Y.-P. Tian, Y.-M. Zhu, H.-P. Zhou, P. Wang, J.-Y. Wu, X.-T. Tao, M.-H. Jiang, Eur. J. Inorg. Chem. (2007) 345;
(f) Q. Yue, J. Yang, G.-H. Li, G.-D. Li, J.-S. Chen, Inorg. Chem. 45 (2006) 4431.

[5] (a) Y.-B. Dong, Q. Zhang, L.-L. Liu, J.-P. Ma, B. Tang, R.-Q. Huang, J. Am. Chem. Soc. 129 (2007) 1514;
(b) W.-G. Lu, C.-Y. Su, T.-B. Lu, L. Jiang, J.-M. Chen, J. Am. Chem. Soc. 128 (2006) 34;
(c) Z.-M. Liu, Y. Liu, S.-R. Zheng, Z.-Q. Yu, M. Pan, C.-Y. Su, Inorg. Chem. 46 (2007) 5814;
(d) S. Ma, D. Sun, M. Ambrogio, J.A. Fillinger, S. Parkin, H.-C. Zhou, J. Am. Chem. Soc. 129 (2007) 1858;
(e) X.-S. Wang, S. Ma, D. Sun, S. Parkin, H.-C. Zhou, J. Am. Chem. Soc. 128 (2006) 16474;
(f) J. Fan, L. Gan, H. Kawaguchi, W.-Y. Sun, K.-B. Yu, W.-X. Tang, Chem. – Eur. J. 9 (2003) 3965;

(g) J.-P. Zhang, S. Horike, S. Kitagawa, Angew. Chem., Int. Ed. 46 (2007) 889;
(h) S. Horike, R. Matsuda, D. Tanaka, S. Matsubara, M. Mizuno, K. Endo, S. Kitagawa, Angew. Chem., Int. Ed. 45 (2006) 7226;
(i) O. Ohmori, M. Kawano, M. Fujita, Angew. Chem., Int. Ed. 44 (2005) 1962;
(j) H. Furukawa, J. Kim, K.E. Plass, O.M. Yaghi, J. Am. Chem. Soc. 128 (2006) 8398.

[6] (a) Q. Ye, Y.-M. Song, G.-X. Wang, K. Chen, D.-W. Fu, P.W.H. Chan, J.-S. Zhu, S.D. Huang, R.-G. Xiong, J. Am. Chem. Soc. 128 (2006) 6554;
(b) O.R. Evans, W.B. Lin, Acc. Chem. Res. 35 (2002) 511;
(c) Q. Ye, Y.-H. Li, Y.-M. Song, X.-F. Huang, R.-G. Xiong, Z. Xue, Inorg. Chem. 44 (2005) 3618.

[7] (a) G. Wu, X.-F. Wang, T.A. Okamura, W.-Y. Sun, N. Ueyama, Inorg. Chem. 45 (2006) 8523;
(b) C.-Y. Li, C.-S. Liu, J.-R. Li, X.-H. Bu, Cryst. Growth Des. 7 (2007) 286;
(c) B. Zhai, L. Yi, H.-S. Wang, B. Zhao, P. Cheng, D.-Z. Liao, S.-P. Yan, Inorg. Chem. 45 (2006) 8471;
(d) X.-D. Chen, H.-F. Wu, X.-H. Zhao, X.-J. Zhao, M. Du, Cryst. Growth Des. 7 (2007) 124.

[8] (a) J.-R. Li, X.-H. Bu, R.-H. Zhang, J. Chem. Soc., Dalton Trans. (2004) 813;
(b) X.-H. Huang, T.-L. Sheng, S.-C. Xiang, R.-B. Fu, S.-M.Y.-M. Li, X.-T. Wu, Inorg. Chem. 46 (2007) 497.

[9] (a) M. Fujita, Chem. Soc. Rev. 27 (1998) 417;
(b) R.E.P. Winpenny, Chem. Soc. Rev. 27 (1998) 447;
(c) D.L. Caulder, K.N. Raymond, Acc. Chem. Res. 32 (1999) 975;
(d) R.W. Saalfrank, E. Uller, B. Demleitner, I. Bernt, Struct. Bond. 96 (2000) 149;
(e) S. Leininger, B. Olenyuk, P.J. Stang, Chem. Rev. 100 (2000) 853;
(f) B.J. Holliday, C.A. Mirkin, Angew. Chem., Int. Ed. 40 (2001) 2022;
(g) S.R. Seidel, P.J. Stang, Acc. Chem. Res. 35 (2002) 972.

[10] (a) B.-H. Ye, M.-L. Tong, X.-M. Chen, Coord. Chem. Rev. 249 (2005) 545;
(b) O. Kahn, Acc. Chem. Res. 33 (2000) 647;
(c) O.M. Yaghi, M. O'Keeffe, N.W. Ockwig, H.K. Chae, M. Eddaoudi, J. Kim, Nature 423 (2003) 705;
(d) S.R. Batten, K.S. Murray, Coord. Chem. Rev. 246 (2003) 103;
(e) B. Kesanli, W. Lin, Coord. Chem. Rev. 246 (2003) 305;
(f) C.-D. Wu, A. Hu, L. Zhang, W. Lin, J. Am. Chem. Soc. 127 (2005) 8940;
(g) S. Thushari, J.A.K. Cha, H.H.-Y. Sung, S.S.-Y. Chui, A.L.-F. Leung, Y.-F. Yen, I.D. Williams, Chem. Commun. (2005) 5515.

[11] (a) X.-M. Chen, M.-L. Tong, Acc. Chem. Res. 40 (2007) 162;
(b) R. Robson, J. Chem. Soc., Dalton Trans. (2000) 3735;
(c) L. Carlucci, G. Ciani, D.M. Proserpio, Coord. Chem. Rev. 246 (2003) 247;
(d) C. Janiak, J. Chem. Soc., Dalton Trans. (2003) 2781;
(e) S. Kitagawa, K. Uemura, Chem. Soc. Rev. 34 (2005) 109.

[12] (a) A. Erxleben, Coord. Chem. Rev. 246 (2003) 203;
(b) S.R. Batten, R. Robson, Angew. Chem., Int. Ed. 37 (1998) 1460;
(c) A.J. Blake, N.R. Champness, P. Hubberstey, W.S. Li, M.A. Withersby, M. Schröder, Coord. Chem. Rev. 183 (1999) 117;
(d) P.J. Hagrman, D. Hagrman, J. Zubieta, Angew. Chem., Int. Ed. 38 (1999) 2639;
(e) M.J. Zaworotko, Angew. Chem., Int. Ed. 39 (2000) 3052;
(f) B. Moulton, M.J. Zaworotko, Chem. Rev. 101 (2001) 1629.

[13] (a) R.-H. Wang, L.-J. Xu, J.-X. Ji, Q. Shi, Y.-M. Li, Z.-Y. Zhou, M.-C. Hong, A.S.C. Chan, Eur. J. Inorg. Chem. (2005) 751;
(b) Y.-L. Wang, D.-Q. Yuan, W.-H. Bi, X. Li, X.-J. Li, F. Li, R. Cao, Cryst. Growth Des. 5 (2005) 1849;
(c) Y.-Q. Xu, D.-Q. Yuan, L. Han, E. Ma, M.-Y. Wu, Z.-Z. Lin, M.-C. Hong, Eur. J. Inorg. Chem. (2005) 2054;
(d) L. Han, H. Valle, X. Bu, Inorg. Chem. 46 (2007) 1511.

[14] (a) J.-R. Li, R.-H. Zhang, X.-H. Bu, Eur. J. Inorg. Chem. (2005) 1913;
(b) J. Wang, S.-L. Zheng, S. Hu, Y.-H. Zhang, M.-L. Tong, Inorg. Chem. 46 (2007) 795–800;
(c) J.P. Reddy, V.R. Pedireddi, Eur. J. Inorg. Chem. (2007) 1150.

[15] (a) J.-F. Wang, R.-Y. Wang, J. Yang, Z.-P. Zheng, M.D. Carducci, T. Cayou, N. Peyghambarian, G.E. Jabbour, J. Am. Chem. Soc. 123 (2001) 6179;
(b) Y.-B. Dong, T. Sun, J.-P. Ma, X.-X. Zhao, R.-Q. Huang, Inorg. Chem. 45 (2006) 10613;
(c) M. Du, Y.-M. Guo, S.-T. Chen, X.-H. Bu, S.R. Batten, J. Ribas, S. Kitagawa, Inorg. Chem. 43 (2004) 1287;
(d) P. Tripathi, A. Pal, V. Jancik, A.K. Pandey, J. Singh, N.K. Singh, Polyhedron 26 (2007) 2597;
(e) O.H. Amin, L.J. Al-Hayaly, S.A. Al-Jibori, T.A.K. Al-Allaf, Polyhedron 23 (2004) 2013;
(f) C.-L. Ma, G.-R. Tian, R.-F. Zhang, Polyhedron 24 (2005) 1773.

[16] (a) Y.-T. Wang, M.-L. Tong, H.-H. Fan, H.-Z. Wang, X.-M. Chen, J. Chem. Soc., Dalton Trans. (2005) 424;
(b) Y.-T. Wang, H.-H. Fan, H.-Z. Wang, X.-M. Chen, Inorg. Chem. 44 (2005) 4148.

[17] (a) Y.-T. Wang, G.-M. Tang, Inorg. Chem. Comm. 10 (2007) 53;
(b) Y.-T. Wang, G.-M. Tang, W.-Y. Ma, W.-Z. Wan, Polyhedron 26 (2007) 782;
(c) Y.-T. Wang, G.-M. Tang, J. Coord. Chem., in press;
(d) M. Du, Z.-H. Zhang, X.-J. Zhao, Q. Xu, Inorg. Chem. 45 (2006) 5785.

[18] Bruker AXS, SAINT Software Reference Manual, Madison, WI, 1998.

[19] G.M. Sheldrick, SHELXTL NT Version 5.1. Program for Solution and Refinement of Crystal Structures, University of Göttingen, Germany, 1997.

[20] G.R. Desiraju, T. Steiner, The Weak Hydrogen Bond in Structural Chemistry and Biology, Oxford University Press, 1999.

[21] A.F. Wells, Three-dimensional Nets and Polyhedra, Wiley-Interscience, New York, 1977.

[22] C. Wang, G. Jung, A.S. Batsanov, M.R. Bryce, M.C. Petty, J. Mater. Chem. 12 (2002) 173.

[23] S.K. Kurtz, T.T. Perry, J. Appl. Phys. 39 (1968) 3798.

Our previous studies have focused on the synthesis of new pcs exhibiting liquid crystal and gas sensor properties [27–29,33–39]. The films of the pcs showing mesomorphic properties at room temperature have been proven to be used as photoconductors and gas sensors in molecular electronic devices. The ordered pc films obtained from liquid crystalline pc compounds are more sensitive than disordered pc films [28,39]. Recently, we have reported the synthesis of peripherally symmetrical substituted octa *p*-tolyl-sulfonyl (tosyl) amido pcs and their NMR and UV spectra investigations in different solvents and pH [40]. We have found that the hydrogen bonding capacity and deprotonation of the tosylamido groups causes interesting spectroscopic properties. Their potential application as chemical gas sensor is being investigated. However, only tosylamido substitution of the pc ring was not enough to exhibit mesogenic properties. Therefore, we designed electron-with-drawing tosylamido and donor alkylthia substituted novel unsymmetrical pcs which are liquid crystals owing to the alkyl chains. The synthesis, characterization and investigation of mesogenic properties are reported here. Also, the influence of the presence of the tosylamido unit on the phthalocyanine core on the mesomorphic properties was determined.

2. Experimental methods

2.1. Materials

The 4,5-dicyano-*N*,*N*′-ditosyl-*o*-phenylenediamine (**1**) [40] and 1,2-di(alkylthio)-4,5-dicyanobenzene derivatives (**2a**–**2c**) [41,42] were synthesized according to published procedures. All other reagents and solvents were reagent-grade quality, obtained from commercial suppliers and dried before use as described by Perrin and Armarego [43].

3. Measurements

Elemental analyses were obtained from Thermo Finnigan Flash 1112. Infrared spectra in KBr pellets were recorded on a Bio-Rad FTS 175C FT IR spectrophotometer. Optical spectra in the UV–Vis region were recorded with a Shimadzu 2001 UV PC spectrophotometer using a 1 cm pathlength cuvette at room temperature The mass spectra were recorded on a LCQ-ion trap (Thermofinnigan, San Jose, CA,USA), equipped with an Electrospray (ES) source. ^{1}H and ^{13}C NMR spectra were recorded in $CDCl_3$ solutions on a Varian 500 MHz spectrometer. Thermogravimetric analyses were carried out on Mettler Toledo Star^e Thermal Analysis System at a rate of 10 °C min^{-1}in a nitrogen flow (50 ml min^{-1}). The phase transition behaviour of these compounds was observed by means of a polarizing microscope (Leitz Wetzler Orthoplan-pol.) equipped with a hot stage (Linkam TMS 93) and temperature-controller (Linkam LNP). Transition temperatures were determined with a scan rate of 10 °C min^{-1} using a Mettler Toledo Star^e Thermal Analysis System/DSC 822^e. The differential scanning calorimeter system was calibrated with indium from 3 to 4 mg samples under nitrogen atmosphere.

3.1. Synthesis of asymmetric phthalocyanines

3.1.1. 2,3,9,10,16,17-Hexakis(hexylthio)-23,24-bis(tosilamido)phthalocyaninato nickel(II) (**3a**)

A mixture of 1,2-di(hexylthio)-4,5-dicyanobenzene (**2a**) (2 mmol), 4,5-dicyano-*N*,*N*′-ditosyl-*o*-phenylenediamine (**1**) (1 mmol), anhydrous $NiCl_2$ (1.5 mmol), 1,8-diazabicyclo[5.4.0]undec-7-ene (DBU, 3 mmol) and 4 ml dried *n*-hexanol were heated to reflux for 18 h under an argon atmosphere. After cooling to room temperature the mixture was treated with ethanol (10 ml), filtered off and washed several times with ethanol. The dark green product was purified by preparative thin layer chromatography (TLC) using a 5:2 CH_2Cl_2/*n*-hexane solvent system. Yield: 8%. Elemental *Anal*. Calc. for $C_{82}H_{102}N_{10}NiO_4S_8$ (1605): C, 61.29; H, 6.40; N, 8.72. Found: C, 61.10; H, 6.35; N, 8.70%. IR (KBr) ν_{max} (cm^{-1}): 3258 (NH), 2956–2856 (CH_2, CH_3), 1599 (C_{ar}=N), 1350, 1163 (SO_2), 560 (CS). MS (ES–MS), *m*/*z* (%): 1606 (100) $[M+H]^+$, 1607 (50) $[M+2H]^+$. ^{1}H NMR ($CDCl_3$) δ: 0.94–1.18 (m, 18H, CH_3), 1.43–2.00 (m, 36H, CH_2), 2.21 (t, 6H, Ar–CH_3), 3.05–3.58 (m, 24H, CH_2), 7.9–8.42 (m, 18H, NH, CH_{ar}). ^{13}C NMR ($CDCl_3$, Decoupled) δ: 13.09 (CH_3), 13.16 (CH_3), 20.59 (CH_2), 21.59 ($C_{ar}CH_3$), 27.72–28.16 (CH_2), 30.50–33.07 (CH_2), 118.5 ($C_{ar}H$), 124.10 ($C_{ar}H$), 127.08 ($C_{ar}H$), 128.8 (C_{ar}), 129.85 ($C_{ar}H$), 132.05 (C_{ar}), 132.72 (C_{ar}), 134.7 (C_{ar}), 138.71 (C_{ar}), 139.11 (C_{ar}), 141.00 (C_{ar}), 143.01 (CN), 143.50 (CN).

3.1.2. 2,3,9,10,16,17-Hexakis(dodecylthio)-23,24-bis(tosilamido) phthalocyaninato nickel(II) (**3b**)

A mixture of 1,2-di(dodecylthio)-4,5-dicyanobenzene (**2b**) (2 mmol), 4,5-dicyano-*N*,*N*′-ditosyl-*o*-phenylenediamine (**1**) (1 mmol), anhydrous $NiCl_2$ (1.5 mmol), 1,8-diazabicyclo[5.4.0]undec-7-ene (DBU, 3 mmol) and 4 ml dried *n*-hexanol were heated to reflux for 18 h under an argon atmosphere. After cooling to room temperature the mixture was treated with ethanol (10 ml), filtered off and washed several times with ethanol. The dark green product was purified by preparative thin layer chromatography (TLC) using a 5:1 CH_2Cl_2/*n*-hexane solvent system. Yield: 7%. Elemental *Anal*. Calc. for $C_{118}H_{174}N_{10}Ni\ O_4S_8$ (2110): C, 67.11; H, 8.30; N, 6.63. Found: C, 67.00; H, 8.31; N, 6.70%. IR (KBr) ν_{max} (cm^{-1}): 3263 (NH), 2957–2856 (CH_2, CH_3), 1598 (C_{ar}=N), 1348, 1164 (SO_2), 559 (CS). MS (ES–MS), *m*/*z* (%): 2111 (100) $[M+H]^+$. ^{1}H NMR ($CDCl_3$) δ: 0.98–1.27 (m, 18H, CH_3), 1.47-2.13 (m, 84H, CH_2), 2.32 (t, 6H, Ar–CH_3), 3.10-3.65 (m, 48H, CH_2), 7.8–8.62 (m, 18H, NH, CH_{ar}). ^{13}C NMR ($CDCl_3$, Decoupled) δ: 13.08 (CH_3), 13.24 (CH_3), 20.59 (CH_2), 21.52 ($C_{ar}CH_3$), 27.80–28.32 (CH_2), 30.56–33.12 (CH_2), 118.67 ($C_{ar}H$), 124.32 ($C_{ar}H$), 127.12 ($C_{ar}H$), 127.54 ($C_{ar}H$), 128.8 (C_{ar}), 129.96 ($C_{ar}H$), 132.15 (C_{ar}), 132.87 (C_{ar}),

134.75 (C_{ar}), 138.79 (C_{ar}), 139.31 (C_{ar}), 141.10 (C_{ar}), 143.01 (CN), 143.65 (CN).

3.1.3. 2,3,9,10,16,17-Hexakis(hexadecylthio)-23,24-bis(tosilamido)phthalocyaninato nickel(II) (3c)

A mixture of 1,2-di(hexadecylthio)-4,5-dicyanobenzene (**2c**) (2 mmol), 4,5-dicyano-*N*,*N*′-ditosyl-*o*-phenylenediamine (**1**) (1 mmol), anhydrous $NiCl_2$ (1.5 mmol), 1,8-diazabicyclo[5.4.0]undec-7-ene (DBU, 3 mmol) and 4 ml dried *n*-hexanol were heated to reflux for 18 h under an argon atmosphere. After cooling to room temperature the mixture was treated with ethanol (10 ml), filtered off and washed several times with ethanol. The dark green product was purified by preparative thin layer chromatography (TLC) using a 5:1 CH_2Cl_2/*n*-hexane solvent system. Yield: 6%. Elemental *Anal*. Calc. for $C_{142}H_{222}N_{10}NiO_4S_8$ (2445): C, 69.65; H, 9.16; N, 5.72. Found: C, 69.60; H, 9.20; N, 5.70%. IR (KBr) ν_{max} (cm^{-1}): 3258 (NH), 2955–2851 (CH_2, CH_3), 1599 (C_{ar}=N), 1350, 1163 (SO_2), 560 (CS). MS (ES–MS), *m*/*z* (%): 2446 (40) $[M+H]^+$. ^{1}H NMR ($CDCl_3$) δ: 0.97–1.29 (m, 18H, CH_3), 1.37–2.17 (m, 108H, CH_2), 2.36 (t, 6H, Ar–CH_3), 3.12–3.69 (m, 52H, CH_2), 7.81–8.60 (m, 18H, NH, CH_{ar}). ^{13}C NMR ($CDCl_3$, Decoupled) δ: 13.06 (CH_3), 13.21 (CH_3), 20.52 (CH_2), 21.50 ($C_{ar}CH_3$), 27.72–28.36 (CH_2), 30.44-33.24 (CH_2), 118.77 ($C_{ar}H$), 124.44 ($C_{ar}H$), 127.24 ($C_{ar}H$), 127.56 ($C_{ar}H$), 128.82 (C_{ar}), 129.76 ($C_{ar}H$), 132.21 (C_{ar}), 132.67 (C_{ar}), 134.70 (C_{ar}), 138.70 (C_{ar}), 139.21 (C_{ar}), 141.105 (C_{ar}), 143.01 (CN), 143.55 (CN).

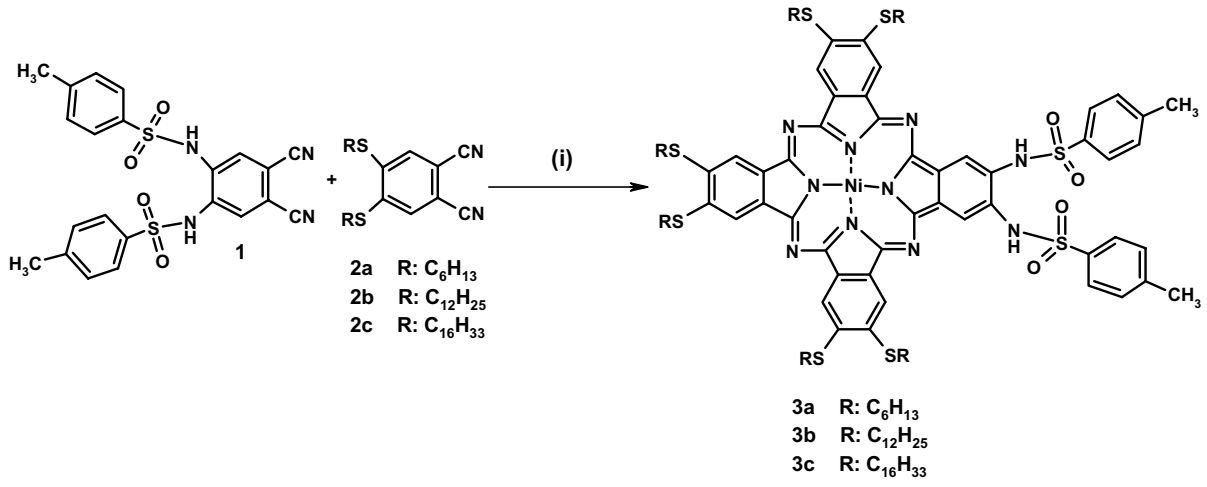
4. Result and discussions

4.1. Synthesis and characterization

The synthetic route of the pcs is shown in Scheme 1. 1,2-Di(alkylthio)-4,5-dicyanobenzenes (**2a**–**2c**) and 4,5-dicyano-*N*,*N*′-ditosyl-*o*-phenylenediamin (**1**) were synthesized according to the published procedures [40–42]. For the preparation of the pcs, we tried two different methods: ring expansion of corresponding sub-pc and statistical condensation of the phthalonitriles. For the first method, the diiminoisondoline derivative of **1** is required. Probably due to hydrolysis of the tosyl groups, it could not be obtained according to the literature [45–47]. Therefore, we adopted the second method (the statistical condensation method) for the preparation of the asymmetric pcs (**3a**–**3c**). Mixed condensation of 1,2-di(alkylthio)-4,5-dicyanobenzene (**2a**–**2c**) and 4,5-dicyano-*N*,*N*′-ditosyl-*o*-phenylenediamin (**1**) in the presence of anhydrous nickel (II) chloride, DBU as a strong nitrogen base and *n*-hexanol as the solvent afforded the asymmetric pcs (**3a–3c**). Generally, this method predicts that the reaction of two different phthalonitriles of the same reactivity in a 3:1 ratio will afford a mixture of products in the following percentages: A_4 33%, A_3B 44%, other cross-condensation products 23% [44]. In our case, the 1,2-di(alkylthio)-4,5-dicyanobenzene derivatives (**2a**–**2c**) are much more reactive than 4,5-dicyano-*N*,*N*′-ditosyl-*o*-phenylenediamine (**1**), therefore the symmetric octaalkylthio phthalocyanine (A_4) derivatives were found to be more preferable than the asymmetric **3a**–**3c** pcs (A_3B). To increase the yield of the asymmetric pcs (**3a**–**3c**) we tried several experiments with different molar ratios, and a 2:1 ratio of two dinitrile derivatives **2a**–**2c** and **1** was found to be the most appropriate. The asymmetric pcs (**3a**–**3c**) were separated by preparative thin layer chromatography from the corresponding symmetric octaalkylthio substituted Ni(II) pc derivatives [$NiPc(SR)_8$] and the other products.

Elemental analysis results and the spectral data (^{1}H NMR, ^{13}C NMR, FT IR, UV–Vis and MS) for the newly synthesized pcs (**3a**–**3c**) were consistent with the assigned formulations. The results are given in the experimental section.

The IR spectral results of the pcs (**3a**–**3c**) are different from the precursors **1** and **2a**–**2c**, so the sharp peak for the C≡N vibrations around 2220–2240 cm^{-1}, associated



Scheme 1. Synthesis of phthalocyanines **3a**–**3c** (i) metal salt, DBU, *n*-hexanol, reflux.

with the nitrile groups, disappeared after conversion into the pcs. The NH groups gave absorption bands at around 3260 cm^{-1} and the characteristic vibration of SO_2 groups appeared at around 1340 and 1160 cm^{-1} in the spectra of all the pcs, and confirmed the presence of the tosylamido groups. In addition, a group of intense absorption bands was also seen in the range 2856–2957 cm^{-1} in the IR spectra of **3a**–**3c**. These can be attributed to the C-H stretching vibrations of the substituted alkyl chains.

A close investigation of the mass spectra of **3a**–**3c** confirmed the proposed structures. The mass spectra of these compounds were obtained by the electron spray (ES) technique. We observed the molecular ion peaks of the pcs at *m/z*: 1606 for **3a**, *m/z*: 2111 for **3b** and *m/z*: 2446 for **3c.**

A common feature of the ^1H NMR spectra of the pcs (**3a**–**3c**) is the broad absorptions probably caused by the aggregation of the pc, which is frequently encountered at the concentrations used for NMR measurements. The ^1H NMR spectra of **3b** and **3c** are similar to that of **3a**. The ^1H NMR spectrum of **3a** exhibits the aromatic and NH protons at 7.90–8.42 ppm as multiplets, the aliphatic CH_2 protons between 1.43 and 3.58 ppm as multiplets, CH_3 protons at δ 0.94–1.18 and ArC–CH_3 protons at around 2.21 ppm. The ratio of aromatic to aliphatic protons appears to show that the benzo groups with two different substituents are present in a 3:1 ratio. The ^{13}C NMR spectral data of **3a**–**3c** given in experimental section are also in accord with the expected structures.

The blue-green pcs show typical electronic spectra with two strong absorption bands: a Soret (B) band at around 300–350 nm and a Q band at around 600–700 nm. The UV–Vis. spectra of **3a**–**c** were obtained in chloroform and the results are given in Table 1. All of these pcs gave very similar spectra; they show the Q band at 697 nm and the B band at 323 nm. Increasing the length of the alkyl chain caused a decrease of the intensity of the Q band as expected. The electronic spectrum is given for compound **3a** (Fig. 1). In addition to this octatosylamido Ni(II) and octahexilthia Ni(II) phthalocyanines are given in Fig. 1 to compare the absorption bands. The electronic absorption spectrum of octatosylamido Ni(II) phthalocyanine gave two Q bands in chloroform: a monomeric Q band around 680 nm together with a blue-shifted intense band around 640 nm corresponding to aggregated species. No additional band around 640 nm corresponding to aggregated species was observed in the electronic spectra of the asymmetric species (**3a**–**3c**). Octahexylthia substituted Ni(II) phthalocyanine also a gave different electronic spectrum from its

Table 1
Electronic spectra of the phthalocyanines in chloroform

Compound	λ_{max}/nm ($\varepsilon/10^4$ dm^3 mol^{-1} cm^{-1})	
	Soret band region	Q band region
3a	322.5(13.32) 413.0(3.64)	697.0(16.61)
3b	323.0(13.00) 414.0(3.22)	697.5(15.82)
3c	323.5(13.10) 413.5(3.50)	698.0(15.11)

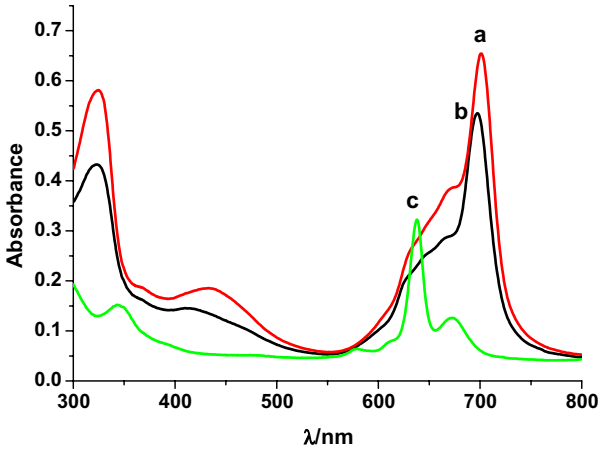


Fig. 1. Visible absorption spectra of octahexzilthia Ni(II) phthalocyanine (a), unsymmetrical substituted Ni(II) pc derivative (**3a**) (b) and octatosilamido Ni(II) phthalocyanine (c) in chloroform. Concentration = 3.74×10^{-6} mol dm^{-3}.

asymmetric derivative (**3a**), with a Q band around 702 nm and a higher extinction coefficient than **3a**.

4.2. Mesomorphic properties

The phase transition behaviours of the compounds **3a**–**3c** were determined by differential scanning calorimetry (DSC) and polarizing microscopic observations. Phase transition temperatures and enthalpy changes of these products are presented in Table 2. The DSC-measurement of compounds **3a**–**3c** show a significant sharp peak in the vicinity of 150 °C, which relates to the melting transition. Furthermore the DSC diagram of **3b** and **3c** depict a weak peak at about 227 °C and 205 °C, respectively that belongs to the clearing point. These investigations indicate that the compounds exhibit a thermotropic liquid crystalline phase between the melting and clearing point [25–28,32–34]. No such additional peak is observed for compound **3a**, which excludes further phase transitions. Only the melting to the mesophase is present. The phthalocyanine derivative **3a** did not give any isotropic transition until 280 °C. Therefore the heating cycles were interrupted before reaching any clearing point to avoid decomposition for **3a**. The thermal stability of the phthalocyanines (**3a**–**3c**) has been investigated by thermal gravimetric analysis (TGA). The initial decomposition of the compounds **3a**, **3b** and **3c** determined

Table 2
Phase transition temperatures and enthalpies for the compound **3a**–**3c** as determined by DSC[a]

Compound	Heating		Cooling	
	C → Col_h → I		I → Col_h → C	
3a	165 (3.90)	not observed	not observed	120 (4.06)
3b	161 (32.54)	227 (1.19)	218 (2.96)	91 (21.11)
3c	144 (42.53)	205 (6.17)	198 (5.52)	23 (50.59)

Heating and cooling rates: 10 °C, heating range: 0–280 °C.
[a] Phase nomenclature: Col_h = discotic hexagonal columnar phase, I = isotropic phase.



Fig. 2. Optical texture of **3b** observed at 170 °C (Magnification ×16).

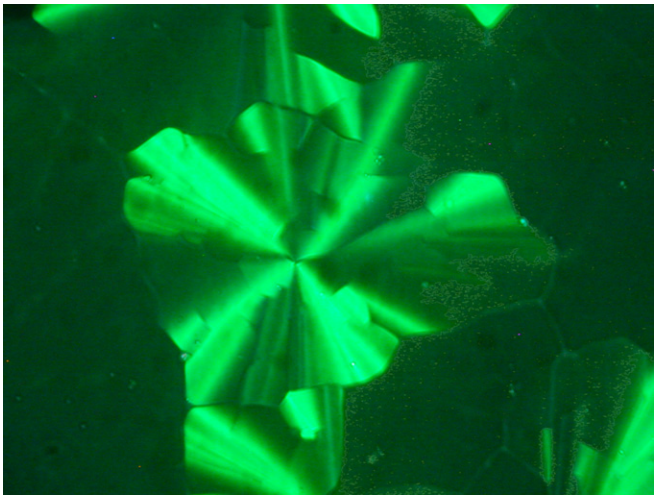


Fig. 3. Optical texture of **3c** observed at 170 °C (Magnification ×50).

by thermogravimetry occur above 298, 290 and 295 °C, respectively, and show negligible differences according to the length of the alkyl-chains. The main decomposition points are 325, 335 and 330 °C, respectively.

Also, the phase transition temperatures of the complexes (**3a**–**3c**) have been surveyed by polarization microscopy. The birefringence textures of the samples were obtained by slow cooling (5 °C min^{-1}) from the isotropic melt. The microscopic observation gave magnificent results for these complexes (**3a**–**3c**). Figs. 2 and 3 shows the photomicrograph of the mesophase of **3b** and **3c**, respectively at 170 °C. For this typical fan-shaped texture, often observed for Col_h, these mesophases could be thus confirmed as the Col_h phases [27–29,33,34].

According to the literature, the mesophase transition temperature of the symmetric hexylthia and dodecylylthia substituted Ni(II) Pcs were 36 and 20 °C [28]. When compared with their asymmetric derivatives (**3a**–**3c**), it could be seen that addition of tosylamido groups to the phthalocyanine core increases the liquid crystal phase transition temperatures but decreases the clearing temperature. The isotropic liquid phase was not observed for hexylthia and dodecylthia substituted Ni(II) Pcs until 300 °C in the literature [28], though isotropic transitions were observed for the asymmetric derivatives (**3b**, **3c**) at 227 and 205 °C respectively. Furthermore, increasing the length of the alkyl chain decreases the melting and isotropic phase transition temperatures of compounds **3a**–**3c**.

5. Conclusions

Asymmetric mesogenic phthalocyanines are rather few. In the present work, the synthesis of new asymmetric Ni(II) phthalocyanines are described and characterized by standard methods (^1H and ^{13}C NMR, elemental analysis, IR, UV/Vis and mass spectrometry). The asymmetric Ni(II) phthalocyanine derivatives **(3a–3c)** exhibit a hexagonal columnar (Col_h) structure. The influence of nature of the side chains upon the mesomorphic properties was compared for the asymmetric pcs (**3a**–**3c**) and also with their symmetric analogous without the tosylamido group [$NiPc(SR)_8$]. It could be seen that addition of the tosylamido group to the phthalocyanine core increases liquid crystal phase transition temperatures but decreases clearing temperatures. In addition to this, increasing the length of alkyl chain decreases the melting and isotropic phase transition temperatures of the compounds **3a**–**3c**.

Acknowledgements

The authors thank to Colette LEBRUN for ES mass spectra and Prof. Ayşe Gül GÜREK for fruitful discussions.

References

[1] N.B. McKeown, Phthalocyanine Materials: Synthesis, Structure and Function, Cambridge University Press, Cambridge, 1998.
[2] C.C. Leznoff, A.B.P. Lever, Phthalocyanines: Properties and Applications, VCH, vols. 1–4, New York, 1989, 1993, 1996.
[3] K.M. Kadish, M.S. Kevin, R. Guilard, The Pophyrin Handbook, Phthalocyanines: Synthesis, vol. 15, Academic Press, 2003.
[4] C. Piechocki, J. Simon, J. Chem. Soc., Chem. Commun. (1985) 259.
[5] G.J. Clarkson, N.B. McKeown, K.E. Treacher, J. Chem. Soc., Perkin Trans. 1 (1995) 1817.
[6] G.J. Clarkson, A. Cook, N.B. McKeown, K.E. Treacher, Z. Ali-Adib, Macromolecules 29 (1996) 913.
[7] M.J. Cook, M.F. Daniel, K.J. Harrison, N.B. McKeown, A.J. Thomson, J. Chem. Soc., Chem. Commun. (1987) 1148.
[8] N.B. McKeown, M.J. Cook, A.J. Thomson, K.J. Harrison, M.F. Daniel, R.M. Richardson, S.J. Roser, Thin Solid Films 159 (1988) 469.
[9] X. Ding, H. Xu, Sensors and Actuators B 65 (2000) 108.
[10] J.W. Winkelman, D. Arad, S. Kimel, J. Photochem. Photobiol. B 18 (1993) 181.
[11] P. Matlaba, T. Nyokong, Polyhedron 21 (2002) 2463.
[12] A. Sastre, B. del Rey, T. Torres, J. Org. Chem. 61 (1996) 8591.
[13] E.M. Maya, C. Garcia, E.M. Garcia-Frutos, P. Vazquez, T. Torres, J. Org. Chem. 65 (2000) 2733.
[14] M. Tian, T. Wada, H. Kimura-Suda, H. Sasabe, J. Mater. Chem. 7 (1997) 861.

[15] S.V. Kudrevich, H. Ali, J.E. van Lier, J. Chem. Soc., Perkin Trans. 1 (1994) 2767.
[16] C.C. Leznoff, P. Snirkaya, B. Khouw, R.L. Cerny, P. Seymour, A.B.P. Lever, J. Org. Chem. 56 (1991) 82.
[17] A. Hirth, A.K. Sobbi, D. Wöhrle, J. Porphyrins Phthalocyanines 1 (1997) 275.
[18] N. Kobayashi, R. Kondo, S. Nakajima, J. Am. Chem. Soc. 112 (1990) 9640.
[19] S. Dabak, A. Gül, Ö Bekaroğlu, Chem.Ber. 127 (1994) 2009.
[20] A. Sastre, T. Torres, M. Hanack, Tetrahedron Lett. 36 (1995) 8501.
[21] E. Musluoğlu, A.G. Gürek, V. Ahsen, Ö Bekaroğlu, Chem. Ber. 125 (1992) 2337.
[22] A. Weitemeyer, H. Kliesch, D. Wöhrle, J. Org. Chem. 60 (1995) 4900.
[23] K. Ohta, L. Jacquemin, C. Sirlin, L. Bosio, J. Simon, New J. Chem. 12 (1988) 751.
[24] D. Masurel, C. Sirlin, J. Simon, New J. Chem. 11 (1987) 455.
[25] C. Piechocki, J. Simon, A. Skoulios, D. Guillon, P. Weber, J. Am. Chem. Soc. 104 (1982) 5245.
[26] D. Guillon, A. Skoulios, C. Piechocki, J. Simon, P. Weber, Mol. Cryst. Liq. Cryst. 100 (1983) 275.
[27] A.G. Gürek, V. Ahsen, F. Heinemann, P. Zugenmaier, Mol. Cryst. Liq. Cryst. 338 (2000) 75.
[28] T.V. Basova, A.G. Gürek, V. Ahsen, Metarials Science and Engineering C 22 (2002) 99.
[29] S. Dabak, V. Ahsen, F. Heinemann, P. Zugenmaier, Mol. Cryst. Liq. Cryst. 338 (2000) 111.
[30] C. Sirlin, L. Bosio, J. Simon, E. Yılmazer, Ö Bekaroğlu, Chem. Phys. Lett. 139 (1987) 362.
[31] C.F. Van Nostrum, S.J. Picken, R.J.M. Nolte, Angew. Chem. Int. Ed. Engl. 33 (1994) 2173.
[32] C.F. Van Nostrum, S.J. Picken, A.J. Schouten, R.J.M. Nolte, J. Am. Chem. Soc. 117 (1995) 9957.
[33] A.G. Gürek, M. Durmuş, V. Ahsen, New J. Chem. 28 (2004) 693.
[34] M. Durmuş, C. Lebrun, V. Ahsen, J. Porphyrins Phthalocyanines 8 (2004) 1175.
[35] F. Yılmaz, D. Atilla, V. Ahsen, Polyhedron 23 (2004) 1931.
[36] M. urmuş, S. Yeşilot, V. Ahsen, New J. Chem. 30 (2006) 675.
[37] V. Ahsen, M. Özdemir, Z.Z. Öztürk, A. Gül, Ö Bekaroğlu, J. Chem. Res. (S) 2 (1995) 348.
[38] T.V. Basova, B.A. Kolesov, A.G. Gürek, V. Ahsen, Thin Solid Films 385 (2001) 246.
[39] T.V. Basova, C. Taşaltın, A.G. Gürek, M.A. Ebeoğlu, Z.Z. Öztürk, V. Ahsen, Sensors Actuators B 96 (2003) 70.
[40] F. Yüksel, A.G. Gürek, C. Lebrun, V. Ahsen, New J. Chem. 29 (2005) 726.
[41] D. Wöhrle, K. Eskes, A. Shigehara, A. Yamada, Synthesis (1993) 194.
[42] A.G. Gürek, Ö Bekaroğlu, J. Chem., Dalton Trans. (1994) 1419.
[43] D.D. Perrin, W.L. Armarego, Purification of Laboratory Chemicals, Pergamon Press, Oxford, 1989.
[44] D. de la Torre, C.G. Claessens, T. Torres, Eur. J. Org. Chem. 16 (2000) 2821.
[45] P.J. Brach, S.J. Grammatica, O.A. Ossanna, L. Weinberger, J. Heterocyclic Chem. 7 (1970) 1403.
[46] E.H. Morkved, S.M. Neset, O. Bjorlo, H. Kjosen, G. Hvistendahl, F. Mo, Acta Chem. Scand. 49 (1995) 658.
[47] E.H. Morkved, H. Kjosen, H. Ossletten, N. Erchak, J. Porphyrins Phthalocyanines 3 (1999) 417.

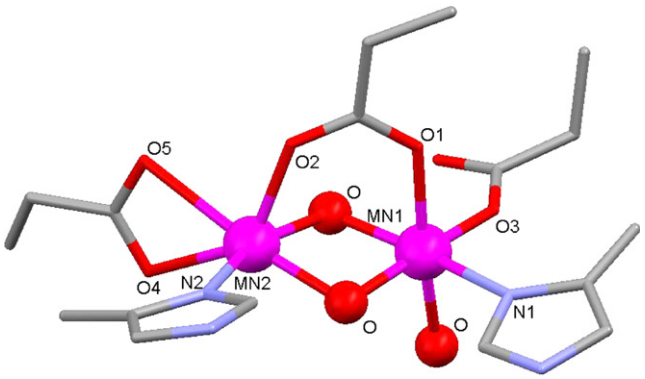


Fig. 1. The dimanganese active site of Mn catalase from *L. plantarum*. The coordinates were obtained from PDB 1JKU and rendered using Mercury 1.4.1 software. Mn(1)–Mn(2), 3.03 Å; Mn(1)–N(1), 2.17 Å; Mn(1)–O(1), 2.11 Å; Mn(1)–O(3), 1.85 Å; Mn(1)-μ-O, 1.92 Å and 2.01 Å; Mn(2)–N(2), 2.16 Å; Mn(2)–O(2), 2.10 Å; Mn(2)–O(4), 2.38 Å; Mn(2)–O5, 2.42 Å; Mn(2)-μ-O, 1.98 Å and 2.23 Å.

The dimanganese redox center of Mn catalase can have at most five oxidation states and four of them have been characterized structurally or spectroscopically. The enzyme isolated under reducing conditions shows the $Mn^{II}Mn^{II}$ oxidation state and is eventually autoxidized to the $Mn^{III}Mn^{III}$ oxidation state through the $Mn^{II}Mn^{III}$ state under air [12]. The autoxidation is more effective under basic conditions. Periodate oxidation of the enzyme results in the superoxidized $Mn^{III}Mn^{IV}$ oxidation state, and the superoxidized Mn catalase is catalytically inactive. It has been suggested that catalytically active manganese catalase utilizes the $Mn^{II}Mn^{II} \leftrightarrow Mn^{III}Mn^{III}$ catalytic cycle [13]. The catalytic activity of Mn catalase in the $Mn^{II}Mn^{II}$ oxidation state is also inhibited in the presence of the chloride ion by the formation of the $Mn^{II}_2(\mu\text{-Cl})(\mu\text{-OH})$ or $Mn^{II}_2(\mu\text{-Cl})$ core [10]. The chloride ion inhibits only the $Mn^{II}Mn^{II}$ oxidation state of the enzyme and the inhibitory effect is reversible [14], but the reactivation mechanism of the inhibited enzyme is not known yet. It has also been reported that the formation of autoxidized Mn catalase is retarded by a high concentration of chloride ion [15].

Due to its easy preparation and versatile coordination chemistry, TPA (tris(2-pyridylmethyl)amine) has been used as a popular biomimetic ligand. Various alkali metal and transition metal complexes of TPA have been synthesized and used for biological model systems such as dioxygen activation by iron non-heme oxygenases [16]. Although many TPA manganese complexes have been reported [17–20], few TPA complexes of $MnCl_2$ have been reported. Although the preparation of $TPAMnCl_2$ has been reported [21], its physical properties and reactivity were not reported. Especially, the synthesis of dinuclear $[TPA_2Mn_2(\mu\text{-Cl})_2]^{2+}$ has never been reported to our knowledge.

Here we report the synthesis, X-ray crystallographic structure, physical properties and catalytic activity of the $[TPA_2Mn^{II}_2(\mu\text{-Cl})_2]^{2+}$ complex. The H_2O_2 dismutation activity of the $[TPA_2Mn^{II}_2(\mu\text{-Cl})_2]^{2+}$ complex was compared with the complexes $TPAMn^{II}Cl_2$ and $[TPA_2Mn^{III}Mn^{IV}(\mu\text{-O})_2]^{3+}$. The $[TPA_2Mn^{II}_2(\mu\text{-Cl})_2]^{2+}$ and $[TPA_2Mn^{III}Mn^{IV}(\mu\text{-O})_2]^{3+}$ complexes are relevant to chloride-inhibited and superoxidized Mn catalase, respectively.

2. Experimental

2.1. General

All experiments and reactions were carried out under a dinitrogen atmosphere using standard Schlenk line techniques or in an inert atmosphere glove box, unless otherwise noted. All solvents were distilled under dinitrogen and nitrogen gas was bubbled through them before each use in the glove box. $MnCl_2$ and $Mn(NO_3)_2 \cdot 4H_2O$ were purchased from Aldrich and were used without further purification. $H_3TPA(ClO_4)_3$ was prepared by the published method [22].

FT-IR spectra were collected on a Nicolet DX V. 4.56 FT-IR spectrometer in KBr pellets and the spectra were corrected for background effects. Elemental analyses were performed in the Microanalytical Laboratory at the University of Michigan. The data were corrected using acetanilide as a standard. ESI-Mass spectra were obtained on a Finnigan LCQ-DECA mass spectrometer by direct injection. Cyclic voltammetry (CV) was performed on a Princeton Applied Research model 263A potentiostat with a K0264 microcell kit. Three electrodes, consisting of a glassy carbon working electrode, a Pt auxiliary electrode and a saturated calomel electrode (SCE) as a reference electrode, were used for the measurements. The complexes of $(Et_3NH)_2[TPA_2Mn_2(\mu\text{-Cl})_2](ClO_4)_4$ (**I**), $TPAMnCl_2$ (**II**) and $[TPA_2Mn_2(\mu\text{-O})_2](ClO_4)_3$ (**III**) were dissolved in MeCN (for **I** and **III**) or CH_2Cl_2 (for **II**), together with 0.1 M $^nBuNPF_6$ as a supporting electrolyte. The scanning rate was 50 mV/s and $E_{1/2}$ of the ferrocene oxidation in MeCN was observed at +0.67 V under these conditions. Magnetic susceptibilities of $(Et_3NH)_2[TPA_2Mn_2(\mu\text{-Cl})_2](ClO_4)_4$ (**I**), $TPAMnCl_2$ (**II**), and $[TPA_2Mn_2(\mu\text{-O})_2](ClO_4)_3$ (**III**) were measured in the temperature range 4–300 K with a Quantum Design MPMS SQUID. The magnetic field of the measurements was 5000 G over the temperature range. The crystalline sample was put into a cellophane capsule under a dinitrogen atmosphere. The magnetic susceptibility of the holder was determined separately for background corrections. Diamagnetic corrections were estimated from Pascal's constants [23]. The temperature-dependent magnetic susceptibility data were fitted using the Origin program. The EPR spectrum of $(Et_3NH)_2[TPA_2Mn_2(\mu\text{-Cl})_2](ClO_4)_4$ (**I**) was obtained at 100 K in the X-band region using a Bruker EMS 4102-ST ESR spectrometer with PC data acquisition.

2.2. Catalytic study

In a 20 ml vial with a stirring bar, the Mn complex was dissolved in 3.0 mL of MeCN under dinitrogen to make a

0.1 mM solution. The vial was sealed with a septum, and connected to the gas volume measurement apparatus through a double-ended needle. The catalysis was initiated by introducing 20% H_2O_2 solution using a syringe. The amount of product formation was calculated from the volume of oxygen gas generated using the ideal-gas equation. The substrate concentration vs. initial velocity graphs were obtained from the triplicate measurements at each substrate concentration.

2.3. $(Et_3NH)_2[TPA_2Mn_2(\mu\text{-}Cl)_2](ClO_4)_4$ (**I**)

$MnCl_2$ (0.43 g, 3.43 mmol) in MeOH (10 mL) was added to 10 mL of a methanol solution of $H_3TPA(ClO_4)_3$ (2.03 g, 3.43 mmol) and NEt_3 (1.43 mL, 10.28 mmol). The reaction mixture was stirred for 2 h at room temperature. The reaction was stopped by filtration and diethyl ether was layered over the filtrate. A pale yellow oil product was isolated by decanting the supernatant. It was dissolved in acetone (10 mL) and filtered to remove insoluble impurities. Diethyl ether was layered over the filtrate to induce incipient crystallization. Greenish yellow rhombic crystals were formed in a few days and isolated by filtration. $(Et_3NH)_2[TPA_2Mn_2(\mu\text{-}Cl)_2](ClO_4)_4$ (870 mg, 0.638 mmol, 37%). FT-IR (KBr, cm^{-1}): 2935(w), 2754(w), 2677(m), 2489(w), 1600(s), 1475(m), 1442(m), 1145(vs), 1108(vs), 1091(vs), 1014(m), 773(m), 763(w), 626(m). *Anal.* Calc. for $C_{48}H_{68}Cl_6Mn_2N_{10}O_{16}$ (MW 1363.72): C, 42.28; H, 5.03; N, 10.27. Found: C, 42.02; H, 5.37; N, 10.21%. ESI-MS^+ (MeOH, *m/z*) 380.4 ($[TPAMnCl]^+$), 444.3 ($[TPAMn(ClO_4)]^+$), 517.2 ($[TPAMnCl_2(Et_3NH)]^+$), 581.1 ($[TPAMnCl(Et_3NH)(ClO_4)]^+$), 795.1 ($[TPA_2Mn_2Cl_3]^+$), 861.1 ($[TPA_2Mn_2Cl_2(ClO_4)]^+$), 925.1 ($[TPA_2Mn_2Cl_2(ClO_4)(MeOH)_2]^+$), 989.0 ($[TPA_2Mn_2Cl_2(ClO_4)(MeOH)_4]^+$). Cyclic voltammetry (MeCN, versus SCE, V) 1.09(qr), 1.30(qr), 1.75(rev), 2.14(qr). EPR(MeOH, 100 K, g) 5.38, 3.33, 1.97. Magnetic susceptibility: 7.89 μ_B (300 K), 2.02 μ_B (4 K).

2.4. $TPAMnCl_2$ (**II**)

Complex **II** was prepared from the perchlorate salt of TPA according to the published method [21], with a slight modification. $MnCl_2$ (0.25 g, 2.01 mmol) in MeOH (20 mL) was added to 20 mL of a methanol solution of $H_3TPA(ClO_4)_3$ (1.19 g, 2.01 mmol) and NEt_3 (0.84 mL, 6.03 mmol). The reaction mixture was stirred for an hour at 50 °C. The solvent was removed under vacuum and the resulting yellow oil was redissolved in MeOH. Solvent diffusion by diethyl ether produced transparent crystals in a day. $TPAMnCl_2$ (290 mg, 0.697 mmol, 35%). FT-IR (KBr, cm^{-1}): 3065(w), 2904(w), 1602(vs), 1442(m), 1423(m), 1014(m), 773(s), 763(m), 638(m). *Anal.* Calc. for $C_{18}H_{18}Cl_2MnN_4$ (MW 416.20): C, 51.94; H, 4.36; N, 13.46. Found: C, 51.54; H, 4.11; N, 13.87%. ESI-MS^+ (MeOH, *m/z*) 380.3 ($[TPAMnCl]^+$), 794.9 ($[TPA_2Mn_2Cl_3]^+$). Cyclic voltammetry (CH_2Cl_2, versus SCE, V) 1.17(rev), 2.04(qr). Magnetic susceptibility: 5.64 μ_B (300 K), 5.54 μ_B (4 K).

2.5. $[TPA_2Mn_2(\mu\text{-}O)_2](ClO_4)_3$ (**III**)

The synthesis of the complex $[TPA_2Mn_2(\mu\text{-}O)_2](S_2O_6)_{3/2} \cdot 7H_2O$ has been reported before [17], and here complex **III** has been prepared by a different method. $H_3TPA(ClO_4)_3$ (355 mg, 0.6 mmol) in 3 mL of MeOH was dissolved by adding NEt_3 (250 μL, 1.8 mmol). To this, $Mn(NO_3)_2 \cdot 4H_2O$ (150 mg, 0.6 mmol) in MeOH (2 mL) was added. The reaction mixture was stirred for 2 h at room temperature, and a few drops of H_2O_2 was added into the reaction mixture until it turned into a black solution. The solvent was removed by N_2 purging, resulting in a black residue. The residue was redissolved in MeCN and slow solvent diffusion by diethyl ether produced a black precipitate. The black precipitate was filtered, washed with diethyl ether several times, and extracted with a minimal amount of MeCN. The solution was kept under air and black plate-type crystals were isolated from the MeCN extract in a day. $[TPA_2Mn_2(\mu\text{-}O)_2](ClO_4)_3$ (120 mg, 0.113 mmol, 37.7%). FT-IR (KBr, cm^{-1}): 3070(w), 2955(w), 2250(w), 1606(s), 1485(m), 1445(m), 1383(m), 1289(m), 1088(vs), 765(s), 623(m). *Anal.* Calc. for $C_{38}H_{39}Cl_3Mn_2N_9O_{14}$ (MW 1062.00): C, 42.98; H, 3.70; N, 11.87. Found: C, 42.17; H, 3.69; N, 11.45%. UV–Vis (green in MeCN): λ_{max} (ε) = 439 nm (2040 $M^{-1}\,cm^{-1}$), 558 nm (1060 $M^{-1}\,cm^{-1}$), 658 nm (890 $M^{-1}\,cm^{-1}$). Cyclic voltammetry (MeCN, versus SCE, V) 0.40(rev), 1.35(rev). Magnetic susceptibility: 1.38 μ_B (300 K), 1.97 μ_B (4 K).

2.6. X-ray crystallography

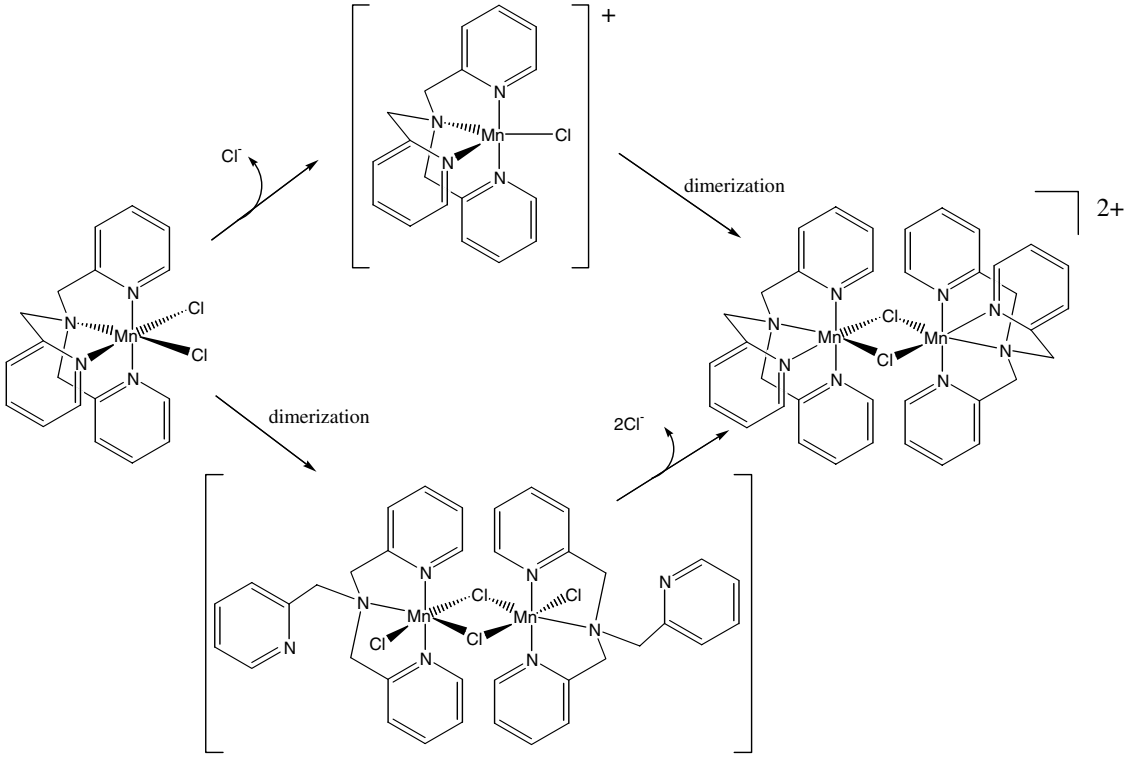
Greenish yellow rhombic crystals of $(Et_3NH)_2[TPA_2Mn_2(\mu\text{-}Cl)_2](ClO_4)_4$ (**I**) and transparent needle-shaped crystals of $TPAMnCl_2$ (**II**) were obtained from the mother liquor after several days. Black plate-shaped crystals of $[TPA_2Mn_2(\mu\text{-}O)_2](ClO_4)_3$ (**III**) were isolated by slow evaporation of MeCN solvent under air. The diffraction data for **I** was collected at 293(2) K and the data for **II** and **III** were collected at 123(2) K using a Bruker SMART area diffractometer equipped with a monochromator in the Mo Kα ($\lambda = 0.71073$ Å) incident beam. The CCD data were integrated and scaled using the Bruker-SAINT software package [24], and the structures were solved and refined using SHEXTL V5.10 [25]. The crystal data and structural parameters are shown in Tables 1 and 2. The structures for compounds **I**, **II** and **III** were solved by direct methods to locate heavy atoms, and the non-hydrogen atoms were located through subsequent difference Fourier syntheses. Structural refinement was carried out by full-matrix least squares on F^2. All non-hydrogen atoms were refined with anisotropic thermal parameters. Hydrogen atoms were located in the calculated positions.

Table 1
Crystal data and structure refinement for $(Et_3NH)_2[TPA_2Mn_2(\mu\text{-}Cl)_2](ClO_4)_4$ (**I**), $TPAMnCl_2$ (**II**) and $[TPA_2Mn_2(\mu\text{-}O)_2](ClO_4)_3$ (**III**)

	I	**II** · MeOH	**III** · MeCN
Empirical formula	$C_{48}H_{68}Cl_6Mn_2N_{10}O_{16}$	$C_{19}H_{22}Cl_2MnN_4O$	$C_{38}H_{39}Cl_3Mn_2N_9O_{14}$
Formula weight	1363.70	448.25	1062.01
Temperature (K)	293(2)	123(2)	123(2)
Wavelength (Å)	0.71073	0.71073	0.71073
Crystal system	monoclinic	monoclinic	triclinic
Space group	$P2_1/c$	$P2_1/n$	$P\bar{1}$
Unit cell dimensions			
a (Å)	11.5784(19)	8.9165(18)	9.853(3)
b (Å)	22.131(4)	15.733(3)	12.002(4)
c (Å)	12.616(2)	14.884(3)	19.691(6)
α (°)			84.186(4)
β (°)	106.570(3)	103.347(3)	84.768(4)
γ (°)			68.620(4)
Volume (Å^3)	3098.5(9)	2031.6(7)	2153.5(11)
Z, D_{calc} (Mg/m^3)	2, 1.462	4, 1.465	2, 1.638
Absorption coefficient (mm^{-1})	0.737	0.929	0.851
$F(000)$	1412	924	1086
Crystal size (mm)	$0.20 \times 0.10 \times 0.10$	$0.40 \times 0.10 \times 0.08$	$0.44 \times 0.38 \times 0.26$
θ Range for data collection (°)	1.84–28.31	1.91–28.55	2.04–28.34
Limiting indices	$-15 \leqslant h \leqslant 14$, $-28 \leqslant k \leqslant 27$, $-16 \leqslant l \leqslant 16$	$-11 \leqslant h \leqslant 11$, $-21 \leqslant k \leqslant 20$, $-19 \leqslant l \leqslant 19$	$-13 \leqslant h \leqslant 13$, $-15 \leqslant k \leqslant 15$, $-26 \leqslant l \leqslant 26$
Reflections collected/unique	19361/7279	44525/5079	39959/10672
R(int)	0.0583	0.0646	0.0322
Completeness to θ	28.31°, 94.3%	28.55°, 98.3%	28.34°, 99.2%
Absorption correction	semi-empirical, (SADABS)	semi-empirical, (SADABS)	semi-empirical, (SADABS)
Refinement method	full-matrix least-squares on F^2	full-matrix least-squares on F^2	full-matrix least-squares on F^2
Data/restraints/parameters	7279/0/374	5079/0/332	10672/0/596
Goodness-of-fit on F^2	0.750	1.048	1.038
R indices [$I > 2\sigma(I)$]	$R_1 = 0.0441$, $wR_2 = 0.0922$	$R_1 = 0.0294$, $wR_2 = 0.0613$	$R_1 = 0.0698$, $wR_2 = 0.1922$
R indices (all data)	$R_1 = 0.1150$, $wR_2 = 0.1008$	$R_1 = 0.0518$, $wR_2 = 0.0691$	$R_1 = 0.0909$, $wR_2 = 0.2104$
Largest difference peak and hole (e Å^{-3})	0.540 and −0.480	0.391 and −0.332	2.013 and −0.874

Table 2
Selected bond lengths (Å) and angles (°) for $(Et_3NH)_2[TPA_2Mn_2(\mu\text{-}Cl)_2](ClO_4)_4$ (**I**), $TPAMnCl_2$ (**II**) and $[TPA_2Mn_2(\mu\text{-}O)_2](ClO_4)_3$ (**III**)

$(Et_3NH)_2[TPA_2Mn_2(\mu\text{-}Cl)_2](ClO_4)_4$ (**I**)		$TPAMnCl_2$ (**II**)		$[TPA_2Mn_2(\mu\text{-}O)_2](ClO_4)_3$ (**III**)	
Mn(1)–N(3)	2.240(2)	Mn(1)–N(1)	2.2617(15)	Mn(1)–N(1)	2.109(4)
Mn(1)–N(1)	2.220(2)	Mn(1)–N(3)	2.2803(15)	Mn(1)–N(3)	2.102(5)
Mn(1)–N(2)	2.259(2)	Mn(1)–N(2)	2.3121(15)	Mn(1)–N(2)	2.035(3)
Mn(1)–N(4)	2.283(2)	Mn(1)–N(4)	2.3643(15)	Mn(1)–N(4)	2.094(3)
Mn(1)–Cl(1)	2.4056(9)	Mn(1)–Cl(2)	2.3996(7)	Mn(1)–O(1)	1.800(3)
Mn(1)–Cl(1)#1	2.6286(10)	Mn(1)–Cl(1)	2.5180(6)	Mn(1)–O(1)#1	1.820(3)
N(1)–Mn(1)–N(3)	150.63(10)	N(1)–Mn(1)–N(3)	146.41(5)	N(1)–Mn(1)–N(3)	156.48(15)
N(3)–Mn(1)–N(2)	83.21(8)	N(1)–Mn(1)–N(2)	85.32(5)	N(1)–Mn(1)–N(2)	84.97(14)
N(1)–Mn(1)–N(2)	94.50(8)	N(3)–Mn(1)–N(2)	84.01(5)	N(3)–Mn(1)–N(2)	84.90(14)
N(3)–Mn(1)–N(4)	76.38(9)	N(1)–Mn(1)–N(4)	73.16(5)	N(1)–Mn(1)–N(4)	78.75(14)
N(1)–Mn(1)–N(4)	74.55(9)	N(3)–Mn(1)–N(4)	73.30(5)	N(3)–Mn(1)–N(4)	78.95(15)
N(2)–Mn(1)–N(4)	77.62(9)	N(2)–Mn(1)–N(4)	74.16(5)	N(2)–Mn(1)–N(4)	82.74(13)
N(3)–Mn(1)–Cl(1)	105.42(7)	N(1)–Mn(1)–Cl(2)	104.64(4)	N(1)–Mn(1)–O(1)#1	95.09(13)
N(1)–Mn(1)–Cl(1)	103.86(7)	N(3)–Mn(1)–Cl(2)	107.50(4)	N(3)–Mn(1)–O(1)#1	93.60(13)
N(2)–Mn(1)–Cl(1)	98.96(7)	N(2)–Mn(1)–Cl(2)	92.15(4)	O(1)#1–Mn(1)–N(2)	176.07(12)
N(4)–Mn(1)–Cl(1)	176.00(6)	N(4)–Mn(1)–Cl(2)	166.20(4)	N(4)–Mn(1)–O(1)#1	93.41(12)
N(3)–Mn(1)–Cl(1)#1	90.76(6)	N(1)–Mn(1)–Cl(1)	93.73(4)	N(1)–Mn(1)–O(1)	102.12(13)
N(1)–Mn(1)–Cl(1)#1	86.30(7)	N(3)–Mn(1)–Cl(1)	90.06(4)	N(3)–Mn(1)–O(1)	100.11(15)
N(2)–Mn(1)–Cl(1)#1	169.12(7)	N(2)–Mn(1)–Cl(1)	167.53(4)	N(2)–Mn(1)–O(1)#1	176.07(12)
N(4)–Mn(1)–Cl(1)#1	92.19(6)	N(4)–Mn(1)–Cl(1)	93.65(4)	N(4)–Mn(1)–O(1)	178.97(14)
Cl(1)–Mn(1)–Cl(1)#1	91.36(3)	Cl(2)–Mn(1)–Cl(1)	100.106(17)	O(1)–Mn(1)–O(1)#1	87.08(11)



Scheme 1. Proposed reaction pathways for the formation of $(Et_3NH)_2[TPA_2Mn_2(\mu\text{-}Cl)_2](ClO_4)_4$ (**I**) from $TPAMnCl_2$ (**II**).

3. Results and discussion

3.1. Syntheses

The iron analog of **I**, $[TPA_2Fe_2(\mu\text{-}Cl)_2](BPh_4)_2$, has been reported as a model compound of diferrous enzyme active centers [26], but the synthesis of the complex $(Et_3NH)_2[TPA_2Mn_2(\mu\text{-}Cl)_2](ClO_4)_4$ (**I**) has never been reported to our knowledge. The synthetic method for **I** is very similar to that for $[TPA_2Fe_2(\mu\text{-}Cl)_2]^{2+}$, and $H_3TPA(ClO_4)_3$ with triethylamine was used in both syntheses for the chelation of the metal ion. When the metallation was tried with free TPA at room temperature, only complex **II** was obtained. In the case of $TPAFeCl_2$, the formation of penta-coordinated $[TPAFeCl]^+$ was observed in the presence of trialkylphosphine and this was suggested as an intermediate during the formation of $[TPA_2Fe_2(\mu\text{-}Cl)_2]^{2+}$ [27]. Likewise, different reaction conditions and crystallization solvent systems would have facilitated the formation of a penta-coordinated $[TPAMnCl]^+$ intermediate, which results in the $[TPA_2Mn_2(\mu\text{-}Cl)_2]^{2+}$ complex. The other possibility of $[TPA_2Mn^{II}_2(\mu\text{-}Cl)_2]^{2+}$ formation is elimination of the terminal chloride ligands from the $TPA_2Mn_2Cl_2(\mu\text{-}Cl)_2$ dimer which could be formed during the reaction (Scheme 1).

The synthesis of $[TPA_2Mn^{III}Mn^{IV}(\mu\text{-}O)_2]^{3+}$ with dithionate counter anions by H_2O_2 oxidation of the Mn(II) complex was first reported by Towle, et al. [17] and the one-electron less oxidized $[TPA_2Mn^{III}Mn^{III}(\mu\text{-}O)_2]^{3+}$ complex was achieved by air-oxidation of $[TPAMn^{II}(DTBSQ)]BPh_4$ [21],[1] The reaction conditions for **III** were different from the published methods. $Mn(NO_3)_2$ was used as a metal reagent and MeOH, instead of water, was used as the reaction solvent. Upon H_2O_2 oxidation, the solution-generated $TPAMn^{II}(\eta^2\text{-}NO_3)(\eta\text{-}ClO_4)$ complex [20] was oxidized and dimerized to complex **III**, which was monitored by color changes of the reaction mixture.

3.2. Structural description

The complex $(Et_3NH)_2[TPA_2Mn_2(\mu\text{-}Cl)_2](ClO_4)_4$ (**I**) crystallized with four perchlorate and two triethylammonium ions in the monoclinic $P2_1/c$ space group (Table 1). The dinuclear manganese core formed a rhombic structure with two distorted octahedral Mn centers (Fig. 2, Table 2). This crystallized with four perchlorate and two triethylammonium counter ions in the unit cell (Fig. 3). The average $Mn–N_{pyr}$ distance is 2.24(1) Å,[2] which is slightly shorter than that of $TPAMnCl_2$ (**II**). The $Mn–N_{amine}$ distance is 2.283(2) Å and is significantly shorter than the corresponding bond of **II**. The average $Mn(1)–N_{pyr}$ distance and $Mn(1)–N_{amine}$ distance are 2.26(2) and 2.3643(15) Å, respectively. The two Mn–Cl bond distances of **I** are

[1] DTBSQ = 3,5-di-tert-butyl-1,2-semiquinonate.

[2] The number in the parenthesis of average bond distances represents the larger of the individual standard deviations or the standard deviation from the mean, $\sigma = \mathrm{SQRT}[\Sigma_{i=1}^{n}(x_i - x)^2/n(n-1)]$, where x_i is an individual standard deviation, x is the average of individual standard deviations.

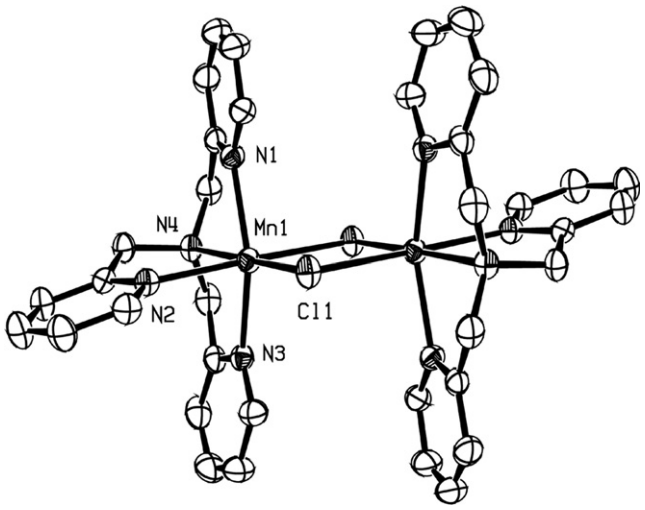


Fig. 2. Crystallographic structure of $[TPA_2Mn_2(\mu\text{-}Cl)_2]^{2+}$ with thermal ellipsoids (50% probability); counter ions and hydrogen atoms are omitted for clarity. The Mn(1)–Mn(1)#1 distance is 3.521(2) Å.

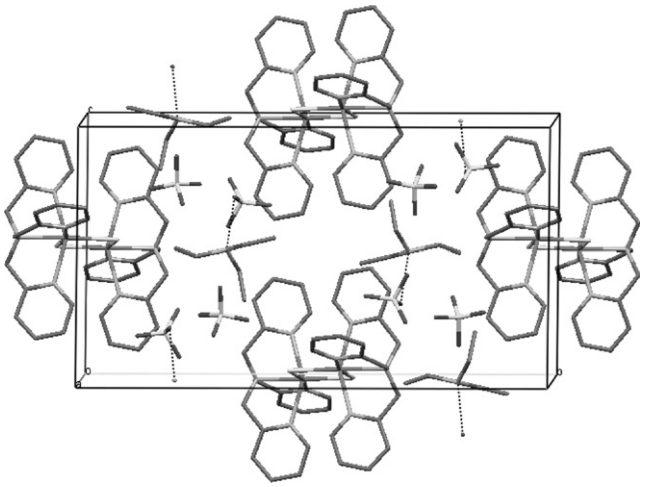


Fig. 3. Packing plot of $(Et_3NH)_2[TPA_2Mn_2(\mu\text{-}Cl)_2](ClO_4)_4$ (**I**). Broken lines indicate hydrogen bonds.

2.4056(9) and 2.6286(10) Å, respectively. Compared to **II**, one of Mn–Cl bonds is elongated by more than 0.1 Å, which is the most distinct bond distance difference between complexes **I** and **II**. The angles between the two axial ligands in **I** and **II** are 166.20(4)° and 176.00(6)°, respectively, and complex **I** shows a more axially-distorted geometry. The distance between the two Mn centers of **I** is 3.521(2) Å, which is much longer than that of the native manganese catalase because it has two chloride bridging ligands instead of water/hydroxide ligands. The protein structure of chloride-inhibited Mn catalase has been reported and a dimanganese center with two bridging chloride ligands was suggested [10]. The distances of the Mn–Mn separation of the chloride-inhibited Mn catalase were obtained from X-ray protein crystallography (3.30 Å) and EPR spectroscopy (3.51 Å) [28]. These values are comparable to the Mn–Mn distance of complex **I**.

The crystallographic structure of $TPAMnCl_2$ (**II**) without a MeOH molecule has been deposited before by others, but the structure was not discussed [29]. The solid state structure of $TPAMnCl_2 \cdot MeOH$ (**II** · MeOH) has been characterized in the monoclinic $P2_1/n$ space group by single crystal X-ray crystallography at 123(2) K (Table 1). The mononuclear Mn complex, **II**, is a six-coordinate Mn^{II} complex with a distorted octahedral coordination geometry (Fig. 4, Table 2). In the coordination sphere of the Mn atom, two chloride ligands are located in a *cis*-configuration at distances of 2.5180(6) and 2.3996(7) Å for Mn(1)–Cl(1) and Mn(1)–Cl(2), respectively. The average Mn(1)–N_{pyr} distance is 2.26(2) Å and the Mn(1)–N_{amine} distance is 2.3643(15) Å, which suggests a high spin configuration of **II** [30]. The average N_{pyr}–Mn(1)–N_{amine} angle and the N(4)–Mn(1)–Cl(1) angle are 73.2(4)° and 93.65(4)°, respectively.

Black crystals of the complex $[TPA_2Mn_2(\mu\text{-}O)_2](ClO_4)_3$ (**III**) were isolated upon solvent evaporation and were stable under air. It crystallized in the triclinic $P\bar{1}$ space group with two unique $[TPA_2Mn_2(\mu\text{-}O)_2]^{3+}$ cations (Table 1). The structure of the same core with dithionate counter anions and water molecules in the unit cell has been reported before [17], but the solved structure showed significantly different structural parameters.

The $[TPA_2Mn_2(\mu\text{-}O)_2]^{3+}$ cation of **III** showed a similar structure to the $[TPA_2Mn_2(\mu\text{-}Cl)_2]^{2+}$ cation of complex **I**. The dimanganese core formed a rhombic structure with distorted octahedral Mn centers (Fig. 5, Table 2). Two different Mn–O bond distances were found from two unique $[TPA_2Mn_2(\mu\text{-}O)_2]^{3+}$ complexes in the unit cell of **III**. The average distance of the short Mn–O bonds is 1.799(3) Å and the average distance of the long Mn–O bonds is 1.817(3) Å. The difference of 0.018 Å is significant but much smaller than the reported value of 0.06 Å in the charge-localized structure [17].

The average distance of the equatorial Mn–N bonds is 2.066(16) Å and the average distance between the Mn

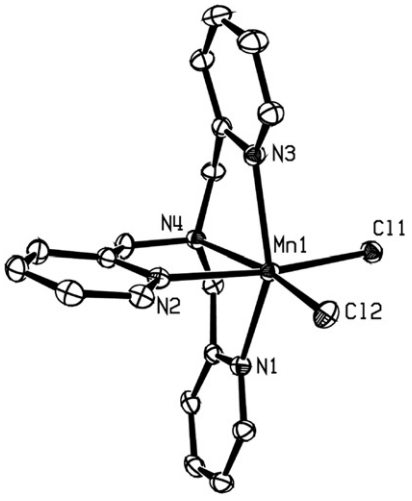


Fig. 4. Crystallographic structure of $TPAMnCl_2$ (**II**) with thermal ellipsoids (50% probability); hydrogen atoms are omitted for clarity.

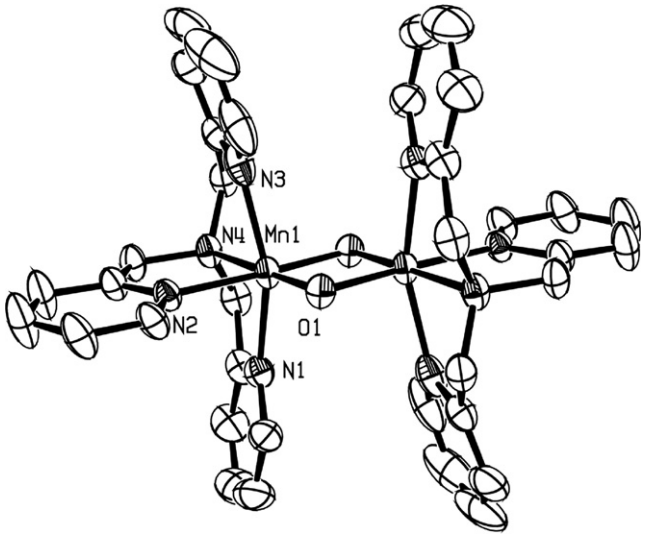


Fig. 5. Crystallographic structure of $[TPA_2Mn_2(\mu\text{-}O)_2]^{3+}$ with thermal ellipsoids (50% probability); counter ions and hydrogen atoms are omitted for clarity.

and axial N atoms is 2.119(9) Å. The average distance of the Mn–N bonds which are *trans* to the longer Mn–O bond is 2.038(3) Å and that of the Mn–N bonds which are *trans* to the shorter Mn–O bond is 2.095(3) Å. It is believed that the Mn–N bonds that are in a *trans*-position to the μ-O ligands (equatorial Mn–N's) are shorter than the other axial Mn–N bonds due to axial Jahn–Teller distortion. The average distance of the Mn–N bonds is 2.092(13) Å, which suggests a high spin configuration of each Mn center in the $Mn^{III}Mn^{IV}$ dinuclear complex [30]. The angles of the two unique Mn–O–Mn bridges are 92.92(11)° and 93.28(11)°, which are much smaller than the reported values, ranging from 94.0° to 94.7° in other complexes with the same $[Mn_2(\mu\text{-}O)_2]^{3+}$ core. Accordingly, the Mn–Mn distances are shorter than the reported values, being 2.6244(12) and 2.6256(13) Å, with an average of 2.6250(13) Å [17]. The Mn–Mn distance of **III** is shorter than 2.70 Å, the distance found from the active site of superoxidized Mn catalase [31]. The angles of the two axial ligands of **III** are 156.48(15)° and 155.53(16)° for N(1)–Mn(1)–N(3) and N(5)–Mn(2)–N(7), respectively.

3.3. Physical properties

FT-IR spectra of $(Et_3NH)_2[TPA_2Mn_2(\mu\text{-}Cl)_2](ClO_4)_4$ (**I**) and $TPAMnCl_2$ (**II**) are almost identical, except that the peaks from the $(Et_3NH)^+$ and $(ClO_4)^-$ ions are found for complex **I**. The peaks from $(Et_3NH)^+$ were found at 2754, 2677 and 2489 cm^{-1}, and the $(ClO_4)^-$ ion showed very strong absorptions at 1200 cm^{-1} and 1050 cm^{-1}. MeCN in the crystal unit cell of $[TPA_2Mn_2(\mu\text{-}O)_2](ClO_4)_3$ (**III**) was observed at 2250 cm^{-1} for the C≡N stretching, and the C=O stretchings of perchlorate in **III** were found at 1088 cm^{-1} [32].

Cyclic voltammetry of complexes **I** and **II** was carried out to see if the two Mn centers in $(Et_3NH)_2[TPA_2Mn_2(\mu\text{-}Cl)_2](ClO_4)_4$ (**I**) communicate electrochemically. $(Et_3NH)_2[TPA_2Mn_2(\mu\text{-}Cl)_2](ClO_4)_4$ (**I**) in MeCN showed multiple oxidation waves, among which the first two oxidation waves at $E_{1/2} = 1.09$ V and $E_{1/2} = 1.30$ V versus SCE were quasireversible (Fig. 5). These oxidations were assigned to the $Mn^{II}Mn^{II}/Mn^{II}Mn^{III}$ and $Mn^{II}Mn^{III}/Mn^{III}Mn^{III}$ oxidation, respectively. The indistinct E_{pa} of the first oxidation ($E_{1/2} = 1.09$ V) and E_{pc} of the second oxidation ($E_{1/2} = 1.30$ V) are probably due to the instability of the $Mn^{II}Mn^{III}$ species. The third reversible oxidation wave found at $E_{1/2} = 1.75$ V can be assigned to the reversible two-electron redox pair of $Mn^{III}Mn^{III}/Mn^{IV}Mn^{IV}$, based on the oxidation current. $TPAMnCl_2$ (**II**) in CH_2Cl_2 showed a reversible oxidation wave at $E_{1/2} = 1.17$ V, corresponding to Mn^{II}/Mn^{III} oxidation (Fig. 5). The next quasi-reversible oxidation wave found at $E_{1/2} = 2.04$ V was assigned to the Mn^{III}/Mn^{IV} redox pair. Experiments at different scan rates confirmed no dimerization of **II** to **I** under the electrochemical conditions. Therefore, the electrochemical property of the dinuclear Mn complex **II** is different from the mononuclear complex **I**. The electrochemical property, as well as the magnetic susceptibility and an EPR study, of $[TPA_2Mn_2(\mu\text{-}O)_2](ClO_4)_3$ (**III**) has been reported before [33]. Complex **III** showed two oxidation potentials at $E_{1/2} = 0.24$ and $E_{1/2} = 1.04$ versus SCE, which are the same as the reported values.

Temperature-dependent magnetic susceptibility data were obtained to study the spin configuration of $(Et_3NH)_2[TPA_2Mn_2(\mu\text{-}Cl)_2](ClO_4)_4$ (**I**) and $TPAMnCl_2$ (**II**). For complex **III**, the magnetic exchange parameter $J = -159$ cm^{-1} was reported [33].

From $(Et_3NH)_2[TPA_2Mn_2(\mu\text{-}Cl)_2](ClO_4)_4$ (**I**), the magnetic moment of 7.89 μ_B at 300 K was much smaller than the spin-only magnetic moment expected for a $S = 5$ spin system (10.95 μ_B) (Fig. 6). The effective magnetic moment decreased as the temperature was lowered and a magnetic susceptibility of 2.02 μ_B was observed at 4 K. The magnetic susceptibility was fitted based on the isotropic Heisenberg

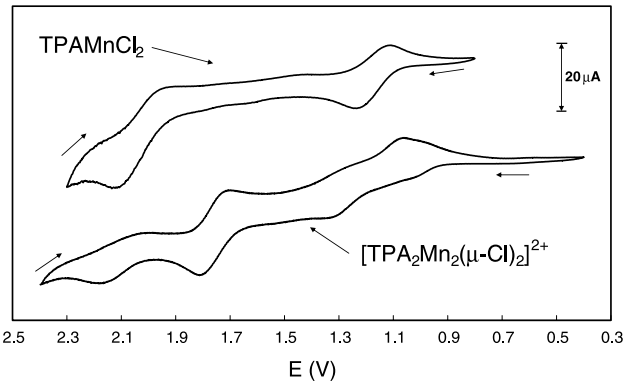


Fig. 6. Cyclic voltammograms of $(Et_3NH)_2[TPA_2Mn_2(\mu\text{-}Cl)_2](ClO_4)_4$ (**I**) and $TPAMnCl_2$ (**II**) at a scan rate of 50 mV/s. Supporting electrolyte: 0.1 M $^nBu_4NPF_6$.

model, $\boldsymbol{H} = -2J\boldsymbol{S}_1 \cdot \boldsymbol{S}_2$ ($\boldsymbol{S}_1 = \boldsymbol{S}_2 = 5/2$), given as follows [34]:

$$\chi = \frac{2Ng^2\beta^2}{kT}\,\frac{e^x + 5e^{3x} + 14e^{6x} + 30e^{10x} + 55e^{15x}}{1 + 3e^x + 7e^{6x} + 9e^{10x} + 11e^{15x}}$$

where $x = J/kT$, and the other symbols have their usual meaning. With $g = 2.0$, the magnetic exchange parameter $J = -8.8\ \mathrm{cm}^{-1}$ was obtained from a fit of experimental data. Thus, complex **I** was characterized as a high spin system with an antiferromagnetic coupling. Although the exchange parameter for chloride-inhibited Mn catalase was not reported, fluoride-inhibited Mn catalase from *L. plantarum* was reported as $J = -1.3\ \mathrm{cm}^{-1}$ [35]. The mononuclear Mn complex of **I** showed a magnetic susceptibility of 5.64 μ_B at 300 K and 5.54 μ_B at 4 K. The calculated spin-only magnetic moment of high spin Mn^{2+} was 5.92 μ_B, which is close to the experimental value. The magnetic moment measurements confirmed the $S = 5/2$ state for $TPAMnCl_2$ (**II**).

Because $TPAMnCl_2$ (**II**) was characterized as a typical high spin Mn^{II} complex and the EPR spectrum of $[TPA_2Mn_2(\mu\text{-}O)_2](ClO_4)_3$ (**III**) was reported before [33], he frozen solution EPR spectrum of $(Et_3NH)_2[TPA_2Mn_2(\mu\text{-}Cl)_2](ClO_4)_4$ (**I**) was only obtained at 100 K (Fig. 7). Complex **I** showed very complicate hyperfine signals at around 1600 G and seven hyperfine signals at 3200 G. It was assigned as a spin-coupled $Mn^{II}Mn^{II}$ core [36]. Mn catalase with a $Mn^{II}Mn^{II}$ core shows very complex signals between 2500 G and 4000 G and is characterized by two 11-line hyperfine signals at 3300 G and 3800 G. The overall spectral shapes of the spectra for complex **I** and the reported chloride-inhibited Mn catalase were similar [15], but the resonances were observed at different magnetic fields, probably due to the different coordination environments of the $Mn^{II}Mn^{II}$ centers.

3.4. Catalytic study

Catalytic dismutation of H_2O_2 by $(Et_3NH)_2[TPA_2Mn_2(\mu\text{-}Cl)_2](ClO_4)_4$ (**I**), $TPAMnCl_2$ (**II**) and $[TPA_2Mn_2(\mu\text{-}O)_2](ClO_4)_3$ (**III**) was studied by volumetric O_2 measurement. All the complexes produced O_2 catalytically. The substrate versus initial velocity plots of the complexes are shown in Fig. 8. Because the catalysis followed sigmoidal kinetics, they were fitted with Hill equation to obtain kinetic parameters.[3] In general, sigmoidal kinetics are observed from multi-subunit enzyme catalysis or from substrate-dependent enzyme activation [37]. In the case of the TPAMn complexes, substrate-activation of the catalysts seems to be the reason for the observed sigmoidal kinetics, and all the complexes seem to act as precatalysts.

The kinetic parameters for complexes **I**, **II** and **III** are shown in Table 3. Catalytic H_2O_2 dismutation by **I** and **II** is reported first here, although preliminary catalytic activity of complex **III** without kinetic parameters has been reported before by others [38]. The kinetic parameters of the K_M and Hill constants for complexes **I** and **II** are very similar, which implies the same reactive species may be involved in the catalysis. Different k_{cat} values result from different relative concentrations of the catalyst formed from complexes **I** and **II**. It seems that $TPAMnCl_2$ (**II**) can be dimerized to $[TPA_2Mn_2(\mu\text{-}Cl)_2]^{2+}$ under the catalytic conditions, so that it exhibits similar catalytic properties to **I** (see Fig. 9).

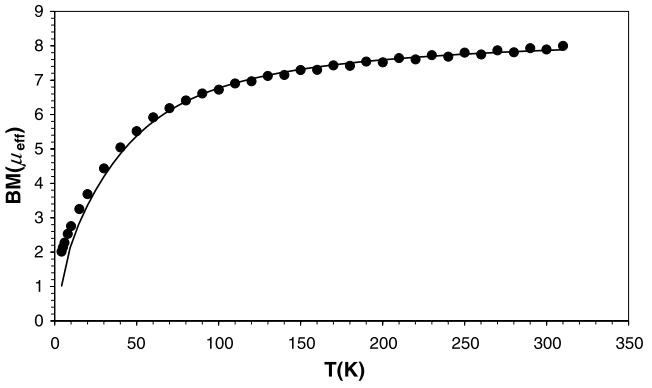


Fig. 7. Molar magnetic susceptibility of $(Et_3NH)_2[TPA_2Mn_2(\mu\text{-}Cl)_2](ClO_4)_4$ (**I**) plotted μ_{eff} vs. temperature. Closed circles represent measured data and the solid line represents the simulated fitting.

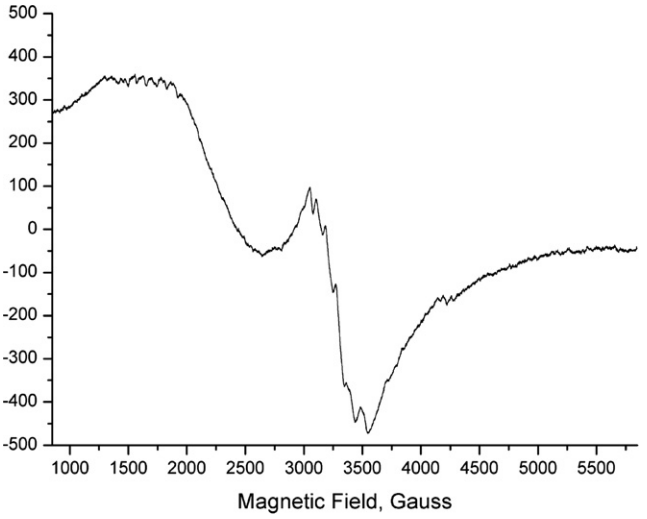


Fig. 8. EPR spectrum of the complex $(Et_3NH)_2[TPA_2Mn_2(\mu\text{-}Cl)_2](ClO_4)_4$ (**I**) at 100 K.

Table 3
Kinetic parameters for $(Et_3NH)_2[TPA_2Mn_2(\mu\text{-}Cl)_2](ClO_4)_4$ (**I**), $TPAMnCl_2$ (**II**) and $[TPA_2Mn_2(\mu\text{-}O)_2](ClO_4)_3$ (**III**)

	I	II	III
k_{cat} (s^{-1})	1.96 ± 0.05	1.28 ± 0.05	3.27 ± 0.05
K_M (M)	1.47 ± 0.04	1.42 ± 0.07	1.09 ± 0.03
Hill constant (n)	4.2 ± 0.4	3.4 ± 0.5	2.7 ± 0.2

[3] Hill equation, $v_i = V_{max}\cdot[H_2O^2]^n/(K_M{}^n + [H_2O^2]^n)$, where v_i is the initial velocity, V_{max} is the maximum velocity, $[H_2O_2]$ is the concentration of substrate, n is the Hill constant, K_M is the Michaelis constant.

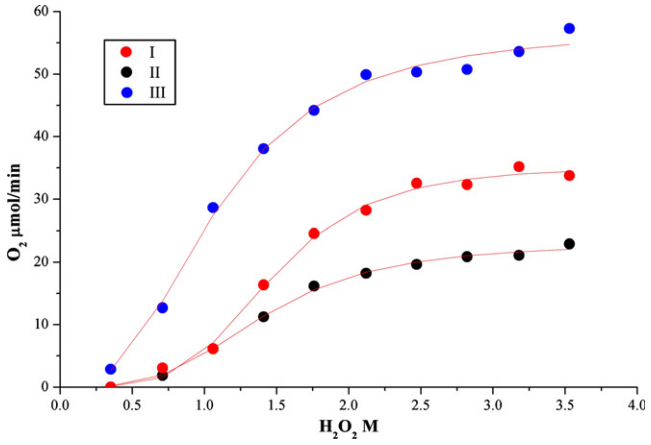


Fig. 9. Reaction rate of O_2 generation by $(Et_3NH)_2[TPA_2Mn_2(\mu\text{-}Cl)_2](ClO_4)_4$ (**I**), $TPAMnCl_2$ (**II**) and $[TPA_2Mn_2(\mu\text{-}O)_2](ClO_4)_3$ (**III**). The plots were simulated with the Hill equation.

The structure of $(Et_3NH)_2[TPA_2Mn_2(\mu\text{-}Cl)_2](ClO_4)_4$ (**I**) with a $Mn^{II}Mn^{II}$ center is similar to the chloride-inhibited active center of Mn catalase (*vide supra*). It was reported that the inhibition is reversible [14], and the catalytic activity of **I** may be relevant to the reactivation of the chloride-inhibited enzyme. Although there is no physical evidence, it is possible that H_2O_2 can act as an acid to protonate the bridging chloride atoms.[4] Chloride ion was also reported to prevent autooxidation of the enzyme, which is fast under basic conditions [15]. During the activation process, all the chloride ligands can be substituted sequentially by H_2O_2 or water to generate active species. The generated catalyst can follow the catalytic cycle which might be relevant to Mn catalase.

4. Conclusion

As a model system of chloride-inhibited manganese catalase, the complex $(Et_3NH)_2[TPA_2Mn_2(\mu\text{-}Cl)_2](ClO_4)_4$ (**I**) has been synthesized. The complex was characterized physically and structurally. Structural features between complex **I** and $TPAMnCl_2$ (**II**) showed little difference, except one of the Mn–Cl bonds was changed. However, the electrochemical properties of **I** and **II** were significantly different, and the dinuclear complex **I** showed multiple redox waves. Both complexes were characterized to have high spin d^5 Mn centers, and complex **I**, with two $S = 5/2$ Mn centers, showed an antiferromagnetic coupling. Catalytic dismutation of H_2O_2 by $(Et_3NH)_2[TPA_2Mn_2(\mu\text{-}Cl)_2](ClO_4)_4$ (**I**) was studied and compared to the related $TPAMnCl_2$ (**II**) and $[TPA_2Mn_2(\mu\text{-}O)_2](ClO_4)_3$ (**III**) complexes. A ctalytic study of **I** suggested that reactivation of chloride-inhibited Mn catalase could require acid-catalyzed bridging ligand substitution.

[4] H_2O_2 is a weak acid with pK_a 11.65.

Acknowledgement

This work was supported by the Korean Research Foundation Grant (KRF-2006-331-F00015) funded by the Korean Government (MOEHRD).

Appendix A. Supplementary material

CCDC 620887, 620886 and 629264 contain the supplementary crystallographic data for $(Et_3NH)_2[TPA_2Mn_2(\mu\text{-}Cl)_2](ClO_4)_4$ (**I**), $TPAMnCl_2$ (**II**) and $[TPA_2Mn_2(\mu\text{-}O)_2](ClO_4)_3$ (**III**). These data can be obtained free of charge via http://www.ccdc.ac.uk/conts/retrieving.html, or from the Cambridge Crystallographic Data Centre, 12 Union Road, Cambridge CB2 1EZ, UK; fax: (+44) 1223-336-033; or e-mail: deposit@ccdc.cam.ac.uk.

References

[1] M.J. Horsburgh, S.J. Wharton, M. Karavolos, S.J. Foster, Trends Microbiol. 10 (2002) 496.
[2] G. Bujacz, M. Jaskolski, J. Alexandratos, A. Wlodawer, G. Merkel, R.A. Katz, A.M. Skalka, Structure 4 (1996) 89.
[3] R.J. Dennis, E. Micossi, J. McCarthy, E. Moe, E.J. Gordon, S. Kozielski-Stuhrmann, G.A. Leonard, S. McSweeney, Acta Cryst. F 62 (2006) 325.
[4] W. Atzenhofer, G. Regelsberger, U. Jacob, G.A. Peschek, P.G. Furtmüller, R. Huber, C. Obinger, J. Mol. Biol. 321 (2002) 479.
[5] M. Balsera, J.B. Arellano, J.L. Revuelta, J. Rivas, J.A. Hermoso, J. Mol. Biol. 350 (2005) 1051.
[6] K.N. Ferreira, T.M. Iverson, K. Maghlaoui, J. Barber, S. Iwata, Science 303 (2004) 1831.
[7] M.M. Whittaker, V.V. Barynin, S.V. Antonyuk, J.W. Whittaker, Biochemistry 38 (1999) 9126.
[8] Z.F. Kanyo, L.R. Scolnick, D.E. Ash, D.W. Christianson, Nature 383 (1996) 554.
[9] V.V. Barynin, M.M. Whittaker, S.V. Antonyuk, V.S. Lamzin, P.M. Harrison, P.J. Artymiuk, J.W. Whittaker, Structure 9 (2001) 725.
[10] S.V. Antonyuk, V.R. Melik-Adamyan, A.N. Popov, V.S. Lamzin, P.D. Hempstead, P.M. Harrison, P.J. Artymiuk, V.V. Barynin, Cryst. Rep. 45 (2000) 105.
[11] M.M. Whittaker, V.V. Barynin, T. Igarashi, J.W. Whittaker, Eur. J. Biochem. 270 (2003) 1102.
[12] S.V. Khangulov, V.V. Barynin, S.V. Antonyuk-Barynina, Biochim. Biophys. Acta 1020 (1990) 25.
[13] G.S. Waldo, J.E. Penner-Hahn, Biochemistry 34 (1995) 1507.
[14] S.V. Khangulov, M.G. Goldfeld, V.V. Gerasimenko, N.E. Andreeva, V.V. Barynin, A.I. Grebenko, J. Inorg. Biochem. 40 (1990) 279.
[15] S.V. Khangulov, V.V. Barynin, N.V. Voevodskaya, A.I. Grebenko, Biochim. Biophys. Acta 1020 (1990) 305.
[16] J.W. Canary, Y. Wang, R. Roy Jr., Inorg. Synth. 32 (1998) 70.
[17] D.K. Towle, C.A. Botsford, D.J. Hodgson, Inorg. Chim. Acta. 141 (1988) 167.
[18] D.F. Xiang, C.Y. Duan, X.S. Tan, Y.L. Liu, W.X. Tang, Polyhedron 17 (1998) 2647.
[19] H. Oshio, E. Ino, I. Mogi, T. Ito, Inorg. Chem. 32 (1993) 5697.
[20] B.-K. Shin, M. Kim, J. Han, Bull. Kor. Chem. Soc. 28 (2007) 417.
[21] Y. Hitomi, A. Ando, H. Matsui, T. Ito, T. Tanaka, S. Ogo, T. Funabiki, Inorg. Chem. 44 (2005) 3473.
[22] J.B. Mandel, C. Maricondi, B.E. Douglas, Inorg. Chem. 27 (1988) 2990.
[23] L.N. Mulay, E.A. Boudreaux (Eds.), Theory and Applications of Molecular Paramagnetism, Wiley Interscience, New York, 1976.

[24] Bruker, SMART and SAINT, Bruker AXS, Inc., Madison, Wisconsin, USA, 1997.
[25] Bruker, SHELXTL, Version 5.10., Bruker AXS, Inc., Madison, Wisconsin, USA, 1998.
[26] Y. Zang, H.G. Jang, Y.-M. Chiou, M.P. Hendrich, L. Que Jr., Inorg. Chim. Acta. 213 (1993) 41.
[27] M. Kim, Y.-U. Kim, J. Han, Polyhedron (2007), doi:10.1016/j.poly.2007.04.041.
[28] G.C. Dismukes, Chem. Rev. 96 (1996) 2909.
[29] S. Ogo, Y. Watanabe, T. Funabiki, Private Communication to CCDC (2003), Deposit # 117555.
[30] Y. Zang, J. Kim, Y. Dong, E.C. Wilkinson, E.H. Appelman, L. Que Jr., J. Am. Chem. Soc. 119 (1997) 4197.
[31] T.L. Stemmler, B.E. Sturgeon, D.W. Randall, R.D. Britt, J.E. Penner-Hahn, J. Am. Chem. Soc. 119 (1997) 9215.
[32] K. Nakamoto, Infrared Spectra of Inorganic Coordination Compounds, second ed., Wiley Interscience, New York, 1970.
[33] M. Suzuki, S. Tokura, M. Suhara, A. Uehara, Chem. Lett. (1988) 477.
[34] O. Kahn, Molecular Magnetism, VCH, New York, 1993.
[35] L. Le Page, E. Perret, I. Michaud-Soret, J.-M. Latour, J. Biol. Inorg. Chem. 7 (2002) 445.
[36] P.J. Pessiki, S.V. Khangulov, D.M. Ho, G.C. Dismukes, J. Am. Chem. Soc. 116 (1994) 891.
[37] S.A. Kuby, A Study of Enzymes, vol. 1, CRC Press, Florida, 1991.
[38] Y. Nishida, T. Akamatsu, K. Tsuchiya, M. Sakamoto, Polyhedron 13 (1994) 2251.

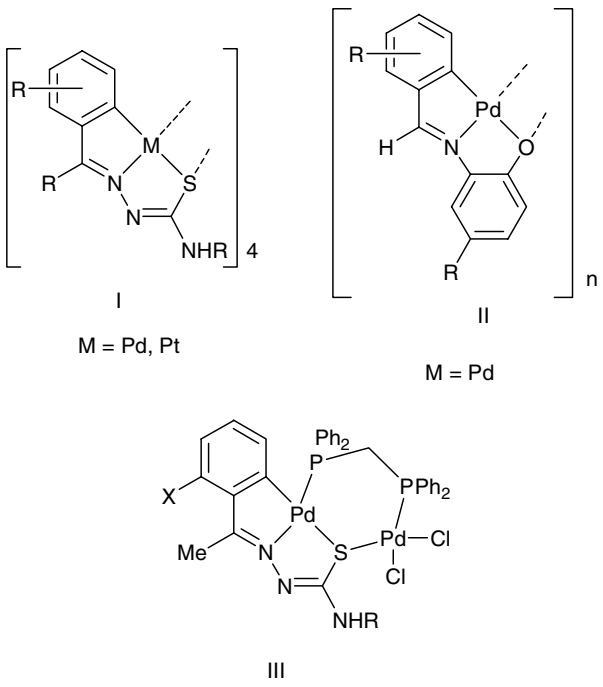


Fig. 1. Cyclometallated complexes with [C, N, X] (X = O, S) ligands.

brings about opening of the tetranuclear structure due to the P–$X_{bridging}$ bond cleavage, whereas the P–$X_{chelating}$ bond persists, even when large excess of the phosphine was used, putting forward its unusual strength. More recently, we have shown that reaction of the tetranuclear tetramers derived from thiosemicarbazones (X = S) with bis(diphenylphosphino)methane caused cleavage of the tetranuclear structure to give new mononuclear complexes, in which the phosphine is monodentate, where one phosphorus atom is uncoordinated. These complexes represent a new class of bidentate [P, S] chelating metalloligands capable of coordinating a second metal centre and, therefore, may be used as building blocks in the construction of polynuclear structures **III** (Fig. 1) [23].

We reasoned that the similar behavior of terdentate [C, N, O] Schiff base species towards nucleophiles, in terms of a strong P–$O_{chelating}$ bond, could be used to explore a new range of compounds upon reaction of the former with phosphines, arsines, and mixed phosphorus/arsenic ligands. Therefore, herein, we report the reactivity of complexes $[Pd\{2,3,4\text{-}(MeO)_3C_6HC(H)=N[2\text{-}(O)\text{-}5\text{-}RC_6H_3]\}]_4$ (**1a**: R = H, **1b**: R = ^{t}Bu) with bidentate [P, O], [P, As], [P, P], [As, As] and [P, N] ligands.

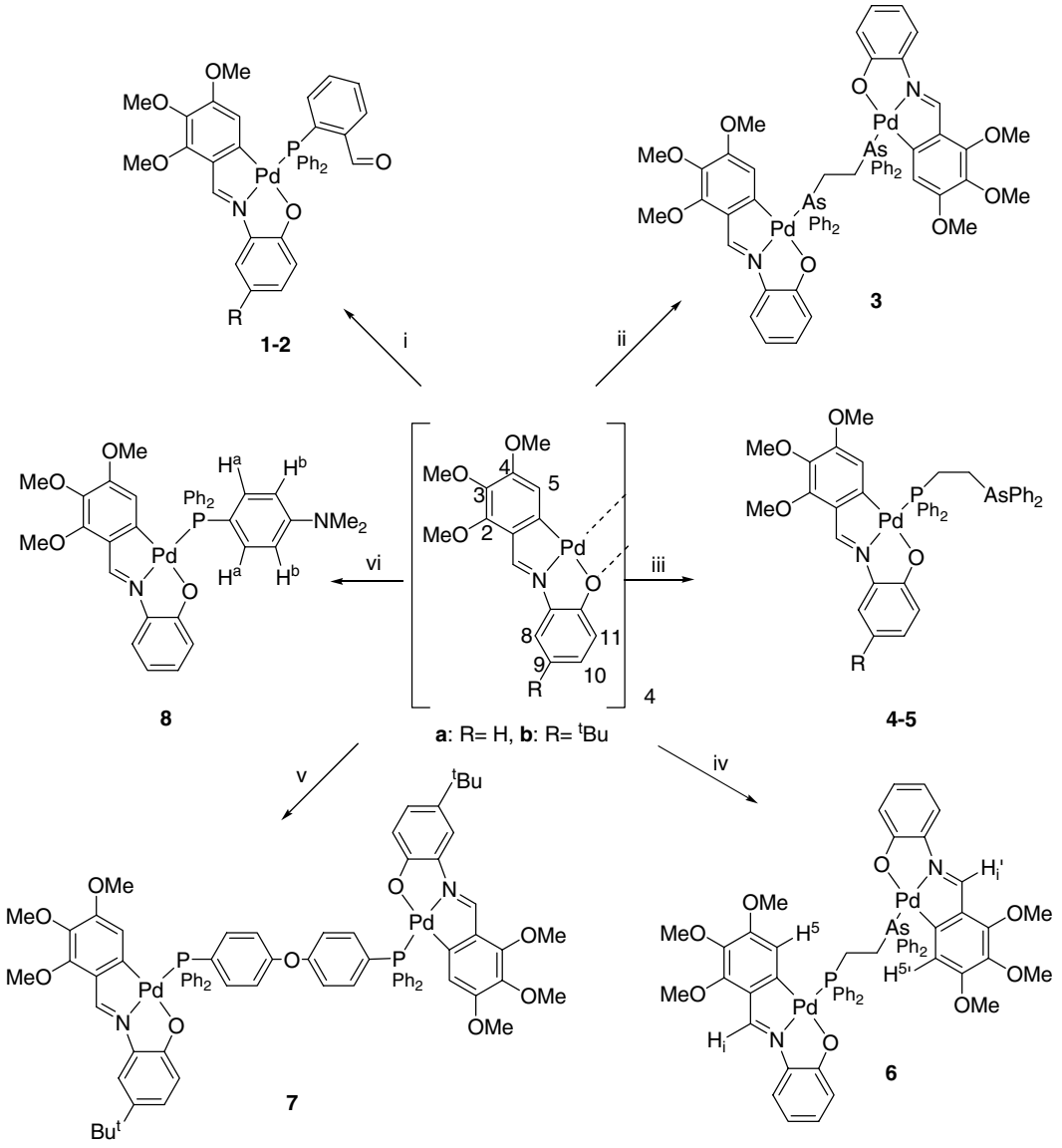
2. Results and discussion

The compounds and reactions are shown in Scheme 1. The compounds were characterised by IR and by ^{1}H, ^{31}P–{^{1}H} spectroscopy and, in part, FAB mass spectrometry; the elemental analysis (C, H, N) supports the expected elemental composition (data in Section 4).

Treatment of **1a** and **1b** with $PPh_2[2\text{-}(COH)C_6H_4]$ in 1:4 molar ratio or with $Ph_2P[4\text{-}(NMe_2)C_6H_4]$ in 1:2 or 1:4 molar ratios, afforded the mononuclear complexes $[Pd\{2,3,4\text{-}(MeO)_3C_6HC(H)=N[2\text{-}(O)C_6H_4\}\{PPh_2[2\text{-}HOC)C_6H_4]\}]$ (**2a**) $[Pd\{2,3,4\text{-}(MeO)_3C_6HC(H)=N[2\text{-}(O)\text{-}5\text{-}^tBuC_6H_3\}\{PPh_2[2\text{-}(HOC)C_6H_4]\}]$ (**2b**) and $[Pd\{2,3,4\text{-}(MeO)_3C_6HC(H)=N[2\text{-}(O)C_6H_4]\}\{PPh_2[4\text{-}(NMe_2)C_6H_4]\}]$ (**7a**), respectively, as air stable solids, in which the tetrameric structure was cleaved after P–$O_{bridging}$ bond cleavage. Coordination of the palladium atom to the C=N moiety was confirmed by the shift to lower wavenumbers of the ν(C=N) band, as compared to the free ligand [21,24,25]. Absence of the ν(OH) band was in agreement with the presence of a phenolate oxygen bonded to the palladium atom [21,22]. These findings were observed for the remaining compounds and shall not be discussed further (see Section 4). The proton resonances were unequivocally assigned (see Section 4); those ascribed to *H*5 and *H*C=N appeared as doublets due to coupling with the ^{31}P nucleus with *J* values of *ca.* 4 and 10 Hz, respectively. In the ^{31}P–{^{1}H} spectra the phosphorus resonance signal appeared as a singlet *ca.* δ 33.0 ppm; these findings were in agreement with a phosphorus *trans* to nitrogen arrangement [21,26–30]. The signals assigned to the *H*5 and 4-O*Me* protons were shifted to lower frequency, as compared to the cyclometallated complexes **1a** and **1b**, due to shielding of phosphine phenyl rings. We have previously observed similar shifts in related complexes, confirming the relative *trans* disposition of the nitrogen atom and the phosphine ligand [17,31]. The FAB mass spectra showed the cluster of peaks characteristic of the $[M]^+$ fragment at 680, **2a**, 738, **2b**, and 697, **7a** uma.

Reaction of **1a** with $AsPh_2(CH_2)_2Ph_2As$ (dppae) in a 1:2 ratio in acetone, gave the dinuclear cyclometallated complex $[\{Pd\{2,3,4\text{-}(MeO)_3C_6HC(H)=N[2\text{-}(O)C_6H_4]\}\}_2\{\mu\text{-}AsPh_2(CH_2)_2Ph_2As\}]$ (**3a**) as an air stable solid. In the ^{1}H NMR spectrum the *H*C=N and H^5 proton resonances appeared as singlets at δ 7.57 and 5.51 ppm, respectively. The H5 and 4-O*Me* resonances were shifted towards lower frequency by *ca.* 0.2 and 1.2 ppm, respectively, due to the shielding effects of the diarsine phenyl rings. Only one set of signals was observed for the proton resonances, indicative of the symmetrical nature of the compounds. The FAB mass spectrum showed two clusters of peaks centred at 1271 and 878 uma, assigned to the molecular ion and to loss of one cyclometallated unit, respectively. Compound **3a** was also isolated when excess dppa was used, establishing the strength of the Pd–$O_{chelating}$ bond, which was not cleaved even under these reaction conditions.

Treatment of **1a** or **1b** with $Ph_2P(CH_2)_2Ph_2As$ (arphos) in the appropriate molar ratio afforded compounds $[Pd\{2,3,4\text{-}(MeO)_3C_6HC(H)=N[2\text{-}(O)C_6H_4]\}\{PPh_2(CH_2)_2Ph_2As\text{-}P\}]$ (**4a**), $[Pd\{2,3,4\text{-}(MeO)_3C_6HC(H)=N[2\text{-}(O)\text{-}5\text{-}^tBuC_6H_3]\}\{PPh_2(CH_2)_2Ph_2As\text{-}P\}]$ (**4b**), and $[\{Pd\{2,3,4\text{-}(MeO)_3C_6HC(H)=N[2\text{-}(O)C_6H_4]\}\}_2\{\mu\text{-}PPh_2(CH_2)_2Ph_2As\}]$ (**5a**). Coordination of the ligand through the phosphorus atom was confirmed by: (a) the multiplicity of the *H*5 and *H*C=N



Scheme 1. (i) Phosphine (acetone, 1:4 molar ratio), (ii) dppae (acetone, 1:2 or 1:4 molar ratio), (iii) arphos (acetone, 1:4 molar ratio), (iv) arphos (acetone, 1:2 molar ratio), (v) diphosphine (acetone, 1:2 or 1:4 molar ratio), (vi) phosphine (dichloromethane, 1:2 or 1:4 molar ratio).

resonances, which were observed as doublets by coupling to the ^{31}P nucleus; (b) the chemical shift of the phosphorus resonance signal at δ 32.5 (**4a**), δ 33.4 (**4b**) and δ 34.0 (**5a**), downfield shifted from its position in the spectrum of the free phosphine, and also in agreement with a phosphorus *trans* to nitrogen coordination to the metal center [21,26–30]. The asymmetric nature of compound **5a** was evidenced by the two distinct sets of proton signals observed for both cyclometallated moieties. Accordingly, two doublet resonances at δ 8.14 and δ 5.42, were assigned to the *H*5 and *HC*=N protons, respectively, coupled to the ^{31}P nucleus with [$^4J(H_iP) = 10.5$ Hz, $^4J(H^5P) = 3.9$ Hz], and two singlets were ascribed to the *H*5′ and *H*′C=N protons at δ 7.58 and δ 5.56, respectively.

In the FAB mass spectra the set of peaks at 834 and 890 uma, for **4a** and **4b**, respectively, were assigned to the $[MH]^+$ ions; their isotopic pattern confirmed the mononuclear formula of the complexes. For compound **5a** a cluster of peaks at 1226 uma was consistent with a dinuclear formula.

Treatment of **2b** with $Ph_2P(C_6H_4)O(C_6H_4)Ph_2P$ in a 1:2 or 1:4 molar ratio at room temperature in acetone gave the dinuclear compound [{Pd{2,3,4-$(MeO)_3C_6HC(H)$=N[2-(O)-^{t}BuC_6H_3]}}$_2${μ-$PPh_2(C_6H_4)O(C_6H_4)Ph_2P$}] (**6b**) (the use of excess phosphine only gave **6b** and unreacted **2b**), after column chromatography (see Section 4). Therefore, the diphosphine could not behave as monodentate through only one phosphorus atom. Thus, both sets of *HC*=N and H5 resonances showed coupling to the phosphorus nuclei [$^4J(HP) = 10.7$ and $^4J(HP) = 3.7$ Hz], and the ^{31}P–{^1H} NMR spectrum revealed a singlet at δ 28.2, in agreement with equivalent phosphorus nuclei.

3. Conclusions

We have shown that Schiff base ligands derived from 2-aminophenols secure three metal coordination sites in cyclometallated palladium(II) compounds and leave but one bonding site for further reaction with nucleophiles, such as tertiary phosphines or arsines. Consequently, the $P–O_{chelating}$ bond remained throughout all the processes in this study, and it was not cleaved upon reaction with the nucleophiles tested. Additional coordinating atoms on the phosphine ligand, such as nitrogen or oxygen, did not show any relevant bonding properties. However, diphosphines or diarsines could bridge two cyclometallated moieties, rendering dinuclear species.

In the case of arphos, this ligand showed to be versatile in its coordination to the cyclometallated complexes **1a** and **1b**. Thus, by adjusting the relative molar ratio, mono- or dinuclear complexes could be prepared, with the ligand behaving as mono- or bidentate, respectively. Still, arphos did not act as a chelating ligand, regardless of the reaction conditions employed.

4. Experimental

4.1. General procedures

Solvents were purified by standard methods [32]. Chemicals were reagent grade. The phosphines PPh_2[2-(HOC)C_6H_4], $PPh_2(CH_2)_2Ph_2As$ (arphos), $Ph_2P(C_6H_4)O(C_6H_4)Ph_2P$ and Ph_2P[4-$(NMe_2)C_6H_4$] were purchased from Aldrich-Chemie. $Ph_2As(CH_2)_2Ph_2As$ (dppae) were purchased from ALFA. Microanalyses were carried out using a Carlo Erba Elemental Analyzer, Model 1108. The cyclometallated complexes **1a** and **1b** were synthesized using the procedure reported recently by us [21]. IR spectra were recorded as KBr discs on a Perkin–Elmer 1330 and on Mattson spectrophotometers. NMR spectra were obtained in $CDCl_3$ and referenced to $CHCl_3$ (^1H and $^{13}C–\{^1H\}$) or 85% H_3PO_4 ($^{31}P–\{^1H\}$) and were recorded on Bruker AC-2005 or Bruker AVANCE 300 spectrometers. All chemical shifts were reported downfield from standards. The FAB mass spectra were recorded using a Quatro mass spectrometer with a Cs ion gun; 3-nitrobenzyl alcohol was used as the matrix.

Analytical and spectroscopic data for the cyclometallated starting complexes **1a** and **1b**.

4.2. [Pd{2,3,4-(MeO)$_3$C$_6$HC(H)=N[2-(O)C$_6$H$_4$]}]$_4$ (**1a**)

Anal. Calc. for $C_{64}H_{60}N_4O_{16}Pd_4$: C, 49.1; H, 3.8; N, 3.6. Found: C, 48.9; H, 3.8; N, 3.5%. IR: ν(C=N), 1589sh, m cm^{-1}. ^1H NMR (200 MHz, $CDCl_3$, δ ppm, *J* Hz): 3.51 [s, 3H, OMe]; 3.82 [s, 3H, OMe]; 4.02 [s, 3H, OMe]; 5.67 [s, 1H, H^5]; 7.57 [s, 1H, HC=N]; 6.62 [dd, 1H, H^8, $^3J(H^8H^9) = 7.6$, $^4J(H^8H^{10}) = 1.5$]; 6.37 [dt, 1H, H^9, $^3J(H^9H^{10}) = 7.5$, $^4J(H^9H^{11}) = 1.5$]; 6.91 [dt, 1H, H^{10}, $^3J(H^{10}H^{11}) = 7.5$, $^4J(H^8H^{10}) = 1.5$]; 7.44 [d, 1H, H^{11}, $^3J(H^{11}H^{10}) = 7.6$, $^4J(H^9H^{11}) = 1.5$]. FAB-MS: $m/z = 1566$ $[M]^+$; 391 $[M/4]^+$.

4.3. [Pd{2,3,4-(MeO)$_3$C$_6$HC(H)=N[2-(O)-5-^{t}BuC$_6$H$_3$]}]$_4$ (**1b**)

Anal. Calc for $C_{68}H_{68}N_4O_{16}Pd_4$: C, 50.3; H, 4.2; N, 3.5. Found: C, 50.1; H, 4.1; N, 3.5%. IR: ν(C=N), 1571sh, m cm^{-1}. ^1H NMR (200 MHz, $CDCl_3$): δ = 1.24 [s, 9H, ^{t}Bu]; 3.38, 3.81, 4.03 [s, 9H, MeO]; 5.81 [s, 1H, H^5]; 6.75 [d, 1H, H^8, $^4J(H^8H^{10}) = 2.2$]; 6.99 [dd, 1H, H^{10}, $^3J(H^{10}H^{11}) = 8.8$, $^4J(H^8H^{10}) = 2.2$]; 7.35 [d, 1H, H^{11}]; 7.54 [s, 1H, HC=N]. FAB-MS: $m/z = 1792$ $[MH]^+$; 896 $[M/2]^+$.

4.4. [Pd{2,3,4-(MeO)$_3$C$_6$HC(H)=N[2-(O)C$_6$H$_4$]}{PPh$_2$[2-(HOC)C$_6$H$_4$]}] (**2a**)

PPh_2(4-(HOC)C_6H_4) (49.8 mg, 0.31 mmol) was added to a suspension of [Pd{2,3,4-$(MeO)_3C_6HC(H)$=N(2-(O)-C_6H_4)] (36.9 mg, 0.31 mmol) in acetone (15 cm^3). The mixture was stirred for 12 h and the solvent removed to give a violet solid which was recrystallized from dichloromethane/hexane. Yield 56%. *Anal.* Calc. for $C_{35}H_{29}NO_5PPd$: C, 61.7; H, 4.3; N, 2.0. Found: C, 61.5; H, 4.3; N, 1.9%. IR: ν(C=O), 1697s cm^{-1}, ν(C=N), 1572s cm^{-1}. FAB-MS: $m/z = 680$ $[M]^+$. ^1H NMR (300 MHz, $CDCl_3$, δ ppm, *J* Hz): 10.37 [d, 1H, *H*C=O, $^4J(HP) = 2.4$], 8.14 [d, 1H, HC=N, $^4J(HP) = 10.8$], 7.59 [t, 1H,$^3J(HH) = 7.6$], 7.10 [d, 1H, H^8, $^3J(H^8H^9) = 7.1$], 6.89 [m, 2H, H^{10}, H^{11}], 6.30 [m, 2H, H^9, H^{11}], 5.54 [s, 1H, H^5, $^4J(H^5P) = 4.9$], 3.94 (s, 3H, MeO), 3.72 (s, 3H, MeO), 2.95 (s, 3H, MeO). $^{31}P–\{^1H\}$ NMR (121.44 MHz, $CDCl_3$, δ ppm): 33.3 s.

Compound **2b** was obtained following a similar procedure as a violet solid.

4.5. [Pd{2,3,4-(MeO)$_3$C$_6$HC(H)=N[2-(O)-5-^{t}BuC$_6$H$_3$]}{PPh$_2$[2-(HOC)C$_6$H$_4$]}] (**2b**)

Yield 66%. *Anal.* Calc. for $C_{39}H_{38}NO_5PPd$: C, 63.4; H, 5.2; N, 1.9. Found: C, 63.4; H, 5.1; N, 1.8%. IR: ν(C=O), 1697s cm^{-1}, ν(C=N), 1571s cm^{-1}. FAB-MS: $m/z = 738$ $[M]^+$. ^1H NMR (200 MHz, $CDCl_3$, δ ppm, *J* Hz): 10.34 [d, 1H, *H*C=O, $^4J(HP) = 2.4$], 8.11 [d, 1H, HC=N, ^4J (HP) = 10.7], 7.02 [d, 1H, H^8, $^4J(H^8H^{10}) = 2.3$], 6.92 [dd, 1H, H^{10}, $^3J(H^{10}H^{11}) = 8.6$, $^4J(H^8H^{10}) = 2.3$], 6.22 [d, 1H, H^{11}, $^3J(H^{10}H^{11}) = 8.6$], 5.52 [s, 1H, H^5, $^4J(H^5P) = 3.9$], 3.98 (s, 3H, MeO), 3.74 (s, 3H, MeO), 2.95 (s, 3H, MeO), 1.24 (s, 9H, ^{t}Bu). $^{31}P–\{^1H\}$ NMR (80.96 MHz, $CDCl_3$, δ ppm) 33.3 s.

Compound **3a** was obtained following a similar procedure, as a red solid, but using a complex cyclometallated/diarsine 1:4 or 1:2 molar ratio.

4.6. [{Pd{2,3,4-(MeO)$_3$C$_6$HC(H)=N[2-(O)C$_6$H$_4$]}}$_2$-{μ-AsPh$_2$(CH$_2$)$_2$Ph$_2$As}] (**3a**)

Yield 49%, using 1:2 molar ratio and 21% using 1:4 molar ratio. *Anal.* Calc. for $C_{58}H_{54}N_2O_8Pd_2As_2$: C, 54.8;

H, 4.3; N, 2.2. Found: C, 54.7; H, 4.2; N, 2.1%. IR: ν(C=N), 1572s cm^{-1}.

FAB-MS: $m/z = 1271$ $[MH]^+$; 878, $[LPd(AsPh_2(CH_2)_2Ph_2As)]^+$. ^1H NMR (200 MHz, $CDCl_3$, δ ppm, J Hz): 7.57 [s, 1H, HC=N], 6.9 [m, 2H, H^8,H^{10}], 6.59 [d, 1H, H^{11}, $^3J(H^{10}H^{11}) = 7.8$], 6.35 [t, 1H, H^9, $J(H^8H^9) = 7.1$], 5.51 [s, 1H, H^5], 3.01 (s, br, 2H, $AsCH_2$), 3.93 (s, 3H, MeO), 3.71 (s, 3H, MeO), 2.63 (s, 3H, MeO).

Compounds **4a**, **4b** were prepared similarly, as violet solids, using a cyclometallated complex/arsinophosphine 1:4 molar ratio.

*4.7. [Pd{2,3,4-(MeO)$_3$C$_6$HC(H)=N[2-(O)C$_6$H$_4$]}-{PPh$_2$(CH$_2$)$_2$Ph$_2$As-P}] (**4a**)*

Yield 64%. *Anal.* Calc. for $C_{42}H_{39}NO_4PPdAs$: C, 60.5; H, 4.7; N, 1.7. Found: C, 60.4; H, 4.6; N, 1.6%. IR: ν(C=N), 1569s cm^{-1}. FAB-MS: $m/z = 834$ $[MH]^+$. ^1H NMR (200 MHz, $CDCl_3$, δ ppm, J Hz): 8.15 [d, 1H, HC=N, $^4J(HP) = 9.7$], 7.13 [dd, 1H, H^8, $^3J(H^8H^9) = 8.0$, $^4J(H^8H^{10}) = 1.4$], 6.96 [dt, 1H, H^{10}, $^3J(H^9H^{10}) = 8.0$, $^4J(H^8H^{10}) = 1.4$], 6.63 [d, 1H, H^{11}, $^3J(H^{10}H^{11}) = 8.0$], 6.39 [t, 1H, H^9, $^3J(H^9H^{10}) = 8.0$], 5.47 [d, 1H, H^5, $^4J(H^5P) = 2.4$], 3.94 (s, 3H, MeO), 3.72 (s, 3H, MeO), 2.95 (s, 3H, MeO), 2.48 (br, 4H, PCH_2CH_2As). ^{31}P–{^1H} NMR (80.96 MHz, $CDCl_3$, δ ppm): 32.5 s.

*4.8. [Pd{2,3,4-(MeO)$_3$C$_6$HC(H)=N[2-(O)-5-^{t}BuC$_6$H$_3$]}{PPh$_2$(CH$_2$)$_2$Ph$_2$As-P}] (**4b**)*

Yield 56%. *Anal.* Calc. for $C_{46}H_{47}NO_4PPdAs$: C, 62.1; H, 5.3; N, 1.6. Found: C, 62.2; H, 5.1; N, 1.5%. IR: ν(C=N), 1571s cm^{-1}. FAB-MS: $m/z = 890$ $[MH]^+$. ^1H NMR (200 MHz, $CDCl_3$, δ ppm, J Hz): 8.13 [d, 1H, H_i,$^4J(H_iP) = 10.2$], 7.08 [d, 1H, H^8, $^4J(H^8H^{10}) = 2.4$], 7.03 [dd, 1H, H^{10}, $^3J(H^{10}H^{11}) = 8.5$, $^4J(H^8H^{10}) = 2.4$], 6.57 [d, 1H, H^{11}, $^3J(H^{10}H^{11}) = 8.5$], 5.48 [s, 1H, H^5, $^4J(H^5P) = 3.4$], 3.97 (s, 3H, MeO), 3.72 (s, 3H, MeO), 2.95 (s, 3H, MeO), 2.47 (br, 4H, PCH_2CH_2As), 1.29 (s, 9H, ^{t}Bu). ^{31}P–{^1H} NMR (80.96 MHz, $CDCl_3$, δ ppm): 33.4 s.

Compound **5a** was obtained following a similar procedure as violet solid but using a complex cyclometallated/arphos 1:2 molar ratio.

*4.9. [{Pd{2,3,4-(MeO)$_3$C$_6$HC(H)=N[2-(O)C$_6$H$_4$]}}$_2$-{μ-PPh$_2$(CH$_2$)$_2$Ph$_2$As}] (**5a**)*

Yield 64%. *Anal.* Calc. for $C_{42}H_{39}NO_4PPdAs$: C, 60.5; H, 4.7; N, 1.7. Found: C, 60.4; H, 4.6; N, 1.6%. IR: ν(C=N), 1572s cm^{-1}. FAB-MS: $m/z = 1226$ $[M]^+$; 834 $[LPd(arphos)]^+$. ^1H NMR (200 MHz, $CDCl_3$, δ ppm, J Hz): 8.14 [d, 1H, HC=N, $^4J(HP) = 10.5$], 7.58 [s, 1H, H′C=N], 7.12 [d, br, 1H, H^8], 6.95 [t, br, 1H, H^{10}], 6.59 [dd, 1H, H^{11}, $^3J(H^{10}H^{11}) = 8.5$, $^4J(H^9H^{11}) = 2.4$], 6.38 [t, br, 1H, H^9], 5.56 [s, 1H, $H^{5\prime}$], 5.42 [d, 1H, H^5, $^4J(H^5P) = 3.9$], 3.95 (s, 6H, MeO), 3.71 (s, 6H, MeO), 2.84 (s, 3H, MeO), 2.81 (s, 3H, MeO), 3.01 (br, 4H, PCH_2CH_2As). ^{31}P–{^1H} NMR (80.96 MHz, $CDCl_3$, δ ppm): 34.0 s.

*4.10. [{Pd{2,3,4-(MeO)$_3$C$_6$HC(H)=N[2-(O)-^{t}BuC$_6$H$_3$]}}$_2${μ-PPh$_2$(C$_6$H$_4$)O(C$_6$H$_4$)Ph$_2$P}] (**6b**)*

A suspension of complex **1b** in acetone was treated with $PPh_2(C_6H_4)O(C_6H_4)Ph_2P$ (cyclometallated complex/diphosphine 1:4 or 1:2 molar ratio) in acetone and the resulting mixture was stirred for 24 h. The solvent was then removed under vacuum to give a violet solid which was chromatographed on a column packed with silica gel. Elution with CH_2Cl_2–C_2H_5OH (99:1) afforded a violet oil after solvent removal, which was recrystallized from dichloromethane–hexane to give the desired product as a violet solid. Yield 27%. *Anal.* Calc. for $C_{76}H_{74}N_2O_9P_2Pd_2$: C, 68.2; H, 5.2; N, 1.4. Found: C, 68.1; H, 5.1; N, 1.3%. IR: ν(C=N), 1565s cm^{-1}. ^1H NMR (300 MHz, $CDCl_3$, δ ppm, J Hz): 8.00 [d, 1H, HC=N, $^4J(HP) = 10.7$], 5.59 [d, 1H, H^5, $^4J(H^5P) = 3.7$], 4.00 (s, 3H, MeO), 3.77 (s, 3H, MeO), 3.02 (s, 3H, MeO), 1.27 (s, 9H, ^{t}Bu). ^{31}P–{^1H} NMR (121.44 MHz, $CDCl_3$, δ ppm): 28.2 s.

Compound **7a** was obtained as a violet solid following a similar procedure to the one used for **6b** but using dichloromethane as solvent.

*4.11. [Pd{2,3,4-(MeO)$_3$C$_6$HC(H)=N[2-(O)C$_6$H$_4$]}-{PPh$_2$[4-(NMe$_2$)C$_6$H$_4$]}] (**7a**)*

Yield 67%, using 1:4 molar ratio, and 36% using 1:2 molar ratio. *Anal.* Calc. for $C_{36}H_{35}N_2PdO_4P$: C, 62.0; H, 5.1; N, 4.0. Found: C, 62.1; H, 5.1; N, 4.1%. IR: ν(C=N), 1572s cm^{-1}. FAB-MS: $m/z = 697$ $[M]^+$. ^1H NMR (300 MHz, $CDCl_3$, δ ppm, J Hz): 8.17 [d, 1H, HC=N, $^4J(HP) = 10.4$], 7.11 [dd, 1H, H^8, $^3J(H^8H^9) = 7.5$, $^4J(H^8H^{10}) = 1.9$], 6.89 [dt, 1H, H^{10}, $^3J(H^{10}H^{11}) = 8.4$, $^4J(H^8H^{10}) = 1.9$], 6.68 [dd, H^b, $^3J(H^aH^b) = 8.0$, $^4J(H^bP) = 1.6$], 6.44 [d, 1H, H^{11}, $^3J(H^{10}H^{11}) = 8.4$], 6.34 [t, 1H, H^9, $^3J(H^9H^{10}) = 7.5$], 5.61 [d, 1H, H^5, $^4J(H^5P) = 4.9$], 3.95 [s, 3H, MeO], 3.73 [s, 3H, MeO], 2.97 [s, 3H, MeO], 2.98 [s, 6H, Me_2]. ^{31}P–{^1H} NMR (121.44 MHz, $CDCl_3$, δ ppm): 32.3 s.

Acknowledgements

We thank the Ministerio de Educación y Ciencia (Project CTQ2006-15621-C02-01/BQU) for financial support.

References

[1] I. Omae, Organometallic Intramolecular-Coordination Compounds, Elsevier Science, Amsterdam New York, 1986.
[2] V.V. Dunina, O.A. Zalevskaya, V.M. Potapov, Russ. Chem. Rev. 571 (1984) 250.
[3] G.R. Newkome, W.E. Puckett, W.K. Gupta, G.E. Kiefer, Chem. Rev. 86 (1986) 451.
[4] A.D. Ryabov, Chem. Rev. 90 (1990) 403.
[5] M. Pfeffer, Recl. Trav. Chim. Pays-Bas 109 (1990) 567.

[6] J. Dupont, C.S. Consorti, J. Spencer, Chem. Rev. 105 (2005) 2527.
[7] V.V. Dunina, O.N. Gorunova, Russ. Chem. Rev. 73 (2004) 309.
[8] V.V. Dunina, O.N. Gorunova, Russ. Chem. Rev. 74 (2005) 871.
[9] (a) F.A. Cotton, B. Hong, Prog. Inorg. Chem. 40 (1992) 179;
(b) L.H. Pignolet, Homogeneous Catalysis with Metal Phosphine Complexes, Plenum Press, New York, 1983.
[10] T.J. Calcot, Chem. Rev. 103 (2003) 3101.
[11] (a) K.I. Na, S. Huh, K.M. Sung, M.J. Jun, Polyhedron 15 (1996) 1841;
(b) J.Y. Kim, M.J. Jun, W.Y. Lee, Polyhedron 15 (1996) 3787.
[12] M. Ito, M. Hirakawa, K. Murata, T. Ikariya, Organometallics 20 (2001) 379.
[13] G.P.C.M. Dekker, A. Buijs, C.J. Elseiver, K. Vrieze, P.W.N.M. van Leeuwen, W.J.J. Smeets, A.L. Spek, Y.F. Wang, C.H. Stam, Organometallics 11 (1992) 1937.
[14] A. Habtemariam, B. Watchman, B.S. Potter, R. Palmer, S. Parsons, A. Parkin, P.J. Sadler, J. Chem. Soc., Dalton Trans. (2001) 1306.
[15] A. Mansour, M. Portnoy, Tetrahedron Lett. 44 (2003) 2195.
[16] J.M. Vila, M. Gayoso, M.T. Pereira, A. Suárez, J.J. Fernández, J.M. Ortigueira, A. Fernández, M. López Torres, Trends Organometal. Chem. 2 (1997) 21.
[17] J.M. Vila, M.T. Pereira, J.M. Ortigueira, M. López-Torres, D. Lata, M. Graña, A. Suárez, J.J. Fernández, A. Fernández, J. Chem. Soc., Dalton Trans. (1999) 4193.
[18] D. Vázquez-García, A. Fernández, J.J. Fernández, M. López-Torres, A. Suárez, J.M. Ortigueira, J.M. Vila, H. Adams, J. Organomet. Chem. 595 (2000) 199.
[19] A.G. Quiroga, J.M. Perez, I. Lopez-Solera, J.R. Masaguer, A. Luque, P. Roman, A. Edwards, C. Alonso, C. Navarro-Ranninger, J. Med. Chem. 41 (1988) 1399.
[20] A. Amoedo, M. Graña, J. Martínez, T. Pereira, M. López-Torres, A. Fernández, J.J. Fernández, J.M. Vila, Eur. J. Inorg. Chem. (2002) 613.
[21] A. Fernández, D. Vázquez-García, J.J. Fernández, M. López-Torres, A. Suárez, S. Castro-Juiz, J.M. Vila, New J. Chem. 26 (2002) 105.
[22] C. López, A. Caubet, S. Pérez, X. Soláns, M. Font-Bardía, J. Organomet. Chem. 681 (2003) 82.
[23] J. Martínez, M.T. Pereira, I. Buceta, G. Alberdi, A. Amoedo, J.J. Fernández, M. López-Torres, J.M. Vila, Organometallics 22 (2003) 5581.
[24] H. Onoue, I. Moritani, J. Organomet. Chem. 43 (1972) 432.
[25] H. Onoue, K. Minami, K. Nakagawa, Bull. Chem. Soc. Jpn. 43 (1970) 3480.
[26] R. Bosque, J. Granell, J. Sales, M. Font-Bardiá, X. Solans, J. Organomet. Chem. 453 (1994) 147.
[27] J.M. Vila, M. Gayoso, M.T. Pereira, M. López-Torres, G. Alonso, J.J. Fernández, J. Organomet. Chem. 445 (1993) 287.
[28] 28 J.M. Vila, M. Gayoso, M.T. Pereira, A. Romar, J.J. Fernández, M. Thornton-Pett, J. Organomet. Chem. 401 (1991) 385.
[29] J. Albert, J. Granell, J. Sales, M. Font-Bardiá, X. Solans, Organometallics 14 (1995) 1393.
[30] P.S. Pregosini, R.W. Kuntz, ^{31}P and ^{13}C NMR of transition metal phosphine complexes, in: P. Diehl, E. Fluck, R. Kosfeld (Eds.), NMR Basic Principles and Progress, vol. 16, Springer, Berlin, 1979.
[31] D. Vázquez-García, A. Fernández, J.J. Fernández, M. López-Torres, A. Suárez, J.M. Ortigueira, J.M. Vila, H. Adams, J. Organomet. Chem. 595 (2000) 199.
[32] D.D. Perrin, W.L.F. Armarego, D.R. Perrin, Purification of Laboratory Chemicals, 4th ed., Butterworth–Heinemann, 1996.

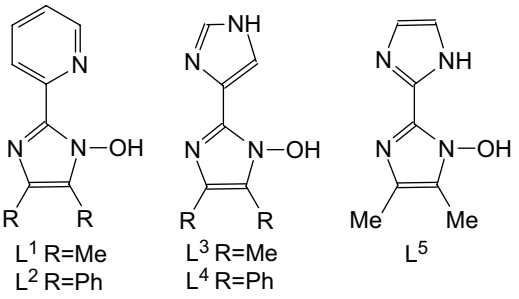


Fig. 1. *N*-hydroxyimidazole ligands.

rate salt with the imidazole ligand in alcohol. The complexes were soluble in a variety of organic solvents and insoluble in water. The complexes formulated with a metal:ligand ratio of 1:2 and were characterised by spectroscopy {IR and NMR (where appropriate)}, microanalysis and X-ray crystallography.

The X-ray crystal structure of $[Cu(L^1)_2](ClO_4)_2 \cdot H_2O$ (Figs. 2a–2c, Tables 1 and 2) shows the Cu(II) ion sitting at a centre of symmetry and with tetragonal geometry. The two L^1 ligands form six-membered, chelate rings with the metal and are *trans* to each other. Both of the NO chelating, neutral *N*-hydroxyimidazole ligands have tautomerised and are in the zwitterion form (Fig. 3), with the uncoordinated imidazole imine N atom being protonated and the oxime O atom deprotonated. There are also long axial bonds to the two perchlorate anions and the solvate water molecule makes three hydrogen bonds to the protonated amine, the oxime O atom and to a perchlorate O atom. The two heterocyclic rings within each ligand are titled at 13.8(1)° to one another. There is π–π stacking (Fig. 2b) creating an infinite two-dimensional network sheet structure. The sheets are linked through the hydrogen bonds between the water molecules and the ligands resulting in the formation of channels which host the water molecules (Fig. 2c).

The three other Cu(II) complexes and one Zn(II) complex all contain two NO chelating zwitterionic *N*-hydroxy-

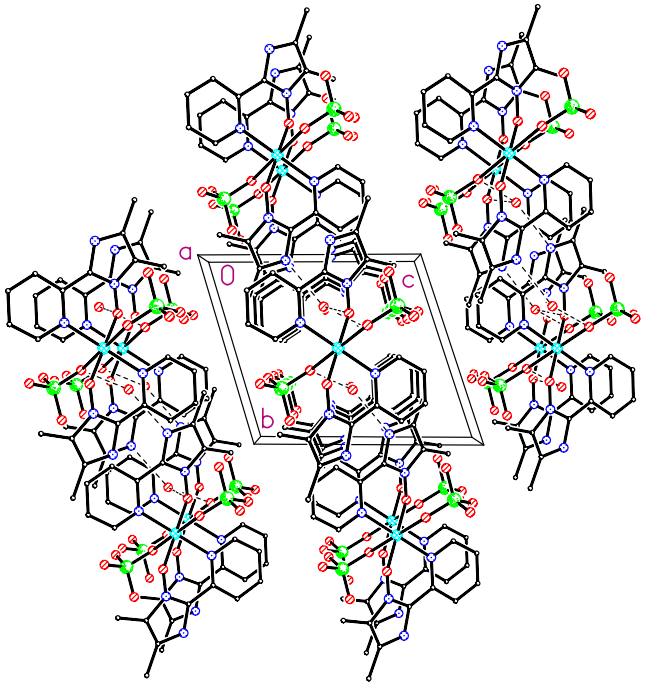


Fig. 2b. π–π stacking in $[Cu(L^1)_2](ClO_4)_2 \cdot H_2O$.

imidazole ligands (Figs. 4–7, Tables 1 and 2) and have core structures similar to $[Cu(L^1)_2](ClO_4)_2 \cdot H_2O$. The three anhydrous Cu(II) complexes have approximate square planar coordination geometry. In the case of $[Cu(L^2)_2](ClO_4)_2$ there are additional hydrogen bonding interactions between the protonated imine N atoms and the perchlorate oxygen atoms stitching neighbouring complexes into infinite chains (for example see Fig. 4). Intermolecular bridging perchlorates and π–π stacking orders the $[Cu(L^3)_2](ClO_4)_2$ units complexes into a supramolecular array (Fig. 5). In the case of $[Cu(L^5)_2](ClO_4)_2$, weak 'Cu–perchlorate–protonated imine' interactions create chains of complex dications (Fig. 7b).

In $[Zn(L^4)_2MeOH](ClO_4)_2 \cdot MeOH$ the cation is a centrosymmetric dimer (Fig. 6a) where the two halves (Fig. 6b) are linked by two bridging deprotonated hydroxyl

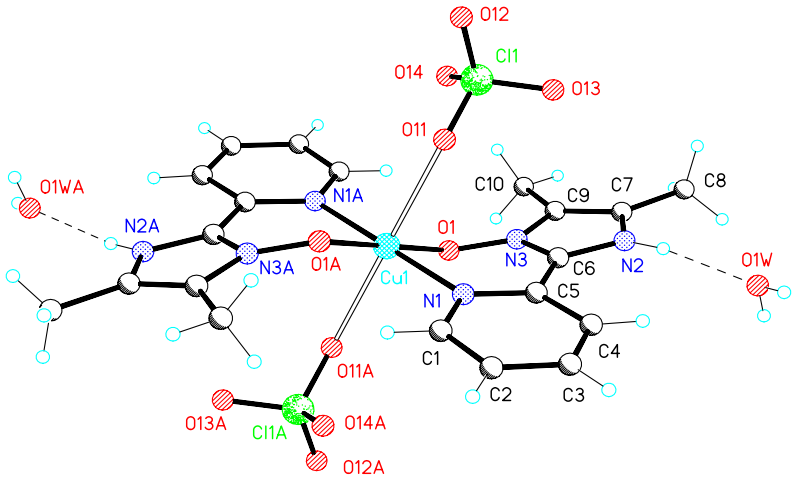


Fig. 2a. X-ray structure of $[Cu(L^1)_2](ClO_4)_2 \cdot H_2O$.

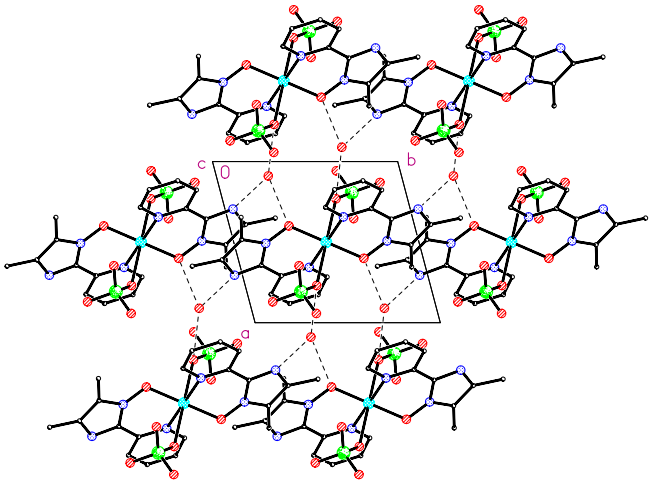


Fig. 2c. Hydrogen-bonded water molecules in the channels formed in $[Cu(L^1)_2](ClO_4)_2 \cdot H_2O$.

O^- atoms (O2). The Zn(II) ions are six-coordinate, the sixth ligand being a methanol solvate molecule. There is extensive hydrogen bonding network involving the coordinated methanol, the methanol of solvation, the perchlorate anion and the hydrogen of the protonated amine N atom. This three-dimensional coordination polymer structure is shown in Fig. 6c.

To our knowledge, the above five complexes are the first documented examples of *N*-hydroxyimidazoles tautomerising to form zwitterions upon complexation to a metal ion and, as such, represent a novel class of ligand.

3. Experimental

Chemicals were purchased from commercial sources and, unless specified, were used without further purification. *N*-Hydroxyimidazoles were prepared by reacting monoximes with aldehydes and ammonia [10,11]. Infrared spectra of solids (in a KBr matrix) were recorded in the region 4000–400 cm^{-1} on a Nicolet FT-IR Impact 400D infrared spectrometer. ^1H NMR spectra were run as solutions in DMSO-d_6 on a Bruker Avance 300 MHz instrument. Microanalytical data were provided by the Microanalytical Laboratory, National University of Ireland, Cork, Ireland. X-ray crystallographic data (Table 3) were collected at 150 K on a Bruker SMART 1000 diffractometer using Mo Kα radiation ($\lambda = 0.71073$ Å). The structures were solved by direct methods and refined by full-matrix least-squares on F^2 using all the reflections. All the non-hydrogen atoms were refined anisotropically and hydrogen atoms bonded to carbon were inserted at calculated positions using a riding model. Hydrogen atoms bonded to O or N were located from difference maps and refined with fixed, isotropic thermal parameters,

Table 2
Hydrogen bonds (Å and °)

D–H...A	*d*(D–H)	*d*(H...A)	*d*(D...A)	⟨(DHA)
$[Cu(L^1)_2](ClO_4)_2 \cdot H_2O$				
N(2)–H(2N)...O(1W)	0.84(3)	1.91(3)	2.723(3)	162(3)
O(1W)–H(1WA)...O(11)#1	0.75(3)	2.16(3)	2.911(2)	177(3)
O(1W)–H(2WB)...O(1)#2	0.78(3)	2.08(3)	2.831(2)	161(3)
$[Cu(L^2)_2](ClO_4)_2 \cdot H_2O$				
N(2)–H(2N)...O(11)	0.82(3)	2.01(3)	2.8284(19)	177(2)
$[Cu(L^3)_2](ClO_4)_2$				
N(2)–H(2N)...O(14)#3	0.79(3)	2.11(3)	2.895(2)	169(3)
N(3)–H(3N)...O(11)	0.84(3)	2.06(3)	2.859(2)	157(3)
$[Zn(L^4)_2MeOH](ClO_4)_2 \cdot MeOH$				
N(12)–H(12)...O(23)#4	0.88	2.02	2.831(3)	153.6
N(13)–H(13)...O(12)	0.88	2.03	2.898(3)	169.9
N(22)–H(22)...O(11)#5	0.88	2.02	2.894(3)	172.2
N(23)–H(23)...O(22)#6	0.88	2.21	3.012(3)	152.1
N(23)–H(23)...O(14)#7	0.88	2.57	3.182(3)	126.9
O(40)–H(40)...O(50)	0.85	1.87	2.717(3)	172.6
O(50)–H(50)...O(24)	0.85	2.23	3.032(3)	158.4
$[Cu(L^5)_2](ClO_4)_2$				
N(2)–H(2N)...O(11)	0.86	1.95	2.787(3)	163.1
N(3)–H(3N)...O(12)	0.88	2.12	2.946(4)	154.7

Symmetry transformations used to generate equivalent atoms: #1 $-x$, $-y+2$, $-z+1$; #2 $-x+1$, $-y+2$, $-z+1$; #3 $-x-1$, $-y+2$, $-z+1$; #4 $-x$, $-y$, $-z+1$; #5 x, $y+1$, z; #6 $-x$, $-y+1$, $-z+1$; #7 $-x+1$, $-y+1$, $-z+1$.

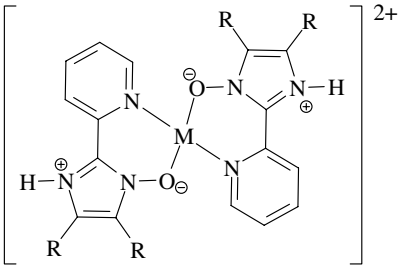


Fig. 3. Zwitterionic form of *N*-hydroxyimidazole ligands chelated to the metal (M^{2+}) centre.

Table 1
Selected bond lengths (Å) and angles (°)

Complex	$[Cu(L^1)_2](ClO_4)_2 \cdot H_2O$	$[Cu(L^2)_2](ClO_4)_2 \cdot H_2O$	$[Cu(L^3)_2](ClO_4)_2$	$[Zn(L^4)_2MeOH](ClO_4)_2 \cdot MeOH$	$[Cu(L^5)_2](ClO_4)_2$
M–O	1.9217(15)	1.9305(12)	1.9297(13)	2.0409(15), 2.0941(15)	1.9299(16)
M–N	2.0523(17)	2.0140(14)	1.9479(15)	2.0550(19), 2.0783(19)	1.9678(19)
O–M–N	90.61(7)	90.25(5)	93.14(6)	90.26(7), 87.77(7)	93.35(7)
O–M–N#1	89.39(7)	89.75(5)	86.86(6)	89.87(7), 92.67(7)	86.65(7)
Symmetry ops #1	$-x+1$, $-y+1$, $-z+1$	$-x+2$, $-y+1$, $-z$	$-x+1$, $-y+1$, $-z+1$	none	$-x+2$, $-y$, $-z+2$

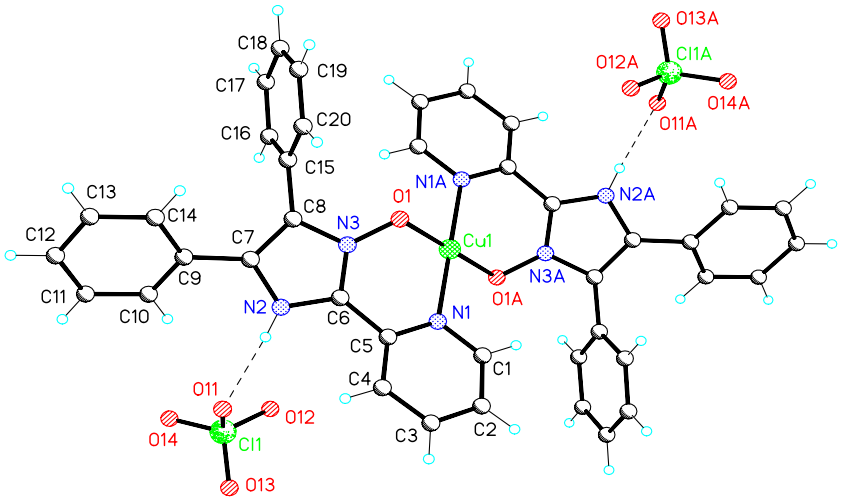


Fig. 4a. X-ray structure of $[Cu(L^2)_2](ClO_4)_2$.

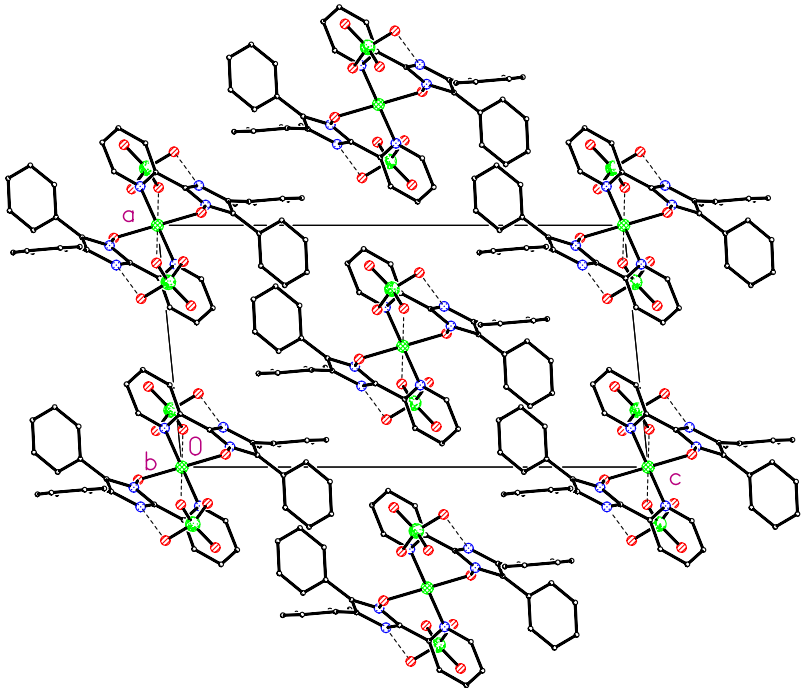


Fig. 4b. Hydrogen bonding interactions forming infinite chains of $[Cu(L^2)_2](ClO_4)_2$ complexes.

except for $[Zn(L^4)_2MeOH](ClO_4)_2 \cdot MeOH$ (where all the H atoms were inserted at calculated positions) and $[Cu(L^5)_2](ClO_4)_2$ (where they were located and not further refined).

3.1. $[Cu(L^1)_2](ClO_4)_2 \cdot H_2O$

A solution of $Cu(ClO_4)_2 \cdot 6H_2O$ and L^1 (1:2 mol ratio) in acetonitrile was refluxed for 4 h and then left to stand overnight. The precipitated green complex was recrystallised from a mixture of acetonitrile and ethanol. Yield = 81%. The complex was soluble in hot acetonitrile and insoluble in water. *Anal.* Calc. for $C_{20}H_{24}N_6O_{11}Cl_2Cu$: C, 36.46; H, 3.67; N, 12.76. Found: C, 36.50; H, 3.29; N, 12.32%. IR: 3456, 3121, 1644, 1605, 1573, 1541, 1491, 1434, 1316, 1288, 1231, 1117, 969, 928, 823, 782, 625, 484 cm^{-1}.

3.2. $[Cu(L^2)_2](ClO_4)_2 \cdot H_2O$

This green complex was prepared and recrystallised in a similar way to $[Cu(L^1)_2](ClO_4)_2 \cdot H_2O$. Yield = 56%. The complex was soluble in hot acetonitrile and insoluble in water. *Anal.* Calc. for $C_{40}H_{32}N_6O_{11}Cl_2Cu$: C, 52.97; H, 3.56; N, 9.27. Found: C, 52.92; H, 3.31; N, 9.33%. IR: 3456, 3126, 1605, 1576, 1544, 1480, 1427, 1309, 1210, 1096, 925, 825, 764, 702, 623, 545 cm^{-1}.

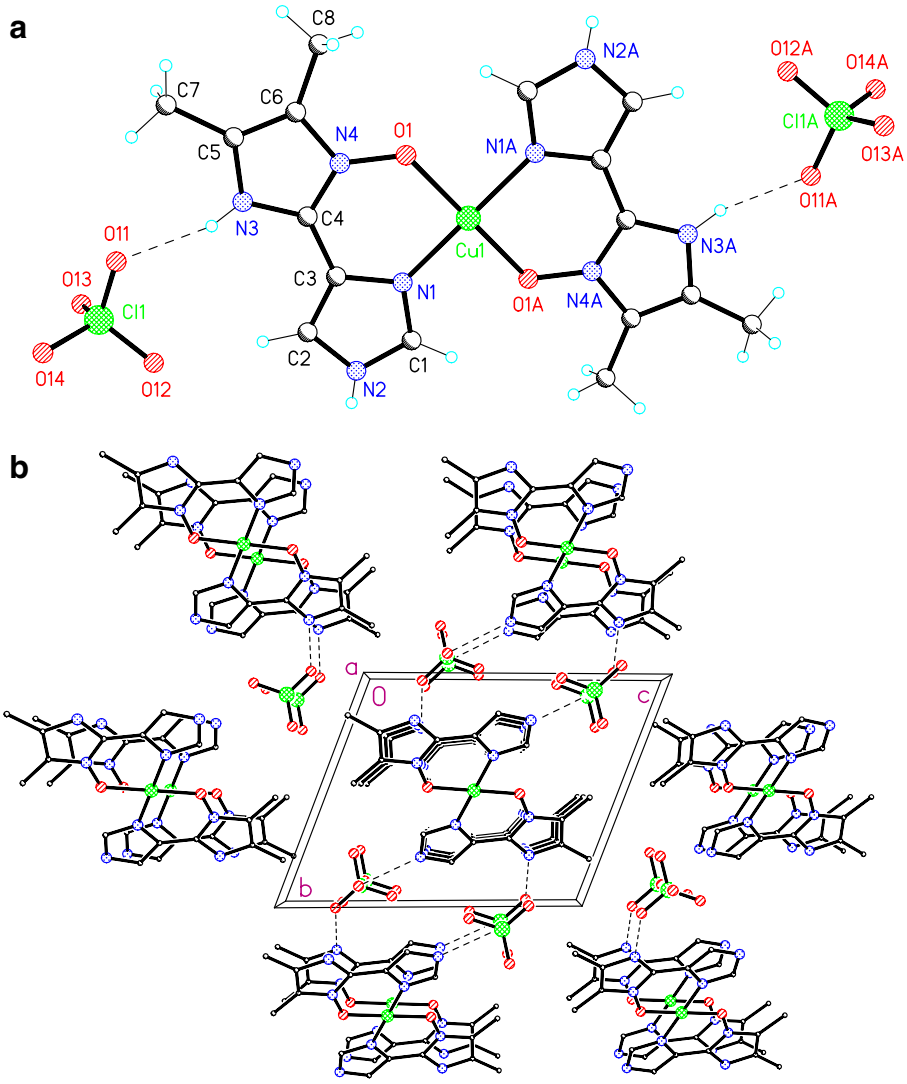


Fig. 5. X-ray structure of $[Cu(L^3)_2](ClO_4)_2$.

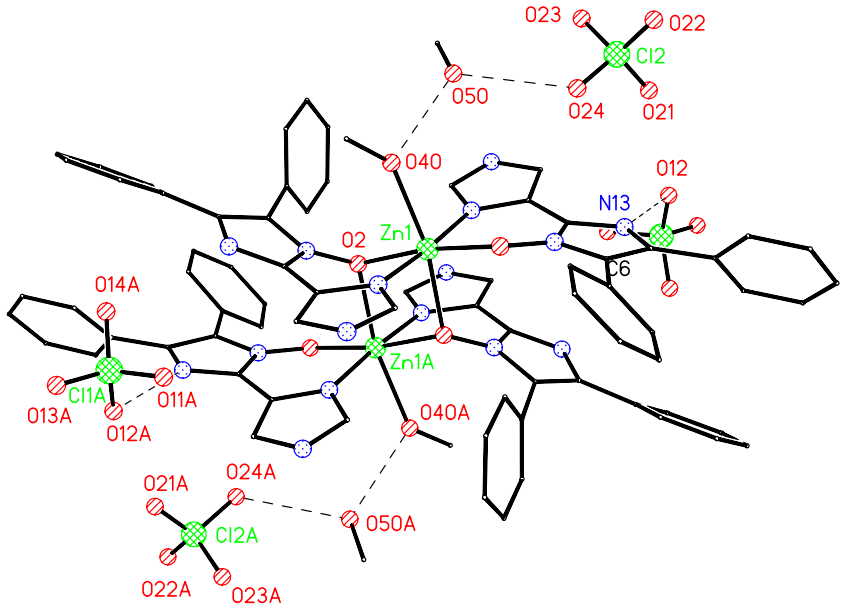


Fig. 6a. X-ray structure of dimeric $[Zn(L^4)_2MeOH](ClO_4)_2 \cdot MeOH$.

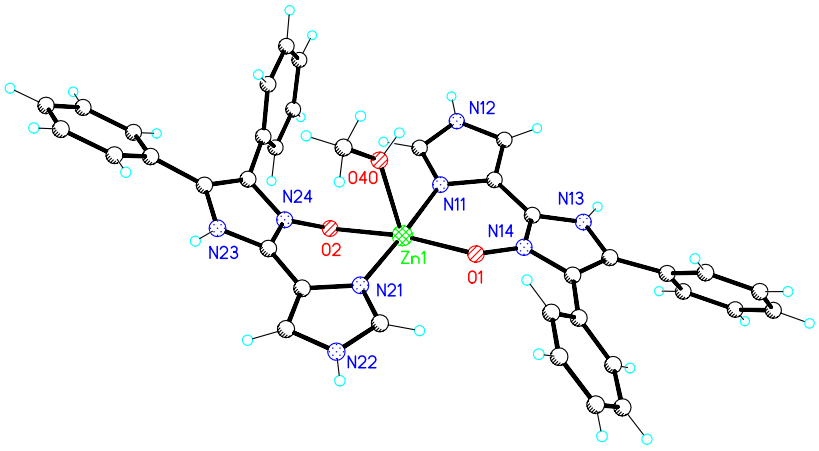


Fig. 6b. One half of dimeric $[Zn(L^4)_2MeOH](ClO_4)_2 \cdot MeOH$.

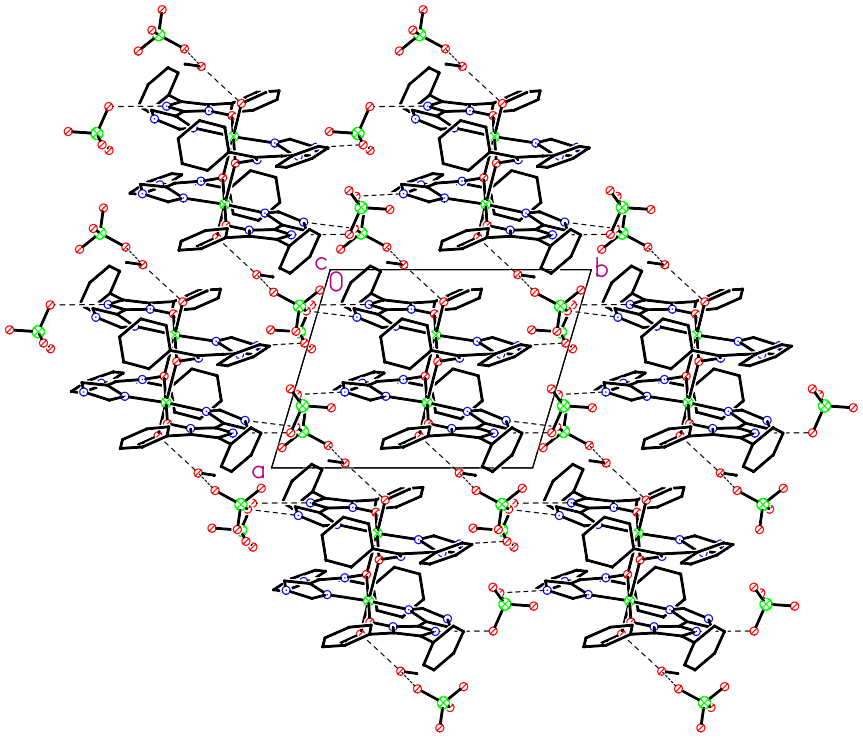


Fig. 6c. Extensive hydrogen bonding network in $[Zn(L^4)_2MeOH](ClO_4)_2 \cdot MeOH$.

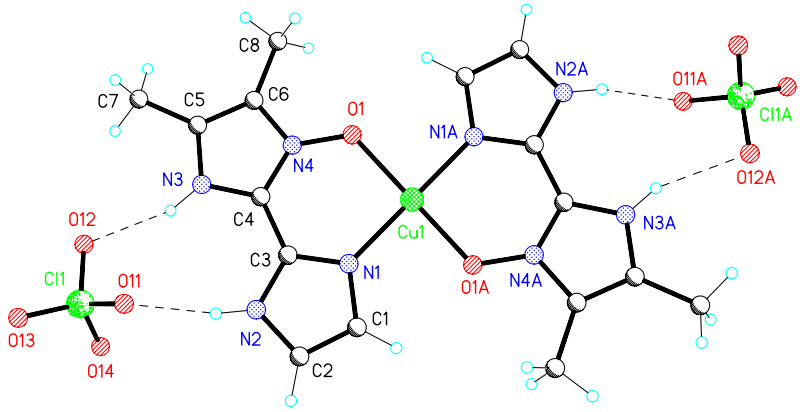


Fig. 7a. X-ray structure of $[Cu(L^5)_2](ClO_4)_2$.

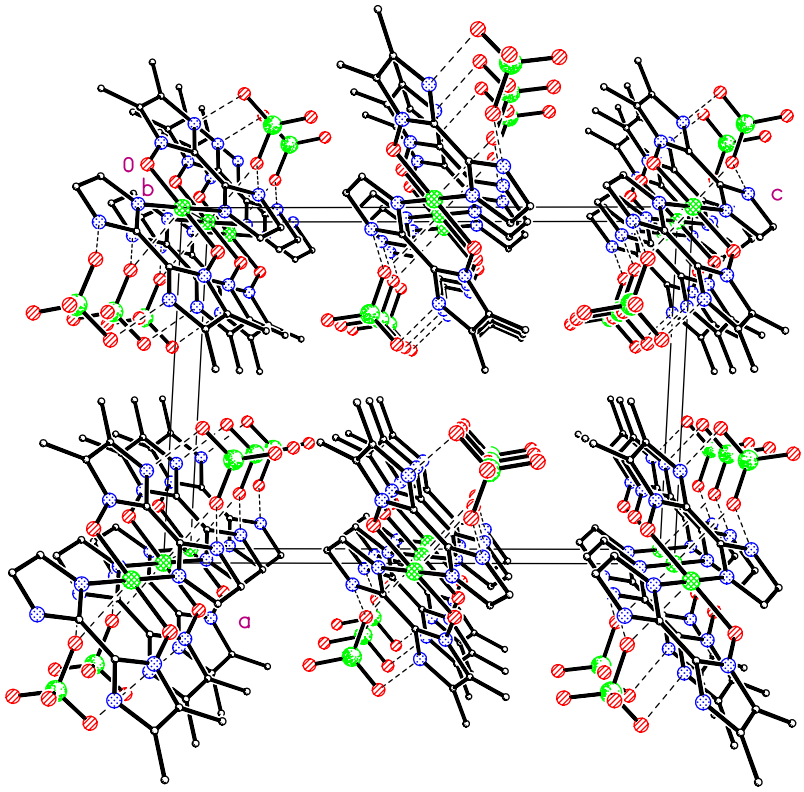


Fig. 7b. Chains of $[Cu(L^5)_2](ClO_4)_2$ formed through 'Cu–perchlorate–protonated imine' interactions.

Table 3
Crystal data and structure refinements

Complex	$[Cu(L^1)_2](ClO_4)_2 \cdot H_2O$	$[Cu(L^2)_2](ClO_4)_2$	$[Cu(L^3)_2](ClO_4)_2$	$[Zn(L^4)_2MeOH](ClO_4)_2 \cdot MeOH$	$[Cu(L^5)_2](ClO_4)_2$
Empirical formula	$C_{20}H_{26}Cl_2CuN_6O_{12}$	$C_{40}H_{30}Cl_2CuN_6O_{10}$	$C_{16}H_{20}Cl_2CuN_8O_{10}$	$C_{38}H_{36}Cl_2N_8O_{12}Zn$	$C_{16}H_{20}Cl_2CuN_8O_{10}$
Formula weight	676.91	889.14	618.84	933.02	618.84
Crystal system	triclinic	monoclinic	triclinic	triclinic	monoclinic
Space group	$P\bar{1}$	$P2_1/n$	$P\bar{1}$	$P\bar{1}$	$P2_1/c$
a (Å)	7.7461(10)	10.0378(8)	4.8193(5)	10.1946(7)	10.8501(9)
b (Å)	9.0192(12)	9.8351(8)	9.9883(10)	12.9732(9)	6.9525(6)
c (Å)	9.9153(13)	19.2452(15)	12.3209(12)	15.7194(11)	15.5483(13)
α (°)	71.879(2)	90	110.492(2)	97.800(1)	90
β (°)	84.956(2)	95.7500(10)	95.627(2)	92.308(1)	93.044(1)
γ (°)	74.375(2)	90	93.404(2)	105.961(1)	90
Volume (Å^3)	634.03(14)	1890.4(3)	550.08(10)	1973.8(2)	1171.24(17)
Z	1	2	1	2	2
D_{calc} (Mg/m)	1.773	1.562	1.868	1.570	1.755
Reflections collected	5122	15171	4690	17260	9520
Independent reflections [R_{int}]	2799 [0.0176]	4386 [0.0205]	2471 [0.0124]	9032 [0.0226]	2745 [0.0185]
Data/restraints/parameter	2799/0/198	4386/0/271	2471/0/177	9032/0/552	2745/0/171
Goodness-of-fit on F^2	1.024	1.031	1.073	1.022	0.896
R_1, wR_2 [$I > 2\sigma(I)$]	0.0310, 0.0720	0.0317, 0.0787	0.0266, 0.0664	0.0390, 0.0880	0.0370, 0.1037
R_1, wR_2 (all data)	0.0427, 0.0773	0.0418, 0.0834	0.0308, 0.0685	0.0573, 0.0973	0.0444, 0.1094

3.3. $[Cu(L^3)_2](ClO_4)_2$

This green complex was prepared and recrystallised in a similar way to $[Cu(L^1)_2](ClO_4)_2 \cdot H_2O$. Yield = 61%. The complex was soluble in hot acetonitrile and insoluble in water. *Anal.* Calc. for $C_{16}H_{20}N_8O_{10}Cl_2Cu$: C, 31.05; H, 3.26; N, 18.11. Found: C, 31.09; H, 3.10; N, 18.34%. IR: 3227, 1619, 1512, 1439, 1292, 1234, 1097, 960, 928, 789, 760, 669, 620, 473 cm^{-1}.

3.4. $[Zn(L^4)_2MeOH](ClO_4)_2 \cdot MeOH$

This white complex was prepared in the same manner as $[Cu(L^1)_2](ClO_4)_2 \cdot H_2O$ and was recrystallised from a

mixture of methanol and acetonitrile. Yield = 83%. The complex was soluble in hot methanol and acetonitrile and insoluble in water. *Anal.* Calc. for $C_{36}H_{28}N_8O_{10}Cl_2Zn$: C, 49.76; H, 3.25; N, 12.89. Found: C, 49.20; H, 3.49; N, 12.76%. ^{1}H NMR: 7.00–7.15 (aromatic H, m), 7.57–7.69 (imidazole H, m). IR: 3272, 1646, 1510, 1436, 1301, 1104, 987, 926, 760, 698, 655, 627, 529 cm^{-1}.

3.5. $[Cu(L^5)_2](ClO_4)_2$

This green complex was prepared and recrystallised in a similar way to $[Cu(L^1)_2](ClO_4)_2 \cdot H_2O$. Yield = 72%. The complex was soluble in hot acetonitrile and ethanol and insoluble in water. *Anal.* Calc. for $C_{16}H_{20}N_8O_{10}Cl_2Cu$: C, 31.05; H, 3.26; N, 18.11. Found: C, 30.74; H, 3.02; N, 17.52%. IR: 3217, 1609, 1531, 1443, 1317, 1126, 1039, 919, 811, 767, 713, 627, 473 cm^{-1}.

Acknowledgement

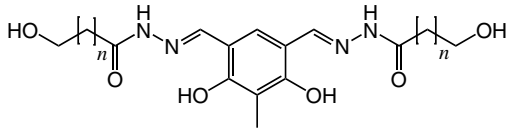
S. Abuskhuna acknowledges financial support from the Libyan Higher Education Department.

Appendix A. Supplementary material

CCDC 638219, 638220, 638221, 638222 and 638223 contain the supplementary crystallographic data for $[Cu(L^1)_2](ClO_4)_2 \cdot H_2O$, $[Cu(L^2)_2](ClO_4)_2 \cdot H_2O$, $[Cu(L^3)_2](ClO_4)_2$, $[Zn(L^4)_2MeOH](ClO_4)_2 \cdot MeOH$ and $[Cu(L^5)_2](ClO_4)_2$. These data can be obtained free of charge via http://www.ccdc.cam.ac.uk/conts/retrieving.html, or from the Cambridge Crystallographic Data Centre, 12 Union Road, Cambridge CB2 1EZ, UK; fax: (+44) 1223-336-033; or e-mail: deposit@ccdc.cam.ac.uk. Supplementary data associated with this article can be found, in the online version, at doi:10.1016/j.poly.2007.06.034.

References

[1] M.R. Grimmett, in: A.R. Katritsky, E.F.V. Scriven (Eds.), Comprehensive Heterocyclic Chemistry II, vol. 3, Pergamon, Oxford, 1996, pp. 77–220.
[2] L. De Luca, Curr. Med. Chem. 13 (2006) 1.
[3] J.N. Delgado, W.A. Remers (Eds.), Wilson and Gisvold's Textbook of Organic Medicinal and Pharmaceutical Chemistry, 10th ed., Lippincott-Raven, Philadelphia, PA, 1998.
[4] J.R. Coura, S.L. de Castro, Mem. Inst. Oswaldo Cruz 97 (2002) 3.
[5] G.G. Allan, C.S. Chopra, T. Mattila, Pest. Sci. 3 (1972) 153.
[6] H.A. Philipp, L.I. Jirkovsky, Am. Home Product Corp. USA (1980) 6.
[7] P. Franchetti, M. Grifantini, C. Lucarelli, Farmaco-Ed. Sci. 27 (1972) 46.
[8] S. Abuskhuna, M. McCann, J. Briody, M. Devereux, V. McKee, Polyhedron 23 (2004) 1731.
[9] S. Abuskhuna, J. Briody, M. McCann, M. Devereux, K. Kavanagh, J. Barreira Fontecha, V. McKee, Polyhedron 23 (2004) 1249.
[10] S. Abuskhuna, M.Sc. thesis, NUI Maynooth, 2004.
[11] K. Akagane, G.G. Allan, Shikizai Kyokaishi 46 (1973) 555.



Scheme 1. The ligands H_6ipa-hyhb ($n = 2$) and H_6ipa-hyhh ($n = 4$).

this context we have recently established an excess to homochiral helical arrays and porous 3D coordination frameworks based on metal complexes containing nucleoside-based salen-type ligands [4] and trinucleating triaminoguanidine-based Schiff-base ligands [5], respectively.

To generate dinuclear *meta*-phenylene-bridged building blocks we synthesized the new Schiff-base ligands H_6ipa-hyhb and H_6ipa-hyhh shown in Scheme 1 providing two [ONO] *N*-salicylidenehydrazide binding pockets bridged through a central resorcinol moiety, which is additionally functionalized by hydroxyl side chains. To date only a scarce number of dinuclear copper(II) complexes with the 1,3-dihydroxybenzene bridging motif have been synthesized which utilize double Schiff-base ligands of 4,6-diacetylresorcinol [6,7], but no crystal structure is reported as yet. In contrast the momonuclear metal complexes of the analogous *N*-salicylidenehydrazide ligands with a variety of different side chain functionalities providing only one binding pocket are well documented [8,9]. In particular, the use of such ligands with hydroxyalkyl side chains leads to supramolecular interactions via hydrogen bonding networks as was shown for vanadium(V) complexes [10]. Moreover, it is interesting to note that in the case of copper(II) complexes of such mononucleating *N*-salicylidenehydrazide ligands the side chain functionality provides a coordinative cross-linking of the phenolate-bridged dinuclear units generating a 2D coordination polymer [11].

In this paper, we report the synthesis and chemical characterization of three novel copper(II) coordination polymers based on the new ω-hydroxyalkyl functionalized double Schiff-base ligands H_6ipa-hyhb and H_6ipa-hyhh (see Scheme 1). The crystal structures of these complexes and their magnetic properties are presented.

2. Experimental

2.1. Materials

4-Hydroxybutanoic acid hydrazide and 6-hydroxyhexanoic acid hydrazide were synthesised by hydrazinolysis of the corresponding lactone. All the other starting materials are commercially available and were used without further purification. Abbreviations used throughout the text: ipa = 4,6-dihydroxy-5-methyl-benzene-1,3-dicarbaldehyde, H_6ipa-hyhb = 4-hydroxy-butanoic acid [1-2,4-dihydroxy-5-[(4-hydroxy-butyryl)-hydrazonomethyl]-3-methyl-phenyl-methylidene]-hydrazide, H_6ipa-hyhh = 6-hydroxy-hexanoic acid [1-2,4-dihydroxy-5-[(6-hydroxy-hexanoyl)-hydrazonomethyl]-3-methyl- phenyl-methylidene]-hydrazide.

2.2. Physical measurement

Melting points were determined via a VEB Analytik Dresden HMK 72/41555. NMR spectra were recorded on Bruker AVANCE 200 and 400 MHz spectrometers at ambient temperatures. The chemical shifts were referenced to tetramethylsilane and are reported in ppm. The infrared spectra were recorded on a Bruker IFS55/EQUINOX spectrometer. Elemental analyses were determined on a Leco CHNS/932 and a VARIO EL III elemental analyzer. Magnetic susceptibilities were obtained from polycrystalline samples using a Quantum-Design MPMSR-5S SQUID magnetometer, measurements were conducted with an applied magnetic field of 2 and 5 kOe in the temperature range from 2 to 300 K. The measured values of χ_M were corrected for their diamagnetic contributions.

2.3. Synthesis of the ligands

2.3.1. 2-Methyl-4,6-diformylresorcinol (ipa)

2-Methylresorcinol (10.0 g, 80 mmol) was mixed with hexamethylenetetramine (22.5 g, 160 mmol) in trifluoroacetic acid (100 mL). Trifluoroacetic acid anhydride (7 mL) was added to the resulting brown reaction solution. This solution was heated at 80 °C for five days under argon atmosphere. The reaction mixture was poured into 4 M HCl (350 mL), stirred for 10 min and extracted with CH_2Cl_2 (7 × 100 mL). The combined organic layers were dried over Na_2SO_4 and the solvent removed under vacuum. The crude product obtained as brown needles was pure enough for the following ligand syntheses (Yield: 5.2 g, 35%). The aqueous layer was allowed to stand in the refrigerator at 8 °C for three days and another fraction of ipa could be isolated as pale pink needles. These were separated by filtration and dried under vacuum (Yield: 2.7 g, 19%). NMR- and IR-spectroscopic measurements revealed that both fractions are identical (overall yield: 7.9 g, 54%). Colorless needles of ipa can be obtained by steam distillation of the combined fractions. M.p. 187 °C. ^{1}H NMR (200 MHz, $CDCl_3$): $\delta = 2.09$ (s, 3H, C*H*$_3$); 7.66 (s, 1H, arom. C*H*); 9.74 (s, 2H, C*H*O); 11.99 ppm (s, 2H, O*H*). ^{13}C NMR (100 MHz, $CDCl_3$): $\delta = 6.5$ (*C*H$_3$); 113.5 (arom. C^2); 115.2 (arom. $C^{4,6}$); 139.9 (arom. C^5); 166.3 (arom. $C^{1,3}$); 194.0 ppm (*C*HO). IR (KBr, cm^{-1}): 2866 vw, 1648 vs, 1610 vs, 1378 m, 1339 m, 1306 s, 1224 w, 1166 vs, 1008 m, 777 m, 726 m, 647 m, 533 m.

2.3.2. H_6ipa-hyhb

4-Hydroxybutanoic acid hydrazide (1.9 g, 16 mmol) was added to a suspension of ipa (1.5 g, 8 mmol) in ethanol (100 mL) and the resulting yellow solution was stirred over night at room temperature. The volume of the reaction mixture was reduced to approximately 30 mL resulting in the precipitation of a pale yellow solid which was filtered off, washed with a small amount of ethanol

and dried under vacuum (Yield: 2.8 g, 96%). M.p. 190 °C (decomposition). As can be seen in the NMR spectra, the ligand is a mixture of two isomers at the ratio of 4:1. *Anal.* Calc. for $C_{17}H_{24}N_4O_6 \cdot H_2O$: C, 51.25; H, 6.58; N, 14.06; Found: C, 51.21; H, 6.73; N, 14.28%. ^{1}H NMR (400 MHz, DMSO-d_6): $\delta = 1.72$ (tt, 4H, $^3J = 7.4$ Hz, CH_2 CH_2OH); 2.06 and 2.07 (s, 3H, CH_3); 2.25 and 2.55 (t, 4H, $^3J = 7.4$ Hz, CH_2C=O); 3.33 (s, 2H, H_2O); 3.42 (dt, 4H, $^3J_t = 6.0$ Hz, $^3J_d = 5.0$ Hz, CH_2OH); 4.51 (t, 2H, $^3J = 5.0$ Hz, CH_2O*H*); 7.36 and 7.37 (s, 1H, arom. C*H*); 8.09 and 8.22 (s, 2H, C*H*=N); 11.18, 11.31, 11.61, 11.62 and 12.43 ppm (s, 4H, arom. O*H* and N*H*). ^{13}C NMR (50 MHz, DMSO-d_6): $\delta = 7.6$ (*C*H_3); 27.1, 28.2, 28.4 and 30.6 (*C*H_2); 60.1 (*C*H_2OH), 110.5, 110.8 and 111.2 (arom. C^2, $C^{4,6}$); 130.8 and 131.1 (arom. C^5); 145.2 and 147.7 (*C*H=N); 157.7 and 158.6 (arom. $C^{1,3}$); 168.3 and 172.9 ppm (*C*=O). IR (KBr, cm^{-1}): 3390 s, 3214 s, 3053 s, 2934 s, 2881 w, 1667 vs, 1629 vs, 1559 s, 1477 w, 1448 w, 1363 s, 1254 m, 1214 m, 1177 s, 1051 s.

2.3.3. H_6ipa-hyhh

6-Hydroxyhexanoic acid hydrazide (0.8 g, 5.5 mmol) was added to a suspension of ipa (0.5 g, 2.8 mmol) in ethanol (50 mL) and stirred for 2 h at room temperature. After removing the volatile components under vacuum at room temperature the ligand was obtained as a pale yellow solid in quantitative yield (Yield: 1.15 g). M.p. 174 °C. As can be seen in the NMR spectra the ligand is a mixture of two isomers at the ratio of 4:1. *Anal.* Calc. for $C_{21}H_{32}N_4O_6 \cdot 0.33H_2O$: C, 57.00; H, 7.44; N, 12.68. Found: C, 56.95; H, 7.43; N, 12.85%. ^{1}H NMR (400 MHz, DMSO-d_6): $\delta = 1.30$ (tt, 4H, $^3J = 7.4$ Hz, CH_2); 1.42 (tt, 4H, $^3J = 6.9$ Hz, CH_2); 1.57 (tt, 4H, $^3J = 7.4$ Hz, C$H_2$$CH_2$OH); 2.04 and 2.05 (s, 3H, CH_3); 2.20 and 2,49 (t, 4H, $^3J = 7.4$ Hz, CH_2C=O); 3.35 (s, 2/3 H, H_2O); 3.37 (dt, 4H, $^3J_t = 6.0$ Hz, $^3J_d = 5.0$ Hz, CH_2OH); 4.36 (t, 2H, $^3J = 5.0$ Hz, CH_2O*H*); 7.38 and 7.36 (s, 1 H, *arom.* C*H*); 8.07 and 8.21 (s, 2H, C*H*=N); 11.19, 11.31, 11.60, 11.62 and 12.43 ppm (s, 4H, arom. O*H* and N*H*). ^{13}C NMR (50 MHz, DMSO-d_6): $\delta = 7.6$ (*C*H_3); 23.7, 24.8, 25.2, 32.2 and 33.9 (*C*H_2); 60.5 (*C*H_2OH); 110.5, 110.8 and 111.2 (arom. C^2, $C^{4,6}$); 130.8 and 131.1 (arom. C^5); 145.2 and 147.7 (*C*H=N); 157.7 and 158.6 (arom. $C^{1,3}$); 168.2 and 172.9 ppm (*C*=O). IR (KBr, cm^{-1}): 3402 s, 3309 m, 3197 s, 3052 s, 2935 s, 2863 m, 1663 vs, 1628 vs, 1561 s, 1458 w, 1364 s, 1223 m, 1176 s, 1068 m, 1052 m.

2.4. Synthesis of the complexes

2.4.1. $\{[Cu_2(H_4ipa\text{-}hyhb)(Hpz)_2](ClO_4)_2\}_n$ (1)

A solution of $Cu(ClO_4)_2 \cdot 6H_2O$ (209 mg, 0.6 mmol) in methanol (3 mL) was added to a suspension of H_6ipa-hyhb (107 mg, 0.3 mmol) in methanol (4 mL). To the resulting dark green solution pyrazole (39 mg, 0.6 mmol) was added and the reaction solution was stirred for 20 min. Aqueous ammonia (2 equiv.) was added generating a green precipitate within 10 min, which redissolves by addition of further methanol (15 mL). Slow evaporation of the solvent afforded after about one week green prisms of $\mathbf{1} \cdot n$MeOH suitable for X-ray diffraction. The crystals were separated by filtration and dried under vacuum, which leads to the loss of the solvent of crystallization (Yield: 126.2 mg, 51%). M.p. > 280 °C (decomposition). *Anal.* Calc. for $C_{23}H_{30}Cl_2Cu_2N_8O_{14}$ (**1**): C, 32.87; H, 3.60; N, 13.33. Found: C, 33.08; H, 3.55; N, 13.33%. IR (KBr, cm^{-1}): 3379 s, 3138 w, 2959 m, 2885 m, 2799 w, 1592 vs, 1565 vs, 1396 m, 1358 m, 1276 m, 1203 s, 1121 vs, 1091 vs, 1047 s, 771 m, 627 m.

2.4.2. $\{[Cu_2(H_4ipa\text{-}hyhb)(Him)_2](ClO_4)_2\}_n$ (2)

The synthesis is analogous to what is described for complex **1**. The use of imidazole (38 mg, 0.6 mmol) instead of pyrazole afforded green prisms of the desired complex as its solvate $\mathbf{2} \cdot \frac{n}{2}H_2O$ (Yield: 170.1 mg, 73%). M.p. > 260 °C (decomposition). *Anal.* Calc. for $C_{23}H_{31}Cl_2Cu_2N_8O_{14.5}$ ($\mathbf{2} \cdot \frac{n}{2}H_2O$): C, 32.52; H, 3.68; N, 13.19. Found: C, 31.78; H, 3.52; N 12.39%. IR (KBr, cm^{-1}): 3330 vs, 3144 w, 2959 m, 2885 w, 1593 vs, 1555 vs, 1425 w, 1396 m, 1366 w, 1277 m, 1201 s, 1141 m, 1121 vs, 1091 vs, 1068 s, 771 w, 626 m.

2.4.3. $\{[Cu_2(H_4ipa\text{-}hyhh)(Hpz)_2](ClO_4)_2\}_n$ (3)

A solution of $Cu(ClO_4)_2 \cdot 6H_2O$ (286 mg, 0.8 mmol) in methanol (2 mL) was added to a suspension of H_6ipa-hyhh (168.3 mg, 0.4 mmol) in methanol (8 mL). After stirring for 15 min a clear dark green solution was obtained. Pyrazole (53 mg, 0.8 mmol) and aqueous ammonia (2 equiv.) were added and the solution was stirred for further 20 min. Slow diffusion of diethylether into this solution afforded within three days green prisms of $\mathbf{3} \cdot n$MeOH suitable for X-ray diffraction. The crystals were filtered off and dried under vacuum, which leads to the loss of the solvent of crystallization (Yield: 195.8 mg, 57%). M.p. > 280 °C (decomposition). *Anal.* Calc. for $C_{27}H_{38}Cl_2Cu_2N_8O_{14}$ (**3**): C, 36.17; H, 4.27; N, 12.50. Found: C, 36.11; H, 4.03; N, 12.37%. IR (KBr, cm^{-1}): 3430 s, 3136 w, 2935 m, 2860 w, 1594 vs, 1569 vs, 1391 m, 1362 m, 1278 m, 1208 s, 1121 vs, 1062 s, 768 m, 625 m.

2.5. X-ray crystallographic studies

X-ray measurements were carried out on a Nonius Kappa CCD diffractometer using graphite monochromated Mo Kα radiation ($\lambda = 71.073$ pm) at 183(2) K. The crystallographic data are summarized in Table 1. Data were corrected for Lorentz and polarization effects, but not for absorption effects [12]. The structures were solved by direct methods with SHELXS-97 and refined by full-matrix least-squares techniques against F_0^2 using SHELXL-97 [13]. The hydrogen atoms were included at calculated positions with fixed thermal parameters. All non-hydrogen atoms were refined anisotropically.

Table 1
Crystallographic and structure refinement data for complexes **1**, **2** and **3**

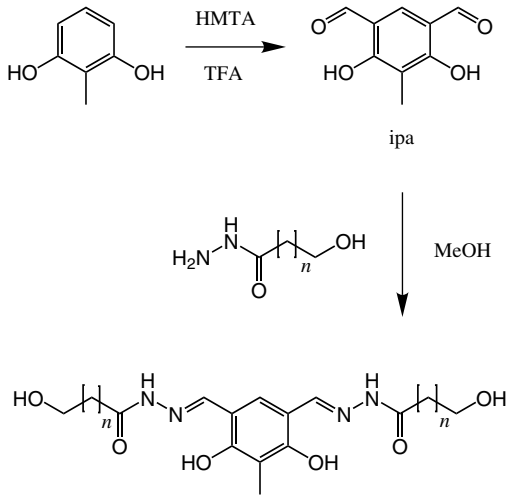
Compound	**1** · *n*MeOH	**2** · $\frac{n}{2}H_2O$	**3** · *n*MeOH
Empirical formula	$C_{24}H_{34}Cl_2Cu_2N_8O_{15}$	$C_{23}H_{31}Cl_2Cu_2N_8O_{14.5}$	$C_{28}H_{42}Cl_2Cu_2N_8O_{15}$
Formula weight	872.57	849.46	928.68
Crystal size (mm)	$1.2 \times 1.2 \times 0.9$	$0.8 \times 0.8 \times 0.6$	$0.8 \times 0.8 \times 0.4$
Crystal system	monoclinic	orthorhombic	triclinic
Space group	$P2_1/n$	*Pbcn*	$P\bar{1}$
a (pm)	1140.52(2)	2623.70(6)	1194.66(4)
b (pm)	2596.81(4)	2221.11(6)	1198.72(6)
c (pm)	2324.29(4)	2199.94(6)	1294.57(5)
α (°)	90	90	96.259(2)
β (°)	102.307(1)	90	97.187(3)
γ (°)	90	90	92.157(2)
V (nm^3)	6.7257(2)	12.8202(6)	1.82590(13)
Z	8	16	2
D_{calc} (Mg m^{-3})	1.723	1.761	1.689
μ (mm^{-1})	1.506	1.576	1.392
θ Range of data collection (°)	1.57, 27.48	1.20, 27.51	2.19, 27.46
Measured reflections	43983	62072	12193
Unique reflections (R_{int})	15388 (0.073)	14667 (0.092)	8108 (0.026)
Goodness-of-fit on F^2	1.035	1.030	1.036
R_1 ($I > 2\sigma(I)$)[a]	0.071	0.092	0.047
wR_2 (all data)[b]	0.198	0.250	0.122

[a] $R_1 = \sum||F_o| - |F_c||/\sum|F_o|$.
[b] $wR_2 = [\sum w(F_o^2 - F_c^2)^2/\sum w(F_o^2)^2]^{1/2}$.

3. Results and discussion

3.1. Synthesis and characterization

The two new ligands H_6ipa-hyhb and H_6ipa-hyhh were synthesized by Schiff base condensation of 2-methyl-4,6-diformylresorcinol (ipa) with two equivalents of the appropriate hydrazides in methanol (Scheme 2). The isophthalaldehyde derivative (ipa) was prepared by a new route with a modified Duff formylation [14] through *ortho*-formylation of 2-methylresorcinol with two equivalents of hexamethylenetetramine (HMTA) in trifluoroacetic acid (TFA). The isophthalaldehyde was isolated analytical pure in 54% overall yield. Reported synthetic routes obtained the aldehyde in lower overall yields of 9% [15] and 36% [16] in time-consuming multi-step-synthesis. Our synthesis is an efficient alternative to the reported literature procedures.



Scheme 2. Synthesis of the ligands H_6ipa-hyhb ($n = 2$) and H_6ipa-hyhh ($n = 4$); HMTA = hexamethylenetetramine.

Each ligand provides two tridentate [ONO] binding pockets with the phenolate oxygen atom, the imine nitrogen atom, and the carbonyl oxygen atom as potential donors. Furthermore, the hydroxyl groups of the alkyl side chains provide additional donors. Depending on the pH value of the solution the phenol groups, the amide groups, and the side chain hydroxyl groups can be deprotonated and therefore the ligands can adopt a variable di-, tetra- or hexaanionic protonation state. The reaction with two equivalents of $Cu(ClO_4)_2 \cdot 6\ H_2O$ in methanol in the presence of two equivalents of aqueous ammonia afforded dark green solutions. Subsequent addition of two equivalents of pyrazole results in the formation of $\{[Cu_2(H_4ipa\text{-}hyhb)(Hpz)_2](ClO_4)_2\}_n$ (**1**) and $\{[Cu_2(H_4ipa\text{-}hyhh)(Hpz)_2](ClO_4)_2\}_n$ (**3**) which can be isolated as green crystals of the corresponding solvent containing compounds **1** · *n*MeOH and **3** · *n*MeOH, respectively. The use of imidazole instead of pyrazole leads to complex $\{[Cu_2(H_4ipa\text{-}hyhb)(Him)_2](ClO_4)_2\}_n$ (**2**) isolated as green crystals of **2** · $\frac{n}{2}H_2O$. In all three complexes the ligands act in their dianionic form. Both phenolate groups are deprotonated, whereas the amide and the hydroxyl groups are still protonated.

The complexes were characterized by X-ray structural analysis, elemental analysis, and IR spectroscopy. The crystals of **1** · *n*MeOH and **3** · *n*MeOH lost the co-crystallized methanol molecules upon drying. The IR-spectra of both ligands exhibit two strong characteristic bands at 1667

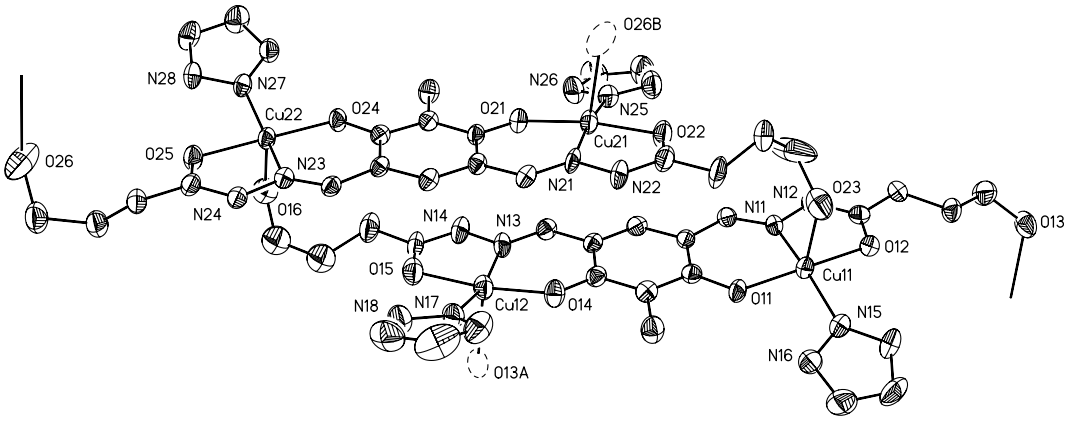


Fig. 1. Structure of the asymmetric unit of compound $\mathbf{1}\cdot n$MeOH. Symmetry-related atoms are labeled with index A and B. The perchlorate ions, methanol molecules and hydrogen atoms are omitted for clarity. Thermal ellipsoids are drawn at the 50% probability level.

and 1629 cm^{-1} (H_6ipa-hyhb) and 1663 and 1628 cm^{-1} (H_6ipa-hyhh), which can be attributed to amide I ($\nu_{C=O}$) and the imine stretching vibration ($\nu_{C=N}$). Both bands were shifted in all three complexes to approximately 1593 and 1565 cm^{-1} due to the coordination of the imine nitrogen atoms and the carbonyl oxygen atoms to the copper ions. In the spectra of the complexes a new strong characteristic broad band can be detected at 1121 cm^{-1} which is attributed to the stretching vibration of the perchlorate ions.

3.2. Description of the structures

3.2.1. $\{[Cu_2(H_4ipa\text{-}hyhb)(Hpz)_2](ClO_4)_2\}_n\cdot nMeOH$ ($\mathbf{1}\cdot n$MeOH)

The compound $\mathbf{1}\cdot n$MeOH crystallizes in the monoclinic space group $P2_1/n$ forming an one-dimensional coordination polymer built up by the dinuclear dicationic complex entities $[Cu_2(H_4ipa\text{-}hyhb)(Hpz)_2]^{2+}$ linked via apical coordination of the hydroxyl groups of both ligand side chains to two adjacent dinuclear complex units.

The molecular structure of the asymmetric unit as well as the atom numbering scheme of the heteroatoms is illustrated in Fig. 1. The asymmetric unit contains four crystallographically independent copper atoms embedded in two ligands. The two binding sites of each ligand are occupied by the copper ions Cu*i*1 and Cu*i*2 ($i = 1, 2$; running number assigned to the independent ligand moieties). The copper atoms are in a distorted square pyramidal coordination environment. The basal square planes are formed by the phenolate oxygen atoms O*i*1/O*i*4, the Schiff base nitrogen atoms N*i*1/N*i*3, the carbonyl oxygen atoms O*i*2/O*i*5, and the nitrogen atoms N*i*5/N*i*7 of the pyrazole co-ligands. The latter are coplanar with the bridging aromatic ligand. The apical positions at the copper ions are occupied by hydroxyl groups O*i*3/O*i*6 of the neighboring complex units. Each dinuclear unit is bound to two adjacent units, this coordination mode leads to the formation of a double hydroxyalkyl-bridged infinite chain structure.

Selected bond lengths and angles are summarized in Table 2. The donor-copper distances within the basal plane are similar for both complex entities and with 189–201 pm in the expected range [17]. The apical bond lengths vary from 225 to 241 pm and are significantly longer due to the weaker coordination of the hydroxyl oxygen atoms and the typical Jahn–Teller distortion of the copper(II) ion. These distances show significant differences for the two independent complex units with values of about 225–229 pm for Cu11–O23 and Cu12–O13A and a considerable elongation for the second moiety with values of about 240 pm (Cu21–O26B and Cu22–O16). Consequently, somewhat different coordination geometries are observed for the copper centers of the two ligand moieties within the asymmetric unit, which reflects in the variation of the τ parameters ($\tau = 0$ for an ideal tetragonal pyramid; $\tau = 1$ for an ideal trigonal bipyramid [18]) of the corresponding polyhedra ($\tau_{Cu11} = 0.11$, $\tau_{Cu12} = 0.14$, $\tau_{Cu21} = 0.03$, $\tau_{Cu22} = 0.02$).

The distance between the copper centers within the dinuclear complex entities across the resorcinol bridge is 827 pm, whereas the shortest non-covalent distances within the coordination chains are found at 465 (Cu11···Cu11A) and 491 pm (Cu22···Cu22A). For the separation between

Table 2
Selected bond lengths (pm) and angles (°) for $\{[Cu_2(H_4ipa\text{-}hyhb)(Hpz)_2](ClO_4)_2\}_n\cdot n$MeOH ($\mathbf{1}\cdot n$MeOH)

Cu11–O11	191.7(4)	Cu21–O21	190.5(3)
Cu11–O12	200.8(3)	Cu21–O22	199.6(4)
Cu11–O23	225.4(4)	Cu21–O26B	238.6(5)
Cu11–N11	192.1(4)	Cu21–N21	191.8(5)
Cu11–N15	195.5(4)	Cu21–N25	194.5(5)
Cu12–O14	190.6(4)	Cu22–O24	189.5(3)
Cu12–O15	198.9(4)	Cu22–O25	198.8(4)
Cu12–O13A	229.5(5)	Cu22–O16	240.5(5)
Cu12–N13	192.4(5)	Cu22–N23	193.5(4)
Cu12–N17	196.4(5)	Cu22–N27	196.2(4)
O11–Cu11–O12	171.43(16)	O21–Cu21–O22	171.36(18)
N11–Cu11–N15	164.77(19)	N21–Cu21–N25	169.97(20)
O14–Cu12–O15	172.17(18)	O24–Cu22–O25	171.35(16)
N13–Cu12–O17	164.39(20)	N23–Cu22–O27	163.37(19)

Symmetry transformations used to generate equivalent atoms: A = $x + 1$, y, z; B = $x + 1$, $y + 1$, z.

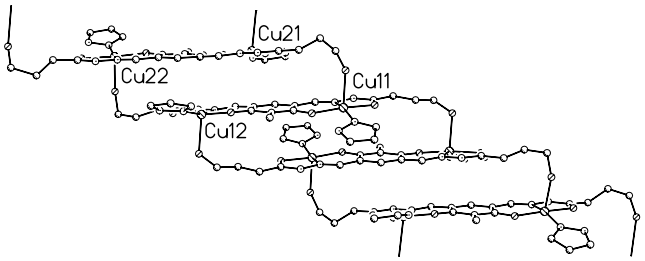


Fig. 2. Polymer structure of complex $\mathbf{1}\cdot n$MeOH. The perchlorate ions and methanol molecules as well as hydrogen atoms are omitted for clarity.

copper centers of adjacent coordination polymer chains distances of at least 706 pm are found. The two ligand molecules are nearly planar with a mean deviation of 5.2 pm for $i = 1$ and 6.0 pm for $i = 2$ from the best least square plane including the ligand atoms except the alkyl side chains. Moreover, the two distinct complex moieties assemble nearly coplanar with a distance of approximately 300 pm and an angle of about 3° between their normal vectors. Due to the coordination of the hydroxyl side chains to adjacent dinuclear complex entities the building blocks assemble to one-dimensional chains along the [0 1 0] direction of the unit cell, which is illustrated in Fig. 2. This results in the formation of a distorted ladder like cationic coordination polymer.

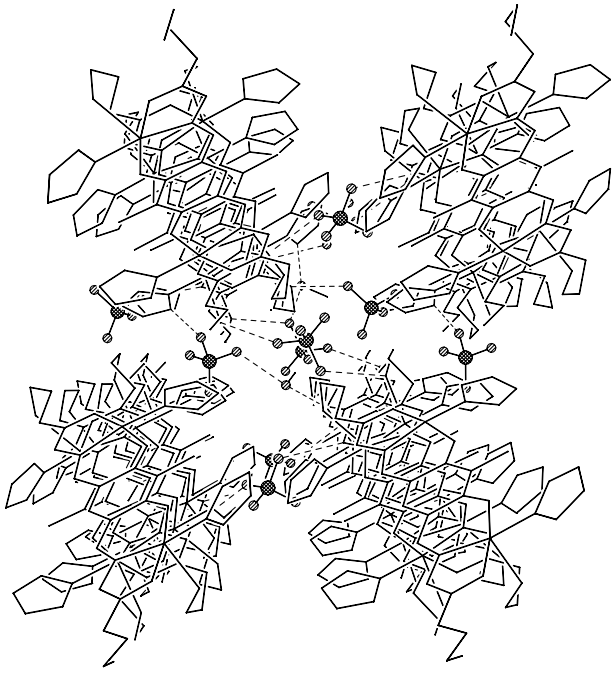


Fig. 3. Assembly of the coordination chains of compound $\mathbf{1}\cdot n$MeOH. View along the coordination chains in [0 1 0] direction. Hydrogen atoms are omitted for clarity. Dashed lines indicate the hydrogen bonds.

In the crystal packing the cationic chains assemble parallel as depicted in Fig. 3. The perchlorate ions located between the chains are cross-linking them by hydrogen bond interactions forming a 3D supramolecular assembly. The perchlorate ions interact through their oxygen atoms via O13–H···O–Cl–O···H–O26 with the protonated hydroxyl groups of the ligand side chains of two adjacent coordination chains. Additional hydrogen bonding links are established through the perchlorate ions by interaction with the amide groups N*i*2–H, N*i*4–H and the uncoordinated pyrazole amine N18–H via O16–H···O–Cl–O···H–N24, N22–H···O–Cl–O···H–N14 and N18–H···O–Cl–O···H–N12.

3.2.2. $\{[Cu_2(H_4ipa\text{-}hyhb)(Him)_2](ClO_4)_2\}_n\cdot\frac{n}{2}H_2O$-($\mathbf{2}\cdot\frac{n}{2}H_2O$)

Reaction of ligand H_6ipa-hyhb with $Cu(ClO_4)_2\cdot 6H_2O$ using imidazole instead of pyrazole results in the formation of a distorted ladder like polymer structure analogous to complex **1**. Complex **2** crystallizes together with one molecule of water per two building block units in the orthorhombic space group *Pbcn*. Again the asymmetric unit contains two independent dinuclear complex fragments, double linked over the hydroxyl oxygen atoms of the side chains as shown in Fig. 4.

Each copper ion is coordinated in the basal plane by the [ONO] ligand binding pocket and the nitrogen atom of the imidazole co-ligand. The apical position is occupied by a hydroxyl oxygen atom. The bond lengths, angles, and dis-

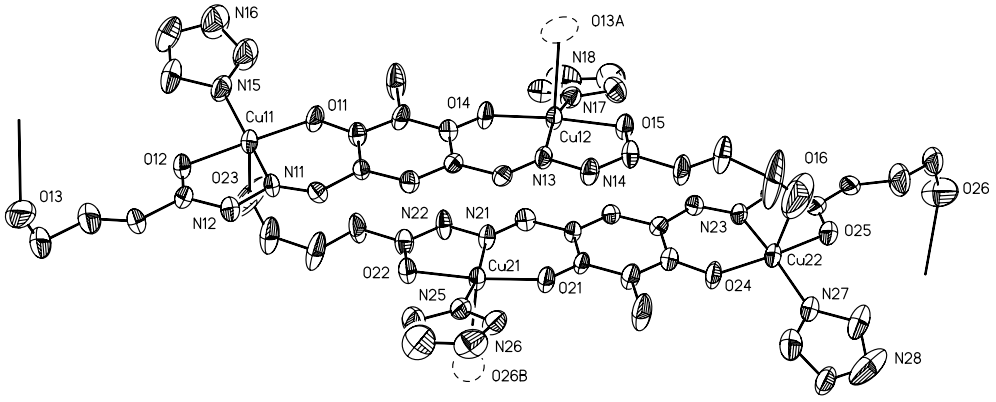


Fig. 4. Structure of the asymmetric unit of compound $\mathbf{2}\cdot\frac{n}{2}H_2O$. Symmetry-related atoms are labeled with index A and B. The perchlorate ions, water molecules and hydrogen atoms are omitted for clarity. Thermal ellipsoids are drawn at the 50% probability level.

tances within the dinuclear complex units are comparable with those of complex **1** (see supporting information). The distances between the axial hydroxyl oxygen atoms and the copper ions (Cu11–O23 247.7, Cu12–O13 246.6, Cu21–O26 261.9, and Cu22–O16 245.0 pm) are significant longer than those to the donor atoms within the basal plane. Therefore, the coordination environment of the copper ions can be best described as (4 + 1) square pyramidal with a weak apical coordination of the hydroxyl oxygen atoms of adjacent dinuclear complex units ($\tau_{Cu11} = 0.12$, $\tau_{Cu12} = 0.15$, $\tau_{Cu21} = 0.08$, $\tau_{Cu22} = 0.10$). All copper centers exhibit small displacements from the best fit mean planes given by the corresponding four basal donor atoms of 16.5 (Cu11), 14.3 (Cu12), 11.9 (Cu21), and 14.2 pm (Cu22) towards the apical position. Within the dinuclear units one copper center is situated above and one below the ligand mean plane defined by all ligand atoms except the hydroxyalkyl side chains. The related absolute displacements of the copper centers from this plane are larger for Cu12 and Cu22 (about 11 pm) as compared to Cu11 (3.9 pm) and Cu21 (0.6 pm), which approximately lie within this plane. In analogy to complex **1** the cationic dinuclear complex units generating the 1D coordination polymer are nearly coplanar (see Fig. 5).

The perchlorate counterions are involved in a hydrogen bonding network which is somewhat different to what is observed for compound **1** · *n*MeOH due to the replacement of the co-ligand by imidazole. Nevertheless, also in this case the 1D coordination chains running along the [1 0 0] direction assemble parallel as depicted in Fig. 6.

3.2.3. {[Cu_2(H_4ipa-hyhh)(Hpz)$_2$](ClO_4)$_2$}$_n$ · *n*MeOH (**3** · *n*MeOH)

The complex cation within the asymmetric unit of the polymeric compound {[Cu_2(H_4ipa- hyhh)(Hpz)$_2$](ClO_4)$_2$}$_n$ · *n*MeOH (**3** · *n*MeOH) is illustrated in Fig. 7. The corresponding bond lengths and angles are given in Table 3. In analogy to compounds **1** and **2** two copper ions are coordinated by one doubly deprotonated ligand molecule, but in contrast to **1** and **2** only one ligand moiety is present in the asymmetric unit.

Both copper centers are coordinated by the phenolate oxygen atoms O1/O4, the Schiff base nitrogen atoms N1/N3, and the carbonyl oxygen atoms O2/O5 of the ligand. The fourth position in the basal plane is occupied by the nitrogen atoms N5/N7 of the pyrazole co-ligands. In the apical position at Cu1 a perchlorate ion is weakly bound through the oxygen atom O14 at a distance of 252 pm, whereas the apical position at Cu2 is occupied by the

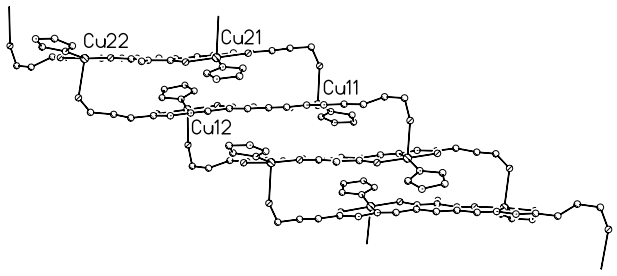


Fig. 5. Polymer structure of compound **2** · $\frac{n}{2}H_2O$. The perchlorate ions and water molecules as well as hydrogen atoms are omitted for clarity.

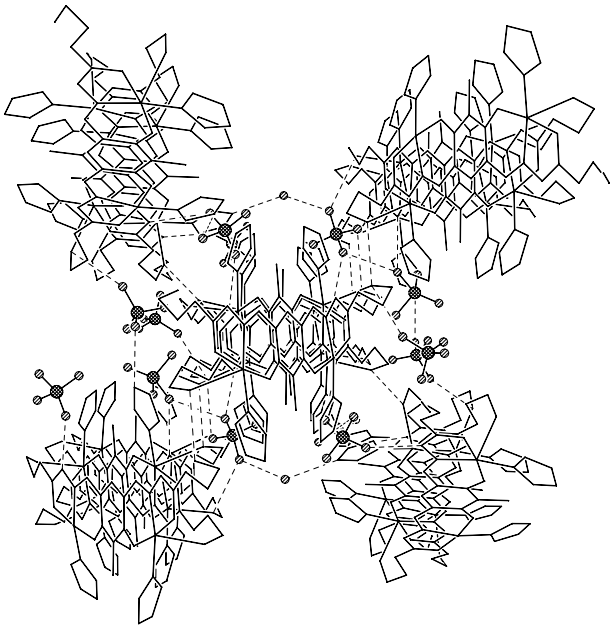


Fig. 6. Assembly of the coordination chains of compound **2** · $\frac{n}{2}H_2O$. View along the coordination chains in [1 0 0] direction. Hydrogen atoms are omitted for clarity. Dashed lines indicate the hydrogen bonds.

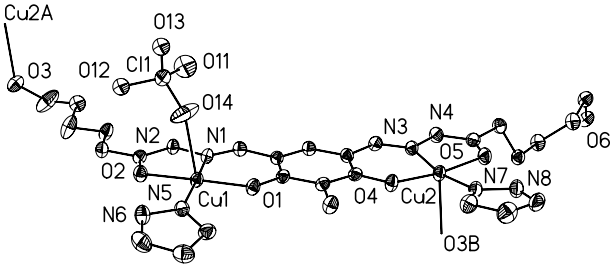


Fig. 7. Structure of the asymmetric unit of compound **3** · *n*MeOH. Symmetry-related atoms are labeled with the index A and B. The second non-coordinated perchlorate ion as well as the methanol molecule and hydrogen atoms are omitted for clarity. Thermal ellipsoids are drawn at the 50% probability level.

Table 3
Selected bond lengths (pm) and angles (°) for {[Cu_2(H_4ipa-hyhh)(Hpz)$_2$]-(ClO_4)$_2$}$_n$ · *n*MeOH (**3** · *n*MeOH)

Cu1–O1	189.9(2)	Cu2–O4	190.6(2)
Cu1–O2	199.0(2)	Cu2–O5	200.3(2)
Cu1–O14	252.2(1)	Cu2–O3B	240.9(3)
Cu1–N1	191.3(3)	Cu2–N3	191.9(3)
Cu1–N5	195.2(3)	Cu2–N7	195.3(3)
O1–Cu1–O2	171.9(1)	O4–Cu2–O5	172.2(1)
N1–Cu1–N5	174.8(1)	N3–Cu2–O7	167.9(1)

Symmetry transformations used to generate equivalent atoms: B = $x - 1$, y, $z - 1$.

hydroxyl oxygen atom O3 of an adjacent building block with a bond distance of 240 pm. The copper ions Cu1 and Cu2 lie approximately within the basal plane of their square-pyramidal coordination polyhedra with a displacement of 6.6 ($\tau = 0.07$) and 12.9 pm towards the apical position ($\tau = 0.04$), respectively.

The dinuclear copper complex cations $[Cu_2(H_4ipahyhh)(Hpz)_2]^{2+}$ assemble to 1D coordination chains linked through the hydroxyl group O3 of one of the two ligand side chains. The 1D coordination polymers are arranged along the [1 0 1] direction of the unit cell. As depicted in Fig. 8 two such chains are cross-linked via hydrogen bonds between the hydroxyl oxygen atom O6 and the amid nitrogen atom N2 of two adjacent chains (O6···N2 278 pm).

The individual dinuclear building blocks of adjacent double chains are stacked through π–π interactions at a distance of about 350 pm as shown in Fig. 9. This leads to a interlaced zipper-like arrangement of the hydrogen bonded double chains. The stacked double chains are further linked by hydrogen bonding interactions between the oxygen atoms of the weakly bound perchlorate ion and the pyrazole nitrogen atom N8 as well as the hydroxyl oxygen atom O6 (O11···N8 282 and O13···O6 283 pm). The second perchlorate counterion is not involved in this network and shows a disorder of all oxygen atoms typical for non-bounded perchlorate ions.

3.3. Magnetochemistry

The magnetization of polycrystalline samples of the compounds **1**, $\mathbf{2}\cdot\frac{n}{2}H_2O$, and **3** were measured in the temperature range between 2 and 300 K. For **1** the temperature dependence of the paramagnetic molar susceptibility χ_M, which is based on the constituting dinuclear building block, and its product with temperature $\chi_M T$ are depicted in Fig. 10. A similar magnetic behavior is observed for the compounds $\mathbf{2}\cdot\frac{n}{2}H_2O$ and **3**. The experimental $\chi_M T$ values at 300 K of 0.88 $cm^3\,K\,mol^{-1}$ for **1**, 0.93 $cm^3\,K\,mol^{-1}$ for $\mathbf{2}\cdot\frac{n}{2}H_2O$, and 0.86 $cm^3\,K\,mol^{-1}$ for **3** are characteristic for the spin-only value of two independent copper(II) ions. Upon lowering the temperature $\chi_M T$ slightly decreases down to 0.75 $cm^3\,K\,mol^{-1}$ at 50 K. Further lowering the temperature leads to a rapid decreases of $\chi_M T$ approaching values close to zero. This behavior is characteristic for an antiferromagnetic coupling between the copper centers with an $S = 0$ ground state.

In order to explain the magnetic properties the experimental $\chi_M T$ data were first analyzed with the alternating chain model derived from the spin Hamiltonian given in Eq. (1) [19,20].

$$\hat{H} = -J\sum_{i=1}^{n/2}[\hat{S}_{A_{2i}}\cdot\hat{S}_{A_{2i-1}} + \alpha\hat{S}_{A_{2i}}\cdot\hat{S}_{A_{2i+1}}]. \quad (1)$$

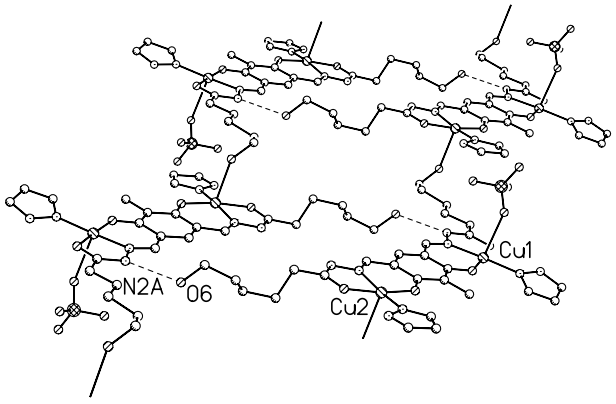


Fig. 8. Double chain structure of compound $\mathbf{3}\cdot n$MeOH. The perchlorate ions as well as the methanol molecules and hydrogen atoms are omitted for clarity. Dashed lines indicate the hydrogen bond O6···N2 (278 pm). The chains run along the [1 0 1] direction of the unit cell.

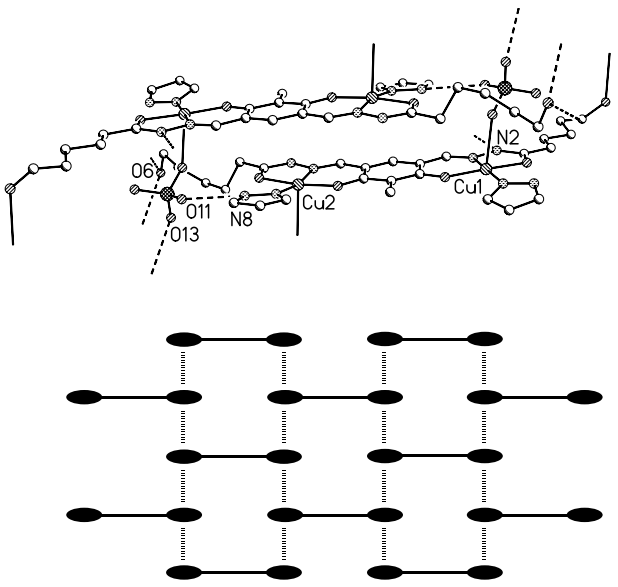


Fig. 9. Top: π–π Stacking and hydrogen bonding interactions between building block units of adjacent double chains of compound $\mathbf{3}\cdot n$MeOH (cf. Fig. 8); dashed lines indicate hydrogen bonds. Bottom: Schematic representation of the arrangement of the hydrogen bonded double chains; the dumb bells represent the 1D coordination polymers linked to double chains; depicted with view along the chains.

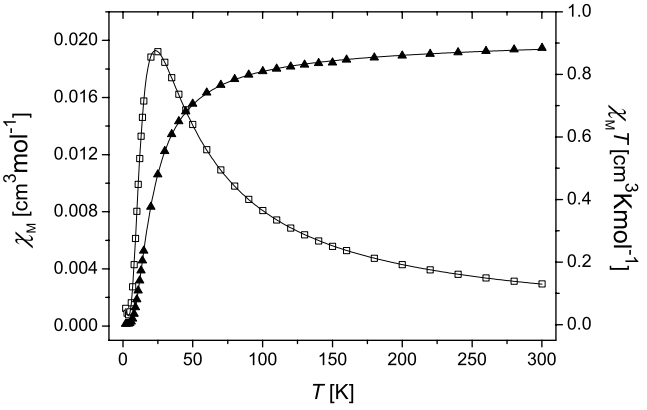


Fig. 10. Plots of χ_M (□) and $\chi_M T$ (▲) vs. T for compound **1**. The corresponding fit functions according to Eq. (2) are drawn as solid lines (for parameters see text and Table 4).

Using the numerical expression reported by Hatfield et al. ($n = 10$ and $S = 1/2$ for data with $T > 9.4$ K) [20] the best fit for compound **1** leads to $J = -26.2\ \mathrm{cm}^{-1}$, $\alpha J = -0.4\ \mathrm{cm}^{-1}$ ($\alpha = 0.016$), $g = 2.20$, and $\chi_{tip} = 2 \times 10^{-5}\ \mathrm{cm}^3\ \mathrm{mol}^{-1}$ with a coefficient of determination of $r^2 = 0.99991$. Herein the J value is assumed to represent the exchange interaction between two copper(II) ions via the resorcinol bridge, whereas the αJ value can be assigned to exchange interaction with adjacent building blocks linked through the hydroxyalkyl side chains of the ligand. The very small values of αJ are consistent with the fact that no efficient exchange pathway (e.g. superexchange or spinpolarisation) is possible along the bridging hydroxyalkyl side chains. Moreover, any kind of through space interaction within the examined temperature range is prohibited by the interatomic distances between non-covalently linked copper centers within and across polymeric chains.

Therefore, the magnetic data were analyzed with the Bleaney–Bowers equation for isolated dinuclear copper(II) complexes ($\hat{H} = -J \cdot \hat{S}_1 \cdot \hat{S}_2$ with $S_1 = S_2 = 1/2$) [21]. The contribution of the paramagnetic impurity (ρ) with $S = 1/2$ as well as the temperature independent paramagnetism (χ_{tip}) were also taken into account according to Eq. (2).

$$\chi_M T = \frac{2N_A g_{eff}^2 \beta^2}{k_B} \left[\frac{(1-\rho)}{\left[3 + e^{\frac{-J}{k_B T}}\right]} + \frac{\rho}{4} \right] + \chi_{tip} T. \qquad (2)$$

The best fit obtained for compound **1** resulted in $J = -26.1\ \mathrm{cm}^{-1}$, $g = 2.18$, $\chi_{tip} = 4 \times 10^{-5}\ \mathrm{cm}^3\ \mathrm{mol}^{-1}$, and $\rho = 0.0026$ with $r^2 = 0.99998$. These values are in very good agreement with those obtained by the fit for the alternating chain model, even leading to a somewhat better coefficient of determination. Therefore, the latter analysis, which is solely based on interactions within the building blocks, was also adopted for compounds $\mathbf{2} \cdot \frac{n}{2}H_2O$ and **3** for which the fit parameters are listed in Table 4.

The exchange coupling constants J are the same for the two dinuclear building blocks with coordinated pyrazole present in **1** and **3**, whereas the coupling is slightly more antiferromagnetic in the case of imidazole as co-ligand as found in compound $\mathbf{2} \cdot \frac{n}{2}H_2O$. To the best of our knowledge there is only one report describing magnetic properties of similarly bridged dinuclear copper(II) complexes with double Schiff-base ligands of 4,6-diacetylresorcinol [6]. These complexes also show antiferromagnetic exchange interactions with a Weiss constants θ ranging from -10 to -20 K depending on the utilized amine ligand side chains.

Table 4
Fit parameters for the magnetic data of the complexes **1**–**3** according to the Bleaney–Bowers equation

Compound	J (cm^{-1})	g_{eff}	ρ	χ_{tip} (cm^3/mol)	r^2
1	−26.12(6)	2.186(1)	0.0026(7)	4×10^{-5}	0.99998
$\mathbf{2} \cdot \frac{n}{2}H_2O$	−28.25(4)	2.193(1)	0.0020(5)	21×10^{-5}	0.99998
3	−26.50(5)	2.171(1)	0.0065(6)	2×10^{-5}	0.99998

Regression of the Curie plots of the compounds **1**–**3** resulted in θ values of about -17 K in all three cases, which is clearly within the reported range. The observed antiferromagnetic behavior can be explained by an intramolecular spin-exchange interaction within the dinuclear complex moieties through the π-pathway of the resorcinol bridge without significant magnetic exchange interactions between adjacent building blocks of the coordination polymer chains.

4. Conclusions

Three polymeric copper(II) complexes were synthesized with two novel double Schiff-base ligands providing two equal [ONO] binding pockets. The dinuclear building blocks, in which the copper ions are linked through a resorcinol bridge, possess additional ω-hydroxyalkyl groups. With pyrazole or imidazole as co-ligands at the copper(II) ions 1D cationic chains are formed, which are linked through an apical coordination of the hydroxyl groups of adjacent building blocks at the copper centers. Depending on the length of the ligand side chains the dinuclear building blocks are assembled to coordination chains of different topology. Due to their cationic nature, the resulting infinite 1D coordination chains are cross-linked by hydrogen bonding interaction with their perchlorate counterions. For **3** additional π–π interactions lead to a stacking of the building block units. The complexes are the first examples exhibiting these types of polymeric 1D topologies. Further studies regarding supramolecular network structures with ligands providing other side chains are under investigation. Temperature-dependent magnetic measurements show antiferromagnetic exchange interactions between the copper(II) centers within the dinuclear building blocks through the π-system of the central resorcinol moiety.

Acknowledgments

We thank the Deutsche Forschungsgemeinschaft (SPP 1137 "Molecular Magnetism") for financial support. D.P. gratefully acknowledges the support by a Graduiertenstipendium of the Freistaat Thüringen.

Appendix A. Supplementary material

CCDC 641597, 641598, and 641599 contain the supplementary crystallographic data for $\mathbf{1} \cdot n$MeOH, $\mathbf{2} \cdot \frac{n}{2}H_2O$, and $\mathbf{3} \cdot n$MeOH. These data can be obtained free of charge via http://www.ccdc.cam.ac.uk/conts/retrieving.html, or from the Cambridge Crystallographic Data Centre, 12 Union Road, Cambridge CB2 1EZ, UK; fax: (+44) 1223-336-033; or e-mail: deposit@ccdc.cam.ac.uk. Supplementary data associated with this article can be found, in the online version, at doi:10.1016/j.poly.2007.06.013.

References

[1] (a) S. Kitagawa, R. Kitaura, S.-i. Noro, Angew. Chem. Int. Ed. 43 (2004) 2334;
(b) C. Janiak, Dalton Trans. (2003) 2781;
(c) O.M. Yaghi, H. Li, C. Davis, D. Richardson, T.L. Groy, Acc. Chem. Res. 31 (1998) 474.

[2] (a) B. Moulton, M.J. Zaworotko, Chem. Rev. 101 (2001) 1629;
(b) M. Eddaoudi, D.B. Moler, H. Li, B. Chen, T.M. Reineke, M. OḰeeffe, O.M. Yaghi, Acc. Chem. Res. 34 (2001) 319;
(c) C.N.R. Rao, S. Natarajan, R. Vaidhyanathan, Angew. Chem. Int. Ed. 43 (2004) 1466;
(d) C.-T. Chen, K.S. Suslick, Coord. Chem. Rev. 128 (1993) 293;
(e) E. Holder, B.M.W. Langeveld, U.S. Schubert, Adv. Mater. 17 (2005) 1109;
(f) W. Plass, Chem. Zeit 32 (1998) 323;
(g) O. Kahn, Acc. Chem. Res. 33 (2000) 647–657.

[3] R.W. Gable, B.F. Hoskins, R. Robson, J. Chem. Soc., Chem. Commun. (1990) 1677.

[4] A. Roth, D. Koth, M. Gottschaldt, W. Plass, Cryst. Growth Des. 6 (2006) 2655.

[5] (a) A. Zharkouskaya, A. Buchholz, W. Plass, Eur. J. Inorg. Chem. (2005) 3400;
(b) A. Zharkouskaya, H. Görls, G. Vaughan, W. Plass, Inorg. Chem. Commun. 8 (2005) 1145;
(c) A.E. Ion, E.T. Spielberg, H. Görls, W. Plass, Inorg. Chim. Acta 360 (2007), doi:10.1016/j.ica.2007.04.014.

[6] N. Manada, H. Okawa, S. Kida, Bull. Chem. Soc. Japan 48 (1975) 64.

[7] (a) A. Taha, Spectrochim. Acta A 59 (2003) 1611;
(b) H.S. Seleem, B.A. El-Shetary, S.M.E. Khalil, M. Mostafa, M. Shebl, J. Coord. Chem. (2005) 479;
(c) A.A.A. Emara, A.A.A. Abou-Hussen, Spectrochim. Acta A 64 (2006) 1010;
(d) A.A.A. Abu-Hussen, J. Coord. Chem. 59 (2006) 157.

[8] (a) M.F. Iskander, A.M. El-Aggan, L.S. Refaat, L. El-Sayed, Inorg. Chim. Acta 14 (1975) 167;
(b) A.A. Aruffo, T.B. Murphy, D.K. Johnson, N.J. Rose, V. Schomaker, Inorg. Chim. Acta 67 (1982) L25;
(c) L. Pickart, W.H. Goodwin, W. Burgua, T.B. Murphy, D.K. Johnson, Biochem. Pharmacol. 32 (1983) 3868;
(d) A.A. Aruffo, T.B. Murphy, D.K. Johnson, N.J. Rose, V. Schomaker, Acta Crystallogr., Sect. C 40 (1984) 1164;
(e) S.C. Chan, L.L. Koh, P.-H. Leung, J.D. Ranford, K.Y. Sim, Inorg. Chim. Acta 236 (1995) 101;
(f) E.W. Ainscough, A.M. Brodie, A.J. Dobbs, J.D. Ranford, J.M. Waters, Inorg. Chim. Acta 267 (1998) 27;
(g) L.L. Koh, O.L. Kon, K. Loh, Y.C. Long, J.D. Ranford, A.L.C. Tan, Y.Y. Tjan, J. Inorg. Biochem. 72 (1998) 155;
(h) N.R. Sangeetha, K. Baradi, R. Gupta, C.K. Pal, V. Manivannan, S. Pal, Polyhedron 18 (1999) 1425;
(i) E.W. Ainscough, A.M. Brodie, W.A. Denny, G.J. Finlay, S.A. Gothe, J.D. Ranford, J. Inorg. Biochem. 77 (1999) 125;
(j) M.F. Iskander, T.E. Khalil, R. Werner, W. Haase, I. Svoboda, H. Fuess, Polyhedron 19 (2000) 1181;
(k) V.V. Lukov, Y.P. Tupulova, V.A. Kogan, L.D. Popov, Russ. J. Coord. Chem. 29 (2004) 335;
(l) M.F. Iskander, L. El-Sayed, N.M.H. Salem, W. Haase, H.J. Linder, S. Foro, Polyhedron 13 (2004) 23.

[9] (a) W. Plass, A. Pohlmann, H.-P. Yozgatli, J. Inorg. Biochem. 80 (2000) 181;
(b) W. Plass, H.-P. Yozgatli, Z. Anorg. Allg. Chem. 629 (2003) 65;
(c) J. Becher, I. Seidel, W. Plass, D. Klemm, Tetrahedron 62 (24) (2006) 5675;
(d) S. Nica, M. Rudolph, H. Görls, W. Plass, Inorg. Chim. Acta 360 (2007) 1743;
(e) M. Mancka, W. Plass, Inorg. Chem. Commun. 10 (2007) 677;
(f) I. Lippold, H. Görls, W. Plass, Eur. J. Inorg. Chem. (2007) 1487.

[10] (a) W. Plass, Coord. Chem. Rev. 237 (2003) 205;
(b) S. Nica, A. Pohlmann, W. Plass, Eur. J. Inorg. Chem. (2005) 2032;
(c) A. Pohlmann, S. Nica, T.K.K. Luong, W. Plass, Inorg. Chem. Commun. 8 (2005) 289.

[11] (a) A. Roth, A. Buchholz, W. Plass, Z. Anorg. Allg. Chem. 633 (2007) 383;
(b) A. Roth, A. Buchholz, M. Gärtner, A. Malassa, H. Görls, G. Vaughan, W. Plass, Z. Anorg. Allg. Chem. 633 (2007), doi:10.1002/zaac.200700249.

[12] (a) SMART COLLECT, Data Collection Software, Nonius B.V., Netherlands;
(b) SMART, Software for the CCD Detektor System, version 5.05: Bruker AXS: Madison, WI.

[13] G.M. Sheldrick, SHELXS97 and SHELXL97, University of Göttingen, Germany.

[14] (a) J.C. Duff, J. Chem. Soc. (1945) 276;
(b) J.C. Duff, E.J. Bills, J. Chem. Soc. (1934) 1305;
(c) J.C. Duff, E.J. Bills, J. Chem. Soc. (1932) 1987;
(d) L.F. Lindoy, G.V. Meehan, N. Svenstrup, Synthesis 7 (1998) 1029.

[15] L.R. Worden, A.W. Burgstahler, K.D. Kaufmann, J.A. Weis, T.K. Schaaf, J. Heterocycl. Chem. 6 (1969) 191.

[16] L.R. Worden, K.D. Kaufman, P.J. Smith, G.N. Widiger, J. Chem. Soc. (C) (1970) 227.

[17] (a) W. Plass, A. Pohlmann, J. Rautengarten, Angew. Chem. Int. Ed. 40 (2001) 4207;
(b) A. Burkhardt, A. Buchholz, H. Görls, W. Plass, Eur. J. Inorg. Chem. (2006) 3400;
(c) A. Roth, J. Becher, C. Herrmann, H. Görls, G. Vaughan, M. Reiher, D. Klemm, W. Plass, Inorg. Chem. 45 (2006) 10066.

[18] A.W. Addison, T.N. Rao, J. Reedijk, J. van Rijn, J.C. Verschoor, J. Chem. Soc., Dalton Trans. (1984) 1349.

[19] (a) O. Kahn, Molecular Magnetism, VCH-Wiley, Weinheim, 1993;
(b) W. Duffy, K.P. Barr, Phys. Rev. 165 (1968) 647.

[20] J.W. Hall, W.E. Marsh, R.R. Weller, W.E. Hatfield, Inorg. Chem. 20 (1981) 1933.

[21] B. Bleaney, K.D. Bowers, Proc. Roy. Soc. (London) Ser. A 214 (1952) 451.

polymers are synthesized. The results of single-crystal X-ray diffraction reveal that $[Pr(mal)(OH)(bipy)\cdot 2H_2O]_n$ (**1**) is a 1-D helical chain with seven-coordinated Pr centers, which is the first sample with a seven coordination number in light lanthanide ionic complexes with carboxylic acids. $\{[Dy^1(SBA)_3(H_2O)_2][Dy^2(SBA)_3(H_2O)_2]\cdot 4H_2O\}_n$ (**2**) forms a 1-D chain-like molecular structure containing two crystallographically unique dysprosium centers, the Dy^1 center is seven-coordinated while Dy^2 is eight-coordinated, which is the first example with a seven coordination number in lanthanide benzene–carboxylate complex systems. Both of $\{[Tb(OHnic)(Onic)(H_2O)_5\cdot(OHnicH)]\cdot H_2O\}_n$ (**3**) and $\{[Sm(OHnic)(Onic)(H_2O)_5\cdot(OHnicH)]\cdot H_2O\}_n$ (**4**) exhibit an interesting 1-D chain-like polymeric structure in which there exist three types of 6-OHnicH ligands, which is rare for lanthanide carboxylate complexes.

Moreover, the photophysical properties of these complexes were studied with ultraviolet absorption spectra, fluorescence excitation and emission spectra. Since hydrothermal products are usually stable and insoluble in common solvents arising from their polymeric structures, both complexes **1** and **2** may be potential candidates for photoactive materials. Especially, for all four complexes, their molecules contain modifiable functional groups such as hydroxyl and sulfo, so they may be used as precursors to synthesize luminescent lanthanide organic-inorganic hybrid materials [42–44].

2. Experimental

2.1. Preparation of complexes

$Ln(NO_3)_3\cdot 6H_2O$ (Ln = Pr, Sm, Tb, Dy) were prepared by dissolving their respective oxides in concentrated nitric acid followed by drying. Maleic acid, 4-sulfobenzoic acid, 6-hydroxynicotinic acid and 2,2′-bipyridine were purchased from Aldrich and were used without further purification. All the other reagents were commercially available and were used as received.

2.1.1. $[Pr(mal)(OH)(bipy)\cdot 2H_2O]_n$ (**1**)

$Pr(NO_3)_3\cdot 6H_2O$ (0.3 mmol), maleic acid (0.45 mmol) and 2,2′-bipyridine (0.3 mmol) were mixed in 15 mL deionized water, and the pH value of the resulting solution was adjusted to be about 6.5 with 0.2 M NaOH solution. After stirring for half an hour, the mixture was placed in a 25 mL Teflon-lined reactor and heated at 160 °C in an oven for 3 days and then slowly cooled to room temperature by air cooling, and well-shaped light colorless single crystals of complex **1** suitable for X-ray single crystal diffraction analysis were obtained. *Anal.* Calc. for $C_{28}H_{30}N_4O_{14}Pr_2$ (928.38): C, 36.19; H, 3.23; N, 6.03. Found: C, 36.01; H, 3.28; N, 5.98%. The IR spectrum exhibits a pattern of bands in the range 4000–400 cm^{-1}: 1423 cm^{-1} ($\nu_s(COO^-)$), 1562 cm^{-1} ($\nu_{as}(COO^-)$).

2.1.2. $\{[Dy^1(SBA)_3(H_2O)_2][Dy^2(SBA)_3(H_2O)_2]\cdot 4H_2O\}_n$ (**2**)

$Dy(NO_3)_3\cdot 6H_2O$ (0.3 mmol) and 4-sulfobenzoic acid (0.9 mmol) were mixed in 15 mL deionized water, and the pH value of the resulting solution was adjusted to be about 6.5 with 0.2 M NaOH solution. After stirring for half an hour, the mixture was placed in a 25 mL Teflon-lined reactor and heated at 160 °C in an oven for 3 days and then slowly cooled to room temperature by air cooling, and well-shaped light colorless single crystals of complex **2** suitable for X-ray single crystal diffraction analysis were obtained. *Anal.* Calc. for $C_{42}H_{46}Dy_2O_{38}S_6$ (1116.15): C, 45.16; H, 4.12. Found: C, 44.96; H, 4.18%. The IR spectrum exhibits a pattern of bands in the range 4000–400 cm^{-1}: 1409 cm^{-1} ($\nu_s(COO^-)$), 1554 cm^{-1} ($\nu_{as}(COO^-)$).

2.1.3. $\{[Ln(OHnic)(Onic)(H_2O)_5\cdot(OHnicH)]\cdot H_2O\}_n$ [Ln = Tb (**3**), Sm (**4**)]

The corresponding lanthanide complexes with 6-OHnicH were prepared by homogeneous precipitation. A stoichiometric amount of lanthanide nitrate $Ln(NO_3)_3\cdot 6H_2O$ (0.5 mmol) and 6-OHnicH acid (1.5 mmol) were dissolved in deionized water and 95% C_2H_5OH, respectively. The pH value of the 6-OHnicH ethanol solution was adjusted to be about 6.5 with 0.2 M NaOH solution. Then the 6-OHnicH acid ethanol solution was added dropwise to the $Ln(NO_3)_3$ aqueous solution and the mixed solution was stirred for 4 h. The resulting solution was filtered and the filtrate was allowed to stand at room temperature. After three weeks, well-shaped light colorless single crystals suitable for analysis were obtained. Data of the Tb complex (**3**): *Anal.* Calc. for $C_{18}H_{24}N_3O_{15}Tb$ (678.30): C, 31.63; H, 3.51; N, 6.15. Found: C, 31.94; H, 3.39; N, 6.08%. The IR spectrum exhibits a pattern of bands in the range 4000–400 cm^{-1}: 1411 cm^{-1} ($\nu_s(COO^-)$), 1544 cm^{-1} ($\nu_{as}(COO^-)$). Data of the Sm complex (**4**): *Anal.* Calc. for $C_{18}H_{24}N_3O_{15}Sm$ (672.75): C, 32.11; H, 3.57; N, 6.24. Found: C 32.31; H, 3.52; N, 6.18%. The IR spectrum exhibits a pattern of bands in the range 4000–400 cm^{-1}: 1411 cm^{-1} ($\nu_s(COO^-)$), 1544 cm^{-1} ($\nu_{as}(COO^-)$).

2.2. Measurements and apparatus

Elemental analyses (C, H, N) were determined with an Elementar Cario EL elemental analyzer. IR spectra were recorded with a Nicolet Nexus 912 AO446 spectrophotometer (KBr pellet), in the 4000–400 cm^{-1} region. Ultraviolet absorption spectra were measured using an Agilent 8453 spectrophotometer. The luminescence (excitation and emission) spectra for the solid complex samples at room temperature and low temperature (77 K) were determined with a Perkin–Elmer LS-55 spectrophotometer, the whole excitation and emission slit widths were 10 and 5 nm, respectively. The phosphorescence spectrum was determined with a Perkin–Elmer LS-55 spectrophotometer.

Table 1
Crystal data and structure refinement for complexes **1**, **2**, **3** and **4**

Complex	**1**	**2**	**3**	**4**
Formula	$C_{28}H_{30}N_4O_{14}Pr_2$	$C_{42}H_{46}Dy_2O_{38}S_6$	$C_{18}H_{24}N_3O_{15}Tb$	$C_{18}H_{24}N_3O_{15}Sm$
Relative molecular weight M	928.38	1116.15	678.30	672.75
Temperature (K)	298(2)	293(2)	293(2)	293(2)
Wavelength (Å)	0.71073	0.71073	0.71073	0.71073
Radiation	Mo Kα	Mo Kα	Mo Kα	Mo Kα
Crystal system	$P2_1/c$	$P\bar{1}$	$P\bar{1}$	$P\bar{1}$
Space group	monoclinic	triclinic	triclinic	triclinic
Unit dimensions				
a (Å)	8.084(2)	13.888(6)	7.1019(17)	7.130(4)
b (Å)	8.805(2)	14.263(7)	10.243(2)	10.287(5)
c (Å)	23.260(6)	16.014(7)	16.654(4)	16.702(8)
α (°)		100.144(7)	73.768(3)	73.543(7)
β (°)	91.181(4)	111.756(6)	88.109(3)	88.191(7)
γ (°)		93.796(7)	88.074(3)	88.176(7)
Volume (Å^3)	1655.3(8)	2870(2)	1174.0(10)	1174.0(10)
Z	2	2	2	2
D_{calc} (Mg/m^3)	1.863	1.292	1.938	1.903
$F(000)$	912	1100	670	670
θ Range for data collection (°)	1.75–25.01	1.40–25.01	2.07–26.01	2.54–25.01
Reflections/collected/unique (R_{int})	6728/2915 (0.0210)	11 761/9759 (0.0405)	5331/4456 (0.0177)	5012/4105 (0.0366)
Refinement method	full-matrix least-squares on F^2	full-matrix least-squares on F^2	full-matrix least-squares on F^2	full-matrix least-squares on F^2
Data/restraints/parameters	2915/7/237	9759/6/798	4456/0/382	4105/0/346
Goodness-of-fit on F^2	1.088	1.082	1.074	1.063
Final R indices [$I > 2\sigma(I)$]	$R_1 = 0.0480$, $wR_2 = 0.1600$	$R_1 = 0.0456$, $wR_2 = 0.1072$	$R_1 = 0.0273$, $wR_2 = 0.0695$	$R_1 = 0.0524$, $wR_2 = 0.1269$
Largest difference in peak and hole (e Å^{-3})	0.903 and −0.558	1.683 and −1.507	1.108 and −1.241	2.285 and −1.890

2.3. Measurement of emission efficiencies

The relative emission quantum efficiencies were calculated according to the previous works by Shinkai and coworkers [45,46]. Using rhodamine B as the standard sample, the calculation equation can be described as $\Phi = \Phi_S \cdot (n^2 \cdot A_S \cdot I / n_S^2 \cdot A \cdot I_S)$, in which I and I_S are absorbency for sample materials and standards, A and A_S are integrated areas under the curves of the lanthanide ions strongest emission lines ($^4F_{9/2} \rightarrow {}^6H_{15/2}$ transition for Dy^{3+} ions, $^5D_4 \rightarrow {}^7F_5$ transition for Tb^{3+} ions and $^4G_{5/2} \rightarrow {}^6H_{7/2}$ transition for Sm^{3+} ions) with regard to sample materials and standards, respectively. In addition, n and n_S are the refractive index of the sample materials and standards. Since the solution concentration is very low (10^{-4} mol dm^{-3}), the refractive index of the solution can be regarded as that of the solvent. At room temperature, the refractive index of ethanol is 1.361. Through the above equation, the relative emission quantum efficiencies of complexes **2**, **3** and **4** were calculated.

2.4. Crystal structure determination

X-ray single crystal diffraction data for complexes **1**–**4** were performed with graphite-monochromated Mo Kα radiation ($\lambda = 0.71073$ Å). The reflections were collected with a Bruker SMART APEX detector. The structures were solved by direct methods. All non-hydrogen atoms were refined anisotropically by full-matrix least-squares methods. The hydrogen atoms were added geometrically and were not refined. All calculations were performed using SHELXS-97 and SHELXL-97 [47,48]. A summary of the crystallographic data and refinement parameters are given in Table 1.

Notes: The packing unit cell diagram for complex **2**, the 1-D chain drawing for complexes **3** and **4**, the absorption and excitation spectra of complexes **3** and **4** and the phosphorescence spectra of the ligands can be seen in Supplementary material.

3. Results and discussion

3.1. Crystal structure of $[Pr(mal)(OH)(bipy)\cdot 2H_2O]_n$ (1)

The complex $[Pr(mal)(OH)(bipy)\cdot 2H_2O]_n$ (**1**) crystallizes in the monoclinic system, with the space group $P2_1/c$. X-ray crystallographic analysis shows that it exhibits a one-dimensional helical chain structure. Fig. 1 shows the structural unit of complex **1**, which contains one praseodymium center, one mal ligand, one OH ligand and one chelating bipy ligand. Each praseodymium center is seven-coordinated by five oxygen atoms and two nitrogen atoms, and the coordination geometry of the praseodymium center can be described as a monocapped octahedral. Among the above-mentioned five oxygen atoms, four

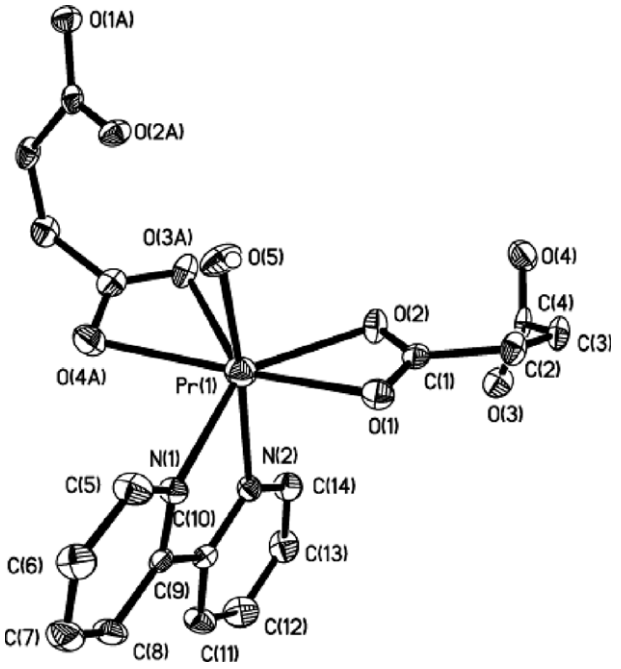


Fig. 1. The ORTEP drawing for complex **1** with the atom labelling scheme.

(O1, O2, O3, O4) are from two different mal ligands and the remaining one (O5) is from one-coordinated OH ligand. The average Pr–O bond distance is 2.336 Å. In addition, the two nitrogen atoms (N1, N2) are from one chelating bipy ligand. Selected bond lengths and angles for complexes **1** and **2** are listed in Table 2, and for complexes **3** and **4** in Table 3.

The important feature of complex **1** is that the coordination number of the praseodymium centers is seven. As is well known, lanthanide ions have high coordination numbers (>6). Especially, the light lanthanide ions (La–Gd) have larger ionic radii than the heavy lanthanide ions (Tb–Lu) due to the lanthanide contraction phenomenon, so the coordination numbers of light lanthanide ions are usually bigger than those of heavy lanthanide ions. For lanthanide aromatic carboxylate complexes, coordination number 8 and 9 are typical, and the number 7 has only been found once previously, in the heavy lanthanide ion complex $[Er(OHCH_2COO)(OCH_2COO)(H_2O)]_n$ [49]. Complex **1** therefore is the first example with a seven coordination number in light lanthanide ionic complexes with carboxylic acids.

In the structure of complex **1**, all the mal anions are deprotonated completely, and they act as tetradentate-bridging ligands towards the seven-coordinated praseodymium centers. For one mal anion, four oxygen atoms from two different carboxyls are coordinated to two praseodymium centers, and the praseodymium centers are connected by mal anions to form a 1-D helical polymeric chain along the *b* axis with a Pr···Pr distance of 5.8661 Å, as shown in Fig. 2. In addition, the bipy planes are on two sides of the zigzag chain alternately and parallel to each other.

Table 2
Selected bond distances (Å) and bond angles (°) for complexes **1** and **2**

Complex **1**		Complex **2**	
Pr(1)–O(5)	2.257(5)	Dy(1)–O(13)	2.215(6)
Pr(1)–N(1)	2.314(6)	Dy(1)–O(7)	2.271(6)
Pr(1)–O(2)	2.317(5)	Dy(1)–O(1)	2.293(6)
Pr(1)–N(2)	2.337(6)	Dy(1)–O(18)	2.305(5)
Pr(1)–O(3)[a]	2.418(5)	Dy(1)–O(11)	2.333(6)
Pr(1)–O(4)[a]	2.457(6)	Dy(1)–O(12)	2.368(7)
Pr(1)–O(1)	2.470(5)	Dy(1)–O(6)[a]	2.393(6)
		Dy(2)–O(23)	2.246(6)
		Dy(2)–O(19)	2.307(6)
		Dy(2)–O(24)[b]	2.338(5)
		Dy(2)–O(14)	2.340(5)
		Dy(2)–O(33)	2.354(6)
		Dy(2)–O(28)	2.404(6)
		Dy(2)–O(34)	2.436(6)
		Dy(2)–O(29)	2.501(6)
O(5)–Pr(1)–N(1)	101.7(2)	O(13)–Dy(1)–O(7)	167.3(2)
O(5)–Pr(1)–O(2)	93.1(2)	O(13)–Dy(1)–O(1)	90.5(2)
N(1)–Pr(1)–O(2)	138.84(3)	O(7)–Dy(1)–O(1)	87.0(2)
O(5)–Pr(1)–N(2)	172.4(2)	O(13)–Dy(1)–O(18)	86.1(2)
N(1)–Pr(1)–N(2)	70.73(2)	O(7)–Dy(1)–O(18)	90.00(2)
O(2)–Pr(1)–N(2)	93.28(2)	O(1)–Dy(1)–O(18)	150.5(2)
O(5)–Pr(1)–O(3)[a]	82.45(2)	O(13)–Dy(1)–O(11)	106.9(2)
N(1)–Pr(1)–O(3)[a]	130.7(2)	O(7)–Dy(1)–O(11)	83.2(2)
O(2)–Pr(1)–O(3)[a]	88.95(2)	O(7)–Dy(1)–O(6)[a]	114.7(2)
N(2)–Pr(1)–O(3)[a]	101.90(2)	O(1)–Dy(1)–O(6)[a]	73.9(2)
O(5)–Pr(1)–O(4)[a]	80.2(2)	O(18)–Dy(1)–O(6)[a]	132.9(2)
N(1)–Pr(1)–O(4)[a]	79.09(2)	O(11)–Dy(1)–O(6)[a]	72.2(2)
O(2)–Pr(1)–O(4)[a]	141.74(2)	O(12)–Dy(1)–O(6)[a]	143.5(2)
N(2)–Pr(1)–O(4)[a]	97.38(2)	O(23)–Dy(2)–O(19)	162.5(2)
O(3)[a]–Pr(1)–O(4)[a]	52.92(2)	O(23)–Dy(2)–O(24)[b]	102.4(2)
O(5)–Pr(1)–O(1)	81.23(2)	O(19)–Dy(2)–O(24)[b]	79.9(2)
N(1)–Pr(1)–O(1)	90.04(2)	O(23)–Dy(2)–O(33)	88.6(2)
O(2)–Pr(1)–O(1)	54.27(2)	O(19)–Dy(2)–O(33)	99.4(2)
N(2)–Pr(1)–O(1)	99.10(2)	O(14)–Dy(2)–O(33)	73.0(2)
O(3)[a]–Pr(1)–O(1)	138.46(2)	O(23)–Dy(2)–O(28)	121.5(2)
O(4)[a]–Pr(1)–O(1)	156.02(2)	O(19)–Dy(2)–O(28)	75.9(2)
		O(14)–Dy(2)–O(28)	136.02(2)
		O(33)–Dy(2)–O(28)	71.2(2)
		O(23)–Dy(2)–O(34)	80.6(2)
		O(19)–Dy(2)–O(34)	83.5(2)

Symmetry transformations used to generate equivalent atoms: for complex **1**: (a) $-x+1,\ y-1/2,\ -z+1/2$; (b) $-x+1,\ y+1/2,\ -z+1/2$. For complex **2**: (a) $-x+2,\ -y+2,\ -z+2$; (b) $-x+1,\ -y+1,\ -z+1$.

Fig. 3 shows the packing view of a unit cell for complex **1**, there exist three types of strong O–H···O intermolecular hydrogen bonds in the structure: one is the O–H···O intermolecular hydrogen bonding between the oxygen atoms of the OH groups and the oxygen atoms of the lattice water molecules (O(5)–H(5A)···O(7)[c]); the second is the O–H···O intermolecular hydrogen bonding between the oxygen atoms of the lattice water molecules and the oxygen atoms of the carboxyl groups (O(6)–H(6A)···O(4)[d], O(6)–H(6B)···O(1)[e] and O(7)–H(7B)···O(3)[f]); the last is the O–H···O intermolecular hydrogen bonding between the oxygen atoms of the lattice water molecules (O(7)–H(7A)···O(6)[f]). In addition, the plane–plane distance between two adjacent bipy ligands from two neighboring helical chains is 3.582 Å, which is within the reasonable

Table 3
Selected bond distances (Å) and bond angles (°) for complexes **3** and **4**

Complex **3**		Complex **4**	
Tb(1)–O(6)[a]	2.361(3)	Sm(1)–O(6)[a]	2.390(5)
Tb(1)–O(11)	2.394(3)	Sm(1)–O(11)	2.446(5)
Tb(1)–O(1)	2.407(3)	Sm(1)–O(1)	2.446(5)
Tb(1)–O(5)	2.422(3)	Sm(1)–O(5)	2.454(5)
Tb(1)–O(9)	2.431(3)	Sm(1)–O(9)	2.477(5)
Tb(1)–O(7)	2.437(3)	Sm(1)–O(4)	2.487(5)
Tb(1)–O(4)	2.455(3)	Sm(1)–O(7)	2.488(5)
Tb(1)–O(10)	2.491(3)	Sm(1)–O(10)	2.538(5)
Tb(1)–O(8)	2.503(3)	Sm(1)–O(8)	2.541(5)
O(6)[a]–Tb(1)–O(11)	73.10(1)	O(6)[a]–Sm(1)–O(11)	73.09(2)
O(6)[a]–Tb(1)–O(1)	140.27(1)	O(6)[a]–Sm(1)–O(1)	140.02(2)
O(11)–Tb(1)–O(1)	76.83(1)	O(11)–Sm(1)–O(1)	76.44(2)
O(6)[a]–Tb(1)–O(5)	143.40(1)	O(6)[a]–Sm(1)–O(5)	143.49(2)
O(11)–Tb(1)–O(5)	120.52(1)	O(11)–Sm(1)–O(5)	119.68(2)
O(6)[a]–Tb(1)–O(9)	5.41(1)	O(6)[b]–Sm(1)–O(9)	76.16(2)
O(11)–Tb(1)–O(9)	148.36(1)	O(11)–Sm(1)–O(9)	149.08(2)
O(6)[a]–Tb(1)–O(7)	118.41(1)	O(11)–Sm(1)–O(7)	134.84(2)
O(11)–Tb(1)–O(7)	135.02(1)	O(1)–Sm(1)–O(7)	68.83(2)
O(1)–Tb(1)–O(4)	75.14(9)	O(11)–Sm(1)–O(4)	68.98(2)
O(5)–Tb(1)–O(4)	53.69(9)	O(1)–Sm(1)–O(4)	75.32(2)
O(5)–Tb(1)–O(10)	79.03(1)	O(5)–Sm(1)–O(10)	78.82(2)
O(7)–Tb(1)–O(10)	132.41(1)	O(9)–Sm(1)–O(10)	71.41(2)
O(6)[a]–Tb(1)–O(8)	70.35(1)	O(11)–Sm(1)–O(8)	73.81(2)
O(5)–Tb(1)–O(8)	143.63(1)	O(1)–Sm(1)–O(8)	76.88(2)

Symmetry transformations used to generate equivalent atoms: (a) $-x$, $y+1$, z; (b) x, $y-1$, z.

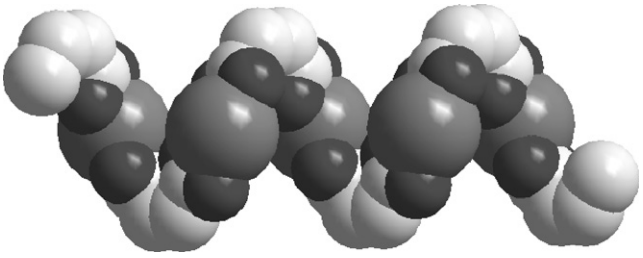


Fig. 2. The 1-D helical chain drawing for complex **1**. For clarity, phen and water molecules are deleted.

range indicating aromatic π–π stacking interactions. The offset angle of the π–π stacking interactions is 33.56°. The interchain hydrogen bonds and π–π stacking interactions are in a novel alternate fashion, and consolidate the stacked arrangement leading to a 3-D supramolecular architecture.

3.2. Crystal structure of $\{[Dy^1(SBA)_3(H_2O)_2]$-$[Dy^2(SBA)_3(H_2O)_2]\cdot 4H_2O\}_n$ (**2**)

The complex $\{[Dy^1(SBA)_3(H_2O)_2][Dy^2(SBA)_3(H_2O)_2]\cdot 4H_2O\}_n$ (**2**) crystallizes in the triclinic system, with the space group $P\bar{1}$. X-ray crystallographic analysis shows that it exhibits a 1-D chain-like structure. As shown in Fig. 4, there are two crystallographically unique dysprosium centers in the crystal structure. The Dy^1 center is seven-coordinated, completed by seven oxygen atoms from five SBA anions and two-coordinated water molecules, and the coordination geometry of the Dy^1 center can be described as a distorted monocapped trigonal prism. Among the above-mentioned seven oxygen atoms, four (O6, O7, O13, O18) are from four bridging SBA ligands, another one (O1) is from a chelating SBA ligand and the remaining two (O11, O12) are from two-coordinated water molecules. The average Dy^1–O bond distance is 2.225 Å. The Dy^2 center is eight-coordinated completely by eight oxygen atoms from five SBA anions and two-coordinated water molecules, the coordination geometry of Dy^2 can be described as a distorted square antiprism. Among the above-mentioned eight oxygen atoms, four (O14, O19, O23, O24) are from four bridging SBA ligands, two (O28, O29) are from a chelating SBA ligand and the remaining two (O33, O34) are from two-coordinated water molecules. The average Dy^2–O bond distance is 2.366 Å. All the Dy^2–O bond distances are much longer than the corresponding Dy^1–O distances.

All the SBA molecules are protonated and take part in the coordination to the dysprosium centers. There are three coordination modes of SBA in the structure: (a) the SBA anion acts as a monodentate ligand towards the Dy^1 center, which causes the coordination number of Dy^1 to be 7, and this coordination mode of carboxyl is seldom seen in the structures of lanthanide aromatic complexes; (b) the SBA anion acts as a bidentate chelating ligand towards the Dy^2 center; (c) the SBA anion acts as a bidentate bridging ligand towards the Dy^1 and Dy^2 centers. Two different typical dysprosium centers are connected by the bridging SBA ligands to form a dimeric fundamental unit with a $Dy^1\cdots Dy^2$ distance of 5.2604(17) Å; then the dimeric units are linked by SBA(c) linking two Dy^1 and Dy^2 centers of neighboring units with a $Dy^1\cdots Dy^1$ distance of 4.4639(14) Å and a $Dy^2\cdots Dy^2$ distance of 4.9355(16) Å; the chains are further linked by interchain hydrogen bonds with both the lattice water molecules and coordinated water molecules as donors and both oxygen atoms of the sulfo group and oxygen atoms of the carboxylate group as acceptors.

To the best of our knowledge, only two lanthanide 4-sulfobenzoic acid complexes $[Ln_2(1,4\text{-BDS})(SBA)_2\cdot 3H_2O]_n$ (Ln = Eu or Gd, 1,4-BDS = benzene-1,4-disulfonic acid) have been reported, and both of them are 3-D networks [50]. In the structures of the two complexes, the sulfonate and carboxyl groups are coordinated to lanthanide centers together, and the coordination number of the lanthanide centers is 9. For complex **2**, only carboxyl groups are coordinated to the lanthanide centers while the sulfonate groups are idle, indicating that the carboxyl groups have a stronger tendency to coordinate to the lanthanide ions than the sulfonate groups in aqueous solution. In addition, the coordination number of the Dy^1 center is seven causing complex **2** to be the first example with a seven coordination number in lanthanide benzene–carboxylate complex systems.

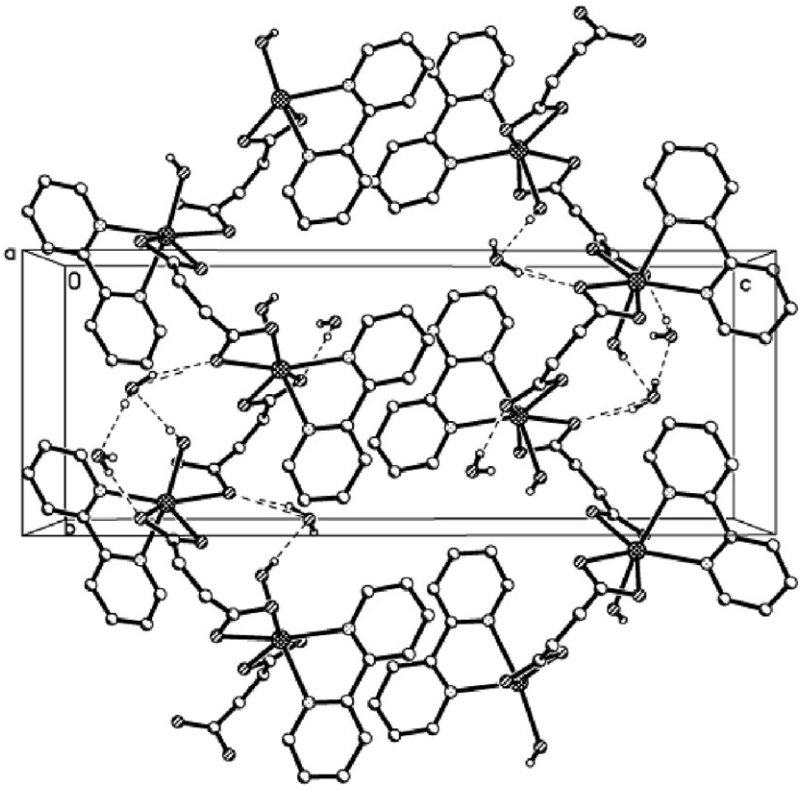


Fig. 3. The packing unit cell diagram for complex **1**.

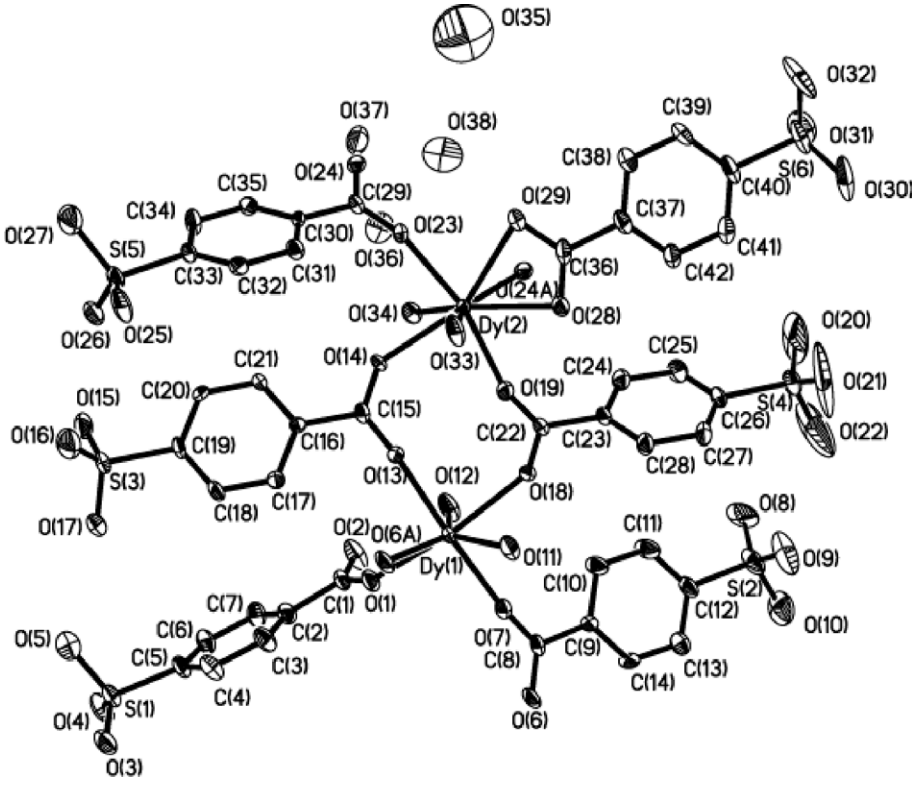


Fig. 4. The ORTEP drawing for complex **2** with the atom labelling scheme.

3.3. Crystal structure of $\{[Ln(OHnic)(Onic)(H_2O)_5 \cdot (OHnicH)] \cdot H_2O\}_n$ [Ln = Tb (3), Sm (4)]

The isomorphous complexes $\{[Tb(OHnic)(Onic)(H_2O)_5 \cdot (OHnicH)] \cdot H_2O\}_n$ (**3**) and $\{[Sm(OHnic)(Onic)(H_2O)_5 \cdot (OHnicH)] \cdot H_2O\}_n$ (**4**) crystallize in the triclinic space group $P\bar{1}$. Fig. 5 shows the crystal structure of complex **3**, whose asymmetric unit contains one terbium center, three 6-OHnic ions, five-coordinated water molecules and one lattice water molecule. Each terbium center is nine-coordinated completely by nine oxygen atoms, and the coordination geometry of terbium center can be described as a distorted monocapped square antiprism. Among the above-mentioned nine atoms, four (O1, O4, O5, O6) are from one bridged $Onic^{2-}$ anion and one monodentate $OHnic^{-}$ anion with a $Tb–O_{hydroxyl}6$ distance of 2.361(3) Å; and the other five are from five-coordinated water molecules with bond distances of 2.394(3)–2.503(3) Å between the terbium center and the oxygen atoms. The average Tb–O distance is 2.433 Å. For complex **4**, the bond distance between the samarium center and the hydroxyl oxygen atom is 2.390(5) Å (Sm–O6) and the average Sm–O distance is 2.474 Å. All the Sm–O bonds are longer than the Tb–O bonds, and the reason for that is the radius of the Sm ion is greater than the Tb ion.

An important feature of complexes **3** and **4**, which does not occur in other lanthanide carboxylate structures to our best knowledge, is that there exist three types of 6-OHnicH ligands in this polymeric structure: (1) the $Onic^{2-}$ anion acts as tridentate-bridging tridentate ligand towards two terbium centers, the Tb centers are connected into a chain-like structure by this coordination mode with the hydroxyl oxygen atoms connecting the terbium center of a neighboring unit; (2) the $OHnic^{-}$ anion acts as a monodentate ligand towards the terbium center; and (3) very interestingly, one neutral OHnicH molecule is not coordinated to a terbium center, but it exists in the structure mostly depending on hydrogen bonding and intermolecular bonding. In the structure of complex **4**, the 6-OHnicH ligands show the same coordination modes.

It is desirable to mention that the $Ln–O_{hydroxyl}$ distances are 2.361(3) Å (Tb-complex) and 2.390(5) Å (Sm-complex), indicating that the hydroxyl groups of the bridging ligands are protonated. Numerous examples of lanthanide–calixarene structures point in this direction, showing phenolate-lanthanide distances of 2.3–2.4 Å [51–55] while protonated phenols are at least 0.2 Å longer [56,57], so it can be determined that the bridging ligand is dianionic and the uncoordinated ligand is neutral. This can be easily understood as the coordination of the carboxylate moiety of the bridging ligand may lead to electron withdrawing effects that decrease the pK of the hydroxyl function, allowing its deprotonation.

Previously, Burns and Baldwin have discussed the structure of $Sm(o\text{-}HOC_6H_4COO)_3 \cdot H_2O$ [56], in which the carboxyl oxygen atoms and the hydroxyl oxygen atoms are coordinated to samarium centers together, and samarium centers are connected to a 1-D chain structure depending on the carboxyl groups linking up the central metal ions completely. In addition, Ni and co-workers have discussed the structures of $Ce(o\text{-}HOC_6H_4COO)_3 \cdot H_2O$ and $Tb(o\text{-}HOC_6H_4COO)_3 \cdot 4H_2O$ [57]. The complex $Ce(o\text{-}HOC_6H_4COO)_3 \cdot H_2O$ shows a similar structure to $Sm(o\text{-}HOC_6H_4COO)_3 \cdot H_2O$, however, in the structure of the Tb complex only carboxyl oxygen atoms are coordinated to Tb ions. These show that the hydroxyl oxygen atom of *o*-hydroxybenzoic acid is coordinated to the central metal ions in the light-lanthanide complexes but not in the heavy-lanthanide complexes. In contrast to *o*-hydroxybenzoic acid, the 6-OHnicH ligand shows some new coordination behaviors: the hydroxyl oxygen atom is coordinated to both light- and heavy-lanthanide ions; especially, lanthanide

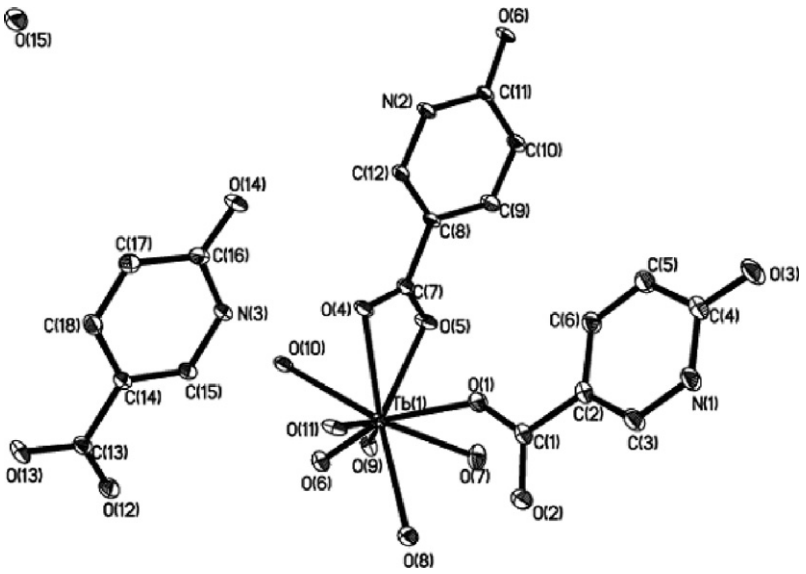


Fig. 5. The ORTEP drawing for complex **3** with the atom labelling scheme, complex **4** shows a very similar structure.

ions are connected into a chain-like structure depending on the hydroxyl oxygen atoms linking up the central metal ion of a neighboring unit.

Fig. 6 shows the packing view of a unit cell for complex **3**, comprising of an infinite chain in which the molecules in the crystal are held together by a system of hydrogen bonding. There exist six types of O–H···O intermolecular hydrogen bonds in the structure of complex **3**: one is the O–H···O intermolecular hydrogen bonding between the oxygen atoms of the lattice water molecules and the hydroxyl oxygen atoms of the monodentate OHnic ions (O(15)–H(15B)···O(3)[c]); the second is the O–H···O intermolecular hydrogen bonding between the oxygen atoms of the coordinated water molecules and the carboxyl oxygen atoms of the uncoordinated 6-OHnicH molecules (O(8)–H(8A)···O(13)[d], O(9)–H(9B)···O(13)[f], O(10)–H(10A)···O(12)[f] and O(11)–H(11B)···O(13)[d]); the third is the O–H···O intermolecular hydrogen bonding between the oxygen atoms of the coordinated water molecules and the hydroxyl oxygen atoms of the uncoordinated 6-OHnicH molecules (O(10)–H(10B)···O(14)[e] and O(11)–H(11A)···O(14)[g]); the fourth is the O–H···O intermolecular hydrogen bonding between the oxygen atoms of the coordinated water molecules and the carboxyl oxygen atoms of the monodentate OHnic ions (O(9)–H(9A)··· O(2)[i]); the fifth is the O–H···O intermolecular hydrogen bonding between the oxygen atoms of the lattice water molecules and the carboxyl oxygen atoms of the monodentate OHnic ions (O(15)–H(15A)···O(2)[g]); the last one is the O–H···O intermolecular hydrogen bonding between the oxygen atoms of the coordinated water molecules and the oxygen atoms of the lattice water molecules (O(7)–H(7A)···O(15)[e] and O(7)–H(7B)···O(15)[h]). In addition, there exists one type of O–H···O intramolecular hydrogen bond: the O–H···O intramolecular hydrogen bonding between the oxygen atoms of the coordinated water molecules and the carboxylic oxygen atoms of the monodentate OHnic ions (O(8)–H(8B)···O(1) and O(8)–H(8B)···O(2)). In the structure of complex **4**, the hydrogen bonds are analogous with these of complex **3**. The interchain hydrogen bonds are in a novel alternate fashion, and consolidate the stacked arrangement leading to a 3-D supramolecular architecture.

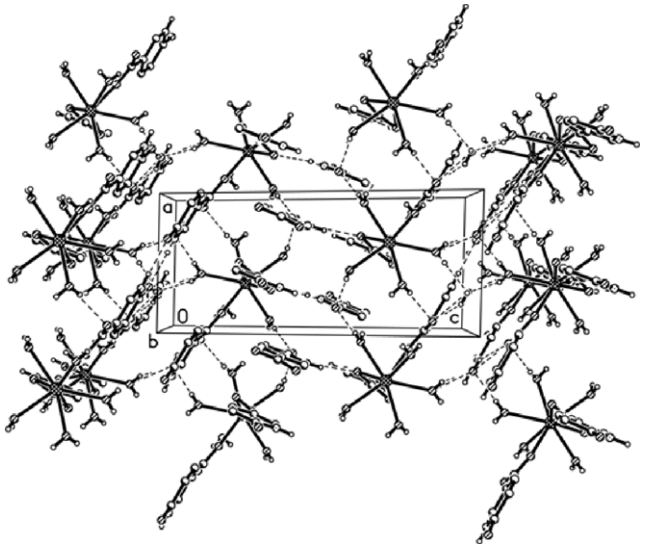


Fig. 6. The packing unit cell diagram for complex **3**, complex **4** shows a very similar unit cell.

3.4. Luminescent properties of complexes *2*, *3* and *4*

The ultraviolet absorption spectrum of $\{[Dy^1(SBA)_3(H_2O)_2][Dy^2(SBA)_3(H_2O)_2]\cdot 4H_2O\}_n$ (10^{-4} mol dm^{-3} ethanol solution) shows a domain absorption band at 212 nm (Fig. 7a), which is attributed to the characteristic absorption of the SBA ligand and the coordination interaction between lanthanide ions and SBA anions to form the more extensive $\pi \rightarrow \pi^*$ conjugated system. The excitation spectrum of complex **2** exhibits that the effective energy absorption (solid state samples) mainly takes place in the spectral range 200–440 nm, and the excitation bands consist of five main peaks at 208, 294, 351, 389 and 417 nm (Fig. 7b). The excitation band at 208 nm is attributed to the absorption of the SBA ligand, indicating that SBA is the energy donor for the luminescence of the Dy^{3+} ion. In addition, the excitation band at 351 nm is due to the own characteristic absorption of the Dy^{3+} ion, which is the direct absorption of the Dy^{3+} excited state. The facts indicate that besides the intramolecular energy transfer mechanism [58,59], there is also a directly excitation mechanism for the Dy^{3+} ions in complex **2**, as follows:

$$Dy^{3+} \xrightarrow{h\nu} Dy^{3+**}(^4F_{9/2}) \xrightarrow{\text{radiative}} {}^6H_J + h\nu' \quad (J = 15/2, 13/2)$$

The emission spectrum shows two apparent emission peaks on excitation at 208 nm: one is at 478 nm and the other is at 572 nm (Fig. 7c), which corresponds to the characteristic emission $^4F_{9/2} \rightarrow H_J$ ($J = 15/2$, 13/2) transition of the Dy^{3+} ion. It is worth pointing out that the blue emission intensity of the $^4F_{9/2} \rightarrow {}^6H_{15/2}$ transition is much stronger than the yellow emission of $^4F_{9/2} \rightarrow {}^6H_{13/2}$. As a result, the title complex exhibits an intense blue photoluminescence upon radiation of UV light in the solid state at room temperature. We further measured the low temperature luminescence spectrum of complex **1** at 77 K, and it still showed the two emissions of the dysprosium ion, at around 482 and 572 nm, the blue emission intensity is also much stronger than the yellow emission (Fig. 7d). The relative emission quantum efficiencies of complexes **2**, **3** and **4** were calculated according to the previous works by Shinkai and co-workers. For complex **2**, the quantum yield value is calculated to be 0.91%, which indicates a good luminescence performance of complex **2**.

The ultraviolet absorption spectra of $\{[Ln(OHnic)(Onic)(H_2O)_5\cdot(OHnicH)]\cdot H_2O\}_n$ (Ln = Tb, Sm) (10^{-4} mol dm^{-3} ethanol solution) exhibit domain absorption peaks in the narrow ultraviolet region in the range of 200–330 nm, and the maximum absorption peaks are located at around 253 and 300 nm, which can be attributed to the characteristic absorption of the 6-OHnicH ligand and

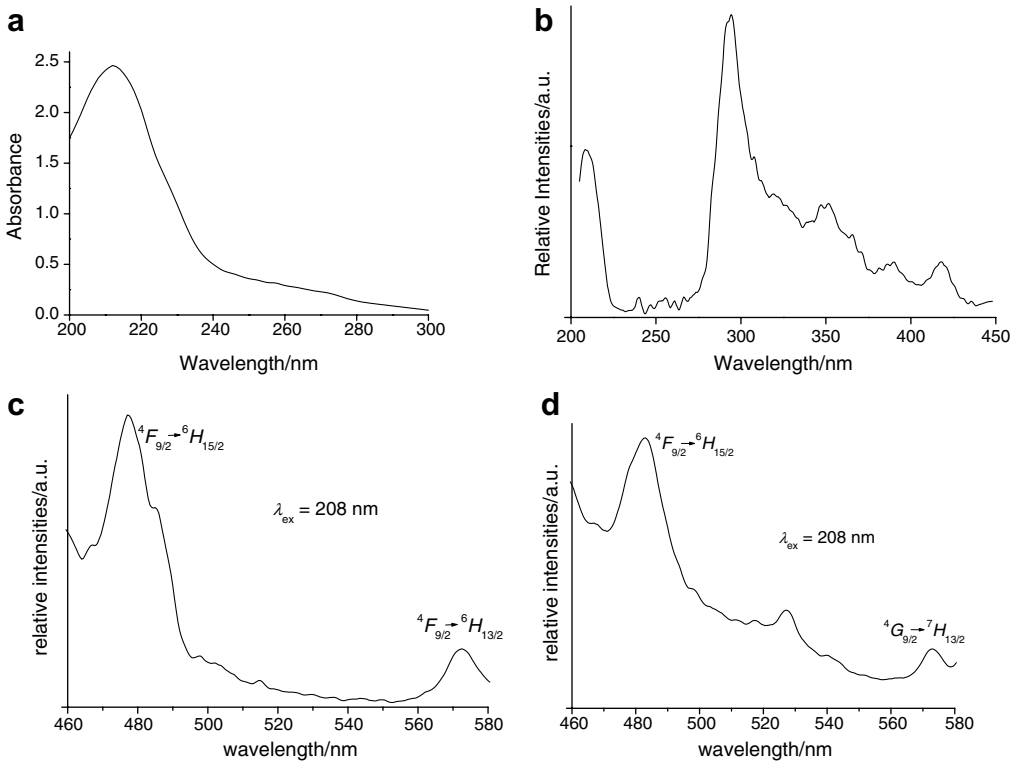


Fig. 7. The absorption, excitation and emission spectra of complex **2**.

the coordination interaction between lanthanide ions and 6-OHnicH anions to form a more extensive $\pi \rightarrow \pi^*$ conjugated system. The excitation spectra of complexes **3** and **4** (solid state samples) show that the effective energy absorption mainly takes place in the long ultraviolet region of 300–400 nm: the excitation bands for complex **3** under the green emission of 543 nm shows two main peaks: 351 nm and 371 nm; the excitation band for complex **4** under the orange emission of 600 nm shows five main peaks: 300 nm, 333 nm, 340 nm, 345 nm and 400 nm. The emission spectrum of complex **3** show two emission peaks on excitation at 371 nm: 488 nm and 543 nm, attributed to the characteristic emission $^5D_4 \rightarrow {}^7F_J$ ($J = 6$, 5) transition of the Tb^{3+} ion. The emission spectrum of complex **4** show two emission peaks on excitation at 400 nm: 560 nm and 594 nm, attributed to the characteristic emission $^4G_{5/2} \rightarrow {}^6H_J$ ($J = 5/2$, 7/2) transition of the Sm^{3+} ion. We further measured the low temperature luminescence spectra of complexes **3** and **4** at 77 K, and both of them show stronger emission luminescence than at room temperature (Figs. 8 and 9). It is worth pointing out that in the structure there are so many water molecules which can decrease the luminescence intensity of a rare earth complex, because the thermal vibration of the water molecules would consume partially the energy absorbed by the ligand; therefore, both complexes **3** and **4** exhibit weak luminescence. In addition, one 6-OHnic ligand is not coor-

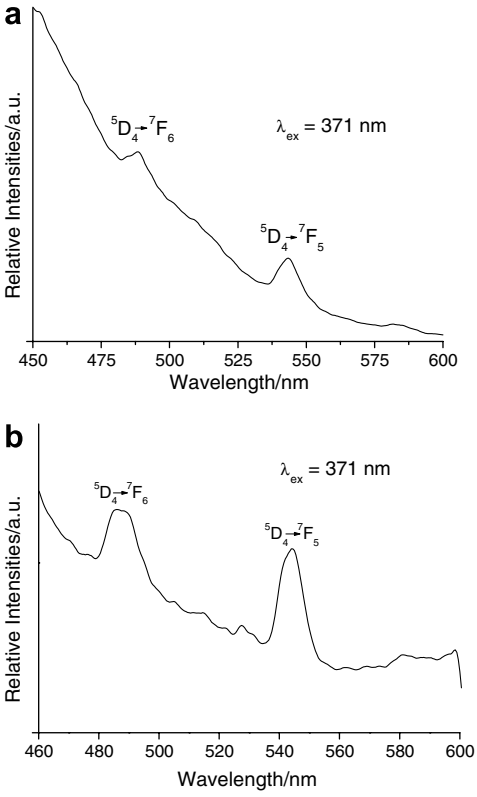


Fig. 8. Luminescence spectra of complex **3** ((a): room temperature; (b): low temperature).

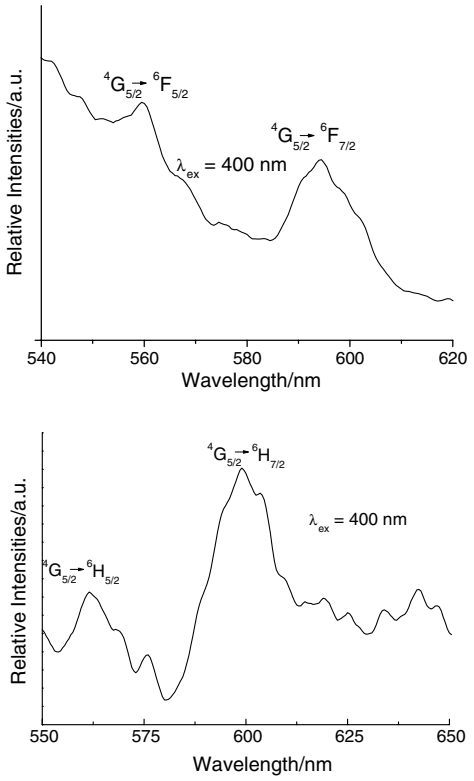


Fig. 9. Luminescence spectra of complex **4** ((a): room temperature; (b): low temperature).

dinated to the central lanthanide ion, and it cannot have a very efficient energy transfer to the central lanthanide metal. So the emission quantum yields for complexes **3** and **4** are not high, and are calculated to be 0.54% and 0.46%, respectively.

4. Conclusion

Four new lanthanide coordination polymers $[Pr(mal)(OH)(bipy)\cdot 2H_2O]_n$ (**1**), $\{[Dy^1(SBA)_3(H_2O)_2][Dy^2(SBA)_3(H_2O)_2]\cdot 4H_2O\}_n$ (**2**), $\{[Tb(OHnic)(Onic)(H_2O)_5\cdot(OHnicH)]\cdot H_2O\}_n$ (**3**) and $\{[Sm(OHnic)(Onic)(H_2O)_5\cdot(OHnicH)]\cdot H_2O\}_n$ (**4**) have been synthesized. Complex **1** is a 1-D helical chain with seven-coordinated praseodymium centers, which is the first example with a seven coordination number in light lanthanide ionic complexes with carboxylic acids. Complex **2** forms a 1-D chain-like molecular structure containing two crystallographically unique dysprosium centers, the Dy^1 center is seven-coordinated while Dy^2 is eight-coordinated, which is the first example with a seven coordination number in lanthanide benzene–carboxylate complex systems. The isomorphous complexes **3** and **4** exhibit an unprecedented 1-D chain-like polymeric structure, and there exist three types of 6-OHnicH ligands in the structural unit, which is rare for lanthanide carboxylate complexes. The photophysical properties of these complexes were studied with ultraviolet absorption spectra, fluorescence excitation and emission spectra.

Acknowledgements

The authors gratefully acknowledged the financial support from the National Natural Science Foundation of China (20671072).

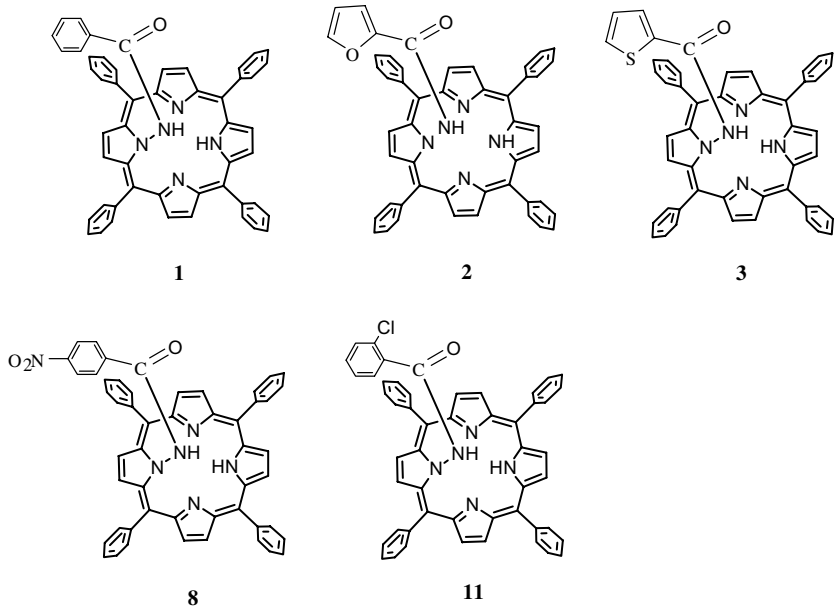
Appendix A. Supplementary material

CCDC 295004, 271342, 254025 and 254026 contain the supplementary crystallographic data (excluding structure factors) for **1**, **2**, **3** and **4**. These data can be obtained free of charge via http://www.ccdc.cam.ac.uk/conts/retrieving.html, or from the Cambridge Crystallographic Data Centre, 12 Union Road, Cambridge CB2 1EZ, UK; fax: (+44) 1223-336-033; or e-mail: deposit@ccdc.cam.ac.uk. Supplementary data associated with this article can be found, in the online version, at doi:10.1016/j.poly.2007.06.018.

References

[1] Q. Silvio, M. Giovanni, F. Alessandra, A. Gianluca, B. Francesco, Inorg. Chem. 43 (2004) 1294.
[2] G. Xu, Z.M. Wang, Z. He, Z. Lu, C.S. Liao, C.H. Yan, Inorg. Chem. 41 (2002) 6802.
[3] B.L. An, M.L. Gong, M.X. Li, J.M. Zhang, J. Mol. Struct. 687 (2004) 1.
[4] S. Faulkner, S.A.P. Pope, J. Am. Chem. Soc. 125 (2003) 10526.
[5] Q. Li, T. Li, J.G. Wu, J. Phys. Chem. B 105 (2001) 12293.
[6] V. Patroniak, P.N.W. Baxter, J.M. Lehn, Z. Hnatejko, M. Kubicki, Eur. J. Inorg. Chem. (2004) 2379.
[7] A.W.H. Lam, W.T. Wong, S. Gao, G. Wen, X.X. Zhang, Eur. J. Inorg. Chem. (2003) 149.
[8] C. Galaup, C. Picard, B. Cathala, L. Cazaux, P. Tisnes, Helv. Chim. Acta 82 (1999) 543.
[9] G. Blasse, G.J. Dirksen, N. Sabbatini, S. Perathoner, Inorg. Chim. Acta 133 (1987) 167.
[10] P.L. Jones, A.J. Amoroso, J.C. Jeffery, J.A. McCleverty, E. Psillakis, L.H. Ree, M.D. Ward, Inorg. Chem. 36 (1997) 10.
[11] D.A. Bardwell, J.C. Jeffery, P.L. Jones, J.A. McCleverty, E. Psillakis, Z. Reeves, M.D. Ward, J. Chem. Soc., Dalton Trans. (1997) 2079.
[12] F.D.M. Ramirez, L. Charbonniere, G. Muller, R. Scopelliti, J.C.G. Bunzli, J. Chem. Soc., Dalton Trans. (2001) 3205.
[13] J.C.G. Bunzli, F. Ihringer, Inorg. Chim. Acta 246 (1996) 195.
[14] P. Thuery, M. Nierlich, J. Vicens, H. Takemura, Polyhedron 19 (2002) 2673.
[15] L. Prodi, S. Pivari, F. Bolletta, M. Hissler, R. Ziessel, Eur. J. Inorg. Chem. (1998) 1959.
[16] S. Przemyslaw, Polyhedron 22 (2003) 337.
[17] A. Beeby, R.S. Dickins, S. Faulkner, D. Parker, J.A.G. Williams, Chem. Commun. (1997) 1401.
[18] W.S. Xia, R.H. Schmehl, C.J. Li, Tetrahedron 56 (2000) 7045.
[19] F.D.S. Gilberto, A.J. Severino, J.P.D.S. Blenio, F.D.S.J. Eronides, Opt. Mater. 11 (1998) 23.
[20] E.J. Nassar, P.S. Calefi, I.L.V. Rosa, O.A. Serra, J. Alloys Compd. (1998) 838.
[21] A.P. Bassett, S.W. Magennis, P.B. Glover, D.J. Lewis, N. Spencer, S. Parsons, R.M. Williams, L.D. Cola, Z. Pikramenou, J. Am. Chem. Soc. 126 (2004) 9413.
[22] R. Cao, D.F. Sun, Y.C. Liang, M.C. Hong, K. Tatsumi, Q. Shi, Inorg. Chem. 126 (2002) 2087.
[23] Y.B. Wang, X.J. Zheng, W.J. Zhuang, L.P. Jin, Eur. J. Inorg. Chem. (2003) 3572.

[24] A.W.H. Lam, W.T. Wong, S. Gao, G.H. Wen, X.X. Zhang, Eur. J. Inorg. Chem. (2003) 149.
[25] Z.M. Wang, L.J. van de Burgt, G.R. Choppin, Inorg. Chim. Acta 310 (2000) 248.
[26] M.P. Oude Wolbers, F.C.J.M. Van Veggel, B.H.M. Snellink-Ruel, J.W. Hofstraat, F.A.J. Geurts, D.N. Reinhoudt, J. Chem. Soc., Perkin Trans. 2 (1998) 2141.
[27] S. Petoud, J.-C.G. Bunzli, K.J. Schenk, C. Piguet, Inorg. Chem. 36 (1997) 1345.
[28] W.W. Horrocks De Jr., P. Bolender, W.D. Smith, R.M. Supkowski, J. Am. Chem. Soc. 119 (1997) 5972.
[29] L.A. Aslanov, I.K. Abdul'minev, M.A. Porai-Koshits, Zh. Fiz. Khim. 47 (1973) 1055.
[30] Y. Koizumi, H. Sawase, Y. Suzuki, T. Takcuchi, M. Shimoi, A. Ouchi, Bull. Chem. Soc. Jpn. 57 (1984) 1809.
[31] Y. Koizumi, H. Sawase, Y. Suzuki, T. Takcuchi, M. Shimoi, A. Ouchi, Bull. Chem. Soc. Jpn. 57 (1984) 1677.
[32] A.E. Kozial, W. Brzyska, B. Klimek, A. Krol, K. Stepmak, J. Coord. Chem. 21 (1990) 183.
[33] M.S. Khiyalov, I.R. Amiraslanov, K.S. Mamedov, E.M. Movsumov, Koord. Khim. 7 (1981) 1255.
[34] M.S. Khiyalov, I.R. Amiraslanov, K.S. Marnedov, E.M. Movsumov, Koord, Khim. 7 (1981) 445.
[35] J.F. Ma, Z.S. Jin, J.Z. Ni, Struct. Chem. 10 (1991) 125.
[36] J.F. Ma, Z.S. Jin, J.Z. Ni, Struct. Chem. 13 (1994) 113.
[37] A.E. Kozial, W. Brzyska, B. Klimek, A. Krol, K. Stepmak, J. Coord. Chem. 15 (1987) 367.
[38] C. Brouca-Cabarrecq, A. Fernandes, J. Jaud, J.P. Costes, Inorg. Chim. Acta 332 (2002) 54.
[39] X.J. Zheng, L.P. Jin, S.Z. Lu, Eur. J. Inorg. Chem. (2002) 3356.
[40] Y.B. Wang, X.J. Zheng, W.J. Zhuangm, L.P. Jin, Eur. J. Inorg. Chem. (2003) 1355.
[41] K.A. GschneidnerJr., J.C.G. Bunzli, V. Pecharsky (Eds.), Handbook on the Physics and Chemistry of Rare Earths, vol. 34, Elsevier, Amsterdam, 2004.
[42] Q.M. Wang, B. Yan, Cryst. Growth Des. 5 (2005) 497.
[43] L.M. Zhao, B. Yan, Appl. Organomet. Chem. 19 (2005) 1060.
[44] H.F. Lu, B. Yan, J. Non-Cryst. Solid 352 (2006) 5331.
[45] N. Sato, J. Yoshida, S. Shinkai, K. Fukuoka, Chem. Lett. (1993) 1261.
[46] N. Sato, J. Yoshida, S. Shinkai, K. Fukuoka, Chem. Lett. (1994) 878.
[47] G.M. Sheldrick, Acta Crysallogr., Sect. A 46 (1990) 467.
[48] G.M. Sheldrick, SHELXS-97: A Program for X-ray Crystal Structure Solution, and SHELXL-97: A Program for X-ray Structure Refinement, University of Göttingen, Göttingen, Germany, 1997.
[49] G. Ingmar, Acta. Chem. Scand. 23 (1969) 1253.
[50] R.G. Xiong, J. Zhang, Z.F. Chen, X.Z. You, C.M. Che, H.K. Fun, J. Chem. Soc., Dalton Trans. (2001) 780.
[51] J.M. Harrowfield, M.I. Ogden, A.H. White, J. Chem. Soc., Dalton Trans. (1991) 979.
[52] B.M. Furphy, J.M. Harrowfield, D.L. Kepert, B.W. Skelton, A.H. White, F.R. Wilner, Inorg. Chem. 26 (1987) 4231.
[53] J.M. Harrowfield, M.I. Ogden, A.H. White, F.R. Wilner, Aust. J. Chem. 42 (1989) 949.
[54] L.J. Charbonniere, C. Balsiger, K.J. Schenk, J.C. Bunzli, J. Chem. Soc., Dalton Trans. (1998) 505.
[55] P.D. Beer, M.G.B. Drew, P.B. Leeson, M.I. Ogden, Inorg. Chim. Acta 246 (1996) 195.
[56] J.H. Burns, W.H. Baldwin, Inorg. Chem. 16 (1977) 289.
[57] J.F. Ma, Z.S. Jin, J.Z. Ni, J. Inorg. Chem. 9 (1993) 160.
[58] G.F.D. Sa, O.L. Malta, C.D. Donega, A.M. Simas, R.L. Longo, P.A. Santa-Cruz, E.F.D. Silva, Coord. Chem. Rev. 196 (2000) 165.
[59] C. Pigust, J.C.G. Bunzli, G. Bernardinelli, G. Hopfgartner, A.F. Williams, J. Am. Chem. Soc. 115 (1993) 8197.



Scheme 1.

of **11**. The lack of study on metal complexes of ligand **11** prompted us to undertake the synthesis and structural investigations of the zinc(II) complexes. Zn(II) is a diamagnetic ion and maintains the d^{10} electron configuration which minimizes intrinsic coordination geometry preferences whilst favoring coordination by ligands of intermediate basicity. In this paper, we describe the X-ray structural investigation on the metallation of **11** leading to the mononuclear zinc(II) complex (*N*-*o*-chlorobenzimido-*meso*-tetraphenylporphyrinato)(methanol)zinc(II) methanol solvate [Zn(*N*-NCO(*o*-Cl)C_6H_4-tpp)(MeOH) · MeOH; **12** · MeOH]. Tsurumaki et al. have reported the electronic structures of oxidized metalloporphyrin complexes by acid-induced cleaveage of Ni(II) complexes of tetraarylporphyrin *N*-oxides at −25 °C [6]. A similar kind of acid hydrolysis was reported by Latos-Grazynski and co-workers for the cleavage of the Ni–O bond in nickel-(II)-6,11,16,21-tetraphenyl-22-hydroxy-*m*-benziporphyrin (TPBPO)Ni^{II}, leading to (TPBPOH)$Ni^{II}Cl$, and for the cleavage of the Ni–C bond in nickel(II)-6,11,16,21-tetraphenyl-*m*-benziporphyrin, leading to chloronickel(II)-22-*H*-6,11,16,21-tetraphenyl-*m*-benziporphyrin [7,8]. We tried to apply acid-hydrolysis to Zn–N bond cleavage in **12** · MeOH. The Zn–N bond in **12** · MeOH is cleaved by addition of aqueous HCl (2%) to a CH_2Cl_2 solution of the complex leading to the desired complex chloro(*N*-*o*-chlorobenzamido-*meso*-tetraphenylporphyrinato)zinc(II) methylene chloride solvate [Zn(*N*-NHCO(*o*-Cl)C_6H_4-tpp)Cl · CH_2Cl_2; **13** · CH_2Cl_2]. Intramolecular hydrogen bonding between the *ortho* chlorine and (*o*-Cl)benzamido hydrogen might enhance the formation of complex **13**. Collectively, we describe the two-stage formation of **13** and the spectroscopic properties of complexes **12** and **13**.

2. Experimental

2.1. *N*-NHCO(*o*-Cl)C_6H_4-Htpp (**11**)

Compound **11** was prepared in 32% yield in the same way as described for *N*-NHCOC_6H_5-Htpp using 2-chlorobenzoyl azide [2]. Compound **11** was dissolved in CH_2Cl_2 and layered with MeOH to give a purple solid. ^{1}H NMR (559.95 MHz, $CDCl_3$, 20 °C) δ: 9.10 [d, 2H, H_β, ^3J(H–H) = 4.2 Hz]; 8.86 [d, 2H, H_β, ^3J(H–H) = 4.8 Hz]; 8.57 [s, 2H, H_β]; 8.15 [s, 2H, H_β]; 8.20 [d, 2H, *ortho* protons *o*-H, ^3J(H–H) = 6.0 Hz]; 8.10 [d, 2H, *o*-H, ^3J(H–H) = 6.6 Hz]; 7.76–7.85 (m, 12H, *meta* and *para* protons); 5.94 [t, 1H, (*o*-Cl)BA-Ph-H_4 (where (*o*-Cl)BA = the *o*-chlorobenzamido ligand), ^3J(H–H) = 7.5 Hz]; 5.70 [d, 1H, (*o*-Cl)BA-Ph-H_3, ^3J(H–H) = 7.8 Hz]; 5.34 [t, 1H, (*o*-Cl)BA-Ph-H_5, ^3J(H–H) = 7.5 Hz]; 2.13 [d, 1H, (*o*-Cl)BA-Ph-H_6, ^3J(H–H) = 7.8 Hz]; −0.26 [bs, 2H, NH]. *Anal.* Calc. for $C_{51}H_{34}ClN_5O$: C, 79.73; H, 4.46; N, 9.12. Found: C, 79.29; H, 4.29; N, 9.05%. MS(FAB): $(M)^+$ 768 (calc. for $C_{51}H_{34}ClN_5O$: 768). UV–Vis spectrum, λ (nm) [$\varepsilon \times 10^{-3}$ (M^{-1} cm^{-1})] in CH_2Cl_2: 429 (213.9), 540 (10.8), 579 (9.7), 637 (7.4). IR (KBr) cm^{-1}: 3052 [ν(CH)], 1624 (amide I band), 1548 (amide II band), 1307 (amide III band), 1594 and 1462 (phenyl ring), 1439 [ν(CN)], 754 [ν(CCl)].

2.2. Zn(*N*-NCO(*o*-Cl)C_6H_4-tpp)(MeOH) · MeOH (**12** · MeOH)

Compound **12** was prepared in 75% yield in the same way as described for Zn(*N*-NCOC_6H_5-tpp)(MeOH) · MeOH using *N*-NHCO(*o*-Cl)C_6H_4-Htpp [2], with a reaction temperature of 30 °C and a reaction time of 30 min.

Compound **12** was dissolved in CH_2Cl_2 and layered with MeOH to obtain purple crystals for single-crystal X-ray analysis. ^{1}H NMR (559.95 MHz, $CDCl_3$, 20 °C) δ: 9.12 [d, 2H, H_β(2,13), ^3J(H–H) = 4.2 Hz]; 8.88 [d, 2H, H_β(3,12), ^3J(H–H) = 4.2 Hz]; 8.78 [s, 2H, H_β(7,8)]; 7.76 [s, 2H, H_β(17,18)]; 8.36 [d, 2H, *ortho* protons *o*-H(26,28), ^3J(H–H) = 7.8 Hz]; 8.09 [d, 2H, *o*-H(22,32), ^3J(H–H) = 6.6 Hz]; 8.84 [bs, 2H, *ortho* protons *o′*-H(38,40)]; 8.21 [bs, 2H, *o′*-H(34,44)]; 7.72–7.87 (m, 12H, *meta* and *para* protons); 6.10 [t, 1H, (*o*-Cl)BA-Ph-H_4, ^3J(H–H) = 7.2 Hz]; 5.91 [d, 1H, (*o*-Cl)BA-Ph-H_3, ^3J(H–H) = 7.8 Hz]; 5.69 [t, 1H, (*o*-Cl)BA-Ph-H_5, ^3J(H–H) = 7.8 Hz]; 3.61 [d, 1H, (*o*-Cl)BA-Ph-H_6, ^3J(H–H) = 7.8 Hz]. *Anal.* Calc. for $C_{53}H_{40}ClN_5O_3Zn$: C, 71.06; H, 4.50; N, 7.82. Found: C, 71.03; H, 4.19; N, 7.47%. MS(FAB): $(M)^+$ 832 (calc. for $C_{51}H_{32}ClN_5OZn$: 832). UV–Vis spectrum, λ (nm) [$\varepsilon \times 10^{-3}$ (M^{-1} cm^{-1})] in CH_2Cl_2: 439 (328.1), 607 (18.8). IR (KBr) cm^{-1}: 3643 [ν(OH)], 3051 [ν(CH)], 1597 (amide I band), 1473 (phenyl and methyl), 1384 (methyl), 1439 [ν(CN)], 753 [ν(CCl)].

2.3. Zn(*N*-NHCO(*o*-Cl)C_6H_4-tpp)Cl · CH_2Cl_2 (**13** · CH_2Cl_2)

Compound **12** (0.06 g, 0.069 mmol) in CH_2Cl_2 (50 ml) was extracted with 2% HCl (50 ml). After the CH_2Cl_2 layer was concentrated to dryness, the residue was redissolved in a minimum of CH_2Cl_2. Removal of the solvent and recrystallization from CH_2Cl_2–CH_3CN [1:1 (v/v)] gave the blue solid **13** (0.059 g, 0.062 mmol, 90%). Compound **13** was dissolved in CH_2Cl_2 and layered with CH_3CN to obtain blue crystals for single-crystal X-ray analysis. ^{1}H NMR (559.95 MHz, $CDCl_3$, 20 °C) δ: 9.03 [d, 2H, H_β(2,13), ^3J(H–H) = 4.8 Hz]; 8.89 [s, 2H, H_β(7, 8)]; 8.89 [d, 2H, H_β(3,12), ^3J(H–H) = 4.2 Hz]; 8.38 [s, 2H, H_β(17,18)]; 8.34 [s, 2H, *ortho* protons *o*-H(26,28)]; 8.12 [s, 2H, *o*-H(22,32)]; 8.77 [s, 2H, *o′*-H(38,40)]; 8.42 [s, 2H, *o′*-H(34,44)]; 7.77–7.94 (m, 12H, *meta* and *para* protons); 6.45 [t, 1H, (*o*-Cl)BA-Ph-H_4, ^3J(H–H) = 7.2 Hz]; 6.23 [t, 1H, (*o*-Cl)BA-Ph-H_5, ^3J(H–H) = 7.8 Hz]; 6.13 [d, 1H, (*o*-Cl)BA-Ph-H_3, ^3J(H–H) = 8.4 Hz]; 5.29 [d, 1H, (*o*-Cl)-BA-Ph-H_6, ^3J(H–H) = 8.1 Hz]; −0.56 [s, 1H, NH]. *Anal.* Calc. for $C_{51}H_{33}Cl_2N_5OZn$: C, 70.56; H, 3.83; N, 8.07. Found: C, 69.99; H, 3.28; N, 8.09%. MS(FAB): $(M - H)^+$ 867 (calc. for $C_{51}H_{33}Cl_2N_5OZn$: 868). UV–Vis spectrum, λ (nm) [$\varepsilon \times 10^{-3}$ (M^{-1} cm^{-1})] in CH_2Cl_2: 440 (306.8), 455 (208.6), 617 (22.2). IR (KBr) cm^{-1}: 3350 [ν(NH)], 3053 [ν(CH)], 1690 (amide I band), 1574 (amide II band), 1274 (amide III band), 1596 and 1480 (phenyl ring), 1441 [ν(CN)], 751 [ν(CCl)].

2.4. Spectroscopy

^{1}H and ^{13}C NMR spectra were recorded at 599.95 and 150.87 MHz, respectively, on Varian Unity Inova-600 spectrometers locked on deuterated solvent, and referenced to the solvent peak. The ^{1}H NMR is relative to $CDCl_3$ at $\delta = 7.24$ and ^{13}C NMR to the center line of $CDCl_3$ at $\delta = 77.0$. HMQC (heteronuclear multiple quantum coherence) was used to correlate protons and carbon through one–bond coupling and HMBC (heteronuclear multiple bond coherence) for two- and three-bond proton–carbon coupling. Nuclear Overhauser effect (NOE) difference spectroscopy was employed to determine the ^{1}H–^{1}H proximity through space over a distance of up to about 4 Å.

The positive-ion fast atom bombardment mass spectrum (FAB MS) was obtained in a nitrobenzyl alcohol (NBA) matrix using a JEOL JMS-SX/SX 102A mass spectrometer. UV–Vis spectra were recorded at 20 °C on a HITACHI U-3210 spectrophotometer. IR spectra were measured at 20 °C in KBr discs on a Bomem, DA8.3 spectrometer. Elemental analyses were obtained using a Heraeus CHN-O-S-Rapid elemental analyzer.

2.5. X-ray crystallography

Table 1 presents the crystal data as well as other information for **12** · MeOH and **13** · CH_2Cl_2. Measurements were taken on a Bruker AXS SMART-1000 diffractometer using monochromatized Mo Kα radiation ($\lambda = 0.71073$ Å) at a temperature of 100(2) K for **12** · MeOH and 297(2) K for **13** · CH_2Cl_2. Empirical absorption corrections were made for both complexes. The structures were solved by direct methods (SHELXL-97) [9] and refined by the full-matrix least-squares method. The (*o*-Cl)BA group within **12** · MeOH is disordered with an occupancy factor of 0.55 for Cl, C(46), C(47), C(48), C(49), C(50), C(51) and

Table 1
Crystal data for **12** · MeOH and **13** · CH_2Cl_2

Compound	**12** · MeOH	**13** · CH_2Cl_2
Empirical formula	$C_{53}H_{40}ClN_5O_3Zn$	$C_{52}H_{35}Cl_4N_5OZn$
Formula weight	895.72	953.02
Space group	$P2_1/n$	$P2_1/c$
Crystal system	monoclinic	monoclinic
a (Å)	14.713(4)	13.8993(16)
b (Å)	16.754(5)	30.995(4)
c (Å)	17.433(5)	11.1975(13)
α (°)	90	90
β (°)	97.933(6)	113.451(2)
γ (°)	90	90
V (Å^3)	4256(2)	4425.5(9)
Z	4	4
F(000)	1856	1952
D_{calc} (g cm^{-3})	1.398	1.430
μ (Mo Kα) (mm^{-1})	0.692	0.843
S	0.961	1.238
Crystal size (mm)	0.25 × 0.15 × 0.10	0.68 × 0.43 × 0.13
θ(°)	28.40	26.02
T (K)	100(2)	297(2)
Number of reflections measured	10496	8684
Number of reflections observed with [$I > 2\sigma(I)$]	7046	6585
R_1^a	0.0610	0.0485
wR_2^b	0.1514	0.1411

[a] $R_1 = [\sum\|\|F_o| - |F_c\|| / \sum|F_o|]$.
[b] $wR_2 = \{\sum[w(F_o^2 - F_c^2)^2] / \sum[w(F_o^2)^2]\}^{1/2}$.

Table 2
Selected bond distances (Å) and angles (°) for compounds **12** · MeOH and **13** · CH_2Cl_2

*Compound **12** · MeOH*			
Bond lengths (Å)			
Zn–N(1)	2.073(3)	Zn–O(2)	2.107(2)
Zn–N(2)	1.944(2)	H(3)···O(1)	1.821(2)
Zn–N(3)	2.067(3)	O(1)···O(3)	2.609(2)
Zn–N(5)	2.013(3)		
Bond angles (°)			
O(2)–Zn–N(1)	88.28(9)	N(1)–Zn–N(2)	94.25(10)
O(2)–Zn–N(2)	111.26(10)	N(1)–Zn–N(3)	169.22(9)
O(2)–Zn–N(3)	95.29(9)	N(1)–Zn–N(5)	84.77(10)
O(2)–Zn–N(5)	117.08(9)	N(2)–Zn–N(3)	95.10(10)
Zn–N(5)–N(4)	95.90(17)	N(2)–Zn–N(5)	131.45(10)
Zn–O(2)–C(52)	131.1(2)	N(3)–Zn–N(5)	85.03(10)
O(3)–H(3)···O(1)	173.65(9)		
*Compound **13** · CH_2Cl_2*			
Bond lengths (Å)			
Zn–N(1)	2.131(2)	Zn–Cl(1)	2.2090(9)
Zn–N(2)	2.007(2)	N(5)···Cl(2)	3.138(2)
Zn–N(3)	2.138(2)	H(5A)···Cl(2)	2.768(2)
Zn···N(4)	2.557(2)		
Bond angles (°)			
Cl(1)–Zn–N(1)	109.81(7)	N(1)–Zn–N(2)	88.65(9)
Cl(1)–Zn–N(2)	120.63(7)	N(1)–Zn–N(3)	136.98(9)
Cl(1)–Zn–N(3)	108.62(7)	N(1)–Zn–N(4)	77.63(9)
Cl(1)–Zn–N(4)	101.04(7)	N(2)–Zn–N(3)	88.05(9)
N(3)–Zn–N(4)	76.78(9)	N(2)–Zn–N(4)	138.30(9)
N(5)–H(5A)···Cl(2)	107.68(9)		

0.45 for Cl′, C(46′), C(47′), C(48′), C(49′), C(50′), C(51′). The phenyl group within **12** · MeOH is disordered with an occupancy factor of 0.5 for C(43), C(44) and 0.5 for C(43′), C(44′). O(1) within **12** · MeOH is disordered with an occupancy factor of 0.9 for O(1) and 0.1 for O(1′). All non–hydrogen atoms were refined with anisotropic thermal parameters, whereas all hydrogen atoms were placed in calculated positions and refined with a riding model. Table 2 lists selected bond distances and angles for complexes **12** · MeOH and **13** · CH_2Cl_2.

3. Results and discussion

3.1. Formation and characterization of *12*

Insertion of $Zn(OAc)_2$ into **11** in a methylene/methanol solution results in the formation of a five-coordinate diamagnetic complex **12** in 75% yield (Scheme 2).

3.2. Crystal structure of *12* · *MeOH*

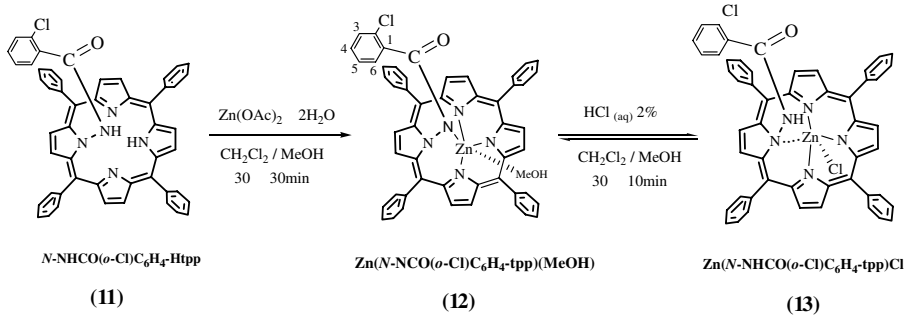
The structure of **12** · MeOH, determined in an X-ray diffraction study, is shown in Fig. 1a. The geometry around Zn in **12** · MeOH is described as a distorted trigonal bipyramid with N(2), N(5) and O(2) lying in the equatorial plane. The Zn–O(2) bond distance is 2.107(2) Å and the mean Zn-4N distance is 2.024(3) Å for **12** · MeOH. The Zn–O(2) (MeOH) distance of 2.107(2) Å is slightly longer than the sum of the covalent radii of Zn and O (1.92 Å) but is significantly shorter than the sum of the van der Waals radii of Zn and O (2.90 Å) [10]. This Zn–O(2) contact may be described as a weak covalent bond. The distortion in five-coordinate complexes can be quantified by the "degree of trigonality" which is defined as $\tau = (\beta - \alpha)/60$, where "$\beta$" is the largest and "$\alpha$" the second largest of the L_{basal}–M–L_{basal} angles [11]. In **12**, we find $\beta = 169.22(9)°$ [N(3)–Zn–N(1)] and $\alpha = 131.45(10)°$ [N(2)–Zn–N(5)] for **12** · MeOH (Table 2) and thus a τ value of 0.63 is obtained for **12** · MeOH. Hence, the geometry around Zn(II) in **12** · MeOH is best described as a distorted trigonal bipyramid. In **12** · MeOH (Fig. 1a), the observed H(3)···O(1) and O(3)···O(1) distances are 1.821(2) and 2.609(2) Å (Table 2), respectively, which fall below those values expected from van der Waals distances (2.60 and 2.80 Å, respectively). The O(3)–H(3)–O(1) angle is 173.65(9)°, and its deviation from linearity is small. Therefore, this intermolecular hydrogen bonding causes an increased polarization of the carbonyl bond in **12** · MeOH. Consequently, the carbonyl carbon C(45) in **12** · MeOH becomes more positive, thereby accounting for its NMR downfield shift of 2.8 ppm observed at 20 °C, i.e. from 161.5 ppm for C(45) in **13** to 164.3 ppm for the same carbonyl carbon in **12** · MeOH (Tables S1 and S2).

3.3. Formation and characterization of *13*

When a solution of **12** in CH_2Cl_2 is treated with aqueous hydrogen chloride (2%), a new species is formed that can be formulated as **13** (Scheme 2). The reaction is reversed by heating the products in CH_2Cl_2/MeOH at 30 °C for 10 min (Scheme 2).

3.4. Crystal structure of *13* · CH_2Cl_2

The structure of **13** · CH_2Cl_2, determined by an X-ray diffraction study, is shown in Fig. 1b. The (*o*-Cl)BA group lies on the side opposite to the chloride Cl(1) in **13** · CH_2Cl_2. The coordination bond lengths Zn–N(1) 2.131(2) Å, Zn–N(2) 2.007(2) Å, Zn–N(3) 2.138(2) Å and Zn–Cl(1) 2.090(9) Å are within the limit found for zinc(II) porphyrins. The (*o*-Cl)BA nitrogen N(5) in **13** · CH_2Cl_2 is no longer bonded to zinc as indicated by its longer internuclear distance, 2.935(2) Å for Zn···N(5). Moreover, the Zn···N(4) distance of 2.557(2) Å for **13** · CH_2Cl_2 is longer than 2.138(2) Å for Zn–N(3) but is significantly shorter than the sum of the van der Waals radii of Zn and N (2.95 Å) [10]. This longer Zn···N(4) contact in **13** · CH_2Cl_2 may be viewed as a secondary intramolecular interaction. This kind of secondary interaction was earlier observed for Zn(*N*-Me-tpp)Cl with Zn···N1 = 2.530(7) Å [12,13]. Most chemists seem to consider this secondary interaction between the metal ion and the fourth N as a weak bond in *N*-substituted porphyrin metal complexes. In the present case, we find $\beta = 138.30(9)°$ [N(2)–Zn–N(4)] and $\alpha = 136.98(9)°$ [N(1)–Zn–N(3)] for **13** · CH_2Cl_2 and thus a τ value of 0.02 is obtained for **13** · CH_2Cl_2. Hence, the



N-NHCO(*o*-Cl)C_6H_4-Htpp (**11**)

Zn(*N*-NCO(*o*-Cl)C_6H_4-tpp)(MeOH) (**12**)

Zn(*N*-NHCO(*o*-Cl)C_6H_4-tpp)Cl (**13**)

Scheme 2.

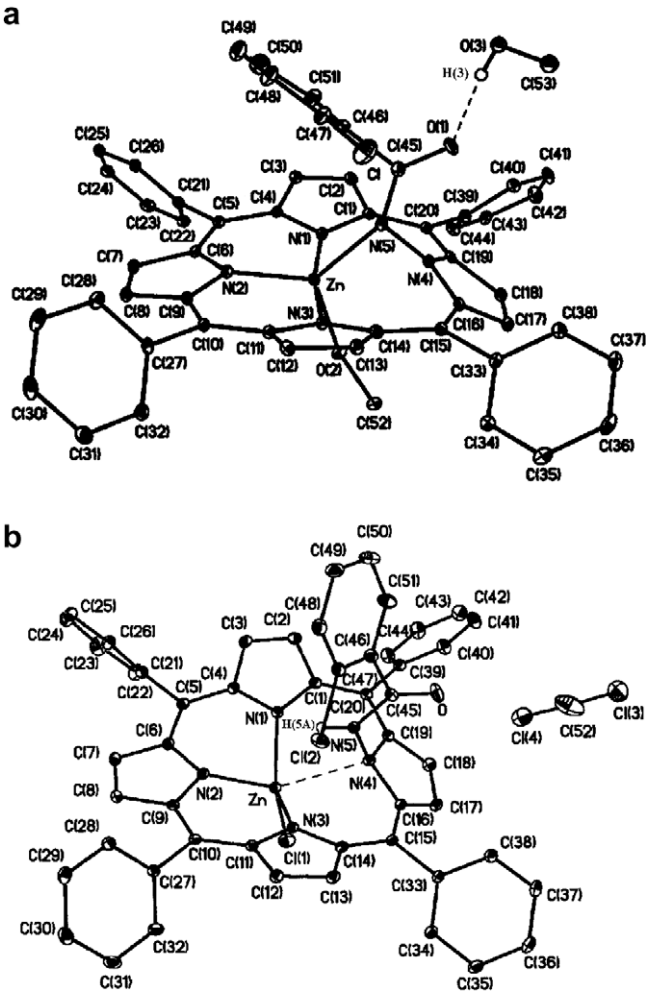


Fig. 1. Molecular configuration and atom-labelling scheme for (a) **12** · MeOH and (b) **13** · CH_2Cl_2, with ellipsoids drawn at 30% probability for both complexes. Hydrogen atoms except H(3) in **12** · MeOH and H(5A) in **13** · CH_2Cl_2 are omitted for clarity.

geometry around Zn(II) in **13** · CH_2Cl_2 is best described as a square-based pyramid with Cl(1) as the apical atom. The τ value of 0.02 obtained for **13** · CH_2Cl_2 is quite close to the value of 0.05 for Zn(*N*-Me-tpp)Cl [12,13]. Hence compounds **13** · CH_2Cl_2 and Zn(*N*-Me-tpp)Cl have a similar coordination geometry around the Zn^{2+} ion. We adopt the plane of three strongly bound pyrrole nitrogen atoms [i.e. N(1), N(2) and N(3)] as a reference plane 3N for **12** · MeOH and **13** · CH_2Cl_2. The zinc ion in **13** · CH_2Cl_2 (or **12** · MeOH) is displaced from the 3N plane by 0.75 Å (or 0.09 Å) toward the chloride [Cl(1)] [or O(2)(MeOH)] (Fig. S1). The occurrence of weak intramolecular hydrogen bonding between the (*o*-Cl)benzamido hydrogen [H(5A)] and the chlorine Cl(2) in **13** is reflected in the long N(5)–H(5A)···Cl(2) bond distance of 2.768(2) Å and acute N(5)–H(5A)···Cl(2) angle of 107.68(9)° (Table 2). This weak intramolecular hydrogen bonding might strengthen the formation of complex **13**.

3.5. ^1H NMR spectroscopy data of 12 and 13 in $CDCl_3$

In solution, the molecule has an effective C_s symmetry with a mirror plane running through the N(2)–Zn–N(5)–N(4) unit for **12** or the N(2)–Zn–N(4)–N(5) unit for **13**. As a result, the ^1H NMR spectra will exhibit four pyrrole resonances [H_β(7,8), H_β(17,18), H_β(3,12), H_β(2,13)] for these two complexes (Fig. 2). Non-equivalence of the two sides of the macrocycle will cause each phenyl ring to have two distinct *ortho* resonances with one set of *ortho* protons, *o*-H(22,32) and *o*-H(26,28), for phenyl C(24) and C(30) and the other set of *ortho* protons, *o′*-H(34,42) and *o′*-H(38,40), for phenyl C(36) and C(42), unless the rotation around the C_{meso}–C_1 [C(5)–C(21), C(10)–C(27) or C(15)–C(33), C(20)–C(39)] bond is sufficiently fast in these two complexes (Fig. 2).

The tautomerism exchange between the two NH protons of **11** in CD_2Cl_2 is fast on the ^1H NMR timescale at both 20 and −90 °C. Hence only one type of N–H proton signal was observed for **11** in CD_2Cl_2 at 20 and −90 °C. At −90 °C, traces of water were frozen from the solution of **11** and **13** in CD_2Cl_2. Thus, the frozen water inhibits intermolecular proton exchange between water and NH protons of **11** and **13**, and allows the observation of a broad singlet for the NH proton at $\delta = -0.51$ ppm ($\Delta\nu_{1/2} = 11.8$ Hz) for **11** and $\delta = -0.69$ ppm ($\Delta\nu_{1/2} = 9.1$ Hz) for **13** at −90 °C. In this case, the NH proton signal for **11** and **13** at −90 °C is broadened by the quadrupolar interaction of the ^{14}N nucleus. The signal arising from the NH proton of **11** in CD_2Cl_2 was observed as a broad singlet at $\delta = -0.29$ ppm ($\Delta\nu_{1/2} = 23$ Hz) at 20 °C. These NMR data suggest that the NH protons of **11** undergo intermediate intermolecular proton exchange with water at 20 °C.

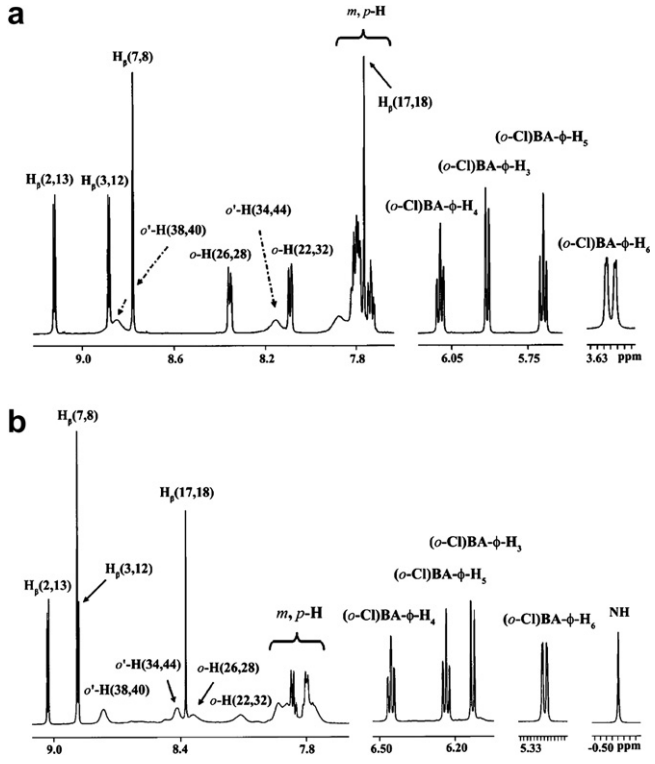


Fig. 2. The 599.95 MHz ^{1}H NMR spectra in $CDCl_3$ at 20 °C for (a) **12** and (b) **13**, where ϕ = Ph (phenyl group).

Moreover, the ^{1}H NMR spectrum of **13** in CD_2Cl_2 showed a sharp singlet at $\delta = -0.58$ ppm ($\Delta\nu_{1/2} = 2.1$ Hz) for the NH proton at 20 °C (see a similar spectrum shown in Fig. 2b). This sharp signal ($\Delta\nu_{1/2} = 2.1$ Hz) is not in agreement with that of $\Delta\nu_{1/2} = 9.1$ Hz found for **13** in the absence of any exchange. Hence, these NMR data for **13** indicate that the NH proton [i.e., H(5A)] bound to N(5) undergoes rapid intermolecular proton exchange with water at 20 °C. Due to the ring current effect, upfield shifts for the ^{1}H resonances of (*o*-Cl)BA-Ph-H_6, (*o*-Cl)BA-Ph-H_3, (*o*-Cl)BA-Ph-H_5 and (*o*-Cl)BA-Ph-H_4 for **13** in $CDCl_3$ at 20 °C are $\Delta\delta = -2.48$ [from 7.77 (obtained from *o*-chlorobenzamide) to 5.29 ppm], −1.29 (from 7.42 to 6.13 ppm), −1.12 (from 7.35 to 6.23 ppm) and −0.95 (from 7.40 to 6.45 ppm), respectively (Fig. 2b). As the distance between the geometrical center (C_t) of the 4N plane and axial protons gets smaller qualitatively, the shielding effect becomes larger [14]. In **13**, the distance for $C_t\cdots$(*o*-Cl)BA-Ph-H_6, $C_t\cdots$(*o*-Cl)BA-Ph-H_3, $C_t\cdots$(*o*-Cl)BA-Ph-H_5 and $C_t\cdots$(*o*-Cl)-BA-Ph-H_4, increases from 5.615, 6.119, 7.138 to 7.312 Å. As the (*o*-Cl)BA-Ph-H_6 proton of **13** is closer to C_t, the shielding gets larger for this (*o*-Cl)BA-Ph-H_6 proton. A similar ring current effect is also observed for **12**. The average distance between $C_t\cdots$(*o*-Cl)BA-Ph-H_6, $C_t\cdots$(*o*-Cl)-BA-Ph-H_5, $C_t\cdots$(*o*-Cl)BA-Ph-H_3 and $C_t\cdots$(*o*-Cl)BA-Ph-H_4 for **12** increases from 3.934, 5.438, 5.684 to 6.166 Å. The fact that all four distances between C_t and (*o*-Cl)BA-Ph protons in **12** are shorter than those distances in **13** indicates that the ring current effect of (*o*-Cl)BA protons in **12** would be larger and in turn the ^{1}H upfield shifts for those protons in the same compound would be still higher. This observation is corroborated by the doublet at 3.61 ppm for (*o*-Cl)BA-Ph-H_6 in **12** and the doublet at 5.29 ppm for the same Ph-H_6 proton in **13**, the triplet at 5.69 ppm for (*o*-Cl)BA-Ph-H_5 in **12** and the triplet at 6.23 ppm for the same Ph-H_5 proton in **13**, the doublet at 5.91 ppm for (*o*-Cl)BA-Ph-H_3 in **12** and the doublet at 6.13 ppm for the same Ph-H_3 proton in **13**, the triplet at 6.10 ppm for (*o*-Cl)BA-Ph-H_4 in **12** and the triplet at 6.45 ppm for the same Ph-H_4 proton in **13** (Fig. 2).

3.6. Solid state IR spectroscopy data of 11, 12 and 13

Compound **12** could be viewed as a tertiary amide and it displayed a unique amide I band at 1597 cm^{-1} in the IR spectrum in the solid state. The two interactions due to a strong intermolecular hydrogen bond between O(1) and H(3) and the covalent bond Zn–N(5) reduces the C=O stretching frequency by 53 cm^{-1} from 1650 cm^{-1} for tertiary amides to 1597 cm^{-1} for **12** [15]. The O–H stretching and methyl bending bands of MeOH in **12** occur near 3643 and 1384 cm^{-1}, respectively. Moreover, compounds **11** and **13** are classified as secondary amides with bands at 1624, 1548 and 1307 cm^{-1} (or 1690, 1574 and 1274 cm^{-1}) being assigned as amide I, II and III bands of **11** (or **13**). These data are quite close to those frequencies of 1680–1630, 1570–1515 and 1300 cm^{-1} reported for amide I, II and III bands of secondary amides [15,16]. The band at 3350 cm^{-1} results from the N(5)–H(5A) stretch of **13**.

4. Conclusion

Two distinct types of zinc complexes, hitherto unreported, have been obtained from *N*-*o*-chlorobenzamido-*meso*-tetraphenylporphyrin (*N*-NHCO(*o*-Cl)C_6H_4-Htpp; **11**). In Zn(*N*-NCO(*o*-Cl)C_6H_4-tpp)(MeOH) (**12**), the N–H bond of the *o*-chlorobenzamido ligand is cleaved and the *o*-chlorobenzamido nitrogen participates in bonding to the zinc ion. In Zn(*N*-NHCO(*o*-Cl)C_6H_4-tpp)Cl (**13**), the *o*-chlorobenzamido [(*o*-Cl)BA] substituent is left intact and the zinc(II) ion is coordinated to the three nitrogens of the macrocycle core. Compound **13** can be synthesized in the reaction of **12** with aqueous HCl (2%).

Acknowledgements

The financial support from the National Science Council of the ROC under Grant NSC 95-2113-M-005-014-MY3 and NSC 95-2113-M-273-002 is gratefully acknowledged.

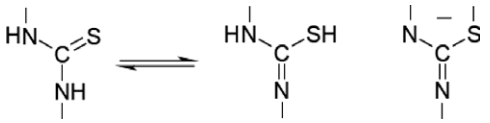
Appendix A. Supplementary material

CCDC 642339 and 642340 contain the supplementary crystallographic data for **12** · MeOH and **13** · CH_2Cl_2. These data can be obtained free of charge via http://www.ccdc.cam.ac.uk/conts/retrieving.html, or from the Cambridge Crystallographic Data Centre, 12 Union Road,

Cambridge CB2 1EZ, UK; fax: (+44) 1223-336-033; or e-mail: deposit@ccdc.cam.ac.uk. Fig. S1 shows the diagram of the porphyrinato ($C_{20}N_4$, Zn, (*o*-Cl)BA, O(MeOH), Cl) unit of **12** · MeOH and **13** · CH_2Cl_2. Tables S1 and S2 show the ^{13}C NMR (150.87 MHz) for **12** and **13** in $CDCl_3$ at 20 °C. Supplementary data associated with this article can be found, in the online version, at doi:10.1016/j.poly.2007.06.021.

References

[1] R.G. Pearson, Inorg. Chem. 27 (1988) 734.
[2] F.A. Yang, J.H. Chen, H.Y. Hsieh, S. Elango, L.P. Hwang, Inorg. Chem. 42 (2003) 4603.
[3] J.Y. Tung, J.H. Chen, Polyhedron 26 (2007) 589.
[4] H.Y. Hsieh, C.W. Cheng, F.A. Yang, J.H. Chen, J.Y. Tung, S.S. Wang, Personal communication.
[5] C.H. Chen, Y.Y. Lee, B.C. Liau, S. Elango, J.H. Chen, H.Y. Hsieh, F.L. Liao, S.L. Wang, L.P. Hwang, J. Chem. Soc., Dalton Trans. (2002) 3001.
[6] H. Tsurumaki, Y. Watanabe, I. Morishima, Inorg. Chem. 33 (1994) 4186.
[7] M. Stepien, L. Latos-Grazynski, Inorg. Chem. 42 (2003) 6183.
[8] M. Stepien, L. Latos-Grazynski, L. Szterenberg, J. Panek, Z. Latajka, J. Am. Chem. Soc. 126 (2004) 4566.
[9] G.M. Sheldrick, SHELXL-97: Program for the Refinement of Crystal Structure from Diffraction Data, University of Göttingen, Göttingen, Germany, 1997.
[10] J.E. Huheey, E.A. Keiter, R.L. Keiter, Inorganic Chemistry, 4th ed., Harper Collins College Publishers, New York, 1993, pp. 117, 292.
[11] A.W. Addison, T.N. Rao, J. Reedijk, J.V. Rijn, G.C. Verschoor, J. Chem. Soc., Dalton Trans. (1984) 1349.
[12] D.K. Lavallee, A.B. Kopelove, O.P. Anderson, J. Am. Chem. Soc. 100 (1978) 3025.
[13] C.K. Schauer, O.P. Anderson, D.K. Lavallee, J.P. Battioni, D. Mansuy, J. Am. Chem. Soc. 109 (1987) 3922.
[14] C.E. Johnson Jr., F.A. Bovey, J. Chem. Phys. 29 (1958) 1012.
[15] K. Nakanishi, P.H. Solomon, Infrared Absorption Spectroscopy – Practical, 2nd ed., Holden Day, San Francisco, 1977, p. 42.
[16] R.M. Silverstein, F.X. Webster, Spectrometric Identification of Organic Compounds, 6th ed., Wiley, New York, 1998, pp. 99, 101.



Scheme 1. Different neutral and anionic forms.

in the resulting complexes, which opens a multiplicity of bonding schemes. The different donor atoms as well as the various structures of thiourea derivatives result in a variety of complexes [3–5,7,18,20].

In recent years various studies have been reported on a derivative group of thiourea with antifungal activity [7], namely *N*-2-pyridine-*N*′-arylthioureas, showing different substitution patterns on either only one or on both rings [22–25]. These different chemical structures create specific properties for each compound, for example a methoxy-substituent can add to the intermolecular hydrogen bonding scheme [26]. In some cases, these intermolecular interactions can form centrosymmetric dimers [27].

In the current study we tried to synthesize derivatives of the *N*-2-pyridine-*N*′-arylthioureas group. The fact that the copper complexes of thiourea derivatives show an antioxidant effect in biological systems [28] encouraged us to produce copper complexes using our synthesized ligands.

Three new ligand types were prepared **L1**: *N*-2-(4-picolyl)-*N*′-(4-methoxyphenyl)thiourea (4PicTu4OMePh), **L2**: *N*-2-(6-picolyl)-*N*′-(4-methoxyphenyl)thiourea (6PicTu4OMePh) and **L3**: *N*-2-(4-picolyl)-*N*′-(4-nitrophenyl)thiourea (4PicTu4NO_2Ph) (Scheme 2).

All these three ligands were reacted with copper(II) acetate. Coordination of ligand **L1** resulted in complex **C1**, [Cu(4PicTz4OMePh)(OAC)(EtOH)], which was obtained as suitable crystals for single crystal X-ray structure analysis.

Also, we report for the first time new compounds that were the product of an oxidation of some reported ligands by copper(II), for example compound **P1**, (PyHTz4OMePh), was isolated and characterized, and was the result of the reaction of the ligand **L4**, *N*-(2-pyridyl)-*N*′-(4-methoxyphenyl)thiourea, [29,30] with copper(II) as we tried to prepare complex **C2**.

2. Experimental

2.1. General procedure

4-Methyl and 6-methyl-2-aminopyridines, 4-methoxy and 4-nitrophenyl isothiocyanates were purchased from Aldrich. Copper(II) acetate monohydrate and solvents were supplied by Merck. All chemicals were used without further purification.

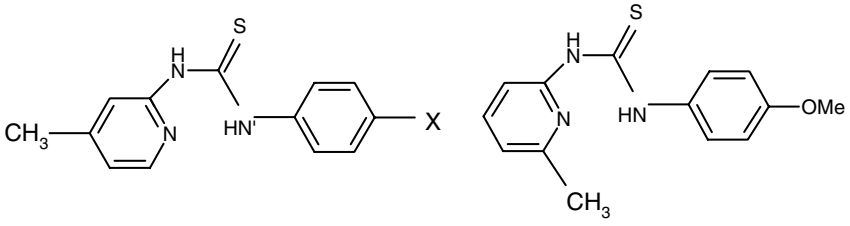
Melting points were determined with the Electro Thermal IA 9000 Series apparatus. FT-IR spectra were obtained with a Nicolet 5SXC spectrometer and using KBr (4000–400 cm^{-1}) pellets. ^1H and ^{13}C NMR spectra in DMSO-d_6 were recorded on a Bruker AVANCE 500 spectrometer at room temperature and with TMS as the internal reference. Elemental analyses for C, H and N were performed on an O-Rapid elemental analyzer.

2.2. Synthesis of the ligands, complexes and precursor

The new ligands, **L1** (4PicTu4OMePh), **L2** (6PicTu4OMePh) and **L3** (4PicTu4NO2Ph) were synthesized using modified protocols from the literature [29,31]. The already reported ligand **L4** (PyTu4OMePh) was prepared as described [29]. The crystals of ligands **L1** and **L2** for X-ray analysis were obtained from recrystallization of an ethanol solution. Percentage yields, melting point, elemental analyses and spectroscopic studies for the ligands **L1**, **L2** and **L3** are as follows.

2.2.1. Ligand *L1* (*4PicTu4OMePh*)

Yield: 0.22 g white powder (82%). Mp: 181–183 °C. FT-IR data (KBr, cm^{-1}): 3490w, 3195m, 3040m, 2920m, 1606s, 1581s, 1524s, 1471s, 1399m, 1346s, 1321s, 1242vs, 1176vs, 1117w, 1095w, 1026s, 824m, 734s, 645m, 603m. ^1H NMR (DMSO-d_6, ppm): 2.29 (s, 3H, H7A, 7B and 7C), 3.75 (s,3H, H19A, 19B and 19C), 6.92 (d, 2H, H14 and 16), 6.93 (d, 1H, H3), 7.05 (s, 1H, H5), 7.51 (d, 2H, H13 and 17), 8.15 (d, 1H, H6), 10.72 (s, 1H, NH), 13.66 (s, 1H, N′H). ^{13}C NMR (DMSO-d_6, ppm): 21.38 (CH_3), 55.74 (OCH_3), 113.12 (C3), 114.12 (C14 and 16), 119.83 (C5), 126.51 (C13 and 17), 132.21 (C12), 145.64 (C6), 150.63 (C4), 154.23 (C2), 157.43 (C15), 179.08 (C=S). *Anal.* Calc.



L1: X = OCH_3 (4PicTu4OMePh)

L3: X = NO_2 (4PicTu4NO_2Ph)

L2: (6PicTu4OMePh)

Scheme 2. Representation of *N*-2-(4-picolyl)-*N*′-(4-methoxyphenyl)thiourea (4PicTu4OMePh), *N*-2-(6-picolyl)-*N*′-(4-methoxyphenyl)thiourea (6PicTu4OMePh) and *N*-2-(4-picolyl)-*N*′-(4-nitrophenyl)thiourea (4PicTu4NO_2Ph).

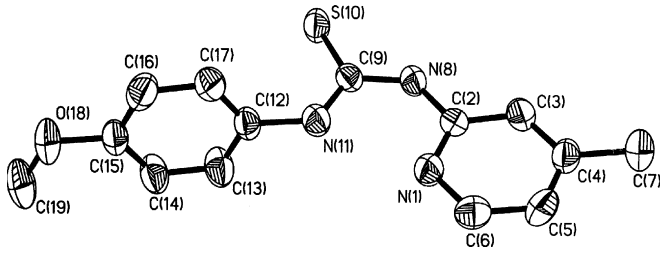


Fig. 1. Molecular structure of **L1** (H atoms are omitted for the clarity; 50% probability level).

for $C_{14}H_{15}N_3OS$: C, 58.60; H, 5.49; N, 15.38. Found: C, 58.72; H, 5.60; N, 15.41%. (The numbers have been clarified in Fig. 1.)

2.2.2. Ligand *L2* (*6PicTu4OMePh*)

Yield: 0.23 g white powder (85%). Mp: 189–190 °C. FT-IR data (KBr, cm^{-1}): 3585vw, 3223m, 3196m, 3030m, 2833w, 1608s, 1562s, 1535m, 1509m, 1451s, 1374m, 1341s, 1299m, 1242vs, 1181s, 1154s, 1111w, 104s, 833s, 795s, 728s, 648m, 624m. ^{1}H NMR (DMSO-d_6, ppm): 2.46 (s, 3H) (H7A, 7B and 7C), 3.75 (s,3H) (H19A, 19B and 19C), 6.94 (d, 3H) (H3, 14 and 16), 7.04 (d, 1H) (H5), 7.59 (d, 2H) (H13 and 17), 7.69 (t, 1H) (H4), 10.73 (s, 1H, NH), 13.92 (s, 1H, N′H). ^{13}C NMR (DMSO-d_6, ppm): 23.69 (CH_3), 55.78 (OCH_3), 110.17 (C3), 114.20 (C14 and 16), 117.63 (C5), 125.65 (C13 and C17), 132.29 (C12), 139.99 (C4), 153.65 (C2), 154.82 (C6), 157.27 (C15), 178.50 (C=S). *Anal.* Calc. for $C_{14}H_{15}N_3OS$: C, 58.60; H, 5.49; N, 15.38. Found: C, 58.48; H, 5.48; N, 15.49%. (The numbers have been clarified in Fig. 2.)

2.2.3. Ligand *L3* (*4PicTu4NO$_2$Ph*)

Yield: 0.18 g pale yellow (62.5%). Mp: 164 °C. FT-IR data (KBr, cm^{-1}): 3285m, 3070w, 2915s, 1592m, 1540s, 1496s, 1377w, 1328vs, 1200s, 1099m, 1031m, 857m, 741m, 676m, 650w. ^{1}H NMR (DMSO-d_6, ppm): 2.30 (s, 3H, H7A, B and C), 6.98 (d, 1H, H3), 7.07 (s, 1H, H5), 8.14 (d, 2H, H13 and 17), 8.21 (d, 2H, H14 and 16), 8.23 (d, 1H, H6), 11.08 (s, 1H, NH), 14.58 (s, 1H, N′H). ^{13}C NMR (DMSO-d_6, ppm): 21.40 (CH_3), 113.45 (C3), 120.40 (C5), 123.20 (C13 and 17), 124.70 (C14, C15 and 16), 143.89 (C12), 145.49 (C6), 151.13 (C4), 153.76 (C2), 178.49 (C=S). *Anal.* Calc. for $C_{13}H_{12}N_4O_2S$: C, 54.17; H, 4.17; N, 19.44. Found: C, 54.12; H, 4.23; N, 19.55%. (The numbers are similar with the numbers in Fig. 1.)

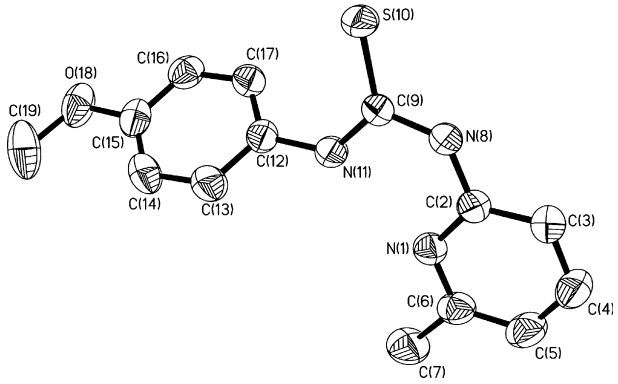


Fig. 2. Molecular structure of **L2** (H atoms are omitted for the clarity; 50% probability level).

2.2.4. Complex *C1*

Complex **C1** [Cu(4PicTz4OMePh)(OAC)(EtOH)] was synthesized from ligand **L1** and copper(II) acetate monohydrate. Copper(II) acetate monohydrate (0.1 g, 0.5 mmol) in 3 mL ethanol was added gradually to the solution of ligand **L1** (0.14 g, 0.5 mmol) in 35 mL ethanol, heated under reflux for 3 h and stirred for 15 h at room temperature. The reaction mixture was filtered off and a slight dark green powder was separated. Dark crystals of the filtrate were obtained after ten days at room temperature. It decomposed at 235 °C. Yield: 0.19 g dark green powder (87%). FT-IR data (KBr, cm^{-1}): 3525w, 2945w, 1616m, 1594m, 1525s, 1459s, 1330m, 1244s, 1159m, 1086w, 1061m, 1027m, 850m, 794m, 630m. *Anal.* Calc. for $C_{18}H_{21}CuN_3O_4S$: C, 49.20; H, 4.78; N, 9.5. Found: C, 48.80; H, 4.80; N, 8.80%.

2.2.5. Complex *C2*

Complex **C2** was synthesized from ligand **L2** and copper(II) acetate monohydrate, using the method as for complex **C1**. The reaction mixture was filtered off and a slight dark olive green powder was separated. It did not melt up to 380 °C. Yield: 0.18 g dark green powder (81%). FT-IR data (KBr, cm^{-1}): 3442w, 2995w, 15869, 1570m, 15462s, 1439s, 1329m, 1259m, 1228m, 1155w, 1047w, 850w, 780m, 680m. *Anal.* Calc. for $C_{16}H_{18}CuN_3O_4S$: C, 48.97; H, 4.59; N, 10.71. Found: C, 47.90; H, 4.30; N, 8.95%.

2.2.6. Complex *C3*

Complex **C3** was also synthesized from ligand **L3** and copper(II) acetate monohydrate, like complexes **C1** and **C2**. An olive green powder as the product was filtered and washed with ethanol and ether, dried in an oven at 80 °C. This compound decomposed at 260 °C. Yield: 0.19 g olive green powder (80%). FT-IR data (KBr, cm^{-1}): 3410vw, 2955w, 1579m, 1521s, 1495s, 1339s, 1290m, 1248s, 1181m, 1084m, 1030m, 841m, 543w. *Anal.* Calc. for $C_{17}H_{20}CuN_4O_5S$: C, 44.80; H, 4.20; N, 12.30. Found: C, 45.11; H, 4.11; N, 12.40%.

2.2.7. Complex *C4*

Complex **C4** was prepared using ligand **L4** and copper(II) acetate monohydrate. 3 mL of an ethanolic solution of copper(II) acetate monohydrate (0.10 g, 0.05 mmol) was added slowly to the ligand **L4** (0.26 g, 0.1 mmol) in 20 mL ethanol, and stirred for 4 h at room temperature. The resulting olive green powder was filtered and washed with

ethanol and ether, dried in an oven at 80 °C. This compound decomposed at 190 °C. Yield: 0.20 g olive green powder (70%). FT-IR data (KBr, cm^{-1}): 3460vw, 2965w, 1553s, 1525m, 1494s, 1443m, 1412s, 1342s, 1289w, 1239s, 1141m, 1024m, 819m, 773m, 722m, 612w. *Anal.* Calc. for $C_{26}H_{20}CuN_6O_2S_2$: C, 54.31; H, 3.50; N, 14.61. Found: C, 54.62; H, 3.27; N, 14.83%.

2.2.8. Precursor *P1* (*PyHTz4OMePh*)

Opaque crystals were obtained from the filtrate of complex **C2** by slow evaporation after three weeks at room temperature. 0.039 g. Mp: 184–186 °C. ^{1}H NMR (DMSO-d_6, ppm): 3.71 (s, 3H, H11A, B and C), 6.85 (s, 1H, H12), 6.9 8 (dd, 1H, H16), 6.95 (s, 1, H6), 7.3 5 (d, 1H, H4), 7.85 (dd, 1H, H17), 7.59 (d, 1H, H3), 7.8 3 (d, 1H, H18), 8.29 (s, 1H, H15). ^{13}C NMR (DMSO-d_6, ppm): 57 (CH_3), 107.24 (C6), 113.16 (C18), 114.85 (C4), 120.15 (C3), 119.81 (C16), 133.58 (C1), 138.38 (C17), 146.94 (C15), 148.96 (C2) 149.15 (C13), 156.69 (C5), 177.78 (C8). *Anal.* Calc. for $C_{13}H_{11}N_3OS$: C, 60.7; H, 4.13; N, 16.34. Found: C, 60.59; H, 4.28; N, 16.18%. (The numbers have been clarified in Fig. 7.)

2.3. X-ray crystallography

Selected crystals of the ligands **L1** and **L2** and the precursor **P1** were mounted on a Bruker-AXS SMART diffractometer with an APEX CCD area detector. Graphite-monochromated Mo Kα radiation (71.073 pm) was used for all measurements. The nominal crystal-to-detector distance was 5.00 cm. A hemisphere of data was collected by a combination of three sets of exposures. Each set had a different ϕ angle for the crystal, and each exposure took 20 s and covered 0.3° in ω. The data were corrected for polarization and Lorentz effects, and an empirical absorption correction (SADABS) [32] was applied. The cell dimensions were refined with all unique reflections. The structures were solved by direct methods (SHELXS-97) [33]. Refinement was carried out with the full-matrix least-squares method based on F^2 (SHELXL-97) with anisotropic thermal parameters for all non-hydrogen atoms. Hydrogen atoms were inserted in calculated positions and refined riding with the corresponding atom.

Complex **C1** was mounted on a Bruker SMART [34] diffractometer with a 1000 CCD area detector. Graphite-monochromated Mo Kα radiation (71.073 pm) was used for measurement. The data were corrected for polarization and Lorentz effects, and an empirical absorption correction (SADABS) [35] was applied. The cell dimensions were refined with SAINTPLUS [36]. The structure was solved first by the direct method and second by the difmap method. Refinement was carried out with the full-matrix least-squares method based on F^2 (SHELXTL-98) [37] with anisotropic thermal parameters for all non-hydrogen atoms. Relevant crystallographic information for the ligands **L1** and **L2**, complex **C1** and precursor **P1** are summarized in Table 1.

3. Results and discussion

3.1. Spectroscopic studies

The solid-state properties of these new compounds were examined by infrared spectroscopy. Selected absorption bands of ligands **L1**, **L2** and **L3**, and complexes **C1**, **C2**, **C3** and **C4** are given in Table 2. The thiourea derivatives can be in the thione or thiol forms. The absence of the ν (S–H) band at about 2570 cm^{-1} and the presence of the ν (N–H) bands in the range of 3000–3300 cm^{-1} in the IR spectra revealed the evidence for thione tautomer formation in the solid state of these compounds. In some cases these bands can be broad as the result of hydrogen bonding. The absorbance bands for different bonds and func-

Table 1
Crystallographic and structure refinement data for **L1**, **L2**, **C1** and **P1**

	L1	**L2**	**C1**	**P1**
Empirical formula	$C_{28}H_{30}N_6O_2S_2$	$C_{14}H_{15}N_3OS$	$C_{18}H_{21}CuN_3O_4S$	$C_{26}H_{22}N_6O_2S_2$
Formula weight	546.70	273.35	438.98	514.62
T (K)	295(2)	299(2)	120(2)	296(2)
Crystal system	monoclinic	monoclinic	monoclinic	triclinic
Space group	$P2_1/c$	$C2/c$	$P2_1/c$	$P\bar{1}$
a (Å)	16.9184(12)	16.6086(11)	14.1605(9)	8.8509(7)
b (Å)	11.7213(8)	12.4244(8)	7.3813(5)	11.9243(10)
c (Å)	14.8123(10)	15.0412(10)	19.2805(13)	12.5385(11)
α (°)				67.945(2)
β (°)				78.958(2)
γ (°)	108.405(2)	115.008(1)	109.5850(10)	82.102(2)
V (Å^3)	2787.1(3)	2812.8(3)	1898.7(2)	1200.66(17)
Z	4	8	4	2
D (Mg m^{-3})	1.303	1.291	1.536	1.423
μ (mm^{-1})	0.228	0.226	1.290	0.260
Final R indices	$R_1 = 0.0763$,	$R_1 = 0.0598$,	$R_1 = 0.0365$,	$R_1 = 0.0533$,
[$I > 2\sigma(I)$]	$wR_2 = 0.1690$	$wR_2 = 0.1420$	$wR_2 = 0.0838$	$wR_2 = 0.1320$
R indices	$R_1 = 0.0927$,	$R_1 = 0.0743$,	$R_1 = 0.0421$,	$R_1 = 0.0754$,
(all data)	$wR_2 = 0.1774$	$wR_2 = 0.1509$	$wR_2 = 0.1320$	$wR_2 = 0.1472$

Table 2
Selected infrared absorption bands for **L1**, **L2**, **L3**, **L4**, **C1**, **C2**, **C3** and **C4** (cm^{-1})

Comp.	NH	C=N C=C (py)	C–N	C=S C–S[a]	C–O (OCH_3)	NO_2[b] COO[c]
L1	3195	1606	1170	1346	1242	
		1581	1117	824	1026	
			1095			
L2	3196	1608	1181	1341	1242	
		1562	1149	833	1034	
L3	3280	1592	1099	1328		1496[b]
		1540	1031	841		1328[b]
						857[b]
L4	3150	1601	1183	1345	1185	
		1580	1137	822	1020	
			1097			
C1	3525[d]	1616	1159	792[a]	1244	1525[c]
		1594			1027	1459[c]
C2	3442	1589	1155	780[a]	1251	1462
		1570			1030	1439
						1495[b]
C3	3410	1579	1181	1335		1339[b]
		1521	1094	841		857[b]
			1036			1521[c]
						1495[c]
C4	3511	1553	1141	773[a]	1180	
		1525			1024	

[a] C–S.
[b] NO_2.
[c] COO.
[d] OH.

tional groups in prepared ligands and complexes have been inserted in Table 2 [10,31,38–42].

^1H and ^{13}C NMR spectroscopy were applied to characterize and define the structural properties, particularly the intra- and intermolecular hydrogen bonding of the ligands **L1**, **L2**, **L3** and **L4** in solution. The presence of NH and N′H resonances in the ^1H NMR (Table 3) and the absence of SH resonances indicate the thione tautomeric form as the stable form in the solutions of the synthesized ligands. The resonance for C=S, shown by the ^{13}C NMR spectra, is an additional evidence for the thione tautomeric form of the ligands.

Corresponding to the literature, the ^1H NMR spectrum of PyTuPh indicates that the N′H and NH resonances appear at 13.86 and 10.90 ppm, but these resonances vary with different parameters, such as the substituted groups on the rings, which release and withdraw electron density in each ring, their positions and intra- and inter-hydrogen bondings [26,27,29,30,43].

Table 3
^1H NMR chemical shifts (ppm) for **L1**, **L2**, **L3** and **L4**[a]

Comp.	N′H[b]	NH[c]	C6H	C4H	OCH_3	CH_3	Ref.
PyTu4OMePh	13.58	10.82	8.37	7.82	3.76		[31]
L4	13.57	10.80	8.29	7.82	3.51		[d]
L1	13.66	10.72	8.15		3.75	2.29	[d]
L2	13.92	10.73		7.69	3.75	2.46	[d]
PyTu2OMePh	13.80	8.53	8.59	7.68	3.92		[43]
4PicTu2OMePh	13.87	8.36	8.61		3.91		[43]
6PicTu2OMePh	14.01	9.00		7.54	3.92		[43]
PyTu4NO_2Ph	14.48	11.20	8.32	7.84			[31]
L3	14.58	11.08	8.23			2.30	[d]

[a] Similar positions are located in each column.
[b] N′H, thiourea connects to the phenyl ring.
[c] NH, thiourea connects to the pyridine ring.
[d] This work.

For example, exchange of a methoxy group in **L1** for a nitro group in **L3** causes that the N′H and NH resonances are shifted further downfield to 14.58 and 11.08 ppm, respectively [31]. The methoxy group in different positions has a small effect on intra-hydrogen interactions and the chemical shift of N′H, but inter-hydrogen bonding and subsequently the chemical shift of NH are influenced by ortho- and meta-substitution positions in comparison to a para-substitution position in the phenyl ring.

In contrast, the different positions of the methyl group in the pyridine ring in ligands **L1** (para-position), **L2** (ortho-position) and PyTu4OMePh (without any substitution) have the same effect on the intermolecular hydrogen bonding and the chemical shifts of NH. On the other hand this position in the phenyl ring has no effect on the chemical shift of NH [29]. The different positions of the methyl group in the pyridine ring affect the intramolecular hydrogen bonding and the chemical shift of N′H (Table 4) [10,43].

^{13}C NMR spectra data reveals (Table 5) no significant differences of the chemical shifts in ligands **L1** and **L2** containing methyl and methoxy groups. In comparison, the nitro group in ligand **L3** causes variations of chemical shifts for C2, C4 and C15 to those of **L1** and **L2**. The chemical shifts of carbon of the C=S bond in all three ligands was about 179 ppm. This similar chemical shift could be due to the isolated position of the thione group in these ligands [44–46].

3.2. Crystal structures of *L1*, *L2*, *C1* and *P1*

Comparison of the molecular structures of ligands **L1**, **L2** (Figs. 1 and 2) and related compounds such as PyTu4OMe [29,30], 4PicTuPh [31], 6PicTuPh [31], 4PicTu2OMePh [43] and 6PicTu2OMePh [43] indicate that the bond distances and angles are similar and are not affected by the substitution patterns on the phenyl or pyridine rings (Table 6).

In the crystal packing of ligand **L1**, weak intermolecular hydrogen bonding interactions were identified between N8–H8···S29 as well as N27–H27···S10, connecting two molecules to each other and forming centrosymmetric dimers in the solid state (Fig. 3). Two strong intramolecular hydrogen bonds, N11–H11···N1 and N30–H30···N20, are formed between NH from thiourea and N from the pyridine ring in each molecule. The centrosymmetric dimer of ligand **L2** (Fig. 4) is also formed by a weak intermolecular hydrogen bonding interaction, N8–H8···S10.

The ligand **L2** contains two strong intramolecular hydrogen bonds, N11–H11···N1 too (Table 8).

The synthesis of complex **C1** starts with the polarization of the C=S bond in ligand **L1** by the copper(II) ion. The transfer of electron density to the sulfur atom results in

Table 4
Intramolecular and intermolecular hydrogen bond distances (Å) and angles (°) (D = donor, A = acceptor) and ^{1}H NMR spectra data for **L1** and **L2**[a]

Comp.	Intramolecular		N′H	D[c]	A	Intermolecular		NH	Ref.
	D–H···A[b] (Å)					D–H···A (Å)	D–H···A (°)		
PyTu4OMePh	2.68(2)	136.8(8)	13.58	N	S	3.42(2)	141.6(2)	10.82	[29]
	2.70(2)	140.2(8)				3.41(1)	152.6(7)		[30]
				N′	O	3.82(1)	116.0(7)		
						3.62(1)	110.3(7)		
PyTu2OMePh	2.668(5)	140.4(3)	13.80	N	S	3.406(3)	149.5(2)	8.53	[43]
				N′	O	3.170(5)	128.7(2)		
4PicTu2OMePh	2.634(9)	141.0(4)	13.87	N	S	3.470(6)	157.9(4)	8.36	[43]
L1	2.642(5)	140.7	13.66	N	S	3.395(3)	168.2	10.72	[d]
	2.647(5)	130.1		N	S	3.400(4)	160.7		
L2	2.632(2)	136.1	13.92	N	S	3.3695(16)	165.5	10.73	[d]
6PicTu2OMePh	2.652(5)	133.2(2)	14.01	N	S	3.421(3)	160.5(2)	9.00	[43]
				N	S	3.418(3)	163.7(2)		
L3			14.58					11.08	[d]
PyTu4NO$_2$Ph	2.655(5)	144.7(3)	14.48	N	S	3.414(3)	163.6(3)	11.20	[31]
				N′	O	3.333(5)	120.2(1)		

[a] Similar positions are located in each column.
[b] D = N′ thiourea connects to the phenyl ring and A = N in the pyridine ring.
[c] D = N thiourea connects to the pyridine ring.
[d] This work.

Table 5
Selected ^{13}C NMR chemical shifts (ppm) for **L1**, **L2** and **L3**[a]

Comp.	C=S	C2	C6	C15	C12	C4	OCH_3	CH_3
L1	179.08	154.23	145.64	157.43	132.21	150.63	55.74	21.38
L2	178.50	153.65	154.82	157.27	132.29	139.99	55.78	23.69
L3	178.49	153.76	145.49	124.70	143. 89	151.13		21.40

[a] Similar positions are located in each column.

Table 6
Selected bond distances (Å) and bond angles (°) for **L1**, **L2** and **P1**

	L1	**L2**		**P1**
N1–C2	1.334(5)	1.329(2)	N14–C13	1.323(3)
C2–N8	1.396(5)	1.400(2)	C13–N12	1.390(3)
N8–C9	1.372(5)	1.368(2)	N12–C8	1.368(2)
C9–N11	1.332(5)	1.328(2)	C8–N9	1.303(3)
C9–S10	1.679(4)	1.6912(19)	C8–S7	1.751(2)
N11–C12	1.440(5)	1.424(2)	N9–C2	1.391(2)
			C1–S7	1.741(2)
N1–C2–N8	118.6(4)	118.63(16)	N14–C13–N12	117.16(18)
C9–N8–C2	130.1(13)	129.88(16)	C8–N12–C13	126.23(18)
N8–C9–S10	119.3(3)	118.83(13)	N12–C8–S7	123.03(15)
N11–C9–N8	117.0(4)	116.72(16)	N9–C8–N12	120.27(18)
N11–C9–S10	123.6(3)	124.43(14)	N9–C8–S7	116.71(15)
C9–N11–C12	125.0(4)	128.20(16)	C8–N9–C2	109.86(16)
			C1–S7–C8	88.33(9)
			N12–C8–S7	123.03(15)
			C6–C1–S7	127.42(16)
			C2–C1–S7	109.72(15)

the polarization and oxidation of the C=S bond [47–49]. The reaction of the sulfur atom with C17 in the phenyl ring eliminates two hydrogen atoms, which are connected to N8 and C17, and a new five-membered ring is formed. The N8–C9 bond length is decreased and the S10–C9 bond length is increased in the complex **C1** [49].

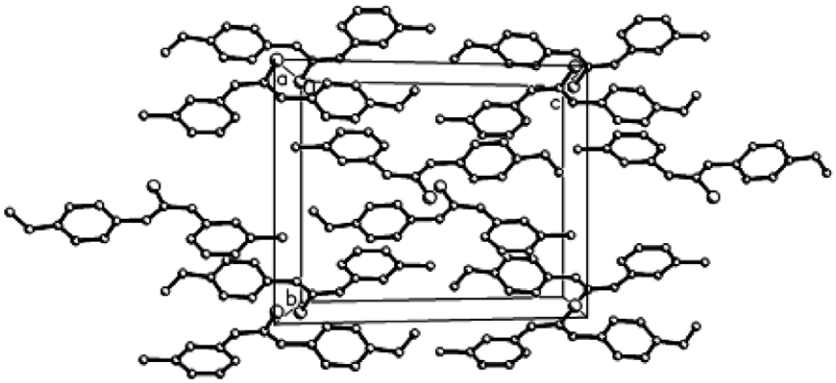


Fig. 3. View of the unit cell **L1**.

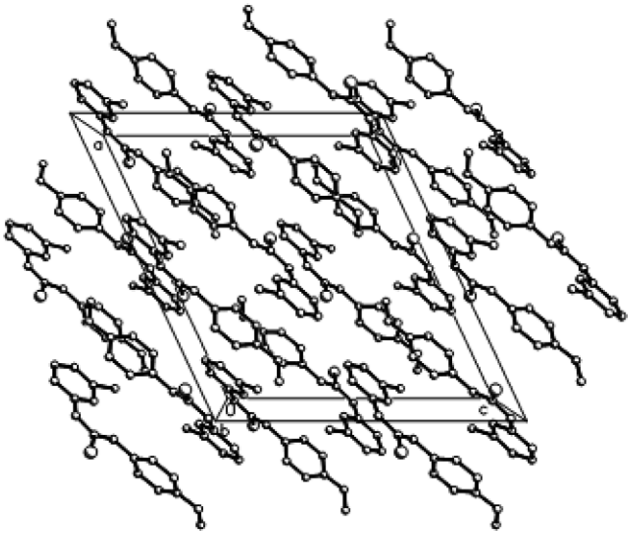


Fig. 4. View of the unit cell **L2**.

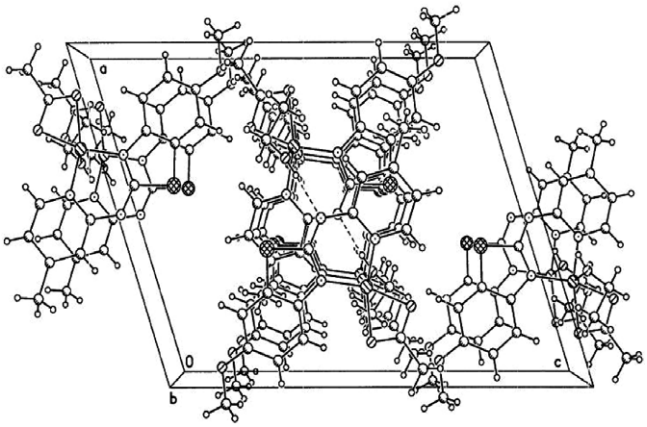


Fig. 6. View of the unit cell of complex **C1** with hydrogen bonding.

The oxidized cyclization form of ligand **L1** communicates with the copper(II) ion as a bidentate chelating agent, via the nitrogens of pyridine and thiourea (Fig. 5).

According to the Pearson principle, the nitrogen atoms of the ligands as a hard base are bound to copper(II) as a hard acid in these complexes [50]. These connections make a six-membered chelate ring around the central ion. This ligand appears as a uninegatively charged form in the complex. In addition, the acetate anion is coordinated to the copper ion in the same plane as **L1**. One solvent molecule occupies the axial position of the complex **C1** via its

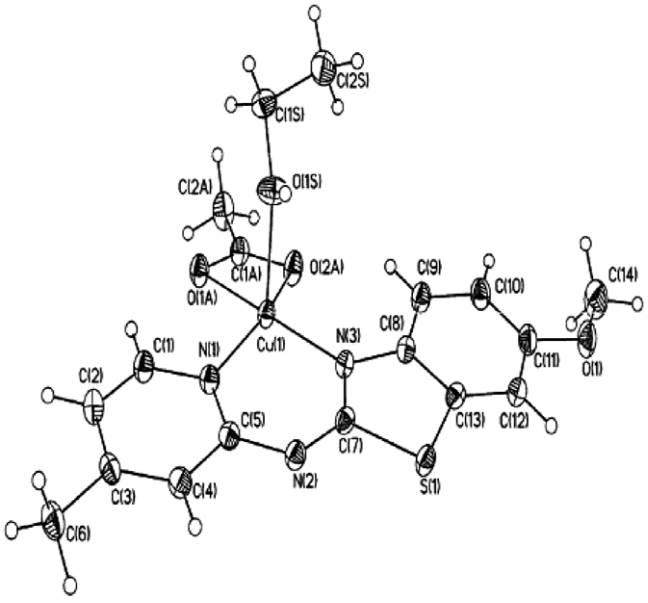


Fig. 5. Molecular structure of complex **C1**.

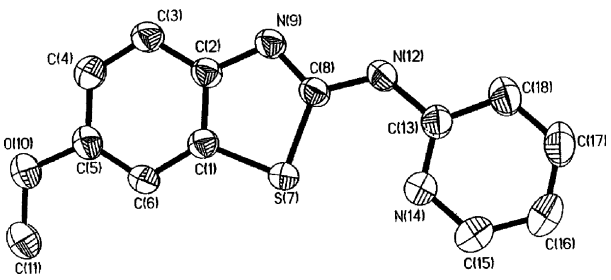


Fig. 7. Molecular structure of **P1** (H atoms are omitted for the clarity; 50% probability level).

Table 7
Selected bond distances (Å) and bond angles (°) for **C1**

	C1		C1
N1–C1	1.367(2)	N3–C8	1.409(2)
N1–C5	1.353(2)	Cu1–N1	1.9657(14)
N2–C5	1.368(2)	Cu1–N3	1.9442(14)
N2–C7	1.324(2)	Cu1–O1A	2.0236(13)
C7–N3	1.339(2)	Cu1–O2A	2.0673(13)
C7–S1	1.7686(16)	Cu1–O1S	2.2013(14)
C1–C13	1.7340(18)		
C5–N1–C1	117.64(15)	N3–Cu1–O2A	103.06(6)
N1–C5–N2	124.07(15)	N1–Cu1–O2A	155.78(6)
C7–N2–C5	124.43(15)	O1A–Cu1–O2A	64.09(5)
N2–C7–S1	114.71(12)	N3–Cu1–O1S	96.83(6)
N2–C7–N3	131.96(15)	N1–Cu1–O1S	99.25(6)
N3–C7–S1	113.34(12)	O1A–Cu1–O1S	91.55(5)
C13–S1–C7	90.41(8)	O2A–Cu1–O1S	95.71(6)
N3–Cu1–N1	93.99(6)	C1A–O1A–Cu1	89.64(10)
N3–Cu1–O1A	165.41(6)	C1A–O2A–Cu1	87.93(11)
N1–Cu1–O1A	96.43(5)		

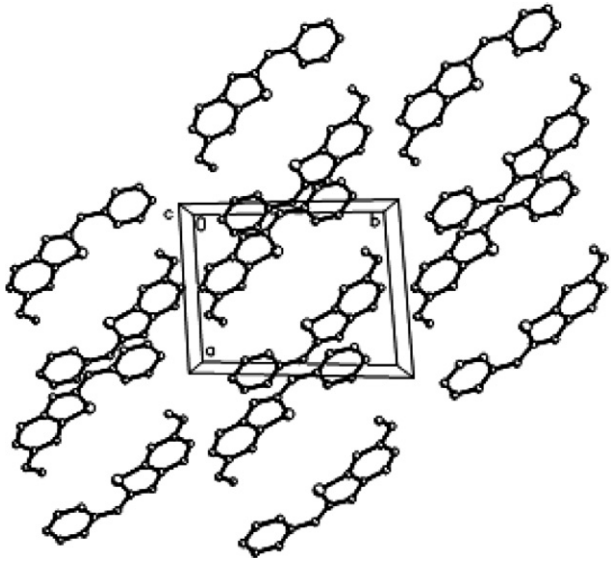


Fig. 8. View of the unit cell of **P1** (H atoms are omitted for clarity).

oxygen atom. Finally, the copper ion is in a five-coordinated environment.

The oxidation of **L1** requires the reduction of another compound in the solution, which is most likely copper(II) [47–49]. The neutral form of complex **C1** containing two negative ligands can be due to the existence of a copper(II) ion that is the result of oxidation of copper(I). The most probable oxidant for the oxidation of the copper(I) ion is dissolved oxygen in the solution.

A five-coordinated complex can be as a trigonal-bipyramid (TBPY), a square-pyramid (SPY) or, an intermediate between these two forms. The structural index parameter ($\tau = (\beta - \alpha)/60$) can be used to determine the structure of the five-coordinated complex [51]. Complex **C1** has a τ value of 0.16, which indicates that the structure of **C1** is very close to SPY [52–62]. Complex **C1** possesses two equal strong intermolecular hydrogen bonds (Fig. 6 and Table 8).

Precursor **P1** is obtained by the oxidative cyclization of ligand **L4** during the preparation of complex **C4** ($C_{26}H_{20}CuN_6O_2S_2$) (Fig. 7). The changes in the bond lengths of **P1** correspond to those of **L1** in complex **C1**. For example, the C–S bond length in precursor **P1** is increased in comparison to that in **L4** (Tables 6 and 7). Two strong hydrogen bonds N12–H12···N27 and N30–H30···N9 form centrosymmetric dimers of **P1** (Fig. 8, Table 8).

4. Conclusion

Characterization of three new pyridyl thiourea derivatives 4PicTu4OMePh, 4PicTu4NO_2Ph and 6PicTu4OMePh and their structures show the existence of hydrogen bonding interactions. The electron withdrawing nitro group has more an effect than the electron donating methoxy group on intra- and intermolecular hydrogen bonding. The position of the methoxy group in the phenyl ring has no effect on intermolecular hydrogen bonding, but the location of the methyl group influences intramolecular hydrogen bonding and the chemical shift of the proton

Table 8
Intra- and intermolecular interactions for **L1**, **L2**, **C1** and **P1**[a]

Compound	D	A	D–H	H···A (Å)	D–H···A (Å)	∠D–H···A (°)
Intramolecular						
L1	N11	N1	0.93	1.85	2.642(5)	140.7
	N30	N20	0.90	1.97	2.647(5)	130.1
L2	N11	N1	0.93	1.88	2.632(2)	136.1
Intermolecular						
L1	N8	S29#1[b]	0.95	1.97	3.395(3)	168.2
	N27	S10#2	0.95	2.48	3.400(4)	160.7
L2	N8	S10[c]	0.93	2.46	3.3695(16)	165.5
C1	O1S	N2[d]	0.813	1.904	2.708(2)	170.34
P1	N12	N27#1[e]	0.87	2.19	3.054(2)	171.5
	N30	N9#2	0.86	2.10	2.944(2)	168.1

[a] Symmetry transformations used to generate equivalent atoms.
[b] #1: $x, y+1, z$; #2: $x, y-1, z$.
[c] #1: $-x+1, -y+1, -z$.
[d] $-x+1, y+2, -z$.
[e] #1: $x-1, y, z+1$; #2: $x+1, y, z-1$.

(NH′). The different positions of the methyl group in the pyridine ring can affect the intramolecular hydrogen bonding and the chemical shift of the proton (NH′).

The reactions of $Cu(OAC)_2$ with the ligands, **L1**, **L2**, **L3** and **L4** result in the new complexes [Cu(4PicTz4OMeTu4NO2Ph)(OAC)], [$Cu(PyHTz4OMePh)_2$] respectively, and a precursor PyHTz4OMePh of **L4**. Oxidative cyclizations of the ligands **L1**, **L2** and **L4** occur during these reactions. The oxidative cyclization in **L1** and **L4** are observed clearly in the molecular structures of **C1** and **P1**. The result of the oxidative cyclization is the appearance of new absorption bands for C–S in the IR spectra of the complexes **C1** and **C4**. The similarity between **L1** and **L2**, and the existence of identical electron donating groups in these ligands, cause oxidative cyclization to be expected in complex **C2**. Also, the new absorbance band in the IR spectrum of this complex shows the formation of a C–S bond. But in complex **C3**, the nitro electron withdrawing group decreases the electron density around the sulfur atom and prevents oxidative cyclization in this complex. Its IR spectrum confirms this point.

In complex **C1**, the copper(II) ion has a square-pyramidal structure and is surrounded by the anionic bidentate oxidative cyclization ligand (4PicTu4OMePh), an acetate anion and ethanol as a solvent. The presence of the precursor (PyHTz4OMePh) in the second reaction shows that first the oxidative cyclizations of the ligands occur and then the complexes are formed.

5. Supplementary material

CCDC 612985, 612986, 285594 and 612987 contain the supplementary crystallographic data for **L1**, **L2**, **C1** and **P1**. These data can be obtained free of charge via http://www.ccdc.cam.ac.uk/conts/retrieving.html, or from the Cambridge Crystallographic Data Centre, 12 Union Road, Cambridge CB2 1EZ, UK; fax: (+44) 1223-336-033; or e-mail: deposit@ccdc.cam.ac.uk.

Acknowledgements

Dr. Zoya Starikova of the Academy of Sciences of Russia is gratefully acknowledged for crystallographic data (complex **C1**). Financial support by the Iran University of Science and Technology is acknowledged.

References

[1] A. Esteves-Souza, K. Pissinate, M.G. Nascimento, N.F. Grynberga, A. Echevarria, Bioorg. Med. Chem. 14 (2006) 492.
[2] R. Ziessel, L. Bonardi, P. Retailleau, G. Ulrich, Org. Chem. 71 (2006) 3093.
[3] D.E. Fuerst, E.N. Jacobsen, J. Am. Chem. Soc. 127 (2005) 8964.
[4] A.G. Wenzel, E.N. Jacobsen, J. Am. Chem. Soc. 124 (2002) 12964.
[5] Y. Tang, L. Deng, Y. Zhang, G. Dong, J. Jiahua, J. Chen, Z. Yang, Org. Lett. 7 (2005) 1657.
[6] C. Fontás, M. Hidalgo, V. Salvadó, E. Anticó, Anal. Chim. Acta 547 (2005) 255.
[7] E. Rodrìguez-Fernandez, J.L. Manzano, J.J. Benito, R. Hermosa, E. Monte, J.J. Criado, J. Inorg. Biochem. 99 (2005) 1558.
[8] T.K. Venkatachalam, E. Sudbeck, F.M. Uckun, J. Mol. Struct. 751 (2005) 41.
[9] S.S. Abdel-Rehim, K.F. Khaled, N.S. Abd-Elshafi, Electrochim. Acta 51 (2006) 3269.
[10] L.M. Fostiak, I. García, J.K. Swearingen, E. Bermejo, A. Castineiras, D.X. West, Polyhedron 22 (2003) 83.
[11] W. Kaminsky, J.P. Jasinski, R. Woudenberg, K.L. Goldberg, D.X. West, J. Mol. Struct. 608 (2002) 135.
[12] W. Zhoua, L. Zhua, Y. Zhanga, Z. Yua, L. Lub, X. Yangb, Vib. Spectrosc. 36 (2004) 73.
[13] U. Bierbach, W. Saak, D. Hasse, S. Pohli, J. Chem. Sci. 45 (1990) 45.
[14] R.C. Boot, G.A. Bomaker, C.A. Davis, G.A. Hope, B.E. Jones, Inorg. Chem. 37 (1998) 651.
[15] H.K. Fun, I.A. Razak, C. Pakaatchai, C. Khaokong, S. Chantrapromma, S. Saithong, Acta Crystallogr. Sect. C 54 (1998) 453.
[16] E.S. Raper, Coord. Chem. Rev. 61 (1985) 115.
[17] U. Bierach, J.D. Roberts, N. Farrell, Inorg. Chem. 37 (1998) 717.
[18] Y.E. Filinchuk, V.V. Oliinik, T. Glovya, M.G. Mys'kiv, Russ. J. Coord. Chem. 27 (2001) 126.
[19] J. Madarasz, P. Bombicz, M. Kaneko, Solid State Ionics 141 (2001) 439.
[20] P. Bombicz, I. Mutikainen, M. Krunks, T. Leskela, J. Madarasz, L. Niinisto, Inorg. Chim. Acta 357 (2004) 513.
[21] A. Castineriras, E. Bermejo, L.J. Akerman, H. Beraldo, D.X. West, J. Mol. Struct. 477 (1999) 1.
[22] D.X. West, A.K. Hermetet, L.J. Ackerman, J. Valdés-Martínes, S. Hernández-Ortega, Acta Crystallogr. Sect. C 55 (1999) 811.
[23] D.R. Kelman, L.F. Szczepura, K.I. Goldberg, W. Kaminsky, A.K. Hermetet, L.J. Ackerman, J.K. Swearingen, D.X. West, J. Mol. Struct. 610 (2002) 143.
[24] W. Kaminsky, D.R. Kelman, J.M. Giesen, K.I. Goldberg, K.A. Claborn, L.F. Szczepura, D.X. West, J. Mol. Struct. 616 (2002) 79.
[25] D.R. Kelman, K.A. Claborn, W. Kaminsky, K.I. Goldberg, D.T. Li, D.X. West, J. Mol. Struct. 654 (2003) 145.
[26] J.M. Giesen, K.A. Claborn, K.I. Goldberg, W. Kaminsky, D.X. West, J. Mol. Struct. 613 (2002) 223.
[27] W. Kaminsky, K.I. Goldberg, D.X. West, J. Mol. Struct. 605 (2002) 9.
[28] J. Vančo, O. Švajlenovà, E. Račanskà, J. Muselik, J. Valentovà, J. Trace Elem. Med. Biol. 18 (2004) 155.
[29] L.F. Szczepura, K.K. Eilts, A.K. Hermetet, L.J. Ackerman, J.K. Swearingen, D.X. West, J. Mol. Struct. 607 (2002) 101.
[30] D.R. Kelman, K.A. Calborn, W. Kaminsky, K.I. Goldenbrg, D.X. West, J. Mol. Struct. 642 (2002) 119.
[31] J. Valdés-Martínes, S. Hernández-Ortega, G. Espinosa-Perez, C.A. Presto, A.K. Hermetet, K.D. Haslow, L.J. Ackerman, L.f. Szczepura, K.I. Goldberg, W. Kaminsky, D.X. West, J. Mol. Struct. 608 (2002) 77.
[32] G.M. Sheldrick, SADABS, University of Göttingen, Germany, 1996.
[33] G.M. Sheldrick, SHELXS97 and SHELXL97, University of Göttingen, Germany, 1997.
[34] Bruker, SMART, Bruker Molecular Analysis Research Tool, V. 5.059. Bruker AXS, Madison, Wisconsin, USA, 1998.
[35] G.M. Sheldrick, SADABS V. 2.01, Bruker/Siemens Area Detector Absorption Correction Program, Bruker AXS, Madison, Wisconsin, USA, 1998.
[36] Bruker, SAINTPlus Data Reduction and Correction Program V. 6.01, Bruker AXS, Madison, Wisconsin, USA, 1998.
[37] G.M. Sheldrick, SHELXTL V. 5.10, Structure Determination Software Suite, Bruker AXS, Madison, Wisconsin, USA, 1998.
[38] K.A. Ketcham, I.B. Garcia, J.K. Swearingen, A.K. El-Sawaf, E. Bermejo, A. Castiñeiras, D.W. West, Polyhedron 21 (2002) 859.
[39] I. García, E. Bermejo, A.K. El-Sawaf, A. Castiñeiras, D.X. West, Polyhedron 21 (2002) 729.
[40] P.N. Yadav, M.A. Demertzis, D. Kovala-Demertzi, S. Stavroula Skoulika, D.X. West, Inorg. Chim. Acta 349 (2003) 30.

[41] A.E. Bolzan, P.L. Schilardi, R.C.V. Piatti, T. Iwasita, A. Cuesta, C. Gutierrez, A.J. Arvia, J. Electroanal. Chem. 571 (2004) 59.
[42] B. Smith, Infrared Spectral Interpretation, A Systematic Approach, CRC LLC, New York, 1999.
[43] D.X. West, J.K. Swearingen, A.K. Hermetet, L.J. Ackerman, J. Mol. Struct. 562 (2001) 95.
[44] S. Ahmad, A.A. Isab, W. Ashraf, Inorg. Chem. Commun. 5 (2002) 816.
[45] A. Vogel, B.S. Furniss, A.J. Hannaford, V. Rogers, P.W.G. Smith, A.R. Tatchell, Vogel's TextBook of Practical Organic Chemistry, Longman, London, 1986.
[46] D. Whittaker, Interpreting Organic Spectra, RSC, London, 2000.
[47] D.X. West, L.F. Szczepura, J.M. Giesen, W. Kamisky, J. Kelley, K.I. Goldberg, J. Mol. Struct. 646 (2003) 95.
[48] O. Estévez-Hernández, E. Otazo-Sánchez, J.L. Cisneros, I. Naranjo-Rodríguez, E. Reguera, Spectrochim. Acta Part A 62 (2005) 964.
[49] D.J. Che, G. Li, Z. Yu, D.P. Zou, C.X. Du, Inorg. Chem. Commun. 3 (2000) 537.
[50] R.G. Pearson, J. Am. Chem. Soc. 85 (1963) 3533.
[51] A.W. Addison, T.N. Rao, J. Reedijk, J. Van Rijin, G.C. Verschoor, J. Chem. Soc., Dalton Trans. (1984) 1349.
[52] J.K. Swearingen, T.J. Romack, I.S. Billen, J.P. Jasinski, Y. Li, R.J. Staples, J. Mol. Struct. 570 (2001) 129.
[53] J. Lee, D. Kim, B. Oh, Y. Soolan, M. Chang, Bull. Korean Chem. Soc. 17 (1996) 836.
[54] K.A. Ketchman, J.K. Swearingen, A. Castineiras, I. Garcia, E. Bermejo, D.X. West, Polyhedron 20 (2001) 3265.
[55] N. Matsumoto, Y. Motoda, T. Matsuo, T. Nakashima, N. Re, F. Dahan, J.P. Tuchagues, Inorg. Chem. 38 (1999) 1165.
[56] Y.B. Dong, M.D. Smith, H.C. Loye, Inorg. Chem. 39 (2000) 1943.
[57] J.T. Tojal, L. Lezama, J.L. Pizarro, M. Insausti, M.I. Arriortua, T. Rojo, Polyhedron 18 (1999) 3703.
[58] M.A. Ali, A.H. Mirza, A.M.S. Hossain, M. Nazimuddin, Polyhedron 20 (2001) 1045.
[59] P. Gómez-Siaz, J. Garcia-Tojal, M.A. Maestro, F.J. Arnaiz, T. Rojo, Inorg. Chem. 41 (2002) 1345.
[60] M.E. Helton, P. Chen, P.P. Paul, Z. Tyeklár, R.D. Sommer, L.N. Zakharov, A.L. Rheingold, E.I. Solomon, K.D. Karlin, J. Am. Chem. Soc. 125 (2003) 1160.
[61] S.K. Chattopadhyay, T.C.W. Mak, Inorg. Chem. Commun. 3 (2000) 111.
[62] P.D. Akirovs, Coord. Chem. Rev. 213 (2001) 181.

Available online at www.sciencedirect.com
ScienceDirect
Polyhedron 26 (2007) 4619
POLYHEDRON
www.elsevier.com/locate/poly

Foreword

Polyhedron Symposia-in-Print, number 28 transition metal chemistry of NO, N_2O and related molecules

Nitric oxide (NO) is an unusual example of a stable diatomic molecule that possesses an odd-electron configuration, the chemistry of which has been extensively studied. In particular, the transition metal chemistry of NO has been studied for many decades, thereby demonstrating that the NO ligand can exhibit a variety of coordination modes. By comparison to NO, the transition metal chemistry of derivatives such as nitroxyl (HNO) and nitrous oxide (N_2O) have been little explored.

This Symposium-in-Print provides a forum that describes not only the transition metal chemistry of NO, but also derivatives such as hyponitrite $[N_2O_2]^{2-}$, nitrite $[NO_2]^-$ nitroxyl (HNO) and other species that share common bonding similarities (e.g. diazenido compounds).

Gerard Parkin
Department of Chemistry, Columbia University, New York, NY 10027, USA
Tel.: +1 212 854 8247; fax: +1 212 932 1289
E-mail address: parkin@columbia.edu

Available online 6 July 2007

0277-5387/$ - see front matter © 2007 Elsevier Ltd. All rights reserved.
doi:10.1016/j.poly.2007.07.001

lable manner, as well as limiting NO exposure to selected sites within the body, we have entrapped [Ru(terpy)(L)-NO](PF$_6$)$_3$ complexes (where terpy = 2,2′:6′,2″-terpyridine and L = 2,2′-bipyridine (bpy) and 3,4-diiminebenzoic acid (NH · NHq) into sol–gel processed polysiloxane and silicone matrices. Recently some physico-chemical properties of nitrosyl complexes entrapped in a silicate sol–gel matrix have been described [19,20]. Although the authors have suggested its use in therapeutic applications due to the controlled NO release, there is no experimental indication that kind of system will work in biological experiments.

In this study, NO measurements were carried out and we have found that [Ru(terpy)(L)NO](PF$_6$)$_3$ complexes can also promote NO-release from the sol–gel and silicone membranes by ultraviolet and visible light irradiation. Some pharmacological properties of the entrapped [Ru(terpy)(NH · NHq)NO](PF$_6$)$_3$ complexes have also been described based on the photolysis at 532 nm showing the versatility of these materials for therapeutic applications.

2. Experimental

2.1. Chemicals and reagents

$RuCl_3 \cdot nH_2O$, terpyridine (terpy) and bipyridine (bpy) were purchased as high purity reagents from Aldrich Chemicals and were used as supplied. Doubly distilled water was used for all experiments. All preparations and measurements were carried out under an argon atmosphere and protected from light.

2.2. Synthesis of ruthenium complexes

The recrystallized complex salt [RuCl(bpy)(terpy)]Cl, [Ru(bpy)(terpy)(NO)](PF$_6$)$_3$, [RuCl(NH · NHq)(terpy)]Cl and [Ru(NH · NHq)(terpy)NO](PF$_6$)$_3$ were prepared as previously published [22–24].

2.3. Preparation of the membranes

The hybrid composite was synthesized by preparing a mixture of 24 mL tetraethoxysilane (Aldrich, Milwaukee, WI, USA) and 19 mL of bidistilled water. The reagents were carefully added and three drops of concentrated HCl were added in order to catalyze the reaction. The nitrosyl ruthenium complexes (*ca*. 0.001 g) were added with constant stirring into 4.5 mL of hydrolyzed. The solution was stirred for 5 min at 60 °C and aliquots (2.0 mL) of the mixture were then transferred to a Petri dish (58 mm diameter) to complete the reaction. The molds remained opened for 3 days until they no longer exhibited weight loss due to evaporation of residual water and solvent.

The silicone resin was prepared by mixing polydimethylsiloxane (PDMS Dow Corning) (2.000 g) with tetraethoxysilane (TEOS, Fluka) (0.500 g) in 2.5 cm^3 of isopropylic alcohol. To this mixture we add the nitrosyl ruthenium compound (0.001 g), previously dissolved in the 0.5 cm^3 of acetonitrile, and five drops of di-*n*-butyltin–dilaurate complex, 5% in hexane (Gelest) as catalyst. The final mixture was stirred for 5 min. The wet gels were air-dried at room temperature for 24 h.

2.4. Apparatus

Ultraviolet-visible (UV–Vis) spectra were recorded on a Hitachi U-3501 and a Hewlett Packard HP8452A diode array spectrophotometer. Infrared (IR) spectra were recorded on either a Protegé 460 series or a MB Bomem 102 FTIR spectrometer. Scanning electron microscopy was performed using a LEO 440 microscope equipped with an Oxford EDS detector. The pH measurements were made using a 430 pH meter from Corning. NO release was measured with an ISO-NOP NO meter from Word Precision Instruments. Continuous photolysis with monochromatic irradiations at 355 and 436 nm was carried out using a 150 W Xenon lamp in a model 6253, Oriel Universal Arc Lamp Source. The irradiation wavelength was selected with an Oriel interference filter, with 10 nm band path, for photolysis at the appropriate wavelengths. The progress of the photoreactions was monitored spectrophotometrically.

2.5. Nitric oxide release measurement

The experiment was performed using a photo-reactor (0.18 m^3) containing 250 W fluorescent lamps (Philips), which were used as a visible light source. The 450–800 nm wavelength range was achieved using a filter. A total of 0.200 g of membrane containing incorporated nitrosyl ruthenium complexes were added to a quartz UV–Vis reservoir containing 10 mL of 0.01 M phosphate buffer solution pH 7.4. This reservoir was connected by a polyethylene tube (20 cm; 1 mm diameter) to another chamber containing 10 mL of phosphate buffer solution where the NO-sensor (amino-700 from Innovative Instruments, Inc) was adapted. Argon flux was bubbling in both reservoirs during the experiment.

The reservoir containing the membrane was submitted to light irradiation and the NO was detected by measuring the current.

2.6. Vessel preparation

Male *Wistar* rats (180–200 g) were killed by decapitation and the thoracic aorta was quickly removed and dissected free and cut into rings 4 mm long. The endothelium was mechanically removed by gently rolling the lumen of the vessel on a thin wire. The aortic rings were placed between two stainless-steel stirrups, and connected to an isometric force transducer (50630-45, Harward Bioscience, South Natick, MA, USA) and the other was connected to a fixed support in the chamber in order to record the tension on a Harward Bioscience Oscillograph polygraph. The rings were placed in a 10 mL organ chamber containing Krebs

solution with the following composition (mmol/L): NaCl 130, KCl 4.7, KH_2PO_4 1.2, $MgSO_4$ 1.2, $NaHCO_3$ 14.9, Glucose 5.5, $CaCl_2$ 1.6. The solution was maintained at pH 7.4 gassed with 95% O_2 and 5% CO_2, at 37 °C. The rings were initially stretched to a basal tension of 1.5 g, before allowing to equilibrate for 60 min in the bath fluid that was changed every 15–20 min. Endothelial integrity was qualitatively assessed by the degree of relaxation caused by acetylcholine (ACh,1 μmol/L) in the presence of contractile tone induced by phenylephrine (0.1 μmol/L). Because our studies require endothelium-denuded aortas, the rings were discharged if there was any degree of relaxation to ACh, in order to avoid possible influence of endothelial factors. The tissues were washed, pre-contracted with the EC_{50} of phenylephrine (0.1 μmol/L). On top of the contraction, the chamber was loaded with $0.134\ g \pm 0.004$ $(n = 7)$ of the membrane containing entrapped $[Ru(NH \cdot NHq)(terpy)NO]^{3+}$, which was added in a dialysis bag to avoid any adverse physiological effect due the organic reagents. Similar experiment was run with the control (membrane without ruthenium complex -0.129 ± 0.004 $(n = 7)$). After addition of the membrane, the light was activated and time-course for relaxation induction was evaluated. Relaxation was calculated as a percentage of the maximal contraction induced by phenylephrine.

Light irradiation for the pharmacological assays was performed using a photo-reactor. The reactor consists of a 0.5 m^3 box inside which aluminum was placed to increase light reflection. Three 250 W fluorescent lamps (Philips) were used as a visible light source with 450–800 nm wavelength range achieved with a filter (7.05 cm^2 area) positioned in front of each channel on the chamber.

2.7. Statistical analysis

Relaxant responses to the NO donor were measured from the plateau of the phenylephrine contraction and were expressed as percent reversal of the phenylephrine pre-contraction. Data are expressed as mean ± SEM. In each set of experiments,*n* indicates the number of rats studied. We considered the maximal relaxing effect for compounds when the concentration used reached the baseline. Statistical significance was tested by one-way ANOVA (Bonferroni's Multiple Comparison Test) and values of $p > 0.05$ were considered to be significant.

3. Results and discussion

The nitrosyl ruthenium complexes, $[Ru(terpy)(L)NO]^{3+}$ (L = bpy; NH · NHq), used in the present study have been proposed as a NO donor agents in aqueous acidic solution by external stimulation [24].

These species react very rapidly in aqueous medium with hydroxide ion to give deep yellow solutions (Eq. (1)).

$$[RuL_5(NO)]^{3+} + 2OH^- \overset{K_{eq}}{\rightleftharpoons} [RuL_5(NO_2)]^{+} + H_2O \qquad (1)$$

Spectral changes accompanying this reaction for $[Ru(bpy)(terpy)NO]^{3+}$ are shown in Fig. 1. The product was characterized as $[Ru(NO_2)(L)(terpy)]^{+}$ (nitro form) based mainly on the similarity of the analogous ruthenium complexes [24]. The spectral profiles show that, above pH 3.00 for $[Ru(bpy)(terpy)NO]^{3+}$ and pH 6.00 for $[Ru(NH \cdot NHq)terpy)NO]^{3+}$, the nitro form exists in significant amounts at equilibrium. Low pH is somehow crucial for both nitrosyl ruthenium species generate NO release by light irradiation. In this regard, novel strategies to preserve the properties of $[Ru(terpy)(L)NO]^{3+}$ should be developed for biomedical applications. We found that silicone and sol–gel matrices could allow stabilizing the nitrosyl species as well be a convenient target delivery system for NO release.

The physico-chemical properties of $[Ru(terpy)(L)NO]^{3+}$ seems to be unaffected by the entrapping process with sol–gel or silicone membranes as judged by the UV–Vis and FTIR analysis. The solid sate absorbance spectra for sol–gel and silicone samples doped with nitrosyl ruthenium complexes show some similarities to those obtained in aqueous solution. Fig. 2 shows the electronic spectrum of $[Ru(bpy)(terpy)NO]^{3+}$, as an example of a [Ru(ter-

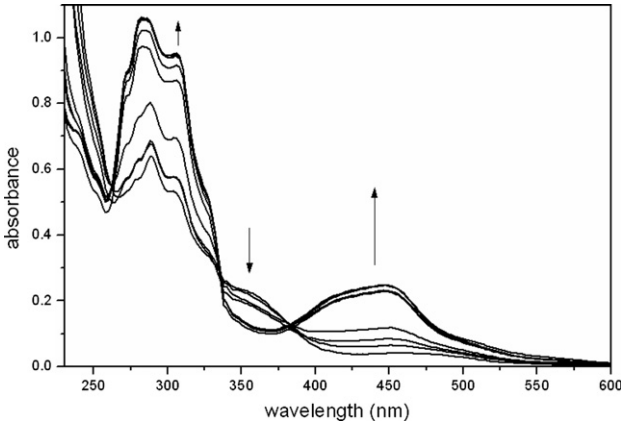


Fig. 1. Spectral profile change with pH for the conversion of $[Ru(NH \cdot NHq)(terpy)NO]^{3+}$ in $[Ru(NH \cdot NHq)(terpy)(NO_2)]^{+}$. Concentration of the complex = 2.6×10^{-5} M. pH 2.02, 2.40, 3.20, 3.58, 6.30, 7.40.

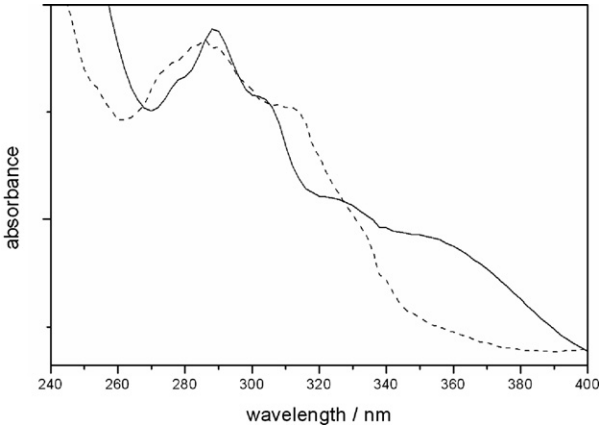


Fig. 2. Electronic spectrum of $[Ru(bpy)(terpy)NO]^{3+}$ in solution pH 2.03 (solid line) and in silicone matrix (dashed line).

py)LNO]$^{3+}$ species in solid state (dashed line) and in aqueous solution (solid line) performed at room temperature. A series of three bands were observed in both spectra in the region of 250–300 nm attributed to intra-ligand transition. However, the electronic spectrum in solution shows a shoulder at 360 nm, attributed to a metal ligand charge transfer band [24], which was not observed in the solid state, probably due the medium effect.

Scanning electron microscopy (SEM) of the studied membranes in this study was applied to determine the distribution pattern and size of particles in the solid matrices. All matrices obtained were found to be amorphous materials (Figure S1: Supporting Material). The SEM micrographs revealed irregularly shaped particles with broad size of 1000 μm for both membranes as well as a homogenous distribution. The samples of [Ru(bpy)(terpy)-NO](PF$_6$)$_3$ complex doped in sol–gel and silicone matrices formed three-dimensional networks while the samples of [Ru(NH · NHq)(terpy)NO](PF$_6$)$_3$ complex showed edges and conchoidal fractures, as well as globular particle shapes with low-dimensional structures.

The entrapped [Ru(terpy)LNO]$^{3+}$ complex on the matrices was submitted to light irradiation at 355 nm, while the [Ru(NH · NHq)(terpy)NO]$^{3+}$ complex was also irradiated at 532 nm. NO monitoring of these photochemical processes in aqueous solution, as observed for [Ru(NH · NHq)-(terpy)NO]$^{3+}$ as an example of nitrosyl ruthenium complex entrapped in silicone matrix, showed NO release (Fig. 3) although in the absence of light no current increase was recorded. The amount of available NO *per* volume of the matrices can be controlled by the amount of [Ru(bpy)(terpy)LNO]$^{3+}$. It implies that tissue exposure to such materials could be convenient because it provides different dosages of NO. After exhaustive photolysis, the UV–Vis spectrum of the entrapped [Ru(terpy)LNO]$^{3+}$ showed [Ru(terpy)-L(H$_2$O)]$^{2+}$ characteristics (Figure S2: Supporting Material).

The stability of the solid matrices to entrap the nitrosyl compounds was tested by rinsing the samples in 0.1 mol L^{-1} HCl and also in phosphate buffer solution at pH 7.40 for 30 min. The electronic spectra of these dispel aliquots showed insignificant absorption, which was considered as a qualitative indicator of the efficiency of the entrapment of ruthenium nitrosyl complexes in sol–gel and silicone matrices.

Due the spectroscopic and photochemical characteristics of [Ru(NH · NHq)(terpy)NO]$^{3+}$ complex in aqueous solution [24] as well encapsulated in a solid matrix, some pharmacological assays was performed. In a vasodilator test, denuded rat aortic rings were previously contracted with phenylephrine and vasorelaxation was verified in the presence of doped matrix. In this experiment, we used the sol–gel matrix (*ca.* 0.200 g), which was kept in a cellulose dialysis tubing to avoid any other side reaction. The addition of the membrane without entrapped compound in the absence of light did not produce vasodilation response. However, as shown in Fig. 4, in the presence of visible light irradiation and after depletion of endogenous photoactivable NO stores, NO release caused relaxation of denuded pre-contracted aorta with maximum within about 100 s. In pre-contracted aortic rings, pre-incubation with oxyhaemoglobin 10 μmol/L for 30 min, a known NO scavenger [25], completely abolished the relaxation induced by the matrix indicating that NO is released in the extracellular medium.

Vasodilation using sol–gel or silicone as target delivery system shows similar vasorelaxation effects observed for [Ru(NH · NHq)(terpy)NO]$^{3+}$ in physiological solution [7]. The entrapped ruthenium complexes induced E_{max}: 29.9 ± 3.6% for sol–gel matrix. It seems to be less effective when compared to the [Ru(NH · NHq)(terpy)NO]$^{3+}$ in physiological solution, which is possibly explained by the fact that activation of guanylyl-cyclase is nitric oxide concentration dependent. In addition, the membrane releases NO extracellularly and some NO amount can be lost outside the cells. In this way, less NO could be available inside the cell to promote the guanylyl-cyclase activation and

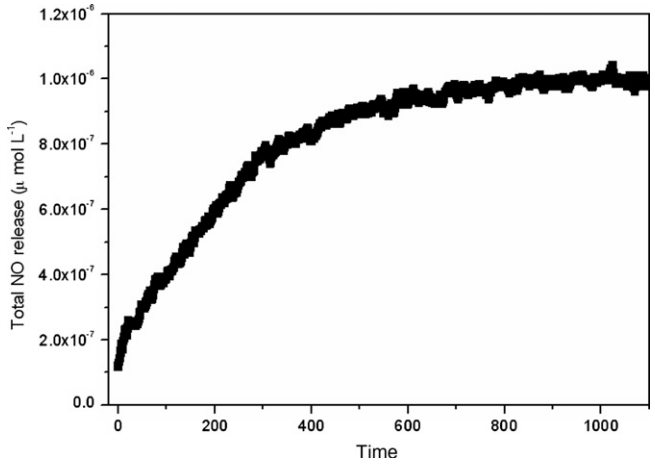


Fig. 3. Time course of NO release from [Ru(NH · NHq)(terpy)NO]$^{3+}$ complex in silicone matrix under 532 nm light irradiation. Mass membrane = 0.200 g.

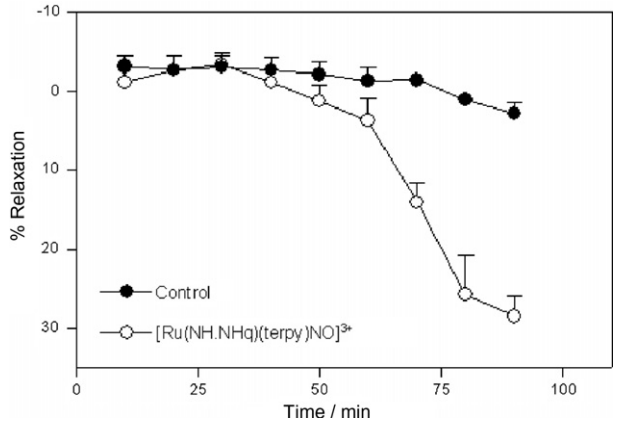


Fig. 4. Time-course for [Ru(NH · NHq)(terpy)NO]$^{3+}$-induced relaxation. Denuded aortic rings were pre-contracted with 100 nmol L^{-1} phenylephrine and [Ru(NH · NHq)(terpy)NO]$^{3+}$ doped in sol–gel matrix (○, $n = 7$) and control (sol–gel matrix) (●, $n = 7$) were added. Data are means ± SEM of n experiments performed on preparations obtained from different animals.

aorta relaxation. Apparently, the observed vasodilation using the target delivery system suggests that local delivery of NO may help increasing the local potency.

4. Conclusions

In the present study, we showed for the first time that the NO released from entrapped $[Ru(NH \cdot NHq)(terpy)\text{-}NO]^{3+}$ by light irradiation induces rat aorta relaxation, as demonstrated by its vasodilatory effect. This NO-release ability might represent an effective mechanism for some therapeutic applications because NO has been shown to prevent biofilm formation. Studies are being conducted at our laboratory to quantify NO optimal amount required to prevent, for example, bacterial adhesion, which may be useful in the development of patch-based topical therapies.

Acknowledgements

Financial support by FAPESP, CNPq, CNPq/milenium, CAPES and FAPESB is grateful acknowledged. We also thank Dr. Neyde Y. Murakami for valuable discussions.

Appendix A. Supplementary material

Supplementary data associated with this article can be found, in the online version, at doi:10.1016/j.poly.2007.03.042.

References

[1] L. Ignarro, Nitric Oxide: Biology and Photobiology, First edition., Academic Press, San Diego, California, USA, 2000.
[2] B.G. Bentz, R.L. Simmons, G.K. Haines, J.A. Radosevich, Head Neck – J. Sci. Spec. 22 (2000) 71.
[3] V. Prevot, S. Bouret, G.B. Stefano, J.C. Beauvillain, Brain Res. 34 (2000) 27.
[4] A.K. Patra, R. Afshar, M.M. Olmstead, P.K. Mascharak, Angew. Chem. Int. 41 (2002) 2512.
[5] P. Vallance, Fundam. Clin. Pharm. 17 (2003) 1.
[6] D. Bonaventura, F.S. Oliveira, V. Togniolo, A.C. Tedesco, R.S. Silva, L.M. Bendhack, Nitric Oxide – Biol. Chem. 10 (2004) 83.
[7] R.G. de Lima, M.G. Sauaia, D. Bonaventura, A.C. Tedesco, R.F.V. Lopez, L.M. Bendhack, R.S. Silva, Inorg. Chim. Acta 358 (2005) 2643.
[8] A.B. Seabra, M.G. de Oliveira, Biomaterials 25 (2004) 3782.
[9] B.J. Nablo, M.H. Schoenfisch, Biomaterials 26 (2005) 4405.
[10] M. Hoshino, L. Laverman, P.C. Ford, Coord. Chem. Rev. 187 (1) (1999) 75102.
[11] M.A. DeLeo, P.C. Ford, Coord. Chem. Rev. 208 (1) (2000) 47.
[12] P. Coppens, I. Novozhilova, A. Kovalevsky, Chem. Rev. 102 (4) (2002) 861.
[13] L. Andrews, A. Citra, Chem. Rev. 102 (4) (2002) 885.
[14] T.W. Hayton, P. Legzdins, W.B. Sharp, Chem. Rev. 102 (4) (2002) 935.
[15] P.C. Ford, I.M. Lorkovic, Chem. Rev. 102 (4) (2002) 993.
[16] M. Clarke, J. Coord. Chem. Rev. 232 (1–2) (2002) 69.
[17] E. Tfouni, M. Krieger, B.R. McGarvey, D.W. Franco, Coord. Chem. Rev. 236 (1–2) (2003) 57.
[18] E. Tfouni, K.Q. Ferreira, F.G. Doro, R.S. da Silva, Z.N. da Rocha, Coord. Chem. Rev. 249 (3–4) (2005) 405.
[19] J. Bordini, P.C. Ford, E. Tfouni, Chem. Comm. (2005) 4169.
[20] K.Q. Ferreira, J.F. Schneider, P.A.P. Nascente, U.P. Rodrigues-Filho, E. Tfouni, J. Coll. Inter. Sci. 300 (2006) 543.
[21] A.A. Eroy-Reveles, Y. Leung, P.K. Mascharak, J. Am. Chem. Soc. 128 (2006) 7166.
[22] K.J. Takeuchi, M.S. Thompson, D.W. Pipes, T.J. Meyer, Inorg. Chem 23 (1984) 1845.
[23] W.R. Murphy, K. Takeuchi, M.H. Barley, T.J. Meyer, Inorg. Chem. 25 (1986) 1041.
[24] R.G. de Lima, M.G. Sauaia, A.C. Tedesco, R.S. Silva, Inorg. Chim. Acta 359 (2006) 2543.
[25] C.Z. Ferezin, F.S. Oliveira, R.S. da Silva, A.R. Simioni, A.C. Tedesco, L.M. Bendhack, Nitric Oxide 13 (2005) 170.

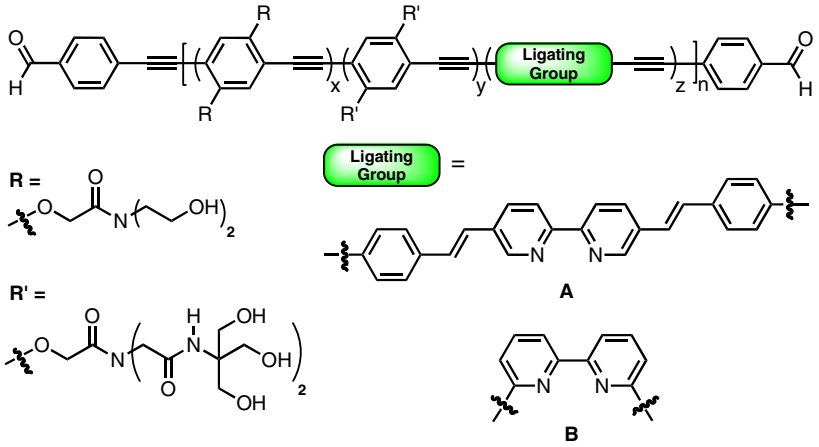


Chart 1. Water-soluble conjugated polymers prepared previously in our laboratory.

under an Ar atmosphere. NMR spectra were recorded in $CDCl_3$ at 22 °C on a 300 MHz Varian instrument and chemical shifts are expressed in ppm relative to residual $CHCl_3$. Air- and/or water-sensitive manipulations were carried out under a dry nitrogen atmosphere using standard Schlenk or glovebox techniques. Nitric oxide gas was purified following a reported procedure [23].

2.1.2. CP1

Compounds **M1** (30 mg, 0.07 mmol), **M2** (50 mg, 0.04 mmol), 5,5′-dibromo-2,2′-bithiophene (10 mg, 0.04 mmol), 4-bromobenzaldehyde (1 mg, 0.007 mmol), $[Pd(PPh_3)_4]$ (8.2 mg, 0.007 mmol), and CuI (1 mg, 0.007 mmol) were combined with morpholine (5 mL) in a pressure tube inside a glove box. The tube was sealed with a Teflon screw cap and removed from the glove box. The reaction mixture was stirred and heated at 70 °C for 25 h. The orange mixture was added to a solution of ethyl acetate to give a precipitate. Isolation of the precipitate and washing with diethyl ether gave an orange solid. The orange solid was purified by using a Chelex column with water as the solvent, and the eluant was removed under reduced pressure to afford the final product (29 mg, 37%). ^{1}H NMR (DMSO): δ 8.0–6.8 (br m, 38 H); 5.4–4.1 (br m, 46 H); 4.0–2.0 (br, overlaps with water and DMSO). $M_n = 9700$ g/mol. Spectroscopic parameters are presented in Table 1.

Table 1
Selected physical properties of **CP1** in various solvents

Property	H_2O	MeCN/H_2O (90:10)	pH 7.4 HEPES/KCl
$\lambda_{\pi\rightarrow\pi^*}$ (nm)	446	425	446
$\log\varepsilon$	3.52	3.46	3.52
λ_{em} (nm)	483	490	483
I_{Cu}/I_0	0.24	0.10	0.10
K_{SV} (M^{-1})	6.1×10^4	4.3×10^5	1.4×10^4
I_{NO}/I_{Cu}	2.1	4.9	0.88
$I_{Angeli's\ Salt}/I_{Cu}$	6.6	3.2	2.1

2.2. Spectrophotometric measurements

2.2.1. General considerations

Absorption spectra were recorded on a Cary 50 spectrophotometer. Fluorescence spectra were acquired on a Photon Technology International Quanta Master 4L fluorimeter. Circulating water baths were used to maintain all samples at 25 ± 1 °C. Samples for fluorescence had a path length of 1 cm in Spectrosil quartz (6Q) or polystyrene cuvettes from Starna, with optical densities <0.05 and 3.0 mL sample solution volumes. Quantum yields (Φ) were determined by averaging the results of at least three trials. Values were referenced to NIST-issued quinine bisulfate (in 0.105 M perchloric acid in Millipore water, $\Phi = 0.546$).

2.2.2. Metal ion selectivity

A 3.0 mL aliquot of a 7.9 μM **CP1** working solution in H_2O was added to each of 17 polystyrene cuvettes. Basal fluorescence spectra were acquired for each sample, and then 2.5 equiv. of each metal salt were introduced by addition of a 10 μL aliquot of a 6.0 mM aqueous stock solution of metal salt to each cuvette. The salts used were NaCl, KNO_3, $MgSO_4$, $CaCl_2$, $BaCl_2$, $EuCl_3$, $Mn(OAc)_2$, $NiSO_4\cdot6H_2O$, K_2PtCl_4, $CuSO_4\cdot5H_2O$, $ZnCl_2$, $CdSO_4$, $Hg(OAc)_2$, $Al_2(SO_4)_3$, and $Pb(OAc)_2\cdot3H_2O$. Fluorescent spectra were recorded within 1 min following addition and again after 10 min. No differences were observed between spectra acquired after 1 or 10 min. The relative quenching efficiency of each metal ion is summarized in Fig. 1 and individual spectra are presented in Fig. S1.

2.2.3. Titration of CP1 with $CuSO_4\cdot5H_2O$

A 3.0 mL aliquot of a 7.9 μM **CP1** solution (in H_2O, 90:10 MeCN/H_2O, or 50 mM HEPES, 100 mM KCl buffer) was added to a polystyrene cuvette. Small aliquots (4.0–20 μL) of 0.60 mM or 6.0 mM $CuSO_4\cdot5H_2O$(aq) were added to the cuvette, where 4.0 μL represents 0.10 or 1.0 equiv. of Cu(II) and 20 μL represents 5.0 equiv. of Cu(II) per mol bithiophene unit in the polymer backbone,

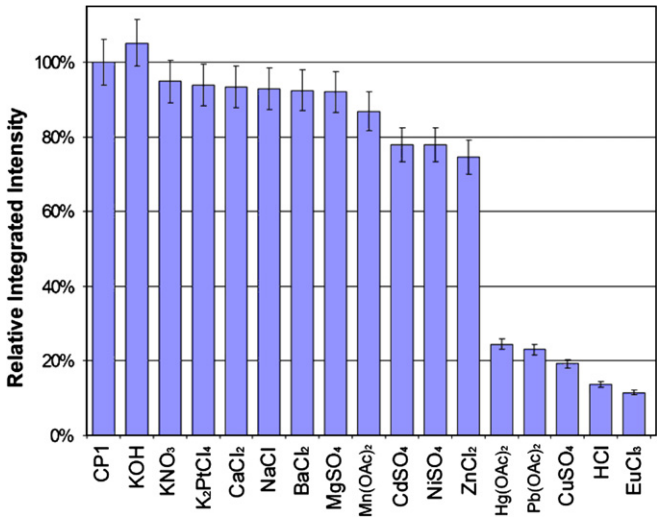


Fig. 1. Relative quenching of **CP1** emission by various species in aqueous solution.

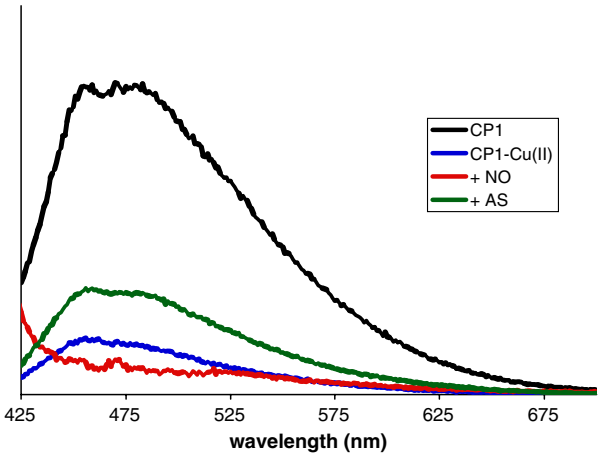


Fig. 2. Emission response of **CP1**–Cu(II) (blue trace) to NO (red trace) and to Angeli's Salt (AS, green trace) in pH 7.4 HEPES/KCl buffer. The fluorescence spectrum of **CP1** (black trace) is given for comparison. (For interpretation of the references to color in the figure legend, the reader is referred to the web version of this article.)

respectively. A total of 42 μL of $CuSO_4 \cdot 5H_2O$ solution was added to the solutions of **CP1** in water and 90:10 MeCN/H_2O, and 118 μL was added to the solutions of **CP1** in pH 7.4, 50 mM HEPES, 100 mM KCl (pH 7.4 HEPES/KCl) buffer. The fluorescence spectra and Stern–Volmer plots are presented in Figs. S2–S4. Relevant photoluminescent parameters are summarized in Table 1.

2.2.4. Response to nitric oxide

2.2.4.1. Response of CP1–Cu(II) complex to excess NO(g) in unbuffered solution. A 3.0 mL aliquot of a 7.9 μM **CP1** solution (in H_2O or 90:10 MeCN/H_2O) was added to a quartz cuvette. A 20 μL aliquot of a 6.0 mM $CuSO_4 \cdot 5H_2O$ solution in H_2O was added to form the **CP1**–Cu(II) complex. The cuvette was sealed with a gastight screw cap equipped with a septum. A 250 μL aliquot of NO(g) (86 equiv. NO per Cu(II) ion) was bubbled through the solution via a gastight syringe inserted through the septum, the solution was vigorously shaken for 3 s, and the fluorescence response was measured. Fluorescence spectra are presented in Figs. S5 and S6 and the fluorescent response is summarized in Table 1.

2.2.4.2. Response of CP1–Cu(II) complex to excess NO(g) in buffered solution. A 3.0 mL aliquot of a 7.9 μM **CP1** solution in pH 7.4 HEPES/KCl buffer was added to a quartz cuvette. A 100 μL aliquot of a 6.0 mM $CuSO_4 \cdot 5H_2O$ solution in H_2O was added to form the **CP1**–Cu(II) complex. The cuvette was sealed with a gastight screw cap equipped with a septum. A 250 μL aliquot of NO(g) (17 equiv. NO per Cu(II) ion) was bubbled through the solution via a gastight syringe inserted through the septum, the solution was vigorously shaken for 3 s, and the fluorescence response was measured. The fluorescence spectrum is presented in Fig. 2 and the fluorescent response is summarized in Table 1.

2.2.5. Selectivity studies

2.2.5.1. Response of CP1–Cu(II) complex to excess SIN-1-Cl in H_2O. A 3.0 mL aliquot of a 7.9 μM **CP1** solution in H_2O was added to a polystyrene cuvette. A 20 μL aliquot of 6.0 mM $CuSO_4 \cdot 5H_2O$ in H_2O was added to form the **CP1**–Cu(II) complex and a basal fluorescence scan was acquired. This solution was transferred to a polystyrene cuvette containing 1.5 mg of SIN-1-Cl (62 equiv. SIN-1-Cl per Cu(II) ion), the cuvette was shaken for 3 s, and the fluorescence was measured. No change in integrated emission was observed.

2.2.5.2. Response of CP1–Cu(II) complex to excess Angeli's Salt in unbuffered solution. A 3.0 mL aliquot of a 7.9 μM **CP1** solution (in H_2O or 90:10 MeCN/H_2O) was added to a polystyrene cuvette. A 20 μL aliquot of a 6.0 mM $CuSO_4 \cdot 5H_2O$ solution in H_2O was added to form the **CP1**–Cu(II) complex and a basal fluorescence scan was acquired. This solution was transferred to a polystyrene cuvette containing 2.4 mg Angeli's Salt (170 equiv. Angeli's Salt per Cu(II) ion), the cuvette was vigorously shaken for 3 s, and the fluorescence was measured. Fluorescence spectra are presented in Figs. S7 and S8 and the fluorescent response is summarized in Table 1.

2.2.5.3. Response of CP1–Cu(II) complex to excess Angeli's Salt in buffered solution. A 3.0 mL aliquot of a 7.9 μM **CP1** solution in pH 7.4 HEPES/KCl buffer was added to a polystyrene cuvette. A 100 μL aliquot of a 6.0 mM $CuSO_4 \cdot 5H_2O$ solution in H_2O was added to form the **CP1**–Cu(II) complex and a basal fluorescence scan was acquired. This solution was transferred to a polystyrene cuvette containing 2.4 mg Angeli's Salt (34 equiv. Angeli's Salt per Cu(II) ion), the cuvette was vigorously shaken for 3 s, and the fluorescence was measured. The fluorescence spectrum is presented in Fig. 2 and the fluorescent response is summarized in Table 1.

3. Results and discussion

3.1. Design and synthesis

We had previously reported water-soluble poly(*p*-phenyleneethynylene) derivatives **A** and **B** with main chain bipyridyl units for metal ion binding, and the Cu(II) CMPs derived from these CPs showed promise for fluorescence turn-on detection of NO [15]. Unfortunately, the Stern–Volmer quenching constant was rather low in water for CPs with bipyridyl ligating groups. In the current study, the reporter module of the CP scaffold comprises the same poly(*p*-phenyleneethynylene) building blocks previously described, but the bipyridyl ligating units have been replaced by bithiophene units. CPs featuring non-ionic water-solubilizing side chains are less sensitive to ionic strength and pH than are CPs with ionic variants [21,22]. Furthermore, CPs with ionic side chains can interact with charged biomolecules such as proteins or DNA to form polyelectrolyte complexes that perturb CP emission [24–28]. Although a number of creative biosensor applications have taken advantage of this feature [25,29,30], emission changes resulting from such 'nonspecific interactions' [24] will yield spurious results for detecting neutral molecules such as NO or HNO. Non-ionic side chains can also interact nonspecifically with biomolecules, but these interactions will be much weaker than for ionic–ionic interactions.

In our previous study [15], we attributed the weak binding of metal ions to the bipyridyl units therein to competition among the side chains, water, and bipyridyl groups for metal binding. One possible strategy to perturb this competitive balance would be to decrease the metal-binding affinity of the water-solubilizing side chains, but this tactic can be synthetically prohibitive and might negatively affect the solubility/biocompatibility of the polymer. An alternative would be to decrease the metal-binding affinity of the main chain receptors. A transition metal could perturb the photoluminescent properties of the polymer without forming a substitutionally inert bond to donor atoms in the main chain.

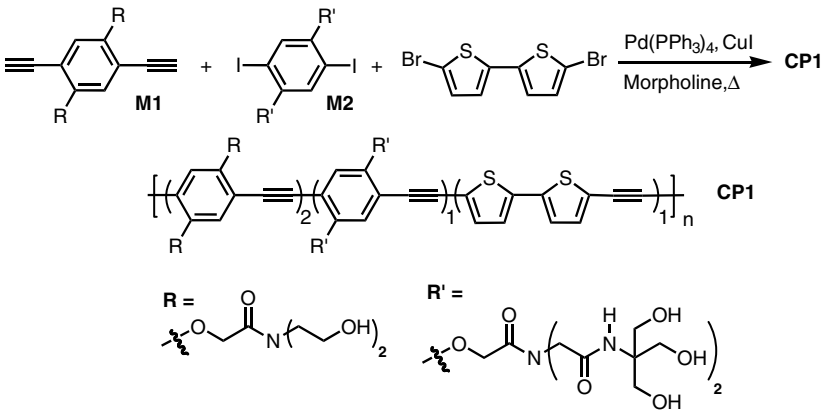
The red-shifted emission of thiophene relative to simple arenes confers upon **CP1** an emission profile that is red-shifted to a range more amenable for biological sensing applications. Thiophene is a poor ligand for metal ions, and the few structurally characterized complexes that exhibit direct M–$S_{thiophene}$ bonds [31,32] reveal that the thiophene can be displaced by coordinating solvents such as MeCN or weakly-coordinating solvents such as CH_2Cl_2. Presumably, this kinetic lability can be attenuated by incorporating the thiophene moiety into a multidentate ligand framework or by supramolecular preorganization that holds the thiophene in proximity to the metal. Although the thiophene–metal bond may be readily broken, a fast kinetic exchange rate will allow a transition metal to quench the main chain emission through transient coordination. Because thiophene red-shifts CP emission similar to pyridine and has much poorer metal-binding affinity, we employed bithiophene as the metal ion receptor for our CP scaffold.

CP1 (Scheme 1) was prepared by Sonogashira coupling of **M1**, **M2**, and 5,5′-dibromo-2,2′-bithiophene under conditions described by others [21,22] and adapted by us [15]. To limit the molecular weight of **CP1**, 4-bromobenzaldehyde was added as an end-capping group. Purification of the material involved precipitation from ethyl acetate and subsequent rinsing with ethyl ether. To ensure full removal of Cu(I) added during the Sonogashira coupling, aqueous CP solutions were passed through a column loaded with Chelex 100 resin [15].

3.2. Spectroscopic properties and emission response to metal ions

CP1 is an orange solid with $\lambda_{max} = 446$ nm and $\lambda_{em} = 483$ nm in water. In a less polar MeCN/H_2O (90:10) mixture, the absorption maximum shifts hypsochromically to 429 nm. The emission maximum does not change as dramatically as the absorption maximum, with only a 7 nm bathochromic shift in MeCN/H_2O (90:10) versus water. Key spectroscopic parameters are summarized in Table 1.

We first examined the response of **CP1** emission to various metal ions and pH values in water. Fig. 1 shows the



Scheme 1. Preparation of **CP1**.

relative integrated emission afforded by the addition of 2.5 equiv. of various metal salts or Brønsted acid/base. Of the metals tested, only Hg(II), Pb(II), Cu(II), and Eu(III) lead to >75% quenching. Hg(II) and Cu(II) also efficiently quenched emission of **A** and **B** (Chart 1), while Eu(III) did not quench the emission of these materials (Pb(II) was not explored).

Fluorescent CP-based NO sensors operating via the reductive nitrosylation mechanism have primarily been Cu(II)–CMPs. Thus, we studied the quenching efficiency of Cu(II) for **CP1** in a more detailed and quantitative fashion. In water, adding 5 equiv. of Cu(II) to **CP1** leads to a 76% quenching of **CP1** emission. The corresponding Stern–Volmer quenching constant (K_{SV}) was measured to be $6.1 \times 10^4\ M^{-1}$, approximately the same value observed for Cu(II) quenching of bipyridyl-functionalized CP **A** in water ($K_{SV} = 5.2 \times 10^4\ M^{-1}$). However, the emission quenching efficiency of **CP1** in MeCN/H_2O ($K_{SV} = 4.3 \times 10^5\ M^{-1}$) was approximately seven times greater than in water. Quenching is somewhat less efficient in buffer ($K_{SV} = 1.4 \times 10^4\ M^{-1}$) than in water. Quenching data and K_{SV} values are listed in Table 1 and Stern–Volmer plots are provided in Figs. S2–S4. In both water and MeCN/H_2O (90:10), the Stern–Volmer plots behave linearly at low [Cu(II)] and begin to level off after 0.5 equiv. Cu(II) per bithiophene unit, suggesting that each Cu(II) center can only access *one* thiophene moiety, consistent with a mixed side chain/main chain coordination environment for copper.

3.3. Emission response to nitric oxide

Addition of 86 equiv. of NO to a 7.9 μM **CP1**–Cu(II) solution in MeCN/H_2O (90:10) afforded an immediate 4.9-fold increase in integrated emission. By comparison, the same experiment in water produced only a 2.1-fold fluorescence turn-on relative to **CP1**–Cu(II). This difference can be rationalized by the difference in **CP1** quenching by Cu(II) in these two solvents. Because the integrated emission of **CP1**–Cu(II) relative to **CP1** is greater in water than MeCN/H_2O (90:10) and is thus less quenched, we would expect the NO-induced turn-on in MeCN/H_2O (90:10) to be greater than in water by the same amount. Indeed, the **CP1**–Cu(II) complex is 2.3 times more quenched in MeCN/H_2O (90:10) compared to water, and the NO-induced turn-on is 2.3 times greater in MeCN/H_2O (90:10) than in water.

Ultimately, we are interested in developing CMPs for sensing NO *in vivo*. Surprisingly, exposure of a 7.9 μM **CP1**–Cu(II) solution in pH 7.4 HEPES/KCl buffer to 17 equiv. NO (relative to Cu) led to a 12% decrease in integrated emission (Fig. 2). Because this decrease was accompanied by an increase in Rayleigh scattering and visual turbidity, it would appear that CMP precipitation is occurring on a small scale and *not* genuine quenching of fluorescence. The same experiment, when performed in pH 7.0 100 mM NH_4OAc, displays no change in integrated emission and no precipitation.

3.4. Emission response to reactive nitrogen species

Despite considerable interest in developing sensors for detecting nitric oxide [13–16,33–40], there has been a surprising lack of progress in sensing other reactive nitrogen species. Only recently has a platform capable of discriminating HNO from NO been disclosed [41]. Our first CMP-based NO sensor employed a bipyridyl-substituted poly(*p*-phenylenevinylene) derivative, and the corresponding Cu(II)–CP complex exhibited a 2.8-fold increase in integrated emission upon addition of excess NO(g) or Angeli's Salt [14]. In this and subsequent work, we have been interested to explore the response of our CMP-based sensors to reactive nitrogen species other than NO.

Addition of 62 equiv. of SIN-1-Cl to a 7.9 μM **CP1**–Cu(II) solution in water produced no change in fluorescence. However, when the same experiment was performed using 170 equiv. of Angeli's Salt, an immediate 5.7-fold turn-on in fluorescence was observed, ultimately leveling off after 20 min at 6.6 times the **CP1**–Cu(II) integrated emission. This result is surprising, given that the integrated emission of **CP1** in water is quenched by 76% with Cu(II), whereby a full restoration in fluorescence can only result in a 4.2-fold enhancement. However, in unbuffered aqueous media Angeli's Salt will dramatically increase the alkalinity of the solution. In the course of our metal selectivity measurements, we observed that increasing the pH of an aqueous solution of **CP1** leads to an increase in integrated emission. Indeed, the pH increases from 6 to 9 upon addition of Angeli's Salt, accounting for 'restored' fluorescence that is higher than the initial fluorescence of **CP1**.

In contrast, when a 7.9 μM **CP1**–Cu(II) solution in MeCN/H_2O (90:10) was exposed to 170 equiv. of Angeli's Salt, an immediate 3.3-fold increase in integrated emission was observed. No restoration beyond initial **CP1** fluorescence occurs in this experiment, presumably because MeCN/H_2O (90:10) undergoes a smaller pH change than pure water. Freshly collected Millipore water has a pH ~ 6 and would quench **CP1** emission relative to biologically relevant milieu. However, MeCN/H_2O (90:10) has only one-tenth the water and therefore one-tenth the available protons for quenching **CP1** emission compared to pure water; thus, the integrated emission of metal-free **CP1** in MeCN/H_2O (90:10) would be greater than in pure water. Furthermore, the large relative MeCN composition of the solvent will substantially influence pK_a values. The pH values for many buffers increase by nearly two log units in going from pure water to MeCN/H_2O (1:1) [42]. This deviation becomes more pronounced for simpler, non-buffering molecules as the percentage of MeCN increases. In the case of ammonia, the pK_a shifts up by more than 7 log units from pure water to pure MeCN [43]. Consequently, the pK_a of water in MeCN/H_2O (90:10) will be substantially higher and thus less susceptible to deprotonation with attendant alkalinity-induced fluorescence enhancement. Because MeCN/H_2O (90:10) is less sensitive to alkalinization, the pH-dependent emissive behavior in

MeCN/H_2O (90:10) is greatly diminished and thus the fluorescence does not increase beyond the initial **CP1** value.

To mimic biological milieu more faithfully and to avoid pH-dependent emission responses, we performed the HNO sensing experiments in pH 7.4 HEPES/KCl buffer. Upon addition of 34 equiv. Angeli's Salt to a 7.9 μM **CP1**–Cu(II) solution in buffer, the integrated emission immediately increased 2.1-fold (Fig. 2). Because the pH is buffered at 7.4, this change in fluorescence is a genuine response to HNO uncomplicated by pH variations.

4. Conclusions

A CMP incorporating bithiophene-based metal binding units, **CP1**, forms a Cu(II) complex that displays good emission enhancement upon exposure to NO(g) in H_2O and MeCN/H_2O (90:10). The fluorescence of **CP1**–Cu(II) shows a 12% decrease in emission upon treatment with NO in pH 7.4 HEPES/KCl buffer, probably a consequence of precipitation, and no change in ammonium acetate solution. Remarkably, a 2.1-fold increase in **CP1**–Cu(II) integrated emission occurs upon exposure to Angeli's Salt in the HEPES buffer, indicating that **CP1**–Cu(II) can sense HNO selectively over NO in buffered aqueous solutions. Because **CP1**–Cu(II) displays greater fluorescence enhancement with Angeli's Salt in MeCN/H_2O (90:10) and water, the selectivity of **CP1**–Cu(II) for HNO over NO in buffer arises not from unique sensitivity to HNO, but rather from an insensitivity to NO. The ability of **CP1**–Cu(II) to react with HNO under conditions in buffered aqueous solution where NO does not represents a significant step towards developing sensors to explore the separate roles of HNO and NO *in vivo*.

Acknowledgements

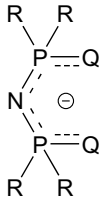
This work was supported by NSF Grant CHE-0234951. We thank Dr. Mi Hee Lim for inspiration and insightful discussion. R.C.S. and A.G.T. thank the NIH and NSF for post- and predoctoral fellowships, respectively. Spectroscopic instrumentation at the MIT DCIF is maintained with funding from NIH Grant 1S10RR13886-01 and NSF Grants CH3-9808063, DBI9729592, and CHE-9808061.

Appendix A. Supplementary material

Stern–Volmer plots, fluorescence spectra for Cu(II) titrations and analyte response. Supplementary data associated with this article can be found, in the online version, at doi:10.1016/j.poly.2007.04.003.

References

[1] R.D. McCullough, Adv. Mater. 10 (1998) 93.
[2] M.O. Wolf, Adv. Mater. 13 (2001) 545.
[3] C. Moorlag, O. Clot, Y. Zhu, M.O. Wolf, Macromol. Symp. 209 (2004) 133.
[4] J.-M. Kern, J.-P. Sauvage, G. Bidan, B. Divisia-Blohorn, J. Polym. Sci. A 41 (2003) 3470.
[5] J. Buey, T.M. Swager, Angew. Chem. Int. Ed. 39 (2000) 608.
[6] P.L. Vidal, M. Billon, B. Divisia-Blohorn, G. Bidan, J.M. Kern, J.P. Sauvage, Chem. Commun. (1998) 629.
[7] S.S. Zhu, T.M. Swager, J. Am. Chem. Soc. 119 (1997) 12568.
[8] B. Jousselme, P. Blanchard, M. Ocąfrain, M. Allain, E. Levillain, J. Roncali, J. Mater. Chem. 14 (2004) 421.
[9] J. Roncali, J. Mater. Chem. 9 (1999) 1875.
[10] P.C. Ewbank, R.S. Loewe, L. Zhai, J. Reddinger, G. Sauvé, R.D. McCullough, Tetrahedron 60 (2004) 11269.
[11] R.D. McCullough, S.P. Williams, Chem. Mater. 7 (1995) 2001.
[12] R.D. McCullough, P.C. Ewbank, R.S. Loewe, J. Am. Chem. Soc. 119 (1997) 633.
[13] R.C. Smith, A.G. Tennyson, S.J. Lippard, Inorg. Chem. 45 (2006) 6222.
[14] R.C. Smith, A.G. Tennyson, M.H. Lim, S.J. Lippard, Org. Lett. 7 (2005) 3573.
[15] L. Do, R.C. Smith, A.G. Tennyson, S.J. Lippard, Inorg. Chem. 45 (2006) 8998.
[16] R.C. Smith, A.G. Tennyson, A.C. Won, S.J. Lippard, Inorg. Chem. 45 (2006) 9367.
[17] K. Tsuge, F. DeRosa, M.D. Lim, P.C. Ford, J. Am. Chem. Soc. 126 (2004) 6564.
[18] P.C. Ford, B.O. Fernandez, M.D. Lim, Chem. Rev. 105 (2005) 2439.
[19] M.D. Bartberger, W. Liu, E. Ford, K.M. Miranda, C. Switzer, J.M. Fukuto, P.J. Farmer, D.A. Wink, K.N. Houk, Proc. Natl. Acad. Sci. USA 99 (2002) 10958.
[20] J.P. Crow, Nitric Oxide 1 (1997) 145.
[21] K. Kuroda, Department of Chemistry Massachusetts, Institute of Technology, Cambridge, MA, 2003, pp. 56–66.
[22] K. Kuroda, T.M. Swager, Chem. Commun. (2003) 26.
[23] D. Tran, B.W. Skelton, A.H. White, L.E. Laverman, P.C. Ford, Inorg. Chem. 37 (1998) 2505.
[24] I.-B. Kim, A. Dunkhorst, U.H.F. Bunz, Langmuir 21 (2005) 7985.
[25] C. Fan, K.W. Plaxco, A.J. Heeger, J. Am. Chem. Soc. 124 (2002) 5642.
[26] I.-B. Kim, U.H.F. Bunz, J. Am. Chem. Soc. 128 (2006) 2818.
[27] M.S. Ayyagari, R. Pande, S. Kamtekar, H. Gao, K.A. Marx, J. Kumar, S.K. Tripathy, J.A. Akkara, D.L. Kaplan, Biotechnol. Bioeng. 45 (1995) 116.
[28] S. Wang, G.C. Bazan, Adv. Mater. 15 (2003) 1425.
[29] B. Liu, G.C. Bazan, Chem. Mater. 16 (2004) 4467.
[30] D. Wang, X. Gong, P.S. Heeger, F. Rininsland, G.C. Bazan, A.J. Heeger, Proc. Natl. Acad. Sci. USA 99 (2002) 49.
[31] M.-G. Choi, R.J. Angelici, Organometallics 10 (1991) 2436.
[32] R.A. Sánchez-Delgado, V. Herrera, C. Bianchini, D. Masi, C. Mealli, Inorg. Chem. 32 (1993) 3766.
[33] T. Nagano, T. Yoshimura, Chem. Rev. 102 (2002) 1235.
[34] K.J. Franz, N. Singh, B. Spingler, S.J. Lippard, Inorg. Chem. 39 (2000) 4081.
[35] M.H. Lim, D. Xu, S.J. Lippard, Nat. Chem. Biol. 2 (2006) 375.
[36] M.H. Lim, S.J. Lippard, J. Am. Chem. Soc. 127 (2005) 12170.
[37] M.H. Lim, S.J. Lippard, Inorg. Chem. 43 (2004) 6366.
[38] S.A. Hilderbrand, M.H. Lim, S.J. Lippard, J. Am. Chem. Soc. 126 (2004) 4972.
[39] K.J. Franz, N. Singh, S.J. Lippard, Angew. Chem. Int. Ed. 39 (2000) 2120.
[40] S.A. Hilderbrand, M.H. Lim, S.J. Lippard, in: C.D. Geddes, J.R. Lakowicz (Eds.), Topics in Fluorescence Spectroscopy, vol. 9, Springer, 2005, pp. 163–188.
[41] M.A. Martí, S.E. Bari, D.A. Estrin, F. Doctorovich, J. Am. Chem. Soc. 127 (2005) 4680.
[42] J. Barbosa, I. Marqués, D. Barrón, V. Sanz-Nebot, Trends Anal. Chem. 18 (1999) 543.
[43] J.F. Coetzee, G.R. Padmanabhan, J. Am. Chem. Soc. 87 (1965) 5005.



R = aryl, alkyl
Q = O, S, Se

Scheme 1.

2. Experimental

All manipulations were carried out under nitrogen by standard Schlenk techniques unless otherwise stated. Solvents were purified, distilled and degassed prior to use. NMR spectra were recorded on a Varian Mercury 300 spectrometer operating at 300, 121.5, and 282.5 MHz for ^{1}H, ^{31}P, and ^{19}F, respectively. Chemical shifts (δ, ppm) were reported with reference to $SiMe_4$ (^{1}H), H_3PO_4 (^{31}P), and $CF_3C_6H_5$ (^{19}F). Infrared spectra (KBr) were recorded on a Perkin–Elmer 16 PC FT-IR spectrophotometer. Elemental analyses were performed by Medac Ltd, Surrey, UK. The ligands $K[N(R_2PQ)_2]$ (R = Ph, Q = O, S, or Se; R = Pr^i, Q = S or Se) [18–21] and $[Ru(NO)Cl_3(PPh_3)_2]$ [22] and $[Rh(NO)Cl_2(PPh_3)_2]$ [23] were prepared according to literature methods. $Ru(NO)Cl_3 \cdot xH_2O$ was purchased from Strem Ltd and used as received.

2.1. Preparation of trans-[Ru(NO)(Cl){N(R$_2$PS)$_2$}$_2$] (R = Ph (1), Pr^i (2))

A suspension of $[Ru(NO)Cl_3(PPh_3)_2]$ (200 mg, 0.26 mmol) and 2 equiv. of $K[N(Ph_2PS)_2]$ (256 mg, 0.53 mmol) in dmf (20 ml) was heated at reflux for 2–3 h, during which the color changed from dark green to orange. The solvent was pumped off, and the residue was washed with Et_2O and then extracted with CH_2Cl_2. Recrystallization from CH_2Cl_2–Et_2O–hexane afforded orange crystals.

Compound **1**: Yield: 83 mg (30%). *Anal.* Calc. for $C_{48}H_{40}ClN_3OP_4RuS_4 \cdot CH_2Cl_2$: C, 51.2; H, 3.7; N, 3.7. Found: C, 51.1; H, 3.9; N, 3.5%. ^{1}H NMR ($CDCl_3$): δ 6.94–7.96 (m, C_6H_5). $^{31}P\{^{1}H\}$ NMR ($CDCl_3$): δ 38.20 (s). IR (KBr, cm^{-1}): 1834 [ν(N≡O)].

Compound **2**: Yield: 28 mg (42%). ^{1}H NMR ($CDCl_3$): δ 2.46–2.60 (m, 4H, C*H*(CH_3)$_2$), 2.10–2.23 (m, 4H, C*H*(CH_3)$_2$), 1.21–1.34 (m, 48H, CH(C*H*$_3$)$_2$). $^{31}P\{^{1}H\}$ NMR ($CDCl_3$): δ 60.84 (s). IR (KBr, cm^{-1}): 1841, 1826 [ν(N≡O)].

2.2. Preparations of trans-[Ru(NO)(Cl){N(Ph$_2$PSe)$_2$}$_2$] (3) and trans-[Ru(NO)(Cl){N(Ph$_2$PSe)$_2$}{Ph$_2$P(Se)NPPh$_2$}] (4)

A mixture of $[Ru(NO)Cl_3(PPh_3)_2]$ (200 mg, 0.26 mmol) and 2 equiv. of $K[N(Ph_2PSe)_2]$ (305 mg, 0.53 mmol) was heated in dmf (20 ml) at reflux for 3 h, during which the color changed from dark green to orange. The solvent was pumped off, and the residue was purified by column chromatography (silica gel) using CH_2Cl_2–hexane (1:1) as eluant. Complexes **3** and **4** were isolated as orange and reddish orange crystals, respectively.

Compound **3**: $R_f = 0.11$. Yield: 125 mg (38%). *Anal.* Calc. for $C_{48}H_{40}ClN_3OP_4RuSe_4 \cdot CH_2Cl_2$: C, 44.1, H, 3.2; N, 3.2. Found: 44.5; H, 3.1; N, 3.1%. ^{1}H NMR ($CDCl_3$): δ 7.20–7.94 (m, 40H, C_6H_5). $^{31}P\{^{1}H\}$ NMR ($CDCl_3$): δ 28.98 (s). IR (KBr, cm^{-1}): 1834 [ν(N≡O)].

Compound **4**: $R_f = 0.23$. Yield: 40 mg (13%). *Anal.* Calc. for $C_{48}H_{40}ClN_3OP_4RuSe_3 \cdot 1.5CH_2Cl_2$: 45.8; H, 3.3; N, 3.2. Found: C, 45.9; H, 3.3; N, 3.4%. ^{1}H NMR ($CDCl_3$): δ 6.89–8.10 (m, 40H, C_6H_5). $^{31}P\{^{1}H\}$ NMR ($CDCl_3$): δ 71.49 (ddd, $J_{PP} = 40.0$ Hz, $J_{PP} = 9.8$ Hz, $J_{PP} = 6.2$ Hz, PPh_2), 55.66 (d, $J_{PP} = 40.0$ Hz, P(Se)Ph_2 *trans* to PPh_2), 31.88 (dd, $J_{PP} = 3.5$ Hz, $J_{PP} = 9.8$ Hz), 26.91 (dd, $J_{PP} = 3.5$ Hz, $J_{PP} = 6.2$ Hz). IR (KBr, cm^{-1}): 1837 [ν(N≡O)].

2.3. Preparation of cis-[Ru(NO)Cl{N(Ph$_2$PO)$_2$}$_2$] (5)

A suspension of $Ru(NO)Cl_3 \cdot xH_2O$ (25 mg, 0.098 mmol) and 2 equiv. of $K[N(Ph_2PO)_2]$ (89 mg, 0.20 mmol) in acetone (15 ml) was heated at reflux for overnight. The solvent was removed, and the residue was extracted with CH_2Cl_2. Recrystallization from CH_2Cl_2–Et_2O–hexane afforded pale reddish brown crystals. Yield: 47 mg (48%). *Anal.* Calc. for $C_{48}H_{40}ClN_3O_5P_4Ru \cdot CH_2Cl_2$: C, 54.3; H, 3.9; N, 3.9. Found: C, 54.1; 3.9; N, 3.8%. ^{1}H NMR ($CDCl_3$): δ 6.85–7.93 (m, 40H, C_6H_5). $^{31}P\{^{1}H\}$ NMR ($CDCl_3$): δ 38.94 (d, $J_{PP} = 4.0$ Hz), 34.74 (d, $J_{PP} = 3.3$ Hz), 34.64 (d, $J_{PP} = 3.7$ Hz), 31.52 (d, $J_{PP} = 3.7$ Hz). IR (KBr, cm^{-1}): 1863 [ν(N≡O)].

2.4. Preparation of [Rh(NO){N(Ph$_2$PQ)$_2$}$_2$] (R = Ph, Q = S (6) or Se (7); R = Pr^i, Q = S (8))

A mixture of $[Rh(NO)Cl_2(PPh_3)_2]$ (50 mg, 0.069 mmol) and $K[N(Ph_2PQ)_2]$ (0.14 mmol) in THF (10 ml) was heated at reflux for 1 h. The solvent was pumped off and the residue was washed with hexane. Recrystallization from CH_2Cl_2–hexane (**6** and **7**) or Et_2O–hexane (**8**) afforded red crystals.

Compound **6**: Yield: 45 mg (63%). *Anal.* Calc. for $C_{48}H_{40}N_3OP_4RhS_4$: C, 56.0; H, 3.9; N, 4.1. Found: C, 55.7; H, 3.9; N, 3.0%. ^{1}H NMR ($CDCl_3$): δ 7.77–7.84 (m, 16H, C_6H_5), δ 7.26–7.37 (m, 24H, C_6H_5). $^{31}P\{^{1}H\}$ NMR ($CDCl_3$): δ 37.85 (d, $J_{RhP} = 3.5$ Hz). IR (KBr, cm^{-1}): 1655 [ν(N≡O)].

Compound **7**: Yield: 46 mg (65%). *Anal.* Calc. for $C_{48}H_{40}N_3OP_4RhSe_4$: C, 47.4; H, 3.3; N, 3.5. Found: C, 47.4; H, 3.3; N, 3.4%. ^{1}H NMR ($CDCl_3$): δ 7.77–7.83 (m, 16H, C_6H_5), 7.26–7.39 (m, 24H, C_6H_5). $^{31}P\{^{1}H\}$ NMR ($CDCl_3$): δ 27.97 (d, $J_{RhP} = 4.1$ Hz). IR (KBr, cm^{-1}): 1629 [ν(N≡O)].

Table 1
Crystallographic data and experimental details for *trans*-[Ru(NO)Cl{N(Pr^i_2PS)$_2$}$_2$] (**2**), *trans*-[Ru(NO)(Cl){N(Ph_2PSe)$_2$}{Ph_2P(Se)NPPh_2}] (**4**), and [Rh(NO){N(Pr^i_2PSe)$_2$}$_2$] (**9**)

Compound	**2**	**4**	**9**
Empirical formula	$C_{24}H_{56}ClN_3OP_4RuS_4$	$C_{48}H_{40}ClN_3OP_4RuSe_3$	$C_{24}H_{56}N_3OP_4RhSe_4$
Formula weight	791.36	1172.11	945.35
Crystal system	triclinic	monoclinic	triclinic
Space group	$P\bar{1}$	$P2_1/c$	$P\bar{1}$
Z	1	4	2
a (Å)	8.4739(5)	22.975(6)	8.559(2)
b (Å)	9.5191(5)	20.593(5)	9.770(2)
c (Å)	13.1320(7)	9.781(3)	24.259(5)
α (°)	106.086(1)		85.945(4)
β (°)	94.173(1)	93.915(4)	84.513(4)
γ (°)	113.566(1)		66.311(3)
V (Å^3)	912.43(9)	4617(2)	1847.8(7)
D_{calc} (g cm^{-3})	1.440	1.686	1.699
Temperature (K)	298(2)	100(2)	298(2)
F(000)	414	2320	940
μ(Mo Kα) (mm^{-1})	0.930	2.942	1.699
Total reflections	5848	33796	17135
Independent reflections	4759	10844	6316
R_{int}	0.0105	0.0389	0.00214
R_1[a], wR_2[b] ($I > 2\sigma(I)$)	0.0225, 0.0617	0.0365, 0.0750	0.0333, 0.0773
R_1, wR_2 (all data)	0.0238, 0.0624	0.0575, 0.0818	0.0402, 0.0798
Goodness-of-fit[c]	1.021	1.005	1.036

[a] $R_1 = \sum||F_o|-|F_c||/\sum|F_o|$.
[b] $wR_2 = [\sum w(|F_o^2| - |F_c^2|)^2/\sum w|F_o^2|^2]^{1/2}$.
[c] GoF $= [\sum w(|F_o| - |F_c|)^2/(N_{obs} - N_{param})]^{1/2}$.

Compound **8**: Yield: 35 mg (67%). *Anal*. Calc. for $C_{24}H_{56}N_3OP_4RhS_4$: C, 38.0; H, 7.4; N, 5.6. Found: C, 38.4; H, 7.5; N, 5.3%. ^{1}H NMR (C_6D_6): δ 2.20–2.40 (m, 8H, C*H*(CH$_3$)$_2$), δ 1.29–1.49 (m, 48H, CH(C*H*$_3$)$_2$). ^{31}P{^{1}H} NMR (C_6D_6): δ 63.17 (s). IR (KBr, cm^{-1}): 1630 [ν(N≡O)].

2.5. Preparation of [Rh(NO){N(Pr^i_2PSe)$_2$}$_2$] (9)

To a suspension of [Rh(NO)Cl$_2$(PPh_3)$_2$] (50 mg, 0.069 mmol) in THF (10 ml) was added 2 equiv. of K[N(Pr^i_2PSe)$_2$] (61 mg, 0.14 mmol), and the reaction mixture was stirred at room temperature for 5 h. The solvent was removed and the residue was extracted with hexane–Et_2O (1:1, v/v). Concentration and cooling at −10 °C afforded deep red crystals. Yield: 46 mg (65%). *Anal*. Calc. for $C_{24}H_{56}N_3OP_4RhSe_4$: C, 30.5; H, 6.0; N, 4.5. Found: C, 30.6; H, 6.1; N, 4.3%. ^{1}H NMR (C_6D_6): δ 2.24–2.47 (m, 8H, C*H*(CH$_3$)$_2$), 1.28–1.57 (m, 48H, CH(C*H*$_3$)$_2$). ^{31}P{^{1}H} NMR (C_6D_6): δ 54.38 (d, $J_{RhP} = 3.2$ Hz). IR (KBr, cm^{-1}): 1618 [ν(N≡O)].

2.6. Preparation of [Rh(NO){NH(Pr^i_2PS)$_2$}$_2$][BF_4]$_2$ (10)

To a solution of **8** (40 mg, 0.053 mmol) in Et_2O (10 ml) was added 2 equiv. of HBF_4 (54% in Et_2O, 15 μl, 0.11 mmol) at 0 °C. The orange solid was collected and washed with Et_2O. Recrystallization from CH_2Cl_2-Et_2O afforded orange crystalline solid. Yield: 31 mg (62%). *Anal*. Calc. for $C_{24}H_{58}B_2F_8N_3OP_4RhS_4 \cdot 0.5CH_2Cl_2$: C, 30.2; H, 6.1; N, 4.3. Found: C, 30.1; H, 6.6; N, 4.2%. ^{1}H NMR (CDCl$_3$): δ 6.80 (s, 2H, N*H*), 2.74–2.88 (m, 8H, C*H*(CH$_3$)$_2$), 1.20–1.46 (m, 48H, CH(C*H*$_3$)$_2$). ^{31}P{^{1}H} NMR (CDCl$_3$): δ 89.45 (s). ^{19}F{^{1}H} NMR (CDCl$_3$): δ −148.96 (s). IR (KBr, cm^{-1}): 1650, 1677 [ν(N≡O)].

2.7. X-ray diffraction analysis

A summary of crystallographic data and experimental details for **2**, **4**, and **9** are summarized in Table 1. Intensity data were collected on a Bruker SMART APEX 1000 CCD diffractometer using graphite-monochromated Mo Kα radiation ($\lambda = 0.71073$ Å) at 100(2) K. The collected frames were processed with the software SAINT. Structures were solved by the direct methods and refined by full-matrix least-squares on F^2 using the SHELXTL software package [24]. Non-hydrogen atoms were refined anisotropically. Selected bond lengths and angles for complexes **2**, **4** and **9** are listed in Tables 2–4, respectively.

3. Results and discussion

3.1. Ruthenium nitrosyl compounds

Treatment of [Ru(NO)Cl$_3$(PPh_3)$_2$] with 2 equiv. of K[N(R_2PS)$_2$] in refluxing dmf afforded the nitrosyl compounds *trans*-[Ru(NO)Cl{N(R_2PS)$_2$}$_2$] (R = Ph (**1**), Pr^i (**2**)) (Scheme 2), isolated as air-stable orange solids. The ^{31}P {^{1}H} NMR spectra for both **1** and **2** exhibit a single resonance (at δ 38.2 (s) and 60.84 (s) ppm, respectively),

Table 2
Selected bond lengths (Å) and angles (°) for *trans*-[Ru(NO)Cl{N($Pr^i_2PS)_2$}$_2$] (**2**)

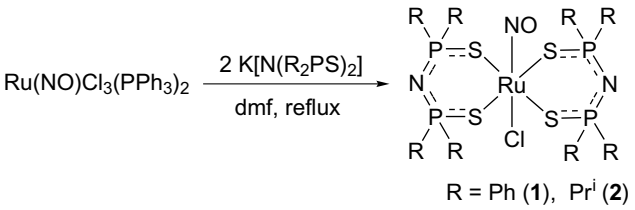
Ru(1)–S(1)	2.4343(13)	Ru(1)–S(2)	2.4369(14)
Ru(1)–S(3)	2.4393(14)	Ru(1)–S(4)	2.4441(14)
Ru(1)–N(1)	1.810(5)	Ru(1)–Cl(1)	2.3392(14)
N(1)–O(1)	1.036(5)	P(1)–S(1)	2.026(2)
P(2)–S(2)	2.0393(19)	P(3)–S(3)	2.0494(19)
P(4)–S(4)	2.031(2)	P(1)–N(2)	1.586(5)
P(2)–N(2)	1.594(4)	P(3)–N(3)	1.591(5)
P(4)–N(3)	1.582(5)		
S(1)–Ru(1)–S(2)	99.90(5)	S(3)–Ru(1)–S(4)	101.26(5)
S(1)–Ru(1)–S(3)	79.58(5)	S(2)–Ru(1)–S(4)	79.15(5)
S(1)–Ru(1)–S(4)	176.64(5)	S(2)–Ru(1)–S(3)	178.08(6)
N(1)–Ru(1)–S(1)	95.92(12)	N(1)–Ru(1)–S(2)	91.04(13)
N(1)–Ru(1)–S(3)	90.85(13)	N(1)–Ru(1)–S(4)	87.33(13)
Cl(1)–Ru(1)–S(1)	85.04(5)	Cl(1)–Ru(1)–S(2)	89.74(5)
Cl(1)–Ru(1)–S(3)	88.38(5)	Cl(1)–Ru(1)–S(4)	91.73(5)
N(1)–Ru(1)–Cl(1)	178.65(14)	Ru(1)–N(1)–O(1)	177.3(5)
P(1)–N(2)–P(2)	134.4(3)	P(4)–N(3)–P(3)	136.4(3)

Table 3
Selected bond lengths (Å) and angles (°) for *trans*-[Ru(NO)(Cl){N(Ph_2P-Se)$_2$}{Ph_2P(Se)NPPh_2}] (**4**)

Ru(1)–Se(1)	2.5765(7)	Ru(1)–Se(2)	2.5321(7)
Ru(1)–Se(3)	2.5060(6)	Ru(1)–P(4)	2.3717(10)
Ru(1)–N(1)	1.719(3)	Ru(1)–Cl(1)	2.3527(10)
N(1)–O(1)	1.139(3)	P(1)–Se(1)	2.1652(10)
P(2)–Se(2)	2.1856(10)	P(3)–Se(3)	2.1932(10)
P(1)–N(2)	1.593(2)	P(2)–N(2)	1.572(2)
P(3)–N(3)	1.579(2)	P(4)–N(3)	1.616(2)
Se(1)–Ru(1)–Se(2)	90.45(2)	Se(2)–Ru(1)–P(4)	94.73(3)
Se(3)–Ru(1)–P(4)	89.60(3)	Se(1)–Ru(1)–Se(3)	83.94(2)
Se(1)–Ru(1)–P(4)	167.44(2)	Se(2)–Ru(1)–Se(3)	171.708(16)
N(1)–Ru(1)–Se(1)	96.99(8)	N(1)–Ru(1)–Se(2)	97.34(8)
N(1)–Ru(1)–Se(3)	89.42(8)	N(1)–Ru(1)–P(4)	93.69(9)
Cl(1)–Ru(1)–Se(1)	85.72(2)	Cl(1)–Ru(1)–Se(2)	84.77(2)
Cl(1)–Ru(1)–Se(3)	88.72(2)	Cl(1)–Ru(1)–P(4)	83.37(3)
N(1)–Ru(1)–Cl(1)	176.53(9)	Ru(1)–N(1)–O(1)	175.9(3)
P(2)–N(2)–P(1)	135.90(17)	P(3)–N(3)–P(4)	123.90(16)

Table 4
Selected bond lengths (Å) and angles (°) for [Rh(NO){N($Pr^i_2PSe)_2$}$_2$] (**9**)

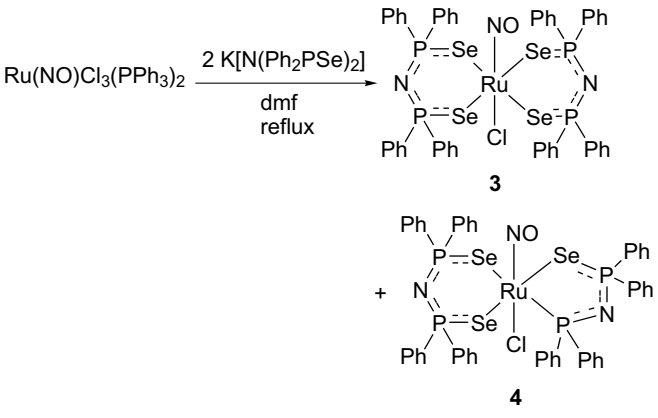
Rh(1)–Se(1)	2.5232(6)	Rh(1)–Se(2)	2.4897(7)
Rh(1)–Se(3)	2.5163(6)	Rh(1)–Se(4)	2.5104(6)
Rh(1)–N(1)	1.905(3)	N(1)–O(1)	1.122(4)
P(1)–Se(1)	2.1872(9)	P(2)–Se(2)	2.2103(10)
P(3)–Se(3)	2.1848(9)	P(4)–Se(4)	2.1979(10)
P(1)–N(2)	1.597(3)	P(2)–N(2)	1.598(3)
P(3)–N(3)	1.605(3)	P(4)–N(3)	1.593(3)
Se(1)–Rh(1)–Se(2)	98.758(14)	Se(3)–Rh(1)–Se(4)	100.784(15)
Se(1)–Rh(1)–Se(3)	169.368(17)	Se(2)–Rh(1)–Se(4)	161.527(19)
Se(1)–Rh(1)–Se(4)	77.687(14)	Se(2)–Rh(1)–Se(3)	79.319(14)
N(1)–Rh(1)–Se(1)	97.65(10)	N(1)–Rh(1)–Se(2)	99.86(9)
N(1)–Rh(1)–Se(3)	92.98(10)	N(1)–Rh(1)–Se(4)	98.58(9)
Rh(1)–Se(1)–P(1)	104.77(3)	Rh(1)–N(1)–O(1)	125.7(3)
P(1)–N(2)–P(2)	132.61(17)	P(4)–N(3)–P(3)	132.93(17)



Scheme 2.

consistent with the *trans* geometry of the compounds. The IR spectrum of **1** shows a strong N–O band at 1834 cm^{-1}, which is similar to that for *trans*-[Ru(NO)Cl(S_2CNEt_2)$_2$] (1840 cm^{-1}) [25]. The splitting for the *v*(NO) band (1826 and 1841 cm^{-1}) for **2** is probably due to a solid-state effect. Photolysis of **2** in THF led to a green species that did not exhibit any *v*(NO) bands in the IR spectrum, indicating that the loss of the nitrosyl ligand. Unfortunately, we have not been able to crystallize this green complex.

Reaction of [Ru(NO)Cl_3(PPh_3)$_2$] with 2 equiv. of K[N($Ph_2PSe)_2$] in refluxing dmf led to a mixture of *trans*-[Ru(NO)Cl{N($Ph_2PSe)_2$}$_2$] (**3**) and *trans*-Ru(NO)Cl{N($Ph_2PSe)_2$}{Ph_2P(Se)NPPh_2}] (**4**) (Scheme 3), which could be separated by column chromatography using CH_2Cl_2–hexane as eluant. Apparently, the formation of **4** involved the Ru-assisted selenium atom abstraction of one [N($Ph_2PSe)_2$]$^-$ ligand in **3**, possibly by PPh_3. It may be noted that in a previous paper, we reported that interaction of [Ru(=CHPh)Cl_2(PCy_3)$_2$] (Cy = cyclohexyl) with K[N($Ph_2PSe)_2$] resulted in selenium atom abstraction from the [N($Ph_2PSe)_2$]$^-$ ligand and the formation of *trans*-[Ru(=CHPh){Ph_2P(Se)NPPh_2}$_2$] along with *trans*-[Ru(=CHPh){N($Ph_2PSe)_2$}$_2$] [26]. Chalcogen atom abstraction occurred for the [N($Ph_2PSe)_2$]$^-$ ligand but not in the sulfide analogue presumably because of the weaker P=Se bond strength compared with that of P=S. The IR N–O stretching frequency of **3** (1834 cm^{-1}) is similar to that of **1**. The ^{31}P {H} NMR spectrum of **3** displays at singlet at δ 28.98 ppm, indicative of the *trans* geometry of the molecule. In the ^{31}P {^{1}H} NMR spectrum of **4**, the doublet



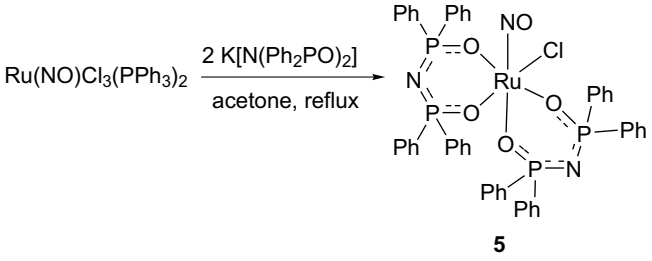
Scheme 3.

of doublets of doublets at δ 71.49 ppm ($^3J_{PP} = 40$, $^2J_{PP} = 9.8$ and $^3J_{PP} = 6.2$ Hz) is assigned to the PPh_2 group, whereas the doublet at δ 55.66 ppm ($^3J_{PP} = 40$ Hz) is assigned to the $P(Se)Ph_2$ group opposite to the PPh_2 group. The remaining two $P(Se)Ph_2$ groups appear as two doublets of doublets at δ 26.91 ($^4J_{PP} = 3.5$, $^3J_{PP} = 6.2$ Hz) and 31.88 ppm ($^4J_{PP} = 3.5$, $^3J_{PP} = 9.8$ Hz) ppm, respectively.

No reaction was found between $[Ru(NO)Cl_3(PPh_3)_2]$ and $K[N(Ph_2PO)_2]$. Refluxing $Ru(NO)Cl_3 \cdot xH_2O$ with $K[N(PPh_2PO)_2]$ in acetone gave *cis*-$[Ru(NO)Cl\{N(Ph_2PO)_2\}_2]$ (**5**) (Scheme 4), isolated as air-stable brown crystals. Unlike the sulfide and selenide analogues, the NO and Cl ligands in **5** are *cis* to each other, as evidenced by the $^{31}P\{^1H\}$ NMR spectrum that displays four doublets at δ 38.94, 34.74, 34.64 and 31.52 ppm ($J \sim 3$–4 Hz). The IR NO stretching frequency for **5** (1863 cm^{-1}) is higher than those of **1** and **3**, suggesting that the P=O group is less electron-releasing than chloride.

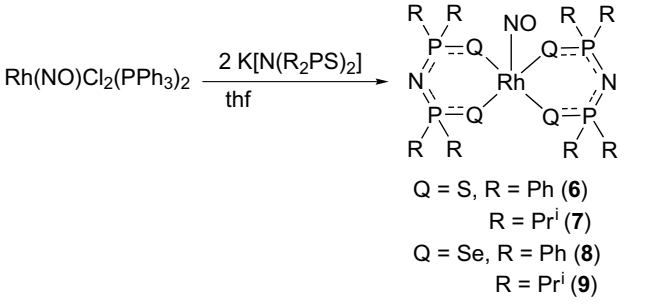
3.2. Rhodium nitrosyl compounds

Treatment of $[Rh(NO)Cl_2(PPh_3)_2]$ with $K[N(R_2PQ)_2]$ in THF afforded $[Rh(NO)\{N(R_2PQ)_2\}_2]$ (R = Ph, Q = S (**6**) or Se (**7**); R = Pr^i, Q = S (**8**) or Se (**9**)) (Scheme 5), isolated as air-stable red crystals. The $^{31}P\{^1H\}$ NMR spectra of **6**, **7**, and **9** display doublets at δ 37.85, 27.97, and 54.38 ppm, respectively, with J_{RhP} values of 3–4 Hz, whereas a singlet at δ 63.17 ppm was found for **8**. The IR N–O stretching frequencies for **6**–**9** of 1618–1655 cm^{-1} are within the range expected for bent nitrosyl compounds [2], although they are higher than that for $[Rh(NO)Cl_2(PPh_3)_2]$ (1559 cm^{-1}) [23]. The ν(NO) for $[Rh(NO)\{N(R_2PQ)_2\}_2]$ was found to



5

Scheme 4.



Scheme 5.

decrease in the order R: Pr^i > Ph, Q: Se > S. This suggests that the selenium ligand is a stronger donor than the sulfur counterpart.

Unlike **1**, no reaction was found when **6** in THF was irradiated with UV light. Attempts have been made to activate the nitrosyl ligand of the Rh nitrosyl compounds by treatment with nucleophiles and electrophiles. No reactions were found when **6** was reacted with MeLi or $LiBEt_3H$. Treatment of **6** with PMe_3 in $CDCl_3$ gave $OPMe_3$ identified by ^{31}P NMR spectroscopy along with an uncharacterized Rh species that showed the absence of ν(NO) in the IR spectrum. We have not been able to crystallize this Rh-containing product. Reaction of **7** with HBF_4 in Et_2O afforded an orange precipitate **10** analyzed as dicationic $[H_2\mathbf{7}][BF_4]_2$. The IR spectrum of **10** shows ν(NO) at 1650 and 1677 cm^{-1}, indicating that the bent nitrosyl ligand remained intact. The $^{31}P\{^1H\}$ NMR spectrum of **10** displays a singlet at δ 89.45 ppm that is considerably more downfield than that for **7**, but similar to that for $HN(Pr^i_2PS)_2$ (δ 91.2 ppm). The observation of a single ^{31}P signal suggests that **10** has a square pyramidal geometry with 2 equivalent $[N(Pr^i_2S)_2]^-$ ligands at the equatorial positions. In addition to the resonances due to the isopropyl protons, the ^1H NMR spectrum displays a broad NH resonance at δ 6.80 ppm that underwent deuterium exchange upon treatment with D_2O. On the basis of the spectroscopic data, **10** is formulated as a dicationic Rh nitrosyl compound containing two protonated dithioimidodiphosphinate ligands, $[Rh(NO)\{HN(Pr^i_2PS)_2\}][BF_4]_2$.

3.3. Crystal structures

The solid-state structure of **2** is shown in Fig. 1; selected bond lengths and angles are listed in Table 2. The geometry about Ru is pseudo octahedral with the nitrosyl ligand opposite to the chloride. The Ru–N–O linkage is linear (177.3(5)°) as expected for the $\{MNO\}^6$ configuration using the Enemark–Feltman notation [27]. The Ru–N distance of 1.810(5) Å is rather long compared with those of reported Ru(II) nitrosyl compounds (e.g. 1.643(8) and 1.687(8) Å for $[Ru(NO)(bdt)_2]^-$ (bdt = 1,2-benzenethiolate) [28] and 1.751(5) Å for *trans*-[Ru(TPP)(NO)(OH)] (TPP = tetraphenylporphyrin dianion [29]). The Ru–S distances (av. 2.4387 Å) are comparable to those in $[Ru\{N(Pr^i_2PS)_2\}_2(PPh_3)]$ (av. 2.405 Å) [16]. Similar to other M–$[N(R_2PS)_2]$ complexes, the P–S distances (2.026(2)–2.049(2) Å) in **2** are longer than those in $HN(Pr^i_2PS)_2$ (1.941(1) and 1.949(1) Å) [20] whereas the P–N distances (1.586(5)–1.594(4) Å) are shorter than those in the latter (1.682(3) and 1.684(2) Å). The P–N–P angles in **2** (134.4(3)° and 136.4(3)°) are slightly larger than that in $HN(Pr^i_2PS)_2$ 131.6(1)°) [20].

The solid-state structure of **4** is shown in Fig. 2; selected bond lengths and angles are listed in Table 3. The geometry around Ru is pseudo octahedral with the nitrosyl group opposite to the chloride. The nitrosyl ligand is linear with the Ru–N–O angle of 175.9(3)°. The Ru–N distance in **4**

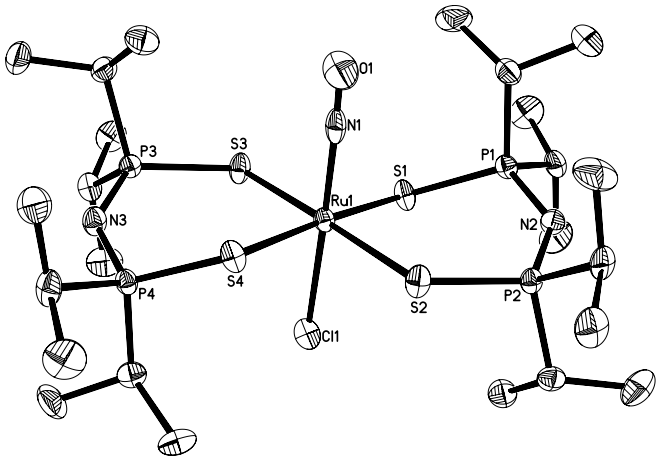


Fig. 1. Molecular structure of *trans*-[Ru(NO)Cl{N(Pr^i_2PS)$_2$}$_2$] (**2**). The ellipsoids are drawn at 30% probability level.

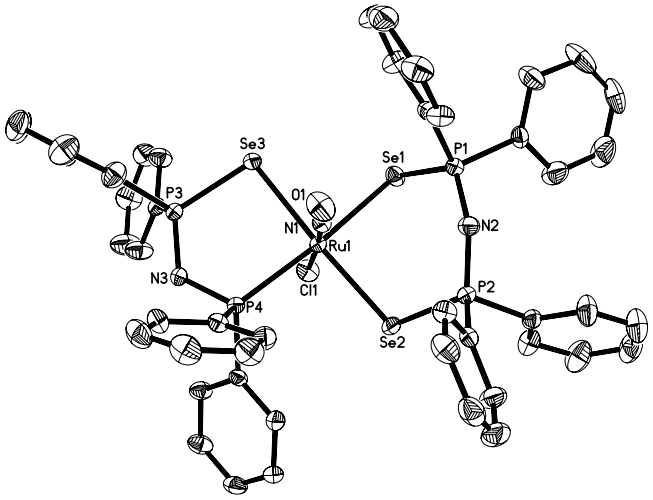


Fig. 2. Molecular structure of *trans*-[Ru(NO)(Cl){N(Ph$_2$PSe)$_2$}{Ph$_2$P(Se)NPPh$_2$}] (**4**). The ellipsoids are drawn at 30% probability level.

(1.719(3) Å) is typical of Ru(II) nitrosyl compounds [7]. The Ru–P distance (2.372(1) Å) is comparable to that in [Ru(=CHPh){Ph$_2$P(Se)NPPh$_2$}$_2$] (av. 2.383 Å) [25]. The Ru–Se (*trans* to P) (2.5765(7) Å) is longer than the Ru–Se (*trans* to Se) (2.5060(6) and 2.5321(7) Å) due to the *trans* influence of the PPh$_2$ group. The N–P distance in the [Pr^i_2P(Se)NPPr^i_2]$^-$ ligand (1.616(2) Å) is slightly longer than the N–P(Se) distances (1.573(2)–1.593(2) Å). The P–N–P angle in the [Pr^i_2P(Se)NPPr^i_2]$^-$ ligand (123.9(2)°) is obviously smaller than that in the [N(Pr^i_2PSe)$_2$]$^-$ ligand (135.9(2)°).

The solid-state structure of **9** is shown in Fig. 3; selected bond lengths and angles are listed in Table 4. The geometry around Rh is pseudo square pyramidal with the nitrosyl ligand occupying the apical position. The Rh–N–O angle is 125.7(3)° that is characteristic for bent nitrosyl compounds [1,2]. A similar bond angle was found for [Rh(NO)Cl$_2$(PPh$_3$)$_2$] (125(1)°) [30]. The bending of the Rh–N–O linkage is in accordance with the {RhNO}^{7} electron configuration [27]. It may be noted that the isoelectronic Co compound [Co(NO)(S$_2$CNEt$_2$)$_2$] also has square pyramidal geometry with an apical bent nitrosyl ligand [31]. The Rh–N distance of 1.905(3) Å is comparable to that in [Rh(NO)Cl$_2$(PPh$_3$)$_2$] (1.91(1) Å) [30]. The Rh atom is displaced above the Se$_4$ mean plane by ca. 0.317 Å. The average Rh–Se distance is 2.5099 Å. The P–Se (2.1848(9)–2.210(1) Å) and P–N (1.593(3) and 1.605(3) Å) distances and P–N–P angles (134.4(3)° and 136.4(3)°) compare well with those in **4**.

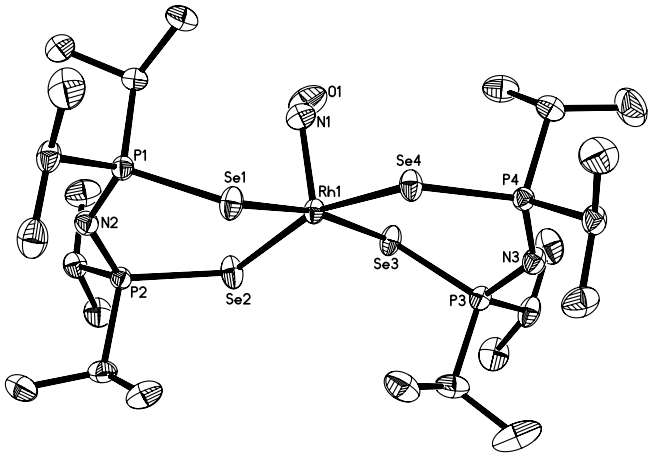


Fig. 3. Molecular structure of [Rh(NO){N(Pr^i_2PSe)$_2$}$_2$] (**9**). The ellipsoids are drawn at 30% probability level.

4. Conclusion

In summary we have synthesized and structurally characterized Ru and Rh nitrosyl compounds with [N(R$_2$PQ)$_2$]$^-$ (Q = O, S, Se) ligands. X-ray crystallography revealed that the nitrosyl ligand in the Ru compounds is linear whereas that in the Rh analogue is bent. Interaction of [Ru(NO)Cl$_3$(PPh$_3$)$_2$] with K[N(Ph$_2$PSe)$_2$] resulted in selenium atom abstraction of the ligand and formation of *trans*-[Ru(NO)(Cl){N(Ph$_2$PSe)$_2$}{Ph$_2$P(Se)NPPh$_2$}]. Treatment of [Rh(NO){N(Pr^i_2PS)$_2$}$_2$] with HBF$_4$ led to protonation of the dithioimidodiphosphinate ligands and formation of dicationic [Rh(NO){HN(Pr^i_2PS)$_2$}$_2$][BF$_4$]$_2$.

Acknowledgements

The work was supported by the Hong Kong Research Grants Council (Project Nos. 602104 and 602203). We thank Dr. Herman Sung for solving the crystal structures. Q.-F. Zhang thanks the Science and Technological Fund of Anhui Province, PR China, for the Outstanding Youth Award (06046100).

Appendix A. Supplementary material

CCDC 632255, 632256 and 632257 contain the supplementary crystallographic data for **2**, **4** and **9**. These data can be obtained free of charge via http://www.ccdc.cam.

ac.uk/conts/retrieving.html, or from the Cambridge Crystallographic Data Centre, 12 Union Road, Cambridge CB2 1EZ, UK; fax: (+44) 1223-336-033; or e-mail: deposit@ccdc.cam.ac.uk. Supplementary data associated with this article can be found, in the online version, at doi:10.1016/j.poly.2007.04.002.

References

[1] J.A. McCleverty, Chem. Rev. 79 (1979) 53.
[2] G.B. Richter-Addo, P. Legzdins, Metal Nitrosyls, Oxford University Press, New York, 1992.
[3] R. Eisenberg, C.D. Meyer, Acc. Chem. Res. 8 (1978) 26.
[4] D.M.P. Mingos, D. Sherman, Adv. Inorg. Chem. 34 (1989) 293.
[5] T.W. Hayton, P. Legzdins, W.B. Sharp, Chem. Rev. 102 (2002) 935.
[6] J.A. McCleverty, Chem. Rev. 104 (2004) 403.
[7] L.J. Ignarro, Nitric Oxide: Biology and Pathology, Academic Press, San Diego, 2000.
[8] I.M. Lorkovic, K.M. Miranda, B. Lee, S. Bernhard, J.R. Schoonover, P.C. Ford, J. Am. Chem. Soc. 120 (1998) 11674.
[9] E. Tfouni, M. Krieger, B.R. McGarvey, D.W. Franco, Coord. Chem. Rev. 236 (2003) 57.
[10] R. Prakash, A.U. Czaja, F.W. Heinemann, D. Sellmann, J. Am. Chem. Soc. 127 (2005) 13758.
[11] I. Haiduc, in: J.A. McCleverty, T.J. Meyer (Eds.), Comprehensive Coordination Chemistry II, vol. 1, Elsevier Pergamon, Amsterdam, 2004, p. 323.
[12] J.D. Woollins, J. Chem. Soc., Dalton Trans. (1996) 2893.
[13] T.Q. Ly, J.D. Woollins, Coord. Chem. Rev. 176 (1998) 451.
[14] I. Haiduc, Coord. Chem. Rev. 158 (1997) 325.
[15] C. Silvestru, J.E. Drake, Coord. Chem. Rev. 223 (2001) 117.
[16] W.-H. Leung, H. Zheng, J.L.-C. Chim, J. Chan, W.-T. Wong, I.D. Williams, J. Chem. Soc., Dalton Trans. (2000) 423.
[17] Q.-F. Zhang, H. Zheng, W.-Y. Wong, I.D. Williams, W.-H. Leung, Inorg. Chem. 39 (2000) 5255.
[18] F.T. Wang, J. Najdzionek, K.L. Leneker, H. Wasserman, D.M. Braitsch, Synth. React. Inorg. Met.–Org. Chem. 8 (1978) 119.
[19] P. Bhattacharyya, A.M.Z. Slawin, D.J. Williams, J.D. Woollins, J. Chem. Soc., Dalton Trans. (1995) 2489.
[20] D. Cupertino, R. Keyte, A.M.Z. Slawin, D.J. Williams, J.D. Woollins, Inorg. Chem. 35 (1996) 2695.
[21] D. Cupertino, D.J. Birdsall, A.M.Z. Slawin, J.D. Woollins, Inorg. Chim. Acta 290 (1999) 1.
[22] J.L. Levison, S.D. Robinson, J. Chem. Soc. A (1970) 2947.
[23] G.R. Crooks, B.F.G. Johnson, J. Chem. Soc. A (1970) 1662.
[24] G.M. Sheldrick, SHELXTL-Plus V5.1 Software Reference Manual, Bruker AXS Inc., Madison, WI, USA, 1997.
[25] J.V. Dubrawski, R.D. Feltham, Inorg. Chem. 19 (1980) 355.
[26] W.-H. Leung, K.-K. Lau, Q.-F. Zhang, W.-T. Wong, B.Z. Tang, Organometallics 19 (2000) 2084.
[27] R.D. Feltham, J.H. Enemark, Top. Stereochem. 2 (1981) 155.
[28] D. Sellmann, K. Hein, F.W. Heinemann, Inorg. Chim. Acta 357 (2004) 3739.
[29] D.S. Bohle, C.-H. Hung, B.D. Smith, Inorg. Chem. 37 (1998) 5798.
[30] S.Z. Goldberg, C. Kubiak, C.D. Meyer, R. Eisenberg, Inorg. Chem. 14 (1975) 1650.
[31] G.A. Brewer, R.J. Butcher, B. Letafat, E. Sinn, Inorg. Chem. 22 (1983) 371.

detection of N_2O is an indirect indicator for the formation of HNO [3], although there are other sources of N_2O in the chemistry of nitric oxide, for example as a product of NO disproportionation mediated by transition metal complexes [12]

$$2HNO \rightarrow N_2O + H_2O \quad (1)$$

2. Experimental

2.1. General

Infrared spectra were obtained using a Nicolet 4700 FTIR and a 0.5 mm-pathlength sealed IR cell. UV–Vis spectra were collected on an HP 8453 diode array spectrophotometer. GC–MS data were obtained using a Hewlett–Packard 6890 Series GC System and a 5973 Mass Selective Detector. Data manipulation was performed using Igor Pro software. Irradiation of samples in IR cells was performed using the 365 nm output of a Mineralight handheld UV lamp. Irradiation in UV–Vis cells was performed using Starna airtight cuvettes equipped with septum caps.

Samples for spectroscopic studies were prepared under a nitrogen atmosphere in the glovebox. Anhydrous chloroform (Aldrich, SureSeal) was transferred via cannula to a Schlenk flask, deaerated, and brought into the glovebox. Solutions of **1** were then prepared and, for studies under nitrogen, loaded into IR cells and removed from the glovebox. For studies performed under CO, samples were placed in airtight flasks equipped with rubber septa and removed from the glovebox, and then CO was bubbled through the solution. These samples were then transferred to IR cells via syringe. Molar concentrations of N_2O in solution were calculated from FTIR data using absorbance values at 2220 cm^{-1}, an extinction coefficient of 910 $M^{-1}\,cm^{-1}$ [13], and a pathlength of 0.05 cm. Molar concentrations of **1** in solution were estimated from FTIR data using absorbance values at 1415 cm^{-1} (a frequency at which there appeared to be little overlap with any other species in solution), an extinction coefficient of 420 $M^{-1}\,cm^{-1}$, and a pathlength of 0.05 cm.

2.2. Synthesis of $Os(N(O)H)(CO)Cl_2(PPh_3)_2$ (1)

Except where noted, all syntheses were carried out under nitrogen. Reagents were used without additional purification. Solvents were deaerated prior to use.

$Os(N(O)H)(CO)Cl_2(PPh_3)_2$ (**1**) was synthesized in a three-step process. First, $Os(H)(CO)Cl(PPh_3)_3$ was synthesized from $OsCl_6^{2-}$ according to a literature method [14]. To a refluxing mixture of triphenylphosphine (1 g) and 2-methoxyethanol (20 mL) was added a slurry of K_2OsCl_6 (330 mg) in 2-methoxyethanol. Then a 10 mL portion of formaldehyde solution (37% in water/methanol) was cannulated into this mixture. The color changed from brownish red to yellowish green, and the mixture was allowed to reflux for 30 min. After cooling, the off-white solid that had settled to the bottom of the flask was isolated and used without further purification.

In the second step, the crude $Os(H)(CO)Cl(PPh_3)_3$ was used for the synthesis of $Os(NO)(CO)Cl(PPh_3)_2$, following literature methods [5,6]. To a mixture of 300 mg $Os(NO)(CO)Cl(PPh_3)_2$ and 100 mg *N*-methyl-*N*-nitrosyl-*p*-toluenesulfonamide (Aldrich, "Diazald") was added 100 mL ethanol. The mixture was allowed to reflux for 3 h, during which time the color changed from yellow to brownish orange. Upon cooling, a brownish orange powder settled to the bottom. The ethanol was removed by cannula, and the solid was washed repeatedly with pentane. The product, $Os(NO)(CO)Cl(PPh_3)_2$, was characterized by its IR spectrum, which was in good agreement with the literature [5].

$Os(N(O)H)(CO)Cl_2(PPh_3)_2$ (**1**) was formed by the reaction of $Os(NO)(CO)Cl(PPh_3)_2$ with gaseous HCl. The synthesis and isolation followed the general method of Wilson and Ibers [5]. To produce gaseous HCl, H_2SO_4 was added to NaCl. In the glovebox, crystals of $Os(NO)(CO)Cl(PPh_3)_2$ (~50 mg) were partially dissolved in dry, deaerated benzene (4 mL) in a test tube with a stir bar. This test tube was placed in a 500 mL three-neck round-bottom flask. HCl gas was flushed through the flask while the benzene solution was stirred. It was then allowed to stand for ~15 min, and then the whole system was flushed with N_2. The flask was then disconnected from the HCl set-up, brought into the glovebox, and allowed to stand for an hour to let the particles settle. The benzene solution was transferred into a separate test tube, leaving behind a yellow/orange powder. Dry, degassed pentane (50 mL) was allowed to slowly effuse into the benzene solution, producing red crystals. The product was characterized by its IR spectrum ($\nu_{CO} = 1980\ cm^{-1}$ and $\nu_{NO} = 1415\ cm^{-1}$ in $CHCl_3$).

3. Results and discussion

The FTIR spectrum of $Os(N(O)H)(CO)Cl_2(PPh_3)_2$ (**1**) shows a strong ν_{CO} absorbance at 1980 cm^{-1}, as well as an absorbance at 1415 cm^{-1}, assigned to the ν_{NO} of coordinated HNO by comparison to the literature data [5]. The peaks at 1435 cm^{-1} and 1483 cm^{-1} are assigned to vibrational modes of the PPh_3 ligands since these peaks are observed for free PPh_3 and other PPh_3-containing osmium species. The UV–Vis spectrum of **1** in $CHCl_3$ shows an absorption maximum at 364 nm (Fig. S1).

3.1. Photochemical reactivity of $Os(N(O)H)(CO)Cl_2(PPh_3)_2$ under nitrogen

When a solution of **1** in $CHCl_3$ under nitrogen was subjected to continuous photolysis at 365 nm, the FTIR absorbance changes shown in Fig. 1 were observed. The peaks at 1415 cm^{-1} and 1980 cm^{-1} decreased in intensity, while a new band grew in at 1925 cm^{-1}. The bands at 1435 cm^{-1} and 1483 cm^{-1} attributed to PPh_3 were nearly unchanged

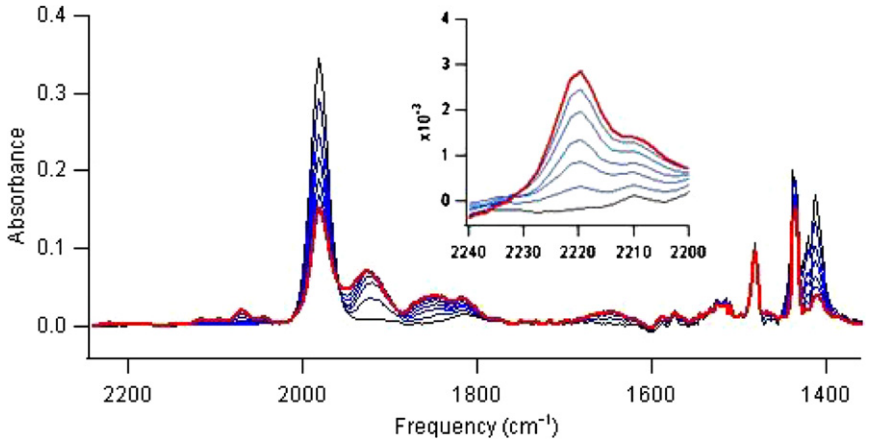


Fig. 1. Infrared spectral changes observed upon 365 nm continuous photolysis of a $CHCl_3$ solution of **1** under nitrogen. The total time of photolysis between the first and last spectrum was 30 min. The spectrum of **1** before photolysis is shown in black. The final spectrum is shown in red. Inset: an enlargement of the spectral region 2200–2240 cm^{-1} showing the growth of a peak indicating the formation of N_2O. (For interpretation of the references to color in this figure legend, the reader is referred to the web version of this article.)

by photolysis. The spectral changes at other frequencies are consistent with photochemical loss of HNO. The decrease in intensity of the bands at 1415 cm^{-1} and 1980 cm^{-1} indicates disappearance of **1**, while the growth of a peak at 1925 cm^{-1} suggests that the product of the photochemical reaction contains a carbonyl ligand. A weak peak was also observed to grow in at 2220 cm^{-1} (inset in Fig. 1), consistent with the appearance of N_2O, which is known to form rapidly from HNO [11]. For comparison, an FTIR spectrum of N_2O-saturated $CHCl_3$ was obtained, and it displayed an analogous peak at the same frequency (2220 cm^{-1}) as the purported N_2O peaks observed in these photochemical studies (Fig. S2). To further confirm the photochemical production of N_2O, a solution of **1** in $CHCl_3$ was irradiated in an air-tight cuvette, and a small sample of this solution was withdrawn and analyzed by GC–MS. A peak with $m/z = 44$ (consistent with N_2O) was observed, overlapping with $m/z = 32$ (O_2) and $m/z = 28$ (N_2) peaks. (The sample had been exposed to air in the transfer and injection process.) The elution time matched well with an authentic sample of N_2O in $CHCl_3$, and this peak was absent in analogous samples not subjected to photolysis.

The disappearance of the HNO peak of **1**, the observation of N_2O formation and the appearance of a new peak attributed to a metal–carbonyl stretch all point to the possible operation of a primary photoreaction involving dissociation of **1** to HNO plus $Os(CO)Cl_2(PPh_3)_2$. A five-coordinate species $OsCl_2(PPh_3)_3$ similar to the proposed osmium product has been reported [15]. The photochemically released HNO would form N_2O through the known dimerization pathway, although a competing pathway might be the reaction of HNO with **1** considering that this is present in greater concentration.

In addition to the peaks attributed to N_2O and the osmium carbonyl product, a broad absorption centered at ~1840 cm^{-1} appeared, possibly due to the ν_{NO} stretching vibration of a linear nitrosyl, and weak peaks appeared above 2000 cm^{-1}, which is an appropriate range for metal-hydride or carbonyl stretches.

Longer term (2 h) photolysis demonstrated that the initial species formed are themselves subject to secondary photolysis (Fig. 2). After 30 min (blue spectrum in Fig. 2), **1** was nearly depleted, as indicated by the relatively small absorbance at 1415 cm^{-1}, and the largest product peak appeared at 1925 cm^{-1}. Upon further photolysis (red spectrum in Fig. 2), the peak at 1925 cm^{-1} decreased in intensity, while peaks grew in at 1973 cm^{-1} and 2040 cm^{-1}. The latter are consistent with the formation of $Os(CO)_2Cl_2(PPh_3)_2$ (**2**), the infrared spectrum of which has been reported [16]. After 60 min of photolysis, the peak at 1415 cm^{-1} is gone, and the peak at 2220 cm^{-1} has stopped growing. Thus appearance of N_2O correlates well with the disappearance of **1**.

3.2. Thermal reactivity of *1* under nitrogen

A portion of the solution of **1** used for photolysis experiments was stored under nitrogen in the dark at room temperature for ~3 h (the duration of the photolysis experiments). During this time, no significant decomposition of **1** occurred, as indicated by the lack of spectral changes (Fig. S3).

3.3. Photochemical reactivity of *1* under CO

When a solution of **1** in $CHCl_3$ was equilibrated with 1 atm CO and subjected to 365 nm irradiation, the major products were **2** and N_2O, according to the changes in the FTIR spectrum (Fig. 3). The evidence for the formation of N_2O is the growth of the peak at 2220 cm^{-1}, coinciding with the disappearance of the peak at 1415 cm^{-1} characteristic of **1**. At the same time, peaks at 2043 cm^{-1} and ~1975 cm^{-1}, corresponding to $Os(CO)_2Cl_2(PPh_3)_2$ [16],

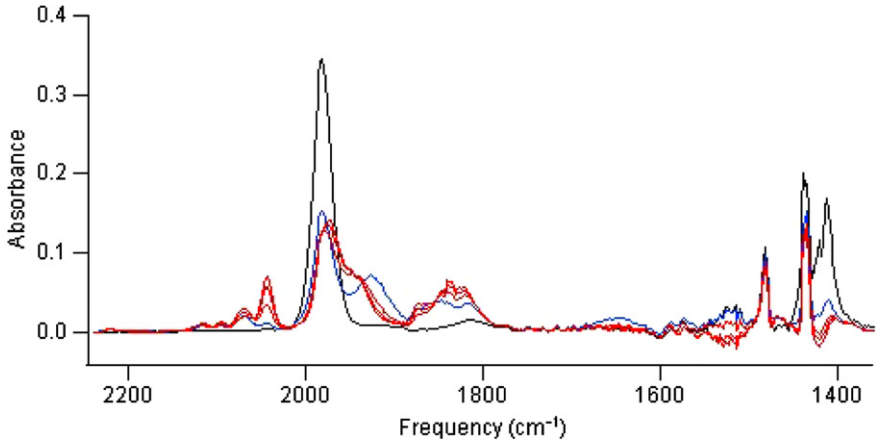


Fig. 2. Spectral changes observed when a $CHCl_3$ solution of **1** under nitrogen in an IR cell was subjected to 365 nm photolysis. Spectra were obtained every 30 min, and the total time of photolysis between the first and last spectrum was 2 h. The spectrum before photolysis is shown in black. The spectrum after 30 min of photolysis is shown in blue. The spectra after 60, 90, and 120 min of photolysis are shown in red. (For interpretation of the references to color in this figure legend, the reader is referred to the web version of this article.)

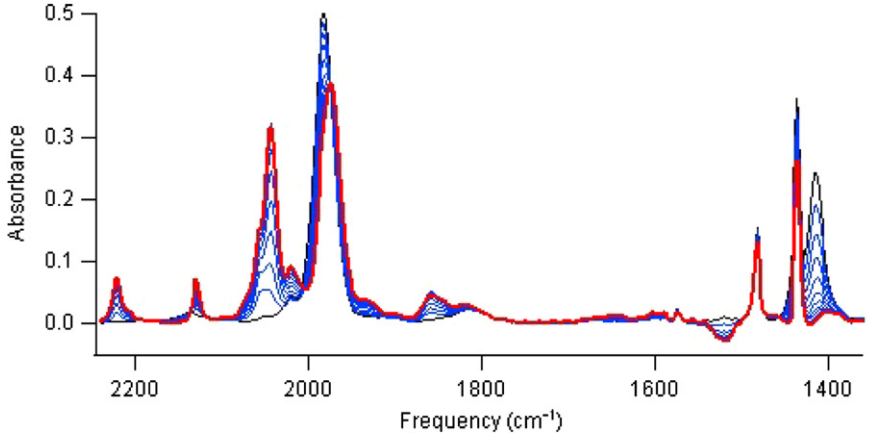


Fig. 3. Infrared spectral changes observed upon 365 nm continuous photolysis of a $CHCl_3$ solution of **1** under ~1 atm CO. The total time of photolysis between the first and last spectrum was 60 min. The initial spectrum is shown in black. The final spectrum is shown in red. (For interpretation of the references to color in this figure legend, the reader is referred to the web version of this article.)

appeared. (The band at 1975 cm^{-1} overlaps with the starting material's strong absorbance at 1980 cm^{-1}, but its presence can be inferred from the fact that the peak at 1980 cm^{-1}, which is stronger than the peak at 1415 cm^{-1}, does not decrease in intensity as quickly as the latter. Also, the final spectrum obtained after exhaustive photolysis clearly shows a peak at 1975 cm^{-1}.) In addition to peaks corresponding to N_2O and **2**, weaker peaks appeared in the 1800–1900 cm^{-1} range and in the 2000–2150 cm^{-1} range, as was observed in reactions under dinitrogen.

3.4. Thermal reactivity of *1* under CO

A portion of the same sample of **1**, equilibrated under 1 atm CO, was allowed to sit in the dark for 80 min, the result being the modest spectral changes shown in Fig. 4. Consistent with the literature reports [8], a small amount of **2** was formed, as indicated by the peak at 2040 cm^{-1}. However, $Os(CO)_2Cl_2(PPh_3)_2$ is formed much faster under irradiation than in the dark. After 60 min of photolysis, **2** was the major product and **1** was almost completely gone, but under analogous conditions in the dark, very little conversion of **1** to **2** took place in a similar time frame.

The accelerated formation of N_2O and $Os(CO)_2Cl_2(PPh_3)_2$ is further evidence that HNO is photochemically liberated from **1**. The dicarbonyl **2** should be formed more rapidly by reaction of CO with the five-coordinate HNO-loss photoreaction intermediate $Os(CO)Cl_2(PPh_3)_2$ than by direct reaction of CO with **1**, the mechanism of which is unknown. The likely pathway is irradiation-induced HNO labilization followed by trapping of the resulting five-coordinate osmium intermediate, as depicted in Scheme 1. The additional FTIR absorbances that appear at 1840 cm^{-1} and in the 2000–2100 cm^{-1} range suggest that other products are formed under photochemical conditions, very likely as the result of CO photodissociation.

The observation that the relative product yields varied with reaction conditions is consistent with this model.

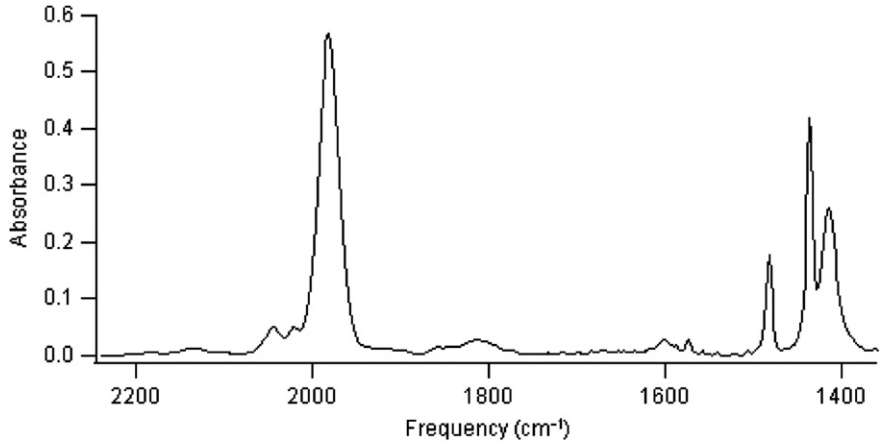
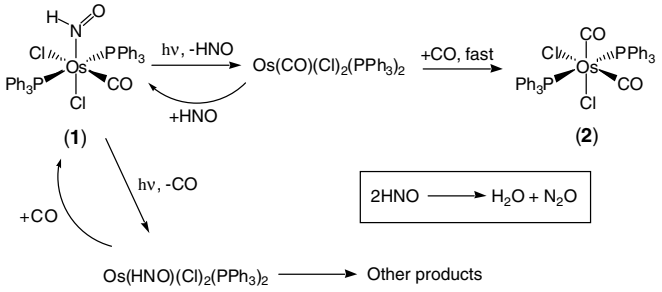


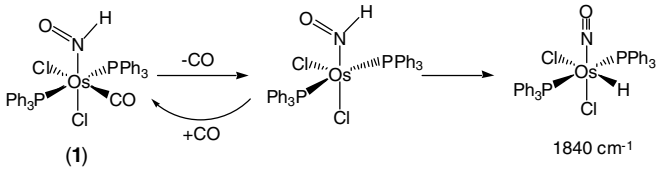
Fig. 4. Infrared spectrum of a sample of **1** under ~1 atm CO after 80 min reaction in the dark at room temperature.



Scheme 1.

The yield of N_2O relative to the amount of **1** consumed is significantly greater under CO than under N_2, as shown in Fig. 5, where the concentration of N_2O generated is plotted against the concentration of **1**. The yield of N_2O relative to disappearance of **1** is given by the negative of the slope of this line. Under N_2, the yield is 0.012, whereas under CO, it is 0.14, more than an order of magnitude larger. (Note that since two HNO are necessary to generate N_2O, the latter number implies that at least 28% of **1** decayed to give nitrous oxide under these conditions. This analysis, however, does not account for other possible fates of nitroxyl.)

According to Scheme 1, the presence of excess CO in the system would affect the net photochemistry in two ways. First, CO could back-react with the five-coordinate intermediate, $Os(N(O)H)Cl_2(PPh_3)_2$, to re-form **1**, thus reducing the net photochemistry along the CO-loss pathway. This would increase the relative importance of the HNO-loss pathway, thus increasing the yield of N_2O relative to disappearance of **1**. The second impact of solution CO would be to trap the HNO-loss photoreaction intermediate, $Os(CO)Cl_2(PPh_3)_2$, to form **2**. This would minimize



Scheme 2.

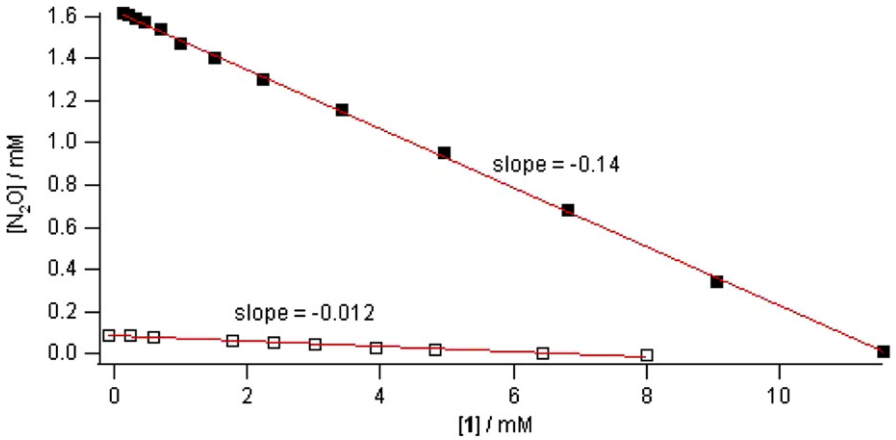


Fig. 5. Molar concentration of N_2O vs. molar concentration of **1**, calculated from the data shown in Figs. 1 and 3. Open squares represent data collected when samples of **1** were irradiated under N_2. Filled squares represent data collected when samples of **1** were irradiated under CO.

back reaction of $Os(CO)Cl_2(PPh_3)_2$ with the HNO generated, thus allowing the latter to react along the N_2O formation pathway. In either case, Scheme 2 predicts that the presence of CO will increase the yield of N_2O relative to depletion of **1**, as was observed. Notably, the reaction of HNO with a metal center to form an HNO complex has a precedent in the reported trapping of nitroxyl with deoxymyoglobin [5].

Although net quantum yields were not measured for this system, the first scenario would lead to a decrease in the overall rate of conversion of **1** to the products, while the second would lead to an increased rate *if* the experiments with and without added CO were carried out under analogous conditions of light intensity, etc. The qualitative experiments illustrated in Fig. S4 show that there is no great difference in the photoinduced decay of **1** regardless of whether or not CO is present although that there was a modest *increase* under CO. In the context of Scheme 1 and the data presented in Fig. 5, this would imply that the major pathway(s) for the depletion of **1** is relatively unaffected by CO but that the pathway generating N_2O is strongly enhanced. Thus, if CO photodissociation is followed by an irreversible unimolecular reaction leading to rapid depletion of the initially formed intermediate $Os(N(O)H)Cl_2(PPh_3)_2$, then the effect of CO on the CO-loss pathway may be small while trapping of $Os(CO)Cl_2(PPh_3)_2$ to form **2**, would enhance the formation of N_2O by inhibiting the back reaction of HNO with that unsaturated intermediate.

What might be a fast irreversible pathway depleting the intermediate $Os(N(O)H)Cl_2(PPh_3)_2$ of the CO-loss pathway? Although the ''other products'' observed were not conclusively elucidated, the appearance of an IR band at 1840 cm^{-1} (Fig. 1) is consistent with the formation of linearly coordinated NO. Furthermore, the absence of a corresponding carbonyl stretch for this species suggests that it was formed via the CO-loss pathway. Hydride migration from the N-coordinated HNO to the vacant coordination site left by CO would give the nitrosyl hydride complex $Os(NO)(H)Cl_2(PPh_3)_2$, as proposed in Scheme 2. An analogous compound, $Os(NO)(H)(O_2CCF_3)_2(PPh_3)_2$, has been reported to have $\nu_{NO} = 1820\ cm^{-1}$ [17], a value similar to that observed in this work (1840 cm^{-1}). While it might be expected that the formation of the nitrosyl product would be inhibited by excess CO owing to back reaction of the intermediate to reform **1**, the effect on the 1840 cm^{-1} band was relatively modest even when the photolysis is carried out under a CO atmosphere. This would be consistent with the unimolecular decay of the intermediate $Os(N(O)H)Cl_2(PPh_3)_2$ (via hydride migration?) being sufficiently fast to compete with the bimolecular back-reaction under the conditions of this study.

4. Summary

Studies of the photochemical and thermal reactivity of **1** indicate that HNO is photochemically liberated from **1**. This conclusion is supported by the detection of N_2O, the product of HNO dimerization, as well as by the spectral characterization of the organometallic products and comparison of reactivities under various conditions. A model for the overall thermal and photochemical reactivity of **1** in $CHCl_3$ is presented in Scheme 1.

Acknowledgements

This work was supported by grants from the National Science Foundation. Carol Buckmann and Professor Randy M. Miller are thanked for their assistance with equipment and instrumentation at CSU Chico.

Appendix A. Supplementary material

Supplementary data associated with this article can be found, in the online version, at doi:10.1016/j.poly.2007.04.044.

References

[1] (a) D.E. Koshland Jr., Science 258 (1992) 1861;
(b) F. Murad, Angew. Chem., Int. Ed. 38 (1999) 1857;
(c) R.F. Furchgott, Angew. Chem., Int. Ed. 38 (1999) 1871;
(d) L.J. Ignarro, Angew. Chem., Int. Ed. 38 (1999) 1883;
(e) P.C. Ford, I.M. Lorkovic, Chem. Rev. 102 (2002) 993;
(f) L.J. Ignarro (Ed.), Nitric Oxide: Biology and Pathobiology, Academic Press, San Diego, 2000;
(g) F.C. Fang (Ed.), Nitric Oxide and Infection, Kluwer Academic Publishers/Plenum Press, Dordrecht/New York, 1999;
(h) R.J. Gryglewski, P. Minuz (Eds.), Nitric Oxide: Basic Research and Clinical Applications, IOS Press, Amsterdam, 2001;
(i) P.C. Ford, B.O. Fernandez, M.D. Lim, Chem. Rev. 105 (2005) 2439.
[2] K.M. Miranda, Coord. Chem. Rev. 249 (2005) 433, and references therein.
[3] P.S.-Y. Wong, J. Hyun, J.M. Fukuto, F.N. Shirota, E.G. DeMaster, D.W. Shoeman, H.T. Nagasawa, Biochemistry 37 (1998) 5362.
[4] (a) M.R. Rhodes, M.H. Barley, T.J. Meyer, Inorg. Chem. 30 (1991) 629;
(b) R. Lin, P.J. Farmer, J. Am. Chem. Soc. 122 (2000) 2393;
(c) A.V. Marchenko, A.N. Vedernikov, D.F. Dye, M. Pink, J.M. Zaleski, K.G. Caulton, Inorg. Chem. 43 (2004) 351;
(d) J. Lee, G.B. Richter-Addo, J. Inorg. Biochem. 98 (2004) 1247.
[5] F. Sulc, C.E. Immoos, D. Pervitsky, P.J. Farmer, J. Am. Chem. Soc. 126 (2004) 1096.
[6] P.J. Farmer, F. Sulc, J. Inorg. Biochem. 99 (2005) 166.
[7] (a) R.D. Wilson, J.A. Ibers, Inorg. Chem. 18 (1979) 336;
(b) D. Sellmann, T. Gottschalk-Gaudig, D. Haussinger, F.W. Heinemann, B.A. Hess, Chem. Eur. J. 7 (2001) 2099;
(c) J.S. Southern, M.T. Green, G.L. Hillhouse, I.G. Guzei, A.L. Rheingold, Inorg. Chem. 40 (2001) 6039;
(d) R. Melenkivitz, G.L. Hillhouse, Chem. Commun. (2002) 660.
[8] K.R. Grundy, C.A. Reed, W.R. Roper, J. Chem. Soc., Chem. Commun. (1970) 1501.
[9] (a) P.C. Ford, J.S. Bridgewater, B. Lee, Photochem. Photobiol. 65 (1997) 57;
(b) J.S. Bridgewater, T.L. Netzel, J.R. Schoonover, S.M. Massick, P.C. Ford, Inorg. Chem. 40 (2001) 1466;
(c) M. Volpe, G. Wu, A. Iretskii, P.C. Ford, Inorg. Chem. 45 (2006) 1861.
[10] M.E. Jacox, D.E. Milligan, J. Mol. Spectrosc. 48 (1973) 536.

[11] (a) F.T. Bonner, M.N. Hughes, Comments Inorg. Chem. 7 (1988) 215;
(b) D.A. Bazylinski, T.C. Hollocher, Inorg. Chem. 24 (1985) 4285.
[12] (a) K.M. Miranda, X. Bu, I. Lorkovic, P.C. Ford, Inorg. Chem. 36 (1997) 4838;
(b) I.M. Lorkovic, K.M. Miranda, B. Lee, S. Bernhard, J.R. Schoonover, P.C. Ford, J. Am. Chem. Soc. 120 (1998) 11674.
[13] I.M. Lorkovic, P.C. Ford, Inorg. Chem. 39 (2000) 632.
[14] N. Ahmad, J.J. Levison, S.D. Robinson, M.F. Uttley, Inorg. Synth. 15 (1974) 53.
[15] P.R. Hoffman, K.G. Caulton, J. Am. Chem. Soc. 97 (1975) 4221.
[16] J.P. Collman, W.R. Roper, J. Am. Chem. Soc. 88 (1966) 3504.
[17] E.B. Boyar, A. Dobson, S.D. Robinson, B.L. Haymore, J.C. Huffman, J. Chem. Soc., Dalton Trans. (1985) 621.

2. Experimental

2.1. Synthesis

All chemicals were purchased and were used as received. *cis*-[Ru(NO)(CH_3O)(pyca)$_2$], *trans*-[Ru(NO)(CH_3O)(pyca)$_2$]-[30], and *cis*-[Ru(NO)(H_2O)(pyca)$_2$]ClO_4 [31] were prepared according to the methods in the literature.

2.1.1. *cis*-[Ru(NO)(CH_3CN)(pyca)$_2$]ClO_4

A suspension of *cis*-[Ru(NO)(H_2O)(pyca)$_2$]ClO_4 (100 mg, 0.20 mmol) in CH_3CN (20 cm^3) was refluxed for 7 h to give a yellow solution. This yellow solution was concentrated to 5 cm^3 using a rotary evaporator, and diethyl ether (2 cm^3) was added to give a yellow precipitate. The product was collected by filtration, washed with diethyl ether and dried in vacuum. Yield: 78 mg (75%). *Anal.* Calc. for $C_{14}H_{11}N_4O_9ClRu$: C, 32.60; H, 2.15; N, 10.86. Found: C, 32.70; H, 2.16; N, 10.68%. IR ν(NO) = 1899 cm^{-1}. ^1H NMR (CD_3CN): δ 2.54 (3H, s, CH_3), 8.00 (1H, t, 5-py), 8.02 (1H, t, 5-py), 8.26 (2H, d, 3-py), 8.40 (1H, t, 4-py), 8.48 (1H, t, 4-py), 8.79 (1H, d, 6-py), 8.87 (1H, d, 6-py). ^{13}C NMR (CD_3CN): δ 118.4 (–CN), 129.5(5-py), 129.6 (5-py), 131.2(3-py), 131.8(3-py), 144.2(4-py), 145.2(4-py), 149.8(6-py), 150.6(6-py), 152.8(2-py), 153.0(2-py), 170.1 (–COO–), 172.2(–COO–).

2.1.2. *trans*-[Ru(NO)(OH)(pyca)$_2$]

$RuCl_3 \cdot nH_2O$ (content of Ru: 41%) (200 mg, 0.81 mmol) and Hpyca (200 mg, 1.62 mmol) were dissolved in C_2H_5OH (50 cm^3). The solution was refluxed for 3 h to give a yellow solution. After 1 day standing and removal of the yellow solid, $(C_2H_5)_4NCl$ (200 mg, 1.21 mmol) was added to the yellow solution to give a yellow solid. The yellow solid, whose main constituent was $(C_2H_5)_4N$[$RuCl_2$(pyca)$_2$], was collected by filtration. Yield: 118 mg (28%). The collected solid, $(C_2H_5)_4N$[$RuCl_2$(pyca)$_2$] (100 mg, 0.18 mmol), was added to an aqueous solution (30 cm^3) of pH 6.22 containing $NaNO_2$ (500 mg, 7.25 mmol). The resultant solution of pH 8.38 was refluxed for 10 h, and then concentrated to dryness using a rotary evaporator to give a yellow solid. This yellow solid was dissolved in CH_3CN (10 cm^3) and the resulted solution was filtrated to remove insoluble matters. The solution was concentrated and allowed to stand till a yellow solid appeared. The product was collected by filtration, washed with diethyl ether and dried in vacuum. Yield: 53 mg (75%). *Anal.* Calc. for $C_{12}H_9N_3O_6Ru$: C, 36.74; H, 2.31; N, 10.71. Found: C, 36.90; H, 2.24; N, 11.05%. IR ν(NO) = 1852 cm^{-1}. ^1H NMR (D_2O): δ 2.07 (1H, s, OH), 8.04 (2H, t, 5-py), 8.30 (2H, t, 4-py), 8.46 (2H, d, 3-py), 8.85 (2H, d, 6-py). ^{13}C NMR (D_2O): δ 128.6 (3-py), 130.8 (5-py), 143.8 (4-py), 149.7 (6-py), 151.1 (2-py), 175.2($-COO^-$).

2.2. Physical measurements

IR spectra were recorded on a Perkin–Elmer FT-1650 FTIR spectrophotometer using samples prepared as KBr disks. Elemental analyses were performed by the Sophia University Analytical Facility. ^1H NMR and ^{13}C NMR spectra were obtained with a JEOL JML-LA500 spectrometer.

2.3. X-ray crystallography

Single crystals of *cis*-[Ru(NO)(CH_3CN)(pyca)$_2$]ClO_4 and *trans*-[Ru(NO)(OH)(pyca)$_2$] were obtained by recrystallization from the acetonitrile solutions and then vapor diffusion of ether into those solutions. The intensity data were collected on a Rigaku Mercury CCD diffractometer, using graphic monochromatized Mo Kα radiation (0.71069 Å). All the calculations were carried out using the Crystal Structure software package [34]. Structures were solved by a direct method, expanded using Fourier techniques and refined using full-matrix least-squares techniques.

2.4. Electrochemical measurements and reduction of ruthenium complexes

Cyclic voltammograms (CVs), normal pulse voltammograms (NPVs), and differential pulse voltammograms (DPVs) of nitrosylruthenium complexes (1.00 mmol dm^{-3}) were made on acetonitrile or dimethylformamide solutions containing 0.1 mol dm^{-3} tetraethylammonium perchlorate, TEAP (Nakarai Tesque. Ltd.), as supporting electrolyte, or on methanol solutions containing 0.1 mol dm^{-3} tetra(*n*-butyl)ammonium hexafluorophosphate, TBAH, (Nakarai Tesque. Ltd.) as supporting electrolyte, with a platinum disk working electrode (ϕ = 1.6 mm) and an Ag|0.01 mol dm^{-3} $AgNO_3$ reference electrode using a BAS 100B/W electrochemical analyzer. Hydrodynamic voltammograms (HDVs) were made with a rotating platinum disk working electrode (ϕ = 3.0 mm) using a BAS RDE-2 rotating electrode. At the end of each measurement, ferrocene was added as an internal standard to correct redox potentials.

Electrochemical reduction of *cis*-[Ru(NO)(CH_3CN)(pyca)$_2$]ClO_4 and *cis*-[Ru(NO)(CH_3O)(pyca)$_2$] in CH_3CN containing 0.1 mol dm^{-3} TEAP and in CH_3OH–CH_3CN (1:4, v/v) containing 0.1 mol dm^{-3} TBAH were performed by the controlled potential electrolysis (CPE) technique. CPE was carried out in a three-compartment cell with a platinum gauze working electrode in the first-compartment, an auxiliary electrode in the second-compartment, and an reference electrode in the third-compartment using a Huso polarograph Model 312 and 343B digital coulometer. After the electrolyses, changes of the reduced species were monitored by CV and HDV.

2.4.1. Isolation of ruthenium complexes from the electrolyzed solution

The CPE experiments of *cis*-[Ru(NO)(CH_3O)(pyca)$_2$] in CH_3CN–CH_3OH (1:4, v/v) containing 0.1 mol dm^{-3} TBAH was performed at the potential of the first reduction

wave (−0.9 V). The CPE consumed 0.05 mol of electrons per mole of *cis*-[Ru(NO)(CH_3O)(pyca)$_2$]. The volume of the electrolyzed solution was reduced by solvent evaporation. The solid material was recrystallized from CH_2Cl_2 and ether for several times. The ruthenium complex was obtained in 65% yield. IR (in CH_3CN) ν(NO) = 1843 cm^{-1}. $E_{1/2} = -1.12$, $E_{pa} = -1.71$ V.

3. Results

3.1. Syntheses and characterization

cis-[Ru(NO)(CH_3CN)(pyca)$_2$]ClO_4 was synthesized by a simple substitution reaction of the H_2O ligand of *cis*-[Ru(NO)(H_2O)(pyca)$_2$]ClO_4 with a CH_3CN solvent under refluxing conditions. *trans*-[Ru(NO)(OH)(pyca)$_2$] was formed by a reaction of *cis*-[$Ru^{III}Cl_2$(pyca)$_2$]$^-$ with NO_2^- in H_2O. The pH value of the reaction mixture changed from 6.22 to 8.38 during this reaction.

Wave numbers of the characteristic N–O stretching mode (ν(NO)) and redox potentials based on reductions of the $(RuNO)^{3+}$ moiety of synthesized and related nitrosylruthenium complexes are presented in Table 1. Each nitrosylruthenium complex having pyca ligands shows a strong NO stretching vibration in the range of 1838–1940 cm^{-1} and CO stretching vibrations(s) of the pyca ligand(s) in 1650–1700 cm^{-1}. Two reduction potentials of the present and previous nitrosyl ruthenium complexes, which can be assigned to the ligand-based reductions of the (RuNO) moiety, $(RuNO)^{3+/2+}$ and $(RuNO)^{2+/+}$, respectively, are summarized in Table 1. The observed values of wave number of the ν(NO) band and redox potetials of the (RuNO) moiety are reasonable, compared with those of similar nitrosylruthenium complexes previously reported [8–33].

In ^{1}H NMR spectra of *cis*-[Ru(NO)(CH_3CN)(pyca)$_2$]ClO_4 and *trans*-[Ru(NO)(OH)(pyca)$_2$], proton signals of the pyca ligands were clearly obtained in the normal aromatic region, indicating these nitrosyl complexes had the diamagnetic property. A ^{1}H NMR spectrum of *cis*-[Ru(NO)(CH_3CN)(pyca)$_2$]ClO_4 showed 8 signals assignable to the methyl group of the acetonitrile ligand and pyridyl protons of the pyca ligands, and the ^{13}C NMR spectrum 14 signals to two carbon atoms of the acetonitrile ligand and 10 of the pyridyl and two of the carboxylate groups of the pyca ligands. These spectra revealed the two pyca ligands were unequivalent to each other and, thus, coordinates in a *cis*-form. A ^{1}H NMR spectrum of *trans*-[Ru(NO)(OH)(pyca)$_2$] showed 5 signals assignable to a hydroxy and pyridyl protons of the hydroxo and the pyca ligands, and a ^{13}C NMR one 6 signals to five of the pyridyl and one carboxylate groups of the pyca ligands. The simpler spectral profile indicated two pyca ligands of *trans*-[Ru(NO)(OH)(pyca)$_2$] symmetrically coordinated to the metal center in a *trans*-form.

3.2. Crystal structures

The crystallographic data are summarized in Table 2. The selected bond distances and angles are summarized in Table 3. *cis*-[Ru(NO)(CH_3CN)(pyca)$_2$]ClO_4 and *trans*-[Ru(NO)(OH)(pyca)$_2$] show pseudo-octahedral coordination with three nitrogen atoms of the nitrosyl and two pyca ligands, two oxygen atoms of two pyca ligands, and one nitrogen of the acetonitrile ligand or one oxygen of the hydroxo ligand, as shown in Figs. 1 and 2.

The geometries around the ruthenium center of *cis*-[Ru(NO)(CH_3CN)(pyca)$_2$]ClO_4 and *trans*-[Ru(NO)(OH)(pyca)$_2$] are consistent with the results of NMR spectroscopy. The nitrosyl ligands are essentially linearly coordinated to the ruthenium centers with Ru–N–O angles 173.4(2) and 171.1(2)°. The Ru–N and N–O bond lengths, 1.759(2) and 1.124(4) Å for *cis*-[Ru(NO)(CH_3CN)(pyca)$_2$]ClO_4 and 1.766(2) and 1.153(2) Å for *trans*-[Ru(NO)(OH)(pyca)$_2$], of the (RuNO) moieties are similar to those of previously reported {RuNO}^{6}-type complexes [8–20,30,31]. The Ru–N(pyca) bond lengths, 2.078(2) and 2.062(2) Å of *cis*-[Ru(NO)(CH_3CN)(pyca)$_2$]ClO_4 and 2.076(1) and 2.059(1) Å of *trans*-[Ru(NO)(OH)(pyca)$_2$] are similar to each other. The Ru–O(pyca) bond lengths

Table 1
Characteristic data of synthesized and related nitrosylruthenium complexes

Complex	$E_{1/2}$ (V)	E_{pc} (V)	ν(NO) (cm^{-1})	Ref.
cis-[Ru(NO)(CH_3CN)(pyca)$_2$]ClO_4	−0.35 [a]	−1.13[a]	1899	this work
cis-[Ru(NO)(H_2O)(pyca)$_2$]ClO_4	−0.57[b]	−1.34[b]	1894	[9,10]
cis-[Ru(NO)(NO_2)(pyca)$_2$]	−0.60[a]	−1.46[a]	1907	[10]
cis-[Ru(NO)Cl(pyca)$_2$][c]	−0.71[a]	−1.48[a]	1890	[10]
cis-[Ru(NO)Cl(pyca)$_2$][d]	−0.71[a]	−1.44[a]	1864	[8]
cis-[Ru(NO)(CH_3O)(pyca)$_2$]	−0.90[a]	−1.68[a]	1861	[8]
trans-[Ru(NO)(H_2O)(pyca)$_2$]ClO_4	−0.53[a]	−1.26[a]	1940	[9]
trans-[Ru(NO)(CH_3O)(pyca)$_2$]	−1.12[a]	−1.71[a]	1838[e]	[9]
trans-[Ru(NO)(OH)(pyca)$_2$]	−1.13[b]	−1.86[b]	1852	this work

[a] In CH_3CN containing TEAP.
[b] In DMF containing TEAP.
[c] The pyca ligands coordinate to the Ru in a *cis*-form with two nitrogen are located at a *trans*-position each other and two oxygen atoms in a *cis*-position.
[d] The pyca ligands coordinate to the Ru in a *cis*-form with two nitrogen and oxygen atoms are located at a *cis*-position each other.
[e] The value of ν(NO) in CH_3CN solution is 1843 cm^{-1}.

Table 2
Crystallographic data

	cis-[Ru(NO)(CH_3CN)-($pyca)_2$]ClO_4	*trans*-[Ru(NO)-(OH)($pyca)_2$]
Formula	$C_{14}H_{11}N_4O_9ClRu$	$C_{12}H_9N_3O_6Ru$
Formula weight	515.79	392.29
Crystal system	monoclinic	monoclinic
Space group	$P2_1/c$	$P2_1/c$
a (Å)	11.035(3)	5.142(1)
b (Å)	13.233(3)	13.040(2)
c (Å)	13.218(4)	19.538(1)
β (°)	106.222(3)	93.383(7)
V (Å^3)	1853.2(9)	1307.8(9)
Z	4	4
D_{calc} (g cm^{-3})	1.848	1.992
μ(Mo Kα) (mm^{-1})	1.048	1.235
T (K)	298	123
Crystal size (mm)	$0.17 \times 0.10 \times 0.07$	$0.16 \times 0.07 \times 0.07$
Data collected	13118	9920
Unique data	4045	2988
R_{int}	0.0190	0.0210
R_1 ($I > 2\sigma(I)$)	0.0396	0.0237
R_w	0.1077	0.0765
Goodness-of-fit	1.289	1.021

Table 3
Selected bond distances (Å) and angles (°)

cis-[Ru(NO)(CH_3CN)($pyca)_2$]ClO_4		*trans*-[Ru(NO)(OH)($pyca)_2$]	
Bond lengths			
Ru–N1	1.759(2)	Ru–N1	1.766(2)
Ru–N2	2.051(2)	Ru–O2	1.937(2)
Ru–N3	2.078(2)	Ru–N2	2.076(1)
Ru–N4	2.062(2)	Ru–N3	2.059(1)
Ru–O2	1.985(2)	Ru–O3	2.041(1)
Ru–O4	2.001(2)	Ru–O5	2.055(1)
N1–O1	1.124(4)	N1–O1	1.153(2)
N2–C1	1.130(3)		
C1–C2	1.436(4)		
O2–C8	1.313(3)	O3–C6	1.293(2)
O3–C8	1.198(4)	O4–C6	1.223(2)
O4–C14	1.312(3)	O5–C12	1.296(2)
O5–C14	1.201(3)	O6–C12	1.224(2)
Bond angles			
N1–Ru–N2	91.94(10)	N1–Ru–N2	93.95(6)
N1–Ru–O2	176.05(9)	N1–Ru–O2	177.45(6)
N2–Ru–N3	90.18(8)	N2–Ru–O5	100.58(5)
N2–Ru–N4	96.58(8)		
N3–Ru–O2	80.18(9)	N2–Ru–O3	80.20(5)
N3–Ru–O4	89.87(8)	N3–Ru–O3	98.06(5)
N4–Ru–O4	81.76(8)	N3–Ru–O5	80.29(5)
Ru–N1–O1	173.4(2)	Ru–N1–O1	171.1(2)
Ru–N2–C1	177.7(2)		
N2–C1–C2	179.0(3)		
O2–C8–O3	123.4(3)	O3–C6–O4	124.3(2)
O4–C14–O5	122.7(3)	O5–C12–O6	124.7(2)

of *cis*-[Ru(NO)(CH_3CN)($pyca)_2$]ClO_4, 1.985(2) and 2.001(2) Å, are slightly shorter than those of *trans*-[Ru(NO)(OH)($pyca)_2$], 2.041(1) and 2.055(1) Å. The C–O bond of the carboxylate groups in the pyca ligands are roughly divided into two types; those of C–O and C=O. The longer bond lengths, 1.313(3) and 1.312(3) Å of *cis*-

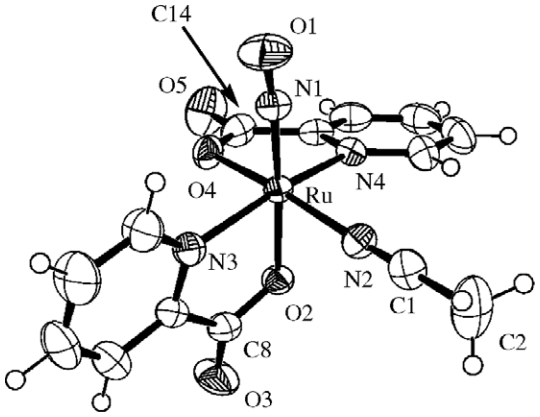


Fig. 1. Structure of *cis*-[Ru(NO)(CH_3CN)($pyca)_2$]$^+$.

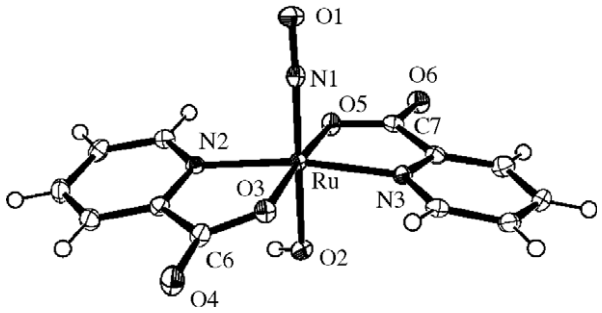


Fig. 2. Structure of *trans*-[Ru(NO)(OH)($pyca)_2$].

[Ru(NO)(CH_3CN)($pyca)_2$]ClO_4 and 1.293(2) and 1.296(2) Å of *trans*-[Ru(NO)(OH)($pyca)_2$], are found between the carboxylate carbon atoms and the oxygen atoms that coordinate to the ruthenium center, and the shorter bond lengths, 1.198(4) and 1.201(3) Å and 1.223(2) and 1.224(2) Å, between the carbon atoms and the non-coordinating ones. The difference in the bond length between the two for *cis*-[Ru(NO)(CH_3CN)($pyca)_2$]-ClO_4, 0.12 Å, is bigger than that for *trans*-[Ru(NO)(OH)-($pyca)_2$], 0.07 Å, while the O–C–O angles are not significantly different between the two.

3.3. Electrochemical properties

Electrochemical properties of this series of nitrosylruthenium complexes having two pyca ligands were studied by cyclic and normal pulse voltammetry. Redox potentials of two new complexes and related complexes are shown in Table 1. CVs of *cis*-[Ru(NO)(CH_3CN)($pyca)_2$]ClO_4 and *trans*-[Ru(NO)(OH)($pyca)_2$] in CH_3CN are shown in Fig. 3. CVs of all the complexes in Table 1 showed a reversible redox couple and an irreversible reduction wave in the potential window of CH_3CN or DMF. The profiles of these CVs were similar to those of {RuNO}^{6}-type complexes. The reversible redox couples of all the complexes were of Nernstian one-electron process, confirmed by the ratio of I_{pa} and I_{pc} of the CVs (the dotted lines in Fig. 3) and the analysis of NPVs.

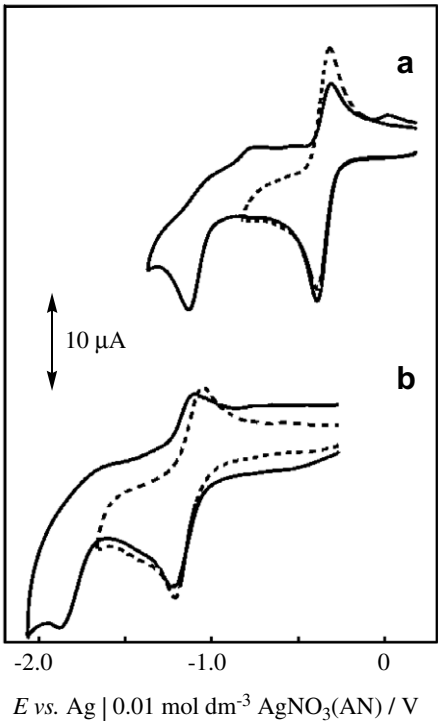


Fig. 3. Cyclic voltammograms in CH_3CN containing 0.10 mol dm^{-3} TEAP at 25 °C (scan rate = 200 mV s^{-1}); (a) *cis*-[Ru(NO)(CH_3CN)(pyca)$_2$]ClO_4, and (b) *trans*-[Ru(NO)(OH)(pyca)$_2$].

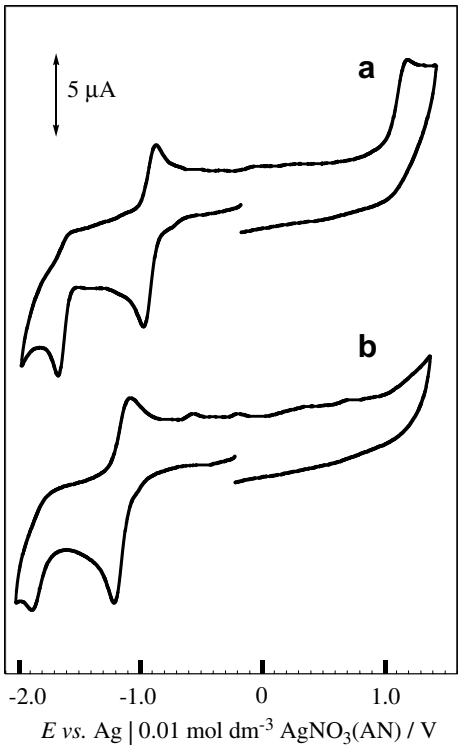


Fig. 4. Cyclic voltammograms in CH_3CN containing 0.10 mol dm^{-3} TEAP (scan rate = 200 mV s^{-1}); (a) *cis*-[Ru(NO)(CH_3O)(pyca)$_2$] and (b) *trans*-[Ru(NO)(CH_3O)(pyca)$_2$].

3.4. Electrochemical reductions based on (RuNO)-moiety

Electrochemical reductions of *cis*-[Ru(NO)(CH_3CN)(pyca)$_2$]ClO_4, *cis*-[Ru(NO)(CH_3O)(pyca)$_2$], and *trans*-[Ru(NO)(CH_3O)(pyca)$_2$] were performed by CPE to determine the number of electrons that participated in a redox reaction and to observe the reaction that followed. CVs of *cis*- and *trans*-[Ru(NO)(CH_3O)(pyca)$_2$] are shown in Fig. 4a and b, respectively.

The CPE for these nitrosylruthenium complexes in CH_3CN containing 0.1 mol dm^{-3} TEAP were performed at the potential of the first reduction wave, −0.40, −1.00, and −1.15 V for *cis*-[Ru(NO)(CH_3CN)(pyca)$_2$]ClO_4, *cis*-[Ru(NO)(CH_3O)(pyca)$_2$], and *trans*-[Ru(NO)(CH_3O)(pyca)$_2$], respectively. The number of electrons was determined by the relation of the change in wave height of HDV (a diffusion current) with the quantity of electricity consumed during electrolysis. The results revealed these waves corresponded to one-electron reduction processes. For the oxidation wave of *cis*-[Ru(NO)(CH_3O)(pyca)$_2$] shown in Fig. 4a, the result of the CPE at 1.50 V revealed the number of electrons was 1.0. The reduction products of *cis*- and *trans*-[Ru(NO)(CH_3O)(pyca)$_2$] in CH_3CN at 25 °C were both stable during the experiments of the CPE at −1.10 V, where the number of electrons was 1.0. Profiles of the first waves of the CVs for *cis*-[Ru(NO)(CH_3O)(pyca)$_2$] in CH_3CN and CH_3OH–CH_3CN (1:4, v/v) are different as shown in Figs. 5a and b. The first wave in CH_3CN was observed as a reversible couple at $E_{1/2} = -0.90$ V,

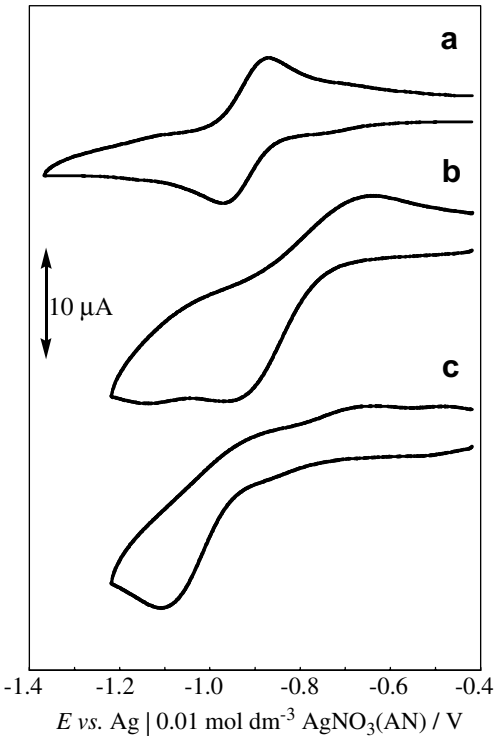


Fig. 5. Cyclic voltammograms of *cis*-[Ru(NO)(CH_3O)(pyca)$_2$]: (a) in CH_3CN, (b) in CH_3OH–CH_3CN (1:4, v/v) before the electrolysis, and (c) after the electrolysis.

while that in CH_3OH–CH_3CN as a quasi-reversible one ($E_{pc} = -0.91$ V) and a small wave appeared in the negative potential region ($E_{pc} = -1.11$ V). The CPE in CH_3OH–CH_3CN at −0.95 V was performed at 25 °C until 0.1 mol of electrons were added per mole of *cis*-[Ru(NO)(CH_3O)-(pyca)$_2$]. The first reduction wave of *cis*-[Ru(NO)(CH_3O)-(pyca)$_2$] at −0.91 V decreased and a new wave at −1.1 V appeared as shown in Fig. 5c.

The reaction product was isolated from the electrolyzed solution in 65% yields as a solid under atmosphere. The isolated ruthenium complex showed ν(NO) at 1843 cm^{-1} in CH_3CN solution and a reversible and irreversible reduction waves at −1.12 and −1.71 V, respectively. Thus, the isolated complex was identified as *trans*-[Ru(CH_3O)-(NO)(pyca)].

4. Discussion

Synthesis of *trans*-[Ru(NO)(OH)(pyca)$_2$] was carried out by using $RuCl_3 \cdot nH_2O$ as a starting material with a pyca ligand in C_2H_5OH under refluxing conditions to afford *cis*-[$Ru^{III}Cl_2$(pyca)$_2$]$^-$, and $NaNO_2$ was used as a nitorsylating and reducing agent in H_2O. The formation reaction of the nitrosyl complex did not proceed only in alcohol such as CH_3OH and C_2H_5OH, because the nitrosylation reaction using the nitrite ion is known to require protic conditions [33]. The geometry around the ruthenium center changed from the *cis*-form to the *trans*-form during the reaction. This geometrical change is explained by the stability of the *trans*-form due to coordination of a strong π-accepter nitrosyl and a π-donor hydroxo ligands in the *trans* position as the same way described in the previous report [30]. The values of ν(NO), the CV profiles showing two one-electron reduction waves in CH_3CN, and the linearly coordinated nitrosyl ligand of *cis*-[Ru(NO)(CH_3CN)-(pyca)$_2$]ClO_4 and *trans*-[Ru(NO)(CH_3O)(pyca)$_2$] indicate that these nitrosyl complexes are classified into the {RuNO}^{6} configuration. The ν(NO) and reduction waves (ν(NO) = 1899 cm^{-1}, $E_{1/2} = -0.35$ V and $E_{pc} = -1.13$ V) of *cis*-[Ru(NO)(CH_3CN)(pyca)$_2$]ClO_4 were, respectively, observed at a higher wave number and in a higher potential region than those of *trans*-[Ru(NO)(OH)(pyca)$_2$] (ν(NO) = 1852 cm^{-1}, $E_{1/2} = -1.13$ V and $E_{pc} = -1.86$ V). These results indicate that the hydroxo ligand of *trans*-[Ru(NO)(OH)(pyca)$_2$] functions as an electronic donating group and the acetonitrile of *cis*-[Ru(NO)(CH_3CN)-(pyca)$_2$]ClO_4 as an electronic accepting group.

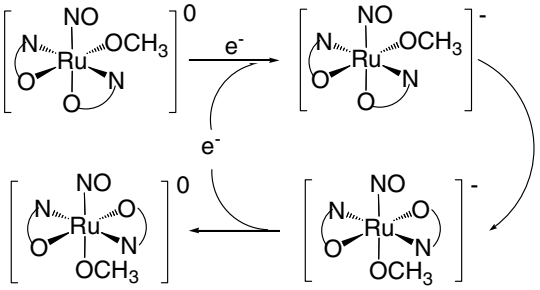
The nitrosyl ligand linearly coordinates to the ruthenium center as would be expected from the results of IR spectroscopy and cyclic voltammetry. The effect of the nitrosyl ligand on the structural parameters of the pyca ligands is observed. The shorter Ru–O(pyca) bond lengths of *cis*-[Ru(NO)(CH_3CN)(pyca)$_2$]ClO_4 than those of *trans*-[Ru(NO)(OH)(pyca)$_2$] are explained by electronic difference between an electronic accepting acetonitrile ligand and an electronic donating hydroxo ligand. For *cis*-[Ru(NO)(CH_3CN)(pyca)$_2$]ClO_4, the Ru–O(pyca) bond length between the ruthenium center and the oxygen atom that in located at the *trans*-position toward the nitrosyl ligand is the shortest due to the strong nitrosyl *trans*-influence. The C–O bond lengths between the carboxylic carbon atom and oxygen atoms in the pyca ligands are also found to show a similar *trans*-influence owing to the existence of an electronic attracting group such as NO and CH_3CN. The lengths of the C–O bonds, where the oxygen atoms coordinate to the ruthenium center, are longer than those of the non-coordinating oxygen atom for *cis*-[Ru(NO)-(CH_3CN)(pyca)$_2$]ClO_4, indicating they are categorized as single and double bonds, respectively, while there is a less significant difference between those for *trans*-[Ru(NO)-(OH)(pyca)$_2$].

Cyclic voltammograms of nitrosylruthenium complexes in CH_3CN generally show a reversible and an irreversible wave that are based on reduction of (RuNO)-moiety as shown in:

$$(RuNO)^{3+} + e^- \rightleftarrows (RuNO)^{2+} \quad (1)$$

$$(RuNO)^{2+} + e^- \rightarrow (RuNO)^{+} \quad (2)$$

The first waves of all nitrosylruthenium complexes in Table 1 are confirmed to be reversible and of one-electron process by analyses of CVs and NPVs and the CPE at the peak potential of the first wave in CH_3CN. The reduction potential of a nitrosylruthenium complex is a good indicator of chemical reactivity of the nitrosyl ligands like the frequency of ν(NO), indicating both *cis*-[Ru(NO)(CH_3CN)(pyca)$_2$]-ClO_4 and *trans*-[Ru(NO)(OH)(pyca)$_2$] belong to the unreactive group. The CV profile of the *cis*-form shows an oxidation wave in CH_3CN, although such is rare. This irreversible oxidation wave is of a Ru(III)/Ru(II) one-electron oxidation process, which is confirmed by changing the diffusion current of the HDV during the CPE in CH_3CN [30]. On the other hand, electrochemical reduction behaviors of *cis*-[Ru(NO)(CH_3O)(pyca)$_2$] in CH_3CN are usual, showing one reversible and one irreversible wave in the normal potential region. The CPE in CH_3CN at −1.15 V reveals that the one-electron reduced complex, *cis*-[Ru(NO)(CH_3O)-(pyca)$_2$]$^-$, is stable within the experimental time, which is consistent with the CV profile. The one-electron reduced complex changes in CH_3OH–CH_3CN (1:4, v/v) within the CV's time scale as shown in Fig. 5b. In fact, the CV after the CPE in CH_3OH–CH_3CN at −0.95 V to generate the one-electron reduced complex shows only a wave at −1.10 V as shown in Fig. 5c. This wave is assigned to *trans*-[Ru(NO)(CH_3O)(pyca)$_2$] by addition of an authentic sample to the electrolyzed solution and confirmed by a DPV (Fig. S2). The formation of *trans*-[Ru(NO)(CH_3O)-(pyca)$_2$] is also confirmed by the CV and IR data for the isolated complex from the electrolyzed solution (Figs. S3 and S4). Thus, *trans*-[Ru(NO)(CH_3O)(pyca)$_2$]$^-$ is generated by an isomerization reaction of the one-electron reduced complex of *cis*-[Ru(NO)(CH_3O)(pyca)$_2$] in CH_3OH–CH_3CN. These results are interpreted by *cis–trans* geometrical isomerization accompanying the electochemical one-



Scheme 1. Possible mechanism for isomerization accompanying one-electron reduction of *cis*-[Ru(NO)(CH_3O)(pyca)$_2$] in CH_3OH–CH_3CN.

electron reduction of *cis*-[Ru(NO)(CH_3O)(pyca)$_2$] as shown in Scheme 1. The second electron transfer step is explained by potential difference between *cis*- and *trans*-[Ru(NO)-(CH_3O)(pyca)$_2$]. The reduction potential of the *cis*-complex is more positive than that of the *trans*-one. Thus, the *cis*-complex is easily reduced by the one-electron reduced form of the *trans*-one.

5. Conclusions

The bis(pyridinecaroboxylato)nitrosylruthenium complexes with a variety of coexisting ligands have been synthesized and characterized. Reactions of these nitrosyl complexes under basic aqueous conditions afforded the nitrosyl complex, $[\{Ru(NO)(pyca)_2\}(H_3O_2)]^+$, which had been characterized in the previous paper [31]. Thus, the nitrosyl ligand of these series of complexes can be classified into unreactive category. The stabilities of the nitrosyl complexes have been explained by considering the electronic interaction between ligands through the ruthenium center. The present *cis–trans* isomerization reaction of [Ru(NO)(CH_3O)(pyca)$_2$] via the one-electron reduction reaction is important for regulating the geometries of these complexes where the electronic interaction occurs between the nitrosyl ligand and other co-existing ligands. It is worthy to note that electrostatic change of the (RuNO)-moiety induces the geometrical isomerization reaction in connection with a photo-induced isomerization of the metal complexes having a nitrosyl ligand.

Appendix A. Supplementary material

CCDC 633232 and 633233 contain the supplementary crystallographic data for *cis*-[Ru(NO)(CH_3CN)(pyca)$_2$]-ClO_4 and *cis*-[Ru(NO)(CH_3O)(pyca)$_2$]. These data can be obtained free of charge via http://www.ccdc.ac.uk/conts/retrieving.html, or from the Cambridge Crystallographic Data Centre, 12 Union Road, Cambridge CB2 1EZ, UK; fax: (+44) 1223-336-033; or e-mail: deposit@ccdc.cam.ac.uk. Supplementary data associated with this article can be found, in the online version, at doi:10.1016/j.poly.2007.04.018.

References

[1] K. Szacilowski, A. Chmura, Z. Stasicka, Coord. Chem. Rev. 249 (2005) 2408, and references therein.
[2] G.B. Richter-Addo, P. Legdzins, J. Burstyn (Ed.), Chem. Rev., 102 (4) (2002) (and references therein).
[3] F. Bottomley, in: P.S. Braterman (Ed.), Reactions of Coordinated Ligands, vol. 2, Plenum Publ. Corp, New York, 1989, and references therein.
[4] B.J. Coe, S.J. Glenwright, Coord. Chem. Rev. 203 (2000) 5, and references therein.
[5] G.B. Richter-Addo, P. Legdzins, Metal Nitrosyls, Oxford, New York, 1992 (and references therein).
[6] R.D. Feltham, J.H. Enemark, Topics in Stereochemistry, Wiley, Inc., New York, 1981, p. 155.
[7] J.H. Enemark, R.D. Feltham, Coord. Chem. Rev. 13 (1974) 339.
[8] M. Videla, J.S. Jacinto, R. Baggio, M.T. Garland, P. Singh, W. Kaim, L.D. Slep, J.A. Olabe, Inorg. Chem. 45 (2006) 8608.
[9] S. Sarkar, B. Sarkar, N. Chanda, S. Kar, S.M. Mobin, J. Fiedler, W. Kaim, G.K. Lahiri, Inorg. Chem. 44 (2005) 6092.
[10] N. Chanda, D. Paul, S. Kar, S.M. Mobin, A. Datta, V.G. Puranik, K.K. Rao, G.K. Lahiri, Inorg. Chem. 44 (2005) 3499.
[11] L.G.F. Lopes, E.E. Castellano, A.G. Ferreira, C.U. Davanzo, M.J. Clarke, D.W. Franco, Inorg. Chim. Acta 358 (2005) 2883.
[12] A.K. Patra, M.J. Rose, K.A. Murphy, M.M. Olmstead, P.K. Mascharak, Inorg. Chem. 43 (2004) 4487.
[13] N. Chanda, S.M. Nobin, V.G. Puranik, A. Datta, M. Niemeyer, G.K. Lahiri, Inorg. Chem. 43 (2004) 1056.
[14] H. Wang, H. Tomizawa, E. Miki, Inorg. Chim. Acta 357 (2004) 4291.
[15] P.G. Zanichelli, A.M. Miotto, H.F.G. Estrela, F.R. Soares, D.M. Grassi-Kassisse, R.C. Spadari-Bratfisch, E.E. Castellano, F. Roncaroli, A.R. Oarise, J.A. Olabe, A. Regina, M.S. de Brito, D.W. Franco, J. Inorg. Biochem. 98 (2004) 1921.
[16] H. Hadadzadeh, M.C. DeRosa, G.P.A. Yap, A.R. Rezvani, R.J. Crutchley, Inorg. Chem. 41 (2002) 6521.
[17] H. Nagao, T. Hirano, N. Tsuboya, S. Shiota, M. Mukaida, T. Oi, M. Yamasaki, Inorg. Chem. 41 (2002) 6267.
[18] B. Serli, E. Zangrado, E. Iengo, E. Alessio, Inorg. Chim. Acta 339 (2002) 265.
[19] R.C.L. Zampieri, G.V. Poelhsitz, A.A. Batista, O.R. Nascimento, J. Ellena, E.E. Castellano, J. Inorg. Biochem. 92 (2002) 82.
[20] D.R. Lang, J.A. Davis, L.G.F. Lopes, A.A. Ferro, L.C.G. Vasconcellos, D.W. Franco, E. Tfouni, A. Wieraszko, M.J. Clarke, Inorg. Chem. 39 (2000) 2294.
[21] R.G. de Lima, M.G. Sauaia, D. Bonaventura, A.C. Tedesco, L.M. Bendhack, R.S. da Silva, Inorg. Chim. Acta 359 (2006) 2543.
[22] M.G. Sauaia, R.G. de Lima, A.C. Tedesco, R.S. da Silva, Inorg. Chem. 44 (2005) 9946.
[23] J.C. Toledo, H.A.S. Silva, M. Scarpellini, V. Mori, A.J. Camargo, M. Bertotti, D.W. Franco, Eur. J. Inorg. Chem. (2004) 1879.
[24] V.R. de Souza, A.M. C Ferreira, H.E. Toma, J. Chem. Soc., Dalton Trans. (2003) 458.
[25] F. Roncaroli, M.E. Ruggiero, D.W. Franco, G.L. Estiú, J.A. Olabe, Inorg. Chem. 41 (2002) 5760.
[26] F.D. Salvo, A. Crespo, D.A. Estrin, F. Doctorovich, Tetrahedron 58 (2002) 4237.
[27] K. Karidi, A. Garoufis, A. Tsipis, N. Hadjiliadis, H. den Dulk, J. Reedijk, J. Chem. Soc., Dalton Trans. (2005) 1176.
[28] A. Czap, F.W. Heinemann, R. van Eldik, Inorg. Chem. 43 (2004) 7832.
[29] M. Ortiz, A. Díaz, R. Cao, R. Suardíaz, A. Otero, A. Antiñolo, J. Fernández-Baeza, Eur. J. Inorg. Chem. (2004) 3353.
[30] T. Hirano, T. Oi, H. Nagao, K. Morokuma, Inorg. Chem. 42 (2003) 6575.
[31] T. Hirano, M. Kuroda, N. Takeda, M. Hayashi, M. Mukaida, T. Oi, H. Nagao, J. Chem. Soc., Dalton Trans. (2002) 2158.

[32] F. Bottomley, E. Hahn, J. Pickadt, H. Schumann, M. Mukaida, H. Kakihana, J. Chem. Soc., Dalton Trans. (1985) 2427.
[33] J.B. Godwin, T.J. Meyer, Inorg. Chem. 10 (1971) 471.
[34] Crystal Structure 3.6.0, Single Crystal Structure Analysis Software; Molecular Structure Corp. and Rigaku Corp.: USA, Japan, 2004.

compounds have been described recently and their electronic structure elucidated [12–14], there is a lack concerning the investigation of capability of these compounds as NO-carrier, as well as about studies of the photochemical NO release. More recently, Siri and coworkers [15] have performed theoretical studies by exploring the reactivity of nitrosyl iron complexes of cyclam, and concluded that only the *cis* isomer is able to release NO, while the *trans*-[Fe(cyclam)(NO)Cl]Cl is stable under the same conditions, and can be further oxidized under oxygen atmosphere [15]. Aiming to understand the reactivity of the nitrosyl iron cyclam complexes concerning the NO release, this article presents a new synthetic route for the *trans*-[Fe(cyclam)(NO)Cl]Cl_2 complex, its characterization and a photochemical study.

2. Experimental

Doubly distilled water was used throughout. Cyclam (1,4,8,11-tetraazacyclotetradecane) was obtained from Aldrich and used without further purification. The *cis*-[Fe(cyclam)Cl_2]Cl complex was prepared according to the literature procedure [16].

2.1. Preparation of trans-[Fe(cyclam)(NO)Cl]Cl_2

The complex *trans*-[Fe(cyclam)(NO)Cl]Cl_2 was prepared by dissolving 0.100 g (0.263 mmol) of *cis*-[Fe(cyclam)Cl_2]Cl in 100 mL of water, under argon atmosphere. A nitric oxide gas flow was passed through the solution for 1 h. The solution was then rotary-evaporated to 2 mL, and the *trans*-[Fe(cyclam)(NO)Cl]Cl_2 complex was precipitated by the addition of 5 mL of ethanol and 10 mL of diethyl ether solution. Recrystallization of *trans*-[Fe(cyclam)-(NO)Cl]Cl_2 in aqueous solution yielded yellow crystals suitable for single crystal X-ray analysis. Crystal data and structure refinement for this complex are summarized in Table 1. The IR spectrum obtained for both crystalline and powder isolated materials in different solvents medium is identical. Elemental analysis: Calc.: C, 30.6; H, 5.1; N, 17.8. Found: C, 30.5; H, 5.0; N, 17.5%.

The characterization of *trans*-[Fe(cyclam)(NO)Cl]Cl_2 complex was carried out by electrochemical techniques, electronic UV–Vis and infrared spectroscopy and X-ray crystallography.

2.2. Quantum yield

Quantum yield was determined from initial spectral changes and was plotted versus reaction percentage and extrapolated back to 0% reaction to minimize inner filter effects. The reported quantum yield is the average of, at least, three independent experiments.

2.3. Apparatus

Single crystals were used for data collection and cell parameter determination on an Enraf–Nonius Kappa-CCD diffractometer, using Mo Kα radiation ($k = 0.71073$ Å). Data collection was made by using the COLLECT program [17]; integration and scaling of the reflections were performed with the HKL Denzo-Scalepack system of programs [18]. Absorption corrections were carried out by using the multi-scan method [19]. The structure was solved by direct methods with SHELXS-97 [20]. The models were refined by full-matrix least-squares on F^2 with SHELXL-97 [20]. All the hydrogen atoms were stereochemically positioned and refined with the riding model [21].

Table 1
Crystal data and structure refinement

Empirical formula	$[C_{10}H_{24}ClN_5OFe]\cdot 2Cl\cdot 4(H_2O)$
Formula weight	464.61
Temperature (K)	120(2)
Wavelength (Å)	0.71073
Crystal system	monoclinic
Space group	*C*2/*c*
Unit cell dimensions	
a (Å)	31.720(2)
b (Å)	7.5121(2)
c (Å)	17.675(1)
β (°)	103.598(2)
Volume (Å^3)	4093.6(4)
Z	8
D_{calc} (Mg/m^3)	1.508
Absorption coefficient (mm^{-1})	1.157
F(000)	1952
Crystal size (mm)	$0.25\times0.03\times0.02$
θ Range for data collection (°)	2.37–25.00
Index ranges	$-35\leqslant h\leqslant 37$, $-8\leqslant k\leqslant 8$, $-21\leqslant l\leqslant 21$
Reflections collected	12565
Independent reflections [R_{int}]	3591 [0.0868]
Completeness to $\theta = 25.00°$ (%)	99.9
Absorption correction	semi-empirical from equivalents
Maximum and minimum transmission	0.996 and 0.907
Refinement method	full-matrix least-squares on F^2
Computing[a]	COLLECT, HKL Denzo-Scalepack SHELXS-97, SHELXL-97
Data/restraints/parameters	3591/0/254
Goodness-of-fit on F^2	1.033
Final *R* indices [$I > 2\sigma(I)$]	$R_1 = 0.0465$, $wR_2 = 0.0982$
R indices (all data)	$R_1 = 0.0783$, $wR_2 = 0.1090$
Extinction coefficient	0.0004(2)
Largest difference in peak and hole (e Å^{-3})	0.403 and −0.658

[a] Data collection, data processing, structure solution and structure refinement respectively.

Electrochemical experiments were performed with an electrochemical analyzer BAS 100W from Bioanalytical Systems at 25.0 ± 0.2 °C. These were generally performed on millimolar solutions of the complexes in 0.10 M CF_3CO_2Na (pH 7.0) aqueous solution by using a conventional three-electrode glass cell with a glassy carbon (ca. 0.13 cm^2 of geometrical area) and Pt foil and Ag/AgCl as the working, auxiliary and reference electrodes, respectively. The electrochemical experiments were performed at room temperature. The reversibility of the electrochemical processes was checked by the linearity of the peak

height for the reduction process as a function of the square root of the scan rate, and the separation between the anodic (E_a) and cathodic potential peaks in the range of 50–80 mV at 25 °C [22]. Elemental analyses were performed with a Perkin–Elmer CHN 2400 analyzer. Electronic spectra were acquired with a HP-8453 diode-array spectrophotometer. IR spectra were obtained in KBr pellets with a Shimadzu IR Prestige-21 spectrophotometer. Monochromatic irradiation at 330 nm was carried out using an Oriel 200-W universal arc lamp source in model 68805. The irradiation wavelength was selected with an Oriel interference filter for photolysis at the appropriate wavelength. The interference filter had an average band pass of 10 nm and the collimated beam intensities ranged from 4×10^{-8} to 1×10^{-9} einstein^{-1} cm^{-2} as determined by ferrioxalate actinometry. The progress of the photoreactions was monitored spectrophotometrically with an HP-8453 diode-array spectrophotometer.

3. Results and discussion

The infrared spectrum of the title complex showed peaks in the range 3190–2856 cm^{-1} that are characteristic of νNH and those in the range 1460–1430 cm^{-1} characteristic of νCH and νCN stretching modes of the cyclam ligand [23,24]. The geometrical configuration assignments are based on the IR fingerprint pattern. Indeed, the IR spectra, in the 800–900 cm^{-1} region, are characteristic of the conformation of the cyclam ligand and can define the coordination scheme of the central metal ion [25,26]. The complexes in the *trans* configuration showed two groups of peaks separated by 80 cm^{-1}. The main peak at lower wavenumber that appears close to 811 cm^{-1} is due to the methylene group, while the absorption peaks close to 891 cm^{-1} can be attributed to the secondary amine vibrations [15]. Also, the IR spectrum exhibits a strong peak at 1888 cm^{-1} assigned to the νNO, which is consistent with the presence of nitrosyl group in the NO^+, $\{FeNO\}^6$ oxidation form [14,27]. The presence of the nitrosyl group in linear form (NO^+) was confirmed by X-ray diffraction studies. The compound crystallizes in the monoclinic space group $P2_1/c$. ORTEP projections are shown in Fig. 1. Bond lengths and angles are given in Table 2. The coordinated nitric oxide forms a linear Fe–NO moiety with a bond angle of 177.4°, and N–O bond length (1.091 Å) are comparable to the angle and distance (177.8° and 1.131 Å) found in *trans*- K{[Fe(cyclam)(NO^0)-Cl] · [FeCl(cyclam)(NO^+)]$_2$}(PF_6)$_6$ complex [14] attributed by oxidation state NO^+. The Fe–N(1) bond length (1.682 Å) is comparable to that of portion $[FeCl(cyclam)(NO^+)]^{2+}$ complex (1.648 Å) [14], which is $\{FeNO\}^6$ type, and shorter than *trans*-[Fe(cyclam)(NO)Cl](ClO_4) (1.820 Å) [12], which is $\{FeNO\}^7$ type. The presence of the two Cl^- ions disordered gives the correct charge balance for the structure. This requires that iron atom is present in the Fe^{2+} oxidation state.

The electronic spectrum of complex presented three bands at 230 nm ($\varepsilon = 1.4 \times 10^4$ M^{-1} cm^{-1}), 315 nm ($\varepsilon = 1.3 \times 10^3$ M^{-1} cm^{-1}) and 335 nm ($\varepsilon = 1.2 \times 10^3$ M^{-1} cm^{-1}). Since the complex is structurally and electronically similar to the *trans*-[Ru(cyclam)(NO^+)Cl]$^{2+}$ species, it is likely that their UV–Vis spectra would be similar [27]. Based on this analogy, the relatively intense band at 230 nm was assigned to the LMCT charge transfer band

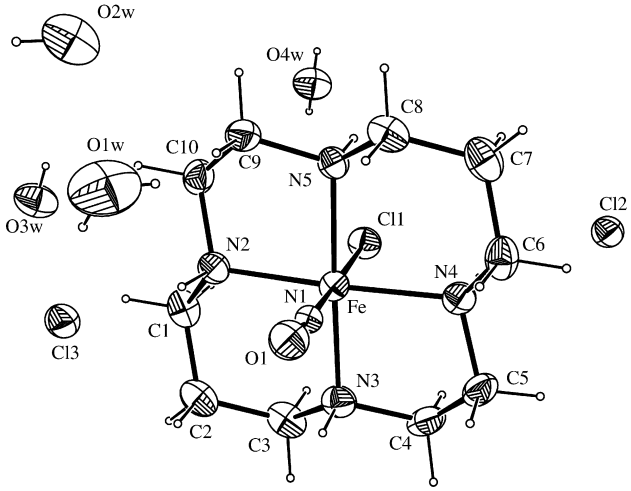


Fig. 1. *ORTEP*[6] view of the complex $[C_{10}H_{24}ClN_5OFe] \cdot 2Cl \cdot 4(H_2O)$, showing the atoms labelling and the 50% probability ellipsoids.

Table 2
Bond lengths (Å) and angles (°)

Bond length (Å)			
Fe–N(1)	1.682(3)	N(4)–C(6)	1.485(5)
Fe–N(2)	2.012(3)	N(4)–C(5)	1.491(5)
Fe–N(3)	2.009(3)	N(5)–C(9)	1.476(5)
Fe–N(4)	1.999(3)	N(5)–C(8)	1.484(5)
Fe–N(5)	2.006(3)	C(1)–C(2)	1.516(6)
Fe–Cl(1)	2.248(1)	C(2)–C(3)	1.522(6)
O(1)–N(1)	1.091(4)	C(4)–C(5)	1.493(6)
N(2)–C(1)	1.482(5)	C(6)–C(7)	1.519(6)
N(2)–C(10)	1.487(5)	C(7)–C(8)	1.510(6)
N(3)–C(3)	1.484(5)	C(9)–C(10)	1.498(5)
N(3)–C(4)	1.487(5)		
Bond angle (°)			
N(1)–Fe–Cl(1)	178.63(11)	N(1)–Fe–N(3)	93.43(14)
N(1)–Fe–N(2)	91.53(13)	N(1)–Fe–N(4)	93.51(13)
N(1)–Fe–N(5)	91.40(14)	C(3)–N(3)–C(4)	112.7(3)
N(2)–Fe–Cl(1)	88.44(9)	C(5)–N(4)–Fe	107.8(2)
N(3)–Fe–Cl(1)	87.94(10)	C(6)–N(4)–Fe	117.4(2)
N(3)–Fe–N(2)	95.36(13)	C(6)–N(4)–C(5)	112.5(3)
N(4)–Fe–Cl(1)	86.50(10)	C(8)–N(5)–Fe	117.2(2)
N(4)–Fe–N(2)	174.80(12)	C(9)–N(5)–Fe	107.9(2)
N(4)–Fe–N(3)	85.61(13)	C(9)–N(5)–C(8)	112.9(3)
N(4)–Fe–N(5)	93.41(13)	N(2)–C(1)–C(2)	112.0(3)
N(5)–Fe–N(3)	175.13(13)	C(1)–C(2)–C(3)	113.8(3)
N(5)–Fe–N(2)	85.20(12)	N(3)–C(3)–C(2)	112.8(3)
N(5)–Fe–Cl(1)	87.24(9)	N(3)–C(4)–C(5)	108.0(3)
O(1)–N(1)–Fe	177.4(3)	N(4)–C(5)–C(4)	108.0(3)
C(1)–N(2)–Fe	118.9(3)	N(4)–C(6)–C(7)	111.3(3)
C(10)–N(2)–Fe	107.6(2)	C(8)–C(7)–C(6)	115.0(3)
C(1)–N(2)–C(10)	112.5(3)	N(5)–C(8)–C(7)	112.6(3)
C(3)–N(3)–Fe	119.0(3)	N(5)–C(9)–C(10)	107.7(3)
C(4)–N(3)–Fe	107.7(2)	N(2)–C(10)–C(9)	107.7(3)

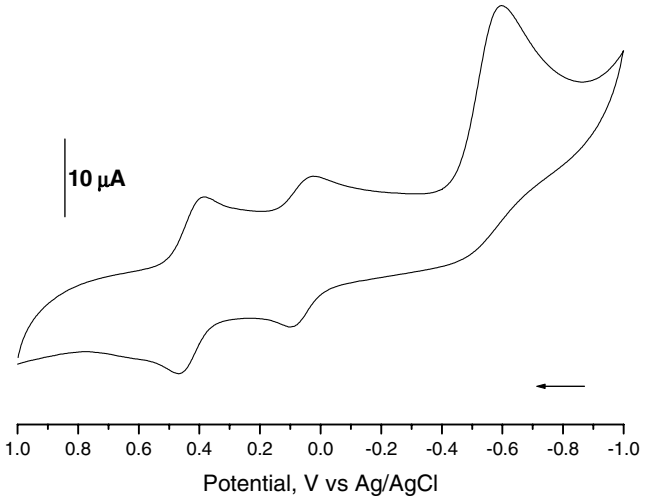


Fig. 2. Cyclic voltammograms for the *trans*-[Fe(cyclam)(NO)Cl]Cl_2 complex in a 0.10 mol L^{-1} CF_3COONa aqueous solution. $E_{initial} = -1.00$ V, $T = 25$ °C, pH 5, $v = 0.10$ V/s.

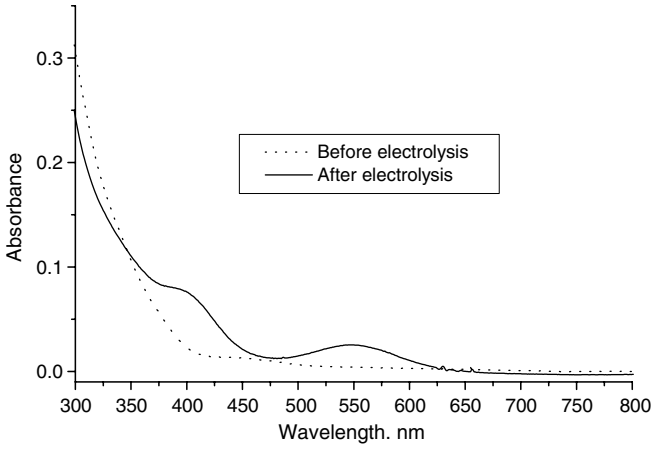


Fig. 3. Electronic spectra of an aqueous solution of *trans*-[Fe(cyclam)(NO)Cl]Cl_2 (dotted line) and the product of electrolysis at 0.2 V.

$[\pi_p(Cl^-) \rightarrow e_g(Fe)]$ and the band at 335 nm was assigned to a spin-allowed d–d transition $^1A_1 \rightarrow {}^1T_1$ [27,28]. The band at 315 nm was assigned to the MLCT $t_{2g} \rightarrow \pi^*(NO^+)$ because upon reduction with zinc amalgam these maxima disappear. Consistent with this assignment, this band shifted to lower energy with increase solvent polarity.

The cyclic voltammetric behavior of complex *trans*-[Fe(cyclam)(NO)Cl]Cl_2 is similar to the *trans*- K{[FeCl-(NO^0)(cyclam)] · [FeCl(NO^+)(cyclam)]$_2$}$(PF_6)_6$ [14] and presented a strong dependence on the potential range investigated, as well as on the initial sweep direction. Fig. 2 shows the cyclic voltammogram for a scan starting at −1.0 V with initial anodic sweep, in which three electrochemical processes are evidenced at −0.70, 0.08 and 0.40 V versus Ag/AgCl.

In harmony with an electrochemical chemical electrochemical (ECE) mechanism, the process centered at 0.08 V is not observed until the potential scan reach the more cathodic potential (Fig. 2).

A reasonable interpretation of the electrochemical results is supported by the electronic, FTIR and EPR spectra obtained for the *trans*-[Fe(cyclam)(NO)Cl]Cl_2 complex acquired after the electrolysis experiments in which the potential was controlled at two different values: −0.7 V and 0.2 V. Upon electrolysis under controlled potential at 0.2 V, the electronic spectrum (Fig. 3) presented two new absorption bands at 398 and 560 nm characteristic of the *trans*-[Fe(cyclam)(NO^0)Cl]$^+$ species formed after the first reduction process. The bands in the visible region of the spectrum are transitions predominantly of d–d character indicating that the *trans*-{Fe–NO}^{6} and *trans*-{Fe–NO}^{7} species must then have different d^n electron configurations, and also suggesting that the one-electron reduction process is centered at the nitric oxide ligand [12].

Furthermore, the IR spectrum of formed species after irradiation, in the solid state, does not present the characteristic of the $\nu(NO^+)$ stretching mode at 1888 cm^{-1}. However, a new peak characteristic of the $\nu(NO^0)$ vibrational stretching mode appeared at 1635 cm^{-1}, [29]. The EPR spectrum (Fig. 4) of formed species in solution at 77 K displays a broad isotropic signal at $g_{iso} = 2.00$. The g value is consistent with an unpaired electron occupying a NO π^* orbital in the {FeNO}^{7} moiety with significant NO^0 character [14,30]. Likewise, the high potential waves ($E_{1/2} = 0.40$ V versus Ag/AgCl) observed in the cyclic voltammogram of the *trans*-[Fe(cyclam)(NO)-Cl]Cl_2 complex are attributed to the *trans*-{FeNO}$^{6/7}$ redox process centered at the nitric oxide ligand.

Upon electrolysis, in which the potential was controlled at −0.7 V, the current intensity of the processes centered at −0.70 and 0.40 V decrease at the expense of the increase in the current intensity for the process centered at 0.08 V. It is reasonable to attribute the process centered at approximately 0.08 V to the $Fe^{III/II}$ redox couple in the

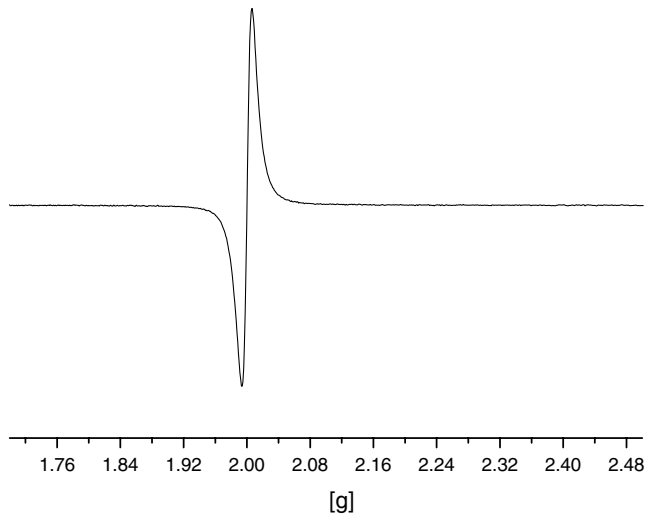


Fig. 4. EPR spectrum, in solid state, of the isolated product of the electrolysis of *trans*-[Fe(cyclam)(NO)Cl]Cl_2 complex at 0.20 V. $T = 77$ K.

trans-[Fe(cyclam)Cl(H_2O)]$^{2+/+}$ generated species after the reduction at −0.70 V. To confirm this assignment, the solution was gently rotary-evaporated and the compound was isolated in the solid state. The IR spectrum of the resulting compound showed no NO peaks (1888 and 1635 cm^{-1}), indicating that the NO dissociation occurred upon the second reduction followed by concomitant generation of the *trans*-[Fe(cyclam)Cl(H_2O)]$^{2+}$ complex. The electronic spectrum of this isolated species in aqueous medium showed two bands at 220 nm and 330 nm. These bands are characteristic of the *trans*-[Fe(cyclam)Cl(H_2O)]$^{2+}$ complex ion [23], reinforcing the assignment for the infrared spectrum discussed above. The following scheme of reactions (Eqs. (1)–(4)) accounts for the voltammetric behavior of the *trans*-[Fe(cyclam)(NO)Cl]$^{2+}$ complex ion, in aqueous media:

$$\textit{trans}\text{-}[Fe^{II}(cyclam)(NO^{+})Cl]^{3+} + e^{-} \overset{E_{1/2}=0.40\ V}{\rightleftharpoons} \textit{trans}\text{-}[Fe^{II}(cyclam)(NO^{0})Cl]^{2+} \quad (1)$$

$$\textit{trans}\text{-}[Fe^{II}(cyclam)(NO^{0})Cl]^{2+} + e^{-} \overset{E_{p}=-0.70\ V}{\rightarrow} \textit{trans}\text{-}[Fe^{II}(cyclam)(NO^{-})Cl]^{+} \quad (2)$$

$$\textit{trans}\text{-}[Fe^{II}(cyclam)(NO^{-})Cl^{2+} + H_2O \rightarrow \textit{trans}\text{-}[Fe^{II}(cyclam)(H_2O)Cl]^{2+} + NO^{-} \quad (3)$$

$$\textit{trans}\text{-}[Fe^{II}(cyclam)(H_2O)Cl]^{2+} \overset{E_{1/2}=0.08\ V}{\rightleftharpoons} \textit{trans}\text{-}[Fe^{III}(cyclam)(H_2O)Cl]^{3+} + e^{-} \quad (4)$$

3.1. Photochemical study

The title complex is stable in solution and in the solid state and only undergoes NO release upon electrolysis and photolysis. In a preliminary investigation, it was observed that photolysis at longer wavelengths (400–600 nm) does not induce photochemical reactivity. Conversely, the irradiation of the complex in aqueous solution, pH 3.4, with light $\lambda_{irradiation} = 330$ nm showed that FeNO moiety undergoes labilization according to Eq. (5)

$$\textit{trans}\text{-}[Fe(cyclam)(NO)Cl^{3+} \xrightarrow{h\nu\ pH\ 3.4} \textit{trans}\text{-}[Fe(cyclam)(H_2O)Cl]^{3+} + NO^{0} \quad (5)$$

Similar photochemical behavior is found for other metal nitrosyl complexes [7].

The aqua complex was identified by comparing the UV–Vis spectrum, electrochemical and infrared data with those of authentic samples of previously characterized *trans*-[Fe(cyclam)Cl(H_2O)]Cl_2. In the electronic spectra changes during the photolysis of the *trans*-[Fe(cyclam)(NO)Cl]Cl_2 complex in 0.1 M NaCl aqueous solution, pH 3.4, it was observed an increase of the LMCT band [$\pi_p(Cl^-) \rightarrow e_g(Fe)$] at 230 nm. This band is characteristic of the *trans*-[Fe(cyclam)Cl(H_2O)]Cl which was generated after NO release according to Eq. (5). Table 3 presents the quantum yield for the photoreaction depicted in Eq. (5) determined from the changes in the electronic spectra, at pH 3.4–6.4 range.

Table 3
Dependence of the ϕ_{NO} with pH

pH	ϕ_{NO}
3.4	0.28 ± 0.05
4.2	0.19 ± 0.03
5.4	0.16 ± 0.03
6.4	0.08 ± 0.02

From these data, it is clearly observed the decreasing in the quantum yield at the expense of the increasing of the pH values. This effect can be explained by the equilibrium illustrated in (Eq. (6)), which favors the *trans*-[Fe(cyclam)-(NO_2)Cl]$^{+}$ formation at high pH values, and the major product is therefore the nitrite species.

$$\textit{trans}\text{-}[Fe(cyclam)(NO)Cl]^{3+} + 2OH^{-} \rightleftharpoons \textit{trans}\text{-}[Fe(cyclam)(NO_2)Cl]^{+} + H_2O \quad (6)$$

In addition, the photolysis of *trans*-[Fe(cyclam)(NO)Cl]Cl_2 dispersed in KBr was performed, and monitored by IR spectroscopy (Fig. 5). The successively acquired IR spectra showed the decrease in the intensity of the νNO^{+} peak at 1888 cm^{-1} at the expense of the appearance of a new peak at 2229 cm^{-1}, which can be assigned to stretching mode of the NO^{+} free of coordination [31].

The photoreaction also was monitored by cyclic voltammetry (Fig. 6). The formation of NO as a photoproduct is confirmed by the increase of the current intensity of the process at 0.85 V, which is attributed to the free $NO^{0/+}$ oxidation. Also, the process centered at approximately 0.40 V versus Ag/AgCl, assigned to the redox process *trans*-$\{FeNO\}^{6/7}$ centered at the NO ligand, is not observed at the first cycle. By performing successive scans, after reduction of the Fe^{III} to Fe^{II} in the aqua species ($E = 0.02$ V), the Fe^{II} complex reacts with free NO regenerating the starting compound which explains the lack of the anodic wave at

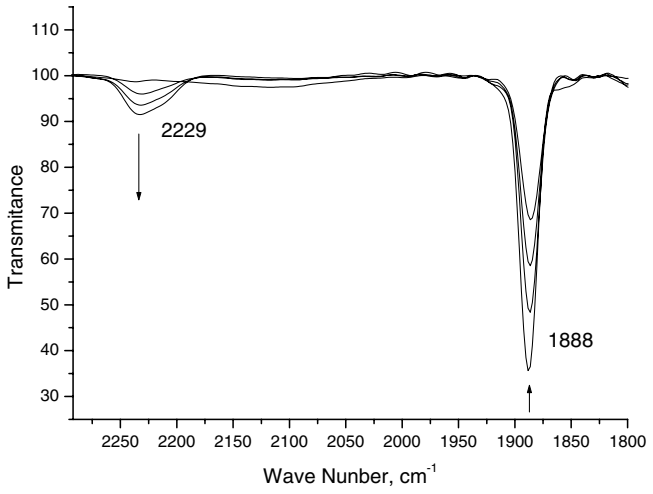


Fig. 5. Infrared spectra of the *trans*-[Fe(cyclam)(NO)Cl]Cl_2 compound dispersed in KBr as function of the irradiation process under 330 nm light.

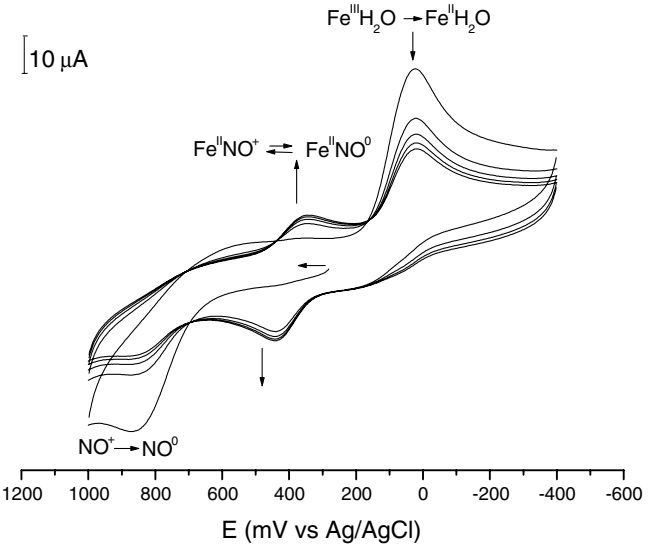


Fig. 6. Changes observed in the cyclic voltammogram of the *trans*-$[Fe(cyclam)(NO)Cl]^{2+}$ complex ion during photolysis at 330 nm, pH 3.4.

0.09 V and the appearance of the process centered at 0.40 V.

A particularly interesting observation is the pH dependence of the photoreaction. When the title compound was irradiated in 0.1 M NaCl aqueous solution, pH 7.0, instead of the release of NO, it was observed the reaction of photoreduction and production of the *trans*-$[Fe (cyclam)(NO^0)Cl]^{+}$ species. The progress of the photoreaction was monitored spectrophotometrically, and it was observed an increase in absorbance at 450 and 550 nm. These spectral changes are consistent with the formation of *trans*-$[Fe(cyclam)(NO^0)Cl]^{+}$ [12]. Hauser and coworkers [12] have observed that the spectra of *trans*-$\{FeNO\}^6$ and *trans*-$\{FeNO\}^7$ are completely different in nature whereas the spectra of *trans*-$\{FeNO\}^8$ are nearly the same.

4. Conclusion

The data collected in this work suggest that, upon irradiation at 330 nm, the *trans*-$[Fe(cyclam)(NO)Cl]Cl_2$ complex releases NO moiety. Since this energy is considered relatively high to indicate this complex as a suitable NO donor model for phototherapy purposes, further experiments are currently under investigation at our laboratories concerning the substitution of the Cl^- ligand in order to obtain a similar complex in which NO releasing could occur at lower energy.

5. Supplementary material

CCDC 633369 contains the supplementary crystallographic data for this paper. These data can be obtained free of charge via http://www.ccdc.cam.ac.uk/conts/retrieving.html, or from the Cambridge Crystallographic Data Centre, 12 Union Road, Cambridge CB2 1EZ, UK; fax: (+44) 1223-336-033; or e-mail: deposit@ccdc.cam.ac.uk.

Acknowledgments

This work was supported by Brazilian agencies: CNPq (LGFL – 301098/2005-0; ISM – 306975/2007), FAPESP, CAPES and FINEP. We are also grateful of Prof. D.W. Franco (IQSC) for affords the EPR equipment.

References

[1] J.A. McCleverty, Chem. Rev. 104 (2004) 403.
[2] S.A. Lipton, J.S. Stamler, Neuropharmacolgy 33 (1993) 1431.
[3] D. Torre, A. Pugliese, F. Speranza, Lancet Infect. Dis. 2 (2002) 273.
[4] L.J. Ignarro, Nitric Oxide Biology and Pathology, Academic Press, San Diego, USA, 2000.
[5] A. Wieraszko, M.J. Clarke, D.R. Lang, L.G.F. Lopes, D.W. Franco, Life Sciences 68 (2001) 1535.
[6] S.F. Fricker, E. Slade, N.A. Powell, O.J. Vayghn, G.R. Henderson, B.A. Murrer, L.L. Megron, S.K. Bisland, F.W.B. Flitney, Br. J. Pharmacol. 122 (1997) 1441.
[7] E. Tfouni, M.H. Krieger, B.R. McGarvey, D.W. Franco, Coord. Chem. Rev. 236 (2003) 57.
[8] R.D. Feltham, J.H. Enemark, Top. Stereochem. 12 (1981) 155.
[9] J.H. Enemark, R.D. Feltham, J. Am. Chem. Soc. 96 (1974) 5002.
[10] G.S. Marks, B.E. McLaughlin, S.L. Jimmo, M. Poklewska-Koziell, J.F. Brien, R. Nakatsu, Drug Metab. Dispos. 23 (1995) 1248.
[11] V.R. Zhelyaskov, D.W. Godwin, Nitric oxide 3 (1999) 419.
[12] C. Hauser, T. Glaser, E. Bill, T. Weyhermüller, K. Wieghardt, J. Am. Chem. Soc. 122 (2000) 4352.
[13] G.B.R. Addo, R.A. Wheeler, C.A. Hixson, L. Chen, M.A. Khan, M.K. Ellison, C.E. Schulz, W.R. Scheidt, J. Am. Chem. Soc. 123 (2001) 6314.
[14] L.G.F. Lopes, E.H.S. Sousa, J.C.V. Miranda, C.P. Oliveira, I.M.M. Carvalho, A.A. Batista, J. Ellena, E.E. Castellano, O.R. Nascimento, I.S. Moreira, J. Chem. Soc., Dalton Trans. (2002) 1903.
[15] O. Siri, A. Tabard, P. Pullumbi, R. Guilard, Inorg. Chim. Acta 350 (2003) 633.
[16] R. Guilard, O. Siri, A. Tabard, G. Broeker, P. Richard, D.J. Nurco, K.M. Smith, J. Chem. Soc., Dalton Trans. (1997) 3459.
[17] Enraf-Nonius, COLLECT, Delft, 1997–2000.
[18] Z. Otwinowski, W. Minor, Meth. Enzymol. 276 (1997) 307.
[19] R.H. Blessing, Acta Crystallogr., Sect. A 51 (1995) 33.
[20] G.M. Sheldrick, SHELXL-97. Program for Crystal Structures Analysis, University of Gottingen, Gottingen, Germany, 1997.
[21] L.J. Farrugia, J. Appl. Cryst. 30 (1997) 565.
[22] I. Taniguchi, Redox Chemistry and Interfacial Behaviour of Biological Molecules, Plenum Press, New York, 1988.
[23] P.K. Chan, C.K. Poon, J. Chem. Soc., Dalton Trans. 10 (1976) 858.
[24] C.K. Poon, C.N. Che, J. Chem. Soc., Dalton Trans. (1981) 1336.
[25] C.K. Poon, Inorg. Chim. Acta 5 (1971) 322.
[26] B.L. Westcott, J.H. Enemark, Inorg. Electr. Struct. Spectrosc. 2 (1999) 403.
[27] D.R. Lang, J.A. Davis, L.G.F. Lopes, A.A. Ferro, L.C.G. Vasconcellos, D.W. Franco, E. Tfouni, A. Wieraszko, M.J. Clarke, Inorg. Chem. 39 (2000) 2294.
[28] A.F. Schreiner, P.J. Hauser, E.S.W. Lin, A. Hopcus, D.J. Hamm, J.D. Gunter, Inorg. Chem. 11 (1972) 90.
[29] M.P. Fontecave, J.L. Pierre, Bull. Soc. Chim. Fr. 131 (1994) 620.
[30] B.R. McGarvey, A.A. Ferro, E. Tfouni, C.W.B. Bezerra, I. Bagatin, D.W. Franco, Inorg. Chem. 39 (2000) 3577.
[31] A.K.M.H. Sousa, J.R. Sousa, M.O. Santiago, E. Longhinotti, A.A. Batista, J. Ellena, E.E. Castellano, L.G.F. Lopes, I.S. Moreira, Tetrahedron Lett. 46 (2005) 1889.

2. Experimental

2.1. General remarks

All manipulations were performed under an atmosphere of argon using standard Schlenk techniques unless otherwise specified. Solvents were dried by refluxing over Na/benzophenone ketyl (THF, toluene, diethyl ether, hexane) or P_2O_5 (dichloromethane), and distilled just before use. Pentane, DMF, CH_3OH, and C_2H_5OH (anhydrous) were purchased from Kanto Chemical and used as received. Cyclohexene were purified by trap-to-trap distillation and stored under argon. IR spectra were recorded on a JASCO FT/IR-610 spectrometer, whereas ^1H (300 MHz) and $^{13}C\{^1H\}$ (75.5 MHz) NMR spectra were obtained on a JEOL JNM-LA300 spectrometer. GC analyses were performed on a GL-Sciences GC353B gas chromatograph equipped with a DB1 J&W capillary column. Elemental analyses were performed by the Analytical Facility at the Research Laboratory of Resources Utilization, Tokyo Institute of Technology.

2.2. Catalytic hydrogenation of cyclohexene

To a stainless steel autoclave containing the catalyst (7.0 μmol) was added cyclohexene (575 mg, 7.0 mmol) and the solvent (4 mL) by a syringe. After hydrogen gas was introduced into the autoclave, the mixture was stirred at 90 °C for 13 h. The amount of cyclohexane was determined by gas chromatography using heptane as an internal standard.

2.3. Preparation of [$Cp^*Ru(NO)(\eta^2$-$C_6H_{10})$] (3)

A mixture of $[Cp^*Ru(NO)(C_6H_5)_2]$ (**1**; 127.1 mg, 0.302 mmol) [5] and cyclohexene (0.62 mL, 6.11 mmol) in toluene (15 mL) was heated at 45 °C for 12 h. After removal of the solvent, the resultant dark red oil was dissolved in hexane and chromatographed on a column of silica gel under argon. After a faint yellow band eluted with hexane was discarded, the second band eluted with toluene/hexane (1:2) was collected and evaporated to dryness. Recrystallization from pentane at −30 °C afforded **3** as red crystals (34.9 mg, 33%). ^1H NMR (C_6D_6): δ 1.59 (m, 4H, $-CH_2(CH_2)_2CH_2-$), 1.66 (s, 15H, Cp^*), 2.56, 2.79, 3.05 (m, 2H each, vinyl and allyl). $^{13}C\{^1H\}$ NMR (C_6D_6): δ 10.1 ($C_5(CH_3)_5$), 23.2 ($-CH_2(CH_2)_2CH_2-$), 31.0 ($=CHCH_2$), 57.6 (=CH), 97.4 ($C_5(CH_3)_5$). IR (KBr): 1673 cm^{-1} (ν_{NO}). *Anal.* Calc. for $C_{16}H_{25}NORu$: C, 55.15; H, 7.23; N, 4.02. Found: C, 54.68; H, 7.34; N, 4.05%.

2.4. X-ray diffraction study

Complex **2** was prepared according to the literature [5], and single crystals suitable for X-ray analysis were obtained from recrystallization from benzene. The crystals of **2** and **3** are mounted on glass fibers. Diffraction experiments were performed on a Rigaku Saturn CCD area detector with graphite-monochromated Mo Kα radiation ($\lambda = 0.710\ 70$ Å). Intensity data were corrected for Lorentz-polarization effects and for absorption. Details of crystal and data collection parameters are summarized in Table 1.

Table 1
X-ray crystallographic data for **2** and **3**

Compound	**2**	**3**
Formula	$C_{20}H_{30}N_2O_2Ru_2$	$C_{16}H_{25}NORu$
Formula weight	532.61	348.45
Space group	$P2_1/c$	$P2_1/c$
Crystal color	dark red	red
Crystal dimension (mm)	$0.6 \times 0.5 \times 0.2$	$0.3 \times 0.3 \times 0.2$
a (Å)	10.693(9)	8.963(4)
b (Å)	14.549(12)	13.879(6)
c (Å)	14.438(12)	13.362(6)
β (°)	114.928(12)	104.373(6)
V (Å^3)	2037.1(30)	1610.2(12)
Z	4	4
T (K)	193	193
D_{calc} (g cm^{-3})	1.737	1.437
μ(Mo Kα) (cm^{-1})	14.99	9.67
Number of measured reflections	16294	14295
Number of unique reflections	4565	3612
Transmission factors	0.572–0.741	0.610–0.824
Number of variables	265	198
R_{int}	0.045	0.052
$R1$ [$I > 2\sigma(I)$]	0.047	0.051
$wR2$ (all data)	0.148	0.136
Goodness-of-fit	1.005	1.011
Maximum and minimum residual electron density (e Å^{-3})	1.99 and −1.49	0.91 and −0.51

Structure solution and refinements were carried out by using the CRYSTALSTRUCTURE program package [6]. The heavy-atom positions were determined by a direct methods program (SIR-92) [7], and remaining non-hydrogen atoms were found by subsequent Fourier syntheses. All non-hydrogen atoms were refined anisotropically by full-matrix least-squares techniques based on F^2, whereas all hydrogen atoms were placed at calculated positions.

3. Results and discussion

3.1. Catalytic hydrogenation of cyclohexene

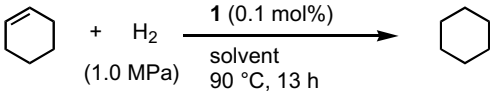
When the (nitrosyl)ruthenium complex **1** was stirred in cyclohexene under 1.0 MPa of H_2 at 90 °C for 13 h, catalytic hydrogenation of cyclohexene took place to afford cyclohexane in moderate yield (Eq. (1), entry 1 in Table 2). Screening of the solvent revealed that use of water gave the best result; the yield of cyclohexane reached to 94% in the reaction with a cyclohexene:**1** ratio of 1000:1 (entry 8). Addition of only 100 equiv. of water per **1** caused a significant decrease in the yield of cyclohexane (entry 9). These results indicate that water seems to serve not only as a simple additive but an efficient reaction media. In the related hydrogenation of alkenes catalyzed by a (nitrosyl)rhodium complex $[Rh(NO)\{P(C_6H_5)_3\}_2$(*p*-benzoquinone)], heterogeneous rhodium(0) metal particles generated by the decom-

Table 2
Hydrogenation of cyclohexene catalyzed by **1**[a]

Entry	Solvent	Yield (%)[b]
1	neat	42
2	CH_2Cl_2	2
3	THF	49
4	CH_3CN	2
5	DMF	27
6	C_2H_5OH	7
7	CH_3OH	27
8	H_2O	94
9	H_2O[c]	80
10[d]	H_2O	67

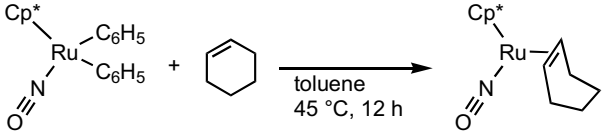
[a] Conditions: S/C = 1000; **1**, 7 μmol; cyclohexene, 7 mmol; solvent, 4 mL; H_2, 1 MPa.
[b] Determined by GC.
[c] Neat plus 12 μL of H_2O (0.7 mmol).
[d] A drop of Hg was added.

position of the complex are proposed to be the true catalyst [8]. In contrast, the mercury poisoning experiment in the present hydrogenation suggests that the catalysis proceeds essentially in the homogeneous phase (entry 10) [9].



(1)

The ^1H NMR spectrum indicated the product mixture contains the dinuclear nitrosyl complex [$Cp^*Ru(\mu_2\text{-}NO)_2RuCp^*$] (**2**), which is a thermolysis product of **1** [5], and a novel (nitrosyl)(cyclohexene)ruthenium complex [$Cp^*Ru(NO)(\eta^2\text{-}C_6H_{10})$] (**3**) as the detectable organometallic species. Complex **3** could be obtained in a pure form by the reaction of **1** with an excess of cyclohexene followed by a chromatographic workup as shown in Eq. (2). The ^1H and $^{13}C\{^1H\}$ NMR spectra of **3** closely resemble to those of the propylene complex [$Cp^*Ru(NO)(\eta^2\text{-}CH_2{=}CHCH_3)$], which has been prepared by the thermolysis of the methyl–vinyl complex [$Cp^*Ru(NO)(CH_3)(CH{=}CH_2)$] [5]. The NO stretching band of **3** at 1673 cm^{-1} is comparable with that of the related η^2-naphthalene complex [$Cp^*Ru(NO)(\eta^2\text{-}C_{10}H_8)$] (1713 cm^{-1}) [10].



(2)

1 **3**

Both **2** and **3** have proved to catalyze the hydrogenation as shown in Table 3. The catalytic activity of the cyclohexene complex **3** was almost equal to that of **1**, whereas the efficiency of the dinuclear catalyst **2** was slightly lower. It is of interest that the ruthenium complex [$Cp^*Ru(CH_3CN)_3$][OSO_2CF_3] [11] without a nitrosyl ligand was less effective for this hydrogenation.

The detailed mechanism of the catalytic hydrogenation is still unclear. Bergman and co-workers have demonstrated that reductive elimination of biphenyl from **1** takes

Table 3
Hydrogenation of cyclohexene catalyzed by ruthenium complexes[a]

Entry	Complex	Yield (%)[b]
1	[$Cp^*Ru(NO)(C_6H_5)_2$] (**1**)	94
2	[$Cp^*Ru(\mu_2\text{-}NO)_2RuCp^*$] (**2**)[c]	82
3	[$Cp^*Ru(NO)(\eta^2\text{-}C_6H_{10})$] (**3**)	94
4	[$Cp^*Ru(CH_3CN)_3$][OSO_2CF_3]	53

[a] Conditions: S/C = 1000; complex, 7 μmol; cyclohexene, 7 mmol; H_2O, 4 mL; H_2, 1 MPa.
[b] Determined by GC.
[c] S/C = 2000.

place at 45 °C to afford a coordinatively unsaturated species [$Cp^*Ru(NO)$] (**A**), which subsequently reacts with a variety of trapping reagents [5,10]. For example, thermolysis of **1** in the presence of triphenylsilane gives rise to the formation of the oxidative addition product [$Cp^*Ru(NO)H\{Si(C_6H_5)_3\}$] [10]. In the catalytic hydrogenation, similar oxidative addition of H_2 to the thermally produced **A** may take place to give the dihydrido species [$Cp^*Ru(NO)H_2$] (**B**). The osmium analogue of **B**, [$Cp^*Os(NO)H_2$], has been isolated from the reaction of [$Cp^*Os(NO)Br_2$] with $NaBH_4$ [12]. The reaction of the dihydride **B** with cyclohexene would lead to the formation of cyclohexane and regeneration of the coordinatively unsaturated species **A**. In this step, bending of the nitrosyl ligand or ring slippage of the Cp^* ligand may take place to facilitate insertion of cyclohexene into the Ru–H bond in **B**. The cyclohexene complex **3** does not seem to be involved in the turnover cycle, because the hydrogenation was much slower in neat cyclohexene, which would be a more favorable condition for the formation of **3**. It is to be noted that **3** could not be observed when isolated **2** was used as the catalyst. This observation indicates that an alternative mechanism without rapture of the dinuclear core of **2** is also possible.

Acceleration of the reaction in water also remains to be clarified. The high polarity of water does not seem to be essential, because the hydrogenation in the less polar organic solvents proceeds faster than that in the polar ones (Table 1). A possible explanation is that the organic substrate/product–water biphasic conditions may cause the local dilution of cyclohexene, which would promote the dissociation of cyclohexene from **3** in the resting state [13]. Further investigation into the mechanism is under way.

3.2. Crystal structures of 2 and 3

The dinuclear complex **2** has previously been characterized only by spectroscopic methods [5]. An X-ray analysis was thus carried out to determine the solid state structure of **2** (Fig. 1). The approximately D_{2h} symmetric structure of **2** with two bridging nitrosyl ligands is almost isostructural with the iron and osmium analogues [$Cp'Fe(\mu_2\text{-}NO)_2FeCp'$] ($Cp' = \eta^5\text{-}C_5H_5$ [14], $\eta^5\text{-}C_5H_4CH_3$ [15]) and [$Cp^*Os(\mu_2\text{-}NO)_2OsCp^*$] [12]. The short metal–metal distance of 2.5366(5) Å is consistent with a formal Ru–Ru double bond as observed in, e.g., [$Cp^*Ru\{Si(CH_3)_3\}(\mu_2$-

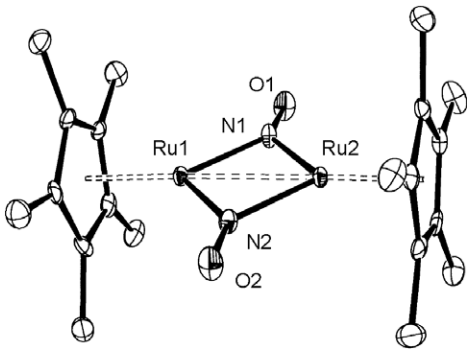


Fig. 1. Crystal structure of **2**. Hydrogen atoms are omitted for clarity. Thermal ellipsoids are drawn at 30% probability level. Selected bond distances (Å) and angles (°): Ru1–Ru2, 2.5366(5); Ru1–N1, 1.924(5); Ru1–N2, 1.915(5); Ru2–N1, 1.933(5); Ru2–N2, 1.918(5); N1–O1, 1.217(7); N2–O2, 1.219(7); Ru1–N1–O1, 139.0(4); Ru1–N2–O2, 140.1(3); Ru2–N1–O1, 138.7(3); Ru2–N2–O2, 137.1(4).

Cl)(μ_2-CH_2)RuCp*] (2.527(1) Å) [16]. The Ru_2N_2 face is almost planar with the dihedral angle of 0.4(2)° around the Ru–Ru vector. The two Cp* ligands are in an almost eclipsed position to each other.

Fig. 2 depicts the molecular structure of the cyclohexene complex **3**. The nitrosyl ligand is essentially linear with the Ru–N–O angle of 175.8(4)°. The cyclohexene ligand adopts an *endo* form to avoid the steric repulsion with the Cp* ligand. The angle defined by the Ru–C11–C12 and C16–C11–C12–C13 planes (ca. 115°) suggests the significant π back donation from the Cp*Ru(NO) moiety to the coordinated alkene. The distance of the coordinated C═C bond is 1.390(9) Å. These structural characteristics are common with the closely related η^2-naphthalene complex [Cp*Ru(NO)(η^2-$C_{10}H_8$)]; the corresponding angle and distance are 115° and 1.418(8) Å, respectively [10].

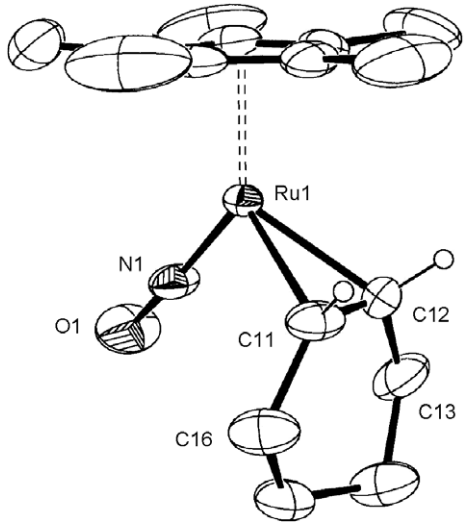


Fig. 2. Crystal structure of **3**. Hydrogen atoms except for the vinyl hydrogens are omitted for clarity. Thermal ellipsoids are drawn at 30% probability level. Selected bond distances (Å) and angles (°): Ru1–N1, 1.732(5); Ru1–C11, 2.161(5); Ru1–C12, 2.163(5); N1–O1, 1.187(7); C11–C12, 1.390(9); Ru1–N1–O1, 175.8(4); Ru1–C11–C16, 122.5(5); Ru1–C12–C13, 120.4(4).

4. Conclusion

We have demonstrated that the (nitrosyl)diphenyl complex **1** serves as a good catalyst precursor for hydrogenation of cyclohexene. Although the mechanistic details have not yet been understood completely, the possible role of the nitrosyl ligand in the catalysis is suggested. In addition, the crystal structures of two catalysts, the nitrosyl-bridged dinuclear complex **2** and mononuclear cyclohexene complex **3** bearing a linear nitrosyl ligand, have been determined.

Acknowledgments

This work was supported by a Grant-in-Aid for Scientific Research Priority Areas (Nos. 14078209 and 18065007) from the Ministry of Education, Culture, Sports, Science and Technology, Japan.

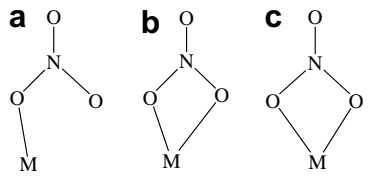
Appendix A. Supplementary material

CCDC 633805 and 633806 contain the supplementary crystallographic data for **2** and **3**. These data can be obtained free of charge via http://www.ccdc.cam.ac.uk/conts/retrieving.html, or from the Cambridge Crystallographic Data Centre, 12 Union Road, Cambridge CB2 1EZ, UK; fax: (+44) 1223-336-033; or e-mail: deposit@ccdc.cam.ac.uk. Supplementary data associated with this article can be found, in the online version, at doi:10.1016/j.poly.2007.04.009.

References

[1] (a) W. Hayton, P. Legzdins, W.B. Sharp, Chem. Rev. 102 (2002) 935;
(b) G.B. Richter-Addo, P. Legzdins, Metal Nitrosyls, Oxford University Press, Oxford, 1992;
(c) I.J. Blackmore, X. Jin, P. Legzdins, Organometallics 24 (2005) 4088;
(d) J.M. Keane, W.D. Harman, Organometallics 24 (2005) 1786.
[2] F. Basolo, Polyhedron 9 (1990) 1503.
[3] (a) S. Matsukawa, S. Kuwata, M. Hidai, Inorg. Chem. 39 (2000) 791;
(b) T. Hattori, S. Matsukawa, S. Kuwata, Y. Ishii, M. Hidai, Chem. Commun. (2003) 510;
(c) K. Arashiba, S. Matsukawa, S. Kuwata, Y. Tanabe, M. Iwasaki, Y. Ishii, Organometallics 25 (2006) 560.
[4] S. Kura, S. Kuwata, T. Ikariya, Angew. Chem., Int. Ed. 44 (2005) 6406.
[5] J. Chang, R.G. Bergman, J. Am. Chem. Soc. 109 (1987) 4298.
[6] D.J. Watkin, C.K. Prout, J.R. Carruthers, P.W. Betteridge, CRYSTALS Issue 10, CRYSTALSTRUCTURE 3.6.0: Crystal Structure Analysis Package, Rigaku and Rigaku/MSC, 9009 New Trails Drive, The Woodlands, TX 77381, USA, 2000–2004.
[7] A. Altomare, G. Cascarano, C. Giacovazzo, A. Guagliardi, M. Burla, G. Polidori, M. Camalli, J. Appl. Crystallogr. 27 (1994) 435.
[8] S. Cenini, R. Ugo, F. Porta, Gazz. Chim. Ital. 111 (1981) 293.
[9] C.M. Hagen, L. Vieille-Petit, G. Laurenczy, G. Süss-Fink, R.G. Finke, Organometallics 24 (2005) 1819.
[10] C.D. Tagge, R.G. Bergman, J. Am. Chem. Soc. 118 (1996) 6908.

[11] P.J. Fagan, M.D. Ward, J.C. Calabrese, J. Am. Chem. Soc. 111 (1989) 1698.
[12] J.L. Brumaghim, J.G. Priepot, G.S. Girolami, Organometallics 18 (1999) 2139.
[13] Regioselective C=C bond hydrogenation of benzylideneacetone in water catalyzed by a water soluble ruthenium complex [$Cp^*RuCl(pta)_2$] (pta = 1,3,5-triaza-7-phosphaadamantane) has been reported although it requires more forcing conditions (130 °C; H_2, 31 MPa): D.N. Akbayeva, L. Gonsalvi, W. Oberhauser, M. Peruzzini, F. Vizza, P. Brüggeller, A. Romerosa, G. Sava, A. Bergamo, Chem. Commun. (2003) 264.
[14] J.L. Calderón, S. Fontana, E. Frauendorfer, V.W. Day, S.D.A. Iske, J. Organomet. Chem. 64 (1974) C16.
[15] K.A. Kubat-Martin, M.E. Barr, B. Spenser, L.F. Dahl, Organometallics 6 (1987) 2570.
[16] W. Lin, S.R. Wilson, G.S. Girolami, Organometallics 13 (1994) 2309.



Scheme 1.

observed by Parkin and co-workers [12] in the study of model complexes of the enzyme carbonic anhydrase. Once again, the identity of the metal ion in a tripodal ligand frameworks determines the coordination geometry of the nitrate ligand.

Yet, in these examples, comparing the electronic properties of the coordinated ligand across such a series of complexes is complicated by the change in metal identity. In order to accurately investigate the effects on the electronic structure of the complexes upon changes in coordination geometry would require a series of related ligand frameworks (excluding the nitrate), all containing the same central metal, but which still allows variations in nitrate geometry. To our knowledge, the ferric porphyrinate complexes [Fe(por)(NO_3)] provide the only example of such a series. Hence we undertook a study of the electronic structure for such a series of complexes aiming to correlate changes in both the Mössbauer and EPR spectra with changes in ligand geometry.

A number of porphyrinate complex structures containing a coordinated nitrate ligand have been reported [13] with a range of coordination modes reported therein. Characterization of a five-coordinate monodentate ferrous complex [Fe(TpivPP)(NO_3)]$^-$ has been published [14]. The structures of the ferric porphyrinate complexes [Fe(por)(NO_3)] based upon the porphyrinates OEP, [15] TPP, [16] and TpivPP [17] demonstrate the geometries illustrated in Scheme 1. Initial attempts at forming a nitrite-coordinated heme complex had resulted in formation of free nitrate as determined by IR spectroscopy following an oxygen atom transfer reaction [18]. A related reaction utilizing picket fence porphyrin (TpivPP) with a protected ligand binding site resulted in nitrate formation with nitrate coordinated to the heme [17]. The crystal structure of [Fe(TpivPP)(NO_3)] [17] displays a symmetrically coordinated bidentate nitrate ligand with the projected plane of the nitrate eclipsing a trans pair of porphyrin nitrogen atoms. Asymmetric bidentate coordination has been reported for [Fe(TPP)(NO_3)] [16] with the projected plane of the nitrate bisecting adjacent pairs of porphyrin nitrogen atoms. The triclinic [Fe(OEP)(NO_3)] [15] exhibits a monodentate nitrate ligand. We have subsequently determined the crystal structure of a monoclinic form of [Fe(OEP)(NO_3)] (reported herein) which also possess a monodentate nitrate ligand.

Initially we undertook to investigate the effects of nitrate coordination mode upon the electronic structure of the ferric porphyrinates. Based upon the reported variations in coordination geometry, the complexes [Fe(por)(NO_3)] provide a means of studying systematic changes in the electronic environment of the iron as the coordination geometry changes. However, seemingly contradictory EPR results were obtained, and led us to reexamine the structure of the asymmetric bidentate coordinated species [Fe(TPP)(NO_3)] [16]. The structure was redetermined at 100 K with crystals having comparable cell constants to those reported previously. Our new structure demonstrates that, rather than a single asymmetric bidentate coordination mode, the nitrate ligand is in fact disordered over two positions. This new structure is discussed particularly in relation to the previous room temperature example [16]. We also present a second crystalline form of [Fe(OEP)(NO_3)], which like the previously reported structure, [15] contains a monodentate nitrate ligand. In addition to the two new crystal structures, we provide electronic characterization of all three [Fe(por)(NO_3)] complexes both in solution and solid state. These reveal marked differences in nitrate coordination geometry between the solid and solution coordination modes for both of the bidentate systems.

2. Experimental

2.1. General information

All reactions were carried out using standard Schlenkware techniques unless otherwise noted. Tetrahydrofuran and hexanes were distilled over sodium and benzophenone prior to use. Methylene chloride was distilled over calcium hydride. H_2OEP was purchased from Midcentury Chemicals. H_2TPP was synthesized according to the method of Adler et al. [19] Metallation reactions to yield [Fe(OEP)(Cl)] and [Fe(TPP)(Cl)] were carried out according to Adler et al. [20] H_2TpivPP was prepared according to a local modification of the reported synthesis [21]. [Fe(TpivPP)(Cl)] was obtained by stirring 150 mg of the free-base overnight with 100 mg of $FeCl_2$ in 25 mL of THF and 0.2 mL of 2,6-lutidine.

Solution UV–Vis spectra were measured on a Perkin–Elmer Lambda 19 UV–Vis–near-IR spectrometer. IR spectra were collected on single crystals ground between two sodium chloride plates with a small amount of Nujol. Spectra were collected on a Nicolet Nexus 870 FT-IR spectrometer. EPR measurements on ground single crystals of [Fe(TpivPP)(NO_3)] were made at 77 K on a Bruker ER 100E spectrometer calibrated with a dpph standard. All other EPR measurements were made on a Bruker EMX-EPR spectrometer. Measurements were made on either frozen methylene chloride solutions or finely ground crystalline solids. Samples were prepared for Mössbauer spectroscopy by grinding approximately 40 mg of crystals, immobilizing in Apiezon M grease to form a mull which was subsequently sealed in an airtight Mössbauer cup.

2.2. Synthesis of [Fe(OEP)(NO$_3$)]

[Fe(OEP)(Cl)] (109.5 mg, 0.176 mmol) was placed in a Schlenk flask with finely ground $AgNO_3$ (35.8 mg, 0.211 mmol). THF (25 mL) was added and the solution stirred overnight. The solvent was removed in vacuo and the reddish-brown solid redissolved in methylene chloride, filtered to remove the inorganic salts and layered with hexanes. X-ray quality crystals were obtained after 7 days.

2.3. Synthesis of [Fe(TPP)(NO$_3$)]

Large single crystals of [Fe(TPP)(NO_3)] were obtained using a similar metathesis pathway. [Fe(TPP)(Cl)] (150 mg, 0.24 mmol) was stirred overnight in 15 mL of THF with 48 mg (0.29 mmol) of $AgNO_3$. Subsequent solvent removal, dissolution in methylene chloride and filtration was carried out prior to layering with hexanes. Large single crystals of up to 2.5 mm length were obtained after 5 days.

Table 1
Crystallographic details for [Fe(OEP)(NO_3)] and [Fe(TPP)(NO_3)]

	[Fe(OEP)(NO_3)]	[Fe(TPP)(NO_3)]
Formula	$C_{36}H_{44}FeN_5O_3$	$C_{44}H_{28}FeN_5O_3$
FW (amu)	650.61	730.56
a (Å)	13.209(3)	10.0271(3)
b (Å)	13.774(3)	16.1341(5)
c (Å)	19.258(4)	16.1341(5)
β (°)	105.50(3)	90.330(2)
V (Å^3)	3376.2(12)	3399.24(17)
Space group	$P2_1/c$	$P2_1/n$
Z	4	4
μ (mm^{-1})	0.489	0.495
Radiation	Mo Kα, $\bar{\lambda} = 0.71073$	Mo Kα, $\bar{\lambda} = 0.71073$
Temperature (K)	293	100(2)
Final R indices [$I > 2\sigma(I)$]	$R_1 = 0.0502$, $wR_2 = 0.1140$	$R_1 = 0.0447$, $wR_2 = 0.1167$
Final R indices (all data)	$R_1 = 0.0802$, $wR_2 = 0.1311$	$R_1 = 0.0704$, $wR_2 = 0.1405$

Determination of the cell constants of the crystals revealed comparable values to those previously reported [16].

2.4. Synthesis of [Fe(TpivPP)(NO$_3$)]

[Fe(TpivPP)(Cl)] (150 mg, 0.14 mmol) was placed in a Schlenk flask with 27 mg (0.16 mmol) of $AgNO_3$ and 15 mL of THF. The mixture was stirred overnight and the solvent evaporated prior to redissolving in CH_2Cl_2 and filtration. UV–Vis spectroscopy of both the THF and CH_2Cl_2 solutions confirmed the formation of [Fe(TpivPP)(NO_3)] yet attempts to obtain a crystalline product were unsuccessful in spite of multiple attempts using variations in crystallization conditions.

2.5. X-ray structure determination

Structures of [Fe(OEP)(NO_3)] and [Fe(TPP)(NO_3)] were solved using the direct methods program SHELXS [22]. All heavy atoms were located using subsequent difference Fourier syntheses. The structures were refined against F^2 with the program SHELXL [23], in which all data collected were used including negative intensities. All nonhydrogen atoms were refined anisotropically. All hydrogen atoms were idealized using the standard SHELXL idealization method. Complete crystallographic details, atomic coordinates, anisotropic thermal parameters and fixed hydrogen coordinates for both are included in the Supplementary material. Table 1 gives brief crystallographic details.

A single crystal of [Fe(OEP)(NO_3)] was mounted on a glass fiber with the long axis approximately collinear with the axis of the fiber. All measurements were performed with graphite monochromated Mo Kα radiation ($\lambda = 0.71073$ Å) on an Enraf-Nonius FAST area detector diffractometer at 127 K as previously described [24]. Intensities of all reflections were reduced using Lorentz and polarization correction factors; the data were also corrected for absorption by an empirical (ψ scans) absorption correction ($\mu = 0.489$ mm^{-1}). Two positions of the methyl carbons of ethyl groups 6 and 7 were observed with this

Table 2
Details of $FeNO_3$ geometry for all [Fe(por)(NO_3)] complexes

Complex	Fe–O1[a]	Fe–O2[a]	δ[a,b]	N5–O1[a]	N5–O2[a]	N5–O3[a]	Ref.
[Fe(OEP)(NO_3)][c]	1.996(2)	3.042(2)	1.076	1.301(3)	1.212(3)	1.199(3)	[15]
[Fe(OEP)(NO_3)][d]	2.016(3)	2.644(3)	0.628	1.206(5)	1.208(6)	1.198(4)	tw
[Fe(TPP)(NO_3)][e]	2.019(4)	2.323(8)	0.304	1.203(6)	1.176(6)	1.188(5)	[16]
[Fe(TPP)(NO_3)][f]	2.125(3)	2.268(3)	0.143	1.199(4)	1.300(3)	1.217(3)	tw
[Fe(TPP)(NO_3)][g]	2.117(4)	2.121(4)	0.004	1.334(4)	1.271(4)	1.217(3)	tw
[Fe(TpivP)(NO_3)]	2.123(3)	2.226(3)	0.103	1.271(4)	1.252(4)	1.214(3)	[17]

Coordination geometries are illustrated in Fig. 4.
[a] Value in Å.
[b] Difference between Fe–O1 and Fe–O2.
[c] Monoclinic form.
[d] Triclinic form.
[e] Room temperature structure.
[f] 100 K structure, major orientation.
[g] 100 K structure, minor orientation.

disorder arising from rotation about the Cm–C(6) and Cm–C(7) bonds. This was resolved by allowing the two possible methyl group positions to refine giving relative occupancies of 65% and 35%. Relevant bond lengths and angles for [Fe(OEP)(NO_3)] are summarized in Table 2.

A single crystal of [Fe(TPP)(NO_3)] was placed in inert oil, mounted on a glass fiber attached to a brass mounting pin and transferred to the cold stream of the diffractometer. Crystal data were collected and integrated using a Bruker Apex system with graphite-monochromated Mo Kα ($\lambda = 0.71073$ Å) radiation. Data collection was carried out at 100 K. [Fe(TPP)(NO_3)] was found to possess a disordered nitrate ligand with two orientations. The two nitrate orientations were refined and determined to have relative occupancies of 60% and 40%. Oxygen atoms of the major orientation are labelled O1A and O2A whilst the minor orientation is labelled O1B and O2B. The central nitrogen atom and the uncoordinated oxygen of the nitrate ligand did not display any disorder. Relevant bond lengths and angles for [Fe(TPP)(NO_3)] are summarized in Table 2.

3. Results

The crystal structures of two five-coordinate nitrate-ligated iron(III) porphyrinate complexes have been obtained. The first of these, monoclinic [Fe(OEP)(NO_3)], represents a second crystalline example of a monodentate nitrate coordinated system in an iron(III) porphyrinate [15]. The second structure, [Fe(TPP)(NO_3)], is a redetermination of a previously reported room temperature structure [16]. Here, we report a revised structure from data collected at 100 K.

Fig. 1 shows the ORTEP diagram and a partial labelling scheme for the monoclinic form of [Fe(OEP)(NO_3)] clearly illustrating the monodentate coordination geometry of the nitrate ligand. Fig. 2a is a schematic representation of the porphyrin core showing the perpendicular displacements

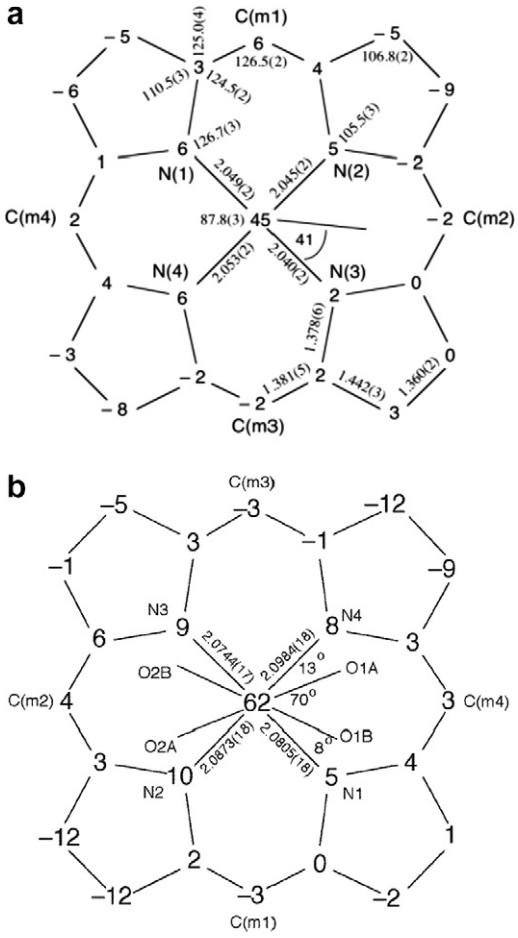


Fig. 2. Formal diagram of the porphyrinato core of (a) [Fe(OEP)(NO_3)] and (b) [Fe(TPP)(NO_3)] displaying perpendicular displacement (in units of 0.01 Å) of the core atoms from the 24-atom mean porphyrin plane. Positive displacements are towards the nitrate coordinated face of the porphyrin. The projections of the nitrate ligand upon the porphyrin plane are also shown. For [Fe(TPP)(NO_3)], the two orientations of the nitrate ligand are shown. (O1A and O2A represent the oxygen atom positions of the major orientation.)

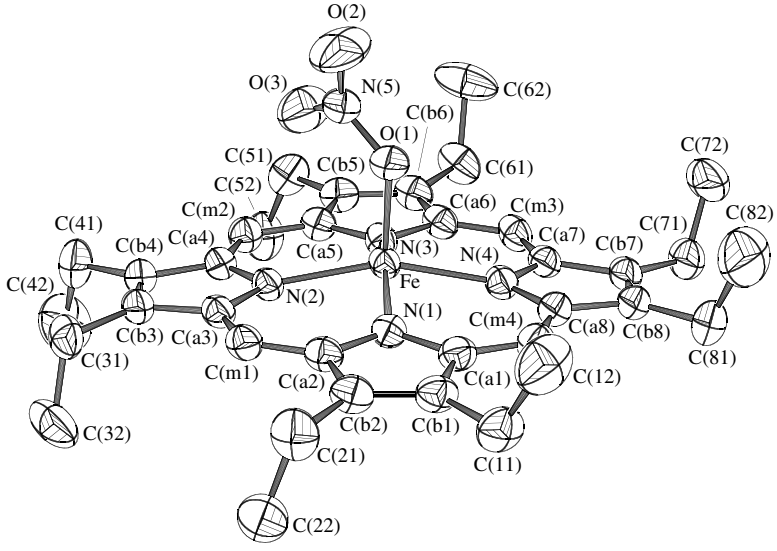


Fig. 1. ORTEP diagram of the monoclinic form of [Fe(OEP)(NO_3)] with 50% probability ellipsoids. The atom labeling scheme is also shown.

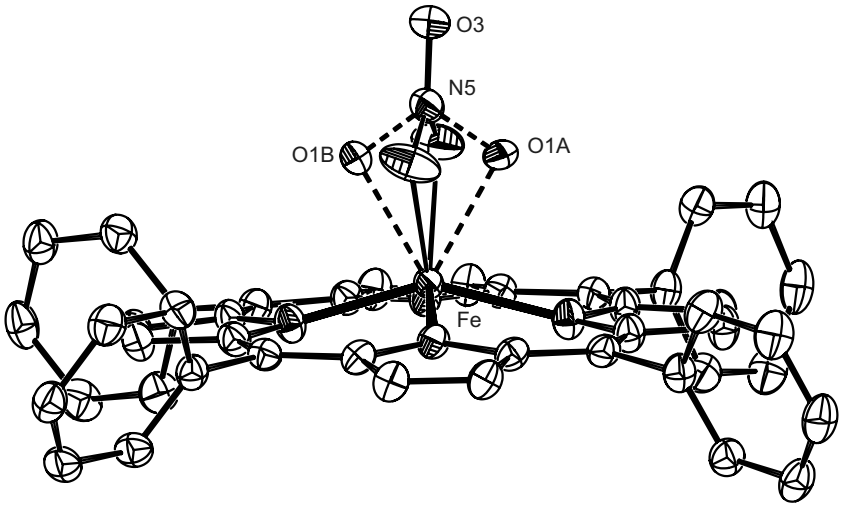


Fig. 3. ORTEP diagram of [Fe(TPP)(NO_3)] with 50% probability ellipsoids. Both orientations of the nitrate ligand is shown with the major orientation labelled O1A, O1B.

Table 3
UV–Vis and IR spectroscopic data for a series of [Fe(por)(NO_3)] complexes

Complex	UV–Vis[a] (nm)	$\nu(NO_3)$[b] (cm^{-1})
[Fe(OEP)(NO_3)]	385, 502, 534, 583, 636	1515, 1385, 1276.
[Fe(TPP)(NO_3)]	412, 513, 574, 658	1531, 1261, 1070
[Fe(TpivP)(NO_3)]	415, 509, 574, 639	1515, 1276, 1071

[a] Measured on CH_2Cl_2 solution.
[b] Measured as KBr disk.

from the 24-atom mean plane. The iron is significantly shifted out of the plane in the direction of the nitrate ligand while the porphyrin core shows a modest combined doming/tenting distortion. An ORTEP diagram for [Fe(TPP)(NO_3)] illustrating both orientations of the nitrate ligand is shown as Fig. 3. The bidentate coordination mode of the nitrate is clearly evident. Fig. 2b shows the porphyrin core of [Fe(TPP)(NO_3)] which also shows a large displacement of the iron in the direction of the nitrate ligand. Projections of both orientations of the nitrate ligand are illustrated with the coordinating oxygens of the major orientation being labeled O1A, O2A. The minor orientation is rotated approximately 70° from the major with both lying close to a pair of opposite Fe–N_p bonds. The dihedral angles (ϕ) which represent the relative orientation of the nitrate ligand with respect to the closest Fe–N_p vector are 13° and 8° for the major and minor orientations respectively. In contrast, for monoclinic [Fe(OEP)(NO_3)] structure, ϕ is 41° with the nitrate ligand lying almost midway between a pair of Fe–N_p bonds. For both the OEP and TPP systems, the nitrate plane lies perpendicular to the plane of the porphyrin. Selected bond lengths for these complexes and related systems are given in Table 2.

Table 3 reports UV–Vis and IR spectroscopic data for the [Fe(por)(NO_3)] complexes. EPR measurements for both ground crystalline solids and solutions were made on all three systems. These data are summarized in Table 4. Solution measurements on all three porphyrin systems made at 4 K are clearly axial with the major feature $g_\perp = 5.7$–6.0 and the minor feature, $g_\parallel \sim 2$. Powder mea-

Table 4
Summary of EPR Data for [Fe(por)(NO_3)] complexes at 4 and 77 K[a]

Complex	Sample	Temperature (K)	Spectrum appearance	g-values
[Fe(OEP)(NO_3)]	cryst. powder	77	axial	$g_\perp = 5.85$
[Fe(OEP)(NO_3)]	cryst. powder	4	axial	$g_\perp = 5.81$, $g_\parallel = 2.018$
[Fe(OEP)(NO_3)]	solution	77	axial	$g_\perp = 5.99$, $g_\parallel = 2.00$
[Fe(OEP)(NO_3)]	solution	4	axial	$g_\perp = 5.86$, $g_\parallel = 1.998$
[Fe(TPP)(NO_3)]	cryst. powder	77	rhombic	$g = 7.71$, 4.04, 1.78
[Fe(TPP)(NO_3)]	cryst. powder	4	rhombic	$g = 8.5$, 4.0, 1.8
[Fe(TPP)(NO_3)]	solution	77	axial	$g_\perp = 5.65$, $g_\parallel$2.001
[Fe(TPP)(NO_3)]	solution	4	axial	$g_\perp = 5.82$, $g_\parallel$1.99
[Fe(TpivPP)(NO_3)]	powder[b]	77	axial	$g_\perp = 5.45$, $g_\parallel = 1.98$
[Fe(TpivPP)(NO_3)]	powder[b]	4	axial	$g_\perp = 5.54$, $g_\parallel = 1.99$
[Fe(TpivPP)(NO_3)]	solution	77	axial	$g_\perp = 5.65$, $g_\parallel = 2.00$
[Fe(TpivPP)(NO_3)]	solution	4	axial	$g_\perp = 5.71$, $g_\parallel = 2.00$
[Fe(TpivPP)(NO_3)]	cryst. powder	77	rhombic	$g_\perp = 6.44$, 3.97, 1.9

[a] All powder samples were prepared from ground single crystals unless otherwise noted. All solution measurements were carried out in frozen CH_2Cl_2.
[b] Powder sample of unknown phase.

Table 5
Mössbauer data for [Fe(por)(NO_3)] complexes

Complex	Temperature (K)	ΔE_q (mm/s)	δ (mm/s)
[Fe(OEP)(NO_3)]	4.2	1.44	0.53
	15	1.39	0.41
	50	1.39	0.42
	100	1.38	0.41
	150	1.36	0.42
	200	1.38	0.38
	RT	1.37	0.36
[Fe(TPP)(NO_3)]	4.2	0.97	0.61
	200	0.98	0.47
	RT	0.97	0.38
[Fe(TpivPP)(NO_3)]	4.2	1.0	0.56
	200	1.10	0.49
	RT	1.07	0.37

surements on the monodentate [Fe(OEP)(NO_3)] also reveal an axial spectrum with $g = 5.8$, 2. By contrast, rhombic spectra are observed for the crystalline bidentate TPP and TpivPP complexes with g values as reported in Table 4. Mössbauer spectra were collected at 4.2 K in zero field for ground crystalline samples of all three porphyrinates. These are fit to a $S = 5/2$ model and data for this fit are given in Table 5. Spectra are illustrated in Fig. 6.

4. Discussion

4.1. Synthetic aspects

We report a straightforward synthetic route for obtaining ferric iron porphyrinate complexes containing a coordinated nitrate ligand. A simple metathesis reaction yields the desired [Fe(por)(NO_3)] complex with the undesirable side-products being removed by a simple filtration. The ease of this synthetic pathway is emphasized when compared with the previous reported methods which either proceeded via an oxygen atom transfer [17], NO attack of a bridged μ-oxo-dimer [15] or in the case of the TPP derivative, reaction of the μ-oxo-dimer with aqueous nitric acid followed by a three-week crystallization [16]. In the latter case, we are able to successfully obtain large crystals in under one week. The only problem encountered with the new reaction system lay in the inability to obtain crystals of the picket-fence porphyrin complex [Fe(TpivPP)(NO_3)]. We were able to show spectroscopically that the species could be obtained in solution yet were unable to prepare a solid crystalline sample. UV–Vis and IR spectroscopic data for all three systems are given in Table 3. In all cases, IR bands associated with the free nitrate ligand were not found, confirming the coordinated nature of the nitrate in all three cases.

4.2. Molecular structures

We report here a new crystalline form and a redetermined structure for two high-spin ferric (nitrato)-porphyrinates. Schematic representations of the porphyrin core for these systems and all other [Fe(por)(NO_3)] complexes are shown in Fig. 4. At the onset of the project, it was thought, based on the reported structures [15–17] that the series of complexes [Fe(por)(NO_3)] exhibited distinct examples of three coordination geometries (Scheme 1). However after evaluation of the EPR data, we decided to redetermine the structure of the asymmetric bidentate coordinated system [Fe(TPP)(NO_3)] [16]. The reported structure [16] showed a nitrate ligand lying midway between a pair of Fe–N_p bonds with two very different Fe–O bond lengths of 2.019(4) and 2.323(8) Å and δ, the difference between the Fe–O bond lengths, of 0.304 Å. The porphyrin core displays a characteristic saddling distortion and the iron is significantly displaced from the mean porphyrin plane in the direction of the nitrate ligand. A similar saddling distortion and iron out-of-plane displacement is observed in the porphyrin core of our redetermined structure at 100 K Fig. 2b. In fact, if we overlay the porphyrin cores of the RT structure and our newly redetermined structure so as to align the saddling patterns, we observe that the originally reported nitrate ligand orientation lies midway between the two orientations found in the 100 K structure. This is consistent with the very large thermal ellipsoids observed for the two *coordinated* oxygen atoms of the nitrate. Based upon

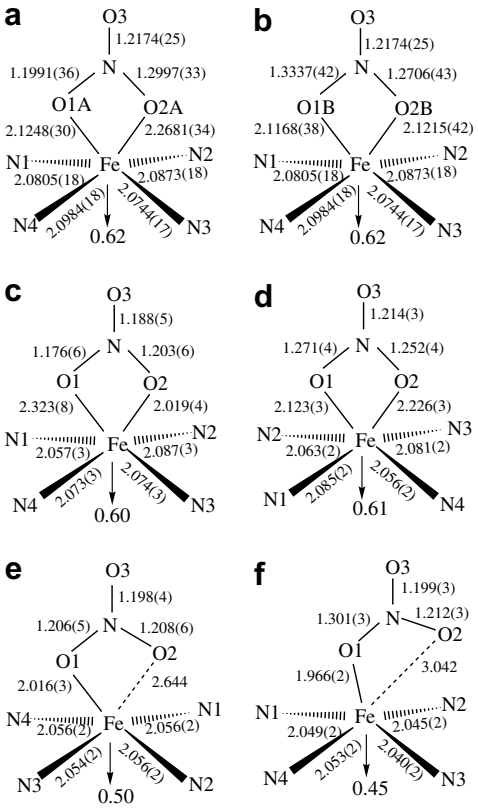


Fig. 4. Schematic representations of the N_4FeNO_3 geometry for all [Fe(por)(NO_3)] complexes. Structures represented are (a) [Fe(TPP)(NO_3)] 100 K, major orientation; (b) [Fe(TPP)(NO_3)] 100 K, minor orientation; (c) [Fe(TPP)(NO_3)]. Room temperature structure (Ref. [16]); (d) [Fe(TpivPP)(NO_3)] (Ref. [17]); (e) [Fe(OEP)(NO_3)] triclinic form (Ref. [15]); (f) [Fe(OEP)(NO_3)] monoclinic form.

this observation, we conclude the previously reported nitrate ligand orientation is in fact an averaging of the two orientations we observe in our 100 K structure. These two orientations present a more eclipsed nitrate position both lying approximately 10° from a Fe–N_p vector. A similar orientation is observed in the other bidentate system [Fe(TpivPP)(NO_3)] [17] where the bidentate nitrate lies 10° from the closest Fe–N_p vector. However, neither of the two new nitrate orientations in the 100 K structure of [Fe(TPP)(NO_3)] display anywhere near the same extent of asymmetric coordination as reported in the RT structure. The major orientation shows the greatest disparity in the two Fe–O bond length ($\delta = 0.1433$ Å) whereas the bond lengths in the minor orientation are practically equivalent ($\delta = 0.0047$ Å). Based upon these results, we reclassify the [Fe(TPP)(NO_3)] system as containing a symmetrically coordinated bidentate nitrate ligand.

We also observe some disparity in the Fe–O distances in the two structures of [Fe(OEP)(NO_3)]. This is most evident in the nonbonded distance between the iron center and the noncoordinating oxygen, O2, in Fig. 4e and f. Although the Fe–O bond length for both of the monodentate nitrates are very similar, the nitrate position with respect to the porphyrin core is significantly different. In the previously reported triclinic form [15], the nitrate adopts an orientation similar to the bidentate systems with the Fe–O2 vector perpendicular to the porphyrin plane and passing through the core center where the iron sits. In the monoclinic form, the Fe–O bond lies more perpendicular to porphyrin plane with the N–O(2) bond shifted significantly from the centered normal to the porphyrin plane. This is reflected in a marked increase in the distance between the iron center and the noncoordinated O(3) from 2.644 Å in the triclinic system to 3.042 Å for the monoclinic system. In both cases, the nitrate ligand still lies close to midway between a pair of Fe–N_p vectors and equivalent iron out-of-plane displacements are observed.

Fig. 4 illustrates the core geometry for all ferric [Fe(por)(NO_3)] systems reported to date. There are a number of features common to all the systems. Each system displays a significant out-of-plane displacement of the iron in the direction of the nitrate ligand. large out-of-plane displacements are common in five-coordinate ferric porphyrinates [25]. No significant differences are observed in the Fe–N_p distances for each system although the distances for the two monodentate OEP derivatives are slightly shorter than the meso-substituted porphyrinates.

The variation in the projection of the nitrate plane onto the plane of the porphyrin has already been discussed briefly. Comparing the data from all systems reveals when the nitrate coordinates in a bidentate fashion, the projection of the ligand plane is close to a Fe–N_p vector with a dihedral angle (ϕ) of ~10°. When the nitrate coordinates in a monodentate fashion, the orientation changes such that it lies midway between the two Fe–N_p vectors, possibly to minimize steric interactions between the pyrrolic nitrogens and the uncoordinated oxygen of the nitrate ligand.

4.3. EPR spectroscopy

EPR spectra on both the powder and solutions of all three nitrate complexes were collected at 77 and 4 K. These data are summarized in Table 4 and displayed in Fig. 5. For the OEP complexes, the EPR spectra for both solid and solution at both temperatures are axial. At 77 K however, the minor $g_\parallel$ feature was too weak to be detected. When the temperature is reduced to 4 K, both $g_\perp$ and $g_\parallel$ features are evident. The observation of axial spectra for both the solid and the solution is consistent with a monodentate coordination mode in both states. Similar axial spectra are observed in other five-coordinate high-spin systems such as [Fe(por)(Cl)] [26]. We have already discussed the differences in coordination mode of the nitrate ligand in the TPP and picket-fence derivatives and we would expect the EPR spectra for these to differ from the simple axial spectra observed for the OEP derivative. Had the previously reported coordination mode of the nitrate in [Fe(TPP)(NO_3)], the highly asymmetric bidentate geometry, been representative of the nitrate geometry at lower temperatures, we would perhaps have expected to see EPR spectra for this system that differ from both that of the OEP and TpivPP systems. Instead, following our new crystallographic determination, we now expect the EPR spectra of the TPP and TpivPP derivatives to be somewhat similar. Indeed, this is true with the EPR of the ground crystalline material displaying rhombic spectra for both of the bidentate coordinated systems. [Fe(TPP)(NO_3)] at 77 K exhibits a complex spectrum from which we identify a major rhombic component has $g = 7.71$, 4.04 and 1.78

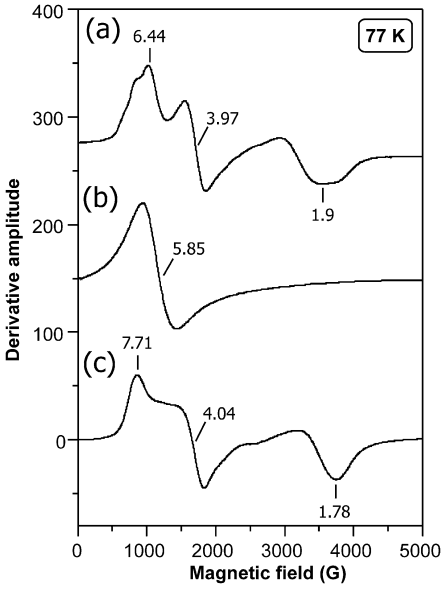


Fig. 5. EPR spectra at 77 K of ground single crystals of (a) [Fe(TpivPP)(NO_3)], (b) [Fe(OEP)(NO_3)], and (c) [Fe(TPP)(NO_3)].

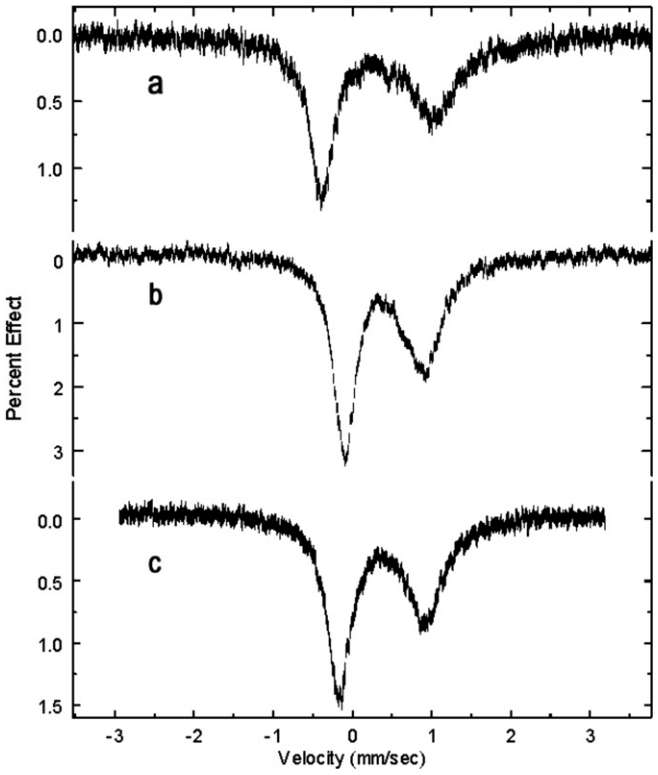


Fig. 6. Mössbauer spectra of (a) [Fe(OEP)(NO_3)], (b) [Fe(TPP)(NO_3)], and (c) [Fe(TpivPP)(NO_3)]. Spectra taken at room temperature.

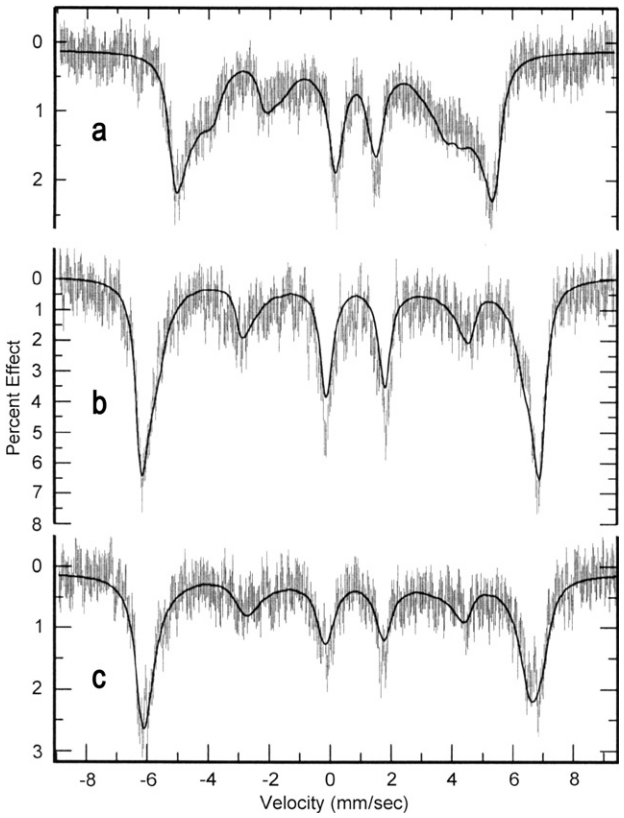


Fig. 7. Mössbauer spectra and calculated fits of the spectra of (a) [Fe(OEP)(NO_3)], (b) [Fe(TPP)(NO_3)], and (c) [Fe(TpivPP)(NO_3)]. Spectra taken at 4.2 K and an applied 4.5 T field parallel to the gamma ray beam.

with the largest g-tensor shifting to 8.5 at 4 K. Correspondingly, the largest g-tensor in the EPR spectrum of the ground crystalline [Fe(TpivPP)(NO_3)] is smaller than that of the TPP derivative ($g = 6.44, 3.97, 1.9$). EPR data from a powder sample of [Fe(TpivPP)(NO_3)] of unknown phase which was prepared using a crude precipitation technique exhibits a characteristic axial spectrum with $g = 5.5, 2$ pattern. Based upon our observations from the OEP system, this likely contains a monodentate nitrate ligand. Similarly, axial EPR spectra are observed for solutions of the TPP and picket fence derivatives. This suggests that the coordination mode of the nitrate ligand in both these systems changes to monodentate upon solvation.

4.4. Mössbauer spectroscopy

Table 5 summarizes the Mössbauer measurements carried out on each of the nitrate complexes collected over a range of temperatures. All three systems were studied at 4 K in an applied magnetic field and the spectra could be satisfactorily fit to a $S = 5/2$ model (Table 6 and Fig. 7). All three systems displayed asymmetric quadrupole doublets at room temperature. Linewidths broadened such that quadrupole splitting fits were inaccessible in the temperature range from 150 K to below 18 K for the TPP and TpivPP derivatives; the OEP derivative did not show the same broadening behavior. The values for the quadrupole splitting are somewhat larger than other high-spin ferric systems such as [Fe(por)(Cl)] ($\Delta E_q \sim 0.9$ mm/s). Since the quadrupole splitting is dependent upon the symmetry of the metal center and we have already observed significant differences in the nature of the g tensors in the ground crystalline samples, we expect here to observe substantial differences in the values of ΔE_q for all three systems. Although differences are observed, the fact that the OEP derivative has the largest value of ΔE_q is unexpected. Moreover, there remains some uncertainty about the exact phase for the picket fence porphyrin measurement.

Table 6
Data from $S = 5/2$ fit to 4.2 K Mössbauer spectra of [Fe(por)(NO_3)] derivatives

Complex	ΔE_q (mm/s)	δ (mm/s)	η	Γ (mm/s)	D (cm^{-1})	E (cm^{-1})	$A_{ii}/g_N\beta_N$ (T)
[Fe(OEP)(NO_3)]	1.44	0.53	0.06	0.52	5.7	0.37	−14.9, −17.3, −2.7
[Fe(TPP)(NO_3)]	0.97	0.61	0.0	0.42	6.9	0.6	−21.8, −20.0, −10.4
[Fe(TpivPP)(NO_3)]	1.0	0.56	0.4	0.57	10	0.2	−23.1, −20.9, −2.0

5. Summary

Nitrate can bind to the iron center in the iron(III) porphyrinates in either a symmetric bidentate or monodentate mode. An earlier report of an asymmetric binding mode is probably not correct. EPR spectra display sensitivity to the coordination mode. An axial high-spin signal is seen for monodentate coordination, whereas a rhombic high-spin spectrum is observed for the bidentate species. Mössbauer spectra do not appear to be as sensitive to the coordination mode.

Acknowledgements

We thank the National Institutes of Health for support of this research under Grant GM-38401. Funds for the purchase of the FAST area detector were provided through NIH Grant RR-06709. We thank the NSF for EPR support through instrumentation Grant NSF-98-70990.

Appendix A. Supplementary material

CCDC 633779 and 633780 contain the supplementary crystallographic data for this paper. These data can be obtained free of charge via http://www.ccdc.cam.ac.uk/conts/retrieving.html, or from the Cambridge Crystallographic Data Centre, 12 Union Road, Cambridge CB2 1EZ, UK; fax: (+44) 1223-336-033; or e-mail: deposit@ccdc.cam.ac.uk. Supplementary data associated with this article can be found, in the online version, at doi:10.1016/j.poly.2007.03.048.

References

[1] B. Averill, Chem. Rev. 96 (1996) 2951.
[2] N. Dudley, Nitrates. The Threat to Food and Water, Green Print, London, 1990.
[3] J. L'hirondel, J.-L. L'hirondel, Nitrate and Man: Toxic, Harmless or Beneficial?, CABI Publishing, New York, NY, 2002.
[4] M. Inoue, Y. Minamiyama, S. Takemura, Meth. Enzymol. 269 (1996) 474.
[5] M.P. Doyle, J.W. Hoekstra, J. Inorg. Biochem. 14 (1981) 351.
[6] R.F. Eich, T. Li, D.D. Lemon, D.H. Doherty, S.R. Curry, J.F. Aitken, A.J. Mathews, K.A. Johnson, R.D. Smith, G.N. Phillips Jr., J.S. Olson, Biochemistry 35 (1996) 6976.
[7] F.A. Cotton, G. Wilkinson, C.A. Murillo, M. Bochmann, Advanced Inorganic Chemistry, sixth ed., Wiley-Interscience, New York, NY, 1999, p. 489.
[8] C.C. Addison, N. Logan, S.C. Wallwork, C.D. Garner, Quart. Rev. 25 (1971) 289.
[9] (a) B.M. Gatehouse, S.E. Livingstone, R.S. Nyholm, J. Chem. Soc. (1957) 4222;
(b) A.B.P. Lever, E. Mantovani, B.S. Ramaswamy, Can. J. Chem. 49 (1971) 1957.
[10] (a) G.J. Van Driel, W.L. Driessen, J. Reedjik, Inorg. Chem. 24 (1985) 2919;
(b) G.J. Kleywegt, W.G.R. Wiesmeijer, G.J. Van Driel, W.L. Driessen, J. Reedjik, J. Chem. Soc., Dalton Trans. (1985) 2717.
[11] Abbreviations used in this paper Por—a generalized porphyrin dianion, OEP dianion of 2,3,7,8,12,13,17,18-octaethylporphyrin, TPP dianion of 5,10,15,20-tetraphenylporphyrin, TpivPP dianion of meso-tetrakis(α-α-α-α-pivalamidophenyl)porphyrin, N_p—pophyrinato nitrogen atom, amtd tris-((3,5-dimethylpyrazoyl-1-yl)methyl)-amine, dpph diphenylpicrylhydrazl.
[12] (a) R. Han, G. Parkin, J. Am. Chem. Soc. 113 (1991) 9707;
(b) C. Kimblin, V.J. Murphy, T. Hascall, B.M. Bridgewater, J.B. Bonanno, G. Parkin, Inorg. Chem. 39 (2000) 967.
[13] G.R.A. Wyllie, W.R. Scheidt, Chem. Rev. 102 (2002) 1067.
[14] H. Nasri, M.K. Ellison, B. Shaevitz, G.P. Gupta, G. Lang, W.R. Scheidt, Inorg. Chem. 45 (2006) 5284.
[15] M.K. Ellison, M. Shang, J. Kim, W.R. Scheidt, Acta Crystallogr., Sect. C 52 (1996) 3040.
[16] M.A. Phillippi, N. Baenziger, H.M. Goff, Inorg. Chem. 20 (1981) 3904.
[17] O.Q. Munro, W.R. Scheidt, Inorg. Chem. 37 (1998) 2308.
[18] M.G. Finnegan, A.G. Lappin, W.R. Scheidt, Inorg. Chem. 29 (1990) 181.
[19] A.D. Adler, F.R. Longo, J.D. Finarelli, J. Goldmacher, J. Assour, L. Korsakoff, J. Org. Chem. 32 (1967) 476.
[20] A.D. Adler, F.R. Longo, F. Kampus, J. Kim, J. Inorg. Nucl. Chem. 32 (1970) 2443.
[21] J.P. Collman, R.R. Gagne, T.R. Halbert, G. Lang, W.T. Robinson, J. Am. Chem. Soc. 97 (1975) 1427.
[22] G.M. Sheldrick, Acta Crystallogr., Sect. A 46 (1990) 467.
[23] G.M. Sheldrick, SHELXL-97: FORTRAN program for crystal structure refinement, University of Göttingen, Göttingen, Germany, 1997.
[24] W.R. Scheidt, I. Turowska-Tyrk, Inorg. Chem. 33 (1994) 1314.
[25] W.R. Scheidt, Systematics of the stereochemistry of porphyrins and metalloporphyrins, in: K.M. Kadish, K. Smith, R. Guilard (Eds.), The Porphyrin Handbook, vol. 3, Academic Press, San Diego, CA and Burlington, MA, 2000 (Chapter 16).
[26] G. Palmer, in: A.B.P. Lever, H.B. Gray (Eds.), Iron Porphyrins Part 2, VCH Publishers Inc., New York, 1983 (Chapter 2).

relevance of the reaction of nitroxyl with thiol compounds probably lies in its oxidative character leading to disulfides, or in the irreversible formation of sulfinamide adducts [14]. While these reactions are specifically associated with the biochemical activity of HNO when critical metals or thiols are involved, the spin forbidden reaction of HNO with molecular oxygen can be regarded as a sink reaction generating a cytotoxic two electron oxidant which is also a hydroxylating agent [15,16]. A comparative study of the reactivity of HNO from the nitroxyl donor Angeli's salt showed that HNO will preferentially react with proteins containing ferric centres or thiols rather than with O_2 or with itself forming N_2O [16].

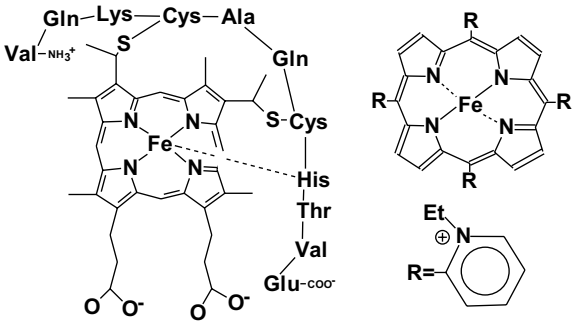
Heme model compounds offer the opportunity to study the reaction kinetics without the complexity arising from ligand interactions with the protein matrix. For example, the heme peptide microperoxidase-11 (MP11) provides a Fe^{III}-histidine pentacoordinated centre that allows the study of the influence of the axial histidine on the reaction. Another perspective of analysis is offered by cationic Mn^{III} porphyrins. The reactions of these porphyrins with HNO donors have been studied by our group and we reported an assisted decomposition of HNO donors leading to the formation of $Mn^{II}NO$ compounds [17]. In this context, we have looked into the reaction between the commonly used nitroxyl donors sodium trioxodinitrate ($Na_2N_2O_3$, Angeli's salt, AS) [18,19] and toluene sulfohydroxamic acid (TSHA), an analogue of Piloty's acid [20,21], with the ferric model compounds Fe^{III}MP11 and the cationic ferric tetrakis *N*-ethylpyridinium-2yl porphyne $[Fe^{III}TEPyP]^{5+}$ (Scheme 1).

2. Materials and methods

2.1. Experimental methods

2.1.1. Reagents

AS and TSHA were synthesized according to published literature [22]. $[Fe^{III}TEPyP]^{5+}$ and MP11 were purchased from Frontier Scientific and Sigma–Aldrich Argentina, respectively, and used as received.



Scheme 1. Structure of Fe^{III}MP11 and $[Fe^{III}TEPyP]^{5+}$.

2.1.2. Reactions of heme models with AS and TSHA

All experiments were done at 25 °C in 0.1 M phosphate buffer, containing EDTA 10^{-4} M to avoid HNO catalytic decomposition by Cu^{II} and other divalent ions. Porphyrin concentration was 5×10^{-6} M, unless otherwise noted. UV–Vis spectra were recorded with a HP 8453 spectrometer in a septum sealed 1 cm path quartz cell. All manipulations were performed under argon atmosphere using septa; solutions were purged for at least 20 min with Ar. All reactions were unaffected by the irradiation of the sample with the light source of the spectrometer. AS and TSHA solutions were freshly prepared for each set of measurements and kept on ice. The donor concentration was checked before each measurement by following its absorbance [21,23]. TSHA was dissolved in ethanol 96%, and added to the porphyrin solutions to a final ethanol/water ratio minor than 1%. The reaction rate was measured by following the absorbance of the porphyrins at the peak position of the Soret and/or Q bands. All reactions were pursued until no more spectroscopic changes were observed, unless otherwise stated. Reaction times ranged from 60 s to 2 h.

Previous studies by our group showed that the reaction is always first order on both reactants, the metalloporphyrin and either the HNO or the donor [17]. To compute the corresponding bimolecular rate constants (k_{on}), the observed first order rate constants (k_{obs}), for several donor or HNO concentrations were obtained for the reactions with $[Fe^{III}TEPyP]^{5+}$ and with MP11 by the initial rate method using the equation:

$$k_{obs} = \frac{v_{on}}{[P]_0} = k_{on}[HNO/Donor]_0$$

where v_{on} is the initial rate of the metalloporphyrin decay, $[P]_0$ is the initial concentration of $[Fe^{III}TEPyP]^{5+}$ or MP11, k_{on} is the second order rate constant and $[HNO/Donor]_0$ is the concentration of the free HNO or of the nitroxyl donor. The HNO concentration was estimated by the following kinetic analysis:

$$\text{Donor(TSHA/ AS)} \xrightarrow{k_d, v_d} \text{HNO} \quad (1)$$

$$\text{HNO} + Fe^{III}P \xrightarrow{k_{on}, v_{on}} Fe^{II}P\text{–NO} \quad (2)$$

$$\text{HNO} \xrightarrow{k_h, v_h} 1\frac{1}{2}N_2O + 1\frac{1}{2}H_2O \quad (3)$$

where the reaction (1) represents the donor decomposition, (2) represents HNO reaction with the metalloporphyrin ($Fe^{III}P$) and (3) represents HNO dimerization. The reaction (1) was considered as an irreversible reaction because its inverse rate is negligible with respect to reactions (2) and (3) at the initial rate condition. Applying the steady state approximation for [HNO], all the HNO produced through reaction (1) must be consumed in reactions (2) and (3), therefore $v_d = v_{on} + v_h$. The donor decomposition first order rate constant k_d [18,20,23,24] ($k_{d(TSHA)} = 3.5 \times 10^{-4}\ s^{-1}$, $k_{d(AS)} = 8 \times 10^{-4}\ s^{-1}$; determined in this work) and the dimerization second order rate constant [15,23,25] k_h ($k_h = 8 \times 10^6\ M^{-1}\ s^{-1}$) [15] are known data. There-

fore, by measuring the initial v_{on} and the donor concentration, [HNO] can be estimated as

$$[\mathrm{HNO}] = \sqrt{\frac{k_d[\mathrm{Donor}] - v_{on}}{k_h}}$$

From the k_{obs} versus [HNO] or [Donor] plots, an estimated $k_{on(HNO)}$ or $k_{on(Donor)}$ can be obtained from the slope. This type of analysis has already been done for studying HNO reaction kinetics [16,17]. Each point showed in the plots corresponds to the mean of at least three independent measurements.

2.2. Computational methods

All computations were performed at the DFT level with the SIESTA code [26,27], which consists on a very efficient DFT implementation which uses pseudopotentials and numerical basis sets. The use of standard norm-conserving pseudopotentials [28] avoids the computation of core electrons, smoothing at the same time the valence charge density. In our study, the nonlinear partial-core correction was applied to the iron atom [29]. Basis functions consist of localized (numerical) pseudoatomic orbitals, projected on a real space grid to compute the Hartree potential and exchange correlation potentials matrix elements. For all atoms, basis sets of double ξ plus polarization quality were employed, with a pseudoatomic orbital energy shift of 25 meV and a grid cutoff of 150 Ry. Calculations were performed using the generalized gradient approximation functional proposed by Perdew et al. [30]. The SIESTA method has shown an excellent performance for medium and large systems and has also proved to be appropriate for heme models with this combination of functional, basis sets, and grid parameters [31,32]. The model used consisted of a porphyrin saturated with hydrogen atoms in all side chains ($Fe^{III}P$) plus the corresponding ligand (5-methylimidazole, NO or AS) optimized in vacuum. We have performed the geometry optimizations of the $[Fe^{III}P(AS)]^{-1}$ complex at the low spin state, which has been found to be the ground state of the system.

3. Results and discussion

3.1. Reaction of $[Fe^{III}TEPyP]^{5+}$ with AS

When AS is added to $[Fe^{III}TEPyP]^{5+}$ solutions under inert atmosphere in equimolar ratio, total conversion of $[Fe^{III}TEPyP]^{5+}$ to $[Fe^{II}TEPyP(NO)]^{4+}$ is observed in less than a minute verifying that the stoichiometry of the reaction is 1:1 in reagent and product (Fig. 1). Although AS decomposes spontaneously with a half life of 866 s, measured under the same reaction conditions at pH 7, as mentioned in Section 2, the equimolar reaction exhibits a half life for AS of just about 5 s, indicating that the decomposition rate is noticeably faster in the presence of the metalloporphyrin. In this scenario, the direct reaction of AS with

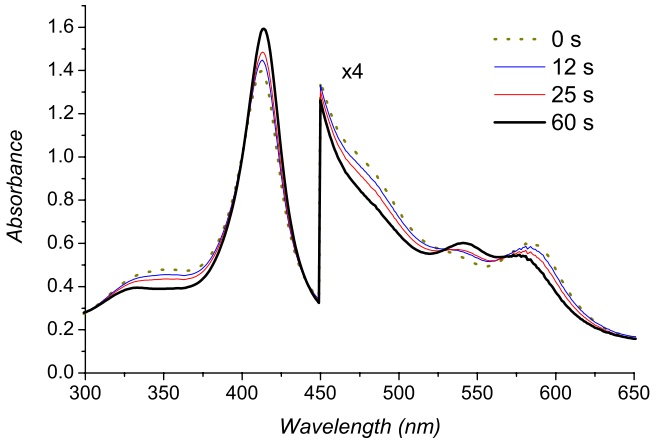


Fig. 1. Spectral changes observed for the addition of AS to a solution $[Fe^{III}TEPyP]^{5+}$ (2×10^{-5} M) (phosphate buffer pH 7, 25 °C). $[Fe^{III}TEPyP]^{5+}$: dotted line, $[Fe^{II}TEPyP\text{-}NO]^{4+}$: thick solid line.

the porphyrin is expected to be the main reaction pathway for AS decomposition. Therefore, the second order rate constant for the reaction ($k_{on(AS)}$) was determined (Table 1) from the slope of the k_{obs} versus [AS] plot (Fig. 2). This results find a precedent in our previous work with Mn^{III} porphyrins, where we demonstrated that the positively charged porphyrin $[Mn^{III}TEPyP]^{5+}$ assists the decomposition of both nitroxyl donors AS and TSHA [17].

3.2. Reaction of $[Fe^{III}TEPyP]^{5+}$ with TSHA

The half life of the spontaneous decomposition of TSHA at pH 10, measured under the experimental conditions described in Section 2.1.2, is 33 min while the half life for the reaction with $[Fe^{III}TEPyP]^{5+}$ is about 10 s, indicating once more that the metalloporphyrin is reacting directly with TSHA. In Fig. 3 is depicted the k_{obs} versus [TSHA]. From the slope of this plot a value for the bimolecular binding constant rate $k_{on(TSHA)}$ is obtained (Table 1).

3.3. Reaction of MP11 with AS

When excess of AS is added to $Fe^{III}MP11$ aqueous solutions under inert atmosphere at pH 7, spectral changes corresponding to the conversion of $Fe^{III}MP11$ to $Fe^{II}MP11(NO)$ are observed (Fig. 4). This product was identified by comparison with the one obtained from the same starting material, sodium dithionite, and nitric oxide (data not shown). The absence of an isosbestic point in Fig. 4 suggests the presence of more than two species. A Principal Factor Analysis predicts the presence of three spectral components in the kinetics which indicates the formation of an intermediate. The rate of HNO production (calculated from known AS concentrations and the decomposition rate constant) and of the reaction of HNO with $Fe^{III}MP11$ are plotted in Fig. 5. As it can be seen in Fig. 5, in all cases HNO production exceeds its consumption by the heme compound indicating that the metalloporphy-

Table 1
Bimolecular reaction rate constants for the binding of nitroxyl donors and HNO to Fe and Mn porphyrins

Porphyrin	pH	Donor	$k_{on(Donor)}$ (M^{-1} s^{-1})	$k_{on(HNO)}$ (M^{-1} s^{-1})
$[Mn^{III}TEPyP]^{5+}$ [17]	7/10	AS/TSHA	$0.8–3.6 \times 10^4$	
$[Fe^{III}TEPyP]^{5+}$	7	AS	$5.4 \pm 0.2 \times 10^3$	
$[Fe^{III}TEPyP]^{5+}$	10	TSHA	$1.1 \pm 0.3 \times 10^4$	
$[Mn^{III}TPPS]^{3-}$ [17]	7/10	AS/TSHA		$\sim 4–9 \times 10^4$
$[Fe^{III}TPPS]^{3-}$ [13]	7	AS	0.5	$\sim 1 \times 10^6$
Fe^{III}MP11	7	AS		$6.4 \pm 0.5 \times 10^4$
Fe^{III}MP11	10	TSHA		$3.1 \pm 0.4 \times 10^4$

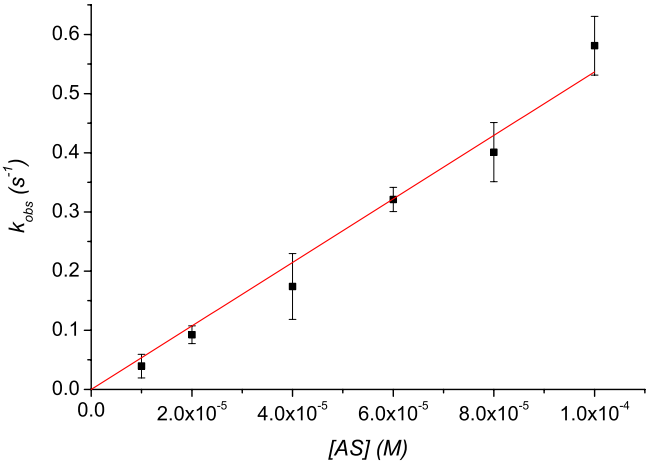


Fig. 2. Initial observed constant rates vs. [AS] (pH 7 phosphate buffer, 25 °C), for the reaction of $[Fe^{III}TEPyP]^{5+}$ (2×10^{-5} M) with AS.

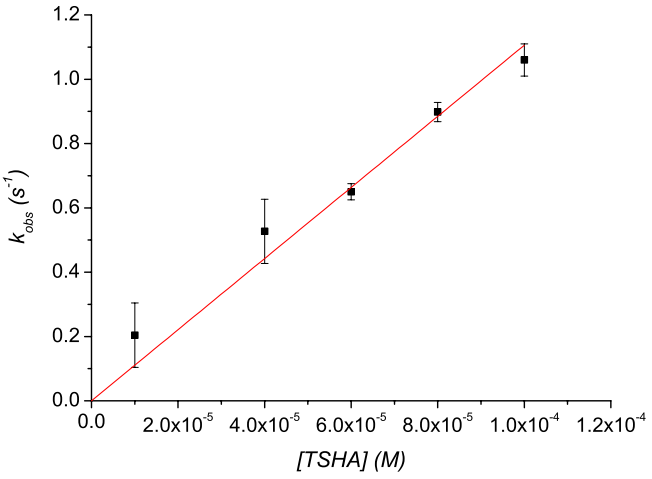


Fig. 3. Initial observed constant rates vs. [TSHA] (pH 10 phosphate buffer, 25 °C), for the reaction of $[Fe^{III}TEPyP]^{5+}$ (2×10^{-5} M) with TSHA.

rin may be reacting directly with the species HNO. Under these circumstances from the plot of the observed rate constant versus [HNO] (Fig. 6) is obtained a value for the bimolecular HNO binding rate constant at pH 7 (Table 1).

3.4. Reaction of MP11 with TSHA

When excess of TSHA is added to Fe^{III}MP11 aqueous solutions under inert atmosphere at pH 10, the spectral changes and kinetics were similar to those observed when AS was the donor (Fig. 7). From the plot of the observed rate constants versus [HNO] (Fig. 8) the rate constant for the bimolecular reaction of HNO at pH 10 is derived (Table 1).

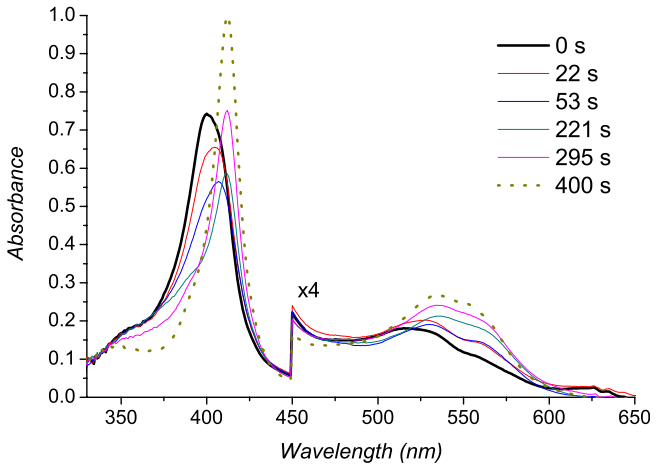


Fig. 4. Spectral changes observed at successive times for the reaction of AS with Fe^{III}MP11 (pH 7 phosphate buffer, 25 °C). Fe^{III}MP11: thick solid line, Fe^{II}MP11-NO: dotted line.

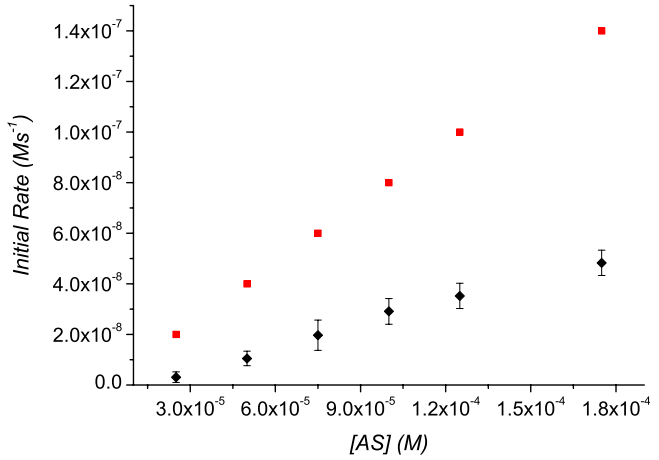


Fig. 5. Calculated initial HNO production rates (squares) and initial reaction rates (diamonds) vs. initial AS concentration (phosphate buffer, 25 °C), for the reaction of Fe^{III}MP11 (5.0×10^{-6} M) with AS (0.2–2.0×10^{-4} M).

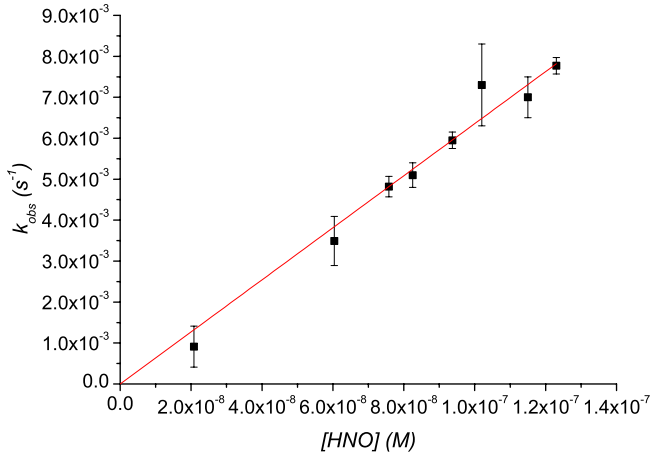


Fig. 6. Initial observed constant rates vs. estimated [HNO] (pH 7 phosphate buffer, 25 °C), for the reaction of Fe^{III}MP11 (5.0×10^{-6} M) with AS (0.2–2.0×10^{-4} M).

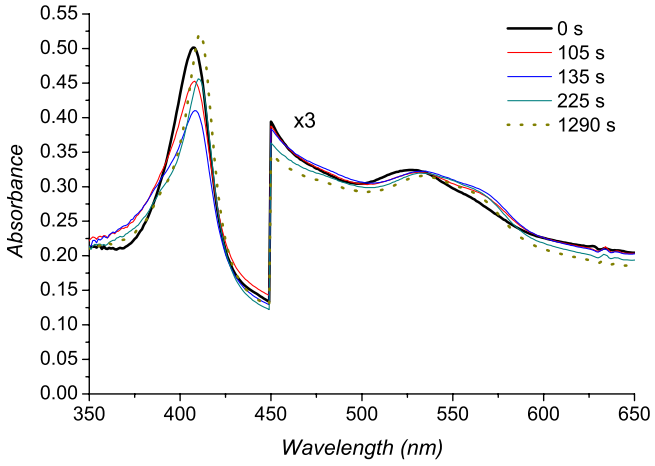


Fig. 7. Spectral changes observed at successive times for the reaction of TSHA with Fe^{III}MP11 (pH 10 phosphate buffer, 25 °C). Fe^{III}MP11: thick solid line, Fe^{II}MP11-NO: dotted line.

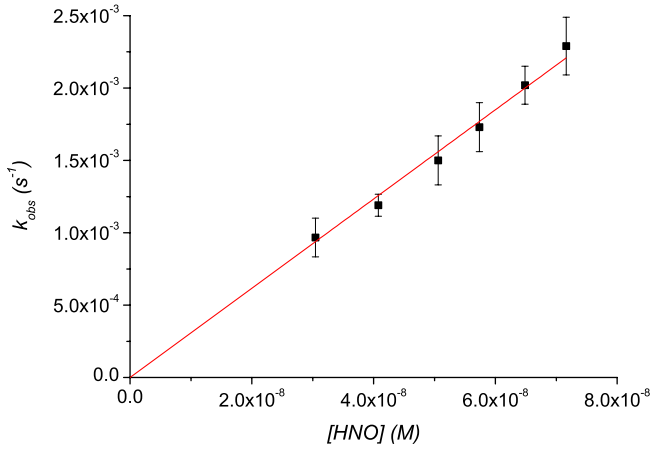


Fig. 8. Initial observed constant rates vs. estimated [HNO] (pH 10 phosphate buffer, 25 °C), for the reaction of Fe^{III}MP11 (5×10^{-6} M) with TSHA (0.3–1.5×10^{-4} M).

In order to gain some insight into the possible nature of the reaction intermediate we followed the reaction by ^{1}H NMR using AS. Fig. 9 shows the ^{1}H NMR spectrum of the starting material, and exhibits the characteristic α-CH_3 chemical displacements between 75 and 55 ppm, attributable to a high spin species [33]. This supports the fact that MP11 is initially pentacoordinated with the proximal histidine as the sole axial ligand or hexacoordinated with water and histidine. The low spin final product is characterized by the α-CH_3 signals between 15 and 30 ppm, suggesting that the product may be the ferrous heme hexacoordinated with NO and histidine as axial ligands [33]. The ^{1}H NMR spectrum scanned during the evolution of the reaction (reaction time: 304 s) shows the α-CH_3 signals in the 30–15 ppm region and an additional signal in this range (pointed in Fig. 9 with an arrow) not observed in the initial and final spectra that indicates the intermediacy of a low spin adduct. The same pattern is observed with both HNO donors and the hemepeptide MP11, while no intermediate is observed for the reaction with free metalloporphyrins. The reaction rate suggest that HNO initially reacts with MP11 in a similar manner to that observed with others negatively charged metalloporphyrins [13,17], but now leading to a low spin reaction intermediate due to the proximal histidine. Subsequently, it is likely that a change occurs in the conformation of the peptide chain,

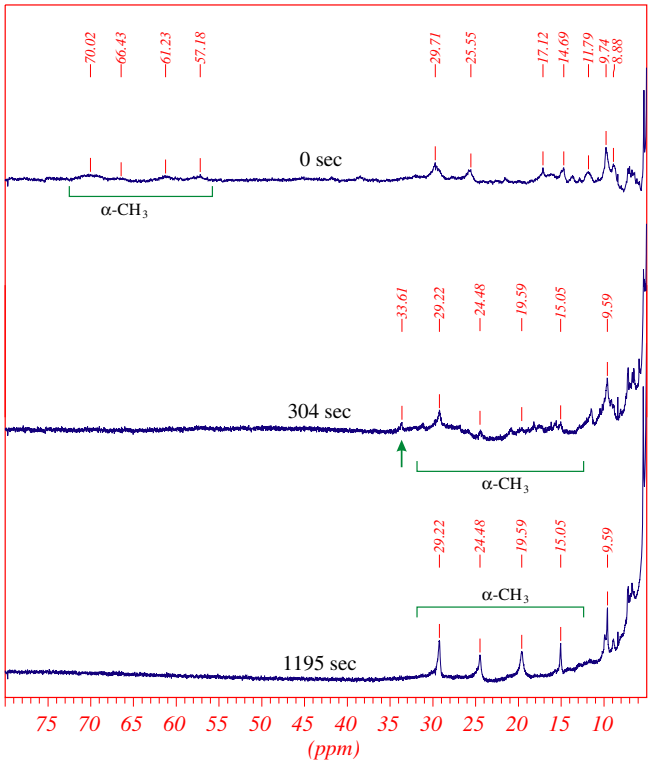


Fig. 9. ^{1}H NMR spectra of the kinetic between MP11 and AS in D_2O at 30 °C under inert atmosphere recorded using a 500 MHz Bruker AM500 spectrometer ($[MP11]_{initial} = 4 \times 10^{-3}$ M and $[AS]_{initial} = 1$ M). 1st spectrum (0 s): MP11; 2nd spectrum (304 s): MP11 (Fe^{III}) + intermediate + Fe^{II}MP11-NO; 3rd spectrum (1195 s): Fe^{II}MP11-NO.

reflected by the UV–Vis and ^{1}H NMR spectroscopic changes, giving rise to the final product.

To obtain additional insight on the intermediate complex between $[Fe^{III}TEPyP]^{5+}$ with AS ($N_2O_3^{2-}$), we have characterized by means of DFT calculations the possible complexes with different coordination patterns (through the N or O atoms) by using a model system of metalloporphyrin, $[Fe^{III}P]^+$. The complex proposed in Scheme 2 and depicted in Fig. 10, coordinated through the N atom, has been found to be the most stable minimum in the potential energy surface. This complex has been found to be more stable than the complexes with AS bound to the metal centre through any of the oxygen atoms. The results also show that the N1–N2(AS) bond length is significantly longer in the $[Fe^{III}P(AS)]^-$ complex than in free AS (2.319 versus 1.371 Å). Furthermore, the N1–N2(AS) bond dissociation energy in the $[Fe^{III}P(AS)]^-$ complex (28.2 kcal/mol), a process which yields as products the $Fe^{II}P$-NO complex and nitrite, is significantly reduced compared to free AS (44.3 kcal/mol). These data support the cleavage of AS assisted by coordination to the metalloporphyrin. The same model system with Mn instead of Fe results in a weaker N1–N2(AS) bond (distance: 2.620 Å, dissociation energy: 19.5 kcal/mol) [17].

The energy of the same process was also calculated for the iron model compound with 5-methylimidazole as sixth ligand, mimicking the coordinated histidine in MP11. Despite the shorter N1–N2 distance in this complex (2.106 Å), the dissociation energy is lower (22.7 kcal/mol) than without the sixth ligand indicating that this intermediate is even less stable than the previous one and probably more difficult to be kinetically detected if formed.

Table 1 summarizes the reported values of k_{on} for nitroxyl donors or nitroxyl and different metalloporphyrins. The data is consistent with two alternative pathways for the reactivity of nitroxyl donors (AS, TSHA) with prophyrin centres in aqueous solutions (Scheme 2). The first one comprises the stepwise assisted decomposition of the donor, enhancing its decomposition rate more than 100 times (through reactions (3) and (4)). Despite the k_{on} for HNO binding are higher than for the donors, the concentration of the donors is four orders of magnitude higher than of the former, leading to a faster pathway for the direct reaction with the donor. This kind of interaction was first observed by our group with Mn^{III} cationic porphyrins [17] and in the present work is also observed with the ferric analogue.

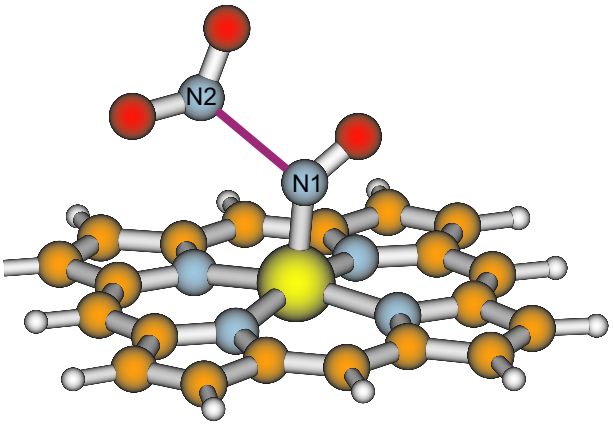
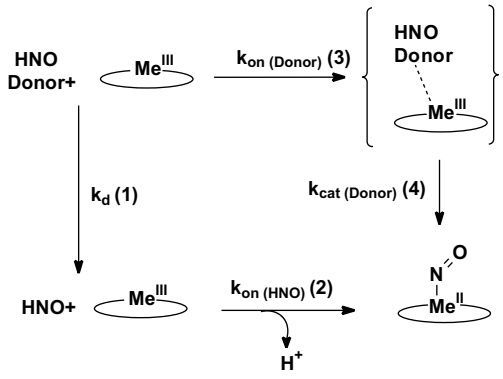


Fig. 10. Optimized DFT structure of the putative intermediate formed by Fe^{III}-Porphyrin and AS.

An interesting point concerning the direct reaction between the donor and the metalloporphyrin is the fact that a possible redox mechanism could be operative for TSHA. Piloty's acid, has been shown to be oxidized by several iron complexes yielding the corresponding radical, which decomposes yielding NO and the reduced metal complex [34]. In our scenario, this mechanism would imply that the reaction proceeds through an intermediate state with the reduced porphyrin (Fe^{II}), radical TSHA and free NO. Afterwards, NO reacts very fast with the reduced iron porphyrin yielding the corresponding nitrosyl complex as the final product, as observed here. However, we cannot discard a mechanism involving an intermediate formed by TSHA and the metalloporphyrin, followed by the NO^- transfer to the porphyrin. Both mechanisms are compatible with our results.

It can be noticed in Table 1 that Fe^{III}MP11 reacts faster with HNO at pH 7 than at pH 10. This is probably due to the fact that in alkaline media the hydroxyl is bound instead of a water molecule, lowering the reaction rate due to the stronger binding.

It is also noteworthy that a positively charged environment seems to be a prerequisite for direct HNO donor–target interaction. Moreover, we found just one study where assisted decomposition of AS by a heme protein (cytochrome P450) is reported [35]. With this picture in mind, direct interaction of HNO donors with biological targets in *in vivo* studies seems to be likely. Furthermore, interpretation of kinetic data from *in vitro* studies under high HNO donor concentrations should be made cautiously. On the other hand, the negatively charged Fe^{III} and Mn^{III} porphyrins and Fe^{III}MP11 react mainly with free HNO. It is not surprising that Fe^{III}MP11 behaves like the anionic porphy-



Scheme 2. Proposed reaction mechanism for HNO donors with metalloporphyrins.

Table 2
Bimolecular rate constants for HNO and NO binding to metalloporphyrins and heme proteins

Target	Reactant	k_{on} (M^{-1} s^{-1})	Ref.
Fe^{III}MP11	HNO	$3.1–6.4 \times 10^4$	this work
Fe^{III}MP11	NO	1.1×10^6	[36]
$[Fe^{III}TPPS]^{3-}$	NO	4.5×10^5	[37]
metMb (Fe^{III})	HNO	8×10^5	[16]
Catalase (Fe^{III})	HNO	3×10^5	[16]
$[Fe^{II}TPPS]^{4-}$	NO	1.5×10^9	[37]
Mb (Fe^{II})	HNO	1.4×10^4	[12]
O_2	HNO	3×10^3	[16]

rins given the proximity of two propionate side chains to the heme pocket. It is also relevant to note that as previously shown [13] free NO possible evolves due to homolytic decomposition of the nitrosyl complexes.

The bimolecular rate constants for HNO binding to the Fe^{III} heme models presented here are quite fast and comparable to the observed reactions rates for NO and HNO reactions with ferric heme systems (Table 2).

It is clear from the data presented in Table 2, that although lacking the protein scaffold, the soluble porphyrins and MP11 display reactivity properties against HNO comparable with the observed reactivity of HNO with heme proteins, which are the main biological targets [16]. The bimolecular rate constants for HNO binding to ferric heme systems are in the order of 10^5–10^6 M^{-1} s^{-1}, similar to the values obtained for NO and probably represent an upper limit for the reaction with ferric hemes. However, these rates are more than 1000 times lower than the corresponding values for NO or CO binding to ferrous hemes [37]. This trend can be explained due to the fact that, for ferric hemes, the ligand binding kinetic is dependent on the lability of the leaving water ligand in contrast with ferrous hemes where the water ligand is weakly bounded [37]. This fact has been shown to play a key role in ligand binding rates in heme proteins [38], therefore it is also expected to be determining towards the reactivity of HNO.

Acknowledgements

This work was financially supported by the University of Buenos Aires, Agencia Nacional de Promoción Científica y Tecnológica, CONICET, and Fundación Antorchas.

References

[1] A.J. Hobbs, J.M. Fukuto, L.J. Ignarro, Proc. Natl. Acad. Sci. U.S.A. 91 (1994) 10992.
[2] H.H.H.W. Schmidt, H. Hofmann, U. Schindler, Z.S. Shutenko, D.D. Cunningham, M. Feelisch, Proc. Natl. Acad. Sci. U.S.A. 93 (1996) 14492.
[3] S. Adak, Q. Wang, D.J. Stuehr, J. Biol. Chem. 275 (2000) 33554.
[4] P. Pagliaro, Life Sci. 73 (2003) 2137.
[5] D.A. Wink, K.M. Miranda, T. Katori, D. Mancardi, D.D. Thomas, L. Ridnour, M.G. Espey, M. Feelisch, C.A. Colton, J.M. Fukuto, P. Pagliaro, D.A. Kass, N. Paolocci, Am. J. Physiol. Heart Circ. Physiol. 285 (2003) H2264.
[6] P. Pagliaro, D. Mancardi, R. Rastaldo, C. Penna, D. Gattullo, K.M. Miranda, M. Feelisch, D.A. Wink, D.A. Kass, N. Paolocci, Free Radical Biol. Med. 34 (2003) 33.
[7] N. Paolocci, T. Katori, H.C. Champion, M.E. St John, K.M. Miranda, J.M. Fukuto, D.A. Wink, D.A. Kass, Proc. Natl. Acad. Sci. U.S.A. 100 (2003) 5537.
[8] D.A. Bazylinski, T.C. Hollocher, J. Am. Chem. Soc. 107 (1985) 7982.
[9] D.A. Bazylinski, J. Goretski, T.C. Hollocher, J. Am. Chem. Soc. 107 (1985) 7986.
[10] M.P. Doyle, S.N. Mahapatro, R.D. Broene, J.K. Guy, J. Am. Chem. Soc. 110 (1988) 593.
[11] K.M. Miranda, R.W. Nims, D.D. Thomasa, M.G. Espey, D. Citrin, M.D. Bartberger, N. Paolocci, J.M. Fukuto, M. Feelisch, D.A. Wink, J. Inorg. Biochem. 93 (2003) 52.
[12] F. Sulc, C.E. Immoos, D. Pervitsky, P.J. Farmer, J. Am. Chem. Soc. 126 (2004) 1096.
[13] S.E. Bari, M.A. Marti, V.T. Amorebieta, D.A. Estrin, F. Doctorovich, J. Am. Chem. Soc. 125 (2003) 15272.
[14] P.S.Y. Wong, J. Hyun, J.M. Fukuto, F.N. Shirota, E.G. DeMaster, D.W. Shoeman, H.T. Nagasawa, Biochemistry 37 (1998) 5362.
[15] V. Shafirovich, S.V. Lymar, Proc. Natl. Acad. Sci. U.S.A. 99 (2002) 7340.
[16] K.M. Miranda, N. Paolocci, T. Katori, D.D. Thomas, E. Ford, M.D. Bartberger, M.G. Espey, D.A. Kass, M. Feelisch, J.M. Fukuto, D.A. Wink, Proc. Natl. Acad. Sci. U.S.A. 100 (2003) 9196.
[17] M.A. Marti, S.E. Bari, D.A. Estrin, F. Doctorovich, J. Am. Chem. Soc. 127 (2005) 4680.
[18] D.A. Bazylinski, T.C. Hollocher, Inorg. Chem. 24 (1985) 4285.
[19] A.S. Dutton, J.M. Fukuto, K.N. Houk, J. Am. Chem. Soc. 126 (2004) 3795.
[20] F.T. Bonner, Y.H. Ko, Inorg. Chem. 31 (1992) 2514.
[21] F. Seel, C. Bliefert, Z. Anorg. Allg. Chem. 394 (1972) 187.
[22] M.N. Hughes, R. Cammack, Nitric Oxide, Pt C 301 (1999) 279.
[23] M.N. Hughes, P.E. Wimbledon, J. Chem. Soc., Dalton Trans. (1976) 703.
[24] F.T. Bonner, B. Ravid, Inorg. Chem. 14 (1975) 558.
[25] M.J. Akhtar, C.A. Lutz, F.T. Bonner, Inorg. Chem. 18 (1979) 2369.
[26] J.M. Soler, E. Artacho, J.D. Gale, A. Garcia, J. Junquera, P. Ordejon, D. Sanchez-Portal, J. Phys. Condens. Matter 14 (2002) 2745.
[27] S. Reich, C. Thomsen, P. Ordejon, Phys. Rev. B 65 (2002) 155411.
[28] N. Troullier, J.L. Martins, Phys. Rev. B 43 (1991) 1993.
[29] S.G. Louie, S. Froyen, M.L. Cohen, Phys. Rev. B 26 (1982) 1738.
[30] J.P. Perdew, K. Burke, M. Ernzerhof, Phys. Rev. Lett. 77 (1996) 3865.
[31] L. Capece, M.A. Marti, A. Crespo, F. Doctorovich, D.A. Estrin, J. Am. Chem. Soc. 128 (2006) 12455.
[32] A. Crespo, M.A. Marti, S.G. Kalko, A. Morreale, M. Orozco, J.L. Gelpi, F.J. Luque, D.A. Estrin, J. Am. Chem. Soc. 127 (2005) 4433.
[33] NMR and EPR, in: K.M. Kadish, K.M. Smith, R. Guilard (Eds.), The Porphyrin Handbook, Academic Press, San Diego, 2000.
[34] P.C. Wilkins, H.K. Jacobs, M.D. Johnson, A.S. Gopalan, Inorg. Chem. 43 (2004) 7877.
[35] Y. Shibata, H. Sato, I. Sagami, T. Shimizu, Biochim. Biophys. Acta Protein Struct. Mol. Enzymol. 1343 (1997) 67.
[36] V.S. Sharma, R.A. Isaacson, M.E. John, M.R. Waterman, M. Chevion, Biochemistry 22 (1983) 3897.
[37] L.E. Laverman, P.C. Ford, J. Am. Chem. Soc. 123 (2001) 11614.
[38] E.E. Scott, Q.H. Gibson, J.S. Olson, J. Biol. Chem. 276 (2001) 5177.

2. Computation details

DFT calculations with the hybrid exchange-correlation functional B3LYP [11] were carried out using the GAUSSIAN03 [12] package. Unless otherwise noted, the geometry of the compounds of interest was optimized in the LanL2DZ [13,14] basis set. The spin-unrestricted UB3LYP method was used for the open-shell systems, and the Kohn–Sham orbital diagrams for these compounds were obtained using the restricted open-shell B3LYP method. Partial atomic charges and orbitals occupations were computed according to the natural atomic orbital (NAO) schemes.[1] Molecular orbitals were plotted using MOLEKEL 4.3 [15].

For the closed-shell systems the Mayer's bond orders [8,9] are calculated as

$$B_{AB} = \sum_{\mu\in A}\sum_{\nu\in B}(\mathbf{DS})_{\mu\nu}(\mathbf{DS})_{\nu\mu}. \quad (1)$$

Here **S** is the overlap matrix and **D** is the spinless density matrix, $\mathbf{D} = \mathbf{P}^{\alpha} + \mathbf{P}^{\beta}$:

$$D_{\mu\nu} = 2\sum_{i}^{occ.} C_{\mu i}C^{*}_{\nu i}; \quad P^{\alpha}_{\mu\nu} = \sum_{i\in\alpha}^{occ.} C_{\mu i}C^{*}_{\nu i}; \quad P^{\beta}_{\mu\nu} = \sum_{i\in\beta}^{occ.} C_{\mu i}C^{*}_{\nu i}, \quad (2)$$

where **C** is the matrix of MO coefficients. In the case of the open-shell systems the Mayer's bond orders are calculated as [8,9]

$$\begin{aligned} B_{AB} &= \sum_{\mu\in A}\sum_{\nu\in B}[(\mathbf{DS})_{\mu\nu}(\mathbf{DS})_{\nu\mu} + (\mathbf{QS})_{\mu\nu}(\mathbf{QS})_{\nu\mu}] \\ &= 2\sum_{\mu\in A}\sum_{\nu\in B}[(\mathbf{P}^{\alpha}\mathbf{S})_{\mu\nu}(\mathbf{P}^{\alpha}\mathbf{S})_{\nu\mu} + (\mathbf{P}^{\beta}\mathbf{S})_{\mu\nu}(\mathbf{P}^{\beta}\mathbf{S})_{\nu\mu}], \end{aligned} \quad (3)$$

where **Q** is the spin density matrix, $\mathbf{Q} = \mathbf{P}^{\alpha} - \mathbf{P}^{\beta}$. For the closed shell systems the Wiberg's bond order indices are calculated in the NAO[2] [18,19] basis as

$$W_{AB} = \sum_{\mu\in A}\sum_{\nu\in B}(D^{NAO}_{\mu\nu})^2 \quad (4)$$

and for the open shell systems [8,9] as

$$\begin{aligned} W_{AB} &= 2\sum_{\mu\in A}\sum_{\nu\in B}[(P^{\alpha,NAO}_{\mu\nu})^2 + (P^{\beta,NAO}_{\mu\nu})^2] \\ &= 2(W^{\alpha}_{AB} + W^{\beta}_{AB}). \end{aligned} \quad (5)$$

We use the local cylindrical symmetry model to break down the A–B bond order index into σ-, π-, and δ-contributions, i.e. $C_{\infty v}$ local symmetry is assumed for each bond. For any given pair of atoms A and B the coordinate system is transformed so, that the *z*-axis would coincide with the bonding line between these two atoms. Depending on the orientation of orbitals μ and ν in respect to the *z*-axis the corresponding term in Eqs. (1), (3), (4), (5) is assigned to σ-, π- or δ-contribution, as illustrated by the Mayer index for the closed shell systems:

$$\begin{aligned} B_{AB} &= \sum_{\substack{\mu\in A\\ \mu\in\sigma}}\sum_{\substack{\nu\in B\\ \nu\in\sigma}}((PS)_{\mu\nu}(PS)_{\nu\mu}) + \sum_{\substack{\mu\in A\\ \mu\in\pi}}\sum_{\substack{\nu\in B\\ \nu\in\pi}}((PS)_{\mu\nu}(PS)_{\nu\mu}) \\ &\quad + \sum_{\substack{\mu\in A\\ \mu\in\delta}}\sum_{\substack{\nu\in B\\ \nu\in\delta}}((PS)_{\mu\nu}(PS)_{\nu\mu}) + \text{residual} \\ &= (B_{AB})_{\sigma} + (B_{AB})_{\pi} + (B_{AB})_{\delta} + (B_{AB})_{res}. \end{aligned} \quad (6)$$

The last term, B_{res}, covers all cases, for which the μ and ν orbitals do not belong to the same type (σ, π or δ). A similar procedure is used for the calculation of W_{AB}. For the open-shell systems the technique is modified appropriately. The method was tested for a set of compounds with various types of chemical bonds, including a number of molecules with cyclic structures.[3] The largest "residual" contributions were found for molecules with small cycles. The validity of this procedure for each bond can be monitored through the B_{res} (or W_{res}) value: if the 'residual component' is not negligible then $B \neq B_{\sigma} + B_{\pi} + B_{\delta}$ and the bond indices analysis discussed above is impossible. Detailed description of the method will be given elsewhere (work in progress).

3. Results and discussion

3.1. Free NO molecule, NO^+ and NO^- ions

Nitric oxide is a stable free radical, the unpaired electron in this molecule resides on a π^* molecular orbital. According to the qualitative molecular orbitals theory, the "classical" bond order in a diatomic molecule is

$$BO = \frac{N_{bond} - N_{antibond}}{2}, \quad (7)$$

where N_{bond} and $N_{antibond}$ are the number of electrons on the bonding and antibonding MO's, respectively. These bond orders can be easily separated into σ, π, and δ-contributions by sorting the MO's according to their symmetry. For the free nitric oxide and its ions the classical bond orders are:

	NO^+	NO^0	NO^-
	$(\sigma)^{10}(\pi)^4(\pi^*)^0$	$(\sigma)^{10}(\pi)^4(\pi^*)^1$	$(\sigma)^{10}(\pi)^4(\pi^*)^2$
BO	3	2.5	2
BO_{σ}	1	1	1
BO_{π}	2	1.5	1

[1] For all dimetal complexes, except $Ru_2(dpf)_4$ and $Ru_2(dpf)_4(NO)_2$, the structural information, MO and NBO analysis are obtained from earlier DFT calculations described in Refs. [16,17].

[2] The possibility of Wiberg indices calculation using the Lowdin orbitals, $W^{(L)}$, has also been considered.

[3] From the B3LYP/cc-pvdz calculation for benzene molecule we found $B_{CC} = 1.46$, $B_{\sigma} = 0.92$, $B_{\pi} = 0.54$, $W_{CC} = 1.44$, $W_{\sigma} = 0.96$, $W_{\pi} = 0.47$, and $B_{res} = W_{res} = 0$. This is in good agreement with the values of $B_{\sigma} = 1.00$ and $B_{\pi} = 0.45$ obtained in Ref. [20] for B3LYP/cc-pvdz using a different scheme of analysis.

Table 1
Bond lengths, r (Å), stretching frequencies ν (cm^{-1}), and bond indices (B, $W^{(L)}$, and W) for the free species NO^+, NO, and NO^-

		NO^+	NO^0	NO^-
LanL2DZ	r	1.106	1.199	1.333
	ν	2220	1770	1289
	B	2.64	2.11	1.64
	B_σ	0.78	0.82	0.89
	B_π	1.86	1.29	0.75
	$W^{(L)}$	3.36	2.58	1.79
	$W_\sigma^{(L)}$	1.48	1.41	1.32
	$W_\pi^{(L)}$	1.88	1.16	0.47
	W	2.80	2.30	1.78
	W_σ	0.97	0.96	0.96
	W_π	1.83	1.34	0.83
6-31G*	r	1.073	1.158	1.279
	ν	2484	1995	1464
	B	2.66	2.18	1.72
	B_σ	0.79	0.84	0.89
	B_π	1.87	1.35	0.82
	$W^{(L)}$	3.39	2.72	1.94
	$W_\sigma^{(L)}$	1.50	1.42	1.32
	$W_\pi^{(L)}$	1.89	1.30	0.62
	W	2.79	2.31	1.80
	W_σ	0.97	0.96	0.96
	W_π	1.83	1.35	0.84
cc-pvdz	r	1.067	1.154	1.277
	ν	2492	1994	1456
	B	2.75	2.26	1.77
	B_σ	0.86	0.91	0.95
	B_π	1.89	1.35	0.82
	$W^{(L)}$	3.37	2.66	1.87
	$W_\sigma^{(L)}$	1.46	1.38	1.29
	$W_\pi^{(L)}$	1.91	1.28	0.58
	W	2.80	2.32	1.80
	W_σ	0.97	0.97	0.96
	W_π	1.83	1.35	0.84

The population of the π^* orbital in the row NO^+, NO^0, NO^- leads to the increase in the bond length (experimental values: 1.06 Å, 1.154 Å, 1.26 Å respectively) and to the decrease in the IR stretching frequencies ν(NO) from 2377 (NO^+) through 1875 (NO) to 1470 cm^{-1} (NO^-) [3,21]. The calculated bond lengths, vibrational frequencies, bond orders and their components for these species are given in Table 1.

As a rule the Wiberg bond indices, computed using the Lowdin orbitals, $W^{(L)}$, are overestimated,[4] especially their σ-component. The quantum chemical bond orders B, B_σ, B_π, W, W_σ, and W_π (Table 1) correlate well with the classical BO values and reliably discriminate between different oxidation states of nitric oxide. The σ-bond order is close to 1 and is almost constant in the series NO^+, NO^0, NO^-. The difference between oxidation states is reflected by B_π or W_π indices. The basis set dependence is more pronounced for the Mayer indices than for the Wiberg indices.

3.2. Ruthenium six-coordinate nitrosyl complexes

The well-known robustness of the linear $\{RuNO\}^n$ group in six-coordinate ruthenium nitrosyls is the obvious explanation of the fact that ruthenium forms more nitrosyls than any other metal [2]. Therefore, we shall start from the analysis of the bonding in these compounds. The calculated values of NO charge (q(NO)), σ- and π-electron population (n_σ and n_π), bond lengths (r) and bond orders for the $[Ru(NO)Cl_5]^{2-}$ complex (symmetry C_{4v}) are given in Table 2. Preferring the NAO-based results to the Mulliken/Mayer scheme, we took into account that: (i) Mulliken populations and Mayer bond orders (q_{Mull}, B_{AB}) are much more dependent on the basis set than corresponding values based on the NAO approach (q_{NAO}, W_{AB}); (ii) the high B(Ru–Cl) indices are not realistic; (iii) negative values of B_{AB} were obtained for some compounds. For these reasons we choose the NAO-based technique for further analysis and discussion. Due to the weak basis set dependence of the bond indices obtained via this approach, the following calculations were performed at the B3LYP/L an L2DZ level.

Since the residual contributions were not found for B and W indices, the analysis of their σ- and π-components is valid. In Fig. 1 the W_{AB} indices for the anionic, neutral, and cationic complexes with linear $\{RuNO\}^6$ group: $[Ru(NO)(CN)_5]^{2-}$, [Ru(NO)hedta] (hedta is the triple-charged anion *N*-(hydroxyethyl)ethylenediaminetriacetate), $[Ru(NO)(NH_3)_5]^{3+}$ are presented. In all cases the N–O σ-bond orders are almost the same as in the free NO, NO^+, and NO^- species. The N–O π-bond orders are close to that for NO^-(Tables 1 and 2; Fig. 1). The prevailing contribution to the Ru–N bonding is brought by the π-component with a bond index of about 1. Note that according to the EDA analysis [27] for the $[Ru(NO)(CN)_5]^{2-}$ complex also there is a significant (ca. 70 %) contribution of the π-orbital interaction to the M–NO covalent bonding [28]. A comparison of Ru–C bond orders in $[Ru(CN)_6]^{4-}$, $[Ru(CN)_6]^{3-}$ ($W_\sigma = 0.43-0.44$, $W_\pi = 0.08-0.09$), and $[Ru(NO)(CN)_5]^{2-}$ complexes (Fig. 1) shows that *cis*- and *trans*-influence of nitric oxide is relatively small, the most noticeable effect being the slight increase of W_σ(Ru–C_{trans}).

For all complexes, regardless of the computational method and basis set used, unusually large values of through-atom indices (TAI) B_{RuO} and W_{RuO} were obtained (see Scheme 1).

The emergence of TAI(Ru–O) is due to the d_π(Ru) and π^*(NO) orbital mixing and, consequently, to large values of $D_{\mu\nu}$ and $(\mathbf{DS})_{\mu\nu}$ for $\mu = d_{xz}$(Ru) and $\nu = p_x$(O), and for $\mu = d_{yz}$(Ru) and $\nu = p_y$(O). Thus, the non-zero TAI suggests delocalization of the π-electron density over the linear fragment and is not likely to be an artefact. It is worth

[4] This effect was also noted in a recent work [24], devoted to the analysis of bond orders in the iso-nitrous acid complexes.

Table 2
Populations of NO σ- and π-orbitals, n(σ) n(π), NO charge, q(NO), bond lengths, r (Å)[a], Mayer (B) and Wiberg (W) bond orders and their components for the $[RuNO(Cl)_5]^{2-}$ complex calculated by the B3LYP method

		3-21G	LanL2DZ	DZVP	DZVP(Ru,Cl)6-31+G*(N,O)
$n(\sigma)_{Mulliken}$		9.81	9.74	9.69	9.48
$n(\pi)_{Mulliken}$		5.32	5.35	5.38	5.36
$q(NO)_{Mulliken}$		−0.12	−0.09	−0.07	+0.16
$n(\sigma)_{NAO}$		9.68	9.64	9.67	9.67
$n(\pi)_{NAO}$		5.31	5.28	5.28	5.31
$q(NO)_{NAO}$		+0.01	+0.08	+0.06	+0.02
N–O	r	1.190	1.206	1.170	1.165
	B	1.58	1.61	1.70	1.69
	B_σ	0.80	0.84	0.88	0.79
	B_π	0.78	0.76	0.82	0.90
	W	1.78	1.80	1.80	1.80
	W_σ	0.97	0.98	0.98	0.98
	W_π	0.81	0.82	0.82	0.81
Ru–N	r	1.794	1.740	1.747	1.745
	B	1.29	1.43	1.56	1.46
	B_σ	0.20	0.33	0.38	0.32
	B_π	1.09	1.10	1.17	1.14
	W	1.46	1.43	1.43	1.45
	W_σ	0.42	0.43	0.42	0.43
	W_π	1.04	1.00	1.01	1.03
Ru–O	r	2.939	2.945	2.917	2.909
	B	0.61	0.53	0.47	0.38
	B_σ	0.06	0.06	0.05	−0.01
	B_π	0.55	0.47	0.42	0.39
	W	0.58	0.50	0.50	0.50
	W_σ	0.03	0.03	0.04	0.03
	W_π	0.54	0.47	0.47	0.47
Ru–Cl_{trans}	r	2.418	2.429	2.405	2.406
	B	0.77	0.81	0.70	0.71
	B_σ	0.58	0.60	0.53	0.55
	B_π	0.19	0.21	0.17	0.16
	W	0.48	0.47	0.48	0.48
	W_σ	0.42	0.39	0.40	0.40
	W_π	0.06	0.08	0.07	0.07
Ru–Cl_{cis}	r	2.511	2.520	2.492	2.490
	B	0.73	0.81	0.64	0.70
	B_σ	0.60	0.65	0.55	0.65
	B_π	0.12	0.14	0.08	0.03
	W	0.47	0.48	0.46	0.46
	W_σ	0.44	0.45	0.44	0.44
	W_π	0.01	0.02	0.02	0.02

[a] Experimental values (Å): r(Ru–N) = 1.738; 1.747; r(N–O) = 1.131; 1.112; r(Ru–Cl_{trans}) = 2.357; r(Ru–Cl_{cis}) = 2.375 [22,23].

mentioning that significant TAI's were found for a number of linear organic and inorganic molecules with multiple bonds, such as CO_2, N_2O, HCNO, $H_2C{=}C{=}C{=}CH_2$, $HC{\equiv}C{-}C{\equiv}CH$, $N{\equiv}C{-}C{\equiv}N$, etc., as well as for carbonyl complexes, though in the latter case the TAI-values are only about a half of those for $\{RuNO\}^6$. The predominant contribution to the TAI is always due to the π-component. For the {RuCN} fragments the Ru–N TAI's are negligibly small (Fig. 1), including those for the bridging CN group in $[(NO)Ru(py)_4{-}N{-}C{-}Ru(py)_4(CN)]^{3-}$ (Scheme 2).

In the $\{RuNO\}^6$ complexes the charge on NO is close to zero, the triple-charged $[Ru(NO)(NH_3)_5]^{3+}$ cation being the only exception to this rule. The total number of electrons on the π-orbitals, n_π(NO), is higher than for the free NO molecule, while for the σ-orbitals n_σ(NO) is lower by approximately the same value. The natural occupancies of ruthenium d-orbitals (Table 4) in octahedral nitrosyl complexes correspond to Ru^{III} oxidation state and d^5 electronic configuration: the $n(d_\pi) = n(d_{xz}) + n(d_{yz})$ values reflect the oxidation state of the metal, at the same time $n(d_{z^2})$ and $n(d_{x^2-y^2})$ values reflect the σ-donor properties of the ligands. In the bridged $[(NO)Ru(py)_4NCRu(py)_4(CN)]^{3-}$ complex both of the Ru atoms are surrounded by π-acceptor ligands, therefore the d_π occupancies (3.12

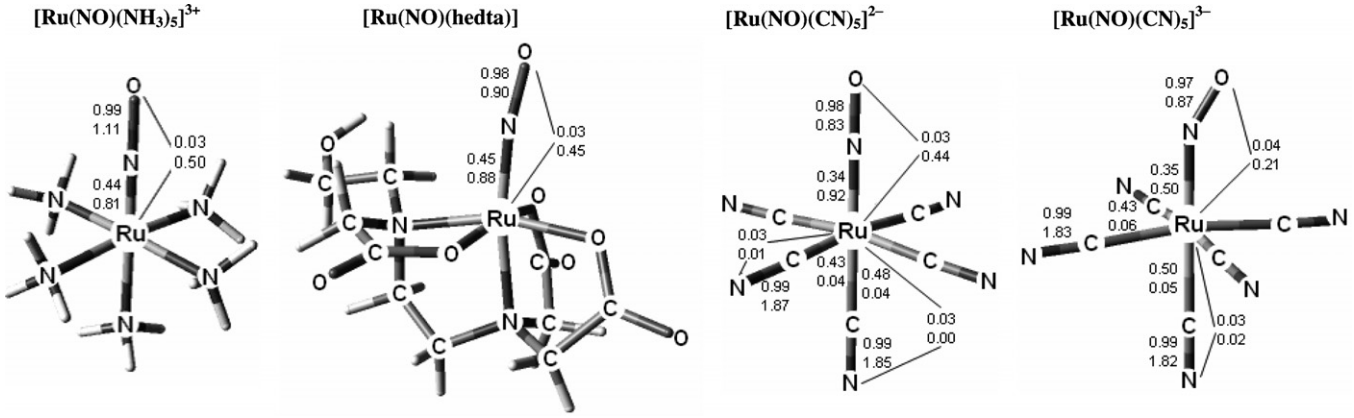
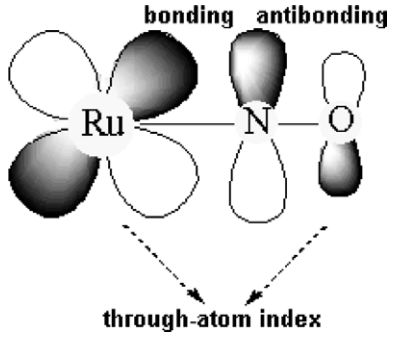
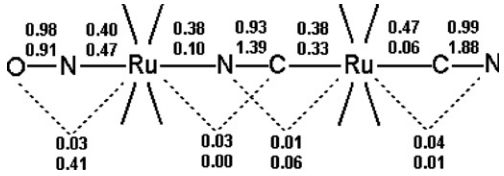


Fig. 1. W_σ (upper value) and W_π (lower value) indices for the six-coordinate nitrosyl complexes of ruthenium.



Scheme 1.



Scheme 2.

and 3.57) are significantly lower than 4, at that binuclear compound exhibits some features of a mixed-valence complex.

Taking into account the calculated charges on the NO ligand, the interpretation of the nitrosyl complexes as compounds of Ru^{III} and NO^0 appears reasonable[5] despite the fact that the N–O bond order is lower than that for the free molecule, and is closer to the value characteristic for NO^-. The latter phenomenon can be explained by the high degree of delocalization in the three-center M–N–O fragment. The unique π-bond order index for Ru–N, which is almost as high as 1, provides sufficient basis to treat Ru–N as a polar covalent bond. Since nitric oxide is a radical with the unpaired electron on a π^* orbital, the optimal conditions for the formation of the covalent M–NO bond are achieved when the d_{xz} and d_{yz} AO of the metal atom are occupied by 1.5 electrons each. In this case the electron pairs $1.5e(d_{xz}) + 0.5e(\pi_x^*)$ and $1.5e(d_{yz}) + 0.5e(\pi_y^*)$ occupy the {MNO}-delocalized orbitals, which are bonding in respect to M–N and antibonding in respect to N–O. Analyzing the M–NO linkage in terms of Green's covalent bond classification [30], Landry et al. [31] conclude that the metal atom is required to contribute three electrons to the metal–nitrosyl bonding interaction, which is in complete agreement with our results. The Ru–N σ-bond is a typical donor acceptor $d_{z^2} \leftarrow \sigma$ (N) bond with $W_\sigma \sim 0.4$, and is localized in the interatomic region.

The increase of the number of electrons in the $\{MNO\}^n$ group to $n = 7$ prohibits the covalent bond formation scheme discussed above. The reasons of M–N–O group bending in complexes with $n > 6$ were discussed in detail in [5,32,33]. We address this issue from the point of view of bond order analysis. Two examples are considered: (i) $[Ru(NO)(CN)_5]^{2-}$ ($n = 6$) and $[Ru(NO)(CN)_5]^{3-}$ ($n = 7$; angle $RuNO = 146^0$ [25]) complexes, and (ii) [Ru(NO)(hedta)] ($n = 6$), $[Ru(NO)(hedta)]^-$ ($n = 7$), $[Ru(NO)(hedta)]^{2-}$ ($n = 8$) series. The N–O bond orders in $[Ru(NO)(hedta)]^q$ were analyzed in Ref. [26] in conjunction with experimental IR stretching frequencies ν(NO). From the Fig. 1 it follows that the π-bond order in $[Ru(NO)(CN)_5]^{3-}$ is almost twice less than $[Ru(NO)(CN)_5]^{2-}$. For the former complex the primary contribution (0.38–0.50) to W_π(Ru–N) is delivered by the π_y component, which is orthogonal to the Ru–N–O plane. This component of the π-bond does not change significantly as compared with the $[Ru(NO)(CN)_5]^{2-}$ complex, which is also true for d_{yz} and π_y^*(NO) orbital occupancies. The in-plane contribution is drastically diminished due to the decrease of the π^*(NO) contribution into the bonding MO (Fig. 2b) and the occupation of the antibonding orbital (Fig. 2c) with

[5] This is in agreement with the calculated bond lengths and the IR stretching frequencies ν(NO). The preferential interpretation of the coordinated nitric oxide as NO^0 is also confirmed by the energy decomposition analysis (EDA) and by the representation of the multiconfigurational wave function in the form of linear combinations of the valence bond structures [28,29].

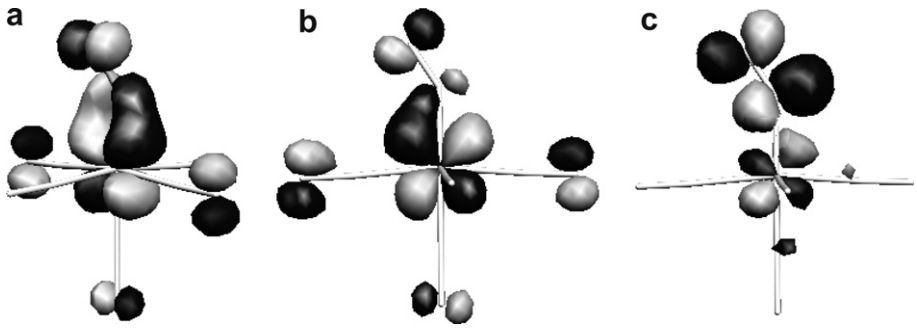


Fig. 2. Molecular π-orbitals of the complex $[Ru(NO)(CN)_5]^{3-}$ with the main contributions of {RuNO} group: orthogonal to the Ru–N–O plane (a), in the Ru–N–O plane (b) and singly occupied molecular orbital (SOMO) in the Ru–N–O plane (c).

consequent compensation of the bonding and antibonding $d_\pi - \pi^*(NO)$ interactions. The TAI(Ru–O) decreases as well. The unpaired electron in the $\{MNO\}^7$complex is distributed between d_{xz} and $\pi_x^*(NO)$, leading to a negative charge on the NO ligand (−0.22).

Similar trends can be observed for the changes of structural parameters and bond orders as we go from $\{RuNO\}^6$ to $\{RuNO\}^7$ in the $[Ru(NO)(hedta)]^q$ (Table 3) series. The further addition of one more electron to $\{RuNO\}^7$ leads to the almost complete destruction of the in-plane Ru–NO π-bond. The out-of-plane π_y-components of the Ru–NO and N–O bonds still remain unchanged. The contribution of s(Ru) into W_σ(Ru–N) is almost the same for these three compounds (0.11–0.12), while the d_{z^2}(Ru) contribution increases from 0.31 ($q = 0$) through 0.36 ($q = -1$) to 0.51 ($q = -2$) due to the mixing of d_{z^2} and π_x^* orbitals in the complexes with the bent {RuNO} group. The increase of π_x^*(NO) population leads to a noticeable negative charge on NO, and is accompanied by the destruction of the intraligand π_x-bond. So, the bond order indices and their components demonstrated sufficient sensitivity to the changes in the {RuNO} group ligand environment and the metal oxidation state and therefore can be used to describe the specific features of MNO bonding.

Table 3
Optimized (B3LYP/LanL2DZ) values of the bond length Ru–N (r, Å) and RuNO angle (°), IR stretching frequency ν(NO) (cm^{-1}), NAO populations for the dπ(Ru), σ(NO), and π(NO)–orbitals, NO charge and Wiberg–NAO bond indices for the complexes $[Ru(NO)(hedta)]^q$; $n = 6 - q$ is the number of π-electrons in the $\{RuNO\}^n$ fragment

q	0	−1	−2
n	6	7	8
r(Ru–N)	1.771	1.867	1.890
∠RuNO	171	144	126
ν(NO)[a]	1819	1567	1350
$n(d_{xz})$	1.48	1.79	1.88
$n(d_{yz})$	1.51	1.59	1.60
n_σ(NO)	9.64	9.70	9.79
n_π(NO)	5.18	5.46	5.77
$n_{\pi x}$(NO)	2.60	3.01	3.36
$n_{\pi y}$(NO)	2.58	2.46	2.41
q(NO)	+0.17	−0.17	−0.57
W(Ru–N)	1.34	1.10	1.14
W_σ	0.45	0.49	0.64
W_π	0.88	0.56	0.44
$W_{\pi x}$	0.44	0.15	0.04
$W_{\pi y}$	0.44	0.41	0.40
W_r	0.01	0.05	0.07
W(N–O)	1.89	1.85	1.61
W_σ	0.98	0.98	0.96
W_π	0.90	0.87	0.65
W(Ru–O)	0.50	0.37	0.37
W_σ	0.03	0.05	0.10
W_π	0.45	0.26	0.02
W_r	0.02	0.06	0.08

[a] Experimental values are 1848, 1858, and 1383 cm^{-1} for $[Ru(NO)(hedta)]$, $[Ru(NO)(hedta)]^-$, and $[Ru(NO)(hedta)]^{-2}$, respectively [26].

3.3. Paddlewheel dimetal $M_2(BL)_4$ and $M_2(BL)_4(L)_2$ complexes

The geometrical parameters of the dimetal carboxylates $M_2(O_2CR)_4$ and $M_2(O_2CR)_4(NO)_2$ (M = Rh and Ru) optimized by the B3LYP method with two basis sets and the results of the NBO analysis were presented earlier [16,17]. In this work the geometries of $Ru_2(dpf)_4$ and $Ru_2(dpf)_4(NO)_2$ were fully optimized without symmetry constraints, and the minimum energy structures were verified by vibration frequencies calculations. We also considered a possibility of replacement of the phenyl fragments in dpf by hydrogen atoms (model complexes $Ru_2(dHf)_4$ and $Ru_2(dHf)_4(NO)_2$). It was found that this model reproduces the main distinctive features of N,N-bridging ligands (electronic configuration of the diruthenium core, Ru–Ru bond length and bond order, etc.), although the values of Ru–N–O and Ru–Ru–$N_{(NO)}$ angles are noticeably underestimated (Table 5).

Paddlewheel dimetal $M_2(BL)_4$ complexes belong to the relatively few polyatomic compounds, for which Eq. (7) is in use. If both metal atoms are placed on the z axis, their d_{z^2}-orbitals are responsible for the σ-bonding, d_{xz} and d_{yz} – for the π-bonding, d_{xy} and $d_{x^2-y^2}$ – for the δ-bonding.[6] The metal–metal bond order is determined by the electron number and consecution of MO's occupation. In the dimetal cores under consideration all bonding MO's $\{\sigma^2\pi^4\delta^2\}$ are

[6] The $d_{x^2-y^2}$ orbitals form the σ-bonds with the bridging ligands, usually they are regarded as unoccupied and so are excluded from consideration at the estimation of the bond order by Eq. (7).

Table 4
Natural d-atomic orbital occupancies of ruthenium in six-coordinate $[RuX_5L]^q$, $[Ru(NO)X_4L]^q$, and binuclear bridged complexes[a]

	d_{z^2}	$d_{x^2-y^2}$	$d_{xz} + d_{yz}$	d_{xy}
$[Ru^{II}(NH_3)_6]^{2+}$	0.63	0.63	3.96	1.98
$[Ru^{II}(NH_3)_5(H_2O)]^{2+}$	0.56	0.64	3.96	1.97
$[Ru^{III}(NH_3)_5(H_2O)]^{3+}$	0.79	0.84	3.05	1.97
$[Ru(NO)(NH_3)_5]^{3+}$	0.95	0.92	3.11	1.98
$[Ru(NO)(NH_3)_4(H_2O)]^{3+}$	0.84	0.92	3.15	1.98
$[Ru^{II}(CN)_6]^{4-}$	1.16	1.16	3.72	1.86
$[Ru^{II}(CN)_5(H_2O)]^{3-}$	1.00	1.15	3.74	1.85
$[Ru^{III}(CN)_5(H_2O)]^{2-}$	1.11	1.24	3.06	1.90
$[Ru(NO)(CN)_5]^{2-}$	1.25	1.33	2.93	1.93
$[(NO)(py)_4RuNCRu(py)_4(CN)]^{3-}$: {Ru(py)$_4$(CN)}	1.09	0.81	3.51	1.92
$[(NO)(py)_4RuNCRu(py)_4(CN)]^{3-}$: {(NO)(py)$_4$Ru}	0.98	0.94	3.12	1.96

[a] L or NO ligands are placed on the z axis.

Table 5
Calculated and experimental metal–metal bond length (Å), angle MNO (°), and stretching frequencies ν(NO) (cm^{-1}) for the complexes $M_2(BL)_4(NO)_2$

M	Rh		Ru				
BL	O_2CH	O_2CCH_3	O_2CH	O_2CCH_3	O_2CCF_3	dHf	dpf
	B3LYP/LanL2DZ						
r(M–M)	2.632	2.610	2.613	2.593	2.613	2.685	2.667
∠MNO	121.07	121.12	149.84	150.68	152.83	141.33	156.18; 157.63
ν(NO)	1652; 1692	1634; 1674	1729; 1749	1711; 1730	1776; 1795	1597; 1611	1659; (1666) 1674
	Experiment [34–37]						
r(M–M)		2.513		2.515 (R = Et)	2.532		2.632
∠MNO		121.04		152.45 (R = Et)	152.83		160.79; 164.44
ν(NO)		1729; 1694		1756	1800		1726

occupied. In the case of $\{Ru_2\}^{4+}$ core there are four electrons on the antibonding π*- and δ*-orbitals (double metal–metal bond; spin-triplet ground state); in the case of $\{Rh_2\}^{4+}$ there are six electrons on these orbitals (single metal–metal bond; closed-shell ground state) (Table 5).

Norman, Renzoni, and Case showed that the highest occupied orbitals of $\{Ru_2\}^{4+}$ compounds, π* and δ*, were likely to be close in energy, and pointed out that the δ*-orbital interacts significantly with the lower lying carboxylate orbitals, while the π* does not [38]. Cotton and Matusz noticed that N,N-ligands may differ a lot from carboxyl groups in their influence on the relative energies of the Ru–Ru bonding and antibonding orbitals [39]. Indeed, the replacement of $BL = O_2CH^-$ by the stronger electron donor dpf^- leads to the increase of the $d_{x^2-y^2}$ population and to the increase of energy splitting for the MO's δ* ($d_{xy} - d_{xy}$) ± π(X) (X = O or N in bridging ligands). As a result, energy of the antibonding MO with dominant δ* contribution is higher than the π*(Ru–Ru) energy level (Fig. 3), therefore the electronic configurations of these complexes are different: $(\pi^*)^2(\delta^*)^2$ ($Ru_2(O_2CR)_4$) and $(\pi^*)^3(\delta^*)^1$ ($Ru_2(dpf)_4$). For the second of these complexes the greater metal–metal distance reflects the smaller strength of δ-bonding in comparison with π-bonding. The calculated W_{MM}, W_σ, W_π, and W_δ values (Table 6) correctly describe the above mentioned distinctions in the bonds between the metal atoms in three complexes. The low (~0.2) values of B_δ(Ru–Ru) and W_δ(Ru–Ru) as compared with the classical bond order $BO_\delta(Ru–Ru) = 0.5$ for the $Ru_2(dpf)_4$ complex can be explained by the participation of δ-orbitals in the bonds with bridging ligands.

Complexes $M_2(BL)_4(NO)_2$ are a remarkable example of compounds in which the NO molecule is in *trans*-position to the covalent metal–metal bond. All dinitrosyl complexes considered here have closed-shell ground states, though for $Ru_2(dpf)_4(NO)_2$ the singlet and triplet states are nearly degenerate. As a result of NO coordination, the orbital diagrams change essentially (Figs. 3 and 4). In the series $Rh_2(O_2CR)_4(NO)_2$, $Ru_2(O_2CR)_4(NO)_2$, and $Ru_2(dpf)_4(NO)_2$ with the increase of the M–N–O angle the M–N bond order approaches the value typical for mononuclear complexes with a linear {MNO} group. The value of TAI(M–$O_{(NO)}$) is growing in the same series. The value of W_π(N–O) is close to that for the free NO^- anion. The residual component for M–M and N–O bonds is equal to zero; for M–N and, especially, for M–$O_{(NO)}$ bonds W_{res} are not negligible (Table 7). Nevertheless, for the paddle-wheel nitrosyl compounds the decomposition of bond indices into σ-, π- and δ-contributions is acceptable for all bonds except M–$O_{(NO)}$. The computed indices are consistent with the following bonding model for these compounds. The NO group may be considered as a neutral

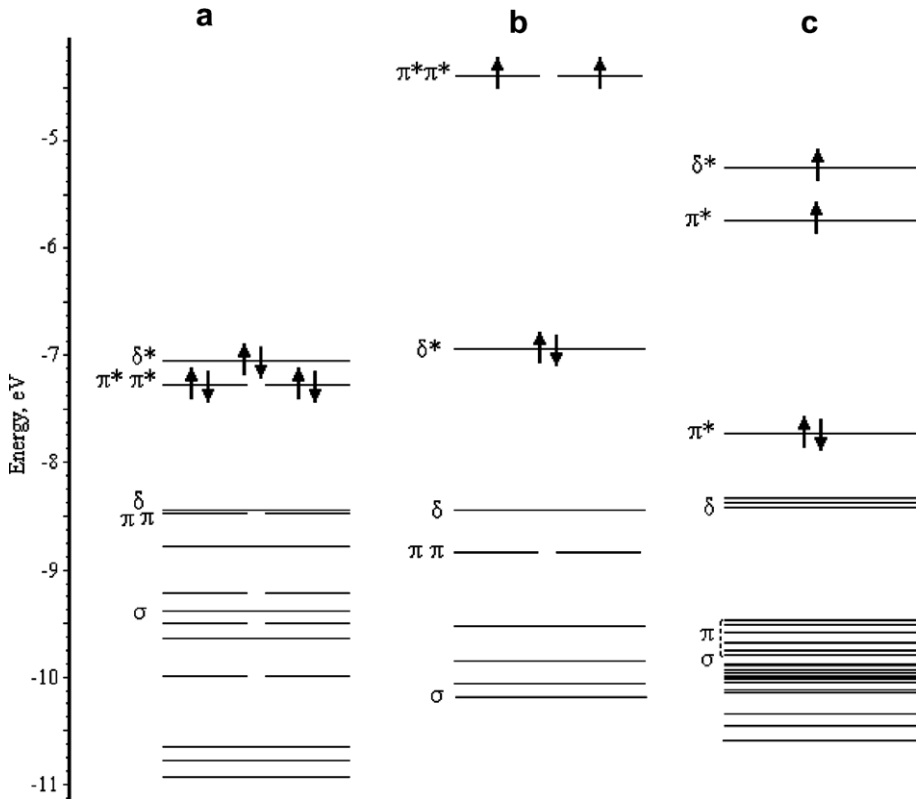


Fig. 3. The molecular orbital diagrams for $Rh_2(O_2CH)_4$ (a), $Ru_2(O_2CH)_4$ (b), $Ru_2(dPf)_4$ (c) complexes according to ROB3LYP/LanL2DZ calculations.

Table 6
The bond orders BO, B, W, and their σ-, π-, and δ-contributions (X is the bridging ligand O or N atom connected to the metal atom)

	$Rh_2(O_2CH)_4$	$Ru_2(O_2CH)_4$	$Ru_2(dpf)_4$
	$\{\sigma^2\pi^4\delta^2\}(\pi^*)^4\,(\delta^*)^2$	$\{\sigma^2\pi^4\delta^2\}(\pi^*)^2\,(\delta^*)^2$	$\{\sigma^2\pi^4\delta^2\}(\pi^*)^3\,(\delta^*)^1$
BO(M–M)	1	2	2
BO_σ	1	1	1
BO_π	0	1	0.5
BO_δ	0	0	0.5
B(M–M)	0.97	1.83	1.58
B_σ	0.89	0.83	0.85
B_π	0.07	0.97	0.55
B_δ	0.01	0.02	0.18
W(M–M)	0.80	1.71	1.40
W_σ	0.79	0.81	0.76
W_π	0.00	0.89	0.48
W_δ	0.01	0.01	0.16
W(M–X)	0.36	0.36	0.41
W_σ	0.33	0.32	0.34
W_π	0.01	0.02	0.04
res	0.02	0.01	0.00

molecule with unpaired electron on π^* MO, in this case the formal configurations of the metal ions are d^6(Ru) and d^7(Rh). The formation of the M–NO bonds occurs according to the same pattern as for mononuclear complexes with a bent {MNO} group: the out-of-plane π_y-component is constructed according to the "1.5e + 0.5e" rule (vide supra) and has the bond index of ca. 0.45; the index for the in-plane π_x-component is reduced as compared to π_y; the σ-bond index is equal to 0.3–0.5 (Table 7).

In the $Rh_2(O_2CH)_4$ complex there are two electrons on each of the antibonding π_{xz}^* and π_{yz}^* orbitals, so these MO's take almost no part in the bond (Tables 7 and 8). Therefore, the axial coordination of nitric oxide is realized by the formation of σ-bond through the interaction between LUMO σ_{dz2}^*(Rh–Rh) of {Rh_2} core and π_x^*(NO) SOMO's of both NO molecules. Such interaction is possible only for the bent {RhNO} group. The occupation of the resulting $\pi_x^*(NO) + \sigma^*(Rh–Rh) + \pi_x^*(NO)$ MO by two electrons leads to the drastic decrease of the metal–metal bond order. These data are consistent with the NBO analysis of the Rh–Rh bond breaking upon the coordination of nitric oxide to $Rh_2(O_2CR)_4$ [16].

In $Ru_2(O_2CH)_4$ π_{xz}^* and π_{yz}^* MO's of the metal core are occupied by a total of two electrons. In $Ru_2(O_2CH)_4(NO)_2$ these electrons together with the electrons on π^* MO's of two NO molecules occupy the $\pi^*(NO) + \pi^*(Ru–Ru) + \pi^*(NO)$ orbitals linking the Ru atoms with NO (Figs. 4 and 5). The increase of π^*(Ru–Ru) population causes diminution of the metal–metal bond order (Table 7). In the case of linear {RuNO} group the donation from σ(NO) to the doubly occupied $d_{z^2}(Ru1) + d_{z^2}(Ru2)$ MO is impossible, therefore the bent structure of this fragment is preferable. The electron density is transferred from NO to the partially occupied $d_{\pi x}$-orbitals, leading to the decrease of π_x^*(Ru–Ru) orbital contribution to the covalent bond with

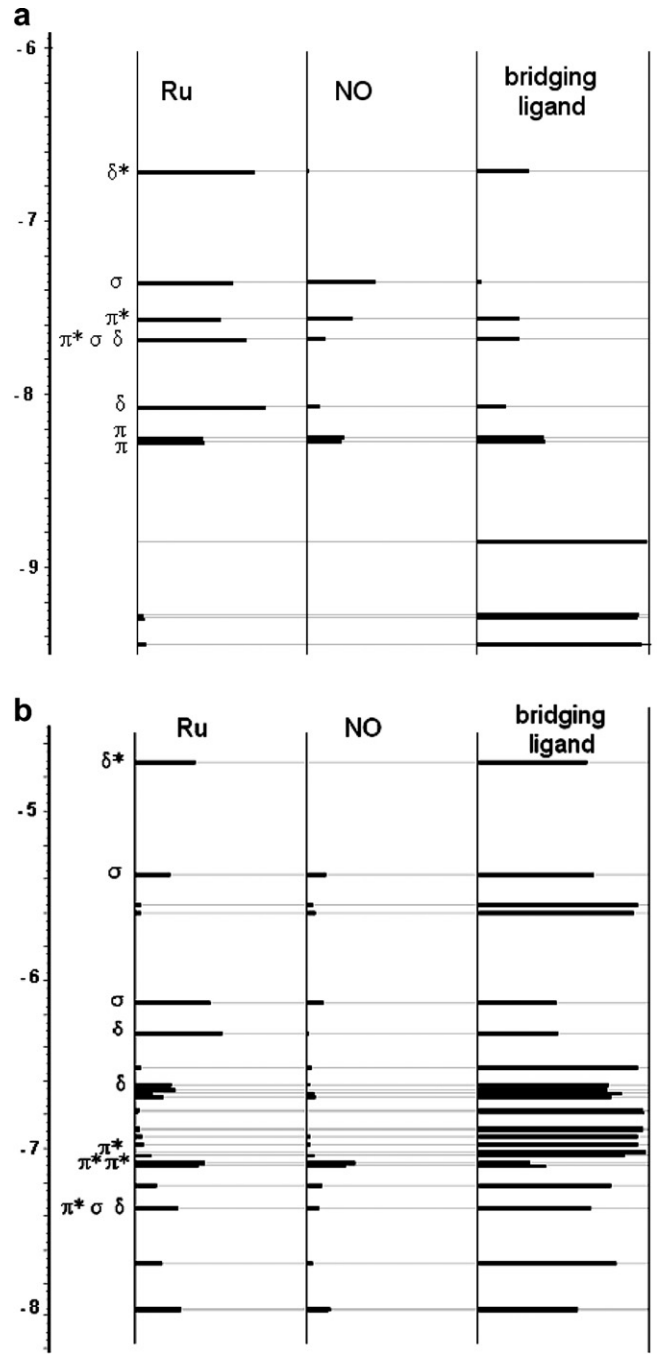


Fig. 4. The molecular orbital diagrams (energies are given in eV) and fragment contributions (percent) for the complexes $Ru_2(O_2CH)_4(NO)_2$ (a) and $Ru_2(dPf)_4(NO)_2$ (b).

NO: the in-plane $W_{\pi x}$(Ru–N) is noticeably less than the out-of plane $W_{\pi y}$(Ru–N), 0.27 and 0.41 respectively. The populations of ruthenium d-AO's remain almost unchanged upon coordination of NO to $Ru_2(O_2CH)_4$ (Table 8). In the case of $Ru_2(dpf)_4$ the addition of two NO molecules changes the electron configuration of the metal atoms (Table 8, Fig. 5). The mechanism of the Ru–Ru π-bond destruction is the same as for the $Ru_2(O_2CH)_4$ complex; the absence of the δ(Ru–Ru) bond

Table 7
Charge of the NO ligand, total population of NO σ- and π-orbitals, bond orders B, W, and their σ-, π-, and δ-contributions (X is the bridging ligand O or N atom connected to the metal atom)

	$Rh_2(O_2CH)_4(NO)_2$	$Ru_2(O_2CH)_4(NO)_2$	$Ru_2(dpf)_4(NO)_2$
q(NO)	0.04	0.07	−0.06
n(σ)	9.93	9.81	9.78
n(π)	5.03	5.12	5.28
W(M–M)	0.15	0.52	0.42
W_σ	0.13	0.46	0.34
W_π	0.01	0.04	0.04
W_δ	0.09	0.01	0.00
W_{res}		0.01	0.03
W(N–O)	2.02	1.92	1.80
W_σ	0.98	0.98	0.97
W_π	1.04	0.94	0.82
W_{res}			
W(M–N)	0.79	1.11	1.19
W_σ	0.49	0.34	0.32
W_π	0.22	0.67	0.79
W_{res}	0.08	0.10	0.08
W(M–O)	0.33	0.47	0.51
W_σ	0.09	0.04	0.04
W_π	0.12	0.25	0.32
W_{res}	0.12	0.17	0.14
W(M–X)	0.34	0.36	0.37
W_σ	0.32	0.33	0.34
W_π	0.01	0.02	0.03
W_{res}	0.02	0.01	0.01

Table 8
Natural d-atomic orbital occupancies (per atom) of ruthenium and rhodium atoms in the dimetal paddlewheel complexes

	$n(d_{z^2})$	$n(d_{xz}) + n(d_{yz})$	$n(d_{x^2-y^2})$	$n(d_{xy})$
$Rh_2(O_2CH)_4$	1.09	4.00	0.70	1.96
$Rh_2(O_2CH)_4(NO)_2$	1.34	3.75	0.74	1.96
$Ru_2(O_2CH)_4$	1.09	3.04	0.64	1.95
$Ru_2(O_2CH)_4(NO)_2$	1.19	3.07	0.69	1.92
$Ru_2(dpf)_4$	1.13	3.47	0.83	1.58
$Ru_2(dpf)_4(NO)_2$	1.25	2.94	0.89	1.94

is a result of δ^* MO population. So, despite the different electron configurations of $\{Ru_2\}^{4+}$ in $Ru_2(BL)_4$ the d-electron configurations for the $Ru_2(BL)_4(NO)_2$ complexes are the same (Table 8). The *cis*-influence of NO on the bonds of metal atoms with the bridging ligands is relatively small (Tables 6 and 7).

The sharp decrease of σ-, π-, and δ- metal–metal bond orders for all paddlewheel complexes is the evidence of the destruction of the bond between the metal atoms in the presence of the axially coordinated nitric oxide molecules (Scheme 3).

The loosening of the direct interaction between the metal atoms and the covalent nature of the M–NO bond explain the long M–M and short M–N distances in the paddlewheel dimetal complexes with nitric oxide molecules as axial ligands.

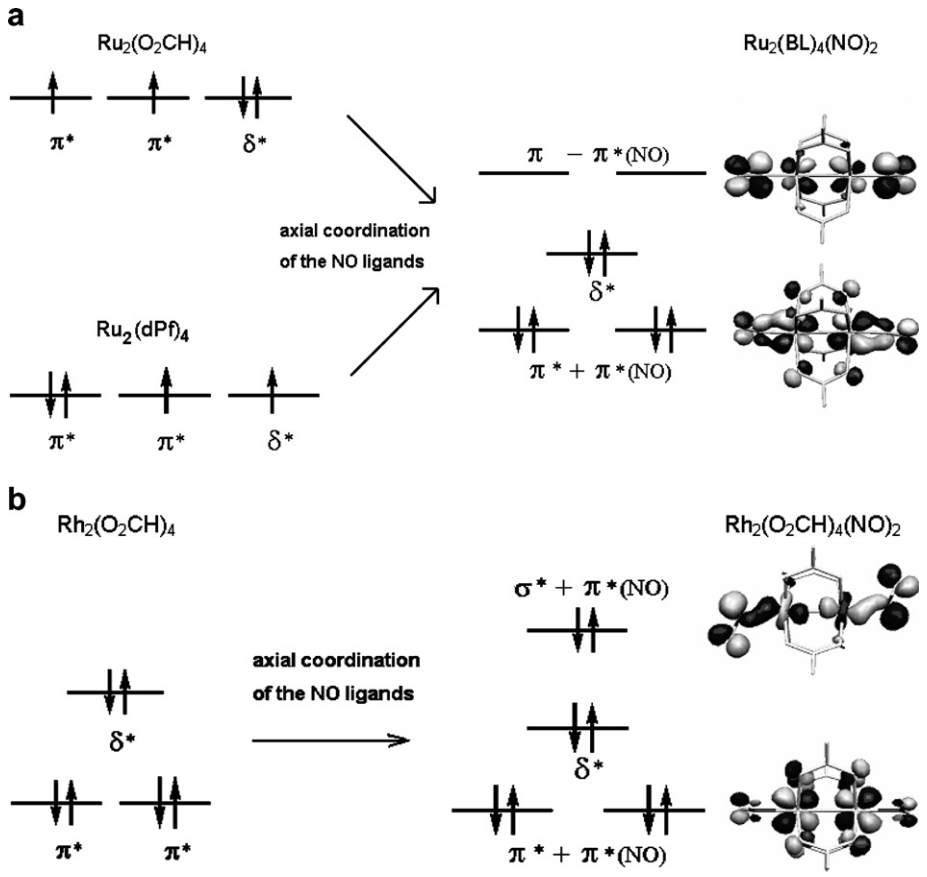
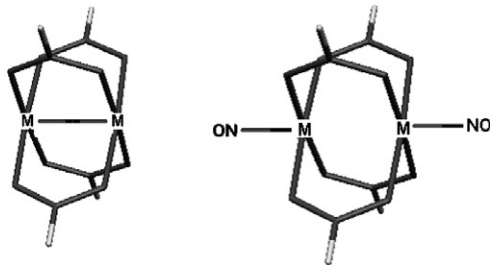


Fig. 5. Scheme of the interaction between the antibonding orbitals of the $\{M_2\}$ core and π^*(NO) orbitals: (a) M = Ru, (b) M = Rh.



Scheme 3.

3.4. Conclusions

In this work, we investigated the electronic structure of transition-metal nitrosyl complexes using Mayer and Wiberg bond order indices, and the proposed novel technique of bond order decomposition into σ-, π-, and δ-contributions. The important advantage of the bond order indices is their independence from any presupposed scheme of bonding in molecules or assumption of metal and NO oxidation states, so the calculated values can be used to derive an unbiased model of the chemical bond. The remarkable property of nitric oxide as a ligand is the ability to form metal–NO bonds with extraordinarily high π-bond order indices, and this gives the basis to treat these bonds as covalent. The noticeable through-atom M–(N)–O indices obtained for the linear {RuNO} group reflect the significant degree of π-electron density delocalization over the triatomic fragment. The analysis of bond orders and their components for the paddlewheel dimetal $M_2(BL)_4(NO)_2$ complexes provides a compact representation of the metal–metal bond destruction caused by the coordination of nitric oxide.

Acknowledgments

The GAUSSIAN03 calculations were carried out using the computational facilities of the Peterhof Telecommunication Center (St. Petersburg State University). Financial support from the Russian Foundation for Basic Research (Project No. 05-03-32463) is gratefully acknowledged.

References

[1] C.K. Jorgensen, Coord. Chem. Rev. 1 (1966) 164.
[2] F. Bottomley, Coord. Chem. Rev. 26 (1978) 7.
[3] G.B. Richter-Addo, P. Legzdins, Metal Nitrosyls, Oxford University Press, Oxford, 1992.
[4] M. Wolak, R. Van Eldik, Coord. Chem. Rev. 230 (2002) 263.
[5] J.N. Enemark, R.D. Feltham, Coord. Chem. Rev. 13 (1974) 339.
[6] M. Sieger, B. Sarkar, S. Zalis, J. Fiedler, N. Escola, F. Doctorovich, J.A. Olabe, W. Kaim, Dalton Trans. (2004) 1797.
[7] K.B. Wiberg, Tetrahedron. 24 (1968) 1083.

[8] I. Mayer, Int. J. Quantum Chem. 29 (1986) 477.
[9] I. Mayer, Simple Theorems, Proofs, and Derivations in Quantum Chemistry, Kluwer/Plenum, New York, 2003.
[10] G. Frenking, N. Frolich, Chem. Rev. 100 (2000) 717.
[11] A. Becke, J. Chem. Phys. 98 (1993) 5648.
[12] M.J. Frisch, G.W. Trucks, H.B. Schlegel, G.E. Scuseria, M.A. Robb, J.R. Cheeseman, J.A. Montgomery Jr., T. Vreven, K.N. Kudin, J.C. Burant, J.M. Millam, S.S. Iyengar, J. Tomasi, V. Barone, B. Mennucci, M. Cossi, G. Scalmani, N. Rega, G.A. Petersson, H. Nakatsuji, M. Hada, M. Ehara, K. Toyota, R. Fukuda, J. Hasegawa, M. Ishida, T. Nakajima, Y. Honda, O. Kitao, H. Nakai, M. Klene, X. Li, J.E. Knox, H.P. Hratchian, J.B. Cross, C. Adamo, J. Jaramillo, R. Gomperts, R.E. Stratmann, O. Yazyev, A.J. Austin, R. Cammi, C. Pomelli, J.W. Ochterski, P.Y. Ayala, K. Morokuma, G.A. Voth, P. Salvador, J.J. Dannenberg, V.G. Zakrzewski, S. Dapprich, A.D. Daniels, M.C. Strain, O. Farkas, D.K. Malick, A.D. Rabuck, K. Raghavachari, J.B. Foresman, J.V. Ortiz, Q. Cui, A.G. Baboul, S. Clifford, J. Cioslowski, B.B. Stefanov, G. Liu, A. Liashenko, P. Piskorz, I. Komaromi, R.L. Martin, D.J. Fox, T. Keith, M.A. Al-Laham, C.Y. Peng, A. Nanayakkara, M. Challacombe, P.M.W. Gill, B. Johnson, W. Chen, M.W. Wong, C. Gonzalez, J.A. Pople, GAUSSIAN 03, Revision B.05, Gaussian, Inc., Pittsburgh, PA, 2003.
[13] W.R. Wadt, P.J. Hay, J. Chem. Phys. 82 (1985) 284.
[14] P.J. Hay, W.R. Wadt, J. Chem. Phys. 82 (1985) 299.
[15] (a) P. Flukiger, H.P. Luthi, S. Portmann, J. Weber, Molekel 4.3, Swiss Center for Scientific Computing, Manno (Switzerland), 2000–2002;
(b) S. Portmann, H.P. Luthi, Chimia 54 (2000) 766.
[16] O.V. Sizova, J. Mol. Struct. Theochem. 760 (2006) 183.
[17] O.V. Sizova, L.V. Skripnikov, A.Yu. Sokolov, O.O. Lubimova, Zh. Strukt. Khim. (Russian Journal of Structural Chemistry) 48 (2007) 33.
[18] A.E. Reed, R.B. Weinstock, F. Weinhold, J. Chem. Phys. 83 (1985) 735.
[19] A.E. Reed, L.A. Curtiss, F. Weinhold, Chem. Rev. 88 (1988) 899.
[20] L.J. Bridgeman, G. Cavigliasso, L.R. Ireland, J. Rothery, J. Chem. Soc., Dalton Trans. (2001) 2095.
[21] J.A. McCleverty, Chem. Rev. 104 (2004) 403.
[22] J.T. Veal, D.J. Hodgson, Inorg. Chem. 11 (1972) 1420.
[23] J.T. Veal, D.J. Hodgson, Acta Crystallogr., Sect. B 28 (1972) 3525.
[24] A.F. Jalbout, M. Solimannejad, J. Mol. Struct. Theochem. 626 (2003) 81.
[25] M.C.G. Lebrero, D.A. Scherlis, G.L. Estiu, J.A. Olabe, D.A. Estrin, Inorg. Chem. 40 (2001) 4127.
[26] Y. Chen, F.-T. Lin, R.E. Shepherd, Inorg. Chem. 38 (1999) 973.
[27] O. Ziegler, A. Rauk, Theoret. Chim. Acta 46 (1977) 1.
[28] O. Lubimova, C. Loschen, G. Frenking, Book of Abstracts of the 10-th V.A. Fock Meeting on Quantum and Computational Chemistry, 2006, p. 62.
[29] O.V. Sizova, V.I. Baranovski, N.V. Ivanova, V.V. Sizov, Mol. Phys. 101 (2003) 715.
[30] M.L.H. Green, J. Organomet. Chem. 500 (1995) 127.
[31] V.K. Landry, K. Pang, S.M. Quan, G. Parkin, Dalton Trans. (2007) 820.
[32] D.M.P. Mingos, Inorg. Chem. 12 (1973) 1209.
[33] J.H. Enemark, R.R. Feltham, Coord. Chem. Rev. 13 (1974) 339.
[34] A.S. Hilderbrand, M.H. Lim, S.J. Lippard, J. Am. Chem. Soc. 126 (2004) 4972.
[35] A.J. Lindsay, G. Wilkinson, M. Motevalli, M.B. Hursthouse, J. Chem. Soc., Dalton Trans. (1987) 2723.
[36] A.J. Lindsay, R.P. Tooze, M. Motevalli, M.B. Hursthouse, G. Wilkinson, Chem. Commun. (1984) 1383.
[37] B. Han, J. Shao, Zh. Ou, T.D. Phan, J. Shen, J.L. Bear, K.M. Kadish, Inorg. Chem. 43 (2004) 7741.
[38] J.G. Norman Jr., G.E. Renzoni, D.A. Case, J. Am. Chem. Soc. 101 (1979) 5256.
[39] F.A. Cotton, M. Matusz, J. Am. Chem Soc. 110 (1988) 5761.

vacuum line, and distilled into vacuum-tight storage flasks. Metallic rhenium was a Chempur (Germany) product, used as received. Phenylhydrazine ($PhNHNH_2$) was an Aldrich product, used as received; *p*-tolylhydrazine (*p*-tolyl-$NHNH_2$) was prepared by treating, under nitrogen, the corresponding *p*-tolyl$NHNH_2 \cdot HCl$ salt with a slight excess of NaOH in aqueous solution. A solid separated out which, after 15 min of stirring, was filtered, washed with water and dried over P_2O_5 under vacuum for 24 h. $PPh(OEt)_2$ and PPh_2OEt were prepared by the method of Rabinowitz and Pellon [10]. Other reagents were purchased from commercial sources in the highest available purity and used as received. Infrared spectra were recorded on a Perkin–Elmer Spectrum One or Nicolet Magna 750 FT-IR spectrophotometer. NMR spectra (^1H, ^{31}P) were obtained on Bruker AC200 or AVANCE 300 spectrometers at temperatures varying between −90 and +30 °C, unless otherwise noted. ^1H spectra are referred to internal tetramethylsilane; $^{31}P\{^1H\}$ chemical shifts are reported with respect to 85% H_3PO_4, with downfield shifts considered positive. COSY NMR experiments were performed using standard programs. The SwaN-MR software package [11] was used to treat NMR data. The conductivity of 10^{-3} M solutions of the complexes in CH_3NO_2 at 25 °C were measured on a Radiometer CDM 83 instrument. Elemental analyses were determined in the Microanalytical Laboratory of the Department of Pharmaceutical Sciences, University of Padova, Italy.

2.1.1. *[$ReBr(ArN_2)_2(PPh_2OEt)_3$] ($BPh_4$)$_2$ (**1**) [Ar = Ph (**a**), p-tolyl (**b**)]*

An equimolar amount of Br_2 (0.16 mmol, 0.42 mL of a 0.38 M solution in CH_2Cl_2) was added to a solution of the appropriate bis(aryldiazenido) [$Re(ArN_2)_2(PPh_2OEt)_3$]-BPh_4 complex (0.16 mmol) in 10 mL of CH_2Cl_2 cooled to −196 °C. The reaction mixture was brought to 0 °C, stirred for 10 min and then evaporated to dryness under reduced pressure. The oil obtained was triturated at 0 °C with ethanol (2 mL) containing an excess of $NaBPh_4$ (0.48 mmol, 0.164 g). A red-brown solid slowly separated out which was filtered and twice crystallised from CH_2Cl_2 and diethyl ether; yield ⩾40% .

Anal. Calc. for $C_{102}H_{95}B_2BrN_4O_3P_3Re$ (**1a**): C, 67.85; H, 5.30; N, 3.10; Br, 4.43. Found: C, 67.61; H, 5.26; N, 3.23; Br, 4.58%. $\Lambda_M = 119.3$ S cm^2 mol^{-1}.

Anal. Calc. for $C_{104}H_{99}B_2BrN_4O_3P_3Re$ (**1b**): C, 68.13; H, 5.44; N, 3.06; Br, 4.36. Found: C, 67.97; H, 5.30; N, 3.17; Br, 4.13%. $\Lambda_M = 126.5$ S cm^2 mol^{-1}.

2.1.2. *[$ReBr_2(PhN_2)_2(PPh_2OEt)_2$]$BPh_4$ (**2a**)*

The complex was prepared following the method used for compounds **1**, starting from the [$Re(PhN_2)_2$-$(PPh_2OEt)_3$]BPh_4 derivative and using a reaction time, at room temperature, of 8 h; yield ⩾55%.

Anal. Calc. for $C_{64}H_{60}BBr_2N_4O_2P_2Re$: C, 57.54; H, 4.53; N, 4.19; Br, 11.96. Found: C, 57.40; H, 4.64; N, 4.11; Br, 12.16%. $\Lambda_M = 53.8$ S cm^2 mol^{-1}.

2.1.3. *[$ReBr_2(ArN_2)_2\{PPh(OEt)_2\}_2$]$BPh_4$ (**3**) [Ar = Ph (**a**), p-tolyl (**b**)]*

An equimolar amount of Br_2 (0.16 mmol, 0.42 mL of a 0.38 M solution in CH_2Cl_2) was added to a solution of the appropriate bis(aryldiazenido) [$Re(ArN_2)_2\{PPh$-$(OEt)_2\}_3$]BPh_4 complex (0.16 mmol) in 10 mL of CH_2Cl_2 cooled to −196 °C. The reaction mixture was brought to 0 °C, stirred for 1 h and then left to reach room temperature. After two hours of stirring, the solvent was removed under reduced pressure to give an oil which was triturated with diethyl ether (5 mL). A red-brown solid slowly separated out which was filtered and crystallised from CH_2Cl_2 and diethyl ether; yield ⩾70% .

Anal. Calc. for $C_{56}H_{60}BBr_2N_4O_4P_2Re$ (**3a**): C, 52.88; H, 4.75; N, 4.41; Br, 12.56. Found: C, 52.69; H, 4.64; N, 4.50; Br, 12.37%. $\Lambda_M = 55.0$ S cm^2 mol^{-1}.

Anal. Calc. for $C_{58}H_{64}BBr_2N_4O_4P_2Re$ (**3b**): C, 53.59; H, 4.96; N, 4.31; Br, 12.29. Found: C, 53.72; H, 4.83; N, 4.42; Br, 12.48%. $\Lambda_M = 54.2$ S cm^2 mol^{-1}.

2.1.4. *$ReBr_2(ArN_2)(ArN{=}NH)(PPh_2OEt)_2$ (**4**) [Ar = Ph (**a**), p-tolyl (**b**)]*

Method A: an equimolar amount of Br_2 (0.20 mmol, 0.53 mL of a 0.38 M solution in CH_2Cl_2) was added to a solution of the appropriate [$Re(ArN_2)_2(PPh_2OEt)_3$]BPh_4 complex (0.20 mmol) in 10 mL of CH_2Cl_2 cooled to −196 °C. The reaction mixture was brought to 0 °C, stirred for 1 h and then left to reach room temperature. The solution was stirred for 8 h until the [$ReBr_2(ArN_2)_2$(P-$Ph_2OEt)_2$]$^+$ (**2**) cations were completely formed. The solvent was removed under reduced pressure to give an oil which was triturated with ethanol (2 mL). After 2–3 h of stirring, a red-brown solid of **4** began to separate out from the resulting solution, which was cooled to −25 °C to complete the precipitation. The solid was filtered and crystallised from ethanol; yield ⩾65%.

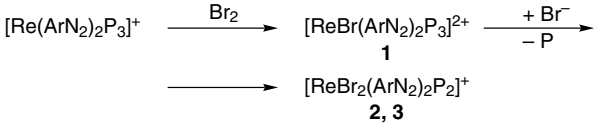
Method B: an equimolar amount of $Li(BHEt_3)$ (0.1 mmol, 100 μL of a 1 M solution in THF) was added to a solution of the appropriate aryldiazenido [$ReBr_2(ArN_2)_2(PPh_2OEt)_2$]$BPh_4$ (**2**) complex (0.1 mmol) in 10 mL of CH_2Cl_2 cooled to −196 °C. The reaction mixture was brought to 0 °C and stirred for 1 h. The solvent was removed under reduced pressure to give an oil which was treated with ethanol (2 mL). A red-brown solid separated out from the resulting solution which was filtered and crystallised from ethanol; yield ⩾75%.

Anal. Calc. for $C_{40}H_{41}Br_2N_4O_2P_2Re$ (**4a**): C, 47.21; H, 4.06; N, 5.50; Br, 15.70. Found: C, 47.38; H, 4.16; N, 5.38; Br, 15.92%.

Anal. Calc. for $C_{42}H_{45}Br_2N_4O_2P_2Re$ (**4b**): C, 48.24; H, 4.34; N, 5.36; Br, 15.28. Found: C, 48.07; H, 4.30; N, 5.48; Br, 15.43%.

3. Results and discussion

Pentacoordinate bis(aryldiazenido) [$Re(ArN_2)_2P_3$]BPh_4 complexes react with equimolar amounts of Br_2 to give first



Scheme 1. P = PPh_2OEt (**1**, **2**), $PPh(OEt)_2$ (**3**); Ar = Ph (**a**) and *p*-tolyl (**b**).

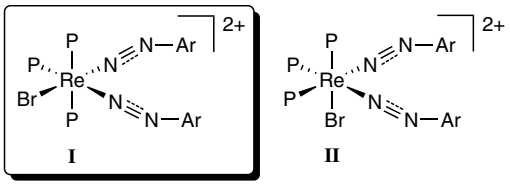


Chart 1.

the tris(phosphine) $[ReBr(ArN_2)_2P_3]^{2+}$ (**1**) species and then the $[ReBr_2(ArN_2)_2P_2]^{+}$ (**2**, **3**) derivatives, as shown in Scheme 1.

The reaction was studied between −80 and +20 °C by ^1H and ^{31}P NMR. Results showed that the addition of an equimolar amount of Br_2 to the $[Re(ArN_2)_2(PPh_2OEt)_3]^{+}$ cation at −80 °C caused the disappearance of precursor signals and the appearance of new signals attributable to the (mono)bromide tris(phosphine) complex cation **1**. Increase in the sample temperature caused a further spectral change, with the appearance of the signals of bis(bromide) complex **2** and free phosphine. The first product of bromination was therefore the dicationic $[ReBr(ArN_2)_2P_3]^{2+}$ (**1**) species and the free Br^- anion, which further reacted with complex **1** to give the final derivative **2**. It may be noted that, with the $PPh(OEt)_2$ ligand, the substitution of one phosphine in the first formed $[ReBr(ArN_2)_2\{PPh(OEt)_2\}_3]^{2+}$ cation is very fast even at low temperature, preventing separation of the complex in pure form. Instead, the final bis(bromide) compounds **2** and **3** were separated with both PPh_2OEt and $PPh(OEt)_2$ phosphines and fully characterised.

Crucial for the successful synthesis of the new bis(aryldiazenido) complexes **1**–**3** was the use of equimolar amounts of Br_2 and beginning the reaction in frozen solutions. Otherwise, large amounts of decomposition products resulted, which prevented purification of the compounds.

Complexes **1**, **2** and **3** were obtained as reddish-brown solids, stable in air and in solution of polar organic solvents, where they behave like 1:2 (**1**) or 1:1 (**2**, **3**) electrolytes [12]. The analytical and spectroscopic data (IR and NMR; Table 1) support the proposed formulations. The IR spectra of the $[ReBr(ArN_2)_2(PPh_2OEt)_3](BPh_4)_2$ (**1a, 1b**) complexes show two bands of medium intensity at 1695 and 1662 cm^{-1} (**1a**), or 1690 and 1659 cm^{-1} (**1b**), attributed to the ν_{N_2} of two aryldiazenido groups in a mutually *cis* position. The ν_{N_2} values, falling above 1600 cm^{-1}, also indicate [4a] singly-bent coordination for both aryldiazenido ligands, which are therefore formally bonded as ArN_2^+ to the central metal, resulting in formal oxidation state I [Re(+1)]. The reaction of $[Re(ArN_2)_2P_3]^{+}$ cations with Br_2 therefore proceeds with the $2e^-$ oxidation of rhenium (from −1 to +1) and formation of one bonded and one free Br^- anion (Scheme 1).

In the temperature range +20 to −80 °C, $^{31}P\{^1H\}$ NMR spectra appear as an AB_2 multiplet, which can be simulated with the parameters listed in Table 1.

These data do not allow us to assign a geometry to the complexes unambiguously, i.e., to decide between geometries **I** and **II** (Chart 1). However, as the ^1H NMR spectra of the $[ReBr(p\text{-tolylN}_2)_2P_3](BPh_4)_2$ (**1b**) complex (Table 1) show two singlets at 2.38 and 2.35 ppm of the methyl substituents of the *p*-tolylN_2 ligands, geometry **I** may tentatively be proposed for both complexes.

The IR spectra of the bis(bromide) bis(aryldiazenido) $[ReBr_2(ArN_2)P_2]BPh_4$ (**2**, **3**) complexes show two bands between 1655 and 1626 cm^{-1} (Table 1), attributed to ν_{N_2} of two aryldiazenido in a mutually *cis* position. The ν_{N_2} values suggest, in this case too, a singly-bent aryldiazenido ligand, formally bonded as ArN_2^+ to a Re(I) central metal [4]. In addition, in the far-IR region the spectrum of the $[ReBr_2(p\text{-tolylN}_2)\{PPh(OEt)_2\}_2]BPh_4$ (**3b**) complex also shows two bands of medium intensity at 185 and 150 cm^{-1}, attributable to ν_{ReBr} of the two Br^- ligands in a mutually *cis* position.

The ^1H NMR spectra of complexes **2** and **3** exhibit the signals of the phosphine and aryldiazenido ligands and of the BPh_4 anion. Only one singlet for the methyl substituent of the *p*-tolylN_2 ligands is observed in the spectra of **3b**, suggesting the magnetic equivalence of the two aryldiazenido ligands. Furthermore, in the temperature range between +20 and −80 °C, the $^{31}P\{^1H\}$ NMR spectra of bis(bromide) complexes **2**, **3** appear as sharp singlets, in agreement with the magnetic equivalence of the two phosphine ligands. On the basis of these data, a *cis–trans* geometry of type **III** (Chart 2) may be proposed for our bis(aryldiazenido) derivatives **2**, **3**.

The $[ReBr_2(ArN_2)_2P_2]^{+}$ (**2**, **3**) cations slowly react in ethanol to give a new complex which, in the case of P = PPh_2OEt, was isolated in pure form and characterised as the aryldiazenido-aryldiazene $ReBr_2(ArN_2)(ArN{=}NH)P_2$ (**4**) derivative (Scheme 2).

The formation of the aryldiazene ArN=NH ligand from the aryldiazenido may be explained by the addition of one H^- species to the ArN_2 group, a hydride which presumably arises from hydrogen abstraction from the ethanol solvent. In order to confirm this reaction and shed light on the properties of bis(aryldiazenido) complexes **2**, **3**, we reacted the $[ReBr_2(ArN_2)_2P_2]^{+}$ cations with an equimolar amount of $LiBHEt_3$, and found that the reaction proceeded to give the same aryldiazene–aryldiazenido complexes **4**, **5**, as shown in Scheme 3. This result therefore shows that the coordinated aryldiazene ArN=NH group is formed by the addition of a hydride to the Nα nitrogen atom of a coordinated aryldiazenido, and consequently supports the reaction of Scheme 2, with the abstraction of one hydride from ethanol to give the aryldiazene species.

Table 1
IR and NMR data for all complexes

	Compound	IR[a] (cm^{-1})	Assignment	^1H NMR[b,c] δ (J, Hz)	Assignment	Spin system	$^{31}P\{^1H\}$ NMR[b,d] δ (J, Hz)
1a	$[ReBr(PhN_2)_2(PPh_2OEt)_3](BPh_4)_2$	1695 s	ν_{N_2}	3.98 m	CH_2	AB_2	δ_A 99.0
		1662 s		1.30 t	CH_3		δ_B 88.4
				1.21 t			$J_{AB} = 22.0$
1b	$[ReBr(p\text{-tolyl}N_2)_2(PPh_2OEt)_3](BPh_4)_2$	1690 s	ν_{N_2}	3.95 m	CH_2	AB_2	δ_A 98.6
		1659 s		2.38 s	CH_3 *p*-tolyl		δ_B 88.5
				2.35 s			$J_{AB} = 22.0$
				1.32 t	CH_3 phos		
				1.23 t			
2a	$[ReBr_2(PhN_2)_2(PPh_2OEt)_2]BPh_4$	1650 s	ν_{N_2}	4.06 qnt	CH_2	A_2	85.2 s
		1626 s		1.24 t	CH_3		
3a	$[ReBr_2(PhN_2)_2\{PPh(OEt)_2\}_2]BPh_4$	1653 s	ν_{N_2}	4.12 m	CH_2	A_2	116.2 s
		1630 s		3.90 m			
				1.35 t	CH_3		
				1.26 t			
3b	$[ReBr_2(p\text{-tolyl}N_2)_2\{PPh(OEt)_2\}_2]BPh_4$	1655 sh	ν_{N_2}	4.17 s	CH_2	A_2	116.7 s
		1637 s		3.89 s			
		185 m	ν_{ReBr}	2.36 s	CH_3 *p*-tolyl		
		150 m		1.34 t	CH_3 phos		
				1.29 t			
4a	$ReBr_2(PhN_2)(PhN{=}NH)(PPh_2OEt)_2$	1622 m	ν_{N_2}	12.73 s, br	NH	A	88.4 s
		177 m	ν_{ReBr}	12.58 s, br		A	85.3 s
		150 m		3.97 m	CH_2		
				1.09 t	CH_3		
				1.07 t			
4b	$ReBr_2(p\text{-tolyl}N_2)(p\text{-tolyl}N{=}NH)(PPh_2OEt)_2$	1628 m	ν_{N_2}	12.70 s, br	NH	A	89.3 s
				12.57 s, br		A	84.9 s
				3.98 m	CH_2		
				2.40 s	CH_3 *p*-tolyl		
				2.37 s			
				2.35 s			
				1.11 t	CH_3 phos		
				1.08 t			

[a] In KBr pellets.
[b] In CD_2Cl_2 at 25 °C.
[c] Phenyl proton resonances are omitted.
[d] Positive shifts downfield from 85% H_3PO_4.

The addition of a hydride to the ArN_2 group may also take place to the Nβ nitrogen atom to give an arylhydrazide(2−) $ReBr_2(ArN_2)[ArN(H)N]P_2$ derivative. However, although the spectroscopic data alone do not allow us to distinguish between a diazene or a hydrazide species, the known precedents [8b,13] seem to suggest as more probable the formation of the aryldiazene derivatives **4**, **5**.

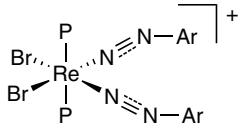
The easy synthesis of aryldiazene complexes **4**, **5** prompted us to prepare bis(aryldiazene) complexes by reacting $[ReBr_2(ArN_2)_2P_2]^+$ with an excess of $LiBHEt_3$. However, although the reaction was carried out at low temperature and proceeded with a color change in the solution from reddish-brown to orange, no stable complex was separated. In addition, the further reaction of $ReBr_2(ArN_2)$-$(ArN{=}NH)P_2$ (**4**, **5**) with $LiBHEt_3$ gave intractable

$$[ReBr_2(ArN_2)_2P_2]^+ \xrightarrow{EtOH} ReBr_2(ArN_2)(ArN{=}NH)P_2$$
2, 3 → **4, 5**

Scheme 2. P = PPh_2OEt (**4**), $PPh(OEt)_2$ (**5**); Ar = Ph (**a**) *p*-tolyl (**b**).

$$[ReBr_2(ArN_2)_2P_2]^+ \xrightarrow[0\ ^\circ C]{LiBHEt_3} ReBr_2(ArN_2)(ArN{=}NH)P_2$$
2, 3 → **4, 5**

Scheme 3. P = PPh_2OEt (**4**), $PPh(OEt)_2$ (**5**); Ar = Ph (**a**) *p*-tolyl (**b**).



III

Chart 2.

mixtures of products, suggesting that only mono-diazene mono-diazenido complexes **4**, **5** are stable and may be isolated. Lastly, it was also noted that the formation of $ReBr_2(ArN_2)(ArN{=}NH)P_2$ from the reaction of **2** and **3** with equimolar amounts of $LiBHEt_3$ proceeded with both PPh_2OEt and $PPh(OEt)_2$ phosphine ligands, but only with PPh_2OEt was a solid obtained (**4**); with $PPh(OEt)_2$, only an oily product was separated.

Aryldiazene complexes were often prepared from coordinated aryldiazenido by means of protonation reaction with Brønsted acid [4,5]. However, the reaction results in $2e^-$ oxidation of the metal center. Direct reaction of the aryldiazenido with a hydride-donor agent is rather rare [8b,13] but does not involve any change in the oxidation number of the metal center. The addition of a hydride anion to the Nα of the aryldiazenido ligand of a Re(I) complex allows easy synthesis of aryldiazene–aryldiazenido complexes **4**, **5**, with the metal in the same oxidation state [Re(I)].

Good analytical data were obtained for aryldiazene complexes **4**, which appear as reddish-orange solids, stable in air and in solution of polar organic solvents, where they behave as non-electrolytes. Spectroscopic data (IR and NMR; Table 1) support the proposed formulation.

The infrared spectra of the aryldiazene–aryldiazenido $ReBr_2(ArN_2)(ArN{=}NH)P_2$ (**4**) complexes show one medium-intensity band at 1622 cm^{-1} (**4a**) and 1628 cm^{-1} (**4b**), attributed to ν_{N_2} of the aryldiazenido ligand. No bands attributable to ν_{NH} or $\nu_{N=N}$ of the aryldiazene group were observed. However, the presence of the ArN=NH ligand was confirmed by the ^1H NMR spectra of the complexes, which show the characteristic [1,4–6], slightly broad, high-frequency signal (15–12 ppm) of the diazene hydrogen atom. The two signals at 12.73 and 12.70 (**4a**) and 12.58 and 12.57 ppm (**4b**) observed in our complexes also suggested the presence of two isomers. This was confirmed by the $^{31}P\{^1H\}$ NMR spectra which, in the temperature range between +20 and −80 °C, show two singlets at 89–85 ppm for both complexes **4a** and **4b**. Lastly, the presence of three singlets at 2.40, 2.37 and 2.35 ppm for the methyl substituents of the 4-$CH_3C_6H_4N_2$ and 4-$CH_3C_6H_4N{=}NH$ ligands in complex **4b** further support the existence of two isomers.

Taking into account the fact that, in the far-region of the IR spectrum, complex **4a** shows two medium-intensity bands at 177 and 150 cm^{-1}, attributable to ν_{ReBr} of the two bromide ligands in a mutually *cis* position, two geometries of type **IV** and **V** (Chart 3) may be proposed for our aryldiazene–aryldiazenido derivatives **4**.

$ReBr_2(ArN_2)(ArN{=}NH)(PPh_2OEt)_2$ (**4**) complexes react with NEt_3 to give, after addition of $NaBPh_4$ and work-up, reddish-orange solids which turned out to be the Re(-1) bis(aryldiazenido) $[Re(ArN_2)_2P_3]BPh_4$ derivatives, used as precursors (see Scheme 1). The yield was rather low, but addition of free phosphine (PPh_2OEt) greatly increased the obtained amount of bis(aryldiazenido) derivatives. Triethylammonium $[NHEt_3]BPh_4$ salt was also separated from the reaction mixture.

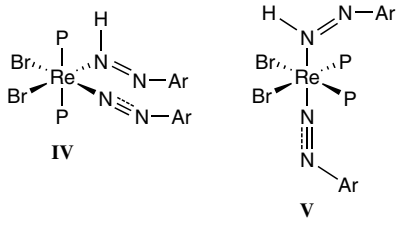
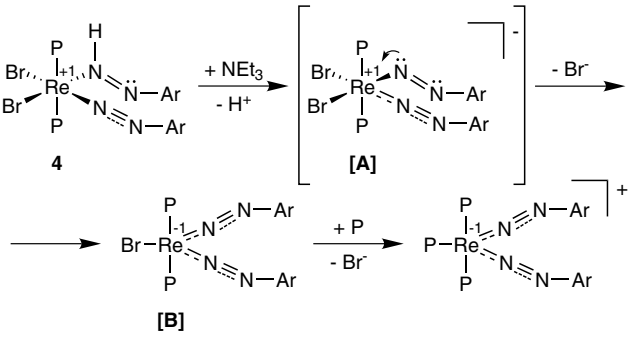


Chart 3.



Scheme 4. P = PPh_2OEt.

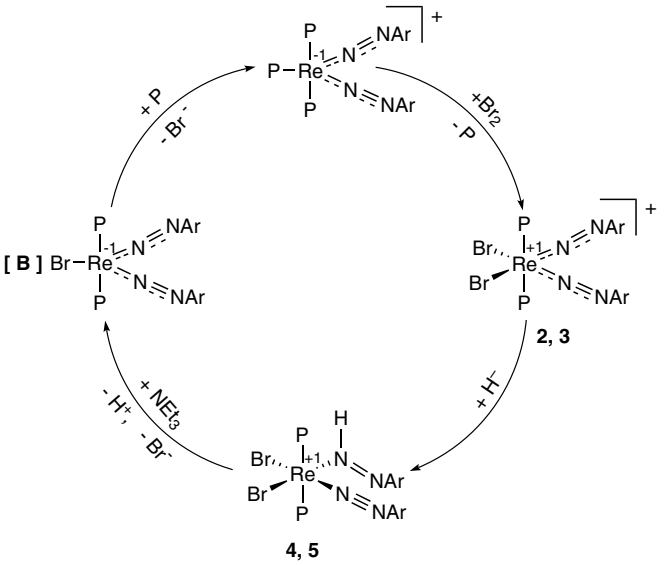
These results may be explained by the fact that the aryldiazene is acidic [1,4–6] and may be deprotonated [1] to give a doubly-bent aryldiazenido ArN_2^- ligand (intermediate **[A]**, Scheme 4).

Upon rearrangement of ArN_2^- to ArN_2^+ and concurrent formal reduction of the central metal to Re(−1), the bis(aryldiazenido) complex **[B]** is formed by the loss of one Br^- ligand, to reach the more stable 18-electron configuration. Substitution of the bromide ligand with PPh_2OEt, through either ligand exchange between the molecules of the complexes, or addition of free phosphite, gives the more stable bis(aryldiazenido)tris(phosphite) $[Re(ArN_2)_2P_3]BPh_4$ species.

These results highlight the interesting properties shown by the bis(aryldiazenido) complexes of rhenium stabilised by phosphite ligands, as shown in Scheme 5.

The starting bis(aryldiazenido) $[Re(ArN_2)_2P_3]^+$ complexes of Re(−1) undergo $2e^-$ oxidation with Br_2 to give the $[ReBr_2(ArN_2)_2P_2]^+$ (**2**, **3**) derivatives, which can add one hydride anion to the aryldiazenido Nα nitrogen atom to give the aryldiazene–aryldiazenido $ReBr_2(ArN_2)(ArN{=}NH)P_2$ (**4**, **5**) complexes. Deprotonation of the aryldiazene ligand in **4** and **5** results in $2e^-$ reduction of the central metal, affording, after dissociation of one bromide ligand, the pentacoordinated Re(−1) $ReBr(ArN_2)_2P_2$ derivatives **[B]**. Substitution of the Br^- ligand with phosphite yields the starting bis(aryldiazenido) $[Re(ArN_2)_2P_3]BPh_4$ complexes.

[1] Separation of $[NHEt_3]BPh_4$ strongly supports the proposed deprotonation reaction.



Scheme 5.

Acknowledgements

The financial support of MIUR (Rome) – Programmi di Ricerca Scientifica di Rilevante Interesse Nazionale, PRIN 2004 – is gratefully acknowledged. We thank Daniela Baldan for technical assistance.

References

[1] (a) D. Sutton, Chem. Rev. 93 (1993) 995;
(b) H. Kisch, P. Holzmeir, Adv. Organomet. Chem. 34 (1992) 67.
[2] (a) H. Zollinger, Diazo Chemistry II, VCH, Weinheim, Germany, 1995;
(b) B.F.G. Johnson, B.L. Haymore, J.R. Dilworth, in: G. Wilkinson, R.D. Gillard, J.A. McCleverty (Eds.), Comprehensive Coordination Chemistry, Vol. 2, Pergamon Press, Oxford, UK, 1987.
[3] (a) M. Hidai, Y. Mizobe, Chem. Rev. 95 (1995) 1115;
(b) A.E. Shilov, Metal Complexes in Biomimetic Chemical Reactions, CRC, Boca Raton, FL, 1997.
[4] (a) B.L. Haymore, J.A. Ibers, Inorg. Chem. 12 (1975) 3060;
(b) B.L. Haymore, J.A. Ibers, J. Am. Chem. Soc. 97 (1975) 5369;
(c) G. Albertin, S. Antoniutti, A. Bacchi, E. Bordignon, G. Pelizzi, P. Ugo, Inorg. Chem. 35 (1996) 6245;
(d) G. Albertin, S. Antoniutti, A. Bacchi, E. Bordignon, F. Busatto, G. Pelizzi, Inorg. Chem. 36 (1997) 1296.
[5] (a) G.W. Parshall, J. Am. Chem. Soc. 87 (1965) 2133;
(b) K.R. Laing, S.D. Robinson, M.F. Uttley, J. Chem. Soc., Dalton Trans. (1973) 2713;
(c) G. Albertin, S. Antoniutti, G. Pelizzi, F. Vitali, E. Bordignon, J. Am. Chem. Soc. 108 (1986) 6627;
(d) G. Albertin, S. Antoniutti, A. Bacchi, G.B. Ballico, E. Bordignon, G. Pelizzi, M. Ranieri, P. Ugo, Inorg. Chem. 39 (2000) 3265;
(e) G. Albertin, S. Antoniutti, E. Bordignon, G. Perinello, J. Organomet. Chem. 625 (2001) 217.
[6] (a) D. Sellmann, A. Brandl, R. Endell, Angew. Chem., Int. Ed. Engl. 12 (1973) 1019;
(b) G. Huttner, W. Gartzke, K. Allinger, Angew. Chem., Int. Ed. Engl. 13 (1974) 822;
(c) D. Sellmann, J. Käppler, M. Moll, F. Knoch, Inorg. Chem. 32 (1993) 960;
(d) M.R. Smith III, R.L. Keys, G.L. Hillhouse, A.L. Rheingold, J. Am. Chem. Soc. 111 (1989) 8312;
(e) T.-Y. Cheng, J.C. Peters, G.L. Hillhouse, J. Am. Chem. Soc. 116 (1994) 204;
(f) G. Albertin, S. Antoniutti, A. Bacchi, M. Bergamo, E. Bordignon, G. Pelizzi, Inorg. Chem. 37 (1998) 479;
(g) A.M. Kirillov, M. Haukka, M.F.C.G. da Silva, A.J.L. Pombeiro, Eur. J. Inorg. Chem. (2005) 2071;
(h) A.M. Kirillov, M. Haukka, A.J.L. Pombeiro, Inorg. Chim. Acta 359 (2006) 4421.
[7] (a) B. Coutinho, J.R. Dilworth, P. Jobanputra, R.M. Thompson, S. Schmid, J. Strähle, C.M. Archer, J. Chem. Soc., Dalton Trans. (1995) 1663;
(b) M.T.A.R.S. da Costa, J.R. Dilworth, M.T. Duarte, J.J.R. Fraústo da Silva, A.M. Galvão, A.J.L. Pombeiro, J. Chem. Soc., Dalton Trans. (1998) 2405;
(c) M.E. Deane, F.J. Lalor, G. Ferguson, B.L. Ruhl, M. Parvez, J. Organomet. Chem. 381 (1950) 213.
[8] (a) G. Albertin, S. Antoniutti, A. Bacchi, B. Fregolent, G. Pelizzi, Eur. J. Inorg. Chem. (2004) 1922;
(b) G. Albertin, S. Antoniutti, M. Bortoluzzi, J. Castro-Fojo, S. García-Fontán, Inorg. Chem. 43 (2004) 4511;
(c) G. Albertin, S. Antoniutti, A. Bacchi, F. De Marchi, G. Pelizzi, Inorg. Chem. 44 (2005) 8947;
(d) G. Albertin, S. Antoniutti, J. Bravo, J. Castro, S. García-Fontán, M.C. Marín, M. Noè, Eur. J. Inorg. Chem. (2006) 3451;
(e) G. Albertin, S. Antoniutti, M. Boato, Inorg. Chim. Acta 357 (2004) 1119;
(f) G. Albertin, S. Antoniutti, F. Bredariol, J. Organomet. Chem. 679 (2003) 208;
(g) G. Albertin, S. Antoniutti, M.T. Giorgi, Eur. J. Inorg. Chem. (2003) 2855;
(h) G. Albertin, S. Antoniutti, E. Bordignon, E. Visentin, Inorg. Chem. 40 (2001) 5465.
[9] G. Albertin, S. Antoniutti, A. Bacchi, E. Bordignon, F. Miani, G. Pelizzi, Inorg. Chem. 39 (2000) 3283.
[10] R. Rabinowitz, J. Pellon, J. Org. Chem. 26 (1961) 4623.
[11] G. Balacco, J. Chem. Inf. Comput. Sci. 34 (1994) 1235.
[12] W.J. Geary, Coord. Chem. Rev. 7 (1971) 81.
[13] L. Fan, F.W.B. Einstein, D. Sutton, Organometallics 19 (2000) 684.

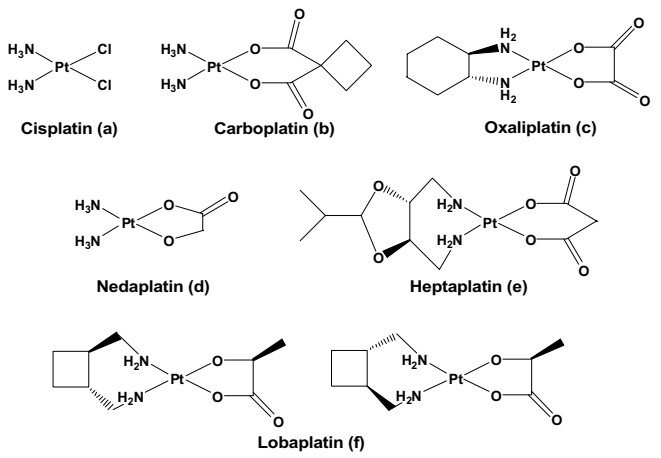


Fig. 1. Structures of cisplatin, carboplatin, oxaliplatin, nedaplatin, heptaplatin and lobaplatin.

of the problems associated with clinically used Pt drugs. They break the cisplatin paradigm by binding to DNA in other ways and may therefore be active against cisplatin-resistant cancer cell lines. Pt^{IV} complexes are also under investigation [7] where they are thought to be activated by reduction in the more reducing environment of cancer cells, thereby acting as prodrugs of the corresponding anti-tumour active Pt^{II} derivatives. An additional strategy to overcome the drawbacks associated with clinically used Pt drugs is to tether biologically-active ligands to the Pt which have, in themselves, inherent anti-tumour properties [1,3].

Nitric oxide (NO) has emerged as one of the most versatile and ubiquitous molecules in the human body with a diverse range of physiological functions including, amongst others, gene regulation, cytostasis, platelet function, vascular smooth muscle relaxation and proliferation, memory, immune stimulation and apoptosis [8–10]. It is derived from L-arginine *via* the catalytic action of a remarkable class of haem-containing metalloenzymes, the NO synthases (NOS), of which three different isoforms are known to exist; endothelial NOS (eNOS), neuronal NOS (nNOS) and inducible NOS (iNOS) [9,10].

Expression of NOS has been demonstrated in a variety of human and murine tumour types including gynecological, breast, head and neck, prostate, bladder and colon cancers and central nervous system tumours such as glioblastomas [11]. The toxic properties of NO are harnessed, within the immune system, in order to facilitate the control of infections and tumour cell growth [11,12]. Generated by iNOS, at high μmol/L concentrations at the site of infection, NO is thought to attack cancer cells by binding to metal centres involved in their respiration, thereby disrupting their function [10,13]. Additionally, NO has been demonstrated to upregulate p53, the tumour suppressor gene [10]. NO-mediated inhibition of DNA synthesis may also be an important mechanism by which macrophages induce cytotoxicity. NO can induce DNA damage by generating reactive nitrogen oxide species (RNOS) such as peroxynitrite and $ONOO^-$, which can oxidise and nitrate DNA and potentially cause single-strand DNA breaks *via* attack on the sugar–phosphate backbone [10,14]. Dinitrogen trioxide, another RNOS derived from NO, can nitrosate amines to form carcinogenic *N*-nitrosamines, which can then alkylate DNA [10,15].

Conflicting reports of pro- and anti-cancer activity associated with NO clearly illustrate the need for further research in this area in order to fully elucidate and understand the precise role of NO in cancer biology. High concentrations of NO, for example, can promote tumour cell death by apoptosis whereas lower concentrations of NO can promote tumour cell proliferation, vascularisation or even resistance to apoptosis [10,11]. In addition to concentration, the cellular effects of NO also depend on its source, latency, cell type and phenotype [10].

NO donors are currently under investigation as therapeutic agents for the treatment of a variety of disease states including cancer [16,17]. We recently reported that hydroxamic acids (RC(O)NHOH), a class of organic bioligands with a diverse range of biological functions [18,19], can act as effective NO donors by virtue of the fact that they readily transfer NO to ruthenium(III) (Ru^{III}) to form stable Ru^{II} nitrosyls. Moreover, in recent years, although there has been a surge of interest in developing novel Ru^{II} nitrosyl complexes, capable of releasing cytotoxic NO [20–23], as yet there is little or no evidence in the literature of NO-releasing Pt-based chemotherapeutics. The potential of NO delivery systems in the enhancement of platinum cytotoxicity has however been demonstrated, by pretreating Chinese hamster V79 lung fibroblast cells with bolus NO or NO delivered from NONOate NO donors. The tumour cells were markedly sensitized to subsequent cisplatin treatment [24]. It was on this premise that we wished to employ a novel synergistic approach, exploiting the well-established anti-cancer properties of Pt and the NO-releasing ability of hydroxamic acids and, in so doing, advance a new class of bifunctional metallodrug with dual DNA-binding and NO-releasing properties. 3- and 4-pyridinehydroxamic acids were specifically chosen with a view to synthesising Pt pyridinehydroxamic acid complexes where the pyridine nitrogen would selectively coordinate Pt^{II} or Pt^{IV} thereby leaving the hydroxamic acid moiety uncoordinated and potentially free to release cytotoxic NO.

Herein, we describe the synthesis, characterisation and NO-releasing ability of a novel class of 3- and 4-pyridinehydroxamic acid (3- and 4-pyhaH) complexes of Pt^{II} and Pt^{IV}. The crystal structure of the Pt^{IV} derivative, *cis*-$[PtCl_4(4\text{-pyhaH})_2]\cdot 2CH_3OH$ is reported. The corresponding 3- and 4-pyridinecarboxylic acid (3- and 4-pycaH) Pt^{II} and Pt^{IV} complexes, together with the Pt^{II} pyridine analogue were also synthesised and characterised to serve as reference standards in biological testing.

2. Experimental

2.1. General

3-Pyridinecarboxylic acid (nicotinic acid) **3**, 4-pyridinecarboxylic acid (isonicotinic acid) **4**, benzohydroxamic acid **5**, methylnicotinate, ethylisonicotinate and pyridine, were all purchased from Aldrich and used without further purification. $K_2[Pt^{II}Cl_4]$ and $K_2[Pt^{IV}Cl_6]$ were used as received from Johnson Matthey. $K[Ru^{III}(Hedta)Cl]\cdot 2H_2O$ was synthesised as previously reported [25].

IR and far-IR spectroscopic measurements were obtained using a Mattson Genesis II CSI FTIR spectrometer. The spectra were analysed using WINFIRST software. Between 4000 and 400 cm^{-1}, KBr discs were employed while between 600 and 200 cm^{-1}, polythene discs (Nujol mull) were used. FTIR grade KBr and nujol were purchased from Aldrich. ^1H NMR spectra were recorded on a Bruker Avance 400 NMR spectrometer and the spectra analysed using TopSpin 1 software. Chemical shifts were measured relative to the undeuterated solvent peak. Elemental analysis was performed by the Microanalytical Laboratory, School of Chemistry & Chemical Biology, University College Dublin, Belfield, Dublin. Electrospray ionisation mass spectroscopy (ESI-MS) experiments were performed on a Quattro Micro quadrupole electrospray mass spectrometer (Micromass, Waters Corp., USA): 10 μL of the samples was injected in 300 μL of acetonitrile:water (60:40, v/v).

2.1.1. Synthesis of 3-pyridinehydroxamic acid (3-pyhaH) (*1*)

Hydroxylamine hydrochloride (5.1 g, 72 mmol) was added to sodium hydroxide (5.8 g, 146 mmol) in deionised water (37 ml). The resulting solution was then added dropwise to methylnicotinate (5.0 g, 36 mmol) in methanol (55 ml). The solution was stirred at room temperature for 72 h, after which the solution was acidified to pH 5.5 using 5% HCl. The solvent was removed *in vacuo* yielding a yellow solid. Methanol (60 ml) was added and sodium chloride filtered. The solvent was removed *in vacuo* yielding a light pink solid, which was recrystallised from water. Yield: 3.0 g, 22 mmol, 66%. *Anal.* Calc. for $C_6H_6N_2O_2$: C, 52.17; H, 4.38; N, 20.28. Found: C, 52.11; H, 4.24; N, 20.14%. ^1H NMR (400 MHz, [d_6]-DMSO, 25 °C): $\delta = 11.25$ (s, 1H, OH), 9.13 (s, 1H, NH), 8.77 (s, 1H, aromatic H), 8.55 (d, 1H, aromatic H), 7.93 (d, 1H, aromatic H), 7.33 (dd, 1H, aromatic H).

2.1.2. Synthesis of 4-pyridinehydroxamic acid (4-pyhaH) (*2*)

4-pyhaH was synthesised from ethylisonicotinate in line with the procedure for 3-pyhaH described in Section 2.1.1 above. Yield: 74%. Anal. Calc. for $C_6H_6N_2O_2$: C, 52.17; H, 4.38; N, 20.28. Found: C, 52.20; H, 4.26; N, 20.18%. ^1H NMR (400 MHz, [d_6]-DMSO, 25 °C): $\delta = 11.42$ (s, 1H, OH), 9.25 (s, 1H, NH), 8.57 (dd, 2H, aromatic H), 7.54 (dd, 2H, aromatic H).

2.1.3. Synthesis of cis-$[Pt^{II}Cl_2(3\text{-pyhaH})_2]\cdot 2H_2O$ (*6*)

3-Pyridinehydroxamic acid (3-pyhaH) (0.146 g, 1.06 mmol) in methanol (7 ml) was added to $K_2[Pt^{II}Cl_4]$ (0.20 g, 0.48 mmol) in deionised water (7 ml). The resulting solution was stirred without protection from light at room temperature for 24 h turning yellow in colour. A yellow precipitate was filtered and dried over P_2O_5. Yield: 0.18 g, 0.31 mmol, 65%. *Anal.* Calc. for $PtC_{12}H_{16}N_4O_6Cl_2$: C, 24.92; H, 2.79; N, 9.69; Cl, 12.26. Found: C, 24.88; H, 2.65; N, 9.64; Cl, 12.35%. ^1H NMR (400 MHz, [d_6]-DMSO, 25 °C): $\delta = 11.48$ (s, 2H, OH), 9.31 (s, 2H, NH), 8.98 (s, 2H, aromatic H), 8.76 (d, 2H, aromatic H), 8.14 (d, 2H, aromatic H), 7.47 (dd, 2H, aromatic H).

The Pt^{II} and Pt^{IV} compounds, **7**–**14**, were synthesised by reaction of the appropriate pyridine derivative or pyridine with either $K_2[Pt^{II}Cl_4]$ or $K_2[Pt^{IV}Cl_6]$, respectively, by the method described in Section 2.1.3 above.

2.1.4. cis-$[Pt^{II}Cl_2(4\text{-pyhaH})_2]\cdot H_2O$ (*7*)

Yield: 70%. *Anal.* Calc. for $PtC_{12}H_{14}N_4O_5Cl_2$: C, 25.73; H, 2.52; N, 10.00; Cl, 12.66. Found: C, 25.94; H, 2.34; N, 9.74; Cl, 12.49%. ^1H NMR (400 MHz, [d_6]-DMSO, 25 °C): $\delta = 11.53$ (s, 2H, OH), 9.43 (s, 2H, NH), 8.78 (dd, 4H, aromatic H), 7.59 (dd, 4H, aromatic H).

2.1.5. cis-$[Pt^{II}Cl_2(3\text{-pycaH})_2]$ (*8*)

Yield: 69%. *Anal.* Calc. for $PtC_{12}H_{10}N_2O_4Cl_2$: C, 28.14; H, 1.97; N, 5.47; Cl, 13.84. Found: C, 28.01; H, 1.90; N, 5.25; Cl, 13.56%. ^1H NMR (400 MHz, [d_6]-DMSO, 25 °C): $\delta = 9.19$ (s, 2H, aromatic H), 8.84 (d, 2H, aromatic H), 8.33 (d, 2H, aromatic H), 7.45 (dd, 2H, aromatic H).

2.1.6. cis-$[Pt^{II}Cl_2(4\text{-pycaH})_2]$ (*9*)

Yield: 77%. *Anal.* Calc. for $PtC_{12}H_{10}N_2O_4Cl_2$: C, 28.14; H, 1.97; N, 5.47; Cl, 13.84. Found: C, 28.11; H, 1.91; N, 5.27; Cl, 13.96%. ^1H NMR (400 MHz, [d_6]-DMSO, 25 °C): $\delta = 8.79$ (dd, 4H, aromatic H), 7.70 (dd, 4H, aromatic H).

2.1.7. cis-$[Pt^{II}Cl_2(py)_2]$ (*10*)

Yield: 75%. *Anal.* Calc. for $PtC_{10}H_{10}N_2Cl_2$: C, 28.31; H, 2.38; N, 6.60. Found: C, 28.21; H, 2.15; N, 6.38%. ^1H NMR (400 MHz, [d_6]-DMSO, 25 °C): $\delta = 8.47$ (d, 4H, aromatic H), 7.49 (t, 4H, aromatic H), 7.32 (m, 2H, aromatic H).

2.1.8. cis-$[Pt^{IV}Cl_4(3\text{-pyhaH})_2]\cdot 2H_2O$ (*11*)

Yield: 63%. *Anal.* Calc. for $PtC_{12}H_{16}N_4O_6Cl_4$: C, 22.20; H, 2.48; N, 8.63; Cl, 21.85. Found: C, 22.47; H, 2.41; N, 8.48; Cl, 21.69%. ^1H NMR (400 MHz, [d_6]-DMSO, 25 °C): $\delta = 11.79$ (s, 2H, OH), 9.51 (s, 2H, NH), 9.13 (s, 2H, aromatic H), 8.88 (d, 2H, aromatic H), 8.26 (d, 2H, aromatic H), 7.48 (dd, 2H, aromatic H).

2.1.9. cis-$[Pt^{IV}Cl_4(4\text{-pyhaH})_2]\cdot 2CH_3OH$ (*12*)

Yield: 63%. *Anal.* Calc. for $PtC_{14}H_{20}N_4O_6Cl_4$: C, 24.83; H, 2.98; N, 8.27; Cl, 20.94. Found: C, 24.77; H, 2.91; N,

8.22; Cl, 20.78%. ^{1}H NMR (400 MHz, [d_6]-DMSO, 25 °C): $\delta = 11.88$ (s, 2H, OH), 9.64 (s, 2H, NH), 8.85 (dd, 4H, aromatic H), 7.97 (dd, 4H, aromatic H).

2.1.10. *cis*-[$Pt^{IV}Cl_4$(3-pycaH)$_2$] (**13**)

Yield: 61%. *Anal.* Calc. for $PtC_{12}H_{10}N_2O_4Cl_4$: C, 24.72; H, 1.73; N, 4.80; Cl, 24.32. Found: C, 24.70; H, 1.69; N, 4.63; Cl, 24.11%. ^{1}H NMR (400 MHz, [d_6]-DMSO, 25 °C): $\delta = 9.23$ (s, 2H, aromatic H), 8.61 (m, 4H, aromatic H), 7.66 (dd, 2H, aromatic H).

2.1.11. *cis*-[$Pt^{IV}Cl_4$(4-pycaH)$_2$] (**14**)

Yield: 67%. *Anal.* Calc. for $PtC_{12}H_{10}N_2O_4Cl_4$: C, 24.72; H, 1.73; N, 4.80; Cl, 24.32. Found: C, 24.56; H, 1.91; N, 4.55; Cl, 24.17%. ^{1}H NMR (400 MHz, [d_6]-DMSO, 25 °C): $\delta = 8.79$ (dd, 4H, aromatic H), 7.98 (dd, 4H, aromatic H).

2.1.12. K[Ru^{II}(Hedta)(NO)Cl] · H_2O (**15**)

cis-[$Pt^{II}Cl_2$(3-pyhaH)$_2$] · $2H_2O$ (**6**) (0.29 g, 0.50 mmol) was added to a yellow aqueous solution (15 ml) of K[Ru^{III}(Hedta)Cl] · $2H_2O$ (0.25 g, 0.50 mmol), resulting in a reddish solution. The reaction was refluxed for 3 h whereupon it turned brown in colour. The reaction was concentrated in vacuo (~5 ml), purified on a sephadex column LH20 using water as eluent to give K[Ru(Hedta)(NO)Cl] · H_2O as a brown solid. Yield: 58%. *Anal.* Calc. for $RuC_{10}H_{15}N_3ClKO_{10}$: C, 23.42; H, 2.95; N, 8.19; Cl, 6.91; K, 7.62. Found: C, 23.45; H, 2.91; N, 8.42; Cl, 6.97; K, 7.46%. ^{1}H NMR (400 MHz, D_2O, 25 °C): $\delta = 4.43$ (d, 2H, CH_2 glycine), 4.34 (s, 2H, CH_2 glycine), 4.09 (2H, s, CH_2 glycine), 3.84 (2H, s, CH_2 glycine) 3.61 (4H, m, CH_2 ethylenediamine); ^{13}C NMR (400 MHz; D_2O; 25 °C): $\delta = 181.8$, 178.5 (CO bound glycinate), 177.7, 168.8 (CO free glycinate), 65.45, 65.4, 64.7, 64.3 (CH_2 glycinate), 62.8, 60.4 (CH_2 ethylenediamine); ν_{max}/cm^{-1} 3345s (OH), 2986s, 2947s (CH, H_2edta), 1894vs (NO), 1726s (CO free glycine arms) and 1649b (CO bound glycine arms); ESI-MS m/z: 456 ([M−H]$^-$).

K[Ru^{II}(Hedta)(NO)Cl] · H_2O (**15**) was likewise obtained by reacting *cis*-[$Pt^{II}Cl_2$(4-pyhaH)$_2$] · H_2O (**7**) with K[Ru^{III}(Hedta)Cl] · $2H_2O$ in line with the procedure described above.

2.2. Structural characterisation of *cis*-[$Pt^{IV}Cl_4$(4-pyhaH)$_2$] · $2CH_3OH$ (**12**)

Crystal data and experimental details for **12** are summarised in Table 1. The structure of **12** was refined in the *Pbcn* space group. Crystal data were collected on a Bruker Smart Apex CCD diffractometer at 100 K using monochromated Mo Kα radiation, ($\lambda = 0.71073$ Å) and the $\phi - \omega$ scan method. The structure was solved by direct method (SHELXS-97) [26] and refined by full-matrix least squares using SHELXL 97-2 package [26]. All hydrogen atoms were localised in the difference fourier map and allowed to refine freely.

Table 1
Summary of crystal data for **12**

Empirical formula	$C_{14}H_{20}N_4O_6Cl_4Pt$
Formula weight	677.23
Temperature (K)	100(2)
Wavelength (Å)	0.71073
Crystal system	orthorhombic
Space group	*Pbcn*
Unit cell parameters	
a (Å)	7.3794(5)
b (Å)	11.9791(8)
c (Å)	24.8071(17)
α (°)	90
β (°)	90
γ (°)	90
Volume (Å^3), Z	2192.9(3), 4
D_{calc} (Mg/m^3)	2.051
Absorption coefficient (mm^{-1})	6.924
F(000)	1304
Crystal size (mm)	0.30 × 0.20 × 0.20
θ Range for data (°)	3.21–29.46
Index ranges	$-9 \leqslant h \leqslant 9$, $-16 \leqslant k \leqslant 16$, $-33 \leqslant l \leqslant 32$
Reflections collected	18484
Independent reflections (R_{int})	2891 (0.0289)
Completeness to $\theta = 29.46°$ (%)	94.8
Absorption correction	semi-empirical from equivalents
Maximum and minimum transmission	0.3381 and 0.2305
Refinement method	full-matrix least-squares on F^2
Data/restraints/parameters	2891/0/172
Goodness-of-fit on F^2	1.049
Final R indices [$I > 2\sigma(I)$]	$R_1 = 0.0217$, $wR_2 = 0.0453$
R indices (all data)	$R_1 = 0.0277$, $wR_2 = 0.0471$
Largest difference in peak and hole (e Å^{-3})	1.713 and −0.904

$R_1 = \sum\|F_o| - |F_c\|/\sum|F_o|$, $wR_2 = [\sum w(F_o^2 - F_c^2)^2/\sum w(F_o^2)^2]^{1/2}$.

2.3. Pharmacological tests

The NO-releasing properties of the test compounds were investigated using an isolated organ bath experiment as follows. Thoracic aorta rings were prepared from male Wistar Hannover rats weighing about 250–400 g purchased from the animal facility of the University of Trieste. The animals were maintained according to the guidelines in force in Italy (DDL 116, 21/02/92 and subsequent addenda) and in compliance with the "Guide for the care and use of laboratory animals" DHIIS Publ. No (NHI) 86-23, Bethesda, MD, NHI (1985). Rat thoracic aortas were carefully removed, after killing of the animals by CO_2 overdose, put into a Petri dish containing Krebs solution (containing 118.3 mM NaCl, 25 mM $NaHCO_3$, 4.8 mM KCl, 2.5 mM $CaCl_2$, 1.2 mM $MgSO_4$, 1.2 mM KH_2PO_4, 11.1 mM glucose, at pH 7.4), and cleaned of fat and of connective tissue. Aorta rings, cut at about 2 mm, were put into a 20 mL organ bath (model 4050, Ugo Basile, Padova Italy) with constant gas flow (95% O_2 + 5% CO_2) at 37 ± 0.5 °C. Two stainless steel hooks were inserted into the aortic lumen to fix the test sample to the bath bottom and to connect it to a force transducer. Aortic rings were equilibrated with Krebs solution and maintained under an optimal ten-

sion of 2 g for 40 min before experiments. Rings were stimulated with 30 mM KCl to assess the integrity of the strips (rings with abnormal contraction were discarded), and responsive rings were rinsed with Krebs solution and allowed to equilibrate for a further 30 min. Contraction was elicited by adding phenylephrine (dissolved in ultrapure water) to the bath (final concentration 3×10^{-7} M). Once sample contraction reached a plateau, the relaxation–response curve was obtained by cumulative additions of acetylcholine (dissolved in ultrapure water) to the organ bath (final concentrations ranging between 10^{-9} M and 10^{-4} M). After their maximal relaxation, aorta rings were rinsed with Krebs solution and allowed to re-equilibrate for 30 min. Contraction was elicited again by phenylephrine, and compounds **1**–**10** were tested in the concentration interval between 10^{-9} and 10^{-4} M (stock solutions were prepared in DMSO with subsequent dilutions in ultra-pure water in order to keep DMSO in the bath to less than 0.1%); cisplatin was used as control, at the same concentrations and conditions.

The vehicle used for dissolving the test complexes was also tested for relaxation. Contraction or relaxation were recorded isometrically *via* a force–displacement transducer (model 7003, Ugo Basile, Padova, Italy) connected to a Unirecord Microdynamometer recorder (model 7050, Ugo Basile, Padova, Italy). Experiments with compounds **6** and **8** were repeated in the presence of 10 μM methylene blue (dissolved in ultrapure water), a guanylate cyclase inhibitor [27]. In this case, methylene blue was added to the organ bath, for 10 min, every time before inducing contraction with phenylephrine. For each compound, experiments were replicated at least three times.

2.4. Statistical analysis

Data were submitted to computer-assisted statistical analysis using ANOVA analysis of variance and Tukey–Kramer multiple comparison post-test or Student *t*-test.

3. Results and discussion

3.1. Synthesis and spectroscopic characterisation of ligands *1–4*

3- and 4-pyridinecarboxylic acid (3- and 4-pycaH) were used as purchased and a selection of IR spectral data are provided in Supplementary data.

The hydroxamic acids were synthesised by reacting the corresponding carboxylic methyl or ethylesters with hydroxylamine in aqueous methanol in line with literature methods [28]. They were obtained in good yields (55–85%) and excellent purity and were characterised by elemental analysis, IR and ^{1}H NMR spectroscopy. The IR spectra of 3-pyhaH **1** and 4-pyhaH **2** contain stretches between 3180–3190 cm^{-1}, 2800–2850 cm^{-1} and 1640–1660 cm^{-1} which may be assigned to ν_{O-H}, ν_{N-H} and $\nu_{C=O}$, respectively. The symmetric and asymmetric stretches corresponding to $\nu_{C=O}$ are found as only one stretch due to intramolecular hydrogen bonding, while the broad ν_{O-H} of the hydroxamato may be attributed to intermolecular hydrogen bonding. These values concur with those previously reported in the literature [29,30]. Selected IR spectral data for **1** and **2** are provided in Supplementary data.

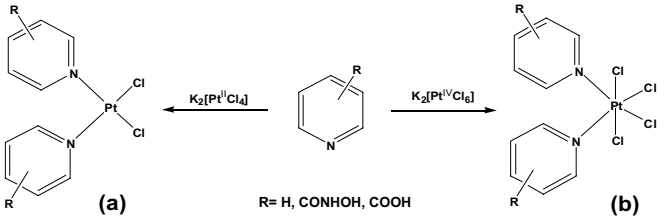
The ^{1}H NMR spectra of the hydroxamic acids **1** and **2** in d_6-DMSO show N–H and O–H resonances at *ca.* 9.2 ppm and 11.3 ppm, respectively, both of which are concentration-dependent due to extensive intermolecular hydrogen bonding at high concentrations. The ^{1}H NMR spectrum of **1** exhibits 4 resonances at 8.77, 8.55, 7.93 and 7.33 ppm corresponding to the four protons of the *meta*-substituted pyridine ring, while that of **2** has two resonances at 8.57 and 7.54 ppm corresponding to the four protons of the *para*-substituted derivative.

3.2. Synthesis and characterisation of Pt^{II} and Pt^{IV} complexes *6–14*

The dichlorido Pt^{II} complexes, **6**–**10** and their Pt^{IV} analogues, **11**–**14** were prepared by reaction of $K_2[Pt^{II}Cl_4]$ or $K_2[Pt^{IV}Cl_6]$, respectively, with the appropriate pyridine derivative (pyd) in aqueous or aqueous/methanolic solutions (Scheme 1).

The previously reported Pt^{II} pyridine analogue, *cis*-$[Pt^{II}Cl_2(py)_2]$ **10** [31], was also synthesised to serve as a reference standard in biological testing. In all cases the yellow Pt^{II} and Pt^{IV} products were obtained in good yield (60–80%) and excellent purity and were further characterised by IR and ^{1}H NMR spectroscopy. The *cis*-configurations of the Pt^{II} complexes, **6**–**10** (Fig. 2), were confirmed by the classic Kurnakov test [32].

The spectroscopic data for the Pt^{II} and Pt^{IV} pyhaH and pycaH complexes are consistent with coordination *via* the pyridine nitrogen and reveal the free nature of the uncoordinated hydroxamic or carboxylic acid moiety as expected. Selected IR and far-IR spectral data for the free ligands and Pt^{II} and Pt^{IV} complexes are provided in Supplementary data (Table 1). Briefly the $\nu_{C=O}$ of the Pt pyhaH and pycaH complexes are found at *ca.* 1660 and 1705 cm^{-1}, respectively, and as expected are comparable to those of the corresponding free ligands. The hydroxamic acid complexes, in addition, display sharp ν_{N-H} and broad ν_{O-H} stretches, again comparable to those of the corresponding free ligands. Far-IR data can also be particularly useful in determining the stereochemistry of the complexes



Scheme 1. Synthesis of (a) *cis*-$[Pt^{II}Cl_2(pyd)_2]$ and (b) *cis*-$[Pt^{IV}Cl_4(pyd)_2]$.

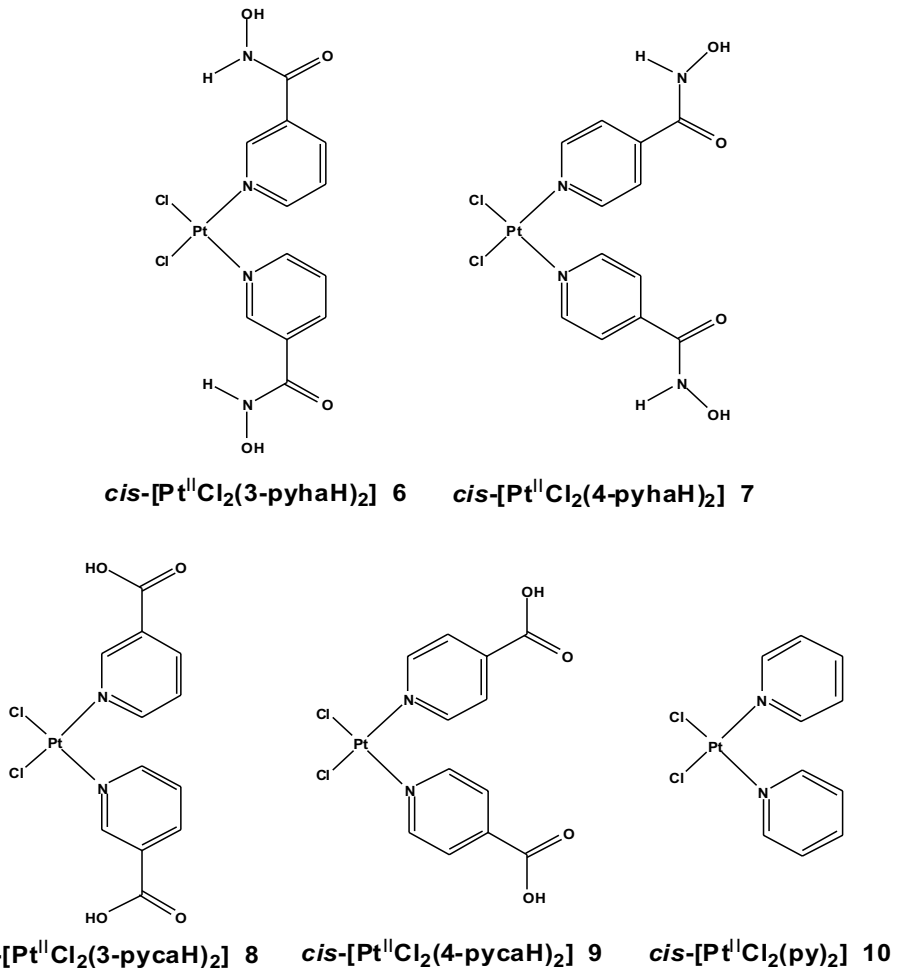


Fig. 2. Structures of the dichlorido Pt^{II} complexes.

synthesised. For a square planar Pt^{II} complex of general formula $PtCl_2L_2$, where L is a monodentate ligand, the *trans*-isomer (D_{2h}) exhibits only one ν_{Pt-Cl} whereas the *cis*-isomer (C_{2v}) exhibits two stretches. For Pt^{IV} complexes of type $PtCl_4L_2$, the *trans*-isomer (D_{4h}) exhibits one ν_{Pt-Cl} and the *cis*-isomer (C_{2v}) exhibits four [33]. The far-IR data support the *cis* configuration for **6** and **8**–**14**. Occasionally the ν_{Pt-Cl} merge as is the case with *cis*-$[Pt^{II}Cl_2(4\text{-pyhaH})_2]$ **7** and the configuration of the complex cannot be accurately determined from far-IR data alone.

The ^1H NMR spectra for all the Pt complexes support the presence of one isomer only. For the pyhaH complexes **6**, **7**, **11** and **12** in d^6-DMSO, N–H and O–H resonances are observed at *ca.* 9.3 ppm and *ca.*11.5 ppm, respectively, and are, as expected, comparable to those of the free ligands. The ^1H NMR spectrum of *cis*-$[Pt^{II}Cl_2(3\text{-pyhaH})_2]$ contains 4 resonances at 8.98, 8.76, 8.14 and 7.47 ppm corresponding to the eight protons of the *meta*-substituted pyridine rings. A similar overall pattern is observed in the ^1H NMR spectra of the Pt^{II} and Pt^{IV} complexes with 4 and 2 resonances integrating well for the complexes with coordinated *meta* and *para*-substituted pyridine rings, respectively, and a shift consistent with complexation.

*3.3. Structural characterisation of cis-[$Pt^{IV}Cl_4$(4-pyhaH)$_2$] · 2CH_3OH (**12**)*

Yellow crystals of **12** suitable for a single crystal X-ray diffraction experiment were obtained by slow evaporation from a methanol solution. The atomic numbering scheme and atom connectivity for **12** are shown in Fig. 3 and a selection of bond lengths and angles reported in Table 2. In **12**, the Pt^{IV} complex displays a near perfect octahedral geometry, not surprisingly given its symmetric nature. The N(1)–Pt–N(1) and the Cl(2)#1–Pt–Cl(2) bond angles are 178.42(6)° and 179.86(4)°, respectively. The N(1)–Pt–Cl(1)#1 and N(1)–Pt–Cl(2)#1 bond angles are 89.91(6)° and 89.21(7)°, respectively. The Pt–Cl bond lengths range from 2.295(1) to 2.308(1) Å and the shorter Pt–N bond lengths are 2.062(2) Å. The two pyhaH ligands lie in the *cis*-configuration where each is present as a monodentate ligand coordinated *via* the pyridine nitrogen only with an uncoordinated hydroxamic acid functional group.

In addition, hydroxamic acids are known to adopt one of two tautomeric forms, the enol and the keto, each of which can exist as *E* or *Z* conformers [19], where the stereodescriptors *E* and *Z* are used to describe the *trans* and *cis*

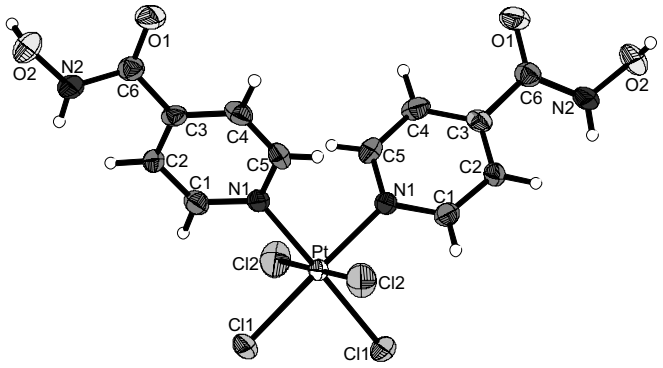


Fig. 3. ORTEP diagram of **12** with solvent molecules omitted. The atomic numbering scheme is displayed (thermal ellipsoids at 80% probability level).

Table 2
Selected bond lengths (Å) and angles (°) with estimated standard deviations for **12**

Bond atoms	Distance (Å)	Angle atoms	Angle (°)
Pt–N(1)	2.062(2)	N(1)–Pt–N(1)#1	91.66(12)
Pt–N(1)#1	2.062(2)	N(1)–Pt–Cl(1)#1	89.91(6)
Pt–Cl(1)#1	2.2951(7)	N(1)#1–Pt–Cl(1)#1	178.42(6)
Pt–Cl(1)	2.2951(7)	N(1)–Pt–Cl(1)	178.42(6)
Pt–Cl(2)#1	2.3084(7)	N(1)#1–Pt–Cl(1)	89.91(6)
Pt–Cl(2)	2.3084(7)	Cl(1)#1–Pt–Cl(1)	88.51(4)
C(3)–C(6)	1.497(3)	N(1)–Pt–Cl(2)#1	89.21(7)
C(6)–O(1)	1.232(3)	N(1)#1–Pt–Cl(2)#1	90.69(7)
C(6)–N(2)	1.330(3)	Cl(1)#1–Pt–Cl(2)#1	89.18(3)
N(2)–O(2)	1.394(3)	Cl(1)–Pt–Cl(2)#1	90.93(3)
		N(1)–Pt–Cl(2)	90.69(7)
		N(1)#1–Pt–Cl(2)	89.21(7)
		Cl(1)#1–Pt–Cl(2)	90.93(3)
		Cl(1)–Pt–Cl(2)	89.18(3)
		Cl(2)#1–Pt–Cl(2)	179.86(4)

orientation of the OH and C=O groups of the hydroxamic acid. The X-ray structural determination of **12** evidenced the free hydroxamic acid moieties in the keto form, adopting *Z* conformation. The hydroxamic acid NH and OH each hydrogen-bond to the oxygen acceptor atoms of different methanol solvent molecules with NH···O and OH···O bond length of approximately 2.00 and 1.81 Å, respectively, while the hydroxamic acid carbonyl oxygen hydrogen-bonds to a third methanol solvent molecule with an O···HO bond length of approximately 1.86 Å (Supplementary data, Fig. 1 and Table 2). With the complex situated on a twofold axis, a three-dimensional hydrogen-bonded lattice results (Fig. 4). The hydrogen-bond distances and angles are presented in Supplementary data (Table 2).

The crystal structure of **12**, together with a comparison of the far-IR spectral data for **12** with those of **11**, **13** and **14**, assist in the definitive assignment of the *cis*-configuration for each of the Pt^{IV} pyhaH and pycaH complexes synthesised (Fig. 5). Selected IR and far-IR spectral data are provided in Supplementary data (Table 1).

3.4. Synthesis and characterisation of $K[Ru^{II}(Hedta)(NO)Cl]\cdot H_2O$ (**15**)

To establish that the free hydroxamic acid moieties in *cis*-$[Pt^{II}Cl_2(x\text{-pyhaH})_2]$ ($x = 3$, 4) are sources of NO, we reacted *cis*-$[Pt^{II}Cl_2(x\text{-pyhaH})_2]$ with the well-known ruthenium (Ru) NO scavenger, $K[Ru^{III}(Hedta)Cl]\cdot 2H_2O$, which resulted in the facile formation of the Ru^{II}-nitrosyl, $K[Ru^{II}(Hedta)(NO)Cl]\cdot H_2O$. Reaction of *cis*-$[PtCl_2(py)_2]$ with $K[Ru^{III}(Hedta)Cl]\cdot 2H_2O$ did not yield a Ru^{II}-nitrosyl product.

The Ru^{II}–NO^+ complex, $K[Ru^{II}(Hedta)(NO)Cl]\cdot H_2O$ (**15**) was obtained upon reaction of *cis*-$[Pt^{II}Cl_2(x\text{-pyhaH})_2]$ ($x = 3$, 4) i.e. **6** or **7** with the well-known NO scavenger, $K[Ru^{III}(Hedta)Cl]\cdot 2H_2O$. Elemental analysis, IR, ^1H and ^{13}C NMR and ESI-mass spectra are consistent with the formulation, $K[Ru^{II}(Hedta)(NO)Cl]\cdot H_2O$ and concur with previously reported examples of Ru^{II}-edta-NO

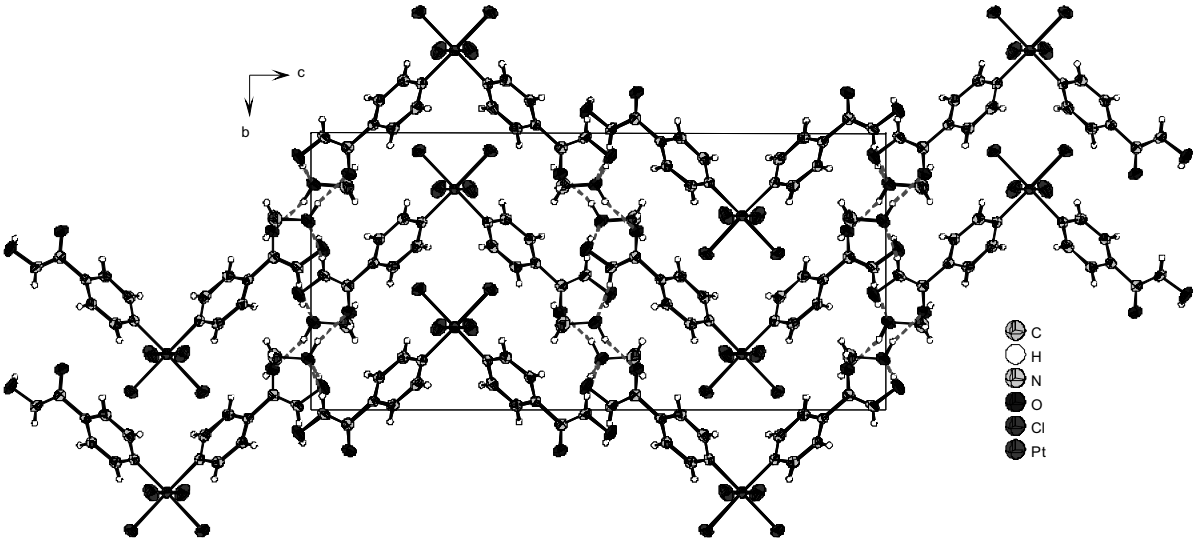
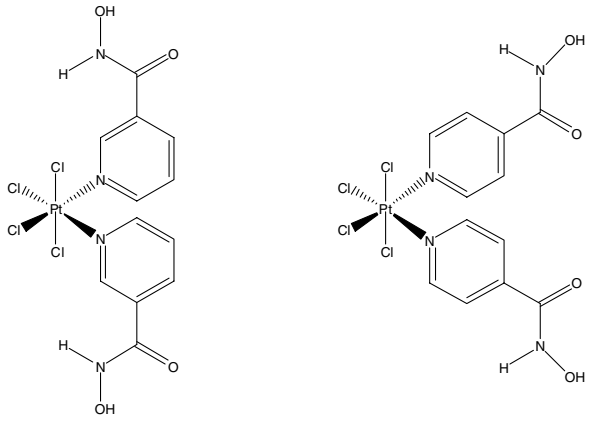
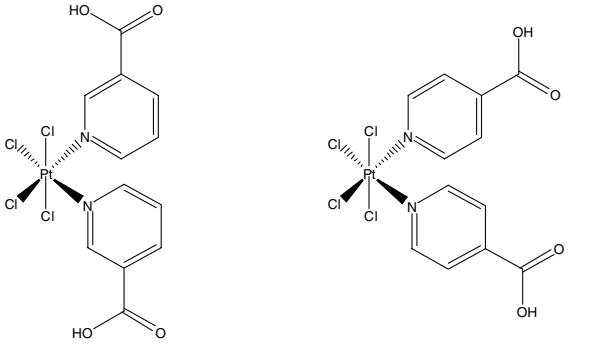


Fig. 4. Crystal packing of **12**. View of three-dimensional hydrogen-bonded lattice along [100] (thermal ellipsoids at 50% probability level).



***cis*-[Pt^{IV}Cl$_4$(3-pyhaH)$_2$] 11** **cis-[Pt^{IV}Cl$_4$(4-pyhaH)$_2$] 12**



***cis*-[Pt^{IV}Cl$_4$(3-pycaH)$_2$] 13** **cis-[Pt^{IV}Cl$_4$(4-pycaH)$_2$] 14**

Fig. 5. Structures of tetrachlorido Pt^{IV} complexes.

complexes in the literature [34]. The IR spectra of **15** contains a distinctive ν_{NO} at 1894 cm^{-1}. ESI-MS in the negative mode was used to unequivocally identify the Ru^{II}–NO$^+$ complex, [Ru^{II}(Hedta)(NO)Cl]$^-$; a mass peak at 456 amu with the correct isotopic abundances was observed. Previous reported reactions of K[Ru^{III}(Hedta)Cl] · 2H$_2$O with hydroxamic acids such as benzohydroxamic acid gave the Ru^{II}–NO$^+$ complex, K$_2$[Ru^{II}(edta)(NO)Cl] [18]. The doubly protonated edta complex Ru(H$_2$edta)(NO)Cl was previously isolated by reacting K[Ru(Hedta)Cl] · 2H$_2$O with *N*-methyl-*N*-nitroso-*p*-toluenesulfonamide or NO gas under argon [34]. Depending on pH, the Ru^{II}-NO$^+$ complexes can be isolated with the free arm of the ethylenediaminetetraacetate in the protonated or the anionic form.

3.5. Pharmacological tests

The free ligands **1**–**4**, benzohydroxamic acid **5** and the Pt^{II} compounds **6**–**10** and their corresponding reference numbers are listed in Table 3.

The effects on vasorelaxation of Pt^{II} compounds **6**–**9**, the hydroxamic acid ligands **1** and **2**, the carboxylic acid ligands **3** and **4** and the control compounds, benzohydroxamic acid **5**, *cis*-[Pt^{II}Cl$_2$(py)$_2$] (**10**), and cisplatin were studied using thoracic aorta rings isolated from rats. Given the fact that Pt^{IV} compounds are thought to be activated by reduction to their corresponding Pt^{II} analogues, the NO-releasing properties of the Pt^{IV} compounds herein described were not investigated.

Table 3
The free ligands, benzohydroxamic acid and the Pt^{II} compounds and their corresponding reference numbers

3-Pyridinehydroxamic acid (3-pyhaH)	**1**
4-Pyridinehydroxamic acid (4-pyhaH)	**2**
3-Pyridinecarboxylic acid (nicotinic acid) (3-pycaH)	**3**
4-Pyridinecarboxylic acid (isonicotinic acid) (4-pycaH)	**4**
Benzohydroxamic acid (bhaH)	**5**
cis-[Pt^{II}Cl$_2$(3-pyhaH)$_2$] · 2H$_2$O	**6**
cis-[Pt^{II}Cl$_2$(4-pyhaH)$_2$] · H$_2$O	**7**
cis-[Pt^{II}Cl$_2$(3-pycaH)$_2$]	**8**
cis-[Pt^{II}Cl$_2$(4-pycaH)$_2$]	**9**
cis-[Pt^{II}Cl$_2$(py)$_2$]	**10**

Compounds **6** and **7**, as well as their ligands **1** and **2**, induce the same extent (~80% at the highest concentration used) of vasorelaxation of aortic rings pre-contracted with phenylephrine, irrespective of the position in the pyridine ring of the hydroxamic acid moiety (Fig. 6). Benzohydroxamic acid, used as a positive control [18], induces vasorelaxation to a lesser extent (Fig. 8). Ligands characterised by the presence of a carboxylic acid group, i.e. compounds **3** and **4**, induce mild relaxation of aorta rings, comparable to that induced by water (the solvent used to dissolve these compounds), that reaches approximately 30% at concentrations $\geqslant 10^{-7}$ M (Fig. 7). In contrast, the corresponding Pt derivatives **8** and **9** cause vasorelaxation statistically (**3** versus **8** $p < 0.02$ for concentrations $\geqslant 10^{-7}$ M) greater than that of the free ligands, with a maximum of approximately 60%, at the highest concentration used (Fig. 7).

Cisplatin and *cis*-[Pt^{II}Cl$_2$(py)$_2$] **10**, studied in the same experimental model (Fig. 8), do not induce relaxation of the aorta rings (relaxation comparable to that induced by

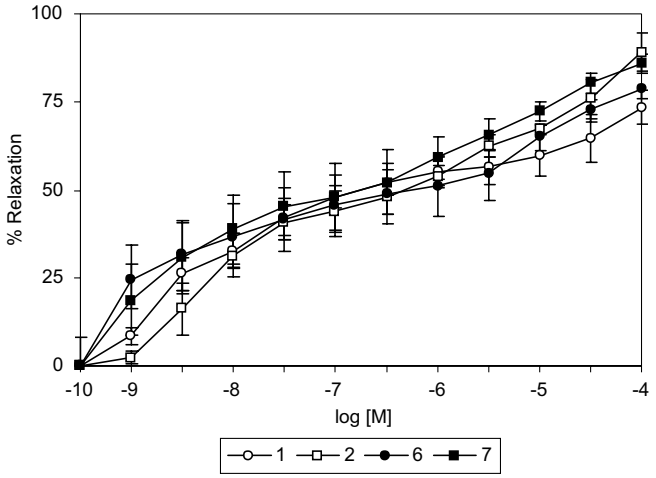


Fig. 6. Effects of compounds 3-pyhaH **1**, 4-pyhaH **2** and of respective platinum compounds *cis*-[Pt^{II}Cl$_2$(3-pyhaH)$_2$] (**6**) and *cis*-[Pt^{II}Cl$_2$(4-pyhaH)$_2$] (**7**) on aortic ring relaxation.

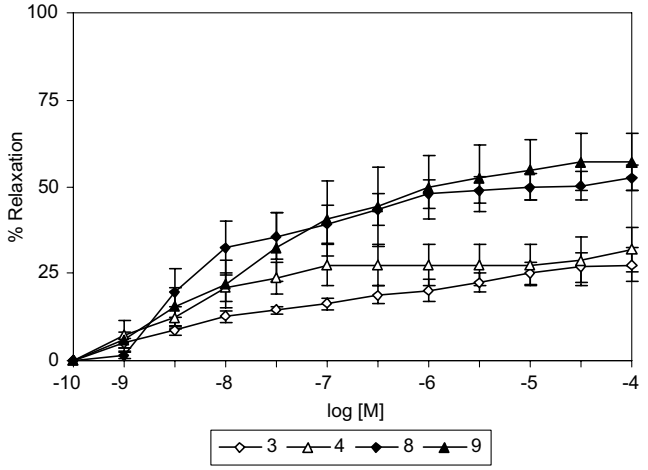


Fig. 7. Effects of compounds 3-pycaH **3**, 4-pycaH **4** and of respective platinum compounds *cis*-[$Pt^{II}Cl_2$(3-pycaH)$_2$] (**8**) and *cis*-[$Pt^{II}Cl_2$-(4-pycaH)$_2$] (**9**) on aortic rings relaxation.

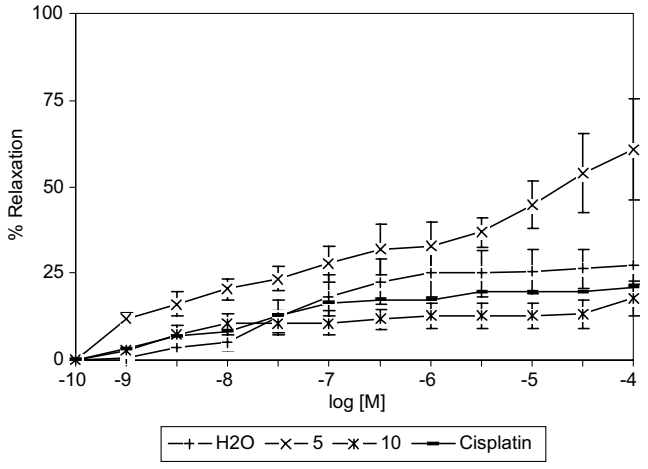


Fig. 8. Effects of water, benzohydroxamic acid **5**, *cis*-[$Pt^{II}Cl_2(py)_2$] (**10**) and cisplatin on aortic rings relaxation.

water) suggesting the lack of any role of the Pt ion *per se* in this phenomenon.

The involvement of NO in the induced vasorelaxation of compounds **6** and **8** was further investigated in the presence and absence of the guanylate cyclase inhibitor methylene blue (Fig. 9). Methylene blue completely abolished the vasorelaxation induced by both compounds **6** and **8**, indicating the involvement of the NO signaling pathway, likewise in the case of compound **8**, a derivative free of the hydroxamic acid moiety.

This data show that both hydroxamic acid and carboxylic acid derivatives in the rat aortic ring model cause NO-dependent releasing properties through a mechanism involving the NO signaling pathway, as supported by the inhibitory effects of the guanylate cyclase inhibitor methylene blue. The former exhibited enhanced NO-dependent releasing properties relative to the latter. It should be stressed that only hydroxamic acid derivatives, *via* the hydroxamic acid functional group, have the potential to

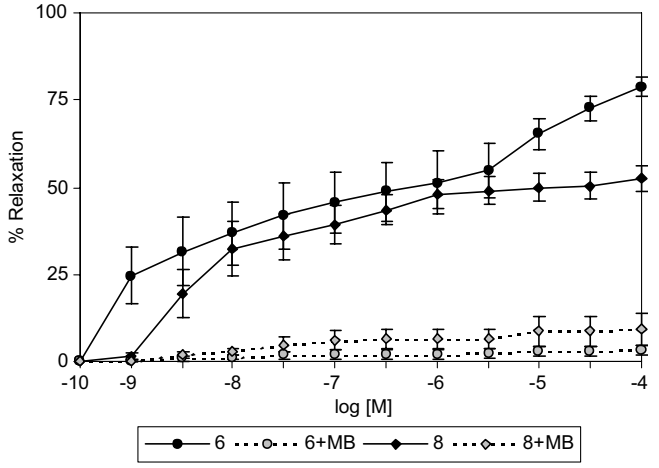


Fig. 9. Effects of *cis*-[$Pt^{II}Cl_2$(3-pyhaH)$_2$] (**6**) and *cis*-[$Pt^{II}Cl_2$(3-pycaH)$_2$] (**8**) in the presence or absence of methylene blue (MB).

release NO. It may therefore be hypothesised that the mechanism of vasorelaxation of aortic rings is probably due to stimulation of NOS activity of the aorta endothelial cells, to which NO-release from compounds **6** and **7** might also contribute, at least at concentrations higher than 3×10^{-5} M.

4. Conclusions

A series of novel Pt^{II} and Pt^{IV} pyridinehydroxamic acid complexes were synthesised with a view to advancing a new class of metallodrug with dual DNA-binding and NO-releasing properties. We can conclude from our investigation that the Pt^{II} pyridinehydroxamic acid derivatives induce potent *in vitro* effects attributable to either NO-release from the hydroxamic acid moiety and/or stimulation of iNOS of the endothelial cells. Considering the role of NO and iNOS activation in the process of proliferation and metastases, the data of the present work suggest further *in vitro* and *in vivo* testing of these compounds on cell proliferation and solid metastasising tumours, respectively. The complexes herein described are not however sufficiently soluble for a full biological investigation. We are currently in the process of developing analogues with superior aqueous solubility.

Acknowledgements

The authors thank Enterprise Ireland under its Basic Research Grant Programme and International Collaboration Scheme, EU COST D20, EU COST D39 and the Programme for Research in Third Level Institutions (PRTLI), administered by the HEA for funding. MADE project at Callerio Foundation is also acknowledged for support. We thank Dr. Dilip Rai (School of Chemistry and Chemical Biology, Science Education and Research Centre, UCD, Belfield, Dublin 4, Ireland) for MS analysis. C.J.M. gratefully acknowledges Johnson Matthey for the generous loan of $K_2[Pt^{II}Cl_4]$ and $K_2[Pt^{IV}Cl_6]$.

Appendix A. Supplementary material

CCDC 251892 contains the supplementary spectroscopic data for **1–4** and **6–14** and the crystallographic data for **12**. These data can be obtained free of charge via http://www.ccdc.cam.ac.uk/conts/retrieving.html, or from the Cambridge Crystallographic Data Centre, 12 Union Road, Cambridge CB2 1EZ, UK; fax: (+44) 1223-336-033; or e-mail: deposit@ccdc.cam.ac.uk. Supplementary data associated with this article can be found, in the online version, at doi:10.1016/j.poly.2007.03.011.

References

[1] M. Galanski, M.A. Jakupec, B.K. Keppler, Curr. Med. Chem. 12 (2005) 2075, and references therein.
[2] A.S. Abu-Surrah, M. Kettunen, Curr. Med. Chem. 13 (2006) 1337, and references therein.
[3] S. van Zutphen, J. Reedijk, Coord. Chem. Rev. 249 (2005) 2845.
[4] G. Natile, M. Coluccia, Met. Ions Biol. Syst. 42 (2004) 209.
[5] N. Farrell, Met. Ions Biol. Syst. 42 (2004) 251.
[6] B.A. Jansen, P. Wielaard, G.V. Kalayda, M. Ferrari, C. Molenaar, H.J. Tanke, J. Brouwer, J. Reedijk, J. Biol. Inorg. Chem. 9 (2004) 403.
[7] M.D. Hall, R.C. Dolman, T.W. Hambley, Met. Ions Biol. Syst. 42 (2004) 297.
[8] C. Napoli, L.J. Ignarro, Annu. Rev. Pharmacol. Toxicol. 43 (2003) 97.
[9] C.J. Marmion, B. Cameron, C. Mulcahy, S.P. Fricker, Curr. Top. Med. Chem. 4 (2004) 1585, and references therein.
[10] B. Bonavida, S. Khineche, S. Huerta-Yepez, H. Garban, Drug. Resist. Update 9 (2006) 157.
[11] L. Morbidelli, S. Donnini, M. Ziche, Curr. Pharm. Des. 9 (2003) 521.
[12] C. Bogdan, Nat. Immunol. 2 (2001) 907.
[13] S.P. Fricker, Platinum Met. Rev. 39 (1995) 150.
[14] C. Szabo, H. Ohshima, Nitric Oxide 1 (1997) 373.
[15] W. Xu, L.Z. Liu, M. Loizidou, M. Ahmed, I.G. Charles, Cell Res. 12 (2002) 311.
[16] G.R. Thatcher, Curr. Top. Med. Chem. 5 (2005) 597.
[17] R. Scatena, P. Bottoni, G.E. Martorana, B. Giardina, Expert Opin. Invest. Drugs 14 (2005) 835.
[18] C.J. Marmion, T. Murphy, J.R. Docherty, K.B. Nolan, Chem. Commun. (2000) 1153.
[19] C.J. Marmion, D. Griffith, K.B. Nolan, Eur. J. Inorg. Chem. 15 (2004) 3003, and references therein.
[20] E. Alessio, G. Mestroni, A. Bergamo, G. Sava, Curr. Top. Med. Chem. 4 (2004) 1525.
[21] M.J. Clarke, Coord. Chem. Rev. 236 (2003) 209.
[22] D. Griffith, E. Zangrando, E. Alessio, C.J. Marmion, Inorg. Chim. Acta 357 (2004) 3770.
[23] K. Karidi, A. Garoufis, A. Tsipis, N. Hadjiliadis, H. den Dulk, J. Reedijk, Dalton Trans. 7 (2005) 1176.
[24] N.P. Konovalova, S.A. Goncharova, L.M. Volkova, T.A. Rajewskaya, L.T. Eremenko, A.M. Korolev, Nitric Oxide 8 (2003) 59.
[25] J. Comiskey, E. Farkas, K.A. Krot-Lacina, R.G. Pritchard, C.A. McAuliffe (the late), K.B. Nolan, Dalton Trans. (2003) 4243.
[26] G.M. Sheldrick, University of Göttingen, 1997.
[27] C.M. Hu, J.J. Kang, C.C. Lee, C.H. Li, J.W. Liao, Y.W. Cheng, Eur. J. Pharmacol. 468 (2003) 37.
[28] B. van't Riet, G.L. Wampler, H.L. Elford, J. Med. Chem. 22 (1979) 589.
[29] D.A. Brown, R.A. Coogan, N.J. Fitzpatrick, W.K. Glass, D.E. Abukshima, L. Shiels, M. Ahlgren, K. Smolander, T.T. Pakkanen, T.A. Pakkanen, M. Perakyla, J. Chem. Soc., Perkin Trans. 2 (1996) 2673.
[30] C. Mulcahy, F.M. Dolgushin, K.A. Krot, D. Griffith, C.J. Marmion, Dalton Trans. (2005) 1993.
[31] N. Farrell, L.R. Kelland, J.D. Roberts, M. Van Beusichem, Cancer Res. 52 (1992) 5065.
[32] J. Arpalahti, B. Lippert, Inorg. Chim. Acta 138 (1987) 171.
[33] K. Nakamoto, Infrared and Raman Spectra of Inorganic and Coordination Compounds, 4th ed., Wiley, New York, 1986.
[34] A.A. Diamantis, J.V. Dubrawski, Inorg. Chem. 20 (1981) 1142.

fundamental roles in biochemical processes, including cardiovascular control, neuronal signaling and as an agent for defense mechanisms against microorganisms and tumors [16,17]. It has been demonstrated that NO is involved as a mediator in one tumor-induced angiogenic process, which is a key step in the formation of metastasis [18]. The possibility of usage of nitrosyl ruthenium complexes as novel antitumor agents which might release cytotoxic NO within tumor cells, leading to cell death, was suggested for the complexes *cis,fac*-$[RuCl_2(NO)(DMSO\text{-}O)_3]BF_4$, *cis,mer*-$[RuCl_2(NO)(py)_3(NO)]BF_4$ and *cis*-$[RuCl_2(NO)$-(terpy)]Cl [19–21]. Additionally it has been claimed that the activity of NAMI-A against disseminated tumors might be related with NO metabolism *in vivo* [20]. Phosphine complexes, including dppf ones (dppf = 1,1′-bis(diphenylphosphino)ferrocene), of various transition metals (Au, Ag, Cu, Ru, Rh, Pt, Pd) have been evaluated as potential antitumor agents in various human tumor cell lines [22–24]. For the Au complexes, for instance, the observed activity has been attributed to the presence of the phosphine ligands, since similar complexes without them had a very low activity [25]. In this sense the metallic center act as carrier of the real drug, protecting it of oxidation or other reactions in the cellular media [26]. The work presented in this paper describes the synthesis, structure, spectroscopic, electrochemical and preliminary *in vitro* antitumor activity of the nitrosyl *fac*-$[RuCl_3(NO)(dppf)]$.

2. Experimental

2.1. Materials for synthesis

Solvents utilized were purified by standard methods. All chemicals used were of reagent grade or comparable purity. The $RuCl_3 \cdot 3H_2O$ was purchased from Aldrich and the dppf ligand was purchased from Strem. The $RuCl_3NO \cdot 2H_2O$, was prepared according to the literature method [27].

2.2. Instrumentation

The infrared spectra were measured from powder samples diluted in KBr or in CH_2Cl_2 solutions using CaF_2 windows on an FTIR Bomem-Michelson 102 spectrometer in the 4000–200 cm^{-1} region for KBr sample and 4000–1000 cm^{-1} for CH_2Cl_2 solution. UV–Vis spectrum was recorded in a HP8452A (diode array) spectrophotometer. All the NMR experiments were recorded on a BRUKER equipment 9.4 T (400 MHz for hydrogen frequency). The $^{31}P\{^1H\}$, ^1H and $^{13}C\{^1H\}$ NMR spectra were recorded in CD_2Cl_2. TMS (^1H, $^{13}C\{^1H\}$) and H_3PO_4 85% ($^{31}P\{^1H\}$) were used for internal and external reference. Cyclic voltammetry (CV) experiments were carried out at room temperature in CH_2Cl_2 and CH_3CN containing 0.10 M $Bu_4N^+ClO_4$ (TBAP) (Fluka Purum) using a BAS-100B/W Bioanalytical Systems Instrument; the working and auxiliary electrodes were stationary Pt foils; a Luggin capillary probe was used and the reference electrode was Ag/AgCl. In these conditions the ferrocene is oxidized at 0.43 V (Fc^+/Fc) in CH_2Cl_2 or in CH_3CN. The microanalyses were performed by Microanalytical Laboratory of Universidade Federal de São Carlos, São Carlos (SP), using a FISIONS CHNS, mod. EA 1108 micro analyser.

2.3. X-ray crystallography

Red crystals of the *fac*-$[RuCl_3(NO)(dppf)]$ complex were grown by slow evaporation of dichloromethane/diethyl ether solution. The crystal was mounted on an Enraf-Nonius Kappa-CCD diffractometer with graphite monochromated Mo Kα ($\lambda = 0.71073$ Å) radiation. The final unit cell parameters were based on all reflections. Data collections were made using the COLLECT program [28]; integration and scaling of the reflections were performed with the HKL DENZO-SCALEPACK system of programs [29]. Absorption correction was carried out using the gaussian method [30]. The structure was solved by direct methods with SHELXS-97 [31]. The model was refined by full-matrix least squares on F2 by means of SHELXL-97 [32]. All hydrogen atoms were stereochemically positioned and refined with the ridging model. The ORTEP showed in Fig. 3 was prepared using ORTEP-3 for windows [33]. Hydrogen atoms of the aromatic rings were set isotropic with a thermal parameter 20% greater than the equivalent isotropic displacement parameter of the atom to which each one is bonded. The data collections and experimental details are summarized in Table 1, and selected bond distances and angles are given in Table 2.

2.4. Synthesis

To a deoxygenated methanolic solution (25 mL) of the $RuCl_3NO \cdot 2H_2O$ precursor (200 mg; 0.72 mmol) was added stoichiometric amount of the dppf ligand (396 mg; 0.72 mmol). The mixture was refluxed under Ar atmosphere for 6 h, leading to the formation of a red suspension. The resultant suspension was concentrated until ca. 5 mL and filtered off. The obtained solid was washed with cold methanol (1 × 5 mL) followed by diethyl ether (2 × 5 mL) and dried *in vacuo*. Yield: 338 mg (60%). ^1H NMR (400.21 MHz, CD_2Cl_2, 298 K): 4.54, 4.66, 4.70, 5.35[1] (s, 2H each, C_5H_4), 7.36 (m, 4H, Ph), 7.44 (t, 6H, Ph), 7.52 (m, 2H, Ph), 7.94 (m, 8H, Ph). $^{13}C\{^1H\}$ NMR (100.64 MHz, CD_2Cl_2, 298 K): 73.8 (t_{AB}, $^3J_{C-P} = 3.3$ Hz, CH of C_5H_4), 74.1 (t_{AB}, $^3J_{C-P} = 3.3$ Hz, CH of C_5H_4), 76.3 (t_{AB}, $^2J_{C-P} = 4.3$ Hz, CH of C_5H_4), 76.9 (t_{AB}, $^2J_{C-P} = 4.3$ Hz, CH of C_5H_4), 78.3 (d, $^1J_{C-P} = 57$ Hz, C of C_5H_4), 127.6 (t_{AB}, $^3J_{C-P} = 5.5$ Hz, C_m of Ph), 128.9 (t_{AB}, $^3J_{C-P} = 5.1$ Hz, C_o of Ph), 131.2 (dd, $^1J_{C-P} = 63$ Hz, $^3J_{C-P} = 3.5$ Hz, C_i of Ph), 131.4 (s, C_p of Ph), 131.9 (dd,

[1] Signal observed in $CDCl_3$. This singlet signal is coincident with the residual CH_2Cl_2 of the CD_2Cl_2 solvent.

Table 1
Crystallographic data and refinement details for *fac*-[$RuCl_3$(NO)(dppf)]

Empirical formula	$C_{34}H_{28}NOP_2Cl_3FeRu$
Formula weight	791.78
Temperature (K)	293(2)
Crystal system	orthorhombic
Space group	*Pnma*
Unit cell dimensions	
a (Å)	17.6531(3)
b (Å)	22.9843(4)
c (Å)	8.6763(2)
Volume (Å^3)	3520.36(12)
Z	4
D_{calc} (Mg/m^3)	1.494
Absorption coefficient (mm^{-1})	1.187
F(000)	1592
Crystal size (mm)	$0.29 \times 0.14 \times 0.12$
θ Range for data collection (°)	3.29–25.00
Limiting indices	$-20 \leqslant h \leqslant 20$, $-27 \leqslant k \leqslant 27$, $-10 \leqslant l \leqslant 9$
Reflections collected	18244
Independent reflections (R_{int})	3166 (0.0448)
Data/restraints/parameters	3166/0/233
Goodness-of-fit on F^2	1.099
Final *R* indices [$I > 2\sigma(I)$]	$R_1 = 0.0402$, $wR_2 = 0.1160$
R indices (all data)	$R_1 = 0.0468$, $wR_2 = 0.1203$
Extinction coefficient	0.0035(8)
Largest difference in peak and hole (e Å^{-3})	0.703 and −0.623

$^1J_{C-P} = 54$ Hz, $^3J_{C-P} = 3.4$ Hz, C_i of Ph), 132.1 (s, C_p of Ph), 134.6 (t_{AB}, $^2J_{C-P} = 8.8$ Hz, C_o of Ph), 136.0 (t_{AB}, $^2J_{C-P} = 8.4$ Hz, C_m of Ph). $^{31}P\{^1H\}$ NMR (162.01 MHz, CD_2Cl_2, 298 K): 28.0 (s). IR (KBr, cm^{-1}): 3110w, 3100w, 3056w, 1852sh, 1837s, 1830m, 1483m, 1435m, 1335w, 1189w, 1123w, 1099w, 1000w, 743m, 698s, 632w, 592w, 581w, 568w, 331w, 290w. UV–Vis (CH_2Cl_2) λ_{max} nm (log ε): 260 (4.28); 306 (3.94); 455 (2.52). ESI mass spectrum (in CH_2Cl_2 with Na^+ addition): *m*/*z* 816, $[M+Na]^+$; 756, $[M-Cl]^+$; 726, $[M-Cl-NO]^+$. *Anal.* Calc. for $C_{34}H_{28}Cl_3FeNOP_2Ru$: C, 51.57; H, 3.56; N, 1.77. Found: C, 51.35; H, 3.57; N, 1.50%.

2.5. Cell culture and cytotoxicity assay

In vitro cytotoxicity assays on cultured human tumor cell lines still represent the standard method for the initial screening of antitumoral agents. Thus, as a first step to assess its pharmacological properties, the new ruthenium complex was assayed toward a human breast tumor cell line MDA-MB-231 (ATCC No. HTB-26). The cells were routinely maintained with Dulbecco's Modified Eagle's medium (DMEM) supplemented with 10% fetal bovine serum (FBS), at 37 °C in a humidified 5% CO_2 atmosphere. After reach confluence, the cells were detached by tripsinization and counted. For the cytotoxicity assay, 4×10^4 cells well^{-1} were seeded in 200 μL of complete medium in 96-well plates (Corning Costar). The plates were incubated at 37 °C in 5% CO_2 for 24 h to allow cell adhesion prior to drug testing. The complex was dissolved in sterile DMSO (stock solution with maximum concentration of 2 mM) and diluted to 1.5, 1.0, 0.5, 0.2, 0.1, 0.05 and 0.02 mM. Two microliters of each complex sample were added to 200 μL medium (without FBS) in such a way that the final concentration of DMSO in each well was approximately 1% and the final concentration of the complex was diluted approximately 100 times. The others compounds evaluated (free dppf, $RuCl_3NO \cdot 2H_2O$ and cisplatin) were also dissolved in sterile DMSO. Cells were exposed to the complex for a 48 h-period. Cell respiration, as an indicator of cell viability, was determined by the mitochondrial-dependent reduction of MTT (3-(4,5-dimethylthiazol-2-yl)-2,5-diphenyltetrazolium bromide) to formazan [34]. MTT solution (0.5 mg/mL) was added to cell cultures and incubated for a 3-h period. Thereafter, 100 μL of isopropanol was added in order to dissolve the formazan crystals. The conversion of MTT to formazan by metabolically viable cells was monitored by an automated microplate reader at 570 nm. The percentage of cell viability was calculated by dividing the average absorbance of the cells treated with the ruthenium complex by that of the control; % cell viability versus drug concentration (logarithmic scale) was plotted to determine the IC_{50} (drug concentration at which 50% of the cells are viable relative to the control), with its estimated error derived from the average of 3 trials.

Table 2
Selected bond distances (Å) and angles (°) for *fac*-[$RuCl_3$(NO)(dppf)]

Ru–N	1.739(4)	N–Ru–Cl(2)	178.94(14)
Ru–Cl(2)	2.3475(14)	N–Ru–P	91.60(9)
Ru–P^i	2.4023(10)	Cl(2)–Ru–P	87.71(3)
Ru–P	2.4023(10)	P^i–Ru–P	98.90(4)
Ru–Cl(1)^i	2.4535(12)	N–Ru–Cl(1)^i	88.09(11)
Ru–Cl(1)	2.4535(12)	Cl(2)–Ru–Cl(1)	92.68(4)
P–C(31)	1.801(4)	P^i–Ru–Cl(1)	173.84(5)
P–C(11)	1.816(4)	P–Ru–Cl(1)	87.27(5)
P–C(21A)	1.850(11)	Cl(1)^i–Ru–Cl(1)	86.57(8)
N–O	1.149(6)	O–N–Ru	177.7(4)

3. Results and discussion

3.1. Characterization

The infrared spectrum of a pure sample of *fac*-[$RuCl_3$(NO)(dppf)] in KBr showed a split nitrosyl stretch with one peak at 1837 cm^{-1} and other at 1830 cm^{-1}. Additionally there was a shoulder at 1852 cm^{-1}. Splitting of NO peaks in solid state IR spectra have been observed for complexes such as *cis*-[RuCl(NO)(en)$_2$]Cl$_2$ [35], *mer*-[RuX_3(NO)(en)] where X = Cl, Br, and I [36] and [RuCl(NO)(bpe) $\cdot$ $2H_2O$] [bpe = *N*,*N*′-bis(2-pyridinecarboxamide)-1,2-ethane dianion [37]. To verify the possibility of some interaction with KBr as the cause of the extra NO stretch, a spectrum was obtained using a NaCl pellet. In this condition only one NO stretch at 1875 cm^{-1} and a shoulder at 1845 cm^{-1} were observed (see Fig. 1). Thus, it might be concluded from these data that bromide might displace chloride when the sample is prepared in KBr, because the

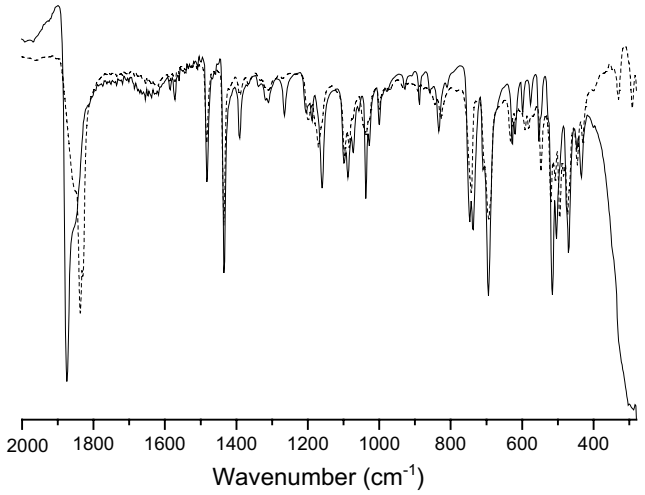


Fig. 1. IR spectra of *fac*-[$RuCl_3$(NO)(dppf)] in KBr (dashed) and NaCl pellets.

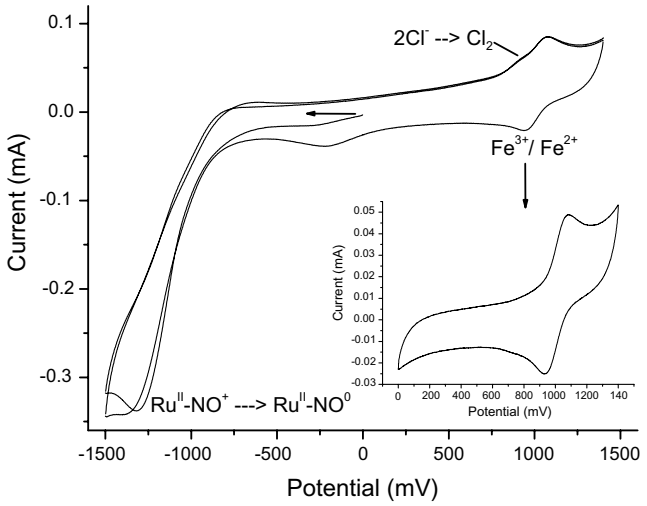


Fig. 2. Cyclic voltammetric response for *fac*-[$RuCl_3$(NO)(dppf)] in CH_2Cl_2 at 100 mV s^{-1}. Inset: same experiment but utilizing a smaller range of potentials (0–1400 mV).

observed peak in NaCl was at higher stretching frequency than that observed in KBr. To avoid this effect the IR spectrum was obtained in CH_2Cl_2 solution and just a single band for the νNO at 1860 cm^{-1} was observed, being another evidence of the solid state effect in the NO stretch split. Other important bands are also those involving the Ru center and the chloride ligands in the low energy region [38]. In the *fac*-[$RuCl_3$(NO)(dppf)] the Ru-Cl bands appeared at 331 and 290 cm^{-1} in KBr pellet as previously observed for the series *fac*-[$RuCl_3$(NO)(P–P)], P–P = dppm, dppe, c-dppen, dppp, dppb and dcpe [27,39,40].

In the $^{31}P\{^1H\}$ NMR spectrum the new complex showed a singlet signal at 28.0 ppm, indicating the magnetic equivalence of the phosphorus atoms, and consequently the *fac* arrangement for the chlorides. The free dppf ligand showed a resonance signal at −16.5 ppm, so the great shift observed indicates the coordination of the ligand to the ruthenium center. The ^1H NMR spectrum of the *fac*-[$RuCl_3$(NO)(dppf)] showed signals for the phenyl groups of the phosphine as multiplets at δ 7.34–7.94 ppm. The ferrocenyl protons show resonances in the region δ 4.50–5.35, appearing as four singlets with relative integrals 1:1:1:1. This is in contrast with the observed in other related 1,1′-disubstituted ferrocene compounds where the ferrocenyl signals usually appear as two triplets corresponding to the AA′BB′ spin system with a coupling constant of ca. 2 Hz for an eclipsed arrangement of the C_5H_4 rings [41]. This is indicative of a staggered arrangement for the two C_5H_4 rings, which has not been confirmed by X-ray crystallographic studies. So, for the title complex there is a difference in the C_5H_4 rings conformation when in solution or in solid state as shown by X-ray structure. Examples of dppf complexes with four singlets for the Cp rings are $[Ru(bipy)_2(dppf)]^{2+}$ [42] and *fac*-[$Re(CO)_3Cl$(dppf)] [43], as indicated by their X-ray analysis where staggered conformations were found. The cyclic voltammetric experiments of *fac*-[$RuCl_3$(NO)(dppf)] were carried out in CH_2Cl_2 and also in CH_3CN solutions. The CV response is dominated by an irreversible reduction, assigned to the reduction of the NO^+ group coordinated to Ru(II) [40,44–46] and a reversible pair corresponding to the pair Fe^{3+}/Fe^{2+} of the dppf ligand as showed in Fig. 2. The reduction of the coordinated NO^+ group is accompanied by a rapid chemical reaction, hence, there is no sign of a return wave even at low temperature (0 °C) and at scan rates up to 5 V s^{-1}. No additional studies were done to determine if NO is released after NO^+ reduction. After the irreversible NO^+ reduction, scanning to positive potential, a new dependent irreversible wave is observed as a shoulder at 0.95 V. This process can be ascribed to the oxidation of free chloride present in the solution indicating that reduction is accompanied by loss of chloride [20,40]. At slightly more positive potentials a reversible wave appeared corresponding to the Fe^{3+}/Fe^{2+} redox pair of the coordinated dppf ligand. In general when coordinated the $E_{1/2}$ of the dppf ligand increases due to the electronic delocalization that stabilizes de Fe^{2+}. This is observed in our complex and the redox potential for the free dppf of 0.74 V [47] is lower than the observed for *fac*-[$RuCl_3$-(NO)(dppf)], 1.0 V. Utilizing CH_3CN as solvent was possible to observe in addition to the previously mentioned waves, an irreversible anodic peak at 2.35 V due the oxidation of the very stable Ru^{II} center, this wave is independent of the NO^+ reduction. The high value for the Ru^{3+}/Ru^{2+}potential is explained by the presence of the NO^+ (strong π acceptor) [48] and it's irreversible character is indicative of instability of the Ru^{III}–NO^+ fragment. Comparing with other species in which the peak potential for the pair Ru^{3+}/Ru^{2+} is not observed, such as the *trans*-$[RuCl(NO)(dppe)_2]^{2+}$ and $[RuCl(NO)(dcpe)(bipy)]^{2+}$ [49,50], the [$RuCl_3$(NO)(dppf)] as well the previously studied [$RuCl_3$(NO)(P–P)] [39,40] complexes show a higher electron density on the metal center because of the presence of two additional chlorides.

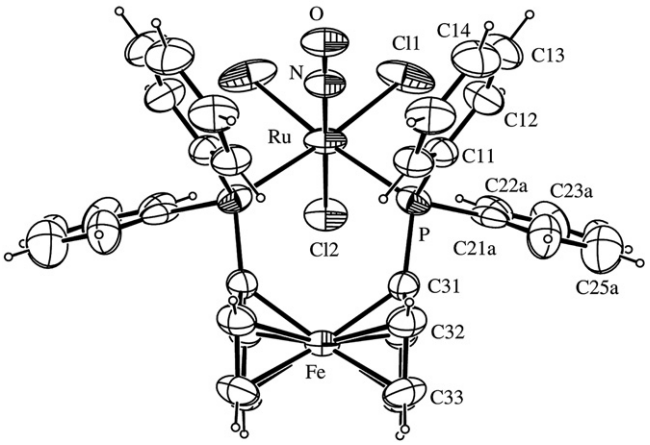


Fig. 3. ORTEP view of *fac*-[$RuCl_3(NO)(dppf)$] showing the atoms labeling and the 50% probability ellipsoids.

3.2. Structural studies

In the structure of the *fac*-[$RuCl_3(NO)(dppf)$] the metal adopts a distorted octahedral geometry as can be seen in the ORTEP (Fig. 3). The nitrosyl group is essentially linear, *trans* positioned to the Cl^-, consistent with the NO stretching vibration band in the IR spectra, both indicating that the NO group is formally bound to the metal as NO^+ [13]. The N–O bond lengths of 1.149(6) Å is consistent with other reported data [27,39,40,51]. The Ru–Cl(1) and Ru-Cl(3) bond lengths 2.4535(12) Å are longer than the Ru–Cl(2) one (*trans* NO; 2.3475(14)) by 0.106 Å, consistent with the *trans* strengthening effect of the NO, also know as 'inverse structural *trans* effect' [52]. The Ru–Cl distances in the range 2.35–2.45 Å are very similar to the related *fac*-[$RuCl_3(NO)(P–P)$] complexes [39,40]. The Ru–P distances of 2.40 Å are similar to the observed in the *fac*-[$RuCl_3$-(NO)(dppb)], but very different from that found in the [$Ru(RCOO)_2(dppf)$] complexes that are close to 2.26 Å [53]. Distances and angles involving the NO group are very similar from that found in the other members of the *fac*-[$RuCl_3(NO)(P–P)$] series [27,39,40,54]. The P(1)–Ru–P(2) angle is 98.90(4)°, which is in the ordinary range for ruthenium compounds with chelated dppf, for example, in the series [$Ru(RCOO)_2(dppf)$], $R = CH_3–CH_3CH_2–C_6H_5$ this angle is in the range 96.53(13)–99.58(5)° [53]. In addition, a variety of bonding parameters typically reported for dppf-containing compounds [55] are presented for some Ru complexes in Table 3. The new *fac*-[$RuCl_3(NO)(dppf)$] and the [$RuCl(dppf)(\eta^6$-*p*-cimeno)]PF_6 [56] present the cyclopentadienyl rings of the dppf ligand in the "synperiplanar eclipsed" conformation while in the [RuClH(dppf)-(CO)(PPh_3)] [57] such rings are in the "synclinal staggered" conformation.

Table 3
Structural parameters of dppf coordination in some Ru complexes [61–62]

	fac-[$RuCl_3(NO)$-(dppf)]	[RuCl(dppf)-(η^6-*p*-cimeno)]PF_6	[RuClH(dppf)-(CO)(PPh_3)]
P–Ru–P (°)	98.90(4)	93.7	102.2
X_A–Fe–X_B[a] (°)	176.92	179.1	178.9
P–Fe–P (°)	63.08	59.5	69.3
τ[b] (°)	0	1.3	50.2
av P–Ru (Å)	2.4023(10)	2.368	2.455
P–P (Å)	3.651	3.46	3.82
av δ_P[c] (Å)	−0.189		

[a] Centroid–Fe–centroid.
[b] The torsion angle C_A–X_A–X_B–C_B, where C is the carbon bonded to the P and X is the centroid.
[c] Deviation of the P atom from de Cp plane, a positive value meaning the P is closer to Fe.

Table 4
IC_{50} values in MDA-MB-231 cell line of *fac*-[$RuCl_3(NO)(dppf)$], $RuCl_3NO \cdot 2H_2O$, free dppf and cisplatin measured in DMSO solutions

Compound	IC_{50} (μM)
fac-[$RuCl_3(NO)(dppf)$]	10 ± 3
$RuCl_3NO \cdot 2H_2O$[a]	>200
dppf	97 ± 8
cisplatin	63 ± 5

[a] The maximum utilized concentration was 200 μM.

3.3. Cytotoxicity results

The cells were exposed to the compound for a relatively long period (2 days), to allow the compound to be able to reach DNA, or another unknown biological target. The complex *fac*-[$RuCl_3(NO)(dppf)$], the uncoordinated dppf and the $RuCl_3NO \cdot 2H_2O$ precursor complex were tested against the MDA-MB-231 cells. For comparison purposes, the cytotoxicity of cisplatin was evaluated under the same experimental conditions. The IC_{50} values, calculated from the dose–survival curves obtained after 48 h drug treatment from MTT assay, are shown in Table 4. The $RuCl_3$-$NO \cdot 2H_2O$ complex proved to be completely ineffective against the tested cell line. The free dppf ligand showed a low activity with an IC_{50} value of 97 ± 8 μM, approximately 10-fold higher than that of the new nitrosyl complex *fac*-[$RuCl_3(NO)(dppf)$]. Even compared with cisplatin (reference metallodrug) our complex is six times more active indicating its potentiality as an antitumor agent. Considering the lack of activity of the $RuCl_3(NO) \cdot 2H_2O$ species seems reasonable to suggest that the activity of *fac*-[$RuCl_3(NO)(dppf)$] is due to the presence of the dppf in its structure which is the real cytotoxic agent and its activity is increased when coordinated to the "$RuCl_3NO$" unity. Studies are been developed in our laboratory to check this possibility.

4. Conclusions

In this work the synthesis and full characterization of the new ruthenium nitrosyl complex *fac*-[$RuCl_3$-(NO)(dppf)] was showed. Spectroscopical, electrochemical and X-ray data indicated a complex of the type {Ru^{II}–

$NO^+\}^6$. Preliminary *in vitro* antitumor activity of this complex showed a moderate to good citotoxicity to the MDA-MB-231 tumor cell line with an IC_{50} of 10 ± 3 μM, a value that is lower than those observed for the $RuCl_3NO \cdot 2H_2O$ precursor, free dppf and cisplatin.

Acknowledgements

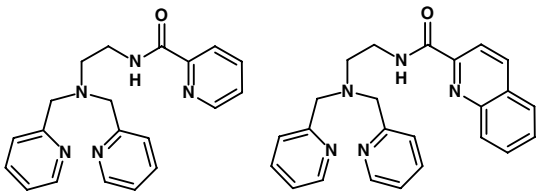
We thank CNPq, CAPES, FINEP, PRONEX and FAPESP for financial support.

Appendix A. Supplementary material

CCDC 634223 contains the supplementary crystallographic data for this paper. These data can be obtained free of charge via http://www.ccdc.cam.ac.uk/conts/retrieving.html, or from the Cambridge Crystallographic Data Centre, 12 Union Road, Cambridge CB2 1EZ, UK; fax: (+44) 1223-336-033; or e-mail: deposit@ccdc.cam.ac.uk. Supplementary data associated with this article can be found, in the online version, at doi:10.1016/j.poly.2007.03.009.

References

[1] E. Wong, C.M. Giandomenico, Chem. Rev. 99 (1999) 2451.
[2] D. Lebwohl, R. Canetta, Eur. J. Cancer 34 (1998) 1522.
[3] M.J. Clarke, F.C. Zhu, D.R. Frasca, Chem. Rev. 99 (1999) 2511.
[4] M. Galanski, V.B. Arion, M.A. Jakupec, B.K. Keppler, Curr. Pharm. Des. 9 (2003) 2078.
[5] C.S. Allardyce, P.J. Dyson, Platinum Met. Rev. 45 (2001) 8.
[6] C.G. Hartinger, S. Zorbas-Seifried, M.A. Jakupec, B. Kynast, H. Zorbas, B.K. Keppler, J. Inorg. Biochem. 100 (2006) 891.
[7] J.M. Rademaker-Lakhai, D. van den Bongard, D. Pluim, J.H. Beijnen, J.H.M. Schellens, Clin. Cancer Res. 10 (2004) 3717.
[8] M.A. Jakupec, V.B. Arion, S. Kapitza, E. Reisner, A. Eichinger, M. Pongratz, B. Marian, N.G.v. Keyserlingk, B.K. Keppler, Int. J. Clin. Pharmacol. Ther. 43 (2005) 575.
[9] W.H. Ang, P.J. Dyson, Eur. J. Inorg. Chem. (2006) 4003.
[10] Y.K. Yan, M. Melchart, A. Habtemariam, P.J. Sadler, Chem. Commun. (2005) 4764.
[11] M.J. Clarke, Coord. Chem. Rev. 232 (2002) 69.
[12] I. Kostova, Curr. Med. Chem. 13 (2006) 1085.
[13] G.B. Richter-Addo, P. Legzdins, Metal Nitrosyls, Oxford University Press, New York, 1992.
[14] R. Eisenberg, C.D. Meyer, Acc. Chem. Res. 8 (1975) 26.
[15] E. Tfouni, M. Krieger, B.R. McGarvey, D.W. Franco, Coord. Chem. Rev. 236 (2003) 57.
[16] L.J. Ignarro (Ed.), Nitric oxide: Biology and Pathobilogy, 1st ed., Academic Press, San Diego, 2000.
[17] S.H. Snyder, D.S. Bredt, Scientific American 266 (1992) 68.
[18] M. Ziche, L. Morbidelli, R. Choudhuri, H.T. Zhang, S. Donnini, H.J. Granger, R. Bicknell, J. Clin. Invest. 99 (1997) 2625.
[19] B. Serli, E. Zangrando, T. Gianferrara, L. Yellowlees, E. Alessio, Coord. Chem. Rev. 245 (2003) 73.
[20] B. Serli, E. Zangrando, E. Iengo, G. Mestroni, L. Yellowlees, E. Alessio, Inorg. Chem. 41 (2002) 4033.
[21] K. Karidi, A. Garoufis, A. Tsipis, N. Hadjiliadis, H. den Dulk, J. Reedijk, Dalton Trans. (2005) 1176.
[22] C. Bincoletto, I.L.S. Tersariol, C.R. Oliveira, S. Dreher, D.M. Fausto, M.A. Soufen, F.D. Nascimento, A.C.F. Caires, Bioorg. Med. Chem. 13 (2005) 3047.
[23] S.J. Berners-Price, R.J. Bowen, P. Galettis, P.C. Healy, M.J. McKeage, Coord. Chem. Rev. 186 (1999) 823.
[24] C. Marzano, M. Pellei, S. Alidori, A. Brossa, G.G. Lobbia, F. Tisato, C. Santini, J. Inorg. Biochem. 100 (2006) 299.
[25] S.J. Bernersprice, R.K. Johnson, A.J. Giovenella, L.F. Faucette, C.K. Mirabelli, P.J. Sadler, J. Inorg. Biochem. 33 (1988) 285.
[26] S.J. Bernersprice, R.E. Norman, P.J. Sadler, J. Inorg. Biochem. 31 (1987) 197.
[27] A.A. Batista, C. Pereira, S.L. Queiroz, L.A.A. de Oliveira, R.H.D. Santos, M.T.D. Gambardella, Polyhedron 16 (1997) 927.
[28] Enraf-Nonius, Collect, Nonius BV, Delft, The Netherlands (1997–2000).
[29] Z. Otwinowski, W. Minor, HKL Denzo and Scalepack, in: C.W. CarterJr., R.M. Sweet (Eds.), Methods in Enzymology, vol. 276, Academic Press, New York, 1997, p. 307.
[30] R.H. Blessing, Acta Crystallographica Section A 51 (1995) 33.
[31] G.M. Sheldrick, Shelxs-97. Program for Crystal Structure Resolution, University of Göttingen, Göttingen, Germany, 1997.
[32] G.M. Sheldrick, Shelxl-97, Program for Crystal Structure Analysis, University of Göttingen, Göttingen, Germany, 1997.
[33] L.J. Farrugia, J. Appl. Crystallogr. 30 (1997) 565.
[34] T. Mosmann, Journal of Immunological Methods 65 (1983) 55.
[35] H. Tomizawa, E. Miki, K. Mizumachi, T. Ishimori, Bull. Chem. Soc. Jp. 67 (1994) 1809.
[36] H. Tomizawa, K. Harada, E. Miki, K. Mizumachi, T. Ishimori, A. Urushiyama, M. Nakahara, Bull. Chem. Soc. Jp. 66 (1993) 1658.
[37] C.F. Fortney, R.E. Shepherd, Inorg. Chem. Commun. 7 (2004) 1065.
[38] K. Nakamoto, Infrared and Raman Spectra of Inorganic and Coordination Compounds, 5th ed., Wiley-Interscience, New York, 1997.
[39] G. Von Poelhsitz, M.P. de Araujo, L.A.A. de Oliveira, S.L. Queiroz, J. Ellena, E.E. Castellano, A.G. Ferreira, A.A. Batista, Polyhedron 21 (2002) 2221.
[40] G. Von Poelhsitz, R.C. de Lima, R.M. Carlos, A.G. Ferreira, A.A. Batista, A.S. de Araujo, J. Ellena, E.E. Castellano, Inorg. Chim. Acta 359 (2006) 2896.
[41] R. Broussier, A. Darold, B. Gautheron, Y. Dromzee, Y. Jeannin, Inorg. Chem. 29 (1990) 1817.
[42] V.W.W. Yam, V.W.M. Lee, K.K. Cheung, J. Chem. Soc., Dalton Trans. (1997) 2335.
[43] T.M. Miller, K.J. Ahmed, M.S. Wrighton, Inorg. Chem. 28 (1989) 2347.
[44] R.W. Callahan, T.J. Meyer, Inorg. Chem. 16 (1977) 574.
[45] D.A. Cavarzan, F.R. Caetano, L.L. Romualdo, F.B. do Nascimento, A.A. Batista, J. Ellena, A. Barison, M.P. de Araujo, Inorg. Chem. Commun. 9 (2006) 1247.
[46] F. Baumann, W. Kaim, L.M. Baraldo, L.D. Slep, J.A. Olabe, J. Fiedler, Inorg. Chim. Acta 285 (1999) 129.
[47] A.E. Gerbase, E.J.S. Vichi, E. Stein, L. Amaral, A. Vasquez, M. Horner, C. MaichleMossmer, Inorg. Chim. Acta 266 (1997) 19.
[48] D.M.P. Mingos, D.J. Sherman, Advances in Inorganic Chemistry 34 (1989) 293.
[49] R.C.L. Zampieri, G. Von Poelhsitz, A.A. Batista, O.R. Nascimento, J. Ellena, E.E. Castellano, J. Inorg. Biochem. 92 (2002) 82.
[50] G. Von Poelhsitz, A.L. Bogado, G.D. de Souza, E. Rodrigues-Filho, A.A. Batista, M.P. de Araujo, Inorg. Chem. Commun. 10 (2007) 133.
[51] R.K. Coll, J.E. Fergusson, V. McKee, C.T. Page, W.T. Robinson, T.S. Keong, Inorg. Chem. 26 (1987) 106.
[52] B.J. Coe, S.J. Glenwright, Coord. Chem. Rev. 203 (2000) 5.
[53] X.L. Lu, S.Y. Ng, J.J. Vittal, G.K. Tan, L.Y. Goh, T.S.A. Hor, J. Organom. Chem. 688 (2003) 100.
[54] A.A. Batista, C. Pereira, K. Wohnrath, S.L. Queiroz, R.H.D. Santos, M.T.D. Gambardella, Polyhedron 18 (1999) 2079.
[55] G. Bandoli, A. Dolmella, Coord. Chem. Rev. 209 (2000) 161.
[56] S.B. Jensen, S.J. Rodger, M.D. Spicer, J. Organom. Chem. 556 (1998) 151.
[57] A. Santos, J. Lopez, J. Montoya, P. Noheda, A. Romero, A.M. Echavarren, Organometallics 13 (1994) 3605.



$PaPy_3H$ $PaPy_2QH$

The $\{Ru–NO\}^6$ nitrosyl $[(PaPy_3)Ru(NO)](BF_4)_2$ exhibits great stability in aqueous solution over a wide range of pH (3–11) for long periods of time. We have employed this nitrosyl to successfully deliver NO to biological targets such as myoglobin, cytochrome c oxidase and soluble guanylate cyclase under *controlled conditions of illumination* [18,21,22]. In order to further improve the NO donating capacity of this NO donor, we recently decided to increase the extent of conjugation in the carboxamide arm of the ligand. We hypothesized that the greater light-harvesting properties of the quinoline moiety (versus pyridine) might enhance the photolability of the Ru–NO unit. In such attempt, we have now synthesized the ligand *N*,*N*-bis (2-pyridylmethyl)amine-*N*-ethyl-2-quinaldine-2-carboxamide ($PaPy_2QH$) that contains a quinoline group in place of pyridine [23]. In this paper we report the synthesis, structure and properties of the $\{Ru–NO\}^6$ nitrosyl $[(PaPy_2Q)Ru(NO)](BF_4)_2$. This nitrosyl indeed exhibits improved photoefficiency when exposed to low-intensity (mW) UV light.

2. Experimental

2.1. Materials and methods

2.1.1. General procedures

The starting Ru(II) salt $[Ru(DMSO)_4Cl_2]$ was prepared from $RuCl_3 \cdot 3H_2O$ as described elsewhere [24]. NO gas was supplied by Spectra Gases, Inc. and purified as described previously [16]. All other reagents were procured from Aldrich Chemical Co. The solvents used in this work were dried according to standard procedures: EtOH and MeOH were distilled from Mg/I_2; MeCN and CH_2Cl_2 from CaH_2; Et_2O from Na; and DMF from BaO. The two ligands $PaPy_3H$ and $PaPy_2QH$ were synthesized by following published procedures [20,23]. $[(PaPy_3)Ru(NO)](BF_4)_2$ was synthesized according to procedures published by us in a previous account [19].

2.1.2. Synthesis of $[(PaPy_2Q)Ru(NO)](BF_4)_2$

A slurry of the yellow starting salt $[Ru(DMSO)_4Cl_2]$ (0.180 g, 0.38 mmol) in 15 ml of EtOH was heated to reflux temperature to generate a clear orange solution. Separately, 0.150 g (0.38 mmol) of the ligand $PaPy_2QH$ was dissolved in 5 ml of EtOH and deprotonated with NaOEt (generated in situ with 10 mg (0.42 mmol) of NaH). The two solutions were then mixed at reflux temperature to generate a dark orange solution. After 35 min of heating, 1 equiv. of solid $NaNO_2$ (0.030 g, 0.42 mmol) was added to the hot solution and the heating was continued for 45 min. A dilute solution of HBF_4 in 3 ml of EtOH was then added to the hot solution and the resulting precipitate was collected by filtration through glass frit under N_2 atmosphere. The reddish-orange solid was washed several times with cold EtOH, then Et_2O and dried under high vacuum. This crude complex was finally stirred in CH_2Cl_2 containing 5% MeOH for several hours. This step provided pure $[(PaPy_2Q)Ru(NO)](BF_4)_2$ (not soluble in CH_2Cl_2/MeOH) as a yellow solid (170 mg) in 65% yield. *Anal*. Calc. for $C_{24}H_{22}B_2F_8N_6O_2Ru$: C, 41.11; H, 3.16; N, 11.99. Found: C, 40.95; H, 3.26; N, 12.07%. Selected IR frequencies (KBr disk, cm^{-1}): 1868 (s, ν_{NO}), 1633 (vs, ν_{CO}), 1457 (w), 1378 (m), 1083 (s), 1035 (s), 767 (m), 533 (w), 521 (w). Electronic spectrum in MeCN, λ_{max} in nm (ε in $M^{-1}\,cm^{-1}$): 245 (19460), 308 (4280), 335 (sh, 3480), 420 (1040). ^1H NMR (CD_3CN) δ: 9.07 d (1H), 8.38 m (2H), 8.23 t (2H), 8.17 m (2H), 8.03 t (1H), 7.90 d (2H), 7.55 d (2H), 7.47 t (2H), 5.31 m (4H), 3.86 (2H), 3.42 t (2H).

2.2. Physical measurements

2.2.1. Spectroscopy

The ^1H NMR spectra were recorded at 298 K on a Varian 500 MHz instrument. A Perkin–Elmer Spectrum-One FT-IR spectrometer was used to monitor the IR spectra. The electronic absorption spectra were obtained with a Carey 50 spectrophotometer (Varian).

2.2.2. Photolysis experiments

Release of NO in solution under aerobic condition was monitored with an *in* NO Nitric Oxide Measuring System (Innovative Instruments, Inc.) using the *ami*NO-2000 electrode. The rates of NO release upon exposure to UV light were measured with a ~0.1 mM solution of the complex in 1 cm× 1 cm quartz cuvette. The light sources employed in this study include (a) an UV Transilluminator (UVP, Inc.) with peak intensity of 5 mW/cm^2 at 300 nm and (b) monochromatic light generated from an Apex Illuminator (150 W Xenon lamp) equipped with a Cornerstone 130 1/8M monochromator (measured intensity of 10 mW at 410 nm). The cuvettes (placed at a distance of 3 cm) were exposed to UV light for no more than 40 s per interval to prevent heating the solution and the electronic spectra were recorded. The apparent rates of NO release were followed at an appropriate wavelength for each compound and the absorbance versus time plots generated in SigmaPlot, and fitted to the 3-parameter exponential equation: $y = y_o + a^*(1 - \exp(-k^*x))$ as done previously. For quantum yield (ϕ) measurements, a ~0.3 mM solution was used to ensure sufficient absorbance ($\geqslant$99%) at the incident wavelength; no more than 20% photolysis occurred in each measurement. Standard actinometry using ferrioxalate was employed to calibrate the light source.

Table 1
Summary of crystal data for $[(PaPy_2Q)Ru(NO)](BF_4)_2 \cdot MeCN$

Empirical formula	$C_{26}H_{25}B_2F_8N_7O_2Ru$
Formula weight	742.22
Crystal color and habit	dichroic yellow needle
Crystal size (mm)	$0.45 \times 0.06 \times 0.05$
Crystal system	triclinic
Space group	$P\bar{1}$
Temperature (K)	90(2)
a (Å)	7.5961(8)
b (Å)	12.4837(13)
c (Å)	15.7711(17)
α (°)	72.844(2)
β (°)	85.539(2)
γ (°)	80.816(2)
Volume (Å^3)	1409.9(3)
Z	2
D_{calc} (Mg/m^3)	1.748
Absorbance coefficient, μ (mm^{-1})	0.650
Reflections collected	18 500
Independent reflections [R_{int}]	8121 [0.0441]
Observed reflections ($I > 2\sigma(I)$)	6629
Maximum and minimum transmission	0.968 and 0.759
Goodness-of-fit on F^2	1.017
Final R indices [$I > 2\sigma(I)$]	$R_1^a = 0.0425$, $wR_2^b = 0.1045$
R indices (all data)	$R_1 = 0.0580$, $wR_2 = 0.1129$

[a] $R_1 = \sum\|F_o| - |F_c\|/\sum|F_o|$.
[b] $wR_2 = \{\sum[w(F_o^2 - F_c^2)^2]/\sum[w(F_o^2)^2]\}^{1/2}$ and $w = 1/[\sigma^2(F_o^2) + (aP)^2 + (bP)]$, where $P = (2F_c^2 + F_o^2)/3$.

Table 2
Selected bond lengths (Å) and bond angles (°) for $[(PaPy_2Q)Ru(NO)](BF_4)_2$ and $[(PaPy_3)Ru(NO)](BF_4)_2$

	$[(PaPy_2Q)Ru(NO)](BF_4)_2$	$[(PaPy_3)Ru(NO)](BF_4)_2$
Ru–N(6)	1.779(2)	1.779(2)
N(6)–O(2)	1.147(3)	1.142(3)
Ru–N(1)	2.133(2)	2.097(2)
Ru–N(2)	1.988(2)	1.997(2)
Ru–N(3)	2.062(2)	2.073(3)
Ru–N(4)	2.084(2)	2.074(2)
Ru–N(5)	2.078(2)	2.086(2)
N(2)–C_{CO}	1.344(3)	1.340(4)
C_{CO}–O(1)	1.231(3)	1.230(4)
Ru–N(6)–O(2)	168.8(2)	170.9(2)
N(6)–Ru–N(1)	105.43(9)	98.63(10)
N(6)–Ru–N(2)	171.29(9)	172.23(11)
N(6)–Ru–N(3)	94.21(9)	101.97(10)
N(6)–Ru–N(4)	88.34(9)	89.91(10)
N(6)–Ru–N(5)	95.67(9)	94.06(10)

2.2.3. X-ray crystallography

Long yellow needles of $[(PaPy_2Q)Ru(NO)](BF_4)_2 \cdot MeCN$ were grown via vapor diffusion of Et_2O into an MeCN solution of the complex at room temperature. Diffraction data were collected at 90 K on a Bruker SMART ApexII instrument using Mo Kα radiation ($\lambda = 0.71073$ Å) and the data were corrected for absorption. The structures were solved using the standard SHELXS-97 package. Additional refinement details are contained in the CIF files (Supplementary material). Instrument parameters, crystal data, and data collection parameters are summarized in Table 1. A comparison of selected bond distances and bond angles for $[(PaPy_2Q)Ru(NO)](BF_4)_2$ and $[(PaPy_3)Ru(NO)](BF_4)_2$ are listed in Table 2.

3. Results and discussion

3.1. Synthesis

The nitrosyl $[(PaPy_2Q)Ru(NO)](BF_4)_2$ was synthesized via acidification of the corresponding Ru(II)–NO_2 precursor in a one-pot reaction (Eq. (1)) [25–27]. The reaction of the deprotonated ligand $PaPy_2Q^-$ with the Ru(II) starting salt $[Ru(DMSO)_4Cl_2]$ followed by the addition of $NaNO_2$ leads to the formation of the Ru(II)–NO_2 precursor (not yet successfully isolated). Acidification of this species, generated *in situ*, with HBF_4 finally affords the nitrosyl in good yield. Coordination of the deprotonated carboxamido nitrogen to the ruthenium center is not affected in this acidification step. Although addition of dilute $HClO_4$

$$Ru^{II}\text{–}NO_2 + 2H^+ \rightarrow \{Ru\text{–}NO\}^6 + H_2O \quad (1)$$

in place of HBF_4 results in formation of the perchlorate salt of the nitrosyl, acids like HCl afford an intractable mixture of species. $[(PaPy_2Q)Ru(NO)](BF_4)_2$ is soluble in a wide variety of polar solvents including H_2O, MeCN, DMF and MeOH.

3.2. Structure of $[(PaPy_2Q)Ru(NO)](BF_4)_2 \cdot MeCN$

The structure of the cation $[(PaPy_2Q)Ru(NO)]^{2+}$ is shown in Fig. 1. The pentadentate $PaPy_2Q^-$ ligand is coordinated to the ruthenium center via three ring nitrogens, the tertiary amine nitrogen and the carboxamido nitrogen. The sixth coordination site, *trans* to the carboxamido nitrogen, is occupied by NO and the overall geometry is pseudo octahedral. Similar binding by the analogous ligand $PaPy_3^-$ to ruthenium has been observed in $[(PaPy_3)$-

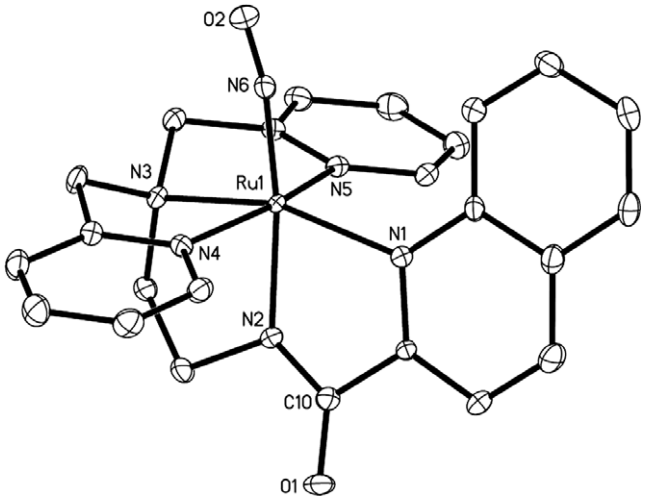


Fig. 1. Thermal ellipsoid (probability level 50%) plot of $[(PaPy_2Q)$-$Ru(NO)]^{2+}$ with the atom-labeling scheme. H atoms are not shown for the sake of clarity.

$Ru(NO)]^{2+}$ [19]. Although the metric parameters of $[(PaPy_2Q)Ru(NO)]^{2+}$ are very similar to those of $[(PaPy_3)Ru(NO)]^{2+}$, there are some differences. For example, the Ru–N(O) bond length of $[(PaPy_2Q)Ru(NO)]^{2+}$ is identical to that of $[(PaPy_3)Ru(NO)]^{2+}$ (both 1.779(2) Å long). Similarly, the N(6)–O(2) bond distances are very close to each other (1.142(3) Å and 1.147(3) Å). In both cases, the shortest bond between the ligand ($PaPy_3^-$ or $PaPy_2Q^-$) and the ruthenium center is the $Ru–N_{amido}$ bond (1.997(2) Å and 1.988(2) Å, respectively). However, the $Ru–N_{quin}$ distance of $[(PaPy_2Q)Ru(NO)]^{2+}$ is longer (2.133(2) Å) than the corresponding $Ru–N_{py}$ distance of $[(PaPy_3)Ru(NO)]^{2+}$ (2.097(2) Å). In addition, the quinoline moiety is slightly tilted away from the coordinated NO (Table 2). The latter difference most possibly arises from the steric bulk of the quinoline unit. The larger quinoline moiety also causes more bending of the Ru–N–O unit in $[(PaPy_2Q)Ru(NO)]^{2+}$ (168.8(2)°) compared to 170.9(2)° in $[(PaPy_3)Ru(NO)]^{2+}$. No π–π stacking has been noted in the structure of $[(PaPy_2Q)Ru(NO)](BF_4)_2 \cdot MeCN$.

3.3. Spectroscopic characterization

$[(PaPy_2Q)Ru(NO)]^{2+}$ exhibits sharp ^1H NMR spectrum in CD_3CN solution at 298 K (Fig. 2), typical of low-spin diamagnetic $\{Ru–NO\}^6$ complexes. The N–O stretching frequency (ν_{NO}) of $[(PaPy_2Q)Ru(NO)]^{2+}$ (1868 cm^{-1}) also falls within the generally accepted range (1800–1950 cm^{-1}) for such nitrosyls. Coordination of the deprotonated carboxamido nitrogen to the metal center is evident in the red-shift of the ν_{CO} value of the complex compared to that of the free ligand (1633 cm^{-1} versus 1667 cm^{-1}).

The electronic absorption spectrum of $[(PaPy_2Q)Ru(NO)]^{2+}$ (Fig. 3) consists of a prominent band at 420 nm ($\varepsilon = 1040\ M^{-1}\ cm^{-1}$) arising from the $d(Ru) \rightarrow \pi^*(NO)$ transition. Similar bands are also observed in other $\{Ru–NO\}^6$ nitrosyls such as [(salen)Ru(NO)(Cl)] ($\lambda_{max} = 376$ nm) and [(bpb)Ru(NO)(Cl)] ($\lambda_{max} = 380$ nm) [28,29]. The small red-shift of the absorption band of $[(PaPy_2Q)Ru(NO)]^{2+}$ compared to that of $[(PaPy_3)Ru(NO)]^{2+}$ ($\lambda_{max} = 410$ nm, Fig. 3) most possibly arises from the extended conjugation of the quinoline moiety [29]. Close inspection of the absorption spectra of $[(PaPy_2Q)Ru(NO)]^{2+}$ and $[(PaPy_3)Ru(NO)]^{2+}$ reveals that introduction of the quinoline moiety in the ligand frame enhances the overall absorption in the UV range of 350–380 nm to a significant extent. As discussed below, this additional absorption due to quinoline has a strong effect on the photoreactivity of $[(PaPy_2Q)Ru(NO)]^{2+}$ compared to $[(PaPy_3)Ru(NO)]^{2+}$.

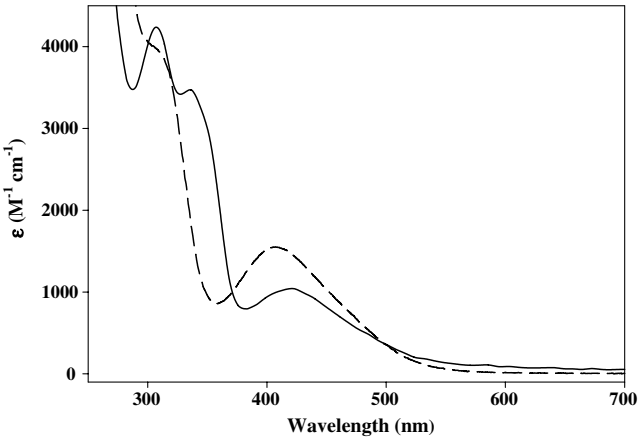


Fig. 3. Electronic absorption spectra of $[(PaPy_2Q)Ru(NO)](BF_4)_2$ (solid line) and $[(PaPy_3)Ru(NO)](BF_4)_2$ (dashed line) in MeCN.

3.4. Photolability of NO

In recent years, we and others have reported a number of $\{Ru–NO\}^6$ nitrosyls that exhibit photolability of the bound NO ligand [19,28–31]. Most of these nitrosyls afford Ru(III) species as the photoproduct (Eq. (2)) in solvents like water. For example, photorelease of NO from $[(PaPy_3)Ru(NO)]^{2+}$ generates $[(PaPy_3)Ru(H_2O)]^{2+}$ that has been characterized by EPR spectroscopy. In the present work, we have studied the photorelease of NO from $[(PaPy_2Q)Ru(NO)]^{2+}$ in both protic and aprotic solvents. As shown in Fig. 4, exposure of a solution of $[(PaPy_2Q)Ru(NO)](BF_4)_2$ in MeCN to low-intensity UV light

$$\{Ru–NO\}^6 + h\nu + solv \rightarrow Ru^{III}–(solv) + NO \quad (2)$$

results in changes in its electronic spectrum consistent with the photorelease of NO. Upon illumination, new peaks are generated at 385 nm and 470 nm and isosbestic points at 360 nm and 305 nm clearly indicate clean conversion of $[(PaPy_2Q)Ru(NO)]^{2+}$ to the solvato species. Release of NO upon illumination can be detected easily by the use of NO-electrode. The resulting NO amperogram (Fig. 4, inset) indicates that NO is released rapidly upon illumina-

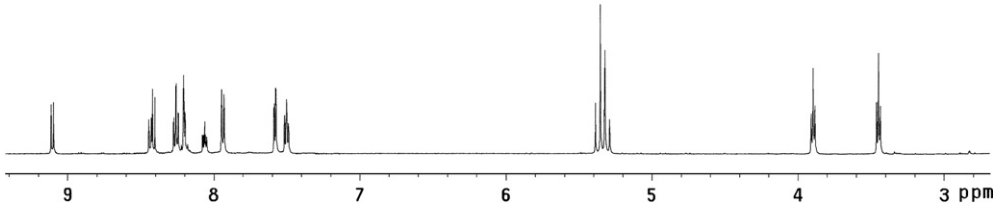


Fig. 2. ^1H NMR spectrum (500 MHz) of $[(PaPy_2Q)Ru(NO)](BF_4)_2$ in CD_3CN at 298 K.

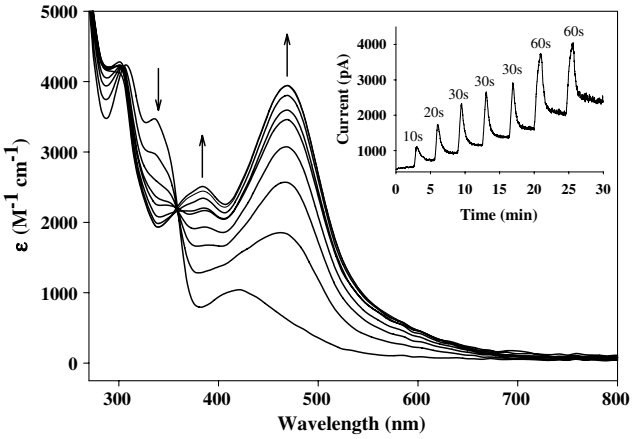


Fig. 4. Changes in electronic spectrum of $[(PaPy_2Q)Ru(NO)](BF_4)_2$ in MeCN observed upon photolysis with low-intensity UV light ($\lambda_{irr} = 300$ nm, 5 mW/cm^2). Inset: NO amperogram indicating release of NO in aqueous solution (pH 7) upon exposure to short pulses of UV light.

tion of an aqueous solution (pH 7) of $[(PaPy_2Q)Ru(NO)]^{2+}$ with low-intensity UV light.

In order to explore the effect(s) of the quinoline moiety on the capacity of NO release by $[(PaPy_2Q)Ru(NO)]^{2+}$, we have compared its photochemical efficiency with that of $[(PaPy_3)Ru(NO)]^{2+}$. The quantum yield value at 300 nm (ϕ_{300}) of $[(PaPy_2Q)Ru(NO)]^{2+}$ in MeCN solution (0.14) is significantly higher than that of $[(PaPy_3)Ru(NO)]^{2+}$ (0.06). Under physiological conditions (H_2O, pH 7), $[(PaPy_2Q)Ru(NO)]^{2+}$ also exhibits a higher quantum efficiency ($\phi_{355} = 0.20$) compared to its pyridine congener $[(PaPy_3)Ru(NO)]^{2+}$ ($\phi_{355} = 0.12$). When the ϕ value of $[(PaPy_2Q)Ru(NO)]^{2+}$ is compared with the ϕ values of other photoactive ruthenium nitrosyls (Table 3), it becomes evident that $[(PaPy_2Q)Ru(NO)]^{2+}$ exhibits sufficient photoactivity for biological purposes.

Close examination of Fig. 3 reveals that ligation of the quinoline-based ligand in $[(PaPy_2Q)Ru(NO)]^{2+}$ shifts the $d(Ru) \rightarrow \pi^*(NO)$ transition (photoactive band) to 420 nm. $[(PaPy_3)Ru(NO)]^{2+}$ exhibits its λ_{max} at 410 nm. In order to examine the effect(s) of irradiation at ~400 nm, we have also determined the quantum yields of both nitrosyls at 410 nm. Interestingly, $[(PaPy_2Q)Ru(NO)]^{2+}$ retains its high level of photoactivity at this wavelength ($\phi_{410} = 0.17$) compared to $[(PaPy_3)Ru(NO)]^{2+}$($\phi_{410} = 0.05$). It is therefore evident that the coordinated quinoline moiety not only increases absorption in the 350–380 nm region (thus acting as a light harvestor) but also enhances the $d(Ru) \rightarrow \pi^*(NO)$ transition and increases the photoactivity at ~400 nm.

Measurements on the time-dependent release of NO from $[(PaPy_3)Ru(NO)]^{2+}$ and $[(PaPy_2Q)Ru(NO)]^{2+}$ (under 300 nm UV light, 5 mW/cm^2) indicate that $[(PaPy_2Q)Ru(NO)]^{2+}$ releases NO faster ($t_{1/2} \approx 0.6$ min) than $[(PaPy_3)Ru(NO)]^{2+}$ ($t_{1/2} \approx 1.4$ min). This fact in conjunction with high ϕ value and greater stability in water makes $[(PaPy_2Q)Ru(NO)]^{2+}$ a very good candidate for the delivery of NO to biological targets.

Ford and co-workers have synthesized several chromium-nitro complexes that include peripheral ''UV antennae'', like pyrene, to increase the overall photochemical efficiency of NO generation [34]. In this work, a *directly coordinated* light-harvesting quinoline unit (Fig. 3) enhances the photoefficiency of $[(PaPy_2Q)Ru(NO)](BF_4)_2$ compared to its pyridine analogue $[(PaPy_3)Ru(NO)](BF_4)_2$. We believe that other photoactive ruthenium nitrosyls could be similarly modified to improve (a) their photoefficiencies and (b) their potential as NO donors in PDT.

Acknowledgement

This research was supported by a grant from the National Science Foundation (CHE-0553405).

Appendix A. Supplementary material

CCDC 634946 contains the supplementary crystallographic data for $[(PaPy_2Q)Ru(NO)](BF_4)_2 \cdot MeCN$. These data can be obtained free of charge via http://www.ccdc.cam.ac.uk/conts/retrieving.html, or from the Cambridge Crystallographic Data Centre, 12 Union Road, Cambridge CB2 1EZ, UK; fax: (+44) 1223-336-033; or e-mail: deposit @ccdc.cam.ac.uk. Supplementary data associated with this article can be found, in the online version, at doi:10.1016/j.poly.2007.03.010.

Table 3
Quantum Yield (ϕ) values for {Ru–NO}^{6} nitrosyls

Complex	Quantum Yield, ϕ (λ_{irr} in nm)			
	MeCN	H_2O	DMF	
$[(PaPy_3)Ru(NO)](BF_4)_2$	0.060 (300), 0.050 (410)	0.12 (355)[a]	0.042 (300)	this work
$[(PaPy_2Q)Ru(NO)](BF_4)_2$	0.14 (300), 0.17 (410)	0.20 (355)[a]	0.075 (300)	this work
[(bpb)Ru(NO)(Cl)]	0.062 (300)			ref. [29]
[(salen)Ru(NO)(Cl)]	0.13 (365)			ref. [28]
$[(NH_3)_4Ru(NO)(py)]^{3+}$		0.11 (330)[b]		ref. [32]
$[(NH_3)_4Ru(NO)(P(OEt)_3)]^{3+}$		0.30 (310)[b]		ref. [33]

[a] pH 7, phosphate buffer.
[b] Measurements made ⩽pH 4.

References

[1] L.J. Ignarro, Nitric Oxide: Biology and Pathobiology, Academic Press, San Diego, 2000.
[2] J. Lincoln, G. Burnstock, Nitric Oxide in Health and Disease, Cambridge University Press, New York, 1997.
[3] F.C. Fang, Nitric Oxide and Infection, Kluwer Academic/Plenum Publishers, New York, 1999.
[4] C.S. Boyd, E. Cadenas, J. Biol. Chem. 383 (2002) 411.
[5] G.C. Brown, FEBS Lett. 369 (1995) 136.
[6] K. Xie, S. Huang, Free Radic. Biol. Med. 34 (2003) 969.
[7] M. Feelisch, J.S. Stamler (Eds.), Nitric Oxide Research, John Wiley and Sons, Chichester, UK, 1996.
[8] J.M. Fukuto, D.A. Wink, Metal Ions Biol. Syst. 36 (1999) 547.
[9] P.G. Wang, T.B. Cai, N. Taniguchi, Nitric Oxide Donors: Pharmaceutical and Biological Applications, Wiley-VCH, Weinheim, 2005.
[10] C. Napoli, L. Ignarro, J. Annu. Rev. Pharmacol. Toxicol. 43 (2003) 97.
[11] L.K. Keefer, R.W. Nims, K.M. Davies, D.A. Wink, Meth. Enzymol. 268 (1996) 281.
[12] P.C. Ford, J. Bourassa, K. Miranda, B. Lee, I. Lorkovic, S. Boggs, S. Kudo, L. Laverman, Coord. Chem. Rev. 171 (1998) 185.
[13] G.B. Richter-Addo, P. Legzdins, Metal Nitrosyls, Oxford University Press, New York, 1992.
[14] R.K. Pandey, J. Porphyr. Phthalocyan. 4 (2000) 368.
[15] A.K. Patra, R. Afshar, M.M. Olmstead, P.K. Mascharak, Angew. Chem., Int. Ed. 41 (2002) 2512.
[16] A.K. Patra, J.M. Rowland, D.S. Marlin, E. Bill, M.M. Olmstead, P.K. Mascharak, Inorg. Chem. 42 (2003) 6812.
[17] R. Afshar, A.K. Patra, M.M. Olmstead, P.K. Mascharak, Inorg. Chem. 43 (2004) 5736.
[18] K. Ghosh, A.A. Eroy-Reveles, B. Avila, T.R. Holman, M.M. Olmstead, P.K. Mascharak, Inorg. Chem. 43 (2004) 2988.
[19] A.K. Patra, M.M. Olmstead, P.K. Mascharak, Inorg. Chem. 42 (2003) 7363.
[20] J.M. Rowland, M.M. Olmstead, P.K. Mascharak, Inorg. Chem. 40 (2001) 2810.
[21] I. Szundi, M.J. Rose, I. Sen, A.A. Eroy-Reveles, P.K. Mascharak, Ó. Einarsdóttir, Photochem. Photobiol. 82 (2006) 1377.
[22] M. Madhani, A.K. Patra, T.W. Miller, A.A. Eroy-Reveles, A.J. Hobbs, J.M. Fukuto, P.K. Mascharak, J. Med. Chem. 49 (2006) 7325.
[23] A.A. Eroy-Reveles, Y.L. Leung, C.M. Beavers, M.M. Olmstead, P.K. Mascharak, Angew. Chem., manuscript is preparation.
[24] I.P. Evans, A. Spencer, G. Wilkinson, J. Chem. Soc., Dalton Trans. (1973) 204.
[25] R.W. Callahan, T.J. Meyer, Inorg. Chem. 16 (1977) 574.
[26] M.G. Gomes, C.U. Davanzo, S.C. Silva, L.G.F. Lopes, P.S. Santos, D.W. Franco, J. Chem. Soc., Dalton Trans. (1998) 601.
[27] H. Nagao, D. Ooyama, T. Hirano, H. Naoi, M. Shimada, S. Sasaki, N. Nagao, M. Mukaida, T. Oi, Inorg. Chim. Acta 320 (2001) 60.
[28] C.F. Works, C.J. Jocher, G.D. Bart, X. Bu, P.C. Ford, Inorg. Chem. 41 (2002) 3728.
[29] A.K. Patra, M.J. Rose, K.M. Murphy, M.M. Olmstead, P.K. Mascharak, Inorg. Chem. 43 (2004) 4487.
[30] P.N. Komozin, V.M. Kazakova, I.V. Miroshnichenko, N.M. Sinitsyn, Zh. Neorg. Khim. 28 (1983) 3186.
[31] J. Bordini, D.L. Hughes, J.D. da Motto Neto, C.J. da Cunha, Inorg. Chem. 41 (2002) 5410.
[32] E. Tfouni, M. Krieger, B.R. McGarvey, D.W. Franco, Coord. Chem. Rev. 236 (2003) 57.
[33] R.M. Carlos, A.A. Ferro, H.A.S. Silva, M.G. Gomes, S.S.S. Borges, P.C. Ford, E. Tfouni, D.W. Franco, Inorg. Chim. Acta 357 (2004) 1381.
[34] F. DeRosa, X. Bu, P.C. Ford, Inorg. Chem. 44 (2005) 4157.

We are currently interested in studying the reaction of $\{MNO\}^7$ complexes with dioxygen in aqueous medium, a study with both fundamental and bioinorganic relevance. Recent reports [11,15] suggest that the rate constant of this process (k_{ox}) might be significantly influenced by the redox potential of the $E_{MNO^+/MNO}$ couple, leading to a linear free-energy relation (LFER) between ln k_{ox} and $E_{NO^+/NO}$ with a negative slope value close to the one predicted by the Marcus model. This result has been rationalized in terms of an associative mechanism that involves the formation of a covalent bond between molecular oxygen and the $\{MNO\}^7$ moiety [15]. Complementary, this same study suggests that six-coordination is crucial to achieve fast oxidation of bound $NO^{\cdot}$ and NO^- complexes, but certainly a more systematic investigation of the autoxidation reaction of hexacoordinated $\{MNO\}^6$ species appears as necessary.

In spite of the large amount of well-described species of this kind, it is not an easy task to find literature examples of water-soluble nitrosyl species with robust coordination spheres that remain unaffected upon redox changes [16]. Examples with the appropriate redox potential to explore their reactions with dioxygen are even scarcer. We explore here one possible alternative to obtain such a species, namely the use of pendant-arm derivatized *N*-macrocyclic ligands. We report the preparation, isolation and characterization of the $\{RuNO\}^6$ species *cis*-$[Ru(L^{py})NO](PF_6)_3$ (**I**) (L^{py} = *N*-(2-methylpyridyl) 1,4,8,11-tetraazacyclotetradecane), focusing on its electronic structure an the possibility of redox interconversion to the one-electron reduced $\{RuNO\}^7$ species.

2. Experimental

2.1. Materials and reagents

The reagents employed in the synthetic procedures were purchased to Aldrich or Merck, and were used without further purification. All the organic solvents employed in synthetic procedures or physical determinations were dried and freshly distilled before used, following standard procedures. The precursor complex $Ru(dmso)_4Cl_2$ [17] and the ligand *N*-(2-methylpyridyl) 1,4,8,11-tetraazacyclotetradecane [18] were synthesized according to previously published procedures. A vacuum line and Schlenk glassware were employed when the manipulations required exclusion of air.

2.2. Synthesis of $[Ru(L^{py})NO](PF_6)_3$ (*I*)

One hundred and seventy milligrams (0.35 mmols) of $Ru(dmso)_4Cl_2$ where added to 35 mL of an ethanolic solution of 102.6 mg of L^{py} (0.35 mmol) under argon. The solution was refluxed for 4 h, reaching a deep orange color. The mixture was allowed to cool down to room temperature. 0.50 g (7.2 mmol) of $NaNO_2$ were added to the reaction mixture, which was further refluxed for 5 h. After cooling down, the reaction mixture was treated with 6.5 mL of HCl 6 M, and the volume reduced to a few mL by vacuum distillation. Addition of 5 mL of a saturated water solution of NH_4PF_6 induced the precipitation of 300 mg of a brownish microcrystalline powder. Recrystallization of this solid by diffusion of diethyl ether into an acetonitrile solution yielded 155 mg (52%) of analytically pure **I**, as revealed by elemental analysis and ^1H and ^{13}C NMR spectroscopy. *Anal.* Calc. for $C_{16}H_{29}F_{18}N_6OP_3Ru$: C, 22.4; H, 3.4; N, 9.8. Found: C, 22.2; H, 3.6; N, 9.7%. ν_{NO} (KBr) = 1917 cm^{-1}. δ_H (CD_3CN): Aromatic protons, 8.59 (1H, d), 8.36 (1H, t), 7.89 (1H, d), 7.85 (1H, t). Amine protons, 9.70 (1H), 9.33 (1H), 6.91 (1H) observed as broad signals. Aliphatic protons, 5.10 (1H, d), 4.88 (1H, d), 3.83 (1H), 3.72 (3H), 3.38 (1H), 3.31 (4H), 3.18 (1H), 3.09 (1H), 2.99 (1H), 2.89 (1H), 2.77 (1H), 2.54 (1H), 2.37 (1H), 2.33 (1H), 2.23 (1H) partially obscured by the solvent, 2.09 (1H), 2.02 (1H). The multiplicity of the signals is not given due to the complexity of the coupling pattern. See text for a detailed discussion. δ_C (CD_3CN): Aromatic carbons, 161.8, 153.9, 144.9, 128.1, 124.9. Aliphatic carbons, 73.6, 65.2, 60.0, 58.2, 56.2, 54.0, 51.0, 50.7, 48.1, 26.6, 23.3.

2.3. Physical measurements

Microanalytical data for C, H, N and O were obtained at INQUIMAE, with a Carlo Erba EA 1108 analyzer. UV–Vis spectra were recorded with either an HP8453 or an HP8452A diode array spectrometer. IR spectral measurements were carried out using alternatively one of two FT spectrophotometers, a Nicolet 150P and a Thermo Nicolet AVATAR 320. Spectra were collected from KBr disks. NMR data were acquired on a Bruker AM500 spectrometer operating at 500.13 MHz for ^1H. Standard pulse sequences were used for two-dimensional (2D) heteronuclear single quantum coherence (HSQC), correlated spectroscopy (COSY) and nuclear Overhauser enhancement spectroscopy (NOESY). Cyclic voltammetry (CV) and square wave voltammetry (SWV) measurements were done in aqueous 0.1 M $HClO_4$ or in organic medium (0.1 M Bu_4NPF_6 as supporting electrolyte) with a standard three electrode cell [19] containing a Pt working electrode (1.5 mm ∅) or a vitreous carbon electrode (3 mm ∅), and a Pt wire as a counterelectrode. As a reference in aqueous media, a commercial Ag/AgCl (BAS) electrode was used. In organic medium, a Ag wire and ferrocene as internal standard was used [20]. Throughout this work, all the reported redox potentials are referred to Ag/AgCl, 3 M NaCl (0.21 V versus NHE). The potential of the working electrode was controlled with one of two commercial potentiostats (Princeton Applied Research 273A or TEQ-03). The spectroelectrochemical experiments in the UV–Vis region were done in a homemade cell containing a quartz cuvette (1 cm path). The potential was controlled with a TEQ-03 potentiostat, using either 0.1 M $HClO_4$ or 0.1 M Bu_4NPF_6 in acetonitrile as supporting electrolyte. A commercial Ag/AgCl reference electrode was used in

aqueous solution whereas a $Ag/AgNO_3$ (0.01 M Ag^+ in acetonitrile) electrode was the reference employed in organic medium. The working and counter electrodes were a Pt net and a Pt wire, respectively. The system was maintained at 25 ± 0.1 °C for the experiments in water and at -30 ± 1 °C for those in acetonitrile (RC6 LAUDA thermostat), and was entirely purged with N_2. In a typical experiment, the solution was electrolyzed at sufficiently low potential (*ca.* 200 mV below the E^0 values registered by CV) in several cathodic steps. Between consecutive reduction periods, the solution was allowed to equilibrate and the open-circuit potential (E_{oc}) together with the UV–Vis spectrum were recorded. Redox potentials and disclosed UV–Vis spectra of the reduced and oxidized species were then obtained by global analysis [21]. This procedure involves a simultaneous multi-wavelength fitting to the Nernst equation [22].

2.4. Theoretical calculations

We employed density functional theory (DFT) computations to fully optimize the geometries of the cations $[Ru(L^{py})NO]^{3+}$, $[Ru(L^{py})NO]^{2+}$, $[Ru(L^{py})NO_2]^{+}$ and $[Ru(L^{py})Cl]^{+}$ in vacuo, without symmetry constraints. The calculations were performed with *Gaussian 03* [23], at the B3LYP level, employing the LanL2DZ basis set, which proved to be suitable for geometry predictions in coordination compounds containing metals of the second and third raw of the transition elements in the Periodic Table [11,24]. We used tight SCF convergence criteria and default settings in the geometry optimizations. Depending on the case (see text below) several minima along the potential energy surface were explored by scanning one particular internal coordinate. The true nature of all the found stationary points, which correspond to (local) minima in the potential energy surface were confirmed by numerical vibrational frequency computations. In all cases the absence of negative frequencies confirmed that the optimized geometries correspond to stable configurations in the potential energy surfaces. Time dependent (TD)DFT computations at the equilibrium geometry were employed as an assistant tool in the interpretation and assignment of the electronic spectra.

3. Results and discussion

3.1. Synthetic strategy and structural characterization of $[Ru(L^{py})NO]^{3+}$

Mono *N*-substitution of 1,4,8,11-tetraazacyclotetradecane (cyclam) can be performed under controlled reaction conditions, employing a large excess of cyclam with respect to the alkylating agent [18,25]. *N*-(2-methylpyridyl) cyclam (L^{py}) is therefore prepared in good yield by the reaction of 2-(chloromethyl)pyridine and a large excess of cyclam in DMF. Separation of the product from the unreacted macrocycle can be easily achieved because of the notoriously different solubility properties of both species. The pentadentate ligand is conveniently incorporated into the coordination sphere of Ru(II) by reaction with $Ru(dmso)_4Cl_2$ in ethanol in the absence of oxygen. This process seems to yield a mixture of products (most probably $[Ru(L^{py})Cl]^{+}$, $[Ru(L^{py})dmso]^{2+}$ and $[Ru(L^{py})(solv)]^{n+}$) that are difficult to isolate and purify. Nevertheless, the reaction of this mixture with nitrite leads to the formation of the nitro derivative $[Ru(L^{py})NO_2]^{+}$. Acidification of the reaction mixture induces acid–base changes in the coordinated ligand as in Eq. (1) [5,26–28], and yields the desired $\{RuNO\}^6$ core.

$$[Ru(L^{py})NO_2]^{+} + 2H^{+} \rightleftarrows [Ru(L^{py})NO]^{3+} + H_2O \quad (1)$$

The ^1H NMR spectrum of **I** in CD_3CN (Supplementary material) consists of 29 partially or totally overlapped signals that also show extensive scalar coupling. This spectrum is a consequence of the rigidity of the macrocycle combined with the lack of symmetry elements, which makes all protons non-equivalent. The ^1H NMR resonances at 8.59, 8.36, 7.89 and 7.85 ppm, referred to as H_{18}, H_{20}, H_{21} and H_{19}, respectively (see Fig. 1 for proton numbering), can be safely ascribed to the pyridine moiety by comparison with the free ligand. Note that complex **I** can potentially present isomerism leading to *cis*- or *trans*-species. However, the observation of a single set of signals for the aromatic protons seems to be consistent with the occurrence of a single isomer.

The three broad features at 9.70, 9.33 and 6.91 ppm, not observed when the spectrum is recorded in D_2O solution, can be attributed to the three exchangeable N*H* protons. The pyridine linker methylene N–CH_2-py protons give rise to two doublets at 4.88 and 5.10 ppm, coupled by one large $^2J(HH) \approx 17.5$ Hz. The remaining features in the range between 2 and 4 ppm, can be altogether assigned to the geminal pairs of CH_2 protons in the cyclam backbone. The ^{13}C NMR spectrum in CD_3CN, shows signals from each one of the 16 macrocyclic ligand carbon atoms (Supplementary material).

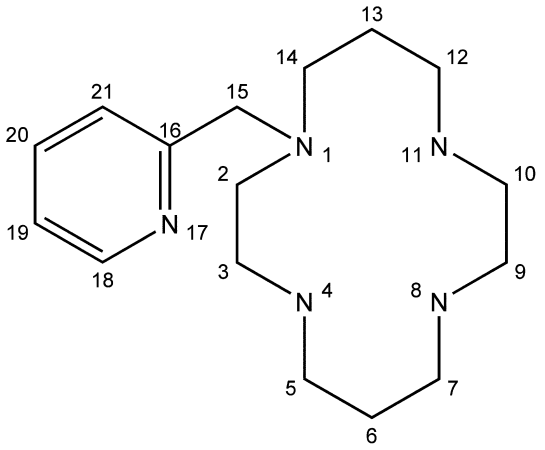


Fig. 1. Atom numbering used to identify the nuclei in the NMR discussion.

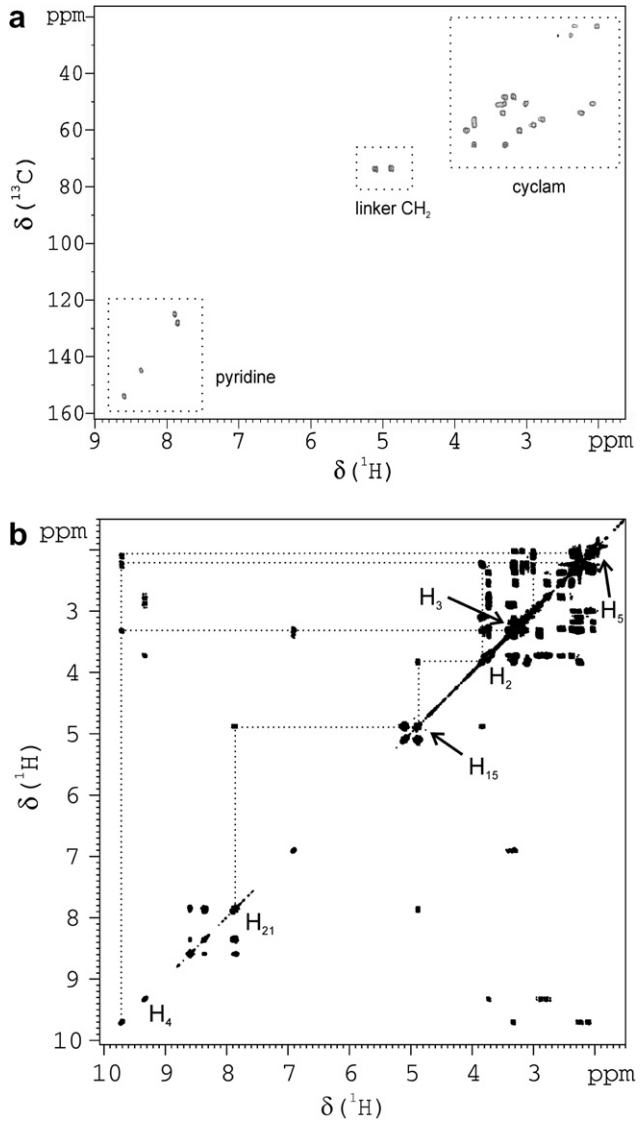


Fig. 2. (a) 2D [^{1}H,^{13}C] HSQC NMR. spectrum of **I** in CD_3CN solution. (b) 2D COSY NMR spectrum of **I** in CD_3CN solution. The dotted lines represent a few steps in the strategy employed in the assignment of the NMR spectrum (see text).

The 2D [^{1}H, ^{13}C] HSQC NMR spectrum (Fig. 2a) shows cross-peaks between 26 of the 29 ^{1}H NMR signals previously described and 16 ^{13}C NMR signals. Among these cross-peaks, it is possible to identify the four single protons from the pyridine moiety, and the 11 paired peaks arising from the geminal CH_2 protons, in agreement with the assignments performed above. Moreover, this NMR experiment confirms the presence of only one spin system (and therefore only one major isomer for **I**) and proved valuable in identifying the geminal pairs of CH_2 protons and assigning them to the corresponding ^{13}C signals.

In combination with all the information gathered up to now, a 2D COSY spectrum (Fig. 2b) allows to find the scalar connectivities and perform a sequential assignment of the ^{1}H NMR spectrum. The pyridine ^{1}H NMR resonance at 7.89 ppm (H_{21}) can be taken as a starting point for the analysis. This proton couples to one that gives rise to a signal at 4.88 ppm, and corresponds to one of the linker methylene protons (H_{15a} or H_{15b}). The latter correlates sequentially with a proton resonating at 3.83 ppm (H_{2a} or H_{2b}). This signal shows additional connectivities with signals at 3.33, 3.09 and 2.23 ppm. From the 2D [^{1}H,^{13}C] HSQC data, protons with chemical shifts of 3.09 and 3.83 ppm are known to be geminal, as well as those at 3.33 and 2.23 ppm. Consequently, these two last resonances can be assigned to their vicinal protons H_{3a}/H_{3b}, both of which are also associated through COSY correlations with the signal at 9.70 ppm. The latter arises from one of the N*H* protons and is now identified as H_4. This proton is scalar-coupled to the one at 2.08 ppm, which in turn couples to a proton at 2.99 ppm. These two last resonances correspond to a pair of geminal protons, that we assign to H_{5a} or H_{5b}. Application of this systematic approach leads to the full assignment of the ^{1}H and ^{13}C NMR spectra. However, the geminal specificity at every CH_2 group still remains unknown. A direct measurement of the $J(^1H^1H)$ coupling constants for these protons helps to eliminate this uncertainty. The *J* values listed in Table 1 reveal two kinds of signals, those split by only one large

Table 1
^{1}H and ^{13}C NMR chemical shifts (δ) in CD_3CN solution, and geminal ^2J(HH) and axial–axial ^3J(HH) scalar coupling constants for compound **I**

^{1}H NMR								^{13}C NMR			
δ (ppm)	Assignment	δ (ppm)	Assignment	δ (ppm)	Assignment	δ (ppm)	Assignment	δ (ppm)	Assignment	δ (ppm)	Assignment
9.70	H_4	4.88	H_{15b}	3.30	H_{7a}	2.37	H_{13b}	161.8	C_{16}	58.2	C_{10}
9.33	H_{11}	3.83	H_{2a}	3.29	H_{14a}	2.33	H_{6a}	153.9	C_{18}	56.2	C_{12}
8.59	H_{18}	3.73	H_{10b}	3.18	H_{7b}	2.23	H_{3a}	144.9	C_{20}	54.0	C_3
8.36	H_{20}	3.71	H_{12b}	3.09	H_{2b}	2.09	H_{5a}	128.1	C_{19}	51.0	C_9
7.89	H_{21}	3.71	H_{14b}	2.99	H_{5b}	2.02	H_{6b}	124.9	C_{21}	50.7	C_5
7.85	H_{19}	3.38	H_{9a}	2.89	H_{10a}			73.6	C_{15}	48.1	C_7
6.91	H_8	3.33	H_{3b}	2.77	H_{12a}			65.2	C_{14}	26.6	C_{13}
5.10	H_{15a}	3.31	H_{9b}	2.54	H_{13a}			60.0	C_2	23.3	C_6

$^2J(H_{15a},H_{15b}) = 17.5$ Hz; $^2J(H_{13a},H_{13b}) = 17.0$ Hz; $^2J(H_{6a},H_{6b}) = 16.4$ Hz; $^2J(H_{7a},H_{7b}) = 15$ Hz; $^2J(H_{2a},H_{2b}) = {}^2J(H_{3a},H_{3b}) = {}^2J(H_{5a},H_{5b}) = 14.0$ Hz; $^2J(H_{9a},H_{9b}) = {}^2J(H_{10a},H_{10b}) = 13.5$ Hz; $^2J(H_{12a},H_{12b}) = {}^2J(H_{14a},H_{14b}) = 13.0$ Hz.

$^3J(H_{2a},H_{3a}) = 14.0$ Hz; $^3J(H_{5a},H_{6a}) = {}^3J(H_{9a},H_{10a}) = 13.5$ Hz; $^3J(H_{6a},H_{7a}) = {}^3J(H_{12a},H_{13a}) = {}^3J(H_{13a},H_{14a}) = 13.0$ Hz; $^3J(H_4,H_{5a}) = {}^3J(H_8,H_{9a}) = {}^3J(H_{10a},H_{11}) = {}^3J(H_{11},H_{12a}) = 11.0$ Hz; $^3J(H_{3a},H_4) = 10.0$ Hz.

^2J(HH) constant, due to geminal coupling exclusively, and those which show at least two large splittings, a ^2J(HH) splitting due to coupling with a geminal partner plus one or two sizeable ^3J(HH) values, depending on whether they are connected to one or two vicinal protons through axial–axial scalar coupling. This information allows discriminating between signals that arise from protons bound to the same carbon atom in the aliphatic backbone. The specific assignment of the methylene N–CH_2-Py resonances requires the study of their dipolar connectivities (see later). Table 1 shows the resulting ^{1}H and ^{13}C NMR assignments.

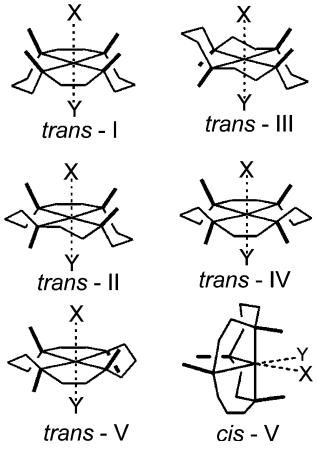


Fig. 3. Different configurations of metal cyclam complexes showing the different alignment of the NH protons.

The NMR analysis presented so far evidences the existence of a single isomer. When attached to a metal center, the macrocyclic 1,4,8,11-tetraazacyclotetradecane (cyclam) could present as much as five configurations at the nitrogen stereogenic centers that give rise to several isomers (labeled *trans*-I–V and *cis*-V, Fig. 3) [29]. In order to determine which of these forms is adopted by compound **I**, a 2D [^{1}H,^{1}H] NOESY NMR data set was recorded in CD_3CN solution. Provided that the difference between configurations resides on the spatial alignment of the NH bonds, special attention has to be paid to these protons. Fig. 4a shows the portion of the NOESY spectrum corresponding to the NH resonances. An intense NOESY cross peak from resonance at 9.70 ppm (H_4) to a signal at 9.33 ppm (H_{11}) indicates that these protons are close in space. They are attached to non-adjacent N atoms and point in the same direction. This observation discards the *trans*-III and *trans*-IV configurations. The remaining NH at 6.91 ppm (H_8) is not dipolar coupled to the other two amine protons (H_{11} or H_4) and is most likely pointing to the opposite side. This last consideration suggests that configurations *trans*-I and *trans*-II should also be disregarded, leaving only two possible configuration, that is *trans*-V or its folded form *cis*-V. The occurrence of NOESY cross-peaks (see Fig. 4b) between protons H_{11}–H_{2a}, H_4–H_{9a}, and H_4–H_{11}

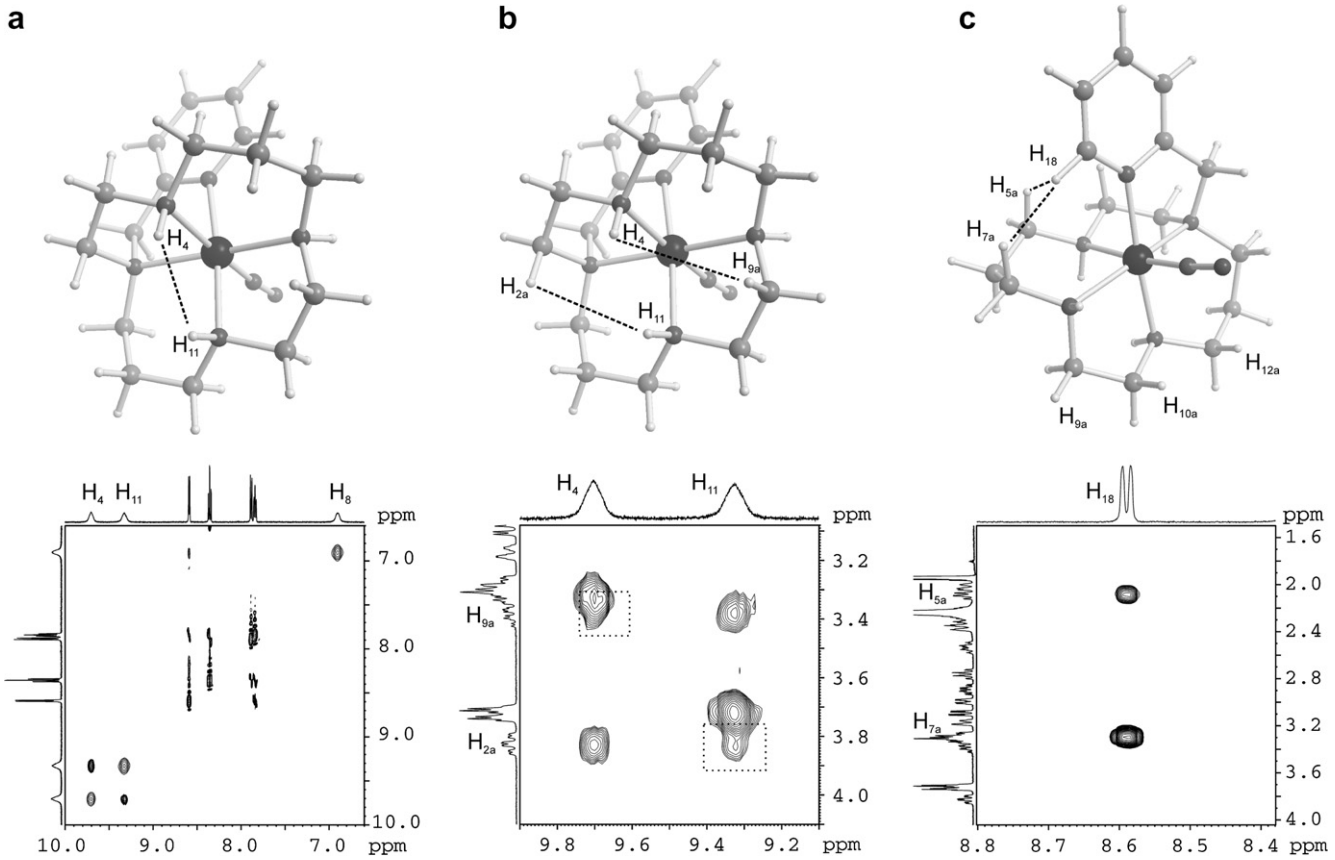


Fig. 4. Selected regions of the 2D [^{1}H,^{1}H] NOESY NMR spectrum of **I** in CD_3CN solution.

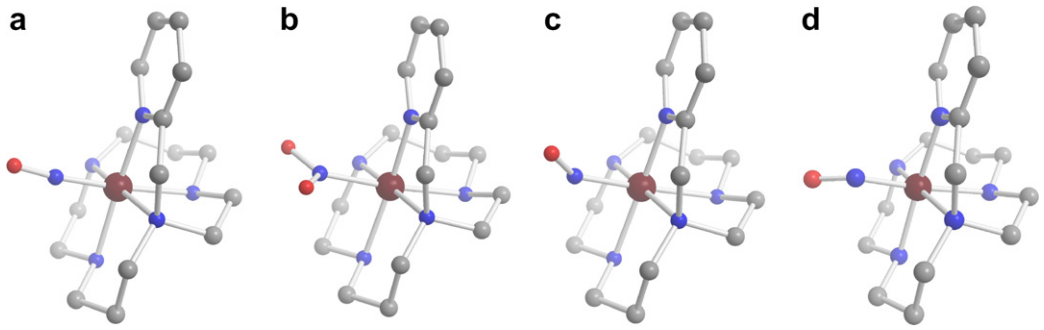


Fig. 5. DFT optimized geometries (in vacuo) for the (a) *cis*-$[Ru(L^{py})NO]^{3+}$ (**I**), (b) *cis*-$[Ru(L^{py})NO_2]^{+}$ (**II**), (c) *cis*-$[Ru(L^{py})NO]^{2+}$ (configuration $\mathbf{III}_a$) and (d) *cis*-$[Ru(L^{py})NO]^{2+}$ (configuration $\mathbf{III}_b$).

disfavors the *trans*-V form. Additionally, the observation of dipolar connectivities between the pyridine H_{18} proton (8.59 ppm) and protons H_{5a} (2.09 ppm) and H_{7a} (3.30 ppm) but not with protons H_{9b}, H_{10a} or H_{12a} (Fig. 4c) confirms a folded *cis*-V configuration. This leaves only two possibilities (actually two pairs of enantiomers) for the structure of **I**, but the only one consistent with all the NMR information and its DFT optimized structure is presented in Fig. 5a. As for the assignment of the methylene N–CH_2-Py protons, the occurrence of NOESY cross-peaks between signals at 4.88 and 3.29 ppm (H_{14a}), and 5.10 and 3.08 ppm (H_{2b}) permitted to know the spatial orientation of these protons. (see Supplementary material for a complete description of the ^{1}H NMR assignment of complex **I**).

It is not trivial to rationalize which factors lead to the isolation of only one configuration. A DFT geometry optimization *in vacuo* of the compound $[Ru(L^{py})Cl]^{+}$ (a presumed intermediate in the preparation of **I**) reveals that the energy of the *cis*-V conformer is *ca.* 10 kJ mol^{-1} lower than the one of the *trans*-III isomer. The situation remains essentially the same if solvation effects are introduced by means of the PCM approximation, where the solvent is treated as a continuum dielectric medium. The computed energy difference suggests a certain degree of thermodynamic control for the reaction. Nevertheless, kinetic effects and even solubility properties cannot be ruled out.

The theoretically optimized *cis*-V geometry obtained for **I**, either in vacuo or with the molecule immersed in a dielectric medium to take into account the influence of the solvent, is consistent with the NMR results. The calculations position the diagnostic H_4–H_{11}, H_4–H_{9a}, H_{11}–H_{2a}, H_{18}–H_{5a}, H_{18}–H_{7a} and H_{18}–H_{9b} pairs of protons at distances of 2.28, 3.06, 3.05, 2.69 and 1.99 Å, respectively. These values are consistent with the observation of the NOESY crossed peaks described above. At the same time, the much larger computed distances H_{18}–H_{9b}, H_{18}–H_{10a} and H_{18}–H_{12b} of 5.05, 5.42 and 6.24 Å, respectively, explain the lack of signals for these proton pairs. Table 2 contains some relevant computed structural parameters and Fig. 5a displays the geometry of the optimized cation. The ruthenium atom is placed in a distorted octahedral N_6 environment, generated by the nitrosyl ligand and the five donor nitrogen atoms of the substituted macrocycle. The Ru–N(nitrosyl) (labeled Ru–N_{22}) bond reveals as significantly shorter than the five remaining Ru–N bonds. The Mayer bond order [30] for this bond (1.08) confirms the higher degree of covalency for Ru–N_{22} compared to the Ru–N(amine) (average of 0.52) and Ru–N(py) (0.53) bonds in the same compound. The computed N_{22}–O_{23} distance and the linear nature of the RuNO moiety are consistent with the expectations for a $\{RuNO\}^6$ species [3,31].

3.2. Vibrational and electronic spectroscopy

The IR spectrum of $[Ru(L^{py})NO](PF_6)_3$ in a KBr disk displays a sharp intense band at 1917 cm^{-1}, assignable to the N–O stretching vibration, ν_{NO}. This value is slightly higher than the ones found for *trans*-[Ru(NO)Cl(cyclam)]$(PF_6)_2$ (1875 cm^{-1}) [32] and $[Ru^{II}(NH_3)_5(NO)]Br_3$ (1913 cm^{-1}) [33], comparable to those reported for several *cis*- and *trans*-$[Ru(NH_3)_4L(NO)]^{3+}$ species (1923–1942 cm^{-1}) [6], and smaller than the values observed in other Ru(II) compounds that carry electron-withdrawing co-ligands (1946 and 1959 cm^{-1} for [Ru(trpy)(bpy)(NO)]-$(PF_6)_3$ and [Ru(tpm)(bpy)(NO)]$(ClO_4)_3$, respectively) [9,11]. This ν_{NO} frequency has been usually employed to qualitatively establish the degree of electronic interaction between the NO ligand and the metal center. In this case the ν_{NO} value suggests an $[Ru^{II}NO^{+}]$ electronic distribution where the NO^{+} character is well preserved [2], in agreement with the DFT bonding picture. The calculated frequency of 1849 cm^{-1} is lower than the measured one. Though this discrepancy is not unusual for calculations at this level of theory [10,11,13,14,24], there might be some contribution to the observed difference arising from hydrogen-bond interactions in the solid state.

The spectral region between 750 and 900 cm^{-1} has been usually employed to differentiate between *cis* and *trans* geometries in cyclam compounds [34,35]. In our case, besides this region is partially obscured by the PF_6^- vibrations, the pendant-arm leaves the complex with no symmetry elements no matter the configuration of the macrocycle. For this reason, the number of signals does not depend on the cyclam configuration and the low energy N–H vibrations are not informative.

Table 2
Selected bond lengths and angles for **I**, **II** and **III** obtained from the DFT optimized structures

Distance	I in vacuo (Å)	I in H_2O (Å)	I in acn (Å)	II in vacuo (Å)	III_a in vacuo (Å)	III_b in vacuo (Å)
$Ru–N_1$	2.17	2.17	2.17	2.19	2.17	2.17
$Ru–N_4$	2.17	2.16	2.16	2.20	2.21	2.21
$Ru–N_8$	2.23	2.20	2.20	2.19	2.22	2.21
$Ru–N_{11}$	2.17	2.15	2.15	2.18	2.17	2.17
$Ru–N_{17}$	2.15	2.15	2.14	2.13	2.14	2.15
$Ru–N_{22}$	1.79	1.78	1.78	2.04	1.90	1.90
$N_{22}–O_{23}$	1.18	1.18	1.18	1.29	1.22	1.22
$N_{22}–O_{24}$				1.31		
Angle	**I in vacuo (°)**	**I in H_2O (°)**	**I in acn (°)**	**II in vacuo (°)**	**III_a in vacuo (°)**	**III_b in vacuo (°)**
$Ru–N_{22}–O_{23}$	174.3	174.7	174.4	122.7	141.6	144.7
$Ru–N_{22}–O_{24}$				118.3		
$O_{23}–N_{22}–O_{24}$				118.8		
$N_1–Ru–N_8$	168.9	170.1	170.0	173.9	171.9	171.6
$N_4–Ru–N_{22}$	174.9	175.7	175.5	175.5	176.5	176.0
$N_{11}–Ru–N_{17}$	174.6	174.6	174.4	172.8	174.3	174.4
$N_1–Ru–N_4$	82.3	82.3	82.3	83.2	82.8	82.8
$N_1–Ru–N_{11}$	93.7	93.8	93.4	95.2	95.1	94.6
$N_1–Ru–N_{17}$	80.9	80.8	81.0	80.9	80.7	80.6
$N_1–Ru–N_{22}$	96.4	96.6	96.5	97.5	95.1	95.4
$N_4–Ru–N_8$	88.1	89.0	88.9	92.3	90.4	90.3
$N_4–Ru–N_{11}$	92.8	91.4	91.4	94.8	94.0	93.5
$N_4–Ru–N_{17}$	86.9	87.2	87.0	90.7	89.4	88.8
$N_8–Ru–N_{11}$	81.0	81.7	82.0	81.1	81.0	80.9
$N_8–Ru–N_{17}$	104.4	103.5	103.4	103.3	103.6	104.2
$N_8–Ru–N_{22}$	93.6	92.4	92.7	87.3	91.9	91.8
$N_{11}–Ru–N_{22}$	92.3	92.9	93.1	89.5	89.0	90.1
$N_{17}–Ru–N_{22}$	88.0	88.5	88.5	85.1	87.5	87.5
$N_{17}–Ru–N_{22}–O_{23}$	−10.4	−16.4	−9.9	86.8	25.2	−147.4
$C_{18}–N_{17}–Ru–N_8$	−2.7	−1.0	−2.0	1.1	0.7	0.7
$C_{16}–N_{17}–Ru–N_8$	−179.4	−178.5	179.7	−174.0	−176.2	−175.5

Fig. 6 displays the electronic spectra of **I** in water (pH 1.0, $HClO_4$) and acetonitrile. Apart from the complete lack of strong bands in the visible region of the spectrum, the most remarkable features when the spectrum was recorded in water include intense absorptions in the UV region, a slight shoulder at *ca.* 236 nm ($\varepsilon = 5770\ M^{-1}\ cm^{-1}$), a much better resolved transition at *ca.* 257 nm ($\varepsilon = 4660\ M^{-1}\ cm^{-1}$), and a progression of weak bands at 313 nm (sh, $\varepsilon = 335\ M^{-1}\ cm^{-1}$), 355 nm (sh, $\varepsilon = 110\ M^{-1}\ cm^{-1}$) and 450 nm ($\varepsilon = 40\ M^{-1}\ cm^{-1}$). Ru(II) species holding amine ligands usually display solvent dependent electronic spectroscopy due to solute–solvent specific (hydrogen-bonding) interactions that can modulate the electronic density on the metal ion [36–39]. This same effect was described for species containing cyclam and π-acceptor ligands [35,40,41]. However, the spectrum of **I** in acetonitrile is virtually identical to the one measured in water, with only minor shifts of the bands to 232 nm ($\varepsilon = 6475\ M^{-1}\ cm^{-1}$), 258 nm ($\varepsilon = 4900\ M^{-1}\ cm^{-1}$), 317 nm (sh, $\varepsilon = 420\ M^{-1}\ cm^{-1}$), 350 nm (sh, $\varepsilon = 180\ M^{-1}\ cm^{-1}$) and 445 nm ($\varepsilon = 40\ M^{-1}\ cm^{-1}$).

The calculations establish that the HOMO is mainly located on the pyridine ring. The degeneracy of the t_{2g} set of metal orbitals is fully lifted because of the symmetry of the compound. One of these orbitals is not properly oriented and remains essentially non-bonding with respect to the nitrosyl moiety, being the majority component of the HOMO − 1 molecular orbital. The other two are strongly stabilized because of the fairly strong π interactions with the nitrosyl, and appear as the main constituents of the bonding HOMO − 5 and HOMO − 6 molecular orbitals. Conversely the LUMO and LUMO + 1 orbitals are mainly located on the NO fragment, but have some metal character resulting from the interaction between the π^* orbitals of the nitrosyl group with $t_{2g}(d_\pi)$ metal orbitals. Thus, the back-donation to the nitrosyl partially shifts electronic density from the metal ion into the π^* orbitals of the coordinated NO^+. The stabilization of the metal centered orbitals and the destabilization of the nitrosyl ones enlarge the HOMO–LUMO energy difference up to 3.2 and 3.6 eV, estimated in vacuum and in solution, respectively. These large values are responsible for the shift of the electronic spectrum to higher energies. The $Ru(II) \rightarrow \pi_{py}$ transition normally expected in the visible region [36–39] is therefore not observed there, but probably at much higher energy. We were not able to observe this band in our experimental conditions, but the analogous transition has been reported at 230 nm in the related systems $[Ru(NH_3)_4L(NO)]^{3+}$ (L = isonicotinamide or pyrazine) [6a,6b]. The π back-donation effect overcomes the subtle electronic changes expected to be induced by the specific interactions with the solvent. This explains the insensitivity of the electronic spectrum toward solvent changes.

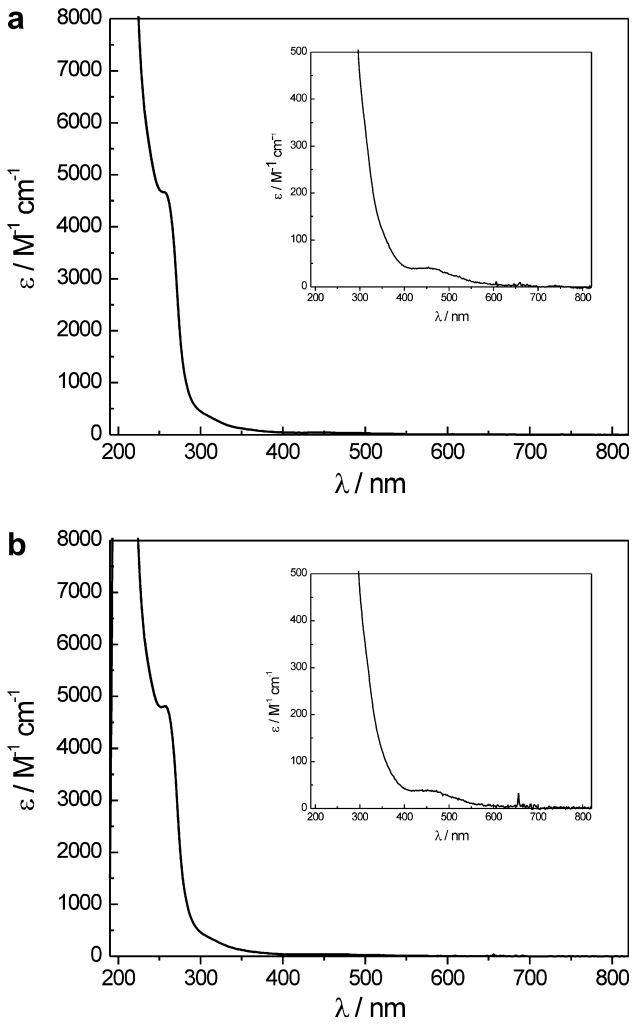


Fig. 6. Experimental UV–Vis spectra of **I** in water and organic medium. (a) Aqueous $HClO_4$ 0.1 M, (b) acetonitrile.

The interpretation of the electronic spectra of nitrosyl complexes is not unambiguous. In our case, the low symmetry of the species might lead to substantial orbital mixing that further complicates the analysis. (TD)DFT has proven as a valuable tool to assist in the assignment of the spectra of several related species [6c]. In the case of **I**, the calculated transitions reproduce qualitatively the experimental spectra. The computations position the Ru(II) $\rightarrow \pi_{py}$ MLCT at 208 nm, though superimposed with d–d and ligand-based transitions, and the lowest lying $\pi_{py} \rightarrow \pi^*_{py}$ intraligand transition at 257 nm. The extra features at lower energy involve several weak transitions with mixed d–d, MLCT (Ru(II) $\rightarrow \pi^*_{NO}$) and LL′CT ($\pi_{py} \rightarrow \pi^*_{NO}$) character. The agreement between the computed and experimental spectra is very good and supports the theoretical treatment.

3.3. Reactions with nucleophiles: formation of $[Ru(L^{py})NO_2]^+$

In spite of the backbonding effect, the coordinated nitrosyl still has a large nitrosonium character. The $[Ru^{II}NO^+]$ electronic distribution manifests experimentally not only in the ν_{NO} values, but also in the expected reaction of **I** with nucleophiles [5,26]. Aqueous solutions of **I** in non-acidic medium undergo rapid spectral changes with formation of $[Ru(L^{py})NO_2]^+$ (**II**), as described by Eq. (1). The reaction with OH^- is reversible and a full recovery of the nitrosyl reactant can be achieved upon acidification. Fig. 7 displays the spectra recorded in the stepwise conversion of the nitrosyl into the nitro compound. The presence of well defined isosbestic points suggests the absence of processes other than the one of interest. A multi-wavelength treatment of the absorption spectra by factor analysis also reveals the presence of only two colored species. This kind of reactions has been extensively studied in the past [5,26–28]. The nucleophilic attack of an OH^- ion leads to the formation of a covalent N–O bond. Afterwards, the intermediate nitrous acid complex deprotonates to yield the nitro derivative [9–11,28,42].

The spectrum of **II** is dominated by strong absorption bands at 264 nm ($\varepsilon = 4260\ M^{-1}\ cm^{-1}$), 308 nm ($\varepsilon = 4440\ M^{-1}\ cm^{-1}$) and 474 nm ($\varepsilon = 5590\ M^{-1}\ cm^{-1}$). As a comparison, the related compound *trans*-$[Ru(NH_3)_4(4\text{-Mepy})(NO_2)]^+$ (4-Mepy = 4-methyl pyridine) displays only one broad MLCT band at 378 nm with a shoulder at higher energies [10].

To understand the electronic structure of this species, we performed a theoretical geometry optimization, whose results are summarized in Table 2 and Fig. 5b. The coordination sphere of the Ru(II) ion in **II** remains very similar to the one described for **I**. The stable structure shows a dihedral N(py)–Ru–N–O angle close to 90° and a slight asymmetry in the coordinated NO_2^-, probably due to the intramolecular hydrogen-bond interaction with the closest N–H at *ca.* 2 Å. A full scan of this dihedral angle shows two minima in the potential energy surface. They correspond to equivalent geometries that result from a 180°

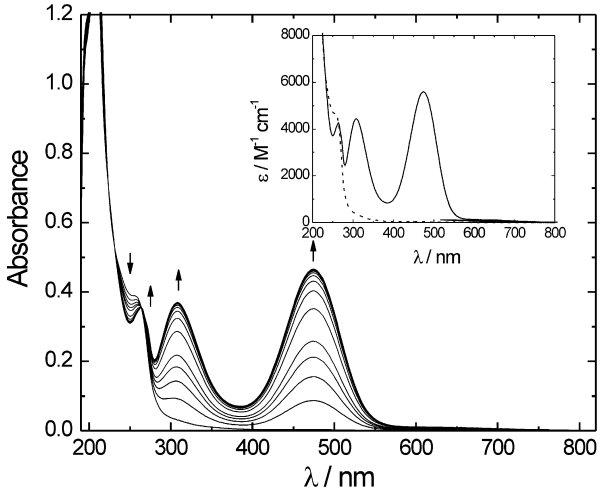


Fig. 7. Consecutive spectra for the reaction of **I** with OH^-. $[OH^-] = ca.\ 10^{-6}$ M, [complex] $= 8.4 \times 10^{-5}$ M. The arrows indicate the spectral changes along the reaction. Inset: Deconvoluted spectra of **I** (dashed line) and **III** (full line).

rotation of the NO_2^- moiety around the Ru–N axis followed by relaxation of the internal coordinates. These two minima are separated by a barrier of 33 kJ mol^{-1} (in vacuo), suggesting that the coordinated nitrite is not freely rotating in this species (or at least rotation around this axis has to be very slow in solution).

The nitro group is a poorer π-acceptor than the nitrosyl (and a better σ-donor). This results in an overall electronic picture with a lower degree of metal–ligand covalency and a higher electronic density located on the metal, as revealed by an average Mayer bond order of 0.36 for Ru–N(cyclam) and 0.49 for $Ru–N_{22}$. The filled frontier orbitals can now be clearly identified as the t_{2g} set. The lowest lying empty molecular orbitals are mostly located on the pyridine and the NO_2^- fragments, but to our surprise the calculations revealed a substantial degree of mixing between pyridine- and nitro-centered orbitals, feasible because of the low symmetry of this species.

The (TD)DFT calculated energy and intensity of the MLCT transitions does not accurately reproduce the experimental observations. This is not completely unexpected, because the electronic structure of this species has to be more sensitive to the medium. Consequently, the theoretical prediction of the electronic spectrum becomes much more difficult. Several approaches [38,43] have been employed in the past to deal with solute–solvent specific interactions, but the implementation of these strategies is beyond the scope of this manuscript. We perform here a tentative assignment of the donor–acceptor charge transfer spectroscopy employing qualitative arguments and comparing with related systems.

The literature values for the MLCT maxima of $[Ru(NH_3)_5NO_2]^+$ and $[Ru(NH_3)_5py]^{2+}$ in water are 368 and 407 nm, respectively [44]. The substitution of an ammonia by the poorer σ-donor pyridine molecule in the coordination sphere of $[Ru(NH_3)_5NO_2]^+$ is expected to shift the $Ru(II) \rightarrow NO_2^-$ MLCT band to higher energies. Using the same argument, the replacement of an ammonia by a nitrite should shift also the band to higher energies (lower wavelengths) than in $[Ru(NH_3)_5py]^{2+}$. This explains reasonably the occurrence of only one band in the spectrum of *trans*-$[Ru(NH_3)_4(4\text{-Mepy})(NO_2)]^+$ that results from the overlap of a $Ru(II) \rightarrow \pi_{py}$ and a $Ru(II) \rightarrow NO_2^-$ absorption both shifted to higher energy if compared to the pentaamine case.

The substantial mixing between the acceptor fragments suggested by the DFT calculations perturbs this description, shifting the two CT bands in opposite directions. We therefore assign the 308 nm band as involving the coordinated nitrite as the acceptor fragment and the 474 nm one as arising from a $Ru(II) \rightarrow \pi_{py}$ MLCT, both of them shifted with respect of the ones in *trans*-$[Ru(NH_3)_4(4\text{-Mepy})(NO_2)]^+$ as a consequence of the orbital mixing.

3.4. $\{RuNO\}^{6,7}$ interconversion

The cyclic voltammogram of **I** in aqueous solution (pH 1, $HClO_4$, $\mu = 0.1$ M) shown in Fig. 8a displays a single reversible wave at −0.02 V, arising from the one-electron interconversion between **I** and the $\{RuNO\}^7$ species $[Ru(L^{py})NO]^{2+}$ (**III**). Further exploration at more reducing potentials was not attempted because of the solvent electrochemical window.

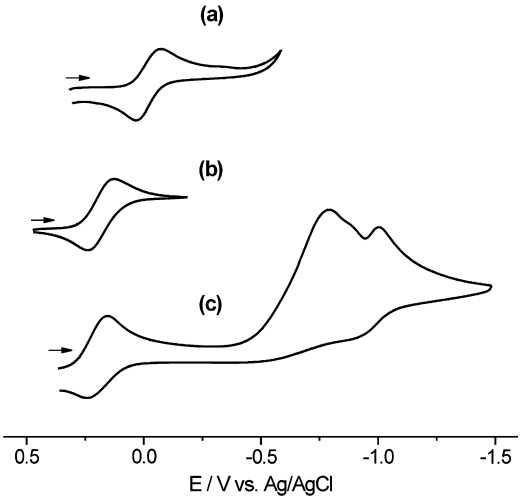


Fig. 8. Cyclic voltammograms of I in H_2O/0.1 M $HClO_4$ (a) and acetonitrile/0.1 M $TBAPF_6$ solution (b and c). Conditions: glassy carbon working electrode, scan rate 200 mV s^{-1}. The arrows indicate the direction of the scan.

The observed redox potential for the reduction of the coordinated nitrosyl is higher than the one reported for the related *trans*-$[Ru(NH_3)_4(4\text{-Mepy})(NO)]^{3+}$, −0.25 V ($\mu = 0.1$ M CF_3COOH/CF_3COONa, pH 4). Even when the difference might be partially ascribed to the differences between *cis*- and *trans*-configurations, it should be noted that a similar shift, which might originate in solvation issues related to the macrocylic ligand was reported when comparing other tetrammine- and cyclam-based nitrosyls [32,35]. For these related systems, the cyclic voltammograms reveal a series of chemical reactions coupled to the electron transfer process, that have been interpreted in terms of labilization of the co-ligands and NO^0 [6,32,35,45]. None of these complications seems to be associated to the $\{RuNO\}^{6,7}$ conversion in our system.

The cyclic voltammograms in acetonitrile (Fig. 9b) reveal the same reversible one-electron reversible process, though shifted to $E^0 = 0.18$ V. An increase of 0.125 V was reported for the same process in *trans*-[Ru(NO)Cl(cyclam)]$^{2+}$, and an even larger difference of *ca.* 0.30 V has been measured in $[Ru(tpm)(bpy)NO]^{3+}$ [11]. The differences can be traced back to changes in the dielectric properties of the solvents, which would favor the reduction process in less polar media. In addition, the larger donor number (DN)[46] of water if compared to acetonitrile (18.1 versus 14.1 for water and acetonitrile, respectively) contributes to increase the electronic density in the coordinated nitrosyl, via specific hydrogen-bond interaction with the amine protons [36]. The general increment in the redox potential, combined with a wider electrochemical window than in water, allowed to explore the reduction of the

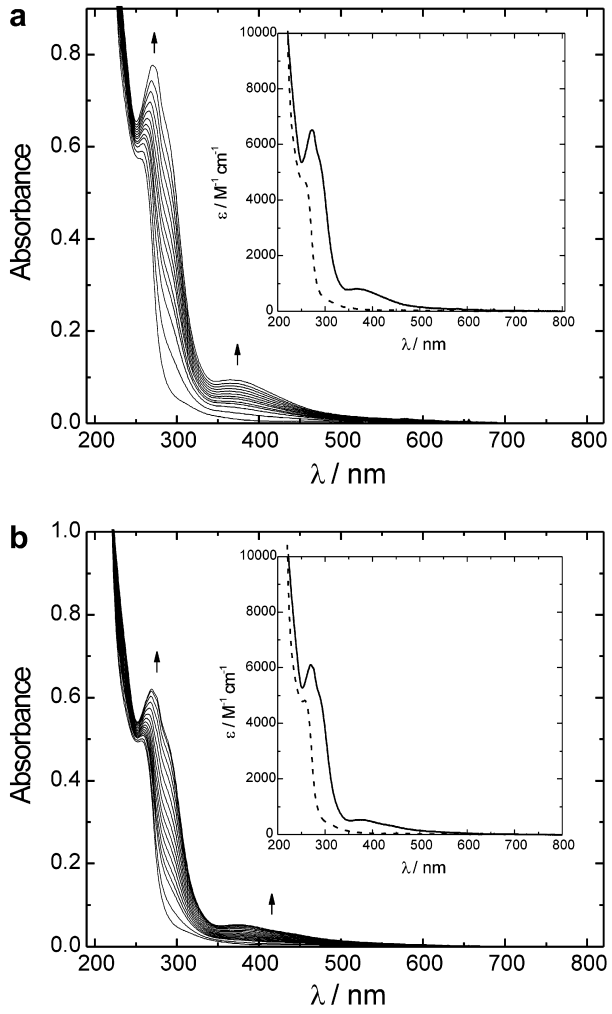


Fig. 9. Spectroelectrochemical conversion of **I** into **III** in water and organic medium under controlled potential conditions. (a) Aqueous $HClO_4$ 0.1 M, (b) acetonitrile/0.1 M $TBAPF_6$, [complex] = 1.2×10^{-4} M and 1.0×10^{-4} M for water and acetonitrile, respectively. The arrows indicate the spectral changes upon reduction. Insets: deconvoluted spectra for **I** (dashed line) and **III** (full line) obtained by factor analysis (see text).

$\{RuNO\}^7$ species. At more negative potentials (*ca.* −0.75 V) a complex pattern involving consecutive electron transfer processes can be detected. All this extra waves appear as irreversible in the CV time scale. The first of such electron transfer process might be tentatively ascribed to the formation of a $\{RuNO\}^8$ species [8,14]. This species appears to be unstable in the CV timescale, even if the experiments are performed at −30 °C and some complementary characterization would be required in order to improve its description.

Fig. 9 shows the stepwise **I** → **III** conversion under controlled potential conditions both in acidic conditions and in acetonitrile solution. The reduction processes proceed smoothly, and the factor analysis of the recorded spectra reveals only two colored species in both solvents. The integrated current, as well as the absorbance versus open-circuit potential curves obtained during the electrolysis are also consistent with a 1-electron process with $E^0_{NO+/NO} = -0.02$ and 0.21 V for water and acetonitrile, respectively. These values are in very good agreement with the ones obtained in the cyclic voltammetry experiments. The slight shift detected in acetonitrile is mostly due to the different temperatures employed in both determination. This experiment confirms the reversibility of the $\{RuNO\}^{6,7}$ redox interconversion. The electrogenerated reduced species in aqueous solution seems to be stable if protected from oxygen, but reoxidizes rapidly in the presence of air to quantitatively regenerate **I**. In acetonitrile, the oxidation by molecular oxygen is much slower, and no spectral changes were observed in the minute timescale. Electrochemical reoxidation leads, in both cases, to quantitative recovery of **I,** even after 2 h. The reversibility of the NO^+/NO conversion indicates that the whole coordination sphere in **III** (including the coordinated NO·) is strongly inert toward substitution reactions. As we mentioned above, this is not always the case, and release of NO or NO-induced *trans* labilization has been observed for several complexes [32,35]. The spectroelectrochemistry confirms that this is not the case with **III**, making this system particularly useful to be studied in both $\{RuNO\}^{6,7}$ oxidation states.

One-electron reduction is expected to induce a bending of the Ru–N–O angle [2,3]. A DFT geometry optimization confirms this expectation. The computation performed in vacuo included a potential energy surface scan of the dihedral O–N–Ru–N(py) angle, which revealed two possible stable geometries $\mathbf{III}_a$ and $\mathbf{III}_b$ for this $\{RuNO\}^7$ species (Fig. 5). The two situations minimize the steric interactions between the NO fragment and the L^{py} ligand. In contrast with **II** and other $\{MNO\}^7$ systems [14], there seem to be no signs of intramolecular N–O ⋯ H–N(cyclam) hydrogen-bond. These two conformers have slightly different thermodynamic stabilities, with $\mathbf{III}_a$ laying 5.4 kJ mol^{-1} below $\mathbf{III}_b$. Overall, the potential energy surface is rather flat and the interconversion of $\mathbf{III}_a$ into $\mathbf{III}_b$ involves a small energy barrier of 6.7 kJ mol^{-1} (1.3 kJ mol^{-1} in the opposite direction). Even when the presence of solvent molecules interacting specifically with the amine protons might hinder the interconversion between conformers, our calculations imply that the NO fragment is freely rotating in the $\{RuNO\}^7$ species. Table 2. collects the most significant structural parameters for $\mathbf{III}_a$ and $\mathbf{III}_b$. The overall features are very similar for both, with a practically identical co-ligand environment. The most significant structural change upon reduction involve, as expected, the lengthening of the Ru–N_{22} and N_{22}–O_{23} to 1.90 and 1.22 Å, and the bending of the Ru–N_{22}–O_{23} angle to *ca.* 143°. These parameters, combined with the reduction of the N_{22}–O_{23} Mayer bond order to 1.56 reflect the population of a formally π-antibonding orbital located mostly on the NO fragment. In fact, the calculations confirm that the SOMO is mostly located on the NO fragment with partial delocalization onto the metal center, a common feature to many $\{RuNO\}^7$ species [9,11,12,16].

The calculations also reveal an overall reduction of the covalency of the Ru–N(L^{py}) bonds, which show an average Mayer bond order of 0.41. Particularly, the Ru–N_4 bond order of 0.38 is the lowest, suggesting the onset of a *trans*-effect. In spite of this, the coordination sphere remains structurally unaffected due to the rigidity of the whole macrocyle. The electronic structure of this species is also affected by π-backbonding. Two metallic orbitals belonging to the t_{2g} set reveal some degree of mixing with the π^* orbitals located on the NO fragment, while the third remains as non-bonding because of the symmetry of the complex. The backbonding interaction is overall smaller than in **I**, revealing NO as a poorer π-acceptor. The lowest lying empty molecular orbitals correspond essentially to the ligand-centered π^* orbitals. Their relatively low energy, in contrast with the computations performed on **I**, permit the development of CT transitions in the visible region. The electronic spectrum of **III** displays an intense absorption at 271 nm ($\varepsilon = 6500\ M^{-1}\ cm^{-1}$), a shoulder at 287 nm ($\varepsilon = 5500\ M^{-1}\ cm^{-1}$) and a weaker band at 365 nm ($\varepsilon = 810\ M^{-1}\ cm^{-1}$), when recorded in water. In acetonitrile the positions of these bands remain almost unchanged at 270 nm ($\varepsilon = 6100\ M^{-1}\ cm^{-1}$), 287 nm ($\varepsilon = 5010\ M^{-1}\ cm^{-1}$) and 369 nm ($\varepsilon = 520\ M^{-1}\ cm^{-1}$).

The (TD)DFT results suggest that the low energy bands, predicted at 378 nm and observed at *ca.* 365 nm are better described as the spin-allowed $\pi_{NO} \rightarrow d_{Ru}$ LMCT with some $\pi_{NO} \rightarrow \pi^*_{py}$ character. The same computations assign the intense absorption at *ca.* 270–290 nm as arising from a $d_{Ru} \rightarrow \pi^*_{py}$ transition, though extensively overlapped with the intraligand $\pi_{py} \rightarrow \pi^*_{py}$, the $d_{Ru} \rightarrow \pi^*_{NO}$ MLCT and weak d–d transitions. It is surprising that even when the absorption bans appear to have CT character, there seems to be little solvent dependency. Though this fact can be indicative of extensive π-backbonding interactions [36,38,39,47], it is not clear that this is the case for **III** and a broader range of solvents has to be explored to asses this issue.

4. Conclusions

This pendant-arm cyclam complex of Ru(II) proved as a valuable platform to investigate the NO^+/NO^0 redox chemistry. The marked inertness of the coordination sphere on both $\{RuNO\}^6$ and $\{RuNO\}^7$ oxidation states, the strong color changes associated to the redox processes and the preliminary results concerning the reaction of this species with O_2 are promising, and open the possibility to a systematic study of redox reactivity. Variations in the identity of the pendant-arm could be used in the future to generate a series of nitrosyl compounds with control over $E^0_{NO^+/NO^0}$ in a region of potentials with scarce examples in the literature.

The abundant experience in connection with the derivatization of cyclam envisages many possible variations leading to macrocyclic species with different donor/acceptor capabilities. The parallelism with the related *trans*-$[Ru(NH_3)_4(4\text{-Mepy})(NO)]^{3+}$ and *trans*-$[Ru(NO)Cl(cyclam)]^{2+}$ series of compounds and the use of theoretical approaches as the ones employed here stand as valuable predictive tools that might be of significant help in the selection of the appropriate substituents. We are currently exploring this possibility.

Acknowledgements

The authors thank the University of Buenos Aires (UBA), the Consejo Nacional de Investigaciones Científicas y Técnicas (CONICET), the Agencia Nacional de Promoción Científica y Tecnológica (ANPCyT) and Fundación Antorchas for economic funding. LDS is a member of the scientific staff of CONICET and AGD is a graduate fellow from UBA.

Appendix A. Supplementary material

IR spectrum of *cis*-$[Ru(L^{py})NO](PF_6)_3$ in the solid state (KBr pellet), ^1H NMR and ^{13}C NMR spectra in CD3CN and full proton assignments. Supplementary data associated with this article can be found, in the online version, at doi:10.1016/j.poly.2007.04.038.

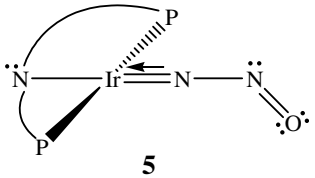
References

[1] G.B. Richter-Addo, P. Legzdins, Metal Nitrosyls, Oxford University Press, New York, 1992.
[2] J.A. Olabe, L.D. Slep, in: J.A. Mc Cleverty, T.J. Meyer (Eds.), Comprehensive Coordination Chemistry II, from Biology to Nanotechnology, vol. 1, Elsevier, Oxford, 2004, p. 603.
[3] (a) J.H. Enemark, R.D. Feltham, Coord. Chem. Rev. 13 (1974) 339;
(b) J.H. Enemark, R.D. Feltham, Top. Stereochem. 12 (1981) 155.
[4] (a) N.J. Armor, M.Z. Hoffman, Inorg. Chem. 14 (1975) 444;
(b) H. Nagao, H. Nishimura, H. Funato, Y. Ichikawa, F.S. Howell, M. Mukaida, H. Kakihana, Inorg. Chem. 28 (1989) 3955;
(c) H. Nishimura, H. Matsuzawa, T. Togano, M. Mukaida, H. Kakihana, F. Bottomley, J. Chem. Soc., Dalton Trans. (1990) 137.
[5] F. Bottomley, Acc. Chem. Res. 11 (1978) 158.
[6] (a) M.G. Gomes, C.U. Davanzo, S.C. Silva, L.G.F. Lopez, P.S. Santos, D.W. Franco, J. Chem. Soc., Dalton Trans. (1998) 601;
(b) S.D.S. Borges, C.U. Davanzo, E.E. Castellano, J. Z-Schpector, S.C. Silva, D.W. Franco, Inorg. Chem. 37 (1998) 2670;
(c) S.I. Gorelsky, S.C. DaSilva, A.B.P. Lever, D.W. Franco, Inorg. Chim. Acta 300–302 (2000) 698.
[7] (a) F. Baumann, W. Kaim, L.M. Baraldo, L.D. Slep, J.A. Olabe, J. Fiedler, Inorg. Chim. Acta 285 (1999) 129;
(b) M. Wanner, T. Scheiring, W. Kaim, L.D. Slep, L.M. Baraldo, J.A. Olabe, S. Zalis, E.J. Baerends, Inorg. Chem. 40 (2001) 5704.
[8] C. Hauser, T. Glaser, E. Bill, T. Weyhermuller, K. Wieghardt, J. Am. Chem. Soc. 122 (2000) 4352.
[9] F. Roncaroli, L.M. Baraldo, L.D. Slep, J.A. Olabe, Inorg. Chem. 41 (2002) 1930.
[10] F. Roncaroli, M.E. Ruggiero, D.W. Franco, G.L. Estiu, J.A. Olabe, Inorg. Chem. 41 (2002) 5760.
[11] M. Videla, J.S. Jacinto, R. Baggio, M.T. Garland, P. Singh, W. Kaim, L.D. Slep, J.A. Olabe, Inorg. Chem. 45 (2006) 8608.
[12] B.R. McGarvey, A.A. Ferro, E. Tfouni, C.W.B. Bezerra, I. Bagatin, D.W. Franco, Inorg. Chem. 39 (2000) 3577.

[13] M. Li, D. Bonnet, E. Bill, F. Neese, T. Weyhermuller, N. Blum, D. Sellman, K. Wieghardt, Inorg. Chem. 41 (2002) 3444.
[14] R.G. Serres, C.A. Grapperhaus, E. Bothe, E. Bill, T. Weyhermuller, F. Neese, K. Wieghardt, J. Am. Chem. Soc. 126 (2004) 5138.
[15] M. Videla, F. Roncaroli, L.D. Slep, J.A. Olabe, J. Am. Chem. Soc. 129 (2007) 278.
[16] S. Frantz, B. Sarkar, M. Sieger, W. Kaim, F. Roncaroli, J.A. Olabe, S. Zalis, Eur. J. Inorg. Chem. (2004) 2902.
[17] I.P. Evans, A. Spencer, G. Wilkinson, J. Chem. Soc., Dalton Trans. (1973) 204.
[18] I. Meunier, A.K. Mishra, B. Hanquet, P. Cocolios, R. Guilard, Can. J. Chem., Rev. Can. Chim. 73 (1995) 685.
[19] A.J. Bard, L.R. Faulkner, Electrochemical Methods, Fundamentals and Applications, John Wiley & Sons, Inc., New York, 1980.
[20] I. Noviandri, K.N. Brown, D.S. Fleming, P.T. Gulyas, P.A. Lay, A.F. Masters, L. Phillips, J. Phys. Chem. B 103 (1999) 6713.
[21] E.R. Malinovsky, Factor Analysis in Chemistry, 2nd edn., Wiley-Interscience, New York, 1991.
[22] A.R. Parise, S. Pollak, L.D. Slep, J.A. Olabe, An. Asoc. Quim. Argent. 83 (1995) 211.
[23] M.J. Frisch et al., Gaussian 03, Rev. D01, Gaussian, Inc., Wallingford CT, 2004.
[24] J. Li, L. Noodleman, D.A. Case, in: E.I. Solomon, A.B.P. Lever (Eds.), Inorganic Electronic Structure and Spectroscopy, vol. I, John Wiley & Sons, New York, 1999, p. 661.
[25] N.F. Curtis, in: J.A. Mc Cleverty, T.J. Meyer (Eds.), Comprehensive Coordination Chemistry II, from Biology to Nanotechnology, vol. 1, Elsevier, Oxford, 2004, p. 447.
[26] F. Bottomley, in: P.S. Braterman (Ed.), Reactions of Coordinated Ligands, vol. 2, Plenum Publ. Corp., New york, 1989.
[27] (a) F. Bottomley, M. Mukaida, J. Chem. Soc., Dalton Trans. (1982) 1933;
(b) P.C. Ford, I.M. Lorkovic, Chem. Rev. 102 (2002) 993;
(c) P.C. Ford, L. Laverman, I. Lorkovic, Adv. Inorg. Chem. 54 (2003) 203;
(d) M.D. Lim, I. Lorkovic, P.C. Ford, J. Inorg. Biochem. 99 (2005) 151.
[28] A.A. Chevalier, L.A. Gentil, J.A. Olabe, J. Chem. Soc., Dalton Trans. (1991) 1959.
[29] B. Bosnich, C.K. Poon, M.L. Tobe, Inorg. Chem. 4 (1965) 1102.
[30] A. Szabo, N.S. Ostlund, Modern Quantum Chemistry. Introduction Advanced Electronic Structure Theory, 1st edn., Dover Publications, Inc., Mineola, NY, 1989.
[31] B.L. Westcott, J.H. Enemark, in: E.I. Solomon, A.B.P. Lever (Eds.), Inorganic Electronic Structure and Spectroscopy, vol. II, John Wiley & Sons, New York, 1999, p. 403.
[32] D.R. Lang, J.A. Davis, L.G.F. Lopes, A.A. Ferro, L.C.G. Vasconcellos, D.W. Franco, E. Tfouni, A. Wieraszko, M.J. Clarke, Inorg. Chem. 39 (2000) 2294.
[33] J.N. Armor, Scheideg Ha, H. Taube, J. Am. Chem. Soc. 90 (1968) 5928.
[34] C.K. Poon, C.M. Che, J. Chem. Soc., Dalton Trans. (1981) 1336.
[35] E. Tfouni, K.Q. Ferreira, F.G. Doro, R.S. da Silva, Z.N. da Rocha, Coord. Chem. Rev. 249 (2005) 405.
[36] C. Creutz, M.H. Chou, Inorg. Chem. 26 (1987) 2995.
[37] (a) C. Creutz, M.D. Newton, N. Sutin, J. Photochem. Photobiol. A-Chem. 82 (1994) 47;
(b) A.M. Zwickel, C. Creutz, Inorg. Chem. 10 (1971) 2395.
[38] Y.G.K. Shin, B.S. Brunschwig, C. Creutz, M.D. Newton, N. Sutin, J. Phys. Chem. 100 (1996) 1104.
[39] (a) Y.K. Shin, B.S. Brunschwig, C. Creutz, N. Sutin, J. Phys. Chem. 100 (1996) 8157;
(b) L.D. Slep, J.A. Olabe, J. Am. Chem. Soc. 123 (2001) 7186.
[40] R.S. da Silva, M.T.P. Gambardella, R.H.A. Santos, B.E. Mann, E. Tfouni, Inorg. Chim. Acta 245 (1996) 215.
[41] R.S. da Silva, E. Tfouni, Inorg. Chem. 31 (1992) 3313.
[42] L.M. Baraldo, M.S. Bessega, G.E. Rigotti, J.A. Olabe, Inorg. Chem. 33 (1994) 5890.
[43] (a) D.A. Estrin, L.M. Baraldo, L.D. Slep, B.C. Barja, J.A. Olabe, L. Paglieri, G. Corongiu, Inorg. Chem. 35 (1996) 3897;
(b) M.C. Gonzalez-Lebrero, A.G. Turjanski, J.A. Olabe, D.A. Estrin, J. Mol. Model. 7 (2001) 201.
[44] (a) F. Bottomley, J.R. Crawford, J. Chem. Soc., Dalton Trans. (1972) 2145;
(b) P. Ford, D.F.P. Rudd, R. Gaunder, H. Taube, J. Am. Chem. Soc. 90 (1968) 1187.
[45] E. Tfouni, M. Krieger, B.R. McGarvey, D.W. Franco, Coord. Chem. Rev. 236 (2003) 57.
[46] V. Gutmann, Electrochim. Acta 21 (1976) 661.
[47] B.S. Brunschwig, C. Creutz, N. Sutin, Coord. Chem. Rev. 177 (1998) 61.

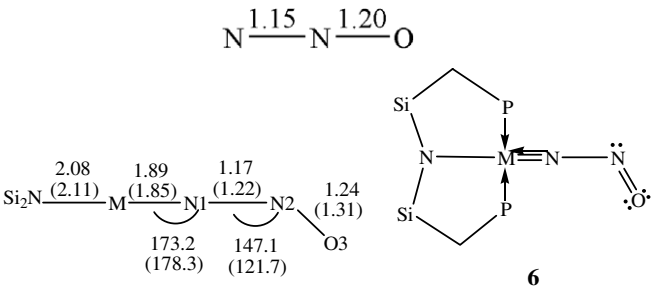
We found a minimum (**4** and Fig. 1) in which N_2O is exactly *trans* (179.1°) to the amide N with an entirely linear RhNNO unit. Bond lengths within the N_2O unit are altered by less than 0.02 Å from those calculated for free N_2O. Results of fixed geometry scan (Table 1) show the minimum.

Apparently (PNP)Rh lacks the reducing power to form N_2O^{2-}, in part because the resulting Rh^{III} would have such an atypical (four-coordinate) coordination geometry for a d^6 configuration. Since a 5d metal is always more reducing than its 4d analog, we did geometry optimization of (PNP)Ir(N_2O). Indeed, this has a minimum (Fig. 2) bent at N_β, but linear at N_α. This is best described by Lewis structure **5**, which indeed has N_2O^{2-} as the ligand, but with additional donation of the N_α lone pair to Ir in the $(PNP)Ir^{2+}$ fragment. Such donation creates an Ir/N_α triple bond but demands localization of the PNP amide lone pair on that N, hence lengthening that bond. The Ir–NSi_2 distance is 2.08 Å in (PNP)Ir(N_2O) but only 1.84 Å in $(PNP)Ir^{2+}$; comparing these, the Mayer Ir–NSi_2 bond order nearly doubles, from 0.80 to 1.51. Table 1 shows that this potential curve is even softer than that for Rh



5

The optimized geometries (Fig. 2) for (PNP)Ir(N_2O) and the isoelectronic and more electron rich $(PNP)Os(N_2O)^{-1}$ are both half-bent, with structural parameters compared in Scheme 1 (where values for Os are shown in parentheses). For the more reducing $(PNP)Os^{-1}$ fragment, the M/N1 distance is shorter and the N1/N2 and N2/O3 distances are longer, while the angle is more linear at N1 and bent to



6

Scheme 1.

Table 1
Bending potential (B3LYP/cc-pVTZ(-f) energies, in kcal mol)

N–N–O (in °)	130	140	150	160	170	180
(PNP)Rh(N_2O)	10.4	6.4	4.4	3.4	2.6	0.0
(PNP)Ir(N_2O)	1.7	−0.2	−0.4	0.3	0.4	0.0

nearly sp^2 at N2. Together, these support the idea of greater participation by structure **6** from Ir to Os. Comparison to the structure of (PNP)Rh(N_2O) shows Rh to be the least reducing, in line with conventional thinking. The Ir/N1 and Os/N1 distances are short enough to qualify as multiple bonds. The M/(amide N) distances become longer when the *trans* distance shortens, consistent with competition between two nitrogens for one empty metal d_π orbital. Atomic charges from an electrostatic potential calculation confirm this: Rh(Ir) are +0.20 and +0.47, while N_2O is −0.14(Rh) and −0.37(Ir).

2.2. Doubly bent N_2O

To probe the claim of Ir/N_α triple bond above, it is necessary to consider N_2O binding geometries when the L_nM fragment already carries 16 valence electrons. For this purpose, we considered two reducing moieties, $(Me_3P)_4Ir^+$ and $(Me_3P)_4Os$, each d^8 and singlet. By removing the π-donor

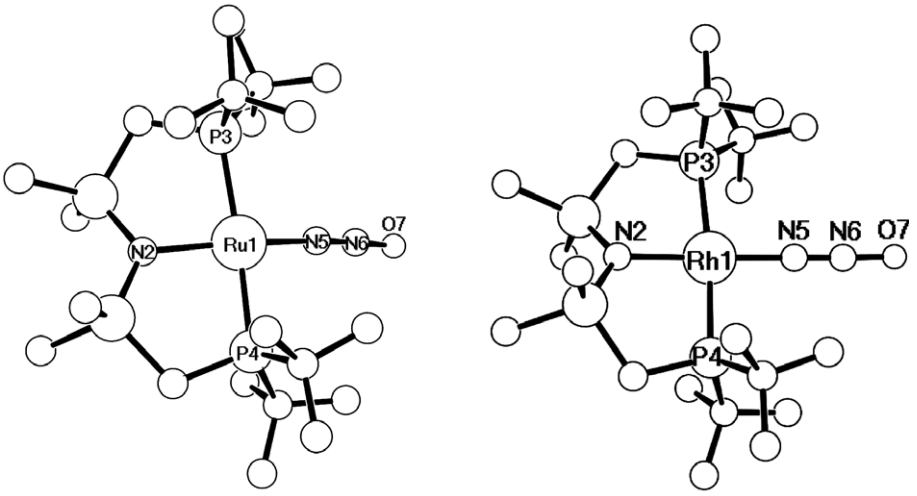


Fig. 1. DFT structures for (PNP)M(N_2O) for M = Ru (left) and Rh (right).

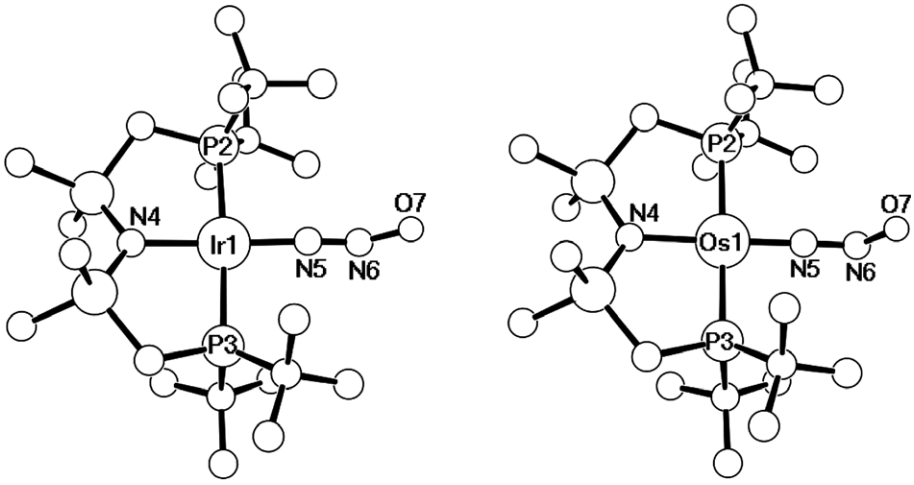
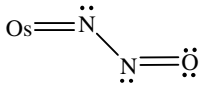


Fig. 2. DFT structures for (PNP)Ir(N_2O) (left) and (PNP)Os(N_2O)$^{-1}$ (right).

amide ligand of PNP, we simplify analysis of the results. The osmium example indeed has an energetic minimum of the sort we seek (Fig. 3), and where the OsNNO unit is *doubly* bent. This is in full accord with Lewis structure **7**. This should then be considered five-coordinate and d^6, and the observed geometry is close to square pyramidal, with the "dominant" ligand, N_2O^{2-}, apical. The small deviation of the Os(PMe_3)$_4$ substructure from C_4 symmetry is attributed to the electronic anisotropy of the Os/N $\sigma + \pi$ bond, causing the NO group to destroy rigorous C_4 symmetry.



7

It is interesting that geometry optimization of doubly bent $(Me_3P)_4Ir(N_2O)^+$, from a variety of starting geometries, dissociates the Ir/N bond, showing the absence of a significant energy minimum and showing N_2O to not be bound to Ir^I in Ir(PMe_3)$_4^+$. Since this cation is clearly less reducing than neutral Os(PMe_3)$_4$, we attribute the purely dissociative character to inadequate reducing power of Ir(PMe_3)$_4^+$, together with the special stability of the d^8 configuration when it is square planar (i.e. the empty d orbital, x^2–y^2, associated with its "unsaturation," has very high energy because it is σ^*_{Ir-P}).

One electron reduction of this Ir^I species, to form the doublet radical $(Me_3P)_4Ir(N_2O)$, gives a species (Fig. 3) which is a minimum (i.e. Ir–N_2O does not dissociate on geometry optimization) and with doubly bent N_2O. Spin densities (0.05 on Ir and 0.89 on N_2O) show this to be Ir^I binding an N_2O^{-1} radical anion, consistent with good reducing power from the 17 electron Ir(PMe_3)$_4$ center. The Ir–N2 distance is 0.18 Å longer than in $(Me_3P)_4Os(N_2O)$, but distances within the N_2O unit differ negligibly.

2.3. More complicated examples

2.3.1. Singlet (PNP)Ru(NO)(N_2O)

The species (PNP)Ru(NO)(N_2O) optimizes to a geometry (Fig. 4) which has linear N_2O (hence 2e donor and

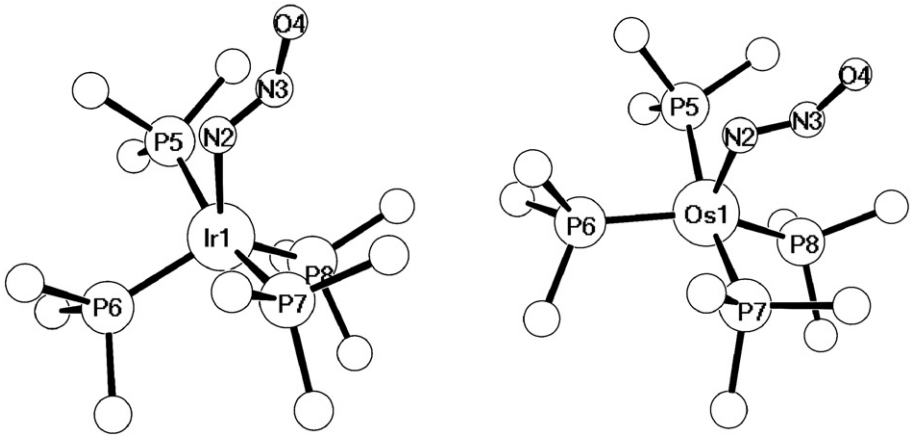


Fig. 3. DFT structures for doublet $(Me_3P)_4Ir(N_2O)$ and singlet $(Me_3P)_4Os(N_2O)$. Selected angles (°) for Ir(Os): M–N2–N3, 119.3 (111.0); N2–N3–O4, 133.7 (134.6).

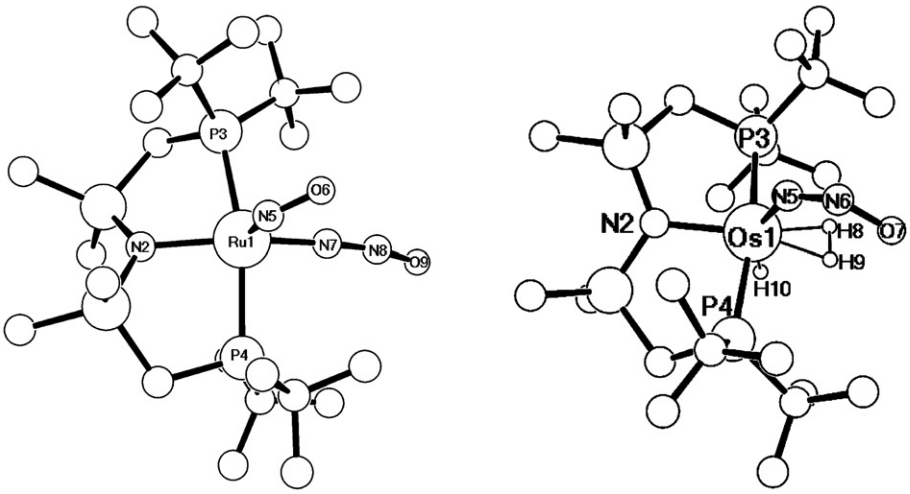
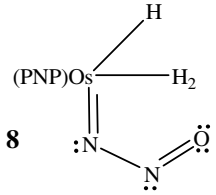


Fig. 4. DFT structures for (PNP)Ru(NO)(N_2O) and (PNP)OsH(H_2)(N_2O).

not reduced) but bent (124.4°) RuNO. This latter bend is needed to achieve an 18-electron configuration (with PNP donating its amide lone pair), and this bend is absent after N_2O is lost from Ru in the planar ground state geometry of (PNP)Ru(NO), which has linear RuNO, hence NO^+ and Ru^0. The distances within N_2O in (PNP)Ru(NO)(N_2O) are only a little changed (<0.02 Å) from those in free N_2O. Altogether then, the (PNP)$Ru^{II}(NO^{-1})$ fragment cannot reduce its coordinated N_2O.

2.3.2. (PNP)Os(H)$_3$ + N_2O

(PNP)$Os(H)_3$ is an operationally unsaturated (16/18 valence e) complex with C_{2v} symmetry and a distorted octahedral structure [2]. When N_2O binds to this molecule *cis* to amide, we located a doubly bent singlet minimum (Fig. 4).[1] The Os/N_α distance, 2.015 Å, is consistent with drawing **8**



8

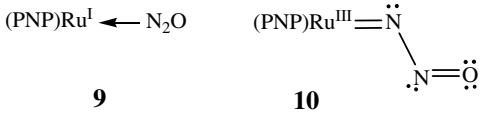
Metal-to-N_2O electron transfer is also evident in an additional characteristic of the minimum found for (PNP)OsH_3(N_2O). When N_2O binds to this trihydride of Os^{IV}, two hydrides respond by reductively coupling (Fig. 4) to form η^2-H_2, with redox transfer of 2e to Os; the product, (PNP)OsH(H_2)(N_2O), thus retains the +4 oxidation state of the reagent. The Os^{VI} alternative is so oxidizing that two hydrides reduce it. In short, the dihydride/dihydrogen outcome is diagnostic of the Os/N_2O interaction having redox character, not mere dative bonding.

2.3.3. The radical (PNP)Ru(N_2O)

Another interesting example is the redox fate of (PNP)Ru^{IV}(≡N) when the NO radical binds Eq. (1) to the nitride nitrogen (Fig. 1). Here N_2O is

$$(PNP)RuN + NO \rightarrow (PNP)Ru(N_2O) \quad (1)$$

formed by N/N bond formation. The resulting $S = 1/2$ complex could be **9** or **10**. The fact that



9 **10**

the minimum found (even starting from a *doubly bent* geometry) has an entirely linear RuNNO structure indicates that d^7 (PNP)Ru^I in the product lacks the reducing power to produce *N*-nitrosoimide. The overall N/N coupling reaction Eq. (1) is thus a 3-electron reduction of Ru^{IV}

$$N^{3-} + NO \rightarrow N_2O + 3e^- \quad (2)$$

Ruthenium is close to planar in this spin doublet species and there is very little change (0.01–0.03 Å) in the bond lengths within the N_2O fragment from those in free N_2O. Structural parameters are within 0.03 Å of those of (PNP)Rh(N_2O), which has one more valence electron. The spin densities, +1.049 on Ru and −0.04 on the N_2O moiety and only +0.02 on the amide N, are consistent with d^7 Ru^I, and support the conclusion that the (PNP)Ru moiety, like (PNP)Rh, lacks 2-electron reducing power.

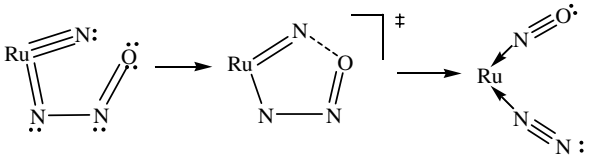
[1] These are not necessarily the most stable of adduct structures, but the structural implication of electron transfer remains true.

3. Discussion

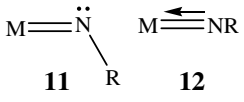
Our initial location of doubly bent N_2O minima involved N_2O addition to $(PNP)Os^{IV}(H)_3$ and to $(PNP)Ru^{IV}N$ [9]. It is remarkable that *one* of these high oxidation states (Ru), and a d^4 electron configuration, retains enough reducing power to transfer 2 electrons to arriving N_2O in the resulting adduct.[1] Reduction of N_2O in the Os case relies on each hydride ligand to furnish one electron. In the osmium case, the bending is central to migration of H-ligands to O, which ultimately forms H–Os ← N≡N:, with liberation of H_2O

$$(PNP)Os(H)_3 + N_2O \rightarrow (PNP)OsH(N_2) + H_2O \quad (3)$$

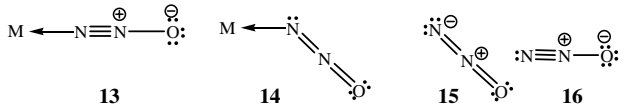
In the latter case, double bending is key to reactivity which transfers O to nitride


(4)

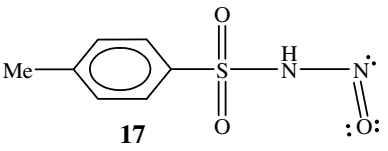
Based on the paucity of examples, N_2O is clearly a very weak ligand (as is its isoelectronic analog CO_2). This can be offered as the cause of why N_2O generally functions only poorly as an oxygen atom transfer reagent (i.e. $N_2O \rightarrow N_2 + O$), in spite of the attractive co-product, N_2. If N_2O binds only poorly to a metal, this becomes the rate determining step, in spite of good thermodynamics of subsequent steps; the O-transfer reaction fails for kinetic reasons. In some sense, it is surprising that the new, 2e redox mode of η^1-binding N_2O to a metal was not proposed until now. While it requires a strongly reducing L_nM reagent, the reaction is wholly analogous to (RN_3-derived) imide binding to a metal; for N_2O^{2-}, the difference focuses on possible conjugation of M=N with N=O when R is the bent nitroso group (**11** and **12**)


11 **12**

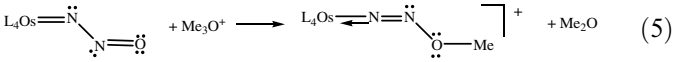
The traditional mode postulated for η^1-N bound coordination of N_2O is always found to be linear at both N, **13**, which is curious given the allene (or cumulene) structure (**14**) normally drawn for N_2O (hence bent at N_α). Structure **15** has more nucleophilic N than any N in structure **16** and structure **15** is more consistent with the observed NN and NO bond lengths (Scheme 1)


13 **14** **15** **16**

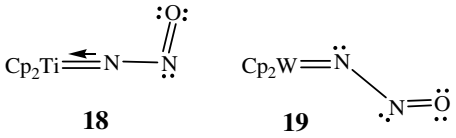
The half-bent versus doubly bent L_nMN_2O structures described here for coordinated N_2O^{2-} have the effect of weakening the N_α/N_β bond (the two reducing equivalents occupy an orbital which is heavily $\pi^*_{N\alpha N\beta}$). This suggests that both bent N_2O ligands may react by NO^q transfer, the value of q being determined by L_nM as well as the specific NO^q receptor reagent. This is a feature shared with the "Diazald" NO transfer reagent **17** [10]: it leaves behind a moiety which can stabilize emerging anion or radical character, as the N/N bond breaks


17

In addition, one can imagine protonation of N_β (or even O) of bent N_2O^{2-}, or attack by an electrophile


(5)

Perhaps the most successful use of N_2O as an oxygen transfer reagent is its reactivity towards low valent, early transition metal metallocenes [11–14], Cp_2M for M = Ti, V, Cr. Here the products are invariably μ-oxo clusters $(CpM)_m(O)_n$. Based on the results presented here, it is possible [15,16] that species like **18** and **19** mediate these reactions and thus that the *N*-nitrosoimide ligand is the source of oxidizing oxygen, with formation, then liberation of N_2. These principles also indicate that binding of N_2O to a solid surface containing reducing equivalents may also involve an *N*-nitrosoimide form


18 **19**

It is interesting that, with the PNP ligand, going to a monovalent 5d metal effects 2-electron reduction of N_2O, whereas a 4d analog does not, in spite of coordination number 4 being unfavorable even for d^6 Ir(III). In that regard, it is important to note [17] that the d^6 (linear) imides (arene)OsNR and Cp*IrNR are both "tetrahedral", or in fact C_{3v}, and this is probably the electronically preferred coordination geometry for L_3MNR, but clearly is structurally impossible for a PNP ligand species.

To encourage experimental discovery of the various structures described here, it will be useful to know their vibrational spectroscopic signatures. Shown in Table 2 are the calculated frequencies of wholly linear, singly bent and doubly bent cases. The wholly linear example has the high frequency characteristic of free N_2O itself, a value which is so high due to strong vibrational coupling of the two different multiple bond stretches (analogous to free

Table 2
Calculated stretching frequencies and bond lengths (Å)

	cm^{-1}	N1–N2	N2–O3
(a) Linear			
Free N_2O	2367	1.15	1.20
(PNP)Rh(N_2O)	2362	1.19	1.21
(PNP)Ru(N_2O)$^{\cdot}$	2330	1.15	1.22
(b) Singly bent			
(PNP)Ir(N_2O)	2059	1.17	1.24
(PNP)Os(N_2O)$^{-1}$	1619	1.22	1.31
(c) Doubly bent			
$(Me_3P)_4$Ir(N_2O)$^{\cdot}$	1591	1.22	1.25
$(Me_3P)_4$Os(N_2O)	1644	1.21	1.26

CO_2), when they are mutually *trans* (high interaction force constant). As the triatomic bends singly, then doubly, the frequencies decrease to the values appropriate to an N=O bond. These values support the conclusions from Lewis structures that reduction (metal-to-ligand redox) weakens bonds within N_2O, and this bodes well for improved predictability of how to do oxygen atom transfer. . ..or NO transfer from coordinated N_2O.

Acknowledgment

This work was supported by the National Science Foundation (NSF).

Appendix A. Supplementary material

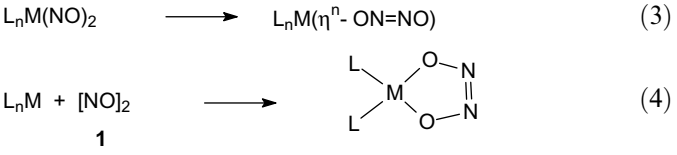
Full computational details and results are available in the online version at http://www.elsevier.com/. Supplementary data associated with this article can be found, in the online version, at doi:10.1016/j.poly.2007.05.035.

References

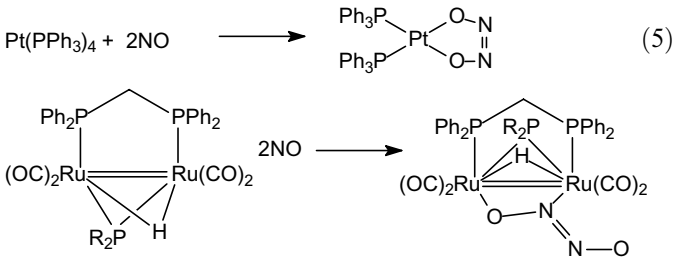
[1] A. Walstrom, M. Pink, X. Yang, J. Tomaszewski, M.-H. Baik, K.G. Caulton, J. Am. Chem. Soc. 127 (2005) 5330.
[2] J.-H. Lee, M. Pink, K.G. Caulton, Organometallics 25 (2006) 802.
[3] S.I. Gorelsky, S. Ghosh, E.I. Solomon, J. Am. Chem. Soc. 128 (2006) 278.
[4] J.-P.F. Cherry, A.R. Johnson, L.M. Baraldo, Y.-C. Tsai, C.C. Cummins, S.V. Kryatov, E.V. Rybak-Akimova, K.B. Capps, C.D. Hoff, C.M. Haar, S.P. Nolan, J. Am. Chem. Soc. 123 (2001) 7271.
[5] P.T. Matsunaga, J.C. Mavropoulos, G.L. Hillhouse, Polyhedron 14 (1995) 175.
[6] J.A. Olabe, G.L. Estiu, Inorg. Chem. 42 (2003) 4873.
[7] F. Bottomley, W.V.F. Brooks, Inorg. Chem. 16 (1977) 501.
[8] M.J. Ingleson, M. Pink, K.G. Caulton, J. Am. Chem. Soc. 128 (2006) 4248.
[9] A. Walstrom, H. Fan, K.G. Caulton (unpublished).
[10] G.B. Richter-Addo, P. Legzdins, Metal Nitrosyls, Oxford University Press, New York, 1992.
[11] F. Bottomley, L. Sutin, Adv. Organomet. Chem. 28 (1988) 339.
[12] F. Bottomley, J. Darkwa, Dalton Transactions: Inorganic Chemistry (1972–1999) (1988) 2505.
[13] F. Bottomley, Polyhedron 11 (1992) 1707.
[14] F. Bottomley, J. Darkwa, J. Chem. Soc. Dalton Trans.: Inorg. Chem. (1972–1999) (1983) 399.
[15] M.R. Smith III, P.T. Matsunaga, R.A. Andersen, J. Am. Chem. Soc. 115 (1993) 7049.
[16] W.A. Howard, G. Parkin, J. Am. Chem. Soc. 116 (1994) 606.
[17] D.E. Wigley, Prog. Inorg. Chem. 42 (1994) 239.

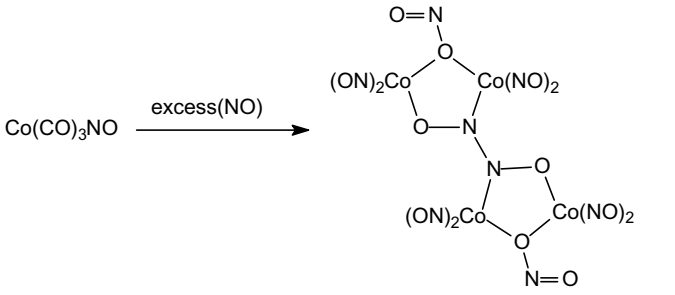
the form of metal catalyzed disproportionation. And of course any disproportionation, metal catalyzed or not, leads to the formation of the very strongly oxidizing nitrogen dioxide. It is significant that the original syntheses of $Cr(NO)_4$ involves a photolytic substitution under a stream of nitric oxide at atmospheric pressure [3,9,10], conditions which favor the binding monomeric nitric oxide and not nitric oxide disproportionation or the reaction of the complex with the nitric oxide dimer.

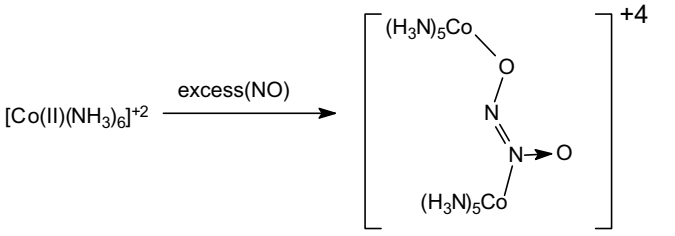
In addition to these fundamental synthetic limitations there is an additional reactivity pattern possible for polynitrosyl complexes which is not observed for polycarbonyls: metal mediated nitric oxide coupling to give N–N bonded derivatives either as hyponitrite [11–14], or nitrous oxide [15] or in some cases ultimately to give dinitrogen [16]. Unfortunately, the evidence for the direct coupling of two nitrosyls in the coordination sphere of a metal is limited and a clear unambiguous example of the reaction in Eq. (3) would help us understand the nature of this transformation. The ambiguity present here is mechanistic: Are either of the nitrosyls coordinated to the metal before N–N bond formation, Eq. (3), or do these N–N coupled products result from the reaction of the dimer **1** with the metal, Eq. (4)?



Examples of metal mediated nitric oxide reductive coupling which give isolable hyponitrite complexes are rare and correspond to the nitrosylation of several electron rich late transition metal complexes, Eqs. (5)–(8) [12–14]. In the ruthenium and platinum examples the corresponding dinitrosyl complexes were not isolated, and have not been reported. The reaction of $Pt(PPh_3)_4$ with nitric oxide proceeds in a straightforward manner involving the reductive dimerization of nitric oxide to yield a *cis*-hyponitrite ligated Pt(II) complex (Eq. (5)) [12]. A more complicated reaction between $Co(CO)_3(NO)$ and excess nitric oxide also proceeds via reductive dimerization of nitric oxide, Eq. (7). In this case the formation of the putative $[Co(NO)_3]$ intermediate is also proposed [13]. Finally, the example shown of the reductive coupling of two Co(II) nitrosyl complexes in Eq. (8), $\{CoNO\}^8$ in the Feltham–Enemark scheme [17], is a well studied [18–20] example known since Werner's pioneering chemistry [21]. In the absence of added reductants nitric oxide coupling can occur with metal oxidation [16] or by nitric oxide disproportionation, Eq. (2). Thus, the reductive nitric oxide coupling which occurs in Eqs. (5)–(8) are likely to be quite common and most likely related to the general metal catalyzed disproportionation of NO by transition metals [15,22] and more recently by lanthanides [23]. The current scarcity of hyponitrite complexes as products of reductive nitrosylation reactions is in part due to their instability and in particular their tendency to lose nitrous oxide [24].





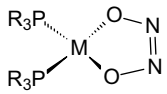


The facile loss of nitrous oxide from the *cis*-hyponitrite complex is one of its key reactivity patterns; it is also important for the uncoordinated ligand. We have attributed this to the instability of the monoalkyl or monoprotonated *cis*-hyponitrite. To demonstrate this point the contrast with *trans*-hyponitrite and its conjugate acid and esters is illustrative. Thus although a series of monoalkylated and protonated *trans*-hyponitrites are now recognized, these correspond to the kinetically activated form which releases nitrous oxide. Unlike *trans*-hyponitrite for which stable dialkylated and diprotonated derivatives can be isolated and characterized, neither is known for the *cis* isomer. We attribute this tendency to the instability of the monoprotonated and monoalkylated *cis*-hyponitrite: addition of the second electrophile can not compete with loss of nitrous oxide. This hypothesis accounts for the instability of *cis*-hyponitrite complexes: any coordination sphere lability which leads to a monohapto *cis* hyponitrite could rapidly lose nitrous oxide. A second consequence of this hypothesis is that the preparation of *cis*-hyponitrite complexes will most likely require prior coordination of the oxygens in the precursor or oxidative addition of the nitric oxide dimer, rather than by direct coordination of the preformed dianion. In this paper, we report: (1) the preparation and characteristics of *cis*-hyponitrite complexes; (2)

the redetermination of the structure of one of these, $Pt(PPh_3)_2(N_2O_2)$, with a significantly improved precision; (3) the syntheses and characterization of new dinitrosyl complexes of ruthenium and osmium with chelating phosphines; and (4) the structures of two of these derivatives, $Ru(dppf)(NO)_2$ and $Os(dppe)(NO)_2$.

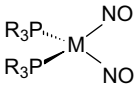
2. Results and discussion

Two streams of experimental data are contrasted in this paper: the stable group 10 M(II) hyponitrite complexes, **2**, for which the corresponding dinitrosyls are not known, and the stable group 8 dinitrosyls, **3**, for which stable mononuclear hyponitrite complexes have not been described



2

M = Pt, Ni



3

M = Ru, Os

2.1. Coordinated hyponitrite

It remains remarkable how few *cis*-hyponitrite complexes there are and how poorly developed the chemistry of this ostensibly simple dianion remains: in part this reflects the extreme reactivity of its simple salts [24], of which the disodium salt was only thoroughly characterized in 1996 [25,26]. In contrast, there are many more reports related to *trans*-hyponitrite, it is easier to prepare and it has greater stability [27,28]. The first and until recently unique example of the mononuclear *cis*-hyponitrite complexes **2a** with $L = PPh_3$ and M = Pt was first prepared by treating $Pt(PPh_3)_4$ with NO [11,12]. In 2002, we described a new way to prepare these derivatives by treating MCl_2L_2, M = Ni, Pt, with the diazeniumdiolate **4**, Eq. (9). In addition to the generality of the possible substrates for the generation of **2** their yields and purity are higher with this synthesis. Detailed spectroscopic and characteristic data are listed in Section 4, **2a**–**e**, and the structure for **2a** has been redetermined since the original had large esd's for the metric parameters for the hyponitrite ligand, and the modeled solution had a very high *R* factor, $R > 10\%$ [12]. Although these crystallographic problems limited the detailed interpretation of the structure of **2a** it did confirm its composition. These limitations are due to the original data being acquired at room temperature, where there is considerable decomposition. Our redetermination corresponds to the −100 °C structure. A side on view of the inner coordination environment of **2a** is shown in Fig. 1, and key metric parameters are included in the caption. The geometry adopted by the *cis*-hyponitrite in **2a** is similar to that in $Ni(dppf)(N_2O_2)$ [24] and the metric parameters are similar to the dianion in its sodium salt [25], but the latter structure is based on the Rietveld refinement of its powder data and the key anion bond lengths and angles have high esd's, cf. O(1)–N(1)=1.40(3); N(1)–N(2) = 1.20(3); N(2)–O(2) = 1.41(3) Å and N(2)–N(1)–O(1) = 120.8(4)°, N(1)–N(2)–O(2) = 117.6(4)° which limits their interpretation.

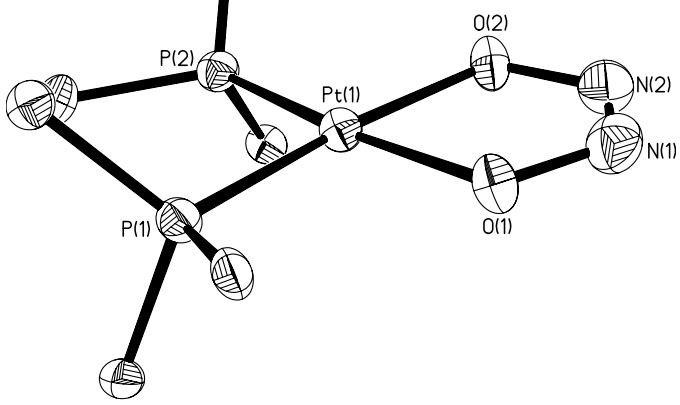
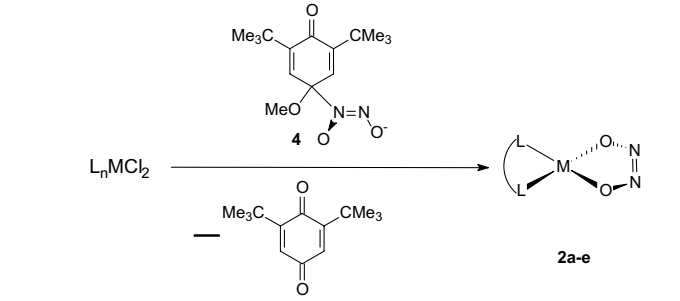


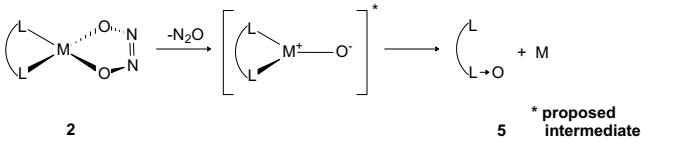
Fig. 1. ORTEP representation of the inner coordination sphere of **2a**. Probability elliposoids shown at 45% and key metric parameters (Å, °): O(1)–N(1) = 1.370(8); N(1)–N(2) = 1.230(9); N(2)–O(2) = 1.363(8); O(1)–Pt(1) = 2.013(4); O(2)–Pt(1) = 2.023(5); Pt(1)–P(1) = 2.2417(17); Pt(1)–P(2) = 2.2671(18) Å; Pt(1)–O(1)–N(1) = 112.1(4); O(1)–N(1)–N(2) = 118.9(7); N(1)–N(2)–O(2) = 118.5(7); N(2)–O(2)–Pt(1) = 112.3(5); O(1)–Pt(1)–O(2) = 78.2(2); O(1)–Pt(1)–P(1) = 93.23(15); O(1)–Pt(1)–P(2) = 168.56(15); O(2)–Pt(1)–P(1) = 171.40(15); O(2)–Pt(1)–P(2) = 90.79.15(15); P(1)–Pt(1)–P(2) = 97.80(7)°.



(9)

In prior work [24], we have termed the reaction in Eq. (9) an umpolung of the C–N bond: on a formal level the bond cleaves heterolytically to give $[N_2O_2]^{2-}$ rather than to generate two NO radicals as do many diazeniumdiolates [29]. The quinone by-product has been quantified and corresponds well to the yield of **2**. Typically, two equivalents of **4** are used for every metal complex, but when the stoichiometry is 1:1 the yield of **2a** is only slightly less than if two equivalents are used. In understanding this transformation the origin of the 4-oxygen of the quinone is crucial, but uncertain. On the one hand the diazeniumdiolate **4** seems

to require the methyloxy substituent as its alkyl substituted relatives do not react as rapidly with acids to release nitrous oxide as readily as **4**. This observation suggests that coordination of **4** might lead to its facile demethylation and that the oxygen is thus retained in the quinone. On the other hand, when the reaction in Eq. (9) is performed for $Pt(PPh_3)_2Cl_2$ with anhydrous solvents the yield drops from 72% to 11%. Thus a hydrolytic mechanism is implicated in Eq. (9). Curiously none of our numerous attempts to adapt this preparation to the related palladium complexes has returned isolable crystalline products or products with the key IR bands at circa 1260, 790 cm^{-1}. Regardless of the mechanistic details of these syntheses, the facile formation of new *cis*-hyponitrite complexes, and the first examples of their nickel complexes, allows for the systematic examination of their chemistry [24].



2 **5**

(10)

These group 10 square planar divalent hyponitrite complexes are sensitive to heat, light, acids, and oxidation. Their thermal decomposition has been monitored by differential scanning calorimetry and they typically decompose exothermally at $T > 85$ °C. To date the only well characterized products of these reactions are the oxide of the phosphine, nitrous oxide, and in the case of the platinum complexes, the colloidal metal. Phosphine oxide is also produced when the decomposition is done with strict exclusion of oxygen. This suggests that decomposition follows the stoichiometry in Eq. (10) where colloidal platinum metal results from the reductive formation of the phosphine oxide, after loss of nitrous oxide. The observed kinetics of nitrous oxide release and complex decomposition are both first order with the same rate constant, within experimental error [24]. The trapping of the oxo intermediate with carbon disulfide and carbon dioxide support its intermediacy [24], and we note that a stable terminal platinum oxide in a Pt(IV) complex has recently been reported [30]. What remains absent in all of the decomposition products of **2** are complexes with nitrosyl ligands as demonstrated by the absence of nitrosyl peaks in their IR spectra. There is no evidence that nitric oxide coupling is reversible in this system, nor is there evidence for stable nitrous oxide complexes in the products.

Based on the yield of $Pt(PPh_3)_2I_2$ and the observed formation of triphenylphosphine oxide, the stoichiometric equation was proposed to involve two moles of **2a** and one mole of iodine:

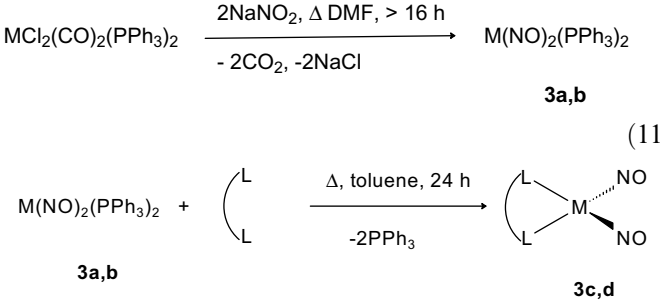
$$2Pt(PPh_3)_2(O_2N_2) + I_2 \rightarrow Pt(PPh_3)_2I_2 + 2N_2O + 2OPPh_3 + Pt(0)$$

When the reaction between **2a** and iodine was monitored by ^{31}P NMR with the proposed stoichiometry, the amount of triphenylphosphine oxide formed was integrated against a triphenylphosphine sulfide standard, and the integrated ratio was identical to the calculated mole ratio.

The oxidative addition reactions of $Pt(PPh_3)_2(N_2O_2)$ with methyl iodide, methyl triflate, iodine, and hydrochloric acid have been examined to determine if it is possible to isolate a Pt(IV) complex with a hyponitrite ligand. With iodine as a solution in methylene chloride there is a rapid reaction which ensues at −78 °C and goes to completion as the reaction is warmed over an hour to give a bright yellow precipitate of *trans*-$Pt(PPh_3)_2I_2$. This same product forms only slowly and in low yield when **2a** is treated with iodomethane under these conditions. In the later case even after 48 h most of the **2a** has not reacted and is recovered from the reaction. In the latter case a peak for *trans*-$Pt(PPh_3)_2(CH_3)I$ is not seen in the ^{31}P NMR spectrum [31]. With methyltriflate a white precipitate of $[Pt(PPh_3)_2(\mu\text{-}OH)]_2[OSO_2CF_3]_2$ forms in 71% yield in the course of the warming the reaction mixture from −78 °C to room temperature.

2.2. Dinitrosyls

Although the dinitrosyls of group 8 metals were some of the first prepared, *cf.* Roussin's red and black salts of iron [32], the isolation of a ruthenium dinitrosyl complex, $[RuCl(NO)_2(PPh_3)_2]BF_4$, with both a bent and linear nitrosyl ligands remains an excellent example of the amphoteric nature of the nitrosyl ligand [6,33]. Perhaps equally remarkable is the reduced neutral analog, $Ru(NO)_2(PPh_3)_2$ which has two linear nitrosyls and remains one of the few isolable tetrahedral low valent ruthenium derivatives [34]. In spite of their early and facile preparation, Eq. (11), which has since been optimized [35], the chemistry of these derivatives remains surprisingly limited to reports of its oxygenation [34], oxidative addition [36–39], catalytic CO/NO metathesis [40–42], and electrochemistry [43].



(11)

(12)

Although nitric oxide exchange is reported to be fast for **3a** [44], attempts to prepare pyridine, 2,2′-bipyridine, and 1,10-phenanthroline complexes by ligand exchange with the triphenylphosphine failed to generate new nitrogen

base analogs of **3a** [35]. The inability of nitrogen based donors, even chelating donors, to substitute for triphenylphosphine is not surprising given that many low oxidation state osmium complexes are known for phosphines but few for ammines. We hypothesized that a chelating phosphine could substitute for the two triphenylphosphine in **3a**,**b** and demonstrated this with the facile preparation of the bisdiphenylphosphinoferrocene complex of ruthenium **3c**, and the diphenylphosphinoethane complex of osmium **3d**, Eq. (12). Both of these substitution reactions have to be carried out in the strict exclusion of oxygen, but the products form in high yield and are readily isolated by recrystallization of the reaction mixtures. All of the dinitrosyl complexes **3** are a red-brown color which is due to a long tailing UV band which has considerable extinction in the visible. In the process of characterizing the UV–Vis activity of **3c,d** a slow oxygen independent photochemical decomposition process was discovered. Nevertheless, **3d** in particular is very reactive towards oxygen in solution or as a solid and rapidly decomposes within 20 min of exposure to oxygen. This is in contrast to the behavior of **3a,d** which decompose much more slowly and are readily purified by recrystallization in the open. As was found for **3b** the product of the reaction of oxygen and **3d** is a mononitrosyl with a coordinated nitrate [34]. There is no precedence in this system for nitrosyl coupling to give a stable or intermediary hyponitrite ligand analogous to **2**.

To understand the structure and reactivity of **3c,d** both complexes have been characterized by single crystal X-ray diffraction. ORTEP representations for both are depicted in Figs. 2 and 3, with representative bond lengths listed in the captions. As with $M(NO)_2(PPh_3)_2$ which have been characterized for M = Os [45] and Ru [46,47] both structures have a distorted tetrahedral geometry at the metal with the angle separating the two nitrosyl ligands being substantially larger, ca 139° as compared to the angle between the two phosphorus atoms which are 101.8° and 84.3° in **3c** and **3d**, respectively. Although the angle between the nitrosyl ligands is very similar to those found for the bistriphenylphosphine complexes, 139.2° and 139.1°, the chelating phosphines in **3c** and **3d** in these structure reduces the angle between the phosphorus atoms from 103.9° and 103.5° for **3a,b**, respectively to 84.3° in **3d**. This change in structure is also reflected in the nitrosyl stretching bands for **3c,d**, which are separated by slightly greater energies than in **3a,b**. It is difficult to attribute the increased reactivity of **3d** with dioxygen to any one particular structural change found by crystallography. In general alkyl phosphines are better donor ligands than their corresponding aryl phosphine analogs. Therefore the increased sensitivity of **3d** to dioxygen may be simply due to increased electron density on the metal from the better donor phosphine.

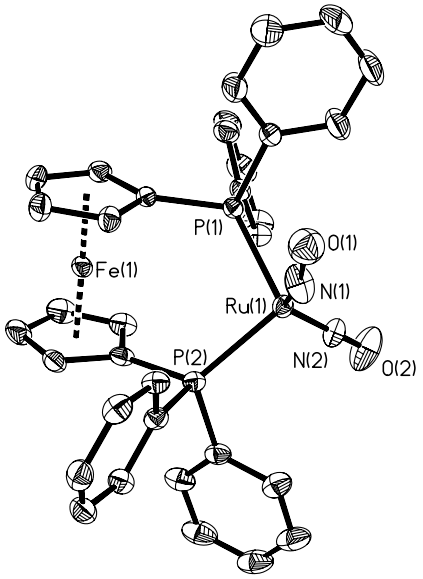


Fig. 2. ORTEP representation of **3c** at 30% probability level and hydrogens omitted. Key metric parameters: Ru(1)–P(1) = 2.3478(14), Ru(1)–P(2) = 2.3667(13), Ru(1)–N(1) = 1.762(5), Ru(1)–N(2) = 1.781(4) Å; N(1)–Ru(1)–N(2) = 132.1(2), P(1)–Ru(1)–P(2) = 101.80(5), P(1)–Ru(1)–N(1) 97.2(2), P(1)–Ru(1)–N(2) 108.98(16), P(2)–Ru(1)–N(1) = 111.50(18), and P(2)–Ru(1)–N(2) = 101.729(16)°.

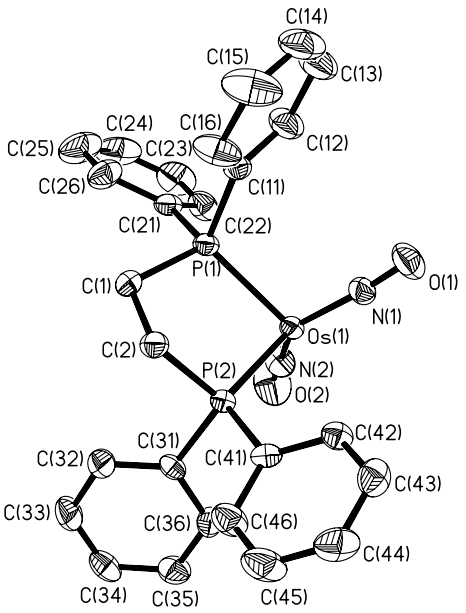


Fig. 3. ORTEP representation of **3d** at 30% probability level and hydrogens omitted. Key metric parameters: Os(1)–P(1) = 2.3143(15), Os(1)–P(2) = 2.3210(14), Os(1)–N(1) = 1.782(5), Os(1)–N(2) = 1.783(4) Å; N(1)–Os(1)–N(2) = 138.7(2), P(1)–Os(1)–P(2) = 84.30(5), P(1)–Os(1)–N(1) 98.80(16), P(1)–Os(1)–N(2) 109.98(19), P(2)–Os(1)–N(1) = 107.42(17), and P(2)–Os(1)–N(2) = 104.42(17)°.

3. Conclusions

While the amphoteric coordination character of nitric oxide, with its concomitant ability to bind in bent and linear geometries, is well known, another potential manifestation of its redox balance with transition metals is its ability to couple to give a hyponitrite complex such as the five examples described in this paper. But does the coordinative

reductive coupling of nitric oxide represent a real reactivity pattern or mechanism? Among the ways to answer this question would be with examples of the formation of a nitrosyl complex from hyponitrite, or alternatively, the formation of hyponitrite complex from a dinitrosyl complex. At this time there are no unambiguous examples of either reaction: the predominant reaction of hyponitrite complexes is elimination of nitrous oxide, and polynitrosyl complexes are not necessarily precursors to hyponitrites. An important origin for this mechanistic uncertainty is nitric oxide's ability to dimerize and thus, as with many of nitric oxides reactions, one of the key questions remains does nitric oxide react as the monomer or dimer? Moreover, is the absence of stable homoleptic polynitrosyls in part due to their tendency to undergo reductive coupling as the first step in an oxidative decomposition pathway? Until we have clear evidence for the presence of these metal bound intermediates in these reactions, this hypothesis remains suggestive.

4. Experimental

4.1. General

The reagents and solvents used were reagent grade and used as supplied. Nitric oxide gas was obtained from Scott Specialty Gases and was purified by passing through a column packed with sodium hydroxide pellets. The nitrosylation apparatus and instrumental methods for these experiments are as described in prior publications [48,49]. Reagents were purchased from Aldrich and used as provided or purified as described in prior reports. Specific precursors were prepared by the literature methods including $PtCl_2(PR_3)_2$ [50,51], $Ni(dppe)Cl_2$ [52], $Pt(dppf)Cl_2$ [53], $Ni(dppf)Cl_2$ [52], $Ru(NO)_2(PPh_3)_2$ [54,34], and $Os(NO)_2(PPh_3)_2$ [34], $Ni(N_2O_2)(dppf)$ [24], sodium-(*Z*)-1-{4-(2,6-di-*tert*-butyl-4-methoxycyclohexadienonyl)}diazen-1-ium-1,2-diolate [49], **4**, and sodium-(*Z*)-1-{4-(2,6-di-*tert*-butyl-4-methylcyclohexadienonyl)}diazen-1-ium-1,2-diolate (**6**) [49].

4.2. Preparation of complexes

4.2.1. $Pt(PPh_3)_2(N_2O_2)$ (**2a**)

$Pt(PPh_3)_2Cl_2$ (0.221 g, 0.280 mmol) is dissolved in 20 mL of acetonitrile/methylene chloride (1:1) and sodium-(*Z*)-1-{4-(2,6-di-*tert*-butyl-4-methoxycyclohexadienonyl)}diazen-1-ium-1,2-diolate (0.196 g, 0.616 mmol), **4**, dissolved in 25 mL of methanol, is added with constant stirring. The solution immediately turns yellow, and the mixture is allowed to stir for 5 min before all solvents are removed in vacuo. The resulting brownish solid material is taken up in 30 mL methylene chloride and allowed to stand for 10 min and filtered to remove any insoluble materials. Ethanol, 30 mL is then added, and solution volume concentrated to roughly half its volume and crystallization induced. Further concentration to 5 mL followed by filtration and successive washes with 5 mL each of ethanol, ether, and hexanes gives 0.158 g, 72.4% of **2a**. DSC: $T_{onset} = 86.9$ °C, $T_{max} = 103.8$ °C, $\Delta H = 68.1$ cal/g (53.1 kcal/mole). IR (KBr, cm^{-1}): 1263 m, 1001 sh, 900.7 m, 793.7 m, 502.4 s.

UV–Vis (CH_2Cl_2, λ_{max}, nm (ε, $M^{-1}\,cm^{-1}$)): 238 (28 674). ^1H NMR (CD_2Cl_2, 400 MHz) δ 7.20 (t, 12H), 7.32–7.40 (m, 18H); ^{13}C NMR (CD_2Cl_2, 400 MHz) δ 134, 131, 129, 128. ^{31}P NMR (CD_2Cl_2, 400 MHz) δ 11.0 ($^1J_{PtP} = 3564$ Hz). The literature method [11] for the preparation of **2a** involves treating $Pt(PPh_3)_4$ with NO in benzene followed by recrystallization. In addition to **2a** a variety of other products appear to be formed and in our hands the synthesis above gives a higher yield of pure *cis*-hyponitrite complex.

4.2.2. $Pt(PPh_2Me)_2(N_2O_2)$ (**2b**)

$Pt(PPh_2Me)_2Cl_2$ (0.3775 g, 0.566 mmol), and **4**, 0.441 g, 1.34 mmol of are treated as for **2a**, to give 0.254 g, 68.4% **2b** as yellow crystals. *Anal*. Calc. for $PtP_2C_{26}H_{26}N_2O_2$: C, 47.64; H, 4.00; N, 4.27. Found: C, 47.54; H, 4.10; N, 3.89%. DSC: $T_{onset} = 87.6$ °C, $T_{max} = 99.0$ °C, $\Delta H = 63.9$ cal/g (41.9 kcal/mole). IR (KBr, cm^{-1}): 1286.4 w, 980.7 w, 851.5 w, 785.9 m, 608.5 m. UV–Vis (CH_2Cl_2, λ_{max}, nm (ε, $M^{-1}\,cm^{-1}$)): 238, 268sh (27 856, 10 585) ^1H NMR (CD_2Cl_2, 400 MHz) δ 1.86 (d, 4H), 7.30 (t, 8H), 7.38–7.48 (m, 12H); ^{13}C NMR (CD_2Cl_2, 100 MHz) δ 133, 132, 129, 128, 15.2. ^{31}P NMR (CD_2Cl_2, 161.9 MHz) δ −11.6.

4.2.3. $Pt(dppf)(N_2O_2)$ (**2c**)

$Pt(dppf)Cl_2$ (0.103 g, 0.13 mmol), and 0.087 g, 0.27 mmol of **4** are treated as for **2a** to give 0.69 g,79% **2b** as yellow crystals. *Anal*. Calc. for $PtFeP_2C_{34}H_{38}N_2O_2$: C, 49.83; H, 4.67, N, 3.42. Found: C, 50.15; H, 3.87; N, 3.55%. DSC: $T_{onset} = 85.1$ °C, $T_{max} = 99.0$ °C, $\Delta H = -52.5$ cal/g, 43.1 kcal/mol. IR (KBr, cm^{-1}): 1330.5 m, 974 m, 890 s, 780.1 s, 611 s. UV–Vis (CH_2Cl_2, λ_{max}, nm (ε, $M^{-1}\,cm^{-1}$)): 238, 268sh (27 856, 10 585) ^1H NMR (CD_2Cl_2, 400 MHz) δ 7.71 (m, 4H), 7.50 (m 8H), 7.40 (m, 8H), 4.41 (m, 4H), 4.24(d, $J = 1.8$ Hz, 4 H); ^{13}C NMR (CD_2Cl_2, 100 MHz) δ 145.7, 134.8, 131.8, 128.8, 77.4 (d, $J = 21$ Hz), 76.4 (t, $J = 2$H), 74.2. ^{31}P NMR (CD_2Cl_2, 161.9 MHz) δ 4.7 ($^1J_{PtP} = 3625.5$ Hz).

4.2.4. $Ni(dppe)(N_2O_2)$ (**2d**)

$Ni(dppe)Cl_2$ (0.2581 g, 0.489 mmol) was dissolved in acetonitrile (120 mL) and a solution of sodium-(*Z*)-1-{4-(2,6-di-*tert*-butyl-4-methoxycyclohexadienonyl)}diazen-1-ium-1,2-diolate (0.3127 g, 0.982 mmol) in 50 mL of methanol was added under nitrogen with constant stirring. The solution immediately turns from reddish to yellow or orange color and stirred for about 15–20 min. The solvent was removed in vacuo. The crude yellow solid material was dissolved in methylene chloride and allowed to stand for 10 min, and the solution filtered to remove any insoluble material. The solvent was removed in vacuo. The crude product was successively washed with ether until the ether

washing is colorless. (Yield: 0.216 g, 77%), *Anal*. Calc. for $NiP_2C_{26}H_{24}N_2O_2$: C, 60.39; H, 4.68; N, 5.42. Found: C, 59.59; H, 4.73; N, 4.92%. DSC: $T_{onset} = 97.3$ °C, $T_{max} = 104.1$ °C, $\Delta H = 136.9$ cal/g (70.8 kcal/mole). IR (KBr, cm^{-1}): New hyponitrite bands are obscured by dppe bands. UV–Vis (CH_2Cl_2, λ_{max}, nm (ε, $M^{-1}\,cm^{-1}$)): 236, 268, 408 (29 513, 19 539, 1012). ^1H NMR (CD_2Cl_2, 400 MHz) δ 2.43 (d, 4H), 7.45–7.52 (m, 12H), 7.87–7.91 (m, 8H); ^{13}C NMR (CD_2Cl_2, 100 MHz) δ 133, 132, 130, 129, 25.9, ^{31}P NMR (CD_2Cl_2, 161.9 MHz) δ 46.4.

4.2.5. *Ru(dppf)(NO)$_2$ (**3c**)*

$Ru(NO)_2(PPh_3)_2$, **3a**, 81 mg, 0.012 mmol, and 1.2 equiv. of dppf, 74 mg, 0.014 mmol, were heated at reflux for 14 h in 20 mL toluene under an atmosphere of nitrogen. After cooling the mixture was brought out of the inert atmosphere box and the solvent removed in vacuo to give a crude red-orange product which was dissolved in 10 mL dichloromethane and recrystallized by the addition of 20 mL ethanol and concentration on a rotory evaporator to give 132 mg, of **3c** in 85% yield. Crystals suitable for X-ray diffraction were grown from dichloromethane/ethanol. *Anal*. Calc. for $C_{34}H_{28}FeN_2O_2P_2Ru$: C, 56.29; H, 5.28; N, 3.86. Found: C, 56.52; H, 3.87; N, 3.54%. IR (cm^{-1}), KBr pellet: ν(NO):1673.2s, 1629.8s, other characteristic bands: 3350 br, 1304.8w, 1264.3w,1164.9m, 836.1w, 819.7m. UV–Vis (CH_2Cl_2), λ_{max}, nm (ε, $M^{-1}\,cm^{-1}$): 422 (1330) ^1H NMR ($CDCl_3$, 400 MHz) δ 4.31 (t, $J = 1.7$, 4H), 4.24 (dd, $J = 1.7$, 1.9, 4H), 7.35–7.37 (m, 12H), 7.53–7.58 (m, 8H); ^{13}C NMR ($CDCl_3$, 100 MHz) δ 71.8(s), 75.1 (t, $J = 4.9$), 84.17 (d, $J = 51.4$), 128.4 (t, $J = 5.8$), 130.1 (s), 133.6 (t, $J = 6.7$), 136.4 (dd, $J = 46.3$, 4.5) ^{31}P NMR ($CDCl_3$, 161.9 MHz) δ 47.5.

4.2.6. *Os(dppe)(NO)$_2$ (**3d**)*

$Os(NO)_2(PPh_3)_2$, (**3b**) 65 mg, 0.0084. mmol, and 2.5 equiv. of bisdiphenylphosphinoethane, dppe, 83 mg, 0.0021 mmol, were heated at reflux for 30 h in 15 mL toluene under an atmosphere of nitrogen. After cooling the mixture was stripped of solvent and the residue crystallized twice in the inert atmosphere box from dichloromethane and ethanol to give 45 mg of **3d** as oxygen sensitive red-brown crystals in 82% yield. Crystals suitable for X-ray diffraction were grown from dichloromethane/ethanol. *Anal*. Calc. for $C_{26}H_{24}N_2O_2P_2Os$: C, 47.99; H, 3.72; N, 4.31. Found: C, 48.28; H, 3.97; N, 4.33%. IR (cm^{-1}), KBr pellet: ν(NO): 1656.8s, 1604.7s. UV–Vis (CH_2Cl_2), λ_{max} 288 nm. ^1H NMR (CD_2Cl_2, 400 MHz) δ 2.51 (d, 4H), 7.48–7.56 (m, 12H), 7.93–7.99 (m, 8H); ^{13}C NMR (CD_2Cl_2, 100 MHz) δ 134, 132, 130, 127, 28.1, ^{31}P NMR (CD_2Cl_2, 161.9 MHz) δ 31.4.

4.3. Reaction of hyponitrite complexes (*2*) with electrophiles

Reaction of HCl with Pt(PPh$_3$)(N$_2$O$_2$) to give cis-Pt(PPh$_3$)$_2$Cl$_2$: **2a** (0.05 g, 0.07 mmol) was dissolved in CH_2Cl_2 (2 mL). HCl (0.15 mmol) in CH_3OH (0.17 mL) was added; gas was observed and a light beige precipitate formed. The solid was collected and washed with hexanes. Yield: 25 mg (40%). The identity of *cis-Pt(PPh$_3$)$_2$Cl$_2$* was confirmed by the absence of the IR bands characteristic of **2a**, as well as a comparison with the literature ^{31}P NMR spectrum of *cis*-$Pt(PPh_3)_2Cl_2$ as prepared by Goel [55].

Compounds **2a**–**c** (0.05 g) were each suspended in ethanol and treated with dilute HCl solution. There was immediate effervescence with gas evolution. The solid residue was collected and characterized by NMR, IR and compared with respective authentic dichloride samples. In order to analyze the evolved gas upon addition of dilute HCl solution, about 0.02 g of compound (**2a**) was placed in an IR gas chamber and HCl gas was bubbled into the gas chamber. The analysis of the evolved gas by FT-IR confirms the presence of N_2O.

Reaction of iodine with Pt(PPh$_3$)$_2$(N$_2$O$_2$) to give trans-Pt(PPh$_3$)$_2$I$_2$: **2a** (0.1 g, 0.13 mmol) and triethylamine (0.05 mL) were dissolved in methylene chloride (10 mL), and degassed by freeze–thaw cycles. The amine is a preventative measure to ensure that the solution remains basic. The solution was cooled to −78 °C and iodine (0.07 g, 0.26 mmol) was added. The reaction was allowed to warm to room temperature over the span of 1 h. A bright yellow precipitate formed and was collected by filtration. Yield: 0.056 g (45%) which is spectroscopically identical by IR, and ^{31}P NMR to literature results for $Pt(PPh_3)_2I_2$ [56] this same product is the only isolable compound from the reaction of methyliodide or hydroiodic acid with **2a**. In the case of methyl iodide there is no evidence for a transitory product corresponding[31] to *trans*-$Pt(PPh_3)_2(CH_3)I$ as its peak at 28.1 ppm ($^1J_{Pt-P} = 3460$ Hz) was not seen by ^{31}P NMR of the monitored reaction mixtures which are dominated by peaks corresponding to the starting material and diiodide product.

4.4. The stoichiometry of the reaction between Pt(PPh$_3$)$_2$(N$_2$O$_2$) with iodine

The platinum complex **2a** (0.025 g, 0.032 mmol) was dissolved in CD_2Cl_2 (0.5 mL) in an NMR tube. Iodine (0.004 g, 0.016 mmol) was added and the mixture was sonicated for 3 h. Once all of the *cis*-hyponitrite had reacted, as confirmed by ^{31}P NMR, a solution of triphenylphosphine sulfide (0.018 g, 0.061 mmol) in CD_2Cl_2 (0.3 mL) was added to the NMR tube and the ^{31}P NMR was measured, with a delay time of 1 s. The integration between triphenylphosphine sulfide and triphenylphosphine oxide was measured and compared to the expected value. Expected ratio ($P(S)Ph_3$:$P(O)Ph_3$) 1.9:1. Measured ratio ($P(S)Ph_3$:$P(O)Ph_3$) 2.1:1.

Reaction of Pt(PPh$_3$)$_2$(N$_2$O$_2$) with CF$_3$SO$_3$CH$_3$: **2a** (0.1 g, 0.13 mmol) was dissolved in methylene chloride (5 mL), and degassed through freeze–thaw methods. The solution was cooled to −78 °C and $CF_3SO_3CH_3$ (0.02 mL, 0.2 mmol) was added. The reaction was allowed

to warm to room temperature in the absence of light over 12 h. The white precipitate which formed was collected filtration. Yield: 0.065 g (71%). The precipitate is insoluble in organic solvents, alcohols, water, acetonitrile, and DMSO. On the basis of IR the compound is determined to be $[Pt(PPh_3)_2(\mu\text{-}OH)]_2[OSO_2CF_3]_2$. IR (KBr, cm^{-1}): 3548 m (ν_{OH}), 1273vs (ν_{SO}), 1032vs (ν_{SO}). An authentic sample of the product was also synthesized for comparison by treating, $Pt(PPh_3)Cl_2$ (0.05 g, 0.06 mmol), in 20 mL chloroform/acetone (1:1) to which water (1 mL) and $AgOSO_2CF_3$ (0.02 g, 0.06 mmol) were then added. After 1 h the silver chloride precipitate was removed by filtration through diatomaceous earth and diethyl ether (10 mL) was added to the filtrate. On standing for 12 h, a white precipitate of $[Pt(PPh_3)_2(\mu\text{-}OH)]_2[OSO_2CF_3]_2$ was collected whose IR spectrum contained the same ν_{OH} band at 3550 cm^{-1}. This band is also present in $[Pt(PPh_3)_2(\mu\text{-}OH)]_2[BF_4]_2$, prepared by Phillips and coworkers [57].

5. X-ray crystallographic data

X-ray diffraction data for **2** · CH_2Cl_2, **3c**, and **3d** were collected on a Bruker P4 diffractometer equipped with a molybdenum tube and a graphite monochromator, Table 1 contains diffraction data for **2** · CH_2Cl_2, **3c**, and **3d**. Unit-cell dimensions were determined from several accurately centered reflections in high 2θ angles using XSCANS program. Three standard reflections measured after every 97 reflections exhibited no significant loss of intensity. The data were corrected for Lorentz-polarization effects and absorption. The structure was solved by direct methods and refined by least-squares techniques on F^2 using SHELXTL.

The *cis* hyponitrite complex **2** is a redetermination of a structure originally reported [12] as a benzene solvate from crystals obtained from benzene/dichloromethane which refined to $R = 10.8\%$. In this original structure the unit cell corresponds to the triclinic space group $P\bar{1}$, with $a = 12.199(6)$, $b = 10.747(6)$, $c = 15.730(8)$ Å, $\alpha = 108.75(4)$, $\beta = 95.57(4)$, and $\gamma = 69.98(4)°$ with $Z = 2$, and $V = 1834.6$ Å^3. In our redetermination crystals were obtained from dichloromethane/ethanol and crystallize in monoclinic space group $P2_1n$, with $a = 13.037(2)$, $b = 15.685(3)$, $c = 17.023(3)$ Å, $\alpha = \gamma = 90$, and $\beta = 98.020(10)°$ with $Z = 4$, and $V = 3446.9(10)$ Å^3. The monoclinic form has a dichloromethane solvate that is well defined and refined anisotropically in the last least squares cycles to give a final R_1 of 3.44%, and S_{gof} of 1.027, and a relatively flat electron density map with the largest difference peak being close to the metal center.

The dinitrosyl complexes **3c** and **3d** were crystallized from dichloromethane/ethanol as large deep orange blocks. The diffraction data collection, solution, and refinement all followed the outline above for **2a** with key data

Table 1
Crystallographic and structure refinement data for compounds **2**, **3c** and **3d**

Compound	**2**	**3c**	**3d**
Molecular formula	$C_{37}H_{32}Cl_2N_2O_2P_2Pt$	$C_{34}H_{30}FeN_2O_3P_2Ru$	$C_{26}H_{24}N_2O_2OsP_2$
Formula weight	864.58	733.46	648.61
Temperature (K)	293(2)	293(2)	293(2)
Crystal system	monoclinic	triclinic	monoclinic
Space group	$P2_1/n$	$P\bar{1}$	$P2_1/n$
a (Å)	13.037(2)	9.363(3)	13.617(3)
b (Å)	15.685(3)	11.892(2)	11.964(2)
c (Å)	17.023(3)	14.870(3)	15.932(3)
α (°)	90	78.29(1)	90
β (°)	98.020(10)	86.38(2)	105.22(2)
γ (°)	90	88.50(2)	90
V (Å^3)	3446.9(10)	1617.9(6)	2504.5(8)
Z	4	2	4
ρ_{calc} (Mg/m^3)	1.666	1.506	1.720
μ (mm^{-1})	4.355	1.050	5.245
$F(000)$	1704	744	1264
Crystal size (mm)	$0.26 \times 0.20 \times 0.14$	$0.70 \times 0.24 \times 0.20$	$0.28 \times 0.22 \times 0.20$
2θ Range (°)	3.54–49.88	4.02–50.00	3.50–50.02
Index ranges	$-1 \leqslant h \leqslant 14$, $-1 \leqslant k \leqslant 16$, $-18 \leqslant l \leqslant 20$	$-1 \leqslant h \leqslant 11$, $-13 \leqslant k \leqslant 13$, $-17 \leqslant l \leqslant 17$	$-16 \leqslant h \leqslant 1$, $-1 \leqslant k \leqslant 14$, $-18 \leqslant l \leqslant 18$
Reflections collected	5853	7074	5458
Independent reflections [R_{int}]	4477 [0.0310]	5663 [0.0229]	4362 [0.0250]
Absorption correction type	psi-scan	psi-scan	psi-scan
Maximum and minimum transmissions	0.1617 and 0.1108	0.3908 and 0.3376	0.1478 and 0.1180
Refinement method	least-squares on F^2	least-squares on F^2	least-squares on F^2
Data/restraints/parameter	4477/0/415	5663/0/388	4362/0/298
Goodness-of-fit on F^2	1.027	1.093	1.006
R [$I > 2\sigma I$]	$R_1 = 0.0344$, $wR_2 = 0.0815$	$R_1 = 0.0494$, $wR_2 = 0.1397$	$R_1 = 0.0296$, $wR_2 = 0.0607$
R (all data)	$R_1 = 0.0422$, $wR_2 = 0.0867$	$R_1 = 0.0607$, $wR_2 = 0.1490$	$R_1 = 0.0494$, $wR_2 = 0.0670$
Largest difference in peak and hole (e Å^3)	2.857 and − 0.955	1.995 and −0.512	0.607 and −0.772

collected in Table 1. During the final stages of the refinement of **3c** an extra intense solvate peak was located in electron difference maps and was modeled as a water solvate whose presence was confirmed by measurement of the IR spectrum of other crystals from the same batch which have a band at 3350 cm^{-1} attributable to the water solvate.

6. Supplementary material

CCDC 633311, 633312 and 635099 contain the supplementary crystallographic data for **2** · $2CH_2Cl_2$, **3c** and **3d**. These data can be obtained free of charge via http://www.ccdc.cam.ac.uk/conts/retrieving.html, or from the Cambridge Crystallographic Data Centre, 12 Union Road, Cambridge CB2 1EZ, UK; fax: (+44) 1223-336-033; or e-mail: deposit@ccdc.cam.ac.uk.

Acknowledgements

We gratefully acknowledge NSERC for support in the form of a Discovery Grant and the Air Force Office of Scientific Research, Grants F49620-96-1-0417 and 98-1-0461, for their financial support of this research.

References

[1] F. Calderazzo, R. Ercoli, G. Natta, in: I. Wender, P. Pino (Eds.), Organic Synthesis via Metal Carbonyls, vol. 1, Wiley Interscience, New York, NY, 1968, pp. 1–272.
[2] T.W. Hayton, W.S. McNeil, B.O. Patrick, P. Legzdins, J. Am. Chem. Soc. 125 (2003) 12935.
[3] M. Herberhold, A. Razavi, Angew. Chem., Int. Ed. Engl. 11 (1972) 1092.
[4] W.P. Griffith, J. Lewis, G. Wilkinson, J. Chem. Soc. (1958) 3993.
[5] I.H. Suberwal, A.B. Burg, J. Chem. Soc., Chem. Commun. (1970) 1001.
[6] C.P. Brock, J.P. Collman, G. Dolcetti, P.H. Farnham, J.A. Ibers, J.E. Lester, C.A. Reed, Inorg. Chem. 12 (1973) 1304.
[7] F. Basolo, Chem. Brit. 5 (1969) 505.
[8] E.W. Abel, Quart. Rev. 17 (1963) 133.
[9] B.I. Swanson, S.K. Satija, J. Chem. Soc., Chem. Commun. (1973) 40.
[10] S.K. Satija, B.I. Swanson, Inorg. Synth. 16 (1976) 1.
[11] S. Cenini, R. Ugo, G. La Monica, S.D. Robinson, Inorg. Chim. Acta 6 (1972) 182.
[12] S. Bhaduri, B.F.G. Johnson, A. Pickard, P.R. Raithby, G.M. Sheldrick, C.I. Zuccaro, J. Chem. Soc., Chem. Commun. (1977) 354.
[13] R. Bau, I.H. Sabherwal, A.B. Burg, J. Am. Chem. Soc. 93 (1971) 4926.
[14] H.-C. Boettcher, M. Graf, K. Mereiter, K. Kirchner, Organometallics 23 (2004) 1269.
[15] J.H. MacNeil, P.A. Berseth, E.L. Bruner, T.L. Perkins, Y. Wadia, G. Westwood, W.C. Trogler, J. Am. Chem. Soc. 119 (1997) 1668.
[16] K. McNeill, R.G. Bergman, J. Am. Chem. Soc. 121 (1999) 8260.
[17] R.D. Feltham, J. Enemark, Coord. Chem. Rev. 13 (1974) 339.
[18] H. Okamura, E. Miki, K. Mizumachi, T. Ishimori, Bull. Chem. Soc. Jpn. 49 (1976) 666.
[19] M.E. Chacon Villalba, A. Navaza, J.A. Guida, E.L. Varetti, P.J. Aymonino, Inorg. Chim. Acta 359 (2006) 707.
[20] B. Jezowska-Trzebiatowska, J. Hanuza, M. Ostern, J. Ziolkowski, Inorg. Chim. Acta 6 (1972) 141.
[21] A. Werner, P. Karrer, Helv. Chim. Acta 1 (1918) 54.
[22] P.C. Ford, I.M. Lorkovic, Chem. Rev. 102 (2002) 993.
[23] G.H. Maunder, M.R. Russo, A. Sella, Polyhedron 23 (2004) 2709.
[24] N. Arulsamy, D.S. Bohle, J.A. Imonigie, S. Levine, Angew. Chem. 41 (2002) 2371.
[25] C. Feldmann, M. Jansen, Angew. Chem. 35 (1996) 1728.
[26] C. Feldmann, M.Z. Jansen, Anorg. Allg. Chem. 623 (1997) 1803.
[27] M.N. Hughes, Quart. Rev., Chem. Soc. 22 (1968) 1.
[28] N. Arulsamy, D.S. Bohle, J.A. Imonigie, E.S. Sagan, Inorg. Chem. 38 (1999) 2716.
[29] J.A. Hrabie, L.K. Keefer, Chem. Rev. 102 (2002) 1135.
[30] T.M. Anderson, W.A. Neiwert, M.L. Kirk, P.M.B. Piccoli, A.J. Schultz, T.F. Koetzle, D.G. Musaev, K. Morokuma, R. Cao, C.L. Hill, Science 306 (2004) 2074.
[31] V.V. Grushin, I.S. Akhrem, M.E. Vol'pin, J. Organomet. Chem. 371 (1989) 403.
[32] E.J. Wharton, J.A. McCleverty, Inorg. Nucl. Chem. Lett. 6 (1970) 549.
[33] C.G. Pierpont, D.G. Van Derveer, W. Durland, R. Eisenberg, J. Am. Chem. Soc. 92 (1970) 4760.
[34] K.R. Grundy, K.R. Laing, W.R. Roper, J. Chem. Soc., Chem. Commun. (1970) 1500.
[35] B.C. Paul, S.C. Sarker, R.K. Poddar, J. Coord. Chem. 28 (1993) 245.
[36] E.B. Boyar, A. Dobson, S.D. Robinson, B.L. Haymore, J.C. Huffman, J. Chem. Soc., Dalton Trans. (1985) 621.
[37] B. Haymore, J.C. Huffman, A. Dobson, S.D. Robinson, Inorg. Chim. Acta 65 (1982) L231.
[38] J.A. McCleverty, C.W. Ninnes, I. Wolochowicz, J. Chem. Soc., Chem. Commun. (1976) 1061.
[39] A. Dobson, S.D. Robinson, J. Organometal. Chem. 99 (1975) C63.
[40] J. Reed, R. Eisenberg, Science 184 (1974) 568.
[41] S. Bhaduri, B.F.G. Johnson, C.J. Savory, J.A. Segal, R.H. Walter, J. Chem. Soc., Chem. Commun. (1974) 809.
[42] S. Bhaduri, B.F.G. Johnson, Trans. Met. Chem. 3 (1978) 156.
[43] G. Piazza, G. Innorta, Inorg. Chim. Acta 70 (1983) 111.
[44] A. Khair, Dhaka University Studies, Part B, Science 31 (1983) 35.
[45] B. Haymore, J.A. Ibers, Inorg. Chem. 14 (1975) 2610.
[46] A.P. Gaughan Jr., B.J. Corden, R. Eisenberg, J.A. Ibers, Inorg. Chem. 13 (1974) 786.
[47] S. Bhaduri, G.M. Sheldrick, Acta Crystallogr., Sect. B 31 (1975) 897.
[48] N. Arulsamy, D.S. Bohle, J.A. Imonigie, E.S. Sagan, J. Am. Chem. Soc. 122 (2000) 5539.
[49] D.S. Bohle, J.A. Imonigie, J. Org. Chem. 65 (2000) 5685.
[50] J. Chatt, R.G. Wilkins, J. Chem. Soc. (1956) 525.
[51] J. Chatt, R.G. Wilkins, J. Chem. Soc. (1952) 273.
[52] A.W. Rudie, D.W. Lichtenberg, M.L. Katcher, A. Davison, Inorg. Chem. 17 (1978) 2859.
[53] G.M. Whitesides, J.F. Gaasch, E.R. Stedronsky, J. Am. Chem. Soc. 94 (1972) 5258.
[54] J.J. Levison, S.D. Robinson, Chem. Ind. (1969) 1514.
[55] R.G. Goel, Inorg. Nucl. Chem. Lett. 15 (1979) 437.
[56] S.H. Mastin, Inorg. Chem. 13 (1974) 1003.
[57] D.A. Phillips, M. Kubota, J. Thomas, Inorg. Chem. 15 (1976) 118.

throughout the experiments. Ruthenium trichloride ($RuCl_3 \cdot 3H_2O$/Johnson Matthey) was the starting reagent for the synthesis of ruthenium complexes. Ionic strength was adjusted with $NaCF_3COO$ ($\mu = 0.3$ mol L^{-1}).

2.2. Synthesis of the ruthenium compounds

The $[Ru(NH_3)_5Cl]Cl_2$ [16], *trans*-$[Ru(NH_3)_4(P(OEt)_3)_2]^{2+}$ [1], *trans*-$[Ru(NH_3)_4P(OEt)_3H_2O]^{2+}$ [1] and *trans*-$[Ru(NH_3)_4P(OEt)_3NO_2](PF_6)$ [17] compounds were prepared and characterized as described in the literature. All syntheses and measurements were performed under inert atmosphere (argon).

2.3. Instrumentation

The UV–Vis measurements were carried out in a 1 cm quartz cell on a Hitachi spectrophotometer U-3501. Infrared spectra measurements were performed in solution using a HATR (Horizontal Attenuated Total Reflectance) Trough Plate System, with 45° ZnSe Crystal in a FTIR Bomen MB-102 spectrometer; the ^{31}P NMR measurements were carried out in D_2O on a Bruker 4.7 T Model AC – 200 spectrophotometer, using hexafluorophosphate as internal standard.

2.4. Formation constant for trans-$[Ru(NH_3)_4P(OEt)_3(NO_2)]^+$

The formation constant for *trans*-$[Ru(NH_3)_4P(OEt)_3NO_2]^+$, K_N, was measured using the Indicator Colorimetric Method [18,19], which considers different values of molar absorptivities (ε) and maximum absorptions of the species involved. The equilibrium constant determination was based on reactions of Eqs. (1)–(3), using pyrazine as the auxiliary ligand.

$$t\text{-}[Ru(NH_3)_4P(OEt)_3H_2O]^{2+} + pz \rightleftharpoons t\text{-}[Ru(NH_3)_4P(OEt)_3pz]^{2+} + H_2O \quad K_{pz} \tag{1}$$

$$t\text{-}[Ru(NH_3)_4P(OEt)_3H_2O]^{2+} + NO_2^- \rightleftharpoons t\text{-}[Ru(NH_3)_4P(OEt)_3NO_2]^{+} + H_2O \quad K_N \tag{2}$$

$$t\text{-}[Ru(NH_3)_4P(OEt)_3pz]^{2+} + NO_2^- \rightleftharpoons t\text{-}[Ru(NH_3)_4P(OEt)_3NO_2]^{+} + pz \quad K_I \tag{3}$$

The spectrum of *trans*-$[Ru(NH_3)_4P(OEt)_3H_2O]^{2+}$ presents λ_{max} at 316 nm ($\varepsilon = 6.5 \times 10^2$ M^{-1} cm^{-1}) [20] and the *trans*-$[Ru(NH_3)_4P(OEt)_3NO_2]^+$ presents λ_{max} at 334 nm ($\varepsilon = 1.8 \times 10^3$ M^{-1} cm^{-1}) [17], at 380 nm ($\varepsilon = 8.0 \times 10^2$ M^{-1} cm^{-1}) and at 400 nm ($\varepsilon = 2.5 \times 10^2$ M^{-1} cm^{-1}). This method allows for the indirect determination of the product formed. Considering that the ligands, pyrazine and NO_2^- should compete for *trans*-$[Ru(NH_3)_4P(OEt)_3H_2O]^{2+}$, and that the equilibrium is rapidly established, is possible to combine the three equations to obtain:

$$K_I = \frac{K_N}{K_{pz}} = \frac{[RuNO_2] \cdot [pz]}{[Rupz] \cdot [NO_2^-]} \tag{4}$$

where $[RuNO_2] = [trans\text{-}[Ru(NH_3)_4P(OEt)_3(NO_2)]^+]$; $[Rupz] = [trans\text{-}[Ru(NH_3)_4P(OEt)_3(pz)]^{2+}]$; and $C_{Ru(II)} = C_{trans-[Ru(NH_3)4P(OEt)3(H2O)](PF6)2}$.

The initial analytical concentration of $C_{Ru(II)}$ was kept constant in all the experiments equal to 1.4×10^{-4} mol L^{-1}. Hence considering $C_{Ru(II)} \ll C_{NO_2^-}$, the nitrite concentration $[NO_2^-]$ should be $\cong C_{NO_2^-}$, and $C_{Ru(II)} \ll C_{pz}$, and thus $[pz] \cong C_{pz}$. The $[Rupz]^{2+}$ concentration was be measured spectrophotometrically ($\varepsilon = 3.8 \times 10^3$ M^{-1} cm^{-1} at 380 nm and 2.5×10^3 M^{-1} cm^{-1} at 400 nm).

The formation constant for the *trans*-$[Ru(NH_3)_4P(OEt)_3pz]^{2+}$ complex, K_{pz}, is 20 M^{-1} [1] while the electronic spectrum of this species did not show any changes for the range of hydrogenionic concentrations studied ($10.5 \leqslant pH \leqslant 11.5$). According to the observations, the values of the absorptivities for NO_2^- are $\varepsilon = 12$ M^{-1} cm^{-1} (380 nm) and < 1 M^{-1} cm^{-1} (400 nm) (see Fig. 1c).

2.5. Nitrite ligand aquation in trans-$[Ru(NH_3)_4P(OEt)_3(NO_2)]^+$

The specific rate constant for the release of nitrite ions in *trans*-$[Ru(NH_3)_4P(OEt)_3(NO_2)]^+$ was measured using pyrazine as auxiliary ligand (Eqs. 5 and 6). These measurements were carried out at pH 10.9; $\mu = 0.3$ mol L^{-1} $NaCF_3COO$ and $T = (25 \pm 0.2)$ °C. The solid *trans*-$[Ru(NH_3)_4P(OEt)_3(NO_2)](PF_6)$ was added into the solutions containing a large excess of pyrazine ($\geqslant 3600$), quickly stirred, and the absorbance changes were followed at 380 nm. The specific rate constant values were calculated through the plots

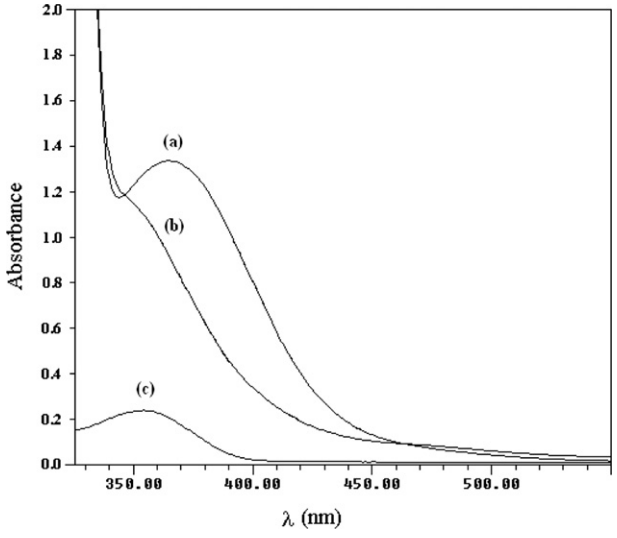


Fig. 1. Electronic spectrum of: (a) the product of reaction between *trans*-$[Ru(NH_3)_4P(OEt)_3(H_2O)](PF_6)_2$ and pyrazine; (b) after the addition of nitrite ions; (c) $NaNO_2$. $C_{Ru} = 4.0 \times 10^{-4}$ mol L^{-1}; $C_{pz} = 1.0$ mol L^{-1}; $C_{NO_2^-} = 0.010$ mol L^{-1}; $\mu = 0.3$ mol L^{-1} ($NaCF_3COO$); pH 11.0; $T = (25 \pm 0.2)$ °C.

of $\ln(A_\infty - A_t)$ versus time and corresponds to the average of five independents experiments.

$$t\text{-}[Ru(NH_3)_4P(OEt)_3NO_2]^+ + H_2O \overset{\text{slow}}{\rightleftharpoons} t\text{-}[Ru(NH_3)_4P(OEt)_3H_2O]^{2+} + NO_2^- \quad (5)$$

$$t\text{-}[Ru(NH_3)_4P(OEt)_3H_2O]^{2+} + pz \overset{\text{fast}}{\rightleftharpoons} t\text{-}[Ru(NH_3)_4P(OEt)_3pz]^{2+} + H_2O \quad (6)$$

2.6. Conversion of the nitro compound into the analogous nitrosyl

The conversion of the nitro, *trans*-$[Ru(NH_3)_4P(OEt)_3(NO_2)]^+$, compound into the corresponding nitrosyl was followed through UV–Vis, ^{31}P NMR and Infra Red spectroscopies.

2.6.1. Infrared measurements in aqueous solutions

Argon degassed solution (1.0×10^{-2} mol L^{-1}) of *trans*-$[Ru(NH_3)_4P(OEt)_3(NO_2)]^+$ at pH 8.0 was added into the HATR Trough Plate System with 45° ZnSe Crystal using syringes and the IR spectrum recorded. The solution pH was then adjusted, with previous degassed 6.0 mol L^{-1} trifluoroacetic acid, to pH 4.5 and new spectrum was recorded.

2.6.2. ^{31}P nuclear magnetic resonance

An alkaline solution (2.0×10^{-3} mol L^{-1}) of *trans*-$[Ru(NH_3)_4P(OEt)_3(NO_2)](PF_6)$ complex was anaerobically injected with a Hamilton gas tight syringe to a NMR tube containing deoxygenated aqueous buffered solution ($T = (25 \pm 0.2)$ °C, 0.2 mol L^{-1} K_2HPO_4, pH 10) to obtain a final concentration of 1.0×10^{-3} mol L^{-1}, and the NMR spectrum recorded. The solution pH was then adjusted to 2.0 with previous degassed 6.0 mol L^{-1} trifluoroacetic acid and another spectrum was obtained.

3. Results and discussion

As a consequence of the reaction between the aqua compound, *trans*-$[Ru(NH_3)_4P(OEt)_3H_2O](PF_6)_2$, and the pyrazine molecule, a band at λ_{max} at 366 nm ($\varepsilon = 4.2 \times 10^3$ M^{-1} cm^{-1}) (Fig. 1a) is developed. In the present study, when nitrite was added to this solution, a decrease in the absorbance was observed (Fig. 1b), due to the conversion of the pyrazine derivate into the nitro compound ($\lambda_{max} =$ 334 nm). This conversion was used to determine the formation constant for the nitro compound, *trans*-$[Ru(NH_3)_4P(OEt)_3NO_2](PF_6)$, as described in Section 2.

The spectra of the final solution obtained for the reaction between the aqua compound *trans*-$[Ru(NH_3)_4P(OEt)_3H_2O](PF_6)_2$ and nitrite ions, in alkaline solution, corresponds to spectra of the *trans*-$[Ru(NH_3)_4P(OEt)_3(NO_2)]^+$ in solution (λ_{max} at 334 nm; $\varepsilon = 1.8 \times 10^3$ mol L^{-1} cm^{-1}) [17].

The concentrations and equilibrium constant data for the nitro complex ion *trans*-$[Ru(NH_3)_4P(OEt)_3NO_2]^+$ formation are resumed in Table 1.

With the pK for reaction (Eq. (7)) having been estimated as 8.6 [3], most of the studies were performed at $C_{H^+} < 10^{-10}$ mol L^{-1} to ensure that the experimental conditions where those for which the nitro species is the predominant product.

$$trans\text{-}[Ru(NH_3)_4P(OEt)_3NO]^{3+} + 2OH^- \overset{k_{OH^-}}{\rightleftharpoons} trans\text{-}[Ru(NH_3)_4P(OEt)_3NO_2]^+ + H_2O \quad (7)$$

By using the experimental data of Table 1, it was possible to determine the formation constant, K_N, as $(5.2 \pm 0.6) \times 10^3$ M^{-1}.

The aquation of the NO_2^- ligand in *trans*-$[Ru(NH_3)_4P(OEt)_3NO_2]^+$ was investigated spectrophotometrically (see Section 2) and k_{-N} was calculate as being $(1.2 \pm 0.3) \times 10^{-1}$ s^{-1}, the latter value being the average of five independent determinations.

Ongoing preliminary studies using stopped-flow technique have shown that the reaction between the *trans*-$[Ru(NH_3)_4P(OEt)_3(H_2O)]^{2+}$ compound and NO_2^- in

Table 1
Concentrations and formation constant[a] for *trans*-$[Ru(NH_3)_4P(OEt)_3NO_2]^+$ for the reaction between *trans*-$[Ru(NH_3)_4P(OEt)_3H_2O]^{2+}$ and nitrite ions in the presence of pyrazine[b]

pH	$C_{RuNO_2} \times 10^4$ (mol L^{-1})	$C_{Rupz} \times 10^4$ (mol L^{-1})	$K_N \times 10^{-3}$ (M^{-1})
10.5	2.99	1.02	5.8 ± 0.8
11.0	2.77	1.09	5.1 ± 0.4
11.5	2.80	1.14	4.9 ± 0.6

[a] Calculated using the Eq. (4), each value corresponds to an average of six independent determinations.
[b] $C_{Ru} = 4.0 \times 10^{-4}$ mol L^{-1}; $C_{pz} = 1.0$ mol L^{-1}; $C_{NO_2} = 0.010$ mol L^{-1}; $\mu = 0.3$ mol L^{-1} ($NaCF_3COO$); $T = (25 \pm 0.2)$ °C.

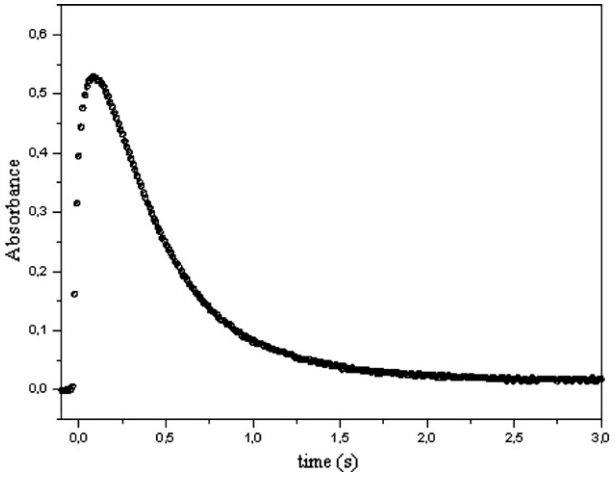


Fig. 2. Plot of absorbance against time for the reaction between *trans*-$[Ru(NH_3)_4P(OEt)_3H_2O]^{2+}$ and nitrite ions. $C_{Ru} = 4.0 \times 10^{-4}$ mol L^{-1}; $C_{NO_2^-} = 1.0 \times 10^{-2}$ mol L^{-1}; pH 10; $\mu = 0.3$ mol L^{-1} ($NaCF_3COO$); 25 °C; 330 nm.

alkaline media ($C_{H^+} < 10^{-10}$ mol L^{-1}) occurs through two distinct steps (Fig. 2), the first process being faster than the second one.

According to study on similar system [21], the first step should account for the formation of both the nitro and nitrito isomers, *trans*-$[Ru(NH_3)_4P(OEt)_3(NO_2)]^+$ and *trans*-$[Ru(NH_3)_4P(OEt)_3(ONO)]^+$, respectively (Eq. (8)).

$$\textit{trans}\text{-}[Ru(NH_3)_4P(OEt)_3H_2O]^{2+} \underset{}{\overset{k_O}{\rightleftharpoons}} \textit{trans}\text{-}[Ru(NH_3)_4P(OEt)_3ONO]^+$$
$$\textit{trans}\text{-}[Ru(NH_3)_4P(OEt)_3H_2O]^{2+} \underset{}{\overset{k_N}{\rightleftharpoons}} \textit{trans}\text{-}[Ru(NH_3)_4P(OEt)_3NO_2]^+ \quad (8)$$

According to preliminary data obtained from plots of k_{obs} versus $C_{NO_2^-}$, k_1 (the sum of $k_N + k_O$) is equal to $(1.25 \pm 0.1) \times 10^3$ M^{-1} s^{-1} (pH 11; $\mu = 0.3$ mol L^{-1}; 25 °C).

The second step should be a consequence of the isomerization of the nitrito into the more stable nitro species (Eq. (9)).

$$\textit{trans}\text{-}[Ru(NH_3)_4P(OEt)_3ONO]^+ \xrightarrow{k_i} \textit{trans}\text{-}[Ru(NH_3)_4P(OEt)_3NO_2]^+ \quad (9)$$

The X-ray structure [17], shown that the isolated product of the reaction between *trans*-$[Ru(NH_3)_4P(OEt)_3(H_2O)]^{2+}$ and NO_2^- in alkaline media, is the nitro isomer. The UV–Vis spectrum of the final product of the reaction between NO_2^- and *trans*-$[Ru(NH_3)_4P(OEt)_3(H_2O)]^{2+}$ is identical to one obtained from dissolving solid *trans*-$[Ru(NH_3)_4P(OEt)_3(NO_2)](PF_6)$ in aqueous solutions at the same experimental conditions. Therefore, it is likely to suppose that the nitro isomer is more stable than the nitrito one and thus the final product of the reaction.

According to the experimental data collected insofar, the rate of this isomerization, k_i, is equal to $(6.9 \pm 1.3) \times 10^2$ M^{-1} s^{-1} (pH 11; $\mu = 0.3$ mol L^{-1}; 25 °C). This system is now under investigation aiming to obtaining a complete understanding of the reactions involved.

From the observed UV–Vis spectrophotometric measurements at pH 10.0, it can be concluded that solutions containing *trans*-$[Ru(NH_3)_4P(OEt)_3(NO_2)]^+$ are stable in basic solutions. However, increasing hydrogenionic concentration leads to the nitro/nitrosyl conversion. At a pH of 4.0 for example, the nitro complex is shown to be quantitatively converted into the nitrosyl in a time scale of minutes ($k_{obs} = 2.2 \times 10^{-3}$ s^{-1}), as illustrated in Fig. 3. This conversion (Eq. (10)) was also observed through ^{31}P NMR and Infrared spectroscopies experiments.

$$\textit{trans}\text{-}[Ru(NH_3)_4P(OEt)_3NO_2]^+ + 2H^+ \rightarrow \textit{trans}\text{-}[Ru(NH_3)_4P(OEt)_3NO]^{3+} + H_2O \quad (10)$$

Conversion was also observed to occur at a pH of 5 (results not shown). However, at this pH, it found to be slower than that at pH 4, thus proving the importance of the hydrogenionic concentrations on this equilibrium.

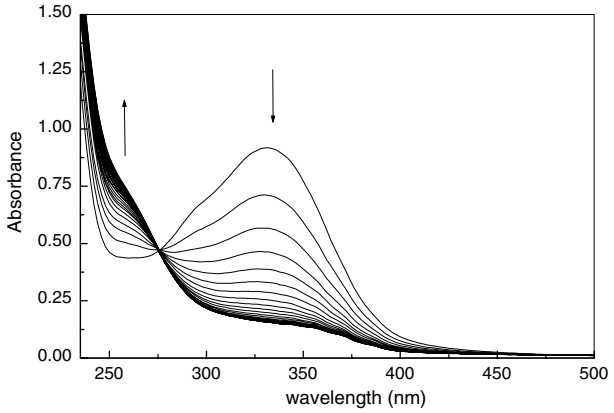


Fig. 3. Spectra changes associated with the quantitative conversion of *trans*-$[Ru(NH_3)_4P(OEt)_3(NO_2)]^+$/ into *trans*-$[Ru(NH_3)_4P(OEt)_3(NO)]^{3+}$. $C_{Ru} = 6.2 \times 10^{-4}$ mol L^{-1}; $\mu = 0.3$ ($NaCF_3COO$) mol L^{-1}; $T = (25 \pm 0.2)$ °C; total time = 1 h, time interval = 2 min; pH 4.

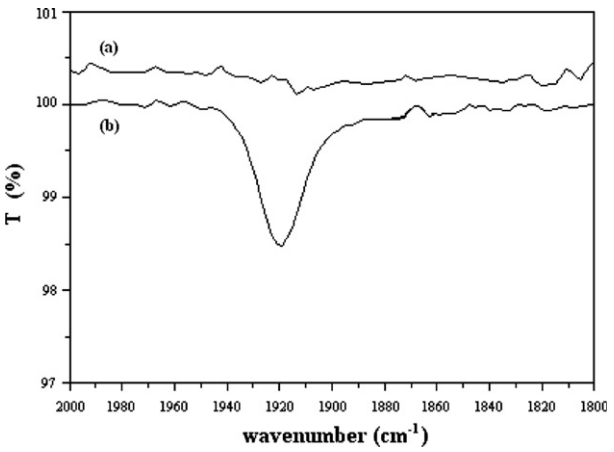


Fig. 4. Infrared spectra of *trans*-$[Ru(NH_3)_4P(OEt)_3NO_2](PF_6)$ in aqueous solution. $C_{Ru} = 2.0 \times 10^{-3}$ mol L^{-1}; pH 8.0 (a) and 4.5 (b); $\mu = 0.3$ ($NaCF_3COO$) mol L^{-1}; $T = (25 \pm 0.2)$ °C.

When the IR spectrum of the nitro compound was obtained at pH 8, no signal that can be attributed to the nitrosyl ligand was observed (Fig. 4). However, after the addition of acid into the solution, a band at 1918 cm^{-1} as observed to form, evidencing the formation of the nitrosyl complex formation since *trans*-$[Ru(NH_3)_4P(OEt)_3NO]^{3+}$ ν_{NO} is observed at 1918 cm^{-1} [3].

As described in the Experimental section, this conversion was also observed through ^{31}P NMR (see Fig. 5).

The ^{31}P NMR spectrum of *trans*-$[Ru(NH_3)_4P(OEt)_3NO_2]^+$ at pH 10 showed a peak at 149 ppm [17], corresponding to nitro species (Fig. 5). Upon solution acidification to pH 2, the signal at 149 ppm was found to completely disappear with a concomitant appearance of another signal at 80 ppm. This new signal strongly enforces the formation of *trans*-$[Ru(NH_3)_4P(OEt)_3NO]^{3+}$ which presents a ^{31}P signal in this area [3].

From the observed results, it can be confirmed that the above reported conversion of the nitro to nitrosyl compound (Eq. (10)) in acid medium is quantitative for the time and under the conditions studied.

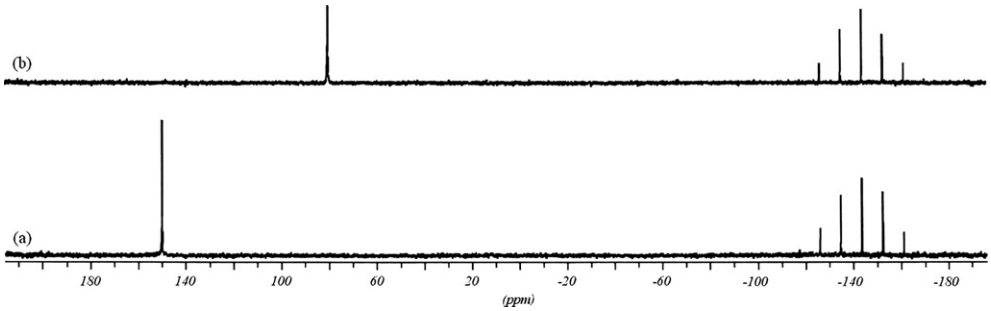


Fig. 5. ^{31}P NMR spectra for *trans*-$[Ru(NH_3)_4P(OEt)_3NO_2]^+$ for different hydrogenionic concentrations. $C_{Ru} = 2.0 \times 10^{-3}$ mol L^{-1}; solvent: deuterated water; (a) pH 10 and (b) pH 2.

The inverse reaction, conversion of the nitrosyl into the nitro compound, has already been described for other compounds in alkaline medium [7,22–24]. Under the conditions studied, the nitrosyl ligand was said to undergo a nucleophilic attack by the hydroxide ion, thus forming the corresponding nitro complex. However, this conversion apparently is not so simple when the studied system involves the phosphite complex *trans*-$[Ru(NH_3)_4P(OEt)_3NO]^{3+}$. Results obtained by the authors strongly suggest that the nucleophilic attack occurs not only at the NO^+ ligand, as expected, but also at the phosphite ligand [25]. These data will be published later.

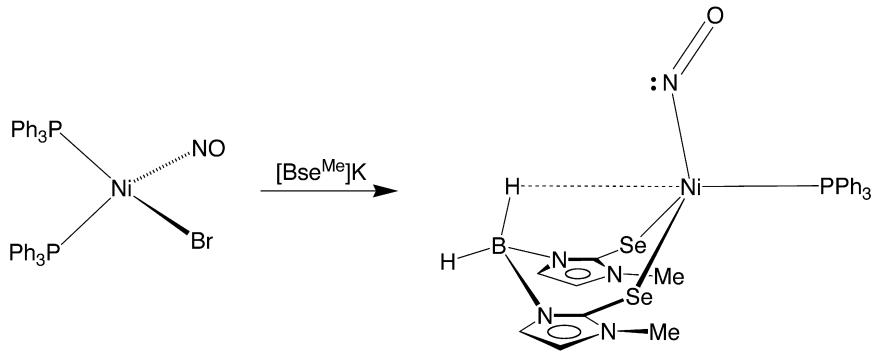
Some studies have also been carried out with the aim of verifying the vasodilator ability of *trans*-$[Ru(NH_3)_4P(OEt)_3NO_2](PF_6)$ in aorta rings without endothelium [26]. In these studies, the observed intensity and time of relaxation of maximum effect were found to be 68% in 114 min. The fact that the nitrosyl exhibits some instability at physiological hydrogenionic concentrations and since the nitro compound is quantitatively converted into the corresponding nitrosyl species at this pH, the use of nitro complexes could be an interesting source of *trans*-$[Ru(NH_3)_4P(OEt)_3(NO)](PF_6)_3$ *in situ*. Furthermore, since the nitro compound has a longer "shelf life" than *trans*-$[Ru(NH_3)_4P(OEt)_3(NO)](PF_6)_3$, storage in the form of the nitro complex instead of nitrosyl could be an interesting alternative. This system is presently under study and results will soon be published.

Acknowledgements

The authors are indebted to Professor José A. Olabe for the interesting discussions and for the financial support of the Brazilian agencies, FAPESP, CNPq and CAPES.

References

[1] D.W. Franco, H. Taube, Inorg. Chem. 17 (1978) 571.
[2] D.W. Franco, Coord. Chem. Rev. 119 (1992) 199.
[3] L.G.F. Lopes, E.E. Castellano, A.G. Ferreira, C.U. Davanzo, M.J. Clarke, D.W. Franco, Inorg. Chim. Acta 358 (2005) 2883.
[4] J.C. Toledo Jr., L.G.F. Lopes, A.A. Alves, L.P. Silva, D.W. Franco, J. Inorg. Biochem. 89 (2002) 267.
[5] B.F. Barros, J.C. Toledo Jr., D.W. Franco, E. Tfouni, M.H. Krieger, Nitric Oxide: Biol. Chem. 7 (2002) 50.
[6] A.S. Torsoni, B.B. Figueiredo, J.C. Toledo Jr., M. Haun, M.H. Krieger, E. Tfouni, D.W. Franco, Nitric Oxide: Biol. Chem. 6 (2002) 247.
[7] E. Tfouni, M. Krieger, B.R. McGarvey, D.W. Franco, Coord. Chem. Rev. 236 (2003) 57.
[8] J.C. Toledo Jr., B.S.L. Neto, D.W. Franco, Coord. Chem. Rev. 249 (2005) 419.
[9] P.G. Zanichelli, H.F.G. Estrela, R.C. Spadari-Bratfisch, D.M. Grassi-Kassisse, D.W. Franco, Nitric Oxide (2006), doi:10.1016/j.niox.2006.10.001.
[10] J.J.N. Silva, A.L. Osakabe, W.R. Pavanelli, J.S. Silva, D.W. Franco, Brit J Pharmacol (2007), doi:10.1038/sj.bjp.0707363.
[11] J.C. Toledo, L.G.F. Lopes, A.A. Alves, L.P. Silva, D.W. Franco, J. Inorg. Biochem. 89 (2002) 267.
[12] D.A. Freedman, D.E. Janzen, J.L. Vreeland, H.M. Tully, K.R. Mann, Inorg. Chem. 41 (15) (2002) 3820.
[13] S.S.S. Borges, C.U. Davanzo, E.E. Castellano, J.Z. Schpector, S.C. Silva, D.W. Franco, Inorg. Chem. 37 (1998) 2670.
[14] M.G. Gomes, S.C. Sebastiao, L.G.F. Lopes, P.S. Santos, D.W. Franco, J. Chem. Soc., Dalton Trans. (1998) 601.
[15] Y. Chen, F.-T. Lin, R.E. Shepherd, Inorg. Chem. 38 (1999) 973.
[16] A.D. Allen, F. Bottomley, R.D. Harris, V.P. Reinslau, C.V. Senoff, Inorg. Synth. 12 (1970) 2.
[17] R.M. Carlos, D.R. Cardoso, E.E. Castellano, R.Z. Osti, A.J. Camargo, L.G. Macedo, D.W. Franco, J. Am. Chem. Soc. 126 (2004) 2546.
[18] A. Berka, J. Vulterin, J. Zýka, in: Newer Redox Titrants, Pergamon Press, London, 1965.
[19] K.B. Yatsimirskii, V.P. Vasil'ev, in: Instability Constants of Complex Compounds, Pergamon Press, London, 1960.
[20] D.W. Franco, Inorg. Chim. Acta 48 (1981) 1.
[21] A.A. Chevalier, L.A. Gentil, J.A. Olabe, J. Chem. Soc., Dalton Trans. 8 (1991) 1959, and references therein.
[22] F. Roncaroli, M.E. Ruggiero, D.W. Franco, G.L. Estiu, J.A. Olabe, Inorg. Chem. 41 (2002) 5760.
[23] H. Nagao, K. Ito, N. Tsuboya, D. Ooyama, N. Nagao, F.S. Howell, M. Mukaida, Inorg. Chim. Acta 290 (1999) 113.
[24] J.H. Swinehart, P.A. Rock, Inorg. Chem. 5 (1966) 573.
[25] J.C. Toledo Jr., R.Z. Osti, D.W. Franco, unpublished results.
[26] P.G. Zanichelli, H.F.G. Estrela, R.C. Spadari-Bratfisch, D.M. Grassi-Kassisse, D.W. Franco, unpublished results.



Scheme 1.

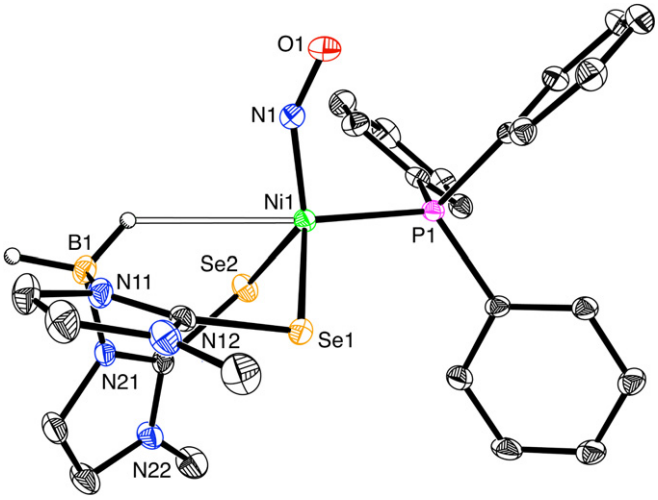


Fig. 1. Molecular structure of [Bse^{Me}]Ni(PPh$_3$)(NO) (only one of the two crystallographically independent molecules is shown).

Structural Database [6] have Ni–N–O bond angles in the range 151.8–179.2°, with a mean value of 169.5°.[2] Since (i) the [Se$_2$P] donor array provided by a [Bse^{Me}] and PPh$_3$ ligand combination is electronically analogous to the [Se$_3$] array of a [Tse^{Mes}] ligand and (ii) both [Bse^{Me}]-Ni(PPh$_3$)(NO) and [Tse^{Mes}]NiNO belong to the same {MNO}^{10} Enemark–Feltham classification [7], the observation of a bent nickel nitrosyl moiety for [Bse^{Me}]-Ni(PPh$_3$)(NO) and a linear nickel nitrosyl moiety for [Tse^{Mes}]NiNO warrants explanation.

Further inspection of the molecular structure of [Bse^{Me}]-Ni(PPh$_3$)(NO) indicates that the [Bse^{Me}] ligand does not coordinate in a simple bidentate κ^2–*Se*$_2$ manner; rather, the B–H group also interacts weakly with the nickel center. Specifically, the Ni···H distances for the two crystallographically independent molecules (2.70 Å and 2.77 Å) are intermediate between the sum of the van der Waals radii (3.2 Å) [8] and sum of the covalent radii (1.5 Å) [9] of nickel and hydrogen. Since both crystallographically independent molecules exhibit this interaction, it is evident that it cannot be simply ascribed to crystal packing forces. As such, the overall coordination geometry of [Bse^{Me}]-Ni(PPh$_3$)(NO) may be described as a distorted trigonal bipyramid, which is of note because there are no five (or six) coordinate nickel nitrosyl compounds listed in the Cambridge Structural Database [6].

In view of the presence of the Ni···H–B interaction, [κ^3–*Se*$_2$*H*–Bse^{Me}] may be viewed as a five-electron [L$_2$X] ligand rather than a three-electron [LX] ligand [1]. On this basis, a simple explanation to account for a bent nitrosyl moiety in [Bse^{Me}]Ni(PPh$_3$)(NO) is that coordination of the B–H group competes effectively with that of the nitrosyl ligand, which thereby bends to prevent the nickel center from adopting a 20-electron configuration. In order to evaluate this proposal in more detail, we have performed density functional theory (DFT) calculations to determine the extent to which the interaction with the B–H group is responsible for the bending of the nitrosyl ligand in [Bse^{Me}]Ni(PPh$_3$)(NO).

The geometry optimized structure of [Bse^{Me}]-Ni(PPh$_3$)(NO) is illustrated in Fig. 2 and reproduces the essential features of the experimental structure with respect to both the Ni–N–O angle (149.2°) and the Ni···H–B interaction (2.74 Å). To evaluate the extent to which the bending of the nitrosyl ligand is caused by the Ni···H–B interaction, additional geometry optimization calculations were performed on [Bse^{Me}]Ni(PPh$_3$)(NO) with constrained Ni–N–O bond angles of 120° and 180° (Fig. 2). As illustrated in Table 1, the Ni···H–B bond distance does correlate with the constrained Ni–N–O bond angle; however, the variation is not large. For example, if the Ni–N–O bond angle is constrained to 180°, the Ni···H–B bond distance increases to 2.89 Å, only 0.1 Å greater than the fully geometry optimized value of 2.79 Å. On this basis, while it is possible that the Ni···H–B interaction does have an effect on the Ni–N–O bond angle, the magnitude of the effect is small and an alternative explanation is required to rationalize the Ni–N–O bond angle.

In this regard, while the occurrence of bent and linear nitrosyl compounds is sometimes predicted by the application of simple electron counting procedures in which these ligands respectively contribute one and three elec-

[2] These values exclude SOQTOH, a metastable state of Cp*NiNO with a side-bound nitrosyl ligand, and CLTPNN01, a disordered structure of (Ph$_3$P)$_2$Ni(NO)Cl.

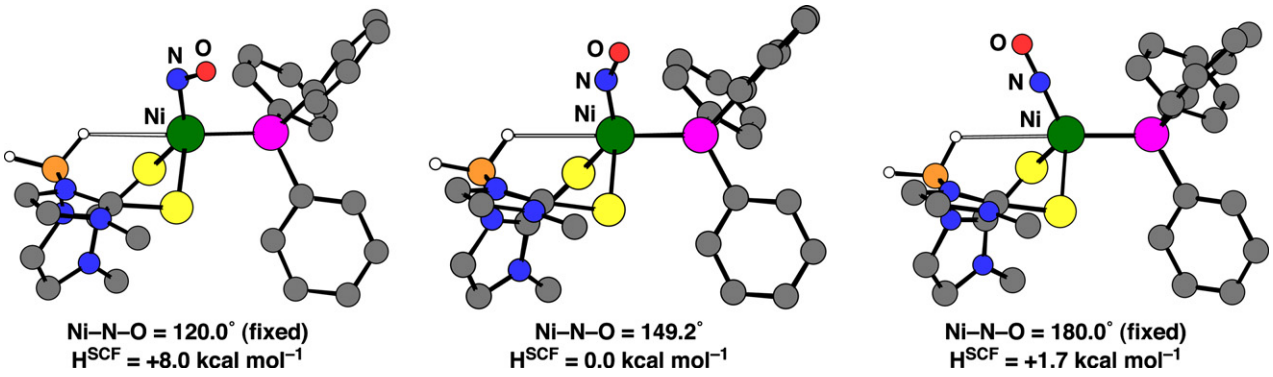


Fig. 2. DFT geometry optimized structures of $[Bse^{Me}]Ni(PPh_3)(NO)$ and their relative H^{SCF} values. The structure in the center is fully geometry optimized, while the left and right structures have been optimized subject to the constraints that the Ni–N–O angles are fixed at 120° and 180°, respectively.

Table 1
Selected data for DFT geometry optimized structures of $[Bse^{Me}]Ni(PPh_3)(NO)$

	"Boat-like"			"Chair-like"
Ni–N–O/°	120.0 (fixed)	149.2	180.0 (fixed)	154.4
Ni···H–B/Å	2.65	2.79	2.89	3.86
H^{SCF}(rel)/ kcal mol^{-1}	8.0	0.0	1.7	3.1

trons to a metal center [10], it is evident that this approach is of limited applicability because exceptions to the 18-electron rule are commonplace [11]. For example, $Ir(PPh_3)_2(NO)Cl_2$ [12] and $Mn(CO)_4(NO)$ [13] are two early examples of five-coordinate complexes that have strongly bent and linear nitrosyl groups, respectively. The latter has an 18-electron configuration, whereas the former has a 16-electron configuration, even though an 18-electron configuration could be achieved if the nitrosyl ligand were to be linear.

A more reliable approach for predicting the geometry of a metal nitrosyl ligand is based on a consideration of the molecular orbital diagrams for the molecule in question [14,15]. Such analyses indicate that, for metal centers with a high d^n configuration, bending provides a means to stabilize orbitals with M–N antibonding character. For example, several previous studies have pointed out that the driving force for bending the M–N–O group in certain complexes is to stabilize the M–N σ^* antibonding orbital [14,15]. Specifically, bending of the nitrosyl ligand reduces the σ-overlap between the sp nitrogen lone pair of the nitrosyl ligand and the metal d_{z^2} orbital (assuming that z is the bond axis) and thereby stabilizes the M–N σ^* antibonding orbital; furthermore, this orbital gains additional stabilization upon bending because one of the NO π^* orbitals is now of appropriate symmetry to interact with the d_{z^2} orbital (Fig. 3) [14,15]. If the $\langle \pi^*(NO), d_{z^2} \rangle$ orbital is occupied, bending provides a means to stabilize the molecule, so long as the higher energy counterpart orbital, $\langle d_{z^2}, \pi^*(NO) \rangle$, is unoccupied. Such bending, however, reduces the π-backbonding component and so the observed geometry reflects a compromise between the two effects which depends critically on the compound in question (*cf.* $Ir(PPh_3)_2(NO)Cl_2$ and $Mn(CO)_4(NO)$ with a common $\{MNO\}^8$ configuration).

To provide further evidence that the nature of the nitrosyl ligand of $[Bse^{Me}]Ni(PPh_3)(NO)$ is not determined by the Ni···H–B interaction, the molecular structure of $[Bse^{Me}]Ni(PPh_3)(NO)$ was geometry optimized with a "chair-like" conformation of the eight-membered $\{[Bse^{Me}]Ni\}$ ring, thereby preventing the B–H group from interacting with the nickel center (Fig. 4). Significantly, geometry optimized "chair-like" $[\kappa^2\text{–}Bse^{Me}]Ni(PPh_3)(NO)$, for which the Ni···H–B separation (3.86 Å) well exceeds the sum of the van der Waals radii of nickel and hydrogen (3.2 Å) [8], also possesses a bent nitrosyl ligand, with a Ni–N–O bond angle of 154.4°. As such, it provides excellent evidence that the Ni···H–B interaction has little effect on the coordination mode of the nitrosyl ligand. The Ni···H–B interaction may, nevertheless, exert an influence with respect to the stability of the molecule, with "chair-like" $[Bse^{Me}]Ni(PPh_3)(NO)$ being 3.1 kcal mol^{-1} higher in energy than the experimentally observed "boat-like" conformation with a Ni···H–B interaction.

Evidence that four-coordinate $[\kappa^2\text{–}Bse^{Me}]Ni(PPh_3)(NO)$, with a "chair-like" conformation that is devoid of Ni···H–B interaction, should also possess a bent nitrosyl ligand is provided by comparison with several other $[L_2X]NiNO$ complexes, such as $(Ph_3P)_2Ni(NO)X$ (X = Cl, N_3, NCS) [16]. However, as noted above, there are also a variety of $[L_2X]NiNO$ complexes that possess linear nitrosyl ligands and data for a selection of these complexes are summarized in Table 2. The feature which distinguishes these two classes of $[L_2X]NiNO$ compounds (which also possess the same $\{NiNO\}^{10}$ Enemark–Feltham description) is that $\{[L_2X]Ni\}$ moieties of the linear nitrosyl compounds are highly symmetric, *e.g.* $\{(R_3P)_3Ni\}$, $\{[Tp^{Me_2}]\}Ni$, $\{[Tse^{Mes}]Ni\}$ and $\{Cp^*Ni\}$, whereas those with bent nitrosyl ligands have lower symmetry. Mingos has pointed out that distortion from linearity is not favored

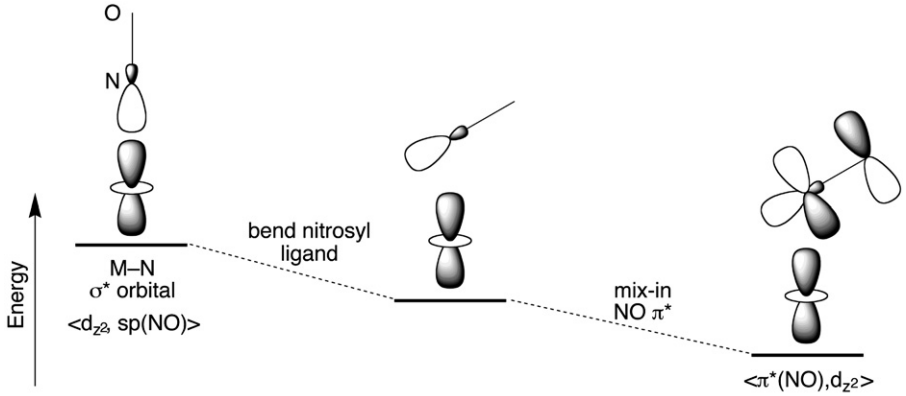


Fig. 3. Influence of bending the nitrosyl ligand on the energy of the M–N σ* orbital of a linear geometry. Bending of the nitrosyl ligand (i) reduces the σ-overlap between the sp nitrogen lone pair and the metal d_{z^2} orbital and (ii) allows one of the NO π* orbitals to interact with the d_{z^2} orbital. See Ref. [14].

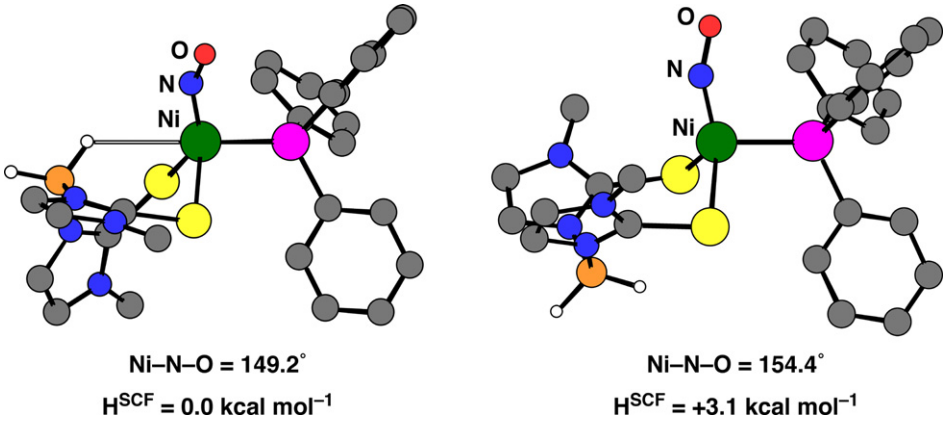


Fig. 4. Comparison of DFT geometry optimized structures of $[Bse^{Me}]Ni(PPh_3)(NO)$ with "boat-like" (left) and "chair-like" (right) conformations, and their relative H^{SCF} values.

Table 2
Selected data for some structurally characterized mononuclear $\{NiNO\}^{10}$ nickel nitrosyl compounds

	ν(NO) (cm^{-1})	d(Ni–N) (Å)	d(N–O) (Å)	Ni–N–O (°)	Reference
$[\kappa^3$–$PhB(CH_2PPh_2)_3]NiNO$	1737	1.624(3)	1.183(3)	176.0(3)	[24]
Cp^*NiNO	1787	1.620(3)	1.177(3)	179.2(3)	[25]
		1.614(3)	1.181(4)	179.1(3)	
$[Tse^{Mes}]NiNO$	1763, 1752	1.633(4)	1.156(5)	180.0	[4]
$[Tp^{Me_2}]NiNO$	1786	1.619(6)	1.170(7)	178.5(6)	[4]
		1.617(6)	1.158(7)	175.3(7)	
$\{[\kappa^3$–$N(CH_2CH_2PPh_2)_3]NiNO\}[BPh_4]$	1755	1.59(2)	1.14(3)	168(2)	[26]
$[(Me_3P)_3NiNO][PF_6]$	1750	1.645(5)	1.139(9)	175.4(5)	[27]
$\{[MeC(CH_2O)_3P]_3NiNO\}[BF_4]$	1867	1.58(1)	1.12(1)	177(2)	[28]
$[(1,3,5\text{-triaza-7-phosphaadamantane})_3NiNO]X$	1778[a]	1.653(4)[b]	1.159(5)[b]	171.5(4)[b]	[29]
$\{[C_6H_4(PPhMe)_2]Ni(NO)$-$[P(OMe)_3]\}[PF_6]$	1825	1.638(5)	1.153(5)	178.0(5)	[30]
$(Me_3P)_2Ni(NO)(NO_2)$	1718	1.652(7)	1.177(7)	166.9(6)	[31]
$[C_6H_4(PPhMe)_2]Ni(NO)NCS$	1755	1.651(3)	1.167(3)	159.5(3)	[30]
$(Ph_3P)_2Ni(NO)(N_3)$		1.686(7)	1.164(8)	152.7(7)	[16a]
$[Bse^{Me}]Ni(PPh_3)(NO)$	1731, 1692	1.675(3)	1.172(3)	149.1(3)	this paper
		1.671(3)	1.162(4)	153.1(3)	

[a] $X = NO_3$.
[b] $X = BPh_4$.

for C_{3v} geometries with $\{NiNO\}^{10}$ configurations because both $\langle \pi^*(NO), d_{z^2} \rangle$ and $\langle d_{z^2}, \pi^*(NO) \rangle$ orbitals are fully occupied, and the stabilization afforded one orbital upon bending is cancelled by the destabilization of the other [14b]. For nitrosyl complexes that are incapable of adopting C_{3v} symmetry, distortions from linearity afford an overall net

stabilization because the orbital that is destabilized upon bending is unoccupied.

Finally, it is noteworthy that the mononitrosyl complex [Bse^{Me}]Ni(PPh$_3$)(NO) is characterized by two frequencies in the ν(NO) region at 1731 cm^{-1} and 1692 cm^{-1}.[3] Possible explanations for this observation are (*i*) the signals correspond to the "boat" and "chair" conformations described above, and *(ii)* the signals correspond to isomers with linear and bent nitrosyl ligands. In this regard, it should be noted that a variety of other mononitrosyl compounds have been reported to exhibit two ν(NO) stretching frequencies which have been suggested to correspond to linear and bent isomers [17].

3. Experimental

3.1. General considerations

All manipulations were performed using a combination of glovebox, high vacuum, and Schlenk techniques under a nitrogen or argon atmosphere unless otherwise specified [18]. Solvents were purified and degassed by standard procedures. ^{1}H NMR spectra were measured on a Bruker 300 DRX spectrometer. ^{1}H chemical shifts are reported in ppm relative to SiMe$_4$ ($\delta = 0$) and were referenced internally with respect to the protio solvent impurity (δ 7.16 for C$_6$D$_5$H) [19]. ^{11}B NMR spectra are reported with reference to external BF$_3$(OEt$_2$) (δ 0.0). Coupling constants are given in hertz. Infrared spectra were recorded on Nicolet Avatar 370 DTGS spectrometer and are reported in cm^{-1}. Mass spectra were obtained on a JMS-HX110/110 Double Focusing mass spectrometer using fast atom bombardment (FAB). [Bse^{Me}]K was obtained by the literature method [5].

3.2. X-ray structure determination

X-ray diffraction data were collected on a Bruker P4 diffractometer equipped with a SMART CCD detector and crystal data, data collection and refinement parameters are summarized in Table 3. The structure was solved using direct methods and standard difference map techniques, and was refined by full-matrix least-squares procedures on F^2 with SHELXTL (Version 5.10) [20].

3.3. Computational details

All calculations were carried out using DFT as implemented in the Jaguar 6.5 suite of *ab initio* quantum chemistry programs [21]. Geometry optimizations were performed with the B3LYP density functional [22] and the 6-31G** (C, H, N, B, P, and O), LAV3P (Se) and LACVP (Ni) [23] basis sets.

[3] The borodeuterated analogue [d$_2$–Bse^{Me}]Ni(PPh$_3$)(NO) has very similar ν(NO) absorptions at 1731 cm^{-1} and 1689 cm^{-1}.

Table 3
Crystal, intensity collection and refinement data

	[Bse^{Me}]Ni(PPh$_3$)(NO)
Lattice	monoclinic
Formula	$C_{26}H_{27}BN_5NiOPSe_2$
Formula weight	683.94
Space group	$P2_1/n$
a (Å)	17.8979(9)
b (Å)	10.4392(5)
c (Å)	31.1556(15)
α (°)	90
β (°)	100.5320(10)
γ (°)	90
V (Å^3)	5723.0(5)
Z	8
Temperature (K)	243
Radiation (λ, Å)	0.71073
ρ (calc.) (g cm^{-3})	1.588
μ (Mo Kα) (mm^{-1})	3.306
θ Max (°)	26.37
Number of data	10825
Number of parameters	683
R_1	0.0336
wR_2	0.0848
Goodness-of-fit	1.034

3.4. Synthesis of [Bse^{Me}]Ni(PPh$_3$)(NO)

A solution of [Bse^{Me}]K (10 mg, 0.027 mmol) in CH$_3$CN (0.5 mL) was added drop-wise to a solution of Ni(PPh$_3$)$_2$(NO)Br (19 mg, 0.027 mmol) in CH$_3$CN (0.5 mL) giving a dark blue solution. The solution was filtered and allowed to evaporate slowly, thereby depositing [Bse^{Me}]Ni(PPh$_3$)(NO) as a dark blue crystalline material, which was isolated by filtration, washed with pentane (1 mL), and dried *in vacuo* (11 mg, 60% yield). X-ray quality crystals were grown from CH$_3$CN. ^{1}H NMR (C$_6$D$_6$): 2.87 [s, 6H of –CH$_3$], 5.76 [br, 2H of imidazole], 6.64 [br, 2H of imidazole], 7.04–7.07 [m, 9H of phenyl], 7.57–7.63 [br, 6H of phenyl]. ^{11}B NMR (CDCl$_3$): −9.4 ppm. Anal. Calc. for $C_{26}H_{27}BN_5NiOPSe_2$: C, 45.7; H, 4.0; N, 10.2. Found: C, 45.8; H, 3.7; N, 10.3%. Mass spectrum: $m/z = 655.3$ {M–NO}$^+$. IR Data (KBr pellet, cm^{-1}): 3158 (w), 3134 (w), 3117 (w), 3064 (w), 3044 (w), 3003 (w), 2978 (w), 2933 (w), 2479 (m), 2394 (m), 2349 (m), 1731 (ν_{NO}, s), 1715 (m), 1692 (ν_{NO}, vs), 1652 (m), 1557 (m), 1539 (m), 1479 (m), 1455 (s), 1434 (s), 1408 (m), 1371 (s), 1325 (m), 1296 (m), 1181 (s), 1151 (s), 1132 (m), 1114 (s), 1094 (s), 1028 (m), 747 (m), 727 (m), 694 (s), 667 (m), 518 (s), 506 (m), 496 (m).

4. Conclusions

In summary, [Bse^{Me}]Ni(PPh$_3$)(NO) has been synthesized by the reaction of Ni(PPh$_3$)$_2$(NO)Br with [Bse^{Me}]K. X-ray diffraction studies demonstrate that the B–H group of the [Bse^{Me}] ligand interacts with the nickel center such that the Ni···H distances for the two crystallographically independent molecules are intermediate between the sum of the van der Waals radii and sum of the covalent radii of nickel and hydrogen. As such, [Bse^{Me}]Ni(PPh$_3$)(NO) is an

uncommon example of a nickel nitrosyl complex with a distorted trigonal bipyramidal geometry. The nickel nitrosyl moieties in both crystallographically independent molecules are significantly bent, with Ni–N–O bond angles of 149.1(3)° and 153.1(3)°, in marked contrast to the linearity observed for [Tse^{Mes}]NiNO (180.0°). A series of DFT geometry optimization calculations demonstrate that the Ni···H–B interaction is not responsible for causing the nitrosyl ligand to bend and that the difference between [Tse^{Mes}]NiNO and [Bse^{Me}]Ni(PPh$_3$)(NO) is due to the [Tse^{Mes}] ligand allowing the molecule to adopt a structure with C_3 symmetry. In contrast, the asymmetry of [Se$_2$P] donor array of the [Bse^{Me}] and PPh$_3$ ligand combination prevents [Bse^{Me}]Ni(PPh$_3$)(NO) from having C_3 symmetry and the nitrosyl ligand bends to stabilize the occupied M–N σ^* antibonding orbital.

Note added in proof

The related *bis*(2-mcrcapto-1-methylimidazolyl)hydroborate complex, [Bm^{Me}]Ni(PPh$_3$)(NO), has been synthesized and structurally characterized by X-ray diffraction. L. S. Maffett, K. L. Gunter, K. A. Kreisel, G. P. A. Yap and D. Rabinovich *Polyhedron* this issue.

Acknowledgements

We thank the National Science Foundation (CHE-03-50498) for support of this research. V.K.L. acknowledges the Department of Defense for a National Defense Science and Engineering Graduate Fellowship.

Appendix A. Supplementary material

CCDC 640150 contains the supplementary crystallographic data for [Bse^{Me}]Ni(PPh$_3$)(NO). These data can be obtained free of charge via http://www.ccdc.cam.ac.uk/conts/retrieving.html, or from the Cambridge Crystallographic Data Centre, 12 Union Road, Cambridge CB2 1EZ, UK; fax: (+44) 1223-336-033; or e-mail: deposit@ccdc.cam.ac.uk. Supplementary data associated with this article can be found, in the online version, at doi:10.1016/j.poly.2007.06.005.

References

[1] For the definition of L, X and Z donor functions, see: M.L.H. Green, J. Organomet. Chem. 500 (1995) 127.
[2] An early example is provided by Ni(PPh$_3$)$_2$(NO)Br. (a) R.D. Feltham, J. Inorg. Nucl. Chem. 14 (1960) 307;
(b) R.D. Feltham, Inorg. Chem. 3 (1964) 116.
[3] Three-coordinate terminal nickel nitrosyl compounds have also been synthesized. See, for example: (a) K.S. Chong, S.J. Rettig, A. Storr, J. Trotter, Can. J. Chem. 57 (1979) 3090;
(b) S.C. Puiu, T.H. Warren, Organometallics 22 (2003) 3974;
(c) V.M. Iluc, A.J.M. Miller, G.L. Hillhouse, Chem. Commun. (2005) 5091.
[4] V.K. Landry, K. Pang, S.M. Quan, G. Parkin, Dalton Trans. (2007) 820.
[5] V.K. Landry, D. Buccella, K. Pang, G. Parkin, Dalton Trans. (2007) 866.
[6] CSD Version 5.28. 3D search and research using the Cambridge Structural Database, in: F.H. Allen, O. Kennard (Eds.), Chemical Design Automation News, vol. 8(1), 1993, pp. 1 & 31–37.
[7] (a) J.H. Enemark, R.D. Feltham, Coord. Chem. Rev. 13 (1974) 339;
(b) R.D. Feltham, J.H. Enemark, In Topics in Inorganic and Organic Stereochemistry, vol. 12, Wiley, New York, 1981, pp. 155–215;
(c) B.L. Westcott, J.H. Enemark, In Inorganic Electronic Structure and Spectroscopy, in: A.B.P. Lever, E.I. Solomon (Eds.), Inorganic Electronic Structure and Spectroscopy, Applications and Case Studies, vol. 2, 1999, pp. 403–450 (Chapter 7).
[8] The van der Waals radii of nickel and hydrogen are 2.0 Å[a] and 1.2 Å,[b] respectively. See: (a) S.S. Batsanov, Inorg. Mater. 37 (2001) 871;
(b) L. Pauling, The Nature of The Chemical Bond, 3rd ed., Cornell University Press, Ithaca, NY, 1960, p. 260.
[9] The covalent radii of nickel and hydrogen are 1.11 Å and 0.37 Å, respectively. See: S.S. Batsanov, Russ. Chem. Bull. 44 (1995) 2245.
[10] B.L. Haymore, J.A. Ibers, Inorg. Chem. 14 (1975) 2610.
[11] G. Parkin, in: R.H. Crabtree, D.M.P. Mingos (Eds.), Comprehensive Organometallic Chemistry III, vol. 1, Elsevier, Oxford, 2006 (Chapter 1).
[12] D.M.P. Mingos, J.A. Ibers, Inorg. Chem. 10 (1971) 1035.
[13] B.A. Frenz, J.A. Enemark, J.A. Ibers, Inorg. Chem. 8 (1969) 1288.
[14] (a) R. Hoffmann, M.M.L. Chen, M. Elian, A.R. Rossi, D.M.P. Mingos, Inorg. Chem. 13 (1974) 2666;
(b) D.M.P. Mingos, Inorg. Chem. 12 (1973) 1209;
(c) C.G. Pierpont, R.J. Eisenberg, Am. Chem. Soc. 93 (1971) 4905.
[15] (a) R. Eisenberg, C.D. Meyer, Acc. Chem. Res. 8 (1975) 26;
(b) D.M.P. Mingos, D.J. Sherman, Adv. Inorg. Chem. 34 (1989) 293;
(c) Reference [7].
[16] (a) J.H. Enemark, Inorg. Chem. 10 (1971) 1952;
(b) K.J. Haller, J.H. Enemark, Inorg. Chem. 17 (1978) 3552.
[17] (a) J.P. Collman, P. Farnham, G.J. Dolcetti, Am. Chem. Soc. 93 (1971) 1788;
(b) G. Booth, J.J. Chatt, Chem. Soc. (1962) 2099;
(c) M.W. Schoonover, E.C. Baker, R.J. Eisenberg, Am. Chem. Soc. 101 (1979) 1880;
(d) C.P. Brock, J.P. Collman, G. Dolcetti, P.H. Farnham, J.A. Ibers, J.E. Lester, C.A. Reed, Inorg. Chem. 12 (1973) 1304.
[18] (a) J.P. McNally, V.S. Leong, N.J. Cooper, in: A.L. Wayda, M.Y. Darensbourg (Eds.), Experimental Organometallic Chemistry, American Chemical Society, Washington, DC, 1987, p. 6 (Chapter 2);
(b) B.J. Burger, J.E. Bercaw, in: A.L. Wayda, M.Y. Darensbourg (Eds.), Experimental Organometallic Chemistry, American Chemical Society, Washington, DC, 1987, p. 79 (Chapter 4);
(c) D.F. Shriver, M.A. Drezdzon, The Manipulation of Air-Sensitive Compounds, 2nd ed., Wiley, Interscience, New York, 1986.
[19] H.E. Gottlieb, V. Kotlyar, A.J. Nudelman, Org. Chem. 62 (1997) 7512.
[20] G.M. Sheldrick, SHELXTL, An Integrated System for Solving, Refining and Displaying Crystal Structures from Diffraction Data, University of Göttingen, Göttingen, Federal Republic of Germany, 1981.
[21] Jaguar 6.5, Schrödinger, New York, NY, 2005.
[22] (a) A.D. Becke, J. Chem. Phys. 98 (1993) 5648;
(b) A.D. Becke, Phys. Rev. A 38 (1988) 3098;
(c) C.T. Lee, W.T. Yang, R.G. Parr, Phys. Rev. B 37 (1988) 785;
(d) S.H. Vosko, L. Wilk, M. Nusair, Can. J. Phys. 58 (1980) 1200;
(e) J.C. Slater, Quantum theory of molecules and solids, The Self-Consistent Field for Molecules and Solids, vol. 4, McGraw-Hill, New York, 1974.
[23] (a) P.J. Hay, W.R. Wadt, J. Chem. Phys. 82 (1985) 270;
(b) W.R. Wadt, P.J. Hay, J. Chem. Phys. 82 (1985) 284;
(c) P.J. Hay, W.R. Wadt, J. Chem. Phys. 82 (1985) 299.
[24] C.E. MacBeth, J.C. Thomas, T.A. Betley, J.C. Peters, Inorg. Chem. 43 (2004) 4645.

[25] (a) J.C. Green, C.J. Underwood, Organomet. Chem. 528 (1997) 91; (b) D.V. Fomitchev, T.R. Furlani, P. Coppens, Inorg. Chem. 37 (1998) 1519.
[26] M. Di Vaira, C.A. Ghilardi, L. Sacconi, Inorg. Chem. 15 (1976) 1555.
[27] G. Elbaze, M. Dartiguenave, Y. Dartiguenave, Inorg. Chim. Acta 87 (1984) 91.
[28] J.H. Meiners, C.J. Rix, J.C. Clardy, J.G. Verkade, Inorg. Chem. 14 (1975) 705.
[29] D.J. Darensbourg, T.J. Decuir, N.W. Stafford, J.B. Robertson, J.D. Draper, J.H. Reibenspies, A. Kathó, F. Joó, Inorg. Chem. 36 (1997) 4218.
[30] A.F.M.M. Rahman, G. Salem, F.S. Stephens, S.B. Wild, Inorg. Chem. 29 (1990) 5225.
[31] J. Kriege-Simondsen, G. Elbaze, M. Dartiguenave, R.D. Feltham, Y. Dartiguenave, Inorg. Chem. 21 (1982) 230.

coworkers [27]. Nickel nitrosyl compounds containing sulfur-donor ligands, examples of which include tetrahedral xanthate derivatives $(Ph_3P)Ni(S_2COR)(NO)$ [28,29] and the heterodinuclear complexes $(Cp'V)_2(\mu\text{-}S)_4\{Ni(NO)\}_2$ [30] and $(ON)Ni\{(\mu\text{-}SCH_2CH_2)_2S\}Fe(NO)_2$ [31], are less common. A compound particularly relevant to our work is the tris(thioether)borate derivative $\{PhB(CH_2SBu^t)_3\}$-Ni(NO), reported almost a decade ago [32], which was until now the only mononuclear nickel nitrosyl complex supported by an $[S_3]$ donor set.

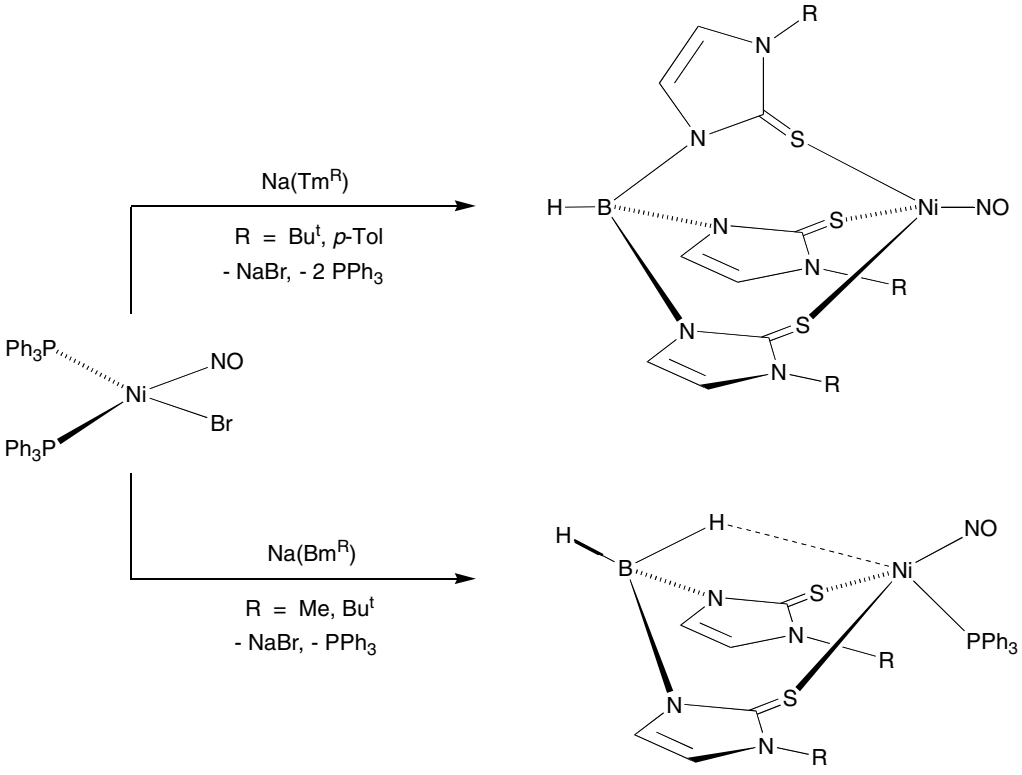
Seeking to further explore the synthesis of nickel nitrosyl complexes in a sulfur-rich environment, we turned our attention to the tris(mercaptoimidazolyl)borate (Tm^R) [33] and bis(mercaptoimidazolyl)borate (Bm^R) [34] ligand systems, which we have previously used to model certain structural elements of the nickel center in [NiFe] hydrogenases [35,36]. We describe in this paper the preparation and characterization of the first nickel nitrosyl complexes containing poly(mercaptoimidazolyl)borate ligands, namely $(Tm^R)Ni(NO)$ and $(Bm^R)Ni(PPh_3)(NO)$ [37,38]. These species, together with Parkin's recently reported tris(pyrazolyl)borate and tris(selenoimidazolyl)borate complexes $(Tp^{Me2})Ni(NO)$ and $(Tse^{Mes})Ni(NO)$ that feature $[N_3]$ and $[Se_3]$ donor groups [39], expand the pool of nickel mononitrosyl complexes now available for the comparative study of their molecular structures and spectroscopic properties.

2. Results and discussion

2.1. Syntheses of nickel nitrosyl complexes

The tris(mercaptoimidazolyl)borate complexes (Tm^R)-Ni(NO) (R = Bu^t, *p*-Tol) were readily prepared by reacting equimolar amounts of the purple triphenylphosphine complex $Ni(PPh_3)_2(NO)Br$ [10] and the corresponding $Na(Tm^R)$ reagents (Scheme 1), and the turquoise (R = Bu^t) or greenish blue (R = *p*-Tol) products were isolated in ca. 40–50% yield after the appropriate work-up. The bis(mercaptoimidazolyl)borate derivatives $(Bm^R)Ni$-$(PPh_3)(NO)$ (R = Me, Bu^t), which are the first transition metal nitrosyl complexes containing Bm^R ligands to be synthesized, were similarly obtained as slate green (R = Me) or indigo (R = Bu^t) microcrystalline solids in ca. 65–80% yield. All the new complexes are air-stable in the solid state and dissolve in a variety of organic solvents, including acetone, acetonitrile, benzene, dichloromethane, tetrahydrofuran (THF), and toluene, to give solutions that are markedly more sensitive to oxygen.

The four new complexes, all of which have a $\{Ni(NO)\}^{10}$ configuration in the Enemark–Feltham notation [40], were characterized by a combination of analytical and spectroscopic techniques, including elemental analyses (CHN) and IR and NMR spectroscopies. The observation of sharp resonances in their ^1H and ^{13}C NMR spectra and the



Scheme 1.

Table 1
IR data (ν_{NO}/cm^{-1}) for selected nickel mononitrosyl complexes

Complex	ν_{NO}/cm^{-1}	Medium	Ref.
[{MeC(CH$_2$O)$_3$P}$_3$Ni(NO)]BF$_4$	1867	Nujol	[23]
CpNi(NO)	1839	Ar, 20 K	[14]
[(Bu^{t}NC)$_3$Ni(NO)]NO$_3$	1828	Nujol	[18]
[(PPh$_3$)$_3$Ni(NO)]PF$_6$	1790	Nujol	[19]
Cp*Ni(NO)	1787	Nujol	[16]
(Tp^{Me2})Ni(NO)	1786	KBr	[39]
{PhB(CH$_2$SBu^t)$_3$}Ni(NO)	1785	CH_2Cl_2	[32]
[(PTA)$_3$Ni(NO)]NO$_3$	1778	KBr	[20]
[{MeC(CH$_2$PEt$_2$)$_3$}Ni(NO)]BPh$_4$	1760	Nujol	[25]
[{N(CH$_2$CH$_2$PPh$_2$)$_3$}Ni(NO)]BPh$_4$	1755	Nujol	[26]
(Tm$^{p\text{-Tol}}$)Ni(NO)	1752	KBr	this work
[(PH$_2$Mes)$_3$Ni(NO)]BF$_4$	1751	KBr	[21]
[(PEt$_3$)$_3$Ni(NO)]PF$_6$	1745	KBr or Nujol	[22]
(Tm$^{t\text{Bu}}$)Ni(NO)	1741	KBr	this work
{PhB(CH$_2$PPh$_2$)$_3$}Ni(NO)	1737	C_6H_6	[27]

magnetic equivalency of the mercaptoimidazolyl groups in the NMR time scale are consistent with the presence in each case of diamagnetic, pseudo-tetrahedral metal complexes in solution. FT-IR spectroscopy was conveniently used to evaluate the electronic nature of the complexes *via* the ν(NO) stretching frequencies of the nitrosyl groups. More specifically, the ν(NO) frequencies of (Tm$^{p\text{-Tol}}$)Ni(NO) (1752 cm^{-1}) and (Tm$^{t\text{Bu}}$)Ni(NO) (1741 cm^{-1}) reflect a considerable degree of backbonding to the NO π^* orbitals and are among the lowest observed for nickel mononitrosyl complexes (Table 1). Thus, there is mounting evidence suggesting that the Tm^{R} ligands are more electron releasing than their hard nitrogen-donor counterparts, the ubiquitous tris(pyrazolyl)borates (Tp$^{RR'}$) [41–43], and that they are electronically comparable to other soft ligands such as the tris(phosphino)borates [27] and the tris(seleno-imidazolyl)borates [39].

The ν(NO) frequencies of the (Bm^{R})Ni(PPh$_3$)(NO) complexes (1688 and 1728 cm^{-1} for R = Me and Bu^t, respectively) are even lower than those found for the (Tm^{R})Ni(NO) derivatives described above. Even though the correlation between ν(NO) frequencies and the extent of bending in the M–N–O moieties of metal nitrosyl complexes is notoriously unreliable [4], this situation suggests that some deviation from linearity in the NiNO units of the (Bm^{R})Ni(PPh$_3$)(NO) compounds may be taking place nevertheless (vide infra). In this regard, a Ni–N–O angle of 152.7° was found in the nickel azide complex Ni(PPh$_3$)$_2$(NO)(N$_3$), which displays a ν(NO) frequency of 1710 cm^{-1} [44]. It is also worth noting that DFT calculations on the closely related bis(selenoimidazolyl)borate complex (Bse^{Me})Ni(PPh$_3$)(NO) suggest that the nitrosyl ligand bends in order to stabilize the occupied M–N σ^* antibonding orbital [45].

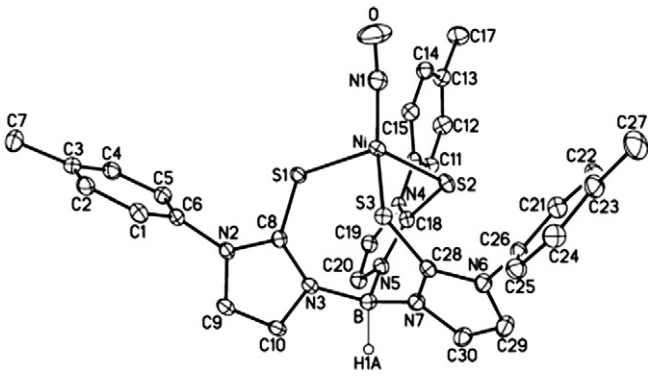


Fig. 1. Molecular structure of (Tm$^{p\text{-Tol}}$)Ni(NO).

2.2. Molecular structures of (Tm$^{p\text{-Tol}}$)Ni(NO) and (Bm^{Me})Ni(PPh$_3$)(NO)

The molecular structure of (Tm$^{p\text{-Tol}}$)Ni(NO) (Fig. 1) was determined using a single crystal obtained at room temperature by slow diffusion of pentane into a THF solution of the complex, and selected bond lengths and angles are given in Table 2. It is a rare example of a structurally characterized mononuclear nickel nitrosyl complex having a [NiS$_3$N] core, second only to Riordan's {PhB(CH$_2$SBu^t)$_3$}-Ni(NO) [32]. As expected, (Tm$^{p\text{-Tol}}$)Ni(NO) presents a slightly distorted tetrahedral geometry, with the three mercaptoimidazolyl groups of the Tm$^{p\text{-Tol}}$ ligand in a propeller-like arrangement around the metal center, canted relative to the pseudo-C_3 axis that contains the boron atom and the fairly linear NO moiety [Ni–N–O = 173.9(4)°]. The average S–Ni–S and S–Ni–N angles (101.5° and 116.6°, respectively) deviate only slightly from the ideal tetrahedral value.

The Ni–S bond distances in (Tm$^{p\text{-Tol}}$)Ni(NO), between 2.319 and 2.350 Å, are longer than those found in a variety of four-coordinate nickel complexes containing thioureas or heterocyclic thiones, which are in the approximate range 2.14–2.30 Å [9]. However, they are shorter than those in Ni(Tm^{Me})$_2$ [2.440(1)–2.483(1) Å] [46], a disparity likely to arise from the higher coordination number of the nickel center in the latter. Despite these differences, the Ni–N

Table 2
Selected bond lengths (Å) and bond angles (°) for (Tm$^{p\text{-Tol}}$)Ni(NO)

Bond lengths	
Ni–S(1)	2.3432(11)
Ni–S(2)	2.3503(11)
Ni–S(3)	2.3190(10)
Ni–N(1)	1.665(3)
N(1)–O	1.131(4)
Bond angles	
S(1)–Ni–S(2)	101.34(4)
S(1)–Ni–S(3)	103.87(4)
S(2)–Ni–S(3)	99.30(4)
S(1)–Ni–N(1)	114.47(10)
S(2)–Ni–N(1)	121.34(11)
S(3)–Ni–N(1)	114.01(11)
Ni–N(1)–O	173.9(4)

and N–O bond lengths [1.665(3) and 1.131(4) Å, respectively] are within the corresponding ranges of values observed for such bonds in four-coordinate nickel nitrosyl complexes (1.58–1.69 and 1.12–1.19 Å, respectively) [9]. It is also worth noting that compelling structural and computational evidence implying that the M–N interactions in linear nitrosyl complexes have actually multiple bond character has recently been provided [39]. More specifically, a combination of X-ray crystallography and DFT calculations performed on $(Tp^{Me2})Ni(NO)$ and $(Tse^{Mes})Ni(NO)$ indicate that a multiply bonded resonance form such as $Ni{\equiv}N^{+}{-}O^{-}$ is a dominant contributor to the bonding scheme in this type of compounds, which exhibit quite short Ni–N bond distances [39].

The molecular structure of $(Bm^{Me})Ni(PPh_3)(NO)$ (Fig. 2) was also determined using a single crystal obtained at room temperature by slow diffusion of pentane into a THF solution of the complex, and selected bond lengths and angles are listed in Table 3. It is the first structurally characterized transition metal nitrosyl complex bearing a Bm^R ligand and only the second having a $[NiS_2PN]$ core, following the cyclopentylxanthate derivative $(PPh_3)Ni(S_2COC_5H_9)(NO)$ [29]. The geometry of the complex can be best described as trigonal pyramidal, with the two thione sulfurs of the Bm^{Me} ligand and a bent NO group [Ni–N–O = 149.6(2)°] that is tilted towards the phosphine making up the base of the pyramid. This spatial arrangement, unprecedented in nickel nitrosyl chemistry, is facilitated by the unique spatial disposition of the Bm^{Me} ligand, which forms an eight-membered ring in an "extended boat" conformation, and the presence of a weak intramolecular Ni···H–B interaction trans to the apical triphenylphosphine ligand. Although $(Bm^{Me})Ni(PPh_3)(NO)$ could be alternatively regarded as a five-coordinate complex displaying a trigonal bipyramidal geometry, we tend to favor the preceding description given the electronic saturation of the metal center (i.e., an 18-electron count) and the ensuing weakness of the Ni···H–B interaction. In this regard, the latter is characterized by a Ni···H separation [2.51(3) Å] that is considerably longer than those previously observed for such interactions, in the range 1.47–2.15 Å [35,36,47–56].

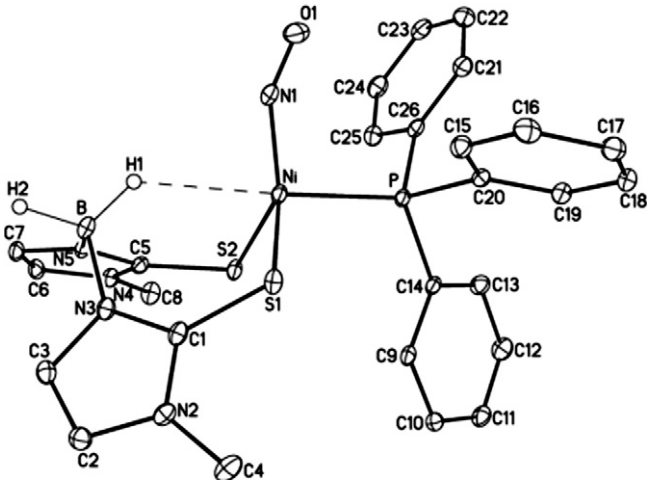


Fig. 2. Molecular structure of $(Bm^{Me})Ni(PPh_3)(NO)$.

Table 3
Selected bond lengths (Å) and bond angles (°) for $(Bm^{Me})Ni(PPh_3)(NO)$

Bond lengths	
Ni–P	2.2260(6)
Ni–S(1)	2.3225(7)
Ni–S(2)	2.3145(7)
Ni···H(1)	2.51(3)
Ni–N(1)	1.6892(19)
N(1)–O(1)	1.170(3)
Bond angles	
S(1)–Ni–S(2)	102.87(2)
N(1)–Ni–S(1)	125.38(7)
N(1)–Ni–S(2)	124.16(7)
S(1)–Ni–P	103.87(2)
S(2)–Ni–P	96.54(3)
N(1)–Ni–P	97.21(6)
S(1)–Ni···H(1)	78.1(6)
S(2)–Ni···H(1)	85.2(6)
P–Ni···H(1)	177.0(6)
N(1)–Ni···H(1)	79.7(6)
Ni–N(1)–O(1)	149.64(17)

A number of metrical parameters suggest that the trigonal pyramidal structure of $(Bm^{Me})Ni(PPh_3)(NO)$ is slightly distorted towards a tetrahedral geometry. This include the observation of moderately obtuse P–Ni–X angles (average = 99.2°) and a sum of angles around the nickel center in the basal plane (352.4°) that is less than a full circle. In the same vein, the nickel atom is located ca. 0.5 Å above the plane defined by S(1), S(2) and N(1), and the calculated four-coordinate geometry index τ_4 recently introduced by Houser [57] (0.78) is somewhat lower than the value corresponding to a perfect trigonal pyramid (0.85). The Ni–S bond distances in $(Bm^{Me})Ni(PPh_3)(NO)$, 2.315(1) and 2.323(1) Å, are virtually identical to those in $(Tm^{p\text{-}Tol})$-Ni(NO) and the Ni–N and N–O bond lengths [1.689(2) and 1.170(3) Å, respectively] are marginally longer but still within the ranges mentioned above for such bonds in four-coordinate nickel nitrosyl complexes.

3. Conclusions

The first bis- and tris(mercaptoimidazolyl)borate nickel nitrosyl complexes have been readily prepared and fully characterized. The observation of fairly low ν(NO) stretching frequencies in their IR spectra provides evidence that the Bm^R and Tm^R ligands are strongly electron-donating tripodal $[S_3]$ ligands. Whereas $(Tm^{p\text{-}Tol})Ni(NO)$ displays the expected slightly distorted tetrahedral geometry and features a linear nitrosyl ligand, $(Bm^{Me})Ni(PPh_3)(NO)$ constitutes the first trigonal pyramidal nickel nitrosyl complex to be structurally characterized. The reactivity of these complexes towards thiols and thiolates, aimed at the generation of *S*-nitrosothiols [58,59], will be investigated in due course.

4. Experimental

4.1. General considerations

All reactions were performed under aerobic conditions unless otherwise noted, solvents were purified and degassed by standard procedures, and all commercially available reagents were used as received. Whereas $Na(Bm^R)$ ($R = Me$, Bu^t) [60] and $Na(Tm^R)$ ($R = Bu^t$, *p*-Tol) [61,62] were prepared as reported, the nickel nitrosyl complex $Ni(PPh_3)_2(NO)Br$ was synthesized by a combination of literature procedures [10,63], as described below. ^1H and ^{13}C NMR spectra were obtained on Varian Gemini (300 MHz) or JEOL ECA-500 (500 MHz) FT spectrometers. Chemical shifts are reported in ppm relative to $SiMe_4$ ($\delta = 0$ ppm) and were referenced internally with respect to the solvent resonances (^1H: δ 2.49 for DMSO-d_5, 7.15 for C_6D_5H, 7.24 for $CHCl_3$; ^{13}C: δ 39.5 for DMSO-d_6, 77.0 for $CDCl_3$, 128.0 for C_6D_6); coupling constants are given in hertz (Hz). IR spectra were recorded from KBr pellets on a Thermo Mattson Satellite 3000 FT-IR spectrophotometer and are reported in cm^{-1}; relative intensities of the absorptions are indicated in parentheses (vs = very strong, s = strong, m = medium, w = weak). Elemental analyses were determined by Atlantic Microlab, Inc. (Norcross, GA).

4.2. Synthesis of $Ni(PPh_3)_2(NO)Br$

Tetrahydrofuran (20 mL) was added to a 100-mL round-bottom flask containing $Ni(PPh_3)_2Br_2$ (1.00 g, 1.346 mmol), triphenylphosphine (0.36 g, 1.373 mmol), and $NaNO_2$ (1.60 g, 23.188 mmol), and the resulting purple suspension was stirred and refluxed under argon for 35 min. The suspension was allowed to cool to room temperature, filtered, and the solvent was removed under reduced pressure from the filtrate to give a purple solid, which was washed with methanol (15 mL) and dried *in vacuo* for 18 h (0.676 g, 73%). IR data: 1733 (vs) [ν_{NO}].

4.3. Synthesis of $(Bm^{Me})Ni(PPh_3)(NO)$

Methanol (5 mL) was added to a 4-dram glass vial containing a mixture of $Ni(PPh_3)_2(NO)Br$ (1.092 g, 1.575 mmol) and $Na(Bm^{Me})$ (0.417 g, 1.591 mmol), resulting in the formation of a purple suspension and, within minutes, a slate green solid suspended in a grey-green solution. After stirring the suspension for 3 h, the product was isolated by filtration and dried *in vacuo* for 18 h (0.740 g, 80%). Mp = 147–149 °C (dec.). NMR data (in C_6D_6): ^1H δ 2.79 (s, 6H, CH_3), 4.60 (br s, 2H, BH_2), 5.63 (d, $^3J_{H-H} = 2.0$, 2H, imidazole *H*), 6.49 (d, $^3J_{H-H} = 2.0$, 2H, imidazole *H*), 7.03 (m, 9H, C_6H_5), 7.56 (m, 6H, C_6H_5); ^{13}C δ 34.3 (q, $^1J_{C-H} = 140$, 2C, CH_3), 118.7 (dd, $^1J_{C-H} = 195$, $^2J_{C-H} = 13$, 2C, imidazole *C*), 122.1 (d, $^1J_{C-H} = 194$, 2C, imidazole *C*), 128.7 (dd, $^1J_{C-H} = 163$, $^3J_{P-C} = 8$, 6C, C_m in C_6H_5), 129.4 (d, $^1J_{C-H} = 163$, 3C, C_p in C_6H_5), 134.4 (dd, $^1J_{C-H} = 160$, $^2J_{P-C} = 16$, 6C, C_o in C_6H_5), 160.4 (s, 2C, C=S), C_{ipso} not observed. IR data: 2918 (w), 2849 (w), 2475 (m), 2396 (m), 2359 (m), 1688 (vs) [ν_{NO}], 1558 (s), 1479 (w), 1456 (m), 1434 (m), 1413 (m), 1381 (s), 1186 (m), 1164 (w), 1123 (m), 1095 (m), 747 (w), 725 (m), 696 (s), 520 (m), 508 (w). *Anal.* Calc. for $C_{26}H_{27}BN_5NiOPS_2$: C, 52.9; H, 4.6; N, 11.9. Found: C, 53.3; H, 4.7; N, 10.9%.

4.4. Synthesis of $(Bm^{tBu})Ni(PPh_3)(NO)$

Under a nitrogen atmosphere, tetrahydrofuran (5 mL) was added to a 4-dram glass vial containing a mixture of $Ni(PPh_3)_2(NO)Br$ (0.202 g, 0.291 mmol) and $Na(Bm^{tBu})$ (0.100 g, 0.291 mmol), resulting in the formation of a purple suspension and, within minutes, a deep blue solution. After stirring for 3 h, the solution was concentrated to ca. 1 mL and addition of pentane (ca. 3 mL) lead to the separation of the product as a dark indigo solid, which was isolated by decantation and dried *in vacuo* for 16 h (0.125 g, 64%). Mp = 121–123 °C (dec.). NMR data (in $CDCl_3$): ^1H δ 1.64 [s, 18H, $C(CH_3)_3$], 6.59 (s, 2H, imidazole *H*), 6.71 (s, 2H, imidazole *H*), 6.90–7.40 (m, 15H, C_6H_5); ^{13}C δ 28.9 [q, $^1J_{C-H} = 126$, 6C, $C(CH_3)_3$], 58.9 [s, 2C, $C(CH_3)_3$], 117.1 (dd, $^1J_{C-H} = 194$, $^2J_{C-H} = 14$, 2C, imidazole *C*), 121.2 (d, $^1J_{C-H} = 193$, 2C, imidazole *C*), 128.7 (d, $^1J_{C-H} = 160$, 6C, C_m in PPh_3), 130.2 (d, $^1J_{C-H} = 154$, 3C, C_p in PPh_3), 132.4 (s, 3C, C_{ipso} in PPh_3), 134.3 (d, $^1J_{C-H} = 159$, 6C, C_o in PPh_3), 158.7 (s, 2C, C=S). IR data: 2974 (m), 2918 (m), 1728 (vs) [ν_{NO}], 1567 (m), 1480 (s), 1434 (s), 1366 (s), 1314 (m), 1237 (m), 1095 (s), 745 (s), 694 (vs), 521 (s). *Anal.* Calc. for $C_{32}H_{39}BN_5NiOPS_2$: C, 57.0; H, 5.8; N, 10.4. Found: C, 58.1; H, 5.9; N, 7.9%. Repeated attempts to obtain a better elemental analysis for this compound have not been successful.

4.5. Synthesis of $(Tm^{tBu})Ni(NO)$

In a Schlenk tube under an atmosphere of argon, a purple stirred suspension of $Ni(PPh_3)_2(NO)Br$ (0.399 g, 0.575 mmol) in methanol (15 mL) was treated dropwise with a solution of $Na(Tm^{tBu})$ (0.288 g, 0.575 mmol) in the same solvent (25 mL), resulting in the formation of a turquoise microcrystalline solid suspended in a blue solution. After stirring for 30 min, the suspension was concentrated under reduced pressure to ca. 5 mL and the product was isolated by filtration and dried *in vacuo* for 1 h (0.156 g, 48%). Mp = 78–79 °C (dec.). ^1H NMR data (in DMSO-d_6): δ 1.92 [s, 27H, $C(CH_3)_3$], 6.61 (s, 3H, imidazole *H*), 7.11 (s, 3H, imidazole *H*), B*H* not observed; ^{13}C NMR data (in $CDCl_3$): δ 29.1 [q, $^1J_{C-H} = 127$, 9C, $C(CH_3)_3$], 59.2 [s, 3C, $C(CH_3)_3$], 115.3 [dd, $^1J_{C-H} = 194$, $^2J_{C-H} = 12$, 3C, imidazole *C*], 122.3 [dd, $^1J_{C-H} = 194$, $^2J_{C-H} = 6$, 3C, imidazole *C*], 159.2 (s, 3C, C=S). IR data: 3206 (w), 3135 (w), 2965 (m), 2916 (w), 2387 (w), 2297 (w), 2233 (w), 1741 (vs) [ν_{NO}], 1565 (m), 1483 (w), 1418 (m), 1398 (m), 1361 (vs), 1302 (m), 1260 (w), 1228 (m), 1198 (s), 1176 (s), 1132 (w), 1071 (w), 1030 (w), 928 (w), 823 (w), 760

(m), 727 (m), 687 (m), 591 (w), 553 (w), 497 (w), 462 (w). *Anal.* Calc. for $C_{21}H_{34}BN_7NiOS_3$: C, 44.5; H, 6.1; N, 17.3. Found: C, 44.4; H, 6.2; N, 17.1%.

4.6. Synthesis of $(Tm^{p\text{-}Tol})Ni(NO)$

In a Schlenk tube under an atmosphere of argon, a purple stirred suspension of $(PPh_3)_2Ni(NO)Br$ (0.300 g, 0.433 mmol) in methanol (20 mL) was treated dropwise with a solution of $Na(Tm^{p\text{-}Tol})$ (0.261 g, 0.433 mmol) in the same solvent (20 mL), resulting in the formation of a greenish-blue microcrystalline solid suspended in a dark blue solution. After stirring for 30 min, the suspension was concentrated under reduced pressure to ca. 5 mL and the spectroscopically pure product was isolated by filtration and dried *in vacuo* for 1 h (0.115 g, 40%). Mp = 70–71 °C (dec.). NMR data (in DMSO-d_6): ^{1}H δ 2.39 (s, 9H, CH_3), 6.97 (s, 3H, imidazole *H*), 7.35 (s, 3H, imidazole *H*), 7.37 (d, $^3J_{H-H} = 8.1$, 6H, H_o or H_m), 7.57 (d, $^3J_{H-H} = 8.1$, 6H, H_o or H_m), B*H* not observed; ^{13}C δ 20.7 (q, $^1J_{C-H} = 125$, 3C, CH_3), 120.6 (d, $^1J_{C-H} = 199$, 3C, imidazole *C*), 124.4 (d, $^1J_{C-H} = 199$, 3C, imidazole *C*), 126.5 (d, $^1J_{C-H} = 162$, 6C, C_o or C_m), 129.4 (d, $^1J_{C-H} = 159$, 6C, C_o or C_m), 135.4 (s, 3C, C_{ipso} or C_p), 138.0 (s, 3C, C_{ipso} or C_p), 158.7 (s, 3C, C=S). IR data: 2919 (w), 2850 (w), 2413 (w), 2368 (w), 2343 (w), 1752 (vs) [ν_{NO}], 1513 (m), 1476 (w), 1428 (m), 1362 (s), 1271 (m), 1192 (s), 1093 (w), 1022 (w), 821 (m), 742 (m), 695 (m). *Anal.* Calc. for $C_{30}H_{28}BN_7NiOS_3$: C, 53.9; H, 4.2; N, 14.7. Found: C, 52.9; H, 4.4; N, 12.8%.

4.7. X-ray structure determinations

X-ray diffraction data were collected on a Bruker-AXS APEX CCD diffractometer using Mo Kα radiation ($\lambda = 0.71073$ Å). A summary of crystal data collection and refinement parameters for $(Bm^{Me})Ni(PPh_3)(NO)$ and $(Tm^{p\text{-}Tol})Ni(NO)$ is presented in Table 4. Crystals were selected and mounted on glass fibers or plastic loops with viscous oil and cooled to the data collection temperature. All data sets were treated with SADABS absorption corrections. Unit cell parameters were determined by sampling three different sections of the Ewald sphere. No symmetry higher than triclinic was observed in the diffraction data and structural solution in the centrosymmetric space group option, $P\bar{1}$, yielded chemically reasonable and computationally stable results of refinement for $(Bm^{Me})Ni(PPh_3)(NO)$. The systematic absences in the diffraction data were uniquely consistent for the reported space group $P2_1/c$ for $(Tm^{p\text{-}Tol})Ni(NO)$. All non-hydrogen atoms were refined with anisotropic displacement parameters. The hydrogen atoms on the boron atoms were located from the difference map and refined with isotropic parameters constrained as $0.20U_{eq}$ of the boron atom. All other hydrogen atoms were treated as idealized contributions. Structure factors are contained in the SHELXTL (version 6.12) program library [64].

Table 4
Crystallographic data for $(Tm^{p\text{-}Tol})Ni(NO)$ and $(Bm^{Me})Ni(PPh_3)(NO)$

	$(Tm^{p\text{-}Tol})Ni(NO)$	$(Bm^{Me})Ni(PPh_3)(NO)$
Formula	$C_{30}H_{28}BN_7NiOS_3$	$C_{26}H_{27}BN_5NiOPS_2$
Formula weight	668.29	590.14
Crystal system	monoclinic	triclinic
Space group	$P2_1/c$ (no. 14)	$P\bar{1}$ (no. 2)
Temperature (K)	120(2)	120(2)
Unit cell dimensions		
a (Å)	19.196(9)	9.747(2)
b (Å)	10.047(5)	11.399(3)
c (Å)	17.976(8)	13.015(3)
α (°)	90	85.365(3)
β (°)	115.262(6)	89.817(3)
γ (°)	90	67.581(3)
V (Å^3)	3135(2)	1331.8(5)
Z	4	2
ρ_{calc} (g cm^{-3})	1.416	1.472
μ(Mo Kα) (mm^{-1})	0.855	0.976
θ_{max} (°)	28.20	28.05
Number of data	7171	5738
Number of parameters	394	342
R_1 ($I > 2\sigma(I)$)[a]	0.0502	0.0368
wR_2 ($I > 2\sigma(I)$)[a]	0.1233	0.0966

[a] $R_1 = \sum(|F_o| - |F_c|)/\sum|F_o|$; $wR_2 = \left\{\sum\left[w(F_o^2 - F_c^2)^2\right]/\sum[w(F_o^2)^2]\right\}^{1/2}$.

5. Supplementary material

CCDC 640731 and 640732 contain the supplementary crystallographic data (excluding structure factors) for $(Bm^{Me})Ni(PPh_3)(NO)$ and $(Tm^{p\text{-}Tol})Ni(NO)$. These data can be obtained free of charge via http://www.ccdc.cam.ac.uk/conts/retrieving.html, or from the Cambridge Crystallographic Data Centre, 12 Union Road, Cambridge CB2 1EZ, UK; fax: (+44) 1223-336-033; or e-mail: deposit@ccdc.cam.ac.uk.

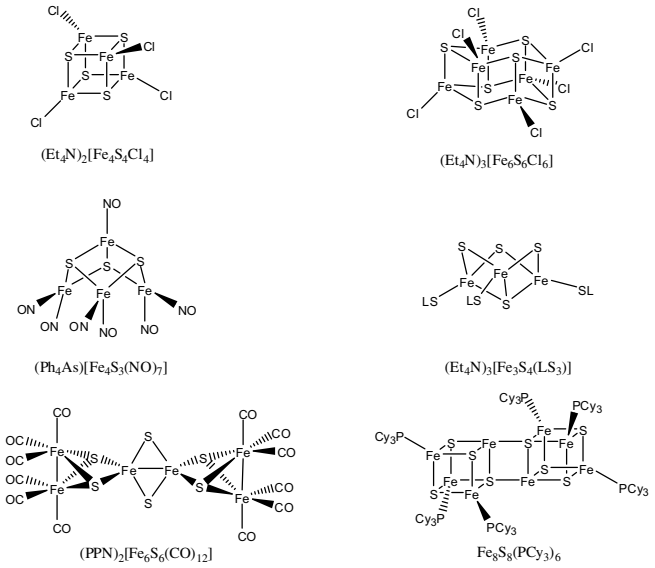
Acknowledgements

We thank the Camille and Henry Dreyfus Foundation, Inc. for a Henry Dreyfus Teacher-Scholar Award to D.R., the donors of the Petroleum Research Fund, administered by the American Chemical Society, and The University of North Carolina at Charlotte for support of this research. We also thank Prof. Marcetta Darensbourg (Texas A&M University) for helpful discussions and Prof. Gerard Parkin (Columbia University) for insightful advice and a preprint of Ref. [45].

References

[1] A.R. Butler, D.L.H. Williams, Chem. Soc. Rev. (1993) 233.
[2] L.J. Ignarro, Angew. Chem., Int. Ed. 38 (1999) 1882.
[3] S.P. Fricker, in: A. Sigel, H. Sigel (Eds.), Metal Ions and Their Complexes in Medication, Metal Ions in Biological Systems, vol. 41, Marcel Dekker, Inc., New York, 2004, p. 421 (Chapter 13).
[4] J.A. McCleverty, Chem. Rev. 104 (2004) 403.
[5] T.W. Hayton, P. Legzdins, W.B. Sharp, Chem. Rev. 102 (2002) 935.
[6] B.L. Westcott, J.H. Enemark, in: E.I. Solomon, A.B.P. Lever (Eds.), Applications and Case Studies, Inorganic Electronic Structure and

Spectroscopy, vol. II, John Wiley & Sons, Inc., New York, 2003, p. 403 (Chapter 7).
[7] D.-H. Lee, B. Mondal, K.D. Karlin, in: W.B. Tolman (Ed.), Activation of Small Molecules, Wiley-VCH, Weinheim, 2006, p. 43 (Chapter 2).
[8] J.A. Olabe, L.D. Slep, in: J.A. McCleverty, T.J. Meyer (Eds.), Comprehensive Coordination Chemistry II, vol. 1, Elsevier Ltd., San Diego, 2004, p. 603 (Chapter 1.31).
[9] Cambridge Structural Database (CSD) version 5.28 (November 2006 + January 2007 update) F.H. Allen, Acta Crystallogr., Sect. B 58 (2002) 380.
[10] R.D. Feltham, Inorg. Chem. 3 (1964) 116.
[11] S.A. Bhaduri, I. Bratt, B.F.G. Johnson, A. Khair, J.A. Segal, R. Walters, C. Zuccaro, J. Chem. Soc., Dalton Trans. (1981) 234.
[12] S. Bhaduri, K.R. Sarma, B.A. Narayan, Transition Met. Chem. 6 (1981) 206.
[13] A.F.M.M. Rahman, G. Salem, F.S. Stephens, S.B. Wild, Inorg. Chem. 29 (1990) 5225.
[14] O. Crichton, A.J. Rest, J. Chem. Soc., Dalton Trans. (1977) 986.
[15] L.X. Chen, M.K. Bowman, Z. Wang, P.A. Montano, J.R. Norris, J. Phys. Chem. 98 (1994) 9457.
[16] J.C. Green, C. Underwood, J. Organomet. Chem. 528 (1997) 91.
[17] D.V. Fomitchev, T.R. Furlani, P. Coppens, Inorg. Chem. 37 (1998) 1519.
[18] S. Otsuka, A. Nakamura, Y. Tatsuno, M. Miki, J. Am. Chem. Soc. 94 (1972) 3761.
[19] S. Bhaduri, B.F.G. Johnson, T.W. Matheson, J. Chem. Soc., Dalton Trans. (1977) 561.
[20] D.J. Darensbourg, T.J. Decuir, N.W. Stafford, J.B. Robertson, J.D. Draper, J.H. Reibenspies, A. Kathó, F. Joó, Inorg. Chem. 36 (1997) 4218.
[21] I.V. Kourkine, S.V. Maslennikov, R. Ditchfield, D.S. Glueck, G.P.A. Yap, L.M. Liable-Sands, A.L. Rheingold, Inorg. Chem. 35 (1996) 6708.
[22] G. Elbaze, F. Dahan, M. Dartiguenave, Y. Dartiguenave, Inorg. Chem. Acta 87 (1984) 91.
[23] J.H. Meiners, C.J. Rix, J.C. Clardy, J.G. Verkade, Inorg. Chem. 14 (1975) 705.
[24] J.O. Albright, F.L. Tanzella, J.G. Verkade, J. Coord. Chem. 6 (1976) 225.
[25] D. Berglund, D.W. Meek, Inorg. Chem. 11 (1972) 1493.
[26] M. Di Vaira, C.A. Ghilardi, L. Sacconi, Inorg. Chem. 15 (1976) 1555.
[27] C.E. MacBeth, J.C. Thomas, T.A. Betley, J.C. Peters, Inorg. Chem. 43 (2004) 4645.
[28] D.P. Kessissoglou, C.A. Tsipis, G.E. Manoussakis, Inorg. Nucl. Chem. Lett. 16 (1980) 245.
[29] I.A. Fanariotis, P.C. Christidis, P.J. Rentzeperis, Z. Kristallogr. 164 (1983) 109.
[30] T.B. Rauchfuss, S.D. Gammon, T.D. Weatherill, S.R. Wilson, New J. Chem. 12 (1988) 373.
[31] W.-F. Liaw, C.-Y. Chiang, G.-H. Lee, S.-M. Peng, C.-H. Lai, M.Y. Darensbourg, Inorg. Chem. 39 (2000) 480.
[32] P.J. Schebler, C.G. Riordan, I.A. Guzei, A.L. Rheingold, Inorg. Chem. 37 (1998) 4754.
[33] M. Garner, J. Reglinski, I. Cassidy, M.D. Spicer, A.R. Kennedy, Chem. Commun. (1996) 1975.
[34] C. Kimblin, T. Hascall, G. Parkin, Inorg. Chem. 36 (1997) 5680.
[35] H.M. Alvarez, M. Krawiec, B.T. Donovan-Merkert, M. Fouzi, D. Rabinovich, Inorg. Chem. 40 (2001) 5736.
[36] H.M. Alvarez, J.M. Tanski, D. Rabinovich, Polyhedron 23 (2004) 395.
[37] L.S. Maffett, K.L. Gunter, D. Rabinovich, Abstracts of Papers, 229th ACS National Meeting, San Diego, CA, United States, March 13–17, 2005, INOR 238.
[38] L.S. Maffett, K.L. Gunter, K.A. Kreisel, G.P.A. Yap, D. Rabinovich, Abstracts of Papers, 231st ACS National Meeting, Atlanta, GA, United States, March 26–30, 2006, INOR 598.
[39] V.K. Landry, K. Pang, S.M. Quan, G. Parkin, Dalton Trans. (2007) 820.
[40] J.H. Enemark, R.D. Feltham, Coord. Chem. Rev. 13 (1974) 339.
[41] M. Garner, M.-A. Lehmann, J. Reglinski, M.D. Spicer, Organometallics 20 (2001) 5233.
[42] L.A. Graham, A.R. Fout, K.R. Kuehne, J.L. White, B. Mookherji, F.M. Marks, G.P.A. Yap, L.N. Zakharov, A.L. Rheingold, D. Rabinovich, Dalton Trans. (2005) 171.
[43] M. Schwalbe, P.C. Andrikopoulos, D.R. Armstrong, J. Reglinski, M.D. Spicer, Eur. J. Inorg. Chem. (2007) 1351.
[44] J.H. Enemark, Inorg. Chem. 10 (1971) 1952.
[45] V.K. Landry, G. Parkin, Polyhedron 26 (2007) 4751.
[46] M. Garner, K. Lewinski, A. Pattek-Janczyk, J. Reglinski, B. Sieklucka, M.D. Spicer, M. Szaleniec, Dalton Trans. (2003) 1181.
[47] B.G. Segal, S.J. Lippard, Inorg. Chem. 16 (1977) 1623.
[48] T. Saito, M. Nakajima, A. Kobayashi, Y. Sasaki, J. Chem. Soc., Dalton Trans. (1978) 482.
[49] N. Carr, D.F. Mullica, E.L. Sappenfield, F.G.A. Stone, Inorg. Chem. 33 (1994) 1666.
[50] T.R. Belderraín, M. Paneque, E. Carmona, E. Gutiérrez-Puebla, M.A. Monge, C. Ruiz-Valero, Inorg. Chem. 41 (2002) 425.
[51] R. Cammi, M. Lanfranchi, L. Marchiò, C. Mora, C. Paiola, M.A. Pellinghelli, Inorg. Chem. 42 (2003) 1769.
[52] P.J. Desrochers, S. LeLievre, R.J. Johnson, B.T. Lamb, A.L. Phelps, A.W. Cordes, W. Gu, S.P. Cramer, Inorg. Chem. 42 (2003) 7945.
[53] M.G. Crestani, M. Muñoz-Hernández, A. Arévalo, A. Acosta-Ramírez, J.J. García, J. Am. Chem. Soc. 127 (2005) 18066.
[54] Y.-L. Wang, R. Cao, W.-H. Bi, Polyhedron 24 (2005) 585.
[55] M. Kandiah, G.S. McGrady, A. Decken, P. Sirsch, Inorg. Chem. 44 (2005) 8650.
[56] Y. Journaux, V. Lozan, J. Klingele, B. Kersting, Chem. Commun. (2006) 83.
[57] L. Yang, D.R. Powell, R.P. Houser, Dalton Trans. (2007) 955.
[58] B. Gaston, Biochim. Biophys. Acta 1411 (1999) 323.
[59] N. Hogg, Annu. Rev. Pharmacol. Toxicol. 42 (2002) 585.
[60] H.M. Alvarez, T.B. Tran, M.A. Richter, D.M. Alyounes, D. Rabinovich, Inorg. Chem. 42 (2003) 2149.
[61] J.L. White, J.M. Tanski, D. Rabinovich, J. Chem. Soc., Dalton Trans. (2002) 2987.
[62] S. Bakbak, V.K. Bhatia, C.D. Incarvito, A.L. Rheingold, D. Rabinovich, Polyhedron 20 (2001) 3343.
[63] A.W.G. Platt, J.F. Gibson, in: J.D. Woollins (Ed.), Inorganic Experiments, Wiley-VCH, Weinheim, 2003, p. 127.
[64] G.M. Sheldrick, Bruker/Siemens Area Detector Absorption Correction Program, Bruker AXS, Madison, WI, 2001.



Scheme 1. Examples of different arrangements of Fe/S clusters.

2. Experimental

All Reactions have been performed under a dinitrogen atmosphere in a glove box and standard shlenck line techniques. All solvents have been distilled and degassed, except of DMF that was not distilled.

$(NH_4)[Fe_4S_3(NO)_7]$ [24], $(PPN)_2[Fe_4(CO)_{13}]$ [25], Benzyl trisulfide (Bz_2S_3) [26], $Mo(CO)_3(MeCN)_3$ [27], $[Ni(MeCN)_6](BF_4)_2$ [28] were synthesized according to published procedures. $[Cu(MeCN)_4]PF_6$, $Fe(CO)_5$, SCl_2 and Bu_4NSH were purchased from commercial sources.

IR spectra were obtained on a Perkin–Elmer BX FT-IR spectrometer (mid-IR) and a Nicolet 740 FT-IR spectrometer (Far-IR) in KBr pellets. Mass Spectra were collected on a Micromass LCT Time-of-Flight mass spectrometer. Elemental analyses were performed by the Microanalytical Laboratory at the University of Michigan. Microbeam Electron Analysis was performed at The University of Michigan Electron Microbeam Analysis Laboratory (EMAL). and Cyclic Voltammetry experiments were carried out on a Glass Carbon working electrode and Ag/AgCl reference electrode with 0.1 M Bu_4NPF_6 supporting electrolyte on a EG&G Princeton Potentiostat/Galvanostat model 263 A. The reduction potentials are reported against a standard calomel electrode SCE.

2.1. Bis(Bis(triphenylphospine)iminium) hexasulfido-octairon-octanitrosyl, $(PPN)_2[Fe_8S_6(NO)_8)]$

An amount of $(NH_4)[Fe_4S_3(NO)_7]$ (0.50 g, 0.87 mmol) and $(PPN)_2[Fe_4(CO)_{13}]$ (2.17 g 1.30 mmol) were dissolved in 20 ml MeCN and allowed to stir for 24 h. The precipitate obtained by filtration was washed with 5 ml MeCN, dissolved in 15 ml DMF and the resulting solution layered with ca. 150 ml ether, affording 0.80 g of a black crystalline product.

Yield 0.41 mmol 94% of $(PPN)_2[Fe_8S_6(NO)_8]$ yield based on $[Fe_4S_3(NO)_7]^-$ as the only source of Fe. Elemental *Anal.* Calc. for $(PPN)_2[Fe_8S_6(NO)_8]\cdot DMF$ $C_{75}H_{67}N_{11}O_9P_4S_6Fe_8$: C, 44.39; H, 3.33; N, 7.59. Found: C, 44.75, H, 3.48, N, 7.36%. IR: 3054(w), 2690(m), 2928(m), 2868(w), 1684(vs)(ν_{N-O}), 1427(m), 1263(m), 1113(m), 797(w), 744(w), 723(m), 690(m), 550(m), 532(m), 526(w), 495(w). MS: (ESI −) 878.6 $Fe_8S_6(NO)_8^-$, 788.2 $Fe_8S_6(NO)_5^-$, 707.2 $Fe_6S_6(NO)_6^-$, 647.3 $Fe_6S_6(NO)_4^-$, 617.3 $Fe_6S_6(NO)_3^-$, 587.3 $Fe_6S_6(NO)_2^-$, 471.5 $Fe_4S_4(NO)_4^-$, 441.5 $Fe_4S_4(NO)_3^-$, 411.52 $Fe_4S_4(NO)_2^-$. MS: (ESI +) 537.8 (PPN^+). CV: (DMF solution, 0.017 M) $E_{1(rev)} = -482$ mV, $E_{2(rev)} = -616$ mV, $E_{3(rev)} = -1202$ mV, $E_{4(rev)} = -1295$ mV.

2.2. Bis(Bis(triphenylphospine)iminium) hexasulfido-hexairon-hexanitrosyl, $(PPN)_2[Fe_6S_6(NO)_6)]$

2.2.1. Method A (Scheme 2, Reaction 2)

An amount of $(PPN)[Fe_4S_3(NO)_7]$ (0.50 g, 0.47 mmol) and $(PPN)_2[Fe_4(CO)_{13}]$ (0.78 g, 0.47 mmol) were dissolved in 20 ml MeCN, and Bz_2S_3 (0.39 g, 1.40 mmol) was added. The resulting mixture was heated under reflux for 24 h. The precipitate formed was washed with 5 ml MeCN, dissolved in 15 ml DMF and layered with ca. 150 ml ether, affording 0.88 g of a black crystalline product. Yield 0.49 mmol, 79% of $(PPN)_2[Fe_6S_6(NO)_6]$, based on total Fe content.

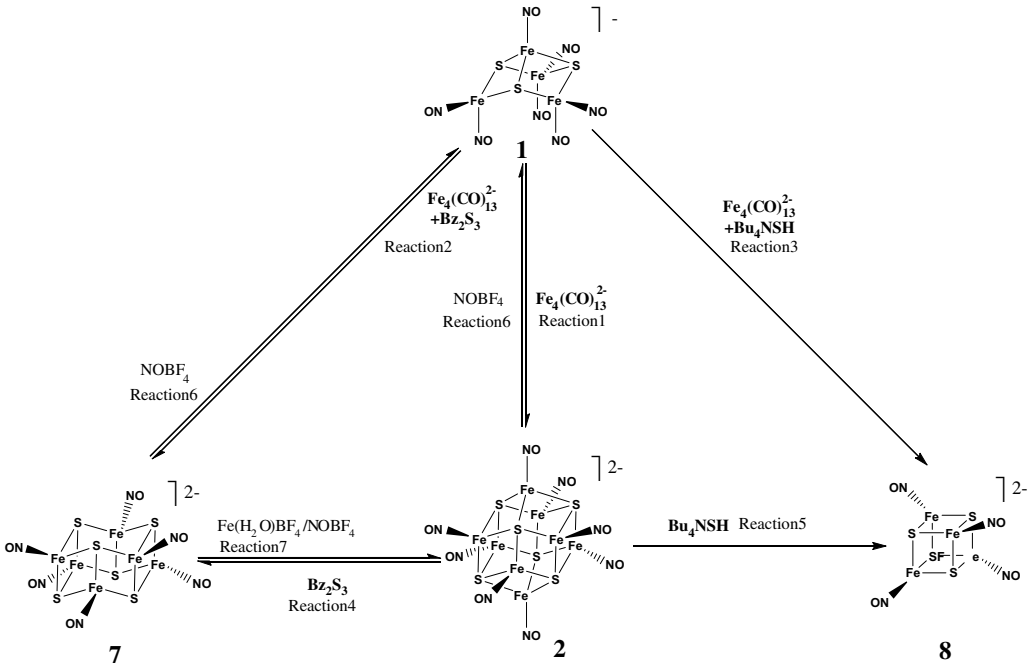
2.2.2. Method B (Scheme 2, Reaction 4)

An amount of $(PPN)_2[Fe_8S_6(NO)_8]$ (0.23 g, 0.12 mmol) was dissolved in 10 ml DMF and Bz_2S_3 (0.1 g, 0.36 mmol) was added and the solution stirred for 24 h. The solution was filtered and layered with ca. 100 ml ether, affording 0.18 g of crystalline product. Yield 0.10 mmol, 84% of $(PPN)_2[Fe_6S_6(NO)_6]$. Elemental *Anal.* Calc. for $(PPN)_2[Fe_6S_6(NO)_6]$, $C_{72}H_{60}N_8O_6P_4S_6Fe_6$: C, 48.46; H, 3.39; N, 6.28. Found: C, 47.90; H, 3.65; N, 7.33%. IR: 2690(m), 2928(m), 2868(w), 1679(vs) (ν_{N-O}), 1669(vs) (ν_{N-O}), 1435(m), 1262(m), 1116(m), 803(w), 743(w), 723(m), 692(m), 687(m), 546(m), 531(m), 523(w), 498(w). MS: (ESI −) *m/z* 1245.31 $(PPN)Fe_6S_6(NO)_6^-$, 707.26 $Fe_6S_6(NO)_6^-$, 647.27 $Fe_6S_6(NO)_4^-$, 617.28 $Fe_6S_6(NO)_3^-$, 587.28 $Fe_6S_6(NO)_2^-$, 557.31 $Fe_6S_6(NO)^-$, 471.49 $Fe_4S_4(NO)_4^-$, 441.49 $Fe_4S_4(NO)_3^-$, 411.52 $Fe_4S_4(NO)_2^-$ and several smaller molecular weight fragments were observed below 400. MS: (ESI +): 537.78 (PPN^+). CV: (DMF solution, 0.019 M) $E_{1(rev)} = -690$ mV, $E_{2(rev)} = -1521$ mV.

2.3. Bis(Bis(triphenylphospine)iminium) tetrasulfido-tetrairon-tetranitrosyl, $(PPN)_2[Fe_4S_4(NO)_4]$

2.3.1. Method A (Scheme 2, Reaction 3)

An amount of $(PPN)[Fe_4S_3(NO)_7]$ (0.50 g, 0.47 mmol) and $(PPN)_2[Fe_4(CO)_{13}]$ (1.17 g, 0.70 mmol) were dissolved in 20 ml MeCN, followed by the addition of Bu_4NSH (0.13 g, 0.47 mmol) in 5 ml MeCN and the mixture was heated under reflux for 24 h. After cooling at room temper-



Scheme 2. Schematic representations of the transformations of Fe/S/NO clusters discussed in this article.

ature the mixture was filtered, and the precipitate was washed with MeCN and extracted with ca. 15 ml DMF and layered with ca. 100 ml ether, affording 0.35 g of microcrystalline product. Yield 0.23 mmol 48.9% of $(PPN)_2$-$Fe_4S_4(NO)_4$ based on $Fe_4S_3(NO)_7^-$. Elemental *Anal.* Calc. for $(PPN)_2[Fe_4S_4(NO)_4]$ $C_{72}H_{60}N_6O_4P_4S_4Fe_4$: C, 55.39; H, 3.90; N, 5.43. Found: C, 51.49; H, 3.49; N, 5.96%.

2.3.2. Method B (Scheme 2, Reaction 5)

An amount of $(PPN)_2[Fe_8S_6(NO)_8]$ (0.20 g, 0.10 mmol) and Bu_4NSH (0.17 g, 0.62 mmol) were dissolved in 10 ml DMF and heated at 80 °C for 24 h. The resulting mixture was cooled at room temperature, filtered, and the solution was layered with ca. 100 ml ether, affording 0.22 g of microcrystalline product. Yield 0.14 mmol, 68.75% of $(PPN)_2Fe_4S_4(NO)_4$. Elemental *Anal.* Calc. for $(PPN)_2$-$[Fe_4S_4(NO)_4]$ $C_{72}H_{60}N_6O_4P_4S_4Fe_4$: C, 55.39; H, 3.90; N, 5.43. Found: C, 52.04; H, 4.10; N, 5.88%. IR:, 2960(m), 2928(m), 2868(w), 1652(vs) (ν_{N-O}), 1435(m), 1262(m), 1116(m), 803(w), 743(w), 723(m), 692(m), 687(m), 546(m), 531(m), 523(w), 498(w). MS: (ESI −) *m/z* 471.5 Fe_4S_4-$(NO)_4^-$, 441.5 $Fe_4S_4(NO)_3^-$, 411.5 $Fe_4S_4(NO)_2^-$ and several smaller molecular weight fragments were observed below 400. MS: (ESI +): 537.7 (PPN^+). CV: (DMF solution, 0.022 M) $E_{1(rev)} = -202$ mV, $E_{2(rev)} = -1279$ mV.

2.4. Bis(Bis(triphenylphospine)iminium) tetrasulfido-tetrairon-hexanitrosyl, $(PPN)_2[Fe_4S_4(NO)_6]$

An amount of $(NH_4)[Fe_4S_3(NO)_7]$ (0.20 g, 0.35 mmol) and $(PPN)_2[Fe_4(CO)_{13}]$ (0.87 g 0.52 mmol) were dissolved in 15 ml MeCN, the mixture was cooled at −20 °C and a solution of Bu_4NSH (0.05 g, 0.19 mmol) in 2 ml MeCN was added. The mixture was stirred for 8 h at −20 °C, filtered, and the precipitate was washed with MeCN and extracted with ca. 5 ml DMF and layered with ca. 50 ml ether, left for 2 days in the freezer, filtered again to remove any $(PPN)_2[Fe_4S_4(NO)_4]$ that formed and the filtrate layered with additional 100 ml ether, affording 0.08 g of green brown microcrystalline product. Yield 0.07 mmol, 14% of $(PPN)_2[Fe_4S_4(NO)_6]$ based on $[Fe_4S_3(NO)_7]^-$. Elemental *Anal.* Calc. for $(PPN)_2[Fe_4S_4(NO)_6]\cdot 2DMF$ $C_{78}H_{74}N_{10}$-$O_8P_4S_4Fe_4$: C, 53.38; H, 4.25; N, 7.98. Found: C, 53.92; H, 4.20; N, 7.33%. IR:, 2962(w), 2930(w), 2861(w), 1700(vs) (ν_{N-O}), 1668(vs) (ν_{N-O}), 1435(m), 1262(m), 1115(m), 840(w), 746(w), 723(m), 692(m), 687(m), 546(m), 531(m), 523(w), 496(w). MS: (ESI −): *m/z* 525.4 $Fe_4S_4(NO)_6^-$, 495.6 $Fe_4S_4(NO)_5^-$, 467.8 $Fe_4S_4(NO)_4^-$ 438.1 $Fe_4S_4(NO)_3^-$. MS: (ESI +): *m/z* 535.3 (PPN^+).

2.5. Bis(Bis(triphenylphospine)iminium) hexasulfido-hexairon-hexanitrosyl bis(tricarbonyl-molybdenum) $(PPN)_2[Mo_2Fe_6(NO)_6(CO)_6]$

An amount of $(PPN)_2[Fe_6S_6(NO)_6]$ (0.5 g, 0.28 mmol) and $Mo(CO)_3(MeCN)_3$ (0.17 g, 0.56 mmol) were dissolved in 15 ml dichloroethane and the solution stirred overnight. The mixture was filtered, and the filtrate layered with ca. 60 ml ether, affording 0.45 g of crystalline material. Yield 0.20 mmol, 71.3% of $(PPN)_2[(CO)_6Mo_2Fe_6S_6(NO)_6]$. Elemental *Anal.* Calc. for $(PPN)_2[(CO)_6Mo_2Fe_6S_6(NO)_6]$ $C_{78}H_{60}N_8O_{12}P_4S_6Fe_6Mo_2$: C, 43.68; H, 2.82; N, 5.22. Found: C, 43.48; H, 2.70; N, 5.16%. IR:, 3055(w), 2957(w), 2926(w), 2861(w), 1926(vs) (ν_{C-O}), 1877(ν_{C-O}), 1723(sh) (ν_{N-O}), 1695(vs) (ν_{N-O}), 1670(sh) (ν_{N-O}), 1437(m), 1384(m), 1258(m), 1113(m), 744(w), 723(m), 691(m), 690(m), 594(m) (ν_{Mo-C}), 548(m), 532(m), 498(w). CV: (DMF solution, 0.031 M) $E_{1(rev)} = -641$ mV, $E_{2(rev)} = -1247$ mV.

2.6. Hexasulfido-hexairon-hexanitrosyl bis(tripropylphosphino-copper) $(PPr_3)_2Cu_2Fe_6S_6(NO)_6$ and Hexasulfido-tetrairon-tetranitrosyl tetrakis(tripropylphosphino-copper) $(PPr_3)_4Cu_4Fe_4S_6(NO)_4$

In 5 ml MeCN, $[Cu(MeCN)_4]PF_6$ (0.21 g, 0.56 mmol) was dissolved and tripropyl phosphine (PPr_3) (0.12 ml, 0.60 mmol) was added dropwise and the solution stirred for 30 min. This solution was added dropwise to a dichloroethane solution (15 ml) containing $(PPN)_2[Fe_6S_6(NO)_6]$ (0.5 g, 0.28 mmol) and the mixture was stirred overnight. The mixture was filtered and the precipitate was washed with small amounts of ether, extracted with a THF/Ether 1:1 mixture and layered with hexanes affording 0.2 g of crystalline $(PPr_3)_2Cu_2Fe_6S_6(NO)_6$. The filtrate was taken to dryness and the residue stirred in ether affording a colored solution and a white powder identified as $PPNPF_6$. Following filtration, the ether solution was dried affording approx. 0.05 g of oily $(PPr_3)_4Cu_4Fe_4S_6(NO)_4$. Crystals suitable for X-ray diffraction were obtained by redissolving in ether and allowing for slow evaporation to occur.

$(PPr_3)_2Cu_2Fe_6S_6(NO)_6$ Elemental *Anal.* Calc. for $(PPr_3)_2Cu_2Fe_6S_6(NO)$ $C_{18}H_{42}N_6O_6P_2S_6Fe_6Cu_2$: C, 18.72; H, 3.67; N, 7.28. Found: C, 18.51; H, 3.63; N, 7.05%. Yield 0.17 mmol, 60% of $(PPr_3)_2Cu_2Fe_6S_6(NO)_6$ based on Fe. IR:, 2957(m), 2927(m), 2867(w), 1766(sh) (ν_{N-O}), 1750(sh) (ν_{N-O}), 1729(vs) (ν_{N-O}), 1660(sh) (ν_{N-O}), 1450(m), 1410(m), 1080(m), 1000(m), 851(w), 736(w). Microprobe analysis confirms the 2:6 ratio of Cu to Fe. CV: (THF solution, 0.029 M) $E_{1(rev)} = -169$ mV, $E_{2(rev)} = -1035$ mV, $E_{3(rev)} = -1667$ mV.

$(PPr_3)_4Cu_4Fe_4S_6(NO)_4$ Elemental *Anal.* Calc. for $(PPr_3)_4Cu_4Fe_4S_6(NO)_4$ $C_{36}H_{84}N_4O_4P_4S_6Fe_4Cu_4$: C, 30.22; H, 5.92; N, 3.92%. Found: C, 32.90; H, 6.35; N, 3.08%. Yield 0.04 mmol 28.5% $(PPr_3)_4Cu_4Fe_4S_6(NO)_4$ based on Cu. IR: 2957(m), 2928(m), 2869(w), 1724(vs) (ν_{N-O}), 1712(vs) (ν_{N-O}), 1457(m), 1080(m), 840(w). Microprobe analysis confirms the 1:1 ratio of Cu to Fe. CV: (THF solution, 0.011 M) $E_{1(rev)} = -153$ mV, $E_{2(rev)} = -1021$ mV, $E_{3(rev)} = -1537$ mV, $E_{4(irr)} = -2077$ mV.

2.7. Hexasulfido-hexairon-hexanitrosyl bis(tripropylphosphino-nickel) $(PPr_3)_2Ni_2Fe_6S_6(NO)_6$ and Hexasulfido-tetrairon-tetranitrosyl tris(tripropylphosphino-nickel) $(PPr_3)_3Ni_3Fe_4S_6(NO)_4$

In 5 ml MeCN, $[Ni(MeCN)_6](BF_4)_2$ (0.27 g, 0.56 mmol) was dissolved and PPr_3 (0.12 ml, 0.60 mmol) was added dropwise and the solution stirred for 30 min. This solution was added dropwise to a dichloroethane solution (15 ml) containing $(PPN)_2[Fe_6S_6(NO)_6]$ (0.5 g, 0.28 mmol) and the mixture was stirred overnight. The mixture was filtered and the precipitate was washed with small amounts of ether and extracted with a THF/Ether 1:1 mixture and layered with hexanes affording 0.15 g of crystalline $(PPr_3)_2Ni_2Fe_6S_6(NO)_6$. The filtrate was taken to dryness and the residue stirred in ether affording a colored solution and a white powder identified as $PPNBF_4$. The resulting ether solution was dried and washed with hexanes and ether and extracted with THF using silica gel as a filtration agent, affording approx. 0.04 g of oily $(PPr_3)_3Ni_3Fe_4S_6(NO)_4$. Crystals suitable for X-ray diffraction were obtained by recrystalization from THF/Hexanes.

$(PPr_3)_2Ni_2Fe_6S_6(NO)_6$ Elemental *Anal.* Calc. for $(PPr_3)_2Ni_2Fe_6S_6(NO)_6$ $C_{18}H_{42}N_6O_6P_2S_6Fe_6Ni_2$ C, 18.88; H, 3.70; N, 7.34. Found: C, 19.12; H, 3.77; N, 7.26%. Yield 0.13 mmol, 46% of $(PPr_3)_2Ni_2Fe_6S_6(NO)_6$ based on Fe. IR: 2958(m), 2927(m), 2868(w), 1763(s) (ν_{N-O}), 1745(sh) (ν_{N-O}), 1725(vs) (ν_{N-O}), 1663(sh) (ν_{N-O}), 1449(m), 1405(m), 12181(m), 1076(m), 1041(m), 851(m), 762(w), 731(m), 586(w), 435(w). Microprobe analysis confirms the 2:6 ratio of Ni to Fe. CV: (THF solution, 0.029 M) $E_{1(rev)} = -1$ mV, $E_{2(rev)} = -717$ mV, $E_{3(rev)} = -1431$ mV.

$(PPr_3)_3Ni_3Fe_4S_6(NO)_4$ Elemental *Anal.* Calc. for $(PPr_3)_3Ni_3Fe_4S_6(NO)_4C_{27}H_{63}N_4O_4P_3S_6Fe_4Ni_3$ C, 27.19; H, 5.32; N, 4.70. Found: C, 31.57; H, 5.91; N, 5.31%. Yield 0.033 mmol, 17.83% $(PPr_3)_3Ni_3Fe_4S_6(NO)_4$ based on Ni. IR: 2957(m), 2927(m), 2868(w), 1720(s) (ν_{N-O}), 1698(vs) (ν_{N-O}), 1679(s) (ν_{N-O}), 1452(m), 1404(m), 1221(m), 1073(m), 1038(m), 849(m), 724(m), 584(w), 440(w). Microprobe analysis confirms the 3:4 ratio of Ni to Fe.

2.8. Reactions of $(PPN)_2[Fe_6S_6(NO)_6]$ with Fe^{2+} or Fe^0

2.8.1. With $Fe(H_2O)_6(BF_4)_2$/ PPr_3 (Scheme 2, Reaction 7)

An amount of $(PPN)_2[Fe_6S_6(NO)_6]$ (0.2 g, 0.11 mmol) and $Fe(H_2O)_6(BF_4)_2$ (0.08 g, 0.24 mmol) were suspended in 20 ml of THF/MeCN 1:1 ratio, and PPr_3 (0.05 ml, 0.25 mmol) was added dropwise. The mixture was stirred overnight, filtered, and the solution layered with ether affording 0.12 g of crystalline material. The material was identified as $(PPN)_2[Fe_8S_6(NO)_8]$ by IR, MS and cyclic voltammetry, without any evidence suggesting the presence of a different species. Yield 0.06 mmol, 55% of $(PPN)_2[Fe_8S_6(NO)_8]$.

2.8.2. With $Fe(CO)_5$

An amount of $(PPN)_2[Fe_6S_6(NO)_6]$ (0.2 g, 0.11 mmol) was dissolved in a solution of 20 ml THF/MeCN 1:1 ratio and $Fe(CO)_5$ (0.03 ml, 0.23 mmol) was added dropwise. The mixture was stirred overnight, filtered, and the filtrate layered with ether affording 0.10 g of a microcrystalline material. The material was identified as $(PPN)_2[Fe_8S_6(NO)_8]$ by IR and MS. Yield 0.05 mmol, 46% of $(PPN)_2[Fe_8S_6(NO)_8]$.

2.9. Reactions of $(PPN)_2[Fe_8S_6(NO)_8]$ with oxidizing agents

2.9.1. With O_2

An amount of $(PPN)_2[Fe_8S_6(NO)_8]$ (0.2 g, 0.11 mmol) was dissolved in 10 ml DMF and O_2 was bubbled through

Table 1
Crystallographic and refinement table of the compounds presented herein

	$[Fe_4S_4(NO)_6]^{2-}$	$[(CO)_6Mo_2Fe_6S_6(NO)_6]^{2-}$	$(PPr_3)_2Cu_2Fe_6S_6(NO)_6$	$(PPr_3)_4Cu_4Fe_4S_6(NO)_4$	$(PPr_3)_2Ni_2Fe_6S_6(NO)_6$	$(PPr_3)_3Ni_3Fe_4S_6(NO)_4$
Color	brown	black	black	black	black	black
Habit	needle	needle	polyhedron	plate	polyhedron	block
Size (mm)	$0.60 \times 0.04 \times 0.04$	$044 \times 0.44 \times 0.34$	$0.44 \times 0.40 \times 036$	$0.30 \times 0.28 \times 0.05$	$0.38 \times 0.34 \times 030$	$0.40 \times 0.24 \times 0.16$
Formula	$C_{78}H_{74}Fe_4N_{10}O_8P_4S_4$	$C_{90}H_{86}Fe_6Mo_2N_{12}O_{16}P_4S_6$	$C_{18}H_{42}Cu_2Fe_6N_6O_6P_2S_6$	$C_{36}H_{84}Cu_4Fe_4N_4O_4P_4S_6$	$C_{18}H_{42}Fe_6Ni_2N_6O_6P_2S_6$	$C_{24}H_{63}Fe_4N_4Ni_3O_4P_3S_6$
Weight	1754.99	2434.93	1155.06	1430.87		1192.61
Crystal system	triclinic	triclinic	cubic	monoclinic	cubic	cubic
Space group	$P\bar{1}$	$P\bar{1}$	$Pa\bar{3}$	$P21/c$	$Pa\bar{3}$	$Pa\bar{3}$
Unit cell dimensions						
a (Å	10.951(6)	12.373(2)	15.9081(9)	11.299(3)	15.7773(10)	21.3741(18)
b (Å)	12.345(7)	14.386(3)	15.9081(9)	15.292(5)	15.7773(10)	21.3741(18)
c (Å)	28.632(15)	15.495(3)	15.9081(9)	17.404(5)	15.7773(10)	21.3741(18)
α (°)	90.021(9)	97.037(3)	90.00	90.00	90.00	90.00
β (°)	94.034(9)	91.936(3)	90.00	98.193(4)	90.00	90.00
γ (°)	90.127(9)	110.014(2)	90.00	90.00	90.00	90.00
Volume	3861(4)	2563.4(8)	4025.8(4)	2976.4(15)	3927.3(4)	9764.8(14)
Z	2	1	4	2	4	8
Temperature (K)	123(2)	123(2)	108(2)	123(2)	108(2)	108(2)
Absorption coefficient	0.991	1.311	3.563	2.700	3.528	2.675
$F(000)$	1808	1234	2320	1472	2312	4912
θ Range (°)	1.80–19.27	1.88–28.39	2.22–28.29	1.78–26.43	2.24–28.30	1.65–28.32
Reflections	32467	81490	82778	51829	85115	194707
Limiting indices	$-10 < h < 10$, $-11 < k < 11$, $-26 < l < 26$	$-16 < h < 16$, $-19 < k < 19$, $-20 < l < 20$	$-21 < h < 21$, $-21 < k < 21$, $-21 < l < 21$	$-14 < h < 14$, $-19 < k < 19$, $-21 < l < 21$	$-21 < h < 21$, $-20 < k < 20$, $-21 < l < 21$	$-28 < h < 28$, $-28 < k < 28$, $-28 < l < 28$
R_{int}	0.1486	0.0292	0.0332	0.0806	0.0383	0.0571
Data/restraints/ parameters	6428/0/978	12725/0/617	1671/0/72	6079/0/286	1636/0/71	4069/0/157
R_1, wR_2 $[I > 2\sigma(I)]$	0.0573, 0.1372	0.0396, 0.1050	0.0134, 0.0343	0.0738, 0.1753	0.0147, 0.0395	0.0199, 0.0413
R_1, wR_2 (all data)	0.1235, 0.1781	0.0456, 0.1098	0.0142, 0.0348	0.1290, 0.2281	0.0158, 0.0399	0.0345, 0.0497
Goodness-of-fit (F^2)	1.029	1.024	1.090	0.990	1.139	1.239

the solution for 5 min. the mixture was stirred for 1 h and filtered to remove a light brown powder and layered with ether affording 0.10 g of crystalline material. The material was identified as $[Fe(DMF)_6][Fe_6S_6(NO)_6]$ by IR, MS and Unit Cell determination. Yield 0.08 mmol, 75.64% of $[Fe(DMF)_6][Fe_6S_6(NO)_6]$.

2.9.2. With $[Fe(Cp)_2]PF_6$

An amount of $(PPN)_2[Fe_8S_6(NO)_8]$ (0.2 g, 0.11 mmol) was dissolved in 10 ml DMF and $[Fe(Cp)_2]PF_6$ (0.14 g, 0.42 mmol) was added. The mixture was stirred overnight, filtered, and the filtrate layered with ether affording 0.05 g of crystalline $[Fe(DMF)_6][Fe_6S_6(NO)_6]$ as identified by IR and MS. Yield 0.04 mmol, 37.8% of $[Fe(DMF)_6]$-$[Fe_6S_6(NO)_6]$.

2.9.3. With SCl_2

An amount of $(PPN)_2[Fe_8S_6(NO)_8]$ (0.2 g, 0.11 mmol) was dissolved in 20 ml dichloroethane and a 10% SCl_2 solution in dichloroethane (0.07 ml, 0.11 mmol) was added dropwise and the solution was stirred for 1 h. The mixture was filtered and the precipitate was dissolved in DMF and layered with ether affording a powder that was identified by IR as $[Fe(DMF)_6]$-$[Fe_6S_6(NO)_6]$.

The filtrate of this solution was layered with ca. 20 ml ether, filtered to remove a white powder of PPNCl, and then layered with additional 40ml ether to obtain 0.08 g light green needle shaped crystals.

The unit cell was identical to the known (PPN)-$[Fe(CO)_3(NO)]$ complex [29], and IR showed characteristic peaks at 1794 cm^{-1} (ν_{N-O}) and 350 cm^{-1} (ν_{Fe-Cl}). Elemental analysis confirmed that the crystals are (PPN)-$[FeCl_3(NO)]$, apparently isomorphous to the (PPN)$[Fe(CO)_3(NO)]$ complex. Yield 0.17 mmol, 80% of (PPN)$[FeCl_3(NO)]$.

Elemental *Anal.* Calc. for (PPN)$[FeCl_3(NO)]C_{36}H_{30}N_2OP_2Cl_3Fe$ C, 59.17; H, 4.14; N, 3.83. Found: C, 58.86; H, 3.99; N, 3.66%. IR:, 3052(w), 2917(w), 2848(w), 1794(vs) (ν_{N-O}), 1436(s), 1244(s), 1114(s), 998(w), 795(w), 749(m), 723(s), 692(s), 550(s), 533(m), 500(m), 350(s) (ν_{Fe-Cl}).

2.10. Crystallographic data

Diffraction data were collected on a Siemens SMART CCD-based X-ray diffractometer, equipped with a Mo Kα probe on a wavelength of 0.71073 Å. Space groups were determined on systematic absences and intensity statistics. Full Matrix least-squares refinement based on F^2 was performed. All non-hydrogen atoms were refined anisotropically, and hydrogen atoms were placed in ideal positions and refined as rigid atoms with individual isotropic thermal displacement parameters. The specific crystallographic data for each compound are presented in Table 1.

3. Results and discussion

The synthesis of the octanuclear iron sulfur nitrosyl cluster $(PPN)_2[Fe_8S_6(NO)_8]$ proceeds through the reaction of $(NH_4)[Fe_4S_3(NO)_7]$ with $(PPN)_2[Fe_4(CO)_{13}]$ in a 2:3 molar ratio affording $(PPN)_2[Fe_8S_6(NO)_8]$ in high yields. The byproducts of this reaction, that were isolated and verified by IR and MS are mainly (PPN)$[Fe(CO)_3(NO)]$ and a small amount of (PPN)$[Fe_4N(CO)_{12}]$. The reaction appears to proceed through the abstraction of nitrosyl ligands from $[Fe_4S_3(NO)_7]^-$ by the $[Fe_4(CO)_{13}]^{2-}$ cluster and the possible formation of an $[Fe_4S_3(NO)_4]^-$ intermediate which subsequently self couples to form the $[Fe_8S_6(NO)_8]^{2-}$ cluster. (PPN)$[Fe(CO)_3(NO)]$ seems to be the main product formed by the reaction of the $[Fe_4(CO)_{13}]^{2-}$cluster with NO^+. The generation of the $[Fe_4N(CO)_{12}]^-$ cluster also is possible considering the reported synthesis of this cluster by the reaction of $Fe_3(CO)_{12}$ with $[Fe(CO)_3(NO)]^-$ [30,31].

In the synthesis of $(PPN)_2[Fe_6S_6(NO)_6]$ (Reaction 2, Scheme 2), the yield of the Fe_6S_6 "prismane" is unreasonably high, assuming that $[Fe_4S_3(NO)_7]^-$ is the only source of Fe. It appears therefore that the $[Fe_4(CO)_{13}]^{2-}$ cluster also provides Fe in the formation of $(PPN)_2[Fe_6S_6(NO)_6]$. In addition, it is known that $[Fe(CO)_3(NO)]^-$ upon reaction with S^0 produces $[Fe_4S_4(NO)_4]^-$ [32] so the pathway to the formation of $(PPN)_2[Fe_6S_6(NO)_6]$ through reaction 2 may be more complicated than the initial formation of $(PPN)_2[Fe_8S_6(NO)_8]$ and further reaction with Bz_2S_3 as shown by reactions 1 and 4 (Scheme 2). The $[Fe_6S_6(NO)_6]^{2-}$ cluster has been synthesized previously with different counter ions but in lower yields [7].

The $[Fe_4S_4(NO)_4]^{2-}$ cluster has not been isolated in this oxidation level previously. The IR spectrum shows a NO stretching vibration at 1652 cm^{-1} which is lower when compared to the 1760 cm^{-1} and 1700 cm^{-1} reported for $Fe_4S_4(NO)_4$ and $[Fe_4S_4(NO)_4]^-$ respectively [32]. The lower frequency of the NO stretching vibration in $(PPN)_2[Fe_4S_4(NO)_4]$ is consistent with the expected increase in the Fe–NO backbonding in the dianionic $(PPN)_2[Fe_4S_4(NO)_4]$. Elemental analysis also is consistent with the $(PPN)_2[Fe_4S_4(NO)_4]$ formula, however we were not able to obtain a satisfactory crystal structure due to high distortion of the PPN^+ cations in the crystal lattice. Nevertheless, the presence of a $[Fe_4S_4(NO)_4]^{2-}$ cluster and two PPN^+ cations has been confirmed.

The synthesis of the $[Fe_4S_4(NO)_6]^{2-}$ (Fig. 1) and $[Fe_4S_4(NO)_4]^{2-}$ clusters from the Roussin anion is not unexpected. The reactions of $[Fe_4S_3(NO)_7]^-$ with SH^-, in polar solvents (L), may well lead in cluster fragmentation and generation of dimeric species such as $\{Fe_2S_2(NO)_3(L)\}^-$ and $\{Fe_2S_2(NO)_2(L)_2\}^-$. Coupling of these units can lead to the formation of the $[Fe_4S_4(NO)_6]^{2-}$ and $[Fe_4S_4(NO)_4]^{2-}$ clusters respectively. As in the case of all $[Fe_4S_3(NO)_7]^-$/$[Fe_4(CO)_{13}]^{2-}$ reactions, the main byproduct in the synthesis of either $[Fe_4S_4(NO)_4]^{2-}$ or $[Fe_4S_4(NO)_6]^{2-}$ is $[Fe(CO)_3(NO)]^-$. The apparent role of $[Fe_4(CO)_{13}]^{2-}$ as a

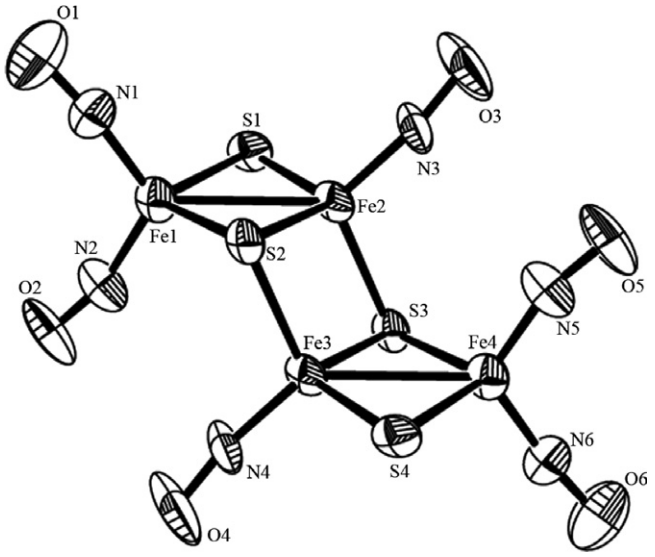


Fig. 1. Ortep diagram of $[Fe_4S_4(NO)_6]^{2-}$ with 50% probability ellipsoids.

NO abstracting reagent is affected by both time and temperature and this explains the formation and isolation of $[Fe_4S_4(NO)_6]^{2-}$ at low temperatures.

The formation of $Fe_4S_4(NO)_4$ from the reaction of $[Fe_4S_3(NO)_7]^-$ and elemental sulfur has been reported [32] and this cluster was studied several years ago, although the mechanism of this reaction is not clear. Based on experimental observations and theoretical calculations by Glidewell and Hoffmann [33,34] the formation of $Fe_4S_4(NO)_4$ from $[Fe_4S_3(NO)_7]^-$ could proceed through a mechanism of fragmentation and reassembly of the latter cluster.

The isolation of $(PPN)_2[Fe_4S_4(NO)_6]$ has been achieved by repeating the reaction that yields $(PPN)_2[Fe_4S_4(NO)_4]$ but at low temperatures. According to the formal oxidation levels, there is a two electron oxidation from $[Fe_4S_3(NO)_7]^-$ to $[Fe_4S_4(NO)_6]^{2-}$ and an additional two electron oxidation to $[Fe_4S_4(NO)_4]^{2-}$. The isolation of this edge fused double dimer can be envisioned as the coupling product of two $\{Fe_2S_2(NO)_3^-\}$ fragments while the cubane as the product of two $\{Fe_2S_2(NO)_2^-\}$ fragments.

The procedure reported here for the synthesis of $(PPN)_2[Fe_4S_4(NO)_6]$ is not an easily reproducible process and seems to be sensitive to time and temperature of crystallization. Both the hypothetical $\{Fe_2S_2(NO)_3(L)\}^-$ and $\{Fe_2S_2(NO)_2(L)\}^-$ fragments possibly involved in the formation of $[Fe_4S_4(NO)_6]^{2-}$ and $[Fe_4S_4(NO)_4]^{2-}$ respectively, may be preset at the same time in various amounts. Therefore isolation of $[Fe_4S_4(NO)_6]^{2-}$ or the more stable $[Fe_4S_4(NO)_4]^{2-}$ will depend on the exact conditions of the experiment, and such conditions are not easily reproduced/obtained. Although $[Fe_4S_4(NO)_6]^{2-}$ has been detected several times in mixtures obtained from this reaction, analytically pure crystalline material has only been obtained once thus far.

3.1. Transformations of $(PPN)_2[Fe_8S_6(NO)_8]$

The $(PPN)_2[Fe_8S_6(NO)_8]$ cluster, stable at high temperatures, upon oxidation transforms to the $[Fe_6S_6(NO)_6]^{2-}$ "prismane". This occurs using O_2, SCl_2 and $[Fe(Cp)_2]PF_6$. In all three cases it seems that there is loss of two {Fe(NO)} fragments rather than rearrangement of the clusters. In coordinating solvents, the main product isolated is $[Fe^{II}(L)_6][Fe_6S_6(NO)_6]$ (L = DMF, THF, MeCN). The $[Fe_6S_6(NO)_6]^{2-}$ anion is structurally related to the $[Fe_8S_6(NO)_8]^{2-}$ pentlandite. The former is obtained from the latter when two {Fe(NO)} moieties are removed from the body diagonal of the pentlandite cube. In addition to the $[Fe_6S_6(NO)_6]^{2-}$ prismane, a yellow brown powder also forms. In the case of the SCl_2 reaction this byproduct was identified and characterised as $(PPN)[FeCl_3(NO)]$ both analytically and spectroscopically (by the NO stretch at 1794 cm^{-1}, the Fe–Cl stretch at 350 cm^{-1} and characteristic PPN stretches in the 800–500 cm^{-1} region). The unit cell dimensions of this byproduct were nearly identical to those of the known $(PPN)[Fe(CO)_3(NO)]$ complex [29]. Although this particular complex has not been synthesized previously, its crystallographic structure determination and further characterizations were not of particular interest in this study and were not further pursued. The $[Fe(L)_6][Fe_6S_6(NO)_6]$ complex isolated has exactly the same infrared spectral pattern for the NO stretching vibrations as the pattern for the previously reported $[Fe(DMF)_6][Fe_6S_6(NO)_6]$ [7]. A counter-ion exchange of $[Fe(DMF)_6]^{n+}$ with PPN^+ gives $(PPN)_2[Fe_6S_6(NO)_6]$. The latter is verified by elemental analysis and confirms that the iron in the $[Fe(L)_6]^{n+}$ counter-ion is divalent ($n = 2$).

For the reaction of $(PPN)_2[Fe_8S_6(NO)_8]$ with eight equivalents of $NOBF_4$ the products isolated are $Fe(DMF)_6[Fe_6S_6(NO)_6]$, $(PPN)[Fe_4S_3(NO)_7]$ and $PPNBF_4$ suggesting that in order to form the more reduced $[Fe_4S_3(NO)_7]^-$ cluster some of the $[Fe_8S_6(NO)_8]^{2-}$ cluster has to be oxidized to produce the necessary electrons since NO^+ cannot act as a reducing agent.

In contrast, when gaseous NO is used both $[Fe_8S_6(NO)_8]^{2-}$ and $[Fe_6S_6(NO)_6]^{2-}$ produce $[Fe_4S_3(NO)_7]^-$ in nearly quantitative yields.

3.2. Reactivity of $(PPN)_2[Fe_6S_6(NO)_6]$

The cyclohexane-like Fe_3S_3 units of the $[Fe_6S_6]$ core can serve as ligands for two additional metal ions and form $[M_2Fe_6S_6]$ clusters, [19,35,36]. The latter were obtained in reactions carried out with coordinatively-unsaturated complexes containing Fe, Mo, Cu and Ni.

In the reaction of $(PPN)_2[Fe_6S_6(NO)_6]$ with $[Fe(H_2O)_6]^{2+}/PPr_3$, or $Fe(CO)_5$, the only product isolated was $[Fe_8S_6(NO)_8]^{2-}$. The formation of $[Fe_8S_6(NO)_8]^{2-}$ even at NO deficient conditions can be explained if fragmentation of the cluster to {Fe(NO)} units occurs. The later under reducing conditions form the $[Fe_8S_6(NO)_8]^{2-}$ preferentially.

In order to increase the yield of $[Fe_8S_6(NO)_8]^{2-}$ the reaction of $(PPN)_2[Fe_6S_6(NO)_6]$ with $[Fe(H_2O)_6]^{2+}$ was carried out in the presence of $NOBF_6$. The only products isolated were $(PPN)[Fe_4S_3(NO)_7]$ and $[Fe(DMF)_6][Fe_6S_6(NO)_6]$ suggesting that the formation of $[Fe_4S_3(NO)_7]^-$ is more favorable in the presence of NO^+.

As in the case of $(Et_4N)_2[Fe_6S_6Cl_6]$, [35] the reaction of $(PPN)_2[Fe_6S_6(NO)_6]$ with $Mo(CO)_3(MeCN)_3$ yields $(PPN)_2[(CO)_6Mo_2Fe_6S_6(NO)_6]$ (Fig. 2) even in molar ratios less than 1:1 suggesting that the $[MoFe_6S_6]$ core, if it forms at all, disproportionates to the $[Mo_2Fe_6S_6]$ and $[Fe_6S_6]$ clusters.

The reaction of $(PPN)_2[Fe_6S_6(NO)_6]$ with $[Cu(MeCN)_4]^+/PPr_3$ affords $(PPr_3)_2Cu_2Fe_6S_6(NO)_6$ (Fig. 3) as the main product, and in a lower yield the $(PPr_3)_4Cu_4Fe_4S_6(NO)_4$ (Fig. 4) cluster. Formation of the $(PPr_3)_4Cu_4Fe_4S_6(NO)_4$ cluster could be explained in terms of fragmentation of the $[Fe_6S_6(NO)_6]^{2-}$ cluster to smaller Fe/S/NO units (i.e. $\{Fe_2S_2(NO)_2\}$ units), The latter in the presence of $Cu(PR_3)$ form $(PR_3)CuS_2Fe(NO)$ units which couple to form the final product. In both cases the Fe_6Cu_2 and Fe_4Cu_4 clusters form due to the superior thermodynamic stability of the Cu–S bond relative to the Fe–S bond. Previously, we have reported on the substitution of Fe atoms by Cu atoms in Fe/S clusters [19,37].

These two products form regardless of the ratio of the Cu used, and their separation was achieved due to their slightly different solubilities. Similar reactions of $[Fe_6S_6(NO)_6]^{2-}$ with $[Ni(MeCN)_6]^{2+}/PPr_3$, give the neutral $(PPr_3)_2Ni_2Fe_6S_6(NO)_6$ (Fig. 5) cluster as the main product, but unlike the case of copper where the byproduct formed

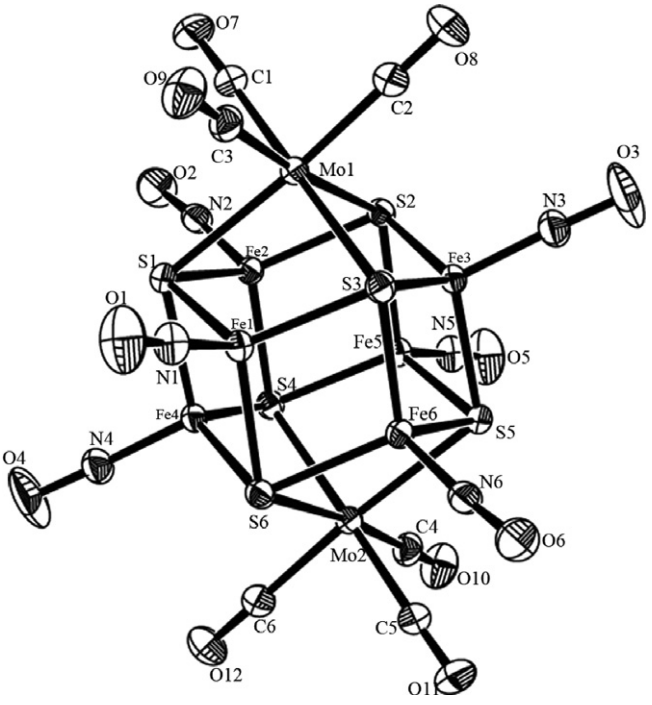


Fig. 2. Ortep diagram of $[(CO)_6Mo_2Fe_6S_6(NO)_6]^{2-}$ showing ellipsoids with 50% probability.

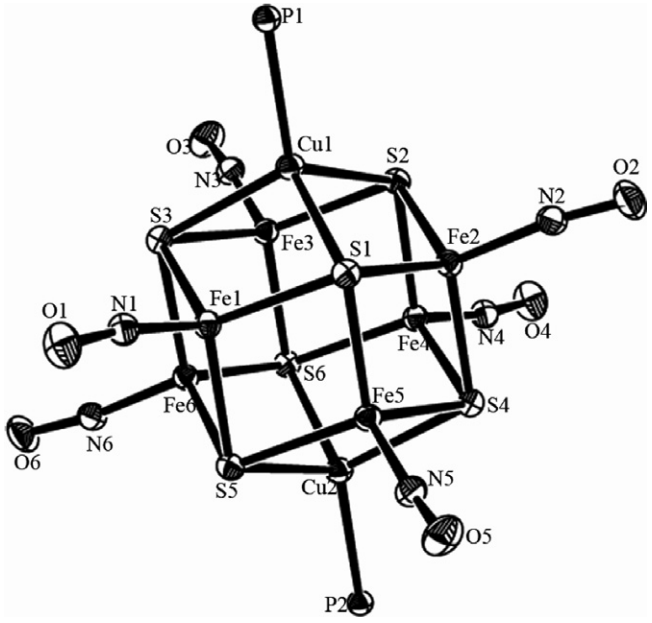


Fig. 3. Ortep diagram of $(PPr_3)_2Cu_2Fe_6S_6(NO)_6$ showing ellipsoids with 50% probability. The carbons of the phosphines have been omitted for clarity.

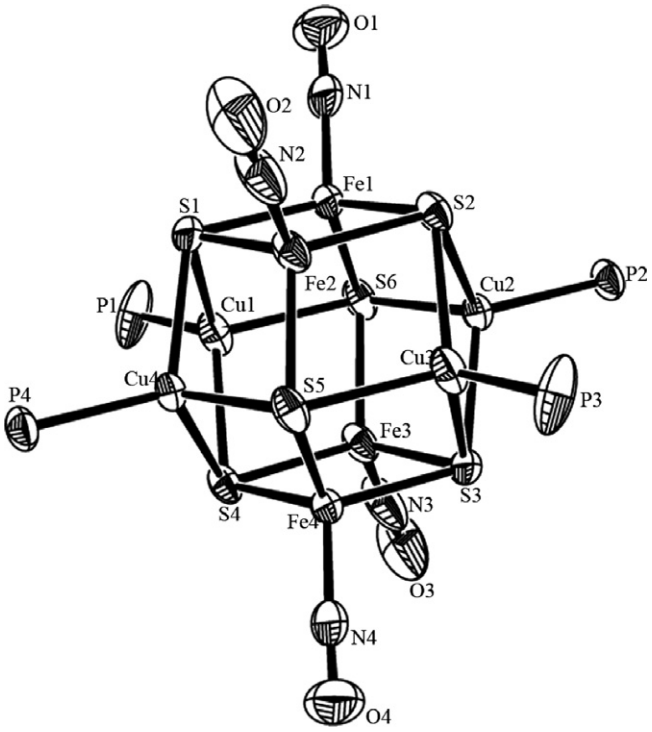


Fig. 4. Ortep diagram of $(PPr_3)_4Cu_4Fe_4S_6(NO)_4$ showing ellipsoids with 50% probability. The carbons of the phosphines have been omitted for clarity.

is $(PPr_3)_4Cu_4Fe_4S_6(NO)_4$, with nickel the other isolable byproduct is the unique Ni/Fe/S cluster $(PPr_3)_3Ni_3Fe_4S_6(NO)_4$ (Fig. 6). This cluster contains the ''voided–cubic'' M_7S_6 core which previously has been found in $(PPr_3)_4Fe_7S_6Cl_3$ [38], $Co_7S_6I_3(PEt_3)_4$ [39], and Co_7S_6-

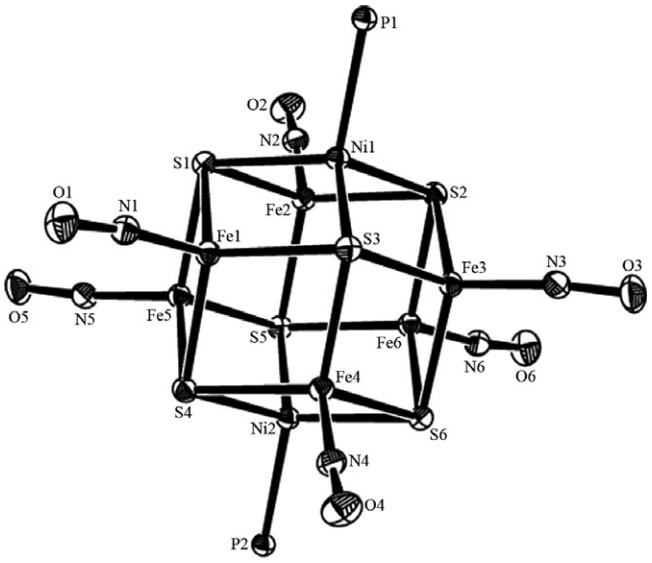


Fig. 5. Ortep diagram of $(PPr_3)_2Ni_2Fe_6S_6(NO)_6$ showing ellipsoids with 50% probability. The carbons of the phosphines have been omitted for clarity.

$X_3(PPh_3)_4$ (X=Cl$^-$ [23], Br$^-$ [40]) but not in mixed metal systems. The $(PPr_3)_3Ni_3Fe_4S_6(NO)_4$ is the only byproduct isolated from a mixture that appears to contain three compounds. The separation of these species is relatively difficult as their solubilities are relatively similar, with $(PPr_3)_3Ni_3Fe_4S_6(NO)_4$ being less soluble in ether and hexanes than the other two species. Unfortunately we ware not able to obtain any crystals from the other two byproducts as they seem relatively unstable. Nevertheless these two species also contain phosphine and nitrosyls as shown by infrared spectroscopy, with the main N–O stretching peak at 1696 cm^{-1} for $(PPr_3)_3Ni_3Fe_4S_6(NO)_4$ (THF fraction), 1739 cm^{-1} (Ether fraction) and 1711 cm^{-1} (Hexanes Fraction). The IR spectra of the Ether fraction is very similar to the pattern of $(PPr_3)_4Cu_4Fe_4(NO)_4$ and since the $[Ni_4Fe_4S_4]$ core is known for $(PPr_3)_4Ni_4Fe_4S_4Cl_4$ [19] and $(PPh_2Me)_4Ni_4Fe_4S_4I_4$ [20], we expect the nitrosyl cluster to have a similar structure.

3.3. Structures

Crystallographic determination of $(PPN)_2[Fe_4S_4(NO)_6]$ reveals a Fe_4S_4 core that can be described as the fusion of two $[(NO)_2Fe(\mu\text{–}S)_2Fe(NO)]^-$ dimers to give a *nido* $[Fe_4S_4(NO)_6]^{2-}$ cluster (Fig. 1) with an inter-dimer Fe–Fe distance of 2.77 Å and an average intra-dimer Fe–Fe distance of 2.68 Å. The Fe–NO distances are almost equivalent at 1.66 Å (1.65–1.67 Å) with average Fe–N–O bond angles of 167° within a range of 163°–171°.

In the $(PPN)_2[(CO)_6Mo_2Fe_6S_6(NO)_6]$ cluster, the M_8S_6 cuboctahedral core exhibits average Mo–Fe and Fe–Fe distances are at 2.89 Å and 2.69 Å, respectively, and Mo–S and Fe–S distances at 2.58 Å and 2.25 Å, respectively. As expected, by comparison to $[Fe_8S_6(NO)_8]^{2-}$, the Mo_2Fe_6 cluster is elongated along the three-fold axis that contains the Mo atoms (Fig. 2). The cluster topology is identical to the MoFe/S/Cl analogues $(Et_4N)_3[(CO)_6Mo_2Fe_6S_6Cl_6]$ and $(Et_4N)_4[(CO)_6Mo_2Fe_6S_6Cl_6]$ [35].

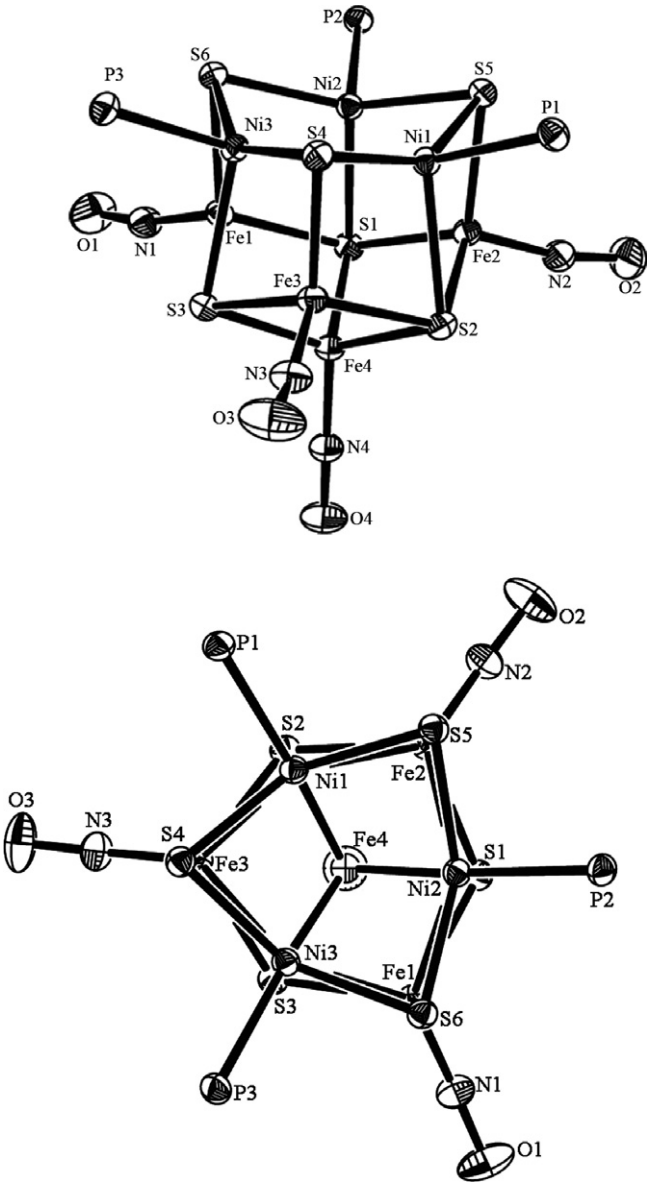


Fig. 6. Ortep diagram of $(PPr_3)_3Ni_3Fe_4S_6(NO)_4$ (side and top view) showing ellipsoids with 50% probability. The carbons of the phosphines have been omitted for clarity.

Both of the Cu/Fe/S/NO structures exhibit the typical cubic arrangement of metals capped by sulfur atoms and have structures similar to those of their Cu/Fe/S/Cl analogues $(Bu_4N)_2[(PPr_3)_2Cu_2Fe_6S_6Cl_6]$ and $(PPr_3)_4Cu_4Fe_4S_6Cl_6$ [19]. In the case of $(PPr_3)_2Cu_2Fe_6S_6(NO)_6$ (Fig. 3) the average Cu–Fe and Fe–Fe distances are 2.70 Å and 2.65 Å and the Cu–S and Fe–S bonds are found at 2.38 Å and 2.24 Å. In $(PPr_3)_4Cu_4Fe_4S_6(NO)_4$ (Fig. 4) the metals in the Cu_4Fe_4 core are arranged in D_{2h} geometry (mutually perpendicular Fe_4 and Cu_4 squares) with average metal–metal distances of 2.74 Å and average Cu–S and Fe–S bond distances of 2.36 Å and 2.26 Å respectively.

The neutral $(PPr_3)_2Ni_2Fe_6S_6(NO)_6$ (Fig. 5) possesses the same core structure as the copper analogue, but is slightly more compact with average Ni–S and Fe–S distances of 2.25 Å and 2.26Å, respectively, and Ni–Fe and Fe–Fe distances at 2.59Å and 2.65Å, respectively. A similar Ni_2Fe_6 core is also found in the Ni/Fe/S/halide analogues, $(Et_4N)_2[(PPr_3)_2Ni_2Fe_6S_6Cl_6]$ [19] and $[PhCH_2NEt_3]_2[(Ph_2MeP)_2Ni_2Fe_6S_6I_6]$ [20].

The $(PPr_3)_3Ni_3Fe_4S_6(NO)_4$ (Fig. 6) cluster can be viewed as a $Fe_4S_3(NO)_4$ unit coupled with a nearly trigonal planar $Ni_3S_3(PPr_3)_3$ unit. In this structure the Iron atoms show a tetrahedral coordination geometry while the Nickel atoms show a trigonal pyramidal geometry. The Fe–Fe distances in the equatorial triangle (defined by Fe1, Fe2 and Fe3) have a mean value of 3.82 Å. These irons are located 2.74 Å from the capping iron. The Ni–Fe distances and Ni–Ni distances are at found at 2.61 and 2.79 Å, respectively, and the Fe–S and Ni–S distances are 2.23 Å and 2.25 Å, respectively.

As shown in Table 2, the M/Fe/S (M=Mo,Cu,Ni) clusters reported in this paper have shorter metal–metal and iron–sulfur distances in a more compact overall structure than their corresponding analogues with halogens. An exception is the $(PPr_3)_3Ni_3Fe_4S_6(NO)_4$ cluster which is of similar size to the structurally similar $[Fe_7S_6]$ and $[Co_7S_6]$ clusters. In the M_7S_6 clusters the "uncapped" M_3S_3 unit shows a triangular M_3 array with distances nearly 1 Å shorter than the distances found in the hexagonal faces of the M_6S_6 prismanes. At present we are exploring the possible function of the "uncapped" unit as a ligand to other metal atoms.

Table 2
Comparison of selected bond distances between different M/Fe/S clusters with the range of distances given in parenthesis along with esd's

Selected bond distances (in Å)	$[(CO)_6Mo_2Fe_6S_6(NO)_6]^{2-}$	$[(CO)_6Mo_2Fe_6S_6Cl_6]^{3-}$	$[(CO)_6Mo_2Fe_6S_6Cl_6]^{4-}$
Mo–Fe	2.893(2.884(6)–2.906(6))	2.930(2)	3.005(2.980(1)–3.031(2))
Fe–Fe	2.672(2.669(6)–2.674(6))	2.742(3)	2.761(2.740(2)–2.781(2))
Octahedron Volume	21.535	22.810	23.983
Mo–S	2.580(2.576(8)–2.674(8))	2.582(3)	2.619(2.611(2)–2.625(2))
Fe–S	2.247(2.230(8)–2.279(8))	2.292(2.280(4)–2.312(4))	2.353 (2.279(2)–2.336(3))
	$(PPr_3)_2Cu_2Fe_6S_6(NO)_6$		$[(PEt_3)_2Cu_2Fe_6S_6Cl_6]^{2-}$
Cu–Fe	2.699(3)		2.784(2.756(10)–2.811(10))
Fe–Fe	2.647(3)		2.772(2.750(11)–2.791(10))
M_8 volume	19.098		21.435
Cu–S	2.381(3)		2.385(2.384(15)–2.392(15))
Fe–S	2.240(2.230(3)–2.247(3))		2.310(2.297(16)–2.322(16))
	$(PPr_3)_4Cu_4Fe_4S_6(NO)_4$		$(PPr_3)_4Cu_4Fe_4S_6Cl_6$
Cu–Cu	2.747(16)		2.733(6)
Cu–Fe	2.747(2.765(17)–2.739(19))		2.787(2.765(6)–2.823(6))
Fe–Fe	2.710(19)		2.784(6)
M_8 volume	20.593		21.431
Cu–S	2.236(2.341(29)–2.376(23))		2.366(2.351(8)–2.380(8))
Fe–S	2.264(2.251(29)–2.281(27))		2.269(2.265(8)–2.275(8))
	$(PPr_3)_2Ni_2Fe_6S_6(NO)_6$	$[(PPr_3)_2Ni_2Fe_6S_6Cl_6]^{2-}$	$[(Ph_2MeP)_2Ni_2Fe_6S_6I_6]^{2-}$
Ni–Fe	2.586(3)	2.615(2.613(15)–2.617(15))	2.645(2.624(2)–2.658(2))
Fe–Fe	2.649(3)	2.752(2.747(18)–2.759(19))	2.719(2.707(2)–2.726(2))
M_8 volume	17.933	19.328	19.281
Ni–S	2.250(3)	2.255(2.245(25)–2.267(25))	2.261(2.257(1)–2.265(1))
Fe–S	2.257(2.236(3)–2.271(3))	2.296(2.297(26)–2.309(26))	2.289 (2.277(2)–2.300(2))
	$(PPr_3)_3Ni_3Fe_4S_6(NO)_4$	$(PEt_3)_4Fe_7S_6Cl_3$	$Co_7S_6Br_3(PPh_3)_4$
Ni–Ni[a]	2.790(4)	2.746(3)	2.883(4)
Ni–Fe	2.618(2.605(4)–2.630(4))	2.624(2.622(2)–2.626(2))	2590 (2.583(3)–2.596(4))
$Fe–Fe_{(planar)}$[b]	3.823(4)	4.148(2)	3.955(4)
$Fe–Fe_{(capping)}$	2.744(4)	2.584(2)	2.607(3)
$Ni–S_{(equatorial)}$	2.144(2.140(5)–2.148(5))	2.179(3)	2.139 (2.129(6)–2.149(5))
$Ni–S_{(axial)}$	2.470(5)	2.231(3)	2.197(6)
$Fe–S_{(capping)}$	2.223(5)	2.193(2)	2.168(4)
$Fe–S_{(equatorial)}$	2.242(5)	2.363(2.361(3)–2.366(3))	2.254 (2.249(5)–2.258(5))
$Fe–S_{(axial)}$	2.204(5)	2.276(3)	2.184(5)

The volume of the metal formed cuboidal unit has been calculated approximating it as a cube, using average metal–metal distances.

[a] The distances of interest are denoted as shown in Fig. 6 using the equivalent metal positions for Fe_7S_6 and Co_7S_6 since in the case of $Ni_3Fe_4S_6$ they are more easily defined and recognized.

[b] The Fe–Fe plane is the trigonal plane defined by Fe1–Fe2–Fe3, and the Fe–Fe(capping) is the distance of Fe4 to the trigonal Fe plane. Fe–S (capping) is the Fe4–S3 distance, Fe–S (equatorial) is the Fe3–S3 distance and Fe–S (axial) is the Fe3–S4 distance.

Table 3
Comparative table of iron–nitrosyl distances and angles and theoretical assignment of oxidation levels based on the three possible oxidation states of the nitrosyl ligands

Compound	ν_{N-O} (cm^{-1})	Fe–N distances (Å)	N–O distances (Å)	Fe–N–O angles (°)	Nitrosyl oxidation state			Enemark–Feltham
					NO^+	$NO^·$	NO^-	
$[Fe_4S_3(NO)_7]^-$ [a]	1731	1.646(2)	1.177(2)	163.4(2)–178.3(2)	Fe(1), 3Fe(−1)	3Fe(1), Fe(II)	4Fe(III)	$\{FeNO\}^7 3\{Fe(NO)_2\}^9$
$[Fe_4S_4(NO)_4]^{2-}$	1652				2 Fe(0), 2Fe(1)	2Fe(1), 2Fe(II)	2Fe(II), 2Fe(III)	$2\{FeNO\}^7 2\{FeNO\}^8$
$[Fe_4S_4(NO)_6]^{2-}$	1700, 1668	1.66(11)	1.18(11)	163(1)–171(1)	4Fe(0)	2Fe(1), 2Fe(II)	4Fe(III)	$2\{FeNO\}^8$ $2\{Fe(NO)_2\}^8$
$[Fe_8S_6(NO)_8]^{2-}$	1684	1.674(2)	1.181(2)	174.6(2)–178.8(2)	6Fe(0), 2Fe(1)	6Fe(1), 2Fe(.II)	6Fe(II), 2Fe(III)	$6\{FeNO\}^8 2\{FeNO\}^7$
$[Fe_6S_6(NO)_6]^{2-}$	1679, 1669	1.669(1)	1.181(2)	172.9(2)– 177.0(2)	2Fe(0), 4Fe(1)	2Fe(1), 4Fe(II)	2Fe(II), 4Fe(III)	$2\{FeNO\}^8 4\{FeNO\}^7$
$(PPr)_2Cu_2Fe_6S_6(NO)_6$ [b]	1766, 1750, 1729, 1660	1.676(1)	1.171(1)	171 (0.1)	2Fe(0), 4Fe(1)	2Fe(1), 4Fe(II)	2Fe(II), 4Fe(III)	$2\{FeNO\}^8 4\{FeNO\}^7$
$(PPr)_4Cu_4Fe_4S_6(NO)_4$ [b]	1724, 1712	1.709(9)	1.14(12)	175–177 (1.1)	4Fe(1)	4Fe(II)	4Fe(III)	$4\{FeNO\}^7$
$(PPr)_2Ni_2Fe_6S_6(NO)_6$ [b]	1763, 1745, 1725, 1663	1.676(1)	1.172(1)	173 (0.1)	4Fe(0), 2Fe(1)	4Fe(1), 2Fe(II)	4Fe(II), 2Fe(III)	$4\{FeNO\}^8 2\{FeNO\}^7$
$(PPr)_3Ni_3Fe_4S_6(NO)_4$ [b]	1720, 1698, 1679	1.668(2)	1.184(3)	168–180 (0.2)	2Fe(0), 2Fe(1)	2Fe(1), 2Fe(II)	2Fe(II), 2Fe(III)	$2\{FeNO\}^8 2\{FeNO\}^7$
$[(CO)_6Mo_2Fe_6S_6(NO)_6]^{2-}$ [b]	1723, 1695, 1670	1.678(2)	1.166(3)	175.5(2)–178.2(3)	2Fe(0), 4Fe(1)	2Fe(1), 4Fe(II)	2Fe(II), 4Fe(III)	$2\{FeNO\}^8 4\{FeNO\}^7$

[a] Crystal structure of $(Et_4N)[Fe_4S_3(NO)_7]$ taken from Ref. [46].
[b] The heterometals are assigned as Cu(I), Ni(II) and Mo(0) assuming that they did not undergo change of oxidation state during the reaction.

3.4. The NO ligands

In metal nitrosyl complexes it is difficult to determine precise oxidation states for the metal atoms since NO could be described as NO^+, NO or NO^-. Thus, in $[Fe_4S_3(NO)_7]^-$ two descriptions have been proposed for the cluster based on the assignment of the NO ligand state. These are: $4Fe^{3+}/NO^-$ [41] and $3Fe^{-1}$,Fe^+/NO^+ [42].

Spectroscopic and structural data for the Fe/S/NO and M/Fe/S/NO clusters (Table 3) show the N–O stretching vibrations in the range from 1652 to 1766 cm^{-1}, the M–N–O angle in the range from 171.8° to 180.0°, the Fe–N bond in the range from 1.67 Å to 1.71 Å and the N–O bond between 1.14 Å and 1.18 Å. Within 3σ (at times as high as .01–.02 Å) the N–O and Fe–NO distances are nearly indistinguishable. The Fe–NO bond is short enough consistent with a considerable amount of multiple bond character. The high standard deviations often associated with the N–O bonds make the bond order difficult to evaluate. The M–N–O angles are all near 180° which is expected for NO^+ coordination as opposed to 120° for NO^- taken in extreme cases, but on the basis of the IR data the NO ligands may be even considered as NO^- given that the typical range for lineal NO is 1450–1950 cm^{-1} and 1400–1720 cm^{-1} for bent NO [10]. Unfortunately there is great overlap in ranges, and given that in a series of $[M(NO)(CN)_5]^{n-}$ complexes (M=V, Cr, Mn, Fe and $n = 2, 3$) the position of ν_{NO} depends upon the cation present and variations up to 100 cm^{-1} have been observed for a given anion [43,44]. This makes the ν_{N-O} vibration unreliable for determining NO oxidation. As described by Enemark and Feltham [45] the transition metal-nitrosyl systems are better described as highly covalent entities using a $\{M–NO\}^n$ notation with n the sum of metal d and NO π^* electrons. Any reference to change of oxidation states of the clusters in this article is in accordance with this notation.

An examination of the structural parameters in the $\{[(R_3P)M]_xFe_{8-x}(L)_{8-x}S_6\}^{n-}$ clusters for L = NO vs Cl^- (Table 2) shows that the NO clusters are characterized by significantly shorter Fe–M, Fe–Fe and Fe–S bond lengths. The data are consistent with the expected π back bonding from the Fe atoms into the NO π^* orbital which in turn results in electron deficient Fe atoms, significant M–Fe and Fe–Fe bonding and Fe–S multiple bonding. At present ^{57}Fe Moessbauer spectroscopy appears to be needed for an assignment of oxidation states to the Fe metals and the NO ligands, by a comparison of the Moessbauer spectra of the NO clusters to those of the corresponding chloro clusters. The Moessbauer spectra of the Cu_2Fe_6, Cu_4Fe_4 and Ni_2Fe_6 clusters (L = Cl^-), with isomer shifts of 0.345 mm/s, 0.341 mm/s and 0.355 mm/s, respectively, are consistent with an Fe oxidation state around +3 and Cu^{+1}, Ni° or Ni^{+1}.

3.5. Electrochemistry

Electrochemical studies of the clusters reported here, show mainly reversible, multielectron reductions (Table 4).

Table 4
Reduction potentials of the four M_2 Fe_6S_6 clusters and comparison with their Fe/S/Cl equivalents

Compound	0/−1 couple			−1/−2 couple			−2/−3 couple			−3/−4 couple		
	$E_{1/2}$ (mV)	ΔE	i_{pc}/i_{pa}	$E_{1/2}$ (mV)	ΔE	i_{pc}/i_{pa}	$E_{1/2}$ (mV)	ΔE	i_{pc}/i_{pa}	$E_{1/2}$ (mV)	ΔE	i_{pc}/i_{pa}
$(PPr_3)_2Cu_2Fe_6S_6(NO)_6$	−169	152	0.84	−1035	148	0.99	−1667	152	1.02			
$(Bu_4N)_2[(PPr_3)_2Cu_2Fe_6S_6Cl_6]$							−228	26		−555	120	
$(PPr_3)_4Cu_4Fe_4S_6(NO)_4$	−153	172	0.39	−1021	156	0.57	−1537	116	0.73	−2065		irr
$(PPr_3)_4Cu_4Fe_4S_6Cl_6$	−17	124		−635	130							
$(PPr_3)_2Ni_2Fe_6S_6(NO)_6$	−1	168	1.10	−717	156	0.61	−1431	334	0.71			
$(Et_4N)_2[(PPr_3)_2Ni_2Fe_6S_6Cl_6]$							−585	156				
$(PPN)_2[(CO)_6Mo_2Fe_6S_6(NO)_6]$							−641	192	0.70	−1247	176	0.68
$(Et_4N)_3[(CO)_6Mo_2Fe_6S_6Cl_6]$										+50	92	1.00

All reductions are reversible unless denoted otherwise.

The $(PPr_3)_2Cu_2Fe_6S_6(NO)_6$ cluster shows three reversible reduction waves (Fig. 7) at −169 mV, −1035 mV, −1667 mV. Following a cyclic scan from 1.8 V to −2 V, the voltammetry shows the appearance of an additional reduction wave at about −633 mV, which suggest that the small peak that appears in that region in the 0 to −2.0 V scan is due to partial oxidation of the cluster during the experiment rather than to the presence of an impurity.

In the case of $(PPr_3)_4Cu_4Fe_4S_6(NO)_4$, although the CV appears to be very similar to $(PPr_3)_2Cu_2Fe_6S_6(NO)_6$ as the first two reductions coincide, (Fig. 8) at high potentials there are different peaks. In addition when two consecutive full scans from −2 V to 1.8 V are performed, there is no appearance of the peak at −0.5 V indicating that it is not a mixture of two species.

For $(PPr_3)_2Ni_2Fe_6S_6(NO)_6$ the cyclic voltammogram (Fig. 9) shows only two reductions at −717 mV and −1431 mV but there is also a reversible wave at −1 mV (not shown), and overall the voltammogram of $(PPr_3)_2Ni_2Fe_6S_6(NO)_6$ is similar to that of $(PPr_3)_2Cu_2Fe_6S_6(NO)_6$ shifted by approx 0.2 V towards more positive potentials. Again after a full range scan there is an emergence of a new reversible wave at −235 V which is also evident in the initial scan but with smaller intensity suggesting that part of the sample had been oxidized during the experimental process.

Contamination of the $(PPr_3)_3Ni_3Fe_4S_6(NO)_4$ cluster with the other unidentified Ni/Fe/S species, did not allow for conclusive electrochemical measurements of this cluster.

For $(PPN)_2[(CO)_6Mo_2Fe_6S_6(NO)_6]$, there are two reduction waves observed at −641 mV and −1247 mV (Fig. 10). In addition there is no significant effect of oxidation as there are no new peaks appearing but the two reductions change in intensity after a full range scan.

As shown in Table 4, by comparison to the corresponding M/Fe/S/Cl species and equivalent couples, the clusters presented herein are more difficult to reduce which is reasonable given that these clusters appear to be more electron rich than their corresponding halogen analogues due to the more covalent nature of the Fe–NO bond that eventually

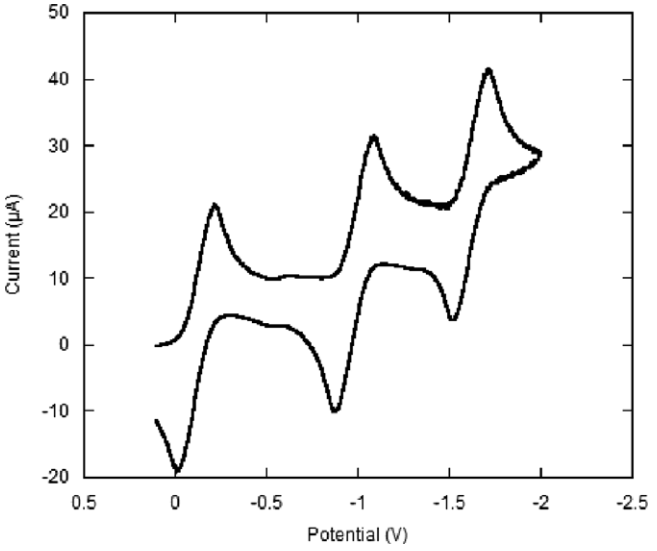


Fig. 7. Cyclic voltammogram of $(PPr_3)_2Cu_2Fe_6(NO)_6$.

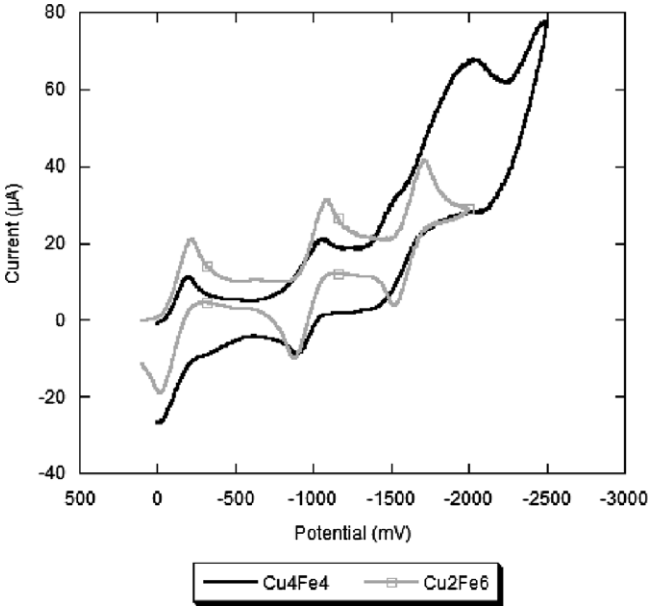


Fig. 8. Cyclic voltammogram of $(PPr_3)_4Cu_4Fe_4S_6(NO)_6$ in comparison with $(PPr_3)_2Cu_2Fe_6S_6(NO)_6$.

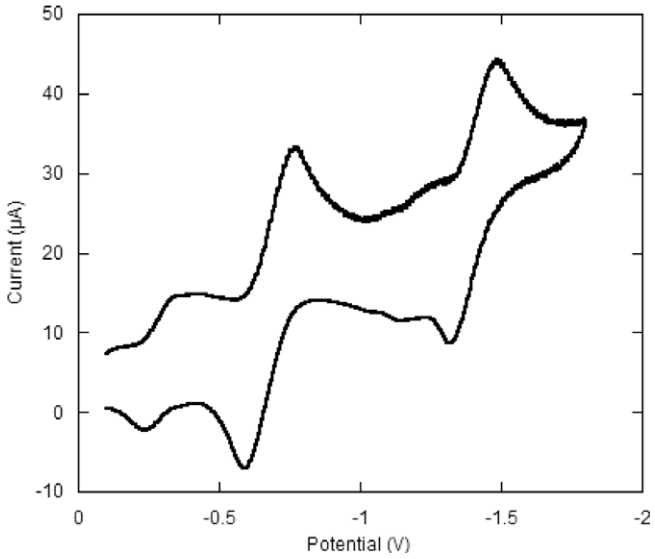


Fig. 9. Cyclyc voltammogram of $(PPr_3)_2Ni_2Fe_6(NO)_6$.

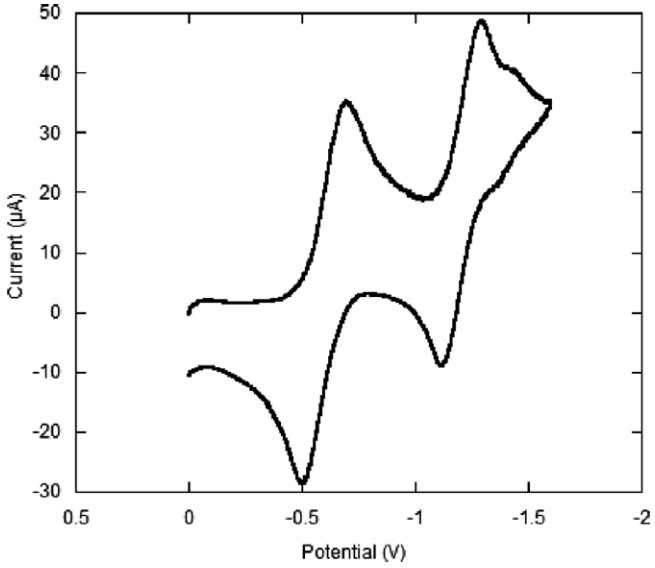


Fig. 10. Cyclyc voltammogram of $(PPN)_2[(CO)_6Mo_2Fe_6(NO)_6]$.

disturbs the ability of the metals to accept additional electrons.

4. Conclusions

In this article we have explored the syntheses and reactivities of the Fe/S/NO clusters. These clusters were found structurally similar to their halo and phosphino analogues, exhibiting similar interconversions between their core structures, and the reactivity of $(PPN)_2[Fe_6S_6(NO)_6]$ towards thiophilic metals such as Mo, Cu and Ni, provides almost identical core structures as the Fe/S/Cl clusters.

The reactivity of the Fe/S/NO clusters presented in this paper are in line with the fragmentation/reassembly mechanism proposed by Glidewell and Hoffmann, as the products obtained through various reactions seem to be the four basic and thermodynamically stable core topologies of Fe_4S_3, Fe_4S_4 Fe_6S_6 and Fe_8S_6, however the isolation of the unique $(PPN)_2[Fe_4S_4(NO)_6]$, ''open-cubane'' and the $(PPr_3)_3Ni_3Fe_4S_6(NO)_4$ clusters provides additional evidence that it is possible to obtain new core topologies by varying reaction conditions and stabilizing inherently metastable structures.

Acknowledgements

We thank Dr. Jeff Kampf for X-ray data collection and Carl Henderson for the Electron Microbeam Analysis. The authors acknowledge the support of this work by a grant from the National Institutes of Health (GM 33080).

Appendix A. Supplementary material

CCDC 643468, 643469, 643470, 643471, 643472 and 643473 contain the supplementary crystallographic data for this paper. These data can be obtained free of charge from The Cambridge Crystallographic Data Centre via www.ccdc.cam.ac.uk/data_request/cif. Supplementary data associated with this article can be found, in the online version, at doi:10.1016/j.poly.2007.06.015.

References

[1] P.V. Rao, R.H. Holm, Chem. Rev. 104 (2004) 527.
[2] H. Ogino, S. Inomata, H. Tobita, Chem. Rev. 98 (1998) 2093.
[3] C.T.W. Chu, L.F. Dahl, Inorg. Chem. 16 (1977) 3245.
[4] J. Zhou, Z.G. Hu, E. Munck, R.H. Holm, J. Am. Chem. Soc. 118 (1996) 1966.
[5] M.G. Kanatzidis, W.R. Hagen, W.R. Dunham, R.K. Lester, D. Coucouvanis, J. Am. Chem. Soc. 107 (1985) 953.
[6] D. Coucouvanis, M.G. Kanatzidis, W.R. Dunham, W.R. Hagen, J. Am. Chem. Soc. 106 (1984) 7998.
[7] M.J. Scott, R.H. Holm, Angew. Chem., Int. Ed. Engl. 32 (1993) 564.
[8] F. Calderoni, F. Demartin, M.C. Iapalucci, F. Laschi, G. Longoni, P. Zanello, Inorg. Chem. 35 (1996) 898.
[9] C. Goh, B.M. Segal, J.S. Huang, J.R. Long, R.H. Holm, J. Am. Chem. Soc. 118 (1996) 11844.
[10] J.A. McCleverty, Chem. Rev. 104 (2004) 403.
[11] A.R. Butler, I.L. Megson, Chem. Rev. 102 (2002) 1155.
[12] T.W. Hayton, P. Legzdins, W.B. Sharp, Chem. Rev. 102 (2002) 935.
[13] F.Z. Roussin, Ann Chim Phys 52 (1858) 285.
[14] F.W. Flitney, I.L. Megson, D.E. Flitney, A.R. Butler, Br. J. Pharmacol. 107 (1992) 842.
[15] F.W. Flitney, I.L. Megson, J.L.M. Thomson, G.D. Kennovin, J. Physiol. (London) 459 (1993) P90.
[16] F.W. Flitney, I.L. Megson, J.L.M. Thomson, G.D. Kennovin, A.R. Butler, Br. J. Pharmacol. 117 (1996) 1549.
[17] H. Kalyvas, D. Coucouvanis, Inorg. Chem. 45 (2006) 8462.
[18] K.C. Misra, M.E. Fleet, Economic Geology 68 (1973) 518.
[19] M. Koutmos, H. Kalyvas, Y. Sanakis, A. Simopoulos, D. Coucouvanis, J. Am. Chem. Soc. 127 (2005) 3706.
[20] C. Junghans, W. Saak, S. Pohl, J. Chem. Soc., Chem. Commun. (1994) 2327.
[21] D. Fenske, H. Krautscheid, M. Muller, Angew. Chem., Int. Ed. Engl. 31 (1992) 321.

[22] D. Fenske, J. Ohmer, J. Hachgenei, K. Merzweiler, Angew. Chem., Int. Ed. Engl. 27 (1988) 1277.
[23] D. Fenske, J. Hachgenei, J. Ohmer, Angew. Chem., Int. Ed. Engl. 24 (1985) 706.
[24] L.L. Martin, L.C. West, B. Wu, Eur. J. Biochem. 268 (2001) 5676.
[25] K. Whitmire, J. Ross, C.B. Cooper, D.F. Shriver, Inorg. Synth. 21 (1982) 66.
[26] D. Coucouvanis, M. Kanatzidis, E. Simhon, N.C. Baenziger, J. Am. Chem. Soc. 104 (1982) 1874.
[27] M.D. Curtis, M.S. Hay, Inorg. Synth. 28 (1990) 150.
[28] R.A. Heintz, J.A. Smith, P.S. Szalay, A. Weisgerber, K.R. Dunbar, Inorg. Synth. 33 (2002) 75.
[29] K.H. Pannell, Y.S. Chen, K. Belknap, C.C. Wu, I. Bernal, M.W. Creswick, H.N. Huang, Inorg. Chem. 22 (1983) 418.
[30] D.E. Fjare, W.L. Gladfelter, Inorg. Chem. 20 (1981) 3533.
[31] D.E. Fjare, W.L. Gladfelter, J. Am. Chem. Soc. 103 (1981) 1572.
[32] C.T.W. Chu, F.Y.K. Lo, L.F. Dahl, J. Am. Chem. Soc. 104 (1982) 3409.
[33] S.S. Sung, C. Glidewell, A.R. Butler, R. Hoffmann, Inorg. Chem. 24 (1985) 3856.
[34] A.R. Butler, C. Glidewell, A.R. Hyde, J.C. Walton, Polyhedron 4 (1985) 797.
[35] D. Coucouvanis, A. Salifoglou, M.G. Kanatzidis, W.R. Dunham, A. Simopoulos, A. Kostikas, Inorg. Chem. 27 (1988) 4066.
[36] S. Pohl, W. Saak, Angew. Chem., Int. Ed. Engl. 23 (1984) 907.
[37] M. Koutmos, D. Coucouvanis, Inorg. Chem. 45 (2006) 1421.
[38] I. Noda, B.S. Snyder, R.H. Holm, Inorg. Chem. 25 (1986) 3851.
[39] F. Cecconi, C.A. Ghilardi, S. Midollini, A. Orlandini, Inorg. Chim. Acta 184 (1991) 141.
[40] F.L. Jiang, L.G. Huang, X.J. Lei, H.Q. Liu, B.S. Kang, Z.Y. Huang, M.C. Hong, Polyhedron 11 (1992) 361.
[41] M. Jaworska, Z. Stasicka, J. Mol. Struct. 785 (2006) 68.
[42] R. Hoffmann, M.M.L. Chen, M. Elian, A.R. Rossi, D.M.P. Mingos, Inorg. Chem. 13 (1974) 2666.
[43] P. Gans, A. Sabatini, L. Sacconi, Inorg. Chem. 5 (1966) 1877.
[44] P.T. Manoharan, H.B. Gray, Inorg. Chem. 5 (1966) 823.
[45] J.H. Enemark, R.D. Feltham, Coord. Chem. Rev. 13 (1974) 339.
[46] S. D' Addario, F. Demartin, L. Grossi, M.C. Iapalucci, F. Laschi, G. Longoni, P. Zanello, Inorg. Chem. 32 (1993) 1153.

remembering excellence comes through living the simple lessons he learned in Coello [10].

Fred dedicated his autobiography [9], "In Loving Memory of My Beloved Wife, Mary and My Parents, Giovanni and Catherina Basolo":

> Regardless of early hardships, I have always considered my early childhood to have been the most enjoyable and most instructive period of my life [9, p. 3].

Most of the miners, including the Basolos, were immigrants from the Piedmont region of northern Italy and spoke the "Piemontese" peasant dialect. Until he attended school, Fred understood but spoke little English. Conditions in the home were primitive—no central heating or plumbing. Watching his mother in the family kitchen made the cooking of Italian dishes one of his favorite hobbies. Fred's legendary concern for his students, colleagues, family, and everyone with whom he came into contact may be traced to his early roots in Coello.

The Great Depression began when Fred was about 10 years old. Since he was too young to work, he attended a four-room elementary school in Coello and then the Christopher Community High School, walking the two miles in all kinds of weather. His first contact with chemistry (he did not even know the meaning of the word) was in high school. The teacher told the class she hated the subject, did not know much about it, and they were going to be largely on their own, which gave Fred the freedom to concentrate on what interested him in both the text and lab experiments.

2. University studies

With a welfare program for college students, Fred enrolled at Southern Illinois Normal School (SIN, now Southern Illinois University, from which he was to receive an honorary doctorate in 1984), where he became a chemistry major and received his B.Ed. degree in 1940. The only person from Coello going to college, today he is still the only Ph.D. from there. Although his parents hoped he would return home as a high school teacher, Chemistry Department chairman James Neckers advised him to go to graduate school. His reaction was, "What is graduate school?" [9, p. 11].

A teaching assistantship allowed Fred to enter the University of Illinois, where he chose as his mentor John C. Bailar, Jr. (1904–1991) [12] (Fig. 1), whom he thought "seemed to be a caring person, with a good understanding of people and their needs" [9, p. 14], qualities for which Fred himself later became well known. The choice was "one of the very best decisions I have ever made" [9, p. 14], and, after his parents, Bailar became his second role model. As most illustrious *Doktorand*, Fred continued Bailar's work with his own students, and after Bailar's death in 1991 he succeeded him as the dean of American coordination chemistry.



Fig. 1. Fred Basolo (left) and John C. Bailar, Jr. (right).

Because Bailar had worked with octahedral cobalt(III) complexes, he wanted to extend his studies to planar platinum(II) and octahedral platinum(IV) complexes. Fred chose for his research the preparation and study of the stereochemical changes that occur during ligand substitution reactions of optically active *cis*-$[PtCl_2\{NH_2CH_2CH_2NH_2\}_2]Cl_2$. His publication [13], describing this research, elicited little interest until more than two decades later, when Barnett Rosenberg serendipitously discovered the antitumor activity of the related *cis*-$[PtCl_2(NH_3)_2]$ (cisplatin), still one of the most widely used anti-cancer drugs [14].

Bailar suggested that Fred finish his research in three years so that he would not be drafted and have to return to Illinois to receive his degree. Fred received his M.S. degree in 1942 and his Ph.D. degree the following year at age 23. He spent three years working on classified research on zirconium fire retardants and mica substitutes at Rohm & Haas Co. in Bridesburg near Philadelphia.

3. University career, marriage, and sabbaticals

In the fall of 1946 Fred accepted a position as Instructor of Chemistry at Northwestern University (NU) in Evanston, Illinois, a Chicago suburb. He married Mary Nutely on June 14, 1947. Their long, happy marriage resulted in three daughters and a son, all of whom became educators and presented the Basolos with 11 grandchildren.

A Guggenheim fellowship enabled the Basolos to spend a year (1954–1955) in Copenhagen, where Fred worked in the laboratory of Jannik Bjerrum [15], whose dissertation popularized the term ligand [16]. They also visited other European countries, including Italy, where they visited Fred's relatives. An enthusiastic golfer, Fred took the opportunity of their time in Scotland to play at the famous course in St. Andrews.

During his Copenhagen year Fred wrote several chapters of the book that was to make an international scientific reputation for him and his NU colleague Ralph G. Pearson, later of hard and soft acid and base (HSAB) fame. Their classic monograph, "Mechanisms of Inorganic

Reactions'' [17], which became the ''Bible of inorganic mechanisms,'' introduced crystal field theory to chemists and showed its ability to explain the properties of coordination compounds and the kinetics and mechanisms of their redox and ligand substitution reactions.

Fred and Mary spent four days during the summer of 1955 at the 3rd International Conference on Coordination Chemistry (3 ICCC) at Amsterdam, where Fred heard the plenary lecture by Technische Universität München's Walter Hieber, the ''father of metal carbonyl chemistry''. In response to Fred's question about the mechanisms involved in the synthesis and reactions of these compounds, Hieber answered him, ''We do chemistry in my laboratory, not the philosophy of chemistry'' [9, p. 101]. Fred realized that here was a neglected field for him and his students to explore.

Fred's doctoral students Andrew J. Wojcicki and Harry B. Gray handled the problem of dealing with toxic metal carbonyls by keeping Linus, a canary who was supposedly more sensitive to fumes than humans, in a cage in the laboratory. Linus died, and his successor, a parakeet named Torpedo, pecked Gray and infected him with parrot fever (psittacosis), from which he recovered quickly, thanks to an early diagnosis and expert care given by the physicians at the Northwestern health center.

The Basolos spent Fred's second sabbatical year, 1961–1962 (he was a Senior NSF Fellow), at Vincenzo Caglioti's institute at the Università di Roma. Fred invited Anthony J. Poë, on his first sabbatical leave from Imperial College, London, to oversee his research group of a dozen graduate students. Poë worked with Fred's student John L. Burmeister on his discovery of linkage isomers of L_nM-NCS and L_nM-SCN [18], the first case of linkage isomerism [19] since Sophus Mads Jørgensen's discovery of the xantho (nitro) ($[Co(NO_2)(NH_3)_5]Cl_2$) and isoxantho (nitrito) $[Co(ONO)(NH_3)_5]Cl_2$ pentaammines of cobalt(III) [20]. Burmeister described the discovery:

> The genesis of this paper [19] may be traced to the moment in 1963 when, hunched over an IR spectrophotometer in a laboratory in Northwestern University's Technological Institute at 1:30 a.m., I watched a pen trace the confirming evidence that I had, indeed, synthesized the first inorganic linkage isomers of the thiocyanate ion. The impacts of this discovery were both immediate and long-range: My doctoral mentor, Fred Basolo, was roused from his slumber by a telephone call to share the joy that always accompanies scientific discovery, light appeared at the end of my Ph.D. tunnel, and, given the green light by Basolo, I initiated a research program that has focused on the coordination chemistry of ambidentate ligands to this very day, some 100 research publications later [21].

During his Rome sabbatical, Fred also wrote the first two chapters of his second book, ''Coordination Chemistry'', a supplementary paperback coauthored with former student Ronald C. Johnson [22,23].

At NU Basolo rose through the ranks—Instructor (1946–1950), Assistant Professor (1950–1955), Associate Professor (1955–1958), Professor (1958–1979), and Charles E. and Emma H. Morrison Professor of Chemistry (1980–1990). He served as Chairman of the Chemistry Department from 1969 to 1972.

4. Basolo and Pearson vs. Ingold and Nyholm

During the second half of the 19th and all of the 20th century, organic chemistry flourished. However, after Alfred Werner's [24] and Sophus Mads Jørgensen's [25] pioneering work, inorganic chemistry languished in the doldrums until World War II, when what Sir Ronald S. Nyholm called the ''Renaissance of Inorganic Chemistry'' occurred [26], a rebirth in which Fred played a preeminent role.

During his work at Rohm and Haas, Fred became interested in studies of the kinetics and mechanisms of substitution reactions on carbon being carried out by organic chemists. He thought that similar studies could be carried out on inorganic coordination compounds such as those of cobalt(III) and platinum(II), with which he was already familiar. He had no experience with kinetics and mechanisms of chemical reactions, but his fellow NU Instructor and physical organic chemist Ralph G. Pearson was performing such studies with carbon compounds. In response to Fred's effort to convince him to collaborate on similar studies on coordination compounds, Ralph first replied, ''There is no interest in inorganic chemistry, so why should I waste my time studying such systems?'' [9, p. 81]. Also, no NU graduate students were interested in inorganic chemistry. Eventually, Fred succeeded in ''seducing'' Ralph into becoming a physical inorganic chemist, and their first joint paper on inorganic kinetics and mechanisms appeared in 1952 [27]. According to Fred,

> Ralph and I arrived at the right place at the right time, resulting in the publication of some 60 co-authored papers on the kinetics and mechanisms of ligand substitution of octahedral and square planar metal complexes. Neither one of us could have done what we did alone, but, by working together, we were *very* successful. The seminal results of our studies are now often used in bioinorganic chemistry research, and in studies on homogeneous catalysis [10, p. 3].

Fred and Ralph and their students discovered that the base hydrolysis of cobalt(III) complexes proceeds by an S_N1CB (substitution, nucleophilic, unimolecular, conjugate base) mechanism. Physical organic chemist Sir Christopher Kelk Ingold (1893–1970) [28], the Nobel-caliber ''high priest of organic mechanisms'', and coordination chemist Sir Ronald Sydney Nyholm (1917–1971) [29,30] – both at University College, London, countered that this view was incorrect, and they published papers stating that the correct mechanism was S_N2 (substitution, nucleophilic, bimolecular). In Fred's words,

> Had our polemic with Ingold and Nyholm, two of the giants of chemistry, not turned out in our favour, we may not have gotten tenure and our department may not now rank among the top four in inorganic chemistry in the U.S. We were very fortunate to have this exchange focus so much favorable attention on our department just at the time when inorganic chemistry in the U.S. was beginning to achieve the importance it now has [9, pp. 90–91].

Considering the significance of their long and intimate collaboration, Pearson's comments, which review the state of the art at the time, are worth quoting:

> Like many others, I owe a large debt of gratitude to Fred. In 1948 he persuaded me to join him in a study of the mechanisms of substitution reactions in coordination compounds. There was almost no work being done in this area. Henry Taube had started to do a little on redox reactions, but there were very few people doing anything that might be called physical inorganic chemistry.
>
> I had already started some work on substitution reactions in organic systems. Physical organic chemistry was already well developed, and the field was dominated by giants like Hughes and Ingold, Winstein and Bartlett. It would have been hard for me to make much of an impression on this field. But, thanks to Fred, he and I became two of the fathers of physical inorganic chemistry.
>
> Our talents were well matched. I knew a lot about studying mechanisms by means of kinetic studies. Fred also knew how to synthesize metal complexes, how to analyze them and how to identify them. We also had just enough in the way of instruments to do what we needed. These included a Cary UV–visible spectrophotometer, a conductivity bridge, and a Rudolph polarimeter.
>
> Our first student was Earl Muetterties, who was a senior at Northwestern, wanting to do some honors research. But graduate students were hard to find. Inorganic chemistry was not popular at that time. It was considered "tombstone chemistry," with a dash of sulfuric acid.
>
> But we were lucky. The atomic energy program had already put some money into the chemistry of metal ions. The success of the Russian Sputnik had increased the interest. There were AEC graduate fellowships available, and Fred and I received a $7000 grant from the AEC to support our work. Such grants were very rare in those days. But we now had graduate students, and very good ones.
>
> We were also fortunate in our choice of research problems for starters. The first, of course, was substitution reactions of octahedral cobalt(III) complexes. The choice was dictated by Fred's doctoral work with John Bailar at Illinois. Cobalt(III) complexes turned out to be the prototype systems for dissociation, or S_N1, mechanisms. We next turned to planar platinum(II) complexes, which were the prototypes for addition, or S_N2, mechanisms. The 16–18 electron rule was working!
>
> Another development in physical inorganic chemistry was happening, and helped us in our interpretation of experimental results. It also increased the interest of the wider chemical community in inorganic chemistry. This was the appearance of crystal field theory, shortly to become ligand field theory, or molecular orbital theory applied to transition metal complexes.
>
> In the 1940s and early 1950s, the theory of inorganic chemistry was dominated by Linus Pauling. His views were based on valence bond theory and mainly used hybrid orbitals and resonance structures to explain things. Actually, it did not work very well. Molecular orbital theory was much better at explanations and approximate calculations. Fred and I published the first edition of "Inorganic Reaction Mechanisms" [17] [The actual title is Mechanisms of Inorganic Reactions—GBK] in 1958. In it we had an introduction to crystal field theory. We also showed pictures of d orbitals and made three-dimensional models of them (Fig. 2).
>
> This was brand new to most chemists. As a result, Fred and I were instrumental in spreading crystal field theory into inorganic chemistry. It had a great impact, since, as one person said, "Inorganic chemistry went from crystal ball to crystal field theory".
>
> We were also lucky that C.K. Ingold and R.S. Nyholm did some work on the mechanism of substitution reactions of metal complexes. Most of what they did was wrong, but Ingold's reputation was so great that much interest in the subject was created. Chemists in other fields began to pay attention.
>
> Fred was also a great teacher. I often quipped that he was a far better teacher than I was. Over the years he taught me much inorganic chemistry, but I was never able to teach him any physical chemistry. He made many other contributions to making inorganic chemistry one of the



Fig. 2. Fred Basolo (left) and Ralph G. Pearson (right) "discover" d-orbitals.

hot research areas of chemistry. Summing up, Fred Basolo was a worthy successor to John Bailar as the Father of American Inorganic Chemistry'' [31].

Fred and Ralph's studies of ligand substitution reactions of octahedral cobalt(III) complexes, acid hydrolysis or aquation of cobalt(III) and chromium(III) metal-ammine complexes, base hydrolysis of metal-ammine complexes, linkage isomers, ligand substitution reactions of Pt(II) square planar complexes, synthetic oxygen carriers, organometallic chemistry, including the indenyl kinetic effect, and biological inorganic chemistry are true chemical classics [32].

The Chemistry Department at Northwestern University is renowned for the strong interaction between its faculty and students. The informal Saturday morning Basolo–Ibers–Pearson (BIP) meetings, where graduate students or postdoctoral fellows present their results on research in progress, are known worldwide and are visited by chemists from around the world.

5. Teaching and professional activities

Like his mentor John Bailar, Fred educated several generations of chemists (58 doctorates, 66 postdoctoral fellows, and countless bachelor's and master's degree candidates). Approximately a third of his students, inspired by his love of teaching, entered academia. The roll of his former students reads like a veritable ''Who's Who'' of inorganic chemistry and chemical education. Like Bailar's, Fred's success as a research supervisor and teacher owed as much to his enduring human qualities as to his profound chemical knowledge.

Fred's former students praise his didactic skills:

> My graduate mentor at Northwestern, Professor Fred Basolo, was a prototypical example of the Mentor Model. . .. he never dealt with us through intermediaries, save for the year he was on sabbatical leave. We discussed our research progress and problems with him on a one-on-one basis, at his behest, at least once a week. We talked about a kaleidoscope of other subjects with him as well, learning a lot about his philosophy of life, in the process. We experienced his culinary and golf skills first hand (get-togethers at his home were frequent, and I never did beat him in a round of golf). In short, he became more than a professor to us—he became a lifelong friend [33].
>
> Fred was the one that taught me how to write a scientific paper. Having taken English composition classes in high school and college, I did not really know how to write a scientific paper, which is very different from a theme for English. So, I spent weeks writing a draft of my first paper. I thought it might be a little long, but overall I was rather pleased with it. A few days after I gave it to Fred, he returned it to me without a mark on it, but it was accompanied by a large stack of yellow hand-written pages. He had rewritten the whole paper! It must have taken many hours. I do not remember talking with him about his version or my version, but I realized what was necessary to write a concise, understandable, accurate, and interesting account of my studies. When I work with my own students who are writing their first papers, I pass on the lessons that I learned from Fred. It is not always an easy process for the student or me, but my expectations for a well-written paper are exactly the same as Fred's [34].
>
> Fred was very flexible and tolerant in his way of directing his PhD students. Fred was a morning person. . ..one of his pet phrases was ''the morning is the mother of the day'', only he first said it in Italian, or more correctly Piemontese, a peasant dialect. He would be in the office at 7:00 AM 6 days a week. .. Fred gave us a long leash; we knew he was there and that he cared, but he did not get in our way of discovering new data and its meaning on our known. .. Fred was a man with an encyclopedia-like mind for chemistry, a quick smile and wink, and a hearty laugh [35].

In his graduate course on coordination chemistry Bailar had lectured on the history of the subject, and Fred condensed Bailar's lecture into a 50-minute lecture for his freshman class to illustrate how science advances. Fred presented this lecture every year for four decades to his students and worldwide to universities and high schools.

Fred was an active force in the Gordon Research Conferences, International Conferences on Coordination Chemistry (ICCC), ACS Petroleum Research Fund Advisory Board, and North Atlantic Treaty Organization (NATO). Elected to the National Academy of Sciences in 1979, he considered among his most important NAS activities his work on ''Opportunities in Chemistry'', a book colloquially known as the ''Pimentel Report'' [36,37]. Despite his numerous professional activities and his more than 380 scientific publications, he was always willing to serve as editor of journals or volumes, write letters of recommendation, award nominations, or forewords to books or monographs.

Fred made a number of speaking tours for the American Chemical Society. In 1970 he was elected Chairman of the ACS Division of Inorganic Chemistry and in 1971 a member of its Executive Committee. Although he thought that he had little chance of being elected President, he agreed to having his name proposed as a petition candidate to oppose the other two candidates loyal to the ACS establishment, who would receive all the establishment votes. To his surprise he was elected 1983 ACS President without any electioneering on his part.

As President, Fred addressed some of his longtime concerns. In his attempts to combat chemophobia he discussed environmental problems with newspaper reporters, radio talk show hosts, and television anchor persons but only if he was given equal time to present the beneficial aspects of chemicals. He also made these views known to congressmen and congressional committees. He received

the ACS George C. Pimentel Award in Chemical Education (1992), the Priestley Medal, the ACS's highest honor (2001) [38], and countless other awards and honorary degrees.

6. Foreign travel

Fred traveled to 40 foreign countries, where his zest for life and remembrance of the humble circumstances of his childhood made him take great delight in each new experience. He considered Italy a second home and traveled there "more times than I can recall" [9, p. 153], lecturing in his "bad, but amusing Italian" [9, p. 156]. He was elected an honorary member of the Società Chimica Italiana (1981) and received honorary doctorates from the Università di Torino (1987), the Università di Padova (1991), and the Università di Palermo (1997) and three Italian medals. He was elected in 1987 to the Accademia Nazionale dei Lincei (Italy's national academy of science), founded in 1603 as the world's oldest scientific society.

Fred made seven trips to China, where he met with Vice-Premier Fang-Yi (the number three governmental official), dined on delicacies like snake soup, drank mao-ti, "which had an odor of kerosene" [9, p. 163], and received an honorary doctorate and a medal. His frequent visits led a Fudan University professor to tell him, "Basolo, you are the Marco Polo of chemistry to China" [9, p. 167].

According to Fred's grandson:

> "He won many awards for his teaching and research. Interestingly, my uncle found most of my grandfather's awards in his sock drawer. My grandfather taught me that you do not hang awards in your house because your work is never more important than your family and you teach to help others and never to win awards" [11].

7. Final years

On August 17–18, 1990, Fred's 70th birthday and his retirement, financially supported by 16 corporations and societies, was celebrated by almost all of his Ph.D. students and postdocs [39]. Sufficient funds were left over from what was known as Basolo 70 (Fig. 3) so that his students and postdoctoral fellows could create an endowment to establish an annual Basolo Medal and Lecture, beginning in 1991. State Governor James Thompson proclaimed August 18, 1990 as "Fred Basolo Day in the state of Illinois".

In 1991 Fred's wife Mary underwent an emergency quadruple heart bypass, after which she began to suffer from Alzheimer's disease. One morning, while driving her to the day-care center, Fred fell asleep at the wheel, probably because of a combination of some new medications and tiredness, and their car hit a tree. Mary succumbed to her injuries and died on February 5, 1997. Five surgeries on Fred's back damaged the nerves from his brain to his legs, and he became unable to walk without two canes, and he used a motorized scooter to get around in the NU Chemistry Building. In spite of pain and shortness of breath, he went to his office every morning, had lunch with his faculty colleagues, and left in the early afternoon.



Fig. 3. George B. Kauffman (left) and Laurie M. Kauffman (right) wearing Basolo 70 T-shirts.

Despite afflictions that would have tested the patience of Job, Fred never felt sorry for himself:

> Men from my grandfather's generation also have a difficult time saying "I Love You". Ironically, it was in his final years that he helped teach the meaning of these words. This previously strong man was confined to a wheel chair. He had become thin and frail. He was unable to garden or play golf. The love of his life, Mary, who he had shared his life with had been killed in a car accident. People had to help him in and out of bed, change him, feed him, and clean him. His final years did not turn out as he had planned. Through all of this though, he never said, "Why Me?" This very strong man allowed himself to become helpless and his body to deteriorate because he knew he was providing a service to God. He was allowing God to use his body to teach the ultimate lesson. That lesson is what "I Love You" means. When my grandfather was very ill one night, I told him "I Love You", and he said, "Those sounds make me feel good." He didn't say those *words*, but those *sounds*. "I Love You" has to be more than words. It must be something we can hear, see, and feel that touches our soul [11].

8. Fred's legacy

Fred Basolo's life is an inspiring tale of an individual committed both to the practice of scientific research and to his profession. In addition to his immense contributions to chemistry, his personality, warmth, sense of humor, charm, and intense interest in people have endeared him to several generations of colleagues and students. Continually aware and proud of his roots, yet humble about his achievements, he wrote:

I can truthfully say that I marvel at what has happened to me during my life. Not in my wildest dreams could I have expected when growing up in the little mining village of Coello that, some day, I would become a successful chemist [9, p. 221].

He will be sorely missed.

Acknowledgements

We are greatly indebted to Robert J. Angelici, John L. Burmeister, Alison Butler, James P. Collman, Alvin L. Crumbliss, James A. Ibers, Ronald C. Johnson, Kazuo Nakamoto, Thomas V. O'Halloran, Ralph G. Pearson, David H. Petering, Anthony J. Poë, Kenneth N. Raymond, William C. Trogler, Andrew J. Wojcicki and Jon Michael Kunzer, and Margaret Ann (Peggy) Basolo Silkaitis for their contributions to this tribute.

References

[1] Fred Basolo's website: <http://66.49.160.113>.
[2] Observer online: News for the Northwestern University Community, March 8, 2007. <http://www.northwestern.edu/observer/issues/2007/03/08/basolo.html>.
[3] T. Jensen, Chicago Tribune (March 7) (2007) 8.
[4] H. Gray, J.S. Magyar, Angew. Chem., Int. Ed. 46 (2007) 1.
[5] R. Petkewich, Chem. Eng. News 85 (10) (2007) 13.
[6] D.R. Shriver, Coord. Chem. Rev. 99 (1990) 3.
[7] J.L. Burmeister, Inorg. Chim. Acta 240 (1995) xxiii.
[8] J.L. Burmeister, Chemtracts—Inorg. Chem. 13 (2000) 73.
[9] F. Basolo, From Coello to Inorganic Chemistry: A Lifetime of Reactions, Kluwer Academic/Plenum Publishers, New York, 2002.
[10] F. Basolo, J.L. Burmeister (Eds.), On Being Well-Coordinated: A Half-Century of Research on Transition Metal Complexes: Selected Papers of Fred Basolo, World Scientific Publishing Co., Singapore, 2003.
[11] J.M. Kunzer, tribute spoken at Fred's funeral by his oldest grandson, courtesy, Margaret Ann (Peggy) Silkaitis (née Basolo).
[12] G.B. Kauffman, G.S. Girolami, D.H. Busch, Coord. Chem. Rev. 128 (1993) 1.
[13] F. Basolo, J.C. Bailar Jr., B.R. Tarr, J. Am. Chem. Soc. 72 (1950) 2433.
[14] B. Rosenberg, I. Van Camp, T. Krigas, Nature 205 (1965) 698.
[15] G.B. Kauffman, J. Chem. Educ. 62 (1985) 1002.
[16] W.H. Brock, K.A. Jensen, C.K. Jørgensen, G.B. Kauffman, Ambix 28 (1981) 171.
[17] F. Basolo, R.G. Pearson, Mechanisms of Inorganic Reactions, Wiley, New York, 1958.
[18] F. Basolo, J.L. Burmeister, A.J. Poë, J. Am. Chem. Soc. 85 (1963) 1700.
[19] J.L. Burmeister, Coord. Chem. Rev. 3 (1968) 225.
[20] S.M. Jørgensen, Z. Anorg. Chem. 5 (1894) 147, 168.
[21] J.L. Burmeister, Curr. Cont.: Phys., Chem. Earth Sci. 28 (27) (1988) 16.
[22] F. Basolo, R.C. Johnson, Coordination Chemistry, Benjamin, New York, 1964.
[23] F. Basolo, R.C. Johnson, Coordination Chemistry, second ed., Science Reviews, Wilmington, DE, 1986.
[24] G.B. Kauffman, Alfred. Werner, Founder of Coordination Chemistry, Springer-Verlag, Berlin, 1966.
[25] G.B. Kauffman, J. Chem. Educ. 36 (1959) 521.
[26] R.S. Nyholm, J. Chem. Educ. 34 (1957) 166.
[27] R.G. Pearson, C.R. Boston, F. Basolo, J. Am. Chem. Soc. 74 (1952) 2943.
[28] R.V. Young, S. Sessine (Eds.), World of Chemistry, Gale Group, Farmington Hills, MI, 2000, p. 552.
[29] R. Porter (Ed.), The Biographical Dictionary of Scientists, second ed., Oxford University Press, New York, 1994, p. 518.
[30] S.E. Livingstone, in: G.B. Kauffman (Ed.), Coordination Chemistry: A Century of Progress, American Chemical Society, Washington, DC, 1994 (Chapter 10).
[31] R.G. Pearson, e-mail to G.B. Kauffman, March 27, 2007.
[32] F. Basolo, Coord. Chem. Rev. 100 (1990) 47.
[33] J.L. Burmeister, Trans. Delaware Acad. Sci. 21 (1994–1995) 9.
[34] R.J. Angelici, e-mail to G.B. Kauffman, March 22, 2007.
[35] A.L. Crumbliss, e-mail to G.B. Kauffman, March 16, 2007.
[36] G.C. Pimentel, J.A. Coonrod, Opportunities in Chemistry, National Academy Press, Washington, DC, 1985.
[37] G.C. Pimentel, J.A. Coonrod, Opportunities in Chemistry Today and Tomorrow, National Academy Press, Washington, DC, 1987.
[38] M. Jacoby, Chem. Eng. News 79 (13) (2001) 59. http://pubs.acs.org/cen/coverstory/7914/7914basolo.html.
[39] J.L. Burmeister, Coord. Chem. Rev. 105 (1990), 269-page issue with 11 papers by former students.

$[HPO_4\{W_2O_2(\mu\text{-}O_2)_2(O_2)_2\}]^{2-}$ denoted "PW_2", etc.) [5,9]. All investigations on the mechanism of epoxidation [8,9,16] under Venturello's conditions [5] ($[MO_4]^{2-}$/$[PO_4]^{3-}$/$[H_3O]^+$/H_2O_2–H_2O/phase-transfer catalyst (PTC)/organic solvent/60 °C) and under Ishii's conditions [19–21] ($H_3[PM_{12}O_{40}]\cdot aq/H_2O_2$–$H_2O$/PTC/organic solvent/40–70 °C) indicate that the two catalyst systems involve common oxodiperoxo anions, despite the fact that each group patented its particular set of precursors as novel chemistry. Since then, additional studies support these results [22–24]. On the other hand, the first cases of oxoperoxometalates, related to the Keggin structure, have also been reported (e.g. $[(Nb^{V}O_2)_3PW_9O_{37}]^{6-}$, $[(Co^{II}O_4)\text{-}W_{11}O_{31}(O_2)_4]^{10-}$, etc.) [25–28]; they were also prepared from aqueous H_2O_2. For the silicon analogues, very drastic conditions ($[H_2O_2]/[W] \approx 8000$; 70 wt% aqueous H_2O_2) are necessary to degrade $H_4[SiW_{12}O_{40}]\cdot aq$ and to generate oxoperoxo species [8]. The corresponding silicopolyoxoperoxomolybdates or tungstates have been synthesized, but are difficult to purify [29]. Furthermore, silica and molybdenum (or tungsten) oxoperoxo moieties $\{MO(O_2)_2\}$ and/or $\{M_2O_2(\mu\text{-}O_2)_2(O_2)_2\}$ interact in aqueous acidic medium to form surface oxoperoxo species with characteristic IR and Raman bands $\tilde{\nu}$(O–O) in the 840–870 cm^{-1} range and $\tilde{\nu}_{asym}(M(O_2))$, $\tilde{\nu}_{sym}(M(O_2))$ at 600–520 cm^{-1} [30]. These observations suggest that it might be possible to synthesize low-nuclearity oxoperoxoheterosiloxanes [29,31] involving the various functionalities on the silica surface (i.e. lone (free) geminal silanols and vicinal silanols from siloxane bridges). These complexes are good models for units such as $\{MO(O_2)_2\}$, $\{M_2O_2(\mu\text{-}O_2)_2(O_2)_2\}$ grafted onto a silica surface (vide supra) via silanols. They also lead to a novel and efficient procedure for molybdenum [32] or tungsten [33,34] insertion into silica MCM-41 mesoporous molecular sieves with high metal dispersion. These syntheses avoid the formation of iso (or hetero) polyoxometalates in the counter-ion-mediated $S^+X^-I^+$ *acidic pathway* [32–34] and favour the presence of low-nuclearity oxoperoxo complexes. These moieties lead to unprecedentedly high incorporation levels [(Si:M) molar ratio ≈ 30:1) not known previously in the SiO_2–MO_3 systems, with a nearly homogeneous distribution of the "MO_x" dopants. These MO_x–SiO_2–MCM-41 are catalysts for gas- or liquid-phase reactions [32–34]. One problem is their sensitivity to the medium where they are employed: leaching of the metal-oxo species is due to nucleophilic attack of the neutral centres by solvents, water and/or reactants or products, but this can be avoided by optimized thermal or hydrothermal treatments. If the leaching problem can be overcome, the MO_x–SiO_2–MCM-41 catalysts and analogues, e.g. SBA-15 [35], etc. may have a promising future on a laboratory and even an industrial scale. To avoid or minimize leaching, a number of organosilanes can be used to generate hybrid organic/inorganic mesoporous materials either by co-condensation or grafting techniques, and thus to allow the control of the surface hydrophilic/hydrophobic balance [36], the objective being the synthesis of silica-based materials highly resistant to nucleophilic attack [37,38]. To open up new possibilities, the synthesis of their model oxoperoxo complexes in *neutral or basic medium* with $R_2Si(OR')_2$ precursors ($R_2 = (CH_3)_2$, $(i\text{-}C_4H_9)_2$ or $(CH_3)(CH_2Cl)$) was investigated. Here we report the synthesis and structural characterization of dimeric molybdenum(VI) and tungsten(VI) polyoxoperoxo complexes: $[PPh_4]_2[R_2SiO_2\{M_2O_2\text{-}(\mu\text{-}O_2)_2(O_2)_2\}]$, M = Mo, W. They not only represent a novel type of silicon-based species for oxidation catalysis, but also models for the preparation of organic/inorganic mesophases or silica-supported molybdenum oxide materials under study in our group [37,38].

2. Experimental

2.1. Materials

Molybdenum trioxide MoO_3 (Fluka) and tungstic acid formulated as $WO_3\cdot H_2O$ (Eurotungstène), 30 wt% aqueous solution of hydrogen peroxide, H_2O_2, (stabiliser: stannate; Prolabo, Aldrich), diethoxydimethylsilane (97%, Aldrich), $(CH_3)_2Si(OEt)_2$, diisobutyldimethoxysilane (97%, Lancaster), $(i\text{-}C_4H_9)_2Si(OMe)_2$, (chloromethyl)methyldiethoxysilane (97%, Lancaster), $(CH_3)(CH_2Cl)Si(OEt)_2$ and $P(C_6H_5)_4Cl$ (≥97%, Fluka) were used without further purification.

Chemical analyses were carried out by the Service Centrale d'Analyse (CNRS, Vernaison, France). All other reagents used (cyclooctene, toluene, chloroform, etc.) were analytical grade.

2.2. Crystal structure determinations: data collection and processing

All measurements were carried out at room temperature using a Enraf-Nonius CAD-4 four-circle diffractometer with graphite-monochromated Mo Kα radiation ($\lambda = 0.71069$ Å). Data were obtained with the ω–2θ scan technique. Two standard reflections showed no significant variation in intensity. Corrections were made for Lorentz and polarization effects; an extinction correction was also applied [39]; an empirical absorption correction on the basis of ψ scan data was introduced. The structures were solved by direct methods (SHELXS-86 program) [40] and subsequent Fourier difference techniques. All non-hydrogen atoms were refined anisotropically. All hydrogen atoms were found on difference Fourier maps; their positions were not refined and they were given one overall isotropic parameter. Refinements were carried out with the CRYSTALS program [41] by minimizing the function $\sum w(|F_o| - |F_c|)^2$, where F_o and F_c are the observed and calculated structure factors.

2.3. Physical measurements

The IR spectra (resolution: 2 cm^{-1}) of the solids as powders, in nujol suspension between two caesium bromide

plates or in dry potassium bromide discs, were measured at 4000–400 cm^{-1} on a Bruker Vector 22 Fourier-transform spectrometer. The ^1H and ^{13}C NMR spectra were recorded using 100 scans at room temperature on a Bruker ASX 300 apparatus, using TMS as reference. CD_3CN, provided by Euriso-top (C.E.A. France), was used as the solvent.

2.4. Syntheses of heteropolyoxoperoxoanions

MoO_3 (0.72 g; 5 mmol) ["H_2WO_4" (1.25 g; 5 mmol)] was added to a 30% solution of aqueous hydrogen peroxide (5 mL; 45 mmol). After 1 h stirring at 60 °C, the yellow [colourless] solution was cooled to room temperature [followed by centrifugation (15 min at 2000 rpm)] to give solution A.

$[PPh_4]_2[(CH_3)_2SiO_2\{M_2O_2(\mu\text{-}O_2)_2(O_2)_2\}]$ **1**: M = Mo and **2**: M = W. NaOH (5 M; 950 μL; 4.75 mmol) and $(CH_3)_2Si(OEt)_2$ (860 μL; 5 mmol) were mixed with 20 mL of ethanol and then added dropwise to solution A. The solution B thus obtained turns slightly orange (B–Mo) [colourless (B–W)] and **1** [**2**] was isolated by addition of an aqueous solution of PPh_4Cl (1.87 g; 4 mL; 5 mmol). After 15 min stirring, the yellow [white] precipitate was filtered off, washed with water (2 × 5 mL) and diethylether (2 × 5 mL), then air-dried. Yield relative to M: 2.10 g; 75% for **1** and 2.33 g; 77% for **2**. (The addition of excess sodium hydroxide would favour the undesired formation of $Na_2[M(O_2)_4]$.)

Anal. Calc. for $C_{50}H_{46}Mo_2O_{12}P_2Si$ (**1**) requires: C, 53.58; H, 4.14; Mo, 17.12; P, 5.53; Si, 2.51. Found: C, 53.77; H, 4.36; Mo, 17.15; P, 5.99; Si, 2.35%. IR (cm^{-1}; nujol mull) 1584 m $\tilde{\nu}$(C–C)$_{arom}$, 1108s δ(C–C)$_{arom}$ + $\tilde{\nu}$(Si–C), 971–958s $\tilde{\nu}$(Mo=O), 916s $\tilde{\nu}$(Si–O), 868vs $\tilde{\nu}$(O–O), 585s $\tilde{\nu}_{asym}(MoO_2)$, 528vs $\tilde{\nu}_{sym}(MoO_2)$; $\delta_H(CD_3CN)$ 0.1 (6H, s, C**H**$_3$–Si) and 7.9 (40H, m, [(C$_6$**H**$_5$)$_4$P$^+$]); δ_C (CD_3CN) 1.9 (2C, s, [**C**H$_3$–Si]), 134.1 (8C, d, [(**C**$_6$H$_5$)$_4$P$^+$]) and 138.2 (40C, m, [(**C**$_6$H$_5$)$_4$P$^+$]).

Anal. Calc. for $C_{50}H_{46}O_{12}P_2SiW_2$ (**2**) requires: C, 46.31; H, 3.57; P, 4.77; Si, 2.16; W, 28.35: Found: C, 46.22; H, 3.92; P, 4.46; Si, 1.92; W, 27.75%. IR (cm^{-1}; nujol mull) 1584m $\tilde{\nu}$(C–C)$_{arom}$, 1106s δ(C–C)$_{arom}$ + $\tilde{\nu}$(Si–C), 984–964s $\tilde{\nu}$(W=O), 916s $\tilde{\nu}$(Si–O), 838vs $\tilde{\nu}$(O–O), 573s $\tilde{\nu}_{asym}(WO_2)$, 525vs $\tilde{\nu}_{sym}(WO_2)$. δ_H (CD_3CN) 0.1 (6 H, s, [C**H**$_3$–Si]) and 7.7 (40H, m, [(C$_6$**H**$_5$)$_4$P$^+$]); δ_C(CD_3CN) 1.7 (2C, s, [**C**H$_3$–Si]), 131.1 (8C, d, [(**C**$_6$H$_5$)$_4$P$^+$]) and 136.2 (40C, m, ([(**C**$_6$H$_5$)$_4$P$^+$]).

Prepared similarly were: $[PPh_4]_2[(i\text{-}C_4H_9)_2SiO_2\{Mo_2O_2(\mu\text{-}O_2)_2(O_2)_2\}]$; **3**: M = Mo and **4**: M = W. $(i\text{-}C_4H_9)_2Si(OMe)_2$ (1.2 mL; 5 mmol) was used as the silicon precursor. Yield relative to M: 2.41 g; 80% for **3** and 2.52 g; 78% for **4**.

Anal. Calc. for $C_{56}H_{58}Mo_2O_{12}P_2Si$ (**3**) requires: C, 55.82; H, 4.85; Mo, 15.92; P, 5.14; Si, 2.33. Found: C, 55.76; H, 4.44; Mo, 16.46; P, 4.70; Si, 2.09%. IR (cm^{-1}; nujol mull) 1585m $\tilde{\nu}$(C–C)$_{arom}$, 1109s δ(C–C)$_{arom}$ + $\tilde{\nu}$(Si–C), 963–948s $\tilde{\nu}$(Mo=O), 918s $\tilde{\nu}$(Si–O), 866vs $\tilde{\nu}$(O–O), 584s $\tilde{\nu}_{asym}(MoO_2)$, 526vs $\tilde{\nu}_{sym}(MoO_2)$.

Anal. Calc. for $C_{56}H_{58}W_2O_{12}P_2Si$ (**4**) requires: C, 48.71; H, 4.23; P, 4.49. Found: C, 48.21; H, 3.95; P, 4.24%. IR (cm^{-1}; nujol mull): 1585m $\tilde{\nu}$(C–C)$_{arom}$, 1108s δ(C–C)$_{arom}$ + $\tilde{\nu}$(Si–C), 973–958s $\tilde{\nu}$(W=O), 918s $\tilde{\nu}$(Si–O), 848vs $\tilde{\nu}$(O–O), 572s $\tilde{\nu}_{asym}(WO_2)$, 527vs $\tilde{\nu}_{sym}(WO_2)$.

Prepared similarly were: $[PPh_4]_2[(CH_3)(CH_2Cl)SiO_2\{Mo_2O_2(\mu\text{-}O_2)_2(O_2)_2\}]$; **5**: M = Mo and **6**: M = W. $(CH_3)(CH_2Cl)Si(OEt)_2$ (920 mL; 5 mmol) was used to generate disilanol $(CH_3)(CH_2Cl)Si(OH)_2$. Yield relative to M: 2.31 g; 80% for **5** and 2.39 g; 77% for **6**.

Anal. Calc. for $C_{56}H_{58}Mo_2O_{12}P_2Si$ (**5**) requires: C, 51.98; H, 3.93; P, 5.36; Cl, 3.07. Found: C, 51.42; H, 3.55; P, 5.02; Cl, 2.90%.

IR data for **5** (cm^{-1}; nujol mull) 1582m $\tilde{\nu}$(C–C)$_{arom}$, 1106s δ(C–C)$_{arom}$ + $\tilde{\nu}$(Si–C), 966s $\tilde{\nu}$(Mo=O), 933s $\tilde{\nu}$(Si–O), 866vs $\tilde{\nu}$(O–O), 801w $\tilde{\nu}$(C–Cl), 585s $\tilde{\nu}_{asym}(MoO_2)$, 525vs $\tilde{\nu}_{sym}(MoO_2)$.

Anal. Calc. for $C_{56}H_{58}W_2O_{12}P_2Si$ **6** requires: C, 45.12; H, 3.41; P, 4.65; Cl, 2.60. Found: C, 44.80; H, 3.15; P, 4.17; Cl, 2.35%.

IR data for **6**: (cm^{-1}; nujol mull) 1582m $\tilde{\nu}$(C–C)$_{arom}$, 1107s δ(C–C)$_{arom}$ + $\tilde{\nu}$(Si–C), 971s $\tilde{\nu}$(W=O), 938s $\tilde{\nu}$(Si–O), 841vs $\tilde{\nu}$(O–O), 801w $\tilde{\nu}$(C–Cl), 580s $\tilde{\nu}_{asym}(WO_2)$, 525vs $\tilde{\nu}_{sym}(WO_2)$.

3. Results and discussion

3.1. Description of structures

According to crystal data (Table 1), chemical analyses and infrared spectra, **1** and **2**; **3** and **4**; **5** and **6** are pairs of isostructural compounds (see also supplementary materials, Table S1). Moreover, a detailed analysis of the crystal data reveals that **1** and **5** are isomorphous. The structures of the anions in complexes **1** and **3** are shown in Figs. 1 and 2 with some selected bond lengths and angles. For compounds **1**, **3** and **5**, they are compared in Table S1.

The anionic structure, in all cases, consists of an assembling anion: $[(CH_3)_2SiO_2)]^{2-}$, $[(i\text{–}C_4H_9)_2SiO_2]^{2-}$ or $[(CH_3)(CH_2Cl)SiO_2]^{2-}$ in **1**, **3** and **5**, respectively, and a dimeric moiety $\{Mo_2O_2(\mu\text{-}O_2)_2(O_2)_2\}$. Both molybdenum centres are 7-coordinated by oxygen atoms in a pentagonal bipyramidal arrangement (see Table S2 in supplementary material). These compounds, i.e. **1**–**6**, possess structures similar to that of the previously reported $[Ph_2SiO_2\{M_2O_2(\mu\text{-}O_2)_2(O_2)_2\}]^{2-}$ (M = Mo, W) complexes, prepared with the diphenylsilanediolato ligand, $[(C_6H_5)_2SiO_2]^{2-}$ [29].

Two oxygen atoms O(6) and O(7) of the $[R_2SiO_2]^{2-}$ anion are corner-sharing with the basal planes of the two different pentagonal bipyramids. The two Mo atoms are connected by two μ_2–η^1:η^2-peroxo bridges [O(4)–O(5) and O(9)–O(8)] also observed in several di- or tetranuclear anionic structures [5,9–11,14,15,29,42]. The two associated pentagonal bipyramids share one edge [O(5)···O(8)] on the non-basal plane. The asymmetric dimeric moiety $\{Mo_2O_2(\mu\text{-}O_2)_2(O_2)_2\}$ thus has two distinct pairs of peroxo ligands: there are both η^2- and μ_2-η^1:η^2-peroxo groups on

Table 1
Crystal data for compounds **1**, **3** and **5** and structure refinement details

	$[PPh_4]_2[(CH_3)_2SiO_2\{Mo_2O_2(\mu\text{-}O_2)_2(O_2)_2\}]$	$[PPh_4]_2[(i\text{-}C_4H_9)_2SiO_2\{Mo_2O_2(\mu\text{-}O_2)_2(O_2)_2\}]$	$[PPh_4]_2[(CH_3)(CH_2Cl)SiO_2\{Mo_2O_2(\mu\text{-}O_2)_2(O_2)_2\}]$
Compound	**1**	**3**	**5**
Formula	$C_{50}H_{46}Mo_2O_{12}P_2Si$	$C_{56}H_{58}Mo_2O_{12}P_2Si$	$C_{50}H_{45}ClMo_2O_{12}P_2Si$
M	1120.83	1204.99	1155.27
Crystal system	triclinic	triclinic	triclinic
Space group	$P\bar{1}$	$P\bar{1}$	$P\bar{1}$
a (Å)	13.395 (3)	10.646 (3)	13.467 (3)
b (Å)	13.474 (6)	11.086 (2)	13.548 (3)
c (Å)	15.877 (3)	24.237 (7)	15.931 (3)
α (°)	76.99 (3)	100.81 (2)	76.03 (2)
β (°)	77.80 (2)	96.56 (2)	79.39 (2)
γ (°)	61.03 (2)	101.36 (2)	61.18 (2)
V (Å^3)	2425 (1)	2721 (1)	2463 (1)
Z	2	2	2
μ (cm^{-1})	6.53	6.37	6.98
Reflections: total, used	8901, 5252	6771, 5194	10103, 7933
Final R	0.046	0.032	0.053
Final R_w^a $I > 3\sigma(I)$	0.053	0.039	0.058

[a] Weighting scheme of the form $w = w'[1 - ((||F_o| - |F_c||)/6\sigma(F_o))^2]^2$ with $w' = 1/\sum_r A_r T_r(X)$ for a Chebyshev series for which $X = F_c/F_c(\max)$ with coefficients for compound **1**: 4.56, −0.91 and 3.40, for compound **3**: 3.78, 0.232, 2.58 and for compound **5**: 8.83, 0.697, 7.24.

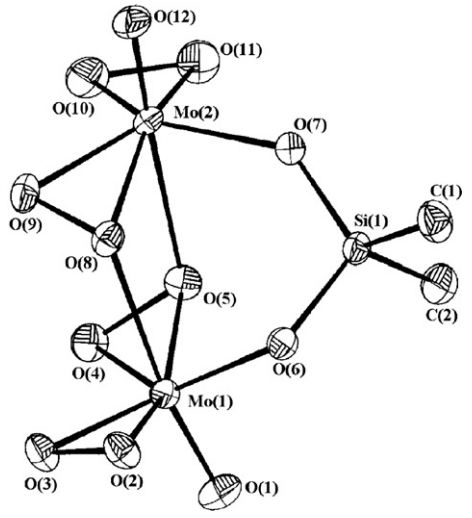


Fig. 1. CAMERON [48] representation of the anion $[(CH_3)_2SiO_2\text{-}\{Mo_2O_2(\mu\text{-}O_2)_2(O_2)_2\}]^{2-}$ in complex (**1**), with 40% thermal probability ellipsoids. Selected bond lengths (Å) and bond angles (°): Mo(1)–O(1), 1.681(5); Mo(1)–O(2), 1.934(4); Mo(1)–O(3), 1.924(4); Mo(1)–O(4), 1.903(4); Mo(1)–O(5), 1.986(4); Mo(1)–O(6), 1.954(4); Mo(1)–O(8), 2.416(4), Mo(2)–O(5), 2.492(4); Mo(2)–O(7), 1.953(4); Mo(2)–O(8), 2.005(4); Mo(2)–O(9), 1.920(4); Mo(2)–O(10), 1.912(5); Mo(2)–O(11), 1.923(5); Mo(2)–O(12), 1.686(4); O(2)–O(3), 1.466(6); O(4)–O(5), 1.474(6); O(8)–O(9), 1.483(6); O(10)–O(11), 1.479(8); Si(1)–O(6), 1.621(4); Si(1)–O(7), 1.617(4); Si(1)–C(1), 1.845(7); Si(1)–C(2), 1.866(8); O(2)–Mo(1)–O(3), 44.7(2); O(4)–Mo(1)–O(5), 44.5(2); O(8)–Mo(2)–O(9), 44.1(2); O(10)–Mo(2)–O(11), 45.4(2); O(1)–Mo(1)–O(8), 171.8(2); O(12)–Mo(2)–O(5), 170.9(2).

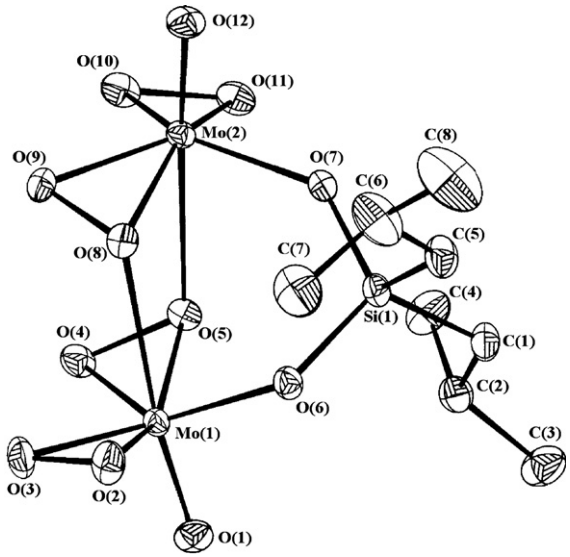


Fig. 2. CAMERON [48] representation of the anion $[(i\text{-}C_4H_9)_2SiO_2\text{-}\{Mo_2O_2(\mu\text{-}O_2)_2(O_2)_2\}]^{2-}$ in complex (**3**), with 40% thermal probability ellipsoids. Selected bond lengths (Å) and bond angles (°): Mo(1)–O(1), 1.682(3); Mo(1)–O(2), 1.926(3); Mo(1)–O(3), 1.926(3); Mo(1)–O(4), 1.909(3); Mo(1)–O(5), 1.996(2); Mo(1)–O(6), 1.960(2); Mo(1)–O(8), 2.429(2), Mo(2)–O(5), 2.484(3); Mo(2)–O(7), 1.959(2); Mo(2)–O(8), 2.006(2); Mo(2)–O(9), 1.934(3); Mo(2)–O(10), 1.911(3); Mo(2)–O(11), 1.924(3); Mo(2)–O(12), 1.678(3); O(2)–O(3), 1.469(4); O(4)–O(5), 1.464(4); O(8)–O(9), 1.479(3); O(10)–O(11), 1.474(5); Si(1)–O(6), 1.641(2); Si(1)–O(7), 1.611(3); Si(1)–C(1), 1.868(4); Si(1)–C(5), 1.857(4); O(2)–Mo(1)–O(3), 44.9(1); O(4)–Mo(1)–O(5), 44.0(1); O(8)–Mo(2)–O(9), 44.0(1); O(10)–Mo(2)–O(11), 45.2(1); O(1)–Mo(1)–O(8), 170.7(1); O(12)–Mo(2)–O(5), 170.8(1).

each metal centre. The pentagonal bipyramids of oxygen atoms surrounding the two molybdenum atoms are almost identical. Each girdle (equatorial plane) is generated by two peroxo groups, one bridging and one non-bridging, and by one oxygen atom of the $[R_2SiO_2]^{2-}$ anion. The oxygen atoms that define the equatorial plane are coplanar to

within 0.006–0.109 Å (Table S2, supplementary materials). As for the octahedral coordination in polyoxometalates and what is also observed with other silicooxoperoxometalates [29], Mo(1) and Mo(2) are located outside the mean plane defined by the five equatorial oxygen atoms (0.37 to 0.40 Å – supplementary materials, Table S2). One of the apical positions of the girdle axis is occupied by the terminal oxo-ligand, and the other by an oxygen atom of the bridging peroxo group with a rather weak and long Mo–O bond (in the range 2.416–2.502 Å for each structure – see Figs. 1 and 2 and Table S1). The non-bridging peroxo groups, [O(2)–O(3) and O(10)–O(11)], are symmetrically coordinated to the Mo atom; the Mo–O distances are nearly equal and correspond to classical single Mo–O bonds (1.911–1.934 Å). In contrast, the bridging peroxo groups μ_2–η^1:η^2 O(5)–O(4) and O(8)–O(9) are dissymmetrically coordinated to Mo(1) and Mo(2), resulting in relatively long Mo(1)–O(5) and Mo(2)–O(8) bonds (1.986–2.006 Å) as expected, and in a shorter bond with the second oxygen atom (1.903–1.934 Å). In all cases, the O–O distances correspond to a classical peroxo bond (1.464–1.483 Å). For instance, in the $[Ph_2SiO_2\{M_2O_2(\mu\text{-}O_2)_2(O_2)_2\}]^{2-}$ anion, the O–O bond lengths were in the range 1.468–1.481 Å [29].

3.2. Infrared spectroscopy

The IR spectra (Fig. 3; Table 2) of complexes **1**–**6** show features comparable to those observed for all other dinuclear species [9–11,29] and support the proposal of isostructural compounds (vide supra). In addition, a band near 1582–1584 cm^{-1} is assigned as $\tilde{\nu}(C\text{–}C)_{arom}$ of the cation and a very sharp band at 1106–1109 cm^{-1} as an in–plane deformation of the phenyl ring with some $\tilde{\nu}$(Si–C) character [29–31]. Consistent with the structural data, there are two strong $\tilde{\nu}$(M=O bands at 971 and 958 cm^{-1} for **1**, at 984 and 964 cm^{-1} for **2**, at 963 and 948 cm^{-1} for **3** and at 973 and 958 cm^{-1} for **4**. For $[(CH_3)(CH_2Cl)SiO_2\{M_2O_2(\mu\text{-}O_2)_2(O_2)_2\}]$ only one very strong maximum at 966 cm^{-1} for M = Mo (**5**) and 971 cm^{-1} for M = W (**6**) can be attributed unambiguously. Si–O stretches appear in the 916–938 cm^{-1} region as very strong maxima for all compounds. Bands at about 865 cm^{-1} for the heteropolyoxoperoxomolybdate anions and near 840 cm^{-1} for tungsten analogues are assigned to $\tilde{\nu}$(O–O) of the peroxo ligands, and bands around 575 and 525 cm^{-1} are assigned to asymmetric and symmetric [$M(O_2)$] stretches, respectively.

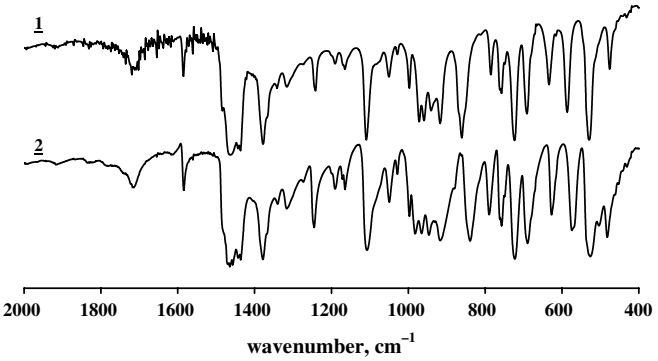


Fig. 3. IR spectra (nujol mull) of $[PPh_4]_2[(CH_3)_2SiO_2\{Mo_2O_2(\mu\text{-}O_2)_2(O_2)_2\}]$ (**1**) and $[PPh_4]_2[(CH_3)_2SiO_2\{W_2O_2(\mu\text{-}O_2)_2(O_2)_2\}]$ (**2**).

4. Conclusion and prospectives

The organosilicate derivatives reported here are structurally related to hydrogenophosphate [9], hydrogenoarsonate [10], sulfate [11], diphenylsilanediolato [29], etc. analogues which belong to a family which is now significantly extended. The chemistry of metallasiloxanes derived from silanediols, disiloxanediols and related Si–OH species is an area of active research, because such compounds are valuable precursors for metal oxides and silicates, and are models for silica-supported or inserted heterogeneous catalysts [37,38]. Novel organically modified silicates have been prepared under alkaline conditions, by direct reaction of $R_2Si(OR')_2$ and oxoperoxo moieties $\{MO(O_2)_2\}$ and/or $\{M_2O_2(\mu\text{-}O_2)_2(O_2)_2\}$ ($R_2 = (CH_3)_2$, $(i\text{-}C_4H_9)_2$ or $(CH_3)(CH_2Cl)$; $R' = CH_3$ or C_2H_5, M = Mo(VI) or W(VI)).

Table 2
Vibrational spectroscopic characteristics (cm^{-1}) of oxodiperoxo complexes **1**–**6** and of three other model complexes

Complexes		$\tilde{\nu}$(M=O)	$\tilde{\nu}$(O–O)	$\tilde{\nu}_{asym}[M(O_2)]$	$\tilde{\nu}_{sym}[M(O_2)]$	Other bands[a]
$[PPh_4]_2[(CH_3)_2SiO_2\{Mo_2O_2(\mu\text{-}O_2)_2(O_2)_2\}]$	**1**	971vs				
		958vs	868vs	585s	528vs	916 $\tilde{\nu}$(Si–O); 1108 $\tilde{\nu}$(Si–C)
$[PPh_4]_2[(CH_3)_2SiO_2\{W_2O_2(\mu\text{-}O_2)_2(O_2)_2\}]$	**2**	984vs				
		964vs	838vs	573s	525vs	916 $\tilde{\nu}$(Si–O); 1106 $\tilde{\nu}$(Si–C)
$[PPh_4]_2[(i\text{-}C_4H_9)_2SiO_2\{Mo_2O_2(\mu\text{-}O_2)_2(O_2)_2\}]$	**3**	963vs				
		948vs	866vs	584s	526vs	918 $\tilde{\nu}$(Si–O); 1109 $\tilde{\nu}$(Si–C)
$[PPh_4]_2[(i\text{-}C_4H_9)_2SiO_2\{W_2O_2(\mu\text{-}O_2)_2(O_2)_2\}]$	**4**	973vs				
		958vs	848vs	572s	527vs	918 $\tilde{\nu}$(Si–O); 1108 $\tilde{\nu}$(Si–C)
$[PPh_4]_2[(CH_3)(CH_2Cl)SiO_2\{Mo_2O_2(\mu\text{-}O_2)_2(O_2)_2\}]$	**5**	966vs	866vs	585s	525vs	933 $\tilde{\nu}$(Si–O); 1106 $\tilde{\nu}$(Si– C)
$[PPh_4]_2[(CH_3)(CH_2Cl)SiO_2\{W_2O_2(\mu\text{-}O_2)_2(O_2)_2\}]$	**6**	971vs	841vs	580s	525vs	938 $\tilde{\nu}$(Si–O); 1107 $\tilde{\nu}$(Si–C)
$(NBu_4)_2[HPO_4\{W_2O_2(\mu\text{-}O_2)_2(O_2)_2\}]$ [9]		983vs	843vs	569s	517vs	1021; 995 $\tilde{\nu}(PO_4)$
$(NHex_4)_3[PO_4\{W_2O_2(\mu\text{-}O_2)_2(O_2)_2\}_2]$ [42]		974vs	845vs	577s	521vs	1084; 1053 $\tilde{\nu}(PO_4)$
$(NHex_4)_3[PO_4\{Mo_2O_2(\mu\text{-}O_2)_2(O_2)_2\}_2]$ [42]		962vs	868vs	590s	542vs	1069; 1040; 1025 $\tilde{\nu}(PO_4)$

[a] $\tilde{\nu}$(Si–O) with a possible contribution of M–O–Si vibration. $\tilde{\nu}$(Si–C) with a possible contribution of $\delta(C\text{–}C)_{arom}$ of the phenyl ring.

The dimers thus characterized, $[PPh_4]_2[R_2SiO_2\{M_2O_2(\mu\text{-}O_2)_2(O_2)_2\}]$, confirm the ability of peroxo ligands to adopt a η^2-bidentate or a bridging unsymmetrical (μ_2-η^2:η^1) role and the ability of disilanol precursors to act as assembling ligands. As in our previous studies [29–31], the alcoholic solvents containing water and hydrogen peroxide provide an environment that promotes the synthesis of low-nuclearity species, even in alkaline hydrogen peroxide (this work), which would favour the formation of $[M(O_2)_4]^{2-}$. These structures would explain the spectroscopic, physical and chemical observations which are involved in the synthesis of organic/inorganic mesophases. Preliminary catalysis tests with not-too-demanding substrates give results poorer than those of the phosphate- or sulfate-based systems [5,9,42–46]. They illustrate the dramatic effects of the assembling ligand, the difficulty encountered in epoxidation with conventional chlorides as phase transfer catalysts and the deleterious effect of sodium chloride, which significantly slows the reaction [46]. The operating conditions of several phase transfer catalysis systems with different anionic mono- to tetranuclear species must be carefully optimized with more demanding alkenes which are of interest in our group as well as the fluxionality of highly active species [22,47]. Catalysis data will be presented later in a fuller report, devoted to comparative studies on d^0 transition metal-based systems and lacunary silicotungstate compounds.

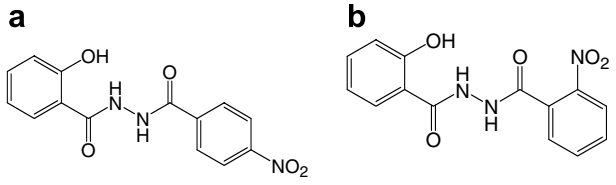
Appendix A. Supplementary material

CCDC 195087, 195088 and 195089 contain the supplementary crystallographic data for **1**, **3** and **5**. These data can be obtained free of charge via http://www.ccdc.cam.ac.uk/conts/retrieving.html, or from the Cambridge Crystallographic Data Centre, 12 Union Road, Cambridge CB2 1EZ, UK; fax: (+44) 1223-336-033; or e-mail: deposit@ccdc.cam.ac.uk. Supplementary data associated with this article can be found, in the online version, at doi:10.1016/j.poly.2007.06.007.

References

[1] H. Mimoun, I. Sérée de Roch, L. Sajus, Bull. Soc. Chim. Fr. (1969) 1481.
[2] R.G. Beiles, Z.E. Rozmanova, O.B. Andreeva, Zh. Neorg. Khim. 14 (1969) 2139–2142.
[3] R.G. Beiles, Z.E. Rozmanova, O.B. Andreeva, Russ. J. Inorg. Chem. 14 (1969) 1122.
[4] J.-M. Brégeault, M. Vennat, L. Salles, J.-Y. Piquemal, Y. Mahha, E. Briot, P.C. Bakala, A. Atlamsani, R. Thouvenot, J. Mol. Catal. A: Chem. 250 (2006) 177, and references therein.
[5] C. Venturello, R. D'Aloisio, J.C.J. Bart, M. Ricci, J. Mol. Catal. 32 (1985) 107.
[6] J.-M. Brégeault, C. Aubry, G. Chottard, N. Platzer, F. Chauveau, C. Huet, H. Ledon, Stud. Surf. Sci. Catal. 66 (1991) 521–529.
[7] J.-M. Brégeault, C. Aubry, G. Chottard, N. Platzer, F. Chauveau, C. Huet, H. Ledon, in: Proceedings of the Fourth Symposium on Dioxygen Activation and Homogeneous Catalytic Oxidation, 9–14 September 1990, Balatonfured, Hungary, 1990.
[8] C. Aubry, G. Chottard, N. Platzer, J.-M. Brégeault, R. Thouvenot, F. Chauveau, C. Huet, H. Ledon, Inorg. Chem. 30 (1991) 4409.
[9] L. Salles, C. Aubry, R. Thouvenot, F. Robert, C. Doremieux-Morin, G. Chottard, H. Ledon, Y. Jeannin, J.-M. Brégeault, Inorg. Chem. 33 (1994) 871.
[10] J.-Y. Piquemal, L. Salles, C. Bois, F. Robert, J.-M. Brégeault, C.R. Acad. Sci., Ser. IIb: Chim. 319 (1994) 1481.
[11] L. Salles, F. Robert, V. Semmer, Y. Jeannin, J.-M. Brégeault, Bull. Soc. Chim. Fr. 133 (1996) 319.
[12] L.J. Csányi, K. Jáky, J. Mol. Catal. 61 (1990) 75.
[13] A.C. Dengel, W.P. Griffith, B.C. Parkin, J. Chem. Soc., Dalton Trans. (1993) 2683.
[14] A.J. Bailey, W.P. Griffith, B.C. Parkin, J. Chem. Soc., Dalton Trans. (1995) 1833.
[15] W.P. Griffith, B.C. Parkin, A.J.P. White, D.J. Williams, J. Chem. Soc., Dalton Trans. (1995) 3131.
[16] D.C. Duncan, R.C. Chambers, E. Hecht, C.L. Hill, J. Am. Chem. Soc. 117 (1995) 681.
[17] N.M. Gresley, W.P. Griffith, B.C. Parkin, A.J.P. White, D.J. Williams, J. Chem. Soc., Dalton Trans. (1996) 2039.
[18] N.M. Gresley, W.P. Griffith, A.C. Laemmel, H.I.S. Nogueira, B.C. Parkin, J. Mol. Catal. A: Chem. 117 (1997) 185.
[19] Y. Ishii, K. Yamawaki, T. Ura, H. Yamada, T. Yoshida, M. Ogawa, J. Org. Chem. 53 (1988) 3587.
[20] Y. Matoba, H. Inoue, J. Akagi, T. Okabayashi, Y. Ishii, M. Ogawa, Synth. Commun. 14 (1984) 865.
[21] S. Sakaguchi, Y. Nishiyama, Y. Ishii, J. Org. Chem. 61 (1996) 5307.
[22] L. Salles, J.-Y. Piquemal, R. Thouvenot, C. Minot, J.-M. Brégeault, J. Mol. Catal. A: Chem. 117 (1997) 375.
[23] M. Hashimoto, K. Itoh, K.Y. Lee, M. Misono, Top. Catal. 15 (2001) 265.
[24] M. Te, C. Fairbridge, Z. Ring, Appl. Catal. A: General 219 (2001) 267.
[25] M.K. Harrup, G.-S. Kim, H. Zeng, R.P. Johnson, D. VanDerveer, C.L. Hill, Inorg. Chem. 37 (1998) 5550.
[26] J. Server-Carrió, J. Bas-Serra, M.E. González-Núñez, A. Garcia-Gastaldi, G.B. Jameson, L.C.W. Baker, R. Acerete, J. Am. Chem. Soc. 121 (1999) 977.
[27] O.A. Kholdeeva, G.M. Maksimov, R.I. Maksimovskaya, L.A. Kovaleva, M.A. Fedotov, V.A. Grigoriev, C.L. Hill, Inorg. Chem. 39 (2000) 3828.
[28] T. Yamase, E. Ishikawa, Y. Asai, S. Kanai, J. Mol. Catal. A: Chem. 114 (1996) 237.
[29] J.-Y. Piquemal, C. Bois, J.-M. Brégeault, Chem. Commun. (1997) 473.
[30] J.-Y. Piquemal, Ph. D. Thesis, P. and M. Curie University, Paris, 28 October 1998.
[31] J.-Y. Piquemal, S. Halut, J.-M. Brégeault, Angew. Chem., Int. Ed. Engl. 37 (1998) 1146.
[32] J.-Y. Piquemal, J.-M. Manoli, P. Beaunier, A. Ensuque, P. Tougne, A.P. Legrand, J.M. Brégeault, Micropor. Mesopor. Mater. 29 (1999) 291.
[33] E. Briot, J.-Y. Piquemal, M. Vennat, J.-M. Brégeault, G. Chottard, J.-M. Manoli, J. Mater. Chem. 10 (2000) 953.
[34] J.-M. Brégeault, J.-Y. Piquemal, E. Briot, E. Duprey, F. Launay, L. Salles, M. Vennat, A.P. Legrand, Micropor. Mesopor. Mater. 44–45 (2001) 409.
[35] E. Briot, J.-Y. Piquemal, J.-M. Brégeault, New J. Chem. 26 (2002) 1443.
[36] A. Stein, B.J. Melde, R.C. Schroden, Adv. Mater. 12 (2000) 1403.
[37] P.C. Bakala, E. Briot, L. Salles, J.-M. Brégeault, Appl. Catal. A: General 300 (2006) 91.
[38] P.-C. Bakala, E. Briot, J.-Y. Piquemal, J.-M. Brégeault, P. Beaunier, Catal. Commun. 8 (2007) 1447.
[39] A.C. Larson, in: F.R. Ahmed, S.R. Hall, C.P. Huber (Eds.), Crystallographic Computing, Munksgaard, Copenhagen, 1970, p. 291.

[40] G.M. Sheldrick, SHELXS-86, Program for the Solution of Crystal Structures, University of Göttingen, 1986.
[41] D.J. Watkin, C.K. Prout, R.J. Carruthers, P.W. Betteridge, CRYSTALS, An Advanced Crystallographic Program System, Chemical Crystallography Laboratory, University of Oxford, 1996.
[42] L. Salles, C. Aubry, F. Robert, G. Chottard, R. Thouvenot, H. Ledon, J.-M. Brégeault, New J. Chem. 17 (1993) 367.
[43] L. Salles, J.-M. Brégeault, R. Thouvenot, C.R. Acad. Sci., Ser. IIc: Chim. 3 (2000) 183.
[44] J.-M. Brégeault, R. Thouvenot, S. Zoughebi, L. Salles, A. Atlamsani, E. Duprey, C. Aubry, F. Robert, G. Chottard, Stud. Surf. Sci. Catal. 82 (1994) 571–581.
[45] J.-M. Brégeault, R. Thouvenot, S. Zoughebi, L. Salles, A. Atlamsani, E. Duprey, C. Aubry, F. Robert, G. Chottard, in: Proceedings of the Second World Congress and Fourth European Workshop Meeting on New Developments in Selective Oxidation, 20–24 September 1993, Benalmadena, Spain, 1993.
[46] Y. Mahha, L. Salles, J.-Y. Piquemal, E. Briot, A. Atlamsani, J.-M. Brégeault, J. Catal. 249 (2007) 338.
[47] L. Salles, R. Thouvenot, J.-M. Brégeault, Dalton Trans. (2004) 904.
[48] D.J. Watkin, C.K. Prout, L.J. Pierce, CAMERON, Chemical Crystallography Laboratory, University of Oxford, 1996.



Scheme 1. Ligands H_3-*o*-nbzshz (a) and H_3-*p*-nbzshz (b).

$Ni_3(shi)_2(Hpko)_2(py)_2$, $[Ni_3(L^2)_2(OAc)_2(MeOH)(H_2O)][BF_4]_2$ and $[Ni_3(oxen)_2(en)][ClO_4]_2$ are reported in the literature [17–19]. Herein, we wish to report the synthesis and crystal structures of three novel trinuclear complexes $[Zn_3(p\text{-nbzshz})_2(C_5H_5N)_4]_n$ (**1**), $Ni_3(p\text{-nbzshz})_2(py)_4$ (**2**) and $Ni_3(o\text{-nbshz})_2(DMF)_2((CH_3)_2O)_2$ (**3**) with two new ligands *N*-*p*-nitrobenzoylsalicylhyldrazidate (H_3-*p*-nbzshz) (Scheme 1a) and *N*-*o*-nitrobenzoylsalicylhydrazidate (H_3-*o*-nbzshz) (Scheme 1b). Complex **1** is the first example of a zinc(II) complex which exhibits a one-dimensional extended polymeric chain structure constructed by *N*-acyl-salicylhydrazides ligands. Complex **2** is the only uncommon bent trinuclear nickel complex with a *N*-acyl-salicylhydrazide, whilst the three nickel atoms in complex **3** are arranged in a strictly linear fashion.

2. Experimental

2.1. General

All reagents for the syntheses were obtained commercially with analytical grade and were used without further purification. Elemental (C, H, N) analysis data were obtained with a Perkin–Elmer Model 240C elemental analyzer. Infrared spectra were collected on an AVATAR 360 FT-spectrometer in the range 4000–400 cm^{-1} (KBr pellets). TG analysis was performed on a Perkin–Elmer DF40 instrument in flowing N_2 with a heating rate of 10 °C min^{-1}.

2.2. Syntheses of the ligands and metal complexes

2.2.1. *N-p-nitrobenzoylsalicylhydrazidate (H_3-p-nbzshz)*

4-Nitro-benzoylchloride (3.10 g, 16.7 mmol), *p*-nitrobenzoic acid (2.78 g, 16.7 mmol), NaOH (0.668 g, 16.7 mmol) and a little tetrabutylammonium bromide were added to chloroform (60 mL). The mixture was filtered after stirring for 4 h at 0 °C. Then salicylhydrazide (4.24 g, 27.7 mmol) was added to the filtrate and it was slowly warmed to room temperature. A light yellow precipitate was obtained and rinsed with chloroform and diethyl ether (yield 1.85 g, 44.37%). Mp: 187–190 °C. *Anal.* Calc. for $C_{14}H_{11}N_3O_5$: C, 55.82; H, 3.68; N, 13.95. Found: C, 55.98; H, 3.46; N, 13.85%. IR (KBr, cm^{-1}): ν(O–H) 3261.64(s), ν(C=O) 1648.04(m), ν_s(>C=N–N=C<) 1614.26(vs), ν_{as}(–NO_2) 1522.90(s), ν_s(–NO_2) 1346.26(s), δ(N–H) + ν(C–N) or ν(C=C) 1507.97(s), ν(C=N) + δ(N–H) 1315.39(m), ν(ArC–O) 1237.52(m).

2.2.2. *N-o-nitrobenzoylsalicylhydrazidate(H_3-o-nbzshz)*

o-Nitrobenzoic acid (1.85 g, 11.1 mmol), 2-nitrobenzoyl chloride (2.07 g, 11.1 mmol) and NaOH (0.445 g, 11.1 mmol) were added to chloroform (60 mL). The mixture was filtered after stirring at 0 °C for half an hour. Then salicylhydrazide (4.24 g, 27.9 mmol) was added to the filtrate to give a light yellow precipitate, which was collected and rinsed with chloroform and diethyl ether (yield 1.60 g, 57.68%). *Anal.* Calc. for $C_{14}H_{11}N_3O_5$: C, 55.82; H, 3.68; N, 13.95. Found: C, 55.88; H, 3.38; N, 13.76%. Mp: 205–207 °C. IR (KBr, cm^{-1}): ν(O–H) 3175.22(s), ν(C=O) 1675.24(w), 1640.68(s), ν_s(>C=N–N=C<) 1608.56(vs), ν_{as}(–NO_2) 1529.39(s), ν_s(–NO_2) 1350.43(s), δ(N–H) + ν(C–N) or ν(C=C) 1562.08(vs), ν(C=N) + δ(N–H) 1308.07(m), ν(ArC–O) 1240.37(m).

2.2.3. *$Zn_3(p\text{-nbzshz})_2(C_5H_5N)_4$ (1)*

A DMF (10 mL) solution of H_3-*p*-nbzshz (0.075 g, 0.25 mmol) was added to a pyridine solution (5 mL) of $Zn(OAc)_2 \cdot 4H_2O$ (0.055 g, 0.25 mmol). The resulting solution was filtered after stirring for 10 min. Orange block crystals were obtained from the filtrate after standing for 10 days. *Anal.* Calc. for $Zn_3(C_{14}H_8N_3O_5)_2(C_5H_5N)_4$: C, 51.99; H, 3.27; N, 12.63. Found: C, 52.18; H, 3.15; N, 12.26%. IR (KBr, cm^{-1}): ν_s(>C=N–N=C<) 1599.13(s), ν_{as}(–NO_2) 1521.25(vs), ν_s(–NO_2) 1343.41(s), ν(C=N) 1545.99(m), ν(C–O) 1399.24(s), ν_s(ArC–O) 1236.63(m), ν(M–O) 593.53(w), 523.55(w), ν(M–N) 471.05(w).

2.2.4. *$Ni_3(p\text{-nbzshz})_2(C_5H_5N)_4$ (2)*

A DMF (10 mL) solution of H_3-*p*-nbzshz (0.075 g, 0.25 mmol) was added to a methanol solution (5 mL) of $Ni(OAc)_2 \cdot 4H_2O$ (0.062 g, 0.25 mmol). The resulting solution was filtered after stirring for 10 min. Crystals were obtained from the filtrate after standing for 4 days. The red block crystals were recrystallized form DMF/pyridine (1:1). *Anal.* Calc. for $Ni_3(C_{14}H_8N_3O_5)_2(C_5H_5N)_4$: C, 52.94; H, 3.33; N, 12.86. Found: C, 53.25; H, 3.01; N, 12.58%. IR (KBr, cm^{-1}): ν_s(>C=N–N=C<) 1600.28(s), ν_{as}(–NO_2) 1518.94(vs), ν_s(–NO_2) 1339.42(s), ν(C=N) 1565.29(s), ν(C–O) 1418.18(s), ν_s(ArC–O) 1265.03(w), ν(M–O) 598.52(w), 540.52(w), ν(M–N) 471.05(w).

2.2.5. *$Ni_3(o\text{-nbzshz})_2(C_3H_7NO)_2(C_2H_6O)_2$ (3)*

A DMF (10 mL) solution of H_3-*o*-nbzshz (0.075 g, 0.25 mmol) was added to a methanol solution (5 mL) of $Ni(OAc)_2 \cdot 4H_2O$ (0.062 g, 0.25 mmol). The resulting solution was filtered after stirring for 10 min. Red block crystals were obtained from the filtrate after 40 days. *Anal.* Calc. for $Ni_3(C_{14}H_8N_3O_5)_2(C_3H_7NO)_2(C_2H_6O)_2$: C, 45.15; H, 4.19; N, 11.08. Found: C, 45.08; H, 3.98; N, 11.48%. IR (KBr, cm^{-1}): ν(C=O) 1653.26(vs), ν_s(>C=N–N=C<) 1600.09(s), ν_{as}(–NO_2) 1526.86(s), ν_s(–NO_2) 1336.56(m), ν(C=N) 1569.52(s), 1553.67(s), ν(C–O) 1412.35(s), δ(N–H) + ν(C–N) 1386.72(m), ν_s(ArC–O) 1263.35(m), ν(M–O) 589.60(w), 547.08(w), ν(M–N) 493.59(w).

Table 1
Crystallographic data of **1**, **2** and **3**

Compound	**1**	**2**	**3**
Formula	$C_{48}H_{36}N_{10}Zn_3O_{10}$	$C_{48}H_{36}N_{10}Ni_3O_{10}$	$C_{38}H_{42}N_8Ni_3O_{14}$
Formula weight	1108.98	1089.00	1010.93
Crystal system	monoclinic	triclinic	monoclinic
Space group	$C2/c$	$P\bar{1}$	$P2_1/n$
a (Å)	23.1644(9)	11.883(1)	9.0314(4)
b (Å)	8.8907(3)	12.214(1)	10.7146(3)
c (Å)	22.8723(7)	17.739(2)	22.0859(7)
α (°)	90	93.643(3)	90
β (°)	93.014(1)	97.021(4)	92.698(1)
γ (°)	90	115.170(3)	90
V (Å^3)	4704.0(3)	2293.4(4)	2134.8(1)
Z	4	2	2
$F(000)$	2256	1116	1044
D_{calc} (Mg m^{-3})	1.566	1.577	1.573
μ (mm^{-1})	1.588	1.291	1.385
T (K)	293	293	293
Dimension (mm)	$0.16 \times 0.20 \times 0.35$	$0.10 \times 0.25 \times 0.50$	$0.08 \times 0.15 \times 0.35$
θ_{max} and θ_{min} (°)	27.48 and 1.53	27.48 and 1.53	27.48 and 1.53
R_{int}	0.0450	0.0532	0.0366
Number of data collected	22210	21274	20572
Number of unique data	5353	10336	4895
Number of observed	3391	5957	3004
Number of variables	321	640	290
R/R_w	0.0330/0.0626	0.0957/0.3666	0.0398/0.0938
Goodness-of-fit	0.896	1.048	0.882
$(\Delta/\sigma)_{max,mean}$	0.001, 0.000	0.009, 0.001	0.001, 0.000
$\Delta\rho_{max}/\Delta\rho_{min}$ (e/Å^3)	0.295/−0.310	1.646/−0.876	0.590/ − 0.491

2.3. X-ray crystallographic studies

Suitable crystals of the three title compounds were mounted on glass fibers. The data were recorded on a Rigaku Weissenberg IP diffractometer with graphite-monochromated Mo Kα radiation ($\lambda = 0.71073$ Å), the scan mode being ω. The structures were solved by direct methods and refined by full-matrix least-squares. All the non-hydrogen atoms were refined with anisotropic thermal parameters. Most of the hydrogen atoms were found from the difference Fourier syntheses and geometrical calculation. All calculations were performed on a Pentium IV PC computer with the SHELXL-97 program package.

Table 2
Selected bond lengths (Å) and angles (°) for complex **1**

Zn(1)–N(1)	2.003(2)	Zn(1)–O(1A)	2.028(1)
Zn(1)–O(3)	2.072(2)	Zn(1)–N(4)	2.080(2)
Zn(1)–O(1)	2.082(2)	Zn(2)–O(2)	2.042(2)
Zn(2)–N(2)	2.149(2)	Zn(2)–N(5)	2.233(2)
Zn(1)···Zn(2)	4.6958(3)	Zn(1)–Zn(1A)	3.1377(5)
N(1)–Zn(1)–O(1A)	144.94(7)	N(1)–Zn(1)–O(3)	78.58(7)
O(1A)–Zn(1)–O(3)	102.67(6)	N(1)–Zn(1)–N(4)	114.96(8)
O(1A)–Zn(1)–N(4)	99.77(7)	O(3)–Zn(1)–N(4)	97.19(8)
N(1)–Zn(1)–O(1)	87.78(6)	O(1A)–Zn(1)–O(1)	80.47(6)
O(3)–Zn(1)–O(1)	160.32(6)	N(4)–Zn(1)–O(1)	101.44(7)
O(2B)–Zn(2)–O(2)	179.8(1)	O(2B)–Zn(2)–N(2)	102.93(7)
O(2)–Zn(2)–N(2)	76.94(7)	N(2)–Zn(2)–N(2B)	103.1(1)
O(2B)–Zn(2)–N(5)	91.48(8)	O(2)–Zn(2)–N(5)	88.67(7)
N(2)–Zn(2)–N(5)	163.45(7)	N(2B)–Zn(2)–N(5)	87.93(8)
N(5)–Zn(2)–N(5B)	84.3(1)	Zn(1A)–O(1)–Zn(1)	99.53(6)
Zn(1)···Zn(2)···Zn(1B)	146.92		

Symmetry codes: (A) $-x, -y+1, -z+1$; (B) $-x, y, -z+1/2$

Table 3
Selected bond lengths (Å) and angles (°) for complex **2**

Ni(1)–O(1)	1.819(7)	Ni(1)–N(1)	1.833(7)
Ni(1)–O(3)	1.864(7)	Ni(1)–N(7)	1.939(8)
Ni(2)–O(2)	2.015(6)	Ni(2)–O(7)	2.015(6)
Ni(2)–N(9)	2.109(8)	Ni(2)–N(8)	2.115(8)
Ni(2)–N(2)	2.152(7)	Ni(2)–N(5)	2.167(8)
Ni(3)–N(4)	1.803(7)	Ni(3)–O(6)	1.818(7)
Ni(3)–O(8)	1.855(7)	Ni(3)–N(10)	1.92(1)
Ni(1)···Ni(2)	4.507(2)	Ni(2)···Ni(3)	4.557(2)
Ni(1)···Ni(3)	4.693(2)		
O(1)–Ni(1)–N(1)	94.4(3)	O(1)–Ni(1)–O(3)	177.1(3)
N(1)–Ni(1)–O(3)	83.8(3)	O(1)–Ni(1)–N(7)	89.8(3)
N(1)–Ni(1)–N(7)	172.9(3)	O(3)–Ni(1)–N(7)	92.2(3)
O(2)–Ni(2)–O(7)	177.4(2)	O(2)–Ni(2)–N(9)	91.0(3)
O(7)–Ni(2)–N(9)	90.2(3)	O(2)–Ni(2)–N(8)	90.4(3)
O(7)–Ni(2)–N(8)	91.9(3)	N(9)–Ni(2)–N(8)	87.4(3)
O(2)–Ni(2)–N(2)	76.5(3)	O(7)–Ni(2)–N(2)	101.1(3)
N(9)–Ni(2)–N(2)	96.3(3)	N(8)–Ni(2)–N(2)	166.4(3)
O(2)–Ni(2)–N(5)	102.1(3)	O(7)–Ni(2)–N(5)	76.6(3)
N(9)–Ni(2)–N(5)	166.1(3)	N(8)–Ni(2)–N(5)	97.3(3)
N(2)–Ni(2)–N(5)	82.2(3)	N(4)–Ni(3)–O(6)	95.7(3)
N(4)–Ni(3)–O(8)	84.3(3)	O(6)–Ni(3)–O(8)	179.6(4)
N(4)–Ni(3)–N(10)	176.0(4)	O(6)–Ni(3)–N(10)	87.7(4)
O(8)–Ni(3)–N(10)	92.3(4)	Ni(1)···Ni(2)···Ni(3)	62.36

Table 4
Selected bond lengths (Å) and angles (°) for complex **3**

Ni(1)–O(1)	1.815(2)	Ni(1)–N(1)	1.824(2)
Ni(1)–O(3)	1.851(2)	Ni(1)–O(6)	1.952(3)
Ni(2)–O(2)	2.015(2)	Ni(2)–N(2)	2.068(2)
Ni(2)–O(7)	2.151(2)	Ni(1)···Ni(2)	4.5573(4)
O(1)–Ni(1)–N(1)	95.3(1)	O(1)–Ni(1)–O(3)	178.7(1)
N(1)–Ni(1)–O(3)	84.61(9)	O(1)–Ni(1)–O(6)	90.3(1)
N(1)–Ni(1)–O(6)	174.0(1)	O(3)–Ni(1)–O(6)	89.8(1)
O(2)–Ni(2)–N(2)	78.83(8)	O(2A)–Ni(2)–N(2)	101.17(8)
O(2)–Ni(2)–O(7)	89.17(8)	N(2)–Ni(2)–O(7)	88.61(8)
O(2A)–Ni(2)–O(7)	90.83(8)	N(2)–Ni(2)–O(7A)	91.39(8)
Ni(1)···Ni(2)···Ni(1A)	180		

Symmetry code: (A) $-x, -y+1, -z+1$

Crystallographic data are summarized in Table 1. Selected bond lengths and angles for complexes **1**–**3** are listed in Tables 2–4.

3. Results and discussions

3.1. Description of the structures

3.1.1. $[Zn_3(p\text{-nbzshz})_2(C_5H_5N)_4]_n$ (1)

Complex **1** is composed of three Zn^{II} atoms, two *p*-nbzshz^{3-} ligands and four pyridine molecules, as shown in Fig. 1 It is the first trinuclear zinc(II) complex with a *N*-acyl-salicylhydrazide ligand. The central Zn(2) atom is located on a crystallographic twofold rotation axis. It is coordinated by two *p*-nbzshz^{3-} ligands through the carbonyl oxygen atoms in *trans* positions [O(2)–Zn(2)–O(2B) 179.8(1)°], two hydrazine nitrogen atoms in *cis* positions [N(2)–Zn(2)–N(2B) 103.1(1)°] and two pyridine molecule *cis* to each other [N(5)–Zn(2)–N(5B) 84.3(1)°]. This N_4O_2 donor set forms a distorted octahedral coordination geometry around the Zn(2) atom. The Zn(2)–O(carbonyl) and Zn(2)–N(hydrazide) bond distances are 2.042(2) Å and 2.149(2) Å, respectively, and Zn(2)–N(py) length is 2.233(2) Å. The Zn(1) and Zn(1B) atoms have a distorted square pyramidal geometry. The basal plane of the square pyramid [root mean square (r.m.s.) deviation 0.1390 Å] is comprised of two phenolic oxygen atoms of two different *p*-nbzshz^{3-} ligands, one carbonyl oxygen atom and one hydrazine nitrogen atom from one *p*-nbzshz^{3-} ligand, and the axial coordination site is occupied by one pyridine ligand with a Zn(1)–N(4) bond distance of 2.080(2) Å. The Zn(II) deviates from the basal mean equatorial plane of the square pyramid towards the apical N(4) atom by 0.4568 Å.

The triply deprotonated *p*-nbzshz^{3-} ligand of compound **1** bridges the neighboring Zn^{2+} cations through its hydrazide N–N group, forming trinuclear zinc units with neighboring Zn···Zn interatomic distances of 4.6958(3) Å. The arrangement of three Zn atoms is slightly curved, with the Zn(1)–Zn(2)–Zn(1B) angle being 146.92°, which is larger than that reported for the trinuclear $Zn_3(2\text{-CEQ})_6 \cdot 2H_2O$ (2-CEQ = 2-[2-(4-cyanophenyl)ethenyl]-8-quinolinolato) (109.2°) [20]. The most remarkable characteristic of this compound is that the adjacent trinuclear zinc units, related by a crystallographic center of symmetry, are linked by two phenolic oxygen atoms of two ligands to form one dimensional wave-like chain structure, as shown in Fig. 2. The bridge is asymmetric and the Zn(1)–O(1) bond [2.082(2) Å] is longer than the Zn(1)–O(1A) bond [2.028(1) Å]. The Zn(1)–O(1)–Zn(1A) bridging angle is 99.53(6)° and the four atoms of the $Zn_2(\mu_2\text{-O})_2$ ring are coplanar with a mean deviation of 0.00 Å from the plane. Di- or poly-nuclear species have been reported for bridging deprotonated phenol groups with two zinc ions [21–24], but a one-dimensional chain structure is rarely reported [25].

3.1.2. $Ni_3(p\text{-nbzshz})_2(py)_4$ (2)

Complex **2** was synthesized from $Ni(OAc)_2 \cdot 4H_2O$ and *N*-*p*-nitrobenzoylsalicylhydrazidate as a ligand in mixed solvents. As illustrated in Fig. 3, the coordination geometry of Ni(2) is octahedral and those of Ni(2) and Ni(3) are square planar. The Ni(2) atom is bound to two carbonyl oxygens, O(2), O(7), two hydrazine nitrogens, N(2), N(5), of two ligands and two nitrogen atoms, N(8), N(9), of solvent pyridine. O(2) is *trans* to O(7) [O(2)–Ni(2)-O7 177.4(2)°], N(2) is *cis* to N(5) [N(2)–Ni(2)–N(5) 82.2(3)°] and N(8) is *cis* to N(9) [N(8)–Ni(2)–N(9) 87.4(3)°]. The

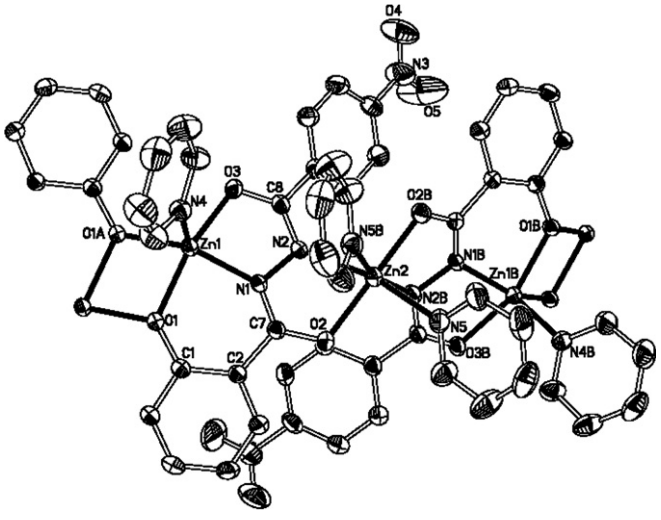


Fig. 1. Molecular structure of $Zn_3(p\text{-nbzshz})_2(C_5H_5N)_4$ with the atom-labelling scheme. Non-hydrogen atoms are represented by their 30% probability thermal ellipsoids. Symmetry operation used to generate equivalent atoms: (A) $-x, -y+1, -z+1$; (B) $-x, y, -z+1/2$.

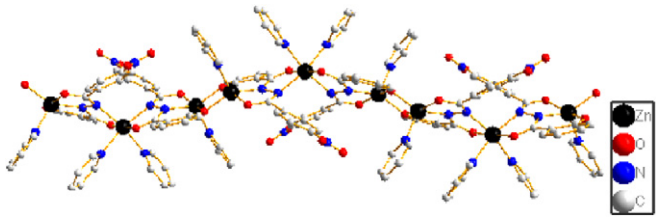


Fig. 2. A view showing the one dimensional wave-like structure of complex $[Zn_3(C_{14}H_8N_3O_5)_2(C_5H_5N)_4]_n$ (**1**).

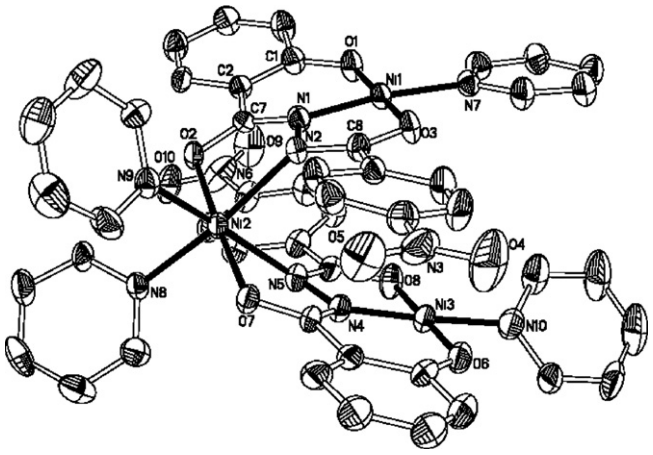


Fig. 3. Molecular structure of $Ni_3(p\text{-nbzshz})_2(C_5H_5N)_4$ with the atom-labelling scheme. Non-hydrogen atoms are represented by their 30% probability thermal ellipsoids.

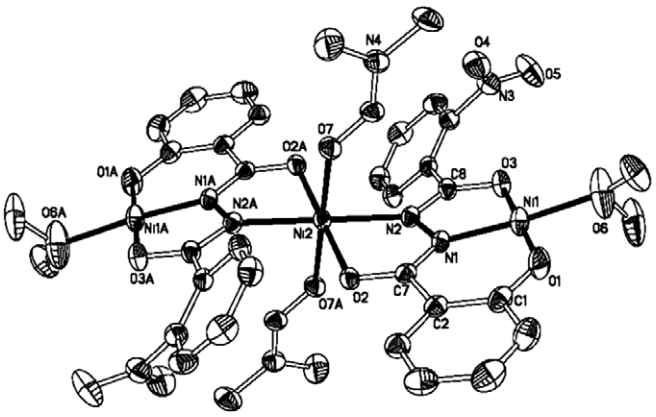


Fig. 4. Molecular structure of $Ni_3(o\text{-nbzshz})_2(DMF)_2((CH_3)_2O)_2$ with the atom-labelling scheme. Non-hydrogen atoms are represented by their 30% probability thermal ellipsoids. Symmetry operation used to generate equivalent atoms: (A) $-x, -y+1, -z+1$.

bond angles above are similar to the corresponding values of 179.8(1)°, 103.1(1)° and 84.3(1)° in complex **1**, but different from those in related complexes [7] which are all close to 180°. The average deviation from the mean plane defined by the N(5)N(9)O(2)O(7) and N(2)N(8)N(5)N(9) sets of atoms is 0.0233 Å and 0.2507 Å, respectively.

For two equivalent Ni(1) and Ni(3) atoms, the regular square planar geometry is realized with carbonyl oxygen, hydrazine nitrogen, phenolic oxygen and pyridine nitrogen atoms. The Ni–N and Ni–O bond distances for Ni(1), Ni(3) atoms (on average, 1.875 Å and 1.839 Å, respectively) are shorter than the corresponding bond lengths of the Ni(2) atom (on average, 2.134 Å and 2.015 Å, respectively). This difference may be attributed to the difference in stereochemistry between the central and terminal Ni^{2+} atoms (octahedral versus square-planar).

The array of three nickel atoms in trinuclear complex **2** is bent with a dihedral angle Ni(1)–Ni(2)–Ni(3) of 62.36°, which is larger than that of the corresponding values of 46.50° in the bent trinuclear Ni(II) complex with a different ligand [17], smaller than the corresponding values of 130.9° and 119.0° in the other two bent trinuclear Ni(II) complex with different ligands [18,19] and is very different from that in other trinuclear nickel complexes [7] with linear metal assemblies. The neighboring Ni···Ni interatomic distances are 4.507(2) Å and 4.557(2) Å, respectively, which are shorter than those in related complexes [7]. The Ni(1)···Ni(3) separation is 4.693 Å, longer by 1.2 Å than that (3.56 Å) reported for the similar bent configuration [17].

3.1.3. $Ni_3(o\text{-nbshz})_2(DMF)_2((CH_3)_2O)_2$ (**3**)

The linear trinuclear structure of complex **3** with a different ligand *N*-*o*-nitrobenzoylsalicylhydrazidate is shown in Fig. 4. The coordination geometry of the three Ni atoms follows a square-planar/octahedral/square-planar mode. The molecule exhibits crystallographic centrosymmetry. The Ni(2) atom, on a symmetry center, is coordinated by the carbonyl oxygen atoms and the hydrazine nitrogen atoms of two ligands and the oxygen atoms of two DMF molecules, giving an all-*trans* octahedral adduct. The two carbonyl oxygen atoms (Ni–O 2.015(2) Å) and the two hydrazine nitrogen atoms (Ni–N 2.068(2) Å) make up a square plane, and two oxygen atoms of two DMF molecules occupy the apical positions with longer distances (Ni–O 2.151(2) Å). The coordination bond angles involving the equivalent *trans* ligands are 180° by symmetry, which is different from that in complex **2**.

For Ni(1) and Ni(1A), the other hydrazine nitrogen (Ni–N 1.824(2) Å), carbonyl oxygen (Ni–O 1.851(2) Å) and phenolic oxygen (Ni–O 1.815(2) Å) of one ligand and methyl ether oxygen atom (Ni–O 1.952(3) Å) form a square plane. The average deviation from the mean plane is 0.0274 Å and the nickel atom is 0.0067 Å out of this plane. The bond distances are normal and are similar to those found in complex **2**, The neighboring nickel distance of 4.5573(4) Å is almost identical with that determined for complex **2**.

3.2. TG analysis of the complexes

The TG curves of compounds **1** and **2** exhibit three steps of weight losses. The first weight loss is 15.73% from 46 to 214 °C and the second is 13.11% in the range 214-363 °C for compound **1**. For compound **2**, the first weight loss is 12.20% in the temperature range 121–232 °C and the second is 13.95% between 232 and 364 °C. Both weight losses are all assigned to the removal of four pyridine molecules. The observed total weight losses in the first and second step (28.84% and 26.15%) are in agreement with the calculated values (28.49% and 29.01%) for the two compounds, respectively. The four pyridine molecules decompose in two steps, which may be due to their different coordination environments. The third weight losses are 25.34% for compound **1** from 363 to 697 °C and 42.73% for compound **2** from 364 to 697 °C, which may result from the decomposition of the ligands.

4. Conclusion

In this paper, we present the syntheses and crystal structures of three trinuclear transition metal complexes with two new ligands *N*-*p*-nitrobenzoylsalicylhydrazidate and *N*-*o*-nitrobenzoylsalicylhydrazidate. Three Zn atoms in compound **1** exhibit alternating square pyramidal and octahedral geometries, while three Ni atoms in compound **2** and **3** follow a square-planar/octahedral/square-planar coordination geometry mode. Complex **1** exhibits a one-dimensional wave-like chain structure resulting from the linkage of the phenolate oxygen donor atoms of neighboring two ligands between two zinc atoms. Complex **2** exhibits a curved Ni_3 metal arrangement with a Ni(1)–Ni(2)–Ni(3) angle of 62.36°, while the three nickel atoms in complex **3** are arranged in a strictly linear fashion with an angle of 180°. It is interesting to note that the molecular structures are remarkably different with the same ligand and same coordinated solvent molecule but different bivalent transition metals in compounds **1** and **2**, while the change of the terminal group location of the ligand and different solvents also results in a remarkably different molecular configuration in compounds **2** and **3**.

Acknowledgements

This work was financially supported by the Natural Science Foundation of Fujian Province, China (No. E0510012) and the National Nature Science Foundation of China.

Appendix A. Supplementary material

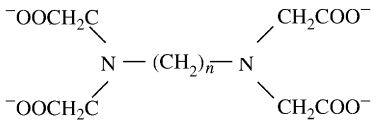
CCDC 299845, 299846 and 299847 contain the supplementary crystallographic data for this paper. These data can be obtained free of charge via http://www.ccdc.cam.ac.uk/conts/retrieving.html, or from the Cambridge Crystallographic Data Centre, 12 Union Road, Cambridge CB2 1EZ, UK; fax: (+44) 1223-336-033; or e-mail: deposit@ccdc.cam.ac.uk. Supplementary data associated with this article can be found, in the online version, at doi:10.1016/j.poly.2007.01.028.

References

[1] R.E.P. Winpenny, Comments Inorg. Chem. 20 (1999) 233.
[2] S. Leininger, B. Olenyuk, P.J. Stang, Chem. Rev. 100 (2000) 853.
[3] E.I. Solomon, R.K. Szilagyi, S.D. George, L. Basumallick, Chem. Rev. 104 (2004) 419.
[4] M. Du, X.J. Zhao, J.H. Guo, X.H. Bu, J. Ribas, Eur. J. Inorg. Chem. (2005) 294.
[5] (a) M. Fujita, Chem. Soc. Rev. 27 (1998) 417;
(b) R.E.P. Winpenny, J. Chem. Soc., Dalton Trans. (2002) 1;
(c) Y.F. Song, G.A. van Albada, M. Quesada, I. Mutikainen, U. Turpeinen, J. Reedijk, Inorg. Chem. Commun. 8 (2005) 975.
[6] (a) S. Lin, S.X. Liu, J.Q. Huang, C.C. Lin, J. Chem. Soc., Dalton Trans. (2002) 1595;
(b) S.X. Liu, S. Lin, B.Z. Lin, C.C. Lin, J.Q. Huang, Angew. Chem. Int. Ed. 40 (2001) 1084;
(c) S. Lin, S.X. Liu, B.Z. Lin, Inorg. Chim. Acta 328 (2002) 69;
(d) S. Lin, S.X. Liu, B.Z. Lin, Chin. J. Inorg. Chem. 18 (2002) 1205;
(e) R.P. John, K.J. Lee, M.S. Lah, Chem. Commun. (2004) 2660;
(f) R.P. John, K.J. Lee, B.J. Kim, B.J. Suh, H. Rhee, M.S. Lah, Inorg. Chem. 44 (2005) 7109;
(g) B. Kwak, H. Rhee, S. Park, M.S. Lah, Inorg. Chem. 37 (1998) 3599;
(h) B. Kwak, H. Rhee, S. Park, M.S. Lah, Polyhedron 19 (2000) 1985;
(i) I. Kim, B. Kwak, M.S. Lah, Inorg. Chim. Acta 317 (2001) 12;
(j) R.P. John, J. Park, D. Moon, K. Lee, M.S. Lah, Chem. Commun. 44 (2006) 3699;
(k) D. Moon, K. Lee, R.P. John, G.H. Kim, B.J. Suh, M.S. Lah, Inorg. Chem. 45 (2006) 7991.
[7] (a) M.X. Yang, S. Lin, L.J. Chen, S.X. Liu, Chin. J. Inorg. Chem. 19 (2003) 433;
(b) M.X. Yang, S. Lin, P. Yu, L.J. Chen, S.X. Liu, Chin. J. Chem. 23 (2005) 1407;
(c) M.X. Yang, S. Lin, Acta Crystallogr., Sect. E 61 (2005) 1095.
[8] S. Akine, T. Nabeshima, Inorg. Chem. 44 (2005) 1205.
[9] E. Simón-Manso, P. Gantzel, C.P. Kubiak, Polyhedron 22 (2003) 1641.
[10] X.H. Bu, M. Du, L. Zhang, D.Z. Liao, J.K. Tang, R.H. Zhang, M. Shionoya, J. Chem. Soc., Dalton Trans. (2001) 593.
[11] V.A. Milway, L. Zhao, T.S.M. Abedin, L.K. Thompson, Z.Q. Xu, Polyhedron 22 (2003) 1271.
[12] J. Heinicke, N. Peulecke, K. Karaghiosoff, P. Mayer, Inorg. Chem. 44 (2005) 2137.
[13] L.K. Thompson, V. Niel, H. Grove, D.O. Miller, M.J. Newlands, P.H. Bird, W.A. Wickramasinghe, A.B.P. Lever, Polyhedron 23 (2004) 1175.
[14] M. Ohashi, J. Yi, D. Shimizu, T. Yamagata, T. Ohshima, K. Mashima, J. Organomet. Chem. 691 (2006) 2457.
[15] G.Q. Zhang, S.Q. Wang, Q. Gan, Y.F. Zhang, G.Q. Yang, J.S. Ma, H.J. Xu, Eur. J. Inorg. Chem. (2005) 4186.
[16] A.L. Harris, A.H. Yang, A. Hegmans, L. Povirk, J.J. Ryan, L. Kelland, N.P. Farrell, Inorg. Chem. 44 (2005) 9598.
[17] M. Alexiou, I. Tsivikas, C. Dendrinou-Samara, A.A. Pantazaki, P. Trikalitis, N. Lalioti, D.A. Kyriakidis, D.P. Kessissoglou, J. Inorg. Biochem. 93 (2003) 256.
[18] H. Adams, D.E. Fenton, P.E. McHugh, Inorg. Chem. Commun. 7 (2004) 147.
[19] Z.N. Chen, H.X. Zhang, K.B. Yu, C.Y. Su, B.S. Kang, Polyhedron 17 (1998) 1535.
[20] J. Zhang, R.G. Xiong, Z.F. Chen, X.Z. You, G.H. Lee, S.M. Peng, Chem. Lett. (2001) 676.
[21] S.R. Korupoju, N. Mangayarkarasi, S. Ameerunisha, E.J. Valente, P.S. Zacharias, J. Chem. Soc., Dalton Trans. (2000) 2845.
[22] S.S. Tandom, S. Chander, L.K. Thompson, Inorg. Chim. Acta 300–302 (2000) 683.
[23] H. Adams, D. Bradshaw, D.E. Fenton, Eur. J. Inorg. Chem. (2001) 859.
[24] N. Mangayarkarasi, M. Prabhakar, P.S. Zacharias, Polyhedron 21 (2002) 925.
[25] Y. Kai, M. Morita, N. Kasai, Bull. Chem. Soc. Jpn. 58 (1985) 1631.

minetetraacetate ion (1,3-pdta), has been used for preparation of hexadentate complexes with many metal ions [1–9]. The structural characteristics of the hexadentate $[M(1,3\text{-pdta})]^-$ (M(III) = Co [1], Cr [2], Rh [2], Fe [3] and V [4]), $[M(1,3\text{-pdta})]^{2-}$ (M(II) = Cu [5], Ni [6], Co [7], Mg [8] and Zn [9]), $[Ca(1,3\text{-pdta})(H_2O)]^{2-}$ [8] and $[Cd(1,3\text{-pdta})(H_2O)]^{2-}$ [9] complexes have been determined by single-crystal X-ray crystallography. Four out of seventeen 1,3-pdta complexes: $Na[Cr(1,3\text{-pdta})]\cdot 3H_2O$ [2], $Na[V(1,3\text{-pdta})]\cdot 3H_2O$ [4], $Na[Fe(1,3\text{-pdta})]\cdot 3H_2O$ [3b] and $K[Co(1,3\text{-pdta})]\cdot 2H_2O$ [1] have been spontaneously resolved by crystallization. Crystals of the first three complexes have been found to be isomorphic (space group $P2_12_12_1$) with those of $Na[Rh(1,3\text{-pdta})]\cdot 3H_2O$ [2] which were resolved based on different solubility of diastereomeric salt pairs using as a resolving agent $(-)_{589}$-$[Co(en)_2(ox)]Br\cdot H_2O$. In the case of $K[Co(1,3\text{-pdta})]\cdot 2H_2O$ [1] the spontaneous resolution has lead to the enantiomerically enriched product which crystallizes in space group $C222_1$ (standard setting). However, the conglomerate crystallization[1] has not been evidenced thus far neither in the case of (1,3-propanediaminetetraacetato)metal(II) [5–9] nor 1,4-bdta [1,4-butanediaminetetraacetate ion] complexes [10,11].[2]. The metal(II) ions of the ionic radii of about 0.8–0.9 Å with 1,3-pdta ligand form octahedral complexes of the $[M(H_2O)_6][M'(1,3\text{-pdta})]\cdot 2H_2O$ type (M(II), M′(II) = Mg,Cu [5a]; Mn,Cu [5b]; Mg,Ni [6]; Mg,Co [7]; Co,Co [7]; Mg,Mg [8]; Mg,Zn [9] and Zn,Zn [9]), which crystallize in the space group *Pnna*, forming the isomorphic series. The 1,3-pdta ligand with spherically symmetric metal ions of the ionic radii greater than 0.9 Å tends to form hexadentate complexes of CN higher than six, as evidenced by the crystal structures of the $[Ca(H_2O)_3Ca(1,3\text{-pdta})(H_2O)]\cdot 2H_2O$ [8] (CN = 8, space group $P\bar{1}$), and isomorphic hexaaquamagnesium(II) crystals of seven-coordinated $[Cd(1,3\text{-pdta})(H_2O)]^{2-}$ [9] and $[Mn(1,3\text{-pdta})(H_2O)]^{2-}$ [12] complexes which crystallize as dihydrates in *Pbcn* space group.

Due to the presence of the six-membered backbone diamine ring in the M-1,3-pdta system, the 1,3-pdta complexes are less strained with respect to the corresponding edta (edta = ethylenediaminetetraacetate ion) complexes [6]. The hexadentate ligand, 1,4-bdta, has lengthened diamine chain with respect to both ligands, edta and 1,3-pdta (Scheme 1), and is able to form a seven-membered backbone diamine ring upon coordination with metal ions. However, stabilization due to chelation, known as a chelate effect, is usually most pronounced for 5- and 6-membered rings. Larger rings offer a rapidly decreasing advantage for coordination to the second site [13]. This might be



n = 2: edta; *n* = 3: 1,3-pdta; *n* = 4: 1,4-bdta

Scheme 1.

one of the reasons why crystallographic results concerned with the hexadentate complexes of 1,4-bdta are rather scarce, being limited to only $[Co(1,4\text{-bdta})]^-$ [10], $[Cr(1,4\text{-bdta})]^-$ [11] and $[V(1,4\text{-bdta})]^-$ [11]. In this paper we report the syntheses of new hexadentate $[Mg(H_2O)_6][Co(1,4\text{-bdta})]\cdot 3H_2O$ (**a**) and $[Mg(H_2O)_6][Ni(1,4\text{-bdta})]\cdot 3H_2O$ (**b**) complexes, as well as the $Ba_2(1,4\text{-bdta})\cdot 2H_2O$ complex which was used for the preparation of the complexes (**a**) and (**b**). For complexes (**a**) and (**b**) we provide electronic absorption spectroscopy characterization and the description of their crystal structures. From the solutions of $[Mg(H_2O)_6][Co(1,4\text{-bdta})]\cdot 3H_2O$ (**a**) and $[Mg(H_2O)_6][Ni(1,4\text{-bdta})]\cdot 3H_2O$ (**b**), conglomerate crystallization has been observed. The incidence of conglomerate crystallization, being a subject of intense study by Bernal and co-workers [14–20], is relatively rare: to the best of our knowledge the reported crystal structures represent the first case of spontaneous resolution involving 1,4-bdta ligand and one of a few reports dealing with conglomerate crystallization of transition metal(II) complexes with N_2O_4 type of ligands [21–25].

2. Experimental

2.1. Compounds preparation

All commercially obtained reagent-grade chemicals were used without further purification.

2.1.1. Preparation of barium 1,4-butanediaminetetraacetate dihydrate, $Ba_2(1,4\text{-bdta})\cdot 2H_2O$

Monochloroacetic acid (86.00 g, 0.91 mol) was dissolved in 100 cm^3 of H_2O and cooled in an ice bath. A cooled solution of NaOH (36.40 g, 0.91 mol) in 90 cm^3 H_2O was added drop by drop, and the rate of addition was adjusted so that the temperature remained below 15 °C. To this solution, 1,4-butanediamine (17.63 g, 0.20 mol) dissolved in 50 cm^3 of H_2O was added, and the solution was allowed to stir for 10 min at 15 °C. Then, the reaction mixture was refluxed (80–90 °C) for 4 h, and an additional amount of NaOH (36.00 g, 0.90 mol) in 60 cm^3 of H_2O was added drop by drop to keep the pH in the range 7–8. The volume of the resulting solution was reduced to 200 cm^3 and the deposited NaCl was filtered out. The filtrate was heated at 90 °C and pH was adjusted to *ca.* 9, then to this filtrate a hot solution of $BaCl_2\cdot 2H_2O$ (98.0 g, 0.40 mol) in 200 cm^3 of H_2O was added. Stirring with maintenance of the temperature at 90 °C was continued for 2 h. The insoluble white precipitate of $Ba_2(1,4\text{-bdta})\cdot 2H_2O$ was collected

[1] Conglomerate crystallization is the phenomenon wherein a solution of racemate precipitates enantiomorphic crystals each of which contains exclusively a single enantiomer (homochiral crystals).

[2] The *P*1 chiral space group, assigned to $K[Cr(1,4\text{-bdta})]\cdot H_2O$ crystals [11a] has been corrected by Herbstein and co-workers [11b] to centrosymmetric $P\bar{1}$.

by filtration, washed with hot water, ethanol, then ether and air-dried. Yield was 117.20 g (93.47%). *Anal.* Calc. for Ba_2(1,4-bdta) · $2H_2O$, $C_{12}H_{20}O_{10}N_2Ba_2$ (*FW* = 626.95): C, 22.99; H, 3.22; N, 4.47. Found: C, 23.01; H, 3.01; N, 4.23%.

2.1.2. Preparation of 1,4-butanediaminetetraacetic acid, H_4 1,4-bdta · $2H_2O$

The 1,4-butanediaminetetraacetic acid ($H_4$1,4-bdta) was prepared according the procedure which is usually used for the preparation of diaminopolycarboxylic acids [26,27]. The solid Ba_2(1,4-bdta) · $2H_2O$ (46.34, 0.074 mol) was added to 1 dm^3 of water and to this suspension 2 equiv. of H_2SO_4 (147.80 cm^3 of 1 M H_2SO_4, 0.148 mol) were added. The obtained mixture was heated at 90 °C with stirring for 5 h. During this time the pH of the solution was kept constant at pH 2.0 by slow addition of 1 M H_2SO_4. The hot reaction mixture was filtered off to remove precipitated $BaSO_4$ and filtrate was evaporated to *ca.* 250 cm^3 and than left to cool at room temperature. White crystals of $H_4$1,4-bdta · $2H_2O$ were collected, washed with ethanol, and air-dried. Yield 22.40 g (85%). The crude product was recrystallized from hot water. *Anal.* Calc. for $H_4$1,4-bdta · $2H_2O$, $C_{12}H_{24}O_{10}N_2$ (*FW* = 356.33): C, 40.45; H, 6.79; N, 7.86. Found: C, 40.57; H, 6.59; N, 7.80%.

2.1.3. Preparation of hexaaquamagnesium (1,4-butanediaminetetraacetato)cobaltate(II) trihydrate, $[Mg(H_2O)_6][Co(1,4\text{-}bdta)] \cdot 3H_2O$ (**a**)

2.81 g (0.01 mol) of $CoSO_4 \cdot 7H_2O$ were dissolved in 50 cm^3 of H_2O at 70 °C. To this solution, solid Ba_2(1,4-bdta) · $2H_2O$ (6.27 g, 0.01 mol) was added and the reaction mixture was heated at 70 °C with stirring for 30 min. The precipitated $BaSO_4$ was removed by filtration. To the obtained dark-purple filtrate, 2.28 g (0.01 mol) of $MgSO_4 \cdot 6\,H_2O$ was added and heating (70 °C) was continued for 30 min. After the precipitated $BaSO_4$ was removed by filtration, to the obtained filtrate 5–6 ml of ethanol was added and the solution was left in a refrigerator overnight. The dark-purple crystals of $[Mg(H_2O)_6][Co(1,4\text{-}bdta)] \cdot 3H_2O$ were collected, washed with ethanol and air-dried. Yield was 2.80 g (50%). The complex was recrystallized by dissolving in hot water, adding of ethanol, and then cooling in a refrigerator. *Anal.* Calc. for $[Mg(H_2O)_6][Co(1,4\text{-}bdta)] \cdot 3H_2O$, $MgCoC_{12}H_{34}O_{17}N_2$ (*FW* = 561.65): C, 25.66; H, 6.10 ; N, 4.99. Found: C, 25.51; H, 6.56; N, 5.00%.

2.1.4. Preparation of hexaaquamagnesium (1,4-butanediaminetetraacetato)nickelate(II) trihydrate, $[Mg(H_2O)_6][Ni(1,4\text{-}bdta)] \cdot 3H_2O$ (**b**)

7.89 g (0.03 mol) of $NiSO_4 \cdot 6H_2O$ were dissolved in 80 cm^3 of H_2O at 80°C. To this solution an equivalent amount of solid Ba_2(1,4-bdta) · $2H_2O$ (18.81 g, 0.03 mol) was added. The obtained mixture was heated at 80°C with stirring for 3 h and then precipitated $BaSO_4$ was removed by filtration. After cooling to room temperature the filtrate was passed through a 5×60 cm column supplied with the Dowex 1-X8 (200–400 mesh) anion-exchange resin in the Cl^- form. The column was then washed with water and then eluted with 0.05 M $MgCl_2$ solution for 3 days. Only one band for a complex with 2- charge appeared. The eluate was evaporated to 5 cm^3 and desalted by passage trough a G-10 Sephadex column, with distilled water as the eluant. The eluate containing $[Mg(H_2O)_6][Ni(1,4\text{-}bdta)] \cdot 3H_2O$ complex was concentrated to a volume of 8 cm^3 and then it was left to stand in a refrigerator for several days. Blue crystals of $[Mg(H_2O)_6][Ni(1,4\text{-}bdta)] \cdot 3H_2O$ were filtered off, washed with ethanol and air-dried. Yield 2.5 g (42%). The complex was recrystallized by dissolving in hot water, and then cooling at a room temperature. *Anal.* Calc. for $[Mg(H_2O)_6][Ni(1,4\text{-}bdta)] \cdot 3H_2O$, $MgNiC_{12}H_{34}O_{17}N_2$ (*FW* = 561.43): C, 25.67; H, 6.10; N, 4.99. Found: C, 25.80; H, 6.00; N, 4.90%.

2.2. Physical measurements

The electronic absorption spectra were recorded on a Perkin–Elmer Lambda 35 spectrophotometer and for these measurements about 5×10^{-2} mol/dm^3 aqua solutions were used. Elemental microanalyses for carbon, hydrogen, and nitrogen were done by the Faculty of Chemistry, University of Belgrade.

2.3. Crystallographic data collection and refinement of the structures

Crystal data for $[Mg(H_2O)_6][Co(1,4\text{-}bdta)] \cdot 3H_2O$ (**a**) and $[Mg(H_2O)_6][Ni(1,4\text{-}bdta)] \cdot 3H_2O$ (**b**) and the parameters of data collection are summarized in Table 1. The intensity data were measured with a KM-4CCD kappa-geometry diffractometer [28] using graphite monochrommated Mo Kα radiation ($\lambda = 0.71073$ Å) at 295(2) K. The structures were solved by direct methods using SHELXS97 [29] and refined by least-squares techniques with SHELXL97 [30]. The intensity data were corrected for Lp effects, as well as, for absorption and extinction. Anisotropic thermal parameters were employed for the non-hydrogen atoms. The positions of the hydrogen atoms attached to the C-atoms were calculated at standardized distances of 0.96 Å. Water hydrogen atoms were located from difference Fourier maps but their bond distances have been standardized to a value of 0.85 Å. All hydrogen atoms were refined using a riding model with the atomic displacement parameters 30% higher than the displacement parameters for the atoms to which they are bonded. The absolute configuration of the $[Co(1,4\text{-}bdta)]^{2-}$ and $[Ni(1,4\text{-}bdta)]^{2-}$ complexes (crystals selected by chance from the optically inactive crystalline masses) was established on the basis of the Flack's absolute structure parameter [31] which refined to a value of 0.027(15) and 0.030(8), respectively, indicating that the corresponding atomic coordinates represent the correct enantiomer (Λ).

Table 1
Crystal data summary for $[Mg(H_2O)_6][Co(1,4\text{-bdta})]\cdot 3H_2O$ (**a**) and $[Mg(H_2O)_6][Ni(1,4\text{-bdta})]\cdot 3H_2O$ (**b**) complexes

	(**a**)	(**b**)
Chemical formula	$C_{12}H_{34}CoMgN_2O_{17}$	$C_{12}H_{34}MgN_2NiO_{17}$
Chemical formula weight	561.65	561.43
Crystal size (mm)	$0.4\times0.3\times0.1$	$0.3\times0.3\times0.2$
Colour, habit	dark-purple, prismatic	blue, prismatic
Crystal system	hexagonal	hexagonal
Space group	$P6_1$	$P6_1$
$a = b$ (Å)	12.029(2)	12.0031(5)
c (Å)	29.215(6)	29.2184(12)
V (Å^3)	3661.0(11)	3645.6(3)
Z	6	6
D_x (Mg m^{-3})	1.529	1.534
Number of reflections for cell parameters	5134	8852
Absorption coefficient (mm^{-1})	0.807	0.903
Diffractometer	kuma KM-4CCD κ-geometry	kuma KM-4CCD κ-geometry
Monochromator	graphite	graphite
Data collection method	*ω scans*	*ω scans*
Number of measured reflections	20260	21716
Number of independent reflections	4399	5225
Number of observed reflections	3639	4651
Criterion for observed reflections	$I > 2\sigma(I)$	$I > 2\sigma(I)$
R_{int}	0.0698	0.0392
θ_{max} (°)	26.05	27.07
Range of h, k, l	$-14 \rightarrow h \rightarrow 14$, $-14 \rightarrow k \rightarrow 14$, $-36 \rightarrow l \rightarrow 31$	$-15 \rightarrow h \rightarrow 15$, $-13 \rightarrow k \rightarrow 15$, $-37 \rightarrow l \rightarrow 36$
Absorption correction	empirical	empirical
$T_{min.}$, $T_{max.}$	0.82083, 0.93319	0.78526, 0.87277
Refinement on	F^2	F^2
$R[F^2 > 2\sigma(F^2)]$	0.0452	0.0305
$wR(F^2)$	0.0838	0.0607
S	0.999	0.984
Number of reflections used in refinement	4399	5225
Number of parameters used	299	299
H-atom treatment	riding model	riding model
Weighting scheme	$w = 1/[\sigma^2(F_o^2) + (0.0384\ P)^2]$ where $P = (F_o^2 + 2F_c^2)/3$	$w = 1/[\sigma^2(F_o^2) + (0.0333\ P)^2]$ where $P = (F_o^2 + 2\ F_c^2)/3$
Flack parameter	0.027(15)	0.030(8)
$\Delta\rho_{max}$ (e Å^{-3})	0.406	0.209
$\Delta\rho_{min}$ (e Å^{-3})	−0.268	−0.222
Extinction method	SHELXL97	SHELXL97
Extinction coefficient	0.0073(5)	0.0117(4)

Siemens computer graphics program XP [32a] and CCDC MERCURY programs [32b] were used to prepare drawings.

3. Results and discussion

*3.1. The crystal structures of $[Mg(H_2O)_6][Co(1,4\text{-bdta})]\cdot 3H_2O$ (**a**) and $[Mg(H_2O)_6][Ni(1,4\text{-bdta})]\cdot 3H_2O$ (**b**) complexes*

Single crystals of the complexes (**a**) and (**b**), grown from racemic solution, are isomorphic and form conglomerates, that is, the Λ and Δ enantiomers crystallize separately in space groups $P6_1$ and $P6_5$, respectively. An ORTEP drawing of the $[Mg(H_2O)_6]^{2+}$ complex cation and $[Co(1,4\text{-bdta})]^{2-}$ complex anion, possessing Λ absolute configuration at the metal center, is depicted in Fig. 1, where the numbering scheme adopted for the respective atoms is also given. As (**a**) and (**b**) form isostructural crystals, a drawing of the unit that constitutes complex (**b**) has not been provided. Selected metal-ligand bond lengths and valence angles are listed in Table 2. For the sake of comparison, the structural data for the $[Co(edta)]^{2-}$ [33], $[Co(1,3\text{-pdta})]^{2-}$ [7], $[Ni(edta)]^{2-}$ [34] and $[Ni(1,3\text{-pdta})]^{2-}$ [6] complexes are also given in Table 2.

The structural units of (**a**) and (**b**) consist of discrete $[M(1,4\text{-bdta})]^{2-}$ (M(II) = Co (**a**) and Ni(**b**)) and $[Mg(H_2O)_6]^{2+}$ octahedra, illustrated in Fig. 1, and three water solvent molecules (O6W, O7W and O8W). For the seven-membered 1,4-butanediamine ring label "B" is introduced. Two out-of-plane glycinate rings (R rings), as well as two in-plane glycinate rings (G rings) are assigned according to the notation suggested by Weakliem and Hoard [35]. The seven-membered 1,4-butanediamine ring (B ring) adopts twist-chair δ conformation (provided that the helicity is defined by the line connecting the two nitrogen

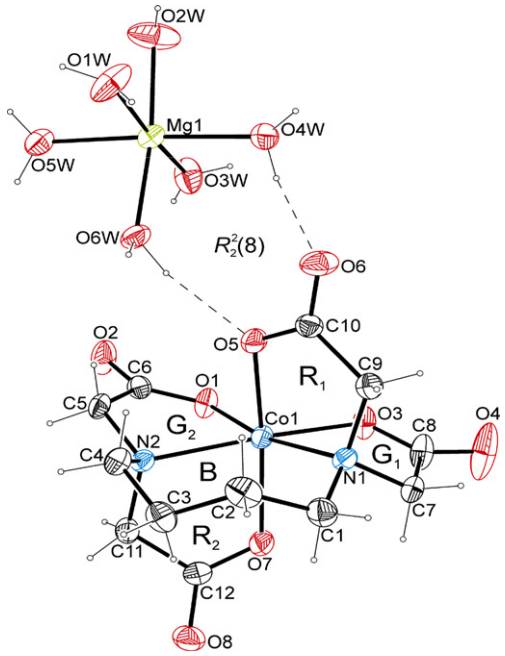


Fig. 1. Molecular structure of the complex cation and anion in $[Mg(H_2O)_6][Co(1,4\text{-bdta})]\cdot 3H_2O$ (**a**). Thermal ellipsoids are drawn at the 40% probability level. Hydrogen atoms are represented as spheres of arbitrary radius.

atoms and the line connecting the methylene carbon atoms that are directly attached to the nitrogen atoms) as expected for the Λ configuration of the complex anion. The highly puckered glycinate rings of the G type are envelopes, while the glycinates of the R type are less strained and have twist form. In $[Co(1,4\text{-bdta})]^{2-}$ and $[Ni(1,4\text{-bdta})]^{2-}$ complexes two out-of plane bond lengths ($M–O_R$) as well as two in-plane bond lengths ($M–O_G$) are comparable both within and between the two sets, whereas in $[Ni(1,3\text{-pdta})]^{2-}$ [6] and $[Co(1,3\text{-pdta})]^{2-}$ [7] complexes, which by virtue of C_2 symmetry have the two $M–O_R$ and the two $M–O_G$ distances equalized, the $M–O_R$ distances are longer than the $M–O_G$ distances. This lengthening of the $M–O_R$ bonds might be a consequence of the constraints imposed by C_2 symmetry of the complex anions. Unlike in pdta, in the asymmetric edta complexes differentiation between the two $M–O_R$ and the two $M–O_G$ distances in both Co(II) and Ni(II) series is significant, so the C_2 molecular symmetry is completely lost. One of the possible reasons why such differentiation takes place might be formation of catena structures by Co(II) and Ni(II) edta complexes and the absence of such motifs in $[M(1,3\text{-pdta})]^{2-}$ and $[M(1,4\text{-bdta})]^{2-}$ (M = Co or Ni) crystals. The mean M–N distances are nearly the same as the mean M–O distances in the $[Ni(edta)]^{2-}$ [34] and $[Ni(1,3\text{-pdta})]^{2-}$ [6] complexes, while in all other complexes listed in Table 2 the mean M–N bond lengths are significantly longer than the mean M–O bond lengths. However, while in the edta and 1,3-pdta complexes the M–N bond lengths are nearly the same in value, they become much longer (weaker) in the analogous 1,4-bdta complexes. Simultaneously, as the size of the backbone diamine ring increases, we observe a steady increase of the N–M–N bite angle. The two geometrical effects might signal an existing disadvantage for coordination to the second nitrogen atom and a consequent loss of chelating properties of the 1,4-bdta ligand, as observed in Hg(1,4-bdta complex) [36]. Unlike the N–M–N bite angle, the O–M–O open angle decreases with an increasing

Table 2
Selected geometrical parameters for the hexadentate Co(II) and Ni(II) complexes with edta, 1,3-pdta and 1,4-bdta ligands

	Co(II)			Ni(II)		
	Edta	1,3-pdta	1,4-bdta	Edta	1,3-pdta	1,4-bdta
$M–O_G$	2.053(6)[i] 2.086(5)[i] 2.039(4)[ii] 2.082(3)[ii]	2.055(1)[iv] 2.054(1)[v]	2.072(3)[vii] 2.081(3)[vii]	2.056(5)[iii] 2.075(5)[iii]	2.026(5)[vi]	2.045(2)[viii] 2.055(2)[viii]
$M–O_R$	2.083(5)[i] 2.103(5)[i] 2.087(3)[ii] 2.123(3)[ii]	2.112(1)[iv] 2.110(1)[v]	2.071(3)[vii] 2.077(3)[vii]	2.034(5)[iii] 2.078(4)[iii]	2.078(5)[vi]	2.055(2)[viii] 2.057(2)[viii]
M–N	2.140(6)[i] 2.163(8)[i] 2.158(3)[ii] 2.161(4)[ii]	2.143(1)[iv] 2.142(2)[v]	2.177(3)[vii] 2.181(3)[vii]	2.070(6)[iii] 2.098(6)[iii]	2.073(6)[vi]	2.126(2)[viii] 2.142(2)[viii]
N–M–N	84.1[i] 84.3(1)[ii]	95.77(7)[iv] 95.71(9)[v]	112.60(12)[vii]	87.3[iii]	96.3(3)[vi]	111.04(7)[viii]
O–M–O	120.8[i] 119.3(1)[ii]	101.63(6)[iv] 101.76(8)[v]	91.51(11)[vii]	112.7[iii]	99.4(3)[vi]	89.89(6)[viii]

edta: [i]Mn/Co (295 K) [33b]; [ii]Co/Co (295 K) [33a]; [iii] Ni/Ni (295 K) [34] – data chosen for one of the three available isomorphic crystal structures differing in the character of the hexaaqua cation.
1,3-pdta: [iv]Co/Co (120 K) [7]; [v]Co/Mg (120 K) [7]; [vi]Mg/Ni (295 K) [6].
1,4-bdta: [vii] Mg/Co (295 K) – this work; [viii] Mg/Ni (295 K) – this work.

size of the backbone diamine ring. In the investigated complexes (**a**) and (**b**), the octahedral O–M–O bond angles are close to the ideal value of 90° (Table 2). The two coordinated oxygen atoms (O1 and O3), situated in the girdle plane and forming the O–M–O angle of 90°, are particularly well suited to act as hydrogen bond acceptors from two water molecules (O1W and O6W) of the hexaaquamagnesium cation also situated at the right angle. The resulting supramolecular $R_2^2(8)$ motif (for description of the graph set notation see Bernstein et al. [37]) can be found in Fig. 2 (right). Constitutionally different, but topologically the same $R_2^2(8)$ motifs are also formed when two neighboring water molecules from the aqua-ion donate their hydrogens to the oxygen atoms constituting the same carboxylate group (Figs. 1 and 2 (right)). Besides, two neighboring water molecules from hexaaquamagnesium cation donate one of their hydrogens to the uncoordinated carboxylate oxygen, which results in $R_2^1(6)$ motif. The described multiple-point hydrogen bond interactions between cationic and anionic species lead to formation of the various types of ring motifs and operate within layers parallel to the symmetry equivalent sets of (1 0 0) planes. One of these layers is illustrated in Fig. 2 (right). At the interception of these ionic layers infinite channels are formed (Fig. 3a), which are filled with uncoordinated water molecules. The channels are chiral as the arrangement of all structural units within and around the channel is dictated by 6_1 screw axis (Fig. 3b). Antidromic hydrogen bonded cycles formed by two uncoordinated carboxylate oxygens (O2 and O4) and all solvent water molecules (O7W, O8W and O9W) fill the center of the channel and are connected in a spiro fashion, with O8W acting as a spiro atom and aspiring to the role of the chirality center at the supramolecular level. This is illustrated in Fig 2 (bottom), while the hydrogen bond parameters are listed in Table 3.

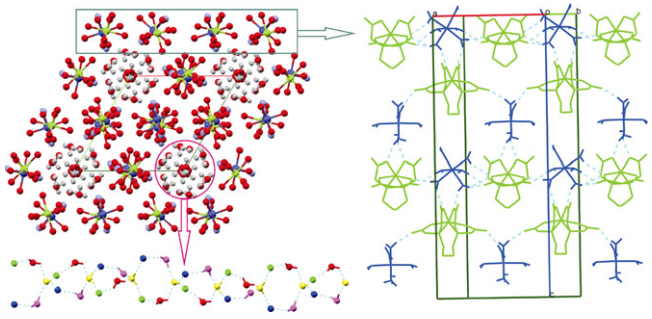


Fig. 2. View along [0 0 1] depicts chiral hydrophilic channels (encircled) and {1 0 0·} ionic layers (marked with a rectangle) in the crystal structures of complex (**a**). The layers contain alternating hydrogen bonded complex anions and cations (right), while the hydrophilic channels contain crystalline water molecules. Mono-spiro chain consisting of twelve-membered hydrogen bond rings (bottom) propagates in a helical manner along the *c*-direction.

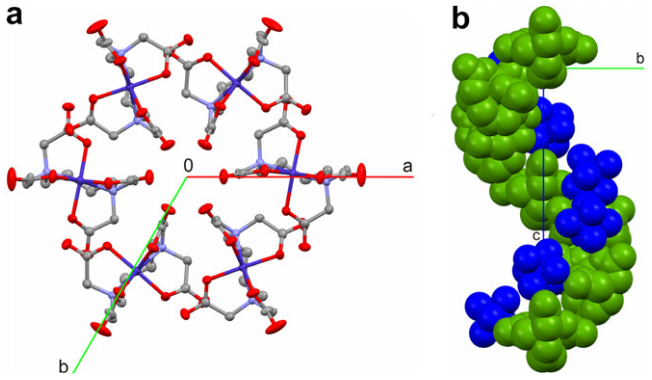


Fig. 3. (a) Top view of the water channels (water molecules not shown) illustrates the concentration of uncoordinated carboxylate oxygens on the channel's walls (b) side view of the channel depicts chiral arrangement of complex cations and anions along the channel dictated by 6_1 screw axis.

3.2. Strain analysis of Co(II)- and Ni(II)-edta-type chelates

The results of a comparative study of the strain characteristics of related series of Co(II)- and Ni(II)-edta-type chelates are given in Table 4. The major contributions to strain were considered to be: (i) the octahedral angles around the metal ion, (ii) the ring angle sums of the various kinds of rings, (iii) the M–O–C bond angles, and (iv) the bond angles that the chelating nitrogen atom makes with its connectors.

Strain-analysis data are available [6,38] for the $[Co(edta)]^{2-}$, $[Ni(edta)]^{2-}$ and $[Ni(1,3\text{-pdta})]^{2-}$ complexes. For the other complexes listed in Table 4 the corresponding data are reported in this paper. In general, the Co(II) complexes with edta-type ligands exhibit greater octahedral strain than the corresponding ones of Ni(II). The total deviation of the octahedral angles for the Ni(II) complexes varies from 60° for $[Ni(1,3\text{-pdta})]^{2-}$ to 85° for $[Ni(edta)]^{2-}$. These values are greater for a group of Co(II) complexes, and vary from 71° for $[Co(1,3\text{-pdta})]^{2-}$ to 106° for $[Co(edta)]^{2-}$. The calculated $\sum\Delta(O_h)$ values for the analyzed structures (Table 4) clearly demonstrate the effect of the diamine ring size on the octahedral distortion of the complex. The Ni(II) and Co(II) complexes with 1,3-pdta ligand are closer to the ideal octahedral geometry than those with 1,4-bdta and edta ligands. In addition, it is interesting to note that the hexadentate $[Co(1,4\text{-bdta})]^{2-}$ and $[Ni(1,4\text{-bdta})]^{2-}$ complexes containing bulky seven-membered diamine ring (5–7–5 ring system in the G plane) are less distorted than the corresponding ones of edta with the 5–5–5 ring system in an equatorial plane.

As expected, the five-membered glycinate rings of the G type are much more strained than those of the R type. The total deviation from the ideal chelate ring bond angle sum (538.5°) varies from −10° to −13° and from +1° to −4° for the G and R type of the glycinate rings, respectively.

Important source of stain in edta-type complexes is the bonding geometry made by the chelating nitrogens. Each N atom makes four bonds with six ideally 109.5° bond angles. The total deviation about the chelating N atoms

Table 3
Hydrogen bond parameters for two isomorphic crystal structures ($[Mg(H_2O)_6][Co(1,4\text{-bdta})]\cdot 3H_2O$ (**a**) and $[Mg(H_2O)_6][Ni(1,4\text{-bdta})]\cdot 3H_2O$ (**b**))

	(**a**)			(**b**)			Symmetry operations on A
	D···A (Å)	H···A (Å)	D–H···A (°)	D···A (Å)	H···A (Å)	D–H···A (°)	
O1W–H1W···O3	2.645(4)	1.85	154	2.650(2)	1.81	170	$x-y+1, x, z+1/6$
O1W–H2W···O8	2.955(4)	2.16	157	2.886(2)	2.10	155	$x+1, y, z$
O1W–H2W···O7	3.088(4)	2.54	123	3.163(2)	2.63	122	$x+1, y, z$
O2W–H3W···O6	2.778(4)	1.93	172	2.831(3)	2.01	161	$y+1, -x+y+1, z-1/6$
O2W–H4W···O7	3.105(5)	2.63	116	2.934(2)	2.10	166	$x+1, y, z$
O3W–H5W···O7W	2.966(4)	2.12	174	2.915(3)	2.13	153	$y, -x+y, z-1/6$
O3W–H6W···O8	2.723(4)	1.95	150	2.737(2)	1.90	168	$y, -x+y, z-1/6$
O4W–H7W···O6	2.834(4)	2.00	164	2.846(2)	2.00	176	
O4W–H8W···O9W	2.704(4)	1.90	158	2.697(3)	1.85	176	
O5W–H9W···O8	2.780(4)	1.94	171	2.776(2)	1.95	164	$x+1, y, z$
O5W–H10W···O7W	2.770(4)	1.98	154	2.749(3)	1.91	170	$x+1, y, z$
O6W–H11W···O1	2.803(4)	2.07	144	2.821(2)	1.99	167	$x-y+1, x, z+1/6$
O6W–H12W···O5	2.804(4)	1.97	167	2.789(2)	1.96	166	
O7W–H13W···O8W	2.786(5)	2.30	117	2.784(3)	1.96	165	$x, y+1, z$
O7W–H14W···O2	2.693(5)	2.04	133	2.707(3)	1.87	169	$x-y, x, z+1/6$
O8W–H15W···O2	2.679(4)	1.86	162	2.711(2)	1.89	162	$x-1, y-1, z$
O8W–H16W···O4	2.662(5)	1.95	141	2.686(3)	1.86	162	
O9W–H17W···O4	2.739(5)	2.04	139	2.756(3)	1.93	163	$x-y+1, x, z+1/6$
O9W–H18W···O8W	2.865(5)	2.03	168	2.844(3)	2.01	166	$x+1, y, z$

Table 4
Strain analysis of hexadentate edta-type chelates of Co(II) and Ni(II)

Complexes[a]	Rings in G-plane	$\sum\Delta\ (O_h)$[b]	$\Delta\sum$[c]			Δ(M–O–C)[d]		$\sum\Delta$(N)[e]	Ref.
			E, T or B	R	G	R	G		
Co(II) (ligand)									
Co(edta)	5–5–5	106	−14	0	−11	+7	+6	21	[33a,38]
Co(1,4-bdta)	5–7–5	95	+70	−4	−12	+6	+6	20	This work
Co(1,3-pdta)[f]	5–6–5	71	+29	+1	−10	+7	+5	11	[7]
Ni(II) (ligand)									
Ni(edta)	5–5–5	85	−14	−1	−13	+2	+3	23	[34,38]
Ni(1,4-bdta)	5–7–5	74	+70	−2	−13	+6	+5	23	This work
Ni(1,3-pdta)	5–6–5	60	+33	+1	−11	+6	+6	11	[6]

[a] Abbreviations of ligands: edta = ethylenediaminetetraacetate, 1,4-bdta = 1,4-butanediaminetetraacetate and 1,3-pdta = 1,3-propanediaminetetraacetate.
[b] $\Sigma\Delta(O_h)$ is the sum of the absolute values of the deviations from 90° of the L–M–L′ bite angles. All values rounded off to the nearest degree.
[c] $\Delta\Sigma$(ring) is the deviation from the ideal of the corresponding chelate rings' bond angle sum. A mean value of the two rings (R or G) is reported for complexes having an approx. C_2 molecular symmetry.
[d] Δ(M–O–C) (ring) is the mean value of the deviation of the corresponding rings' M–O–C bond angle from 109.5°.
[e] $\Sigma\Delta$(N) is the sum of the absolute values of the deviations from 109.5° of the six bond angles made by the nitrogen atoms. A mean value for the two nitrogens is reported.
[f] The average values are given for the two complexes: $Co[Co(1,3\text{-pdta})]\cdot 8H_2O$ and $Mg[Co(1,3\text{-pdta})]\cdot 8H_2O$ that form isomorphic crystals.

in edta and 1,4-bdta complexes varies from 21° to 23°, and from 20° to 23°, respectively, while this value for 1,3-pdta complexes sums 11°. The greatest deviation about the N atoms in edta structures is not consistently and specifically due to any one of the six bond angles. However, the considerable strain formed about the N atoms in the investigated $[Ni(1,4\text{-bdta})]^{2-}$ and $[Co(1,4\text{-bdta})]^{2-}$ structures can be attributed to the strain formed in the M–N–C(B) bond angles. Obviously, this strain could be released if the 1,4-bdta ligand, which has a relatively long chain, spanned between two different metal centers, instead of chelating only one metal center.

*3.3. Electronic absorption spectra of $[Mg(H_2O)_6][Co(1,4\text{-bdta})]\cdot 3H_2O$ (**a**) and $[Mg(H_2O)_6][Ni(1,4\text{-bdta})]\cdot 3H_2O$ (**b**) complexes*

The electronic absorption spectrum of $[Co(1,4\text{-bdta})]^{2-}$ complex is presented in Fig. 4 and for comparison in the same figure the spectrum of $[Co(1,3\text{-pdta})]^{2-}$ complex, containing six-membered 1,3-propanediamine ring in the equatorial plane [7], is also given. The electronic absorption data of these two complexes are reported in Table 5 and these data are compared with those for the $[Co(H_2O)_6]^{2+}$ complex [33a]. The electronic absorption spectra of

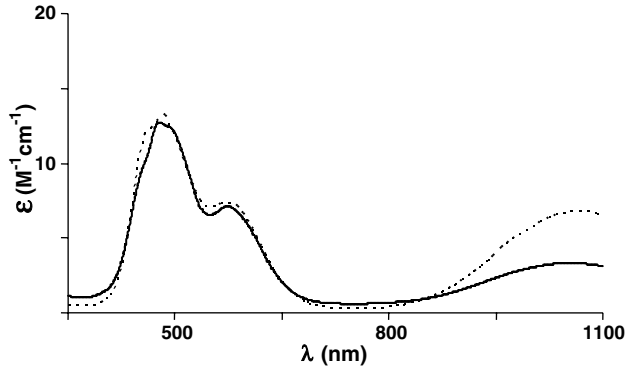


Fig. 4. Electronic absorption spectra of $[Mg(H_2O)_6][Co(1,4\text{-bdta})]\cdot 3H_2O$ (—) and $[Mg(H_2O)_6][Co(1,3\text{-pdta})]\cdot 2H_2O$ (· · · · · ·) [7] complexes.

Table 5
Electronic absorption data of $[Mg(H_2O)_6][Co^{II}(1,4\text{-bdta})]\cdot 3H_2O$. For comparison corresponding data for $[Co^{II}(H_2O)_6]^{2+}$ and $[Co^{II}(1,3\text{-pdta})]^{2-}$ complexes have been also given

Complex	Absorption		
	λ (nm)	ε (M^{-1} cm^{-1})	
$[Co^{II}(H_2O)_6]^{2+}$ [33a]	1234.0	1.4	$^4T_{1g} \rightarrow {}^4T_{2g}$
	625.0	0.3	$^4T_{1g} \rightarrow {}^4A_{2g}$
	515.0	4.9	$^4T_{1g} \rightarrow {}^4T_{1g}(P)$
	462.0(sh)		
$[Mg(H_2O)_6][Co^{II}$	1062.8	6.6	
$(1,3\text{-pdta})]\cdot 2H_2O$ [7]	572.5	7.3	
	483.0	12.9	
	460.0(sh)	11.7	
$[Mg(H_2O)_6]$	1053.1	3.5	
$[Co^{II}(1,4\text{-bdta})]\cdot$	574.0	7.4	
$3H_2O$ [This work]	487.4	13.2	
	457.2(sh)	10.2	

$[Co(1,4\text{-bdta})]^{2-}$ and $[Co(1,3\text{-pdta})]^{2-}$ complexes are similar in the shape and positions of the absorption maxima and both of these spectra with C_2 symmetry and Co^{II}–N_2O_4 chromophore of the ligand field showed similar multiplicity and band positions with those for octahedral $[Co(H_2O)_6]^{2+}$ complex with O_h symmetry assigned as: $^4T_{1g} \rightarrow {}^4T_{2g}$; $^4T_{1g} \rightarrow {}^4A_{2g}$; $^4T_{1g} \rightarrow {}^4T_{1g}(P)$ (Fig. 4 and Table 5). However, the electronic absorption spectra of $[Co(edta)]^{2-}$ [33a] and $[Co(o\text{-phdta})]^{2-}$ (*o*-phdta = *o*-phenylenediaminetetraacetate ion) [33a] complexes with the same Co^{II}-N_2O_4 chromophore as the investigated $[Co(1,4\text{-bdta})]^{2-}$ and $[Co(1,3\text{-pdta})]^{2-}$ [7] complexes, exhibit higher multiplicity and clear bands separation. This can be explained by taking into account that the 1,3-pdta- and 1,4-bdta-Co(II) systems, with flexible 1,3-propanediamine six-membered and 1,4-butanediamine seven-membered rings in the equatorial plane are less strained and much closer to the ideal octahedral configuration than $[Co(edta)]^{2-}$ and $[Co(o\text{-phdta})]^{2-}$ complexes. This has been clearly demonstrated previously by comparison of edta- and 1,3-pdta-Co(II) complexes [7], and it is additionally supported in this paper by analyzing $[Co(1,4\text{-bdta})]^{2-}$ system (octahedral strain is released in the order edta, 1,4-bdta, 1,3-pdta; see Section 3.2. and Table 4).

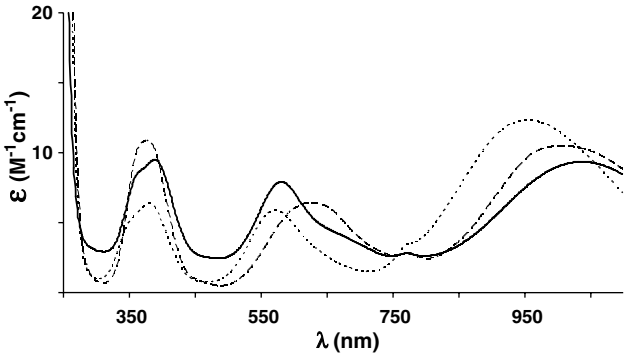


Fig. 5. Electronic absorption spectra of $[Mg(H_2O)_6][Ni(1,4\text{-bdta})]\cdot 3H_2O$ (——), $[Mg(H_2O)_6][Ni(1,3\text{-pdta})]\cdot 2H_2O$ (· · · · · ·) [6] and *trans*(O_5)-$[Ni_2(1,3\text{-pddadp})(H_2O)_4]\cdot 4H_2O$ (– – – –) [39] complexes.

The electronic absorption spectrum of $[Ni(1,4\text{-bdta})]^{2-}$ complex is given in Fig. 5. This spectrum has been compared with the corresponding spectra for $[Ni(1,3\text{-pdta})]^{2-}$ [6] and *trans*(O_5)-$[Ni(1,3\text{-pddadp})]^{2-}$ [39] complexes. The corresponding numerical data for these Ni(II) complexes are given in Table 6. The electronic absorption spectra of $[Ni(1,3\text{-pdta})]^{2-}$ [6] and *trans*(O_5)-$[Ni(1,3\text{-pddadp})]^{2-}$ [39] complexes have been previously discussed in detail and here they have only been repeated for the sake of comparison with the spectrum of $[Ni(1,4\text{-bdta})]^{2-}$ complex. In general, it has been shown, that the spectra of Ni(II)-1,3-pdta-type complexes containing the six-membered diamine ring (T ring), with respect to Ni(II)-edta-type complexes containing the five-membered diamine ring (E ring), exhibit broadening of the first absorption band located at the lowest energy due to the influence of tetragonality on the spectrochemical behavior of these complexes (D_{4h} model) [6,38,39]. In accordance to previously established results for the Ni(II)-edta-type [38] and most other Ni(II) complexes [40–44], the interpretation of the electronic absorption spectrum of $[Ni(1,3\text{-pdta})]^{2-}$ complex [6] has been done by using an octahedral model (O_h): $^3A_{2g} \rightarrow {}^3T_{2g}$ (*F*) (band I); $^3A_{2g} \rightarrow {}^3T_{1g}$ (*F*) (band III) and $^3A_{2g} \rightarrow {}^3T_{1g}$ (*P*) (band IV) (Table 6). Due to the general similarities in the shape between the electronic absorption spectra of

Table 6
Electronic absorption data of nickel(II) complexes with hexadentate 1,3-pdta, 1,3-pddadp and 1,4-bdta ligands

Complex		Absorption		Assignments O_h
		λ (nm)	ε ($M^{-1}cm^{-1}$)	
$[Mg(H_2O)_6][Ni(1,$	I	959.9	15.4	$^3A_{2g} \rightarrow {}^3T_{2g}(F)$
$3\text{-pdta})]\cdot 2H_2O$ [6]	II	770.3	3.9	$\rightarrow {}^1E_g(D)$
	III	571.5	7.3	$\rightarrow {}^3T_{1g}(F)$
	IV	379.7(sh)	7.9	$\rightarrow {}^3T_{1g}(P)$
Trans(O_5)-$[Ni_2(1,$	I	1005.3	13.1	
$3\text{-pddadp})(H_2O)_4]\cdot$	II	773.5	3.5	
$4H_2O$ [39]	III	626.9	8.0	
	IV	376.2	13.6	
$[Mg(H_2O)_6][Ni(1,$	I	1038.7	11.7	
$4\text{-bdta})]\cdot 3H_2O$	II	771.1	3.5	
[This work]	III	581.0	9.9	
	IV	388.7(sh)	11.9	

$[Ni(1,3\text{-pdta})]^{2-}$ [6] and $[Ni(1,4\text{-bdta})]^{2-}$ complexes the same octahedral (O_h) model can be applied for interpretation of the corresponding spectrum of the examined $[Ni(1,4\text{-bdta})]^{2-}$ complex.

The shape of the electronic spectrum of *trans*(O_5)-$[Ni(1,3\text{-pddadp})]^{2-}$ is different from those for $[Ni(1,3\text{-pdta})]^{2-}$ [6] and $[Ni(1,4\text{-bdta})]^{2-}$ complexes. These differences are mainly manifested in the fourth absorption maximum located at the highest energy, where the later two complexes exhibit a tendency for splitting of this absorption band. The absence of the resolution of this absorption band for *trans* (O_5)-$[Ni(1,3\text{-pddadp})]^{2-}$ can be attributed to the fact that this complex with two 3-propionate six-membered rings in an equatorial position constitutes a less strained system than the other two complexes. Additionally, a slight difference between electronic absorption spectra of $[Ni(1,4\text{-pdta})]^{2-}$ and $[Ni(1,3\text{-bdta})]^{2-}$ complexes can be observed in Fig. 5. These differences, manifested through the broadening and splitting in the region of the fourth absorption maximum, as well as in the slight broadening and splitting in the region of the third absorption band for the electronic spectrum of $[Ni(1,4\text{-bdta})]^{2-}$ complex, can be attributed to the fact that this complex with a seven-membered 1,4-butanediamine ring (B ring) in an equatorial plane constitutes a more strained system than $[Ni(1,3\text{-pdta})]^{2-}$ complex having six-membered 1,3-propanediamine ring. The fact that $[Ni(1,4\text{-bdta})]^{2-}$ is more strained system in comparison with $[Ni(1,3\text{-pdta})]^{2-}$ complex can be notified by observing of the strain analysis data given in Table 4.

Finally, in each electronic spectrum of these three Ni(II) complexes there is a shoulder at approximately 770 nm (band II, Table 6) that occurs on the higher-energy side of the spin-allowed band. Previously, it has been discussed that this band probably arises from a spin-forbidden triplet-to-singlet transition [6,39].

4. Concluding remarks

Stereochemically labile hexadentate cobalt(II) and nickel(II) complexes with 1,4-bdta ligand have been shown to undergo a spontaneous resolution upon crystallization, an unprecedented instance with this type of ligand, and to form isostructural, high symmetry crystals. Even though the bridging 1,4-butanediamine group is longer than in other edta-like ligands and thus provides less rigidification, the metal/ligand complexation is enhanced by strong CFSE, and by topological constraints through ligand and water supramolecular structures. The geometry around the Co(II) and Ni(II) ions is flexibly changed by the chelate-ring size, as evidenced by a steady increase of N–M(II)–N and decrease of O_G–M(II)–O_G valence angles on going from E, through T to B rings. The strain of octahedral complex anion is more severe when either edta or 1,4-bdta ligand is used as compared with a less strained 1,3-pdta complex, which is reflected in their electronic absorption spectra.

Supplementary material

CCDC 636017 and 636018 contain the supplementary crystallographic data for $[Mg(H_2O)_6][Co(1,4\text{-bdta})]\cdot 3H_2O$ (**a**) and $[Mg(H_2O)_6][Ni(1,4\text{-bdta})]\cdot 3H_2O$ (**b**). These data can be obtained free of charge via http://www.ccdc.cam.ac.uk/conts/retrieving.html, or from the Cambridge Crystallographic Data Centre, 12 Union Road, Cambridge CB2 1EZ, UK; fax: (+44) 1223-336-033; or e-mail: deposit@ccdc.cam.ac.uk.

Acknowledgement

This work was funded in part by the Ministry of Science and Environmental Protection of the Republic of Serbia (Project No.: 142008B).

References

[1] R. Nagao, F. Marumo, Y. Saito, Acta Crystallogr. Sect. B28 (1972) 1852.
[2] R. Herak, G. Srdanov, M.I. Djuran, D.J. Radanovic, M. Bruvo, Inorg. Chim. Acta 83 (1984) 55.
[3] (a) T. Yamamoto, K. Mikata, K. Miyoshi, H. Yoneda, Inorg. Chim. Acta 150 (1988) 237;
(b) K. Okamoto, K. Kanamori, J. Hidaka, Acta Crystallogr. Sect. C46 (1990) 1640;
(c) H.P. Bommeli, G. Anderegg, W. Petter, Z. Kristallogr. 174 (1986) 23.
[4] J.C. Robles, Y. Matsuzaka, S. Inomata, M. Shimoi, W. Mori, H. Ogino, Inorg. Chem. 32 (1993) 13.
[5] (a) U. Rychlewska, D.D. Radanovic, V.S. Jevtovic, D.J. Radanovic, Polyhedron 19 (2000) 1;
(b) M. Hernandez-Padilla, E. Chinea, S. Dominguez, A. Mederos, M.C. Munoz, F. Lloret, Polyhedron 19 (2000) 1175.
[6] D.J. Radanovic, T. Ama, H. Kawaguchi, N.S. Draškovic, D.M. Ristanovic, S. Janicijevic, Bull. Chem. Soc. Jpn. 74 (2001) 701, and references therein.
[7] D.D. Radanović, U. Rychlewska, M.I. Djuran, N.S. Drašković, M.M. Vasojević, I.M. Hodžić, D.J. Radanović, Polyhedron 22 (2003) 2745.
[8] D.D. Radanović, U. Rychlewska, M.I. Djuran, B. Warżajtis, N.S. Drašković, D.M. Gurešić, Polyhedron 23 (2004) 2183.
[9] U. Rychlewska, D.M. Gurešić, B. Warżajtis, D.D. Radanović, M.I. Djuran, Polyhedron 24 (2005) 2009.
[10] L.M. Shkolnikova, G.V. Polyanchuk, A.L. Poznyak, V.G. Yashunskii, A.B. Ilyukhin, Koord. Khim. 17 (1991) 626.
[11] (a) K. Kanamori, A. Kyotoh, K. Fujimoto, K. Nagata, H. Suzuki, K. Okamoto, Bull. Chem. Soc. Jpn. 74 (2001) 2113;
(b) F.H. Herbstein, Hu Shengzhi, M. Kapon, Acta Crystallogr. B58 (2002) 884.
[12] U. Rychlewska, B. Warżajtis, D. Cvetić, D.D. Radanović, D.M. Gurešić, M.I. Djuran, Polyhedron 26 (2007) 3437.
[13] N.N. Greenwood, A. Earnshaw, Chemistry of the Elements, Pergamon Press Ltd., Oxford, 1984.
[14] I. Bernal, J. Cetrullo, J. Myrczek, J. Cai, W.T. Jordan, J. Chem. Soc., Dalton Trans. (1993) 1771.
[15] I. Bernal, J. Cetrullo, J. Myrczek, J.S. Ricci Jr., D.J. Radanovic, S.R. Trifunovic, in: W. Gans, J.C.A. Boyens (Eds.), Intermolecular Interactions, Plenum Press, New York, 1998, pp. 155–164.
[16] I. Bernal, J. Myrczek, J. Cai, Polyhedron 12 (1993) 1149.
[17] I. Bernal, J. Cetrullo, J. Coord. Chem. 20 (1989) 237.
[18] I. Bernal, J. Cetrullo, J. Coord. Chem. 20 (1989) 247.
[19] I. Bernal, J. Cetrullo, J. Coord. Chem. 20 (1989) 259.

[20] I. Bernal, J. Cetrullo, Inorg. Chim. Acta 150 (1988) 75.
[21] C.J. Kepert, T.J. Prior, M.J. Rosseinsky, J. Am. Chem. Soc. 122 (2000) 5158.
[22] C.J. Kepert, M.J. Rosseinsky, Chem. Commun. (1998) 31.
[23] T.J. Greenhough, M.F.C. Ladd, Acta Crystallogr. B34 (1978) 2744.
[24] T.B. Mikhailova, E.V. Pakhmutova, A.E. Malkov, I.F. Golovaneva, A.A. Sidorov, I.G. Fomina, G.G. Aleksandrov, V.N. Ikorskii, V.M. Novotortsev, I.L. Eremenko, I.I. Moiseeva, Russian Chem. Bull., Int. Edit. 52 (2003) 2105.
[25] S. Ianelli, C. Pelizzi, G. Pelizzi, P. Tarasconi, J. Chem. Crystallogr. 26 (1996) 195.
[26] J.A. Weyh, R.E. Hamm, Inorg. Chem. 7 (1968) 2431.
[27] D.J. Radanović, S.R. Trifunović, M.S. Cvijović, C. Maricondi, B.E. Douglas, Inorg. Chim. Acta 196 (1992) 161.
[28] CrystAlis CCD software. Version 1.171 Oxford Diffraction, Oxfordshire (England), 2000.
[29] G.M. Sheldrick, Acta Crystallogr. Sect. A 46 (1990) 467.
[30] G.M. Sheldrick SHELXL97, Program for the Refinement of Crystal Structures, University of Göttingen, Germany, 1997.
[31] H.D. Flack, Acta Crystallogr. Sect. A 39 (1983) 876.
[32] (a) Stereochemical Workstation Operation Manual, Release 3.4. Siemens Analytical X-Ray Instruments Inc., Madison, WI, 1989;
(b) Mercury, Ver. 1.4.1., Cambridge Crystallographic Data Center, 12 Union Road, Cambridge, England, 2004.
[33] (a) E.F.K. McCandlish, T.K. Michael, J.A. Neal, E.C. Lingafelter, N.J. Rose, Inorg. Chem. 17 (1978) 1383;
(b) X. Solans, M. Font-Altaba, J. Oliva, J. Herrera, Acta Crystallogr. Sect. C 39 (1983) 435.
[34] E. Coronado, M. Drillon, A. Fuertes, D. Beltran, A. Mosset, J. Galy, J. Am. Chem. Soc. 108 (1986) 900.
[35] H.A. Weakliem, J.L. Hoard, J. Am. Chem. Soc. 81 (1959) 549.
[36] A. Albinati, V. Gramlich, G. Anderegg, F. Lianza, W. Petter, H. Bommeli, Inorg. Chim. Acta 274 (1998) 219.
[37] J. Bernstein, R.E. Davis, L. Shimoni, N.L. Chang, Angew. Chem., Int. Ed. Engl. 34 (1995) 1555.
[38] D.J. Radanović, S. Ianelli, G. Pelosi, Z. D Matović, S. Tasić-Stojanović, B.E. Douglas, Inorg. Chim. Acta 278 (1998) 66.
[39] Z.D. Matović, S. Ianelli, G. Pelosi, S.K. Janicijevic, V.M. Ristanović, G. Ponticelli, D.J. Radanović, Polyhedron 21 (2002) 2667.
[40] C.K. Jørgensen, Acta Chem. Scand. 9 (1955) 1362.
[41] C.K. Jørgensen, Acta Chem. Scand. 10 (1956) 887.
[42] N.J. Rose, C.A. Root, D.H. Busch, Inorg. Chem. 6 (1967) 1431.
[43] W.C.E. Higginson, S.C. Nyburg, J.S. Wood, Inorg. Chem. 3 (1964) 463.
[44] O. Bostrup, C.K. Jørgensen, Acta Chem. Scand. 11 (1957) 1223.

subject has been reviewed [10]. The SO_4^{2-} anion is the exclusive product in the oxidation with substitution inert complexes whereas both SO_4^{2-} and $S_2O_6^{2-}$ ions are the products in the oxidation by labile complexes [11]. The oxidation of S(IV) has been extensively studied mainly by one-electron oxidants[1] The oxidation by $Os(bpy)_3^{3+}$ [12], Cu(III) [13], dodecatungstocobaltate(III) [14] and Fe^{3+}(aq) [15] are sensitive to dissolved oxygen in the distilled water whereas no such effect is observed in the oxidations by alkaline MnO_4^- [16], [Mn(acac)$_3$] (Hacac = acetylacetone) [17], [Mn(III)(cydta)] [18] and in the presence of excess Fe^{3+}(aq) ion [19].

Oxidation with the Tl^{3+}(aq) ion [20] involved the formation of weak sulfite-complexes whereas the oxidation with $AuCl_4^-$ and $AuCN_2X_2^-$ (X = Cl, Br) ions [21] proceeded directly. These ions did not participate in any catalytic cycle [22,23], and a free radical chain was not initiated as in the photo induced auto-oxidation of S(IV) [24]. It was considered imperative to examine the oxidation by the $[Ag(H_2L)]^{3+}$ ion with the view of whether it binds itself with S(IV), since its electron affinity is high [25] and structurally it can have axial coordination [26] as reported in the oxidation of H_2O_2 [27] and aliphatic and aromatic alcohols [28].

2. Experimental

2.1. Materials

The orange red ethylenebis(biguanide)silver(III) nitrate, $Ag(H_2L)(NO_3)_3$, was prepared using the method of Ray and Chakravorty [29]. The purity of the prepared sample and its concentration in solution was checked with a HP8452A spectrophotometer[2] (λ_{max} 372 nm, $\varepsilon = 1205$; λ_{max} 370 nm, $\varepsilon = 1210$ in solution $0.01 < [H^+] < 0.1$ mol dm^{-3} [30]).

The suitably diluted $HClO_4$ (E. Merck, GR) was standardised against a standard alkali solution. The $LiClO_4$ solution was prepared by neutralising LiOH (Sigma) by standard $HClO_4$ and standardised as described [31]. The solutions of Na_2SO_3 (Baker, AR) were freshly prepared and standardised as described earlier [18]. The estimated concentration includes the concentrations of the SO_2(aq), HSO_3^- and SO_3^{2-} species and is represented by [S(IV)]. All the chemicals used were either analytical or purified grade and all the solutions were prepared in twice-distilled water.

2.2. Kinetic measurements

Initially solutions of $Ag(H_2L)^{3+}$ and Na_2SO_3 were freshly prepared in distilled water degassed with nitrogen for a sufficient time and diluted suitably with stock solutions of degassed $HClO_4$ and $LiClO_4$ to have the desired concentrations. However, the solutions were not degassed later since the rate constants from the degassed and non-degassed solutions agreed within the experimental limits (3–4%). The S(IV) solution was used within 2 h of preparation because such a solution in perchloric acid is stable over this period [20]. The ionic strength was maintained at 0.5 mol dm^{-3} with $LiClO_4$ unless stated otherwise.

A photoelectric SFA 11 colorimeter, working on the principle of a stopped-flow instrument and connected to a programmable printer to print the absorbance at fixed intervals of time, was used to measure the rate. The temperature of the stock syringes, filled with the reactant solutions, and the cell compartment was maintained at the desired temperature (±0.1 °C) by circulating water from a Haake D8G refrigerated circulatory water bath. The reactant solutions were manually pushed into the reaction cell. The start switch was activated by the piston of the syringe collecting the waste solution from the reaction cell.

The kinetics, under pseudo first-order reaction conditions ($[S(IV)] \gg [Ag(H_2L)]^{3+}$), were studied by following the disappearance of $Ag(H_2L)^{3+}$ at 420 nm [17], at which the Ag(III) complex absorbs and the S(IV) solution is transparent. The absorbance of the reaction mixtures at infinite time was measured the next day.

Each run was studied at least thrice. The plots of $\ln(A_t - A_\infty)$ against time, obtained by using the EXCEL PROGRAM, were linear for more than three half-lives of the reaction. The k_{obs} (s^{-1}) value was computed from the slope of the plots. The deviation between the mean k_{obs} value, reported in the Tables, and those obtained from multiple runs was within ±3–4%.

2.3. Test for free radical

Acrylonitrile (1–2 ml) was added to each of the reactant solutions purged with nitrogen. The solutions, remaining clear over few minutes, were mixed to initiate the reaction. The appearance of a white precipitate in the reaction mixture indicated the formation of free radicals during the course of the reaction.

2.4. Stoichiometry

In one set of experiments the stoichiometry was studied under the kinetic conditions (excess of [S(IV)]) and in the other set $[Ag(H_2L)^{3+}]$ was taken in slight excess over [S(IV)]. Each set consisted of several reaction mixtures with different $[H^+]$, and these were left for sufficient time in glass stoppered flasks to ensure completion of the reaction. The unreacted S(IV) and $Ag(H_2L)^{3+}$ were estimated volumetrically [18], and spectrophotometrically at 370 nm respectively.

Reaction mixtures with similar concentrations were prepared in another set of experiments and after the completion of the reaction, nitrogen was bubbled through the

[1] The exhaustive reference to the studies by various one-electron oxidants is given in Ref. [20].

[2] The instrument could not be used for the kinetic study because its cell compartment could not be thermostated for a constant temperature.

spent reaction mixtures for sufficient time to expel excess $SO_2 \cdot H_2O$. Thereafter a slight excess of $BaClO_4$ solution was added to precipitate the SO_4^{2-} ion for its gravimetric estimation. The estimated amount of SO_4^{2-} ion from these sets agreed within $(99.8 \pm 0.6)\%$.

The results based on the estimation of unreacted S(IV) and Ag(III) and SO_4^{2-} ion indicated a stoichiometric ratio, $\Delta[Ag(enbbg)^{3+}]/\Delta[S(IV)]$, of 1.02 ± 0.02 and therefore the stoichiometry is represented by Eq. (1).

$$Ag(H_2L)^{3+} + H_2SO_3 + H_2O \rightarrow Ag(H_2L)^{+} + SO_4^{2-} + 4H^{+} \quad (1)$$

2.5. Absence of Ag^+ and free ethylenebis(biguanide) in the spent reaction mixtures

The addition of NaCl solution to the spent reaction mixtures did not result in the precipitation of AgCl indicating that the free Ag^+ ion was absent as a reaction product. A similar absence of a precipitate in the reaction mixtures treated with $CuSO_4$ solution was an indication that free ethylenebis(biguanide) was also absent in the spent reaction mixture. Hence, it is concluded that the reduction product of $Ag(H_2L)^{3+}$ is the $Ag(H_2L)^{+}$ ion.

2.6. Absence of $S_2O_6^{2-}$ in the reaction product

The spent reaction mixtures with a deficient amount of S(IV) were treated with a known amount of Cr(VI) solution in 1 mol dm^{-3} H_2SO_4. The Cr(VI) in these reaction mixtures was estimated at 348 nm [32] after some time. The results of estimation indicated that no Cr(VI) was used by the reaction mixtures. It was, therefore, concluded that no detectable amount of $S_2O_6^{2-}$ ion was produced during the reaction. This method is suitable for the detection of $S_2O_6^{2-}$ concentrations as low as 5×10^{-6} mol dm^{-3}.

2.7. Spectral studies

The rapid scanning of the reaction mixture ($10^5[Ag(H_2L)]^{3+} = 7.0$, $10^3[S(IV)] = 1.5$ and $[HClO_4] = 0.2$ mol dm^{-3}) on a HP UV–Vis 8452A spectrophotometer was similar to that of $Ag(H_2L)^{3+}$ solution of the same concentration at 370 and 420 nm. This indicated that either there is no formation of complex(es) between $[Ag(H_2L)]^{3+}$ and [S(IV)] or the complexes were weak if such complexes were formed.

2.8. Distribution of S(IV) species

The three forms of S(IV) which are in equilibrium in aqueous solution are considered in the equilibria (2)–(4). The relative concentrations of these species are pH dependent and the hydrated species, $(SO_2 \cdot H_2O)$, is the dominant species at pH values <2 [33].

$$SO_2H_2O \overset{K_{a1}}{\rightleftharpoons} HSO_3^- + H^+ \quad (2)$$

$$HSO_3^- \overset{K_{a2}}{\rightleftharpoons} SO_3^{2-} + H^+ \quad (3)$$

$$2HSO_3^- \overset{K_d}{\rightleftharpoons} S_2O_5^{2-} + H_2O \quad (4)$$

The fractional concentrations of these species, based on the equilibria (2) and (3), were calculated for a total $[S(IV)] = 0.02$ mol dm^{-3} over $0.01 \leqslant [H^+] \leqslant 0.5$ mol dm^{-3} using the equilibrium constants $K_{a1} = 4.30 \times 10^{-2}$ and $K_{a2} = 4.57 \times 10^{-7}$ mol dm^{-3}, respectively, at 25 °C [34]. The fraction is equal to the quotient of the concentration of the particular species divided by the total [S(IV)]. The calculated values of the fraction for each of the species are given in Table 1 and the distribution is graphically illustrated in Fig. 1. From the distribution plot it is inferred that not only the fraction concentration of SO_3^{2-} (found between 10^{-6} and 10^{-8} mol dm^{-3}) but its significance as a possible reaction partner is negligible. Hence, the reactive S(IV) species are $SO_2 \cdot H_2O$ and the HSO_3^- ion.

The reason for neglecting equilibrium (4), $K_d = 8.8 \times 10^{-2}$ dm^3 mol^{-1} at 25 °C [35], while calculating the concentrations of the above species was circumscribed by the fact that no second-order dependence in S(IV) was observed and $S_2O_6^{2-}$ was not the reaction product. Hence, equilibrium (4) has no kinetic significance in the present investigation.

2.9. Distribution of Ag(III)-complex species

The distribution of the fractions of Ag(III)-complex species, governed by equilibria (5) and (6), was similarly calculated for [Ag(III)-complex] $= 3 \times 10^{-4}$ mol dm^{-3} over the same range of $[H^+]$ as in the case of S(IV) using $K_{Ag1a} = 1.58 \times 10^{-4}$ and $K_{Ag2a} = 1.58 \times 10^{-7}$ mol dm^{-3} at 25 °C [36]. The values, in Table 2, are plotted in Fig. 2 from which it is contingent that the fraction of the $Ag(H_2L)^{3+}$ species is ~1, even at the lowest hydrogen ion concentration. The fraction values of $Ag(HL)^{2+}$ and $Ag(L)^{+}$ decrease with increase in hydrogen ion concentration. The $Ag(L)^{+}$

Table 1
The distribution of H_2SO_3, HSO_3^- and SO_3^{2-} species as fractions (= concentration of the species/$[S(IV)]_o$) at different hydrogen ion concentrations at 25 °C

$[H^+]$	0.01	0.02	0.03	0.04	0.05	0.1	0.15	0.2	0.25	0.3	0.4	0.5
H_2SO_3	0.187	0.315	0.408	0.478	0.535	0.695	0.775	0.82	0.85	0.87	0.9	0.915
HSO_3^-	0.81	0.685	0.59	0.52	0.465	0.302	0.225	0.178	0.148	0.126	0.098	0.08
$10^6 \times SO_3^{2-}$	37	15.5	8.95	5.9	4.23	1.37	0.68	0.406	0.27	0.191	0.111	0.0725

$[S(IV)]_o = 0.02$ mol dm^{-3}.

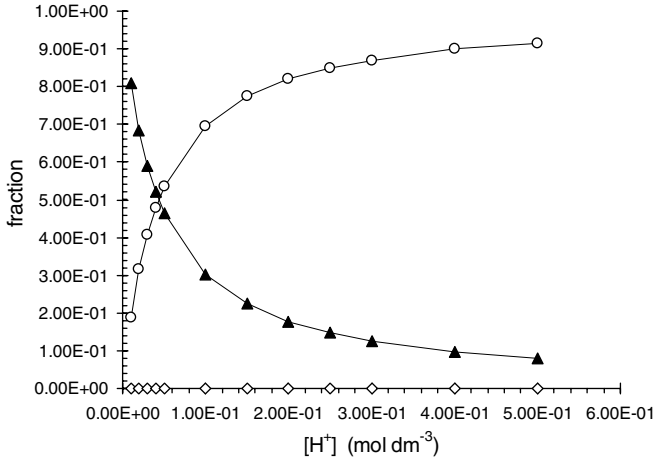


Fig. 1. The plot of the distribution of SO_2(aq), HSO_3^- and SO_3^{2-} species as fractions (= concentration of the species/ $[S(IV)]_o$) at different hydrogen ion concentrations at 25 °C. SO_3(aq) (○),HSO_3^- (▲) and SO_3^{2-} (◇). $[S(IV)]_o = 0.02$ mol dm^{-3}.

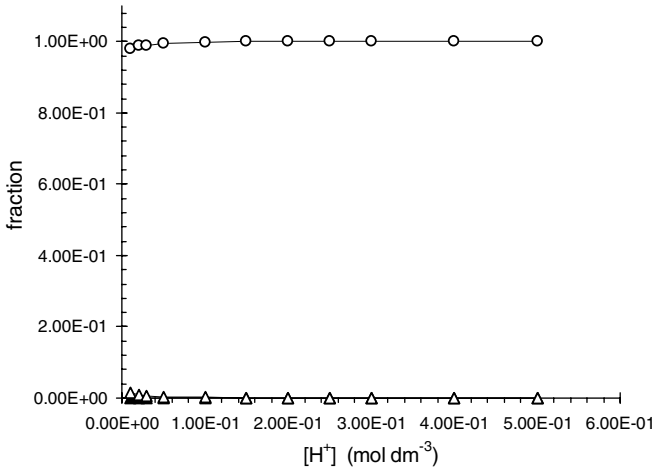


Fig. 2. The distribution of AgH_2L^{3+}, $AgHL^{2+}$ and AgL^+ species as fractions (= concentration of the species/$[Ag(III)\ complex]_o$) at different hydrogen ion concentrations at 25 °C. AgL^+ (▲), $AgHL^{2+}$ (△) and AgH_2L^{3+} (○). $[Ag(III)\text{-complex}]_o = 3 \times 10^{-4}$ mol dm^{-3}.

fraction (found between 10^{-7} and 10^{-8} mol dm^{-3}) is hardly visible in the plot whereas the $Ag(HL)^{2+}$ fraction is about one thousandth of the total concentration of the Ag(III)-complex. Thus, the species $Ag(HL)^{2+}$ and $Ag(L)^+$ are unlikely to contribute to the observed rate of the reaction and therefore can be neglected. Equilibrium (6), for the same reason, has no kinetic significance:

$$Ag(H_2L)^{3+} \overset{K_{Ag1}}{\rightleftharpoons} Ag(HL)^{2+} + H^+ \quad (5)$$

$$Ag(HL)^{2+} \overset{K_{Ag2}}{\rightleftharpoons} Ag(L)^+ + H^+ \quad (6)$$

3. Results

The invariance of $10^4 k_{obs} = 6.73 \pm 0.15$ s^{-1}, ($10^2[S(IV)] = 5.0$; $[H^+] = 0.2$ and ionic strength $\mu = 0.5$ mol dm^{-3}), over a 20-fold variation in $[Ag(H_2L)^{3+}]$ at 30 °C is consistent with the first-order dependence in the $Ag(H_2L)^{3+}$ ion. There is a proportionate increase in k_{obs} with [S(IV)], Table 3, and the plots between k_{obs} and [S(IV)], Fig. 3, are linear and pass through the origin indicating the first-order dependence in [S(IV)]. k_{obs} decreased with the increase in $[H^+]$ and the k_{obs} values at four temperatures are in Table 4. The plot of $k_{obs}(1 + K_{a1}[H^+]^{-1})/[S(IV)]$ against $[H^+]^{-1}$, Fig. 4, is non-linear whereas the plot of $k_{obs}/[S(IV)]$ against $[H^+]^{-1}$, Fig. 5, is linear.

The k_{obs} value was independent of [Ag(I)], (Table 5), suggesting that the electron transfer does not take place in a reversible step in which Ag(I) is a product. The rate was also independent of free ligand L (= ethylenebis(biguanide)) indicating that there is no substitution of L by S(IV) species. An increase in ionic strength (μ, $LiClO_4$), Table 6, decreased k_{obs}, indicating that ions of opposite charges are involved in the reaction. The Davies equation (7) is applicable at the relatively high ionic strength [37,38], and accordingly the plot of $\log k_{obs}$ against $(\sqrt{\mu}/1 + \sqrt{\mu}) - 0.01\mu$, Fig. 6, is linear with the slope $(z_a z_b) = -3.07$:

$$\log k_{obs} = \log k_o + z_a z_b \left(\frac{\sqrt{\mu}}{1 + \sqrt{\mu}} - 0.01\mu \right) \quad (7)$$

4. Mechanism and discussion

The retardation in the rate with increasing $[H^+]$ indicates the presence of a deprotonation equilibrium preceding the rate limiting step. In the present reaction both S(IV) and the Ag(III) complex have a deprotonation equilibrium, as considered in Eqs. (2) and (3) for S(IV), and (6) and (7) for the Ag(III) complex. However, the discussion on the distribution of the S(IV) and Ag(III) complex species had indicated that the effective equilibrium are (2) and (5), respectively.

Table 2
The distribution of AgH_2L^{3+}, $AgHL^{2+}$and AgL^+ species as fractions (= concentration of the species/$[Ag(III)\ complex]_o$) at different hydrogen ion concentrations at 25 °C

$[H^+]$	0.01	0.02	0.03	0.05	0.1	0.15	0.2	0.25	0.3	0.4	0.5
AgH_2L^{3+}	0.98	0.989	0.988	0.996	0.998	1.0	1.0	1.0	1.0	1.0	1.0
$10^3 \times AgHL^{2+}$	15.6	7.87	5.23	3.16	1.59	1.06	0.793	0.633	0.53	0.397	0.317
$10^9 \times AgL^+$	248	62.3	27.7	10.0	2.52	1.12	0.63	0.40	0.28	0.157	0.10

$[Ag(III)\ complex]_o = 3 \times 10^{-4}$ mol dm^{-3}.

Table 3
The dependence of k_{obs} on [S(IV)] at 30 °C $10^4[Ag(H_2L)]^{3+} = 3.0$, $[H^+] = 0.2$ and $[\mu] = 0.5$ mol dm^{-3}

10^2[S(IV)] (mol dm^{-3})	0.1	0.25	0.5	1.0	1.5	2.0	3.0	4.0	5.0
10^4k_{obs} (s^{-1})	0.136	0.333	0.684	1.32	2.05	2.77	4.06	5.33	6.71
10^2k_2 (=k_{obs}/[S(IV)])	1.36	1.33	1.37	1.32	1.37	1.38	1.35	1.33	1.34

Mean $10^2k_2 = 1.35 \pm 0.02$ dm^3 mol^{-1} s^{-1}.

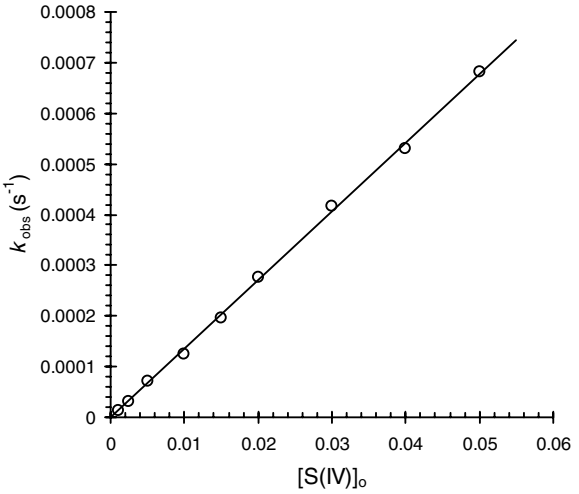


Fig. 3. The linear plot of k_{obs} against $[S(IV)]_o$ passing through the origin at 30 °C.

Table 4
The dependence of k_{obs} on $[H^+]$ at different temperatures $10^4[Ag(H_2L)]^{3+} = 3.0$; $[S(IV)] = 0.02$ and $[\mu] = 0.5$ mol dm^{-3}

$[H^+]$ (mol dm^{-3})	0.01	0.02	0.05	0.10	0.20	0.30	0.40	0.50
10^4k_{obs} (s^{-1}, 25 °C)	29.7	15.9	6.02	3.84	1.95	1.71	1.47	1.09
10^4k_{obs} (s^{-1}, 30 °C)	36.5	18.7	8.06	4.48	2.73	2.15	1.85	1.67
10^4k_{obs} (s^{-1}, 35 °C)	43.7	22.8	10.1	5.85	3.73	3.01	2.67	2.47
10^4k_{obs} (s^{-1}, 40 °C)	54.3	28.5	12.9	7.85	5.33	4.41	3.97	3.77
10^4k_{obs} (s^{-1}, 45 °C)	64.5	32.1	16.2	9.71	7.12	6.23	5.65	4.37

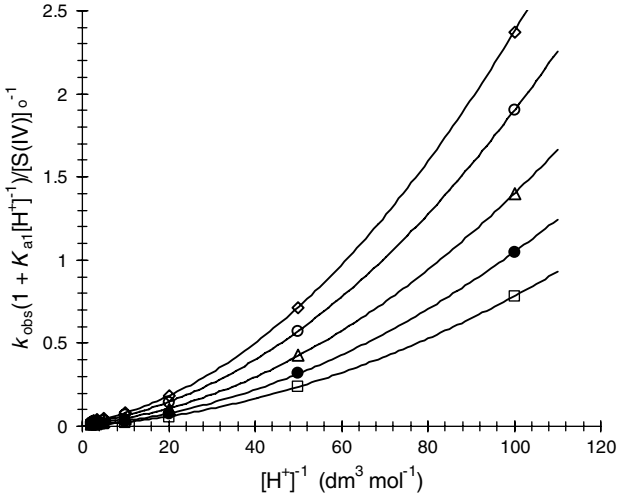


Fig. 4. The plot of the left side of Eq. (17) against $[H^+]^{-1}$ at temperatures: 25 °C (□), 30 °C (■), 35 °C (△), 40 °C (○) and 45 °C (◇) is non-linear. The plot is concave and the experimental conditions are the same as in Fig. 3.

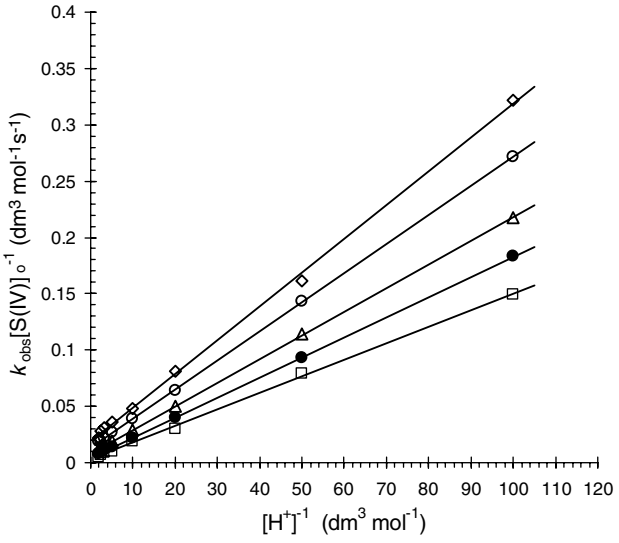


Fig. 5. The linear plots of $k_{obs}/[S(IV)]$ against $[H^+]^{-1}$ with intercepts at temperatures: 25 °C (□), 30 °C (●), 35 °C (△), 40 °C (○) and 45 °C (◇) is consistent with Eq. (26). $10^4[Ag(H_2L)]^{3+} = 3.0$; $[S(IV)] = 0.02$ and $[\mu] = 0.5$ mol dm^{-3}.

Table 5
The dependence of k_{obs} on [Ag(I)] at 35 °C $10^4[Ag(H_2L)]^{3+} = 3.0$, $[\mu] = 0.5$, $[S(IV)] = 0.02$, $[H^+] = 0.3$ mol dm^{-3}

10^4 [Ag$^+$] (mol dm^{-3})	0.01	0.02	0.05	0.10	0.20	0.30	050
10^4k_{obs} (s^{-1})	3.05	3.00	3.02	3.07	3.01	3.03	3.01

Table 6
The dependence of k_{obs} on ionic strength at 45 °C $10^4[Ag(H_2L)]^{3+} = 3.0$, $[S(IV)] = 0.02$ and $[H^+] = 0.1$ mol dm^{-3}

μ (mol dm^{-3})	0.1	0.2	0.3	0.4	0.5	0.6	0.8	1.0
10^4k_{obs} (s^{-1})	34.4	18.5	12.8	11.0	9.68	8.80	6.97	5.05

On consideration of the stoichiometry of the reaction, a first-order dependence of the reaction in Ag(III) complex and S(IV), and the SO_4^{2-} ion being the product of the reaction with no indication for the formation of an intermediate from the UV–Vis spectra of the reaction mixture, the following reactions are likely to be part of the proposed mechanism under Scheme I, where reactions (8) and (9) are rate determining.

Scheme I:

$$SO_2(aq) \overset{K_{a1}}{\rightleftharpoons} HSO_3^- + H^+ \quad (2)$$

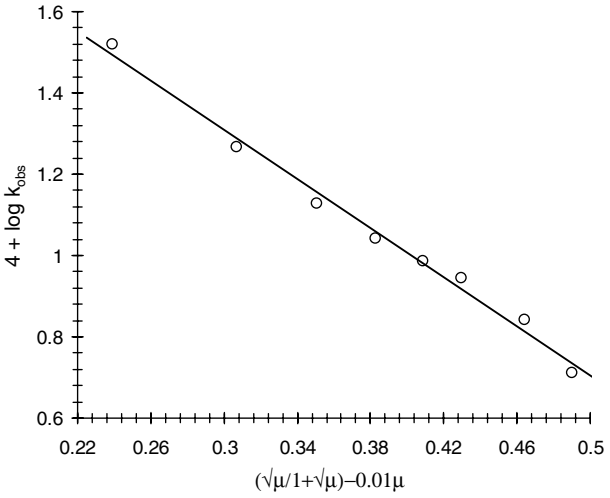


Fig. 6. The linear plot of log k_{obs} against $(\sqrt{\mu}/(1+\sqrt{\mu}) - 0.01\mu)$ has a slope = -3.07 ± 0.16 $10^4[Ag(H_2L)]^{3+} = 3.0$, [S(IV)] = 0.02 and $[H^+]$ = 0.1 mol dm^{-3} at 45 °C.

$$Ag(H_2L)^{3+} \overset{K_{Ag1}}{\rightleftharpoons} Ag(HL)^{2+} + H^+ \quad (5)$$

$$Ag(H_2L)^{3+} + SO_2(aq) \overset{k}{\rightarrow} SO_3^{-\cdot} + Ag(H_2L)^{2+} + 2H^+ \quad (8)$$

$$Ag(H_2L)^{3+} + HSO_3^- \overset{k_o}{\rightarrow} SO_3^{-\cdot} + Ag(H_2L)^{2+} + H^+ \quad (9)$$

$$Ag(H_2L)^{2+} + SO_3^{-\cdot} + H_2O \overset{k_3(fast)}{\rightarrow} Ag(H_2L)^{+} + SO_4^{2-} + 2H^+ \quad (10)$$

The free radical $SO_3^{-\cdot}$ in aqueous solution is supported by esr spectroscopy [39]. The rate law in view of the reactions (2), (5) and (8)–(10) is expressed by the following equation:

$$\text{rate} = \frac{-d[Ag(III)]_o}{dt} = (k + k_o K_1[H^+]^{-1})[SO_2(aq)][Ag(H_2L)^{3+}] \quad (11)$$

The correlation of the concentrations of $SO_2(aq)$ with the analytical concentration $[S(IV)]_o$ in view of equilibria (2) and (3) is expressed by Eq. (12), which changes to Eq. (13) on the assumption that $(1 + K_{a1}[H^+]^{-1}) \gg K_{a2}K_{a1}[H^+]^{-2}$ which is consistent with the fraction of the respective species shown in Fig. 1 over a given range of hydrogen ion concentrations:

$$[SO_2] = \frac{[S(IV)]_o}{1 + K_{a1}[H^+]^{-1} + K_{a1}K_{a2}[H^+]^{-2}} \quad (12)$$

or

$$[SO_2(aq)] = [S(IV)]_o(1 + K_{a1}[H^+]^{-1})^{-1} \quad (13)$$

Similarly, the correlation of the concentration of $Ag(H_2L)^{3+}$ with its analytical concentration, [Ag(III) complex]$_o$, in view of equilibria (5) and (6) is given by Eq. (14), which with the assumption that $1 \gg K_{Aga1}[H^+]^{-1} + K_{Aga1}$-$K_{Aga2}[H^+]^{-2}$ is reduced to Eq. (15). Eq. (15) is consistent with the plot in Fig. 2 where the fraction value of Ag-$(H_2L)^{3+} \sim 1$ even at the lowest hydrogen ion concentration:

$$[Ag(H_2L)^{3+}] = \frac{[Ag(III)\text{-complex}]_o}{1 + K_{Ag1a}[H^+]^{-1} + K_{Ag1a}K_{Ag2a}[H^+]^{-2}} \quad (14)$$

$$[Ag(H_2L)^{3+}] = [Ag(III)\text{-complex}]_o \quad (15)$$

Eq. (16) is obtained on substituting the respective values of $[SO_2(aq)]$ and $[Ag(H_2L)^{3+}]$ from Eqs. (13) and (15) into Eq. (11):

$$\frac{-d[Ag(III)]}{dt} = \left(\frac{k + k_o K_{a1}[H^+]^{-1}}{1 + K_{a1}[H^+]^{-1}}\right)[S(IV)]_o[Ag(III)\text{-complex}]_o \quad (16)$$

or

$$k_{obs}(1 + K_{a1}[H^+]^{-1})/[S(IV)]_o = (k + k_o K_{a1}[H^+]^{-1}) \quad (17)$$

The desired plot of the left side of Eq. (17) against $[H^+]^{-1}$ is illustrated in Fig. 4, which is concave indicating that $k_{obs}(1 + K_{a1}[H^+]^{-1})/$ [S(IV)] increased more rapidly than the $[H^+]^{-1}$ value. Since the term $(1 + K_{a1}[H^+]^{-1})$ cannot be neglected, Scheme I is unlikely to represent the mechanism of the reaction.

The alternate Scheme II considers the involvement of the weak intermediates most likely. The intermediates evaded both kinetic and spectrophotometric detections because of their weak nature.

Scheme II

$$SO_2(aq) \overset{K_{a1}}{\rightleftharpoons} HSO_3^- + H^+ \quad (2)$$

$$Ag(H_2L)^{3+} \overset{K_{Ag1}}{\rightleftharpoons} Ag(HL)^{2+} + H^+ \quad (5)$$

$$Ag(H_2L)^{3+} + SO_2(aq) \overset{K_1}{\rightleftharpoons} Ag(H_2L)SO_2^{3+} \quad (18)$$

$$Ag(H_2L)^{3+} + HSO_3^- \overset{K_2}{\rightleftharpoons} Ag(H_2L)HSO_3^{2+} \quad (19)$$

$$Ag(H_2L)SO_2^{3+} \overset{k'}{\rightarrow} Ag(H_2L)^{2+} + SO_3^{-\cdot} \quad (20)$$

$$Ag(H_2L)HSO_3^{2+} \overset{k''}{\rightarrow} Ag(H_2L)^{2+} + SO_3^{-\cdot} + H^+ \quad (21)$$

$$Ag(H_2L)^{2+} + SO_3^{-\cdot} + H_2O \overset{k_3(fast)}{\rightarrow} Ag(H_2L)^{+} + SO_4^{2-} + 2H^+ \quad (10)$$

The proposed inner-sphere mechanism has similarity with those of alcohols [28], H_3PO_2 [40] and ascorbic acid [41], and $Tl^{3+}(aq)$ oxidation of $SO_2(aq)$ under similar conditions of H^+ ions [20]. The rate in terms of reactions (17)–(20) and (14) is given by the following equation:

$$\text{rate} = \frac{-d[Ag(III)]_o}{dt} = (k'K_1 + k''K_2K_1[H^+]^{-1})[Ag(H_2L)^{3+}][SO_2(aq)] \quad (22)$$

The correlation between $[Ag(H_2L)]^{3+}$ and [Ag(III) complex]$_o$ in terms of Eqs. (18) and (19) is given by Eq. (23), whereas Eq. (13) holds good for the correlation between $[SO_2(aq)]$ and [S(IV)]:

$$[Ag(H_2L)^{3+}] = \frac{[Ag(III)]_o}{1 + K_1[SO_2(aq)] + K_1K_2[SO_2(aq)][H^+]^{-1}} \quad (23)$$

The substitution of the proper values of $[SO_2(aq)]$ from Eq. (13) and that of $[Ag(H_2L)^{3+}]$ from Eq. (23) into Eq. (22) gives the following equation:

$$\frac{-d[Ag(III)]}{dt} = \frac{(k'K_1 + k''K_2K_1[H^+]^{-1})[Ag(III) - complex]_o[S(IV)]_o/(1 + K_{a1}[H^+]^{-1})}{(1 + (K_1 + K_1K_2[H^+]^{-1}))[S(IV)]_o/(1 + K_{a1}[H^+]^{-1})} \quad (24)$$

The terms $(1 + K_{a1}[H^+]^{-1})$, appearing both in the numerator and denominator, cancel each other and therefore Eq. (24) is transformed into Eq. (25):

$$\frac{-d[Ag(III)]}{dt} = \frac{(k'K_1 + k''K_2K_1[H^+]^{-1})[Ag(III) - complex]_o[S(IV)]_o}{(1 + (K_1 + K_1K_2[H^+]^{-1}))[S(IV)]_o} \quad (25)$$

Since $1 \gg (K_1 + K_1K_2[H^+]^{-1})[S(IV)]_o$ because of the microscopic values of K_1 and K_2, the Eq. (25) is reduced to Eq. (26) where $k_1 = k'K_1$ and $k_2 = k''K_2K_{a1}$:

$$k_{obs}/[S(IV)]_o = (k_1 + k_2[H^+]^{-1}) \quad (26)$$

Eq. (26) is consistent with the linear plot of $k_{obs}/[S(IV)]_o$ against $[H^+]^{-1}$ in Fig. 5, with intercepts on the rate ordinate. The inner-sphere mechanism is thereby supported. The formation of the intermediate $Ag(H_2L)HSO_3^{2+}$ through reaction (19) is preferred because it is consistent with the slope value ($z_az_b = -3.07$) of the plot in Fig. 6. The alternate route in Eq. (27) is kinetically indistinguishable from the reaction in Eq. (19) because of the identity that $K_2K_{a1} = K'_2K_1$, as shown below:

$$Ag(H_2L)SO_2(aq)^{3+} \overset{K'_2}{\rightleftharpoons} Ag(H_2L)HSO_3^{2+} + H^+ \quad (27)$$

or

$$[Ag(H_2L)HSO_3^{2+}] = K'_2K_1[Ag(H_2L)^{3+}][SO_2(aq)][H^+]^{-1} \quad \text{(from (27) and (18))} \quad (28)$$

$$= K_2K_{a1}[Ag(H_2L)^{3+}][SO_2(aq)][H^+]^{-1} \quad \text{(from (19) and (2))} \quad (29)$$

The values of the estimated rate constants k_1 and k_2 from the least square values of the intercepts and slopes, at different temperatures, are given in Table 7. It is noted that at lower temperatures $k_2 > k_1$, but the difference narrows as the temperature increases. The Arrhenius plots corresponding to k_1 and k_2 are given in Figs. 7 and 8, respectively. The significance of the activation parameters is not discussed because these are based on the product of the rate limiting and equilibrium constants and the values of the equilibrium constants remain indeterminate. However, it seems that the combination of reactions (18) and (20) is enthalpy controlled ($\Delta H^{\ddagger}_{k1} = 70 \pm 3$ kJ mol^{-1} and $\Delta S^{I}_{k1} = -42 \pm 10$ J K^{-1} mol^{-1}), and the combination of reactions (2), (19) and (21) is driven by the entropy, ($\Delta H^{I}_{k2} = 9 \pm 1$ kJ mol^{-1} and $\Delta S^{I}_{k2} = -225 \pm 2$ J K^{-100} mol^{-1}). The trend that $\Delta S^{I}_{k1} > \Delta S^{I}_{k2}$ is similar to that observed in the oxidation of alcohols for which $\Delta H^{\ddagger}_{k1}$ and ΔH^{I}_{k2} are fairly similar [28]. Both ΔH^{I}_{k2} and ΔS^{I}_{k2} are almost of the same magnitude as in the oxidation of H_3PO_2 for a similar path [40]. Such a similarity is a pointer and supportive of the proposed inner-sphere mechanism.

The coordination number in Ag(III) (d^8) could be either four (planar) or six (octahedral). The diamagnetic $[Ag(H_2L)]^{3+}$ complex is square planar and the Ag(III) ion is tetra-coordinated by four nitrogen atoms of the ethylene-bisbiguanidinium ion. Thus $SO_2(aq)$ has to be axially coordinated. A water molecule is also axially coordinated to make the sulfito-complex octahedral.

It seems that the generalisation that the one or two-electron oxidation of S(IV) by metal ions and their complexes results in the formation of $S_2O_6^{2-}$ or SO_4^{2-}, respectively [11] needs reconsideration. The oxidation by one electron

Table 7
Values of k_1 and k_2 (dm^3 mol^{-1} s^{-1})

Temp (°C)	25	30	35	40	45
10^3k_1 (dm^3 mol^{-1} s^{-1})	3.23	4.73	8.27	13.4	18.9
10^3k_2 (dm^3 mol^{-1} s^{-1})	34.4	37.4	39.6	43.9	46.1

$\Delta H^{\ddagger}_{k1} = 70 \pm 3$.
$\Delta H^{\ddagger}_{k2} = 9 \pm 1$ kJ mol^{-1}.
$\Delta S^{\ddagger}_{k1} = -42 \pm 10$.
$\Delta S^{\ddagger}_{k2} = -225 \pm 2$ J K^{-1} mol^{-1}.

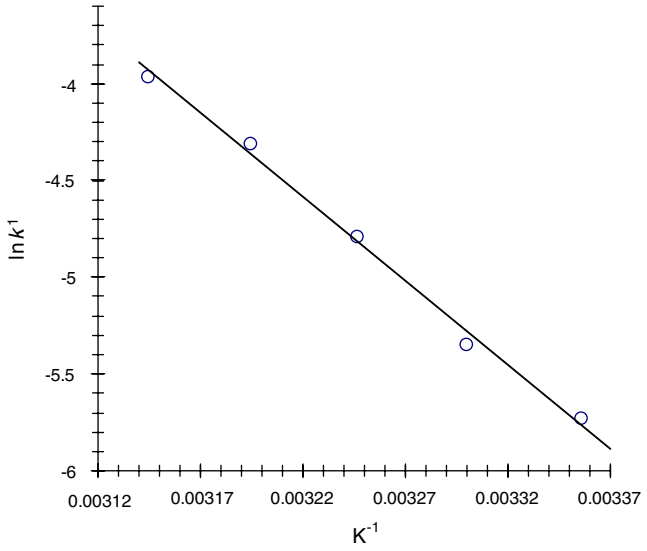


Fig. 7. The linear Arrhenius plot of $\ln k_1$ against K^{-1}.

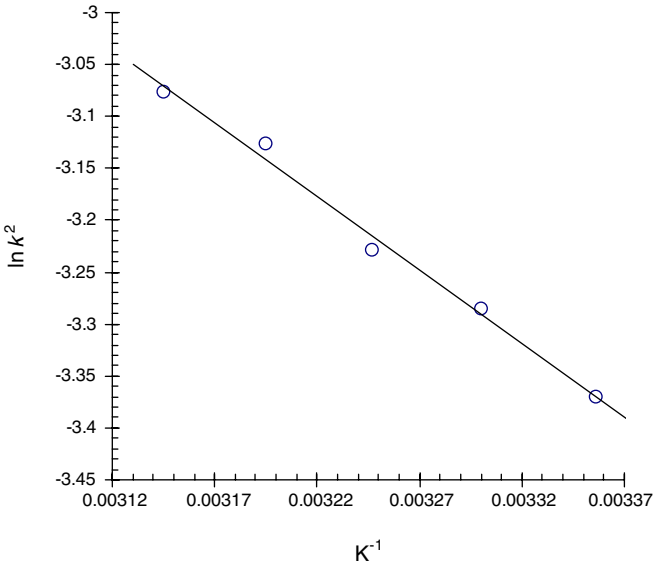


Fig. 8. The linear Arrhenius plot of ln k_2 against K^{-1}.

oxidants such as $IrCl_2^-$ and $[Os(bpy)_3]^{3+}$ [12], $[Mn(acac)_3]$ [17], $Fe^{3+}(aq)$ [19], alkaline MnO_4^- [16] and $[Fe(edta)]^-$ [42] results in the formation of SO_4^{2-} as the sole product. On the other hand one electron oxidants such as 12-tungstocobaltate(III) [14], $[Ni^{IV}L^1_2]^{2+}$ and $[Ni^{IV}L^2]^{2+}$ (HL^1 = 6-amino-3-methyl-4-azahex-3-en-2-one oxime, $H_2L^2 = 3$, 14-dimethyl-4,7,10,13-tetra-azahexadeca-3,13-diene-2,15-dione dioxime) [43], *trans*-(diaqua)(*N*,*N*′)-propylene 1,2 bis(salicylidinim inato)Fe(III) [44], (tetraethylenepentamine)Fe(III) [45] produce both SO_4^{2-} and $S_2O_6^{2-}$ ions, though in certain cases $S_2O_6^{2-}$ is the exclusive product at high [S(IV)] [14,43].

The exclusive formation of SO_4^{2-} or $S_2O_6^{2-}$ or both in different proportions is dependent on the fate of $SO_3^{-\cdot}$ formed during the oxidation of S(IV) by one electron oxidants. The exclusive product is SO_4^{2-} ion if k_3 (see reaction (10)) $\gg k_4$ (see reaction (30)) and if $k_4 \gg k_3$, the exclusive product would be the $S_2O_6^{2-}$ ion. When k_3 and k_4 are of comparable magnitude, the product ratio SO_4^{2-}:$S_2O_6^{2-}$ would depend on the k_3:k_4 ratio.

$$SO_3^{-\cdot} + SO_3^{-\cdot} \xrightarrow{k_4(\text{fast})} S_2O_6^{2-} \qquad (30)$$

Acknowledgements

The financial grants from UGC (F.12-59/1997) and (F.12-147/2001) are acknowledged with thanks. Thanks are also due to Dr. R.S. Sindal, Head of the Department, for laboratory facilities.

References

[1] L.J. Kirschenbaum, J.H. Ambrus, G. Atkinson, Inorg. Chem. 12 (1973) 283.
[2] R.N. Mehrotra, L.J. Kirschenbaum, Inorg. Chem. 28 (1989) 4327, and references cited therein.
[3] L.J. Kirschenbaum, J.D. Rush, J. Am. Chem. Soc. 106 (1984) 1003.
[4] L.J. Kirschenbaum, R.K. Panda, E.T. Borish, E. Mentasti, Inorg. Chem. 28 (1989) 3623.
[5] D. Sen, N.N. Ghosh, P. Ray, J. Indian Chem. Soc. 27 (1950) 619.
[6] K. Das, R. Banerjee, A. Das, S. Dasgupta, Bull. Electrochem. 5 (1989) 477.
[7] J. Veprek Siska, D.M. Wagnerava, K. Eckschalag, Collect. Czech. Chem. Commun. 31 (1966) 1248.
[8] R. Banerjee, Proc. Indian Acad. Sci. (Chem. Sci.) 106 (1994) 655, and references cited therein.
[9] S. Solanki, R. Saha, S. Arora, A. Prakash, Raj N. Mehrotra, Indian J. Chem. 40A (2001) 256.
[10] C. Brandt, R. van Eldik, Chem. Rev. 95 (1995) 119, There is a good bibliography on the oxidation of S(IV) by transition metal ions up to 1994.
[11] (a) K.K. Sengupta, S. Das, P.K. Sen, Trans. Met. Chem. 12 (1987) 33; (b) E.L. Stapp, D.W. Carlyle, Inorg. Chem. 13 (1974) 834; (c) A. Brown, W.C.E. Higginson, J. Chem. Soc., Dalton Trans. (1972) 166; (d) R. Sarala, M.A. Islam, S.B. Robin, D.M. Stanbury, Inorg. Chem. 29 (1990) 1133.
[12] R. Sarala, D.M. Stanbury, Inorg. Chem. 29 (1990) 3456, and references cited therein.
[13] J.M. Anast, D.M. Margerum, Inorg. Chem. 20 (1981) 2319.
[14] M. Ali, S.K. Saha, P. Banerjee, J. Chem. Soc., Dalton Trans. (1990) 187.
[15] C. Brandt, I. Fávián, R. van Eldik, Inorg. Chem. 33 (1994) 687.
[16] (a) L.I. Simandi, M. Jaky, C.R. Savage, Z.A. Schelly, J. Am. Chem. Soc. 107 (1985) 4220; (b) T. Ernst, M. Gifert, M. Wilgosky, Int. J. Chem. Kinetic 24 (1990) 887.
[17] S. Mukhopadhyay, Rupendranath Banerjee, J. Chem. Soc., Dalton Trans. (1993) 933.
[18] U. Chandrawat, A. Prakash, R.N. Mehrotra, Can. J. Chem. 73 (1995) 1531.
[19] Gábor Lente, István Fábián, J. Chem. Soc., Dalton Trans. (2002) 778.
[20] J. Berglund, P. Werndrup, L.I. Elding, J. Chem. Soc., Dalton Trans. (1994) 1435.
[21] J. Berglund, L.I. Elding, Inorg. Chem. 34 (1995) 513.
[22] R van Eldik, N. Coichev, K. Bal Reddy, A. Gerhard, Ber. Bunsenges. Phys. Chem. 96 (1992) 478.
[23] J. Berglund, S. Fronaeus, L.I. Elding, Inorg. Chem. 32 (1993) 4527.
[24] .U. Diester, P. Warneck, J. Phys. Chem. 94 (1990) 2191, and references cited therein.
[25] D.A. Zatko, J.W. Prather, J. Electron Spectrosc. Relat. Phenom. 2 (1973) 191.
[26] (a) M.L. Simms, J.L. Atood, D.A. Zatko, J. Chem. Soc., Chem. Commun. (1973) 46; (b) L. Coghi, G. Pellizzi, Acta Crystallogr. Sect. B 31 (1975) 131.
[27] R. Banerjee, A. Das, S. Dasgupta, J. Chem. Soc., Dalton Trans. (1989) 1645.
[28] R. Banerjee, A. Das, S. Dasgupta, J. Chem. Soc., Dalton Trans. (1990) 1207.
[29] P. Ray, N.C. Chakravarty, J. Indian Chem. Soc. 21 (1944) 47.
[30] R. Banerjee, D. Banerjea, Indian J. Chem. 17A (1979) 246.
[31] S. Dholiya, A. Prakash, Raj N. Mehrotra, J. Chem. Soc., Dalton Trans. (1992) 819.
[32] D.W. Carlyle, J. Am. Chem. Soc. 94 (1972) 4525.
[33] H.G. Maahs, J. Geophys. Res. 88 (1983) 10721.
[34] R.M. Smith, A.E. Martell, Critical Stability Constants, vol. 6, Plenum Press, New York, 1989, pp. 16 & 450.
[35] R.E. Connick, T.M. Tam, E. von Deuster, Inorg. Chem. 21 (1982) 103.
[36] R. Banerjee, K. Das, A. Das, S. Dasgupta, Inorg. Chem. 28 (1989) 585.
[37] C.W. Davies, Ion Association, Butterworth, London, 1962, p. 39.
[38] C.W. Davies, J. Chem. Soc. (1938) 2093.

[39] (a) R.O.C. Norman, P.M. Storey, J. Chem. Soc. B (1971) 1009;
(b) B.D. Flockhart, K.J. Irvin, R.C. Pink, B.D. Sharma, J. Chem. Soc., Chem. Commun. (1971) 339.
[40] R. Banerjee, R. Das, S. Mukhopadhyay, J. Chem. Soc., Dalton Trans. (1992) 1317.
[41] S. Dasgupta, E. Herlinger, W. Linert, J. Chem. Soc., Dalton Trans. (1993) 567.
[42] M. Dellert-Ritter, R. van Eldik, J. Chem. Soc., Dalton Trans. (1992) 1045.
[43] S. Bhattacharya, M. Ali, S. Gangopadhyay, P. Banerjee, J. Chem. Soc., Dalton Trans. (1994) 3733.
[44] A. Das, A.C. Dash, Indian J. Chem. 40A (2001) 65.
[45] A.C. Dash, A.K. Patnaik, N. Das, Indian J. Chem. 36A (1997) 268.

2. Results and discussion

Scheme 1 shows the synthetic route to the complexes. The bis-pyrene ligand, $\mathbf{L}^{pyr}$, was accessed by the reaction of 2 equiv. of 1-aminopyrene with diethylenetriaminepentaacetic diacidanhydride (DTPAA), in the presence of triethylamine. The reaction mixture was stirred at room temperature for 24 h and the resultant crude product was purified, first by washing with dichloromethane, and then chromatographically (silica). The free ligand was isolated as a light brown solid and the corresponding lanthanide complexes $\mathbf{Ln}\cdot\mathbf{L}^{pyr}$ (Ln = Nd, Gd, Er, Yb) were prepared by addition of 1 equiv. $Ln(OTf)_3$. The purity of the complexes was assessed using thin layer chromatographic analysis to ensure that no free ligand remained following complexation.

The free ligand $\mathbf{L}^{pyr}$ was characterised using ^1H NMR, elemental analyses, mass spectrometry, IR and UV–Vis. The complexes were isolated in good yields. MALDI-TOF spectra were obtained for each of the complexes and gave peak clusters with the correct isotopic distributions, corresponding to the parent ion $\{M-H\}^+$, in each case. Vibrational IR studies are insightful for carboxylate derivatives of this type, and for the complexes they show a low energy shift for ν(C=O) when compared to the free ligand [16]. The hygroscopic nature of the complexes prevented reproducible elemental analyses from being obtained.

3. Photophysical studies

The absorption spectra of $\mathbf{L}^{pyr}$ showed a typical spectral profile associated with a pyrene containing species. The distinctive features at 300–350 nm correspond to IL π–π^* transitions. The spectra of the corresponding complexes $\mathbf{Ln}\cdot\mathbf{L}^{pyr}$ revealed very similar properties with only minor deviations in absorption maxima from the free ligand.

The luminescence features of these species were then analysed. Fig. 1 shows the steady state UV–Vis emission spectra of the free ligand, $\mathbf{L}^{pyr}$, and corresponding complexes, $\mathbf{Ln}\cdot\mathbf{L}^{pyr}$, in air-equilibrated methanolic solutions at a concentration of approximately 1×10^{-6} M. An excitation wavelength of 340 nm was utilised and corresponds to selective irradiation of the pyrene chromophore. Fig. 1 shows that, for $\mathbf{L}^{pyr}$, pyrenyl emission dominates with vibronically structured features between 300 and 450 nm, assigned to intraligand transitions ($^1\pi\pi^*$). Pyrene luminescence in this region corresponds to monomeric pyrene as opposed to aggregated pyrene units, which are prone to excimer emission. The significantly weaker, broadened feature from 450 to 550 nm may be due to the presence of a pyrene excimer. However, at the concentration used in this study intermolecular excimer formation (usually observed around 480 nm) should not be favoured [13]. For the complexes, $\mathbf{Ln}\cdot\mathbf{L}^{pyr}$, the fluorescence emission spectra are again dominated by pyrenyl emission although the relative intensities of the vibronic transitions between 350 and 455 nm have changed and there is a slightly more pronounced broad band around 450–550 nm. Although weak in comparison to the higher energy transitions, the intensity of the excimer band in the complexes is twofold that of the parent ligand, $\mathbf{L}^{pyr}$. However, the absence of a dominating band at 450–500 nm suggests that the pyrene units are probably kept sufficiently separated, due to the coordination geometry of the ligand.

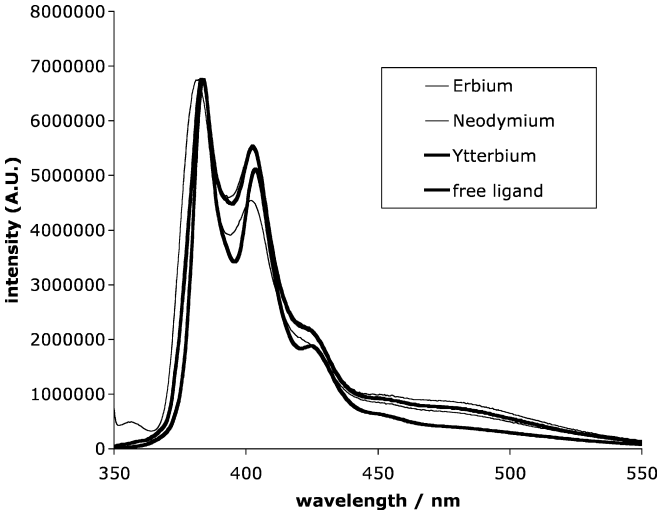
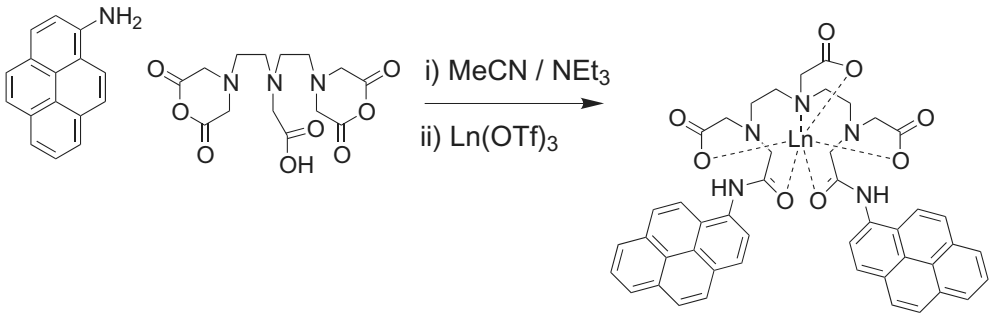


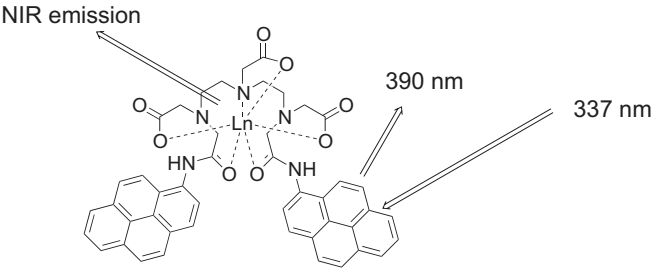
Fig. 1. Comparison of the pyrene based emission from the free ligand and complexes. Spectra are normalised about the 384 nm peak. Samples were prepared as 8×10^{-7} M methanol solutions (λ_{ex} = 340 nm).



Scheme 1. Synthesis of $\mathbf{Ln}\cdot\mathbf{L}_{pyr}$ (Ln = Nd, Gd, Er and Yb).

Time-resolved emission studies on the pyrene-based fluorescence were undertaken on aerated solutions of the complexes. A rapidly pulsed excitation source (NanoLED at 355 nm operating at 500 kHz) was used in conjunction with a time-correlated single photon counting apparatus monitoring the emission at 390 nm. In each case, two lifetimes were obtained when analysing the decay profile: typically these were one component of ~6 ns and another much shorter of ~0.5 ns. The relative weightings of the contributions are shown in Table 1. The observation of these short-lived components, in aerated solution, is consistent with the excited states being singlet in nature. The existence of two components may well be a conformational effect on the pyrenyl groups. For comparison, the Gd^{III} complex was also measured. The emissive state of Gd^{III} lies above the excited states of pyrene thus rendering the metal ion non-emissive, but a useful analogue for studying the excited states of chromophoric units. The results in this study show that the time-resolved emissive characteristics of the ligand do not vary much between the lanthanides, suggesting that the dominant energy transfer mechanism between the pyrene units and emissive lanthanide ions probably involves the pyrene triplet state as observed in related systems (see Scheme 2).

The emission of the lanthanide ions was analysed using near-infrared luminescence (see Figs. 2–4). An excitation wavelength of 337 nm was used and ideally suited to effectively sensitising the pyrene chromophoric units ($\lambda_{max} = 343$ nm). Measurements were conducted in deuteriated and non-deuteriated methanolic solutions and lifetime values were obtained by iterative reconvolution with the detector response using established procedures. In each case sensitised lanthanide emission was observed, the lifetimes for which are shown in Table 1 and the wavelengths for which are consistent with the metal present [Nd^{III}, $^4F_{3/2} \rightarrow {}^4F_{13/2}$ at 1055 and 1340 nm, respectively; Er^{III}, $^4F_{13/2} \rightarrow {}^4F_{15/2}$ at 1530 nm; Yb^{III}, $^2F_{5/2} \rightarrow {}^2F_{7/2}$ at 980 nm]. Time-resolved emission spectra (TRES) were recorded for each of the complexes (see Fig. 2) in CD_3OD and reveal the spectral profile in relation to the lifetime. In the cases of $\mathbf{Ln} \cdot \mathbf{L}^{pyr}$ (Ln = Nd, Yb), the lifetimes are unremarkable and typical of dtpa- or dota-like complexes in protic media [4,17]. However, the observation of Er^{III} emission in protic, non-deuteriated solvent is noteworthy and rare (see Fig. 3). The observed lifetime of 134 ns is shorter than both the Nd^{III} and Yb^{III} analogues reflecting the more pronounced sensitivity of Er^{III} to quenching *via* O–H oscillators. In CD_3OD, the lifetime is of microsecond order and comparable to previous observations for related Er^{III} species in deuteriated media [17].



Scheme 2. Possible mode of lanthanide sensitisation.

For the Yb^{III} example it is possible to utilise the lifetime measurements to deduce an approximation of inner sphere solvent coordination (denoted q) by application of the following equation based originally on Horrocks' work and developed further by Parker, Beeby and co-workers:

$$q = 2[(k_{CH_3OH} - k_{CD_3OD}) - 0.05]$$

where k_{CH_3OH} and k_{CD_3OD} are the observed rate constants for luminescence in CH_3OH and CD_3OD, respectively. This results in an inner-sphere hydration number (q) of 0.84 for $\mathbf{Yb} \cdot \mathbf{L}^{pyr}$. For Nd^{III} the equation used is:

$$q = 290(k_{CH_3OH} - k_{CD_3OD}) - 0.4$$

Here deduction of the inner sphere hydration state of Nd^{III} species is less clear cut due to non-radiative quenching *via* other oscillators such as C–H and N–H [18,19]. Despite this the above equation has been shown to hold well for aminocarboxylate ligands and is thus applied in this case. From the lifetimes of $\mathbf{Nd} \cdot \mathbf{L}^{pyr}$ q, is obtained as 0.53. Thus for both examples $q < 1$ which is entirely reasonable given that the ligand itself possesses eight potential donor atoms and large hydrophobic chromophores which may inhibit the approach of protic solvent molecules. In the Yb^{III} and Er^{III} cases, the quality of the data fits was significantly

Table 1
Photophysical data for the free ligand ($\mathbf{L}^{pyr}$) and its complexes ($\mathbf{Ln} \cdot \mathbf{L}^{pyr}$ where Ln = Nd, Er and Yb)

Compound	Visible emission	NIR emission					q[e]
	τ_{MeOH}/ns[a]	λ_{em}/nm[b]	τ_{rise}/ns (CH_3OH)[c]	τ_{MeOH}/ns[d]	τ_{rise}/ns (CD_3OD)[c]	τ_{CD3OD}/ns[d]	
$\mathbf{Nd} \cdot \mathbf{L}^{pyr}$	0.6 (40%), 6.0 (60%)	1340	<5	203	<5	576	0.53
$\mathbf{Gd} \cdot \mathbf{L}^{pyr}$	0.5 (40%), 5.8 (60%)						
$\mathbf{Er} \cdot \mathbf{L}^{pyr}$	0.5 (54%), 5.9 (46%)	1530	<5	134	9	1009	
$\mathbf{Yb} \cdot \mathbf{L}^{pyr}$	0.6 (46%), 6.1 (54%)	980	18	1802	28	9047	0.84

[a] $\lambda_{ex} = 355$ nm, $\lambda_{em} = 390$ nm, percentages in parentheses are the relative weightings of each lifetime.
[b] Wavelength of emission.
[c] $\lambda_{ex} = 337$ nm, rise time of lanthanide emission.
[d] $\lambda_{ex} = 337$ nm.
[e] Inner sphere hydration number.

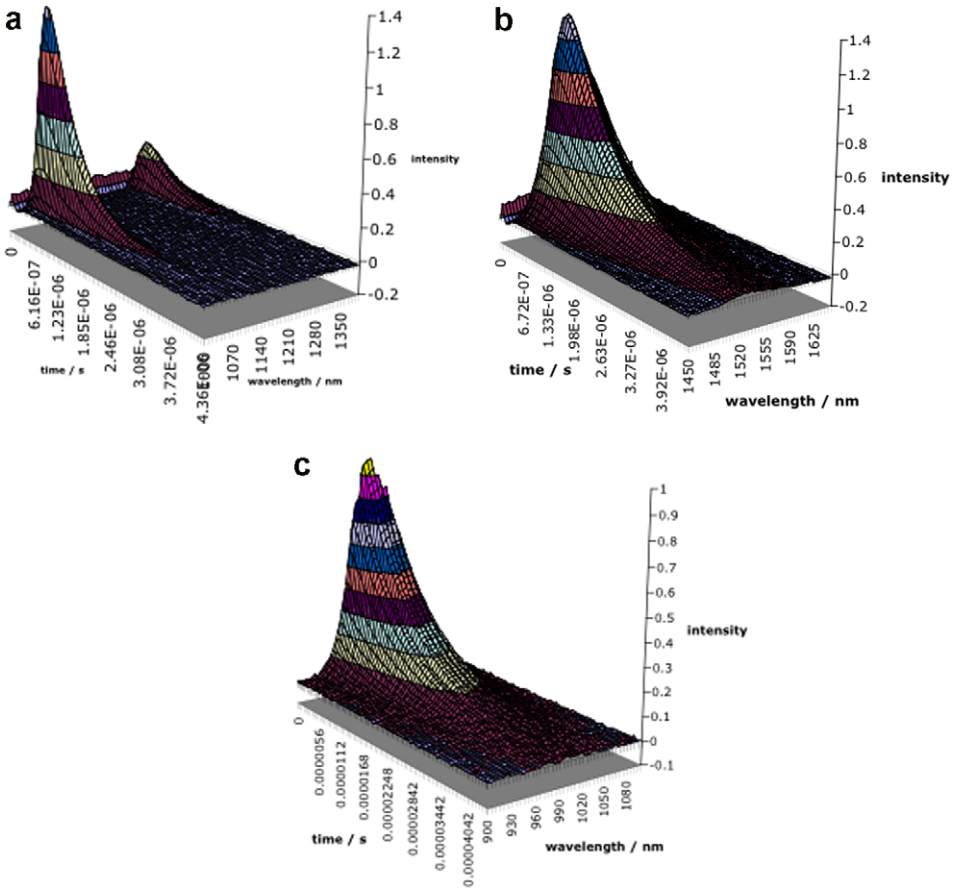


Fig. 2. Time-resolved emission spectra for $\mathbf{Ln} \cdot \mathbf{L}^{pyr}$ in CD_3OD ($\lambda_{ex} = 337$ nm).

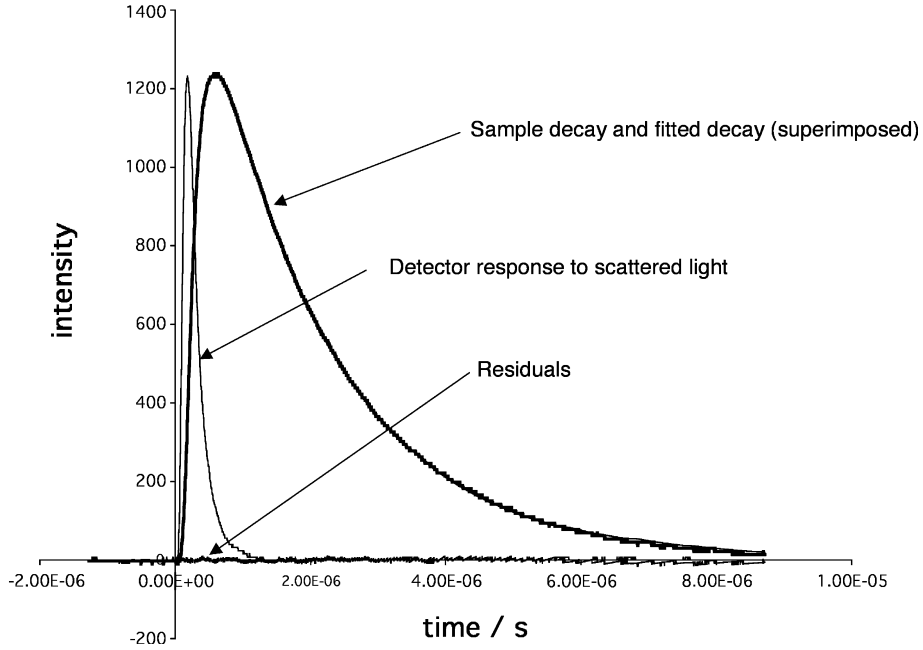


Fig. 3. Lifetime decay profile for $\mathbf{Yb} \cdot \mathbf{L}^{pyr}$ in CH_3OH. The lifetime is 1802 ns, the rise-time 18 ns following excitation at 337 nm and detection at 980 nm.

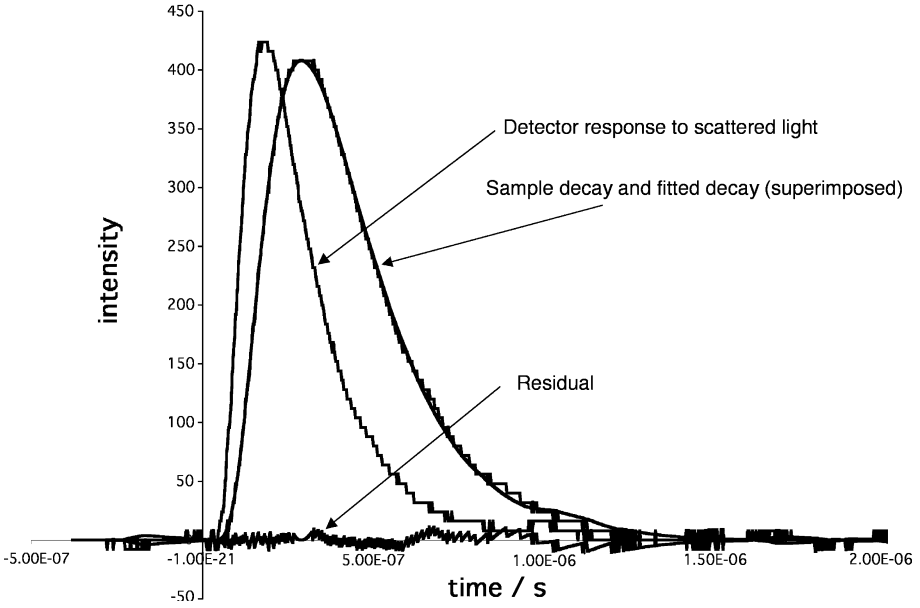


Fig. 4. Lifetime decay profile for $\mathbf{Er} \cdot \mathbf{L}^{pyr}$ in CH_3OH. The lifetime is 134 ns following excitation at 337 nm and detection at 1530 nm.

improved by incorporating short rise-time components (of equal weighting to the decay component). Rise-time data can often be informative when considering energy transfer efficiency. A short rise time within the duration of the laser pulse (<5 ns) implies efficient energy transfer whilst longer values may well be indicative of less efficient processes. We have shown previously with pyrene appended DOTA-like complexes that increasing the length of the spacer linking the chromophore to the complex reduces energy transfer efficiency as evidenced in a longer rise time [4]. For $\mathbf{Ln} \cdot \mathbf{L}^{pyr}$ (Ln = Er, Yb) the rise times are all <30 ns and therefore comparable to previous examples where the linker between chromophore and complex is short, and consequently energy transfer, regardless of the mechanism, seems reasonably efficient. Rise-time exponentials were not required for the Nd^{III} indicating an even more efficient energy transfer process from the pyrene to Nd^{III}. Mechanisms involving Förster [20] energy transfer and Dexter [21,22] exchange have previously been proposed to elucidate sensitisation of lanthanide ions by organic chromophores. The Förster mechanism is a through space dipole–dipole process which shows a distance dependency of r^{-6} (where r is the donor–acceptor separation) whereas Dexter exchange should proceed with e^{-r} and occurs in cases where there is a significant electronic interaction between the donor and acceptor. Assuming energy transfer occurs *via* the conventional triplet excited state of the pyrene we need to consider the phosphorescence spectrum. Unfortunately, room temperature measurements conducted on a de-aerated solution of $\mathbf{Gd} \cdot \mathbf{L}^{pyr}$ did not allow the triplet state of the pyrenyl components to be obtained. However, it is likely that Nd^{III} possesses f–f levels which overlap with the $^3pyr^*$ level (which usually resides between 600 and 700 nm) and this may explain the apparent efficiency of energy transfer in $\mathbf{Nd} \cdot \mathbf{L}^{pyr}$ where the rise time <5 ns [23]. In contrast Yb^{III} has just one f–f level at ~980 nm which will overlap less effectively with $^3pyr^*$ and hence the observation of a rise time >5 ns. However, because of the structure of the complexes $\mathbf{Ln} \cdot \mathbf{L}^{pyr}$ where the pyrenyl amide is coordinated to the lanthanide, it is possible that Dexter exchange may also contribute to the energy transfer process. Additionally, in the case of $\mathbf{Yb} \cdot \mathbf{L}^{pyr}$ it is also important to consider the formation of Yb^{II} intermediates *via* LMCT [24].

4. Conclusions

This paper demonstrates how pyrene can act as an effective sensitiser for neodymium, erbium and ytterbium in protic media. This includes a rare report of Er^{III} emission in non-deuteriated protic solvent and in the future may allow a more detailed study into the non-radiative quenching pathways associated with this lanthanide ion. Despite the incorporation of two pyrene chromophores within the ligand, the formation of the complexes induces only subtle changes in the relative intensities of the luminescent signals originating from monomer and excimer emissions. This suggests that the chromophores are distant from one another and that the coordination requirements of the lanthanide ion dominate the solution state structure of the ligand.

5. Experimental

Diethylenetriaminepentaacetic dianhydride, lanthanide trifluoromethanesulfonate salts and 1-aminopyrene were all purchased from the Aldrich Chemical company. Infrared spectra were recorded as solids using an ATR (Attenuated Total Reflectance)-fitted Bruker Equinox 55 spectrometer over the range 4000–800 cm^{-1} for 64 scans. Mass spectra were obtained using positive or negative

electrospray in acetonitrile solutions on a Micromass Platform II, or by MALDI using methanol solutions with an ALPHA matrix on a Micromass Tofspec2. Electronic absorption spectra were obtained on a double-beam Cary Varian 500 Scan UV–Vis–NIR spectrophotometer as methanol solutions. ^{1}H and $^{13}C\{^{1}H\}$ NMR spectra were recorded on a Bruker Avance 400 MHz spectrometer at 298 K. CHN analyses were performed by the Microanalytical Laboratory, University of Manchester using a Carlo Erba Instruments CHNS-O EA 1108 Elemental Analyser. The steady state luminescence measurements were determined using a Horiba Yobin-Yvon Fluorolog. In the case of near-IR measurements of the Nd^{III}, Er^{III} and Yb^{III} complexes, the sample was excited using a pulsed nitrogen laser (PTI-3301, 337 nm) operating at 10 Hz. Light emitted perpendicular to the excitation beam was focused onto the slits of a monochromator (PTI120), which was used to select the appropriate wavelength. The growth and decay of the luminescence at selected wavelengths was detected using a germanium photodiode (Edinburgh Instruments, EI-P) and recorded using a digital oscilloscope (Tektronix TDS220) before being transferred to a PC for analysis. Time-resolved emission spectra (TRES) were obtained by measuring the growth and decay of the luminescence at each of a series of wavelengths. Luminescence lifetimes were obtained by iterative reconvolution of the detector response (obtained by using a scatterer) with exponential components for growth and decay of the metal-based luminescence, using a spreadsheet running in Microsoft Excel. The details of this approach have been discussed elsewhere [19]. Fitting to a double exponential decay yielded no improvement in fit, as judged by minimisation of residual squared and reduced χ^2, except where indicated.

6. Synthesis of L^{pyr}

A 2.2 equiv. of 1-aminopyrene (0.4 g, 1.85 mmol) were added to 1 equiv. of DTPAA (0.3 g, 0.84 mmol) in stirring acetonitrile under a dinitrogen atmosphere. Excess triethylamine was added dropwise and the solution allowed to stir, initially at room temperature (2 h) and then at 50 °C for a further 18 h. The volume was reduced to dryness in vacuo and the dark brown residue was taken up in the minimum volume of methanol. This concentrate was then added to rapidly stirring, ice cold, diethylether to form a cream precipitate which was isolated by filtration using Schlenk apparatus. The solid was washed with more diethylether and dichloromethane to remove unreacted aminopyrene. The product can be further purified by being introduced to a silica loaded column and eluted initially with 10% MeOH in DCM (to remove any unreacted amino pyrene) and then 50% MeOH in DCM to isolate the desired product (yield, 0.41 g, 62%). IR (KBr disc) $\nu = 3036$, 2962, 2842, 1636, 1522, 1444, 1404, 1328, 1286, 1162, 1104, 990, 962, 924, 842, 712 cm^{-1}. UV–Vis (MeOH) λ_{max} (ε/mol^{-1} dm^3 cm^{-1}) 348 (31 700), 325 (34 000), 275, (66 900), 267 (64 500), 245 (81 600) nm. ES^- MS (MeCN): m/z 790 $\{M-H\}^-$. *Anal.* Calc. for $C_{46}H_{41}N_5O_8 \cdot 2H_2O$: C, 66.74; H, 5.48; N, 8.46. Found: C, 66.79; H, 5.17; N, 8.41%. ^{1}H NMR (400 MHz, MeOD, 300 K) $\delta_H = 8.25$–7.31 (18H, m, pyr), 4.20-2.10 (18H, m, CH_2).

7. Synthesis of $Nd \cdot L^{pyr}$

L^{pyr} (0.05 g, 0.063 mmol) was dissolved in methanol (5 cm^3) and 1 equiv. of $Nd(OTf)_3$ (0.037 g, 0.063 mmol) added. The mixture was stirred at 50 °C for 24 h. The reaction mixture was then cooled and the reaction volume reduced to a minimum. The concentrate was then added dropwise to stirring, ice cold diethyl ether (20 cm^3) inducing precipitation (yield, 0.051 g, 86%). IR (KBr disc) $\nu = 3042$, 2968, 1618, 1540, 1438, 1406, 1272, 1250, 1164, 1030, 994, 962, 914, 846, 714 cm^{-1}. UV–Vis (MeOH) λ_{max} (ε/mol^{-1} dm^3 cm^{-1}) 339 (14 500), 326 (14 100), 276 (23 900), 266 (22 300), 241 (37 800) nm: MALDI (3-NOBA) m/z 933 $\{M+H\}^+$ with correct isotopic distribution.

8. Synthesis of $Er \cdot L^{pyr}$

As for $\mathbf{Nd \cdot L^{pyr}}$ but using $Er(OTf)_3$ (0.039 g, 0.063 mmol). (Yield 0.052 g, 87%). IR (KBr disc) $\nu = 3044$, 2976, 2922, 1624, 1538, 1438, 1406, 1242, 1164, 1084, 1030, 714 cm^{-1}. UV–Vis (MeOH) λ_{max} (ε/mol^{-1} dm^3 cm^{-1}) 341 (19 600), 323 (21 300), 275 (40 600), 266 (39 400), 244 (49 500) nm. MALDI (3-NOBA): m/z 957 $\{M+H\}^+$ with correct isotopic distribution.

9. Synthesis of $Yb \cdot L^{pyr}$

As for $\mathbf{Nd \cdot L^{pyr}}$ but using $Yb(OTf)_3$ (0.039 g, 0.063 mmol). (Yield 0.051 g, 84%). IR (KBr disc) $\nu = 3042$, 2970, 2922, 1618, 1540, 1436, 1404, 1272, 1250, 1166, 1092, 1031, 712 cm^{-1}. UV–Vis (MeOH) λ_{max} (ε/mol^{-1} dm^3 cm^{-1}) 348 (17 100), 312 (20 100), 264 (39 800), 248 (43 400) nm. MALDI (3-NOBA): m/z 963 $\{M+H\}^+$ with correct isotopic distribution.

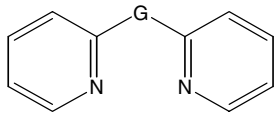
Acknowledgements

The author thanks the Universities of Cardiff and Manchester for support. Mrs. Valerie Boote of the School of Chemistry, The University of Manchester is acknowledged for mass spectrometry, and Dr. Rebecca Laye for assistance with the infrared measurements.

References

[1] (a) D. Parker, Coord. Chem. Rev. 205 (2000) 109;
(b) S. Faulkner, J.L. Matthews, in: M.D. Ward (Ed.), Comprehensive Coordination Chemistry, 2nd ed., vol. 9, Elsevier, Oxford, UK, 2004, p. 913, and references therein;
(c) J.-C. Bünzli, C. Piguet, Chem. Soc. Rev. 34 (2005) 1048;
(d) S. Faulkner, S.J.A. Pope, B.P. Burton-Pye, Appl. Spec. Rev. 40 (2005) 1;
(e) T. Gunnlaugsson, J.P. Leonard, Chem. Commun. (2005) 3114.

[2] (a) For examples A. Beeby, S. Faulkner, D. Parker, J.A.G. Williams, J. Chem. Soc., Perkin Trans. 2 (2001) 1268;
(b) S.J.A. Pope, S.L. Heath, A.M. Kenwright, S. Faulkner, Chem. Commun. (2003) 1550;
(c) S. Quici, M. Cavazzini, G. Marzanni, G. Accorsi, N. Armaroli, B. Ventura, F. Barigelletti, Inorg. Chem. 44 (2005) 529;
(d) T. Lazarides, M.A.H. Alamiry, H. Adams, S.J.A. Pope, S. Faulkner, J.A. Weinstein, M.D. Ward, Dalton Trans. (2007) 1484.
[3] (a) S.I. Klink, H. Keizer, F.C.J.M. van Veggel, Angew. Chem., Int. Ed. Engl. 39 (2000) 4319;
(b) A. Beeby, R.S. Dickins, S. Fitzgerald, L.J. Govenlock, C.L. Maupin, D. Parker, J.P. Riehl, G. Siligardi, J.A.G. Williams, Chem. Commun. (2000) 1183;
(c) D. Imbert, M. Cantuel, J.-C. Bünzli, G. Bernardinelli, C. Piguet, J. Am. Chem. Soc. 125 (2003) 15698;
(d) S.J.A. Pope, B.J. Coe, S. Faulkner, E.V. Bichenkova, X. yu, K.T. Douglas, J. Am. Chem. Soc. 126 (2004) 9490;
(e) D. Guo, C. Duan, F. Lu, Y. Hasegawa, Q. Meng, S. Yanagida, Chem. Commun. (2004) 1486;
(f) P.B. Glover, P.R. Ashton, L.J. Childs, A. Rodger, M. Kercher, R.M. Williams, L. DeCola, Z. Pikramenou, J. Am. Chem. Soc. 125 (2003) 9918;
(g) F. Kennedy, N.M. Shavaleev, T. Koullourou, Z.R. Bell, J.C. Jeffery, S. Faulkner, M.D. Ward, Dalton Trans. (2007) 1492.
[4] S. Faulkner, M.-C. Carrie, S.J.A. Pope, J. Squire, A. Beeby, P.G. Sammes, Dalton Trans. (2004) 1405.
[5] (a) J.S. Kim, O.J. Shon, J.A. Rim, S.K. Kim, J. Yoon, J. Org. Chem. 67 (2002) 2348;
(b) T. Jin, Chem. Commun. (1999) 2491.
[6] A.-J. Tong, A. Yamauchi, T. Hayashita, Z.-Y. Zhang, B.D. Smith, N. Termae, Anal. Chem. 73 (2001) 1530.
[7] K-S. Foscaneanu, J.C. Scaiano, Photochem. Photobiol. Sci. 4 (2005) 817.
[8] H.K. Cho, D.H. Lee, J.-I. Hong, Chem. Commun. (2005) 1690.
[9] D.Y. Sakaki, B.E. Padilla, Chem. Commun. (1998) 1581.
[10] S. Leroy, T. Soujanya, F. Fages, Tetrahedron Lett. 42 (2001) 1665.
[11] A.C. Benniston, A. Harriman, D.J. Lawrie, A. Mayeux, K. Rafferty, O.D. Russell, Dalton Trans. (2003) 4762.
[12] X. Guo, D. Zhang, T. Wang, D. Zhu, Chem. Commun. (2003) 914.
[13] B. Bodenant, F. Fages, M.-H. Delville, J. Am. Chem. Soc. 120 (1998) 7511.
[14] J.Y. Lee, S.K. Kim, J.H. Jung, J.S. Kim, J. Org. Chem. 70 (2005) 1463.
[15] A. Okamoto, T. Ichiba, I. Saito, J. Am. Chem. Soc. 126 (2004) 8364.
[16] S.J.A. Pope, V.A. Boote, A.M. Kenwright, S. Faulkner, Dalton Trans. (2003) 3780.
[17] S.J.A. Pope, B.J. Coe, S. Faulkner, Chem. Commun. (2003) 1551.
[18] A. Beeby, I.M. Clarkson, R.S. Dickins, S. Faulkner, L. Royle, D. Parker, A.S. de Sousa, J.A.G. Williams, J. Chem. Soc., Perkin Trans. 2 (1999) 493.
[19] (a) A. Beeby, S. Faulkner, Chem. Phys. Lett. 266 (1997) 116;
(b) M.H.V. Werts, J.W. Hofstraat, F.A.J. Guerts, J.W. Verhoeven, Chem. Phys. Lett. 276 (1997) 196.
[20] (a) T. Förster, Ann. Phys. 2 (1948) 55;
(b) I.M. Clarkson, A. Beeby, J.I. Bruce, L.J. Govenlock, M.P. Lowe, C.E. Matthieu, D. Parker, K. Senanayake, New. J. Chem. (2000) 377.
[21] D.L. Dexter, J. Chem. Phys. 21 (1953) 836.
[22] F. Barigelletti, L. Famigni, V. Balzani, J.P. Collin, J.P. Sauvage, A. Sour, E.C. Constable, A.W.M.C. Thompson, Coord. Chem. Rev. 132 (1994) 209.
[23] A. Salinas Castillo, A. Segura Carretero, J.M. Costa Fernandez, W.J. Jin, A. Fernandez Gutierrez, Anal. Chim. Acta 516 (2004) 213.
[24] W.D. Horrocks, J.P. Bolender, W.D. Smith, R.M. Supkowski, J. Am. Chem. Soc. 119 (1997) 5972.



G= CH_2, $C(OH)_2$, C(OH)(OMe), C=O, NH, O, S

Fig. 1. Di-(2-pyridyl) ligands.

2. Experimental

2.1. Reagents and general procedures

All manipulations of air and moisture sensitive materials were carried out under dinitrogen using Schlenk techniques. Solvents were dried before use by standard methods. Di-(2-pyridyl)ketone, $NaS_2CNEt_2 \cdot 3H_2O$ and $PdCl_2$ were obtained commercially (Aldrich) and used as received. Melting points were recorded on a Mel-Temp II apparatus and are uncorrected. EI mass spectra were recorded on a Hewlett Packard 5989A spectrometer and FAB-mass spectra on a Jeol JMS-AX505HA mass spectrometer. Elemental analyses were performed on a Finnigan Flash EA 1112NC. IR spectra were recorded on a FT-IR 200 Perkin–Elmer spectrophotometer in the 4000–400 cm^{-1} range using KBr and CsI pellets. NMR spectra were recorded on a Jeol GSX 400 spectrometer. ^1H (399.78 MHz) and ^{13}C (100.53 MHz) spectra were obtained in DMSO-d_6. Chemical shifts (ppm) are relative to $Si(CH_3)_4$. NMR assignments of **1**–**7** were made by two-dimensional heteronuclear and homonuclear correlation experiments (hetcor, coloc and cosy). Single-crystal X-ray structures determination of compounds **3**–**7** were performed at room temperature on a Bruker Smart 6000 CCD diffractometer using graphite monochromated Mo Kα radiation (0.71073 Å). Structures of compounds **3**–**6** were solved by direct methods and the structure of the compound **7** was solved by Patterson method (SHELXTL NT 5.10) [18]. All non-hydrogen atoms were refined anisotropically. The positions of the hydrogen atoms were kept fixed with a common isotropic displacement parameter.

2.2. Synthesis of di-(2-pyridyl)methane ligands **1**–**4**

Ligands **1** [19], **2** and **3** [20] were prepared as previously described; these ligands were characterized by means of NMR in $CDCl_3$ solution; for the sake of this work we have characterized them in DMSO-d_6 solution and reported below.

2.2.1. Di-(2-pyridyl)-N-methylimine (**1**)

Moisture-sensitive yellow solid. M.p. 67–68 °C. ^1H NMR (DMSO-d_6) δ: 8.66 (dd, 1H, H-12, $^3J_{H12-H11} = 4.85$ Hz, $^4J_{H12-H10} = 1.83$ Hz), 8.43 (dd, 1H, H-6, $^3J_{H6-H5} = 4.76$ Hz, $^4J_{H6-H4} = 1.83$ Hz), 8.14 (d, 1H, H-9, $^3J_{H9-H10} = 8.05$ Hz), 7.89 (m, 2H, H-4, H-10), 7.42 (m, 2H, H-5, H-11,), 7.32 (dd, 1H, H-3, $^3J_{H3-H4} = 7.68$, $^4J_{H3-H5} = 1.09$ Hz), 3.19 (s, 3H, N-CH_3); ^{13}C {^1H} NMR (DMSO-d_6) δ: 168.4 (C-13), 157.0 (C-2), 155.3 (C-8), 149.8 (C-12), 148.9 (C-6), 137.2 (C-4), 136.7 (C-10), 125.0 (C-5), 124.2 (C-3), 123.6 (C-11), 121.8 (C-9), 41.3 (N-CH_3).

2.2.2. Di-(2-pyridyl)methanol (**2**)

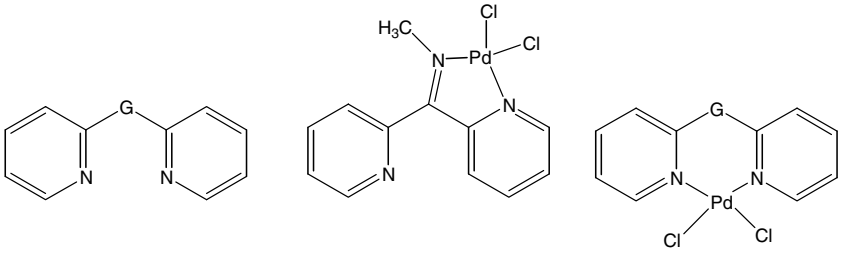
Yellow oil. ^1H NMR (DMSO-d_6) δ: 8.47 (d, 1H, H-6, $^3J_{H6-H5} = 4.40$ Hz), 7.78 (dd, 1H, H-4, $^3J_{H4-H3} = 7.68$, $^3J_{H4-H5} = 7.72$ Hz), 7.57 (d, 1H, H-3, $^3J_{H3-H4} = 7.68$ Hz), 7.22 (ddd, 1H, H-5, $^3J_{H5-H6} = 4.40$ Hz, $^3J_{H5-H4}$=7.72 Hz, $^4J_{H4-H6} = 1.48$ Hz), 6.28 (d, 1H, OH, $^3J_{OH14-H13} = 4.76$ Hz), 5.83 (d, 1H, CH-13, $^3J_{H13-OH14} = 5.12$ Hz); ^{13}C {^1H} NMR (DMSO-d_6) δ: 163.2 (C-2), 148.9 (C-6), 137.2 (C-4), 122.9 (C-5), 121.7 (C-3), 77.5 (C-13).

2.2.3. Di-(2-pyridyl)methylchloride (**3**)

Colorless solid. Dec. 67–69 °C. ^1H NMR (DMSO-d_6) δ: 9.03 (d, 1H, H-6, $^3J_{H6-H5} = 5.12$ Hz); 8.19 (dd, 1H, H-4, $^3J_{H4-H3} = 7.32$ Hz, $^3J_{H4-H5} = 7.60$ Hz); 7.95 (d, 1H, H-3, $^3J_{H3-H4} = 7.32$ Hz); 7.68 (dd, 1H, H-5, $^3J_{H5-H6} = 5.12$ Hz, $^3J_{H5-H4} = 7.60$ Hz); 7.18 (s, 1H, CH-13). ^{13}C {^1H} NMR (DMSO-d_6) δ: 155.3 (C-6); 151.9 (C-2); 142.0 (C-4); 126.8 (C-5); 126.6 (C-3); 60.8 (C-13).

2.2.4. Di-(2-pyridyl)methyl-N,N-diethyldithiocarbamate (**4**)

A mixture of **3** (0.100 g, 0.443 mmol) and sodium diethyldithiocarbamate trihydrate (0.120 g, 0.532 mmol) in



1 G= CNMe
2 G= CH(OH)
3 G= CH(Cl)
4 G= $CH(S_2CNEt_2)$

5

6 G= CH(OH)
7 G= $CH(S_2CNEt_2)$

Fig. 2. Ligands and complexes synthesized.

25 mL of dry $CHCl_3$ was refluxed for 16 h. The colorless solution obtained was cooled to room temperature, filtered and dried by means of a column of Celite and Na_2SO_4. The solvent was evaporated to dryness in vacuum to give colorless crystals. Yield: 78% (0.120 g). M.p. 69 °C. *Anal*. Calc. for $C_{16}H_{19}N_3S_2$; C, 60.53; H, 6.03; N, 13.24. Found: C, 60.30; H, 6.18; N, 12.92%. IR (KBr, cm^{-1}) $\nu = 3066$, 3040 (Ar–H); 2979, 2860 (Aliph-H); 1642 (C=N); 1582, 1493, 1471 (C=C); 1271 (C=S). ^{1}H NMR (DMSO-d_6) δ: 8.48 (d, 1H, H-6, $^3J_{H6–H5} = 4.02$ Hz); 7.75 (ddd, 1H, H-4, $^3J_{H4–H5} = 7.68$ Hz, $^3J_{H4–H3} = 8.05$ Hz, $^4J_{H4–H6} = 1.83$ Hz); 7.58 (d, 1H, H-3, $^3J_{H3–H4} = 8.05$ Hz); 7.24 (dd, 1H, H-5, $^3J_{H5–H4} = 7.68$ Hz, $^3J_{H5–H6} = 4.02$ Hz); 6.64 (s, 1H, CH-13), 3.91 (q, 2H, CH_2, $^3J_{H18–H19} = 7.00$ Hz), 3.77 (q, 2H, CH_2, $^3J_{H20–H21} = 7.00$ Hz); 1.21 (t, 3H, CH_3 $^3J_{H19–H18} = 17.00$ Hz), 1.13 (t, 3H, CH_3, $^3J_{H21–H20} = 7.00$ Hz). ^{13}C {^{1}H} NMR (DMSO-d_6) δ: 192.7 (C=S); 159.5 (C-2); 149.7 (C-6); 137.4 (C-4); 123.7 (C-3); 122.9 (C-5); 63.2 (C-13); 49.9 (CH_2-18), 47.2 (CH_2-20); 13.1 (CH_3-19), 11.9 (CH_3-21).

2.3. Synthesis of cis-dichloropalladium(II) complexes (5–7)

2.3.1. cis-Dichloro[di-(2-pyridyl)-N-methylimine]palladium(II) (5)

0.112 g (0.56 mmol) of **1** were added to a solution of $PdCl_2$ (0.100 g, 0.56 mmol) in 25 mL of dry acetonitrile. The mixture was refluxed for 16 h, cooled to room temperature and after the solvent was evaporated to dryness in vacuum to give yellow crystals. Yield: 90% (0.190 g). Dec. 187–190 °C. *Anal*. Calc. for $C_{12}H_{11}Cl_2N_3Pd$: C, 38.48; H, 2.96; N, 11.22. Found: C, 37.17; H 2.69; N, 11.22%. IR (KBr, cm^{-1}) $\nu = 3093$, 3059 (Ar–H); 2980, 2926 (Aliph-H); 1615 (C=N); 1582, 1568, 1468 (C=C). ^{1}H NMR (DMSO-d_6) δ: 9.12 (d, 1H, H-12, $^3J_{H12–H11} = 4.76$ Hz); 8.87 (d, 1H, H-6, $^3J_{H6–H5} = 4.76$ Hz); 8.21 (ddd, 1H, H-10, $^3J_{H10–H9} = 7.69$ Hz, $^3J_{H10–H11} = 7.87$ Hz, $^4J_{H10–H12} = 1.46$ Hz); 8.15 (ddd, 1H, H-4, $^3J_{H4–H3} = 7.70$ Hz, $^3J_{H4–H5} = 7.51$ Hz, $^4J_{H4–H6} = 1.46$ Hz); 7.91 (m, 2H, H-3, H-11); 7.72 (dd, 1H, H-5, $^3J_{H5–H4} = 7.51$ Hz, $^3J_{H5–H6} = 4.76$ Hz); 7.26 (d, 1H, H-9, $^3J_{H9–H10} = 7.69$ Hz); 3.34 (s, 3H, N-CH_3). ^{13}C {^{1}H} NMR (DMSO-d_6) δ: 176.4 (C-13); 157.3 (C-2); 151.1 (C-6); 151.0 (C-12); 148.7 (C-8); 141.9 (C-10); 138.5 (C-4); 129.6 (C-9); 129.4 (C-11); 126.6 (C-5); 125.5 (C-3); 44.6 (N-CH_3).

2.3.2. cis-Dichloro[di-(2-pyridyl)methanol]palladium(II) (6)

0.500 g (2.70 mmol) of **2** were added to a solution of $PdCl_2$ (0.480 g, 2.70 mmol) in 40 mL of dry acetonitrile. The solution was refluxed for 16 h and after the solvent was evaporated to dryness in vacuum to give yellow crystals. Yield: 92% (0.90 g). Dec. 244–248 °C. *Anal*. Calc. for $C_{12}H_{10}Cl_2N_2OPd$: C, 36.34; H, 2.77; N, 7.71. Found: C, 36.51; H, 2.79; N, 8.82%. IR (KBr, cm^{-1}) ν: 3430 (O–H); 3115 (Ar–H); 2900 (Aliph-H); 1601 (C=N, C=C); 1568, 1463 (C=C). ^{1}H NMR (DMSO-d_6) δ: 8.77 (d, 1H, H-6, $^3J_{H6–H5} = 5.12$ Hz); 8.13 (dd, 1H, H-4, $^3J_{H4–H5} = {}^3J_{H4–H3} = 7.68$ Hz); 7.84 (d, 1H, H-3, $^3J_{H3–H4} = 7.68$ Hz); 7.81 (d, 1H, OH, $^3J_{OH14–H13} = 4.94$ Hz); 7.48 (dd, 1H, H-5, $^3J_{H5–H4} = 7.68$ Hz, $^3J_{H5–H6} = 5.12$ Hz); 6.72 (d, 1H, CH-13, $^3J_{H13–OH14} = 5.12$ Hz). ^{13}C {^{1}H} NMR (DMSO-d_6) δ: 158.2 (C-2); 153.2 (C-6); 141.5 (C-4); 125.3 (C-5); 122.2 (C-3); 75.8 (C-13).

2.3.3. cis-Dichloro[di-(2-pyridyl)methyl-N,N-diethyldithiocarbamate]palladium(II) (7)

0.0685 g (0.215 mmol) of **4** were added to a solution of $PdCl_2$ (0.038 g, 0.214 mmol) in 25 mL of dry acetonitrinile. The suspension was refluxed for 24 h and then cooled to room temperature. The cold suspension was filtered. From the saturated solution were obtained yellow-brown crystals by slow evaporation. Yield: 90% (0.09 g). M.p: 243–245 °C. *Anal*. Calc. for $C_{16}H_{19}Cl_2N_3PdS_2$: C, 38.84; H, 3.87; N, 8.49. Found: C, 38.85; H, 4.44; N, 7.90%. IR (KBr, cm^{-1}) $\nu = 3097$, 3071 (Ar–H); 2920, 2851 (Aliph-H); 1619 (C=N); 1601, 1472, 1438 (C=C); 1183(C=S). ^{1}H NMR (DMSO-d_6) δ: 8.91 (d, 1H, H-6, $^3J_{H6–H5} = 4.76$ Hz); 8.12 (dd, 1H, H-4, $^3J_{H4–H3} = 7.15$ Hz, $^3J_{H4–H5} = 6.90$ Hz, $^4J_{H4–H6} = 1.46$ Hz); 8.03 (d, 1H, H-3, $^3J_{H3–H4} = 7.15$ Hz); 7.58 (dd, 1H, H-5, $^3J_{H5–H4} = 6.90$, $^3J_{H5–H6} = 4.76$ Hz); 7.09 (s, 1H, CH-13); 3.96 (q, 2H, CH_2, $^3J_{H18–H19} = 6.96$ Hz), 3.84 (q, 2H, CH_2, $^3J_{H20–H21} = 6.96$ Hz); 1.27 (t, 3H, CH_3, $^3J_{H19–H18} = 6.96$ Hz); 1.18 (t, 3H, CH_3, $^3J_{H21–H20} = 6.96$ Hz). ^{13}C {^{1}H} NMR (DMSO-d_6) δ: 189.9 (C=S); 153.6 (C-2); 154.5 (C-6); 141.4 (C-4); 127.0 (C-3); 125.9 (C-5); 61.9 (C-13); 50.6 (CH_2-18), 47.8 (CH_2-20); 13.1 (CH_3-19), 11.7 (CH_3-21).

3. Results and discussion

3.1. Synthesis of derivatives of di-(2-pyridyl)methane (1–4)

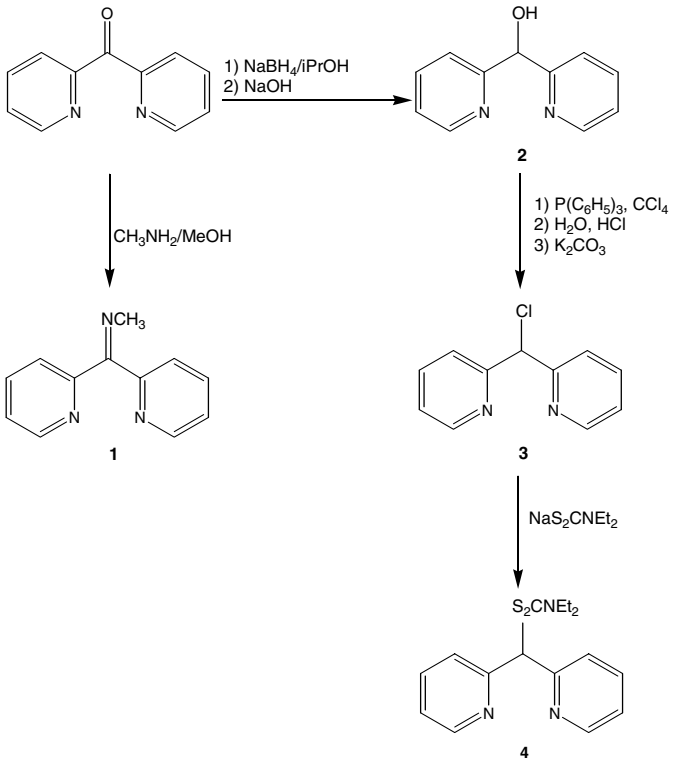
Ligands **1**–**3** were prepared as previously described [19,20], whereas the ligand **4** was synthesized from the reaction of **3** with an excess of sodium diethyldithiocarbamate trihydrate in hot $CHCl_3$, see Scheme 1.

3.2. Synthesis of palladium(II) complexes (5–7)

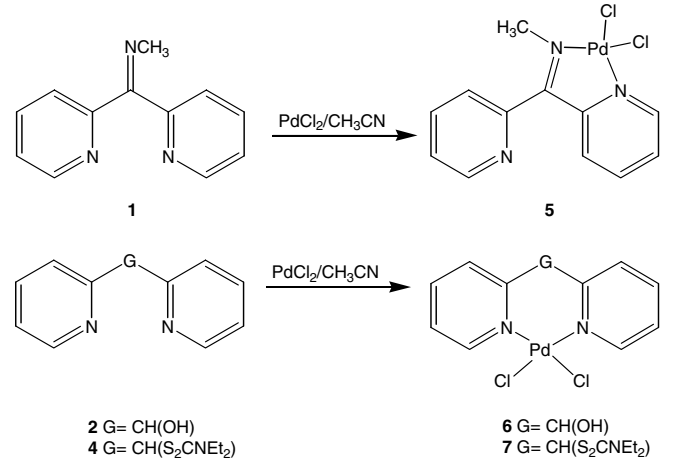
The *cis*-palladium(II) complexes **5**–**7** were synthesized from the reaction of di-(2-pyridyl)methane derivatives **1**, **2** and **4** with $PdCl_2$ in equimolar ratios in hot acetonitrile, see Scheme 2.

3.3. Mass spectrometry

EI mass spectra of ligands **1** and **2** showed the molecular ion peaks [$M^{\cdot+}$] at m/z (% intensity) = 197 (38%) and 186 (3%), respectively. For **3** was observed the peak [M^+−H] at 203 (1%) and for **4** was observed the peak [M^+−2H] at 315 (1%). In complexes **5** and **7**, FAB mass spectra showed the [$M^{\cdot+}$−Cl] peaks with the appropriate isotopic ratio at $m/z = 340$ (5%) and 460 (10%), respectively. In complex **6**



Scheme 1.



Scheme 2.

only was observed the $[M^+-PdCl_2H]$ peak at 185 (30%), assigned to the deprotonate free ligand **2**. No more peaks could be assigned.

3.4. Infrared spectroscopy

In ligands **1**–**4**, IR spectra showed a weak band at 1683, 1684, 1645 and 1642 cm^{-1} respectively, assignable to the ν(C=N) absorption. For complexes **5** and **7** the ν(C=N) absorption is shifted to lower wave numbers (1615 and 1619 cm^{-1}, respectively). In **6** the ν(C=N) absorption is overlapped with the ν(C=C) absorption at 1601 cm^{-1}. The ν(C=N) absorption analysis indicates the coordination of the nitrogen atoms to the palladium atom.

3.5. NMR spectra

^1H and ^{13}C NMR spectra of **1**–**7** were obtained at room temperature in DMSO-d_6.

^1H NMR spectra of ligands **2**–**4** displayed four signals in the aromatic region. On the other hand, in the ^1H spectrum of **1** were observed six signals in the same region. In **2**, **3** and **4** the CH group was observed as a single signal at 5.83, 7.18 and 6.64 ppm, respectively, whereas in **1** the N-CH_3 group was observed as a single signal at 3.19 ppm. In **4** the ethyl groups are magnetically nonequivalent. The CH_2 groups were observed at 3.91 and 3.77 ppm as triplet signals and the CH_3 groups as quartet signals at 1.21 and 1.13 ppm. In **4** we used the line-shape analysis method at 20–90 °C in DMSO-d_6 with increments of 10 °C. The activation free energy ($\Delta G_c^{\neq}$) was calculated to be 22.1 kcal/mol with $T_c = 75$ °C. The $\Delta G_c^{\neq}$ value obtained in **4** confirms the restricted C–N bond rotation in the dithiocarbamate fragment as has previously been described in analogue molecules [21].

In **1** the ^{13}C spectrum showed ten signals as reported [19] but ^{13}C spectra of **2**–**4** showed five signals for the pyridinic rings. In ^{13}C spectra the bridging C13 carbon atom was observed at 77.5 for **2**, 60.8 for **3** and 63.2 ppm for **4**. The C=S group in **4** was observed at 192.7 ppm; the magnetically nonequivalent CH_2 and CH_3 groups were observed at 49.9, 47.2 and 13.1, 11.9 ppm, respectively.

^1H and ^{13}C NMR data for ligands **2**–**4** at room temperature suggest that the bonds formed between the *ipso* carbon of the pyridinic rings and the carbon bridging group rotate freely in solution. The presence of the rigid C=N bond in **1** produces a different environment for pyridinic rings respect to the methyl group (*E*–*Z* position). Due to the existence of signals attributable to two nonequivalent pyridinic rings in the spectra, we can conclude that the iminic bond does not isomerize or the isomerization is very slow [19]. This *E*–*Z* isomerization process has been studied in *N*-substituted imines analogues to **1** and explained by a nitrogen inversion mechanism [22].

^1H NMR spectra of dichloropalladium(II) complexes **5**–**7** and those of ligands **1**, **2** and **4** did not show significant variations in the chemical shifts. On the other hand, ^{13}C data of complexes **5**–**7** showed important variations in the chemical shifts for the C2, C6, C8, C12 and C13 carbons closer to the coordination sites, with respect to the free ligands **1**, **2** and **4**. In Table 1 is showed the variation of chemical shifts, $\Delta\delta$. Negative values of $\Delta\delta$ indicate variations in the chemical shift towards higher frequencies after coordination, whereas $+\Delta\delta$ indicate chemical shifts to lower frequencies (Table 1). In **5**, the C8 and C13 atoms in the five-membered chelate ring are the most protected and unprotected, respectively. These large values can be attributable to the coordination of the iminic nitrogen to the palladium atom. In contrast, in the complexes **6** and

Table 1
Variation of chemical shifts ($\Delta\delta$) of ^{13}C in ppm for the complexes **5**–**7** respect to the free ligands

Complexes	C-2	C-6	C-8	C-12	C-13
5	−0.3	−2.2	+6.6	−1.2	−8.0
6	+5.0[a]	−4.3[b]	+5.0[a]	−4.3[b]	+1.7
7	+5.9[a]	−4.8[b]	+5.9[a]	−4.8[b]	+1.3

[a–b] Carbon atoms observed as averaged signals.

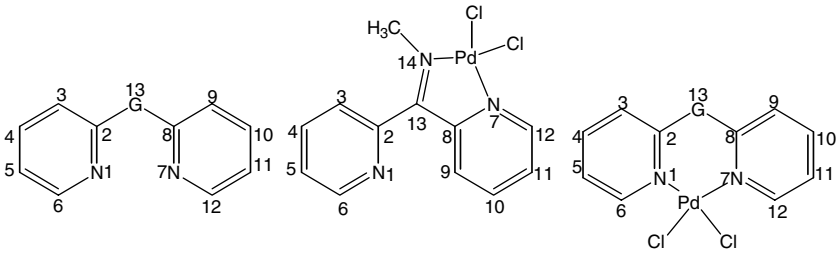
7 where six-membered chelate rings are formed, the C13 carbon atom is slightly protected (small $\Delta\delta$) whilst the C2 and C8 *ipso* carbons are the most protected upon coordination. The metallic coordination also affects the C6 and C12 *ortho* carbons, displaying deshielding effects. These variations of $\Delta\delta$ values for complexes **6** and **7** confirm the coordination of both pyridinic nitrogen atoms to the palladium atom.

3.6. X-ray crystallography

The structures in the crystalline solid state of compounds **3**–**7** were determined by single-crystal X-ray diffraction analyses. Crystallographic data are given in Table 2 and selected bond lengths and angles are given in Table 3.

Molecular structures of ligands **3** and **4** are showed in Figs. 3 and 4. In the unit cell of **3** there are two crystallographic independent molecules named **3a** and **3b**, Fig. 3.

The X-ray structures of **3** and **4** showed that they are not planar; in **3a**, the pyridinic rings are twisted around the bridging carbon and the *ipso* carbon bonds. In order to describe the conformation of the ligands **3** and **4**, we assume a *syn* conformation if the N–C–C–Y torsional angle (Y = Cl for **3** and Y = S for **4**) is lesser than 90 °



1 G= CNMe
2 G=CH(OH)
4 G= CH(S_2CNEt_2)

5

6 G=CH(OH)
7 G=CH(S_2CNEt_2)

Table 2
Selected crystallographic data for compounds **3**–**7**

Compound	**3**	**4**	**5**	**6**	**7**
Empirical formula	$C_{11}H_9ClN_2$	$C_{16}H_{19}N_3S_2$	$C_{12}H_{11}Cl_2N_3Pd$	$C_{11}H_{10}Cl_2N_2OPd$	$C_{16}H_{19}Cl_2N_3PdS_2$
M_r (g/mol)	204.65	317.46	374.54	363.51	494.76
Crystal size (mm)	0.55 × 0.40 × 0.11	0.46 × 0.20 × 0.18	0.48 × 0.18 × 0.16	0.29 × 0.18 × 0.10	0.26 × 0.18 × 0.05
$F(000)$	424	336	368	712	496
Crystal system	triclinic	triclinic	triclinic	monoclinic	triclinic
Space group	$P\bar{1}$	$P\bar{1}$	$P\bar{1}$	$P2(1)/n$	$P\bar{1}$
a (Å)	7.990(2)	8.6754(6)	8.5863(7)	9.3363(8)	8.8764(10)
b (Å)	10.816(3)	9.0674(6)	9.4614(7)	8.4242(7)	10.2641(12)
c (Å)	12.605(3)	11.8203(8)	9.4939(8)	16.7951(14)	12.3173(14)
α (°)	108.504(5)	86.141(2)	82.568(2)	90	80.686(3)
β (°)	92.748(5)	74.826(2)	70.920(2)	105.799(2)	80.676(4)
γ (°)	99.491(5)	68.771(2)	68.974(2)	90	65.934(3)
V (Å^3)	1013.0(4)	836.12(10)	680.30(9)	1271.05(19)	1005.4(2)
Z	4	2	2	4	2
$\rho_{calc.}$ (Mg/m^3)	1.342	1.261	1.828	1.900	1.634
μ (mm^{-1})	0.335	0.315	1.740	1.863	1.399
$F(000)$	424	336	368	712	496
Goodness-of-fit	1.030	1.025	1.052	1.164	0.827
Temperature (K)	292(2)	293(2)	290(2)	293(2)	293(2)
θ Range (°)	2.02–26.10	1.79–25.02	2.27–25.00	2.27–25.01	1.68–25.03
Reflections collected	6788	5119	4141	7514	6229
Unique reflections	4001	2936	2386	2227	3559
Absorption correction	SADABS	SADABS	SADABS	SADABS	SADABS
Solution method	direct	direct	direct	direct	Patterson
R_{int}	0.0409	0.0381	0.0284	0.0462	0.0685
R_1; wR_2 [$I > 2\sigma(I)$]	0.0719, 0.1832	0.0497, 0.1297	0.0468, 0.1273	0.0311, 0.0851	0.0560, 0.1122
R_1; wR_2 [all data]	0.1413, 0.2243	0.0629, 0.1395	0.0493, 0.1312	0.0393, 0.1007	0.1206, 0.1570
Largest residuals (e Å^{-3})	0.659/−0.520	0.384/−0.466	0.890/−1.352	0.489/−0.695	0.714/ −0.595

Table 3
Selected bond lengths (Å) and bond angles (°) of compounds **3**–**7**

Compound	**3**[a]	**4**	**5**	**6**	**7**
Y14	Cl	S	N	O	S
Pd1–Cl1			2.286(1)	2.289(1)	2.292(2)
Pd1–Cl2			2.288(1)	2.300(1)	2.281(2)
Pd1–N1				2.028(4)	2.038(7)
Pd1–N7			2.033(4)	2.030(3)	2.045(7)
Pd1–N14			2.027(4)		
C13–Y14	1.799(5)	1.823(2)	1.297(6)	1.408(5)	1.82(1)
C15–S14		1.786(2)			1.77(1)
C15–S16		1.663(2)			1.67(1)
C15–N17		1.336(3)			1.34(1)
Cl1–Pd1–Cl2			89.74(6)	90.50(5)	92.3(1)
N1–Pd1–N7				87.3(2)	87.2(3)
N14–Pd1–N7			80.4(2)		
Cl1–Pd1–N1				91.0(1)	90.2(2)
Cl1–Pd1–N14			174.5(1)		
Cl2–Pd1–N7			175.8(1)	91.3(1)	90.4(2)
Cl1–Pd1–N7			94.4(1)	178.1(1)	176.4(2)
Cl2–Pd1–N1				176.8(1)	177.3(2)
Cl2–Pd1–N14			95.5(1)		
C15–N17–C18		124.3(2)			124.0(1)
C15–N17–C20		120.5(2)			121.2(1)
C18–N17–C20		115.1(2)			115.0(1)
C2–C13–C8	113.1(4)	113.6(2)	119.5(4)	110.3(4)	109.4(8)
S14–C15–S16		123.3(1)			123.4(6)
N1–C2–C13–C8	−51.9(5)	39.0(3)		60.9(5)	60.4(1)
N7–C8–C13–C2	−85.0(4)	−93.9(3)	−176.9(4)	−61.5(5)	−60.0(1)
N1–C2–C13–Y14	72.2(4)	−86.5(2)	−76.3(5)	−177.7(4)	−59.2(9)
N7–C8–C13–Y14	152.4(3)	30.1(3)	1.2(6)	177.0(4)	63.3(1)

[a] Averaged distances for the two crystallographic independent molecules.

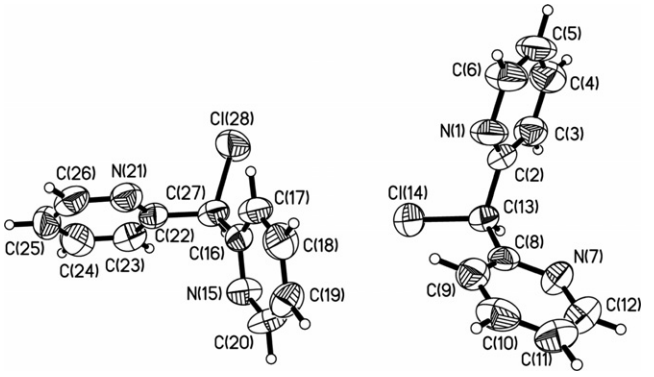


Fig. 3. Molecular structure of **3** with labeled atoms and 50% probability displacement ellipsoids.

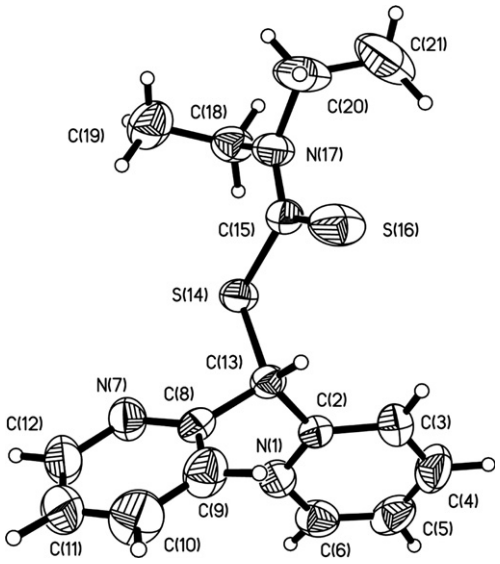


Fig. 4. Molecular structure **4** with labeled atoms and 50% probability displacement ellipsoids.

and *anti* if it is larger [19]. In **3** one of the torsional angles is 72.2(4)° and the other one is 152.4(3)° (see Table 3). Hence, the conformation of **3** can be described as *syn–anti*. In **4**, the torsional angles are 86.5(2)° and 30.1(3)°. The magnitude of these angles indicates that **4** exhibits in solid state a *syn–syn* conformation. There are three sulphur–carbon distances (1.823(2), 1.786(2) and 1.663(2) Å). The first two are consistent with a single bond and the last one with a double bond; they are similar to that found in analogue compounds [1.807(3), 1.758(3) and 1.664(3) Å in ethylene bis(dimethyl–dithiocarbamate) and 1.812(2), 1.778(2) and 1.675(2) Å in butane-1,4-diyl bis(dimethyldithiocarbamate)] [23]. The sum of the angles around nitrogen is close to 360° indicating a planar geometry.

Crystallographic data showed that the ligands **1**, **2** and **4** behave as bidentate ligands when coordinate to Pd(II). The X-ray structures of the palladium complexes **5**–**7** consist of neutral molecules with square planar Pd(II) (Figs. 5–7).

The N–Pd distances in these compounds are significantly the same [2.027(4) and 2.033(4) Å in **5**; 2.028(4) and 2.030(3) Å in **6** and 2.038(7) and 2.045(7) Å in **7**] and are similar to other previously reported for dipyridinic and pyridinic complexes containing N–Pd bonds [13,14,24–26]. The main difference between **5** and the **6** and **7** pair is the coordination mode; in **5** the iminic nitrogen and one pyridinic nitrogen are coordinated to Pd forming a five-membered chelate ring, whereas in **6** and **7** both pyridinic rings are coordinated, forming six-membered chelate rings with bite angles of 80.4(2)°, 87.3(2)° and 87.2(3)°, respectively. These data confirm the results obtained by the NMR analyses. In addition, complexes **6** and **7** are also not planar (dihedral angles between the pyridinic rings are 118.4° and 113.2° for **6** and **7**, respectively).

In the palladium complexes **5**–**7** the pyridinic rings are also twisted as in the free ligands **1** and **4** in solid state. In **5**, the torsional angles N7–C8–C13–N14 and N1–C2–C13–N14 measured around the bridging carbon and the ipso carbon bonds are 1.2(6)° and 76.3(5)°; displaying a *syn–syn* conformation [19]. In **6**, the torsional angles are 177.0(4)° and 177.7(4)° displaying an *anti–anti* conformation, whereas that in **7** the conformer is *syn–syn* with torsional angles of 63.3(1)° and 59.2(9)°.

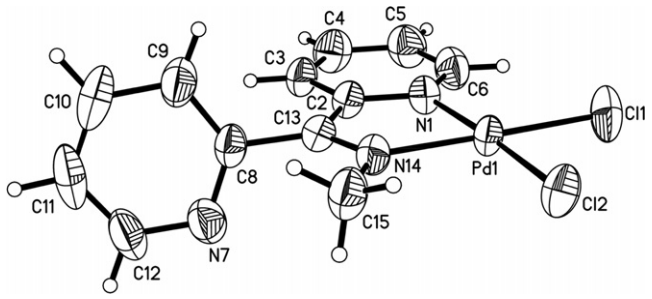


Fig. 5. Molecular structure of **5** with labeled atoms and 50% probability displacement ellipsoids.

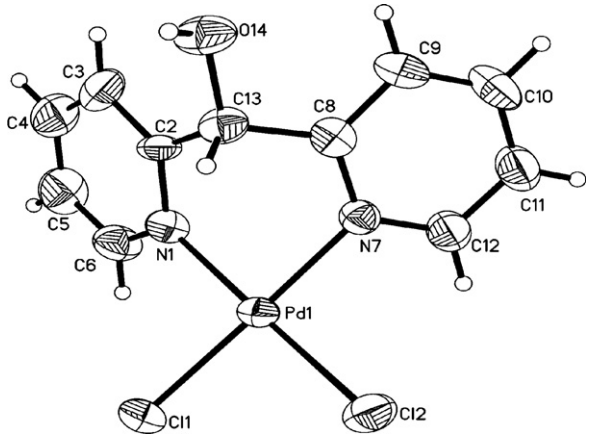


Fig. 6. Molecular structure of **6** with labeled atoms and 50% probability displacement ellipsoids.

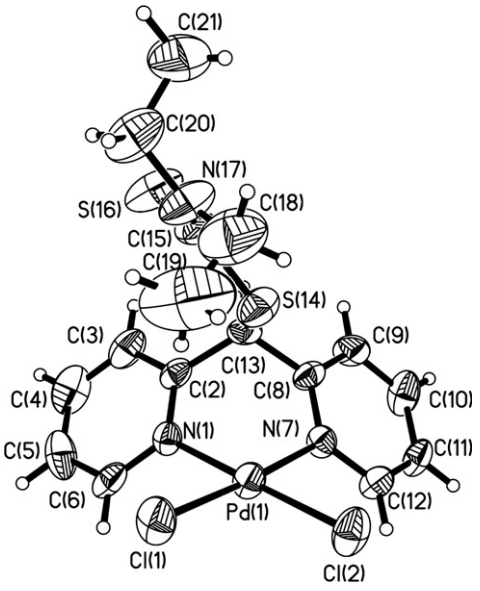


Fig. 7. Molecular structure of **7** with labeled atoms and 50% probability displacement ellipsoids.

Respect to the complexes **6** and **7** where six-membered chelate rings are formed, the central ring in both complexes is in a boat conformation, however the position of the exocyclic ligands is very different. The –OH ligand in **6** is in a bowsprit position whereas the $-S_2CNEt_2$ ligand in **7** is in a flagpole position as the predominant conformers in solid state. This difference can be attributable to an intramolecular contact between the soft acid palladium and the soft base sulphur (Pd—S = 3.054 Å) that is shorter than the van der Waals radii sum ($\sum r_{vdW}(Pd,S) = 3.43$ Å) but longer than the covalent radii sum ($\sum r_{cov}(Pd,S) = 2.33$ Å) [27].

4. Conclusion

Complexes *cis*-dichloro[di-(2-pyridyl)-*N*-methylimine]-palladium(II) (**5**), *cis*-dichloro[di-(2-pyridyl)methanol]palladium(II) (**6**) and *cis*-dichloro[di-(2-pyridyl)methyl-*N*,*N*-diethyldithiocarbamate]palladium(II) have been characterized and synthesized. The presence of donor *N*-methylimine, hydroxy and *N*,*N*-diethyldithiocarbamate fragments bound to the methylene bridge opens the possibility in the free ligands **1**, **2** and **4** to act as a tridentate ligands, however, they solely coordinate to the palladium atom in a bidentate fashion. The complexes differ in the size of the chelate ring; in **6** and **7** the rings are six-membered whereas in **5** is five-membered sized. The difference in the coordination mode can be attributable to the rigidity of the iminic carbon present in **5**.

5. Supplementary material

CCDC 634227, 634228, 634225, 634226 and 634229 contain the supplementary crystallographic data for **3**, **4**, **5**, **6**

and **7**. These data can be obtained free of charge via http://www.ccdc.cam.ac.uk/conts/retrieving.html, or from the Cambridge Crystallographic Data Centre, 12 Union Road, Cambridge CB2 1EZ, UK; fax: (+44) 1223-336-033; or e-mail: deposit@ccdc.cam.ac.uk.

Acknowledgements

S.G.M. and M.G.R.M. acknowledge the CONACYT scholarships. Financial support by CONACYT (Grant No. 35085-E) is acknowledged.

References

[1] F. Sinner, M.R. Buchmeiser, T. Tessadri, M. Mupa, K. Wurst, G.K. Bonn, J. Am. Chem. Soc. 120 (1998) 2790.
[2] M.R. Buchmeiser, K. Wurst, J. Am. Chem. Soc. 121 (1999) 11101.
[3] J. Silberg, T. Schareina, R. Kempe, K. Wurst, M.R. Buchmeiser, J. Organomet. Chem. 622 (2001) 6.
[4] M.R. Buchmeiser, T. Schareina, R. Kempe, K. Wurst, J. Organomet. Chem. 634 (2001) 39.
[5] T. Kawano, T. Shinomaru, I. Ueda, Org. Lett. 4 (2002) 2545.
[6] C. Nájera, J. Gil-Moltó, S. Karlström, L.R. Falvello, Org. Lett. 5 (2003) 1451.
[7] Y. Wen-Rui, L. Ze-Hau, Z. Qian-Feng, Acta Crystallogr., Sect., C 59 (2003) m139.
[8] M.J. Rauterkus, S. Fakih, C. Mock, I. Puscasu, B. Krebs, Inorg. Chim. Acta 350 (2003) 355.
[9] G.R. Newkome, V.K. Gupta, K.J. Theriot, J.C. Ewing, S.P. Wicelinsky, W.R. Huie, F.R. Fronczek, S.F. Watkins, Acta Crystallogr., Sect. C 40 (1984) 1352.
[10] A.J. Canty, G. Hayhurst, J. Chem. Soc., Chem. Commun. (1980) 316.
[11] A.J. Canty, N. Chaichit, B.M. Gatehouse, E.E. George, G. Hayhurst, Inorg. Chem. 20 (1981) 2414.
[12] A.M. García, J. Manzur, Acta Crystallogr., Sect. C 50 (1994) 1882.
[13] P.J. Steel, C.J. Sumby, Dalton Trans. (2003) 4505.
[14] G. Annibale, L. Canovese, L. Cattalini, G. Natile, M. Biagini-Cingi, A.-M. Manotti-Lanfredi, A. Tiripicchio, J. Chem. Soc., Dalton Trans. (1981) 2280.
[15] B. Milani, G. Mestroni, E. Zangrando, Croat. Chem. Acta 74 (2001) 851.
[16] A.J. Canty, N.J. Minchin, B.W. Skelton, A.H. White, Aust. J. Chem. 45 (1992) 423.
[17] C. Jian-Kai, L. Zhao-Ji, K. Yao, C. Yu-Biao, Q. Ye-Yang, W. Yi-Hang, Y. Yuan-Gen, Acta Crystallogr., Sect. E: Struct. Rep. Online 58 (2002) m768.
[18] SHELXTL 5.10 Bruker AXS, Inc., Madison, WI, USA (1998).
[19] B. Flores-Chávez, B.A. Martínez-Ortega, J.G. Alvarado-Rodríguez, N. Andrade-López, J. Chem. Cryst. 35 (2005) 451.
[20] R.M. La Crois, Manganese Complexes as Catalysts in Epoxidation Reactions, A Ligand Approach, University Library of Groningen, Groningen, Netherlands, 2002 (Chapter 2).
[21] M. Bordbar, H.R. Bijanzadeh, N. Alizadeh, J. Chin. Chem. Soc. 51 (2004) 471.
[22] W.B. Jennings, S. Al-Showiman, D.R. Boyd, R.M. Campbell, J. Chem. Soc. Perkin II (1976) 1501.
[23] J. Fangfang, Z. Dunru, F. Hoong-Kun, C. Kandasamy, I.A. Razak, Y. Xiaozeng, Acta Crystallogr., Sect. C 55 (1999) 940.
[24] T. Schareina, G. Hillebrand, H. Fuhrmann, R. Kempe, Eur. J. Inorg. Chem. (2001) 2421.
[25] A.J. Canty, N.J. Minchin, L.M. Engelhardt, B.W. Skelton, A.H. White, J. Chem. Soc., Dalton Trans. (1986) 645.
[26] C. Mock, I. Puscasu, M.J. Rauterkus, G. Tallen, J.E.A. Wolff, B. Krebs, Inorg. Chim. Acta 319 (2001) 109.
[27] W.W. Porterfield, Inorganic Chemistry: A Unified Approach, 2nd ed., Academic Press, Inc., USA, 1993, pp. 214.

structure of transition metal complexes. It meets with the requirements of being accurate, easy to use and fast enough to allow the study of relatively large molecules of transition metal complexes [15]. Recent studies have also supported the TD-DFT method to be applicable for open- and closed-shell 5d-metal complexes, giving good assignment of experimental spectra [16–18].

2. Experimental

2.1. General procedure

All the reagents used for the syntheses were commercially available and were used without further purification. The $[ReCl_3(MeCN)(PPh_3)_2]$ complex was prepared as reported previously [12], and bis(pyrazol-1-yl)methane was synthesised according to the modified literature method [19].

The IR spectrum were recorded on a Nicolet Magna 560 spectrophotometer in the spectral range 4000–400 cm^{-1} with the sample in the form of KBr pellets. The electronic spectrum was measured on a spectrophotometer Lab Alliance UV–Vis 8500 in the range 1000–200 nm in dichloromethane solution. Elemental analyses (C H N) were performed on a Perkin–Elmer CHN-2400 analyzer.

2.2. Preparation of bis(pyrazol-1-yl)methane (bpzm)

Pyrazole (9.6 g, 0.1 mol), $Bu_4N^+HSO_4^-$ (1.7 g, 0.005 mol), potassium carbonate (13.8 g, 0.1 mol), powdered KOH (5,6 g, 0.1 mol), and an excess of dry methylene chloride (300 cm^3) were intensively stirred and refluxed in a water bath for 6 h. After this time, a second portion of KOH (5.6 g, 0.1 mol) and $Bu_4N^+HSO_4^-$ (1.7 g, 0.005 mol) was added and the mixture was intensively stirred and refluxed for an additional 6 h. The liquid layer was removed and the residue was washed three times with 100 cm^3 of methylene chloride. The combined organic layers were dried with anhydrous magnesium sulfate and methylene chloride was removed on a rotary evaporator. The pale yellow residue was purified by vacuum sublimation as previously described [19] (isolated yield 87%, 8.9 g).

2.3. Preparation of $[ReCl_3(bpzm)(PPh_3)] \cdot CH_2Cl_2$

$[Re(MeCN)Cl_3(PPh_3)_2]$ (0.50 g, 0.58 mmol) and bpzm (0.1 g, 0.67 mmol) in dichloromethane (40 cm^3) were refluxed for 4 h. The starting material gradually dissolved and the colour of the reaction solution became dark brown. The volume was condensed to 10 cm^3, diethyl ether (50 cm^3) was added and a brown microcrystalline solid was filtered. The product was washed with EtOH and cold ether, and dried in vacuo (yield 90%). The crystals suitable for X-ray investigation were obtained by recrystallization from a mixture of dichloromethane/methanol.

IR (KBr; ν/cm^{-1}): 1587(w), 1574(w), 1518(m) and 1510 (w) ν_{CN} and $\nu_{C=C}$;

Anal. Calc. for $C_{26}H_{25}Cl_5N_4PRe$: C, 39.63; H, 3.20; N, 7.11. Found: C, 39.75; H, 3.30; N, 7.29%.

2.4. X-ray diffraction studies

A brown crystal of $[ReCl_3(bpzm)(PPh_3)] \cdot CH_2Cl_2$ was mounted on a KM-4-CCD automatic diffractometer equipped with a CCD detector, and used for data collection. X-ray intensity data were collected with graphite monochromated MoKα radiation ($\lambda = 0.71073$ Å) at 295(1) K. Details concerning crystal data and refinement are given in Table 1. Lorentz, polarization and numerical absorption corrections [20] were applied. The structure was solved by the Patterson method and subsequently completed by difference Fourier recycling. All the non-hydrogen atoms were refined anisotropically using the full-matrix, least-squares technique. The hydrogen atoms were treated as ''riding'' on their parent carbon atoms and assigned isotropic temperature factors equal to 1.2 times the value of the equivalent temperature factor of the parent atom. SHELXS97 [21], SHELXL97 [22] and SHELXTL [23] programs were used for all the calculations. Atomic scattering factors were those incorporated in the computer programs.

2.5. Computational details

The GAUSSIAN03 program [24] was used in the calculations. The geometry optimisation of the $[ReCl_3(bpzm)(PPh_3)]$ complex was carried out with the DFT method

Table 1
Crystal data and structure refinement for $[ReCl_3(bpzm)(PPh_3)] \cdot CH_2Cl_2$

Empirical formula	$C_{26}H_{25}Cl_5N_4PRe$
Formula weight	787.92
Temperature (K)	295(1)
Wavelength (Å)	0.71073
Crystal system	monoclinic
Space group	$P2_1/n$
Unit cell dimensions	
a (Å)	10.2233(3)
b (Å)	19.7599(6)
c (Å)	15.1285(2)
β (°)	101.411(2)
Volume (Å^3)	2995.72(13)
Z	4
D_{calc} (Mg/m^3)	1.747
Absorption coefficient (mm^{-1})	4.579
$F(000)$	1536
Crystal size (mm)	$0.06 \times 0.12 \times 0.24$
θ range for data collection (°)	2.86–25.00
Index ranges	$-9 \leqslant h \leqslant 12$
	$-23 \leqslant k \leqslant 23$
	$-17 \leqslant l \leqslant 17$
Reflections collected/independent	18,634/5267 [$R_{int} = 0.0294$]
Completeness to $2\theta = 50.2°$	96.6%
Maximum and minimum transmission	0.749 and 0.518
Data/restraints/parameters	5267/0/334
Goodness-of-fit on F^2	1.037
Final R indices [$I > 2\sigma(I)$]	$R_1 = 0.0214$ $wR_2 = 0.0518$
R indices (all data)	$R_1 = 0.0300$ $wR_2 = 0.0518$
Largest difference peak and hole (e Å^{-3})	0.863 and −0.832

with the use of the B3LYP functional [25,26]. The electronic spectrum of the $[ReCl_3(bpzm)(PPh_3)]$ complex was calculated with the TDDFT method [27]. The calculations were performed by using an ECP basis set on the rhenium atom, the standard 6-31+g** basis for chlorine, phosphorus and nitrogen, 6-31g* basis for carbon and 6-31G basis for hydrogen atoms. The Xe core electrons of Re were replaced by an effective core potential and a DZ quality Hay and Wadt Los Alamos ECP basis set (LANL2DZ) [28] was used for the valence electrons. An additional *d* function with exponent $\alpha = 0.3811$ and *f* function with exponent $\alpha = 2.033$ on the rhenium atom were added.

2.6. Magnetic measurement

Magnetic measurements in the temperature range 1.8–300 K were performed using a Quantum Design SQUID-based MPMSXL-5-type magnetometer. The SQUID magnetometer was calibrated with the palladium rod sample (Materials Research Corporation, measured purity 99.9985%). The superconducting magnet was generally operated at a field strength ranging from 0 to 5 T. Measurements were made at a magnetic field of 0.5 T. Corrections are based on subtracting the sample-holder signal and contribution χ_D estimated from the Pascal constants [29] and equal $-363 \times 10^{-6}\,cm^3\,mol^{-1}$ for complex $[ReCl_3(bpzm)(PPh_3)]$. The effective magnetic moment was calculated from the equation, $\mu_{eff} = 2.83(\chi_M T)^{1/2}$ (*B.M.*).

Table 2
Hydrogen bonds for $[ReCl_3(bpzm)(PPh_3)]$

D	A	H ··· A (Å)	D ··· A (Å)	D—H ··· A (°)
C(12)	Cl(3)	2.60	3.433(4)	148.8
C(18)	Cl(3)	2.79	3.497(4)	133.9
C(18)	N(3)	2.59	3.248(5)	128.5
C(22)	Cl(3)	2.49	3.249(4)	134.7

3. Results and discussion

The $[ReCl_3(bzpm)(PPh_3)]$ complex was prepared in good yield by a ligand exchange reaction starting from $[ReCl_3(MeCN)(PPh_3)_2]$ and bis(pyrazol-1-yl)methane (bpzm):

$$[ReCl_3(MeCN)(PPh_3)_2] + bpzm \rightarrow [ReCl_3(bzpm)(PPh_3)] + MeCN + PPh_3$$

It was isolated as a brown microcrystalline solid, soluble in common organic solvents. The elemental analysis of the complex is in good agreement with its formulation. The characteristic bands corresponding to the ν(CN) and ν(C=C) modes of the bpzm ligand appear at 1600–1500 cm^{-1} in the IR spectrum of $[ReCl_3(bzpm)(PPh_3)]$ [30].

3.1. Crystal structure

$[ReCl_3(bzpm)(PPh_3)]$ crystallises as the dichloromethane solvate, and the dichloromethane molecule is not bonded to any atom of the Re(III) complex. No intermolecular interactions with enough strength to govern crystal packing or molecule conformation were found in the structure of $[ReCl_3(bzpm)(PPh_3)]$, only some weak intramolecular hydrogen bonds [31,32] were detected in the $[ReCl_3(bzpm)(PPh_3)]$ molecule and they are gathered in Table 2.

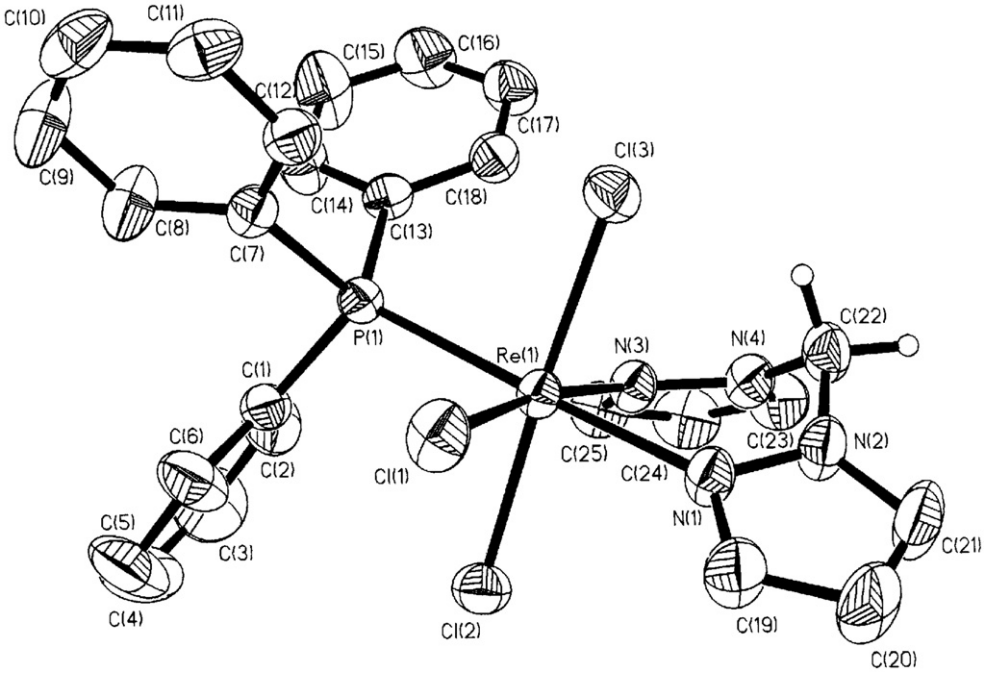


Fig. 1. The molecular structure of $[ReCl_3(bpzm)(PPh_3)]$ (50% probability ellipsoids). The hydrogen atoms of the phenyl and pyrazole rings are omitted for clarity.

The molecular structure of $[ReCl_3(bpzm)(PPh_3)]$ is given in Fig. 1. The pseudooctahedral environment of the Re center in $[ReCl_3(bpzm)(PPh_3)]$ shows clear distortions, induced by the bite angle of the chelating bpzm ligand. Upon coordination of bis(pyrazol-1-yl)methane to the rhenium centre, a six-membered cycle (made by the four nitrogen atoms, the rhenium atom and the carbon atom) is formed, and the formed ring shows a *boat* distorted toward *sofa* conformation with the rhenium and the carbon atoms off the plane defined by the four nitrogen atoms (with deviations from the least squares plane of 0.624(5) and 0.640(5) Å, respectively). The planar, in the range of experimental error, pyrazole rings are inclined at 57.1(2)°.

The chloride ions of $[ReCl_3(bpzm)(PPh_3)]$ are arranged in a *meridional* fashion, and the nitrogen atom of the bpzm ligand occupies the *trans* position to the Cl(1) ion. The *mer* geometry of the ReX_3 fragment has been confirmed for the $[ReCl_3(pzH)_2(PPh_3)]$ and $[ReCl_3(3,5\text{-}Me_2pzH)_2(PPh_3)]$ complexes [14], but in the $[ReX_3(L–L)(PPh_3)]$ compounds with bipy-like ligands the *mer* geometry is definitely rarer than the *fac* arrangement [33]. It seems that electronic factors favour the *meridional* configuration in $[ReCl_3(bpzm)(PPh_3)]$. The *facial* disposition of halide ions in the $[ReCl_3(L–L)(PPh_3)]$ complexes is preferred by the strong π acceptor L–L ligand, as it maximizes the back-bonding effect. It is significant that the Re–N distances in

Table 3
The experimental and optimized bond lengths (Å) and angles (°) for $[ReCl_3(bpzm)(PPh_3)]$

Bond lengths	Experimental	Optimized	Bond angles	Experimental	Optimized
Re(1)–N(1)	2.146(3)	2.165	N(3)–Re(1)–N(1)	84.97(11)	85.76
Re(1)–N(3)	2.122(3)	2.158	N(3)–Re(1)–Cl(2)	86.43(8)	84.34
Re(1)–Cl(1)	2.3983(9)	2.450	N(1)–Re(1)–Cl(2)	87.90(9)	86.96
Re(1)–Cl(2)	2.3552(9)	2.405	N(3)–Re(1)–Cl(3)	92.89(8)	90.53
Re(1)–Cl(3)	2.3718(9)	2.446	N(1)–Re(1)–Cl(3)	88.87(9)	89.04
Re(1)–P(1)	2.4199(9)	2.492	Cl(2)–Re(1)–Cl(3)	176.75(3)	173.71
			N(3)–Re(1)–Cl(1)	170.69(8)	171.84
			N(1)–Re(1)–Cl(1)	86.98(8)	87.30
			Cl(2)–Re(1)–Cl(1)	88.62(3)	91.00
			Cl(3)–Re(1)–Cl(1)	91.61(3)	93.65
			N(3)–Re(1)–P(1)	95.88(8)	97.89
			N(1)–Re(1)–P(1)	177.66(9)	176.08
			Cl(2)–Re(1)–P(1)	94.32(3)	94.79
			Cl(3)–Re(1)–P(1)	88.91(3)	89.51
			Cl(1)–Re(1)–P(1)	92.34(3)	89.16

Table 4
The energy and character of the selected molecular orbitals with α and β spins for $[ReCl_3(bpzm)(PPh_3)]$

	MOs with α spin		MOs with β spin	
	E (eV)	Character	*E* (eV)	Character
HOMO − 10	−7.188	π(Cl), π(PPh_3), n(P), n(N)	−7.262	π(Cl), π(PPh_3), π(bpzm)
HOMO − 9	−6.988	π(PPh_3), π(Cl)	−7.178	π(Cl), π(PPh_3)
HOMO − 8	−6.899	π(PPh_3), π(Cl)	−7.074	π(Cl), π(PPh_3)
HOMO − 7	−6.745	π(PPh_3), π(Cl)	−6.939	π(PPh_3), π(Cl)
HOMO − 6	−6.654	π(PPh_3), π(Cl)	−6.868	π(PPh_3), π(Cl)
HOMO − 5	−6.568	π(Cl), π(PPh_3)	−6.686	π(PPh_3), π(Cl), n(P)
HOMO − 4	−6.431	π(PPh_3), n(P) π(Cl)	−6.607	π(PPh_3), π(Cl)
HOMO − 3	−6.307	π(PPh_3), n(P) π(Cl)	−6.450	π(Cl), π(PPh_3)
HOMO − 2	−5.559	d_{yz}(Re), π(Cl)	−6.381	π(PPh_3), π(Cl), n(P)
HOMO − 1	−5.304	d_{xz}(Re), π(Cl)	−6.227	π(Cl), π(PPh_3)
HOMO	−5.198	d_{xy}(Re), π(Cl)	−4.770	d_{xz}(Re), π(Cl)
LUMO	−1.064	π*(bpzm)	−2.550	d_{yz}(Re), π(Cl), π*(bpzm)
LUMO + 1	−0.790	π*(bpzm), π*(PPh_3)	−2.162	d_{xy}(Re), π(Cl), π*(bpzm)
LUMO + 2	−0.700	π*(bpzm), π*(PPh_3), d_{z2}(Re)	−0.888	π*(bpzm)
LUMO + 3	−0.541	π*(PPh_3), d_{z2}(Re)	−0.750	π*(PPh_3), π*(bpzm)
LUMO + 4	−0.378	π*(PPh_3), d_{x2-y2}(Re)	−0.548	π*(bpzm)
LUMO + 5	−0.269	d_{x2-y2}(Re), π*(PPh_3)	−0.431	π*(PPh_3), d_{z2}(Re)
LUMO + 6	−0.080	π*(PPh_3)	−0.320	π*(PPh_3)
LUMO + 7	0.038	π*(PPh_3)	−0.106	π*(PPh_3)
LUMO + 8	0.062	π*(bpzm)	0.036	π*(PPh_3)
LUMO + 9	0.346	π*(PPh_3)	0.064	π*(bpzm)
LUMO + 10	0.516	π*(bpzm)	0.147	d_{x2-y2}(Re), π*(PPh_3)

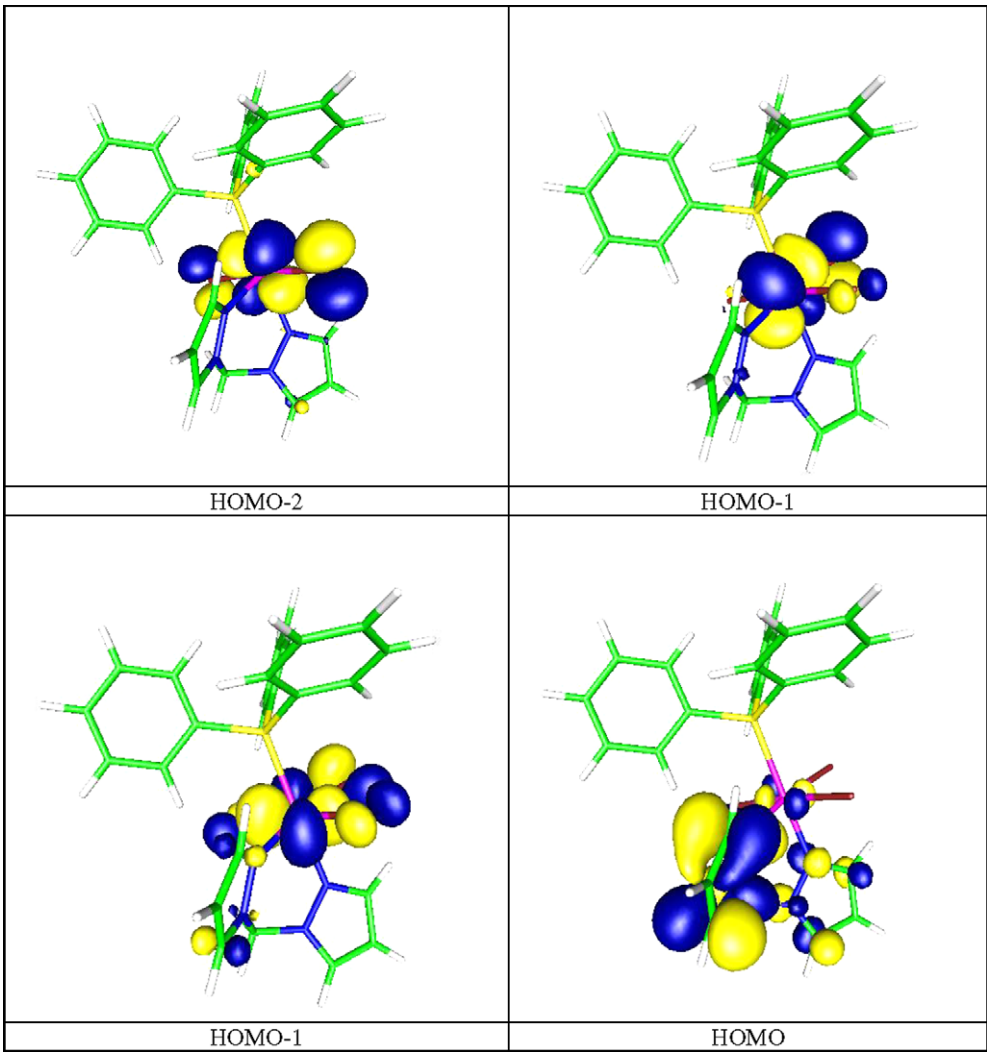


Fig. 2. The selected HOMO and LUMO orbitals with α spin for $[ReCl_3(bpzm)(PPh_3)]$. Positive values of the orbital contour are represented in blue (0.04 au) and negative values – in yellow (−0.04 au). (For interpretation of the references to colour in this figure, the reader is referred to the web version of this article.)

$[ReCl_3(bpzm)(PPh_3)]$ (2.146(3) and 2.122(3) Å) are longer than those in $[ReX_3(bipy)(PPh_3)]$ (2.099(8) and 2.094(8) Å), with the facial disposition of the halide ions [34]. On the other hand, these values are shorter than comparable distances for saturated amine complexes where metal-to-ligand π-back bonding is not possible, for instance, the Re–NH_2 distance in the compound $[Re(N_2)(ampy)(tbpy)(PPh_3)]PF_6$ is 2.197(7) Å [35]. Some differences are observed between the Re(1)–N(1) and Re(1)–N(3) bond lengths as the Re(1)–N(3) distance is affected by the *trans* influence of the triphenylphosphine ligand. The presence of Re–PPh_3 back-bonding diminishes the demand on π*(bpzm) orbitals. The most important experimental bond lengths and angles of $[ReCl_3(bzpm)(PPh_3)]$ are reported in Table 3.

3.2. Geometry optimisation

The geometry of $[ReCl_3(bpzm)(PPh_3)]$ was optimized in the triplet and singlet states using the DFT method with

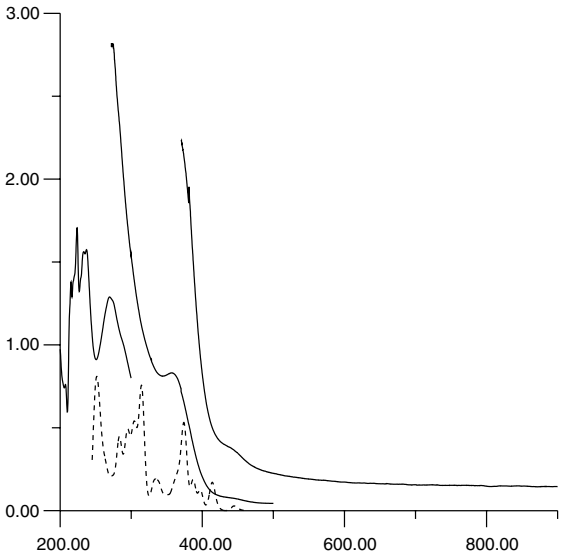


Fig. 3. The experimental (—) and calculated (---) electronic absorption spectra of $[ReCl_3(bpzm)(PPh_3)]$.

the B3LYP functional. The energy of the singlet state is 12.7 kcal higher. The optimized geometric parameters of the triplet state are gathered in Table 3. In general, the predicted bond lengths and angles are in agreement with the values based upon the X-ray crystal structure data, and the general trends observed in the experimental data are well reproduced in the calculations.

3.3. Molecular orbitals

The energies and characters of several highest occupied and lowest unoccupied molecular orbitals of [$ReCl_3$(bpzm)(PPh_3)] are presented in Table 4. The selected HOMO and LUMO orbitals of [$ReCl_3$(bpzm)(PPh_3)] with α spin are depicted in Fig. 2. Among the highest occupied MOs of [$ReCl_3$(bpzm)(PPh_3)], the largest numbers constitute π orbitals of the phenyl rings of PPh_3 and π_{Cl} orbitals. The H-2, H-1 and HOMO orbitals with α-spin and HOMO orbital with β-spin have π_{Re-Cl} character. The lowest unoccupied molecular orbital with α-spin is localised on the π-antibonding orbitals of the bpzm ligand. The LUMO and L+1 orbitals with β-spin can be represented as a combination of π_{Re-Cl}, and π_{bpzm}, with predominant involvement of the former component.

3.4. Electronic spectrum

The experimental and calculated electronic spectra of [$ReCl_3$(bpzm)(PPh_3)] are presented in Fig. 3. Each calculated transition is represented by a gaussian function

Table 5
The spin-allowed triplet–triplet electronic transitions calculated with the TDDFT method and the assignments of the calculated transitions to the experimental absorption bands for [$ReCl_3$(bpzm)(PPh_3)]

The most important orbital excitations	Character	λ (nm)	E (eV)	f	Experimental Λ (nm) (E (eV)) ε
H-1(β) → L(β)	π(Cl)/π(PPh_3) → d	451.2	2.75	0.0004	435.0 (2.85) 320
H(β) → L + 2(β)	d → π*(bzpm)	444.3	2.79	0.0015	
H(α) → L(α)	d → π*(bzpm)	421.4	2.94	0.0011	
H(α) → L(α)	d → d/π*(PPh_3)				
H(β) → L + 2(β)	d → π*(bzpm)	415.6	2.98	0.0034	
H-2(β) → L(β)	π(PPh_3)/n(P)/π(Cl) → d	413.2	3.00	0.0064	
H-3(β) → L(β)	π(Cl)/π(PPh_3) → d	406.4	3.05	0.0009	
H(β) → L + 2(β)	d → π*(bzpm)	397.2	3.12	0.0068	
H(β) → L + 4(β)					
H-1(β) → L + 1(β)	π(Cl)/π(PPh_3) → d	387.1	3.20	0.0102	
H(β) → L + 3(β)	d → π*(PPh_3)/π*(bpzm)	377.0	3.29	0.0066	
H(α) → L(α)	d → π*(bpzm)				
H(β) → L + 3(β)	d → π*(PPh_3)/π*(bpzm)	376.3	3.29	0.0045	
H(α) → L(α)	d → π*(bpzm)				
H-5(β) → L(β)	π(PPh_3)/n(P)/π(Cl) → d	373.0	3.32	0.0196	356.8 (3.47) 2700
H-1(α) → L(α)	d → π*(bpzm)				
H-1(α) → L(α)	d → π*(bpzm)	366.5	3.38	0.0066	
H(β) → L + 3(β)	d → π*(PPh_3)/π*(bpzm)				
H(β) → L + 10(β)	d → d	345.0	3.59	0.0025	
H(β) → L + 6(β)	d → π*(PPh_3)	332.1	3.73	0.0062	
H(β) → L + 5(β)					
H-8(β) → L + 1(β)	π(Cl)/π(PPh_3) → d	315.7	3.93	0.0188	
H-9(β) → L + 1(β)					
H-10(β) → L(β)	π(Cl)/π(PPh_3)/π(bpzm) → d	314.4	3.94	0.0150	
H-1(α) → L + 2(α)	d → π*(PPh_3)/π*(bpzm)	312.1	3.97	0.0065	
H-11(β) → L(β)	π(Cl)/π(bpzm) → d	304.8	4.07	0.0122	269.4 (4.60) 13400
H-2(α) → L + 1(α)	d → π*(PPh_3)/π*(bpzm)	301.9	4.11	0.0123	
H-9(β) → L + 1(β)	π(Cl)/π(PPh_3) → d	295.3	4.20	0.0127	
H-13(β) → L(β)	π(Cl)/π(bpzm) → d	292.8	4.23	0.0057	
H-11(β) → L + 1(β)	π(Cl)/π(bpzm) → d	284.4	4.36	0.0120	
H-10(β) → L + 1(β)	π(Cl)/π(PPh_3)/π(bpzm) → d				
H-15(β) → L(β)	π(Cl) → d	282.7	4.39	0.0082	
H-17(β) → L(β)	π(Cl)/π(PPh_3)/n(P)/n(N) → d	255.5	4.85	0.0065	
H-15(β) → L + 1(β)	π(Cl) → d				
H-1(β) → L + 3(β)	π(Cl)/π(PPh_3) → π*(bpzm)/π*(PPh_3)	254.9	4.86	0.0082	226.8 (5.47) 13780
H-2(α) → L + 7(α)	d → π*(PPh_3)	249.9	4.96	0.0062	
H-18(β) → L(β)	n(P) → d				
H-2(β) → L + 2(β)	π(PPh_3)/n(P)/π(Cl) → π*(bpzm)	249.5	4.97	0.0063	
H-2(α) → L + 7(α)	d → π*(PPh_3)	248.4	4.99	0.0061	
					215.2 (5.76) 14370

$y = ce^{-bx^2}$ with the height (c) equal to the oscillator strength and b equal to 0.04 nm^{-2}.

The spin-allowed triplet–triplet electronic transitions calculated with the TDDFT method for [$ReCl_3$(bpzm)-(PPh_3)] are gathered in Table 5. For the high energy part of the spectrum, only transitions with oscillator strengths larger than 0.0050 are listed in Table 5.

The investigated complex is of large size, the number of basis functions is equal to 605. A hundred electron transitions calculated by the TDDFT method do not comprise all the experimental absorption bands. The UV–Vis spectrum of [$ReCl_3$(bpzm)(PPh_3)] was calculated only to 240 nm, so the shortest wavelength experimental band cannot be assigned to the calculated transitions, and the assignment of the band at 226.8 nm is not complete. Some additional intraligand and interligand transitions are expected to be found at higher energies in the calculation for [$ReCl_3$(bzpm)(PPh_3)].

The electronic absorption spectrum of [$ReCl_3$(bpzm)-(PPh_3)] is similar to those observed for [$ReCl_3$(pzH)$_2$-(PPh_3)] and [$ReCl_3$(3,5-Me_2pzH)$_2$(PPh_3)] [14]. Some intense bands are observed below 300 nm and two considerably weaker absorptions exist in the low energy range. In contrast, the solution spectra of *fac*-[$ReCl_3$(L–L)(PPh_3)] display multiple transitions of moderate intensity in the form of peaks and shoulders in the visible region (400–1000 nm) [34,36].

The experimental bands of [$ReCl_3$(bpzm)(PPh_3)] at 435.0, 356.8 and 269.4 nm are attributed to Ligand–Metal Charge Transfer (π(Cl) → d and π(PPh_3) → d) and Metal–Ligand Charge Transfer (d → π*(PPh_3) and d → π*(bpzm)) transitions.

The absorption band at 226.8 nm results mainly from Ligand–Ligand Charge Transfer and intraligand (IL) transitions.

3.5. Magnetic properties

The magnetic properties of [$ReCl_3$(bpzm)(PPh_3)] under the form μ_{eff} versus T (μ_{eff} the effective magnetic moment) is shown in Fig. 4. The chloro-derivative of rhenium(III), shows a room temperature magnetic moment of 1.74 B.M. (0.379 $cm^3mol^{-1}K$). The magnetic moment of the solid is temperature dependent between 300 and 60 K. Only a slight magnetic anomaly is observed in the temperature range 55–14 K, and below 14 K the value of the χ_{MT} product decreases with temperature lowering. This behavior is characteristic of mononuclear d^4 low-spin octahedral Re(III) complexes ($^3T_{1g}$ ground state) [37–45] and arises because of the large spin–orbit coupling (ζ = 2500 cm^{-1} [46]), which gives a diamagnetic ground state. It seems that at room temperature, in accordance with Boltzmann's distribution, the higher magnetic state is populated, and it is depopulated with temperature lowering and a decrease of the magnetic moment is observed.

The variation of the magnetization M versus the magnetic field H for the complex [$ReCl_3$($OPPh_3$)(dppt)] at

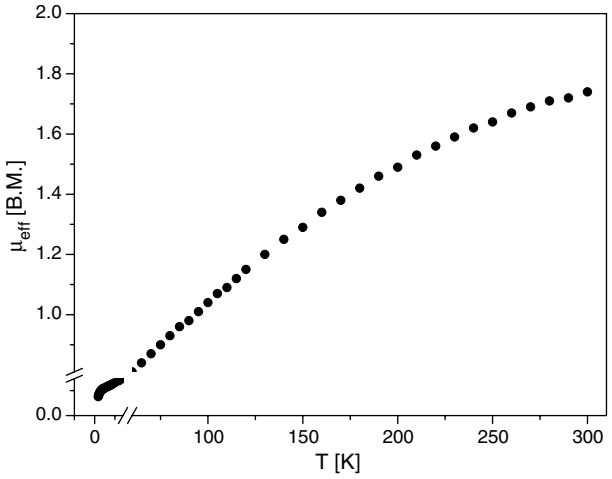


Fig. 4. Plots of the experimental effective magnetic moment μ_{eff} (●) vs. temperature for the complex [$ReCl_3$(bpzm)(PPh_3)].

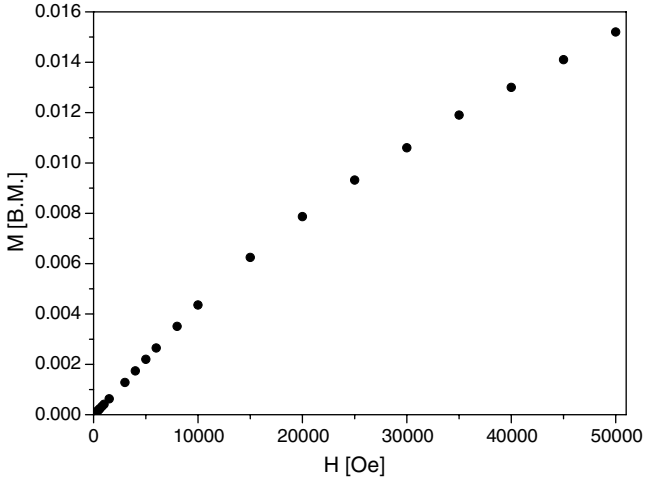


Fig. 5. Field dependence of the magnetization for the complex [$ReCl_3$(bpzm)(PPh_3)] at 2 K.

2 K is shown in Fig. 5. The M versus H curve for the complex very slowly increases and indicates a value of the magnetization near to zero (0.015 B.M.) at 5 T. The magnetization of the sample confirms that the ground state is diamagnetic.

4. Supplementary material

CCDC 640910 contains the supplementary crystallographic data for $C_{26}H_{25}Cl_5N_4PRe$. These data can be obtained free of charge via http://www.ccdc.cam.ac.uk/conts/retrieving.html, or from the Cambridge Crystallographic Data Centre, 12 Union Road, Cambridge CB2 1EZ, UK; fax: (+44) 1223-336-033; or deposit@ccdc.cam.ac.uk.

Acknowledgements

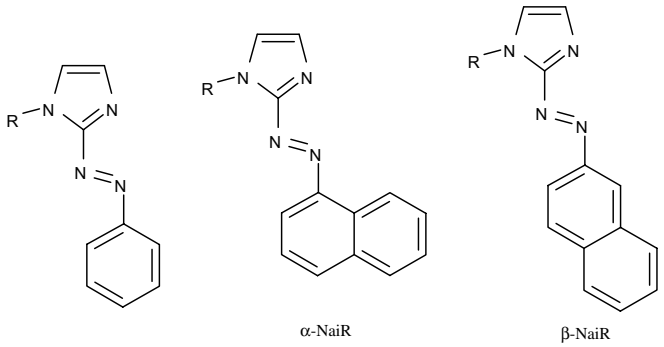
The GAUSSIAN03 calculations were carried out in the Wrocław Centre for Networking and Supercomputing,

WCSS, Wrocław, Poland under calculational Grant No. 51/96. The work was supported by the Polish Ministry of Science and Higher Education Grant No. 1T09A12430.

References

[1] C. Pettinari, R. Pettinari, Coord. Chem. Rev. 249 (2005) 663.
[2] L.-F. Tang, Z.-H. Wang, Y.-M. Xu, J.-T. Wang, H.-G. Wang, X.-K. Yao, Polyhedron 18 (1999) 2383.
[3] L.-F. Tang, Z.-H. Wang, W.-L. Jia, Y.-M. Xu, J.T. Wang, Polyhedron 19 (2000) 381.
[4] E. Teuma, M. Loy, C. Le Berre, M. Etienne, J.C. Daran, P. Kalck, Organometallics 22 (2003) 5261.
[5] K.A. Van Langenberg, B. Moubaraki, K.S. Murray, E.R.T. Tiekink, Z. Kristallogr, New Cryst. Struct. 218 (2003) 345.
[6] J. Ruiz, V. Rodriguez, C. De Haro, J. Perez, G. Lopez, Inorg. Chim. Acta 357 (9) (2004) 2331.
[7] J. Ruiz, N. Cutillas, C. Vincente, M.D. Villa, G. Lopez, J. Lorenzo, F.X. Aviles, V. Moreno, D. Bautista, Inorg. Chem. 44 (2005) 7365.
[8] Ch.-Ch. Chou, Ch.-Ch. Su, H.-L. Tsai, K.-H. Lii, Inorg. Chem. 44 (2005) 628.
[9] A.S. Potapov, A.I. Khlebnikov, Polyhedron 25 (2006) 2683.
[10] D.L. Reger, J.R. Gardinier, P.J. Pellechia, M.D. Smith, K.J. Brown, Inorg. Chem. 42 (2003) 7635.
[11] M. Porchia, G. Papini, C. Santini, G.G. Lobia, M. Pellei, F. Tisato, G. Bandoli, A. Dolmella, Inorg. Chem. 44 (2005) 4045.
[12] G. Rouschias, G. Wilkinson, J. Chem. Soc. A (1967) 993.
[13] P. Ghosh, A. Pramanik, N. Bag, A. Chakravorty, J. Chem. Soc., Dalton Trans. (1992) 1883.
[14] B. Machura, M. Jaworska, R. Kruszynski, Polyhedron 23 (2004) 1819.
[15] H. Chermette, Coord. Chem. Rev. 178–180 (1998) 699.
[16] M.C. Aragoni, M. Arca, T. Cassano, C. Denotti, F.A. Devillanova, F. Isaia, V. Lippolis, D. Natali, L. Niti, M. Sampietro, R. Tommasi, G. Verani, Inorg. Chem. Commun. 5 (2002) 869.
[17] P. Romaniello, F. Lelj, Chem. Phys. Lett. 372 (2003) 51.
[18] P. Norman, P. Cronstrand, J. Ericsson. Chem. Phys. 285 (2002) 207.
[19] S. Julia, P. Sala, J. del Mazo, M. Sancho, C. Ochoa, J. Elguero, J.P. Fayet, M.C. Vertut, J. Heterocycl. Chem. 19 (1982) 1141.
[20] CrysAlis RED, Oxford Diffraction Ltd., Version 1.171.29.2.
[21] G.M. Sheldrick, Acta Crystallogr. Sect., A 46 (1990) 467.
[22] G.M. Sheldrick, SHELXL97. Program for the Refinement of Crystal Structures. University of Göottingen, Germany, 1997.
[23] G.M. Sheldrick, SHELXTL: release 4.1 for Siemens Crystallographic Research Systems, 1990.
[24] M.J. Frisch, G.W. Trucks, H.B. Schlegel, G.E. Scuseria, M.A. Robb, J.R. Cheeseman, J.A. Montgomery, Jr., T. Vreven, K.N. Kudin, J.C. Burant, J.M. Millam, S.S. Iyengar, J. Tomasi, V. Barone, B. Mennucci, M. Cossi, G. Scalmani, N. Rega, G.A. Petersson, H. Nakatsuji, M. Hada, M. Ehara, K. Toyota, R. Fukuda, J. Hasegawa, M. Ishida, T. Nakajima, Y. Honda, O. Kitao, H. Nakai, M. Klene, X. Li, J.E. Knox, H.P. Hratchian, J.B. Cross, C. Adamo, J. Jaramillo, R. Gomperts, R.E. Stratmann, O. Yazyev, A.J. Austin, R. Cammi, C. Pomelli, J.W. Ochterski, P.Y. Ayala, K. Morokuma, G.A. Voth, P. Salvador, J.J. Dannenberg, V.G. Zakrzewski, S. Dapprich, A.D. Daniels, M.C. Strain, O. Farkas, D.K. Malick, A.D. Rabuck, K. Raghavachari, J.B. Foresman, J.V. Ortiz, Q. Cui, A.G. Baboul, S. Clifford, J. Cioslowski, B.B. Stefanov, G. Liu, A. Liashenko, P. Piskorz, I. Komaromi, R.L. Martin, D.J. Fox, T. Keith, M.A. Al-Laham, C.Y. Peng, A. Nanayakkara, M. Challacombe, P.M.W. Gill, B. Johnson, W. Chen, M.W. Wong, C. Gonzalez, J.A. Pople, GAUSSIAN03, Revision B.03, Gaussian, Inc., Pittsburgh PA, 2003.
[25] A.D. Becke, J. Chem. Phys. 98 (1993) 5648.
[26] C. Lee, W. Yang, R.G. Parr, Phys. Rev. B 37 (1988) 785.
[27] M.E. Casida, in: J.M. Seminario (Ed.), Recent Developments and Applications in Modern Density Functional Theory, Theoretical and Computational Chemistry, Vol. 4, Elsevier, Amsterdam, 1996.
[28] P.J. Hay, W.R. Wadt, J. Chem. Phys. 82 (1985) 299.
[29] E. König, Magnetic Properties of Coordination and Organometallic Transition Metal Compounds, Springer-Verlag, Berlin, 1966.
[30] K. Nakamoto, Infrared and Raman Spectra of Inorganic and Coordination Compounds, 4th ed., Wiley-Interscience, New York, 1986.
[31] G.R. Desiraju, T. Steiner, The Weak Hydrogen Bond in Structural Chemistry and Biology, Oxford University Press (1999).
[32] G.A. Jeffrey, W. Saenger, Hydrogen Bonding in Biological Structures, Springer-Verlag, 1994.
[33] F.H. Allen, Acta Crystallogr. Sect., B 58 (2002) 380.
[34] B. Machura, R. Kruszynski, M. Jaworska, P. Lodowski, Polyhedron 24 (2005) 701.
[35] S.D. Orth, J. Barrerra, M. Sabat, W.D. Harman, Inorg. Chem. 33 (1994) 3026.
[36] S. Sengupta, J. Gangopadhyay, A. Chakravorty, J. Chem. Soc., Dalton Trans. (2003) 4635.
[37] J.E. Fergusson, Coord. Chem. Rev. 1 (1966) 459.
[38] B.N. Figgis, J. Lewis, Prog. Inorg. Chem. 6 (1964) 37.
[39] B.N. Figgis, Introduction to Ligand Field, Wiley-Interscience, New York, 1966, p. 248.
[40] J. Chatt, G.J. Leigh, D.M.P. Mingos, E.W. Randall, D. Shaw, J. Chem. Soc., Chem. Commun. (1968) 419.
[41] H.P. Gunz, G.J. Leigh, J. Chem. Soc. (1971) 2229.
[42] B. Coutinho, J.R. Dilworth, P. Jobanputra, R.M. Thompson, S. Schmidt, J. Strähle, C.M. Archer, J. Chem. Soc., Dalton Trans (1995) 1663.
[43] M. Hirsch-Kuchma, T. Nicholson, A. Davison, W.M. Davis, A.G. Jones, Inorg. Chem. 36 (1997) 3237.
[44] C.A. McConnachie, E.I. Stiefel, Inorg. Chem. 36 (1997) 6144.
[45] C. Pearson, A.L. Beauchamp, Can. J. Chem. 75 (1997) 220.
[46] A. Earnshaw, B.N. Figgis, J. Lewis, R.D. Peacok, J. Chem. Soc. (1961) 3132.

electron donating ability. Herein we present the kinetic and mechanistic studies of the reaction of picolinic acid (picH) with Pd(α/β-NaiR)Cl_2. Picolinic acid which is a naturally occurring degradation product of tryptophan [35], a DNA base, is a cheap and safe drug facilitating Zn/Cu ion absorption from intestine because of its metal ion chelating activity. Also picolinic acid has an extra clinical antimicrobial chemo-theraupteic application. Phenylazoimidazole (**i**) Naphthylazoimidazole (**ii**)



Phenylazoimidazole (**i**)

Naphthylazoimidazole (**ii**)

2. Experimental

2.1. Reagents/materials

The complexes were prepared by a reported procedure [36,37]. Picolinic acid (picH) (SRL, Mumbai) was purified by recrystallization from boiling toluene. Acetonitrile (MeCN) (SRL, Mumbai) was purified by a known procedure [38,39]. All kinetic and spectroscopic measurements were recorded on an Agilent 8453E UV-Vis Spectroscopy System. Quartz cells (1.0 cm path length) from Hellma were used. IR spectra (KBr pellet) were recorded on a FT-IR Spectrophotometer Spectrum RX1, Perkin–Elmer. ^{1}H NMR spectra were drawn from 300 MHz Bruker NMR instrument in CD_3CN using TMS as an internal standard. Microanalyses were carried out on a Perkin–Elmer 2400 CHN elemental analyzer. The specific conductance was measured on a JENCONS 4010 Conductivity Meter. The pH was measured on a SYSTRONICS 361 Digital pH meter. Rate constants and standard deviations were calculated by linear regression using a PC-based programmed Microcal-origin version Origin-6.1.

2.1.1. Kinetic measurements

For kinetic measurements, stock solutions of the complexes (*ca.* 10^{-3} mol dm^{-3}) and of picolinic acid (picH) (*ca.* 10^{-2} mol dm^{-3}) were prepared in dry MeCN. Solutions of different concentrations were prepared by quantitative dilution of stock solutions using dry MeCN. All experiments were performed at 298 K (unless otherwise mentioned) by mixing required volumes of the thermostated reactants and transferring the mixture to the absorption cell (1.0 cm length). On addition of picolinic acid (picH) to the solution of Pd(NaiR)Cl_2 in MeCN the orange solution changes to yellow–orange. The influence of the addition of picolinic acid (picH) on the spectra of Pd(α-NaiEt)Cl_2 is shown in the Fig. 1. The change proceeds through a single isosbestic point at *ca.* 489 nm. The decrease in absorbance of the reaction mixture was recorded automatically at *ca.* 530 nm as a function of time (s) for at least three halves of the reaction and up to maximum 1000 s. A_∞ was measured after $\sim$ 24 h of mixing, when the absorbance became constant. In all experiments, initial molar concentration of picH, $[picH]_0$, was kept at least ten times in excess so as to maintain pseudo-first-order kinetic condition. Pseudo-first-order rate constants, k_{obs}, were obtained from the slopes of the plots of $(A_t - A_\infty)$ *versus* time (s) (Fig. 2) where A_t is the absorbance of the reaction mixture at time, t (s) after mixing of picH solution and A_∞ is the absorbance of same reaction mixture after completion of the reaction.

2.2. Synthesis of [Pd(α-/β-NaiR)(pic)](ClO$_4$) (α-NaiR,3; β-NaiR,4)

A representative synthesis of [Pd(α-NaiEt)(pic)](ClO_4) (**3a**) is given below.

To a MeCN solution (15 ml) of the complex, Pd(α-NaiEt)Cl_2 (0.025 g, 5.84×10^{-2} mmol), picH (0.0216 g, 17.52×10^{-2} mmol) was added and the orange colored solution was stirred for about 24 h. It was filtered and allowed to evaporate to dryness at room temperature. The mass was then dissolved in MeOH and $NaClO_4$ (aq) (1 g) was added to it. A brown precipitate was filtered and washed with water. Dried product was then chromatographed over silica gel and MeCN eluted orange band. Yield: 0.021 g (65.22%).

All other complexes were prepared by the same procedure and yield varied 60–70%.

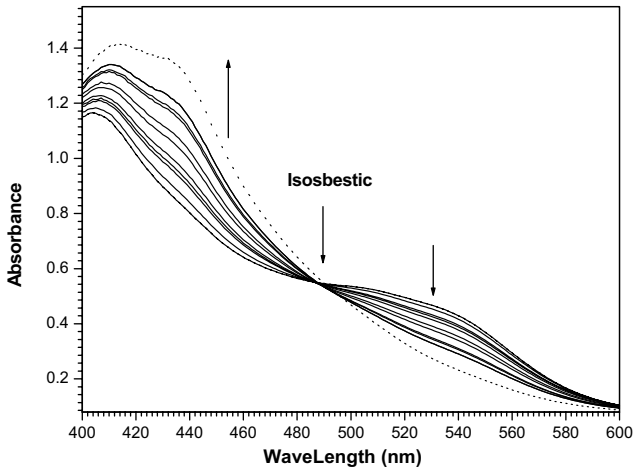


Fig. 1. Spectra of Pd(α-NaiEt)Cl_2(…) in MeCN and a reaction mixture of Pd(α-NaiEt)Cl_2 and picH in MeCN solution at 298 K. The arrows indicate decrease and increase of band intensities as reaction proceeds.

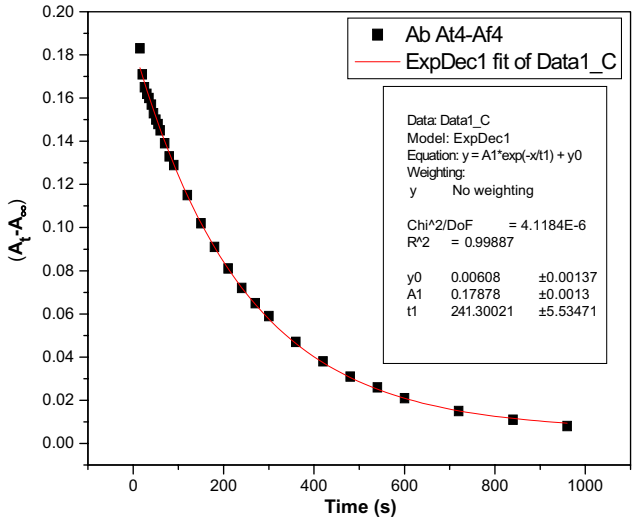


Fig. 2. Plot of $(A_t - A_\infty)$ vs. time (s) for reaction: Pd(α-NaiEt)Cl_2 + picH in MeCN. $[Pd(\alpha\text{-NaiEt})Cl_2]_0 = 1.00 \times 10^{-4}$ mol dm^{-3}, $[picH]_0 = 7 \times 10^{-3}$ mol dm^{-3} and temperature = 298 K.

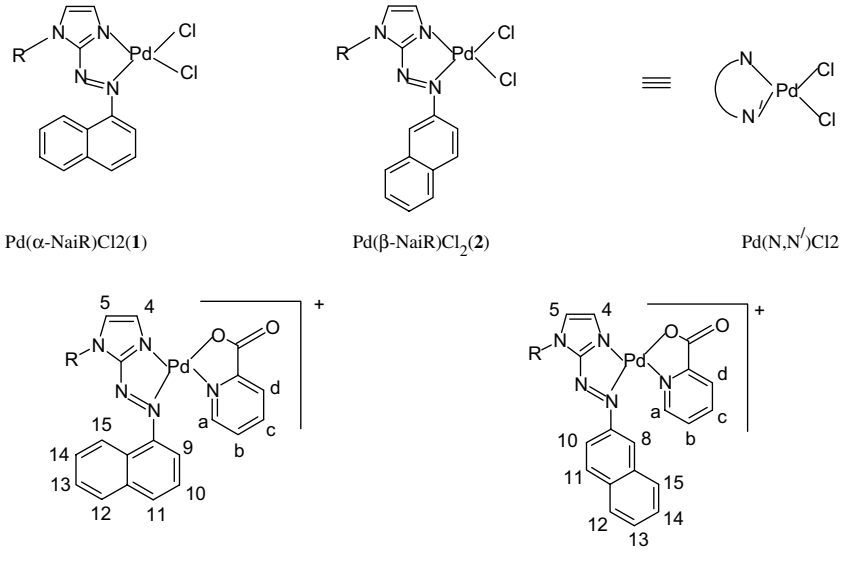
Microanalytical data of the complexes are as follows: For [Pd(α-NaiMe)(pic)](ClO_4) (**3a**): *Anal.* Calc. for $C_{20}H_{16}O_6N_5PdCl$: C, 42.56; H, 2.84; N, 12.41. Found: C, 42.50; H, 2.96; N, 12.36%. For [Pd(α-NaiEt)(pic)](ClO_4) (**3b**): *Anal.* Calc. for $C_{21}H_{18}O_6N_5PdCl$: C, 43.61; H, 3.11; N, 12.11. Found: C, 43.56; H, 3.10; N, 12.13%. For [Pd(α-NaiBz)(pic)](ClO_4) (**3c**): *Anal.* Calc. for $C_{26}H_{20}O_6N_5PdCl$: C, 48.76; H, 3.13; N, 10.94. Found: C, 48.72; H, 3.15; N, 11.01%. For [Pd(β-NaiMe)(pic)](ClO_4) (**4a**): *Anal.* Calc. for $C_{20}H_{16}O6N_5PdCl$: C, 42.56; H, 2.84; N, 12.41. Found: C, 42.52; H, 2.81; N, 12.44%. For [Pd(β-NaiEt)-(pic)](ClO_4) (**4b**): *Anal.* Calc. for $C_{21}H_{18}O_6N_5PdCl$: C, 43.61; H, 3.11; N, 12.11. Found: C, 43.68; H, 3.16; N, 12.12%. For [Pd(β-NaiBz)(pic)](ClO_4) (**4c**): *Anal.* Calc. for $C_{26}H_{20}O_6N_5PdCl$: C, 48.76; H, 3.13; N, 10.94. Found: C, 48.72; H, 3.16; N, 10.89%.

3. Results and discussion

3.1. Kinetics and mechanism

Two classes of naphthylazoimidazole complexes of palladium(II) have been used in this work. They are Pd(α-NaiR)Cl_2 (**1**) (α-NaiR = 1-alkyl-2-(naphthyl-α-azo)-imidazole) and Pd(β-NaiR)Cl_2 (**2**)(β-NaiR = 1-alkyl-2-(naphthyl-β-azo)imidazole) [where R = Me (**a**)/Et(**b**)/Bz(**c**)]. The ligands belong to the unsymmetric bidentate *N*,*N*′-donor type and form dichloropalladium(II) complexes, here after we abbreviate the complex as Pd(*N*,*N*′)Cl_2 (Scheme 1). The reaction kinetics between Pd(*N*,*N*′)Cl_2 and picolinic acid (picH) was studied spectrophotometrically. The reaction is first order in Pd(II) complex as k_{obs}-values are almost constant when all variants are constant except the complex concentration. The k_{obs}-values (Table 1) and the linear plots for the k_{obs} *versus* $[picH]_0$ (Figs. 3 and 4) indicate the reaction is first order in picH. The slope of the plot is second order rate constant (k_2) of the reaction. The presence of intercept (k_0) indicates the existence of a minor solvent assisted path to the overall reaction products (MeCN is a coordinating solvent).

The rate increases with rise of temperature, as expected from the Eyring equation. The second order rate constants (k_2) were measured at different temperatures in the range of 293–313 K for each reaction. Activation parameters, standard enthalpy of activation ($\Delta^{\ddagger}H^{\circ}$) and standard entropy of activation ($\Delta^{\ddagger}S^{\circ}$) were calculated from Eyring plots



Scheme 1.

Table 1
Pseudo-first-order rate constants (k_{obs}) for reactions of picolinic acid with Pd(R′aiR)Cl_2 in MeCN at 298 K

Pd(R′aiR)Cl_2	10^3 [picH]$_0$ (mol dm^{-3})	10^3k_{obs} (s^{-1})	$10k_2$ (dm^3 mol^{-1} s^{-1})	10^3k_0 (s^{-1})
Pd(α-NaiMe)Cl_2 (**1a**)	1.0	0.88	6.2	0.36
	3.0	2.20		
	5.0	3.62		
	7.0	4.68		
	10.0	6.43		
Pd(α-NaiEt)Cl_2 (**1b**)	1.0	0.81	5.6	0.17
	3.0	1.79		
	5.0	2.90		
	7.0	4.14		
	10.0	5.79		
Pd(α-NaiBz)Cl_2 (**1c**)	1.0	0.96	7.4	0.21
	3.0	2.42		
	5.0	3.97		
	7.0	5.42		
	10.0	7.65		
Pd(β-NaiMe)Cl_2 (**2a**)	1.0	1.12	9.2	0.174
	3.0	2.91		
	5.0	4.78		
	7.0	6.65		
	10.0	9.40		
Pd(β-NaiEt)Cl_2 (**2b**)	1.0	1.00	8.2	0.168
	3.0	2.59		
	5.0	4.25		
	7.0	5.90		
	10.0	8.33		
Pd(β-NaiBz)Cl_2 (**2c**)	1.0	1.20	10.2	0.16
	3.0	3.19		
	5.0	5.32		
	7.0	7.29		
	10.0	10.40		

[Pd(R′aiR)Cl_2]$_0 = 1.00 \times 10^{-4}$ mol dm^{-3}.

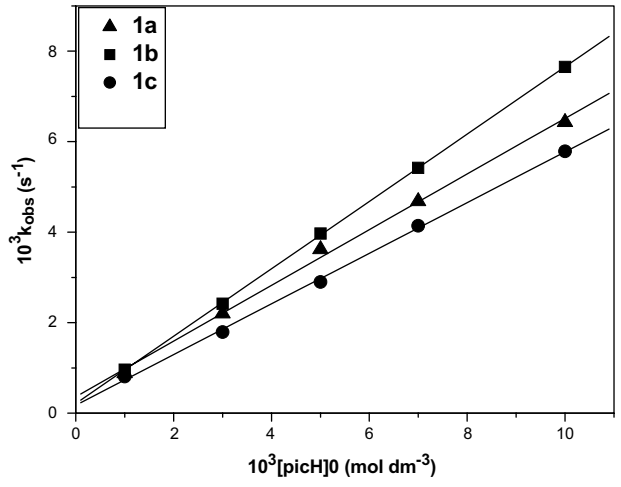


Fig. 3. Plots of k_{obs} vs. [picH]$_0$ for the reactions: Pd(α-NaiR)Cl_2 + picH in MeCN. [Pd(α-NaiR)Cl_2]$_0 = 1.00 \times 10^{-4}$ mol dm^{-3} and temperature = 298 K.

(Figs. 5 and 6) and are recorded in Table 2. The activation parameter values corroborate with the experimental k_2-values. The order for $\Delta^{\ddagger}H^{\circ}$ and $\Delta^{\ddagger}S^{\circ}$ are: Pd(NaiEt)Cl_2>

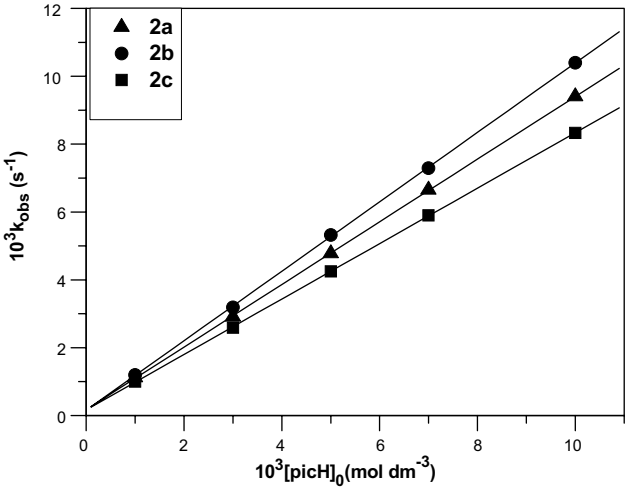


Fig. 4. Plots of k_{obs} vs. [picH]$_0$ for the reactions: Pd(β-NaiR)Cl_2 + picH in MeCN. [Pd(β-NaiR)Cl_2]$_0 = 1.00 \times 10^{-4}$ mol dm^{-3} and temperature = 298 K.

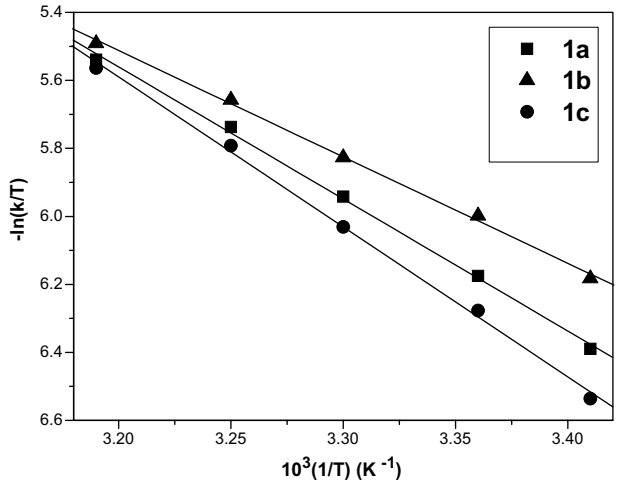


Fig. 5. Plots of ln(k/T) vs. (1/T) for the reactions: Pd(α-NaiR)Cl_2 + picH in MeCN.

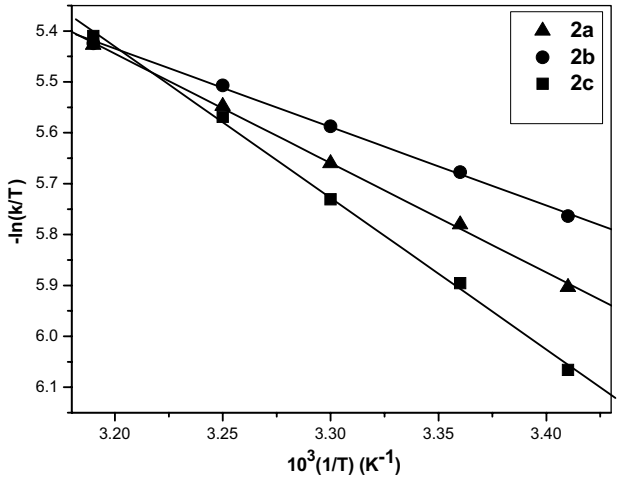
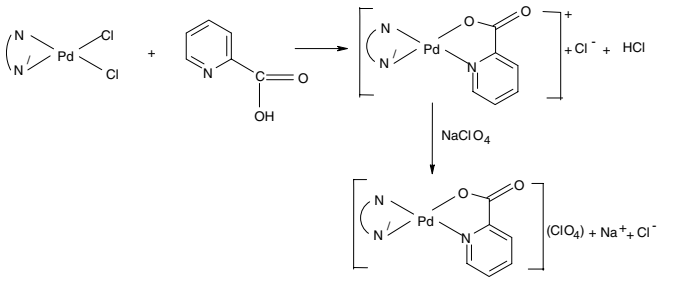


Fig. 6. Plots of ln(k/T) vs. (1/T) for the reactions: Pd(β-NaiR)Cl_2 + picH in MeCN.

Table 2
Second order rate constants (k_2) at different temperatures and activation parameters of the reactions

Pd(R′aiR)Cl$_2$	Temperature (K)	10k (dm^3 mol^{-1} s^{-1})	$\Delta^{\ddagger}H^{\circ}$ (kJ mol^{-1})	$\Delta^{\ddagger}S^{\circ}$ (J K^{-1} mol^{-1})
Pd(α-NaiMe)Cl$_2$	293	4.92	32.62(±4)	−139.35(±25)
(**1a**)	298	6.20		
	303	7.96		
	308	9.93		
	313	12.30		
Pd(α-NaiEt)Cl$_2$	293	4.25	37.05(±5)	−125.46(±30)
(**1b**)	298	5.60		
	303	7.28		
	308	9.40		
	313	12.00		
Pd(α-NaiBz)Cl$_2$	293	6.05	26.27(±3)	−159.29(±18)
(**1c**)	298	7.40		
	303	8.93		
	308	10.75		
	313	12.90		
Pd(β-NaiMe)Cl$_2$	293	8.00	18.05(±2)	−184.99(±15)
(**2a**)	298	9.20		
	303	10.55		
	308	12.00		
	313	13.75		
Pd(β-NaiEt)Cl$_2$	293	6.80	24.99(±3)	−162.70(±20)
(**2b**)	298	8.20		
	303	9.83		
	308	11.75		
	313	14.00		
Pd(β-NaiBz)Cl$_2$	293	9.20	12.95(±2)	−201.28(±12)
(**2c**)	298	10.20		
	303	11.35		
	308	12.50		
	313	13.80		

Pd(NaiMe)Cl$_2$ > Pd(NaiBz)Cl$_2$ and Pd(α-NaiR)Cl$_2$ > Pd(β-NaiR)Cl$_2$. The iso-kinetic plot (Fig. 7) supports an identical mechanism for the reaction of Pd(N,N')Cl$_2$ with picH. Kinetic studies in the presence of externally added Cl$^-$ (LiCl) reveal that the rate as well as k_{obs} decreases inversely with [Cl$^-$]$_0$ (Table 3), which supports the mechanism given in Scheme 2. The dissociation of the second Pd–Cl bond is the rate-determining step and the dissociation of the first Pd–Cl bond is affected by externally added Cl$^-$ ion. The product was isolated and characterized as [Pd(N,N')(pic)](ClO$_4$). The nucleophilic substitution process involves direct displacement of 2 Cl$^-$ ions by picolinic acid (Eq. (1)). In the MeCN medium picH will exist largely in the undissociated form [40].



(1)

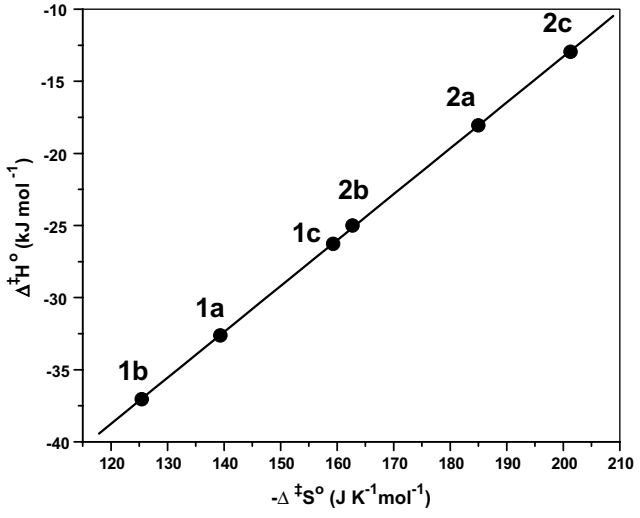
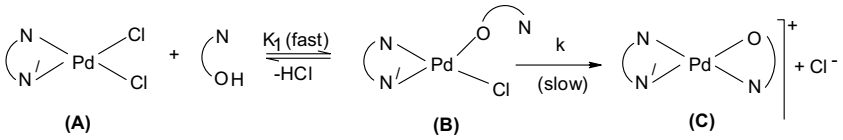


Fig. 7. Plot of $\Delta^{\ddagger}H^{\circ}$ vs. $\Delta^{\ddagger}S^{\circ}$ i.e., iso-kinetic plot for the reactions: Pd(R′aiR)Cl$_2$ + picH in MeCN.

Table 3
Effect of externally added LiCl on pseudo-first-order rate constants (k_{obs}) for reactions of picolinic acid with Pd(R′aiR)Cl$_2$ in MeCN at 298 K

Pd(R′aiR)Cl$_2$	10^3 [LiCl]$_0$ (mol dm^{-3})	10$^3 k_{obs}$ (s^{-1})
Pd(α-NaiMe)Cl$_2$ (**1a**)	0.2	2.05
	0.4	1.16
	0.6	0.82
	0.8	0.65
	1.0	0.57
Pd(α-NaiEt)Cl$_2$ (**1b**)	0.2	1.71
	0.4	0.93
	0.6	0.65
	0.8	0.52
	1.0	0.45
Pd(α-NaiBz)Cl$_2$ (**1c**)	0.2	2.35
	0.4	1.28
	0.6	1.00
	0.8	0.75
	1.0	0.62
Pd(β-NaiMe)Cl$_2$ (**2a**)	0.2	2.78
	0.4	1.56
	0.6	1.12
	0.8	0.85
	1.0	0.73
Pd(β-NaiEt)Cl$_2$ (**2b**)	0.2	2.49
	0.4	1.35
	0.6	0.98
	0.8	0.74
	1.0	0.62
Pd(β-NaiBz)Cl$_2$ (**2c**)	0.2	3.02
	0.4	1.55
	0.6	1.14
	0.8	0.87
	1.0	0.75

[Pd(R′aiR)Cl$_2$]$_0$ = 1.00×10^{-4} mol dm^{-3}, [picH]$_{0=}$$3.00 \times 10^{-3}$ mol dm^{-3}.



Scheme 2.

The observed rate is

$$\text{Rate} = [k_0 + k_2[\text{picH}]_0]\{\text{Pd(R}'\text{aiR)Cl}_2\}$$
$$= k_{\text{obs}}[\text{Pd(R}'\text{aiR)Cl}_2]$$

(where $k_2 = \frac{kK_1}{[\text{Cl}^-]_0}$, which is constant at constant $[\text{Cl}^-]_0$ and $k_{\text{obs}} = k_0 + k_2[\text{picH}]_0$).

The k_0 and k_2 are the intercept and the slope of the plot of k_{obs} *versus* $[\text{picH}]_0$ respectively. It is probable that the highly negative O donor will coordinate first with the positively charged metal centre, with fast dissociation of the first Pd–Cl bond, and finally forms a stable four coordinated square planar complex (**B**). Then picolinate-N (which remains free in **B**) slowly coordinates with Pd(II) as a compulsion of chelate stability. Obviously the later rate is slower than the former rate. Therefore the second Pd–Cl bond cleavage is the rate-determining step. This is also supported by the effect of externally added Cl^- ions (LiCl). The plausible mechanism is given in Scheme 2. There are two parallel pathways: one is the existence of a minor solvent assisted path where MeCN substitutes Cl^- initially, then MeCN is displaced by picH and finally forms the reaction product (**C**) (Scheme 3).

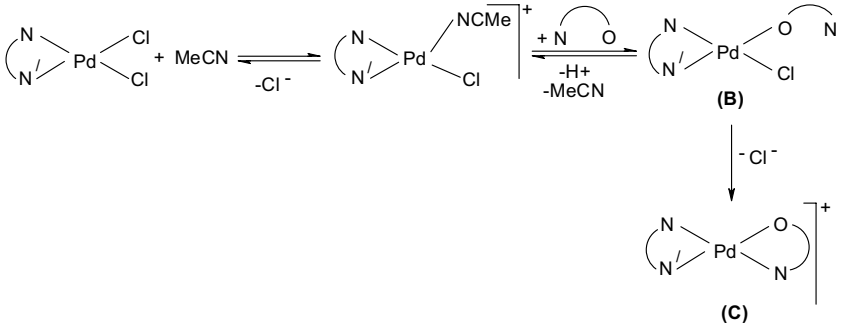
Although the steric crowding of α-/β-naphthyl group in the *N*,*N*′ chelating ligand is significant, its electron withdrawing property, due to conjugation, stabilizes the Pd(*N*,*N*′) chelated species in preference to de-chelation.

The kinetic data in Table 1 reveal that the magnitude of k increases in the order: $\text{Pd}(\alpha\text{-NaiEt})\text{Cl}_2 < \text{Pd}(\alpha\text{-NaiMe})\text{Cl}_2 < \text{Pd}(\alpha\text{-NaiBz})\text{Cl}_2$. This is because of the electron withdrawing tendency of Bz group is greater than Me which in turn is slightly greater than Et.

3.2. Product characterization

To MeCN solution of the complex, $\text{Pd}(N,N')\text{Cl}_2$, picH was added and the orange colored solution was stirred for about 24 h. It was filtered and allowed to evaporate almost to dryness at room temperature. Mass so produced was then dissolved in MeOH and NaClO_4 (aq) was added. A brown precipitate formed which was filtered and then washed with water and cold MeCN. Dried product was chromatographed over silica gel and MeCN eluted an orange-red band. Finally the dried product was characterized by micro-analytical data (experimental section), ^{1}H NMR (Table 4) spectral data. The molar conductance data in MeCN solution ($\Lambda_M = 90$–$106\ \text{S cm}^2\ \text{mol}^{-1}$) show 1:1 electrolytic nature of the complexes. The IR spectra of the complexes display a sharp stretch at 1380–1410 cm^{-1} which corresponds to ν(N=N) and is red shifted by 5–10 cm^{-1} from that of Pd(NaiR)Cl_2 [36]. This may be attributed to better charge delocalization from coordinated pic^- to the chelated NaiR motif than that of Cl in precursor. The binding is indirectly established by the disappearance of two ν(Pd–Cl) bands corresponding to the *cis*-PdCl_2 configuration [21,36,41] and appearance of new bands at 1450–1460 and 460–500 cm^{-1} due to ν(COO) and ν(Pd–O), respectively. All the complexes exhibit a structure less band at 1050–1100 cm^{-1} corresponding to $\nu(\text{ClO}_4)$ suggesting lack of any significant interaction in the solid state [42].

The ^{1}H NMR spectra of the complexes were recorded in CD_3CN and the data are collected in Table 4. The proton-numbering pattern is shown in Scheme 1. Data reveal that the signals in the spectra of the complexes are shifted downfield relative to the free ligand values [33]. This supports the coordination of the ligand to Pd(II). An important feature of the spectra is the shifting of imidazole protons 4H and 5H to lower δ-values, in general, relative to the naphthyl protons (6H–13H). The imidazole protons suffer downfield shifting by 0.1–0.2 ppm compared to the free ligand position. This supports the strong preference of imidazole-N binding to Pd(II). The naphthyl protons appear as multiplets except a broad singlet of 6H and doublet of 8H (in $[\text{Pd}(\beta\text{-NaiR})(\text{pic})](\text{ClO}_4)$) in the complexes



Scheme 3.

Table 4
^{1}H NMR spectral data of [Pd(α/β-NaiR)(pic)](ClO$_4$) in CD$_3$CN

Compound	δ, ppm (J, Hz)											
	4H[a]	5H[a]	8H[b]	9H	10H	11–15H[c]	N(1)–CH$_3$	N(1)–CH$_2$	[N(1)–CH$_2$–]CH$_3$	a-H[d]	b-H[e]	c-H[e]	d-H[d]
[Pd (α-NaiMe)(pic)] (ClO$_4$) (**3a**)	7.50	7.30		7.72 (7.0) d	7.55 m	7.55	4.10			9.00 (7.0)	7.88 (7.0)	7.88 (7.0)	8.05 (7.0)
[Pd(α-NaiEt)(pic)] (ClO$_4$) (**3b**)	7.52	7.35		7.72 (7.0) d	7.57 m	7.57		4.61 (9.0)q	1.64 (7.0)t	9.03 (7.0)	7.91 (7.0)	7.91 (7.0)	8.08 (7.0)
[Pd(α-NaiBz)(pic)] (ClO$_4$) (**3c**)	7.55	7.38		7.75 (7.0) m	7.60 m	7.60		5.60[f]		9.05 (7.0)	7.95 (7.0)	7.95 (7.0)	8.10 (7.0)
[Pd(β-NaiMe)(pic)] (ClO$_4$) (**4a**)	7.50	7.32	8.00		7.85 (7.0) d	7.50	4.13			9.02 (7.0)	7.85 (7.0)	7.85 (7.0)	8.08 (7.0)
[Pd(β-NaiEt)(pic)] (ClO$_4$) (**4b**)	7.53	7.35	8.05		7.88 (7.0) d	7.50		4.55 (9.0)q	1.60 (7.0)t	9.05 (7.0)	7.88 (7.0)	7.88 (7.0)	8.10 (7.0)
[Pd(β-NaiBz)(pic)] (ClO$_4$) (**4c**)	7.58	7.40	8.14		7.95 (7.0) d	7.54		5.65[f]		9.10 (7.0)	7.92 (7.0)	7.92 (7.0)	8.15 (7.0)

[a] Broad singlet.
[b] Singlet.
[c] Multiplet.
[d] Doublet.
[e] Triplet.
[f] Ph-H: 7.40–7.50 ppm.

and a doublet of 15H in case of all the complexes. The 1-alkyl group appears as singlet for 1-Me in [Pd(α/β-NaiMe)(Q)](ClO$_4$), a quartet to –N–CH$_2$– and a triplet for the –CH$_3$ group in [Pd(α/β-NaiEt)(pic)](ClO$_4$) and a singlet for –CH$_2$– and benzyl protons in [Pd-(α/β-NaiCH$_2$Ph)(pic)](ClO$_4$) complexes. The pic protons (a–d) appear at higher δ, 8–9 ppm.

4. Conclusion

The kinetics of the reactions between Pd(*N*,*N*′)Cl$_2$ and picolinic acid (picH) were studied spectrophotometrically at 530 nm under pseudo-first-order condition in MeCN. The reactions are first order in Pd-complex and picH. The rate of reaction is largely influenced by the π-acidity of the chelating ligand; substitution in the naphthylazoimidazole backbone influences much the rate of the substitution process. Activation parameters $\Delta^{\ddagger} H^{\circ}$ and $\Delta^{\ddagger} S^{\circ}$ of reactions were measured which corroborates the kinetic rate data. The products isolated from the reaction between Pd(NaiR)Cl$_2$ and picH in MeCN have been characterized by spectral data and support the composition [Pd(NaiR)-(pic)](ClO$_4$).

Acknowledgements

Financial help from Jadavpur University is gratefully acknowledged. We thank Dr. C. Sinha, Professor of Chemistry, Jadavpur University for his sincere all round help and support.

References

[1] S.J. Lippard, in: I. Bertini, H.B. Gray, S.J. Lippard, J.S. Valentine (Eds.), Bioinorganic Chemistry, University Science Books, Mill Valley, CA, 1994, p. 505.
[2] P.D. Beer, Acc. Chem. Res. 31 (1998) 71.
[3] Y.S. Yoo, Y.S. Sohn, Y.K. Do, J. Inorg. Biochem. 73 (1999) 187.
[4] J. Li, L.M. Zheng, I. King, T.W. Doyle, S.H. Chan, Curr. Med. Chem. 8 (2001) 121.
[5] P. Banerjee, Coord. Chem. Rev. 19 (1999) 190.
[6] B. Lippert, Coord. Chem. Rev. 18 (1999) 263.
[7] M. Kato, J. Takahashi, Y. Sugimoto, C. Kosuge, S. Kishi, S. Yano, J. Chem. Soc. Dalton Trans. (2001) 747.
[8] H. Chen, J.A. Parkinson, S. Pearsons, R.A. Coxall, R.O. Gould, P.J. Sadler, J. Am. Chem. Soc. 124 (2002) 3064.
[9] A.H. Velders, H. Kooijman, A.L. Spek, J.G. Hassnoot, D. Vos, D. Reedijk, J. Inorg. Chem. 39 (2000) 2966.
[10] D. Kovala-Demertzi, A. Boccarelli, M.A. Demertzis, M. Coluccia, Chemotherapy 53 (2007) 148.
[11] A. Divsalar, A.A. Saboury, H. Mansoori-Torshizi, B. Hemmatinejad, Bull. Korean Chem. Soc. 27 (2006) 1801.
[12] J.L. Butour, S. Wimmer, F. Wimmer, P. Castan, Chemico-Biol. Interact. 104 (1997) 165.
[13] D.S. Umreiko, D.N. Kachurina, I.E. Chernikova, G.G. Novitskii, N.M. Sinitsyn, T.M. Buslaeva, V.I. Efanov, Zdravookhranenie Belorussii 12 (1986) 22.
[14] M.M.L. Fiallo, A. Garnier-Suillerot, Biochemistry 25 (1986) 924.
[15] T.K. Misra, D. Das, C. Sinha, P.K. Ghosh, C.K. Pal, Inorg. Chem. 37 (1998) 1672.
[16] P. Byabartta, P.K. Santra, T.K. Misra, C. Sinha, C.H.L. Kennard, Polyhedron 20 (2001) 905.

[17] P.K. Santra, T.K. Misra, D. Das, C. Sinha, A.M.Z. Slawin, J.D. Woollins, Polyhedron 18 (1999) 2869.
[18] S. Pal, D. Das, P. Chattopadhyay, C. Sinha, K. Panneerselvam, T.H. Lu, Polyhedron 19 (2000) 1263.
[19] G.K. Rauth, S. Pal, D. Das, C. Sinha, A.M.Z. Slawin, J.D. Woollins, Polyhedron 20 (2001) 363.
[20] R. Roy, P. Chattopadhyay, C. Sinha, S. Chattopadhyay, Polyhedron 15 (1996) 3361.
[21] D. Das, M.K. Nayak, C. Sinha, Transition Met. Chem. 22 (1997) 172.
[22] D. Das, C. Sinha, Transition Met. Chem. 23 (1998) 309.
[23] Ž.D. Bugarčić, S.T. Nandibewoor, M.S.A. Hamza, F. Heinemann, R. van Eldik, Dalton Trans. (2006) 2984.
[24] E. Breet, R. van Eldik, Berichte der Bunsen-Gesellschaft 102 (1998) 1418.
[25] A. Shoukry, T. Rau, M. Shoukry, R. van Eldik, J. Chem. Soc. Dalton Trans. (1998) 3105.
[26] H. Hohmann, S. Suvachittanont, R. van Eldik, Inorg. Chim. Acta 177 (1990) 51.
[27] J. Berger, M. Kotowski, R. van Eldik, U. Frey, L. Helm, A.E. Merbach, Inorg. Chem. 28 (1989) 3759.
[28] S. Saha, P.K. Ghosh, A. Mahapatra, Transition Met. Chem. 30 (2005) 706.
[29] S. Saha, T. Majumdar, A. Mahapatra, Inorg. React. Mech. 6 (2006) 19.
[30] S. Saha, T. Majumdar, A. Mahapatra, Transition Met. Chem. 31 (2006) 1017.
[31] S. Saha, T. Majumdar, A. Mahapatra, Indian J. Chem. 45A (2006) 877.
[32] S. Saha, P.K. Sarkar, A. Mahapatra, Transition Met. Chem. 31 (2006) 389.
[33] S. Saha, A. Mahapatra, Inorg. React. Mech. 6 (2006) 71.
[34] P.K. Ghosh, S. Saha, A. Mahapatra, Polyhedron 26 (2007) 2655.
[35] G.W. Evans, P.E. Johnson, Characterization and quantization of Zn-binding ligand in human milk, Pediatr. Res. 14 (1980) 876.
[36] J. Dinda, P.K. Santra, C. Sinha, L.R. Falvello, J. Organomet. Chem. 629 (2001) 28.
[37] S. Pal, D. Das, P. Chattopadhyay, C. Sinha, K. Panneerselvam, T.H. Lu, Polyhedron 19 (2000) 1263.
[38] R. Roy, T.K. Misra, C. Sinha, A. Mahapatra, A. Sanyal, Transition Met. Chem. 22 (1997) 453.
[39] R. Roy, D. Das, M. Banerjee, A. Mahapatra, Transition Met. Chem. 26 (2001) 205.
[40] T. Suganuma, A. Tanada, H. Tomizawa, M. Tanaka, E. Miki, Inorg. Chim. Acta 320 (2001) 22.
[41] C.K. Pal, S. Chattopadhyay, C. Sinha, D. Bandyopadhyay, A. Chakravorty, Polyhedron 13 (1994) 999.
[42] S. Goswami, W. Kharmawphlang, A.K. Deb, S.M. Peng, Polyhedron 15 (1996) 3635.

complexes bearing dps [28–34], there have been several acentric coordination networks constructed from dps, reported for their interesting solvent capture and release [31] and good photoluminescent properties [33]. In addition, the study of copper(II) as a metal center is seldom reported except for a 3D non-interpenetrating framework of $[\{Cu(\mu\text{-dps})_2(SO_4)\}\cdot 3H_2O\cdot DMF]_\infty$ exhibiting an unusual third-order NLO property [34] and a 3D interpenetrating framework of $[Cu_4(\mu\text{-dps})_4(Mo_8O_{26})\cdot 2H_2O]_n$ [35].

In this contribution, we describe the preparation and characterization of a series of Cu(II)/dps complexes. Five novel acentric or chiral Cu(II)/dps coordination compounds were obtained by utilizing different counteranions and solvents: $\{[Cu_3(\mu\text{-dps})_4(\mu\text{-}SO_4)_2(SO_4)(H_2O)_5]\cdot 10H_2O\}_\infty$ (**1** · $10H_2O$) (3D framework), $[Cu(dps)_4(H_2O)_2]\cdot(ClO_4)_2\cdot H_2O$ (**2** · H_2O) (mononuclear complex), $\{[Cu(\mu\text{-dps})_2(DMF)_2](ClO_4)_2\}_\infty$ (**3**) (2D undulating grid), $\{[Cu(\mu\text{-dps})_2(H_2O)_2]\cdot(NO_3)_2\cdot 2H_2O\}_\infty$ (**4** · $2H_2O$) (1D double-stranded chain) and $\{[Cu_3(\mu\text{-dps})_6(DMF)_2(H_2O)_4]\cdot(NO_3)_6\cdot(DMF)\cdot 6H_2O\}_\infty$ (**5** · DMF · $6H_2O$) (2D undulating grid). It was found that the counteranion and solvent have profound effects on the formation of the framework. Three copper salts (sulfate, nitrate and perchlorate) were used as precursors, and the reaction media were DMF or aqueous solutions. All these non-centrosymmetric complexes are SHG-active (second harmonic generation).

2. Experimental

General: All chemicals and solvents are reagent grade. The solvents were used after drying. *CAUTION!* Metal perchlorates with organic ligands are potentially explosive. Only a small amount of material should be handled with great caution. The elemental analysis of C, H and N was obtained by the Elemental Analysis Service with an EA1110-CHNS elemental analyzer. Infrared spectra were measured as KBr disks on a MagNa-550 FT-IR system. The single crystal X-ray diffraction data were recorded on a Rigaku Mercury CCD X-ray diffractometer. Thermal gravimetric (TG) analysis was conducted on a Universal V3.7A TA instrument for **1**, **4** and **5** in flowing N_2 with a heating rate of 10 °C/min^{-1}. The strength of second harmonic generation (SHG) efficiency of the compounds was estimated by measuring a powder pellet. The experimental arrangement includes a high power mode-locked Nd: YAG laser with 200 ps pulse at a repetition rate of 5 Hz at a selected wavelength of 1064 nm. The laser beam is split into two parts, one to generate the SHG signal in the sample and the other to generate the SHG signal in the reference of urea [36].

2.1. Synthesis of $\{[Cu_3(\mu\text{-dps})_4(\mu\text{-}SO_4)_2(SO_4)(H_2O)_5]\cdot 10\,H_2O\}_\infty$ (**1** · $10H_2O$)

Dps (0.15 g, 0.8 mmol) in ethanol (3 mL) was carefully layered onto a blue aqueous solution (5 mL) of $CuSO_4\cdot 5H_2O$ (0.1 g, 0.4 mmol), and a mixture of diethyl ether and methanol was then layered onto the ethanol solution. Blue prisms of $\{[Cu_3(\mu\text{-dps})_4(\mu\text{-}SO_4)_2(SO_4)(H_2O)_5]\cdot 10H_2O\}_\infty$ (**1** · $10H_2O$) were obtained after one day and were isolated by filtration. Yield: 0.16 g (80%). *Anal.* Calc. for $C_{40}H_{62}Cu_3N_8O_{27}S_7$ (1502.0): C, 31.98; H, 4.16; N, 7.46. Found: C, 32.23; H, 4.27; N, 7.38%. IR (KBr pellet, cm^{-1}): 3426 (m), 3048 (w), 1659 (m), 1582 (s), 1535 (m), 1482 (m), 1412 (m), 1188 (s), 1111 (s), 1065 (m), 1026 (m), 996 (s), 810 (m), 725 (m), 617 (m), 540 (m), 494 (m).

2.2. Synthesis of $[Cu(dps)_4(H_2O)_2]\cdot(ClO_4)_2\cdot H_2O$ (**2** · H_2O)

The preparation of **2** is similar to that of **1**, except that $CuSO_4$ was replaced by $Cu(ClO_4)_2$ (0.1 g, 0.4 mmol). Blue crystals of $[Cu(dps)_4(H_2O)_2]\cdot(ClO_4)_2\cdot H_2O$ (**2** · H_2O) were obtained in a few days and isolated by filtration. Yield: 0.34 g (80%). *Anal.* Calc. for $C_{40}H_{38}Cl_2CuN_8O_{11}S_4$ (1069.5): C, 44.92; H, 3.58; N, 10.48. Found: C, 44.52; H, 3.78; N, 10.61%. IR (KBr pellet, cm^{-1}): 3383 (s), 2442 (w), 1670 (w), 1597 (s), 1577 (vs), 1539 (m), 1481 (s), 1412 (s), 1385 (m), 1319 (w), 1219 (m), 1092 (vs), 1061 (s), 1022 (m), 1003 (m), 872 (w), 829 (m), 814 (w), 725 (m), 706 (m), 621 (s), 540 (m), 492 (m), 455 (w).

2.3. Synthesis of $\{[Cu(\mu\text{-dps})_2(DMF)_2](ClO_4)_2\}_\infty$ (**3**)

The preparation of **3** is similar to that of **1**, except that $CuSO_4$ in aqueous solution was replaced by $Cu(ClO_4)_2$ (0.1 g, 0.4 mmol) in acetonitrile solution. Blue crystals of $\{[Cu(\mu\text{-dps})_2(DMF)_2](ClO_4)_2\}_\infty$ (**3**) were obtained in a few days and isolated by filtration. Yield: 0.19 g (60%). *Anal.* Calc. for $C_{26}H_{30}Cl_2CuN_6O_{10}S_2$ (785.1): C, 39.77; H, 3.85;N, 10.70. Found: C, 40.02; H, 3.82; N, 10.81%. IR (KBr pellet, cm^{-1}): 1652 (s), 1606 (s), 1506 (s), 1447 (m), 1384 (m), 1279 (w), 1237 (w), 1167 (m), 1094 (vs), 980 (m), 828 (w), 724 (w), 661 (w), 634 (s).

2.4. Synthesis of $\{[Cu(\mu\text{-dps})_2(H_2O)_2]\cdot(NO_3)_2\cdot 2H_2O\}_\infty$ (**4** · $2H_2O$)

The preparation of **4** is similar to that of **1**, except that $CuSO_4\cdot 5H_2O$ was replaced by $Cu(NO_3)_2\cdot 6H_2O$ (0.12 g, 0.4 mmol). Blue crystals of $\{[Cu(\mu\text{-dps})_2(H_2O)_2]\cdot(NO_3)_2\cdot 2H_2O\}_\infty$ (**4** · $2H_2O$) were obtained in a few days and isolated by filtration. Yield: 0.19 g (76%). *Anal.* Calc. for $C_{20}H_{24}CuN_6O_{10}S_2$ (636.1): C, 37.76; H, 3.80; N, 13.21. Found: C, 37.38; H, 3.95; N, 13.02%. IR (KBr pellet, cm^{-1}): 3457 (m), 3065 (w), 1590 (s), 1482 (m), 1382 (vs), 1212 (m), 1104 (w), 1057 (m), 1026 (w), 826 (m), 725 (m), 540 (m), 494 (m).

2.5. Synthesis of $\{[Cu_3(\mu\text{-dps})_6(DMF)_2(H_2O)_4]\cdot(NO_3)_6\cdot(DMF)\cdot 6H_2O\}_\infty$ (**5** · DMF · $6H_2O$)

The preparation of **5** is similar to that of **3**, but $Cu(ClO_4)_2$ was replaced by $Cu(NO_3)_2\cdot 6H_2O$ (0.12 g, 0.4 mmol). Blue crystals of $\{[Cu_3(\mu\text{-dps})_6(DMF)_2(H_2O)_4]\cdot$

Table 1
Summary of crystallographic data of **1**–**5**

Compound	**1** · $10H_2O$	**2** · H_2O	**3**	**4** · $2H_2O$	**5** · DMF · $6H_2O$
Formula	$C_{42}H_{62}Cu_3N_8O_{27}S_7$	$C_{40}H_{38}Cl_2CuN_8O_{11}S_4$	$C_{26}H_{30}Cl_2CuN_6O_{10}S_2$	$C_{20}H_{24}CuN_6O_{10}S_2$	$C_{69}H_{89}Cu_3N_{21}O_{31}S_6$
Formula weight	1502.02	1069.46	785.12	636.11	2091.59
Crystal system	monoclinic	tetragonal	orthorhombic	trigonal	orthorhombic
Space group	$P2_1(4)$	$P4_32_12(96)$	$Pca2_1(29)$	$P3_121(152)$	$Pca2_1(29)$
a (Å)	11.809(2)	16.3919(10)	18.144(2)	9.5830(9)	18.094(3)
b (Å)	22.188(3)		10.9450(13)		11.3809(18)
c (Å)	12.509(2)	16.9063(10)	16.6741(17)	25.280(3)	44.077(6)
β (°)	112.777(4)				
γ (°)				120.00	
V (Å^3)	3022.0(9)	4542.6(5)	3311.2(6)	2010.6(3)	9077(2)
Z	2	4	4	6	4
D_{calc} (Mg m^{-1})	1.651	1.564	1.575	1.576	1.531
$F(000)$	1546	2196	1612	981	4324
Crystal size (mm)	$0.36 \times 0.35 \times 0.22$	$0.58 \times 0.38 \times 0.23$	$0.30 \times 0.20 \times 0.14$	$0.40 \times 0.17 \times 0.13$	$0.32 \times 0.22 \times 0.15$
θ Range (°)	3.03–25.35	3.03–25.35	3.07–25.35	3.45–27.48	3.02–25.35
Reflections collected	28,711	44,709	31,560	22,306	42,729
Unique (R(int))	10,966 [0.0461]	4169 [0.0309]	5876 [0.0631]	3091 [0.0530]	14,737 [0.0891]
Data/restraints/parameters	10966/3/780	4169/3/312	5876/3/429	3091/4/194	14737/109/1133
Goodness-of-fit	1.103	1.106	1.106	1.124	1.098
Flack parameter	0.504(16)	0.003(11)	0.02(2)	0.03(2)	0.5(3)
R_1, wR_2 [$I > 2\sigma(I)$]	0.0652, 0.1664	0.0249, 0.0605	0.0552, 0.1243	0.0567, 0.1172	0.1185, 0.2688
The largest and smallest final difference electron density (e A^{-3})	1.871, −0.613	0.381, −0.295	0.751, −0.442	0.652, −0.697	0.813, −1.398

$(NO_3)_6 \cdot (DMF) \cdot 6H_2O\}_\infty$ (**5** · DMF · $6H_2O$) were obtained in a few days and isolated by filtration. Yield: 0.24 g (85%). *Anal.* Cacl. for $C_{69}H_{89}Cu_3N_{21}O_{31}S_6$ (2091.6): C, 39.62; H, 4.29; N, 14.06. Found: C, 39.78; H, 4.12; N, 14.11%. IR (KBr pellet, cm^{-1}): 3411(m), 2925 (w), 2855 (w), 1636 (m), 1574 (m), 1536 (m), 1482 (m), 1381(s), 1211 (s), 1142 (w), 1104 (m), 1065 (m), 810 (m), 725 (m), 656 (m), 602 (m), 540 (m), 494 (m).

Table 2
Selected bond lengths (Å) and bond angles (°) of **1** · $10H_2O$

Cu(1)–N(7)	2.031(6)	Cu(2)–N(2)	2.002(6)
Cu(1)–N(5)	2.049(6)	Cu(2)–N(8)$^{\#1}$	2.007(6)
Cu(1)–N(1)	2.048(6)	Cu(3)–N(4)	1.992(6)
Cu(1)–N(3)	2.059(6)	Cu(3)–N(6)$^{\#2}$	2.007(6)
Cu(1)–O(5)	2.334(5)	Cu(3)–O(16)	2.062(6)
Cu(1)–O(1)	2.420(5)	Cu(3)–O(15)	2.067(6)
Cu(2)–O(14)	1.970(6)	Cu(3)–O(9)	2.187(7)
Cu(2)–O(13)	1.996(5)	Cu(3)–O(3)$^{\#3}$	2.385(6)
O(3)–Cu(3)$^{\#4}$	2.385(6)		
N(7)–Cu(1)–N(5)	93.9(2)	N(4)–Cu(3)–N(6)$^{\#2}$	178.4(3)
N(7)–Cu(1)–N(1)	87.6(3)	N(4)–Cu(3)–O(16)	95.1(2)
N(5)–Cu(1)–N(1)	178.3(3)	N(6)#2–Cu(3)–O(16)	86.5(2)
N(7)–Cu(1)–N(3)	178.9(3)	N(4)–Cu(3)–O(15)	92.0(3)
N(5)–Cu(1)–N(3)	87.2(2)	N(6)$^{\#2}$–Cu(3)–O(15)	86.4(2)
N(7)–Cu(1)–O(5)	90.2(2)	O(16)–Cu(3)–O(15)	170.3(3)
N(3)–Cu(1)–O(1)	92.7(2)	N(4)–Cu(3)–O(9)	87.1(3)
N(5)–Cu(1)–O(5)	88.7(2)	N(6)$^{\#2}$–Cu(3)–O(9)	93.1(3)
N(1)–Cu(1)–O(5)	92.1(2)	O(16)–Cu(3)–O(9)	86.4(3)
N(3)–Cu(1)–O(5)	90.0(2)	O(15)–Cu(3)–O(9)	100.4(3)
N(7)–Cu(1)–O(1)	87.1(2)	N(4)–Cu(3)–O(3)$^{\#3}$	89.9(2)
N(5)–Cu(1)–O(1)	89.8(2)	N(6)$^{\#2}$–Cu(3)–O(3)$^{\#3}$	90.1(2)
N(1)–Cu(1)–O(1)	89.3(2)	O(16)–Cu(3)–O(3)$^{\#3}$	84.5(2)
O(5)–Cu(1)–O(1)	176.8(2)	O(15)–Cu(3)–O(3)$^{\#3}$	89.0(2)
O(14)–Cu(2)–O(13)	174.5(2)	C(3)–S(1)–C(8)	102.6(3)
O(14)–Cu(2)–N(2)	86.7(3)	C(13)–S(2)–C(18)	104.7(4)
O(13)–Cu(2)–N(2)	88.3(2)	C(23)–S(3)–C(28)	103.1(4)
O(14)–Cu(2)–N(8)$^{\#1}$	90.0(3)	C(33)–S(4)–C(38)	102.9(4)
O(13)–Cu(2)–N(8)$^{\#1}$	95.0(2)	N(2)–Cu(2)–N(8)$^{\#1}$	176.1(3)

Symmetry transformations used to generate equivalent atoms: #1 $-x+2$, $y-1/2$, $-z+2$, #2 $-x-1$, $y-1/2$, $-z$, #3 $x-1$, y, $z-1$.

2.6. X-ray diffraction crystallography

All measurements were made on a Rigaku Mercury CCD X-ray diffractometer (3 kV, sealed tube) at −80 °C by using graphite monochromatic MoKα radiation ($\lambda = 0.71070$ Å) and a suitable single crystal was mounted

Table 3
Selected bond lengths (Å), angles (°) and hydrogen bonds (Å, °) of **2** · H_2O

Cu(1)–N(3)	2.033(2)	Cu(1)–N(1)		2.059 (2)
Cu(1)–O(1)	2.354(2)			
N(3)–Cu(1)–N(3)$^{\#1}$	90.4 (1)	N(1)–Cu(1)–O(1)$^{\#1}$		89.3(6)
N(3)–Cu(1)–N(1)$^{\#1}$	174.4(7)	N(3)–Cu(1)–O(1)		96.0(6)
N(3)$^{\#1}$–Cu(1)–N(1)$^{\#1}$	91.5(7)	N(3)$^{\#1}$–Cu(1)–O(1)		86.6(6)
N(3)–Cu(1)–N(1)	91.5(6)	N(1)$^{\#1}$–Cu(1)–O(1)		89.3(6)
N(3)$^{\#1}$–Cu(1)–N(1)	174.4(7)	N(1)–Cu(1)–O(1)		88.0(6)
N(1)$^{\#1}$–Cu(1)–N(1)	87.0(1)	O(1)$^{\#1}$–Cu(1)–O(1)		176.4(8)
N(3)–Cu(1)–O(1)$^{\#1}$	86.6(6)	C(8)–S(1)–C(3)		101.3(1)
N(3)$^{\#1}$–Cu(1)–O(1)$^{\#1}$	96.0(6)	C(18)–S(2)–C(13)		100.3(1)
N(1)$^{\#1}$–Cu(1)–O(1)$^{\#1}$	88.0(6)			
D–H···A	d(D–H)	d(H···A)	d(D···A)	∠(DHA)
O(1)–H(1A)···O(6)	0.813(10)	1.966(11)	2.776(2)	174(3)
O(1)–H(1B)···N(2)$^{\#2}$	0.811(10)	2.040(11)	2.847(2)	173(3)
O(6)–H(6A)···N(4)$^{\#3}$	0.825(10)	2.040(11)	2.847(2)	173(3)

Symmetry transformations used to generate equivalent atoms: #1 y, x, $-z+1$, #2 $-y+3/2$, $x-1/2$, $z-1/4$, #3 $-x+1/2$, $y+1/2$, $-z+3/4$.

Table 4
Selected bond lengths (Å) and bond angles (°) of **3**

Cu(1)–N(2)$^{\#1}$	2.020(5)	Cu(1)–N(1)	2.047(5)
Cu(1)–N(3)	2.023(5)	Cu(1)–O(2)	2.331(4)
Cu(1)–N(4)$^{\#2}$	2.023(5)	Cu(1)–O(1)	2.423(4)
N(2)$^{\#1}$–Cu(1)–N(3)	178.5(2)	N(4)$^{\#2}$–Cu(1)–O(2)	89.2(2)
N(2)$^{\#1}$–Cu(1)–N(4)$^{\#2}$	89.9(1)	N(1)–Cu(1)–O(2)	90.8(2)
N(3)–Cu(1)–N(4)$^{\#2}$	88.8(2)	N(2)$^{\#1}$–Cu(1)–O(1)	89.8(2)
N(2)$^{\#1}$–Cu(1)–N(1)	91.0(2)	N(3)–Cu(1)–O(1)	89.1(2)
N(3)–Cu(1)–N(1)	90.2(2)	N(4)$^{\#2}$–Cu(1)–O(1)	87.9(2)
N(4)$^{\#2}$–Cu(1)–N(1)	179.1(2)	N(1)–Cu(1)–O(1)	92.1(2)
N(2)$^{\#1}$–Cu(1)–O(2)	89.0(2)	O(2)–Cu(1)–O(1)	176.9(2)
N(3)–Cu(1)–O(2)	92.0(2)	C(80– S(1)–C(3)	101.3(3)
C(18)–S(2)–C(13)	103.6(3)		

Symmetry transformations used to generate equivalent atoms: #1 $x-1/2$, $-y+1$, z, #2 $x-1/2$, $-y$, z, #3 $x+1/2$, $-y+1$, z, #4 $x+1/2$, $-y$, z.

at the top of a glass fiber. Diffraction data were collected in the ω mode and the collected data were reduced by using the program Crystal-Clear (Rigaku and MSC, Ver. 1.3, 2001), and a semi-empirical absorption correction was applied. The reflection data were also corrected for Lorentz and polarization effects.

The structure was solved by SHELXS-97 (Sheldrick, 1990) and refined using full-matrix least-squares on F^2 with the SHELXL-97 program [38] (Sheldrick, 1997). For **1** · $10H_2O$, all copper atoms, sulfate anions and dps ligands were refined anisotropically and all coordinated water molecules, solvated water and ethanol molecules were refined isotropically without placing any hydrogen atoms. O27 of a solvated water molecule is twofold disordered. Only 32 Hydrogen atoms corresponding to 4 organic ligands were introduced at calculated positions and included in the structure-factor calculations. For **2** · H_2O, **3** and **4** · $2H_2O$, all non-hydrogen atoms were refined anisotropically and hydrogen atoms were introduced at calculated positions and included in the structure-factor calculations. For **5** · DMF · $6H_2O$, the oxygen atoms of free water molecules refined isotropically without placing the hydrogen atoms. The Flack parameters of **1** and **5** were refined together with all the other parameters using twin.

All calculations were performed on a Dell workstation using the SHELX software package. A summary of the key crystallographic information for **1**–**5** is given in Table 1. The selected atomic distances and bond angles of **1**–**5** are listed in Tables 2–6 respectively. The selected atomic distances and bond angles of **5** and the hydrogen bonds of **2** and **4** are listed in the Supplementary material.

3. Results and discussion

3.1. Synthesis and general characterization

Compounds **1**, **2** and **4** were prepared by the reaction of the corresponding Cu(II) salts in aqueous solution with 2 equiv of dps in ethanol solution (Scheme 1). Compounds **3** and **5** were prepared with a similar procedure except that the aqueous solution was replaced by DMF. All of the compounds are blue, air-stable and dissolve in DMF or DMSO solution. Compounds **1**–**5** are characterized by elemental analysis, IR spectra and thermal analysis. The FT-IR spectra of **1**, **2**, **4** and **5** showed a broad band centered at ca. 3400 cm^{-1}, which can be attributed to the O–H stretching of water molecules. The characteristic absorption bands of SO_4^{2-} groups for **1** appear at 1065–1105 and 615 cm^{-1}, and the ClO_4^- anion stretching vibrations appear at 1092 (vs) and 621 (s) cm^{-1} for **2** and 1094 (vs) and 634 (s) cm^{-1} for **3**. For **4** and **5**, the characteristic bands of NO_3^- anions appear at 1382 and 1381 cm^{-1}, respectively.

3.2. Description of crystal structures

3.2.1. $\{[Cu_3(\mu\text{-dps})_4(\mu\text{-}SO_4)_2(SO_4)(H_2O)_5]\cdot 10H_2O\}_\infty$ $(1\cdot 10H_2O)$

Complex **1** · $10H_2O$ consists of a three-dimensional $[Cu(\mu\text{-dps})_2SO_4]$ structure, different from other analogous

Table 5
Selected bond lengths (Å), angles (°) and hydrogen bonds (Å, °] of **4** · $2H_2O$

Cu(1)–N(1)	2.031(3)	Cu(1)–N(2)$^{\#1}$		2.029(3)
Cu(1)–O(1)	2.443(3)			
N(2)#1–Cu(1)–N(2)#2	89.8(2)	N(2)#1–Cu(1)–N(1)		178.0(1)
N(2)#2–Cu(1)–N(1)	89.4(1)	N(2)#1–Cu(1)–N(1)#3		89.4(1)
N(2)#2–Cu(1)–N(1)#3	178.0(1)	N(1)–Cu(1)–N(1)#3		91.5(2)
N(2)#1–Cu(1)–O(1)	91.0(1)	N(2)#2–Cu(1)–O(1)		90.5(1)
N(1)–Cu(1)–O(1)	90.8(1)	N(1)#3–Cu(1)–O(1)		87.7(1)
C(8)–S(1)–C(3)	97.6(2)			
D–H···A	*d*(D–H)	*d*(H···A)	*d*(D···A)	∠(DHA)
C(6)–H(6)···O(5)$^{\#6}$	0.95	2.40	3.328(5)	166.9
C(5)–H(5)···O(2)$^{\#7}$	0.95	2.47	3.406(7)	167.5
C(2)–H(2)···O(5)	0.95	2.51	3.450(6)	171.8
O(1)–H(1B)···O(3)$^{\#8}$	0.819(10)	2.33(3)	3.114(7)	160(7)
O(1)–H(1A)···O(5)$^{\#9}$	0.819(10)	2.07(2)	2.866(5)	164(6)
O(5)–H(5A)···O(3)$^{\#10}$	0.818(10)	2.49(3)	3.218(8)	149(5)
O(5)–H(5A)···O(4)$^{\#10}$	0.818(10)	2.28(3)	3.049(9)	157(6)
O(5)–H(5B)···O(4)$^{\#11}$	0.822(10)	2.031(13)	2.852(7)	176(7)

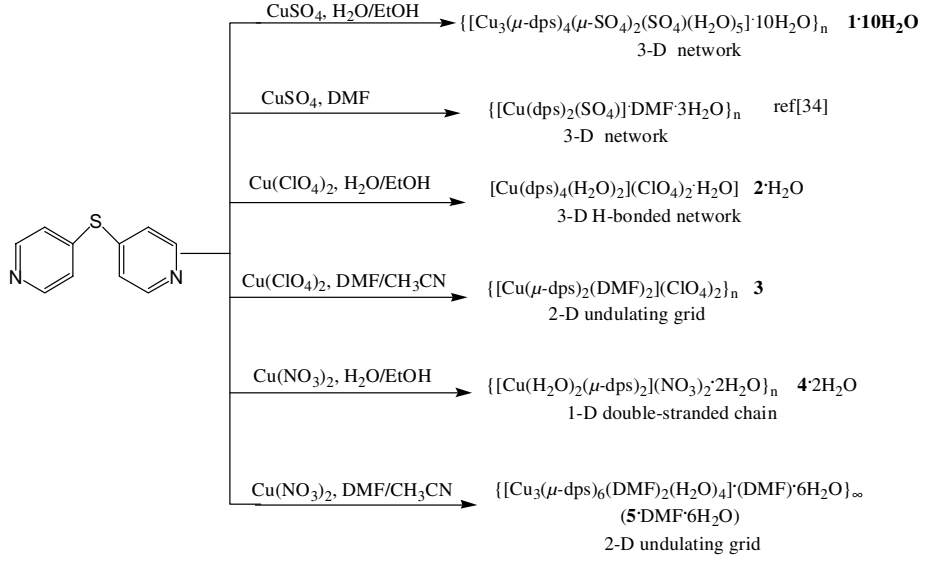
Symmetry transformations used to generate equivalent atoms: #1 $y-2$, x, $-z+1$, #2 $x-1$, $y-1$, z, #3 $y-1$, $x+1$, $-z+1$, #4 $x+1$, $y+1$, z, #6 y, $x+1$, $-z+1$, #7 $x-1$, $y+1$, z, #8 y, x, $-z+1$, #9 $y-1$, x, $-z+1$, #10 $-x+1$, $-x+y+1$, $-z+4/3$, #11 $x-1$, y, z.

Table 6
Selected bond lengths (Å) and angles (°) of **5** · DMF · $6H_2O$

Cu(1)–N(1)	2.007(11)	Cu(2)–N(9)$^{\#4}$	2.052(11)
Cu(1)–N(3)	2.024(11)	Cu(2)–O(3)	2.298(11)
Cu(1)–N(2)$^{\#1}$	2.029(11)	Cu(2)–O(4)	2.494(9)
Cu(1)–N(4)$^{\#2}$	2.054(10)	Cu(3)–N(13)	1.975(11)
Cu(1)–O(1)	2.341(10)	Cu(3)–N(12)$^{\#1}$	2.004(10)
Cu(1)–O(2)	2.515(9)	Cu(3)–N(11)	2.003(11)
Cu(2)–N(7)$^{\#3}$	1.998(10)	Cu(3)–N(14)$^{\#5}$	1.995(11)
Cu(2)–N(8)	2.021(10)	Cu(3)–O(5)	2.381(9)
Cu(2)–N(6)	2.031(11)	Cu(3)–O(6)	2.846(12)
N(1)–Cu(1)–N(3)	175.5(5)	N(8)–Cu(2)–O(4)	90.4(4)
N(1)–Cu(1)–N(2)$^{\#1}$	92.1(4)	N(6)–Cu(2)–O(4)	91.1(3)
N(3)–Cu(1)–N(2)$^{\#1}$	88.6(4)	N(9)$^{\#4}$–Cu(2)–O(4)	89.0(4)
N(1)–Cu(1)–N(4)$^{\#2}$	88.8(4)	O(3)–Cu(2)–O(4)	178.8(4)
N(3)–Cu(1)–N(4)$^{\#2}$	90.8(4)	N(13)–Cu(3)–N(12)$^{\#1}$	177.9(5)
N(2)$^{\#1}$–Cu(1)–N(4)$^{\#2}$	178.1(4)	N(13)–Cu(3)–N(11)	88.6(5)
N(1)–Cu(1)–O(1)	93.6(4)	N(12)$^{\#1}$–Cu(3)–N(11)	89.5(4)
N(3)–Cu(1)–O(1)	90.9(4)	N(13)–Cu(3)–N(14)$^{\#5}$	90.6(4)
N(2)$^{\#1}$–Cu(1)–O(1)	87.0(4)	N(12)$^{\#1}$–Cu(3)–(14)$^{\#5}$	91.1(4)
N(4)$^{\#2}$–Cu(1)–O(1)	91.1(4)	N(11)–Cu(3)–N(14)$^{\#5}$	170.8(5)
N(1)–Cu(1)–O(2)	86.3(4)	N(13)–Cu(3)–O(5)	91.2(4)
N(3)–Cu(1)–O(2)	89.3(3)	N(12)$^{\#1}$–Cu(3)–O(5)	88.1(4)
N(2)$^{\#1}$–Cu(1)–O(2)	89.8(4)	N(11)–Cu(3)–O(5)	95.7(4)
N(4)$^{\#2}$–Cu(1)–O(2)	92.0(3)	N(14)$^{\#5}$–Cu(3)–O(5)	93.0(4)
O(1)–Cu(1)–O(2)	176.8(3)	N(13)–Cu(3)–O(6)	91.8(4)
N(7)$^{\#3}$–Cu(2)–N(8)	88.6(4)	N(12)$^{\#1}$–Cu(3)–O(6)	89.0(4)
N(7)$^{\#3}$–Cu(2)–N(6)	91.4(4)	N(11)–Cu(3)–O(6)	87.8(4)
N(8)–Cu(2)–N(6)	178.5(4)	N(14)$^{\#5}$–Cu(3)–O(6)	83.0(4)
N(7)$^{\#3}$–Cu(2)–N(9)$^{\#4}$	176.2(4)	O(5)–Cu(3)–O(6)	175.3(4)
N(8)–Cu(2)–N(9)$^{\#4}$	89.9(4)	C(8)–S(1)–C(3)	101.3(6)
N(6)–Cu(2)–N(9)$^{\#4}$	90.2(4)	C(18)–S(2)–C(13)	105.1(6)
N(7)$^{\#3}$–Cu(2)–O(3)	93.3(4)	C(26)–S(3)–C(31)	101.2(7)
N(8)–Cu(2)–O(3)	88.7(4)	C(36)–S(4)–C(41)	103.7(6)
N(6)–Cu(2)–O(3)	89.8(4)	C(49)–S(5)–C(54)	100.3(6)
N(9)$^{\#4}$–Cu(2)–O(3)	90.1(4)	C(64)–S(6)–C(59)	104.7(7)
N(7)$^{\#3}$–Cu(2)–O(4)	87.5(4)		

Symmetry transformations used to generate equivalent atoms: #1 $x-1/2, -y+1, z$ #2 $x+1/2, -y+2, z$ #3 $x-1/2, -y, z$ #4 $x+1/2, -y+1, z$ #5 $x-1/2, -y+2, z$.

CuL_2SO_4 complexes (L = bipyridyl ligand) reported previously [13,34,37]. As shown in Fig. 1a, there are three crystallographically independent Cu(II) atoms in the asymmetric unit. The proximal coordination at the Cu(1) center consists of $[CuN_4O_2]$ units, in which the basal sites are occupied by four pyridyl nitrogen donors from four dps ligands, with Cu–N distances of 1.992(6)–2.059(6) Å, and the axial positions are occupied by two oxygen donors from two sulfate bridges with two elongated Cu–O distances (2.334(5) and 2.420(5) Å). The geometry about the Cu(2) site is defined by *trans* nitrogen donors from two dps ligands and two water molecules in the basal sites, with a sulfate oxygen group and an aqua ligand in the axial positions forming a $[CuN_2O_4]$ unit. The Cu(2)–O(22) (H_2O) distance of 2.559 Å is significantly larger than the equatorial Cu–O (H_2O) distances, whereas the Cu(2)–O(8) distance of 2.455 Å is indicative of a weak Cu–sulfate interaction. The coordination geometry of Cu(3) may be described as a $[CuN_2O_4]$ unit, in which the basal plane consists of two *trans*-N donors and two water molecules and the axial positions are occupied by two oxygen donors of the sulfate ligand. The Cu(3)–O(9) distance of 2.187(7) Å is smaller than Cu(3)–O(3′) 2.385(6) Å, indicating the terminal sulfate anion has a stronger interaction with the copper center than that of the bridging sulfate. Eight copper atoms link into a rhombic $[Cu(\mu\text{-dps})]_8$ ring, including four Cu(1) atoms occupying the grid corners and two Cu(2) and Cu(3) atoms occupying the midpoints of four Cu(dps) lines. The rhombic $[Cu(\mu\text{-dps})]_8$ ring with dimensions of 20.3×20.8 Å (Cu(1)···Cu(1^a)), gives an area of ca. 400 Å^2 (Fig. 1b), which is obviously larger than the reported complexes CuL_2SO_4 (L = bipyridyl ligand) [13,34,37]. Sulfate anions, water molecules are all occupied in the $[Cu(\mu\text{-dps})]_8$ cavities (Fig. 1c). The adjacent [Cu(μ-dps)] layers interlink forming a 3D network via unusual short Cu(2)–sulfate–Cu(1)–sulfate–Cu(3)–sulfate chains



Scheme 1. Preparation of compounds **1**–**5**.

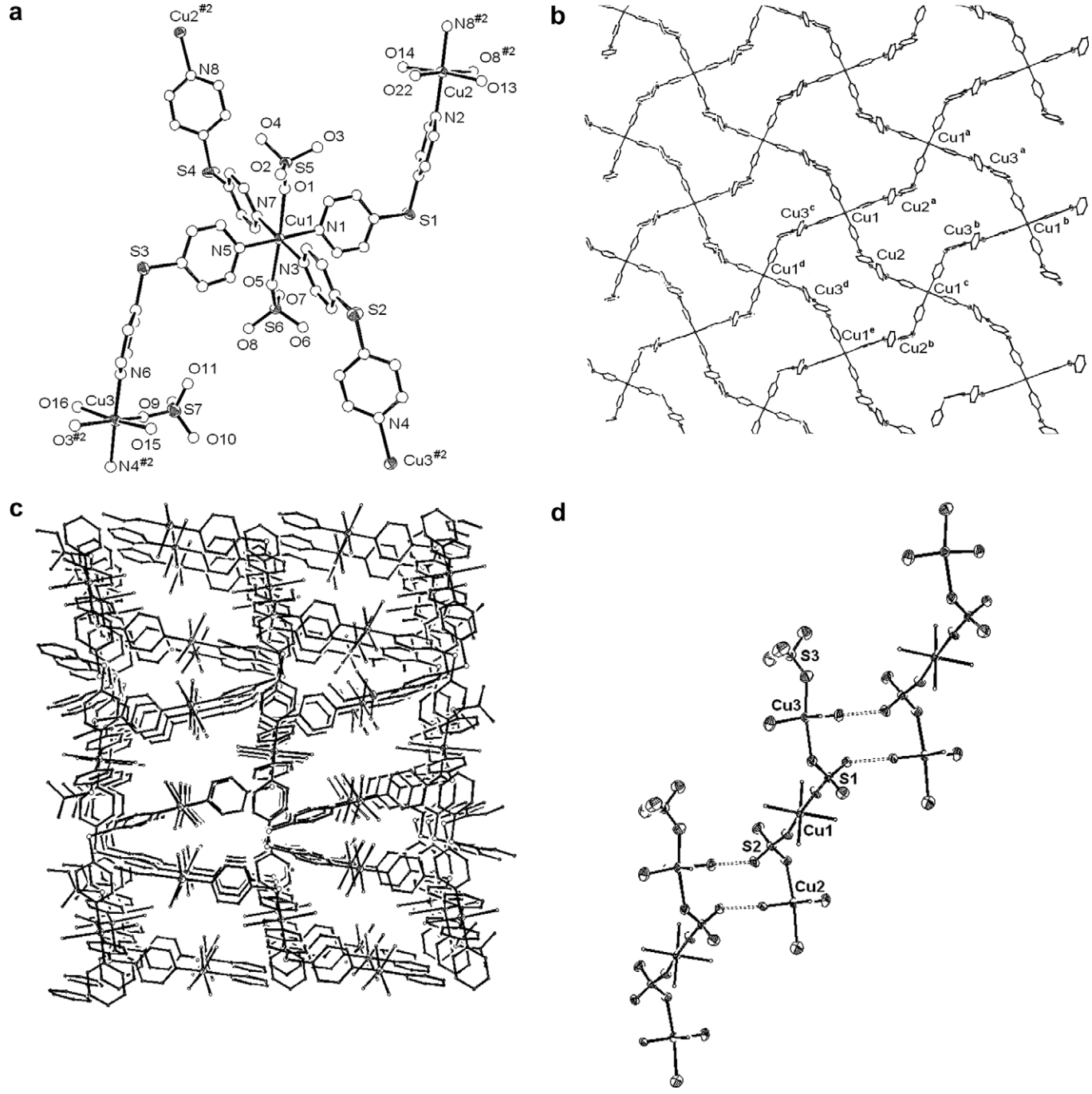


Fig. 1. Structure of $\mathbf{1} \cdot 10H_2O$: (a) the local coordination environment of three Cu^{2+} atoms (hydrogen atoms are omitted for clarity); (b) the lattice layer bridged by dps (sulfate anions, coordinated water molecules and free solvent molecules are omitted); (c) the 3D network bridged by sulfate, viewed along the *a*-axis (free solvent molecules and all hydrogen atoms are omitted for clarity); (d) the short Cu(2)–sulfate–Cu(1)–sulfate–Cu(3)–sulfate chain (dps except N atom, free solvent molecules and all hydrogen are omitted for clarity).

along the *a*-axis, different from the usual infinite Cu–sulfate–Cu chain found in CuL_2SO_4 [17,34] (Fig. 1d).

3.2.2. $\{[Cu(dps)_4(H_2O)_2](ClO_4)_2 \cdot H_2O\}$ ($\mathbf{2} \cdot H_2O$)

The structure of **2** consists of a mononuclear $[Cu(dps)_4(H_2O)_2]^{2+}$ cation, two free ClO_4^- anions and a free water molecule in the asymmetry unit, which is similar to the reported $[Zn(dps)_4(H_2O)_2](ClO_4)_2 \cdot H_2O$ [33], but quite different from other copper–dps coordination polymers. The coordination geometry of the copper atom adopts the typical $[CuN_4O_2]$ octahedral arrangement. Dps in this case acts as a monodentate ligand, in which the bent angles of the sulfur atoms (C–S–C–C) are 101.30(10)° and 100.29(11)°, which is smaller than the bridging ligands in **1** (av. 103.2°). The other N atom of each dps ligand is involved in H-bonding to give a box-like structure

(Fig. 2a). It is the weak non-covalent interaction (H-bond) that blocks the formation of the expected coordination bond (Cu–N(dps)). The O(6) atom of the free water molecule behaves as a double donor and double acceptor, whereas the oxygen atom of the coordinated water molecule (O(1)) acts as a double donor. Three kinds of H-bonds appear in this H-bonded network. The free water molecule (O(6)) H-bonds with the coordinated water molecule (the O(1) atom, forming the O(1)–H···O(6) bond), and with the uncoordinated *cis* N(4) atom, forming the O(1)–H···N(4) bond chain. The coordinated O(1) also links the uncoordinated N(2) atom from the next unit, forming the O(1)–H···N(2) bond. Thus, the O(1)–H···O(6) bond links the complexes along the *c*-axis forming an infinite chain while both O–H···N bonds extend parallel to the *ab*-plane finally forming a 3D H-bonded network (Fig. 2b).

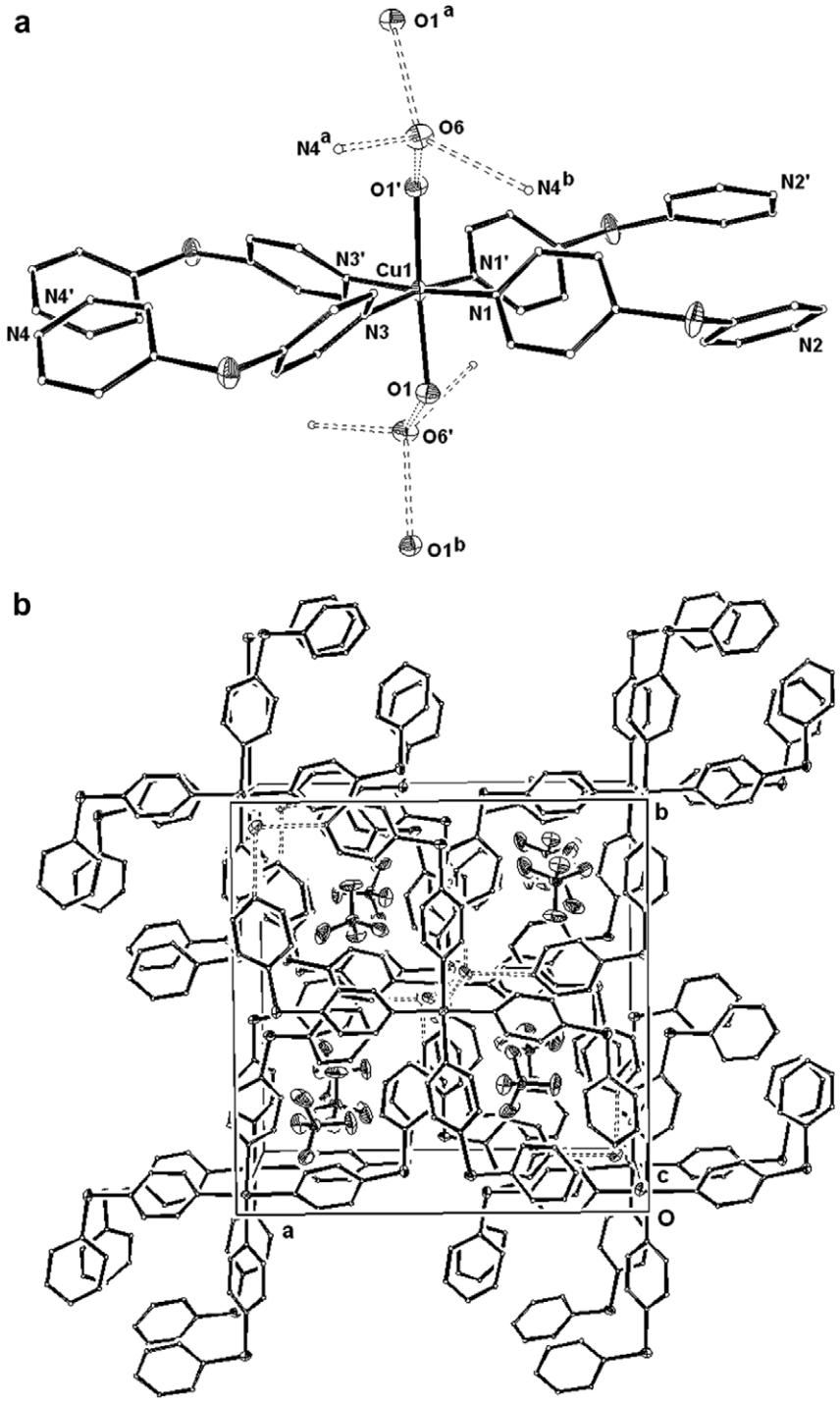


Fig. 2. Structure of $\mathbf{2}\cdot H_2O$: (a) the local coordination environment of the Cu^{2+} atom (hydrogen atoms are omitted for clarity); (b) the packing diagram of $\mathbf{2}\cdot H_2O$, hydrogen bonds are illustrated (hydrogen atoms are omitted for clarity).

3.2.3. $\{[Cu(\mu\text{-dps})_2(DMF)_2](ClO_4)_2\}_\infty$ (3)

The structure of **3** consists of a usual 2D cationic network constructed by $[Cu(\mu\text{-dps})]_4$ metallaboxes which has been observed in $[Co(\mu\text{-dps})_2Cl_2]_\infty$ [29], but the counteranions in this case only provide the appropriate charge balance. The local coordination geometry around the Cu(II) center is also similar with that described in **2**, an octahedral geometry in which four basal sites are occupied by four pyridine nitrogen atoms and two apical sites are occupied by oxygen atoms from DMF solvent molecules (Fig. 3a). The bent angles of the sulfur atoms (C–S–C) in **3** are 101.3(3)–103.6(3)°, comparable with those in **1** and **2**. The Cu···Cu edge dimensions of the 40-membered ring formed by four copper(II) ions and four dps ligands are 10.7×0.5 Å^2, similar to those reported previously [29]. The anions and solvent molecules are occupied in the channels formed by stacking of the cavities (Fig. 3b).

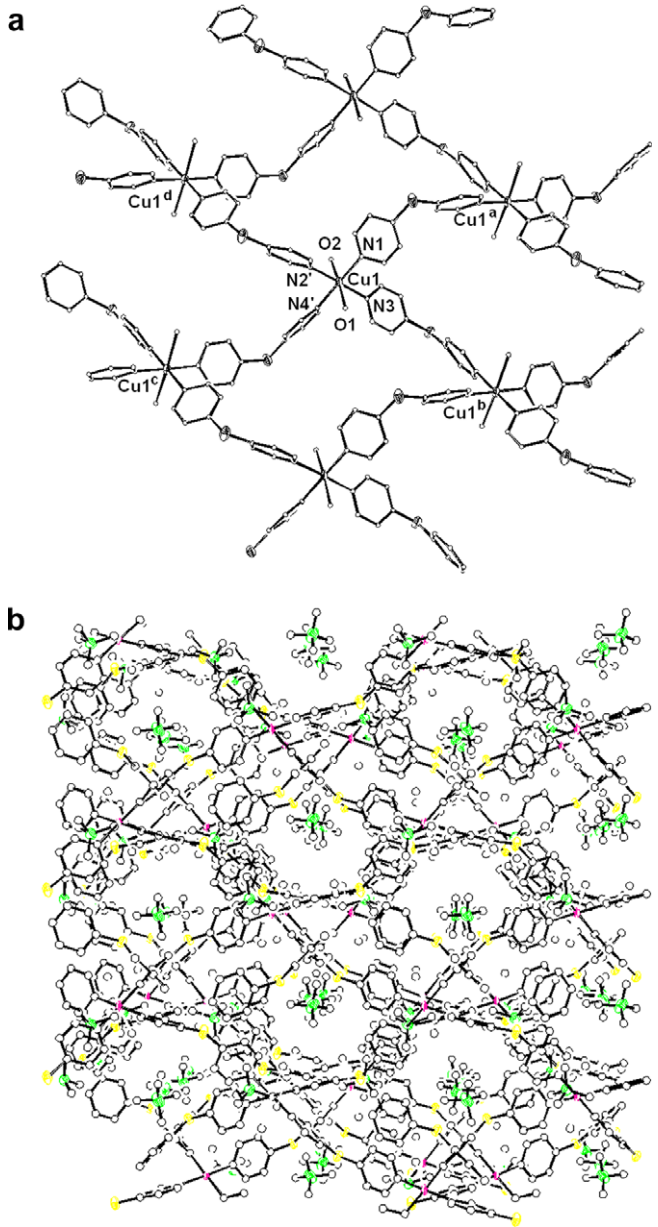


Fig. 3. Structure of **3**: (a) the local coordination environment of the Cu^{2+} atom (only the coordinated oxygen atom of the solvent molecule is preserved and hydrogen atoms of dps molecules are omitted for clarity); (b) view along the [0 0 1] plane showing the 10.69×10.53 Å^2 channels of **3**, the anions are shown in the channels (hydrogen atoms are omitted for clarity).

3.2.4. $\{[Cu(\mu\text{-dps})_2(H_2O)_2]\cdot(NO_3)_2\cdot 2H_2O\}_\infty$ ($4\cdot 2H_2O$)

The structure of complex **4** consists of a cationic 1D infinite double stranded $[Cu(\mu\text{-dps})_2]$ chain, two NO_3^- counteranions and two free water molecules. In **4**, the copper(II) center has an octahedral geometry, being coordinated to two water molecules and four pyridyl groups from four different dps ligands. Dps spacers are linked to the copper(II) atoms in a double-stranded bridge fashion along the *a*-axis, resulting in a 20-membered ring with a smaller cavity (Fig. 4a), which is different from the 1D zigzag chain of $[Zn(\mu\text{-dps})_4(CH_3COO)_2]$, but similar to that of $[Co(\mu\text{-dps})_2(NCS)_2\cdot 2H_2O]_\infty$ and $[Ni(\mu\text{-dps})_2(NO_3)_2\cdot EtOH]_\infty$ [29]. The bent angle of the sulfur atom (C–S–C = 97.6(2)°) is obviously smaller than those of **1**–**3** and those reported previously [29–34]. The closest Cu···Cu intra-chain distance is 9.754 Å, slightly larger than that of the inter-chain Cu···Cu distance (9.583 Å). NO_3^- is not coordinated to the metal, and provides the appropriate charge balance. The free water molecule acts as a double H-bond donor, linking with the nitrate and coordinated water molecule parallel to the $Cu(\mu\text{-dps})_2$ chain. The $Cu(\mu\text{-dps})_2$ chains run parallel to the *ab* plane forming layers, and the adjacent layers are rotated by 90° to produce small rhombic channels in the projection along the *c*-axis (Fig. 4b).

3.2.5. $\{[Cu_3(\mu\text{-dps})_6(DMF)_2(H_2O)_4]\cdot(NO_3)_6\cdot(DMF)\cdot 6H_2O\}_\infty$ ($5\cdot DMF\cdot 6H_2O$)

Complex $5\cdot DMF\cdot 6H_2O$ consists of a usual 2D cationic network constructed by $[Cu(\mu\text{-dps})]_4$ metallaboxes, which has been observed in **3**, and the nitrate counteranions only provide the appropriate charge balance. In the asymmetric unit, there are three crystallographic independent copper atoms with two kinds of coordination mode. The coordination around the Cu(1) and Cu(2) atoms are similar, an octahedral geometry in which four basal sites are occupied by four pyridine nitrogen atoms and two apical sites are occupied by oxygen atoms from a DMF molecule and a water molecule. The Cu–O (DMF) distances are 2.341(10) Å (Cu(1)–O(1)) and 2.298(11) Å Cu(2)–O(3)), and the Cu–O (H_2O) distances are 2.515(9) Å (Cu(2)–O(2)) and 2.494(9) Å (Cu(2)–O(4)), indicating weak interactions between the copper centers and solvated molecules. The Cu(3) center has a more distorted octahedral geometry in which four basal sites are occupied by four pyridine nitrogen atoms and two apical sites are occupied by oxygen atoms from two H_2O molecules, with elongated Cu–O interactions (2.381(19) and 2.846(12) Å). Each copper center coordinates with bridging dps, forming a 2D cat-

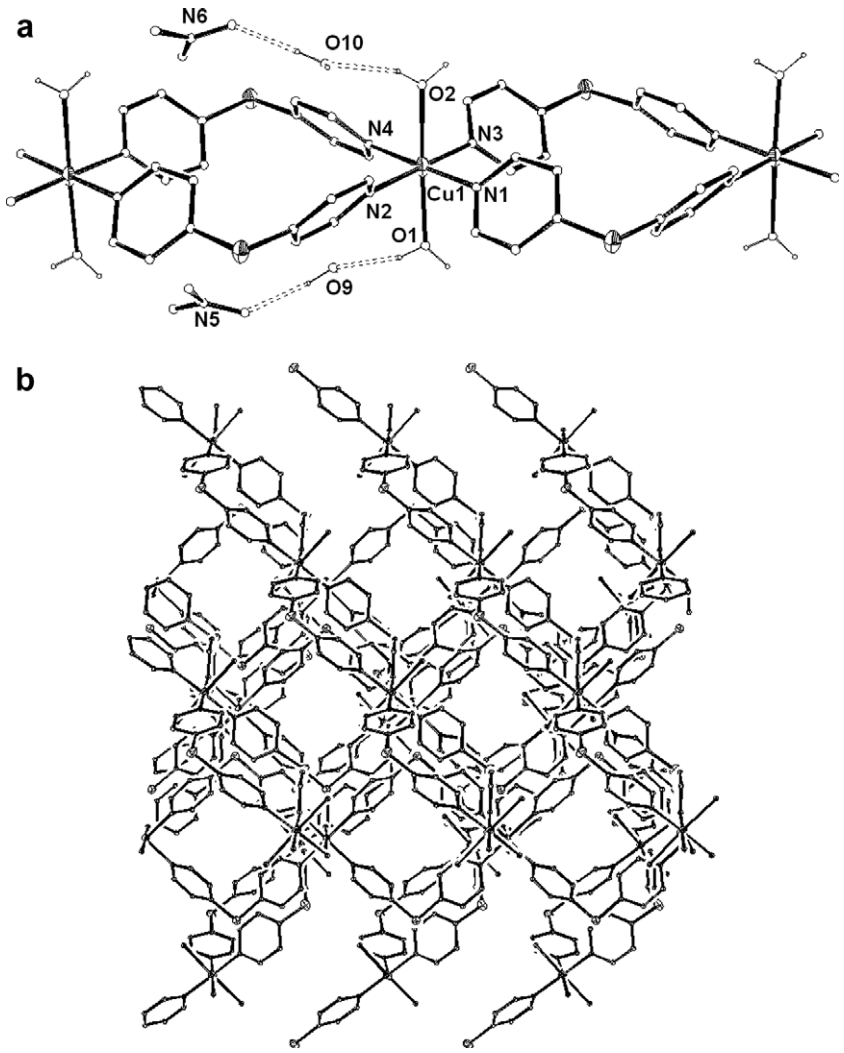


Fig. 4. Structure of $\mathbf{4}\cdot 2H_2O$: (a) the local coordination environment of the Cu^{2+} atom (hydrogen atoms of dps molecules are omitted for clarity) and (b) the stacking of the chains in $\mathbf{4}\cdot 2H_2O$, viewed along the *c*-axis (all hydrogen atoms are omitted for clarity).

ionic network independently. The Cu···Cu edge dimensions of the 40-membered ring formed by the four copper(II) ions and four 4,4′-dps ligands are 10.63×10.74 Å^2, similar with that found in **3** and $[\{Cu(\mu\text{-dps})_2(SO_4)\}\cdot 3H_2O\cdot DMF]_\infty$ [34]. The anions and solvent molecules are occupied in the channels formed by stacking of the cavities (Fig. 5a). The stacking diagram of **5** is shown in Fig. 5b and three different [Cu(μ-dps)] layers stack in turn, but the distances between adjacent layers is different: the smallest interlayer Cu(1)···Cu(2) distance is 8.43 Å and Cu(2)–Cu(3) distance is 8.55 Å and Cu(1′)–Cu(3) distance is 8.59 Å respectively. In addition, it should be noted that nitrate has a stronger inclination to form H-bonds with water molecules than perchlorate, so that more free water molecules are preserved in the unit cell.

3.3. TGA study

To understand the thermal stabilities of the three copper(II)/dps compounds (**1**, **4** and **5**), the samples were analyzed by TGA (the TGA curve is provided in the Supplementary material). Upon heating, samples show a gradual weight loss (18.4%) between 70 and 200 °C for **1**, which ascribes to the loss of all water molecules of crystallization and coordination (18.0% calculated value). There is a further gradual weight loss (60.0%) in two steps in the region 200–693 °C, which is attributed to the release of dps molecules (50.1%, calculated value) and release of sulfate or oxygen (11.4%, calculated value). The final residue of **1** is 21.6%, consistent with the calculated value (21.5%) if a mixture of CuS and Cu_2O is the final product.

The thermal decomposition of **4** is characterized by a dehydration step (8.6%) from 50 to 100 °C, corresponding to the loss of two water molecules of crystallization and a water molecule of coordination (8.5%, calculated value). The second weight loss (38.4%) between 100 and 270 °C is attributed to the release of an additional coordinated water molecule (2.8%, calculated value) and the decomposition of nitrates (19.5%, calculated value) and partly dps molecules. Due to the incomplete decomposition at

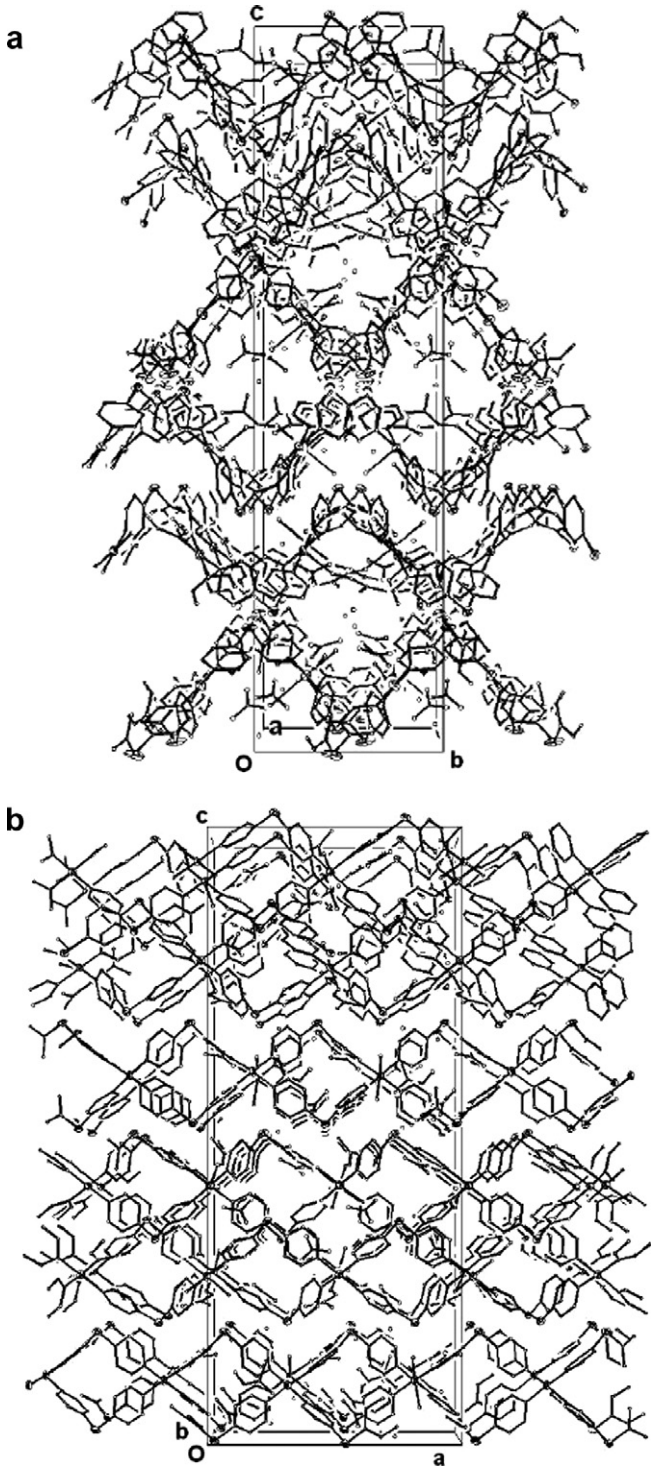


Fig. 5. Structure of $\mathbf{5} \cdot DMF \cdot 6H_2O$: (a) view along the *b*-axis showing the stacking of the grids (hydrogen atoms are omitted for clarity); (b) view along the *a*-axis showing the 10.63x10.74 $Å^2$ channels of $\mathbf{5} \cdot DMF \cdot 6H_2O$, the anions are shown in the channels (hydrogen atoms are omitted for clarity).

300 °C, the residue (40.8%) includes CuS, S (20.1%, calculated value) and organic fragments (totally calculated value of dps except S is 49.1%).

The thermal decomposition of **5** is similar to that of **4**, characterized by a slow dehydration step (11.7%) from 50 to 140 °C corresponding to the loss of all the water molecules of crystallization and coordination (calculated value is 8.6%). The second (42.8%) between 140 and 260 °C is attributed to the release of three DMF molecules (calculated value is 10.5%) and the decomposition of nitrate (17.8%) and partly dps molecules. Due to the incomplete decomposition at 300 °C, the residue (40.5%) includes CuS, S (calculated value is 18.3%) and mainly organic fragments (totally calculated value of dps except S is 46.5%).

As shown by their X-ray crystal structures, all of these samples contain a considerable amount of solvated water and other solvents in their crystalline structures, and hence a considerable weight loss at lower temperature ranges is observed as expected.

3.4. Non-linear optical properties

The second-order non-linear optical properties of the five compounds were also investigated qualitatively. Powder SHG measurements indicate that compounds **1**–**5** are all SHG-active, in agreement with their non-centrosymmetric structures. However, their SHG signals are weaker than that of urea and the intensities are 20% for **1** and **5**, 30% for **2** and **4** and 50% for **3** less than that of urea [37].

3.5. Conclusion

In this paper, a series of non-centrosymmetric Cu/dps complexes have been synthesized and structurally characterized. Among the five compounds **1**–**5**, the coordination geometries of copper atoms adopt a similar (4+2) octahedral arrangement and consist of $[CuN_4O_2]$ or $[CuN_2O_4]$ units. All the structural architectures strongly depend on the counteranions with different coordination abilities. Sulfate coordinates to the copper(II) center in $\{[Cu_3(\mu\text{-dps})_4(\mu\text{-}SO_4)_2(SO_4)(H_2O)_5] \cdot 10H_2O\}_\infty$ ($\mathbf{1} \cdot 10H_2O$) to produce a 3D network with a large cavity, while ClO_4^- and NO_3^- remain as non-coordinating counteranions, and the extended structures more depend on the coordination mode of the copper atom itself, forming 1D or 2D networks. However, the different shapes (tetrahedral, trigonal) of the anions (ClO_4^-, NO_3^-) can affect the topological structures. The tetrahedral ClO_4^- anion in **3** may induce the target product of a 2D grid extended structure, whilst the planar NO_3^- anion in **4** induces a 1D chain. In addition, solvent is another important factor that affects the target structures. Its participation in coordination with the metal center and the formation of hydrogen bonds may result in more complicated assemblies. For instance, compound **1** is obtained from water and owns larger cavities than its analogous complex $[\{Cu(\mu\text{-dps})_2(SO_4)\} \cdot DMF \cdot 3H_2O]_\infty$, obtained from DMF solution [34]. In **2**, the weak non-covalent interaction (H-bond) blocks the formation of the expected coordination bond (Cu–N(dps)).

More interestingly, all these copper complexes are SHG-active. It may provide an effective method to synthesize

non-symmetrical materials by using an achiral flexible ligand under appropriate conditions.

Acknowledgements

Authors gratefully thank Chinese Natural Science Foundation No.20476066 and 20571054, Jiangsu Province Natural Science Foundation No. BK 2005031 and the innovation plan for Graduate students in Jiangsu Province.

Appendix A. Supplementary material

CCDC 611821, 610353, 278776, 609975 and 611822 contain the supplementary crystallographic data for **1**, **2**, **3**, **4** and **5**. These data can be obtained free of charge via http://www.ccdc.cam.ac.uk/conts/retrieving.html, or from the Cambridge Crystallographic Data Centre, 12 Union Road, Cambridge CB2 1EZ, UK; fax: (+44) 1223 336 033; or e-mail: deposit@ccdc.cam.ac.uk.

The TG curves of **1**, **4** and **5** are provided as Supplementary material. Supplementary data associated with this article can be found, in the online version, at doi:10.1016/j.poly.2007.06.033.

References

[1] J.M. Lehn, J.L. Atwood, J.E.D. Davis, D.D. MacNicol, F. Vögtle, Comprehensive Supramolecular Chemistry, vol. 1–11, Pergamon Press, Oxford, UK, 1996.
[2] F.A. Cotton, G. Wilkinson, C.A. Murrillo, M. Bochmann, Advanced Inorganic Chemistry, Wiley-Interscience Publication, New York, USA, 1999.
[3] O.M. Yaghi, H. Li, C. Davis, D. Richardson, T. Groy, Acc. Chem. Res. 31 (1998) 474.
[4] S.R. Seidel, P.J. Stang, Acc. Chem. Res. 35 (2002) 972.
[5] S.H. Feng, R.R. Xu, Acc. Chem. Res. 34 (2001) 239.
[6] S. Kitagawa, K. Uemura, Chem. Soc. Rev. 34 (2005) 109.
[7] M.J. Zaworotko, Cryst. Growth Des. 7 (2007) 4.
[8] M.C. Hong, Y.J. Zhao, W.P. Su, R. Cao, M. Fujita, Z.Y. Zhou, A.S.C. Chan, J. Am. Chem. Soc. 122 (2002) 4819.
[9] M.H. Zeng, B. Wang, X.Y. Wang, W.X. Zhang, X.M. Chen, S. Gao, Inorg. Chem. 45 (2006) 7069.
[10] Z.J. Guo, P.J. Sadler, Angew. Chem., Int. Ed. 38 (1999) 1512.
[11] R.G. Xiong, X.Z. You, B.F. Abrahams, Z.L. Xue, C.M. Che, Angew. Chem., Int. Ed. 40 (2001) 4422.
[12] B.Q. Ma, S. Gao, G. Su, G.X. Xu, Angew. Chem., Int. Ed. 40 (2001) 434.
[13] S. Noro, R. Kitaura, M. Kondo, S. Kitagawa, T. Ishii, H. Matsuzaka, M. Yamashita, J. Am. Chem. Soc. 124 (2002) 2568.
[14] D. Hagrman, R. Hammond, R. Haushalter, J. Zubieta, Chem. Mater. 10 (1998) 2091.
[15] Z. Huang, M. Du, H.B. Song, X.H. Bu, Cryst. Growth Des. 4 (2004) 71.
[16] M. Du, X.H. Bu, Z. Huang, S.T. Chen, Y.M. Guo, Inorg. Chem. 42 (2003) 552.
[17] M.A. Withersby, A.J. Blake, N.R. Champness, P. Hubberstey, W.S. Li, M. Schröder, Angew. Chem., Int. Ed. 36 (1997) 2327.
[18] D.F. Sun, D.J. Collins, Y.X. Ke, J.L. Zuo, H.C. Zhou, Chem. Eur. J. 12 (2006) 3768.
[19] Q.R. Fang, G.S. Zhu, M. Xue, J.Y. Sun, Y. Wei, S.L. Qiu, R.R. Xu, Angew. Chem., Int. Ed. 44 (2005) 3845.
[20] Q.R. Fang, G.S. Zhu, M. Yue, J.Y. Sun, F.X. Sun, S.L. Qiu, Inorg. Chem. 45 (2006) 3582.
[21] G. Tian, G.S. Zhu, X.Y. Yang, Q.R. Fang, M. Xue, J.Y. Sun, Y. Wei, S.L. Qiu, Chem. Commun. (2005) 1396.
[22] Q.R. Fang, G.S. Zhu, M. Xue, J.Y. Sun, F.X. Sun, S.L. Qiu, Inorg. Chem. 45 (2006) 3582.
[23] M.C. Hong, Cryst. Growth Des. 7 (2007) 10.
[24] O.R. Evans, R.G. Xiong, G.K. Wong, W. Lin, Angew. Chem., Int. Ed. 38 (1999) 536.
[25] O.R. Evans, Z. Wang, R.G. Xiong, B.M. Foxman, W. Lin, Inorg. Chem. 38 (1999) 2969.
[26] O.R. Evans, W. Lin, Acc. Chem. Res. 35 (2002) 511.
[27] M. Du, Y.M. Guo, S.T. Chen, S.R. Batten, J. Ribas, S. Kitagawa, Inorg. Chem. 43 (2004) 1287.
[28] J.P. Lang, Q.F. Xu, W.H. Zhang, H.X. Li, Z.G. Ren, J.X. Chen, Y. Zhang, Inorg. Chem. 45 (2006) 10487.
[29] O.S. Jung, S.H. Park, D.C. Kim, Inorg. Chem. 37 (1998) 610.
[30] O.S. Jung, S.H. Park, C.H. Park, J.K. Park, Chem. Lett. 27 (1999) 923.
[31] M. Kondo, Y. Shimizu, M. Miyazawa, Y. Irie, A. Nakamura, T. Naito, K. Maeda, F. Uchida, T. Nakamoto, A. Inaba, Chem. Lett. 33 (2004) 514.
[32] Z. Ni, J.J. Vittal, Cryst. Growth Des. 1 (2001) 195.
[33] S. Muthu, Z. Ni, J.J. Vittal, Inorg. Chim. Acta 358 (2005) 595.
[34] Y. Niu, Z. Li, Y. Song, M. Tang, B. Wu, X. Xin, J. Solid State Chem. 179 (2006) 4003.
[35] D. Hagrman, J. Zubieta, C.R. Acad. Sci., Serie IIc: Chim. 3 (2000) 231.
[36] X.Z. You, J. Photochem. Photobiol. A: Chem. 106 (1997) 85.
[37] X.C. Su, S.R. Zhu, H.K. Lin, X.B. Leng, Y.T. Chen, J. Chem. Soc., Dalton Trans. (2001) 3163.
[38] G.M. Sheldrick, SHELX97, University of Göttingen, Göttingen, Germany, 1997.

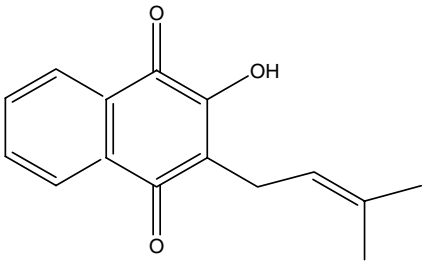


Chart 1. Chart of lapachol.

lapachol were added, giving immediately a bright-red solution. The solution was left at room temperature for 1 h, during which time the product appeared as red needles. The product is moderately soluble in MeOH, EtOH, soluble in diethyl ether. Yield 54 mg (86%). X-ray quality crystals were obtained after slow evaporation of a diluted ethanolic solution. *Anal*. Calc. for $CoC_{34}H_{38}O_8$: C, 64.45; H, 6.05. Found: C, 64.47; H, 5.70%. FAB-MS *m/e* 542 (15%, CoL_2^+), 307 (35%), 289 (10%). IR (4000–400 cm^{-1}, KBr): 3410 vs, 2913 s, 2847 s, 1798 w, 1635 s, 1575 s, 1558 m, 1432 s, 1388 m, 1334 s, 1307 m, 1274 m, 1209 w, 1137 m, 1982 m, 1017 s, 870 w, 597 s broad.

2.2. *[NiL$_2$(EtOH)$_2$] (**2**)*

This compound was prepared in a completely analogous way from 11.4 mg (0.045 mmol) of $Ni(CH_3COO)_2 \cdot 4H_2O$ and 22.2 mg (0.09 mmol) of lapachol, as red needle-shaped crystals. Yield 21 mg (72%). *Anal*. Calc. for $NiC_{34}H_{38}O_8$: C, 64.48; H, 6.05. Found: C, 64.77; H, 5.98%. FAB-MS *m/e* 541 (10%, NiL_2^+), 307 (23%), 289 (7%), 176 (9%). IR (4000–400 cm^{-1}, KBr): 3400 s (br), 2959 w, 2910 m, 2843 w, 1627 s, 1578 vs, 1551 vs, 1355 s, 1337 s, 1288 s, 1266 s, 1239 m, 1222 w, 1186 w, 1957 w, 950 m, 861 w, 785 w.

2.3. *[CuL$_2$py$_2$] (**3**)*

$Cu(CH_3COO)_2 \cdot 2H_2O$ (10 mg, 0.05 mmol) was reacted with lapachol (25 mg, 0.10 mmol) in 5 ml of methanol in the same manner. Then 10 drops of pyridine were added, producing a massive separation of red prismatic crystals. Single crystals of X-ray quality were obtained by ethanol vapour diffusion into a solution in CH_2Cl_2. Yield 26 mg (81%). *Anal*. Calc. for $CuC_{40}H_{36}O_6N_2$: C, 68.22, H, 5.15; N, 3.98. Found: C, 67.92; H, 5.09; N, 3.85%. FAB-MS *m/e* 541 (8%, CuL_2^+), 367 (9%), 307 (19%), 176 (7%).

Table 1
Crystal data and structure refinement for **1**–**3**

Compound	**1**	**2**	**3**
Empirical formula	$C_{34}H_{38}CoO_8$	$C_{34}H_{38}NiO_8$	$C_{40}H_{36}CuN_2O_6$
Formula weight	633.59	633.35	704.27
Temperature (K)	293(2)	293(2)	293(2)
Wavelength (Å)	0.71073	0.71073	0.71073
Crystal system	triclinic	monoclinic	monoclinic
Space group	$P\bar{1}$	$P2_1/c$	$P2_1/c$
Unit cell dimensions			
a (Å)	8.1832(11)	12.3319(13)	8.4255(4)
b (Å)	9.4848(10)	9.3180(14)	17.1110(12)
c (Å)	10.9722(14)	17.3069(15)	12.0788(7)
α (°)	112.503(11)	90	90
β (°)	91.423(11)	128.196(5)	90.988(3)
γ (°)	92.675(11)	90	90
Volume (Å^3)	785.08(17)	1562.9(3)	1741.13(18)
Z	1	2	2
d_{calc} (Mg/m^3)	1.336	1.342	1.343
Absorption coefficient (mm^{-1})	0.597	0.671	0.677
$F(000)$	331	664	734
Crystal size (mm)	$0.09 \times 0.05 \times 0.01$	$0.09 \times 0.06 \times 0.01$	$0.10 \times 0.04 \times 0.02$
θ Range for data collection	6.42–27.50	2.10–28.28	2.06–28.66
Index ranges	$-10 \le h \le 10$, $-12 \le k \le 11$, $-14 \le l \le 14$	$-16 \le h \le 15$, $-11 \le k \le 11$, $-22 \le l \le 23$	$-8 \le h \le 10$, $-23 \le k \le 22$, $-15 \le l \le 16$
Reflections collected	21 376	26 895	29 085
Independent reflections [$R_{(int)}$]	3558 [0.0355]	3789 [0.0945]	4360 [0.0630]
Completeness to $\theta = 28.66°$ (%)	98.5	97.6	97.2
Refinement method	full-matrix least-squares on f^2	full-matrix least-squares on f^2	full-matrix least-squares on f^2
Data/restraints/parameters	3558/0/227	3789/0/199	4360/0/225
Goodness-of-fit on F^2	1.054	1.289	1.215
Final R indices [$I > 2\sigma(I)$]	$R_1 = 0.0442$, $wR_2 = 0.1102$	$R_1 = 0.0901$, $wR_2 = 0.2170$	$R_1 = 0.0489$, $wR_2 = 0.1235$
R indices (all data)	$R_1 = 0.0659$, $wR_2 = 0.1186$	$R_1 = 0.1223$, $wR_2 = 0.2397$	$R_1 = 0.0736$, $wR_2 = 0.1440$
Largest difference in peak and hole (e Å^{-3})	0.620 and −0.311	1.184 and −0.907	0.515 and −0.882

2.4. Crystallography

Diffraction data were collected at room temperature using a Bruker-Nonius Kappa CCD diffractometer with graphite monochromated Mo Kα radiation ($\lambda = 0.71073$ Å). Frames were collected with the COLLECT program [13], indexed and processed using Denzo SMN and the files scaled together using the HKL2000 program [14]. The absorption correction was applied using a semi-empirical method based on multiple scanned reflections in PLATON program [15]. The structure solution was obtained by direct methods, using the SIR2004 [16] and refined with the SHELXL-97 program [17]. Crystallographic parameters are given in Table 1.

CCDC reference numbers 644610–644612.

2.5. Electrochemistry

Electrochemical measurements were carried out with an AMEL 5000 potentiostat–galvanostat system controlled by a Pentium PC. The electrochemical cell was a conventional one with three electrodes. The reference electrode was Ag/AgCl, the counter electrode was a platinum sheet (Radiometer) and the working electrode was glassy carbon (Metrohm). As supporting electrolyte 0.1 M Bu_4NClO_4 in dichloromethane, deoxygenated by bubbling argon through, was used. The ferrocene/ferrocenium couple was used as an internal reference ($E^{\circ\prime}$ 0.440 V vs NHE). The changes were identified as $1e^-$ processes from bulk electrolysis experiments. $E^{\circ\prime}$ values defined as $1/2(E_a + E_c)$ and ΔE_p defined as $[E_c - E_a]$, where E_a and E_c are the anodic and cathodic peak potentials, were obtained from cyclic voltammetry experiments. From repeated determinations the reproducibility was ±5 mV. The data obtained are summarized in Table 3.

3. Results and discussion

Synthesis. The synthesis of **1**–**3** is rather straightforward and produces the complexes with the M/L ratio 1:2 in high yields. Since a base, acetate, is already present, it is not necessary to add an external base to deprotonate lapachole, and the reaction is driven to completion by the chelate effect and low solubility of the final products in alcohols. An alternative method for the preparation of ZnL_2, CdL_2 and CuL_2 used electrochemical oxidation of the sacrificial metal electrodes in the presence of dissolved lapachol with variable yields (30–75%). Lapachol reduction into semiquinone form (or further) also takes place under the conditions of electrolysis, which may account for lower yields [9–11]. Therefore the method based on the methathesis reactions with acetate salts is more suitable. We also prepared ZnL_2 from $Zn(CH_3COO)_2 \cdot 4H_2O$ and lapachol in the same manner as **1** and **2** in almost quantitative yield, and confirmed its identity by elemental analysis, NMR and FAB-MS. Alternatively, the sodium lapacholate can be prepared first from NaOH and lapachol, and then reacted with a suitable metal salt. This procedure was used to prepare $[ZnL_2(EtOH)_2]$ [9–11].

Structures. The Co and Ni complexes, CoL_2 and NiL_2, form octahedral *trans* adducts **1** and **2** with two molecules of ethanol upon recrystallization from this solvent. Their main geometrical parameters are given in Table 2. The coordination of the two bidentade lapacholate ligands and of two ethanol molecules is all-*trans*. This is different form the *cis*-arrangement of the lapacholate rings observed in $[ML_2(H_2O)(DMF)]$ [11]. In **1** the coordination around Co is distorted octahedral with three sets of Co–O bond lengths, decreasing in the order Co–O(quinonic) 2.15 Å > Co–O(EtOH) 2.10 Å > Co–O(enolic) 2.02 Å. The same order was found in $[ZnL_2(EtOH)_2]$ [10]. In the Ni complex **2** this order is partially reversed: Ni–O(EtOH) 2.10 Å > Ni–O(quinonic) 2.08 Å > Ni–O(enolic) 2.00 Å. In **3** the axial ligands are pyridines, and the distortion is much greater: Cu–O(quinonic) 2.42 Å > Cu–N 2.02 > Cu–O(enolic) 1.95 Å. This can be explained by the well-known tetragonal Jahn–Teller distortion for Cu^{2+}. Apart from this, the three sets of M–O distances differ less between them in the Ni complex, than in the Co or Zn complex, which is probably due to the highest ligand field stabilization energy for high-spin octahedral d^8 configuration (Ni^{2+}) [18]. There is no clear trend in the M–O distances. A 2,2′-bipy adduct, $[CuL_2(bipy)]$, has been structurally characterized. In that case the *cis*-geometry is imposed by the 2,2′-bipy, but this

Table 2
Main bond distances in **1**–**3** and related complexes (Å)

Complex	$M–O_{(quinonic)}$	$M–O_{(enolic)}$	$M–O_{(EtOH)}/M–N_{(py)}$	C=O free	C=O coordinated	C–O enolic
1	2.15(2)	2.021(8)	2.10(2)	1.239(5)	1.227(5)	1.280(9)
2	2.079(4)	2.003(4)	2.097(9)	1.231(7)	1.235(6)	1.289(6)
3	2.415(4)	1.948(2)	2.018(3)	1.234(3)	1.223(3)	1.290(3)
$[CuL_2(bipy)]$[a]	2.40(1)	1.950(6)	1.999(7)	1.24(1)	1.22(1)	1.29(1)
	2.44(1)	1.923(6)	2.026(7)	1.23(1)	1.23(1)	1.30(1)
$[ZnL_2(EtOH)_2]$[b]	2.183(2)	1.991(2)	2.152(2)	1.243(3)	1.226(3)	1.279(3)
LH (lapachol) [20]				1.225		1.347
				1.232		1.350

[a] Ref [9].
[b] Ref. [10].
[c] Ref [19].

hardly affects Cu–O distances: 1.92–1.95 Å for enolic coordination, and 2.40–2.44 Å for quinonic coordination [9]. Thus the coordination around Cu both in this complex and in **3** can be described as two isomeric types of square planar CuN_2O_2 coordination (*trans*-CuN_2O_2 in **3** and *cis* in [CuL_2(bipy)]), plus two weakly coordinated quinonic oxygens in the axial positions. The structural difference between the quinonic and enolic C–O groups persists upon coordination: the former are perceptibly shorter (1.22–1.24 Å) than the latter (1.28–1.29 Å). Metal coordination does not affect the quinonic bond distances. The same situation is observed in [CuL_2(bipy)] [9]. Inversely, the C–O enolic distances shorten dramatically upon deprotonation and metal coordination, as compared with free lapachone. This may reflect some degree of bond delocalization within the chelate rings. The M–O distances do not follow the order (Co < Ni < Zn) in which the ionic radii of M^{2+} decrease. Within the quinonoid ring, the C–C bonds inside the MO_2C_2 chelate are the longest and can be regarded as single bonds (1.50 Å), while those between enolic carbon atom and alkyl-substituted carbon atom are shortest (1.38 Å), approaching the normal double bond (1.32 Å) in the 3-methyl-2-butenyl rest.

The molecules are packed in the crystals in a way to permit stacking of the aromatic rings.

The mass-spectra show peaks of the ML_2^+ species which arise from the coordinated solvent loss. Further fragmentation is also observed Figs. 1,2.

In CV (Fig. 3, Table 3) both **1** and **2** show quasi reversible one-electron reduction waves, which most probably correspond to the ligand reduction to the semiquinonic form. The possibility of stabilization of the electrogenerated anion radical by intramolecular hydrogen bonding in different classes of quinones has been extensively

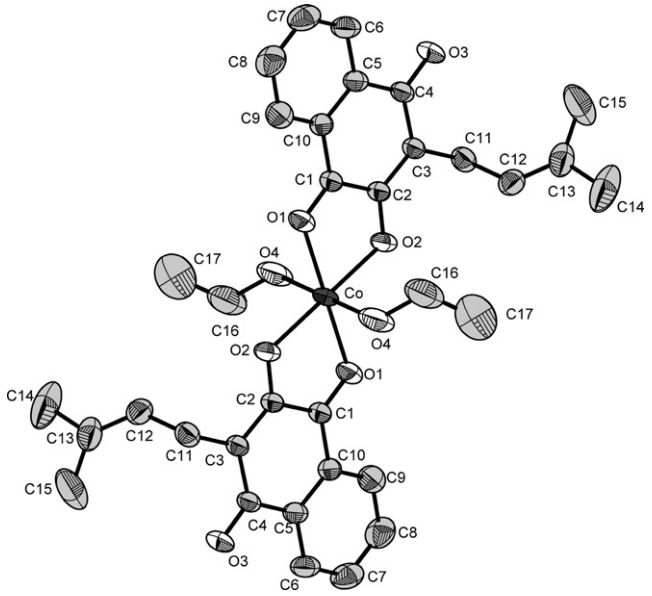


Fig. 1. ORTEP view of **1**. Ellipsoids are drawn at the 50% probability level. The H atoms are omitted for clarity. **2** has the same structure.

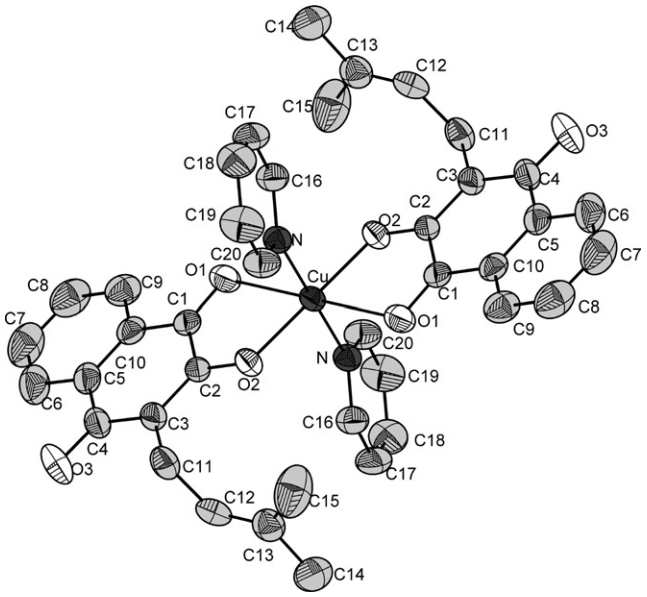


Fig. 2. ORTEP view of **3**. Ellipsoids are drawn at the 50% probability level. The H atoms are omitted for clarity.

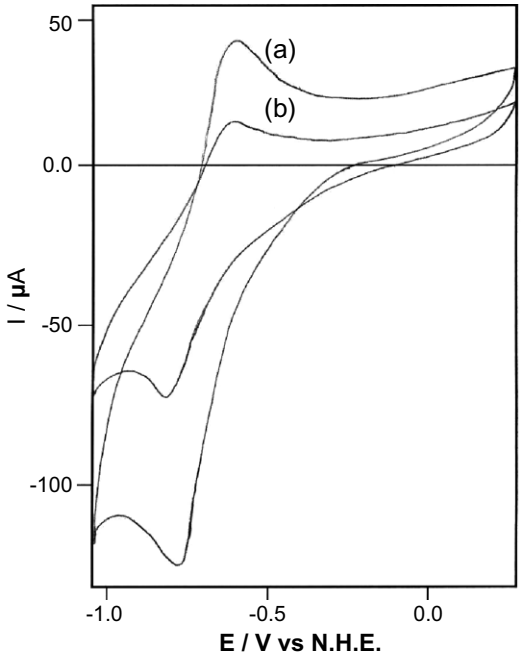


Fig. 3. Cyclic voltammograms of (a) 1 mM $NiL_2(EtOH)_2$ (**2**) and (b) 1 mM $CoL_2(EtOH)_2$ (**1**) in 0.1 M Bu_4NClO_4 at scan rate 100 mV s^{-1}.

Table 3
CV data (potentials in V converted vs NHE) for (a) 1 mM $NiL_2(EtOH)_2$ and (b) 1 mM $CoL_2(EtOH)_2$ 0.1 M Bu_4NClO_4 at scan rate 100 mV s^{-1}

Compound	$E^{\circ\prime}$	E_a	E_c	ΔE_p
$NiL_2(EtOH)_2$	**−0.685**	−0.548	−0.786	0.234
$CoL_2(EtOH)_2$	**−0.717**	−0.596	−0.837	0.241

reviewed [20]. The values observed for the redox potentials of compounds **1** and **2** are in the first monoelectronic reduction potential range of isolated lapachol and derivatives compounds [21]. Bubbling CO into the cell does not affect the reduction process which rules out the possibility of metal reduction to M(I) (CO coordination to the reduced metal would shift the reduction waves, as reported for Ni(I) complexes [22]).

Acknowledgements

R.H.M is grateful to the Spanish Ministerio de Educación y Ciencia through Project CTQ2005-09270-C02-02. The authors thank the Servicio General de Cristalografía de la Universidad de La Laguna for X-ray facilities.

Appendix A. Supplementary material

CCDC 644610, 644611, 644612 contain the supplementary crystallographic data for **1**, **2**, **3**. These data can be obtained free of charge via http://www.ccdc.cam.ac.uk/conts/retrieving.html, or from the Cambridge Crystallographic Data Centre, 12 Union Road, Cambridge CB2 1EZ, UK; fax: (+44) 1223-336-033; or e-mail: deposit@ccdc.cam.ac.uk. Supplementary data associated with this article can be found, in the online version, at doi:10.1016/j.poly.2007.06.022.

References

[1] K.V. Rao, T.J. McBride, J.J. Olenson, Cancer Res. 28 (1968) 1952.
[2] J.B. Block, A.A. Serpick, W. Miller, P.H. Wiernick, Cancer Chemother. Rep. Part 2 4 (1974) 27.
[3] N.A. de Sandoval, C.P. Rodriguez, N.R. de Martinez, Acta Phisiol. Pharmacol. Ther. Latinoam. 46 (4) (1996) 257.
[4] T.A. Annan, C. Peppe, D.G. Tuck, Can. J. Chem. 68 (1990) 423.
[5] T.A. Annan, C. Peppe, D.G. Tuck, Can. J. Chem. 68 (1990) 1598.
[6] K.H. Thompson, C.A. Barta, C. Orvig, Chem. Soc. Rev. 35 (2006) 545.
[7] A.R. Ravelo, A. Estevez-Braun, E. Perez-Sacau, Stud. Nat. Products Chem. 29 (2003) 719.
[8] A. Dufresne, C.G. de Lima, J. Knudsen, J.E. Moreira, J. Inorg. Nucl. Chem. 35 (1973) 789.
[9] E.H. de Oliveira, G.A. Medeiros, C. Peppe, M.A. Brown, D.G. Tuck, Can. J. Chem. 75 (1997) 499.
[10] M.A. Martínez, M.C.L. de Jiménez, E.E. Castellano, O.E. Piro, P.J. Aymonino, J. Coord. Chem. 56 (2003) 803.
[11] M.A. Martinez, M.C.L. de Jimenez, E.E. Castellano, O.E. Piro, P.J. Ayomino, J. Argent. Chem. Soc. 93 (2005) 183.
[12] O.G. de Lima, I.L. D'Albuquerque, C.G. de Lima, M.H.D. Maia, Rev. Inst. Antibióticos 4 (1962) 3.
[13] Bruker–Nonius (1997–2000): Collect Program Suite, Bruker-Nonius, The Netherlands.
[14] Z. Otwinowski, W. Minor, in: C.W. CarterJr., R.M. Sweet (Eds.), Processing of X-ray Diffraction Data Collected in Oscillation Mode, vol. 276, Academic Press, New York, 1997, p. 307, Pt. A.
[15] A.L. Spek, Acta Crystallogr. A46 (1990) C34.
[16] M.C. Burla, R. Caliandro, M. Camalli, B. Carrozzini, G.L. Cascarazo, L. De Caro, C. Giacovazzo, G. Polidori, R. Spagna, J. Appl. Crystallogr. 38 (2005) 381.
[17] G.M. Sheldrick, SHELXL-97, Program for the refinement of Crystal Structures, University of Göttingen, 1997.
[18] M. Gerloch, E.C. Constable, Transition Metal Chemistry, VCH, Weinheim, 1994.
[19] I.K. Larsen, L.A. Andersen, B.F. Pedersen, Acta Crystallogr. C48 (1992) 2009.
[20] P.A.L. Ferraz, F.C. De Abreu, J. Tonholo, E. Chiari, A.V. Pinto, V. Glezer, M.O.F. Goulart, J. Electrochem. Soc. 507 (2001) 275.
[21] N.M.F. Lima, C.S. Correia, P.A.L. Ferraz, A.V. Pinto, M.C.R.F. Pinto, A.E.G. Santana, M.O.F. Goulart, J. Braz. Chem. Soc. 13 (2002) 822.
[22] Hyun Jin Jung, Hyochoon Bang, Myunghyun Paik Suh, Bull. Korea Chem. Soc. 22 (5) (2001) 523.

R = Ph whilst with the bulkier ligand (R = Cy) only a 1:1 complex was isolated [3c] and $[Li(R_2PC(N^iPr)_2]_n$ forms a dimer with R = Ph, but a less sterically crowded hexamer for R = Cy [7].

We examined a series of lanthanide nitrate complexes with tricyclohexylphosphine oxide to investigate the effect of increasing the steric bulk of the ligand on the structural properties of the resulting complexes. The increased lipophilicity of Cy_3PO compared to Ph_3PO may make its complexes more suited to solvent extraction. In this respect any transition from a neutral to cationic complex may also provide a mechanism for increased selectivity in extraction, with ionic complexes having lower affinity to a non-aqueous phase.

2. Results and discussion

2.1. Synthesis and structures

The reaction of lanthanide nitrates with tricyclohexylphosphine oxide in metal to ligand ratios between 1:3 and 1:4 led to the isolation of $Ln(NO_3)_3(OPCy_3)_3$ as ethanol solvates except for the Eu and Er complexes. The 1:4 complexes which can be formed with Ph_3PO [5] and the smaller Ph_2MePO [8] cannot be obtained with the more bulky Cy_3PO under these conditions. The complexes formed in high yield giving crystals suitable for X-ray diffraction.

The structures comprise two molecules in the unit cell for the La, Nd, Eu and Er complexes and one for Tm and Yb. Details of the data collection and refinement are given in Table 1 and selected bond lengths and angles in Table 2. The geometries about the metals are all distorted *mer*-octahedra if the nitrate ligands are considered to act as pseudo-monodentate ligands bonded via the nitrogen atoms. The "*cis*" angles range from 104.5° to 74.0° with an average of 90.9° over all the complexes, whilst the "*trans*" angles range from 153.4° to 176.9° with an average of 164.7°.

The coordination mode of the nitrate ligands changes with the decrease in the ionic radius of the lanthanide ion. Thus for the larger ions La–Eu the nitrates all act as bidentate ligands and the complexes are 9-coordinate. Where the unit cells contain ethanol molecules, they are not hydrogen bonded to any of the nitrate ligands. The structure of one of the molecules in the unit cell of the lanthanum complex is shown in Fig. 1. The Er structure has two molecules in the unit cell which differ in the binding of the nitrates. One molecule has three bidentate nitrates and a similar overall structure to those of the La, Nd and Eu complexes, whilst the other has two bidentate and one monodentate nitrate and is hence eight-coordinate. It is interesting to note here that the monodentate nitrate is not hydrogen bonded to the lattice ethanol, and this appears to lead to relatively symmetrical bonding to the metal with non-bonded distances between the O–Er of 3.940(6) and 3.979(5) Å. The structures of the Tm and Yb complexes have one molecule in the unit cell in which there are two bidentate and one monodentate nitrate ligands. The structure of the Tm complex is shown in Fig. 2.

In these complexes the monodentate nitrate is hydrogen bonded to the lattice ethanol and this causes a distinct asymmetry in the bonding of the monodentate nitrate. The H-bonded oxygen–Ln distance is over 4.4 Å whilst the non-H-bonded distances are in the region of 3.5 Å for the Tm and Yb complexes.

The Ln–O distances have a good linear correlation with the nine-coordinate (La to Er) and eight-coordinate (Er to Yb) ionic radii of the respective lanthanide ions [9]. A plot of the Ln–O($N_{bidentate}$) and Ln–O(P) distances versus ionic radius is shown in Fig. 3.

In the Er structure the monodentate nitrate has an Er–O(N) distance of 2.287(5) Å compared with longer distances for the Tm (2.310(2) Å) and Yb (2.304(2) Å), respectively. This discrepancy can be explained by the hydrogen bonding between the nitrate and ethanol. In the Tm and Yb complexes, the O···O contacts between the nitrate and ethanol of 2.932(5) Å (Tm) and 2.943(5) Å (Yb) are shorter than the sum of the Van der Waals radius for oxygen (3.04 Å) and are thus indicative of a hydrogen bond.

2.2. Infrared spectroscopy

Infrared spectroscopy has routinely been used as a means of identifying the coordination mode of nitrate ligands to metals [10]. Thus although monodentate and bidentate coordinated nitrates have the same local symmetry the splitting of the N–O stretching modes has been taken as a means of assigning structures. Further, ionic nitrate, with a higher local symmetry should be readily distinguishable by the number of bands observed alone.

We have recently encountered complexes in which formally ionic nitrates are hydrogen bonded to lanthanide coordinated ligands or lattice solvent molecules [11]. The spectra in these instances are typical of bidentate nitrates. It was thus apparent that the use of spectroscopy alone in determining the coordination mode of nitrate ligands was prone to uncertainties when H-bonding ligands were present.

The infrared spectra of the Cy_3PO complexes are as expected for complexes of phosphine oxides with lanthanide nitrates. The P=O stretch decreases on coordination from 1146 cm^{-1} to about 1100 cm^{-1} on coordination to the metal. The spectra of the N–O region in these complexes differ only subtly despite the presence of monodentate nitrates in the Er, Tm and Yb complexes. All complexes show absorptions typical of coordinated nitrate with strong bands in the 1480–1450 cm^{-1} and 1300–1290 cm^{-1} region and a weaker absorption around 1040 cm^{-1}. Complexes which contain both monodentate and bidentate nitrates do not display features which would allow unambiguous identification of the presence of monodentate nitrates.

Table 1
Crystal data, data collection and refinement parameters

Compound	$[La(Cy_3PO)_3(NO_3)_3]\cdot 0.25EtOH$	$[Nd(Cy_3PO)_3(NO_3)_3]\cdot 0.25EtOH$	$[Eu(Cy_3PO)_3(NO_3)_3]$	$[Er(Cy_3PO)_3(NO_3)_3]$	$[Tm(Cy_3PO)_3(NO_3)_3]\cdot EtOH$	$[Yb(Cy_3PO)_3(NO_3)_3]\cdot EtOH$
Crystal data						
Molecular formula	$C_{108}H_{198}La_2N_6O_{24}P_6 + CH_3O_{0.5}$	$C_{108}H_{198}N_6Nd_2O_{24}P_6 + CH_3O_{0.5}$	$C_{108}H_{198}Eu_2N_6O_{24}P_6$	$C_{108}H_{198}Er_2N_6O_{24}P_6$	$C_{54}H_{99}N_3O_{12}P_3Tm + C_2H_6O$	$C_{54}H_{99}N_3O_{12}P_3Yb + C_2H_6O$
Molecular weight, M_r	2451.40	2462.06	2454.46	2485.06	1290.27	1294.38
Crystal system	monoclinic	monoclinic	monoclinic	monoclinic	orthorhombic	orthorhombic
Space group	$P2_1$	$P2_1$	$P2_1$	$P2_1$	$Pc2_1n$	$Pc2_1n$
Unit cell dimensions						
a (Å)	11.7015(7)	11.6360(4)	11.6216(2)	11.62110(10)	14.2639(2)	14.25470(10)
b (Å)	18.7997(6)	18.7227(12)	18.7278(4)	18.6661(2)	22.2990(4)	22.3444(2)
c (Å)	28.6979(16)	28.4733(17)	28.4435(6)	27.9691(4)	19.1100(3)	19.13000(10)
α (°)	90	90	90	90	90	90
β (°)	100.953(2)	101.063(3)	101.5490(10)	99.1778(4)	90	90
γ (°)	90	90	90	90	90	90
Cell volume, V (Å^3)	6198.3(5)	6087.8(6)	6065.3(2)	5989.40(12)	6078.33(17)	6093.15(8)
Formula units/unit cell, Z	2	2	2	2	4	4
D_{calc} (Mg m^{-3})	1.313	1.343	1.344	1.378	1.410	1.411
$F(000)$	2594	2606	2592	2612	2720	2724
Reflections to obtain cell parameters	98420	55177	135855	102414	28935	75486
θ (°)	2.91–26.73	2.92–26.01	2.91–27.48	2.95–27.46	2.91–27.48	2.91–27.49
λ (Mo Kα) (Å)	0.71073	0.71073	0.71073	0.71073	0.71073	0.71073
μ (mm^{-1})	0.825	0.991	1.171	1.540	1.600	1.675
T (K)	120(2)	120(2)	120(2)	120(2)	120(2)	120(2)
Crystal description	block	plate	block	block	prism	shard
Colour	colourless	colourless	colourless	colourless	colourless	colourless
Dimensions (mm)	$0.3\times0.16\times0.14$	$0.1\times0.1\times0.02$	$0.1\times0.08\times0.04$	$0.2\times0.1\times0.1$	$0.3\times0.2\times0.2$	$0.38\times0.18\times0.12$
Data collection and SORTAV *absorption correction [19]*						
T_{max}	0.97779	1.01367	1.35378	1.09172	1.00179	0.80646
T_{min}	0.92571	0.95229	0.68948	0.86566	0.90410	0.72406
Measured reflections	34864	37736	73696	80937	13116	68372
Independent reflections	20342	19181	24697	26588	13116	13420
Observed reflections ($F_o > n\sigma F_o$))	14127 ($n=4$)	14798 ($n=4$)	20285 ($n=4$)	20777 ($n=4$)	11568 ($n=4$)	11804 ($n=4$)
R_{int}	0.0703	0.0706	0.1465	0.1293	0.0000	0.0710
θ_{max} (°)	26.73	26.01	27.45	27.46	27.48	27.49
h	$-14\rightarrow13$	$-12\rightarrow14$	$-15\rightarrow14$	$-15\rightarrow15$	$-18\rightarrow18$	$-18\rightarrow18$
k	$-23\rightarrow20$	$-23\rightarrow21$	$-22\rightarrow24$	$-24\rightarrow24$	$-28\rightarrow28$	$-27\rightarrow29$
l	$-28\rightarrow36$	$-34\rightarrow35$	$-36\rightarrow36$	$-36\rightarrow36$	$-24\rightarrow24$	$-24\rightarrow24$
Refinement on F^2						
Scattering factors from International Tables for Crystallography (vol. C)						
Reflections	20342	19181	24697	26588	13116	13420
Parameters/restraints	1342/1	1342/1	1317/37	1307/1	691/1	690/1

(*continued on next page*)

Table 1 (*continued*)

Compound	$[La(Cy_3PO)_3(NO_3)_3]\cdot 0.25EtOH$	$[Nd(Cy_3PO)_3(NO_3)_3]\cdot 0.25EtOH$	$[Eu(Cy_3PO)_3(NO_3)_3]$	$[Er(Cy_3PO)_3(NO_3)_3]$	$[Tm(Cy_3PO)_3(NO_3)_3]\cdot EtOH$	$[Yb(Cy_3PO)_3(NO_3)_3]\cdot EtOH$
Weighting scheme, w[a]	$[\sigma^2(F_o^2)+(0.0354P)^2]^{-1}$	$[\sigma^2(F_o^2)+(0.0331P)^2]^{-1}$	$[\sigma^2(F_o^2)+(0.0901P)^2+7.72P]^{-1}$	$[\sigma^2(F_o^2)+(0.0599P)^2+0.81P]^{-1}$	$[\sigma^2(F_o^2)+(0.0426P)^2+14.02P]^{-1}$	$[\sigma^2(F_o^2)+(0.0365P)^2]^{-1}$
Final R indices[b] ($F_o > n\sigma F_o$)	$n=4$	$n=4$	$n=4$	$n=4$	$n=4$	$n=4$
R (F)	0.0585	0.0546	0.0734	0.0634	0.0307	0.0305
$wR_2(F^2)$	0.0981	0.0889	0.1756	0.1339	0.0630	0.0646
S	0.987	1.007	1.091	1.031	1.046	1.014
Final R indices[b] (all data)						
$R(F)$	0.1093	0.0862	0.0924	0.0887	0.0416	0.0395
$wR_2(F^2)$	0.1086	0.0960	0.1867	0.1456	0.0663	0.0679
$(\Delta/\sigma)_{max}$	0.001	0.002	0.001	0.001	0.002	0.002
$\Delta\rho_{max}$ (e Å^{-3})	1.24	0.51	2.77	1.07	0.999	1.08
$\Delta\rho_{min}$ (e Å^{-3})	−1.38	−0.77	−3.17	−1.85	−0.623	−0.99
Extinction correction	none	none	none	none	none	none
Absolute structure parameter	−0.011(10)	−0.014(8)	−0.017(10)	−0.020(7)	0.520(5)[c]	−0.030(4)

[a] $P = [\max(F_o^2, 0) + 2F_c^2]/3$.

[b] $R_1 = \sum\|F_o\| - F_c\|/\sum|F_o|$; $wR_2 = [\sum[w(F_o^2 - F_c^2)^2]/\sum[w(F_o^2)^2]]^{0.5}$.

[c] Batch scale factor for TWIN refinement.

Table 2
Selected bond lengths (Å), bond angles (°) and geometry between non-bonded atoms of $Ln(NO_3)_3(Cy_3PO)_3$

	$[Ln(Cy_3PO)_3(NO_3)_3]\cdot 0.25C_2H_5OH$		$[Ln(Cy_3PO)_3(NO_3)_3]$		$[Ln(Cy_3PO)_3(NO_3)_3]\cdot C_2H_5OH$		
	La	Nd	Eu	Er	Tm	Yb	
Ln(1)–O(1a)	2.596(5)	2.534(5)	2.493(6)	2.444(5)	2.449(3)	2.450(2)	Ln(1)–O(1)
Ln(1)–O(3a)	2.609(5)	2.552(5)	2.515(6)	2.431(5)	2.411(2)	2.405(2)	Ln(1)–O(3)
Ln(1)–O(4a)	2.616(5)	2.549(5)	2.526(6)	2.441(5)	2.442(2)	2.439(2)	Ln(1)–O(4)
Ln(1)–O(6a)	2.610(5)	2.533(5)	2.509(7)	2.443(6)	2.440(2)	2.428(2)	Ln(1)–O(6)
Ln(1)–O(7a)	2.635(5)	2.558(5)	2.499(7)	2.287(5)	2.310(2)	2.304(2)	Ln(1)–O(7)
Ln(1)–O(9a)	2.618(5)	2.575(5)	2.546(7)				Ln(1)–O(9)
Ln(1)–O(10a)	2.420(5)	2.360(5)	2.313(6)	2.279(6)	2.219(2)	2.202(2)	Ln(1)–O(10)
Ln(1)–O(11a)	2.419(5)	2.348(4)	2.314(6)	2.225(4)	2.241(2)	2.228(2)	Ln(1)–O(11)
Ln(1)–O(12a)	2.424(4)	2.363(4)	2.333(6)	2.254(5)	2.220(2)	2.203(2)	Ln(1)–O(12)
Ln(1)···N(1a)	3.014(7)	2.954(7)	2.944(8)	2.857(7)	2.852(3)	2.848(3)	Ln(1)···N(1)
Ln(1)···N(2a)	3.049(7)	2.977(7)	2.950(7)	2.880(7)	2.860(3)	2.854(3)	Ln(1)···N(2)
Ln(1)···N(3a)	3.030(7)	2.959(6)	2.961(9)	3.275(6)	3.322(3)	3.321(3)	Ln(1)···N(3)
Ln(1)···P(1a)	3.8906(20)	3.8263(20)	3.8029(22)	3.7423(22)	3.6995(9)	3.6858(8)	Ln(1)···P(1)
Ln(1)···P(2a)	3.9284(21)	3.8604(17)	3.8409(23)	3.7453(18)	3.7531(10)	3.7452(9)	Ln(1)···P(2)
Ln(1)···P(3a)	3.8809(19)	3.8175(19)	3.7959(21)	3.7195(20)	3.7129(9)	3.6971(8)	Ln(1)···P(3)
Ln(2)–O(1b)	2.610(5)	2.534(5)	2.487(7)	2.422(5)			
Ln(2)–O(3b)	2.623(4)	2.541(5)	2.531(6)	2.459(5)			
Ln(2)–O(4b)	2.640(5)	2.567(5)	2.529(7)	2.461(6)			
Ln(2)–O(6b)	2.605(4)	2.526(5)	2.511(6)	2.410(6)			
Ln(2)–O(7b)	2.653(5)	2.581(5)	2.545(6)	2.497(6)			
Ln(2)–O(9b)	2.663(5)	2.596(4)	2.584(7)	2.545(7)			
Ln(2)–O(10b)	2.408(4)	2.340(4)	2.303(5)	2.262(4)			
Ln(2)–O(11b)	2.432(4)	2.366(3)	2.336(5)	2.273(4)			
Ln(2)–O(12b)	2.400(5)	2.338(5)	2.312(6)	2.255(6)			
Ln(2)···N(1b)	3.031(6)	2.958(7)	2.912(7)	2.859(6)			
Ln(2)···N(2b)	3.041(7)	2.979(7)	2.925(7)	2.880(7)			
Ln(2)···N(3b)	3.066(9)	3.001(6)	2.967(9)	2.955(8)			
Ln(2)···P(1b)	3.8787(20)	3.8079(17)	3.7875(19)	3.7329(18)			
Ln(2)···P(2b)	3.9323(18)	3.8644(14)	3.8375(20)	3.7668(16)			
Ln(2)···P(3b)	3.8818(22)	3.8062(22)	3.7677(25)	3.7242(24)			
N(3a)···Ln(1)···P(2a)	168.70(15)	167.40(13)	167.07(19)	172.35(13)	167.55(6)	167.30(6)	N(3)···Ln(1)···P(2)
N(1a)···Ln(1)···N(2a)	174.68(19)	175.52(19)	176.91(21)	173.39(20)	176.24(9)	176.44(8)	N(1)···Ln(1)···N(2)
N(1a)···Ln(1)···N(3a)	91.43(21)	92.21(20)	92.61(24)	83.19(19)	90.79(9)	91.00(9)	N(1)···Ln(1)···N(3)
N(2a)···Ln(1)···N(3a)	87.01(19)	86.29(19)	86.99(24)	93.08(19)	90.02(9)	89.52(8)	N(2)···Ln(1)···N(3)
N(3a)···Ln(1)–O(11a)	168.72(19)	167.31(16)	166.64(24)	174.18(17)	166.75(9)	166.55(9)	N(3)···Ln(1)–O(11)
P(1a)···Ln(1)···P(3a)	162.64(4)	162.30(4)	161.57(5)	158.16(5)	156.19(2)	156.02(2)	P(1)···Ln(1)···P(3)
O(10a)–Ln(1)–O(11a)	86.61(16)	87.06(16)	86.95(22)	97.50(18)	92.91(11)	92.90(10)	O(10)–Ln(1)–O(11)
O(10a)–Ln(1)–O(12a)	156.51(15)	156.58(15)	155.10(21)	157.67(20)	160.15(9)	159.80(8)	O(10)–Ln(1)–O(12)
O(11a)–Ln(1)–O(12a)	85.42(16)	85.83(16)	85.83(22)	90.37(18)	95.61(9)	95.94(8)	O(11)–Ln(1)–O(12)

(*continued on next page*)

Table 2 (*continued*)

	[Ln(Cy$_3$PO)$_3$(NO$_3$)$_3$] · 0.25C$_2$H$_5$OH		[Ln(Cy$_3$PO)$_3$(NO$_3$)$_3$]		[Ln(Cy$_3$PO)$_3$(NO$_3$)$_3$] · C$_2$H$_5$OH	
	La	Nd	Eu	Er	Tm	Yb
N(3b)···Ln(2)···P(2b)	161.83(17)	162.63(13)	163.55(18)	163.49(18)		
N(1b)···Ln(2)···N(2b)	172.42(17)	173.71(19)	174.28(20)	175.38(19)		
N(1b)···Ln(2)···N(3b)	101.69(19)	99.76(18)	98.11(22)	96.44(21)		
N(2b)···Ln(2)···N(3b)	84.98(19)	84.97(18)	86.11(22)	85.32(20)		
N(3b)···Ln(2)–O(11b)	160.92(19)	161.65(16)	162.51(23)	162.68(21)		
P(1b)···Ln(2)···P(3b)	159.10(5)	159.22(4)	159.73(5)	158.08(5)		
O(10b)–Ln(2)–O(11b)	87.17(15)	86.86(13)	86.79(19)	87.35(15)		
O(10b)–Ln(2)–O(12b)	156.47(15)	156.60(16)	155.86(20)	154.61(19)		
O(11b)–Ln(2)–O(12b)	91.87(17)	90.97(16)	90.11(24)	88.59(20)		

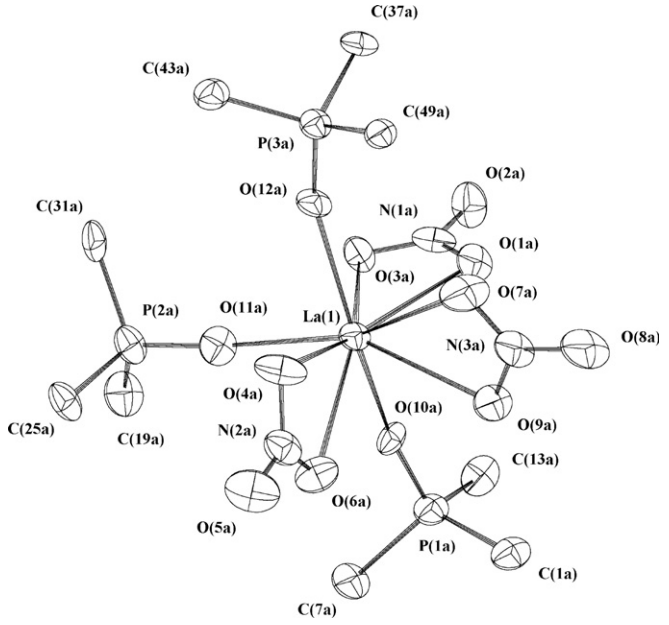


Fig. 1. The structure of one of the molecules of La(Cy$_3$PO)$_3$(κ^2-NO$_3$)$_3$. Thermal ellipsoids are drawn at the 50% probability level and cyclohexyl groups have been omitted for clarity.

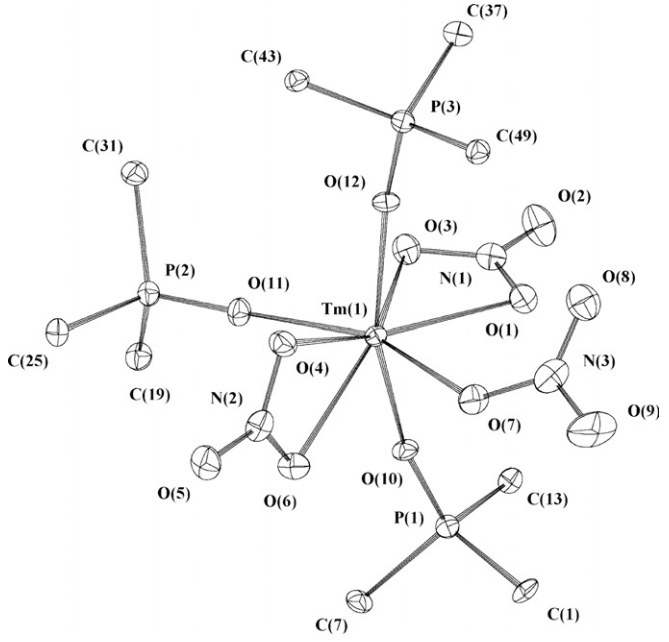


Fig. 2. The structure of Tm(Cy$_3$PO)$_3$(κ^1-NO$_3$)(κ^2-NO$_3$)$_2$. Thermal ellipsoids are drawn at the 50% probability level and cyclohexyl groups have been omitted for clarity.

2.3. Electrospray mass spectrometry

The solution properties of the complexes were examined by electrospray mass spectrometry in methanol solution, and the data and assignments for the complexes studied are given in Table 3. Assignments are made on the basis of calculated *m*/*z* ratios, all of which are within 0.5 Da of the theoretical values and the observation of analogous

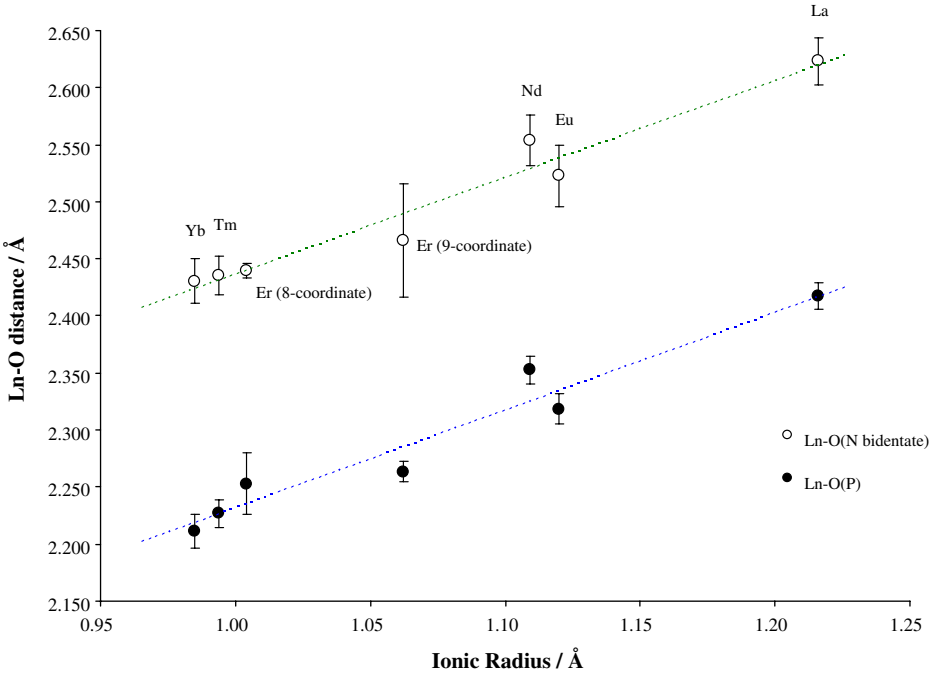


Fig. 3. The variation in Ln–O distances with ionic radius of the lanthanide ion.

Table 3
The electrospray mass spectra[a] of $Ln(NO_3)_3L_3$ in methanol/water

	$[Ln(NO_3)_2L_3]^+$	$[Ln(NO_3)L_4]^{2+}$	$[Ln(NO_3)L_3]^{2+}$	$[Ln(OH)L_4]^{2+}$	$[Ln(OMe)L_4]^{2+}$	$[Ln(OMe)L_3]^{2+}$
La	1151.6(<5)	692.9(10)	544.8(<5)	670.4(10)		529.3(20)
Nd	1156.6(15)	695.5(50)	547.3(10)	672.8(30)	679.8(15)	531.7(20)
Eu	1165.7(<5)	700.0(10)	501.0(<5)	677.5(<5)		536.3(10)
Gd	1170.6(5)	702.3(15)	554.0(5)	680.0(15)	686.5(5)	538.8(10)
Tb	1171.6(20)	703.2(75)	554.5(15)	680.7(65)	687.0(10)	539.5(40)
Ho	1177.6(20)	705.9(50)	557.5(10)	683.4(45)	690.0(5)	542.3(25)
Tm	1181.6(20)	709.9(10)	559.5(5)	685.4(10)		544.4(20)
Yb	1186.7(25)	710.4(50)	562.2(15)	687.9(45)	694.8(<5)	546.8(20)
Tandem mass spectra						
Precursor ion	$[Ln(NO_3)_2L_3]^+$	$[Ln(NO_3)L_4]^{2+}$		$[Ln(OH)L_4]^{2+}$		$[Ln(OMe)L_3]^{2+}$
Fragment ion	$[Ln(NO_3)_2L_2]^+$	$[Ln(NO_3)L_3]^{2+}$		$[Ln(OH)L_3]^{2+}$		$[Ln(OMe)L_2]^{2+}$
La	855.1	544.6		522.1		380.8
Ho	881.2	557.5		534.9		394.0
Yb	890.0	562.1		539.6		398.4[b]

[a] *m/z* (relative intensity %).
[b] Significant fragmentation of this ion was observed as discussed in the text.

species for the series of complexes studied. In addition the theoretical isotope patterns give excellent agreement with those observed. An example for the $[Gd(NO_3)_2L_3]^+$ ion is typical and shown in Fig. 4. The spectra all show strong signals from $[L+H]^+$, $[L+Na]^+$, $[2L+H]^+$ whilst those from lanthanide containing ions indicate that the complexes undergo redistribution reactions in solution. Such redistribution reactions are common for lanthanide complexes and have previously been observed for β-diketonate [12] and a variety of phosphine oxide [13] complexes. Peaks from $[Ln(NO_3)_2L_3]^+$ are observed for all complexes, often as low intensity clusters of signals. The main lanthanide containing signals are derived from loss of nitrate to give $[Ln(NO_3)L_3]^{2+}$ and from loss of nitrate and attachment of further ligand to give $[Ln(NO_3)L_4]^{2+}$. There appears to be no correlation between the abundance of +2 cations and the presence of the monodentate nitrates observed in the solid state structures. In addition to these processes solvolysis reactions are also apparent giving rise to intense signals assigned to $[Ln(OH)L_4]^{2+}$, $[Ln(OMe)L_3]^{2+}$ and $[Ln(OMe)L_4]^{2+}$. Such solvolysis processes have been observed in the spectra of lanthanide salts and complexes before [14] and are thought to be due to gas phase processes rather than reflecting the nature of solution species. The mass spectra of several of the complexes were recorded again after the solutions had aged for about three weeks

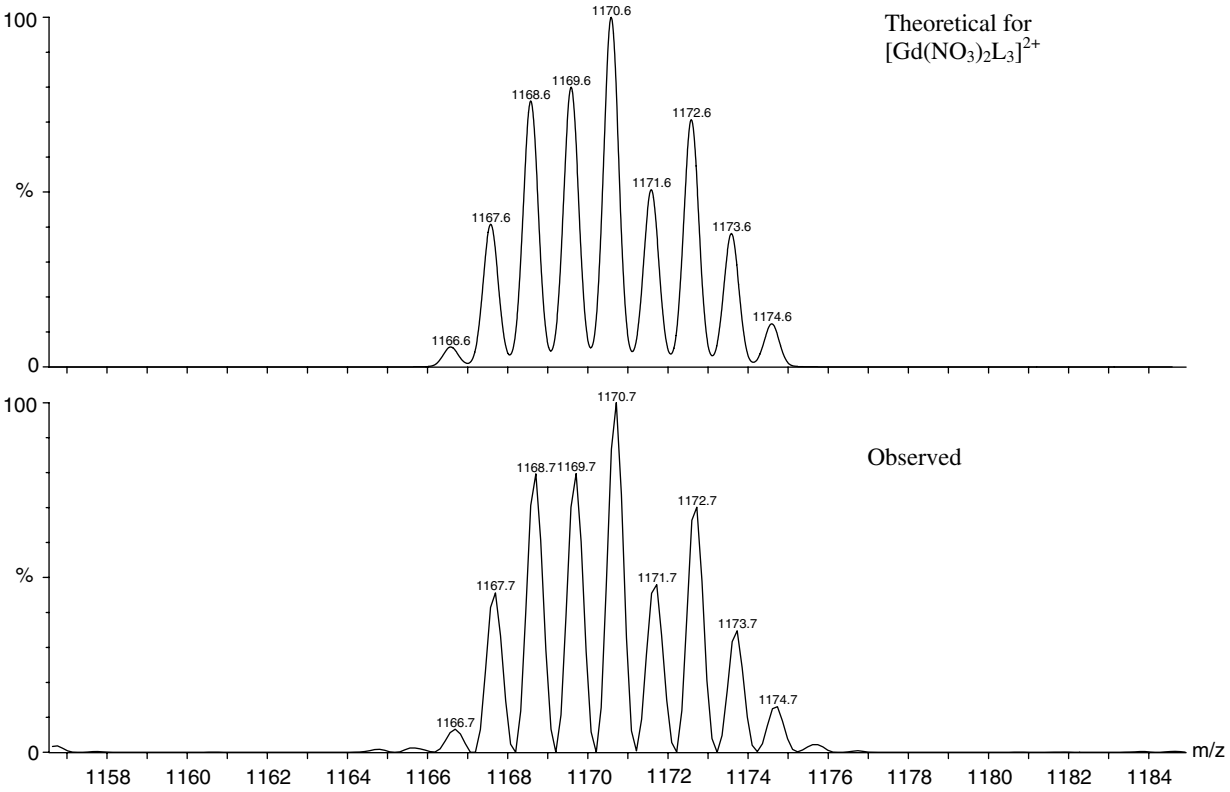


Fig. 4. Theoretical isotope pattern for $[Gd(NO_3)_2L_3]^+$ (L = Cy_3PO) and that observed in the positive ion electrospray mass spectrum.

and showed no significant differences with spectra obtained from fresh solutions. The positive ion ESMS of $Ho(NO_3)_3L_3$ is representative of the spectra obtained and is shown in Fig. 5.

Selected ions were also examined by tandem mass spectrometry to investigate their behaviour in the gas phase. The ions were chosen to represent species which might be expected initially to be present in solution namely

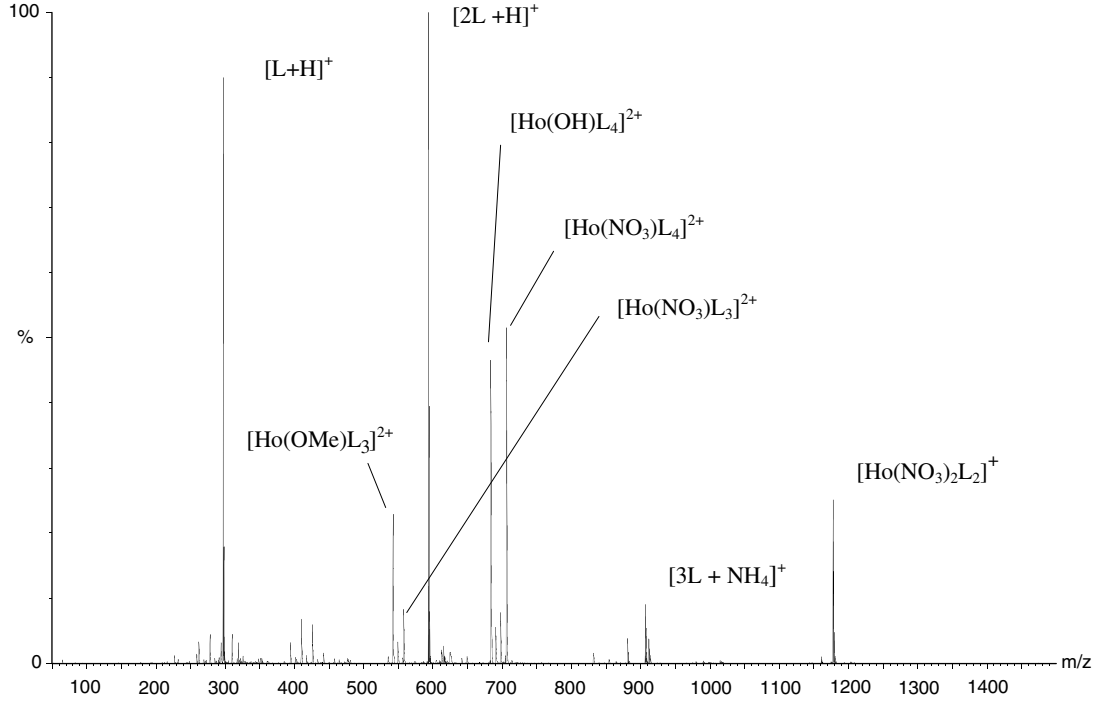


Fig. 5. The positive ion Electrospray mass spectrum of $Ho(NO_3)_3L_3$ (L = Cy_3PO) in methanol/water with principal assignments.

$[Ln(NO_3)_2L_3]^+$ and $[Ln(NO_3)L_4]^{2+}$ and also ions which are more likely to have been formed as part of the electrospray process such as $[Ln(OH)L_4]^{2+}$ and $[Ln(OMe)L_3]^{2+}$. The lanthanum, holmium and ytterbium complexes were studied to represent the range of lanthanides. The tandem mass spectra of most of the ions are simple, showing loss of only one tricyclohexylphosphine oxide ligand for all ions studied. The exception to this was $[Yb(OMe)L_3]^{2+}$ which

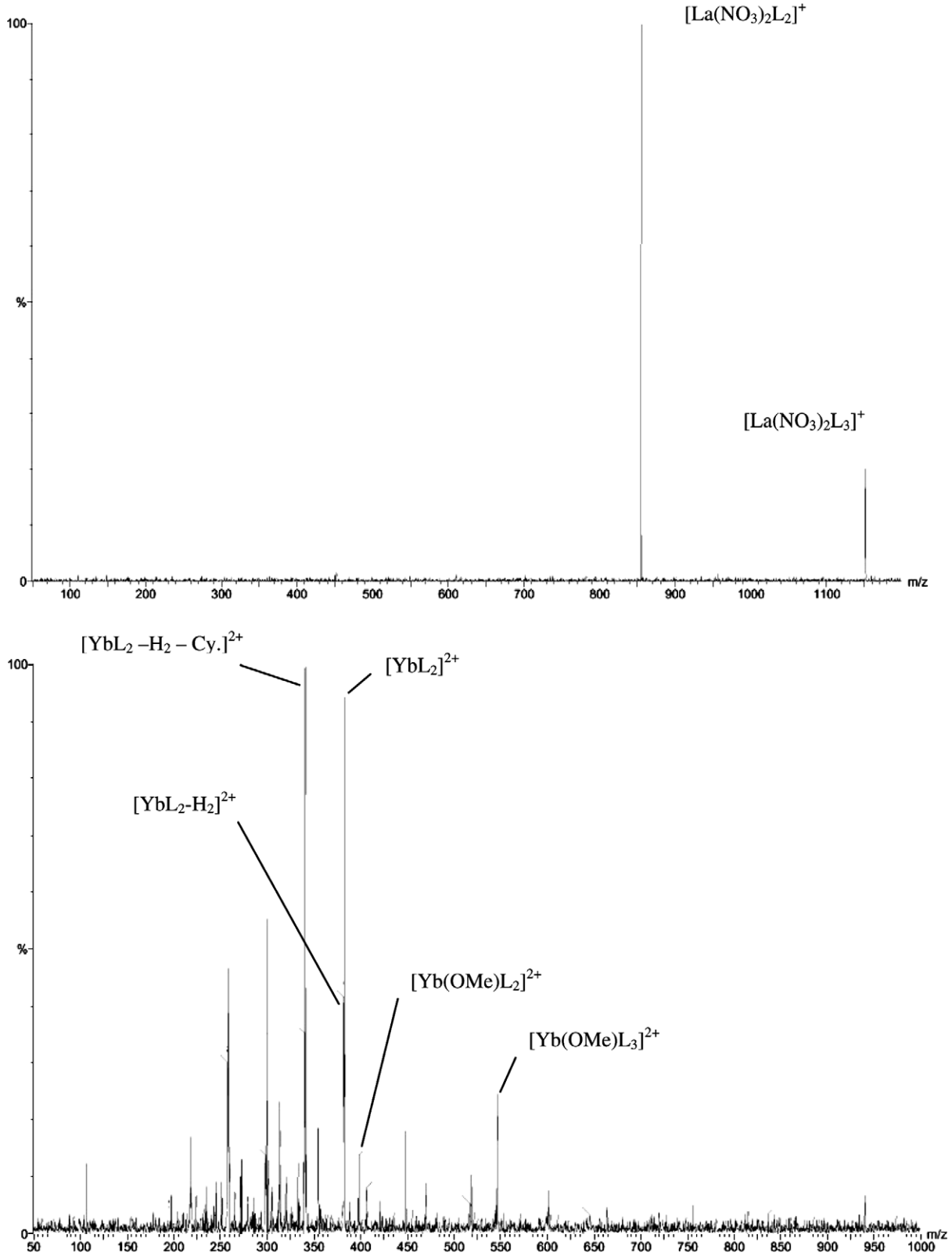


Fig. 6. The tandem mass spectra of the $[La(NO_3)_2L_3]^+$ (upper) and $[Yb(OMe)L_3]^{2+}$ ($L = Cy_3PO$) (lower) ions.

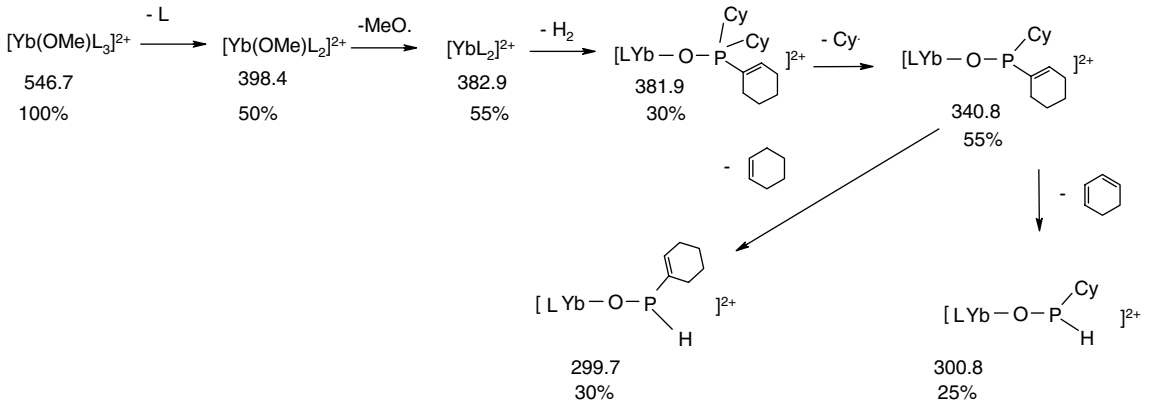


Fig. 7. A possible fragmentation pathway for $[Yb(OMe)L_3]^{2+}$ (L = Cy_3PO).

required a higher collision offset (COFF) to induce fragmentation similar to that of the La and Ho complex ions. Typical spectra for the La and Yb complexes are shown in Fig. 6. The Yb complex ion required COFF 50 eV, whilst the corresponding La and Ho ions yielded simple and meaningful fragment ions with COFF 30–40 eV. The stability of the Yb complex to loss of ligand is presumably due to the higher charge density on the metal ion. Under the harsher conditions required for its fragmentation a more complex spectrum was produced. This showed loss of Cy_3PO with further fragmentation due to loss of MeO·, cyclohexyl radicals and possibly cyclohexadiene. Loss of cyclohexene and cyclohexyl radicals under electron impact has been observed previously in the mass spectra of aromatic cyclohexyl ethers [15] and in $Cy_2P(O)C_2H_4P(O)Cy_2$ [16] and whilst electrospray ionisation is generally less energetic, the application of higher COFF in the tandem mass spectra of the Yb complex presumably supplies sufficient energy for radical formation.

The loss of H_2 from a 2+ charged ion was also apparent by the presence of peaks separated by one *m*/*z* unit. Fig. 7 illustrates a possible fragmentation pathway which accounts for the presence of the major ions observed. It must be noted that the mechanism is tentative. Cleavage of the Yb–OMe bond leading to loss of MeO· generates an Yb(II) fragment which may explain why whilst further decomposition of $[Yb(OMe)L_2]^{2+}$ was observed the corresponding ion for La and Ho, for which the divalent states are less stable, does not undergo this decomposition.

3. Experimental

3.1. Crystal structure determinations

Data were collected by the EPSRC National Crystallography Service at the University of Southampton using previously described procedures [17–19].

The positions of the metal atoms in the La and Yb structures were estimated by Patterson methods using SHELXS-97 [20], and all remaining non-H atom positions were obtained through subsequent Fourier syntheses (SHELXL-97) [21]. Refinement was by full-matrix least-squares on F^2 data using SHELXL-97 [21]. Solutions and all refinements were conducted using SHELX-97 from within the WinGX [22] suite of software.

The Nd, Eu and Er structures were each refined in space group $P2_1$ after isomorphous replacement into the La structure. The Tm structure was solved by similar replacement into the Yb structure (space group $Pc2_1n$) after re-indexing the data and transforming the unit cell axes from the alternative space group setting, $Pbn2_1$ for which the data were collected. The asymmetric unit in each of the La–Er structures consisted of two discrete lanthanide-containing molecules. The asymmetric units of the Tm and Yb structures each consisted of a single lanthanide-containing molecule.

Attempts to refine the Er structure after initial substitution into the La structure showed the positions of the atoms of one of the bidentate nitrate groups in one of the two molecules to be unstable. After deletion of nitrate atoms, peaks were re-located in subsequent Fourier syntheses to build a stable model containing a monodentate nitrate group – consistent with the molecular structure observed in the Yb and Tm complexes.

In each of the structures, non-H atoms were refined anisotropically with the exception of the C atoms of one of the cyclohexyl groups in each of the La and Nd structures and two cyclohexyl groups in the Er structure. The initial, fully anisotropic, models of the La–Er structures displayed marked librational elongation of the thermal ellipsoids of the C-atoms in these groups, and their geometry deviated from that expected for the cyclohexyl moiety. A disordered, isotropic, model consisting of two alternative sites with complementary site occupation factors was adopted for the La, Nd, and Er structures. SIMU restraints were applied to C-atoms of the corresponding group in the Eu structure for which data were poorer.

An ethanol molecule was located near to one of the nitrate groups in each of the La, Nd, Tm and Yb structures. The site occupation factors of the solvent molecules in the La and Nd lattices were initially refined, and finally

fixed at half occupancy. A similar solvent molecule was located in the Er structure apparently H-bonded to one of the bidentate nitrate groups. This site occupation factor of this solvent refined to <0.6%, and made little improvement to the figures of merit. It was excluded from the final structure. No similar solvent could be located in the difference Fourier maps of the Eu structure.

All H atoms were included in the refinements at idealised positions riding on the atoms to which they were bonded (methane C–H = 1.00 Å, methylene C–H = 0.99 Å, methyl C–H = 0.98 Å, O–H = 0.84 Å) The H-atoms of each functional group were assigned a single, refined isotropic displacement parameter, except those of solvent molecules which were assigned a common, refined isotropic displacement parameter.

The non-centrosymmetric structures refined to give Flack absolute structure parameters of −0.011(10), −0.014(8), −0.017(10), −0.020(7), −0.030(4) for the La, Nd, Eu, Er and Yb structures, respectively. The absolute structure of the Tm complex could not be unambiguously determined. ROTAX analysis [23] of the Tm data indicated merohedral or pseudo-merohedral twinning. The Tm structure refinement was repeated assuming racemic twinning by using the default TWIN setting in SHELXL-97 [21], and refinement converged to yield a batch scale factor of 0.520(5).

Molecular graphics were generated using SNOOPI [24]

3.2. Mass spectrometry

Electrospray mass spectra were recorded on a either a Waters ZQ-4000 or a Micromass Quattro II for the MS/MS measurements. Samples in methanol solution were loop injected into a flow of 1:1 methanol: water running at 40μL/min into the electrospray capillary. Nebulisation was pneumatically assisted by a flow of $N_{2(g)}$ at 15 L/min and a drying gas of $N_{2(g)}$ at 100 L/min warmed by a source temperature of 80 °C. The spray voltage was 3.5 kV and the cone voltage varied between 20 V and 90 V depending on the mass and charge of the ions of interest. For tandem mass spectra, $Ar_{(g)}$ at a pressure of 2×10^{-3} mbar was introduced into the collision chamber (termed quadrupole 2 or Q2); ions formed during the ES process and mass selected for individual analysis by the first quadrupole (Q1), were accelerated through this region of relatively high pressure by a voltage termed the collision offset (COFF). The COFF voltage was adjusted to obtain optimal fragmentation for each precursor ion, and the resulting fragment ions analysed by Q3.

3.3. Infrared spectroscopy

Infrared spectra were recorded in the range 400–4000 cm^{-1} on a Thermo Nicolet Avatar 370 instrument operating in ATR mode. Samples were analysed without pre-treatment other than crushing onto the optical surface.

3.4. Synthesis and characterisation

Tricyclohexylphosphine oxide was prepared by oxidation of an acetone solution of tricyclohexylphosphine with 30% H_2O_2. In a typical preparation the phosphine (20.04 g) was suspended in 100 ml of acetone and hydrogen peroxide (9.00 g 30% aqueous solution) was added in portions allowing the vigorous reaction to subside before the next addition. The resulting clear solution was allowed to cool to room temperature and the resulting crystalline solid filtered, washed with a little cold acetone and dried at the pump to give 19.18 g of a waxy colourless solid. NMR (acetone) δ^{31}P 51.6, literature 50.0 [25] ν_{PO} 1146 cm^{-1}.

The nitrate complexes were prepared by mixing hot solutions of tricyclohexylphosphine oxide with the appropriate lanthanide nitrate in ethanol. On cooling crystals formed in 80–100% yield. Representative syntheses and characterisation are described below.

$La(NO_3)_3(Cy_3PO)_3 \cdot 0.5EtOH$. $La(NO_3)_3 \cdot 5H_2O$ (0.23 g 0.55 mmol) in 10 ml hot ethanol was mixed with Cy_3PO (0.71 g 2.4 mmol) in 10 ml hot ethanol. The resulting solution was warmed for 15 min during which time crystals began to form. The mixture was cooled to room temperature and allowed to stand overnight. The colourless crystals were filtered, washed with a small quantity of cold ethanol and dried at the pump to give 0.65 g (99%), ν_{PO} 1097 cm^{-1}.

Anal. Calc. for $La(NO_3)_3(Cy_3PO)_3 \cdot 0.5EtOH$: C, 53.39; H, 8.31; N, 3.40. Found: C, 52.88; H, 8.20; N, 3.28%.

$Nd(NO_3)_3(Cy_3PO)_3 \cdot 0.5EtOH$. $Nd(NO_3)_3 \cdot 6H_2O$ (0.26 g 0.59 mmol) in 5 ml hot ethanol was mixed with Cy_3PO (0.66 g 2.2 mmol) in 10 ml hot ethanol. The mixture was cooled to room temperature and allowed to stand overnight. The lilac crystals which formed were filtered, washed with a small quantity of cold ethanol and dried at the pump to give 0.65 g (99%), ν_{PO} 1099 cm^{-1}.

Anal. Calc. for $Nd(NO_3)_3(Cy_3PO)_3 \cdot 0.5EtOH$: C, 53.16; H, 8.27; N, 3.38. Found: C, 52.63; H, 8.19; N, 3.32%.

$Eu(NO_3)_3(Cy_3PO)_3$. $Eu(NO_3)_3 \cdot 6H_2O$ (0.26 g 0.58 mmol) in 10 ml hot ethanol was mixed with Cy_3PO (0.72 g 2.4 mmol) in 10 ml hot ethanol. The mixture was cooled to room temperature and allowed to stand overnight. The colourless crystals which formed were filtered, washed with a small quantity of cold ethanol and dried at the pump to give 0.63 g (88%) ν_{PO} 1102 cm^{-1}.

Anal. Calc. for $Eu(NO_3)_3(Cy_3PO)_3$: C, 52.85; H, 8.13; N, 3.42. Found: C, 52.38; H, 8.15; N, 3.23%.

$Tm(NO_3)_3(Cy_3PO)_3$. $Tm(NO_3)_3 \cdot 6H_2O$ (0.24 g 0.52 mmol) in 5 ml hot ethanol was mixed with Cy_3PO (0.62 g 2.0 mmol) in 10 ml hot ethanol. The mixture was cooled to room temperature and allowed to stand overnight. The colourless crystals which formed were filtered, washed with a small quantity of cold ethanol and dried at the pump to give 0.55 g (84%), ν_{PO} 1104 cm^{-1}.

Anal. Calc. for $M(NO_3)_3(Cy_3PO)_3$: C, 52.13; H, 8.02; N, 3.38. Found: C, 52.05; H, 8.20; N, 3.15%.

Acknowledgements

We are grateful to the Royal Society of Chemistry for support through the research fund and EPSRC for access to the X-ray data collection service at Southampton University.

Appendix A. Supplementary material

CCDC 602138 to 602143 contain the supplementary crystallographic data for La to Yb. These data can be obtained free of charge via http://www.ccdc.cam.ac.uk/conts/retrieving.html, or from the Cambridge Crystallographic Data Centre, 12 Union Road, Cambridge CB2 1EZ, UK; fax: (+44) 1223-336-033; or e-mail: deposit@ccdc.cam.ac.uk. Supplementary data associated with this article can be found, in the online version, at doi:10.1016/j.poly.2007.06.023.

References

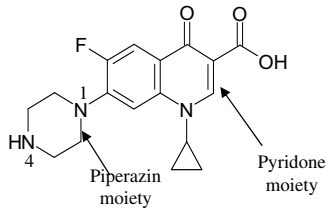
[1] (a) For reviews, see: S.A. Cotton, in: J.A. McCleverty, T.J. Meyer (Eds.), Comprehensive Coordination Chemistry II, vol. 3, Elsevier, Amsterdam, 2004, p. 93;
(b) T.S. Lobana, in: F.R. Hartley (Ed.), The Chemistry of Organophosphorus Compounds, vol. 2, Wiley, New York, 1992, p. 409.
[2] (a) K.L. Nash, C. Lavallette, M. Borkowski, R.T. Paine, X. Gan, Inorg. Chem. 41 (2002) 5849;
(b) A.N. Turanov, V.K. Karandashev, A.N. Yarkevich, Z.V. Safronova, Solvent Extr. Ion Exc. 22 (2004) 391.
[3] (a) X. Gan, R.T. Paine, E.N. Duesler, H. Nöth, J. Chem. Soc., Dalton Trans. (2003) 153;
(b) X. Gan, E.N. Duesler, R.T. Paine, Inorg. Chem. 40 (2001) 4420;
(c) X. Gan, B.M. Rapko, E.N. Duesler, I. Binyamin, R.T. Paine, B.P. Hay, Polyhderon 24 (2005) 469.
[4] W. Levason, E.H. Newman, M. Webster, Acta Crystallogr., Sect. C 56 (2000) 1308.
[5] W. Levason, E.H. Newman, M. Webster, Polyhedron 19 (2000) 2697.
[6] M.J. Glazier, W. Levason, M.L. Matthews, P.L. Thornton, M. Webster, Inorg. Chim. Acta 357 (2004) 1083.
[7] N.E. Mansfield, M.P. Coles, P.B. Hitchcock, J. Chem. Soc., Dalton Trans. (2006) 2052.
[8] M. Bosson, W. Levason, T. Patel, M.C. Popham, M. Webster, Polyhedron 20 (2001) 2055.
[9] R.D. Shannon, Acta Crystallogr., Sect. A 32 (1976) 751.
[10] K. Nakamoto, Infrared and Raman Spectra of Inorganic and Coordination Compounds, 5th ed., Wiley, New York, 1997.
[11] A.M.J. Lees, A.W.G. Platt, Inorg. Chem. 42 (2003) 4673.
[12] J.M. Curtis, P.J. Derrick, A. Schnell, E. Constantin, R.T. Gallagher, J.R. Chapman, Inorg. Chim. Acta 201 (1992) 197.
[13] (a) J. Fawcett, A.W.G. Platt, Polyhedron 22 (2002) 967;
(b) J. Fawcett, A.W.G. Platt, S. Vickers, M.D. Ward, Polyhedron 23 (2004) 2561;
(c) A.M.J. Lees, A.W.G. Platt, Polyhedron 24 (2005) 427.
[14] (a) I.I. Stewart, G. Horlick, Anal. Chem. 66 (1994) 3983;
(b) R. Colton, A. D'Agostino, J.C. Traeger, Mass Spectrom. Rev. 14 (1995) 79;
(c) S. Colette, B. Amekraz, C. Madic, L. Berthon, G. Cote, C. Moulin, Inorg. Chem. 42 (2003) 2215.
[15] T.A. Molenaar-Langeveld, L.M. Van der Burg, J.W.H. Peeters, C.G. De Koster, S. Ingemann, J. Mass Spectrom. 39 (2004) 1075.
[16] L.C. Baldwin, M.J. Fink, J. Organomet. Chem. 646 (2002) 230.
[17] DENZO – Data collection and processing software Z. Otwinowski, W. Minor, in: C.W. Carter Jr., R.M. Sweet (Eds.), Methods in Enzymology, Macromolecular Crystallography, Part A, vol. 276, Academic Press, London, 1997, pp. 307–326.
[18] R. Hooft, COLLECT – Data collection software, Nonius B.V., 1998.
[19] (a) SORTAV – absorption correction software package: R.H. Blessing, Acta Crystallogr., Sect. A 51 (1995) 33;
(b) R.H. Blessing, J. Appl. Crystallogr. 30 (1997) 421.
[20] (a) G.M. Sheldrick, SHELXS-97, Release 97-2: A Program for Automatic Solution of Crystal Structures, University of Göettingen, Göettingen, Germany, 1997;
(b) G.M. Sheldrick, Z. Dauter, K.S. Wilson, H. Hope, L.C. Sieker, Acta Crystallogr., Sect. D 49 (1993) 18.
[21] G.M. Sheldrick, SHELXL-97, Release 97-2: A Program for Crystal Structure Refinement, University of Göettingen, Göettingen, Germany, 1997.
[22] (a) L.J. Farrugia, WinGX: A Windows Program for Crystal Structure Analysis, University of Glasgow, Glasgow, 1998;
(b) L.J. Farrugia, J. Appl. Crystallogr. 32 (1999) 837.
[23] ROTAX: Simon Parsons & Bob Gould, University of Edinburgh with additions by Richard Cooper (Oxford) and Louis Farrugia (Glasgow), November, 2001.
[24] K. Davies, SNOOPI – Molecular Plotting Program, Chemical Crystallography Laboratory, University of Oxford, 1983.
[25] M.M. Crutchfield, C.H. Dungan, J.H. Letcher, V. Mark, J.R. Van Wazer, Topic in Phosphorus Chemistry, vol. V, Interscience, New York, 1967.

(Scheme 1) and a mechanism, in which a hypomanganate is formed in a two-electron reduction followed by a rapid oxidation of the hypomanganate ion [11] (Scheme 2).

The manganese chemistry involved in these multistep redox reactions is an important source of information as the manganese intermediates are relatively easy to identify when they have sufficiently long life time and oxidation states of the intermediates permit useful conclusions as to the possible reaction mechanisms including the nature of intermediates.

Ciprofloxacin [cyclopropyl-6-fluoro-1,4-dihydro-4-oxo-7-(piperazinyl)-quinolone-3-carboxylic acid] is one of the potent synthetic fluoroquinolone antibacterial agents, that are widely used in human and veterinary medicines [12] and also used in the treatment of infections due to *Bacillus anthracis* (i.e., anthrax infections) [13]. Due to their extensive usage, fluoroquinolones may enter the environment via wastewater effluent and biosolids from sewage treatment plants and via manure and litters from food-producing animal husbandry. There are studies on the modified pharmacological and toxicological properties of these drugs in the form of metallic complexes [14–16].

The presence and accumulation of fluoroquinolone antibiotics in aquatic environments, albeit at low concentrations, may pose threats to the ecosystem and human health by inducing increase and spread of bacteria drug-resistance due to long-term exposure. Chemical oxidation using permanganate has been widely used for treatment of pollutants in drinking water and wastewater applications for over 50 years. The title reaction was extensively investigated to elucidate the behavior of this fluoroquinolone antibacterial agent during wastewater treatment by permanganate. The structure of ciprofloxacin is shown below which consists of piperazine and pyridone moieties.



$$\mathrm{Mn(VII)} + \mathrm{S} \xrightarrow{k_1} \mathrm{Mn(VI)} + \mathrm{S}^{\bullet}$$

$$\mathrm{Mn(VII)} + \mathrm{S}^{\bullet} \xrightarrow{k_2} \mathrm{Mn(VI)} + \mathrm{Products}$$

S=substrate $k_2 >> k_1$

Scheme 1.

$$\mathrm{Mn(VII)} + \mathrm{S} \xrightarrow{k_3} \mathrm{Mn(V)} + \mathrm{Products}$$

$$\mathrm{Mn(VII)} + \mathrm{Mn(V)} \xrightarrow{k_4} 2\mathrm{Mn(VI)}$$

S=substrate $k_4 >> k_3$

Scheme 2.

In view of potential pharmaceutical importance of ciprofloxacin and lack of the literature on the oxidation of this drug by any oxidant except in two cases [17,18] and the complexity of the reaction, a detailed study of the reaction becomes important. The present study deals with the title reaction to investigate the redox chemistry of permanganate in such media and to arrive at a suitable mechanism for oxidation of ciprofloxacin by permanganate on the basis of kinetic results.

2. Experimental

All chemicals used were of analytic reagent grade and double distilled water was used throughout the work. The solution of ciprofloxacin (Bayer AG) was prepared by dissolving known amount of its hydrochloride salt in distilled water. The permanganate (SISCO-CHEM Ltd.) solution was prepared and standardized against oxalic acid by standard procedure [19]. Potassium manganate solution was prepared as described by Carrington and Symons [20]. KOH (BDH, Analar) and KNO_3 (BDH, Analar) were employed to maintain the required alkalinity and ionic strength, respectively, in reaction solutions.

2.1. Instruments used

(a) For kinetic measurements: UV–Vis spectrophotometer (Varian CARY 50 Bio) connected to a rapid kinetic accessory (Hitech SFA-12).

(b) For product analysis:
LC-ESI-MS technique. Hewlet Packard 1100 reverse phase high performance liquid chromatography (HPLC) system with a phenomenes C18 column, hp 1100 series diode array UV/Visible detector and hp 1100 MSD Series mass analyzer.
LC-ESI-MS/MS technique. AGILENT 1100 series high performance liquid chromatography (HPLC) system, AGILENT 1100 variable wavelength detector and Esquire 3000 plus (BRUKER DALTONICS, Germany) mass analyzer.
Twelve microliters of acidified reaction mixture was injected. The mobile phase consisted of acetonitrile (eluent A) and water (Containing 0.1% CH_3COOH) at a flow rate of 1 ml/min. Gradient elution was run to separate substrate and reaction products. Gradient 0 min/20% A–40 min/95% A–45 min/95% A–47 min/20% A. UV detection at 226 and 280 nm.

2.2. Kinetic procedure

The oxidation of ciprofloxacin by permanganate was followed under pseudo-first order conditions where [ciprofloxacin] was excess over [permanganate] at 25 ± 0.1 °C unless otherwise stated. The reaction was initiated by mixing the required quantities of previously thermostatted solutions of ciprofloxacin and permanganate, which also

contained definite quantities of KOH and KNO_3 to maintain the required alkalinity and ionic strength. The progress of reaction was followed by measuring the absorbance of unreacted permanganate in the reaction mixture present in 1 cm cell in a thermostatted compartment of a Varian CARY 50 Bio UV–Vis. spectrophotometer at 526 nm. It was verified that other constituents of the reaction mixture do not absorb significantly at this wavelength. The application of Beer's law to permanganate at 526 nm had been verified and $\varepsilon = 2100 \pm 50\ dm^3\ mol^{-1}\ cm^{-1}$. The reaction was followed more than three half lives. The first order rate constants, k_{obs} were obtained from the plots of $\log(A_t - A_\infty)$ *versus* time. Where A_t refers to absorbance at any time t and A_∞ is at infinite time which excludes the absorbance of any Mn(VI) during the reaction. The plots were linear over 70% completion of the reaction and rate constants were reproducible within ±5%.

The effect of dissolved oxygen on the reaction was studied by preparing the reaction mixture and following the reaction in an atmosphere of nitrogen. No significant difference between the results was observed. In view of ubiquitous contamination of carbonate in basic solutions, the effect of carbonate on the reaction was also studied. Added carbonate had no effect on reaction rate. However, fresh solutions were used during the experiments. Regression analysis of experimental data to obtain the regression coefficient, r and standard deviation, S of points from the regression line was performed using microsoft excel-2003 programme.

3. Results

3.1. Oxidation products of ciprofloxacin

LC-ESI-MS analysis of ciprofloxacin reaction indicated the presence of three products with molecular ions of m/z 348 (Fig. 1(a) (iv)) (Yield 5%), 306 (Fig. 1(a) (ii)) (Yield 32%) and 263 (Fig. 1(a) (iii)) (Yield 55%), respectively. The molecular ion of ciprofloxacin is m/z 332. The m/z 348 corresponds to *N*-oxide product. The m/z 306 (i.e., the M−26 product with respect to ciprofloxacin) corresponds to partial dealkylation of the piperazine ring while the m/z 263 corresponds to full dealkylation of the piperazine ring (i.e., the –NH2 product). These two products were also identified previously as oxidation products [17] and photodegradation products of ciprofloxacin [21].

3.2. Reaction orders

The reaction orders were determined from the slope of $\log k_{obs}$ *versus* log (concentration) plots by varying the concentrations of ciprofloxacin and alkali in turn while keeping all other concentrations and conditions constant.

3.3. Effect of [oxidant]

The oxidant $KMnO_4$ concentration was varied in the range of 4.0×10^{-5}–4.0×10^{-4} mol dm^{-3} and the constant k_{obs} values (Table 1) indicate that order with respect to [$KMnO_4$] was unity. This was also confirmed by linearity and parallel plots of $\log[A_t - A_\infty]$ *versus* time (Fig. 2) ($r \geqslant 0.983$, $S \leqslant 0.016$) up to 75% completion of the reaction.

3.4. Effect of [ciprofloxacin]

The effect of ciprofloxacin concentration on the reaction was studied at constant concentrations of alkali and permanganate and at a constant ionic strength of 0.04 mol dm^{-3} at 25 °C. The substrate, ciprofloxacin was varied in the range of 2.0×10^{-3}–2.0×10^{-2} mol dm^{-3}. The k_{obs} values increased with increase in concentration of ciprofloxacin (Table 1). The order with respect to [ciprofloxacin] was found to be less than unity (0.48) ($r \geqslant 0.9859$, $S \leqslant 0.008$).

3.5. Effect of [alkali]

The effect of increase in concentration of alkali on the reaction was studied at constant concentrations of ciprofloxacin and permanganate at a constant ionic strength of 0.04 mol dm^{-3} at 25 °C. The rate constants increased with increase in alkali concentration (Table 1). The order with respect to [OH^-] was found to be less than unity (0.64).

3.6. Effect of ionic strength and solvent polarity

The effect of ionic strength was studied by varying the potassium nitrate concentration from 0.02 to 0.2 mol dm^{-3} at constant concentrations of permanganate, ciprofloxacin and alkali. It was found that increasing ionic strength had no effect on the rate constant. The effect of relative permittivity ($\in_T$) was studied by varying the *t*-butanol–water content (v/v) in the reaction mixture with all other conditions being maintained constant. Decreasing the dielectric constant of the medium had no effect on the rate of the reaction.

3.7. Effect of initially added products

The manganate ion concentration was varied from 4.0×10^{-5} to 4.0×10^{-4} at constant concentrations of permanganate, ciprofloxacin, alkali and ionic strength. It was found that initially added manganate ion had no effect on the rate constant.

The experimental rate law is given as follows:

$$\frac{-d[MnO_4^-]}{dt} = k[MnO_4^-][CF]^{0.48}[OH^-]^{0.64}$$

3.8. Effect of temperature

The kinetics was studied at four different temperatures under varying concentrations of ciprofloxacin and alkali, keeping other conditions constant. The rate constants were

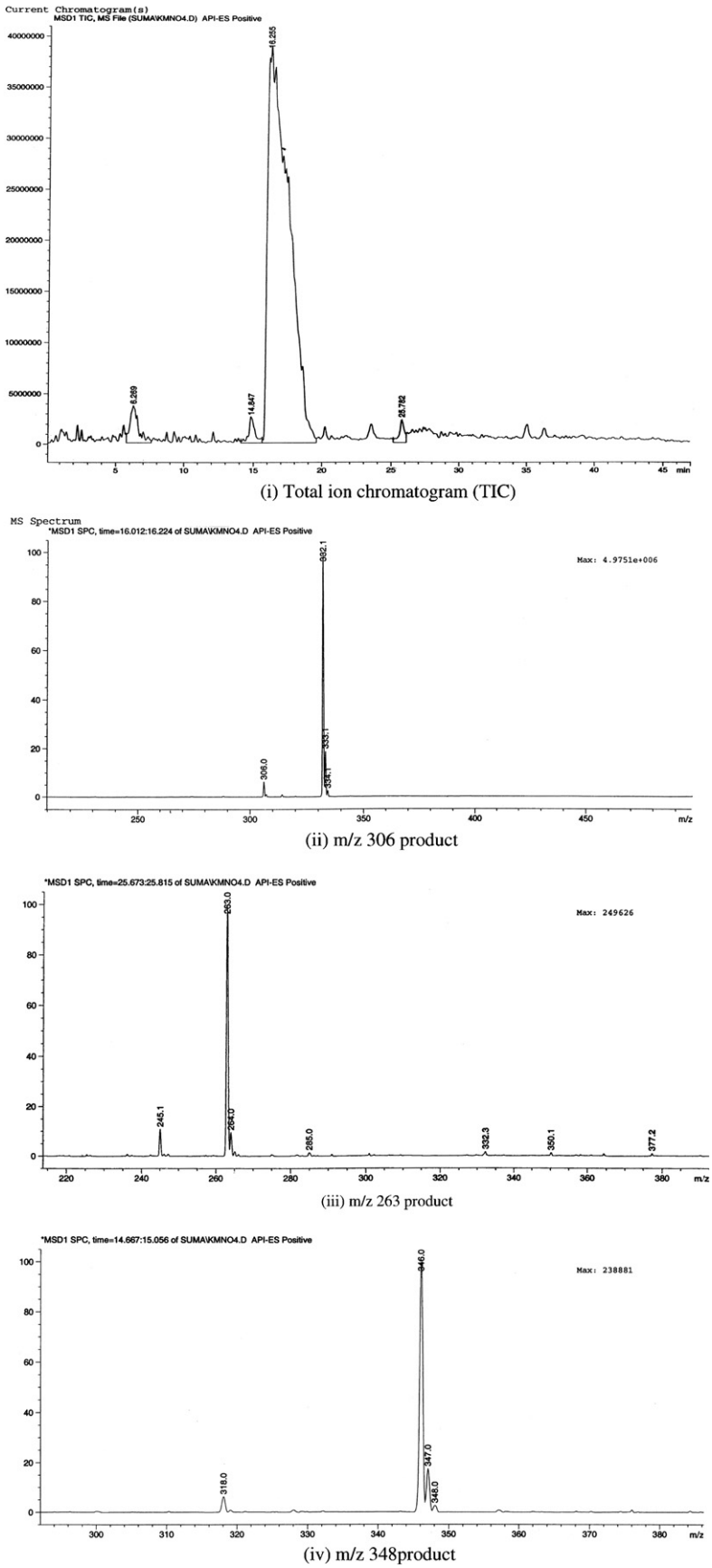


Fig. 1(a). LC-ESI-MS spectra of oxidation products of ciprofloxacin.

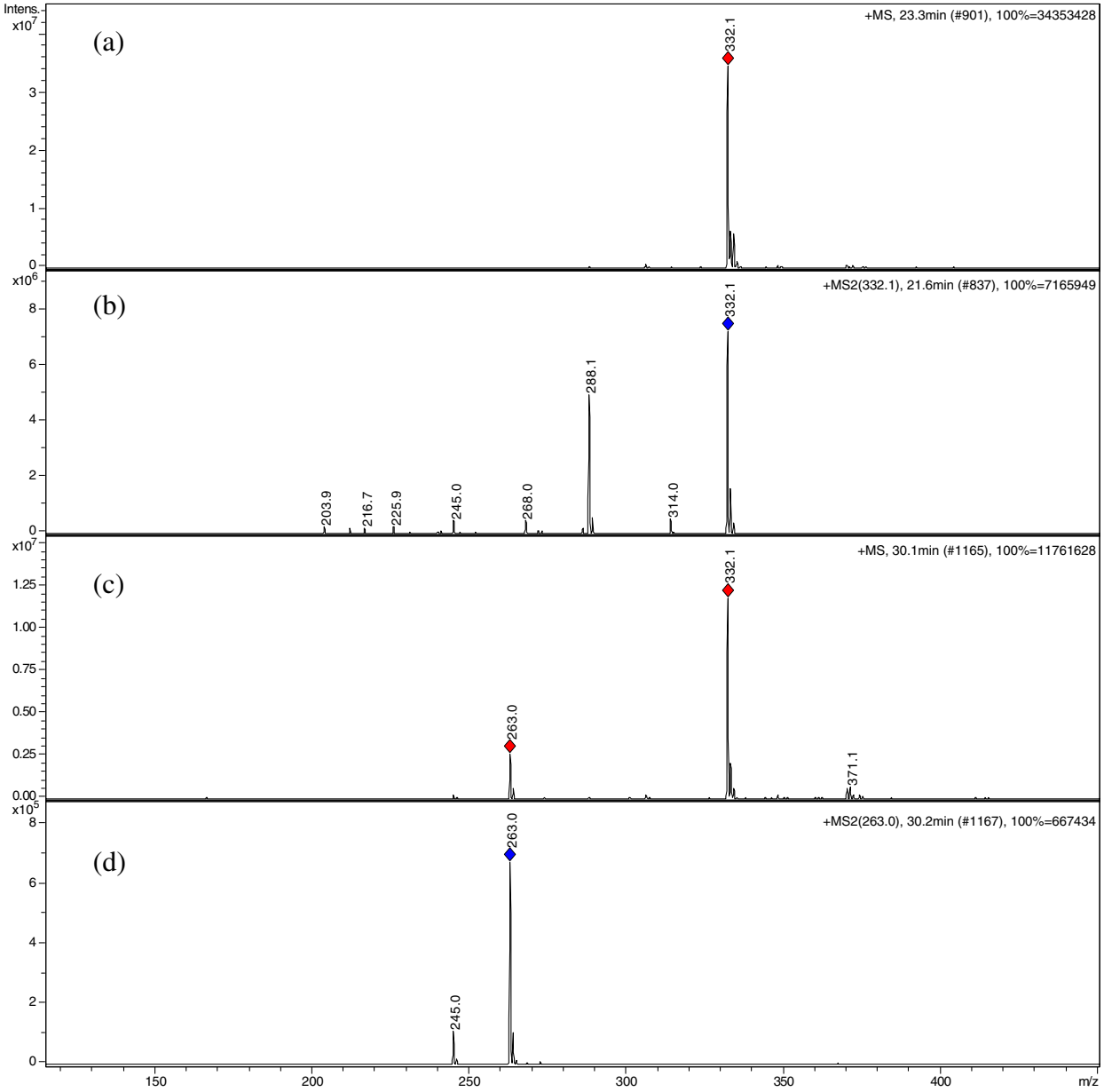


Fig. 1(b). LC-ESI-MS-MS spectra of oxidation products of ciprofloxacin. (a) Molecular ion peak $(M + H)^+$ of ciprofloxacin. (b) Fragmentation of $(M + H)^+$. (c) Molecular ion peaks of *m/z* 332 $(M + H)^+$ and *m/z* 263 (M−69). (d) Fragmentation of (M−69) product.

found to increase with increase in temperature. The rate constant (k) of the slow step of Scheme 1 were obtained from the slopes and intercepts of $1/k_{obs}$ *versus* 1/[CF] and $1/k_{obs}$ *versus* $1/[OH^-]$ plots at four different temperatures. The energy of activation corresponding to these rate constants was evaluated from the Arrhenius plot of $\log k$ *versus* $1/T$ ($r \geqslant 0.9802$, $S \leqslant 0.009$) and from which other activation parameters were obtained (Table 2).

4. Discussion

Permanganate ion, MnO_4^-, is a powerful oxidant in an aqueous alkaline medium. As it exhibits many oxidation states, the stoichiometric results and pH of reaction media play an important role. Under the prevailing experimental conditions at pH > 12, the reduction product of Mn(VII) is stable and further reduction of Mn(VI) might be stopped [10,22]. But during this study, colour of the solution changed from violet to blue and then to green. The spectrum of green solution was identical to that of MnO_4^{2-}. It is probable that blue colour originated from the violet of permanganate and the green from manganate, excluding the accumulation of hypomanganate. The spectral changes during the reaction are shown in Fig. 3. It is evident from the figure that the concentration of MnO_4^- decreases at 526 nm due to Mn(VII) and increases at 603 and 453 nm due to Mn(VI). As the reaction proceeds, slowly yellow turbidity develops, after keeping for a long time the solution turns to colourless resulting in a brown precipitate. This suggests that, the products formed might have undergone

Table 1
Effect of variation of $[MnO_4^-]$, [CF] and $[OH^-]$ on the oxidation of ciprofloxacin by alkaline MnO_4^- at 25 °C and $I = 0.04$/mol dm^{-3}

10^4 $[MnO_4^-]$ (mol dm^{-3})	10^3 [CF] (mol dm^{-3})	10^2 $[OH^-]$ (mol dm^{-3})	10^3 k_{obs} (s^{-1})	10^3 $k^*_{Calc.}$ (s^{-1})
0.4	3.0	2.0	6.71	6.51
0.8	3.0	2.0	6.81	6.51
1.0	3.0	2.0	6.70	6.51
2.0	3.0	2.0	6.78	6.51
3.0	3.0	2.0	6.69	6.51
4.0	3.0	2.0	6.62	6.51
3.0	2.0	2.0	5.36	5.44
3.0	3.0	2.0	6.69	6.41
3.0	4.0	2.0	7.00	6.85
3.0	8.0	2.0	7.64	7.36
3.0	16.0	2.0	8.46	8.42
3.0	20.0	2.0	8.93	8.65
3.0	3.0	0.4	3.02	3.20
3.0	3.0	0.8	4.59	4.69
3.0	3.0	1.0	4.90	5.18
3.0	3.0	2.0	6.70	6.51
3.0	3.0	4.0	7.20	7.47

* Calculated from Eq. (6) using k, K_1 and K_2 obtained from verification plot for different experimental conditions.

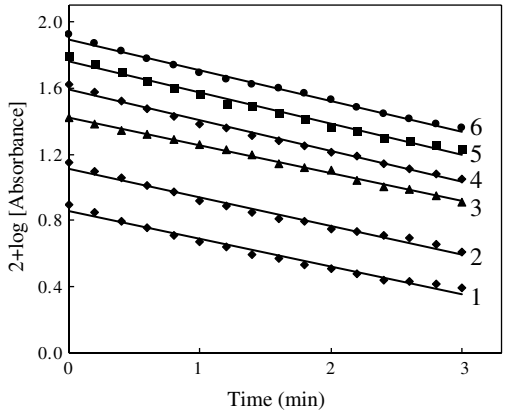


Fig. 2. First order plots of the oxidation of ciprofloxacin by permanganate in aqueous alkaline medium. $[CF] = 3.0 \times 10^{-3}$ $[OH^-] = 2.0 \times 10^{-2}$ $I = 0.04$/mol dm^{-3}. $[MnO_4^-] \times 10^4$ mol dm^{-3} = (1) 0.4, (2) 0.8, (3) 1.0, (4) 2.0, (5) 3.0, (6) 4.0.

Table 2
Activation and thermodynamic parameters for the oxidation of ciprofloxacin by MnO_4^- in aqueous alkaline medium with respect to slow step of Scheme 3

Temperature (K)		10^3 k (s^{-1})
(a) Effect of temperature		
298		9.4
303		10.1
308		11.2
313		12.1
Parameters		Values
(b) Activation parameters		
E_a (kJ mol^{-1})		13.4 ± 0.3
$\Delta H^{\#}$ (kJ mol^{-1})		10.9 ± 0.2
$\Delta S^{\#}$ (J K^{-1} mol^{-1})		-247 ± 6
$\Delta G^{\#}$ (kJ mol^{-1})		84.5 ± 3.0
Temperature (K)	K_1 (dm^3 mol^{-1})	10^{-3} K_2 (dm^3 mol^{-1})
(c) Equilibrium constants K_1 and K_2 at different temperatures		
298	6.6	6.2
303	9.3	4.2
308	14.9	2.6
313	22.2	2.2
Quantities	Using K_1 values	Using K_2 values
(d) Thermodynamic quantities using K_1 and K_2 values		
ΔH (kJ mol^{-1})	63.9 ± 1.5	-54.6 ± 1.5
ΔS (J K^{-1} mol^{-1})	230 ± 5	-111 ± 4
ΔG (kJ mol^{-1})	-6.3 ± 0.2	-20.7 ± 0.3

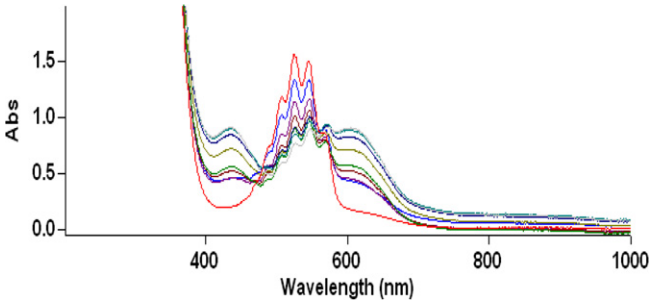
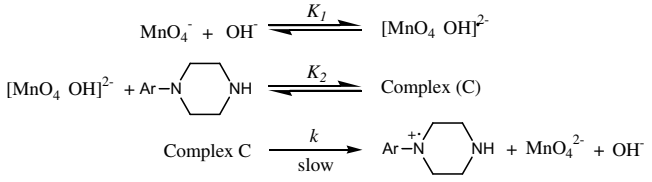


Fig. 3. Spectral changes during the oxidation of ciprofloxacin (CF) by $KMnO_4^-$ at 5 °C. $[MnO_4^-] = 3.0 \times 10^{-4}$, $[CF] = 3.0 \times 10^{-3}$, $[OH^-] = 2.0 \times 10^{-2}$, $I = 0.04$/mol dm^{-3}.

further oxidation resulting in lower oxidation state of manganese, Mn(IV). The results imply that first the alkali combines with permanganate to give an alkali-permanganate species $[MnO_4 \cdot OH]^{2-}$ in a prior equilibrium step [23]. The fractional order with respect to ciprofloxacin presumably results from the complex formation between oxidant and substrate prior to the slow step. Indeed it is to be noted that a plot of $1/k_{obs}$ *versus* 1/[CF] (Michaelis–Menten plot) shows an intercept in agreement with complex formation. The evidence for complex formation was obtained from UV–Vis spectra of oxidant, substrate and reaction mixture, in which bathochromic shift of 7 nm from 315 to 322 nm and hyperchromicity at 322 nm was observed at lower temperature (5 °C). The literature points out that piperazine ring of ciprofloxacin is the reactive moiety towards oxidation [17].

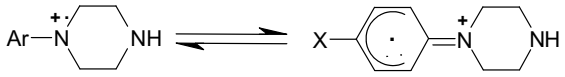
Within the complex one-electron is transferred from ciprofloxacin to Mn(VII). The breaking of this complex (C) is considered to be the slow step, forming ciprofloxacin radical intermediate and product, Mn(VI). The formed radical intermediate may subsequently undergo several different reaction pathways to yield a range of products. Such oxidant–ciprofloxacin complex formation and electron transfer step is considered as rate-limiting step in earlier report also [17]. The effect of ionic strength and dielectric constant on the rate explains qualitatively the involvement of a neutral molecule in the reaction. All the results may be interpreted in the form of following Scheme 3.

Since Scheme 3 is in accordance with the generally well-accepted principle of non-complementary oxidations taking place in sequence of one-electron steps, the reaction



Scheme 3.

between the substrate and oxidant would afford a radical intermediate. This type of radical intermediate shown in the slow step has also been observed in the literature [18]. This formed radical intermediate can be stabilized by resonance of the aromatic ring.

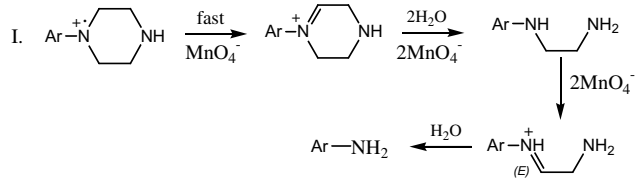


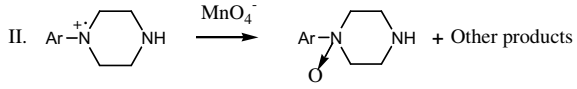
4.1. Further reactions of radical intermediates

Scheme 3 shows that the radical intermediates may undergo several subsequent reactions to generate a range of products observed in this study. Earlier studies have demonstrated that anilinyl radicals most likely undergo coupling via the amino group (head) or the *para* position of the benzene ring (tail) to form head-to-head, head-to-tail, or tail-to-tail coupling products [24]. Coupling of flouroquinolone radicals, however, is likely difficult (as pointed out in Ref. [17]) because of steric hindrance at the N1 position and the blockage at the *para* position in the aromatic ring. This radical formation is followed by other fast steps as given in the following two pathways, which could explain the formation of the oxidation products identified Fig. 1(b).

Pathway I is a *N*-dealkylation process (Scheme 3), in which one electron is transferred from the radical N1 to Mn(VII), yielding an iminium ion [24b,25]. Hydrolysis of the iminium ion follows immediately. Although hydrolysis of an iminium ion with the N atom connecting to an aromatic ring is a relatively slow reaction [17], it may still kinetically compete with the oxidation reaction at the N4 atom. Similar oxidation and hydrolysis occurs at the N4 atom, leading to the production of the partially dealkylated M−26 product. In a similar fashion, the M−26 product is oxidized to its corresponding iminium ion at its inner N1 and finally hydrolyzed to the fully dealkylated M−69 product [26]. In the presence of an excess amount of permanganate, the M−69 product can be further oxidized in a manner similar to oxidation of aniline. Since Scheme 3 is in accordance with the generally well-accepted principle of non-complementary oxidations taking place in sequence of one-electron steps, the reaction between the substrate and oxidant would afford a radical intermediate. This type of radical intermediate shown in the slow step has also been observed in the literature [18]. This radical formation is followed by other fast steps as given in the following two pathways, which could explain the formation of the oxidation products identified.

Pathway II. Based on the kinetic results and product analysis, the possibility of reaction pathways other than the one discussed above cannot be excluded (listed as pathway II in Scheme 3). One example is a pathway leading to the formation of *N*-oxide product (i.e. M+16). Despite the high complexity of the radical reactions, one can expect that the likelihood of the N1 radical intermediate to undergo either of the reaction pathways will be affected by electronic and steric effects on the radical and result in different yields among the various products





Scheme 3 leads to the rate law (6) as follows:
According to Scheme 3

$$\text{Rate} = \frac{-\mathrm{d}[\mathrm{MnO_4^-}]}{\mathrm{d}t} = kK_1K_2[\mathrm{MnO_4^-}][\mathrm{CF}]_\mathrm{f}[\mathrm{OH^-}]_\mathrm{f} \quad (1)$$

The total $[MnO_4^-]$ can be written as

$$\begin{aligned}[\mathrm{MnO_4^-}]_\mathrm{T} &= [\mathrm{MnO_4^-}]_\mathrm{f} + [\mathrm{MnO_4 \cdot OH}]^{2-} + [\mathrm{Complex}] \\ &= [\mathrm{MnO_4^-}]_\mathrm{f} + K_1[\mathrm{MnO_4^-}][\mathrm{OH^-}] + K_1K_2[\mathrm{MnO_4^-}][\mathrm{OH^-}][\mathrm{CF}] \\ &= [\mathrm{MnO_4^-}]_\mathrm{f}(1 + K_1[\mathrm{OH^-}] + K_1K_2[\mathrm{OH^-}][\mathrm{CF}])\end{aligned}$$

where t and f stands for total and free

$$[\mathrm{MnO_4^-}]_\mathrm{f} = \frac{[\mathrm{MnO_4^-}]_\mathrm{T}}{1 + K_1[\mathrm{OH^-}] + K_1K_2[\mathrm{OH^-}][\mathrm{CF}]} \quad (2)$$

Similarly, total $[OH^-]$ can be calculated as

$$[\mathrm{OH^-}]_\mathrm{T} = [\mathrm{OH^-}]_\mathrm{f} + [\mathrm{MnO_4 \cdot OH}]^{2-} + [\mathrm{Complex}]$$

In view of low concentration of MnO_4^- and ciprofloxacin used, above equation can be written as

$$[\mathrm{OH^-}]_\mathrm{T} = [\mathrm{OH^-}]_\mathrm{f} \quad (3)$$

Similarly,

$$[\mathrm{CF^-}]_\mathrm{T} = [\mathrm{CF^-}]_\mathrm{f} \quad (4)$$

Substituting Eqs. (2)–(4) in Eq. (1) we get,

$$\text{Rate} = \frac{kK_1K_2[\mathrm{MnO_4^-}][\mathrm{OH^-}][\mathrm{CF}]}{1 + K_1[\mathrm{OH^-}] + K_1K_2[\mathrm{OH^-}][\mathrm{CF}]} \quad (5)$$

$$\frac{\text{Rate}}{[\mathrm{MnO_4^-}]} = k_\mathrm{obs} = \frac{kK_1K_2[\mathrm{OH^-}][\mathrm{CF}]}{1 + K_1[\mathrm{OH^-}] + K_1K_2[\mathrm{OH^-}][\mathrm{CF}]} \quad (6)$$

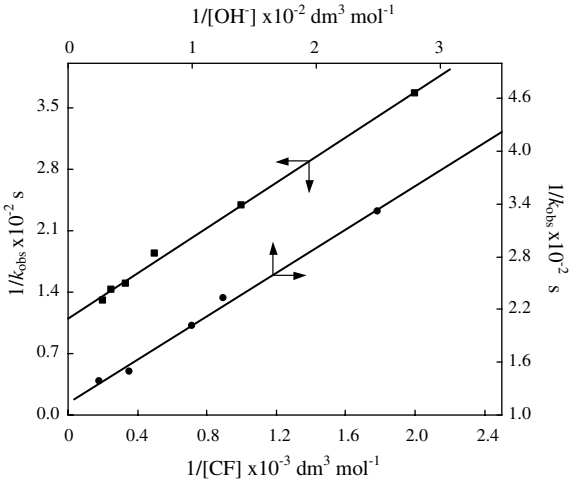


Fig. 4. Plots of $1/k_{obs}$ *versus* 1/[CF] and $1/k_{obs}$ *versus* $1/[OH^-]$ for verification of rate law (6) in the form of (7) on the MnO_4^- oxidation of ciprofloxacin in aqueous alkaline medium at 25 °C. (Conditions as in Table 1.)

Eq. (6) confirms all the observed orders with respect to different species, which can be verified by rearranging it to.

$$\frac{1}{k_{obs}} = \frac{1}{kK_1K_2[OH^-][CF]} + \frac{1}{kK_2[CF]} + \frac{1}{k} \quad (7)$$

According to Eq. (7), other conditions being constant, plots of $1/k_{obs}$ *versus* 1/[CF] ($r \geqslant 0.996$, $S \leqslant 0.012$) and $1/k_{obs}$ *versus* $1/[OH^-]$ ($r \geqslant 0.997$, $S \leqslant 0.013$) should be linear and are found to be so (Fig. 4). The slopes and intercepts of such plots lead to the values of K_1, K_2 and k (Table 2). The value of K_1 is in agreement with the literature [27].

The thermodynamic quantities for the first and second equilibrium steps of Scheme 3 can be evaluated as follows. The [CF] and $[OH^-]$ (as in Table 1) were varied at four different temperatures. The plots of $1/k_{obs}$ *versus* 1/[CF] and $1/k_{obs}$ *versus* $1/[OH^-]$ should be linear. From the slopes and intercepts, the values of K_1 and K_2 were calculated at different temperatures and these values are given in Table 2. van't Hoff's plots were made for variation of K_1 and K_2 with temperature $\log K_1$ *versus* $1/T$ ($r \geqslant 0.9939$, $S \leqslant 0.009$) and $\log K_2$ *versus* $1/T$ ($r \geqslant 0.926$, $S \leqslant 0.0074$). The values of enthalpy of reaction ΔH, entropy of reaction ΔS and free energy of reaction ΔG, were calculated for the first, and second equilibrium steps. These values are given in Table 2. A comparison of the later values (from K_2) with those obtained for the slow step of the reaction shows that these values mainly refer to the rate-limiting step, supporting the fact that the reaction before rate determining step is fairly fast and involves low activation energy [28].

The moderate values of $\Delta H^{\#}$ and $\Delta S^{\#}$ were both favorable for electron transfer processes. The value of $\Delta S^{\#}$ within the range for radical reaction has been ascribed to the nature of electron pairing and unpairing processes and to the loss of degrees of freedom formerly available to the reactants upon the formation of rigid transition state [29]. The negative value of $\Delta S^{\#}$ indicates that the complex (C) is more ordered than the reactants [30].

The observed modest enthalpy of activation and a relatively low value of the entropy of activation as well as a higher rate constant of the slow step indicate that the oxidation presumably occurs via inner-sphere mechanism [31].

5. Conclusion

The results of this investigation indicate that ciprofloxocin of antibiotic class is substantially degraded under conditions yielding lower mass degradates. The results demonstrate that in carrying out this reaction, the role of pH in the reaction medium is crucial. The literature [32] reports that dealkylated products of ciprofloxacin have reduced antimicrobial activity. Since dealkylated products were obtained by permanganate oxidation of ciprofloxacin, it is evident that the products of this title reaction have reduced antimicrobial activity after oxidation. This permanganate oxidation can be effectively used in the wastewater treatment at the sites contaminated by flouroquinolone antibiotics. Insoluble manganese dioxide formed, provides advantages in the removal of phenol and other organic contaminants from the wastewater. Rate constant of slow step and other equilibrium constants involved in the mechanism are evaluated and activation parameters with respect to slow step of reaction were computed. The overall mechanistic sequence described here is consistent with product, mechanistic and kinetic studies.

References

[1] A. Shaabani, F. Tavasoli-Rad, D.G. Lee, Synth. Commun. 35 (2005) 571.
[2] S. Caron, R.W. Dugger, S.G. Ruggeri, J.A. Ragan, D.H. Brown Ripin, Chem. Rev. 106 (2006) 2943.
[3] D.G. Lee, in: W.S. Trahanovsky (Ed.), Oxidation in Organic Chemistry, Part D, Academic Press, New York, 1982, p. 147.
[4] L.I. Simandi, in: S. Patai, Z. Rappoport (Eds.), The Chemistry of Functional Groups, Wiley, Chichester, 1983, Suppl. C.
[5] D.G. Lee, E.J. Lee, K.C. Brown, Phase Transfer Catalysis, New Chemistry, Catalysis and Applications, ACS Symposium Series, vol. 326, American Chemical Society, Washington, DC, 1987.
[6] A.J. Fatiadi, Synthesis 106 (1987) 85.
[7] J.F. Perez-Benito, D.G. Lee, J. Org. Chem. 52 (1987) 3239.
[8] R. Stewart, K.A. Gardner, L.L. Kuehnert, J.M. Mayer, Inorg. Chem. 36 (1997) 2069.
[9] L.I. Simandi, M. Jaky, C.R. Savage, Z.A. Schelly, J. Am. Chem. Soc. 107 (1985) 4220.
[10] P.L. Timmanagoudar, G.A. Hiremath, S.T. Nandibewoor, Transition Met. Chem. 22 (1997) 193;
S. Nadimpalli, R.A. Rallabandi, L.S. Dikshitulu, Transition Met. Chem. 18 (1993) 510.
[11] (a) R.G. Panari, R.B. Chougale, S.T. Nandibewoor, Polish J. Chem. 72 (1998) 99;
(b) A. Bohm, M. Adam, H. Mauermann, S. Stein, K. Mullen, Tetrahedron Lett. 33 (1992) 2795.
[12] A.I. Darkopoulos, P.C. Ioannou, Anal. Chem. 354 (1997) 197.
[13] R. Williams, J.C. Riviere, Chem. Health Safety 1 (2003) 7.
[14] M. Ruyz, L. Perello, R. Ortiz, A. Castineiras, C. Maichle-Mossmer, E. Canton, J. Inorg. Biochem. 59 (1995) 801;

M. Ruyz, L. Perello, J. Server-Carrio, R. Ortiz, S. Garcýa-Granda, M.R. Dýaz, E. Canton, J. Inorg. Biochem. 69 (1998) 231.
[15] I. Turel, I. Leban, N. Bukovec, J. Inorg. Biochem. 66 (1997) 241.
[16] M.P. Lopez-Gresa, R. Ortiz, L. Parello, J. Latorre, M. Liu-Gonzalez, S. Garcia-Granda, M. Perez-Priede, E. Canton, J. Inorg. Biochem. 92 (2002) 65.
[17] Huichun Zhang, Ching-Hua Huang, Environ. Sci. Technol. 39 (2005) 4474, and references there in.
[18] Michael C. Dodd, Amisha D. Shah, Urs Von Gunten, Ching-Hua Huang, Environ. Sci. Technol. 39 (2005) 4474.
[19] G.H. Jeffery, J. Bassett, J. Mendham, R.C. Denny, in: Vogel's Textbook of Quantitative Chemical Analysis, 5th ed., ELBS, Longman, Essex, UK, 1996, p. 370.
[20] A. Carrington, M.C.R. Symons, J. Chem. Soc. (1956) 3373.
[21] J. Burhenne, Environ. Sci. Pollut. Res. 4 (1997) 10.
[22] L.I. Simandi, M. Jaky, C.R. Savage, Z.A. Schelly, J. Am. Chem. Soc. 107 (1985) 4220.
[23] R.G. Panari, R.B. Chougale, S.T. Nandibewoor, J. Phys. Org. Chem. 11 (1998) 448.
[24] (a) S. Laha, R.G. Luthy, Environ. Sci. Technol. 24 (1990) 363;
(b) M. Bietti, A. Cuppoletti, C. Dagostin, C. Florea, C. Galli, P. Gentili, H. Petride, C. Russo Caia, Eur. J. Org. Chem. 11 (1998) 2425.
[25] (a) Y. Seto, F.P. Guengerich, J. Biol. Chem. 268 (1993) 9986;
(b) J. Iley, R. Tolando, J. Chem. Soc., Perkin Trans. 2 (2000) 2328;
(c) J.R.L. Smith, D.N. Mortimer, J. Chem. Soc., Perkin Trans. 2 (1986) 1743;
(d) A. Cuppoletti, C. Dagostin, C. Florea, C. Galli, P. Gentili, O. Lanzalunga, A. Petride, H. Petride, Chem. Eur. J. 5 (1999) 2993.
[26] F. Wang, L.M. Sayre, J. Am. Chem. Soc. 114 (1992) 248.
[27] D.C. Bilehal, R.M. Kulkarni, S.T. Nandibewoor, Z. Phys. Chem. (2003) 1.
[28] (a) K.S. Rangappa, M.P. Raghavendra, D.S. Mahadevappa, D. Channegouda, J. Org. Chem. 63 (1998) 531;
(b) D.C. Bilehal, R.M. Kulkarni, S.T. Nandibewoor, Can. J. Chem. 79 (2001) 1926.
[29] C. Walling, Free Radicals in Solution, Academic Press, New York, 1957, p. 38.
[30] (a) K.S. Rangappa, N. Anitha, N.M. Madegouda, Synth. React. Inorg. Met. Org. Chem. 31 (2001) 1499;
(b) Z.D. Bugarcic, S.T. Nandibewoor, M.S.A. Hamza, F. Heimemann, Rudi van Eldik, Dalton Trans. (2006) 2984.
[31] (a) K.W. Hicks, J. Inorg. Nucl. Chem. 38 (1976) 1381;
(b) S.A. Farokhi, S.T. Nandibewoor, Tetrahedron 59 (2003) 7595.
[32] G. Phillips, B.E. Johnson, J. Ferguson, J. Antimicrob. Chemother. 26 (1990) 783.

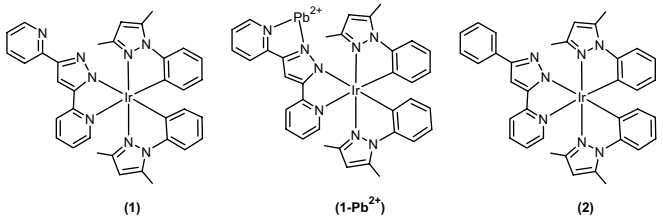
Ca^{2+}, Hg^{2+} or Pb^{2+}, can be obtained. Moreover, it may allow the design of ''light-controlled ion switches'', for which the cation ejection from, e.g. the crown ether can be triggered by the effective reduction of electron donation at the receptor on excitation of the nearby chromophore [11]. As many of heavy metals are known as fluorescence quenchers via enhanced spin–orbit coupling [12], it is thus intriguing and of both fundamental and application importance to examine the interaction between environmental hazard metals such as Pb^{2+} (or Hg^{2+}) and heavy metal complexes that mainly exhibit room-temperature phosphorescence in solution due to the strong spin–orbit coupling effect.

Aiming at this goal, we present a novel phosphorescence sensor, in which an 3,5-di(pyridyl)pyrazole (py_2pz) moiety is attached to the heteroleptic Ir(III) complex (**1**). This design provides three inherent advantages [13]. First, the Ir(III) metal atom forms highly stable, octahedral coordinated structure and inherits strong phosphorescent emission due to the heavy atom effect induced by the Ir(III) metal center. Moreover, the ancillary cyclometalated *N*-phenyl pyrazole ligands, for which their $\pi\pi^*$ energy levels are far greater than those of the respective MLCT and other ligand-centered $\pi\pi^*$ excited states [14], enable both the HOMO and LUMO to reside predominantly on the ancillary py_2pz segment. Thirdly, the py_2pz fragment is attached to the Ir(III) metal center and then forming a neutral metal complex. Such a charge-neutral characteristic is similar to that of the Re(I) and Pt(II) based sensor complexes, but is in sharp contrast to most of the Ru(II) based polypyridyl sensors [15], for which the net cationic charge on the overall metal complex is expected to reside, in part, at the ligand site, giving a much reduced sensitivity in recognizing metal cations [16]. Finally, the nitrogen atoms of the py_2pz moiety would act as the effective donor site, allowing the direct recognition of the incoming cationic analytes. In other words, the py_2pz segment acts as crab chela and can potentially be used for distinguishing metal ions, simplifying the design strategy (see Scheme 1).

2. Experimental

2.1. General information and materials

Elemental analyses and Mass spectra (operating in FAB mode) were carried out at the NSC Regional Instrument Centre at National Chiao Tung University, Taiwan. ^1H and ^{13}C NMR spectra were recorded on a Varian Mercury 400 instrument; chemical shifts are quoted with respect to internal standard Me_4Si. All synthetic manipulations were performed under N_2 atmosphere, while solvents were used as received. Synthesis of 3,5-di(2-pyridyl) pyrazole (py_2pz)H, 3-phenyl-5-(2-pyridyl) pyrazole (ppypz)H and 1-phenyl-3,5-dimethyl pyrazole (pdpz)H follows the procedures documented in the literature [17]. Treatment of (pdpz)H with $IrCl_3 \cdot nH_2O$ in refluxing methoxyethanol afforded the chloride bridged dimer $[(pdpz)_2IrCl]_2$ in 75% yield [14]; it was then used for subsequent reactions without further purification.



Scheme 1.

2.2. Preparation of [(pdpz)$_2$Ir(py$_2$pz)] (1)

A mixture of $[(pdpz)_2IrCl]_2$ (150 mg, 0.13 mmol), 3, 5-di(2-pyridyl) pyrazole (py_2pzH, 64 mg, 0.29 mmol) and Na_2CO_3 (93 mg, 0.88 mmol) in 2-methoxyethanol (25 mL) was heated to reflux for 6 hours. Excess of water was added after cooling the solution to room temperature. The precipitate was collected by filtration and subjected to silica gel column chromatography, eluting with a mixture of ethyl acetate and methanol (9:1). Pale yellow crystals of $[(pdpz)_2Ir(py_2pz)]$ (**1**) were obtained from repeated recrystallization using a mixture of THF and pentane at room temperature (49 mg, 0.065 mmol, 50%).

Spectral data of **1**: MS (FAB, ^{193}Ir): *m*/*z* 756 (M^+). ^1H NMR (400 MHz, DMSO-d_6, 298 K): δ 8.43 (d, 1H, $J_{HH} = 4.8$ Hz), 7.99 (d, 1H, $J_{HH} = 7.6$ Hz), 7.84 (t, 1H, $J_{HH} = 7.8$ Hz), 7.63 (t, 1H, $J_{HH} = 7.6$ Hz), 7.60 (t, 1H, $J_{HH} = 8.0$ Hz) 7.53 (d, 1H, $J_{HH} = 5.6$ Hz), 7.47 (d, 1H, $J_{HH} = 8.0$ Hz), 7.42 (d, 1H, $J_{HH} = 8.4$ Hz), 7.39 (s, 1H), 7.07 (t, 2H, $J_{HH} = 6.4$ Hz), 6.95 (t, 1H, $J_{HH} = 8.0$ Hz), 6.86 (t, 1H, $J_{HH} = 8.0$ Hz), 6.75 (t, 1H, $J_{HH} = 7.6$ Hz), 6.65 (t, 1H, $J_{HH} = 7.6$ Hz), 6.28 (d, 1H, $J_{HH} = 7.2$ Hz), 6.23 (d, 1H, $J_{HH} = 8.0$ Hz), 6.20 (s, 1H), 6.16 (s, 1H), 2.75 (s, 3H, Me), 2.72 (s, 3H, Me), 1.50 (s, 3H, Me), 1.47 (s, 3H, Me). *Anal.* Calc. for $C_{35}H_{31}IrN_8$: C, 55.61; N, 14.82; H, 4.13. Found: C, 55.37; N, 14.46; H, 4.20%.

2.3. Preparation of [(pdpz)$_2$Ir(ppypz)] (2)

A mixture of $[(pdpz)_2IrCl]_2$ (200 mg, 0.17 mmol), 3-phenyl-5-(2-pyridyl) pyrazole (ppypzH, 85 mg, 0.38 mmol) and Na_2CO_3 (214 mg, 0.21 mmol) in 2-methoxyethanol (25 mL) was heated to reflux for 6 h. Excess of water was added after cooling the solution to room temperature. The precipitate was collected by filtration and subjected to silica gel column chromatography, eluting with a mixture of ethyl acetate and methanol (9:1). Pale yellow crystals of $[(pdpz)_2Ir(ppypz)]$ (**2**) were obtained from repeated recrystallization using a mixture of THF and pentane at room temperature (68 mg, 0.009 mmol, 53%).

Spectral data of **2**: MS (FAB, ^{193}Ir): *m*/*z* 755 (M^+). ^1H NMR (400 MHz, DMSO-d_6, 298 K): δ 7.91 (d, 1H, $J_{HH} = 7.6$ Hz), 7.82 (t, 1H, $J_{HH} = 7.2$ Hz), 7.59 (d, 1H, $J_{HH} = 7.2$ Hz), 7.52 (d, 1H, $J_{HH} = 6.2$ Hz), 7.46 (d, 1H,

$J_{HH} = 8.0$ Hz), 7.40 (d, 1H, $J_{HH} = 8.0$ Hz), 7.24 (t, 2H, $J_{HH} = 8.0$ Hz), 7.19 (s, 1H), 7.08 (t, 1H, $J_{HH} = 7.2$ Hz), 7.04 (t, 1H, $J_{HH} = 6.2$ Hz), 6.93 (t, 2H, $J_{HH} = 7.6$ Hz), 6.84 (t, 1H, $J_{HH} = 8.0$ Hz), 6.74 (t, 1H, $J_{HH} = 7.6$ Hz), 6.63 (t, 1H, $J_{HH} = 7.6$ Hz), 6.27 (d, 1H, $J_{HH} = 7.2$ Hz), 6.22 (d, 1H, $J_{HH} = 7.2$ Hz), 6.19 (s, 1H), 6.15 (s, 1 H), 2.77 (s, 3H, Me), 2.74 (s, 3H, Me), 1.52 (s, 3H, Me), 1.50 (s, 3H, Me). *Anal.* Calc. for $C_{36}H_{32}IrN_7$: C, 57.28; N, 12.99; H, 4.27. Found: C, 57.14; N, 13.01; H, 4.28%.

2.4. Preparation of $[(pdpz)_2Ir(py_2\ pz)Pb(ClO_4)_2]$-(**1**-$Pb^{2+}$)

$Pb(ClO_4)_2 \cdot H_2O$ (18.7 mg, 0.046 mmol) was dissolved in 6 mL acetonitrile and then added into a glass tube with solid sample of **1** (17.4 mg, 0.023 mmol). The light green-yellow crystal suitable for single crystal X-ray diffraction was grown by ether diffusion for several days.

2.5. X-ray diffraction study

Single crystal X-ray diffraction data were measured on a Bruker SMART Apex CCD diffractometer using (Mo Kα) radiation ($\lambda = 0.71073$ Å). The data collection was executed using the SMART program. Cell refinement and data reduction were performed with the SAINT program. The structure was determined using the SHELXTL/PC program and refined using full-matrix least squares.

Crystal data for **1**-Pb^{2+}: $C_{35}H_{31}Cl_2IrN_8O_8Pb$, $M = 1161.97$, monoclinic, space group $P2_1/n$, $T = 150$ K, $a = 19.0572(12)$, $b = 9.9577(6)$, $c = 19.2354(12)$ Å, $\beta = 91.354(2)°$, $U = 3649.2(4)$ Å^3, $Z = 4$, μ (Mo Kα) $= 8.462$ mm^{-1}, 24 109 reflections collected, 8360 unique ($R_{int} = 0.0604$), final $R_1[I > 2\sigma(I)] = 0.0391$, wR_2 (all data) $= 0.0898$.

2.6. UV–Vis and phosphorescence titration of compounds *1* with Pb^{2+} ions

The stock solution of compound **1** (2×10^{-5} M) was prepared by using spectroscopic grade CH_3CN. The solution of Pb^{2+} ions (1×10^{-3} M) was prepared by using $Pb(ClO_4)_2$ hydrate dissolved in CH_3CN. The solutions of **1** in the titration range exhibited a linear dependence of absorption and emission. The absorption and emission spectrum of **1** (3.2 mL of 2×10^{-5} M stock solution) in a quartz cell (1 cm width) were recorded at 298 K. The absorption titration of **1** with Ca^{2+} and Hg^{2+} ions were carried out by a procedure similar to that for Pb^{2+} ion.

2.7. Measurements

Steady-state absorption and emission spectra were recorded by a Hitachi (U-3310) spectrophotometer and an Edinburgh (FS920) fluorimeter, respectively. The association constant K_a of 1:1 **1**/guest complex formation calculated by the UV–Vis absorption method is obtained by the following equation [18]:

$$\frac{A_0}{A_0 - A} = \left(\frac{\varepsilon_M}{\varepsilon_M - \varepsilon_p}\right)\left[\frac{1}{K_a C_g} + 1\right] \quad (1)$$

where C_g is the added guest (e.g. Pb^{2+}) concentration. A_0 (ε_M) and A (ε_p) denote the absorbance (molar extinction coefficient) of free **1**, and solution after adding, e.g. Pb^{2+}, respectively, at a selective wavelength. Eq. (1) can be further extended to the emission titration experiment expressed as

$$\frac{F_0}{F_0 - F} = \frac{\Phi_M \varepsilon_M}{(\Phi_M \varepsilon_M - \Phi_p \varepsilon_p)}\left(\frac{1}{K_a C_g} + 1\right) \quad (2)$$

where $F_0(\Phi_M)$ and $F(\Phi_p)$ denote the photoluminescence (quantum yield) of free **1**, and that of solution after adding Pb^{2+}, respectively, at a selective wavelength. Details of nanosecond lifetime measurements have been described in previous publication [19].

3. Results and discussions

As shown in Fig. 1, ion-free **1** in CH_3CN exhibits a weak 426 nm ($\varepsilon = 235$ M^{-1} cm^{-1}) absorption band, which is assigned to the spin-forbidden $^3\pi\pi^*$ (^{3}ILCT) transition perhaps mixed with a small amount of the ^{3}MLCT transition to the py_2pz ligands. The absorption band around 300 nm ($\varepsilon \sim 10^4$ M^{-1} cm^{-1}) is attributed to the $^1\pi\pi^*$ transition, while transitions associated with ^{1}MLCT are relatively weak and thus are possibly hidden underneath the $^1\pi\pi^*$ bands. In degassed or N_2 purged CH_3CN, **1** exhibits a 485 nm emission with moderate intensity ($\Phi \sim 0.04$, $\tau \sim 70$ ns). Upon aeration, the emission yield is reduced to 0.01 ($\tau \sim 21$ ns). The strong O_2 quenching and a calculated long radiative lifetime of ~2.6 μs lead us to conclude that the emission unambiguously originates from phosphorescnece.

The absorption and luminescence spectra recorded for **1** upon titrated with Pb^{2+} are also depicted in Fig. 1. Note that the titration was performed in the aerated solution.

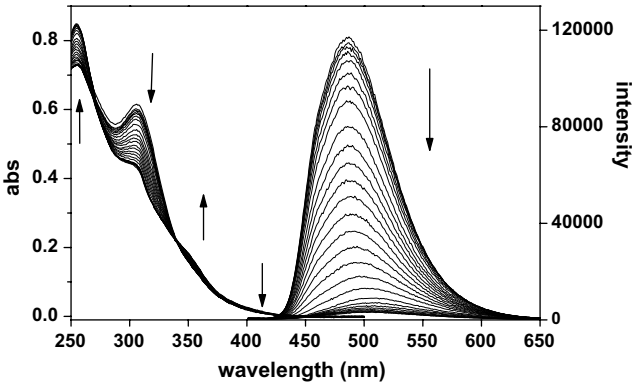


Fig. 1. The absorption and emission spectra of **1** (2.0×10^{-5} in aerated CH_3CN) upon addition of increasing amounts of Pb^{2+} at (a) 0, (b) 0.07, (c) 0.13, (d) 0.20, (e) 0.33, (f) 0.47, (g) 0.60, (h) 0.80, (i) 1.07, (j) 1.27, (k) 1.43, (l) 1.60, (m) 1.77, (n) 1.93, (o) 2.10, (p) 2.27, (q) 2.43, (r) 2.60, (s) 2.77, (t) 2.93, (u) 3.10, (v) 3.27, (w) 3.43, (x) 3.60, (y) 3.77, (z) 3.93, (aa) 4.10, (ab) 4.27 μM of **1**, λ_{ex}: 339 nm.

Evidently, the addition of Pb^{2+} caused a significant change of the absorption spectral profile with an isosbestic point appearing at ~340 nm, indicating the existence of ground-state equilibrium between two species, namely the free and Pb^{2+} linked **1**-Pb^{2+} complexes. Concomitantly, upon excitation at the isosbestic point, the 485 nm phosphorescence was gradually red shifted toward 505 nm, accompanied by the drastic decrease of the emission intensity. Taking the emission peak intensity of **1** and **1**-Pb^{2+} to be F_0 and F, respectively, a straight line plot of $F_0/(F_0 - F)$ versus $\mathbf{1}/[Pb^{2+}]$ at, e.g. 485 nm is depicted in Fig. 2, supporting the 1:1 complexation ratio. Additional evidence was provided by the Job's plot analysis [20], in which decreases of the 485 nm were plotted against molar fractions of **1** and Pb^{2+} under a condition of the constant total concentration. As such, the concentration of **1**-Pb^{2+} reached a turning point when the molar fraction of [**1**]/([Pb^{2+}]+[**1**]) was about 0.5 (see insert of Fig. 2). Accordingly, the association constant K_a was deduced to be as large as $(7.0 \pm 0.3) \times 10^5\ M^{-1}$.

The key-role of crab chela made by the py_2pz segment can be envisaged by the synthesis of complex **2**, in which the pyridyl lariate was replaced by the essentially inert phenyl group. As a result, negligible spectral changes were observed during the Pb^{2+} titration for complex **2** up addition to 10^{-3} M, providing a preliminary spectral evidence for the high activity of py_2pz functional group in **1**. Moreover, the definitive support for the **1**-Pb^{2+} structure is rendered by the single crystal X-ray structural analyses, for which the single crystals of **1**-Pb^{2+} adduct were obtained from a slow diffusion of Et_2O into a concentrated acetonitrile solution of a 1:1 mixture of **1** and $Pb(ClO_4)_2$. Its ORTEP diagram was depicted in Fig. 3, showing the typical pseudo-octrahedral coordination arrangement around the Ir(III) center. Similar to those of related cyclometalated Ir(III) complexes [21], the nitrogen atoms of the pdpz

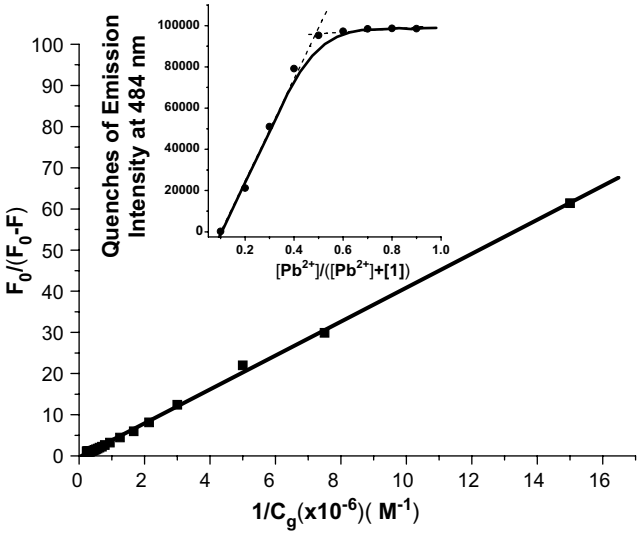


Fig. 2. The plot of $F_0/F_0 - F$ against $1/C_g$ at 486 nm. Insert: Job's plot of a 1:1 complex of **1** and Pb^{2+} cation, where the quenches of emission intensity at 484 nm was plotted against the mole fraction of Pb^{2+}.

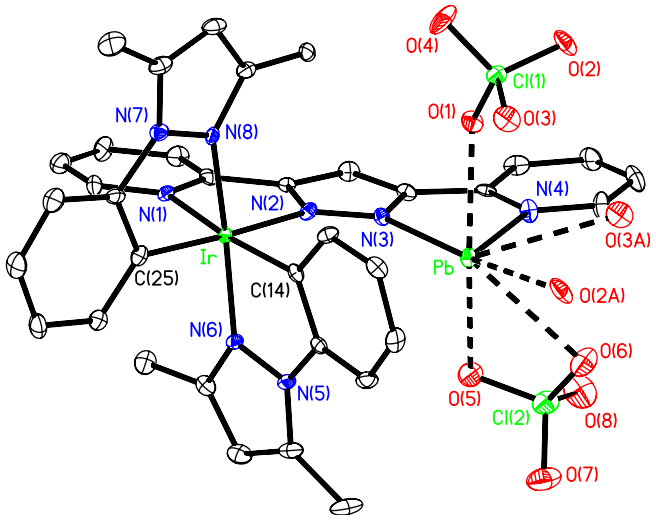


Fig. 3. ORTEP diagram of **1**-Pb^{2+} with thermal ellipsoids shown at 50% probability level; Ir–N(6) = 2.023(5) Ir–N(8) = 2.028(5), Ir–N(1) = 2.167(6), Ir–N(2) = 2.082(5), Ir–C(25) = 1.997(7), Ir–C(14) = 2.002(7), Pb–N(3) = 2.415(6), Pb–N(4) = 2.471(5) Å.

ligands resided at the mutual *trans*-disposition, while the coordinated N atoms of py_2pz ligands occupied the positions trans to the phenyl group of the pdpz ligands. All the Ir–C and Ir–N bond distances are unremarkable, as they falled in the range typical for these heteroleptic Ir(III) complexes reported in literatures. On the other hand, it is notable that the Pb^{2+} ion is linked to the outer pocket of py_2pz ligand with Pb-N distances being 2.415(6) and 2.471(5) Å, which fall within the literature value [22]. Such a bridged py_2pz bonding is akin to those of homodinuclear py_2pz complexes [23] and hybid complex containing lanthanide and transition metal elements such as $[(hfac)_3Ln(py_2pz)Cr(acac)_2]$ [24].

Competitive experiments have been performed using the same titration method for other metal cations, including alkali, alkaline earth metals and certain heavy metals. While there is apparently no spectral changes for alkali metal ions, the associated absorption spectra revealed a small amount of changes for alkaline and Hg^{2+} ions (see Figs. 4 and 5 for Ca^{2+} and Hg^{2+}titration). However, except for Hg^{2+}, none of them revealed appreciable changes in terms of emission profile and intensity in the range of 10^{-6}–10^{-3} M (also see Fig. 6). Addition of Hg^{2+} exhibited an emission quenching effect but with a smaller K_a. Based on a similar approach with that used for the Pb^{2+} titration, the association constant was determined to be $(5.9 \pm 0.3) \times 10^4\ M^{-1}$ and $(1.0 \pm 0.2) \times 10^4\ M^{-1}$ for Hg^{2+} and Ca^{2+} (absorption titration), respectively. The association constant for those selected metal ions are all less than that for Pb^{2+} by more than one order of the magnitude. This can also be illustrated by the phosphorescence intensity ratio of **1** (2×10^{-5} M in acetonitrile) in the presence of selected metal ion (10^{-3} M) before and after adding 10^{-3} M of Pb^{2+} shown in Fig. 6. The highly selective effect can be qualitatively rationalized by the amount of charge

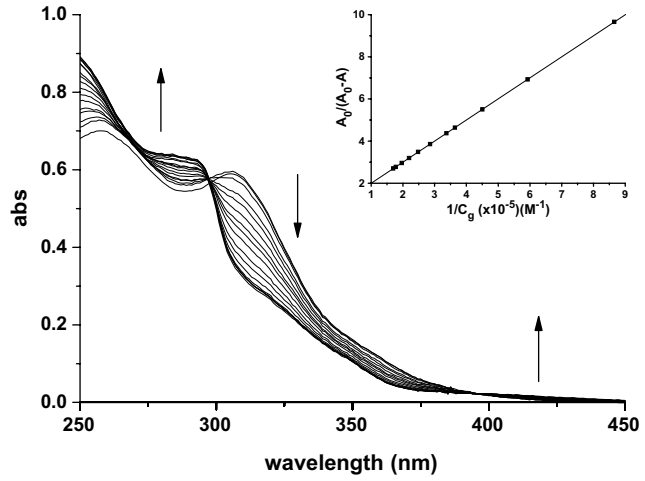


Fig. 4. The absorption spectra of **1** (2.0×10^{-5} in aerated CH_3CN) upon addition of increasing amounts of Ca^{2+} at (a) 0, (b) 1.16×10^{-5}, (c) 1.69×10^{-5}, (d) 2.22×10^{-5}, (e) 2.75×10^{-5}, (f) 2.97×10^{-5}, (g) 3.50×10^{-5}, (h) 4.03×10^{-5}, (i) 4.56×10^{-5}, (j) 5.09×10^{-5}, (k) 5.63×10^{-5}, (l) 5.89×10^{-5} M of **1**. Insert: the plot of $A_0/(A_0-A)$ against $\mathbf{1}/C_g$ at 306 nm.

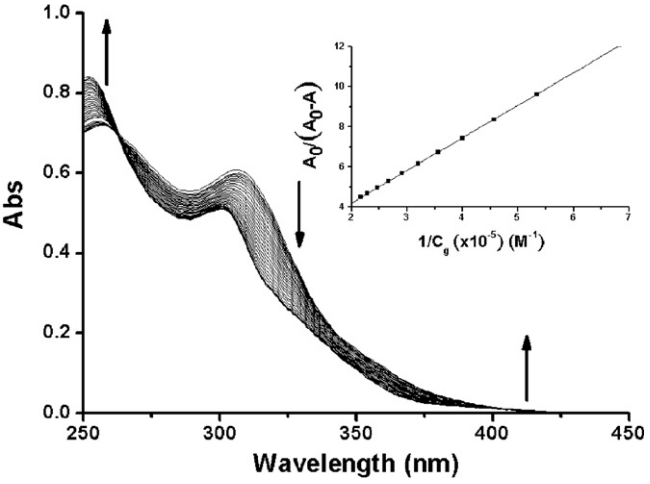


Fig. 5. The absorption spectra of **1** (2.0×10^{-5} in aerated CH_3CN) upon addition of increasing amounts of Hg^{2+} at (a) 0, (b) 0.31, (c) 0.63, (d) 0.94, (e) 1.25, (f) 1.47, (g) 1.88, (h) 2.19, (i) 2.50, (j) 2.81, (k) 3.13, (l) 3.44, (m) 3.75, (n) 4.06, (o) 4.38, (p) 4.61, (q) 5.00, (r) 5.31, (s) 5.63 (t) 5.94, (u) 6.25, (v) 6.56, (w) 6.87, (x) 7.19, (y) 7.50, (z) 7.81, (aa) 8.13, (ab) 8.44, (ac) 8.75, (ad) 9.06, (ae) 9.38 μM of **1**. Insert: the plot of $A_0/(A_0-A)$ against $1/C_g$ at 306 nm.

density, ρ, specified as $\rho = g/(4/3\pi r^3)$ where g and r are the corresponding formal charge (+1 or +2) and radius, respectively. For example, the reciprocal of r^3 (the Shannon effective ionic radius with coordination number of 8: $Pb^{2+}\sim1.29$, $Hg^{2+}\sim1.16$, and $Ca^{2+}\sim1.12$) [25] correlates well with the trend of the association constants.

We have also examined whether a similar recognition capability can be applied in the heterogeneous solid film in aqueous solution. Since **1** is insoluble in water, to simplify the process, a silica-based TLC plate was used as a solid support to soak **1** in CH_3CN so that a complex **1** coated TLC plate was prepared with an optical density of

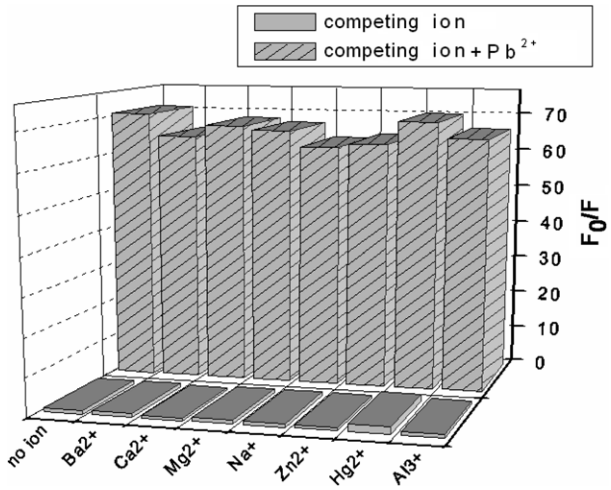


Fig. 6. (Grey) The phosphorescence intensity ratio of ion-free **1** (F_0, 2×10^{-5} M in acetonitrile) versus **1** in the presence of the selected metal ions (10^{-3} M). The phosphorescence intensity ratio of ion-free **1** vs. **1** in the presence of the selected metal ions (10^{-3} M), followed by addition of 10^{-3} M of Pb^{2+} ion (Slash-Grey).

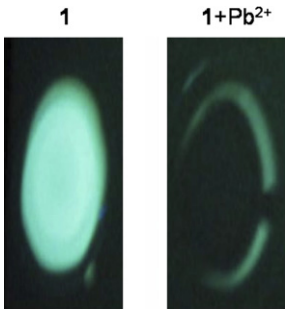


Fig. 7. The color of the sensor developed on a TLC plate with **1** in CH_3CN (left) and with Pb^{2+} solution in H_2O (right) was illuminated under 365 nm (UV lamp) for visualization (see text for the experimental detail). (For interpretation of the references to colour in this figure legend, the reader is referred to the web version of this article.)

$\sim$1.0 at 350 nm. Then we transfer a drop ($\sim$10 μL) of an aqueous solution (pH $\sim$ 7.0) containing $\sim10^{-4}$ M of $Pb(ClO_4)_2$ solution onto the plate, and then vacuum-dried to remove water. With the use of a commercially available UV-lamp (365 nm), photograph demonstrates a salient change of emission from blue–green (complex **1**) to a nearly dark state upon complexation with Pb^{2+} ion (see Fig. 7), implying the feasibility of **1** in sensing Pb^{2+} in aqueous solution down to nanomolar scales.

4. Conclusions

In conclusion, we apply complex **1** to demonstrate the concept of sensing Pb^{2+} ion based on the rare metal–ion sensitive phosphorescence. The ligated chromophores act as both recognition and signal-transmitting units, while the heavy metal, i.e. both Ir(III) ion and guest Pb^{2+}, serve as perturbing bases to enhance and quench

the phosphorescence, respectively. The emission quenching effect must be due to the affected core chromophores, i.e., the di(2-pyridyl) pyrazolate, that directly linked with Pb^{2+}, provoking the intersystem crossing to another lower-lying triplet state for the host molecule via an enhanced spin–orbit coupling. Consequently, the emission intensity will plausibly be quenched due to a smaller T_1–S_0 energy gap.

On the other hand, the internal motion of the uncoordinated pyridyl substituent can play some crucial role in the emission quenching mechanism. To obtain an enhanced emission, in future, one can design a host molecule which will increase its rigidity after the complexation without affecting its chromophore. In this approach, the current system is versatile in that the functionalization can be achieved with methods similar to that have been strategically designed for the $^1\pi\pi^*$ (i.e. fluorescence) chromophores. In view of oxygen quenching, in a steady state approach, one can then saturate the solution with N_2 so that the enhanced phosphorescence can also serve as an additional signaling to distinguish it from the fluorescence interference. The success in the recognition of Pb^{2+}(aq) in the TLC plate demonstrates its suitability for the conceptual development of a practical recognization device. The results may spark a broad range of interest in both fundamental approach and applications relevant to third-row transition metal complexes.

Acknowledgements

We thank the National Science Council of Taiwan, ROC for the financial Support.

Appendix A. Supplementary material

CCDC 643498 contains the supplementary crystallographic data for **1**-Pb^{2+}. These data can be obtained free of charge via http://www.ccdc.cam.ac.uk/conts/retrieving.html, or from the Cambridge Crystallographic Data Centre, 12 Union Road, Cambridge CB2 1EZ, UK; fax: (+44) 1223-336-033; or e-mail: deposit@ccdc.cam.ac.uk. Supplementary data associated with this article can be found, in the online version, at doi:10.1016/j.poly.2007.06.029.

References

[1] C.-T. Chen, W.-P. Huang, J. Am. Chem. Soc. 124 (2002) 6246.
[2] http://www.epa.gov/safewater/mcl.html.
[3] (a) V. Amendola, L. Fabbrizzi, M. Lincchelli, C. Mangano, P. Pallavicini, L. Parodi, A. Poggi, Coord. Chem. Chem. Rev. 190–192 (1999) 649;
(b) J. Liu, Y. Lu, J. Am. Chem. Soc. 125 (2003) 6642;
(c) J. Li, Y. Lu, J. Am. Chem. Soc. 122 (2000) 10466;
(d) M. Sun, D. Shangguan, H. Ma, L. Nie, X. Li, S. Xiong, G. Liu, W. Thiemann, Biopolymers 72 (2003) 413;
(e) F.-Y. Wu, S.W. Bae, J.-I. Hong, Terahedron Lett. 47 (2006) 8851;
(f) M. Kadarkaraisamy, G.A. Sykes, Inorg. Chem. 45 (2006) 779;
(g) D.P. Wernette, C.B. Swearingen, D.M. Cropek, M. Donald, Y. Lu, J.V. Sweedler, P.W. Bohn, Analyst 131 (2006) 41.
[4] S. Deo, H.A. Godwin, J. Am. Chem. Soc. 122 (2000) 174.
[5] M.-Y. Chae, J. Yoon, A.W. Czarnik, J. Mol. Recognit. 9 (1996) 297.
[6] J.Y. Kwon, Y.J. Jang, Y.J. Lee, K.M. Kim, M.S. Seo, W. Nam, J. Yoon, J. Am. Chem. Soc. 127 (2005) 10107.
[7] (a) R. Slone, D.I. Yoon, R.M. Calhoun, J.T. Hupp, J. Am. Chem. Soc. 117 (1995) 11813;
(b) P.K.M. Siu, S.-W. Lai, W. Lu, N. Zhu, C.-M. Che, Eur. J. Inorg. Chem. (2003) 2749;
(c) Q.-Z. Yang, L.-Z. Wu, H. Zhang, B. Chen, Z.-X. Wu, L.-P. Zhang, C.-H. Tung, Inorg. Chem. 43 (2004) 5195;
(d) M.-J. Li, B.W.-K. Chu, N. Zhu, V.W.-W. Yam, Inorg. Chem. 46 (2007) 720.
[8] (a) Y. Shen, B.P. Sullivan, Inorg. Chem. 34 (1995) 6235;
(b) V.W.-W. Yam, C.-L. Chan, C.-K. Li, K.M.-C. Wong, Coord. Chem. Rev. 216–217 (2001) 173;
(c) V.W.-W. Yam, R.P.-L. Tang, K.M.-C. Wong, X.-X. Lu, K.-K. Cheung, N. Zhu, Chem. Eur. J. 8 (2002) 4066;
(d) L.J. Charbonniere, R.F. Ziessel, C.A. Sams, A. Harriman, Inorg. Chem. 42 (2003) 3466.
[9] (a) J. Ohshita, T. Uemura, T. Inoue, K. Hino, A. Kunai, Organometallics 25 (2006) 2225;
(b) S.A. McFarland, D. Magde, N.S. Finney, Inorg. Chem. 44 (2005) 4066;
(c) M.-J. Li, B.W.-K. Chu, V.W.-W. Yam, Chem. Eur. J. 12 (2006) 3528.
[10] (a) J.F. Michalec, S.A. Bejune, D.G. Cuttell, G.C. Summerton, J.A. Gertenbach, J.S. Field, R.J. Haines, D.R. McMillin, Inorg. Chem. 40 (2001) 2193;
(b) J.D. Lewis, L. Bussotti, P. Foggi, R.N. Perutz, J.N. Moore, J. Phys. Chem. A 106 (2002) 12202;
(c) J.D. Lewis, J.N. Moore, Dalton Trans. (2004) 1376;
(d) W.-S. Tang, X.-X. Lu, K.M.-C. Wong, V.W.-W. Yam, J. Mater. Chem. 15 (2005) 2714.
[11] M.-L. Ho, F.-M. Hwang, P.-N. Chen, Y.-H. Hu, Y.-M. Cheng, K.-S. Chen, G.-H. Lee, Y. Chi, P.-T. Chou, Org. Biomol. Chem. (2006) 98.
[12] D.S. McClure, J. Chem. Phys. 20 (1952) 682.
[13] (a) P.-T. Chou, Y. Chi, Chem. Eur. J. 13 (2007) 380;
(b) P.-T. Chou, Y. Chi, Eur. J. Inorg. Chem. (2006) 3319.
[14] (a) C.-H. Yang, S.-W. Li, Y. Chi, Y.-M. Cheng, Y.-S. Yeh, P.-T. Chou, G.-H. Lee, C.-H. Wang, C.-F. Shu, Inorg. Chem. 44 (2005) 7770;
(b) C.-J. Chang, C.-H. Yang, K. Chen, Y. Chi, C.-F. Shu, M.-L. Ho, Y.-S. Yeh, P.-T. Chou, Dalton Trans. (2007) 1881.
[15] (a) Y. Shen, B.P. Sullivan, J. Chem. Edu. 74 (1997) 685;
(b) P.D. Beer, S.W. Dent, N.C. Fletcher, T.J. Wear, Polyhedron 15 (1996) 2983;
(c) M.E. Padilla-Tosta, J.M. Lloris, R. Martinez-Manez, M.D. Marcos, M.A. Miranda, T. Pardo, F. Sancenon, J. Soto, Eur. J. Inorg. Chem. (2001) 1475.
[16] T. Lazarides, T.A. Miller, J.C. Jeffery, T.K. Ronson, H. Adams, M.D. Ward, Dalton Trans. (2005) 528.
[17] W.-S. Yu, C.-C. Cheng, Y.-M. Cheng, P.-C. Wu, Y.-H. Song, Y. Chi, P.-T. Chou, J. Am. Chem. Soc. 125 (2003) 10800.
[18] (a) P.-T. Chou, G.-R. Wu, C.-Y. Wei, C.-C. Cheng, C.-P. Chang, F.–T. Hung, J. Phys. Chem. B 103 (1999) 10042;
(b) P.-T. Chou, G.-R. Wu, C.-Y. Wei, C.-C. Cheng, C.-P. Chang, F.-T. Hung, J. Phys. Chem. B 104 (2000) 7818;
(c) P.-T. Chou, C.-Y. Wei, C.-R.C. Wang, F.-T. Hung, C.-P. Chang, J. Phys. Chem. A 103 (1999) 1939.
[19] C.Y. Chen, C.T. Cheng, J.K. Yu, S.C. Pu, Y.M. Cheng, P.T. Chou, Y.H. Chou, H.T. Chiu, J. Phys. Chem. B 108 (2004) 10687.
[20] K.A. Connors, Binding Constants, Wiley, New York, 1987.
[21] (a) Y.-H. Song, S.-J. Yeh, C.-T. Chen, Y. Chi, C.-S. Liu, J.-K. Yu, Y.-H. Hu, P.-T. Chou, S.-M. Peng, G.-H. Lee, Adv. Funct. Mater. 14 (2004) 1221;

(b) F.-M. Hwang, H.-Y. Chen, P.-S. Chen, C.-S. Liu, Y. Chi, C.-F. Shu, F.-I. Wu, P.-T. Chou, S.-M. Peng, G.-H. Lee, Inorg. Chem. 44 (2005) 1344;
(c) C.-H. Yang, Y.-M. Cheng, Y. Chi, C.-J. Hsu, F.-C. Fang, K.-T. Wong, P.-T. Chou, C.-H. Chang, M.-H. Tsai, C.-C. Wu, Angew. Chem., Int. Ed. 46 (2007) 2418.

[22] E. Psillakis, J.C. Jeffery, J.A. McCleverty, M.D. Ward, Chem. Commun. (1997) 1965.

[23] J. Casabo, J. Pons, K.S. Siddiqi, F. Teixidor, E. Molins, C. Miravitlles, J. Chem. Soc., Dalton Trans. (1989) 1401.

[24] R. Kawahata, T. Tsukuda, T. Yagi, M.A. Subhan, H. Nakata, A. Fuyuhiro, S. Kaizaki, Chem. Lett. 32 (2003) 1084.

[25] Q.-Z. Yang, Q.-X. Tong, L.-Z. Wu, Z.X. Wu, L.P. Zhang, C.H. Tung, Eur. J. Inorg. Chem. (2004) 1948.

2. Results and discussion

A priori the most efficient route of reaction is expected to be the same as for iodides – the direct reaction of an organic sulfide with an alkyl halide, bromide or chloride

$$R_2S + R'X \rightarrow (R'R_2S^+)X^- \quad (1)$$

Although iodides may be prepared without solvent or in non-polar solvents under ambient conditions, bromides and chlorides are expected to react extremely slowly under such conditions. Obviously, the reaction conditions must be optimized with respect to the influence of solvent, temperature and reactant concentrations.

2.1. Choice of solvent

Reaction (1) is a typical example of a second-order substitution, S_N2-type. This means that polarity and solvation properties of the solvent will play a very important role in the stabilization of the transition state and thus affect the reaction rate. Product stability ought to be affected as well.

The most commonly used solvents for such reactions are those with a high dielectric constant, e.g., water, methanol, ethanol, acetone or nitromethane. Also, 2,2,2-trifluoroethanol, sulphuric and hydrofluoric acid have been used in some cases [11].

One should also consider that Reaction (1) is reversible and that the product can decompose into the reactants. The decomposition products may of course also interact with all compounds in the reaction mixture. Consequently, the most common side-reactions observed involve alkyl metathesis

$$R_2S + R'X \rightarrow (R'R_2S^+)X^- \rightarrow RX + RR'S \quad (2)$$

As shown by Pocker and Parker [12], the rate of decomposition is higher in non-polar solvents with low ion solvation ability. These observations correspond to the predictions made above. The solvation of the halide anion will give the major contribution to the stabilization of a sulfonium salt in solution. Thus, the higher the dielectric constant of the solvent the better. Strong electrophilic properties of the solvent will enhance the solvation of the halide anion and thereby render a stabilization of the desired product.

From these considerations, water ought to be a good solvent candidate; it has a dielectric constant ε of 81 and quite strong electrophilic properties. Nevertheless, the nucleophilic properties of water are also quite pronounced causing efficient solvolysis, hydrolysis, of sulfonium salts in water.

Therefore, the choice of trifluoroacetic acid may be more suitable, since it combines a high dielectric constant ($\varepsilon = 37$) and marked electrophilic properties, whereas the nucleophilic properties are insignificant.

For the synthesis of dodecyl dimethyl sulfonium iodide it is not necessary to make any other improvements. The synthesis of dodecyl dimethyl sulfonium iodide was reported already in 1940 by Kuhn and Dann [13]:

$$\{n\text{-}CH_3(CH_2)_{11}\}(CH_3)S + MeI \rightarrow [\{n\text{-}CH_3(CH_2)_{11}\}(CH_3)_2S]I \quad (3)$$

The sulfonium iodide was prepared by direct reaction between dodecyl methyl sulfide and methyl iodide without any solvent and during 36 h; the yield was 58%. Using trifluoroacetic acid as a solvent we obtained a yield of 95% in 15 min, and the subsequent analysis of the product demonstrated that recrystallization does not lead to any significant increase in product purity.

A control experiment for the synthesis of dodecyl dimethyl sulfonium bromide was also made: dodecyl bromide and dimethyl sulfide were mixed without solvent. The mixture required more than one year before a significant yield was achieved.

It is notable that some sulfonium salts, especially chlorides, demonstrate a pronounced hygroscopic behaviour, implicating that any presence of water, and even contact with water adsorbed on glass surface, should be avoided. The neglect of dry conditions of synthesis leads to the formation of syrups and product decomposition.

An excess of diethyl ether was used to precipitate, and thus separate, the sulfonium salts from solution. Although the sulfonium iodides required quite small portions of diethyl ether, the bromides and chlorides required much higher amounts. In the case of sulfonium chlorides the separation technique may be further developed.

2.2. Choice of temperature and duration of synthesis

The set of useful temperatures is rather narrow because of the low boiling point of dimethyl sulfide (b.p. 36 °C). However, performing syntheses in sealed glass tubes allow temperatures of at least 70–90 °C. The solvent is expected to stabilize the product and prevent it from decomposition into by-products.

In the present work, the yield of synthesis as a function of applied temperature and reaction time was systematically studied. The yields were determined by argentometric titration of the reaction mixtures (*vide infra*). The results are presented in Table 1.

Table 1
Yield, %, of dodecyl dimethyl sulfonium bromide as a function of temperature and reaction time

T (°C)	Time (h)											
	0.25	0.5	1	2	4	7	10	14	18	22	26	63
90	25.5	44.4	68.2	85.5	88.3	90.9			89.6	91.6	91.4	
70			30.2	45.3	68.1	82.4	90.5	90.8	88.6			85.3

These results show that an increase in reaction temperature does not lead to a decrease of maximum yield indicating that decomposition of the products is considerably slower than the formation. ^{1}H and ^{13}C NMR spectra of the reaction mixtures show that the amount of by-products is low during the synthesis and that the main product is the desired sulfonium halide. These observations are also the motivation for using the observed amount of halide anion as a measure of product yield. The main conclusion is that higher temperatures are preferable for the synthesis yield.

2.3. Choice of reactants and their concentrations

The main factor determining suitable concentrations and the ratio between alkyl halide and organic sulfide reactants is the target sulfonium salt. Sulfonium salts can be used as alkylating agents, and as it was shown by Ray and Levine [14] that improper choice of reactant conditions may cause loss of product through dealkylation of the sulfonium salt, especially in the case when the organic sulfide is in excess with respect to the alkyl halide. One should also consider that decomposition of sulfonium salts leads to the formation of new alkyl halides, which can react with the original organic sulfide. The results by Siegel and Graefe [15] support such explanations and provide further useful information: the higher the ratio of sulfide to alkyl halide, the less are yield and purity.

For these reasons an excess of alkyl halide to organic sulfide was used in this work; normally, two times more alkyl halide than organic sulfide.

For the synthesis of dimethyl dodecyl sulfonium iodide methyl iodide and dodecyl methyl sulphide were used. Methyl iodide has the advantage of being liquid under ambient conditions and is expected to react more readily than the dodecyl one. For syntheses of other salts, dodecyl halides and dimethyl sulfide were used because methyl bromide and chloride are gases and rather difficult to handle under ambient conditions.

After successful experiments using dodecyl derivatives, also hexadecyl dimethyl sulfonium bromide and chloride of good quality and with good yields were synthesized.

2.4. Recrystallization

Recrystallization was used in order to ensure the purity of the prepared samples of the sulfonium salts. Acetone was the primary solvent for this purpose based on the work by Yano et al. [2]. Titration, comparison of signals in NMR spectra and melting points were used to determine the amount of impurities in crude and recrystallized products.

From the results obtained it was concluded that recrystallization does not lead to significant decrease of impurities, and this step in the synthetic procedure is considered facultative. The results showed that samples of dodecyl dimethyl sulfonium bromide contain less than 1% (mol.) of impurities, and after recrystallization the amount of impurities is less than 0.5% (mol.). Samples of dodecyl dimethyl sulfonium chloride contain less than 2% (mol.) of impurities, and after recrystallization their amount is unchanged. It should be noted that dodecyl dimethyl sulfonium chloride is rather difficult to recrystallize because of its hygroscopy and tendency to form syrups. It is not obvious that recrystallization should provide an enhanced purity, since potential decomposition in solvents of low polarity (low dielectric constants) may lead to an overall decrease of purity and yield.

Nevertheless, if recrystallization is desired, the use of ethyl acetate as the medium is recommended. The above described bromides, as well as dodecyl dimethyl sulfonium iodide, recrystallize easily and with high yields. Chlorides are still harder to recrystallize.

2.5. Note about product stability

Trialkylsulfonium bromides are fine white crystals; they are very stable under ambient conditions and could be stored for months.

Trialkylsulfonium chlorides are fine white crystals, which tend to "melt" in contact with an ambient atmosphere, due to water absorption. The product tends to be unstable even when stored in PET-flasks and moisture-free atmosphere. One can speculate that both high hygroscopicity as well as natural instability, caused by a chloride anion attack on the sulfonium cation, lead to an inherent trialkyl sulfonium chloride instability. This could explain some deviations in the results of elemental analysis.

2.6. Crystal structure of $[\{CH_3(CH_2)_{15}\}(CH_3)_2S]Br$

Crystalline products are obtained of all synthesized compounds in this study. The structure of $[\{CH_3(CH_2)_{11}\}(CH_3)_2S]I$ is previously known [16].

Crystals suitable for detailed single crystal diffraction were obtained for the $[\{CH_3(CH_2)_{15}\}(CH_3)_2S]Br$ compound described below. The compound crystallizes in the triclinic system, space group $P\bar{1}$. The structure consists of hexadecyldimethylsulfonium cations and bromide anions. Fig. 1 shows the arrangement of structure in the unit cell.

For this type of compound, typically the inorganic anions form layers in close proximity to the cationic end of the organic ions. The cation tails represent the most predominant structure-driving entity forming double-layers. The present compound is no exception. Two more rare structural features can be identified; (1) the aliphatic tails do not interpenetrate; (2) the angle between the layers formed by the bromide ions and the aliphatic tails is very low, about 32°. The later feature gives quite thin double-layers in relation to the extended hexadecyl tails. The distance between bromide ions in adjacent layers is just over 24 Å. The closest distance between bromide ions within the inorganic layer is about 6 Å. The packing of ions is shown in Fig. 1.

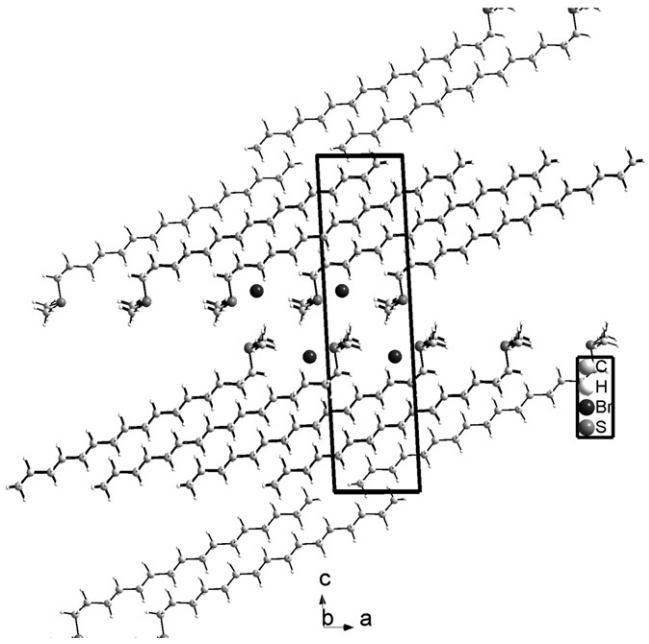


Fig. 1. The structure of $[\{CH_3(CH_2)_{15}\}(CH_3)_2S]Br$.

3. Conclusions

The usage of trifluoroacetic acid as solvent is strongly recommended for the synthesis of trialkyl sulfonium salts. A higher temperature shortens the time of synthesis. In order to prevent loss of product, an excess of alkyl halide should be used. The syntheses give products of quite good quality and suitable for further use without additional purification. If purification is required, ethyl acetate ought to be used for recrystallization.

The designed method for synthesis of non-symmetrical alkyl dimethyl sulfonium halides appears to be universal and was used for the production of a variety of compounds. These compounds have already been used for the subsequent synthesis of low-dimensional organic–inorganic compounds displaying for instance magnetic properties [17].

4. Experimental

Trifluoroacetic acid was distilled over phosphorus pentaoxide (1% mass) to remove traces of water. Standard C, H and S elemental analyses were performed by MikroKemi AB, Uppsala, Sweden. Halogens, Cl, Br and I, were analyzed by argentometric titration. NMR spectra were recorded on a Bruker DMX 500 MHz spectrometer. Solutions for NMR spectroscopic investigations were prepared by dissolving 6–8 mg of reaction products in 1 ml of deuturated chloroform at ambient temperature.

4.1. Synthesis of dodecyl dimethyl sulfonium iodide

3.17 g (22.3 mmol) of methyl iodide, 1.83 g (8.47 mmol) of dodecylmethylsulfide and 3.12 g (27 mmol) of trifluoroacetic acid were mixed in a 25 ml round-bottom flask and the flask was closed with a stopper. The reaction was performed at room temperature without stirring. After 15 min diethyl ether (100 ml) was added to precipitate the product. Yield: 2.89 g (95%), m.p.: 80–82 °C; after recrystallization in 5 ml of acetone, 1.58 g (52%), m.p.: 80–82 °C. *Anal.* Calc. for $(C_{14}H_{31}S)I$: I, 35.4. Found: I, 34.8%. ^1H NMR (500 MHz, $CDCl_3$) δ 3.39 (s, 6H), 3.78 (t, *J* 8.6, 2H), 1.83 (~tt/m, *J* 7–9, 2H), 1.53 (~tt/m, *J* 7–9, 2H), 1.43–1.20 (group, 16H), 0.90 (t, *J* 7.1, 3H).

4.2. Synthesis of dodecyl dimethyl sulfonium bromide

Reaction in sealed tube: 3.30 g (13 mmol) of 1-bromododecane, 0.40 g (6.5 mmol) of dimethylsulfide and 3.00 g (26 mmol) of trifluoroacetic acid were mixed in a glass tube. The mixture was frozen in liquid nitrogen and the tube sealed. The sealed tube was heated in a water bath to the reaction temperature for a known period of time. After the reaction time the sealed tube was cooled in a cold water bath. For the subsequent argentometric titration all contents of the sealed tube was transferred to a 50 ml metric flask and diluted with distilled water.

If precipitation of the product was desired, the content of the sealed tube was instead diluted with diethyl ether (200 ml). Yield: 80% (90 °C, 3 h), m.p.: 62–64 °C. *Anal.* Calc. for $(C_{14}H_{31}S)Br$: C, 54.0; H, 10.0; S, 10.3; Br, 25.5. Found: C, 53.1; H, 10.0; S, 10.5; Br, 25.3%. ^1H NMR (500 MHz, $CDCl_3$) δ 3.40 (s, 6H), 3.78 (t, *J* 8.5, 2H), 1.81 (~tt/m, *J* 7–9, 2H), 1.51 (~tt/m, *J* 7–9, 2H), 1.42–1.22 (group, 16H), 0.90 (t, *J* 7.1, 3H).

Reaction in open system. 6.45 g (25.9 mmol) of 1-bromododecane, 0.53 g (8.6 mmol) of dimethylsulfide and 5.60 g (49 mmol) of trifluoroacetic acid were mixed in a 25 ml round-bottom flask. A long water cooler with absorption tube was connected to the flask. The synthesis was carried out during 3 h at approximately 65–70 °C and intensive boiling was observed. A new portion of 0.26 g (4.3 mmol) of dimethylsulfide was added to the reaction mixture and the reaction continued. After another 3 h the reaction mixture was cooled to room temperature and diethyl ether (600 ml) was added to precipitate the product. Yield: 3.90 g (97%), m.p.: 62–64 °C. A recrystallization from acetone (20 ml) was made to ensure the quality of product. Yield: 3.22 g (80%), m.p.: 62–64 °C. *Anal.* Calc. for $(C_{14}H_{31}S)Br$: Br, 25.5. Found: Br, 25.3%. ^1H NMR (500 MHz, $CDCl_3$) δ 3.40 (s, 6H), 3.78 (t, *J* 8.5, 2H), 1.81 (~tt/m, *J* 7–9, 2H), 1.51 (~tt/m, *J* 7–9, 2H), 1.42–1.22 (group, 16H), 0.90 (t, *J* 7.1, 3H).

Reaction without solvent. 1.94 g (7.79 mmol) of dodecyl bromide and 0.24 g (3.90 mmol) of dimethyl sulphide were mixed in a 5 ml round-bottom flask. Some crystals precipitated on the bottom of the flask after one month. After 18 months the amount of precipitate was enough to allow separation. Yield: 0.61 g (50%).

4.3. Synthesis of dodecyl dimethyl sulfonium chloride

2.52 g (11 mmol) of 1-chlorododecane, 0.35 g (5.6 mmol) of dimethylsulfide and 2.40 g (21 mmol) of trifluoroacetic acid were mixed in a glass tube. The mixture was frozen at liquid nitrogen temperature and the tube sealed. The sealed tube was heated in a water bath to the appropriate temperature for a known period of time. After reaction the sealed tube was cooled in a cold water bath. For the subsequent argentometric titration all contents of the sealed tube was transferred to a 50 ml metric flask and diluted with distilled water.

If precipitation of product was desired, the contents of the sealed tube instead was diluted with diethyl ether (300 ml). Yield: 66% (90 °C, 72 h), m.p.: 58–60 °C; after recrystallization in 10 ml acetone (46%), m.p.: 58–60 °C. *Anal.* Calc. for $(C_{14}H_{31}S)Cl$: C, 63.0; H, 11.7; S, 12.0; Cl, 13.3. Found: C, 49.2; H, 8.1; S, 7.6; Cl, 9.3%. ^1H NMR (500 MHz, $CDCl_3$) δ 3.24 (s, 6H), 3.61 (t, J 8.9, 2H), 1.82 (~tt/m, J 7–9, 2H), 1.51 (~tt/m, J 7–9, 2H), 1.42–1.22 (group, 16H), 0.90 (t, J 7.1, 3H).

4.4. Synthesis of hexadecyl dimethyl sulfonium bromide

24.5 g (80 mmol) of 1-bromohexadecane, 2.54 g (41 mmol) of dimethylsulfide, 19.1 g (168 mmol) of trifluoroacetic acid were mixed in a 100 ml round flask and stirred for 2 days at 60–65 °C. Diethyl ether (400 ml) was added to precipitate the product. Yield: 9.80 g (66%), m.p.: 75 °C. After recrystallization from ethyl acetate: 9.43 g (63%), m.p.: 75 °C. *Anal.* Calc. for $(C_{18}H_{39}S)Br$: C, 59.82; H, 9.20; S, 8.87; Br, 22.11. Found: C, 59.0; H, 10.7; S, 9.0; Br, 21.7%.

4.5. Synthesis of hexadecyl dimethyl sulfonium chloride

20.00 g (77 mmol) of 1-chlorohexadecane, 2.40 g (39 mmol) of dimethylsulfide and 30.00 g (263 mmol) of trifluoroacetic acid were mixed in a 250 ml round-bottom flask. A long water cooler with absorption tube was connected to the flask. The synthesis was carried out during 7 days at approximately 65–70 °C and intensive boiling was observed. Then the reaction mixture was cooled to room temperature and diethyl ether (1000 ml) was added to precipitate the product. Yield: 6.5 g (53%). A recrystallization from ethyl acetate (100 ml) was made to ensure the quality of product. Yield: 3.45 g (28%). m.p.: 73 °C.

4.6. Synthesis of 1,12-dodecanediylbis[dimethylsulfonium]dibromide

3.00 g (9.1 mmol) of 1,12-dibromododecane, 1.14 g (18.4 mmol) of dimethyl sulfide and 15.2 g (133 mmol) of trifluoroacetic acid were placed in 50 ml round flask and stirred at 60–65 °C for 1 day. Diethyl ether (300 ml) was added to precipitate the product. Yield: 1.98 g (48%). Recrystallization from ethylacetate: 1.75 g (44%). *Anal.* Calc. for $(C_{12}H_{24}S_2)Br_2$: C, 42.5; H, 8.0; S, 14.2; Br, 35.3. Found: C, 42.8; H, 8.0; S, 14.1; Br, 39.7%.

4.7. Argentometric titration

A solution of silver nitrate of the approximate concentration 0.05 mol/l was prepared from recrystallized, chemically pure silver nitrate and then standardized using a solution of potassium thiocyanate. For this purpose, a solution of potassium thiocyanate of the concentration 0.1000 mol/l was prepared from a standard sample. A concentrated solution of iron–ammonia alums was used as indicator.

Fifteen milliliters of the standardized solution of silver nitrate was added to 4 ml (or 8 ml for the samples of short reaction times, 0.25 and 0.5 h) of the diluted reaction mixtures (*vide supra*). Subsequently, the excess of silver nitrate was titrated with the standard solution of potassium thiocyanate in the presence of iron–ammonia alums. The yields of the syntheses were determined and compared to the theoretically expected ones.

4.8. Crystal structure determination of $[\{CH_3(CH_2)_{15}\}(CH_3)_2S]Br$

X-ray diffraction data were collected using a Bruker Nonius KappaCCD diffractometer. The compound crystallizes in the triclinic system, space group $P\bar{1}$. All

Table 2
Crystallographic data for $[\{CH_3(CH_2)_{15}\}(CH_3)_2S]Br$

Compound number	**1**
Empirical formula	$C_{18}H_{39}SBr$
Unit cell dimensions	
a (Å)	6.8270(7)
b (Å)	7.1230(3)
c (Å)	24.2150(15)
α (°)	90.36(1)
β (°)	92.08(1)
γ (°)	116.25(1)
Cell volume (Å^3)	
V	1055.0(1)
Z	2
ρ (calc.) (g/cm^3)	1.157
Crystal system, space group	triclinic, $P\bar{1}$ (No. 2)
Diffractometer	Bruker-Nonius KappaCCD
Temperature (K)	297
Radiation	radiation: Mo Kα
θ Range	$4.5 < \theta < 27.5$
Number of measured reflections	19912
Number of unique reflections	4809
R_{int}	0.0809
Number of refined parameters	181
Ratio reflections/parameters	27
Residuals R_1 (all reflections)	0.0751
R_1 (3655 observed reflections)	0.0503
wR_2 (all reflections)	0.128
Goodness-of-fit	1.129
Difference electron density	0.94/−0.56
CCDC number	266633

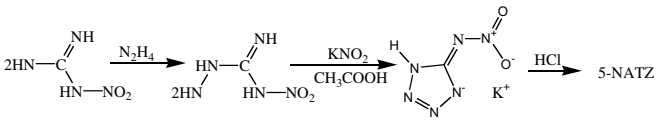
non-hydrogen atoms were refined with anisotropic displacement parameters. Crystallographic details of the structure determination are presented in Table 2.

5. Supplementary material

CCDC 266633 contains the supplementary crystallographic data for this paper. These data can be obtained free of charge via http://www.ccdc.cam.ac.uk/conts/retrieving.html, or from the Cambridge Crystallographic Data Centre, 12 Union Road, Cambridge CB2 1EZ, UK; fax: (+44) 1223-336-033; or e-mail: deposit@ccdc.cam.ac.uk.

References

[1] (a) H. Paulsson, A. Hagfeldt, L. Kloo, J. Phys. Chem. B 107 (49) (2003) 13665;
(b) H. Paulsson, M. Berggrund, E. Svantesson, A. Hagfeldt, L. Kloo, Sol. Energy Mater. Sol. Cells 82 (3) (2004) 345.
[2] K. Yamauchi, Y. Hisanaga, M. Kinoshita, J. Chem. Soc., Perkin Trans. I 8 (1983) 1941.
[3] B. Badet, M. Julia, M. Ramirez-Munoz, C.A. Sarrazin, Tetrahedron 39 (19) (1983) 3111.
[4] H. Paulsson, M. Berggrund, A. Fischer, L. Kloo, Z. Anorg. Allg. Chem. 630 (3) (2004) 413.
[5] M. Nyman, D. Ingersoll, S. Singh, F. Bonhomme, T.M. Alam, C.J. Brinker, M.A. Rodriguez, Chem. Mater. 17 (2005) 2885.
[6] M.L. Rojas-Cervantes, B. Casal, P. Aranda, M. Saviron, J.C. Galvan, E. Ruiz-Hitzky, Colloid Polym. Sci. 279 (10) (2001) 990.
[7] Minhua Cao, Xiaoyan He, Jun Chen, Changwen Hu, Cryst. Growth Des. 7 (1) (2007) 170.
[8] Y. Yano, T. Okonogi, W. Tagaki, J. Org. Chem. 38 (22) (1973) 3912.
[9] M. Rosenberger, W. Jackson, G. Saucy, Helv. Chim. Acta 63 (6) (1980) 1665.
[10] D. Landini, A. Maia, F. Montanari, M. Mikolajczyk, A. Zatorski, Nov. J. Chem. 4 (12) (1980) 723.
[11] H. Heydt, E. Vilsmaier, Triorgano-sulfonium-Salze. Houben-Weyl. Methoden der Organische Chemie. Teil I, E11, Georg Thieme Verlag, Stuttgart, New York, 1985, pp. 405–502.
[12] Y. Pocker, A.J. Parker, J. Org. Chem. 31 (5) (1966) 1526.
[13] R. Kuhn, O. Dann, Chem. Ber. 73B (1940) 1092.
[14] F.E. Ray, I. Levine, J. Org. Chem. 2 (1937) 267.
[15] S. Siegel, A.F. Graefe, J. Am. Chem. Soc. 75 (1953) 4521.
[16] (a) P.H. Svensson, L. Kloo, Structural investigations of the dodecyldimethylsulfonium polyiodides (submitted for publication).;
(b) P.H. Svensson, Synthesis, Structure and bonding in polyiodide and binary metal iodide–iodine systems. Ph.D. thesis, Lund University, 1998, p. 16.
[17] I. Sokka, L. Kloo, unpublished work.



Scheme 1.

The latter was investigated in general, from the standpoint of its energetic properties. The thermal decomposition and crystal structure of 5-H_2NATZ have been described in detail in [18–20]. The heat of decomposition is equal to 3520 J/g [18], the calculated value of the heat of formation is approximately 500 kJ/mol [19–21]. Activation energies were calculated for 5-H_2NATZ and its mercury and lead salts [22]. The structural chemistry of alkaline metal and ammonium 5-nitroaminotetrazolates are well investigated. Crystal structures of $NH_4CN_6O_2H$ [23], $(NH_4)_2CN_6O_2$ [24], MCN_6O_2H (M = Cs [25], Na [26], Li [27]) $Rb_3(CN_6O_2)(CNNNO_2)\cdot H_2O$ [25] and the K^+ salt of 3-methyl-5-nitroaminotetrazole [28] have been reported. Complexes of 5-NATZ with transition metals are poorly studied, only the crystal structure of the nickel dimeric complex, $Ni_2(NH_3)_6(CN_6O_2)_2$ [29], has been determined. However, 5-H_2NATZ and its derivatives should be an interesting class of ligands, due to the following reasons: (i) 5-H_2NATZ is a dibasic acid that can be easily transformed into mono and di-substituted salts; (ii) anions of 5-NATZ have many sites for coordination by metal ions; and (iii) conjugated systems of five-member rings of tetrazoles can form π–π intermolecular interactions in the crystal structure to build extended 2D and 3D networks. It worth mentioning that the anionic form of tetrazole considered can be strictly controlled by using appropriate conditions. In this context, 5-NATZ is the perspective ligand for construction of high energetic network structures with a combination of physicochemical and explosive properties.

In this work, we present the syntheses and crystal structures of the mono-substituted complex of lead(II) as well as a disubstituted complex of mercury(II). Furthermore, the interpretation of the coordination mode through electronic features of 5-NATZ and its mono- and dianion was performed by means of theoretical modelling.

2. Experimental

2.1. Materials and methods

The guanidine carbonate, potassium nitrite, mercury, silver, lead and copper nitrates were obtained from the Aldrich Chemical Company Ltd. and Fluka, and were used without purification. *N*-Nitro-*N*-aminoguanidine was obtained from nitroguanidine [30], which was obtained from guanidine nitrate [31]. Chemical analyses of the samples dried to a constant weight were performed with a Fisons Instruments 1108 CHNS-O Elemental analyzer. IR spectra in the range 4000–400 cm^{-1} were recorded on a Perkin–Elmer System 2000 FT-IR spectrometer. Decomposition temperatures were determined on an IA 8100 Electrothermal instrument. Lead and silver contents were determined by weight analysis in the forms of $PbMoO_3$ and AgBr. The copper content was determined by iodometric titration.

2.2. Synthesis

2.2.1. Synthesis of potassium 5-nitroaminotetrazolate (*1*)

Complex **1** was prepared by interaction of *N*-nitro-*N*-aminoguanidine with KNO_2 and acetic acid, as described in [17]. Yield: 65%. $T_{decom.} = 248$ °C. *Anal.* Calc. for $KHCN_6O_2$: C, 7.14; H, 0.60; N, 49.98. Found: C, 6.92; H, 0.53; N, 50.13%. IR (Nujol, cm^{-1}): 2726 (*ν*N–H), 1544 (*ν*C–N), 1450 (*ν*N–O), 1318 (*ν*N–NO_2),1224 (*ν*C–N–NO_2), 1146 (*ν*N–N), 1094, 1058 (*ν*N–N), 1030 (*δ*N–H), 998 (*ν*N–N), 864, 774 (*δ*N–NO_2), 746, 698 (*δ*N–H), 462, 418 (*ν*O–K).

2.2.2. Synthesis of bis-potassium 5-nitroaminotetrazolate (*2*)

Complex **2** was obtained by reaction of equimolar amounts of **1** and KOH. Yield: 85%. $T_{decom.} = 400$ °C. *Anal.* Calc. for $K_2CN_6O_2$: C, 5.82; N, 40.78. Found: C, 5.54; N, 40.33%. IR (Nujol, cm^{-1}): 1396 (*ν*N–NO_2), 1294 (*ν*N–O), 1146 (*ν*N–N), 1028 (*ν*C–N), 1010 (*ν*N–N), 862 (*δ*C–N–NO_2), 462, 418 (*ν*O–K).

2.2.3. Synthesis of 5-NATZ (*3*)

Compound **3** was prepared by the procedure described in [17]. The pure product was isolated by extraction with diethyl ether. Yield: 48%. *Anal.* Calc. for $H_2CN_6O_2$: C, 9.23; H, 1.55; N, 64.61. Found: C, 9.11; H, 1.63; N, 64.62%.

2.2.4. Synthesis of lead 5-nitroaminotetrazolate (*4*)

To a solution of $Pb(NO_3)_2$ (0.44 g, 0.625 mmol) in 3 ml of water, a solution of 0.21 g (1.25 mmol) of **1** in 3 ml of water was added. After 1 h, salt **3** started to crystallize as large prisms. The crystals were separated by filtration. Yield: 76%. $T_{decom.} = 230$ °C. *Anal.* Calc. for $PbH_2C_2N_{12}O_4\cdot 4H_2O$: Pb, 38.56; C, 4.47; H, 1.88; N, 31.28. Found: Pb, 38.47; C, 4.68; H, 1.74; N, 31.13%. IR (Nujol, cm^{-1}): 3376 (*ν*O–H), 2726 (*ν*N–H), 1650, 1526 (*ν*C–N), 1462(*ν*N–O), 1342 (*ν*N–NO_2),1254 (*ν*C–N–NO_2), 1158 (*ν*N–N), 1120, 1066 (*ν*N–N), 1034 (*δ*N–H), 996 (*ν*N–N), 866, 770 (*δ*N–NO_2), 740, 700 (*δ*N–H), 416.

2.2.5. Synthesis of copper 5-nitroaminotetrazolate (*5*)

To a solution of $Cu(NO_3)_2\cdot 3H_2O$ (0.242 g, 1 mmol) in 2 ml of water, a solution of 0.168 g (1 mmol) of **1** in 3 ml of water was added. After 5 h, complex **3** precipitated as a dark-green fine crystallized powder, and was separated by filtration. Yield: 69%. $T_{decom.} = 240$ °C. *Anal.* Calc. for $CuCN_6O_2(H_2O)_3$: Cu, 25.92; C, 4.86; H, 2.43; N,

34.01. Found: Cu, 26.13; C, 4.76; H, 2. 32; N, 34.07%. IR (Nujol, cm^{-1}): 3380 (νO–H), 2735 (νN–H), 1630, 1500 (νC–N), 1406 (νN–NO_2), 1298, 1268 (νN–O), 1182 (νN–N), 1020 (νN–N), 1010 (νN–N), 872 (δC–N–NO_2), 748 (δC–N–C), 560, 492.

2.2.6. Synthesis of silver 5-nitroaminotetrazolate (6)

A solution of 0.168 g (1 mmol) of **1** in 3 ml of water was added to solution of $AgNO_3$ (0.34 g, 1 mmol) in 1 ml of water. A white precipitate formed immediately. This substance was separated by filtration. Yield: 83%. $T_{decom.}$ = 345 °C. *Anal.* Calc. for $Ag_2CN_6O_2(H_2O)_3$: Ag, 54.18; C, 3.01; H, 1.50; N, 21.05. Found: Ag, 53.65; C, 2.94; H, 1.67; N, 21.28%. IR (Nujol, cm^{-1}): 3650 (νO–H), 1612, 1546 (νC–N), 1350 (νN–NO_2), 1316 (νN–O), 1238 (νC–N), 1054 (νN–N), 1002 (νN–N), 880 (δC–N–NO_2), 760 (δC–N–C), 736.

2.2.7. Synthesis of mercury 5-nitroaminotetrazolate (7)

To a solution of $Hg(NO_3)_2$ (0.34 g, 1 mmol) in 1 ml of water, a solution of 0.168 g (1 mmol) of **1** in 3 ml of water was added. A white precipitate formed immediately. This substance was separated by filtration. Yield: 83%. $T_{decom.}$ = 165 °C. *Anal.* Calc. for $HgCN_6O_2(H_2O)_2$: C, 3.29; H, 1.11; N, 23.05. Found: C, 3.24; H, 1.23; N, 22.87%. IR (Nujol, cm^{-1}): 3450 (νO–H), 1618, 1488 (νC–N), 1328 (νN–NO_2), 1286 (νN–O), 1184 (νC–N), 1026 (νN–N), 962 (νN–N), 863 (δC–N–NO_2), 756 (δC–N–C).

2.3. Single-crystal X-ray structure determination

Single crystals of **4** suitable for X-ray structure determination were obtained by slow evaporation of the water solution. The crystals of **7** were grown by slow diffusion of mercury(II) nitrate through silica gel containing potassium 5-nitroaminotetrazolate.

Data collection for crystals of **4** was carried out at room temperature on a four-cycle diffractometer using graphite-monochromated Mo Kα radiation (λ = 0.71973 Å), whereas data collection for **7** was carried out on a Stoe IPDS diffractometer (Imaging Plate Detector System) with graphite-monochromated Mo Kα radiation (λ = 0.71073 Å) at 183(2) K using a cold N_2-gas stream. The direct method was used to solve the crystal structures by applying the software options of the program SHELXS-97. The structure refinement was performed with the program SHELXL-97. Non-hydrogen atoms were refined anisotropically by full-matrix least-squares techniques based on F^2. The hydrogen atoms of organic groups were placed in calculated positions within a riding model approximation with a fixed temperature factor. Hydrogen atoms of water molecules were located based on the difference electron-density maps and were refined isotropically with a fixed bond length. Twining was observed for the crystal of **7**, the twining matrix was calculated using the PLATON program. Details of data collection and refinement are given in Table 1.

Table 1
Crystallographic data and details of structure refinements for **4** and **7**

Formula	$C_2H_{10}N_{12}O_8Pb$	$HgCN_6O_4H_4$
Formula weight	537.35	365.41
Crystal system	orthorhombic	monoclinic
Space group	*Pbcn*	$P2_1/n$
a (Å)	20.816 (4)	14.958 (3)
b (Å)	9.630 (2)	6.590 (1)
c (Å)	6.273 (1)	14.958 (3)
β (°)	90	111.99 (3)
V (Å^3)	1257.5 (4)	1367.1 (5)
Z	4	8
D_{calc} (Mg/m^3)	2.796	3.500
T (K)	150	150
F(000)	976	960
Crystal dimensions (mm)	0.60 × 0.40 × 0.30	0.1 × 0.05 × 0.05
Θ_{max} (°)	28.27	27.48
Reflections collected	3124	6868
Independent reflections	1562	3036
Parameters	109	198
Goodness-of-fit	1.081	0.905
R_1	0.0316	0.0582
wR_2 (F^2)	0.0715	0.1427
Largest difference in peak and hole (e Å^{-3})	2.593 and −1.579	2.301 and −4.282

2.4. Calculation details

Full geometry optimization of the molecular structures were performed at the DFT level of theory using the hybrid Perdew–Burke–Ernzerhof parameter free exchange-correlation functional (PBE0) [32–34] as it is implemented in the PC GAMESS [35] version of the GAMESS-US [36] program package. Standard triple-split 6-311G(d,p) basis sets were used for all atoms of the systems under consideration. Geometry optimization of all the molecules was performed without any symmetry constrains (C_1 point group). The gradient norm was taken to be 10^{-5} a.u. The true minimum was controlled by the Hessian matrix and, as a consequence, harmonic frequencies calculation. The lack of imaginary frequencies indicates that the true minimum was achieved.

Based on the optimized geometry configurations, natural bond orbital (NBO) analysis [37,38] was performed for all systems. Computed data were visualized with help of the CHEMCRAFT program package [39].

In accord with Pearson [40], the chemical hardness (η) can be calculated by the following formula:

$$\eta = \frac{1}{2}\left(\frac{\partial^2 E}{\partial N^2}\right)_v = \frac{1}{2}\left(\frac{\partial \mu}{\partial N}\right)_v = \frac{1}{2}(I - A)$$

where I – ionization potential, A – electron affinity, E – the energy of N-electrons system, N – amount of electrons in the molecule, v – external potential, and μ – chemical potential. However, the Koopmans theorem allows the estimation of the hardness by using only orbital energies of the highest occupied molecular orbital (HOMO) and the lowest unoccupied molecular orbital (LUMO) of the molecule in its ground state as follows:

$$\eta \approx -\frac{1}{2}(\text{HOMO–LUMO})$$

Applicability of the Koopmans theorem to DFT MOs was found and confirmed by Baerends and co-workers [41] and Stowasser and Hoffmann [42].

3. Results and discussion

Potassium 5-nitroaminotetrazolate, obtained from guanidine carbonate, was used as the starting material. Other salts were obtained from the potassium salt **1** and the corresponding metal nitrates in water solution in accordance with the following reactions:

$$2KHCN_6O_2 + Pb(NO_3)_2 = Pb(HCN_6O_2)_2(H_2O)_4 + 2KNO_3$$

$$KHCN_6O_2 + Cu(NO_3)_2 = Cu(CN_6O_2)(H_2O)_3 + KNO_3 + HNO_3$$

$$KHCN_6O_2 + 2AgNO_3 = Ag_2(CN_6O_2)(H_2O)_3 + KNO_3 + HNO_3$$

$$KHCN_6O_2 + Hg(NO_3)_2 = [Hg(CN_6O_2)(H_2O)_2]_n + KNO_3 + HNO_3$$

The main difference between these reactions is that lead forms a mono-substituted salt, while copper, mercury and silver form di-substituted ones. It reflects the great affinity of Cu^{2+}, Hg^{2+} and Ag^{+} to soft ligands, and the propensity of silver to form completely substituted salts. The silver salt has high chemical stability and cannot be destructed by boiling with concentrated nitric acid. All the transition metal salts considered contain water molecules of crystallization. The hydrate composition has been calculated from the elemental analysis. In the case of lead and mercury derivatives, it was further confirmed by the crystal structure determinations.

IR spectra of 5-NATZ and alkali metal salts have been fully described previously [25]. Coordination of the ligand by a metal ion leads to an increase in the stretching vibrations in which atoms of the nitro-group are involved (Table 2).

Stretching displacements in the lead salt are in accordance with its crystal structure, where the metal atom is coordinated by the NO_2 group. Since the nitro-group is fixed, the energy of the stretching vibrations of the N–NO_2 and C–N–NO_2 fragments increases. There are two bands involving NO_2 asymmetric stretching in the copper complex.

Complex **4** crystallizes in the orthorhombic space group *P*bcn with four molecules in the unit cell. This compound has a polymeric structure formed by chains of $(PbO_2)_n$ and anions of 5-NATZ. The coordination number of lead is found to be 10. The lead ion is bound with three different types of oxygen atoms (Fig. 1): (i) oxygen atoms from bridging water molecules, (ii) oxygen atoms from terminal water molecules, and (iii) oxygens from nitro-groups.

The coordination polyhedron can be derived from the icosahedron by removal of two apexes with subsequent compression. The Pb–O bond lengths are in the range 2.653(5) to 2.888(5) Å (Table 3).

The Pb–O(terminal water) distance is equal to 2.653(5) Å, while the Pb–O(NO_2) bond length is 2.888(5) Å. The average Pb–O distance is 2.764(5) Å, being slightly greater than that in $Pb(CH_3COO)_2(H_2O)$, 2.742(6) Å [43], which has a similar polymeric crystal structure.

The anion of 5-NATZ in **4** is found to be monodeprotonated. Bond lengths in the ligand are similar to those for $MHCN_6O_2$, M = Li, Na, Cs [22–24]. The main difference between the 5-nitroaminotetrazolate anion in the lead salt and in alkali metal salts is observed for the bond lengths in the nitro group. The distances considered are significantly different (1.255(5) and 1.283(5) Å), and are longer than those in the case of $CsHCN_6O_2$ (1.243(5) and 1.260(5) Å). The latter can be the result of the coordination of the oxygen atoms with lead. The oxygen atom involved in the shortest Pb–O distance forms the longest N–O bond. The distance C(1)–N(2) (1.370(5) Å) shows the best correlation with the nitro-iminium form of the ligand [15,26]. Hydrogen atoms are connected to the N(6) nitrogen atom.

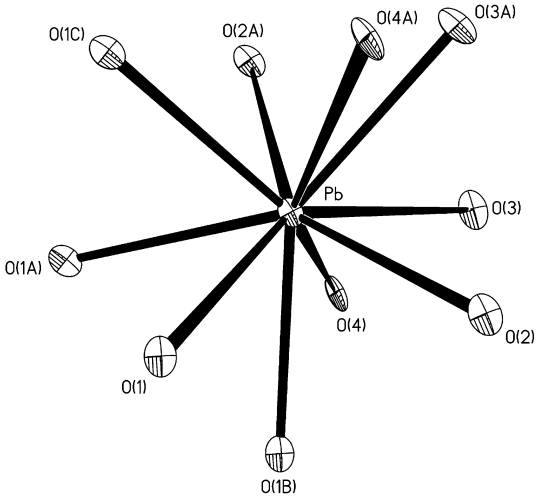


Fig. 1. Coordination environment of the lead ion.

Table 2
Frequencies of vibrational modes in metal complexes of 5-NATZ

	NO_2 asymmetric stretch	N–NO_2 stretch	C–N–NO_2 asymmetric stretch	N_3–N_4 stretch	N_2–N_3 stretch	C–N–NO_2 bending
$KHCN_6O_2$	1450	1318	1224	1058		
$Pb(HCN_6O_2)_2$	1460	1342	1254	1066		
$K_2CN_6O_2$	1294	1396			1010	862
$Ag_2CN_6O_2$	1316	1350			1002	880
$CuCN_6O_2$	1298, 1268	1406			1020	872
$HgCN_6O_2$	1286	1328			1026	863

Table 3
Selected bond lengths (Å) and angles (°) for $Pb(CHN_6O_2)_2(H_2O)_4$

Bond lengths (Å)		Bond angles (°)	
Pb–O(1)	2.888(5)	O(1)–Pb–O(2)	45.5(1)
Pb–O(2)	2.753(5)	O(1)–Pb–O(3)	62.5(1)
Pb–O(3)	2.784(5)	O(1)–Pb–O(3a)	122.9(2)
Pb–O(3a)	2.741(5)	O(1)–Pb–O(4)	99.4(2)
Pb–O(4)	2.652(5)	O(2)–Pb–O(3)	88.1(1)
O(2)–N(6)	1.283(7)	O(2)–Pb–O(3a)	144.1(2)
O(1)–N(6)	1.255(7)	O(2)–Pb–O(4)	71.9(2)
N(6)–N(5)	1.311(8)	O(3)–Pb–O(3a)	63.1(2)
N(5)–C(1)	1.370(8)	O(3)–Pb–O(4)	73.0(2)
N(4)–C(1)	1.328(8)	O(3a)–Pb–O(4)	79.0(1)
N(4)–N(3)	1.352(7)	N(6)–O(2)–Pb	100.5(4)
N(3)–N(2)	1.302(7)	O(1)–N(6)–O(2)	118.8(5)
		O(1)–N(6)–N(5)	125.1(6)
		O(2)–N(6)–N(5)	116.2(5)
		N(6)–N(5)–C(1)	115.7(6)
		C(1)–N(4)–N(3)	106.7(5)
		N(2)–N(3)–N(4)	110.8(5)
		N(3)–N(2)–N(1)	106.6(5)
		N(2)–N(1)–C(1)	108.6(5)
		N(4)–C(1)–N(1)	107.2(6)
		N(4)–C(1)–N(5)	119.7(6)
		N(1)–C(1)–N(5)	133.1(6)

Intramolecular and intermolecular hydrogen bonds are present in the crystal (Fig. 2); the former being observed between the O(4) atom and N(6) atom, the N(6)···O(4) distance is equal to 2.599(6) Å. Each 5-nitroaminotetrazolate ion is connected with a water molecule and adjacent ligands through five hydrogen bonds. All nitrogen atoms except N(2) and N(1) take part in hydrogen bonding. The intermolecular hydrogen bonds are characterized by the distances N–N 2.705(6) Å, N–O 2.828(6) Å and O–O 2.828(6) Å.

$(PbO_2)_n$ chains are stacked in the plane *bc* and form layers consisting only of lead ions and water molecules. 5-NATZ anions are located between the layers (Fig. 3). They

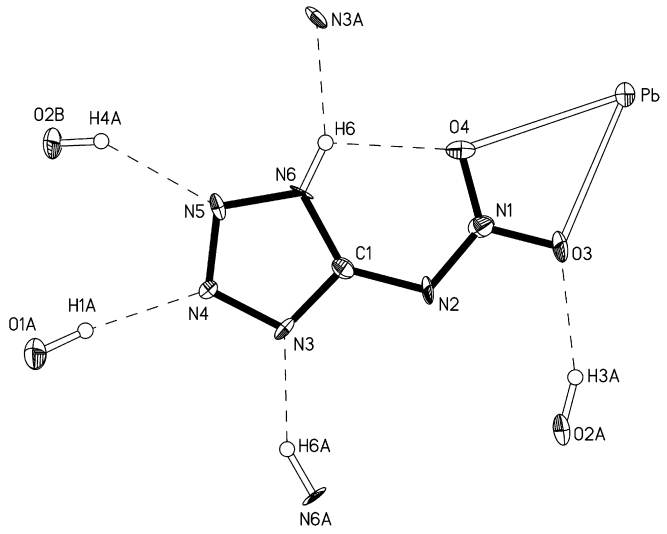


Fig. 2. System of hydrogen bonds around the 5-nitroaminotetrazolate ion, hydrogen bonds are shown as dashed lines.

are linked with lead by Pb–O bonds and are held together by hydrogen bonds, as described in the previous paragraph, and by stacking interactions. The distances between the planes of the tetrazole rings are equal to 3.143(6) Å. From such a point of view, the crystal structure of **4** has a hybrid structure that can be described as an intermediate step between an organometallic coordination polymer and an organic–inorganic hybrid material [44].

The polymeric crystal structure of **7** consists of infinite chains, $[–Hg–CN_6O_2–]_n$, fragments of which are presented in Fig. 4. The formal coordination number of mercury is equal to six. At the same time, the two Hg–N distances are significantly shorter than the Hg–O distances, 2.05(2) Å versus 2.60(2)–2.71(2) Å, respectively. In accord with these, the coordination geometry of mercury can be better described as linear, the N(3)–Hg–N(9) angle is 169° (Table 4). The Hg–N bond lengths are equivalent in the range of standard deviations, its value of 2.05(2) Å is slightly smaller than that for mercury nitrotetrazolate [45]. The difference in length of Hg–O and Pb–O bonds is due to the smaller radius of the Hg atom [46].

The structure of the $5\text{-}NATZ^{2-}$ anion shows differences from the corresponding structure in the alkali metal salts, Ni salt and the calculated geometry. Nitrogen atoms N(3) and N(6) have long N–N (1.40(2) Å) and C–N (1.35(2)–1.42(2) Å) bonds. These lengths are closer to single N–N and C–N bonds and consequently the Hg–N bonds have strong covalent character.

The $[–Hg–CN_6O_2–]_n$ chains are connected by bridged water in the 3D-network, Fig. 5. An extended networks of hydrogen bonds are observed in the crystal structure of the mercury derivative of 5-NATZ.

We have provided theoretical calculations on the equilibrium geometry, charge distribution (Figs. 8a–8c) and chemical hardness of $5\text{-}H_2NATZ$, $5\text{-}HNATZ^-$ and $5\text{-}NATZ^{2-}$ (Table 5) for interpretation of X-ray data and for in-depth consideration of 5-nitroaminotetrazolate coordination properties (for further details see Supplementary material). General numerations of the 5-NATZ atoms in this part are reflected in Fig. 6, and the main possible coordination modes are presented in Fig. 7.

Equilibrium geometrical parameters (Tables S1–S3) are in good agreement with the experimental X-ray diffraction data of $5\text{-}H_2NATZ$ [18] and its salts [25]. The C–N(2) distances, 1.307 and 1.349 Å for $5\text{-}H_2NATZ$ and $5\text{-}HNATZ^-$, respectively, confirm the nitroimino structure of this form. This distance in $5\text{-}NATZ^{2-}$ is 1.394 Å, being closer to the nitroamino form.

Charge distribution in $5\text{-}H_2NATZ$ shows a general pattern in which negative charges are concentrated on the oxygen atoms of the nitro group and the nitrogen atoms N(3) and N(6), but these nitrogen atoms are connected with hydrogens and consequently cannot be coordinated by metal. Therefore, neutral $5\text{-}H_2NATZ$ can really coordinate only through the oxygen atoms, type 1, 6. One hydrogen atom is omitted in the mono-deprotonated form $5\text{-}HNATZ^-$, enabling chelating coordination, type 2. The

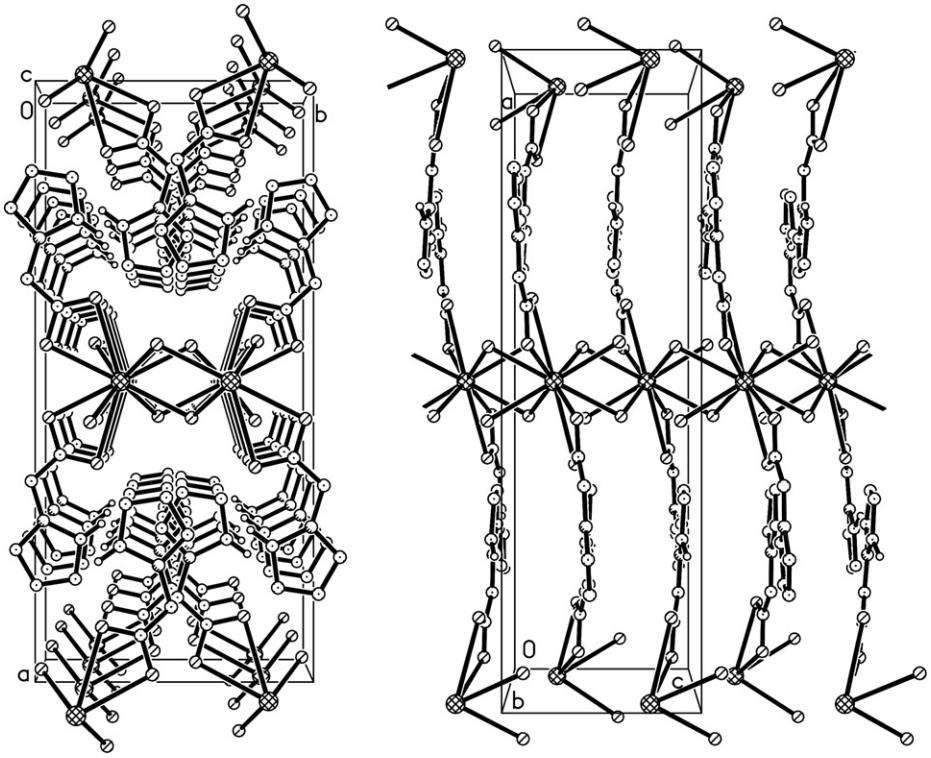


Fig. 3. Packing of $Pb(CHN_6O_2)_2(H_2O)_4$.

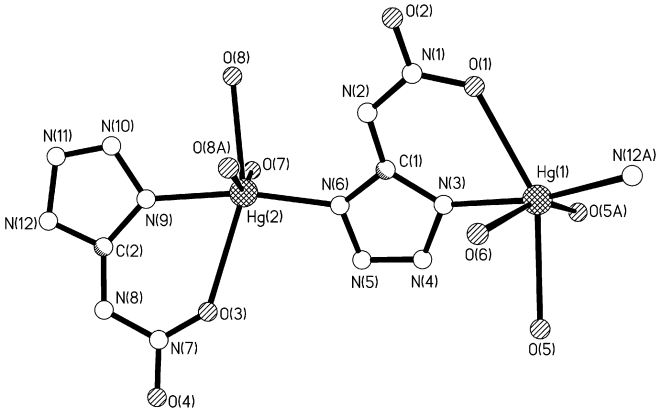


Fig. 4. Fragment of chain in **7**.

Table 4
Selected bond lengths (Å) and angles (°) for $[Hg(CN_6O_2)(H_2O)_2]_n$

Bond lengths (Å)		Bond angles (°)	
Hg(1)–N(3)	2.06(2)	N(3)–Hg(1)–N(12)	168.9(9)
Hg(1)–N(12)	2.05(2)	N(3)–Hg(1)–O(1)	70.4(8)
Hg(1)–O(1)	2.63(2)	N(3)–Hg(1)–O(5)	88.7(8)
Hg(1)–O(5)	2.60(2)	N(12)–Hg(1)–O(5)	101.9(8)
Hg(1)–O(5a)	2.71(2)	N(3)–Hg(1)–O(5a)	88.8(8)
Hg(1)–O(6)	2.70(2)	N(3)–Hg(1)–O(6)	84.6(8)
Hg(2)–N(6)	2.10(2)	N(9)–Hg(2)–N(6)	168.9(9)
Hg(2)–N(9)	2.07(2)	N(9)–Hg(2)–O(3)	70.4(8)
Hg(2)–O(3)	2.64(2)	N(9)–Hg(2)–O(8)	87.6(7)
Hg(2)–O(7)	2.65(2)	N(6)–Hg(2)–O(8)	103.5(7)
Hg(2)–O(8)	2.52(2)	N(9)–Hg(2)–O(7)	88.0(7)
Hg(2)–O(8a)	2.70(2)	N(9)–Hg(2)–O(8a)	91.2(7)

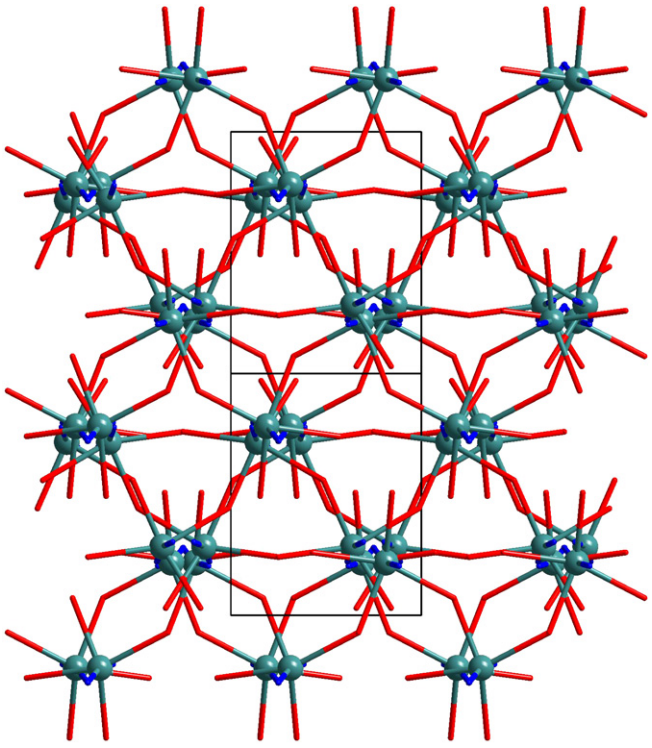


Fig. 5. Packing diagram of **7**, view along chains. Atoms, which are not connected with mercury, are omitted for clarity.

negative charges on N(4) and N(5) are increased relative to 5-H_2NATZ, but coordination through these nitrogen atoms is not probable in this case. The di-deprotonated form of

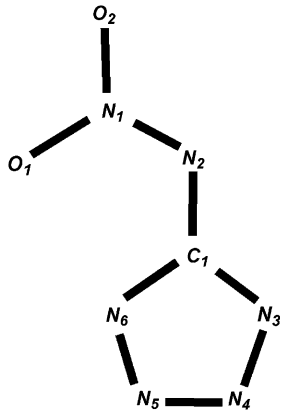


Fig. 6. Numeration scheme for 5-NATZ.

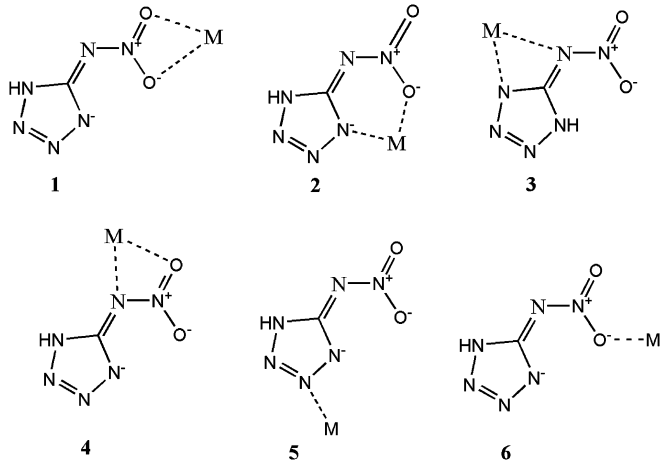


Fig. 7. Possible coordination modes for 5-nitroaminotetrazolates.

5-NATZ^{2-} shows the maximum possible coordination types, the negative charges on N(4) and N(5) continue to increase and that makes coordination through these atoms possible, e.g. as reported for the nickel derivative [29].

The hardness of the system decreases when we pass from the neutral to the di-deprotonated form, and it can lead to

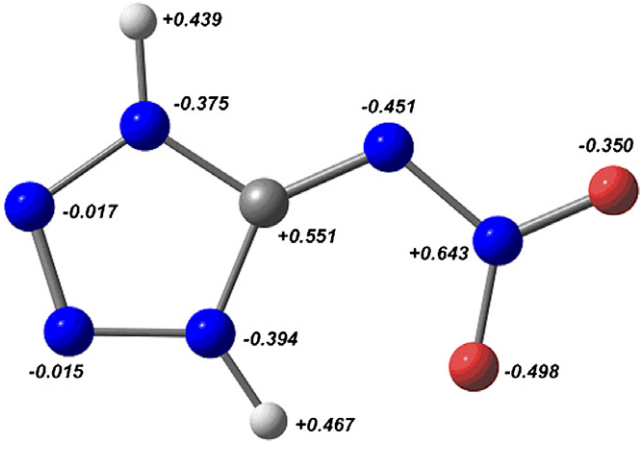


Fig. 8a. Charge distribution scheme for 5-H_2NATZ.

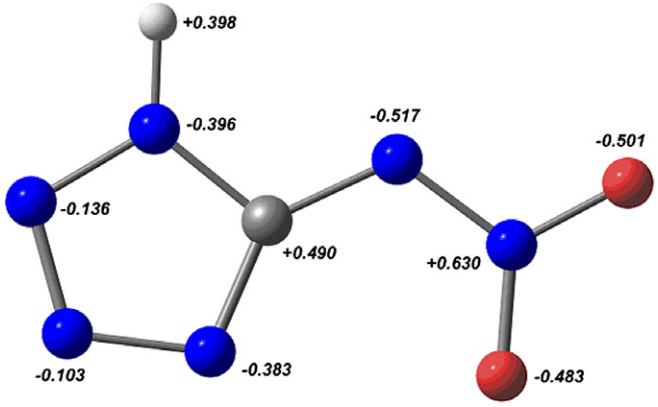


Fig. 8b. Charge distribution scheme for 5-HNATZ^{-}.

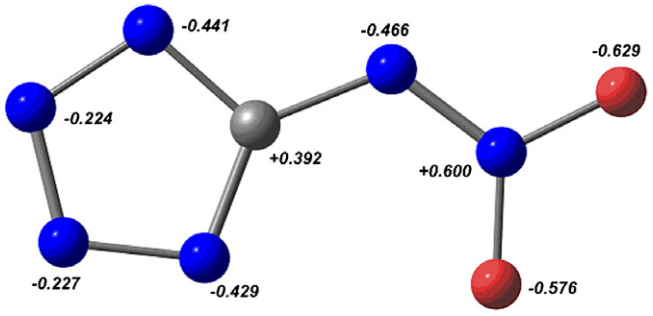


Fig. 8c. Charge distribution scheme for 5-NATZ^{2-}.

Table 5
Hardness of systems considered

System	Hardness (eV)
5-H_2NATZ	3.08
5-HNATZ^{-}	2.86
5-NATZ^{2-}	2.76

a preferred formation of di-substituted complexes in the case of soft metals such as silver and mercury. In this work such a tendency was illustrated with the structures of the lead and mercury derivatives. Interplay of the values of ionic radii and effective positive charge may play an important role in defining the coordination environment (CN Pb = 10, CN Hg = 6). In our opinion, there are two main reasons why the coordination numbers of lead and mercury differ: (i) the ionic radius of mercury is smaller than that of lead; (ii) the effective positive charge of the Hg atom is lowered due to the mostly covalent character of the Hg–N bond.

The temperatures of decomposition of the salts were determined (Table 6). The tendencies which were found for alkali metal salts [22] are also retained for the salts of heavy metals. The temperature of decomposition of the mono-substituted derivative salt is 1.5 times lower than

Table 6
Temperatures of onset of exothermic decomposition

Substance	T (°C)
$KHCN_6O_2$	245
Pb $(HCN_6O_2)_2$	230
$K_2CN_6O_2$	400
$Ag_2CN_6O_2$	345
$CuCN_6O_2$	240
$HgCN_6O_2$	165

that for the di-substituted silver one. The low temperature of decomposition of the copper(II) salt can be caused by the catalytic properties of the copper ion in oxidation reactions.

4. Conclusion

In this work, we showed the possibility of building chain-like extended networks using 5-nitroaminotetrazole (5-NATZ) as a ligand, with examples of lead and mercury salts. Calculations of charge distribution and chemical hardness of the systems showed that soft metal ions should give completely replaced salts with N-coordination. On the other hand, a hard metal can form acidic salts with O-coordination. This can be justified based on the crystal structures presented here. Both structures are polymeric, but the lead structure consists of $(PbO_2)_n$ chains with 5-HNATZ$^-$ acting as a terminal ligand coordinated through oxygen atoms. At the same time, use of the mercury ion gave rise to only the completely replaced salt consisting of $[–Hg–CN_6O_2–]_n$ chains with strongly covalent Hg–N bonds. The crystal structures of these salts give information about their potential applications, such as initiators for explosive materials. The lead derivative includes strongly coordinated water molecules that probably cannot be eliminated by heating in a vacuum. Thus, the lead salt is not a perspective initiator. Water molecules in mercury salt are weakly connected with the metal and are likely to be eliminated by heating in a vacuum. The anhydrous compound should exhibit better explosive properties.

Appendix A. Supplementary material

CCDC 626662 and 639048 contain the supplementary crystallographic data for **4** and **7**. These data can be obtained free of charge via http://www.ccdc.cam.ac.uk/conts/retrieving.html, or from the Cambridge Crystallographic Data Centre, 12 Union Road, Cambridge CB2 1EZ, UK; fax: (+44) 1223-336-033; or e-mail: deposit@ccdc.cam.ac.uk. Cartesian coordinates for all the calculated molecules; full sets of both experimental and theoretical geometrical parameters for all the molecules; full sets of NBO atomic charges in all the computed molecules; table with absolute energies for all the calculated molecules. Supplementary data associated with this article can be found, in the online version, at doi:10.1016/j.poly.2007.06.035.

References

[1] P.J. Koningsbruggen, Y. Garcia, H. Kooijman, A.L. Spek, J.G. Haasnoot, O. Kahn, J. Linares, E. Codjovi, F. Varret, J. Chem. Soc., Dalton Trans. (2001) 466.
[2] X.-M. Zhang, Y.-F. Zhao, H.-S. Wu, S.R. Batten, S.W. Ng, J. Chem. Soc., Dalton Trans. (2006) 3170.
[3] M. Friedrich, J.C. Galvez-Ruiz, T.M. Klapoetke, P. Mayer, B. Weber, J. Weigand, Inorg. Chem. 44 (2005) 8044.
[4] R.-G. Xiong, X. Xue, H. Zhao, X.-Z. You, B.F. Abrahams, Z.-L. Xue, Angew. Chem., Int. Ed. 41 (2002) 3800.
[5] X.-S. Wang, Y.-Z. Tang, X.-F. Huang, Z.-R. Qu, C.-M. Che, P.W.H. Chan, R.-G. Xiong, Inorg. Chem. 44 (2005) 5278.
[6] T. Wu, B.-H. Yiand, D. Li, Inorg. Chem. 44 (2005) 4130.
[7] P. Lin, W. Clegg, R.W. Harrington, R.A. Henderson, J. Chem. Soc., Dalton Trans. (2005) 2388.
[8] M. Dinca, A.F. Yu, J.R. Long, J. Am. Chem. Soc. 128 (2006) 8913.
[9] T. Wu, R. Zhou, D. Li, Inorg. Chem. Commun. 9 (2006) 341.
[10] A.J. Blake, N.R. Champness, P. Hubberstey, W.-S. Li, M.A. Withersby, M. Schröder, Coord. Chem. Rev. 183 (1999) 117.
[11] J.-R. Li, X.-H. Bu, G.-C. Jia, S.R. Batten, J. Mol. Struct. 828 (2007) 142.
[12] A. Hammerl, G. Holl, T.M. Klapotke, P. Mayer, H. Noth, H. Piotrowski, M. Warchhold, Eur. J. Inorg. Chem. (2002) 834.
[13] J.C. Gálvez-Ruiz, G. Holl, K. Karaghiosoff, T.M. Klapötke, K. Löhnwitz, P. Mayer, H. Nöth, K. Polborn, C.J. Rohbogner, M. Suter, J.J. Weigand, Inorg. Chem. 44 (2005) 4237.
[14] H. Xue, Y. Gao, B. Twamley, J.M. Shreeve, Inorg. Chem. 44 (2005) 5068.
[15] R.P. Singh, R.D. Verma, D.T. Meshri, J.M. Shreeve, Angew. Chem., Int. Ed. 45 (2006) 3584.
[16] R. Wang, H. Gao, C. Ye, B. Twamley, J.M. Shreeve, Inorg. Chem. 46 (2007) 932.
[17] E. Lieber, E. Sherman, R.A. Henry, J. Cohen, J. Am. Chem. Soc. 73 (1951) 2327.
[18] A. Gao, A.L. Rheingold, T.B. Brill, Prop. Explos. Pyrotech. 16 (1991) 97.
[19] A.M. Astahov, R.S. Stepanov, L.A. Kruglikova, A.A. Nefedov, Russ. J. Org. Chem. 37 (2001) 611.
[20] B.C. Tappan, R.W. Beal, T.B. Brill, Thermochem. Acta 388 (2002) 227.
[21] Z.X. Chen, J.M. Xiao, H.M. Xiao, Y.N. Chiu, J. Phys. Chem. A 103 (1999) 8062.
[22] Z.-X. Chen, H. Xiao, Int. J. Quantum Chem. 79 (2000) 350.
[23] A.D. Vasiliev, A.M. Astakhov, A.A. Nefedov, R.S. Stepanov, J. Struct. Chem. 44 (2003) 322.
[24] A.M. Astakhov, A.D. Vasiliev, M.S. Molokeev, A.M. Sirotinin, L.A. Kruglyakova, J. Struct. Chem. 45 (2004) 175.
[25] B.C. Tappan, C.D. Incarvito, A.L. Rheingold, T.B. Brill, Thermochem. Acta 384 (2002) 113.
[26] A.M. Astakhov, A.D. Vasiliev, M.S. Molokeev, J. Struct. Chem. 45 (2004) 537.
[27] A.M. Astakhov, A.D. Vasiliev, M.S. Molokeev, A.M. Sirotinin, L.A. Kruglyakova, J. Struct. Chem. 45 (2004) 360.
[28] A.G. Mayanc, V.S. Klimenko, V.V. Erina, K.G. Pireseva, S.S. Gordeichuk, V.N. Leibzon, V.S. Kuzmin, Y.N. Burcev, Chim. Getcyc. Comp. (1991) 1067.
[29] S.F. Palopoli, S.J. Geib, A.L. Rheingold, T.B. Brill, Inorg. Chem. 27 (1988) 2963.
[30] A. Henry, R.C. Makosky, G.B.L. Smith, J. Am. Chem. Soc. 73 (1951) 474.
[31] H. Gilman (Ed.), Organic Syntheses, Russian Translation, vol. 1, Moscow, 1949, p. 298.
[32] J.P. Perdew, K. Burke, M. Erzenhorf, Phys. Rev. Lett. 77 (1996) 3865.
[33] J.P. Perdew, K. Burke, M. Erzenhorf, Phys. Rev. Lett. 78 (1997) 1396.

[34] C. Adamo, V. Barone, J. Chem. Phys. 110 (1999) 6158.
[35] A.A. Granovsky. Available from: <http://lcc.chem.msu.ru/gran/gamess/index.html>.
[36] M.W. Schmidt, K.K. Baldridge, J.A. Boatz, S.T. Elbert, M.S. Gordon, J.H. Jensen, S. Koseki, N. Matsunaga, K.A. Nguyen, S. Su, T.L. Windus, M. Dupuis, J.A. Montgomery, J. Comput. Chem. 14 (1993) 1347.
[37] A.E. Reed, L.A. Curtiss, F. Weinhold, Chem. Rev. 88 (1988) 899.
[38] F. Weinhold, C.A. Landis, Valency and Bonding: A Natural Bond Orbital Donor–Acceptor Perspective, Cambridge University Press, Cambridge, 2005, 760p.
[39] http://www.chemcraftprog.com.
[40] R.G. Pearson, Chemical Hardness: Applications from Molecules to Solids, Wiley–VCH Verlag GmbH, Weinheim/New York, 1997, 198p.
[41] E.J. Baerends, O.V. Gritsenko, R. van Leeuwen (Eds.), Chemical Applications of Density Functional Theory, ACS Symposium Series No. 269, vol. 20, American Chemical Society, 1996, p. 20.
[42] R. Stowasser, R. Hoffmann, J. Am. Chem. Soc. 121 (1999) 3414.
[43] R.G. Bryant, V.P. Chacko, M.C. Etter, Inorg. Chem. 23 (1984) 3580.
[44] P.J. Hagrman, D. Hagrman, J. Zubieta, Angew. Chem., Int. Ed. 38 (1999) 2638.
[45] J. Xianglin, S. Meicheng, H. Haochuan, W. Jinming, Z. Yu, Huaxue Tongbao (Chin.) (Chem. Bull.) (1982) 336.
[46] R.D. Shannon, Acta Crystallogr., Sect. A 32 (1976) 751.

a Bruker AC-300 MHz spectrometer operating in the quarter mode. The spectra were collected over a 50-kHz band width with 16 K data points and a 5-μs of 45° pulse. For a typical spectrum, between 1000 and 5000 transients were accumulated with a 50-ms delay time. The signal-to-noise ratio was improved by apodization of the free induction decay. Melting points are uncorrected and were obtained on a Kofler Heizbank Rechart type 7841 melting point apparatus.

2.2. Synthesis of complex [Fe(bipy)Cl_4][bipy · H] (1)

2,2′-Bipyridine (0.31 g, 2 mmol) in 0.1 M HCl (20 ml) was added to a solution of $FeCl_3 \cdot 6H_2O$ (0.27 g, 1 mmol) in water (15 ml) and the resulting red solution was stirred at 55–60 °C for 3 h. The orange colored precipitated product was recrystallized from CH_3CN. After 3 days, orange prismatic crystals of **1** were isolated (yield: 0.39 g, 76.3%, m.p.: 216 °C). IR (KBr, cm^{-1}): 3060m (*ν*(CH)), 1615m, 1599s, 1583s, 1529s, 1494w, 1473m, 1456m, 1443s, 1433m, 1384w, 1367w, 1320m, 1311s, 1270m, 1248w, 1229w, 1174m, 1158m, 110w, 1102w, 1088w, 1068w, 1058w, 1020m, 1010m, 993sh, 929m, 908w, 881m, 808w, 764s, 733m, 724m, 652m, 630m, 610m, 524w, 425w, 441w, 418m, 400w, 393w, 362w, 333w, 308s (*ν*(Fe–Cl)), 290s (*ν*(Fe–Cl)), 255s (*ν*(Fe–N)). *Anal.* Calc. for **1**: C, 46.96; H, 3.33; N, 10.95. Found: C, 46.58; H, 3.51; N, 10.76%.

2.3. Synthesis of complex [Fe(bipy)Cl_3(DMSO)] (2)

Dimethyl sulfoxide (0.44 ml, 6.4 mmol) was added to a solution of [Fe(bipy)Cl_4][bipy · H] (0.4 g, 0.8 mmol) in CH_3OH (40 ml) and the resulting orange solution was stirred at 40–45 °C for 2 h. This solution was left to evaporate slowly at room temperature. After 5 days, yellow prismatic crystals of **2** were isolated (yield: 0.23 g, 72.5%, m.p.: 268 °C). IR (KBr, cm^{-1}): 3060m, 2998m, 2918m (*ν*(CH)), 1605m, 1598s, 1563s, 1493s, 1471s, 1309s 1220m, 1205m, 1152s, 1102m, 1070w, 1059w, 1031m, 1025m, 1014w, 985s, 952s, 939s, 908w, 894w, 810w, 768s, 731s, 717w, 653m, 632m, 546w, 434s, 417m, 361w, 345m, 311s (*ν*(Fe–Cl)), 291s (*ν*(Fe–Cl)), 255s (*ν*(Fe–N)). *Anal.* Calc. for **2**: C, 36.32; H, 3.53; N, 7.06. Found: C, 36.18; H, 3.71; N, 6.89%.

2.4. Synthesis of complex [Fe(phen)Cl_4][phen · H] (3)

1,10-Phenanthrolinum chloride monohydrate (0.474 g, 2 mmol) in 10 ml water was added to a solution of $FeCl_3 \cdot 6H_2O$ (0.273 g, 1 mmol) in water (15 ml) and the resulting red solution was stirred at 55–60 °C for 3 h. The orange colored precipitated product was recrystallized from CH_3CN. After 3 days, orange prismatic crystals of **3** were isolated (yield: 0.44 g, 78.6%, m.p.: 268–270 °C). IR (KBr, cm^{-1}): 3053m (*ν*(CH)), 1616m, 1609m, 1596s, 1583s, 1539s, 1525s, 1518m, 1493m, 1464s, 1423s, 1341m, 1312m, 1278m, 1239m, 1185s, 1145m, 1101m, 1071w, 1036w, 991w, 974w, 965w, 898w, 883w, 868w, 851s, 840s, 817m, 781w, 767s, 723s, 715s, 641m, 620w, 537w, 506w, 461m, 426m, 410w, 399w, 305s (*ν*(Fe–Cl)), 286s (*ν*(Fe–Cl)), 269s (*ν*(Fe–N)). *Anal.* Calc. for **3**: C, 51.51; H, 3.04; N, 10.02. Found: C, 51.21; H, 3.11; N, 9.88%.

2.5. Synthesis of complex [Fe(phen)Cl_3(DMSO)] (4)

Dimethyl sulfoxide (0.92 ml, 13 mmol) was added to a solution of [Fe(phen)Cl_4][phen · H] (0.30 g, 0.54 mmol) in CH_3OH (40 ml) and the resulting orange solution was stirred at 40–45 °C for 2 h. This solution was left to evaporate slowly at room temperature. After 5 days, deep yellow prismatic crystals of **4** were isolated (yield: 0.17 g, 74.8%, m.p.: 233–235 °C). IR (KBr, cm^{-1}): 3072m, 2998m, 2918m (*ν*(CH)), 1623m, 1605m, 1582s, 1563s, 1509s, 1494m, 1425s, 1342s, 1224s, 1146m, 1105s, 1029m, 983s, 948s, 937s, 868m, 810w, 781w, 724s, 642m, 556w, 481w, 436s, 427s, 344m, 311s (*ν*(Fe–Cl)), 264s (*ν*(Fe–N)). *Anal.* Calc. for **4**: C, 39.95; H, 3.33; N, 6.66. Found: C, 39.76; H, 3.24; N, 6.48% (see Table 1).

2.6. Crystal structure determination and refinement

The X-ray diffraction measurements were made on a STOE IPDS-II diffractometer with graphite-monochromated Mo Kα radiation. For [Fe(bipy)Cl_3(DMSO)] (**2**), a yellow prismatic crystal with dimensions $0.40 \times 0.20 \times 0.20$ mm and for [Fe(phen)Cl_3(DMSO)] (**4**), a deep yellow prismatic crystal with dimensions of $0.25 \times 0.20 \times 0.15$ mm was mounted on a glass fiber and used for data collection. Cell constants and an orientation matrix for data collection were obtained by least-squares refinement of the diffraction data from 3396 unique reflections for **2** and 3542 for **4**. Data were collected at a temperature of 293(2) K to a maximum 2θ value of 53.48° for **2** and 53.46° for **4** and in a series of ω scans in 1° oscillations and integrated using the Stoe X-AREA [19] software package. The numerical absorption coefficient, μ, for Mo Kα radiation is 1.555 mm^{-1} for **2** and 1.446 mm^{-1} for **4**. A numerical absorption correction was applied using X-RED [20] and X-SHAPE [21] software. The data were corrected for Lorentz and polarizing effects. The structures were solved by direct methods [22] and subsequent difference Fourier maps and then refined on F^2 by a full-matrix least-squares procedure using anisotropic displacement parameters [22]. All of the hydrogen atoms were located in a difference Fourier map and then after refined isotropically. Subsequent refinement then converged with R factors and parameters errors significantly better than for all attempts to model the solvent disorder. Atomic factors are from the International Tables for X-ray Crystallography [23]. All refinements were performed using the X-STEP 32 crystallographic software package [24]. A summary of the crystal data, experimental details and refinement results is given in Table 2.

Table 1
Selected IR frequencies of bipyridine, phenanthroline, dimethyl sulfoxide and complexes **1**–**4** (cm^{-1})

Compound	ν(C=C), ν(C=N)	ν(ring deformation)	ν(C–H)	ν(Fe–N)	ν(S=O)	ν(Fe–Cl)	ν(Fe–O)
Bipy	1414, 1453, 1554, 1578	616, 649, 738, 757, 892	3060				
Phen	1429, 1510, 1593	630, 720, 754, 850, 863	3070				
DMSO			2913, 2996		1050		
[Fe(bipy)Cl_4][bipy · H]	1433, 1473, 1583, 1599	630, 652, 764, 808, 881	3060	255		290, 308	
[Fe(phen)Cl_4][phen · H]	1464, 1493, 1539, 1569	641, 767, 781, 868, 883	3053	269		286, 305	
[Fe(bipy)Cl_3(DMSO)]	1471, 1493, 1563, 1598	632, 653, 731, 768, 810, 894	2918, 2998, 3060	255	985	311, 291	434
[Fe(phen)Cl_3(DMSO)]	1494, 1509, 1563, 1582	642, 724, 781, 810, 868	2998, 2998, 3072	264	984	311	436

Table 2
Crystallographic and structure refinements data for complexes **2** and **4**

Complex	**2**	**4**
Formula	$C_{12}H_{14}Cl_3FeN_2OS$	$C_{14}H_{14}Cl_3FeN_2OS$
Formula weight	396.51	420.53
Temperature (K)	293(2)	293(2)
Wavelength λ (Å)	0.71073	0.71073
Crystal system	Triclinic	Orthorhombic
Space group	$P\bar{1}$	$Pn2_1/a$
Crystal size (mm)	$0.40 \times 0.20 \times 0.20$	$0.25 \times 0.20 \times 0.15$
a (Å)	7.498(1)	8.631(1)
b (Å)	9.982(2)	12.204(1)
c (Å)	11.492(2)	16.541(2)
α (°)	89.30(1)	90
β (°)	82.62(1)	90
γ (°)	71.21(1)	90
Volume ($Å^3$)	807.2(2)	1442.4(4)
Z	2	4
D_{calc} (g cm^{-1})	1.631	1.603
θ Ranges for data collection (°)	1.79–26.74	2.07–26.73
F(000)	402	852
Absorption coefficient	1.555	1.446
Index ranges	$-9 \leqslant h \leqslant 9$, $-12 \leqslant k \leqslant 12$, $0 \leqslant l \leqslant 14$	$-10 \leqslant h \leqslant 10$, $-14 \leqslant k \leqslant 15$, $-20 \leqslant l \leqslant 20$
Data collected	7226	12 703
Unique data (R_{int})	3396 (0.0416)	3542 (0.0365)
Parameters/restrains	182/0	202/1
Final R_1, wR_2^a (observed data)	0.0245, 0.0618	0.0266, 0.0705
Final R_1, wR_2^a (all data)	0.0293, 0.0638	0.0277, 0.0711
Goodness of fit on F^2 (S)	1.043	1.069
Extinction coefficient	0.0043(16)	0.0014(11)
Absolute structure parameter		0.023(15)
Largest difference in peak and hole (e $Å^{-3}$)	0.260 and −0.225	0.203 and −0.348

[a] $R_1 = \sum||F_o| - |F_c||/\sum|F_o|$, $wR_2 = [\sum(w(F_o^2 - F_c^2)^2)/\sum w(F_o^2)^2]^{1/2}$.

3. Results and discussion

3.1. Synthesis of compounds 1–4

Compounds **1** and **3** were synthesised according to the reported procedure for the preparation of compound **1** [25]. Treatment of one equivalent of $FeCl_3 \cdot 6H_2O$ with 2 equivalents of the bidentate chelating ligand, N–N, in the presence of HCl solution affords a compound with the general formula [Fe(N–N)Cl_4][N–N · H] in high yield, 76–78%, Eq. (1):

$$FeCl_3 \cdot 6H_2O + 2N\text{–}N \cdot HCl \xrightarrow{H_2O} [Fe(N\text{–}N)Cl_4][N\text{–}N \cdot N] \quad (1)$$

where **1** when N–N is bipyridine and **3** when N–N is phenanthroline.

The structures of complexes **1** and **3** were obtained by X-ray crystallography and confirmed by means of IR and ^{1}H NMR spectroscopic techniques, so they are unambiguously identified [25,26]. Addition of DMSO to the methanolic solution of **1** and **3** results in the formation of **2** and **4**, respectively, Eq. (2):

$$[Fe(N\text{–}N)Cl_4][N\text{–}N \cdot H] \xrightarrow{CH_3OH/DMSO} [Fe(N\text{–}N)Cl_3(DMSO)] + N\text{–}N \cdot HCl \quad (2)$$

where **2** when N–N is bipyridine and **4** when N–N is phenanthroline.

Solution studies of **1** and **3** show that exchange of a chloride ion by a donor ligand such as DMSO, CH_3OH, DMF and pyridine is fast. Dissolution of **1** and **3** in a donor solvent and subsequent recrystallization produces the neutral complex [Fe(N–N)Cl_3(D)] where D stands for donor ligands. We were able to determine the crystal structure of [Fe(phen)Cl_3(CH_3OH)] by dissolving and recrystallising **3** in CH_3OH solvent, and although the structure was reported before it further proves the formation of the aforementioned complex [26]. The structures of **2** and **4** also were characterized by X-ray diffraction in addition to IR and ^{1}H NMR spectroscopies. Therefore, we introduce the synthesis of complexes with a general formula $[Fe(N\text{–}N)Cl_4]^-[N\text{–}N \cdot H]^+$ as useful precursors for the synthesis of hetro ligand complexes of labile high spin Fe^{III} with the general formula $[Fe^{III}(N\text{–}N)Cl_3(D)]$ were N–N stands for diimines and D stands for donor ligands.

The structures of complexes **1** and **3** consist of alternating stacks of $[Fe(bipy)Cl_4]^-$ and $[Fe(phen)Cl_4]^-$ anions and $(bipy \cdot H)^+$ and $(phen \cdot H)^+$ cations, respectively, linked together by hydrogen bonds. Each anion binds to organic donors through N–H···Cl hydrogen bonds (H···Cl is 2.33(0.029) Å and N–H···Cl is 153.47(7.00)° for **1** and H···Cl is 2.61(0.025) Å and N–H···Cl is 138.15(2.21)° for **3**). It seems that hydrogen bonding between the acidic hydrogen of the cation with one of the coordinated chloride ligands in the anionic part of **1** or **3** has a promoting

effect for the removal of Cl as HCl in the presence of an entering donor ligand [25–27].

The only well-characterized compound with this general formula is [Fe(phen)$Cl_3(H_2O)$], which is prepared in very low yield from the reaction of $FeCl_3 \cdot 6H_2O$ and phenanthroline in 10 M HCl, maybe as a by-product. In contrast, the analytical yields of formation of complexes **2** and **4** are near quantitative [18].

3.2. ^1H NMR investigation

Although iron phenanthroline and bipyridine complexes were made in the last century, most of them were characterized by X-ray analysis and IR spectroscopy, and NMR analyses are rare [18,28–38]. Trace A in Fig. 1 shows the ^1H NMR spectrum of compound **1** in CD_3OD/CH_3OH (98:2). This spectrum was obtained right after dissolution of **1** in the aforementioned solvent. The proton signals of bipyridine are observed at 8.7, 8.4, 8.1 and 7.6 ppm, consistant with the C_2 symmetry of this structure in the solid state. The proton signals of the coordinated bipy are not resolved from bipy · H counter ions under these conditions. The ^1H NMR spectrum of [Fe(bipy)Cl_3(DMSO)] in CD_3OD is indicated in trace B of Fig. 1. Trace C is the spectrum of **1** in CD_3OD:CH_3OH (98:2) 1 h after dissolution of **1** in CD_3OD, and Trace D is the same spectrum after 24 h. In a separate experiment, [Fe(bipy)Cl_3-(CH_3OH)] (**5**), was synthesized [26] and its spectrum was obtained in CD_3OD. ^1H NMR demonstrate this spectrum is the exact spectrum as that in trace D in Fig. 1. This data confirms that the coordinated protons of DMSO are presented as a broad signal at 45.8 ppm in CD_3OD solution at 20 °C. In addition the proton signal of CH_3 for coordinated methanol was observed at 104.6 ppm. ^1H NMR investigation has shown that dissolution of **1** in methanol converts **1** to **5**, and in DMSO **1** is converted to **3**. A similar behavior and ^1H NMR spectrum was obtained for compounds **2**, **4** and [Fe(bipy)Cl_3(CH_3OH)], which proves generality of the method. For phenanthroline complexes, again the proton signal of the CH_3 group in methanol was observed at 104.5 ppm and the methyl group of coordinated DMSO at 45.3 ppm, almost in the same places as the bipyridine complexes. Addition of H_2O or taking the spectrum of **1** in D_2O produces a new feature for the proton signals, and we are working to characterize this. However, addition of 10 μl HCl/D_2O in CD_3OD results in a new complex with a new signal at −5.7 ppm, which may belong to the compound [Fe(bipy)$Cl_3(H_2O)$]. Fig. 2 demonstrates the ^1H NMR spectrum of compound **4**, [Fe(phen)Cl_3(DMSO)], in DMSO-d_6 solvent. In this spectrum, two broad signals appear at 45.4 ppm, which is in the same region as for the methyl signal of DMSO in **4** in accordance with the results presented in Fig. 1. However, another broad signal appears under these conditions at around 13 ppm, with the same intensity as the signal at 45.4 ppm. This can be an indication of [Fe(phen)-Cl_2(DMSO)$_2$]Cl formation according to the following equation:

$$[Fe(phen)Cl_3(DMSO)] \xrightarrow{DMSO} [Fe(phen)Cl_2(DMSO)_2]Cl \quad (3)$$

Notably, the titration process of DMSO in methanol was checked and the results show that the optimum amount for [Fe(phen)Cl_3(DMSO)] formation is about 24 equivalents of DMSO to one equivalent of complex **3**.

3.3. IR and UV–Vis of investigation

IR spectroscopy is a strong tool for identification of iron phenanthroline and iron bipyridine complexes, since a

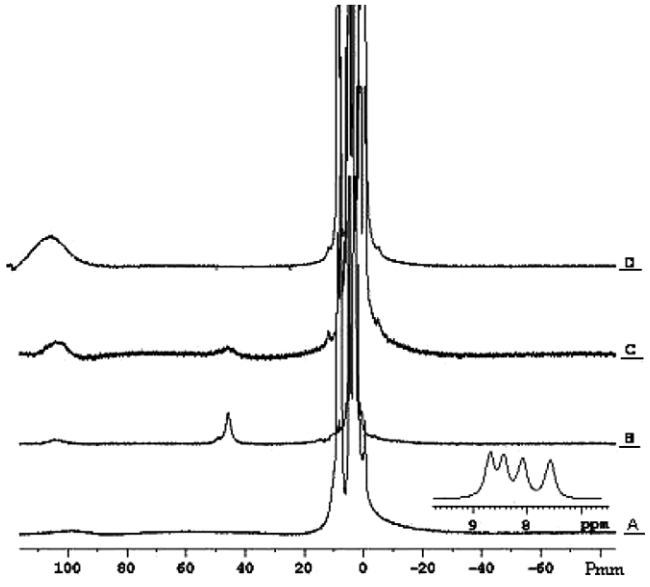


Fig. 1. ^1H NMR spectra of (A) complex **1** in CD_3OD:CH_3OH (98:2) right after dissolution, (B) complex **2** in the above-mentioned solvent, (C) complex **1** after 1 h and (D) complex **1** after 1 day in the above-mentioned solution.

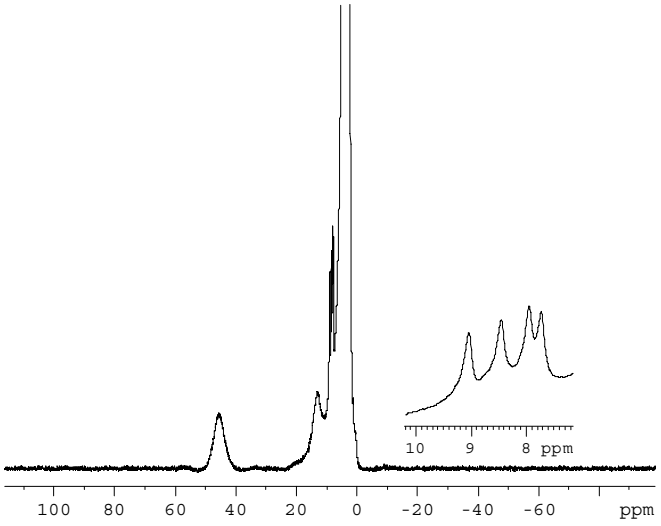


Fig. 2. ^1H NMR of compound **4**, [Fe(phen)Cl_3(DMSO)], in DMSO-d_6 solvent.

Table 3
Selected bond distances (Å) and bond angles (°) for complexes **2** and **4**

Complex	**2**	**4**
Bond distances (Å)		
Fe1–N1	2.181(2)	2.222(2)
Fe1–N2	2.194(2)	2.203(2)
Fe1–Cl1	2.309(1)	2.294(1)
Fe1–Cl2	2.316(1)	2.295(1)
Fe1–Cl3	2.305(1)	2.342(1)
Fe1–O1	2.090(1)	2.069(2)
O1–S1	1.525(1)	1.525(2)
Bond angles (°)		
N1–Fe1–N2	74.17(6)	75.49(2)
N1–Fe1–Cl1	167.14(4)	168.29(8)
N2–Fe1–Cl2	163.03(4)	166.77(6)
Cl3–Fe1–O1	170.74(4)	166.70(6)
Cl1–Fe1–Cl2	98.39(2)	99.26(3)
N1–Fe1–O1	82.83(5)	84.95(8)
N2–Fe1–O1	79.11(6)	82.57(8)

wealth of information is presented in the literature. IR absorption of the free ligands and compounds **1**–**4** are presented in Table 3. The Fe–Cl and Fe–N frequencies in **2** and **4** are mainly distinguishable in comparison with the known complex **1** [26]. In addition new signals at 985 and 984 cm^{-1} in the IR spectra of **2** and **4**, respectively, are assigned to ν(S=O). Other iron(III) DMSO complexes reported in the literature have shown ν(S=O) in the 910–960 cm^{-1} region [38]. The bands at 434 and 436 cm^{-1} were assigned to Fe–O stretching in **2** and **4**, respectively. The IR information confirm the high spin character of the iron center in **2** and **4**, since low spin iron(III) complexes have shown 50–70 cm^{-1} higher Fe^{III}–N frequencies [39]. Magnetic susceptibility measurements for **2** and **4** by the Evans method confirms the high spin character of these complexes ($\mu_{eff} \approx 6$ BM) [40].

UV–Vis spectra of **2** and **4** have no spin allowed signals for d–d transitions (their color is yellow in solution), but a

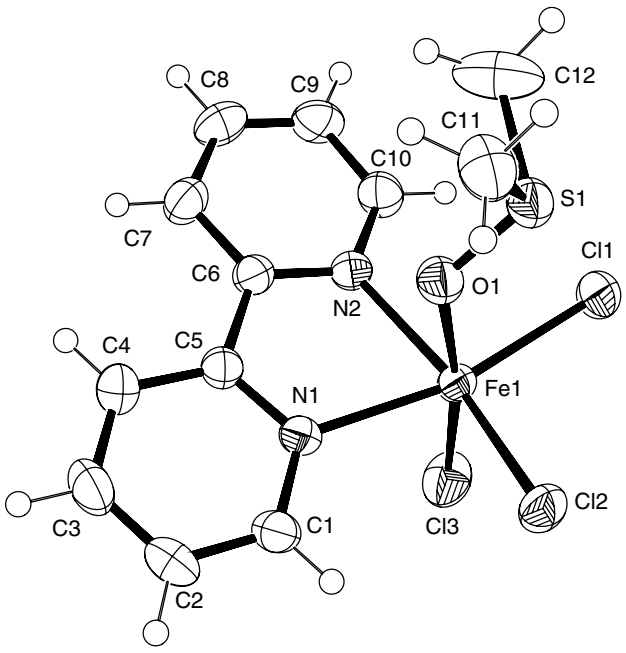


Fig. 3. The labelled diagram of [Fe(bipy)Cl_3(DMSO)] (**2**). Thermal ellipsoids are at the 50% probability level.

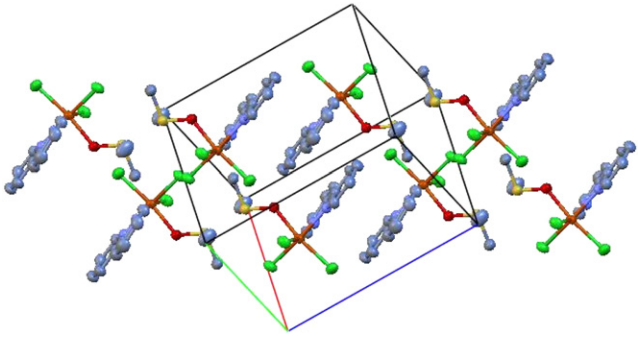


Fig. 4. Crystal packing diagram for complex **2**. Hydrogen atoms are omitted for clarity.

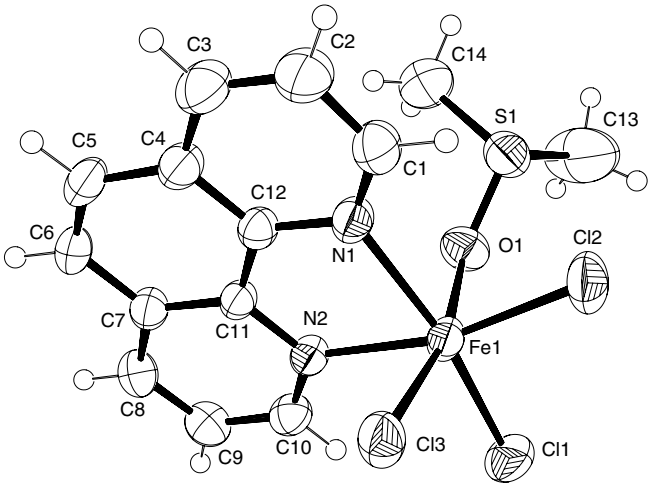


Fig. 5. The labelled diagram of [Fe(phen)Cl_3(DMSO)] (**4**). Thermal ellipsoids are at the 50% probability level.

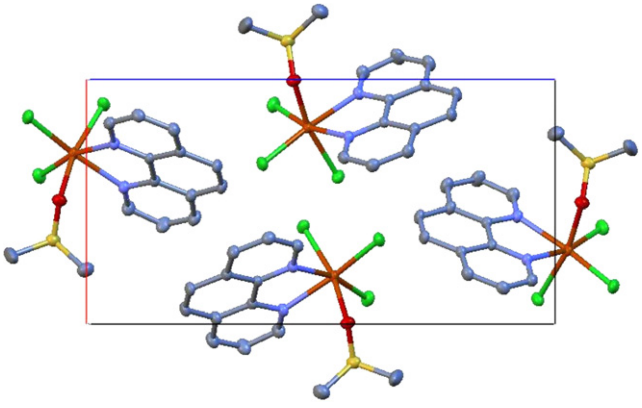


Fig. 6. Crystal packing diagram for complex **4** viewed in the *b*-direction. Hydrogen atoms are omitted for clarity.

Table 4
The mean bond distances (Å) and angles (°) of some phenanthroline and bipyridine iron(III) complexes

Iron complex	⟨Fe–N⟩ (Å)	⟨Fe–Cl⟩ (Å)[a]	⟨Fe–Cl⟩ (Å)[b]	∠N–Fe–N (°)	Spin state	Reference
$[Fe(phen)Cl_4]^-$	2.2012(14)	2.3195(9)	2.3824(8)	75.04(6)	H.S.	Present work
$[Fe(bipy)Cl_4]^-$	2.193(3)	2.392(1)	2.299(1)	73.91(1)	H.S.	[25]
$[Fe(bipy)Cl_3(DMSO)]$	2.187(14)	2.309(6)	2.3046(7)	74.17(6)	H.S.	Present work
$[Fe(phen)Cl_3(DMSO)]$	2.213(2)	2.294(8)	2.3421(7)	75.49(8)	H.S.	Present work
$[Fe(phen)Cl_3(H_2O)]$	2.174(3)	2.276	2.276	75.6(1)	H.S.	[18]
$[Fe(phen)_2Cl_2]^+$	2.250(11)	2.240			H.S.	[42]
$[Fe(phen)_3]^+$	1.973			83.0(3)	L.S.	[43]

[a] Equatorial.
[b] Axial.

charge transfer bond is seen around 353 nm, in accordance with the high spin character of the iron(III) center.

3.4. Description of the molecular structures of *[Fe(bipy)Cl₃(DMSO)]* (**2**) and *[Fe(phen)Cl₃(DMSO)]* (**4**)

Yellow prismatic crystals of **2** and **4** were grown by recrystallization of their respective microcrystals in CH_3CN over a week. Table 2 shows details of the data collection and refinement of the X–ray crystal structure determinations for **2** and **4**. Selected bond lengths and bond angles are presented in Table 3. The crystal structures of complexes **2** and **4** consist of three chloride ions, one chelating bipyridine (or phenanthroline in **4**) and one DMSO molecule. The ORTEP view with the numbering schemes and packing diagrams for compounds **2** and **4** are shown in Figs. 3–6. The complexes have distorted octahedral geometries. The differences between coordinated ligands, different bond distances for *cis* and *trans* chloride ligands relative to diimine in **2** and **4** are the main factors accounting for these distortions, Table 3. The structures of **2** and **4** are mainly similar. The Fe–N (ave.) distance for complex **2** is 2.19 Å, which is slightly smaller than that found for **4** (2.21 Å), which is compensated by the Fe–Cl bond distances on the opposite sites, in which the Fe–Cl bonds are slightly larger in **2** than those in **4**. DMSO is coordinated to the Fe(III) center by oxygen and the Fe–O bond distances are almost similar in **2** and **4**, as expected.

The metal ligand bond lengths were used to obtain the spin state of the metal center, Table 4. The Fe–N (ave.) bond distances in high spin iron(III) phenanthroline and bipyridine complexes are around 2.2 Å in high spin complexes, and in low spin Fe^{III} complexes Fe–N distances less than 2 Å were reported [18,41]. Therefore, the Fe–N bond distances here show the present complexes are unambiguously high spin d^5. The Fe–O bond distances for **2** and **4** are 2.09 Å and 2.07 Å, respectively. The Fe–O bond distance in $[Fe^{III}(phen)Cl_3(H_2O)]$ was reported to be 2.19 Å, which is considerably longer than the Fe–O bond distances in **2** and **4** [18]. This elongation in the former complex is due to hydrogen bond formation. There are no hydrogen bonds present in complexes **2** and **4**.

As it is shown in Fig. 4, in complex **2** the bipy ligands form π bonding stacks in which each bipy ligand lies between two bipy ligands of adjacent iron complexes. The close contact distance between adjacent aromatic rings is 3.18 Å. In the complex **4**, there are no π–π aromatic interactions between the phen ligands, Fig. 6, and the angles between phen planes are about 25° and 63° in the lattice.

4. Supplementary material

CCDC 298949 and 651953 contain the supplementary crystallographic data for **2** and **4**. These data can be obtained free of charge via http://www.ccdc.cam.ac.uk/conts/retrieving.html, or from the Cambridge Crystallographic Data Centre, 12 Union Road, Cambridge CB2 1EZ, UK; fax: (+44) 1223-336-033; or e-mail: deposit@ccdc.cam.ac.uk.

Acknowledgments

We thank the Iranian National Science Foundation and Research and Graduate Study Councils of Shahid Beheshti University for financial support.

References

[1] S.J. Chalk, J.F. Tyson, Anal. Chem. 66 (1994) 660.
[2] N. Mudasir, Inoue H. Yoshioka, Anal. Chem. 29 (1996) 2239.
[3] R. Sariego, L. Farias, N.A. Moya, Polyhedron 16 (1997) 3487.
[4] P.B. Samnani, P.K. Bhattacharya, P.A. Ganeshpure, V.J. Koshy, N. Satish, J. Mol. Catal. 110 (1996) 89.
[5] L.G. Bachas, L. Cullen, R.S. Hutchins, D.L. Scott, J. Chem. Soc., Dalton Trans. (1997) 1571.
[6] O. Fussa-Reydel, H.T. Zang, J.ccT. Hump, C.R. Leidner, Inorg. Chem. 28 (1989) 1533.
[7] P.G. Pickup, R.A. Osteryoung, Inorg. Chem. 24 (1985) 2707.
[8] C.S. Chow, F.M. Bogdan, Chem. Rev. 97 (1997) 1489.
[9] P.G. Sammes, G. Yahioglu, Chem. Soc. Rev. 23 (1994) 327.
[10] V. Balzani, A. Juris, M. Venturi, S. Campagna, S. Serroni, Chem. Rev. 96 (1996) 759.
[11] F. Calderazzo, G. Pampaloni, V. Passarelli, Inorg. Chim. Acta 330 (2002) 136.
[12] J.W. Steed, J.L. Atwood, Supramolecular Chemistry, Wiley, Chichester, 2000.

[13] K. Larsson, L. Öhrström, Inorg. Chim. Acta 357 (2004) 657.
[14] K. Binnemans, P. Lenaerts, K. Driesen, C. Görller-Walrand, J. Mater. Chem. 14 (2004) 191.
[15] P. Lenaerts, A. Storms, J. Mullens, J. D'Haen, C. Görller-Walrand, K. Binnemans, K. Driesen, Chem. Mater. 17 (2005) 5194.
[16] Ph. Thomas, M. Benedix, H. Henning, Z. Anorg. Allg. Chem. 468 (1980) 213.
[17] P.N. Hawker, M.V. Twigg, in: G. Wilkinson, R.D. Gillard, J.A. McCleverty (Eds.), Comprehensive Coordination Chemistry, vol. 4, Pergamon press, Oxford, 1987.
[18] P. Kulkarni, S. Padhye, E. Sinn, Polyhedron 17 (1998) 2623, and references therein.
[19] Stoe & Cie, X-AREA, Version 1.30: Program for the Acquisition and Analysis of Data, Stoe & Cie GmbH, Darmatadt, Germany, 2005.
[20] Stoe & Cie, X-RED, Version 1.28b: Program for Data Reduction and Absorption Correction, Stoe & Cie GmbH, Darmatadt, Germany, 2005.
[21] Stoe & Cie, X-SHAPE, Version 2.05: Program for Crystal Optimization for Numerical Absorption Correction, Stoe & Cie GmbH, Darmatadt, Germany, 2004.
[22] G.M. Sheldrick, SHELX-97: Program for Crystal Structure Solution and Refinement, University of Göttingen, Göttingen, Germany, 1997.
[23] K. Lonsdale, International Tables for X-ray Crystallography, vol. C, Kluwer Academic Publisher, Doordrecht, The Netherlands, 1995.
[24] Stoe & Cie, X-STEP32, Version 1.07b: Crystallographic Package, Stoe & Cie GmbH, Darmstadt, Germany, 2000.
[25] V. Amani, N. Safari, H.R. Khavasi, Polyhedron (2007) (accepted for publication), doi:10.1016/j.poly.2007.05.050.
[26] P.C. Healy, J.M. Patrick, B.W. Skelton, A.H. White, Aust. J. Chem. 36 (10) (1983) 2031.
[27] M.V. Veids, E.H. Witten, W.M. Reiff, Inorg. Chim. Acta 53 (1981) L237.
[28] B. Hutchinson, J. Takemoto, K. Nakamato, J. Am. Chem. Soc. 3 (1970) 3335.
[29] J.H. Takemoto, B. Hutchinson, Inorg. Chem. 12 (3) (1973) 705.
[30] Y. Saito, J. Takemoto, B. Hutchinson, K. Nakamoto, Inorg. Chem. 11 (9) (1972) 2003.
[31] P. Gütlich, A. Hauser, H. Spiering, Angew. Chem., Int. Ed. Engl. 33 (1994) 2024, and references therein.
[32] C.J. Pouchert, The Aldrich Library of Infrared Spectra, 3rd ed., Aldrich Chemical Company, Milwaukee, WI, 1981.
[33] W.M. Reipf, B. Dockum, M.A. Weber, R.B. Frankel, Inorg. Chem. 14 (4) (1975) 800.
[34] P. Kople, Z. Trávníček, R. Zbořil, J. Marek, Polyhedron 23 (2004) 2193.
[35] R.D. Poulsen, A. Hazell, Acta Crystallogr., Sect. E 57 (2001) m186.
[36] D.F. Xiang, X.S. Tan, S.W. Zhang, Y. Han, K.B. Yu, W.X. Tang, Polyhedron 17 (1998) 2095.
[37] F.F. Jian, H.L. Xiao, Q.X. Wang, K. Jiao, Struct. Chem. 16 (2005) 117.
[38] B. Yan, Z.-D. Chen, S.-X. Wang, J. Chin. Chem. Soc. 47 (2000) 1211.
[39] K. Nakamato, Infrared and Raman Spectra of Inorganic and Coordination Compounds: Part B, 5th ed., Wiley, New York, 1997.
[40] D.F. Evans, J. Chem. Soc. (1959) 2003.
[41] P.C. Healy, B.W. Skelton, A.H. White, Aust. J. Chem. 36 (1983) 2043.
[42] H.J. Goodwin, M. McPartlin, H.A. Goodwin, Inorg. Chim. Acta 25 (1977) L74.
[43] J. Baker, L.M. Engelhardt, B.N. Figgis, A.H. White, J. Chem. Soc., Dalton Trans. (1975) 530.

1. Introduction

Hg(II) is a diamagnetic ion and maintains d^{10} electron configuration which minimizes intrinsic coordination geometry preferences while favoring coordination by softer ligands. In 1979, a homo-dinuclear structure was proposed for the bischloromercury(II) complex of *N*-tosylaminoctaethylporphyrin, $C_{45}H_{51}N_5OSCl_2Hg_2$ [or $(HgCl)_2$(N-NTs-OEP); **1**] (NTs = tosylimido, OEP = dianion of octaethylporphyrin), which represented the first X-ray structural proof for the existence of mercury(II) porphyrin sitting-atop (SAT) complexes [1]. Later, the mononuclear mercury(II) porphyrin sitting-atop structure of a *N*-monoalkylated porphyrin, i.e., [chloro(*N*-methyl-*meso*-tetraphenylporphyrinato) mercury(II)] [Hg(*N*-Me-tpp)Cl; **2**] (tpp = dianion of *meso*-tetraphenylporphyrin) was reported [2].

The preparation of *N*-substituted-*N*-aminoporphyrins has been described by three groups [3–7]. Upon replacement of CH_3^- of tosyl by a bulkier and heavier $^tBu^-$ group, the free base *N*-*p*-$HNSO_2C_6H_4CH_3$-Htpp (**3**) became 21-(4-*tert*-butyl-benzenesulfonamido)- 5,10,15,20-tetraphenylporphyrin *N*-*p*-$NSO_2C_6H_4{}^tBu$-Htpp (**4**) [8]. In *N*-substituted-*N*-aminoporphyrin, the H atom of NH_2 when replaced by 2-thiophenecarboxyamino group, it forms a new free aminated porphyrin, namely, *N*-2-thiophenecarboxamido-*meso*-tetraphenylporphyrin (*N*-NHCO-2-C_4H_3S-Htpp; **5**) which is a derivative of 2-acyl-thiophenes [9]. The phenylmercury(II) cation which binds to a variety of ligand sites ranging from N, O and C atoms serves as a good probe ion because it is unifunctional, gives complexes with a well defined stereochemistry and participates readily in electrophilic substitution [10]. A thorough review of the literature shows that there is no prior report on phenylmercury(II) with free bases **4** and **5** [8,9]. The coordination chemistry of phenylmercury(II) explored with anions derived from bases **4** and **5** reveals the formation of the phenylmercury(II) complex of (phenylato)(*N*-2-thiophenecarboxamido-*meso*-tetraphenylporphyrinato) mercury(II) [HgPh(*N*-NHCO-2-C_4H_3S-tpp); **6**] and bisphenylmercury(II) complex of 21-(4-*tert*-butyl-benzenesulfonamido)-5,10,15,20-tetraphenylporphyrin, $[(HgPh)_2$(*N*-*p*-$NSO_2C_6H_4{}^tBu$-tpp); **7**], respectively. The lack of previous work on metal complexes of these two ligands prompted us to undertake the synthesis and structural studies of Hg(II) complexes. Apparently, upon replacing Cl^-, OEP^{2-}, and CH_3^- with $C_6H_5^-$, tpp^{2-}, and the *tert*-butyl anion respectively, the complex **1** became **7** [1]. Likewise, upon replacement of Cl^- and N–CH_3 by $C_6H_5^-$ and N–NHCO-2-C_4H_3S, respectively, the complex **2** became **6** [2]. The compounds **6** and **7** are the first two organomercury(II) porphyrin complexes with the $HgPh^+$ moiety. The ring current effect of the porphyrin was employed to unambiguously assignment of the ^1H resonances of the phenyl group coordinated to Hg(1) in **6** or that group coordinated either to Hg(1) or Hg(2) in **7**. The bulky ^tBu group in this system enhances the crystallization of complex **7** [8]. The complexes **6** and **7** were investigated by ^{199}Hg NMR spectroscopy in order to clarify the coordination behavior of **6** in CD_2Cl_2 and **7** in $CDCl_3$ solutions. In this paper, we describe here on the synthesis, ^1H, ^{13}C and ^{199}Hg NMR spectroscopic characterization of complexes **6** and **7**. Our hope is that such structure-spectroscopic correlations will prove useful in the further development of the degradation reactions for environmental poisoning of mercury.

2. Experimental

2.1. HgPh(N-NHCO-2-C_4H_3S-tpp) (6)

A mixture of PhHgOAc (0.05 g, 1.48×10^{-4} mol) in MeOH (10 cm^3) and *N*-NHCO-2-C_4H_3S-Htpp (**5**) (0.07 g, 9.46×10^{-5} mol) in CH_2Cl_2 (20 cm^3) and CH_3CN (20 cm^3) was refluxed overnight [5,9]. After concentrating, the residue was dissolved in a trace amount of toluene, dried with anhydrous Na_2SO_4, and filtered. The filtrate was concentrated and recrystallized from CH_2Cl_2–hexane [1:2 (v/v)] yielding a bluish purple solid of **6** (0.056 g, 5.49×10^{-5} mol, 58%) which was again dissolved in CH_2Cl_2 and layered with hexane to get bluish purple crystals for single crystal X-ray analysis. ^1H NMR (599.94 MHz, CD_2Cl_2, 20 °C): δ 8.86 [s, H_β(7,8)]; 8.73 [d, H_β(2,13), ^3J(H–H) = 4.8 Hz]; 8.71 [d, H_β(3,12), ^3J(H–H) = 4.8 Hz]; 7.70 [s, H_β(17,18)]; 8.21 [s, *o*-H(22,32) and *o*-H(26,28)]; 8.48 [bs, *o*′-H(38,40) and *o*′-H(34,44)]; 7.76–7.83 (m, *m*, *p*-H), 6.15[d, S–H_5 or H(49), ^3J(H–H) = 5.1 Hz], where S = thiophene group; 6.03 [t, Hg–Ph–H_4 or H(53), ^3J(H–H) = 7.5 Hz], where Hg–Ph is the phenyl group (Ph) coordinated to Hg atom; 5.82 [t, Hg–Ph–H_3,5 or H(52, 54), ^3J(H–H) = 7.8 Hz and ^4J(Hg–H) = 50 Hz]; 5.27 [t, S–H_4 or H(48), ^3J(H–H) = 3.6 Hz]; 3.13 [d, Hg–Ph–H_2,6 or H(51,55), ^3J(H–H) = 6.0 Hz and ^3J(Hg–H) = 194 Hz]; 1.78 [d, S–H_3 or H(47), ^3J(H–H) = 3.0 Hz]; −0.10 [s, NH]. ^{199}Hg NMR (107.24 MHz, CD_2Cl_2, 20 °C): δ −1108 [s, Hg(1)]. MS (FAB): M^+ 1017 (calc. for $C_{55}H_{34}Hg_1N_5O_1S_1$:1017). UV/Vis spectrum, λ(nm) [$\varepsilon\times10^{-3}$ (M^{-1} cm^{-1})] in CH_2Cl_2: 430 (585.2), 546 (26.7), 582 (25.3), 637 (16.6).

2.2. (HgPh)2(N-p-$NSO_2C_6H_4{}^tBu$-tpp) (7)

A mixture of PhHgOAc (0.081 g, 2.41×10^{-4} mol) in MeOH (10 cm^3) and *N*-*p*-$HNSO_2C_6H_4{}^tBu$-Htpp (**4**) (0.05 g, 6.03×10^{-5} mol) in CH_2Cl_2 (20 cm^3) and CH_3CN (20 cm^3) was refluxed for 12 h [5,8]. After concentrating, the residue was dissolved in a trace amount of toluene, dried with anhydrous Na_2SO_4 and filtered. The filtrate was concentrated and recrystallized from $CHCl_3$–hexane [1:1 (v/v)] yielding bluish purple solid of **7** (0.055 g, 3.98×10^{-5} mol, 66%) which was again dissolved in $CHCl_3$ and layered with hexane to get bluish purple crystals for single crystal X-ray analysis. ^1H NMR (299.95 MHz, $CDCl_3$, 20 °C) : δ 8.84 [d, H_β(3,12), ^3J(H–H) = 4.2 Hz]; 8.79 [d, H_β(2,13), ^3J(H–H) = 4.2 Hz]; 8.56 [s, H_β(7,8)];

6.78 [s, H_β(17,18)]; 8.21 (bs) and 8.12 (s) for *o*-H(26,28) and *o*-H (22,32); 7.69–7.78 (m, *m*, *p*-H), 7.04 [d, ^{t}BuBS-$H_{3,5}$ or H(47, 49), ^3J(H–H) = 8.4 Hz], where ^{t}BuBS = 4-*tert*-butylbenzenesulfonyl; 6.72 [t, Hg(1)–Ph–H_4 or H(58), ^3J(H–H) = 7.5 Hz], where Hg(1)–Ph is the phenyl group (Ph) coordinated to Hg(1) atom; 6.63 [t, Hg(1)–Ph–H_3,5 or H(57, 59), ^3J(H–H) = 7.2 Hz]; 6.09 [d, ^{t}BuBS-$H_{2,6}$ or H(46, 50), ^3J(H–H) = 8.4 Hz]; 5.99 [t, Hg(2)–Ph–H_4 or H(64), ^3J(H–H) = 7.5 Hz], where Hg(2)-Ph is the phenyl group (Ph) coordinated to Hg(2) atom; 5.74 [t, Hg(2)–Ph–$H_{3,5}$ or H(63, 65), ^3J(H–H) = 7.5 Hz and ^4J(Hg–H) = 53 Hz]; 4.72 [d, Hg(1)–Ph–$H_{2,6}$ or H(56, 60), ^3J(H–H) = 7.2 Hz and ^3J(Hg–H) = 196 Hz]; 3.08 [d, Hg(2)–Ph–$H_{2,6}$ or H(62, 66), ^3J(H–H) = 7.5 Hz and ^3J(Hg–H) = 198 Hz]; 1.15 [s, t-butyl protons]. ^{199}Hg NMR (107.24 MHz, $CDCl_3$, 20 °C) : δ −1074 [s, Hg(2)]; −1191 [s, Hg(1)]. MS (FAB): M^+ 1379 (calcd for $C_{66}H_{51}Hg_2N_5O_2S$: 1379). UV/Vis spectrum, λ (nm) [$\varepsilon \times 10^{-3}$ (M^{-1} cm^{-1})] in CH_2Cl_2: 433 (516.5), 461 (67.0), 549 (23.1), 585 (24.8), 638 (22.5).

2.3. Spectroscopy

Proton and ^{13}C NMR spectra were recorded at 299.95 (or 599.94) and 75.43 (or 150.87) MHz, respectively, on Varian VXR-300 (or Varian Unity Inova-600) spectrometers locked on deuterated solvent, and referenced to the solvent peak. Proton NMR is relative to CD_2Cl_2 or $CDCl_3$ at $\delta = 5.30$ or 7.24 and ^{13}C NMR to the center line of CD_2Cl_2 or $CDCl_3$ at $\delta = 53.6$ or 77.0. ^{199}Hg NMR was obtained at 107.24 MHz on a Bruker DMX-600 spectrometer locked on deuterated solvent. Chemical shifts of ^{199}Hg were measured relative to an external reference of 0.5 M phenylmercury(II) acetate in DMSO-d6 (−1439.5 ppm) but reported relative to dimethylmercury (0.0 ppm). HMQC (heteronuclear multiple quantum coherence) was used to correlate protons and carbon through one-bond coupling and HMBC (heteronuclear multiple bond coherence) for two- and three-bond proton–carbon coupling. Nuclear Overhauser effect (NOE) difference spectroscopy was employed to determine the ^{1}H–^{1}H proximity through space over a distance of up to about 4 Å.

The positive ion fast atom bombardment mass spectrum (FAB MS) was obtained in a nitrobenzyl alcohol (NBA) matrix using a JEOL JMS-SX/SX 102 A mass spectrometer. UV/Vis spectra were recorded at 20 °C on a HITACHI U-3210 spectrophotometer.

2.4. Crystallography

Table 1 presents the crystal data as well as other information for $\mathbf{6}\cdot CH_2Cl_2\cdot 0.5C_6H_{14}$ and **7**. Measurements were taken on a Bruker AXS SMART-1000 diffractometer using monochromatized Mo Kα radiation ($\lambda = 0.71073$ Å). Empirical absorption corrections were made for both complexes. The structures were solved by direct methods (SHELXTL97) [11] and refined by the full-matrix least-squares method. The phenyl group coordinated to Hg(1) within $\mathbf{6}\cdot CH_2Cl_2\cdot 0.5C_6H_{14}$ is disordered with an occupancy factor of 0.65 for C(52)–C(55) and 0.35 for C(52′)–C(55′). S(1)

Table 1
Crystal data and structure refinement for HgPh(*N*–NHCO-2-C_4H_3S-tpp)·($CH_2Cl_2\cdot 0.5C_6H_{14}$) ($\mathbf{6}\cdot CH_2Cl_2\cdot 0.5C_6H_{14}$) and (HgPh)2(*N*-*p*-NSO2C6H4^{t}Bu-tpp) (**7**)

Empirical formula	$C_{59}H_{46}C_{12}HgN_5OS$ ($\mathbf{6}\cdot CH_2Cl_2\cdot 0.5C_6H_{14}$)	$C_{66}H_{51}Hg_2N_5O_2S$ (**7**)
Formula weight	1144.56	1379.36
Space group	$P\bar{1}$	$P\bar{1}$
Crystal system	triclinic	triclinic
a (Å)	13.1989(9)	9.7004(12)
b (Å)	14.4506(10)	18.148(2)
c (Å)	14.7071(10)	19.241(2)
α (°)	90.1320(10)	72.233(2)
β (°)	112.0980(10)	82.798(2)
γ (°)	95.8480(10)	88.430(2)
V (Å^3)	2583.0(3)	3200.0(7)
Z	2	2
F(000)	1146	1348
D_{calc} (g cm^{-3})	1.472	1.432
μ (Mo Kα) (mm^{-1})	3.169	4.868
S	0.864	0.981
Crystal size (mm)	0.80 × 0.46 × 0.46	0.35 × 0.10 × 0.04
θ (°)	2.02–26.01	1.36–28.26
T (*K*)	293(2)	293(2)
Number of reflections measured	10163	15835
Number of reflections observed	8988	8424
R_1^a [$I > 2\sigma(I)$]	0.0360	0.0522
wR_2^b	0.0996	0.1289

[a] $R_1 = [\sum||F_o| - F_c||/\sum|F_o|]$.
[b] $wR_2 = \{\sum[w(F_o^2 - F_c^2)^2]/\sum[w(F_o^2)^2]\}^{1/2}$.

Table 2
Selected bond lengths (Å) and angles (°) for compounds $\mathbf{6}\cdot CH_2Cl_2\cdot 0.5C_6H_{14}$ and **7**

Complex $\mathbf{6}\cdot CH_2Cl_2\cdot 0.5C_6H_{14}$			
Bond lengths (Å)			
Hg(1)–N(1)	2.589(3)	Hg(1)–C(50)	2.047(4)
Hg(1)–N(2)	2.119(3)	Hg(1)···N(4)	3.171(3)
Hg(1)–N(3)	2.627(3)	Hg(1)···N(5)	3.402(3)
Bond angles (°)			
C(50)–Hg(1)–N(1)	107.20(15)	N(1)–Hg(1)–N(2)	76.11(11)
C(50)–Hg(1)–N(2)	173.58(12)	N(1)–Hg(1)–N(3)	105.97(10)
C(50)–Hg(1)–N(3)	107.66(15)	N(2)–Hg(1)–N(3)	76.19(11)
Complex **7**			
Bond lengths (Å)			
Hg(1)–N(5)	2.103(5)	Hg(2)–N(1)	2.566(6)
Hg(1)–C(55)	2.065(8)	Hg(2)–N(2)	2.155(6)
Hg(1)···Hg(2)	3.622(6)	Hg(2)–N(3)	2.583(6)
Hg(1)···N(1)	3.033(6)	Hg(2)–C(61)	2.064(7)
Hg(1)···N(2)	2.860(6)	Hg(2)···N(4)	3.182(6)
Hg(1)···N(3)	2.850(6)	Hg(2)···N(5)	3.669(6)
Hg(1)···N(4)	3.203(6)		
Bond angles (°)			
N(5)–Hg(1)–C(55)	160.7(3)	N(1)–Hg(2)–N(2)	76.0(2)
C(61)–Hg(2)–N(1)	103.4(3)	N(1)–Hg(2)–N(3)	104.42(17)
C(61)–Hg(2)–N(2)	167.4(2)	N(2)–Hg(2)–N(3)	75.1(2)
C(61)–Hg(2)–N(3)	116.8(2)		

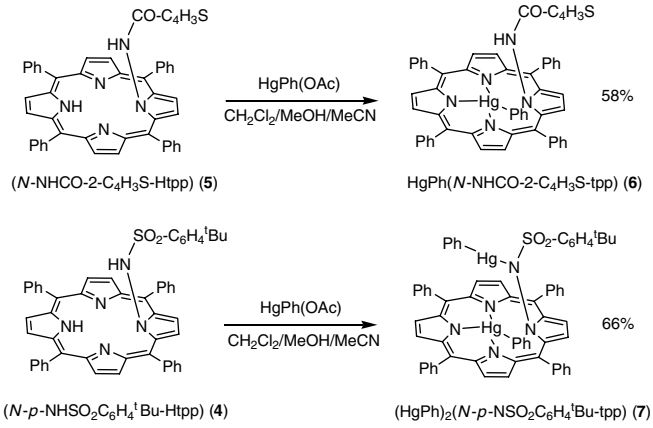
[or O(1)] within $\mathbf{6}\cdot CH_2Cl_2\cdot 0.5C_6H_{14}$ is also disordered with an occupancy factor of 0.55 [or 0.55] for S(1) [or O(1)] and 0.45 [or 0.45] for S(1′) [or O(1′)], respectively. One equivalent of CH_2Cl_2 solvent in $\mathbf{6}\cdot CH_2Cl_2\cdot 0.5C_6H_{14}$ is disordered with an occupancy factor of 0.62 [or 0.51] for Cl(1) [or Cl(2)] and 0.38 [or 0.49] for Cl(1′) [or Cl(2′)], respectively. The *tert*-butyl group within **7** is disordered with an occupancy factor of 0.46 [or 0.53] for C(52) [or C(53)] and 0.54 [or 0.47] for C(52′) [or C(53′)], respectively. All disordered atoms and solvent (CH_2Cl_2) were refined with isotropic displacement parameters. All non-hydrogen atoms, except the disordered atoms and solvent (CH_2Cl_2), were refined with anisotropic thermal parameters, whereas all hydrogen atoms were placed in calculated positions and refined with a riding model. Table 2 lists selected bond lengths and angles for complexes $\mathbf{6}\cdot CH_2Cl_2\cdot 0.5C_6H_{14}$ and **7**.

3. Results and discussion

3.1. Molecular structures of $\mathbf{6}\cdot CH_2Cl_2\cdot 0.5C_6H_{14}$ and 7

Using the d^{10} metal mercury(II), new mononuclear mercury $\mathbf{6}\cdot CH_2Cl_2\cdot 0.5C_6H_{14}$ and new bismercury **7** complexes were synthesized. The synthetic strategy is outlined in Scheme 1.

During the metallation of free base *N*-NHCO-2-C_4H_3S-Htpp (**5**) with PhHg(OAc) (Scheme 1) [9], the soft acid Hg^{2+} prefers to retain one phenyl ligand (soft base) and coordinates to the N [i.e., N(2)] of **5** to form a four-coordinate complex $\mathbf{6}\cdot CH_2Cl_2\cdot 0.5C_6H_{14}$ with a seesaw geometry and the angle of N(2)–Hg(1)–C(50) is 173.58(12)° in $\mathbf{6}\cdot CH_2Cl_2\cdot 0.5C_6H_{14}$ (Table 2). The complex $\mathbf{6}\cdot CH_2Cl_2\cdot 0.5C_6H_{14}$ is first example of an *N*-substituted *N*-aminoporphyrin-mercury complex with retention of the *N*-2-thiophenecarboxamido group. Two strongly electronegative oxygen atoms of the sulfonamide group in the free base *N*-*p*-$HNSO_2C_6H_4{}^tBu$-Htpp (**4**) enhance the acidity of the amido proton of $HNSO_2C_6H_4{}^tBu$ ligand in **4** [8]. During the metallation of *N*-*p*-$HNSO_2C_6H_4{}^tBu$-Htpp (**4**) with PhHg(OAc) one Hg^{2+} prefers to retain the phenyl group and coordinate to nitrogen [i.e., N(5)] of the *N*-*p*-HNSO2C6H4^{t}Bu group to form a two-coordinate, linear coordination around Hg(1) atom and with an angle of N(5)–Hg(1)–C(55) = 160.7(3)° in **7**. The other Hg^{2+} retains the phenyl group and attacks the nitrogen [i.e., N(2)] of the porphyrin ring to form a four-coordinate with a seesaw coordination around Hg(2) atom with an angle of N(2)–Hg(2)–C(61) = 167.4(2)° in **7**. The molecular frameworks are depicted in Fig. 1a for $\mathbf{6}\cdot CH_2Cl_2\cdot 0.5C_6H_{14}$ and Fig. 1b for **7**. The metal–ligand bond distances and the angles are summarized in Table 2. The covalent bond of Hg(1)–C(50) = 2.047 (4) Å in $\mathbf{6}\cdot CH_2Cl_2\cdot 0.5C_6H_{14}$ and of Hg(2)–C(61) = 2.064(7) Å and Hg(1)–C(55) = 2.065(8) Å in **7** are smaller than the sum of the covalent radii of Hg and C (2.26 Å) [12]. The mercury nitrogen bond distances [Hg(1)–N(1) = 2.589(3), Hg(1)–N(2) = 2.119(3), and Hg(1)–N(3) = 2.627(3) Å] in $\mathbf{6}\cdot CH_2Cl_2\cdot 0.5C_6H_{14}$ and [Hg(2)–N(1) = 2.566(6), Hg(2)–N(2) = 2.155(6), and



Scheme 1.

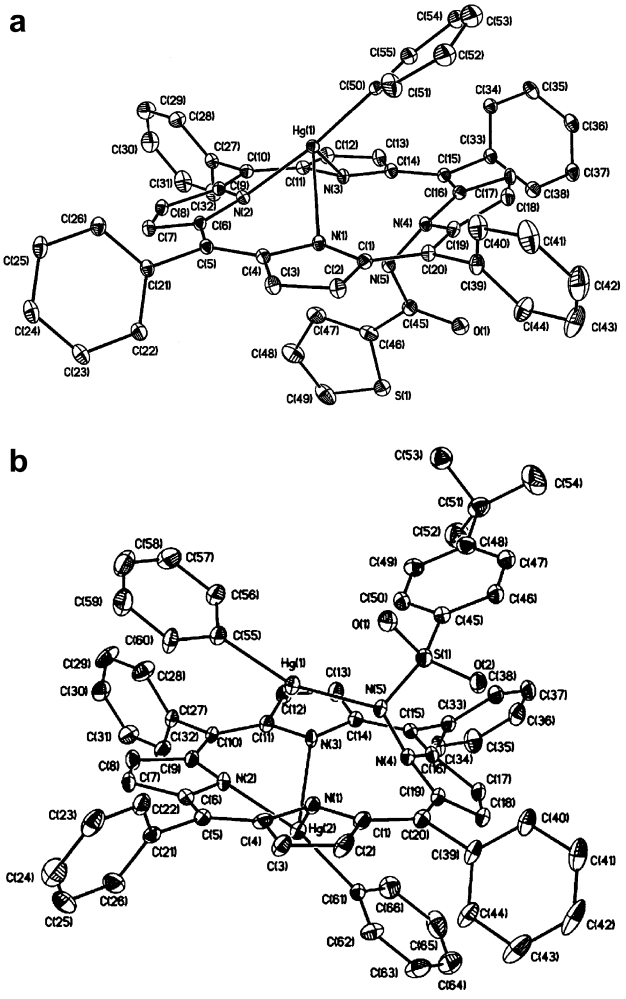


Fig. 1. Molecular configuration and atom-labeling scheme for (a) $\mathbf{6}\cdot CH_2Cl_2\cdot 0.5C_6H_{14}$, and (b) **7**, with ellipsoids drawn at 30% probability. Hydrogen atoms for both compounds and solvent CH_2Cl_2 for $\mathbf{6}\cdot CH_2Cl_2\cdot 0.5C_6H_{14}$ are omitted for clarity.

Hg(2)–N(3) = 2.583(6) Å] in **7**, are well below the upper limit of a typical Hg–N covalent bond [2.75(2) Å] [2,13]. The pyrrole nitrogen N(4) is no longer bonded to the Hg(1) in **6** · CH_2Cl_2 · $0.5C_6H_{14}$ and Hg(2) in **7** as indicated by their longer internuclear distances, 3.171(3) Å for Hg(1)···N(4) in **6** · CH_2Cl_2 · $0.5C_6H_{14}$ and 3.182(6) Å for Hg(2)···N(4) in **7**. Hence, C(50), N(1), N(2), and N(3) are bonded covalently to the Hg(1) atom in **6** · CH_2Cl_2 · $0.5C_6H_{14}$. Hg(1) is bonded to fewer than four nitrogen atoms, and so compound **6** · CH_2Cl_2 · $0.5C_6H_{14}$ may be considered as a Tsutsui's sitting-atop (SAT) complex [14]. In a similar way, the Hg(2) is tetracoordinated with three nitrogen atoms [i.e., N(1), N(2), and N(3)] of porphyrins and one carbon atom [i.e., C(61)] of phenyl group in **7**. The coordination around Hg(2) in **7** is also a mercury(II) porphyrin SAT complex. The similar kind of SAT complex was previously reported for complexes **1** and **2** [1,2].

We adopt the plane of three strongly bound pyrrole nitrogen atoms [i.e., N(1), N(2), N(3)] as a reference plane 3N for **6** · CH_2Cl_2 · $0.5C_6H_{14}$ and **7**. Because of the larger size of Hg^{2+} [$\gamma(Hg^{2+}) = 1.10$ Å with coordination number (CN) = 4 and $\gamma(Hg^{2+}) = 0.83$ Å with CN = 2] [12], Hg(1) and N(5) lie 1.47 and −1.29 Å respectively, above the 3N plane in **6** · CH_2Cl_2 · $0.5C_6H_{14}$, compared to −1.49 Å for Hg(2) and 1.36 Å for N(5) in**7**. The Hg(1) of **7** is 2.12 Å out of its 3N plane in the opposite direction of the Hg(2) atom. The separation between atoms Hg(1) and Hg(2) in **7** is 3.622(6) Å, which is larger than the sum of van der Waals radii of two Hg(II), 3.50(7) Å [13]. Hence, no metallophilic Hg(II)···Hg(II) interaction in **7** may be anticipated. The porphyrin macrocycle is indeed distorted because of the presence of the 2-thiophenecarboxamido (NCO-2-C_4H_3S) and the NSO2C6H4^{t}Bu group in **6** · CH_2Cl_2 · $0.5C_6H_{14}$ and **7**, respectively (Figure S1 in Supplementary material). Thus, N(4) pyrrole rings bearing the 2-thiophenecarboxamido (NCO-2-C_4H_3S) and the $NSO_2C_6H_4{}^tBu$ group in **6** · CH_2Cl_2 · $0.5C_6H_{14}$ and **7** deviate most from the 3N plane and as oriented separately with a dihedral angle of 33.3° and of 42.9°, whereas small angles of 4.9°, 21.0° and 8.7° occur with N(1), N(2), and N(3) pyrroles for **6** · CH_2Cl_2 · $0.5C_6H_{14}$ and 7.7°, 15.2°, and 11.1° with N(1), N(2), and N(3) pyrroles for **7**. In **6**, such a large deviation from planarity for the N(4) pyrrole is also reflected by observing a 10–12 ppm upfield shift in the ^{13}C NMR spectrum of $C_\beta(17,18)$ at 121.0 ppm compared to 133.4 ppm for $C_\beta(3,12)$, 133.2 ppm for $C_\beta(2,13)$, and 131.2 ppm for $C_\beta(7,8)$ (Table S1 in Supplementary material). In **7**, a similar deviation is also found for the N(4) pyrrole by observing a 14–15 ppm upfield shift of the $C_\beta(17,18)$ at 118.8 ppm compared to 134.2 ppm for $C_\beta(2,13)$, 133.4 ppm for $C_\beta(7,8)$, and 132.7 ppm for $C_\beta(3,12)$ (Table S2 in Supplementary material). The dihedral angles between the mean plane of the skeleton (3N) and the plane of the phenyl group are 56.7° [C(24)], 64.4° [C(30)], 49.7° [C(36)], and 59.7° [C(42)] for **6** · CH_2Cl_2 · $0.5C_6H_{14}$ and the corresponding angles are 60.1°, 81.4°, 45.3°, and 50.3° for **7**. Likewise, the dihedral angles between the mean plane of the 3N and the plane of the phenyl group coordinated to the Hg atom are 45.1° [C(53)] for **6** · CH_2Cl_2 · $0.5C_6H_{14}$ and 43.7° [C(58)], and 43.1° [C(64)] for **7**.

3.2. ^1H and ^{13}C NMR for 6 in CD_2Cl_2 and 7 in $CDCl_3$

Complexes **6** and **7** were characterized by ^1H and ^{13}C NMR spectra. In solution, the molecules have effective Cs symmetry with a mirror plane running through the N(2)–Hg(1)–C(50)–N(4) unit for **6** or N(2)–Hg(2)–Hg(1)–N(4) unit for **7**. There are four distinct β-pyrrole protons H_β, four β-pyrrole carbons C_β, four α-pyrrole carbons C_α, two different *meso* carbons C_{meso} and two phenyl-C1 carbons for these two complexes (Tables S1 and S2 in Supplementary material).

Due to the solubility problem, we observed the NMR spectra of **6** in CD_2Cl_2 and **7** in $CDCl_3$. The NMR spectra for a 0.01 M solution of **6** in CD_2Cl_2 (Fig. 2a) and for a

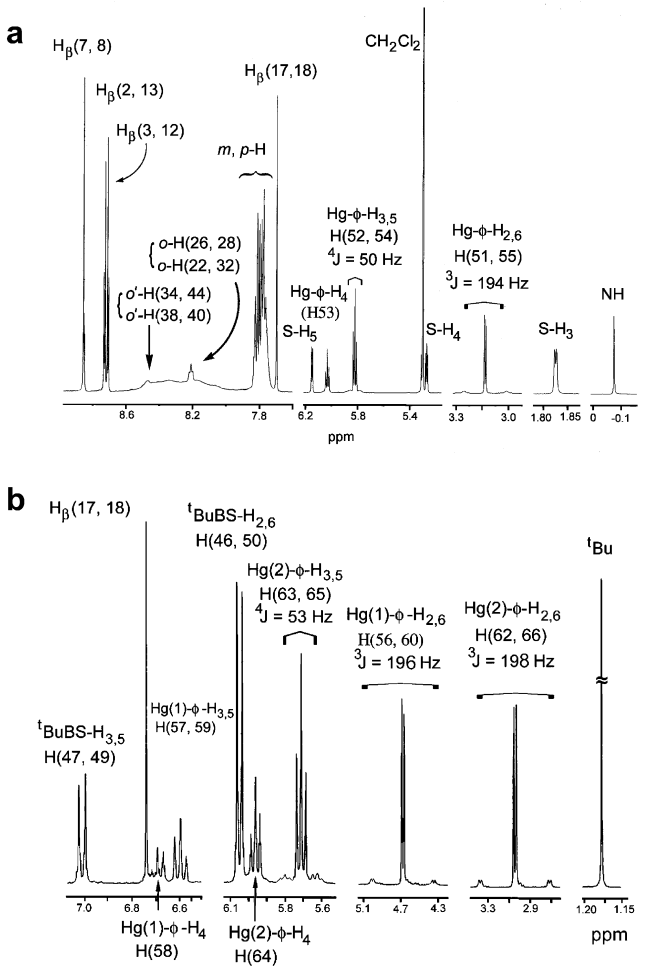


Fig. 2. ^1H NMR spectra at 20 °C (a) for a 0.01 M solution of **6** in CD_2Cl_2 at 599.94 MHz, entire spectrum; (b) for a 0.05 M solution of **7** in $CDCl_3$ at 299.95 MHz, showing Hg(1)-ϕ, Hg(2)-ϕ protons and ^{t}BuBS protons, where S = thiophene group, in **6** and ^{t}BuBS = 4-*tert*-butylbenzenesulfonyl group in **7**, ϕ = phenyl group.

0.05 M solution of **7** in $CDCl_3$ (Fig. 2b and Figure S2 in Supplementary material) showed four different types of H_β at 20 °C. In **6**, the singlet at 8.86 ppm is assigned to $H_\beta(7,8)$ and the doublet at 8.73 ppm to $H_\beta(2,13)$ with $^3J(H–H) = 4.8$ Hz. The doublet at 8.71 ppm is assigned to $H_\beta(3,12)$ with $^3J(H–H) = 4.8$ Hz and the singlet at 7.70 ppm to $H_\beta(7,8)$ (Fig. 2a). Likewise, in **7** the doublet at 8.84 ppm is due to $H_\beta(3,12)$ with $^3J(H–H) = 4.2$ Hz and the other doublet 8.79 ppm is due to $H_\beta(2,13)$ with $^3J(H–H) = 4.2$ Hz. The singlet at 8.56 ppm is due to $H_\beta(7,8)$ and the other singlet at 6.78 ppm is due to $H_\beta(17,18)$ (Fig. 2b and Figure S2 in Supplementary material).

All ^{t}BuBs, Hg–Ph protons in **6** and 2-thiophenecarboxamido (where Hg–Ph = the phenyl group (Ph) coordinated to Hg atom), Hg(2)–Ph, Hg(1)–Ph protons in **7** are shifted upfield compared to their counterparts on free ^{t}BuBs, Hg–Ph, 2-thiophenecarboxamido, Hg(2)–Ph,and Hg(1)–Ph. Such a shift is presumably attributed to the ring current effect. On the basis of the ring model [15], as the distance between the geometrical center (Ct) of the 4N [i.e., N(1), N(2), N(3), and N(4) for **6** and **7**] plane and axial protons gets smaller, the shielding effect becomes larger. In **7**, the average distance between Ct···Hg(2)–Ph–$H_{2,6}$, Ct···Hg(2)–Ph–$H_{3,5}$ and Ct···Hg(2)–Ph–H_4 increases from 3.937, 5.886 to 6.616 Å. Likewise, the average distance between Ct···Hg(1)–Ph–$H_{2,6}$, Ct···Hg(1)–Ph–$H_{3,5}$ and Ct···Hg(1)–Ph–H_4 increases from 4.558, 6.657 to 7.433 Å. The fact that all three distances between Ct···Hg(2)–Ph are shorter than those of Ct···Hg(1)–Ph in **7** indicates that the ring current effect in Hg(2)–Ph protons would be larger and in turn the ^{1}H upfield shifts for Hg(2)–Ph protons would be still higher. This observation is corroborated by the doublet at 3.08 ppm with satellites of $^3J(Hg–H) = 198$ Hz for Hg(2)–Ph–$H_{2,6}$ and the doublet at 4.72 ppm with $^3J(Hg–H) = 196$ Hz for the Hg(1)–Ph–$H_{2,6}$, the triplet at 5.74 ppm with well-resolved $^4J(Hg–H)$ of 53 Hz for the Hg(2)–Ph–$H_{3,5}$ and the triplet at 6.63 ppm with $^4J(Hg–H) = 50$ Hz for Hg(1)–Ph–$H_{3,5}$, the triplet at 5.99 ppm for Hg(2)–Ph–H_4 and the triplet at 6.72 ppm for Hg(1)–Ph–H_4. The ^{1}H NMR also revealed that the aromatic protons of the ^{t}BuBS group in **7** appear as two doublets at 7.04 ppm (^{t}BuBS-$H_{3,5}$) with $^3J(H–H) = 8.4$ Hz and at 6.09 ppm (^{t}BuBS-$H_{3,5}$) with $^3J(H–H) = 8.4$ Hz. This observation is consistent with the fact that the average distance between Ct···^{t}BuBS-$H_{2,6}$ and Ct···^{t}BuBS-$H_{3,5}$ in **7** increases from 5.139 to 6.933 Å. X-ray diffraction analysis unambiguously confirms that **7** is a dimercury complex. In addition, FAB MS indicates that molecular ion (M^+) of **7** is 1379. This further supports that **7** is a dimercury species in the solid phase. The strong diamagnetic shielding observed for all six resonances of the Hg(2)-Ph and the Hg(1)–Ph protons in the ^{1}H NMR spectrum of **7** suggests that **7** remains in a dinuclear mercury(II) complex in the solution phase (Fig. 2b).

In a similar fashion, in compound **6**, the average distance between Ct···Hg–Ph–$H_{2,6}$, Ct···Hg–Ph–$H_{3,5}$ and Ct···Hg–Ph–H_4 increases from 3.932, 5.808 to 6.638 Å. The ^{1}H NMR indicates that the aromatic protons of Hg–Ph in **6** appears as a doublet at 3.13 ppm with a coupled satellites $^3J(Hg–H)$ of 194 Hz for Hg–Ph–$H_{2,6}$, a triplet at 5.82 ppm with $^4J(Hg–H) = 50$ Hz for Hg–Ph–$H_{3,5}$, and a triplet at 6.03 ppm for Hg–Ph–H_4. Broadly, the ^{1}H NMR for phenyl protons of Hg–Ph in **6** is similar to those of Hg(2)–Ph in **7**. Due to the ring current effect, upfield shifts for the ^{1}H resonances of S–H_5, S–H_4 and S–H_3 in **6** with O, S-*cis* conformer in CD_2Cl_2 at 20 °C are $\Delta\delta = -1.48$ [from 7.63 (obtained from 2-acetylthiophene) to 6.15 ppm], −2.42 (from 7.69 to 5.27 ppm) and −5.35 ppm (from 7.13 to 1.78 ppm), respectively.

Heteronuclear coupling constants for ^{199}Hg in alkyl mecurials have been determined to decrease in the order $^1J \gg {}^3J > {}^2J > {}^4J$ [16]. Recently, a Karplus-type relationship was suggested for the magnitude of $^3J(Hg–H)$ which would predict weak coupling for torsion angle (Ψ) close to 90° and the largest coupling for torsion angles that approach 0 or 180° [17]. In **6**, the average torsion angle (Ψ) between Hg(1) and H (51A) [or H(55A)] was 10.5°. In **7**, the average torsion angle (Ψ) between Hg(1) and H(56A) [or H(60A)] was 5.0° while that angle between Hg(2) and H(62A) [or H(66A)] was 11.2°. In **6** and **7**, all the average torsion angles (Ψ) were within 12° of either 0 or 180°. Hence, $^3J(Hg–H)$ of 194 Hz for the Hg–Ph–$H_{2,6}$ protons in **6** was observed and was approximate to that of 197 ± 1 Hz for the Hg(2)–Ph–$H_{2,6}$ and Hg(1)–Ph–$H_{2,6}$ protons in **7**. The proton spectra clearly show $^3J(Hg–H)$ coupling. The presence of the mercury–proton coupling is an important indicator of slow ligand exchange in **6** and **7** [18,19]. The $^4J(Hg–H)$ of 50 Hz was observed for the Hg–Ph–$H_{3,5}$ protons in **6** and for the Hg(2)–Ph–$H_{3,5}$ and Hg(1)–Ph–$H_{3,5}$ protons in **7**. In **6** and **7**, the coupling constant of $^3J(Hg–H) = 197 \pm 1$ Hz is larger than that of $^4J(Hg–H) = 50$ Hz. These two coupling constants are consistent with those of $^3J(Hg–H) = 204$ Hz and $^4J(Hg–H) = 54$ Hz, respectively, for PhHgOAc in DMSO-d6 at ambient temperature [20].

3.3. ^{199}Hg NMR for 6 in CD_2Cl_2 and 7 in $CDCl_3$

The ^{199}Hg spectrum at 20 °C shows a sharp signal at −1074 ppm for a 0.05 M solution of **7** in $CDCl_3$, which is near the position of the Hg(1) signal observed in the spectrum for a 0.01 M solution of **6** in CD_2Cl_2, −1108 ppm (Fig. 3). Hence the signal at δ −1074 ppm of **7** is assigned to the Hg(2) nucleus with a coordination number of four. Therefore, the other signal at δ −1191 ppm of **7** is assigned to the Hg(1) nucleus with a smaller coordination number of two. It is known in the case of Hg NMR spectroscopy that on increasing coordination number generally lowers the chemical shift [16]. This fact explained that the ^{199}Hg signal of the Hg(2) nucleus in **7** lies at a downfield shift of 117 ppm from that of the Hg(1) nucleus. The ^{199}Hg chemical shift δ of Hg(1) in **7** is quite close to that of −1147 ppm for HgPh (DABRd) [where HDABRd = 5-(4′-dimethyl-

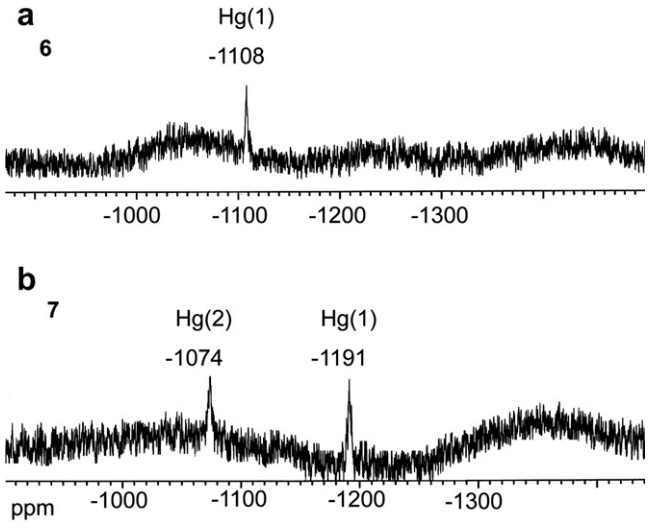


Fig. 3. The ^{199}Hg NMR spectra at 107.24 MHz (a) for a 0.01 M solution of **6** in CD_2Cl_2 at 20 °C and (b) for a 0.05 M solution of **7** in $CDCl_3$ at 20 °C.

aminobenzylidene)rhodanine] [21],−1152 ppm for HgPh (TRd) [where HTRd = 5-(2′-thiophenomethylene)rhodanine] [21] and −1156 ∼ −1346 ppm for the *N*-phenylmecury derivatives of *N*-aryl- and *N*-alkyl-substituted benzenesulfonamides (Ph–Hg–N(R)SO2Ph; R = Me, Et, Pr^i, Bu^t, Ph, 2-NO_2-C_6H_4, 4-NO_2–C_6H_4) [22]. The ^{199}Hg NMR data in $CDCl_3$ solution clearly reveal that there are two different Hg nuclei, i.e. Hg(1) and Hg(2), in **7**. These ^{199}Hg NMR data provide a second evidence that **7** remains as a dimercury(II) species in $CDCl_3$ solution. The chemical shift of ^{13}C for HgPh carbons was controlled by the paramagnetic term and not by the ring current effect [23–25]. Hence, the ^{13}C NMR data revealed that HgPh carbons in Hg(2)–Ph of **7** and Hg(1)–Ph of **6** · CH_2Cl_2 · $0.5C_6H_{14}$ are marginally affected (Tables S1 and S2 in Supplementary material). Moreover, the ^{13}C chemical shift of Hg(2)–Ph–C_1(C61) at an upfield of 3.3 ppm from that of Hg(1)–Ph–C_1(C55) (Table S2 in Supplementary material). This upfield shift is correlated with the ^{199}Hg signal of Hg(2) nucleus that shows a downfield shift from that of the Hg(1) nucleus in **7**.

4. Conclusions

We have investigated two new diamagnetic porphyrin complexes, namely, a mononuclear mercury(II) complex **6** · CH_2Cl_2 · $0.5C_6H_{14}$ and a dinuclear mercury(II) complex **7**, and their X-ray structures are established. These two porphyrin complexes are of a SAT type. NOE difference spectroscopy, HMQC and HMBC were employed to unambiguously assign the ^{1}H and ^{13}C NMR resonances of **6** in CD_2Cl_2 and **7** in $CDCl_3$ at 20 °C. Our results demonstrate the tetracoordination for Hg(1) in **6** · CH_2Cl_2 · $0.5C_6H_{14}$and Hg(2) in **7**. On the other hand, a linear coordination is described for Hg(1) in **7**. The transmetallation and degradation reactions for **6** and **7** are under investigation.

Acknowledgment

The financial support from the National Science Council of the ROC under Grant NSC 95-2113-M-005-014-MY3 and NSC 95-2113-M-273-002 is gratefully acknowledged.

Appendix A. Supplementary material

CCDC 637230 and 637231 contain the supplementary crystallographic data for **6** · CH_2Cl_2 · $0.5C_6H_{14}$ and **7**. These data can be obtained free of charge via http://www.ccdc.cam.ac.uk/conts/retrieving.html, or from the Cambridge Crystallographic Data Centre, 12 Union Road, Cambridge CB2 1EZ, UK; fax: (+44) 1223-336-033; or e-mail: deposit@ccdc.cam.ac.uk. Supplementary data associated with this article can be found, in the online version, at doi:10.1016/j.poly.2007.06.019. Figure S1 showing the diagram of the porphyrinato (C20N4, Hg, ^{t}BuBS, and thiophene) of **6** · CH_2Cl_2 · $0.5C_6H_{14}$ and **7**. Figure S2 showing the ^{1}H NMR spectra for **7** at 299.95 MHz in $CDCl_3$ at 20 °C. Tables S1 and S2 showing the ^{13}C NMR (150.87 MHz) data of **6** CH_2Cl_2 · $0.5C_6H_{14}$ in CD_2Cl_2 and **7** in $CDCl_3$ at 20 °C, respectively.

References

[1] H.J. Callot, B. Chevrier, R. Weiss, J. Am. Chem. Soc. 101 (1979) 7729.
[2] M.C. Wang, L.S. Sue, B.C. Liau, B.T. Ko, S. Elango, J.H. Chen, Inorg. Chem. 40 (2001) 6064.
[3] H.J. Callot, Tetrahedron 35 (1979) 1455.
[4] H.J. Callot, J. Fischer, R. Weiss, J. Am. Chem. Soc. 104 (1982) 1272.
[5] H.J. Callot, B. Chevrier, R. Weiss, J. Am. Chem. Soc. 100 (1978) 4733.
[6] K. Ichimura, Bull Chem. Soc. Jpn. 51 (1978) 1444.
[7] F.A. Yang, J.H. Chen, H.Y. Hsieh, S. Elango, L.P. Hwang, Inorg. Chem. 42 (2003) 4603.
[8] W.Z. Shil, K.Y. Cho, C.W. Cheng, J.H. Chen, S.S. Wang, F.L. Liao, J.Y. Tung, H.Y. Hsieh, S. Elango, Polyhedron 25 (2006) 1864.
[9] J.Y. Tung, J.H. Chen, Polyhedron 26 (2007) 589.
[10] G.C. Stocco, A. Tamburello, M.A. Girasoli, Inorg. Chem. Acta 78 (1983) 57.
[11] G.M. Sheldrick, SHELXL97, A Program for Crystal Structures Refinement, University of Göttingen, Germany, 1997.
[12] J.E. Huheey, E.A. Keiter, R.L. Keiter, Inorganic Chemistry, fourth ed., Harper Collins College Publishers, New York, 1993, pp. 114, 292.
[13] S. Das, C.H. Hung, S. Goswami, Inorg. Chem. 42 (2003) 8592.
[14] J.P. Macquet, M.M. Millard, T. Theophanides, J. Am. Chem. Soc. 100 (1978) 4741.
[15] C.E. Johnson Jr., F.A. Bovey, J. Chem. Phys. 29 (1958) 1012.
[16] B. Wrackmeyer, R. Contreres, Annu. Rep. NMR Spectrosc. 24 (1992) 267.
[17] R.P. Blake, B. Lee, M.F. Summers, J.B. Park, Z.H. Zhou, M.W.W. Adams, New. J. Chem. 18 (1994) 387.
[18] M.L. Helm, G.P. Helton, D.G. VanDerveer, G.P. Grant, Inorg. Chem. 44 (2005) 5696.
[19] T.S. Lobana, A. Sanchez, J.S. Casas, A. Castineiras, J. Sordo, M.S. Garcia-Tasende, E.M. Vazquez-Lopez, J. Chem. Soc., Dalton Trans. (1997) 4289.

[20] W. McFarlane, J. Chem. Soc. A (1968) 2280.
[21] J.S. Casas, E.E. Castellano, A. Macias, N. Playa, A. Sanchez, J. Sordo, J.M. Varela, E.M. Vazquez-Lopez, Polyhedron 20 (2001) 1845.
[22] Y.K. Grishin, Y.A. Ustynyuk, T.I. Voevodskaya, A.S. Peregudov, D.N. Kravtsov, Bull. Acad. Sci. USSR Div. Chem. Sci. 34 (1985) 1399.
[23] S.J. Lin, T.N. Hong, J.Y. Tung, J.H. Chen, Inorg. Chem. 36 (1997) 3886.
[24] A. Carrington, A.D. McLachlan, Introduction to Magnetic Resonance, Harper and Row, New York, 1967, p. 57.
[25] J.A. Pople, W.G. Schneider, H.J. Bernstein, High-Resolution Nuclear Magnetic Resonance, McGraw-Hill, New York, 1959, p. 172.

derivative with azide [25], topologically similar to the sulfate salt. It is worth noting that in these copper systems bpds is always doubly bridged irrespective of the metal–ligand ratio. However, bulkier and chelating coordinating anions, such as hexafluoroacetylacetonate [26], malate [27a], acetate, benzoate, and hexanoate [27b], lead to polymers with single bridging bpds ligand. The above facts suggest that dimensionality of the Cu–bpds networks entirely depends on the anion. These observations stimulated us to pursue further studies using different anions. On the other hand, Ryu et al. reported a 2D coordination polymer with bridging bpp [28] using metal/ligand ratio of 1:2. The authors did not give an account on the effect of changing this ratio, but we have obtained a new complex varying the metal–ligand stoichiometry. The present contribution reports the synthesis, crystal structure and magnetic property of two Cu(II) coordination polymers, $[Cu(bpp)(H_2O)_2(ClO_4)_2]_n$ (**1**) and $\{[Cu(bpds)_2(ClO_4)_2]\cdot 1.5\,(H_2O)\}_n$ (**2**) [bpp, 1,3-bis(4-pyridyl)propane and bpds, 4,4′-bipyridyl disulfide].

2. Experimental

2.1. Materials

High purity 1,3-bis(4-pyridyl)propane (98%) (bpp) and 4,4′-bipyridyl disulfide (Aldrithiol-4; 98%) (bpds) were purchased from the Aldrich Chemical Co. Inc. and were used as received. All other chemicals were of AR grade.

2.2. Physical measurements

Elemental analyses (carbon, hydrogen and nitrogen) were performed using a Perkin–Elmer 240C elemental analyzer. IR spectra were measured from KBr pellets on a Nicolet 520 FTIR spectrometer. Magnetic measurements were carried out in the "Servei de Magnetoquímica (Universitat de Barcelona)" on polycrystalline samples (40 mg) with a Quantum Design SQUID MPMS-XL magnetometer working in the 2–300 K range. The magnetic field was 0.1 T. The diamagnetic corrections were evaluated from Pascal's constants.

2.3. Synthesis of complexes

2.3.1. $[Cu(bpp)(H_2O)_2(ClO_4)_2]_n$ (1)

A methanolic solution (10 ml) of bpp (1 mmol, 0.198 g) was added drop wise to an aqueous solution (10 ml) of $Cu(ClO_4)_2\cdot 6H_2O$ (1 mmol, 0.370 g). The reaction mixture was stirred for 30 min and filtered. The filtrate was kept in a $CaCl_2$ desiccator and deep blue single crystals suitable for X-ray analysis were obtained after a few days. Yield: 74%. *Anal.* Calc. for $C_{13}H_{18}Cl_2CuN_2O_{10}$ (496.73): C, 31.40; H, 3.62; N, 5.67%. Found: C, 30.81; H, 3.75; N, 5.44%. The infrared spectra exhibited the following absorptions: 3109–3500(sbr), 2966(s), 2864(s), 1618(vs), 1558(s), 1506(s), 1452(s), 1433(vs), 1363(w), 1278(vs), 1244(vw), 1228(w), 1211(w), 1139(vs), 1114(vs), 1087(vs), 1068(vs), 1029(s), 983(w), 931(vw), 860(w), 817(s), 767(vw), 702(s), 624(vs), 572(s), 518(s) cm^{-1}.

2.3.2. $\{[Cu(bpds)_2(ClO_4)_2]\cdot 1.5(H_2O)\}_n$ (2)

Complex **2** were synthesized following the same procedure adopted for **1** using bpds (1 mmol, 0.220 g) instead of bpp. Blue crystals suitable for X-ray diffraction analysis were obtained from the filtrate kept in $CaCl_2$ desiccator. Yield: 78%. *Anal.* Calc. for $C_{20}H_{19}Cl_2CuN_4O_{9.50}S_4$(730.07) : C, 32.87; H, 2.60; N, 7.67%. Found: C, 32.23; H, 3.10; N, 7.92%. The infrared spectra exhibited the following absorptions: 3120–3579(sbr), 3091(s), 3040(s), 1629(vw), 1589(vs), 1544(s), 1481(vs), 1417(vs), 1321(s), 1222(vs), 1114(vs), 1087(vs), 1058(vs), 1026(s), 987(w), 933(vw), 831(vs), 811(s), 802(s), 717(vs), 624(vs), 499(s), 445(w) cm^{-1}.

2.4. Crystallographic data collection and refinement

Crystal data and details of data collections and refinements for the structures reported are summarized in Table 1. The data collections were carried out at 293(3) K using Mo-Kα radiation ($\lambda = 0.71073$ Å) on a Nonius DIP-1030H system, 30 frames with a φ rotation of 6° and exposure time of 15–20 min. Cell refinements, indexing and scaling of the data sets were performed using programs MOSFLM and SCALA [29]. Two residuals in **2** were assigned to water molecules at 0.5 and 0.25 occupancy factor (H atoms not located). The contribution of hydrogen atoms at calculated positions were included in final cycles of refinements.

Table 1
Crystal data and details of the structure determination for complexes **1** and **2**

Complex	**1**	**2**
Empirical formula	$C_{13}H_{18}Cl_2CuN_2O_{10}$	$C_{20}H_{19}Cl_2CuN_4O_{9.50}S_4$
Formula weight (g mol^{-1})	496.73	730.07
Crystal system	Monoclinic	Orthorhombic
Space group	*C*2/*c*	*Ccc*2
a (Å)	20.068(5)	13.771(3)
b (Å)	7.466(3)	19.682(4)
c (Å)	13.194(3)	10.702(3)
β (°)	93.04(2)	
V (Å^3)	1974.0(10)	2900.7(12)
Z	4	4
D_{calc} (g cm^{-3})	1.671	1.672
μ (Mo Kα) (mm^{-1})	1.431	1.281
F(000)	1012	1480
θ Range (°)	2.91–29.06	2.62–27.10
Reflections collected	6902	11084
Unique reflections	2531	3077
R_{int}	0.0449	0.0267
Data $I > 2\sigma(I)$	2079	2635
Refined parameters	137	192
R_1^a/wR_2^a [$I > 2\sigma(I)$]	0.0445/0.1151	0.0500/0.1254
R_1/wR_2 [all data]	0.0544/0.1250	0591/0.1429
Goodness-of-fit[b]	1.064	1.110
Residuals (e Å^{-3})	0.489, −0.418	0.531, −0.396

[a] $R_1 = \Sigma|F_o| - |F_c|/\Sigma|F_o|$, $wR_2 = [\Sigma w(F_o^2 - F_c^2)^2/\Sigma w(F_o^2)^2]^{1/2}$.
[b] Goodness-of-fit $= \{\Sigma[w(F_o^2 - F_c^2)^2]/(n-p)\}^{1/2}$.

The structures were solved by Patterson and Fourier analyses and refined by the full-matrix least-squares method based on F^2 with all observed reflections [30]. All the calculations were performed using the WinGX System, Ver 1.64 [31].

3. Results and discussion

3.1. Description of the structures

3.1.1. Complex *1*

As shown in Fig. 1, complex **1** consists of undulated polymers elongated in the [1 0 1] direction built up by $[Cu(H_2O)_2(ClO_4)_2]$ centrosymmetric units connected by bpp ligands. The metal presents octahedral coordination geometry with axial bond distances considerably distorted for the Jahn-Teller effect, while deviations of bond angles from ideal values do not exceed 2.0°. The Cu–O(perchlorate) bond lengths are 2.568(2) Å, while the Cu–N and Cu–OH_2 distances are of 2.046(2) and 2.010(2) Å, respectively (Table 2). The bpp linker, having central propyl carbon positioned on a twofold axis, adopts a GG (*gauche–gauche*) conformation, with torsion angles about the propane chain of 72.3(2)°, that leads the collinear metals to be separated by 12.298(3) Å. Longer metal–metal distances measured in other polymeric chains (see below) are a direct consequence of the preference for *anti* torsion angles along the propyl chain. In fact, the flexibility of bpp ligand leads to different conformations with a range of N–N distances from 3.9 to 10.1 Å [32], the present being of 8.66 Å. This feature allowed obtaining supramolecular architectures of different dimensionality and topology by using different counter anions [33] or solvent system [34].

The water molecule is located at a distance of 3.00 Å from the coordinated perchlorate oxygen O(2) (Fig. 1), but also at 3.02 and 3.21 Å from two symmetry related ClO_4^- oxygens of adjacent polymers (O(3) and O(2) at $-x+1/2,\ -y+1/2,\ -z+1$ and at $x,\ -y+1,\ z+1/2$, respectively). The positions of water H atoms were successfully refined in the direction of the latter acceptors; however, it is not to be excluded that water H atoms are likely to be disordered giving rise to a 3D architecture where polymers are weakly bound by H bond connections. Among the numerous copper(II)–bpp polymers reported to date, only a few examples show 1D coordination chains with single metals connected by bridging bpp ligands.

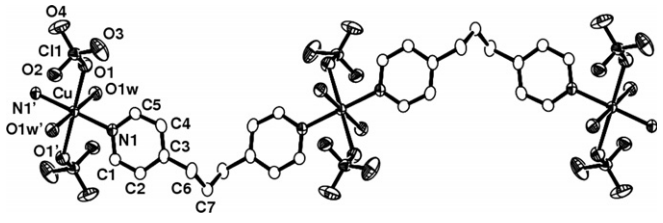


Fig. 1. Polymeric chain (ORTEP drawing) of **1** with atom labeling scheme.

The complex **1** joins those containing thiopheneacetate [21c] (Cu–Cu separation of 12.169 Å), hexafluoroacetonate [22a,22b] (12.848 Å), 2-methylacrylate [22d] (12.385 Å), and chloride [34] (13.480 Å) as metal-bound counter anion. Interestingly all of these are chelating ligands, while in the chloride derivative, the metal coordination sphere is completed by monocoordinated pendant bpp. As a matter of fact, the lacking of water molecules in the perchlorate compounds $[Cu(bpp)_2(ClO_4)_2]_n$ [28,33b] gives rise to 2D layered structures of 4,4 topology, of which one exhibits parallel interpenetration.

3.1.2. Complex *2*

The crystal structure analysis of **2** evidences a double stranded coordination chain and Fig. 2 shows a view of the polymeric arrangement with the atom numbering scheme of the crystallographic independent unit. The metal, which resides on a twofold axis, has a distorted octahedral environment, being surrounded by four nitrogen donors from four bpds ligands in the equatorial plane, and by two oxygen atoms from perchlorate anions occupying the axial positions. The Cu–N bond lengths are 2.031(5) and 2.025(5) Å, and the Cu–O distance is 2.508(4) Å. The *trans* N(1)–Cu–N(2′) bond angle is 173.57(19)° and the *cis* N–Cu–N bond angles are in a close range from 89.8(2) to 90.4(3)° (Table 2). The *gauche* conformation of the bpds spacer is indicated by the C–S–S–C torsion angle of 91.7(2)°, that falls in the range of 83.8(6)–95.5(8)°, found in a series of coordination polymers containing bpds ligands [35]. The py ring mean planes form a dihedral angle of 81.8(2)°. This bpds conformation spans the copper ions at a distance of 10.702(3) Å. Excluding bpds polymers containing Cu_2I_2 fragments and Cu_4I_4 cubane frameworks [23g], the latter value is slightly shorter than that of 10.839 Å found in the 2D network of $[Cu(bpds)_2(N_3)](ClO_4)$ reported by us [25], but sensibly longer than the intermetallic separation of 10.528 Å measured in the 1D $[Cu(bpds)_2(H_2O)](NO_3)_2$ and of 10.547 Å in the 2D assembly $[Cu(bpds)_2(SO_4)]$ [24]. The two-dimensional grid of 4,4 topology, detected in $[Cu(bpds)_2(N_3)](ClO_4)$ [25] and in $[Cu(bpds)_2(SO_4)]$ [24] complexes, has a

Table 2
Selected bond lengths (Å) and angles (°) for complexes **1** and **2**

1		**2**	
Cu–N(1)	2.046(2)	Cu–N(1)	2.031(5)
Cu–O(1w)	2.010(2)	Cu–N(2)	2.025(5)
Cu–O(1)	2.568(2)	Cu–O(1)	2.508(4)
N(1)–Cu–N(1′)	180.0	N(1)–Cu–N(1′)	89.8(2)
O(1w)–Cu–O(1w′)	180.0	N(1)–Cu–N(2)	90.23(16)
O(1′)–Cu–O(1)	180.0	N(1)–Cu–N(2′)	173.57(19)
N(1)–Cu–O(1w)	89.81(9)	N(2′)–Cu–N(2)	90.4(3)
N(1)–Cu–O(1w′)	90.19(9)	N(1)–Cu–O(1)	83.81(17)
N(1)–Cu–O(1)	89.66(8)	N(1)–Cu–O(1′)	87.32(18)
N(1)–Cu–O(1′)	90.34(8)	N(2)–Cu–O(1)	99.07(17)
O(1w)–Cu–O(1)	91.72(9)	N(2)–Cu–O(1′)	89.78(17)
O(1w)–Cu–O(1′)	88.28(9)	O(1)–Cu–O(1′)	167.5(3)

Primed atom (′) **1** at $-x+1/2, -y+5/2, -z$, **2** at $-x+3/2, -y+1/2, z$.

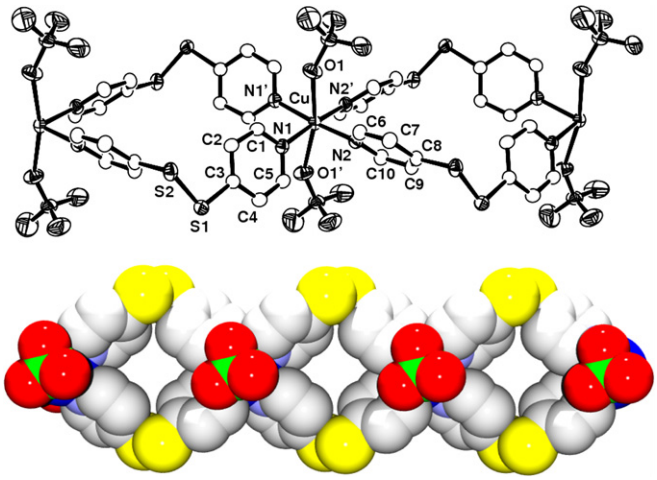


Fig. 2. Polymeric chain (ORTEP drawing) of **2** with atom labeling scheme and space-filling representation.

comparable topology with the nodes occupied by copper ions, the edges by double bpds connectors and by single anion μ-(1,3-N_3) or μ-(SO_4), respectively (Fig. 4). Correspondently the Cu–Cu distance spanned by the azide and sulfate anions are of 6.703 and 7.118 Å, while the shortest intermetallic distance between adjacent polymers in the crystal of **2** is 8.720 Å. It is interesting to note that in the present case the use of ClO_4^- as counter anion induces the formation of 1D polymers which are packed in the crystal in a cogging arrangement (Fig. 3), and no π–π interaction occurs between bpds pyridine rings of adjacent polymeric chains. The packing leaves 11.5% of void space in the unit cell with cavities filled by disordered lattice water molecules, which accounts for a total of 1.5 per metal ion.

3.2. Magnetic properties

3.2.1. Complex *1*

The magnetic properties of complex **1** as $\chi_M T$ versus T plot (χ_M is the molar magnetic susceptibility for one Cu^{II} ion) and the reduced magnetization ($M/N\beta$ versus H) are shown in Fig. 5. The value of $\chi_M T$ at 300 K is 0.437 $cm^3\ mol^{-1}$ K, which is as expected for one magnetically quasi-isolated spin doublet ($g > 2.00$). Starting from room temperature, $\chi_M T$ values are practically constant up to 50 K, then below 50 K they decrease quickly to 0.42 $cm^3\ mol^{-1}$ K at 2 K. This feature is characteristic of weak (almost negligible) antiferromagnetic interactions. The reduced molar magnetization at 2 K (Fig. 5, inset) clearly corroborates that the antiferromagnetic coupling is very small. The $M/N\beta$ value at 5 T is close to 1.0 Nβ and the curve follows the Brillouin function for a g value of 2.18.

Complex **1** is, actually, a 1D copper(II) entity. Thus, we have fitted the experimental data applying the formula for an uniform 1D copper(II) system, given by Bonner and Fisher [36]. The best-fit parameters obtained are

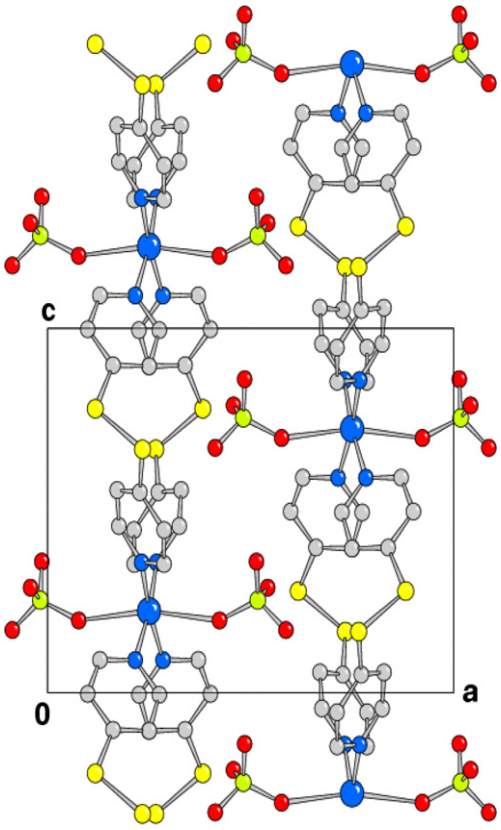


Fig. 3. Crystal packing of **2** viewed down *b*-axis.

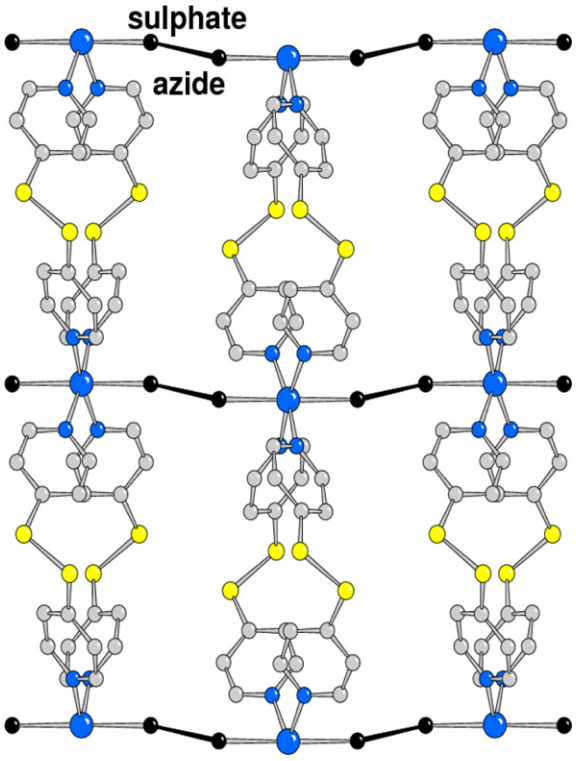


Fig. 4. Sketch of crystal packing of Cu(bpds) polymers in the $[Cu(bpds)_2(SO_4)]$ [24] and $[Cu(bpds)_2(N_3)](ClO_4)$ [25] complexes.

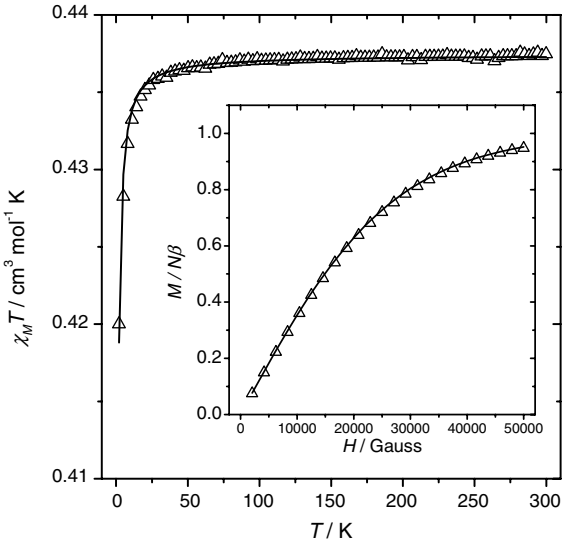


Fig. 5. Plot of $\chi_M T$ vs T for complex **1**. Open points are the experimental data and solid lines represent the best-fit obtained. Inset: plot of the reduced magnetization at 2 K.

$J = -0.1 \pm 0.01$ cm^{-1}, $g = 2.16 \pm 0.01$ and $R = 8.7 \times 10^{-6}$. The very small (negligible) J value can be interpreted as a consequence of the negligible overlap between the copper(II) ions through the long bridge [37].

3.2.2. Complex 2

The magnetic properties of complex **2** as $\chi_M T$ versus T plot (χ_M is the molar magnetic susceptibility for one Cu^{II} ion) and the reduced magnetization ($M/N\beta$ versus H) are shown in Fig. 6. It is also a 1D system and the magnetic data was fitted adopting the same procedure as in **1**. The best-fit parameters obtained are $J = -0.21$ cm^{-1} and $g = 2.11$.

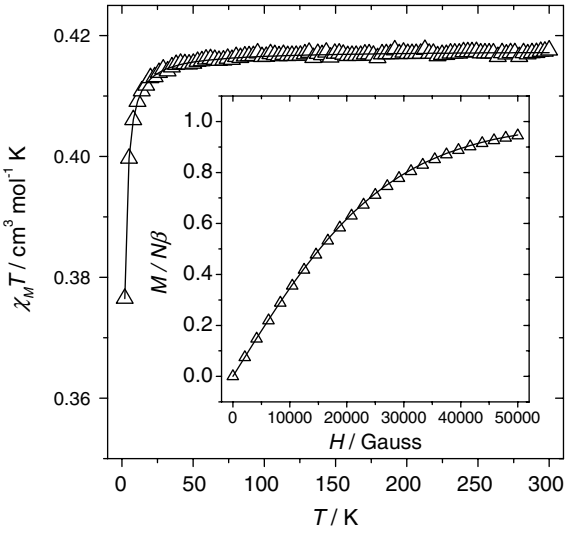


Fig. 6. Plot of $\chi_M T$ vs T for complex **2**. Open points are the experimental data and solid lines represent the best-fit obtained. Inset: plot of the reduced magnetization at 2 K.

4. Conclusion

Here, we have presented the synthesis, crystal structure and magnetic study of two Cu(II) coordination polymers using bpp and bpds as bridging ligand and perchlorate as counter anion. Both complexes show 1D coordination chains: complex **1** displays $Cu(H_2O)_2(ClO_4)_2$ units linked through bridging bpp and **2** has $Cu(ClO_4)_2$ fragments connected by double bpds ligands. The former, synthesized changing the metal–ligand ratio with respect to previously reported complexes, undergoes weak H-bonding interactions resulting a 3D supramolecular architecture. We have showed that dimensionality of the Cu–bpds network depends on the anion: in complex **2** perchlorate acts as mono-coordinated ligand leading to 1D chain, while using azide or sulfate 2D networks are obtained, and conversely the anion remains as lattice moiety, balancing the charge only, in the nitrate derivative.

Appendix A. Supplementary material

CCDC 646196 and 646197 contain the supplementary crystallographic data for **1** and **2**. These data can be obtained free of charge via http://www.ccdc.cam.ac.uk/conts/retrieving.html, or from the Cambridge Crystallographic Data Centre, 12 Union Road, Cambridge CB2 1EZ, UK; fax: (+44) 1223 336 033; or e-mail: deposit@ ccdc.cam.ac.uk. Supplementary data associated with this article can be found, in the online version, at doi:10.1016/j. poly. 2007.06.031.

References

[1] (a) S.R. Batten, R. Robson, Angew. Chem., Int. Ed. 37 (1998) 1460;
(b) G.R. Desiraju, Angew. Chem., Int. Ed. Engl. 34 (1995) 2311;
(c) D. Braga, F. Grepioni, A.G. Orpen, Crystal Engineering: From Molecules and Crystals to Materials, NATO Science Series, Series C, vol. 538, Kluwer Academic, Dordrecht, 1999;
(d) S.C. Manna, E. Zangrando, A. Bencini, C. Benelli, N. Ray Chaudhuri, Inorg. Chem. 45 (2006) 9114;
(e) S. Konar, P.S. Mukherjee, E. Zangrando, F. Lloret, N. Ray Chaudhuri, Angew. Chem., Int. Ed. 41 (2002) 1561.

[2] (a) P.J. Hagrman, D. Hagrman, J. Zubieta, Angew. Chem., Int. Ed. 38 (1999) 2638;
(b) S. Kitagawa, R. Kitaura, S. Noro, Angew. Chem. Int. Ed. 43 (2004) 2334;
(c) S.C. Manna, E. Zangrando, J. Ribas, N. Ray Chaudhuri, Dalton Trans. (2007) 1383;
(d) S.C. Manna, E. Zangrando, M.G.B. Drew, J. Ribas, N. Ray Chaudhuri, Eur. J. Inorg. Chem. (2006) 481.

[3] (a) K. Hegetschweiler, B. Morgenstern, J. Zubieta, P.J. Hagrman, N. Lima, R. Sessoli, F. Totti, Angew. Chem., Int. Ed. 43 (2004) 3436;
(b) B. Morgenstern, S. Steinhauser, K. Hegetschweiler, E. Garribba, G. Micera, D. Sanna, L. Nagy, Inorg. Chem. 43 (2004) 3116;
(c) L. Applegarth, A.E. Goeta, J.W. Steed, Chem. Commun. (2005) 2405;
(d) S.C. Manna, J. Ribas, E. Zangrando, N. Ray Chaudhuri, Inorg. Chim. Acta 360 (2007) 2589;
(e) S. Masaoka, D. Tanaka, Y. Nakanishi, S. Kitagawa, Angew. Chem., Int. Ed. 43 (2004) 2530;

(f) D. Sun, Y. Ke, T.M. Mattox, B.A. Ooro, H.-C. Zhou, Chem. Commun. (2005) 5447.
[4] (a) M. Okeeffe, M. Eddaoudi, H. Li, T. Reineke, O.M. Yaghi, J. Solid State Chem. 153 (2000) 3;
(b) M. Fujita, K. Umemoto, M. Yoshizawa, N. Fujita, T. Kusukawa, K. Biradha, Chem. Commun. (2001) 509;
(c) S.R. Seidel, P.J. Stang, Acc. Chem. Res. 35 (2002) 972.
[5] A.K. Ghosh, D. Ghoshal, E. Zangrando, J. Ribas, N. Ray Chaudhuri, Dalton Trans. (2006) 1554.
[6] (a) S.C. Manna, K. Okamoto, E. Zangrando, N. Ray Chaudhuri, CrystEngComm 9 (2007) 199;
(b) X.-C. Huang, D. Li, X.-M. Chen, CrystEngComm 8 (2006) 355;
(c) T.L. Hennigar, D.C. MacQuarrie, P. Losier, R.D. Rogers, M.J. Zaworotko, Angew. Chem., Int. Ed. 36 (1997) 972.
[7] (a) B. Moulton, M.J. Zaworotko, Chem. Rev. 101 (2001) 1629;
(b) R.K. Seddon, M.J. Zaworotko, Crystal engineering: the design and application of functional solids (NATO Science Series), 1999.
[8] (a) I.G. Dance, in: G.R. Desiraju (Ed.), The Crystals as a Supramolecular Entity, John Wiley, NewYork, 1996;
(b) D.J. Hill, M.J. Mio, R.B. Prince, T.S. Hughes, J.S. Moore, Chem. Rev. 101 (2001) 3893.
[9] A.K. Ghosh, D. Ghoshal, T.-H. Lu, G. Mostafa, N. Ray Chaudhuri, Cryst. Growth Des. 4 (2004) 851.
[10] (a) S. Grimme, C. Diedrich, M. Korth, Angew. Chem., Int. Ed. 45 (2006) 625;
(b) E. Barratt, R.J. Bingham, D.J. Warner, C.A. Laughton, S.E.V. Phillips, S.W. Homans, J. Am. Chem. Soc. 127 (2005) 11827.
[11] S.A. Bourne, L.J. Moitsheki, CrystEngComm 7 (2005) 674.
[12] (a) L.R. MacGillivray, S. Subramamian, M.J. Zaworotko, J. Chem. Soc., Chem. Commun. (1994) 1325;
(b) O.M. Yaghi, H. Li, J. Am. Chem. Soc. 117 (1995) 10401;
(c) L. Carlucci, G. Ciani, D.M. Proserpio, A. Sironi, J. Chem. Soc., Dalton Trans. (1997) 1801.
[13] M. Fujita, Y.J. Kwon, O. Sasaki, K. Yamaguchi, K. Ogura, J. Am. Chem. Soc. 117 (1995) 7287.
[14] L. Carlucci, G. Ciani, D.M. Proserpio, New J. Chem. (1998) 1319.
[15] (a) A.J. Blake, N.R. Champness, S.S.M. Chung, W.-S. Li, M. Schröder, Chem. Commun. (1997) 1005;
(b) M.J. Zaworotko, Chem. Soc. Rev. (1994) 283.
[16] K.N. Power, T.L. Hennigar, M.J. Zaworotko, Chem. Commun. (1998) 595.
[17] (a) T. Soma, H. Yuge, T. Iwamoto, Angew. Chem., Int. Ed. Engl. 33 (1994) 1665;
(b) L. Carlucci, G. Ciani, D.M. Proserpio, A. Sironi, Angew. Chem., Int. Ed. Engl. 34 (1995) 1895.
[18] P. Losier, M.J. Zaworotko, Angew. Chem., Int. Ed. Engl. 35 (1996) 2779.
[19] (a) M.L. Tong, B.H. Ye, J.W. Cai, X.M. Chen, S.W. Ng, Inorg. Chem. 37 (1998) 2645;
(b) M.L. Tong, X.M. Chen, X.L. Yu, T.C.W. Mak, J. Chem.Soc., Dalton Trans. (1998) 5.
[20] D. Hagrman, C. Zubieta, D.J. Rose, J. Zubieta, R.C. Haushalter, Angew. Chem., Int. Ed. 36 (1997) 873.
[21] (a) W.J. Belcher, C.A. Longstaff, M.R. Neckenig, J.W. Steed, Chem. Commun. (2002) 1602;
(b) L. Carlucci, G. Ciani, A. Gramaccioli, D.M. Proserpio, S. Rizzato, CrystEngComm 29 (2000) 1;
(c) M.V. Marinho, M.I. Yoshida, K.J. Guedes, K. Krambrock, A.J. Bortoluzzi, M. Horner, F.C. Machado, W.M. Teles, Inorg. Chem. 43 (2004) 1539;
(d) L. Carlucci, G. Ciani, M. Moret, D.M. Proserpio, S. Rizzato, Angew. Chem., Int. Ed. 39 (2000) 1506.
[22] (a) Y.-B. Dong, M.D. Smith, R.C. Layland, H.-C. Loye, Inorg. Chem. 38 (1999) 5027;
(b) M.J. Plater, M.R.S.J. Foreman, A.M.Z. Slawin, Inorg. Chim. Acta 303 (2000) 132;
(c) R. Wang, L. Han, Y. Sun, Y. Gong, D. Yuan, M. Hong, J. Mol. Struct. 694 (2004) 79;
(d) R.S. Rarig, J.J. Zubieta, Polyhedron 22 (2003) 177;
(e) X.-J. Luan, Y.-Y. Wang, D.-S. Li, P. Liu, H.-M. Hu, Q.-Z. Shi, Shie-Ming Peng, Angew. Chem., Int. Ed. 44 (2005) 3864.
[23] (a) S.C. Manna, S. Konar, E. Zangrando, K. Okamoto, J. Ribas, N. Ray Chaudhuri, Eur. J. Inorg. Chem. (2005) 4646;
(b) H. Kessler, W. Rundel, Chem. Ber. 101 (1968) 3350;
(c) R.R. Fraser, G. Boussard, J.K. Saunder, J.B. Lambert, C.E. Mixan, J. Am. Chem. Soc. 93 (1971) 3822;
(d) H. Kessler, A. Rleker, W. Rundel, J. Chem. Soc., Chem. Commun. (1968) 475;
(e) F. Seel, W. Gombler, R. Bundez, Justus Liebigs Ann. Chem. 735 (1970) 1;
(f) M. Hong, W. Su, R. Cao, M. Fujita, J. Lu, Chem. Eur. J. 3 (2000) 427;
(g) A.J. Blake, N.R. Brooks, N.R. Champness, M. Crew, D.H. Gregory, P. Hubberstey, M. Schröder, A. Deveson, D. Fenske, L.R. Hanton, Chem. Commun. (2001) 1432;
(h) S.C. Manna, A.K. Ghosh, J. Ribas, M.G.B. Drew, C.-N. Lin, E. Zangrando, N. Ray Chaudhuri, Inorg. Chim. Acta 359 (2006) 1395.
[24] J. Luo, M. Hong, R. Wang, D. Yuan, R. Cao, L. Han, Y. Xu, Z. Lin, Eur. J. Inorg. Chem. (2003) 3623.
[25] S.C. Manna, S. Konar, E. Zangrando, M.G.B. Drew, J. Ribas, N. Ray Chaudhuri, Eur. J. Inorg. Chem. (2005) 1751.
[26] (a) F.M. Tabellion, S.R. Seidel, A.M. Arif, P.J. Stang, J. Am. Chem. Soc. 123 (2001) 7740;
(b) R. Horikoshi, T. Mochida, H. Moriyama, Inorg. Chem. 40 (2001) 2430.
[27] (a) R. Carballo, B. Covelo, N. Fernandez-Hermida, E. Garcia-Martinez, A.B. Lago, M. Vazquez, E.M. Vazquez-Lopez, Cryst. Growth Des. 6 (2006) 629;
(b) R. Horikoshi, M. Mikuriya, Bull. Chem. Soc. Jpn. 78 (2005) 827.
[28] J.Y. Ryu, C. Kim, D.W. Park, L.O. Park, Y. Kim, A.J. Lough, Acta Crystallogr. Sect., E 61 (2005) m1489.
[29] Collaborative Computational Project, Number 4. Acta Crystallogr., Sect. D, 50 (1994) 760.
[30] G.M. Sheldrick, SHELX97 Programs for Crystal Structure Analysis (Release 97-2), University of Göttingen, Germany, 1998.
[31] L.J. Farrugia, J. Appl. Crystallogr. 32 (1999) 837.
[32] L. Carlucci, G. Ciani, D.M. Proserpio, S. Rizzato, CrystEngComm 4 (2002) 121.
[33] (a) M.J. Plater, M.R.St.J. Foreman, A.M.Z. Slawin, J. Chem. Res. 74 (1999) 728;
(b) K. Jin, X. Huang, L. Pang, J. Li, A. Appel, S. Wherland, Chem. Commun. (2002) 2872.
[34] L. Carlucci, G. Ciani, M. Moret, D.M. Proserpio, S. Rizzato, Chem. Mater. 14 (2002) 12.
[35] R. Horikoshi, T. Mochida, N. Maki, S. Yamada, H. Moriyama, J. Chem. Soc., Dalton Trans. (2002) 28.
[36] J.C. Bonner, M.E. Fisher, Phys. Rev. A 135 (1964) 640.
[37] C. Janiak, Dalton Trans. (2003) 2781.

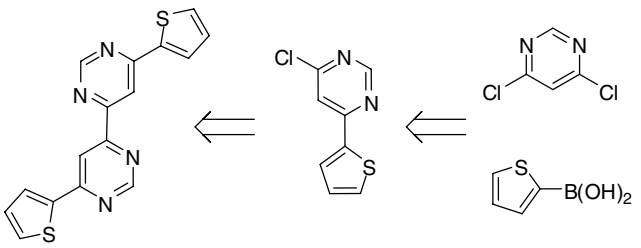
gap law [9,11]. We were thus interested to see if electron rich pendant groups had a significant effect on the properties of red-emitting Ru(II) complexes of bidentate ligands.

We chose thiophene as both an electron-rich pendant sub-unit and the π-accepting bidentate ligand 4,4′-bipyrimidine (bpm) as the metal-binding subunit as it binds to a wide range of metal ions to form complexes with interesting properties [12]. Previous studies of 2,2′-bipyridine (bpy) [13], 1, 10-phenanthaline (phen) [14], and 2,2′:6′,2″-terpyridine (tpy) [15] containing thiophenes as polymerizable units did not discuss the optical properties of the subunits in great detail. In this case, the bpm chelating motif has the advantage of forming complexes with lower energy excited-states than bpy, phen and tpy, particularly with metal ions such as Ru(II) [16] . In particular, Ru(II) complexes of bpm are low energy, red emitters, a much sought after property for biomedical applications [2]. Herein we describe the synthesis and properties of the ligand 6,6′-di(2″-thienyl)-4,4′-bipyrimidine (th_2bpm) and its hetero- and homo-leptic Ru(II) complexes.

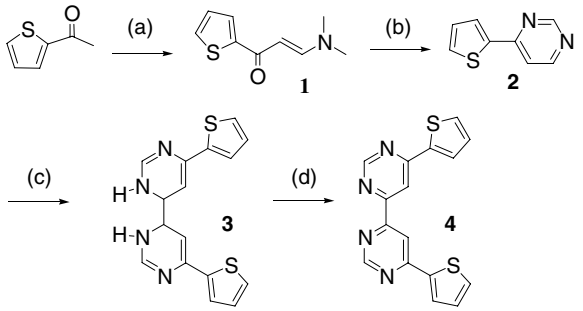
2. Results and discussions

The most straightforward synthesis of the th_2bpm ligand (**4**) would have two thienyl–pyrimidine halves coupled together (Scheme 1). Although one could envisage palladium catalyzed heterocoupling reactions, such as the Suzuki reaction, followed by nickel catalyzed homocoupling reactions [17], we opted to use a catalyst-free approach (Scheme 2). Thus, ligand **4** was obtained in three steps, as outlined in Scheme 2, without the need of oxygen-sensitive catalysts.

In the first step (Scheme 2, step a), enaminone **1** was synthesized from 2-acetylthiophene using a small excess of *N*,*N*-dimethylformamide dimethylacetal following a previously established method [18]. The condensation of **1** (Scheme 2, step b) with three equivalents of formamidine acetate in the presence of three equivalents of sodium ethoxide resulted in the formation of the corresponding 4-(2-thienyl) pyrimidine **2** in moderate yields. The Michael addition of the free amidine on the enaminone followed by the intramolecular cyclisation gives **2** after column chromatography [19].



Scheme 1. Retrosynthetic route to 6,6′-di(2″-thienyl)-4,4′-bipyrimidine (th_2bpm, **4**) via Suzuki heterocoupling reaction and a Ni-catalyzed Ullmann reaction.

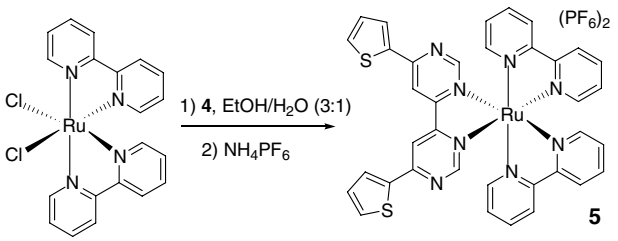


Scheme 2. Synthesis of 6,6′-di(2-thienyl)-4,4′-bipyrimidines **4.** Reagents and conditions: (a) EtOH, reflux, 6 h, yield 53%; (b) 3 equiv. formamidine acetate, 3 equiv. NaOEt, EtOH, reflux, 24 h, yield 48%; (c) 3 equiv. Na(s), THF, 36 h, r.t.; (d) air, 1 h, yield 61%.

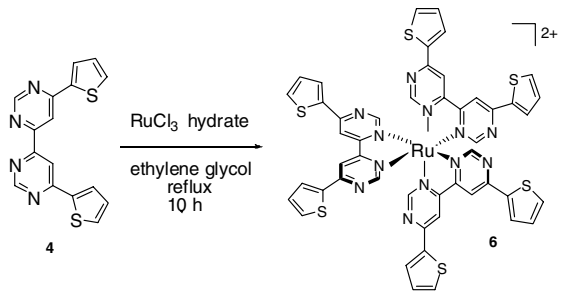
The desired 6,6′-di(2-thienyl)-4,4′- bipyrimidine **4** was obtained by the radical anion coupling of two molecules of 4-(2-thienyl)-pyrimidine, **2** (Scheme 2, step c). The pyrimidine dimerizes upon treatment with 3 equivalents of sodium in anhydrous THF. As the initial radical anion is generated the solution turns dark purple, then yellow with the formation of dihydrobipyrimidine **3**, which is oxidized by bubbling air through the solution product **4** was then purified by recrystallization from methanol. A radical anion mechanism was previously established for this type of reaction [20].

The heteroleptic complex **5** was readily prepared by allowing a slight excess of th_2bpm to react with the dehydrate of $Ru(bpy)_2Cl_2$ in a boiling mixture of ethanol/water (3:1) overnight (Scheme 3). The addition of a saturated aqueous solution of NH_4PF_6 to the reaction mixture precipitated the complex as its bis(hexafluorophosphate) salt, which was then purified by column chromatography on silica gel eluting with the supernatant of a mixture of acetonitrile: potassium nitrate (7:1). The pure dark red complex was obtained after reprecipitating its PF_6 salt by the addition of NH_4PF_6.

Several attempts to prepare the homoleptic complex $[Ru(6,6'\text{-bis(2-thienyl)-4,4'- bipyrimidine})_3](PF_6)_2$, **6** adopting the same synthetic strategy as for the preparation of complex **5** failed, leading to a uncharacterized green product. However, complex **6** could be successfully prepared by refluxing $RuCl_3 \cdot xH_2O$ with a small excess of 6,6′-bis(2-thienyl)-4,4′-bipyrimidine using more drastic conditions, replacing the $EtOH/H_2O$ solvent mixture by refluxing ethylene glycol, which affords a higher reaction temperature



Scheme 3. Synthesis of heteroleptic complex **5**.



Scheme 4. Synthesis of homoleptic complex **6**.

and a readily oxidized solvent in order to reduce Ru(III) to Ru(II) (Scheme 4).

The ^{1}H NMR data for th_2bpm and its Ru(II) complexes are given in Table 1. The assignment of signals was based on the 2D COSY spectra of the complexes and by comparison of the various spectra with known compounds such as $[Ru(bpy)_2bpm]^{2+}$ and $[Ru(bpm)_3]^{2+}$ [21]. In the ^{1}H NMR spectra of complexes, the proton H_5 of the pyrimidine ring is shifted downfield compared to those of the free ligands, while the proton H_2 is shielded due to the shielding planes of the ancillary ligands. All the aromatic protons of the thienyl subunits resonate downfield compared to those of the free ligand and can be easily recognized by their coupling constants (see Chart 1).

Several attempts were made to obtain single crystals of ligand **4** that would diffract to wide angles; however, the best results from recrystallization in $CHCl_3$/hexane provided yellow crystals of **4** which were only suitable for refinement at small angles. The ORTEP representation of ligand **4** with its atoms labeling scheme is presented in Fig. 1. Details of data collection and refinement are given in Table 2. Ligand **4** crystallizes with four molecules in the asymmetric unit. The *N*-atoms of the central pyrimidine rings are in a *trans* orientation to one another, thereby minimizing the unfavourable electronic interaction between the lone pairs on N(2) and N(3). The thienyl rings are essentially co-planar to their respective pyrimidine rings while the two pyrimidines are almost so, with an angle of 3.2° between the two rings. There is an intermolecular π-stacking interaction between molecules in the solid state. The electron rich thiophene ring of one molecule is stacked above the electron-poor pyrimidine of another, with an intermolecular distance of approximately 3.7 Å (Fig. 2).

The redox potentials of ligand **4** and its Ru(II) complexes **5** and **6**, as determined by cyclic voltammetry and square wave techniques in acetonitrile solution, are summarized in Table 3. For each complex, the cyclic voltammograms exhibit at least one quasi-reversible oxidation wave and three quasi-reversible reduction waves. The oxidation potentials of complexes **5** and **6** are found at +1.39 V and +1.57 V, respectively, and are associated with the removal of an electron from the metal center. The metal-centered oxidation of $[Ru(bpy)_3]^{2+}$ (+1.27 V) suggests that the metal-based orbitals in **5** and **6** are stabilized due to the increased π-acceptor properties of the th_2bpm ligand as compared to bpy. The fact that three th_2bpm ligands are coordinated to the Ru(II) center in **6** leads to a more positive Ru(III/II) oxidation potential in **6** as compared to **5**.

Table 1
^{1}H NMR resonances for compounds **4**–**6** in ppm[a]

cmpd	bpm		Thiophene			bpy				
	2	5	3′	4′	5′	$B_{3,3'}$	$B_{4,4'}$	$B_{5,5'}$	B_6	$B_{6'}$
4	9.28	8.73	8.00	7.23	7.66					
5	8.54	8.94	8.30	7.36	7.72	8.51	8.09	7.44	8.00	7.85
6	8.63	8.98	8.31	7.39	7.86					
Ru(bpy)$_2$bpm^{2+}[b]	8.49	9.07				8.54	8.10	7.42	7.81	7.70

[a] CD_3CN at 400 MHz, referred to the residual solvent peak.
[b] From Ref. [21].

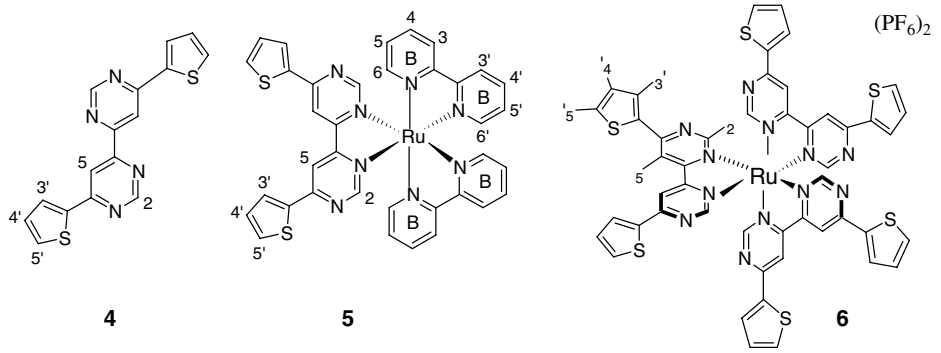


Chart 1. The 6,6′-di(2-thienyl)-4,4′-bipyrimidine ligand (**4**), its hetero- (**5**) and homo- (**6**) leptic Ru(II) complexes and their ^{1}H NMR labels.

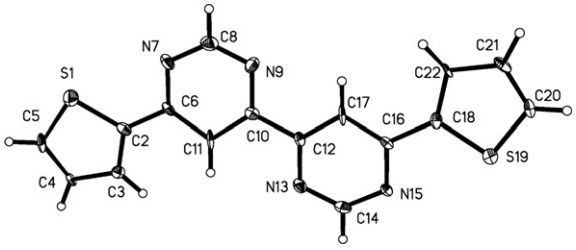


Fig. 1. X-ray structure of **4** as an ORTEP representation.

Table 2
Crystallographic data for **4**

Empirical formula	$C_{16}H_{10}N_4S_2$
M	322.40
Crystal system	monoclinic
Temperature	100 (2) K
Space group	$P2_1/c$
a (Å)	9.4379 (3)
b (Å)	21.3331(6)
c (Å)	7.3658 (2)
β (°)	110.720 (1)
V (Å^3)	1387.11 (7)
Z	4
R	0.0764
wR_2	0.1914

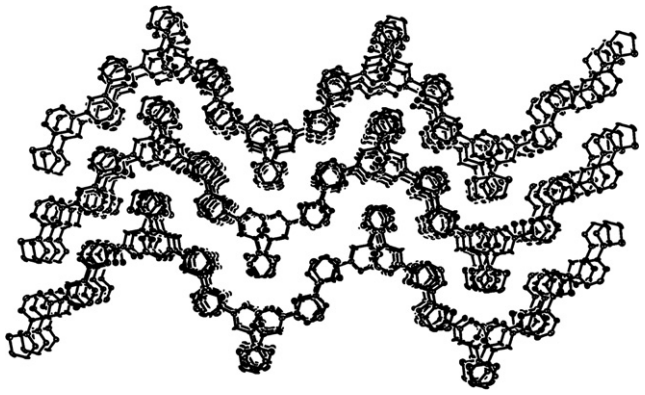


Fig. 2. Intermolecular π-stacking in the solid state structure of **4**.

Table 3
Redox potentials in acetonitrile for the ruthenium(II) complexes[a]

Complex	$E_{1/2}$(ox)	$E_{1/2}$(red)			$\Delta E_{1/2}$
4	1.62	−1.36	−1.75	−2.28[c]	2.98
5	1.39	−0.68	−1.25	−1.70	2.07
6	1.57[c]	−0.66[b,c]	−0.94[b,c]	−1.39	2.23
$[Ru(bpy)_3]^{2+}$[d]	1.27	−1.31	−1.50	−1.77	2.58
$[Ru(bpy)_2bpm]^{2+}$[e]	1.45	−0.67	−1.30	−1.59	2.12

[a] Potentials are in volts versus SCE corrected to internal ferrocene, 0.1 M in TBAP, recorded at a sweep rate of 200 mV/s.
[b] Values determined from square wave voltammetry.
[c] Irreversible.
[d] Ref. [22].
[e] Ref. [23].

The thiophene oxidation in **4** is not seen in complexes **5** and **6** as it is beyond the solvent potential window.

The two complexes exhibit three successive one-electron ligand-centered reductions. The potential reductions are anodically shifted with respect to those of the bpy ligand due to the fact that the lowest π*-orbital of the substituted bpm ligand is much lower in energy than the lowest π*-orbital of the bpys. However, in both of the cases the ligand reduction processes occur more readily in the complex than in the free ligand (−1.36 V).

The first reduction of the complex is assigned to the reduction of the th$_2$bpm ligand as 4,4′-bipyrimidine is more easily reduced than 2,2′-bipyridine. The first reduction potential of the all complexes is anodically shifted compared to the analogous unsubstituted bpm-based complex $[Ru(bpm)(bpy)_2]^{2+}$ as the lowest π*-orbital of th$_2$bpm is lower in energy than the lowest π*-orbital of the unsubstituted bpm as a result of electron delocalization. The second one-electron reduction of the complex also occurs on the 4,4′-bipyrimidine unit as each pyrimidine can accept an electron much more readily than the bpy ligands, albeit at a more negative potential. The third reduction of complexes **5** and **6** is assigned to the reduction of the bpy ligand (−1.70 V) and to a th$_2$bpm ligand (−1.39 V), respectively.

The difference $\Delta E_{1/2}$ between the oxidation E_{ox} potential and the first reduction E_{red1} potential for the complexes is also included in Table 3. The $\Delta E_{1/2}$ is a measure of the difference between the energy of the HOMO and the LUMO of the Ru(II) complexes and is in good correlation with the ^{1}MLCT absorption energy maxima and reinforces the attribution of this band mainly to the d(Ru) → π*(bpm) transition.

The UV–Vis spectra of the compounds **4**–**6** were recorded in acetonitrile solution and are illustrated in Fig. 3. The absorption data and extinction coefficients are displayed in Table 4. The free ligand and the Ru(II) complexes exhibit intense absorption bands in the UV region, assigned to ligand-centered π → π* transitions. The pyrimidine and pyridine π → π* transitions dominate the 280–

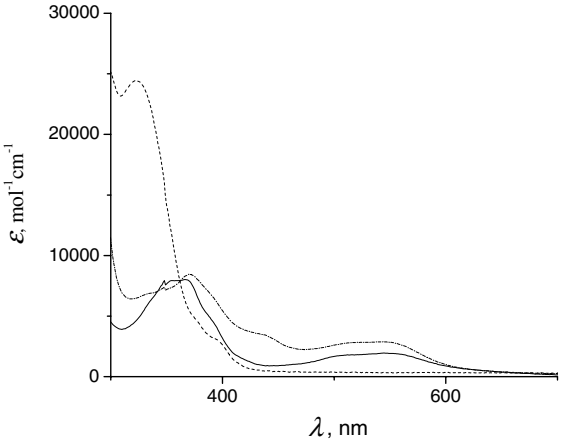


Fig. 3. Absorption spectra of **4** (···), **5** (-·-·-), and **6** (—) recorded in acetonitrile at room temperature.

Table 4
Spectroscopic data for **4**–**6** in deaerated CH_3CN solution

Complex	Absorption	Emission[a]
	λ_{max} (nm) (ε, $M^{-1}\,cm^{-1}$)	λ_{max} (nm)
4	322 (24400) 394 (sh)	
5	548 (2800) 512 (sh) 438 (3400)	770
6	544 (1900) 392 (sh)	722
$[Ru(bpm)_3]^{2+}$[b]	496 (6460) 462 (sh)	700
$[Ru(bpy)_2(bpm)]^{2+}$[b]	526 (3980) 506 (sh) 427 (5620)	742

[a] At 298 K.
[b] Ref. [23].

360 nm region of the spectra and overlap with the band due to the absorption by the thiophene group. The visible region of the spectra is characterized by the presence of two bands that can be attributed to two separate ^{1}MLCT transitions. The band at longer wavelength is associated with a d(Ru) $\rightarrow\pi^*$ (th_2bpm ligand) transitions, whereas the band at 438 nm in **5** is attributed to a d(Ru) $\rightarrow \pi^*$ (bpy) process. In complex **6**, the d(Ru) $\rightarrow \pi^*$ (th_2bpm ligand) transition is bathochromically shifted relative to those of the unsubstituted bpm tris-chelate complex $[Ru(bpm)_3]^{2+}$ (Table 4), as a consequence of the extension of the delocalization in the acceptor th_2bpm ligands. Concomitant with the red shift of the ^{1}MLCT absorption bands in the visible spectrum is a red shift in the ^{3}MLCT emission bands.

The emission spectra of the complexes were recorded in acetonitrile solution and are displayed in Table 4. As complexes **5** and **6** exhibit similar lower-energy MLCT bands in their absorption spectra as compared to $Ru(bpy)_2(bpm)^{2+}$ and $[Ru(bpm)_3]^{2+}$, respectively, the ^{3}MLCT emission bands are also red-shifted (see Table 4). This effect is consistent with the bathochromic shift in absorption and emission λ_{max} complexes with substituted bpm ligands as compared with the unsubstituted bpm ligand [24]. As aryl substituents with extended π systems permit greater delocalization of the excited state, there are fewer bond displacement changes, and, therefore, a concomitant decrease in nonradiative decay.

3. Conclusion

Two new ruthenium (II) complexes with thiophene-substituted 4,4′-bipyrimidine were synthesized and characterized. It has been demonstrated that substitution on the bipyrimidine ligand is an efficient way to tune the energy of the ground and excited states and, consequently, the photophysical properties of the complexes. The low-lying π^* acceptor orbitals of the substituted bidiazine ligands allow the reduction of the complexes at less negative potentials. A more extended π-conjugation of the substituted bipyrimidines stabilizes the empty π^* orbitals of the ligands and thus lowers the absorption and emission energies as compared to the parent $[Ru(bpm)_3]^{2+}$ complex. The new complexes emit at low energy in the red region of the visible spectrum. Although the presence of the 2-thiophene moiety does not produce new π-conjugated polymers by electrochemical polymerization [25], the possibility of introducing 3-thiophene units into the same position or electropolymerizing the free ligand does exist.

4. Experimental

4.1. Materials and methods

$Ru(bpy)_2Cl_2 \cdot 2H_2O$ was prepared by a literature method [26]. The metal complexes were purified by column chromatography on Kiesegel 60 (230–400 mesh) silica gel. Ammonium hexafluorophosphate and potassium nitrate were purchased from Aldrich and used without further purification. Tetrabutylammonium hexafluorophosphate was purchased from Aldrich and purified by recrystallization from toluene–methanol. Acetonitrile for photophysical and electrochemical experiments was of spectroscopic grade. Elemental analyses were performed by Laboratoire d'Analyse Elementaire de l'Université de Montréal.

Nuclear magnetic resonance (NMR) spectra were recorded in CD_3CN at room temperatutre (r.t.) on a Bruker AV400 spectrometer at 400 MHz for ^{1}H NMR and at 100 MHz for ^{13}C NMR. Chemical shifts are reported in part per million (ppm) relative to residual solvent protons (1.93 ppm for acetonitrile-d_3) and carbon resonance (1.79 ppm for methyl resonance of acetonitrile-d_3) of the solvent. Routine absorption spectra and emission spectra were measured in deaerated acetonitrile at r.t. on a Cary 500i UV–Vis–NIR Spectrophotometer and a Cary Eclipse Fluorescence Spectrophotometer, respectively, with errors of ±2 nm. Electrochemistry data were collected in deaerated acetonitrile with 0.1 M Bu_4NPF_6 on a BAS CV-50W Voltammetric Analyzer. Redox potentials were corrected by internal reference ferrocene (395 mV vs SCE).

4.2. Preparation of 2-thienyl enaminone (*1*)

N,*N*-Dimethylformamide dimethyl acetal (24.6 mL, 0.18 mol) was added dropwise to a stirred solution of 2-acetylthiophene (20 mL, 0.18 mol) in boiling absolute EtOH (20 mL) and the stirring was continued for 6 h, at which time hexane was added. A yellow solid precipitated which was isolated by filtration (17.29 g). Yield: 53%. ^{1}H NMR ($CDCl_3$, 400 MHz): δ 8.7 (d, $J = 12.2$ 1 H, H_1), 7.85 (d, $J = 3.7$, 1H, $H_{3'}$), 7.71 (d, $J = 4.9$, 1H, $H_{5'}$), 7.07 (t, $J = 8.6$, 1H, $H_{4'}$), 5.65 d, $J = 12.2$, 1H, H_2), 3.14 (s, 3H, N-CH_3), 2.94 (s, 3H, *N*-CH_3). ^{13}C NMR ($CDCl_3$): δ

181.1, 154.1, 147.7, 130.7, 128.8, 128.0, 92.0, 45.3, 37.4. MS: $m/z = 182.1$. *Anal.* Calc. for $C_9H_{11}NOS$: C, 59.64; H, 6.12; N, 7.73; S, 17.69. Found: C, 59.51; H, 6.17; N, 7.71; S, 17.15%.

4.3. Preparation of 4-(2′-thienyl)-pyrimidine (2)

To a stirred solution of **1** (5.0 g, 0.027 mol) in absolute ethanol (10 mL) at reflux was added formamidine acetate (8.6 g, 0.083 mol) and stirring was continued for 10 min. A solution of Na (1.9 g, 0.083 mol) in absolute EtOH (20 mL) was added to the reaction mixture and the reflux was maintained for 16 h, after which time the reaction mixture was allowed to cool to r.t. The solution was concentrated under vacuum and the solid residue dissolved in CH_2Cl_2 (50 mL). The precipitate was filtered and the filtrate concentrated. The desired compound was purified by column chromatography on alumina (EtOAc:hexane = 1:5) to give 4-(2′-thienyl)- pyrimidine as a white crystalline powder (2.10 g). Yield: 48%. ^{1}H NMR ($CDCl_3$, 400 MHz): δ 9.14 (s, 1H, H_2), 8.70 (d, $J = 5.4$, 1H, H_5), 7.82 (d, $J = 3.7$, 1H, $H_{3'}$), 7.63 (d, $J = 5.5$, 1H, H_6), 7.60 (d, $J = 5.1$, 1H, $H_{5'}$), 7.19 (t, $J = 8.7$, 1H, $H_{4'}$). ^{13}C NMR ($CDCl_3$): δ. 159.3, 159.2, 157.4, 142.5, 130.9, 128.9, 128.1, 115.5. MS: $m/z = 163.2$. *Anal.* Calc. for $C_8H_6N_2S$: C, 59.23; H, 3.73; N, 17.27; S, 19.77. Found: C, 59.03; H, 3.68; N, 17.17; S, 18.98%.

4.4. Preparation of 6,6′-bis(2-thienyl)-4,4′-bipyrimidine (4)

To a solution of **2** (1.13 g, 0.0069 mol) in THF (5 mL) was added sodium metal (0.48 g, 0.020 mol). The solution turned purple and then yellow. The reaction was quenched with EtOH (4 mL) and triethylamine (0.2 mL) to afford **3**, which was then oxidized by bubbling air through the solution for 1 h. The reaction mixture was dissolved in CH_2Cl_2 and washed three times with water. The extract was purified by recrystallization from methanol to afford a cream-coloured product (0.678 g). Yield: 61%. ^{1}H NMR ($CDCl_3$, 400 MHz): δ 9.23 (s, 2H, H_2), 8.78 (s, 2H, H_5), 8.00 (d, $J = 3.5$, 2H, $H_{3'}$), 7.66 (d, $J = 5.1$, 2H, $H_{5'}$), 7.23 (t, $J = 8.6$, 1H, $H_{4'}$). ^{13}C NMR ($CDCl_3$): δ 161.4, 161.1, 159.4, 142.4, 131.3, 129.1, 128.9, 116.0. MS: $m/z = 323.1$. HRMS: calcd [M + 1] for $C_{16}H_{10}N_4S_2$, 323.1942; found, 323.1935.

4.5. Preparation of [Ru(bpy)$_2$(4)](PF$_6$)$_2$ (5)

The complex *cis*-$[Ru(bpy)_2Cl_2] \cdot 2H_2O$ (0.010 g, 0.019 mmol) was suspended in a mixture of ethanol and water (8 mL, 75:25) and was heated for 30 min. 6,6′-Bis(2-thienyl)-4,4′-bipyrimidine (1.2 equiv., 0.0074 g, 0.023 mmol) was added and the mixture was refluxed overnight. The resulting solution was cooled to room temperature and the ethanol was removed under reduced pressure. After filtration, a saturated solution of ammonium hexafluorophosphate was added dropwise to the filtrate to complete precipitation of the product. The precipitate was collected by filtration, washed with water and diethyl ether, and dried. The complex was purified by column chromatography (SiO_2, acetonitrile: KNO_3(aq.), 7:1). The nitrate salt was metathesized to the PF_6 salt and the solvent removed under reduced pressure. The red product (10.7 mg) was finally collected by filtration after dissolving the solid in acetonitrile and precipitating by its addition to ether. Yield: 55%. ^{1}H NMR (CD_3CN, 400 MHz): δ 8.94 (s, 2H, H_5), 8.54 (s, 2H, H_2), 8.51 (d, $J = 5.4$ Hz, 4H, $B_{3,3'}$), 8.30 (d, $J = 5.6$ Hz, 2H, $H_{3'}$), 8.09 (t, $J = 11.7$ Hz, 4H, $B_{4,4'}$), 8.00 (d, $J = 4.9$ Hz, 2H, B_6), 7.85 (d, $J = 4.9$ Hz, 2H, $B_{6'}$), 7.72 (d, $J = 5.5$ Hz, 2H, $H_{5'}$), 7.44 (t, $J = 12.2$ Hz, 4H, $B_{5,5'}$), 7.36 (d, $J = 8.6$ Hz, 2H, $H_{4'}$). ^{13}C (CD_3CN): δ 165.1, 163.7, 160.4, 157.3, 152.8, 143.3, 138.3, 131.6, 129.6, 129.0, 124.8, 124.16, 117.2. ES-MS: $m/z = 367.7$ (M-2 PF_6^+).

4.6. Preparation of [Ru(6,6′-bis(2-thienyl)-4,4′-bipyrimidine)$_3$] (PF$_6$)$_2$ (6)

A solution of $RuCl_3 \cdot 3H_2O$ (0.0065 g, 0.031 mmol) and 6,6′-bis(2-thienyl)-4,4′-bipyrimidine (0.030 g, 0.093 mmol) in ethylene glycol (10 mL) was refluxed overnight. A saturated solution of ammonium hexafluorophosphate was added dropwise to the reaction mixture to complete precipitation. The precipitate was collected by filtration, washed by water and diethyl ether and dried. The complex was purified by column chromatography (SiO_2, acetonitrile:aq.KNO_3, 7:1). The nitrate salt was metathesized to the PF_6 salt and the solvent removed under reduced pressure. The red product (11.4 mg) was finally collected by dissolving the solid in acetonitrile and precipitated by addition to water. Yield: 27%. ^{1}H NMR (CD_3CN, 400 MHz): δ 8.98 (s, 6H, H_5), 8.63 (s, 6H, H_2), 8.31 (d, $J = 3.8$ Hz, 6H, $H_{3'}$), 7.86 (d, $J = 4.7$ Hz, 6H, $H_{5'}$), 7.39 (t, $J = 8.8$ Hz, 6H, $H_{4'}$). ^{13}C (CD_3CN): δ 162.4, 161.8, 159.9, 142.7, 132.0, 129.2, 117.5. ES-MS: $m/z = 533.7$ (M-2 PF_6^+).

5. Supplementary material

CCDC 284567 contains the supplementary crystallographic data for this paper. These data can be obtained free of charge via http://www.ccdc.cam.ac.uk/conts/retrieving.html, or from the Cambridge Crystallographic Data Centre, 12 Union Road, Cambridge CB2 1EZ, UK; fax: (+44) 1223-336-033; or e-mail: deposit@ccdc.cam.ac.uk.

Acknowledgements

We thank the NSERC of Canada and the Université de Montréal for financial support and Johnson Matthey PLC for a loan of $RuCl_3$. E.A.M. thanks the Commonwealth Foundation for a doctoral fellowship.

References

[1] (a) V. Balzani, F. Scandola, Supramolecular Photochemistry, Horwood, Chichester, 1991;
(b) V. Balzani, L. De Cola, Supramolecular Chemistry, Kluwer, Dordrecht, 1992;
(c) V. Balzani, A. Credi, M. Venturi, Molecular Devices and Machines, Wiley-VCH, Weinheim, 2003;
(d) F. Scandola, C. Chiorboli, M.T. Indelli, M.A. Rampi, in: V. Balzani (Ed.), Electron Transfer in Chemistry, vol. 3, VCH-Wiley, 2001, p. 337.

[2] K.K.-W. Lo, W.-K. Hui, C.-K. Chung, K.H.-K. Tsang, D.C.-M. Ng, N. Zhu, K.-K. Cheung, Coord. Chem. Rev. 249 (2005) 1434, and references therein.

[3] (a) K. Kalyanasundaram, M. Grätzel, Coord. Chem. Rev. 77 (1998) 347;
(b) K. Kalyanasundaram, Coord. Chem. Rev. 46 (1982) 159.

[4] B. O'Reagan, M. Grätzel, Nature 35 (1991) 737.

[5] (a) A. Juris, V. Balzani, F. Barigelletti, S. Campagna, P. Belser, A. von Zelewsky, Coord. Chem. Rev. 84 (1988) 85;
(b) A.J. Bard, M.A. Fox, Acc. Chem. Res. 28 (1995) 141.

[6] D.M. Roundhill, Photochemistry and photophysics of metal complexes, in: John P. FacklerJr. (Ed.), Modern Inorganic Chemistry, Plenum Press, New York, 1994.

[7] V. Balzani, A. Juris, M. Venturi, S. Campagna, S. Serroni, Chem. Rev. 96 (1996) 759.

[8] (a) A. Von Zelewsky, Stereochemistry of Coordination Compounds, John Wiley & Sons Ltd., New York, 1996;
(b) E. Baranoff, J.-P. Collin, L. Flamigni, J.-P. Sauvage, Chem. Soc. Rev. 33 (2004) 147;
(c) J.P. Sauvage, J.P. Collin, J.C. Chambron, S. Guillerez, C. Coudret, V. Balzani, F. Barigelletti, L. De Cola, L. Flamigni, Chem. Rev. 94 (1994) 993.

[9] T.J. Meyer, Pure Appl. Chem. 58 (1986) 1193.

[10] M. Maestri, N. Armaroli, V. Balzani, E.C. Constable, A.M.W.C. Thompson, Inorg. Chem. 34 (1995) 2759.

[11] (a) E.A. Medlycott, G.S. Hanan, Chem. Soc. Rev. 34 (2005) 133;
(b) E.A. Medlycott, G.S. Hanan, Coord. Chem. Rev. 250 (2006) 1763.

[12] (a) S. Ernst, W. Kaim, J. Am. Chem. Soc. 108 (1986) 3578;
(b) E. Ioachim, G.S. Hanan, Can. J. Chem. 83 (2005) 1114;
(c) W. Kaim, H.E.A. Kramer, C. Vogler, J. Rieker, J. Organomet. Chem. 367 (1989) 107;
(d) E. Ioachim, E.A. Medlycott, G.S. Hanan, Inorg. Chim. Acta. 359 (2006) 766.

[13] (a) S.S. Zhu, R.P. Kingsborough, T.M. Swager, J. Mater. Chem. 9 (1999) 2123;
(b) S.S. Zhu, T.M. Swager, Adv. Mater. 8 (1996) 497.

[14] (a) K. Araki, H. Endo, G. Masuda, T. Ogawa, Chem. Eur. J. 10 (2004) 3331;
(b) P.-L. Vidal, B. Divisia-Blohorn, G. Bidan, J.-M. Kern, J.-P. Sauvage, J.-L. Hazemann, Inorg. Chem. 38 (1999) 4203;
(c) S.S. Zhu, T.M. Swager, J. Am. Chem. Soc. 119 (1997) 12568;
(d) S.S. Zhu, P.J. Carroll, T.M. Swager, J. Am. Chem. Soc. 118 (1996) 8713.

[15] (a) J. Hjelm, R.W. Handel, A. Hagfeldt, E.C. Constable, C.E. Housecroft, R.J. Forster, Inorg. Chem. 44 (2005) 1073;
(b) J. Hjelm, E.C. Constable, E. Figgemeier, A. Hagfeldt, R. Handel, C.E. Housecroft, E. Mukhtar, E. Schofield, Chem. Commun. (2002) 284.

[16] S. Ernst, W. Kaim, Inorg. Chem. 28 (1989) 1520.

[17] We had previously shown that this approach was not well suited to coupling pyridyl-pyrimidines, K.O. Johansson, C. Tong, A. Coté, G.S. Hanan, Chem. Commun. (2000) 709, however, that it is well suited to non-coordinating aryl-pyrimidines: S. Dufresne, G.S. Hanan, F. Laverdière, M. Li Fraine, W.G. Skene, unpublished results.

[18] R.S. Beredereck, F. Effenberger, Chem. Ber. 97 (1964) 3407.

[19] E. Bejan, H.A. Haddou, J.C. Daran, G.G.A. Balavoine, Synthesis (1996) 1012.

[20] (a) E. Ioachim, E.A. Medlycott, M.I.J. Polson, G.S. Hanan, Eur. J. Org. Chem (2005) 3775;
(b) M.I.J. Polson, J.A. Lotoski, N.J. Taylor, G.S. Hanan, B. Hasenknopf, R. Thouvenot, F. Loiseau, R. Passalaqua, S. Campagna, Eur. J. Inorg. Chem. (2002) 2549.

[21] S. Ernst, W. Kaim, Angew. Chem, Int. Ed. Engl. 24 (1985) 430.

[22] D.P. Rillema, G. Allen, T.J. Meyer, D. Conrad, Inorg. Chem. 22 (1983) 1617.

[23] S. Ernst, W.J. Kaim, Inorg.Chem. 28 (1989) 1520.

[24] G.F. Strouse, J.R. Schoonover, R. Duesing, S. Boyde, W.E. Jones Jr., T.J. Meyer, Inorg. Chem. 34 (1995) 473.

[25] Attempts to electropolymerize complexes 5 and 6 failed, presumably due to the poor geometry of the 4-substituted bpm ligand: S. Dufresne, G.S. Hanan, F. Laverdière, M. Li Fraine, W.G. Skene, unpublished results.

[26] B.P. Sullivan, D.J. Salmon, T.J. Meyer, Inorg. Chem. 17 (1978) 3334.

formed *in vacuo* using the hybrid DFT B3LYP method [5] without symmetry constrains, in combination with the polarized, ECP-based LACVP** basis set [6]. The "restricted" formalism was applied in all calculations. An initial refinement of the geometries was obtained using the restricted semi-empirical PM3 calculations [7]. All the resultant stationary points were characterized as true minima (*i.e.*, no imaginary frequencies). Atomic charges derived from Natural population analysis [8]. All calculations were carried out with computers equipped with Intel Pentium 4 660 processors (Prescott 2M) operating at 3.6 GHz frequency. The software used was the SPARTAN '02 [9].

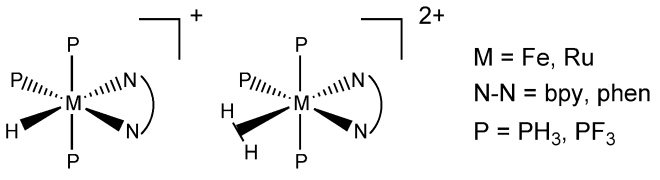
3. Results and discussion

The molecules considered are iron and ruthenium classical and non-classical hydrides of the type *mer*-$[MH(N–N)P_3]^+$ and *mer*-$[M(\eta^2\text{-}H_2)(N–N)P_3]^{2+}$ {M = Fe, Ru; N–N = bpy, phen; P = PH_3, PF_3}, as depicted in Scheme 1. To speed up calculations, the small PH_3 and PF_3 phosphines were considered. Moreover, the use of these ligands strongly reduces the number of possible molecular conformers, thus helping the attainment of the molecular energy minimum during the geometry optimisations. From a chemical point of view PH_3 and PF_3 are quite interesting, having a strongly different co-ordinating behaviour: PF_3 is, in fact, a much more π-acidic ligand than PH_3 and the phosphites considered in Ref. [3] have a π-back-donation ability which is intermediate between that of PH_3 and PF_3 [10], thus the ligands considered in this work can be thought from an electronic point of view as two "borderline cases". Steric effects are usually negligible in acid–base reactions, thus the use of PH_3 and PF_3 instead of the bulkier phosphites did not appear to be too great a simplification.

The experimentally observed [3] acidity differences between iron(II) and ruthenium(II) hydride derivatives for the equilibrium reaction:

$$[M(\eta^2\text{-}H_2)(N–N)P_3]^{2+} \rightleftharpoons [MH(N–N)P_3]^+ + H^+$$

can be correlated with some ground-state calculated properties of the $[MH(N–N)P_3]^+$ and $[M(\eta^2\text{-}H_2)H(N–N)P_3]^{2+}$ cations, such as charge distributions and bond lengths. Table 1 reports the charge distribution on the hydride ligands resulting from the Natural population analyses performed on the geometry-optimised models of the $[MH(N–N)P_3]^+$ cations {M = Fe, Ru; N–N = bpy, phen; P = PH_3, PF_3}.



Scheme 1. $[MH(N–N)P_3]^+$ and $[M(\eta^2\text{-}H_2)(N–N)P_3]^{2+}$ cations.

Table 1
Hydride Natural charge of $[MH(N–N)P_3]^+$ cations

Complex	Natural charge
$[FeH(bpy)(PH_3)_3]^+$	−0.237
$[FeH(phen)(PH_3)_3]^+$	−0.234
$[FeH(bpy)(PF_3)_3]^+$	−0.195
$[FeH(phen)(PF_3)_3]^+$	−0.191
$[RuH(bpy)(PH_3)_3]^+$	−0.127
$[RuH(phen)(PH_3)_3]^+$	−0.123
$[RuH(bpy)(PF_3)_3]^+$	−0.125
$[RuH(phen)(PF_3)_3]^+$	−0.122

As depicted in Fig. 1, the co-ordinated hydrogen atoms have a more negative charge in the Fe(II) derivatives. The more negative charge of the co-ordinated hydrogen atom in the $[FeH(N–N)P_3]^+$ classical hydrides means a greater basicity of the iron(II) derivatives. It is to be noted that the hydride-character of the Fe(II) complexes is strongly influenced by the nature of the considered phosphine, while for both the Fe(II) and Ru(II) hydrides there are not important variations by changing the nitrogen-donor chelate ligand.

Also for the doubly charged non-classical hydrides $[M(\eta^2\text{-}H_2)(N–N)P_3]^{2+}$ {M = Fe, Ru; N–N = bpy, phen; P = PH_3, PF_3} the charge distribution was studied and in Table 2 the average Natural charges of the H atoms of the co-ordinated di-hydrogen molecule are reported.

In the doubly-charged $[M(\eta^2\text{-}H_2)(N–N)P_3]^{2+}$ non-classical hydrides the co-ordinated di-hydrogen molecule has a more positive charge in the Ru(II) derivatives (see Fig. 2). As for the classical hydrides $[MH(N–N)P_3]^+$, the 2,2′-bipyridine and the 1,10-phenanthroline derivatives show practically the same electronic properties. Also the variation of phosphine from PH_3 to PF_3 does not significantly affect the charge of the $\eta^2\text{-}H_2$ fragments. The more positive charge of the co-ordinated di-hydrogen molecule in the $[Ru(\eta^2\text{-}H_2)(N–N)P_3]^{2+}$ non-classical hydrides agrees with the greater acidity of the ruthenium(II) species as compared with the iron(II) analogues.

The computed $r_{H–H}$ bond lengths, reported in Table 3, highlight the differences between $[Fe(\eta^2\text{-}H_2)(N–N)P_3]^{2+}$ and $[Ru(\eta^2\text{-}H_2)(N–N)P_3]^{2+}$ cations. The more acidic character of Ru(II) non-classical hydrides corresponds, in fact, to a slightly longer H–H bond of the co-ordinated $\eta^2\text{-}H_2$ di-hydrogen molecule, as depicted in Fig. 3. The average difference between iron and ruthenium derivatives is 0.033 Å. As expected from the previous considerations, for both the Fe(II) and Ru(II) hydrides there are not meaningful variations by changing the N-donor chelate ligand.

By varying the co-ordinated phosphines from PH_3 to PF_3, a shortening of the H–H bond lengths, which principally affects the $[Ru(\eta^2\text{-}H_2)(N–N)P_3]^{2+}$ derivatives, is observed. It is known [1] that the bond between di-hydrogen and a transition metal can be qualitatively described on

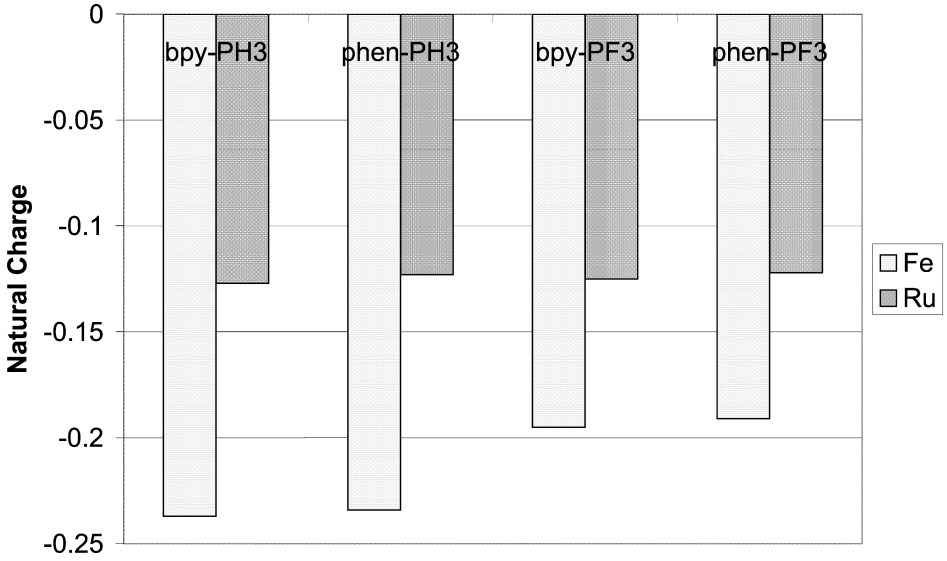


Fig. 1. Natural charge of the co-ordinated hydrogen atoms in the $[MH(N–N)P_3]^+$ cations.

Table 2
Average Natural charge of the H atoms in $[M(\eta^2\text{-}H_2)(N–N)P_3]^{2+}$ cations

Complex	Natural charge
$[Fe(\eta^2\text{-}H_2)(bpy)(PH_3)_3]^{2+}$	0.063
$[Fe(\eta^2\text{-}H_2)(phen)(PH_3)_3]^{2+}$	0.065
$[Fe(\eta^2\text{-}H_2)(bpy)(PF_3)_3]^{2+}$	0.061
$[Fe(\eta^2\text{-}H_2)(phen)(PF_3)_3]^{2+}$	0.063
$[Ru(\eta^2\text{-}H_2)(bpy)(PH_3)_3]^{2+}$	0.097
$[Ru(\eta^2\text{-}H_2)(phen)(PH_3)_3]^{2+}$	0.098
$[Ru(\eta^2\text{-}H_2)(bpy)(PF_3)_3]^{2+}$	0.091
$[Ru(\eta^2\text{-}H_2)(phen)(PF_3)_3]^{2+}$	0.089

Table 3
$r_{H–H}$ bond lengths of $[M(\eta^2\text{-}H_2)(N–N)P_3]^{2+}$ cations

Complex	$r_{H–H}$ (Å)
$[Fe(\eta^2\text{-}H_2)(bpy)(PH_3)_3]^{2+}$	0.843
$[Fe(\eta^2\text{-}H_2)(phen)(PH_3)_3]^{2+}$	0.844
$[Fe(\eta^2\text{-}H_2)(bpy)(PF_3)_3]^{2+}$	0.838
$[Fe(\eta^2\text{-}H_2)(phen)(PF_3)_3]^{2+}$	0.840
$[Ru(\eta^2\text{-}H_2)(bpy)(PH_3)_3]^{2+}$	0.881
$[Ru(\eta^2\text{-}H_2)(phen)(PH_3)_3]^{2+}$	0.882
$[Ru(\eta^2\text{-}H_2)(bpy)(PF_3)_3]^{2+}$	0.865
$[Ru(\eta^2\text{-}H_2)(phen)(PF_3)_3]^{2+}$	0.868

the basis of a σ-bond between the HOMO of H_2 and a d_σ orbital of the metal, enforced by an interaction between a d_π filled orbital of the metal and the LUMO of H_2. The greater π-acidity of PF_3 [10] causes a decrease of the π-electron density of the metal centres, which consequently reduces the back-donation towards the $H_2\sigma^*$ molecular orbital and decreases the H–H elongation.

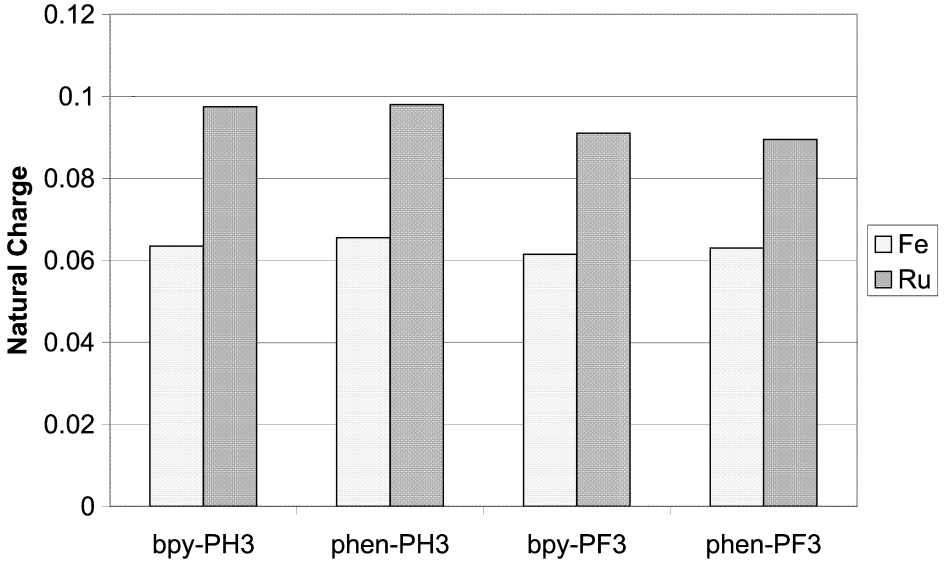


Fig. 2. Natural charge of the co-ordinated hydrogen atoms in the $[M(\eta^2\text{-}H_2)(N–N)P_3]^{2+}$ cations.

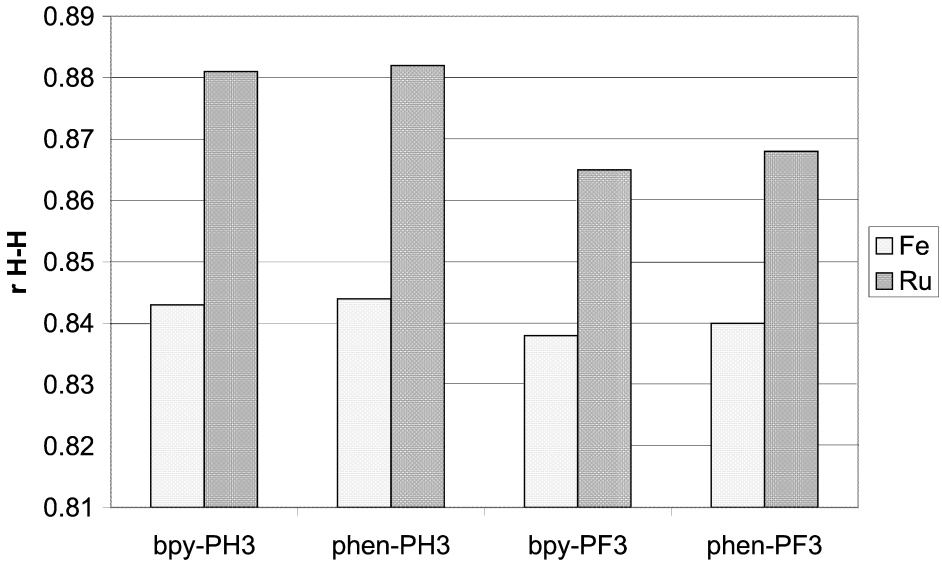


Fig. 3. r_{H-H} bond lengths of $[M(\eta^2\text{-}H_2)(N\text{–}N)P_3]^{2+}$ non-classical hydrides.

The comparison of the global energies of the $[MH(N\text{–}N)P_3]^+$ hydrides ($E_{[M]H}$) and of their conjugated acids $[M(\eta^2\text{-}H_2)(N\text{–}N)P_3]^{2+}$ ($E_{[M]H2}$) represents a more quantitative approach to the different acidities of iron(II) and ruthenium(II) non-classical hydrides. The energy differences between the *in vacuo* dissociation of the iron and ruthenium non-classical hydrides, $\Delta E_{Fe\text{–}Ru}$, can be easily calculated from the $E_{[M]H}$ and $E_{[M]H2}$ values:

$$[Fe(\eta^2\text{-}H_2)(N\text{–}N)P_3]^{2+} \rightarrow [FeH(N\text{–}N)P_3]^{+} + H^{+}$$

$$[Ru(\eta^2\text{-}H_2)(N\text{–}N)P_3]^{2+} \rightarrow [RuH(N\text{–}N)P_3]^{+} + H^{+}$$

$$\begin{aligned}\Delta E_{Fe\text{–}Ru} &= \{E_{[M]H}(Fe) + E_{H+} - E_{[M]H2}(Fe)\} \\ &\quad - \{E_{[M]H}(Ru) + E_{H+} - E_{[M]H2}(Ru)\} \\ &= \{E_{[M]H}(Fe) + E_{[M]H}(Ru)\} \\ &\quad - \{E_{[M]H2}(Fe) - E_{[M]H2}(Ru)\}\end{aligned}$$

The $\Delta E_{Fe\text{–}Ru}$ values reported in Table 4 agree with the experimentally observed higher acidity of the ruthenium(II) species, showing that the dissociation of the Fe(II) non-classical hydrides is always more than 3 Kcal/mol higher than that of the analogues Ru(II) derivatives. As expected from the previous results, the loss of an H^+ ion is energetically more favourable for the ruthenium non-classical hydrides.

The Natural charge distributions of the $[MH(N\text{–}N)P_3]^+$ and $[M(\eta^2\text{-}H_2)(N\text{–}N)P_3]^{2+}$ cationic hydrides allow to better understand the role of both the metal centres and the ancillary ligands in the acidity of these species. As described before (see Tables 1 and 2), the higher acidity of the ruthenium derivatives can be correlated to a more positive charge of the hydride and di-hydrogen ligands. In Table 5 the partial charge of the N-donor chelate ligands (N–N), the sum of charges of the P-donor ligands (P_3) and the Natural charge of the metal ion (M) are reported. It can be clearly observed that the greater charge of the –H and $-(\eta^2\text{-}H_2)$ ligands in Ru(II) derivatives is principally correlated to a strongly reduced partial charge of the metal ion. Quite surprisingly, both the N-donor and P-donor ligands show an increased partial charge in ruthenium classical and non-classical hydrides, as depicted in Fig. 4 for $[MH(bpy)(PH_3)_3]^+$ and $[M(\eta^2\text{-}H_2)(bpy)(PH_3)_3]^{2+}$ complexes {M = Fe, Ru}.

In our opinion, the data on the Natural charge distribution presented in Tables 1, 2 and 5 can be explained in a really simple way, by considering that the electronegativity of ruthenium is greater than that of iron: in fact, commonly

Table 4
$\Delta E_{Fe\text{–}Ru}$ values

N ligand	P ligands	$\Delta E_{Fe\text{–}Ru}$ (Kcal/mol)
bpy	PH_3	3.7
bpy	PF_3	3.7
phen	PH_3	3.9
phen	PF_3	3.2

Table 5
Natural charges of the N-donor (N–N), sum of the Natural charges of the P-donors (P_3) and charge of the metal ion (M)

Complex	N–N	P_3	M
$[FeH(bpy)(PH_3)_3]^+$	0.278	0.667	0.292
$[FeH(phen)(PH_3)_3]^+$	0.275	0.668	0.291
$[FeH(bpy)(PF_3)_3]^+$	0.369	0.803	0.023
$[FeH(phen)(PF_3)_3]^+$	0.367	0.804	0.020
$[Fe(\eta^2\text{-}H_2)(bpy)(PH_3)_3]^{2+}$	0.476	0.912	0.485
$[Fe(\eta^2\text{-}H_2)(phen)(PH_3)_3]^{2+}$	0.471	0.913	0.485
$[Fe(\eta^2\text{-}H_2)(bpy)(PF_3)_3]^{2+}$	0.550	1.037	0.290
$[Fe(\eta^2\text{-}H_2)(phen)(PF_3)_3]^{2+}$	0.552	1.030	0.292
$[RuH(bpy)(PH_3)_3]^+$	0.282	0.878	−0.033
$[RuH(phen)(PH_3)_3]^+$	0.282	0.878	−0.037
$[RuH(bpy)(PF_3)_3]^+$	0.353	0.946	−0.174
$[RuH(phen)(PF_3)_3]^+$	0.354	0.943	−0.175
$[Ru(\eta^2\text{-}H_2)(bpy)(PH_3)_3]^{2+}$	0.540	1.174	0.100
$[Ru(\eta^2\text{-}H_2)(phen)(PH_3)_3]^{2+}$	0.531	1.173	0.100
$[Ru(\eta^2\text{-}H_2)(bpy)(PF_3)_3]^{2+}$	0.595	1.259	−0.036
$[Ru(\eta^2\text{-}H_2)(phen)(PF_3)_3]^{2+}$	0.594	1.264	−0.037

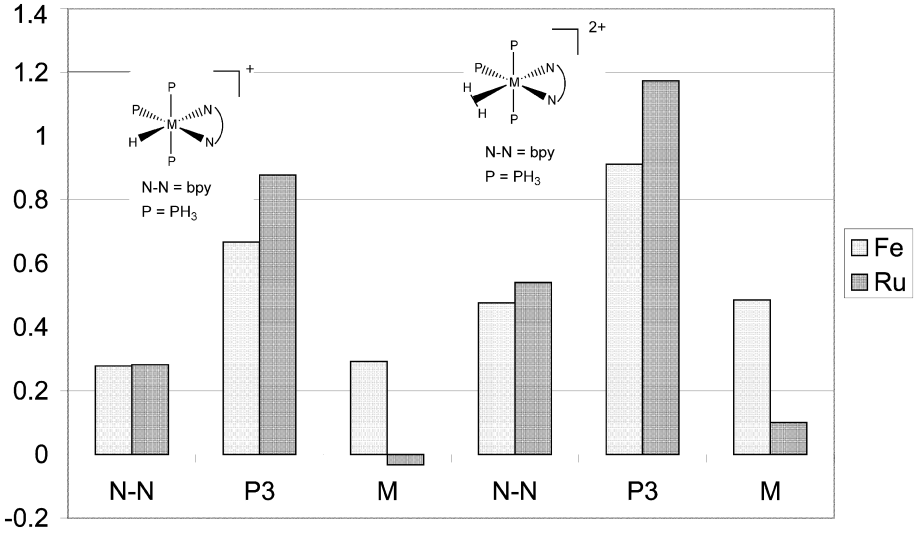


Fig. 4. Partial charges of ancillary ligands and metal ion for $[MH(bpy)(PH_3)_3]^+$ and $[M(\eta^2\text{-}H_2)(bpy)(PH_3)_3]^{2+}$ {M = Fe, Ru}.

reported Pauling's electronegativity [11] of Ru is 2.2, while the one of Fe is 1.8. The experimentally observed acidity differences between iron and ruthenium non-classical hydrides of the type $[M(\eta^2\text{-}H_2)(N\text{–}N)P_3]^{2+}$, together with the charge distributions of the ancillary ligands in both the classical and non-classical hydrides, can be considered as a consequence of the different electronegativities of the two metal ions.

4. Concluding remarks

In this work, a good correlation between various computed molecular properties and experimental data reported in the literature was highlighted. The observed reactivity of N_2P_3-donor-set Fe(II) and Ru(II) di-hydrogen derivatives found a correlation with ground-state properties such as bond lengths, charge distributions and H^+ dissociation energies. Finally, the charge distributions obtained from DFT calculations allowed to hypothesize that the different acidities of iron and ruthenium non-classical hydrides could be mainly justified on the basis of the difference of electronegativity of the two metal ions considered.

Acknowledgement

We sincerely thank Ca' Foscari University of Venice for financial support (Ateneo fund 2005).

References

[1] (a) G.J. Kubas, Metal Dihydrogen and Sigma-Bond Complexes, Kluwer, New York, 2001;
(b) M. Peruzzini, R. Poli, Recent Advances in Hydride Chemistry, Elsevier, Amsterdam, 2001;
(c) A. Dedieu, Transition Metal Hydrides, Wiley-VCH, New York, 1992;
(d) P.G. Jessop, R.H. Morris, Coord. Chem. Rev. 121 (1992) 155;
(e) D.M. Heinekey, W.J. Oldham Jr., Chem. Rev. 93 (1993) 913;
(f) M.A. Esteruelas, L.A. Oro, Chem. Rev. 98 (1998) 577.
[2] (a) B.P. Sullivan, J.V. Caspar, S.R. Johnson, T.J. Meyer, Organometallics 3 (1984) 1241;
(b) T.A. Luther, D.M. Heinekey, Inorg. Chem. 37 (1998) 127;
(c) D.F. Mullica, J.M. Farmer, J.A. Kautz, S.L. Gipson, Y.F. Belay, M.S. Windmiller, Inorg. Chim. Acta 285 (1999) 318;
(d) P.S. Hallman, B.R. McGarvey, G.J. Wilkinson, J. Chem. Soc. (A) (1968) 3143;
(e) D.M. Heinekey, H. Mellows, T. Pratum, J. Am. Chem. Soc. 122 (2000) 6498;
(f) J.M. Kelly, J.G. Vos, J. Chem. Soc., Dalton Trans. (1986) 1045.
[3] (a) G. Albertin, S. Antoniutti, M. Bortoluzzi, Inorg. Chem. 43 (2004) 1328;
(b) G. Albertin, S. Antoniutti, A. Bacchi, C. D'Este, G. Pelizzi, Inorg. Chem. 43 (2004) 1336;
(c) M. Bortoluzzi, PhD Thesis, Venice, 2004.
[4] W.D. Harman, H. Taube, J. Am. Chem. Soc. 112 (1990) 2261.
[5] (a) R.G. Parr, W. Yang, Density-Functional Theory of Atoms and Molecules, Oxford University Press, Oxford, 1989;
(b) J.K. Labanowski, J. Andzelm, Density Functional Methods in Chemistry, Springer-Verlag, New York, 1991;
(c) P. Geerlings, F. De Proft, W. Langenaker, Chem. Rev. 103 (2003) 1793;
(d) T. Ziegler, Chem. Rev. 91 (1991) 651.
[6] (a) W.J. Henre, R. Ditchfield, J.A. Pople, J. Chem. Phys. 56 (1972) 2257;
(b) P.J. Hay, R.W. Wadt, J. Chem. Phys. 82 (1985) 299;
(c) M. Dolg, in: J. Grotendorst (Ed.), Modern Methods and Algorithms of Quantum Chemistry, NIC series, vol. 1, John Neumann Institute for Computing, Jülich, 2000, pp. 479–508.
[7] J.J.P. Stewart, J. Comput. Chem. 10 (1989) 209.
[8] A.E. Reed, L.A. Curtiss, F. Weinhold, Chem. Rev. 88 (1988) 899.
[9] SPARTAN '02, Wavefunction Inc., Irvine CA, 2002. We sincerely thank Prof. S. Cossu for the use of his software package.
[10] C.A. McAuliffe, Comprehensive Coordination Chemistry (Ligands), vol. 2, Pergamon Press, Oxford, 1987 (Chapter 14).
[11] L. Pauling, J. Am. Chem. Soc. 54 (1932) 3570.

2. Experimental

2.1. Materials

Colloidal borosilicate (CBS) and colloidal silica (CS) were stable dispersions obtained from Nalco Company. Both were samples of commercial products. The content of dispersed phase in CBS was 8.68% by weight and the B/Si molar ratio was 0.04. Colloidal silica contained 15.67% SiO_2 by weight. Sodium tetraborate decahydrate (borax) was purchased from Sigma–Aldrich, while the catechol and DL-tartaric acid were acquired from Alfa Aesar. Both of these reagents were used without further purification.

2.2. Preparation of colloidal silica–borax blend

The blends of colloidal silica with borax having B/Si molar ratio of 0.04 were prepared by mixing 6.64 g of 3% borax solution with 20.0 g of CS dispersion in a 60 ml capped glass jar. The samples were thoroughly mixed, and their pH adjusted to 9.5 with a small amount of hydrochloric acid solution.

2.3. Treatment of borosilicates and silica–borax blends with catechol and tartaric acid

Since catechol is susceptible to oxidation, especially in the alkaline medium, all experiments were carried out in a glove box under a continuous flow of nitrogen. First, solutions of catechol in water were prepared. For the reaction with colloidal borosilicate 0.37 g of catechol was dissolved in 9.56 g of water, while for the reaction with borax/silica blends, 0.69 g of catechol was dissolved in 28.1 g of water. These amounts of catechol were chosen to yield boron-to-chelant molar ratio of 1:3. The prepared catechol solutions were, respectively, added to 20 g of CBS and to 26.64 g of CS/borax blends. The resulting mixtures were shaken thoroughly and their pH was adjusted to 9.5 with a small amount of NaOH solution. All the colloids and solutions (including DI water used to dissolve catechol and solutions used to adjust the pH) were deaerated by bubbling nitrogen through them.

The treatment of borosilicates and colloidal silica/borax blends with the tartaric acid (H_2T) was carried out in the same way as described above. For the reaction with CBS 0.5 g of tartaric acid was dissolved in 9.5 g of deionized water, while for the reaction with CS/borax blend 0.94 g of tartaric acid was dissolved in 27.54 g of deionized water. After complete dissolution, these tartaric acid solutions were added to 20 g of CBS and 26.64 g of CS/borax blend, respectively. These amounts of tartaric acid yielded B:H_2T molar ratio of 1:3. No pH adjustment of the final solutions was performed. Since tartaric acid is stable towards oxidation by air, there was no need to prepare solutions in a glove box.

2.4. NMR spectroscopy

NMR spectra were acquired on a Varian INOVA spectrometer operating at 59 MHz ^{29}Si or 96 MHz ^{11}B. A 10 mm broadband probe fitted with quartz decoupler and broadband inserts, and proprietary top and lower insulators was used. Wilmad 6010 tubes, made of PTFE-FEP, were used in these studies. The hole of a 5 mm spinner turbine was enlarged to accommodate the approximately 8 mm o.d. PTFE tube. In the ^{29}Si spectra, a 90° observe pulse and a 15 s relaxation delay were used. Chemical shifts are referenced to tetramethylsilane (0 ppm) in $CDCl_3$. All ^{11}B NMR spectra were acquired at 27 °C, with a 90° observe pulse and a 2.5 s relaxation delay. In one experiment H_3BO_3 (0.1 M) was used as an external chemical shift standard. All chemical shifts are reported relative to $(CH_3CH_2)_2O \cdot BF_3$.

3. Results and discussion

3.1. Characterization of CBS and CS/borax blends by ^{11}B NMR

The ^{11}B NMR spectra of CBS and CS/borax blend at pH 9.5 are shown in Fig. 1. In the spectrum of CBS the lar-

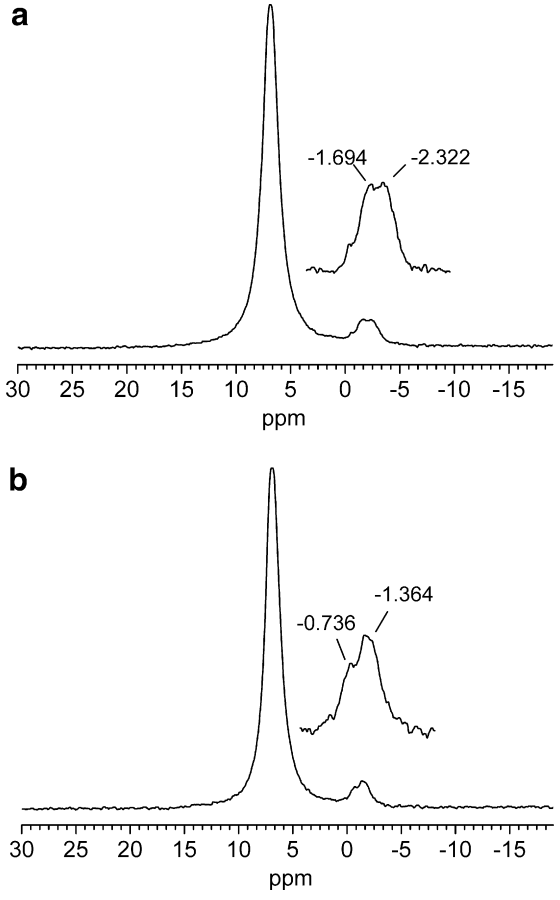


Fig. 1. ^{11}B NMR spectra of colloidal borosilicate (a) and colloidal silica blended with borax (b).

ger, more downfield resonance at 6.858 ppm results from free borate, and the smaller, more upfield group of peaks at −1 to −3 ppm arises from borosilicate species [7]. The ^{11}B NMR spectrum of a mixture of CS with borax solution is similar to the spectrum of CBS, with a large free borate peak at 6.820 ppm, and a group of smaller peaks near 0 to −2 ppm. In both cases boron is associated with the structure of colloidal particle via compounds that can be described by a general formula $B(OSi)_n(OH)_m$, where $n + m = 3$, $n \neq 0$. Overlapping peaks in the 0 to −2 ppm region are probably due to the presence of these compounds in different ratios. Although the spectra look similar, they are not identical: the smaller group of peaks in CBS resonates slightly more upfield than the group of similar peaks in the mixture of CS and borax, indicating differences in the structure of CBS and CS/borax blends. Indeed, in agreement with [2], a more upfield position of peaks in CBS suggests that boron probably forms mostly B–(O–Si)$_3$ bonds, consistent with incorporation into the colloidal particle. In the case of boron-modified colloidal silica, surface silanol groups would interact with soluble boron to form mostly $(OH)_2$–B–O–Si bonds. This is consistent with the observed relative downfield position in the spectrum of CS/borax blend.

3.2. Chelation of borates in CBS and CS/borax blends with catechol

The ^{11}B NMR spectra of CBS and CS/borax mixtures with catechol, acquired immediately after preparation, are shown in Fig. 2. The same figure also shows the ^{11}B spectrum of a mixture of catechol with borax solution. The addition of catechol to CBS, CS/borax blend and borax solution has resulted in the formation of 1:1 and 1:2 catechol:borate complexes at 7.5 and 13.0 ppm, respectively [13–15] via complexation of the free borate (Fig. 1, 6.858 ppm peak). In CBS/catechol mixture, in the region from 0 to −5 ppm, only the upfield component of the group of peaks seen in Fig. 1 is visible at −2.522, while the downfield component, at −1.694 ppm, is not visible. The stability of the upfield component toward catechol complexation must be a consequence of stable, covalent B–O–Si bonding present in the particle interior. In contrast, the facile complexation of the downfield component indicates that the boron–silica interaction is weaker, and is probably an interaction on the surface of the colloidal silica particle. The peaks characteristic of borosilicate remained present in the spectrum recorded on the second day after mixing CBS with the catechol. The peaks became significantly smaller after 6 days of aging.

In the spectrum of mixtures of the CS/borax blend and catechol, no peaks are present in the region between 0 and −5 ppm, indicating the absence of any borosilicate. The peaks that were visible in this region prior to complexation (Fig. 1) are no longer detectable, because the surface borosilicate of the colloidal silica particle is easily complexed by catechol and thereby removed.

Since catechol is known to be aggressive towards colloidal silica, the CS/borax blend was also examined by ^{29}Si NMR prior to and after catechol addition (Fig. 3). Both spectra are typical of colloidal silica [16,17]. Although the chemical shift of a sharp peak at ∼−144 ppm agrees with that of a complex between catechol and silicon [18], the relative amounts of Q^0, Q^1, Q^2, Q^3, and Q^4 appear to be approximately the same in both spectra. This indicates that under current experimental conditions dissolution of substrate in catechol is insignificant and probably limited to the surface of silica particle. The fact that in the ^{11}B NMR spectrum of CBS the borosilicate peak remains present after treatment with catechol, suggests that B–O–Si chemical bonds are within the colloidal particle and not just at the particle surface, as it is in the case with CS/borax blend.

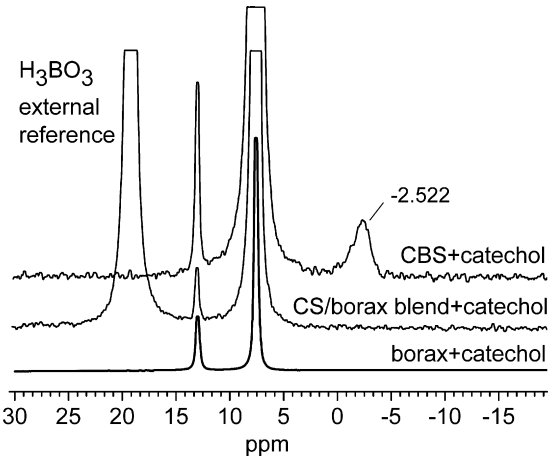


Fig. 2. ^{11}B NMR spectra of borosilicate and colloidal silicaborax blend treated with 3:1 molar excess of catechol.

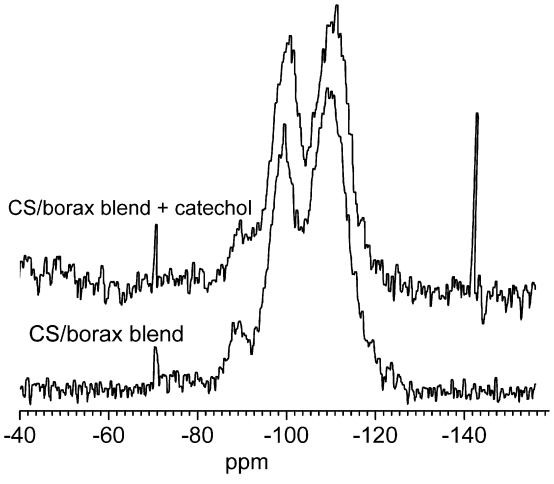


Fig. 3. ^{29}Si NMR spectra of a blend of colloidal silica with borax in the presence and absence of catechol.

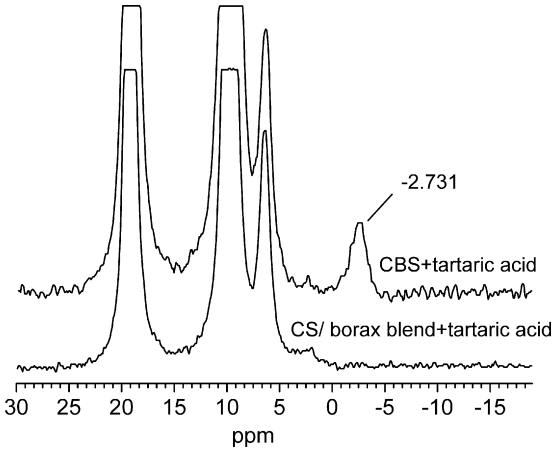


Fig. 4. ^{11}B NMR spectra of borosilicate and colloidal silicaborax blend treated with 3:1 molar excess of tartaric acid.

3.3. Chelation of borates in CBS and CS/borax blends with tartaric acid

Tartaric acid is also known to form complexes with soluble borates [19–21]. However, in contrast to catechol, it does not form complexes with silicon. As such, the risk of degrading colloidal silica and borosilicate particles is greatly diminished. The pH of the CBS and tartaric acid mixture was 3.05, and the pH of the blend and tartaric acid mixture was 3.40. The pH was not adjusted as it was expected that the amount of NaOH that would be required to adjust the pH from ~3 to 9.5 would have likely caused dissolution of a significant portion of the colloidal silica or borosilicate particles.

The spectra of CBS–H_2T mixture and CS/borax blend–H_2T mixture are shown in Fig. 4. The spectrum of H_2T treated CBS exhibits four distinct resonances, at 19.201, 8.710, 6.360, and −2.731 ppm. The resonance at 19.201 ppm represents free borate. The resonances at 8.710 and 6.360 ppm result from acid–borax complexes [21]. The most upfield resonance, at −2.731 ppm, arises from boron incorporated as colloidal borosilicate [7]. No changes were observed in the spectrum of this mixture recorded on the following day.

In the spectrum of tartaric acid added to the CS/borax blend, no signals characteristic of borosilicate are seen between 0 and −5 ppm. The boron species that had been present in this region (Fig. 1) were fully complexed by tartaric acid. These findings confirm the conclusion that boron species at −1.364 and −0.736 ppm in the spectrum of CS/borax blend arise from boron associated with the surface of the colloidal silica particle, which was accessible to tartaric acid contained in the continuous phase. The signals in the spectrum of mixtures of tartaric acid and the blend of CS/borax at 9.691 and 6.360 ppm result from tartaric acid–borate complexes, and the signal at 19.176 results from uncomplexed borate.

4. Conclusions

The results of conducted experiments prove that in CBS boron is incorporated throughout the colloidal particles as stable B–O–Si bonds. Although the chemical shifts of the boron in the CBS and CS/borax blend are similar, they are not equivalent, and represent chemically different boron species. Our complexation studies with catechol and tartaric acid illustrate the obvious difference between the boron species in colloidal borosilicate and colloidal silica/borax blends. The species in the blend were complexed by catechol and tartaric acid, indicating that these boron species are associated with the surface of the colloidal silica particle. In contrast, the observed borosilicate was stable toward the action of catechol and tartaric acid.

References

[1] M.R. Klotz, S.R. Ely, Method of preparing a metal cation-deficient crystalline borosilicate, US Patent No. 4, 285, 919, 1981.
[2] A.D. Irwin, J.S. Holmgren, T.W. Zerda, J. Jonas, J. Non-Cryst. Solids 89 (1987) 191.
[3] A.D. Irwin, J.S. Holmgren, J. Jonas, J. Non-Cryst. Solids 101 (1988) 249.
[4] H. Emme, M. Valldor, R. Pottgen, H. Huppertz, Chem. Mater. 17 (2005) 2707.
[5] R.K. Iler, The Chemistry of Silica, Wiley, New York, 1979.
[6] B.A. Keiser, J.E. Whitten, Colloids comprising amorphous borosilicate, US Patent No. 6, 372, 805, 2002.
[7] J. Fu, A. Gerli, B.A. Keiser, A. Zelenev, Stud. Surf. Sci. Catal. 132 (2001) 247.
[8] B.A. Keiser, J.E. Whitten, Method of increasing retention in papermaking using colloidal borosilicates, US Patent No. 6,361,653, 2002.
[9] R.F. Mortlock, A.T. Bell, C.J. Radke, J. Phys. Chem. 95 (1991) 37.
[10] J. Ma,Y. Peng, Z. Li, Preparation process for boron-modified particle silica sol, China Patent 1613759, 2005.
[11] J. Ma, Y. Peng, Z. Li, Zhonghua Zhiye 26 (6) (2005) 49.
[12] J. Ma, Y. Peng, Z. Li, Trans. China Pulp Paper 20 (2) (2005) 139.
[13] Y. Kazuo, M. Kotaka, M. Okamoto, H. Kakihana, Bul. Chem. Soc. Japan 52 (10) (1979) 3005.
[14] M. Pasdeloup, C. Brisson, Org. Magn. Res. 16 (2) (1981) 164.
[15] R.D. Pizer, P.J. Ricatto, C.A. Tihal, Polyhedron 12 (17) (1993) 2137.
[16] A.P. Legrand, H. Hommel, J.B. d'Espinosede la Caillerie, Colloids Surf A. 158 (1999) 157.
[17] C.T. Knight, J. Chem. Soc., Dalton Trans. (1988) 1457–1460.
[18] C. Shao, X. Li, S. Qiu, F.-S. Xiao, Micropor. Mesopour. Mater. 33 (1999) 215.
[19] K. Kustin, R. Pizer, J. Am. Chem. Soc. 91 (2) (1969) 317.
[20] L. Lamande', D. Boyer, A. Munoz, J. Organomet. Chem. 329 (1987) 1.
[21] M. Van Duin, J.A. Peters, A.P.G. Kieboom, H. van Bekkum, Tetrahedron 41 (16) (1985) 3411.

Among the nucleobases, adenine and its derivatives shows the widest range of binding possibilities because it can exhibit five donor sites, namely N9 [13], N7 [14], N3 [15], N1 [16–23] and N6 [24] or combinations of them [25–52] and a great variety of complexes with different metal ion binding patterns have been reported with both adenine and 9-substituted adenine.

Following our current research of crystallographic studies on metal–nucleobase systems, we studied reactivity of adenine towards Mg(II) and Mn(II) metal ions through the analysis of their complexes. In terms of ionic radius, coordination geometry, and ligand preferences, Mn^{2+} is considered a good mimic of Mg^{2+} in solution [53], although it is known its rather enhanced preference for soft donor sites such as N and S [54]. However, crystallographic report on coordinative Mn–N linkages, involving isolated nucleobases and their derivatives are scarce [55], being Mn(II) ion usually coordinated to water molecules, exocyclic oxygen atoms of purine or pirimidine rings or phosphate groups [55c–61].

We report herein the synthesis of new adenine containing compounds, $[Mg(H_2O)_6X_2 \cdot 2ade]$ (with $X = Cl^-$ (**1**), Br^- (**2**), ClO_4^- (**3**)), $[Mn(H_2O)_4 \cdot (ade)_2 \cdot (ClO_4)_2]$ (**4**), and $[Mn_2(H_2O)_6 \cdot (ade)_2 \cdot (NO_3)_4 \cdot 2H_2O]$ (**5**), (where ade = adenine) and their characterization by X-ray crystallography. Compounds **1**, **2** and **3** consist of hexaaquo metal ions, ade molecules and chloride (**1**), bromide (**2**) or perchlorate (**3**) ions self-assembled through an extended network of hydrogen bonding interactions. Compound **4** is made up of $[Mn(H_2O)_4 \cdot (ade)_2]^{2+}$ units, with the ade molecules directly coordinated to the metal centres through the N(3) atoms, while compound **5** contains $[Mn_2(H_2O)_6 \cdot (ade)_2]^{2+}$ dimers, with the ade ligands coordinated to the metal centres *via* N(3) and N(9) in a bidentate fashion. Compounds **1**, **2** and **3** represent additional examples of supramolecular assemblies containing Mg(II) hexaaquo ions [62a,63]. Compounds **4** and **5** represent the first example of direct binding between the Mn(II) ion and the adenine molecule. Furthermore, only few complexes containing Mn(II) metal ion directly linked to the N donor site of isolated nucleobases are known [55]. Our results reasonably suggest the greater reactivity of Mn(II) ion toward ade and an increased preference for soft donor sites such as N, when compared with Mg(II) ion, in which case the supramolecular assembly does not evolve towards the species containing direct metal-base links. Another interesting feature in compounds **1**, **2** and **4** is the protonation state of ade, which exists in the less common N9-deprotonated/N7-protonated tautomeric form [64].

2. Experimental

2.1. Materials

All the solvents and reagents for synthesis were commercially available and used as received. Elemental analyses (C, H, N) were performed by the Microanalytical Service of the Università della Calabria.

2.2. Synthesis of the complexes

Single crystals of **1**–**5** (colourless parallelepipeds) have been obtained by slow evaporation at room temperature and in the darkness of equimolar aqueous solutions of MgX_2 ($X = Cl^-$ (**1**), Br^- (**2**), ClO_4^- (**3**)) or MnX_2 ($X = ClO_4^-$ (**4**), NO_3^- (**5**)) and ade. In a typical experiment, the aqueous solution of ade was added dropwise to the aqueous solution containing the Mg(II) or Mn(II) salt with continuous stirring. Yields: 70% (**1**), 75% (**2**) and 70% (**3**), 65% (**4**) and 60% (**5**). Analytical data: *Anal.* Calc. for $C_{10}H_{22}N_{10}O_6Cl_2Mg_1$ (**1**): C, 25.36; H, 4.68; N, 29,58. Found: C, 25.45; H, 4.88; N, 29.21%. *Anal.* Calc. for $C_{10}H_{22}N_{10}O_6Br_2Mg_1$ (**2**): C, 21.35; H, 3.94; N, 24.90. Found: C, 21.56; H, 3.47; N, 24.69%. *Anal.* Calc. for $C_{10}H_{22}N_{10}O_{14}Cl_2Mg_1$ (**3**): C, 19.97; H, 3.69; N, 23.28. Found: C, 19.45; H, 3.36; N, 23.77%. *Anal.* Calc. for $C_{10}H_{18}N_{10}O_{12}Cl_2Mn_1$ (**4**): C, 20.15; H, 3.04; N, 23.50. Found: C, 20.45; H, 3.36; N, 23.79%. *Anal.* Calc. for $C_{10}H_{26}N_{14}O_{20}Mn_2$ (**5**): C, 15.55; H, 3.39; N, 25.39. Found: C, 15.41; H, 3.32; N, 25.77%.

2.3. Crystallographic data collection and structure determinations

X-ray diffraction data were collected using a Bruker R3m/V automatic four-circle for compound **1**–**3** and a Bruker-Nonius X8APEXII CCD area detector diffractometer for the other complexes. Graphite-monochromated Mo Kα radiation ($\lambda = 0.71073$ Å) was used in both cases. Lorentz-polarization and empirical absorption corrections through the ψ-scan program [65] was applied for **1**–**3**. The data for compounds **4**–**5** were processed through the SAINT [66] reduction and SADABS [67] absorption software. The structures were solved by direct methods and subsequently completed by Fourier recycling using the SHELXTL software package [68]. Non-hydrogen atoms were refined anisotropically. The hydrogen atoms of the water molecules were located on a ΔF map and refined with three restraints for each molecule (O–H and H–H distances) with thermal factors fixed to 0.06 Å^2. The H7 hydrogen atoms of adenine molecules in compounds **1**, **2** and **4** were located on a ΔF map and refined with thermal factors fixed to 0.06 Å^2, whereas all the others hydrogen atoms of the adenine ligand in all compounds were set in calculated positions and refined as riding atoms. Full-matrix least-squares refinements on F^2, carried out by minimizing the function $\sum w(|F_o| - |F_c|)^2$, reached convergence with values of the discrepancy indices given in Table 1. The graphical manipulations were performed using the XP utility of the SHELXTL system and Crystal Maker Software [69]. Crystallographic data are listed in Table 1 while selected bond lengths and angles around the metal atoms are given in Tables 2 (**1**–**3**), 3 (**4**) and 4 (**5**).

Table 1
Crystal data and structure refinement for compounds **1**–**5**

Compound	**1**	**2**	**3**	**4**	**5**
Empirical formula	$C_5H_{11}N_5O_3ClMg_{0.5}$	$C_5H_{11}N_5O_3BrMg_{0.5}$	$C_5H_{11}N_5O_7ClMg_{0.5}$	$C_5H_9N_5O_6ClMn_{0.5}$	$C_5H_{13}N_7O_{10}Mn$
Crystal system	triclinic	triclinic	triclinic	triclinic	monoclinic
Space group	$P\bar{1}$	$P\bar{1}$	$P\bar{1}$	$P\bar{1}$	$P2(1)/c$
Z	2	2	2	2	4
T (K)	293	293	293	293	293
Formula weight	236.79	281.25	300.79	298.09	386.16
a (Å)	8.236(2)	8.317(1)	6.811(2)	7.6718(3)	10.4411(4)
b (Å)	8.289(2)	8.524(2)	8.482(2)	8.4545(3)	19.2855(8)
c (Å)	9.104(2)	9.030(1)	11.192(3)	9.1032(3)	7.4539(3)
α	70.68(3)	71.91(1)	91.77(2)	73.355(2)	90
β	71.26(3)	71.26(1)	107.13(2)	75.613(2)	103.415(1)
γ	61.57(3)	61.77(1)	104.21(2)	76.574(2)	90
V (Å^3)	505.65	524.48	595.26	539.65	1459.98
D_{calc} (g cm^{-3})	1.555	1.781	1.678	1.834	1.757
μ (mm^{-1})	0.40	3.94	0.39	0.94	0.97
[a]R_1 [$I > 2\sigma(I)$]	0.0348	0.0332	0.0686	0.0345	0.0347
[b,c]wR_2	0.0978	0.0847	0.2015	0.1087	0.1346

[a] $R_1 = \sum||F_o| - |F_c||/\sum|F_o|$.
[b] $wR_2 = \{\sum[w(F_o^2 - F_c^2)^2]/[(w(F_o^2)^2]\}^{1/2}$.
[c] $w = 1/[\sigma^2(F_o^2) + (aP)^2 + bP]$ with $P = [F_o^2 + 2F_c^2]/3$, $a = 0.0675$ (**1**–**2**), 0.1394 (**3**), 0.1000 (**4**–**5**), and $b = 0$ (**1**–**5**).

Table 2
Selected bond distances (Å) and angles (°) for compounds **1**–**3**[a,b]

Compound	**1**	**2**	**3**
Mg(1)–O(1)	2.016(1)	2.010(2)	2.039(3)
Mg(1)–O(2)	2.078(1)	2.089(2)	2.070(3)
Mg(1)–O(3)	2.087(1)	2.080(2)	2.092(3)
O(1)–Mg(1)–O(2)	89.35(7)	89.69(9)	86.8 (1)
O(1)–Mg(1)–O(2a)	90.65(7)	90.31(9)	93.2(1)
O(1)–Mg(1)–O(3)	89.75(6)	90.39(9)	89.0(1)
O(1)–Mg(1)–O(3a)	90.25(6)	89.61(9)	90.9(1)
O(2)–Mg(1)–O(3)	87.26(6)	87.06(9)	89.1(1)
O(2)–Mg(1)–O(3a)	92.74(6)	92.94(9)	90.9(1)

[a] Estimated standard deviations in the last significant digits are given in parentheses.
[b] Symmetry code: (a) $-x+1$, $-y$, $-z+1$ for **1** and **2**, (b) $-x$, $-y$, $-z+1$ for **3**.

Table 3
Selected bond distances (Å) and angles (°) for compound **4**[a,b]

Mn(1)–O(2)	2.165(1)
Mn(1)–O(1)	2.209(1)
Mn(1)–N(3)	2.294(1)
O(1)–Mn(1)–N(3)	89.74(4)
O(1)–Mn(1)–N(3a)	90.26(4)
O(1)–Mn(1)–O(2)	87.81(5)
O(1) –Mn(1)–O(2a)	92.19(5)
O(2)–Mn(1)–N(3)	89.90(4)
O(2)–Mn(1)–N(3a)	90.10(4)

[a] Estimated standard deviations in the last significant digits are given in parentheses.
[b] Symmetry code: (a) $-x+1$, $-y$, $-z+1$.

Table 4
Selected bond distances (Å) and angles (°) for compound **5**[a,b]

Mn(1)–O(1)	2.1123(12)
Mn(1)–O(2)	2.1170(12)
Mn(1)–N(9a)	2.2379(10)
O(1)–Mn(1)–O(2)	94.72(6)
O(1)–Mn(1)–N(9a)	90.17(5)
O(2)–Mn(1)–N(9a)	99.23(5)
O(1)–Mn(1)–N(3)	104.63(5)
O(2)–Mn(1)–N(3)	97.31(5)
N(9a)–Mn(1)–N(3)	156.77(4)
O(1)–Mn(1)–O(3a)	88.52(5)
O(2)–Mn(1)–O(3a)	176.57(5)
Mn(1)–N(3)	2.2492(11)
Mn(1)–O(3a)	2.2955(11)
Mn(1)–O(3)	2.2968(10)
N(9a)–Mn(1)–O(3a)	79.63(4)
N(3)–Mn(1)–O(3a)	82.90(4)
O(1)–Mn(1)–O(3)	169.41(5)
O(2)–Mn(1)–O(3)	90.36(5)
N(9a)–Mn(1)–O(3)	79.83(4)
N(3)–Mn(1)–O(3)	83.88(4)
O(3a)–Mn(1)–O(3)	86.26(4)

[a] Estimated standard deviations in the last significant digits are given in parentheses.
[b] Symmetry code: (a) $-x+1$, $-y+1$, $-z+1$.

3. Results and discussion

Compounds **1**, **2** and **3** consist of hexaaquo Mg(II) ions, ade molecules and chloride (**1**), bromide (**2**) or perchlorate (**3**) ions. The asymmetric unit of compounds **1**–**3** contains a chloride (**1**), bromide (**2**) or a perchlorate ion (**3**), an ade ligand and an Mg(II) ion, lying on a crystallographic inversion centre with a 0.5 occupancy factor, coordinated to three water molecules. Each Mg(II) metal ion is in a distorted octahedral environment, being bonded to six water molecules. The Mg(II)–O bond distances [mean values 2.060(1) Å (**1**), 2.060(2) Å (**2**) and 2.067(3) Å (**3**)] are in agreement with the values reported for other similar Mg(II) hexaaquo complexes [62,63]. Supramolecular architectures in the isostructural compounds **1**–**2**, and in **3** are different depending on the nature of counterions. In **1** and **2** each

$[Mg(H_2O)_6]^{2+}$ ion is linked through four H-bonds to two molecules of ade, involving two *cis*-coordinated water molecules [O(1) and O(2)] and the N(9) and N(3) atoms of the nucleobase [O(1)···N(3) 2.701(2) Å (**1**) and 2.707(3) Å (**2**); O(2)···N(9) 2.878(2) Å (**1**) and 2.889(3) Å (**2**)], leading to non-covalent stabilization of the 7H-adenine tautomer (Fig. 1a). The existence in the lattice of adenine nucleobase in its 7H-tautomer form has been unambiguously determined by the location of the H7 proton on the ΔF map and confirmed by the careful analysis of the hydrogen bonding pattern, and the observation of the internal angle at N7 (C(8)–N(7)–C(5) 106.1(1) in **1** and 106.6(2) in **2**) which is significantly larger than that involving the deprotonated N9 position (C(8)–N(9)–C(4) 103.6(1) in **1** and 103.4(2) in **2**). It is known that the protonation at N sites in the adenine does not modify substantially the bond distances but it enlarges the endocyclic C–N–C angle up to ca. 4° [70]. For comparison, these angles are 103.5 and 105.6° in the compound (9H-adenine) · $2H_2O$ [71]. The titled compounds represent the second examples of characterization at the solid-state of this minor tautomer as free molecule (without metal coordination) stabilized through non-covalent interactions. The first example of non-covalent stabilization of H7-adenine tautomer has been recently reported for the compound of formula [Mn(μ-ox)(H_2O)]-(7H-ade) [13q], (ox = oxalate). Even in this case, the N3 and N9 atoms of adenine establish strong O_w–H_w···N hydrogen bonds with coordinated water molecules.

The supramolecular architecture in **1**–**2** is built up by means of H-bonding and stacking interactions. Chloride (**1**) or bromide (**2**) anions are held with the cationic moiety $[Mg(H_2O)_6(ade)_2]^{2+}$ by means of H-bonds involving the oxygen atoms of the coordinated water molecules [O(3)···Cl(1) 3.142(2) Å (**1**) and O(3)···Br(1) 3.291(2) Å (**2**)], [O(3)···Cl(1b) 3.203(2) Å (**1**) and O(3)···Br(1b) 3.313(2) Å (**2**); (b) = $-x+1$, $-y+1$, $-z+1$], [Cl(1)···O(1e) 3.206(2) Å (**1**) and Br1)···O(1e)3.334(2) Å (**2**); (e) = $x-1$, $y+1$, z], generating layers developing in

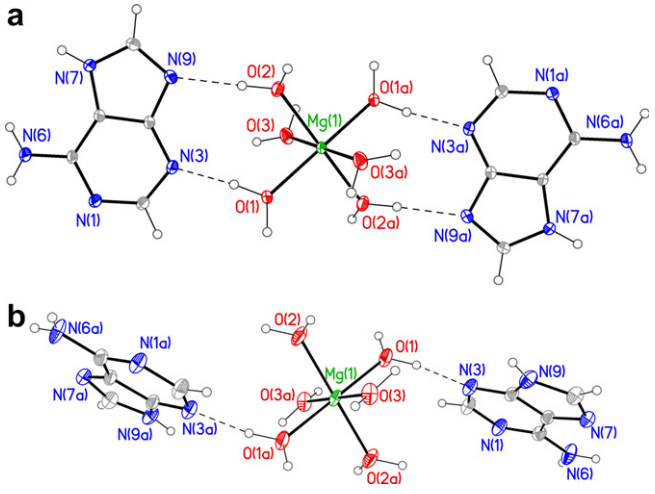


Fig. 1. Ortep drawing and atomic labeling scheme of compounds **1** (a) and **3** (b). Thermal ellipsoids are drawn at the 30% probability level.

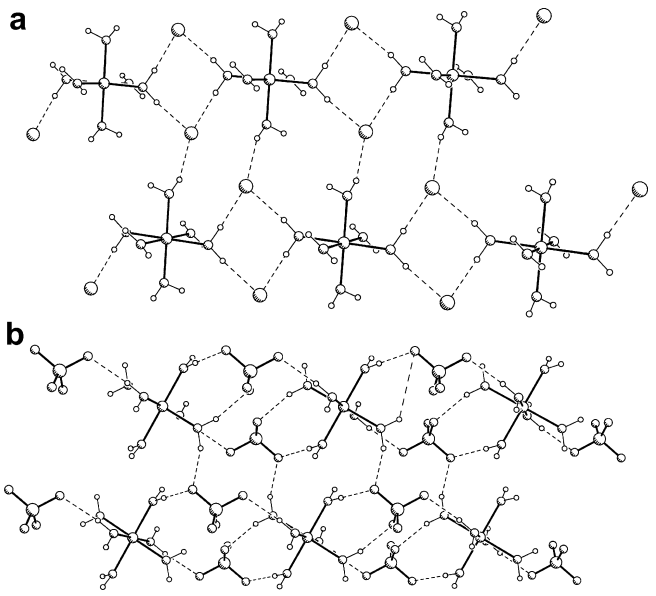


Fig. 2. View along *z*-axis of the inorganic layers of compounds **1**–**2** (a) and **3** (b) showing the H-bonding network.

the *xy* plane (Fig. 2). Layers of ade molecules, which are sandwiched between the planes defined by the $[Mg(H_2O)_6]^{2+}$ cations and the Cl^- or Br^- anions, alternate with the inorganic ones (Fig. 3a). The distances between consecutive Mg(II) ions along *x* and *y* directions correspond to the *a* and *b* crystallographic axes, respectively. The ade molecules within each organic layer are held to the inorganic planes also by means of H-bond interactions between O(2) and the N(1) atoms developing along the *x* direction [O(2)···N(1c) 2.808(2) Å (**1**) and 2.849(3) Å (**2**); (c) = $x-1$, y, z] (Fig. 4). The 3D arrangement is realized by π stacking interactions between purine rings, the interplanar distances being 3.35 (**1**) and 3.36 (**2**) Å (Fig. 5a).

In compound **3** each $[Mg(H_2O)_6]^{2+}$ ion is linked through two hydrogen bonds to two molecules of ade, involving two *trans*-coordinated water molecules [O(1) and O(1a); (a) = $-x$, $-y$, $1-z$] and the N(3) atoms of the nucleobase [O(1)···N(3) 2.712(5) Å] (Fig. 1b). Unlike **1** and **2**, in **3** the N(9) atom is protonated according to the more stable 9H-tautomer of ade, being the non-covalent stabilization of the 7H-tautomer not active in this case. In fact, the N9 atom is not involved in H-bonding interactions with the O(2) coordinated water molecules, as in **1** and **2**, being the suitable H_w on the O(2) atom already engaged in an H-bonding interaction with a ClO_4^- ion. The supramolecular architecture is built up by means of H-bonding and stacking interactions. Perchlorate anions are held with the cationic moiety $[Mg(H_2O)_6(ade)_2]^{2+}$ by means of H-bonds involving the oxygen atoms of the coordinated water molecules [O(2)···O(4) 3.039(6) Å, O(1)···O(6b) 3.105(6) Å, O(3)···O(6c) 2.890(6) Å, O(3)···O(7d) 2.990(6) Å; (b) = x, $y-1$, z; (c) = $-x+1$, $-y+1$, $-z+1$; (d) = $-x$, $-y+1$, $-z+1$], generating layers developing in the *xy* plane (Fig. 2b). The distances between consecutive Mg(II) ions along *x* and *y* directions correspond to the *a* and *b*

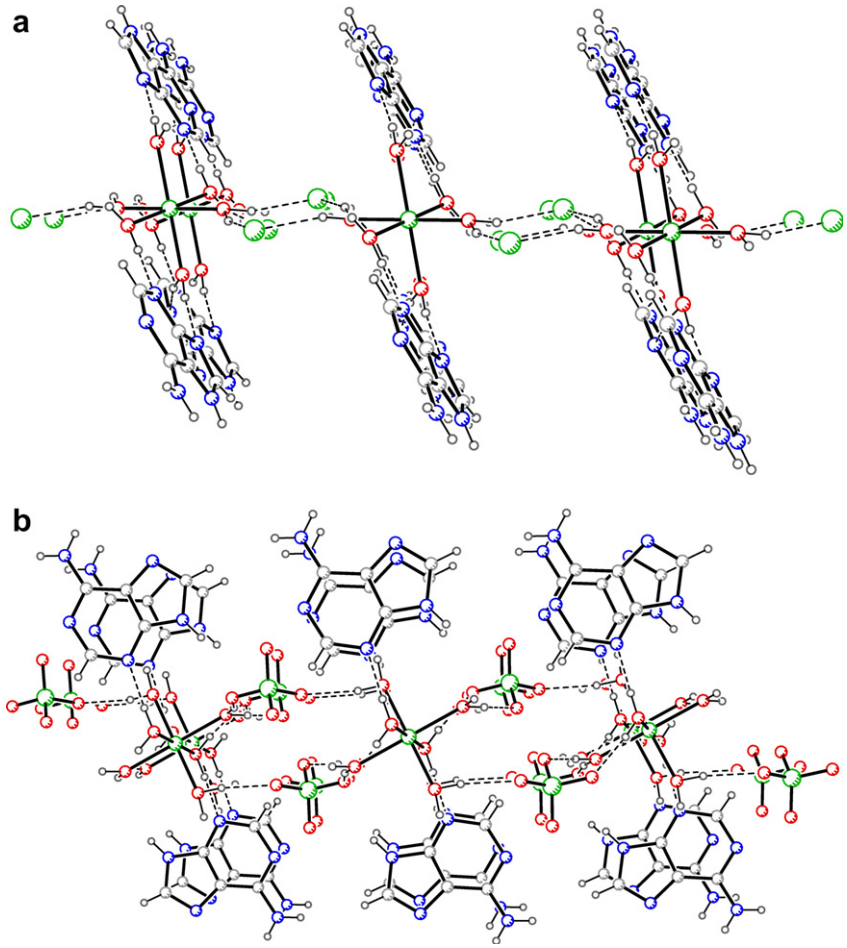


Fig. 3. View of the alternated inorganic and organic layers in *xy* plane in **1**, **2** (a) and **3** (b). Ade rings lie in the *xz* planes in **1**–**2** and in the *yz* plane in **3**.

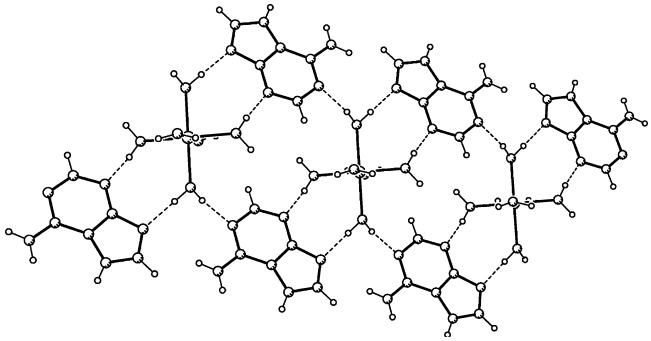


Fig. 4. Perspective view along *y*-axis of the H-bonding interactions between O(2) and the N(1) atoms in **1**–**2**.

crystallographic axes, respectively. Layers of ade molecules, which are sandwiched between the planes defined by the $[Mg(H_2O)_6]^{2+}$ cations and the ClO_4^- anions alternate to the inorganic ones (Fig. 3b). Unlike compounds **1**–**2**, where the ade molecules lie in the *xz* planes, in **3** the purine rings are positioned in the *yz* plane. Ade molecules H-bonded to consecutive inorganic layer are linked each other by means of interactions between the Watson–Crick edges, N1 and N6H [N(6)···N(1e) 2.956(6) Å; (e) = $-x+1, -y-1, -z+2$] (Fig. 6) and to the adjacent inorganic layers by means of the H-bond interactions between O(2) and N(7) [O(2)···N(7f) 2.751(5) Å; (f) = $x-1$, y, $z-1$]. These interactions together with the π-stacking between purine rings [interplanar distances being 3.28 Å] produce a 3D arrangement (Fig. 5b).

We can reasonably presume that the structural differences encountered in compound **1**–**2** and **3** rely on the nature and shape of the counterions.

The non-covalent stabilization of the 7H-adenine tautomer in **1**–**2** is the more evident difference compared with the perchlorate containing compound. From an accurate analysis of the crystal structures of compounds **1**–**2** and **3** it is possible to point out the differences that can leads to the stabilization of the two different 3D supramolecular networks and, consequently, of the 7H- (**1**, **2**) or 9H- (**3**) tautomers. In **1** and **2** each $Mg(H_2O)_6^{2+}$ ion is surrounded by six anions and four ade molecules (Fig. S1a). Four chloride (bromide) ions are H-bonded to O(3) and O(3a) water molecules, while the other two are H-bonded to O(1) and O(1a). Two ade molecules are H-bonded *via* N(3) with O(1) and O(1a), while the O(2) and O(2a) water molecules, not interacting with the anions, are H-bonded to the unprotonated N9 binding site, this non-covalent interaction leading to the stabilization of the H7-tautomer. Two

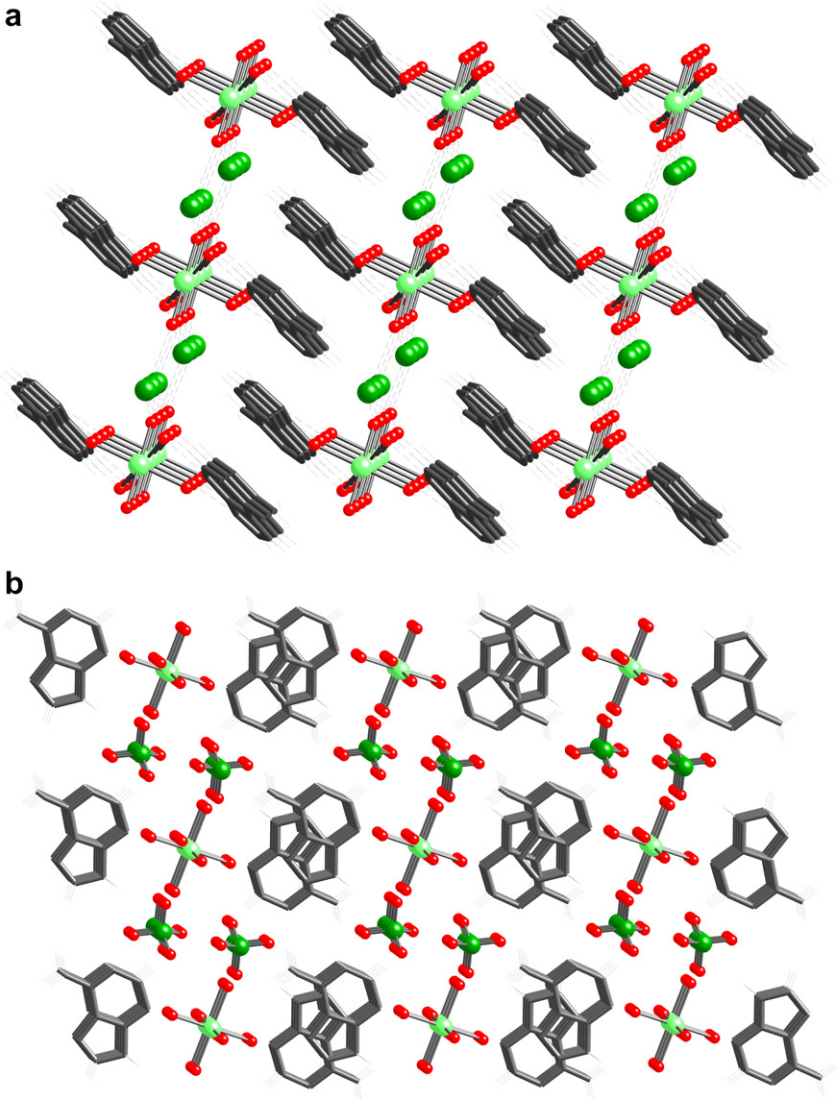


Fig. 5. View of the crystal packing of (a) **1**–**2**, and (b) **3**.

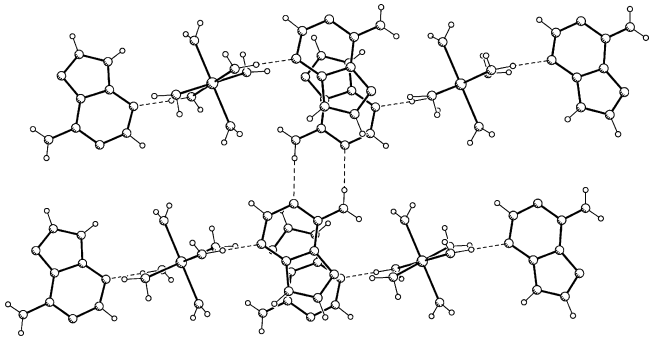


Fig. 6. View along *x*-axes of the Watson–Crick interactions between ade molecules H-bonded to consecutive inorganic layers in **3**.

other ade molecules are H-bonded *via* N1 to O(2). The second coordination sphere of the $Mg(H_2O)_6^{2+}$ ion in **3** is still formed by six anions and four ade molecules. Two of the four perchlorate ions interacting with O(3) and O(3a) water molecules are H-bonded to O(1) and O(1a) as well. Consequently, the remaining two perchlorate ions are H-bonded to O(2) and O(2a), creating sterical hindrance and making the suitable H_w no more available for H-bonding interaction with N(9), which is in this case protonated. Other two ade molecules interact with O(2) *via* N(7). This analysis let us suppose that the H-bonding interactions between the hexaaquo cations and the anions are the driving forces for the supramolecular assembling of the nucleobases, leading as consequential effect to the stabilization of one or the other tautomeric form.

Another observation can support this last hypothesis. A supramolecular architecture similar to that observed in compounds **1**–**2** has been recently described for the 1-Mecyt-containing compounds of formula $[Mg(H_2O)_6(1\text{-Mecyt})_2]Cl_2$, $[Ni(H_2O)_6(1\text{-Mecyt})_2]Cl_2$ [63]. In particular, compounds **1** and **2** present *quasi*-identical inorganic layers, comprising for only difference the lacking of an H-bond between chloride ions and O(2) water molecules if compared with the 1-Mecyt containing compounds. This

difference does not cause modification in the final arrangement of the inorganic net. The nucleobases 1-Mecyt and ade are H-bonded *via* N3/O2 and N3/N9, respectively, to the O(1) and O(2) water molecules in an identical manner. This results also support the hypothesis that H-bonding interactions in the inorganic networks drive the supramolecular assembling of the organic layers, producing very similar 3D architecture, which are independent from the nature of nucleobase.

Crystal structure of compound **4** is made up of $[Mn(H_2O)_4(ade)_2]^{2+}$ units and perchlorate ions. In the complex cation the manganese atom lies on a crystallographic inversion centre and is coordinated to four water molecules and to two *trans* unidentate adenine molecules directly linked *via* N3 (Fig. 7). Similar complexes have been reported in the case of Co(II) and Cu(II) metal ions, containing, respectively, ade and 9-substituted ade as ligand. In both case ade and 9Me-ade act as monodentate ligand, in the first case *via* N9 [13a], while in the second one the coordination occurs *via* N7, being N9 alkilated [14a]. The metal co-ordination in **4** is almost undistorted octahedral, with the ade ligand occupying the apical position of an elongated octahedron [Mn–N(3) = 2.295(1) Å]. The N9 atom of each ade ligand is involved in H-bonding interactions with the coordinated water molecules [O(2)···N(9a) 2.770(2) Å; (a) = $-x+1$, $-y$, $-z+1$], leading to stabilization of the 7H-adenine tautomer. Even in this case, the stabilization of the minor tautomer of ade is due to the existence of non-covalent interaction rather than the coordination to the metal centre. Other two examples exist in literature on complexes containing the tautomer 7H-adenine as ligand coordinated *via* N3 [15b,15f]. The perchlorate ion is anchored to the $[Mn(H_2O)_4(ade)_2]^{2+}$ cation by means of H-bonds involving O(5) and the coordinated water molecule O(1) [O(1)···O(5a) 3.054(2) Å]. The H-bonding interaction between the O(1) atom of a $[Mn(H_2O)_4(ade)_2]^{2+}$ unit and N(1) of another one [O(1)···N(1b) 2.775(2) Å; (b) = $-x$, $-y$, $-z+1$] defines a ribbon-like motif along *x*-axis (Fig. 8). The alternate of these ribbons with the perchlorate anions [O(2)···O(3c) 2.932(2) Å; (c) = $-x+1$, $-y$, $-z+2$] produce layers in the *xz* plane. The hydrogen bonds occurring between adjacent layers [N(6)···O(3d) 3.031(2), N(7)···O(5e) 3.036(2) Å; (d) = $x-1$, $y+1$, $z-1$, (e) = $-x+1$, $-y+1$, $-z+1$] give rise to the 3D supramolecular network.

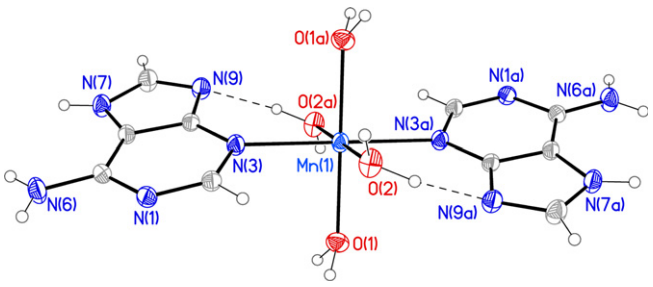


Fig. 7. Ortep drawing and atomic labeling scheme of compound **4**. Thermal ellipsoids are drawn at the 25% probability level.

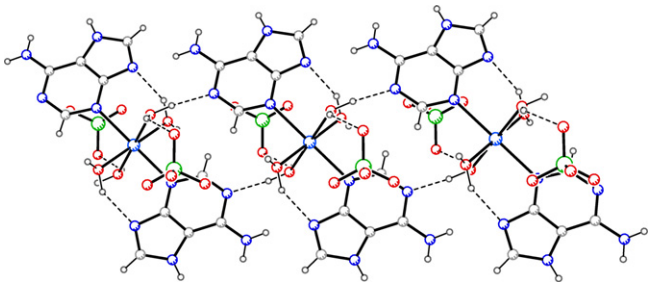


Fig. 8. View along *z*-axis of the ribbon motif in compound **4**.

The structure of **5** contains the centrosymmetric dimeric $[Mn_2(H_2O)_6(ade)_2]^{4+}$ cations, nitrate ions and crystallization water molecules. The two manganese of the dimeric units are bridged by two water molecules and two bidentate adenine ligands, coordinated *via* N3 and N9 (Fig. 9). This mode of base binding to metal ions is not unprecedented [25–29], even if never observed for Mn(II)-ade complexes. Each Mn(II) metal centre is in a distorted octahedral environment. The best equatorial plane is defined by the oxygen atoms O(1), O(2), O(3) and O(3a) of coordinated water molecules [(a) = $-x+1$, $-y+1$, $-z+1$], the maximum deviation being 0.082(1) Å at O(1), with the Mn(II) atom 0.097(1) Å out of this plane. The mean distorsion from octahedral geometry is due to the bidentate coordination of adenine, with the major deviation at the O(1)–Mn(1)–N(3) angle (104.63(5)°). The Mn···Mn distance within the dimeric unit is 3.3514(4) Å.

Anions and crystallization water molecules are held to the dimeric unit by means of hydrogen bonding interactions involving coordinated water molecules [O(2)···O(6) 2.743(2) Å; O(2)···O(10) 2.780(2) Å; O(3)···O(9) 2.657(2) Å; O(10)···O(9) 2.734(2) Å]. The dimeric units are held each other by means of H-bonds running along *z* axis involving the bridging water molecule O(3), the crystallization water molecule and the nitrate anions [O(1)···O(7a) 2.759(2) Å, O(3)···O(10b) 2.689(1) Å; (a) = $-x+1$, $-y+1$, $-z+1$, (b) = $-x+1$, $-y+1$, $-z+2$]. A

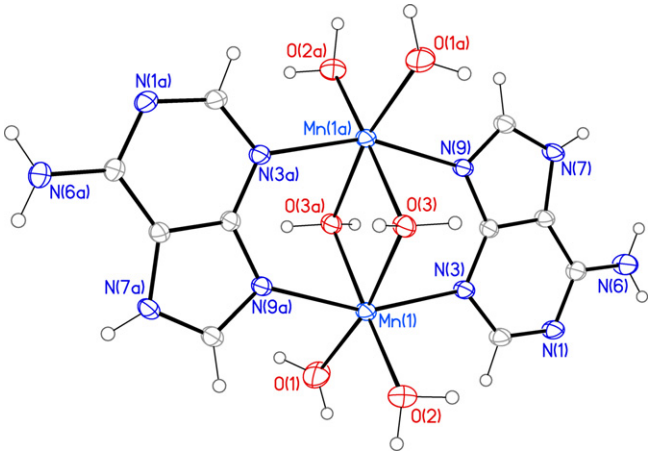


Fig. 9. Ortep drawing and atomic labeling scheme of compound **5**. Thermal ellipsoids are drawn at the 25% probability level.

bidimensional motif in the *xy* plane is obtained by the interaction of adenine ligands and nitrate ions [N(7)···O(6c) 2.792(2) Å, N(6)···O(4c) 2.906(2) Å, (c) = *x*-1,*y*,*z*-1]. The 3D supramolecular arrangement is achieved by further H-bonds [O(1)···O(4d) 2.764(2) Å, O(10)···N(1e) 2.808(2) Å, N(6)···O(8d) 3.077(2) Å; (d) = *x*, $-y+3/2$, $z-1/2$, (e) = *x*, $-y+3/2$, $z+1/2$].

4. Conclusions

Five new complexes with ade and M = Mg(II) or Mn(II) have been synthesized and structurally characterized. Their structural features are related to the different Mg(II) and Mn(II) reactivity with ade nucleobase. The greater reactivity of Mn(II) ion toward ade and an increased preference for soft donor sites such as N has been proved by obtaining two complexes (**4**, **5**), where the direct coordination of ade ligand *via* N3 (**4**) and N3/N9 (**5**) has been observed, in contrast to the Mg(II) ion, that in the same reaction condition, does not form complexes containing direct metal–nucleobase bonds. The detailed analysis of all the non-covalent interactions working in compounds **1**–**3** gives a comprehensive evidence of the influence of counterions on determining the H-bonds pattern involving the $[Mg(H_2O)_6]^{2+}$ cations and ade molecules. The strong H-bonding interactions between coordinated water molecules and the N9 binding site of ade in **1** and **2** lead to the non-covalent stabilization of the less common N9-deprotonated/N7-protonated tautomeric form of ade. A similar driving force is operative in compound **4**. On the contrary, these interactions are hindered by the presence of perchlorate ions in **3**, where the ade exist in the more stable N9-protonated form.

Acknowledgement

Thanks are due to the Italian MIUR, the Università della Calabria and Regione Calabria (POR Calabria 2000/2006, misura 3.16, progetto PROSICA) for financial support.

Appendix A. Supplementary materials

CCDC 638585, 638586, 638587, 638588 and 638589 contain the supplementary crystallographic data for this paper. These data can be obtained free of charge via http://www.ccdc.cam.ac.uk/conts/retrieving.html, or from the Cambridge Crystallographic Data Centre, 12 Union Road, Cambridge CB2 1EZ, UK; fax: (+44) 1223-336-033; or e-mail: deposit@ccdc.cam.ac.uk. X-ray crystallographic files of compounds **1**–**5** in CIF format; view of second coordination sphere of **1** and **2** (Fig. S1) and interdimeric H-bonding interaction in **5** (Fig. S2). This material is available free of charge via the Internet at http://pubs.acs.org. Supplementary data associated with this article can be found, in the online version, at doi:10.1016/j.poly.2007.06.037.

References

[1] S. Sivakova, S. Rowan, J. Chem. Soc. Rev. 34 (2005) 9.
[2] J.A.R. Navarro, B. Lippert, Coord. Chem. Rev. 222 (2001) 219.
[3] (a) W. Saenger, Principles of Nucleic Acid Structure, Springer-Verlag, New York, 1984, pp. 201–219;
(b) V.K. Misra, D.E. Draper, Biopolymers 48 (1998) 113;
(c) I. Tinoco Jr., C. Bustamante, J. Mol. Biol. 293 (1999) 271.
[4] (a) A.M. Pyle, in: A. Sigel, H. Sigel (Eds.), Metal Ions in Biological Systems: Interactions of MetalIons with Nucleotides, Nucleic Acids, and their Constituents, vol. 32, Marcel Dekker, New York, 1996, pp. 452–480;
(b) A.L. Feig, O.C. Uhlenbeck, in: R.F. Gesteland, T.R. Cech, J.F. Atkins (Eds.), The RNA World, second ed., Cold Spring Harbor Laboratory Press, Cold Spring Harbor, New York, 1999, pp. 287–319;
(c) E.A. Doherty, J.A. Doudna, Annu. Rev. Biochem. 69 (2000) 597.
[5] E.A. Meyer, R.K. Castellano, F. Diederich, Angew. Chem., Int. Ed. 42 (2003) 1211.
[6] A.C. Chen, A.D. Frankel, J. Am. Chem. Soc. 126 (2004) 434.
[7] S.J. Berners-Price, P.J. Sadler, Coord. Chem. Rev. 151 (1996) 1.
[8] B. Lippert, in: K.D. Karlin (Ed.), Progress in Inorganic Chemistry, vol. 54, John Wiley and Sons, New York, 2005, p. 385.
[9] B. Lippert, Coord. Chem. Rev. 200 (2000) 487.
[10] B. Lippert, J. Chem. Soc., Dalton Trans. (1997) 3971.
[11] E. Bugella-Altamirano, D. Choquesillo-Lazarte, J.M. González-Pérez, M.J. Sánchez-Moreno, R. Marín-Sánchez, J.D. Martín-Ramos, B. Covelo, R. Carballo, A. Castiñeiras, J. Niclós-Gutiérrez, Inorg. Chim. Acta 339 (2002) 160.
[12] A. Marzotto, D.A. Clemente, A.G. Ciccarese Valle, J. Crystallogr. Spectrosc. Res. 23 (1993) 119.
[13] (a) P. de Meester, A.C. Skapski, J. Chem. Soc., Dalton Trans. (1973) 424;
(b) P. de Meester, A.C. Skapski, J. Chem. Soc., Dalton Trans. (1973) 1596;
(c) T.J. Kistenmacher, Acta Crystallogr., Sect. B: Struct. Cryst. Chem. 30 (1974) 1610;
(d) D.B. Brown, J.W. Hall, H.M. Helis, E.G. Walton, D.J. Hodgson, W.E. Hatfield, Inorg. Chem. 16 (1977) 2675;
(e) W.M. Beck, J.C. Calabrese, N.D. Kottmair, Inorg. Chem. 18 (1979) 176;
(f) L. Prizant, M.J. Olivier, R. Rivest, A.L. Beauchamp, Can. J. Chem. 59 (1981) 1311;
(g) J.P. Charland, A.L. Beauchamp, Croat. Chem. Acta 57 (1984) 697;
(h) Y. Rosopulos, U. Nagel, W. Beck, Chem. Ber. 118 (1985) 931;
(i) E.R.T. Tiekink, T. Kurucsev, B.F. Hoskins, J. Crystallogr. Spectrosc. Res. 19 (1989) 823;
(j) A. Marzotto, A. Ciccarese, D.A. Clemente, G. Valle, J. Chem. Soc., Dalton Trans. (1995) 1461;
(k) D. Badura, H. Vawhrenkamp, Inorg. Chem. 41 (2002) 6013;
(l) U.E.I. Horvath, S. Cronje, J.M. McKenzie, L.J. Barbour, H.G.Z. Raubenheimer, Naturforforsch. B: Chem. Sci. 59 (2004) 1605;
(m) Md. A. Salam, K. Aoki, Inorg. Chim. Acta 314 (2001) 71;
(n) T. Suzuki, Y. Hirai, H. Monjushiro, S. Kaizaki, Inorg. Chem. 43 (2004) 6435;
(o) A.C. Morel, D. Choquesillo-Lazarte, C. Alarçon-Payer, J.M. Gonzáles-Pérez, A. Castiñeiras, J. Niclós-Gutiérrez, Inorg. Chem. Commun. 6 (2003) 1354;
(p) M. Odoko, N. Okabe, Acta Crystallogr., Sect. E: Struct. Rep. Online 61 (2005) m2670;
(q) J.P. Gárcia-Téran, O. Castillo, A. Luque, U. Gárcia-Courceiro, G. Beobide, P. Román, Dalton Trans. (2006) 902.
[14] (a) E. Sletten, M. Ruud, Acta Crysrallogr., Sect. B: Struct. Crystallogr. Cryst. Chem. 31 (1975) 982;
(b) M.R. Taylor, L.M. Vikins, M.J. McCall, Acta Crystallogr., Sect. C: Cryst. Struct. Commun. 45 (1989) 1625;

(c) A. Schreiber, M.S. Luth, A. Erxeleben, E.C. Fusch, B. Lippert, J. Am. Chem. Soc. 118 (1996) 4124;
(d) M.B. Janik, A. Hegmans, E. Freisinger, B. Lippert, J. Biol. Inorg. Chem. 4 (1999) 130;
(e) J. Arpalahti, K.D. Kilka, S. Molander, Eur. J. Inorg. Chem. (2000) 1007;
(f) M.A. Salam, K. Aoki, Inorg. Chim. Acta 311 (2000) 15;
(g) O. Sigel, S.M. Thompson, E. Freisinger, F. Glahe, B. Lippert, Chem. Eur. J. 7 (2001) 1968;
(h) M.S. Luth, E. Freisinger, B. Lippert, Chem. Eur. J. 7 (2001) 2104;
(i) E. Bugella-Altamirano, D. Choquesillo-Lazarte, J.M. González-Pérez, M.J. Sánchez-Moreno, R. Marín-Sánchez, J.D. Martín-Ramos, B. Covalo, R. Carballo, A. Castiñeiras, J. Niclós-Gutiérrez, Inorg. Chim. Acta 339 (2002) 160;
(j) A. Gaballa, H. Schmidt, G. Hempel, D. Reichert, C. Wagner, E. Rusanov, D. Steinbom, J. Inorg. Biochem. 98 (2004) 439;
(k) M. Roitzsch, B. Lippert, J. Am. Chem. Soc. 126 (2004) 2421;
(l) P. Amo-Ochoa, S.S. Alexandre, C. Pastor, F. Zamora, J. Inorg. Biochem. 99 (2005) 2226;
(m) A. Egger, V.B. Arion, E. Reisner, B. Cebrian-Losantos, S. Shova, G. Trettenhahn, B.K. Keppler, Inorg. Chem. 44 (2005) 122;
(n) C.G. Barry, C.S. Day, U. Bierbach, J. Am. Chem. Soc. 127 (2005) 1160;
(o) K. Aoki, Md. A. Salam, Inorg. Chim. Acta 339 (2002) 427;
(p) M. Mikola, K.D. Kilka, J. Arpalahti, Chem. Eur. J. 6 (2000) 3404;
(q) M.A. Shipman, C. Price, A.E. Gibson, M.R.J. Elsegood, W. Clegg, A. Houlton, Chem. Eur. J. 6 (2000) 4371;
(r) I.B. Rother, M. Willermann, B. Lippert, Supramol. Chem. 14 (2002) 189;
(s) E.Y. Bivian-Castro, M. Roitzsch, D. Gupta, B. Lippert, Inorg. Chim. Acta 358 (2005) 2395.

[15] (a) M.J. Sánchez-Moreno, D. Choquesillo-Lazarte, J.M. González-Pérez, R. Carballo, A. Castiñeiras, J. Niclós-Gutiérrez, Inorg. Chem. Commun. 5 (2002) 800;
(b) C.G. Barry, C.S. Day, U. Bierbach, J. Am. Chem. Soc. 127 (2005) 1160;
(c) C. Price, M.A. Shipman, N.H. Rees, M.R.J. Elsegood, A.J. Edwards, W. Clegg, A. Houlton, Chem Eur. J. 7 (2001) 1194;
(d) J.P. García-Terán, O. Castillo, A. Luque, U. García-Couceiro, P. Román, F. Lloret, Inorg. Chem. 43 (2004) 5761;
(e) C. Price, B.R. Horrocks, A. Mayeux, M.R.J. Elsegood, W. Clegg, A. Houlton, Angew. Chem., Int. Ed. 41 (2002) 1047;
(f) A. Marzotto, D.A. Clemente, A. Ciccarese, G. Valle, J. Crystallogr. Spectrosc. Res. 23 (1993) 119;
(g) J.E. Kickham, S.J. Loeb, S.L. Murphy, Chem. Eur. J. 3 (1997) 1203;
(h) D. Amantia, C. Price, M.A. Shipman, M.R.J. Elsegood, W. Clegg, A. Houlton, Inorg. Chem. 42 (2003) 3047;
(i) E. Bugella-Altamirano, D. Choquesillo-Lazarte, J.M. González-Pérez, M.J. Sánchez-Moreno, R. Marín-Sánchez, J.D. Martín-Ramos, B. Covalo, R. Carballo, A. Castiñeiras, J. Niclós-Gutiérrez, Inorg. Chim. Acta 339 (2002) 160;
(j) M.A. Shipman, C. Price, A.E. Gibson, M.R.J. Elsegood, W. Clegg, A. Houlton, Chem. Eur. J. 6 (2000) 4371;
(k) C. Price, M.R.J. Elsegood, W. Clegg, A. Houlton, Chem Commun. (1995) 2285.

[16] M.J. McCall, M.R. Taylor, Biochim. Biophys. Acta 390 (1975) 137.
[17] M.J. Olivier, A.L. Beauchamp, Inorg. Chem. 19 (1980) 1064.
[18] F. Schwartz, B. Lippert, H. Schollborn, U. Thewalt, Inorg. Chim. Acta 176 (1990) 113.
[19] O. Krizanovic, M. Sabat, R. Beyerle-Pfnur, B. Lippert, J. Am. Chem. Soc. 115 (1993) 5538.
[20] J. Arpalahti, K.D. Klika, R. Sillanpaa, R.J. Kivekas, Chem. Soc., Dalton Trans. (1998) 1397.
[21] J. Arpalahti, K.D. Klika, Eur. J. Inorg. Chem. (1999) 1199.
[22] M. Roitzsch, B. Lippert, Inorg. Chem. 43 (2004) 5483.
[23] M. Roitzsch, I.B. Rother, M. Willermann, A. Erxleben, B. Costisella, B. Lippert, Inorg. Chem. 41 (2002) 5946.
[24] J. Arpalahti, K.D. Kilka, Eur. J. Inorg. Chem. (2003) 4195.
[25] P. De Meester, A.C. Skapski, J. Chem. Soc., Dalton Trans. (1972) 2400.
[26] C. Gagnon, J. Hubert, R. Rivest, A.L. Beauchamp, Inorg. Chem. 16 (1977) 2469.
[27] A. Terzis, A.L. Beauchamp, R. Rivest, Inorg. Chem. 12 (1973) 1166.
[28] C.H. Wei, K.B. Jacobson, Inorg. Chem. 20 (1981) 356.
[29] J.W. Suggs, M.J. Dube, M. Nichols, Chem. Commun. (1993) 307.
[30] L. Prizant, M.J. Olivier, R. Rivest, A.L. Beauchamp, Acta Crystallogr., Sect. B: Struct. Cryst. Chem. B38 (1982) 88.
[31] W.S. Sheldrick, P. Gross, Inorg. Chim. Acta 156 (1989) 139.
[32] W.S. Sheldrick, H.S. Hagen-Eckhard, S. Heeb, Inorg. Chim. Acta 206 (1993) 15.
[33] P.X. Rojas-Gonzáles, A. Castiñeras, J.M. Gonzáles-Pérez, D. Choquesillo-Lazarte, J. Niclós-Gutiérrez, Inorg. Chem. 41 (2002) 6190.
[34] S. Kom, W.S.J. Sheildrick, Chem. Soc., Dalton Trans. (1997) 2191.
[35] J. Viljanen, K.D. Kilka, R. Sillanpaa, J. Arpalahti, Inorg. Chem. 38 (1999) 4924.
[36] N. Shan, S.J. Vickers, H. Adams, M.D. Ward, J.A. Thomas, Angew. Chem., Int. Ed. 43 (2004) 3938.
[37] E.F. Day, C.A. Crawford, K. Folting, K.R. Dunbar, G. Christou, J. Am. Chem. Soc. 116 (1994) 9339.
[38] S. Das, C. Madhavaiah, S. Verma, P.K. Bharadwaj, Inorg. Chim. Acta 358 (2005) 3236.
[39] S. Jaworski, S. Menzer, B. Lippert, M. Sabat, Inorg. Chim. Acta 205 (1993) 31.
[40] R.K.O. Sigel, S.M.M. Thompson, E. Freisinger, B. Lippert, Chem. Commun. (1999) 19.
[41] M.S. Luth, E. Freisinger, B. Lippert, Chem. Eur. J. 7 (2001) 2104.
[42] M. Roitzsh, I.B. Rother, M. Willermann, A. Erxleben, B. Costisella, B. Lippert, Inorg. Chem. 41 (2002) 5946.
[43] I.B. Rother, M. Willermann, B. Lippert, Supramolecular Chem. 14 (2002) 189.
[44] M. Roitzsh, B. Lippert, Chem. Commun. (2005) 5991.
[45] M.A. Shipman, C. Price, M.R.J. Elsegood, W. Clegg, A. Houlton, Angew. Chem., Int. Ed. 39 (2000) 2360.
[46] M.A. Shipman, C. Price, A.E. Gibson, M.R.J. Elsegood, W. Clegg, A. Houlton, Chem. Eur. J. 6 (2000) 4371.
[47] C.S. Purohit, S. Verma, J. Am. Chem. Soc. 128 (2006) 400.
[48] I.B. Rother, E. Freisinger, A. Erxleben, B. Lippert, Inorg. Chim. Acta 300 (2000) 339.
[49] M.S. Luth, E. Freisinger, F. Glahe, J. Muller, B. Lippert, Inorg. Chem. 37 (1998) 3195.
[50] J. Hubert, A.L. Beauchamp, Acta Crystallogr., Sect. B: Struct. Cryst. Chem. B36 (1980) 2613.
[51] J. Gárcia- Téran, O. Castillo, A. Luque, U. Gárcia-Couceiro, P. Róman, L. Letama, Inorg. Chem. 43 (2004) 4549.
[52] J.M. González-Pérez, C. Alarcón-Payer, A. Castiñeiras, T. Pivetta, L. Lezama, D. Choquesillo-Lazarte, G. Crisponi, J. Niclós-Gutiérrez, Inorg. Chem. 45 (2006) 877.
[53] C.G. Hoogstraten, C.V. Grant, T.E. Horton, V.J. De Rose, R.D. Britt, J. Am. Chem. Soc. 124 (2002) 834.
[54] (a) C.W. Bock, A.K. Katz, G.D. Markham, J.P. Glusker, J. Am. Chem. Soc. 121 (1999) 7360;
(b) G.H. Reed, R.R. Poyner, in: A. Sigel, H. Sigel (Eds.), Metal Ions in Biological Systems: Manganese and its Role in Biological Processes, vol. 37, Marcel Dekker, New York, 2000, pp. 183–207;
(c) C.G. Hoogstraten, C.V. Grant, T.E. Horton, V.J. DeRose, R.D. Britt, J. Am. Chem. Soc. 124 (2002) 384.

[55] (a) P. de Meester, D.M.L. Goodgame, T.J. Jones, A.C. Skapski, Biochem. J. 139 (1974) 791;
(b) M.V. Capparelli, D.M.L. Goodgame, P.B. Hayman, A.C. Skapski, Inorg. Chim. Acta 125 (1986) L47;
(c) J.P. García-Terán, O. Castillo, A. Luque, U. García-Couceiro, G. Beobide, P. Román, Dalton Trans. (2006) 902.

[56] D. Dobrzynska, L.B. Jerzykiewicz, J. Am. Chem. Soc. 126 (2004) 11118.

[57] M. Sabat, R. Cini, T. Haromy, M. Sundaralingam, Biochemistry 24 (1985) 7827.
[58] G. De Munno, M. Medaglia, D. Armentano, J. Anastassopoulou, T. Theophanides, J. Chem. Soc., Dalton Trans. (2000) 1625.
[59] K. Aoki, Chem. Commun. (1976) 748.
[60] B. Lippert, U. Schubert, Inorg. Chim. Acta 56 (1981) 15.
[61] P. Castan, C. Viala, P.L. Fabre, F. Nepveu, J.P. Souchard, G. Bernardinelli, Can. J. Chem. 76 (1998) 205.
[62] (a) M.A. Geday, G. De Munno, M. Medaglia, J. Anastassopoulou, T. Theophanides, Angew. Chem., Int. Ed. 36 (1997) 511;
(b) E. Freisinger, A. Schimanski, B. Lippert, J. Biol. Inorg. Chem. (JBIC) 6 (2001) 378;
(c) W.-L. Liu, Y. Zou, C.-L. Ni, Z.-P. Ni, Y.-Z. Li, Y.-G. Yao, Q.-J. Meng, Polyhedron 23 (2004) 849;
(d) J.A.R. Kennedy, B.A. Kirkhouse, K.M. Mc Carney, O. Puissegur, W.E. Smith, E. Staunton, S.J. Teat, J.C. Cherryman, R. James, Chem.-Eur. J. 10 (2004) 4606;
(e) F. Gao, B.-H. Meng, Y.-B. Wei, Acta Crystallogr., Sect. C: Cryst. Struct. Commun. 60 (2004) m360;
(f) Q. Yang, S. Gao, L.-H. Huo, Acta Crystallogr., Sect. E: Struct. Rep. Online 61 (2005) m277;
(g) D.D. Radanovic, U. Rychlewska, M.I. Djuran, N.S. Draskovic, M.M. Vasojevic, I.M. Hodzic, D.J. Radanovic, Polyhedron 22 (2003) 2745;
(h) Z.-H. Zhou, Y.-F. Deng, Y.-Q. Jiang, H.-L. Wan, S.W. Ng, Dalton Trans. (2003) 2636.
[63] T.F. Mastropietro, D. Armentano, N. Marino, G. De Munno, J. Anastassopoulou, T. Theophanides, Cryst. Growth Des. 7 (2007) 609.
[64] N.C. Gonnella, H. Nakanishi, J.B. Holtwick, D.S. Horowitz, K. Kanamori, N.J. Leonard, J.D. Roberts, J. Am. Chem. Soc. 105 (1983) 2050.
[65] A.C.T. North, D.C. Philips, F.S. Mathews, Acta Crystallogr., Sect. A 24 (1968) 351.
[66] SAINT – Ver. 6.45 Copyright (c) Bruker Analytical X-ray Systems Inc., Madison, Wisconsin, USA, 2003.
[67] G.M. Sheldrick. SADABS Program for Absorption Correction, Version 2.10, Analytical X-ray Systems, Madison, Wisconsin, USA, 2003.
[68] SHELXTL; Bruker Analytical X-ray Instruments, Madison, WI, 1998.
[69] CrystalMaker – Ver. 6.3.1, CambridgeSoft Corporation, Oxfordshire OX26 3TA, UK, 2003.
[70] A. Marzotto, A. Ciccarese, D.A. Clemente, G. Valle, J. Chem. Soc., Dalton Trans. (1995) 1461.
[71] S.M. Tretyak, V.V. Mitkevich, L.F. Sukhodub, Crystallogr. Rep. 32 (1987) 1268.

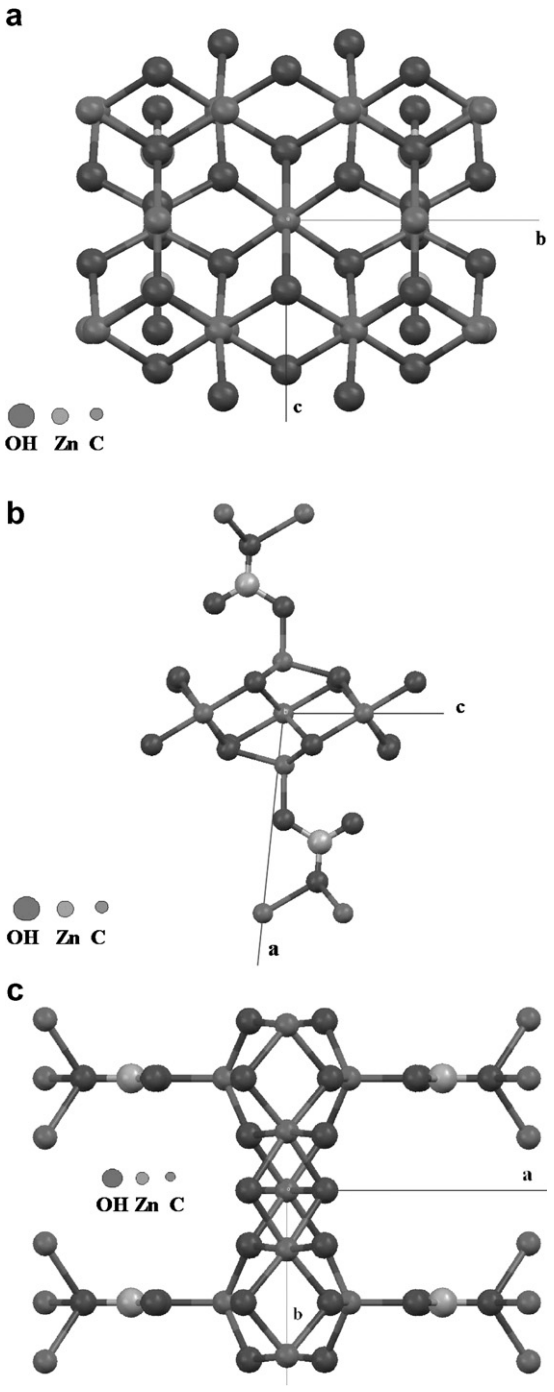


Fig. 1. Model of hydrozincite along the *a*, *b* and *c* axes.

figure displays the structure of hydrozincite looking along the *a*, *b* and *c* axes, respectively.

It is important to study the malachite–hydrozincite–hydrocerrusite assemblage and the stability of the system. The reason is that these minerals are the stable minerals at one atmosphere. One essential method is to use vibrational spectroscopic techniques. Infrared and Raman spectroscopy have been used to investigate carbonates including azurite and malachite [6,7]. A detailed single crystal Raman study of selected mineral carbonates has been undertaken [6,8]. This would seem important in the context of the stability of the hydroxy carbonates of Zn, Cu and Pb. However the vibrational spectroscopy of hydrozincite has not been undertaken. This may be due to the amorphous nature of the hydrozincite crusts. Few infrared spectral studies of related minerals such as the rosasite group have been forthcoming [7,9–11]. An infrared stretching vibration of the hydroxyl unit of azurite was observed at 3425 cm^{-1}, whereas two bands were reported for malachite at 3400 and 3320 cm^{-1}. The observation of two bands for malachite suggests coupling of the hydroxyl stretching vibrations [8]. This coupling was not observed for azurite [8]. Azurite and malachite form the basis of pigments in samples of an archaeological or medieval nature [12–15]. It is not known if hydrozincite was used in medieval paintings. Malachite has a characteristic infrared active intense band at ~430 cm^{-1} and for azurite an intense band at ~400 cm^{-1}. The deformation modes of azurite were reported at 1035 and 952 cm^{-1} and at 1045 and 875 cm^{-1} for malachite [7,16]. Hydrozincites from different origins showed differences in the infrared spectra in the OH stretching region [4]. These variations were accounted for by differences in stacking of the minerals [4]. Minerals in the rosasite mineral group, (a group of copper hydroxy carbonates) namely, rosasite, glaukosphaerite, kolwezite, mcguinnessite, nullaginite and pokrovskite have been studied by Raman spectroscopy at 298 and 77 K [17,18].

Vibrational spectroscopic studies of carbonate minerals have been undertaken over an extended period of time [19–21]. Adler and Kerr showed that differences in the infrared absorption spectra of carbonates were a function of cation size [19]. Some NIR studies have been undertaken [22,23]. Raman studies also have been forthcoming but not in recently [24–26]. Farmer reported the vibrational wavenumbers of calcite structured minerals (Table 12. IX p. 239) [2]. In this table the band positions for smithsonite were listed as 1093 cm^{-1} (v_1 symmetric stretching mode), 1412 and 1440 cm^{-1} (v_3 antisymmetric stretching mode), 870 cm^{-1} (v_2 in-plane bending mode), 733 and 743 cm^{-1} (v_4 out of plane bending mode) with lattice modes at 307, 200, 165 cm^{-1}. Some variation of band positions is found in the literature. Very little spectroscopic information on hydrozincite is available. However a comparison may be made with the mineral aurichalcite. The mineral aurichalcite $(Zn,Cu^{2+})_5(CO_3)_2(OH)_6$ is also monoclinic as are many of the other hydroxy carbonates such as malachite [27–29]. Aurichalcite forms in the oxidation zones of zinc–copper deposits. Crystals are similar to that of hydrozincite and are acicular and fibrous and often found in aggregates. Anthony et al. [1 reports aurichalcite to be acicular to lath-like crystals with prominent crystal growth along the [0 1 0] axis, commonly striated parallel to [0 0 1] axis. The mineral is of point group 2/*m* and space group $P2_1/m$ [1]. The accurate X-ray crystallography of aurichalcite is difficult to obtain because of its very small interwoven needles which makes obtaining single crystal studies difficult [1,3,29,30]. Harding [3 showed that the positions in the structure of

aurichalcite are octahedrally coordinated. The atom positions occupied by zinc have tetrahedral coordination [3]. Spectroscopic studies of aurichalcites and related minerals such as hydrozincite have been sparse. Reports regarding the chemical analysis, ESR, electronic and some limited infrared spectroscopic studies have been published [31]. These workers reported optical spectra revealing the presence of copper in D_{4h} symmetry with crystal field (Dq) and tetragonal field (Ds and Dt). This research was further extended in a comparison of rosasite and aurichalcite [32]. Optical and EPR spectra of aurichalcite accounted for Cu^{2+} ion in the distorted octahedron site [32]. Stoilova et al. [33] reported the infrared spectra of a series of synthetic hydroxy carbonates containing Cu^{2+}.

Raman spectroscopy has proven very useful for the study of minerals [34–36]. Indeed Raman spectroscopy has proven most useful for the study of diagentically related minerals often occurring with carbonate minerals [37–41]. Some previous studies have been undertaken by the authors using Raman spectroscopy to study complex secondary minerals formed by crystallisation from concentrated sulphate solutions [42]. The aim of this paper is to present Raman and infrared spectra of synthetic hydrozincites and smithsonite and to discuss the spectra from the structural point of view. The paper is a part of systematic studies of vibrational spectra of minerals of secondary origin in the oxide supergene zone and their synthetic analogs.

2. Experimental

2.1. Synthesis of hydrozincite and smithsonite

Three different synthesis techniques were trialled during the synthesis of hydrozincite. The first involved weighing out equimolar amounts of the Zinc (II) salt and the carbonate salt, dissolving in a minimum volume of deionised water and combining rapidly in a beaker of adequate size. The two Zinc salts used in the experiment were zinc chloride $ZnCl_2$ and zinc nitrate $Zn(NO_3)_2$. Sodium hydrogen carbonate $NaHCO_3$ was the source of the carbonate ion used for both experiments. The following chemical reaction occurs:

$$5ZnCl_2\ (s) + 10NaHCO_3\ (soln) \leftrightarrow Zn_5(CO_3)_2(OH)_6\ (s) + 8CO_2\ (g) + 10NaCl\ (soln) + 2H_2O$$

Smithsonite is formed according to the following reaction:

$$ZnCl_2\ (soln) + 2NaHCO_3\ (soln) \leftrightarrow ZnCO_3\ (s) + CO_2\ (g) + 2NaCl\ (soln) + H_2O$$

The second experiment involved a similar process of mixing the reactants but at a controlled rate using a peristaltic pump system operating at 10 cm min^{-1}. Both the zinc salt and carbonate salt were made up as standard solutions of equal concentration 0.5 M so that adding equivalent volumes 50 cm^3 of reagents gave the desired amounts of reagents according to the stoichiometry of the reaction. The pH of the reaction was monitored but remained essentially constant at pH = 7.2. The following alternative reaction is envisaged for the formation of smithsonite:

$$Zn_5(CO_3)_2(OH)_6\ (s) + 3CO_2\ (g) \leftrightarrow 5ZnCO_3\ (s) + 3H_2O\ (g).$$

The third synthesis method involved hydro-thermally treating some of the products from the previous two methods in a hydrothermal bomb at 100 °C for 48 h with adequate washing of the products after removal from the bomb. Adequate washing was achieved when the silver chloride test was negative. Thus indicating that all free chloride ions were removed. All of the samples were then washed and dried with ethanol and were placed in an oven at 80 °C over night to dry thoroughly.

From the XRD analysis, it was found that there was an impurity of another synthetic mineral found in the samples that had both used zinc chloride and had then been hydrothermally treated. It can be seen that hydrothermal treatment actually promotes the formation of this synthetic mineral identified as simonkolleite, a zinc chloride hydroxide hydrate mineral with the formula of $Zn_5(OH)_8Cl_2H_2O$. It is apparent that if the sample was synthesised using the $ZnCl_2$ and then hydro-thermally treated, the carbonate yield decreased significantly thereby increasing the yield of simonkolleite.

2.2. X-ray diffraction

XRD analyses were performed on a Philips PANalytical X'Pert PRO X-ray diffractometer (radius: 240.0 mm). Incident X-ray radiation was produced from a line focused PW3373/10 Cu X-ray tube, operating at 40 kV and 40 mA, providing a $K\alpha_1$ wavelength of 1.54 Å. The incident beam was monochromated through a 0.020 mm Ni filter then passed through a 0.04 rad. Soller slit, a 15 mm fixed mask and a 1/2° fixed anti scatter slit. After interaction with the sample, the diffracted beam passed though a secondary 0.04 rad. Soller slit and a 0.25° progressive divergence slit before detection by an X'Celerator RTMS detector. The detector was set in scanning mode, with an active length of 2.022 mm. Samples were analysed utilising Bragg-Brentano geometry over a range of 1.5–70° 2θ with a step size of 0.02° 2θ, with each step measured for 12.1 s. For all XRD analyses, the samples were dispersed in hexane and dropped onto low background quartz plates, forming a thin film upon evaporation of the hexane.

2.3. Raman microprobe spectroscopy

The crystals of hydrozincite or smithsonite were placed and oriented on the stage of an Olympus BHSM microscope, equipped with 10× and 50× objectives and part of a Renishaw 1000 Raman microscope system, which also includes a monochromator, a filter system and a Charge Coupled Device (CCD). Raman spectra were excited by a HeNe laser (633 nm) at a resolution of 2 cm^{-1} in the range

between 100 and 4000 cm^{-1}. Repeated acquisition using the highest magnification was accumulated to improve the signal to noise ratio. Band positions were calibrated using the 520.5 cm^{-1} line of a silicon wafer. In order to ensure that the correct spectra are obtained, the incident excitation radiation was scrambled. Previous studies by the authors provide more details of the experimental technique [43–46].

2.4. Mid-IR spectroscopy

Infrared spectra were obtained using a Nicolet Nexus 870 FTIR spectrometer with a smart endurance single bounce diamond ATR cell. Spectra over the 4000–525 cm^{-1} range were obtained by the co-addition of 64 scans with a resolution of 4 cm^{-1} and a mirror velocity of 0.6329 cm/s. Spectra were co-added to improve the signal to noise ratio.

Spectral manipulation such as baseline adjustment, smoothing and normalisation were performed using the Spectracalc software package GRAMS (Galactic Industries Corporation, NH, USA). Band component analysis was undertaken using the Jandel 'Peakfit' software package, which enabled the type of fitting function to be selected and allows specific parameters to be fixed or varied accordingly. Band fitting was done with the lowest possible number of Lorentz–Gauss cross-product functions. The Lorentz–Gauss ratio was maintained at values greater than 0.7 and fitting was undertaken until reproducible results were obtained with squared correlations of r^2 greater than 0.995.

3. Results and discussion

3.1. Relative stability of hydrozincite and smithsonite

The relative stability of hydrozincite and smithsonite are of importance to understand their formation in nature. Of the secondary minerals containing zinc only smithsonite and hydrozincite are known. The formation of these minerals is controlled by the partial pressure of CO_2 [47,48],

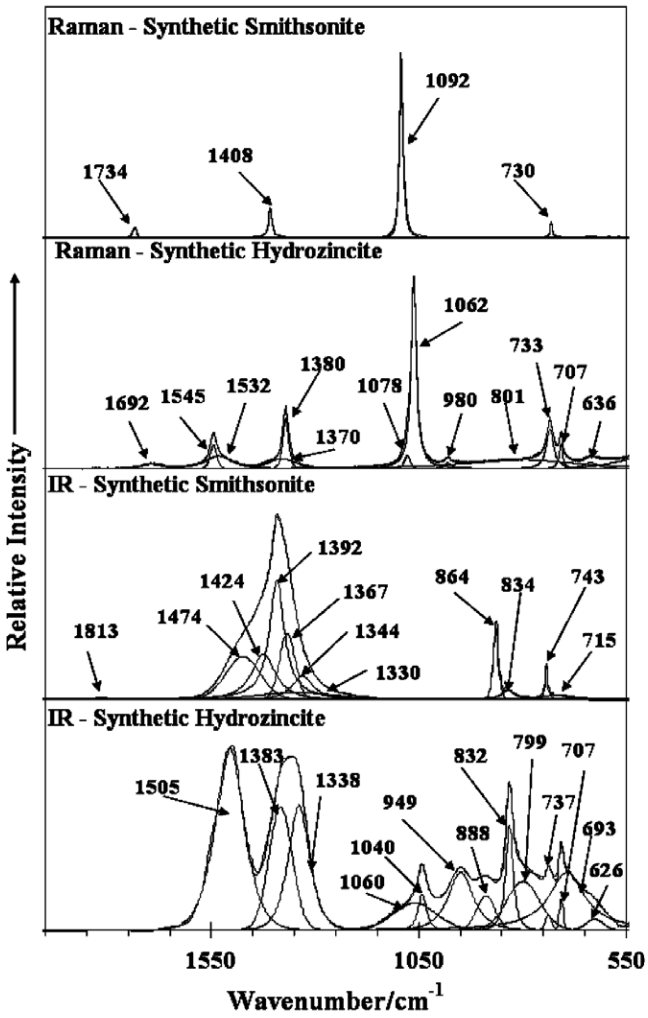


Fig. 3. Raman and infrared spectra of synthetic hydrozincite and smithsonite in the 550–1800 cm^{-1} region.

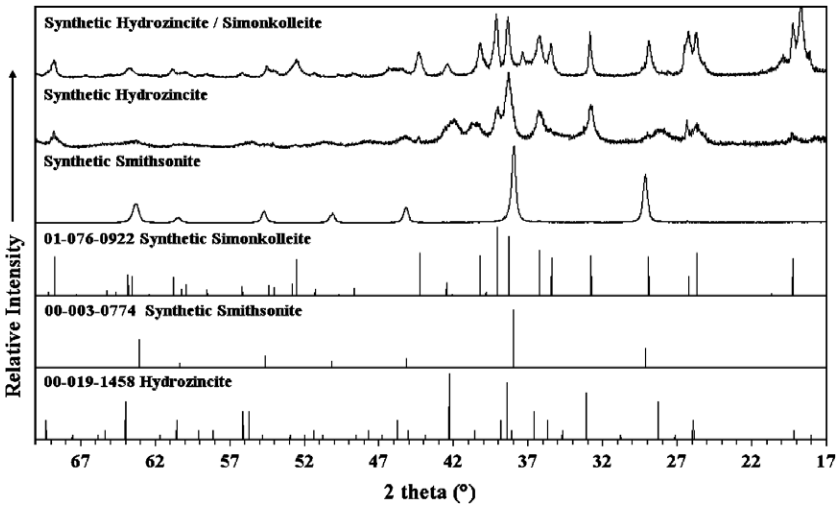


Fig. 2. XRD patterns of synthetic hydrozincite, smithsonite and simonkolleite and the reference patterns.

according to the equation for the formation of hydrozincite with $\log K = 10.32$ [47]. Thus ZnO is unstable with respect to hydrozincite at partial pressures above $10^{-5.16}$. If the partial pressure of CO_2 increases above $10^{-1.41}$ smithsonite formation is favoured according to the reaction $Zn_5(CO_3)_2(OH)_6$ (s) + $3CO_2$ (g) ↔ $5ZnCO_3$ (s) + $3H_2O$ (g). These results provide implications for the relative stability of hydrozincite and smithsonite. It is noted that hydrozincite may form from solutions resulting from oxidised zone of a Pb–Zn ore body [47]. Thus zincite (ZnO) is a rare mineral and smithsonite is only stable at elevated CO_2 partial pressures. The partial pressure range for the stability of hydrozincite according to Williams is limited and no doubt this accounts for the rarity of the mineral in nature [48]. The mineral can be readily synthesised in the laboratory and is often found in corrosion products of zinc [14,29,49]. In the presence of tenerite (CuO) the formation of malachite and/or azurite is favoured at the expense of hydrozincite [48]. Often the assembalge malachite–hydrozincite–hydrocerrusite is the stable system at 1 atm CO_2 pressure. Bouchard and Smith [14] reported the formation of a significant number of phases on metal coins including hydrozincite.

An impurity of simonkolleite with hydrozincite may be synthesised depending upon the starting materials. The conditions for the formation of simonkolleite are the same as that for hydrozincite. It was found that if zinc chloride was used in the synthesis and the sample was

Table 1
Results of the Raman and infrared spectra of synthetic smithsonite and hydrozincite

IR – synthetic smithsonite			IR – synthetic hydrozincite			Raman – synthetic smithsonite			Raman – synthetic hydrozincite		
Center	FWHM	%	Center	FWHM	%	Center	FWHM	%	Center	FWHM	%
			3478	189	6.07				3541	137	3.01
						3472	234	12.92			
									3407	142	17.06
3356	310	7.26									
			3291	282	31.44				3286	251	29.67
						3265	288	8.86			
			3063	222	4.74						
									2934	131	1.71
			2895	231	3.83						
2498	32	0.28									
									2330	3	0.10
1813	29	0.24									
						1734	10	1.71			
									1692	58	0.61
									1545	17	0.97
									1532	74	2.37
			1505	81	16.05						
1474	96	16.87									
1424	67	14.84				1408	10	6.03			
1392	43	30.44	1383	65	8.12				1380	77	1.61
									1370	15	1.91
1367	43	11.78									
1344	220	5.74	1338	59	8.12						
1330	57	6.54									
						1092	9	33.57			
									1078	15	0.47
			1060	119	3.20				1062	15	9.40
			1042	23	0.96				980	19	0.35
			949	69	2.28						
864	14	4.60	888	51	1.76						
834	34	1.87	832	20	2.64						
			799	93	2.25				801	294	7.72
743	7	1.37	737	16	0.25	730	6	1.98	733	20	2.37
715	88	2.07	707	10	0.32				707	9	0.76
			693	103	7.73						
			626	45	0.24				636	41	0.74
									417	244	10.71
									385	18	3.02
						350	453	11.90	346	43	2.18
						304	15	19.83			
									272	38	0.95
									227	33	1.49
						198	12	3.21	198	38	0.52

hydrothermally treated, a significant yield of simonkolleite was produced. The sample proved to be a mixed phase of simonkolleite and hydrozincite. It is also interesting that when smithsonite is formed, simonkolleite was not. The XRD patterns together with standard XRD reference patterns of synthetic smithsonite and hydrozincite are shown in Fig. 2. Clearly the pure hydrozincite and smithsonite phases were synthesised as single phases.

3.2. Spectroscopy

The Raman and infrared spectra of synthetic hydrozincite and smithsonite in the 550–1800 cm^{-1} region are shown in Fig. 3. The results of the band component analysis are reported in Table 1. Raman bands are assigned according to published data and by comparison with data for other minerals [18,45,50–58]. The Raman spectrum of synthetic hydrozincite shows an intense sharp band at 1062 cm^{-1}. Other low intensity bands are observed at 1078 and 980 cm^{-1}. The latter Raman band at 980 cm^{-1} is assigned to the δ OH deformation mode. The Raman spectrum of synthetic smithsonite shows a sharp band at 1092 cm^{-1}. These bands are assigned to the v_1 symmetric stretching mode of the carbonate unit. Infrared bands in this position are not observed for smithsonite. However a band at 1040 cm^{-1} is found in the infrared spectrum of synthetic hydrozincite. The $(CO_3)^{2-}$ v_1 band of the hydrozincite compound should not be infrared active. However, because of symmetry reduction of the carbonate anion through distortion the infrared band becomes activated.

A number of low intensity Raman bands are observed in the 1300–1500 cm^{-1} region (Fig. 3). A single band for synthetic smithsonite is observed at 1408 cm^{-1} and for hydrozincite bands at 1545 and 1380 cm^{-1} are found. These bands may be ascribed to the v_3 $(CO_3)^{2-}$ antisymmetric stretching modes. In the infrared spectrum of synthetic smithsonite a broad spectral profile centred on 1392 cm^{-1} is observed and is assigned to the v_3 $(CO_3)^{2-}$ antisymmetric stretching modes. In the infrared spectrum of synthetic hydrozincite bands are observed at 1505, 1383 and 1338 cm^{-1}. The difference in the number of bands in this spectral region of smithsonite and hydrozincite is ascribed to the symmetry reduction of the hydrozincite.

The v_2 bending mode for carbonates varies from around 890 to 850 cm^{-1}. For smithsonite Farmer reported an infrared band at 870 cm^{-1} [2]. For hydrozincite the infrared band was observed at 837 cm^{-1} [2]. In this work no Raman bands are observed for synthetic smithsonite or hydrozincite in this position. In the infrared spectrum of synthetic hydrozincite bands are observed at 888, 832 cm^{-1} with a broad feature at 799 cm^{-1}. In the infrared spectrum of smithsonite two bands are observed at 864 and 834 cm^{-1}. These bands are assigned to the carbonate v_2 bending mode. The observation of more than one v_2 mode suggests symmetry reduction of the carbonate anion in the structure. A comparison may be made with the spectra of other hydroxycarbonates. A mineral similar to hydrozincite is aurichalcite $(Zn,Cu)_5(CO_3)_2(OH)_6$. For aurichalcite two Raman bands may be resolved at 860 and 845 cm^{-1}. Only a single band at 817 cm^{-1} is observed in this region for malachite $Cu_2(CO_3)(OH)_2$. The FTIR spectrum of malachite showed two bands at 879 and 821 cm^{-1} [8]. This FTIR spectral region is more complex for azurite $Cu_3(CO_3)_2(OH)_2$ with bands observed at 872, 837, 815 and 796 cm^{-1}.

Multiple bands are observed for the carbonate v_4 in phase bending modes in the Raman spectrum of hydrozincite with bands at 733, 707 and 636 cm^{-1}. The number of bands observed in this spectral region may be attributed to the structural distortion of the mineral. For smithsonite only a single band at 730 cm^{-1} is observed. Farmer (based upon the work of Moenke [21]) reported two infrared bands for hydrozincite at 738 and 710 cm^{-1} [2]. Farmer also reported only a single band for smithsonite at 733 cm^{-1}. In the infrared spectrum of synthetic hydrozincite a broad complex spectral profile with two bands resolved at 737 and 707 cm^{-1} is observed. In the infrared spectrum of synthetic smithsonite two bands at 743 and 715 cm^{-1} are observed. It is interesting that in the Raman

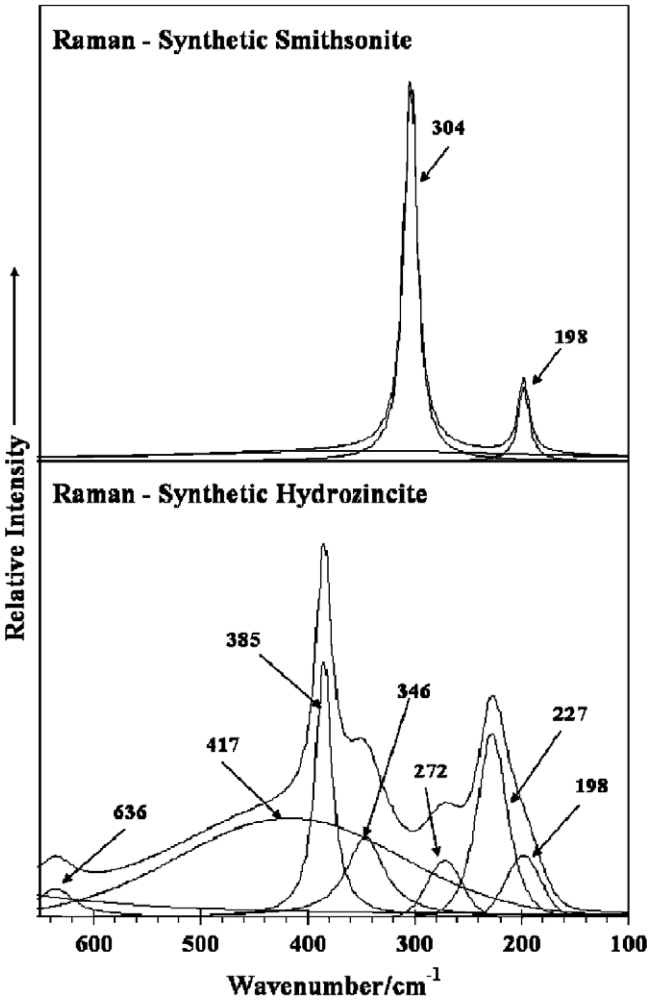


Fig. 4. Raman and infrared spectra of synthetic hydrozincite and smithsonite in the 100–600 cm^{-1} region.

spectrum of aurichalicte three bands are observed at 752, 733 and 708 cm^{-1}. The equivalent Raman bands for malachite are observed at 752 and 717 cm^{-1}. In the infrared spectra bands are observed at 779, 754 and 701 cm^{-1} for azurite and at 780, 750 and 715 cm^{-1} for malachite [8].

In the Raman spectrum of smithsonite in the 100 to 600 cm^{-1} region, two prominent bands are observed at 304 and 198 cm^{-1} (Fig. 4). These bands are assigned to lattice modes. Farmer reported lattice modes in the infrared spectrum of smithsonite at 307, 200 and 165 cm^{-1} [2]. For hydrozincite Raman bands are observed at 385, 346, 272 and 227 cm^{-1}. Bands in this spectral region have not been previously defined. The Raman spectra of the OH stretching region of the three aurichalcite mineral samples are shown in Fig. 5. The Raman spectrum of smithsonite shows two bands at 3472 and 3265 cm^{-1} and the infrared spectrum a single band at 3356 cm^{-1}. These bands are attributed to adsorbed water. For synthetic hydrozincite infrared bands are observed at 3291, 3063 and 2895 cm^{-1} and Raman bands are found at 3541, 3407, 3286 cm^{-1}. Farmer based upon the work of Moenke reported bands for hydrozincite at 3300 and 3260 cm^{-1}. A single symmetric band is observed for aurichalcite at 3338 cm^{-1}. A comparison can be made with rosasite where two distinct bands are observed at 3387 and 3319 cm^{-1}. The bands are assigned to the OH stretching vibration. Bouchard and Smith [14] reported a noticeably broad band in the Raman spectrum of aurichalcite at 3331 cm^{-1}. This value is in good agreement with the results reported in this work. Infrared bands for aurichalcite are observed at 3491, 3350, 3244 and a broad band at 3173 cm^{-1}. The infrared spectrum of a second aurichalcite mineral gave bands at 3359, 3249 and 3106 cm^{-1}. The broad band at around 3163 cm^{-1} may be ascribed to adsorbed water. The first two bands are assigned to OH stretching vibrations.

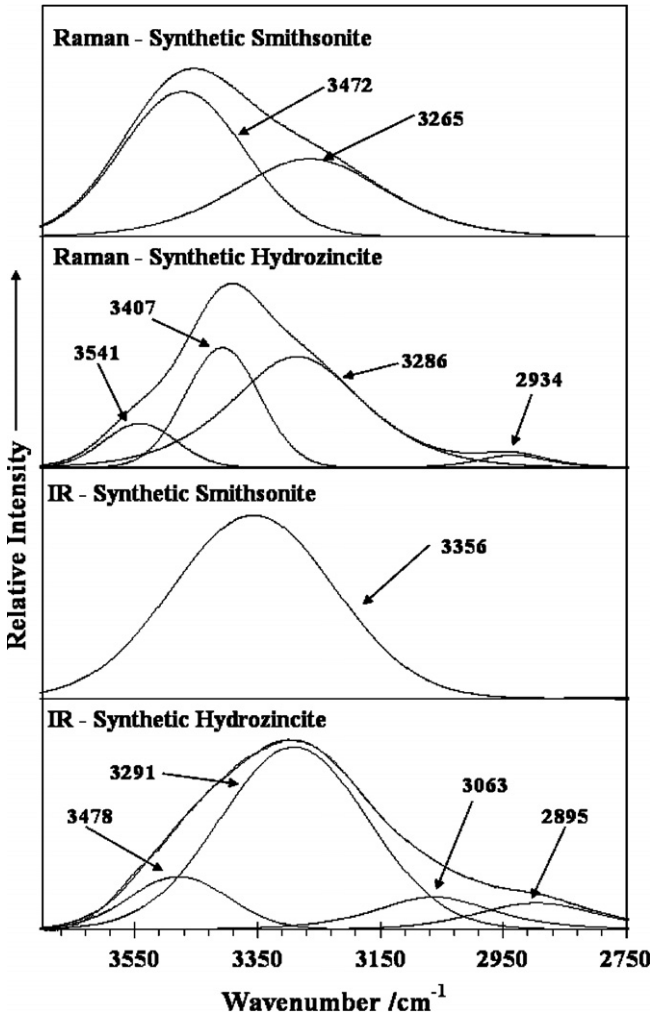


Fig. 5. Raman and infrared spectra of synthetic hydrozincite and smithsonite in the 2750–3600 cm^{-1} region.

4. Conclusions

Of the secondary minerals of zinc only two minerals are known, namely smithsonite and hydrozincite and their formation of is controlled by the partial pressure of CO_2according to the reactions $5ZnO(s) + 2CO_2\ (g) \leftrightarrow Zn_5(CO_3)_2(OH)_6\ (s)$ and $Zn_5(CO_3)_2(OH)_6\ (s) + 3CO_2\ (g) \leftrightarrow 5ZnCO_3\ (s) + 3H_2O\ (g)$. An impurity of simonkolleite with hydrozincite was synthesised depending upon the starting materials

The Raman spectra of synthetic hydrozincite and smithsonite show intense sharp bands at 1062 and 1092 cm^{-1}, assigned to the v_1 symmetric stretching mode of carbonate. Raman bands for synthetic smithsonite is observed at 1408 cm^{-1} and for hydrozincite bands at 1545 and 1380 cm^{-1} and are ascribed to the v_3 $(CO_3)^{2-}$ antisymmetric stretching modes. Multiple bands are observed for the carbonate v_4 in phase bending modes in the Raman spectrum of hydrozincite with bands at 733, 707 and 636 cm^{-1}. The number of bands observed in this spectral region may be attributed to the structural distortion of the mineral. For smithsonite only a single band at 730 cm^{-1} is observed. No Raman bands are observed for synthetic smithsonite or hydrozincite around 850 cm^{-1}. This is the expected position of the v_2 mode. In the infrared spectrum of synthetic hydrozincite bands are observed at 888, 832 cm^{-1} with a broad feature at 799 cm^{-1}.

Acknowledgements

The financial and infra-structure support of the Queensland University of Technology, Inorganic Materials Research Program is gratefully acknowledged. The Australian Research Council (ARC) is thanked for funding the instrumentation.

References

[1] J.W. Anthony, R.A. Bideaux, K.W. Bladh, M.C. Nichols, Handbook of Mineralogy, Mineral Data Publishing, Tiscon, AZ, USA, 2003.
[2] V.C. Farmer, Mineralogical Society Monograph 4: The Infrared Spectra of Minerals, 1974.

[3] M.M. Harding, B.M. Kariuki, R. Cernik, G. Cressey, Acta Crystallogr. Sect. B: Struct. Sci. B50 (1994) 673.
[4] W. Zabinski, Can. Mineral. 8 (1966) 649.
[5] S. Ghose, Acta Cryst. 17 (1964) 1051.
[6] J.A. Goldsmith, S.D. Ross, Spectrochim. Acta, Part A: Mol. Biomol. Spectrosc. 24 (1968) 2131.
[7] C. Rodriguez P, Bol. Soc. Quim. Peru 35 (1969) 38.
[8] R.L. Frost, W.N. Martens, L. Rintoul, E. Mahmutagic, J.T. Kloprogge, J. Raman Spectrosc. 33 (2002) 252.
[9] K. Wada, Kanzei Chuo Bunsekishoho 19 (1978) 133.
[10] P. Tarte, in: Proceedings of the International Meeting on Molecular Spectrometry, 4th, Bologna, 1959, vol. 3, 1962, pp. 1041–1049.
[11] P. Tarte, M. Deliens, Bull. Soc. Roy. Sci. Liege 43 (1974) 96.
[12] R.J.H. Clark, J. Mol. Struct. 480–481 (1999) 15.
[13] L. Burgio, D.A. Ciomartan, R.J.H. Clark, J. Raman Spectrosc. 28 (1997) 79.
[14] M. Bouchard, D.C. Smith, Asian Chem. Lett. 5 (2001) 157.
[15] B. Guineau, Stud. Conserv. 29 (1984) 35.
[16] C. Rocchiccioli, Compt. Rend. 259 (1964) 4581.
[17] R.L. Frost, D.L. Wain, W.N. Martens, B.J. Reddy, Polyhedron 26 (2007) 275.
[18] R.L. Frost, J. Raman Spectrosc. 37 (2006) 910.
[19] H.H. Adler, P.F. Kerr, Am. Mineral. 48 (1963) 124.
[20] C.K. Huang, P.F. Kerr, Am. Mineral. 45 (1960) 311.
[21] H. Moenke, W. Zabinski, Geologie (Berlin) 12 (1963) 1221.
[22] J.M. Hunt, M.P. Wisherd, L.C. Bonham, Anal. Chem. 22 (1950) 1478.
[23] G.R. Hunt, J.W. Salisbury, Mod. Geol. 2 (1971) 23.
[24] W.P. Griffith, Nature (London, United Kingdom) 224 (1969) 264.
[25] R.G. Herman, C.E. Bogdan, A.J. Sommer, Mater. Sci. Res. 19 (1985) 113.
[26] W.P. Griffith, J. Chem. Soc. [Sect.] A: Inorg. Phys. Theor. (1970) 286.
[27] R.S. Braithwaite, G. Ryback, Mineral. Mag. 33 (1963) 441.
[28] R.G. Herman, C.E. Bogdan, P.L. Kumler, D.M. Nuszkowski, Mater. Chem. Phys. 35 (1993) 233.
[29] J.L. Jambor, Can. Mineral. 8 (1964) 92.
[30] J.L. Jambor, I.D. MacGregor, Paper – Geological Survey of Canada, 74-1, Pt. B, 1974, p. 172.
[31] S. Vedanand, B.M. Sudhana, B.J. Reddy, P.S. Rao, Bull. Mater. Sci. 19 (1996) 1089.
[32] B.J. Reddy, F. Nieto, A.S. Navas, Monatshefte (2004) 302.
[33] D. Stoilova, V. Koleva, V. Vassileva, Spectrochim. Acta, Part A: Mol. Biomol. Spectrosc. 58A (2002) 2051.
[34] R.L. Frost, S.J. Palmer, J.M. Bouzaid, B.J. Reddy, J. Raman Spectrosc. 38 (2007) 68.
[35] R.L. Frost, D.A. Henry, M.L. Weier, W. Martens, J. Raman Spectrosc. 37 (2006) 722.
[36] R.L. Frost, A.W. Musumeci, J.T. Kloprogge, M.O. Adebajo, W.N. Martens, J. Raman Spectrosc. 37 (2006) 733.
[37] R.L. Frost, J. Cejka, M. Weier, W.N. Martens, J. Raman Spectrosc. 37 (2006) 879.
[38] R.L. Frost, M.L. Weier, J. Cejka, J.T. Kloprogge, J. Raman Spectrosc. 37 (2006) 585.
[39] R.L. Frost, J. Cejka, M.L. Weier, W. Martens, J. Raman Spectrosc. 37 (2006) 538.
[40] R.L. Frost, M.L. Weier, B.J. Reddy, J. Cejka, J. Raman Spectrosc. 37 (2006) 816.
[41] R.L. Frost, M.L. Weier, W.N. Martens, J.T. Kloprogge, J. Kristof, J. Raman Spectrosc. 36 (2005) 797.
[42] R.L. Frost, R.-A. Wills, M.L. Weier, W. Martens, J. Raman Spectrosc. 36 (2005) 435.
[43] R.L. Frost, D.A. Henry, K. Erickson, J. Raman Spectrosc. 35 (2004) 255.
[44] R.L. Frost, Spectrochim. Acta, Part A 60A (2004) 1469.
[45] R.L. Frost, O. Carmody, K.L. Erickson, M.L. Weier, J. Cejka, J. Mol. Struct. 703 (2004) 47.
[46] R.L. Frost, O. Carmody, K.L. Erickson, M.L. Weier, D.O. Henry, J. Cejka, J. Mol. Struct. 733 (2004) 203.
[47] A.K. Alwan, P.A. Williams, Transition Met. Chem. (Dordrecht, Netherlands) 4 (1979) 128.
[48] P.A. Williams, Oxide Zone Geochemistry, Ellis Horwood Ltd, Chichester, West Sussex, England, 1990.
[49] F. Zhu, D. Persson, D. Thierry, Corrosion (Houston, TX, United States) 57 (2001) 582.
[50] R.L. Frost, P.A. Williams, W. Martens, Mineral. Mag. 67 (2003) 103.
[51] R.L. Frost, M.L. Weier, Thermochim. Acta 406 (2003) 221.
[52] R.L. Frost, M.L. Weier, J.T. Kloprogge, J. Raman Spectrosc. 34 (2003) 760.
[53] R.L. Frost, M.L. Weier, Thermochim. Acta 409 (2004) 79.
[54] W.N. Martens, L. Rintoul, J.T. Kloprogge, R.L. Frost, Am. Mineral. 89 (2004) 352.
[55] R.L. Frost, K.L. Erickson, M.L. Weier, O. Carmody, J. Cejka, J. Mol. Struct. 737 (2005) 173.
[56] L. Frost Ray, L. Weier Matt, J. Cejka, A. Ayoko Godwin, Mol. Biomol. Spectrosc. 65 (2006) 529.
[57] R.L. Frost, B.J. Reddy, D.L. Wain, M.C. Hales, J. Near Infrared Spectrosc. 14 (2006) 317.
[58] R.L. Frost, B.J. Reddy, D.L. Wain, W.N. Martens, Spectrochim. Acta, Part A 66 (2007) 1075.

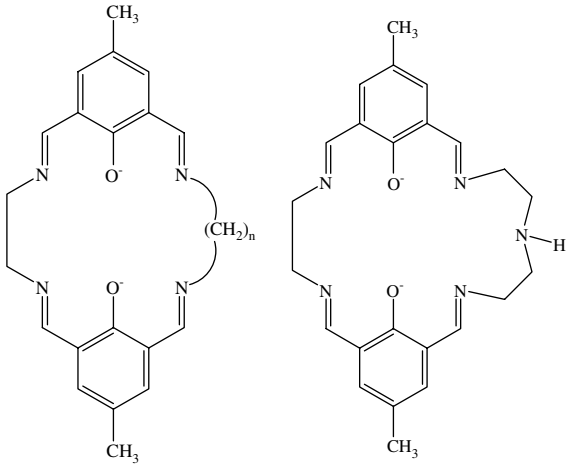


Chart 1.

if one were to use various polyamines with methyl(s) or other groups on the lateral diimine chain, and further to evaluate the biological activities. Although a considerable amount of work has been performed on the biological activity of mononuclear, homo- and heterodinuclear complexes [24–29], the quest for the development of new bioactive substances still persists. Consequently the structural study and screening of antibacterial and antifungal activity of the new heterodinuclear complexes will be of interest.

In this report, we describe the synthesis of eight new heterodinuclear complexes (Chart 2), by the template reaction of the Okawa mononuclear Cu(II) precursor, CuL, with *N*,*N*-bis(2-aminoethyl)benzylamine, *N*,*N*-bis(2-aminoethyl)-2-phenyl ethylamine, 2,2-dimethyl-1,3-propanediamine and 1,2-diaminopropane in the presence of Zn^{2+} and/or Pb^{2+} ions, which finally were isolated as solids and characterized. The macrocycles L^1 and L^2 bear a 4-coordination site with a N_2O_2 "salen-like" donor set and a 5-coordination site with a N_3O_2 "saldien-like" donor set. The macrocycles L^3 and L^4 bear two 4-coordination sites with N_2O_2 "salen-like" donor sets.

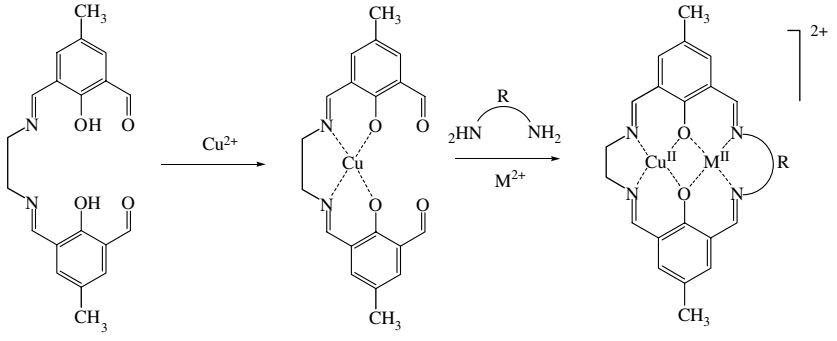
The structure of $[CuZnL^3(H_2O)](ClO_4)_2$ has been determined by X-ray diffraction and shows that the Zn(II) and Cu(II) centres reside in the N_2O_2 "salen-like" sites of the macrocyclic ligand, sharing the bridging phenolic oxygen atoms. The fifth coordination site for the Zn centre is occupied by a water ligand. The spectral study of all the complexes is reported together with the microanalysis and molar conductivity data.

We also explored the antibacterial and antifungal activities of all the prepared heterodinuclear complexes, as well as CuL, against *Escherichia coli*, *Candida albicans* and *Staphyloccocus aureus*.

2. Experimental

2.1. General Information

All of the chemicals and solvents were purchased from Aldrich and Merck. 2,6-Diformyl-4-methylphenol, *N*,*N*-bis(2-aminoethyl)-2-phenyl-ethylamine three hydrobromide and *N*,*N*′-bis(3-formyl-5-methylsalicylidene)ethane-1,2-diamine (H_2L) and [*N*,*N*′-bis(3-formyl-5-methylsalicylidene)ethane-1,2-diaminato]copper(II), (CuL), were prepared according to the literature method [23,30,31]. ^1H and $^{13}C\{^1H\}$ NMR spectra were obtained on a Bruker Avance 300 MHz spectrometer. IR spectra were recorded as pressed KBr discs, using a Unicom Galaxy Series FTIR 5000 spectrophotometer (200–4000 cm^{-1}). Electronic spectral measurements were carried out using a Perkin–Elmer Lamda spectrophotometer in the range 200–900 nm. C, H and N analyses were performed on a Vario EL III elemen-



H_2L CuL M=Zn, Pb

ligands	R
L^1	$-CH_2CH_2N(CH_2Ph)CH_2CH_2-$
L^2	$-CH_2CH_2N(CH_2CH_2Ph)CH_2CH_2-$
L^3	$-CH_2C(CH_3)_2CH_2-$
L^4	$-CH(CH_3)CH_2-$

Chart 2. The template condensation between CuL and polyamines in the presence of M(II) ions (M = Zn, Pb).

tal analyser. Metal analyses were made on a Perkin–Elmer 2380 atomic absorption/flame emission spectrophotometer. Conductivity measurements were carried out at 20 °C with a Metrohm 712 conductometer using 10^{-3} M solutions of the complexes in DMF.

2.2. X-ray crystal structure determination

Vapor diffusion of diethyl ether into a solution of $[CuZn(L^3)(H_2O)(ClO_4)]$ ClO_4 (**6**) in acetonitrile afforded crystals suitable for study by X-ray crystallography. Crystal data were collected on a STOE IPDS-II diffractometer with graphite monochromated Mo Kα radiation ($\lambda = 0.71073$ Å). Cell constants and an orientation matrix for the data collection were obtained by least-squares refinement of diffraction data from 7150 unique reflections. Data were collected at a temperature of 293(2) K to a maximum 2θ value of 53.74° and in a series of ω scans in 1° oscillations, and integrated using the Stoe X-AREA [32] software package. The numerical absorption coefficients, μ, for Mo Kα radiation are 1.132 mm^{-1} for 1, 1.314 mm^{-1} for 2 and 1.446 mm^{-1} for 3. The numerical absorption coefficient, μ, for Mo Kα radiation is 1.566 mm^{-1}. A numerical absorption correction was applied using X-RED [33] and X-SHAPE [34] software. The data were corrected for Lorentz and Polarizing effects. The structure was solved by direct methods and subsequent difference Fourier maps and then refined on F^2 by a full-matrix least-squares procedure using anisotropic displacement parameters [35]. All of the hydrogen atoms were located in a difference Fourier map and then after refined isotropically. Subsequent refinement then converged with R factors and parameters errors significantly better than for all attempts to model the solvent disorder. All refinements were performed using the X-STEP32 crystallographic software package [36]. Additional details of the data collection and refinement for the structure is given in Table 1.

2.3. Antibacterial and antifungal study

CuL and all the prepared complexes were screened for their activity against *E. coli*, *S. aureus* and *C. albicans* (CA) strains by the disc diffusion method as gram negative, gram positive and fungal organisms, respectively. Muller Hinton agar and Sabouraud dextrose agar were used to culture bacteria and fungi, respectively. The culture media was poured into sterile plates and microorganisms were introduced on the surface of the agar plates individually. The blank sterile discs, measuring 6.4 mm in diameter, were soaked in a known concentration of the test compounds. Then the soaked discs were implanted on the surface of the plates. A blank disc was soaked in the solvent (DMSO) and implanted as a negative control on each plate along with the standard drugs. The plates were incubated at 37 °C (24 h) and 27 °C (48 h) for bacterial and fungal strains, respectively. The inhibition zones were measured and compared with standard drugs. The zone of inhibition values are given in Table 4.

Table 1
Crystallographic data and refinement details for **6**

	6
Empirical formula	$C_{25}H_{29}Cl_2CuN_4O_{11}Zn$
Formula weight	761.39
Crystal system, space group	orthorhombic, *Pnca*
a (Å)	14.5300(18)
b (Å)	17.562(2)
c (Å)	26.296(4)
α (°)	90.0
β (°)	90.0
γ (°)	90.0
V (Å)^3	6710.1(15)
Z	8
Crystal size (mm)	$0.35 \times 0.20 \times 0.10$
Wavelength (Å)	0.71073
ρ_{calc} (g cm^{-3})	1.507
$F(000)$	3104
Temperature (K)	293(2)
θ (°)	1.39–26.87
Index ranges	$-18 \leqslant h \leqslant 16$, $-22 \leqslant k \leqslant 19$, $-33 \leqslant l \leqslant 33$
Number of reflections measured	35 567
R_{int}	0.0879
Number of unique reflections	7150
Goodness-of-fit	1.128
Number of reflections used in refinement ($F^2 > 2\sigma(I)$)	4236
R^a, wR_2^b	0.1757, 0.1924
Final shift/error$_{max}$	0.000
Maximum residual peak (e Å^{-3})	0.654
Minimum residual peak (e Å^{-3})	−0.427

[a] $R = \sum |F_o| - |F_c| / \sum |F_0|$ for $F^2 > 2\sigma F^2$.

[b] $wR_2 = \left[\left[\sum w(F_o^2 - F_c^2)^2 \right] / \sum w(F_o^2)^2 \right]^{1/2}$, where $w = [\sum^2(F_o^2) + (xP)2]^{-1}$ and $P = [F_o^2 + 2F_c^2]/3$.

2.4. Synthesis of N,N-bis(2-aminoethyl)benzylamine trihydrobromide (aeba.3HBr)

N,*N*-bis(2-aminoethyl)benzylamine three hydrobromide was prepared by the reaction of benzylamine with *N*-tosylaziridine (1:2) in acetonitrile at room temperature for 5 days followed by detosylation with HBr/AcOH, as described previously for *N*,*N*-bis(2-aminoethyl)-2-phenylethylamine trihydrobromide (aepa.3HBr) [31]. Overall Yield: 54%. ^{1}H NMR (D_2O, ppm) δ 3.35 (t, 4 H), 3.51 (t, 4H), 4.39 (s, 2H), 7.45 (m, 5H).^{13}C{^{1}H}NMR (D_2O, ppm) δ 135.4, 129.3, 129.1, 127.7, 49.7, 33.9, 29.5. *Anal.* Calc. for $C_{11}H_{22}N_3Br_3$: C, 30.29; H, 5.04; N, 9.63. Found: C, 30.2; H, 5.2; N, 9.4%.

Safety note: Perchlorate complexes are potentially explosive. While we have not experienced any problems with the compounds described, they should be treated with caution and handled in small quantities.

2.5. General procedure for the synthesis of **1**, **2**, **3** and **4**

A solution of KOH (1.5 mmol) in absolute EtOH (10 ml) was added to a suspension of the triamine salt (aeba.3HBr or aepa. 3HBr) (0.5 mmol) in absolute EtOH

(10 ml) and the mixture was stirred at room temperature for 15 min. The mixture was filtered and the precipitate was washed well with absolute EtOH (10 ml). This solution was added dropwise to a stirring suspension of CuL (0.5 mmol) and metal salt ($Pb(NO_3)_2 \cdot 3H_2O$ or $Zn(ClO_4)_2 \cdot 6H_2O$) (0.5 mmol) in DMF (30 ml) over a period of 15 min. $NaClO_4$ (1 mmol) was added, and the mixture was stirred for an additional 20 min at ambient temperature. The solution was allowed to settle for 12 h at 0 °C. The resultant product was collected by filtration and washed successively with diethyl ether.

$[CuPb(L^1)(dmf)(ClO_4)](ClO_4)$ (**1**): The solid product was filtered off, washed with EtOH and dissolved in acetonitrile-DMF (1:1). The resulting solution was left to crystallize at room temperature to afford **1** as a brown powder. Yield: 42%. *Anal.* Calc. for $C_{34}H_{40}N_6O_{11}Cl_2CuPb$: C, 38.89; H, 3.81; N, 8.00; Cu, 6.05. Found: C, 38.6; H, 3.5; N, 8.2; Cu, 6.3%. IR (KBr) cm^{-1}: 1640, 1625(C=N), 1327 (C–O), 1092, 1075, 1055, 621, 509, 448, 378, 334. Λ_M: 223 Ω^{-1} cm^2 mol^{-1}. UV–Vis λ_{max} (nm) (ε (M^{-1} cm^{-1})): 274, 380 (12 500), 549 (160) in DMF.

$[CuZn(L^1)(H_2O)](ClO_4)_2$ (**2**): The solid product was filtered off, washed with EtOH and dissolved in acetonitrile–THF (1:1). The resulting solution was left to crystallize at room temperature to afford **2** as a green powder. Yield 53%. *Anal.* Calc. for $C_{31}H_{35}N_5O_{11}Cl_2CuZn$: C, 43.64; H, 4.10; N, 8.20; Cu, 7.44. Found: C, 43.8; H, 4.4; N, 8.5; Cu, 7.8%. IR (KBr) cm^{-1}: 1660, 1639 (C=N), 1340 (C–O), 1087, 621, 502, 485, 356, 338. Λ_M: 232 Ω^{-1} cm^2 mol^{-1}. UV–Vis λ_{max}(nm) (ε (M^{-1} cm^{-1})): 270, 377 (11 800), 480–650 (100) in DMF.

$[CuPb(L^2)(dmf)](ClO_4)_2 \cdot dmf$ (**3**): The solid product was filtered off, washed with EtOH and dissolved in acetonitrile–DMF (1:1). The resulting solution was left to crystallize at room temperature to afford **3** as red microcrystals. Yield 41%. *Anal.* Calc. for $C_{38}H_{49}N_7O_{12}Cl_2CuPb$: C, 40.13; H, 4.31; N, 8.62; Cu, 5.59. Found: C, 40.2; H, 4.4; N, 8.6; Cu, 5.7%. IR (KBr) cm^{-1}: 1642, 1628 (C=N), 1329 (C–O), 1093, 623, 661, 507, 440, 374, 337. Λ_M: 238 Ω^{-1} cm^2 mol^{-1}. UV–Vis λ_{max} (nm) (ε (M^{-1} cm^{-1})): 276, 380 (12 100), 560 (150) in DMF.

$[CuZn(L^2)(H_2O)](ClO_4)_2$ (**4**): The solid product was filtered off, washed with EtOH and dissolved in acetonitrile. The resulting solution was left to crystallize at room temperature to afford **4** as a green powder. Yield 40%. *Anal.* Calc. for $C_{32}H_{37}N_5O_{11}Cl_2CuZn$: C, 44.31; H, 4.27; N, 8.07; Cu, 7.33. Found: C, 44.3; H, 4.3; N, 8.1; Cu, 7.2%. IR (KBr) cm^{-1}:1649, 1620 (C=N), 1327 (C–O), 1091, 623, 510, 486, 359, 336. Λ_M: 242 Ω^{-1} cm^2 mol^{-1}. UV–Vis λ_{max} (nm) (ε (M^{-1} cm^{-1})): 272, 398(12 400), 595(180) in DMF.

2.6. General procedure for the synthesis of *5*, *6*, *7* and *8*

A solution of di-amine (2,2-dimethyl-1,3-propanediamine or 1,2-diaminopropane) (0.5 mmol) in EtOH (20 ml) was added dropwise to a stirred suspension of CuL (0.5 mmol) and metal salt ($Pb(NO_3)_2 \cdot 3H_2O$ or $Zn(ClO_4)_2 \cdot 6H_2O$) (0.5 mmol) in CH_2Cl_2–MeOH (1:1) (20 ml) over a period of 10 min. Except for **5**, $NaClO_4$ (1 mmol) was added. The mixture was stirred for 3 h at ambient temperature. The solution was allowed to settle for 12 h at 0 °C. The resultant product was collected by filtration and washed successively with diethyl ether.

$[CuPb(L^3)(NO_3)](NO_3) \cdot H_2O$ (**5**): The solid product was filtered off, washed with EtOH and dissolved in CH_3OH. The resulting solution was left to crystallize at room temperature to afford **5** as a red powder. Yield 38%. *Anal.* Calc. for $C_{25}H_{30}N_6O_9CuPb$: C, 36.22; H, 3.62; N, 10.13; Cu, 7.66. Found: C, 36.2; H, 3.5; N, 10.0; Cu, 7.4%. IR (KBr) cm^{-1}: 1650, 1630 (C=N), 1324 (C–O), 1449, 1384, 1310, 1040, 610, 567, 502, 469, 423, 348. Λ_M: 215 Ω^{-1} cm^2 mol^{-1}. UV–Vis λ_{max} (nm) (ε (M^{-1} cm^{-1})): 273, 389 (12 300), 580 (130) in DMF.

$[CuZn(L^3)(H_2O)](ClO_4)_2$ (**6**): The product was dissolved in acetonitrile and the solution was diffused with diethyl ether to afford **6** as reddish microcrystals. Yield 43%. *Anal.* Calc. for $C_{25}H_{29}N_4O_{11}Cl_2CuZn$: C, 39.43; H, 3.80; N, 7.35; Cu, 8.34. Found: C, 39.3; H, 3.9; N, 7.5; Cu, 8.0%. IR (KBr) cm^{-1}: 1641, 1620 (C=N), 1321 (C–O), 1109, 624, 509, 453, 334. Λ_M: 240 Ω^{-1} cm^2 mol^{-1}. UV–Vis λ_{max} (nm) (ε (M^{-1} cm^{-1})): 271, 365 (12 100), 518 (170) in DMF.

$[CuPb(L^4)(ClO_4)(CH_3OH)](ClO_4)$ (**7**): The product was dissolved in acetonitrile-methanol (1:1) mixture and the solution was diffused with diethyl ether to afford **7** as red microcrystals. Yield 46%. *Anal.* Calc. for $C_{24}H_{28}N_4O_{11}Cl_2$-CuPb: C, 32.39; H, 3.15; N, 6.29; Cu, 7.13. Found: C, 32.2; H, 3.3; N, 6.5; Cu, 7.3%. IR (KBr) cm^{-1}: 1610, 1634 (C=N), 1317 (C–O), 1101, 1078, 1046, 621, 560, 501, 454, 410, 353. Λ_M: 228 Ω^{-1} cm^2 mol^{-1}. UV–Vis λ_{max} (nm) (ε (M^{-1} cm^{-1})): 270, 370 (12 800), 530 (190) in DMF.

$[CuZn(L^4)(CH_3OH)](ClO_4)_2$ (**8**): The solid product was filtered off, washed with EtOH and dissolved in acetonitrile-methanol (1:1). The resulting solution was left to crystallize at room temperature to afford **8** as a red powder. Yield 43%. *Anal.* Calc. for $C_{24}H_{28}N_4O_{11}Cl_2CuZn$: C, 38.53; H, 3.74; N, 7.48; Cu, 8.49. Found: C, 38.6; H, 3.5; N, 7.6; Cu, 8.9%. IR (KBr) cm^{-1}: 1615, 1639 (C=N), 1320 (C–O), 1097, 623, 507, 449, 352, 338. Λ_M: 235 Ω^{-1} cm^2 mol^{-1}. UV–Vis λ_{max} (nm) (ε (M^{-1} cm^{-1})): 271, 365 (12 200), 520 (180) in DMF.

3. Results and discussion

Schiff base condensation of a mononuclear precursor, such as CuL, with various polyamines in the presence of second metal ion is one of the most classical reactions to synthesise heterodinuclear complexes.

The synthesis of the heterodinuclear Cu(II)–M(II) (M = Pb and Zn) complexes was carried out in DMF (for **1**–**4**) or CH_2Cl_2–MeOH (1:1) (for **5**–**8**) via the template condensation of [*N*,*N*′-bis(3-formyl-5-methylsalicylidene)ethane-1,2-diaminato]copper(II), CuL, and various polyamines in the presence of Zn(II) and/or Pb(II) (Chart 2). The prepared complexes were fully characterized by

microanalysis, IR and UV–Vis spectroscopy. The observed products are air stable solids, moderately soluble in DMF and/or CH_3CN and had elemental analyses consistent with the formulations given in Section 2.

3.1. Infrared spectra

In order to clarify the mode of bonding, the IR spectra of H_2L, the mononuclear fragment CuL, and the heterodinuclear complexes were studied and assigned on the basis of a careful comparison of the latter with the former.

In the IR spectrum of CuL the bands at 1672 and 1633 cm^{-1} can be assigned to the C=O and C=N stretching vibrations, respectively [23]. The υ(C=N) band in CuL is red-shifted by 10 cm^{-1} from that of the H_2L value. This can be ascribed to the withdrawal of electron density from the nitrogen atom owing to coordination. The υ(C–O) band (phenolic) in CuL, at 1298 cm^{-1}, appears at a higher frequency compared to the H_2L value by 44 cm^{-1}. This is in agreement with the phenolato–O single bonded to the metal ion [37,38].

The total absence of the CuL υ(C=O) absorption in the IR spectrum of each heterodinuclear complex together with the appearance of new υ(C=N) absorptions in the range 1647–1657 cm^{-1} clearly indicates that a cyclic Schiff-base has formed in each case. In all the prepared complexes, **1**–**8**, the υ(C–O) band (phenolic) appears at 1317–1340 cm^{-1} and is blue-shifted by 63–86 cm^{-1} from that of H_2L. On comparing with the literature [39], the greater shifting of the υ(C–O) (phenolic) frequency may be due to the phenolato–O bridging two metal centres.

The IR spectrum for the nitrate complex, **5**, show bands at ca. 1449 (υ_5), 1310 (υ_1) and 1040 (υ_2) cm^{-1}, suggesting the presence of a coordinated nitrate group, as well as a band at ca. 1384 cm^{-1} attributable to ionic NO_3^- [40–42]. The $\Delta\upsilon$ separation between the two highest frequency bands of coordinated nitrate falls in the range 130–200 cm^{-1}, suggesting bidentate coordination of the nitrate anion [40,42,43].

The complexes **2**, **3**, **4** and **8** exhibit bands attributable to ionic perchlorate at *ca.* 1090 cm^{-1} (υ_3) and *ca.* 623 cm^{-1} (υ_4). Bands attributable to the perchlorate groups are present in the spectra of **1**, **6** and **7** at *ca.* 1050, 1080 and 1105 cm^{-1}, suggesting the presence of coordinated perchlorate groups [40].

Complexes **1** and **3** show an intense band at ca. 1653 cm^{-1} that can be attributed to the υ(C=O) vibration of a coordinated DMF molecule. The presence of water molecules is confirmed by the appearance of an intense broad band centered at about 3400–3300 cm^{-1} in the IR spectra of **2**, **4** and **6**.

Some new bands with medium to weak intensities appear in the region 630–500 cm^{-1} and 480–330 cm^{-1} in the spectra of all the complexes, which are assigned to υ(M–O) and υ(M–N) vibration modes, respectively [40,44]. These bands are in accordance with data found in the literature and strongly support the involvement of the azomethine nitrogen and the phenolic oxygen atoms in the coordination.

3.2. Description of the crystal structure

The solid-state structure of the cation in **6**, determined by single crystal X-ray diffraction studies, together with the atom labelling scheme is illustrated in Fig. 1. Selected bond lengths (Å), bond angles (°) and torsion angles (°) with estimated standard deviations are given in Tables 2 and 3.

The Cu–N and Cu–O bond lengths in **6** (Table 2) fall in the range reported for CuL, and are shorter than the Zn–N and Zn–O bond lengths for the Zn(II) ion in the N_2O_2 cavity with the propylene lateral chain [45–47].

The Cu–Zn interatomic separation, bridged by two phenolic oxygen atoms, is about 3.0 Å. The Zn in the N_2O_2 site has a square–pyramidal geometry together with one water molecule at the axial site. The in-plane Zn-to-donor bond distances range from 2.010(7) to 2.049(7) Å and the axial Zn–O (water) bond distance is 2.022(7) Å. The structure shows that the equatorial plane for the Zn center is slightly distorted. The sum of the angles subtended by the macrocycle donor atoms at Cu and Zn is 360.0° and 349.7°, respectively, and Zn is displaced from the basal N(amine)$_2$O$_2$ least-squares plane towards the water oxygen. The plane containing N(3), N(4), O(1) and O(2) has a r.m.s. deviation of 0.320 Å with the metal atom being 0.429 (2) Å out of this plane.

3.3. Conductivity measurements and electronic spectra

The molar conductance (Λ_M) of all the prepared complexes, presented in Section 2, fall within the range

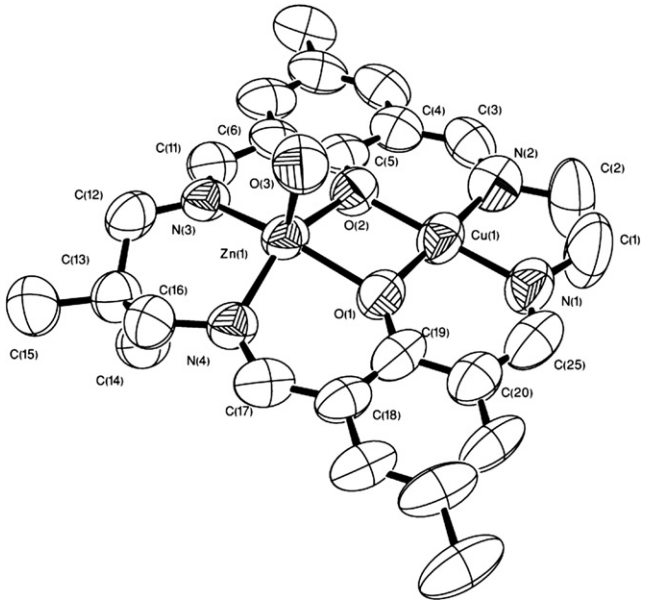


Fig. 1. The molecular structure of **6** showing displacement ellipsoids at the 50% probability level. H atoms are omitted for clarity.

Table 2
Selected bond lengths (Å) and angles (°) for **6**

Bond lengths			
Cu(1)–N(1)	1.918(10)	Zn(1)–N(3)	2.010(7)
Cu(1)–N(2)	1.886(11)	Zn(1)–N(4)	2.041(8)
Cu(1)–O(1)	1.904(7)	Zn(1)–O(1)	2.047(6)
Cu(1)–O(2)	1.887(6)	Zn(1)–O(2)	2.049(7)
Cu(1)–Zn(1)	3.0271(17)	Zn(1)–O(3)	2.022(7)
Bond angles			
Cu(1)–O(1)–Zn(1)	100.0(3)	N(3)–Zn(1)–O(3)	108.1(3)
Cu(1)–O(2)–Zn(1)	100.5(3)	N(4)–Zn(1)–O(3)	103.5(3)
N(1)–Cu(1)–N(2)	86.3(5)	O(1)–Cu(1)–O(2)	83.0(3)
N(1)–Cu(1)–O(1)	94.9(4)	O(1)–Zn(1)–O(3)	96.9(3)
N(2)–Cu(1)–O(2)	95.8(4)	O(2)–Zn(1)–O(3)	98.2(3)
N(3)–Zn(1)–N(4)	99.5(3)		
N(3)–Zn(1)–O(1)	87.6(3)		

reported for 1:2 electrolytes in DMF [48]. This implies that in **1**, **5** and **7** the weakly bonded counter ions in the solid state must be dissociated, at least in DMF solution.

The electronic spectra of the complexes in DMF display main features at 360–400 nm and 540–620 nm. The band at 360–400 nm may be assigned to the π–π^* electronic transition associated with the C=N linkages [10–16,20–22], and that of 540–620 nm to the d–d transitions. The intense absorption band at short wavelengths ca. 270 nm, may be assigned to intraligand π–π^* transitions [49].

The spectra for some of these complexes were also recorded in CH_3CN and DMSO, in an attempt to confirm the nature of these bands, by observing their position in different solvents; unfortunately, the co-presence of different kinds of chromophores, such as imine groups, phenol or phenyl rings, made it impossible to differentiate the exact nature of the bands (Fig. 2).

In some cases, the intensity of the absorption bands changed when the spectra were recorded after a period of 2 days, suggesting the displacement of some coordinated

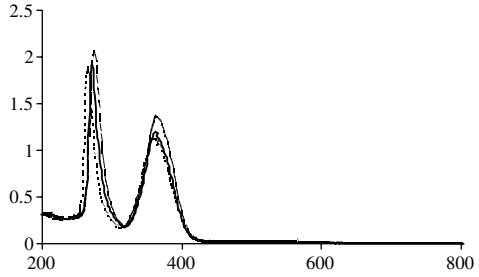


Fig. 2. UV spectra of **6** in DMF(---), CH_3CN (. . .) and DMSO (—).

anions or water molecules by solvent molecules, or a demetallation process [50].

3.4. Biological activities

CuL and all the synthesized heterodinuclear complexes, **1**–**8**, were tested for their anti-microbial activity against bacteria (*E. coli* and *S. Aureus*) and fungi (CA). The results of their biological activity are presented in Table 4. The anti-microbial activity of hetero- and homodinuclear complexes of similar phenol-based macrocyclic [25] and macroacyclic [24,26,29] ligands has been reported. In our study there was no activity observed by the prepared complexes against *E. coli* and CA, whereas compounds **2**, **4**, **6** and **8** had an inhibition zone between 9 and 14 mm on the culture of *S. aureus*. The anti-*S. aureus* activity of **6**, with an inhibition zone of 14 mm, is better than that of the other compounds (Table 4). An interesting result is that the Cu–Zn complexes of all the macrocyclic ligands showed a growth inhibition property, as it was reported for similar heterodinuclear complexes [25,26]. It can be concluded that the presence of the Zn(II) ion is important to have anti-bacterial activity, as the presence of Pb(II) in place of Zn(II) as the second metal ion gives complexes which showed no activity. The biological activ-

Table 3
Selected torsion angles (°) for **6**

N(1)–C(1)–C(2)–N(2)	−2(3)	C(11)–N(3)–Zn(1)–O(2)	−0.1(9)
N(1)–Cu(1)–Zn(1)–N(4)	−29.9(5)	C(11)–N(3)–Zn(1)–Cu(1)	−11.9(10)
N(2)–Cu(1)–Zn(1)–N(3)	30.7(5)	C(11)–N(3)–Zn(1)–O(1)	−53.2(12)
Cu(1)–O(1)–Zn(1)–N(3)	62.4(7)	C(12)–N(3)–Zn(1)–N(4)	24.9(7)
Cu(1)–O(1)–Zn(1)–O(3)	−89.9(3)	C(13)–C(12)–N(3)–Zn(1)	−48.9(11)
Zn(1)–O(2)–Cu(1)–O(1)	7.3(3)	C(13)–C(16)–N(4)–Zn(1)	47.1(11)
Zn(1)–O(2)–Cu(1)–N(1)	−43(7)	C(16)–N(4)–Zn(1)–N(3)	−23.8(7)
Zn(1)–O(1)–Cu(1)–N(2)	12(18)	C(16)–N(4)–Zn(1)–O(3)	87.5(7)
C(1)–C(2)–N(2)–Cu(1)	5(2)	C(17)–N(4)–Zn(1)–O(3)	−87.2(8)
C(2)–N(2)–Cu(1)–N(1)	−4.4(10)	C(17)–N(4)–Zn(1)–O(1)	9.2(8)
C(2)–C(1)–N(1)–Cu(1)	−2(2)	C(17)–N(4)–Zn(1)–O(2)	57.4(11)
C(3)–N(2)–Cu(1)–O(2)	−10.4(10)	C(17)–N(4)–Zn(1)–Cu	19.0(9)
C(3)–N(2)–Cu(1)–O(1)	−29(18)	C(19)–O(1)–Cu(1)–N(1)	−8.0(8)
C(4)–C(3)–N(2)–Cu	1.4(17)	C(19)–O(1)–Zn(1)–N(4)	−14.9(8)
C(5)–O(2)–Zn(1)–N(3)	4.3(8)	C(19)–O(1)–Zn(1)–O(3)	88.4(8)
C(5)–O(2)–Zn(1)–O(3)	−103.6(8)	C(25)–N(1)–Cu(1)–O(1)	1.3(10)
C(5)–O(2)–Zn(1)–N(4)	111.1(9)	O(2)–Cu(1)–Zn(1)–N(3)	19.5(4)
C(6)–C(11)–N(3)–Zn(1)	−4.8(16)	O(1)–Cu(1)–Zn(1)–N(4)	−15.9(4)
C(6)–C(5)–O(2)–Zn(1)	−3.6(13)		

Table 4
Zone of inhibition of the compounds

Compounds	*Staphylococcus aureus*	*Escherichia coli*	*Candida albicans*
CuL	–	–	–
1	–	–	–
2	9	–	–
3	–	–	–
4	9	–	–
5	–	–	–
6	14	–	–
7	–	–	–
8	11	–	–
DMSO	–	–	–
Standard drugs	Penicillin 39 mm	Gentamicin 17	Nistatin 25 mm

–, Indicates bacteria are resistant to the compounds. Zones of inhibition are reported for diameters in mm. Disks were inoculated with 5 mg of the compounds dissolved in DMSO.

ity in compound **6**, as mentioned earlier, is still more than **8**, which can be correlated to the presence of coordinated water [51] as well as one additional methyl group. The presence of coordinated water in **2** and **4** also can be a reason for the biological activity of these compounds. More detailed studies are recommended to understand the possible mechanisms involve in the inhibition of the growth of staph. aureus and to evaluate the differences of the growth inhibition mechanism between the organisms used in this study.

4. Conclusions

A series of Cu^{II}–M^{II} (M = Zn and Pb) heterodinuclear complexes of the macrocycles $(L^n)^{2-}$ ($n = \mathbf{1}$–$\mathbf{4}$) were obtained by cyclocondensation of the Okawa mononuclear Cu(II) precursor, CuL, with various di- and/or tri-amines in the presence of Pb(II) and Zn(II) metal ions. The site selectivity of the metal ions was demonstrated by X-ray crystallography for $[CuZn\ L^3(H_2O)](ClO_4)_2 \cdot CuL$ and its Cu(II)–M(II) (M = Zn and Pb) complexes were tested for anti-microbial activity and the compounds were found to have no activity against the bacteria *E. coli* and CA, but the Cu–Zn complexes were found to be active against *S. aureus*.

Acknowledgements

We thank the Arak University for financial support throughout this research work.

Appendix. Supplementary material

CCDC 648356 contains the supplementary crystallographic data for this paper. These data can be obtained free of charge via www.ccdc.ac.uk/conts/retrieving.html, or from the Cambridge Crystallographic Data Centre, 12 Union Road, Cambridge CB2 1EZ, UK; fax: (+44) 1223-336-033; or e-mail: deposit@ccdc.cam.ac.uk.

References

[1] P.A. Vigato, S. Tamburini, Coord. Chem. Rev. 248 (2004) 1717.
[2] E.J. O'Neil, B.D. Smith, Coord. Chem. Rev. 250 (2006) 3068.
[3] H. Ōkawa, H. Furutachi, D.E. Fenton, Coord. Chem. Rev. 174 (1998) 51.
[4] S. Tamburini, P.A. Vigato, M. Gatos, L. Bertolo, U. Casellato, Inorg. Chim. Acta 359 (2006) 183.
[5] M. Thirumavalavan, P. Akilan, M. Kandaswamy, Polyhedron 24 (2005) 781.
[6] T. Chattopadhyay, K. Sabnam Banu, A. Banerjee, J. Ribas, A. Majee, M. Nethaji, D. Das, J. Mol. Struct. 833 (2007) 13.
[7] L. Salmon, P. Thuéry, M. Ephritikhine, Polyhedron 25 (2006) 1537.
[8] B. Dutta, P. Bag, K. Nag, New J. Chem. 29 (2005) 1182.
[9] A. Hori, Y. Mitsuka, M. Ohba, H. Ōkawa, Inorg. Chim. Acta 337 (2002) 113.
[10] K. Abe, K. Matsufuji, M. Ohba, H. Ōkawa, Inorg. Chem. 41 (2002) 4461.
[11] M. Yonemura, K. Arimura, K. Inoue, N. Usuki, M. Ohba, H. Ōkawa, Inorg. Chem. 41 (2002) 582.
[12] S. Kita, H. Furutachi, H. Ōkawa, Inorg. Chem. 38 (1999) 4038.
[13] K. Ikeda, K. Matsufuji, M. Ohba, M. Kodera, H. Ōkawa, Bull. Chem. Soc. Jpn. 77 (2004) 733.
[14] K. Danjobara, Y. Mitsuka, Y. Miyasato, M. Ohba, H. Ōkawa, Bull. Chem. Soc. Jpn. 76 (2003) 1769.
[15] H. Furutachi, S. Fujinami, M. Suzuki, H. Ōkawa, J. Chem. Soc., Dalton Trans. (1999) 2197.
[16] H. Ōkawa, J. Nishio, M. Ohba, M. Tadokoro, N. Matsumoto, M. Koikawa, S. Kida, D.E. Fenton, Inorg. Chem. 32 (1993) 2949.
[17] H. Ohtsu, S. Itoh, S. Nagatomo, T. Kitagawa, S. Ogo, Y. Watanabe, S. Fukuzumi, Chem. Commun. (2000) 1051.
[18] S.C. Lee, R.H. Holm, J. Am. Chem. Soc. 115 (1993) 11789.
[19] R.T. Volbeda, M.H. Charon, C. Piras, E.C. Hatchikian, M. Frey, J.C. Fontecilla-Camps, Nature 373 (1995) 580.
[20] H. Furutachi, A. Ishida, H. Miyasaka, N. Fukita, M. Ohba, H. Ōkawa, M. Kioikawa, J. Chem. Soc., Dalton Trans. (1999) 367.
[21] H. Furutachi, S. Fujinami, M. Suzuki, H. Ōkawa, J. Chem. Soc., Dalton Trans. (2000) 2761.
[22] M. Sasaki, K. Manseki, H. Horiuchi, M. Kumagai, M. Sakamoto, H. Sakiyama, Y. Nishida, M. Sakai, Y. Sadaoka, M. Ohba, H. Ōkawa, J. Chem. Soc., Dalton Trans. (2000) 259.
[23] H. Ōkawa, S. Kida, Bull, Chem. Soc. Jpn. 45 (1972) 1759.
[24] A.D. Naik, S.M. Annigeri, U.B. Gangadharmath, V.K. Revankar, V.B. Mahale, Spectrochim. Acta Part A 58 (2002) 1713.
[25] B.H.M. Mruthyunjayaswamy, O.B. Ijare, Y. Jadegoud, J. Braz. Chem. Soc. 16 (2005) 783.
[26] R.N. Patel, N. Singh, K.K. Shukla, U.K. Chauhan, S. Chakraborty, J. Niclós-Gutiérrez, A. Castiñeiras, J. Inorg. Biochem. 98 (2004) 231.
[27] S. Chandra, N. Gupta, R. Gupta, Spectrochim. Acta Part A 63 (2006) 587.
[28] N.M. Agh-Atabay, B. Dulger, F. Gucin, Eur. J. Med. Chem. 40 (2005) 1096.
[29] M. Tümer, D. Ekinci, F. Tümer, A. Bulut, Spectrochim. Acta Part A 67 (2007) 916.
[30] N.C. Verani, E. Rentschler, T. Weyhermuller, E. Bill, P. Chaudhuei, J. Chem. Soc., Dalton Trans. (2000) 151.
[31] D.E. Fenton, P.C. Hellier, Inorg. Chim. Acta 198–200 (1992) 577.
[32] Stoe & Cie, X-AREA, vesion 1.30: program for the acquisition and analysis of data, Stoe & Cie GmbH, Darmstadt, Germany, 2005.
[33] Stoe & Cie, X-RED, vesion 1.28b: Program for data reduction and absorption correction, Stoe & Cie GmbH, Darmstadt, Germany, 2005.

[34] Stoe & Cie, X-SHAPE, version 2.05: Program for crystal optimization for numerical absorption correction, Stoe & Cie GmbH, Darmstadt, Germany, 2004.
[35] G.M. Sheldrick, SHELX97 Program for crystal structure solution and refinement, University of Göttingen, Germany, 1997.
[36] Stoe & Cie, X-STEP32, Version 1.07b: Crystallographic package, Stoe & Cie GmbH, Darmstadt, Germany, 2000.
[37] N.H. Pilkington, R. Robson, Aust. J. Chem 23 (1970) 2225.
[38] S.K. Gupta, Y.S. Kushwah, Polyhedron 20 (2001) 2019.
[39] J.K. Nag, D. Das, S. Pal, C. Sinha, Proc. Indian Acad. Sci.(Chem. Sci) 113 (2001) 11.
[40] K. Nakamoto, Infrared and Raman Spectra of Inorganic and Coordination Compounds, Wiley-Interscience, New York, 1978.
[41] N.F. Curtis, Y.M. Curtis, Inorg. Chem. 4 (1965) 804.
[42] M. Vicente, C. Lodeiro, H. Adams, R. Bastida, A. De Blas, D.E. Fenton, A. Macias, A. Rodriguez, T. Rodriguez-Blas, Eur. J. Inorg. Chem (2000) 1015.
[43] R.J. Frerrano, J. Inorg. Nucl. Chem. 10 (1959) 319.
[44] K. Goluck, A. Altun, S. Guner, M. Kumru, B. Aktas, Spectrochim. Acta Part A 60 (2004) 303.
[45] S.K. Dutta, U. Flörke, S. Mohanta, K. Nag, Inorg. Chem. 37 (1998) 5029.
[46] P. Biswas, M. Ghosh, S.K. Dutta, U. Flörke, K. Nag, Inorg. Chem. 45 (2006) 4830.
[47] M. Yonemura, N. Usuki, Y. Nakamura, M. Ohba, H. Ōkawa, J. Chem. Soc., Dalton Trans (2000) 3624.
[48] W.J. Geary, Coord. Chem. Rev. 7 (1971) 81.
[49] Q. Shi, R. Cao, X. Li, J. Luo, M. Hong, Z. Chen, New J. Chem. 26 (2002) 1397.
[50] C. Lodeiro, R. Bastida, E. Bertolo, A. Macías, A. Rodríguez, Polyhedron 22 (2003) 1701.
[51] A. Tamilselvi, M. Nethaji, G. Mugesh, Chem. Eur. J. 12 (2006) 7797.

We were interested to study the conformational and complexation behaviour of trisubstitued calix[4]arene with Na^+ and K^+ ions with an emphasis to achieve selectivity for K^+ over Na^+. In this paper, we report the synthesis and structural characterization of calix[4]arene derivatives having substituents at three out of the four OH groups in the lower rim, their complexation properties with Na^+ and K^+ ions and also the effect of various substituents on the molecular structure/packing.

2. Experimental

2.1. Materials

The compounds calix[4]arene [8] and 2-(2-chloroethoxy)-ethanol *p*-toluenesulfonate [9] were synthesized following the literature procedures. All the reagents used in this study were purchased from Aldrich and S. D. Fine Chemicals. All solvents were analytical grade and purified by standard procedures before use [10].

2.2. Physical measurements

Elemental analyses (C, H and N) were performed on a model 2400 Perkin–Elmer elemental analyzer. NMR spectra were recorded on a model DPX 200 Bruker FT-NMR instrument. Infrared spectra were recorded on a Perkin–Elmer Spectrum GX FT-IR system. Mass spectra were recorded on a Q-Tof micro™ LC–MS instrument. The UV–Vis spectra were recorded on a CARY 500 scan Varian spectrophotometer. Single crystal structures were determined using a Bruker SMART 1000 (CCD) diffractometer.

2.3. Synthesis of ligands

2.3.1. Synthesis of 25,27-bis(1-propyloxy)calix[4]arene (***L*^{1})

This compound was synthesized following the literature procedure [11], Yield 60%. ^{1}H NMR (200 MHz, $CDCl_3$) δ 8.30 (s, 2H, OH), 7.05, 6.90 (d, $J = 7.4$ Hz, 4H each, Ar), 6.72, 6.67 (t, $J = 7.4$ Hz, 2H each, Ar), 4.30 (d, $J = 13.0$ Hz, 4H, ArCH_2Ar), 3.97 (t, $J = 6.2$ Hz, 4H, OCH_2), 3.37 (d, $J = 13.0$ Hz, 4H, ArCH_2Ar), 2.05 (m, 4H, CH_2), 1.30 (t, $J = 7.4$ Hz, 6H, CH_3). LC–MS *m/z* 531.91 ($\mathbf{L^1} + Na^+$).

2.3.2. Synthesis of 25,26,27-tris(1-propyloxy)calix[4]arene (***L*^{2})

To a suspension of calix[4]arene (0.848 g, 2 mmol) in acetonitrile (80 mL) was added iodopropane (2.04 g, 12 mmol) and K_2CO_3 (1.66 g,12 mmol) in excess and the reaction mixture was stirred under reflux for 34 h. The solvent was then removed under reduced pressure and the residue was treated with 10% HCl (50 mL) and extracted with CH_2Cl_2 (100 mL). The organic phase was separated, washed twice with distilled water (100 mL × 2) and dried over $MgSO_4$. The solvent was removed by rotary evaporation and the product was purified by column chromatography using silica gel as the packing material and ethyl acetate–hexane (1:9) as the eluent. The solvent was removed from the desired fraction and the solid compound was dried under vacuo (yield 330 mg, 30%). Single crystals suitable for X-ray crystallography were obtained by slow evaporation of a dilute solution of the compound dissolved in acetonitrile–hexane (1:1). IR (KBr pellet, cm^{-1}) 3408 (OH). UV–Vis ($CHCl_3$, λ_{max} nm, ε $M^{-1}\,cm^{-1}$), 285 sh (2.57×10^3), 277 (3.46×10^3), 243 (3.3×10^3). ^{1}H NMR (200 MHz, $CDCl_3$) δ 7.25 (s, 1H, OH), 7.06–6.81 (m, 9H, Ar), 6.73–6.62 (m, 3H, Ar), 4.08 (d, $J = 13.2$ Hz, 2H, ArCH_2Ar), 3.95 (m, 2H, OCH_2), 3.84 (s, 2H, ArCH_2Ar), 3.82 (s, 2H, ArCH_2Ar), 3.59 (m, 2H, OCH_2), 3.24 (d, $J = 13.0$ Hz, 2H, ArCH_2Ar), 3.14 (t, $J = 7.6$ Hz, 2H, OCH_2), 1.79 (m, 4H, CH_2), 1.33 (m, 2H, CH_2), 0.99 (t, $J = 7.2$ Hz, 6H, CH_3), 0.57 (t, $J = 7.4$ Hz, 3H, CH_3). LC–MS *m/z* 573.40 ($\mathbf{L^2} + Na^+$). *Anal.* Calc. for $C_{38}H_{45}O_4N$: C, 79.15; H, 7.66; N, 2.36. Found: C, 78.45; H, 7.53; N, 2.21%.

2.3.3. Synthesis of 25,27-bis(1-propyloxy)-26(5-chloro-3-oxapentyloxy)calix[4]arene (***L*^{3})

A mixture of dipropyl calix[4]arene (0.740 g, 1.45 mmol), 2-(2-chloroethoxy)-ethanol *p*-toluenesulfonate (0.405 g, 1.45 mmol) and Cs_2CO_3 (0.474 g, 1.45 mmol) in acetonitrile (50 mL) was heated at reflux for 24 h under nitrogen atmosphere. The reaction mixture was allowed to cool to room temperature, solvent was then removed under reduced pressure and the residue was treated with 10% HCl (50 mL) and 100 mL of CH_2Cl_2. The organic phase was separated, dried over $MgSO_4$ and evaporation of the solvent under reduced pressure afforded a brownish oil. The compound was purified by column chromatography using silica gel as the packing material and ethyl acetate–hexane (1:11) as the eluent. Yield 0.358 g, (40%). Single crystals suitable for X-ray study were grown by slow evaporation of the solution containing THF–hexane (1:5). IR (KBr pellet, cm^{-1}) 3268 (OH). UV–Vis ($CHCl_3$, λ_{max} nm, ε $M^{-1}\,cm^{-1}$) 285 sh (3.46×10^3), 277 (4.1×10^3), 243 (3.75×10^3). ^{1}H NMR (200 MHz, $CDCl_3$) δ 7.32 (s, 1H, OH), 7.24 (d, $J = 3.8$ Hz, 2H, Ar), 7.07–6.89 (m, 7H, Ar), 6.80–6.63 (m, 3H, Ar), 4.10 (d, $J = 13.0$ Hz, 2H, ArCH_2Ar), 3.95 (m, 2H, OCH_2), 3.89 (s, 2H, ArCH_2Ar), 3.87 (s, 2H, ArCH_2Ar), 3.65–3.55 (m, 4H, OCH_2), 3.33 (t, $J = 5.2$ Hz, 2H, OCH_2), 3.26 (d, $J = 13.0$ Hz, 2H, ArCH_2Ar), 2.92 (t, $J = 5.0$ Hz, 2H, OCH_2), 2.64 (t, $J = 5.0$ Hz, 2H, CH_2Cl), 1.73 (m, 4H, CH_2), 0.98 (t, $J = 7.4$ Hz, 6H, CH_3). LC–MS *m/z* 638.30 ($\mathbf{L^3} + Na^+$). *Anal.* Calc. for $C_{38}H_{43}O_5Cl$: C, 74.19; H, 7.04. Found: C, 73.94; H, 6.92%.

2.3.4. Synthesis of 25(o-p-toluenesulfonate)26,28-bis(1-propyloxy)calix[4]arene (***L*^{4})

A mixture containing dipropyl calix[4]arene (0.762 g, 1.5 mmol), *p*-toluenesulfonyl chloride (0.286 g, 1.5 mmol) and Cs_2CO_3 (0.489 g,1.5 mmol) in acetonitrile (50 mL)

was heated at reflux for 20 h under nitrogen atmosphere. The reaction mixture was allowed to cool to room temperature and solvent was removed by rotary evaporation. The residue was treated with 10% HCl (50 mL) and CH_2Cl_2 (100 mL). The organic phase was separated and dried over $MgSO_4$ and evaporation of the solvent under reduced pressure afforded a yellow oil. The compound was purified by column chromatography using silica gel as the packing material and ethyl acetate–hexane (1:16) as the eluent. The desired compound was obtained as a white solid. Yield 0.397 g (40%). Single crystals suitable for X-ray study were grown by slow evaporation of a THF–hexane (1:5) solution. IR (KBr pellet, cm^{-1}) 3452 (OH). UV–Vis ($CHCl_3$, λ_{max} nm, ε $M^{-1}\,cm^{-1}$) 284 sh (3.46×10^3), 276 (4.01×10^3), 243 (4.55×10^3). ^{1}H NMR, (200 MHz, $CDCl_3$) δ 7.34 (d, $J = 7.4$ Hz, 2H, Ar), 7.20 (s, 1H, OH), 7.15 (d, $J = 7.2$ Hz, 2H, Ar), 7.07–7.01 (m, 4H, Ar), 6.75–6.68 (m, 6H, Ar), 6.38 (t, $J = 7.6$ Hz, 2H, Ar), 4.10 (d, $J = 14.8$ Hz, 2H, ArCH_2Ar), 4.04 (d, $J = 13.2$ Hz, 2H, ArCH_2Ar), 3.98–3.87 (m, 2H, OCH_2), 3.75 (d, $J = 14.8$ Hz, 2H, ArCH_2Ar), 3.65–3.53 (m, 2H, OCH_2), 3.22 (d, $J = 13.2$ Hz, 2H, ArCH_2Ar), 2.39 (s, 3H, Ts-CH_3), 1.84–1.53 (m, 4H, CH_2), 0.99 (t, $J = 7.2$ Hz, 6H, CH_3). LC–MS m/z 685.53 ($\mathbf{L^4} + Na^+$). *Anal.* Calc. for $C_{41}H_{42}O_6S$: C, 74.29; H, 6.39; S, 4.84. Found: C, 73.87; H, 6.15; S, 4.58%.

2.4. In situ complexation study by NMR

^{1}H NMR spectra of ligands $\mathbf{L^2}$–$\mathbf{L^4}$ (0.01 mmol each) in $CDCl_3$–CD_3OH (0.5 mL, 4:1) were recorded. Then metal (Na^+/K^+) iodide (20 times molar equivalents) was added into the solution in the NMR tube, the reaction mixture was shaken well to dissolve the metal salt and the NMR spectra of the solutions were recorded at different time intervals. Compound $\mathbf{L^3}$ with KI showed significant changes in the NMR spectra within 6 h. Compounds $\mathbf{L^2}$, $\mathbf{L^3}$ and $\mathbf{L^4}$ with NaI and compounds $\mathbf{L^2}$ and $\mathbf{L^4}$ with KI did not show any significant change in the NMR spectra even after 4 days.

2.5. Synthesis of Na^+ and K^+ complexes

Each of the three ligands (15 mg) were dissolved in a chloroform–methanol mixture (10 mL, 4:1), the required metal iodide (20 M equiv) was added into the solution and the reaction mixture was stirred at room temperature for 4 days. The reaction mixture was filtered using a sintered crucible to remove undissolved metal iodide. The solvent was then removed at reduced pressure, the resulting solid mass was dissolved in $CDCl_3$–CD_3OH (4:1) and filtered, and ^{1}H NMR spectra of the solutions were recorded. The observations are consistent to that found in the in situ NMR experiments. Data for the K^+complex of $\mathbf{L^3}$: IR (KBr pellet, cm^{-1}) 3459, 1624 and 801 cm^{-1} (H_2O), 3269 (OH). ^{1}H NMR (200 MHz, $CDCl_3$) δ 7.45 (s, 1H, OH), 7.32 (d, $J = 7.4$ Hz, 2H, Ar), 7.17–6.96 (m, 7H, Ar), 6.89 (d, $J = 7.4$ Hz, 2H, Ar), 6.83–6.72 (m, 1H, Ar), 4.26 (s, 4H, $2H_2O$),4.10 (d, $J = 13.4$ Hz, 2H, ArCH_2Ar), 4.03–3.99 (m, 2H, OCH_2), 3.95 (s, 2H, ArCH_2Ar), 3.92 (s, 2H, ArCH_2Ar), 3.86–3.81 (m, 2H, OCH_2), 3.67–3.50 (m, 4H, OCH_2), 3.34 (d, $J = 13.2$ Hz, 2H, ArCH_2Ar), 3.20–3.15 (m, 2H, OCH_2), 3.05–3.00 (m, 2H, CH_2Cl), 1.84–1.71 (m, 4H, CH_2), 1.00 (t, $J = 7.4$ Hz, 6H, CH_3). LC–MS m/z = 1305.0 ($2\mathbf{L^3} + K^+ + 2H_2O$), 1287.23 ($2\mathbf{L^3} + K^+ + H_2O$).

2.6. Determination of the association constant (K_a) by NMR titration

A stock solution of the host compound ($\mathbf{L^3}$, 5.176×10^{-3} M) was prepared in 4:1 $CDCl_3$–MeOH. A portion of this solution (0.5 mL) was taken in an NMR tube and used as the host, in the remaining solution KI was dissolved (16.64×10^{-3} M) and it was used as the guest so that the host concentration remained constant throughout the titration. Successive aliquots (0.1 mL each time) of the guest solution were added to the host in the NMR tube and after 30 min from each addition the ^{1}H NMR spectra were recorded. The changes in chemical shift of the CH_2 protons of the 2-(2-chloroethoxy)-ethanol moiety of the host was measured as a function of guest concentration, and the binding constant (K_a) was calculated following the procedure described in the literature for 2:1 host:guest complexes [12]. The value of K determined is 1.4×10^5 M^{-1}.

2.7. X-ray crystallography for $\mathbf{L^2}$–$\mathbf{L^4}$

The crystallographic data and details of data collection for all the three compounds are given in Table 1. Crystals of a suitable size were selected from the mother liquor and immersed in partone oil, then mounted on the tip of a glass fiber and cemented using epoxy resin. Intensity data for all three crystals were collected at 100 K using Mo Kα ($\lambda = 0.71073$ Å) radiation on a Bruker SMART APEX diffractometer equipped with a CCD area detector. The data integration and reduction were processed with SAINT [13] software. An empirical absorption correction was applied to the collected reflections with SADABS [13b]. The structures were solved by direct methods using SHELXTL [14] and were refined on F^2 by the full-matrix least-squares technique using the SHELXL-97 [15] program package. Graphics are generated using PLATON [16] and MERCURY 1.3 [17]. In all the compounds, non-hydrogen atoms were refined anisotropically until convergence was reached and the hydrogen atoms attached to the ligand moieties were stereochemically fixed.

3. Results and discussion

3.1. Synthesis of ligands $\mathbf{L^1}$–$\mathbf{L^4}$

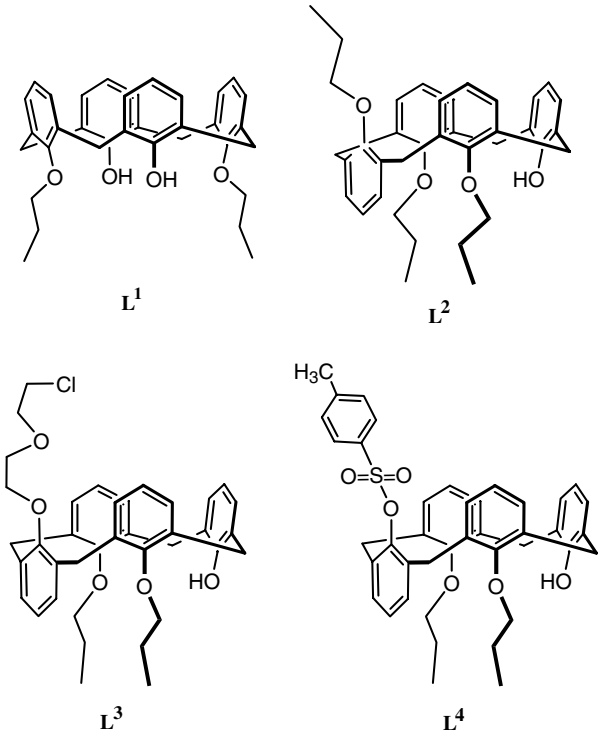
Compounds $\mathbf{L^1}$–$\mathbf{L^4}$ are shown in Chart 1. For the synthesis of these trisubstituted derivatives, the reaction conditions and the molar proportions of the reactants are crucial to control the reaction to achieve the maximum yield of the desired

Table 1
Summary of crystallographic data for $\mathbf{L^2}$, $\mathbf{L^3}$ and $\mathbf{L^4}$

Compound	$\mathbf{L^2}$	$\mathbf{L^3}$	$\mathbf{L^4}$
Empirical formula	$C_{39}H_{45}NO_4$	$C_{38}H_{43}Cl_1O_5$	$C_{41}H_{42}O_6S_1$
Formula mass	591.76	615.17	662.81
Crystal colour	colourless	colourless	yellow
Crystal size (mm)	$0.29 \times 0.19 \times 0.10$	$0.22 \times 0.14 \times 0.09$	$0.45 \times 0.28 \times 0.22$
Temperature (K)	100	100	100
Crystal system	monoclinic	monoclinic	monoclinic
Space group	$P2_1/n$	$P2_1/c$	$P2_1$
a (Å)	11.1795(12)	11.5711(8)	9.3129(9)
b (Å)	20.227(2)	13.9153(9)	35.339(3)
c (Å)	15.2139(16)	20.6531(14)	11.0407(10)
α (°)	90	90	90
β (°)	94.964(2)	105.7560(10)	106.340(2)
γ (°)	90	90	90
Z	4	4	4
V (Å^3)	3427.4(6)	3200.5(4)	3486.8(6)
Density (Mg/m^3)	1.147	1.277	1.263
Absorption coefficient (mm^{-1})	0.073	0.163	0.140
$F(000)$	1272	1312	1408
Reflections collected	16789	18628	17170
Independent reflections	6011 [$R_{int} = 0.0359$]	7382 [$R_{int} = 0.0256$]	6218 [$R_{int} = 0.0685$]
Number of parameters	402	400	873
S (Goodness-of-fit) on F^2	1.054	1.029	1.072
Final R_1 , wR_2 ($I > 2\sigma(I)$)	0.0679, 0.1949	0.0430, 0.1063	0.0627, 0.1322
Weighted R_1, wR_2 (all data)	0.1128, 0.2278	0.0548, 0.1152	0.0830, 0.1442
Largest difference in peak and hole (e Å^{-3})	0.511 and −0.228	0.361 and −0.258	0.318 and −0.331

product. All these reactions were carried out in acetonitrile under reflux conditions using Cs_2CO_3 as a base. In the case of $\mathbf{L^2}$, double of the required amount of iodopropane was used whereas for $\mathbf{L^3}$ and $\mathbf{L^4}$, molar proportions of the reactants have been used to achieve the maximum yield. These compounds were obtained with low to moderate yield after purification by extensive column chromatography.

All of these compounds gave satisfactory C, H and N analysis. Mass spectra of all these compounds were recorded by LC–MS and the observed e/m values show excellent agreement with the calculated values. It may be noted that e/m values (100%) of all the compounds correspond to the Na^+ adduct (ligand + Na^+), which is a well-known phenomenon when LC–MS is used for the measurement of mass [5]. In the IR spectra, the strong bands at 3408, 3268 and 3452 cm^{-1} for $\mathbf{L^2}$, $\mathbf{L^3}$ and $\mathbf{L^4}$, respectively suggest the presence of an OH group. The difference in band positions is due to various degrees of O–H···O interactions with the adjacent oxygen atom of the calixarene moiety, as evident from the crystal structures. Conformational analysis of the molecules was done by NMR and single crystal X-ray study.



$\mathbf{L^1}$ $\mathbf{L^2}$ $\mathbf{L^3}$ $\mathbf{L^4}$

Chart 1. Structures of the compounds $\mathbf{L^1}$–$\mathbf{L^4}$.

3.2. Conformational study of ligands by NMR spectroscopy

^{1}H NMR spectra of all the compounds were recorded in $CDCl_3$ and the data, with assignment of the signals, are presented in the experimental section. However, signals for the bridged methylene groups (ArCH_2Ar) are noteworthy, particularly in the context of conformational analysis. They exhibit four signals, two doublets and two closely spaced singlets for $\mathbf{L^2}$ and $\mathbf{L^3}$, whereas $\mathbf{L^4}$ exhibits four doublets. The appearance of doublets for the bridged methylene protons is an indication of a typical AB pattern with non-equivalent axial and equatorial hydrogen atoms. The doublets around δ 4.10 (2H) and around δ 3.25 (2H) for $\mathbf{L^2}$ and $\mathbf{L^3}$ suggest that two of the four methylene groups are equivalent. The other two methylene groups exhibit two closely spaced singlets, indicating that the two protons (axial and equatorial) of each methylene group are equivalent but the two methylene groups are non-equivalent. In the case of $\mathbf{L^4}$, the J values indicate that the doublets at δ 4.10 ($J = 14.8$ Hz, 2H) and at δ 3.75 ($J = 14.8$ Hz, 2H) correspond to two equivalent methylene groups with non-equivalent axial and equatorial protons. Similarly, the doublets at δ 4.04 ($J = 13.2$ Hz, 2H) and at δ 3.22 ($J = 13.2$ Hz, 2H) correspond to two equivalent methylene groups with AB type protons. This kind of splitting pattern for the bridged methylene groups suggest a partial cone conformation for these molecules [6b,7,18]. For $\mathbf{L^2}$–$\mathbf{L^4}$, two substituents are common, the third substituent in $\mathbf{L^2}$ and $\mathbf{L^3}$ are similar, but for $\mathbf{L^4}$ it is significantly different. This third substituent has affected the precise geometry of the calix unit and because of this effect the splitting patterns

of the bridged methylene groups for L^2 and L^3 are similar but are different from L^4.

3.3. Molecular structures of the ligands

The ORTEP diagrams of compounds L^2–L^4 are shown in Fig. 1. For all the three compounds, the bond lengths and bond angles are in the usual ranges [1g,1i,5a], and the following discussion refers mainly to the conformation and shape of the calixarene skeleton. The crystal structures clearly show that all the three compounds have adopted partial cone conformations, however the precise shape of the molecules differ due to variations in the substituent. The conformation of the calixarene can also be described by a typical sequence of the signs of the torsion angles around the aromatic units and the σ-bonds connecting

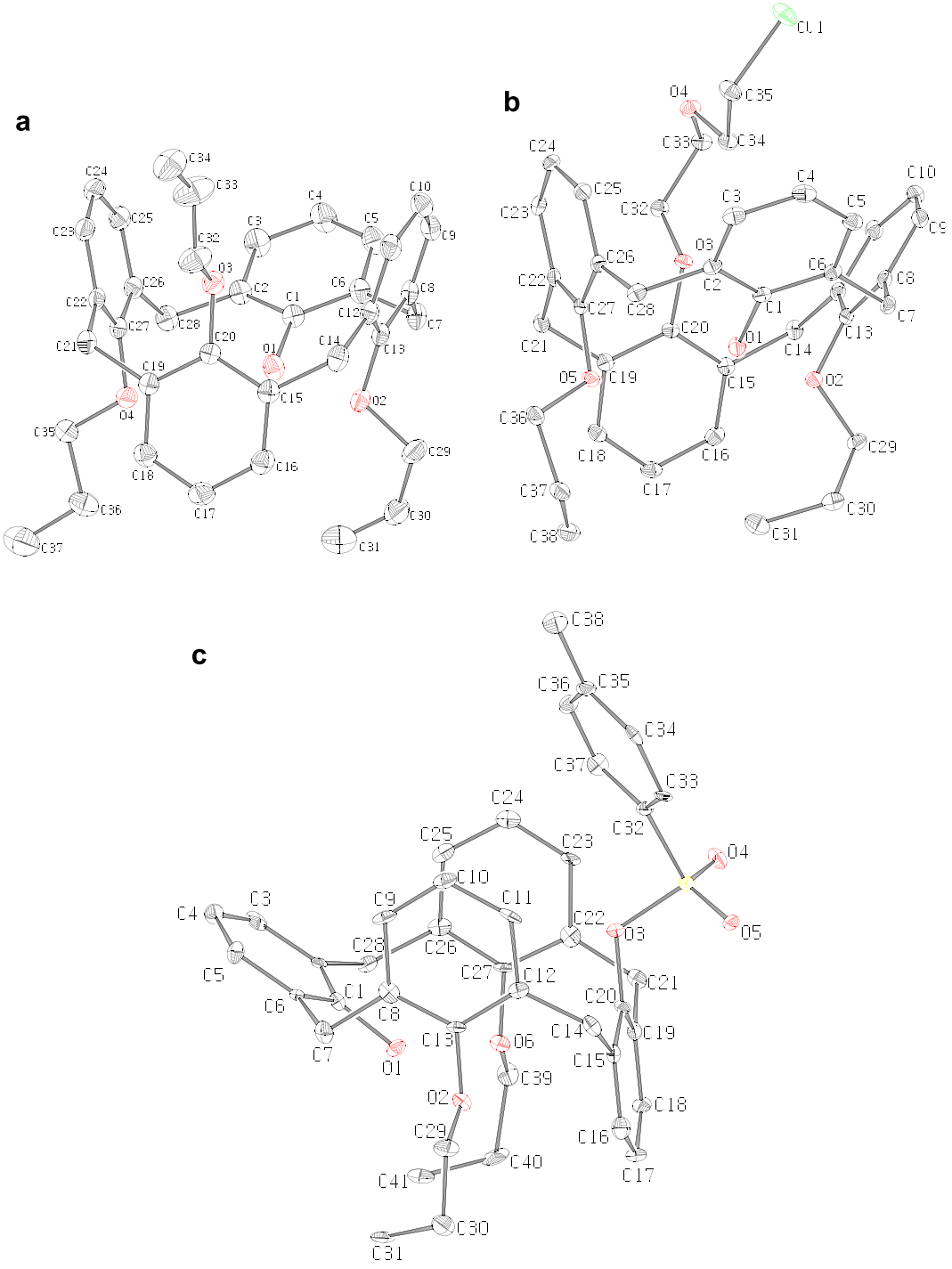


Fig. 1. ORTEP diagrams with the atom numbering scheme depicting the conformation of the calixarene moiety for compounds L^2 (a), L^3 (b) and L^4 (c) (hydrogen atoms are omitted for clarity).

the methylene bridges [19]. These sequences for all the three compounds (Table S1, Supplementary material) are (+,−)(+,+)(−,−)(+,−), which corresponds to the partial cone (paco) conformation.

Compound $\mathbf{L^2}$ encapsulates an acetonitrile molecule inside the calix cone with a strong C–H···π interaction between the hydrogen atoms of the acetonitrile and the centroid of the calix phenyl rings, as depicted in Fig. 2. Details of this C–H···π interaction are given in Table 2. A similar mode of guest encapsulation has also been reported with different substituted calixarene molecules [20]. It may be noted that the phenolic hydrogen H1 makes a strong intramolecular H-bond with O2 of the neighboring *O*-propyl group (Table 3), as depicted in Fig. 2. The propyl groups attached to the third and fourth phenyl rings are in an extended conformation whereas that attached to the second phenyl ring is in a folded conformation, as indicated by the torsion angles (O3–C32–C33–C34 = 175.30°, O4–C35–C36–C37 = 176.94° and O2–C29–C30–C31 = 48.69°). The folded conformation of the propyl group is attributed to the involvement of O2 in intramolecular H-bonding interactions with the adjacent phenolic oxygen O1.

The packing diagram of $\mathbf{L^2}$ viewed down the *a*-axis is shown in Fig. 3, with an offset π stacked array of calix moieties along the *b*-axis. The calixarene molecules are oriented with Cg1 and Cg3 phenyl centroids of adjacent molecules making offset π···π stacking interactions from either side, extending the array along the *b*-axis, Cg1···Cg3 = 4.86 Å with a Cg···Cg perpendicular distance of 3.52 Å, where Cg1 and Cg3 are the centroids of the C1–C6 and C15–C20

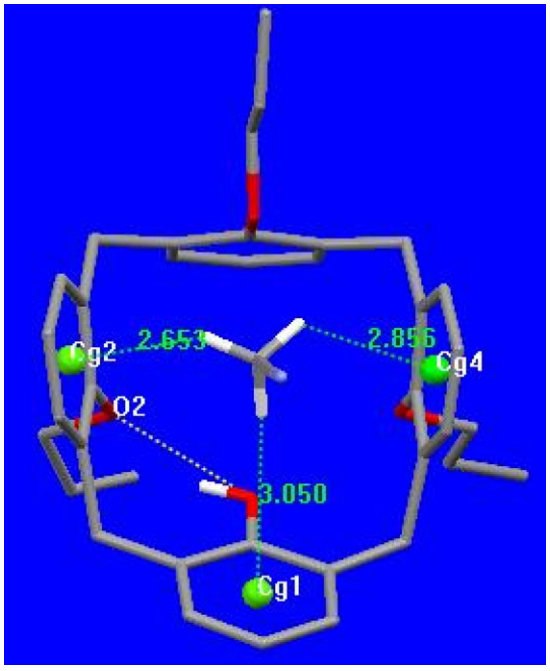


Fig. 2. MERCURY diagram depicting the encapsulated acetonitrile molecule inside the calixarene cone in $\mathbf{L^2}$, and also showing the intramolecular O–H···O interaction.

Table 2
C–H···π interactions for $\mathbf{L^2}$, $\mathbf{L^3}$ and $\mathbf{L^4}$ (Å and °)

C–H···Cg	*d*(H···Cg)	*d*(C···Cg)	∠C–H···Cg
Compound $\mathbf{L^2}$			
C39–H39B···Cg1	3.05	3.987(4)	166
C39–H39A···Cg2	2.65	3.452(5)	141
C39–H39C···Cg4	2.86	3.505(5)	126
Compound $\mathbf{L^3}$			
C34–H34A···Cg2	2.86	3.731(6)	150
C34–H34B···Cg4	2.89	3.689(6)	142
Compound $\mathbf{L^4}$			
C70-H70···Cg1[a]	2.98	3.640(7)	126
C79–H79A···Cg2	2.85	3.574(7)	133

[a] $1-x, 1/2+y, -z$; Cg1, Cg2 and Cg4 are the centroids of the phenyl rings C1–C6, C8–C13 and C22–C27, respectively for all compounds.

Table 3
Hydrogen bond distances for $\mathbf{L^2}$, $\mathbf{L^3}$ and $\mathbf{L^4}$ (Å and °)

D–H···A	*d*(H···A)	*d*(D···A)	∠D–H···A
Compound $\mathbf{L^2}$			
O1–H1···O2	1.96	2.733(3)	156
Compound $\mathbf{L^3}$			
O1–H1···O2	1.85	2.653(3)	166
Compound $\mathbf{L^4}$			
O1–H1···O6	2.04	2.840(5)	167
O7–H7···O12	2.42	3.209(5)	161
C21–H21A···O4	2.43	3.216(7)	138
C55–H55A···O10	2.44	3.193(7)	134
C7–H7A···O4[a]	2.59	3.506(7)	158
C38–H38A···O5[b]	2.41	3.322(8)	158
C69–H69A···O10[c]	2.52	3.458(7)	163
C79–H79C···O11[d]	2.38	3.284(7)	156

[a] $x, y, -1+z$.
[b] $1+x, y, z$.
[c] $x, y, 1+z$.
[d] $-1+x, y, z$.

phenyl rings. Thus the stabilization of the compound in the crystal lattice can be mainly attributed to intermolecular phenyl offset π···π stacking interactions and intramolecular O–H···O and C–H···π interactions.

In the case of $\mathbf{L^3}$, both the methylene hydrogen atoms of 2-(2-chloroethoxy)-ethanol are involved in strong intramolecular C–H···π interactions with the opposite phenyl rings of the calix moiety (Fig. 4), bringing this group in towards to the calix cone and thus preventing the entry of any solvent molecule for encapsulation in the cavity. The phenolic hydrogen H1 is involved in strong intramolecular O–H···O hydrogen bonding with the neighboring oxygen atom attached to the benzene ring. Details of the C–H···π and O–H···O interactions are given in Tables 2 and 3, respectively. The distances and angles of these interactions are well within the values reported by Meyer et al. in their review article [21]. The propyl groups attached to the second and fourth phenyl rings are in a folded conformation (torsion angles O2–C29–C30–C31 = 62.99°, O5–C36–C37–C38 = −65.48°)

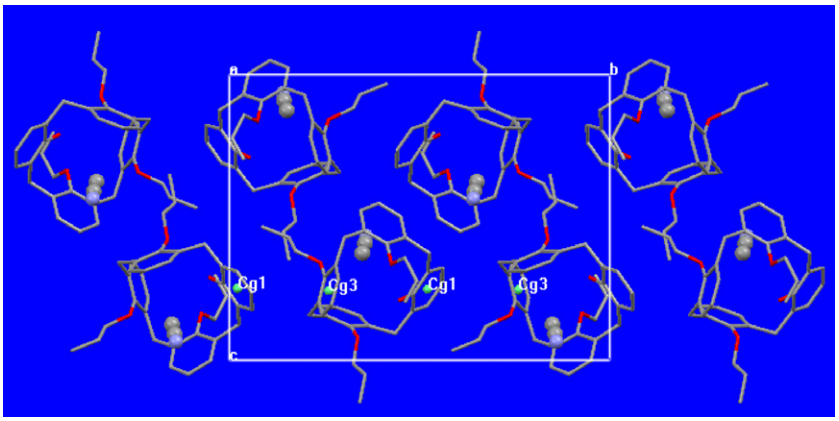


Fig. 3. Packing diagram of $\mathbf{L^2}$ viewed down the *a*-axis showing the orientation of the calixarene moiety with the encapsulated acetonitrile molecule; the calixarene molecules are oriented with Cg1 and Cg3 phenyl centroids of adjacent molecules making offset π···π stacking interactions from either side, extending the array along the *b*-axis.

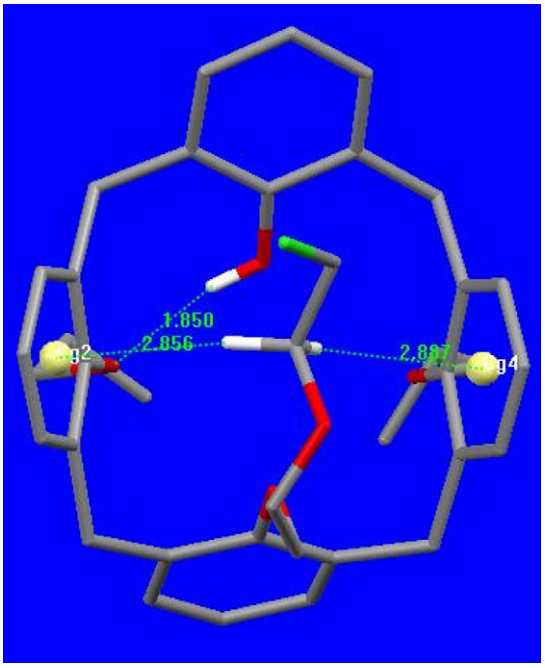


Fig. 4. MERCURY diagram of $\mathbf{L^3}$ depicting the intramolecular O–H···O interaction and C–H···π interaction between the aromatic rings of the calixarene unit and the methylene hydrogen atoms of the attached 2-(2-chloroethoxy)-ethanol moiety.

and are projected outwards from the calix cone. The torsion angle of the attached 2-(2-chloroethoxy)-ethanol moiety (O3–C32–C33–O4 = 66.02°, C32–C33–O4–C34 = 78.66°, C33–O4–C34–C35 = 163°, O4–C34–C35–Cl1 = −68.22°) clearly shows that except for the middle portion of the string, all other parts are in a folded conformation to attain the right orientation for an effective C–H···π interaction of the methylene hydrogens with the phenyl rings, as mentioned above.

The packing arrangement of $\mathbf{L^3}$ is similar to that of $\mathbf{L^2}$, however no significant intermolecular C–H···π interaction is observed between adjacent calix moieties, as in the case of $\mathbf{L^2}$ (Fig. S1, Supplementary material). Intramolecular C–H···π interactions dominate in governing the conformation of the calix moiety and effective crystal packing in $\mathbf{L^3}$.

The packing diagram of $\mathbf{L^4}$ shows that the calix molecules are arranged as hydrogen bonded offset layers along the *c*-axis and can be viewed as a corrugated layer along the *b*-axis (Fig. S2). The screw related calix moieties of the asymmetric units are associated via C–H···π interactions to form a corrugated arrangement along the *b*-axis (Fig. 5). Details of these C–H···π interactions between the calix ring C1–C6 and the methyl hydrogen H79A of the *p*-toluenesulfonate, and C8–C13 and the methylene hydrogen of the propyl moiety are given in Table 2. The offset layers of the ligands oriented along the *c*-axis are formed by strong C–H···O interactions of the sulfonate oxygen atoms from both molecules in the asymmetric unit. Thus sulfonate oxygens O4 and O5 of the first molecule are involved in intermolecular C–H···O interactions with the rim methylene hydrogen H7A along the *c*-axis and with H38A along the *a*-axis, respectively. It is interesting to note that O4 is further involved in an intramolecular C–H···O interaction with the rim methylene hydrogen H21A. The sulfonate oxygen atoms O10 and O11 of the second calix molecule are also involved in C–H···O interactions in similar fashion to that of O4 and O5. Details of all these H-bonding interactions with their pertinent symmetry codes are summarized in Table 3. Thus concomitant C–H···O interactions along the *a*- and *b*-axes with C–H···π interactions create a supramolecular three dimensional network.

3.4. Complexation study with Na^+ and K^+ ions

3.4.1. In situ NMR study

A complexation study of $\mathbf{L^2}$–$\mathbf{L^4}$ with Na^+ and K^+ by NMR experiments was carried out following the method as described in the experimental section. ^{1}H NMR spectra of the ligands and those with excess metal (Na^+/K^+) iodide were recorded at different time intervals in $CDCl_3$–CD_3OH (4:1) at room temperature. The ligand $\mathbf{L^3}$ with the K^+ ion

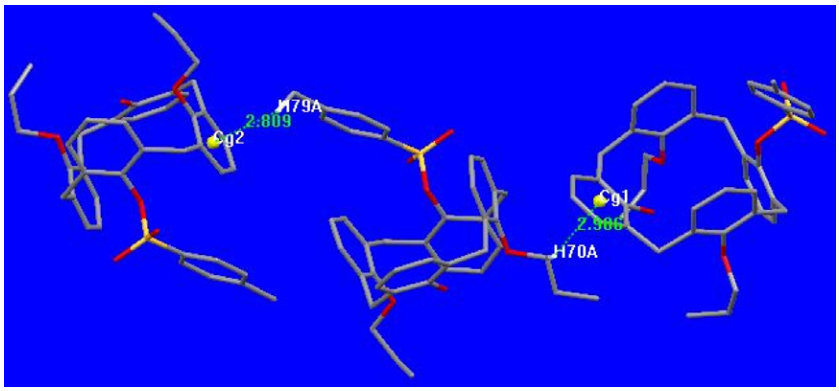


Fig. 5. C–H···π interactions between the aromatic rings of the calixarene moiety and methylene hydrogen (H70A) and methyl hydrogen (H79A) atoms of the propyl and *p*-toluenesulfonate groups, respectively, in $\mathbf{L^4}$.

exhibits a significant downfield shift of all the signals due to the protons of the 2-(2-chloroethoxy)-ethanol moiety ($-OCH_2CH_2OCH_2CH_2Cl$) and also some changes in the aromatic region compared to that of parent compound ($\mathbf{L^3}$), however in all other cases no significant change in the NMR spectra was observed. This observation suggests that complex formation takes place only between $\mathbf{L^3}$ and K^+ and not in any other cases under the experimental conditions. The relevant portions of the NMR spectra of $\mathbf{L^3}$, ($\mathbf{L^3}$ + NaI) and ($\mathbf{L^3}$ + KI) are shown in Fig. 6. It may be noted that in the spectra of ($\mathbf{L^3}$ + KI), the chemical shifts of all the CH_2 protons of the $-OCH_2CH_2OCH_2CH_2Cl$ moiety have moved downfield by 0.23, 0.30, 0.33 and 0.52 ppm, respectively, while the chemical shifts due to all other aliphatic protons remain almost at the same positions as observed for $\mathbf{L^3}$. This data suggests that only the $-OCH_2CH_2OCH_2CH_2Cl$ moiety is involved in complex formation with K^+. For further confirmation, an attempt has been made to synthesize and isolate solid complexes of Na^+ and K^+ with these ligands.

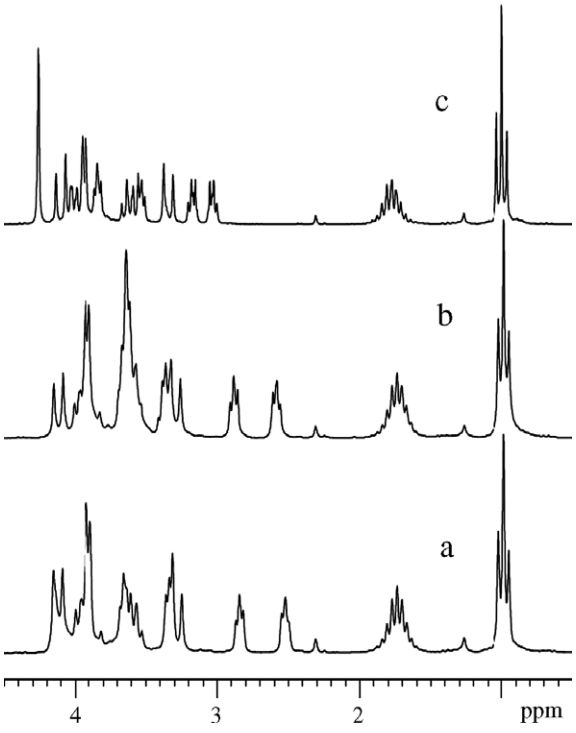


Fig. 6. Selected portion of the ^1H NMR spectra of (a) $\mathbf{L^3}$, (b) [$\mathbf{L^3}$ + NaI] and (c) [$\mathbf{L^3}$ + KI]; recorded in $CDCl_3$–CD_3OH (4:1) at room temperature.

The association constant (K_a) of $\mathbf{L^3}$ with K^+ was determined by NMR titration following the method described in the experimental section. For calixarene, determination of K_a by NMR titration is not very common because of the fact that it is difficult to find a clean separate peak of the host, which shifts with increasing metal ion (guest) concentrations. The value of K_a obtained ($1.4 \times 10^5\ M^{-1}$) is comparable to that found by Beer et al. by NMR titration for K^+ with calix[4]semitubes, where two calix[4]arene units are bridged by two ethylene chains and the K^+ ion is encapsulated in the cavity formed by the calix units and the ethylene bridge [22].

3.4.2. Synthesis of solid complexes

An attempt has been made to synthesis Na^+ and K^+ complexes of these ligands following the method described in Section 2. A solid mass was isolated and the ^1H NMR spectra of all samples were recorded in $CDCl_3$–CD_3OH. The observations are consistent to that found in the in situ NMR experiment; the spectra of the K^+complex of $\mathbf{L^3}$ is similar to that obtained from in situ NMR experiment, whereas for all other cases minor or no changes were observed.

The mass spectra of the K^+ complex of $\mathbf{L^3}$ exhibits a peak with low intensity at $m/z = 1305.0$ and a peak with moderate intensity at $m/z = 1287.23$. The first peak corresponds to the composition [$2\mathbf{L^3} + K^+ + 2H_2O$] and the second peak corresponds to [$2\mathbf{L^3} + K^+ + H_2O$], the observed m/z values are in excellent agreement with the calculated values, 1305.52 and 1287.51, respectively. The data suggest that complex formation takes place with two molecules of ligand, a K^+ ion and two molecules of water. The proposed structure of the complex is shown in Fig. 7. A similar observation was also noted by Beer et al., for calix tubes consisting of two calix units (M), where the proposed com-

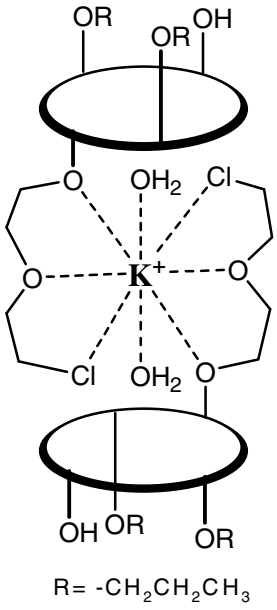


Fig. 7. Proposed structure for the K^+ complex of $\mathbf{L^3}$.

position was ($M+K^+ + 2H_2O$) [23]. In the K^+ complex, the involvement of water molecules in the coordination is also indicated by IR and NMR spectra. The IR spectra of $\mathbf{L^3}$ and its K^+ complex is shown in Fig. 8. Three new strong peaks (compared to $\mathbf{L^3}$), which appear at 3459, 1624 and 801 cm^{-1} are due to ν_s(O–H), the bending mode of H–O–H and the wagging mode of a coordinated water molecule [24]. In the ^1H NMR spectra, a new singlet at δ 4.3 (Fig. 6c), which corresponds to 4H, is assigned to the coordinated water molecules. A free water molecule used to appear at δ 4.8, and the signal due to a coordinated water molecule is expected to move downfield, however in this case it has moved upfield by ~0.5 ppm. From the possible structure of the complex it appears that the protons of the coordinated water molecules are inside or close to the cavity of the calixarene, which is a highly π-electron rich zone due to the presence of four aromatic rings. Because of this high π-electron density in the vicinity, the protons of the water molecules moved to the upfield region. Coordination of an alkali metal ion with chlorine in the presence of a crown ether has also been demonstrated crystallographically [25]. The selective complexation with K^+ is probably because of hole-size matching, the size of the cavity formed by the two 2-(2-chloroethoxy)-ethanol moieties fits well with the ionic size of K^+, the size of Na^+ is probably too small to make strong interactions with all the coordination sites as is required to form a stable complex.

4. Conclusions

A family of calix[4]arenes with three substituents at the lower rim have been synthesized and structurally characterized. Of the three substituents, one is different and the effect of this variable substituent on the metal binding ability and structural arrangement has been investigated. The calixarene moiety of all these three compounds adopts a partial cone conformation, however, all the three compounds exhibit different types of intra- and intermolecular C–H···π interactions, which provide them with different unique structural arrangements. Compound $\mathbf{L^2}$ encapsulates an acetonitrile molecule in the cavity of the calix moiety, whereas in $\mathbf{L^3}$ the third substituent itself moves in towards the cavity to make a strong C–H···π interaction with the phenyl rings, which prevents entry of the solvent molecule in the calix cone. Compound $\mathbf{L^4}$, which contains *p*-toluenesulfonate groups as the third substituent, behaves differently; no encapsulation in the cavity is observed but CH_2 of the propyl group and CH_3 of the *p*-toluenesulfonate group make strong intermolecular C–H···π interactions with the centroid of the phenyl groups of adjacent molecules. The packing diagram of $\mathbf{L^2}$ shows strong π···π stacking interactions, making an array along the *b*-axis, whereas $\mathbf{L^4}$ exhibits intermolecular C–H···O interactions to form a layered three dimensional architecture. A complexation study of all these compounds with Na^+ and K^+ ions reveal that the conformation of $\mathbf{L^3}$ is such that it forms a complex

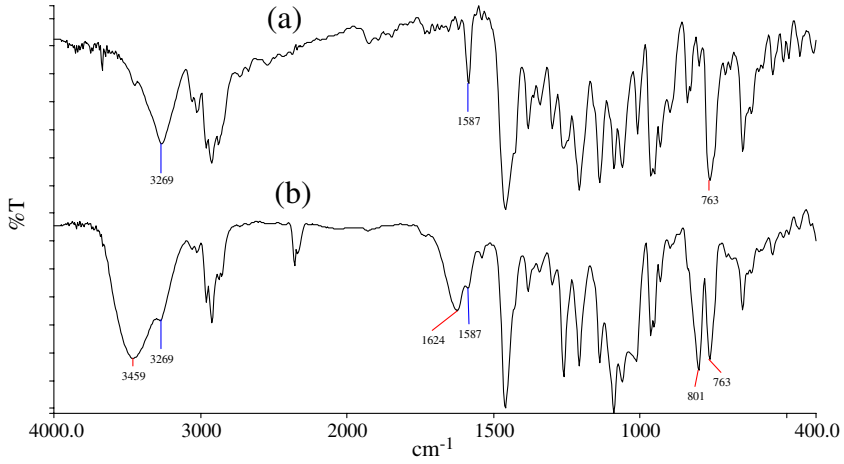


Fig. 8. IR spectra of compound $\mathbf{L^3}$ (a) and its K^+ complex (b).

selectively with K^+, the association constant also indicates strong complex formation, and therefore it may be used as a K^+ selective ionophore in the presence of Na^+.

Acknowledgements

We are grateful to the Department of Science and Technology (DST), Government of India, for financial support. We also thank CSIR, New Delhi, for generous support towards infrastructures and core competency development. We thank Mr. V. Boricha, Mr. A.K. Das and Mr. V. Agarwal for recording NMR, mass and IR spectra, respectively.

Appendix A. Supplementary material

CCDC 635311, 635312 and 635313 contain the supplementary crystallographic data for **L²**, **L³** and **L⁴**. These data can be obtained free of charge via http://www.ccdc.cam.ac.uk/conts/retrieving.html, or from the Cambridge Crystallographic Data Centre, 12 Union Road, Cambridge CB2 1EZ, UK; fax: (+44) 1223-336-033; or e-mail: deposit@ccdc.cam.ac.uk. Supplementary data associated with this article can be found, in the online version, at doi:10.1016/j.poly.2007.07.012.

References

[1] (a) C.D. Gutsche, Calixarenes, Royal Society of Chemistry, Cambridge, UK, 1989;
(b) J. Vicens, V. Boehmer (Eds.), Calixarenes, A Versatile Class of Macrocyclic Compounds, Kluwer, Dordrecht, Netherlands, 1991;
(c) V. Boehmer, Angew. Chem. 107 (1995) 785;
V. Boehmer, Angew. Chem., Int. Ed. Engl. 34 (1995) 713;
(d) A. Ikeda, S. Shinkai, Chem. Rev. 97 (1997) 1713;
(e) C.D. Gutsche, Calixarene Revisited, Royal Society of Chemistry, Cambridge, UK, 1998;
(f) S. Leon, D.A. Leigh, F. Zerbetto, Chem. Eur. J. (2002) 4854;
(g) A. Shivanyuk, M. Saadioui, F. Broda, I. Thondorf, M.O. Vysotsky, K. Rissanen, E. Kolehmainen, V. Boehmer, Chem. Eur. J. (2004) 2138;
(h) K. Kobayashi, K. Ishii, S. Sakamoto, T. Shirasaka, K. Yamaguchi, J. Am. Chem. Soc. 125 (2003) 10615;
(i) A. Dubes, K.A. Udachin, P. Shahgaldian, A.N. Lazar, A.W. Coleman, J.A. Ripmeester, New J. Chem. 29 (2005) 1141;
(j) H.M. Chawla, S.P. Singh, S.N. Sahu, S. Upreti, Tetrahedron 62 (2006) 7854.

[2] (a) A. Casnati, A. Pochini, R. Ungaro, F. Ugozzoli, F. Arnaud, S. Fanni, M.-J. Schwing, R.J.M. Egberink, F. De Jong, D.N. Reinhoudt, J. Am. Chem. Soc. 117 (1995) 2767;
(b) J.S. Kim, O.J. Shon, J.W. Ko, M.H. Cho, I.Y. Yu, J. Vicens, J. Org. Chem. 65 (2000) 2386;
(c) O. Tatsuya, I. Katsutoshi, F. Shintaro, G. Masahiro, J. Membr. Sci. 217 (2003) 87;
(d) P.M. Marcos, J.R. Ascenso, Tetrahedron 62 (2006) 3081.

[3] (a) H.-F. Ji, R. Dabestani, G.M. Brown, J. Am. Chem. Soc. 122 (2000) 930;
(b) N.R. Cha, M.Y. Kim, Y.H. Kim, J.-I. Choe, S.-K. Chang, J. Chem. Soc., Perkin Trans. 2 (2002) 1193;
(c) J.S. Kim, O.J. Shon, J.A. Rim, S.K. Kim, J. Yoon, J. Org. Chem. 67 (2002) 2348;
(d) J.Y. Lee, S.K. Kim, J.H. Jung, J.S. Kim, J. Org. Chem. 70 (2005) 1463;
(e) S.K. Kim, J.H. Bok, R.A. Bartsch, J.Y. Lee, J.S. Kim, Org. Lett. 7 (2005) 4839;
(f) S.K. Kim, S.H. Kim, H.J. Kim, S.H. Lee, S.W. Lee, J. Ko, R.A. Bartsch, J.S. Kim, Inorg. Chem. 44 (2005) 7866.

[4] (a) J.M. Notestein, E. Iglesia, A. Katz, J. Am. Chem. Soc. 126 (2004) 16478;
(b) R. Cacciapaglia, A. Casnati, L. Mandolini, D.N. Reinhoudt, R. Salvio, A. Sartori, R. Ungaro, J. Org. Chem. 70 (2005) 624.

[5] (a) P. Agnihotri, E. Suresh, P. Paul, P.K. Ghosh, Eur. J. Inorg. Chem. (2006) 3369;
(b) A. Ikeda, T. Tsudera, S. Shinkai, J. Org. Chem. 62 (1997) 3568;
(c) V. Csokai, A. Grün, B. Balàzs, A. Simon, G. Tóth, I. Bitter, Tetrahedron 62 (2006) 10215.

[6] (a) E. Ghidini, F. Ugozzoli, R. Ungaro, S. Harkema, A.A. El-Fadl, D.N. Reinhoudt, J. Am. Chem. Soc. 112 (1990) 6979;
(b) K. Iwamoto, S. Shinkai, J. Org. Chem. 57 (1992) 7066;
(c) A. Ikeda, S. Shinkai, J. Am. Chem. Soc. 116 (1994) 3102.

[7] (a) K. Iwamoto, K. Araki, S. Shinkai, Tetrahedron 47 (1991) 4325;
(b) K. Iwamoto, K. Araki, S. Shinkai, J. Org. Chem. 56 (1991) 4955;
(c) J. Luo, Qi-Yu. Zheng, C.-F. Chen, Z.-T. Huang, Chem. Eur. J. 11 (2005) 5917;
(d) X. Zeng, L. Weng, L. Chen, F. Xu, Q. Li, X. Leng, X. He, Z.-Z. Zhang, Tetrahedron 58 (2002) 2647.

[8] (a) C.D. Gutsche, M. Iqwal, Org. Synth. 68 (1990) 234;
(b) C.D. Gutsche, J.A. Levine, P.K. Sujeeth, J. Org. Chem. 50 (1985) 5802.

[9] M. Ouchi, Y. Inoue, T. Kanzaki, T. Hakushi, J. Org. Chem. 49 (1984) 1408.

[10] D.D. Perrin, W.L.F. Armarego, D.R. Perrin, Purification of Laboratory Chemicals, second ed., Pergamon Press, Oxford, UK, 1980.

[11] A. Casanti, A. Pochini, R. Ungaro, F. Ugozzoli, F. Arnaud, S. Fanni, M.-J. Schwing, R.J.M. Egberink, F. De Jong, D.N. Reinhoudt, J. Am. Chem. Soc. 117 (1995) 2767.

[12] Ya-Q. Hao, Y. Wu, J. Liu, G. Luo, G. Yang, J. Inclusion Phenom. Macro. Chem. 54 (2006) 171.

[13] (a) G.M. Sheldrick, SAINT and XPREP, 5.1 Ed, Siemens Industrial Automation Inc., Madison, WI, 1995;
(b) SADABS, Empirical Absorption Correction Program, University of Göttingen, Göttingen, Germany, 1997.

[14] G.M. Sheldrick, SHELXTL Reference Manual: Version 5.1, Bruker AXS, Madison, WI, 1997.

[15] G.M. Sheldrick, SHELXL-97: Program for Crystal Structure Refinement, University of Göttingen, Göttingen, Germany, 1997.

[16] A.L. Spek, PLATON-97, University of Utrecht, Utrecht, The Netherlands, 1997.

[17] MERCURY 1.3, Supplied with Cambridge Structural Database, CCDC, Cambridge, UK, 2003.

[18] (a) W. Verboom, S. Datta, Z. Asfari, S. Harkema, D.N. Reinhoudt, J. Org. Chem. 57 (1992) 5394;
(b) J. Guillon, J.-M. Leger, P. Sonnet, C. Jarry, M. Robba, J. Org. Chem. 65 (2000) 8283;
(c) C.D. Gutsche, P.A. Reddy, J. Org. Chem. 56 (1991) 4783;
(d) G. Ferguson, J.F. Gallagher, L. Giunta, P. Neri, S. Pappalardo, M. Parisi, J. Org. Chem. 59 (1994) 42.

[19] C. Danila, M. Bolte, V. Böhmer, Org. Biomol. Chem. 3 (2005) 172.

[20] A. Arduini, F. Nachtigall, A. Pochini, A. Secchi, F. Ugozzoli, Supramol. Chem. 12 (2000) 273, and references therein.

[21] E.A. Meyer, R.K. Castellano, F. Diederich, Angew. Chem., Int. Ed. 42 (2003) 1210, and references therein.

[22] P.R.A. Webber, A. Cowley, M.G.B. Drew, P.D. Beer, Chem. Eur. J. 9 (2003) 2439.

[23] S.E. Matthews, P. Schmitt, V. Felix, M.G.B. Drew, P.D. Beer, J. Am. Chem. Soc. 124 (2002) 1341.

[24] K. Nakamoto, Infrared Spectra of Inorganic and Coordination Compounds, John Wiley and Sons, New York, 1963, p. 155.

[25] (a) J. Hu, L.J. Barbour, G.W. Gokel, Chem. Commun. (2002) 1808;
(b) D.-Q. Wang, J.-M. Dou, M.-J. Niu, D.-C. Li, Y. Liu, Acta Chim. Sinica 60 (2002) 2145.

Fc–C_6H_4–C≡CH and C_6H_5–C≡CH. Complexes [Fc–C_6H_4–$(C≡C)_n$–R][$Co_2(CO)_6$]$_{n'}$[Fc = $C_5H_5FeC_5H_4$, R = H, $n = 1$, $n' = 1$ (**1**); R = C_6H_5, $n = 2$, $n' = 2$ (**2**); R = Fc–C_6H_4, $n = 2$, $n' = 2$ (**3**)] were obtained by the reactions of compounds Fc–C_6H_4–C≡CH [24], Fc–C_6H_4–C≡C–C≡C–C_6H_5 (**L**) and Fc–C_6H_4–$(C≡C)_2$–C_6H_4–Fc [25] with excess $Co_2(CO)_8$, respectively (see Scheme 1). Compound **L** contains a linear C_5H_4–C_6H_4–$(C≡C)_2$–C_6H_5 linkage. One alkyne bond (for **1**) or two alkyne bonds (for **2** and **3**) coordinate with the Co–Co bonds in complexes **1**, **2** and **3**. Compound **L** is an orange yellow, air-stable crystalline compound that is soluble in both non-polar solvents such as benzene and polar solvents such as diethyl ether or chloroform. Complexes **2** and **3** are black, air-stable crystalline compounds, with solubilities similar to compound **L**. Complex **1** is a purple-black, air-stable crystalline compound, but it is air-sensitive in solution.

The absorbing peaks of the FT-IR spectra in the region 2100–2013 cm^{-1} correspond to the stretching vibrations of the coordinated CO groups, which confirm that there are coordinated $Co_2(CO)_6$ species. ^1H and ^{13}C NMR spectra reflect that there are the appropriate Fc, Ph, C≡C and CO groups in **L**, **1**, **2** and **3**. The structure and composition of compounds **L**, **1**, **2** and **3** are proven further by their elemental analyses and MS data.

2.2. Molecular structures of compounds *L* and *2*

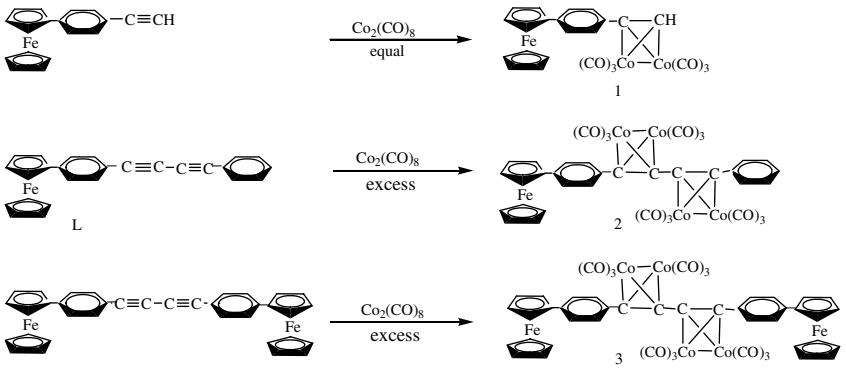
The crystal and molecular structures of compounds **L** and **2** were determined by X-ray single crystal analysis. Crystal data and relevant structural parameters are given in Table 1. The structures with the atom numbering schemes are shown in Figs. 1 and 2, and the selected bond lengths and angles are listed in Table 2.

The molecule of compound **L** contains a butadiynyl chain, of which the terminal groups are phenyl and *p*-ferrocenylphenyl groups (see Fig. 1). The bond distances C(12)–C(13) [1.198(5) Å] and C(14)–C(15) [1.195(5) Å] show there are two C≡C triple bonds in **L**. The shorter C(9)–C(12) [1.436(5) Å], C(13)–C(14) [1.370(6) Å] and C(15)–C(16) [1.437(5) Å] bond distances, compared to the classical single bond length, are the result of electron delocalization of the C_4 diyne chain, phenyl and ferrocenylphenyl units. The data of the bond angles [C(9)–C(12)–C(13), 178.9(4)°; C(12)–C(13)–C(14), 177.1(4)°; C(13)–C(14)–C(15), 178.8(4)°; C(14)–C(15)–C(16), 178.7(4)°] demonstrate the carbon chain C(9)C(12)C(13)C(14)C(15)C(16) has a nearly linear structure.

The molecule of complex **2** contains two approximately tetrahedral μ-alkyne dicobalt moieties bound to the ferr-

Table 1
Crystal data and structure refinement for **L**, **2**

Identification code	**L**	**2**
Empirical formula	$C_{26}H_{18}Fe$	$C_{38}H_{18}O_{12}Co_4Fe$
Formula weight	386.25	958.09
Temperature (K)	298(2)	298(2)
Wavelength (Å)	0.71073	0.71073
Crystal system	triclinic	monoclinic
Space group	$P\bar{1}$	$P2(1)/n$
Unit cell dimensions		
a (Å)	7.158(3)	19.051(4)
b (Å)	9.875(4)	9.6101(19)
c (Å)	14.643(6)	22.547(4)
α (°)	76.357(6)	90
β (°)	82.288(5)	113.143(2)
γ (°)	69.624(5)	90
Volume (Å^3), Z	941.4(6), 2	3795.7(13), 4
Calculated density (Mg/m^3)	1.363	1.677
Absorption coefficient (mm^{-1})	0.807	2.146
$F(000)$	400	1904
Crystal size (mm)	0.15 × 0.15 × 0.10	0.15 × 0.12 × 0.08
θ Range for data collection (°)	1.43–26.01	1.19–26.00
Limiting indices	$-8 \leqslant h \leqslant 8$, $-12 \leqslant k \leqslant 10$, $-16 \leqslant l \leqslant 18$	$-22 \leqslant h \leqslant 23$, $-11 \leqslant k \leqslant 5$, $-27 \leqslant l \leqslant 27$
Reflections collected	4300	16 124
Independent reflections (R_{int})	3591 (0.0286)	7419 (0.0361)
Completeness to θ	97.2%	99.4%
Maximum and minimum transmission	0.9236 and 0.8885	0.8470 and 0.7390
Data/restraints/parameters	3591/0/244	7419/0/496
Goodness-of-fit on F^2	0.987	1.237
Final R indices [$I > 2\sigma(I)$]	$R_1 = 0.0572$, $wR_2 = 0.1102$	$R_1 = 0.0691$, $wR_2 = 0.1463$
R indices (all data)	$R_1 = 0.0861$, $wR_2 = 0.1186$	$R_1 = 0.0899$, $wR_2 = 0.1534$
Largest difference peak and hole (e Å^{-3})	0.506 and −0.277	0.478 and −0.422



Scheme 1.

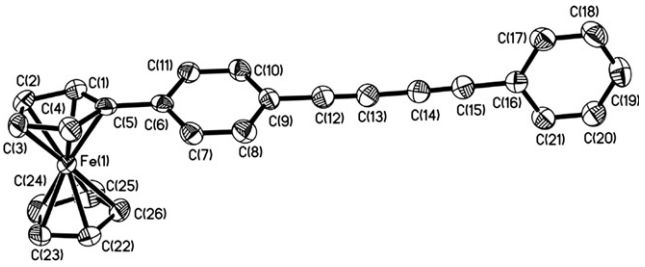


Fig. 1. Molecular structure of **L**.

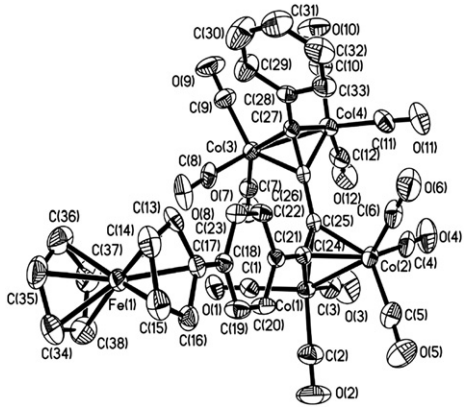


Fig. 2. Molecular structure of **2**.

ocenylphenyl and phenyl units. In **2** the CO ligands coordinated to the Co atoms are terminal (vide IR) and the alkyne bonds adopt the typical μ_2-η^2 coordination fashion, with the alkyne bond lying essentially perpendicular to the Co–Co bond in the C_2Co_2 units. The Co–Co bond distances, in the range 2.452–2.461 Å, are classical values for Co–Co bond lengths of similar complexes. The coordinated alkyne bond lengths of **2** [C(24)–C(25)1.349(7) Å; C(26)–C(27)1.355(8) Å] are longer than that of **L** [C(12)–C(13) (1.198(5) Å) and C(14)–C(15) (1.195(5) Å)] and are similar to the classical alkene bond length due to $Co_2(CO)_6$ units coordinated by diyne bonds. In complex **2** the bond angle data [C(21)–C(24)–C(25), 140.2(5)°; C(24)–C(25)–C(26), 141.1(5)°; C(25)–C(26)–C(27), 141.3(5)°; C(26)–C(27)–C(28), 144.9(5)°] demonstrate the construction of **L** is altered from a linear to a non-linear structure while **L** is coordinated to the $Co_2(CO)_6$ units. It is noteworthy that the $Co_2(CO)_6$ units are coordinated to the alkyne bond in a *trans* arrangement and the two terminal groups (phenyl and ferrocenylphenyl) are in a *cis* arrangement (see Fig. 2). Because of the large ferrocenylphenyl substituted group, the molecular structure of **2** is quite different from [Fc–C≡C–C≡C–C_6H_5][$Co_2(CO)_6$]$_2$ [20].

In **L** the dihedral angle [1.85(0.28)°] between plane 1 [C(22)C(23)C(24)C(25)C(26)] and plane 2 [C(1)C(2)C(3)-C(4)C(5)] shows that the two Cp planes in the Fc group are nearly parallel. The dihedral angle [16.15(0.21)°] between plane 2 and plane 3 [C(6)C(7)C(8)C(9)C(10)C(11)] is deviated from parallel, and the dihedral angle [74.39(0.13)°] between the two phenyl rings, that is plane 3 and plane 4 [C(16)C(17)C(18)C(19)C(20)C(21)], is nearly perpendicular.

In **2** the dihedral angle [0.45(0.59)°] of the two Cp rings shows that they are nearly parallel. It is interesting that the dihedral angle [9.20(0.47)°] between the planes of the Cp ring [C(13)C(14)C(15)C(16)C(17)] and the phenyl ring [C(18)C(19)C(20)C(21)C(22)C(23)] becomes smaller than that of **L**. The dihedral angle between the two phenyl rings [C(18)C(19)C(20)C(21)C(22)C(23)] and [C(28)C(29)C(30)-C(31)C(32)C(33)] alters from 74.39(0.13)° to 86.71(0.23)°. The changes of the dihedral angles in **2** show that the increased steric requirements on the coordinated $Co_2(CO)_6$ groups lead to a twisting of the substituents away from each other.

3. Experimental

3.1. General procedures

All reactions and manipulations were carried out using standard Schlenk techniques under an atmosphere of pure

Table 2
Selected bond lengths (Å) and angles (°) for **L**, **2**

Bond lengths				Bond angles			
L							
C(1)–C(5)	1.432 (5)	C(12)–C(13)	1.198(5)	C(3)–C(4)–C(5)	109.1(4)	C(12)–C(13)–C(14)	177.1(4)
C(5)–C(6)	1.468(5)	C(13)–C(14)	1.370(6)	C(4)–C(5)–C(6)	127.2(4)	C(13)–C(14)–C(15)	178.8(4)
C(6)–C(11)	1.390(5)	C(14)–C(15)	1.195(5)	C(5)–C(6)–C(7)	121.4(3)	C(14)–C(15)–C(16)	178.7(4)
C(8)–C(9)	1.395(5)	C(15)–C(16)	1.437(5)	C(8)–C(9)–C(12)	120.7(4)	C(16)–C(17)–C(18)	120.6(4)
C(9)–C(12)	1.436(5)	C(16)–C(17)	1.387(5)	C(9)–C(12)–C(13)	178.9(4)	C(15)–C(16)–C(21)	121.4(4)
2							
Co(1)–Co(2)	2.452(1)	Co(4)–C(26)	1.952(5)	C(24)–Co(1)–Co(2)	51.8(2)	C(15)–C(16)–C(17)	108.7(6)
Co(1)–C(24)	1.952(5)	Co(4)–C(27)	1.968(5)	C(24)–Co(2)–Co(1)	51.0(2)	C(17)–C(18)–C(19)	121.1(5)
Co(1)–C(25)	1.989(6)	C(20)–C(21)	1.385(8)	C(25)–Co(1)–Co(2)	51.3(2)	C(20)–C(21)–C(24)	122.0(5)
Co(2)–C(24)	1.975(5)	C(21)–C(24)	1.449(7)	C(25)–Co(2)–Co(1)	52.1(2)	C(21)–C(24)–C(25)	140.2(5)
Co(2)–C(25)	1.967(5)	C(24)–C(25)	1.349(7)	C(26)–Co(3)–Co(4)	50.9(2)	C(24)–C(25)–C(26)	141.1(5)
Co(3)–Co(4)	2.461(1)	C(25)–C(26)	1.435(8)	C(26)–Co(4)–Co(3)	51.3(2)	C(25)–C(26)–C(27)	141.3(5)
Co(3)–C(26)	1.963(5)	C(26)–C(27)	1.355(8)	C(27)–Co(3)–Co(4)	51.5(2)	C(26)–C(27)–C(28)	144.9(5)
Co(3)–C(27)	1.942(6)	C(27)–C(28)	1.463(8)	C(27)–Co(4)–Co(3)	50.5(2)	C(27)–C(28)–C(29)	121.5(6)

nitrogen. Solvents were purified, dried and distilled under a nitrogen atmosphere prior to use. Reactions were monitored by TLC. Chromatographic separations and purifications were performed on 200–300 mesh silica gel. $Co_2(CO)_8$ was purchased from Alfa Aesar. The ligands Fc–C_6H_4–C≡CH and Fc–C_6H_4–(C≡C)$_2$–C_6H_4–Fc were prepared according to the literature methods [24,25].

IR spectra were recorded on a Nicolet FT-IR spectrometer, as KBr discs. Elemental analyses were carried out on an Elementar var III-type analyzer. ^{1}H and ^{13}C NMR spectra in $CDCl_3$ were recorded on a Bruker Avance-500 MHz spectrometer. The mass spectra were determined by using a Polaris Q MS, Micromass LCT instrument. Melting points were determined by using XT-4 melting point apparatus.

3.2. Synthesis of compound Fc–C_6H_4–(C≡C)$_2$–C_6H_5 (**L**)

Fc–C_6H_4–C≡CH (57 mg, 0.2 mmol), C_6H_5–C≡CH (40 mg, 0.40 mmol) and CuCl (9 mg, 0.09 mmol) were dissolved in 8 ml pyridine. This solution was stirred for 3 h in air at 60 °C. The solvent was removed under reduced pressure. The resulting mixture was washed with saturated NH_4Cl solution and extracted with CH_2Cl_2. The organic phase was incorporated and then dried using the dehydrated $MgSO_4$ and filtrated. The solvent was removed under reduced pressure. The residue was purified by neutral alumina column chromatography using hexane as the eluant. Crystals of **L** were obtained by recrystallizing solid **L** from hexane at −15 °C. Yield: 28%. m.p. 212–213 °C. *Anal*. Calc. for $C_{26}H_{18}Fe$: C, 80.83; H, 4.66. Found: C, 80.43; H, 4.70%. IR (KBr disk, cm^{-1}) ν 815s, 1004m, 1173 m, 1593s, 1521 m, 2146 m, 2208 m, 2852 m, 2924 m, 2960 m. ^{1}H NMR ($CDCl_3$, δ): 4.07–4.70 (m, 9H, Fc), 7.26–7.54 (m, 9H, C_6H_5, C_6H_4). ^{13}C NMR ($CDCl_3$, δ): 66.7–70.0 (Cp), 73.9–82.1 (2C≡C), 118.7–141.2 (2Ph). MS (EI) 386 (M^+).

3.3. Synthesis of complex [Fc–C_6H_4–C≡C–H][$Co_2(CO)_6$] (**1**)

A benzene solution of $Co_2(CO)_8$ (120 mg, 0.35 mmol) and Fc–C_6H_4–C≡CH (100 mg, 0.35 mmol) was stirred for 4 h at room temperature. The solvent of the resulting dark purple mixture was removed in vacuum. The residue was dissolved in a minimal amount of benzene and subjected to chromatographic separation on a silica gel column (2.0 × 40 cm). Elution with hexane afforded a purple-red band (**1**). Crystals of **1** were obtained by recrystallizing solid **1** from hexane at −20 °C. Complex **1**: Yield: 60%. m.p. 132–134 °C. *Anal*. Calc. for $C_{24}H_{14}O_6Co_2Fe$: C, 50.35; H, 2.45. Found: C, 49.90; H, 2.47%. IR (KBr disk, cm^{-1}) ν_{CO} 2013vs, 2054s, 2095s. ^{1}H NMR ($CDCl_3$, δ): 4.07–4.65 (m, 9H, Fc), 6.4 (s, 1H, –C≡C–H), 7.26–7.43 [m, 4H, C_6H_4]. ^{13}C NMR ($CDCl_3$, δ): 66.6–72.7 (Cp), 90.3, 84.7 (–C≡CH), 126.5–139.9 (C_6H_4), 199.5 (CO). MS (ESI): 572 (M^+).

3.4. Synthesis of complex [Fc–C_6H_4–(C≡C)$_2$–C_6H_5][$Co_2(CO)_6$]$_2$ (**2**)

A benzene solution of $Co_2(CO)_8$ (240 mg, 0.70 mmol) and compound **L** (135 mg, 0.35 mmol) was stirred for 4 h at room temperature. The solvent of the resulting dark mixture was removed in vacuum. The residue was dissolved in a minimal amount of benzene and subjected to chromatographic separation on a silica gel column (2.0 × 40 cm). Elution with hexane afforded a dark band (**2**). Crystals of **2** were obtained by recrystallizing solid **2** from hexane at −20 °C. Complex **2**: Yield: 65%. m.p. 164–165 °C. *Anal*. Calc. for $C_{38}H_{18}O_{12}Co_4Fe$: C, 47.60; H, 1.88. Found: C, 47.08; H, 1.85%. IR (KBr disk, cm^{-1}) ν_{CO} 2013vs, 2054vs, 2084s, 2100s. ^{1}H NMR ($CDCl_3$, δ): 4.04–4.67 (m, 9H, Fc), 7.26–7.51 (m, 9H, C_6H_5, C_6H_4). ^{13}C NMR ($CDCl_3$, δ): 66.5–69.7 (Cp), 84.4 (C≡C), 126.1–139.7 (C_6H_5, C_6H_4), 198.5 (CO). MS (ESI): 959 (M^++1).

3.5. Synthesis of complex [Fc–C_6H_4–(C≡C)$_2$–C_6H_4–Fc][$Co_2(CO)_6$]$_2$ (**3**)

A benzene solution of $Co_2(CO)_8$ (240 mg, 0.70 mmol) and Fc–C_6H_4–(C≡C)$_2$–C_6H_4-Fc (200 mg, 0.35 mmol) was stirred for 4 h at room temperature. The solvent of the resulting dark mixture was removed in vacuum. The residue was dissolved in a minimal amount of benzene and subjected to chromatographic separation on a silica gel column (2.0 × 40 cm). Elution with hexane afforded a black band (**3**). Crystals of **3** were obtained by recrystallizing solid **3** from hexane at −20 °C. Complex **3**: Yield: 69%; m.p. 300 °C (dec.). *Anal*. Calc. for $C_{48}H_{26}O_{12}Co_4Fe_2$: C, 50.44; H, 2.28. Found: C, 50.14; H, 2.91%. IR (KBr disk, cm^{-1}) ν_{CO} 2088vs, 2047vs, 2014s, 2000s. ^{1}H NMR ($CDCl_3$, δ): 4.05–4.67 (m, 18H, Fc), 7.26–7.44 (m, 8H, 2C_6H_4). ^{13}C NMR ($CDCl_3$, δ): 66.5–69.7 (Cp), 84.3–99.7 (2C≡C), 126.1–139.7 (2C_6H_4), 198.5 (CO). MS (ESI): 1142 (M^+).

3.6. X-ray crystallography of compounds **L** (**2**)

The black crystals of compounds **L** and **2** were mounted on a glass fibers. All measurements were made on a Bruker SMART APEX CCD diffractometer with graphite monochromated Mo Kα ($\lambda = 0.71073$ Å) radiation. All data were collected at 20 °C using the ϕ and ω scan techniques. All structures were solved by direct methods and expanded using the Fourier technique [26]. An absorption correction based on SADABS was applied [27]. All non-hydrogen atoms were refined by full matrix least-squares on F^2. Hydrogen atoms were located and refined by the geometry method. The cell refinement, data collection and reduction were done by Bruker SMART and SAINT [28]. The structure solution and refinement were performed by SHELXSL 97 [29]. The further crystal data and details of measurements are shown in Table 1.

4. Conclusion

A new ferrocenylphenyl butadiynyl ligand Fc–C_6H_4–$(C{\equiv}C)_2$–C_6H_5 has been synthesized by the Glaser cross-coupling reaction and three new cobalt coordinated complexes **1**, **2**, **3** have successfully been obtained by the addition reaction of $Co_2(CO)_6$ units to the alkyne bonds of *p*-ferrocenylphenylacetylene compounds. The synthesis and structure of compounds **L** and **2** are reported for the first time. The molecular structure of complex **2** shows that the $Co_2(CO)_6$ units coordinated to the alkyne bonds are in a *trans* arrangement. The molecular structure data demonstrate that the butadiynyl groups of ligand **L** are nearly linear and the coordinated butadiynyl groups in **2** have deviated from a linear structure.

Acknowledgements

We are grateful to the Specialized Research Fund for the Doctoral Program of Higher Education of China (20060128001) and the Natural Science Foundation of Inner Mongolia for financial support of this work.

Appendix A. Supplementary material

CCDC 648852 and 648853 contain the supplementary crystallographic data for **L** and **2**. These data can be obtained free of charge via http://www.ccdc.cam.ac.uk/conts/retrieving.html, or from the Cambridge Crystallographic Data Centre, 12 Union Road, Cambridge CB2 1EZ, UK; fax: (+44) 1223-336-033; or e-mail: deposit@ccdc.cam.ac.uk.

References

[1] A. Tarraga, P. Molina, D. Curiel, M.D. Velasco, Organometallics 20 (2001) 2145.
[2] R. Dembinski, T. Bartik, B. Bartik, M. Jaeger, J.A. Gladysz, J. Am. Chem. Soc. 122 (2000) 810.
[3] (a) J.M. Tour, Chem. Rev. 96 (1996) 537;
(b) A.C. Ribou, J.P. Launay, M.L. Sachtleben, H. Li, C.W. Spangler, Inorg. Chem. 35 (1996) 3735.
[4] (a) F. Paul, C. Lapinte, Coord. Chem. Rev. 180 (1998) 431;
(b) F. Paul, W.E. Meyer, L. Toupet, H.J. Jiao, J.A. Gladysz, C. Lapinte, J. Am. Chem. Soc. 122 (2000) 9405.
[5] B. Jacques, J.P. Tranchier, F.R. Munch, E. Rose, Organometallics 23 (2004) 84.
[6] T.M. Friedrichsen, H. Wong, M.H. Prosenc, J.E. Heck, Eur. J. Inorg. Chem. 5 (2003) 936.
[7] F. Paul, C. Lapinte, Coord. Chem. Rev. 178–180 (1998) 431.
[8] N.J. Long, C.K. Williams, Angew. Chem. Int. Ed. 42 (2003) 2586.
[9] C.J. McAdam, N.W. Duffy, B.H. Robinson, J. Simpson, Organometallics 15 (1996) 3935.
[10] C.J. McAdam, N.W. Duffy, B.H. Robinson, J. Simpson, J. Organomet. Chem. 527 (1997) 179.
[11] R.D. Adams, O.S. Kwon, B. Qu, M.D. Smith, Organometallics 20 (2001) 5225.
[12] M.I. Bruce, K. Costuas, T. Davin, B.G. Ellis, J.F. Halet, C. Lapinte, P.J. Low, M.E. Smith, B.W. Skelton, L. Toupet, A.H. White, Organometallics 24 (2005) 3864.
[13] A. Klein, O. Lavastre, J. Fiedler, Organometallics 25 (2006) 635.
[14] N. Duffy, J. McAdam, C. Nervi, D. Osella, M. Ravera, B. Robinson, J. Simpson, Inorg. Chim. Acta 247 (1996) 99.
[15] C.J. McAdam, N.W. Duffy, B.H. Robinson, J. Simpson, Organometallics 15 (1996) 3935.
[16] M.C. Chung, A. Sakurai, M. Akita, Y.M. Oka, Organometallics 18 (1999) 4684.
[17] T.J.J. Müller, J. Blümel, J. Organomet. Chem. 683 (2003) 354.
[18] P. Butler, J.F. Gallagher, A.R. Manning, H.M. Bunz, C.J. McAdam, J. Simpson, B.H. Robinson, J. Organomet. Chem. 690 (2005) 4545.
[19] R.D. Adams, B. Qu, M.D. Smith, Organometallics 21 (2002) 3867.
[20] N. Zhu, Q.L. Suo, Y.B. Wang, L.M. Han, Y.G. Bai, L.H. Weng, Polyhedron 26 (2007) 981.
[21] Q.L. Suo, N. Zhu, L.M. Han, Y.B. Wang, Y.G. Bai, L.H. Weng, Polyhedron 25 (2006) 3209.
[22] L.M. Han, Q.L. Suo, Y.B. Wang, J.H. Ye, N. Zhu, X.B. Leng, J. Sun, Polyhedron 24 (2005) 759.
[23] C. Glaser, Ber. Dtsch. Chem. Ges. 2 (1869) 422.
[24] C.R. Simionescu, T. Lixandru, I. Mazilu, L. Tataru, J. Organomet. Chem. 113 (1976) 23.
[25] W.Y. Wong, K.Y. Ho, S.L. Ho, Z.Y. Lin, J. Organomet. Chem. 683 (2003) 341.
[26] G.M. Sheldrick, Acta Crystallogr., Sect. A 46 (1990) 467.
[27] G.M. Sheldrick, SADABS. Siemens Area Detector Absorption, Correction Software. University of Göttingen, Germany, 1997.
[28] Bruker. SMART and SAINT. Area Detector Control and Integration Software. Bruker Analytical X-ray Instruments Inc., Madison, WI, USA, 1998.
[29] Bruker. SHELXTL. Bruker Analytical X-ray Instruments Inc., Madison, WI, USA 1997.

2. Results and discussion

2.1. Synthesis and spectroscopic characterization of complexes 1–4

By reaction of $[(C_5H_4SiMe_2{}^tBu)_2Ln(\mu\text{-}Me)]_2$ with 2 equiv of elemental sulfur in toluene at room temperature, we synthesized new complexes $[(C_5H_4SiMe_2{}^tBu)_2Ln(\mu\text{-}SMe)]_2$ [Ln = Yb (**1**), Er (**2**), Dy (**3**), Y (**4**)] in good yields. The formation of complexes **1-4** was interpreted as one sulfur atom insertion into the Ln–C(Me) bond of $[(C_5H_4SiMe_2{}^tBu)_2Ln(\mu\text{-}Me)]_2$, as shown in Scheme 1.

Complexes **1**–**4** are highly soluble in THF and soluble in toluene and *n*-hexane. They are sensitive to moisture and air. The four methylthiolate complexes were characterized by elemental analysis, IR and MS spectroscopies, which were in good agreement with the proposed structures. The spectroscopic properties of **1**–**4** are very similar, indicating that they have similar structures. Compounds **1** and **3** were also characterized crystallographically. The IR spectra of these complexes show characteristic absorptions of the η^5-$C_5H_4SiMe_2{}^tBu$ group at about 3085, 1460, 1007, 774 cm^{-1}. Although the molecule ion peaks of these complexes are not observed in the mass spectra, their main fragments are observed, such as $[M/2]^+$, $[M/2-Me]^+$, and $[M/2-SMe]^+$.

Complex **1** crystallized from the solvent mixture of tetrahydrofuran and toluene in triclinic system, space group $P\bar{1}$. An ORTEP diagram of **1** is shown in Fig. 1. Selected bond distances and angles are given in Table 1. The X-ray structure of **1** definitively proves that only one sulfur atom is inserted into the Yb–C bond, giving a thiolate ligand. Complex **1** is a solvent-free dimeric structure with each ytterbium coordinated by two η^5-$C_5H_4SiMe_2{}^tBu$ groups and two bridging sulfur atoms. The coordination number of ytterbium atom is eight, which is common as those of many lanthanocene thiolates complexes. The average Yb–S distance of 2.706 Å is comparable with the values found in the related thiolate-bridged complexes $[Cp_2Yb(\mu\text{-}SMe)]_2$ (2.706(4) Å) and $[Cp_2Yb(\mu\text{-}S^nBu)]_2$ (2.707(3) Å) [7], but is shorter than that found in $Cp_2Yb(SBT)(THF)$ (SBT = benzothiazole-2-thiolate) (2.843 Å) [6d]. The S–C bond distance of 1.826(5) Å is in the normal range for a sulfur–carbon (sp^3) single bond [9] and is similar to the values reported in other complexes containing thiolate ligands [7]. In the Yb_2S_2 bridging unit, the angles of Yb–S–Yb and S–Yb–S are respectively 97.4(1)° and 82.6(1)°, which are similar to the corresponding values in $[Cp_2Yb(\mu\text{-}SMe)]_2$ and $[Cp_2Yb(\mu\text{-}S^nBu)]_2$ [7], but very different from the observations in $[(Me_3CC_5H_4)_2Ce(\mu\text{-}SCHMe_2)]_2$ [6c].

As shown in Fig. 1, complex **3** is isostructural to complex **1** and is also a symmetrical dimeric structure. The

$$[(C_5H_4SiMe_2{}^tBu)_2LnMe]_2 \xrightarrow[\text{toluene}]{1/4\ S_8} [(C_5H_4SiMe_2{}^tBu)_2Ln(\mu\text{-}SMe)]_2$$

Ln = Yb(**1**), Er(**2**), Dy(**3**), Y(**4**)

Scheme 1.

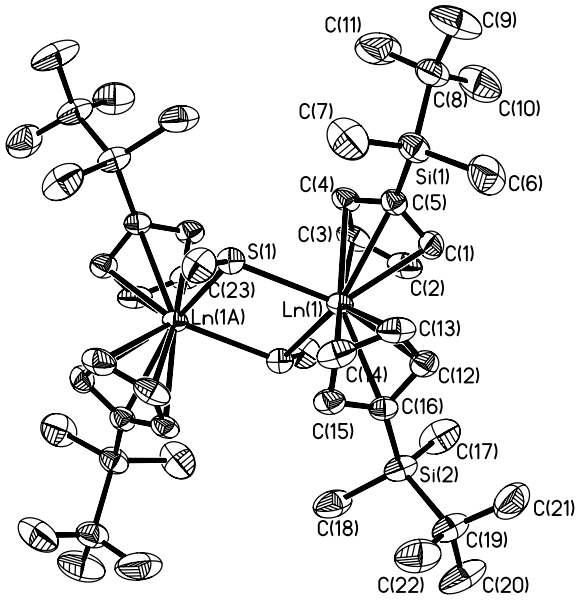


Fig. 1. ORTEP diagram of $[(C_5H_4SiMe_2{}^tBu)_2Ln(\mu\text{-}SMe)]_2$ [Ln = Yb (**1**), Dy (**3**)] with the probability ellipsoids drawn at the 30% level. Hydrogen atoms are omitted for clarity.

Table 1
Selected bonds lengths (Å) and angles (°) for complex **1** and **3**

	Ln = Yb (**1**)	Ln = Dy (**3**)
Ln(1)–C(1)	2.580(5)	2.655(4)
Ln(1)–C(2)	2.576(5)	2.615(4)
Ln(1)–C(3)	2.602(5)	2.628(4)
Ln(1)–C(4)	2.610(5)	2.661(5)
Ln(1)–C(5)	2.609(5)	2.657(4)
Ln(1)–C(12)	2.578(5)	2.646(4)
Ln(1)–C(13)	2.588(5)	2.619(5)
Ln(1)–C(14)	2.616(5)	2.626(5)
Ln(1)–C(15)	2.617(5)	2.644(5)
Ln(1)–C(16)	2.632(4)	2.640(5)
S(1)–C(23)	1.826(5)	1.825(5)
Ln(1)–S(1)	2.6987(14)	2.7350(14)
Ln(1A)–S(1)	2.7130(15)	2.7536(14)
C(23)–S(1)–Ln(1)	118.8(2)	118.67(18)
Ln(1)–S(1)–Ln(1A)	97.40(4)	96.70(4)
C(23)–S(1)–Ln(1A)	117.0(2)	117.34(19)
S(1)–Ln(1)–S(1A)	82.60(4)	83.30(4)

structural parameters of **3** (Table 1) are very similar to those for complex **1**. The Dy–C(Cp) distances range from 2.615(4) to 2.661(4) Å, and the average value of 2.639(5) Å is similar to those found in other Cp_2Ln-containing lanthanide complexes, such as $Cp_2Dy(SBT)(THF)$ (2.65(3) Å) [6d]. The Dy–S and Dy–C distances are comparable to the corresponding distances in complex **1**, respectively, when the difference in the metal ionic radii is considered [10].

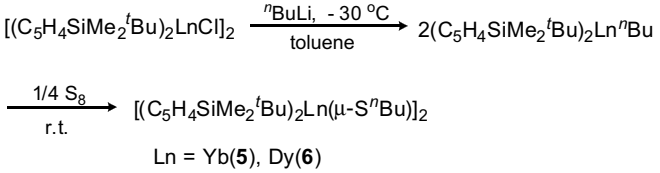
2.2. Synthesis and spectroscopic characterization of complexes 5 and 6

In order to understand the factors affecting the insertion of sulfur into the lanthanide–carbon bond, the reactivity of

the corresponding *n*-butyl complexes with elemental sulfur was also studied. In contrast to the previously observation that reaction of $Cp_2Y(^nBu)$ with elemental sulfur in 1:1 stoichiometric ratio at room temperature yields $[(Cp_2Y)_2(\mu_3\text{-}S)(THF)]_2$ as the metal-containing product with the extrusion of $^nBuS^nBu$ and $^nBuSS^nBu$ [7], under the same conditions $(C_5H_4SiMe_2{}^tBu)_2Ln^nBu$ (prepared in situ from $[(C_5H_4SiMe_2{}^tBu)_2LnCl]_2$ and Li^nBu) undergo smooth insertion of sulfur into Ln–C bond to give the insertion products $[(C_5H_4SiMe_2{}^tBu)_2Ln(\mu\text{-}S^nBu)]_2$ [Ln = Yb (**5**), Dy (**6**)] (Scheme 2). Attempts to obtain the corresponding lanthanocene sulfide or disulfide complexes by reacting $(C_5H_4SiMe_2{}^t\text{-}Bu)_2Ln^nBu$ with a slight excess of elemental sulfur were unsuccessful. The reasons why $[(C_5H_4SiMe_2{}^tBu)_2Ln(\mu\text{-}S^nBu)]_2$ are more stable in solution with S_8 than $[(C_5H_5)_2Ln(\mu\text{-}S^nBu)]_2$ are as yet unclear, but may reflect the greater steric hindrance of *tert*-butyldimethylsilylcyclopentadienyl in comparison to cyclopentadienyl. These results demonstrate that the nature of cyclopentadienyl co-ligands has great influence on the final product from the reaction of lanthanocene alkyls with elemental sulfur. The formation of complexes **5** and **6** further proves that substituted lanthanocene alkyl complexes exhibit high activity toward elemental sulfur, leading to thiolate ligands.

The two butylthiolate complexes are air- and moisture-sensitive. They are readily dissolved in THF and soluble in toluene and *n*-hexane. Complexes **5** and **6** were characterized by elemental analysis, IR, mass spectroscopies and X-ray single crystal diffraction analysis, which were in agreement with the proposed structures. The IR spectra of these complexes show that the characteristic absorptions of the $\eta^5\text{-}C_5H_4SiMe_2{}^tBu$ group.

Complexes **5** and **6** crystallize from the solvent toluene in monoclinic system, space group $P2(1)/c$. The X-ray structures of **5** and **6** definitively prove that only one sulfur atom is inserted into the Ln–C(^{n}Bu) bond, giving a thiolate ligand. Fig. 2 shows the molecule structure of **5** and **6** and their selected bond distances and angles are listed in Table 2. Complexes **5** and **6** are isostructural and centresymmetrical dimeric structures. In the two complexes, each Ln^{3+} ion is coordinated by two $\eta^5\text{-}C_5H_4SiMe_2{}^tBu$ groups and two sulfur atoms. The Yb–S distances are similar to that found in complex **1**. The S–C bond distance of 1.841(12) Å is in the normal range for a sp^3 sulfur–carbon single bond and similar to the distances reported in other complexes containing SR groups [9]. All the distances and angles of complex **6** (Table 2) are in normal range,



Scheme 2.

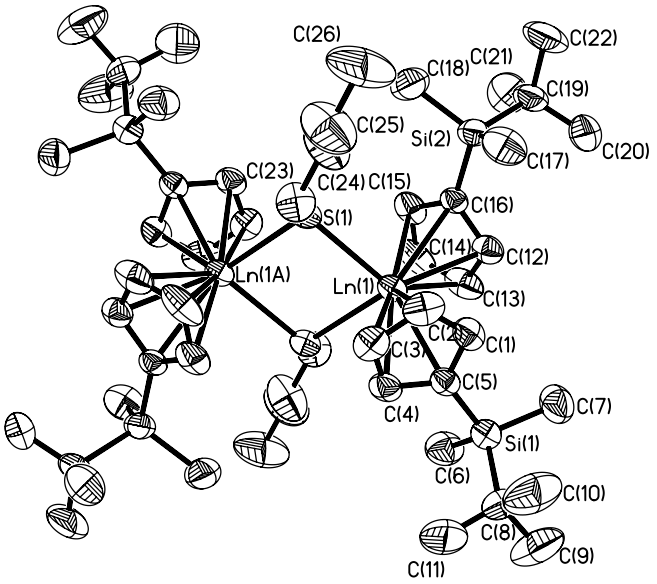


Fig. 2. ORTEP diagram of $[(C_5H_4SiMe_2{}^tBu)_2Ln(\mu\text{-}S^nBu)]_2$ [Ln = Yb (**5**), Dy (**6**)] with the probability ellipsoids drawn at the 30% level. Hydrogen atoms are omitted for clarity.

Table 2
Selected bonds lengths (Å) and angles (°) for complex **5** and **6**

	Ln = Yb (**5**)	Ln = Dy (**6**)
Ln(1)–C(1)	2.606(13)	2.638(9)
Ln(1)–C(2)	2.596(12)	2.642(8)
Ln(1)–C(3)	2.579(12)	2.643(9)
Ln(1)–C(4)	2.585(12)	2.638(9)
Ln(1)–C(5)	2.595(12)	2.642(8)
Ln(1)–C(12)	2.601(13)	2.636(9)
Ln(1)–C(13)	2.592(14)	2.634(9)
Ln(1)–C(14)	2.583(14)	2.646(9)
Ln(1)–C(15)	2.604(12)	2.662(9)
Ln(1)–C(16)	2.632(12)	2.667(8)
S(1)–C(23)	1.841(12)	1.850(9)
Ln(1)–S(1A)	2.713(3)	2.761(3)
S(1A)–Ln(1)–S(1)	84.19(11)	84.65(7)
Ln(1A)–S(1)–Ln(1)	95.81(11)	95.35(7)
C(23)–S(1)–Ln(1)	118.0(5)	117.3(4)
C(23)–S(1)–Ln(1A)	116.5(5)	116.4(4)

and the angles of Dy–S–Dy [95.4(1)°] and S–Dy–S [84.6(1)°] are similar to the corresponding values in complex **5**, when the different ionic radii of the center metals is considered.

3. Conclusion

The results of this study offer an interesting contrast to the known cyclopentadienyl-type organolanthanide alkyl complexes. With a cyclopentadienyl group as a co-ligand, insertion of sulfur into the Ln–C bond is only available for methyl complexes at room temperature, whereas the *n*-butyl complexes undergo facile conversion to lanthanocene

sulfides via the competitive interaction of the resultant thiolate intermediate with the remaining sulfur, followed by the intermolecular elimination of thioether or organic disulfide. The corresponding insertion intermediate $[Cp_2Ln(\mu\text{-}S^nBu)]_2$ could be only isolated in the presence of excess $Cp_2Ln(^nBu)$ under more mild reaction conditions. In contrast, for the present *tert*-butyldimethylsilylcyclopentadienyl ligand system, under the same reaction conditions, insertion is available for both methyl and butyl complexes, and these complexes undergo smooth insertion of sulfur into lanthanide–alkyl bond to give the corresponding insertion products $[(C_5H_4SiMe_2{}^tBu)_2Ln(\mu\text{-}SMe)]_2$ and $[(C_5H_4SiMe_2{}^tBu)_2Ln(\mu\text{-}S^nBu)]_2$, respectively. All these results confirm that the insertion of sulfur into the lanthanide-alkyl bond is general.

4. Experimental

4.1. General procedures

All operations involving air- and moisture-sensitive compounds were carried out under an inert atmosphere of purified nitrogen using standard Schlenk techniques. The solvents of THF, toluene and *n*-hexane were refluxed and distilled over sodium benzophenone ketyl under nitrogen immediately prior to use. $[Cp^t_2Ln(\mu\text{-}Cl)]_2$ [11], $[Cp^t_2Ln(\mu\text{-}Me)]_2$ [12] and $Cp^t_2Ln^nBu$ ($Cp^t = \eta^5\text{-}C_5H_4SiMe_2{}^tBu$) [13] were prepared by the literature procedures. Methyllithium and *n*-Butyllithium were purchased from Aldrich and were used without further purification. Elemental analyses for C and H were carried out on a Rapid CHN–O analyzer. Infrared spectra were obtained on a NICOLET FT-IR 360 spectrometer with samples prepared as Nujol mulls. Mass spectra were recorded on a Philips HP5989A instrument operating in EI mode. Crystalline samples of the respective complexes were rapidly introduced by the direct inlet techniques with a source temperature of 200 °C. The values of *m*/*z* are referred to the isotopes ^{12}C, ^{1}H, ^{16}O, ^{32}S, ^{28}Si, ^{174}Yb, ^{166}Er, ^{164}Dy, ^{89}Y.

4.2. Synthesis of $[(C_5H_4SiMe_2{}^tBu)_2Yb(\mu\text{-}SMe)]_2$ (1)

To a solution of $[Cp^t_2Yb(\mu\text{-}Me)]_2$ (0.290 g, 0.266 mmol) in toluene (30 mL) was added S_8 (17 mg, 0.066 mmol). After stirring for 10 h, the reaction mixture was concentrated by reduced pressure to give a yellow powder. Recrystallization of the powder from the mixture solution of THF and toluene at −15 °C afforded **1** as orange-red crystals. Yield: 0.211 g (68.6%). *Anal.* Calc. for $C_{46}H_{82}S_2Si_4Yb_2$: C, 47.72; H, 7.14. Found: C, 47.65; H, 7.10%. IR (Nujol, cm^{-1}): 3080 w, 1469 s, 1444 w, 1377 w, 1358 m, 1249 s, 1179 s, 1069 w, 1042 s, 1008 m, 903 m, 860 w, 846 w, 828 s, 805 s, 788 w, 777 s, 665 m, 643 s. EI-MS: *m*/*z* [fragment, relative intensity (%)] = 767 (M−2Cp^{t}H−2Me−1, 2), 737 (M−2Cp^t−SMe−Me−1, 13), 578 (M/2−1, 6), 564 (M/2−Me, 4), 532 (M/2−SMe, 23), 476 (M/2−SMe−^{t}Bu+1, 4), 417 (M/2−SMe−SiMe$_2{}^t$Bu, 5), 353 (M/2−Cp^t−SMe, 5), 295 (M/2−SMe−Cp^t−^{t}Bu−1, 2), 239 (M/2−SMe−Cp^t−SiMe$_2{}^t$Bu+1, 4), 180 (Cp^{t}H, 4) ($Cp^t = C_5H_4SiMe_2{}^tBu$).

4.3. Synthesis of $[(C_5H_4SiMe_2{}^tBu)_2Er(\mu\text{-}SMe)]_2$ (2)

Following the procedure described above for **1**, reaction of $[Cp^t_2Er(\mu\text{-}Me)]_2$ (0.291 g, 0.27 mmol) with S_8 (17 mg, 0.066 mmol) gave complex **2** as pink crystals. Yield: 0.201 g (65%). *Anal.* Calc. for $C_{46}H_{82}S_2Si_4Er_2$: C, 48.20; H, 7.21. Found: C, 48.08; H, 7.16%. IR (Nujol, cm^{-1}): 3085 w, 2923 s, 2854 s, 1470 s, 1443 w, 1377 w, 1358 m, 1248 s, 1179 s, 1069 w, 1042 s, 1007 m, 902 m, 864 w, 846 w, 828 s, 805 s, 788 w, 777 s, 664 m, 643 s. EI-MS: *m*/*z* [fragment, relative intensity (%)] = 570 (M/2−1, 2), 558 (M/2−Me+2, 2), 526 (M/2−SMe+2, 54), 482 (M/2−SMe−C_3H_6, 6), 466 (M/2−SMe−^{t}BuH, 5), 424 (M/2−SMe−C_3H_6−^{t}BuH, 3), 408 (M/2−SMe−SiMe$_2{}^t$Bu–1, 4), 392 (M/2−Cp^t, 3), 352 (M/2−SMe−SiMe$_2{}^t$Bu–^{t}Bu, 5), 303 (M/2−SMe−Cp^t–C_3H_6, 3), 290 (M/2−SMe−Cp^t–^{t}Bu+2, 2), 180 (Cp^{t}H, 5).

4.4. Synthesis of $[(C_5H_4SiMe_2{}^tBu)_2Dy(\mu\text{-}SMe)]_2$ (3)

Following the procedure described above for **1**, reaction of $[Cp^t_2Dy(\mu\text{-}Me)]_2$ (0.557 g, 0.52 mmol) with S_8 (33 mg, 0.13 mmol) gave complex **3** as pale-yellow crystals. Yield: 0.410 g (69%). *Anal.* Calc. for $C_{46}H_{82}S_2Si_4Dy_2$: C, 48.61; H, 7.27. Found: C, 48.47; H, 7.45%. IR (Nujol, cm^{-1}): 3081 w, 1469 s, 1443 w, 1377 w, 1358 m, 1249 s, 1179 s, 1069 w, 1042 s, 1007 m, 903 m, 860 w, 846 w, 828 s, 805 s, 788 w, 777 s, 664 m. EI-MS: *m*/*z* [fragment, relative intensity (%)] = 746 (M−2Cp^{t}H−2CH$_4$, 2), 716 (M−2Cp^{t}H−S Me−Me, 13), 568 (M/2−1, 2), 554 (M/2−Me, 3), 522 (M/2−SMe, 38), 480 (M/2−SMe−C_3H_6, 4), 464 (M/2−SMe−^{t}BuH, 4), 406 (M/2−SMe−SiMe$_2{}^t$Bu−1, 5), 390 (M/2−Cp^t, 3), 350 (M/2−SMe−SiMe$_2{}^t$Bu−^{t}Bu, 5), 301 (M/2−SMe−Cp^t−C_3H_6, 3), 286 (M/2−SMe−Cp^t−^{t}Bu, 2), 180 (Cp^{t}H, 5).

4.5. Synthesis of $[(C_5H_4SiMe_2{}^tBu)_2Y(\mu\text{-}SMe)]_2$ (4)

Following the procedure described above for **1**, reaction of $[Cp^t_2Y(\mu\text{-}Me)]_2$ (0.217 g, 0.235 mmol) with S_8 (15 mg, 0.059 mmol) gave complex **4** as colorless crystals. Yield: 0.140 g (60%). *Anal.* Calc. for $C_{46}H_{82}S_2Si_4Y_2$: C, 55.84; H, 8.35. Found: C, 55.79; H, 8.26%. IR (Nujol, cm^{-1}): 3081 w, 2923 s, 2853 s, 1469 s, 1443 w, 1377 w, 1358 m, 1249 s, 1179 s, 1069 w, 1042 s, 1007 m, 903 m, 860 w, 846 w, 828 s, 805 s, 788 w, 778 s, 664 m, 645 s. EI-MS: *m*/*z* [fragment, relative intensity (%)] = 794 (M−Cp^t–Me, 4), 749 (M−Cp^t−Me−SMe+2, 40), 628 (M−2Cp^{t}H, 56), 598 (M−2Cp^{t}H−2Me, 26), 583 (M−2Cp^t−SMe, 13), 536(M−2Cp^t−2SMe, 12), 511 (M−2Cp^t−SMe−Me−^{t}Bu, 3), 494 (M/2, 4), 479 (M/2−Me, 5), 447 (M/2−SMe, 60), 391 (M/2−SMe−^{t}Bu+1, 5), 302 (M/2−SMe−SiMe$_2{}^t$Bu, 5), 317 (M/2−Cp^t+2, 3), 243 (M/2−SMe−SiMe$_2{}^t$Bu–^{t}Bu–2, 5), 227 (M/2−SMe−Cp^t–C_3H_6+1, 3), 180 (Cp^{t}H, 7).

4.6. Synthesis of $[(C_5H_4SiMe_2{}^tBu)_2Yb(\mu\text{-}S^nBu)]_2$ (5)

To a solution of $[(C_5H_4SiMe_2{}^tBu)_2YbCl]_2$ (0.533 g, 0.47 mmol) in toluene (30 mL) was added ^{n}BuLi (1.60 M, 0.588 mL in hexane) at −30 °C. After stirring for 1 h at the low temperature, the reaction solution was slowly warmed to room temperature and stirred for 1 h, forming a colorless precipitate (LiCl). Then, to the mixture was added S_8 (30 mg 0.117 mmol) at ambient temperature. After stirring for 12 h, the precipitate was removed by centrifugation. Removal of the solvent gave pink powder. Recrystallization of the powder from toluene at −15 °C afforded **5** as orange–red crystals. Yield: 0.327 g (56%). *Anal.* Calc. for $C_{52}H_{94}S_2Si_4Yb_2$: C, 50.29; H, 7.63. Found: C, 50.22; H, 7.72%. IR (Nujol, cm^{-1}): 3086 w, 1463 s, 1377 s, 1360 w, 1249 s, 1179 s, 1043 s, 1007 m, 903 w, 829 s, 805 s, 776 s, 669 w, 665 w. EI-MS: *m*/*z* [fragment, relative intensity (%)] = 620 (M/2−1, 3), 564 (M/2−^{n}Bu, 2), 534 (M/2−S^{n}Bu+2, 80), 404 (M/2−S^{n}Bu−SiMe$_2{}^t$Bu−CH$_3$+2, 4), 362 (M/2−S^{n}Bu−SiMe$_2{}^t$Bu−^{t}Bu+2, 7), 298 (M/2−S^{n}Bu−Cp^t − ^{t}Bu+2, 2), 180 (Cp^{t}H, 6).

4.7. Synthesis of $[(C_5H_4SiMe_2{}^tBu)_2Dy(\mu\text{-}S^nBu)]_2$ (6)

Following the procedure described above for **5**, reaction of $[(C_5H_4SiMe_2{}^tBu)_2DyCl]_2$ (0.450 g, 0.405 mmol) ^{n}BuLi (1.60 M, 0.506 mL in hexane) and subsequently with S_8 (26 mg, 0.10 mmol) gave pale yellow powder. Recrystallization of the powder from toluene at −15 °C afforded **6** as pale yellow crystals. Yield: 0.371 g (75%). *Anal.* Calc. for $C_{52}H_{94}S_2Si_4Dy_2$: C, 51.16; H, 7.76. Found: C, 51.06; H, 7.80%. IR (Nujol, cm^{-1}): 3085 w, 1463 s, 1443 w, 1377 s, 1360 w, 1249 s, 1178 s, 1043 s, 1007 m, 902 w, 829 s, 805 s, 774 s, 721 m, 668 w, 643 w. EI-MS: *m*/*z* [fragment, relative intensity (%)] = 717 (M−2Cp^t−S^{n}Bu−BuH, 13), 610 (M/2−1, 4), 554 (M/2−^{n}Bu, 2), 522 (M/2−S^{n}Bu, 80), 406 (M/2−S^{n}Bu−SiMe$_2{}^t$Bu−1, 6), 390 (M/2−S^{n}Bu−SiMe$_2{}^t$Bu

Table 3
Crystal and data collection parameters of complexes of **1**, **3**, **5** and **6**

	1	**3**	**5**	**6**
Formula	$C_{46}H_{82}S_2Si_4Yb_2$	$C_{46}H_{82}S_2Si_4Dy_2$	$C_{52}H_{94}S_2Si_4Yb_2$	$C_{52}H_{94}S_2Si_4Dy_2$
Molecular weight	1157.68	1136.60	1241.83	1220.75
Crystal dimensions (mm)	0.20 × 0.10 × 0.08	0.20 × 0.10 × 0.10	0.20 × 0.20 × 0.15	0.25 × 0.20 × 0.20
Crystal system	triclinic	triclinic	monoclinic	monoclinic
Space group	$P\bar{1}$	$P\bar{1}$	$P2(1)/c$	$P2(1)/c$
a (Å)	8.320(23)	8.411(3)	8.435(4)	8.523(4)
b (Å)	13.132(4)	13.114(4)	26.792(14)	26.918(12)
c (Å)	13.158(4)	13.208(4)	13.881(7)	13.761(6)
α (°)	100.021(4)	100.716(4)	90	90
β (°)	95.441(4)	95.189(4)	101.160(7)	101.185(6)
γ (°)	102.107(4)	101.648(4)	90	90
V (Å^3)	1371.3(7)	1385.9(8)	3078(3)	3097(2)
Z	1	1	2	2
D_{calc} (g cm^{-3})	1.402	1.362	1.340	1.309
μ (mm^{-1})	3.579	2.863	3.194	2.568
F(000)	586	578	1268	1252
Radiation (λ = 0.710730 Å)	Mo Kα	Mo Kα	Mo Kα	Mo Kα
Temperature (K)	293(2)	293(2)	293(2)	293(2)
Scan type	ω–2θ	ω–2θ	ω–2θ	ω–2θ
θ Range (°)	1.59–25.01	1.62–25.01	1.52–25.01	1.69–25.01
h, k, l Range	$-9 \leqslant h \leqslant 9$, $-13 \leqslant k \leqslant 15$, $-15 \leqslant l \leqslant 13$	$-9 \leqslant h \leqslant 9$, $-12 \leqslant k \leqslant 15$, $-15 \leqslant l \leqslant 13$	$-10 \leqslant h \leqslant 9$, $-31 \leqslant k \leqslant 29$, $-16 \leqslant l \leqslant 16$	$-10 \leqslant h \leqslant 10$, $-28 \leqslant k \leqslant 32$, $-16 \leqslant l \leqslant 13$
Number of reflections measured	5755	5835	12712	12885
Number of unique reflections	4760 (R_{int} = 0.0142)	4812 (R_{int} = 0.0188)	5415 (R_{int} = 0.0584)	5448 (R_{int} = 0.0405)
Completeness to θ (%)	98.4 (θ = 25.01)	98.6 (θ = 25.01)	99.8 (θ = 25.01)	99.6 (θ = 25.01)
Maximum and minimum transmission	0.7627 and 0.5346	0.7627 and 0.5982	0.6458 and 0.5675	0.6277 and 0.5662
Refinement method	full-matrix least-squares on F^2	full-matrix least-squares on F^2	full-matrix least-squares on F^2	full-matrix least-squares on F^2
Data/restraints/parameters	4760/1/244	4812/1/244	5415/0/271	5448/0/271
Goodness-of-fit on F^2	1.038	0.979	1.352	1.289
Final R indices [$I > 2\sigma(I)$]	R_1 = 0.0297, wR_2 = 0.0651	R_1 = 0.0298, wR_2 = 0.0689	R_1 = 0.0839, wR_2 = 0.1385	R_1 = 0.0687, wR_2 = 0.1143
R indices (all data)	R_1 = 0.0369, wR_2 = 0.0691	R_1 = 0.0381, wR_2 = 0.0728	R_1 = 0.1237 wR_2 = 0.1474	R_1 = 0.0915, wR_2 = 0.1214
Largest difference in peak and hole (e Å^{-3})	0.880 and −0.540	1.056 and −0.465	1.603 and −0.843	1.056 and −0.579

$-CH_4-$1, 4), 350 (M/2−S^{n}Bu−SiMe$_2$^{t}Bu−^{t}Bu, 7), 286 (M/2−S^{n}Bu−Cp^t−^{t}Bu, 2), 180 (Cp^{t}H, 11).

4.8. X-ray crystal structure determination of complexes *1*, *3*, *5* and *6*

Suitable crystals of complexes **1**, **3**, **5** and **6** were selected and sealed in a thin-walled glass capillary under N_2 for structural analysis. Diffraction data were collected on a Bruker SMART Apex CCD diffractometer using graphite-monochromated Mo Kα ($\lambda = 0.71073$ Å) radiation. During the collection of the intensity data, no significant decay was observed. For **1**, frames were integrated to the maximum 2θ angle of 50.02° with the Siemens SAINT program to yield a total of 5755 reflections, of which 4760 were independent ($R_{int} = 0.0142$). For **3**, frames were integrated to the maximum 2θ angle of 50.02° with the Siemens SAINT program to yield a total of 5835 reflections, of which 4812 were independent ($R_{int} = 0.0188$). For **5**, frames were integrated to the maximum 2θ angle of 50.02° with the Siemens SAINT program to yield a total of 12 712 reflections, of which 5415 were independent ($R_{int} = 0.0584$). For **6**, frames were integrated to the maximum 2θ angle of 50.02° with the Siemens SAINT program to yield a total of 12 885 reflections, of which 5448 were independent ($R_{int} = 0.0405$). The final unit cell parameters were determined from the full-matrix least-squares on F^2 refinement of three-dimensional centroids of 5755 reflections for **1**, 5835 reflections for **3**, 5415 reflections for **5** and 5448 reflections for **6**. The intensities were corrected for Lorentz-polarization effects and empirical absorption with SADABS program [14]. A summary of the crystallographic data and selected experimental information is given in Table 3.

The structures were solved by the direct method using the SHELXL-97 program [15]. All non-hydrogen atoms were found from the difference Fourier syntheses. The H atoms were included in calculated positions with isotropic thermal parameters related to those of the supporting carbon atoms, but were not included in the refinement. All calculations were performed using the Bruker Smart program.

Supplementary material

CCDC 645443, 645447, 645446 and 645445 contain the supplementary crystallographic data for **1**, **3**, **5** and **6**. These data can be obtained free of charge via htpp://www.ccdc.cam.ac.uk/conts/retrieving.html, or from the Cambridge Crystallographic Data Centre, 12 Union Road, Cambridge CB2 1EZ, UK; fax: (+44) 1223-336-033; or e-mail: deposit@ccdc.cam.ac.uk.

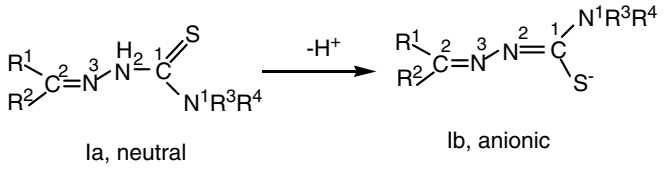
Acknowledgement

We thank the NNSF of China and the Fund of the New Century Distinguished Scientist of the Education Ministry of China for financial support.

References

[1] (a) H. Schumann, J.A. Meese-Marktscheffel, L. Esser, Chem. Rev. 95 (1995) 865;
(b) F. Nief, Coord. Chem. Rev. 178–180 (1998) 13;
(c) H.X. Li, Z.R. Ren, Y. Zhang, W.H. Zhang, J.P. Lang, Q. Shen, J. Am. Chem. Soc. 127 (2005) 1122;
(d) M. Roger, N. Barros, T. Arliguie, P. Thuéry, L. Maron, M. Ephritikhine, J. Am. Chem. Soc. 128 (2006) 8790;
(e) H.X. Li, M.L. Cheng, Z.G. Ren, W.H. Zhang, J.P. Lang, Q. Shen, Inorg. Chem. 45 (2006) 1885;
(f) A. Cofone, M. Niemeyer, Z. Anorg. Allg. Chem. 632 (2006) 1930;
(g) Q. Shen, H.R. Li, C.S. Yao, Y.M. Yao, L.L. Zhang, K.B. Yu, Organometallics 20 (2001) 3070;
(h) M. Roger, L. Belkhiri, P. Thuéry, T. Arliguie, M. Fourmigué, A. Boucekkine, M. Ephritikhine, Organometallics 24 (2005) 4940.
[2] (a) C.M. Zhang, R.T. Liu, X.G. Zhou, Z.X. Chen, L.H. Weng, Y.H. Lin, Organometallics 23 (2004) 3246;
(b) J. Zhang, L.P. Ma, R.F. Cai, L.H. Weng, X.G. Zhou, Organometallics 24 (2005) 738;
(c) C.M. Zhang, R.T. Liu, Z.X. Chen, X.G. Zhou, Chin. J. Chem. 24 (2006) 231.
[3] (a) Y. Nakayama, T. Shibahara, H. Fukumoto, A. Nakamura, Macromolecules 29 (1996) 8014;
(b) Z.M. Hou, Y.G. Zhang, H. Tezuka, P. Xie, O. Tardif, T. Koizumi, H. Yamazaki, Y. Wakatsuki, J. Am. Chem. Soc. 122 (2000) 10533;
(c) J. Dowsland, F. McKerlie, D.J. Procter, Tetrahedron Lett. 41 (2000) 4923;
(d) H.M. Sun, H.R. Li, C.S. Yao, Y.M. Yao, H.T. Sheng, Q. Shen, Chin. J. Chem. 23 (2005) 1541.
[4] (a) M. Roger, T. Arliguie, P. Thuéry, M. Fourmigué, M. Ephritikhine, Inorg. Chem. 44 (2005) 584;
(b) M.A. Katkova, A.V. Borisov, G.K. Fukin, E.V. Baranov, A.S. Averyushkinc, A.G. Vitukhnovsky, M.N. Bochkarev, Inorg. Chim. Acta 359 (2006) 4289.
[5] (a) T.D. Tilley, R.A. Andersen, A. Zalkin, D.H. Templeten, Inorg. Chem. 21 (1982) 2644;
(b) Z.Z. Wu, Z.E. Huang, R.F. Cai, X.G. Zhou, Z. Xu, X.Z. You, X.Y. Huang, J. Organomet. Chem. 506 (1996) 25;
(c) S.D. Stults, R.A. Anderson, A. Zalkin, Organometallics 9 (1990) 1623;
(d) L.X. Zhang, X.G. Zhou, Z.E. Huang, R.F. Cai, X.Y. Huang, Polyhedron 18 (1999) 1533;
(e) W.J. Evans, K.A. Miller, D.S. Lee, J.W. Ziller, Inorg. Chem. 44 (2005) 4326.
[6] (a) I.P. Beletskaya, A.Z. Voskoboynikov, A.K. Shestakova, H. Schumann, J. Organomet. Chem. 463 (1993) C1;
(b) W.E. Piers, D.J. Parks, L.R. MacGillivray, M.J. Zaworotko, Organometallics 13 (1994) 4547;
(c) W.E. Piers, L.R. MacGillivray, M. Zaworotko, Organometallics 12 (1993) 4723;
(d) L.K. Knight, W.E. Piers, R. Mcdonald, Chem. Eur. J. 6 (2000) 4322;
(e) H.X. Li, Y.J. Zhu, M.L. Chenga, Z.G. Ren, J.P. Lang, Q. Shen, Coord. Chem. Rev. 250 (2006) 2059.
[7] Y.R. Li, C.F. Pi, J. Zhang, X.G. Zhou, Z.X. Chen, L.H. Weng, Organometallics 24 (2005) 1982.
[8] (a) C.J. Schaverien, Adv. Organomet. Chem. 36 (1994) 283;
(b) P.W. Roesky, C.L. Stern, T.J. Marks, Organometallics 16 (1997) 4705.
[9] F.H. Allen, O. Kennard, D.G. Watson, L. Brammer, A.G. Orpen, J. Chem. Soc., Perkin Trans. (1987) S1.
[10] R.D. Shannon, Acta Crystallogr., Sect. A 32 (1976) 751.
[11] X.G. Zhou, L.X. Zhang, C.M. Zhang, J. Zhang, M. Zhu, J. Organomet. Chem. 655 (2002) 120.

[12] H. Schumann, M.R. Keitsch, J. Demtschuk, G.A. Molander, J. Organomet. Chem. 582 (1999) 70.
[13] X.G. Zhou, L.B. Zhang, M. Zhu, R.F. Cai, L.H. Weng, Organometallics 20 (2001) 5700.
[14] G.M. Sheldrick, SADABS, A Program for Empirical Absorption Correction, Göttingen, Germany, 1998.
[15] G.M. Sheldrick, SHELXL-97, Program for the Refinement of the Crystal Structure, University of Göttingen, Germany, 1997.



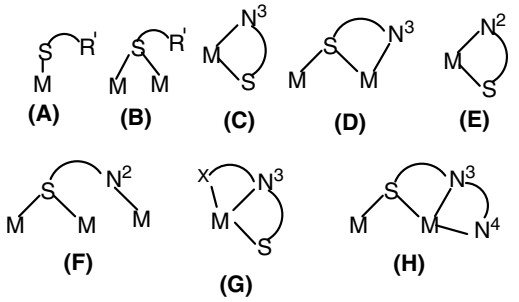


Chart 1.

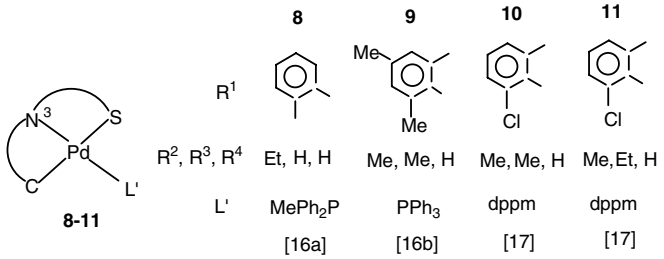


Chart 2.

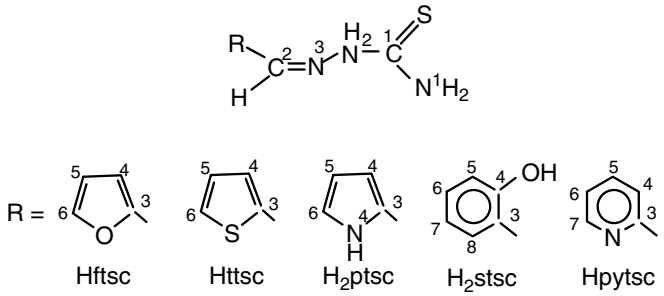


Chart 3.

carbaldehyde thiosemicarbazone (Httsc), pyrrole-2-carbaldehyde thiosemicarbazone (H_2ptsc), salicylaldehyde thiosemicarbazone (H_2stsc) and pyridine-2-carbaldehyde thiosemicarbazone (Hpytsc), which have been used to observe the effect of the different rings at the C^2 carbon on the nature of bonding with palladium (II). In this paper, we report a series of Pd^{II} complexes [18] that have been characterized using analytical data, spectroscopic techniques and X-ray crystallography.

2. Experimental

2.1. Materials and techniques

Furan-2-carbaldehyde, thiophene-2-carbaldehyde, pyrrole-2-carbaldehyde, salicylaldehyde, pyridine-2-carbaldehyde, Ph_3P and $PdCl_2$ were procured from Aldrich Sigma Ltd. The thiosemicarbazone ligands were prepared by the reported methods [19]. Trans-$PdCl_2(PPh_3)_2$ was prepared by reacting a solution of $PdCl_2$ in CH_3CN with two moles of PPh_3 [20]. Elemental analysis for C, H and N were carried out using a thermoelectron FLASHEA1112 analyser. The melting points were determined with a Gallenkamp electrically heated apparatus. The IR spectra were recorded using KBr pellets on a Pye-Unicam SP3-300 spectrophotometer. ^{1}H NMR spectra were recorded on a JEOL AL300 FT spectrometer at 300 MHz in $CDCl_3$ with TMS as the internal reference. The ^{31}P NMR spectra were recorded at 121.5 MHz with $\{(CH_3O)_3P\}$ as the external reference taken as the zero position.

2.2. Synthesis of [Pd(η^2-N^3, S-ftsc)(PPh_3)Cl] (1)

To the *trans*-$PdCl_2(PPh_3)_2$ precursor (0.05 g, 0.07 mmol) suspended in toluene (15 mL) was added solid Hftsc (0.012 g, 0.07 mmol), followed by the addition of Et_3N base (1 mL), and the mixture was stirred for 3 h, during which time a clear light orange solution was formed along with $Et_3NH^+Cl^-$, separating from the solution at the bottom of the flask. The solution was filtered to remove $Et_3NH^+Cl^-$ and allowed to evaporate at room temperature, and after evaporation, a yellow orange crystalline product was formed. Yield: 0.026 g, 65%; m.p. 233–235 °C. *Anal.* Calc. for $C_{24}H_{21}ClN_3OPPdS$: C, 50.30; H, 3.84; N, 7.30. Found: C, 50.83; H, 3.87; N, 7.46%. Main I.R. peaks (KBr, cm^{-1}): ν(NH) 3495s, 3292s, ν(C–H) 3050w, ν(C=N) + δNH_2 + ν(C=C) 1606s, 1589s, 1514s, ν(C=S) 819s, ν(P–C) 1095s. ^{1}H NMR ($CDCl_3$, δ, ppm): 8.60 (d, 1H, C^2H), 7.70–7.77 (m, 6H, *o*-Ph), 7.40–7.54 (m, 11H, *m,p*-Ph + $C^{4,6}$), 6.53 (dd, 1H, C^5H), 4.84 (s, 2H, NH_2). ^{31}P NMR ($CDCl_3$, δ, ppm): −80.5. $\Delta\delta(\delta_{complex}-\delta_{PPh_3}) =$ 32.6 ppm.

2.3. Synthesis of [Pd(η^2-N^3, S-ttsc)(PPh_3)Cl] (2)

Compound **2** was prepared similarly to **1**.

Yield: 0.024 g, 65%, m.p. 233–235 °C. *Anal.* Calc. for $C_{24}H_{21}N_3S_2PClPd$: C, 49.0; H, 3.50; N, 7.13. Found: C, 49.2; H, 3.48; N 7.4%. I.R. (KBr, cm^{-1}): ν(N–H) 3350m, ν(C=N) + δNH_2 + ν(C=C) 1581m, 1514s, 1459sh, ν(C=S) 808s, ν(P–C) 1095s. ^{1}H NMR ($CDCl_3$, δ, ppm): 8.80 (d, 1H, C^2H), 7.71–7.78 (m, 6H, *o*-Ph), 7.63 (d, 1H, C^6), 7.54 (d, 1H, C^4), 7.40–7.52 (m, 9H, m&p-Ph), 7.09 (dd, 1H, C^5), 4.87 (s, 2H, NH_2). ^{31}P NMR($CDCl_3$, δ, ppm): −80.5. $\Delta\delta(\delta_{complex} - \delta_{PPh_3}) = 32.6$ ppm.

2.4. Synthesis of [Pd(η^2-N^3,S-ftsc)$_2$] (3)

To $PdCl_2(PPh_3)_2$ (0.05 g, 0.07 mmol) suspended in toluene (20 mL) was added Hftsc (0.026 g, 0.14 mmol), followed by the addition of Et_3N base (2 mL). The solution was refluxed for around 2 h, and then filtered to remove $Et_3NH^+Cl^-$. A red crystalline product started forming after

a few days. Yield: 0.018 g, 51%, m.p. 188 °C *Anal.* Calc. for $C_{12}H_{12}N_6S_2O_2Pd$: C, 32.6; H, 2.71; N, 19.00. Found: C, 32.0; H, 2.84; N, 18.8%. ^{1}H NMR data ($CDCl_3$, δ, ppm): 8.60 (d, 1H, C^2H), 6.53 (dd, 1H, C^5H), 4.84 (s, 2H, NH_2). Crystals for X-ray study were grown from acetonitrile.

2.5. Synthesis of [Pd(η²-N³,S-ttsc)₂] (4)

Compound **4** was prepared similarly to **3**.

Yield: 0.019 g, 54%, m.p. 223–225 °C. *Anal.* Calc. for $C_{12}H_{12}N_6S_4Pd$: C, 30.37; H, 2.53; N, 17.7. Found: C, 30.81; H, 2.48; N, 17.4%. I.R. (KBr, cm^{-1}): ν(N–H) 3384m, 3363w, 3278s, ν(C–H) 3176m, ν(C=N) + δNH_2 + ν(C=C) 1577s, 1595sh, ν(C–S) 811s. ^{1}H NMR data ($CDCl_3$, δ, ppm): 7.73 (s, 2H, C^2H), 7.65 (d, 2H, C^6H), 7.40 (d, 2H, C^4H), 7.08 (dd, 2H, C^5H), 5.07 (s, 4H, NH_2).

2.6. X-ray crystallography

The data for compounds **1** and **2** were collected at 293 and 295 K, respectively, on a Siemens P4 diffractometer. The θ–2θ technique was used to measure the intensities up to a maximum of $2\theta = 50°$ with graphite monochromatised Mo Kα radiation ($\lambda = 0.71073$ Å). Cell parameters were refined in the θ range 10–12.5° using XSCANS [21]. The data were corrected for Lorentz and polarization factors. An empirical psi absorption correction was applied. The structure was solved by direct methods and refined by full matrix least squares methods based on F^2. All non-hydrogen atoms were refined anisotropically, and hydrogen atoms were assigned calculated positions. Scattering factors from the International Tables for X-ray crystallography were used [22]. Data reduction, structure solution, refinement and molecular graphics were performed using SHELXTL-PC [23] and WINGX [24].

Single crystals of compounds **3** and **4** were mounted on a CCD area detector diffractometer, equipped with a graphite monochromator using Mo Kα radiation ($\lambda = 0.71073$ Å) for **3** and Cu Kα radiation ($\lambda = 1.54178$ Å) for **4**. The unit cell dimensions and intensity data were measured at 273(2) (**3**) and 296(2) K (**4**). The structures were solved by the direct methods and refined by full matrix least square methods based on F^2 with anisotropic thermal parameters for the non-hydrogen atoms, using Bruker SMART (data collection and cell refinement), Bruker SHELXTL (data reduction and computing molecular graphics), SHELXS-97 (structure solution) and SHELXL-97 (structure refinement)] [25]. An empirical psi absorption correction was applied. The calculated positions for the H atoms were used in structure factor (SF) calculations with ω scan to 56° 2θ.

3. Results and discussion

3.1. Synthesis and IR spectroscopy

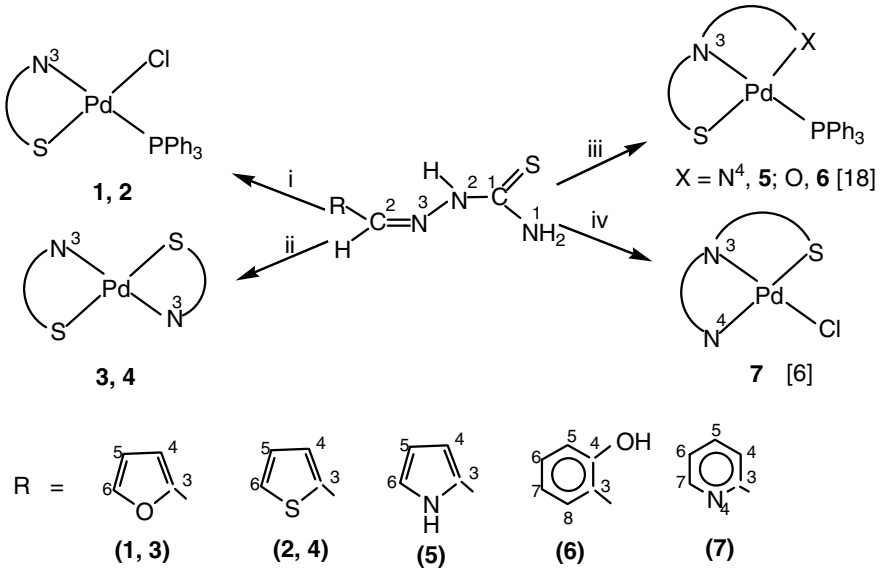
Scheme 1 depicts the formation of complexes **1**–**6** using a series of thiosemicarbazone ligands, namely Hftsc, Httsc, H_2ptsc, H_2stsc and Hpytsc. The formation of compounds [Pd(η²-N^3,*S*-ftsc)(PPh_3)Cl] (**1**) and [Pd(η²-N^3,*S*-ttsc)-(PPh_3)Cl] (**2**) required the addition of one equivalent of Hftsc or Httsc to the *trans*-$PdCl_2(PPh_3)_2$ precursor, while the addition of two equivalents of thiosemicarbazone to *trans*-$PdCl_2(PPh_3)_2$ yielded compounds [Pd(η²-N^3,*S*-ftsc)$_2$] (**3**) and [Pd(η²-N^3,*S*-ttsc)$_2$] (**4**). In all these complexes, the thiosemicarbazone ligands coordinate via the N^3,*S* donor atoms. Interestingly, the addition of one equivalent of H_2ptsc or H_2stsc to the $PdCl_2(PPh_3)_2$ precursor removed both the Cl anions, forming compounds [Pd(η³-N^4,N^3,*S*-ptsc)(PPh_3)] (**5**) and [Pd(η³-O, N^3,*S*-stsc)(PPh_3)] (**6**) [18]. There was no effect on the stoichiometry when two equivalents of H_2ptsc or H_2stsc were used. It may be noted that in compounds **1**–**4**, only the hydrazinic hydrogen (–N^2H) is removed, whereas in complexes **5** and **6**, both –N^2H as well as –N^4H (pyrrole, **5**) or –OH (**6**) groups were deprotonated [18]. Thus, the presence of acidic hydrogens in the rings at the C^2 carbon (pyrrole, 2-hydroxyphenyl) modulated the dentacy of the H_2ptsc or H_2stsc ligands from the usual bidentate mode to a tridentate mode. Pyridine-2-carbaldehyde thiosemicarbazone (Hpytsc) with $PdCl_2(PPh_3)_2$ formed only a square planar complex [Pd(η³-N^4,N^3,*S*-pytsc)Cl] (**7**) [6], and its stoichiometry is unaffected by the addition of two equivalents of Hpytsc [18].

The IR spectra of the complexes reveal the presence of ν(N–H) bands due to the (–NH_2) group in the range 3278–3495 cm^{-1}. The bands in the region 3100–3150 cm^{-1}, expected due to the –N^2H group in the free ligands [19], are found to be absent in the spectra of their complexes **1**–**4**, thus supporting the anionic form of the ligands. The ν(C–H) bands due to the aromatic ring are observed for all the complexes in the region near 3050 cm^{-1}. Further, $\delta(NH_2)$ + ν(C=N) + ν(C–C) vibration modes are unresolved, and are assigned to the range 1635–1515 cm^{-1}. However, the thioamide bands due to the ν(C–S) mode are shifted to lower energy (at ~810 cm^{-1}) as compared with the similar free ligand bands, and this is consistent with its single bond character in the anionic form [19]. The presence of PPh_3 in complexes **1** and **2** is confirmed by the presence of a characteristic ν(C–P) band in the range 1095–1099 cm^{-1} (see Table 1).

3.2. Crystal structures

The atomic numbering schemes for complexes **1**–**4** are given in Figs. 1–4, respectively, and selected bond angles and bond lengths are listed in Table 2. Compounds **1**–**4** crystallized in the monoclinic crystal systems (**1**, **2**), the trigonal system (**3**) or the triclinic system (**4**).

In complex **1**, furan-2-carbaldehyde thiosemicarbazonate ($ftsc^-$) binds via N^3 and *S* donor atoms to the Pd^{II} center, with the furan ring (C_4H_3O) remaining pendant. The other two sites are occupied by the Cl and PPh_3 ligands. The bite angle N^3–Pd–S is 83.09(11)° while the other three angles around the Pd^{II} center, namely, S–Pd–P, P–Pd–Cl and N^3–Pd–Cl, are 91.49(5)°, 90.39(5)° and



Scheme 1. $PdCl_2(PPh_3)_2$ (i,iii,iv); 1/2 $PdCl_2(PPh_3)_2$ (ii); toluene, Et_3N (i–iv).

Table 1
Crystal data and refinement details for complexes **1**–**4**

	1	**2**	**3**	**4**
Empirical formula	$C_{24}H_{21}ClN_3OPPdS$	$C_{24}H_{21}ClN_3PPdS_2$	$C_{12}H_{14}N_6O_2PdS_2$	$C_{12}H_{12}N_6PdS_4$
M	572.32	588.43	444.61	474.92
T (K)	293(2)	295(2)	273(2)	296(2)
Crystal system	monoclinic	monoclinic	trigonal	triclinic
Space group	$P2_1/c$	$P2_1/n$	$R\bar{3}$	$P\bar{1}$
Unit cell dimensions (mm^3)	$0.18 \times 0.17 \times 0.13$	$0.18 \times 0.16 \times 0.16$	$0.30 \times 0.20 \times 0.20$	$0.38 \times 0.14 \times 0.08$
a (Å)	14.160(5)	10.1020 (10)	14.2620(3)	9.8828(2)
b (Å)	12.093(5)	14.5190 (10)	14.2620(3)	11.1201(2)
c (Å)	16.103(5)	17.1340 (10)	20.9708(11)	12.6224(2)
α (°)	90	90	90	87.6440(10)
β (°)	114.17(1)	99.96(1)	90	74.8790(10)
γ (°)	90	90	120	81.0800(10)
V ($Å^3$)	2515.7(16)	2477.4(3)	3694.1(2)	1322.95(4)
Z	4	4	9	3
D_{calcd} ($Mg\ m^{-3}$)	1.511	1.578	1.800	1.788
μ (mm^{-1})	1.011	1.108	1.402	12.972
Reflections collected	3255	4886	16838	14681
Unique reflections (R_{int})	3057 (0.0366)	4612 (0.0215)	2049	4131
Reflections with $[I > 2\sigma(I)]$	2380	3782	1889	3352
R indices (all data)	$R_1 = 0.0427$, $wR_2 = 0.0857$	$R_1 = 0.0377$, $wR_2 = 0.0789$	$R_1 = 0.0218$, $wR_2 = 0.0597$	$R_1 = 0.0636$, $wR_2 = 0.1313$
Final R indices $[I > 2\sigma(I)]$	$R_1 = 0.0303$, $wR_2 = 0.0741$	$R_1 = 0.0293$, $wR_2 = 0.0764$	$R_1 = 0.0194$, $wR_2 = 0.0575$	$R_1 = 0.0528$, $wR_2 = 0.1250$

95.02(11)°, respectively. Compound **2**, with the thiophene ring (C_4H_3S) in lieu of furan (C_4H_3O), has similar corresponding bond angles, namely 83.00(7)° (N^3–Pd–S), 91.73(3)° (S–Pd–P), 92.08(3)° (P–Pd–Cl) and 94.14(7)° (N^3–Pd–Cl). Among the trans bond angles, the N^3–Pd–P angles are similar, {174.58(11)°, **1**; 171.63(8)°, **2**}, while the S–Pd–Cl angles are different {177.98(16)°, **1**; 169.86 (4)°, **2**}. The bite angles of **1** and **2** (Table 3) are similar to that of complex **8** (Chart 2) {N^3–Pd–S, 83.19(11)°} [16a], but the N^3–Pd–P and S–Pd–X (X = Cl, **1**, **2**; C, **8**) trans angles of **1** and **2** are different from that of **8** {N^3–Pd–P, 178.75(11)°; S–Pd–C 164.5(2)°} [16a]. Further, the Pd–P bond distances of **1**, **2** and **8** are comparable (Table 3), but the Pd–N^3 and Pd–S distances are different due to the difference in the chemical environments in the three cases (Table 3). It is concluded from the above that there is no metallation involving the furan or thiophene rings in compounds **1** and **2**, a behaviour unlike that observed

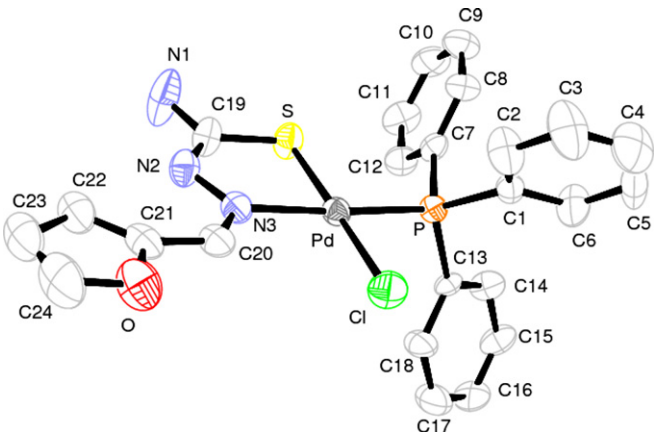


Fig. 1. Structure of the complex [Pd(η^2-N^3,*S*-ftsc)(PPh_3)Cl] (**1**) with the atomic numbering scheme.

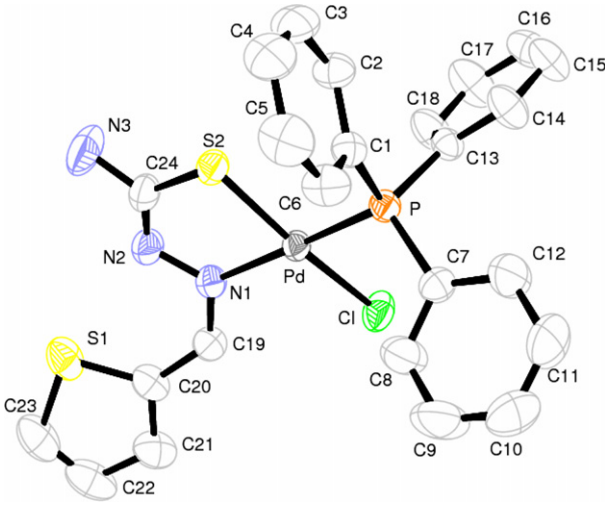


Fig. 2. Structure of the complex [Pd(η^2-N^3,*S*-ttsc)(PPh_3)Cl] (**2**) with the atomic numbering scheme.

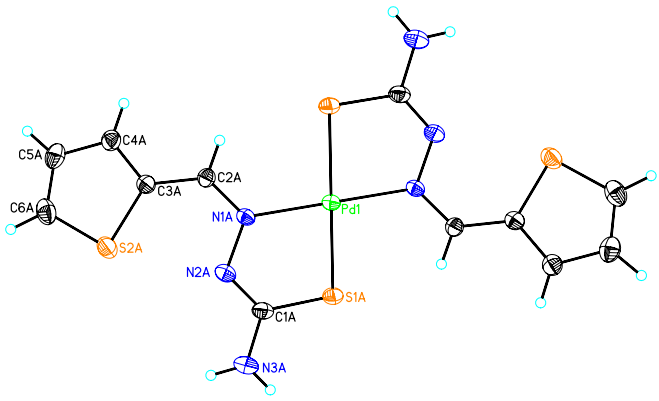


Fig. 4a. Structure of the complex [Pd(η^2-N^3,*S*-ttsc)] (**4**) with the atomic numbering scheme.

for compound **8** and its other analogues as listed in Chart 2.

A second mole of the Hftsc or Httsc ligand was added to the reaction systems of complexes **1** and **2**, with the objective that the coordination might proceed in one of three ways: (i) it may coordinate via the S-donor atom of the anionic thiosemicarbazone by replacing a chloride ion, (ii) it may chelate via N^3, S donor atoms and replace the chloride as well as PPh_3, and (iii) the pendant ring might metallate during the attempt to remove chloride by the presence of a second mole of ligand. The formation of compounds *trans*-[Pd(η^2-N^3,*S*-ftsc)$_2$] (**3**), and *trans*-[Pd(η^2-N^3,*S*-ttsc)$_2$] (**4**), has demonstrated that it is the second path which has been adopted by the reaction systems. It may be attributed to the chelate effect of the anionic thiosemicarbazones (ftsc$^-$ and ttsc$^-$), which have removed both Cl^- as well as PPh_3, and yielded the most symmetric products **3** and **4**. No metallation occurred, however, under these conditions.

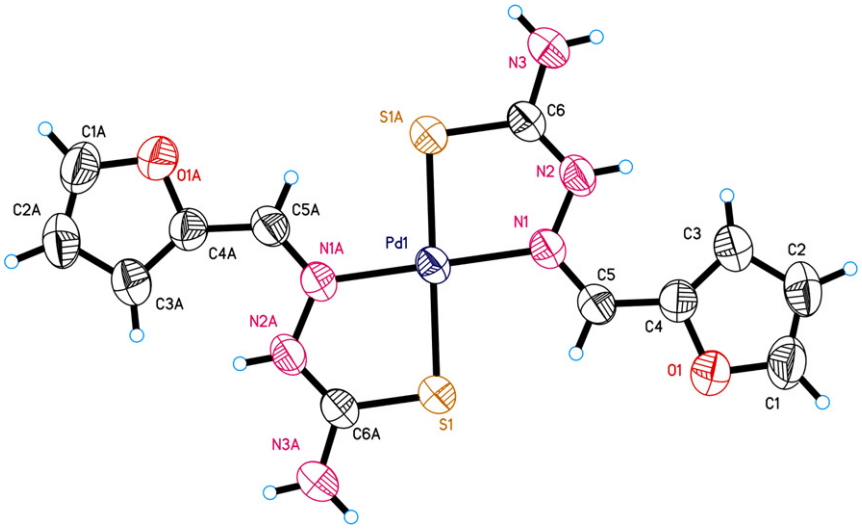


Fig. 3. Structure of the complex [Pd(η^2-N^3,*S*-ftsc)$_2$] (**3**) with the atomic numbering scheme.

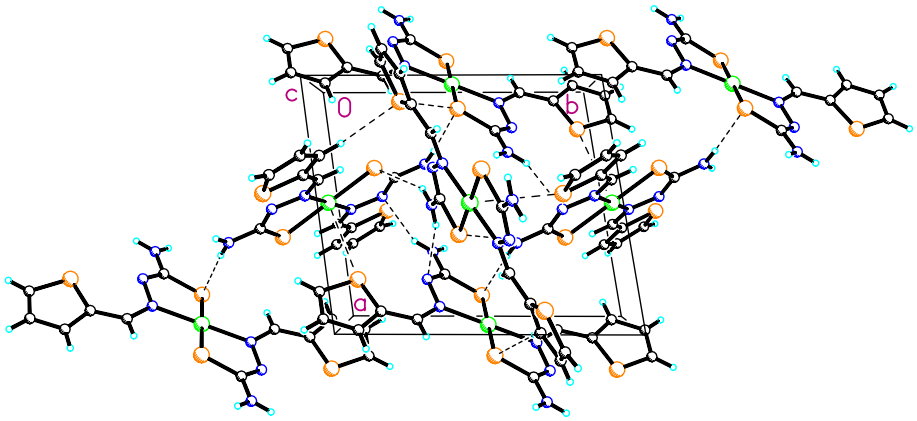


Fig. 4b. Intermolecular H-bond interactions between three molecules in the unit cell of complex **4**.

Table 2
Selected bond lengths and bond angles for **1**–**4**

1			
Pd–N(3)	2.105(4)	Pd–P	2.2582(15)
Pd–S	2.2428(14)	C(19)–S	1.753(5)
Pd–Cl	2.3458(13)	N(2)–C(19)	1.301(6)
N(3)–Pd–S	83.09(11)	N(3)–Pd–Cl	95.02(11)
N(3)–Pd–P	174.58(11)	S–Pd–Cl	177.98(6)
S–Pd–P	91.49(5)	P–Pd–Cl	90.39(5)
2			
Pd–N(1)	2.083(2)	Pd–P	2.2609(7)
Pd–S(2)	2.2398(7)	C(24)–S(2)	1.753(3)
Pd–Cl	2.3451(8)	C(24)–N(2)	1.306(4)
N(1)–Pd–S(2)	83.00(7)	N(1)–Pd–Cl	94.14(7)
N(1)–Pd–P	171.67(7)	S(2)–Pd–Cl	169.87(3)
S(2)–Pd–P	91.79(3)	P–Pd–Cl	92.08(3)
3			
Pd(1)–N(1)#	2.0305(13)	Pd(1)–N(1)	2.0305(13)
Pd(1) S(1)#	2.2710(5)	Pd(1)–S(1)	2.2710(5)
C(6)–S(1)	1.7291(18)	C(6)–N(2)	1.307(2)
N(1)#1–Pd(1)–N(1)	180.0	N(1)–Pd–S(1)	83.67(4)
S(1)–Pd(1)–S(1)#1	180.0		
4			
Pd(1)–N(1A)#	2.031(5)	Pd(1)–N(1A)	2.031(5)
Pd(1)–S(1A)#	2.2869(15)	Pd(1)–S(1A)	2.2869(15)
N(1)#1–Pd(1)–N(1)	179.999(1)	N(1A)–Pd(1)–S(1A)	82.89(14)
S(1)–Pd(1)–S(1)#1	179.998(1)	N(1A)#1–Pd(1)–S(1A)#1	82.89(14)
Pd(2)–N(1B)#	2.019(5)	Pd(2)–N(1B)	2.019(5)
Pd(2)–S(1B)#	2.2981(14)	Pd(2)–S(1B)	2.2981(14)
N(1B)#2–Pd(2)–N(1B)	180.0	N(1B)–Pd(2)–S(1B)	82.75(13)
S(1B)–Pd(2)–S(1B)#2	179.997(2)	N(1B)#2–Pd(2)–S(1B)#2	82.75(13)
Pd(3)–N(1C)#	2.030(5)	Pd(3)–N(1C)	2.030(5)
Pd(2)–S(1B)#	2.2860(15)	Pd(2)–S(1B)	2.2860(15)
N(1C)–Pd(3)–N(1C)#3	179.999(2)	N(1C)–Pd(3) S(1C)	83.37(14)
S(1C)–Pd(3)–S(1C)#3	180.0	N(1C)#3–Pd(3)–S(1C)#3	83.37(14)

In complexes **3** and **4**, the Pd^{II} ion is coordinated by two thiosemicarbazonate moieties (ftsc$^-$ and ttsc$^-$, respectively) via N^3 and S donor atoms in a *trans*-N_2S_2 manner with pendant heterocyclic rings. The bite angles {N^3–Pd–S, 83.67°, **3**; 82.89°, **4**} are similar to those in complexes **1** and **2**. The trans angles N^3–Pd–N^3 and S–Pd–S for both the complexes are linear (180.0° each). Interestingly, crystals of complex **4** reveal that there are three independent

Table 3
Comparison of bond lengths (Å) and bond angles (°) of complexes **1**–**6** with some literature values

	Pd–P	Pd–S	Pd–N^3	Pd–Cl	N–Pd–S	*trans* angles
1	2.2580	2.2430	2.103	2.3459	83.09	177.98, 174.58
2	2.2609	2.2395	2.085	2.3450	82.95	171.63, 169.86
3		2.2710	2.0305		83.67	180, 180
4		2.2869	2.031		82.89	179.99, 179.99
5 [18]	2.275	2.2453	2.0190		84.16	176.53, 164.22
6 [18]	2.2364	2.2566	2.005		83.44	177.14, 173.99
7 [6]		2.2439	1.962	2.3025	84.14	179.14, 165.44
8 [16a]	2.2527	2.3270	2.029		83.19	178.75, 164.5

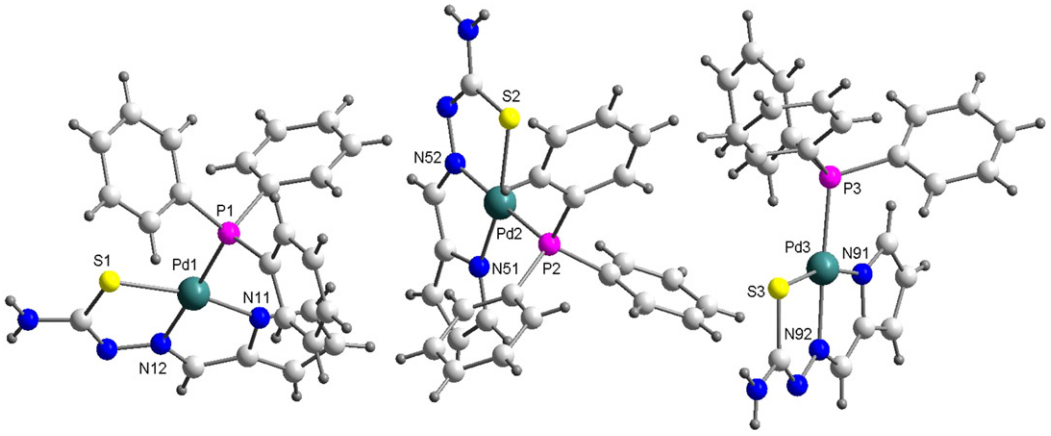


Fig. 5. Three molecules in the unit cell of complex **5**.

molecules with different orientations in the same unit cell (Fig. 4b), and with minor differences in bond parameters (Table 2). The existence of the three different types of molecules appears to be due to the presence of different intermolecular hydrogen bonds between the amino hydrogens ($-NH_2$) and the coordinated sulfur atom, as is shown in its packing diagram. The Pd–S and Pd–N bond lengths of complexes **3**, {2.2710(5) and 2.0305(13) Å}, and **4** {2.2869(15) and 2.031(5) Å}, are also similar. On comparing the bond lengths of **1** and **3**, it is found that the Pd–S distance of **1** is shorter than that of complex **3**, whereas the Pd–N distance is longer (Table 3). Similar differences in bond lengths are observed for complexes **2** and **4**. It may be added here that the N^3–Pd–S bite angles shown by complexes **1**–**4** are similar to those of complexes **5** and **6**. Further, compound **5** also showed three types of independent molecule with different bond parameters (Fig. 5) [18], similar to those shown by compound **4**.

3.3. NMR spectroscopy

The signals due to $-N^2H$ protons in the free ligands [19] were absent in complexes **1**–**4**, thus supporting deprotonation during complexation in all the complexes. The $-NH_2$ protons appear as single peaks in all the complexes due to the free rotation of the N^1H_2 group along the C^1-N^1 bond axis, instead of two broad peaks as observed in the free ligands due to the restricted rotation of the $-N^1H_2$ group along the C^1-N^1 bond axis at room temperature [19]. The peaks due to C^2H and ring protons are given in the experimental section. The ^{31}P NMR spectra of complexes **1** and **2** show a coordination shift of 32.6 ppm each, which is close to the shift observed for complexes **5** and **6** [18].

4. Conclusion

It may be concluded that for R = furan or thiophene at the C^2 carbon, the thiosemicarbazone ligands (Hftsc and Httsc) act as uninegative bidentate coordinating ligands to the metal center via N^3,*S*-donor atoms, forming five membered chelate rings, and the resulting products (**1**–**4**) are dependent on the metal to ligand molar ratio. For R = pyrrole or 2-hydroxyphenyl, the ligands act as dinegative tridentate coordinating ligands via N^4,N^3,*S*- or *O*,N^3,*S*-donor atoms (**5**, **6**), and for R = pyridyl, the ligand is uninegative tridentate (N^4,N^3,*S*) (**7**). There was no effect on stoichiometry when two equivalents of H_2ptsc, H_2stsc or Hpytsc were used.

5. Supplementary material

CCDC 650112, 650113, 650114 and 650115 contain the supplementary crystallographic data for **1**, **2**, **3** and **4**. These data can be obtained free of charge via http://www.ccdc.cam.ac.uk/conts/retrieving.html, or from the

Cambridge Crystallographic Data Centre, 12 Union Road, Cambridge CB2 1EZ, UK; fax: (+44) 1223-336-033; or e-mail: deposit@ccdc.cam.ac.uk.

Acknowledgements

Financial assistance to one of us (G.B.) from CSIR New Delhi (F.No. 9/254(155)-EMR-1) is gratefully acknowledged. We thank the referees for healthy comments.

References

[1] D.X. West, A.E. Liberta, S.B. Padhye, R.C. Chikate, P.B. Sonawane, A.S. Kumbhar, R.G. Yerande, Coord. Chem. Rev. 123 (1993) 49.
[2] T.S. Lobana, Rekha, R.J. Butcher, A. Castineiras, E. Bermejo, P.V. Bharatam, Inorg. Chem. 45 (2006) 1535.
[3] (a) T.S. Lobana, A. Sanchez, J.S. Casas, A. Castineiras, J. Sordo, M.S. Garcia-Tasende, Polyhedron 17 (1998) 3701;
(b) J.S. Casas, E.E. Castellano, M.C. Rodriguez-Arguelles, A. Sanchez, J. Sordo, J. Zukerman-Schpector, Inorg. Chim. Acta 260 (1997) 183;
(c) R. Carballo, A. Castineiras, T. Perez, Z. Naturforsch. B. Chem. Sci. 56 (2001) 881.
[4] F. Basuli, S.-M. Peng, S. Bhattacharya, Inorg. Chem. 39 (2000) 1120.
[5] L.A. Ashfield, A.R. Cowley, J.R. Dilworth, P.S. Donnely, Inorg. Chem. 43 (2004) 4121.
[6] D. Kovala-Demertzi, J.R. Miller, N. Kourkoumelis, S.K. Hadjikakou, M.A. Demertzis, Polyhedron 18 (1999) 1005.
[7] D. Kovala-Demertzi, P.N. Yadav, M.A. Demertzis, J.P. Jasiski, F.J. Andreadaki, I.D. Kostas, Tetrahedron Lett. 48 (2004) 2923.
[8] J. Garcia-Tojal, L. Lezama, J.L. Pizarro, M. Insausti, M.I. Arriortua, T. Rojo, Polyhedron 18 (1999) 3703.
[9] S. Baylak, A. Balaban, A.R. Turker, B. Erk, J. Anal. Chem. 61 (2006) 476.
[10] R.K. Mahajan, I. Kaur, T.S. Lobana, Talanta 59 (2003) 101.
[11] B. Asci, G. Alpdogan, S. Sungur, Anal. Lett. 39 (2006) 997.
[12] R. Alonso, E. Bermejo, A. Castineiras, T. Perez, R. Carballo, Z. Anorg. Allg. Chem. 623 (1997).
[13] P. Souza, A.I. Matesanz, C. Pastor, Inorg. Chem. Comm. 5 (2002) 344.
[14] D. Kovala-Demertzi, N. Kourkoumelis, M.A. Demertzis, J.R. Miller, C.S. Frampton, J.K. Swearingen, D.X. West, Eur. J. Inorg. Chem. (2000) 727.
[15] P.N. Yadav, M.A. Demertzis, D. Kovala-Demertzi, A. Castineiras, D.X. West, Inorg. Chim. Acta 332 (2002) 204.
[16] (a) J.M. Vila, M.T. Pereira, J.M. Ortigueira, M. Grana, D. Lata, A. Suarez, J.J. Fernandez, A. Fernandez, M. Lopez-Torres, H. Adams, J. Chem. Soc., Dalton Trans. (1999) 4193;
(b) A. Amoeda, M. Grana, J. Martinez, T. Pereira, M. Lopez-Torres, A. Fernandez, J.J. Fernandez, J.M. Vila, Eur. J. Inorg. Chem. (2002) 613.
[17] J. Martinez, L.A. Adiro, J.M. Antelo, M. Teresa-Pereira, J.J. Fernandez, J.M. Vila, Polyhedron 25 (2006) 2848.
[18] T.S. Lobana, G. Bawa, A. Castineiras, R.J. Butcher, Inorg. Chem. Comm. 10 (2007) 506.
[19] T.S. Lobana, A. Sánchez, J.S. Casas, A. Castiñeíras, J. Sordo, M.S. García-Tasende, E.M. Vázquez-López, J. Chem. Soc., Dalton Trans. (1997) 4289.
[20] W.L. Steffen, G.J. Palenik, Inorg. Chem. 15 (1976) 2432.
[21] XSCANS, Siemens Analytical X-ray Instruments Inc., Madison, WI, USA, 1994.
[22] International Tables for X-ray Crystallography, vol. C, Kluwer, Dordrecht, The Netherlands, 1995.
[23] G.M. Sheldrick, SHELXTL-PC, release 5.03, Siemens Analytical X-ray Instruments Inc., Madison, WI, USA, 1995.
[24] G.X. Win, L.J. Farrugia, J. Appl. Cryst. 32 (1999) 837.
[25] G.M. Sheldrick, SHELXL-97, Program for the Refinement of Crystal Structures, University of Göttingen, Göttingen, Germany, 1997.

$C_6H_{14}N_4O_2$) and several counter ions. In the solid state, these compounds show interesting supramolecular structures, self-assembly and self-organization, with infinite single-, double- or triple-stranded helicates. As a consequence of the versatility of the positively charged guanidinium group, a binding site for H-bonds, arginine forms many complexes on reaction with organic and inorganic acids, and also incorporating metal ions [13,14]. The self-assembly is governed by hydrogen bonding, by the coordination of the metal ions, as well as by the nature of the counter ions. The metal compounds studied by Yamauchi and collaborators are essentially three dimensional and we are not aware of any dinuclear or polynuclear metal complex formation either with arginine or with other amino acid. As pointed out by Dey et al. [15] the ligands obtained by forming dinuclear metal complexes are effective devices for the recognition and assembly of external species, and also to mimic sites in which two metal ions cooperate to form a biologically relevant active centre. Thus, as part of our working lines on metal derivatives of amino acids, we found interesting to obtain and characterize dinuclear or polynuclear copper–arginine compounds using appropriate counter ions.

In recent years, Youngme and collaborators [16–18] prepared and characterized structurally and magnetically double and triply bridged dinuclear Cu(II) complexes containing the aromatic ligands 1,10-phenanthroline, 2,2′-bipyridine and di-2-pyridylamine and the $H_xPO_4^{(3-x)-}$ ($x = 1, 2$) oxoanions. In these compounds, the phosphate groups form bridges of different coordination types supporting weak antiferromagnetic interactions between neighbour copper ions. Here we exploited the bridging capabilities of phosphate groups as counter ions and report the synthesis, X-ray crystal structure and magnetic measurements of $[Cu_2(\text{L-arg})_2(\mu\text{-}HPO_4\text{-}O)(\mu\text{-}HPO_4\text{-}O,O')(\mu\text{-}OH)]^- \cdot (H_3O)^+ \cdot (H_2O)_6$ (**1**), a new dinuclear copper complex of L-arginine bridged by hydrogenphosphate and hydroxyl groups exhibiting unusual dinuclear interactions with a Cu(II) coordination and bridging mode which has not been observed previously for copper–amino acid complexes.

2. Material and methods

The growth solutions were prepared in a two-step process. In the first step, L-arginine phosphate ($C_6H_{14}N_4O_2 \cdot H_3PO_4 \cdot H_2O$) was synthesized by dissolving equimolar quantities of L-arginine (Ajinomoto Co.) and orthophosphoric acid (Merck) in a saturated water solution. The pH value of this solution was adjusted to 4.25. In the second step, Cu(II) ions as copper acetate with mole fractions 0.275 and 0.50, were added to the solution. All reagents were of analytical grade. Slow solvent evaporation at constant temperature was employed in the crystal growth and plate like crystals of **1** with intense blue colour and elongated along one direction, were obtained after few weeks. Atomic Absorption Spectroscopy (Perkin–Elmer Analyst 200) and a CHN analyser (Perkin–Elmer Series II 2400) were used for elemental analyses of C, H, N and Cu contents in **1**. *Anal.* Calc. for $C_{12}H_{46}Cu_2N_8O_{20}P_2$: C, 17.76; H, 5.71; Cu, 15.66; N, 13.81; O, 39.43; P, 7.63. Found: C, 17.98; H, 5.59; Cu, 15.8; N, 13.76%. Oxygen and phosphorus were not measured. The crystal density obtained by the Arquimedes' method is (1.682 ± 0.004) Mg/m^3. The experimentally measured composition and density are in good agreement with the values obtained from the X-ray diffraction structural determination.

Diffraction data were collected at 153 K with an Enraf-Nonius Kappa-CCD diffractometer with sealed tube source and graphite-monochromated Mo Kα radiation ($\lambda = 0.71073$ Å). The unit cell parameters were derived from least squares refinement of 10451 reflections from $\theta = 0.998°$ to $\theta = 27.485°$. The data collection was within $\theta = 27.485°$; however, the final refinement improved when the weakest reflections beyond the usual $\theta = 25.000°$ were removed, and this condition was maintained. Data collection was made using the COLLECT program [19] and the integration and scaling of the reflections were performed with the HKL Denzo-Scalepack system of programs [20]. Absorption correction was carried out using the multi-scan method [21]. The structure of the complex was solved by the Patterson method using SHELXS-97 [22] and refined by full-matrix least-squares method on $(F_{obs})^2$ using SHELXL-97 [23]. The crystal data and details of the refinement are given in Table 1. Only one H atom of the phosphate groups was found in the difference Fourier maps, and had their coordinates refined. The hydrogen atoms of the water molecules could not be unequivocally assigned from the difference Fourier maps and those of the N atoms were found on Fourier maps, although the free refinement resulted in an unacceptable geometry. Thus, the H-atoms were refined with restraints N–H = 0.96 Å for N1A and N1B, H···H distances of 1.60 Å compatible with tetrahedral geometry, and N–H = 0.86 Å for other N atoms, with H···H distances of 1.80 Å, compatible with amino group geometry. The remaining H atoms were placed at calculated positions, assigned a fixed displacement and restrained to ideal geometry with C–H = 0.99 Å. The thermal parameters of all hydrogen atoms were related to those of their parent atoms by $U(\text{H}) = 1.2U_{eq}(\text{C,N})$. The absolute configuration of the arginine molecule was determined by the anomalous dispersion method from 3582 Friedel pairs with a Flack parameter of −0.01(1) [24]. The final value of R was 0.0433 for 4995 observed reflections ($F_0 > 4\sigma(F_0)$) and the final value of R_w was 0.1309 for 5174 unique reflections which were not merged before the last refinement cycle. The weighting scheme was $w^{-1} = [\sigma^2(F_o^2) + (0.0894P)^2 + 0.09P]$ where $P = [\max(F_o^2, 0) + 2F_c^2]/3$. The final difference map showed a peak of 1.36 e Å^{-3}, without exhibiting significant features.

The magnetic susceptibility of a powdered sample of 140 mg of **1** placed in a gelatine capsule sample holder was measured between 2 and 300 K with applied magnetic fields $B_0 = \mu_0 H = 0.2$ and 0.5 T (μ_0 being the vacuum per-

Table 1
Crystal data and structure refinement for **1**

Empirical formula	$C_{12}H_{46}Cu_2N_8O_{20}P_2$
Formula weight	811.59
Temperature (K)	153(2)
Wavelength (Å)	0.71073
Crystal system	triclinic
Space group	$P\bar{1}$ (no. 1)
Unit cell dimensions	
a (Å)	7.234(1)
b (Å)	11.395(1)
c (Å)	11.429(1)
α (°)	109.74(1)
β (°)	107.20(1)
γ (°)	100.31(1)
Volume (Å^3)	805.3(2)
Z	1
D_{calc} (Mg/m^3)	1.678
Absorption coefficient (mm^{-1})	1.509
F(000)	422
Crystal size (mm)	$0.20 \times 0.18 \times 0.18$
Colour	blue
Index ranges	$-8 \leqslant h \leqslant 8$, $-13 \leqslant k \leqslant 13$, $-13 \leqslant l \leqslant 13$
Reflections collected	10451
Independent reflections (R_{int})	5174 (0.0341)
Maximum and minimum transmission	1.045 and 0.960
Refinement method	full-matrix least-squares on F^2
Data/restraints/parameters	5174/23/443
Goodness-of-fit on F^2	1.195
Final R indices [$I > 2\sigma(I)$]	$R_1 = 0.0433$, $wR_2 = 0.1142$
R indices (all data)	$R_1 = 0.0493$, $wR_2 = 0.1309$
Absolute structure parameter	−0.013(12)
Extinction coefficient	0.118(7)
Largest difference in peak and hole (e Å^{-3})	1.364 and −0.939

meability) with a PPMS magnetometer (Quantum Design, Inc.). Measurements of the magnetization isotherm at a temperature $T = 2.29(1)$ K were performed with applied magnetic fields up to 9 T.

3. Results and analysis

3.1. Crystal structure of *1*

An ORTEP [25] view of the basic structural unit with the corresponding numbering system is depicted in Fig. 1. Selected bond lengths and bond angles are given in Table 2. The crystal structure contains two $[Cu(L\text{-arg})]^{2+}$ cations, two $(HPO_4)^{2-}$ anions, one OH^- anion, one H_3O^+ hydronium and six water molecules in the unit cell. These two Cu(L-arg) units are connected by three bridges: a didentate hydrogenphosphate anion, a monodentate hydrogenphosphate anion and a hydroxyl anion. FT-IR spectrum showed a band at 969 cm^{-1} and a shoulder around 3452 cm^{-1} that are assigned to the vibration modes of the OH [26]. In comparison with the other six water molecules, the geometrical analysis of the structure around the isolated oxygen atom O7W shows a tetrahedral environment with the shortest distances with respect to neighbouring oxygen atoms, which leads us to attribute this oxygen to the location of a hydronium ion. This hypothesis is corroborated by thermogravimetric measurements that show two stages. The first is associated to the loss of the six water

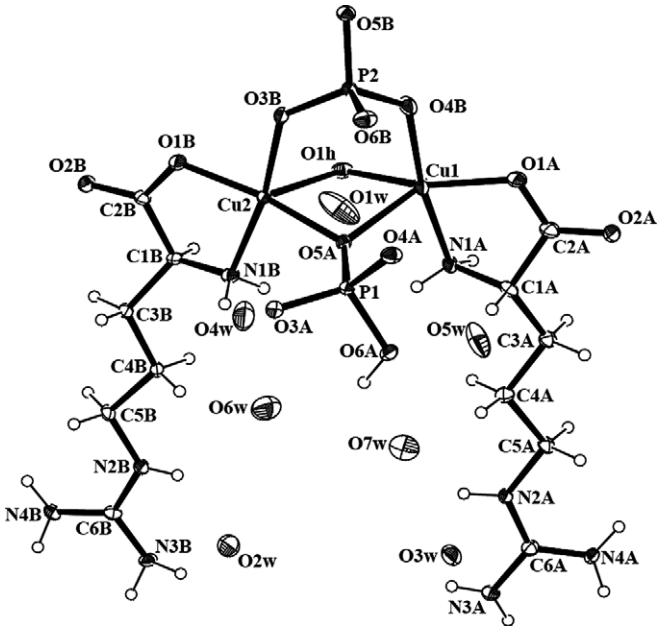


Fig. 1. ORTEP drawing at 30% probability level of **1**. Hydrogen atoms are represented as spheres of arbitrary size, except those of the water molecules which were not found, as explained in the text.

Table 2
Selected bond lengths (Å) and angles (°) for **1**

Cu1–O4B	1.909(4)	O1h–Cu1–O5A	81.14(13)
Cu1–O1A	1.956(4)	O3B–Cu2–O1B	88.18(14)
Cu1–N1A	1.995(4)	O3B–Cu2–O5A	95.73(14)
Cu1–O1h	2.061(4)	O1B–Cu2–O5A	170.25(14)
Cu1–O5A	2.243(3)	O3B–Cu2–N1B	170.25(16)
Cu2–O3B	1.920(3)	O1B–Cu2–N1B	83.16(16)
Cu2–O1B	1.949(4)	O5A–Cu2–N1B	92.15(15)
Cu2–O5A	1.955(3)	O3B–Cu2–O1h	91.06(13)
Cu2–N1B	2.011(4)	O1B–Cu2–O1h	109.34(14)
Cu2–O1h	2.392(4)	O5A–Cu2–O1h	79.58(13)
P1–O3A	1.502(4)	N1B–Cu2–O1h	96.02(15)
P1–O4A	1.516(3)	O3A–P1–O4A	115.7(2)
P1–O5A	1.546(3)	O3A–P1–O5A	110.64(19)
P1–O6A	1.599(3)	O4A–P1–O5A	109.97(18)
P2–O3B	1.516(3)	O3A–P1–O6A	108.54(19)
P2–O4B	1.517(4)	O4A–P1–O6A	105.13(19)
P2–O5B	1.518(3)	O5A–P1–O6A	106.27(19)
P2–O6B	1.605(4)	P1–O5A–Cu2	124.88(19)
O4B–Cu1–O1A	88.08(16)	P1–O5A–Cu1	132.63(18)
O4B–Cu1–N1A	170.87(16)	Cu2–O5A–Cu1	98.89(13)
O1A–Cu1–N1A	82.79(16)	O3B–P2–O4B	112.9(2)
O4B–Cu1–O1h	92.82(16)	O3B–P2–O5B	111.44(19)
O1A–Cu1–O1h	153.65(17)	O4B–P2–O5B	110.7(2)
N1A–Cu1–O1h	95.40(15)	O3B–P2–O6B	108.8(2)
O4B–Cu1–O5A	95.04(14)	O4B–P2–O6B	109.3(2)
O1A–Cu1–O5A	125.04(16)	O5B–P2–O6B	103.26(19)
N1A–Cu1–O5A	90.16(15)	Cu1–O1h–Cu2	91.40(13)

molecules and the second is consistent with the loss of the H_3O^+ and OH^- groups. The six free water molecules and the hydronium ion which lead to solvent channels parallel to the crystallographic *a*-axis are involved in a complicated hydrogen bonding network and contribute to stabilize the structure of the complex and the crystal packing. Since the H atoms of the water molecules and the hydronium ion were not located on difference maps, detailed description of the H-bonding network is difficult.

The two phosphate groups show two longer lengths consistent with P–OH bonds. The O6B atom at 2.705(5) Å from the O4A atom, is a good candidate for an H donor because it has the longest distance P2–O6B = 1.609(6) Å.

Both chemically different Cu atoms in the dinuclear unit are in distorted square-pyramidal coordination with different basal planes (see Fig. 1). The Cu1 ion coordinates one carboxylate oxygen (O1A) and one amino nitrogen (N1A) of the associated L-arginine molecule. In its basal plane it also coordinates two oxygen atoms, one from the didentate hydrogenphosphate group (O4B) and the other from the hydroxyl anion (O1h). The apical position of the Cu1 centre is occupied by one oxygen atom from the monodentate hydrogenphosphate group [Cu1–O5A = 2.243(3) Å]. The Cu1 atom is 0.249(2) Å above the basal plane, towards the O5A oxygen atom. The Cu2 ion coordinates one carboxylate oxygen (O1B) atom and one amino nitrogen atom (N1B) of the second L-arginine molecule in a square planar geometry together with two oxygen atoms from both di- (O3B) and monodentate (O5A) hydrogenphosphate groups. In this case, the apical position is occupied by the OH^- anion [Cu2–O1h = 2.396(4) Å]. The Cu2 atom is 0.118(2) Å above the basal plane, towards the OH^- anion. The two pyramids share the edge made by O1h–O5A = 2.803(5) Å, resulting in two strained angles O1h–Cu1–O5A = 81.1(1)° and O1h–Cu2–O5A = 79.6(1)°. The dihedral angle between the least squares planes defined by the basal atoms O1h–N1A–O1A–O4B and O1B–N1B–O3B–O5A is 13.8(2)°. Both basal planes are close to the planes of the corresponding L-arginine molecule. The quasi-planar conformation of the L-arginine molecules in **1** is markedly different from that observed in L-arginine phosphate monohydrate [27].

Each $[Cu(L\text{-arg})]^{2+}$ is connected to adjacent ones through two hydrogen bonds with similar lengths. One of these bonds is between one of the guanidinium NH_2 moieties and the oxygen atom of the coordinated carboxylate group. The other is between the second guanidinium NH_2 moiety and the oxygen atom of the uncoordinated carbonyl group. The result is a layered structure (see Fig. 2) with layers nearly parallel to the plane defined by four atoms of four neighbouring molecules of the dinuclear complex: N3B, $N3B^{i}$, $N4A^{ii}$ and $N4A^{iii}$, with translational symmetry operations (i) = $-1+x$, $-1+y$, $-2+z$; (ii) = $2+x$, $1+y$, $1+z$; (iii) = $1+x$, y, $-1+z$, having Miller indices (1 −3 1), and interplanar distance 3.552 Å.

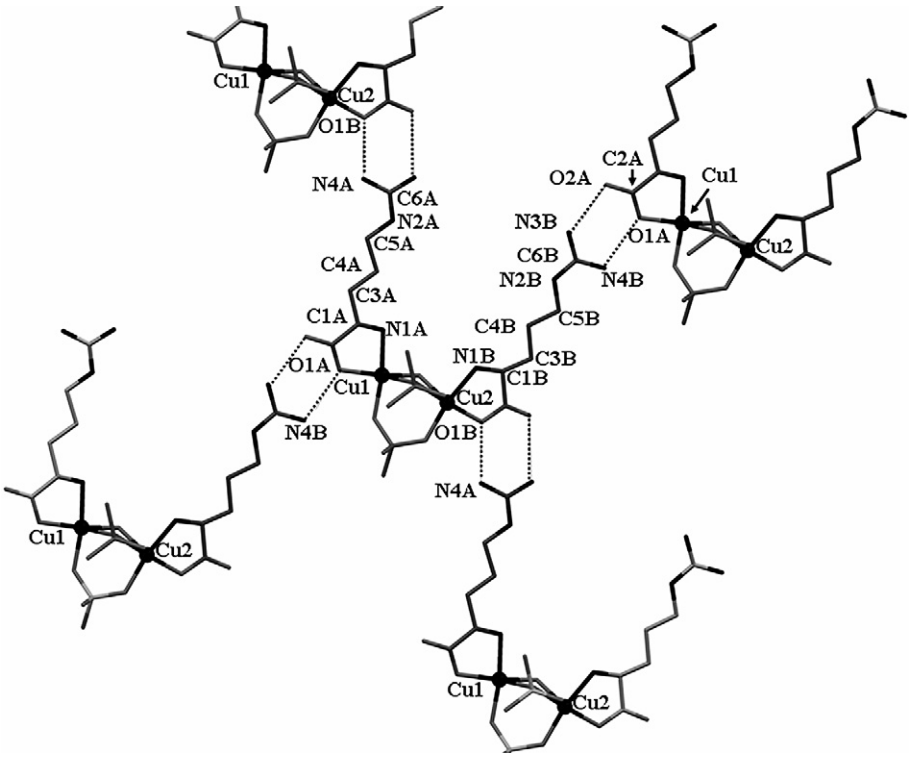


Fig. 2. Crystallographic packing of structure **1.** Cu1 and Cu2 ions of neighbour dinuclear units in a layer are bridged through a pair of H-bonds connecting the tale of the guanidinium group associated to one Cu, to the oxygens of the L-arginine carboxylate group coordinated to the other neighbour copper in the layer. Dashed lines indicate H-bonds. The bridge includes nine diamagnetic atoms plus the proton in the H-bond. The distance between coppers is 13.339 Å and that measured along the bond is 17.006 Å.

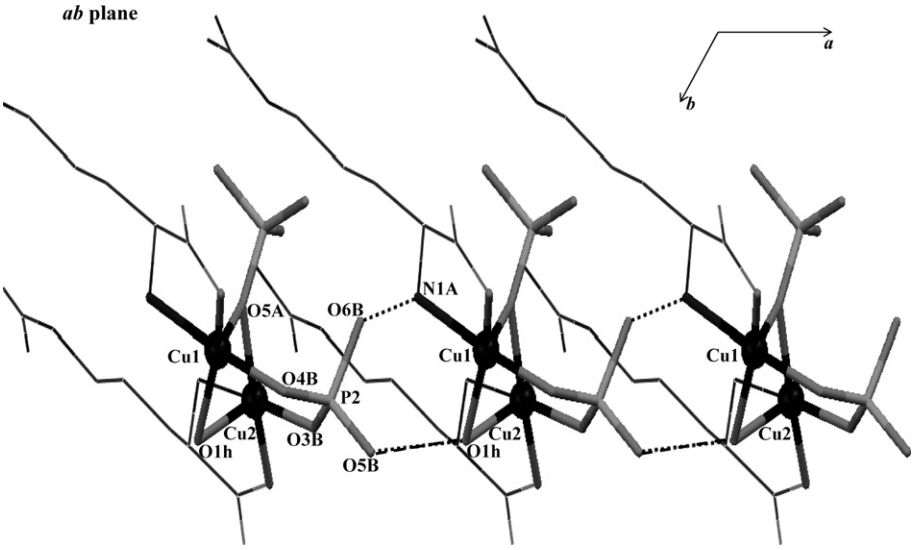


Fig. 3. Chemical bridges connecting dinuclear units in neighbour layers. Oxygens O5B and O6B belonging to the phosphate group providing the O–P–O bridge in dinuclear units are H-bonded to the N1A and O1h ligands to the Cu1 of the neighbour dinuclear unit. This bridge contains 4 diamagnetic atoms plus the H-bond. The distance between Cu1 atoms is 7.234 Å and that measured along the bond is 11.201 Å.

The copper ions are 3.1948(8) Å apart and the chemical paths connecting them are the two equatorial–apical bridges with bond lengths d[Cu1–O1h–Cu2] = 4.417 Å and d[Cu1–O5A–Cu2] = 4.194 Å, and one O–P–O bridge with bond length d[Cu1–O4B–P2–O3B–Cu2] = 6.863 Å, that support the intradinuclear exchange interaction. The bridging angles Cu1–O5A–Cu2 and Cu1–O1h–Cu2 are 98.97° and 91.25°, respectively.

The connections between rotated copper ions in neighbouring dinuclear units in the same layer are described in Fig. 2. One of them has 10 diamagnetic atoms including one moderate H-bond (Cu1–N1A–C1A–C3A–C4A–C5A–N2A–C6A–N4A–H42A···O1B–Cu2) with total bond length of 17.006 Å, and Cu1–Cu2 distance of 13.339 Å. The other similar connection, Cu1–O1A···H42B–N4B–C6B–N2B–C5B–C4B–C3B–C1B–N1B–Cu2 has a total bond length of 15.633 Å and the distance between copper atoms is 13.263 Å. The chemical bridges connecting Cu dinuclear units in adjacent layers of **1** are shown in Fig. 3; all of them being through the phosphate groups. The distance between two Cu1 atoms or two Cu2 atoms is the same, d = 7.234 Å, and the total bond lengths are 11.201 Å and 9.958 Å, respectively. The first path (Cu1–O4B–P2–O6B···H11A–N1A–Cu1) contains four diamagnetic atoms and a weak H-bond defined according to Steiner's criteria [28] (dotted line in the figure) with d[O6B–N1A] = 3.039 Å, while the second path (Cu2–O3B–P2–O5B–O1h–Cu2) is similar to the first one but includes one short contact d[O5B–O1h] = 2.068 Å. The third chemical path connect Cu1 to Cu2 (Cu1–O4B–P2–O5B–O1h–Cu2) separated by a distance of 7.943 Å, with total bond length of 9.949 Å containing four diamagnetic atoms and one short contact O5B–O1h. Finally, the fourth chemical path connect Cu2 to Cu1 (Cu2–O3B–P2–O6B···H11A–N1A–Cu1) separated by a distance of 7.872 Å, with total bond length of 11.210 Å containing four diamagnetic atoms and one H-bond. Considering the different number of diamagnetic atoms and the lengths of the chemical paths connecting dinuclear units described in Figs. 2 and 3, we conclude that the most relevant paths in supporting exchange interactions are those coupling each dinuclear unit with two dinuclear units in neighbour layers (Fig. 3).

3.2. Magnetic results

The dc magnetic susceptibility data corresponding to one mol of Cu_2 dinuclear units in **1** measured with B_0 = 0.5 T at temperatures T between 2 and 300 K are displayed in Fig. 4 as $T\chi(T)$. The values measured with

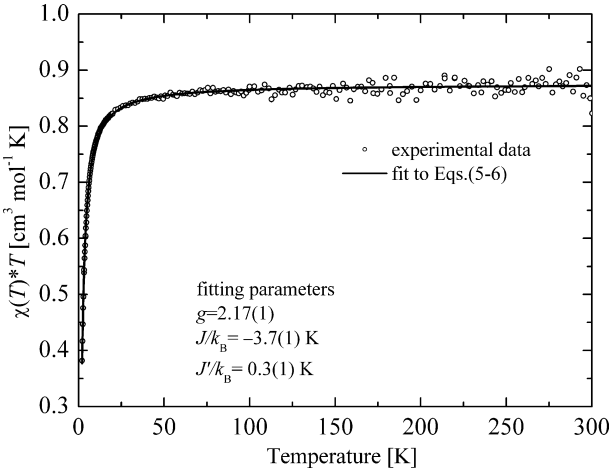


Fig. 4. Values of $T\chi(T)$ obtained with an applied field B_0 = 0.5 T at temperatures T between 2 and 300 K in a powder sample of **1** (circles). The solid line displays the best global fit of Eqs. (5) and (6) to the susceptibility, obtained for a dinuclear unit within a molecular field approximation. The values of the parameters obtained in the fit are shown.

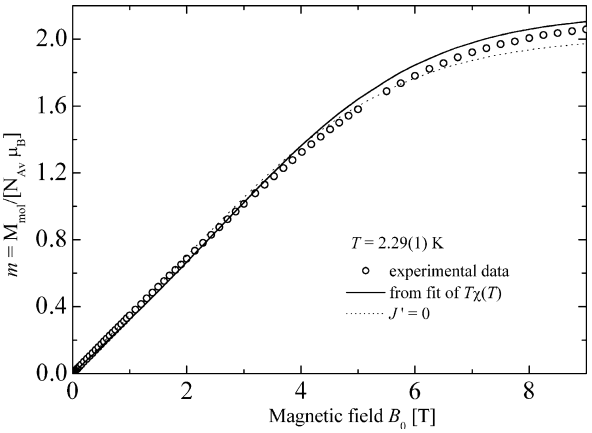


Fig. 5. Values of the molecular magnetization $m(B_0)$ observed with applied fields $0 < B_0 < 9$ T at $T = 2.29(1)$ K in a powder sample of **1** (symbols). The solid line displays the magnetization calculated with a molecular field approximation using Eqs. (2) and (3), considering the intradinuclear and interdinuclear interactions evaluated from the susceptibility data. The dashed line is obtained as the best fitting with a model ignoring the interactions between dinuclear units.

$B_0 = 0.2$ T (not shown) agree within the experimental uncertainty with those in Fig. 4. The molecular magnetization measured at 2.29(1) K as a function of B_0 is shown in Fig. 5. The contributions of the sample holder, the diamagnetism and temperature independent paramagnetism of the sample have been already subtracted from the data displayed in Figs. 4 and 5. At room temperature $T\chi(T) = 0.871$ cm^3 K/mol. This value is reduced to $T\chi(T) = 0.38$ cm^3 K/mol at 2 K, indicating a predominant antiferromagnetic coupling between copper ions (Fig. 4). The magnetic moment per dinuclear unit at 2.29 K and at the highest field (9 T), where still is not fully saturated, amounts 2.06 μ_B (Fig. 5).

The susceptibility data were fitted assuming a Hamiltonian involving equal values for the angular average of the g-factor of the two copper ions, and isotropic intra- and interdinuclear exchange interactions J and J', respectively. The interdinuclear interactions J' with the relevant $z = 2$ neighbouring dinuclear units are identical (see the structural description and Fig. 3), so in the molecular field approximation the Hamiltonian of a dinuclear unit can be written as:

$$\mathscr{H} = \mu_B g(S_{1z} + S_{2z})B_0 - J\mathbf{S}_1 \cdot \mathbf{S}_2 - zJ'(S_{1z} + S_{2z})\langle S_z\rangle \qquad (1)$$

In the last term, $\langle S_z\rangle$ is the thermal average of the component along B_0 of the spin of a neighbour dinuclear unit. Thus, in units of μ_B, the molecular magnetization m of a dinuclear unit under an effective field B acting on each copper ion pair at temperature T is:

$$m = (M_m/N_{Av}) = 2g\exp(J/k_BT)\sinh(g\mu_B B/k_BT)/Z \qquad (2)$$

where Z is the partition function:

$$Z = 1 + \exp(J/k_BT)[1 + 2\cos h(g\mu_B B/k_BT)] \qquad (3)$$

In the molecular field model used in Eq. (1), the effective field B is the sum of the applied field B_0 plus a contribution due to the interaction with the neighbour dinuclear units:

$$B = B_0 - \frac{zJ'}{g\mu_B}\langle S_z\rangle = B_0 - \frac{zJ'}{g^2\mu_B^2}m \qquad (4)$$

As shown by O'Connor [29] and Kahn [30] the Bleaney–Bowers equation [31] for the magnetic susceptibility of this dinuclear unit is:[1]

$$T\chi(T) = \frac{2N_{Av}g^2\mu_B^2}{3k_B}\frac{T}{(T-\theta)[1+\frac{1}{3}\exp(-J/k_BT)]} \qquad (5)$$

with:

$$\theta = \frac{-2zJ'/k_B}{3 + \exp(-J/k_BT)} \qquad (6)$$

A least squares fit of Eqs. (5) and (6) to the susceptibility data in Fig. 4 gives $g = 2.17(1)$, $J/k_B = -3.7(1)$ K and $zJ'/k_B = 0.6(1)$ K, indicating antiferromagnetic intradinuclear exchange interaction, as indicated by the low temperature behaviour of $T\chi(T)$ in Fig. 4, and an effective ferromagnetic coupling $J'/k_B = 0.3$ K (considering $z = 2$) between neighbour dinuclear units. The solid line in Fig. 4 is calculated with these parameters. They were also used to evaluate the molecular magnetization m considering Eqs. (2) and (4) and the results are shown as a solid line in Fig. 5. The prediction for the molecular magnetization m is not as good as that for $T\chi(T)$. The two types of data correspond to well separate regions in the phase diagram of the generalized susceptibility through the quantity $T\frac{1}{N_{Av}}\left(\frac{\partial M_m}{\partial B_0}\right)$ versus T and B_0. Consequently, it is not surprising to find small discrepancies between the predictions in the values of M_m versus B_0 using the parameters obtained from the $T\chi(T)$ data. To emphasize the role of the interdinuclear interactions, we also display in Fig. 5 results obtained by fitting these data with a model that neglects the interdinuclear coupling J'.

The antiferromagnetic intra-dinuclear interaction $J/k_B = -3.7$ K is associated with the Cu–O–Cu and Cu–O–P–O–Cu bridges shown in Fig. 1. We propose that the smaller ferromagnetic coupling $J'/k_B = 0.3$ K between dinuclear units in neighbour layers is supported by the paths described in Fig. 3.

4. Discussion and conclusions

Our single crystal X-ray diffraction measurements indicate that the synthesized ternary copper compound **1** is triclinic with two chemically different copper ions in dinuclear units. Each copper ion is in a square pyramidal geometry coordinated to a nitrogen from the α-amino group and to an oxygen from the carboxylate group of the L-arginine molecules. They are bridged by two HPO_4^{2-} and one OH^- anions, showing a dinuclear copper structure that is not common in metal derivatives of amino acids. This structure appears as a consequence of the bonding possibilities offered by the phosphate groups bridging these units,

[1] See Eq. (6.5.12) in Ref. [30].

combined with the ample possibilities of bonding of the guanidinium group of arginine. The magnetic measurements indicate a weak antiferromagnetic intradinuclear coupling ($J/k_B = -3.7$ K) between copper ions supported by Cu–O–Cu and phosphate bridges, and a smaller ferromagnetic coupling ($J'/k_B = 0.3$ K) between dinuclear units in neighbour layers, supported by bridges containing four diamagnetic atoms plus the H-bond (Fig. 3). As discussed earlier, the distance between the connected Cu1 atoms in neighbour dinuclear units 7.234 Å and that measured along the path is 11.201 Å.

Our structural results for the dinuclear units in **1** show two equatorial–apical paths, one involving a phosphate oxygen (O5A) and the other through an O1h. Because of the distortion of the pyramidal units one may guess that the ground orbital states of the individual Cu ions in dimeric units are not a pure $d_{x^2-y^2}$ orbital (supported by a $g = 2.17$). Thus, one expects some small contributions to the antiferromagnetic coupling caused by this distortion. The basal planes around each Cu are not parallel producing a lack of orthogonality between apical and equatorial electronic densities. A third connection between the Cu ions is produced by an equatorial–equatorial path –O4B–P2–O3B– that will also contribute to the coupling, in spite that this occurs through three diamagnetic atoms.

A search in the Cambridge Crystallographic Database [32–34] was performed without much success to locate other compounds with similar intradinuclear chemical bridges. Dinuclear copper compounds with hydrogenphosphate bridges were reported recently by Youngme and collaborators [16–18] for dinuclear compounds with the aromatic ligands di-2-pyridylamine, 1,10-phenanthroline and 2,2′-bipyridine bipyridine ($[Cu(dpyam)(\mu\text{-}H_2PO_4)(H_2PO_4)]_2$, $[Cu_2(phen)_2(\mu\text{-}H_2PO_4\text{-}O,O')_2(H_2PO_4)]$, $[Cu_2(phen)_2(\mu\text{-}H_2PO_4\text{-}O,O')(\mu\text{-}H_2PO_4\text{-}O)(\mu\text{-}HPO_4\text{-}O)]_2(H_2O)_9$, and $[Cu_2(bpy)_2(\mu,\eta^2\text{-}HPO_4)\text{-}(\mu,\eta^1\text{-}H_2PO_4)(\mu,\eta^2\text{-}H_2PO_4)]_n$). In order to make comparisons or find similarities, it is worth to remark that in the compound studied here the Cu1–Cu2 coupling in the dinuclear unit is supported by three bonds (see Fig. 3).

In Ref. [16], two compounds with di-2-pyridylamine are reported. In the first one, there are two equatorial–equatorial didentate dihydrogenphosphate bridging ligands connecting copper ions at 5.14 Å. The reported exchange interaction $J/k_B \sim -4$ K is similar to that observed for **1**, but the two equatorial–equatorial bridges supporting the interaction and the distance between coppers are too different to allow comparisons. The second compound is polymeric, and the magnitude J of the interaction, supported by an equatorial–equatorial tridentate hydrogenphosphate bridge is much larger than that in compound **1**. Reference [17] reports a compound containing phenanthroline having two chemically different dinuclear units in the unit cell. One of them (unit B) is similar to compound **1**, with a distance $d = 3.074(3)$ Å between coppers and similar bridges and they attribute to this unit a *ferromagnetic* coupling $J/k_B \sim 1.4$ K. However, the experimental uncertainty of this value introduced by the coexistence of two different dinuclear units may be large, and a comparison with our result for **1** is hard to make. Our situation seems to be closer to that reported by Phuengphai et al. [18] for their compound named 1, except for the non-existence of the equatorial–apical bond formed through O1h. They estimate $J/k_B = -7.4$ K for that compound. Even if, the structure of the phosphate bridge is different from ours as to establish a clear cut comparison of the magnetic interaction observed in **1**, one is tempted to speculate that the lack of the equatorial–apical bond formed through O1h, tend to enhance the antiferromagnetic behaviour, as observed in Ref. [18].

Regarding the observed interactions between dinuclear units, Chattopadhyay et al. [35] claimed that bridges containing H-bonds propagate antiferromagnetic interactions between metal centres. However, for the title compound and for the compounds reported in Refs. [16,17], the coupling J' is ferromagnetic. Clarifying this point would require more experimental information in other similar situations and detailed calculations.

5. Supplementary material

CCDC 292513 contains the supplementary crystallographic data for **1**. These data can be obtained free of charge via http://www.ccdc.cam.ac.uk/conts/retrieving.html, or from the Cambridge Crystallographic Data Centre, 12 Union Road, Cambridge CB2 1EZ, UK; fax: (+44) 1223-336-033; or e-mail: deposit@ccdc.cam.ac.uk.

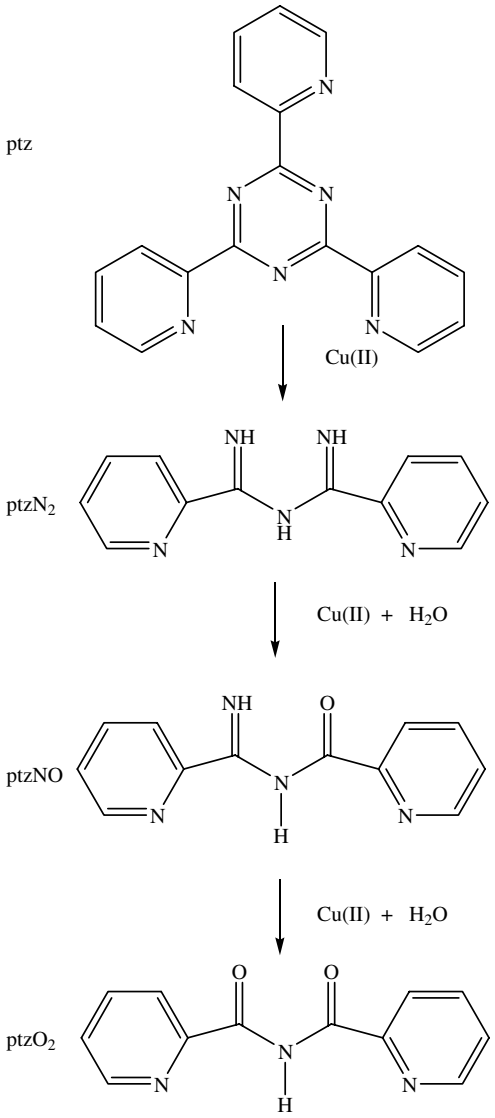
Acknowledgements

We thank Dr. E.E. Castellano (Instituto de Física de São Carlos – USP) for X-ray data collection and to Dr. Mireille Perec (INQUIMAE, University of Buenos Aires and CONICET) for helpful comments on the manuscript. We also thank to the Spanish Research Council (CSIC) for providing some of us with free-of-charge licenses to the Cambridge Structural Database [32–34]. The work in Brazil was supported by FUNAPE, CNPq, FAPERJ and CAPES. The work in Argentina was supported by Grants CAI+D-UNL, PIP 5274 and ANPCyT PICT 06-13782. M.C.G.P. and R.C. are members of CONICET.

References

[1] B.T. Matthias, C.E. Miller, J.P. Remeika, Phys. Rev. 104 (1956) 849 .
[2] F. Jona, G. Shirane, Ferroelectric Crystals, Dover, New York, 1993.
[3] D. Xu, M. Jiang, Z. Tan, Acta Chem. Sinica 41 (1983) 570.
[4] S.B. Monaco, L.E. Davis, S.P. Velsko, F.T. Wang, D. Eimerl, A. Zalkin, J. Cryst. Growth 85 (1987) 252.
[5] D. Eimrel, S. Velsko, L. Davis, F. Wang, G. Loiacono, G. Kennedy, IEEE J. Quantum Electron. 25 (1989) 179.
[6] R.C. Santana, J.F. Carvalho, S.R. Amaral, I. Vencato, F. Pelegrini, M.C. Terrile, A.C. Hernandes, R. Calvo, J. Phys. Chem. Solids 63 (2002) 1857.
[7] S.J. Lippard, J.M. Berg, Principles of Bioinorganic Chemistry, University Science Books, Mill Valley, CA, 1994.

[8] H. Masuda, A. Odani, T. Yamazaki, T. Yahima, O. Yamauchi, Inorg. Chem. 32 (1993) 1111.
[9] N. Ohata, H. Masuda, O. Yamauchi, Angew. Chem., Int. Ed. Engl. 35 (1996) 531.
[10] N. Ohata, H. Masuda, O. Yamauchi, Inorg. Chim. Acta 286 (1999) 37.
[11] N. Ohata, H. Masuda, O. Yamauchi, Inorg. Chim. Acta 300–302 (2000) 749.
[12] O. Yamauchi, A. Odani, M. Takani, J. Chem. Soc., Dalton Trans. (2002) 3411.
[13] M.T.L.S. Duarte, M.A.A.F.C.T. Carrondo, M.L.S.S. Gonçalves, M.B. Hursthouse, N.P.C. Walker, H.M. Dawes, Inorg. Chim. Acta 124 (1986) 41.
[14] R.C. Santana, R.O. Cunha, J.F. Carvalho, I. Vencato, R. Calvo, J. Inorg. Biochem. 99 (2005) 415.
[15] S.K. Dey, N. Mondal, M.S. El Fallah, R. Vicente, A. Escuer, X. Solans, M. Font-Bardía, T. Matsushita, V. Gramlich, S. Mitra, Inorg. Chem. 43 (2004) 2427.
[16] S. Youngme, P. Phuengphai, N. Chaichit, C. Pakawatchai, G.A. van Albada, O. Roubeau, J. Reedijk, Inorg. Chim. Acta 357 (2004) 3603.
[17] P. Phuengphai, S. Youngme, C. Pakawatchai, G.A. van Albada, M. Quesada, J. Reedijk, Inorg. Chem. Commun. 9 (2006) 147.
[18] P. Phuengphai, S. Youngme, N. Chaichit, C. Pakawatchai, G.A. van Albada, M. Quesada, J. Reedijk, Polyhedron 25 (2006) 2198.
[19] B.A. Frenz, COLLECT: Enraf-Nonius CAD-4 Software, Delft, The Netherlands, 1997.
[20] Z. Otwinowski, W. Minor, in: C.W. CarterJr., R.M. Sweet (Eds.), Processing of X-ray Diffraction Data Collected in Oscillation Mode: Methods in Enzymology, Academic Press, New York, 1997, p. 307.
[21] R.H. Blessing, Acta Crystallogr., Sect. A 51 (1995) 33.
[22] G.M. Sheldrick, SHELXS-97: Program for Crystal Structure Resolution, University of Göttingen, Göttingen, Germany, 1997.
[23] G.M. Sheldrick, SHELXL-97: Program for Crystal Structure Refinement, University of Göttingen, Göttingen, Germany, 1997.
[24] H.D. Flack, Acta Crystallogr., Sect. A 39 (1983) 876.
[25] L.J. Farrugia, J. Appl. Crystalogr. 30 (1997) 565.
[26] J.R. Ferraro, W.R. Walker, Inorg. Chem. 4 (1965) 1382.
[27] K. Aoki, K. Nagano, Y. Iitaka, Acta Crystallogr., Sect. B 27 (1971) 11.
[28] T. Steiner, Angew. Chem.. Int. Ed. 41 (2002) 48.
[29] C.J. O'Connor, Prog. Inorg. Chem. 29 (1982) 203.
[30] O. Kahn, Molecular Magnetism, Wiley–VCH, New York, 1993.
[31] B. Bleaney, K.D. Bowers, Proc. Roy. Soc. Lond. A 214 (1952) 451.
[32] F.H. Allen, Acta Crystallogr., Sect. B 58 (2002) 380.
[33] A.G. Orpen, Acta Crystallogr., Sect. B 58 (2002) 398.
[34] I.J. Bruno, J.C. Cole, P.R. Edington, M. Kessler, C.F. Macrae, P. McCabe, J. Pearson, R. Taylor, Acta Crystallogr., Sect. B 58 (2002) 389.
[35] S. Chattopadhyay, M. Sinha Ray, M.G.B. Drew, A. Figuerola, C. Diaz, A. Ghosh, Polyhedron 25 (2006) 2241.



Scheme 1.

anion, which is formed upon deprotonation of bis(2-pyridylcarbonyl)amine Hbpca (see Scheme 1). Mononuclear, dinuclear (homonuclear and heteronuclear), and trinuclear complexes have been identified for various divalent and trivalent metal ions [M(II) = Cu(II), Fe(II), Mn(II), Co(II), Ni(II), and Zn(II); M(III) = Fe(III), Rh(III)] [8–14]. Among these compounds, a ternary complex of copper(II) with one $bpca^-$ and another derivative formed during the hydrolysis process, namely 2-picolinamide, has been described [9]. The ptO_2^- is obtained by means of a Cannizzaro-type reaction of pyridine-2-carboxaldehyde and NaNCO in the presence of a copper metal ion [15]. Recently, we have determined the crystal structures of different copper carboxylates and fluoride complexes with ptO_2^- [16].

In this paper, we describe for the first time the crystal structures of copper(II)–chlorobenzoate complexes with ptO_2^-. The influence of the chlorine atom in positions 2, 3, and 4 of the chlorobenzoate anions on the crystal structures and the spectroscopic properties of the copper complexes with ptO_2^- has also been studied.

2. Experimental

2.1. Materials and physical measurements

Reagents and solvents were commercially available and used without further purification.

Elemental analyses (C, N, H) were performed on a Carlo Erba AAS instrument. IR spectra (KBr disks) were taken on a Mattson satellite FT-IR in the range 4000–400 cm^{-1}. Diffuse reflectance spectra (nujol mulls) of the complexes were carried out on a Shimadzu UV-2101 PC spectrophotometer. UV–Vis spectra of the complex solutions were carried out on an HP 8453 spectrophotometer. Electronic paramagnetic resonance (EPR) spectra were taken at the Q-band frequency at room temperature with a Bruker ELEXSYS spectrometer. Electrochemical measurements were made with the aid of a Princeton Applied Research Model 273A potentiostat/galvanostat. Cyclic voltammograms were obtained for acetonitrile and DMF solutions of the complexes with [TBA][ClO_4] as the supporting electrolyte under argon atmosphere. The electrochemical cell employed had a standard three-electrode configuration: a platinum working electrode, a platinum wire counter electrode, and an Ag–AgCl reference electrode.

2.2. Synthesis of the complexes [Cu(ptO_2)(2-Clbenz)(H_2O)] (1), [Cu(ptO_2)(3-Clbenz)] (2), and [Cu(ptO_2)(4-Clbenz)(DMF)] (3)

Ten millilitres of an aqueous solution of $Cu(ClO_4)_2 \cdot 6H_2O$ (370 mg, 1 mmol) were added to 40 mL of a yellow DMF solution containing 137 mg (1 mmol) of chlorobenzoic acid (2-chloro, 3-chloro, or 4-chloro), 312 mg (1 mmol) of ptz and 2 ml of a methanolic solution of KOH 2 N. A dark green solution was formed immediately; after 30 min it turned blue-green in color and overnight it became blue. Slow evaporation of the solution yielded blue, needle-like crystals. Yield: 57, 72, and 68% respectively. Analytical data for **1**: *Anal.* Calc. for $C_{19}H_{14}ClCuN_3O_5$: C, 49.25; H, 3.04; N, 9.07. Found: C, 49.01; H, 3.12; N, 8.98%. Analytical data for **2**: *Anal.* Calc. for $C_{19}H_{12}ClCuN_3O_4$: C, 51.24; H, 2.71; N, 9.43. Found: C 50.98; H 2.69; N 9.28%. Analytical data for **3**: *Anal.* Calc. for $C_{22}H_{19}ClCuN_4O_5$: C, 50.97; H, 3.69; N, 10.81. Found: C 51.07; H 3.75; N 10.98%.

2.3. X-ray crystallography

Crystals were mounted on glass fibers and these samples were used for data collection. Data for **1** was collected with a Bruker X8Kappa APEXII diffractometer and for **2** and **3** with a Nonius Kappa CCD 2000 diffractometer. The data for **1** was processed with APEX2 [17] and corrected for

Table 1
Crystal data and structure refinement for [Cu(ptO$_2$)(2-Clbenz) (H$_2$O)], [Cu(ptO$_2$)(3-Clbenz)] and [Cu(ptO$_2$)(4-Clbenz)(DMF)]

	[Cu(ptO$_2$)(2-Clbenz)(H$_2$O)] (**1**)	[Cu(ptO$_2$)(3-Clbenz)] (**2**)	[Cu(ptO$_2$)(4-Clbenz)(DMF)] (**3**)
Empirical formula	$C_{19}H_{14}ClCuN_3O_5$	$C_{19}H_{12}ClCuN_3O_4$	$C_{22}H_{19}ClCuN_4O_5$
Formula weight	463.32	445.31	518.40
Temperature (K)	100(2)	293(2)	293(2)
Wavelength (Å)	0.71073	0.71073	0.71073
Crystal system	monoclinic	orthorhombic	triclinic
Space group	*P*2(1)/*n* (No. 14)	*P*212121	$P\bar{1}$
Unit cell dimensions			
a (Å)	7.43560(10)	5.3540(2)	9.9360(2)
b (Å)	24.1903(3)	16.4790(7)	10.3590(2)
c (Å)	0.34180(10)	20.2130(8)	12.3830(3)
α (°)	90	90	99.2910
β (°)	99.2770(10)	90	108.1690(9)
γ (°)	90	90	105.2670(10)
Volume (Å^3)	1835.84(4)	1783.36(12)	1126.26(4)
Z	4	4	2
D_{Calc} (Mg/m^3)	1.676	1.659	1.529
Crystal size	0.20 × 0.18 × 0.10	0.28 × 0.08 × 0.04	0.1 × 0.08 × 0.05
Absorption coefficient	1.374 mm^{-1}	1.407 mm^{-1}	1.130 mm^{-1}
F(000)	940	900	536
Limiting indices	$-10 \leqslant h \leqslant 10$, $0 \leqslant k \leqslant 34$, $0 \leqslant l \leqslant 14$	$-6 \leqslant h \leqslant 6$, $-21 \leqslant k \leqslant 21$, $-25 \leqslant l \leqslant 26$	$-11 \leqslant h \leqslant 12$, $-13 \leqslant k \leqslant 11$, $-16 \leqslant l \leqslant 15$
Reflections collected/ unique	31,550/5362 [*R*(int) = 0.0308]	3930/3930 [*R*(int) = 0.0000]	8225/5125 [*R*(int) = 0.0286]
Data/restraints/ parameters	5362/0/262	3930/0/248	5125/0/300
Final *R* indices [$I > 2\sigma(I)$]	$R_1 = 0.0291$, $wR_2 = 0.0692$	$R_1 = 0.0650$, $wR_2 = 1636$	$R_1 = 0.0538$, $wR_2 = 0.1575$
R indices (all data)	$R_1 = 0.0365$, $wR_2 = 0.0718$	$R_1 = 0.1386$, $wR_2 = 0.2156$	$R_1 = 0.0882$, $wR_2 = 0.2005$

absorption using SADABS [18]. The data for **2** and **3** were processed with collect and HKL DENZO and SCALEPACK programs [19,20]. The structures were solved by direct methods [21,22], which revealed the position of all non-hydrogen atoms. These atoms were refined on F^2 by a full-matrix least-squares procedure using anisotropic displacement parameters [23]. The hydrogen atoms were located from difference syntheses or in their calculated positions (C–H, 0.93–0.97 Å), and were refined using a riding model [24,25]. Atom scattering factors were taken from the International Tables for Crystallography [26]. Crystal and refinement data are listed in Table 1.

3. Results and discussion

3.1. Crystal structures

[Cu(ptO$_2$)(2-Clbenz)(H$_2$O)] (**1**): Fig. 1 shows an ORTEP view of the molecule with the atomic numbering scheme. Selected bond distances and angles are listed in Table 2. The coordination sphere of copper(II) is best described as a distorted square based pyramid, as can be deduced from the τ value of 0.16 [27]. The basal positions are occupied by the three nitrogen atoms from the ptO$_2^-$ ligand and one oxygen atom from the monodentate 2-chlorobenzoate anion. The apical site is occupied by the oxygen atom from the coordinated water molecule. The Cu–N bond distances, ranging from 1.9470(13) to 2.0140(13) Å, are very similar to those found in other previously reported

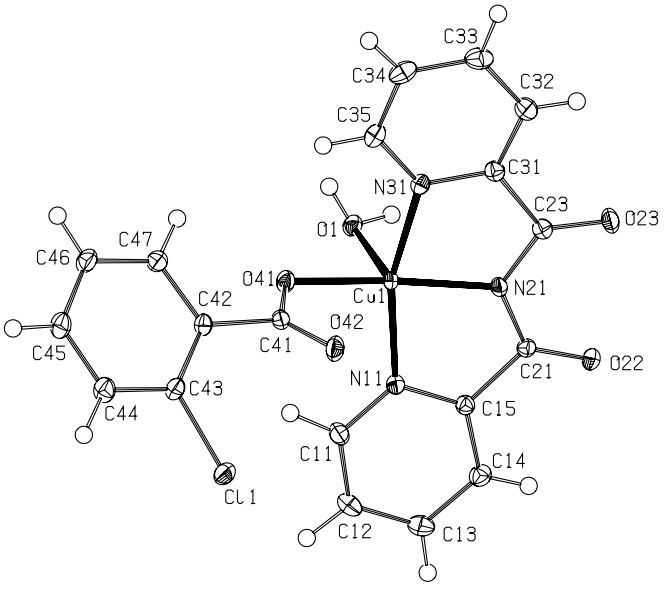


Fig. 1. ORTEP drawing of [Cu(ptO$_2$)(2-Clbenz)(H$_2$O)] (**1**).

copper(II) complexes with ptO$_2^-$ [8,16]. The Cu–O(2–chlorobenzoate) and the Cu–O water bond distances are 1.9465(11) and 2.3180(11) Å, respectively. The four basal atoms are quasi coplanar, and the copper ion is displaced 0.143 Å below the plane. A distorted octahedron could be considered due to fact that the Cu–O(42) distance is 2.6890(12) Å. In this case, the carboxylate acts as a

Table 2
Selected bond lengths (Å) and angles (°) for [Cu(ptO$_2$)(2-Clbenz) (H$_2$O)], [Cu(ptO$_2$)(3-Clbenz)] and [Cu(ptO$_2$)(4-Clbenz)(DMF)]

[Cu(ptO$_2$)(2-Clbenz) (H$_2$O)] (**1**)		[Cu(ptO$_2$)(3-Clbenz)] (**2**)		[Cu(ptO$_2$)(4-Clbenz)(DMF)] (**3**)	
Cu(1)-O(41)	1.9465(11)	Cu(1)-N(21)	1.928(7)	Cu(1)-O(41)	1.951(3)
Cu(1)-N(21)	1.9470(13)	Cu(1)-O(41)	1.939(6)	Cu(1)-N(21)	1.950(3)
Cu(1)-N(11)	2.0115(13)	Cu(1)-N(11)	2.000(7)	Cu(1)-N(11)	2.012(3)
Cu(1)-N(31)	2.0140(13)	Cu(1)-N(31)	2.002(7)	Cu(1)-N(31)	2.018(3)
Cu(1)-O(1)	2.3180(11)			Cu(1)-O(1)	2.284(3)
Cu(1)-O(42)	2.6890(12)				
O(41)-Cu(1)-N(21)	171.50(5)	N(21)-Cu(1)-O(41)	177.1(3)	O(41)-Cu(1)-N(21)	164.24(13)
O(41)-Cu(1)-N(11)	97.93(5)	N(21)-Cu(1)-N(11)	82.5(3)	O(41)-Cu(1)-N(11)	98.94(13)
N(21)-Cu(1)-N(11)	81.50(5)	O(41)-Cu(1)-N(11)	99.6(3)	N(21)-Cu(1)-N(11)	81.89(13)
O(41)-Cu(1)-N(31)	97.67(5)	N(21)-Cu(1)-N(31)	82.3(3)	O(41)-Cu(1)-N(31)	96.09(13)
N(21)-Cu(1)-N(31)	81.70(5)	O(41)-Cu(1)-N(31)	95.5(3)	N(21)-Cu(1)-N(31)	81.65(14)
N(11)-Cu(1)-N(31)	161.86(5)	N(11)-Cu(1)-N(31)	164.8(3)	N(11)-Cu(1)-N(31)	163.28(14)
O(41)-Cu(1)-O(1)	87.21(4)			O(41)-Cu(1)-O(1)	91.09(11)
N(21)-Cu(1)-O(1)	101.29(5)			N(21)-Cu(1)-O(1)	104.61(12)
N(11)-Cu(1)-O(1)	93.81(5)			N(11)-Cu(1)-O(1)	92.72(12)
N(31)-Cu(1)-O(1)	96.15(5)			N(31)-Cu(1)-O(1)	94.29(12)

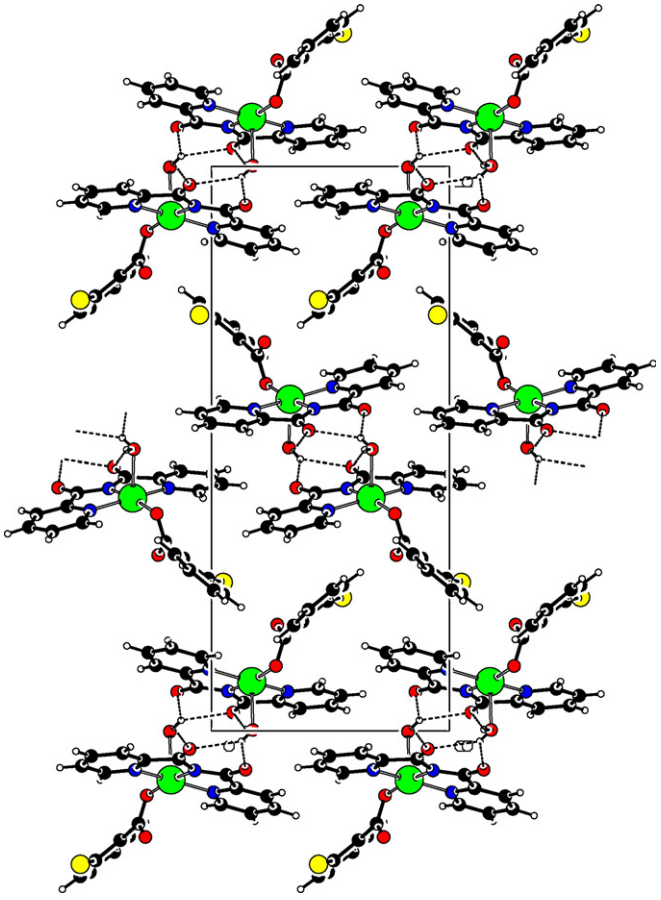


Fig. 2. Crystal packing of [Cu(ptO$_2$)(2-Clbenz)(H$_2$O)] (**1**) showing the hydrogen bonds.

bidentate ligand as is also the case in the [Cu(ptO$_2$)(benz)]·(H$_2$O) complex [16].

The crystal packing is achieved by intermolecular hydrogen bonds (see Fig. 2). A moderate hydrogen bond is formed between the O1W and the carbonyl O23 [O1W ··· O23 = 2.9127(15) Å, O1W–H1A–O23 = 137.3°].

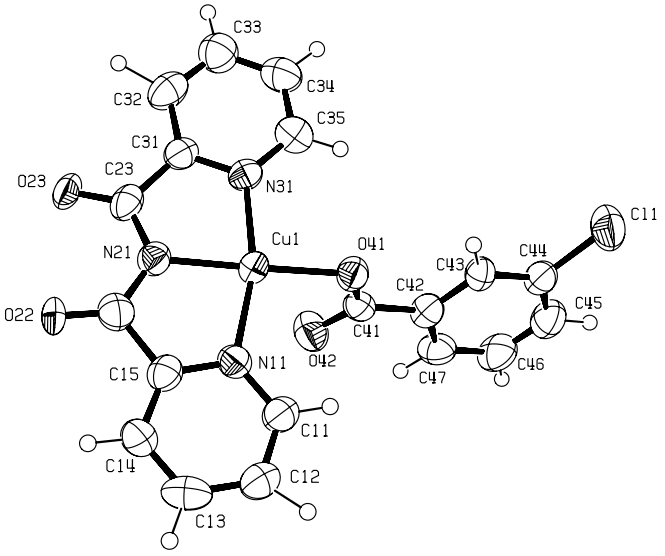


Fig. 3. ORTEP drawing of [Cu(ptO$_2$)(3-Clbenz)] (**2**).

In addition, the O1W forms two moderate hydrogen bonds with the other carbonyl O22 [O1W ··· O22, 2.8838(14) and 3.0218(16) Å, O1W–H1A–O22 = 160.3° and O1W–H1B–O22 = 142.3°] [28].

*[Cu(ptO$_2$)(3-Clbenz)] (**2**):* Fig. 3 displays the structure of the complex with the labeling scheme. Selected interatomic distances and angles are listed in Table 2. The geometry of the copper(II) ion can best be described as very slightly distorted square planar. The distortion of the square planar geometry is determined by the dihedral angle between the CuN$_2$ and CuNO planes. Thus, when the dihedral angle is 0°, the geometry is planar while when the angle is 90°, the stereochemistry is tetrahedral. In this complex, the dihedral angle value is 1.91(0.23)°, which indicates a very slightly distorted square planar configuration [29]. The coordination polyhedron is formed by a ptO$_2^-$, which functions as a tridentate ligand through the nitrogen atoms, and one carboxylate O atom from the 3-chloro-

benzoate ligand. The three Cu–N bond distances, which are all within the 1.928(7)–2.002(7) Å range, are comparable not only to those of the complex described above, but also to those found for other copper(II)–ptO_2 complexes [8]. The distance between the other $O_{carboxylate}$ and the copper(II) is 2.6120(64) Å, which is too large to be considered coordinated, but a semicoordination might be possible. Moreover, the bond distance between one of the $O_{carbonyl}$ atoms of the ptO_2^- and the copper(II) of the contiguous molecule is 2.7189(65) Å, thus the crystal structure is a linear chain in which the ptO_2^- acts as bridging ligand (Fig. 4). The influence of this semicoordination of one of the $O_{carbonyl}$ atoms is confirmed by the differences found in the two carbonyl bond distances [C(21)–O(22) 1.207(11) and C(23)–O(23) 1.235(10) Å, respectively]. In contrast, the C=O bond lengths are similar in the two other chlorobenzoate copper complexes, [(1.2299(18) and 1.2202(19) Å for **1** and 1.214(5) and 1.219(5) Å for **3**]. This Cu–$O_{carbonyl}$ semicoordinated bond probably helps stabilize the structure.

*[Cu(ptO₂)(4-Clbenz)DMF] (**3**):* An ORTEP view of the complex with the atom numbering scheme is shown in Fig. 5. Selected bond distances and angles are presented in Table 2. The coordination sphere of copper(II) in this complex can best be described as a very slightly distorted square based pyramid, as can be deduced from the τ value of 0.016 [27]. The basal positions are occupied by the three nitrogen atoms from the ptO_2^- ligand and one oxygen atom from the monodentate 4-chlorobenzoate anion. The apical site is occupied by the oxygen atom from the coordinated DMF molecule. The Cu–N bond distances, ranging from 1.950(3) to 2.018(3) Å, are very similar to those found in other previously reported copper(II) complexes with ptO_2^- [8,16]. The Cu–O(4–chlorobenzoate) and the Cu–O(DMF) bond distances are 1.951(3) and 2.284(3) Å, respectively. The four basal atoms are quasi coplanar, with the copper ion displaced 0.1836 Å above the plane. The second oxygen of the 4-chlorobenzoate anion is located at the long distance of 2.7410(38) Å from copper(II). As in the compound described above, if we consider this distance to be a semicoordination, the geometry of the copper(II) can be defined as a distorted octahedron.

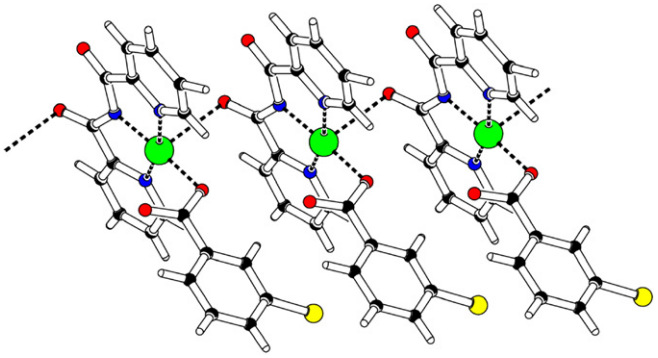


Fig. 4. Crystal packing of [Cu(ptO_2)(3-Clbenz)] (**2**).

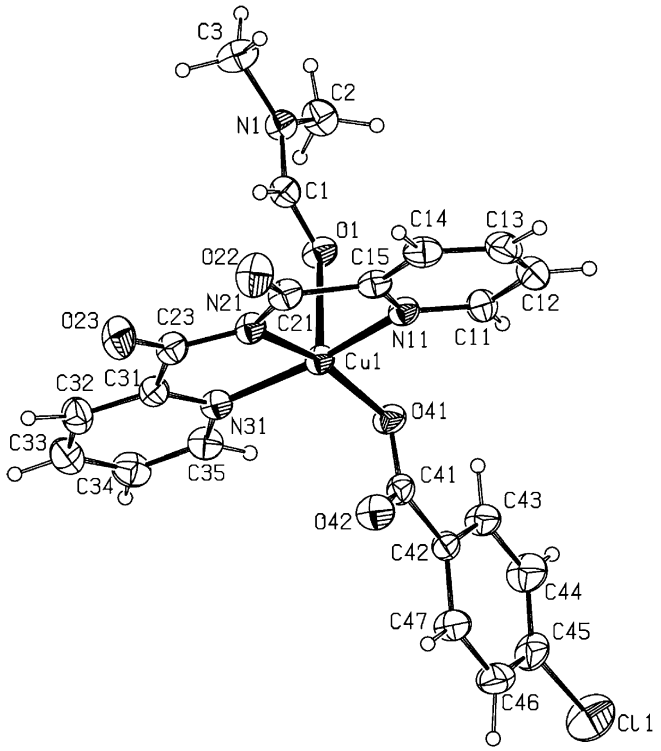


Fig. 5. ORTEP drawing of [Cu(ptO_2)(4-Clbenz)(DMF)] (**3**).

The individual pyrimidyl rings of the ptO_2^- ligand in the three complexes are planar; indeed, the largest deviation from planarity is less than 0.0073 Å.

The crystal packing, displayed in Fig. 6, shows π–π stacking interactions between the ptO_2^- rings. No hydrogen bonds were observed.

3.2. Spectroscopic properties

The most important feature in the IR spectra of the three complexes is the presence of a high-intensity band centered at 1712 cm^{-1} [ν(C=O) vibration], which indicates that the hydrolysis of ptz has occurred [8]. Another remarkable aspect of the ν(C=O) vibration of the ptO_2^- in complex **2** is the presence of a strong, sharp band at 1650 cm^{-1} that can be attributed to a second ν(C=O) vibration. This is probably due to the semicoordination of one of the oxygen atoms of the carbonyl group to the copper(II) ion of a contiguous molecule, a hypothesis that is corroborated by the differences observed in the C=O bond distances (C(21)–O(22) and C(23)–O(23) 1.207(11) and 1.235(10), respectively). All the spectra exhibit bands at about 1600 and 1350 cm^{-1} which correspond to the ν_{as} (COO^-) and ν_s(COO^-) vibrations from the chlorobenzoate group. The $\Delta\nu = \nu_{as}(COO)-\nu_s(COO) = 250\ cm^{-1}$ indicates that the carboxylate acts as a monodentate ligand [30], in agreement with the crystal structures. The band that appears at 1621 cm^{-1} in the IR spectrum of **3** can be assigned to the ν(C=O) of the DMF. The high region of the IR spectrum of **1** shows a strong, sharp band at 3523 cm^{-1} due to the presence of coordinated water [31].

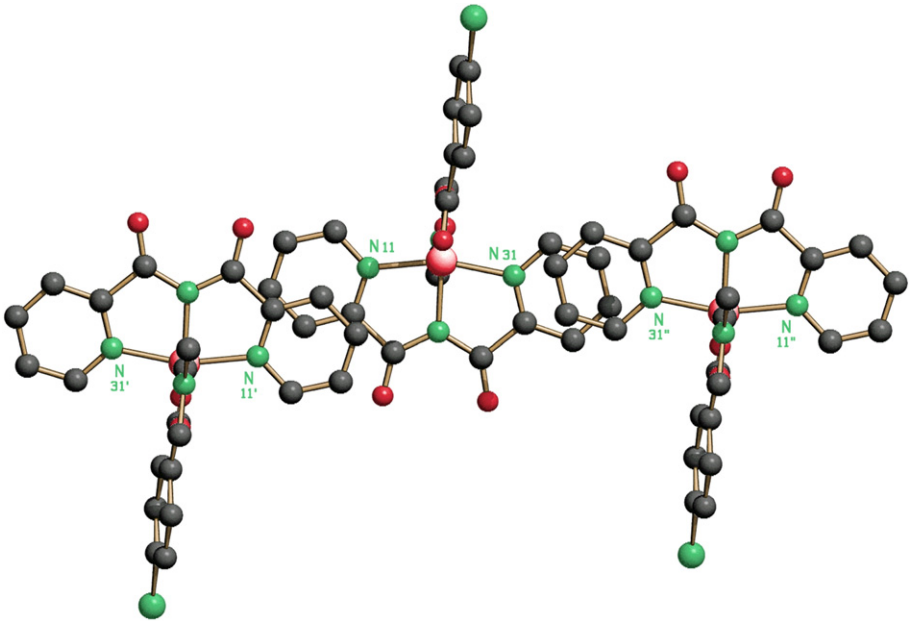


Fig. 6. Crystal packing of [Cu(ptO$_2$)(4-Clbenz)(DMF)] (**3**).

The reflectance spectra of the three complexes show an unresolved d–d band at 633, 643, and 598 nm, respectively, and a shoulder at about 432 nm. The latter can be attributed to a MLCT band.

The UV–Vis spectra of saturated aqueous solutions of the three complexes show the same maxima at 634 nm, indicating that in solution the three compounds have the same chromophore as a result of the coordination of water molecules and the dissociation of the carboxylate anions. Moreover, a weak LMCT band at about 400 nm, similar to that observed in the solid state spectra, is observed. The spectrum of 5.3 mM acetonitrile solutions of **1** exhibits a band at 609 nm ($\varepsilon = 115\ M^{-1}\ cm^{-1}$) and a shoulder at ≈406 nm. The spectrum of **1** in DMF solution at 1.4 mM shows a band at 631 nm ($\varepsilon = 150\ M^{-1}\ cm^{-1}$). The differences in the position of the d–d maximum among the spectra in solution may be due to the different donor properties of the solvents themselves. The spectrum of **3** in DMSO solution at 3.8 mM shows a band at 635 nm ($\varepsilon = 105\ M^{-1}\ cm^{-1}$). In any case, the spectra of the three complexes are similar to those reported in a previous study, in which acetate, formate and benzoate were used. These findings all confirm that the main species in solution is the CuptO$_2^+$ cation [16].

3.3. EPR spectroscopy

The Q-band spectra of polycrystalline samples of the complexes were recorded at room temperature. Powder samples of **1**–**3** were prepared from single crystals. The EPR parameters were obtained from simulations made with WINEPRSimphonia [32]. The Q-band EPR spectra of the three compounds are axial, with $g_\parallel = 2.244$; 2.215; 2.24 and $g_\perp = 2.061$; 2.045; 2.049 for **1**, **2** and **3**, respectively. These results point to a mainly copper(II) d_{x2-y2} orbital ground state ($g_\parallel > g_\perp$). The pattern of the EPR spectra is in good agreement with the crystal structures.

3.4. Electrochemical behavior

The cyclic voltammogram of **1** in the electroactive domain of acetonitrile/Bu$_4$NClO$_4$ is shown in Fig. 7. First, a reduction peak around −1.0 mV (versus SCE) was observed towards cathodic potentials; this can be attributed to the reduction of Cu(II) to Cu(I). On the reverse scan, an anodic peak at about −0.034 mV was found. The voltammogram is clearly irreversible, probably

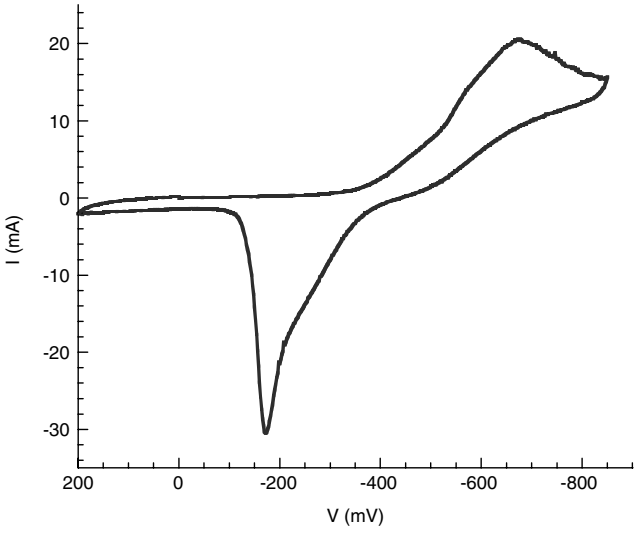


Fig. 7. Cyclic voltammogram of [Cu(ptO$_2$)(2-Clbenz)(H$_2$O)] (**1**) in acetonitrile.

because after the reduction of Cu(II), the Cu(I) species thus formed is unstable. The reduction peak at −1.0 mV relative to SCE corresponds to −0.78 mV relative to NHE. Irreversible cyclic voltammograms are also obtained from the complex in DMF solution, which shows a reduction peak at −0.654 mV relative to SCE. The negative values indicate a strong stabilization of the copper(II) state through the formation of the complex.

4. Conclusions

In this paper, we present the crystal structures of three copper(II) chlorobenzoate complexes with the hydrolysis derivative of 2,4,6-tris(2-pyridyl)-1,3,5-triazine (ptz), the ptO_2^- ligand. An in-depth study of these crystal structures has revealed several interesting differences. In the [Cu(ptO_2)(3-Clbenz)] (**2**) complex, the copper(II) ion is semicoordinated to a carbonyl oxygen atom of the ptO_2^- of another contiguous molecule with a Cu–O distance of 2.719 Å. In the other two complexes, the corresponding distances are 3.929 Å and 4.707 Å for [Cu(ptO_2)(2-Clbenz)(H_2O)] (**1**) and [Cu(ptO_2)(4-Clbenz)(DMF)] (**3**), respectively. These differences are influenced by the position of the chlorine atom in the benzoate. When the chlorine atom is in position 2 or 4, the donor effect of the carboxylate oxygen atoms involved in the metal complexation is reinforced whereas a chlorine in position 3 reduces this effect. In this last case, the electronic density on the copper(II) is lower, which leads the metal ion in the [Cu(ptO_2)(3-Clbenz)] (**2**) complex to form a semicoordinative bond with a contiguous ptO_2^-, which, in turn, gives rise to a chain structure.

Acknowledgements

J.B., G.A., and M.G.-A. acknowledge financial support from the Spanish CICYT (CTQ2004-03735). B.M. acknowledges financial support from the Junta de Castilla y León (SA056A05). A.C. acknowledges financial support from Spanish CICYT (CTQ2006-15329-C02/BQU). F.E. gratefully thanks Generalitat Valenciana (Proyect GV06/376) for financial support.

Appendix A. Supplementary material

CCDC 644942, 644943 and 644944 contain the supplementary crystallographic data for **1**, **2** and **3**. These data can be obtained free of charge via http://www.ccdc.cam.ac.uk/conts/retrieving.html, or from the Cambridge Crystallographic Data Centre, 12 Union Road, Cambridge CB2 1EZ, UK; fax: (+44) 1223 336 033; or e-mail: deposit@ccdc.cam.ac.uk.

References

[1] E.M. Smolin, L. Rapoport, *S*-Triazines and Derivatives, Interscience, New York, 1959, p. 163.
[2] E.I. Lerner, S.J. Lippard, J. Am. Chem. Soc. 98 (1976) 5397.
[3] E.I. Lerner, S.J. Lippard, Inorg. Chem. 16 (1977) 1546.
[4] J. Faus, M. Julve, J.M. Amigo, T. Debaerdemaeker, J. Chem. Soc., Dalton Trans. (1989) 1681.
[5] P.A. Gillard, P. A Williams, Trans. Metal Chem. 4 (1979) 18.
[6] P. Paul, B. Tyagi, M.M. Bhadbhade, E. Suresh, J. Chem. Soc., Dalton Trans. (1997) 2273.
[7] P. Paul, B. Tyagi, A.K. Bilakhiya, M.M. Bhadbade, G. Ramachandaiah, Inorg. Chem. 37 (1998) 5733.
[8] X.-P. Zhou, D. Li, S.-L. Zheng, X. Zhang, T. Wu, Inorg. Chem. 45 (2006) 7119.
[9] J.V. Folgado, E. Coronado, D. Beltrán-Porter, R. Burriel, A. Fuertes, C. Miratvilles, J. Chem. Soc., Dalton Trans. (1988) 3041.
[10] A. Cantarero, J.M. Amigo, J. Faus, M. Julve, T. Debaerdemaeker, J. Chem. Soc., Dalton Trans. (1988) 2033.
[11] J.V. Folgado, E. Martinez-Tamayo, A. Beltrán-Porter, D. Beltrán-Porter, Polyhedron 8 (1989) 1077.
[12] A. Kamiyama, T. Noguchi, T. Kajiwara, T. Ito, Inorg. Chem. 41 (2002) 507.
[13] T. Glaser, T. Lugger, R. Fröhlich, Eur. J. Inorg. Chem. (2004) 394.
[14] B. Casellas, F. Constantino, A. Mandonnet, A. Caneschi, D. Gatteschi, Inorg. Chim. Acta 358 (2005) 177.
[15] S.A. Cotton, V. Franckevicius, M.F. Mahon, L.L. Ooi, P.R. Taithby, Polyhedron 25 (2006) 1057.
[16] J. Borrás, G. Alzuet, M. González-Alvarez, J.L. García-Giménez, B. Macías, M. Liu-González, Eur. J. Inorg. Chem. (2007) 822.
[17] Bruker, APEX2 Software, Bruker AXS Inc. V2.0-1, Madison, Wisconsin, USA, 2005.
[18] G.M. Sheldrick, SADABS. Program for Empirical Absorption Correction of Area Detector Data, University of Goettingen, Germany, 1997.
[19] COLLECT, Nonius BV, 1997–2000.
[20] Denzo-Scalepack Z. Otwinowski, W. Minor, Processing of X-ray Diffraction Data Collected in Oscillation Mode, in: C.W. CarterJr., R.M. Sweet (Eds.), Methods in Enzymology, Macromolecular Crystallography, Part A, vol. 276, Academic Press, 1997, p. 307.
[21] G.M. Sheldrick, Acta Crystallogr. Sect., A 46 (1990) 467.
[22] SIR97 A. Altomare, M.C. Burla, M. Camalli, G.L. Cascarano, C. Giacovazzo, A. Guagliardi, A.G.G. Moliterni, G. Polidori, R. Spagna, J. Appl. Cryst. 32 (1999) 115.
[23] G.M. Sheldrick, SHELXL-97. Program for the Refinement of Crystal Structures, University of Goettingen, Germany, 1997.
[24] A.L. Spek, PLATON. A Multipurpose Crystallographic Tool, Utrecht University, Utrecht, The Netherlands, 2003.
[25] (a) PARST. M. Nardelli, Comput. Chem. 7 (1983) 95;
(b) M. Nardelli, J. Appl. Crystallogr. 28 (1995) 659.
[26] A.J.C. Wilson, International Tables for Crystallography, vol. C, Kluwer Academic Publishers, Dordrecht, The Netherlands, 1995.
[27] W. Addison, T.N. Rao, J. Reedijk, J. van Rijn, C.G. Verschoor, J. Chem. Soc., Dalton Trans. (1984) 1349.
[28] G.A. Jefrey, An Introduction to Hydrogen Bonding, Oxford University Press, Oxford, 1997.
[29] L.P. Battaglia, A. Bonamartini-Corradi, G. Marcotrigiano, L. Menabue, G.C. Pellacani, Inorg. Chem. 18 (1979) 148.
[30] G.G.B. Deacon, R.J. Phillips, Coord. Chem. Rev. 33 (1980) 227.
[31] K. Nakamoto, Infrared and Raman Spectra of Inorganic and Coordination Compounds, 4th ed., Wiley, New York, 1986, p. 228.
[32] WINEPR-Simphonia 1.25 Bruker Analytic Gmbh, Kalrsruhe, FRG, 1994.

reduction reactions of vanadium is of great importance. Bis(2,4-pentanedionato-O,O′) oxovanadium(IV) [VO-(acac)$_2$], was found to have insulin-mimetic properties superior to those of $VOSO_4$ in cell culture studies [9].

4-Acyl-5-pyrazolones are an interesting class of β-diketones, containing a pyrazole ring fused to a chelating arm [10]. The interest in the coordination chemistry of pyrazolones has increased greatly in the last decade [11]. Due to the presence of two oxygen donor atoms and facile keto–enol tautomerism, they easily coordinate with metal ions after deprotonation of the enolic hydrogen and provide stable metal complexes with six-membered chelate rings. Pyrazolones are used in analytical chemistry for the determination and isolation of almost all metal ions due to their high extracting ability, intense colour of the complex extracts and low solubility of the complex in some solvents [12,13]. Square pyramidal oxovanadium(IV) compounds with 4-acyl-5-pyrazolones have been reported [10]. However, to the best of our knowledge nobody has reported the reduction of oxovanadium(V) salts with 4-acyl-5-pyrazolones.

Herein, we report the reduction of oxovanadium(V) by 1-phenyl-3-methyl-4-toluoyl-5-pyrazolone at neutral and acidic pH conditions. The resulting vanadium complex was characterized by electron paramagnetic resonance spectroscopy, magnetic susceptibility, FT-IR, UV–Vis and mass spectroscopy. Finally, the probable structure of the oxovanadium(IV) complex was deduced from the spectral data and further confirmed by molecular modelling investigations.

2. Experimental

2.1. Materials

Vanadyl sulfate, ammonium monovanadate and the starting materials for the synthesis of the ligand was obtained from Sigma–Aldrich. All the other chemicals used were of analytical reagent grade and were used without further purification.

2.2. Physical measurements

Absorbance was measured using a Shimadzu UV-2450 spectrophotometer. Deconvolution of UV spectra was done using Peak Fit 4.12 software. Elemental analyses were performed with a Perkin–Elmer Series 2 Elemental Analyser 2400. The mass of the complexes were determined by fast atom bombardment high-resolution mass spectrometry (FAB-HRMS; JEOL JSM600). A Nicolet FT-IR 560 Magna spectrometer using KBr (neat) was used to obtain IR spectral data and a Bruker 300 MHz NMR spectrometer was used to obtain ^{1}H NMR and ^{13}C NMR spectra of the compounds in $CDCl_3$. The EPR spectra were recorded on a Varion E-112 spectrometer at liquid nitrogen as well as room temperature. The magnetic moments were measured using a model 155 vibrating sample magnetometer system.

Cyclic voltammetric experiments were conducted using a Cypress Systems Model CS-1090 computer-controlled voltammetric analyzer (BAS 100 electrochemical analyzer Graphtec WX 1200 recorder). All the experiments were done under a nitrogen atmosphere at ambient temperature in solutions with 0.1 M tetrabutylammonium hexafluorophosphate as the supporting electrolyte. Cyclic voltammograms (CVs) were obtained using a three-electrode system consisting of glassy-carbon working, Pt wire auxiliary and SCE reference electrodes. The ferrocenium/ferrocene couple was used to monitor the reference electrode and was observed at 0.450 V with $\Delta E_p = 0.120$ V and $i_{pc}/i_{pa} \approx 1.0$ in acetonitrile under these conditions.

2.3. Synthesis

1-Phenyl-3-methyl-4-toluoyl-5-pyrazolone, Hpmtp, was synthesized from 1-phenyl-3-methyl-5-pyrazolone and para-toluoyl chloride and is summarised in Scheme 1 [12].

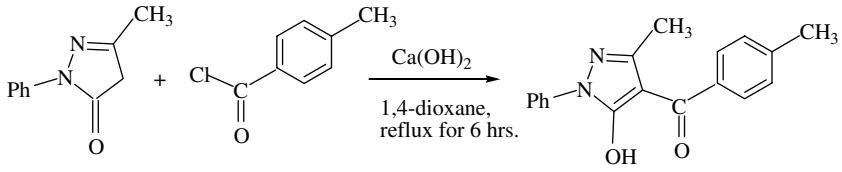
2.3.1. Preparation of vanadium complexes

The complex of oxovanadium(V) with Hpmtp was prepared at both acidic and neutral pH conditions. The exact preparation steps adopted are described below.

To a well-stirred ethanol solution of 2.0 mM Hpmtp, an aqueous solution of NaOH (2.0 mM) was added. The pH was adjusted to 7 ($VO(pmtp)_2$ (**1**)) and 1 ($VO(pmtp)_2$ (**2**)) after the complete dissolution of Hpmtp and 1.0 mM ammonium monovanadate was then added, and the reaction mixture was stirred for 8 h. The precipitate formed was filtered, washed with ethanol, then with distilled water, and dried in a desiccator over fused calcium chloride. M.p.: 259.1 °C. IR (KBr) data ν (cm^{-1}): 1566, 1519, 962, 752. Mass spectrum: (M+1) peak 650.53 (Figs. 1 and S1).

2.3.2. Polymerization

In order to identify the formation of a free radical in the reduction process, the polymerization reaction of 5% (v/v) acrylonitrile has been carried out at room temperature in an inert atmosphere in the presence of oxovanadium(V) (0.001 mol dm^{-3}) and Hpmtp (0.01 mol dm^{-3}). A cloudy suspension was observed within a few minutes after the addition of the metal solution. The reaction was then kept, under stirring, for 2 h. A large amount of polymer was then precipitated by adding methanol to the reaction mixture. On the other hand, in the absence of either Hpmtp or oxovanadium(V) no detectable polymerization was noticed. Although these experiments are not helpful in finding out the free-radical species formed during the reduction of oxovanadium(V) by Hpmtp, they definitely indicate the formation of a free radical in the process, which is ultimately responsible for the acrylonitrile polymerization.



Scheme 1.

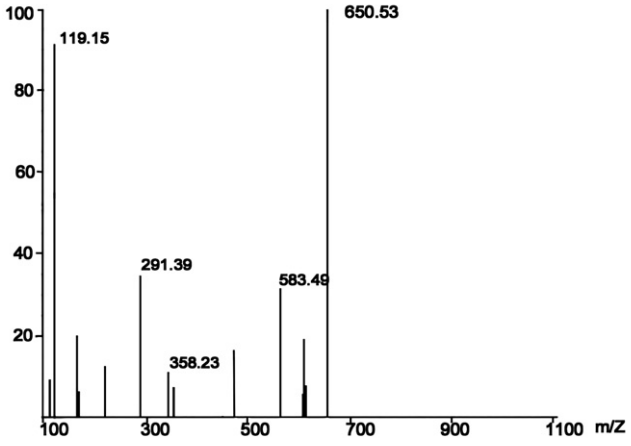


Fig. 1. Mass spectrum of $VO(pmtp)_2$ (**1**).

2.3.3. DFT calculations

The electronic structure of the complex $VO(pmtp)_2$ was calculated with the unrestricted density functional theory (DFT) using the B3LYP functional [14–16] as implemented in the GAUSSIAN-03 suite of programs [17]. For the V atom, the LANL2DZ basis set was selected together with the effective core potential of Hay and Wadt [18–20]. For the other elements, the 6-31G* basis sets were selected [21]. The geometry of the ligand system pmtp was also optimized at the B3LYP/6-31G* level of theory.

2.3.4. X-ray crystallography data collection and processing

X-ray single crystal data were recorded at room-temperature on a Bruker Smart 6000 diffractometer equipped with a CCD detector and a copper tube source. Data were processed using SAINTPLUS (SAINTPLUS, program suite for data processing, Bruker AXS, Inc., Madison, Wisconsin, USA). Structures were solved and refined using SHELXL-97 [22]. Non-hydrogen atoms were refined anisotropically and a riding model was used for C–H hydrogen atoms. The hydroxyl protons were placed in positions calculated for optimum hydrogen bonding.

3. Results and discussion

3.1. Characterization of Hpmtp

The synthesized Hpmtp was characterized by IR and ^1H NMR spectral data and elemental analysis. ^1H NMR ($CDCl_3$) data δ (ppm): 7.2–7.98 (m, 9H, phenyl), 2.14 (s, 3H, methyl of pyrazole ring), 2.45 (s, 3H, methyl of aromatic ring). IR (KBr) data ν (cm^{-1}): 1598, 1537, 753. Elemental Anal. Calc. for $C_{18}H_{16}N_2O_2$: C, 73.97; H, 5.48; N, 9.59. Found: C, 74.64; H, 5.66; N, 9.57%. In the ^1H NMR spectrum of Hpmtp, no peak corresponding to the enolic OH was observed. However, the absence of a peak at δ 3.4 ppm, corresponding to the methyne proton at the fourth position of the pyrazolone ring, confirms the existence of Hpmtp in the enolic form. The structure of Hpmtp was finally confirmed by the single crystal X-ray analysis (Fig. 2).

The single crystal X-ray diffraction study on this compound clearly indicates that the compound exists in the enol form. The structural data shows that the C(9)–O(1) distance in this compound is 1.327 Å, comparable with the distance found for C–OH in some pyrazolone derivatives [23] and the C(11)–O(2) distance is 1.258 Å, which is in the range of C=O distances in similar compounds [24].

3.2. Electron transfer from Hpmtp to oxovanadium(V)

In order to understand the redox chemistry of Hpmtp in the presence and absence of oxovanadium(V), cyclicvoltametric studies have been conducted in the range from 2.0 to −2.0 V and the corresponding voltammograms are depicted in Fig. 3. The voltammogram of Hpmtp (Fig. 3a) in acetonitrile solution (Hpmtp = 25 mM) has an irreversible oxidation peak around 1.37 V, which indicates the formation of a stable oxidised species of Hpmtp. Existence of a similar stable oxidised species of 1-phenyl-3-methyl-4-benzoyl-5-pyrazolone has been well documented elsewhere [25]. As can be seen from the voltammogram (Fig. 3b) of Hpmtp (5.0 cm^3 of 25 mM) in acetonitrile solution in the presence of 25 mM (2.0 cm^3) of oxovanadium(V), the peak current corresponding to the oxidation of the ligand at 1.37 V gradually decreases with the increase of concentration of oxovanadium(V), and a new peak

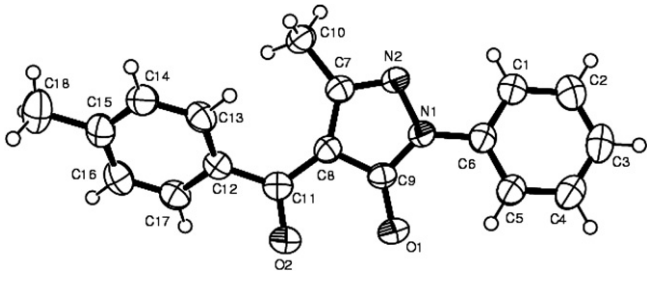


Fig. 2. Single crystal X-ray structure of Hpmtp.

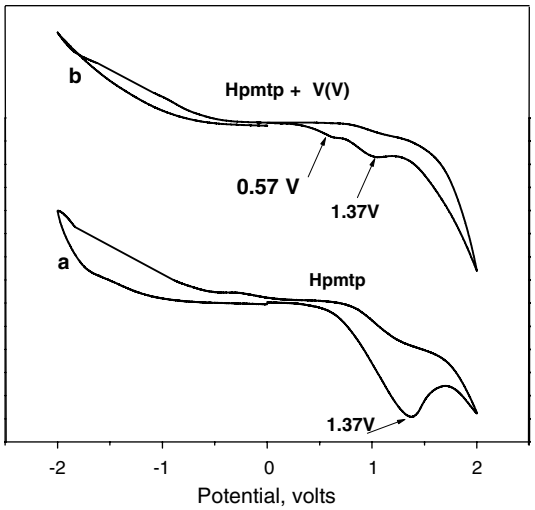


Fig. 3. Cyclicvoltammograms recorded in acetonitrile: (a) Hpmtp; (b) Hpmtp (5 ml of 25 mM) in presence of oxovanadium(V) (2 ml of 25 mM). Solute concentration 25 mM. Scan rate 50 mV s^{-1}. SCE was used as the reference electrode.

corresponding to the oxidation of oxovanadium(IV) to oxovanadium(V) appears at ~0.57 V. Since the reduction of oxovanadium(V) to oxovanadium(IV) occurs at a potential [26] lower than the oxidation potential of the ligand, the transfer of one electron is possible from the ligand to oxovanadium(V). An electron transfer process has also been reported for 1-phenyl-3-methyl-4-benzoyl-5-pyrazolone by Toropchina et al. [25].

3.3. Formation of a free-radical intermediate of Hpmtp

It is clear from the cyclic voltammetric studies that the ligand, Hpmtp transfers one electron to oxovanadium(V) and forms a free-radical intermediate, as indicated in Scheme 2. An indirect evidence for the formation of a free-radical intermediate has been ascertained by investigating the polymerization of acrylonitrile in the presence of oxovanadium(V) and Hpmtp. In the absence of either Hpmtp or oxovanadium(V), no detectable polymerization was noticed. This is an indirect evidence for the formation of a free-radical intermediate during the complexation process. Thus in the present study, it has been presumed that the reaction proceeds *via* a free-radical mechanism wherein oxovanadium(V) undergoes a one-electron reduction, as is evident from the cyclic voltammetric studies. The free radical thus generated finally couples with another free radical and forms a stable dimer. The dimeric species of the ligand has been isolated from the filtrate of the complexing medium and characterized by IR, ^{1}H NMR and ^{13}C NMR spectra (Figs. S2 and S3). In the ^{1}H NMR spectrum of the dimer, the δ values show a considerable shift from that of Hpmtp which indicates the formation of a new species. The IR spectrum of the dimer shows two strong absorptions in the region 1668–1610 cm^{-1}, indicating the presence of two C=O groups. Upon dimerisation, the sp^2 hybridised (δ 110–140 ppm) carbon in the pyrazole ring (C_4) of Hpmtp becomes an sp^3 hybridised one (δ 0–80 ppm), which can be clearly seen from the ^{13}C NMR spectrum of the dimer and Hpmtp (Fig. S4).

3.4. Stoichiometry

Hpmtp reduces aqueous oxovanadium(V) in both acidic and neutral media according to the following equation:

$$2VO_2^+ + 6HL \rightarrow 2VOL_2 + \text{Dimer} + 2H_2O + 2H^+$$

The 1:3 stoichiometry of the metal to ligand was confirmed at pH 1 and 7 by analysing both the filtrate of the complexing media and the resultant complex formed.

3.5. Mechanism of reduction of oxovanadium(V) to oxovanadium(IV) and subsequent complexation by Hpmtp

Based on the above studies the detailed scheme for the reduction of vanadium(V) to vanadium(IV) and subsequent complexation can be expressed in Scheme 2.

3.6. Spectroscopic characterization of $VO(pmtp)_2$

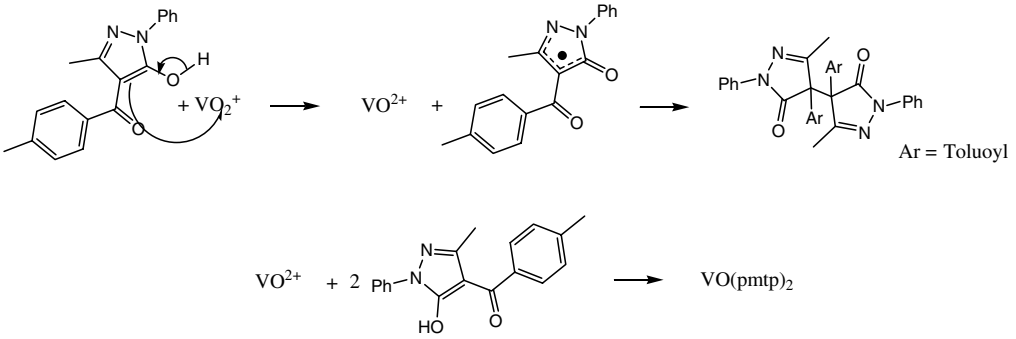
The elemental analyses and HRMS studies of the complexes prepared at both acidic and neutral pH conditions show a metal-to-ligand ratio of 1:2. Further, these values correspond to a oxovanadium(IV) species rather than a oxovanadium(V) species.

3.6.1. Infrared spectroscopy

The vanadium complex exhibits strong absorption bands at 1600–1515 cm^{-1} assigned to the stretching ν(C=O), ν(C=C) and ν(C=N) modes of the arylpyrazolone ring coordinated to the metal ion. Further, a signal at about 960 cm^{-1} in the region for a ν(V=O) stretch of the complex is observed. On the other hand, Uzouwku [27] has reported the V=O asymmetric stretching frequency at 895 cm^{-1} in a series of oxovanadium(IV) complexes of 4-acyl-5-pyrazolones. Usually, ν(V=O) stretches in most oxovanadium(IV) complexes are observed in the region 930–1010 cm^{-1} [28]. The low ν(V=O) value may arise from the presence of a bridging vanadyl group [29,30]. The absence of a broad absorption in the region 3000–3500 cm^{-1}, due to the –OH group of H_2O in the complex, indicates the absence of coordinated water. This is consistent with the thermogravimetric analysis of the complex in that there is no weight loss with an increase in temperature from 50 to 400 °C.

3.6.2. Magnetic and EPR measurements

The room-temperature magnetic susceptibility data for $VO(pmtp)_2$, prepared under acidic and neutral pH conditions, show essentially paramagnetic behaviour attributed to the d^1 system. The effective magnetic moments obtained for the oxovanadium(IV) complexes (1.79–1.83 BM) were within the normal range (1.57–2.1 BM) [31,32]. These



Scheme 2. Reduction and complexation of oxovanadium(V) with 1-phenyl-3-methyl-4-benzoyl pyrazolone.

values are as expected for the spin only μ_s of a d^1-system when the orbital contribution is completely quenched [33].

The X-band EPR spectra (Figs. 4 and S5) of the vanadium complexes exhibit a set of eight hyperfine lines arising from the interaction of the unpaired electron with the $^{51}V(IV)$ ($I = 7/2$) nucleus. The eight lines in the spectra of the complexes are an indication of their monomeric structure [32]. Symmetry reduction due to geometry distortion produces significant changes in EPR spectra. For square pyramidal complexes with C_{4v} symmetry, where the V=O bond is along the z-axis and the four donor atoms are along the x and y axes, an anisotropic EPR spectrum is expected, exhibiting two g ($g_z = g_\| < g_| = g_x = g_y$) and two A ($A_z = A_\| > A_| = A_x = A_y$) values. A distortion from the square pyramidal geometry can give three g and three A values. It is clear from the EPR parameters of the complexes **1** and **2** listed in Table S2 that both the complexes have a slightly distorted square pyramidal geometry. The

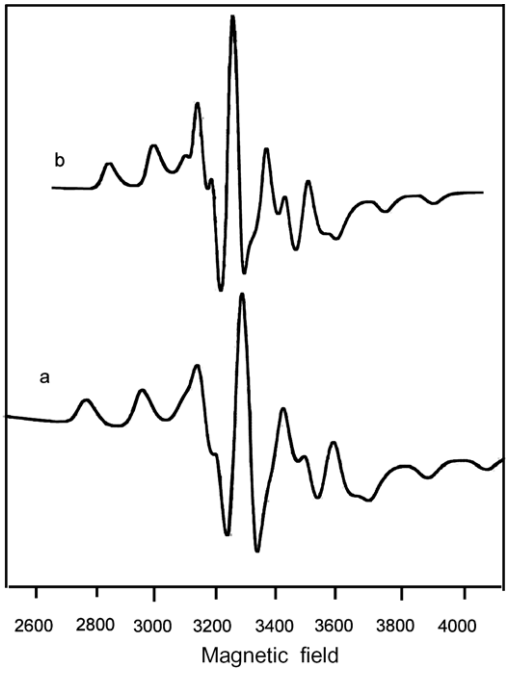


Fig. 4. ESR spectra of $VO(pmtp)_2$ (**1**). (a) Solid at 77 K; (b) dissolved in acetonitrile at 77 K.

g-values lie in the 1.9–1.99 range and agree with the fact that when the d-shell is less than half filled the spin–orbit effect reduces the g value from that of a free electron (2.0023) [3]. The order and magnitude of the resonance parameters are typical of the spectra displayed by a slightly distorted square pyramidal oxovanadium(IV) complexes with the unpaired electron in an orbital of mostly d_{xy} character.

3.6.3. Electronic absorption spectra

In the electronic spectra of Hpmtp in acetonitrile solution, the n–π^* transition of the carbonyl group was observed at around 285 nm, and the π–π^* transition of the phenyl group was observed at 245 nm and both transitions had an ε value of the order of 10^5 mol^{-1} cm^{-1}. In the complex, these absorption bands are red shifted to 305 and 250 nm, respectively, indicating the involvement of the carbonyl group in the complex formation with the metal ion. A similar behaviour has been reported elsewhere for the electronic spectral analysis of a series of oxovanadium(IV) 4-acyl-5-pyrazolone complexes [27]. The UV–Vis spectrum of the complex has overlapping peaks in the 400–800 cm^{-1} region. Hence, curve fitting of the spectrum was carried out using Peak Fit 4.12 software. In the curve fitting procedure, the peaks were assumed to be a number of Gaussian peaks, but no physical significance was attached to these peaks apart from the fact that their presence results in satisfactory curve fitting. The deconvoluted spectra of $VO(pmtp)_2$ prepared at acidic (Fig. 5) and neutral (Fig. S6) pH conditions have four transitions in the visible region. The observed absorption peaks correspond to transitions from the d_{xy} orbital to the d_{xz} (794 nm), d_{yz} (643 nm), $d_{x^2-y^2}$ (501 nm) and d_{z^2} (424 nm) orbitals in accordance with reports on the transitions of oxovanadium(IV) complexes having distorted square pyramidal geometries. The d–d absorption spectra of square pyramidal oxovanadium(IV) complexes are generally interpreted by the scheme proposed by Ballhausen and Gray [34]. The V=O bond defines the z-axis, and the x and y axes are in the equatorial plane. The energy levels predicted for the 3d orbitals in this scheme follow the order: $d_{xy}(b_2) < d_{xz}, d_{yz}(e) < d_{x^2-y^2}(b_1) < d_{z^2}(a_1)$. The three transitions, $b_2 \rightarrow e$, $b_2 \rightarrow b_1$ and $b_2 \rightarrow a_1$, are typical of a square pyramidal complex.

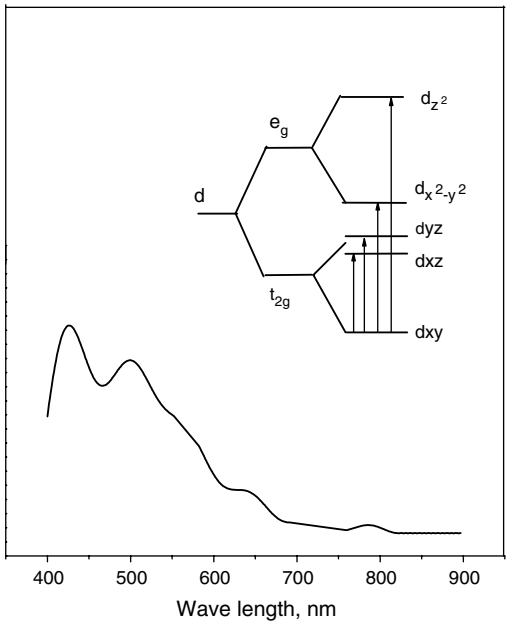


Fig. 5. Deconvoluted UV spectrum of $VO(pmtp)_2$ (**1**).

A distortion from the square pyramidal geometry removes the degeneracy between the d_{xz} and d_{yz} orbitals. The *e* level will then split into two, $b_1(d_{xz})$ and $b_2(d_{yz})$, and accordingly four transitions will be observed in the case of a complex with a distorted square pyramidal geometry [31,32]. This type of d–d transitions is also observed by Fukuda et al. [35] and Klich et al. [36]. It can be concluded from the above spectral data that the oxovanadium(IV) ion with two coordinating ligands will be present in a slightly distorted square pyramidal geometry.

3.6.4. Optimized geometry of a distorted square pyramidal oxovanadium(IV) complex

A square pyramidal geometry containing two $pmpt^-$ moieties is considered as the most probable oxovanadium(IV) complex. The optimized geometry of this system at the B3LYP/6-31G* level of DFT is depicted in Fig. 6. In this structure, the four oxygen atoms from the two $pmpt^-$ ligands are at the base and a VO double bond of length 1.584 Å is pointing towards the apex of the pyramid. Two different V–O single bonds can be seen, a short one of length 1.963 Å with the pyrazolone oxygen and a long one of 1.994 Å with the toluoyl oxygen. The high coordination power of the pyrazolone oxygen is reflected in its short V–O bond, in accordance with the highest negative MESP of −157.6 kcal/mol observed for this oxygen in the $pmpt^-$ system (Fig. S7). The molecular orbital and the spin density analysis of the complex showed that the unpaired electron of the vanadium atom is mainly localized on the d_{xy} orbital, further supporting the earlier mentioned electronic transitions originating from this orbital. The V–O bond distances to $pmtp^-$ are significantly longer than the VO double bond, as observed in the X-ray crystal structure of $VO(acac)_2$ (acac = acetylacetone) [35] and $VO(acac\text{-}NMe_2)_2$ (acac-NMe_2 = *N*,*N*-dimethoxyacetylacetamido) [37]. Further, the VO double bond of length in $VO(pmtp)_2$ (1.584 Å), deduced by DFT, is in the same range as observed in $VO(acac)_2$ (1.592 Å) [32]. The electronic transitions of $VO(pmtp)_2$ predicted using GAUSSIAN-03 [782 nm (d_{xy} orbital to d_{xz}), 654 nm (to d_{yz}), 520 nm (to $d_{x^2-y^2}$) and 420 nm (to d_{z^2})] were in good agreement with the experimental data [794 nm (d_{xy} orbital to d_{xz}), 643 nm (to d_{yz}), 501 nm (to $d_{x^2-y^2}$) and 424 nm (to d_{z^2})].

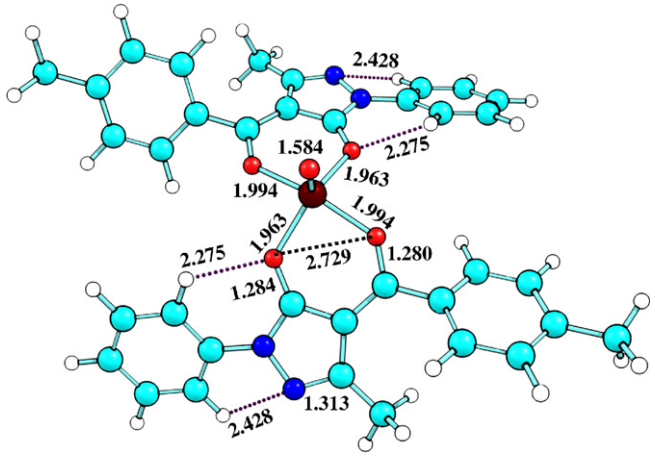


Fig. 6. The optimized geometry of this system at the B3LYP/6-31G* level of DFT.

The distortion of a square pyramidal structure to a trigonal bipyramid is measured in terms of the τ parameter [34]. This parameter is $(\alpha - \beta)/60$ where α is the angle formed by the two pseudo-axial atoms at the vanadium atom and β is the angle formed by the two pseudo-equatorial atoms. For purely square pyramidal complexes τ is zero. Complexes with $0 < \tau < 0.5$ will be distorted square pyramid and those with $0.5 < \tau < 1$ will be distorted trigonal bipyramid. For $VO(pmtp)_2$ the τ value obtained is 0.1, indicating a slight distortion from the square pyramidal geometry. It can be concluded from the DFT calculations that the vanadium ion exhibits a distorted square pyramidal coordination environment in $VO(pmtp)_2$. A similar geometry has been observed earlier in the oxovanadium(IV) complexes of β-diketonates as evidenced by X-ray single crystal studies [38].

4. Conclusions

Hpmtp instantaneously reduces vanadium(V) over the pH range 1–7 and forms $VO(pmtp)_2$ by the transfer of one electron to VO_2^+, via the formation of a free-radical intermediate. The voltammogram of Hpmtp has an irreversible oxidation peak around 1.37 V indicating the formation of a stable oxidised species. Further, the oxidation potential of Hpmtp is higher than the redox potential of vanadium(V), which clearly highlights that the ligand can reduce vanadium(V) to vanadium(IV) by transferring one electron. The existence of vanadium(IV) in the complex has been ascertained by electron paramagnetic

resonance spectroscopy, magnetic susceptibility and electronic spectroscopy. These reduction reactions occur under physiological conditions and thus could be important for the reduction of vanadium(V)-containing coordination compounds used as insulin-enhancing agents for treatment of diabetics.

Acknowledgements

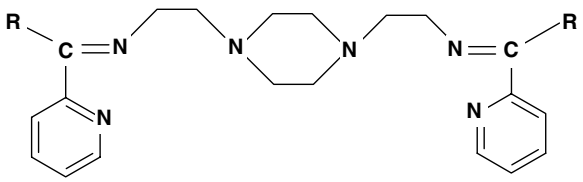
The authors thank Prof. T.K. Chandrashekhar, Director, Regional Research Laboratory, Trivandrum, for his constant encouragement. One of the authors (R.P.N.) wishes to thank the Council of Scientific & Industrial Research for the award of a Senior Research Fellowship.

Appendix A. Supplementary material

Elemental analysis data for $VO(pmtp)_2$ (**1** and **2**), ESR paramers for $VO(pmtp)_2$ (**1** and **2**), mass spectrum of $VO(pmtp)_2$ (**2**), ^1H NMR spectrum of the dimer, ^{13}C NMR spectrum of the dimer, ^{13}C NMR spectrum of Hpmtp, ESR spectrum of $VO(pmtp)_2$ (**2**), deconvoluted UV spectrum of $VO(pmtp)_2$ (**2**) and the MESP-painted van der Waals surface of $pmpt^-$ are provided as supplementary data. Supplementary data associated with this article can be found, in the online version, at doi:10.1016/j.poly.2007.07.020.

References

[1] D.C. Crans, J.J. Smee, E. Gaidamauskas, L. Yang, Chem. Rev. 104 (2004) 849.
[2] A. Levina, P.A. Lay, N.E. Dixon, Inorg. Chem. 39 (2000) 385.
[3] K. Kustin, D.L. Toppen, Inorg. Chem. 12 (1973) 1404.
[4] P.C. Wilkins, M.D. Johnson, A.A. Holder, D.C. Crans, Inorg. Chem. 45 (2006) 1471.
[5] J.S. Littler, W.A. Waters, J. Chem. Soc. (1959) 1299.
[6] J.S. Littler, W.A. Waters, J. Chem. Soc. (1959) 3014.
[7] C.F. Wells, L.V. Kurtisyn, J. Chem. Soc. A (1970) 1372.
[8] (a) K.C. Thompson, J.H. McNeil, C. Orvig, Chem. Rev. (1999) 2561; (b) K.C. Thompson, C. Orvig, J. Chem. Soc., Dalton Trans. (2000) 2885.
[9] (a) S.S. Amin, K. Cryer, B. Zhang, S.K. Dutta, S.S. Eaton, O.P. Anderson, S.M. Miller, B.A. Reul, S.M. Brichard, D.C. Crans, Inorg. Chem. 39 (2000) 406;
(b) J. Li, G. Elberg, D.C. Crans, Y. Shechter, Biochemistry 35 (1996) 8314.
[10] F. Marchetti, C. Pettinari, R. Pettinari, Coord. Chem. Rev. 249 (2005) 2909.
[11] C. Pettinari, F. Marchetti, A. Drozdov, Comprehensive Coordination Chemistry II, vol. 1, Elsevier, New York, 2003.
[12] P.N. Remya, R. Pavithran, M.L.P. Reddy, Solvent Extr. Ion Exch. 24 (2005) 501.
[13] R. Meera, M.L.P. Reddy, Solvent Extr. Ion Exch. 22 (2004) 761.
[14] A.D. Becke, Phys. Rev. A 38 (1988) 3098.
[15] A.D. Becke, J. Chem. Phys. 98 (1993) 5648.
[16] C. Lee, W. Yang, R.G. Parr, Phys. Rev. B 37 (1988) 785.
[17] M.J. Frisch, G.W. Trucks, H.B. Schlegel, G.E. Scuseria, M.A. Robb, J.R. Cheeseman, J.A. Montgomery, T. Vreven, K.N. Kudin, J.C. Burant, J.M. Millam, S.S. Yengar, J. Tomasi, V. Barone, B. Mennucci, M. Cossi, G. Scalmani, N. Rega, G.A. Petersson, H. Nakatsuji, M. Hada, M. Ehara, K. Toyota, R. Fukuda, J. Hasegawa, M. Ishida, T. Nakajima, Y. Honda, O. Kitao, H. Nakai, M. Klene, X. Li, J.E. Knox, H.P.J.B. Hratchian, V. Cross, C. Bakken, J. Adamo, R. Jaramillo, R.E. Gomperts, O. Stratmann, A.J. Yazyev, R. Austin, C. Cammi, J.W. Pomelli, P.Y. Ochterski, K. Ayala, G.A. Morokuma, P. Voth, J.J. Salvador, V.G. Dannenberg, S. Zakrzewski, A.D. Dapprich, M.C. Daniels, O. Strain, D.K. Farkas, A.D. Malick, K. Rabuck, J.B. Raghavachari, J.V. Foresman, Q. Ortiz, A.G. Cui, S. Baboul, J. Clifford, B.B. Cioslowski, G. Stefanov, A. Liu, P. Liashenko, I. Piskorz, R.L. Komaromi, D.J. Martin, T. Fox, M.A. Keith, C.Y. Al-Laham, A. Peng, M. Nanayakkara, P.M.W. Challacombe, B. Gill, W. Johnson, M.W. Chen, C. Wong, J.A. Gonzalez, A. Pople, GAUSSIAN-03, Revision C.02, Gaussian, Inc., Wallingford, CT, 2004.
[18] P.J. Hay, W.R. Wadt, J. Chem. Phys. 82 (1985) 299.
[19] P.J. Hay, W.R. Wadt, J. Chem. Phys. 82 (1985) 270.
[20] W.R. Wadt, P.J. Hay, J. Chem. Phys. 82 (1985) 284.
[21] P.C. Hariharan, J.A. Pople, Mol. Phys. 27 (1974) 209.
[22] G.M. Sheldrick, SHELXL-97: Program for X-ray Crystal Structure Refinement, University of Göttingen, Göttingen, Germany, 1997.
[23] R.N. Jadeja, J.R. Shah, Polyhedron 26 (2007) 1677, and references cited therein.
[24] B. Peng, G. Liu, D. Jia, K. Yu, J. Mol. Struct. 692 (2004) 217.
[25] A.V. Toropchina, V.V. Yanilkin, V.I. Morozov, L.P. Sysoeva, A.I. Movchan, B.I. Buzykin, G.A. Chumutova, Russ. J. Electrochem. 39 (2003) 1181.
[26] J.D. Lee, Concise Inorganic Chemistry, 5th ed., Blackwell Science Ltd., Osney Mead, Oxford OX2 0EL, USA, 1996.
[27] B.A. Uzoukwu, Synth. React. Inorg. Met.-Org. Chem. 22 (1992) 185.
[28] M.R. Maurya, Coord. Chem. Rev. 237 (2003) 163.
[29] A.P. Ginsberg, H.J. Williams, Inorg. Chem. 5 (1966) 1656.
[30] J. Selbin, Coord. Chem. Rev. 1 (1960) 293.
[31] J.C. Pessoa, J.A.L. Silva, A.L. Vieira, L. Vilas-Boas, P. O'Brien, P. Thornton, J. Chem. Soc., Dalton Trans. (1992) 1745.
[32] J. Selbin, Chem. Rev. 65 (1965) 153.
[33] A.S. Orabi, M.I. Ayad, A.E.-M.M. Ramadan, Transition Met. Chem. 23 (1998) 391.
[34] C.J. Ballhausen, H.B. Gray, Inorg. Chem. 1 (1962) 111.
[35] I. Fukuda, H. Matsushima, K. Maeda, M. Koikawa, T. Tokii, Chem. Lett. 26 (1997) 463.
[36] P.R. Klich, A.T. Daniher, P.R. Challen, D.B. McConville, W.J. Youngs, Inorg. Chem. 35 (1996) 347.
[37] R.P. Dodge, D.H. Temleton, A. Zalkin, J. Chem. Phys. 35 (1961) 55.
[38] D.C. Crans, A.R. Khan, M. Mahroof-Tahir, S. Mondal, S.M. Miller, O.P. Colour Anderson, T. Jakusch, T. Kiss, J. Chem. Soc., Dalton Trans. (2001) 3337.



Scheme 1.

and luminescence behaviour of a dinuclear compound of the type $[Cd_2(pbap)(OH_2)_2(N_3)_4]$ (**1**) [pbap = *N*-(1-pyridin-2-ylbenzylidene)-*N*-[2-(4-{2-[(1-pyridin-2-ylbenzylidene)amino]ethyl}piperazin-1-yl)ethyl]amine (Scheme 1)] and a polymeric compound of the type $[Cd_2(pfap)(\mu_{1,3}\text{-NCS})(\mu_{1,3}\text{-SCN})(NCS)_2]_n$ (**2**) [pfap = *N*-(1-pyridin-2-ylformy-lidene)-*N*-[2-(4-{2-[(1-pyridin-2ylformy-lidene)amino]ethyl}piperazin-1-yl)ethyl]amine (Scheme 1)] in combination with tailored hexadentate N-donor Schiff bases (pbap/pfap) and azide/thiocyanate.

2. Experimental

2.1. Materials

High purity 2-benzoylpyridine (Fluka, Germany), pyridine-2-carboxaldyde (Fluka, Germany), 2-[4-(2-aminoethyl)piperazin-1-yl]ethylamine (Aldrich, USA), sodium azide (Aldrich, USA), ammonium thiocyanate (E. Merck, India) and cadmium(II) nitrate tetrahydrate (E. Merck, India) were purchased from the respective concerns and were used as received. Cadmium(II) perchlorate hexahydrate was prepared by treatment of cadmium(II) carbonate (E. Merck, India) with perchloric acid (E. Merck, India) followed by slow evaporation on steam-bath, filtration through a fine glass-frit and preservation in a desiccator containing concentrated sulfuric acid (E. Merck, India) for subsequent use. All other chemicals and solvents were AR grade and were used as received.

2.2. Physical measurements

Elemental analyses (carbon, hydrogen and nitrogen) were measured using a Perkin–Elmer 2400 CHNS/O elemental analyser. IR spectra (KBr discs, 4000–300 cm^{-1}) were recorded using a Perkin–Elmer FTIR model RX1 spectrometer. Molar conductances were measured using a Systronics conductivity meter where the cell constant was calibrated with 0.01 (M) KCl solution and DMF was used as the solvent. Thermal analysis was recorded using a Perkin–Elmer Diamond TG/DTA system under a flow of nitrogen (30 ml min^{-1}). The sample was heated at a rate of 10 °C min^{-1} with inert alumina as a reference. Ground state absorption and steady-state fluorescence measurements were made with a Jasco model V-530 UV–Vis spectrophotometer and Hitachi model F-4010 spectrofluorimeter, respectively. Time-resolved fluorescence measurements were carried out using a time-correlated single photon counting (TCSPC) spectrometer Edinburgh Instruments, model 199; a hydrogen filled coaxial flash lamp with a pulse width of 1.2 ns at FWHM and a Philips XP-2020Q photomultiplier tube were used as the excitation source and the fluorescence detector.

2.3. Preparation of the Schiff bases

2.3.1. N-(1-Pyridin-2-ylbenzylidene)-N-[2-(4-{2-[(1-pyridin-2-ylbenzylidene)amino]ethyl}piperazin-1-yl)ethyl]amine (pbap)

2-[4-(2-Aminoethyl)piperazin-1-yl]ethylamine (0.172 g, 1 mmol) with 2-benzoylpyridine (0.366 g, 2 mmol) was refluxed in dehydrated alcohol in a 1:2 molar ratio. After 10 h reflux the reaction solution was evaporated under reduced pressure to a gummy mass, which was dried and stored *in vacuo* over $CaCl_2$ for subsequent use; yield, 1.928 g (70%). IR (KBr disc, cm^{-1}): ν(C=N) 1594. UV–Vis (λ_{max}, nm): 245, 293.

2.3.2. N-(1-Pyridin-2-ylformylidene)-N-[2-(4-{2-[(1-pyridin-2ylformylidene)amino]ethyl}pipera-zin-1-yl)ethyl]amine (pfap)

2-[4-(2-Aminoethyl)piperazin-1-yl]ethylamine (0.172 g, 1 mmol) and pyridine-2-carboxaldyde (0.214 g, 2 mmol) were mixed together and refluxed in anhydrous ethanol (25 cm^3) for 10 h. The yellowish brown solution that resulted was concentrated on a steam bath and dried *in vacuo* over $CaCl_2$ to a yellowish brown semi-solid for subsequent use. Yield: 1.525 g (75%). IR (KBr disc, cm^{-1}): ν(C=N) 1592. UV–Vis (λ_{max}, nm): 242, 290.

2.4. Preparation of the complexes

2.4.1. $[Cd_2(pbap)(OH_2)_2(N_3)_4]$ (1)

Pbap (0.476 g, 1 mmol) dissolved in methanol (20 cm^3) was added to an acetonitrile solution (20 cm^3) of cadmium perchlorate hexahydrate (0.622 g, 2 mmol) with continuous stirring. To this, a methanolic solution (20 cm^3) of sodium azide (0.260 g, 4 mmol) was added. The resulting light yellow solution was filtered and kept for slow evaporation. After 7 days colourless crystals were separated, washed with toluene and dried *in vacuo* over silica gel indicator. Yield: 0.823 g (50%). *Anal.* Calc. for $C_{32}H_{38}N_{18}O_2Cd_2$ (**1**): C, 41.3; H, 4.0; N, 27.0. Found: C, 41.2; H, 4.1; N, 27.1%. IR (KBr, cm^{-1}): $\nu(N_3)$ 2070; ν(OH) 3300–3500 (broad). UV–Vis (λ, nm) 340. Λ_M (MeOH, Ω^{-1} cm^2 mol^{-1}): 5.

2.4.2. $[Cd_2(pfap)(\mu_{1,3}\text{-NCS})(\mu_{1,3}\text{-SCN})(NCS)_2]_n$ (2)

An acetonitrile solution (5 cm^3) of pfap (0.175 g, 1 mmol) was added dropwise to a solution of $Cd(NO_3)_2 \cdot 4H_2O$ (0.308 g, 2 mmol) in methanol (5 cm^3). NH_4NCS (0.152 g, 4 mmol) in methanol (5 cm^3) was added slowly to this solution. The resultant solution was filtered and kept for slow evaporation. After 5 days **2** was separated, washed with methanol and dried *in vacuo* over $CaCl_2$. Yield: 1.570 g (60%). *Anal.* Calc. for $C_{24}H_{26}N_{10}S_4Cd_2$ (**2**): C, 35.7; H, 3.2;

N, 17.4. Found: C, 35.8; H, 3.3; N, 17.3%. IR (KBr, cm^{-1}): ν_{as}(SCN) 2105, 2125. UV–Vis (λ, nm) 312. Λ_M (MeOH, Ω^{-1} cm^2 mol^{-1}): 5.

2.5. Crystallographic data collection and refinement

Single-crystals suitable for X-ray work were grown by slow evaporation of a methanol–acetonitrile solution of **1** and **2** at 298 K [crystal size: **1**, $0.10 \times 0.10 \times 0.07$ mm^3; **2**, $0.12 \times 0.05 \times 0.05$ mm^3]. Data were collected on a Siemens SMART CCD area diffractometer equipped with a graphite-monochromator Mo Kα radiation ($\lambda = 0.71073$ Å). The intensity data were corrected for Lorentz and polarization effects and an empirical absorption correction was employed using the SAINT [16] and SADABS [17] programs for the crystals. Diffraction data for the crystals were measured using the φ- and ω-scan techniques. Systematic absence led to the identification of space groups $P2(1)/c$ for **1** and $C2/c$ for **2**. A summary of the crystallographic data and structure refinement parameters are given in Table 1.

Table 1
Crystallographic data and structure refinement for $[Cd_2(pbap)(OH_2)_2(N_3)_4]$ (**1**) and $[Cd_2(pfap)(\mu_{1,3}\text{-NCS})(\mu_{1,3}\text{-SCN})(NCS)_2]_n$ (**2**)

Compound	**1**	**2**
Empirical formula	$C_{32}H_{38}N_{18}O_2Cd_2$	$C_{24}H_{26}N_{10}S_4Cd_2$
Formula weight	931.60	807.59
Temperature (K)	200(2)	200(2)
Wavelength (Å)	0.71073	0.71073
Crystal system	monoclinic	monoclinic
Space group	$P2(1)/c$	$C2/c$
a (Å)	14.7967(13)	27.549(3)
b (Å)	10.4236(9)	7.8073(8)
c (Å)	12.4202(10)	14.6330(15)
β (°)	100.515(2)°	106.758(2)
V (Å^3)	1883.5(3)	3013.6(5)
Z	2	4
D_{calc} (Mg m^{-3})	1.643	1.780
μ (mm^{-1})	1.186	1.722
$F(000)$	936	1600
Crystal size (mm)	$0.10 \times 0.10 \times 0.07$	$0.12 \times 0.05 \times 0.05$
θ Ranges (°)	2.40 to 28.27	2.72 to 26.64
$h/k/l$	−19, 15/−11, 13/ −16, 16	−35, 35/−10, 8/ −18, 18
Reflections collected	11 344	3523
Independent reflections (R_{int})	4325 (0.0421)	2381 (0.0641)
Completeness to theta (%)	92.6 (28.27°)	91.5 (28.27°)
Data/restraints/ parameters	4325/0/252	2381/0/181
T_{max} and T_{min}	1.000 and 0.794	1.000 and 0.805
Goodness-of-fit on F^2	1.011	0.996
Final R indices [$I > 2\sigma(I)$]	$R_1 = 0.0379$, $wR_2 = 0.0794$	$R = 0.0476$, $wR_2 = 0.1003$
R indices (all data)	$R_1 = 0.0510$, $wR_2 = 0.0843$	$R = 0.0767$, $wR_2 = 0.1107$
Largest peak and hole (e Å^{-3})	0.934 and −0.355	1.04 and −0.42

Weighting Scheme: $R_1 = \sum|F_o| - |F_c||/\sum|F_o|$, $wR_2 = [\sum w(F_o^2 - F_c^2)_2/\sum w(F_o^2)^2]^{1/2}$, Calc. $w = 1/[\sigma^2(F_o^2) + (0.0495P)^2 + 0.0000P]$ for **1** and $w = 1/[\sigma^2(F_o^2) + (0.0341P)^2 + 0.0000P]$ for **2** where $P = (F_o^2 + 2F_c^2)/3$.

The structures were solved by direct methods and the structure solution and refinement were based on $|F|^2$. Of the 11344 (**1**) and 3523 (**2**) reflections, 4325 and 2381 with $I > 2\sigma(I)$ were used for the structure solution. All non-hydrogen atoms were refined with anisotropic displacement parameters whereas hydrogen atoms were placed in calculated positions when possible and given isotropic U values 1.2 times that of the atom to which they are bonded. At convergence, the final residual were $R_1 = 0.0379$ (**1**) and 0.0476 (**2**); $wR_2 = 0.0794$ (**1**) and 0.1003 (**2**) with $I > 2\sigma(I)$, goodness-of-fit = 1.011 (**1**) and 0.996 (**2**). The final differences Fourier map showed the maximum and minimum peak heights of 0.934 and −0.355 e Å^{-3} for **1**, and 1.04 and −0.42 e Å^{-3} for **2**. All crystallographic calculations were conducted with SHELXL-97 [18], ORTEP-32 [19] and PLATON [20] programs.

3. Results and discussion

3.1. Synthesis and formulation

The Schiff bases, *N*-(1-pyridin-2-ylbenzylidene)-*N*-[2-(4-{2-[(1-pyridin-2-ylbenzylidene)amino]ethyl}piperazin-1-yl)ethyl]amine (pbap) or *N*-(1-pyridin-2-ylformylidene)-*N*-[2-(4-{2-[(1-pyridin-2-ylformylidene)amino]ethyl}piperazin-1-yl)ethyl]amine (pfap) were synthesized by refluxing 2-[4-(2-aminoethyl)piperazin-1-yl]ethylamine (1 mol) with 2-benzoylpyridine or pyridine-2-carboxaldehyde (2 mol) in dehydrated alcohol. The reaction of cadmium(II) chlorate hexahydrate/cadmium(II) nitrate tetrahydrate, pbap/pfba and sodium azide/ammonium thiocyanate in a 2:1:4 molar ratio in MeOH–MeCN solvent mixture at room temperature results in a dimeric and a polymeric compound, as shown in Eqs. (1) and (2):

$$2\,Cd(ClO_4)_2.6H_2O + pbap + 4\,NaN_3 \xrightarrow[298\ K]{\text{MeOH-MeCN}} [Cd_2(pbap)(OH_2)_2(N_3)_4] + 4\,NaClO_4 + 10\,H_2O \quad (\mathbf{1}) \tag{1}$$

$$2n\,Cd(NO_3)_2.4H_2O + n\,pfap + 4n\,NH_4SCN \xrightarrow[298\ K]{\text{MeOH-MeCN}} [Cd_2(pfap)(\mu_{1,3}\text{-NCS})(\mu_{1,3}\text{-SCN})(NCS)_2]_n + 4n\,NH_4NO_3 + 8n\,H_2O \quad (\mathbf{2}) \tag{2}$$

The air-stable, moisture-insensitive compounds are powders, soluble in a range of common organic solvents such as methanol, ethanol, acetonitrile, dimethylformamide and dimethylsulfoxide, but insoluble in water. Microanalytical (C, H and N) results and spectroscopic data are useful to formulate the product. In methanolic solution they behave as non-electrolytes, as reflected from their low conductivity values (~5 ohm^{-1} cm^2 mol^{-1}). In the IR spectra, **1** shows a strong absorption band at 2070 cm^{-1}, which is assignable to the stretching vibration of the terminal azide $\nu(N_3)$, and also shows a broad band in the region 3300–3500 cm^{-1} due to ν(O–H), indicating the presence of

the coordinated water molecules [21]. Two strong peaks at 2125 and 2105 cm^{-1}, assignable to ν_{as}(SCN) stretching vibrations of the thiocyanate [21], are observed for **2**. The position (>2100 cm^{-1}) and number of signals strongly suggest a mutual *cis* alignment as well as N- and S-coordination of the bound thiocyanates. The solutions are colourless and exhibit absorptions at 340 nm for **1** and 312 nm for **2**. Reflectance (in Nujol) and electronic (in MeOH solution) spectra are akin in each complex, reflecting a similar gross structure and electronic structure in the solid state and in solution. The transition may correspond to an intramolecular n–π^*/π–π^* charge transfer [22]. According to the thermal study (TG-DTA), compound **1** upon heating loses two molecule of water at ~140 °C, suggesting that the water molecules are involved in coordination and in strong hydrogen bonding interactions.

3.2. X-ray crystal structures

3.2.1. Crystal structure of $[Cd_2(pbap)(OH_2)_2(N_3)_4]$ (1)

The dinucleating hexadentate character or alternatively bis(tridentate) view of the ligand and two pairs of donor set arrangements through the incorporation of the ring within the bridge, is clearly evident and is shown in Fig. 1. Relevant bond distances and bond angles in **1** are listed in Table 2. C–H···π and O–H···N hydrogen bondings leading to the superstructure formation are shown in Figs. 2–5. The structure of **1** is a centrosymmetric dimer linked by the bis(tridentate) congregator. Cd(1) is surrounded by two terminal azide nitrogen atoms [N(4), N(7)], one coordinated water molecule [O(1)] and three N atoms [N(1), N(2), N(3)] of the new Schiff base ligand (pbap), whereas the neighboring Cd(1A) is ligated to the other three N donor set atoms [N(1A), N(2A), N(3A)] of the same pbap ligand, completing its bis(tridentate) mode, two terminal azides [N(4A), N(7A)] and one water [O(1A)] molecule. The basal dimeric plane consists of a six N-donor set of the congregator and two terminal azide nitrogen atoms, while the axial coordination sites of each cadmium center are occupied by an azide nitrogen [N(4)/N(4A)] and the coordinated water [O(1)/O(1A)]. The cadmium(II) centers are six-coordinate (CdN_5O) with a substantial departure from an ideal octahedral geometry [*cisoid* angles: 68.88(9)–122.47(10)°; *transoid* angles: 141.95(9)–175.42(10)°]. Cd–N(pbap) distances are in the range 2.335(3)–2.459(2) Å, and Cd–N(azido) distances are within the range 2.243(3)–2.335(3) Å. It is worth mentioning that none of the azido anions behave as a bridging ligand; this is an unusual azido coordination mode [15,16]. The intramolecular Cd···Cd distance in **1** is quite large [6.473(2) Å]. The azido ligands are quasi-linear with N(4)–N(5)–N(6) and N(7)–N(8)–N(9) angles of 178.0(5)° and 177.7(4)°; The N4–N5 and N(7)–N(8) bond lengths [1.181(4) Å] are larger than N(5)–N(6) [1.149(5) Å] and N(8)–N(9) [1.148(4) Å], indicating coordination of N(4) and N(7) to the cadmium center.

Table 2
Selected bond distances (Å) and angles (°) for **1** and **2**

Compound **1**		Compound **2**	
Bond distances (Å)			
Cd(1)–N(1)	2.414(3)	Cd(1)–N(1)	2.387(5)
Cd(1)–N(2)	2.335(3)	Cd(1)–N(2)	2.250(5)
Cd(1)–N(3)	2.459(2)	Cd(1)–N(3)	2.524(4)
N(4)–N(5)	1.181(4)	Cd(1)–N(4)	2.295(4)
N(5)–N(6)	1.149(5)	Cd(1)–N(5)	2.395(4)
Cd(1)–N(4)	2.335(3)	Cd(1)–S(1)	2.6161(14)
Cd(1)–N(7)	2.243(3)	N(2)–C(2)	1.121(7)
Cd(1)–O(1)	2.317(2)	C(2)–S(2)	1.624(5)
N(7)–N(8)	1.181(4)		
N(8)–N(9)	1.148(4)		
Bond angles (°)			
N(1)–Cd(1)–N(2)	68.88(9)	N(1)–Cd(1)–N(2)	177.80(18)
N(1)–Cd(1)–N(3)	141.95(9)	N(1)–Cd(1)–N(3)	89.13(14)
N(1)–Cd(1)–N(4)	89.73(10)	N(1)–Cd(1)–N(4)	81.86(15)
N(1)–Cd(1)–N(7)	95.24(10)	N(1)–Cd(1)–N(5)	87.39(15)
N(1)–Cd(1)–O(1)	93.14(9)	N(1)–Cd(1)–S(1)	93.77(11)
N(2)–Cd(1)–N(3)	93.14(9)	N(2)–Cd(1)–N(3)	88.70(16)
N(2)–Cd(1)–N(4)	87.95(10)	N(2)–Cd(1)–N(4)	97.85(16)
N(2)–Cd(1)–N(7)	164.12(10)	N(2)–Cd(1)–N(5)	94.57(16)
N(2)–Cd(1)–(O1)	96.42(10)	N(2)–Cd(1)–S(1)	86.78(12)
N(3)–Cd(1)–N(7)	122.47(10)	N(3)–Cd(1)–N(4)	73.24(15)
N(3)–Cd(1)–N(4)	93.38(9)	N(3)–Cd(1)–N(5)	143.66(14)
N(3)–Cd(1)–O(1)	86.56(9)	N(3)–Cd(1)–S(1)	113.82(10)
N(4)–Cd(1)–N(7)	92.14(9)	N(4)–Cd(1)–N(5)	70.45(15)
N(7)–Cd(1)–O(1)	84.05(10)	N(4)–Cd(1)–S(1)	171.78(12)
N(4)–Cd(1)–O(1)	175.42(10)	N(5)–Cd(1)–S(1)	102.51(10)
N(8)–N(7)–Cd(1)	127.5(2)	N(1)*–C(1)–S(1)	178.5(5)
N(6)–N(5)–N(4)	178.0(5)	N(2)–C(2)–S(2)	176.4(5)
N(9)–N(8)–N(7)	177.7(4)		

The C–H···π interaction joins two adjacent molecules and constructs a supramolecular 1D chain (Fig. 2) in the 110 direction (D–H···π: C(3)–H(3A)···Cg(1), D–H: 0.93(3) Å, H···Cg: 2.88 Å, X···Cg: 3.712(5) Å, < X–

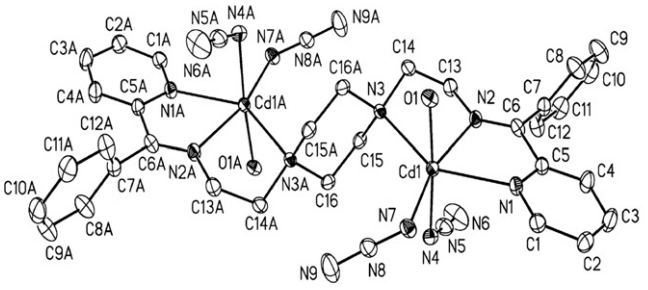


Fig. 1. Thermal ellipsoid plot of the dinuclear $[Cd_2(pbap)(OH_2)_2(N_3)_4]$ (**1**) with the atom labelling scheme and 20% probability ellipsoids for all non-hydrogen atoms.

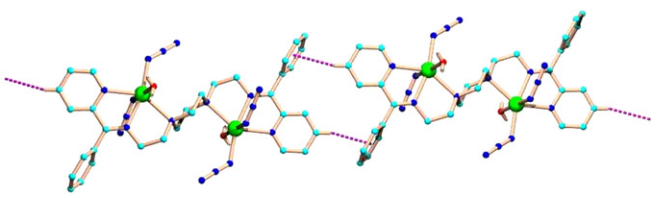


Fig. 2. C–H···π interactions in 1 forming a 1D chain in the 110 direction.

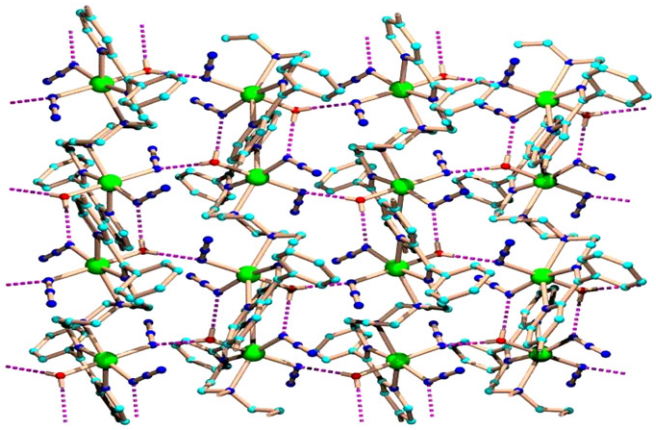


Fig. 3. O–H···N hydrogen bonding in **1** forming a sheet in the *bc* plane.

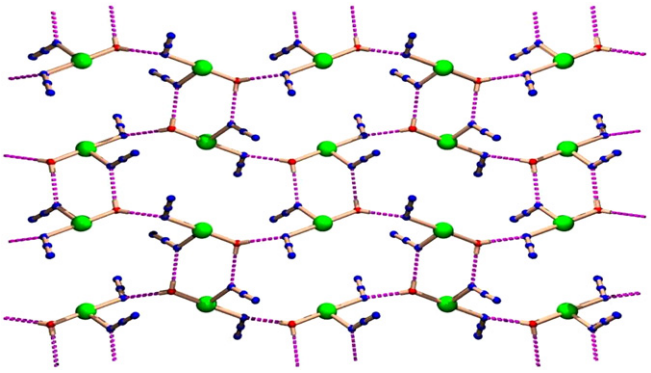


Fig. 4. Sheet formation in **1** in the *bc* plane through hydrogen bonding (omitting the ligand frame for clarity).

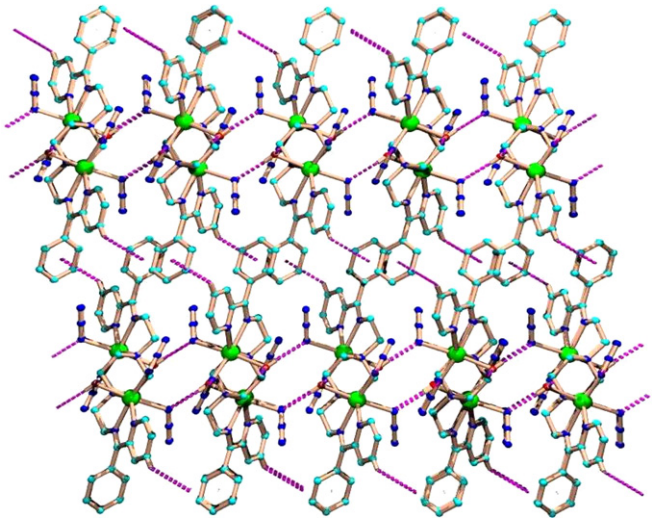


Fig. 5. O–H···N hydrogen-bonded sheet interwoven by C–H···π interactions in **1** forming a 3D network.

H···Cg: 147°, symmetry code: $1-x$, y, $2-z$). Two types of O–H···N hydrogen bonds (O(1)–H(1)···N(4): H···A:2.02(4) Å, D···A: 2.767(4) Å, angle D–H···A: 177(3)°, symmetry code x, $1/2-y$, $-1/2+z$ and O(1)–H(2)···N(7): H···A: 0.72(4) Å, D···A: 2.840(4) Å, angle D–H···A: 177(4)°, symmetry code $2-x$, y, $2-z$) form a 2D sheet in the *bc* plane (Figs. 3 and 4). These hydrogen bonds and C–H···π interactions are interwoven to form a 3D network (Fig. 5).

3.2.2. Crystal structure of $[Cd_2(pfap)(\mu_{1,3}\text{-NCS})(\mu_{1,3}\text{-SCN})(NCS)_2]_n$ (2)

A single crystal X-ray diffraction study of **2** shows that the crystal lattice consists of a $[Cd_2(pfap)(\mu_{1,3}\text{-NCS})(\mu_{1,3}\text{-SCN})(NCS)_2]_n$ unit (Fig. 6). The layer structure for **2**, through π···π interactions, is displayed in Fig. 7. Selected bond distances and bond angles relevant to the metal ion coordination sphere are given in Table 2. The polynuclear unit of **2** contains two symmetry related cadmium(II) centers [Cd(1), Cd(1*)] connected by a Schiff base acting as a bis(tridentate) ligand, and two end-to-end ($\mu_{1,3-}$) bi-bridged thiocyanate/isothiocyanate intermediaries and one N-coordinated isothiocyanate are attached to each of the two cadmium(II) centers completing the hexacoordination of the metal ions with a distorted octahedral CdN_5S coordination environment, which propagates forming the 1D polymeric chain. The N-coordination of the terminal NCS^- ligands indicates that the three N-atoms of the Schiff base (pfba) and the N-donation of the $\mu_{1,3-}$ bridged NCS^- ligand create a hardness in cadmium(II) center that enforces the ambidentate ligand to be bound in such a fashion. Cd(1) is attached by three nitrogen atoms, viz. the piperazine nitrogen [N(3)], the imine nitrogen [N(4)] and the pyridine nitrogen [N(5)], of the Schiff base and two end-to-end ($\mu_{1,3-}$) bi-bridged nitrogen [N(1)] and sulfur [S(1)] atoms and one terminal nitrogen [N(2)] atom of the thiocyanate ligands, whereas the neighbouring symmetry related Cd(1*) is ligated to the other three N donor set of the same Schiff base, completing its bis(tridentate)mode, and the counter ends [S(1*) and N(1*)] of two end-to-end ($\mu_{1,3-}$) bi-bridged thiocyanate ligands and the one terminal nitrogen [N(2*)] of the pseudohalide. Each metal center contains one eight-membered bridging loop and two five-membered chelate loops. The eight-membered Cd–$(SCN)_2$–Cd bridging loops adopt a chair confirmation. The equatorial plane of Cd(1) consists of three nitrogen atoms [N(3), N(4), N(5)] of the bis(tridentate) Schiff base and one sulfur atom [S(1)] of a bridging thiocyanate, whereas the axial positions are occupied by a bridging nitrogen atom [N(1)] and a terminal nitrogen atom [N(2)] of the thiocyanate ligands. The maximum deviation of the Cd(1) center from the mean plane is 0.1713 Å. The degrees of distortion from an ideal octahedral geometry are reflected in the *cisoid* [70.45(15)–113.82(10)°] and *transoid* [143.66(14)–177.80(18)°] angles. The Cd–N [2.250(5)–2.524(4) Å] bond lengths are shorter than the bridging Cd–S [2.6161(14) Å] distance, as expected, and are consistent [15] with the corresponding values of the cadmium(II) thiocyanato bridging system. The Cd(1)–N(3) [piperazine] distance [2.524(4) Å] is longer than the Cd(1)–N(5) [pyridine] distance [2.395(4) Å] and Cd(1)–N(4) (imine) bond length [2.295(4) Å]. The intradimer Cd···Cd separation

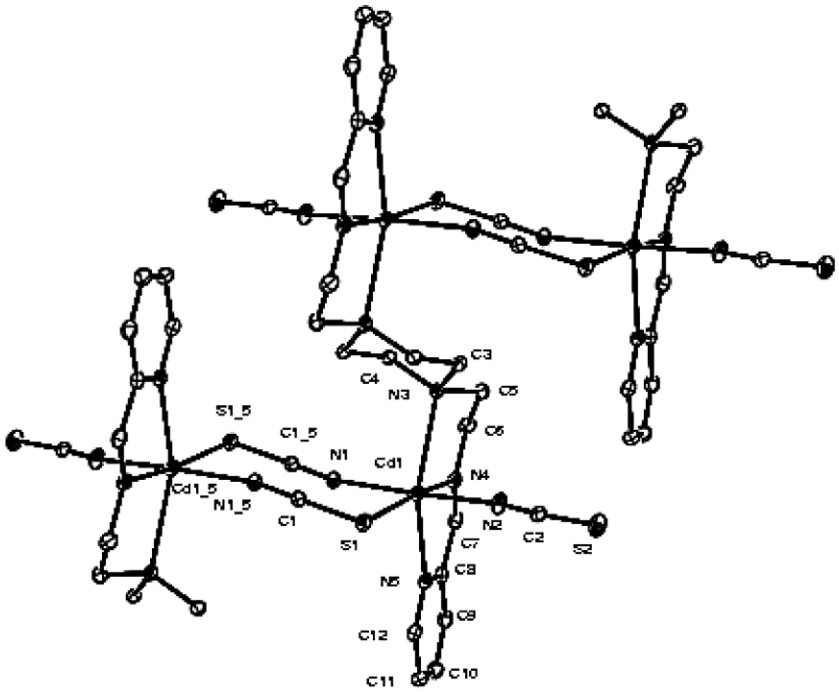


Fig. 6. Thermal ellipsoid plot of the polynuclear $[Cd_2(pfap)(\mu_{1,3}\text{-NCS})(\mu_{1,3}\text{-SCN})(NCS)_2]_n$ (**2**) with the atom labelling scheme and 30% probability ellipsoids for all non-hydrogen atoms.

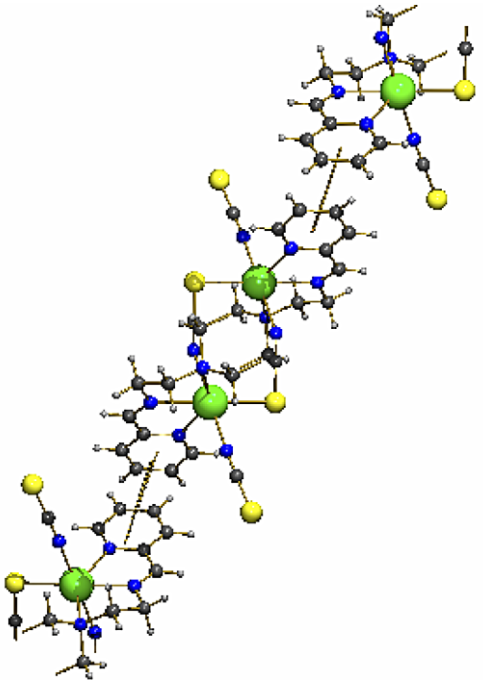


Fig. 7. Layer structure in **2** through π···π interactions.

[6.640(5) Å], through the bis(tridentate) bridge of the Schiff base is larger than the Cd···Cd separation [5.849(5) Å] through the bi-bridged thiocyanates. The angle between the terminal and bridging thiocyanates [S(1)–Cd(1)–N(2)] is 86.78(12)°, reflecting the *cis* alignment of the N- and S-coordination of the bound thiocyanates. N(1) and S(1) from two bridging isothiocyanate and thiocyanate ligands, and N(2) from the terminal isothiocyanate are in the meridional position of the distorted octahedron. The thiocyanates are coordinated in a linear fashion as seen from the N(1*)–C(1)–S(1) and N(2)–C(2)–S(2) angles [178.5(5) and 176.4(5)°]. The N(2)–C(2) length [1.121(7) Å] is shorter than C(2)–S(2) [1.624(5) Å], reflecting N-coordination of the terminal thiocyanate.

In crystal lattice the 1D covalent chain of **2** forms a layer structure with a face-to-face π···π interaction from two terminal pyridine rings [Ring(4)-ring(4)]: Cg(4)–Cg(4) [(a)] separation: 5.1732(3) Å, vertical displacement of Cg: 4.873 Å; [(a)] $1/2 - x,\ -1/2 + y,\ 3/2 - z$; Cg(4) = N(5)–C(8)–C(9)–C(10)–C(11)–C(12)] (Fig. 7).

3.3. Luminescence spectra

The fluorescence behaviour of **1** and **2** has been examined. The fluorescent emission was measured in MeOH solution at 298 K. Upon photoexcitation at 340 and 312 nm an intense fluorescent band was observed with a maximum at 465 and 410 nm and a lifetime of 2.63 and 2.58 ns for **1** and **2**, respectively. The higher lifetime may be due to the presence of stronger weak interactions, which are mainly responsible [23,24] for fluorescence. In glassy solutions (77 K) a red shift is observable at 535 and 510 nm for **1** and **2**, which is presumably due to $^3(\pi\text{–}\pi^*)$ phosphorescence.

4. Conclusion

In conclusion, X-ray crystallographic characterization of new dimeric cadmium(II) azido and polymeric cad-

mium(II) thiocyanato compounds is reported herein. To the best of our knowledge, this the first report of a Schiff base containing polymeric cadmium(II) pseudohalide compound, where the versatility of the tailored hexadentate blocker is realized through its bis(tridentate) congregation behaviour encapsulating two metal ions instead of the classical hexacoordination binding a single metal ion. Again, intermolecular cooperative [25] forces are harnessed to engineer novel crystalline architectures. Both the compounds are examples of good luminous materials.

Acknowledgements

We are thankful to the Department of Science and Technology (DST) and the Council of Scientific and Industrial Research (CSIR), New Delhi, India for financial support. The authors thank Prof. M. J. Zaworotko, The University of South Florida, USA for the X-ray study.

5. Supplementary material

CCDC 205911 and 205912 contain the supplementary crystallographic data for **1** and **2**. These data can be obtained free of charge via http://www.ccdc.cam.ac.uk/conts/retrieving.html, or from the Cambridge Crystallographic Data Centre, 12 Union Road, Cambridge CB2 1EZ, UK; fax: (+44) 1223-336-033; or e-mail: deposit@ccdc.cam.ac.uk.

References

[1] (a) M. Fujita, Chem. Soc. Rev. 6 (1998) 417;
(b) B. Kesanli, W. Lin, Coord. Chem. Rev. 246 (2003) 305.
[2] (a) B. Cornils, W.A. Hermann, R. Scholgl, C.-H. Wong (Eds.), Catalysis from A to Z: A Concise Encyclopedia, John Wiley & Sons, New York, 2000;
(b) I. Beletskaya, C. Moberg, Chem. Rev. 106 (2006) 2320.
[3] (a) J.R. Farraro, J.M. Williams, Introduction to Synthetic Electrical Conductors, Academic Press, New York, 1987;
(b) O. Kahn, Molecular Magnetism, VCH, New York, 1993;
(c) J.S. Miller, M. Drillon (Eds.), Magnetism: Molecules to Materials V, Wiley-VCH, Weinheim, 2005.
[4] (a) S.R. Marder, in: D.W. Bruce, D. O'Hare (Eds.), Metal Containing Materials for Non-Linear Optics in Inorganic Materials, second ed., Wiley, Chichester, 1996, p. 121;
(b) D. Demus, J.W. Goodby, G.W. Gray, H.-W. Spiess, V. Vill (Eds.), Handbook of Liquid Crystals, Wiley-VCH, Weinheim, 1998;
(c) Special issue on Chemical Sensors:, Chem. Rev. 10 (2000) 7.
[5] S.T. Hyde, B. Ninham, S. Anderson, Z. Blum, T. Landh, K. Larsson, S. Liddin, The Language of Shape, Elsevier, Amsterdam, 1997.
[6] (a) E. Uller, B. Demleitner, I. Bernt, R.W. Saalfrank, in: M. Fujita (Ed.), Structure and Bonding, vol. 96, Springer, Berlin, 2000, p. 149;
(b) S. Leininger, B. Olenyuk, P.J. Stang, Chem. Rev. 100 (2000) 853.
[7] (a) G.A. Jeffrey, An Introduction to Hydrogen Bonding, Oxford University Press, Oxford, 1997;
(b) G.R. DesirajuT. Steiner, The Weak Hydrogen Bond in Structural Chemistry and Biology, Oxford University Press, Oxford, 1999;
(c) M. Meot-Ner, Chem. Rev. 105 (2005) 213.
[8] (a) C. Janiak, Angew. Chem., Int. Ed. Engl. 36 (1997) 1431;
(b) K.-M. Detlefs, P. Hobza, Chem. Rev. 100 (2000) 143.
[9] (a) M. Nishio, M. Hirota, Y. Umezawa, The CH/π Interaction, Wiley-VCH, New York, 1998;
(b) H. Takahasi, S. Tsuboyama, Y. Umezawa, K. Honda, M. Nishio, Tetrahedron 56 (2000) 6185.
[10] (a) Special issue on Focus on Self-Assembly: , Acc. Chem. Res. 32 (1999) 4;
(b) B.J. Holliday, C.A. Mirkin, Angew. Chem., Int. Ed. 40 (2001) 2022.
[11] (a) T.K. Karmakar, S.K. Chandra, J. Ribas, G. Mostafa, T.-H. Lu, B.K. Ghosh, Chem. Commun. (2002) 2364;
(b) S.H. Rahaman, R. Ghosh, G. Mostafa, B.K. Ghosh, Inorg. Chem. Commun. 8 (2005) 700;
(c) S.H. Rahaman, R. Ghosh, G. Mostafa, B.K. Ghosh, Inorg. Chem. Commun. 8 (2005) 1137.
[12] (a) D. Bose, S.H. Rahaman, G. Mostafa, R.D.B. Walsh, M.J. Zaworotko, B.K. Ghosh, Polyhedron 23 (2004) 545;
(b) S.H. Rahaman, D. Bose, H. Chowdhury, G. Mostafa, H.-K. Fun, B.K. Ghosh, Polyhedron 24 (2005) 1837.
[13] (a) A.M. Golub, H. Kohler, V.V. Skopenko (Eds.), Chemistry of Pseudohalides, Elsevier, Amsterdam, 1986;
(b) J. Ribas, C. Diaz, R. Costa, J. Tercero, X. Solans, M. Font-Bardia, H. Stoeckli-Evans, Inorg. Chem. 37 (1998) 233, and references cited therein;
(c) J.-M. Shi, Y.-M. Sun, Z. Liu, L.D. Liu, W. Shi, P. Chen, J. Chem. Soc., Dalton Trans. (2006) 376, and references cited therein.
[14] (a) V. Alexander, Chem. Rev. 95 (1995) 273;
(b) A.D. Garnovskii, A.L. Nivorozhkin, V.I. Minkin, Coord. Chem. Rev. 126 (1993) 1.
[15] (a) S.R. Marder, J.E. Sohn, G.B. Stuckey (Eds.), Materials for Non-Linear Optics: Chemical Perspectives, ACS Symp. Ser., Washington, DC, 1991;
(b) O.R. Evans, W. Lin, Acc. Chem. Res. 35 (2002) 511.
[16] G.M. Sheldrick, SAINT, V4, Software Reference Manual Siemens Analytical X-ray Systems, Madison, WI, USA, 1996.
[17] G.M. Sheldrick, SADABS, Program for Empirical Absorption Correction of Area Detector Data, University of Gottingen, Germany, 1996.
[18] G.M. Sheldrick, SHELXL-97, Program for Refinement of Crystal Structures, University of Gottingen, Germany, 1997.
[19] L.J. Farrugia, J. Appl. Crystallogr. 30 (1997) 565.
[20] A.L. Spek, PLATON99, Molecular Geometry Program, University of Utrecht, The Netherlands, 1999.
[21] K. Nakamoto, Infrared and Raman Spectra of Inorganic and Coordination Compounds, part B: Applications in Coordination, Organometallic and Bioinorganic Chemistry, John Wiley & Sons Inc., New York, 1997, p. 171.
[22] A.B.P. Lever, Inorganic Electronic Spectroscopy, second ed., Elsevier, New York, 1984.
[23] (a) B. Dutta, P. Bag, U. Florke, K. Nag, Inorg. Chem. 44 (2005) 147;
(b) Y. Kang, J. Zhang, Z.-J. Li, Y.-Y. Qin, Y.-G. Yao, Inorg. Chem. Commun. 8 (2005) 722.
[24] (a) K.-Y. Ho, W.-Y. Yu, K.-K. Cheung, C.-M. Che, Chem. Commun. (1998) 2101;
(b) K.-Y. Ho, W.-Y. Yu, K.-K. Cheung, C.-M. Che, J. Chem. Soc., Dalton Trans. (1999) 1581.
[25] (a) D. Braga, F. Grepioni, A.G. Orpen, Crystal Engineering: From Molecules and Crystals to Materials, Kluwer, Dordrecht, 1999;
(b) G.R. Desiraju, Nature 412 (2001) 397.

and M(II) 3d metal ions (M = Ni, Mn) bridged by thiocyanate groups. Due to its ambident character, the thiocyanate group, like cyanide, may serve as a bridging ligand. It is interesting to learn how the arrangement of molecules in the crystal lattice, configuration of the nitrogen atom ligands and the type of paramagnetic centers in the heterometallic systems influence the magnetic properties of the compounds studied (Scheme 1).

2. Experimental

2.1. Materials

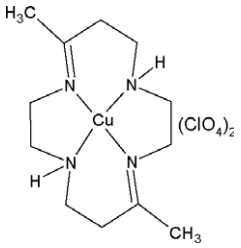
All materials used in this work were of the reagent grade purity. They were used as commercially obtained. $[CuL_\alpha](ClO_4)_2$ was prepared as previously reported [5].

2.2. Synthesis of the complex $\{CuL_\alpha[Ni(NCS)_4(H_2O)_2]\}$ (1)

A solution of $[CuL_\alpha](ClO_4)_2$ (73.02 mg, 0.15 mmol) in CH_3CN (10 mL) was added dropwise to an aqueous solution (10 mL) containing KSCN (58.31 mg, 0.6 mmol) and $NiCl_2 \cdot 4H_2O$ (35.64 mg, 0.15 mmol). The mixture was subsequently stirred. After a few days, a dark-pink crystalline solid was formed from the violet solution by slow evaporation. It was filtered and washed using diethyl ether (2×10 mL). Yield: 86.15 mg (93%). Violet crystals suitable for X-ray diffraction studies were obtained by slow evaporation of a solution of all the reagents in CH_3CN–H_2O (1:1) at room temperature. IR/cm^{-1}: bands associated with the thiocyanate ligand appear at 2121 (vs), 2088 (vs), 815 (vw), 480 (w), 474 (w), 460 (w). *Anal.* Calc. for $C_{16}H_{28}N_8O_2S_4NiCu$ (614.95): C, 31.25; H, 4.59; N, 18.22; S, 20.86. Found: C, 31.16; H, 4.38; N, 18.21; S, 19.56%. The copper and manganese content was determined by the ICP method: Calc. Ni 9.54, Cu 10.33. Found: Ni 9.22, Cu 10.02.

2.3. Synthesis of complex $\{CuL_\alpha[Mn(NCS)_4(H_2O)_2]\}$ (2)

A solution of $[CuL_\alpha](ClO_4)_2$ (73.02 mg, 0.15 mmol) in CH_3CN (10 mL) was added dropwise to an aqueous solution (10 mL) containing KSCN (58.31 mg, 0.6 mmol) and $MnCl_2 \cdot 4H_2O$ (29.68 mg, 0.15 mmol). The mixture was subsequently stirred. The resulting orange precipitate was filtered off, washed with diethyl ether (2×10 ml) and dried at room temperature. Yield: 80.35 mg (88%). Violet crystals of **2** suitable for X-ray diffraction studies were obtained by slow evaporation of a CH_3CN–H_2O (1:1) solution of the previously prepared precipitate. IR/cm^{-1}: bands associated with the thiocyanate ligand appear at 2103 (vs), 2071 (vs), 814 (vw), 470 (w). *Anal.* Calc. for $C_{16}H_{28}N_8O_2S_4MnCu$ (611.18): C, 31.44; H, 4.62; N, 18.33; S, 20.99. Found: C, 31.02; H, 4.58; N, 18.12; S, 19.88. The nickel and manganese content was determined by the ICP method: Calc. Mn 8.99, Cu 10.40. Found: Mn 8.44, Cu 9.96.



Scheme 1. Schematic view of the macrocyclic copper(II) complex.

2.4. Magnetic measurement

Magnetic measurements in the temperature range 1.8–300 K were performed using a Quantum Design SQUID-based MPMSXL-5-type magnetometer. The SQUID magnetometer was calibrated with a palladium rod sample (Materials Research Corporation, measured purity 99.9985%). The superconducting magnet was generally operated at a field strength ranging from 0 to 5 T. Measurements were undertaken at a magnetic field of 0.5 T. Corrections are based on subtracting the sample holder signal and the contribution χ_D estimated from Pascal constants [6].

2.5. EPR spectra

EPR spectra were recorded at room temperature and 77 K on a Bruker ESP 300 spectrometer operating at X-band equipped with an ER 035M Bruker NMR gaussmeter and HP 5350B Hewlett-Packard microwave frequency counter. The spectra at a temperature of 4.2 K were measured with an X-band Radiopan SE/X 2543 spectrometer.

2.6. X-ray crystallographic analysis

Single-crystal X-ray measurements of complexes **1** and **2** were accomplished on a Kuma KM4CCD κ-axis diffractometer with graphite–monochromated MoKα radiation at 100 K. The crystals were positioned 65 mm from the KM4CCD camera. 1204 frames were measured at 1.0° intervals with a counting time of 20 s for complex **1** and 17 s for complex **2**. The data were corrected for Lorentz and polarization effects. A numerical absorption correction was applied. Data collection, cell refinement and data reduction were carried out with the Kuma Diffraction programs: CrysAlisCCD and CrysAlisRED [7]. The structures were solved by direct methods [8] and refined using SHELX [9]. The refinement was based on F^2 for all reflections except those with very negative F^2. Weighted R factors wR and all goodness-of-fit S values are based on F^2. Conventional R factors are based on F with F set to zero for negative F^2. The $F_0^2 > 2s(F_0^2)$ criterion was used only for calculating R factors and is not relevant to the choice of reflections for the refinement. The R factors based on F^2 are about twice as large as those based on F. Most of

Table 1
Crystal data and structure refinement

Identification code	$\{CuL_\alpha[Ni(NCS)_4(H_2O)_2]\}$	$\{CuL_\alpha[Mn(NCS)_4(H_2O)_2]\}$
Empirical formula	$C_{16}H_{28}N_8O_2S_4NiCu$	$C_{16}H_{28}N_8O_2S_4MnCu$
Formula weight	614.95	611.18
Temperature (K)	100	100 K
Wavelength (Å)	0.71073	0.71073
Crystal system	triclinic	triclinic
Space group	$P\bar{1}$	$P\bar{1}$
Unit cell dimensions		
a (Å)	7.4732(6)	7.4762(6)
b (Å)	7.8580(6)	7.9492(6)
c (Å)	11.1708(8)	11.2395(8)
α (°)	98.403(6)	97.906(6)
β (°)	94.726(6)	95.251(6)
γ (°)	107.695(7)	107.393(7)
Volume (Å^3)	612.63(8)	625.11(8)
Z	1	1
D_{calcd} (Mg/m^3)	1.667	1.624
Absorption coefficient (mm^{-1})	2.008	1.720
$F(000)$	317	314
Crystal size (mm^3)	$0.39 \times 0.19 \times 0.14$	$0.61 \times 0.35 \times 0.18$
θ Range for data collection (°)	3.22–24.99	3.70–24.99
Index ranges	$-8 \leqslant h \leqslant 8$, $-9 \leqslant k \leqslant 9$, $-13 \leqslant l \leqslant 13$	$-8 \leqslant h \leqslant 8$, $-9 \leqslant k \leqslant 9$, $-13 \leqslant l \leqslant 13$
Reflections collected	13	13
Independent reflection	9002	8949
Absorption correction	2161 ($R_{int} = 0.0311$)	2196 ($R_{int} = 0.0512$)
Maximum and minimum transmission	numerical	numerical
Refinement method	0.76193 and 0.52627	0.75300 and 0.51327
Data/restraints/parameters	full-matrix least-squares on F^2	full-matrix least-squares on F^2
Goodness-of-fit on F^2	2161/0/203	2196/0/191
Final R indices [$I > 2\sigma(I)$]	1.070	1.063
R indices (all data)	$R_1 = 0.0341$, $wR_2 = 0.0842$	$R_1 = 0.0415$, $wR_2 = 0.1061$
Largest diffraction peak and hole	$R_1 = 0.0369$, $wR_2 = 0.0866$	$R_1 = 0.0432$, $wR_2 = 0.1078$
[e Å^{-3}]	1.914 and −0.582	1.904 and −0.583

the hydrogen atoms were located from a difference map and refined isotropically. All remaining hydrogen atoms were located at the idealized averaged geometrical positions and allowed to ride on the heavy atoms. Scattering factors were taken from Tables 6.1.1.4 and 4.2.4.2 in Ref. [10]. Details concerning crystal data and refinement are given in Table 1.

3. Results and discussion

3.1. Structural description

The molecular structure of the complex $\{CuL_\alpha[Ni(NCS)_4(H_2O)_2]\}$ (**1**) is isostructural with the complex $\{CuL_\alpha[Mn(NCS)_4(H_2O)_2]\}$ (**2**). They both crystallize in the triclinic $P\bar{1}$ space group with only half of the molecule in the independent part of the unit cell {1/2 CuL_α^{2+} and 1/2 $[Ni(NCS)_4(H_2O)_2]^{2-}$ for complex **1** and 1/2 $[Mn(NCS)_4(H_2O)_2]^{2-}$ anion for complex **2**}. The anions and the CuL_α^{2+} cations are located at the inversion centers, therefore only halves of the moieties are independent (Fig. 1).

The Mn(II) and Ni(II) ions are connected with the Cu(II) ions via thiocyanate bridges, thus complexes **1** and **2** create infinite polymeric zig-zag chains in the crystal lattice (Fig. 2). These chains are assembled from the repeating units of the CuL cations and $[Ni(NCS)_4(H_2O)_2]$ (**1**) or $[Mn(NCS)_4(H_2O)_2]$ (**2**) complex anions. The molecular packing of the polymeric chains is shown in Fig. 3. The 3D structure consists of regular columns of stacked molecules.

Each Cu(II) cation is octahedrally coordinated by four nitrogen atoms of the macrocyclic ring and two sulfur atoms from the bridging ligand. The Cu–S distances are equal, 2.922 and 2.949 Å in complexes **1** and **2**, respectively. The Cu–N distances are similar for both complexes and vary from 1.982 to 2.001 Å. The coordination geometry of the Ni(II) and Mn(II) ions is close to a slightly distorted octahedron. The nickel and manganese ions are bound to two bridging and two non-bridging thiocyanate ions through four nitrogen atoms. The last two coordination sites are occupied by water molecules. In **1**, the Ni–N distances are equal to 2.070 and 2.064 Å, whereas the Ni–O distances are 2.116 Å. In the case of complex **2**, the corresponding distances are longer and are equal to 2.204 and 2.215 Å, and 2.240 Å for Mn–N and Mn–O, respectively. The thiocyanate groups are almost linear. All remaining distances and angles are provided in Table 2. Two non-bridging thiocyanate ligands create hydrogen bonds with the oxygen atoms from water molecules belonging to neighboring polymeric chains. Hydrogen bonds are

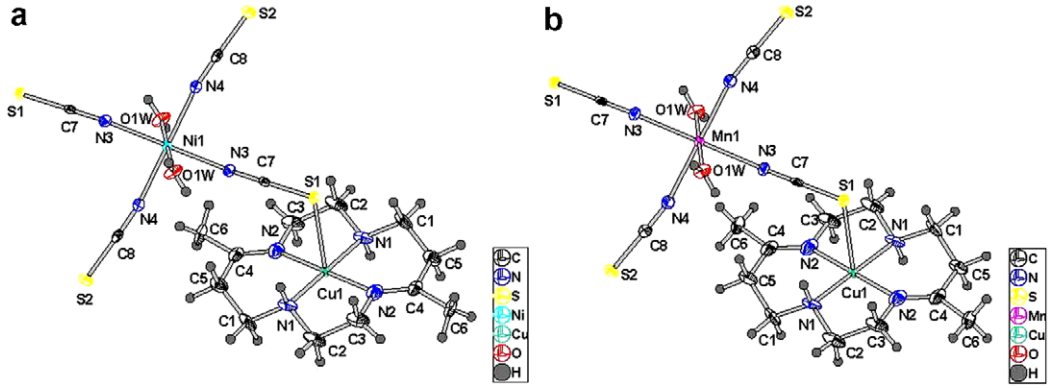


Fig. 1. Thermal ellipsoid representation of (a) complex **1** and (b) complex **2** with atom labels. Both macrocyclic ligand and anion are located at the inversion centers.

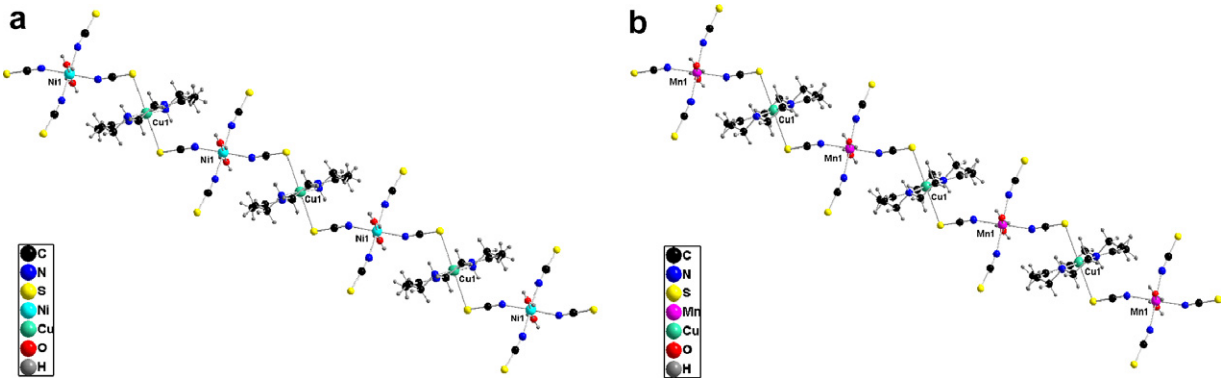


Fig. 2. Polymeric chains created by moieties of (a) complex **1** and (b) complex **2**.

also formed between the nitrogen atoms of the macrocyclic ring and the sulfur atoms (Table 3). The shortest intramolecular distances between the metallic centres in the same chain are *ca.* 6.342 Å (Cu1···Ni1) and 6.421 Å (Cu1···Mn1). The distances between the metallic ions in neighboring chains are equal to 7.283 Å (X, $1+Y$, Z) (Cu1···Ni1) and 7.473 Å ($1+X$, Y, Z) (Cu1···Cu1). The corresponding values in complex **2** are: 7.316 Å (X, $1+Y$, Z) (Cu1···Mn1) and 7.476 Å ($1+X$, Y, Z) (Cu1···Cu1). In the crystal lattice both complexes creates 1D polymeric chains.

3.2. Magnetic properties

The magnetic behavior of **1** is shown in Fig. 4 in the form of a $\chi_M T$ versus T plot, where χ_M stands for the magnetic susceptibility per Cu(II)Ni(II) unit. The value of $\chi_M T$ at room temperature is 1.53 $cm^3\ mol^{-1}$ K for compound **1**, which is as expected for a magnetically non-interacting Cu(II)Ni(II) entity with the local spins $S_{Cu} = 1/2$ and $S_{Ni} = 1$.

$\chi_M T$ smoothly decreases over a wide range of decreasing temperatures, and rapidly decreases at the lowest temperatures. The slight decrease of $\chi_M T$ can either be due to the zero-field splitting effect of the Ni^{II} ions and/or to intra- or intermolecular exchange interactions characterised by J_{Ni-Ni} and J_{Cu-Ni}. As mentioned in the structural discussion, this complex can be viewed as a heterobimetallic pseudo one-dimensional chain. It is interesting why in the present case a minimum for $\chi_M T$ is not observed. Since the J_{Cu-Ni} interaction is relatively large, the ratio $|D|/|J|$, where D is due to both local anisotropy and anisotropic exchange, is likely to be much too small to account for the absence of the minimum. On the other hand, no other relatively efficient interchain exchange pathways seem to be possible. The distances between the metallic ions in the neighboring chains are equal to 7.283 Å (Cu(II)–Ni(II)) and 7.473 Å (Cu(II)–Cu(II)), a little longer than the intermolecular distances between the metallic centers in the same chain 6.342 Å (Cu(II)–Ni(II)). This might provide an interchain exchange pathway. The same kind of magnetic interaction was observed in other Cu(II)–Ni(II) complexes, $CuNi(C_2O_4)_2 \cdot 4H_2O$ [11] and $CuZn(C_2O_4)_2 \cdot 4H_2O$ [12]. In such cases, the magnetic exchange parameter may be expressed as a sum of contributions, including pairs of magnetic orbitals, according to the formulae:

$$J_{CuCu} = J_{b_1b_1}$$
$$J_{NiNi} = 1/4(J_{b_1b_1} + J_{a_1a_1} + 2J_{a_1b_1})$$
$$J_{CuNi} = 1/2(J_{b_1b_1} + J_{a_1b_1})$$

where a_1 and b_1 are magnetic orbitals.

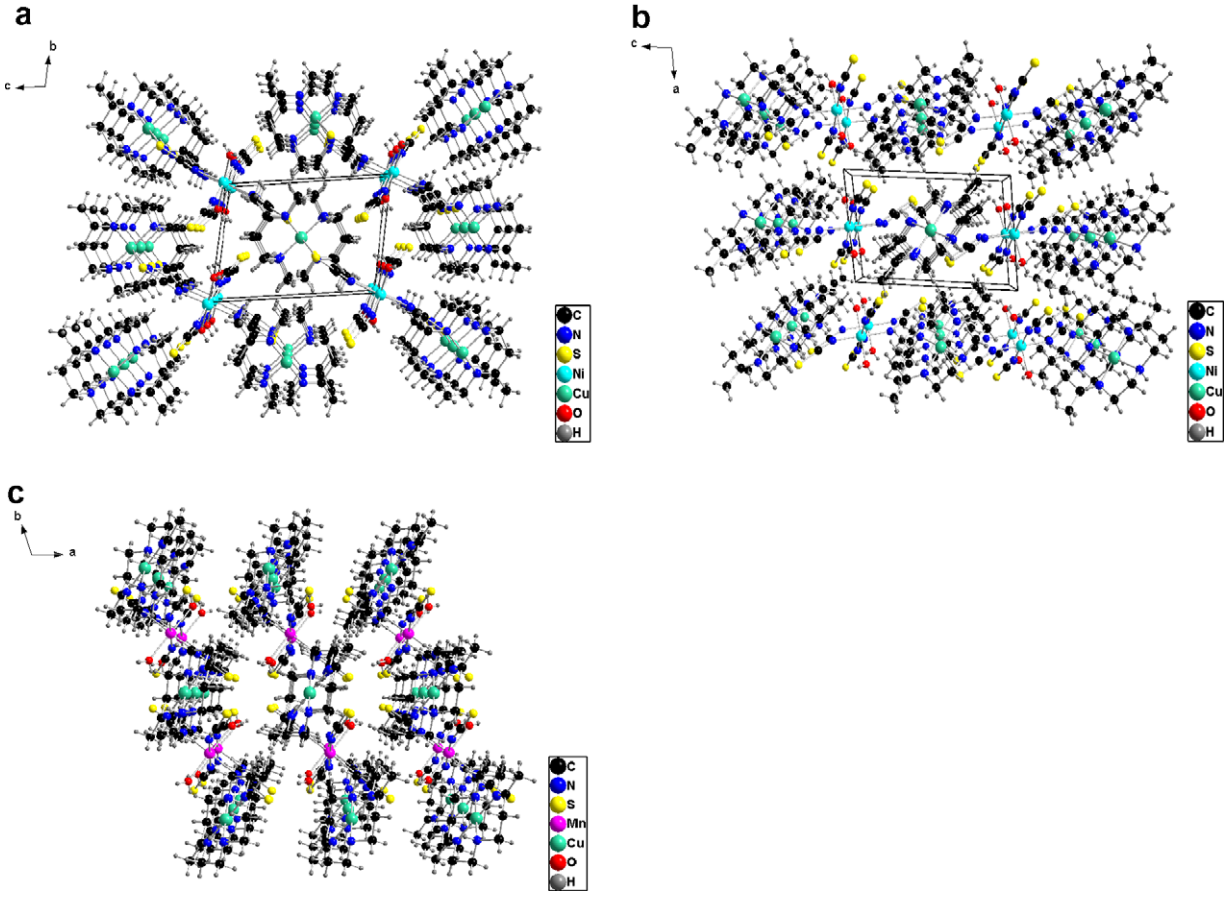


Fig. 3. Perspective views along: (a) *x*-axis (complex **1**), (b) *y*-axis (complex 1) and (c) *z*-axis (complex **2**). Because of the isostructural nature of the crystals, the other crystal views for complex **2** look exactly the same as for complex **1**.

Table 2
Selected bond lengths (Å) and bond angles (°) for complexes **1** and **2**

$\{CuL_\alpha[Ni(NCS)_4(H_2O)_2]\}$		$\{CuL_\alpha[Mn(NCS)_4(H_2O)_2]\}$	
Cu1⋯ Ni1	6.3419(5)	Cu1⋯ Mn1	6.4214(5)
Cu1⋯ Ni1#1	7.2834(5)	Cu1⋯ Mn1#1	7.3160(5)
Cu1⋯ Cu1#2	7.4732(6)	Cu1⋯ Cu1#2	7.4762(6)
Cu1⋯ Cu1#3	12.684(1)	Cu1⋯ Cu1#3	12.843(1)
Ni1⋯ Ni1#3	12.684(1)	Mn1⋯ Mn1#3	12.843(1)
Cu1–N1	1.987(3)	Cu1–N1	1.982(3)
Cu1–N2	2.001(3)	Cu1–N2	1.997(3)
Cu1–S1	2.9220(8)	Cu1–S1	2.9486(8)
Ni1–N3	2.070(3)	Mn1–N3	2.204(3)
Ni1–N4	2.064(3)	Mn1–N4	2.215(3)
Ni1–O1W	2.116(3)	Mn1–O1W	2.240(3)
S1–C7	1.649(3)	S1–C7	1.644(3)
S2–C8	1.659(3)	S2–C8	1.657(3)
N3–C7	1.166(4)	N3–C7	1.173(5)
N4–C8	1.158(4)	N4–C8	1.159(5)
N3–Ni1–N4	88.5(1)	N3–Mn1–N4	88.5(1)
N3–Ni1–O1W	86.7(1)	N3–Mn1–O1W	86.0(1)
N4–Ni1–O1W	93.5(1)	N4–Mn1–O1W	93.8(1)
C7–S1–Cu1	99.9(1)	C7–S1–Cu1	98.5(1)
C7–N3–Ni1	155.3(2)	C7–N3–Mn1	153.0(3)
C8–N4–Ni1	169.6(2)	C8–N4–Mn1	167.5(3)
N3–C7–S1	179.4(3)	N3–C7–S1	179.8(3)
N4–C8–S2	178.4(3)	N4–C8–S2	178.7(3)

Symmetry transformations used to generate equivalent atoms: #1 = X, $1+Y$, Z; #2 = $1+X$, Y, Z; #3 = X, $1+Y$, $1+Z$.

On the other hand, the chains are linked together through hydrogen bonding formed between the nitrogen atoms of the macrocyclic ring and the sulfur atoms or between the non-bridging thiocyanate ligands and the oxygen atoms of water molecules. These facts create further possibilities of a magnetic exchange pathway.

On the basis of the above hypothesis, the magnetic susceptibility of the chain χ_{chain} was calculated by Eq. (1), where the first term describes an infinite Ni(II) chain (Eq. (1)), according to the polynomial expression of Hiller [13], and the second term is a temperature independent contribution from Cu(II).

$$\chi_{chain} = \frac{Ng_{Mn}^2\beta^2}{kT}[A + Bx^2][1 + Cx + Dx^3]^{-1} + \frac{Ng_{Cu}^2\beta^2}{3kT}S_{Cu}(S_{Cu}+1) + TIP \quad (1)$$

where $x = |J|/kT$, $A = 0.6667$, $B = 2.5823$, $C = 3.6035$ and $D = 39.558$. J is the exchange coupling constant and TIP is the temperature-independent paramagnetism (60×10^{-6} $cm^3\,mol^{-1}$). Taking into account the 2D interactions, we modified the molar magnetic susceptibility χ_m employing Eq. (2) [14], where J' is the interchain coupling constant and $z = 2$, the number of nearest Ni(II) neighbours. Other symbols have their usual meaning.

Table 3
Hydrogen bonds formed by complexes **1** and **2** [Å and °]

D-H···A	Symmetry	*d*(D–H)	*d*(H···A)	*d*(D···A)	<(DHA)
{CuL$_\alpha$[Ni(NCS)$_4$(H$_2$O)$_2$]}					
N1–H1N···S1	*X*, *Y*, *Z*	0.90(5)	2.92(5)	3.416(3)	117(3)
N1–H1N···S2	*X*, 1 + *Y*,*Z*	0.90(5)	2.72(5)	3.549(3)	154(4)
O1W–H1W···S2	*X*, 1 + *Y*, *Z*	0.74(5)	2.66(5)	3.392(3)	172(4)
O1W–H2W···S2	2−*X*, −*Y*, −*Z*	0.69(5)	2.73(5)	3.373(3)	158(5)
{CuL$_\alpha$[Mn(NCS)$_4$(H$_2$O)$_2$]}					
N1–H1N···S1	*X*, *Y*, *Z*	0.97(5)	2.91(5)	3.449(3)	116(3)
N1–H1N···S2	*X*, 1 + *Y*, *Z*	0.97(5)	2.63(5)	3.528(3)	155(4)
O1W–H1W···S2	*X*, 1 + *Y*, *Z*	0.76(5)	2.61(5)	3.372(3)	174(4)
O1W–H2W···S2	2−*X*, −*Y*, −*Z*	0.79(6)	2.56(6)	3.344(3)	169(5)

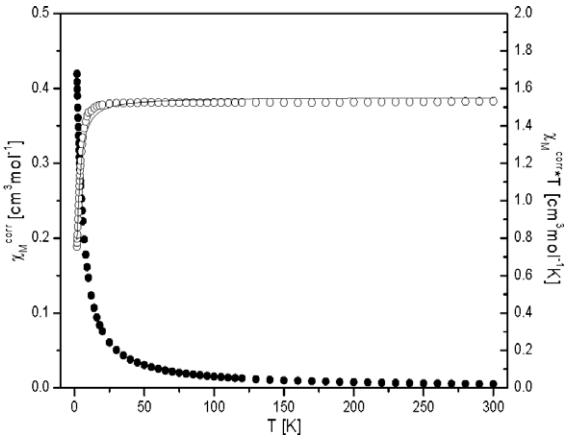


Fig. 4. Thermal dependence of χ_M (●) and $\chi_M T$ (○) for {CuL$_\alpha$[Ni(NCS)$_4$(H$_2$O)$_2$]} (**1**). The solid line is the calculated curve.

$$\chi_M^{corr} = \chi_{chain}/[1 - \chi_{chain}(2zJ'/Ng^2\beta^2)] \quad (2)$$

The least-squares fit of Eq. (2) to the data gives $J = -1.35 \times 10^{-5}$ cm^{-1}, zJ′ = −1.0 cm^{-1}, $g_{Cu} = g_{Ni} = 2.33$, and the agreement factor, defined as $R = [(\chi_M)^{obsd} - (\chi_M)^{cald}]^2/[(\chi_M)^{obsd}]^2$, equals 5.06×10^{-4}. This result suggests that there is no interaction (J) between the nearest Ni(II) ions in the chain and the antiferromagnetic interchain interaction (*J*′) possibility cannot be ruled out.

Since the decrease of $\chi_M T$ at low temperature can be attributed to the zero-field splitting (ZFS) of the Ni(II) ions, we used the following Eqs. (3)–(5) [15] for isolated Ni(II) and Cu(II) ions with ZFS:

$$\chi_M = \frac{\chi_\parallel + 2\chi_\perp}{3} + \frac{Ng^2\beta^2}{4kT} \quad (3)$$

$$\chi_\parallel = \frac{2Ng_\parallel^2\beta^2}{kT}\frac{\exp(-D/kT)}{1 + 2\exp(-D/kT)} \quad (4)$$

and

$$\chi_\perp = \frac{2Ng_\perp^2\beta^2}{D}\frac{1 - \exp(-D/kT)}{1 + 2\exp(-D/kT)} \quad (5)$$

where *D* (axial zero-field splitting parameter) is the energy difference between $M_s = \pm 1$ and $M_s = 0$ levels. The best fit leads to the values $|D| = 5.51$ cm^{-1} (the sign of *D* cannot be determined from powder magnetic susceptibility data) and $g_{avNi} = 2.19$, $g_{Cu} = 2.00$ ($R = 9.59 \times 10^{-5}$). The calculated value of the *D* parameter suggests that the zero-field splitting effect of the Ni(II) ions is dominant in the examined compound.

One can conclude that according to the above results the magnetic susceptibility of compound **1** can be calculated by Eq. (6), as a sum of independent contributions from the Ni(II) and Cu(II) paramagnetic ions with a molecular field correction (Eq. (2)).

$$\chi = \frac{Ng_{Ni}^2\beta^2}{3kT}S_{Ni}(S_{Ni} + 1) + \frac{Ng_{Cu}^2\beta^2}{3kT}S_{Cu}(S_{Cu} + 1) \quad (6)$$

The least-squares fitting allows exactly the same values of g_{Cu}, g_{Ni} and zJ' parameters to be obtained and confirms our conclusions.

The molar magnetization as a function of magnetic field up to 50 KOe at 2 K is shown in Fig. 5. It (M) is expressed in B.M. units and M_s is the expected saturation value. The magnetization increases gradually to a saturation value of $M_S = 2.23$ B.M., as expected for the zero-field splitting effect for the Ni(II) ions, and antiferromagnetic coupling of the pair of metal ions (Cu, Ni) cannot be ruled out.

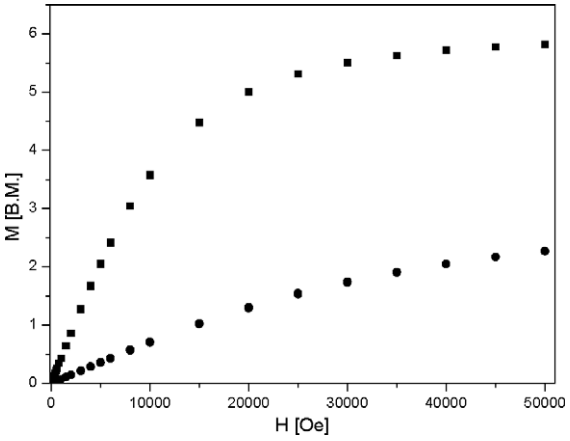


Fig. 5. Field dependence of the magnetization for complexes (●){CuL$_\alpha$[Ni(NCS)$_4$(H$_2$O)$_2$]} (**1**) and (■) {CuL$_\alpha$[Mn(NCS)$_4$(H$_2$O)$_2$]} (**2**).

Complex **2** exhibits similar magnetic properties (Fig. 6). At room temperature, the $\chi_M T$ value is 4.57 cm^3Kmol^{-1}, close to that (4.57 cm^3Kmol^{-1}) expected for the $S = {}^5/_2$ and $S = ½$ spins. This value remains nearly constant over a wide range of temperature, and smoothly decreases below 3 K.

According to Kahn's theory, in an antiferromagnetic exchange ($J < 0$) within an alternating Mn(II)–Cu(II) chain, the net spins ($S = S_{Mn}–S_{Cu} = 2$) are parallel to each other in the ground state, and $\chi_M T$ should diverge below the critical temperature. In the examined compound there is no minimum on the $\chi_M T$ versus T curve, which is typical for ferrimagnetic behaviour.

In the absence of the minimum, the decrease of $\chi_M T$ observed at the lowest temperature for this compound is attributed to either very weak Mn(II)···Mn(II) antiferromagnetic interactions within the chain or, alternatively, cooperative interchain Mn(II)···Cu(II) interactions, which gives rise to the ferrimagnetic behaviour (or may lead to a cancellation of the spins (Scheme 2)).

As already mentioned, the $Mn(NCS)_4(H_2O)_2$ fragment approaches a distorted octahedral symmetry. The copper ions are located in an almost octahedral environment with the bridging SCN groups occupying the axial positions. For this kind of symmetry the unpaired electron on the copper ion is described by the xy-like orbital transformed as dz^2 and localized on the nitrogen ligand only.

Under these circumstances, the Mn···Mn superexchange within the chain propagated by the filled dz^2-like orbital of the NCS–Cu–SCN pathway may prevail over the Mn···Cu and Cu···Cu interactions. A similar situation is observed in the $[Cu(en)_2[Mn(NCS)_4(H_2O)_2]_n$ [16] and $Cu(en)_2MnCl_4$ [17] complexes. For the purpose of magnetic analysis, the magnetic susceptibility equation for χ_{chain} (Eq. (7)) was used with a correction for the molecular field (Eq. (2)). The first term describes an infinite Mn(II) chain [13] and the second term is a temperature independent contribution from Cu(II).

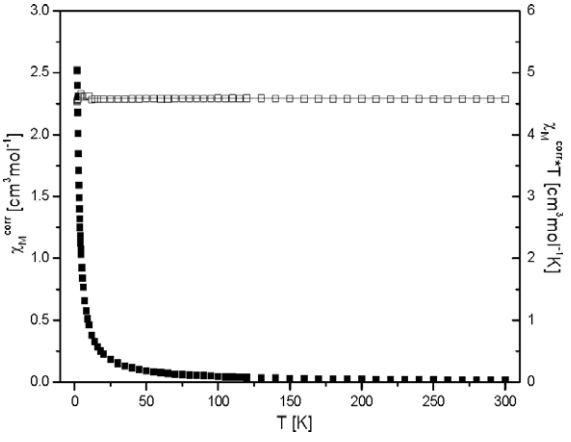
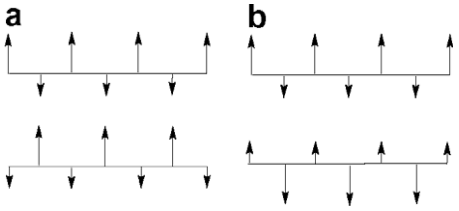


Fig. 6. Thermal dependence of χ_M (■) and $\chi_M T$ (□) for $\{CuL_\alpha[Mn(NCS)_4(H_2O)_2]\}$ (**2**). The solid line is the calculated curve.



Scheme 2. Schematic representation of two modes of interchain metal–metal magnetic interactions: (a) antiferromagnetic interchain interaction between the nearest manganese and copper ions, giving rise to a ferrimagnetic behaviour; (b) on the contrary, a cancellation of the spins.

$$\chi_{chain} = \frac{Ng_{Mn}^2\beta^2}{kT}[A + Bx^2][1 + Cx + Dx^3] + \frac{Ng_{Cu}^2\beta^2}{3kT}S_{Cu}(S_{Cu} + 1) + TIP \quad (7)$$

where $x = |J|/kT$, $A = 2.9167$, $B = 208.04$, $C = 15.543$ and $D = 2707.2$, J is the exchange coupling constant and TIP is the temperature-independent paramagnetism (60×10^{-6} cm^3mol^{-1}). The least-squares fit of the formula from Eq. (7) to the experimental data gives $J = -0.002$ cm^{-1}, $zJ' = -0.01$ cm^{-1}, $g_{Cu} = g_{Mn} = 1.98$, and the agreement factor, defined as $R = [(\chi_M T)^{obsd} - (\chi_M T)^{cald}]^2/[(\chi_M T)^{obsd}]^2$ equals 2.21×10^{-5}. These results suggest that inside the chain non-interacting magnetic centers exist, so this system may be treated as isolated.

As a second step, we tried to analyse the magnetic behavior, including the zero-field splitting effect, within the $S = 5/2$ local ground states of the Mn(II) ions. For this purpose we used the modified Eqs. (8) and (9) presented in the literature [18]:

$$\chi_{ZFS} = \frac{Ng_{Mn}^2\beta^2}{4kT}\left[\frac{1 + 9\exp(2D/kT) + 25\exp(6D/kT)}{1 + \exp(2D/kT) + \exp(6D/kT))}\right] \quad (8)$$

$$\chi_m = \chi_{ZFS} + \frac{Ng_{Cu}^2\beta^2}{3kT}S_{Cu}(S_{Cu} + 1) + TIP \quad (9)$$

where D is the axial zero-field splitting parameter for Mn(II). Least-squares fitting gives $D = 6 \times 10^{-4}$ cm^{-1}, $g_{Cu} = 2.25$, $g_{Mn} = 1.94$, and the agreement factor R is equal to 4.96×10^{-5}. In this case, the magnetic susceptibility may by expressed as a combination of the Mn···Mn interaction and the zero-field splitting. The expression of Hiller [13] then was modified by replacing the $NS(S + 1)g_{Mn}{}^2\beta^2/3kT$ term with χ_{ZFS}, which is shown by Eq. (9) [19]. The final expression is then as follows:

$$\chi_{chain} = \frac{12}{35}\chi_{ZFS}[A + Bx^2][1 + Cx + Dx^3] + \frac{Ng_{Cu}^2\beta^2}{3kT}S_{Cu}(S_{Cu} + 1) + TIP$$
$$\chi_M^{corrr} = \chi_{chain}/[1 - \chi_{chain}(2zJ'/Ng^2\beta^2)] \quad (10)$$

This leads to the parameters $J = -0.002$ cm^{-1}, $zJ' = -0.01$ cm^{-1}, $D = 2 \times 10^{-4}$ cm^{-1}, $g_{Cu} = g_{Mn} = 1.98$. The agreement factor R is equal to 6.72×10^{-5}. As a con-

sequence, one obtains a near zero value of the D parameter which allows us to conclude that in the examined compound a very weak antiferromagnetic interaction between the Mn(II) ions in the neighboring chain is dominant. Finally, the magnetic susceptibility data of compound **2** can be calculated by Eq. (11), as a sum of independent contributions from Mn(II) and Cu(II) paramagnetic ions with molecular field correction.

$$\chi = \frac{Ng_{\mathrm{Mn}}^2\beta^2}{3kT} S_{\mathrm{Mn}}(S_{\mathrm{Mn}}+1) + \frac{Ng_{\mathrm{Cu}}^2\beta^2}{3kT} S_{\mathrm{Cu}}(S_{\mathrm{Cu}}+1) \qquad (11)$$

Least-squares fitting gives exact values of the g_{Cu}, g_{Mn} and zJ' parameters and confirms our expectations. This fully confirms the magnetization versus field dependence at 2 K illustrated in Fig. 5. In such a case, the ground state is $S_{\max} = 1/2 + {}^5/_2 = {}^6/_2$ and the magnetization (per Cu–Mn unit) should saturate to the value of $M = 6\mu_{\mathrm{B}}$. Experimental data show that at a magnetic field $B = 5$ T and temperature as low as $T = 2.0$ K, the magnetization M is equal 5.82 μ_{B}, very close to the theoretical value. This fact evidences a very small role of the zero-field splitting effect.

It is interesting to compare the magnetic behavior of complex **2** with the results obtained for the $[CuL]_2[Mn(NCS)_4](ClO_4)_2$ trimer (L = *N*-dl-5,5,7,1212,14-hexamethyl-1,4,8,11-tetraazacyclotetradeca-4,11-diene) [20]. The differences in the crystalline structures of the two complexes have a significant influence on the values of the magnetic properties. A partial conversion of the macrocyclic ring conformation in the trimer is caused by increasing the number of methyl groups in the macrocyclic rings. As a consequence of the methyl group in a Cu–Mn–Cu trimer block, one of the axial sites at the CuL^{2+} ion is occupied and only one vacant site at the central cooper(II) ion is available. The macrocyclic ion, with a Cu^{II} magnetic center, is only linked by a thiocyanate bridge to one Mn unit to form a ferromagnetically interacting trimer structure, very much different from the chain structure in compound **2**. Also the change of bond lengths and valence angles, (e.g., the Cu–S distances in **1** are 2.9486(8) and 2.841(1) Å in the trimer, and the Mn–N lengths are 2.204(3) and 2.075(2) Å in the trimer) seem to play a role. These results suggest that when the Cu–S distances increase, the magnitude of the exchange coupling constant decreases, as expected for a weak overlap of the magnetic orbitals.

It is also worthwhile to compare the magnitude of the intrachain exchange parameter in the reported binuclear Cu(II)–M(II) species, containing the same bridging and terminal ligands but different M(II) ions. The literature data for similar $Cu^{II}Ni^{II}$[11] and $Cu^{II}Mn^{II}$ [16,17] complexes suggest that, according to Kahn's theory [2], the J_{CuM} parameter can be related to the contributions from pairs of magnetic orbitals by $J_{\mathrm{CuM}} = \left(\sum_{\mu} J_{\mu b_1}\right) n_{\mathrm{M}}$, where n_{M} is the number of magnetic orbitals around M, b_1 stands for the symmetry of the unique magnetic orbitals ($d_{x^2-y^2}$) around Cu, and μ for the symmetry of the magnetic orbital around M. The magnetic orbital for the bimetallic systems will be as follows:

$$J_{\mathrm{CuNi}} = \frac{1}{2}(J_{b_1b_1} + J_{a_1b_1})$$

$$J_{\mathrm{CuMn}} = \frac{1}{5}(J_{b_1b_1} + J_{a_1b_1} + J'_{a_1b_1} + J_{a_2b_1} + J_{b_2b_1})$$

where $J_{b_1b_1}$ are the magnetic orbitals located in the plane of the bridging network with the predominant antiferromagnetic contribution, dependent on M. Mn(II) and Ni (II) ions are 3d transition metals. The 3d orbital energy for Mn is higher than for Ni. This is because of the increase of the nuclear charge. A lower 3d energy means a smaller energy gap between the singly occupied 3d orbital of M and the symmetry adapted orbital of the bridging ligand. On the other hand, the M–N distance also decreases. Both effects result in an increasing overlap between the b_1 – type magnetic orbitals of Cu and M because of an increase of delocalization of the magnetic orbital from M towards the bridge. As a consequence, the antiferromagnetic contribution $J_{b_1b_1}$ also increases. In complexes **1** and **2**, a stronger antiferromagnetic exchange reaction is observed for the $Cu^{II}Ni^{II}$ compound than for that of $Cu^{II}Mn^{II}$.

3.3. EPR spectra

The EPR spectrum of a polycrystalline sample of complex **1** at 293 shows an isotropic signal at $g = 2.041$ with a peak-to-peak linewidth of 75 G (Fig. 7). Only one other signal at $g = 2.042$ ($\delta_{\mathrm{Hpp}} = 80$ G) is observed at 77 K. The EPR spectrum at 4.2 K is composed of two lines at $g = 2.091$ and 2.218. The structure is associated only with the electronic configuration ($S = 1/2$) of the cooper centers in an octahedral ligand field.

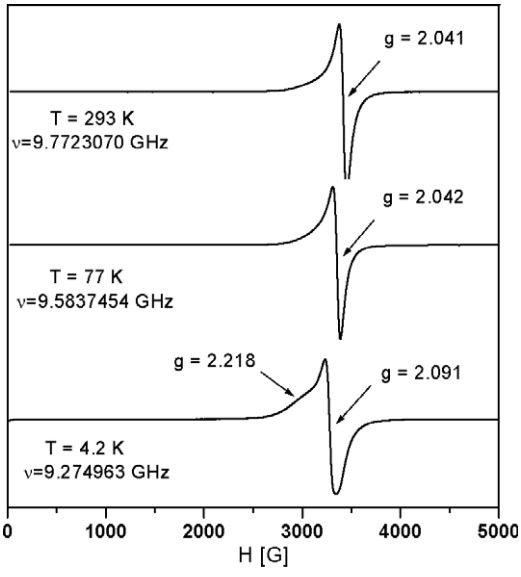


Fig. 7. EPR spectra for $\{CuL_\alpha[Ni(NCS)_4(H_2O)_2]\}$ at room temperature, 77 K and 4.2 K.

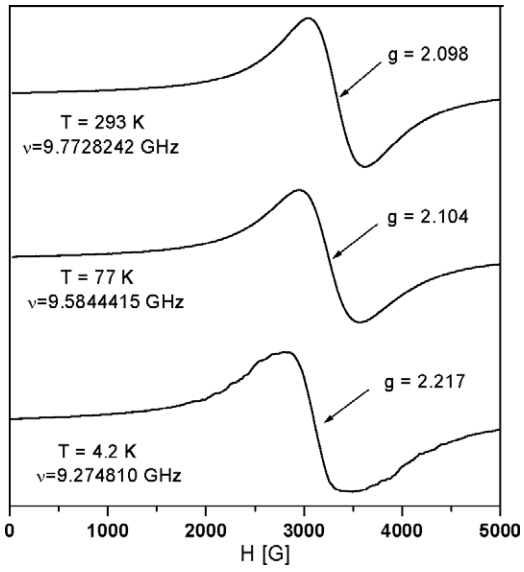


Fig. 8. EPR spectra for $\{CuL_\alpha[Mn(NCS)_4(H_2O)_2]\}$ at room temperature, 77 K and 4.2 K.

The EPR spectrum of a polycrystalline powdered sample of **2** at 293 K shows an isotropic line at $g = 2.098$ with a peak-to-peak linewidth of 575 G (Fig. 8). At 77 K the spectrum displays the same isotropic line at $g = 2.104$, but with a larger peak-to-peak linewidth amounting to 610 G. These results suggest that in the temperature range from 77 to 293 K only one signal is observed as a result of superposition of copper(II) and manganese(II) signals. At 4.2 K the fine structure consists of the stronger asymmetric line at $g = 2.217$ ($\delta_{Hpp} = 730$ G).

4. Conclusion

We would like to finish the present work with a brief comment on its chemical relevance. Up until now only a few $Mn^{II}Cu^{II}$ [21,22] and $Ni^{II}Cu^{II}$ [11] ordered bimetallic chains have been described. In these complexes, the metals ions were connected by dithiooxalato or oxalate bridges. The magnetic behaviour of these compounds is different from that of **1** and **2** (for example, the presence of a minimum and maximum in the $\chi_M T$ versus T plot). The differences result from the fact that the dithiooxalato or oxalate ligands are more efficient than the thiocyanide bridge in transmitting the antiferromagnetic interactions between the two metal ions. Complexes **1** and **2** are apparently very poor one-dimensional systems and the minimum of the $\chi_M T$ versus T plot is quenched by the interchain interactions. The dominant interchain interactions in **1** and **2** correspond to the shortest metal···metal interchain distances, i.e., $Cu^{II}Cu^{II}$, $Mn^{II}Mn^{II}$ and $Ni^{II}Ni^{II}$. Although being further apart from each other, the chains can interact through a hydrogen bond network. Additionally, in complex **2** a larger D value than J indicates a dominant zero-field splitting with the $S = 1$ local ground states of the Ni(II) ions.

Supplementary material

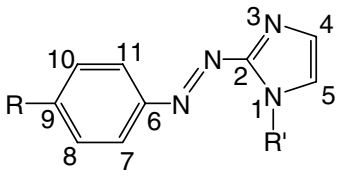
CCDC 288834 and 288835 contain the supplementary crystallographic data for **1** and **2**. These data can be obtained free of charge via http://www.ccdc.cam.ac.uk/conts/retrieving.html, or from the Cambridge Crystallographic Data Centre, 12 Union Road, Cambridge CB2 1EZ, UK; fax: (+44) 1223 336 033; or e-mail: deposit@ccdc.cam. ac.uk.

Acknowledgement

This work was financially supported by the Polish Ministry of Science and Higher Education (Grant No. 1 T09A12430 and 3 T09A 018 28).

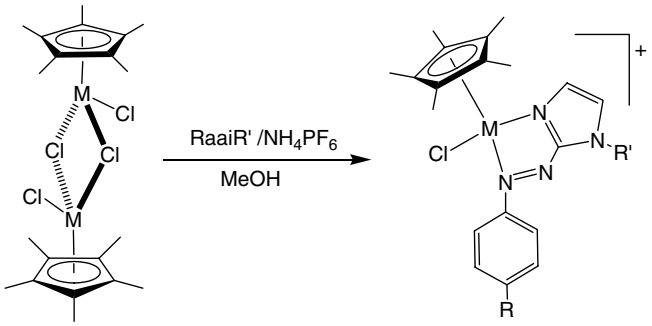
References

[1] O. Kahn (Ed.), Magnetism: A Supramolecular Function, NATO ASI Series, vol. C484, Kluwer Academic Publishers, Dordrecht, 1996.
[2] O. Kahn, Molecular Magnetism, VCH, New York, 1993.
[3] G. Francese, S. Ferlay, H.W. Schmalle, S. Decurtins, New J. Chem. (1999) 267.
[4] S. Ferlay, T. Mallah, J. Vaissermann, F. Bartolomé, P. Veillet, M. Verdaguer, Chem. Commun. (1996) 2481.
[5] J. Mrozinski, J. Bull. Acad. Polon.: Chim. 26 (1978) 789.
[6] E. König, Magnetic Properties of Coordination and Organometallic Transition Metal Compounds, Springer-Verlag, Berlin, 1966.
[7] Oxford Diffraction, CrysAlis CCD and CrysAlis RED. Oxford Diffraction Poland, Wrocław, Poland, 2001.
[8] G.M. Sheldrick, Acta Crystallogr. Sect., A 46 (1990) 467.
[9] G.M. Sheldrick, SHELXL93. Program for the Refinement of Crystal Structures, University of Göttingen, Germany.
[10] A.J.C. Wilson (Ed.), International Tables for Crystallography, vol. C, Kluwer, Dordrecht, 1992.
[11] M. Verdaguer, M. Julve, A. Michalowicz, O. Kahn, Inorg. Chem. 22 (1983) 2624.
[12] J. Girerd, M. Verdaguer, O. Kahn, Inorg. Chem. 19 (1980) 274.
[13] W. Hiller, J. Strähle, A. Datz, M. Hanack, W.E. Hatfield, L.W. ter Haar, P. Gütlich, J. Am. Soc. 106 (1984) 329.
[14] J. Samuel Smart, Effective Field Theories of Magnetism, W.B. Saunders Comp., Philadelphia and London, 1966.
[15] E. Calacio, I.B. Maimoun, F. Lloret, J. Suarez-Varela, Inorg. Chem. 44 (2005) 3771.
[16] H.-Z. Kou, D.-Z. Liao, P. Cheng, Z.-H. Jiang, S.-P. Yan, G.-L. Wang, X.-K. Yao, H.-G. Wang, Can. J. Chem. 76 (1998) 1102.
[17] B. Chiari, O. Piovesana, P.F. Zanazzi, Inorg. Chem. 34 (1995) 2652.
[18] C.J. O'Connor, Prog. Inorg. Chem. 29 (1982) 203.
[19] M.L. Kirk, M.S. Lah, C. Raptopoulou, D.P. Kessissoglou, W.E. Hatfield, L. Pecoraro, Inorg. Chem. 30 (1991) 3900.
[20] A. Bieńko, J. Kłak, J. Mroziński, R. Boča, I. Brüdgam, H. Hartl, J. Chem. Soc., Dalton Trans. (2007) 2681.
[21] A. Gleizes, M. Verdaguer, J. Am. Chem. Soc. 103 (1981) 7373.
[22] M. Verdaguer, A. Gleizes, J. Renard, P. Seiden, J. Phys. Rev. B: Conndens. Matter 29 (1984) 514.



R, R' = H (Pai-H)
R, R' = H, CH_3 (Phai-Me)
R, R' = H, C_2H_5 (Phai-Et)
R, R' = CH_3, H (Tai-H)
R, R' = CH_3 (Tai-Me)
R, R' = CH_3, C_2H_5

Scheme 1.



M = Rh, Ir

R, R' = H; M = Rh (**1**), M = Ir (**7**)
R, R' = H, CH_3; M = Rh (**2**), M = Ir (**8**)
R, R' = H, C_2H_5; M = Rh (**3**), M = Ir (**9**)
R, R' = CH_3, H; M = Rh (**4**), M = Ir (**10**)
R, R' = CH_3; M = Rh (**5**), M = Ir (**11**)
R, R' = CH_3, C_2H_5; M = Rh (**6**), M Ir (**12**)

Scheme 2.

synthesis of cyclopentadienyl ruthenium [11], indenyl-ruthenium [12] and arene-ruthenium [13] complexes with a variety of nitrogen-based ligands. However, the analogous pentamethylcyclopentadienyl rhodium(III) and iridium(III) azo complexes have not been explored as much as the corresponding isoelectronic cyclopentadienyl and arene-ruthenium(II) complexes. As a part of our continuing study, we would like to report herein the syntheses and characterization of new cationic pentamethylcyclopentadienyl rhodium(III) and iridium(III) complexes with N,N-donor arylazoimidazole ligands.

2. Results and discussion

1-Methyl-2-(arylazo)imidazole (aai-Me), 1-ethyl-2-(arylazo)imidazole (aai-Et) and 2-(arylazo)imidazole (aai-H) were synthesized by coupling the aryldiazonium ions with imidazole in aqueous sodium carbonate solution (pH 7) and purified by the reported method [26]. The alkylation was carried out by adding alkyl halide in dry THF solution to the corresponding 2-(arylazo)imidazole in the presence of sodium hydride [14].

Six arylazoimidazole (RaaiR′) (see Scheme 1) ligands have been used in this work. Ligands are unsymmetrical N,N′-bidentate chelates, where N and N′ abbreviated to N (imidazole) and N′ (azo) donor centers, respectively. The pentamethylcyclopentadienyl rhodium and iridium dimers $[\{(\eta^5\text{-}C_5Me_5)M(\mu\text{-}Cl)Cl\}_2]$ where M = Rh and Ir reacted with arylazoimidazoles (RaaiR′) in the presence of ammonium salts in methanol to form mononuclear cationic complexes having the general formula $[(\eta^5\text{-}C_5Me_5)MCl(RaaiR')]^+$ (C_5Me_5 = pentamethylcyclopentadienyl; M = Rh or Ir) (Scheme 2). The cationic complexes **1**–**6** are orange, while the complexes **7**–**12** are brown in colour. These complexes are non-hygroscopic, air-stable, shiny crystalline solids. They are sparingly soluble in methanol and benzene, soluble in dichloromethane, chloroform, acetone, acetonitrile, and insoluble in hexane, petroleum ether and diethyl ether.

The analytical data of these complexes are consistent with the formulations (Table 1). The formation of cationic complexes **1**–**6** and **7**–**12** are confirmed by the appearance of the strong band at around 840 cm^{-1} due to the $\nu_{(P-F)}$ of the PF_6^- anion. The bands appearing at around 1600 and 1400 cm^{-1} are assigned for $\nu_{(C=N)}$ and $\nu_{(N=N)}$, respectively, of the ligand [15].

The ^1H NMR spectrum of complexes shows a singlet for the pentamethylcyclopentadienyl protons in the range 1.38–1.71 ppm, indicating downfield shift from the starting dimeric complexes. A downfield shift in the position of the pentamethylcyclopentadienyl protons might result from a change in electron density on the metal center due to chelation of the arylazoimidazole ligand through its nitrogen atoms. The N–H proton of complexes **1**, **4**, **7** and **10** is exhibited a singlet in the range 8.2–9.2 ppm. The N-methyl protons (N-Me) of complexes **2**, **5**, **8** and **11** appear as a singlet at 3.82–4.19 ppm. The N-methylene proton (N-CH_2) of complexes **3**, **6**, **9** and **12** appears as a quartet in the range 4.14–4.55 ppm. All these complexes show doublet and multiplet in the range of 5.75–7.96 ppm due to the phenyl protons of the azoimine ligand.

The ^{31}C $\{^1H\}$ NMR spectrum of complexes **1**–**6** and **7**–**12** contain resonances for the pentamethylcyclopentadienyl ring carbons at around 90 ppm. The resonance observed at 155 ppm may be due to the azoimine (C=N) carbon of the ligand. The spectra also show resonances in the range of 122.1–162.2 ppm for the aromatic carbons and carbons of imidazole C–H group.

2.1. Electronic spectra

The low spin d^6 configuration of the mononuclear complexes provides filled orbitals of proper symmetry, which can interact with low lying π^* orbitals of the arylazoimidazole ligands (RaaiR′). A band attributable to the MLCT ($t_{2g} \rightarrow \pi^*$) transition is therefore expected in the electronic spectra [16], where the transition energy of these bands varies with the nature of the ligands acting as π-acceptors. The presence of electron donating groups (H, CH_3, C_2H_5) on the imidazole nitrogen of the azoimine ligand should decrease the energy of transition, causing a red shift in

Table 1
Analytical,[a] FT IR, ^{1}H NMR[b] and ^{13}C NMR of complexes [**1**–**12**][PF_6]

Complex	Analyses (%)			IR (KBr pellets (cm^{-1}))	^{1}H NMR δ [multiplicity, nH, J (Hz)]	^{13}C NMR (δ)
	C	H	N			
1	38.6 (38.5)	3.9 (3.9)	9.4 (9.3)	3204 (ν_{N-H}), 1639 ($\nu_{C=N}$), 1434 ($\nu_{N=N}$), 844 (ν_{P-F})	1.38 (s, 15H, C_5Me_5), 6.97 (d, 2H, $^{3}J = 7.5$ Hz, Ph), 7.32–7.53 (m, 3H, Ph), 7.69 (d, 1H, $^{3}J = 6.4$ Hz, CH), 8.24 (d, 1H, CH), 9.21 (s, 1H, NH)	8.96, 96.47, 122.41, 124.36, 127.32, 129.49, 131.16, 134.90, 151.18
2	39.7 (40.0)	4.2 (4.2)	9.3 (9.1)	1633 ($\nu_{C=N}$), 1427 ($\nu_{N=N}$), 850 (ν_{P-F})	1.47 (s, 15H, C_5Me_5), 3.24 (s, 3H, CH_3), 7.47 (d, 2H, $^{3}J = 6.4$ Hz, Ph), 7.52–7.77 (m, 3H, Ph), 8.02 (d, 1H, $^{3}J = 7.2$ Hz, CH), 8.46 (d, 1H, CH)	8.91, 40.13, 92.92, 122.13, 126.42, 127.47, 130.27, 135.56, 142.55, 156.17
3	40.8 (40.8)	4.4 (4.3)	9.1 (9.1)	1633 ($\nu_{C=N}$), 1434 ($\nu_{N=N}$), 844 (ν_{P-F})	1.32 (s, 15H, C_5Me_5), 1.46 (t, 3H, $^{3}J = 4.5$ Hz, CH_3), 4.42 (q, 2H, CH_2), 7.07 (d, 2H, $^{3}J = 6.2$ Hz, Ph), 7.15–7.32 (m, 3H, Ph), 7.47 (d, 1H, $^{3}J = 6.1$ Hz, CH), 7.84 (d, 1H, CH)	8.91, 16.14, 44.16, 98.14, 122.19, 125.32, 127.62, 128.72, 133.74, 139.92, 146.11
4	39.7 (39.9)	4.2 (4.3)	9.3 (9.2)	3423 (ν_{N-H}), 1600 ($\nu_{C=N}$), 1447 ($\nu_{N=N}$), 850 (ν_{P-F})	1.71 (s, 15H, C_5Me_5), 2.53 (s, 3H, CH_3), 6.79 (d, 2H, $^{3}J = 6.1$ Hz, Ph), 6.93 (d, 2H, Ph), 7.58 (d, 1H, $^{3}J = 6.8$ Hz, CH), 7.99 (d, 1H, CH), 8.16 (s, 1H, NH)	9.26, 15.79, 86.19, 124.68, 127.38, 130.92, 131.17, 133.12, 136.19, 142.36
5	40.8 (40.6)	4.4 (4.4)	9.1 (9.2)	1606 ($\nu_{C=N}$), 1447 ($\nu_{N=N}$), 844 (ν_{P-F})	1.39 (s, 15H, C_5Me_5), 2.14 (s, 3H, CH_3), 3.42 (s, 3H, CH_3), 7.18 (d, 2H, $^{3}J = 6.8$ Hz, Ph), 7.42 (d, 2H, Ph), 7.71 (d, 1H, $^{3}J = 4.4$ Hz, CH), 8.24 (d, 1H, CH)	8.90, 22.46, 42.34, 97.16, 126.32, 127.41, 130.67, 132.31, 136.31, 141.46, 152.56
6	41.8 (41.7)	4.6 (4.4)	8.9 (8.9)	1626 ($\nu_{C=N}$), 1434 ($\nu_{N=N}$), 849 (ν_{P-F})	1.48 (t, 3H, $^{3}J = 6.9$ Hz, CH_3), 1.53 (s, 15H, C_5Me_5), 2.45 (s, 3H, CH_3), 4.55 (q, 2H, CH_2), 7.52 (d, 2H, $^{3}J = 8.4$ Hz, Ph), 7.86 (d, 2H, Hz, Ph), 8.01 (d, 1H, CH), 8.26 (d, 1H, CH)	9.31, 16.09, 21.76, 43.93, 99.21 124.22, 129.11, 130.59, 131.03, 144.79, 150.30, 155.01
7	33.6 (33.5)	3.4 (3.4)	8.2 (8.5)	3151 (ν_{N-H}), 1619 ($\nu_{C=N}$), 1467 ($\nu_{N=N}$), 850 (ν_{P-F})	1.47 (s, 15H, C_5Me_5), 7.13 (d, 2H, $^{3}J = 8.2$ Hz, Ph), 7.22–7.49 (m, 3H, Ph), 7.82 (d, 1H, $^{3}J = 8.1$ Hz, CH), 8.47 (d, 1H, CH), 9.12 (s, 1H, NH)	8.90, 92.86, 123.74, 124.29, 129.93, 130.42, 130.53, 133.17, 152.99
8	34.6 (34.4)	4.2 (4.3)	8.1 (8.2)	1633 ($\nu_{C=N}$), 1434 ($\nu_{N=N}$), 844 (ν_{P-F})	1.53 (s, 15H, C_5Me_5), 3.36 (s, 3H, CH_3), 7.69 (d, 2H, $^{3}J = 6.9$ Hz, Ph), 7.78–7.82 (m, 3H, Ph), 7.98 (d, 1H, CH), 8.30 (d, 1H, CH)	8.92, 39.89, 93.20, 124.46, 129.67, 130.01, 133.63, 151.68, 152.96, 160.96
9	35.6 (35.4)	3.8 (3.9)	7.9 (8.0)	1626 ($\nu_{C=N}$), 1440 ($\nu_{N=N}$), 844 (ν_{P-F})	1.36 (s, 15H, C_5Me_5), 1.52 (t, 3H, $^{3}J = 6.1$ Hz, CH_3), 4.26 (q, 2H, CH_2), 7.13 (d, 2H, $^{3}J = 7.3$ Hz, Ph), 7.23–7.41 (m, 3H, Ph), 7.53 (d, 1H, $^{3}J = 7.14$ Hz, CH), 7.91 (d, 1H, CH)	8.92, 14.13, 42.46, 94.36, 124.61, 126.52, 127.37, 130.49, 135.18, 146.63, 155.23
10	34.6 (34.6)	4.2 (4.6)	8.1 (8.7)	2925 (ν_{N-H}), 1606 ($\nu_{C=N}$), 1394 ($\nu_{N=N}$), 850 (ν_{P-F})	1.50 (s, 15H, C_5Me_5), 2.46 (s, 3H, CH_3), 7.46 (d, 2H, $^{3}J = 8.4$ Hz, Ph), 7.71 (d, 2H, Ph), 7.89 (d, 1H, $^{3}J = 10.6$ Hz, CH), 8.71 (d, 1H, CH), 9.07 (s, 1H, NH)	8.93 21.63, 92.65, 124.38, 127.47, 130.17, 130.32, 143.95, 150.93, 162.19
11	35.6 (35.4)	3.8 (3.7)	7.9 (7.9)	1633 ($\nu_{C=N}$), 1434 ($\nu_{N=N}$), 844 (ν_{P-F})	1.41 (s, 15H, C_5Me_5), 2.06 (s, 3H, CH_3), 3.53 (s, 3H, CH_3), 7.09 (d, 2H, $^{3}J = 6.4$ Hz, Ph), 7.44 (d, 2H, Ph), 7.68 (d, 1H, $^{3}J = 6.1$ Hz, CH), 8.09 (d, 1H, CH)	8.97, 21.37, 44.08, 99.42, 122.28, 125.37, 128.14, 130.36, 133.18, 139.92, 148.74
12	36.6 (36.6)	4.0 (4.1)	7.8 (7.7)	1637 ($\nu_{C=N}$), 1434 ($\nu_{N=N}$), 844 (ν_{P-F})	1.38 (s, 15H, C_5Me_5), 1.43 (t, 3H, $^{3}J = 5.4$ Hz, CH_3), 2.26 (s, 3H, CH_3), 4.44 (q, 2H, CH_2), 7.31 (d, 2H, $^{3}J = 6.6$ Hz, Ph), 7.82 (d, 2H, Ph), 8.14 (d, 1H, $^{3}J = 5.6$ Hz, CH), 8.32 (d, 1H, CH)	9.18, 15.69, 22.43, 46.15, 97.43, 123.72, 125.36, 128.93, 130.83, 133.68, 142.39, 152.35

[a] Calculated values are in parentheses.
[b] In $CDCl_3$; s, singlet; d, doublet; m, multiplet; $J_{(H-H)}$ in Hz.

Table 2
UV–Visible absorption data in dichloromethane at 298 K

Sl. no.	Complexes	λ_{max} (nm)			
1	$[(\eta^5\text{-}C_5Me_5)RhCl(Phai\text{-}H)]PF_6$	415	326		
2	$[(\eta^5\text{-}C_5Me_5)RhCl(Phai\text{-}Me)]PF_6$	407	370	358	
3	$[(\eta^5\text{-}C_5Me_5)RhCl(Phai\text{-}Et)]PF_6$	410	391	364	335
4	$[(\eta^5\text{-}C_5Me_5)RhCl(Tai\text{-}H)]PF_6$	423	365	313	
5	$[(\eta^5\text{-}C_5Me_5)RhCl(Tai\text{-}Me)]PF_6$	665	406	364	311
6	$[(\eta^5\text{-}C_5Me_5)RhCl(Tai\text{-}Et)]PF_6$	408	395	312	
7	$[(\eta^5\text{-}C_5Me_5)IrCl(Phai\text{-}H)]PF_6$	414	388	321	
8	$[(\eta^5\text{-}C_5Me_5)IrCl(Phai\text{-}Me)]PF_6$	446	393	316	
9	$[(\eta^5\text{-}C_5Me_5)IrCl(Phai\text{-}Et)]PF_6$	452	375	309	
10	$[(\eta^5\text{-}C_5Me_5)IrCl(Tai\text{-}H)]PF_6$	436	397	317	
11	$[(\eta^5\text{-}C_5Me_5)IrCl(Tai\text{-}Me)]PF_6$	407	333	311	
12	$[(\eta^5\text{-}C_5Me_5)IrCl(Tai\text{-}Et)]PF_6$	407	333	311	

MLCT maxima [17], while an electron withdrawing group should increase the transition energy. The electronic spectra of pentamethylcyclopentadienyl rhodium azoimine complexes (**1**–**6**) with the formulations $[\eta^5\text{-}C_5Me_5RhCl(RaaiR')]^+$ displayed very weak bands at 408–423 nm, a medium absorption band at ~390 nm and a very strong absorption band at ~330 nm (Table 2). The band at 390 nm has been assigned to a MLCT transitions [t_{2g} {Rh(III) → π*(azoimine)}]. The λ_{max} value of this band is consistent with those of the azoimine ligand bound to the complexes of rhodium [18].

The free ligand itself shows intraligand charge-transfer transitions (n–π*, π–π*) of high intensity ($\varepsilon \sim 10^4$–$10^5\ M^{-1}\ cm^{-1}$) at <400 nm. The transitions at ~350 nm and below are thus not considered further. Other two transitions at longer wavelength region (410–460 nm and 370–390 nm) differ in their intensities. The first transition (410–460 nm) is of moderate intensity and has been assigned to the MLCT band dπ(Rh) → π*(azoimine) in the complexes [19] or else from the hybrid orbitals composed of dπ(Rh) and π(Cp*) to the π*(azoimine) orbitals of the ligand. The weak transition at ~650 nm may originate from a singlet–triplet transition, particularly that allowed by the strong spin–orbit coupling in rhodium [20].

Electronic spectra of iridium complexes (**7**–**12**) display bands in the region ~450 nm, ~380 nm and ~320 nm. The broad medium intensity bands centering around 450 nm are assigned to MLCT bands arising from drift of electron density from the filled Ir(III) → dπ(t_{2g}) orbitals to the low lying π* orbitals of the RaaiR′ ligand. The position of this band is consistent with those in other metal-azo complexes [21]. The band around 320 nm is assigned to an MLCT transition [Ir(III) → dπ* on the Cp* ring].

2.2. Molecular structure of complex $[(\eta^5\text{-}C_5Me_5)RhCl(Me\text{–}C_6H_4\text{–}N{=}N\text{–}C_3H_3N_2)]^+$ (**4**)

The complex **4**[PF_6] crystallizes in the monoclinic $P2_1/n$ space group. The ORTEP drawing of the molecule along with the atom-numbering scheme is shown in Fig. 1. The asymmetric unit consists of a rhodium atom displaying

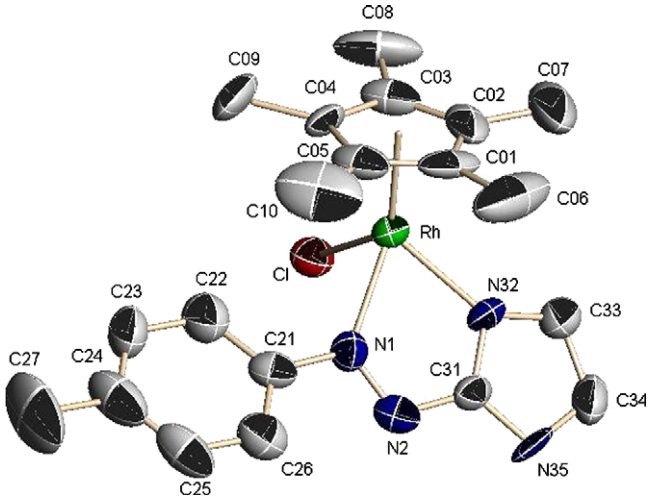


Fig. 1. ORTEP diagram of complex **4** at 50% probability level with hydrogen atoms and hexafluorophosphate anion omitted for clarity. Selected bond lengths (Å) and bond angles (°): Rh–N(1) 2.132(7), Rh–N(32) 2.105(8), Rh–Cl 2.423(3), N(1)–N(2) 1.275(10), Rh–C* 1.795 (* centroid is at $x = 0.7413$, $y = 0.1825$, $z = 0.9899$ at 1.795 Å to Rh); N(1)–Rh–N(32) 74.9(3), N(1)–Rh–Cl 92.5(2), N(32)–Rh–Cl 86.9(2).

the three-legged 'piano-stool' geometry. The metal is coordinated to one $\eta^5\text{-}C_5Me_5$ group, one chloride and two nitrogen atoms of Tai-H which binds to the metal in a bidentate chelating mode, as postulated from experimental data.

The pentamethylcyclopentadienyl ligand is symmetrically bound to the metal ion. All the Cp* atoms lie in a plane, and indicated by the similar bond distances between carbons. The Rh–Cl bond length is 2.432(3) Å which is slightly longer than the other two-coordinated chelating Schiff base rhodium complex $[(\eta^5\text{-}C_5Me_5)RhCl(C_5H_4N\text{-}2\text{-}CH{=}N\text{–}C_6H_4\text{-}p\text{-}Cl)]^+$ [2.3756(7) Å] [22].

The Rh–N distances are unequal with Rh–N(1), 2.132(7) Å and Rh–N(32), 2.105(8) Å. This has been observed in other complexes involving bidentate rhodium terpyridine $[(\eta^5\text{-}C_5Me_5)RhCl(Ph\text{-}terpy)]BF_4$ [23]. Rhodium to pentamethylcyclopentadienyl ring centroid distance is 1.759 Å and is consistent with those reported for the other rhodium(III) Cp* complexes [22]. The bond angles N(1)–Rh–Cl and N(32)–Rh–Cl are 92.5(2) and 86.9(2), respectively, indicating a piano stool type of structure at rhodium center. The N=N bond distance, N(1)–N(2) is 1.275(10) Å which is longer than free ligand value [1.250(1) Å] [24]. This refers to significant charge delocalization from metal d-orbital, dπ(Rh) → π*(azo) in the coordinated Tai-H.

3. Experimental

3.1. General remarks

$[\{(\eta^5\text{-}C_5Me_5)M(\mu\text{-}Cl)Cl\}_2]$ (M = Rh, Ir) [25] and arylazoimidazole (RaaiR′) ligands [26] were prepared according to published methods. All other reagents were

commercially available and were used as received. UV/visible absorption spectra were recorded on a Hitachi – 300 spectrophotometer using precision cells made of quartz (1 cm). The ^{1}H and ^{13}C $\{^{1}H\}$NMR spectra were recorded in $CDCl_3$ solvent with TMS as internal standard and recorded on JEOL 500 (500 MHz) or Bruker ACF-300 (300 MHz) spectrometers, the coupling constants J are given in Hz. Infrared spectra were recorded as KBr pellets on a Perkin–Elmer-model-983 spectrophotometer. Microanalyses were performed on a Perkin–Elmer-2400 CHN/O analyzer, SAIF-NEHU, Shillong, India.

3.2. Synthesis of $[(\eta^5\text{-}C_5Me_5)RhCl(L)]PF_6$ {L = Phai-H (1), Phai-Me (2), Phai-Et (3), Tai-H (4), Tai-Me (5), Tai-Et (6)}

A mixture of $[(\eta^5\text{-}C_5Me_5)RhCl_2]_2$ (100 mg, 0.16 mmol), arylazoimidazole (RaaiR′) (0.36 mmol) and potassium hexafluorophosphate (0.41 mmol) was stirred in dry methanol (20 mL) at 0 °C for 3 h. The solution becomes clear before the product precipitates. After 3 h the orange solid precipitated and the product was filtered, washed with diethylether (3 × 10 ml) and then dried *in vacuo* to afford 70–80% yield of the complexes.

3.3. Synthesis of $[(\eta^5\text{-}C_5Me_5)IrCl(L)]PF_6$ {L = Phai-H (7), Phai-Me (8), Phai-Et (9), Tai-H (10), Tai-Me (11), Tai-Et (12)}

These compounds was prepared by the same procedure as described above for [**1**–**6**][PF_6] using $[(\eta^5\text{-}C_5Me_5)Ir(\mu\text{-}Cl)(Cl)]_2$ (100 mg, 0.125 mmol), arylazoimidazole (RaaiR′) (0.26 mmol) and potassium hexafluorophosphate (0.41 mmol). Brown solid, Yield 65–75%.

4. Structure analysis and refinement

X-ray quality crystals of the complex **4**[PF_6] were grown by slow diffusion of hexane into dichloromethane solution. An orange crystal of complex **4**[PF_6] was mounted on a Bruker Apex CCD diffractometer in a full reciprocal sphere equipped with CCD detector and used for data collection. X-ray intensity data were collected with graphite monochromated Mo Kα radiation (0.71073 Å) at 293(2) K, with 0.3° scans in ω scan in mode and 10 s per frame. The intensity data were corrected for Lorentz and polarization effects. An empirical absorption correction was made by modeling a transmission surface by spherical harmonics employing equivalent reflections with $I > 2\sigma(I)$ (program SADABS) [27]. The structure was solved by direct methods [28]. All the non-hydrogen atoms were refined anisotropically using the full-matrix, least-squares technique on F^2 using the SHELXL-97 software [29]. All the hydrogen atoms were found from difference Fourier synthesis after four cycles of anisotropic refinement using a ''riding'' model. A summary of crystal data, data collection parameters and convergence results is compiled in Table 3.

Table 3
Crystal data and structure refinement for complex **4**[PF_6]

Empirical formula	$C_{20}H_{25}ClF_6N_4PRh$
Formula weight	604.77
Temperature (K)	293(2)
Wavelength (Å)	0.71073
Crystal system	Monoclinic
Space group	$P21/n$
Unit cell dimensions	
a (Å)	8.386(9)
b (Å)	27.72(3)
c (Å)	10.717(12)
β (°)	91.11(2)
Volume (Å^3)	2491(5)
Z	4
D_{calc} (Mg/m^3)	1.613
Absorption coefficient (mm^{-1})	0.917
$F(000)$	1216
Crystal size (mm)	0.15 × 0.10 × 0.07
θ Range for data collection (°)	1.47–28.26
Index ranges	$-9 \leqslant h \leqslant 9$, $-35 \leqslant k \leqslant 17$ $-13 \leqslant l \leqslant 4$
Reflections collected	7814
Independent reflections [R_{int}]	4514 [0.0796]
Completeness to theta (°, %)	28.26, 73.2
Absorption correction	Empirical
Refinement method	Full-matrix least-squares on F^2
Data/restraints/parameters	4514/0/284
Goodness-of-fit on F^2	0.999
Final R indices [$I > 2\sigma(I)$]	$R_1 = 0.0791$, $wR_2 = 0.1360$
R indices (all data)	$R_1 = 0.1839$, $wR_2 = 0.1696$
Largest difference peak and hole (e Å^{-3})	0.657 and −0.513

Appendix A. Supplementary material

CCDC 272064 contains the supplementary crystallographic data for **4**[PF_6]. These data can be obtained free of charge via http://www.ccdc.cam.ac.uk/conts/retrieving.html, or from the Cambridge Crystallographic Data Centre, 12 Union Road, Cambridge CB2 1EZ, UK, fax: (+44) 1223-336-033, or e-mail: deposit@ccdc.cam.ac.uk. Supplementary data associated with this article can be found, in the online version, at doi:10.1016/j.poly.2007.07.007.

References

[1] (a) P.M. Maitlis, J. Organomet. Chem. 500 (1995) 239;
(b) E.W. Abel, F.G.A. Stone, G. WilkinsonSir (Eds.), Comprehensive Organometallic Chemistry II: A Review of the Literature, vol. 8, 1982–1994, p. 175.
[2] (a) C. Joubran, D.B. Grotjahn, J.L. Hubbard, Organometallics 15 (1996) 1230;
(b) E. Carmona, A. Cingolani, F. Marchetti, C. Pettinari, R. Pettinari, B.W. Skelton, A.H. White, Organometallics 22 (2003) 1820;
(c) T. Steinke, C. Gemel, M. Cokoja, M. Winter, R.A. Fischer, Chem. Commun. 9 (2003) 1066;
(d) I. Ara, J.R. Berenguer, E. Eguizabal, J. Fornies, E. Lalinde, A. Martin, Eur. J. Inorg. Chem. 6 (2001) 1631.
[3] (a) T.C. Higgis, M. Helliwell, C.D. Carner, J. Chem. Soc., Dalton Trans. (1996) 2101;

(b) J. Abe, Y. Shirai, J. Am. Chem. Soc. 118 (1996) 4705;
(c) C. Tejel, B.F. Villiarroya, M.A. Ciriano, A. Oro, M. Lanfranchi, A. Tiripicchio, M.T. Camellini, Inorg. Chem. 35 (1996) 4360.
[4] (a) M. Melnik, L. Macaskova, C.E. Holloway, Coord. Chem. Rev. 126 (1993) 71;
(b) R. Rajan, R. Rajaram, B.U. Nair, T. Ramasami, S.K. Mondal, J. Chem. Soc., Dalton Trans. (1996) 2019.
[5] S. Belanger, A.L. Beauchamp, Inorg. Chem. 35 (1996) 7836.
[6] (a) C. Anderson, A.L. Beauchamp, Inorg. Chem. 34 (1995) 6065;
(b) A. Hatzidimitriou, A. Gourdon, J. Devillers, J.-P. Launay, E. Mena, E. Amouyal, Inorg. Chem. 35 (1996) 2212;
(c) B.K. Keppler, D. Wehe, H. Endres, N. Rupp, Inorg. Chem. 26 (1987) 8440.
[7] (a) J. Dinda, D. Das, P.K. Santra, C. Sinha, L.R. Falvello, J. Organomet. Chem. 629 (2001) 28;
(b) J. Dinda, S.K. Jasimuddin, G. Mostafa, C.-H. Hung, C. Sinha, Polyhedron 23 (2004) 793.
[8] U.S. Ray, S.K. Jasimuddin, B.K. Ghosh, M. Monfort, J. Ribas, G. Mostafa, T.-H. Lu, C. Sinha, Eur. J. Inorg. Chem. (2004) 250.
[9] (a) U.S. Ray, D. Banerjee, J.-C. Liou, C.-N. Lin, T.-H. Lu, C. Sinha, Inorg. Chim. Acta 358 (2005) 1019;
(b) J. Dinda, U. Ray, G. Mostafa, T.-H. Lu, A. Usman, I.A. Razak, S. Chantrapromma, H.-K. Fun, C. Sinha, Polyhedron 22 (2003) 247;
(c) J.K. Nag, P.K. Santra, C. Sinha, F.-L. Liao, T.-H. Lu, Polyhedron 20 (2001) 2253.
[10] (a) P. Govindaswamy, C. Sinha, M.R. Kollipara, J. Organomet. Chem. 690 (2005) 3465;
(b) P. Govindaswamy, P.J. Carroll, C. Sinha, Mohan Rao Kollipara, J. Coord. Chem. 60 (2007) 97.
[11] R. Lalrempuia, P. Govindaswamy, Y.A. Mozharivskyj, Mohan Rao Kollipara, Polyhedron 23 (2004) 1069.
[12] Mohan Rao Kollipara, E.K. Rymmai, Polyhedron 22 (2003) 307.
[13] (a) P. Govindaswamy, Y.A. Mozharivskyj, Mohan Rao Kollipara, J. Organomet. Chem. 689 (2004) 3265;
(b) P. Govindaswamy, H.P. Yennawar, Mohan Rao Kollipara, J. Organomet. Chem. 689 (2004) 3108;
(c) P. Govindaswamy, P.J. Carroll, Y.A. Mozharivskyj, Mohan Rao Kollipara, J. Organomet. Chem. 690 (2005) 885;
(d) P. Govindaswamy, Y.A. Mozharivskyj, Mohan Rao Kollipara, Polyhedron 23 (2004) 3115.
[14] D. Das, M.K. Nayak, C. Sinha, Transit. Met. Chem. 22 (1997) 172.
[15] (a) N. Nag, G.K. Lahiri, A. Chakravorty, Inorg. Chem. 31 (1992) 40;
(b) G.K. Lahiri, S. Goswami, L.R. Falvello, A. Chakravorty, Inorg. Chem. 26 (1987) 3365.
[16] (a) H.-K. Fun, K. Chinnakali, X.-F. Chen, X.-H. Zhu, X.-Z. You, Acta Crystallogr. 25 (1999) 99;
(b) B.K. Ghosh, A. Chakravorty, Coord. Chem. Rev. 95 (1989) 239;
(c) P. Byabartta, S.K. Jasimuddin, B.K. Ghosh, C. Sinha, A.M.Z. Slawin, J.W. Woollins, New J. Chem. 26 (2002) 1415.
[17] (a) A.G. Del, V. Morena, N.E. Katz, J. Olabe, P.J. Aymonino, Inorg. Chim. Acta 35 (1979) 183;
(b) D.W. Herlocker, R.S. Drago, V.I. Meek, Inorg. Chem. 5 (1966) 2009;
(c) D.K. Lavallee, M.D. Baughman, M.P. Phillips, J. Am. Chem. Soc. 99 (1977) 718.
[18] (a) A.P. Szecsy, S.S. Millen, A. Haim, Inorg. Chim. Acta 28 (1978) 189;
(b) A. Mishra, K. Mishra, U.C. Agarwala, Polyhedron 9 (1990) 863.
[19] (a) J. Dinda, D. Das, P.K. Santra, C. Sinha, L.R. Falvello, J. Organomet. Chem. 629 (2001) 28;
(b) S. Pal, D. Das, C. Sinha, C.H.L. Kennard, Inorg. Chim. Acta 313 (2001) 21.
[20] E.M. Kobler, T.J. Meyer, Inorg. Chem. 21 (1982) 3967.
[21] I. Chakraborty, S. Sengupta, S. Das, S. Banerjee, A. Chakravorty, J. Chem. Soc., Dalton Trans. (2003) 134.
[22] P. Govindaswamy, Y.A. Mozharivskyj, M.R. Kollipara, Polyhedron 24 (2005) 1710.
[23] H. Aneetha, P.S. Zacharias, B. Srinivas, G.H. Lee, Y. Wang, Polyhedron 18 (1999) 299.
[24] H.-K. Fun, K. Chinnakali, X.-F. Chen, X.-H. Zhu, X.-Z. You, Acta Crystallogr. 25 (1999) 99.
[25] (a) J.W. Kang, K. Moseley, P.M. Maitlis, J. Am. Chem. Soc. 91 (1969) 5970;
(b) R.G. Ball, W.A.G. Graham, D.M. Heinekey, J.K. Hoyano, A.D. McMaster, B.M. Mattson, S.T. Michel, Inorg. Chem. 29 (1990) 2023;
(c) C. White, A. Yates, P.M. Maitlis, Inorg. Synth. 29 (1992) 228.
[26] T.K. Misra, D. Das, C. Sinha, P.K. Ghosh, C.K. Pal, Inorg. Chem. 37 (1998) 1672.
[27] XRD Single crystal software, Bruker Analytical X-ray systems, Madison, USA, 2002.
[28] G.M. Sheldrick, SHELXS 86, Program for Crystal Structure Solution, University of Göttengen, Göttengen, Germany, 1986.
[29] M. Sheldrick, SHELXS 97, Program for Crystal Structure Refinement, University of Göttengen, Göttengen, Germany, 1997.

observed only in films consisting of a mixture of monoclinic grains and the amorphous phase, but not in films having a triclinic phase structure. In this connection, there have been some works that were devoted to structural studies of evaporated PbPc films [21,22].

Substituted lead phthalocyanines are not so thoroughly investigated as compared to the unsubstituted Pb(II)Pc. Non-peripheral 1,4,8,11,15,18,22,25-octakis(hexylsulfanyl)phthalocyanine has been synthesized and characterized by X-ray crystallography in the work of Cook and co-workers [10]. Furthermore, non-peripheral tetraalkoxy [16], tetra- and octa-diethoxymalonyle substituted [17], (cumylphenoxy) [12] tetranitro- and tetraamino substituted [18] lead phthalocyanines were synthesized and characterized. The first mesomorphic lead phthalocyanines were reported in 1987 [11,19]. Simon and co-workers [11] have shown that alkoxymethyl substituted phthalocyaninato lead(II) complexes [$PbPcR_8$, with $R = -CH_2OC_nH_{2n+1}$ ($n = 8$, 12, 18)] form a hexagonal columnar mesophase, which is stable at room temperature when $n = 8$ and 12; since then Ford et al. indicated that octa-(2-ethylhexyloxy) lead phthalocyanines exist in mesophases from −100 to +200 °C [13–15]. These derivatives have been alkoxy [13–15] and alkoxy methyl [11] octasubstituted mesogens with side chains substituted at the 2,3-positions on the benzene ring, but mesomorphic alkylthio-substituted lead pc compounds have not been synthesized yet.

In this work, the synthesis of new octakis (alkylthio)-substituted lead phthalocyanines (**1a** and **2a**) is described. The mesogenic properties of these new materials are studied by differential scanning calorimetry and optical microscopy. The preparation of thin films of these phthalocyanines and their investigation by the method of UV–Vis absorption spectroscopy are also reported. The current–voltage characteristics and electrical switching behaviour in the sandwich structures of Au/$PbPcR_8$ (**1a**)/Au are also discussed.

2. Experimental

2.1. Materials

1,2-Di(13,17-dioxanonacosane-15-sulfanylmethyl) phthalonitrile (**1**) [23] and 1,2-di(13,17-dioxanonacosane-15-sulfanyl) phthalonitrile (**2**) [24] were synthesized according to the reported procedures. All other reagents and solvents were reagent-grade quality, obtained from commercial suppliers and were dried as described by Perrin and Armarego [25] before use.

2.2. Measurements

Elemental analyses were obtained from a Thermo Finnigan Flash 1112. Infrared spectra in KBr pellets were recorded on a Bio-Rad FTS 175C FT-IR spectrophotometer. Optical spectra in the UV–Vis region were recorded with a UV–Vis-3101PC Shimadzu using 1 cm pathlength cuvettes at room temperature. Mass spectra were obtained from an Esquire 6000 Ion Trap LC/MS(n)-System (Bruker Daltonik GmbH). ^1H and ^{13}C NMR spectra were recorded in $CDCl_3$ solutions on a Varian 500 MHz spectrometer. A domestic microwave oven ARÇELİK, model MD 272 (max. 850 W, min. 60 W) with five select power levels was used to carry out the synthesis with the microwave. The phase transition behaviour of these compounds was observed by means of a polarizing microscope (Leitz Wetzler Orthoplan-pol.) equipped with a hot stage (Linkam TMS 93) and temperature-controller (Linkam LNP). Transition temperatures were determined with a scan rate of 5 °C min^{-1} using a Mettler Toledo Star^e Thermal Analysis System/DSC 822^e. A differential scanning calorimeter system was calibrated with indium from 3 to 4 mg samples under a nitrogen atmosphere.

2.3. Synthesis

2.3.1. 2,3;9,10;16,17;23,24-Octakis(13,17-dioxanonacosane-15-sulfanylmethyl) phthalocyaninato lead (II) (*1a*)

2.3.1.1. Method A. A round-bottomed flask fitted with a condenser was degassed and flame-dried under dry argon. The flask was charged under argon with 1,2-di(13,17-dioxanonacosane-15-sulfanylmethyl) phthalonitrile (**1**) (0.600 g, 0.576 mmol) and anhydrous Pb(II)O (0.064 g, 0.288 mmol). The mixture was heated at 210 °C with stirring under an argon atmosphere for 5 h without solvent. The reaction mixture was dissolved in chloroform then centrifuged and the precipitate, including inorganic impurities, was removed. Thus the inorganic impurities were eliminated. The solvent was evaporated and the crude product was passed through a Bio Beads column (Bio-Rad Laboratories) using CH_2Cl_2 as the eluent to eliminate organic impurities. This purification step was repeated two times. Purification was further achieved by preparative thin layer chromatography [silica gel; eluent CH_2Cl_2/*n*-hexane, 1:1 (v/v)]. Yield: 55 mg (9%).

*2.3.1.2. Method B (Microwave-assisted synthesis method for compound **1a**).* A mixture of dinitrile **1**, (0.300 g, 0.288 mmol), anhydrous Pb(II)O (0.032 g, 0.144 mmol), 1,8-diazabicyclo[5.4.0]undec-7-ene (DBU, 0.2 ml) and 2 ml *n*-pentanol was irradiated in a microwave (350 W) for 8 min. Compound **1a** was purified by the same procedure as described for method A. Yield: 60 mg (19%). *Anal.* Calc. for $C_{256}H_{464}N_8PbO_{16}S_8$ requires: C, 70.29; H, 10.69; N, 2.56. Found: C, 70.50; H, 10.43; N, 2.25%. IR (KBr) [υ, cm^{-1}] 3040, 2926, 2855, 1621, 1464, 1421, 1373, 1340, 1329, 1261, 1105. MS (APPI-MS), *m*/*z* (%): 4371 $[M + H]^+$ (100). ^1H NMR (500 MHz, $CDCl_3$): δ 0.87 (t, 48H, CH_3), 1.02–1.45 (m, 288H, CH_2), 1.60 (m, 32H, CH_2), 3.22–3.67 (m, 64H, OCH_2), 3.78 (t, 8H, CH), 4.70 (s, 16H, CH_2S), 9.53 (s, 8H, CH_{ar}). ^{13}C NMR (500 MHz, $CDCl_3$): δ 14.35 (CH_3), 22.94 (CH_2), 26.46 (CH_2), 29.51–32.18 (CH_2), 33.39–33.69 (CH_2), 38.72 (CH_2S), 46.18 (CH), 71.58

(OCH_2), 71.80 (CH_2O), 125.41 ($C_{ar}H$), 137.18 (C_{ar}), 139.75 (C_{ar}), 154.20 (C_{ar} C=N).

*2.3.2. 2,3;9,10;16,17;23,24-Octakis (13,17-dioxanonacosane-15-sulfanyl) phthalocyaninato lead (II) (**2a**)*

2.3.2.1. Method A. Compound **2a** was prepared by the same procedure as described for **1a** by starting with 1,2-di(13,17-dioxanonacosane-15-sulfanyl) phthalonitrile (**2**) (0.400 g, 0.394 mmol), and anhydrous Pb(II)O (0.043 g, 0.197 mmol). The reaction mixture was dissolved in chloroform then centrifuged, and the precipitate including inorganic impurities was removed. The solvent was evaporated and the crude product was passed through a Bio Beads column using CH_2Cl_2 as the eluent to eliminate organic impurities. Furthermore, this product was purified with preparative thin layer chromatography [silica gel, eluent CH_2Cl_2/*n*-hexane, 2:3 (v/v)]. Yield: 40 mg (10%).

*2.3.2.2. Method B (Microwave-assisted synthesis method for compound **2a**).* A mixture of dinitrile **2**, (400 mg, 0.394 mmol), anhydrous Pb(II)O (0.043 g, 0.197 mmol), 1,8-diazabicyclo[5.4.0]undec-7-ene (DBU, 0.3 ml) and 2.5 ml *n*-pentanol was irradiated in a microwave (350 W) for 8 min. Compound **2a** was purified by the same procedure as described for method A. Yield: 85 mg (20%). *Anal.* Calc. for $C_{248}H_{448}N_8PbO_{16}S_8$ requires: C, 69.89; H, 10.60; N, 2.63. Found: C, 70.10; H, 10.35; N, 2.53%. IR (KBr) [υ, cm^{-1}] 3040, 2950, 2855, 1600, 1460, 1370, 1330, 1120, 1105. MS (APPI-MS), *m*/*z* (%): 4259 $[M + H]^+$ (100). ^1H NMR (500 MHz, $CDCl_3$): δ 0.77 (t, 48H, CH_3), 1.05–1.34 (m, 288H, CH_2), 1.61 (m, 32H, OC–CH_2), 3.52 (t, 32H, OCH_2), 3.93 (d, 32H, CH_2O), 4.05 (m, 8H, CH), 9.42 (s, 8H, CH_{ar}). ^{13}C NMR (500 MHz, $CDCl_3$): δ 14.36 (CH_3), 22.91 (CH_2), 26.50 (CH_2), 29.58–30.05 (CH_2), 32.16 (CH_2), 48.12 (CH), 70.55 (OCH_2), 71.90 (O CH_2-CHS), 126.05 ($C_{ar}H$), 138.12 (C_{ar}), 140.60 (C_{ar}–S), 154.10 (C_{ar} C=N).

2.4. Film preparation and characterization

Small volumes of solutions of the derivatives **1a** and **2a** in chloroform (10 mg/ml) were dispensed via a glass pipette onto an ultrasonically cleaned substrate held onto a photoresist spinner (Microsystem model 4000). The speed of substrate rotation was 2000 rpm, and spinning was continued for 30 s during which time the solvent had evaporated to generate a film of the phthalocyanine derivative. Some films were annealed at 50 °C for 1 h in a nitrogen atmosphere for comparison with the as-deposited layers. The substrates used were varied according to the experimental requirements for different characterization.

Absorption spectra of the films on quartz substrates were recorded with a UV–Vis scanning spectrophotometer (UV–Vis-3101PC "Shimadzu") in the range 350–800 nm. Spectroscopic ellipsometric measurements on spun films on silicon substrates were performed by using a Woolam *TM V M* 2000 – rotating analyzer spectroscopic ellipsometer in the spectral range 370–1000 nm. The angle of incidence was fixed at 60°. Dedicated software was used for data acquisition and analysis of the measured ellipsometric parameters $\Psi(\lambda)$ and $\Delta(\lambda)$.

A silicon slide covered by an Au layer was used as a substrate for the measurements of conductivity. For electrical measurements on samples in the form of a sandwich structure, top electrodes of Au 100 nm in thickness were deposited by thermal evaporation in a vacuum of about 10^{-6} torr.

Current–voltage measurements were performed using a Keithley 236 electrometer in a microprocessor controlled measuring system. The bias voltage was taken to be positive when the bottom contact was at a higher voltage than the top electrode. All electrical measurements were performed in air at room temperature and at −10 °C. The *I*–*V* characteristics were recorded for two sweep directions (+V to −V and −V to +V) and also in voltage loops (0 to +V to −V to +V).

3. Results and discussion

3.1. Synthesis and general properties

Generally, substituted phthalocyanines are prepared by cyclotetramerization of substituted 1,2-dicyanobenzenes or 1,3-diimino-1H-isoindolines [26]. Fig. 1 shows the synthesis of the lead phthalocyanines (**1a** and **2a**). PbPc can be prepared by heating PbO or $Pb(OAc)_2$ with the respective phthalonitrile derivative without solvent [12–17] or in *n*-pentanol [16]. Addition of anhydrous lead(II) acetate to a solution of Li_2Pc or H_2Pc in anhydrous alcohol gives PbPc [16,27]. PbPc can also be obtained by a microwave method [18]. In this work, we performed melting and microwave methods to prepare the target PbPcs. Firstly cyclotetramerization of the dinitrile compounds was carried out in the presence of dried PbO without any solvent. In this method, we obtained the PbPcs in a low yield. Therefore, the synthesis of the desired PbPcs was carried out in *n*-pentanol and DBU by a microwave method. The yields using microwave irradiation were in all cases higher than that obtained with the classical method. Although the microwave technique has been used to synthesize other Pcs, this technique is fairly new for PbPcs. To the best of the authors' knowledge there has been only one publication about this so far [18]. To increase the yield of the pcs (**1a**, **2a**) we tried two experiments with different molar ratios, 4:1 and 2:1, and the 2:1 ratio of the dinitrile derivatives and PbO was found to be the most appropriate. Also, in the literature an excess of the lead salts was used for the synthesis of the lead pcs [11,13].

The crude product was firstly passed through a Bio Beads column for eliminating organic impurities and then the lead phthalocyanines (**1a** and **2a**) were purified by using preparative thin layer chromatography as quickly as

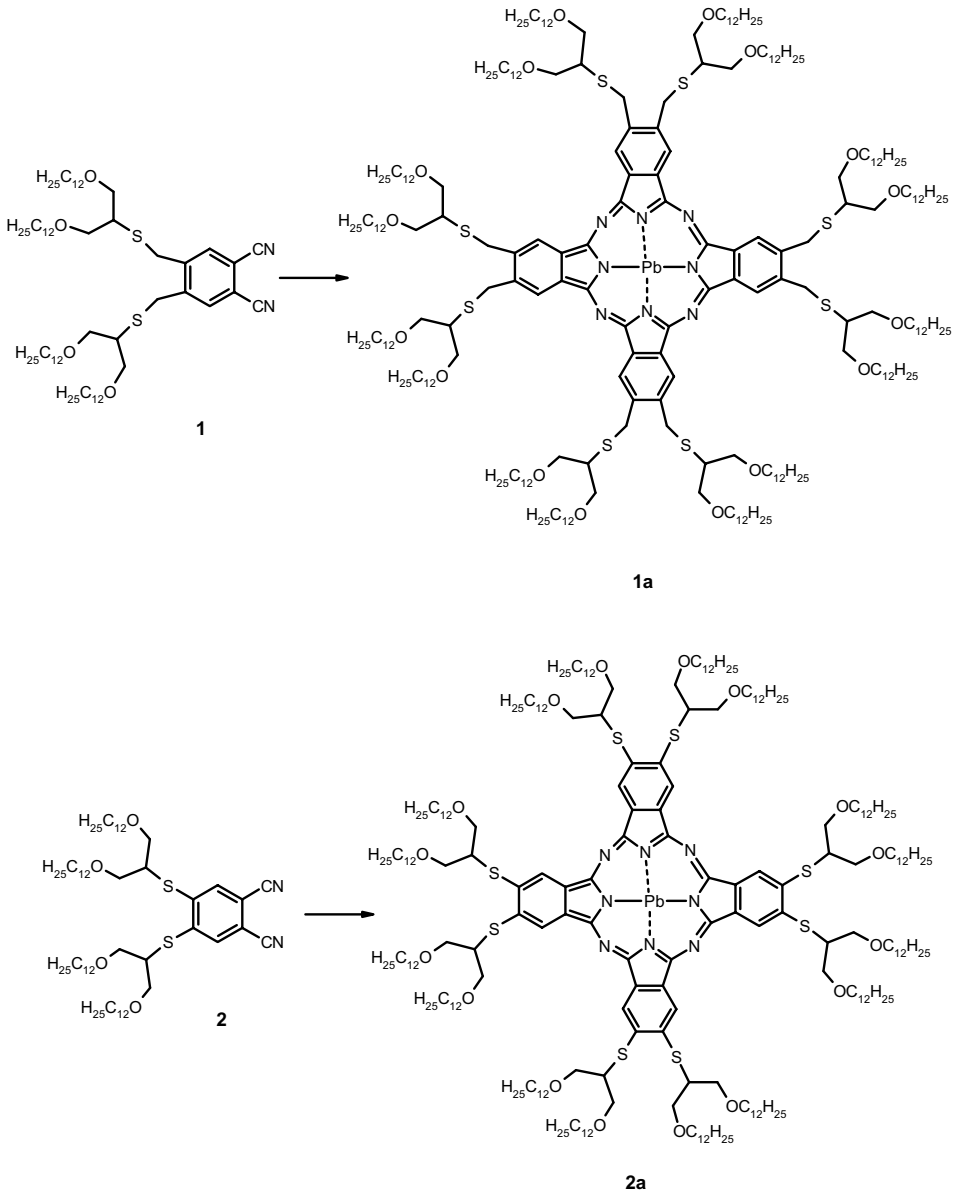


Fig. 1. Synthetic route of the compounds **1a** and **2a**.

possible because the PbPcs turned into the metal-free analogues on the preparative card. The intense brownish-green waxy products are very soluble in polar and non-polar solvents, such as chloroform, benzene, carbontetrachloride and tetrahydrofuran.

3.2. Spectroscopic characterization

The new (phthalocyaninato)lead complexes **1a** and **2a** were characterized by elemental analysis and various spectroscopic methods. The mass spectra of the phthalocyanines were obtained by the atmospheric pressure photoionization (APPI) technique and the full scan mass spectra of these compounds clearly showed intense signals for the protonated molecular ion $[M + H]^+$. The diamagnetic lead(II) compounds **1a** and **2a** gave well-resolved ^1H NMR spectra in $CDCl_3$. Fig. 2 shows the spectrum of **2a** in which there is one singlet at δ 9.42 for one set of the phthalocyanine ring protons. The aliphatic protons' signals can also be assigned unambiguously due to well-resolved multiplicity and integration of all the signals. The triplet at δ 4.05, the multiplet at δ 3.93 and the triplet at δ 3.52 are due to the CH, OCH_2 and CH_2O protons, respectively. Methyl group peaks belonging to the alkyl chain appeared as multiplets in the range δ 1.59–1.08. The ^1H NMR spectrum of compound **1a** shows similar spectral features except for a singlet peak at δ 4.70 ppm corresponding to Ar–CH_2.

In the ^{13}C NMR spectra of compounds **1a** and **2a**, the carbon atom of the N=C–N group in the phthalocyanine core could be assigned by comparison of the chemical shift measured with data reported in the literature [23,24].

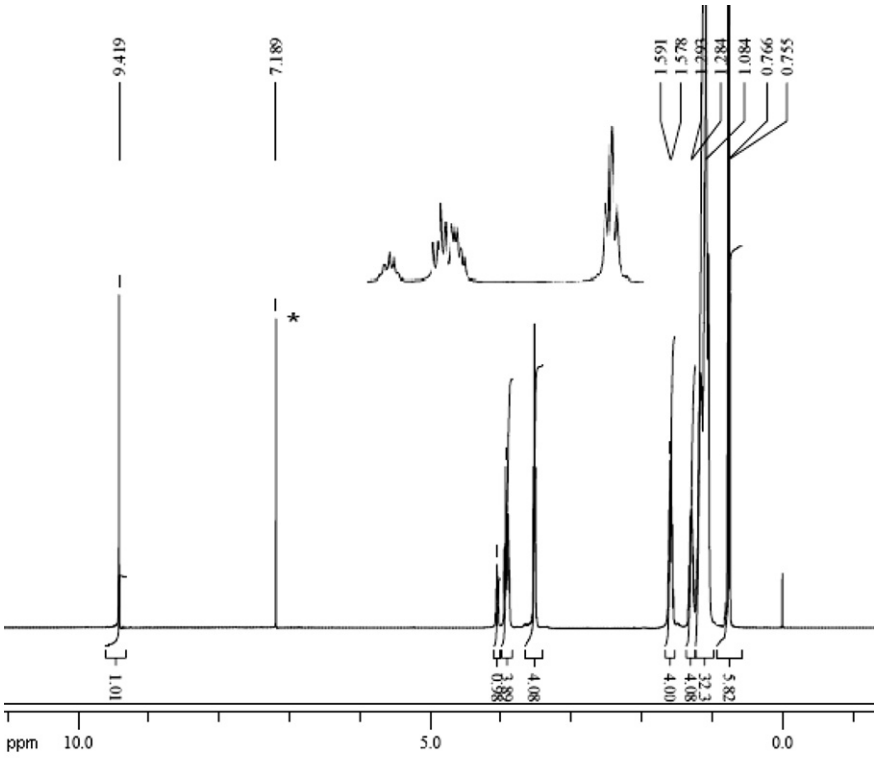


Fig. 2. ^{1}H NMR spectrum of **2a** in $CDCl_3$. The signal due to residue $CHCl_3$ is denoted as ∗.

^{13}C NMR spectra of the phthalocyanines show signals for four aromatic carbon atoms between ca. 125 and 154 ppm.

The IR spectral results of the phthalocyanine derivatives (**1a**, **2a**) are different from the phthalocyanine precursors **1** and **2**, so the sharp peak for the C≡N vibrations around 2220–2235 cm^{-1} associated with nitrile groups disappeared after phthalocyanine formation. In addition, a group of absorption bands were also seen in the range 2850–2955 cm^{-1} in the IR spectra of **1a** and **2a**. These can be attributed to the C–H stretching vibrations of the substituted alkyl chains.

In the electronic spectra of the Pcs, the phthalocyanine derivatives (**1a** and **2a**) show intense Q absorption bands above 700 nm (Figs. 4 and 5). The presence of methylene bridges in compound **1a**, distinct from **2a**, shifts the Q-band to a shorter wavelength by about 27 nm. The reason for the shifting to shorter wavelengths is that the methylene bridges reduce the electron releasing ability of the sulfur atoms to the pc core [23,24,28]. Furthermore, the effect of the central metal ion shows a shift of these intense Q-bands to higher wavelengths in comparison with their nickel and metal free derivatives [24].

3.3. The mesogenic properties of the PbPc complexes (*1a* and *2a*)

The phase transition temperatures were determined by differential scanning calorimetry (DSC). The DSC measurements were performed on the virgin materials with a scanning rate of 5 °C/min. Phase transition temperatures and the corresponding enthalpy changes of the PbPc complexes (**1a** and **2a**) are summarized in Table 1. The DSC measurements of **1a** and **2a** show a significant sharp peak in the vicinity of −10 °C which relates to an isotropic phase transition. The sharpness of the isotropic point gives an indication of the purity of the compound. No additional peaks are observed for compounds **1a** and **2a**, which excludes further phase transitions (see Table 1).

Also, the phase transition temperatures of the complexes (**1a** and **2a**) have been surveyed by polarization microscopy. The birefringence textures observed by polarizing optical microscopy were best observed by slowly cooling from the isotropic phase to the mesophase. The textures observed by microscopy for these studied complexes (**1a** and **2a**) are very similar to those described in the literature [23,24,29]. Fig. 3 shows the photomicrograph of the

Table 1
Phase transition temperatures and enthalpies for the compounds **1a** and **2a** as determined by DSC[a]

Compound	$T_{Col\ h \rightarrow I}$/°C [ΔH/kJ mol^{-1}]	
	Heating	Cooling
1a	−1.91 [115.25]	−9.26 [119.17]
2a	−9.62 [189.29]	−13.16 [177.99]

Heating and cooling rates: 5 °C, heating range: −50 to 100 °C.
[a] Phase nomenclature: Col_h = discotic hexagonal columnar mesophase, I = isotropic phase.

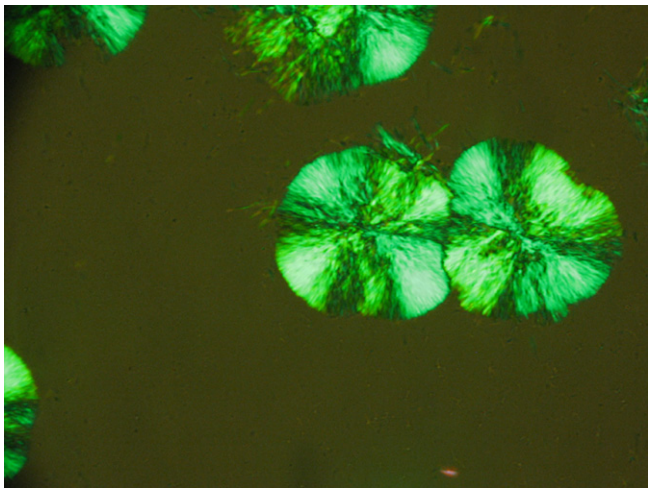


Fig. 3. Optical texture of **2a** at −20°C.

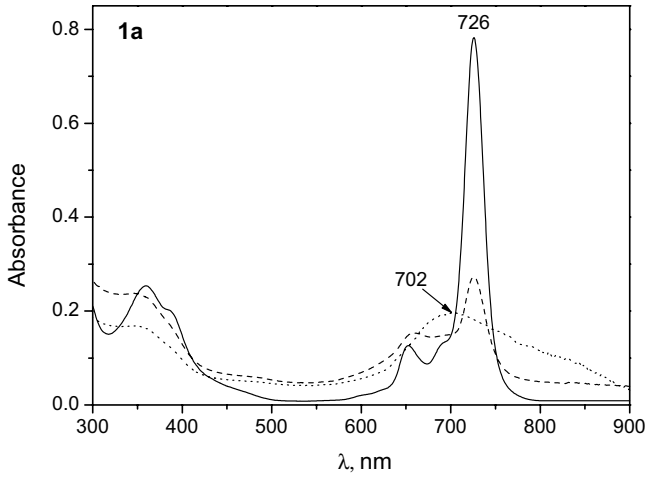


Fig. 4. Absorption spectra of **1a**: solutions in chloroform (——); films on quartz at room temperature (– – – – –) and slowly cooled down to −10 °C (· · · · · · · · ·).

mesophase of **2a** at −20 °C. This typical fan-shaped texture is often observed for Col_h, hence these mesophases could thus be confirmed as the Col_h phases [30–37].

In mesogen metalleted Pcs, Pb(II) sterically destabilizes the cofacial columnar structure and dramatically reduces both crystal-to-mesophase and mesophase-to-isotropic transition temperatures [1a]. A decrease in the clearing point temperatures was observed for the coordination of Pb^{2+} for **1a** and **2a** in comparasion with their Ni(II) and free derivatives [23,24]. Also, when compared to the influence of substition with alkylthiamethyl and alkylthia upon the mesomorphic properties of the Pc derivatives (**1a** and **2a**), the clearing point of **1a** subtituted with alkylthiamethyl was lower than that of **2a** subtituted with alkylthia. It could be seen that the addition of methylene bridges to the phthalocyanine core decreases the clearing point temperature as given in the literature [23,24]. According to the literature, the same behaviour was observed for the alkoxy and alkoxymethyl derivatives [14,15].

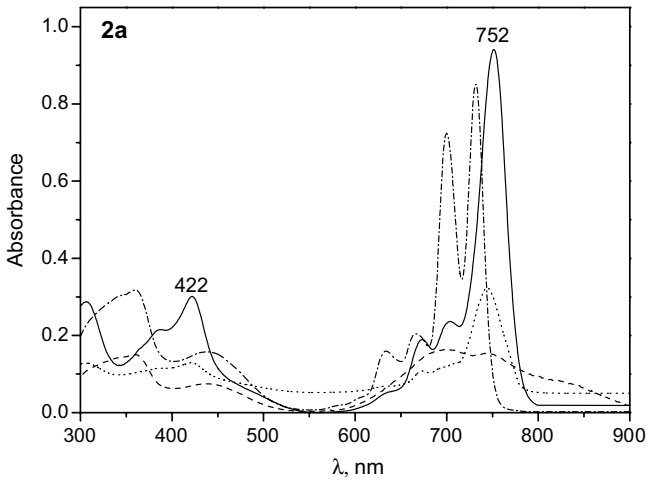


Fig. 5. Absorption spectra of **2a**: solutions in chloroform (——); films on quartz immediately after deposition (· · · · · · · · ·) and 3 h (– – – –) after deposition, and solution in chloroform obtained by washing away the films 3 h after deposition (–·–·–·).

3.4. Film investigation

The absorption spectra of **1a** and **2a** solutions in chloroform are presented in Figs. 4 and 5, respectively. The spectra of solutions are characterized by an intense electronic absorption in the visible region, with the Q-band at 726 and 752 nm for **1a** and **2a**, respectively. Compound **2a** is characterized by low chemical stability and loses the Pb^{2+} central ion during storage in chloroform in the room atmosphere after some hours to form the metal-free phthalocyanine (H_2Pc). It decomposes both in solution and in the form of a thin film. Fig. 5 shows the absorption spectra of the film of **2a** immediately after deposition and 3 h later. The loss of the Pb^{2+} central ion is clearly observed. This is further confirmed when the film was washed away by chloroform and the spectrum of the resulting solution was recorded. The splitting of the Q-band indicates the formation of H_2Pc [24,26]. Therefore, transformation of this derivative to the metal free phthalocyanine makes further investigation of **2a** films difficult.

Compound **1a** is characterized by a higher stability and does not lose the central metal at least for some weeks. Therefore the data of the electrical properties investigation are presented for thin films of compound **1a** only.

It has already been shown in a previous publication [37,38] that the slow cooling of phthalocyanines exhibiting mesogenic properties from the isotropic liquid leads to the formation of films with an ordered structure. These compounds are liquid at room temperature (Table 1). To obtain a film with an ordered structure, thin films of compound **1a** were slowly cooled from room temperature down to −10 °C. The absorption spectrum of **1a** film at room temperature, as well as at −10 °C, is given in Fig. 4. The spectrum for a solution of **1a** in chloroform is also included

for comparison. The absorption spectrum of the film at room temperature (Fig. 4, dashed line) is similar to that of the chloroform solution. The spectrum of **1a** film at −10 °C is completely different (Fig. 4, dotted line). Indeed, the position of the Q-band absorption provides good evidence for a change of the molecular ordering [39]. The broadened and blue-shifted Q-bands in the visible absorption spectra of the film provide good evidence for molecular ordering and indicate a stacking arrangement of the molecules in the film [40].

Unsubstituted lead phthalocyanine is known to have unique electronic properties which originate from its one dimensional structure. Earlier publications [20,41] reported an electrical switching effect in the film of unsubstituted PbPc of the monoclinic structure and suggested an electric field-induced order–disorder transition mechanism in the stacking direction.

It is therefore interesting to examine the electrical switching in thin films of substituted phthalocyanines. Sandwich structures of the type Au/PbPc (**1a**)/Au were prepared for the investigation of the electrical properties. *I–V* characteristics of Au/PbPc (**1a**)/Au have been recorded for two sweep directions; in the first case, the film was at room temperature and in the second case, the film was slowly cooled down to −10 °C. The Au/$PbPcR_8$ (**1a**)/Au structure, in which the film of PbPc (**1a**) is disordered at room temperature, shows *I–V* dependence close to symmetric with no switching effect being observed. A typical *I–V* curve for the structure cooled down slowly to −10 °C is shown in Fig. 6. The figure shows that when the dc bias was swept from a positive voltage ($V_{max} = 1$ V), the device current was very small for both polarities until about −0.9 V. The state of phthalocyanine can be termed as the OFF state, which then switches to the ON state at −1 V. During the sweep from negative voltage, PbPc retained the high-conducting ON state. When the device is in its OFF state, the shape of the *I–V* dependence is almost symmetric. In contrast to the OFF state, the ON state displays an asymmetrical *I–V* characteristic, thus suggesting that the charge injection is modified. The switching behaviour is asymmetric with a larger ON/OFF ratio (∼50) for negative voltage. The device could be cycled between the two states many times without degradation. This characteristic was stable for an applied bias between −1 V and +1 V. Exceeding those limits resulted in an irreversible transition to a lower resistance switching state. These molecular devices show repeatable switching and may be applicable to memory cells and other logic devices in the future. However, in order to get reproducible and reliable device characteristics it is very important to understand the basic transport mechanisms in these diodes and measure quantitative switching characteristics of the devices.

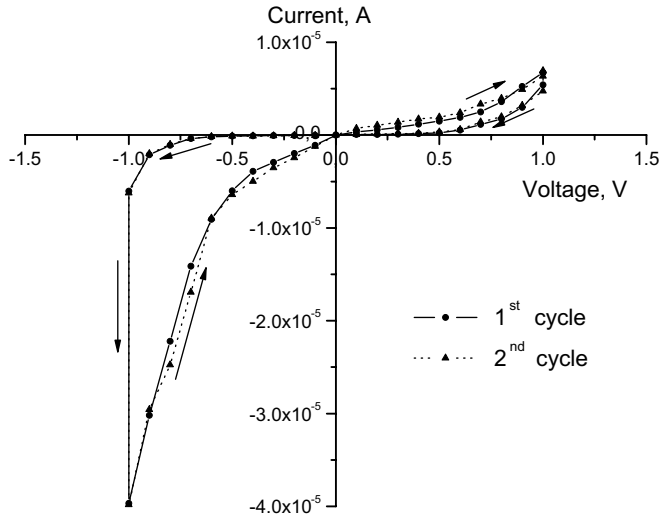


Fig. 6. *I–V* characteristics of the Au/$PbPcR_8$ (**1a**)/Au sandwich cell slowly cooled to −10 °C for two voltage sweeping directions (shown by arrows).

4. Conclusions

In this work, the synthesis of new mesomorphic octakis (alkylthio)-substituted phthalocyanines of Pb(II) were described, using microwave irradiation with higher yield and heating without solvent methods. The Pb(II) pcs were characterized using different spectroscopic techniques (NMR, UV–Vis, FT-IR and MS). The microwave technique is a fairly novel approach for the synthesis of lead phthalocyanines. These complexes are viscous waxy liquids at room temperature and form liquid crystalline phases in the vicinity of −10 °C. Compound **2a** loses Pb^{2+} during storage in atmosphere after some hours to form the metal-free phthalocyanine (H_2Pc). Compound **1a** is characterized by higher stability and loses the central metal ion after some weeks at least. The Au/PbPc (**1a**)/Au structure, in which the film of PbPc (**1a)** is disordered at room temperature, shows *I–V* dependence close to symmetric and does not display any switching effect. To obtain films with an ordered structure the film of **1a** was slowly cooled from room temperature down to −10 °C. It was shown that the slowly cooled Au/PbPc(**1a**)/Au structure shows repeatable and stable switching for applied bias voltages between −1 V and +1 V.

When Pc is substituted with alkylthiamethyl chains, the Q-band shifts to shorter wavelength and the clearing point temperatures decrease compared with alkylthia chains. Furthermore, the coordination of Pb^{2+} with the Pc core was responsible for lower the clearing temperature and Q band absorption occurring at longer wavelenghts for compounds **1a** and **2a**, compared with other derivatives.

References

[1] (a) N.B. McKeown, Phthalocyanine Materials: Synthesis, Structure, Function, Cambridge University Press, Cambridge, 1998;
(b) J. Simon, P. Bassoul, Design of Molecular Materials: Supramolecular Engineering, Wiley-VCH, Weinheim, Germany, 2000.
[2] R.D. Gould, T.S. Shafai, Thin Solid Films 373 (2000) 89.
[3] S. Ambily, F.P. Xavier, C.S. Menon, Mater. Lett. 41 (1999) 5.

[4] M.E. Azim-Araghi, D. Campbell, A. Krier, R.A. Collins, Semicond. Sci. Technol. 11 (1996) 39.
[5] K. Ukei, Acta Crystallogr. 29 B (1973) 2290.
[6] K. Ukei, J. Phys. Soc. Jpn. 40 (1976) 140.
[7] Y. Iyechika, K. Yakushi, I. Ikemoto, H. Kurado, Acta Crystallogr. B 38 (1982) 776.
[8] F. Przyborowski, C. Hamann, Cryst. Res. Technol. 17 (1982) 1041.
[9] T.L. Bluhm, H.J. Wagner, R.O. Loutfy, J. Mater. Sci. Lett. 2 (1983) 85.
[10] P.M. Burnham, M.J. Cook, L.A. Gerrard, M.J. Heeney, D.L. Hughes, Chem. Commun. (2003) 2064.
[11] C. Piechocki, J.C. Boulou, J. Simon, Mol. Cryst. Liq. Cryst. 149 (1987) 115.
[12] A.W. Snow, N.L. Jarvis, J. Am. Chem. Soc. 106 (1984) 4706.
[13] W.T. Ford, L. Sumner, W. Zhu, Y.H. Chang, P.-J. Um, K.H. Choi, P.A. Heiney, N.C. Maliszewskyj, New J. Chem. 18 (1994) 495.
[14] C. Piechocki, J. Simon, A. Skoulios, D. Gullion, P. Weber, J. Am. Chem. Soc. 104 (1982) 5245.
[15] J.F. Wan der Pol, E. Neeleman, J.W. Zwikker, R.J.M. Nolte, W. Drenth, J. Aerts, R. Wissers, S.J. Picken, Liq. Cryst. 5 (1989) 577.
[16] Y. Bian, L. Li, J. Dou, D.Y. Y Cheng, R. Li, C. Ma, D.K.P. Ng, N. Kobayashi, J. Jiang, Inorg. Chem. 43 (2004) 7539.
[17] H.A. Dinçer, H. Çerlek, A. Gül, M.B. Koçak, Main Group Chem. 4 (2005) 209.
[18] B.N. Achar, T.M.M. Kumar, K.S. Lokesh, J. Porphyr. Phthalocya. 9 (2005) 872.
[19] M. Hanack, A. Beck, H. Lehmann, Synthesis 8 (1987) 703.
[20] Y. Machida, Y. Saito, A. Taomoto, K. Nichogi, K. Waragai, S. Asakawa, Jap. J. Appl. Phys. 28 (1989) 297.
[21] A. Miyamoto, K. Nichogi, A. Taomoto, T. Nambu, M. Murakami, Thin Solid Films 256 (1995) 64.
[22] L. Ottaviano, L. Lozzi, A.R. Phani, A. Ciattoni, S. Santucci, S. DiNardo, Appl. Surf. Sci. 136 (1998) 81.
[23] A.G. Gürek, V. Ahsen, F. Heineman, P. Zugenmaier, Mol. Cryst. Liq. Cryst. 338 (2000) 75.
[24] D. Atilla, G. Aslıbay, A.G. Gürek, H. Can, V. Ahsen, Polyhedron 26 (2007) 1061.
[25] D.D. Perrin, W.L. Armarego, Purification of Laboratory Chemical, Pergamon Press, Oxford, 1980.
[26] C.C. Leznoff, in: C.C. Leznoff, A.B.P. Lever (Eds.), Phthalocyanines: Properties and Applications, vol. 1, VCH, Weinheim, 1989, p. 1 (Chapter 1).
[27] D. Wöhrle, M. Eskes, A. Shigehara, A. Yamada, Synthesis 2 (1993) 194.
[28] N. Kobayashi, H. Ogata, N. Nonaka, E.A. Luk'yanets, Chem. Eur. J. 9 (2003) 5123.
[29] K. Ban, K. Nishizawa, K. Ohta, A.M. van de Craats, J.M. Warman, I. Yamamoto, H. Shirai, J. Mater. Chem. 11 (2001) 321.
[30] A.M. van de Craats, J.M. Warman, H. Hasebe, R. Naito, K. Ohta, J. Phys. Chem. B 101 (1997) 9224.
[31] J. Sleven, C. Görller-Wallard, K. Binnemans, Mater. Sci. Eng. C 18 (2001) 229.
[32] F. Maeda, K. Hatsuska, K. Ohta, M. Kimura, J. Mater. Chem. 13 (2003) 243.
[33] H. Eichhorn, D. Wöhrle, D. Pressner, Liq. Cryst. 5 (1997) 643.
[34] K. Ban, K. Nishizawa, K. Ohta, H. Shirai, J. Mater. Chem. 10 (2000) 1083.
[35] A.G. Gürek, M. Durmuş, V. Ahsen, New J. Chem. 28 (2004) 693.
[36] T. Basova, E. Kol'tsov, A.K. Hassan, A. Nabok, A.K. Ray, A.G. Gürek, V. Ahsen, J. Mat. Sci. Mater. Electron. 15 (2004) 623.
[37] A.G. Gürek, T. Basova, D. Luneau, C. Lebrun, E. Kol'tsov, A. Hassan, V. Ahsen, Inorg. Chem. 4 (2006) 1667.
[38] T. Basova, A.G. Gürek, V. Ahsen, Mater. Sci. Eng. C 22 (2002) 99.
[39] B.M. Hassan, H. Li, N.B. McKeown, J. Mater. Chem. 10 (2000) 39.
[40] M. Kasha, H.R. Rawls, A. El-Bayoumi, Pure Appl. Chem. 11 (1965) 371.
[41] T. Frauenheim, C. Hamann, M. Müller, Phys. Status Solidi A 86 (1984) 735.

2. Experimental

2.1. General procedures

All air-sensitive manipulations, unless stated otherwise, were performed using standard Schlenk techniques under an atmosphere of high-purity argon or glovebox techniques. Toluene and *n*-hexane were dried by refluxing over sodium and benzophenone and distilled under argon prior to use. C_6D_6 was dried over activated 4 Å molecular sieves and vacuum-transferred to a sodium-mirrored air-free flask. $CDCl_3$ was dried over CaH_2 for 48 h and vacuum-transferred to an air-free flask. $ZnEt_2$ was purchased from Aldrich and used as received. The 7-amino-2,4-dimethylquinoline [10], 3,5-di-*tert*-butyl-2-hydroxyl-benzaldehyde [11a], 5-bromo-2-hydroxyl-benzaldehyde [11b] and 3,5-dibromo-2-hydroxyl-benzaldehyde [11c] were synthesized according to the literature methods. NMR spectra were measured using a Varian Mercury-300 or Bruker AVANCE-500 NMR spectrometer. IR spectra were recorded on a Nicolet Impact 410 FTIR spectrometer using KBr pellets. The elemental analyses were performed on a Perkin–Elmer 2400 analyzer. UV–Vis absorption spectra were recorded on a UV-3100 spectrophotometer. Fluorescent measurements were carried out on a RF-5301PC spectrophotometer. Mass spectra were recorded on an 1100 LC/MS system (Agilent Technology Corporation). All melting points were determined by an X-5 micro-melting point apparatus and are uncorrected.

2.2. General procedure for the salicylaldimine ligands

The condensation of salicylaldehydes with 1 equiv. of 7-amino-2,4-dimethylquinoline was carried out by refluxing the two reactants in ethanol for 8 h. Upon cooling the resulting reaction solution to room temperature, a yellow or orange-red solid precipitated from the solution. The solid product was filtered and washed with cold ethanol and then dried in vacuo to give the desired salicylaldimine ligand in excellent yields.

2.3. Synthesis of $C_{18}H_{16}N_2O$ (**1a**)

2-Hydroxyl-benzaldehyde (2.10 mL, 18.6 mmol) and 7-amino-2,4-dimethylquinoline (3.21 g, 18.6 mmol) in 35 ml of refluxing ethanol afforded 4.16 g of compound **1a** as a yellowish solid. Yield: 81%. m.p.: 137–138.6 °C. ES–MS (MeOH) *m/z*: 277.0 [$(M+1)^+$]. *Anal.* Calc. for $C_{18}H_{16}N_2O$ (276.33): C, 78.24; H, 5.84; N, 10.14. Found: C, 78.36; H, 5.77; N, 10.10%. ^{1}H NMR (300 MHz, $CDCl_3$, 298.3 K): δ (ppm) 2.70 (s, 3H, quinolyl-CH_3), 2.75 (s, 3H, quinolyl-CH_3), 6.97 (t, $J = 7.5$ Hz, 1H, aryl), 7.05 (d, $J = 7.5$ Hz, 1H, Ph-H), 7.15 (s, 1H, quinolyl-H), 7.39–7.44 (m, 2H, Ph-H), 7.51 (d, $J = 8.7$ Hz, 1H, quinolyl-H), 7.94 (s, 1H, quinolyl-H), 8.01 (d, $J = 8.7$ Hz, 1H, quinolyl-H), 8.77 (s, 1H, CH=N), 13.11 (s, 1H, OH).^{13}C NMR (75.4 MHz, $CDCl_3$, 298.3 K): δ (ppm) 18.6 (quinolyl-CH_3), 25.0 (quinolyl-CH_3), 117.2, 118.3, 119.2, 121.3, 122.6, 124.8, 125.4, 132.5, 133.5, 144.5, 148.1, 149.3 (quinolyl-7-C), 159.5 (Ph-2-C), 161.2 (quinolyl-2-C), 163.7 (CH=N). IR (KBr, cm^{-1}): υ 3377 (br) 3046 (w), 2984 (m), 2951 (m), 2921 (m), 1972 (w), 1926 (w), 1622 (s), 1605 (vs), 1574 (vs), 1514 (s), 1497 (vs), 1460 (s), 1372 (s), 1336 (m), 1284 (vs), 1259 (s), 1191 (vs), 1161 (vs), 1136 (s), 1030 (m), 1001 (w), 972 (m), 959 (w), 943 (m), 901 (m), 874 (vs), 826 (vs), 666 (m), 630 (m), 595 (w), 570 (w), 541 (w), 470 (m), 450 (w), 428 (w).

2.4. Synthesis of $C_{26}H_{32}N_2O$ (**1b**)

Similarly, 3,5-di-*tert*-butyl-2-hydroxybenzaldehyde (1.72 g, 7.36 mmol) and 7-amino-2,4-dimethylquinoline (1.27 g, 7.36 mmol) in 25 ml of refluxing ethanol afforded 2.36 g of complex **1b** as an orange solid. Yield: 85%. m.p.: 185.5–186.5 °C. ES–MS (DMSO) *m/z*: 389.2 [$(M+1)^+$]. *Anal.* Calc. for $C_{26}H_{32}N_2O$ (388.55): C, 80.37; H, 8.30; N, 7.21. Found: C, 80.29; H, 8.25; N, 7.23%. ^{1}H NMR (300 MHz, $CDCl_3$, 298.3 K): δ (ppm) 1.34 (s, 9H, $C(CH_3)_3$), 1.50 (s, 9H, $C(CH_3)_3$), 2.70 (s, 3H, quinolyl-CH_3), 2.75 (s, 3H, quinolyl-CH_3), 7.15 (s, 1H, Ph-H), 7.25 (s, 1H, Ph-H), 7.49–7.54 (m, 2H, quinolyl-H), 7.94 (s, 1H, quinolyl-H), 7.99 (d, $J = 8.7$ Hz, 1H, quinolyl-H), 8.80 (s, 1H, CH=N), 13.56 (s, 1H, OH). ^{13}C NMR (75.4 MHz, $CDCl_3$, 298.3 K): δ (ppm) 18.6 (quinolyl-CH_3), 24.9 (quinolyl-CH_3), 29.4 ($C(CH_3)_3$), 31.4 ($C(CH_3)_3$), 34.1 ($C(CH_3)_3$), 35.1 ($C(CH_3)_3$), 117.7, 118.3, 121.9, 122.4, 124.7, 125.2, 127.1, 128.5, 137.0, 140.8, 144.4, 148.4, 149.9 (quinolyl-7-C), 158.4 (Ph-2-C), 159.3 (quinolyl-2-C), 165.0 (CH=N). IR (KBr, cm^{-1}): υ 3493 (br), 2960 (m), 2912 (w), 2868 (w), 1603 (m), 1580 (s), 1509 (w), 1472 (w), 1438 (m), 1392 (w), 1369 (w), 1361 (w), 1378 (w), 1273 (w), 1251 (w), 1193 (w), 1168 (m), 1139 (w), 1029 (w), 1004 (w), 962 (w), 933 (w), 888 (m), 862 (w), 838 (w), 809 (w), 764 (w), 726 (w), 662 (w), 641 (w), 601 (w), 572 (w), 524 (w), 497 (w).

2.5. Synthesis of $C_{18}H_{15}BrN_2O$ (**1c**)

Similarly, 5-bromo-2-hydroxybenzaldehyde (0.92 g, 4.6 mmol) and 7-amino-2,4-dimethylquinoline (0.79 g, 4.6 mmol) in 35 ml of refluxing ethanol afforded 1.42 g of compound **1c** as an orange solid. Yield: 87%. m.p.: 177.7–178.7 °C. ES–MS (MeOH) *m/z*: 357.0 [$(M+1)^+$]. *Anal.* Calc. for $C_{18}H_{15}BrN_2O$ (355.23): C, 60.86; H, 4.26; N, 7.89. Found: C, 60.92; H, 4.16; N, 7.78%. ^{1}H NMR (300 MHz, $CDCl_3$, 298.3 K): δ (ppm) 2.72 (s, 3H, quinolyl-CH_3), 2.79 (s, 3H, quinolyl-CH_3), 6.95 (d, $J = 8.7$ Hz, 1H, Ph-H), 7.14 (s, 1H, Ph-H), 7.47–7.54 (m, 3H, quinolyl-H and Ph-H), 8.01–8.04 (m, 2H, quinolyl-H), 8.70 (s, 1H, CH=N), 13.10 (s, 1H, OH). ^{13}C NMR (75.4 MHz, $CDCl_3$, 298.3 K): δ (ppm) 18.9 (quinolyl-CH_3), 24.2 (quinolyl-CH_3), 110.7, 117.2, 119.3, 120.5, 122.0, 122.8, 123.1, 125.2, 125.4, 125.6, 134.6, 136.3, 159.0 (Ph-2-C), 160.3 (quinolyl-2-C), 162.8 (CH=N). IR

(KBr, cm^{-1}): υ 3444 (br), 3038 (w), 2967 (w), 2917 (m), 1896 (w), 1717 (w), 1601 (vs), 1555 (vs), 1511 (m), 1476 (s), 1449 (m), 1412 (m), 1370 (s), 1340 (s), 1281 (s), 1212 (m), 1195 (s), 1167 (vs), 1130 (m), 1092 (w), 1072 (w), 1028 (w), 993 (w), 955 (w), 935 (w), 897 (s), 859 (s), 824 (vs), 770 (m), 743 (w), 691 (w), 674 (m), 656 (s), 623 (m), 595 (w), 540 (m), 465 (w), 441 (w).

2.6. Synthesis of $C_{18}H_{14}Br_2N_2O$ (**1d**)

Similarly, 3,5-di-bromo-2-hydroxybenzaldehyde (2.37 g, 8.46 mmol) and 7-amino-2,4-dimethylquinoline (1.46 g, 8.46 mmol) in 35 ml of refluxing ethanol afforded 3.01 g of compound **1d** as an orange-red solid. Yield: 82%. m.p.: 174.7–175.7 °C. ES–MS (DMSO) *m/z*: 434.9 [$(M+1)^+$]. *Anal.* Calc. for $C_{18}H_{14}Br_2N_2O$ (434.12): C, 49.80; H, 3.25; N, 6.45. Found: C, 49.73; H, 3.20; N, 6.54%. ^{1}H NMR (300 MHz, $CDCl_3$, 298.3 K): δ (ppm) 2.72 (s, 3H, quinolyl-CH_3), 2.78 (s, 3H, quinolyl-CH_3), 7.47–7.54 (m, 3H, quinolyl-H and Ph-H), 8.01–8.04 (m, 2H, quinolyl-H), 7.10 (s, 1H, Ph-H), 7.13 (s, 1H, Ph-H), 7.36 (s, 1H, quinolyl-H), 7.78–7.89 (m, 2H, quinolyl-H), 8.05 (s, 1H, quinolyl-H), 8.70 (s, 1H, CH=N), 14.21 (s, 1H, OH). ^{13}C NMR (75.4 MHz, d_6-DMSO, 298.3 K): δ (ppm) 18.5 (quinolyl-CH_3), 24.7 (quinolyl-CH_3), 109.4, 111.6, 117.8, 118.6, 118.9, 119.4, 119.9, 120.9, 122.7, 125.6, 126.4, 134.4, 137.6, 157.3 (Ph-2-C), 159.4 (quinolyl-2-C), 163.0 (CH=N). IR (KBr, cm^{-1}): υ 3492 (br), 3069 (w), 2982 (w), 2956 (w), 2918 (w), 1917 (w), 1898 (w), 1753 (w), 1733 (w), 1720 (w), 1594 (vs), 1554 (s), 1513 (m), 1435 (s), 1370 (s), 1349 (m), 1339 (m), 1294 (m), 1272 (m), 1211 (m), 1197 (m), 1161 (vs), 1138 (s), 1029 (m), 1000 (m), 961 (m), 933 (m), 878 (s), 861 (s), 816 (s), 769 (w), 741 (m), 690 (m), 678 (w), 661 (w), 651 (m), 597 (w), 556 (w), 540 (w), 496 (w), 441 (w).

2.7. Synthesis of $C_{36}H_{30}N_4O_2Zn$ (**2a**)

To a solution of ligand **1a** (0.30 g, 1.07 mmol) dissolved in 30 ml of dry toluene was added a solution of $ZnEt_2$ (0.51 mmol) in toluene (5 ml) at −78 °C with stirring. The reaction mixture was allowed to warm to room temperature for 2 h, and heated at 80 °C for an additional 8 h. The solvent was removed under vacuum and the residue was washed with dry ^{n}hexane (3×20 ml). Then the crude product was further purified by recrystallization from toluene/^{n}hexane (1:6 in v/v) to give yellowish-green plate crystals (0.27 g, 86%) m.p.: 263.3–264.2 °C. *Anal.* Calc. for $C_{36}H_{30}N_4O_2Zn$ (616.04): C, 70.19; H, 4.91; N, 9.09. Found: C, 70.13; H, 4.85; N, 9.14%. ^{1}H NMR (300 MHz, $CDCl_3$, 298.3 K): δ (ppm) 2.57 (s, 3H, quinolyl-CH_3), 2.59 (s, 3H, quinolyl-CH_3), 6.78 (t, $J = 6.9$ Hz, 1H, Ph-H), 6.98 (d, $J = 8.4$ Hz, 1H, Ph-H), 7.05 (s, 1H, quinolyl-H), 7.22 (dd, $J = 6$ Hz, 1.8 Hz, 1H, quinolyl-H), 7.36–7.46 (m, 2H, Ph-H), 7.54 (s, 1H, quinolyl-H), 7.78 (d, $J = 9$ Hz, 1H, quinolyl-H), 8.57 (s, 1H, CH=N). ^{13}C NMR (75.4 MHz, $CDCl_3$, 298.3 K): δ (ppm) 18.5 (quinolyl-CH_3), 25.1 (quinolyl-CH_3), 115.4, 118.4, 118.8, 121.3, 122.7, 123.8, 125.3, 125.4, 136.6, 136.9, 144.2, 148.3, 149.5, 159.7 (quinolyl-2-C), 170.1 (Ph-2-C), 171.7 (CH=N). IR (KBr, cm^{-1}): υ 3039 (w), 3020 (w), 2953 (w), 2911 (w), 1604 (m), 1582 (m), 1531 (m), 1510 (w), 1462 (w), 1435 (w), 1392 (w), 1343 (w), 1315 (w), 1248 (w), 1187 (w), 1170 (w), 1170 (w), 1151 (w), 1125 (w), 1030 (w), 991 (w), 949 (w), 915 (w), 887 (w), 858 (w), 839 (w), 817 (w), 775 (w), 758 (w), 677 (w), 629 (w), 599 (w), 568 (w), 541 (w), 525 (w), 505 (w), 472 (w), 452 (w).

2.8. Synthesis of $C_{52}H_{62}N_4O_2Zn$ (**2b**)

Complex **2b** was synthesized by the same procedures as those used for **2a** with **1b** (0.45 g, 1.17 mmol) as a starting material. Pure **2b** (0.45 g, 91%) was obtained as a yellow powder by recrystallization from toluene/^{n}hexane (1:6 in v/v). m.p.: 246.1–248 °C. *Anal.* Calc. for $C_{52}H_{62}N_4O_2Zn$ (840.46): C, 74.31; H, 7.44; N, 6.67. Found: C, 74.35; H, 7.36; N, 6.64%. ^{1}H NMR (300 MHz, C_6D_6, 298.3 K): δ (ppm) 1.34 (s, 9H, $C(CH_3)_3$), 1.77 (s, 9H, $C(CH_3)_3$), 1.94 (s, 3H, quinolyl-CH_3), 2.39 (s, 3H, quinolyl-CH_3), 6.45 (s, 1H, quinolyl-H), 6.78 (d, $J = 2.7$ Hz, 1H, Ph-H), 7.39 (d, $J = 8.7$ Hz, 1H, quinolyl-H), 7.58 (dd, $J = 8.7$ Hz, 2.4 Hz, 1H, quinolyl-H), 7.74 (d, $J = 2.7$ Hz, 1H, Ph-H), 7.86 (d, $J = 2.1$ Hz, 1H, quinolyl-H), 8.16 (s, 1H, CH=N). ^{13}C NMR (75.4 MHz, C_6D_6, 298.3 K): δ (ppm) 18.0 (quinolyl-CH_3), 25.1 (quinolyl-CH_3), 29.9 ($C(CH_3)_3$), 31.5 ($C(CH_3)_3$), 34.0 ($C(CH_3)_3$), 36.0 ($C(CH_3)_3$), 118.7, 119.7, 121.4, 122.3, 125.2, 125.4, 131.3, 131.6, 136.1, 142.3, 143.3, 149.4, 150.3 (Ph-2-C), 159.5 (quinolyl-2-C), 170.8 (CH=N). IR (KBr, cm^{-1}): υ 2953 (s), 2912 (s), 2869 (m), 1590 (vs), 1550 (m), 1530 (vs), 1511 (s), 1460 (s), 1426 (vs), 1385 (s), 1361 (m), 1340 (m), 1325 (m), 1271 (m), 1254 (s), 1236 (m), 1218 (m), 1194 (s), 1164 (vs), 1133 (s), 1024 (w), 1002 (w), 988 (w), 963 (w), 940 (w), 914 (w), 879 (w), 830 (w), 816 (w), 788 (w), 772 (w), 746 (w), 681 (w), 662 (w), 637 (w), 595 (w), 571 (w), 539 (w), 511 (w), 485 (w).

2.9. Synthesis of $C_{36}H_{28}Br_2N_4O_2Zn$ (**2c**)

Complex **2c** was synthesized by the same procedures as those used for **2a** with **1c** (0.25 g, 0.71 mmol) as a starting material. Pure **2c** (0.23 g, 83%) was obtained as a brown-yellow powder by recrystallization from toluene/^{n}hexane (1:6 in v/v). m.p.: 184.3–187.8 °C. *Anal.* Calc. for $C_{36}H_{28}Br_2N_4O_2Zn$ (773.83): C, 55.88; H, 3.65; N, 7.24. Found: C, 55.79; H, 3.71; N, 7.27%. ^{1}H NMR (300 MHz, $CDCl_3$, 298.3 K): δ (ppm) 2.58 (s, 3H, quinolyl-CH_3), 2.59 (s, 3H, quinolyl-CH_3), 6.86 (d, $J = 8.7$ Hz, 1H, Ph-H), 7.06 (s, 1H, Ph-H), 7.16 (d, $J = 7.8$ Hz, 1H, quinolyl-H), 7.23 (s, 1H, quinolyl-H), 7.42 (d, $J = 8.7$ Hz, 1H, quinolyl-H), 7.50 (s, 1H, quinolyl-H), 7.79 (d, $J = 8.7$ Hz, 1H, Ph-H), 8.40 (s, 1H, CH=N). ^{13}C NMR (75.4 MHz, $CDCl_3$,

298.3 K): δ (ppm) 18.5 (quinolyl-CH_3), 25.2 (quinolyl-CH_3), 118.8, 119.8, 120.7, 122.9, 125.5, 125.8, 128.2, 130.0, 137.8, 139.0, 144.2, 148.2, 148.8, 160.0 (quinolyl-2-C), 168.9 (Ph-2-C), 170.4 (CH=N). IR (KBr, cm^{-1}): υ 3033 (w), 2952 (m), 2912 (m), 2856 (w), 1602 (vs), 1515 (vs), 1456 (vs), 1414 (vs), 1381 (vs), 1335 (s), 1310 (vs), 1240 (m), 1156 (vs), 1073 (m), 1027 (m), 1006 (m), 984 (m), 963 (w), 943 (m), 922 (w), 876 (m), 826 (s), 787 (s), 748 (w), 713 (w), 682 (w), 652 (s), 605 (w), 540 (m), 525 (w), 504 (w), 471 (w), 453 (w).

2.10. Synthesis of $C_{36}H_{26}Br_4N_4O_2Zn$ (2d)

Complex **2d** was synthesized by the same procedures as those used for **2a** with **1d** (0.52 g, 1.19 mmol) as a starting material. Pure **2d** (0.49 g, 88%) was obtained as a yellow powder by recrystallization from toluene/^{n}hexane (1:6 in v/v). m.p.: 281.3–285 °C. *Anal.* Calc. for $C_{36}H_{26}Br_4N_4O_2Zn$ (931.62): C, 46.41; H, 2.81; N, 6.01. Found: C, 46.52; H, 2.84; N, 5.90%. ^{1}H NMR (300 MHz, d_6-DMSO, 298.3 K): δ (ppm) 2.56 (s, 3H, quinolyl-CH_3), 2.61 (s, 3H, quinolyl-CH_3), 7.21 (s, 1H, quinolyl-H), 7.71–7.72 (br, 3H, Ph-H and quinolyl-H), 7.90–7.95 (br, 2H, quinolyl-H), 8.65 (s, 1H, CH=N). ^{13}C NMR (75.4 MHz, d_6-DMSO, 298.3 K): δ (ppm) 18.0 (quinolyl-CH_3), 24.7 (quinolyl-CH_3), 118.0, 120.4, 121.0, 122.2, 124.5, 125.3, 128.2, 128.9, 137.7, 138.1, 143.7, 147.7, 151.0, 158.9 (quinolyl-2-C), 164.5 (Ph-2-C), 168.4 (CH=N). IR (KBr, cm^{-1}): υ 3059 (w), 2911 (w), 1752 (w), 1588 (s), 1558 (w), 1506 (m), 1428 (m), 1402 (m), 1372 (w), 1342 (w), 1307 (w), 1214 (w), 1196 (w), 1144 (s), 1119 (w), 1029 (w), 1001 (w), 932 (w), 868 (w), 815 (w), 751 (w), 713 (w), 682 (w), 651 (w), 643 (w), 633 (w), 621 (w), 611 (w), 600 (w), 590 (w), 580 (w), 570 (w), 559 (w), 548 (w), 539 (w), 528 (w), 517 (w), 507 (w), 496 (w), 487 (w), 476 (w), 465 (w), 454 (w), 444 (w), 433 (w), 423 (w), 413 (w), 403 (w).

2.11. X-ray structure determination of 2b

Single crystals of **2b** suitable for X-ray structural analysis were obtained from a saturated solution of **2b** in toluene/^{n}hexane (1:6, v/v) at room temperature. Diffraction data were collected at 293 K on a Bruker Smart diffractometer equipped with graphite-monochromated Mo Kα radiation (λ = 0.71073 Å) for **2b**. The structure was solved by direct methods [12] and refined by full-matrix least-squares on F^2. Most non-hydrogen atoms, except those in the disordering groups, were refined anisotropically. All hydrogen atoms, except those on disordered carbon atoms, were calculated and their contributions in structural factor calculations were included. All calculations were performed using the SHELXTL crystallographic software packages [13]. Details of the crystal data, data collection and structure refinements are summarized in Table 1.

Table 1
Crystal data and structure refinement for complex **2b**

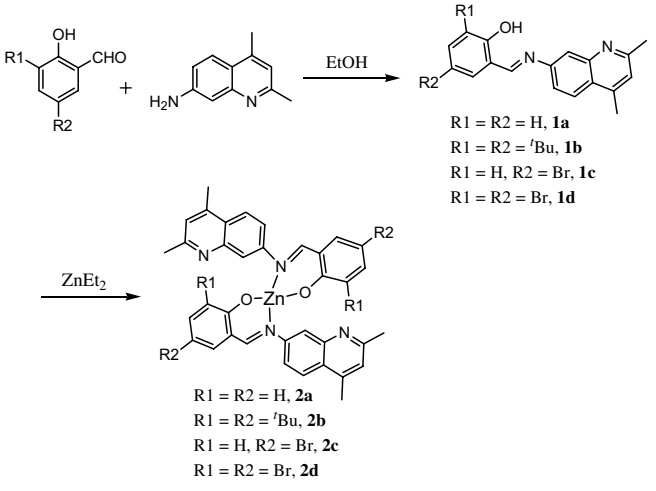
Data	2b
Formula	$C_{53.50}H_{65.50}N_4O_2Zn$
Fw	861.97
Temperature (K)	293(2)
Crystal system	triclinic
Space group	$P\bar{1}$
a (Å)	12.5327 (11)
b (Å)	14.8692 (13)
c Å	15.4913 (14)
α (°)	77.809 (2)
β (°)	85.060 (2)
γ (°)	69.277 (2)
Volume (Å^3)	2639.0 (4)
Z	2
D_{calc} (Mg m^{-3})	1.058
$F(000)$	896
θ Range for data collection (°)	1.74–28.31
Limiting indices	$-14 \leqslant h \leqslant 16$, $-16 \leqslant k \leqslant 19$, $-20 \leqslant l \leqslant 20$
Data/restraints/parameters	12965/115/553
Goodness-of-fit on F^2	1.030
Final R indices [$I > 2\sigma(I)$]	$R_1^a = 0.0743$, $wR_2^b = 0.2136$
R indices (all data)	$R_1^a = 0.1304$, $wR_2^b = 0.2662$
Largest difference in peak and hole (e A^{-3})	0.820 and −0.505

[a] $R_1 = \sum \|F_o| - |F_c\| / \sum |F_o|$.
[b] $wR_2 = [\sum[w(F_o^2 - F_c^2)^2] / \sum[w(F_o^2)^2]]^{1/2}$.

3. Results and discussion

3.1. Synthesis of the ligands

Ligands **1a**–**1d** were readily prepared by simple condensation of salicyaldehydes with 7-amino-2,4-dimethylquinoline in EtOH in high yields (Scheme 1). Compounds **1a**–**1d** were characterized via ^{1}H, ^{13}C NMR and IR spectroscopies, as well as elemental analysis. The ^{1}H NMR spectra of **1a**–**1d** exhibit resonances at δ = 8.77, 8.80, 8.70 and 8.70 ppm, respectively, for the CH imino protons, with



Scheme 1. Synthetic route for ligands **1a**–**1d** and complexes **2a**–**2d**.

the corresponding ^{13}C resonance at $\delta = 163.7$, 165.0, 162.8, 163.0 ppm, respectively. The OH resonances appear at characteristically low field shifts ($\delta = 13.11$ ppm for **1a**, 13.56 ppm for **1b**, 13.10 ppm for **1c** and 14.21 ppm for **1d**). The infrared absorption band of the imine C=N stretching vibration occurs in the region 1594–1605 cm^{-1}.

3.2. Synthesis of the zinc complexes

The bis-salicylaldiminato zinc complexes **2a**–**2d** were conveniently synthesized in higher yields (83–91%) by the reaction of $ZnEt_2$ with two equivalents of the corresponding ligand by alkane elimination (Scheme 1). Complexes **2a**–**2d** were always obtained when the molar ratio of ligand/$ZnEt_2$ was 1:1 or 2:1 in toluene, which is due to the fact that the salicylaldiminato ligands are not sterically bulky enough to inhibit the formation of bis-ligand species [14]. Complexes **2a**–**2d** have different solubilities in common solvents. Complexes **2a** and **2c** are well soluble in methylene chloride, diethyl ether and THF, moderately soluble in toluene, and sparingly soluble in saturated hydrocarbon solvents. Complex **2b** is well soluble in common solvents. Complex **2d** is soluble in DMSO (dimethyl sulfone), moderately soluble in methylene chloride and sparingly soluble in other common solvents. Complexes **2a**–**2d** were all characterized by elemental analyses, ^1H, ^{13}C NMR and IR spectroscopies, and satisfactory analytical results were obtained. In the ^1H NMR spectra of these complexes, the resonance for the CH imino protons in **2a** (8.57 ppm), **2b** (8.16 ppm), **2c** (8.40 ppm) and **2d** (8.65 ppm) shifts by about 0.2 ppm, 0.64 ppm, 0.30 ppm and 0.05 ppm, respectively, towards high field compared to the corresponding signals of the free ligands. However the resonances (171.7 ppm for **2a**, 170.8 ppm for **2b,** 170.4 ppm for **2c** and 168.4 ppm for **2d**) for the CH imino carbons in the ^{13}C NMR spectra shift by about 8 ppm, 5.8 ppm, 7.6 ppm and 5.4 ppm, respectively, to low field in comparison with the corresponding ones of the free ligands. The O–H proton signals of the free ligands disappear in the ^1H NMR and IR spectra of the complexes **2a**–**2d**, which indicates the formation of a Zn–O bond in these complexes. All the complexes are stable to air and moisture in the solid state and can be left in the air for several days without obvious decomposition.

3.3. The crystal structure of complex *2b*

Crystals of complex **2b** suitable for X-ray crystal structure determination were grown from toluene/^{n}hexane at room temperature. The ORTEP drawing of the molecular structure of **2b** is shown in Fig. 1, top. Selected bond lengths and angles for complex **2b** are given in Table 2.

There are two ^{n}hexane solvent molecules in the unit cell of complex **2b**, and the ^{n}hexane solvate exhibits molecular disorder. The high residual peaks in a difference fourier map with suitable geometry were refined isotropically with occupancies factors (0.25:0.25) for each ^{n}hexane moiety.

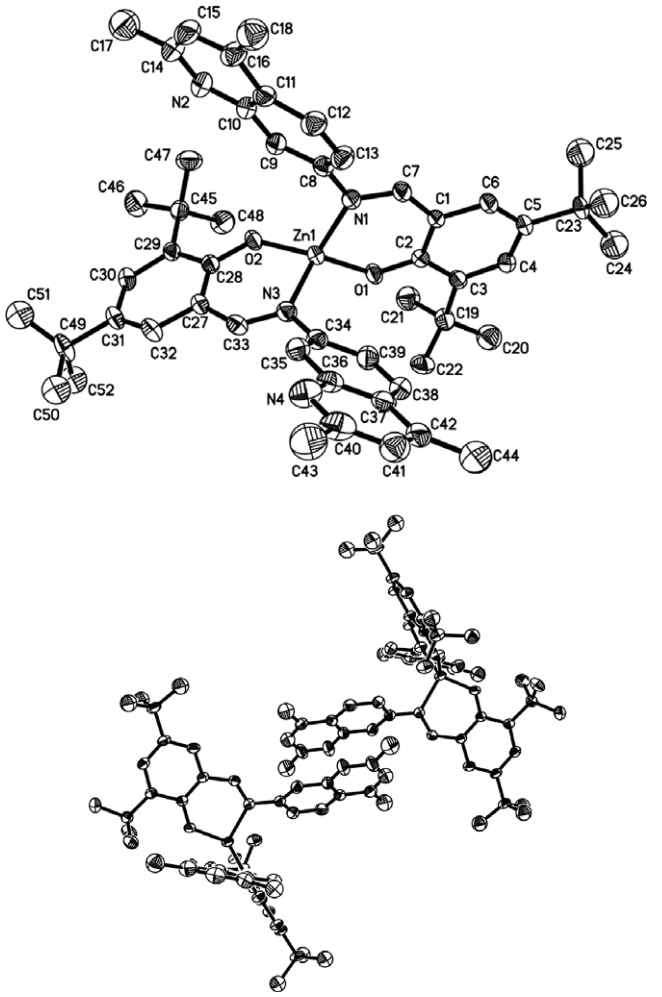


Fig. 1. Top: Molecular structure of complex **2b**; bottom: Crystal packing diagram between two adjacent molecules of complex **2b** showing the existence of the π–π stacking interaction in the solid state. (Thermal ellipsoids are drawn at 30% probability. All H atoms and the disordered ^{n}hexane solvate are omitted for clarity.)

Table 2
Selected bond lengths (Å) and angles (°) for complex **2b**

Complex **2b**			
Zn(1)–N(1)	1.994(3)	N(1)–Zn(1)–N(3)	110.98(13)
Zn(1)–N(3)	2.016(3)	N(3)–Zn(1)–O(1)	115.21(13)
Zn(1)–O(1)	1.903(3)	N(3)–Zn(1)–O(2)	95.65(12)
Zn(1)–O(2)	1.901(3)	O(1)–Zn(1)–O(2)	121.66(12)
N(1)–C(7)	1.305(5)	C(7)–N(1)–Zn(1)	120.9(3)
N(3)–C(33)	1.298(5)	C(8)–N(1)–Zn(1)	121.5(2)
N(1)–Zn(1)–O(1)	121.66(12)	C(33)–N(3)–Zn(1)	119.9(3)
N(1)–Zn (1)–O(2)	118.79(13)	C(34)–N(3)–Zn(1)	123.1(3)

The X-ray analysis reveals that complex **2b** adopts a distorted tetrahedral geometry with the metal center chelated by two bidentate ligands via the phenolate oxygen atom and imine nitrogen atom. The O–Zn–O angle in **2b** (121.66(12)°) is larger than those values (105–112.5°) in the similar bis-salicylaldiminato zinc complexes $(NR^2C_7H_{5-x}(R^1)_xO)_2Zn$ [$x = 1$ or 2; R^1 = Me, ^{t}Bu, Cl, OMe;

$R^2 = 2,6\text{-}^iPr_2C_6H_3$] [14], while the N–Zn–N angle in **2b** (110.98(13)°) is smaller than those in the latter complexes (122.9–128.9°). The two dihedral angles between the quinolyl ring and the six-membered chelating ring are 46.5 and 48.9°, respectively. The two six-membered chelating rings are nearly planar with the zinc atoms lying 0.0454 and 0.0328 Å out of the plane, and they are closely perpendicular to each other with the dihedral angle being 88.7°. The imino C=N bonds in complex **2b** retain their double bond character, being 1.305(5) and 1.298(5) Å. In addition, the X-ray diffraction analysis reveals that an intermolecular π–π interaction appears in the solid state of complex **2b**, forming an antiparallel dimeric structure (Fig. 1, bottom). One quinolyl ring in complex **2b** stacks together with the corresponding one in an adjacent molecule by the π–π interaction with a distance of 3.64 Å [15]. Moreover, one thing that should be mentioned is that all the methyl groups of the ^{t}Bu group at the 5-position of the salicylene ring in **2b** display rotational disordering over two sites, with 50% occupancy factors for each site. The H-atoms are placed in calculated positions on the disordered atoms.

3.4. Luminescent property

Table 3 summarizes the absorption and emission data for compounds **1a**–**1d** and **2a**–**2d** in solution and the solid state. As shown in Table 3, it can be seen that the four complexes **2a**–**2d** show three main absorption bands similar to those in the ligands **1a**–**1d** in the UV region. The electronic absorption spectra of those complexes in the maximum absorption wavelength are red-shifted relative to the ligands due to the perturbation of the intraligand π–π* transition of the salicylaldiminato unit by the metal atom.

Fig. 2 shows the emission spectra of **1a**–**1d** and **2a**–**2d** in solution. And Fig. 3 shows the emission spectra of **1a**–**1d** and **2a**–**2d** in the solid state. In comparison with the corresponding free ligands ($\lambda_{max} = 476$, 524, 478 and 486 nm, respectively, for **1a**–**1d**), complexes **2a**–**2d** in solution exhibit red-shifts with $\lambda_{max} = 503$, 532, 514 and 515 nm, respectively. The coordinated zinc atom plays a dual role in the luminescence of **2a**–**2d** as pointed out in the literature for coordination complexes [16]. First, the formation of covalent bonds between the Zn and O atoms *via* π-donation of

Table 3
Photoluminescent data for ligands **1a**–**1d** and complexes **2a**–**2d**

Compound	Absorption (nm) ε ($dm^3\ mol^{-1}\ cm^{-1}$)	Excitation (λ, nm)	Emission (λ_{max}, nm)	Quantum yields (Φ)[a]	Conditions
1a	272(18847) 348(13659)	404	476	0.003	CH_2Cl_2, 298 K
		404	536		solid, 298 K
1b	277(41670), 328(28384), 363(24353)	432	524	0.004	CH_2Cl_2, 298 K
		393	553		solid, 298 K
1c	272(27519), 329(17234), 357(18484)	390	478	0.001	CH_2Cl_2, 298 K
		390	558		solid, 298 K
1d	275(27906), 334(12169), 363(sh, 10503)	407	486	0.001	CH_2Cl_2, 298 K
		407	578		solid, 298 K
2a	277(44266), 323(29571), 407(18194)	407	503	0.059	CH_2Cl_2, 298 K
		407	493		solid, 298 K
2b	283(48358), 322(33104), 428(20292)	428	532	0.151	CH_2Cl_2, 298 K
		428	519		solid, 298 K
2c	276(41691), 321(26805), 417(19710)	438	514	0.016	CH_2Cl_2, 298 K
		438	535		solid, 298 K
2d	284(33089), 325(27703), 422(21188)	420	515	0.005	CH_2Cl_2, 298 K
		420	526		solid, 298 K

[a] Determined using quinine sulfate in 0.1 M sulfuric acid as a standard.

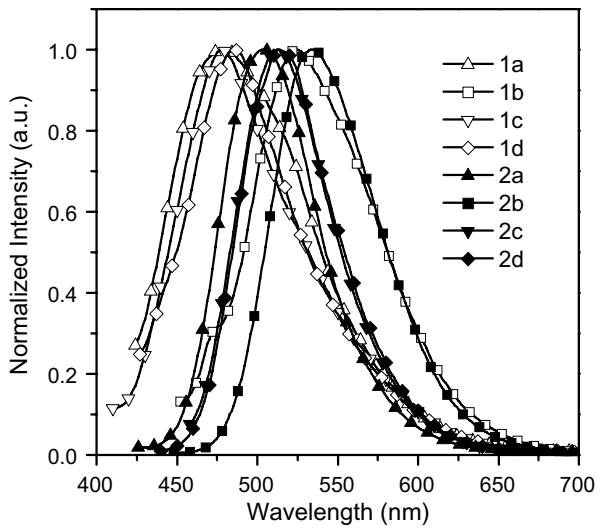


Fig. 2. Emission spectra of ligands **1a**–**1d** and complexes **2a**–**2d** in CH_2Cl_2.

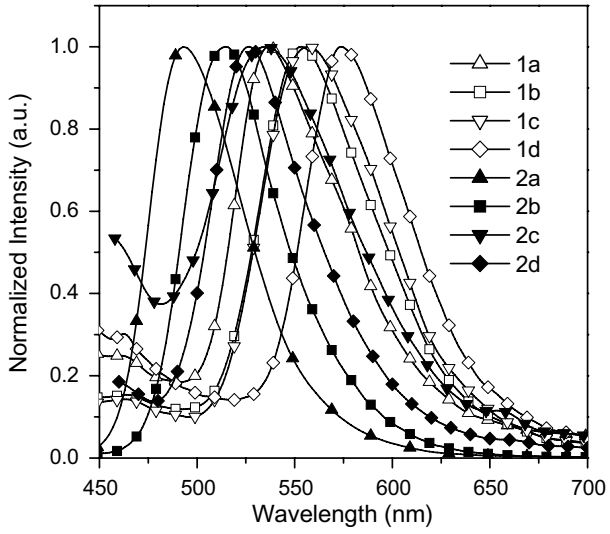


Fig. 3. Emission spectra of ligands **1a**–**1d** and complexes **2a**–**2d** in the solid state.

a lone-pair electrons of the O atom to the Zn atom changes the emission energy, due to the lowering of the energy gap between π* and π. Second, the coordination of the ligands with the Zn atom increases the rigidity of the ligands, which can diminish the loss of energy *via* vibrational motions and increase the emission efficiency. The emission maximum of complexes **2b**–**2d** in solution is red-shifted by about 29, 11 and 12 nm, respectively, compared to that of the complex **2a**, which is possibly due to the fact that the electron-donating nature of the *tert*-butyl group and bromo group on the phenyl ring lowers the energy gap between π* and π. The quantum yields of all the compounds have been determined in solution. It was found that the quantum yields of the complexes are higher than those of the corresponding ligands, considering that the coordination of the ligands to the zinc atom increases the rigidity of the molecule. The quantum yields of complexes **2c** and **2d** are lower than those of **2a** and **2b** due to the fact that the bromo atom can quench the fluorescence and results in luminescence decay. All compounds **1a**–**1d** and **2a**–**2d** emit bright fluorescence in the solid state at room temperature. Complexes **2a**–**2d** exhibit a bright emission with $\lambda_{max} = 493$, 519, 535 and 526 nm, respectively ($\lambda_{max} = 536$, 553, 558 and 578 nm for ligands **1a**–**1d**). The emission maxima of these complexes are blue-shifted compared to those of the corresponding free ligand in the solid state, which is probably due to the disappearance of the intramolecular hydrogen bonding in compounds **1a**–**1d** after coordination with the zinc atom [17]. The emission maxima of complexes **2a** and **2b** in the solid state are blue-shifted compared to their corresponding emission maxima in solution, while the emission maxima of complexes **2c** and **2d** in the solid state are red-shifted compared to their corresponding emission maxima in solution. Blue shifting probably results from the diminished conjugated extent of the two complexes **2a** and **2b** since the free rotation of the quinolyl ring in these complexes is blocked in the solid state. Red shifting of emission maximum can be normally observed for most fluorescent compounds in the solid state, probably due to π–π stacking of the aromatic rings in the molecules.

4. Conclusions

A series of bis-salicylaldiminato zinc complexes have been synthesized and characterized. Our research results indicate that the chelating bidentate salicylaldiminato conjugated ligands are well suitable for synthesizing four-coordinate zinc complexes by the reaction of $ZnEt_2$ with the corresponding ligands. These complexes produce bright fluorescence in both solution and the solid state, and the emission color in solution can be tuned by the 3- and 5-position substituents on the salicylene rings of the ligands. The four-coordinate zinc complexes are a new class of luminescent material with potential applications in opto-electronic devices.

5. Supplementary material

CCDC 634611 contains the supplementary crystallographic data for **2b**. These data can be obtained free of charge via http://www.ccdc.cam.ac.uk/conts/retrieving.html, or from the Cambridge Crystallographic Data Centre, 12 Union Road, Cambridge CB2 1EZ, UK; fax: (+44) 1223-336-033; or e-mail: deposit@ccdc.cam.ac.uk.

Acknowledgements

This work was supported by the National Natural Science Foundation of China (No. 20674024) and the Ministry of Science and Technology of China (No. 2002CB6134003).

References

[1] (a) F. Loiseau, C.D. Pietro, S. Serroni, S. Campagna, A. Licciardello, A. Manfredi, G. Pozzi, S. Quici, Inorg. Chem. 40 (2001) 6901;
(b) A. Bencini, E. Bemi, A. Bianchi, P. Fornasari, C. Giorgi, J.C. Lima, C. Loderio, M.J. Melo, J.S.D. Melo, A.J. Parola, F. Pina, J. Pina, B. Valtancoli, J. Chem. Soc., Dalton Trans. (2004) 2180;
(c) Y. Mikata, M. Wakamatsu, S. Yano, J. Chem. Soc., Dalton Trans. (2005) 545;
(d) K.M. Hendrickson, J.P. Geue, O. Wyness, S.F. Lincoln, A.D. Ward, J. Am. Chem. Soc. 125 (2003) 3889;
(e) S.P. Man, D.M. Benoit, E. Buchaca, F. Esan, M. Motevalli, J. Wilson, A. Sullivan, Inorg. Chem. 45 (2006) 5328;
(f) Y.J. Mikata, M. Wakamatsu, A. Kamanaka, S. Yano, A. Odani, K. Morihiro, S. Tamotsu, Inorg. Chem. 45 (2006) 9262;
(g) P.J. Jiang, Z.J. Guo, Coor. Chem. Rev. 248 (2004) 205;
(h) L. Gao, Y. Wang, J.Q. Wang, L. Huang, L.Y. Shi, X.X. Fan, Z.G. Zou, T. You, M. Zhu, Z.S. Li, Inorg. Chem. 45 (2006) 6844.

[2] (a) S.N. Wang, Coord. Chem. Rev. 215 (2001) 79;
(b) C.H. Chen, J. Shi, Coord. Chem. Rev. 171 (1998) 161.

[3] C.M. Che, S.C. Chan, H.F. Xiang, M.C.W. Chan, Y. Liu, Y. Wang, Chem. Commun. (2004) 1484.

[4] (a) Y. Hamada, T. Sano, M. Fujita, T. Fujii, Y. Nishio, K. Shibata, Jpn. J. Appl. Phys. 32 (1993) L511;
(b) T. Sano, Y. Nishio, Y. Hamada, H. Takahashi, T. Usuki, K. Shibata, J. Mater. Chem. 10 (2000) 157;
(c) P.F. Wang, Z.R. Hong, Z.Y. Xie, S.W. Tong, O.Y. Wong, C.S. Lee, N.B. Wong, L.S. Hung, S.T. Lee, Chem. Commun. (2003) 1664;
(d) K.H. Chang, C.C. Huang, Y.H. Liu, Y.H. Hu, P.T. Chou, Y.C. Lin, J. Chem. Soc., Dalton Trans. (2004) 1731;
(e) D. Das, B.G. Chand, K.K. Sarker, J. Dinda, C. Sinha, Polyhedron 25 (2006) 2333;
(f) R. Ghosh, S.H. Rahaman, C.N. Lin, T.H. Lu, B.K. Ghosh, Polyhedron 25 (2006) 3104;
(g) O. Lavastre, I. IIIitchev, G. Jegou, P.H. Dixneuf, J. Am. Chem. Soc. 124 (2002) 5278;
(h) L.S. Sapochak, F.E. Benincasa, R.S. Schofield, T.L. Baker, K.K.C. Riccio, D. Fogarty, H. Kohlmann, K.F. Ferris, P.E. Burrows, J. Am. Chem. Soc. 124 (2002) 6119;
(i) M.R. Bermejo, M. Vazquez, J. Sanmartin, A.M. García-Deibe, M. Fondo, C. Lodeiro, New J. Chem. 26 (2002) 1365.

[5] A.C.W. Leung, J.H. Chong, B.O. Patrick, M.J. Maclachlan, Macromolecules 36 (2003) 5051.

[6] H. Tanaka, S. Tokito, Y. Taga, A. Okada, J. Mater. Chem. 8 (1998) 1999.

[7] G. Yu, S.W. Yin, Y.Q. Liu, Z.G. Shuai, D.B. Zhu, J. Am. Chem. Soc. 125 (2003) 14816.

[8] (a) W.K. Wong, X.P. Yang, R.A. Jones, J.H. Rivers, V. Lynch, W.K. Lo, D. Xiao, M.M. Oye, A.L. Holmes, Inorg. Chem. 45 (2006) 4340;
(b) X.P. Yang, R.A. Jones, W.K. Wong, V. Lynch, M.M. Oye, A.L. Holmes, Chem. Commun. (2006) 1836;
(c) X.P. Yang, R.A. Jones, Q.Y. Wu, M.M. Oye, W.-K. Lo, W.-K. Wong, A.L. Holmes, Polyhedron 25 (2006) 277.

[9] (a) R. Pohl, V.A. Montes, J. Shinar, P. Anzenbacher Jr., J. Org. Chem. 69 (2004) 1723;
(b) X.M. Liu, W. Gao, Y. Mu, G.H. Li, L. Ye, H. Xia, Y. Ren, S.H. Feng, Organometallics 24 (2005) 1614, and references herein.

[10] (a) C.K. Bradsher, Chem. Rev. 38 (1946) 447;
(b) W.S. Johnson, F.J. Mathews, J. Am. Chem. Soc. 66 (1944) 210.

[11] (a) Y.J. Zhang, M. Hao, H. Wang, X.B. Lu, Dyestuffs and Coloration 41 (2004) 284;
(b) Y.J. Fan, Q.Q. Zhao, Y.L. Sheng, Y.X. Ma, Chemical World (2005) 352;
(c) Q.Q. Zhao, C.Y. Neu, D.F. Wang, A.H. Yu, Chem. Res. Appl. 10 (1998) 179.

[12] G.M. Sheldrick, SHELXTL PC Siemens Analytical X-ray Instruments, Madison WI, 1993.

[13] G.M. Sheldrick, SHELXTL Structure Determination Programs, Version 5.0; PC Siemens Analytical Systems, Madison, WI, 1994.

[14] D.J. Darensbourg, P. Rainey, J. Yarbrough, Inorg. Chem. 40 (2001) 986.

[15] C. Janiak, J. Chem. Soc., Dalton Trans. (2000) 3885.

[16] (a) D. Rendell (Ed.), Fluorescence and Phosphorescence, Wiley, New York, 1987;
(b) H. Yersin, A. Vogler (Eds.), Photochemistry and Photophysics of Coordination Compounds, Springer-Verlag, Berlin, 1987;
(c) A.W. Adamson, P.D. Fleischauer (Eds.), Concepts of Inorganic Photochemistry, Wiley, New York, 1975;
(d) N.I. Nijegorodov, W.S. Downey, J. Phys. Chem. 98 (1994) 5639.

[17] N.J. Xiang, T.H. Lee, L.M. Leung, S.K. So, J.X. Shi, M.L. Gong, Chem. J. Chin. Univ. 27 (2006) 808.

Recently, the importance of metallo-organic complexes has been associated with supramolecular chemistry. In addition, there has been considerable interest for inorganic metal clusters, coordination complexes and organic molecules into extended motifs held together either by strong metal-ligand bonding or by weaker bonding forces such as hydrogen-bonding, π–π interactions (face-to-face) and C–H–π interactions (T-shaped geometry, edge-face or herringbone interactions) [23–25]. These weak non-covalent bonds can sustain supramolecular synthons which are structure determining.

We report here the template synthesis of phenylmercury(II) and cadmium(II) complexes of a tridentate N_2S donor ligand, diacetylmonoximemorpholine *N*-thiohydrazone (Hdammth) (H_2dammthiol, the thiol form of this hydrazone is actually involved in the complex formation) and their characterization by elemental analyses, spectral data (electronic, infrared and ^{1}H NMR), and by X-ray crystal structure analysis. The supramolecular structure of these complexes is also reported.

2. Experimental

2.1. Physical measurements

The elemental analyses were carried out at the Sophisticated Analytical Instrument Facility, Central Drug Research Institute, Lucknow, India. The electronic spectra were recorded on a Shimadzu UV-1601 spectrophotometer, infrared spectral data were collected (KBr pellets) on a Perkin-Elmer L120-000A spectrophotometer, and NMR spectra were recorded at the Indian Institute of Chemical Biology, Kolkata, India.

2.2. Materials

The solvents and chemicals were purified and dried prior to use by standard procedures. Diacetylmonoxime was purchased from Aldrich and morpholine *N*-thiohydrazide was prepared by published methods [26,27]. [PhHg(OAc)] and $[Cd(OAc)_2]\cdot 2H_2O$ were purchased from SRL Mumbai, India. The molar conductance was measured using an Elico CM-180 conductivity bridge in chloroform (10^{-3} M solution).

2.3. Synthesis of [PhHg(Hdammthiol)] (1)

A mixture of diacetylmonoxime (0.2 g, 0.002 mol) and morpholine *N*-thiohydrazide (0.32 g, 0.002 mol) was heated under gentle reflux in the presence of [PhHg(OAc)] (0.67 g, 0.002 mol). The concentrated yellow solution produced yellow colored crystals upon cooling. This compound was recrystallized from chloroform, which gave suitable single crystals for X-ray study. Yield: ~0.68 g, (65%).

Anal. Calc. for $C_{15}H_{20}O_2N_4SHg$: C, 34.58; H, 3.87; N, 10.75; Hg, 38.50. Found: C, 34.31; H, 3.79; N, 10.86; Hg, 38.65%. $\Lambda_M = 12.9\ \Omega^{-1}\ cm^2\ mol^{-1}$. λ (max) (in chloroform) 242 nm, 314 nm, 374 nm and 480 nm (shoulder).

Table 1
Crystallographic data for compounds **1** and **2**

	1	**2**
Formula	$C_{15}H_{20}HgN_4O_2S$	$C_{18}H_{30}CdN_8O_4S_2$
Molecular weight	521.00	599.02
Crystal class	Triclinic	Triclinic
Space group	$P\bar{1}$	$P\bar{1}$
λ (Å)	0.71073	0.71073
a (Å)	7.979(3)	8.741(4)
b (Å)	9.917(4)	10.697(5)
c (Å)	11.395(4)	13.926(6)
α (°)	97.858(7)	102.686(7)
β (°)	99.302(7)	105.158(7)
γ (°)	111.231(6)	97.743(8)
V (Å^3)	810.5(5)	1200.3(9)
Z	2	2
D_c (g cm^{-1})	2.135	1.657
Colour	yellow	yellow
μ (Mo Kα) (mm^{-1})	9.639	1.126
F(000)	500	612
T (K)	100(2)	100(2)
θ Range (°)	2.25–28.43	1.57–28.25
h,*k*,*l* Ranges	−10,9; −12,12; −15,13	−6,11; −13,12; −17, 15
R	0.0245	0.0297
wR_2	0.0619	0.0825
T_{min}	0.163	0.696
T_{max}	0.249	0.848
Total number of reflection measured	5217	7520
Number of unique reflections, R_{int}	3548, 0.0245	5031, 0.0315
Number of reflections with $I > 2\sigma(I)$, parameters	3746, 211	5395, 304
Goodness-of-fit, *S*	1.018	1.060

2.4. Synthesis of [Cd(Hdammthiol)$_2$] (2)

This compound was prepared by the same method described above. To the refluxing solution of a mixture of diacetylmonoxime (0.5 g, 0.005 mol) and morpholine *N*-thiohydrazide (0.8 g, 0.005 mol), $[Cd(OAc)_2]\cdot 2H_2O$ (0.67 g, 0.0025 mol) was added and further refluxed for another 30 min. The resulting yellow solution was filtered and concentrated to yield a yellow compound. This compound was recrystallized from chloroform, which gave suitable single crystals for X-ray study. Yield: ~1.12 g, (75%).

Anal. Calc. for $C_{18}H_{30}O_4N_8S_2Cd$: C, 36.09; H, 5.05; N, 18.71; Cd, 18.77. Found: C, 35.93; H, 5.14; N, 18.86; Zn, 18.91%. $\Lambda_M = 13.54\ \Omega^{-1}\ cm^2\ mol^{-1}$. λ (max) (in chloroform) 247 nm, 323 nm, 382 nm and 487 nm (shoulder).

2.5. X-ray crystallography

Crystallographic data and refinement details are given in Table 1. Intensity data were measured on a Bruker APEX CCD based diffractometer employing Mo Kα radiation. Data processing and absorption correction were accomplished with SAINT [28]. The structures were solved by direct methods [28] and refinement (anisotropic displacement

parameters, hydrogen atoms in the riding model approximation and weighting scheme of the form $w = 1/[\sigma^2(F_o^2) + (0.0434P)^2]$, where $P = (F)_o^2 + 2F_c^2)/3$ was on F^2). Graphics were obtained with ORTEP 3 for Windows at the 50% probability level [29,30]. Additional figures were drawn with PLATON for Windows [31,32].

3. Results and discussion

Metal template reactions of diacetylemonoxime with morpholine *N*-thiohydrazide in the presence of [PhHg(OAc)] and $[Cd(OAc)_2] \cdot 2H_2O$ produced [PhHg(Hdammthiol)] (**1**) and $[Cd(Hdammthiol)_2]$ (**2**), respectively, with good yields. Elemental analyses confirm these formulations. The molar conductance values suggest their non-electrolytic nature in chloroform. Taking these results and considering the X-ray crystal structures of these complexes (see later discussion), we conclude that the hydrazone ligand transformed to its thiol form (H_2dammthiol) and functions as a monobasic bidentate (NS) donor in the phenylmercury(II) complex and as a monobasic tridentate (NNS) donor ligand in the cadmium(II) complex.

3.1. Crystal structure of [PhHg(Hdammthiol)] (1)

The phenylmercury(II) compound **1** crystallizes in the space group $P\bar{1}$ (2) and the molecule adopts a tricoordinated T-shaped geometry within the crystal (Fig. 1). The mercury(II) atom (Hg1) is coordinated by the phenyl carbon and by S1 and N3 of the hydrazone ligand. The Hg(II) atom is 0.027(1) Å above the plane. Selected bond lengths and angles are given in Table 2.

The Hg1–C1 bond distance of 2.035(4) Å is in the accepted range for unperturbed mercury–carbon bonds (2.05–2.09 Å) [33]. This Hg–C bond distance is shorter than that in the analogous methylmercury(II) compound where Hg–C = 2.09 Å [34]. This may be due to a contribution of electron flow from mercury to the π^* orbitals of the phenyl group in the phenylmercury(II) compound. The Hg–S bond distance of 2.3351(14) Å is similar to that of methylmercury(II) compounds [2.380(3) Å] with a sulfur containing ligand [34]. The Hg–N bond distance 2.543(4) is comparable to the Hg–N distance of an earlier reported organomercury(II) compound [34]. The coordination of nitrogen and sulfur of the thiohydrazone ligand to mercury leads to the formation of a five-membered chelate ring, necessitating deviation of the C_{ph}–Hg–S bond angles from linearity (166.92(10)°), as also shown by the methylmercury(II) compound [34].

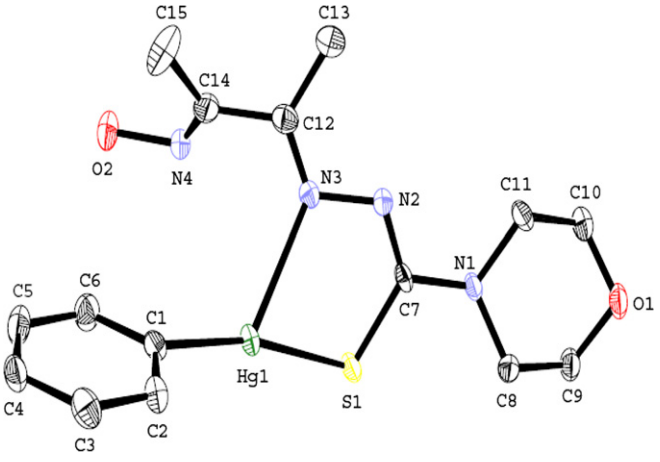


Fig. 1. ORTEP diagram of [PhHg(Hdammthiol)] (**1**) with 50% probability ellipsoids.

The C–S bond distance 1.744(4) Å is shorter than a C–S single bond (1.81 Å) but longer than a C–S double bond (1.62 Å) [35,36] suggesting partial double bond character in the complex, similar to related thiosemicarbazonates of methylmercury(II) and dimethylthallium(III) [34,37,38].

The C–N bond distance of N(3)–C(12) [d(C=N) = 1.270(6) Å] and N(4)–C(14) [d(C=N) = 1.262(6) Å] conform to the double-bond distances and deprotonation of hydrazinic NH proton also induces double bond character to the N(2)–C(7) [d(C=N) = 1.287(5) Å] bond [34,35,37,38].

It is interesting to note that there is no intermolecular π–π interaction between the phenyl rings. But a weak interaction between C(8)–H(8A) and a π group (phenyl ring) links the two phenylmercury molecules into a supramolecular dimer having a C–H···π synthon (Fig. 2). The C–H···π interaction is characterized by the H···Cg distance of 2.84 Å (Cg being the mid point of the phenyl ring) with a C(8)–H(8A)···Cg angle of 136°.

Besides this C–H···π interaction, intermolecular hydrogen bonds (C(2)–H(2)···O(1)[a]; a = $-x$, $1-y$, $1-z$ and C(4)–H(4)···O(2)[b] b = $1-x$, $-y$, $-z$) form a two-dimensional sheet in the *ac* plane (Fig. 3). The D···A separations are 3.228(6) and 3.327(6) Å and the D–H···A angles are 148° and 147°, respectively. The intermolecular hydrogen bonding between O(2)–H(2A) and N(4)[c] (c = $1-x$, $1-y$, $-z$) form a $R_2^2(6)$ synthon. The D···A bond separation is 2.763(5) Å with a D–H···A angle of 147° (Fig. 3).

3.2. Crystal structure of [Cd(Hdammthiol)$_2$] (2)

The cadmium compound crystallizes in the triclinic space group $P\bar{1}$ (2). The cadmium(II) atom is coordinated by two thiohydrazone ligands. The coordination sphere of the Cd(II) centre is best described as a trapezoidal bipyramid (Fig. 4). The S1, N3, N4, N7 atoms define the equatorial plane. The axial positions are occupied by N8 and S2 atoms with a N8–Cd–S2 angle of 142.08(5)°.

The Cd(1)–S(1) and Cd(1)–S(2) bond distances are 2.5684(14) and 2.5646(14) Å, respectively. The Cd(1)–N(3) (2.342(2) Å) and Cd(1)–N(7) (2.331(2) Å) distances are longer than Cd(1)–N(4) (2.495(2) Å) and Cd(1)–N(8) (2.427(2) Å), which are consistent with the Cd–N bond distance of a cadmium hexamine complex [33].

The C–S bond distances of the cadmium complex are 1.735(2) and 1.738(3) Å, and these are shorter than those

Table 2
Selected bond lengths (Å) and bond angles (°) for [PhHg(Hdammthiol)] (**1**) and [Cd(Hdammthiol)$_2$] (**2**)

Complex **1**		Complex **2**			
Bond lengths					
Hg(1)–S(1)	2.3351(14)	Cd(1)–S(1)	2.5684(14)	Cd(1)–N(7)	2.331(2)
Hg(1)–N(3)	2.543(4)	Cd(1)–S(2)	2.5646(14)	Cd(1)–N(8)	2.427(2)
Hg(1)–C(1)	2.035(4)	Cd(1)–N(3)	2.342(2)	S(1)–C(1)	1.735(2)
S(1)–C(7)	1.744(4)	Cd(1)–N(4)	2.495(2)	S(2)–C(10)	1.738(3)
Bond angles					
S(1)–Hg(1)–N(3)	72.92(8)	S(1)–Cd(1)–N(7)	121.94(5)	S(1)–Cd(1)–N(4)	139.64(5)
S(1)–Hg(1)–C(1)	166.92(10)	S(1)–Cd(1)–N(8)	93.76(5)	N(3)–Cd(1)–N(4)	66.54(7)
N(3)–Hg(1)–C(1)	119.97(13)	S(2)–Cd(1)–N(3)	98.22(5)	N(3)–Cd(1)–N(7)	155.62(6)
		S(2)–Cd(1)–N(7)	74.92(5)	N(3)–Cd(1)–N(8)	95.31(6)
		S(2)–Cd(1)–N(8)	142.08(5)	N(4)–Cd(1)–N(7)	92.99(6)
		S(1)–Cd(1)–S(2)	109.28(2)	N(4)–Cd(1)–N(8)	80.94(6)
		S(1)–Cd(1)–N(3)	74.26(5)		

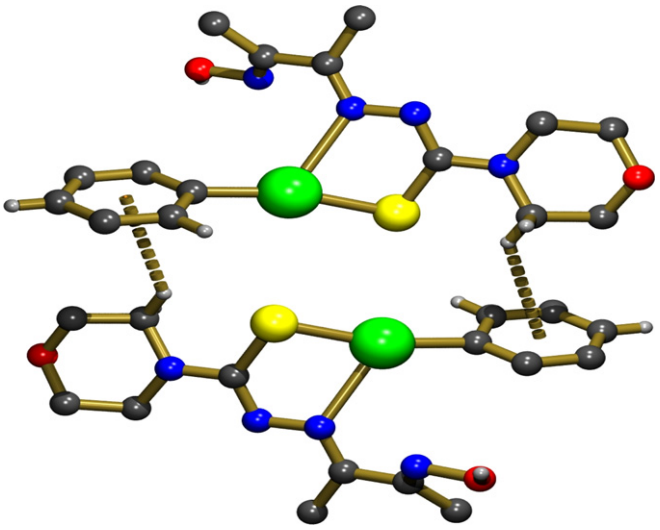


Fig. 2. Two-dimensional supramolecular dimer having a C–H···π synthon of [PhHg(Hdammthiol)] (**1**).

of the mercury complex (d(C–S) = 1.744(4) Å). These bond distances are also shorter than a C–S single bond (1.81 Å) but longer than a C–S double bond (1.62 Å), suggesting partial double bond character in the complex as found in related thiosemicarbazonates [39].

The C–N average bond distance of N(3)–C(12) [d(C=N) = 1.270(6) Å] and N(4)–C(14) [d(C=N) = 1.262(6) Å] conforms to double-bond distances and deprotonation of the hydrazinic NH proton induces double bond character with the result that N(2)–C(7) [d(C=N) = 1.287(5) Å] is close to that of a double bond [34,35,37,38].

Complex **2** forms a 2D supramolecular sheet in the *bc* plane through hydrogen bonding interactions (O–H···O and C–H···O) (Fig. 5). The average D···A separations of O–H···O (O(2)–H(2)···O (3)[d]; d = 1 − x, −y, 1−z and O(4)–H(4)···O(1)[e] d = 2 − x, 2 − y, 2 − z) hydrogen bonds are 2.69 (3) Å and the average D–H···A angle is 144°. The D···A separation of the C–H···O (C(14)–H(14A)···O(4)[f]; f = 1 − x, 1 − y, 1 − z) hydrogen bond is 3.394(3) Å and the D–H···A angle is 145°. These supramolecular sheets stack along [1 0 0] (Fig. 6). No directional weak interactions (π–π, C–H···π, hydrogen bonding) are operative between the two sheets. Thus, an intermolecular Van der Waals interaction is responsible for this stacking. The methyl terminals of the ligand from adjacent sheets face each other in this arrangement.

The crystal structure possesses an impressively short intermolecular C(sp3)···O(sp3) contact [C9···O4* 2.958(3) Å; * = 1 − x, 1 − y, 2 − z]. A CSD search was carried out to query for the intermolecular distance from a

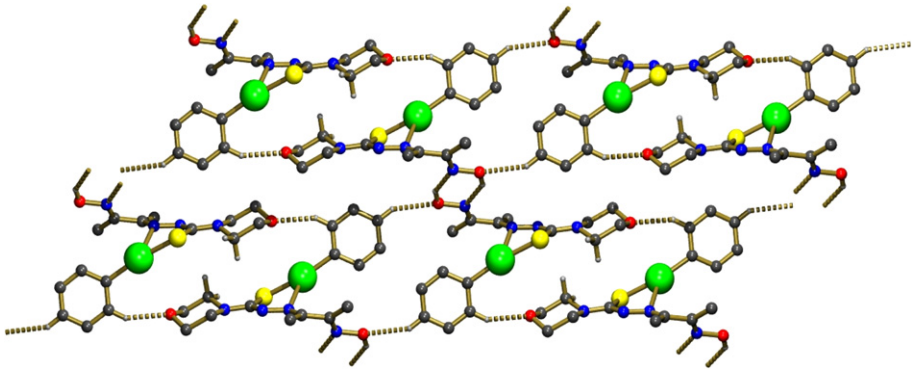


Fig. 3. Two-dimensional O–H···O and C–H···O hydrogen bonded sheet and O–H···N synthons of [PhHg(Hdammthiol)] (**1**).

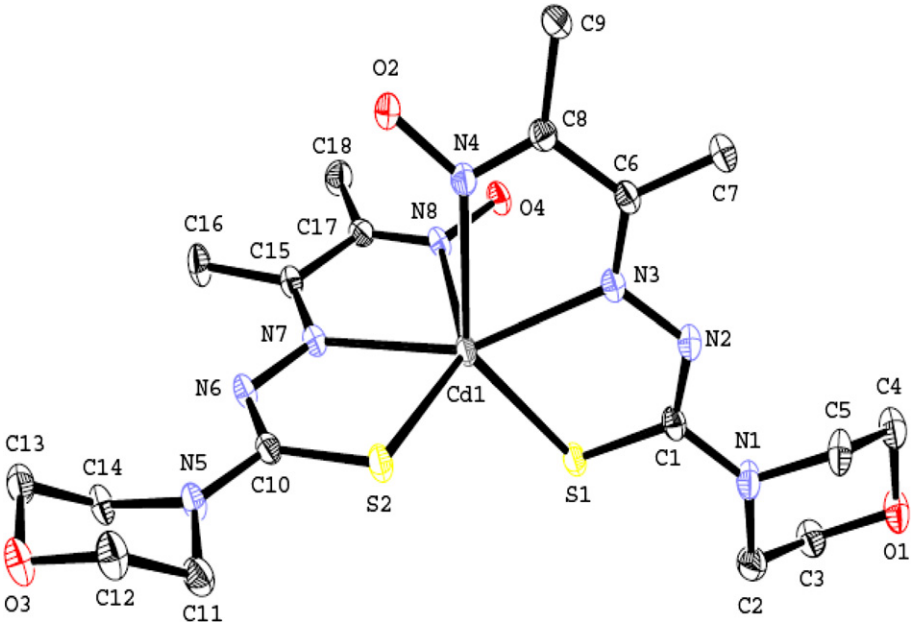


Fig. 4. ORTEP diagram of [Cd(Hdammthiol)$_2$] (**2**) with 50% probability ellipsoids.

N=C(CH3)–C(CH3) = N moiety to an oxime NOH moiety. When the non-bonding interaction between the two fragments was constrained with the O···C distance being less than 3.22 Å, the search resulted in 27 hits with a range 3.033–3.218 Å, and the three shortest distances were 3.033, 3.073 and 3.078 Å [40–42]. A closer look at the geometry of the O(sp3)···C (sp3) contact reported here reveals an interesting packing force using an uncommon interaction (Fig. 7). The O4 atom of the oxime is directed towards the centre of the plane formed by three H atoms (H9A, H9B, H9C) of the methyl group of the propylidene moiety, and is evidenced by the angle ∠C8–C9···O4* of 172.0°. The C9–H9A···O4*, C9–H9B···O4* and C9–H9C···O4* angles are 89.0°, 83.8° and 97.6°, respectively. It is interesting to note that if the strength of the C···O attraction is greater, the ∠C–H···O angle will be less in contrast to the normal C–H···O interaction. So, the angles rendered by the interaction are less than the generally accepted ∠C–H···O angles (~110°). The cooperative effect of the three individual interactions acts on the face of the plane of the three methyl hydrogens of the C9 atom due to their high acidic character. This non-conventional interaction could prove to be a good supramolecular synthon. We may term it as a CH_3···O interaction.

3.3. Comparison between the supramolecular structures

In summary, the hydrogen-bonding motifs of complexes **1** and **2** exhibit unique synergy through linear and cyclic supramolecular assemblies. In complex **1**, the primary structure directing agent is the oxime–oxime interaction which leads to a complimentary hydrogen-bonding $R_2^2(6)$ synthon. Linear C–H···O bonds to both oxime and morpholinic oxygen acceptors guide the assembly into a 2D sheet in the *ac* plane. Further, despite the presence of an aromatic ring no π···π interaction appears, but C–H···π interactions between the 2D sheets lead to the crystal synthesis. In complex **2**, a complimentary hydrogen bond (O–H···O) between the morpholine–oxime moieties prevails along with a C–H···O hydrogen bond. Bertolasi et al., have shown that oximes are able to form three types of hydrogen bonds where the oxygen atom of the oxime can act as a donor as well as an acceptor [43]. Our investigation supports this. The linear O–H···O and C–H···O supramolecular glue generate an infinite sheet architecture in the *bc* plane involving C(3) synthons.

In the literature, molecules (organic or metal complex) bearing non-deprotonated oximes showed the capability of generating aesthetic extended networks with the potential to be a crystal engineering tool [44–46]. The most common hydrogen bonding network arrangement reigning in these systems is the oxime–oxime $R_2^2(6)$ ring, and less often the C(3) chain and $R_2^4(6)(12)$ rings [47,48]. The first two synthons exist in our case also. Aakeröy et al., investigated silver complexes of pyridine–oxime ligands. They showed that the oxime–oxime interaction [$R_2^2(6)$] is not disrupted and is able to withstand the potentially disruptive influences of anions and pyridine–oxime interactions. In complex **2**, we have the opportunity to notice that the morpholine substituted moiety disrupts the $R_2^2(6)$ synthons to C(3) [morpholine···oxime O–H···O] synthons. This shows that morpholine···oxime C(3) synthon is even stronger for this complex.

3.4. ^{1}H NMR and infrared spectra

The ^{1}H NMR spectrum of the mercury complex [PhHg(Hdammthiol)] (**1**) in $CDCl_3$ at room temperature exhibits sharp singlets at δ 3.17 ppm and δ 3.6 ppm due to N–CH_2 (4 H) and O–CH_2 (4H), respectively, of the mor-

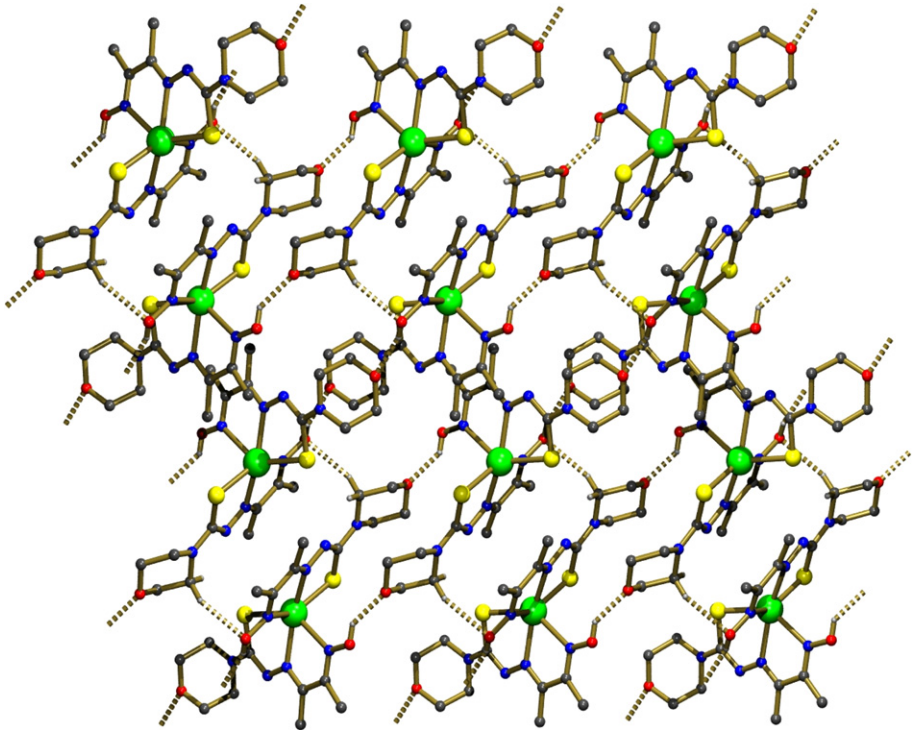


Fig. 5. Two-dimensional hydrogen bonding sheet of [Cd(Hdammthiol)$_2$] (**2**) along the *bc* plane.

pholine ring. Whereas in the cadmium(II) complex [Cd(Hdammthiol)$_2$] (**2**), these resonances are observed at δ 3.27 ppm and δ 3.69 ppm, respectively. These values are consistent with earlier reported values [49]. Two singlets, one at δ 2.50 ppm and another at δ 1.92 ppm, are tentatively assigned to the methyl protons of the mercury com-

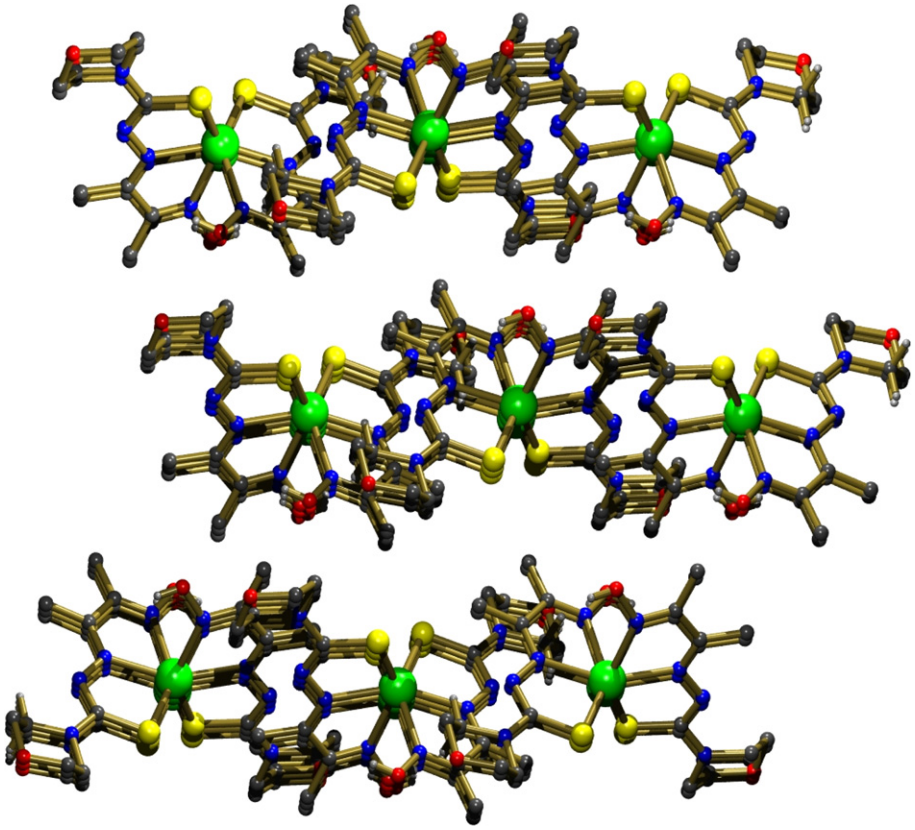


Fig. 6. Two-dimensional intermolecular Van der Waals interactions of terminal methyl groups in [Cd(Hdammthiol)$_2$] (**2**).

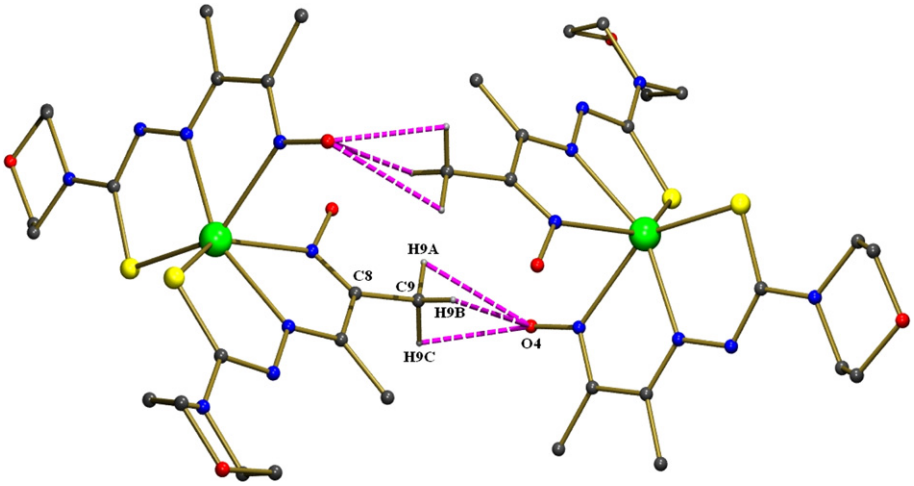


Fig. 7. Trifurcated $CH_3\cdots O$ hydrogen bonding between O4 and hydrogens on C9 of [Cd(Hdammthiol)$_2$] (**2**).

pound [50], while the methyl resonances of the cadmium complex are observed at δ 2.32 ppm and δ 2.04 ppm [50]. The aromatic proton resonances of phenylmercury(II) are observed as multiplets in the range δ 7.23–7.44 ppm.

The ν(C=S) of the thioketo form of the ligand generally absorbs at around 800 cm^{-1} in the infrared spectrum [51]. In the phenylmercury(II) and cadmium(II) complexes no such bands were observed in this region; instead bands at 730 cm^{-1} for the phenylmercury(II) complex and 745 cm^{-1} for the cadmium(II) complex were observed and assigned to ν(C–S). This suggests coordination of the phenylmercury(II) and cadmium(II) ions through the thiol sulfur via deprotonation [52]. The broad infrared spectral bands around 3350 cm^{-1} may be assignable to ν_{oxime}(OH), suggesting non-involvement of this group in bond formation in both complexes [53]. The observed bands, one at 1605 cm^{-1} and another at 1580 cm^{-1}, are tentatively assigned to ν_{oxime}(C=N) and $\nu_{hydrazone}$(C=N) groups, respectively [53,54].

4. Conclusion

We have synthesized two new complexes, one with the phenylmercury(II) ion and another with the cadmium(II) ion, involving the thiol form of the ligand diacetylmonoximemorpholine *N*-thiohydrazone. X-ray structure crystallography shows that the phenylmercury(II) complex has an tricoordinated distorted T-shaped topology, while a trapezoidal bipyramidal geometry is present in the cadmium(II) complex. Very few such tricoordinated distorted T-shaped structures for a phenylmercury(II) complex have been reported. Two-dimensional supramolecular assemblies of both the complexes and a new non-conventional $CH_3\cdots O$ interaction in cadmium complex are postulated.

Acknowledgements

One of us (K.D.) is thankful to the University Grants Commission, New Delhi for Emeritus Fellowship and Financial grants to conduct this work. We are also thankful to the Sophisticated Instrumentation Facility, Central Drug Research Institute, Lucknow, India for elemental analysis and spectroscopic data. Facilities provided by the DST, Govt. of India, New Delhi under FIST are also gratefully acknowledged. We are also grateful to the referees for their valuable comments.

Appendix A. Supplementary material

CCDC 653350 and 653351 contain the supplementary crystallographic data for complexes **1** and **2**. These data can be obtained free of charge via http://www.ccdc.cam.ac.uk/conts/retrieving.html, or from the Cambridge Crystallographic Data Centre, 12 Union Road, Cambridge CB2 1EZ, UK; fax: (+44) 1223-336-033; or e-mail: deposit@ccdc.cam.ac.uk. Supplementary data associated with this article can be found, in the online version, at doi:10.1016/j.poly.2007.07.027.

References

[1] S.S. Djbbar, B.O. Benali, J.P. Deloume, Polyhedron 16 (1997) 2175.
[2] P. Bhattacharya, J. Parr, A.T. Ross, J. Chem. Soc., Dalton Trans (1998) 3149.
[3] J.C. Wu, N. Tang, W.S. Liu, M.Y. Tan, A.C.S. Chan, Chin. Chem. Lett. 12 (2001) 757.
[4] L. He, S.H. Gou, Q.F. Shi, J. Chem. Crystallogr. 29 (1999) 207.
[5] D.X. West, A.E. Liberta, S.B. Padhye, P.B. Chikate, A.S. Sonawani, O. Kumbhar, R.G. Yerande, Coord. Chem. Rev. 123 (1993) 49.
[6] D. Kovala-Dermertzi, A. Domopoulou, M. Demertzis, C. Raptopoulou, A. Terzis, Polyhedron 13 (1994) 1917.
[7] D.X. West, M.S. Lockwood, A. Castineiras, Trans. Met. Chem. 22 (1997) 447.
[8] D.X. West, H. Gebremedhin, R.J. Butcher, J.P. Jasinski, Trans. Met. Chem. 20 (1995) 84.
[9] D. Kovala-Dermertzi, A. Domopoulou, M.A. Demertzis, G. Valle, A. Papageorgiou, J. Inorg. BioChem. 68 (1997) 47.
[10] Z.H. Liu, C.Y. Duan, J. Hu, X.Z. You, Inorg. Chem. 38 (1999) 1719.
[11] Y.P. Tian, C.Y. Duan, Z.L. Lu, X.Z. You, T.C.W. Mak, Z.Y. Zhang, Inorg. Chem. 36 (1997) 1247.

[12] Z.H. Liu, C.Y. Duan, J. Hu, J.H. Li, Y.J. Liu, Y.H. Mei, X.Z. You, New J. Chem. 24 (2000) 1057.
[13] E.S. Raper, Coord. Chem. Rev. 61 (1985) 115.
[14] E.S. Raper, Coord. Chem. Rev. 153 (1996) 199.
[15] M.J.M. Campbell, Coord. Chem. Rev. 15 (1975) 279.
[16] S. Padhye, G.B. Kauffmann, Coord. Chem. Rev. 63 (1985) 127.
[17] D.X. West, S.B. Padhye, P.B. Sonawane, Struc. Bonding (Berlin) 76 (1991) 4.
[18] D.X. West, A.E. Liberta, S.B. Padhye, R.C. Chilate, P.B. Sonawane, A.S. Kumbhar, R.G. Yerande, Coord. Chem. Rev. 123 (1993) 49.
[19] T.S. Lobna, P.K. Bhatia, J. Sci. Ind. Res. 48 (1989) 394.
[20] M.C. Rodrìguez-Argüelles, M.B. Ferrari, G.G. Fava, C. Pelizzi, G. Tarasconi, R. Albertini, P.P. Dall'Aglio, P. Lunghi, S. Pinelli, J. Inorg. Biochem. 58 (1995) 157.
[21] J.S. Casas, M.S. García-Tasende, C. Maichele-Mössmer, M.C. Rodrìguez- Argüelles, A. Sánchez, J. Sordo, A. Vázquez-lópez, S. Pinelli, P. Lunghi, R. Albertini, J. Inorg. Biochem. 62 (1996) 41.
[22] M.B. Ferrari, G.G. Fava, G. Tarasconi, R. Albertini, S. Pinelli, R. Starcich, J. Inorg. Biochem. 53 (1994) 13.
[23] B. Chen, M. Eddaoudi, S.T. Hyde, M. O'Keeffe, O.M. Yaghi, Science 291 (2001) 1021 (and references cited therein).
[24] S.S.-Y. Chui, S.M.-F. Lo, A.G. Orpen, I.D. Williams, Science 283 (1999) 1148, and references cited therein.
[25] J.S. Seo, D. Whang, H. Lee, S.I. Jun, J. Oh, Y.J. Jeon, K.A. Kim, Nature 404 (2000) 982, and references cited therein.
[26] D.J. Baner, P.W. Sadler, Brit. 1026401 (Cl. CO7c, d) April 20, 1966.
[27] D.J. Baner, P.W. Sadler, Chem. Abst. 65 (1966) 2224e.
[28] G.M. Sheldrick, SHELXS-97, SHELXL-97 Programs for Crystal Structure Analysis, University of Göttingen, Germany, 1997.
[29] L.J. Farrugia, ORTEP 3 for Windows, Version 1.076, University of Glasgow, (1997–2002).
[30] L.J. Farrugia, J. Appl. Cryst. 30 (1997) 565.
[31] A.L. Spek, J. Appl. Cryst. 36 (2003) 7.
[32] A.L. Spek, PLATON Version 1.11, 2007.
[33] L.G. Kuz'mina, Y.T. Struchkov, Croat. Chem. Acta 57 (1984) 701.
[34] J. Zukerman-Schpector, M.C. Rodrìguez-Argüelles, M.I. Suárez, A. Sánchez, J.S. Casas, J. Sordo, J. Coord. Chem. 24 (1991) 177.
[35] P. Pauling, The Nature of Chemical Bond, third ed., Cornell University Press, New York, 1960.
[36] J.D. Curry, R.J. Jandacer, J. Chem. Soc., Dalton Trans. (1972) 1120.
[37] A. Macias, M.C. Rodrìguez-Argüelles, M.I. Suárez, A. Sánchez, J.S. Casas, J. Sordo, U. Englert, J. Chem. Soc., Dalton Trans. (1989) 1787.
[38] J.S. Casas, M.V. Castaňo, M.S. García-Tasende, I. Martinez-Santamarta, A. Sánchez, J. Sordo, E.E. Castellano, J. Zukerman-Schpector, J. Chem. Res. (1992) 324.
[39] G. Park, N. Ye, R.D. Rogers, M.W. Brechbiel, R.P. Planalp, Polyhedron 19 (2000) 1155.
[40] C.A. Otter, R.M. Hartshorn, J. Chem. Soc., Dalton Trans. (2002) 4193.
[41] N. Bresciani-Pahor, L. Randaccio, P.J. Toscano, J. Chem. Soc., Dalton Trans. (1982) 1559.
[42] U. Englert, A. Haring, C. Hu, I. Kalf, Z. Anorg. Allg. Chem. 628 (2002) 1173.
[43] V. Bertolasi, G. Gilli, A.C. Veronese, Acta Crystallogr., Sect. B 38 (1982) 502.
[44] V.Y. Kukuskin, T. Nishioka, D. Tudela, K. Isobe, I. Kinoshita, Inorg. Chem. 36 (1997) 6157.
[45] R.J. Butcher, R.S. Bendre, A.S. Kuwar, Acta Crystallogr., Sect. E 61 (2005) 3511.
[46] S. Naskar, D. Mishra, R.J. Butcher, S.K. Chattopadhyay, Polyhedron (2007), doi:10.1016/j.poly.2007.03.063.
[47] E.A. Bruton, L. Brammer, F.C. Pigge, C.B. Aakeröy, D.S. Leinen, New J. Chem. 27 (2003) 1084.
[48] C.B. Aakeröy, A.M. Beatty, D.S. Leinen, Cryst. Eng. Comm 4 (2002) 310.
[49] E. Tas, M. Ulusoy, M. Guler, Synth. React. Inorg. Met-Org. Chem. 34 (2004) 1211.
[50] J.P. Naskar, S. Chowdhury, M.G.B. Drew, D. Datta, Cryst. Eng, Commun. 6 (2002) 556.
[51] G.C. Perey, D.A. Thoruton, Inorg. Nucl. Chem. Lett. 7 (1971) 599.
[52] K. Dey, D. Bandyopadhya, Indian J. Chem. 31A (1992) 34.
[53] M.M. Mostafa, K.M. Ibrahim, M.N.H. Mousa, Trans. Met. Chem. 9 (1984) 243.
[54] S.P. Ghosh, T. Bandyopadhyay, Trans. Met. Chem. 10 (1985) 57.

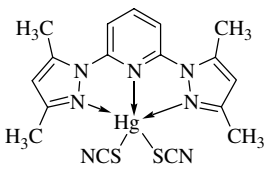


Fig. 1. Chemical structure of the title compound.

point apparatus. The IR spectra were obtained by using IR grade KBr disks on a Perkin–Elmer 1600 Series FTIR spectrophotometer in the range of 4000–250 cm^{-1}. The electronic spectra were obtained using a Cary 1E UV–Visible spectrophotometer (Varian). The thermogravimetry/differential thermal analysis (TG/DTA) measurements were run on a Shimadzu DTG-60H. In this study, thermogravimetric curves were obtained with a flow rate of the carrier gas of 100 mL/min and a heating rate of 10 °C/min in nitrogen (3 bar) with an alumina pan. The experiments were carried out in the range 35–750 °C and with a cleaned up range of 750–800 °C under oxygen atmosphere. The recorded data were analyzed with the help of the TA-60 WS Version 2.01 software.

2.2. Synthesis

2.2.1. Ligand (bdmpp)

The ligand bdmpp was prepared from 2,6-dichloropyridine and the potassium salt of 3,5-dimethyl-*N*-pyrazol by refluxing in diglime as described previously in the literature (Scheme 1) [10]. 3,5-Dimethylpyrazol was synthesized by the reaction of hydrazine hydrate and 2,4-pentandione [11].

2.2.2. [Hg(bdmpp)(SCN)$_2$] (1)

A 20 ml solution of 2,6-bis(3,5-dimethyl-*N*-pyrazolyl)pyridine (bdmpp) (0.266 g, 1 mmol) in hot acetonitrile was added to a 20 ml hot methanolic solution of $Hg(SCN)_2$ (0.316 g, 1 mmol). The mixture was filtered off while the solution was hot. The resulting mixture was set aside for two days and colourless fine crystals formed. The crystals were filtered off and dried in the open air. Yield: 80%, mp: 201–203 °C, ^{1}H NMR (400 MHz, 25 °C, $CDCl_3$,) 2.44 (s, 6H), 2.60 (s, 6H), 6.20 (s, 2H), 7.42 (d, 2H, $J = 8.12$ Hz), 8.06 (t, 1H, $J = 8.08$ Hz). *Anal.* Calc. for $C_{17}H_{17}HgN_7S_2$: C, 34.96; H, 2.93; N, 16.79. Found: C, 34.62; H, 2.78; N, 16.07. Suitable crystals were selected for the XRD study.

2.3. Computational details

GAUSSIAN03 program package [12] was used in the calculations. The geometry of the title complex was optimized by semi-empirical molecular orbital treatment at both the PM3 level and density functional theory (DFT) using Becke's three-parameter hybrid method (B3) [13] and the exchange functional of Lee, Yang and Parr (LYP) [14] in conjuction with the LANL2DZ basis set, which includes the effective core potential (ECP) proposed by Hay and Wadt, plus double basis-ξ for Cl- and I-atoms [15]. Whether the stationary points were minima or first-order saddle points was determined by analytical computation of vibrational frequencies at the level of geometry optimization.

2.4. X-ray structure determination

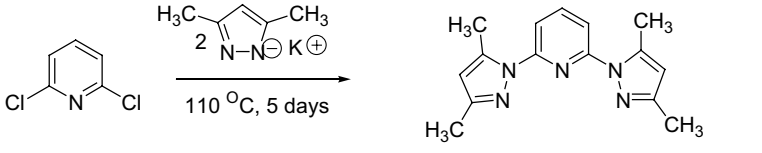
Diffraction measurements were made on a three-circle CCD diffractometer using graphite monochromated Mo-K(α) radiation ($\lambda = 0.71073$ Å) at −100 °C for compound **1**. The intensity data were integrated using the SAINT [16] program. Absorption, Lorentz and polarisation corrections were applied. The structure was solved by direct methods and refined by full-matrix least-squares against F^2 using SHELXTL [17]. All non-hydrogen atoms were assigned anisotropic displacement parameters and were refined without positional constraints. Hydrogen atoms were included in idealised positions with isotropic displacement parameters constrained to 1.5 times the U_{eq} of their attached carbon atoms for methyl hydrogens, and 1.2 times the U_{eq} of their attached carbon atoms for all others.

3. Results and discussion

3.1. Description of the crystal structure

Crystal data collection and refinement of the title compound [Hg(bdmpp)(SCN)$_2$] (L = 2,6-bis(3,5-dimethyl-*N*-pyrazolyl)pyridine) is summarized in Table 1. The ORTEP and molecular packing diagrams are displayed in Figs. 2 and 3. Selected bond lengths and angles in the complex are listed in Table 2.

The Hg(II) atom is pentacoordinated, with three nitrogen atoms (N1, N3 and N5) from the 2,6-bis(3,5-dimethyl-*N*-pyrazolyl ligand and two sulfur atoms from the thiocyanate ligand. Both mercury and sulfur atoms



2,6-bis(3,5-dimethyl-N-pyrazolyl)pyridine

Scheme 1.

Table 1
Crystallographic and refinement data for the title compound

Formula	$C_{17}H_{17}HgN_7S_2$
Formula weight	584.09
Temperature (K)	100(2)
Wavelength (Å)	0.71073
Crystal system	triclinic
Space group	$P\bar{1}$
Unit cell dimensions	
a (Å)	7.312(2)
b (Å)	11.804(2
c (Å)	12.407(3)
α (°)	114.25(3)
β (°)	94.14(3)
γ (°)	100.64(3)
Volume (Å^3)	946.3(4)
Z	2
D_{calc} (g cm^{-3})	2.050
Absorption coefficient (mm^{-1})	8.371
$F(000)$	560
θ Range for data collection (°)	1.83–27.48
Index ranges	$-9 \leqslant h \leqslant 9$, $-15 \leqslant k \leqslant 15$, $-16 \leqslant l \leqslant 16$
Reflections collected	10,878
Independent reflections	4338 [$R_{(int)} = 0.1559$]
Refinement method	full-matrix least-squares on F^2
Data/restraints/parameters	4338/0/248
Goodness-of-fit on F^2	1.060
Final R indices [$I \geqslant 2\sigma(I)$]	$R_1 = 0.0486$, $wR_2 = 0.1175$
R indices (all data)	$R_1 = 0.0500$, $wR_2 = 0.1184$

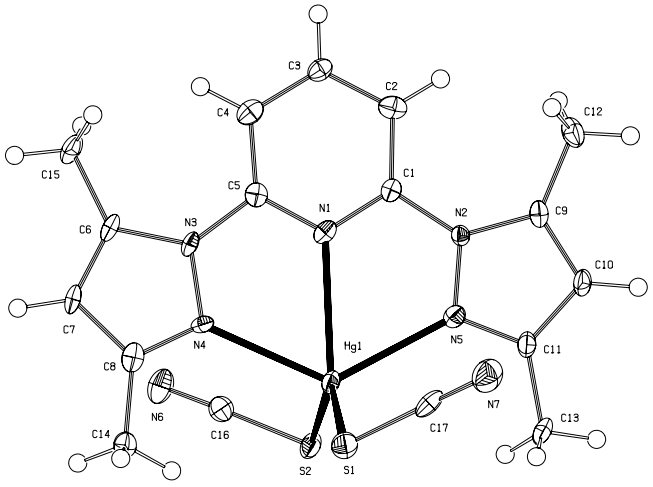


Fig. 2. The molecular structure of the title compound. Displacement ellipsoids are plotted at the 50% probability level.

are soft according to Pearson theory [18], so the thiocyanate ions that are bonded to metal terminally are the S atoms. In five coordinate compounds, the coordination sphere could be described either as square-pyramidal or trigonal bipyramidal, depending on the parameter, $\tau = (\beta - \alpha)/60$ (α and β are the two largest bond angles around the metal ion). When τ is 0, the coordination is assumed to be an ideal square pyramid; for an ideal trigonal bipyramid τ is 1 [19]. The largest bond angles in the coordination sphere are 127.89° [N5–Hg–N4] and 116.36° [S2–Hg–N3], which give a τ value of 0.1921. This value is closer to that of a distorted square-pyramid around the mercury atom.

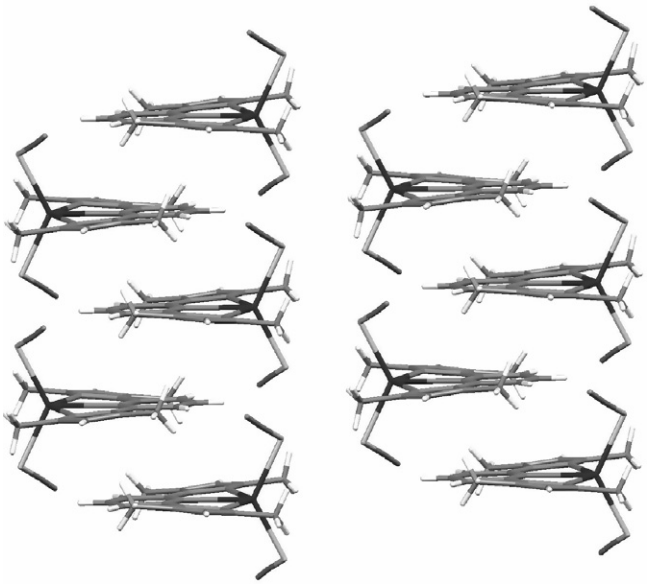


Fig. 3. Packing diagram of the title complex.

The Hg–N bond distances are in the range 2.385(6)–2.557(4) Å, and the Hg–S1 and Hg–S2 bond distances are 2.462(2) and 2.472(2) Å, respectively (Table 2). All the bond lengths and angles are comparable with similar structures [20–22].

3.2. Geometry

PM3 calculations are generally satisfactory for the prediction of structure of organic and organotin compounds [23]. On the other hand, DFT methods are very successful in modelling organic systems [24]. To compare their results for the organomercury compound, the geometry of $[Hg(bdmpp)(SCN)_2]$ was optimized in a singlet state using PM3 and B3LYP/LanL2DZ methods. Selected calculated bond lengths, bond angles and dihedral angles of **1** are gathered in Table 1. The differences among the calculated values of geometrical parameters are insignificant for the PM3 and B3LYP/LanL2DZ methods used. For both calculations, bond angles and dihedral angles remain in sufficient agreement, except for the Hg(1)–S(1)–C(17) bond angle. In particular, the B3LYP/LanL2DZ results are better than those obtained by using PM3. On the contrary, the theoretical bond lengths at the B3LYP/LanL2DZ level are overestimated by 1.5, 5.3, 9.4 and 3.9% for the Hg(1)–N(1), Hg(1)–N(4), Hg(1)–S(1) and S(1)–C(17) bonds, respectively. The bond lengths calculated at the PM3 level are more overestimated for the first two bonds by 15.1% and 5.6%, respectively, but less overestimated for the last two bonds by 0.3% and 2.1%, respectively. Our calculations

Table 2
Selected observed and calculated bond lengths (Å) and angles (°) for the [Hg(bdmpp)(SCN)$_2$] complex

	Observed	Calculated			
		B3LYP/LANL2DZ	% error	PM3	% error
Bond lengths					
Hg(1)–N(1)	2.557	2.519	1.5	2.171	15.1
Hg(1)–N(4)	2.408	2.536	−5.3	2.273	5.6
Hg(1)–S(1)	2.462	2.694	−9.4	2.470	−0.3
S(1)–C(17)	1.676	1.741	−3.9	1.640	2.1
C(1)–N(1)	1.320	1.331	−0.8	1.367	−3.6
C(1)–N(2)	1.414	1.417	−0.2	1.433	−1.3
C(9)–N(2)	1.385	1.396	−0.8	1.418	−2.4
C(16)–N(6)	1.141	1.157	−1.4	1.173	−2.8
C(1)–C(2)	1.396	1.408	−0.9	1.403	−0.5
C(9)–C(12)	1.502	1.500	0.1	1.474	1.9
N(2)–N(5)	1.376	1.405	−2.1	1.405	−2.1
Bond angles					
S(1)–Hg(1)–N(1)	115.2	110.8	3.8	119.2	−3.5
Hg(1)–S(1)–C(17)	99.2	92.3	7.0	87.2	12.1
C(1)–N(1)–C(5)	120.2	120.6	−0.3	120.1	0.1
N(1)–C(1)–N(2)	115.6	114.7	0.8	114.0	1.4
N(3)–N(4)–C(8)	106.7	105.9	0.7	107.5	−0.7
C(1)–C(2)–C(3)	116.9	117.8	−0.8	118.6	−1.5
C(6)–C(7)–C(8)	106.8	107.1	−0.3	107.9	−1.0
C(9)–C(12)–H(12A)	109.5	111.0	−1.4	110.8	−1.2
C(1)–C(2)–H(2)	121.5	121.5	0.0	121.1	0.3
Dihedral angles					
Hg(1)–N(1)–C(1)–C(2)	177.3	178.9	−0.9	179.5	−1.2
N(1)–C(1)–C(2)–H(2)	−178.6	176.6	1.1	178.7	−0.1
N(2)–N(5)–C(11)–C(13)	−179.7	178.8	0.5	179.5	0.1

prove that the quality of the data obtained with the DFT method (B3LYP/LanL2DZ) is not much better than that of the semi-empirical data (PM3). The discrepancy between the experimental (X-ray) and calculated values for the atomic coordinates might result from the different environments of a molecule in the experimental crystalline state and in the theoretical gas phase. However, it may be stated that the modelling techniques applied in the present work properly reflect the main properties of the actual structure and can be successfully applied for predicting the features of the [Hg(bdmpp)(SCN)$_2$] complex.

3.3. Spectroscopic properties

3.3.1. FTIR spectra

The IR spectrum of [Hg(bdmpp)(SCN)$_2$] in KBr pellets exhibits two strong bands corresponding to ν(C=N) at 2340 and 2360 cm^{-1}. The band corresponding to the ν(C=S) stretching vibration appears at 785 cm^{-1}. The FTIR spectrum of the free ligand shows weak peaks at 2977, 2921 cm^{-1} and 3134, 3106 cm^{-1}, assignable to CH_3 and aromatic hydrogen bonds, respectively.

For the [Hg(bdmpp)(SCN)$_2$] complex, the experimental IR spectral frequencies were 3054, 2118 and 1599 cm^{-1}, those in the DFT computation were 3051, 2139 and 1631 cm^{-1} and those in the PM3 computations were 3040, 2290 and 1689 cm^{-1}. As can be seen from Table 3, the PM3 results are always higher than the experimental ones. On the contrary, there is no such apparent tendency for the DFT results.

Table 3
The observed and calculated vibrational frequencies of B3LYP/LanL2DZ and PM3 for [Hg(bdmpp)(SCN)$_2$]

Observed frequency	Calculated frequency	
	B3LYP/LanL2DZ	PM3
518	514	616
735	742	677
786	759	726
833	832	857
985	865	994
1039	1011	1074
1138	1130	1093
1303	1324	1292
1347	1351	1339
1383	1385	1389
1447	1410	1460
1560	1604	1578
1599	1631	1689
2118	2139	2290
3054	3051	3040

To make a comparison with the experimental observation, we present correlation graphics in Fig. 4 based on the calculations. It can be seen that both graphs match each other well, but the experimental vibrational frequencies are especially in better agreement with the DFT results at the B3LYP/LanL2DZ level than the semi-empirical results at the PM3 level.

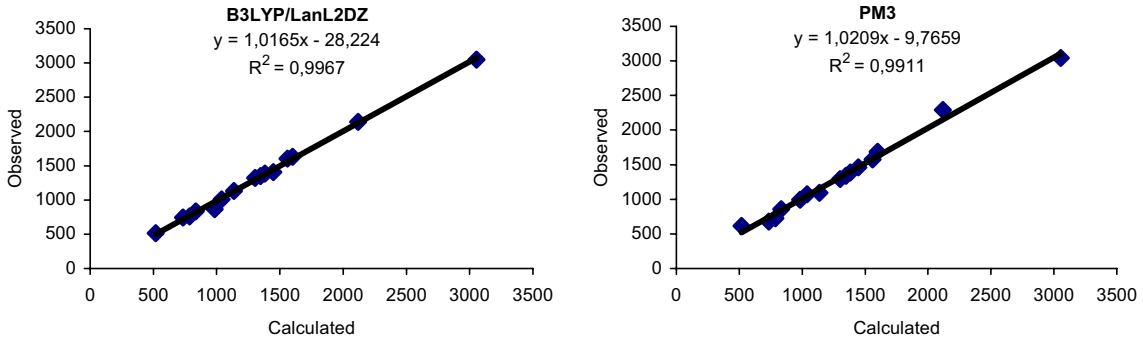


Fig. 4. Correlation graphics of observed and calculated (B3LYP/LanL2DZ and PM3 level) frequencies (cm^{-1}) of $[Hg(bdmpp)(SCN)_2]$.

3.3.2. Absorption spectra

The absorption spectra of the ligand (bdmpp) and complex $[Hg(bdmpp)(SCN)_2]$ were recorded in dimethylformamide. The UV spectra for the ligand and complex show two absorptions bands between 250 and 310 nm. For the bdmpp complex, a band occurs near 267 nm ($\varepsilon_1 = 16{,}000$ M^{-1} cm^{-1}) and 298 nm ($\varepsilon_2 = 17{,}340$ M^{-1} cm^{-1}). The spectrum of the free ligand exhibits intense peaks at 258 (12,800 M^{-1} cm^{-1}) and 300 nm. This indicates ligand-centered bands occur in this region, though other charge-transfer transitions also may contribute significant intensity. A similar observation was mentioned by Willison et al. [25].

3.4. Thermal analysis

The TGA and DTA analysis of $[Hg(bdmpp)(SCN)_2]$ was investigated both under inert and open-air atmosphere. Thermal analysis shows the weight lost under a nitrogen atmosphere between 188 and 227 °C is about 44–45%, which is nearly the same with the mass of the bdmpp ligand in the complex and, at 201 °C the melting peak point can be observed easily. Between 277 and 440 °C there is a new decomposition observed and approximately at 700 °C the mass nearly vanishes. This situation shows that $Hg(SCN)_2$ in the medium turns to gas by decomposing first fast and then slowly.

3.5. Orbitals

In the conjugated molecules, the frontier molecular orbital energies play an important role in the electric and optical properties, as well as in UV–Vis spectra and chemical reactions [26]. (Fig. 5) shows the distributions and energy levels of the HOMO − 1, HOMO, LUMO and LUMO + 1 orbitals computed at the B3LYP/LanL2DZ level for the HgSCN complex. The HOMO–LUMO gap is 0.141 eV, so electron movement between these orbitals could easily occur so that we observe a peak around 310 nm in the UV–Vis spectrum. Moreover, one can see that the HOMO − 1 and HOMO are substantially localized on the SCN parts of the complex. On the contrary, LUMO and LUMO + 1 are mainly confined in the aromatic part of the complex.

4. Conclusion

Pseudohalide ions are attractive as co-ligands due to their bridging of metal ions to each other and neutralizing the charges of the complexes. In addition, the aim of this study was to form mononuclear complex structures coordinated by bdmpp with the help of cyanate. The structure of the title complex has been characterized by X-ray diffraction and by means of elemental analyses, IR and electronic spectra. Studies along these lines are currently in progress in our laboratory.

Acknowledgements

The financial support of the Scientific and Technical Research Council of Turkey (TUBİTAK) Grants No: TBAG-2452-104T064 and 104T371, and Balikesir University is gratefully acknowledged. Hulya Kara also thanks the

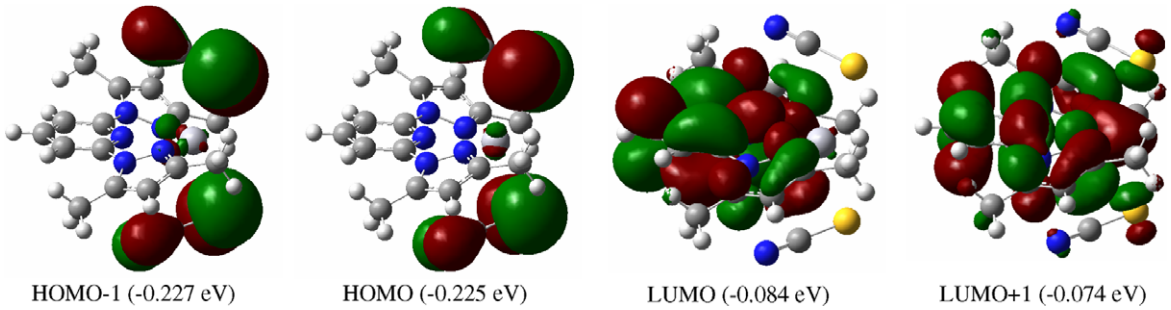


Fig. 5. Molecular orbital surfaces and energy levels given in parantheses for the HOMO − 1, HOMO, LUMO and LUMO + 1 of $[Hg(bdmpp)(SCN)_2]$ complex computed at B3LYP/LanL2DZ level.

Nato-B1-TUBITAK for funding and Prof. Guy Orpen (School of Chemistry, University of Bristol, UK) for his hospitality.

Appendix A. Supplementary material

CCDC 635128 contains the supplementary crystallographic data for [2,6-bis(3,5-dimethyl-*N*-pyrazolyl)pyridine]-(dithiocyanato)mercury(II). These data can be obtained free of charge via http://www.ccdc.cam.ac.uk/conts/retrieving.html, or from the Cambridge Crystallographic Data Centre, 12 Union Road, Cambridge CB2 1EZ, UK; fax: (+44) 1223 336 033; or e-mail: deposit@ccdc.cam.ac.uk. Supplementary data associated with this article can be found, in the online version, at doi:10.1016/j.poly.2007.07.021.

References

[1] M.A. Halcrow, Coord. Chem. Rev. 249 (2005) 2880.
[2] F. Ercan, C. Arıcı, D. Ülkü, R. Kurtaran, M. Aksu, O. Atakol, Z. Kristallogr. 219 (2004) 295.
[3] C. Arıcı, D. Ülkü, R. Kurtaran, Ü. Ergün, O. Atakol, Cryst. Res. Technol. 41 (2006) 309.
[4] G. Mahmoudi, A. Morsali, L-G. Zhu, Polyhedron (2007), doi:10.1016/j.poly. 2007.01.047.
[5] W. Huang, T. Ogawa, J. Mol. Struct. 785 (2006) 21.
[6] Z.-H. You, H.-L. Zhu, Z. Anorg. Allg. Chem. 630 (2004) 2754.
[7] F.A. Mautner, R. Vicente, S.S. Massoud, Polyhedron 25 (2006) 1673.
[8] R. Kurtaran, H. Namli, C. Kazak, O. Turhan, O. Atakol, J. Coord. Chem. in press (2006).
[9] R. Kurtaran, C. Arıcı, S. Durmuş, D. Ülkü, O. Atakol, Anal. Sci. 19 (2003) 335.
[10] D.L. Jameson, K.A. Goldsby, J. Org. Chem. 55 (1990) 4992.
[11] B.S. Furniss, A.J. Hannaford, P.W.G. Smith, A.R. Tatchell, Vogel's Textbook of Practical Org.Chem, Fifth ed., Longman, Science and Technical, 1991, p. 1149.
[12] M.J. Frisch, G.W. Trucks, H.B. Schlegel, G.E. Scuseria, M.A. Robb, J.R. Cheeseman, J.A. Montgomery Jr., T. Vreven, K.N. Kudin, J.C. Burant, J.M. Millam, S.S. Iyengar, J. Tomasi, V. Barone, B. Mennucci, M. Cossi, G. Scalmani, N. Rega, G.A. Petersson, H. Nakatsuji, M. Hada, M. Ehara, K. Toyota, R. Fukuda, J. Hasegawa, M. Ishida, T. Nakajima, Y. Honda, O. Kitao, H. Nakai, M. Klene, X. Li, J.E. Knox, H.P. Hratchian, J.B. Cross, C. Adamo, J. Jaramillo, R. Gomperts, R.E. Stratmann, O. Yazyev, A.J. Austin, R. Cammi, C. Pomelli, J.W. Ochterski, P.Y. Ayala, K. Morokuma, G.A. Voth, P. Salvador, J.J. Dannenberg, V.G. Zakrzewski, S. Dapprich, A.D. Daniels, M.C. Strain, O. Farkas, D.K. Malick, A.D. Rabuck, K. Raghavachari, J.B. Foresman, J.V. Ortiz, Q. Cui, A.G. Baboul, S. Clifford, J. Cioslowski, B.B. Stefanov, G. Liu, A. Liashenko, P. Piskorz, I. Komaromi, R.L. Martin, D.J. Fox, T. Keith, M.A. Al-Laham, C.Y. Peng, A. Nanayakkara, M. Challacombe, P.M.W. Gill, B. Johnson, W. Chen, M.W. Wong, C. Gonzalez, J.A. Pople, Gaussian 03, Revision C.2, Gaussian, Inc., Pittsburgh PA, 2003.
[13] A.D. Becke, J. Chem. Phys. 98 (1993) 5648.
[14] C. Lee, W. Yang, R.G. Parr, Phys. Rev. B 37 (1988) 785.
[15] P.J. Hay, W.R. Wadt, J. Chem. Phys. 82 (1985) 284.
[16] SAINT integration software version 7.06A, Bruker AXS, Madison, WI, 1997-2003.
[17] SHELXTL program system version 6.14, Bruker AXS Inc., Madison, WI, 2000-2003.
[18] R.G. Pearson, Inorg. Chem. 27 (1988) 734.
[19] A.W. Addison, T. Nageswara Rao, J. Reedijk, J. van Rijn, G.C. Verschoor, J. Chem. Soc., Dalton Trans. (1984) 1349.
[20] .R. Choudhury, S.K. Dey, N. Mondal, S. Mitra, V. Gramlich, Inorg. Chim. Acta 353 (2003) 217.
[21] T.K. Maji, S. Sain, G. Mostafa, D. Das, T-H. Lu, N.R. Chaudhuri, J. Chem. Soc., Dalton Trans. (2001) 3149.
[22] T.J. Emge Cbeng, J.G. Brennan, Inorg. Chem. 33 (1994) 3711.
[23] (a) R.B. de Alencastro, J.A.S. Bomfim, C.A.L. Filgueiras, R.A. Howie, J.L. Wardell, Appl. Organomet. Chem. 19 (2005) 479;
(b) A. Azizoglu, Struct. Chem. 14 (2003) 575.
[24] (a) T. Tugsuz, F. Sevin, J. Mol. Struct. (Theochem) 775 (2006) 29;
(b) B. Kilbas, A. Azizoglu, M. Balci, Helv. Chim. Acta 89 (2006) 1449;
(c) M.L. McKee, M. Swart, Inorg. Chem. 44 (2005) 6975.
[25] S.A. Willison, H. Jude, R.M. Antonelli, J.M. Rennekamp, N.A. Eckert, A. Jeanette Krause Bauer, W.B. Connick, Inorg. Chem. 43 (2004) 2548.
[26] I. Fleming, Frontier Orbitals and Organic Chemical Reactions;, Wiley, London, 1976.

employed as either homogeneous [2] or heterogeneous [3] catalysts in a variety of chemical reactions. Rhodium-based homogeneous catalysts in particular may be used *inter alia* in carbon–carbon bond formation [4], cyclopropanation [5], decarbonylation of aldehydes [6], hydroboration of olefins [7], hydroformylation of olefins [8], hydrogenation [9], hydrosilation [10] and carbon monoxide insertion reactions [11–13]. Oxidative addition of iodomethane to square planer rhodium(I) or iridium(I) complexes and subsequent CO insertion reactions is important in the Monsanto and Cativa industrial processes [12,14] for the production of acetic acid from methanol. The rate-determining step in the rhodium-based Monsanto process is the oxidative addition of methyl iodide to $[Rh(CO)_2I_2]^-$. In contrast, during *cis*-$[Ir(CO)_2I_2]^-$-catalyzed methyl carbonylation in the Cativa process, CO insertion in $[CH_3Ir(CO)_2I_3]^-$ to give $[(CH_3CO)Ir(CO)_2I_3]^-$ is rate-determining. It is known [15–17] that rhodium(I) complexes of the type $[Rh(L,L')(CO)(PPh_3)]$, L,L′ = mono charged bidentate ligands, can also facilitate the formation of an acetyl species following oxidative addition of methyl iodide. Depending on what L,L′ is, a variety of reaction mechanisms for this reaction has been reported. These mechanisms are summarized in Eq. (1) (L,L′) = methyl(2-methyl-amino-1-cyclopentene-1-dithiocarboxylato, [17]), (2) (L,L′ ¯thioacetylacetonato [15d]), (3) (L,L′ = *inter alia* 1,1,1-trifluoro-2,4-pentanedionato [15a]) and (4) (L,L′ = *inter alia* 2,4-pentanedionato [15b]) below. The notation Rh^{III}-alkyl1 and Rh^{III}-acyl1 in the four equations below indicates the first formed alkylated, $[Rh^{III}(R)]$, or acylated rhodium(III) species, $[Rh^{III}(COR)]$. When the last number in the notation changes to "2", such as in Rh^{III}-alkyl2 in Eqs. (3) and (4), it shows that after the first alkylated or acylated species has formed, it converted to a second, different but more stable, alkylated or acylated geometrical isomer.

$$Rh^{I} + CH_3I \underset{k_{-1}}{\overset{k_1,K}{\rightleftharpoons}} Rh^{III}\text{-alkyl1} \xrightarrow{k_2} Rh^{III}\text{-acyl1} \quad (1)$$

$$Rh^{I} + CH_3I \xrightarrow{k_1} Rh^{III}\text{-alkyl1} \xrightarrow{k_2} Rh^{III}\text{-acyl1} \quad (2)$$

$$Rh^{I} + CH_3I \underset{k_{-1}}{\overset{k_1,K}{\rightleftharpoons}} Rh^{III}\text{-alkyl1} \overset{k_2}{\mapsto} Rh^{III}\text{-acyl1} \xrightarrow{k_3} Rh^{III}\text{-alkyl2} \quad (3)$$

$$Rh^{I} + CH_3I \underset{k_{-1}}{\overset{k_1,K}{\rightleftharpoons}} Rh^{III}\text{-alkyl1} \underset{k_{-2}}{\overset{k_2}{\rightleftharpoons}} Rh^{III}\text{-acyl1} \underset{k_{-3}}{\overset{k_3}{\rightleftharpoons}} Rh^{III}\text{-alkyl2} \quad (4)$$

In, for example, Eq. (4), $[Rh(H_3CCOCHCOCH_3)(CO)(PPh_3)(CH_3)(I)]$ would be a typical formula describing the two different Rh^{III}-alkyl1 or Rh^{III}-alkyl2 geometrical isomers. The first example of a single crystal structure determination of a Rh^{III}-alkyl species of this type is described later in this publication and Fig. 8 shows clearly the coordination modes. For the Rh^{III}-acyl1 isomer of Eq. (4), the formula $[Rh(H_3CCOCHCOCH_3)(COCH_3)(PPh_3)(I)]$ is representative. Structurally it differs from the alkyl species in that the CO ligand inserted between the Rh center and the alkyl, here a methyl ligand, to generate an acyl ligand.

We were interested to establish whether a ferrocenyl (Fc) fragment as part of the β-diketonato ligand in complexes of the type [Rh(β-diketonato)(CO)(PPh$_3$)] may enhance acyl formation during oxidative addition. Utilizing L,L′ = $(FcCOCHCOCF_3)^-$ = fctfa, we show with this communication that incorporation of the ferrocenyl group in the β-diketonato ligand significantly enhances the rate of acyl formation as well as the ensuing carbonyl insertion and deinsertion to form new Rh^{III}-alkyl and Rh^{III}-acyl species during the oxidative addition of CH_3I to [Rh(fctfa)-(CO)(PPh$_3$)]. We especially demonstrate how a variety of different spectroscopic techniques (UV/Vis, IR, ^{1}H and ^{31}P NMR) may be used to obtain different information packages and a better insight into the overall process that takes place during this general type of reaction. Especially satisfying was the realization that each of the previous proposed mechanisms (Eqs. (1)–(4)) are only special cases of the more general mechanism given in the abstract for the reaction between [Rh(fctfa)(CO)(PPh$_3$)] and CH_3I.

2. Experimental

2.1. Materials and apparatus

NMR measurements, at 298 K unless otherwise stated, were recorded on a Bruker Advance DPX 300 NMR spectrometer [^{1}H (300.130 MHz), and ^{31}P (121.495 MHz)]. Chemical shifts are reported as δ values relative to $SiMe_4$ at 0 ppm for the ^{1}H spectra or relative to 85% H_3PO_4 at 0 ppm for the ^{31}P spectra. Infrared spectra were recorded on a Hitachi 270-50 infrared spectrometer either in a KBr matrix or in chloroform or acetone solutions. UV measurements were recorded on a GBC-916 UV/Vis spectrometer. Liquid reactants and solvents were distilled prior to use, water was double distilled. DMF was dried according to published methods [18]. Solutions of [Rh(fctfa)(CO)(PPh$_3$)] in acetone, methanol, ethyl acetate, benzene and chloroform [19] were tested for stability by means of ^{1}H NMR and overlay IR and UV spectra for at least 24 h.

Synthesis of [Rh(fctfa)(CO)(PPh$_3$)(CH$_3$(I)]: Methyl iodide (1.9 g, 13.4 mmol) was added to [Rh(fctfa)-(CO)(PPh$_3$)] [20] (75 mg, 0.1 mmol) dissolved in hexane (70 ml) at 30 °C. N_2 was purged through the reaction vessel before it was sealed and left at room temperature in the dark. After 5 days crystals suitable for X-ray structure determination were obtained from the reaction mixture, 90% yield, m.p.: 235 °C; C, 47.5; H 3.2, $C_{34}H_{28}F_3FeO_3$-RhPI requires C, 47.6; H, 3.3%). IR (KBr), ν_{max}/cm^{-1}: 2056 (C=O); ^{1}H NMR($CDCl_3$): isomer A: 1.78 (3H, d d, CH_3), 4.30 (5H, s, C_5H_5 and 1H, m, C_5H_4), 4.40 (1H, m, C_5H_4), 4.48 (1H, m, C_5H_4), 4.77 (1H, m, C_5H_4), 5.31 (1H, s, CH) and 7.25–7.50 (15H, m, aromatic); isomer B: 1.78 (3H, d d, CH_3), 4.24 (5H, s, C_5H_5 and 1H, m, C_5H_4), 4.38 (1H, m, C_5H_4), 4.60 (1H, m, C_5H_4), 4.80

(1H, m, C_5H_4), 5.45 (1H, s, CH) and 7.25 – 7.50 (15H, m, aromatic).

2.2. Crystallography

Crystal density of [Rh(fctfa)(CO)(PPh_3)CH_3(I)] was determined by flotation in sodium iodide solution. A crystal of dimensions $0.075 \times 0.150 \times 0.650$ mm was used for data collection on a Syntex P-1 diffractometer with Nb filtered utilizing Mo Kα radiation. The $\omega/2\theta$-scan technique was used with variable scan width $\Delta\omega = (0.43 + 0.34 \tan\theta)°$, scan speed 5.49° min^{-1} in ω and a maximum scan time of 60 s per reflection. Unit cell parameters were determined from least-squares refinement of 25 reflections with $15 < \theta < 20°$ (total measuring range $3 < \theta < 25°$). Empirical absorption corrections [21] were applied with minimum and maximum correction factors of 0.4529 and 0.7413, respectively. The mean intensity of three standard reflections, measured over 7200 s of X-ray exposure time, varied from the initial value by less than −1%. All possible reflections with $(\sin\theta)/\lambda < 0.59$ Å^{-1} in the range $-12 < h < 12.0 < k < 18.0 < l < 24$ were measured, giving 4420 unique reflections of which 4414 were considered observed [$I > 2.0\sigma(I)$]. The structure was solved by the heavy-atom method using SHELXS86 [22] and was subjected to anisotropic full-matrix least-squares refinement on F (a total of 380 parameters refined) using SHELXS93 [23]. The H-atom positions were calculated riding on the adjacent C atoms assuming C–H = 0.930 Å, and were refined with an overall temperature factor. Neutral-atom scattering factors were taken from Cromer and Mann [24] and anomalous-dispersion corrections for rhodium from *International Tables for X-ray Crystallography* [25]. Final $R = 0.0588$ and $wR = 0.1692$ (unit weights), $(\Delta\rho)_{max} = 1.841$, $(\Delta\rho)_{min} = -1.087$ e Å^{-3} and $(\Delta/\sigma)_{max} = -0.745$. The high value of the maximum residual electron density $(\Delta\rho)_{max}$ of 1.841 is due to irrelevant peaks near the heavy Rh-atom.

2.3. Kinetic measurements

The kinetic rate constants were determined utilizing UV/Vis (by monitoring the change in absorbance at 375, 400, 530 and 580 nm), IR (by monitoring formation and disappearance of the carbonyl peaks at 2082, 2064, 1990, 1729 and 1714 cm^{-1}), ^1H and ^{31}P NMR spectroscopy (by monitoring the change in integration units of the various signals with time as specified in Table 2 and Fig. 6). A linear relationship between UV absorbance, A, and concentration, C, confirmed the validity of the Beer Lambert law ($A = \varepsilon Cl$ with l = path length = 1 cm) for the [Rh(fctfa)(CO)(PPh_3)] complex. All kinetic measurements were monitored under pseudo first-order conditions with CH_3I concentrations 7–10 000 times the concentration of the [Rh(fctfa)(CO)(PPh_3)] complex. At least five different concentrations within this range were utilized. The concentration of [Rh(fctfa)(CO)(PPh_3)] was $\leqslant 0.0004$ mol dm^{-3} for UV/Vis measurements and $\leqslant 0.01$ mol dm^{-3} for IR and NMR measurements. The activation parameters $\Delta H^{\#}$, $\Delta S^{\#}$ and $\Delta G^{\#}$ for the reaction in chloroform and acetone were obtained from kinetic runs between 15.0 and 35.0 °C. At least three temperatures, held constant within 0.1 °C, were employed to establish the temperature dependence for each substitution reaction.

2.4. Calculations

Pseudo first-order rate constants, k_{1obs}, for reaction set 1 were calculated by fitting kinetic data to the first-order equation [26]

$$[A]_t = [A]_0 \exp(-k_{1obs} t) \tag{5}$$

with $[A]_t$ and $[A]_0$ the absorbance of the indicated species at time t and 0 (UV/Vis or IR experiments), or integral values for the specified peaks on NMR spectra, and were converted to second order rate constants, k_1, by determining the slope of the linear plots of k_{1obs} against the concentration of the incoming CH_3I ligand with

$$k_{obs} = k_{-1} + k_1[CH_3I] \tag{6}$$

Here k_{-1} is the first-order rate constant for the reverse step [26] in the general mechanism

$$A + CH_3I \underset{k_{-1}}{\overset{k_1}{\rightleftharpoons}} B$$

with A = [Rh(fctfa)(CO)(PPh_3)] and B = {[Rh(fctfa)(CH_3)(CO)(PPh_3)(I)] ⇌ [Rh(fctfa)($COCH_3$)(PPh_3)(I)]}, or more conveniently expressed as [Rh^{III}-alkyl1 ⇌ Rh^{III}-acyl1]. First-order rate constants for reaction set 2, k_3, and reaction set 3, k_4, were also determined from Eq. (5) by replacing k_{1obs} with k_3 or k_4. Kinetic data for the consecutive reaction treatment [26] of IR data obtained in acetone and applicable to the general reaction $A \xrightarrow{k_1} B \xrightarrow{k_3} C$ were fitted to Eq. (5) when monitoring the disappearance of A, Eq. (7) for monitoring the appearance and disappearance of B and Eq. (8) for monitoring the appearance of C, here Rh^{III}-alkyl2. A and B were defined above.

$$[B]_t = \frac{k_{1obs}[A]_0}{k_3 - k_{1obs}} [\exp(-k_{1obs} t) - \exp(-k_3 t)] \tag{7}$$

$$[C]_t = [A]_0 \left\{ 1 - \frac{1}{k_3 - k_{1obs}} [k_3 \exp(-k_{1obs} t) - k_{1obs} \exp(-k_3 t)] \right\} \tag{8}$$

Activation parameters [26] were obtained from a fit on Eq. (9) with k_i ($i = 1, 3$) the kinetic rate constants for reaction steps 1 and 3.

$$\ln \frac{k_i}{T} = -\frac{\Delta H^{\#}}{RT} + \frac{\Delta S^{\#}}{R} + \ln \frac{k_B}{h} \tag{9}$$

All kinetic mathematical fits were done utilizing the fitting program MINSQ [27]. The error of all the data is presented according to crystallographic conventions. For example $k_{1obs} = 0.0446(1)$ s^{-1} implies $k_{1obs} = 0.0446 \pm 0.0001$ s^{-1}.

3. Results and discussion

3.1. The UV/Vis study, solvent and temperature dependence

As illustrated in Fig. 1, three general reaction steps for the oxidative addition reaction between CH_3I and [Rh(fctfa)(CO)(PPh_3)] could be identified by UV/Vis spectrophotometry. Due to the larger change in absorbance for the second and third reaction step at 375 nm, more accurate k_3 and k_4 rate constants were obtainable at this wavelength. For reaction step 1, data obtained at 530 nm gave more accurate k_1 and k_{-1} rate constants.

The first reaction showed a first-order dependence on CH_3I, while the second and third (not illustrated) reactions are independent (i.e. zero order) of CH_3I concentration, Fig. 2. It is clear that the relationship between k_{1obs} and [CH_3I] in chloroform does not pass through the origin. This implies [26] that reaction step one is an equilibrium process of the form

$$A + B \underset{k_{-1}}{\overset{k_1}{\rightleftharpoons}} C$$

However, when the reaction was studied in methanol, acetone, ethyl acetate and benzene, k_{-1} was found to be so small as to be undetected. The temperature dependence in chloroform for the first and second stages of the oxidative addition reaction is also demonstrated in Fig. 2.

The increase in the rate of the first step of oxidative addition depends linearly on the dielectric constant, DE [28], of each solvent, Fig. 3. Chloroform does not fit the trend suggested by the other solvents because it follows a different mechanism (k_{-1} is measurable).

Rate constants, results of the solvent dependence study and activation parameters which were obtained from the temperature dependence study utilizing Eq. (9) are summarized in Table 1.

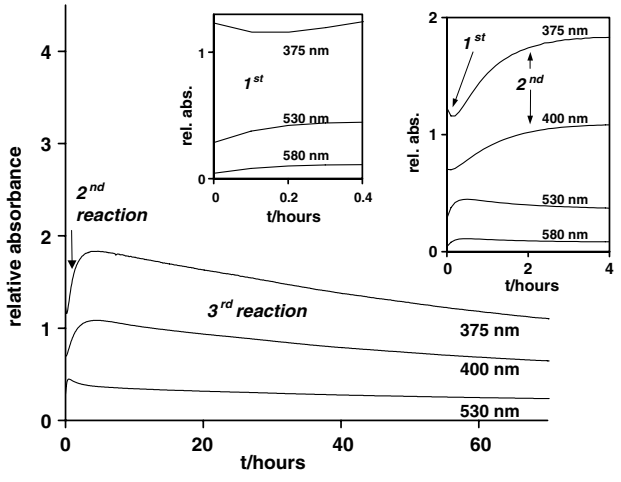


Fig. 1. Relative absorbance *vs.* time data at 25 °C for the UV/Vis monitored oxidative addition of CH_3I to [Rh(fctfa)(CO)(PPh_3)] in chloroform at the indicated wavelengths for the first reaction step (insert top left), the second reaction step (insert top right) and the third reaction step (main graph, starting at approximately 5 h), [Rh(fctfa)(CO)(PPh_3)] = 0.00015 mol dm^{-3}, [CH_3I] = 0.1416 mol dm^{-3}.

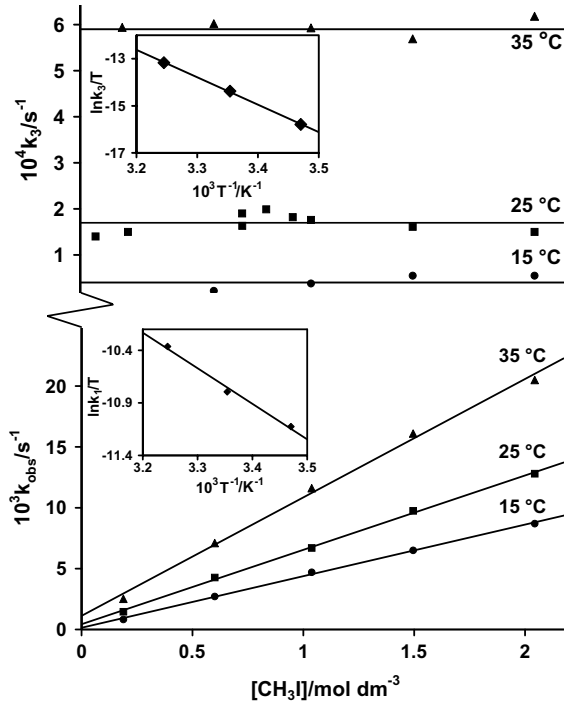


Fig. 2. CH_3I concentration dependence for the UV/Vis monitored oxidative addition of CH_3I to [Rh(fctfa)(CO)(PPh_3)] in chloroform at 530 nm for the first reaction step, bottom, and for the second reaction step, top. Insets: The linear dependence between $\ln(k/T)$ and $1/T$ allowed the determination of activation parameters.

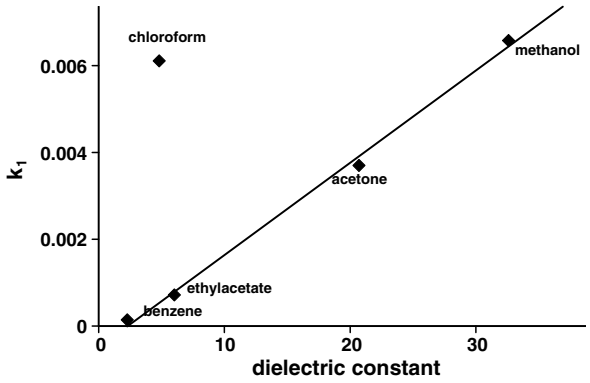


Fig. 3. Relationship between the second-order rate constant, k_1, in units of $dm^3\ mol^{-1}\ s^{-1}$, and the dielectric constant of the solvent during the UV monitoring of the first reaction set of the oxidative addition of CH_3I to [Rh(fctfa)(CO)(PPh_3)] at 25 °C.

Of special interest is the observation that $\Delta S^{\#}$ values for all the reaction steps that are independent of [CH_3I] (the k_{-1} and k_3 steps), approaches zero within experimental error, whereas $\Delta S^{\#}$ for the second order reaction step related to k_1 are large negative. This is consistent with an interpretation that the transition state for the forward step 1 reaction occurs via an associative mechanism where the coordination number changes from 4 to 6. For the other reaction steps, the coordination number changes from 6 to 5 implying the transition state undergoes much less dramatic coordination changes. This results in $\Delta S^{\#}$ approaching zero.

Table 1
Kinetic rate constants for the oxidative addition reaction of CH_3I to [Rh(fctfa)(CO)(PPh_3)] as obtained by various spectroscopic methods at 25 °C by considering each reaction step in isolation during data work-up with Eq. (5), as well as by a consecutive reaction treatment of data with Eqs. (7) and (8)

Method	Solvent (DE),[a] (λ/nm)	Reaction sequence 1[b] $\Delta H^{\#} = 29(3)$, $\Delta S^{\#} = -188(9)$ k_1 ($dm^3\ mol^{-1}\ s^{-1}$)	Reaction sequence 1[b] $\Delta H^{\#} = 81(6)$, $\Delta S^{\#} = -40(20)$ k_{-1} (s^{-1})	Reaction sequence 2[b,c] $\Delta H^{\#} = 93(1)$, $\Delta S^{\#} = -5(3)$ k_3 (s^{-1})	RS 3[b,c] 10^6 k_4 (s^{-1})
UV/Vis	$CHCl_3$ (4.8) $\lambda = 580$	0.0060(1)	0.0005(1)	0.00016(2)	
	$\lambda = 530$	0.0061(1)	0.0005(1)	0.00017(2)	4.4(1)
	$\lambda = 400$			0.00021(2)	4.3(1)
	$\lambda = 375$			0.00020(1)	3.7(1)
	C_6H_6 (2.27)	0.000141(2)	~0		
	CH_3COOEt (6.02)	0.000716(4)	~0		
	$(H_3C)_2CO$ (20.7)	0.00370(4)[d]	~0		
	CH_3OH (32)	0.00658(3)	~0		
IR[c]	$CHCl_3$	0.0061(2)	0.0006(2)	0.00017(1)	4.7(4)
	$(H_3C)_2CO$, Eq. (5)[e]	0.0041(1)	~0	0.00020(4)	2.6(5)
	$(H_3C)_2CO$, Eq. (7)[e]	0.0046(4)	~0	0.00010(1)	
	$(H_3C)_2CO$, Eq. (8)[e]	0.008(2)	~0	0.00018(1)	
	$(H_3C)_2CO$, Eq. (7)[e]			0.00016(1)	5.5(3)
^1H NMR	$CHCl_3$ (4.8)	0.006(1)		0.00011(1)	5(2)
^{31}P NMR	$CHCl_3$ (4.8)	0.005(1)		0.00012(2)	

Activation parameters in $CHCl_3$ are summarized in the table heading. RS is the reaction sequence and Et is the ethyl.

[a] DE is the dielectric constant at 25 °C, except for $CHCl_3$ where DE is at 20 °C. The sited wave lengths were used to monitor the reaction by UV/Vis in $CHCl_3$.

[b] Units of $\Delta H^{\#}$ is kJ mol^{-1}, that of $\Delta S^{\#}$ is J mol^{-1} K^{-1}. For the extremely slow reaction sequence 3 ($t_{1/2} < 35$ h), no activation parameters were determined. Also, k_{-3} and $k_{-4} \neq 0$ but *very* small.

[c] Cited rate constants are the average from several reactions with different CH_3I concentrations.

[d] In acetone, $\Delta H^{\#} = 50(4)$ kJ mol^{-1}, $\Delta S^{\#} = -124(4)$ J mol^{-1} K^{-1}.

[e] IR data for each reaction set fitted to the indicated kinetic model Eqs. (5), (7) or (8), conditions for the consecutive reaction treatment of IR data were $[CH_3I] = 0.2604$ mol dm^{-3}, [Rh(fctfa)(CO)(PPh_3)] = 0.002 mol dm^{-3}, $T = 25$ °C.

Results of the UV/Vis section only of this study are interpreted to imply that the first reaction step represents an oxidative addition process whereby the Rh^{I} nucleus converts to a Rh^{III} nucleus. The product of this oxidative addition step may be either an alkyl or acyl species, [Rh(fctfa)(CH_3)(CO)(PPh_3)(I)] or [Rh(fctfa)($COCH_3$)(PPh_3)(I)] (or both), but the UV/Vis technique cannot distinguish between these possibilities. Since the second and third reaction steps are independent of [CH_3I], one may deduce that these two reactions either involve slow solvent exchange with any of the ligands of the newly formed Rh^{III} complex or it may be isomerization from an alkyl to an acyl product (or *vice versa*). To obtain more insight on the nature of the Rh^{III}-products, an infrared study of the reaction was conducted as this technique is ideal to distinguish between metal–CO bonds that vibrates at ~1900–2100 cm^{-1}, and metal–$COCH_3$ bonds that vibrates at ~1600–1800 cm^{-1}.

3.2. Infrared study

3.2.1. Chloroform as solvent

Three reaction steps could also be identified by IR spectroscopy, Fig. 4. In the first reaction step, the rate of disappearance of the Rh^{I} species [Rh^{I}(fctfa)(CO)(PPh_3)] in chloroform at 25 °C, as monitored by the disappearance of the CO peak at 1990 cm^{-1} corresponds exactly with the rate of formation of *both* a Rh^{III}-alkyl1 species, [Rh^{III}-(fctfa)(CH_3)(CO)(PPh_3)(I)], monitored by the appearance of the CO-peak at 2082 cm^{-1}, and a Rh^{III}-acyl1 species, [Rh^{III}(fctfa)($COCH_3$)(PPh_3)(I)], monitored at 1729 cm^{-1}. The half-life of the first reaction step under pseudo first-order conditions with [CH_3I] = 1.673 mol dm^{-3} and at 25 °C, Fig. 4, is 63 s. Since it is highly unlikely that the Rh^{III}-acyl1 species can be formed by fast isomerization of an *undetected* Rh^{III}-alkyl species with total different ligand coordination pattern than the *detected* Rh^{III}-alkyl1 species at *exactly* the same rate as the detected Rh^{III}-alkyl1 species, this result is considered to imply that an equilibrium exist between the Rh^{III}-alkyl1 and Rh^{III}-acyl1 species that is fast enough to be maintained on the time scale of [Rh(fctfa)-(CO)(PPh_3)] disappearance. The same conclusion could be drawn using ^1H NMR data and will be discussed under the NMR heading. This first set of reactions may, therefore, be presented by reaction sequence (10) where k_i represents forward rate constants and k_{-i} reverse rate constants, $i = 1$ or 2.

$$[Rh^{I}(fctfa)(CO)(PPh_3)] + CH_3I \underset{k_{-1}}{\overset{k_1}{\rightleftharpoons}} \left[Rh^{III}\text{-alkyl1} \underset{k_{-2}}{\overset{k_2}{\rightleftharpoons}} Rh^{III}\text{-acyl1}\right] \quad (10)$$

The k_{-1} step in Eq. (10) was only detected in $CHCl_3$ solutions. The equilibrium constant between the Rh^{III}-alkyl1 and Rh^{III}-acyl1 species is defined as $K_2 = k_2/k_{-2}$. Pseudo first-order rate constants k_{1obs} for reaction 10 utilizing nine different CH_3I concentrations between 0.12 and 1.70 mol dm^{-3} were determined. A graph (not shown) of k_{1obs} *versus* [CH_3I] in chloroform solution, was linear with *y*-intercept 0.0006(2) s^{-1}. This satisfies Eq. (6) with

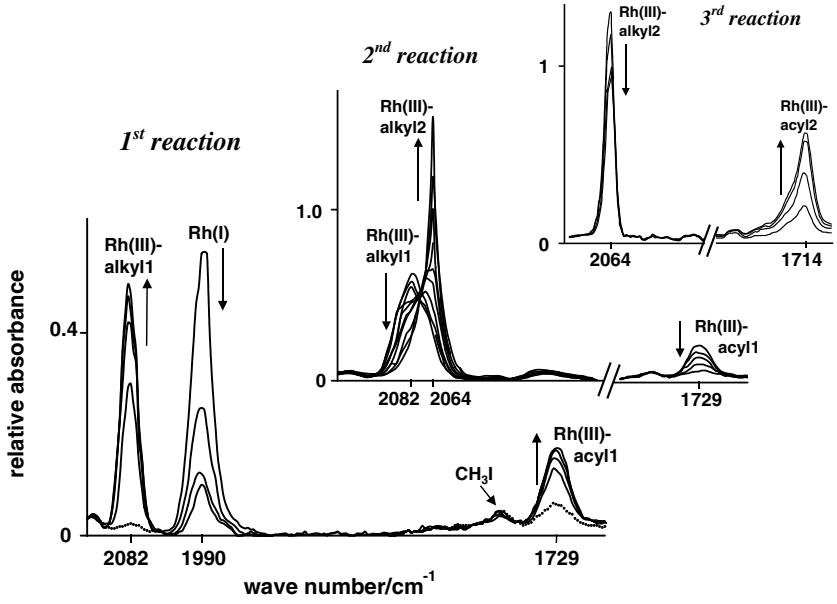


Fig. 4. The reaction between CH_3I (1.673 mol dm^{-3}) and [Rh(fctfa)(CO)(PPh_3)] (0.0100 mol dm^{-3}) in chloroform at 25 °C as monitored by IR spectroscopy. The first set of reactions (bottom spectrum, spectrum times are $t = 0$ (.....), not shown for Rh^{I} due to high amplitude), 74, 149, 224 and 299 s) shows the disappearance of Rh(I) at 1990 cm^{-1} ($k_{1obs} = 0.011\ s^{-1}$) and the simultaneous appearance at the same rate of a Rh^{III}-alkyl1, at 2082 cm^{-1}, and a Rh^{III}-acyl1 species at 1729 cm^{-1}. The middle insert illustrates the simultaneous disappearance of Rh^{III}-alkyl1 ($t = 554$, 734, 1094, 1919, 2819, 3719, 4905, 7605, 10305 and 20205 s) and Rh^{III}-acyl1 ($t = 554$, 1919, 3719, 7605 and 20205 s) and the formation of a Rh^{III}-alkyl2 species at 2064 cm^{-1} ($k_3 = 0.00017(3)\ s^{-1}$ for all three cases) during the second set of reactions. The third set of reactions (top right inset) is illustrated by the disappearance of the Rh^{III}-alkyl2 species (spectra were recorded at $t = 40408$, 121558, 248726 and 335308 s) and the simultaneous formation of a new Rh^{III}-acyl2 species at 1714 cm^{-1} ($k_4 = 4.3(2) \times 10^{-6}\ s^{-1}$).

k_1 the second order forward rate constant and k_{-1} the first-order reverse rate constant for reaction (10). Individual values for k_1 and k_{-1} are tabulated in Table 1. The mutual consistency of k_1 and k_{-1} values as determined by the UV/Vis and IR methods are obvious.

A second, much slower ($t_{1/2} \approx 1.1$ h ≈ 4000 s) set of reactions that are CH_3I independent is illustrated in the middle insert in Fig. 4, where the Rh^{III}-acyl1 species at 1729 cm^{-1} and the Rh^{III}-alkyl1 species at 2082 cm^{-1} both disappear at the same rate ($k_2 = 0.00017(1)$ s^{-1}) as the formation of a new Rh^{III}-alkyl2 geometrical isomer ($k_3 = 0.00017(3)$ s^{-1}) at 2064 cm^{-1}. Again, this is regarded as additional proof that the equilibrium between the Rh^{III}-acyl1 species and the Rh^{III}-alkyl1 species is fast. The $[CH_3I]$-independent second reaction step is $0.011/0.00017 \approx 65$ times slower (from rate constants from Fig. 4) than the $[CH_3I]$-dependent first reaction at $[CH_3I] = 1.673$ mol dm^{-3}. Kinetic data of the second reaction is consistent with the equilibrium

$$A \underset{k_{-3}}{\overset{k_3}{\rightleftharpoons}} B \tag{11}$$

where $A = [Rh^{III}\text{-alkyl1} \rightleftharpoons Rh^{III}\text{-acyl1}]$ and $B = Rh^{III}$-alkyl2. As discussed later, $k_{-3} \lll k_3$. The structure of the Rh^{III}-alkyl2 geometrical isomer having the molecular formula $[Rh^{III}(fctfa)(CH_3)(CO)(PPh_3)(I)]$ has also been solved and is reported later in this publication.

The second set of reactions was followed by a very slow ($t_{1/2} \approx 40$ h) $[CH_3I]$-independent third reaction and corresponds to the slow first-order disappearance of the Rh^{III}-alkyl2 species ($k_4 = 4.9(5) \times 10^{-6}$ s^{-1}) at 2064 cm^{-1} and the appearance, at the same rate, of a new Rh^{III}-acyl2 geometrical isomer at 1714 cm^{-1} ($k_4 = 4.4(2) \times 10^{-6}$ s^{-1}, Fig. 4, top right inset). The long half-life of the third reaction implied that it could not be followed with great accuracy, as solvent evaporation became difficult to control. The kinetic data of the third reaction is consistent with the general reaction sequence

$$Rh^{III}\text{-acyl2} \xrightarrow{k_4} Rh^{III}\text{-alkyl2} \tag{12}$$

Utilizing the combined information obtained by the UV/Vis and IR study only, the overall reaction sequence for this oxidative addition reaction may therefore be represented as

$$\begin{array}{c} [Rh^{I}(fctfa)(CO)(PPh_3)] + CH_3I \\ k_{-1} \uparrow\downarrow k_1 \\ \left[\begin{array}{c} [Rh^{III}(fctfa)(CH_3)(CO)(PPh_3)(I)]^1 \\ k_{-2} \uparrow\downarrow k_2 \\ [Rh^{III}(fctfa)(COCH_3)(PPh_3)(I)]^1 \end{array}\right] \\ \downarrow k_3 \\ [Rh^{III}(fctfa)(CH_3)(CO)(PPh_3)(I)]^2 \\ \downarrow k_4 \\ [Rh^{III}(fctfa)(COCH_3)(PPh_3)(I)]^2 \end{array} \tag{13}$$

where the superscripts "1" and "2" refer to Rh^{III}-alkyl1, Rh^{III}-acyl1, and Rh^{III}-alkyl2 or Rh^{III}-acyl2, respectively. As was the case with the first set of reactions, k_3 and k_4 obtained by the IR method are consistent with the results from the UV/Vis method.

3.2.2. Consecutive reaction treatment in acetone as solvent

In chloroform, the k_{obs} *versus* $[CH_3I]$ graph for the first step did not pass through the origin for both the UV/Vis and IR detection methods, and this is indicative of a noticeable equilibrium in the first reaction step of the total reaction. However, IR results in acetone indicate, in agreement with the UV/Vis results in acetone (Table 1), that this equilibrium was shifted so far to the right that the k_{-1} step is not observable. The apparent absence of a k_{-1} step in acetone allowed us to treat results from an IR study in acetone utilizing consecutive reaction kinetic models.

The IR observed reaction sequence of this reaction in acetone in the range 1960–2100 cm^{-1} was basically the same as observed in chloroform. However, the formation of the Rh^{III}-acyl complexes could not be measured due to the strong IR absorbance of the solvent, acetone, in the 1650–1800 cm^{-1} region. The Rh^{I} peak was monitored at 1987 cm^{-1} and the Rh^{III}-alkyl1 and Rh^{III}-alkyl2 species at 2082 and 2059 cm^{-1}, respectively. By treating data for every reaction sequence in isolation utilizing Eq. (5), as was done in chloroform, rate constants was determined for all the reaction steps and corresponded to those of the UV/Vis study. Rate constants are listed in Table 1.

Because the equilibrium K_2 was found to be fast enough to be maintained during Rh(I) depletion, and since CH_3I was in large excess over Rh(I), it was possible to determine the rate constants k_1, k_3 and k_4 for the studied reaction in acetone by using the consecutive reaction treatment on the general reaction sequence, $A \xrightarrow{k_1} B \xrightarrow{k_3} C \xrightarrow{k_4} D$ (A, B and C was defined in Sections 3.1 and 3.2.1, $D = Rh^{III}$-acyl2). By ignoring the very slow k_4 step (i.e. D) in the reaction sequence and upon performing a least-squares fit of the available IR absorbance *vs.* time data of the Rh^{III}-alkyl1 peak for the reaction in acetone to Eq. (7), see graph shown in Fig. 5, top, the rate constants were determined as $k_{1obs} = 0.0012(1)$ s^{-1} ($k_1 = 0.0046$ dm^3 mol^{-1} s^{-1}), and $k_3 = 0.00010(1)$ s^{-1}. The value of k_{1obs} corresponds very close with those obtained from data treatment utilizing Eq. (5) (values summarized in Table 1). The value of k_3 was slightly (37%) smaller than the value of 0.00016(2) s^{-1} which was determined by treating reaction 2 in isolation.

In addition, fitting of the available absorbance/time data of the Rh^{III}-alkyl2 peak to Eq. (8), see Fig. 5, bottom, resulted in $k_{1obs} = 0.0022(6)$ s^{-1} ($k_1 \approx 0.0084$ dm^3 mol^{-1} s^{-1}), while $k_3 = 0.00018(1)$ s^{-1}. This value of k_3 corresponds well to the value obtained by treating data sets as separate, isolated quantities for each reaction according to Eq. (5). Utilizing Eq. (8), k_1 was 83% (1.83 times) larger than the value obtained from Eq. (5) but it is still kinetically equivalent. This drift in k_1 and k_3 was accentuated because of the difficulty of obtaining large

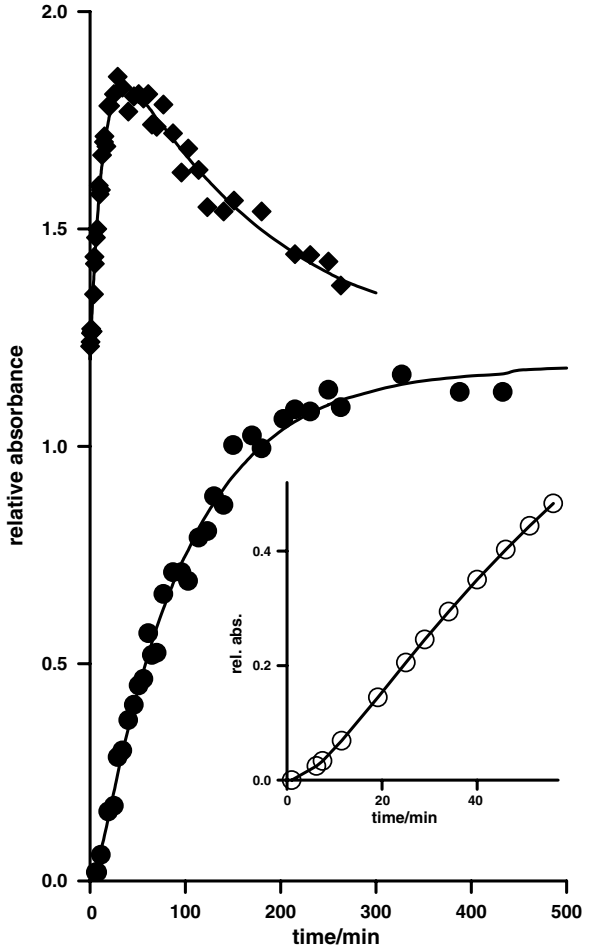


Fig. 5. Relative IR absorbance *vs.* time data of the reaction between CH_3I (0.2604 mol dm^{-3}) and [Rh(fctfa)(CO)(PPh_3)] (0.002 mol dm^{-3}) in acetone at 25 °C. Top: Kinetic data were fitted to the consecutive reaction model Eq. (7), relative absorbancies of the Rh^{III}-alkyl1 species are illustrated. Bottom: A data fit of Rh^{III}-alkyl2 IR absorbances to Eq. (8) is shown. Inset: An enlargement of the initial stages of Rh^{III}-alkyl2 formation. The slow initial formation of the Rh^{III}-alkyl2 species in the region $t < 10$ min is apparent.

amounts of data points for relatively fast reactions quickly enough with overlay spectra utilizing an infrared spectrophotometer. It led to too little available data to fit complicated equations.

By ignoring the fast k_1 step (i.e. A) in $A \xrightarrow{k_1} B \xrightarrow{k_3} C \xrightarrow{k_4} D$ and by applying the consecutive reaction kinetic model, Eq. (7), to intermediate C for the compound series B, C and D, values of k_3 and k_4 were found to $1.6(1) \times 10^{-4}$ and $5.5(3) \times 10^{-6}$ s^{-1}. The value for k_3 corresponded well to the previously determined values. The value for k_4 is larger by a factor 2 than the value obtained from the treatment of data in isolation, which gave $k_4 = 2.6(5) \times 10^{-6}$ s^{-1}. This twofold difference between the k_4 values are again not regarded as significant. Eq. (8) could not be fitted to formation data of D, from the reaction in acetone as solvent, due to interference of the acetone carbonyl peak in the region of Rh^{III}-acyl2 detection.

All things considered, the calculated rate constants obtained by the consecutive reaction treatment (Eqs. (7) and (8)) and as individual data sets utilizing Eq. (5) are regarded as mutually consistent and confirm the proposed mechanism. It is, however, important to note that consistency between the consecutive reaction treatment of data and treatment of kinetic data of each reaction step in isolation would not have been observed if reaction step 1 was not much faster than reaction step 2 and if reaction step 3 was not much slower than reaction step 2. If the rates did not differ as much as demonstrated by the half lives cited in Section 3.2.1, reaction steps 1, 2 and 3 would be overlapping so much that accurate rate constants would not be obtainable by regarding each reaction step in isolation.

When the consecutive reaction treatment of data was applied to reactions performed in *chloroform* (data for Section 3.2.1), the mathematical models (Eqs. (7) and (8)) were not found to be appropriate as data could not be satisfactorily fitted to it. The breakdown of the model is attributed to the detected k_{-1} step in the mechanism

$$A \underset{k_{-1}}{\overset{k_1}{\rightleftharpoons}} B \xrightarrow{k_3} C$$

The mathematical treatment of such monophasic reversible reactions is quite complex [29].

3.3. ^1H and ^{31}P NMR study

The reaction between CH_3I and [Rh(fctfa)(CO)(PPh_3)] was also monitored by ^1H and ^{31}P NMR in order to obtain additional insight into this reaction. By carefully comparing the positions and integrals of the different signals, the spectral parameters of different isomers could be identified, Table 2, see also Ref. [19]. The same reaction sequence as observed by IR and UV/Vis, was observed utilizing ^1H NMR, Fig. 6 and ^{31}P NMR, Fig. 7. The new feature introduced by the NMR study is the existence of more than one geometrical isomer for each intermediate. The two main isomers of each intermediate will be referred to as A and B, *e.g.* Rh^{III}-alkyl1A and Rh^{III}-alkyl1B, the choice of the labels are arbitrary and have no significance. The A and B isomers of each species exist in a fast equilibrium with each other, because the observed rate constant for the disappearance or formation of an A and a B isomer of the same species was found to be within experimental error the same and also because the ratio Rh(I)A/Rh(I)B = 1.5 (obtained by integral evaluation) is not the same as the ratio Rh^{III}-alkyl1A/Rh^{III}-alkyl1B = 0.39 or the ratio Rh^{III}-acyl1A/Rh^{III}-acyl1B = 1.0 (Table 2). If the reaction was ($Rh^{I}A + CH_3I \rightleftharpoons$ {Rh^{III}-alkyl1A $\rightleftharpoons$ Rh^{III}-acyl1A}) for the A isomers and separately ($Rh^{I}B + CH_3I \rightleftharpoons$ {Rh^{III}-alkyl1B $\rightleftharpoons$ Rh^{III}-acyl1B}) for the B isomers, and if no equilibrium between isomers A and B existed, the ratio A:B of these isomers would have been the same throughout the entire reaction sequence involving steps 1, 2 and 3.

Rate constants obtained from ^1H NMR are summarized in Table 1. It can be seen good agreement exist between the

Table 2
The equilibrium constant K_c and ^{1}H and ^{31}P NMR spectral parameters of the different isomeric forms of [Rh(fctfa)(CO)(PPh$_3$)] and the Rh^{III} complexes formed during the oxidative addition reaction of CH_3I to [Rh(fctfa)(CO)(PPh$_3$)]

Compound	K_c[a]	δ–^{31}P (ppm)	^1J(^{31}P–^{103}Rh) (Hz)	% of each isomer by		δ–^{1}H (CH)[b] (ppm)	δ–^{1}H (CH_3) (ppm)	δ–^{1}H (Fc)[c] (ppm)		
				^{31}P NMR	^{1}H NMR			5H	2H	2H
Rh^{I}A	0.68	48.04	176.4	[d]	60	6.045		3.94	4.09	4.27
Rh^{I}B		48.04	176.4	[d]	40	6.045		4.20	4.50	4.83
Rh^{III}-alkyl 1A	2.57	33.23	125	28	28	6.055	1.47	4.29	4.73	[e]
Rh^{III}-alkyl 1B		32.80	124	72	72	6.055	1.42	4.34	[e]	[e]
Rh^{III}-acyl 1A	1.00	38.38	155	50	50	6.08	3.05	4.17	[e]	[e]
Rh^{III}-acyl 1B		37.57	155	50	50	6.08	2.98	3.94	[e]	[e]
Rh^{III}-alkyl 2A	4.56	27.09	115.2	19	18	5.45	1.78	4.23	[e]	[e]
Rh^{III}-alkyl 2B		29.33	116.5	81	82	5.30	1.77	4.31	4.31	4.47
									4.39	4.76
Rh^{III}-acyl 2A	1.65						2.91			
Rh^{III}-acyl 2B							3.01			

[a] K_c = [Rh-species B]/[Rh-species A] for the equilibrium Rh-species A ⇌ Rh-species B.
[b] In the text the CH group of fctfa is referred to as the methine proton.
[c] Fc = ferrocenyl.
[d] Peaks of the two isomers overlapped.
[e] Peaks could not uniquely be identified due to excessive overlapping.

kinetic rate constants obtained by utilizing UV/Vis, IR, ^{1}H NMR and ^{31}P NMR spectroscopic methods.

The structure of one of the isomers of the [Rh^I(fctfa)-(CO)(PPh$_3$)] is reported elsewhere [20], while the structure of the [Rh^{III}(fctfa)(CH$_3$)(CO)(PPh$_3$)(I)]^{2B} species is reported in this communication. The structure of the other Rh^{III} acyl compounds is as yet unknown and the indicated formulas relate to molecular stoichiometry only and not to a specific geometry. The ^{1}H and ^{31}P NMR spectrum of the crystalline isolated Rh^{III}-alkyl2B isomer were identical to the spectrum of isomer Rh^{III}-alkyl2B as observed during the monitoring of the second set of reactions during the oxidative addition reaction of [Rh(fctfa)(CO)(PPh$_3$)] with CH_3I in $CDCl_3$ solutions. An important observation was that upon dissolving the solid crystalline Rh^{III}-alkyl2B isomer in $CDCl_3$, isomerization to the Rh^{III}-alkyl2A isomer sets in. After 4 days, traces of Rh(I), Rh^{III}-alkyl1 and Rh^{III}-acyl1 were also observed on ^{1}H and ^{31}P NMR. This means that Eq. (13) also has a k_{-3} and k_{-4} step, but these rate constants are so small that the k_{-3} and k_{-4} steps are simply not kinetically determinable. Taking into account there exist two main isomers of each reactant and reaction product, the complete reaction sequence for the oxidative addition of CH_3I to [Rh(fctfa)(CO)(PPh$_3$)] is therefore

$$\begin{bmatrix} [Rh^I(fctfa)(CO)(PPh3)]_A \\ \Updownarrow K_{c1} \\ [Rh^I(fctfa)(CO)(PPh3)]_B \end{bmatrix} + CH_3I$$

$$k_{-1} \Updownarrow k_1 \quad \textit{First set of reactions}$$

$$\begin{bmatrix} [Rh^{III}\text{-alkyl1A}] & & [Rh^{III}\text{-acyl1A}] \\ \Updownarrow K_{c2} & K_2=k_2/k_{-2} & \Updownarrow K_{c3} \\ [Rh^{III}\text{-alkyl1B}] & & [Rh^{III}\text{-acyl1B}] \end{bmatrix} \quad (14)$$

$$k_{-3} \Updownarrow k_3 \quad \textit{Second set of reactions}$$

$$\begin{bmatrix} [Rh^{III}\text{-alkyl2A}] \\ \Updownarrow K_{c4} \\ [Rh^{III}\text{-alkyl2B}] \end{bmatrix} \underset{k_{-4}}{\overset{k_4}{\rightleftharpoons}} \begin{bmatrix} [Rh^{III}\text{-acyl2A}] \\ \Updownarrow K_{c5} \\ [Rh^{III}\text{-acyl2B}] \end{bmatrix}$$

Third set of reactions

The above mechanism is a completely general mechanism. As such it caters for all previously encountered special cases sighted in Eqs. (1)–(4). Each one of these four equations can be generated by careful manipulation of the size of the individual rate constants. For example, Eq. (14) will simplify to Eq. (3) provided $k_{-2} = k_{-3} = k_4 = k_{-4} = 0\ s^{-1}$. The equilibrium constants for the equilibrium between the isomers, defined as K_{ci} = [RhB-species]/[RhA-species], $i = 1, 2, \ldots 5$, were determined from the ^{1}H NMR integration data of suitable identifiable and well resolved peaks at 25 °C in $CDCl_3$ and are documented in Table 2.

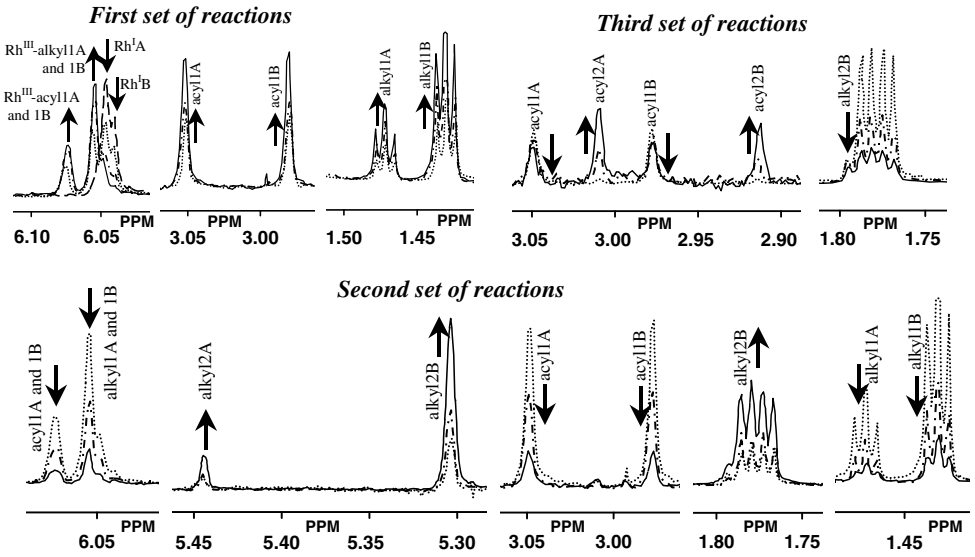


Fig. 6. Fragments of the ^{1}H NMR spectra in $CDCl_3$ illustrating reaction sequences during the oxidative addition and the ensuing carbonyl insertion and deinsertion reactions of 0.3674 mol dm^{-3} CH_3I to 0.0183 mol dm^{-3} [Rh(fctfa)(CO)(PPh_3)] in $CDCl_3$ at $T = 25$ °C. *Top left*: Selected spectra for the first set of reactions illustrating changes in the signal of the methine proton of the β-diketonato ligand of the indicated isomers in the region 6.04–6.08 ppm, the growing signals of the CH_3-group of indicated Rh^{III}-acyl isomers at 3.05 and 2.98 ppm and of Rh^{III}-alkyl isomers at 1.47 and 1.42 ppm. *Bottom*: Signal intensity changes of the second reaction sequence showing the methine proton of the β-diketonato ligand of the indicated isomers at 5.30–6.08 ppm, the CH_3 signal disappearance for the Rh^{III}-acyl isomers at 3.05 and 2.98 ppm and Rh^{III}-alkyl isomers at 1.47 and 1.42 ppm, and the increase in signal intensity of the CH_3-group of the overlapping alkyl 2 isomers at 1.78 ppm. *Top right*: The third set of reactions is illustrated by changes in signal intensity of the CH_3-group of the Rh^{III}-alkyl2 isomers at 1.78 ppm, and of the Rh^{III}-acyl2A and 2B species at 3.01 and 2.92 ppm. The multiplicity of the signal of the CH_3 group of the Rh^{III}-alkyl1 and 2 isomers is due to coupling with Rh (spin 1/2) and P (spin 1/2). Supplementary data shows further spectra highlighting NMR changes.

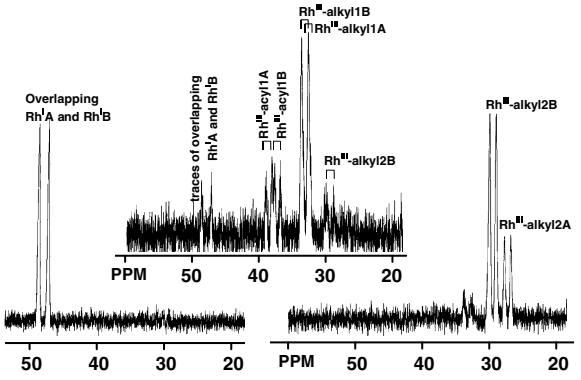


Fig. 7. Selected ^{31}P NMR spectra illustrating doublet ^{31}P peaks of the indicated reactants and products during the three sets of reactions for the oxidative addition of 0.500 mol dm^{-3} CH_3I to 0.021 mol dm^{-3} [Rh(fctfa)(PPh_3)(CO)] in $CDCl_3$ at 25 °C. Bottom left: at time $t = 0$ (reagent). Middle top: $t = 1070$ s (towards the end of the first set of reactions). Bottom right: $t = 69520$ s (near the end of the second set of reactions).

3.4. The crystal structure data of [Rh(fctfa)(CO)(PPh_3)(CH_3)(I)]

The numbering system of the atoms in [Rh(fctfa)-(CO)(PPh_3)(CH_3)(I)] is shown in Fig. 8 while the crystal data are summarized in Table 3. Selected bond lengths and bond angles are given in Table 4. An obvious feature of [Rh(fctfa)(CO)(PPh_3)(CH_3)(I)] and similar known Rh^{III}-alkyl complexes in which the fctfa ligand is replaced with other bidentate ligands [15,30] is that the iodo ligand, I, is bonded in the axial position of the octahedron, above or below the equatorial plane of the octahedron formed by O(1), O(2), C(5)O and C(6)H_3. The Rh–I bond axis deviated 3.6(1)° towards O(2) from the expected 90° and the Rh–P bond deviates by more than 2° away from O(1) and O(2).

This resulted in a 2.26(5)° deviation from linearity for the I–Rh–P bond axis. A similar deviation from linearity (3.4°) for the I–Rh–P bond axis was found for [Rh(cupf)-(CO)(PPh_3)(CH_3)(I)] [15]. The Rh^{III}–I bond length of the present study, 2.716(1) Å, is shorter (~0.1 Å) than Rh–I bonds in complexes having the CH_3 group *trans* to the iodine atom [30] and this is the result of the smaller *trans* influence of PPh_3 compared to that of an alkyl group. The various ligand–rhodium–ligand bond angles in the equatorial plane formed by O(1), O(2), C(6) and C(5), *viz.* C(5)–Rh–C(6) = 88.4(4)°, C(5)–Rh–O(2) = 97.3(3)°, O(2)–Rh–O(1) = 88.0(2)° and O(1)–Rh–C(6) = 86.1(3)°, deviate 2–7° from 90°. The Rh–C(5)–O(3) bond angle, 175.7(8)°, is not completely linear, with the C(5)–O(3) bond length 1.12(1) Å, significantly shorter than the C(5)–O(3) bond distance of 1.147(5) Å in [Rh^{I}(fctfa)(CO)(PPh_3)] [20].

In accordance with the π bonding concept [31] the Rh–C(5) bond length of 1.830(8) Å is larger than the corresponding bond length, 1.801(5) Å, in [Rh^{I}(fctfa)-(CO)(PPh_3)] because decreasing electron density on the rhodium center in changing the oxidation state from I to III, imply less electron donating capability from the metal

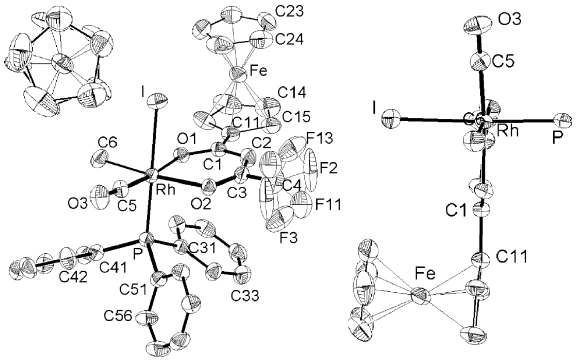


Fig. 8. A perspective view of [Rh(fctfa)(CO)(PPh_3)(CH_3)(I)] showing atom labelling. Thermal ellipsoids were drawn at a 30% probability level. The view from above down the ferrocenyl axis (top left) shows the cyclopentadienyl ring deviates 12.7° from a fully eclipsed conformation. Right: The cyclopentadienyl rings are planar and almost parallel, they deviate 3.1(5)° from co-planarity with the plane through the Rh chelate.

d-orbital into the π^* orbital of the carbonyl ligand. This leads to a longer (weaker) Rh–C bond length and a stronger C–O bond. The Rh–O(1) bond is 0.085 Å shorter than the Rh–O(2) bond which indicates the structure is not symmetric around the β-diketonato ligand. However, both Rh–O(1) and Rh–O(2) bonds in [Rh^{III}(fctfa)(CO)(PPh_3)(CH_3)(I)] are longer than the corresponding bonds in [Rh^{I}(fctfa)(CO)(PPh_3)] [20], 2.048(3) Å and 2.070(3) Å. The Rh–O(1) bond in both the Rh(I) and Rh(III) complexes is *trans* to the CO group, but Rh–O(2) is *trans* to the PPh_3 group in [Rh^{I}(fctfa)(CO)(PPh_3)] and *trans* to the CH_3 group in [Rh^{III}(fctfa)(CO)(PPh_3)(CH_3)(I)]. The C(3)–O(2) and C(1)–O(1) bonds in the β-diketonato skeleton of the [Rh(β-diketonato)(CO)(PPh_3)(CH_3)(I)] complex are similar, 1.271(9) Å and 1.265(8) Å, respectively, and both bonds are smaller than the corresponding bonds in free Hfctfa [32]. The change in oxidation state from Rh(I) to Rh(III) did not influence the C(3)–O(2) and C(1)–O(1) bond lengths. The C(1)–C(2) and C(2)–C(3) bonds of the present Rh(III) complex are similar, contrary to what was found for both [Rh^{I}(fctfa)(CO)(PPh_3)] (corresponding bonds were 1.413(5) and 1.368(6) Å), or the free Hfctfa ligand where asymmetric enolization was observed (C(1)–C(2) = 1.432(6) Å, C(2)–C(3) = 1.345(6) Å). As was the case for [Rh(fctfa)(CO)(PPh_3)], deviations up to 10° from the expected 120° for sp^2 hybridization for the C atoms of the β-diketonato skeleton were found, Table 4. The largest deviations were at the C atoms bound to O(1) and O(2). In the case of the free Hfctfa [32] the corresponding bond angles were all within experimental error 120°.

Table 4
Selected bond lengths (Å) and angles (°) for [Rh(fctfa)(CO)(PPh_3)(CH_3)(I)]

Atoms	Bond	Atoms	Bond
Rh–C(5)	1.830(8)	F(1)–C(4)	1.39(3)
Rh–O(1)	2.075(5)	C(1)–C(2)	1.40(1)
Rh–C(6)	2.076(8)	C(2)–C(3)	1.38(1)
Rh–O(2)	2.160(5)	C(3)–C(4)	1.51(1)
Rh–P	2.320(2)	C(1)–C(11)	1.47(1)
Rh–I	2.716(1)	C(11)–C(12)	1.41(1)
P–C(51)	1.822(7)	C(11)–C(15)	1.45(1)
O(3)–C(5)	1.12(1)	C(12)–C(13)	1.40(1)
O(2)–C(3)	1.271(9)	C(21)–C(22)	1.39(2)
F(2)–C(4)	1.40(3)	C(41)–C(42)	1.40(1)
	Angles	Atoms	Angles
C(5)–Rh–O(1)	173.8(3)	O(1)–C(1)–C(2)	126.5(6)
O(1)–Rh–O(2)	88.0(2)	O(2)–C(3)–C(2)	129.3(7)
O(2)–Rh–P	92.9(2)	C(2)–C(3)–C(4)	118.9(7)
O(1)–Rh–I	89.7(1)	C(3)–C(2)–C(1)	125.3(7)
O(1)–C(1)–C(11)	114.2(7)	Rh–C(5)–O(3)	175.7(8)
O(2)–C(3)–C(4)	111.9(7)	P–Rh–I	177.74(5)
C(34)–C(33)–C(32)	119.6(9)		

The standard deviation of the last decimal is given in brackets.

The cyclopentadienyl rings are within experimental error, planar and almost parallel [dihedral angle 1.4(6)°] while the average angle of deviation from a fully eclipsed configuration is 12.7°, Fig. 8. The cyclopentadienyl ring which is bonded to the β-diketonato chelate ring at C(1) deviates 3.1(5)° from co-planarity with the plane defined by atoms O(1), O(2), C(1), C(2), C(3) and Rh, i.e. the plane through the chelate ring.

The average C–C bond distance, 1.38(1) Å, in the phenyl rings is within experimental error near the normal value (1.394 Å) for the aromatic C–C bond [33]. The bond angles around P differ no more than 7° from 109°28′, the angle for a regular tetrahedron. The mean P–C distance is 1.82(1) Å, and almost the same [20] as in the parent rhodium(I) complex [Rh^{I}(fctfa)(CO)(PPh_3)], where it was 1.824 Å. The Rh^{III}–P bond distance for the present complex of

Table 3
Crystal data and structure refinement for [Rh(fctfa)(CO)(PPh_3)(CH_3)(I)]

Empirical formula	$C_{34}H_{28}F_3FeO_3RhPI$	*Z*, density (calculated) (g/cm^3)	4, 1.716
Formula weight	858.2219	Temperature (K)	293(2)
Crystal system	Monoclinic	Wavelength (Å)	0.71073
Space group	$P2_1/c$	Absorption coefficient (mm^{-1})	1.961
Unit cell dimensions			
a (Å)	10.769(2)	Reflections collected	4717
b (Å)	15.153(3)	Unique reflections	4420 [$R_{int} = 0.0588$]
c (Å)	20.413(5)	Refinement method	Full-matrix least-squares on F^2
β (°)	94.31(2)	Data [$I > 2\sigma(I)$]; parameters	4414; 429
Volume (Å^3)	3221(1)	Final *R* indices [$I > 2\sigma(I)$]	$R = 0.0588$, $R_w = 0.1692$

2.320(2) Å is, however, much longer than the Rh–P bond distance for [Rh^{I}(fctfa)(CO)(PPh_3)], 2.232(1) Å, indicating a change in oxidation state from Rh(I) to Rh(III) results in a weaker Rh–P bond. The Rh^{III}–P bond length for the [Rh(fctfa)(CO)(PPh_3)(CH_3)(I)] complex is, however, in the same order as was found for a variety of other Rh^{III}-alkyl complexes including [Rh(cupf)(CO)(PPh_3)(CH_3)(I)] [15c], 2.327(4) Å, and [Rh(ox)(CO)(PPh_3)(CH_3)I] [30b], 2.321(2) Å, (average of two molecules found in one unit cell, Hcupf = *N*-hydroxy-*N*-nitroso-benzeneamine).

The trifluoromethyl group in [Rh(fctfa)(CO)(PPh_3)-(CH_3)(I)] is disordered, similar to what was found for the free β-diketone Hfctfa [32]. An intermolecular interaction was observed between F and either a hydrogen on a ferrocenyl group, or a hydrogen on a phenyl ring from *another* molecule (indicated by H′): F(3)–H′(53) = 2.661 Å, F(3)–H′(12) = 2.669 Å, F(12)–H′(53) = 2.652 Å, F(12)–H′(13) = 2.667 Å, F(13)–H′(36) = 2.606 Å. These intermolecular interactions link one molecule to another in the unit cell and it is partially the cause of the CF_3 disorder. However, the CF_3 disorder is also the result of intramolecular interaction that prevents rotation of the CF_3 group. Two preferred CF_3 orientations are observed. The first involves a strong intramolecular interaction between F(2) and H(2) (the hydrogen bonded to C(2)) and a weak interaction between both F(1) and F(3) with O(2). The contact distances are F(2)–H(2) = 2.362 Å, F(1)–O(2) = 2.702 Å and F(3)–O(2) = 2.718 Å, respectively. The other CF_3 orientation, involving F(12), F(11) and F(13), is the result of a strong interaction between F(12) and O(2) and a weak interaction of both F(11) and F(13) with H(2). The intramolecular contact distances are F(12)–O(2) = 2.485 Å, F(11)–H(2) = 2.727 Å and F(13)–H(2) = 2.624 Å, respectively.

4. Conclusion

A three-step reaction sequence was found for the oxidative addition of iodomethane to [Rh(fctfa)(CO)(PPh_3)], the final product of the reaction was found to be a Rh^{III}-acyl species. UV/Vis studies alone could only provide reaction rates and the amount of reaction steps. Utilizing IR spectroscopic techniques, alkyl and acyl Rh^{III} species could be identified, but only NMR spectroscopy revealed that each reaction product exists in solution as two main isomers in a fast equilibrium with each other. This study is the first to observe a fast equilibrium between Rh^{III}-alkyl and Rh^{III}-acyl intermediates (equilibrium K_2) and it was the first to determine the actual rate of conversion from a Rh^{III}-alkyl2 species to a Rh^{III}-acyl2 species. The incorporation of a ferrocenyl group in the β-diketonato ligand slightly accelerated the rate of CH_3I oxidative addition when compared with the rate of oxidative addition to either the corresponding $CH_3COCHCOCF_3^-$ [15a] or PhCOCH-$COCF_3^-$ complex [34]. A completely general mechanism for the oxidative addition of CH_3I to [Rh(β-diketonato)(CO)(PPh_3)] could be derived and all previously proposed mechanisms for a variety of such reactions are special cases of the general mechanism that emanated from this study. The structure of the intermediate Rh^{III}-alkyl2B geometric isomer, [Rh(fctfa)(CO)(PPh_3)(CH_3)(I)], was solved. It was asymmetric in nature and the phosphine and iodo ligands were found to be the axial ligands.

Acknowledgements

Financial assistance by the South African NRF under Grant 2054243 and the Central Research Fund of the University of the Free State is gratefully acknowledged.

Appendix A. Supplementary material

CCDC 646438 contains the supplementary crystallographic data for [Rh(fctfa)(CO)(PPh_3)(CH_3)(I)]. These data can be obtained free of charge via http://www.ccdc.cam.ac.uk/conts/retrieving.html, or from the Cambridge Crystallographic Data Centre, 12 Union Road, Cambridge CB2 1EZ, UK; fax: (+44) 1223-336-033; or e-mail: deposit@ccdc.cam.ac.uk. Supplementary data associated with this article can be found, in the online version, at doi:10.1016/j.poly.2007.07.004.

References

[1] S.E. Sherman, S.J. Lippard, Chem. Rev. 87 (1987) 1153.
[2] W.A. Herrmann, Kontakte 1 (1991) 22.
[3] W.A. Herrmann, Kontakte 3 (1991) 29.
[4] C. Mercier, P. Chabardes, Pure Appl. Chem. 66 (1994) 1509.
[5] (a) J. Adams, D.M. Spero, Tetrahedron 47 (1991) 1765;
(b) A.J. Anciaux, A. Demonceau, A.F. Noels, R. Warin, A.J. Hubert, P. Teyssié, Tetrahedron 24 (1983) 2169.
[6] J.M. O' Connor, J. Ma, Tetrahedron 57 (1992) 5075.
[7] (a) K. Burgess, M.J. Ohlmeyer, Chem. Rev. 91 (1991) 1179;
(b) D.A. Evans, G.C. Fu, A.H. Hoveyda, J. Am. Chem. Soc. 114 (1992) 6671.
[8] (a) N. Sakai, S. Mano, K. Nozaki, H. Takaya, J. Am. Chem. Soc. 115 (1993) 7033;
(b) G.D. Cuny, S.L. Buchwald, J. Am. Chem. Soc. 115 (1993) 2066.
[9] (a) M.J. Burk, Y.M. Wang, J.R. Lee, J. Am. Chem. Soc. 118 (1996) 5142;
(b) D.A. Evans, G.C. Fu, Chem. Rev. 93 (1993) 1307;
(c) W.R. Cullen, S.J. Rettig, F.B. Wickenheiser, J. Mol. Catal. 66 (1991) 251.
[10] W.R. Cullen, F.B. Wickenheiser, J. Organomet. Chem. 370 (1989) 141.
[11] J.H. Jones, Platinum Metals Rev. 44 (2000) 94.
[12] P.M. Maitlis, A. Haynes, G. J Sunley, M.J. Howard, J. Chem. Soc., Dalton Trans. (1996) 2187.
[13] J.D. Atwood, Coord. Chem. Rev. 83 (1988) 93.
[14] (a) A. Haynes, B.E. Mann, G.E. Morris, P.M. Maitlis, J. Am. Chem. Soc. 115 (1993) 4093;
(b) A. Haynes, P.M. Maitlis, G.E. Morris, G.J. Sunley, H. Adams, P.W. Badger, C.M. Bowers, D.B. Cook, P.I.P. Elliot, T. Ghaffer, H. Green, T.R. Griffin, M. Payne, J.M. Pearson, M.J. Taylor, P.W. Vickers, R.J. Watt, J. Am. Chem. Soc. 126 (2004) 2847.
[15] (a) S.S. Basson, J.G. Leipoldt, J.T. Nel, Inorg. Chim. Acta 84 (1984) 167;
(b) S.S. Basson, J.G. Leipoldt, A. Roodt, J.A. Venter, T.J. van der Walt, Inorg. Chim. Acta 119 (1986) 35;

(c) S.S. Basson, J.G. Leipoldt, A. Roodt, J.A. Venter, Inorg. Chim. Acta 128 (1987) 31;
(d) J.G. Leipoldt, S.S. Basson, L.J. Botha, Inorg. Chim. Acta 168 (1990) 215;
(e) J.A. Venter, J.G. Leipoldt, R. van Eldik, Inorg. Chem. 30 (1991) 2207.

[16] D.M.C. Smit, Synthesis and kinetic study of rhodium(I) complexes containing organic tripod ligands (in Afrikaans), Ph.D. thesis, University of the Orange Free State, R.S.A., 1995.

[17] (a) G.J.J. Steyn, A. Roodt, J.G. Leipoldt, Inorg. Chem. 31 (1992) 3477;
(b) G.J.J. Steyn, A. Roodt, J.G. Leipoldt, Rhodium Ex. 1 (1993) 25.

[18] B.S. Furniss, A.J. Hannaford, P.W.G. Smith, A.R. Tatchell, Vogel's Textbook of Practical Organic Chemistry, 5th ed., John Wiley & Sons, New York, 1994, p. 409.

[19] J. Conradie, G.J. Lamprecht, S. Otto, J.C. Swarts, Inorg. Chim. Acta 328 (2002) 191.

[20] G.J. Lamprecht, J.C. Swarts, J. Conradie, J.G. Leipoldt, Acta Crystallogr., Sect. C 49 (1993) 82.

[21] L.G. Akselrud, Yu. N. Grin, P. Yu. Zavalii, V.K. Pacharsky, V.S. Fundamensky, CSD-universal program package for single crystal and/or powder structure data refinement, XII European Crystallographic Meeting, Moscow, August 1989, Collected Abstracts, v.3, p. 155.

[22] G.M. Sheldrick, Acta Crystallogr., Sect. A 46 (1990) 467.

[23] G.M. Sheldrick, SHELX93, Program for Crystal Structure Determination, University of Göttingen, Germany, 1993.

[24] D.T. Cromer, J. Mann, Acta. Crystallogr., Sect. A 24 (1968) 321.

[25] A.J.C. Wilson (Ed.), International Tables for X-ray Crystallography, vol. C, Kluver Academic Publishers, Dortrecht, 1992.

[26] J.H. Espenson, Chemical Kinetics and Reaction Mechanisms, 2nd ed., McGraw-Hill, New York, 1995, pp. 15, 49, 70–75, 156.

[27] MINSQ, Least Squares Parameter Estimation, Version 3.12, MicroMath, 1990.

[28] R.C. Weast, Handbook of Chemistry and Physics, 49th ed., The Chemical Rubber Co., Ohio, 1969, pp. E58–E59.

[29] R.G. Wilkins, Kinetics and Mechanism of Reactions of Transition Metal Complexes, 2nd thoroughly revised ed., VCH, Weinheim, 1991, p. 15.

[30] (a) J.P. Collman, P.A. Christian, S. Current, P. Denisevich, T.R. Halbert, E.R. Schmittou, K.O. Hodgson, Inorg. Chem. 15 (1976) 223;
(b) K.G. van Aswegen, J.G. Leipoldt, I.M. Potgieter, G.J. Lamprecht, A. Roodt, G.J. van Zyl, Trans. Met. Chem. 16 (1991) 369.

[31] F.A. Cotton, G. Wilkinson, Basic Inorganic Chemistry, John Wiley & Sons, New York, 1976, pp. 473–480.

[32] (a) W.C. du Plessis, T.G. Vosloo, J.C. Swarts, J. Chem. Soc., Dalton Trans. (1998) 2507;
(b) W.C. du Plessis, J.C. Erasmus, G.J. Lamprecht, J. Conradie, T.S. Cameron, M.A.S. Aquino, J.C. Swarts, Can. J. Chem. 77 (1999) 378.

[33] L.E. Sutin, Tables of Interatomic Distances and Configuration in Molecules and Ions, Supplement 1956–1959, The Chemical Society, London, p. S16s.

[34] D. Lamprecht, G.J. Lamprecht, unpublished results.

and potassium thiocyanate (Merck) were used as supplied and solvents were purified by standard procedures before use. *Caution:* Perchlorate complexes of metals with organic ligands are potentially explosive and should be handled with care.

2.2. Syntheses of ligands

The thiosemicarbazone ligands (Scheme 1) were synthesized by adopting and modifying a reported procedure of Scovill et al. [9]. The syntheses of HL^1 [7], HL^2 [10] and HL^3 [7] have been published earlier.

2.3. Syntheses of complexes

2.3.1. Syntheses of $[MnL^1_2] \cdot H_2O \cdot EtOH$ (*1*) and $[MnL^1_2] \cdot 3H_2O$ (*3*)

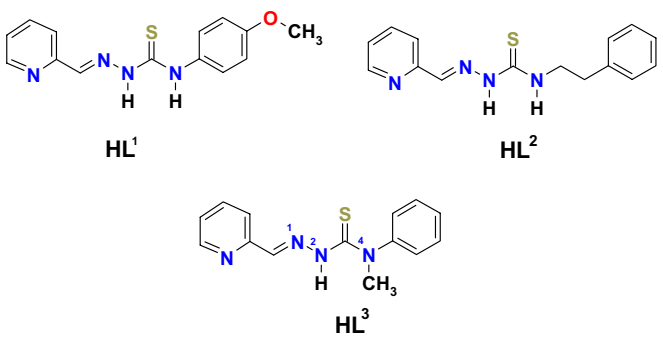
To a solution of the respective ligand (2 mmol) in hot ethanol (25 ml) was added $MnCl_2 \cdot 4H_2O$ (1 mmol), and the resulting solution was heated at reflux for 2 h and then kept at room temperature (overnight). The complexes formed were filtered, washed thoroughly with water, ethanol and then ether and dried *in vacuo* over P_4O_{10}. However compound **1** crystallized as $[MnL^1_2] \cdot H_2O$ (**1a**) on slow evaporation of its solution in ethanol in air.

2.3.2. Synthesis of $[Mn(L^1)(HL^1)]OAc$ (*2*)

To a solution of HL^2 (2 mmol) in hot ethanol (25 ml) was added $Mn(OAc)_2 \cdot 4H_2O$ (1 mmol), and the resulting solution was heated at reflux for 2 h and then kept at room temperature (overnight). The complex formed was filtered, washed thoroughly with water, ethanol and then ether and dried *in vacuo* over P_4O_{10}.

2.3.3. Synthesis of $[MnL^3_2] \cdot 3H_2O$ (*4*)

To a solution of HL^3 (2 mmol) in hot ethanol (25 ml) was added $Mn(ClO_4)_2 \cdot 6H_2O$ (1 mmol), and the resulting solution was heated at reflux for 2 hours and then kept at room temperature (overnight). The complex formed was filtered, washed thoroughly with water, ethanol and then ether and dried *in vacuo* over P_4O_{10}.



Scheme 1. The thiosemicarbazones HL^1, HL^2 and HL^3. The numbering scheme used is shown for HL^3.

2.3.4. Synthesis of $[Mn(HL^3)_2](SCN)_2 \cdot MeOH$ (*5*)

To a solution of HL^3 (2 mmol) in hot ethanol (25 ml) was added $MnCl_2 \cdot 4H_2O$ (1 mmol), and the resulting solution was heated at reflux for 2 h. The mixture was then cooled and stirred with KCNS for 30 min and kept at room temperature (overnight). The complex formed was filtered, washed thoroughly with water, ethanol and then ether and dried *in vacuo* over P_4O_{10}.

2.4. Physical measurements

Elemental analyses of the ligands and the complexes were done on a Heracus elemental analyzer at the CDRI, Lucknow, India and on a Vario EL III CHNS analyzer at SAIF, Kochi, India. The IR spectra were recorded on a Thermo Nicolet AVATAR 370 DTGS model FT-IR spectrophotometer with KBr pellets at the SAIF, Kochi. Electronic spectra of the complexes were recorded on a Cary 5000, version 1.09 UV–Vis–NIR spectrophotometer from solutions in $CHCl_3$. The EPR spectra of the complexes in the solid state at 298 K and in DMF solution at 77 K were recorded on a Varian E-112 spectrometer using TCNE as the standard, with 100 kHz modulation frequencies and 0.2 mT modulation amplitude at the SAIF, IIT, Bombay, India. The magnetic susceptibility measurements were carried out at the Indian Institute of Technology, Roorkee, India, at room temperature in the polycrystalline state on a PAR model 155 Vibrating Sample Magnetometer at 5 kOe field strength. The molar conductivities of the complexes in dimethylformamide solutions (10^{-3} M) at room temperature were measured using a direct reading conductivity meter.

2.5. X-ray crystallography

Single crystals of compound $[MnL^1_2] \cdot H_2O$ (**1a**) of X-ray diffraction quality were grown from a solution of **1** in ethanol by slow evaporation at room temperature in air. The crystallographic data and structure refinement parameters are given in Table 1. Intensity data and cell parameters were recorded at room temperature (293 K) on a Nonius, MACH3 diffractometer equipped with graphite monochromated Mo Kα ($\lambda = 0.71073$ Å) radiation. A single crystal of dimensions $0.35 \times 0.30 \times 0.30$ mm^3 was used for data collection. The Maxus (Nonius software) was used for data reduction [11]. The trial structure was solved using SHELXS-97 [12] and refinement was carried out by full-matrix least squares on F^2 (SHELXL) [12]. The non-hydrogen atoms were refined with anisotropic thermal parameters. All hydrogen atoms, with the exception of those on N4, were geometrically fixed and refined using a riding model. The hydrogen atoms of the N4 atoms were located from difference Fourier maps. However, the hydrogen atoms of the water molecule could not be located and were ignored. The molecular graphics employed were ORTEP-III [13] and PLATON [14].

Table 1
Crystal refinement parameters of compound $[MnL^1_2]\cdot H_2O$ (**1a**)

Parameters	$[MnL^1_2]\cdot H_2O$
Empirical formula	$C_{28}H_{28}Mn_1N_8O_3S_2$
Formula weight (M)	643.63
Temperature (T) (K)	293(2)
Wavelength (Mo Kα) (Å)	0.71073
Crystal system	monoclinic
Space group	$C2/c$
Lattice constants	
a (Å)	15.1640(12)
b (Å)	18.7930(15)
c (Å)	11.8960(11)
α (°)	90.00
β (°)	109.310(8)
γ (°)	90.00
Volume V (Å^3)	3199.4(5)
Z	8
D_{calc} (ρ) (g cm^{-3})	1.332
Absorption coefficient, μ (mm^{-1})	0.585
F(000)	1324
Crystal size (mm)	$0.35\times0.30\times0.30$
Color, nature	brown, block
Limiting indices	$0\leqslant h\leqslant 18$, $-22\leqslant k\leqslant 0$, $-14\leqslant l\leqslant 13$
Reflections collected	2855
Independent reflections [R(int)]	2750 [0.0177]
Refinement method	full-matrix least-squares on F^2
Data/restraints/parameters	2750/0/200
Goodness-of-fit on F^2	1.060
Final R indices [$I>2\sigma(I)$]	$R_1=0.0582$, $wR_2=0.1515$
R indices (all data)	$R_1=0.1229$, $wR_2=0.1762$
Largest difference peak and hole (e Å^{-3})	0.703 and −0.280

3. Results and discussion

All the five compounds are bis(thiosemicarbazone) complexes. In the compounds **1**, **3** and **4**, the thiosemicarbazones deprotonate and chelate in the thiolate form, as proven by the IR spectral data. In **5**, the ligand moieties are in the thione form, whereas in **2**, one of them is in the thione form and the other in the thiolate form. Elemental analyses and conductivity data are in agreement with the general empirical formula $[MnL_2]$ for the complex part of compounds **1**, **3** and **4**. Compound **2** is found to be [Mn(L)(HL)]OAc and **5** turned out to be $[Mn(HL)_2](SCN)_2$. The colors, partial elemental analyses, molar conductivities and magnetic susceptibilities of the metal complexes are shown in Table 2. The room temperature magnetic moments of powdered samples of all the complexes are consistent with manganese in the +2 oxidation state, with no significant exchange interactions between adjacent metal centers [15]. The molar conductivity values for 10^{-3} M DMF solutions of complexes **1**, **3** and **4** suggest that these complexes are non-electrolytes and the values for **2** and **5** show that they are probably 1:1 and 1:2 electrolytes respectively [16].

3.1. Crystal structure of $[MnL^1_2]\cdot H_2O$ (*1a*)

The molecular structure of $[MnL^1_2]\cdot H_2O$, obtained from single crystal X-ray diffraction studies, showed a six coordinate Mn(II) center in a distorted octahedral geometry. The molecular structure of the compound along with the atom numbering scheme is given in Fig. 1. The asymmetric unit contains one half of the molecule and the other half is generated by a twofold axis passing through the metal center. The Mn(II) center is coordinated in an N_4S_2 *meridional* manner by two anionic ligand moieties using pairs of *cis* pyridyl-*N*, *trans* azomethine-*N* and *cis* thiolate-*S* atoms. The coordination of sulfur occurs through deprotonation after enolization, and was confirmed by the partial single and double bond nature of the C7–S1 [1.735(4) Å] and N3–C7 [1.316(5) Å] bonds [17].

The bond parameters (Table 3) show that the geometry around Mn(II) is distorted significantly from a perfect octahedron. The metal center is shared by four fused five membered chelate rings. The planes comprising Mn1, S1, C7, N2, N3 and Mn1, N1, C5, C6, N2, with a maximum deviation from the mean plane of 0.013(4) Å for N3 and −0.020(4) Å for C5 respectively, make an angle of 1.79(12)°. The mean plane of the bicyclic chelate rings Mn1, N1, C5, C6, N2, N3, C7, S1, having a maximum deviation of −0.059(4) Å for the C5 atom, makes a dihedral angle of 87.84(7)° with its counterpart. The Mn–$N_{azomethine}$, Mn–N_{py} and Mn–S bond lengths are comparable with the previously reported manganese complexes [5,6,17].

The molecules are connected in the crystal lattice through an intermolecular hydrogen bond N4–H4···S1 [symmetry code: $-x$, $-y$, $-z$; with a H···S distance of 2.62(6) Å and angle 148(5)°] interactions and make six

Table 2
Colors, partial elemental analyses, magnetic susceptibilities and molar conductivities of the complexes

Complex	Color	μ (BM)	λ_M^a	Found(calc.) %			
				C	H	N	S
$[MnL^1_2]\cdot H_2O\cdot EtOH$ (**1**)	brown	6.02	1.5	52.57(52.24)	4.75(4.97)	16.23(16.25)	9.34(9.30)
$[Mn(L^1)(HL^1)]OAc$ (**2**)	brown	5.62	69	52.85(52.55)	4.46(4.41)	16.42(16.34)	9.82(9.35)
$[MnL^2_2]\cdot 3H_2O$ (**3**)	orange	5.33	18	53.78(53.32)	5.19(5.37)	16.93(16.58)	9.53(9.49)
$[MnL^3_2]\cdot 3H_2O$ (**4**)	brown	5.56	12	44.67(44.95)	3.90(4.45)	14.76(14.98)	8.41(8.57)
$[Mn(HL^3)_2](SCN)_2\cdot MeOH$ (**5**)	brown	5.81	138	49.99(50.05)	4.03(4.34)	19.19(18.83)	16.63(17.24)

[a] Molar conductivity of 10^{-3} M DMF solution, in Ω^{-1} cm^2 mol^{-1}.

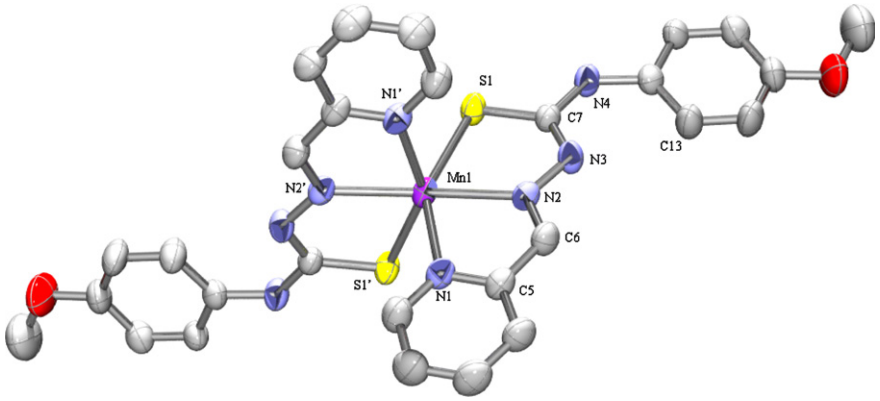


Fig. 1. ORTEP diagram of $[MnL^1_2] \cdot H_2O$ with 25% probability ellipsoids. The hydrogen atoms and a water molecule are omitted for clarity.

Table 3
Selected bond lengths (Å) and bond angles (°) of $[MnL^1_2] \cdot H_2O$

Bond lengths (Å)		Bond angles (°)	
Mn(1)–N(2)	2.257(3)	N(2′)–Mn(1)–N(2)	163.63(18)
Mn(1)–N(1)	2.293(4)	N(2′)–Mn(1)–N(1)	96.44(13)
Mn(1)–S(1)	2.5349(13)	N(2)–Mn(1)–N(1)	71.78(13)
C(7)–S(1)	1.735(4)	N(2′)–Mn(1)–N(1′)	71.78(13)
N(1)–C(1)	1.317(6)	N(2)–Mn(1)–N(1′)	96.44(13)
N(1)–C(5)	1.340(6)	N(1)–Mn(1)–N(1′)	90.47(18)
N(2)–C(6)	1.291(5)	N(2′)–Mn(1)–S(1)	117.10(9)
N(2)–N(3)	1.379(5)	N(2)–Mn(1)–S(1)	74.25(9)
N(3)–C(7)	1.316(5)	N(1)–Mn(1)–S(1)	146.00(10)
N(4)–C(7)	1.364(6)	N(1′)–Mn(1)–S(1)	94.66(10)
N(4)–C(8)	1.419(6)	N(2′)–Mn(1)–S(1′)	74.25(9)
		N(2)–Mn(1)–S(1′)	117.10(9)
		N(1)–Mn(1)–S(1′)	94.66(10)
		N(1′)–Mn(1)–S(1′)	146.00(10)
		S(1)–Mn(1)–S(1′)	99.46(6)
		C(7)–S(1)–Mn(1)	98.86(15)

membered rings leading to a three dimensional network (Figs. 2 and 3).

A weak intramolecular hydrogen bond C13–H13···N3 [with an H···N distance of 2.33 Å and an angle of 121°] stabilizes each molecule, while π···π interactions between rings comprised of the N1, C1, C2, C3, C4 and C5 atoms [Cg(5)–Cg(5), symmetry code: $1/2 - x$, $1/2 - y$, $-z$; with a distance of 3.738(3) Å between the ring centroids] reinforces the crystal structure cohesion in the packing (Fig. 3).

3.2. Infrared and electronic spectra

The shifts in IR spectral bands assigned in the spectra of the ligands because of coordination are given in Tables 4 and 5. A medium band in the range 3129–3158 cm^{-1} in the free ligands HL^1, HL^2 and HL^3, due to a $\nu(^2N–H)$

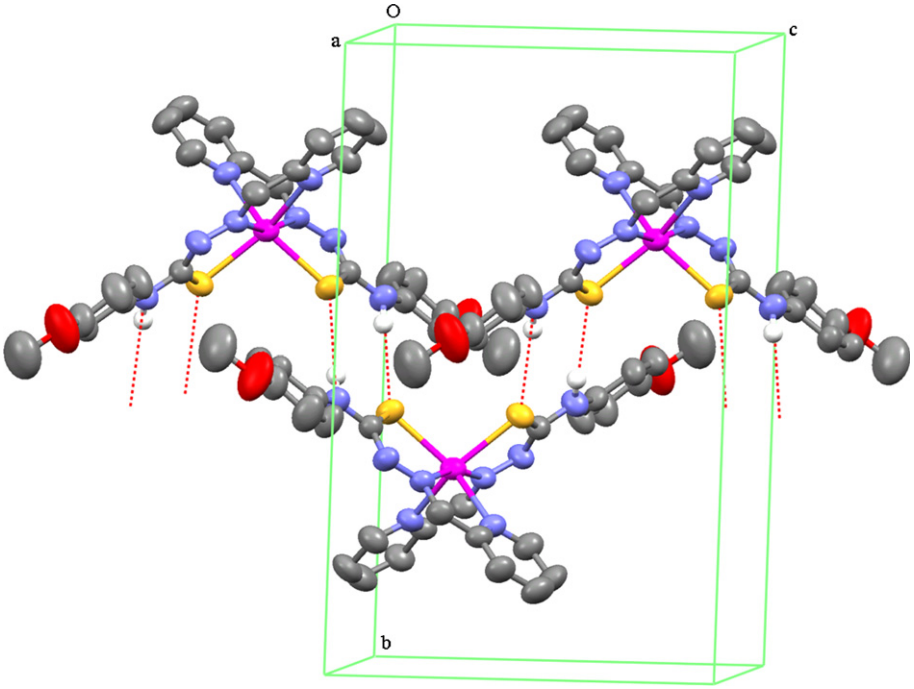


Fig. 2. The intermolecular hydrogen bonds in $[MnL^1_2] \cdot H_2O$ with 25% probability ellipsoids. Hydrogen atoms engaged in hydrogen bonds are shown with an arbitrary radius while others are omitted for clarity.

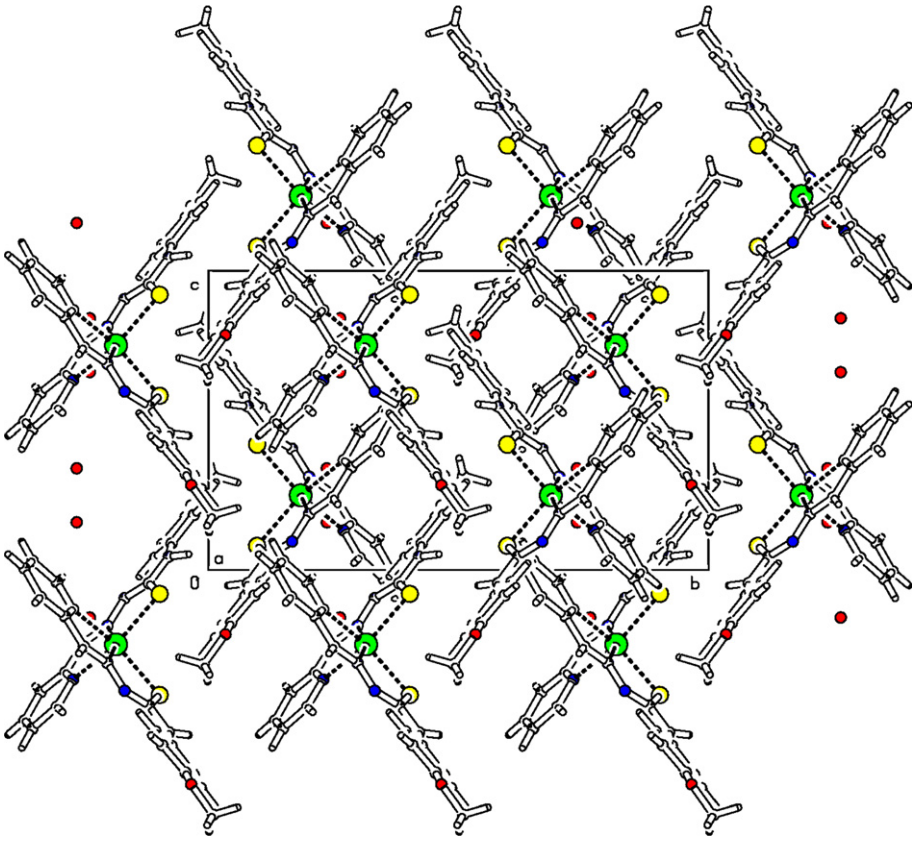


Fig. 3. A view of the unit cell packing of $[MnL^1_2] \cdot H_2O$ along the *a* axis.

vibration, disappears in the spectra of complexes **1**, **3** and **4**, providing strong evidence for ligand coordination to the manganese(II) ion in the deprotonated thiolate form [6]. In complexes **2** and **5**, the $\nu(^2N–H)$ bands are present since these complexes have the ligands in the thione form. The strong bands at 3310 and 3374 cm^{-1} in the spectra of HL^1 and HL^2, assigned to $\nu(^4N–H)$, shift to higher energies. The ν(C=N) bands of thiosemicarbazones are found to be shifted to lower frequencies in all the complexes indicating coordination *via* the azomethine nitrogen. The coordination of this nitrogen is also supported by a shift in ν(N–N) to higher frequencies [5]. In the spectra of all the complexes the bands corresponding to the newly formed N=C bond $[\nu(^2N=^3C)]$ due to the enolization of the ligands are present at *ca.*1600 cm^{-1}. Coordination *via* the thiolate sulfur is indicated by the negative shift of the two bands assigned to ν(C–S + C–N) and δ(C–S + C–N) vibrations. The out-of-plane and in-plane bending vibrations of the pyridine ring in the uncomplexed ligands shift to higher frequencies on complexation, confirming the coordination of the ligands to the metal *via* the pyridine nitrogen [18]. The manganese-donor atom stretching frequencies in the ranges 402–420 $cm^{-1}[\nu(Mn–N_{imine})]$, 352–381 cm^{-1} $[\nu(Mn–S)]$ and 248–289 $cm^{-1}[\nu(Mn–N_{py})]$. provide further evidence for the coordination of the azomethine nitrogen, thione/thiolate sulfur and pyridyl nitrogen.

The strong band at 2054 cm^{-1} $[\nu(CN)]$ and a medium band at 481 cm^{-1} $[\delta(SCN)]$ indicates the presence of ionic thiocyanate in **5** [19]. The spectrum of the acetate-containing complex **3** displays relatively strong bands at 1628 $[\nu_a(COO)]$ and 1397 cm^{-1}, $[\nu_s(COO)]$ indicating the ionic nature of the acetate in this compound [20].

Electronic transition intensities of octahedral manganese(II) complexes are very low since the transitions from the ground state $^6A_{1g}$ are doubly forbidden. The absorptions of the organic ligands tailing into the visible region obscure the very weak d–d absorption bands of the manganese(II) complexes. The broad band at *ca.* 23000 cm^{-1}, typical of octahedral manganese(II) complexes due to the $^4T_{2g} \leftarrow {}^6A_{1g}$ transitions, is observed for all the complexes. The very weak bands at *ca.* 18000 cm^{-1} are assigned to $^4T_{1g} \leftarrow {}^6A_{1g}$ transitions. The electronic spectral assignments are summarized in Table 6.

3.3. EPR spectra

The spin Hamiltonian used to represent the EPR spectra of Mn(II) is given by

$$\widehat{H} = g\beta HS + D[S_z^2 - S(S+1)/3] + E(S_x^2 - S_y^2)$$

where H is the magnetic field vector, g is the spectroscopic splitting factor, β is the Bohr magneton, D is the

Table 4
Infrared spectra (cm^{-1}) of *N*(4)-substituted thiosemicarbazones and their manganese(II) complexes

Compound	νC=N	ν^2N=^{3}C	νN–N	ν/δC–S	py(ip)	py(op)	ν^2N–H	ν^4N–H
HL^1	1584		1024	1334, 837	613	401	3134	3310
$[MnL^1_2]$ (**1**)	1562	1607	1081	1296, 836	646	409		3427
$[Mn(L^I)(HL^1)]OAc$ (**2**)	1534	1598	1093	1296, 832	654	408	3304	3411
HL^2	1586		1079	1324, 897	622	406	3129	3374
$[MnL^2_2]$ (**3**)	1560	1592	1143	1300, 837	632	409		3441
HL^3	1590		1035	1307, 779	614	421	3158	
$[MnL^3_2]$ (**4**)	1541	1596	1144	1301, 774	635	457		
$[Mn(HL^3)_2](SCN)_2$ (**5**)	1574	1598	1132	1294, 773	632	451	3434	

Table 5
Metal–ligand stretching frequencies (cm^{-1}) of the complexes

Complex	Mn–N_{azo}	Mn–S	Mn–N_{py}
$[MnL^1_2]$ (**1**)	402	364	248
$[Mn(L^I)(HL^1)]OAc$ (**2**)	410	354	289
$[MnL^2_2]$ (**3**)	411	381	279
$[MnL^3_2]$ (**4**)	420	362	276
$[Mn(HL^3)_2](SCN)_2$ (**5**)	410	352	288

Table 6
Electronic spectral assignments of the ligands and the complexes

Compound	$\pi \rightarrow \pi^*$	$n \rightarrow \pi^*$	$^4T_{1g} \leftarrow {}^6A_{1g}$	$^4T_{2g} \leftarrow {}^6A_{1g}$
HL^1	42735, 38760	30769		
$[MnL^1_2]$ (**1**)	42841, 37879	33898	18248	22936
$[Mn(L^I)(HL^1)]OAc$ (**2**)	42194, 37492	35481	18051	23810
HL^2	42194, 36630	30960		
$[MnL^2_2]$ (**3**)	41841, 37453	33728	18903	23419
HL^3	43290, 38610	30842		
$[MnL^3_2]$ (**4**)	42194, 38610	33003	18867	23148
$[Mn(HL^3)_2](SCN)_2$ (**5**)	42118, 38786	33416	18478	23542

axial zero field splitting term, E is rhombic zero field splitting parameter and S is the electron spin vector [21]. If D and E are very small compared to $g\beta HS$, five EPR transitions are expected. The solid state EPR spectra of complexes **1**, **3** and **5**, at 298 K are characterized by broad signals with g values of 1.99, 2.03 and 2.02, respectively. The signals of **2** and **4** were very broad due to dipolar interactions and a random orientation of the Mn^{2+} ions [18]. In the spectra from DMF solutions at 77 K, a hyperfine sextet is observed with g values 1.98, 1.99, 1.99 and 1.98, and A values 98, 98, 100 and 100 G, respectively, for **1**, **3**, **4** and **5** (Fig. 4). The six hyperfine lines are due to the interaction of the electron spin with the nuclear spin (^{55}Mn, $I = 5/2$). However, hyperfine splitting is not observed for **2**.

The observed g values are very close to the free electron spin value, suggestive of the absence of spin orbit coupling in the ground state. The A_{iso} values are consistent with an octahedral coordination, since A_{iso} in tetrahedral sites is 20–25% lower than in octahedral sites. The A_{iso} values are somewhat lower than pure ionic compounds, which reflects the covalent nature of the metal–ligand bond in the complexes. The mixing of the nuclear hyperfine levels with the zero field splitting factor produces low intensity forbidden lines with an average spacing of 38 G, lying between each of the two main hyperfine lines in the frozen solution spectra of the complexes [5].

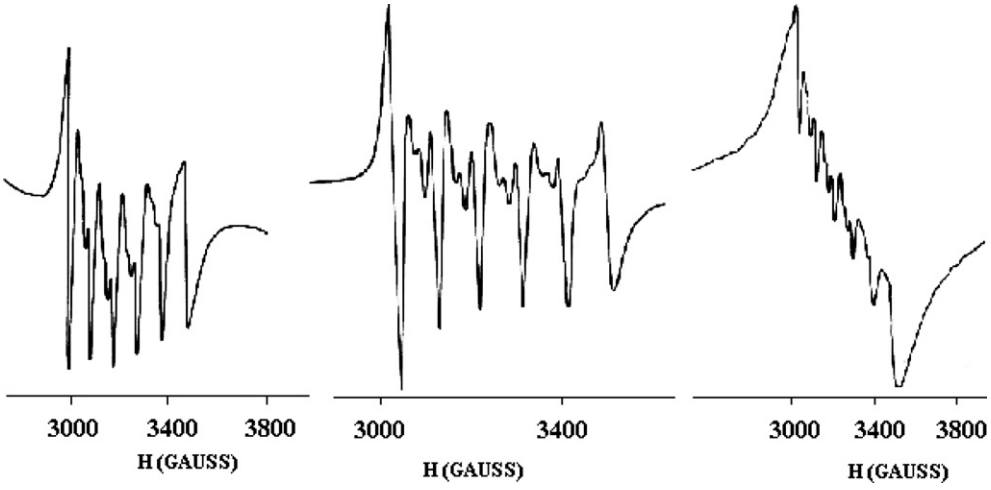


Fig. 4. EPR spectrum of **3** (left), **4** (middle) and **5** (right) in DMF at 77 K.

Acknowledgements

P.F. Rapheal and E. Manoj thank the University Grants Commission, New Delhi, India, for financial support. M.R.P. Kurup is thankful to the CSIR, New Delhi, India, for financial support. We are thankful to the National Single Crystal X-ray Diffraction Facility, IIT, Bombay, India, for providing single crystal XRD results.

Appendix A. Supplementary material

CCDC 622077 contains the supplementary crystallographic data for $[MnL^1{}_2] \cdot H_2O$. These data can be obtained free of charge via http://www.ccdc.cam.ac.uk/conts/retrieving.html, or from the Cambridge Crystallographic Data Centre, 12 Union Road, Cambridge CB2 1EZ, UK; fax: (+44) 1223-336-033; or e-mail: deposit@ccdc.cam.ac.uk. Supplementary data associated with this article can be found, in the online version, at doi:10.1016/j.poly.2007.07.028.

References

[1] S.N. Pandeya, J.R. Dimmock, Pharmazie 48 (1993) 659, and Refs. therein.
[2] A.K. El-Sawaf, D.X. West, R.M. El-Bahnasawy, F.A. El-Saied, Transit. Met. Chem. 23 (1998) 227.
[3] M. Joseph, M. Kuriakose, M.R.P. Kurup, E. Suresh, A. Kishore, S.G. Bhat, Polyhedron 25 (2006) 61.
[4] R.P. John, A. Sreekanth, M.R.P. Kurup, H.-K. Fun, Polyhedron 24 (2005) 601.
[5] A. Sreekanth, M. Joseph, H.-K. Fun, M.R.P. Kurup, Polyhedron 25 (2006) 1408.
[6] V. Philip, V. Suni, M.R.P. Kurup, M. Nethaji, Spectrochim. Acta, Part A 64 (2006) 171.
[7] P.F. Rapheal, E. Manoj, M.R.P. Kurup, E. Suresh, Polyhedron 26 (2007) 607.
[8] P.F. Rapheal, E. Manoj, M.R.P. Kurup, Polyhedron 26 (2007) 818.
[9] J.P. Scovill, D.L. Klayman, C.F. Franchino, J. Med. Chem. 25 (1982) 1261.
[10] H.-K. Fun, S. Chantrapromma, P.F. Rapheal, V. Suni, M.R.P. Kurup, Acta Crystallogr., Sect. E 62 (2006) o125.
[11] Nonius, MACH3 software, B.V. Nonius, Delft, The Netherlands, 1997.
[12] G.M. Sheldrick, SHELXS97 and SHELXL97, Program for the solution of Crystal Structures, University of Gottingen, Germany, 1997.
[13] L.J. Farrugia, J. Appl. Cryst. 30 (1997) 565.
[14] A.L. Spek, J. Appl. Cryst. 36 (2003) 7.
[15] M. Devereux, M. McCann, V. Leon, R. Kelly, D. OSheaa, V. McKee, Polyhedron 22 (2003) 3187.
[16] W.J. Geary, Coord. Chem. Rev. 7 (1971) 81.
[17] A. Usman, I.A. Razak, S. Chantrapromma, H.-K. Fun, A. Sreekanth, S. Sivakumar, M.R.P. Kurup, Acta Crystallogr., Sect. C 58 (2002) m461.
[18] B.S. Garg, M.R.P. Kurup, S.K. Jain, Y.K. Bhoon, Trans. Met. Chem. 13 (1988) 92.
[19] D.N. Sathyanarayana, Vibrational Spectroscopy, New Age International, New Delhi, 2004, p. 400.
[20] K. Nakamoto, Infrared and Raman Spectra of Inorganic and Coordination Compounds, Wiley-Interscience, New York, 1986, p. 60.
[21] D.J.E. Ingram, Spectroscopy at Radio and Microwave Frequencies, second ed., Butterworth, London, 1967.

(H-TFA), which circumvent the solubility, volatility, and carbonate problems [1,2].

Since the TFA ligand has the potential to adopt numerous binding modes such as terminal (TFA), chelating (TFA_c), bridging (μ-TFA), and bridging chelating (μ_c-TFA) it is difficult to predict the final A^E-TFA structure; however, in order to fully optimize the final materials' properties, it is critical to know the precursors' structural properties. While several alkaline earth TFA derivatives are now crystallographically available [23–36], half were solved in the presence of a transition metal [24–28,31,34], which is not of use for production of complex ceramic materials. Of the remaining A^E homocationic species [29,30,32,33,35,36], most were solved in the presence of crown ether modifiers [29,30,35] or had water present [33,35,36]. Both of these conditions are unattractive for materials processing due to the potential for increased carbon contamination or uncontrolled reactivity.

Therefore, we undertook the synthesis of the simple A^E-TFA congeners, to investigate the structural properties of simple A^E homocationic species, following Eq. (1). The synthesis, and subsequent crystallization from a Lewis basic solvent [tetrahydrofuran (THF) or pyridine (py)] yielded: $Mg(TFA)_2(py)_4$ (**1**), $\{[Ca_2(\mu\text{-}TFA)_3(THF)_4](\mu\text{-}TFA)\}_n$ (**2**), $\{[(\mu\text{-}TFA)_2Sr(\mu_c\text{-}TFA)][H\text{-}py]py\}_n$ (**3**), and $\{[Ba(\mu_c\text{-}TFA)_2(\mu_c\text{-}TFA)(py)][H\text{-}py]\}_n$ (**4**). The synthesis and characterization of **1**–**4** are presented in this report.

$$M^0 + (xs)H\text{-}TFA \xrightarrow{solv} \text{“}M(TFA)_2(solv)\text{”}$$
$$M^0 = Mg,\ Ca,\ Sr,\ Ba;\ Solv = THF,\ py. \quad (1)$$

2. Experimental

All compounds described below were handled with rigorous exclusion of air and water using standard Schlenk line and glove box techniques. All reactions were run under an argon atmosphere in a glovebox. All solvents were stored under argon and used as received (Aldrich) in SureSeal™ bottles, including tetrahydrofuran (THF) and pyridine (py). The following chemicals were used as received (Aldrich and Alfa Aesar): Mg^0, Ca^0, Ba^0, Sr^0, and H-TFA.

FT-IR data were obtained on a Bruker Vector 22 Instrument using KBr pellets under an atmosphere of flowing nitrogen. Elemental analysis was performed on a Perkin-Elmer 2400 CHN-S/O Elemental Analyzer. All NMR samples were prepared from dried crystalline materials that were handled and stored under an argon atmosphere. Solution NMR data were obtained on a 400 MHz Bruker NMR spectrometer with the materials dissolved in the parent solvent. The solution ^{19}F NMR data were obtained at 376.23 MHz with the chemical shifts referenced to an external standard of $CFCl_3$ ($\delta = 0.00$ ppm), while the solution ^{13}C NMR data were obtained at 100.1 MHz, and referenced to residual protonated solvent signal. The solid-state MAS NMR spectra were obtained on a Bruker Avance 400 using either a 4 or 2.5 mm MAS probe using a 15 kHz spinning speed. Both direct polarization (DP) decays (^{19}F and ^{13}C) and cross-polarization (CP) experiments ($^{13}C\{^1H\}$) were obtained. The ^{13}C MAS NMR spectra being obtained using either ^{19}F or ^1H TPPM decoupling, but because of instrumental limitations we were not able to obtain both ^1H and ^{19}F decoupling simultaneously. The solid-state ^{19}F MAS NMR chemical shifts were referenced to a secondary standard Teflon™, ($\delta = -122$ ppm) with respect to $CFCl_3$ $\delta = 0.0$ ppm. The solid-state ^{13}C MAS NMR spectra were referenced to the secondary standard adamantane $\delta = 28.5$ ppm with respect to TMS, $\delta = 0.0$ ppm.

2.1. General synthesis of "A^E-TFA_2 (solv)"

The appropriate metal was added to a stirring solution of H-TFA in a flat bottom flask. The reaction immediately began to bubble and was allowed to stir for 12 h. After this time, the bubbling was complete and if the metal was not dissolved, the reaction mixture was heated at reflux temperatures on a Schlenk line until all of the metal was consumed. The solution was dried *in vacuo* to yield off-white powders. This material was assumed to be '$A^E(TFA)_2$' was redissolved in a minimum of the appropriate Lewis basic solvent and X-ray quality crystals were allowed to form by slow evaporation of the volatile component of the reaction.

2.2. $Mg(TFA)_2(py)_4$ (**1**)

Used Mg^0 (5.00 g, 206 mmol), H-TFA (93.8 g, 823 mmol). "$Mg(TFA)_2$" Yield: 99.8% (51.5 g). Used "$Mg(TFA)_2$" (1.00 g, 3.99 mmol), py (~10 mL). Yield: 79.5% (1.80 g). FT-IR (KBr, cm^{-1}) 3152(w), 3112(m), 3084(m), 2967(w), 2918(w), 2862(w), 1740(w,sh), 1700(s), 1604(m,sh), 1538(w), 1490(w,sh), 1469(m), 1447(m,sh), 1210(s), 1150(s,sh), 1069(m), 1041(m), 1006(w,sh), 845(m), 802(m), 759(m), 721(w,sh), 705(m), 629(w,sh), 608(m), 522(m), 474(m), 427(w,sh). ^{13}C NMR (100.5 MHz, py-d_5) δ 162.6 (q, O_2CCF_3, $J_{C-F} = 293$ Hz), 117.9 (q, O_2CCF_3, $J_{C-F} = 29$ Hz). Elemental analysis for $C_{24}H_{20}F_6MgN_4O_4$ for **1** (%): C, 50.86; H, 3.55; N, 9.88; O 11.292. $C_{12.75}H_{8.75}MgF_6N_{1.75}O_4$ (**1** − 2.25 py) Calc. C, 39.39; H, 2.27; N, 6.30. Found: C, 39.90; H, 2.55; N, 6.30%.

2.3. $\{[Ca_2(\mu\text{-}TFA)_3(THF)_4](\mu\text{-}TFA)\}_n$ (**2**)

Used Ca^0 (5.00 g, 125 mmol), H-TFA (56.8 g, 499 mmol). "$Ca(TFA)_2$" Yield: 99.8% (33.2 g). Used "$Ca(TFA)_2$" (1.00 g, 3.76 mmol), THF (~10 mL). Yield: 65.4% (1.01 g). FT-IR (KBr, cm^{-1}) 3431(w), 2964(w), 2902(w), 1745(w,sh), 1687(s), 1462(m), 1208(s), 1149(s,sh), 1036(m), 866(m), 802(m), 726(m), 674(w), 608(w), 522(w), 430(w). ^{13}C NMR (100.5 MHz, THF-d_8) δ 160.4 (q, O_2CCF_3, $J_{C-F} = 293$ Hz), 116.8 (q, O_2CCF_3, $J_{C-F} = 39$ Hz). Elemental analysis for $C_{24}H_{32}Ca_2F_{12}O_{12}$ for **2** (%): C, 35.12; H, 3.93. $C_{15}H_{14}Ca_2F_{12}O_{9.75}$ (**2** − 2.25

THF) Calc. C, 27.36; H, 2.15; N, 0. Found: C, 27.55; H, 2.44; N, 0.37%.

2.4. $\{[(\mu\text{-TFA})_2Sr(\mu_c\text{-TFA})][H\text{-py}]py\}_n$ (3)

Used Sr^0 (5.00 g, 57.0 mmol), H-TFA (26.0 g, 228 mmol). "$Sr(TFA)_2$(H-TFA)" Yield: 99.9% (24.3 g). Used "$Sr(TFA)_2$(H-TFA)" (1.00 g, 2.34 mmol), py (~10 mL). Yield: 80.77% (1.11 g). FT-IR (KBr, cm^{-1}) 3444(w), 3252(w), 3177(w), 3111(m), 3080(m), 2964(m), 2904(m), 2854(m), 1661(s), 1546(m), 1490(m), 1454(m), 1204(s), 1141(s,sh), 850(m,sh), 801(m), 752(m,sh), 725(m,sh), 682(m), 604(w), 519(w), 417(w). ^{13}C NMR (100.5 MHz, py-d_5) δ 164.9 (q, O_2CCF_3, $J_{C-F} = 292$ Hz), 119.7 (q, O_2CCF_3, $J_{C-F} = 40$ Hz). Elemental analysis for $C_{16}H_{11}F_9N_2O_6Sr$ **3** (%): C, 32.80; H, 1.89; N, 4.78. $C_{14.75}H_{9.75}SrF_9N_{1.75}O_6$ (**3** − 0.25 py) Calc. C, 31.29; H, 1.74; N, 4.33. Found: C, 31.12; H, 1.74; N, 4.15%.

2.5. $\{[Ba(\mu_c\text{-TFA})_2(\mu_c\text{-TFA})(py)][H\text{-py}]\}_n$ (4)

Used Ba^0 (5.00 g, 36.4 mmol), H-TFA (16.6 g, 146 mmol), "$Ba(TFA)_2$(H-TFA)" Yield: 76.3% (13.2 g). Used "$Ba(TFA)_2$(H-TFA)" (1.00 g, 2.10 mmol), py (~10 mL). Yield: 97.4% (1.28 g). FT-IR (KBr, cm^{-1}) 3444(w), 3255(w), 3185(w), 3112(m), 3080(m), 2966(w), 2894(m), 2850(m), 1661(s), 1546(m), 1491(m), 1443(m), 1202(s), 1137(s,sh), 1059(w,sh), 843(m), 798(m), 753(m), 723(m), 682(m), 605(w), 518(w). ^{13}C NMR (100.5 MHz, py-d_5) δ 165.6 (q, O_2CCF_3, $J_{C-F} = 293$ Hz), 119.7 (q, O_2CCF_3, $J_{C-F} = 35$ Hz). Elemental analysis for $C_{16}H_{11}BaF_9N_2O_6$ **4** (%): C, 30.24; H, 1.74; N, 4.41. $C_{13.5}H_{8.5}BaF_9N_{1.5}O_6$ (**4** + 0.50 py) Calc. C, 27.20; H, 1.44; N, 3.52. Found: C, 27.43; H, 1.48; N, 3.44%.

2.6. General X-ray crystal structure information [37]

Each crystal was mounted onto a thin glass fiber from a pool of Fluorolube™ and immediately placed under a liquid N_2 stream, on a Bruker AXS diffractometer. The radiation used was graphite monochromatized Mo Kα radiation ($\lambda = 0.7107$ Å). The lattice parameters were optimized from a least-squares calculation on centered reflections. Lattice determination and data collection were carried out using SMART Version 5.054 software. Data reduction was performed using SAINT Version 6.01 software. The structure refinement was performed using XSHELL 3.0 software. The data were corrected for absorption using the SADABS program within the SAINT software package.

Each structure was solved using direct methods. This procedure yielded the heavy atoms, along with a number of the C, F, and O atoms. Subsequent Fourier synthesis yielded the remaining atom positions. The final refinement of each compound included anisotropic thermal parameters on all atoms. For the non-centrosymmetric structure **3**, the coordination of the TFA ligands about the Sr atoms is dictated by a 2_1-screw axis along the polymer propagation direction (*c*-axis). The polymer chain occupies both the edge of the cell along the c-axis as well as propagating through the center of the cell (through the center of the *a*–*b*-plane), which disallows the screw axis a center of inversion, resulting in the non-centrosymmetric symmetry. Additional information concerning the data collection and final structural solutions (Table 1) of these compounds can be found in the supplemental information or by accessing CIF files through the Cambridge Crystallographic Data Base.

3. Results and discussion

As mentioned previously, there are only a hand-full of A^E-TFA derivatives that have been crystallographically characterized [23–36], wherein most homocationic A^E species utilized crown ether modifications to increase their volatility for metal organic chemical vapor deposition (MOCVD) applications [29,30,35]. However, the characteristics that make these excellent MOCVD precursors, also make them ineffective for sol–gel processes. The other derivatives without a crown ether possess water, such as $\{[Sr(TFA)(\mu\text{-}TFA)(H_2O)_2]_n[N_2H_5C_3][TFA]\}$ [33] and $[Ca(TFA)_2(H_2O)_2]_n$ [36], which will introduce uncontrolled reactivity to precursor solution. Due to the void of simple TFA derivatives of A^E precursors, we proceeded to characterize this set of precursors.

3.1. Synthesis

The A^E-TFA adducts were synthesized simply by dissolving the bulk A^E metal in TFA(neat) (Eq. (1)). After the extensive effervescence was complete, if any metal remained, the mixture was heated until the metal was completely consumed. Attempts to isolate crystals of these compounds directly from the reaction mixtures were not successful which is most likely due to the formation of extended polymeric networks based on the large cation size to ligand charge ratio the A^E-TFA system will posses. Therefore, the reaction mixture was dried to a powder that displayed only limited solubility in standard non-polar solvents. However, using Lewis basic solvents (i.e., py or THF) – chosen due to their compatibility with the materials processing parameters employed and their known ability to act as a Lewis bases for A^E cations [3] – the powders were easily solubilized. Crystals were isolated for each congener as **1**–**4**, shown in Figs. 1–4, respectively. Data collection parameters are available in Table 1 and select metrical data are tabulated in Table 2.

The structure of **1**, the smallest cation of the A^E congener set, was found to be monomeric. Each Mg cation was found to adopt a 6-coordinated octahedral (Oh) geometry by binding four equatorial py solvent molecules and two axial, terminal TFA ligands (Fig. 1). It is of note that there are two unique monomeric molecules in this structure, which are chemically identical and differ only in their packing

Table 1
Data collection parameters for **1**–**4**

Compound	**1**	**2**	**3**	**4**
Chemical formula	$C_{24}H_{20}F_6MgN_4O_4$	$C_{24}H_{32}Ca_2F_{12}O_{12}$	$C_{16}H_{11}F_9N_2O_6Sr$	$C_{16}H_{11}BaF_9N_2O_6$
Formula weight	566.75	820.66	585.89	635.61
Temperature (K)	168	168	168	168
Space group	triclinic	monoclinic	orthorhombic	monoclinic
	$P\bar{1}$	$P2_1/c$	$Pna2_1$	$P2_1/c$
a (Å)	9.085 (3)	10.0952 (6)	18.967 (13)	13.177 (3)
b (Å)	16.764 (5)	20.8523 (13)	14.068 (10)	19.169 (4)
c (Å)	18.141 (6)	17.1268 (11)	8.310 (6)	8.5978 (17)
α (°)	70.307 (5)			
β (°)	85.569 (6)	90.580 (1)		102.418 (3)
γ (°)	89.840 (5)			
V (Å^3)	2592.8 (14)	3605.1 (4)	2217 (3)	2120.9 (7)
Z	4	4	4	4
D_{calc} (Mg/m^3)	1.452	1.512	1.755	1.991
μ, (Mo Kα) (mm^{-1})	0.150	0.431	2.542	1.988
R_1^a (%) (all data)	10.80 (14.86)	9.61 (11.23)	5.39 (11.22)	3.95 (5.49)
wR_2^b (%) (all data)	28.07 (30.55)	25.22 (26.80)	10.11 (12.16)	7.67 (8.24)

[a] $R_1 = \sum|F_o| - |F_c| / \sum|F_o| \times 100$.
[b] $wR_2 = [\sum w (F_o^2 - F_c^2)^2 / \sum (w|F_o|^2)^2]^{1/2} \times 100$.

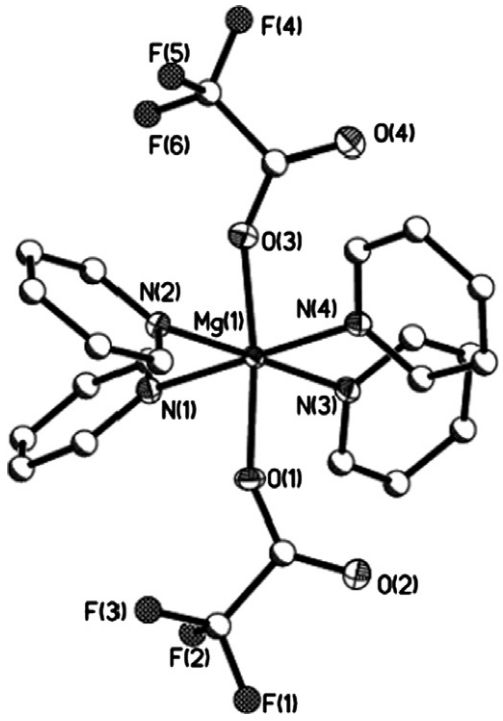


Fig. 1. Structure plot of **1**. Heavy atoms thermal ellipsoids drawn at 30% level. Carbon and fluorine atoms drawn as ball and stick for clarity.

behavior. For this reason, we present only one of the observed molecules in Fig. 1 to represent this structure which is the first report of a Mg-TFA derivative[23] and only the second structurally characterized A^E-TFA that employs a py solvent molecule, the other of which is [(py)(TFA)-(TFA$_c$)Ba(18-Crown-6)$_2$]$_2$ [30]. Of the alkaline earth TFA derivatives, only seven possess a terminal TFA molecule [23–25,30,31] and only two of those possess *only* A^E cations. For the later molecules, the TFA is forced to be terminal due to the steric crowding of crown ether ligands [30]; whereas for **2**, the multiple bound py solvent molecules and small Mg cation limit the chelating behavior of the TFA ligands.

Compound **2** was solved as a polymeric species (see Fig. 2). The molecule is constructed from two Ca metal centers bridged by three μ-TFA ligands to form the initial moiety. Two of these dinuclear moieties are linked together using a fourth μ-TFA ligand yielding the general constructs of **2**. The slightly distorted Oh geometry of each Ca was completed through the binding of two THF molecules in a *cis* equatorial arrangement. This is the first A^E-TFA system noted with bound THF [23–32,36]. The Ca–O distances were found to range from 2.27 to 2.38 Å with similar distances noted for THF ligands. The bite angle of the TFA ligands are all nearly identical at ~130°. It is of note that a water solvated Ca-TFA identified as {[(H$_2$O)$_2$Ca-(μ-TFA)(μ-TFA)$_2$]$_2$Ca}$_n$ has been reported, however, a μ-TFA ligand cross-links the chains in this molecule [36]. This is not present in **2** where the chains were not found to interact. The structure displays disorder on some of the CF_3 and THF ligands; however, this disorder was not modeled due to the inability to obtain a stable refinement while modeling potential disordered C sites (THF) or F sites (CF_3).

Compound **3** was also found to be an asymmetric polymeric chain as noted Fig. 3a and b. Each Sr atom possesses two μ-TFA and one μ_c-TFA ligand and completes its irregular 7-coordination by binding to each of the TFA ligands from the next Sr metal center (Fig. 3a). The μ- and μ_c-TFA ligands are arranged in a *trans* arrangement down the polymer chain (Fig. 3b). The μ_c-TFA binding mode has only been previously observed for Ba-TFA derivatives [23,29,31]. The Sr–O distance range from 2.49 to 2.70 Å with the longer distances associated with the μ_c-TFA ligands. The Sr—Sr distance was found to be 4.32 Å. The bite angle of the

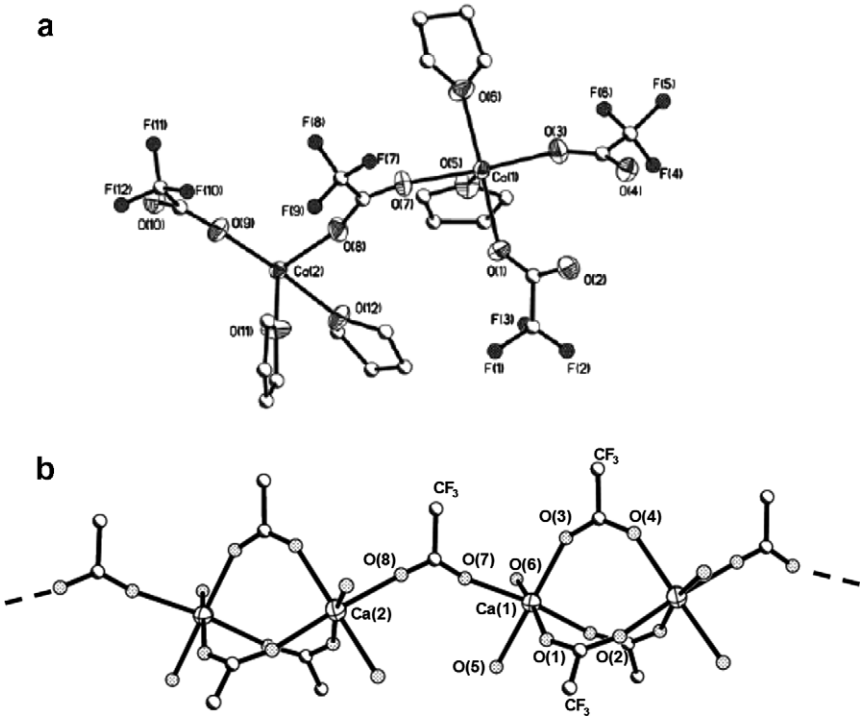


Fig. 2. Structure plot of **2**: (a) Unit cell – heavy atoms thermal ellipsoids drawn at 30% level and carbon and fluorine atoms drawn as ball and stick for simplicity. (b) Diagram of core to show extended network. H- and F- and some C-removed for clarity.

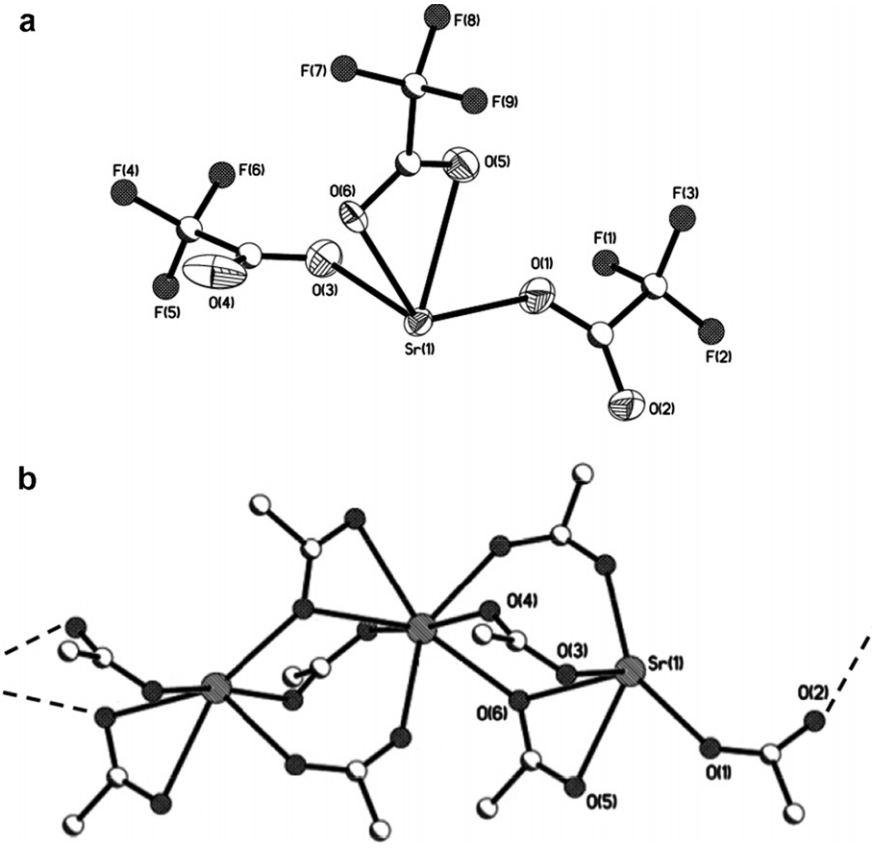


Fig. 3. Structure plot of **3**: (a) Unit cell – heavy atoms thermal ellipsoids drawn at 30% level and carbon and fluorine atoms drawn as ball and stick for simplicity. (b) Diagram of core to show extended network. H- and F- and some C-removed for clarity.

μ_c-TFA (128.6°) and the two μ-TFA (129.2° and 130.0°) are nearly identical. For **3**, a proton is needed to have a charge neutral molecule. In the lattice two pyridine solvent molecules are readily identified and a search of the electron density map indicates a proton was located *between* these two pyridine rings. The bond distances suggest that one of these is a pyrdinium molecule that solves the charge balance issue; however, the 'free' pyridine appears to have a substantial interaction with the pyridinium atom as well. For orientation, the Sr polymer chain is meshed in between this py–H—py complex along the edge of the cell and down the middle. This arrangement is relatively unusual with only four examples of the structural characterization of the py–H—py interaction noted for a variety of derivatized pyridines [38–41]. The bond lengths of the N(1)-C(7) in **3** are 1.33 Å, which is consistent with literature values, however, the N(1)–C(11) distance is slightly shorter at 1.30 Å. Structure **3** also displays disorder on some of the CF_3 ligands but again as noted for **2**, the disorder was not modeled due to the inability to obtain a stable refinement while modeling potential disordered of the F sites (CF_3).

Again, an asymmetric polymeric structure was observed for **4**, with one molecule of co-crystallized py (Fig. 4a). Each Ba adopts an irregular 10-coordinated geometry using the six O atoms of three μ_c-TFA ligands and three O atoms from the neighboring μ_c-TFA (Fig. 4b). The coordination was completed through the binding of a py solvent molecule. The Ba metal centers are separated by nearly 4.40 Å with Ba–O distances ranging from 2.74 to 2.99 Å, wherein the μ-TFA distances being the longest. The bite angles of the three μ_c-TFA (128.5°, 128.2°, and 127.5°) are similar to each other but significantly smaller than those noted for the other congeners. Again, a proton must be included for formal charge balance and was located between one of the oxygens of the TFA ligand and the lattice py (Fig. 4c). The N(2)–H(1)–O(3A) angle is ~169.7°

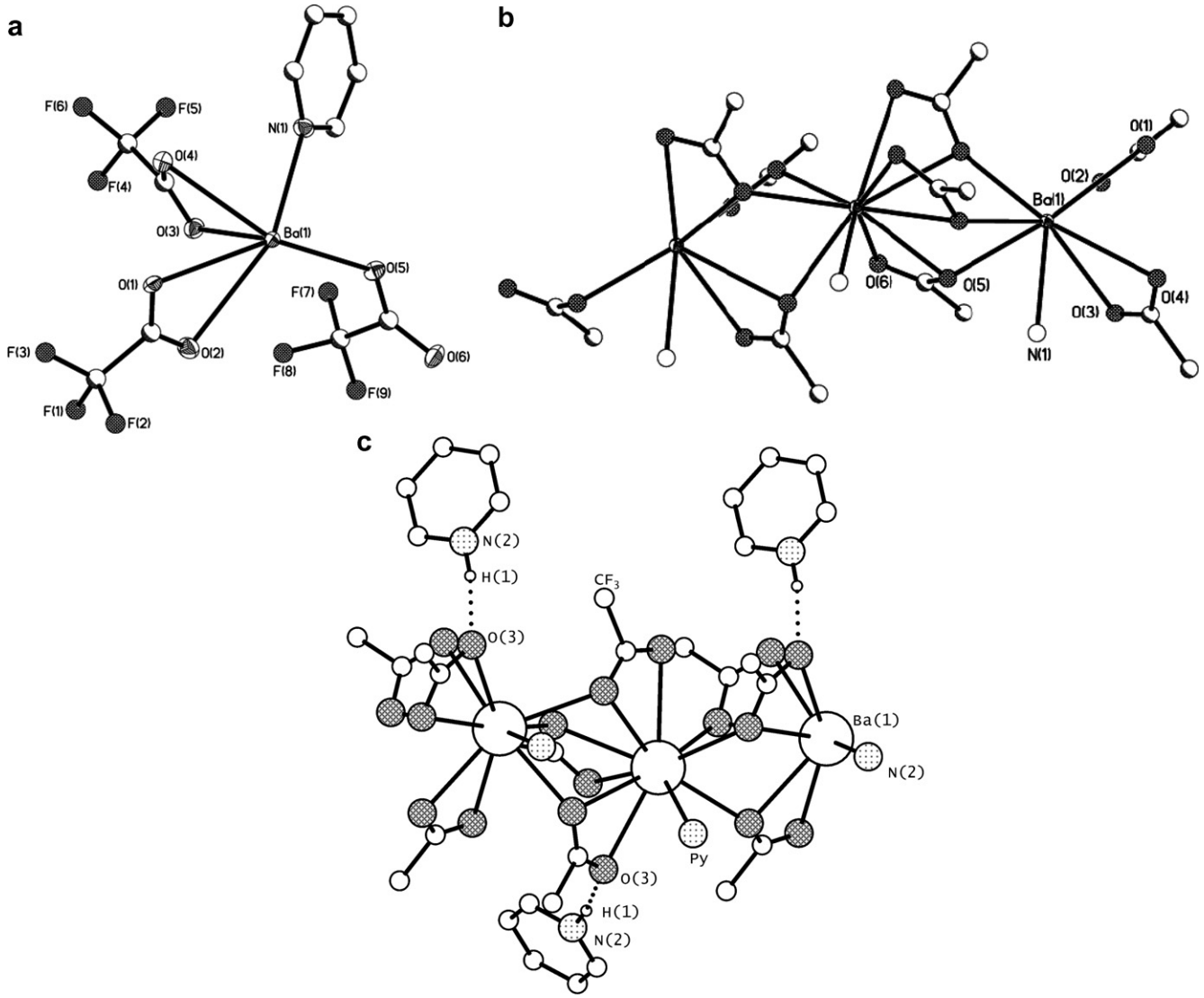


Fig. 4. Structure plot of **4**: (a) Unit cell – heavy atoms thermal ellipsoids drawn at 30% level and carbon and fluorine atoms drawn as ball and stick for simplicity. (b) Diagram of core to show extended network. H- and F- and some C-removed for clarity. (c) Diagram of pyridinium coordination via hydrogen bonding to the O3 atom of a chealated TFA.

Table 2
Selected metrical data for **1**–**4**

Compound	Bond distance (Å)	Average	Bond angles (°)	Average
1	Mg–O	2.02	O–Mg–O	173.2
	Mg–N	2.23	O–Mg–N	90.0
			O–C–O	129.6
2	Ca–O	2.32	O–Ca–O	89.6
	$Ca–O_{THF}$	2.32	$O–Ca–O_{THF}$	171.6
			O–C–O	130.5
3	Sr–O	2.51	O–Sr–O	81.2
			$O–Sr–O_c$	48.9
			O–C–O	129.3
4	Ba–O	2.85	O–Ba–O	76.5
	Ba–N	2.93	$O–Ba–O_c$	44.7
			O(1)–Ba(1)–N(1)	133.26(11)
			O(2)–Ba(1)–N(1)	134.73(11)
			O(3)–Ba(1)–N(1)	66.65(11)
			O(4)–Ba(1)–N(1)	65.15(10)
			O–C–O	128.2

with a N–H distance of 0.92 Å versus a 1.77 Å for the H-TFA distance. Based on these distances and comparison to the literature bond distances, this molecule is also a pyrdinium salt as noted in **3** [38–41]. As mentioned previously, the μ-TFA ligand has been observed in Ba-TFA derivatives [23,29,31], however, this molecule is unique in both arrangement, py coordination, and salt formation.

The transition from the smallest to the largest congener of this series reveals the different bonding modes available to the TFA ligand dependant upon the size of the cation. For instance, the smallest cation Mg only has terminal monodentate TFA ligands noted in **1**; whereas, Ba the largest, **4**, has only μ_c-TFA. For **3**, Ca is of such a size as to only form both μ- and μ_c-TFA ligand arrangements. This occurs even while there is room to solvate the cation, as noted for **2** and **4**. There was no sign of simple chelation by the TFA ligand in these systems that must be due to a combination of the electron donation by the Lewis basic solvents, their occupation of open coordination sites, and the size of the various A^E cations explored. Interestingly, the use of py has serendipitously yielded pyridinium ions for **3** and **4**, which appears to facilitate crystallization.

Analyses of the bulk powders were undertaken to verify they were consistent with the solid-state X-ray structures isolated. Not surprisingly, the elemental analyses of **1**–**4** were not consistent with the simple structures reported. The variations between the bulk powder and single crystal structure were associated with the bound solvents noted for **1**,**2**, and **4** as well as the free solvents or pyridinium salts found in **3** and **4**, that notoriously cause discrepancies in the elemental analyses [3,12–19]. Removal of fractional solvent molecules show an agreement can be rendered for these compounds; however, this is less than desirable in identifying these compounds.

Therefore, solid-state NMR data were collected to further characterize the bulk powders (listed in Table 3). For the majority of samples, a single ^{19}F MAS NMR resonance was observed resulting from the TFA fluoro-methyls. However, compound **2** revealed an overlap of multiple ^{19}F resonances with very similar chemical environments. These most likely represent crystal packing inequivalencies. The inability to distinguish the different TFA bonding motifs led to the analysis of both the $^{13}C\{^{19}F\}$ and $^{13}C\{^{1}H\}$ MAS NMR spectra. For the TFA moiety, a carboxyl (HOC(O)R) ^{13}C resonance around 165 ppm and a trifluoro-(CF_3) group around 114 ppm should be observed. The spectra of **1**–**4** (Fig. 5) all possess the expected TFA resonances but in general these peaks are either very broad or composed of a cluster of closely overlapping resonances. It was not possible to distinguish between the different μ_c-TFA, μ-TFA, and TFA carbon environments in the solid-state ^{13}C MAS experiments. Compounds **1** and **4** also display broad pyridine resonances whereas **2** displays a set of broad THF resonances all associated with the coordinated solvents within their respective crystal structures. Interestingly, **3** also display an additional set of py resonances that may reflect the py–H—py salt observed in the solid-state structure. These

Table 3
NMR data for **1**–**4**

Compound	Solid-state		Solution (solv)	
	δ $^{13}C\{^{19}F\}$ ppm (assignment)	δ ^{19}F (FWHM Hz)	^{13}C ppm δ (assignment)	^{19}F ppm δ (CF_3-TFA)
1	162.2 (O_2C–CF_3)	−75.5 (930)	162.6(O_2C–CF_3)	−74.8
	117.6 (CF_3)		117.9 (CF_3)	−76.0
	149.9–126.4 (py)		(py-d_5)	
2	160.0 (O_2C–CF_3)	−74.7 (383)	160.4(O_2C–CF_3)	−70.2
	115.5 (CF_3)	−75.7 (531)	116.8 (CF_3)	
	68.7–25.1 (THF)	−76.6 (443)	(THF-d_8)	
		−77.4 (442)		
3	162.2	−75.9 (880)	164.9(O_2C–CF_3)	−75.0
	116.5 (CF_3)		119.7 (CF_3)	
	147.6–128.2 (py)		(py-d_5)	
4	162.0 (O_2C–CF_3)	−75.6 (815)	165.6(O_2C–CF_3)	−75.2
	116.9 (CF_3)		119.7 (CF_3)	
	149.8–126.4 (py)		(py-d_5)	

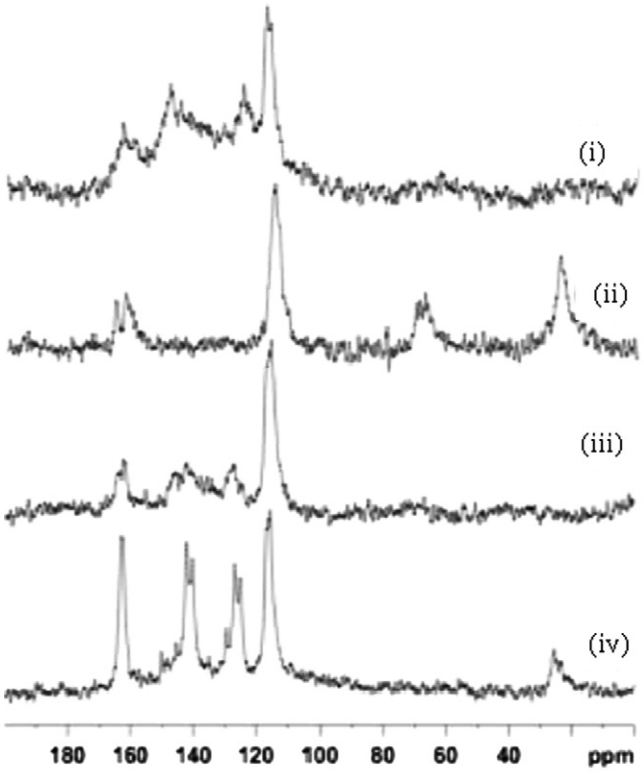


Fig. 5. The $^{13}C\{^{19}F$ decoupled} MAS NMR spectra (i) **1**, (ii) **2**, (iii) **3**, and (iv) **4**.

py and THF solvent resonances reveal very poor CP efficiencies (thus the ^{13}C NMR were obtained using DP) suggesting a high degree of mobility of these pyridine and THF environments at room temperature.

Solution $^{13}C\{^{1}H\}$ and ^{19}F NMR spectra of the materials dissolved in THF were also obtained (Table 3). The standard resonances associated with the bound solvent and a multiplet for the carboxylate ligand due to J_{C-F} splitting was observed. The ^{19}F NMR spectrum of **1** revealed two resonances in a 60:40 ratio, which is in contrast to the single resonance observed in the solid-state ^{19}F MAS NMR. The two ^{19}F NMR resonances at δ −74.8 and −76 ppm may represent a nuclearity change associated with a monomer-dimer equilibrium. Low temperature studies could not be undertaken due to the low solubility of these compounds. For **2**–**4** only a single ^{19}F resonance δ −75 ppm was observed in solution. As noted above in the solid-state, compound **2** has four overlapping resonances but in solution these packing variations averaged out yielding the single resonance noted in Table 3.

Since the carboxylate ligand is indicative of binding modes, the FT-IR spectra of these compounds were collected to further assist in identifying the bulk powder. The spectra indicated that the TFA ligand had fully reacted based on the lack of OH stretches coupled with significant changes in the C=O stretch of the TFA. For **1** two stretches (1778 and 1690 cm^{-1}) were present which would correspond to the terminally bound TFA ligands present in the observed structure. In contrast, for **2**, only one stretch was noted at 1668 cm^{-1} that would be consistent with μ-TFA ligands; for **4**, two peaks at 1773 and 1672 cm^{-1} were observed and associated with μ_c-TFA ligands; however, for **3**, three peaks at 1753, 1678, and 1665 cm^{-1} were observed. By combining the stretches noted for **2** and **4**, it is apparent that **3** have both μ- and μ_c-TFA ligands present. These FTIR spectra, along with the above data, indicate that the bulk powders of **1**–**4** were consistent with the single crystal structures noted.

4. Summary and conclusion

The structural aspects of solvated TFA alkaline earth derivatives have been solved with several novel aspects present, such as the first: Mg-TFA species, THF solvated species, pyridinium salts derivatives. The TFA ligand coordination were found to bind in several arrangements including terminal, μ-TFA, and μ_c-TFA, the nature of which is determined by the size of the cation and bound solvent molecules. Interestingly, the above conditions were not conducive to the formation of TFA_c in any instance but the use of py as a Lewis basic solvent for the system led to the formation of pyridinium salts for two of the congeners. While each of these types of binding modes have been observed in the literature [23–32,36], this family of compounds is unusual for alkaline earth carboxylates due to their lack of crown ethers and the inclusion of Lewis bases which may lend some insight into the processing of superconductor or other alkaline earth based materials.

Acknowledgements

For support of this research, the authors thank the Office of Basic Energy Science and the US Department of Energy under Contract DE-AC04-94AL85000. Sandia is a multiprogram laboratory operated by Sandia Corporation, a Lockheed Martin Company, for the United States Department of Energy.

Appendix A. Supplementary material

CCDC 643339, 643340, 643341 and 643342 contain the supplementary crystallographic data for **1**, **2**, **3** and **4**, respectively. These data can be obtained free of charge via http://www.ccdc.cam.ac.uk/conts/retrieving.html, or from the Cambridge Crystallographic Data Centre, 12 Union Road, Cambridge CB2 1EZ, UK; fax: (+44) 1223-336-033; or e-mail: deposit@ccdc.cam.ac.uk. Supplementary data associated with this article can be found, in the online version, at doi:10.1016/j.poly.2007.07.009.

References

[1] J.T. Dawley, P.G. Clem, T.J. Boyle, L.M. Ottley, D.L. Overmyer, M.P. Siegal, Physica C 1–2 (2004) 143.
[2] M.P. Siegal, P.G. Clem, J.T. Dawley, R.J. Ong, M.A. Rodriguez, D.L. Overmyer, Appl. Phys. Lett. 80 (2002) 2710.

[3] B.A. Hernandez-Sanchez, T.J. Boyle, C.M. Baros, L.N. Brewer, T.J. Headley, D.R. Tallant, M.A. Rodriguez, B.A. Tuttle, Chem. Mater. 19 (2007) 1459.
[4] T.J. Boyle, B.A. Hernandez-Sanchez, C.M. Baros, L. Brewer, M.A. Rodriguez, Chem. Mater. 19 (2007) 2016.
[5] D.C. Bradley, Chem. Rev. 89 (1989) 1317.
[6] D.C. Bradley, R.C. Mehrotra, D.P. Gaur, Metal Alkoxides, Academic Press, New York, 1978.
[7] D.C. Bradley, R.C. Mehrotra, I.P. Rothwell, A. Singh, Alkoxo and Aryloxo Derivatives of Metals, Academic Press, New York, 2001, pp. 704.
[8] C.D. Chandler, C. Roger, M.J. Hampden-Smith, Chem. Rev. 93 (1993) 1205.
[9] L.G. Hubert-Pfalzgraf, New. J. Chem. 11 (1987) 663.
[10] N.Y. Turova, Uspekhi Khimi 73 (2004) 1131.
[11] N.Y. Turova, E.P. Turevskaya, V.G. Kessler, M.I. Yanovskaya, The Chemistry of Metal Alkoxide, Kluwer Academic Publishers., Boston, 2002, p. 568.
[12] T.J. Boyle, N.L. Andrews, M.A. Rodriguez, C. Campana, T. Yiu, Inorg. Chem. 42 (2003) 5357.
[13] T.J. Boyle, S.D. Bunge, T.M. Alam, G.P. Holland, T.J. Headley, G. Avilucea, Inorg. Chem. 44 (2005) 1309.
[14] T.J. Boyle, S.D. Bunge, N.L. Andrews, L.E. Matzen, K. Sieg, M.A. Rodriguez, T.J. Headley, Chem. Mater. 16 (2004) 3279.
[15] T.J. Boyle, S.D. Bunge, P.G. Clem, J. Richardson, J.T. Dawley, L.A.M. Ottley, M.A. Rodriguez, B.A. Tuttle, G. Avilucea, R.G. Tissot, Inorg. Chem. 44 (2005) 1588.
[16] T.J. Boyle, D.M. Pedrotty, T.M. Alam, S.C. Vick, M.A. Rodriguez, Inorg. Chem. 39 (2000) 5133.
[17] T.J. Boyle, L.J. Tribby, S.D. Bunge, Eur. J. Inorg. Chem. (2006) 4553.
[18] T.J. Boyle, R.P. Tyner, T.M. Alam, B.L. Scott, J.W. Ziller, B.G. Potter, J. Am. Chem. Soc. 121 (1999) 12104.
[19] S.D. Bunge, T.J. Boyle, H.D. Pratt, T.M. Alam, M.A. Rodriguez, Inorg. Chem. 43 (2004) 6035.
[20] Conquest Version 1.9, Cambridge Crystallographic Data Centre, 2004. Available from: <www.ccdc.cam.ac.uk>.
[21] J. Zhao, K.H. Dahmen, H.O. Marcy, L.M. Tonge, B.W. Wessels, T.J. Marks, C.R. Kannewurf, Solid State Commun. 69 (1989) 187.
[22] G. Paz-Pujalt, Physica C 166 (1990) 177, March.
[23] F.D. Rochon, R. Melanson, P.-C. Kong, Inorg. Chim. Acta (1997) 303.
[24] S.R. Breeze, S. Wang, Inorg. Chem. 33 (1994) 5113.
[25] S.R. Breeze, S. Wang, L.K. Thompson, Inorg. Chim. Acta 250 (1996) 163.
[26] N.K. Karan, B. Samanta, S. Mitra, V. Gramlich, Z. Naturforsch B; Chem. Sci. 60 (2005) 640.
[27] N. Kuzmina, M. Ryazanov, S. Troyanov, Polyhedron 18 (1999) 2177.
[28] S. Wang, S.J. Trepanier, M.J. Wagner, Inorg. Chem. 32 (1993) 833.
[29] W.A. Wojtczak, P. Atanassova, M.J. Hampden-Smith, E.N. Duesler, Inorg. Chem. 35 (1996) 6995.
[30] W.A. Wojtczak, M.J. Hampden-Smith, E.N. Duesler, Inorg. Chem. 1998 (1998) 1781.
[31] J. Zhang, L.G. Hubert-Pfalzgraf, D. Luneau, Inorg. Chem. Commun. 7 (2004) 979.
[32] J. Zhang, L.G. Hubert-Pfalzgraf, D. Luneau, Polyhedron 24 (2005) 1185.
[33] F. Marchetti, C. Pettinari, R. Pettinari, A. Cingolani, R. Gobetto, M.R. Chierotti, A. Drozdov, S.I. Troyanov, Inorg. Chem. 45 (2006) 3074.
[34] B. Samanta, J. Chakraborty, N.K. Karan, R.k.B. Singh, G.P.A. Yap, C. Marschner, J. Baumgertner, S. Mitra, Struct. Chem. 17 (2006) 139.
[35] S. Mishra, J. Zhang, L.G. Hubert-Pfalzgraf, Eur. J. Inorg. Chem. (2007) 602.
[36] M. Khristov, P. Peshev, O. Angelova, R. Petrova, J. Macicek, Montash. Chem. 129 (1998) 1093.
[37] H. Miyasaka, K. Nakata, L. Lecren, C. Coulon, Y. Nakazawa, T. Fujisaki, K. Sugiura, M. Yamashita, R. Clerac, J. Am. Chem. Soc. 128 (2006) 3770.
[38] N. Kobayashi, T. Naito, T. Inabe, Bull. Chem. Soc. Jpn. 76 (2003) 1351.
[39] C. Glidewell, H.D. Holden, Acta Crystallogr., Sect. B 38 (1982) 667.
[40] J.V. Brencic, B. Ceh, I. Leban, Z. Anorg. Allg. Chem. 549 (1987) 233.
[41] F.A. Mautner, M.A.S. Goher, Polyhedron 18 (1999) 553.

Lewis acid activation of the substrate, generation of a reactive nucleophile (Zn-OH) and stabilization of the leaving group [19]. Schiff bases can act as useful blockers due to their preparational accessibility, structural varieties and varied denticities. Pseudohalides are efficient intermediates; of them the flexidentate homoatomic azide and ambidentate heteroatomic cyanate and thiocyanate ions form various networks with several transition and non-transition metal ions together with organic spacers of varied denticities [15]. In an effort to isolate and study new forms of such aggregates, we have been exploring the coordination behaviour of a potentially tetradentate Schiff base ligand (**LH**, Scheme 1), the condensation product of *o*-vanillin and 2-dimethylaminoethylamine, towards zinc(II) centers in combination with pseudohalides (azide, cyanate and thiocyanate ions).

Moreover, luminescent compounds are attracting much current research interest because of their many applications including emitting materials for organic light emitting diodes, light harvesting materials for photocatalysis and fluorescent sensors for organic or inorganic analytes [20]. Introduction of electron-donating groups into the salicylidene moiety of Zn(II) complexes enhances the quantum yield of photoluminescence [21]. Hence it is important to understand the coordination chemistry and luminescence between Group 12 metal ions for developing new materials which can function as fluorescent sensors [20].

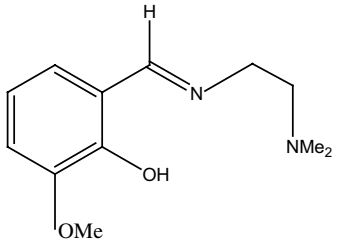
Our research group has already reported some mono- and dinuclear transition metal complexes using the ligand **LH** [3,7,22]. In continuation, using zinc trichloroacetate hydrate as the metal salt, three new dinuclear zinc(II) complexes, $[Zn(L)(\mu_{1,1}\text{-}N_3)Zn(L)(N_3)]\cdot 1.5H_2O$ (**1**), $[Zn(L)(\mu_{1,1}\text{-}NCO)Zn(L)(NCO)]\cdot 1.5H_2O$ (**2**) and $[Zn(L)(\mu_{1,1}\text{-}NCS)Zn(L)(NCS)(OH_2)]$ (**3**), have been synthesized with **LH**. In this paper, we have reported the synthetic details, spectral characterizations, thermal investigations, along with X-ray crystal structures and fluorescence studies of **1**, **2** and **3**, where pseudohalides act as terminal ligands as well as adopting an *end-on* bridging mode in the presence of a potentially tetradentate Schiff base (**LH**).

2. Experimental

2.1. Materials

2-Dimethylaminoethylamine (Fluka, Germany), *o*-vanillin (Lancaster, UK), sodium azide, sodium cyanate and sodium thiocyanate (Aldrich, USA) were used as received. Zinc(II) trichloroacetate hydrate was prepared by treatment of zinc carbonate (E. Merck, India) with trichloroacetic acid (E. Merck, India) followed by slow evaporation on a steam-bath, then filtration through a fine glass-frit, and it was preserved in a desiccator containing $CaCl_2$ for subsequent use. All the solvents were of AR grade and were used as received.

Caution! Azido compounds of metal ions are potentially explosive, especially in the presence of organic ligands. Only a small amount of material should be prepared and it must be handled with care.



Scheme 1. **LH**.

2.2. Physical measurements

The infrared spectra of the complexes were recorded on a Perkin-Elmer RX I FT-IR spectrophotometer with KBr discs (4000–300 cm^{-1}). Elemental analyses (C, H, N) were carried out using a Perkin-Elmer 2400 II elemental analyzer. ^1H NMR spectra were recorded on a Bruker 300 MHz FT-NMR spectrometer using trimethylsilane as an internal standard in $CDCl_3$ for complexes **1** and **2**, and in d^6-DMSO for complex **3**. The thermal analyses of **2** and **3** were done on a Mettler Toledo TGA/SDTA-851e thermal analyzer system in a dynamic atmosphere of dinitrogen (flow rate: 30 cm^3 min^{-1}) in an alumina crucible at a heating rate of 10 °C min^{-1}. Ground state absorptions for the ligand and the complexes were made with a Perkin-Elmer Lambda 40 (UV–Vis) spectrophotometer in methanol. A "JOBIN YVON Fluoro Max 3. A" spectrofluorimeter model was used for the steady state fluorescence measurements for all the three complexes and the Schiff base ligand at room temperature (298 K). The solutions of the ligand and complexes **1**, **2** and **3** were prepared in a 2:1 water–methanol mixed solvent ratio and the OD for each of the solutions at the wavelength for fluorescence excitation was recorded. The fluorescence quantum yields of the Schiff base (**LH**) and its zinc-pseudohalides complexes were determined using quinine sulfate as the reference with a known φ_R of 0.70 in methanol. The complexes, along with ligand and the reference compound, were excited at 370 nm and the emission spectra were recorded from 385 to 700 nm. The area of the emission spectrum was integrated using the software available in the instrument and the quantum yield was calculated according to the following equation:

$$\varphi_S/\varphi_R = [A_S/A_R] \times [(OD)_R/(OD)_S] \times [\eta_S^2/\eta_R^2]$$

Here φ_S and φ_R are the fluorescence quantum yields of the sample and reference, respectively, A_S and A_R are the areas under the fluorescence spectra of the sample and the reference, respectively. $(OD)_S$ and $(OD)_R$ are the respective optical densities of the sample and the reference solution at the wavelength of excitation, and η_S and η_R are the values of refractive index for the respective solvents used for the sample and reference [23].

2.3. Synthesis of the Schiff base ligand and metal complexes

2.3.1. Schiff base $[(CH_3)_2NCH_2CH_2N{=}CHC_6H_3(OH)(OMe)]$ (**LH**)

The Schiff base was obtained by refluxing a methanolic solution (50 ml) of *o*-vanillin (10 mmol) and 2-dimethylaminoethylamine (10 mmol) for 30 min. The resulting orange yellow solution containing the required product was used without further purification.

2.3.2. $[Zn(L)(\mu_{1,1}\text{-}N_3)Zn(L)(N_3)]\cdot 1.5H_2O$ (**1**)

To an aqueous methanolic solution (30 ml) of zinc trichloroacetate hydrate (0.390 g, 1 mmol), a solution of the Schiff base **LH** (1 mmol) was added, followed by a solution of sodium azide (0.065 g, 1 mmol) in a minimum volume of methanol with constant stirring for 10 min. This mixture was kept at room temperature, yielding light yellow hexagonal crystals suitable for X-ray diffraction after 10 days. The crystals were isolated by filtration and air-dried. Yield: 61%. *Anal.* Calc. for $C_{24}H_{37}N_{10}O_{5\cdot5}Zn_2$: C, 42.08; H, 5.40; N, 20.45. Found: C, 42.02; H, 5.38; N, 20.41%.

2.3.3. $[Zn(L)(\mu_{1,1}\text{-}NCO)Zn(L)(NCO)]\cdot 1.5H_2O$ (**2**)

Complex **2** was synthesized in a similar manner as described above, but adding sodium cyanate (0.065 g, 1 mmol) instead of sodium azide. Light yellow, hexagonal crystals suitable for X-ray diffraction were obtained after 2 weeks. The crystals were collected by filtration and air-dried. Yield: 53%. *Anal.* Calc. for $C_{26}H_{37}N_6O_{7\cdot5}Zn_2$: C, 45.59; H, 5.40; N, 12.27. Found: C, 45.52; H, 5.37; N, 12.22 %.

2.3.4. $[Zn(L)(\mu_{1,1}\text{-}NCS)Zn(L)(NCS)(OH_2)]$ (**3**)

Complex **3** was prepared following the same procedure as for **1** and **2**, except by adding sodium thiocyanate (0.0808 g, 1 mmol) as the bridging ligand instead of NaN_3 or NaOCN. Light yellow block shaped crystals suitable for X-ray diffraction were obtained after 7 days. The crystals were collected by filtration and air-dried. Yield: 68%. *Anal.* Calc. for $C_{26}H_{36}N_6O_5Zn_2S_2$: C, 44.14; H, 5.13; N, 11.88. Found: C, 44.08; H, 5.09; N, 11.81%.

2.4. Crystallographic data collection and structure refinements

Intensity data for the light yellow coloured crystals of **1** and **2** were collected on a Bruker X8 Apex 2 diffractometer whilst data for **3** were collected on a Rigaku AFC7 four circle serial diffractometer. Data were corrected for absorption empirically by means of multi-scans (SADABS) (**1**, **2**) and psi scans (**3**). The structures were solved by direct and difference Fourier methods and refined by full-matrix least-squares on F^2. All non-hydrogen atoms were refined with anisotropic displacement parameters. The crystallographic computing was performed using SHELXTL [24] programs. Further details have been given in Table 1.

Table 1
Experimental, crystallographic and refinement data for complexes **1**, **2** and **3**

Complex	**1**	**2**	**3**
Empirical formula	$C_{24}H_{37}N_{10}O_{5\cdot5}Zn_2$	$C_{26}H_{37}N_6O_{7\cdot5}Zn_2$	$C_{26}H_{36}N_6O_5S_2Zn_2$
Formula weight	684.38	684.36	707.47
Temperature (K)	100(2)	100(2)	120(2)
Wavelength (Å)	0.71073	0.71073	0.71073
Crystal system	monoclinic	monoclinic	monoclinic
Space group	$P2_1/c$	$P2_1/c$	$P2_1/c$
Unit cell dimensions			
a (Å)	15.6250(6)	15.7633(5)	15.970(3)
b (Å)	13.8467(6)	13.7198(4)	13.790(2)
c (Å)	13.9116(6)	13.9833(4)	13.891(2)
α (°)	90	90	90
β (°)	105.193(2)	105.29209(10)	103.324(3)
γ (°)	90	90	90
Volume (Å^3)	2904.6(2)	2917.09(15)	2976.9(8)
Z	4	4	4
D_{calc} (Mg/m^3)	1.565	1.558	1.579
Absorption coefficient (mm^{-1})	1.707	1.701	1.799
$F(000)$	1420	1420	1464
Crystal size (mm)	$0.32\times0.20\times0.16$	$0.56\times0.40\times0.35$	$0.24\times0.22\times0.10$
θ Range for data collection (°)	2.11–36.76	1.34–36.61	1.31–23.27
Reflections collected	74253	35256	10573
Independent reflections [R_{int}]	13806 [0.0375]	12535 [0.0343]	4283 [0.0254]
Goodness-of-fit on F^2	1.000	0.997	1.040
Final R indices [$I>2\sigma(I)$]	$R_1=0.0317$, $wR_2=0.0673$	$R_1=0.0333$, $wR_2=0.0716$	$R_1=0.0259$, $wR_2=0.0623$
R indices (all data)	$R_1=0.0576$, $wR_2=0.0757$	$R_1=0.0621$, $wR_2=0.0814$	$R_1=0.0306$, $wR_2=0.0651$
Largest difference in peak and hole (e Å^{-3})	0.616 and −0.785	0.573 and −0.553	0.438 and −0.388

3. Results and discussion

3.1. Description of crystal structures of 1, 2 and 3

Complex **1** is isostructural with complex **2**, but it contains N_3^- instead of NCO^-. However **3**, which differs only in the pseudohalide (SCN^-) has some significant structural differences when compared to **1** and **2**.

The ORTEP diagrams of **1**, **2** and **3** are shown in Figs. 1–3, respectively with selected bond dimensions given in Tables 2–5. Complex **1** and **2** contain two geometrically distinct zinc(II) centers. Zn1 has a predominantly square pyramidal geometry (N_4O donor set) with $\tau = 0.02$ and 0.017 for **1** and **2**, respectively ($\tau = 0$ and 1 for the perfect square pyramidal and trigonal bipyramidal geometries, respectively) [25] whilst Zn2 has a distorted octahedral geometry (N_3O_3 donor set). The two Zn(II) centers in all the three complexes are doubly bound together by a μ_2-phenolato oxygen atom O1 of the deprotonated Schiff base $\mathbf{L}^-$ and a $\mu_{1,1}$-pseudohalide nitrogen atom N1 (of azide for **1**, cyanate for **2** and thiocyanate for **3**). The distance between the two non-bonded Zn(II) centers are 3.2130(2) Å (**1**), 3.1745(2) Å (**2**) and 3.1918(5) Å (**3**), which is comparable to similar systems [22]. In **1** and **2**, the N6 atom of the terminal pseudohalide ligand binds to the apical site on Zn1 whilst the N_2O donors (N2, N3 and O1 atoms) of the deprotonated Schiff base $\mathbf{L}^-$ together with the bridging N_3^-/NCO^- nitrogen atom N1 form the square base. Conversely the Zn2 center has a distorted octahedral coordination geometry composed of a N_3O_3 donor set (N1, N4, N5, O1, O2 and O3 atoms) from both Schiff base ligands and the bridging pseusohalide ligand. However in **3**, the geometry around both zinc(II) centers is distorted octahedral with a N_3O_3 donor set for Zn1 and a N_4O_2 donor set for Zn2. The water to Zn distance is much shorter [Zn2–O4, 2.369(2) Å] than that found in **1** and **2**, where there is a water molecule near the vacant sixth site of the square pyramidal Zn centers [O5–Zn1, 2.774(1) Å (**1**) and 2.873(1) Å (**2**)]. The square base around Zn1 is formed by phenolato and methoxy oxygen atoms (O1 and O2, respectively) from the bridging $\mathbf{L}^-$, imino nitrogen N3 from chelating $\mathbf{L}^-$ and bridging thiocyanato nitrogen N1, whereas the axial sites are occupied by the phenolato oxygen O3 and amino nitrogen N2 atom of the chelating $\mathbf{L}^-$. On the other side the N_2O donor set (N4, N5 and

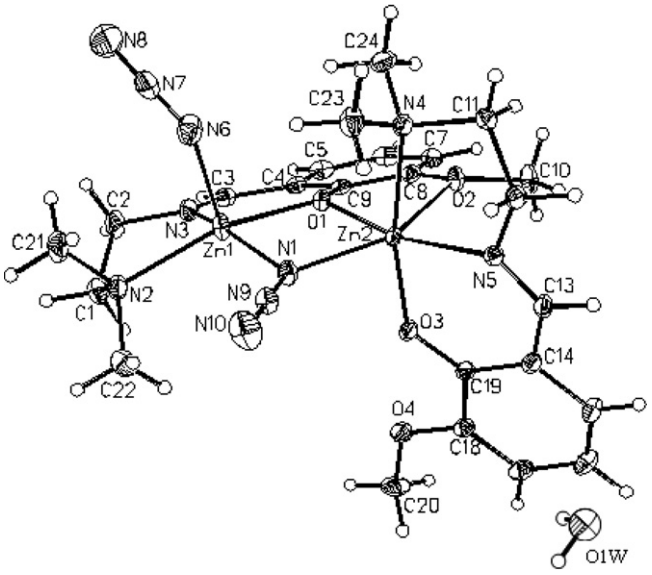


Fig. 1. View of the dimeric unit of **1**, with atomic labels. Displacement ellipsoids are shown at the 50% probability level.

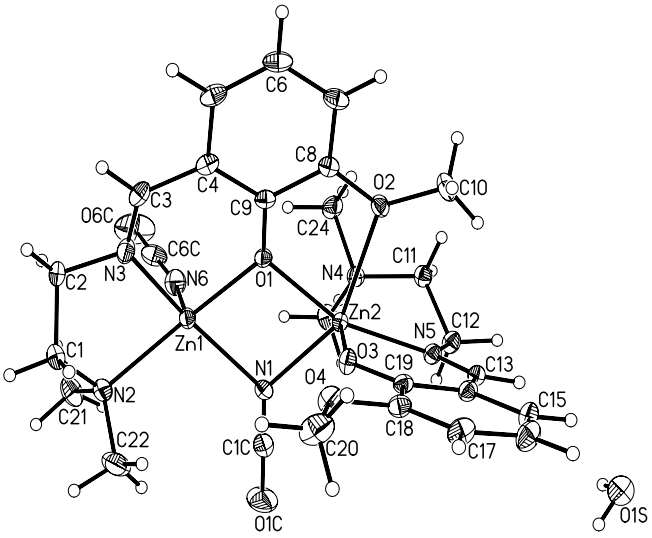


Fig. 2. View of the dimeric unit of **2**, with atomic labels. Displacement ellipsoids are shown at the 50% probability level.

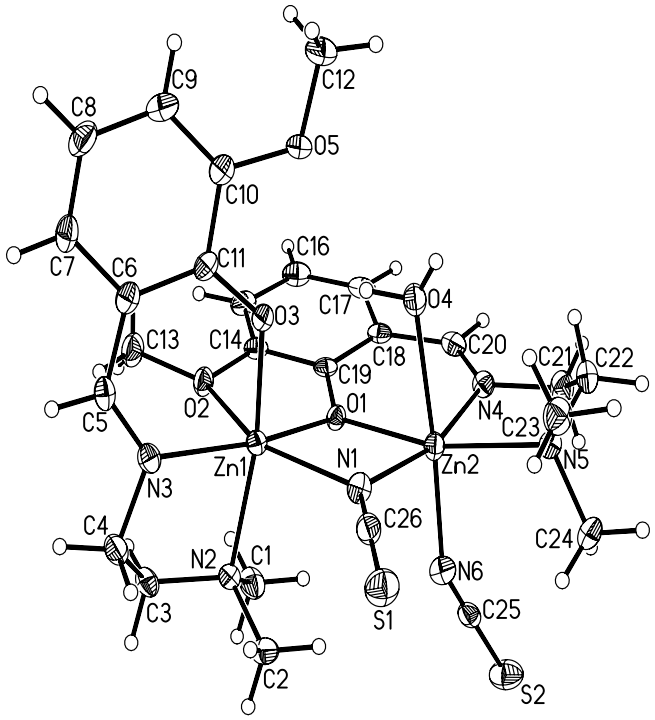


Fig. 3. View of the dimeric unit of **3**, with atomic labels. Displacement ellipsoids are shown at the 50% probability level.

Table 2
Molecular dimensions (bond lengths in Å and angles in °) about the zinc atoms in complexes **1**, **2** and **3**

1		**2**		**3**	
Zn(1)–N(6)	2.0648(12)	Zn(1)–N(6)	2.0033(14)	Zn(1)–O(2)	2.4077(17)
Zn(1)–O(1)	2.0433(8)	Zn(1)–O(1)	2.0442(9)	Zn(1)–N(1)	2.235(2)
Zn(1)–N(3)	2.0633(11)	Zn(1)–N(3)	2.0725(14)	Zn(1)–N(2)	2.235(2)
Zn(1)–N(1)	2.1088(10)	Zn(1)–N(1)	2.1274(13)	Zn(1)–N(3)	2.041(2)
Zn(1)–N(2)	2.1992(11)	Zn(1)–N(2)	2.2032(12)	Zn(1)–O(1)	2.0130(16)
Zn(2)–O(1)	2.0336(8)	Zn(2)–O(1)	2.0210(10)	Zn(1)–O(3)	2.0131(17)
Zn(2)–O(3)	2.0236(8)	Zn(2)–O(3)	2.0215(10)	Zn(2)–O(4)	2.369(2)
Zn(2)–N(5)	2.0481(10)	Zn(2)–N(5)	2.0478(12)	Zn(2)–N(5)	2.193(2)
Zn(2)–N(1)	2.1570(10)	Zn(2)–N(1)	2.1361(12)	Zn(2)–N(1)	2.159(2)
Zn(2)–N(4)	2.2501(10)	Zn(2)–N(4)	2.2811(12)	Zn(2)–N(6)	2.089(2)
Zn(2)–O(2)	2.4223(9)	Zn(2)–O(2)	2.4499(10)	Zn(2)–N(4)	2.063(2)
O(1)–Zn(1)–N(3)	87.09(4)	N(6)–Zn(1)–O(1)	103.41(5)	Zn(2)–O(1)	2.0531(16)
O(1)–Zn(1)–N(6)	101.17(4)	N(6)–Zn(1)–N(3)	102.12(6)	O(1)–Zn(2)–N(4)	87.82(7)
N(3)–Zn(1)–N(6)	103.71(5)	O(1)–Zn(1)–N(3)	86.24(5)	O(1)–Zn(2)–N(6)	95.51(8)
O(1)–Zn(1)–N(1)	79.55(4)	N(6)–Zn(1)–N(1)	101.18(6)	N(4)–Zn(2)–N(6)	96.15(8)
N(3)–Zn(1)–N(1)	157.54(4)	O(1)–Zn(1)–N(1)	80.34(4)	O(1)–Zn(2)–N(1)	82.09(7)
N(6)–Zn(1)–N(1)	96.58(5)	N(3)–Zn(1)–N(1)	155.25(5)	N(4)–Zn(2)–N(1)	165.92(8)
O(1)–Zn(1)–N(2)	158.84(4)	N(6)–Zn(1)–N(2)	99.23(5)	N(6)–Zn(2)–N(1)	94.57(8)
N(3)–Zn(1)–N(2)	82.38(4)	O(1)–Zn(1)–N(2)	156.27(5)	O(1)–Zn(2)–N(5)	166.45(7)
N(6)–Zn(1)–N(2)	99.14(4)	N(3)–Zn(1)–N(2)	82.17(5)	N(4)–Zn(2)–N(5)	83.17(8)
N(1)–Zn(1)–N(2)	104.00(4)	N(1)–Zn(1)–N(2)	102.22(5)	N(6)–Zn(2)–N(5)	95.50(8)
O(3)–Zn(2)–O(1)	92.76(3)	O(1)–Zn(2)–O(3)	93.14(4)	N(1)–Zn(2)–N(5)	104.87(8)
O(3)–Zn(2)–N(5)	88.96(4)	O(1)–Zn(2)–N(5)	160.29(4)	O(1)–Zn(2)–O(4)	80.57(7)
O(1)–Zn(2)–N(5)	161.79(4)	O(3)–Zn(2)–N(5)	88.97(4)	N(4)–Zn(2)–O(4)	84.96(7)
O(3)–Zn(2)–N(1)	93.78(4)	O(1)–Zn(2)–N(1)	80.65(4)	N(6)–Zn(2)–O(4)	175.89(8)
O(1)–Zn(2)–N(1)	78.63(4)	O(3)–Zn(2)–N(1)	95.71(4)	N(1)–Zn(2)–O(4)	83.73(7)
N(5)–Zn(2)–N(1)	119.37(4)	N(5)–Zn(2)–N(1)	118.66(5)	N(5)–Zn(2)–O(4)	88.56(8)
O(3)–Zn(2)–N(4)	167.98(3)	O(1)–Zn(2)–N(4)	94.86(4)	O(3)–Zn(1)–O(1)	93.29(7)
O(1)–Zn(2)–N(4)	95.62(3)	O(3)–Zn(2)–N(4)	166.72(4)	O(3)–Zn(1)–N(3)	88.80(8)
N(5)–Zn(2)–N(4)	80.41(4)	N(5)–Zn(2)–N(4)	79.96(4)	O(1)–Zn(1)–N(3)	161.65(7)
N(1)–Zn(2)–N(4)	96.31(4)	N(1)–Zn(2)–N(4)	96.04(5)	O(1)–Zn(1)–N(2)	96.19(7)
O(3)–Zn(2)–O(2)	87.23(3)	O(1)–Zn(2)–O(2)	70.25(4)	N(3)–Zn(1)–N(2)	81.01(8)
O(1)–Zn(2)–O(2)	70.60(3)	O(3)–Zn(2)–O(2)	86.34(4)	O(3)–Zn(1)–N(1)	90.18(7)
N(5)–Zn(2)–O(2)	91.40(4)	N(5)–Zn(2)–O(2)	90.36(4)	O(1)–Zn(1)–N(1)	81.10(7)
N(1)–Zn(2)–O(2)	149.22(3)	N(1)–Zn(2)–O(2)	150.90(4)	N(3)–Zn(1)–N(1)	117.15(8)
N(4)–Zn(2)–O(2)	87.45(3)	N(4)–Zn(2)–O(2)	86.41(4)	N(2)–Zn(1)–N(1)	94.96(8)
Zn(2)–O(1)–Zn(1)	104.02(4)	Zn(2)–O(1)–Zn(1)	102.69(4)	O(3)–Zn(1)–O(2)	89.64(6)
Zn(1)–N(1)–Zn(2)	97.73(4)	Zn(1)–N(1)–Zn(2)	96.25(5)	O(1)–Zn(1)–O(2)	71.30(6)
				O(3)–Zn(1)–N(2)	169.80(7)
				N(3)–Zn(1)–O(2)	90.50(7)
				N(2)–Zn(1)–O(2)	89.86(7)
				N(1)–Zn(1)–O(2)	152.34(7)
				Zn(1)–O(1)–Zn(2)	103.43(7)
				Zn(2)–N(1)–Zn(1)	93.17(8)

Table 3
Hydrogen bond dimensions for **1** (Å) and (°)

D–H...A	*d*(D–H)	*d*(H...A)	*d*(D...A)	∠(DHA)
O(5)–H(51W)...O(3)	0.81(2)	2.02(2)	2.7947(13)	160(2)
O(5)–H(51W)...O(4)	0.81(2)	2.51(2)	3.0970(14)	130.3(19)
O(5)–H(52W)...N(10)#1	0.82(2)	2.47(2)	3.2624(18)	165(2)
O(1W)–H(11W)...N(8)#2	0.93(3)	1.81(3)	2.739(3)	178(4)
O(1W)–H(11W)...N(7)#2	0.93(3)	2.74(4)	3.644(3)	164(3)

Symmetry transformations used to generate equivalent atoms: #1 $-x+1$, $-y+2$, $-z+1$; #2 x, $y-1$, z.

O1) from the bridging $\mathbf{L}^-$ and the *end-on* bridging thiocyanato nitrogen N1 form the square base around Zn2 and the terminal thiocyanato nitrogen N6 and oxygen atom O4 of the coordinated water molecule take up two axial positions of the octahedron. The distortion in the geometry from regular octahedron is evidenced from the respective *cis*-and *trans*-angles about the Zn1 and Zn2 centers (Table 2).

Table 4
Hydrogen bond dimensions for **2** (Å) and (°)

D–H...A	*d*(D–H)	*d*(H...A)	*d*(D...A)	∠(DHA)
O(1S)–H(11S)...O(3)#1	0.85(2)	1.98(2)	2.7780(16)	158(2)
O(1S)–H(11S)...O(4)#1	0.85(2)	2.45(2)	3.0730(17)	131.0(19)
O(1S)–H(12S)...O(1C)#2	0.81(2)	2.34(2)	3.125(2)	164(2)

Symmetry transformations used to generate equivalent atoms: #1 x, $-y+3/2$, $z-1/2$; #2 $-x+1$, $y+1/2$, $-z+1/2$.

Table 5
Hydrogen bond dimensions for **3** (Å) and (°)

D–H...A	*d*(D–H)	*d*(H...A)	*d*(D...A)	∠(DHA)
O(4)–H(41W)...O(3)	0.88(4)	1.86(4)	2.690(3)	158(3)
O(4)–H(41W)...O(5)	0.88(4)	2.48(4)	3.110(3)	130(3)
O(4)–H(42W)...S(1)#1	0.76(3)	2.70(3)	3.455(2)	170(3)

Symmetry transformations used to generate equivalent atoms: #1 $-x+1$, $-y+2$, $-z$.

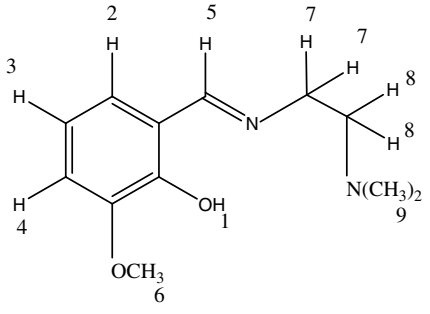
The two Schiff base ligands also display flexible coordination modes in all the three structures such that one is tetradenate (N_2O_2 donor set) whilst the other is tridentate (N_2O donor set) with a non-bonded methoxy (–OMe) group. Further variation is found in the pseudohalide coordination as one binds two metal centers in an *end-on* bridging mode and the other as a terminal ligand.

In **1**, the unbound (O1W) water participates in the shortest hydrogen bond with the azido nitrogen, whilst the weakly bound water molecule O5 interacts with the phenolato and methoxy oxygen atoms of the Schiff base (Table 3, Supplementary material 1). The zinc complexes interact directly with each other with $\pi-\pi$ stacking between the rings (C4 to C9), where the C4...C6i distance (where i is the symmetry code $2-x, -y, 1-z$) is 3.317 Å. The hydrogen bonding patterns are similar in **2**, the shortest hydrogen bond involves the pseudohalide and solvent water (although the H atoms were not located for O2s, the O...O distance is 2.686 Å). There is also π–π stacking between adjacent aromatic rings where the C4...C6i distance (where i is the symmetry code $-x, 1-y, 1-z$) is 3.348 Å. (Supplementary material 2, Table 4). In **3**, unlike **1** and **2**, the zinc complexes are directly connected as a centrosymmetric dimer *via* two intermolecular hydrogen bonds involving the weakly coordinated water molecule with S1 of the bridging thiocyanate. This may be because the SCN^- ligand is significantly larger than N_3^- or NCO^- and **3** has to take on a slightly different packing motif to incorporate this difference. However, the intramolecular hydrogen bonds involving the methoxy and phenoxo O atoms are very similar to those found for **1** and **2** (Table 5, Supplementary material 3).

3.2. Infrared spectra

The infrared spectra of the complexes are consistent with the structural data given in this paper. The bifurcated bands at 2082, 2051 cm^{-1} for **1**, 2208, 2187 cm^{-1} for **2** and 2067, 2028 cm^{-1} for **3** are attributed to the bridging azido (N_3^-), cyanato (NCO^-) and thiocyanato (SCN^-) groups in **1**, **2** and **3**, respectively [26]. The strong $\nu_{C=N}$ bands occurring at 1630, 1632 and 1629 cm^{-1} for **1**, **2** and **3** respectively are shifted considerably towards lower frequencies compared to that of the free Schiff base ligand (1635 cm^{-1}),

Table 6
^{1}H NMR spectral data with assignments for the Schiff base **LH**, and complexes **1**, **2** and **3**



LH

Proton numbering scheme

Schiff base/complex	δ (in ppm)
LH	2.06 (6H, s, H9); 2.64 (2H, t, $J=3.4$ Hz, H8); 3.42 (2H, t, $J=4.5$ Hz, H7); 3.86 (3H, s, H6); 5.26 (1H, s, H1); 6.35 (1H, d, $J=7.2$ Hz, H2); 6.61 (1H, d, $J=7.5$ Hz, H4); 8.01 (1H, t, $J=7.8$ Hz, H3); 8.30 (1H, s, H5)
1	2.14 (12H, s, H9); 2.65 (4H, t, $J=3.4$ Hz, H8); 3.46 (4H, t, $J=4.2$ Hz, H7); 4.01 (6H, s, H6); 3.88 (3H, s, H6′); 6.50 (2H, d, $J=7.2$ Hz, H2); 6.83 (2H, d, $J=7.4$ Hz, H4); 8.13 (2H, t, $J=7.6$ Hz, H3); 8.33 (2H, s, H5)
2	2.14 (12H, s, H9); 2.65 (4H, t, $J=3.2$ Hz, H8); 3.46 (4H, t, $J=3.9$ Hz, H7); 4.03 (6H, s, H6); 3.86 (3H, s, H6′); 6.51 (2H, d, $J=6.8$ Hz, H2); 6.83 (2H, d, $J=7.4$ Hz, H4); 8.13 (2H, t, $J=7.8$ Hz, H3); 8.35 (2H, s, H5)
3	2.14 (12H, s, H9); 2.59 (2H, s, H10); 2.65 (4H, t, $J=3.2$ Hz, H8); 3.46 (4H, t, $J=3.9$ Hz, H7); 4.02 (6H, s, H6); 3.87 (3H, s, H6′); 6.50 (2H, d, $J=6.8$ Hz, H2); 6.82 (2H, d, $J=7.4$ Hz, H4); 8.12 (2H, t, $J=7.8$ Hz, H3); 8.34 (2H, s, H5)

indicating coordination of the imino nitrogen atom [27]. Ligand coordination to the metal centers is substantiated by two bands appearing for ν_{M-N} at 459, 448, 448 cm^{-1} and for ν_{M-O} at 372, 368, 370 cm^{-1} for **1**, **2** and **3**, respectively.

3.3. ^1H NMR spectra

^1H NMR spectroscopy has been used to extract information regarding the coordination mode of the ligand with the metal ions for the complexes **1**, **2** and **3**; the NMR data are summarized in Table 6. The ^1H NMR spectra (Fig. 5) of **1** and **2** are almost indistinguishable and are slightly different from that of **3**, which contains only one additional singlet peak for the coordinated water molecule. In all the complexes **1**, **2** and **3**, the signal due to the phenolic hydrogen (H1) of the free molecule (5.2623 ppm) is absent, indicating the coordination of a deprotonated ligand in these complexes. The signals for the amino methyl group (H9) show downfield shifts (0.08 ppm) from its position of the free molecule due to the coordination of the amino nitrogen atom with the metal centers. The singlet due to the proton (H5) attached to the imino (–C=N) group shows a downfield shift (0.03–0.05 ppm) compared to its position in the free molecule, reflecting the coordination of the deprotonated Schiff base ligand ($\mathbf{L}^-$) to the metal centers through the imine nitrogen atom. In the spectra of all the complexes, the signals for the methoxy hydrogens (H6 and H6′) give two bands with close δ values, one with significant downfield shifts (0.15–0.17 ppm, H6), and another with minor shifts (0.02 ppm, H6′) suggesting the presence of two types of methoxy group in the complexes, one coordinating and the other non-coordinating. The phenyl hydrogens show significant shifts [0.15–0.16 ppm (H2), 0.22 ppm (H4), 0.12 ppm (H3)] indicating the involvement of the phenolato oxygen in coordination with the metal centers. For the complexes, the protons (H7) of the CH_2 group attached to the imine nitrogen and the protons (H8) of the CH_2 group associated with the amine nitrogen show downfield shifts of 0.04 ppm and 0.01 ppm, respectively from the free ligand values. The spectrum of complex **3** contains one extra singlet signal at 2.59 ppm due to the hydrogen atoms (H10) of the water molecule attached to the Zn2 center. The results obtained from the NMR spectra support the structures obtained by the X-ray analysis and suggest that the structures of complexes **1** and **2** are retained in $CDCl_3$ solution and **3** in d^6-DMSO. The NMR spectrum of **3** is recorded in the solution phase and it is different from those of **1** and **2**, which indicates that the different structure of **3** shown in the solid state is also maintained in solution.

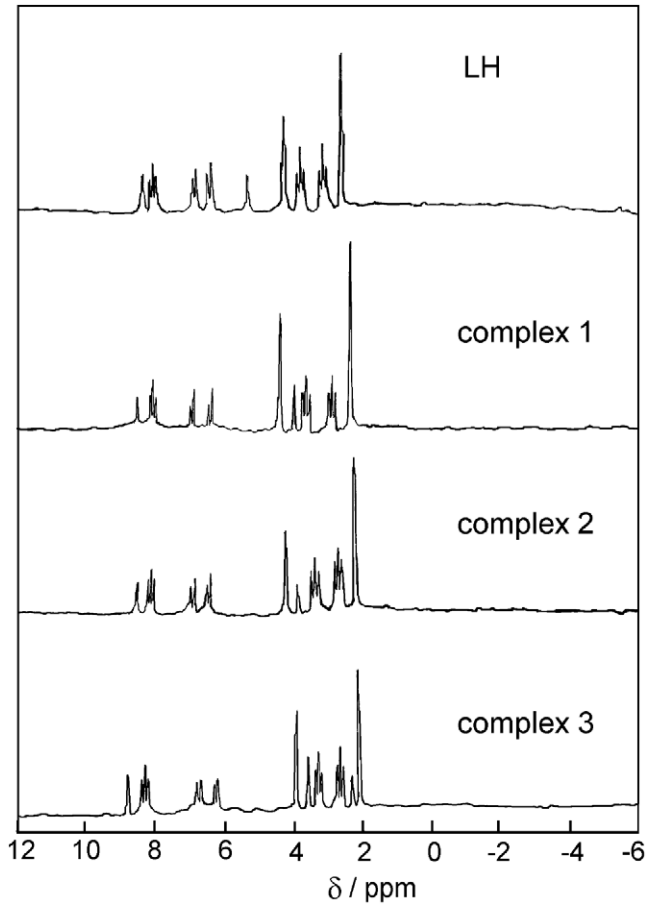


Fig. 5. NMR spectra of LH and complexes **1**, **2** and **3**.

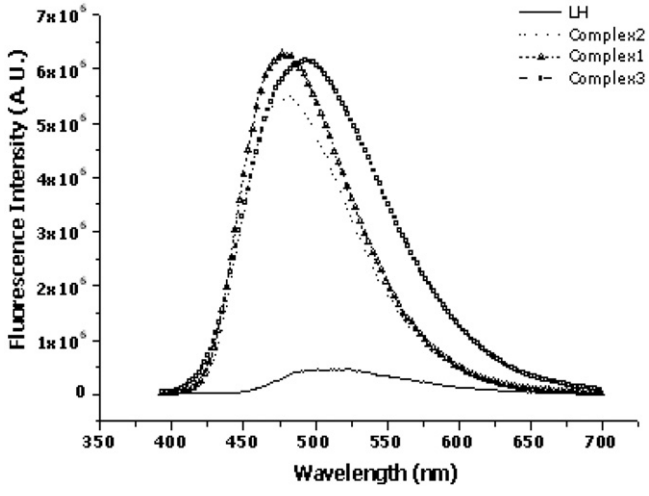


Fig. 4. Fluorescence spectra of LH and complexes **1**, **2** and **3** in methanol-water (λ_{exc} = 370 nm).

3.4. Thermogravimetric analyses

The thermal study of complex **1** was not carried out in order to avoid an explosion of the azide compound. The TGA experiments for **2** and **3** indicated that the crystals of **2** and **3** are stable up to ~100 °C and ~168 °C, respectively. At temperatures above ~100 °C and ~168 °C, the crystals of the respective complexes started to lose weight. For complex **2**, the first stage of weight loss (~3.92%) occurs between 100 °C and 110 °C, which corresponds to

Table 7
Photophysical parameters of **LH** and complexes **1**, **2** and **3** in methanol–water at 298 K; excitation at 370 nm; reference compound is quinine sulfate ($\varphi_R = 0.07$ in methanol)

Compound	Abs (λ_{max}), nm	Emission (λ_{max}), nm	Quantum yield (φ)
LH	417	524	0.0021
1	375	475	0.1385
2	375	475	0.0077
3	370	495	0.0162

the loss of the intramolecular hydrogen bonded water molecule present in the crystal lattice. For complex **3**, the first stage of weight loss (~2.61%) takes place between 168 °C and 178 °C, corresponding to the loss of one coordinated water molecule.

3.5. Fluorescence spectral studies

The fluorescence properties of the Schiff base ligand (**LH**) and its Zn(II) complexes (**1**, **2** and **3**) were studied at room temperature (298 K) in methanol–water solutions (Fig. 4). All the three complexes exhibit strong fluorescence in comparison to **LH**. For Zn(II) complexes, no emission originating from metal-centered MLCT/LMCT excited states are expected, since the Zn(II) ion is difficult to oxidize or reduce due to its stable d^{10} configuration. Thus, the emission observed in the complexes is tentatively assigned to the $^1(\pi–\pi^*)$ intraligand fluorescence [23]. It is interesting that the Zn(II) complexes show a higher intensity than that of the free ligand. This is supported from their calculated quantum yield values (Table 7) with reference to quinine sulfate. Metal ions can enhance or quench the fluorescence emission of some Schiff base ligands containing an aromatic ring. Quenching of fluorescence of a ligand by transition metal ions during complexation is a rather common phenomenon which is explained by processes such as magnetic perturbation, redox activity, electronic energy transfer, etc. Enhancement of fluorescence through complexation is, however, of much interest as it opens up the opportunity for photochemical applications of these complexes [28]. In the absence of metal ions the fluorescence of the ligand is probably quenched by the occurrence of a photoinduced electron transfer (PET) process due to the presence of a lone pairs of electrons of the donor atoms in the ligand. Such a PET process is prevented by the complexation of **LH** with metal ions; thus the fluorescence intensity may be greatly enhanced by the coordination of Zn(II). The chelation of the ligand to Zn(II) increases the rigidity of the ligand and thus reduces the loss of energy by thermal vibrational decay [23].

4. Conclusion

The Schiff base **LH** forms three dinuclear Zn(II) complexes with the $Zn(TCA)_2 \cdot \times H_2O$ metal salt, where the two Zn(II) centers are bridged by a μ_2-phenolato O atom of $\mathbf{L}^-$ and a $\mu_{1,1}$- pseudohalide nitrogen atom. The deprotonated Schiff base $\mathbf{L}^-$ shows flexible coordination (both tridentate and tetradentate coordination modes) in all the complexes. The azido and cyanato complexes are isostructural but the thiocyanato species has two, rather than one, six coordinated Zn centers owing to the coordination of solvent water. This may be because the SCN^- ligand is significantly larger than N_3^- and NCO^- and so chooses a slightly different packing motif. Although the zinc TCA salt has been used to prepare the complexes, the TCA anion is totally absent from the crystal lattice in all the complexes. This is in contrast to the previously reported zinc complex of zinc acetate dihydrate [22]. This may be explained by the fact that the −I effect of the three chlorine atoms in the TCA anion decreases the coordination ability and thus it is a weaker nucleophile compared to the pseudohalide ligands forming the bridge between the two metal centers. Furthermore, the three dinuclear Zn(II) complexes each displays intense fluorescence at room temperature. It is suggested that these compounds exhibit the potential for use in applications as photoactive materials.

Acknowledgements

We gratefully acknowledge Jadavpur University, Kolkata, India for providing Laboratory facilities. We are thankful to Dr. Andrés Ibañez M. for the structural data analysis of complex **3**. Our thanks are also extended to Dr. S. Das, Department of Chemistry, Jadavpur University, Kolkata, India and Mr. P.S. Guin, Saha Institute of Nuclear Physics, Kolkata, India for recording the fluorescence spectra. We are grateful to Mr. J. Chakraborty, Jadavpur University, Kolkata for modification of Fig. 4.

Appendix A. Supplementary material

CCDC 628347, 628348 and 637863 contain the supplementary crystallographic data for **1**, **2** and **3**. These data can be obtained free of charge via http://www.ccdc.cam.ac.uk/conts/retrieving.html, or from the Cambridge Crystallographic Data Centre, 12 Union Road, Cambridge CB2 1EZ, UK; fax: (+44) 1223-336-033; or e-mail: deposit@ccdc.cam.ac.uk. Supplementary data associated with this article can be found, in the online version, at doi:10.1016/j.poly.2007.07.025.

References

[1] P. Zanello, S. Tamburini, P.A. Vigato, G.A. Mazzochim, Coord. Chem. Rev. 77 (1987) 165.
[2] P.A. Vigato, S. Tamburini, D.E. Fenton, Coord. Chem. Rev. 106 (1990) 105.
[3] C.R. Choudhury, S.K. Dey, R. Karmakar, C.D. Wu, C.Z. Lu, M.S. El. Fallah, S. Mitra, New J. Chem. 27 (2003) 1360, and references therein.
[4] S. Chandra, X. Sangeetika, Spectrochim. Acta A 60 (2004) 147.

[5] (a) D. Kessel, A.F.A. Sayyab, E.M.H. Jaffar, A.H.H.A. Lanil, Iraqi J. Sci. 22 (1981) 312;
(b) E.M. Hodnett, W.J. Dunn, J. Med. Chem. 13 (1970) 768.
[6] (a) E.M. Hodnett, W.J. Dunn, J. Med. Chem. 15 (1972) 339;
(b) J. Chakraborty, R.N. Patel, J. Indian Chem. Soc. 73 (1996) 191.
[7] S.K. Dey, N. Mondal, M.S. El. Fallah, R. Vicente, A. Escuer, X. Solans, M.F. Bardía, T. Matsushita, V. Gramlich, S. Mitra, Inorg. Chem. 43 (2004) 2427, and references therein.
[8] (a) D. Bose, S.H. Rahaman, G. Mostafa, R.D.B. Walsh, M.J. Zaworotko, B.K. Ghosh, Polyhedron 23 (2004) 545, and references therein;
(b) J. Pons, J. Rius, J. Ros, Inorg. Chim. Acta 359 (2006) 379;
(c) Z.M. Hao, X.-M. Zhang, Inorg. Chem. Commun. 9 (2006) 57.
[9] (a) S.-Q. Bai, E.-Q. Gao, Z. He, C.-J. Fanga, C.-H. Yan, Cryst. Eng. Commun. 6 (2004) 606;
(b) F.J. Barros-Garcý, F. Luna-Giles, M.A. Maldonado- Rogado, E. Viñuelas- Zahý'nos, Polyhedron 25 (2006) 43.
[10] (a) J. Wang, X. Qian, Chem. Commun. (2006) 109;
(b) A.A. Mohamed, H.E. Abdou, J.P. Fackler Jr., Inorg. Chem. 45 (2006) 11;
(c) K.K. Sarker, B.G. Chand, A.D. Jana, G. Mostafa, C. Sinha, Inorg. Chim. Acta 359 (2006) 695.
[11] (a) B. Cornils, W.A. Hermann, R. Schlogl (Eds.), Catalysis from A to Z: A Concise Encyclopedia, Wiley, New York, 2000;
(b) C. Janiak, Coord. Chem. Rev. 250 (2006) 66;
(c) Catalyst for Fine Chemical Synthesis, vol. 3, Wiley, New York, 2004.
[12] (a) D. Demus, J.W. Goodby, G.W. Grey, H.-W. Spiess, V. Vill (Eds.), Handbook of Liquid Crystal, Wiley-VCH, Weinheim, 1998;
(b) I.M. Saez, J.W. Goodby, J. Mater. Chem. 15 (2005) 26.
[13] (a) J.R. Farraro, J.M. Williams, Introduction to Synthetic Electrical Conductors, Academic Press, New York, 1987;
(b) S.R. Marder, in: D.W. Bruce, D. O'Hare (Eds.), Metal Containing Materials for Non-linear Optics in Inorganic Materials, Wiley, Chichester, 1996;
(c) S.R. Marder, Chem. Commun. (2006) 131.
[14] (a) O. Kahn, Molecular Magnetism, VCH, New York, 1993;
(b) J.S. Miller, M. Drillon (Eds.), Magnetism: Molecules to Materials V, Wiley-VCH, Weinheim, 2005;
(c) Special Issue on Chemical Sensors, Chem. Rev. 100 (2000) 7.
[15] R. Ghosh, S.H. Rahaman, C.-N. Lin, T.-H. Lu, B.K. Ghosh, Polyhedron 25 (2006) 3104, and references therein.
[16] S. Sen, S. Mitra, P. Kundu, M.K. Saha, C. Krüger, J. Bruckmann, Polyhedron 16 (1997) 2481.
[17] H. Sigel (Ed.), Metal Ions in Biological Systems, vol. 10, Dekker, New York, Basel, 1979.
[18] C.R. Choudhury, A. Datta, V. Gramlich, G.M.G. Hossain, K.M.A. Malik, S. Mitra, Inorg. Chem. Commun. 6 (2003) 790.
[19] A. Erxleben, J. Hermann, J. Chem. Soc., Dalton Trans. (2000) 569.
[20] L.D.L. Durantaye, T. McCormick, X.-Y. Liu, S. Wang, Dalton Trans. (2006) 5675, and references therein.
[21] H.-C. Lin, C.-C. Huang, C.-H. Shi, Y.-H. Liao, C.-C. Chen, Y.-C. Lin, Y.-H. Liu, Dalton Trans. (2007) 781.
[22] S. Sen, P. Talukder, S.K. Dey, S. Mitra, G. Rosair, D.L. Hughes, G.P.A. Yap, G. Pilet, V. Gramlich, T. Matsushita, Dalton. Trans. (2006) 1758, and references therein.
[23] D. Das, B.G. Chand, K.K. Sarker, J. Dinda, C. Sinha, Polyhedron 25 (2006) 2333.
[24] G.M. Sheldrick, Programs for the Solution and Refinement of Crystal Structures, SHELXTL version 5.1., Bruker AXS P4 Inc., Madison, WI, USA, 1999.
[25] A.W. Addison, T.N. Rao, J. Reedijk, J. van Rijn, G.C. Verschoor, J. Chem. Soc., Dalton Trans. (1984) 1349.
[26] K. Nakamoto, Infrared and Raman Spectra of Inorganic and Coordination Compounds, 5th ed., Wiley, New York, 1997.
[27] M. Tanaka, M. Kitaoka, H. Ökawa, S. Kida, Bull. Chem. Soc. Jpn. 42 (1976) 677.
[28] A. Majumder, G.M. Rosair, A. Mallick, N. Chattopadhyay, S. Mitra, Polyhedron 25 (2006) 1753, and references therein.

Presently we report on the syntheses, crystal structures, thermal- and magnetic properties of two novel 3D carboxylato-bridged coordination polymers of Mn(II) with two different dicarboxylate ligands, $\{[Mn(aip)(DMF)]\}_n$, CPO-9, and $\{[Mn_3(Hatp)_2(atp)_2](H_2O)_2(DEF)_4\}_n$, CPO-10 [aip = 5-aminoisophthalate, atp = 2-aminoterephthalate, DMF = dimethylformamide, DEF = diethylformamide].

2. Experimental

2.1. Synthesis

$\{[Mn(aip)(DMF)]\}_n$, CPO-9. Dark brown single crystals were prepared from a starting mixture of $MnCl_2 \cdot 4H_2O$ (148 mg, 0.75 mmol), 5-aminoisophthalic acid (aip, 272 mg, 1.5 mmol), tetrahydrofuran (THF, 4.0 mL) and dimethylformamide (DMF, 8.0 mL). The crystallization took place in a teflon lined steel autoclave at 110 °C for 24 h. The product was filtered and washed with DMF, and dried at ambient overnight. The yield was 75% based on Mn. *Anal.* Calc. for $C_{11}H_{12}MnN_2O_5$: C, 43.01; H, 3.94; N, 9.12. Found: C, 42.80; H, 4.02; N, 8.56%.

$\{[Mn_3(Hatp)_2(atp)_2]\ (H_2O)_2(DEF)_4\}_n$, CPO-10. Light brown single crystals were obtained from a reaction conducted at 110 °C for 24 h. The starting mixture was composed of $MnCl_2 \cdot 4H_2O$ (148 mg, 0.75 mmol), 2-aminoterephthalic acid (atp, 272 mg, 1.5 mmol), tetrahydrofuran (THF, 4.0 mL) and diethylformamide (DEF, 8.0 mL). The reaction took place in a teflon lined steel autoclave. The product was filtered and washed with DMF, and dried at ambient overnight. The yield was 70% based on Mn. *Anal.* Calc. for $C_{52}H_{70}Mn_3N_8O_{22}$: C, 47.17; H, 5.33; N, 8.47. Found: C, 46.53; H, 5.04; N, 8.21%.

2.2. Single-crystal X-ray diffraction

Single-crystal X-ray diffraction data were collected using a Bruker ApexII diffractomer with a graphite monochromator and Mo Kα radiation ($\lambda = 0.71073$ Å). The crystals were glued to glass fibres, and data were collected at room temperature. Data reduction and empirical absorption correction were carried out using the programs SAINT [17] and SADABS [18], respectively. The crystal structures were solved by direct methods and refined using the WINGX program package [19]. For CPO-9 the refinement of the structure was straightforward with all non-hydrogen atoms being refined anisotropically, and the organic hydrogen atoms being generated geometrically and refined in the riding mode. In case of CPO-10, the aminogroups of the 2-aminoterephthalate anions are disordered over two positions. The solvent molecules inside the pores of CPO-10 were severely disordered, and no satisfactory model for the disorder could be found. The electron density was taken into account with the SQUEEZE procedure in PLATON [20]. In the same way as for CPO-9, the non-hydrogen atoms were refined anisotropically, and the organic hydrogen atoms were generated geometrically and refined in the riding mode. The crystallographic data and details on the refinements for both compounds are listed in Table 1, and selected bond distances and angles are given in Table 2.

2.3. Thermogravimetric analysis (TGA)

TGA was performed on a Perkin–Elmer TGA. The samples of CPO-9 and CPO-10 (about 20 mg) were heated to 700 °C in flowing nitrogen gas at a heating rate of 5 °C/min.

2.4. High-temperature powder X-ray diffraction (HT-PXRD)

HT-PXRD data for CPO-9 and -10 were collected in transmission mode with a Siemens D5000 diffractometer using Cu $K\alpha_1$ radiation selected with an incident beam Ge monochromator. The detector was a Braun PSD. The sample was kept in a rotating 0.5 mm quartz capillary

Table 1
Crystal data and structure refinement data for CPO-9 and -10

Identification code	CPO-9	CPO-10
Empirical formula	$C_{11}H_{12}MnN_2O_5$	$C_{52}H_{70}Mn_3N_8O_{22}$
Formula weight	307.17	1323.98
Temperature (K)	295	295
Wavelength (Å)	0.71073	0.71073
Crystal system	orthorhombic	monoclinic
Space group	$Pna2_1$ (no. 33)	$C2/c$ (no. 15)
a (Å)	7.7808(7)	34.370(3)
b (Å)	15.2752(13)	10.0755(10)
c (Å)	10.8529(9)	17.9793(17)
β (°)	90	97.8570(10)
V (Å^3)	1289.90(19)	6167.7(10)
Z	4	4
D_{calc} (g cm^{-3})	1.582	1.424
Absorption coefficient (mm^{-1})	1.041	0.686
$F(000)$	628	2748
Θ Range for data collection (°)	2.30–26.43	2.11–26.49
Miller index ranges	$-9 \leqslant h \leqslant 9$, $-17 \leqslant k \leqslant 18$, $-13 \leqslant l \leqslant 13$	$-42 \leqslant h \leqslant 43$, $-12 \leqslant k \leqslant 12$, $-22 \leqslant l \leqslant 22$
Reflections collected	15457	23947
Independent reflections [R_{int}]	2615 [0.0208]	6380 [0.0899]
Reflections observed ($>2\sigma$)	2469	3009
Refinement method	full-matrix least-squares on F^2	full-matrix least-squares on F^2
Data/restraints/parameters	2615/1/172	6380/1/270
Goodness-of-fit on F^2	1.094	0.860
Final R indices [$I > 2\sigma(I)$]	$R_1 = 0.0223$, $wR_2 = 0.0596$	$R_1 = 0.0561$, $wR_2 = 0.1364$
R indices (all data)	$R_1 = 0.0239$, $wR_2 = 0.0601$	$R_1 = 0.1105$, $wR_2 = 0.1495$
Largest difference in peak and hole (e Å^{-3})	0.323 and −0.213	0.712 and −0.457

Calculated standard deviations in parentheses.

Table 2
Selected bond lengths (Å) and bond angles (°) for CPO-9 and CPO-10

CPO-9			
Mn(1)–O(3)	2.073(2)	O(3)–Mn(1)–O(2)	84.58(7)
Mn(1)–O(4)	2.089(2)	O(4)–Mn(1)–O(2)	92.43(7)
Mn(1)–O(1)	2.102(2)	O(1)–Mn(1)–O(2)	97.66(8)
Mn(1)–O(2)	2.147(2)	O(3)–Mn(1)–O(5)	88.46(9)
Mn(1)–O(5)	2.177(2)	O(4)–Mn(1)–O(5)	79.95(9)
O(3)–Mn(1)–O(4)	125.87(7)	O(1)–Mn(1)–O(5)	97.74(8)
O(3)–Mn(1)–O(1)	132.38(7)	O(2)–Mn(1)–O(5)	163.92(9)
O(4)–Mn(1)–O(1)	101.64(7)		
CPO-10			
Mn(1)–O(7)	2.076(3)	O(3)–Mn(1)–O(4)	57.35(9)
Mn(1)–O(5)	2.090(3)	O(7)–Mn(1)–O(2)	146.20(12)
Mn(1)–O(1)	2.195(3)	O(5)–Mn(1)–O(2)	85.37(12)
Mn(1)–O(3)	2.264(2)	O(1)–Mn(1)–O(2)	56.71(12)
Mn(1)–O(4)	2.297(3)	O(3)–Mn(1)–O(2)	101.50(10)
Mn(1)–O(2)	2.343(3)	O(4)–Mn(1)–O(2)	88.20(11)
Mn(2)–O(6)	2.085(2)	O(6)–Mn(2)–O(6)	180.00(15)
Mn(2)–O(6)	2.085(2)	O(6)–Mn(2)–O(8)	86.86(12)
Mn(2)–O(8)	2.130(3)	O(6)–Mn(2)–O(8)	93.14(12)
Mn(2)–O(8)	2.130(3)	O(6)–Mn(2)–O(8)	93.14(12)
Mn(2)–O(3)	2.250(2)	O(6)–Mn(2)–O(8)	86.86(12)
Mn(2)–O(3)	2.250(2)	O(8)–Mn(2)–O(8)	180.0
O(7)–Mn(1)–O(5)	103.76(12)	O(6)–Mn(2)–O(3)	92.06(9)
O(7)–Mn(1)–O(1)	89.60(12)	O(6)–Mn(2)–O(3)	87.94(9)
O(5)–Mn(1)–O(1)	106.41(13)	O(8)–Mn(2)–O(3)	89.19(10)
O(7)–Mn(1)–O(3)	110.50(10)	O(8)–Mn(2)–O(3)	90.81(10)
O(5)–Mn(1)–O(3)	91.79(10)	O(6)–Mn(2)–O(3)	87.94(9)
O(1)–Mn(1)–O(3)	149.08(11)	O(6)–Mn(2)–O(3)	92.06(9)
O(7)–Mn(1)–O(4)	99.81(11)	O(8)–Mn(2)–O(3)	90.81(10)
O(5)–Mn(1)–O(4)	146.43(12)	O(8)–Mn(2)–O(3)	89.19(10)
O(1)–Mn(1)–O(4)	97.25(12)	O(3)–Mn(2)–O(3)	180.00(9)

Calculated standard deviations in parentheses.

which was heated from 30 to 270 °C with a gas blower. Diffraction patterns were collected continuously while heating the samples. The measurement time for each powder pattern was 2 h, meaning that each pattern represents an average for a temperature interval of about 24 °C.

2.5. Magnetic measurements

The magnetization measurements were performed using a Quantum Design MPMS SQUID system. Data for zero field cooled samples were collected in the range 2–300 K in an applied field of 1000 G. Gelatin sample holders were used. A Pd standard was used for calibration.

3. Result and discussion

3.1. Crystal structures

CPO-9 crystallizes in the orthorhombic space group $Pna2_1$ (no. 33). The asymmetric unit of CPO-9 contains one aip^{2-}, one Mn(II) and one DMF molecule. The Mn(II) ion exhibits five-coordination with a distorted trigonal bipyramidal geometry (Fig. 1). Four of the oxygen atoms (O1, O2, O3 and O4) originate from four distinct aip

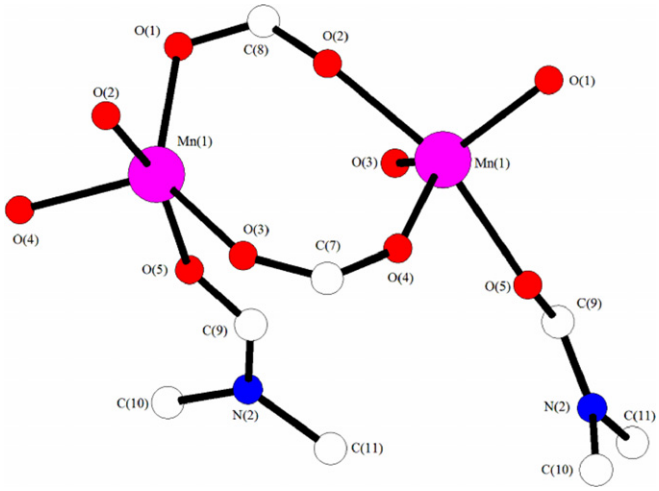


Fig. 1. Coordination environment for Mn in CPO-9.

ligands, while the last oxygen atom, O5, comes from a DMF molecule. Mn–O bonding distances in the range 2.073(2)–2.177(2) Å are fully consistent with previously reported results [21–23]. The adjacent Mn(II) centres are doubly bridged by the carboxylate groups of the aip ligands to form infinite chains of Mn–O polyhedra running along [1 0 0]. The two carboxylate groups bridging subsequent Mn atoms adopt a syn–syn and a syn–anti conformation, respectively. The Mn–Mn distance within the chains is 4.1177(4) Å.

Each of the infinite chains is connected to four adjacent chains by the ring system of the aip ligands to form a 3D coordination polymer. The structure contains 1D channels running along [1 0 0] (Fig. 2). The dimensions of these channels are 8.3×8.3 Å (measured between atom centres). The DMF molecules and the amino groups of the aip ligands protrude into the channels. Crystal structures containing similar infinite chains of five-coordinated Mn being doubly bridged by carboxylate groups as in CPO-9 are known in literature. One 1D and two 3D coordination polymers show the same structural motif [24–26]. However, the

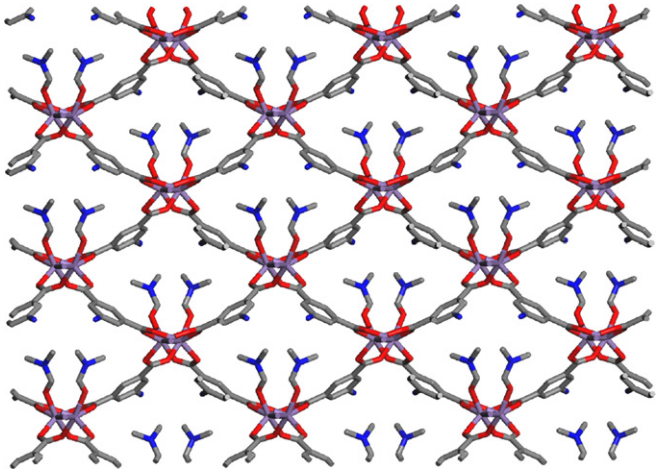


Fig. 2. The crystal structure of CPO-9 seen along [1 0 0].

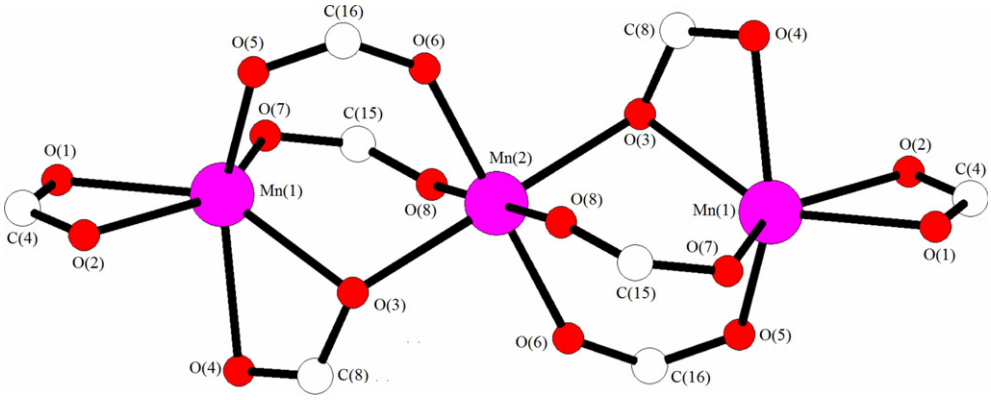


Fig. 3. The trinuclear Mn_3 building units observed in CPO-10.

connectivity within the chains differs between these structures. In addition to CPO-9, one more Mn(II) compound based on aip have been identified in the literature [27,28].

CPO-10 crystallizes in the monoclinic space group $C2/c$ (no. 15). A linear trinuclear Mn_3 unit forms the fundamental building unit of CPO-10 (Fig. 3). Such trinuclear units exist in a number of molecular complexes containing Mn(II) [29–35], and also in three dimensional coordination polymers based on Ni [36], Zn [37] and Mg [38]. The central Mn(2) atom in the Mn_3 units shows a rather regular octahedral coordination geometry involving six carboxylate oxygen atoms, while the terminal Mn(1) atoms in the Mn_3 units show a far more irregular six-coordination involving carboxylate oxygen atoms, Table 2. The bonding distances of 2.076(3)–2.343(3) Å for Mn(1) and 2.085(2)–2.250(2) Å for Mn(2) are within the expected range for divalent Mn(II). The divalent nature of the Mn atoms is further confirmed by bond valence calculations [39]. The Mn–Mn distance of 3.5232(6) Å within the Mn_3 units is consistent with findings for similar trinuclear compounds [29,34]. The Mn atoms in the Mn_3 units are connected by two syn-syn bridging bidentate carboxylate groups and one bridging/chelating carboxylate group. The trinuclear units are terminated by bidentate chelating carboxylate groups.

The linear Mn_3 units are linked via the atp ligands to form a 3D coordination polymer containing channels of dimension 10.1×10.4 Å (measured between atom centers) running along [0 0 1] (Fig. 4). These channels are occupied by two water molecules and four DEF molecules per formula unit. Because of disorder, the channel contents could not be established on the basis of the single crystal X-ray diffraction data, and is therefore determined on the basis of TGA and elemental analysis. The solvent accessible void volume of the crystal structure was calculated by PLATON [20] as 51.9% of the unit cell volume, i.e. a rather high value compared with other materials so far described.

In order to achieve charge neutrality of the CPO-10 material, either some atp ligands have extra protons attached or the channel content must be protonated. Since all the oxygen atoms of carboxylate groups are involved in bonding to Mn, it is most likely that hydrogen atoms are attached to the nitrogen atoms of the amino groups. These amino groups are, however, disordered over two positions, and thus the hydrogen atoms cannot be located by difference Fourier analysis of the X-ray diffraction data. The disorder of the channel content also makes it impossible to locate any protons. Formally we suggest that two atp ligands per formula units are protonated in order to obtain charge neutralization of CPO-10.

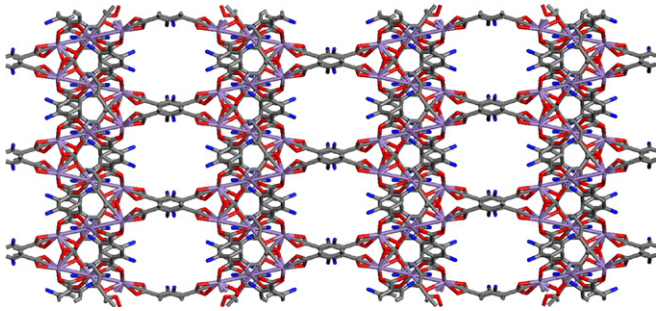


Fig. 4. The crystal structure of CPO-10 seen along [0 0 1].

3.2. Thermal properties

A three dimensional representation of the progressive change in the high temperature powder X-ray diffraction patterns for CPO-9 over the temperature range 30–270 °C is shown in Fig. 5. The patterns reveal that CPO-9 transforms into an amorphous phase at 250 °C. The TGA curve (Fig. 6) shows that this transformation correlates with a partial loss of DMF molecules at 180–250 °C. From 250 to 400 °C, there is a gradual weight loss involving the rest of the DMF molecules, presumably also an OH group being bonded to Mn (observed 23.16 wt%, calculated 23.80 wt%). The final weight loss starting at 400 °C reflects the decomposition of the aip ligands.

The thermal behaviour of CPO-10 is analogous to CPO-9, and exhibits low thermal stability by being transformed into an amorphous phase at 250 °C. The TGA curve shows two weight losses up to 250 °C involving the loss of two

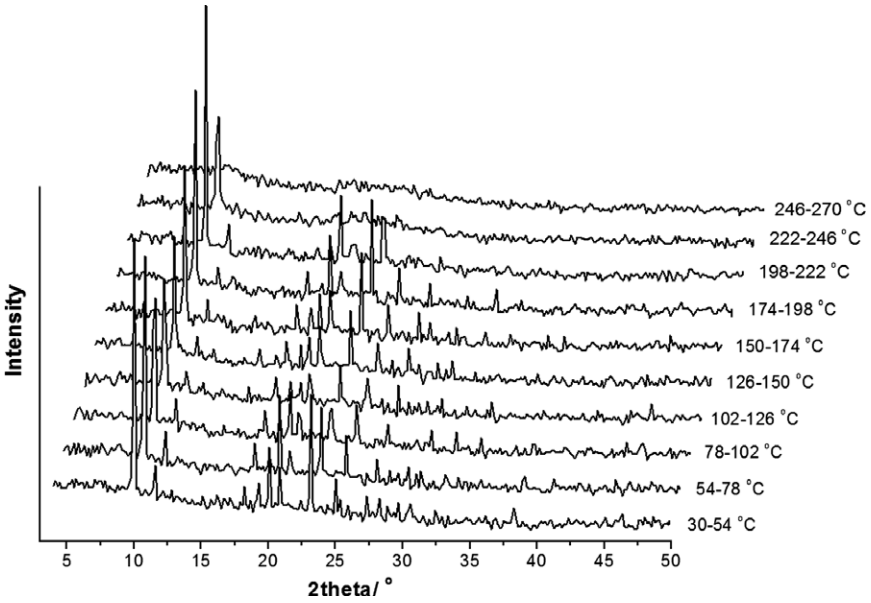


Fig. 5. Three-dimensional representation of high-temperature powder X-ray data for CPO-9 between 30 and 270 °C.

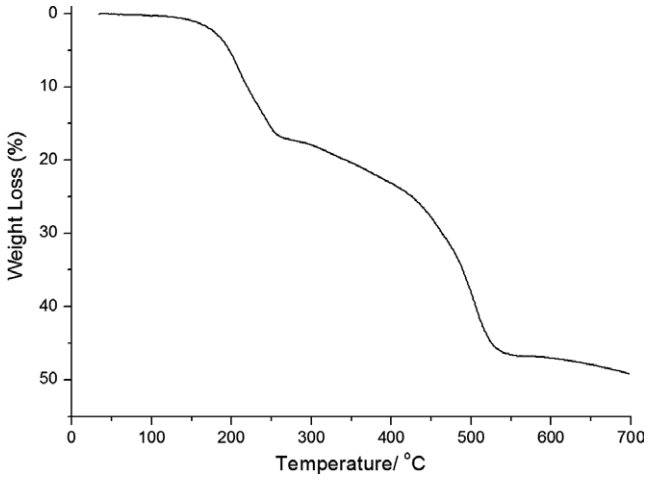


Fig. 6. TGA curve for CPO-9 heated in N_2 at a rate of 5 K/min.

water molecules (observed 2.77 wt%, calculated 2.73 wt%) and four DEF molecules (observed 30.12 wt%, calculated 30.61 wt%). These weight losses are followed by the decomposition of the atp ligands starting gradually already at 250 °C.

3.3. Magnetic properties

Variable-temperature magnetic susceptibility data for CPO-9 is presented in Fig. 7. At room-temperature, $\chi_m T$ is 4.32 cm^3 K mol^{-1}, which is slightly lower than the value of 4.38 cm^3 K mol^{-1} expected for uncoupled Mn(II) atoms ($S = 5/2$ and $g = 2$). As the temperature is lowered, $\chi_m T$ decreases gradually down to around 50 K and thereafter sharply to reach 0.43 cm^3 K mol^{-1} at 2 K. This behaviour indicates that weak antiferromagnetic interactions between the Mn(II) ions dominate the magnetic properties of

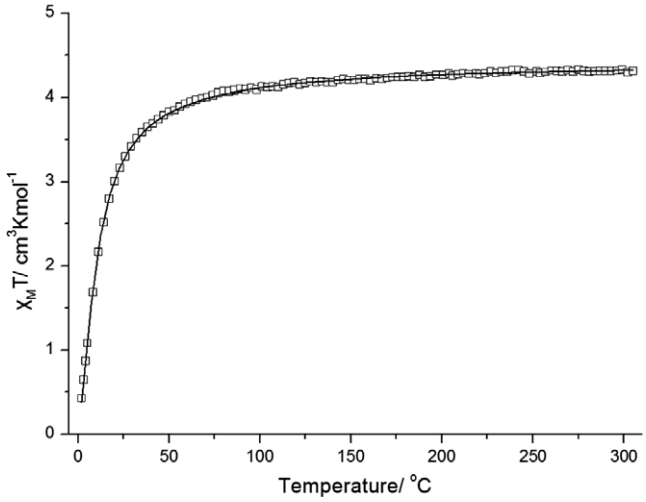


Fig. 7. $\chi_m T$ versus T for CPO-9; the solid line represents the best theoretical fit, see text.

CPO-9. On basis of the crystal structure of CPO-9, there are two possible exchange pathways; an intrachain interaction through the carboxylate bridges and an interchain interaction via the extended aip ligand. Thus the magnetic behaviour can be interpreted by means of the analytical expression derived by Fisher [40] for an infinite chain of classical spins based on the Hamiltonian $H = -J\Sigma S_i S_{i+1}$. The interchain interaction is taken into account by combining this expression with interchain interactions (J') under the molecular field approximation [41]. The analytical expression will then be: $\chi_m = [Ng^2\beta^2F(S,T)]/[1 - 2zJ'F(S,T)]$ where $F(S,T) = [S(S+1)(1+u)]/[3kT(1-u)]$ and $u = \coth(JS(S+1)/kT) + (JS(S+1)/kT)^{-1}$. With allowance for all parameters to vary, the best least squares fit shown in Fig. 7 gives $g = 2.010 \pm 0.001$, $J/k = -1.55 \pm 0.02$ K and $zJ'/k = 0.35 \pm 0.03$ K. The J/k value, which is comparable to previously reported results for doubly bridged carboxylate Mn(II) compounds [42], indicate weak antiferromagnetic interactions through the carboxylate bridges. The positive zJ'/k value indicate a weak interchain ferromagnetic interaction through the 5-aminoisophthalo ligand. Such an interaction has also been earlier reported for an Mn(II) terephthalte compound [43].

The variable-temperature magnetic susceptibility data for CPO-10 (Fig. 8) also reveal an overall antiferromagnetic behaviour. The value of $\chi_m T$ decreases gradually from 13.07 at room temperature to 4.58 cm^3 K mol^{-1} at 2 K. The room temperature value is slightly lower than the expected value of 13.125 cm^3 K mol^{-1} for three uncoupled Mn(II) ions, each with $S_i = 5/2$ and $g_i = 2$. Considering the crystal structure of CPO-10 with linear trinuclear units of Mn(II), the spin Hamilitonian would be $H_s = J(S_1S_2 + S_2S_1) + J'(S_1S_1)$, where S_i is the spin of the Mn(II) atom with number i (Fig. 3). However, the magnetic interactions between the Mn(1) terminal manganese ions is assumed to be negligible in this linear complex ($J' = 0$), and hence only the Mn(1)···Mn(2) interaction (J) is considered. The energies of the states are then given by $E(S_{11},S) = -J[S(S+1) - S_{11}(S_{11}+1)]$ where S is the total spin of the Mn_3 unit and $S_{11} = S_1 + S_1$ is the spin quantum number associated with the spin of the terminal Mn ions. We have the conditions $0 \leqslant S_{11} \leqslant 5$ and $|S_{11} - 5/2| \leqslant S \leqslant S_{11} + 5/2$. The Van Vleck expression for the susceptibility is then $\chi_m = [Ng^2\beta^2\Sigma S(S+1)(2S+1)\exp(-E(S_{11},S)/kT)]/[3kT\Sigma(2S+1)\exp(-E(S_{11},S)/kT)]$. In addition the magnetic interactions between trinuclear units through the atp ligands are taken into account by the molecular field approximation [41]. The expression for the susceptibility is then $\chi_{MFC} = \chi_m/[1 - (2zJ'\chi_m)/(Ng^2\beta^2)]$. The best least squares fit shown in Fig. 8 gives $g = 2.072 \pm 0.001$, $J/k = -4.72 \pm 0.04$ K, $zJ'/k = 0.0006 \pm 0.005$ K. The J/k value of CPO-10 are well within the range reported for other Mn(II) compounds containing the same trinuclear units [29–33,35], and indicates weak antiferromagnetic coupling mediated by the carboxylate bridges. The zJ'/k value is close to zero indicating no magnetic couplings between the trinuclear units.

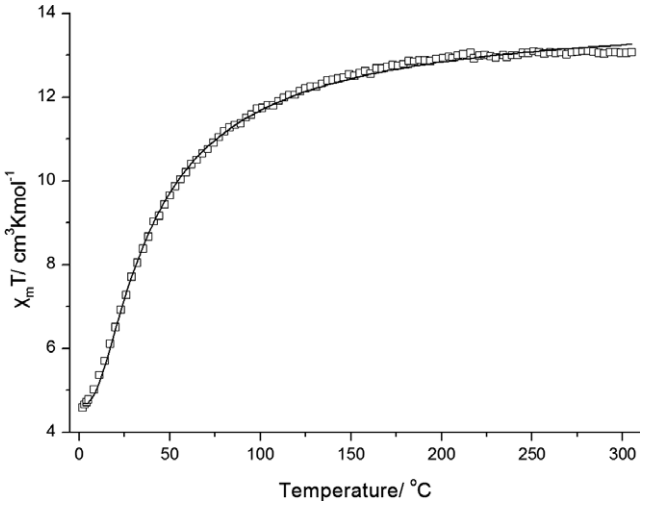


Fig. 8. $\chi_m T$ versus T for CPO-10; the solid line represents the best theoretical fit, see text.

4. Conclusions

In conclusion, two novel 3D coordination based on Mn(II) have been obtained by solvothermal methods. Both structures contain void volumes filled with solvent molecules. However, these molecules cannot be removed without the structures collapsing into amorphous phases at 250 °C. There are antiferromagnetic couplings between the Mn(II)ions in both compounds.

Acknowledgement

This work has received support from the Norwegian Research Council (Grant 151502/ 210).

Appendix A. Supplementary material

CCDC 299264 and 299265 contain the supplementary crystallographic data for CPO-9 and CPO-10. These data can be obtained free of charge via http://www.ccdc.cam.ac.uk/conts/retrieving.html, or from the Cambridge Crystallographic Data Centre, 12 Union Road, Cambridge CB2 1EZ, UK; fax: (+44) 1223-336-033; or e-mail: deposit@ ccdc.cam.ac.uk.

References

[1] C. Janiak, Dalton Trans. (2003) 2781.
[2] O.M. Yaghi, M. O'Keeffe, N.W. Ockwig, H.K. Chae, M. Eddaoudi, J. Kim, Nature 423 (2003) 705.
[3] S. Kitagawa, R. Kitaura, S. Noro, Angew. Chem. Int. Ed. 43 (2004) 2334.
[4] M.J. Rosseinsky, Micropor. Mesopor. Mater. 73 (2004) 15.
[5] G. Ferey, C. Mellot-Draznieks, C. Serre, F. Millange, Acc. Chem. Res. 38 (2005) 217.
[6] X.M. Zhang, M.L. Tong, H.K. Lee, X.M. Chen, J. Solid State Chem. 160 (2001) 118.

[7] Z.Z. Lin, F.L. Jiang, D.Q. Yuan, L. Chen, Y.F. Zhou, M.C. Hong, Eur. J. Inorg. Chem. (2005) 1927.
[8] H.K. Chae, D.Y. Siberio-Perez, J. Kim, Y. Go, M. Eddaoudi, A.J. Matzger, M. O'Keeffe, O.M. Yaghi, Nature 427 (2004) 523.
[9] G. Ferey, C. Mellot-Draznieks, C. Serre, F. Millange, J. Dutour, S. Surble, I. Margiolaki, Science 309 (2005) 2040.
[10] R. Tannenbaum, Chem. Mater. 6 (1994) 550.
[11] J.S. Seo, D. Whang, H. Lee, S.I. Jun, J. Oh, Y.J. Jeon, K. Kim, Nature 404 (2000) 982.
[12] C.-D. Wu, A. Hu, L. Zhang, W. Lin, J. Am. Chem. Soc. 127 (2005) 8940.
[13] R.B. Fu, S.C. Xiang, S.M. Hu, L.S. Wang, Y.M. Li, X.H. Huang, X.T. Wu, Chem. Commun. (2005) 5292.
[14] M.J. Plater, M.R. St. J. Foreman, E. Coronado, C.J. Gómez-García, A.M.Z. Slawin, J. Chem. Soc., Dalton Trans. (1999) 4209.
[15] K. Barthelet, K. Adil, F. Millange, C. Serre, D. Riou, G. Férey, J. Mater. Chem. 13 (2003) 2208.
[16] P.D.C. Dietzel, Y. Morita, R. Blom, H. Fjellvåg, Angew. Chem. Int. Ed. 44 (2005) 6354.
[17] SAINT+, version 6.22. Bruker AXS Inc., Madison, WI, USA, 2001.
[18] G.M. Sheldrick, SADABS: Empirical Absorption Corrections Program, University of Göttingen, Germany, 1997.
[19] L.J. Farrugia, J. Appl. Crystallogr. 32 (1999) 837.
[20] A.L. Spek, Acta Crystallogr. Sect A 46 (1990) C34.
[21] S.P. Perlepes, J.C. Huffman, G. Christou, Chem. Commun. (1991) 1657.
[22] S. Yano, M. Doi, S. Tamakoshi, W. Mori, M. Mikuriya, A. Ichimura, I. Kinoshita, Y. Yamamoto, T. Tanase, Chem. Commun. (1997) 997.
[23] H.J. Eppley, H.L. Tsai, N. de Vries, K. Folting, G. Christou, D.N. Hendrickson, J. Am. Chem. Soc. 117 (1995) 301.
[24] M.A. Kiskin, I.G. Fomina, G.G. Aleksandrov, A.A. Sidorov, V.M. Novotortsev, Y.V. Rakitin, Z.V. Dobrokhotova, V.N. Ikorskii, Y.G. Shvedenkov, I.L. Eremenko, I.I. Moiseev, Inorg. Chem. Commun. 8 (2005) 89.
[25] M.L. Tong, J. Wang, S. Hu, J. Solid State Chem. 178 (2005) 1518.
[26] K.O. Kongshaug, H. Fjellvåg, Solid State Sci. 4 (2002) 443.
[27] Q.X. Liao, Y.G. Yao, Chin. J. Struct. Chem. 25 (2006) 465.
[28] X.J. Li, D.Q. Yuan, X.D. Zhang, R. Cao, J. Coord. Chem. 59 (2006) 969.
[29] V. Tangoulis, D.A. Malamatari, K. Soulti, V. Stergiou, C.P. Raptopoulou, A. Terzis, T.A. Kabanos, D.P. Kessissoglou, Inorg. Chem. 35 (1996) 4974.
[30] S. Menage, S.E. Vitols, P. Bergerat, E. Codjovi, O. Kahn, J.J. Girerd, M. Guillot, X. Solans, T. Calvet, Inorg. Chem. 30 (1991) 2666.
[31] R.L. Rardin, P. Poganiuch, A. Bino, D.P. Goldberg, W.B. Tolman, S.C. Liu, S.J. Lippard, J. Am. Chem. Soc. 114 (1992) 5240.
[32] J.B. Vincent, G. Christou, Adv. Inorg. Chem. Radiochem. 33 (1989) 197.
[33] R.A. Reynolds, W.R. Dunham, D. Coucouvanis, Inorg. Chem. 37 (1998) 1232.
[34] K. Tsuneyoshi, H. Kobayashi, H. Miyamae, Acta Crystallogr., Sect. C 49 (1993) 233.
[35] C.J. Milios, T.C. Stamatatos, P. Kyritsis, A. Terzis, C.P. Raptopoulou, R. Vicente, A. Escuer, S.P. Perlepes, Eur. J. Inorg. Chem. (2004) 2885.
[36] K.O. Kongshaug, H. Fjellvåg, Solid State Sci. 5 (2003) 303.
[37] H. Li, C.E. Davis, T.L. Groy, D.G. Kelley, O.M. Yaghi, J. Am. Chem. Soc. 120 (1998) 2186.
[38] M. Dinca, J.R. Long, J. Am. Chem. Soc. 127 (2005) 9376.
[39] N.E. Brese, M. O'Keeffe, Acta Crystallogr., Sect. B 47 (1991) 192.
[40] M.E. Fischer, Am. J. Phys. 32 (1964) 343.
[41] C.J. O'Conner, Prog. Inorg. Chem. 29 (1982) 203.
[42] S. Durot, C. Policar, G. Pelosi, F. Bisceglie, T. Mallah, J.P. Mahy, Inorg. Chem. 42 (2003) 8072.
[43] C.S. Hong, Y. Do, Inorg. Chem. 36 (1997) 5684.

Table 1
Crystal data and structure refinement details of $[(PPh_3)_2RuH(CO)(C_{10}H_8NO_3)]\cdot 0.5CH_3OH$ (**1**) and $[(PPh_3)_2RuCl(CO)(C_9H_6O_2)]$ (**2**)

	1	**2**
Empirical formula	$C_{49.50}H_{45}NO_{5.50}P_2Ru$	$C_{47}H_{36}ClNO_3P_2Ru$
Formula weight	904.88	861.23
Temperature (K)	293(2)	293(2)
Crystal system	monoclinic	monoclinic
Space group	$P2_1/n$	$P2_1/n$
Unit cell dimensions		
a (Å)	12.3516(5)	10.9441(5)
b (Å)	15.1962(5)	21.2302(11)
c (Å)	22.7646(9)	16.8572(8)
β	97.205(4)	92.153(4)
Volume (Å^3)	4239.1(3)	3913.9(3)
Z	4	4
D_{calc} (Mg/m^3)	1.418	1.462
Absorption coefficient (mm^{-1})	0.496	0.595
$F(000)$	1868	1760
Crystal dimensions (mm)	$0.08\times0.08\times0.28$	$0.04\times0.12\times0.38$
θ Range for data collection (°)	2.83–25.00	2.91–25.00
Index ranges	$-14\leqslant h\leqslant 14,\ -8\leqslant k\leqslant 18,\ -27\leqslant l\leqslant 26$	$-7\leqslant h\leqslant 13,\ -25\leqslant k\leqslant 25,\ -20\leqslant l\leqslant 20$
Reflections collected	26 145	24 198
Independent reflections [R_{int}]	7333 [0.0371]	6860 [0.0467]
Data/restraints/parameters	7333/0/543	6860/0/496
Goodness-of-fit on F^2	0.915	0.977
Final R indices [$I>2\sigma(I)$]	$R_1=0.0338$	$R_1=0.0267$
	$wR_2=0.0746$	$wR_2=0.0627$
R indices (all data)	$R_1=0.0669$, $wR_2=0.0793$	$R_1=0.0467$, $wR_2=0.0652$
Largest difference in peak and hole (e Å^{-3})	0.857 and −0.508	0.516 and −0.357

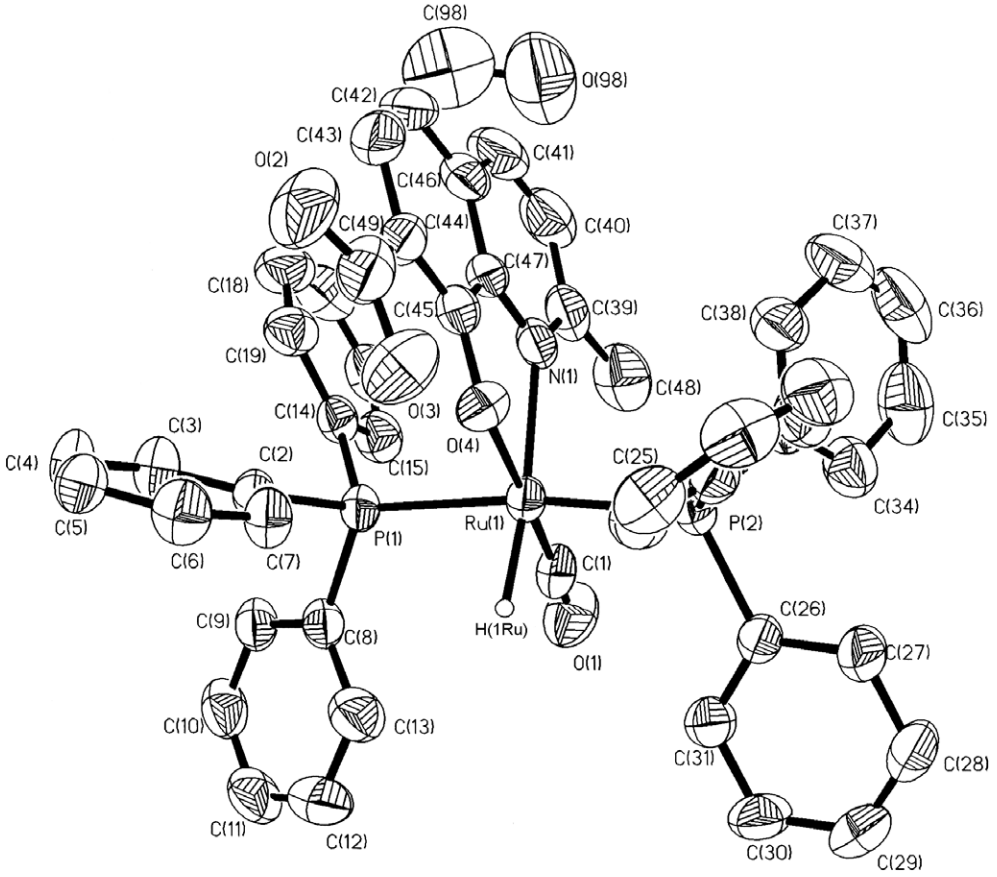


Fig. 1. Drawing of $[(PPh_3)_2RuH(CO)(C_{10}H_8NO_3)]\cdot 0.5CH_3OH$ with 50% probability displacement ellipsoids. The hydrogen atoms except H(1Ru) are omitted.

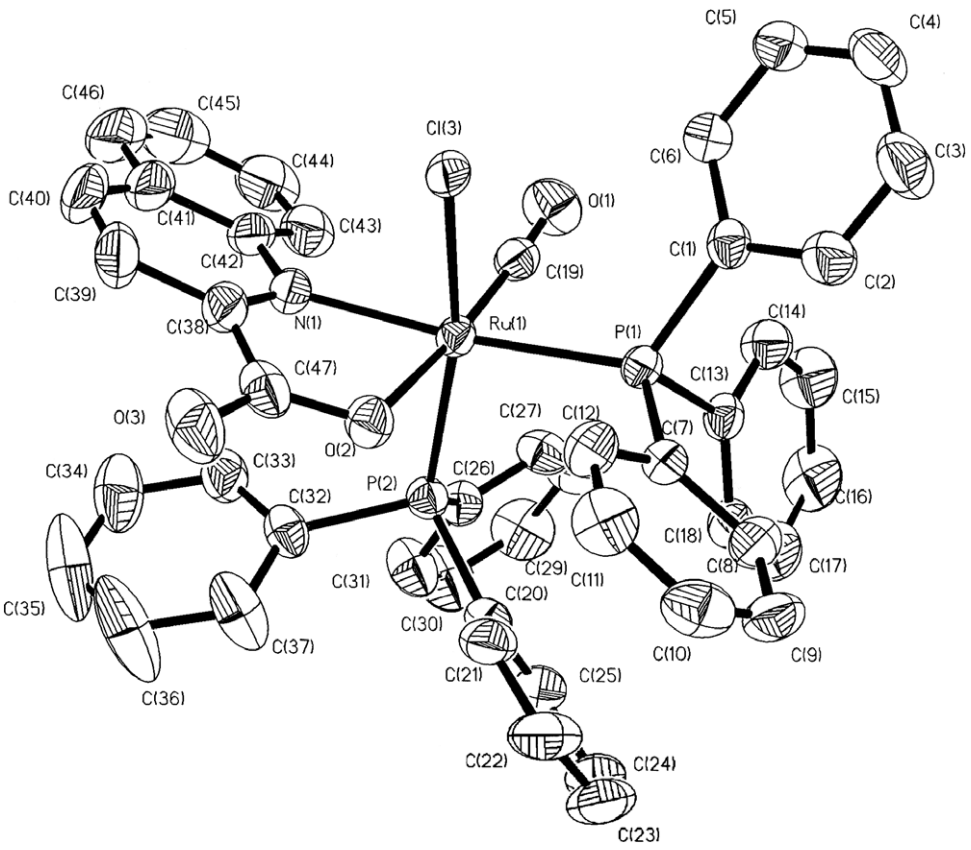


Fig. 2. Drawing of $[(PPh_3)_2RuCl(CO)(C_9H_6O_2)]$ with 50% probability displacement ellipsoids. The hydrogen atoms are omitted for clarity.

with the samples in the form of KBr pellets. Electronic spectra were measured on a Lab Alliance UV–Vis 8500 spectrophotometer in the range 800–200 nm in dichloromethane solution. Elemental analyses (C, H, N) were performed on a Perkin–Elmer CHN–2400 analyzer.

All reagents, except the 8-hydroxy-2-methylquinoline-7-carboxylic acid, used for the synthesis of the complexes are commercially available and were used without further purification. The $[RuHCl(CO)(PPh_3)_3]$ complex was synthesised using a literature method [22]. The 8-hydroxy-2-methylquinoline-7-carboxylic acid was synthesised as described in the literature [13].

2.2. Synthesis of $[(PPh_3)_2RuH(CO)(C_{10}H_8NO_3)]$ (1) and $[(PPh_3)_2RuCl(CO)(C_9H_6O_2)]$ (2)

A suspension of $[RuHCl(CO)(PPh_3)_3]$ (0.95 g, 1×10^{-3} mol) and 8-hydroxy-2-methyl-quinoline-7-carboxylic acid (0.21 g) or quinoline-2-carboxylic acid (0.18 g) in methanol (100 cm^{-3}) was refluxed until the solid dissolved, then the solution was cooled and filtered. Crystals suitable for X-ray crystal analysis were obtained by slow evaporation of the reaction mixture. Yield 78% (**1**) and 82% (**2**).

Anal. Calc. for **1**: $C_{47}H_{36}ClNO_3P_2Ru$: C, 63.94; H, 4.58; N, 3.64. Found: C, 64.01; H, 4.53; N, 3.66%.

2: $C_{50}H_{42}ClNO_3P_2Ru$: C, 66.48; H, 4.69; N, 1.55. Found: C, 66.28; H, 4.59; N, 1.51%.

IR (KBr, cm^{-1}): **1**: 3055 ν_{CH}; 2925 $\nu_{CH-phenyl}$; 1945 ν_{Ru-H}; 1918 ν_{CO}; 1610 ν_{CN}; 1590 asν_{COO}; 1482 $\delta_{(C-CH\ in\ the\ plane)}$; 1436 $\nu_{Ph(P-Ph)}$; 1378 sν_{COO}; 1121 $\delta_{(C-CH\ in\ the\ plane)}$; 996 $\delta_{(C-C\ out\ of\ the\ plane)}$; 756 $\delta_{(C-C\ out\ of\ the\ plane)}$; 697 $\delta_{(C-C\ in\ the\ plane)}$.

2: 3060 ν_{CH}; 1938 ν_{CO}; 1650 ν_{CN}; 1596 asν_{COO}; 1482 $\delta_{(C-CH\ in\ the\ plane)}$; 1434 $\nu_{Ph(P-Ph)}$; 1348 sν_{COO}; 1089 $\delta_{(C-CH\ in\ the\ plane)}$; 750 $\delta_{(C-C\ out\ of\ the\ plane)}$; 696 $\delta_{(C-C\ in\ the\ plane)}$.

UV–Vis [nm] in CH_3OH (logε): **1**: 400 (3.48); 357 sh (3.59); 332 (3.77); 281 (4.31); 210 (4.40).

2: 350 (3.01); 283 (3.38); 238 (4.20); 206 (4.32).

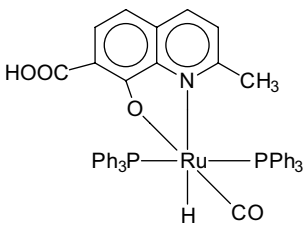


Fig. 3. Structural drawing of $[(PPh_3)_2RuH(CO)(C_{10}H_8NO_3)]$.

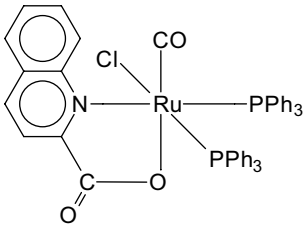


Fig. 4. Structural drawing of $[(PPh_3)_2RuCl(CO)(C_9H_6O_2)]$.

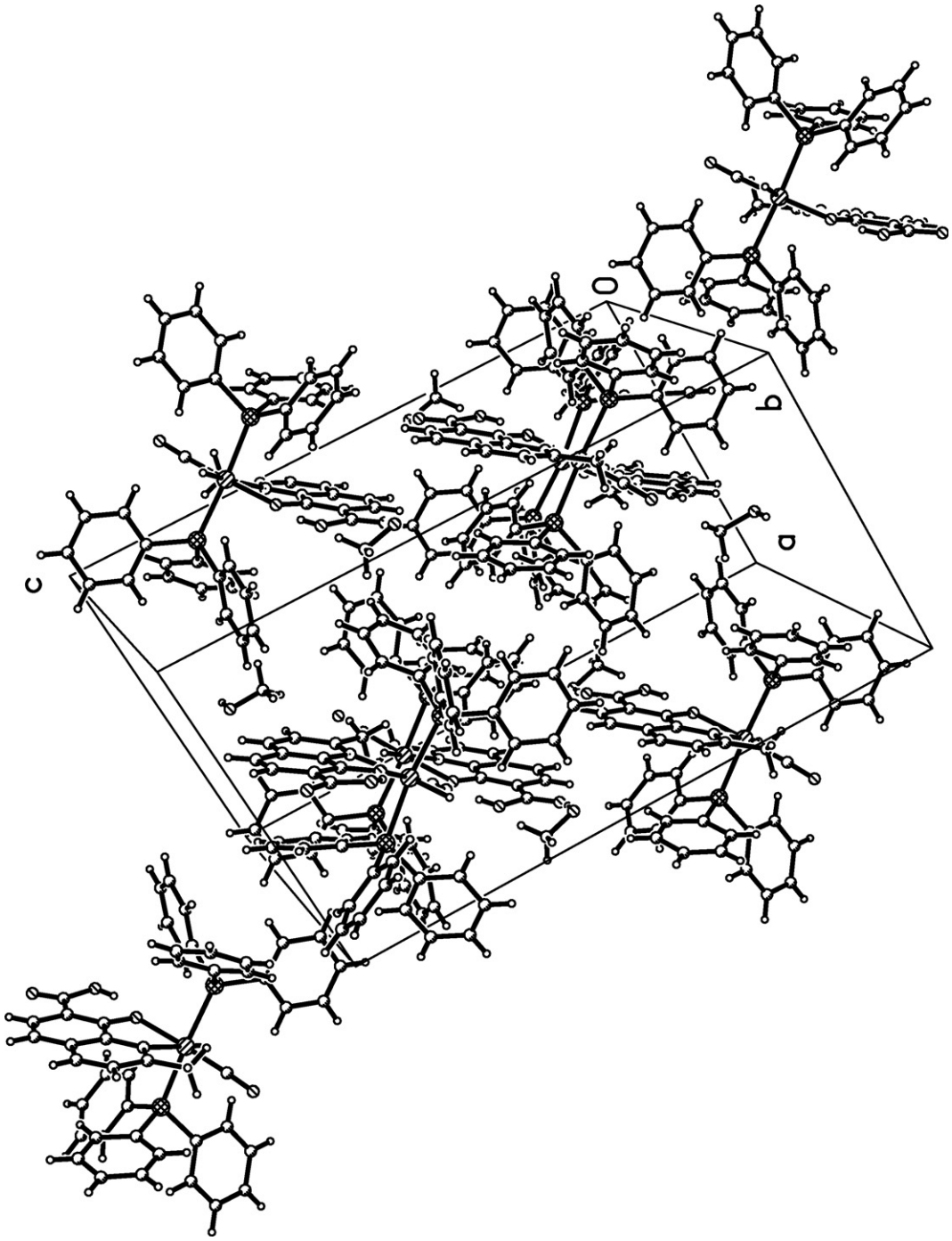


Fig. 5. Part of the molecular packing of $[(PPh_3)_2RuH(CO)(C_{10}H_8NO_3)]$.

2.3. DFT calculations

The GAUSSIAN-03 program [23] was used for the calculations. The geometry optimisation was carried out using the DFT method with the B3LYP functional [24,25]. The electronic transitions were calculated with the PCM model [26] with dichloromethane as the solvent. The calculation was performed using the DZVP basis set [27] with f functions and with exponents 1.94722036 and 0.748930908 on the ruthenium atom and polarisation functions for all other atoms: 6–31g(2d,p) – chlorine, 6–31g** – carbon, nitrogen, oxygen, and 6–31g(d,p) – hydrogen. Natural bond orbital (NBO) calculations were performed using the NBO code [28] included in GAUSSIAN-03.

2.4. Crystal structure determination and refinement

A green prism of complex **1** and a white prism of **2** were mounted in turn on a KM-4-CCD automatic diffractometer equipped with a CCD detector, and were used for data

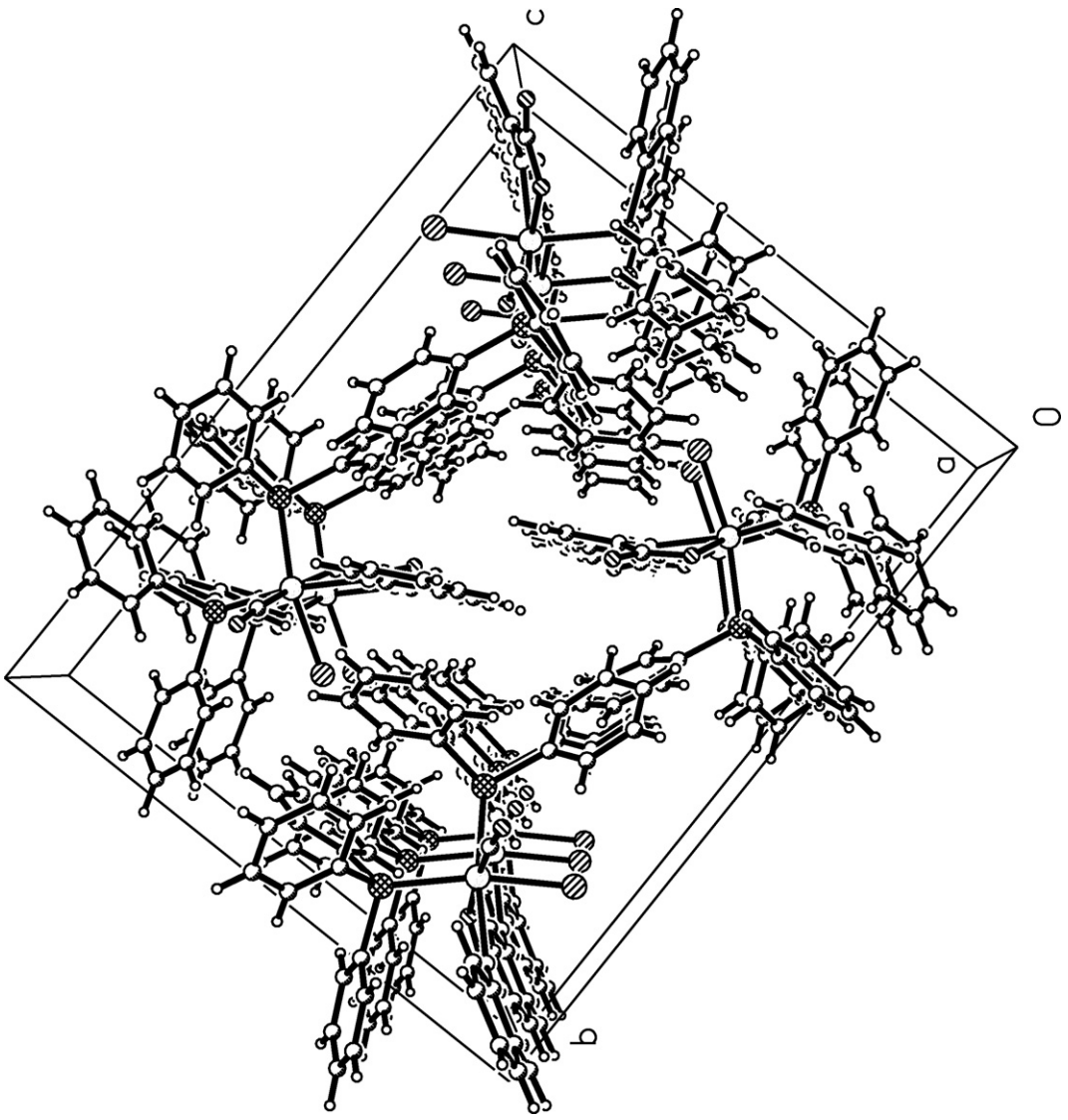


Fig. 6. Part of the molecular packing $[(PPh_3)_2RuCl(CO)(C_9H_6O_2)]$.

collection. X-ray intensity data were collected with graphite monochromated Mo Kα radiation ($\lambda = 0.71073$ Å) at the temperature 295.0(3) K, with the ω scan mode. The Ewald sphere reflections were collected up to $2\theta = 50.0°$ for both complexes. The unit cell parameters were determined from least-squares refinement of the setting angles of 7333 and 6860 strongest reflections for complexes **1** and **2**, respectively. Details concerning the crystal data and refinement are gathered in Table 1. The reference frames, monitored every 40 measurement frames, show 1.01% decay for the crystal of compound **1** and no decay for the crystal of compound **2**. During the data reduction of compound **1** a decay correction was taken into account. Lorentz, polarisation and numerical absorption [29] corrections were applied. The structures were solved using the Patterson method combined with a partial structure expansion procedure. All the non-hydrogen atoms were refined anisotropically using the full-matrix, least-squares technique on F^2. The hydrogen atoms were found from difference Fourier synthesis after four cycles of anisotropic refinement, and refined as ''riding'' on the adjacent atom with an individual isotropic temperature factor equal to 1.2 times the value of the equivalent temperature factor of the parent atom. The H(1Ru) atom in complex **1** was placed in a calculated position (Ru–H distance 1.6 Å) according to similar compounds [30–36]. SHELXS97 [37], SHELXL97 [38] and SHELXTL [39] programs were used for all calculations. Atomic scattering factors had values incorporated in the computer programs.

3. Results and discussion

The reaction between the $[RuHCl(CO)(PPh_3)_3]$ complex and 8-hydroxy-2-methyl-quinoline-7-carboxylic acid or quinoline-2-carboxylic acid in methanolic solution gives the mononuclear ruthenium(II) compounds $[(PPh_3)_2RuH-$

$(CO)(C_{10}H_8NO_3)]$ (green, air-stable, crystalline solid) and $[(PPh_3)_2RuCl(CO)(C_9H_6O_2)]$ (white solid). Infrared spectra of the complexes exhibit characteristic bands of coordinated ligands – quinoline carboxylic acid, CO, PPh_3 and the hydride group.

The strong bands at 1938 and 1918 cm^{-1} for complex **1** and **2**, respectively, are assigned to the ν_{CO} stretching vibrations of the ruthenium bonded carbonyl group, and the band at 1945 cm^{-1} corresponds to ν_{Ru-H} of the hydride ligand (complex **1**). The ν_{CO} and ν_{Ru-H} stretching vibrations in the $[RuHCl(CO)(PPh_3)_3]$ complex are at 2020 and 1903 cm^{-1}, respectively. The bands at 1610 and 1650 cm^{-1} are attributed to the CN stretching vibration of the quinoline ligand. The asymmetric and symmetric ν_{COO} stretching bands are at 1590, 1596 cm^{-1} and 1378, 1348 cm^{-1} for compounds **1** and **2**, respectively.

The positions of the ν_{CO} and ν_{Ru-H} bands in the IR spectrum of complex **1** indicate a decrease of the metal–carbonyl carbon interaction and an increase of the Ru–H bond order. Taking into account the IR spectra of both complexes, the quinoline type ligand is a σ-donor that induces a large Ru–CO back-bonding.

3.1. Crystal structure

Both obtained complexes crystallise in the monoclinic space group $P2_1/n$. The crystal data of complexes **1** and **2** are given in Table 1. The molecular structures of **1** and **2** are presented in Figs. 1 and 2 (see Figs. 3, 4), respectively, and molecular packing is depicted, receptively, in Figs. 5 and 6. The ruthenium atom in the complex $[(PPh_3)_2RuH(CO)(C_{10}H_8NO_3)]$ is in a distorted octahedral environment with *trans*-triphenylphosphine ligands (angle P(1)–Ru(1)–P(2) 172.19(3)°). The carbonyl ligand is in a *trans*-position to the O donor atom (C(1)–Ru(1)–O(4) 178.12(11)°) and the hydrido ion lies *trans* to the coordinated nitrogen from the quinoline ligand – with an angle of 170.0°. The Ru–N bond distance is longer in complex **1** than in complex **2** due to the *trans* effect of the hydride ligand. The interatomic distances in the carbonyl and triphenylphosphine ligands are normal.

In the structure of compound **1** one very weak intramolecular O(4)–HO(3) hydrogen bond (D···A distance 2.554(3) Å and D–H···A angle 151.7°) and one very weak intermolecular C(40)–H(40)O(98) hydrogen bond (D···A distance 3.290(10) Å and D–H···A angle 139.5°) can be found.

The ruthenium atom of complex **2**, $[(PPh_3)_2RuCl(CO)(C_9H_6O_2)]$, is also in a distorted octahedral environment with *cis*-triphenylphosphine ligands (angle P–Ru–P 99.28(2)°). The carbonyl ligand is in a *trans* position to the carboxylic O donor atom (O(2)–Ru–C(19) 174.95(9)°) and the chloride ion is *trans* to the P(2) atom −166.11(2)°. All Ru–ligand distances, namely Ru–Cl 2.4250(6), Ru–P 2.3763(7), 2.3861(7), Ru–N 2.169(2), Ru–C 1.826(3) and Ru–O 2.1035(16) Å, are normal and comparable with distances in other ruthenium complexes containing heterocyclic ligands.

Table 2
Selected bond lengths (Å) and angles (°) for $[(PPh_3)_2RuH(CO)(C_{10}H_8NO_3)]$ (**1**) and $[(PPh_3)_2RuCl(CO)(C_9H_6O_2)]$ (**2**)

	1			**2**	
	Experimental	Calculated		Experimental	Calculated
Bond lengths (Å)					
Ru(1)–C(1)	1.805(4)	1.806	Ru(1)–C(19)	1.826(3)	1.865
Ru(1)–O(4)	2.127(19)	2.126	Ru(1)–O(2)	2.1035(16)	2.108
Ru(1)–N(1)	2.221(3)	2.225	Ru(1)–N(1)	2.169(2)	2.243
Ru(1)–P(2)	2.355(8)	2.354	Ru(1)–P(2)	2.3861(7)	2.456
Ru(1)–P(1)	2.360(8)	2.361	Ru(1)–P(1)	2.3763(7)	2.438
Ru(1)–H(1Ru)	1.6042	1.604	Ru(1)–Cl(3)	2.4250(6)	2.458
C(1)–O(1)	1.231(4)	1.159	C(19)–O(1)	1.155(3)	1.164
Angles (°)					
C(1)–Ru(1)–O(4)	178.12(11)	178.14	C(19)–Ru(1)–O(2)	174.95(9)	178.18
C(1)–Ru(1)–N(1)	103.76(12)	103.67	N(1)–Ru(1)–C(19)	98.15(10)	101.67
O(4)–Ru(1)–N(1)	75.66(9)	75.83	O(2)–Ru(1)–N(1)	77.43(7)	76.57
C(1)–Ru(1)–P(2)	92.83(10)	92.87	P(1)–Ru(1)–C(19)	84.89(8)	87.79
O(4)–Ru(1)–P(2)	89.02(6)	88.97	P(1)–Ru(1)–O(2)	99.05(5)	94.03
N(1)–Ru(1)–P(2)	97.25(6)	97.33	N(1)–Ru(1)–P(1)	169.76(6)	163.87
C(1)–Ru(1)–P(1)	86.66(10)	86.68	C(19)–Ru(1)–P(2)	99.86(8)	97.02
O(4)–Ru(1)–P(1)	91.55(6)	91.53	O(2)–Ru(1)–P(2)	82.70(5)	82.57
N(1)–Ru(1)–P(1)	90.44(6)	90.44	N(1)–Ru(1)–P(2)	89.87(6)	90.77
P(2)–Ru(1)–P(1)	172.19(3)	172.10	P(2)–Ru(1)–P(1)	99.28(2)	101.11
C(1)–Ru(1)–H(1Ru)	85.4	85.30	C(19)–Ru(1)–Cl(3)	92.45(8)	93.27
O(4)–Ru(1)–H(1Ru)	95.1	95.09	O(2)–Ru(1)–Cl(3)	84.56(5)	86.92
N(1)–Ru(1)–H(1Ru)	170.0	170.21	N(1)–Ru(1)–Cl(3)	81.98(6)	80.28
P(2)–Ru(1)–H(1Ru)	86.1	85.99	P(1)–Ru(1)–Cl(3)	88.14(2)	86.21
P(1)–Ru(1)–H(1Ru)	86.1	86.12	P(2)–Ru(1)–Cl(3)	166.11(2)	167.56

The molecules in the crystal are connected by four very weak C–H···O intramolecular hydrogen bonds: C(12)–H(12)···O(2) (D···A distance 3.059(3) Å, D–H···A angle 120.0°), C(21)–H(21)···O(2) (D···A distance 3.074(3) Å, D–H···A 145.6°), C(6)–H(6)···Cl(3) (D···A distance 3.208(3) Å, D–H···A angle 108.90°) and C(43)–H(43)···O(1) (D···A distance 3.267(4) Å, D–H···A angle 132.6°).

3.2. Geometry optimisation

The geometries of the studied complexes were optimised by the DFT method with the B3LYP functional. The geometry parameters for the optimised complexes are gathered in Table 2. In general, the predicted bond lengths and angles are in agreement with the X-ray structural data. The largest difference is found for the C(1)–O(1) bond (~0.072 Å) (compound **1**). The maximum differences between the optimised and experimental geometry of compound **2** are exhibited in the Ru(1)–N(1) distance (0.074 Å) and N(1)–Ru(1)–P(1) angle (5.9°).

3.3. Charge distribution and NBO analysis

The calculated charges on the ruthenium atom in the studied complexes are considerable lower than the formal charge of +2 and are close to −0.01 and 0.26 for **1** and **2**, respectively. The charges on the P atoms are positive and close to 1.15 (1.20); the charge on the chloride ligand in $[(PPh_3)_2RuCl(CO)(C_9H_6O_2)]$ is larger than −1 (−0.55), the charge on the quinoline carboxylic acid ligands is close to −0.64 for **1** and −0.52 for **2**. The occupancies of the ruthenium d orbitals, obtained from the NBO analysis, are as follow: $d_{xy} - 1.73$; $d_{xz} - 1.84$; $d_{yz} - 1.21$; $d_{x^2-y^2} - 1.23$; $d_{z^2} - 1.61$ for $[(PPh_3)_2RuH(CO)(C_{10}H_8NO_3)]$ and $d_{xy} - 1.80$; $d_{xz} - 1.74$; $d_{yz} - 1.75$; $d_{x^2-y^2} - 1.13$; $d_{z^2} - 0.96$ for $[(PPh_3)_2RuCl(CO)(C_9H_6O_2)]$.

The Ru–C bond orbitals in the two studied complexes are polarised towards the carbon atom, and the C≡O bond orbitals are polarised towards the oxygen end. The oxygen atoms of the carbonyl ligands have one lone pair (LP) orbital. The occupancies of the Ru–C bonds are (*anti*-bonding NBOs are given in round brackets)

Table 3
The energy and character of selected occupied and virtual MOs for $[(PPh_3)_2RuH(CO)(C_{10}H_8NO_3)]$ (**1**) and $[(PPh_3)_2RuCl(CO)(C_9H_6O_2)]$ (**2**)

	$[(PPh_3)_2RuH(CO)(C_{10}H_8NO_3)]$ (**1**)		$[(PPh_3)_2RuCl(CO)(C_9H_6O_2)]$ (**2**)	
	E (eV)	Character	*E* (eV)	Character
HOMO − 20	−7.902	$\pi_{qu} + n_P$	−7.728	$\pi_{Cl} + n_P$
HOMO − 19	−7.788	π_{qu}	−7.510	π_{Cl}
HOMO − 18	−7.393	$\pi_{qu} + \sigma_H$	−7.282	π_{Ph}
HOMO − 17	−7.306	$\pi_{phosphine}$	−7.219	π_{Ph}
HOMO − 16	−7.249	$\pi_{phosphine}$	−7.203	$\pi_{qu} + \pi_{Cl}$
HOMO − 15	−7.200	π_{COOH}	−7.099	$\pi_{Ph} + \pi_{COO}$
HOMO − 14	−7.067	π_{Ph}	−7.061	$\pi_{Cl} + \pi_{Ph}$
HOMO − 13	−6.999	π_{Ph}	−7.040	$\pi_{COO} + d$
HOMO − 12	−6.983	π_{Ph}	−6.949	π_{Ph}
HOMO − 11	−6.966	π_{Ph}	−6.931	π_{Ph}
HOMO − 10	−6.893	π_{Ph}	−6.865	π_{Ph}
HOMO − 9	−6.860	π_{Ph}	−6.838	π_{Ph}
HOMO − 8	−6.787	π_{Ph}	−6.819	π_{Ph}
HOMO − 7	−6.776	$\pi_{Ph} + d + \pi_{CO}$	−6.770	π_{Ph}
HOMO − 6	−6.708	$\pi_{Ph} + d + \pi_{CO}$	−6.721	π_{Ph}
HOMO − 5	−6.669	$\pi_{Ph} + d$	−6.675	$\pi_{Ph} + d + \pi_{CO}$
HOMO − 4	−6.615	π_{Ph}	−6.596	π_{Ph}
HOMO − 3	−6.400	$d + \pi_{CO} + n_P$	−6.588	$\pi_{Ph} + d + \pi_{CO}$
HOMO − 2	−6.313	$d + \pi^*_{CO}$	−6.487	$\pi_{Cl} + \pi_{qu}$
HOMO − 1	−5.886	$d + n_P$	−6.248	$d + \pi^*_{Cl}\pi_{Co}$
HOMO	−5.255	$d + \pi^*_{qu}$	−6.119	$d + \pi^*_{Cl}$
LUMO	−1.567	π^*_{qu}	−2.025	π^*_{qu}
LUMO + 1	−0.838	$d_{z^2} + \pi^*_{qu}$	−1.518	$d - \sigma_{Cl} - n_p$
LUMO + 2	−0.759	$\pi^*_{qu} + \pi^*_{Ph}$	−0.999	π^*_{qu}
LUMO + 3	−0.631	$d + \pi^*_{Ph}$	−0.882	$d + \pi^*_{qu}$
LUMO + 4	−0.571	$d + \pi^*_{Ph}$	−0.811	$d + \pi^*_{Ph}$
LUMO + 5	−0.484	π^*_{Ph}	−0.713	π^*_{Ph}
LUMO + 6	−0.272	π^*_{Ph}	−0.555	π^*_{Ph}
LUMO + 7	−0.179	π^*_{Ph}	−0.539	π^*_{Ph}
LUMO + 8	−0.160	π^*_{Ph}	−0.433	$d + \pi^*_{CO} + \pi^*_{Ph}$
LUMO + 9	−0.098	π^*_{Ph}	−0.248	$d + \pi^*_{CO} + \pi^*_{Ph}$
LUMO + 10	0.041	π^*_{Ph}	−0.218	$\pi^*_{Ph} + \pi^*_{CO}$
LUMO + 11	0.065	π^*_{Ph}	−0.174	$d + \pi^*_{CO} + \pi^*_{Ph}$
LUMO + 12	0.201	$d + \pi^*_{CO} + \pi^*_{Ph}$	−0.063	π^*_{Ph}
LUMO + 13	0.234	$d + \pi^*_{CO} + \pi^*_{Ph}$	−0.052	π^*_{Ph}

for complex **1**: 1.976 (0.398) and for complex **2**: 1.938 (0.272).

3.4. Electronic structure

The energies and characters of several highest occupied and lowest unoccupied molecular orbitals of the studied complexes are presented in Table 3. The HOMO–LUMO gaps of complexes **1** and **2** are 3.69 and 4.09 eV, respectively. In both cases, the ruthenium atom possesses a d^6 configuration. The highest MO is d_{xz} with a contribution of the p_π antibonding orbitals from the quinoline ligand in the case of complex **1** and from the chlorine ligands of compound **2**. The π_{Ru-CO} bonding interaction contribute in the H-2 and H-3 orbitals of compounds **1** and **2**. The π^*_{Ru-CO} orbitals are also distributed among several unoccupied molecular orbitals. They contribute in L + 12, L + 13 (complex **1**) and L + 9, L + 11 for **2**. The LUMO orbitals are localised on the quinoline ring. The d_{z^2} orbital of the Ru atom

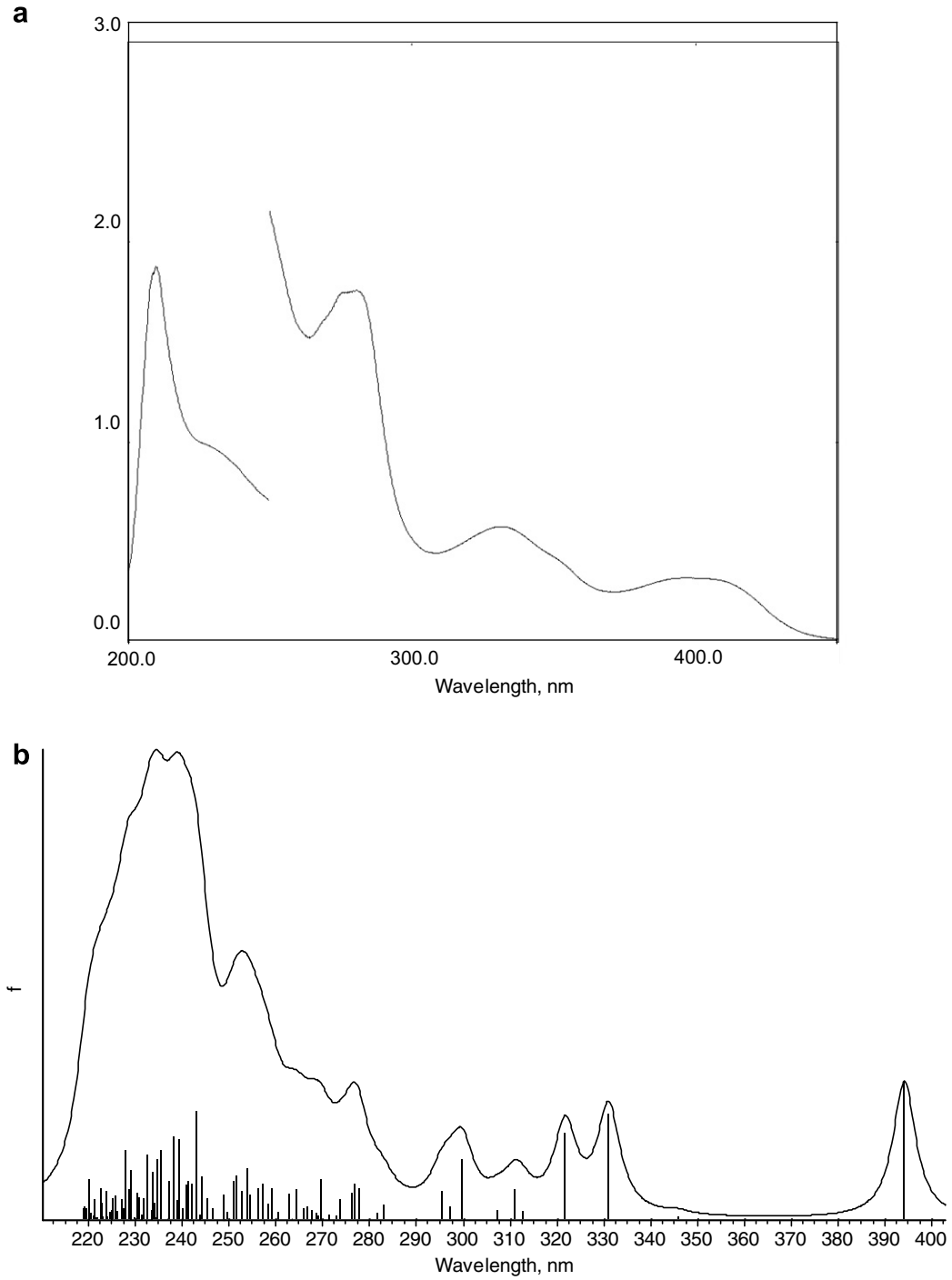


Fig. 7. The UV–Vis spectra of $[(PPh_3)_2RuH(CO)(C_{10}H_8NO_3)]$: (a) experimental; (b) calculated.

makes the largest contribution into L + 3, whereas the L + 4 molecular orbital has $d_{x^2-y^2}$ character in the studied complexes.

3.5. Electronic spectrum

The experimental and calculated electronic spectra of allowed singlet transitions, calculated with the TDDFT method, are presented in Figs. 7 and 8, respectively, for complexes **1** and **2**. The contour of the calculated spectrum was broadening by the Lorentzian function, calculated by the equation:

$$I = \frac{I_0}{1 + \left(\frac{\nu - \nu_0}{\gamma}\right)^2}; \quad \text{where}$$

$\gamma = 1/2$ the spectral width at $1/2$ height.

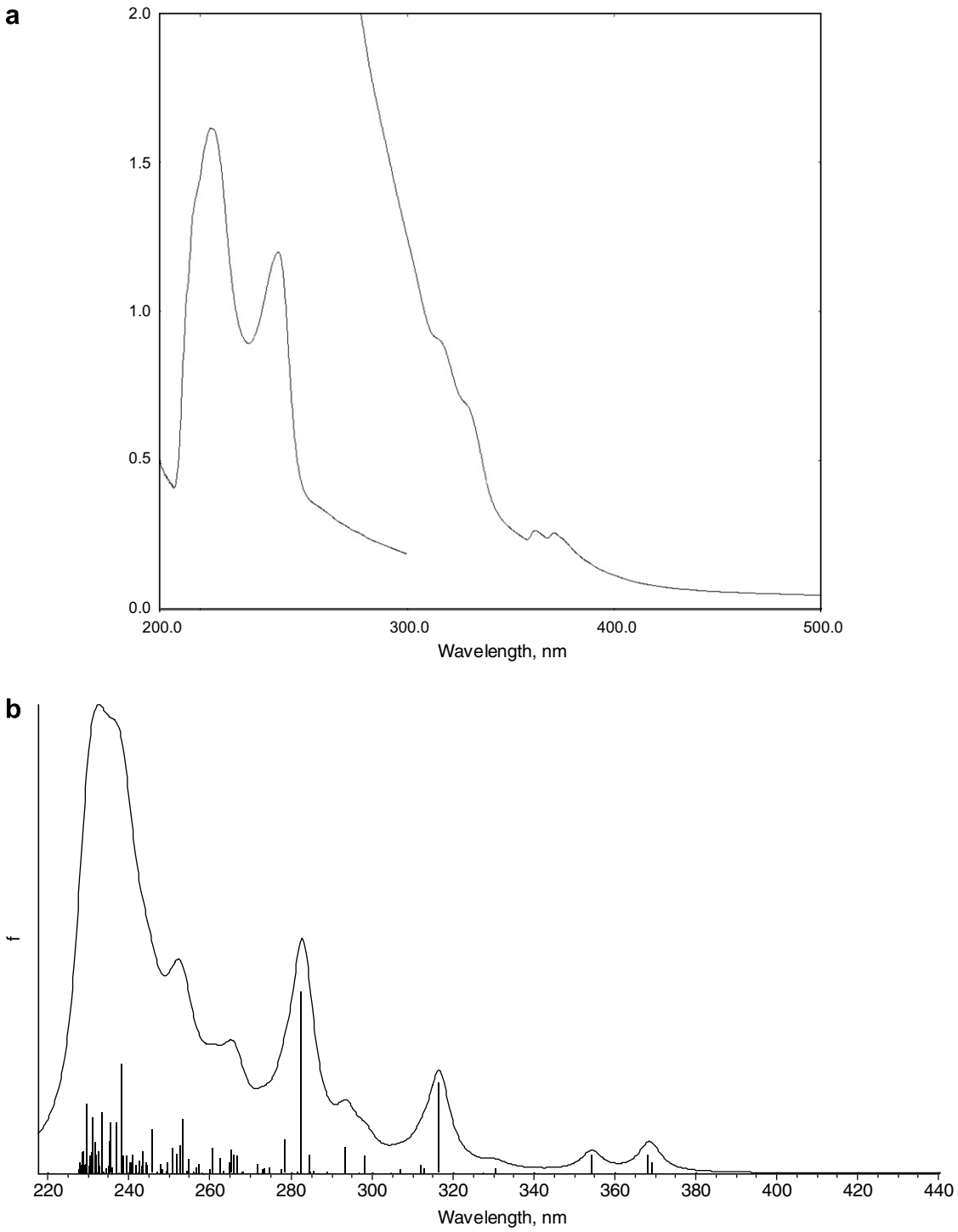


Fig. 8. The UV–Vis spectra of $[(PPh_3)_2RuCl(CO)(C_9H_6O_2)]$: (a) experimental; (b) calculated.

Hundred electronic transitions were calculated for the studied complexes using the DZVP with the f functions basis set on the ruthenium atom, and they do not comprise all the experimental absorption bands. The UV–Vis spectra were calculated up to ~225 nm, so the shortest wavelength experimental bands cannot be assigned to calculated transitions. However, considering that the solution spectra of PPh_3 and quinoline type ligands exhibit intense absorption bands in the 260–200 nm region, some additional intraligand and interligand transitions are expected to be found at higher energies in the calculations.

The assignments of the calculated transitions to the experimental bands are based on the criterion of the energy and oscillator strength of the calculated transitions. In the description of the electronic transitions only the main components of the molecular orbitals are taken into consideration.

The first experimental bands at 400 and 357 nm in $[(PPh_3)_2RuH(CO)(C_{10}H_8NO_3)]$ (**1**) and at 350.0 nm in $[(PPh_3)_2RuCl(CO)(C_9H_6O_2)]$ (**2**) consist of $d \rightarrow \pi^*_{qu}$ MLCT (Metal–Ligand Charge Transfer) transitions (HOMO/H-1 → LUMO). The next bands with maxima at 332 and 280 nm for complex **1** and 283 nm for **2** were calculated as the d → d LF (Ligand Field) transitions with contributions of MLCT excitation between *d* ruthenium and $\pi^*_{phosphine/qu}$ orbitals. For the higher energy band (maximum at 238 nm) of complex **2**, mainly intra- and interligand transitions are observed ($\pi_{qu} \rightarrow \pi^*_{Ph}$; $\pi_{qu} \rightarrow \pi^*_{qu}$; $\pi_{Cl} \rightarrow \pi^*_{Ph}$; $\pi_{CO} \rightarrow \pi^*_{Ph}$; $\pi_{CO} \rightarrow \pi^*_{qu}$). The bands at 210 and 206 nm for complexes **1** and **2**, respectively, were not calculated but in the energy region some additional intraligand and interligand transitions are expected.

Acknowledgement

The crystallographic part was financed by funds allocated by the Ministry of Science and Higher Education to the Department of X-ray Crystallography and Crystal Chemistry, Institute of General and Ecological Chemistry, Technical University of Łódź.

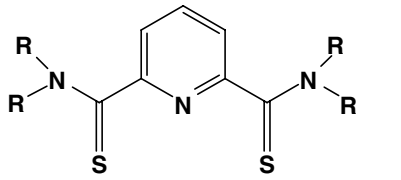
Appendix A. Supplementary material

CCDC 649418 and 649903 contain the supplementary crystallographic data for **1** and **2**. These data can be obtained free of charge via http://www.ccdc.cam.ac.uk/conts/retrieving.html, or from the Cambridge Crystallographic Data Centre, 12 Union Road, Cambridge CB2 1EZ, UK; fax: (+44) 1223-336-033; or e-mail: deposit@ccdc.cam.ac.uk.

References

[1] H.J. Roth, H. Fenner, in: Arzneistoffe, third ed., Deutscher Apotheker Verlag, Stuttgart, 2000, pp. 51–114.
[2] C.R. Harris, A. Thorarensen, Curr. Med. Chem. 11 (2004) 2213.
[3] K. Andries, P. Verhasselt, J. Guillemont, H.W. Gohlmann, J.M. Neefs, H. Winkler, J. Van Gestel, P. Timmerman, M. Zhu, E. Lee, P. Williams, D. de Chaffoy, E. Huitric, S. Hoffner, E. Cambau, C. Truffot-Pernot, N. Lounis, V. Jarlier, Science 307 (2005) 223.
[4] S. Vangapandu, M. Jain, R. Jain, S. Kaur, P.P. Singh, Bioorg. Med. Chem. 12 (2004) 2501.
[5] C. Sissi, M. Palumbo, Curr. Med. Chem. Anti-Canc. Agents 3 (2003) 439.
[6] E. Bossu, A.M. Agliano, N. Desideri, I. Sestili, R. Porra, M. Grandilone, M.G. Quaglia, J. Pharm. Biomed. Anal. 19 (1999) 539.
[7] T.C. Ko, M.J. Hour, J.C. Lien, C.M. Teng, K.H. Lee, S.C. Kuo, L.J. Huang, Bioorg. Med. Chem. Lett. 11 (2001) 279.
[8] J. Jampilek, M. Dolezal, J. Kunes, P. Vichova, D. Jun, I. Raich, R. O'Connor, M. Clynes, J. Pharm. Pharmacol. 56 (2004) 783.
[9] J. Jampilek, M. Dolezal, J. Kunes, P. Vichova, D. Jun, I. Raich, R. O'Connor, M. Clynes, Curr. Org. Chem. 8 (2004) 1235.
[10] J. Jampilek, M. Dolezal, V. Opletalova, J. Hartl, Curr. Med. Chem. 13 (2006) 117.
[11] J.L. Marco, C.M. Carmo, Mini Rev. Med. Chem. 3 (2003) 518.
[12] K. Mekouar, J.F. Mouscadet, D. Desmaele, F. Subra, H. Leh, D. Savoure, C. Auclair, J. d'Angelo, J. Med. Chem. 41 (1998) 2846.
[13] J. Polanski, F. Zouhiri, L. Jeanson, D. Desmaele, J. d'Angelo, J. Mouscadet, R. Gieleciak, J. Gasteiger, M. Le Bret, J. Med. Chem. 45 (2002) 4647.
[14] J. Polanski, H. Niedbala, R. Musiol, D. Tabak, B. Podeszwa, R. Gieleciak, A. Bak, A. Palka, T. Magdziarz, Acta Pol. Pharm. Drug Res. 61 (2004) 3.
[15] Y. Pommier, A.A. Johnson, C. Marchand, Nat. Rev. Drug. Discov. 4 (2005) 236.
[16] F. Zouhiri, M. Danet, C. Bernard, M. Normand-Bayle, J.F. Mouscadet, H. Leh, C.M. Thomas, G. Mbemba, J. d'Angelo, D. Desmaele, Tetrahedron Lett. 46 (2005) 2201.
[17] R. Musiol, J. Jampilek, V. Buchta, L. Silva, H. Niedbala, B. Podeszwa, A. Palka, K.A. Majerz-Maniecka, B. Oleksyn, J. Polanski, Bioorg. Med. Chem. 14 (2006) 3592.
[18] J. Jampilek, M. Dolezal, J. Kunes, V. Buchta, K. Kralova, Med. Chem. 1 (2005) 591.
[19] R. Musiol, J. Jampilek, K. Kralova, B. Podeszwa, J. Finster, H. Niedbala, A. Palka, J. Polanski. ECSOC-9 2005, November 1–30, http://www.usc.es/congresos/ecsoc/9/BOCNP/c005/index.htm.
[20] R. Musiol, J. Jampilek, K. Kralova, D.R. Richardson, D. Kalinowski, B. Podeszwa, J. Finster, H. Niedbala, A. Palka, J. Polanski. Bioorg. Med. Chem. 15 (2007) 1280.
[21] A.H. Velders, A.C.G. Hotze, G.A. van Albada, J.G. Haasnoot, J. Reedijk, Inorg. Chem. 39 (2000) 4073.
[22] N. Ahmad, J.J. Levinson, S.D. Robinson, M.F. Uttely, Inorg. Synth. 15 (1974) 48.
[23] M.J. Frisch, G.W. Trucks, H.B. Schlegel, G.E. Scuseria, M.A. Robb, J.R. Cheeseman, J.A. Montgomery Jr., T. Vreven, K.N. Kudin, J.C. Burant, J.M. Millam, S.S. Iyengar, J. Tomasi, V. Barone, B. Mennucci, M. Cossi, G. Scalmani, N. Rega, G.A. Petersson, H. Nakatsuji, M. Hada, M. Ehara, K. Toyota, R. Fukuda, J. Hasegawa, M. Ishida, T. Nakajima, Y. Honda, O. Kitao, H. Nakai, M. Klene, X. Li, J.E. Knox, H.P. Hratchian, J.B. Cross, C. Adamo, J. Jaramillo, R. Gomperts, R.E. Stratmann, O. Yazyev, A.J. Austin, R. Cammi, C. Pomelli, J.W. Ochterski, P.Y. Ayala, K. Morokuma, G.A. Voth, P. Salvador, J.J. Dannenberg, V.G. Zakrzewski, S. Dapprich, A.D. Daniels, M.C. Strain, O. Farkas, D.K. Malick, A.D. Rabuck, K. Raghavachari, J.B. Foresman, J.V. Ortiz, Q. Cui, A.G. Baboul, S. Clifford, J. Cioslowski, B.B. Stefanov, G. Liu, A. Liashenko, P. Piskorz, I. Komaromi, R.L. Martin, D.J. Fox, T. Keith, M.A. Al-Laham, C.Y. Peng, A. Nanayakkara, M. Challacombe, P.M.W. Gill, B. Johnson, W. Chen, M.W. Wong, C. Gonzalez, J.A. Pople, GAUSSIAN 03, Revision B.03, Gaussian, Inc., Pittsburgh, PA, 2003.
[24] D. Becke, J. Chem. Phys. 98 (1993) 5648.
[25] W. Lee, R. Yang, G. Parr, Phys. Rev. B 37 (1988) 785.
[26] J. Mennucci, J. Tomasi, Chem. Phys. 106 (1997) 5151.

[27] K. Eichkorn, F. Weigend, O. Treutler, R. Ahlrichs, Theor. Chim. Acc. 97 (1997) 119.
[28] D. Glendening, A.E. Reed, J.E. Carpenter, F. Weinhold, NBO (version 3.1).
[29] D. Becke, J. Chem. Phys. 98 (1993) 5648.
[30] M.V. Ovchinnikov, A.M. Ellern, I.A. Guzei, R.J. Angelici, Inorg. Chem. 40 (2001) 7014.
[31] S.M. Boniface, G.R. Clark, T.J. Collins, W.R. Roper, J. Organomet. Chem. 206 (1981) 109.
[32] H. Werner, W. Stuer, B. Weberndorfer, J. Wolf, Eur. J. Inorg. Chem. (1999) 1707.
[33] P.C. Junk, J.W. Steed, J. Organomet. Chem. 587 (1999) 191.
[34] A. Romero, A. Vegas, A. Santos, A.M. Cuadro, J. Chem. Soc., Dalton Trans (1987) 183.
[35] J.G. Haasnoot, W. Hinrichs, O. Weir, J.G. Vos, Inorg. Chem. 25 (1986) 4140.
[36] E. Bonfada, C. Maichle-Mossmer, J. Strahle, U. Abram, Z. Anorg. Allg. Chem. 625 (1999) 1327.
[37] G.M. Sheldrick, Acta Cryst. A46 (1990) 467.
[38] G.M. Sheldrick, SHELXL97, Program for the Solution and Refinement of Crystal Structures, University of Göttingen, Germany, 1997.
[39] G.M. Sheldrick, shelxtl: Release 4.1 for Siemens Crystallographic Research Systems, 1990.



Scheme 1.

tetrahedral geometry, whereas the cationic units contain two slightly distorted square planar mononuclear fragments with different types of interactions:

(i) square planar entities interacting through the S atoms yielding a dinuclear complex with a $[Cu_2(\mu\text{-}S)_2]$ core;
(ii) square planar moieties joined through the Cl ligands forming a dinuclear complex containing a $[Cu_2(\mu\text{-}Cl)_2]$ core.

It appeared that the mode of bridging was being governed by the choice of solvent. Magnetic susceptibility studies showed that both compounds showed an overall antiferromagnetic behaviour. For a better understanding of superexchange mechanisms in binuclear Cu(II) complexes [2,3] and in order to investigate the influence of increased steric bulk brought about by the replacement of ethyl groups by *i*-Pr and *i*-Bu at the terminal positions of the carboxamide side arms [Scheme 1], we have studied the structure, and magnetic behaviour of two new tetranuclear Cu(II) compounds containing *N*,*N*,*N*′,*N*′-tetraalkylpyridine-2,6-dithiocarboxamide (R = *iso*-butyl and *iso*-propyl) chelating ligands. The X-ray structures and magnetic data are discussed.

2. Experimental

2.1. Materials

All reactions were carried out in anhydrous solvents under dry N_2 atmosphere. Solvents and other reagents were dried using standard techniques as described previously [1]. The ligands *N*,*N*,*N*′,*N*′-tetraisopropylpyridine-2,6-dithiocarboxamide (S-dppt) and *N*,*N*,*N*′,*N*′-tetraisobutylpyridine-2,6-dithiocarboxamide (S-dbpt) were prepared as per the method given for S-dept [1] except that *N*,*N*,*N*′,*N*′-tetraisopropylpyridine-2,6-dicarboxamide(DPAP) [4] and *N*,*N*,*N*′,*N*′-tetraisobutylpyridine-2,6-dicarboxamide(DBAP) were respectively used as the starting materials. The latter compound was obtained as a white crystalline solid by using a similar method as reported for the preparation of DPAP. M.p., 61 °C. *Anal.* Calc. for $C_{23}H_{39}N_3O_2$: C, 70.95; H, 10.02; N, 10.79. Found: C, 70.68; H, 9.92; N, 10.60%. $\nu_{C=O}$: 1640 cm^{-1}. ^1H NMR ($CDCl_3$, TMS): $\delta = 0.82$ (d, 12H, CH_3), 0.94 (d, 12H, CH_3), 1.67 (hept, 2H, CH), 2.04 (d, 2H, CH), 3.20 (d, 4H, CH_2), 3.26 (d, 4H, CH_2), 7.49 (d, 2H, py), 7.77 (t, 1H, py). S-dppt is a yellow crystalline solid. M.p., 141 °C. *Anal.* Calc. for $C_{19}H_{31}N_3S_2$: C, 62.46; H, 8.49; N, 11.50. Found: C, 63.12; H, 7.84; N, 11.23%. S-dbpt is also a yellow crystalline solid. M.p. 87 °C. *Anal.* Calc. for $C_{23}H_{39}N_3S_2$: C, 65.55; H, 9.26; N, 9.97. Found: C, 66.13; H, 9.80; N, 9.47%.

2.2. $[\{Cu(S\text{-}dbpt)\}_2(\mu\text{-}Cl)_2][\{CuCl_2\}_2(\mu\text{-}Cl)_2]$ (**1**) and $[CuCl(S\text{-}dppt)]_2[\{CuCl_2\}_2(\mu\text{-}Cl)_2]$ (**2**)

Both compounds were prepared following exactly the same experimental procedure as that used for $[Cu_2Cl_2(\mu\text{-}S\text{-}dept)_2][Cu_2Cl_4(\mu\text{-}Cl)_2]$ [1] but by using S-dbpt and S-dppt as ligands and isobutanol/acetonitrile (1:1) and isopropanol/acetonitrile (1:1) as the reaction solvents for the preparation of **1** and **2**, respectively. **1**: M.p., 232 °C. *Anal.* Calc. for $C_{23}H_{39}N_3S_2Cl_4Cu_2$: C, 40.00; H, 5.65; N, 6.08; Cl, 20.6. Found: C, 39.69; H, 5.27; N, 5.86; Cl, 20.2%. IR (KBr pellet, cm^{-1}): 1598s, 1561m, 1528m, 1465s, 1342m, 1279m, 1252m, 1192w, 1150m, 1116m, 1088m, 1040m, 1026m, 983m, 925w, 814m, 780w, 722w, 702w, 640w, 602w, 568m. Molar conductance (Ω^{-1} cm^2 mol^{-1}): 194 (CH_3CN). UV–Vis [λ_{max}, nm ($\in$, M^{-1} cm^{-1})] in MeOH: 767 (198). **2**: M.p., 220 °C. *Anal.* Calc. for $C_{19}H_{31}N_3S_2Cl_4Cu_2$: C, 35.96; H, 4.88; N, 6.62; Cl, 22.4 Found: C, 35.14; H, 5.02; N, 6.41; Cl, 22.0%. IR (KBr pellet, cm^{-1}): 1597s, 1582m, 1518m, 1460s, 1375m, 1355m, 1294m, 1264m, 1138m, 1099m, 1026m, 1017w, 959w, 814w, 760w, 722w, 634m, 438w. Molar conductance (Ω^{-1} cm^2 mol^{-1}): 186 (CH_3CN). UV–Vis [λ_{max}, nm ($\in$, M^{-1} cm^{-1})] in MeOH: 762 (283).

2.3. Physical methods

Elemental analyses (C, H, N) were performed on a Perkin–Elmer model 2400 CHN elemental analyzer. Chlorine was estimated as chloride by Volhard's method. IR spectra were recorded as KBr pellets on a Perkin–Elmer RX-1 FTIR spectrophotometer. Molar conductances were measured using a digital conductivity bridge model CC601. The UV–Vis spectra were recorded on a JASCO V-530 UV–Vis spectrophotometer. Magnetic susceptibility measurements for powdered samples of **1** and **2** were carried out at the "Unitat de Mesures Magnètiques" of the Universitat de Barcelona with a Quantum design SQUID MPMS-XL susceptometer. The magnetic susceptibility data were recorded in the 2–300 K temperature range under magnetic fields of 500 G (2–30 K) and 10 000 G (2–300 K).

2.4. X-ray crystallography

Crystallization of $[\{Cu(S\text{-}dbpt)\}_2(\mu\text{-}Cl)_2][\{CuCl_2\}_2(\mu\text{-}Cl)_2]$ **1** and $[CuCl(S\text{-}dppt)]_2[\{CuCl_2\}_2(\mu\text{-}Cl)_2]$ **2** by slow evaporation of their saturated solutions in acetonitrile and isopropanol, respectively, at room temperature yielded good single crystals. The data were collected on a Siemens P4 single crystal diffractometer using graphite

Table 1
Crystal data and structure refinement for $[\{Cu(S\text{-}dbpt)\}_2(\mu\text{-}Cl)_2][\{CuCl_2\}_2(\mu\text{-}Cl)_2]$ **1** and $[CuCl(S\text{-}dppt)]_2[\{CuCl_2\}_2(\mu\text{-}Cl)_2]$ **2**

Identification code	**1**	**2**
Empirical formula	$C_{46}H_{78}Cl_8Cu_4N_6S_4$	$C_{19}H_{31}Cl_4Cu_2N_3S_2$
Formula weight	1381.22	634.47
Temperature (K)	293(2)	293(2)
Wavelength (Å)	0.71069	0.71069
Crystal system	triclinic	monoclinic
Space group	$P\bar{1}$ (#2)	$P2_1/c$
Unit cell dimensions		
a (Å)	8.547(5)	7.708(5)
b (Å)	13.695(5)	29.127(5)
c (Å)	13.849(5)	12.016(5)
α (°)	75.370(5)	93.280(5)
β (°)	87.430(5)	
γ (°)	89.120(5)	
Volume (Å^3)	1566.9(12)	2693(2)
Z	1	4
D_{calc} (Mg/m^3)	1.464	1.565
Absorption coefficient (mm^{-1})	1.849	2.143
$F(000)$	712	1296
Crystal size (mm)	$0.3 \times 0.2 \times 0.2$	$0.3 \times 0.15 \times 0.15$
θ Range for data collection (°)	1.52–25.00	2.65–25.02
Limiting indices	$0 \leqslant h \leqslant 8$, $-15 \leqslant k \leqslant 15$, $-16 \leqslant l \leqslant 16$	$0 \leqslant h \leqslant 9$, $0 \leqslant k \leqslant 34$, $-14 \leqslant l \leqslant 14$
Reflections collected/ unique [R_{int}]	5577/5179 [0.0299]	5168/4692 [0.1063]
Completeness to theta	25.00°, 94.0%	25.02°, 98.5%
Absorption correction	empirical psi scan	empirical psi scan
Refinement method	full-matrix least-squares on F^2	full-matrix least-squares on F^2
Data/restraints/parameters	5179/0/307	4692/0/271
Goodness-of-fit on F^2	0.962	1.022
Final R indices [$I > 2\sigma(I)$]	$R_1 = 0.0454$, $wR_2 = 0.1134$	$R_1 = 0.1224$, $wR_2 = 0.2977$
Largest difference peak and hole (e A^{-3})	0.508 and −0.715	0.768 and −0.770
CCDC number	620447	620448

monochromatized Mo Kα radiation ($\lambda = 0.71073$ Å). Table 1 shows the unit cell parameters and other crystallographic details. The quality of the crystals for compound **2** was not good as is apparent from high value for R_{int} for the measured data. Data collection and cell refinement were done with XSCANS [5]. The data were corrected for Lorentz and polarization effects. Emperical absorption corrections were performed for both the compounds using psi scans. The structures were solved by direct methods and refined anisotropically by the full matrix least squares method. All the hydrogen atoms were fixed geometrically as riding atoms with a displacement parameter equal to 1.2 (CH, CH_2) or 1.5 (CH_3) times that of the parent atoms. Data reduction, structure solutions, refinement and molecular graphics were performed using SHELXLTL-PC [6]. Torsion angles and least square planes were calculated by using PARST [7].

3. Results and discussion

3.1. Synthesis and structure

Compounds **1** and **2** were obtained in about 80% yield by refluxing anhydrous $CuCl_2$ with S-dbpt and S-dppt, respectively in anhydrous CH_3CN mixed with the corresponding alcohol (isobutanol or isopropanol) in a 1:1 ratio (on a volume basis). The same product was obtained in each case irrespective of whether the metal–ligand ratio was 1:1 or 2:1. Both compounds are air and moisture stable and were characterized through elemental analyses, IR data, conductivity measurements, X-ray crystallography and low temperature magnetic measurements. The compounds readily dissolve in many polar organic solvents. Millimolar solutions of complexes **1** and **2** in CH_3CN show significant dissociation but due to the large sizes of the cation and anion, the conductivities are less than the expected values for bi-bivalent and uni-bivalent electrolytes [8].

Crystallization of **1** and **2** by slow evaporation of their saturated solutions in acetonitrile and isopropanol, respectively, at room temperature yields good single crystals. The relevant crystallographic data and selected bond lengths and bond angles are summarized in Tables 1 and 2, respectively. The crystal structure for **1** is depicted in Fig. 1. The compound contains a cationic binuclear unit, $[\{Cu(S\text{-}dbpt)\}_2(\mu\text{-}Cl)_2]^{2+}$ and an anionic binuclear unit $[\{CuCl_2\}_2(\mu\text{-}Cl)_2]^{2-}$. In the cationic fragment, each copper atom is pentacoordinated by the pyridine N atom, two S atoms of the S-dbpt ligand and by two chloro ligands acting in the bridging mode. The bridging through chloro groups is unsymmetrical with one distance being 2.233(2) Å and the other being 2.723(2) Å. Each metal atom has a slightly distorted square pyramidal geometry [Reedijk's factor is 0.05, denoting an almost regular square

Table 2
Important bond angles and distances in complexes **1** and **2**

	1	2
Cu(1)–N(1)	1.993(4)	1.985(1)
Cu(1)–Cl(1)	2.233(2)	2.201(4)
Cu(1)–S(1)	2.305(2)	2.272(4)
Cu(1)–S(2)	2.331 (2)	2.281(4)
Cu(1)–Cl(1)	2.723(2)$^{\#1}$	
Cu(2)–Cl(4)	2.169(2)	2.198(5)
Cu(2)–Cl(3)	2.176(2)	2.202(6)
Cu(2)–Cl(2)	2.303(2)	2.327(4)
Cu(2)–Cl(2)	2.328(2)$^{\#2}$	2.322(5)$^{\#3}$
Cu(2)···Cu(2)	3.354	3.330
Cl(3)–Cu(2)–Cl(4)	104.4	103.9
Cl(4)–Cu(2)–Cl(2)$^{\#4}$	98.90$^{\#4}$	97.62$^{\#5}$
Cl(3)–Cu(2)–Cl(2)$^{\#4}$	136.0$^{\#4}$	139.2$^{\#5}$
Cl(4)–Cu(2)–Cl(2)	139.9	137.4
Cl(3)–Cu(2)–Cl(2)	97.58	97.97
Cl(2)–Cu(2)–Cl(2)$^{\#4}$	87.17$^{\#4}$	88.50$^{\#5}$

Symmetry transformations used to generate equivalent atoms for this table: #1 $-x, -y, -z+2$; #2 $-x+1, -y+1, -z+1$; #3 $-x+2, -y, -z+2$; #4 $1-x, 1-y$; #5 $1-z; 2-x, -y, 2-z$.

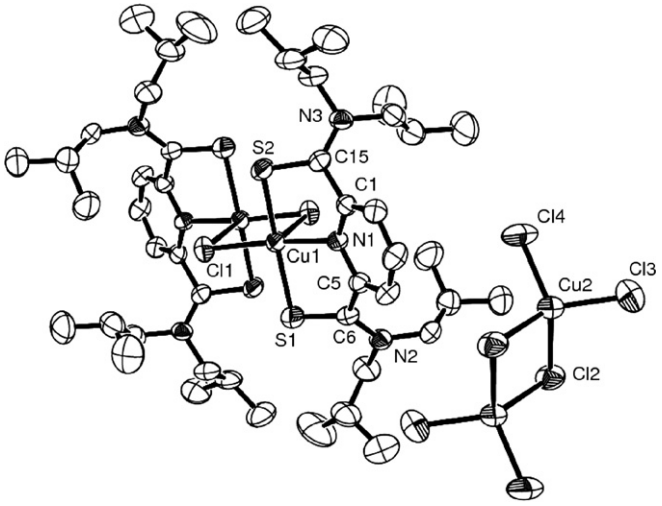


Fig. 1. ORTEP drawing of compound **1** and the numbering scheme used in the structure analysis.

pyramidal geometry] [9], where the basal plane is defined by N1, S1, S2 and Cl1. The apical position of the square pyramid is occupied by one of the chlorine atoms coordinated to the second Cu metal center, acting as a bridging ligand. The structure may be imagined as two square pyramids sharing a basal to apical edge. The Cu1 atom is 0.223(1) Å above the mean plane defined by the four basal atoms. The Cu1···Cu1* distance is 3.355 Å and the Cu–Cl–Cu angle is 84.6°. Complexes containing a $Cu_2(\mu\text{-}Cl)_2$ core, containing five coordinated metal ions in a square pyramid geometry, generally have a base sharing arrangement in which the apical groups point in opposite directions. The other two possible arrangements of the polyhedra are parallel (parallel disposition of the basal planes) and perpendicular (perpendicular disposition of the basal planes) [2b]. The present dinuclear unit is in the parallel mode, which makes the basal atoms of the two sharing polyhedra parallel to each other (Fig. 2). A mean plane passing through the two thioamide groups indicates that the C1, C15, S2, N3 and C5, C6, S1, N2 planes are twisted with respect to the pyridine ring by 47.7(1)° and 46.1(1)°, respectively.

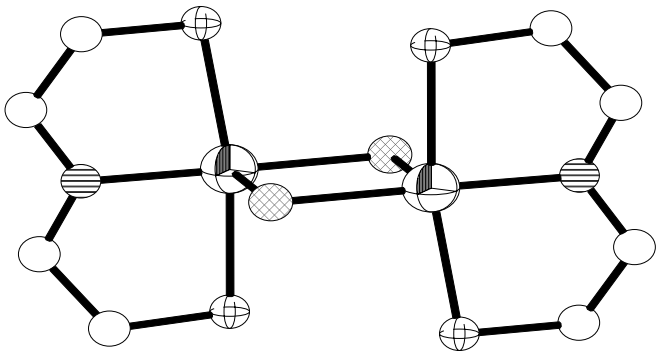


Fig. 2. Core plot of the cationic complex present in compound **1**, showing the parallel disposition of the basal planes of the square pyramids around each Cu(II) ion.

The anionic moiety in complex **1**, $[\{CuCl_2\}_2(\mu\text{-}Cl)_2]^{2-}$, consists of two tetracoordinated Cu metal centers bridged by two chloro anions and each Cu atom is also bonded to two terminal Cl ligands. The $[Cu_2(\mu\text{-}Cl)_2]$ core is planar and the Cu···Cu^{i} distance is 3.354(1) Å (where i = $-x$, $-y$, $2-z$) and the Cu–(μ-Cl)–Cu^{i} angle is 92.8°. Torsion angles of 40° and 44° are observed for Cu(2)–Cl(2)–Cu(2)^{i}–Cl(4) and Cu(2)–Cl(2)–Cu(2)^{i}–Cl(3), respectively. All the chlorine atoms in the anion $[Cu_2Cl_4(\mu\text{-}Cl)_2]^{2-}$ interact with hydrogen atoms of neighboring symmetry related cations (Fig. 3). The non-bridging chloro ligand Cl(3)^{ii} (where ii = $-x+1$, $-y+1$, $-z+2$) is an acceptor to two interactions, i.e., with the pyridine H(4) and Bu H(13B) hydrogen atoms of a cationic complex [2.885(2) and 2.883(3) Å, respectively]. The other non-bridging chloro group Cl(4)^{iii} (where iii = $-x+1$, $-y+1$, $-z+2$) is involved in one H-bonding interaction with the butyl H16B hydrogen atom of another cationic complex [2.837(2) Å]. The bridging chloro groups Cl(2)^{iv} (where iv = $-x+1$, $-y+1$, $-z+2$) are each involved in interactions with H(8) to form a C(8)–H(8)···Cl(2)^{iv} hydrogen bond, each one with a different cationic complex [2.839(1) Å]. In all cases, the C–H···Cl distances are shorter than 2.95 Å (the sum of van der Waals radii of H and Cl) [10]. The anion is thus involved in a total of eight weak H-bonding interactions of the type C–H···Cl (six between non-bridging and two between bridging chloro groups), with six dinuclear cationic complexes.

The structure of compound **2** consists of two cationic units, $[CuCl(S\text{-}dppt)]^{+}$, and the anionic dinuclear $[Cu_2Cl_4(\mu\text{-}Cl)_2]^{2-}$ (Fig. 4). The cationic fragment is monomeric with a distorted square planar geometry around the Cu(1) atom. Mean plane calculations indicated that N1, S1, S2 and Cl1 do not lie in one plane. The ligand coordinates through the two thioamide S atoms and pyridine N atom. The fourth coordination site is occupied by the chlorine atom Cl(1).

The anionic fragment in complex **2** shows identical structural features as those observed for **1**. The Cu2···Cu2^{i} distance is 3.330 Å and the twist angle phi, Cu2^{i}–Cl2–Cu2–Cl4 (where i = $-x$, $-y$, $-z$), is 42.3°. Comparison of bond distances of compounds **1** and **2** (Table 2) reveals that all the metal ligand bond distances are shorter in **2**. This may suggest that the metal ion is more tightly held by the S-dppt ligand. This is further borne by the fact that in compound **2**, Cu(1) lies 0.0343(4) Å above the mean plane, whereas the metal ion is 0.223(1) Å above the mean plane in the case of the S-dbpt compound. This probably decreases the area available around the Cu^{2+} ion in the case of compound **2** for coordination by another ligand, and so only a monomer having a square planar geometry is formed. It appears that the mode of bridging is governed by the nature of the solvent and the steric factors due to the increased size of the groups attached to the carboxamide N atoms of the side arms [1].

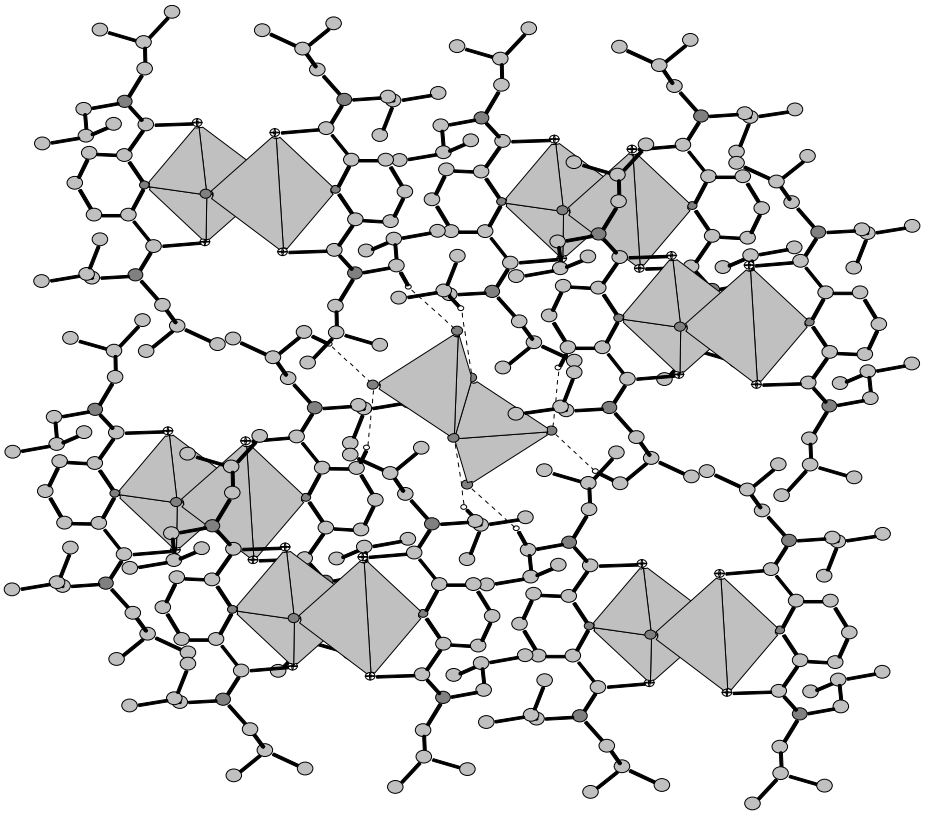


Fig. 3. Plot showing the weak C–H···Cl interaction between the anionic dinuclear complex $[Cu_2Cl_4(\mu\text{-}Cl)_2]^{2-}$ and the cationic dinuclear complex in compound **1**.

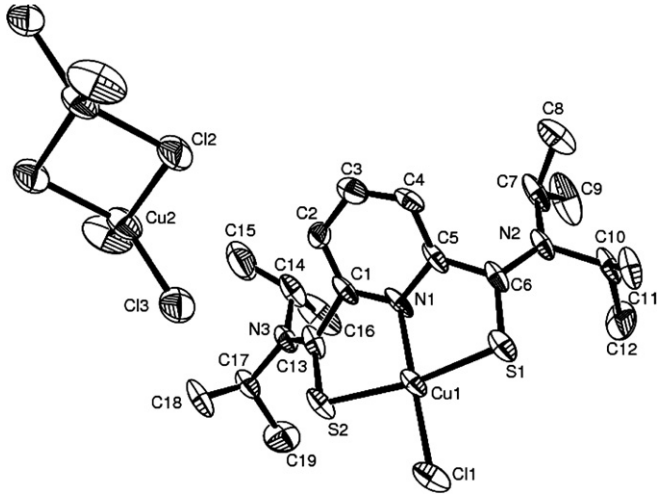


Fig. 4. The coordination modes of compound **2**.

3.2. Magnetic properties

The magnetic behaviour of compounds **1** and **2** has been investigated in the 2–300 K temperature range. Fig. 5 shows a plot of $\chi_M T$ *versus* T for compound **1**. The $\chi_M T$ product at room temperature is 1.68 $cm^3\ mol^{-1}$ K and this value increases upon cooling, reaching a maximum value at 2 K (1.82 $cm^3\ mol^{-1}$ K). This behaviour is indicative of a ferromagnetic interaction. Consequently, bearing in mind that this compound is constituted of two dinuclear species, at least one of them must show a ferromagnetic interaction between the Cu(II) ions.

The experimental data corresponding to the two dinuclear species in compound **1**, $\chi_M T = (\chi_M T)_1 + (\chi_M T)_2$, were fitted in Eq. (1), which was obtained using the Bleaney–Bowers equation [11] based on the spin Hamiltonian $H = -JS_1 \cdot S_2$ for each dinuclear species.

$$\chi_M T = (2Ng_1^2\beta^2/[k(3+\exp(-J_1/kT))]) + (2Ng_2^2\beta^2/[k(3+\exp(-J_2/kT))]) \quad (1)$$

The best fit was obtained with $J_1 = -0.77\ cm^{-1}$, $g_1 = 2.0$, $J_2 = 3.19\ cm^{-1}$, $g_2 = 2.21$ and $R = 1.6 \times 10^{-5}$.

For compound **2**, the $\chi_M T$ *versus* T plot is shown in Fig. 6. This compound is constituted of two mononuclear cationic species and one dinuclear anionic species, thus the $\chi_M T$ values correspond to four Cu(II) ions. The $\chi_M T$ values are around 1.5 $cm^3\ mol^{-1}$ K, from room temperature to 13 K. On cooling below this temperature, $\chi_M T$ decreases reaching a value of 1.38 $cm^3\ mol^{-1}$ K at 2 K. For this compound, the $\chi_M T$ values are the sum of two contributions, from the dinuclear complex and from the two mononuclear complexes, $\chi_M T = (\chi_M T)_{dinuclear} + 2(\chi_M T)_{mononuclear}$, therefore the experimental data were fitted by

$$\chi_M T = (2Ng_d^2\beta^2/[k(3+\exp(-J/kT))]) + 2(Ng_m^2\beta^2/4k) \quad (2)$$

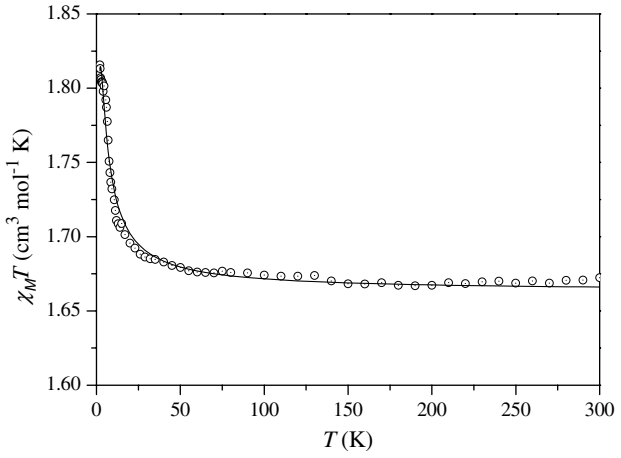


Fig. 5. $\chi_M T$ *vs.* T plot for **1**. Solid line corresponds to the best fit obtained.

The best fit was obtained with $J = -0.83\ \text{cm}^{-1}$, $g_d = g_m = 2.0$ and $R = 9.9 \times 10^{-6}$.

Compound **1**, with anionic and cationic dinuclear complexes, shows two kinds of magnetic interactions, ferromagnetic and antiferromagnetic, and for assignment of these to each appropriate dinuclear entity it is necessary to compare the magneto-structural values with analogous compounds. A number of compounds containing the $[\{CuCl_2\}_2(\mu\text{-}Cl)_2]^{2-}$ anion are reported in the literature. The magnetic interaction in this species is very sensitive to the structural parameters, and the magnetic coupling constant is generally found between +53 and $-93\ \text{cm}^{-1}$. In most compounds, this species is planar [12–16], in some cases, the counter cation could be coordinated in an axial position [14,16,17,20]. In several compounds, an interaction between the dinuclear anions is observed and the compound is described as a one-dimensional system [14–16,20]. In other cases, the compound is formulated as $MCuCl_3$ and shows an alternating chain structure [18–20]. Very few systems show isolated dinuclear anions, and in these cases, the geometry around the Cu(II) ions is very sensitive to the volume of the counter cation. Complexes with EPh_4^+ (E = P, As, Sb) as a cation show a pseudo-tetrahedral distortion

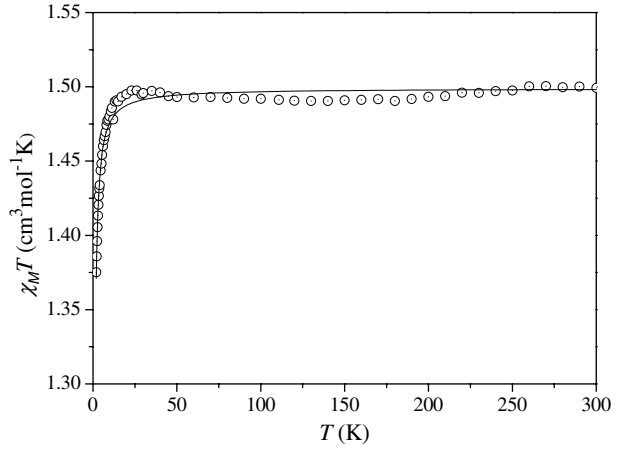


Fig. 6. $\chi_M T$ *vs.* T plot for **2**. Solid line corresponds to the best fit.

and the magnetic interaction is ferromagnetic [21,22]. For these compounds the ferromagnetic interaction decreases from $+80\ \text{cm}^{-1}$ for the PPh_4^+ $+40\ \text{cm}^{-1}$ for the $AsPh_4^+$ complex, due to the diminution of the Cu–Cl_b–Cu angle from 93.7° to 93.3°.

It is well known that for complexes with a planar Cu_2X_2 core, the magnetic interaction is very sensitive to the CuXCu angle, being ferromagnetic when this angle is close to 90° [12]. Some studies are reported in the literature about the effect of the distortions around the Cu(II) ions on the magnetic properties [1,23–25]. Deviation from planarity between the Cl_tCuCl_t and Cl_bCuCl_b planes affects the energy of the ϕ_a and ϕ_s orbitals. The minimum energy gap is expected for angles around 35–45°, for larger angles, this gap increases again. For the PPh_4^+ compound, the dihedral angle between the Cl_tCuCl_t and Cl_bCuCl_b planes (τ) is 50° [21,22].

Structural parameters for the $[\{CuCl_2\}_2(\mu\text{-}Cl)_2]^{2-}$ anion in **1** and **2** are very close, consequently the magnetic coupling constant J must be similar. As it was indicated, compound **2** contains only this dinuclear species with a very weak antiferromagnetic coupling ($J = -0.83\ \text{cm}^{-1}$), therefore the magnetic coupling constant for this anionic species in compound **1** could be assigned to J_1 ($-0.77\ \text{cm}^{-1}$). However, for the analogous compound reported in the literature with the ethyl derivative ligand, $[\{Cu(S\text{-}dept)\}_2(\mu\text{-}Cl)_2][\{CuCl_2\}_2(\mu\text{-}Cl)_2]$ [1], the magnetic interaction due to the anionic species was antiferromagnetic, with a J value of $-19\ \text{cm}^{-1}$. As it was indicated, a ferromagnetic interaction could be found for $\alpha \sim 90°$ and $\tau \sim 40°$. The three complexes show Cu–Cl_b–Cu angles (α) close to 90°, and quite different dihedral angles between the Cl_tCuCl_t and Cl_bCuCl_b planes (τ): for the species present in **1** and **2** this angle is 56°, while for the ethyl compound it was 63° [1]. Therefore the τ angle for the species in compounds **1** and **2** are closest to the ferromagnetic situation.

So, if the magnetic properties of the anionic species of **1** are described by J_1, the cationic species $[\{Cu(S\text{-}dbpt)\}_2(\mu\text{-}Cl)_2]^{2+}$ must show ferromagnetic behaviour with a magnetic coupling constant $J_2 = 3.19\ \text{cm}^{-1}$. The kind and magnitude of the magnetic interaction is similar to the reported value for the analogous cationic complex $[\{Cu(S\text{-}dept)\}_2(\mu\text{-}Cl)_2]^{2+}$ [1], in agreement with the resemblance of the structural parameters in the two complexes.

For dinuclear dichlorobridged pentacoordinated copper complexes, the local geometry around the Cu(II) ions is generally square pyramid, and three relative arrangements of the square pyramids have been found: (a) the square pyramids sharing basal edge (coplanar bases); (b) the square pyramids sharing a base-to-apex edge so that the Cl atom situated at the vertex of one base becomes the apical vertex of the other square pyramid, and just the opposite happens for the other Cl bridging ligand (parallel bases); and (c) the two square pyramids sharing a base-to-apex edge, but in this case, the apical chloro ligand of one pyramid is also the apical atom of the other square pyramid (perpendicular bases) [2].

Table 3
Structural and magnetic data of some di-μ-chloro-bridged Cu(II) complexes with parallel basal planes ($H = -JS_1 \cdot S_2$)

Complex	α (°)	α/R[a]	J (cm^{-1})	d(Cu–Cl$_b$)[b] (Å)	R (Å)
[{Cu(TMSO)$_2$Cl}$_2$(μ-Cl)$_2$] [27]	88.5	29.3	−16.0	2.28	3.02
[{Cu(2-pic)Cl}$_2$(μ-Cl)$_2$] [28]	100.6	29.9	−7.4	2.29	3.36
[{Cu(dmgH)Cl}$_2$(μ-Cl)$_2$] [29]	88.0	32.6	0.6	2.24	2.70
[{Cu(terpy)}$_2$(μ-Cl)$_2$](PF$_6$)$_2$ [30]	89.9	33.0	−5.9	2.22	2.72
[{Cu(dien)}$_2$(μ-Cl)$_2$](ClO$_4$)$_2$ [31]	92.0	33.5	+0.4	2.29	2.75
[{Cu(apyhist)}$_2$(μ-Cl)$_2$](ClO$_4$)$_2$ [32]	87.5	31.9	−3.1	2.27	2.74
[Cu(HL^1)Cl$_2$]$_2$(ClO$_4$)$_2$ [33]	94.7	32.4	+10.7	2.29	2.92
[{Cu(L^2)Cl}$_2$(μ-Cl)$_2$(ClO$_4$)](ClO$_4$) [33]	86.1	32.7	−1.9	2.28	2.64
[{Cu(Mebta)$_2$Cl}$_2$(μ-Cl)$_2$] [34]	88.1	33.5	+6.7	2.30	2.63
[{Cu(S-dept)}$_2$(μ-Cl)$_2$][CuCl$_3$(EtOH)] [1]	84.3	30.0	+4.5	2.23	2.81
[{Cu(S-dbpt)}$_2$(μ-Cl)$_2$][{CuCl$_2$}$_2$(μ-Cl)$_2$]	84.6	31.1	+3.2	2.23	2.72

Ligand abbreviation: TMSO: tetramethylene sulfoxide; baamo; 8-amino-5-aza-4-methyl-3-octene-2-onate; 2-pic: 2-methylpyridine; dmgH: dimethylglyoxime; terpy: 2,2′:6′,2″-terpyridine; dien: diethylenetriamine; apyhist: (4-imidazolyl)ethylene-2-amino-1-ethylpyridine; L^1: 1,5-bis(pyridin-4-ylmethyl)-1,5-diazacyclooctane; L^2: 1-(pyridin-2-ylmethyl)-1,4-diazacycloheptane; Mebta: methylbenzotriazole; S-dept: *N*,*N*,*N*′,*N*′-tetraethylpyridine-2,6-dithiocarboxamide.

[a] $R = d(\text{Cu–Cl}_{\text{apical}})$.

[b] $\text{Cl}_b = \text{Cl}_{\text{basal}}$.

Extensive magneto-structural correlations for these kinds of complexes have been reported. These studies show that the Cu–Cl–Cu (α) angle and the longer Cu–Cl distance (*R*) have a strong influence on the magnetic interaction. A correlation between the singlet–triplet gap (ΔE_{S-T}) and α/*R* [26] was found, with a ferromagnetic behaviour observed for α/*R* values between 32.6 and 34.8. However, this rule is only valid for complexes with similar arrangement of the square pyramids [2b].

Table 3 summarizes the most relevant structural parameters and magnetic coupling constants for complexes with parallel basal planes. These compounds show a weak ferro or antiferromagnetic interaction, with coupling constant values between −16 and +11 cm^{-1}. For Cu(II) ions in a square pyramidal geometry, the d orbital of each copper involved in the magnetic interaction is the x^2–y^2 orbital, and these orbitals are parallel. So, in an ideal case, the overlap through the chloride bridges must be negligible, and a ferromagnetic behaviour must be attended. However, a small distortion of the coordination polyhedron and Cu–Cl–Cu angles different from 90° create an overlap route through the bridge, and an antiferromagnetic coupling could be observed.

In agreement with the Hatfield's rule [26], the majority of ferromagnetic compounds reported in Table 3 show a quotient α/*R* between 32.6 and 34.8. However, the cationic complexes [{Cu(S-dept)}$_2$(μ-Cl)$_2$]$^{2+1}$ and [{Cu(S-dbpt)}$_2$(μ-Cl)$_2$]$^{2+}$ (**1**) show minor values of α/*R*. These complexes have two sulfur atoms coordinated to the Cu(II) ions in the basal plane of the square pyramid, while the other compounds have N or O donor ligands.

3.3. Molecular orbitals

Extended Hückel calculations based on the crystallographic coordinates of compounds **1** and **2** have been carried out with the CACAO program [35], with the aim to compare the present results with the analogous complex formed with the S-dept ligand [1]. For the cationic species a major overlap of population between the Cu-donor atom (N, S or Cl) was observed for the complex in **2**, more than in complex **1**, in agreement with the shorter distances found in **2**. Moreover, the singly occupied molecular orbital (SOMO), with an important contribution of the x^2–y^2 orbital of the Cu(II) ion, shows a small contribution of the pyridine ring in complex **2**, and it is not present in **1** or in the analogous dinuclear cationic species obtained with the S-dept ligand [1].

A comparison of the energy gap between the two SOMO's for the dinuclear species with S-dbpt (in **1**) (0.042 eV) and S-dept (0.011 eV) [1] agrees with the magnetic properties. Both compounds show a very small energy gap and a ferromagnetic interaction is observed. Moreover, the smaller gap corresponds to the compound with a major ferromagnetic coupling constant (4.5 cm^{-1} as compared to 3.2 cm^{-1} for **1**).

For the anionic species [{CuCl$_2$}$_2$(μ-Cl)$_2$]$^{2-}$ the energy gap is greater than for the cationic species, and is similar for both compounds (0.367 eV for complex **1** and 0.354 eV for complex **2**). A major value was reported for [{CuCl}$_2$(μ-S-dept)$_2$] [{CuCl$_2$}$_2$(μ-Cl)$_2$]^1 (0.435 eV), which showed greater antiferromagnetic coupling ($J = -19$ cm^{-1}).

Acknowledgement

Montse Corbella thanks the Ministerio de Educación y Ciencia for financial support (CTQ2006-01759/BQU).

Appendix A. Supplementary material

CCDC 620447 and 620448 contain the supplementary crystallographic data for **1** and **2**. These data can be obtained free of charge via http://www.ccdc.cam.ac.uk/

conts/retrieving.html, or from the Cambridge Crystallographic Data Centre, 12 Union Road, Cambridge CB2 1EZ, UK, fax: (+44) 1223-336-033, or e-mail: deposit@ccdc.cam.ac.uk. Supplementary data associated with this article can be found, in the online version, at doi:10.1016/j.poly.2007.07.022.

References

[1] R. Kapoor, A. Kataria, P. Venugopalan, P. Kapoor, M. Corbella, M. Rodriguez, I. Romero, A. Llobet, Inorg. Chem. 43 (2004) 6699.

[2] (a) P. Kapoor, A. Pathak, R. Kapoor, P. Venugopalan, M. Corbella, M. Rodriguez, J. Robles, A. Llobet, Inorg. Chem. 41 (2002) 6153;
(b) M. Rodriguez, A. Llobet, M. Corbella, Polyhedron 19 (2000) 2483;
(c) M. Rodriguez, A. Llobet, M. Corbella, A.E. Martell, J. Reibenspies, Inorg. Chem. 38 (1999) 2328.

[3] (a) E. Pardo, J. Faus, M. Julve, M.C. Munoz, J. Cano, X. Ottenwaelder, Y. Journaux, R. Carrasco, G. Blay, I. Fernandez, R. Ruiz-Garcia, J. Am. Chem. Soc. 125 (2003) 10770;
(b) G. Psomas, C.P. Raptopoulou, L. Jordanidis, C. Dendrinou-Samara, V. Tangoulis, D.P. Kessissoglou, Inorg. Chem. 39 (2000) 3042;
(c) S. Ferlay, A. Jouaiti, M. Loi, M.W. Hosseini, A. De Cian, P. Turek, New J. Chem. (2003) 1801;
(d) J. Cano, E. Ruiz, P. Alemany, F. Lloret, S. Alvarez, J. Chem. Soc., Dalton Trans. (1999) 1669.

[4] T.L. Borgne, J. Benech, S. Floquet, G. Beernardinelli, C. Aliprandini, P. Bettens, C. Piguet, J. Chem. Soc., Dalton Trans. (2003) 3856.

[5] XSCANS, X-ray Single Crystal System, Version 2.1, Siemens Analytical X-ray Instruments Inc., Madison, WI, USA, 1994.

[6] G.M. Sheldrick, SHELXTL-PC, Release 5.03, Siemens Analytical X-ray Instruments Inc., Madison, WI, USA, 1995.

[7] M. Nardelli, Comput. Chem. (1983) 95.

[8] W.J. Geary, Coord. Chem. Rev. (1971) 81.

[9] A.W. Addison, T.N. Rao, J. Reedijk, J.V. Rijn, G.C. Verschoor, J. Chem. Soc., Dalton Trans. (1984) 1349.

[10] L. Brammer, E.A. Bruton, P. Sherwood, Cryst. Growth Des. (2001) 277.

[11] B. Bleaney, K.D. Bowers, Proc. Royal Soc., Ser. A 214 (1952) 451.

[12] A. Kobayashi, A. Sato, E. Arai, H. Hobayashi, C. Faulmann, N. Kushch, P. Cassoux, Solid State Commun. 103 (1997) 371.

[13] R.D. Willet, R. Butcher, C.P. Landee, B. Twamley, Polyhedron 24 (2005) 2222.

[14] B. Scott, U. Geiser, R.D. Willet, B. Patyal, C.P. Landee, R.E. Greeney, T. Manfredini, G.C. Pellacani, A.B. Corradi, L.P. Battaglia, Inorg. Chem. 27 (1988) 2454.

[15] A. Colombo, L. Menabue, A. Motori, G.C. Pellacani, W. Porzio, F. Sandrolini, R.D. Willet, Inorg. Chem. 24 (1985) 2900.

[16] B. Scott, R.D. Willet, Inorg. Chim. Acta 141 (1988) 193.

[17] J.T. Blanchette, R.D. Willet, Inorg. Chem. 27 (1988) 843.

[18] S. O'Brien, R.M. Gaura, C.P. Landee, B.L. Ramakhrishna, R.D. Willet, Inorg. Chim. Acta 141 (1988) 83.

[19] U. Geiser, R.M. Gaura, R.D. Willet, D.X. West, Inorg. Chem. 25 (1986) 4203.

[20] L.W. Ter Haar, W.E. Hatfield, Inorg. Chem. 24 (1985) 1022.

[21] M. Textor, E. Dubler, H.R. Oswald, Inorg. Chem. 13 (1974) 1361.

[22] W.E. Estes, J.R. Wasson, J.W. Hall, W.E. Hatfield, Inorg. Chem. 17 (1978) 3657.

[23] P.J. Hay, J.C. Thibeault, R. Hoffmann, J. Am. Chem. Soc. 20 (1975) 4884.

[24] O. Castell, J. Miralles, R. Caballol, Chem. Phys. 179 (1994) 377.

[25] A. Bencini, D. Gatteschi, J. Am. Chem. Soc. 108 (1986) 5763.

[26] W.E. Marsh, K.C. Patel, W.E. Hatfield, D.J. Hodgson, Inorg. Chem. 22 (22) (1983) 511.

[27] D.D. Swank, G.F. Needham, R.D. Willet, Inorg. Chem. 18 (1979) 761.

[28] W.E. Marsh, W.E. Hatfield, D.J. Hodgson, Inorg. Chem. 2 (1982) 2679.

[29] M. Mégnamisi-Bélombé, M.A. Novotny, Inorg. Chem. 19 (1980) 2470.

[30] T. Rojo, M.I. Arriortua, J. Ruiz, J. Chem. Soc., Dalton Trans. (1987) 285.

[31] (a) S.K. Hoffmann, D.K. Towle, W.A. Hatfield, K. Wieghardt, P. Chaudhuri, J. Weiss, Mol. Cryst. Liq. Cryst. 107 (1984) 161;
(b) S.K. Hoffmann, D.K. Towle, W.A. Hatfield, P. Chaudhuri, K. Wieghardt, Inorg. Chem. 24 (1985) 1307.

[32] W.A. Alves, R.H. Almeida Santos, A. Paduan-Filho, C.C. Becerra, A.C. Borin, A.M. Da Costa Ferreira, Inorg. Chim. Acta 357 (2004) 2269.

[33] M. Du, Y.-M. Guo, X.-H. Bu, J. Ribas, M. Monfort, New J. Chem. 26 (2002) 645.

[34] O.K. Skorda, T.C. Stamatatos, A.P. Vafiadis, A.T. Lithoxoidou, A. Terzis, S.P. Perlepes, J. Mrozinski, C.P. Raptopoulou, J.C. Plakatouras, E.G. Bakalbassis, Inorg. Chim. Acta 358 (2005) 565.

[35] C. Mealli, D.M. Proserpio, A. Lenco, J. Chem. Educ. 67 (1990) 399.

to multinuclear systems [5–7]. Tridentate and tetradentate ligands such as salen-type Schiff bases are quite capable of forming complexes with certain metal ions which can exhibit unusual coordination, high thermodynamic stability and kinetic inertness. The coordination geometry of these complexes depends upon the electronic configuration and size of the metal ions, repulsions between non-bonded atoms in different ligand arms, and the inherent rigidity due to the presence of aromatic rings, etc. [8]. Such topologies are also based on strong metal–ligand covalent bonds [9] and multiple weak non-covalent forces like hydrogen bonding [10] and π–π interactions [11]. The role of different transition and non-transition metal ions as templates, Schiff bases as blocking units and pseudohalides or carboxylates as bridges are very much noteworthy in this regard [12–15]. Pseudohalides, especially azide, thiocyanate or dicyanamide, have long been known for their versatile coordination modes to exploit the desired architectures. Cadmium(II), well suited with its d^{10} configuration, permits a wide range of symmetries and coordination numbers and hence reports on hexacoordinated cadmium(II) complexes are well documented [14,15]. However, heptacoordinated cadmium(II) complexes are not very common [12,16]. All these features have prompted us to develop new coordination complexes with increased dimensionality using the variation of donor sites. Both the Schiff bases used to prepare the reported complexes are symmetric in nature. The most interesting fact is that although the ligands are quite symmetric in nature, their coordination behaviour to the metal atoms is not at all similar. The geometry of the coordination around the metal centers is mostly distorted octahedral, but one of the complexes shows a unique presence of both hexa- and heptacoordinated metal centers. From the report, it is very much clear that the coordination environment around the metal centre is largely influenced by the steric demand of the long chain multidentate ligand.

We have successfully prepared three trinuclear Cd(II) complexes and characterised them on the basis of microanalytical, spectroscopic and other physicochemical properties. X-ray crystallographic studies have been made to establish their structures. The present paper reports a systematic study of three new trimeric Cd(II) complexes with two multidentate Schiff bases. In addition, the investigation of the coordination properties of cadmium is of interest because of the environmental aspects and biological activity of Cd(II). The details of syntheses, structures and other spectroscopic behaviours are described below.

2. Experimental

2.1. Materials

All the chemicals and solvents used for the syntheses were of analytical grade. Cadmium nitrate, tetrahydrate; salicylaldehyde; 3-methoxysalicylaldehyde; sodium thiocyanate; sodium dicyanamide and diethylenetriamine were purchased from Aldrich Chemical Co. Inc. and were used without any further purification. Methanol and *N*,*N*-dimethylformamide ($HCONMe_2$) were used as solvents. Both the solvents were super dried before use. AR grade methanol was distilled with a good fractionating column for the exclusion of moisture. In this method, the water content was reduced to *ca*. 100 ppm. The solvent dimethyl formamide (AR) was distilled over di-phosphorus pentoxide before use in order to minimise the moisture content in the solvents. Hydrated cadmium (II) trifluoroacetate $[Cd(CF_3COO)_2 \cdot xH_2O]$ was prepared by the treatment of cadmium(II) carbonate, $CdCO_3$, (AR grade, E. Merck, India) with 60% trifluoroacetic acid (AR grade, E. Merck, India) followed by slow evaporation on a steam bath. It was then filtered through a fine glass-frit and preserved in a $CaCl_2$ desiccator.

2.2. Syntheses

Caution! Although no problems were encountered in this work, trifluoroacetic acid and its vapour are potentially corrosive to human skin. It should be handled with every care.

2.2.1. Synthesis of the Schiff base ligands

2.2.1.1. Synthesis of $(OH)C_6H_4CH{=}N(CH_2)_2NH(CH_2)_2N{=}CHC_6H_4(OH)$ ($\boldsymbol{H_2L^1}$). The Schiff base chelator H_2L^1 was prepared following a reported [17] procedure with a slight modification. Salicylaldehyde (0.244 g, 2 mmol) was refluxed with diethylenetriamine (0.103 g, 1 mmol) in dehydrated methanol. After 1 h, a deep orange yellow solution was obtained. It was subjected to TLC which revealed the presence of some unreacted starting materials along with the Schiff base product. The Schiff base product was isolated by column chromatography in order to get it in the purified form. The purified ligand was then evaporated under reduced pressure to yield a gummy mass, which was dried and stored *in vacuo* over $CaCl_2$ for subsequent use. Yield: 0.264 g (85%). *Anal*. Calc. for $C_{18}H_{21}N_3O_2$: C, 69.43; H, 6.80; N, 13.49. Found: C, 69.40; H, 6.82; N, 13.50%. Mass spectrum (EI): *m*/*z* 311($M^+ = L^+$). FT-IR (KBr, cm^{-1}): *ν*(C=N) 1640. UV–Vis (*λ*, nm): 242, 369.

2.2.1.2. Synthesis of $(OH)(OCH_3)C_6H_3CH{=}N(CH_2)_2NH(CH_2)_2N{=}CHC_6H_3(OH)(OCH_3)$ ($\boldsymbol{H_2L^2}$). The Schiff base chelator H_2L^2 was prepared following the same procedure as adopted for H_2L^1 except 3-methoxysalicylaldehyde (0.305 g, 2 mmol) was refluxed with diethylenetriamine (0.103 g, 1 mmol) in dehydrated methanol. Yield: 0.304 g (82%). *Anal.* Calc. for $C_{20}H_{25}N_3O_4$: C, 64.67; H, 6.78; N, 11.31. Found: C, 64.65; H, 6.80; N, 11.30%. Mass spectrum (EI): *m*/*z* 371 ($M^+ = L^+$). FT-IR (KBr, cm^{-1}): *ν*(C=N) 1641. UV–Vis (*λ*, nm): 240, 372.

2.2.2. Syntheses of the Schiff base complexes

2.2.2.1. Synthesis of $[Cd_3(L^1)_2(SCN)_2(CF_3COO)_2]$ (**1**). The appropriate quantity of solid Schiff base ligand H_2L^1

(0.622 g, 2 mmol) was dissolved in dry methanol (20 ml). A solution of $Cd(CF_3COO)_2 \cdot 2H_2O$ (1.123 g, 3 mmol) in dry methanol (10 ml) was added to this solution (3:2 molar ratio, M:L) followed by the addition of a 5 ml methanolic solution of 0.162 g (2 mmol) NaSCN. The mixture was refluxed for 2 h at 80 °C. The resulting yellow coloured solution was then filtered off and the filtrate was left undisturbed. After 5 days fine colourless needle shaped X-ray diffraction quality single crystals separated out. They were filtered, washed with methanol and dried *in vacuo* over $CaCl_2$. Yield: 85%. *Anal.* Calc. for $C_{42}H_{40}Cd_3F_6N_8O_8S_2$: C, 38.80; H, 3.10; N, 8.62. Found: C, 38.82; H, 3.07; N, 8.65%.

*2.2.2.2. Synthesis of $[Cd_3(L^1)_2(SCN)_2(HCONMe_2)]$ (**2**).* 0.622 g (2 mmol) of the solid Schiff base ligand H_2L^1 was dissolved in dry methanol (20 ml). A gently warm solution of $Cd(NO_3)_2 \cdot 4H_2O$ (0.930 g, 3 mmol) in dry methanol (10 ml) was added to this solution (3:2 molar ratio, M:L) followed by the addition of 5 ml NaSCN solution (0.162 g, 2 mmol). The solution turned turbid. *N*,*N*-Dimethylformamide was added dropwise till the turbidity just disappeared. The mixture was refluxed for 3 h at 80 °C. The resulting yellow coloured solution was then filtered off and the filtrate was left undisturbed. After 2 h colourless plate shaped X-ray diffraction quality single crystals separated out. They were filtered, washed with methanol and dried *in vacuo* over $CaCl_2$. Yield: 65%. *Anal.* Calc. for $C_{41}H_{43}Cd_3N_9O_5S_2$: C, 43.08; H, 3.79; N, 11.03. Found: C, 43.05; H, 3.80; N, 11.00%.

*2.2.2.3. Synthesis of $[Cd_3(L^2)_2\{N(CN)_2\}_2]$ (**3**).* 0.742 g (2 mmol) of the solid Schiff base ligand H_2L^2 was dissolved in 10 ml methanol. The solution was then added to a 10 ml gently warm solution of $Cd(NO_3)_2 \cdot 4H_2O$ (0.930 g, 3 mmol) followed by the slow dropwise addition of 5 ml sodium dicyanamide solution (0.178 g, 2 mmol). The mixture was then refluxed for 45 min at 85 °C. The resulting yellow coloured solution was filtered off and the filtrate was left undisturbed. After 5 days, yellow block shaped X-ray diffraction quality single crystals separated out from the medium. They were filtered, washed with methanol and dried *in vacuo* over $CaCl_2$. Yield: 87%. *Anal.* Calc. for $C_{44}H_{46}Cd_3N_{12}O_8$: C, 43.74; H, 3.84; N, 13.91. Found: C, 43.76; H, 3.80; N, 13.94%.

2.3. Physical measurements

The Fourier Transform infrared spectra of the ligands and the complexes were recorded on a Perkin–Elmer RX-I FT-IR spectrophotometer with a KBr disc in the range 4000–200 cm^{-1}. Elemental analyses (C, H, N) were carried out using a Perkin–Elmer 2400 II elemental analyser. The electronic spectra of the ligands were recorded on a Perkin–Elmer Lambda 40 (UV/Vis) spectrometer in methanol. Steady state fluorescence measurements were performed using a Spex Fluorolog-II spectrofluorimeter. For spectroscopic measurements, the concentration of the solutions were *ca.* 2×10^{-5} M. Mass spectra were obtained with a MAT 8200 (electron ionization, EIMS) instrument.

2.4. Single crystal X-ray structure determination

A good diffraction quality air stable single crystal of **1** (dim $0.01 \times 0.01 \times 0.01$ mm) was mounted in a Nonius KappaCCD diffractometer while that of **2** (dim $0.12 \times 0.12 \times 0.03$ mm) and **3** (dim $0.40 \times 0.50 \times 0.50$ mm) in Bruker X8 APEXII CCD and Bruker AXS P4 diffractometers, respectively. All the diffractometers were equipped with graphite monochromated Mo Kα radiation ($\lambda = 0.71069$ Å for **1** and 0.71073 Å for **2** and **3**). Crystal data were collected using the software COLLECT [18a] at a temperature of 293 K for **1** and using Bruker SMART [18b] and Bruker XCANS [18c] softwares at a temperature 123 K for **2** and **3**, respectively. Cell refinements were carried out using DENZO-SCALEPACK [18a], Bruker SAINT and Bruker XCANS for **1**, **2** and **3**, respectively. No significant intensity variation was observed for each of them. A total of 8876 reflections (6368 unique reflections, $R_{int} = 0.021$), 16 582 reflections (8470 unique reflections, $R_{int} = 0.087$) and 27 073 reflections (6801 unique reflections, $R_{int} = 0.049$) for **1**, **2** and **3** were collected applying the boundary condition $I > 3\sigma(I)$ for **1** and $I \geqslant 2\sigma(I)$ for **2** and **3**. No absorption correction was applied to the data sets for **1** and **3**. Multiscan absorption correction was applied to the intensity values ($T_{max} = 0.9533$, $T_{min} = 0.8302$) empirically using SADABS for **2** [18d]. Data reduction was performed using DENZO-SCALEPACK for **1** [18a], while Bruker SAINT [18e] and Bruker SHELXTL [18f] softwares were used for **2** and **3**, respectively. According to the observed systematic extinctions, the structure of **1** was solved by direct methods using the SIR97 [18g] program combined with Fourier difference syntheses and refined against F using reflections maintaining the boundary condition $I/\sigma(I) > 3$ (CRYSTALS program [18(h)]). For **2** and **3**, the final structures were solved by direct methods using the program SHELXS-97 and refined with full-matrix least-squares based on F^2 using SHELXL-97 [18i]. The molecular graphics and crystallographic illustrations were prepared using the CAMERON [18j], ORTEP-III [18k] and CRYSTALMAKER [18l], Bruker SHELXTL [18f] programs for **1**, **2** and **3**, respectively. For all non-hydrogen atoms, the anisotropic displacement parameters have been refined successfully. Hydrogen atoms of the aromatic rings and the imino groups were placed geometrically and refined as a riding model taken from a difference Fourier map and refined with isotropic thermal parameters. Maximum and minimum peaks (e $Å^{-3}$) in the final difference Fourier synthesis were found as 1.96 and −1.99, 1.363 and −1.273, 1.12 and −0.84 for **1**, **2** and **3**, respectively. Relevant crystallographic data and structure refinement parameters for all the three complexes are summarised in Table 1.

Table 1
Crystallographic parameters for complexes **1**, **2** and **3**

Complex	**1**	**2**	**3**
Formula	$C_{42}H_{40}Cd_3F_6N_8O_8S_2$	$C_{41}H_{43}Cd_3N_9O_5S_2$	$C_{44}H_{46}Cd_3N_{12}O_8$
Formula weight	1300.17	1143.16	1208.16
Crystal system	triclinic	triclinic	monoclinic
Space group	$P\bar{1}$(no. 2)	$P\bar{1}$(no. 2)	$C2/c$(no. 15)
a (Å)	10.506(5)	10.148(15)	10.142(10)
b (Å)	10.832(5)	11.456(11)	24.684(3)
c (Å)	12.362(5)	21.100(3)	18.492(3)
α (°)	68.288(5)	75.374(6)	90
β (°)	67.608(5)	88.362(6)	99.924 (10)
γ (°)	72.489(5)	66.317(6)	90
V (Å^3)	1187.3(9)	2166.1(5)	4560.2(10)
Z	1	2	4
T (K)	293	123	123
$\lambda_{\text{Mo K}\alpha}$ (Å)	0.71069	0.71073	0.71073
D_{calc} (g cm^{-3})	1.818	1.753	1.760
μ (mm^{-1})	1.502	1.610	1.453
$F(000)$	642	1136	2408
Crystal dimension (mm)	$0.01 \times 0.01 \times 0.01$	$0.12 \times 0.12 \times 0.03$	$0.40 \times 0.50 \times 0.50$
θ (°)	1.9, 29.5	2.3, 26.0	3.4, 30.4
Total, unique data, R_{int}	8876, 6368, 0.021	16582, 8470, 0.087	27073, 6801, 0.049
Observed data	4853 [$I > 3\sigma(I)$]	5259 [$I \geqslant 2\sigma(I)$]	5728 [$I \geqslant 2\sigma(I)$]
R^a, R_w^b	0.0526, 0.0742	0.0812, 0.1556	0.0282, 0.0679
Goodness-of-fit	1.125	1.082	1.033
$\Delta\rho_{\text{max, min}}$ (e Å^{-3})	1.96, −1.99	1.36, −1.27	1.12, −0.84

[a] $R = \sum(|F_o - F_c|)/\sum|F_o|$.
[b] $R_w = \{\sum[w(|F_o - F_c|)^2]/\sum[w|F_o|^2]\}^{1/2}$.

3. Results and discussion

3.1. Fourier Transform infrared spectra

The solid state Fourier Transform infrared spectra of all the complexes, recorded on a FT-IR spectrophotometer in the range 4000–200 cm^{-1} are fully consistent with their single crystal structures. The samples were studied as powders dispersed in KBr pellets. The spectral region for all the complexes is more or less similar due to the similarity in coordination modes of the ligands with the metal centres. Sharp peaks were found at 1640 cm^{-1} and 1641 cm^{-1} for H_2L^1 and H_2L^2, respectively, which can be correlated to the stretching frequency of the azomethine (CH=N) group in the Schiff base ligands. This stretching frequency of the azomethine (CH=N) group observed near about 1640 cm^{-1}, is shifted to lower frequency values upon complexation with the metal by 20–40 cm^{-1} [19,20], suggesting coordination via the azomethine nitrogen in all the complexes. ν(N–H) at 3435 cm^{-1} in the IR spectrum of complex **1**, suggests the presence of a protonated nitrogen atom in the ligand [21]. Several sharp weak peaks observed for the complexes in the range 3180–2855 cm^{-1} are likely to be due to the aromatic stretches [22]. Sharp bands appearing at 455 and 375 cm^{-1} correspond to ν(Cd–N), and ν(Cd–O), respectively in all the complexes. The ν(C–O) mode is present as a very strong band at about 1240 cm^{-1}. Complex **1** also shows asymmetric and symmetric stretching vibrations of the trifluoroacetate groups at 1600 and 1450 cm^{-1}, respectively. The difference between ν_{asym}(COO) and ν_{sym}(COO) ($\Delta\nu = 150$ cm^{-1}), which is smaller than 164 cm^{-1} observed in ionic trifluoroacetate, reflects the bidentate bridging coordination mode [21]. In the mid energy range, characteristic absorption peaks for terminal SCN^- groups were found at 2105 cm^{-1}and 2109 cm^{-1}, respectively for **1** and **2**, along with the distinctive peaks in the low energy region near 1215 cm^{-1} attributable to δ_{CN} vibrations [22]. In the case of complex **3**, sharp characteristic peaks are found at 2300, 2245 and 2185 cm^{-1}, which may be assigned to $\nu_{\text{sym}} + \nu_{\text{asym}}$(CN), ν_{asym}(CN) and ν_{sym}(CN) stretching frequencies, respectively. The characteristic peaks invariably prove the presence of a terminal dicyanamide group in complex **3** [12a].

3.2. UV/Vis spectra

Electronic spectra of all the complexes have been measured in HPLC grade methanol. In a like manner, the bands in the 465–335 nm range can be assigned to the n–π^* transition from the azomethine (CH=N) group [4]. In the spectra of the complexes, these n–π^* transitions, are shifted to lower frequencies indicating that the imine nitrogen atom is involved in coordination to the Cd(II) metal ion. The bands at higher energies (300–210 nm range) are associated with benzene π–π^* transitions. The spectra of the complexes show intense bands in the high-energy region at 305–375 nm which can be attributed to L → M charge transfer bands [23]. Although the precise nature of this transition involving the phenoxide group is not fully

clear (it has been considered to be an O(phenoxide) → Cd(II) LMCT [24] or a Cd(II) → π* (phenoxide) MLCT [25] transition), it is agreed that a higher energy component should exist near 330 nm [26].

3.3. X-ray crystal structures of the complexes

3.3.1. $[Cd_3(L^1)_2(SCN)_2(CF_3COO)_2]$ (1)

The crystal structure of **1** consists of only one crystallographically independent molecule. Fig. 1 gives a labelled ORTEP diagram of **1**. Selected bond lengths and angles are presented in Table 2a. The complex crystallises in the $P\bar{1}$ space group. The structure found for complex **1** is a linear trinuclear array of three Cd(II) atoms coupled by both doubly μ-phenolato oxygens of the Schiff base ligand and simultaneously two trifluoroacetate anions in the *syn–syn* bridging mode. The crystal structure is also well supported and documented by different characterisation data found for the complex through elemental analysis and detailed spectral investigation. The coordination geometry around the terminal Cd(II) centers may be regarded as distorted octahedral. The equatorial plane of each of the two equivalent terminal Cd atoms are formed by the two imine nitrogen atoms [N(9), N(15)] and two phenolic oxygen atoms [O(1), O(23)] coming from the same ligand [N(9)–Cd(2)–O(23) = 138.99(18)° and N(15)–Cd(2)–O(1) = 142.36(17)°]. The apical positions are occupied by one sulfur atom (S37) from the terminal SCN^- ligand and another oxygen atom (O25) from the bridging trifluoroacetate group [S(37)–Cd(2)–O(25) = 161.55(18)°]. The Cd(2)–imine nitrogen [2.318(5) and 2.399(5) Å], Cd(2)–phenolic oxygen [2.284(4) and 2.342(3) Å] bond distances are in the range observed for similar systems [12,27]. The average bite angle of the extremely puckered eight membered chelate ring N(9)–C(10)–C(11)–N(12)–C(13)–C(14)–N(15)–Cd(2) is ~139.46°, thus introducing considerable steric strain in the fragment, enhancing a considerable distortion to the octahedral Cd(2) centre (Fig. 2). In the Schiff base ligand, the N(12) atom is protonated (Fig. 2), which is supported by the comparatively larger distance [Cd(2)–N(12): 2.446 Å] than for the other nitrogen atoms of the ligand [Cd(2)–N(9): 2.318(5) and Cd(2)–N(15): 2.399(5) Å]. However, the coordination geometry of the central Cd(1) atom deviates very slightly from an ideal octahedron

Table 2a
Selected bond distances (Å) and angles (°) for **1**

	Bond lengths	(Å)	Bond angles	(°)
1	Cd(1)–O(1)	2.287(3)	Cd(1)–O(1)–Cd(2)	98.35(13)
	Cd(1)–O(23)	2.266(3)	Cd(1)–O(23)–Cd(2)	100.72(17)
	Cd(1)–O(24)	2.363(4)	O(1)–Cd(1)–O(1*)	180.00
	Cd(2)–O(1)	2.342(3)	O(23)–Cd(1)–O(23*)	180.00
	Cd(2)–O(23)	2.284(4)	O(24)–Cd(1)–O(24*)	180.00
	Cd(2)–O(25)	2.356(4)	O(1)–Cd(2)–O(23)	74.25(15)
	Cd(2)–N(9)	2.318(5)	O(1)–Cd(2)–S(37)	112.82(19)
	Cd(2)–N(15)	2.399(5)	N(9)–Cd(2)–N(15)	139.5(2)
	Cd(2)–S(37)	2.546(6)	N(9)–Cd(2)–O(23)	138.99(18)
	C(8)–N(9)	1.287(9)	N(15)–Cd(2)–O(1)	142.36(17)
	C(16)–N(15)	1.261(9)	C(38)–S(37)–Cd(2)	149.5(6)
	C(26)–O(25)	1.224(7)	S(37)–Cd(2)–O(25)	161.55(18)

*: $-x, -y, -z$.

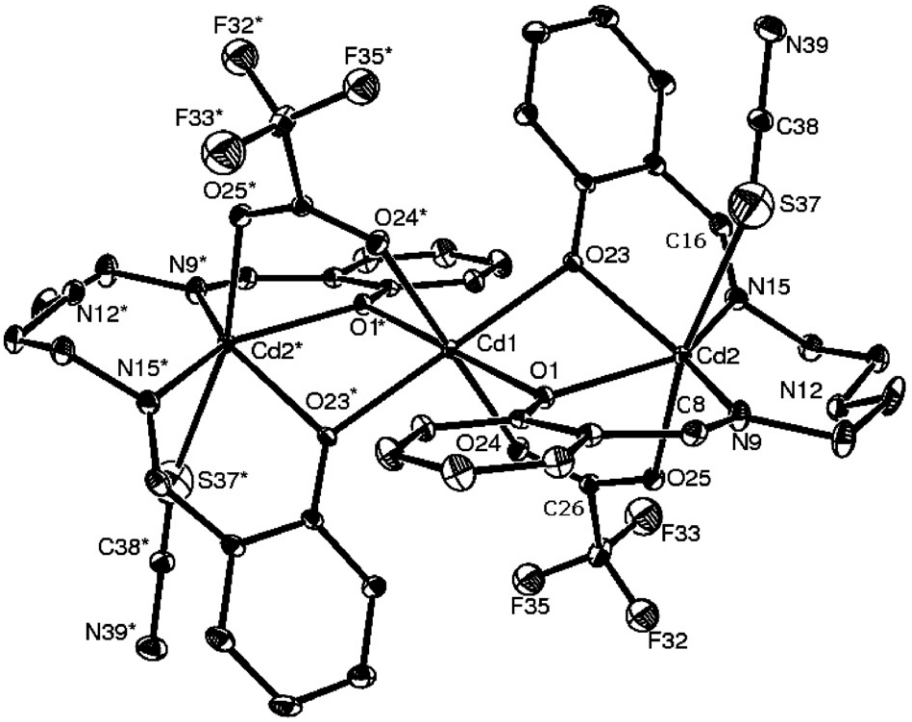


Fig. 1. ORTEP diagram of **1** with the atom numbering scheme (non-hydrogen atoms have been shown at 40% ellipsoid probability). Symmetry operation *: $-x, -y, -z$.

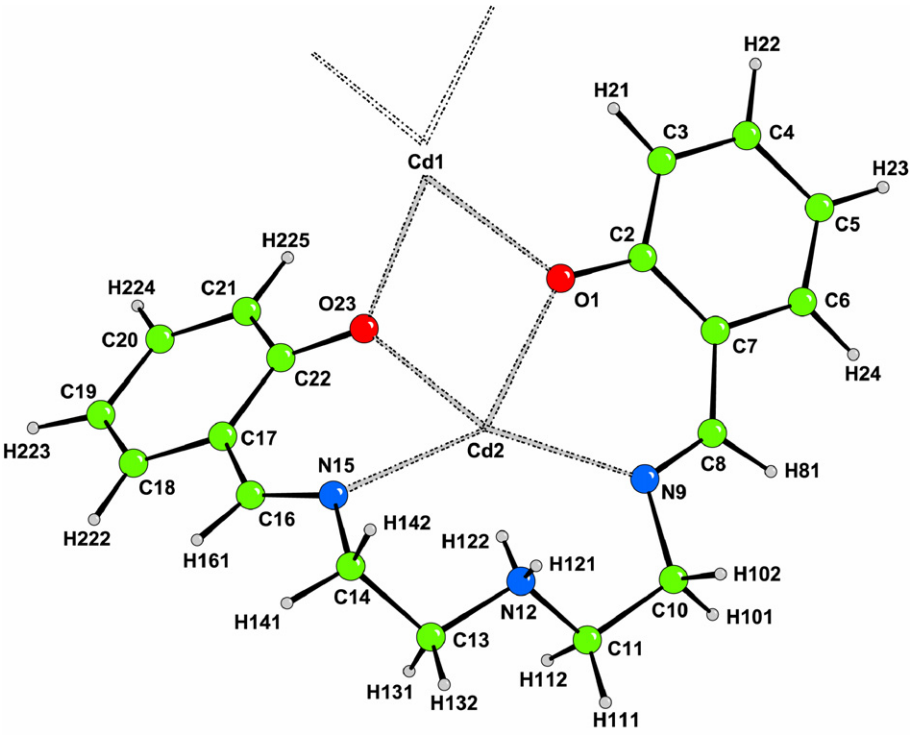


Fig. 2. Isolated view of the Cd(2) centre of **1** showing the imposed strain by the ligand (trifluoroacetate ligands have not been shown for picture clarity).

[O(1)–Cd(1)–O(1*), O(23)–Cd(1)–O(23*), O(24)–Cd(1)–O(24*) are each 180°]. The central Cd(1) atom has an O_2O_2 donor set from the two ligands. Again each of the two trifluoroacetate anions bridges the terminal Cd(2) and central Cd(1) atoms in a *syn–syn* fashion, but remaining to each other coordinated in a *trans*-fashion. Hence the central Cd(1) atom finally has an $O_2O_2O_2$ donor set (four equatorial oxygens coming from four deprotonated phenolic oxygens of the two ligands and two axial oxygens from the bridging trifluroacetates). The complex appears to be the most symmetric in nature with an inversion centre lying on the central Cd(1) atom, which is reflected by exactly the same *trans*-Cd–O(phenolate)–Cd bond angles [Cd(1)–O(1)–Cd(2): 98.35(13)°, Cd(1)–O(1*)–Cd(2*): 98.35(13)°, Cd(1)–O(23)–Cd(2): 100.72(17)°, Cd(1)–O(23*)–Cd(2*): 100.72(17)°]. The closest distance between two neighbouring cadmium atoms in the molecule is 3.503(3) Å and it is just half of the distance between the terminal cadmium centres (7.006 Å). In the crystal packing, each of the neutral metal–ligand clusters is isolated from another one. No interaction is found between the isolated clusters because the shortest distance between clusters is equal to ~8.204 Å (Fig. 3).

3.3.2. $[Cd_3(L^1)_2(SCN)_2(HCONMe_2)]$ (**2**)

Unlike the previous complex, complex **2** is a novel example of a doubly μ_3-phenoxo bridged cyclic Cd(II) trimer (Fig. 4). According to the best of our knowledge, it is the first of its kind reported in the literature where both six and seven coordinated Cd(II) centres are coexisting in the same μ_3-phenoxo bridged cyclic Cd(II) trimeric system. In the complex all the three metal centers bear dissimilar coordination patterns. Among them, the Cd(1) and Cd(3) centres are six coordinated whilst the remaining Cd(2) metal centre is seven coordinated. Both the Cd(1) and Cd(3) centres display a highly distorted octahedral environment. The Cd(1) centre is enjoying a N_3O_3 donor set. The severely strained equatorial plane is constructed by a N_2O_2 donor set [among them N(1) and N(3) are imine nitrogens; O(1) and O(3) are phenolate oxygen atoms] while the apical sites are occupied by O(2) coming from the phenolate oxygen atom of the Schiff base ligand and N(2), the free secondary nitrogen donor site present within the ligand backbone [O(2)–Cd(1)–N(2): 135.5(3)°, the highest among all the Cd(1) centred bond angles]. The average bite angles of the five membered chelate rings range from ~70° to 77°. It is also clearly reflected by the reduction in the bond angles around the Cd(1) centre (Table 2b). The Cd(3) centre also shows a distorted octahedral geometry with the equatorial plane constructed by an O_3N donor set [all the oxygen atoms are phenolate oxygens and the nitrogen atom N(8) is from the terminal thiocyanate]. The axial sites are occupied by one nitrogen atom N(7) from another terminal thiocyanate and O(2), a phenolate oxygen atom coming from the Schiff base ligand [N(7)–Cd(3)–O(2): 172.3(3)°]. The Cd(3) atom is shifted from the mean basal plane O(1)O(3)O(4)N(8) by 0.425(3) Å towards the apically coordinated N(7) atom. The most interesting coordination environment in this complex is manifested by the Cd(2) centre which is heptacoordinated, in contrast to its hexaco-

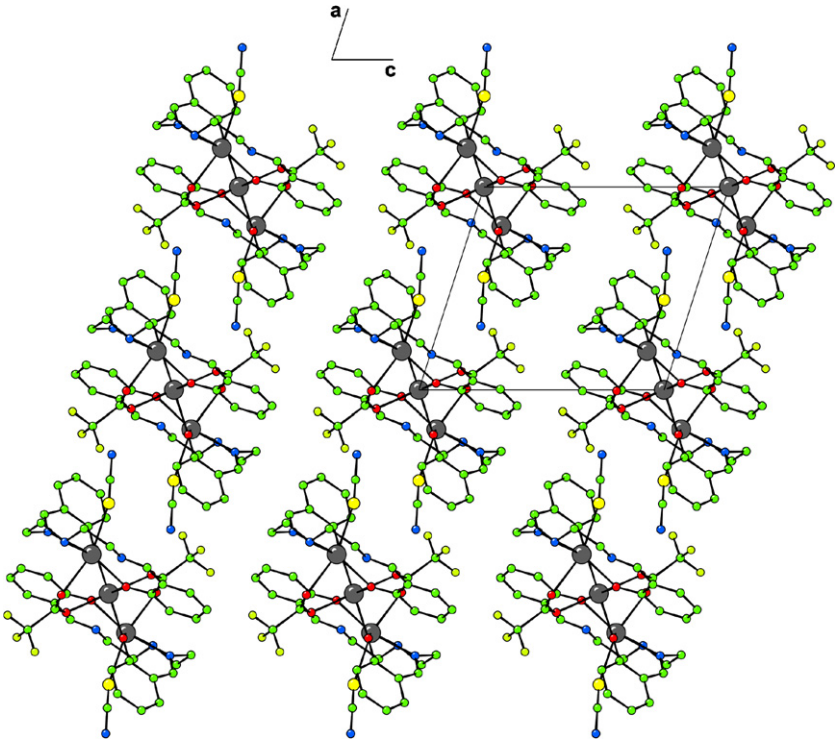


Fig. 3. Packing diagram of **1** along the *ac* plane.

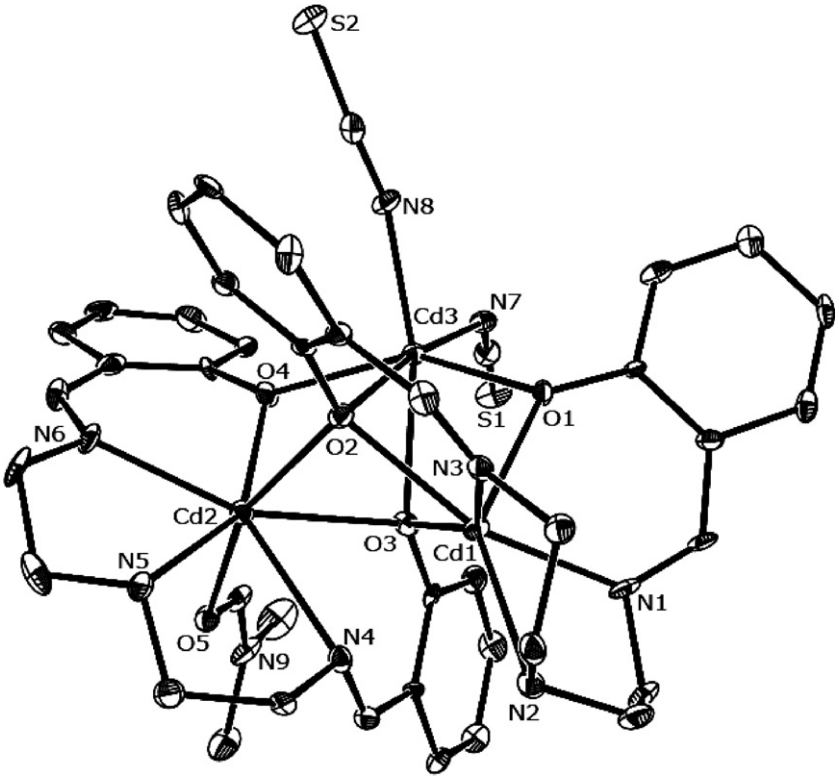


Fig. 4. ORTEP diagram of **2** with the atom numbering scheme (non-hydrogen atoms have been shown at 40% ellipsoid probability).

ordinated neighbours Cd(1) and Cd(3). The geometry around the metal centre can be best described as a severely distorted monocapped octahedron. The equatorial plane is constructed by a O_3N donor set [among them N(4) is an imine nitrogen; O(4) is a μ-phenolato oxygen bridging the Cd(2) and Cd(3) centres; O(2) is a μ_3-phenolato oxygen

Table 2b
Selected bond distances (Å) and angles (°) for **2**

Bond lengths		(Å)	Bond angles	(°)
2	Cd(1)–O(1)	2.325(8)	O(1)–Cd(1)–O(2)	76.9(3)
	Cd(1)–O(2)	2.348(7)	O(2)–Cd(1)–O(3)	68.8(2)
	Cd(1)–O(3)	2.382(7)	O(1)–Cd(1)–N(1)	77.9(3)
	Cd(1)–N(1)	2.281(10)	O(2)–Cd(1)–N(2)	135.5(3)
	Cd(1)–N(2)	2.585(11)	O(3)–Cd(2)–N(4)	65.3(3)
	Cd(1)–N(3)	2.255(8)	O(2)–Cd(2)–O(5)	157.1(3)
	Cd(2)–O(2)	2.277(6)	O(4)–Cd(2)–O(5)	91.4(3)
	Cd(2)–O(3)	2.398(7)	N(4)–Cd(2)–O(3)	65.3(3)
	Cd(2)–O(4)	2.331(9)	N(8)–Cd(3)–O(3)	157.0(3)
	Cd(2)–O(5)	2.316(6)	N(7)–Cd(3)–O(4)	102.8(3)
	Cd(2)–N(4)	2.594(10)	N(7)–Cd(3)–O(2)	172.3(3)
	Cd(2)–N(5)	2.380(11)	Cd(1)–O(1)–Cd(3)	98.5(3)
	Cd(2)–N(6)	2.343(9)	Cd(1)–O(2)–Cd(2)	97.5(3)
	Cd(3)–O(1)	2.223(8)	Cd(2)–O(2)–Cd(3)	88.4(2)
	Cd(3)–O(2)	2.549(8)	Cd(1)–O(2)–Cd(3)	89.3(2)
	Cd(3)–O(3)	2.393(8)	Cd(1)–O(3)–Cd(2)	93.3(2)
	Cd(3)–O(4)	2.266(8)	Cd(2)–O(3)–Cd(3)	89.4(2)
	Cd(3)–N(7)	2.285(10)	Cd(1)–O(3)–Cd(3)	92.4(2)
	Cd(3)–N(8)	2.211(10)	Cd(2)–O(4)–Cd(3)	94.3(3)

which simultaneously bridges all the three Cd centres and O(5) comes from the coordinated $HCONMe_2$ molecule]. The *trans*-axial sites are occupied by one nitrogen atom N(5) from the secondary nitrogen donor site of the diamine fragment and O(3), a μ_3-phenolato oxygen. Another bond, Cd(2)–N(6), is directed through the centre of the trigonal face furnished by N(5), O(4) and O(5). It fulfils the seven coordinated geometry around the metal centre [the Cd(2)–N(4), Cd(2)–O(2), Cd(2)–O(4) and Cd(2)–O(5) bond lengths are 2.594(10), 2.277(6), 2.331(9) and 2.316(3) Å, respectively in the equatorial plane; Cd(2)–N(5) and Cd(2)–O(3) are 2.380(11) and 2.398(7) Å, respectively in the apical zone and Cd(2)–N(6) is 2.343(9) Å]. The apparent anomaly in the corresponding bond lengths around the Cd(2) centre is probably due to the severe strain imposed by the ligand system to the metal atom [the Cd(2) centre is deviated from the mean plane constructed by N(4), O(2), O(4) and O(5) by 0.6561(2) Å towards the apical N(5) atom]. The most noteworthy structural novelty of complex **2** lies in the interesting variation of the coordination behaviour of the "salen" moieties present in the two fag ends of the completely symmetric ligand H_2L^1. In the doubly deprotonated ligand (L^{2-}), one phenoxo oxygen [O(1) or O(4)] is μ-bridged between two adjacent metal centres [Cd(1)–Cd(3) or Cd(2)–Cd(3)] while its immediate neighbour on the other end [O(2) or O(3)] bridges three Cd(II) centers simultaneously, which is a very rare phenomenon observed in the chemical literature in the case of such salen-type Schiff base complexes. Thus there are actually two different kinds of phenolato oxygen atoms present in the ligand: one of them doubly coordinated to the adjacent metal centres and the other kind shows a μ_3 bridging mode which helps to afford a cyclic trimer of Cd(II). The average M–O(phenolate)–M bond angles are around 93°. All other relevant bond lengths and bond angles are given in Table 2b. The nearest Cd–Cd distances are: Cd(1)–Cd(2), 3.477(3); Cd(2)–Cd(3), 3.370(5); Cd(1)–Cd(3), 3.445(2) Å, thereby showing the least chance of interactions among the adjacent metal centres. Again from the view of crystal packing, any sort of non-covalent or weak interaction is absent amongst the neutral metal-Schiff base clusters, with them being isolated at large distances.

3.3.3. $[Cd_3(L^2)_2\{N(CN)_2\}_2]$ (**3**)

A perspective view of the trimeric asymmetric unit of complex **3** has been represented in Fig. 5 as an ORTEP plot and a packing diagram is shown in Fig. 6. Coordi-

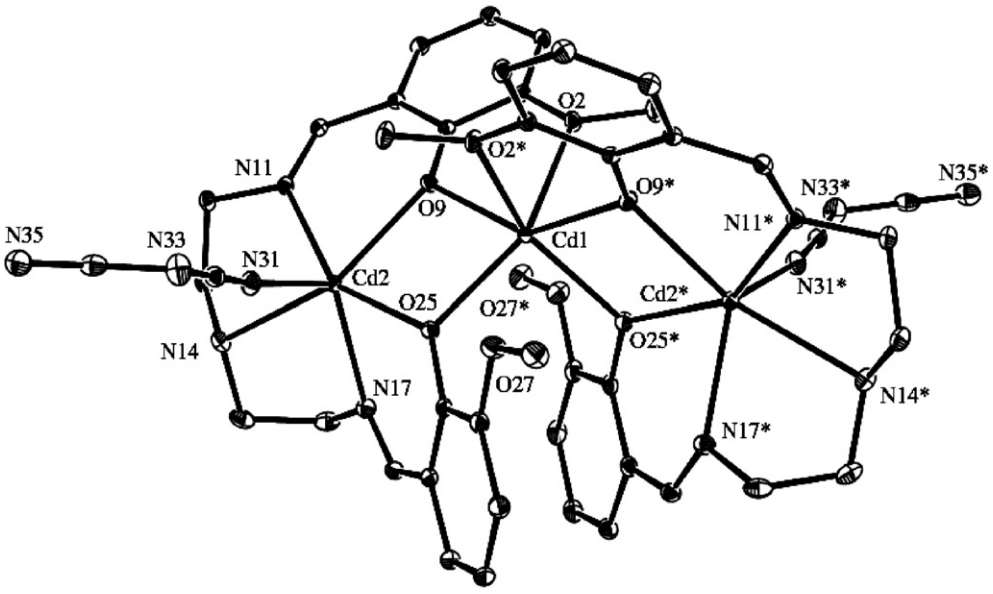


Fig. 5. ORTEP diagram of **3** with the atom numbering scheme (non-hydrogen atoms have been shown at 40% ellipsoid probability). Symmetry operation *: $1 - x$, y, $1/2 - z$.

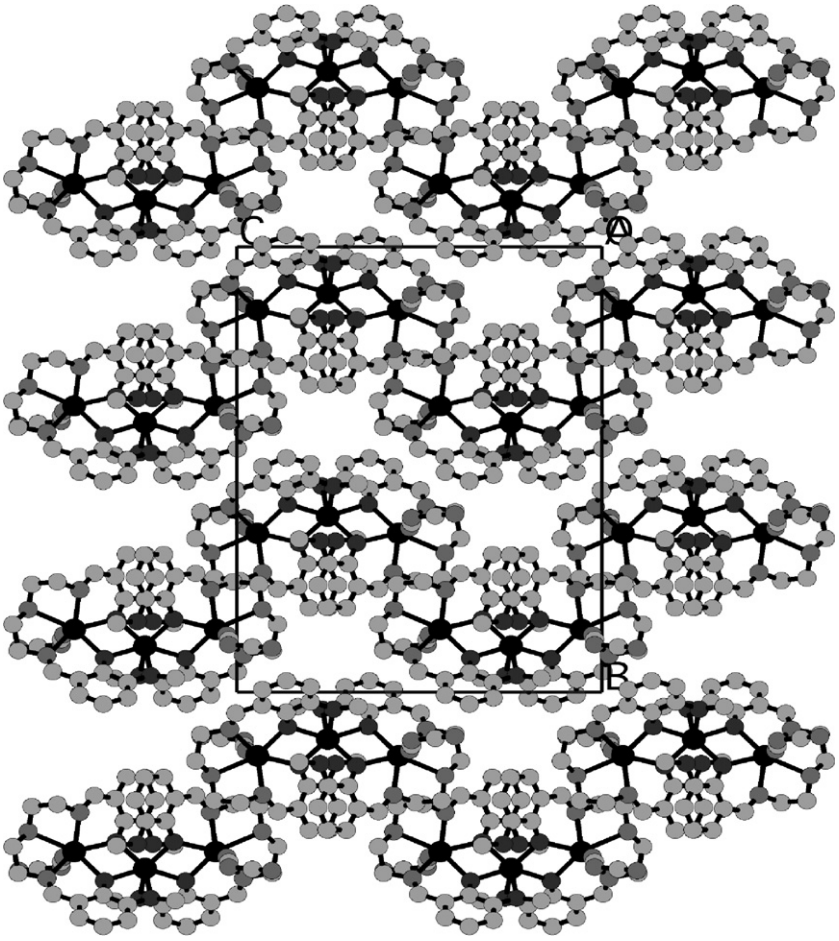


Fig. 6. Packing diagram of **3**.

nates of the non-hydrogen atoms, and selected bond distances and bond angles are given in Table 2c. The structure is a linear trimeric one, bearing two equivalent terminal Cd(II) centres. Complex **3** crystallises in the *C*2/*c* (monoclinic) space group. Adjacent Cd(II) atoms in the linear trinuclear array are coupled to each other doubly with μ-phenoxo bridges. The crystal structure is also well supported and documented by different characterisation data found for the complex through elemental analysis and detailed spectroscopic investigation. The coordination geometry around the central Cd(1) can be best described as a distorted octahedron. The central Cd(1) has an $O_2O_2O_2$ donor set from the two ligands, among the four equatorial oxygens, two are from two deprotonated phenolic oxygens [O(25) and O(25*)] while the other two are from two methoxy oxygens [O(2) and O(2*)] from the two different ligands. The two axial sites are occupied by two phenolic oxygens [O(9) and O(9*)]. The O(9)–Cd(1)–O(9*) angle of 145.12(5)° is the highest among all the *trans*-bond angles. The other *trans*-equatorial bond angles, O(2)–Cd(1)–O(25) and O(2*)–Cd(1)–O(25*), are same [142.84(5)°]. The coordination geometry around each symmetrically equivalent terminal Cd(II) centre may be regarded as a distorted octahedron. The terminal Cd(2) centre enjoys a N_4O_2 donor set. The severely strained equatorial plane is constructed by a N_3O donor set [among them N(17) is a imine nitrogen, N(14) is the free secondary nitrogen donor site and O(9) is a phenolate oxygen atom of the same Schiff base ligand, while N(31) comes from the terminal dicyanamide ligand]. The apical sites are occupied by O(25) coming from the phenolate oxygen atom and N(11), the imine nitrogen donor site

Table 2c
Selected bond distances (Å) and angles (°) for **3**

Bond lengths		(Å)	Bond angles	(°)
3	Cd(1)–O(2)	2.3702(17)	O(9)–Cd(1)–O(9*)	145.12(5)
	Cd(1)–O(2*)	2.3702(17)	O(2)–Cd(1)–O(25)	142.84(5)
	Cd(1)–O(9)	2.2601(15)	O(2*)–Cd(1)–O(25*)	142.84(5)
	Cd(1)–O(9*)	2.2601(15)	O(25)–Cd(1)–O(25*)	95.97(6)
	Cd(1)–O(25)	2.2134(15)	N(11)–Cd(2)–O(25)	149.63(6)
	Cd(1)–O(25*)	2.2134(15)	N(14)–Cd(2)–O(9)	147.90(6)
	Cd(2)–O(9)	2.3256(15)	N(17)–Cd(2)–N(31)	115.55(8)
	Cd(2)–O(25)	2.3077(15)	O(9)–Cd(2)–O(25)	71.99(5)
	Cd(2)–N(11)	2.2932(18)	N(11)–Cd(2)–N(14)	71.96(6)
	Cd(2)–N(14)	2.560(2)	O(9)–Cd(2)–N(11)	77.80(6)
	Cd(2)–N(17)	2.290(2)	Cd(1)–O(9)–Cd(2)	105.36(6)
	Cd(2)–N(31)	2.246(2)	Cd(1)–O(25)–Cd(2)	107.52(6)

*: $1 - x, y, 1/2 - z$.

present in the same Schiff base ligand. The *trans*-axial bond angle N(11)–Cd(2)–O(25) is 149.63(6)°. The average bite angles of the two puckered five and six membered chelate rings are ~71.31° and 77.25°, respectively, which initiate a considerable distortion to the octahedral Cd(2) centre (Fig. 5). The comparatively larger distance [Cd(2)–N(14): 2.560(2) Å] than for the other nitrogen atoms of the Schiff base ligand [Cd(2)–N(11): 2.2932(18) and Cd(2)–N(17): 2.290(2) Å] may be attributed to the considerable steric strain present in the fragment. The most interesting feature lies in the variation of the coordination pattern of the *o*-vanilin moieties at the two ends of the Schiff base ligand (H_2L^2). In the doubly deprotonated ligand L^{2-}, one –OMe group is coordinated to the central Cd(1) centre while its counterpart in the other end of the same ligand remains free. The same behaviour is also observed for the other ligand. The closest distance between two terminal Cd atoms in the molecule is 7.050 Å and it is approximately double that between the neighbouring Cd centres (3.647 Å). In the packing diagram we did not find any trace of non-covalent or weak interactions among the neutral metal-Schiff base clusters (Fig. 6).

3.4. Luminescence properties

Steady-state fluorescence studies have been performed to establish the metal Schiff base coordination for all the three complexes. Fluorescence spectra for both the Schiff base ligands and their respective Cd(II) complexes have been measured in methanol (Fig. 7). All of them show characteristic broad fluorescence emissions indicating a ligand-to-metal charge transfer (LMCT) nature of the bands. Significant differences in the positions of the emission maximum of the complexes from that of the ligands may be considered as an evidence of metal–ligand complexation. All the complexes show intense bands at *ca.* 360 nm, which may be assigned to intraligand $^1(\pi-\pi^*)$ transitions. The emission energy of all the complexes in methanol solutions at 298 K is almost same and is assignable to intraligand fluorescence [12,28–30]. The lifetimes of the complexes are in range 2.50–2.60 ns. In glassy solutions (methanol at 77 K) both fluorescence and $^3(\pi-\pi^*)$ phosphorescence are observed at 525 nm.

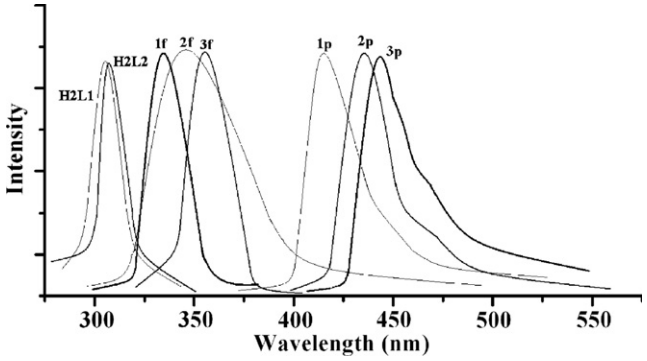


Fig. 7. Luminescence spectra for the ligands and the complexes H2L1: fluorescence spectra for the ligand H_2L^1, H2L2: fluorescence spectra for the ligand H_2L^2, **1f**, **2f**, **3f**: fluorescence spectra of **1**, **2**, **3** in MeOH solution at 298 K, respectively. 1p, 2p, 3p: Phosphorescence spectra of **1**, **2**, **3** in MeOH glassy solution at 77 K, respectively.

4. Conclusion

The present study shows that the reaction of long chain multidentate salen-type Schiff base ligands with various metal salts can afford a variety of fascinating metal-cluster frameworks. Both the ligands are flexible enough due to their long chain lengths and hence they are able to adjust their conformations in order to fit with the geometries of the metal ion thereby reducing the steric strain within the ligand backbone. We have been able to synthesise three novel trinuclear coordination complexes with two analogous multidentate Schiff base ligands. The novelty of the work lies in the interesting variation of the coordination pattern of the different donor sites due to the flexibility of the long chain ligand backbone.

Acknowledgements

Joy Chakraborty is especially grateful to the University Grants Commission, New Delhi, Government of India for the award of a Senior Research Fellowship to him. J.C. is also thankful to Dr. Arnab Mukherjee, Department of Chemical Engineering, University Institute of Chemical Technology, Mumbai for the technical support to the luminescence studies of the complexes. Santarupa Thakurta is grateful to the CSIR, Govt. of India for a Junior Research Fellowship.

Appendix A. Supplementary material

CCDC 636959, 636961, 636960 contain the supplementary crystallographic data for **1**, **2** and **3**. These data can be obtained free of charge via http://www.ccdc.ac.uk/conts/retrieving.html, or from the Cambridge Crystallographic Data Centre, 12 Union Road, Cambridge CB2 1EZ, UK; fax: (+44) 1223-336-033; or e-mail: deposit@ccdc.cam.ac.uk.

References

[1] Z.-F. Chen, Y.-Z. Tang, H. Liang, H.-K. Fun, K.-B. Yu, J. Coord. Chem. 59 (2006) 207.
[2] Q. Shi, L. Xu, J. Ji, Y. Li, R. Wang, Z. Zhou, R. Cao, M. Hong, A.S.C. Chan, Inorg. Chem. Commun. 7 (2004) 1254.
[3] (a) Z.-L. You, H.-L. Zhu, W.-S. Liu, Z. Anorg. Allg. Chem. 630 (2004) 1617;
(b) Z.-L. You, H.-L. Zhu, Z. Anorg. Allg. Chem. 630 (2004) 2754.
[4] A. Golcu, M. Tumer, H. Demirelli, R.A. Wheatley, Inorg. Chim. Acta 358 (2005) 1785.
[5] S. Brooker, Coord. Chem. Rev. 222 (2001) 33.
[6] V. Amendola, L. Fabbrizzi, C. Mangano, P. Pallavicini, A. Poggi, A. Taglietti, Coord. Chem. Rev. 219 (2001) 821.
[7] P.A. Vigato, S. Tamburini, Coord. Chem. Rev. 248 (2004) 1717.

[8] S. Sen, P. Talukder, S.K. Dey, S. Mitra, G. Rosair, D.L. Hughes, G.P.A. Yap, G. Pilet, V. Gramlich, T. Matsushita, Dalton Trans. (2006) 1758.
[9] (a) S. Leininger, B. Olenyuk, P.J. Stang, Chem. Rev. 100 (2000) 853;
(b) W. Meier, Chem. Soc. Rev. 29 (2000) 295.
[10] (a) T. Steiner, Angew. Chem., Int. Ed. Engl. 41 (2002) 48;
(b) G.R. Desiraju, Acc. Chem. Res. 35 (2002) 565;
(c) N.V. Belkova, E.S. Subina, L.M. Epstein, Acc. Chem. Res. 38 (2005) 624.
[11] (a) C. Janiak, J. Chem. Soc., Dalton Trans. (2000) 3885;
(b) M.J. Zaworotko, Chem. Commun. (2002) 199;
(c) M.K. Milcic, V.B. Medakovic, D.N. Sredojevic, N.O. Juranic, S.D. Zaric, Inorg. Chem. 45 (2006) 4755.
[12] (a) J. Chakraborty, B. Samanta, G. Pilet, S. Mitra, Inorg. Chem. Commun. 10 (2007) 40;
(b) A. Majumder, G. Rosair, A. Mallick, N. Chattopadhyay, S. Mitra, Polyhedron 25 (2006) 1753.
[13] (a) P. Comba, T.W. Hambley, Molecular Modelling of Inorganic and Coordination Compounds, second ed., VCH, Weinheim, 2000;
(b) J. Wang, X. Qian, Chem. Commun. (2006) 109.
[14] (a) V. Alexander, Chem. Rev. 95 (1995) 273;
(b) T.K. Karmakar, S.K. Chandra, J. Ribas, G. Mostafa, T.-H. Lu, B.K. Ghosh, Chem. Commun. (2002) 2364.
[15] (a) A.M. Golub, H. Kohler, V.V. Skopenko (Eds.), Chemistry of Pseudohalides, Elsevier, Amsterdam, 1986;
(b) J. Ribas, A. Escuer, M. Monfort, R. Vicente, R. Cortes, L. Lezama, T. Rojo, Coord. Chem. Rev. 193 (1999) 1027.
[16] (a) H. Zhang, X. Wang, K. Zhang, B.K. Teo, Coord. Chem. Rev. 183 (1999) 157;
(b) S.H. Rahaman, R. Ghosh, G. Mostafa, B.K. Ghosh, Inorg. Chem. Commun. 8 (2005) 700, and refs. therein;
(c) V. Haber, I. Cisaova, J. Fabry, Polyhedron 22 (2003) 3451.
[17] (a) C.-M. Liu, R.-G. Xiong, X.-Z. You, Y.-J. Liu, K.-K. Cheung, Polyhedron 15 (1996) 4565;
(b) C.-M. Liu, R.-G. Xiong, X.-Z. You, H.-K. Fun, K. Sivakumar, Polyhedron 16 (1997) 119;
(c) M.S. Ray, R. Bhattacharya, S. Chaudhuri, L. Righi, G. Bocelli, G. Mukhopadhyay, A. Ghosh, Polyhedron 22 (2003) 617.
[18] (a) Nonius COLLECT, DENZO, SCALEPACK, SORTAV: KAPPACCD Program B.V., Delft, The Netherlands 1999;
(b) SMART: Data Collection Program for the CCD Area-Detector System;
(c) XCANS: Data Collection Program for the Bruker P4 system;
(d) G.M. Sheldrick, SADABS, Programs for Area Detector Adsorption Correction, Institute for Inorganic Chemistry, University of Göttingen, Germany, 1996;
(e) SAINT: Data Reduction, Frame Integration Program for the CCD Area-Detector System, Bruker Analytical X-ray Systems Ltd., Madison, Wisconsin, USA, 2005;
(f) G.M. Sheldrick, SHELXTL version 5.1: Program for the Solution and Refinement of Crystal Structures, Bruker AXS P4, Inc., Madison, WI, USA, 1999;
(g) G. Cascarano, A. Altomare, C. Giacovazzo, A. Guagliardi, A.G. Moliterni, D. Siliqi, M. Burla, G. Polidori, M. Camalli, Acta Crystallogr. A52 (1996) C-79;
(h) D.J. Watkin, C.K. Prout, J.R. Carruthers, P.W. Betteridge, CRYSTALS Issue 11, Chemical Crystallography Laboratory, Oxford, UK, 1999;
(i) G.M. Sheldrick, SHELX-97 (SHELXS and SHELXL) Program for Solution and Refinement of Crystal structures, University of Göttingen, Germany, 1997;
(j) D.J. Watkin, C.K. Prout, L.J. Pearce, CAMERON, Chemical Crystallography Laboratory, OXFORD, UK, 1996;
(k) L.J. Farrugia, ORTEP-3 for Windows, J. Appl. Crystallogr. 30 (1997) 565;
(l) D.C. Palmer, CRYSTAL MAKER 7.04, Crystal Maker Software, Yarnton, UK, 2005.
[19] S.H. Rahaman, R. Ghosh, T.-H. Lu, B.K. Ghosh, Polyhedron 24 (2005) 1525.
[20] M. Dolaz, M. Tümer, M. Dıgrak, Trans. Met. Chem. 29 (2004) 528.
[21] M.T.H. Tarafder, A. Kasbollah, K.A. Crouse, A.M. Ali, B.M. Yamin, H.-K. Fun, Polyhedron 20 (2001) 236.
[22] (a) K. Nakamoto, Infrared and Raman Spectra of Inorganic and Coordination Compounds, fifth ed., John Wiley, New York, 1997, Part A and B;
(b) R.T. Conley, Infrared Spectroscopy, Allyn & Bacon, Boston, 1966.
[23] M. Tümer, Synth. React. Inorg. Met. Org. Chem. 30 (2000) 1139.
[24] R. Atkins, G. Brewer, E. Kokot, G.M. Mockler, J.E. Sinn, Inorg. Chem. 24 (1985) 127.
[25] A.G. Suillerot, J.P. Albertini, A. Collet, L. Faury, J.M. Pastor, L.J. Tosi, J. Chem. Soc., Dalton Trans. 44 (1981) 2544.
[26] A.R. Amundsen, J. Whelan, B. Bosnich, J. Am. Chem. Soc. 99 (1977) 6730.
[27] A.G. Blackman, Polyhedron 24 (2005) 1.
[28] L.-Z. Cai, W.-T. Chen, M.-S. Wang, G.-C. Guo, J.-S. Huang, Inorg. Chem. Commun. 7 (2004) 611.
[29] J.-X. Chen, S.-X. Liu, E.-Q. Gao, Polyhedron 23 (2004) 1877.
[30] D. Bose, J. Banerjee, Sk. H. Rahaman, G. Mostafa, H.-K. Fun, R.D. Bailey Walsh, M.J. Zaworotko, B.K. Ghosh, Polyhedron 23 (2004) 2045.

properties. Several recently synthesized nickel complexes have been tested for inhibition of cancer cell proliferation [20–22].

Among the compounds tested a bis(citronellal thiosemicarbazonato)nickel(II), [Ni(tcitr)2], and the corresponding free ligand Htcitr showed a remarkable activity in apoptosis induction [23]. In accordance, we have decided to extend our research to other nickel complexes of aliphatic long-chain thiosemicarbazones that differ from those previously studied in the apoptosis assay for the chain length and for the substituents on the thiosemicarbazone terminal nitrogen atom. In this frame we have synthesized, modifying a procedure described in the literature [24], and characterized nine ligands and prepared the corresponding nickel derivatives starting from nickel acetate. Five of these complexes and namely bis(heptanal thiosemicarbazonato)nickel(II) (**10**), bis(decanal thiosemicarbazonato) nickel(II) (**13**), bis(N^1-methyldecanal thiosemicarbazonato) nickel(II) (**14**), bis(N^1-allyldecanal thiosemicarbazonato) nickel(II) (**15**) and bis(N^1-allylundecanal thiosemicarbazonato)nickel(II) (**18**), were characterized by X-ray diffractometry. Among the synthesized compounds the two that overcame an initial screening on solubility and stability in the culture broth of leukemia cells (human lymphoma) were chosen: the heptanal thiosemicarbazone and its nickel complex. These two compounds were then used to test the biological activity on leukemia line U937 in order to compare the effect of the simple ligand versus the action of the complex.

2. Experimental

2.1. Materials and methods

Undecanal 97% (Lancaster), decanal 97% (Alfa Aesar), heptanal 97% (Alfa Aesar), 4-methylthiosemicarbazide 97% (Aldrich), 4-allylthiosemicarbazide 97% (Aldrich), $Ni(CH_3COO)_2 \cdot 4H_2O$ (Carlo Erba) were commercially available and used without further purification. Elemental analyses (C, H, N, S) were performed with a Carlo Erba model EA 1108 automatic analyzer. IR spectra (4000–400 cm^{-1}) for KBr discs were recorded on a Nicolet 5PC FT. Chemical ionization-mass (*m*/*z*, 70 eV) fragmentation patterns were obtained, using samples dissolved in methanol, with a Finnegan 1020 6c mass spectrometer equipped with a quadrupole mass selector MATSSQ 710. The ^1H NMR spectra were recorded on a Bruker 300 spectrometer. Chemical shifts are reported in parts per million referenced to that of residual solvent protons. Melting points were determined with a Gallenkamp instrument. UV–Vis measurements were performed on a Perkin–Elmer UV/Vis Lambda 25 spectrometer with quartz cuvettes.

2.2. Preparation of the ligands

In a typical procedure to a methanol solution (45 mL) of appropriate thiosemicarbazide (0.90 mmol) obtained by magnetic stirring and slight heating, an equimolar amount of aliphatic aldehyde was added dropwise (Scheme 1). For the synthesis of the compounds **1**–**5**, **7** and **8** was necessary boiling the respective reaction mixtures under reflux condition, while for **6** and **9** stirring at room temperature was sufficient. By following this general procedure after 8 h a transparent and colorless solution was obtained for all the ligands except for **6** and **9** which it appear pale yellow. From standing solution separates a white microcrystalline product (yellow for **6** and **9**) that was then isolated by filtration and analyzed.

2.2.1. Heptanal thiosemicarbazone (*1*)

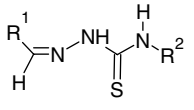
(Yield: 0.132 g, 78%). M.p.: 80 °C. IR(KBr, cm^{-1}): 3404(m) and 3256(m) $\nu(NH_2)$; 3159(s) ν(NH); 2970(m) $\nu(CH_{al})$; 1594(vs) ν(C=N); 1540(vs) ν(C=N); 1369 and 1283(w) ν(C–N); 824(w) ν(C=S). Mass spectrum (%, *m*/*z*): 188 (100, MH^+). *Anal.* Calc. for $C_8H_{17}N_3S$: C, 51.3; H, 9.2; N, 22.4; S, 17.1. Found: C, 51.1; H, 9.2; N, 22.3; S, 17.3%. ^1H NMR (300 MHz, $CDCl_3$): δ_H (ppm) 9.76 (s, 1H, N*H*CS), 7.56 (t, 1H, C*H*=N), 7.15 and 6.82 (2 bs, 1H each, NH_2), 2.33 (m, 2H, CH_2 in C2), 1.75–1.50 (m, 4H, CH_2 in C3 + C4), 1.45–1.20 (m, 4H, CH_2 in C5 + C6), 0.91 (t, 3H, CH_3).

2.2.2. N^1-Methyl heptanal thiosemicarbazone (*2*)

(Yield: 0.136 g, 75%). M.p.: 85 °C. IR(KBr, cm^{-1}): 3268(w) ν(NH); 3163(m) ν(NH); 2986(s) $\nu(CH_{al})$; 1552(vs) ν(C=N); 1310(vw) and 1252(s) ν(C–N); 789(w) ν(C=S). Mass spectrum (%, *m*/*z*): 202 (100, MH^+). *Anal.* Calc. for $C_9H_{19}N_3S$: C, 53.7; H, 9.5; N, 20.9; S, 15.9. Found: C, 54.0; H, 9.8; N, 20.5; S, 16.1%. ^1H NMR (300 MHz, $CDCl_3$): δ_H (ppm) 9.74 (s, 1H, N*H*CS), 7.58 (t, 1H, C*H*=N), 6.84 (q, 1H, N*H*CH_3), 3.14 (d, 3H, CH_3N*H*), 2.38 (m, 2H, CH_2 in C2), 1.74–1.53 (m, 4H, CH_2 in C3 + C4), 1.40–1.21 (m, 4H, CH_2 in C5 + C6), 0.90 (t, 3H, CH_3).

2.2.3. N^1-Allyl heptanal thiosemicarbazone (*3*)

(Yield: 0.174 g, 85%). M.p.: 90 °C. IR(KBr, cm^{-1}): 3273(w) and 3173(m) ν(NH); 2981(s) $\nu(CH_{al})$; 1552(vs) ν(C=N); 1310 (vw) and 1252(s) ν(C–N); 789(w) ν(C=S). Mass spectrum (%, *m*/*z*): 228 (100, MH^+). *Anal.* Calc. for $C_{11}H_{21}N_3S$: C, 58.1; H, 9.3; N, 18.5; S, 14.1. Found: C, 58.3; H, 9.7; N, 18.4; S, 14.2%. ^1H NMR (300 MHz, $CDCl_3$): δ_H (ppm) 9.85 (s, 1H, N*H*CS), 7.92 (t, 1H, N*H*CH_2), 7.60 (t, 1H, C*H*=N), 5.88 (m, 1H, CH_2=C*H*-CH_2), 5.16 (dd, 1H, CH_2=CH, Hβ), 5.07 (dd, 1H,



R^1= C_6H_{13}- R^2= H- (**1**); CH_3- (**2**); CH_2=CH-CH_2- (**3**)
R^1= C_9H_{19}- R^2= H- (**4**); CH_3- (**5**); CH_2=CH-CH_2- (**6**)
R^1= $C_{10}H_{21}$- R^2= H- (**7**); CH_3- (**8**); CH_2=CH-CH_2- (**9**)

Scheme 1.

CH_2=CH, Hα), 4.21 (dd, 2H, CH–CH_2–NH), 2.35 (m, 2H, CH_2 in C2), 1.72–1.51 (m, 4H, CH_2 in C3 + C4), 1.38–1.21 (m, 4H, CH_2 in C5 + C6), 0.91 (t, 3H, CH_3).

*2.2.4. Decanal thiosemicarbazone (**4**)*

(Yield: 0.132 g, 64%). M.p.: 97 °C. IR(KBr, cm^{-1}): 3392 and 3260(m) $\nu(NH_2)$; 3159(m) ν(NH); 2918(s) and 2851(m) $\nu(CH_{al})$; 1598(vs) ν(C=N); 1365 and 1287(w) ν(C–N); 832(w) ν(C=S). Mass spectrum (%, *m*/*z*): 230(100, MH^+). *Anal.* Calc. for $C_{11}H_{23}N_3S$: C, 57.6; H, 10.1; N, 18.3; S, 14.0. Found: C, 57.2; H, 10.1; N, 18.2; S, 13.8%. ^{1}H NMR (300 MHz, $CDCl_3$): δ_H (ppm) 9.80 (s, 1H, N*H*CS), 7.58 (t, 1H, C*H*=N), 7.18 and 6.84 (2 bs, 1H each, NH_2), 2.43 (m, 2H, CH_2 in C2), 1.75–1.55 (m, 4H, CH_2 in C3 + C4), 1.45–1.12 (m, 10H, CH_2 in C5 + C6 + C7 + C8 + C9), 0.92 (t, 3H, CH_3).

*2.2.5. N^1-Methyl decanal thiosemicarbazone (**5**)*

(Yield: 0.149 g, 68%). M.p.: 48 °C. IR(KBr, cm^{-1}): 3365(m) and 3159(m) ν(NH); 2995(m) $\nu(CH_{al})$; 1555(vs) ν(C=N); 1334(w) and 1271(s) ν(C–N); 800(w) ν(C=S). Mass spectrum (%, *m*/*z*): 244(100, MH^+). *Anal.* Calc. for $C_{12}H_{25}N_3S$: C, 59.2; H, 10.4; N, 17.3; S, 13.2. Found: C, 59.5; H, 10.5; N, 17.3; S, 12.9%. ^{1}H NMR (300 MHz, $CDCl_3$): δ_H (ppm) 9.78 (s, 1H, N*H*CS), 7.56 (t, 1H, C*H*=N), 6.80 (q, 1H, N*H*CH_3), 3.14 (d, 3H, CH_3NH), 2.42 (m, 2H, CH_2 in C2), 1.74–1.54 (m, 4H, CH_2 in C3 + C4), 1.43–1.11 (m, 10H, CH_2 in C5 + C6 + C7 + C8 + C9), 0.92 (t, 3H, CH_3).

*2.2.6. N^1-Allyl decanal thiosemicarbazone (**6**)*

(Yield: 0.146 g, 60%). M.p.: 57 °C. IR(KBr, cm^{-1}): 3365(s) and 3155(m) ν(NH); 2941(vs) $\nu(CH_{al})$; 1555 (vs) ν(C=N); 1295 and 1225(m) ν(C–N); 800(w) ν(C=S). Mass spectrum (%, *m*/*z*): 270 (100, MH^+). *Anal.* Calc. for $C_{14}H_{27}N_3S$: C, 62.4; H, 10.1; N, 15.6; S, 11.9. Found: C, 62.7; H, 10.1; N, 15.8; S, 11.5%. ^{1}H NMR (300 MHz, $CDCl_3$): δ_H (ppm) 9.77 (s, 1H, N*H*CS), 7.55 (t, 1H, C*H*=N), 6.79 (q, 1H, N*H*CH_2), 5.89 (m, 1H, CH_2=C*H*–CH_2), 5.15 (dd, 1H, CH_2=CH, H*β*), 5.10 (dd, 1H, CH_2=CH, Hα), 4.20 (dd, 2H, CH–CH_2–NH), 2.43 (m, 2H, CH_2 in C2), 1.73–1.54 (m, 4H, CH_2 in C3 + C4), 1.43–1.14 (m, 10H, CH_2 in C5 + C6 + C7 + C8 + C9), 0.93 (t, 3H, CH_3).

2.2.7. Undecanal thiosemicarbazone (7)

(Yield: 0.147 g, 67%). M.p.: 75.6 °C. IR(KBr, cm^{-1}): 3417(m) and 3264(m) $\nu(NH_2)$; 3161(s) ν(NH); 2936(vs) and 2839(s) $\nu(CH_{al})$; 1527(vs) ν(C=N); 1363(m) ν(C–N); 830(w) ν(C=S). Mass spectrum (%, *m*/*z*): 244 (100, MH^+). *Anal.* Calc. for $C_{12}H_{25}N_3S$: C, 59.2; H, 10.4; N, 17.3; S, 13.2. Found: C, 58.8; H, 10.7; N, 17.0; S, 12.8%. ^{1}H NMR (300 MHz, $CDCl_3$): δ_H (ppm) 9.78 (s, N*H*CS), 7.56 (t, 1H, C*H*=N), 7.19 and 6.83 (2 bs, 1H each, NH_2), 2.42 (m, 2H, CH_2 in C2), 1.74–1.55 (m, 4H, CH_2 in C3 + C4), 1.45–1.12 (m, 12H, CH_2 in C5 + C6 + C7 + C8 + C9 + C10), 0.93 (t, 3H, CH_3).

*2.2.8. N^1-Methyl undecanal thiosemicarbazone (**8**)*

(Yield: 0.118 g, 51%). M.p.: 51.2 °C. IR(KBr, cm^{-1}): 3357(m) and 3159(m) ν(NH); 2981(m) $\nu(CH_{al})$; 1540(vs) ν(C=N); 1326(w) and 1264(vs) ν(*C–N*); 793(w) ν(C=S). Mass spectrum (%, *m*/*z*): 258(100, MH^+). *Anal.* Calc. for $C_{13}H_{27}N_3S$: C, 60.6; H, 10.6; N, 16.3; S, 12.4. Found: C, 60.4; H, 10.8; N, 16.0; S, 12.8%. ^{1}H NMR (300 MHz, $CDCl_3$): δ_H (ppm) 9.78 (s, 1H, N*H*CS), 7.54 (t, 1H, C*H*=N), 6.80 (q, 1H, N*H*CH_3), 3.12 (d, 3H, CH_3N*H*), 2.42 (m, 2H, CH_2 in C2), 1.75–1.54 (m, 4H, CH_2 in C3 + C4), 1.42–1.11 (m, 12H, CH_2 in C5 + C6 + C7 + C8 + C9 + C10), 0.92 (t, 3H, CH_3).

*2.2.9. N^1-Allyl undecanal thiosemicarbazone (**9**)*

(Yield: 0.153 g, 60%). M.p.: 50 °C. IR(KBr, cm^{-1}): 3357(s) and 3159(m) ν(NH); 2999(w) and 2921(m) $\nu(CH_{al})$; 1552(vs) ν(C=N); 1295(m) and 1228(m) ν(C–N); 804(w) ν(C=S). Mass spectrum (%, *m*/*z*): 284(100, MH^+). *Anal.* Calc. for $C_{15}H_{29}N_3S$: C, 63.6; H, 10.3; N, 14.8; S, 11.3. Found: C, 64.0; H, 10.6; N, 14.3; S, 10.9%. ^{1}H NMR (300 MHz, $CDCl_3$): δ_H (ppm) 9.78 (s, 1H, N*H*CS), 7.59 (t, 1H, C*H*=N), 6.81 (q, 1H, N*H*CH_2), 5.91 (m, 1H, CH_2=C*H*–CH_2), 5.18 (dd, 1H, CH_2=CH, Hβ), 5.13 (dd, 1H, CH_2=CH, Hα), 4.22 (dd, 2H, CH–CH_2–NH), 2.44 (m, 2H, CH_2 in C2), 1.76–1.54 (m, 4H, CH_2 in C3 + C4), 1.44–1.13 (m, 12H, CH_2 in C5 + C6 + C7 + C8 + C9 + C10), 0.96 (t, 3H, CH_3).

2.3. Preparation of the complexes

All nickel complexes were prepared by reacting $Ni(CH_3COO)_2$ (1 mmol dissolved in methanol, 20 mL) and the corresponding ligand (2 mmol, dissolved in methanol, 30 mL) in a 1:2 ratio. After stirring for 2 h at room temperature the resulting brown solution is placed standing to allow the solvent to evaporate and the product is formed as microcrystals or a microcrystalline powder. UV spectra of complexes (CH_3OH) show absorption bands in the region 650–400 nm (*ε*, 50–500 $L \times cm^{-1} \times mol^{-1}$) due to d–d transitions together to very strong absorptions below 300 nm due to ligand $n \rightarrow \sigma^*$ and $n \rightarrow \pi^*$ transitions.

*2.3.1. Bis(heptanal thiosemicarbazonato)nickel(II) (**10**)*

Yield: 0.324 g, 75%. M.p.: 156 °C. IR(KBr, cm^{-1}): 3424 (s) and 3299(m) $\nu(NH_2)$; 2921(m) $\nu(CH_{al})$; 1633(s) δNH; 1520(vs) ν(C=N); 1345(m) and 1147(w) ν(C–N); 765(w) ν(C=S). *Anal.* Calc. for $C_{16}H_{32}N_6NiS_2$: C, 44.6; H, 7.5; N, 19.5; S, 14.9. Found: C, 45.0; H, 7.6; N, 19.2; S, 15.1%. ^{1}H NMR (300 MHz, DMSO-d_6): δ_H (ppm) 7.80 (bs, 1H, NH_2), 7.65 (t, 1H, C*H*=N), 7.16 (bs, 1H, NH_2), 2.34 (m, 2H, CH_2 in C2), 1.76–1.51 (m, 4H, CH_2 in C3 + C4), 1.46–1.21 (m, 4H, CH_2 in C5 + C6), 0.92 (t, 3H, CH_3).

*2.3.2. Bis(N^1-methyl heptanal thiosemicarbazonato)nickel(II) (**11**)*

Yield: 0.368 g, 80%. M.p.: 88 °C. IR(KBr, cm^{-1}): 3172(m) ν(NH); 2988(s) $\nu(CH_{al})$; 1531(vs) ν(C=N);

1262(s) ν(C–N); 780(w) ν(C=S). *Anal.* Calc. for $C_{18}H_{36}N_6NiS_2$: C, 47.1; H, 7.9; N, 18.3; S, 14.0. Found: C, 47.2; H, 7.8; N, 18.2; S, 14.1%. ^{1}H NMR (300 MHz, DMSO-d_6): δ_H (ppm) 7.68 (t, 1H, C*H*=N), 6.61 (q, 1H, N*H*CH$_3$), 3.10 (d, 3H, CH_3NH), 2.39 (m, 2H, CH_2 in C2), 1.74–1.53 (m, 4H, CH_2 in C3 + C4), 1.44–1.21 (m, 4H, CH_2 in C5 + C6), 0.93 (t, 3H, CH_3).

2.3.3. Bis(N^1-allyl heptanal thiosemicarbazonato)nickel(II) (**12**)

Yield: 0.368 g, 72%. M.p.: 74 °C. IR(KBr, cm^{-1}): 3182(m) ν(NH); 2980(s) ν(CH$_{al}$); 1531(vs) ν(C=N); 1242(s) ν(C–N); 777(w) ν(C=S). *Anal.* Calc. for $C_{22}H_{40}N_6NiS_2$: C, 51.7; H, 7.9; N, 16.4; S, 12.5. Found: C, 51.8; H, 7.6; N, 16.7; S, 12.5%. ^{1}H NMR (300 MHz, DMSO-d_6): δ_H (ppm) 7.69 (t, 1H, C*H*=N), 7.53 (t, 1H, N*H*CH$_2$), 5.91 (m, 1H, CH$_2$=C*H*–CH$_2$), 5.18 (dd, 1H, CH_2=CH, Hβ), 5.10 (dd, 1H, CH_2=CH, Hα), 4.23 (dd, 2H, CH–CH_2–NH), 2.37 (m, 2H, CH_2 in C2), 1.74–1.50 (m, 4H, CH_2 in C3 + C4), 1.39–1.23 (m, 4H, CH_2 in C5 + C6), 0.94 (t, 3H, CH_3).

2.3.4. Bis(decanal thiosemicarbazonato)nickel(II) (**13**)

Yield: 0.423 g, 82%. M.p.: 124 °C. IR(KBr, cm^{-1}): 3431(m) and 3303(m) and 3178(m) ν(NH); 2918(s) ν(CH$_{al}$); 1629(s) δNH; 1520(vs) ν(C=N); ν(*C–N*); 789(w) ν(C=S). *Anal.* Calc. for $C_{22}H_{44}N_6NiS_2$: C, 51.3; H, 8.6; N, 16.3; S, 12.4. Found: C, 51.5; H, 8.6; N, 15.9; S, 12.3%. ^{1}H NMR (300 MHz, DMSO-d_6): δ_H (ppm) 7.90 (bs, 1H, NH_2), 7.67 (t, 1H, C*H*=N), 7.19 (bs, 1H, NH_2), 2.44 (m, 2H, CH_2 in C2), 1.76–1.56 (m, 4H, CH_2 in C3 + C4), 1.46–1.13 (m, 10H, CH_2 in C5 + C6 + C7 + C8 + C9), 0.93 (t, 3H, CH_3).

2.3.5. Bis(N^1-methyl decanal thiosemicarbazonato)nickel(II) (**14**)

Yield: 0.435 g, 80%. M.p.: 77 °C. IR(KBr, cm^{-1}): 3416(vs) ν(NH); 2994(s) ν(CH$_{al}$); 1532(vs) ν(C=N); 1260(m) and 1174(w) ν(C–N); 734(vw) ν(C=S). *Anal.* Calc. for $C_{24}H_{48}N_6NiS_2$: C, 53.0; H, 8.9; N, 15.5; S, 11.8. Found: C, 53.4; H, 9.0; N, 15.2; S, 11.8%. ^{1}H NMR (300 MHz, DMSO-d_6): δ_H (ppm) 7.63 (t, 1H, C*H*=N), 6.64 (q, 1H, N*H*CH$_3$), 3.16 (d, 3H, CH_3NH), 2.46 (m, 2H, CH_2 in C2), 1.76–1.56 (m, 4H, CH_2 in C3 + C4), 1.44–1.13 (m, 10H, CH_2 in C5 + C6 + C7 + C8 + C9), 0.94 (t, 3H, CH_3).

2.3.6. Bis(N^1-allyl decanal thiosemicarbazonato)nickel(II) (**15**)

Yield: 0.417 g, 70%. M.p.: 55 °C. IR(KBr, cm^{-1}): 3375(s) ν(NH); 2942(vs) ν(CH$_{al}$); 1529(vs) ν(C=N); 1290 and 1215(m) ν(C–N); 747(w) ν(C=S). *Anal.* Calc. for $C_{28}H_{52}N_6NiS_2$: C, 56.5; H, 8.8; N, 14.1; S, 10.8. Found: C, 56.8; H, 9.1; N, 14.4; S, 11.0%. ^{1}H NMR (300 MHz, DMSO-d_6): δ_H (ppm) 7.63 (t, 1H, C*H*=N), 6.43 (q, 1H, N*H*CH$_2$), 5.91 (m, 1H, CH$_2$=C*H*–CH$_2$), 5.17 (dd, 1H, CH_2=CH, Hβ), 5.12 (dd, 1H, CH_2=CH, Hα), 4.22 (dd, 2H, CH–CH_2–NH), 2.45 (m, 2H, CH_2 in C2), 1.75–1.56 (m, 4H, CH_2 in C3 + C4), 1.45–1.16 (m, 10H, CH_2 in C5 + C6 + C7 + C8 + C9), 0.95 (t, 3H, CH_3).

2.3.7. Bis(undecanal thiosemicarbazonato)nickel(II) (**16**)

Yield: 0.418 g, 77%. M.p.: 138 °C. IR(KBr, cm^{-1}): 3307(m) and 3194(m) ν(NH); 2921(s) ν(CH$_{al}$); 1629(s) δNH; 1520(vs) ν(C=N); 1330(s) ν(C–N); 789(w) ν(C=S). *Anal.* Calc. for $C_{24}H_{48}N_6NiS_2$: C, 53.0; H, 8.9; N, 15.5; S, 11.8. Found: C, 53.1; H, 9.3; N, 15.4; S, 11.7%. ^{1}H NMR (300 MHz, DMSO-d_6): δ_H (ppm) 7.91 (bs, 1H, NH_2), 7.64 (t, 1H, C*H*=N), 7.20 (bs, 1H, NH_2), 2.42 (m, 2H, CH_2 in C2), 1.75–1.55 (m, 4H, CH_2 in C3 + C4), 1.46–1.13 (m, 12H, CH_2 in C5 + C6 + C7 + C8 + C9 + C10), 0.94 (t, 3H, CH_3).

2.3.8. Bis(N^1-methyl undecanal thiosemicarbazonato)nickel(II) (**17**)

Yield: 0.429 g, 75%. M.p.: 74 °C. IR(KBr, cm^{-1}): 3400(s) ν(NH); 2921(vs) ν(CH$_{al}$); 1540(vs) ν(C=N); 1260(m) ν(C–N); 711(vw) ν(C=S). *Anal.* Calc. for $C_{26}H_{52}N_6NiS_2$: C, 54.6; H, 9.2; N, 14.7; S, 11.2. Found: C, 55.0; H, 9.3; N, 14.6; S, 10.9%. ^{1}H NMR (300 MHz, DMSO-d_6): δ_H (ppm) 7.61 (t, 1H, C*H*=N), 6.58 (q, 1H, N*H*CH$_3$), 3.14 (d, 3H, CH_3NH), 2.44 (m, 2H, CH_2 in C2), 1.77–1.56 (m, 4H, CH_2 in C3 + C4), 1.44–1.13 (m, 12H, CH_2 in C5 + C6 + C7 + C8 + C9 + C10), 0.94 (t, 3H, CH_3).

2.3.9. Bis(N^1-allyl undecanal thiosemicarbazonato)nickel(II) (**18**)

Yield: 0.436 g, 70%. M.p.: 62 °C. IR(KBr, cm^{-1}): 3404(s) ν(NH); 2921(s) ν(CH$_{al}$); 1536(vs) ν(C=N); 1497(s) and 1271(m) ν(C–N); 723(w) ν(C=S). *Anal.* Calc. for $C_{30}H_{56}N_6NiS_2$: C, 57.8; H, 9.0; N, 13.5; S, 10.3. Found: C, 58.1; H, 9.2; N, 13.8; S, 10.5%. ^{1}H NMR (300 MHz, DMSO-d_6): δ_H (ppm) 7.68 (t, 1H, C*H*=N), 6.45 (q, 1H, N*H*CH$_2$), 5.93 (m, 1H, CH$_2$=C*H*–CH$_2$), 5.20 (dd, 1H, CH_2=CH, Hβ), 5.15 (dd, 1H, CH_2=CH, Hα), 4.24 (dd, 2H, CH–CH_2–NH), 2.46 (m, 2H, CH_2 in C2), 1.78–1.56 (m, 4H, CH_2 in C3 + C4), 1.46–1.12 (m, 12H, CH_2 in C5 + C6 + C7 + C8 + C9 + C10), 0.95 (t, 3H, CH_3).

2.4. X-ray crystallography

Single crystals of complexes **10**, **13**, **14**, **15** and **18** were mounted on glass fibers and used for X-ray diffraction experiments. Data were collected at room temperature for compounds **15** and **18** on a Bruker-Siemens SMART AXS 1000 equipped with CCD detector, while those of **10**, **13**, **14** on a Philips PW1100 diffractometer; in both cases graphite monochromated Mo Kα radiation ($\lambda = 0.71069$ Å) was used. Data collection details for the Bruker-Siemens SMART AXS 1000 are: crystal to detector distance = 5.0 cm, 2424 frames collected (complete sphere mode), time per frame = 20 s, oscillation $\Delta\sigma = 0.300°$. No crystal decay was observed in all cases. Data reduction was performed up to a 0.90 Å resolution by the SAINT pack-

age [25] and data were corrected for absorption effects by the SADABS [26] procedure; in the data collection carried out on the Philips PW1100 diffractometer the intensities were measured using a modified version [27] of the profile analysis method of Lehman and Larsen [28] and were corrected for Lorentz and polarization effects. The phase problem was solved by direct methods [29] and the structures were refined by full-matrix least-squares on all F^2 performed using SHELXL97 [30], as implemented in the WINGX [31]. Anisotropic displacement parameters were refined for non-hydrogen atoms in all complexes except in complex **15** for the carbon atoms of the allyl substituent which is disordered on two positions with occupancy factor of 0.5. All hydrogen atoms were located from Fourier maps and refined isotropically except those of the disordered allyl group in **15**. Only five hydrogen atoms were introduced in calculated positions, and more exactly those on the last two carbons of compound **18**.

Analytical expressions of neutral atom scattering factors were employed according to the International Tables [32]. Molecular geometry calculations were performed using the PARST [33] computer program and the structure drawings obtained with the ORTEPIII [34] and PLATON [35] programs. Further details for structural analysis are summarized in Tables 2a and 2b.

2.5. Biological activity testing

The compounds were tested for their solubility in the culture medium and in DMSO. At the same time the biological action of the solvent has been evaluated at the different concentration used. Compound **1** and its nickel derivative **10** were chosen as suitable for biological testing for their solubility and their purity. Cells were also treated with the inorganic nickel salt at the same concentrations used for 11 and no effect was observed on cell proliferation. Compounds were evaluated *in vitro* for their cytotoxicities, using peripheral blood mononuclear cells (PBMC) as a control, on human leukemic cell line U937 from a patient with histiocytic lymphoma. This line was grown in RPMI-1640 medium added of antibiotics (penicillin 100 U/ml, streptomycin 100 μg/ml), L-glutamine 2 mM and fetal bovine serum (FBS) 10% and kept at 37 °C in humid atmosphere at 5% CO_2.

2.5.1. Cell growth

The cells were seeded in a 96-well tray at a concentration of 1×10^5/ml in culture medium and kept in culture for 24 h until they reach a concentration of about 2×10^5/ml in exponential phase. The cells were then treated with the compounds in different concentrations in order to evaluate the IC50 through the ProCheckTM cell viability assay (Intergen). In each well were placed 100 μl of cell culture with 20 μl of ProCheckTM reagent to a final volume of 120 μl. After 1–4 h of incubation at 37 °C and under a 5% CO_2 humidified atmosphere the measurement was carried out through an ELX800 Packard spectrophotometer at 475 nm wavelength. Cell mortality was evaluated after 24 h by the trypan blue exclusion method and determined by using a hemocytometer.

2.5.2. Apoptosis assay

To evaluate apoptosis the cytofluorimetric method was followed, through the Mebcyto Apoptosis Kit, where Annexin-V and Propidium Iodide are used to discriminate early and late apoptosis. Early during the process of apoptosis, cells lose their phospholipid membrane asymmetry and expose phosphatidylserine (PS) at the cell surface. This

Table 1
Selected bond distances (Å) and angles (°)

	10	**13**	**14**	**15**	**18**
Ni1–S1	2.174(1)	2.168(1)	2.181(2)	2.175(1)	2.175(1)
Ni1–N3	1.909(2)	1.918(2)	1.927(2)	1.916(2)	1.914(2)
S1–C1	1.739(2)	1.739(2)	1.737(2)	1.736(4)	1.733(3)
N1–C1	1.343(3)	1.334(3)	1.341(2)	1.350(5)	1.352(3)
N2–N3	1.402(2)	1.410(2)	1.394(2)	1.400(4)	1.405(3)
N2–C1	1.309(3)	1.306(4)	1.302(2)	1.290(5)	1.289(3)
N3–C2	1.297(3)	1.288(2)	1.292(2)	1.295(5)	1.289(3)
C2–C3	1.491(3)	1.493(3)	1.490(4)	1.474(5)	1.486(3)
N3–Ni1–S1	85.49(5)	85.37(6)	85.73(8)	85.65(9)	85.71(6)
N3–Ni1–S1^I	94.51(5)	94.63(6)	94.27(8)	94.35(9)	94.29(6)
C1–S1–Ni1	95.24(7)	96.61(8)	96.60(9)	96.06(13)	96.23(9)
C1–N2–N3	111.7(2)	111.4(2)	112.8(1)	111.9(3)	111.9(2)
C2–N3–N2	114.8(2)	113.6(2)	112.1(1)	111.0(3)	110.8(2)
C2–N3–Ni1	125.5(1)	125.1(2)	126.4(1)	127.4(3)	127.7(2)
N2–N3–Ni1	119.7(1)	121.3(1)	121.5(1)	121.6(2)	121.5(2)
N2–C1–N1	119.1(2)	119.6(2)	119.0(2)	117.8(4)	117.6(3)
N2–C1–S1	123.0(2)	123.2(2)	123.2(1)	123.9(3)	124.1(2)
N1–C1–S1	117.9(2)	117.2(2)	117.8(1)	118.3(3)	118.3(2)
	$I = 1-x, -1-y, -1-z$	$I = -x, 1-y, 1-z$	$I = 1-x, 1-y, -z$	$I = -x, -y, 1-z$	$I = -x, -y, 1-z$

Table 2a
Experimental data for crystallographic analyses

Compound	**10**	**13**	**14**
Formula	$C_{16}H_{32}N_6NiS_2$	$C_{22}H_{44}N_6NiS_2$	$C_{24}H_{48}N_6NiS_2$
a (Å)	8.272(1)	8.174(5)	7.467(7)
b (Å)	8.486(1)	8.226(4)	9.239(7)
c (Å)	8.810(1)	11.414(2)	11.745(17)
α (°)	78.88(1)	110.14(3)	107.75(8)
β (°)	66.18(1)	91.19(2)	100.73(7)
γ (°)	68.05(1)	107.49(4)	105.10(8)
V (Å^3)	524.1(1)	680.6(6)	713(1)
Z	1	1	1
Formula weight	431.30	515.46	543.51
Space group	$P\bar{1}$	$P\bar{1}$	$P\bar{1}$
D_{calc} (Mg/m^3)	1.366	1.258	1.265
μ (mm^{-1})	1.14	0.89	0.85
θ_{max}	30	25	30
Observed reflections	3056	1955	4153
Unique reflections	2789	1736	3521
Number of parameters	179	142	247
R^a (observed reflections)	0.0545	0.0290	0.0387
wR_2^b (all reflections)	0.1626	0.0774	0.1114

[a] $R = \sum(||F_o| - |F_c||)/\sum|F_o|$.
[b] $wR_2 = [\sum w(|F_o|^2 - |F_c|^2)^2/\sum w(F_o^2)]^{1/2}$.

Table 2b
Experimental data for crystallographic analyses

Compound	**15**	**18**
Formula	$C_{28}H_{52}N_6NiS_2$	$C_{30}H_{56}N_6NiS_2$
a (Å)	5.477(1)	5.328(1)
b (Å)	9.133(1)	9.170(1)
c (Å)	17.736(3)	18.739(3)
α (°)	92.69(1)	91.670(2)
β (°)	96.24(1)	95.333(2)
γ (°)	104.46(1)	101.723(2)
V (Å^3)	851.46(2)	891.5(2)
Z	1	1
Formula weight	595.59	623.64
Space group	$P\bar{1}$	$P\bar{1}$
D_{calc} (Mg/m^3)	1.162	1.162
μ (mm^{-1})	0.71	0.69
θ_{max}	25	24.5
Unique reflections	2979	2542
Observed reflections	1985	1883
Number of parameters	231	270
R^a (observed reflections)	0.0612	0.0379
wR_2^b (all reflections)	0.1487	0.0933

[a] $R = \sum(||F_o| - |F_c||)/\sum|F_o|$.
[b] $wR_2 = [\sum w(|F_o|^2 - |F_c|^2)^2/\sum w(F_o^2)]^{1/2}$.

process can be monitored by using Annexin-V which is a Ca^{2+}-dependent, phospholipid-binding protein with high affinity for PS, and is useful for identifying apoptotic cells with exposed PS. Translocation of PS to the external cell surface is not unique to apoptosis, but occurs also during cell necrosis. The difference between these two forms of cell death is that during the initial stages of apoptosis the cell membrane remains intact, while at the very moment that necrosis occurs the cell membrane looses its integrity and becomes leaky. Therefore, necrotic cells easily stained with Propidium Iodide as well as Annexin-V, whereas apoptotic cells are stained only with Annexin-V.

3. Results and discussion

The ligands synthesized are characterized by a long hydrophobic tail and by a polar thiosemicarbazone head. By varying the length of the tail and the substitution on the polar head with a methyl or an allyl fragment their physicochemical properties have been modified. The presence of substituents on the terminal nitrogen of the thiosemicarbazide group influences the hydrogen bond pattern of the molecules and this is particularly apparent in the crystal packing. These compounds were synthesized as part of a wider screening project in order to gain an insight into the causes that render many thiosemicarbazone metal complexes so active on cell proliferation inhibition and apoptosis induction.

3.1. Crystal and molecular structure

The crystals of compounds **10** and **13** are made up of complex molecules of formula $[Ni(C_8H_{17}N_3S)_2]$ and $[Ni(C_{11}H_{23}N_3S)_2]$, respectively. The structure of the complex units, as can be seen in the Ortep plot reported in Figs. 1 and 2, is formed by a nickel(II) ion, lying on a center of symmetry that coordinates two molecules of the ligand in its monodeprotonated form. In the asymmetric unit the coordinated thiosemicarbazonate unit chelates through the sulfur and the iminic nitrogen forming a 5-member chelation rings. The metal to donor distances are only slightly different: the Ni1–N3 bonds are 1.909(2) Å and 1.918(2) Å and the Ni1–S1 bonds of 2.174(1) Å and 2.168(1) Å for **10** and **13**, respectively. Also the corresponding N–Ni–S angles are quite similar: 85.49(5)° in the first and in the second 85.37(6)°. Another feature that these two compounds have in common is the

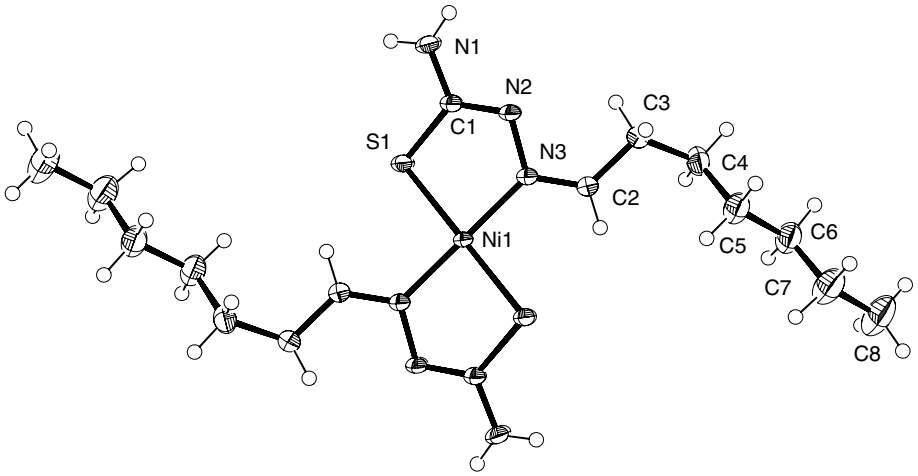


Fig. 1. ORTEP drawing of complex **10** with thermal ellipsoids at the 50% probability level.

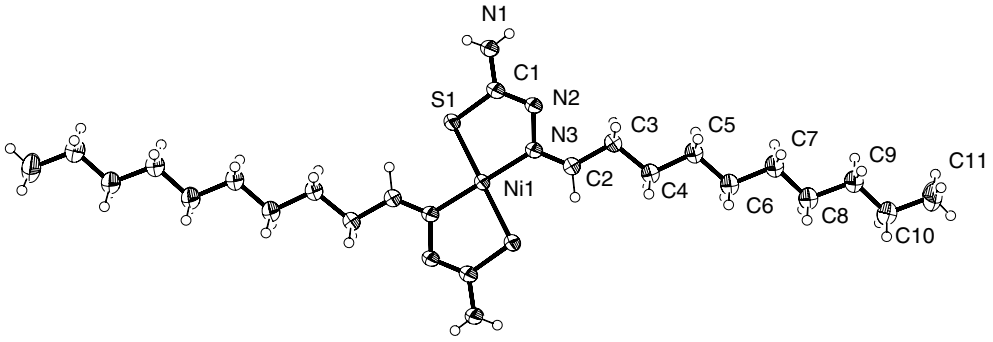


Fig. 2. ORTEP drawing of complex **13** with thermal ellipsoids at the 50% probability level.

terminal amine nitrogen that is involved in two hydrogen bonds. One of the hydrogens is used for a hydrogen bond with the deprotonated hydrazinic nitrogen of an adjacent molecule and the second hydrogen binds the sulfur of another adjacent molecule. In **10** the hydrogens bonds are N1–H2···N2 $(-x+1, -y+2, -z+2)$ 3.036(3) Å 168(4)° and N1—H1···S1 $(-x+1, -y+2, -z+1)$ 3.638(3) Å 162(4)° while in **13** N1–H2···N2 $(-x-1, -y, -z+1)$ 3.132(4) Å 171.4(2)° and N1–H1···S1 $(-x-1, -y+1, -z+1)$ 3.618(3) Å 138.7(2)°. These two hydrogen bonds generate bidimensional sheets that are distorted by the presence of the hydrophobic tails. The strain can be perceived by the more significant differences that can be found in the puckering amplitude [36] of the coordination ring that in **10** is larger than in **13** [**10** $q2 = 0.268(2)$ Å $\varphi 2$ di $-1.9(5)°$; **13** $q2 = 0.175(1)$ Å $\varphi 2 = -3.8(6)°$]. The sheets are then packed through hydrophobic interaction between the lipophilic chains protruding from the hydrogen bonds planes. Noteworthy in compound **13** is the lengthening of the chain that causes a change in the angle between the average line defined by the hydrophobic chain and the normal to the coordination plane defined by the nickel and the four donor atoms. In compound **10** the angle is 71.03(5)° while in compound **13** it increases up to 79.26(5)°.

The structure of compound **14**, **15** and **18** $[Ni(C_{12}H_{24}N_3S)_2]$, $[Ni(C_{15}H_{26}N_3S)_2]$ and $[Ni(C_{15}H_{28}N_3S)_2]$ are reported as ORTEP plots in Figs. 3–5. In these molecules one hydrogen of the terminal nitrogen is substituted with a methyl or an allyl group and the formation of the NH···N hydrogen bond is thus prevented. In these crystals the complexes are arranged as ribbons flanked by alternating protruding hydrophobic chains. The lack of a second hydrogen bond allow the aliphatic chains to lie in the coordination planes and this change influences the strain on the coordination moiety as can be seen from the puckering amplitude that drops to an average value of 0.081(2) Å.

The hydrogen bonds observed in the three packings are N1–H21···S1 $(-x, -y, -z+1)$ 3.607(3) Å 151(3)° in **14**, N1–H21···S1 $(-x, -y+1, -z+1)$ 3.550(4) Å 154(4)° in **15** and N1–H20···S1 $(-x, -y+1, -z+1)$ 3.572(3) Å 151.4(2)° in **18** and these bonds are slightly tighter than the ones found in the first two compounds in agreement with a lesser strain.

To sum up, the five complexes can be classified into two groups: those with two possible hydrogen bonds and those with one (Fig. 6). In the former the packing is based on planes generated by hydrogen bonds that developed in two different directions and these planes are subsequently stacked one upon the other to form the crystal through

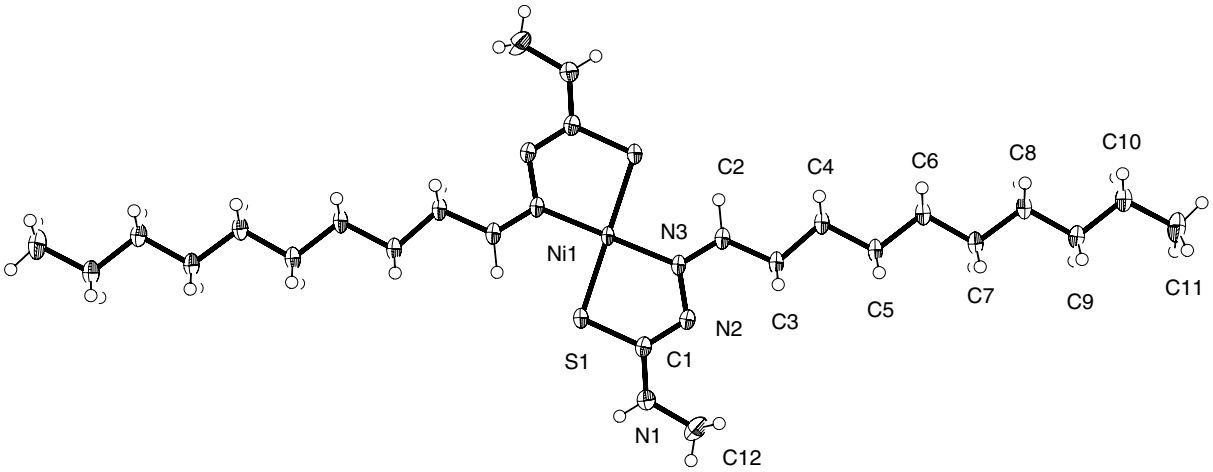


Fig. 3. ORTEP drawing of complex **14** with thermal ellipsoids at the 50% probability level.

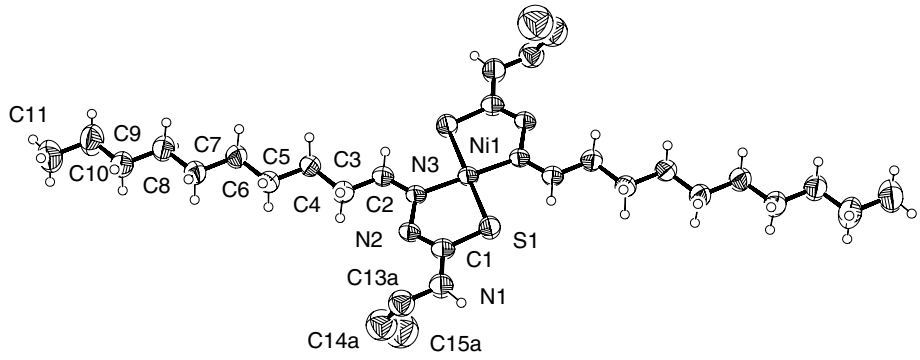


Fig. 4. ORTEP drawing of complex **15** with thermal ellipsoids at the 50% probability level. Atoms labelled with "a" correspond to one of the two possible positions occupied by the disordered allyl group.

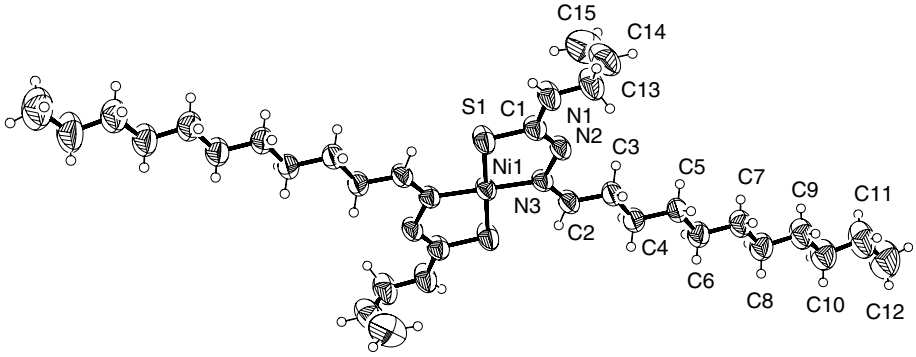


Fig. 5. ORTEP drawing of complex **18** with thermal ellipsoids at the 50% probability level.

van der Waals interactions. In the second group ribbons of molecules are formed by the only possible hydrogen bond interaction and the second dimension is obtained by the intercalation of the hydrophobic tails and all this approximately in a plane. These planes are then piled up through hydrophobic interactions to form the third dimension. In this second group the packing is looser and the lack of one of the hydrogen bond can be identified as the main cause of their lower melting points (**14**, **15** and **18** m.p. 77°, 55° and 62°) with respect to those of the complexes obtained from unsubstituted thiosemicarbazones (**10** and **13** m.p. 156° and 124°). Selected bond distances and angles are reported in Table 1.

3.2. Effects on cell proliferation and apoptosis

Before carrying out biological tests to compare the *in vitro* apoptotic activity of the thiosemicarbazones and

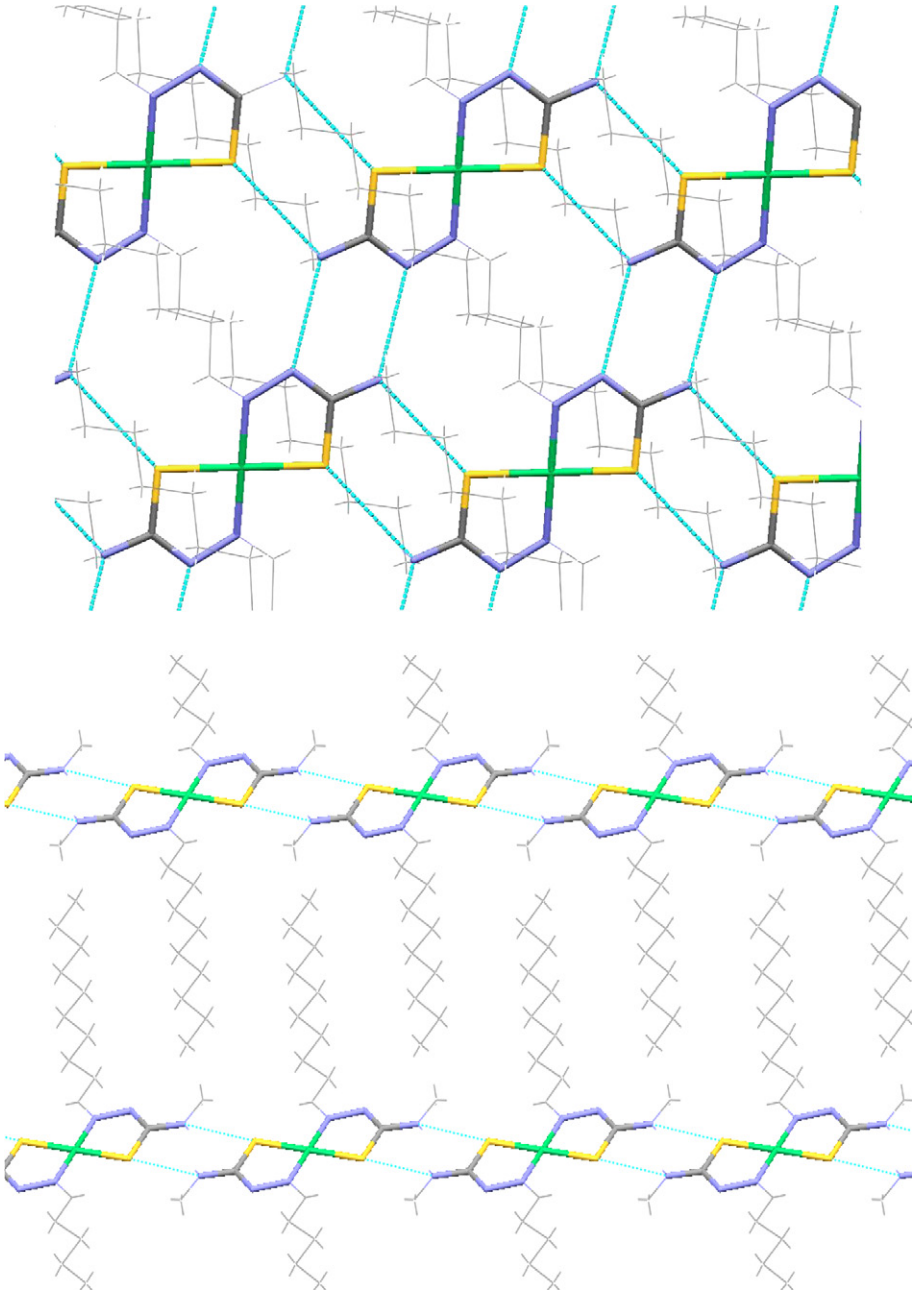


Fig. 6. Hydrogen bond patterns found in the structures: group 1 (above) and group 2 (below).

their corresponding nickel complexes, the compounds were dissolved in DMSO and the solution was tested in the culture medium to check that the compounds remain in solution. The biological action of DMSO could above certain concentrations be responsible for inhibition, and was therefore evaluated in blank experiments. Based on the solubility of the 18 compounds our biological investigations were carried out with ligand **1** and its nickel complex **10**, considered the most suitable for the biological tests.

To evaluate the IC50 for cell line U937 using a modified MTT test, ligand **1** was used in a range between 1 and 54 μM and the corresponding complex between 0.5 and 4.61 μM. From these tests resulted that, after 24 h, the ligand did not show any significant effect on proliferation even at high concentrations (54 μM) while complex **10** was able to inhibit cell proliferation at 50% with a concentration of 3.46 μM with DMSO lower than 0.02%. The data were obtained using the MTT test and were confirmed by controlling the cell vitality with Trypan blue after 24 h.

The complex has been therefore tested to verify if it acts by inducing apoptosis. What has been found is that in short times (2 and 6 h) there are no signs of apoptosis in the cells while after 12 h of incubation in the presence of an IC_{50} concentration of the complex a 8.6% of cells in early apoptosis with respect to the untreated control and after 24 h this percentage increased to 16% (Fig. 7).

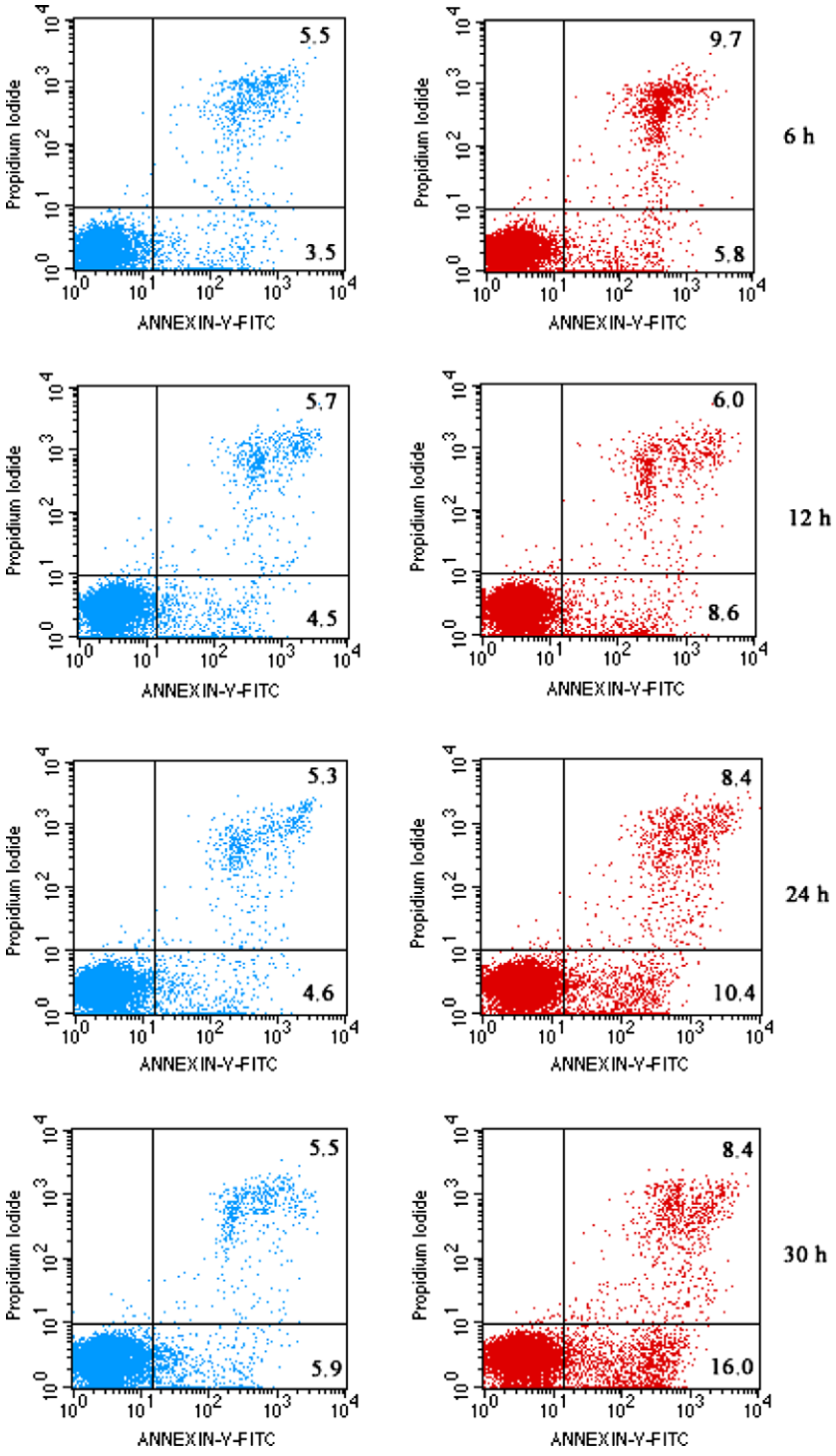


Fig. 7. Apoptosis assays: the dot plots represent the % of cells in early apoptosis, Annexin-V positive (lower right quadrant), and cells in late apoptosis, Annexin-V and Propidium Iodide positive (upper left quadrant), the dot plots on the left refer to the untreated cells.

4. Conclusions

At present an accepted theory concerning the action of this class of compounds centers on the ability of thiosemicarbazones to sequester iron and to inhibit the iron-dependent enzyme ribonucleotide reductase [37,38]. This inhibition would prevent cells to accomplish their DNA synthesis step in their duplication cycle. The properties of thiosemicarbazones through which ribonucleotide reductase is deactivated are two and namely their ability to sequester iron, the metal center in ribonucleotide reductase, and their capacity to react with a radical species present in the vicinity of the active site involved in the attack on ribose to transform it in deoxyribose. An hindrance in

the synthesis phase of the cell cycle is one of those events that ultimately lead the cell to the apoptotic process. This theory has its drawbacks and in particular it does not explain the systematic higher activity of complexes with respect to the ligands for instance, and also the fact that we observed in a previous work where the cell cycle stopped after the DNA duplication had been completed (G2/M phase) [39].

Besides these interactions with ribonucleotide reductase concomitant processes such as the generation of reactive oxygen species (ROS) that can cause damages within the cell or interactions with external cell receptors that stimulate programmed cell death are equally conceivable.

From our experiments with compounds **1** and **10** three facts are relevant and more precisely that the ligand by itself, even at higher concentrations, gives no interference in the cell cycle, secondly also a nickel acetate solution with the same concentration shows no effect on cell proliferation and thirdly that the nickel complex has no effect on a normal cell line taken as a reference. An hypothesis that can be proposed is that since the molecules presented in this work are characterized by hydrophobic tails, they can easily cross the cell membrane and could also get inserted into the mitochondrial lipidic bilayer. A redox center anchored to a mitochondrion is particularly subject to generate ROS being exposed to oxygen and to the electrons of the respiratory chain and can become a real Troy horse for the cell. Damages on the lipidic bilayer of mitochondria caused by ROS could eventually lead to a leak of cytochrome c that is one of the key events that leads to apoptosis: the assembly of the so called ''apoptosome'' and the consequent triggering of the caspase cascade. A further point that could support our hypothesis is that mitochondria of tumoral and in particular leukemic cells are characterized by a decreased activity of radical scavenging enzyme Mn SOD [40] and this could explain the selectivity of compound **10** towards leukemia cell line U937 with respect to healthy peripheral blood mononuclear cells.

A further hypothesis of action, given the planarity of the nickel complexes and the consequent unsaturated coordination sphere of the metal, is the intercalation of these molecules between the nucleic bases and subsequent reactions that could include hydrolysis of the DNA backbone, formation of nickel adducts and even oxidative damage to the nucleobases.

Acknowledgment

This work was supported by the Italian Ministry of University and Research (MIUR, PRIN.2004059078).

Appendix A. Supplementary material

CCDC 616867, 616868, 616869, 616870 and 616871 contains the supplementary crystallographic data for **10**, **13**, **14**, **15** and **18**. These data can be obtained free of charge via http://www.ccdc.cam.ac.uk/conts/retrieving.html, or from the Cambridge Crystallographic Data Centre, 12 Union Road, Cambridge CB2 1EZ, UK; fax: (+44) 1223-336-033; or e-mail: deposit@ccdc.cam.ac.uk. Supplementary data associated with this article can be found, in the online version, at doi:10.1016/j.poly.2007.07.014.

References

[1] S. Padhyé, G.B. Kauffman, Coord. Chem. Rev. 63 (1985) 127.
[2] R.W. Byrnes, M. Mohan, W.E. Antholine, R.X. Xu, D.H. Petering, Biochemistry 29 (1990) 7046.
[3] A. Kolocouris, K. Dimas, C. Pannecouque, M. Witvrouw, G.-B. Foscolos, G. Stamatiou, G. Fytas, G. Zoidis, N. Kolocouris, G. Andrei, R. Snoeck, E. De Clercq, Bioorg. Med. Chem. 12 (2002) 723.
[4] K.C. Agrawal, A.C. Sartorelli, J. Med. Chem. 12 (1969) 771.
[5] W.E. Antholine, J. Knight, H. Whelan, D.H. Petering, Mol. Pharm. 13 (1977) 89.
[6] D.L. Klayman, J.F. Bartosovich, T.S. Griffin, C.J. Mason, J.P. Scovill, J. Med. Chem. 22 (1979) 855.
[7] D.L. Klayman, J.P. Scovill, J.F. Bartosovich, C.J. Mason, J. Med. Chem. 22 (1979) 1367.
[8] Z. Lakovidou, A. Papageorgiou, M.A. Demertzis, E. Mioglou, D. Mourelatos, A. Kotsis, P.N. Yadav, D. Kovala-Demertzi, Anticancer Drugs 12 (2001) 65.
[9] R.C. Condit, R. Easterly, R.F. Pacha, Z. Fathi, R.J. Meis, Virology 185 (1991) 857.
[10] M. Manowitz, G. Walter, J. Pharm. Sci. 53 (1964) 220.
[11] O.E. Offiong, Transition Met. Chem. 23 (1998) 553.
[12] R.H.U. Borges, E. Paniago, H. Beraldo, J. Inorg. Biochem. 65 (1997) 267.
[13] M. Belicchi Ferrari, G. Gasparri Fava, P. Tarasconi, R. Albertini, S. Pinelli, R. Starcich, J. Inorg. Biochem. 53 (1994) 13.
[14] M. Belicchi Ferrari, F. Bisceglie, E. Leporati, G. Pelosi, P. Tarasconi, S. Pinelli, Bull. Chem. Soc. Jpn. 75 (2002) 781.
[15] M. Belicchi Ferrari, G. Gasparri Fava, E. Leporati, G. Pelosi, R. Rossi, P. Tarasconi, R. Albertini, A. Bonati, P. Lunghi, S. Pinelli, J. Inorg. Biochem. 70 (1998) 145.
[16] M. Belicchi Ferrari, F. Bisceglie, G. Pelosi, P. Tarasconi, R. Albertini, A. Bonati, P. Lunghi, S. Pinelli, J. Inorg. Biochem. 83 (2001) 169.
[17] M. Baldini, M. Belicchi-Ferrari, F. Bisceglie, G. Pelosi, S. Pinelli, P. Tarasconi, Inorg. Chem. 42 (2003) 2049.
[18] M. Belicchi-Ferrari, S. Capacchi, F. Bisceglie, G. Pelosi, P. Tarasconi, Inorg. Chim. Acta 312 (2001) 81.
[19] S.W. Ragsdale, Curr. Opin. Chem. Biol. 2 (2) (1998) 208.
[20] M.C. Rodriguez-Arguelles, M.B. Ferrari, F. Bisceglie, C. Pelizzi, G. Pelosi, S. Pinelli, M. Sassi, J. Inorg. Biochem. 98 (2) (2004) 313.
[21] F. Liang, P. Wang, X. Zhou, T. Li, Z. Li, H. Lin, D. Gao, C. Zheng, C. Wu, Bioinorg. Med. Chem. Lett. 14 (2004) 1901.
[22] Z. Afrasiabi, E. Sinn, W. Lin, Y. Ma, C. Campana, S. Padhye, J. Inorg. Biochem. 99 (7) (2005) 1526.
[23] M. Belicchi-Ferrari, F. Bisceglie, G. Pelosi, M. Sassi, P. Tarasconi, M. Cornia, S. Capacchi, R. Albertini, S. Pinelli, J. Inorg. Biochem. 90 (2002) 113.
[24] Peter P.T. Sah, T.C. Daniels, Recueil 69 (1954) 1545.
[25] SAINT: SAX, Area Detector Integration Program, Siemens Analytical Instruments Inc., Madison, WI, USA, 1995.
[26] G. Sheldrick, SADABS: Siemens Area Detector Absorption Correction Software, University of Goettingen, Germany, 1996.
[27] D. Belletti, A. Cantoni and G. Pasquinelli, Gestione on line di diffrattometro a cristallo singolo Siemens AED con sistema IBM PS 2/30, Internal Report 1/88, Centro di Studio per la Strutturistica Diffrattometrica del CNR, 1988.
[28] M.S. Lehman, F.K. Larsen, Acta Crystallogr., Sect. A 30 (1974) 580.
[29] A. Altomare, M.C. Burla, M. Camalli, G. Cascarano, C. Giacovazzo, A. Guagliardi, A.G. Moliterni, G. Polidori, R. Spagna, SIR97: A New Program For Solving And Refining Crystal Structures, Istituto di

Ricerca per lo Sviluppo di Metodologie Cristallografiche, C.N.R., Bari, Italy.
[30] G. Sheldrick, SHELXL97. Program for Structure Refinement, University of Goettingen, Germany, 1997.
[31] L.J. Farrugia, J. Appl. Crystallogr., Sect. A 32 (1999) 837.
[32] International Tables for X-ray Crystallography, vol. 4, Kynoch Press, Birmingham, UK, 1974.
[33] M. Nardelli, J. Appl. Cryst. 28 (1995) 659.
[34] C.K. Johnson, M.N. Burnett, ORTEPIII. Report ORNL-6895, Oak Ridge National Laboratory, Tennessee, USA, 1996.
[35] A.L. Spek, PLATON. A Multipurpose Crystallographic Tool, Utrecht University, Utrecht, The Netherlands, 1999.
[36] D. Cremer, J.A. Pople, J. Am. Chem. Soc. 97 (1975) 1354.
[37] D.R. Richardson, Crit. Rev. Oncol. Hemat. 42 (2002) 267.
[38] D.B. Lovejoy, D.R. Richardson, Blood 100 (2002) 666.
[39] M. Belicchi-Ferrari, F. Bisceglie, C. Casoli, S. Durot, Morgenstern-Badarau, G. Pelosi, E. Pilotti, S. Pinelli, P. Tarasconi, J. Med. Chem. 48 (2005) 1671.
[40] L.W. Oberlay, Superoxide dismutase and cancer, in: L.W. Oberlay (Ed.), Superoxide Dismutase, vol. II, CRC Press, Boca Raton, FL, 1982, p. 127.

which are used as fluorescent brighteners as well. The first optical brightener, 2-styryl-1,3-benzothiazole (styryl = phenylethenyl) was prepared for the first time in the XIXth century. Apart from the above-mentioned properties of benzothiazole and its derivatives, they are of chemical interest from a coordination point of view since these molecules contain both S and N heteroatoms besides the π-aromatic system and show a wide variety of metal complexes.

As a part of our comprehensive investigation of the coordination chemistry of the 12th group of metals with various ligands, we recently started to explore the complexes of Zn and Hg with benzothiazole derivatives acting as dominantly monodentate neutral ligands through the N donor atom [8–10]. To our best knowledge there is only one article published so far on 2-styryl-1,3-benzothiazole complexes with mercury(II) halides [11] in which Battaglia and co-workers reported the existence of a few other mercury(II) complexes of the formula Hg_2Cl_4(sb), $HgBr_2$(sb), HgI_2(sb) and HgI_2(sb)$_2$. Complex **5**, $HgBr_2$(sb)$_2$, isolated and characterized by us, is isostructural with the later one.

In this paper, we report the synthesis and structural characterization of 2-styryl-1,3-benzothiazole and our results of a study on its coordinating ability with mercury(II) chloride and bromide. We also report, for the first time, the crystal and molecular structures of the cycloaddition reaction products of 2-styryl-1,3-benzothiazole as well as of 2-(4-chlorostyryl)-1,3-benzothiazole.

2. Experimental

2.1. Materials and physical measurements

Mercury(II) chloride and mercury(II) bromide were used as received from Aldrich without further purification. CHNS analyses were performed in the Analytical Services Laboratories of the Institute Ruđer Bošković. The mercury content was determined by complexometric titration with sodium diethyldithiocarbamate of the solution obtained after decomposition of the specimen in *aqua regia* [12].

The IR spectra were obtained from KBr pellets in the range 4000–450 cm^{-1} with a Perkin–Elmer Spectrum RX I FT-spectrometer. The Raman spectra in the range 600–100 cm^{-1} were obtained with a Bruker Equinox 55 spectrometer. The thermal measurements were performed using a simultaneous TGA–DTA analyser (Mettler-Toledo TGA/SDTA 851^e). The TGA and DTA curves were obtained by placing the samples (approximately 10 mg in mass) in small alumina pans, with heating rate of 10 °C/min and nitrogen (purity above 99.996%) flowing at a rate of 20 mL/min.

2.2. Preparations

2.2.1. 2-Styryl-1,3-benzothiazole (sb) (*1*)

2-Styryl-1,3-benzothiazole was previously prepared in our laboratory by the condensation of benzaldehyde with 2-methylbenzothiazole, using the described procedures [13,14]. The single crystals of sb were obtained by the liquid diffusion crystallization method of an ethanol/*n*-pentane solution.

M.p. = 111 °C. IR ν_{max} (cm^{-1}): 3058w, 3028w, 2992w, 1628m, 1616w, 1572w, 1554w, 1497s, 1475m, 1453m, 1445vs, 1434s, 1315s, 1281w, 1261w, 1242m, 1233m, 1219w, 1190s, 1173w, 1155w, 1123w, 1073w, 1012m, 961vs, 942m, 880w, 760vs, 727vs, 691vs, 670m, 511w, 485w.

2.2.2. (2-Styrylbenzothiazole-N)mercury(II) chloride-μ-chlorobis(2-styrylbenzothiazole-N)mercury(II), $[Hg_2Cl_4(sb)_3]$ (*2*)

A solution of 2-styryl-1,3-benzothiazole (0.15 g, 0.632 mmol) in 15 mL of ethanol was added slowly to a solution of mercury(II) chloride (0.085 g, 0.313 mmol) in 7 mL of ethanol. The reaction mixture was refluxed for 5 h and then left to evaporate at room temperature. After 10 days yellow-green crystals were filtered off, washed several times with ethanol and dried. Yield: 0.16 g (81.6%). *Anal.* Calc. for $C_{45}H_{33}Hg_2Cl_4N_3S_3$ (1254.96): C, 43.07; H, 2.65; Hg, 31.98; N, 3.35; S, 7.66. Found: C, 42.95; H, 2.71; Hg, 32.05; N, 3.60; S, 7.79%. M.p. = 216 °C (dec.). IR ν_{max} (cm^{-1}): 3057w, 3024w, 1624m, 1576w, 1560w, 1497m, 1469m, 1455m, 1447m, 1432s, 1318m, 1274w, 1244w, 1224w, 1199w, 1183w, 1153w, 1106w, 1068w, 1017w, 951m, 888w, 854w, 759s, 750vs, 725m, 720s, 698m, 680s, 614w, 512w, 477w.

2.2.3. 1,3-Bis(1,3-benzothiazol-2-yl)-2,4-diphenylcyclobutane (*3*)

Two weeks after the isolation of compound **2**, a small amount of yellow crystals was obtained from filtrate. Yield: few crystals. IR ν_{max} (cm^{-1}): 3055m, 3023m, 2996w, 2371w, 2344w, 1931w, 1895w, 1800w, 1734w, 1653w, 1629m, 1575w, 1554w, 1500m, 1478m, 1455m, 1446s, 1434s, 1340w, 1332w, 1316m, 1282w, 1191m, 1183m, 1164w, 1155w, 1123w, 1109w, 1072w, 106w, 1011m, 999w, 964m, 956vs, 935m, 913w, 964m, 867w, 849w, 756vs, 750vs, 724vs, 710m, 670m, 686vs, 664s, 612w, 584w, 547w, 522w, 511m, 503w, 480m, 453w.

2.2.4. 1,3-Bis(1,3-benzothiazol-2-yl)-2,4-bis(4-chlorophenyl)cyclobutane (*4*)

Compound **4** was previously prepared in our laboratory by condensation of *p*-chlorobenzaldehyde with 2-methylbenzothiazole, using the described procedures [14,15]. Yield: 8.2%. Compound **4** is soluble in CH_2Cl_2, $CHCl_3$, less soluble in EtOH and acetone.

Single crystals of **4** were obtained by the liquid diffusion crystallization method of an ethanol/*n*-pentane solution i.e. in contrast to compound **1**, cycloaddition occurred during crystallization.

2.2.5. Dibromobis(trans-2-styrylbenzothiazole-N)mercury(II), $[HgBr_2(sb)_2]$ (*5*)

A solution of 2-styryl-1,3-benzothiazole (0.14 g, 0.590 mmol) in 15 mL of ethanol was added slowly to a solution of mercury(II) bromide (0.10 g, 0.277 mmol) in

5 mL of ethanol. The reaction mixture was refluxed for 3 h and then left to evaporate at room temperature. After two weeks yellow crystals were filtered off, washed several times with ethanol and dried. Yield: 0.15 g (75.0%). *Anal*. Calc. for $C_{30}H_{22}HgBr_2N_2S_2$ (835.24): C, 43.14; H, 2.66; Hg, 24.02; N, 3.35; S, 7.68. Found: C, 43.62; H, 2.91; Hg, 24.11; N, 3.80; S, 7.94%. M.p. = 196 °C. IR ν_{max} (cm^{-1}): 3052w, 3024w, 1624m, 1576w, 1560w, 1497m, 1469m, 1455m, 1447m, 1432s, 1318m, 1274w, 1244w, 1224w, 1199m, 1183, 1153w, 1106w, 1068w, 1017w, 951s, 887w, 854w, 759s, 750vs, 725m, 720m, 699m, 680m, 614w, 512w, 477w.

2.3. X-ray diffraction experiment

The general and crystal data and summary of intensity data collection and structure refinement for compounds **1**–**5** are given in Table 1.

The data collection for all the structures were carried out on an Xcalibur four-circle kappa geometry single-crystal diffractometer with an Xcalibur Sapphire 3 CCD detector by applying the CrysAlis Software system, Versions 171.23 and 171.26 at ambient temperature [16]. The Lorentz-polarization effect was corrected and intensity data reduced by the CrysAlis RED application of the CrysAlis Software system, Version 171.23 [16]. The diffraction data for **2** and **5** were corrected for absorption by the multi-scan procedure.

The structure solution procedure for all five structures were performed by direct methods with the SHELXS program [17]. The coordinates and anisotropic thermal displacement parameters for all non-hydrogen atoms were refined by the least-squares methods based on F^2 using the SHELXL-97 program [18]. The all hydrogen atoms, which belong to phenyl and ethenyl carbon atoms were generated at ideal geometrical positions [Csp^2–H 0.93 Å, Csp^3–H 0.98 Å; U_{iso}(-H) = 1.2U_{eq}(C)] and refined applying the riding model. The molecular graphics were done using the PLATON-98 program [19].

3. Results and discussion

3.1. Preparation

We have examined reactions of sb with mercury(II) chloride and bromide in ethanol solution. The molar ratio of sb to mercury halide was 2:1. The halide complexes described herein have different formulae from those reported by Battaglia and co-workers [11]. The complexes were only sparingly soluble in common organic solvents (ethanol, methanol, DMSO, DMF).

3.2. IR and Raman spectra

The IR spectra of styrylbenzothiazoles and their metal complexes in the range 1650–1380 cm^{-1} can be associated with overall ring-skeletal (benzene and thiazole ring) stretching modes [20,21]. Ring-breathing and CH in-plane deformations fall into range 1320–935 cm^{-1}. Vibration modes in the 880–720 cm^{-1} range can be attribute to the CH out-of-plane deformations. 2-Styryl-1,3-benzothiazole exhibits an absorption band assigned to ν(CN) at 1475 cm^{-1}, which is shifted upon coordination to the mercury atom to 1469 cm^{-1} in both complexes and is in accordance with the literature data regarding other metal complexes containing the bta moiety [22,23]. A small shift towards lower energy indicates decreased C=N double bond character due to coordination of the ligand through the ring nitrogen atom.

Complementary information is obtained from low frequency Raman spectra. The spectra of the halide complexes in the range 300–150 cm^{-1} show bands which are not seen in the spectrum of the free ligand. These bands are assigned to terminal and bridging ν(Hg–halide) modes [11,24–26]. The strong bands in the spectrum of the chloride complex at 289 and 181 cm^{-1} are attributed to the Hg–Cl terminal and Hg–Cl bridging stretching modes, respectively. The mononuclear bromide complex shows only a Hg–Br terminal stretching vibration at 178 cm^{-1}.

The IR and Raman spectra of the mercury(II) complexes are in agreement with their crystal structures.

3.3. Crystal structure description

ORTEP plots of the molecular structures for compounds **1**–**5** are depicted in Fig. 1. The selected molecular geometries are listed in Table 2 for organic molecules **1**, **3** and **4** and Table 3 for complexes **2** and **5**.

3.3.1. Compounds *1*, *3* and *4*

On surveying of the CSD (Version 5.28, November 2006, update January 2007) [27], only one organic derivative of 2-styryl-1,3-benzothiazole was found, 2-[2-(3,4-dichlorophenyl)vinyl]benzo[*d*]thiazole [28].

The 2-styryl-1,3-benzothiazole molecule, sb, **1** is essentially planar (Fig. 1a) with a dihedral angle of only 2.9(1)° between the benzothiazole and phenyl rings. The benzothiazole and phenyl rings are essentially planar, with a maximum deviation from the least-squares plane of only 0.017(2) and −0.007(2) Å for atoms C7 and C15, respectively. The S1–C2 bond distance of 1.731(2) Å is slightly shorter than the S1–C1 bond distance of 1.766(3) Å (1.739(4) Å and 1.760(4) Å in the structure of 2-[2-(3,4-dichlorophenyl)vinyl]benzo[*d*]thiazole [28]) due to the pronounced delocalization in the –S–C=N– fragment of the thiazole ring of the ligands, but both of them are between a pure σ S–C bond (1.82 Å) and a double S=C bond (1.56 Å) [29]. A similar trend is observed for the N1–C1 and N1–C7 bond distances (1.278(3) and 1.379(3) Å, respectively). The bond angle around the S1 atom (C2–S1–C1 89.07(11)°) is in agreement with that found in the structure of 2-[2-(3,4-dichlorophenyl)vinyl]benzo[*d*]thiazole (89.1(2)°) [28]. The configuration around C8=C9 is *E*. The molecules are arranged with antiparallel stacking, attracted

Table 1
General and crystal data and summary of intensity data collection and structure refinement for compounds **1**, **2**, **3**, **4** and **5**

Compound	**1**	**2**	**3**	**4**	**5**
Chemical name	2-styryl-1,3-benzothiazole (sb)	(2-styrylbenzothiazole-*N*)mercury(II) chloride-μ-chlorobis(2-styrylbenzothiazole-*N*)mercury(II)	1,3-bis(1,3-benzothiazole-2-yl)-2,4-diphenylcyclobutane	1,3-bis(1,3-benzothiazole-2-yl)-2,4-bis(4-chlorophenyl)cyclobutane	dibromobis(*trans*-2-styrylbenzothiazole-*N*)mercury(II)
Formula	$C_{15}H_{11}NS$	$C_{45}H_{33}Cl_4Hg_2N_3S_3$	$C_{30}H_{22}N_2S_2$	$C_{30}H_{20}Cl_2N_2S_2$	$C_{30}H_{22}Br_2HgN_2S_2$
Molecular weight	237.31	1254.90	474.62	543.50	835.03
Crystal system	monoclinic	triclinic	orthorhombic	triclinic	monoclinic
Colour and habit	colourless and plate	yellow and block	colourless and prism	colourless and plate	yellow and prism
Space group	$P2_1/c$	$P\bar{1}$	*Pbca*	$P\bar{1}$	$C2/c$
Crystal dimensions (mm)	$0.29 \times 0.26 \times 0.17$	$0.48 \times 0.32 \times 0.23$	$0.36 \times 0.28 \times 0.12$	$0.41 \times 0.32 \times 0.22$	$0.67 \times 0.30 \times 0.24$
Unit cell parameters					
a (Å)	6.1436(2)	12.756(2)	10.8113(2)	5.9048(9)	14.5676(6)
b (Å)	14.5189(5)	14.107(2)	11.0592(2)	9.3087(13)	13.3433(5)
c (Å)	13.3588(6)	14.3614(19)	19.8087(4)	12.075(2)	15.7051(5)
α (°)	90	60.972(14)	90	96.23(1)	
β (°)	93.465(4)	75.233(13)	90	97.71(1)	110.049(4)
γ (°)	90	87.153(13)	90	99.45(1)	
V (Å^3)	1189.40(8)	2176.6(5)	2368.41(8)	643.00(17)	2867.75(18)
Z	4	2	4	1	4
D_{calc} (g cm^{-3})	1.325	1.915	1.331	1.404	1.934
μ (mm^{-1})	0.246	7.471	0.247	0.438	8.322
$F(000)$	496	1200	992	280	1592
2θ Range (°)	3.84–27.00	3.83–27.00	3.83–27.00	3.83–27.00	3.87–29.99
h, k, l Range	−7 to 7, −18 to 18, −16 to 16	−16 to 16, −18 to 18, −18 to 18	−13 to 13, −14 to 14, −25 to 25	−7 to 7, −11 to 11, −14 to 14	−20 to 20, −18 to 18, −22 to 22
Scan type	ω	ω	ω	ω	ω
Number of measured reflections	18 809	44 531	35 719	10 506	31 337
Number of individual reflections (R_{int})	2561 (0.0158)	9440 (0.0276)	2555 (0.0698)	2552 (0.0311)	4162 (0.0737)
Number of refined parameters	154	514	154	163	169
Number of observed reflections [$I \geqslant 2\sigma(I)$]	2194	7190	1810	1752	1356
g_1, g_2 in w[a]	0.0888, 0.7866	0.1321, 0.000	0.0635, 1.2133		0.2000, 0.000
R[b], wR[c] [$I \geqslant 2\sigma(I)$]	0.0611, 0.1692	0.0317, 0.1735	0.0551, 0.1485	0.0692, 0.2147	0.0937, 0.3341
R, wR (all data)	0.0706, 0.1580	0.0551, 0.1103	0.0846, 0.1257	0.0975, 0.1999	0.1772,0.2798
Goodness-of-fit on F^2, S[d]	1.05	1.058	1.075	1.044	0.947
Minimum and maximum electron density (e Å^{-3})	−0.27 and 0.79	−0.895 and 2.058	−0.295 and 0.235	−0.249 and 0.410	−2.207 and 3.410
Maximum Δ/σ	<0.001	0.001	<0.001	<0.001	0.001
Extinction coefficient					0.0028(7)

[a] $w = 1/[\sigma^2(F_o^2)] + [g_1P + g_2P]$ where $P = (F_o^2 + 2F_c^2)/3$.
[b] $R = \sum\|F_o| - |F_c\|/\sum|F_o|$.
[c] $wR = [\sum(F_o^2 - F_c^2)^2/\sum w(F_o^2)^2]^{1/2}$.
[d] $S = \sum[w(F_o^2 - F_c^2)^2/(N_{obs} - N_{param})]^{1/2}$.

by π–π interactions (Fig. 2a). The intramolecular distance H9···S1 of 2.837(1) Å cannot be regarded as a C–H···S hydrogen bond, rather it is a consequence of molecular stereochemistry. Otherwise, only van der Waals interactions are present.

The molecular structures of compounds **3** and **4** are characterized by three moieties defined by the atoms of the benzothiazole, phenyl and cyclobutane rings (Figs. 1 b and c). Since the ring centroids lie at a crystallographic centre of symmetry, the cyclobutane rings in **3**

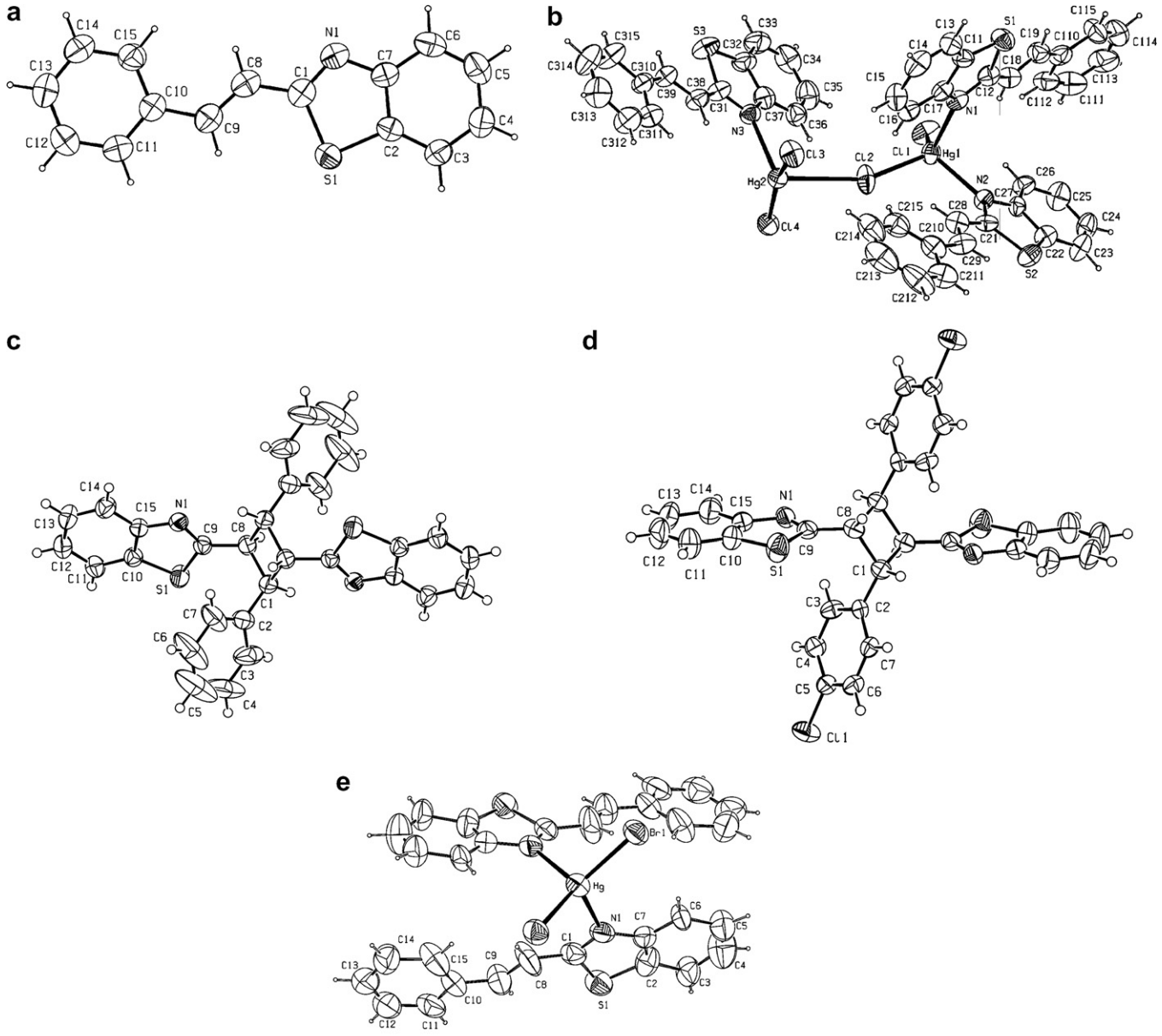


Fig. 1. ORTEP drawing of 2-styryl-1,3-benzothiazole (sb) (**1**) (a), $[Hg_2Cl_4(sb)_3]$ (**2**) (b), 1,3-bis(1,3-benzothiazol-2-yl)-2,4-diphenylcyclobutane (**3**) (c), 1,3-bis(1,3-benzothiazol-2-yl)-2,4-bis(4-chlorophenyl)cyclobutane (**4**) (d), and $[HgBr_2(sb)_2]$ (**5**) (e) with the atomic numbering scheme of asymmetric unit. The thermal ellipsoids are drawn at the 50% probability level at 293 K, except in the case of compound **5** (e) (30% probability at 293 K).

and **4** are strictly planar. The cyclobutane ring bond distances are in agreement with those found for planar cyclobutane rings according to Allen [30] (Table 2). The mean C–C value for planar cyclobutane rings according to Ref. [30] is 1.558(3) Å and it is marginally longer in relation to the value for puckered rings. The cyclobutane ring geometry reflects the balance between ring strain forces (which are minimized in the planar form) and repulsive interactions between substituents, and it is not influenced by possible conjugative interactions with π-substituents.

The shortness of the exocyclic C8–C9 bond, the distance being 1.494(3) and 1.484(6) Å in **3** and **4**, respectively, is related to higher s character in the orbitals involved in the exocyclic C–C bonds.

The dihedral angles between the benzothiazole and cyclobutane rings are 61.4(3)° and 52.9(2)° for **3** and **4**, respectively. The dihedral angles between the benzothiazole and phenyl rings are 70.2(2)° and 51.3(2)° for **3** and **4**, respectively.

The S1–C9 and S1–C10 bonds are 1.750(2) and 1.729(2) Å in **3** and 1.743(5) and 1.732(6) Å in **4**. The molecules are arranged into antiparallel pairs of benzothiazole rings attracted by π–π interactions in both structures **3** and **4** (Fig. 2b and c). Except these and van der Waals interactions, there are no other contacts in these structures.

Table 2
Selected interatomic distances (Å) and valence and torsion angles (°) for the compounds **1**, **3** and **4**

Compound	1	3	4
Selected interatomic distances (Å)			
S1–C1 (S1–C9 in **3** and **4**)	1.766(3)	1.750(2)	1.743(5)
S1–C2 (S1–C10 in **3** and **4**)	1.731(2)	1.729(2)	1.732(6)
N1–C1 (N1–C9 in **3** and **4**)	1.278(3)	1.292(3)	1.307(6)
N1–C7 (N1–C15 in **3** and **4**)	1.379(3)	1.396(3)	1.395(6)
C8–C9	1.314(4)	1.494(3)	1.484(6)
C1–C8		1.571(3)	1.589(6)
C1–C8^{i}		1.548(3)	1.555(6)
C1–C2		1.499(4)	1.514(6)
Cl1–C5			1.740(5)
Selected bond angles (°)			
C9–C8–C1	127.8(2)		
C8–C9–C10	126.1(2)		
C1–C8–C9		118.9(2)	120.1(4)
C1^{i}–C8^{i}–C9^{i}		116.3(2)	116.0(4)

Symmetry codes: i = $-x+2, -y, -z+1$ in **3** and $-x+2, -y+3, -z$ in **4**.

Table 3
Selected interatomic distances (Å) and valence and torsion angles (°) for the compounds **2** and **5**

Compound	2	5
Bond distances (Å)		
Hg1–Cl1	2.396(2)	
Hg1–Cl2	2.452(2)	
Hg1–N1	2.368(6)	
Hg1–N2	2.316(6)	
Hg2–Cl2	2.939(2)	
Hg2–Cl3	2.326(2)	
Hg2–Cl4	2.359(2)	
Hg2–N3	2.468(6)	
Hg–Br1		2.515(2)
Hg–N1		2.387(12)
Bond angles (°)		
N2–Hg1–N1	93.6(2)	
N2–Hg1–Cl1	116.5(2)	
N1–Hg1–Cl1	113.8(2)	
N2–Hg1–Cl2	108.2(2)	
N1–Hg1–Cl2	108.3(2)	
Cl1–Hg1–Cl2	114.4(1)	
Cl3–Hg2–Cl4	160.7(1)	
Cl3–Hg2–N3	100.6(2)	
Cl4–Hg2–N3	98.5(2)	
Cl3–Hg2–Cl2	93.9(1)	
Cl4–Hg2–Cl2	84.7(1)	
N3–Hg2–Cl2	103.9(2)	
N1–Hg–N1^{i}		93.2(7)
N1^{i}–Hg–Br1		105.6(3)
N1–Hg–Br1		111.6(3)
N1^{i}–Hg–Br1^{i}		111.6(3)
N1–Hg–Br1^{i}		105.6(3)
Br1–Hg–Br1^{i}		124.82(9)

Symmetry codes: i = $-x, y, 1/2-z$.

3.3.2. Compound *2*

In **2**, the sb ligand is coordinated to the mercury atom as a neutral monodentate ligand through the thiazolyl nitrogen atom (Fig. 1b). The crystal and molecular structure of $Hg_2Cl_4(sb)_3$ reveals a dinuclear complex with two differently coordinated mercury(II) ions, with the Cl^- ion participating in a very non-symmetrical linear bridge. One Hg(II) ion is tetrahedrally coordinated with two Cl^- ions (Hg1–Cl1(terminal) 2.396(2) Å, Hg1–Cl2 (bridging) 2.452(2) Å), and two thiazole N nitrogen atoms from two ligand molecules (Hg1–N1 2.368(6) Å and Hg1–N2 2.316(6) Å). The bond angles values are in the range 93.6(2)° (for the N2–Hg1–N1 angle) to 116.5(2)° (for the N2–Hg1–Cl1 angle) revealing, along with the Hg1–Cl1 bond value of 2.396(2) Å, that the terminal Cl1 atom is more strongly bound to the Hg(II) ion than the N atom from the ligand. The sum of the covalent radii of Hg and Cl amounts to 2.48 Å (tetrahedral mercury covalent radius of 1.48 Å + covalent radius of Cl 0.99 Å) [31–34]. According to that value, Hg1–Cl1(terminal) and Hg1–Cl2 (bridging) bond values of 2.396(2) and 2.452(2) Å, respectively, are shorter than the calculated sum. On the other hand, the sum of the covalent radii of Hg and N amounts to 2.18 Å. Therefore, the Hg1–N1 and Hg1–N2 bond values of 2.368(6) and 2.316(6) Å, respectively, are longer than 2.18 Å, and thus belong to contacts slightly longer than the sum of the covalent radii, but shorter than the sum of the van der Waals radii for Hg (1.55–1.65 Å) [34] and N (1.5–1.55 Å) [30]. Such bond distance values are followed up by bond angle values.

The other Hg(II) ion is coordinated by three Cl^- ions (two terminal Hg2–Cl3 and Hg2–Cl4 of 2.326(2) and 2.359(2) Å, respectively, and one bridging Hg2–Cl2 of 2.939(2) Å) and one N atom from the ligand (Hg2–N3 of 2.468(6) Å) in a 2+2 fashion, rather than in a deformed tetrahedral form. The Hg2–Cl(terminal) bond distance values are inbetween the calculated sum for diagonal and tetrahedral mercury coordination (1.30 + 0.99 = 2.29 Å for a diagonal Hg–Cl environment) [31–34]. On the other hand, the Hg2–Cl2 bond value is close to the van der Waals sum for Hg and Cl (3.05 Å). Similar rather long Hg–Cl bond values are found in the structure of $[Hg\{(CH_3)_2(C_2H_5)P\}_2Cl]^+[Hg\{(CH_3)_2(C_2H_5)P\}Cl_3]^-$ [36] where complex cations and anions are linked by Cl bridges with Hg–Cl(bridging) distances of 3.07(1) and 3.25(1) Å. Some authors consider that a cut-off is at 3.35 Å, and all Hg–Cl distances up to this value are considered to be a part of the mercury coordination sphere [37].

The largest angle around mercury is for Cl3–Hg2–Cl4, 160.7(1)°, correspondingly followed by the shortest bond value. This value is in the range 158–170° established for diagonal mercury coordination with additional contacts, as is given by Holloway and Melnik in their classification and analysis of crystallographic and structural data for mercury coordination compounds [35]. The smallest angle around mercury is for Cl4–Hg2–Cl2, 84.7(1)°.

The coordinated ligand molecules in compound **2** are essentially planar with dihedral angles of only 1.03(1)° and 2.00(1)° between the benzothiazole and phenyl rings (C21–C215) and (C31–C315), respectively, except for the

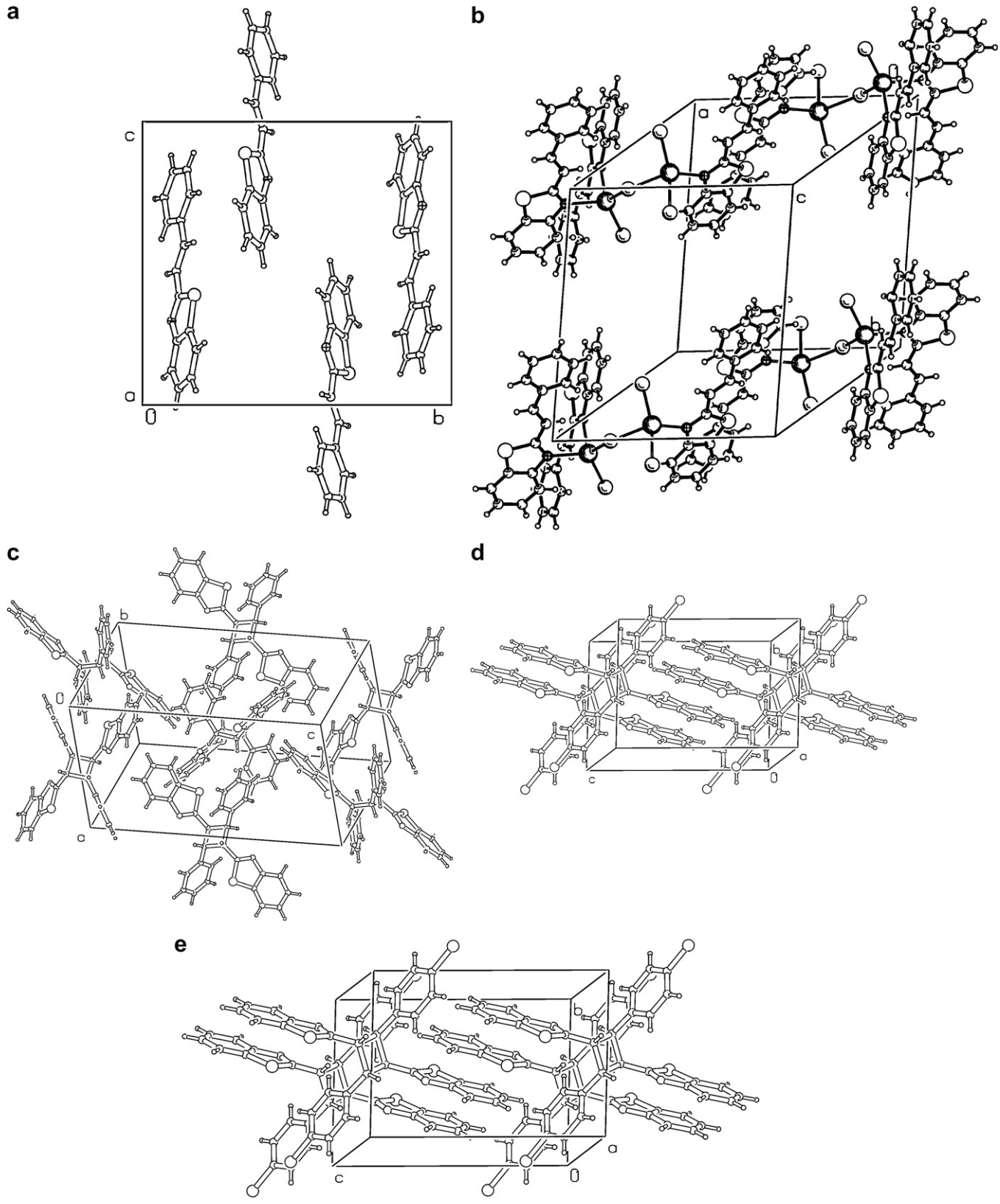


Fig. 2. PLATON view of crystal structures of (**1**) (a), (**2**) (b), (**3**) (c), (**4**) (d) and (**5**) (e).

first molecule (C11–C115), which is almost planar with a corresponding angle of 6.41(1)°. The dihedral angles between the planes defined by the atoms of the ligands as a whole amount 89.00(1)° (molecules C11–C115 and C21–C215), 76.83(1)° (molecules C11–C115 and C31–C315) and 12.28(1)° (molecules C21–C215 and C31–C315).

All approaches of the type C–H···Cl and C–H···S (3.10(1)–3.64(1) Å) are intramolecular in character and could not be recognized as hydrogen bonds (Fig. 2d).

3.3.3. Compound 5

Compound **5** has a deformed tetrahedral geometry around the mercury(II) ion with the neutral monodentate ligand 2-styryl-1,3-benzothiazole **1** coordinated through the thiazolyl nitrogen atom (Fig. 1e). The mercury(II) ion is situated at the crystallographic twofold axis with the distances Hg–Br1 2.515(2) Å and Hg–N1 2.387(12) Å. An indication of the tetrahedral deformation from ideal bond angles values is represented by the angle Br1–Hg–$Br1^{i}$ ($i = -x, y, 1/2 - z$), 124.82(9)°. The Hg–Br1 bond distance value is shorter than the sum of the covalent radii of Hg and Br ($1.48 + 1.14 = 2.62$ Å) [31–34], while the Hg–N1 bond distance value is the only contact shorter than the van der Waals radii sum of Hg and N. That is accompanied by a decrease in the N1–Hg–$N1^{i}$ ($i = -x, y, 1/2 - z$) bond angle of 93.2(7)°.

The ligand is almost planar with a dihedral angle of 6.7(1)° between the planes calculated through the atoms of the benzothiazole and phenyl rings.

The molecules are mutually joined only by van der Waals interactions with two contacts C6–H6···Br1 and C9–H9···S1 of 3.780(17) and 3.16(2) Å (H6···Br1 and H9···S1 are 2.919 and 2.731 Å with the angles of 155° and 109°, respectively) (Fig. 2e).

3.4. Thermal analysis (TGA–DTA)

Samples of the mercury(II) complexes **2** and **5** were heated from room temperature up to 600 °C. The TGA curves of **2** and **5** show a continuous thermal decomposition which starts at around 210 °C for **2** and at around 190 °C for **5**. The decomposition of the halide complexes is represented by exothermic peaks at 235.2 °C for **2** and at 202.2 °C for **5**. Exothermic peaks in the DTA curves can be connected with sublimation of the corresponding mercury(II) halides.

4. Conclusions

Two novel mercury(II) halide complexes with 2-styryl-1,3-benzothiazole (sb) have been prepared. $Hg_2Cl_4(sb)_3$ and $HgBr_2(sb)_2$ were characterized by elemental analysis, IR, Raman spectroscopy and thermal methods. Their crystal and molecular structures were determined by X-ray crystal structure analysis as well as the structure of the uncoordinated sb. 2-Styryl-1,3-benzothiazole and 2-(4-chlorostyryl)-1,3-benzothiazole undergo intermolecular cycloaddition and the corresponding dimeric cyclobutane derivatives have been obtained and structurally characterized. IR and Raman data of the mercury(II) complexes are in good agreement with the data obtained by structural analysis.

Acknowledgements

Financial support of the Ministry of Science, Education and Sport of the Republic of Croatia is greatly appreciated (Grant No. 119-1193079-1332).

Appendix A. Supplementary material

CCDC 648475, 648476, 648477, 648478 and 648479 contain the supplementary crystallographic data for this paper. These data can be obtained free of charge via http://www.ccdc.cam.ac.uk/conts/retrieving.html, or from the Cambridge Crystallographic Data Centre, 12 Union Road, Cambridge CB2 1EZ, UK; fax: (+44) 1223-336-033; or e-mail: deposit@ccdc.cam.ac.uk. A structure factors table is available from the authors.

References

[1] B. Rosenberg, L. Van Camp, J.E. Trosko, V.H. Mansour, Nature 222 (1969).
[2] J.A. Muir, G.M. Gomez, M.M. Muir, O. Cox, M.E. Cadiz, Acta Crystallogr., Sect. C 43 (1987) 1258.
[3] M.M. Muir, G.M. Gomez, J.A. Muir, M.E. Cadiz, O. Cox, C.L. Barnes, Acta Crystallogr., Sect. C 44 (1988) 803.
[4] G.M. Gomez, M.M. Muir, J.A. Muir, O. Cox, Acta Crystallogr., Sect. C 44 (1988) 1554.
[5] M.M. Muir, G.M. Gomez, M.E. Cadiz, J.A. Muir, Inorg. Chim. Acta 168 (1990) 47.
[6] C.M. Lozano, M.M. Muir, X. Tang, Y. Li, J. Chem. Crystallogr. 24 (1994) 639.
[7] C.M. Lozano, O. Cox, M.M. Muir, J.D. Morales, J.L. Rodríguez-Cabán, P.E. Vivas-Mejía, F.A. Gonzales, Inorg. Chim. Acta 271 (1998) 137.
[8] Z. Popović, D. Mrvoš-Sermek, Ž. Soldin, V. Tralić-Kulenović, Acta Crystallogr., Sect. C 57 (2001) 20.
[9] Z. Popović, Ž. Soldin, G. Pavlović, D. Matković-Čalogović, D. Mrvoš-Sermek, M. Rajić, Struct. Chem. 13 (5/6) (2002) 425.
[10] Z. Popović, G. Pavlović, Ž. Soldin, V. Tralić-Kulenović, L. Racanè, Acta Crystallogr., Sect. C 59 (2003) m4.
[11] L.P. Battaglia, A. Bonamartini Corradi, M.R. Cramarossa, J. Gelsomini Giusti, Polyhedron 12 (1993) 2235.
[12] P. Gouverner, W. Hoedeman, Anal. Chim. Acta (1964) 30.
[13] W. Ried, S. Hinschung, Justus Liebigs Ann. Chem. 600 (1956) 47.
[14] V. Tralić-Kulenović, L. Fišer-Jakić, Spectrochim. Acta 53 (1997) 271.
[15] V. Dryanska, C. Ivanov, C.C.R. Acad. Bulg. Sci. 23 (1970) 1227.
[16] Xcalibur CCD System, CrysAlis Software System, Version 171.23, Oxford Diffraction, Oxford Diffraction Ltd., 2004.
[17] G.M. Sheldrick, Acta Crystallogr., Sect. A 46 (1990) 467.
[18] G.M. Sheldrick, SHELXL-97: Program for the Refinement of Crystal Structures, University of Göttingen, Göttingen, Germany, 1997.
[19] A.L. Spek, Acta Crystallogr., Sect. A 46 (1990) 34.
[20] N.B. Colthup, L.H. Daly, S.E. Wiberley, Introduction to Infrared and Raman Spectroscopy, Academic Press, New York, 1964.
[21] C.N.R. Rao, R. Venkataraghavan, Can. J. Chem. 42 (1964) 43.
[22] F. Téllez, A. Peña-Hueso, N. Barba-Behrens, R. Contrerea, A. Flores-Parra, Polyhedron 25 (2006) 2363.
[23] M. Aresta, Inorg. Chim. Acta 44 (1980) L3.
[24] A. Giusti, G. Peyronel, Spectrochim. Acta A 38 (1982) 975.
[25] N.A. Bell, T.N. Branston, W. Clegg, L. Parker, E.S. Raper, C. Sammon, C.P. Constable, Inorg. Chim. Acta 319 (2001) 130.
[26] N.A. Bell, S.J. Coles, C.P. Constable, D.E. Hibbs, M.B. Hursthouse, R. Mansor, E.S. Raper, C. Sammon, Inorg. Chim. Acta 323 (2001) 69.

[27] Cambridge Structural Database, Version 5.28, Cambridge Crystallographic Data Centre, 12 Union Road, Cambridge, England, 2007.
[28] J. Yang, P. Kumar, J.R. Dimmock, J.W. Quail, Acta Crystallogr., Sect. C 51 (1995) 2700.
[29] N. Trinajstić, Tetrahedron Lett. 12 (1968) 1529.
[30] F.H. Allen, Acta Crystallogr., Sect. B 40 (1984) 64.
[31] L. Pauling, General Chemistry, 3rd ed., W.H. Freeman, San Francisco, CA, 1970.
[32] D. Grdenić, Quart. Rev. 19 (1965) 303.
[33] A. Bondi, J. Phys. Chem. 68 (1964) 441.
[34] D. Matković-Čalogović, Ph.D. Thesis (in Croatian; Abstract in English), University of Zagreb, Zagreb, 1994.
[35] C.E. Holloway, M. Melnik, Main Group Chem. 17 (11–12) (1994) 799.
[36] N.A. Bell, M. Goldstein, T. Jones, I.W. Nowell, Acta Crystallogr., Sect. B 36 (1980) 708.
[37] D.A. House, W.T. Robinson, V. McKee, Coord. Chem. Rev. 135/136 (1994) 533.

$\{[Cu_3(CN)_3(4\text{-PyHBIm})_4]\cdot 2H_2O\}_n$ (**3**) and $[Cu_5(CN)_3(4\text{-PyBIm})_2]_n$ (**4**) have been prepared and structurally characterized. Their structures vary from one- to two-dimensions along with the change of the position of pyridyl N atom. Herein, we report their syntheses, crystal structures, thermal stabilities and luminescent properties.

2. Experimental

2.1. Materials and methods

The ligands 2-(*n*-pyridyl)benzimidazole ($n = 2,3,4$) were prepared according to the literature method [12]. Other chemicals were of reagent grade and used as received without further purification. Elemental analyses were performed on a Vario EL III elemental analyzer. Infrared spectra were recorded with a Nicolet A370 FT-IR spectrometer by KBr pellets in the range 400–4000 cm^{-1}. Thermogravimetric analyses were completed on a Netzsch STA 449C thermal analyzer at a heating rate of 10 °C min^{-1} in air. Fluorescent spectra were recorded on a Shimadzu RF-5301 spectrophotometer.

2.2. Synthesis

$[Cu_2(CN)(2\text{-PyBIm})]_n$ (**1**). A mixture of CuCN (0.50 mmol), $K_3[Fe(CN)_6]$ (0.25 mmol), 2-PyHBIm (0.25 mmol) in 7 mL water was added 3 drops of aqueous NH_3 and then sealed in a 15-mL Teflon-lined reactor. The mixture was heated in an oven at 180 °C for 72 h and slowly cooled to room temperature at a rate of 10 °C h^{-1}. Yellow block crystals of **1** were obtained with 50% yield based on 2-PyHBIm. *Anal*. Calc. for $C_{13}H_8Cu_2N_4$: C, 44.95; H, 2.32; N, 16.13. Found: C, 44.71; H, 2.29; N, 16.20%. IR (KBr pellet, cm^{-1}): 2136s, 1599s, 1453m, 1422s, 1403s, 790w, 733s.

$[Cu_2(CN)_2(3\text{-PyHBIm})]_n$ (**2**). The reaction was carried out in a method similar to that for **1**, used 3-PyHBIm instead of 2-PyHBIm and sealed at 170 °C for 12 h. Yellow block crystals were obtained with 42% yield based on 3-PyHBIm. *Anal*. Calc. for $C_{14}H_9Cu_2N_5$: C, 44.92; H, 2.42; N, 18.71. Found: C, 45.03; H, 2.39; N, 18.50%. IR (KBr pellet, cm^{-1}): 3361s, 2127s, 1597m, 1447s, 1393m, 811m, 750s, 697s, 568s.

$\{[Cu_3(CN)_3(4\text{-PyHBIm})_4]\cdot 2H_2O\}_n$ (**3**) and $[Cu_5(CN)_3(4\text{-PyBIm})_2]_n$ (**4**). The reaction was carried out in a method similar to that for **1**, used 4-PyHBIm instead of 2-PyHBIm and sealed at 170 °C for 12 h. Two kinds of crystals, yellow block crystals of **3** and red stick crystals of **4**, were obtained with 35% yield of **3** and 24% yield of **4** based on 4-PyHBIm. Complex **3**: *Anal*. Calc. for $C_{51}H_{40}Cu_3N_{15}O_2$: C, 56.43; H, 3.714; N, 19.35. Found: C, 56.43; H, 3.61; N, 19.40%. IR (KBr pellet, cm^{-1}): 3534m, 3387m, 3053m, 2119s, 1612s, 1435s, 1317m, 835m, 745s. Complex **4**: *Anal*. Calc. for $C_{27}H_{16}Cu_5N_9$: C, 41.35; H, 2.06; N, 16.07. Found: C, 41.89; H, 2.05; N, 16.29%. IR (KBr pellet, cm^{-1}): 2137s, 1606s, 1426s, 1389m, 828m, 750s.

2.3. X-ray crystallography

The well-shaped single crystals of **1**–**4** were selected for X-ray diffraction study. The diffraction data were collected on a Bruker Smart Apex-II CCD diffractometer with graphite monochromated Mo Kα radiation ($\lambda = 0.71073$ Å) at 293(2) K. Determinations of the crystal system, orientation matrix and cell dimensions were performed according to the established procedures. Empirical absorption corrections were applied using the SADABS program. The structures

Table 1
Crystallographic data and structure refinements for **1**–**4**

	1	**2**	**3**	**4**
Empirical formula	$C_{13}H_8Cu_2N_4$	$C_{14}H_9Cu_2N_5$	$C_{51}H_{40}Cu_3N_{15}O_2$	$C_{27}H_{16}Cu_5N_9$
Formula weight	347.31	374.34	1085.60	784.19
Crystal system	monoclinic	triclinic	triclinic	triclinic
Space group	$P2(1)/n$	$P\bar{1}$	$P\bar{1}$	$P\bar{1}$
a (Å)	9.887(10)	8.4196(8)	12.796(2)	8.6442(9)
b (Å)	6.911(7)	9.2078(10)	13.742(2)	11.0859(12)
c (Å)	18.336(19)	9.390(1)	14.772(2)	14.2907(15)
α (°)	90	98.709(1)	103.362(3)	108.567(1)
β (°)	90.178(13)	97.918(1)	99.382(2)	91.523(2)
γ (°)	90	109.316(1)	90.307(3)	91.791(1)
V (Å^3)	1253(2)	665.16(12)	2491.0(7)	1296.6(2)
Z	4	2	2	2
D_{calc} (g cm^{-3})	1.841	1.869	1.447	2.009
μ (mm^{-1})	3.382	3.195	1.326	4.072
Reflections collected	3995	3441	19180	6748
Unique reflections, R_{int}	1504, 0.0386	2289, 0.0118	7617, 0.0267	4483, 0.0149
Data/restraint/parameters	1504/0/172	2289/0/194	7617/0/640	4483/0/373
R_1, wR_2 [$I > 2\sigma(I)$]	0.0376, 0.0629	0.0285, 0.0715	0.0693, 0.1640	0.0335, 0.0819
R_1, wR_2 (all data)	0.0691, 0.0683	0.0351, 0.0759	0.1306, 0.2038	0.0562, 0.0945
Goodness-of-fit on F^2	0.833	1.027	0.999	1.034
Largest diffraction peak and hole (e Å^{-3})	0.430 and −0.254	0.515 and −0.519	0.523 and −0.557	0.568 and −0.400

Table 2
Selected bond lengths (Å) and angles (°) for **1**–**4**

1[a]			
Cu(1)–N(1)	1.823(4)	Cu(2)–C(1)	1.830(5)
Cu(1)–N(2)	1.857(4)	Cu(2)–N(3)	1.969(5)
C(1)–N(1)#1	1.153(6)	Cu(2)–N(4)	2.130(5)
N(2)–Cu(1)–N(1)	173.6(2)	C(1)–Cu(2)–N(4)	134.3(2)
C(1)–Cu(2)–N(3)	145.2(2)	N(3)–Cu(2)–N(4)	80.3(2)
2[b]			
Cu(1)–N(1)	2.073(3)	Cu(2)–N(3)	2.061(3)
Cu(1)–C(14)#1	1.865(3)	Cu(2)–N(4)	1.916(4)
Cu(1)–C(13)#2	1.889(3)	Cu(2)–N(5)	1.917(3)
N(4)–C(13)	1.131(5)	N(5)–C(14)	1.148(4)
N(1)–Cu(1)–C(14)#1	116.4(1)	N(3)–Cu(2)–N(4)	114.6(1)
N(1)–Cu(1)–C(13)#2	103.5(1)	N(3)–Cu(2)–N(5)	109.4(1)
C(14)#1–Cu(1)–C(13)#2	139.7(1)	N(4)–Cu(2)–N(5)	135.9(1)
3[c]			
Cu(1)–N(1)	1.913(8)	Cu(2)–N(9)	2.040(6)
Cu(1)–N(2)	1.891(8)	Cu(2)–C(1)	1.823(8)
Cu(1)–N(3)	2.093(6)	Cu(2)–C(51)	1.818(8)
Cu(1)–N(6)	2.100(6)	Cu(3)–C(2)	1.810(7)
Cu(3)–N(12)	2.060(6)	Cu(3)–N(15)	1.903(9)
N(1)–Cu(1)–N(2)	120.4(4)	C(1)–Cu(2)–N(9)	120.4(3)
N(1)–Cu(1)–N(3)	105.9(3)	C(1)–Cu(2)–C(51)	136.2(4)
N(2)–Cu(1)–N(3)	114.2(3)	C(51)–Cu(2)–N(9)	103.4(3)
N(2)–Cu(1)–N(6)	107.3(3)	C(2)–Cu(3)–N(15)	136.5(3)
N(15)–Cu(3)–N(12)	103.7(3)	C(2)–Cu(3)–N(12)	119.8(3)
4[d]			
Cu(1)–N(1)	1.869(3)	Cu(3)–C(14)	1.849(4)
Cu(1)–N(1) #1	1.870(3)	Cu(3)–N(3)	1.920(4)
Cu(2)–C(8)	1.806(4)	Cu(3)–N(4)	2.097(3)
Cu(2)–N(2)	1.865(3)	Cu(4)–C(20)	1.853(4)
Cu(5)–N(6)	1.859(4)	Cu(4)–N(5)	1.903(4)
Cu(5)–N(8)	1.861(3)	Cu(4)–N(7)	2.116(3)
N(1)–Cu(1)–N(1)#1	180.0	C(20)–Cu(4)–N(5)	148.2(2)
C(8)–Cu(2)–N(2)	174.7(2)	C(20)–Cu(4)–N(7)	103.2(1)
C(14)–Cu(3)–N(3)	147.4(2)	N(5)–Cu(4)–N(7)	108.5(1)
C(14)–Cu(3)–N(4)	110.1(1)	N(6)–Cu(5)–N(8)	174.9(1)
N(3)–Cu(3)–N(4)	102.5(1)		

[a] #1 $x+1/2, -y+1/2, z-1/2$; #2 $x-1/2, -y+1/2, z+1/2$.
[b] #1 $-x+1, -y, -z+1$; #2 $-x+1, -y+1, -z+1$.
[c] #1 $x+1, y, z$; #2 $x-1, y, z$.
[d] #1 $-x+1, -y-1, -z+1$; #2 $-x, -y+3, -z$; #3 $x+1, y-1, z$; #4 $x-1, y+1, z$.

were solved by direct method with SHELXS-97 program and refined by full-matrix least squares on F^2 with SHELXL-97 program [13]. All non-hydrogen atoms were refined anisotropically, and hydrogen atoms were located and included at their calculated positions. The crystal data and structure refinement results are summarized in Table 1. Selected bond lengths and angles are listed in Table 2.

3. Results and discussion

3.1. General characterization

The hydrothermal reactions of CuCN, $K_3Fe(CN)_6$ with 2-PyHBIm or 3-PyHBIm in a 2:1:1 molar ratio afforded complex $[Cu_2(CN)(2\text{-PyBIm})]_n$ (**1**) or $[Cu_2(CN)_2(3\text{-PyHBIm})]_n$ (**2**). Similar reaction using 4-PyHBIm instead of 2/3-PyHBIm afforded a mixture of $\{[Cu_3(CN)_3(4\text{-PyHBIm})_4]\cdot 2H_2O\}_n$ (**3**) and $[Cu_5(CN)_3(4\text{-PyBIm})_2]_n$ (**4**). Herein, $K_3[Fe(CN)_6]$ acts as cyanide source [14]. Try to prepare complexes **1**–**4** without $K_3[Fe(CN)_6]$ failed. Three drops of aqueous NH_3 was used as base in each reaction. Complexes **1** and **4** possess deprotonated 2/4-PyBIm ligands, while complexes **2** and **3** contain neutral 3/4-PyHBIm ligands. Their formulas have been confirmed by elemental analysis data.

Corresponding to transition metal cyanides, IR absorption bands in the region of 2000–2200 cm^{-1} are due to the presence of CN^- stretching vibrations [15]. The characteristic strong absorption of cyanide for **1**–**4** appears at 2136, 2127, 2119, 2137 cm^{-1}, respectively. Single peak of CN^- indicates that the cyanide groups coordinate to Cu(I) in sole mode. The characteristic absorption bands of *n*-PyBIm exist in the spectra of **1**–**4**. However, complexes **2** and **3** show N–H stretching vibration near 3361, 3387 cm^{-1}, respectively, while complexes **1** and **4** have not N–H absorption bands. This phenomenon also indicates that the 2/4-PyHBIm ligands are deprotonated in complexes **1** and **4**.

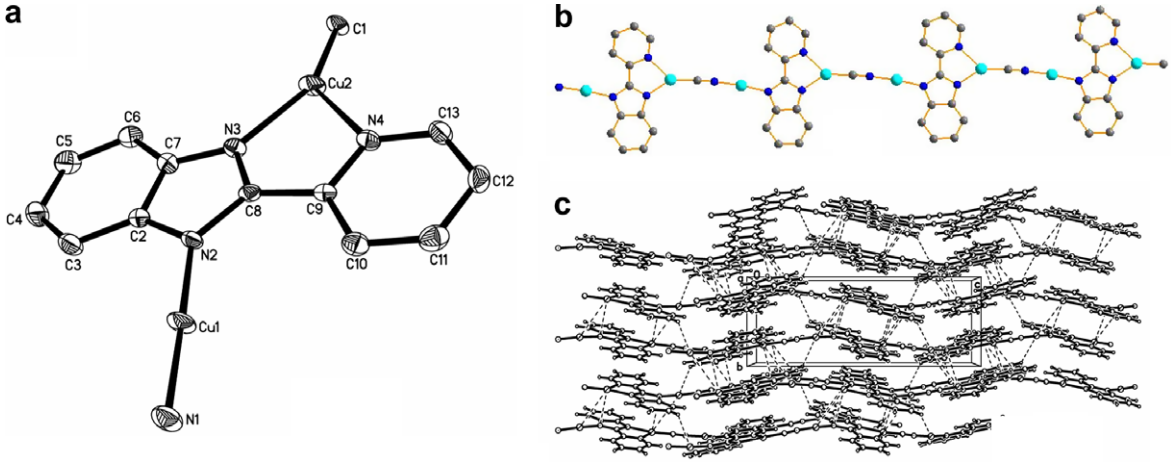


Fig. 1. Views of asymmetric structural unit (a), one-dimensional chain (b), and packing diagram (c) of **1**.

3.2. Description of crystal structures

X-ray structural analysis reveals that the complex **1** is a one-dimensional coordination polymer in which 2-(2-pyridyl)benzimidazole is deprotonated and adopts a tridentate coordination mode. As shown in Fig. 1a, there are two unique metal sites in complex **1**. Cu1 is two-coordinated by a cyanide group and a 2-PyBIm ligand via N_{BIm}-donor atom (Cu1–N1 = 1.823(4), Cu1–N2 = 1.857(4) Å, N1–Cu1–N2 = 173.6(2)°). Cu2 is in a planar trigonal coordination environment and coordinates to a 2-PyBIm via N_{Py}, N_{BIm} and a cyanide group (Cu2–N3 = 1.969(5), Cu2–N4 = 2.130(5), Cu2–C1 = 1.830(5) Å). In 2-PyBIm ligand, the pyridyl ring is almost coplanar with benzimidazole aromatic plane. However, the adjacent 2-PyBIm ligands have a dihedral angle of 33.4°. 2-PyBIm acting as a tridentate ligand links $Cu_2(CN)$ units to form a one-dimensional infinite chain (Fig. 1b). As packing diagram showing (Fig. 1c), the linear chains stack face to face with the 2-PyBIm ligands in a distance of 3.422 Å, falling in a separation of π–π interaction.

Complex **2** consists of infinite Cu(I)-cyanide zigzag chains and bidentate 3-PyHBIm bridging ligands. As shown in Fig. 2a, the structure possesses two unique metal sites. Both Cu1 and Cu2 are in trigonal geometries. However, the detail coordination environment of these two sites is some different. Cu1 is coordinated by a N_{Py}-donor atom and two cyanide groups, while Cu2 is coordinated by a N_{Bim}-donor atom and two cyanide groups. Different from the deprotonated 2-PyBIm ligand in **1**, the 2-(3-pyridyl)benzimidazole ligand of **2** does not deprotonate and acts as a neutral bidentate ligand. The bridging cyanide ligands connect the Cu(I) atoms to form one-dimensional chain and each bidentate 3-PyHBIm bridging ligand links

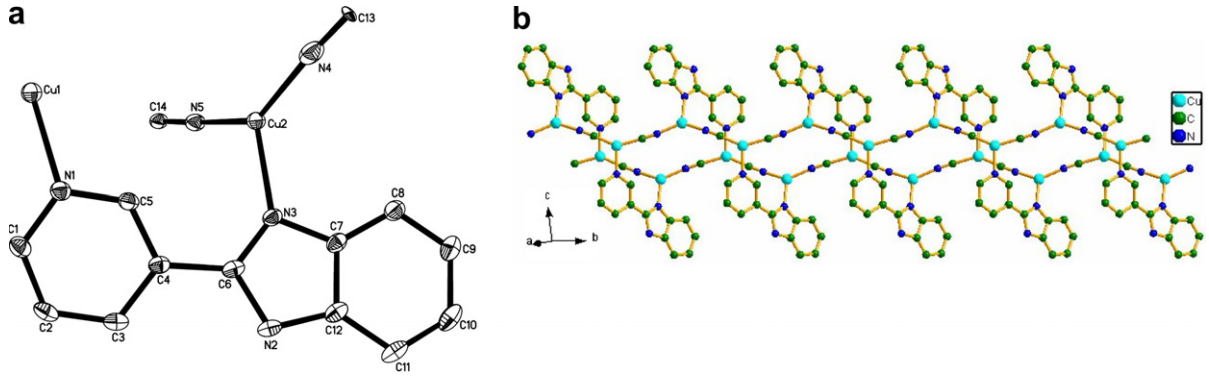


Fig. 2. Views of asymmetric structural unit (a) and ladder-like double chain (b) of **2**.

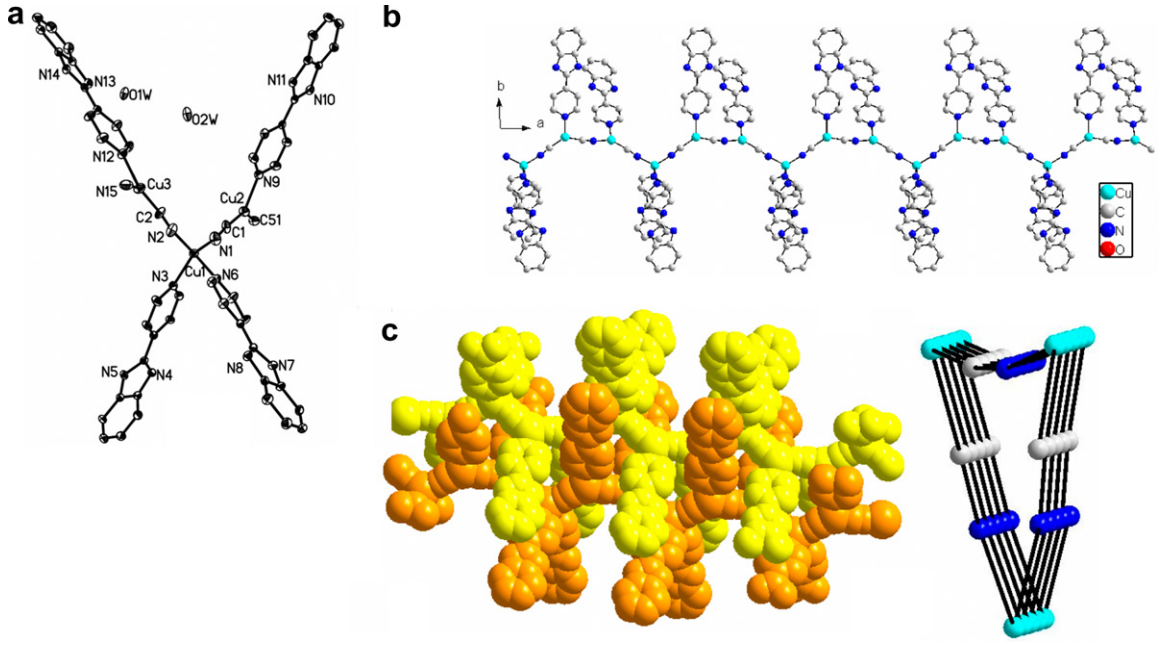


Fig. 3. Views of asymmetric structural unit (a), one-dimensional chain (b), and interpenetrating structure (c) of **3**.

two Cu(I) atoms of adjacent $[Cu–CN]_n$ chains to form ladder structure (Fig. 2b). The distance between the aromatic rings of adjacent 3-PyBIm is *ca.* 3.682 Å, indicating the presence of some π–π stacking interaction.

Complexes **3** and **4** were separated in same preparation reaction. X-ray analysis reveals that the complex **3** is constructed as one-dimensional helical chain architecture. As shown in Fig. 3a, there are three distinct copper atoms in the asymmetric structural unit. All the cyanide groups playing μ_2-bridge link Cu(I) atoms to form a one-dimensional helical chain (Fig. 3b). 4-PyHBIm does not deprotonate and adopts monodentate coordination mode through pyridyl nitrogen atom. Cu1 atom is in a distorted tetrahedral geometry. In addition to two N_{Py}-donor atoms from two 4-PyHBIm ligands, Cu1 is yet bonded to two cyanide groups. Two 4-PyHBIm ligands coordinated to Cu1 have a dihedral angle of 63.6°. Both Cu2 and Cu3 are in trigonal geometry and coordinate to two cyanide groups and a N_{Py}-donor atom. 4-PyHBIm ligands coordinated to Cu(I) atoms outstretching to four directions display a saddle-shaped structure. The one-dimensional helical chains containing saddle-shaped structural units pack in an interpenetrating mode (Fig. 3c), through weak π–π interaction of the lateral 4-PyBIm ligands with a separation of 3.702 Å, into a two-dimensional network.

Complex **4** is attributed to a two-dimensional network, wherein 2-(4-pyridyl)benzimidazole is deprotonated and acts as a tridentate bridging ligand. There are five crystallographically independent Cu(I) atoms which adopt two kinds of coordination geometries, namely two- and three-coordination (Fig. 4a). Cu3 and Cu4 atoms are trigonally three-coordinated by two μ_2-cyanide groups and a 4-PyBIm ligand via N_{Py}-donor atom, while Cu1, Cu2 and Cu5 atoms are all in two coordinating environment. Cu1 is coordinated by two N_{BIm}-donor atoms belong to different 4-PyBIm ligands. Cu2 and Cu5 both coordinate to a μ_2-cyanide group and a N_{BIm}-donor atom. All these kinds of Cu(I) atoms are connected by μ_2-cyanide groups and N_{BIm}-donor atoms into infinite zigzag chains, which are further connected through N_{Py}-donor atoms of 4-PyBIm into a two-dimensional layer polymeric structure (Fig. 4b). The pyridyl ring deviates from the aromatic plane of benzimidazole with a dihedral angle of 20.8° and 32.5°, respectively, for both independent 4-PyBIm ligands.

3.3. Thermal stabilities and luminescent properties

Thermal analyses for complexes **1**–**4** were performed in the temperature range of 20–900 °C. These coordination polymers were stable up to 200 °C, and then took place two steps of weight-loss. Complex **1** decomposed in the temperature range 440–500 °C and 540–740 °C, which corresponds to the releases of a cyanide group (found: 11.36%, calc. 7.49%) and a 2-PyBIm ligand (found: 42.20%, calc. 46.70%) [16,17]. The final, thermal stable residue is CuO (found: 46.44%, calc. 45.81%). Complex **2** lost two cyanide groups in the range 220–340 °C (found: 15.36%, calc. 13.90%) and a 3-PyHBIm ligand in 440–880 °C (found: 44.08%, calc. 43.60%) with CuO residue left (found: 40.56%, calc. 42.50%). Complex **3** released lattice water in 160–210 °C (found: 3.72%, calc. 3.32%). The decomposition occurred in the range of 230–290 °C may be assigned to a mixed process of three cyanide groups released and two benzimidazole groups decomposed (found: 26.92%, calc. 28.59%). The pyridyl residues and other two 4-PyHBIm ligands were released in 410–570 °C (found: 45.82%, calc. 43.32%) with thermal stable CuO residue left (found: 23.54%, calc. 21.98%). Complex **4** lost three cyanide groups and a benzimidazole group in 220–310 °C (found: 22.15%, calc. 24.63%). The pyridyl residue and another 4-PyBIm ligand decomposed in 400–690 °C with CuO residue left (found: 38.29%, calc. 50.72%). The reason leading to less CuO residue left is unclear. It is also possible to produce metal Cu residue (calc. 40.51%) [18,19]. Usually, the detailed decomposition mechanisms of metal cyanide and 2-(*n*-pyridyl)benzimidazole are too complicated to explain [20,21]. Comparing the complex structures and their thermal stabilities, 2-PyBIm adopts chelating and bridging coordination mode, which leads to the higher thermal stability of polymer **1**.

In the solid states, complexes **1**–**4** exhibit photoluminescence under 365 nm light excitation (Fig. 5). Amongst

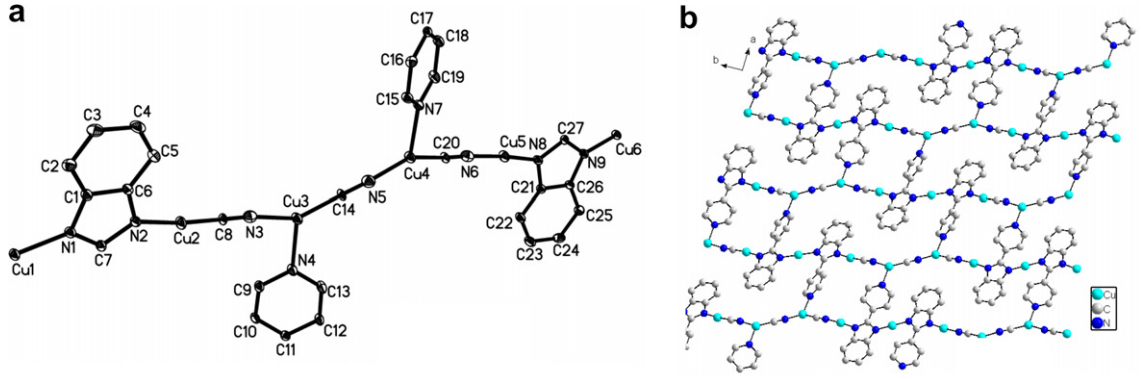


Fig. 4. Views of asymmetric structural unit (a) and two-dimensional polymeric network (b) of **4**.

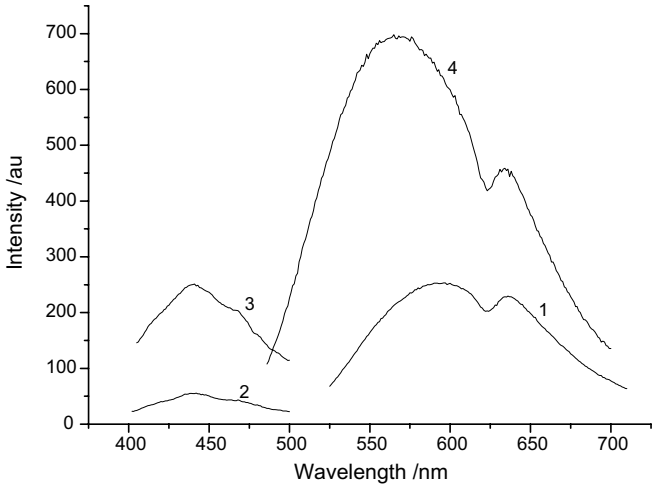


Fig. 5. Emission spectra of **1**–**4**.

them, complexes **1** and **4** constructed through deprotonated 2/4-PyBIm gave strong emission peak maximum at 595, 575 nm with shoulder peak at 640, 635 nm, respectively. While complexes **2** and **3** containing neutral 3/4-PyHBIm gave weak emission peak maximum at 440, 435 nm. It has been reported that organic compound 4-PyHBIm has weak emission band centered at 492 nm, while 4-PyHBIm-Ag(I) complexes exhibit intense luminescence near 540 nm [23]. Generally, metal-to-ligand charge transfer (MLCT) is the most common assignment for the luminescence of d^{10} transition metal complexes [22]. Most of copper(I)-cyanide complexes exhibit luminescence in the range 400–500 nm [5]. So the luminescence of title complexes may be assigned to MLCT where the electron is transferred from Cu(I) to 2/4-PyBIm ligand for **1**, **4**, and transferred from Cu(I) to cyanide group for **2**, **3**.

4. Conclusions

Four copper(I) cyanide coordination polymers containing 2-(*n*-pyridyl)benzimidazole ligands have been prepared by hydrothermal reactions. These complexes possess one-dimensional linear chain, ladder-like double chain, saddle-shaped helical chain, and two-dimensional layer polymeric structures. The cyanide groups in four complexes all act as bidentate bridging ligands. The ratio of Cu/CN, the position of pyridine N atom in three 2-(*n*-pyridyl)benzimidazole ($n = 2, 3, 4$) ligands, and the deprotonated or neutral ligands influence the coordination structures, thermal stabilities and luminescent properties.

Acknowledgements

Financially supported by the Research Foundation for Returned Chinese Scholars Overseas of Chinese Education Ministry (7A14219), and the Development Foundation of Shanghai Education Commission (03AK35).

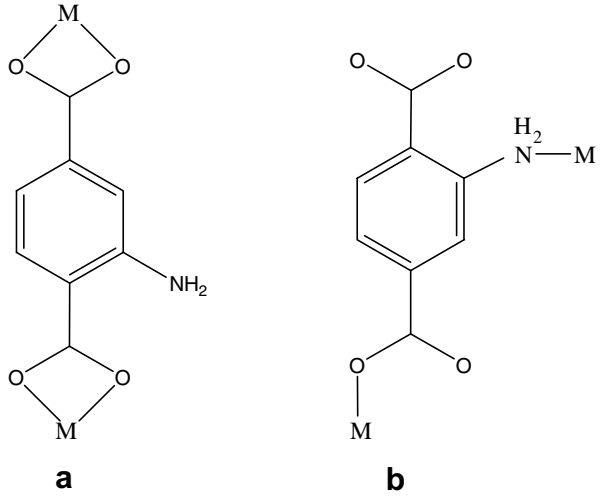
Appendix A. Supplementary material

CCDC 647549, 647554, 647550 and 647551 contain the supplementary crystallographic data for **1**, **2**, **3** and **4**. These data can be obtained free of charge via http://www.ccdc.cam.ac.uk/conts/retrieving.html, or from the Cambridge Crystallographic Data Centre, 12 Union Road, Cambridge CB2 1EZ, UK; fax: (+44) 1223-336-033; or e-mail: deposit@ccdc.cam.ac.uk. Supplementary data associated with this article can be found, in the online version, at doi:10.1016/j.poly.2007.07.013.

References

[1] O.M. Yaghi, M. O'Keeffe, N.W. Ockwig, H.K. Chae, M. Eddaoudi, J. Kim, Nature 423 (2003) 705.
[2] P.J. Stang, B. Olenyuk, Acc. Chem. Res. 30 (1997) 502.
[3] M. Ohba, H. Okawa, Coord. Chem. Rev. 198 (2000) 313.
[4] X. He, C.Z. Lu, D.Q. Yuan, S.M. Chen, J.T. Chen, Eur. J. Inorg. Chem. 11 (2005) 2181.
[5] S.W. Liang, M.X. Li, M. Shao, Z.X. Miao, Inorg. Chem. Commun. 9 (2006) 1312.
[6] X. He, C.Z. Lu, C.D. Wu, L.J. Chen, Eur. J. Inorg. Chem. 12 (2006) 2491.
[7] L.J. Zhou, Y.Y. Wang, C.H. Zhou, C.J. Wang, Q.Z. Shi, S.M. Peng, Cryst. Growth Des. 7 (2007) 300.
[8] S.M. Peng, J. Coord. Chem. 59 (2006) 1107.
[9] L.J. Chen, X. He, Q.Z. Zhang, X.Y. Wu, C.Z. Lu, Inorg. Chem. Commun. 9 (2006) 740.
[10] S.M. Yue, H.B. Xu, J.F. Ma, Z.M. Su, Y.H. Kan, H.J. Zhang, Polyhedron 25 (2006) 635.
[11] X.F. He, C.M. Vogels, A. Decken, S.A. Westcott, Polyhedron 23 (2004) 155.
[12] E. Alcalde, I. Dinares, L. Perez-Garcia, T. Roca, Synthesis (1992) 395.
[13] G.M. Sheldrick, SHELXS-97 and SHELXL-97. Program for Crystal Structure Solution and Refinement, University of Göttingen, Germany, 1997.
[14] H. Mao, C. Zhang, C. Xu, H. Zhang, X. Shen, B. Wu, Y. Zhu, Q. Wu, H. Wang, Inorg. Chim. Acta 358 (2005) 1934.
[15] H.L. Shyu, H.H. Wei, Y. Wang, Inorg. Chim. Acta 258 (1997) 81.
[16] S.W. Liang, M.X. Li, M. Shao, H.J. Liu, J. Mol. Struct. in press doi:10.1016/j.molstruc.2006.11.063.
[17] C.K. Xia, C.Z. Lu, X.Y. Wu, Q.Z. Zhang, J.J. Zhang, D.M. Wu, Polyhedron 26 (2007) 91.
[18] J. Cernak, J. Chomic, C. Kappenstein, R. Brahmi, D. Duprez, Thermochim. Acta 276 (1996) 209.
[19] V.T. Kilmaz, A. Karadag, Thermochim. Acta 348 (2000) 121.
[20] C.K. Xia, C.Z. Lu, D.Q. Yuan, Q.Z. Zhang, X.Y. Wu, J.J. Zhang, D.M. Wu, J. Mol. Struct. 831 (2007) 195.
[21] X. Liu, G. Guo, A. Wu, L. Cai, J. Huang, Inorg. Chem. 44 (2005) 4282.
[22] E. Colacio, R. Kivekas, F. Lloret, M. Sunberg, J. Suarez-Varela, M. Bardaji, A. Laguna, Inorg. Chem. 41 (2002) 5141.
[23] C.K. Xia, C.Z. Lu, Q.Z. Zhang, X. He, J.J. Zhang, D.M. Wu, Cryst. Growth Des. 5 (2005) 1569.

emitting units with suitable metal ions and weak interactions could fabricate a variety of luminescent materials. H_2atpt is a more suitable candidate for assembling such compounds due to its interesting structural features. Compared with tpt ligand (H_2tpt = terephthalic acid), the introduction of an amino group in H_2atpt results in the following two effects at least: (i) a supramolecular effect, namely providing more hydrogen-bonding donor or acceptor sites in the construction of the supramolecular packing; (ii) a coordination effect, namely, adding a new coordination site to coordinate with more metal centers. To the best of our knowledge, there are no Cd(II) compounds and rare Zn(II) compounds which have been structurally characterized by X-ray analysis among all the reported compounds with the atpt ligand [35–46]. So, we have started a systematic study on M(II) coordination to the atpt ligand (M = Cd and Zn). One of the aims of this project is to analyze the influence that factors, such as hydrogen bonding, rigidity and the possibility of specific attractive interactions between aromatic rings, can exert on the structure and photoluminescent properties of atpt–containing M(II) compounds. Furthermore, the introduction of N-containing aromatic ligands (bipy and phen, *etc.*) may induce a new structural evolution. A N-containing aromatic ligand is important in maintaining the desired low dimensional coordination polymer and may provide potential recognition sites for π–π aromatic stacking interactions. So, we assumed that the atpt ligand could be useful in the formation of supramolecular networks with some important features in the presence of N-containing aromatic ligands. Here we report the syntheses, structures, properties and weak interactions of two novel coordination compounds [Cd(atpt)phen-$(H_2O)]\cdot H_2O$ (**1**) and $[Zn_2(atpt)_2(bipy)_2(H_2O)_2]$ (**2**) with the atpt ligand. X-ray analysis reveals that compound **2** exhibits an unusual coordination mode of the atpt ligand, which has been observed for the first time (Scheme 1b). There are altogether nine crystallographically established coordination modes of the atpt ligand among the reported compounds, which have been summarized by Cheng et al., besides the one reported by Jin et al. [40,41]. To the best of our knowledge, compound **1** is the first structurally characterized Cd(II) complex with the atpt ligand, although Decker and Frye had reported the synthesis but no crystal structure of one Cd(II) compound with this ligand [46]. So far, there is only one structural report that the amino group of the atpt ligand coordinates to trivalent lanthanide ions [41]. Compound **2** is the first structurally characterized case where the amino group of the atpt ligand coordinates to divalent metal ions. Compounds **1** and **2** exhibit green photoluminescence in the solid state at room temperature.



Scheme 1. Coordination modes of the atpt ligand in the title compounds: (a) (**1**); (b) (**2**).

2. Experimental

2.1. Materials and instruments

All reagents were purchased commercially. Elemental analyses (C, H and N) were carried out on a 240 C Elemental analyzer. FT-IR spectra (400–4000 cm^{-1}) were recorded from KBr pellets in a Magna 750 FT-IR spectrophotometer. Solid state emission spectra were recorded using a 48000DSCF fluorescence spectrometer. Thermogravimetric analyses (TG) were taken on a NETZSCH STA 409 PG/PC instrument.

2.2. Synthesis

2.2.1. $[Cd(atpt)phen(H_2O)]\cdot H_2O$ (**1**)

Phen (0.0131 g, 0.066 mmol) was dissolved in methanol (3 ml) and then a solution of $Cd(NO_3)_2\cdot 4H_2O$ (0.0204 g, 0.066 mmol) in water (3 ml) was added. To this solution a mixture of H_2atpt (0.0120 g, 0.066 mmol) and NaOH (0.0053 g, 0.132 mmol) in water (10 ml) was added and then the resulting solution was filtered. The filtrate was kept at ambient temperature for several days and yellow crystals formed. They were filtered and washed with methanol and dried in vacuum (yield: 30% based on H_2atpt). *Anal.* Calc. for $C_{20}H_{15}CdN_3O_{5.5}$: C, 48.61; H, 3.23; N, 8.43. Found: C, 48.75; H, 3.26; N, 8.31%.

2.2.2. $[Zn_2(atpt)_2(bipy)_2(H_2O)_2]$ (**2**)

Bipy (0.0156 g, 0.100 mmol) was dissolved in methanol (4 ml) and then a solution of $Zn(NO_3)_2\cdot 4H_2O$ (0.0297 g, 0.100 mmol) in water (5 ml) was added while stirring. To this solution a mixture of H_2atpt (0.0181 g, 0.100 mmol) and NaOH (0.0088 g, 0.200 mmol) in water (10 ml) was added and then the resulting solution was filtered. The filtrate was kept at ambient temperature for several days and yellow crystals formed. They were filtered and washed with methanol and dried in vacuum (yield: 60% based on H_2atpt). *Anal.* Calc. for $C_{18}H_{17}N_3O_6Zn$: C, 49.50; H, 3.92; N, 9.62. Found: C, 49.60; H, 3.74; N, 9.61%.

Table 1
Crystallographic data and structure refinement for the title compounds

Compound	1	2
Empirical formula	$C_{20}H_{15}CdN_3O_{5.50}$	$C_{18}H_{17}N_3O_6Zn$
Formula weight	497.75	436.72
Temperature (K)	293(2)	293(2)
Wavelength (Å)	0.71073	0.71073
Crystal system	triclinic	monoclinic
Space group	$P\bar{1}$	$P2(1)/c$
a (Å)	9.6483(14)	10.979(4)
b (Å)	9.9256(17)	13.652(5)
c (Å)	11.5794(17)	11.745(5)
α (°)	67.193(2)	90
β (°)	68.372(2)	98.865(5)
γ (°)	80.077(2)	90
Volume (Å^3)	949.7(3)	1739.3(12)
Z	2	4
d_{calc} (Mg/m^3)	1.741	1.668
Absorption coefficient (mm^{-1})	1.191	1.456
$F(000)$	496	896
θ Range for data collection (°)	3.13–25.01	1.88–25.01
Limiting indices	$-11 \leqslant h \leqslant 11$, $-11 \leqslant k \leqslant 11$, $-13 \leqslant l \leqslant 11$	$-13 \leqslant h \leqslant 13$, $-16 \leqslant k \leqslant 16$, $-13 \leqslant l \leqslant 11$
Reflections collected/ unique [$R_{(int)}$]	5176/3291 [0.0380]	9226/3042 [0.0273]
Completeness to $\theta = 25.02°$ (%)	98.1	99.6
Maximum and minimum transmission	1.0000 and 0.708565	1.0000 and 0.722779
Data/restraints/ parameters	3291/0/280	3042/0/253
Goodness-of-fit on F^2	1.008	1.043
Final R indices [$I > 2\sigma(I)$]	$R_1 = 0.0641$, $wR_2 = 0.1669$	$R_1 = 0.0274$, $wR_2 = 0.0658$
R indices (all data)	$R_1 = 0.0954$, $wR_2 = 0.1798$	$R_1 = 0.0371$, $wR_2 = 0.0688$
Largest difference in peak and hole (e Å^{-3})	1.295 and −1.664	0.217 and −0.287

2.3. X-ray single-crystal structure determination

Crystallographic data for all the compounds were collected at 293(2) K with a Siemens SMART CCD diffractometer using graphite-monochromated (Mo Kα) radiation ($\lambda = 0.71073$ Å), ψ and ω scans modes. The structures were solved by direct methods and refined by the full-matrix least-squares on F^2 method using the SHELXL-97 program [47]. Intensity data were corrected for Lorenz and polarization effects and an empirical absorption correction was performed. All non-hydrogen atoms were refined anisotropically. The carbon-bound hydrogen atoms were added geometrically and allowed to ride on their respective parent atoms. The oxygen-bound hydrogen atoms were located in the difference Fourier map and kept fixed in those positions. The contribution of these hydrogen atoms was included in the structure factor calculations. Details of crystal data, collection and refinement are listed in Table 1.

3. Results and discussion

3.1. Preparation

The ligand atpt was chosen as a bridging ligand and the N-containing ligands as chelating ligands and π-stacking moieties. Synthesis conditions, such as starting materials, solvents, reaction temperature, pH, molar ratio and the method to grow single crystals, usually have a great effect on the structure of the compound. Compounds **1** and **2** were obtained by a solution-mixed method under the addition of NaOH (H_2atpt:NaOH = 1:2). These compounds are insoluble in water and common organic solvents, such as methanol, acetone and DMF, *etc*. Therefore, single-crystals used for X-ray analysis were directly grown from the reaction medium.

3.2. Structural analysis of [Cd(atpt)phen(H_2O)] · H_2O (1)

Compound **1** is a 1D zigzag chain (Fig. 1). It is interesting that the center of the benzene ring of the atpt ligand in **1** lies on the crystallographic inversion center, so its amino group is disordered over two sites. In the asymmetric unit of **1** there is one Cd atom, one atpt ligand, one phen ligand, one coordinated water and one lattice water molecule. The Cd atom is seven-coordinated by two nitrogen atoms from the phen ligand and five oxygen atoms from the atpt ligand and H_2O molecule. The coordination geometry of the Cd(II) center can be described as a distorted monocapped octahedral geometry (Table 2).

The atpt ligand in **1** shows the usual bis-chelating coordination mode reported in the literature (Scheme 1a) [41]. The Cd atoms are linked into a 1D zigzag chain with a nearest Cd···Cd distance of 11.417 Å. The dihedral angles between the carboxylate group O1C17O2 and C18C19C20C18bC19bC20b is 7.45°, which is smaller than that between the carboxylate group O3C13O4 and C14C15C16C14aC15aC16a (17.01°). The phen ligands are arranged on two sides of the 1D chain, alternatively. The benzene ring C18C19C20C18bC19bC20b of the atpt ligand is almost in the same plane as the phen ligand (dihedral angle: 2.22°), while the adjacent benzene ring C14C15C16C14aC15aC16a of the atpt ligand is almost perpendicular to the phen ligand (dihedral angle: 83.29°). 1D zigzag chains are further linked by interchain C–H···π and π–π stacking interactions and hydrogen bonds (Fig. 2). The centeroid···centeroid distance between the nearest benzene ring of the atpt ligand and the aromatic ring C2C3C4C5N2 of phen in the nearest adjacent chain is 3.905 Å. The distance, 2.697 Å, between the H10 atom attached to the C10 atom of the phen ligand in one chain and the centeroid of the nearest benzene ring of the atpt ligand in the nearest chain shows that there are interchain C10–H10···π interactions in the compound

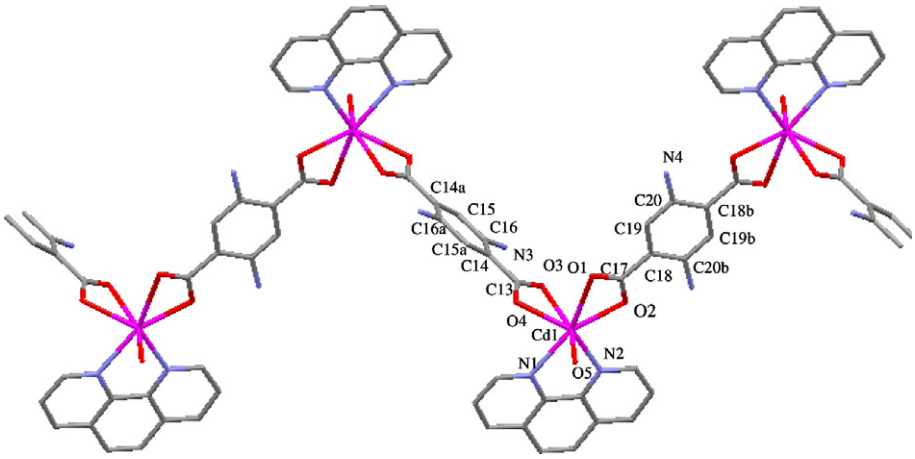


Fig. 1. View of the coordination environment of the Cd atom and the coordination mode of the atpt ligand in **1**.

Table 2
Selected bond lengths (Å) and angles (°) for the compounds

Compound **1**			
Cd(1)–O(5)	2.261(7)	Cd(1)–O(2)	2.277(7)
Cd(1)–O(4)	2.331(6)	Cd(1)–N(2)	2.353(6)
Cd(1)–N(1)	2.418(8)	Cd(1)–O(3)	2.440(6)
Cd(1)–O(1)	2.672(4)		
O(5)–Cd(1)–O(2)	99.6(3)	O(5)–Cd(1)–O(4)	148.6(3)
O(2)–Cd(1)–O(4)	96.8(3)	O(5)–Cd(1)–N(2)	96.4(3)
O(2)–Cd(1)–N(2)	84.1(2)	O(4)–Cd(1)–N(2)	111.8(2)
O(5)–Cd(1)–N(1)	86.2(3)	O(2)–Cd(1)–N(1)	152.3(3)
O(4)–Cd(1)–N(1)	91.5(3)	N(2)–Cd(1)–N(1)	68.3(2)
O(5)–Cd(1)–O(3)	93.6(2)	O(2)–Cd(1)–O(3)	124.6(2)
O(4)–Cd(1)–O(3)	55.2(2)	N(2)–Cd(1)–O(3)	147.4(2)
N(1)–Cd(1)–O(3)	81.5(2)		
Compound **2**			
Zn(1)–O(1)	2.0237(16)	Zn(1)–O(5)	2.0623(16)
Zn(1)–N(1)	2.1053(19)	Zn(1)–N(2)	2.120(2)
Zn(1)–O(6)	2.1662(18)	Zn(1)–N(3)#1	2.461(2)
O(1)–Zn(1)–O(5)	94.92(7)	O(1)–Zn(1)–N(1)	95.52(7)
O(5)–Zn(1)–N(1)	169.03(7)	O(1)–Zn(1)–N(2)	169.10(7)
O(5)–Zn(1)–N(2)	92.59(7)	N(1)–Zn(1)–N(2)	77.54(8)
O(1)–Zn(1)–O(6)	95.16(7)	O(5)–Zn(1)–O(6)	88.61(7)
N(1)–Zn(1)–O(6)	87.13(7)	N(2)–Zn(1)–O(6)	92.90(7)
O(1)–Zn(1)–N(3)#1	86.89(7)	O(5)–Zn(1)–N(3)#1	97.10(6)
N(1)–Zn(1)–N(3)#1	86.80(7)	N(2)–Zn(1)–N(3)#1	84.35(7)
O(6)–Zn(1)–N(3)#1	173.76(6)		

Symmetry codes for **1**: #1 $x+1/2$, $-y+3/2$, $z+1/2$ #2 $-x+1/2$, $-y+3/2$, $-z$; **3**: #1 $-x$, $-y+1$, $-z$; **4**: #1 $-x$, $y+1/2$, $-z+3/2$; #2 $-x+1$, $y-1/2$, $-z+3/2$.

(C–H···Cg = 3.583 Å; ∠ C–H···Cg = 159.65°). This kind of contact further stabilizes the 3D supramolecular framework.

Hydrogen bonds exist extensively in **1** (Table 3). There are two strong intramolecular hydrogen bonds: one exists between the coordinated carboxylate oxygen atom O2 and the nitrogen atom N4 [N4–H5A···O2 2.555(5) Å], while the other exists between the nitrogen atom N(3) of the amino group and the coordinated carboxylate oxygen atom O4 [N3–H3B···O4 2.6653 Å]. The 1D chains are further assembled by strong intermolecular hydrogen bonds [N3–H3A···O2 $(1-x, -y, 1-z)$ 2.9956 Å; N4–H4A···O5 $(1-x, -y, 2-z)$ 3.0285 Å; O5–H5A···O6 $(-1+x, y, 1+z)$ 2.7039 Å; O5–H5B···O3 $(-x, -y, 2-z)$ 2.7263 Å]. Thus a 3D supramolecular framework featuring a 1D channel with the dimensions 11.477×11.579 Å^2 occupied by the phen ligand is formed (Fig. 3).

3.3. Structural analysis of $[Zn_2(atpt)_2(bipy)_2(H_2O)_2]$ (2)

Compound **2** exhibits a center-symmetrical binuclear structure (Fig. 4). The zinc atom exhibits a distorted octahedral geometry (Table 2). The atpt ligand employs its one carboxylate groups and an amino group in turn to coordinate to the two zinc centers (Scheme 1b). Quite different from the coordination modes in all the other compounds with the atpt ligand, the coordination mode of the atpt ligand in **2** is new. One of its two carboxylate groups acts as a monodentate ligand, whereas the other carboxylate group does not participate in coordination to Zn(II). To the best of our knowledge, this is the first case where only one carboxylate group of atpt coordinates with metal ions, from the reported compounds with the atpt ligand [35–46]. The amino group of atpt coordinates to the other zinc(II) center. Thus, a dinuclear compound is formed as a result of atpt ligand bridging, with an intramolecular Zn···Zn distance of 7.638 Å.

The other interesting characteristic in this structure is that the benzene ring of the atpt ligand C11C12C13C14C15C16 is approximately parallel to the bipy ring. The bipy ligand is almost planar, the dihedral angle between the two pyridyl planes is 6.90° and its bond lengths and angles are almost the same as those for free bipy [48]. The dihedral angle between the benzene ring and the pyridyl plane C1C2C3C4C5N1 is 11.28°. The centeroid–centeroid distance between them is 3.484 Å. Thus an unusual intramolecular strong π–π stacking interaction between the benzene ring of the atpt ligand and the Zn(II)-coordinated bipy ring takes place.

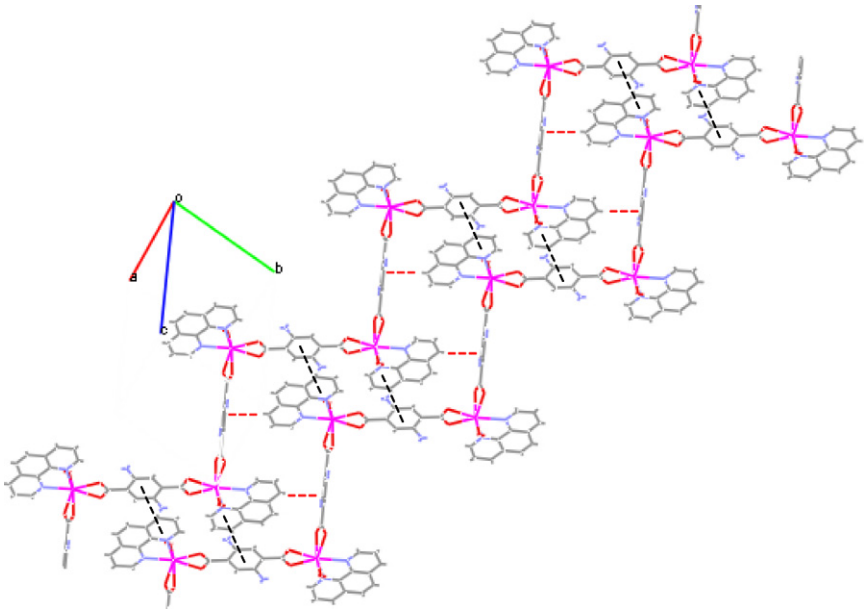


Fig. 2. View of the C–H···π (the red dashed line) and the π–π (the black dashed line) stacking interactions between the nearest chains in **1**.

Table 3
The details of the hydrogen bonds for the title compounds

D–H···A	*d*(D–H)	*d*(H···A)	*d*(D···A)	∠DHA	Symmetry of A
Compound **1**					
N3–H3A···O2	0.8600	2.2400	2.9956	146.00	$1-x, -y, 1-z$
N3–H3B···O4	0.8600	2.0400	2.6653	129.00	
N4–H4A···O5	0.8600	2.5100	3.0285	119.00	$1-x, -y, 2-z$
N4–H4B···O2	0.8600	1.8900	2.5555	133.00	
O5–H5A···O6	0.8500	1.9300	2.7039	151.00	$-1+x, y, 1+z$
O5–H5B···O3	0.8500	1.9600	2.7263	149.00	$-x, -y, 2-z$
Compound **2**					
N3–H3A···O3	0.9000	2.4000	3.0623	131.00	$x, 1/2-y, 1/2+z$
N3–H3B···O4	0.9000	1.9900	2.7337	139.00	
O5–H5A···O2	0.8500	1.9400	2.6910	146.00	
O5–H5B···O3	0.8500	1.8500	2.6959	174.00	$1+x, 1/2-y, 1/2+z$
O6–H6A···O2	0.8500	2.1800	2.9494	151.00	$x, 1/2-y, 1/2+z$
O6–H6B···O4	0.8500	1.7900	2.6291	171.00	$1+x, 1/2-y, 1/2+z$

Hydrogen bonds exist extensively in **2** (Table 3). There are two kinds of intramolecular hydrogen bonds: one exists between the uncoordinated carboxylate oxygen atom O2 and oxygen atom O5 from the coordinated water molecule [O5–H5A···O2 $(1+x, -1+y, z)$ 2.691(8) Å], while the other exists between the nitrogen atom N3 of the amino group and the uncoordinated carboxylate oxygen atom O4 [N3–H3B···O4 2.7337 Å]. The binuclear zinc(II) units are further linked by strong intermolecular hydrogen bonds [N3–H3A···O3 $(x, 1/2-y, 1/2+z)$ 3.0623 Å; O5–H5B···O3 $(1+x, 1/2-y, 1/2+z)$ 2.6959 Å; O6–H6A···O2 $(x, 1/2-y, 1/2+z)$ 2.9494 Å; O6–H6B···O4 $(1+x, 1/2-y, 1/2+z)$ 2.6291 Å]. Thus a 3 D supramolecular network is formed (Fig. 5). The distance, 2.697 Å, between the H4 atom attached to the C4 atom of the bipy ring and the centeroid of the benzene ring of the atpt ligand, shows there are intermolecular C4–H4···π interactions (C–H···Cg = 3.488 Å; ∠C–H···Cg = 143.40°). This kind of contact further stabilizes the 3D network.

3.4. FT-IR spectra

The FT-IR spectra of compounds **1** and **2** show broad peaks in the range of 3600–3200 cm^{-1} due to the existence of water molecules and the amino group of the atpt ligand. The IR results are commonly employed to distinguish the coordination modes of the carboxylate groups. A correlation of the carboxylate coordination mode to metal ions is usually made by examining the difference $\Delta\nu(COO) = \nu_{as}(COO) - \nu_{s}(COO)$ of the compound [49]. The vibrations of $\nu_{as}(COO)$ and $\nu_{s}(COO)$ are at 1619, 1549 cm^{-1} and 1427, 1375 cm^{-1} for **1** and at 1580, 1563 cm^{-1} and 1440, 1372 cm^{-1} for **2**, respectively. These facts indicate that the carboxylate groups

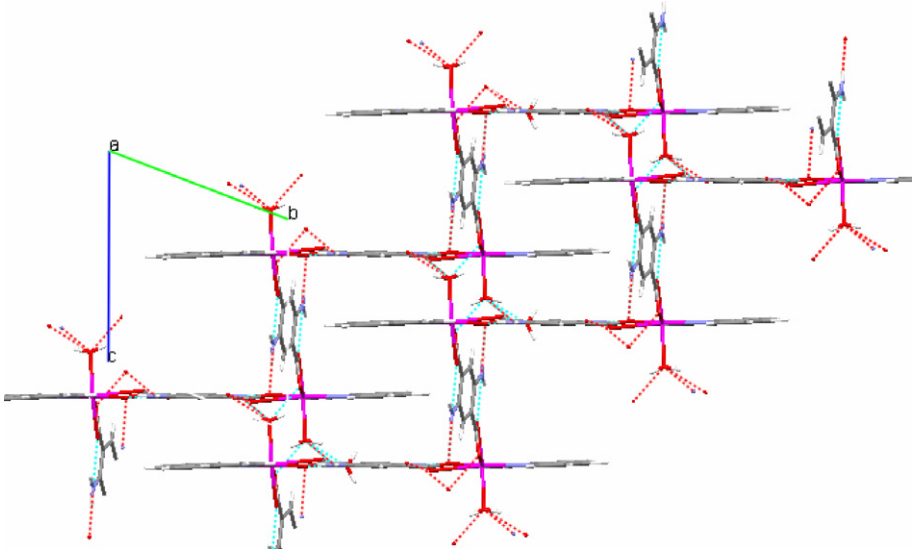


Fig. 3. View of the 3D supramolecular network formed by hydrogen bonding, π–π and C–H···π interactions (down the *a* axis) in **1**.

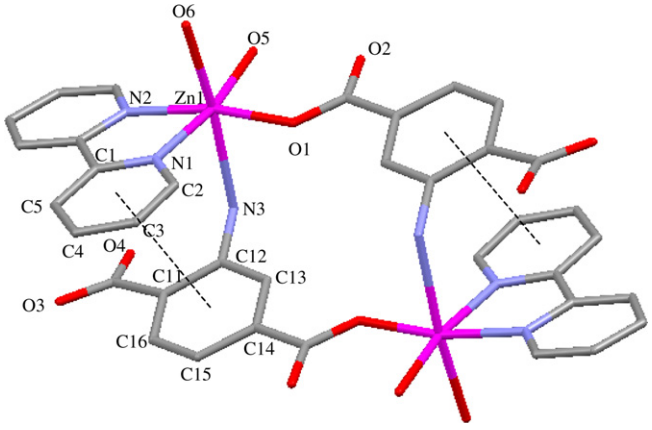


Fig. 4. Molecular structure of **2**, the black dashed line indicates the intramolecular π–π stacking interactions.

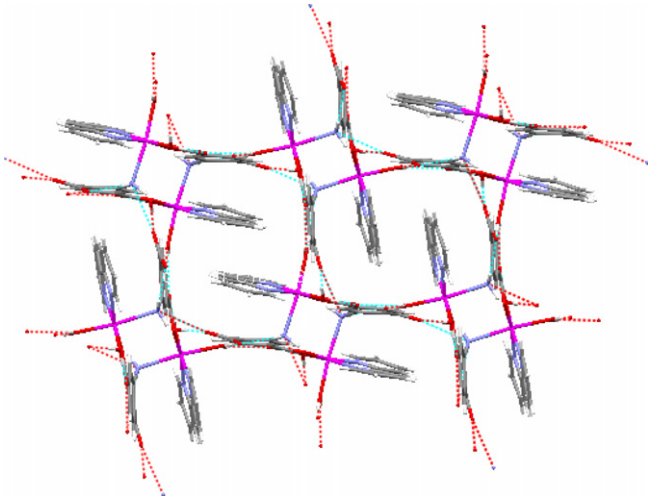


Fig. 5. View of the 3D supramolecular network formed by hydrogen bonding and C4–H4···π interactions between the C4 atom of the bipy ring and the centroid of the benzene ring of the atpt ligand in **2** (down the *a* axis).

of the atpt ligand exhibit the bis-chelating coordination mode in **1**. One of the two carboxylate groups of the atpt ligand in **2** displays a monodentate motif. In all these cases, the results of the X-ray analysis allowed the unambiguously assignment of the binding modes of the carboxylate groups.

3.5. Thermogravimetric analysis

To study the thermal stability of the compounds, thermogravimetric analysis (TG) was performed on polycrystalline samples under a nitrogen atmosphere in flowing N_2 with a heating rate of 10 °C min^{-1} (Fig. 6). Compound **1** releases the coordinated H_2O and lattice H_2O molecules from 46 to 148 °C with a weight loss of 5.3% (calcd. 5.4%). Compound **1** decomposes at 279 °C. TGA for **2**shows that two H_2O molecules are lost in the temperature range 51–160 °C (calc. 8.3%; obsd. 8.1%) and this compound decomposes at 241 °C.

3.6. Photoluminescence properties

The solid-state photoluminescence spectra of H_2atpt and the title complexes at room temperature are depicted in Fig. 7. H_2atpt exhibits a broad strong fluorescent emission centered on 588 nm with an excitation maximum at 358 nm. Green fluorescence for both **1** and **2** can be observed, where the maximum emission wavelengths, λ_{em}, are at 538 nm and 553 nm, respectively, by exciting the solid sample under UV at $\lambda_{ex} = 385$ nm and 335 nm, respectively. The excited-state origins for **1** and **2** seem to be due to a metal-to-ligand charge-transfer transition (MLCT). The fluorescent intensity of **1** is stronger than that of **2**, which may be attributed to the fact that the conjugation degree of the phen ligand is larger than that of the bipy ligand.

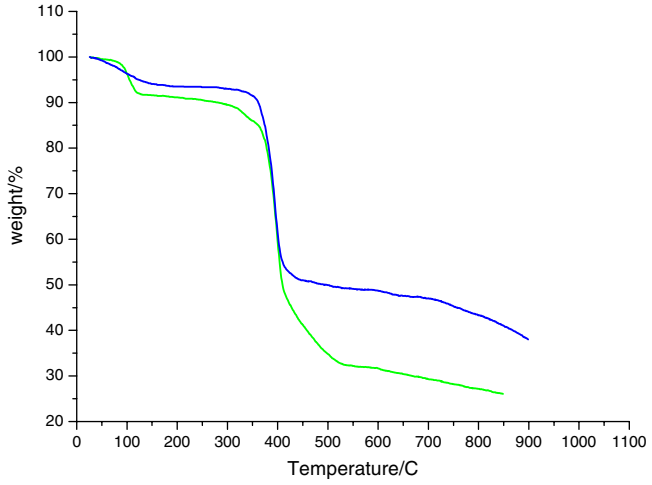


Fig. 6. TG curves of **1** (blue) and **2** (green). (For interpretation of the references to colour in this figure legend, the reader is referred to the web version of this article.)

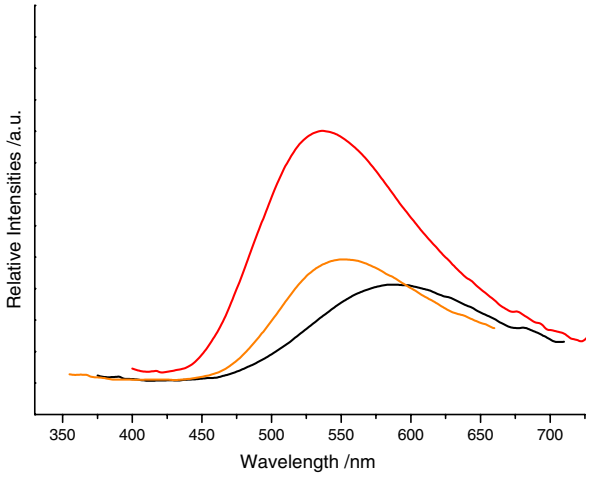


Fig. 7. The emission spectra of H_2atpt (black), **1** (red) and **2** (orange) in the solid state at 298 K. The corresponding excitation wavelengths, λ_{ex}, are 358, 385 and 335 nm, respectively. (For interpretation of the references to colour in this figure legend, the reader is referred to the web version of this article.)

4. Conclusions

In conclusion, two new coordination compounds based on the H_2atpt ligand have been obtained. Compound **1** is the first structurally characterized Cd complex with the atpt ligand. The amino group of the atpt ligand in **2** coordinates to the divalent metal ions for the first time. The atpt ligand exhibits different coordination modes in these two compounds. Furthermore, the atpt ligand in **2** exhibits a newly observed coordination mode compared with all the reported compounds with the atpt ligand. Compound **1** is a 1D zigzag chain, which further assembles into a 3D supramolecular framework. Compound **2** exhibits a binuclear structure with intramolecular π–π stacking interactions. The strong intermolecular hydrogen bonding and C4–H4···π interactions in **2** lead to the formation of a 3D supramolecular network. Green fluorescence can be observed for both **1** and **2**.

Acknowledgements

We gratefully acknowledge the Foundation of Jiangsu Provincial Key Program of Physical Chemistry in Yangzhou University for financial support of this work.

Appendix A. Supplementary material

CCDC 607818 and 607815 contain the supplementary crystallographic data for **1** and **2**. These data can be obtained free of charge via http://www.ccdc.cam.ac.uk/conts/retrieving.html, or from the Cambridge Crystallographic Data Centre, 12 Union Road, Cambridge CB2 1EZ, UK; fax: (+44) 1223-336-033; or e-mail: deposit@ccdc.cam.ac.uk. Supplementary data associated with this article can be found, in the online version, at doi:10.1016/j.poly.2007.07.031.

References

[1] F.A. Cotton, C. Lin, C.A. Murillo, Acc. Chem. Res. 34 (2001) 759.
[2] T.K. Maji, K. Uemura, H.-C. Chang, R. Matsuda, S. Kitagawa, Angew. Chem. Int. Ed. 43 (2004) 3269.
[3] S. Kawata, S. Kitagawa, H. Kumagai, C. Kudo, H. Kamesaki, T. Ishiyama, R. Suzuki, M. Kondo, M. Katada, Inorg. Chem. 35 (1996) 4445.
[4] A. Morsali, A.R. Mahjoub, Polyhedron 23 (2004) 2427.
[5] D. Dobrzyńska, T. Lis, L.B. Jerzykiewicz, Inorg. Chem. Commun. 8 (2005) 1090.
[6] A.C. Sudik, A.P. Côté, O.M. Yaghi, Inorg. Chem. 44 (2005) 2998.
[7] J.P. García-Terán, O. Castillo, A. Laque, U. Garcia-Couceivo, P. Román, F. Lloret, Inorg. Chem. 43 (2004) 5761.
[8] A.M. Chippindale, M.R. Grimshaw, A.V. Powell, A.R. Cowley, Inorg. Chem. 44 (2005) 4121.
[9] S.J. Loeb, Chem. Commun. (2005) 1511.
[10] T.K. Maji, G. Mostafa, H.-C. Chang, S. Kitagawa, Chem. Commun. (2005) 2439.
[11] Q. Wei, M. Nieuwenhuyzen, F. Meunier, C. Hardacre, S.L. James, J. Chem.Soc., Dalton Trans. (2004) 1807.
[12] A.R. Millward, O.M. Yaghi, J. Am. Chem. Soc. 127 (2005) 17998.
[13] B.J. Holliday, C.A. Mirkin, Angew. Chem. Int. Ed. 40 (2001) 2022.
[14] P.J. Hagraman, D. Hagrman, J. Zubieta, Angew. Chem. Int. Ed. 38 (1999) 2638.
[15] S.-I. Noro, H. Miyasaka, S. Kitagawa, T. Wada, T. Okubo, M. Yamashita, T. Mitani, Inorg. Chem. 44 (2005) 133.
[16] P. Diaz, J. Benet-Buchholz, R. Vilar, A.J.P. White, Inorg. Chem. 45 (2006) 1617.
[17] F.S. Delgado, J. Sanchiz, C. Ruiz-Pérez, F. Lloret, M. Julve, Inorg. Chem. 42 (2003) 5938.
[18] H.W. Roesky, M. Andruh, Coord. Chem. Rev. 236 (2003) 91.
[19] E. Colacio, F. Lloret, R. Kivekäs, J. Ruiz, J. Suārez-Varela, M.R. Sunberg, Chem. Commun. (2002) 592.
[20] X.-J. Li, R. Cao, D.-F. Sun, W.-H. Bi, Y.-Q. Wang, X. Li, M.-C. Hong, Cryst. Growth Des. 4 (2004) 775.
[21] C. Janiak, J. Chem.Soc., Dalton Trans. (2003) 2781.
[22] X.H. Bu, W. Weng, J.R. Li, W. Chen, R.H. Zhang, Inorg. Chem. 41 (2002) 413.
[23] N.S. Gunning, C.L. Cahill, J. Chem.Soc., Dalton Trans. (2005) 2788.
[24] A. Kraft, A.C. Grimsdale, A.B. Holmes, Angew. Chem. Int. Ed. Engl. 33 (1998) 402.

[25] Y.-Q. Huang, B. Ding, H.-B. Song, B. Zhao, P. Ren, P. Cheng, H.-G. Wang, D.-Z. Liao, S.-P. Yan, Chem, Commun. (2006) 4906.
[26] R. Carballo, B. Covelo, C. Lodeiro, E.M. Vázquez-López, CrystEngComm. 7 (2005) 294.
[27] H.-K. Fun, S.S. Sundara Raj, R.-G. Xiong, J.-L. Zuo, Z. Yu, J. Chem. Soc., Dalton Trans. (1999) 1915.
[28] D.M. Ciurtin, N.G. Pschirer, M.D. Smith, U.H.F. Bunz, H.C. zur Loye, Chem. Mater. 13 (2001) 2743.
[29] E. Cariati, X. Bu, P.C. Ford, Chem. Mater. 12 (2000) 3385.
[30] J.-H. He, J.-H. Yu, Y.-T. Zhang, Q.-H. Pan, R.-R. Xu, Inorg. Chem. 44 (2005) 9279.
[31] Y.-X. Ke, D.J. Collins, D.-F. Sun, H.-C. Zhou, Inorg. Chem. 45 (2006) 1897.
[32] M. Du, X.-J. Jiang, X.-J. Zhao, H. Cai, J. Ribas, Eur. J. Inorg. Chem. 6 (2006) 1245.
[33] L. Hao, M.A. Mansour, R.J. Lachicotte, H.J. Gysling, R. Eisenberg, Inorg. Chem. 39 (2000) 5520.
[34] N.W. Alock, P.R. Barker, J.M. Haider, M.J. Hannon, C.I. Painting, Z. Pikramenou, E.A. Plummer, K. Rissanen, P. Saarenketo, J. Chem. Soc., Dalton Trans. (2000) 1447.
[35] C.-B. Liu, C.-Y. Sun, L.-P. Jin, S.-Z. Lu, New J. Chem. 28 (2004) 1019.
[36] M.E. Braun, C.D. Steffek, J. Kim, P.G. Rasmussen, O.M. Yaghi, Chem. Commun. (2001) 2532.
[37] Z.-Y. Fu, X.-T. Wu, J.-C. Dai, S.-M. Hu, W.-X. Du, H.-H. Zhang, R.-Q. Sun, Eur. J. Inorg. Chem. (2002) 2730.
[38] H.T. Xu, N.W. Zheng, X.L. Jin, R.Y. Yang, Z.Q. Li, Chem. Lett. (2002) 350.
[39] H.T. Xu, N.W. Zheng, X.L. Jin, R.Y. Yang, Y.G. Wu, E.Y. Ye, Z.Q. Li, J. Mol. Struct. 655 (2003) 339.
[40] X.-Y. Chen, B. Zhao, W. Shi, J. Xia, P. Cheng, D.-Z. Liao, S.-P. Yan, Z.-H. Jiang, Chem. Mater. 17 (2005) 2866.
[41] C.-B. Liu, X.-J. Zhang, Y.-Y. Yang, L.-P. Jin, Inorg. Chem. Commun. 8 (2005) 1045.
[42] M. Eddaoudi, J. Kim, N. Rosi, D. Vodak, J. Wachter, M. OKeeffe, O.M. Yaghi, Science 295 (2002) 469.
[43] A.L. Grzesiak, F.J. Uribe, N.W. Ockwig, O.M. Yaghi, A.J. Matzger, Angew. Chem. Int. Ed. 45 (2006) 2553.
[44] H.T. Xu, N.W. Zheng, X.L. Jin, R.Y. Yang, Z.Q. Li, J. Mol. Struct. 646 (2003) 197.
[45] Y.G. Wu, N.W. Zheng, R.Y. Yang, H.T. Xu, E.Y. Ye, J. Mol. Struct. 610 (2002) 181.
[46] J.S. Decker, H.Z. Frye, Naturforsch. Teil B 21 (7) (1966) 626.
[47] G.M. Sheldrick, SHELXL 97, Programs for Crystal Structure Analysis (Release 97-2), University of Götinggen, Germany, 1997.
[48] L.L. Merrit, E.D. Schroeder, Acta Crystallogr. 9 (1956) 801.
[49] K. Nakamoto, Infrared and Raman Spectra of Inorganic and Coordination Compounds, John Wiley and Sons, New York, 1997.

the stable analogous neutral ReO complexes starting with Ph–XN_2S-type ligands acting as a trianionic ligand $XN^-N^-S^-$ (X = OMe, SMe, NMe_2).

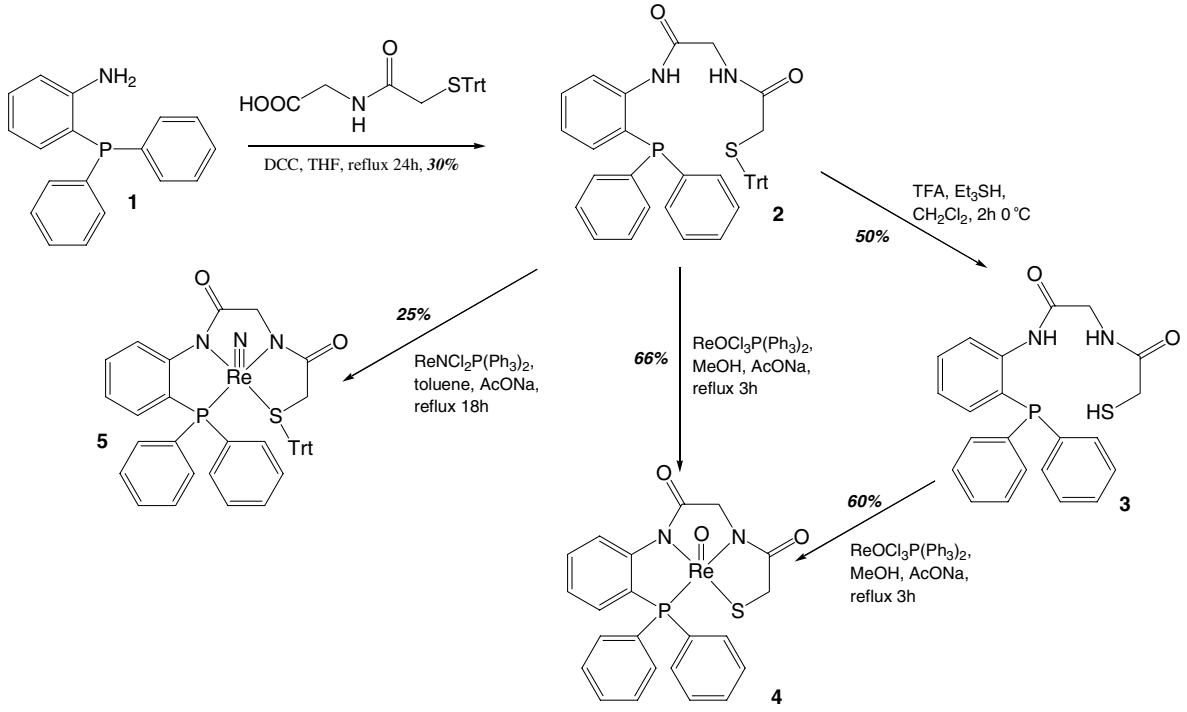
Due to their tendency to delocalize the electron density on the metal – a result of their σ-donor and π-acceptor character – phosphines often lead to the stabilization of the complexes in which they are contained [5]. This led us to anticipate that the incorporation of one phosphine group in the chelate ring should enhance the reactivity of the ligand towards the MO^{3+} core (M = Tc or Re) and consequently increase the stability of the resulting neutral metallic complexes. This expectation has been realized in the isolation of two neutral semi-rigid PN_2S rhenium(V) complexes and the structural characterization of one of them, [ReO{Ph-P(Ph_2)N_2S}] (**4**). To our knowledge, these compounds are the first Re^VN and Re^VO species including a semi-rigid PN_2S framework, the only previous examples in ReO chemistry being the PN_2S-tetradentate monooxorhenium complexes obtained with the non-semi-rigid ligands 3-diphenylphosphinoglycyl-L-(S-protected)cysteine and its methyl ester [6]. It is noteworthy that a Re^VO species including a semi-rigid Ph-P_2N_2 framework has been reported by Tisato et al. [7].

2. Results and discussion

The ligands of this study have been prepared under a strictly inert atmosphere according to the method outlined in Scheme 1. Thus, reaction of 2-iodoaniline with diphenylphosphine in the presence of NEt_3 and $Pd(PPh_3)_4$ as a catalyst in warm acetonitrile afforded the 2-diphenylphosphinoaniline (**1**), in quite good yield [8]. A conventional carbodiimide amide coupling of *N*-[(S-trityl)acetyl]glycine [3b] with **1** in THF, followed by the cleavage of the trityl group under acidic conditions (TFA, Et_3SiH) [9] gave the ligands [Ph-P(Ph_2)N_2S(Trt)] (**2**) and [Ph-P(Ph_2)N_2SH] (**3**), respectively. The ligands showed good solubility in methanol, ethanol, dichloromethane, chloroform and acetonitrile. They were characterized by elemental analysis, ^1H and ^{31}P NMR spectroscopy, all consistent with the formula shown in Scheme 1. In particular, the ^{31}P spectra of **2** and **3** revealed only one peak at ≈−21.5 ppm corresponding to P^{III} species. The IR spectrum of **3** exhibited an absorption band at 2482 cm^{-1}, which corresponds to the S–H stretching vibration.

Ligand-exchange reactions in warm methanol of labile $ReOCl_3(PPh_3)_2$ with a slight excess of the relevant tritylated or detritylated ligand (1:1.2 metal:ligand ratio) in the presence of a methanolic sodium acetate solution as a deprotonating agent led to the same neutral complex **4** in satisfactory yield (Scheme 1). The cleavage of the trityl group of **2**, accomplished during the coordination of the ligand to the ReO^{3+} core, is explained by the acidic contribution of the metal (Lewis acid) in the mechanism of sulfur detritylation. Complex **4** crystallised from CH_2Cl_2/hexane solution by slow evaporation and afforded purple crystals suitable for X-ray analysis.

The spectroscopic characteristics of the oxo-rhenium complex **4** of the general formula [ReO{Ph-P(Ph_2)N_2S}], as evident from the elemental analysis, were similar to the analogous anionic complexes described previously [3b,10], i.e. (i) the characteristic rhenium(V) oxo isotopic pattern



Scheme 1. Synthesis of compounds **4** and **5**.

consistent with the presence of a neutral mononuclear complex ([M+H$^+$] = 607/609), (ii) an intense band in the IR spectrum attributable to the Re=O stretching vibration at 966 cm^{-1}, (iii) a non-equivalence of the two hydrogens of each methylene group (AX pattern) of the tetradentate ligand framework in the proton NMR spectrum, the downfield signal of both AX patterns being assigned to the *endo* protons (*syn* to the Re=O group) and the upfield signals to the *exo* ones (*anti* to the Re=O group) [6b,11]. The ^{31}P NMR spectrum showed a singlet peak in agreement with phosphine coordination,[12] the pertinent peak moving downfield to the +38.7 ppm positive region from the −21.6 and −21.2 ppm values exhibited by the uncoordinated detritylated and tritylated ligands, respectively. Thus only one single isomer was produced. The formation of a single isomer is important as isomerism can markedly influence the pharmacokinetics of a radiopharmaceutical [13].

As shown in Fig. 1, the crystal structure of **4** consists of a discrete monomeric and neutral monooxo complex packed with no intermolecular contacts shorter than the van der Waals radii sum. Selected interatomic distances and bond angles are listed in Table 2. The coordination geometry about the metal is distorted square pyramidal with the phosphorous of the linked phosphine, the two amide nitrogen and the sulfur atom occupying the equatorial plane and the oxo group directed in the apical position. The description in terms of a square pyramid is supported by the nearly equal N(2)–Re(1)–S(1) and N(1)–Re(1)–P(1) angles, leading to a very low trigonality index τ of 0.05 (N(2)–Re(1)–S(1) = 135.91(15)° and N(1)–Re(1)–P(1) = 138.88(14)°) [14]. This value is similar to those found for our analogous anionic complexes ($0.00 < \tau < 0.07$) [4,10] and the semi-rigid neutral complex [ReO{Ph-N$_3$O}] recently developed by Papachristou et al. [15] ($\tau = 0.01$). The Re atom lies 0.78 Å above the basal plane, which is reflected by the O=Re–N and O=Re–S/P angles ranging from 106.73(15)° to 114.1(2)°. This value is in agreement with the displacement normally observed for square-pyramidal rhenium complexes [4,16]. The tetradentate coordination mode of the triply deprotonated ligand leads to a three (5,5,5)-membered chelate ring system around the rhenium atom. The two phenyl rings of the phosphine are roughly perpendicular to the Ph–PN$_2$S plane; the mean planes passing through them make angles of 87.9° and 125.0° with the pyramidal basal plane. The same planes define an angle to each other of 64.2°.

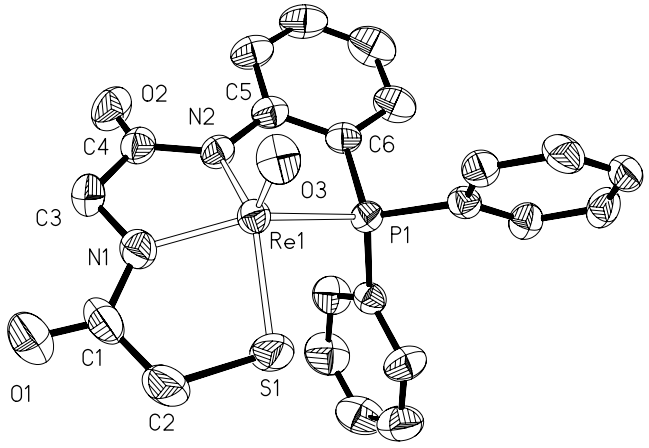


Fig. 1. ORTEP diagram of **4** with 50% probability thermal ellipsoids showing the atomic labelling scheme.

The valence bond distances are unexceptional and are within the range observed for Re-oxo (1.675(4) Å), Re–N$_{amide}$ (ca. 1.99 Å) and Re–S$_{thiolate}$ (2.2614(17) Å) bonds in ReO five-coordinate square-pyramidal complexes. The dominating feature of this structure is the Re–P distance. The latter is 2.4052(14) Å, and it is far shorter than that reported for the non-semi-rigid [ReO{P(Ph$_2$)N$_2$S}] compound developed by Mazzi et al. [6b] 2.4446(2) Å. The rigidity imposed by the aromatic ring conjugated with the strained five-membered chelate ring Re(1)–P(1)–C(6)–C(5)–N(2) instead of a six-membered chelate ring for the Mazzi complex explains this difference. Consequently, the P(1)–Re(1)–N(2) angle is shorter in our complex than in Mazzi's one (78.84(14)° versus 90.5(2)°). It is noteworthy that the length of the X–Re bond in our [ReO(Ph–XN$_2$S)] complexes (X = O, S, NH, PPh$_2$) is greatly influenced by the nature of the X atom. As expected, the bulkier is the X atom, the longer is the X–Re bond, with the following order: d_{N-Re} 1.968(2)Å $< d_{O-Re}$ 2.000(4) Å $\ll d_{S-Re}$ 2.2969(18) Å $< d_{P-Re}$ 2.4052(14) Å. In return, there are no significative differences for the other Re–N or Re–S bonds.

By using the above coordination conditions, treatment of **2** with the ReNCl$_2$(PPh$_3$)$_2$ precursor afforded an intractable mixture, from which the isolation of pure and defined species was not possible. Surprisingly, use of solid sodium acetate as a deprotonating agent and toluene instead of methanol as the solvent allowed us to isolate an unprecedented non-detritylated neutral nitridorhenium(V) complex in 25% yield, as sketched in Scheme 1. [ReN{Ph-P(Ph$_2$)N$_2$S(Trt)}] (**5**) was characterized by spectroscopical methods, even though crystals suitable for X-ray work could not be obtained. In particular, both ^{31}P and ^{1}H NMR spectra demonstrated that **5** is diamagnetic, suggesting a low-spin d^2 configuration, typical of distorted octahedral or distorted square-pyramidal species bearing a multiple oxo- or nitrido-core [17]. The presence of the trityl group is revealed by the integration ratio of total aromatic/aliphatic protons (29/4), consistent with three more phenyl rings in the complex. As expected, the methylene protons of the tetradentate ligand framework were found to be diastereotopic (AX pattern) with coupling constants in the range 17.5–19.5 Hz (Fig. 2). The DCI-MS spectrum of complex **5** showed the production of molecular cations at *m/z* 848/850 ([M+H$^+$]) and *m/z* 865/867 ([M+NH$_4^+$]), with a detectable fragment ion at *m/z* 243 ([Trt$^+$]), revealing the loss of the trityl group. The IR spectrum of **5** exhibited an absorption band at 1098 cm^{-1} assigned to the characteristic ReN stretching vibration. No multiple strong bands were detected in the ranges 1500–1560 and 3200–3400 cm^{-1} of complex **5**, confirming the deprotonation of the amide functions. The complex is

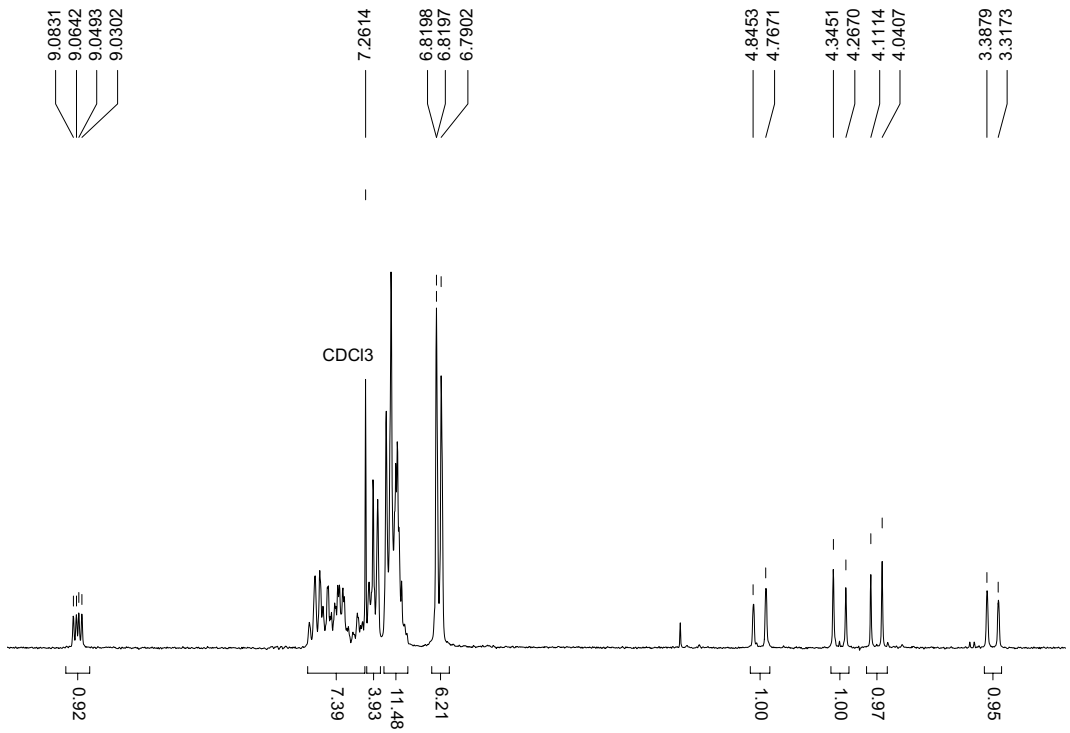


Fig. 2. ^{1}H NMR spectrum of [ReN{Ph-P(Ph$_2$)N$_2$S(Trt)}] (**5**) ($CDCl_3$; 250 MHz; 25 °C).

non-conducting in acetonitrile solutions, as expected [18]. So, chelation of the ReN core proceeds by coordination with the PN_2S^{2-} donor atom set formed from one neutral phosphine, two deprotonated amide groups and one neutral thioether. This is the first example where metal catalysed removal of the trityl group does not occur during a Re^{V} complexation.

The isolation of these two complexes conjugated with the fact that we never succeeded in isolating a neutral Re^{V} complex with [Ph–X(Me)N$_2$S(Trt)] ligands (X = O or S) suggested that the phosphorus atom of the chelate (i) enhances the reactivity of the ligand towards the ReO^{3+} core, (ii) binds first to the metal and this bond acts as the driving force for coordination. The latter hypothesis is consistent with the mechanism proposed by Visentin et al. for their similar ReO complexes with a P,N,N,S donor atom set [6b]. Our complexes are extremely stable in the solid state as well as in organic solvents for long periods of time, as shown by NMR spectroscopy. Their stability is not affected by the presence of air. The mixing of a π-donor S atom with a π-acceptor P atom ensures an appropriate electronic balance around the ReO or ReN core and this event contributes to the overall robustness of the system.

3. Conclusion

In conclusion, the new semi-rigid PN_2S ligand studied here exhibits high chelating affinity for the rhenium(V) core. A neutral stable monooxorhenium(V) complex was produced as a single isomer by reacting the tritylated or detritylated ligand with a ReO precursor, in good yield. The high affinity of the PN_2S set toward $Re^{V}O$ can be expected also for ^{99m}TcO, making this ligand potentially useful as a ^{99m}TcO-based brain perfusion or brain receptor imaging agent. A radio-labelling study with ^{99m}Tc will start soon. Investigations on the unexpected neutral complex [ReN{Ph-P(Ph$_2$)N$_2$S(Trt)}], isolated during the complexation of the tritylated ligand with $ReNCl_2(PPh_3)_2$, are still going on to better understand the formation of this complex.

4. Experimental

4.1. General methods

All preparations and manipulations were carried out under a nitrogen atmosphere using standard Schlenk techniques. All chemicals were of the highest purity commercially available. Rhenium(VII) oxide was purchased from Aldrich Chem. Co. It was converted to $ReOCl_3(PPh_3)_2$ and $ReNCl_2(PPh_3)_2$ according to published protocols [19]. Solvents were dried and distilled by standard methods before use and stored over 0.3 nm molecular sieves. 2-(diphenylphosphino)aniline (**1**) [8] and *N*-[(S-trityl)acetyl]glycine [3b] were prepared as described previously. Silica gel (0.060–0.200 nm) was purchased from Acros. TLC was performed using precoated Kieselgel 60 plates F_{254} (TLC plates, Merck) and was visualised by UV or iodine. Column chromatography was carried out using "gravity" silica (Merck). Infrared spectra (4000–400 cm^{-1}) were recorded as KBr pellets on a Vector 22 Bruker spectrophotometer. NMR spectra were recorded on a Bruker AC 200 (81.015 MHz for ^{31}P) and AC 250

apparatus (250.133 MHz for ^1H). Chemical shifts are indicated in δ values (ppm) downfield from internal TMS. For the $^{31}P\{^1H\}$ spectra the external standard was H_3PO_4 (82% D_2O, $\delta = 0.0$ ppm). DCI-Mass spectra were obtained on a NERMAG R10-10 mass spectrometer. Microanalysis was performed by the Microanalytical Department of the Ecole Nationale Supérieure de Chimie de Toulouse.

4.2. Synthetic work

4.2.1. N-[2-(diphenylphosphino)phenyl]-2-[(triphenylmethylmercapto)methylcarbonylamino] ethanamide (2)

N-[(S-trityl)acetyl]glycine (1.957 g, 5 mmol) and **1** (1.385 g, 5 mmol) were dissolved in anhydrous degassed THF (25 mL). Dicyclohexylcarbodiimide (1.135 g, 5.5 mmol) was added and the mixture was heated at reflux for 24 h. After cooling to room temperature, the insoluble dicyclohexylurea was removed by filtration and the filtrate evaporated under reduced pressure. The obtained brown oil was dissolved in AcOEt (20 mL) and cooled at 0 °C. A white solid was collected by filtration and washed with cold AcOEt. The solid was purified by column chromatography on silica gel (eluent: CH_2Cl_2/AcOEt, 96/4) to give **2** as a white powder (1.002 g, 30%).

Anal. Calc. for $C_{41}H_{35}N_2O_2PS$: C, 75.67; H, 5.42; N, 4.30; S, 4.93. Found: C, 75.37; H, 5.22; N, 4.10; S, 5.22%; IR (KBr): ν (cm^{-1}) 3328, 3269 (NH); 3052 (CH_{Ar}), 1702, 1652 (CO); 1026 (P–C); MS (DCI/NH_3) *m/z* 243 [Trt^+], 651 [$M+H^+$]; 667, [$M+NH_4^+$]; $^{31}P\{^1H\}$ NMR ($CDCl_3$): δ (ppm): −21.2 (s); ^1H NMR ($CDCl_3$) δ (ppm): 3.15 (s, 2H, SCH_2); 3.49 (d, 2H, $J = 5.5$ Hz, CH_2N); 6.42 (broad s, 1H, NH); 6.85–7.56 (m, 28H, CH_{Ar}); 8.09 (broad s, 1H, NH); 8.22 (m, 1H, CH_{Ar}).

4.2.2. N-[2-(diphenylphosphino)phenyl]-2-[mercaptomethylcarbonylamino]ethanamide (3)

To a chilled solution of **2** (0.250 g, 0.38 mmol) in degassed CH_2Cl_2 (30 mL) were added TFA (13 mL) and triethylsilane (121 μL, 0.76 mmol). The solution became colourless and it was stirred for 2 h. After removal of the solvents under vacuum, the resulting residue was crystallised as a white powder upon addition of hexane (77 mg, 50%).

Anal. Calc. for $C_{22}H_{21}N_2O_2PS$: C, 64.69; H, 5.18; N, 6.86; S, 7.85. Found: C, 64.80; H, 5.01; N, 6.50; S, 7.64%; IR (KBr) ν (cm^{-1}) 3338, 3241 (NH); 2482 (SH); 1696, 1640 (CO); MS (DCI/NH_3): *m/z* 409 [$M+H^+$]; $^{31}P\{^1H\}$ NMR ($CDCl_3$): δ (ppm): −21.6 (s) ; ^1H NMR ($CDCl_3$) δ (ppm): 1.33 (t, 1H, $J = 8.8$ Hz, SH); 3.22 (d, 2H, $J = 8.8$ Hz, SCH_2); 3.93 (d, 2H, $J = 5.5$ Hz, CH_2N); 6.90 (m, 1H, NH); 6.92 (m, 1H, CH_{Ar}); 7.06-7.41 (m, 11H, CH_{Ar}); 7.55 (m, 1H, CH_{Ar}); 8.10 (broad s, 1H, NH); 8.35 (m, 1H, CH_{Ar}).

4.2.3. [N-(2-diphenylphosphinophenyl)-2-(mercaptomethylcarbonylamino)ethanamido(4-)-κ^4P,N,N′,S]oxorhenate(V) or [ReO{Ph-P(Ph$_2$)N$_2$S}] (4)

Method 1: To a suspension of **2** (200 mg, 0.308 mmol) and $ReOCl_3(PPh_3)_2$ (307 mg, 0.370 mmol) in degassed MeOH (30 mL) was added a 1 M solution of sodium acetate in degassed MeOH (3 mL, 3 mmol). After refluxing for 3 h, the solution turned violet and clear. After cooling, the solution was filtered off and evaporated to dryness. The obtained brown violet solid was recrystallised from CH_2Cl_2/hexane (2/1) to afford **4** as a violet powder (123 mg, 66%).

Method 2: The same procedure as method 1 starting with **3** (50 mg, 0.122 mmol), $ReOCl_3(PPh_3)_2$ (122 mg, 0.147 mmol) and sodium acetate in MeOH (1 mL, 1 mmol). After recrystallisation, **4** was obtained as a violet powder (44 mg, 60%).

Anal. Calc. for $C_{22}H_{18}N_2O_3PReS$: C, 43.49; H, 2.99; N, 4.61; S, 5.28. Found: C, 43.60; H, 3.12; N, 4.58; S, 5.12%; IR (KBr): ν(cm^{-1}) 1665, 1647 (CO); 966 (ReO); MS (DCI/NH_3): *m/z* (%) 607 (11), 609 (20) [$M+H^+$], 623 (1), 625 (2) [$M+NH_4^+$]; $^{31}P\{^1H\}$ NMR ($CDCl_3$): δ (ppm): 38.7 (s); ^1H NMR ($CDCl_3$) δ (ppm): 3.88 (d, 1H, $J = 17.4$ Hz, SCH_2); 4.04 (d, 1H, $J = 17.4$ Hz, SCH_2); 4.78 (d, 1H, $J = 19.0$ Hz, CH_2N); 5.22 (d, 1H, $J = 19.0$ Hz, CH_2N); 7.20 (t, 1H, $J = 7.3$ Hz, CH_{Ar}); 7.28–7.91 (m, 12H, CH_{Ar}); 9.10 (dd, 1H, $J_{HH} = 8.5$ Hz, $J_{HP} = 4.6$ Hz, CH_{Ar}).

4.2.4. [N-(2-diphenylphosphinophenyl)-2-{(triphenylmethylmercapto) methylcarbonylamino}ethanamido(4-)-κ^4P,N,N′,S]nitridorhenate(V) or [ReN{Ph-P(Ph$_2$)N$_2$S(Trt)}] (5)

To a suspension of **2** (200 mg, 0.308 mmol) and $ReNCl_2(PPh_3)_2$ (294 mg, 0.370 mmol) in degassed toluene (30 mL) was added sodium acetate (304 mg, 3.7 mmol). After refluxing for 18 h the solution turned brown and clear. After cooling, the solution was filtered off and evaporated to dryness. Addition of ether (10 mL) gave a precipitate which was filtered off. The precipitate was dissolved in CH_2Cl_2. Addition of hexane gave a precipitate which was filtered off. The filtrate was concentrated to give **5** as a reddish-brown powder (65 mg, 25%).

Anal. Calc. for $C_{41}H_{33}N_3O_2PReS$: C, 58.00; H, 3.92; N, 4.95; S, 3.78. Found: C, 58.08; H, 4.20; N, 4.60; S, 3.56%; IR (KBr): ν(cm^{-1}) 3050 (CH_{Ar}); 1661, 1637 (CO); 1098 (ReN); MS (DCI/NH_3): *m/z* (%) 243 (14) [Trt^+], 848 (60), 850 (100) [$M+H^+$], 865 (3), 867 (6) [$M+NH_4^+$]; $^{31}P\{^1H\}$ NMR ($CDCl_3$): δ (ppm): 39.0 (s); ^1H NMR ($CDCl_3$) δ (ppm): 3.31 (d, 1H, $J = 17.6$ Hz, SCH_2); 4.04 (d, 1H, $J = 17.6$ Hz, SCH_2); 4.26 (d, 1H, $J = 19.5$ Hz, CH_2N); 4.76 (d, 1H, $J = 19.5$ Hz, CH_2N); 6.70–6.82 (m, 6H, CH_{Ar}); 7.05–7.60 (m, 22H, CH_{Ar}); 9.05 (dd, 1H, $J_{HH} = 8.5$ Hz, $J_{HP} = 4.7$ Hz, CH_{Ar}). Λ_M (CH_3CN): 21.10 Ω^{-1} cm^2 mol^{-1} (neutral).

4.3. X-ray crystal structure determination of complex 4

[ReO{Ph-P(Ph_2)N_2S}] (**4**) was crystallised by slow evaporation of a CH_2Cl_2/hexane solution. A purple crystal of **4** thus produced was mounted on a Nonius Kappa CCD diffractometer equipped with a CDD detector, and was used for data collection. X-ray intensity data were collected with

Table 1
Summary of the crystal data for complex **4**

Complex	[ReO{Ph-P(Ph$_2$)N$_2$S}]
Empirical formula	$C_{22}H_{18}N_2O_3PReS$
Molecular weight	607.635
Crystal system	monoclinic
Space group	$P2_1/n$
Crystal size (mm)	$0.56 \times 0.16 \times 0.06$
a (Å)	9.2572(6)
b (Å)	13.0513(3)
c (Å)	17.6436(14)
β (°)	100.107(6)
V (Å^3)	2098.6(2)
Z	4
d [g/cm^3]	1.923
F(000)	1176
Total reflections	39174
Independent reflections	3621
Parameters	272
Observed reflections [$I > 2\sigma(I)$]	3621
Final R indices [$I > 2\sigma(I)$]	$R_1 = 0.0351$, $wR_2 = 0.0817$
R indices (all data)	$R_1 = 0.0471$, $wR_2 = 0.0917$
Goodness-of-fit	1.109

Table 2
Selected bonds lengths (Å) and angles (°) for complex **4**

Bond lengths			
Re(1)–O(3)	1.675(4)	C(2)–S(1)	1.821(7)
Re(1)–P(1)	2.4052(14)	C(1)–N(1)	1.364(9)
Re(1)–N(2)	2.046(5)	C(4)–N(2)	1.402(7)
Re(1)–N(1)	1.981(6)	C(6)–P(1)	1.806(6)
Re(1)–S(1)	2.2614(17)		
Bond angles			
O(3)–Re(1)–N(1)	113.8(2)	N(2)–Re(1)–N(1)	78.9(2)
O(3)–Re(1)–P(1)	106.73(15)	N(1)–Re(1)–S(1)	82.53(16)
O(3)–Re(1)–N(2)	114.1(2)	P(1)–Re(1)–S(1)	90.01(6)
O(3)–Re(1)–S(1)	110.00(17)	N(2)–Re(1)–S(1)	135.91(15)
P(1)–Re(1)–N(2)	78.84(14)	P(1)–Re(1)–N(1)	138.88(14)

graphite-monochromated Mo Kα radiation ($\lambda = 0.71073$ Å) at a temperature of 298 K. The most significant details of the crystallographic study are reported in Table 1. A collection of selected bond distances and angles are shown in Table 2. The structure was solved by direct methods. All the non-hydrogen atoms were refined anisotropically using the full-matrix, least-squares procedure based on F^2. Structure determination and refinement were performed using the maXus [20] and shelx-97 [21] programs. 3621 independent reflections with $I \geqslant 2\sigma(I)$ were used for refinement of the unit cell ($\theta \leqslant 25°$). Hydrogens for the mater molecule were not located.

Appendix A. Supplementary material

CCDC 651266 contains the supplementary crystallographic data for this paper. These data can be obtained free of charge via http://www.ccdc.cam.ac.uk/conts/retrieving.html, or from the Cambridge Crystallographic Data Centre, 12 Union Road, Cambridge CB2 1EZ, UK; fax: (+44) 1223-336-033; or e-mail: deposit@ccdc.cam.ac.uk. Supplementary data associated with this article can be found, in the online version, at doi:10.1016/j.poly.2007.07.032.

References

[1] (a) J.R. Dilworth, S.J. Parrot, Chem. Soc. Rev. 27 (1998) 43;
(b) K. Hashimoto, K. Yoshihara, Top. Curr. Chem. 176 (1996) 79.
[2] E. Deutsch, K. Libson, Comments Inorg. Chem. 3 (1984) 83.
[3] (a) J. Le Gal, E. Benoist, M. Gressier, Y. Coulais, M. Dartiguenave, Tetrahedron Lett. 43 (2002) 9295;
(b) J. Le Gal, L. Latapie, M. Gressier, Y. Coulais, M. Dartiguenave, E. Benoist, Org. Biomol. Chem. 2 (2004) 876.
[4] J. Le Gal, F. Tisato, G. Bandoli, M. Gressier, J. Jaud, S. Michaud, M. Dartiguenave, E. Benoist, J. Chem. Soc., Dalton Trans. (2005) 3800.
[5] A.F. Cotton, G. Wilkinson, P.L. Gaus, Basic Inorganic Chemistry, 2nd ed., Wiley, New York, 1987.
[6] (a) M. Santamaria, U. Mazzi, S. Gatto, A. Dolmella, G. Bandoli, M. Nicolini, J. Chem. Soc., Dalton Trans. (1997) 1765;
(b) R. Visentin, R. Rossin, M.C. Giron, A. Dolmella, G. Bandoli, U. Mazzi, Inorg. Chem. 42 (2003) 950.
[7] F. Tisato, F. Refosco, A. Moresco, G. Bandoli, A. Dolmella, C. Bolzati, Inorg. Chem. 34 (1995) 1779.
[8] O. Herd, A. Hessler, M. Hingst, M. Tepper, O. Stelzer, J. Organomet. Chem. 522 (1996) 69.
[9] D.H. Hunter, L.G. Luyt, J. Labelled Cpd. Radiopharm. 43 (2000) 403.
[10] (a) J. Le Gal, E. Benoist, M. Gressier, F. Bélanger-Gariépy, A.L. Beauchamp, Acta Crystallogr., Sect. E 63 (2007) m865;
(b) J. Le Gal, E. Benoist, M. Gressier, F. Bélanger-Gariépy, A.L. Beauchamp, Acta Crystallogr., Sect. E 63 (2007) m647.
[11] J.P. O'Neil, S.R. Wilson, J.A. Katzenellenbogen, Inorg. Chem. 33 (1994) 319.
[12] C. Bolzati, A. Boshi, L. Ucceli, F. Tisato, F. Refosco, A. Cagnolini, A. Duatti, S. Prakash, G. Bandoli, A. Vittadini, J. Am. Chem. Soc. 124 (2002) 11468.
[13] S. Liu, Chem. Soc. Rev. 33 (2004) 445.
[14] A.W. Addison, T.N. Rao, J. Reedijk, G.C. Verschoor, J. Chem. Soc., Dalton Trans. (1984) 1349.
[15] M. Papachristou, I. Permettis, T. Siatra-Papastaikoudi, M. Pelecanou, C. Tsoukalas, C.P. Raptopoulou, A. Terzis, E. Chiotellis, M. Papadopoulos, Eur. J. Inorg. Chem. (2003) 3826.
[16] (a) E. Wong, T. Fauconnier, S. Bennet, J. Valliant, T. Nguyen, F. Lau, L. Lu, A. Pollack, R.A. Bell, J.R. Thornback, Inorg. Chem. 36 (1997) 5799;
(b) R.A. Bell, B.E. McCarry, J.F. Valliant, Inorg. Chem. 37 (1998) 3517;
(c) L. Hansen, M. Lipowska, E. Meléndez, X. Xu, S. Hirota, A.T. Taylor, L.G. Marzilli, Inorg. Chem. 38 (1999) 5351.
[17] (a) G. Bandoli, A. Dolmella, M. Pochia, F. Refosco, F. Tisato, Coord. Chem. Rev. 214 (2001) 43;
(b) F. Tisato, F. Refosco, G. Bandoli, Coord. Chem. Rev. 135/136 (1994) 325.
[18] W.J. Geary, Coord. Chem. Rev. 7 (1971) 81.
[19] (a) N. Johnson, C.J.L. Lock, G. Wilkinson, Inorg. Synth. 9 (1967) 145;
(b) P. Sullivan, J. Brewer, H.B. Gray, Inorg. Synth. 29 (1992) 146.
[20] S. Mackay, C.J. Gilmore, C. Edwards, N. Stewart, K. Shankland, maXus, Computer Program for the Solution and Refinement of Crystal Structures, Nonius, The Netherlands, MacScience, Japan, and The University of Glasgow, UK, 1999.
[21] G.M. Sheldrick, shelxl-97. Program for the Refinement of Crystal Structures, University of Göttingen, Germany, 1997.

Available online at www.sciencedirect.com
ScienceDirect
Polyhedron 26 (2007) 5191
POLYHEDRON
www.elsevier.com/locate/poly

Corrigendum

Corrigendum to "Structural diversities and spectroscopic properties of bis and tris (1,10-phenanthroline)copper(II) complexes" [Polyhedron 26 (2007) 1459–1468]

Sujittra Youngme [a,*], Nanthawat Wannarit [a], Chaveng Pakawatchai [b], Narongsak Chaichit [c], Eakasit Somsook [d], Urho Turpeinen [e], Ilpo Mutikainen [e]

[a] *Department of Chemistry, Faculty of Science, Khon Kaen University, Khon Kaen 40002, Thailand*
[b] *Department of Chemistry, Faculty of Science, Prince of Songkla University, Hat Yai, Songkla 90112, Thailand*
[c] *Department of Physics, Faculty of Science and Technology, Thammasat University Rangsit, Pathumthani 12121, Thailand*
[d] *Department of Chemistry, Faculty of Science, Mahidol University, Bangkok 10400, Thailand*
[e] *Laboratory of Inorganic Chemistry, Department of Chemistry, P.O. Box 55 (A.I.Virtasen aukio 1), 00014 University of Helsinki, Finland*

Available online 21 August 2007

In Table 1 on page 1461, the cell parameters of compound **3** should be

a (Å)	7.5403(10)
b (Å)	10.5766(15)
c (Å)	16.288(2)
α (°)	97.334(2)
β (°)	102.990(2)
γ (°)	108.981(2)

and not

a (Å)	7.6058(14)
b (Å)	9.6820(18)
c (Å)	15.577(3)
α (°)	79.244(3)
β (°)	81.927(3)
γ (°)	83.155(3)

as listed.

DOI of original article: 10.1016/j.poly.2006.11.036
* Corresponding author. Fax: +66 4320 2373.
E-mail address: sujittra@kku.ac.th (S. Youngme).

0277-5387/$ - see front matter © 2007 Elsevier Ltd. All rights reserved.
doi:10.1016/j.poly.2007.07.008

On the other hand, an interest in the chemistry of Nb(V) and Ta(V) fluorides is essentially connected with the development of suitable methods for concentration (separation) of these elements, the processes being based on the recrystallization or extraction of the proper complexes from acidic aqueous solutions [3]. Recently, we revealed some interesting features of the "host–guest" complexes formed as a result of the interaction of Nb and Ta pentafluorides with crown ethers. Two synthetic routes were applied: the interaction of the corresponding M_2O_5 oxides with hydrofluoric acid in the presence of the CE, and the direct interaction of MF_5, also in the presence of HF, with the same crown ethers. These two pathways resulted in crystalline complexes of the composition $[CE \cdot H_3O][MF_6]$ for the hexadentate benzo-18-crown-6 [4], *cis-syn-cis*-dicyclohexyl-18-crown-6 [5] and diphenyl-20-crown-6 [6], $[(1.5DB18C6)_2 \cdot H_7O_3][MF_6]$ complexes for 1.5-dibenzo-18C6 [6] and $[TB30C10 \cdot H_5O_2][MF_6]$ for tetrabenzo-30-crown-10 (M = Nb, Ta) [7]. Complexes with B18C6 and *cis-syn-cis*-DCH18C6 provided examples of supramolecular isomers: monoclinic ($P2_1/n$) and orthorhombic (*Pbca*) polymorphs for $[B18C6 \cdot H_3O][TaF_6]$ that are distinct by the subtle packing changes [4], and monoclinic again ($P2_1/n$) and triclinic ($P\bar{1}$) polymorphs for [*cis-syn-cis*-$DCH18C6 \cdot H_3O][TaF_6]$, differing by the pronounced conformational changes in the macrocyclic molecule and in the crystal packing [5]. The occurrence of supramolecular isomerism (SI) [8] implies a superstructural diversity for a given building block. Complexes with conformationally flexible CEs and aza-macrocycles give some examples of supramolecular isomers [9].

The next intriguing feature of the studied complexes is a diversity of the encapsulated oxonium ions [10]. The use of hexadentate B18C6, *cis-syn-cis*-DCH18C6 and DP20C6 resulted in crystalline complexes of the general formula $[CE \cdot H_3O][MF_6]$, where the macrocyclic cavity includes the simplest oxonium cation H_3O^+ (also called an Eigen core [10]), while the use of TB30C10 afforded the opportunity for the extraction of the $[H_5O_2]^+$ Zundel cation, $[H_2O\cdots H\cdots OH_2]^+$ [10] within the complex of the same stoichiometry. The decrease in number of oxygen atoms accessible for interaction with the tripodal oxonium cation in the case of [1.5] DB18C6 resulted in the storage of the three-membered oxonium cluster $[H_7O_3]^+$ within the cage formed by two [1.5] DB18C6 molecules in the complex of composition $[(1.5DB18C6)_2 \cdot H_7O_3][MF_6]$ (M = Nb, Ta) [6].

In this paper, we selected gradually diminishing in size classic 18-crown-6 (18C6), 15-crown-5 (15C5), benzo-15-crown-5 (B15C5) and benzo-12-crown-4 (B12C4) as macrocyclic ligands to react with Nb and Ta pentafluorides. Five new complexes, $[18C6 \cdot H_3O][NbF_6]$ (**1**), $[18C6 \cdot H_3O][TaF_6]$ (**2**), $[15C5 \cdot H_5O_2][TaF_6]$ (**3**), $[(B15C5)_2 \cdot H_5O_2][(B15C5)_2 \cdot H_3O)\ ][TaF_6]_2$ (**4**) and $[(B12C4)_2 \cdot H_3O][TaF_6]$ (**5**), were obtained. The crystals were obtained by the two above described synthetic routes, resulting in both cases (four crown ethers used) in crystallographically identical complexes. The details of their synthesis and structure are reported.

2. Experimental

2.1. Materials and apparatus

Caution! Hydrofluoric acid should be treated as an extremely aggressive liquid. All crown ethers were purchased from ACROS, Ta_2O_5/Nb_2O_5 and TaF_5/NbF_5 were purchased from Aldrich and were used without further purification. Complexes $[18C6 \cdot H_3O][NbF_6]$ (**1**), $[18C6 \cdot H_3O][TaF_6]$ (**2**), $[15C5 \cdot H_5O_2][TaF_6]$ (**3**), $[(B15C5)_2 \cdot H_5O_2][TaF_6]$ $[(B15C5)_2 \cdot H_3O][TaF_6]$ (**4**) and $[(B12C4)_2 \cdot H_3O][TaF_6]$ (**5**) were obtained by two synthetic pathways: by an interaction of the corresponding oxides with 40% aqueous HF followed by treatment of the resulting solution with the corresponding crown ether, and by the interaction of the initial corresponding metal pentafluoride, NbF_5/TaF_5, with the CE in a medium of 40% HF. All the complexes were analyzed for C, H and F in a Perkin–Elmer 240 °C instrument. The X-ray structural analysis revealed the identity of the complexes obtained under the different synthetic conditions, the best crystallographic results are discussed in this paper.

2.2. Synthesis

I route: To Nb_2O_5/Ta_2O_5 (0.5 mmol) dissolved in 45% HF (6–7 ml), the corresponding CE (1 mmol) dissolved in 8–10 ml methanol was added. The resulting solution was stored at 20–25 °C in a Teflon exsiccator for a low evaporation of solvent to a volume of 5–6 ml over several days.

II route: To solution of CE (1 mmol) was added a solution of NbF_5/TaF_5 (1 mmol) in 10–12 ml of 45% hydrofluoric acid. The resulting solution was stored at 20–25 °C in a Teflon exsiccator for a low evaporation of solvent to a volume of 5–6 ml over several days.

2.2.1. $[18C6 \cdot H_3O][NbF_6]$ (1)

Crystals of complex **I** separated in a yield of 72% (0.350 g), and are colorless transparent prisms, soluble in methanol, ethanol; m.p.: >220 °C (decomp). *Anal.* Calc. for $C_{12}H_{27}F_6NbO_7$: C, 29.40; H, 5.55; F, 23.25. Found: C, 29.33; H, 5.58; F, 23.45%.

2.2.2. $[18C6 \cdot H_3O][TaF_6]$ (2)

Crystals of **2** separated in a yield of 75% (0.430 g), and are colorless transparent prisms, soluble in methanol, ethanol; m.p.: >195 °C (decomp). *Anal.* Calc. for $C_{12}H_{27}F_6TaO_7$: C, 29.42; H, 4.71; F, 19.71. Found: C, 24.87; H, 4.68; F, 19.70%.

2.2.3. $[15C5 \cdot H_5O_2][TaF_6]$ (3)

Crystals of **3** separated in a yield of 74% (0.280 g), and are colorless transparent prisms, soluble in methanol, ethanol; m.p.: 124–125 °C (decomp). *Anal.* Calc. for

$C_{10}H_{25}F_6O_7Ta$: C, 31.10; H, 5.87; F, 14.76. Found: C, 31.13; H, 5.92; F, 14.82%.

2.2.4. $[(B15C5)_2 \cdot H_5O_2][TaF_6][(B15C5)_2 \cdot H_3O][TaF_6]$ (4)

Crystals of **4** were separated in a yield of 82% (0.350 g), and are colorless transparent crystals, soluble in methanol, ethanol; m.p.: 126–127 °C (decomp). *Anal.* Calc. for $C_{56}H_{88}F_{12}O_{23}Ta_2$: C, 39.12; H, 5.16; F, 13.26. Found: C, 39.59; H, 5.17; F, 13.34%.

2.2.5. $[(B12C4)_2 \cdot H_3O][TaF_6]$ (5)

Crystals of **5** were separated in a yield of 95% (0.360 g), and are colorless transparent crystals, soluble in methanol, ethanol; m.p.: >180 °C (decomp). *Anal.* Calc. for $C_{24}H_{35}F_6O_9Ta$: C, 37.81; H, 4.63; F, 14.95. Found: C, 37.78; H, 4.67; F, 14.91%.

2.3. X-ray diffraction determination

The X-ray intensity data for complexes **1**, **2**, **4** and **5** were recorded at 123 K on a Bruker SMART 1000 CCD area detector diffractometer employing graphite monochromatized Mo Kα radiation ($\lambda = 0.71073$ Å) in the ϕ and ω scan mode. Final unit cell dimensions and positional data were obtained and refined on the entire data set. Integration and scaling resulted in a data set corrected for Lorentz and polarization effects using DENZO [11]. The scaling as well as the global refinement of the crystal parameters were performed by SCALEPACK [11]. The experimental data for complex **3** were recorded at ambient temperature (295 K) on an Xcalibur S with a CCD detector (Mo-Kα radiation, graphite monochromator, ω scan mode). The absorption correction for **2**–**5** was applied using SADABS [12]. The structure solution and refinement proceeded similarly using the SHELX-97 program package [13] for all the structures. Direct methods yielded all non-hydrogen atoms of the asymmetric unit. These atoms were treated anisotropically (full-matrix least squares method on F^2). In complexes **1** and **2** the macrocycle and oxonium cation occupy the special position 2/*m*, that makes it impossible to localize the oxonium hydrogen atoms, and in the next section only O···O distances will be discussed. In complex **3** the mirror plane *m* bisects the macrocycle through the O(1) atom and the C(5)–C(5′) valent bond, both oxygen atoms and one hydrogen atom of the $(H_5O_2)^+$ oxonium cation. The crown oxygen atom O(3) is disordered over two positions with equal occupancies. In complexes **4** and **5** the oxonium ion occupies a position on a two-fold axis, being equally disordered. C-bound H atoms were placed in calculated positions, with C–H distances of 0.93 or 0.97 Å, and were treated using a riding-model approximation with $U_{iso}(H) = 1.2\,U_{eq}(C)$. H atoms of water molecules and oxonium ions were determined from difference Fourier maps and were then allowed to refine isotropically with $U_{iso}(H) = 1.5U_{eq}(O)$ and O–H distances subjected to DFIX restraints.

The X-ray data and details of the refinement for **1**–**5** are summarized in Table 1, selected geometric parameters are given in Table 2 and the hydrogen bonding geometries for **3**–**5** are given in Table 3.

3. Results and discussion

3.1. Description of the structures

Complexes **1** and **2** are isostructural (Table 1), so only complex **2** is further discussed. Both complexes crystallize in the orthorhombic space group *Pbam*. The NbF_6^- anion in complex **1** resides on an inversion centre and is characterized by an octahedral core with Nb–F distances ranging from 1.844(2) up to 1.876(2) Å and F–Nb–F valent angles between *cis*-fluorine atoms practically being equal to 90°. The geometry of the NbF_6^- anion is close to that found in 3-chloro-1,3,4,2,5-thiadiselenadiazolium hexafluoroniobium [14] and in bis(pyrazine)dicopper bis(hexafluoroniobium) piperazine solvate [15]. The TaF_6^- anions in complexes **2**–**5** also adopt the usual octahedral geometry with Ta–F distances ranging from 1.854(5) to 1.877(7) Å in **2**, from 1.868(8) to 1.887(7) Å in **3**, from 1.845(4) to 1.874(4) Å in **4**, and from 1.881(3) to 1.888(2) Å in **5**, the maximal deviation for the F–Ta–F valent angle between *cis*-fluorine atoms from a right angle being 1.5°. This geometry is close to that found in catena-[(μ-chloro)-bis(μ-fluoro)tetrafluoro-hexamethyltantalum)] ditin [16] and in methyltriphenylphosphonium hexafluorotantalate [17].

3.1.1. $[18C6 \cdot H_3O][TaF_6]$ (2)

The ORTEP view for complex **2** is shown in Fig. 1. The 18C6 molecule and oxonium cation $(H_3O)^+$ are situated in the 2/*m* position: the *m* plane passes through the O(1) and O(1′) atoms, and the twofold axis bisects the C(3)–C(3′) bond. The arrangement of both macrocycle and oxonium ion on a special position explains the availability of only two different O(oxonium)···O(crown) distances, being equal to 2.777(6) Å [to O(1) and its symmetry-related counterpart], and 2.708(5) Å [to O(2) and its three symmetry-related counterparts]. The 18C6 molecule is characterized by the idealized D_{3d} symmetry with the *trans-gauche-trans*-sequence of torsion angles and ±0.171(5) Å deviation of oxygen atoms from the mean plane.

3.1.2. $[15C5 \cdot H_5O_2][TaF_6]$ (3)

Complex **3**, of the composition $[15C5 \cdot H_5O_2][TaF_6]$, crystallises in the orthorhombic crystal system, space group *Pnma*. The ORTEP view for complex **3** is shown in Fig. 2. The asymmetric unit of **3** comprises of one half of the TaF_6^- anion, one half of the 15C5 molecule and one half of the $(H_5O_2)^+$ Zundel cation, all these species residing on a mirror plane. Within the Zundel cation, the water molecule and oxonium ion are held together *via* a strong OH···O hydrogen bond, the O···O separation being 2.462(12) Å. Its interaction with two neighboring crown molecules related by the glide plane occurs in such a way

Table 1
Crystal data and structure refinement parameters for complexes **1**–**5**

	1	**2**	**3**	**4**	**5**
Composition	$C_{12}H_{27}F_6NbO_7$	$C_{12}H_{27}F_6O_7Ta$	$C_{10}H_{25}F_6O_7Ta$	$C_{56}H_{88}F_{12}O_{23}Ta_2$	$C_{24}H_{35}F_6O_9Ta$
CCDC number	652989	652990	652991	652992	652993
Formula weight	490.25	578.29	552.25	1719.16	762.47
Crystal system	orthorhombic	orthorhombic	orthorhombic	monoclinic	triclinic
Space group	*Pbam*	*Pbam*	*Pnma*	*C*2/*c*	$P\bar{1}$
a (Å)	9.0639(8)	9.0655(13)	12.2350(16)	28.293(5)	8.7701(15)
b (Å)	10.1656(9)	10.1316(14)	12.6607(16)	16.023(3)	8.8881(15)
c (Å)	10.9854(13)	10.9474(16)	11.9124(16)	15.943(3)	10.0280(17)
α (°)	90.0	90.0	90.0	90.0	72.114(3)
β (°)	90.0	90.0	90.0	106.05(3)	83.909(3)
γ (°)	90.0	90.0	90.0	90.0	73.275(3)
V (Å^3)	1012.19(17)	1005.5(2)	1845.3(4)	6946(2)	712.3(2)
Z	2	2	4	8	1
D_{calc} (Mg/m^3)	1.609	1.910	1.988	1.644	1.778
μ (mm^{-1})	0.676	5.548	6.041	3.252	3.945
F(000)	500	564	1072	3448	378
Reflections collected/unique	942/942	5421/1054	14070/1791	15382/6162	3978/2730
Reflections with $I > 2\sigma(I)$	677	733	1423	4730	2730
Goodness-of-fit	1.064	1.055	1.170	1.022	1.075
R_1, wR_2 [$I > 2\sigma(I)$]	0.0517, 0.1441	0.0289, 0.0862	0.0566, 0.1099	0.0378, 0.0783	0.0227, 0.0604

that the $(H_3O)^+$ oxonium part is involved in two equal OH···O bifurcated hydrogen bonds to the O(2) and O(3A) atoms, the O···O separations being 2.646 and 2.945 Å, while the 'water part' *via* O(4) is involved in the O(4)···O(3) interaction, the O···O separation being 2.995(15) Å (Table 3). The crown molecules and $(H_5O_2)^+$ cations alternate in the infinite chain. The atom O(4) deviates by 1.692(4) Å from the mean plane of crown oxygen atoms that are coplanar to within ±0.28 Å, while atom O(5) deviates by 1.692(4) Å from the same atoms of the next crown molecule. In the macrocyclic framework all the C–O–C–C torsion angles are *anti*-, four O–C(sp^3)–C(sp^3)–O angles are *gauche*-and the O(3)–C(5)–C5′–O3′ angle is 0.0° due to the mirror symmetry (Table 2).

3.1.3. *[(B15C5)$_2$ · H$_5$O$_2$] [(B15C5)$_2$ · H$_3$O][TaF$_6$]$_2$ (**4**)*

Complex **4**, of the composition [(B15C5)$_2$ · H$_5$O$_2$][(B15C5)$_2$ · H$_3$O][TaF$_6$]$_2$, crystallises in the monoclinic crystal system, space group *C*2/*c*. It is built of two different in composition sandwich cations (associated with A and B macrocycles) and two TaF_6^- anions. The ORTEP view for complex **4** is shown in Fig. 3. The asymmetric unit of **4** comprises two halves of the TaF_6^- anions, (one is situated on an inversion center and the other is situated on a twofold axis), two B15C5 molecules (designated A and B) in general positions, and two oxonium oxygen atoms O(6A) and O(6B) (associated with the similarly labelled macrocycles), the former being located on a twofold axis, the latter being located in a general position in the vicinity of an inversion center and forming a $(H_5O_2)^+$ Zundel cation. In sandwich **A** the oxonium ion is equally disordered over the inversion center, forming correspondingly two and one hydrogen bonds to two crown molecules in the sandwich, the O(oxonium)···O(crown) separations falling in the range 2.742(3)–3.031(3) Å. The O(6A) oxygen atom deviates by 1.811(2) Å from the mean plane of the crown oxygen atoms that are coplanar to within ±0.28 Å. In molecule **A** the dihedral angle between the plane through the phenyl ring and 5 oxygens is equal to 26.2(1)°. Along the 15-membered heterocyclic framework all O–C(sp^3)–C(sp^3)–O torsion angles are *gauche*-, while O–C(sp^2)–C(sp^2)–O that belongs to the phenyl ring is *cis*, of 10 C–C–O–C torsions 8 are *anti*- and two adopt the *gauche*-conformation, giving rise to the sequence of two *gauche*-torsion angles meeting at C(3A) and C(6A) atoms (Table 2). In sandwich **B**, having the composition [(B15C5)$_2$ · H$_5$O$_2$], the O···O separation of 2.409 Å within the Zundel cation is the shortest among the corresponding O···O distances that are of concern in the cited data [9]. The other O···O distances to crown oxygens range from 2.651 to 3.012 Å (Table 3). The atom O(6B) deviates by 1.692(4) Å from the mean plane of crown oxygen atoms that are coplanar to within ±0.28 Å. In molecule **B** the dihedral angle between the planes through the phenyl ring and 5 oxygens is equal to 17.5(1)°, all C–O–C–C torsion angles are *anti*-, all O–C(sp^3)–C(sp^3)–O angles are *gauche*-, and the O–C(sp^2)–C(sp^2)–O angle is *cis* (Table 2). The dependence of the hydrogen bonding on the system is evident on changing the crown ether conformation.

3.1.4. *[(B12C4)$_2$ · H$_3$O][TaF$_6$] (**5**)*

Complex **5**, of the composition [(B12C4)$_2$ · H$_3$O][TaF$_6$], crystallises in the triclinic space group $P\bar{1}$. The ORTEP view for this complex is shown in Fig. 4. The TaF_6^- anion occupies a position on an inversion center. The macrocyclic cation has a typical B12C4 sandwich-like structure with the oxonium ion enclosed between two inversion-related macrocycles with three main O···O separations to crown oxygens equal to 2.652(3), 2.819(3) and 2.881(3) Å. The oxonium cation O(5) deviates by 1.953(2) Å from the mean

Table 2
Selected bond distances (Å) and angles (°) for complexes **2**–**5**

Complex **2**			
Ta(1)–F(2)	1.856(5)	Ta(1)–F(1)	1.877(7)
Ta(1)–F(3)	1.854(5)		
F(2)–Ta(1)–F(3)	89.5(3)	F(2)–Ta(1)–F(1)	90.0(1)
F(3)–Ta(1)–F(1)	90.0(1)		
C(2)#1–C(1)#1–O(1)–C(1)	−179.3(5)	C(1)–C(2)–O(2)–C(3)	174.4(8)
C(1)#1–O(1)–C(1)–C(2)	179.3(5)	C(2)–O(2)–C(3)–C(3)#2	178.4(13)
O(1)–C(1)–C(2)–O(2)	64.0(8)	O(2)–C(3)–C(3)#2–O(2)#2	−52(2)
Complex **3**			
Ta(1)–F(1)	1.868(8)	Ta(1)–F(3)	1.883(6)
Ta(1)–F(4)	1.877(8)	Ta(1)–F(2)	1.887(7)
F(1)–Ta(1)–F(4)	179.8(4)	F(1)–Ta(1)–F(2)	90.4(3)
F(1)–Ta(1)–F(3)	90.1(3)	F(4)–Ta(1)–F(2)	89.7(3)
F(4)–Ta(1)–F(3)	89.7(3)	F(3)–Ta(1)–F(2)	90.2(4)
F(3)–Ta(1)–F(3)#3	88.6(4)	F(2)#3–Ta(1)–F(2)	91.0(6)
F(3)–Ta(1)–F(2)#3	178.7(3)		
C(1)#4–O(1)–C(1)–C(2)	−168.2(6)	O(2)–C(3)–C(4)–O(3)	−45(3)
O(1)–C(1)–C(2)–O(2)	64(1)	C(3)–C(4)–O(3)–C(5)	170(2)
C(1)–C(2)–O(2)–C(3)	−168(1)	C(4)–O(3)–C(5)–C(5)#4	−151(1)
C(2)–O(2)–C(3)–C(4)	141(2)		
Complex **4**			
Ta(1)–F(3)	1.853(3)	Ta(2)–F(6)	1.845(4)
Ta(1)–F(2)	1.864(3)	Ta(2)–F(5)	1.866(3)
Ta(1)–F(1)	1.866(3)	Ta(2)–F(4)	1.874(4)
F(3)–Ta(1)–F(2)	89.0(2)	F(5)#5–Ta(2)–F(5)	91.1(3)
F(3)–Ta(1)–F(1)	90.0(2)	F(6)#5–Ta(2)–F(4)	90.0(2)
F(2)–Ta(1)–F(1)	91.5(2)	F(5)#5–Ta(2)–F(4)	179.7(2)
F(6)–Ta(2)–F(6)#5	175.2(3)	F(5)–Ta(2)–F(4)	89.0(2)
F(6)–Ta(2)–F(5)#5	93.1(2)	F(4)–Ta(2)–F(4)#5	90.8(3)
F(6)–Ta(2)–F(5)	90.3(2)	F(6)–Ta(2)–F(4)	86.7(2)
O(1A)–C(1A)–C(2A)–O(2A)	−69.4(5)	O(1B)–C(1B)–C(2B)–O(2B)	−64.3(6)
C(1A)–C(2A)–O(2A)–C(3A)	167.2(4)	C(1B)–C(2B)–O(2B)–C(3B)	167.4(5)
C(2A)–O(2A)–C(3A)–C(4A)	−91.4(5)	C(2B)–O(2B)–C(3B)–C(4B)	−163.9(5)
O(2A)–C(3A)–C(4A)–O(3A)	−63.6(5)	O(2B)–C(3B)–C(4B)–O(3B)	68.0(6)
C(3A)–C(4A)–O(3A)–C(5A)	179.8(4)	C(3B)–C(4B)–O(3B)–C(5B)	−165.0(4)
C(4A)–O(3A)–C(5A)–C(6 A)	−172.8(4)	C(4B)–O(3B)–C(5B)–C(6B)	170.0(4)
O(3A)–C(5A)–C(6A)–O(4A)	60.9(5)	O(3B)–C(5B)–C(6B)–O(4B)	−70.9(6)
C(5A)–C(6A)–O(4A)–C(7A)	82.2(5)	C(5B)–C(6B)–O(4B)–C(7B)	158.0(5)
C(6A)–O(4A)–C(7A)–C(8A)	−170.3(4)	C(6B)–O(4B)–C(7B)–C(8B)	−169.5(4)
O(4A)–C(7A)–C(8A)–O(5A)	66.3(5)	O(4B)–C(7B)–C(8B)–O(5B)	60.9(5)
C(7A)–C(8A)–O(5A)–C(9A)	−175.6(3)	C(7B)–C(8B)–O(5B)–C(9B)	178.2(3)
C(8A)–O(5A)–C(9A)–C(10A)	176.3(3)	C(8B)–O(5B)–C(9B)–C(10B)	171.8(4)
O(5A)–C(9A)–C(10A)–O(1A)	0.8(5)	O(5B)–C(9B)–C(10B)–O(1B)	1.1(5)
C(9A)–C(10A)–O(1A)–C(1A)	−158.8(3)	C(9B)–C(10B)–O(1B)–C(1B)	−156.1(3)
C(10A)–O(1A)–C(1A)–C(2A)	171.1(4)	C(10B)–O(1B)–C(1B)–C(2B)	176.9(4)
Complex **5**			
Ta(1)–F(3)	1.881(3)	Ta(1)–F(2)	1.888(2)
Ta(1)–F(1)	1.885(2)		
F(3)–Ta(1)–F(1)	90.5(1)	F(1)–Ta(1)–F(2)	90.7(1)
F(3)–Ta(1)–F(2)	90.3(1)		
O(1)–C(1)–C(2)–O(2)	61.2(4)	O(3)–C(5)–C(6)–O(4)	63.5(5)
C(1)–C(2)–O(2)–C(3)	−136.0(3)	C(5)–C(6)–O(4)–C(7)	−157.0(3)
C(2)–O(2)–C(3)–C(4)	75.5(4)	C(6)–O(4)–C(7)–C(12)	73.3(4)
O(2)–C(3)–C(4)–O(3)	65.8(4)	O(4)–C(7)–C(12)–O(1)	−9.3(4)
C(3)–C(4)–O(3)–C(5)	−171.0(4)	C(7)–C(12)–O(1)–C(1)	157.0(3)
C(4)–O(3)–C(5)–C(6)	84.7(5)	C(12)–O(1)–C(1)–C(2)	−172.7(3)

Symmetry transformations used to generate equivalent atoms: (#1) $x, y, -z$; (#2) $-x, -y+1, z$ for **2**; (#3) $x, -y+3/2, z$; (#4) $x, 1/2-y, z$ for **3** and (#5) $-x+1, y, -z+3/2$ for **4**.

plane of the four crown oxygens, which are coplanar to within ±0.294 Å. The dihedral angle between the plane through the phenyl ring and the 4 oxygens is equal to 17.2(2)°. Within the 12-membered heterocyclic framework three O–C–C–O torsion angles are *gauche* and the one that belongs to the phenyl ring is *cis*-; of 8 C–O torsion angles

Table 3
Hydrogen bond distances (Å) and angles (°) for complexes **3**–**5**

D–H···A	*d*(D–H)	*d*(H···A)	*d*(D···A)	∠(DHA)	Symmetry transformation for acceptor
Complex **3**					
O(4)–H(1O4)···O(3)	0.90(1)	2.24(2)	2.995(15)	142(2)	*x*, *y*, *z*
O(5)–H(1O5)···O(4)	0.86(2)	1.61(3)	2.462(12)	171(14)	*x*, *y*, *z*
O(5)–H(2O5)···O(2)	0.85(2)	1.84(4)	2.646(9)	156(9)	$x-1/2$, *y*, $-z+1/2$
O(5)–H(2O5)···O(3A)	0.85(2)	2.41(8)	2.945(15)	121(7)	$x-1/2$, *y*, $-z+1/2$
Complex **4**					
O(6A)–H(61)···O(4A)	0.87(2)	1.95(6)	2.740(3)	150(10)	$-x+1$, *y*, $-z+3/2$
O(6A)–H(61)···O(5A)	0.87(2)	2.44(8)	3.031(3)	126(8)	$-x+1$, *y*, $-z+3/2$
O(6A)–H(62)···O(2A)	0.87(2)	2.09(6)	2.868(3)	150(10)	*x*, *y*, *z*
O(6A)–H(62)···O(3A)	0.87(2)	2.28(9)	2.866(4)	125(9)	*x*, *y*, *z*
O(6A)–H(63)···O(2A)	0.87(2)	2.05(4)	2.868(3)	159(10)	$-x+1$, *y*, $-z+3/2$
O(6B)–H(16)···O(2B)	0.84(2)	1.81(2)	2.648(5)	179(6)	*x*, *y*, *z*
O(6B)–H(26)···O(6B)	0.85(2)	1.55(3)	2.402(5)	173(15)	$-x+3/2$, $-y+1/2$, $-z+1$
O(6B)–H(36)···O(4B)	0.83(2)	1.92(3)	2.710(4)	158(5)	*x*, *y*, *z*
O(6B)–H(36)···O(5B)	0.83(2)	2.50(4)	3.014(4)	121(4)	*x*, *y*, *z*
Complex **5**					
O(5)–H(51)···O(4)	0.88(2)	1.95(3)	2.819(3)	172(12)	*x*, *y*, *z*
O(5)–H(52)···O(2)	0.88(2)	1.79(3)	2.652(3)	167(12)	*x*, *y*, *z*
O(5)–H(53)···O(1)	0.88(2)	2.17(9)	2.881(3)	138(11)	$-x+1$, $-y+1$, $-z+1$

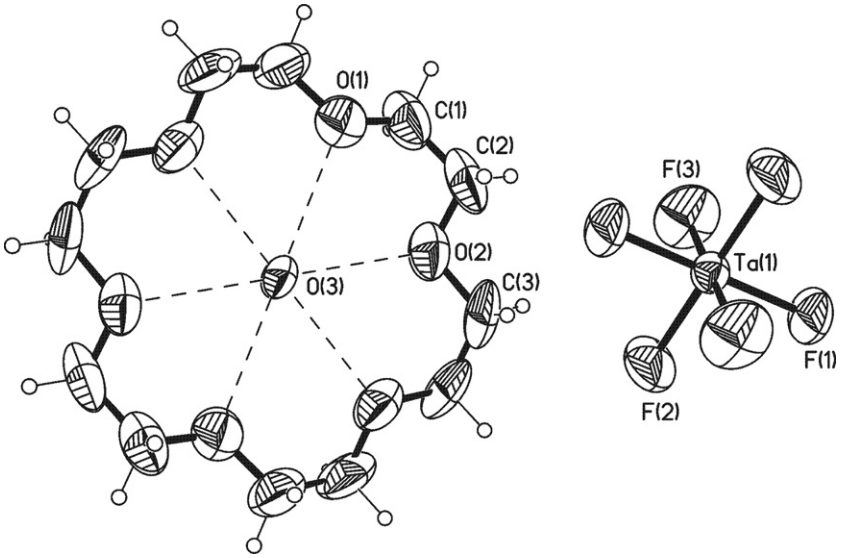


Fig. 1. ORTEP drawing of **2** with the numbering scheme and the shortest O···O distances shown by dashed lines. Thermal ellipsoids are shown at the 50% probability level.

three adopt a *gauche*-conformation and give rise to two corner fragments with a sequence of two *gauche*-torsion angles at the C(3) and C(5) atoms and meets with a *cis*-torsion angle at the C(7) atom (Table 2).

Analysis of CSD [18] data for oxonium-containing crown complexes of the composition $[CE \cdot H(H_2O)_n^+ \cdot An]$ (where CE – crown ether, An – halogen-containing anion) reveals that 18C6 and its benzo-, dicyclohexano- and tetracarboxylic derivatives are highly selective for H_3O^+ because of the size and symmetry fit between them, allowing the inclusion of the oxonium ion within the 18-membered crown ether cavity with the formation of three strong OH···O hydrogen bonds [19]. However, both larger and smaller in size macrocycles are capable of accommodating the Eigen core as well. As examples, dibenzo-30C10 simultaneously contains two H_3O^+ cations within the cavity [20], two B15C5 molecules enclose the oxonium cation in a sandwich structure [21] similar to complex **4**, two dibromo-15C5 molecules incapsulate two H_3O^+ cations within sandwich structure [22]. Smaller in size, benzo-15C5 and 12C4 are also capable of fixing the oxonium ion either in a sandwich mode [23] or through an additional contact with the anion [24]. The next in size $[H_2O\cdots H\cdots OH_2]^+$Zundel cation is perfectly displayed on one side of the DB18C6 macrocycle in the DB18C6 oxonium perchlorate trihydrate [25], within 24- and 30-

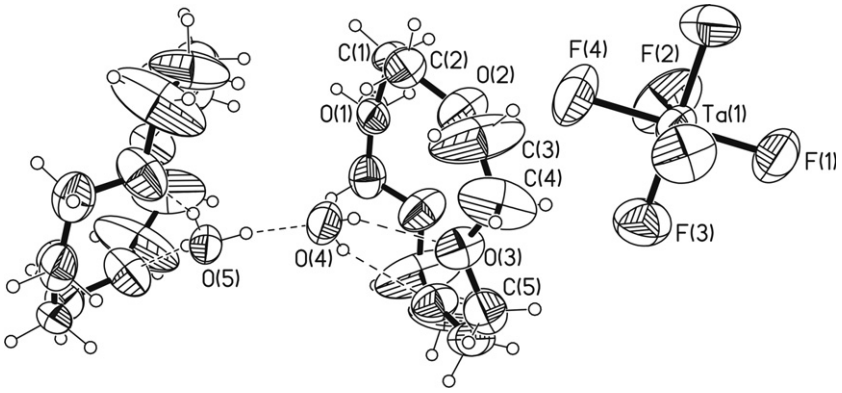


Fig. 2. ORTEP drawing of **3** with the numbering scheme and the shortest O···O distances shown by dashed lines. Thermal ellipsoids are shown at the 50% probability level.

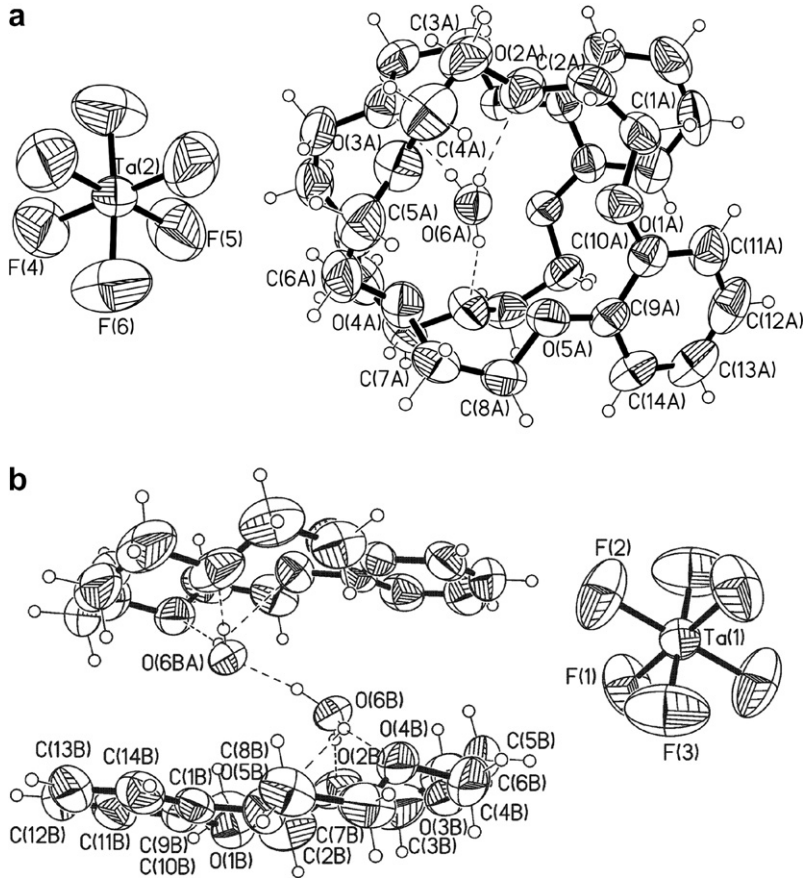


Fig. 3. ORTEP drawing of **4** with the partial numbering scheme and hydrogen bonding shown by dashed lines. Thermal ellipsoids are shown at the 50% probability level.

membered macrocycles [19u] or between two molecules of B15C5, as in bis(B15C5) tetrachloro-aurate(III) oxonium monohydrate [2] and in our complex **3**, while tetrabenzo30C10 excellently stores the Zundel cation within one cavity [7]. On the contrary, the fixation of the $[H_7O_3]^+$ cation by crown ethers is relatively uncommon and only few examples are known so far where $[H_7O_3]^+$ oxonium cations alternate with crown ether in hydrogen-bonded chains with long-range interactions to the anions [2,26] or are encapsulated within the cage formed by two crown molecules [6]. A comparison of novel compounds with the known literary examples shows the reproducibility of the crown ether–oxonium ion supramolecular architecture for 18C6, 15C5 and B15C5. A reliable comparison of subtle effects (hydrogen bond lengths and angles) for these units cannot be made due to the location of the oxonium species on the crystallographic symmetry elements.

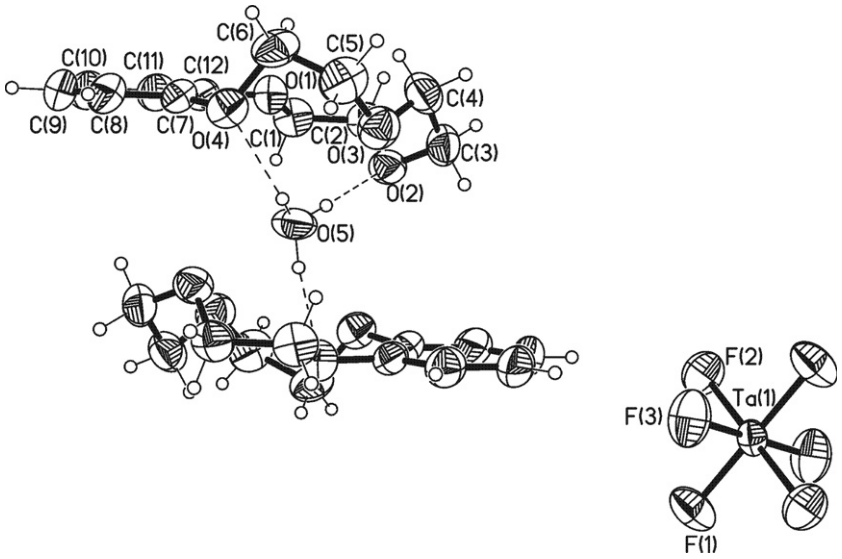


Fig. 4. ORTEP drawing of **5** with the numbering scheme and hydrogen bonding shown by dashed lines. Thermal ellipsoids are shown at the 50% probability level.

The crystal packing in **1**–**5** exhibits common structural features. The all H-bonding coordination abilities of the $[H_3O]^+$ or $[H_5O_2]^+$ cations are used to interact with the crown ether oxygen atoms since both NbF_6^- and TaF_6^- behave as very non-coordinating anions, being much poorer hydrogen bond acceptors than for example $AuCl_4^-$ which contributes to the interactions with oxonium species [2]. The decisive factor in the supramolecular organization are weak CH(crown)···F interactions. Similar to all previously reported complexes of this family [4–7], the crystal packing in **1**–**5** represents an alternation of rows of organic (macrocyclic cations in **1**–**2**, or macrocyclic sandwiches in **3**–**5**) and inorganic (Nb_6^-/TaF_6^- anions) components (Fig. 5), being held together by CH···F interactions. The simplest case of crystal packing is evident for **1**–**2**. For the perfectly regular structure **2**, shown in Fig. 4a, the C(3)H···F(2) contact (H···F 2.61, C···F 3.394(15) Å, CHF angle 138° slightly exceeds the accepted limit (H···Acceptor = 2.6 Å). In **5**, due to the shortest C(1)H···F(1) contact (H···F 2.52, C···F 3.211(5) Å, CHF angle 128°, charged components alternate in the chain. In the layer structure **4** two independent TaF_6^- anions fulfill different structural functions: the $Ta(1)F_6$ anion is located on an inversion center and acts as a bridge between two different macrocyclic sandwiches (**A** and **B**) *via* the F(1) atom, [C(7A)–H(7A1)···F(1)(x, $1-y$, $0.5+z$) 2.55, C···F 3.250(6) Å, CHF angle 129° and C(5B)–H(5B2)···F(1) 2.55, C···F 3.343(6) Å, CHF angle 140°], while the second anion, $Ta(2)F_6$, located on a two-fold axis, bridges only **B** sandwiches *via* C(14B)···F(5) interactions [C(14B)–H(14B)···F(5)(3/2−x, $-0.5+y$, 3/2 − z) 2.54, C···F 3.312(6) Å, CHF angle 141°].

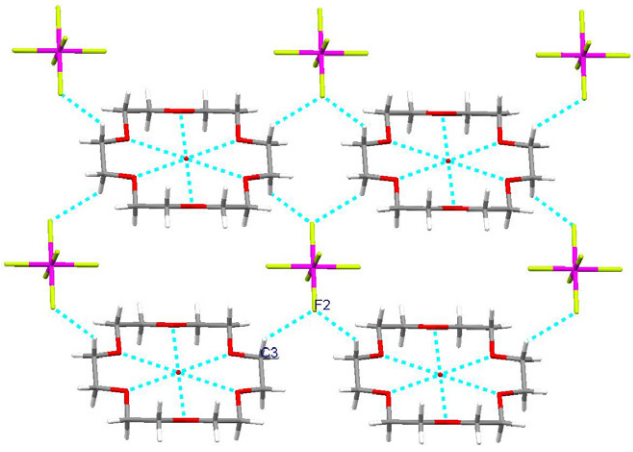


Fig. 5. Fragment of the crystal packing for **2**. Only atoms responsible for short CH···F contacts are labelled.

4. Conclusion

The interaction of Nb_2O_5/Ta_2O_5 or NbF_5/TaF_5 with 18-,15- and 12-membered CEs in the presence of hydrofluoric acid results in complexes of the compositions $[18C6 \cdot H_3O][NbF_6]$ (**1**), $[18C6 \cdot H_3O][TaF_6]$ (**2**), $[15C5 \cdot H_5O_2][TaF_6]$ (**3**) $[(B15C5)_2 \cdot H_5O_2]$ $[(B15C5)_2 \cdot H_3O][TaF_6]_2$ (**4**) and $[(B12C4)_2 \cdot H_3O][TaF_6]$ (**5**). All compounds represent ionic species with direct interactions between the oxonium ion and oxygen atoms of the macrocyclic molecule and a lack of any interactions between the oxonium ion and the anion. According to the X-ray data, the $[H_3O]^+$ oxonium cation centers the 18-membered crown cavity in isostructural complexes **1**–**2**, and bridges two smaller 12-membered macrocycles in **5**. Compound **5** is the first example of an oxonium ion direct interaction with the small B12C4 macrocycle. The crystal **3** contains the $[H_5O_2]^+$ dioxonium cation and alternates with 15C5 molecules in the infinite chains, whereas complex **4** represents a unique example

of the co-existence of both the $[H_3O]^+$ Eigen core and $[H_2O\cdots H\cdots OH_2]^+$ Zundel cations within one structure, both being incorporated in two sandwich-type organized macrocyclic cations. The B15C5 molecules that form these sandwiches differ by their conformations.

Acknowledgements

This work was supported by the Russian Foundation for Basic Research and the Academy of Sciences of Moldova (Project No. 06-03-90894-Mol-a). W.J.W. and E.V.G. acknowledge the support of the National Council of Science of Taiwan (Grant No. 94-2811-M-032).

Appendix A. Supplementary material

CCDC 652989, 652990, 652991, 652992 and 652993 contains the supplementary crystallographic data for **1**, **2**, **3**, **4** and **5**. These data can be obtained free of charge via http://www.ccdc.cam.ac.uk/conts/retrieving.html, or from the Cambridge Crystallographic Data Centre, 12 Union Road, Cambridge CB2 1EZ, UK; fax: (+44) 1223 336 033; or e-mail: deposit@ccdc.cam.ac.uk. Supplementary data associated with this article can be found, in the online version, at doi:10.1016/j.poly.2007.07.037.

References

[1] J.L. Atwood, S.G. Bott, P.C. Junk, M.T. May, J. Coord. Chem. 37 (1996) 89.
[2] (a) M. Calleja, K. Johnson, W.J. Belcher, J.W. Steed, Inorg. Chem. 40 (2001) 4978, and references cited therein;
(b) M. Calleja, S.A. Mason, P.D. Prince, J.W. Steed, C. Wilkinson, New J. Chem. 25 (2001) 1475.
[3] A.G. Babkin, V.G. Maiorov, A.I. Nikolaev, Nauka 224 (1988).
[4] M.S. Fonari, N.G. Furmanova, W.-J. Wang, E.V. Ganin, I.A. Verin, Yu.A. Simonov, V.O. Gelmboldt, Kristallografiya (Russ.) 51 (2006) 856.
[5] M.S. Fonari, O.A. Alekseeva, N.G. Furmanova, K.A. Lysenko, W.-J. Wang, S.-W. Tang, E.V. Ganin, V.O. Gelmboldt, Yu.A. Simonov, Kristallografiya (Russ.) 52 (2007) 271.
[6] Ed.V. Ganin, V.O. Gelmboldt, L.V. Koroeva, M.S. Fonari, Yu.A. Simonov, J. Lipkowski, S.A. Kotlyar, G.L. Kamalov, J. Incl. Phenom. 56 (2006) 345.
[7] N.G. Furmanova, M.X. Rabadanov, T.S. Chernaya, M.S. Fonari, Yu.A. Simonov, Ed.V. Ganin, V.O. Gelmboldt, R.Ya. Grygorash, S.A. Kotlyar, G.L.Kamalov, Kristallografiya, submitted for publication.
[8] (a) B. Moulton, M.J. Zaworotko, Chem. Rev. 101 (2001) 1629;
(b) G.R. Desiraju, Science 278 (1997) 404.
[9] (a) M.A. Xiang Hao, S. Siegler, C. Parkin, P. Brock, Cryst. Growth Des. 5 (2005) 2225;
(b) L.-Q. Kong, J.-M. Dou, Da-C. Li, Da-Qi Wan, J. Mol. Struct. 785 (2006) 186;
(c) M.S. Fonari, V.Ch. Kravtsov, Yu.A. Simonov, E.V. Ganin, V.O. Gelmboldt, Russ. J. Struct. Chem. 40 (1999) 1002;
(d) M.S. Fonari, Yu.A. Simonov, Yu.M. Chumakov, G. Bocelli, E.V. Ganin, V.O. Gelmboldt, Acta Crystallogr., Sect. C 59 (2003) m168.
[10] (a) M. Eigen, Angew. Chem., Int. Ed. Engl. 3 (1964) 1;
(b) G. Zundel, in: Sandorfy (Ed.), The Hydrogen Bond – Recent Developments in Theory and Experiments, North-Holland, Amsterdam, 1976, p. 683;
(c) J. Xu, M.A. Sharpe, L. Qin, S. Ferguson-Miller, G.A. Voth, J. Am. Chem. Soc. 129 (10) (2007) 2910;
(d) F. Garczarek, K. Gerwert, Nature 439 (2006) 109.
[11] Z. Otwinowski, W. Minor, in: C.W. Carter, R.M. Sweet (Eds.), Methods. Enzymol., Macromolecular Crystallography, Part A, vol. 276, Academic Press, London, 1996, p. 307.
[12] G.M. Sheldrick, SADABS, Bruker AXS Inc., Madison, WI-53719, USA, 1997.
[13] G.M. Sheldrick: SHELXS97 and shelxl97, Programs for Crystal Structure Solution and Refinement, University of Göttingen, Germany, 1997.
[14] A. Haas, J. Kasprowski, K. Angermund, P. Betz, C. Kruger, Yi-Hung Tsay, S. Werner, Chem. Ber. 124 (1991) 1895.
[15] P. Halasyamani, K.R. Heier, M.J. Willis, C.L. Stern, K.R. Poeppelmeier, Z. Anorg. Allg. Chem. 622 (1996) 479.
[16] O.I. Guzyr, M. Schormann, J. Schimkowiak, H.W. Roesky, C. Lehmann, M.G. Walawalkar, R. Murugavel, H.-G. Schmidt, M. Noltemeyer, Organometallics 18 (1999) 832.
[17] M.A. McLoughlin, N.L. Keder, W.C. Kaska, Acta Crystallogr., Sect. C 48 (1992) 1098.
[18] F.N. Allen, Acta Crystallogr., Sect. B 58 (2002) 380.
[19] (a) B.M. Bulychev, V.K. Bel'sky, Zh. Neorg. Khim. (Russ.) (Russ. J. Inorg. Chem.) 40 (1995) 1834;
(b) H. Feinberg, I. Columbus, S. Cohen, M. Rabinovitz, H. Selig, G. Shoham, Polyhedron 12 (1993) 1811;
(c) L.J. Barbour, L.R. MacGillivray, J.L. Atwood, J. Chem. Cryst. 26 (1996) 59;
(d) B. Neumuller, M. Plate, K. Dehnicke, Z. Kristallogr. 209 (1994) 92;
(e) V.S. Sergienko, L.Kh. Minacheva, N.Kh. Ashurova, M.A. Porai-Koshits, K.G. Yakubov, V.G. Sakharova, Russ. J. Inorg. Chem. 36 (1991) 381;
(f) V.S. Sergienko, L.Kh. Minacheva, G.G. Sadikov, N.Kh. Ashurova, V.V. Minin, K.G. Yakubov, V.M. Sherbakov, Russ. J. Inorg. Chem. 37 (1992) 346;
(g) H. Feinberg, I. Columbus, S. Cohen, M. Rabinovitz, H. Selig, G. Shoham, Polyhedron 12 (1993) 2913;
(h) P.C. Junk, J.L. Atwood, J. Chem. Cryst. 24 (1994) 247;
(i) R. Chenevert, D. Chamberland, M. Simard, F. Brisse, Can. J. Chem. 68 (1990) 797;
(j) J.L. Atwood, S.G. Bott, P.C. Junk, M.T. May, J. Organomet. Chem. 487 (1995) 7;
(k) J.L. Atwood, S.G. Bott, C.M. Means, A.W. Coleman, Hongming Zhang, M.T. May, Inorg. Chem. 29 (1990) 467;
(l) P.C. Junk, L.R. MacGillivray, M.T. May, K.D. Robinson, J.L. Atwood, Inorg. Chem. 34 (1995) 5395;
(m) S.A. El Khalik, M. El Essawi, I. Dombrowski, K.-F. Tebbe, Z. Naturforsch. B54 (1999) 136;
(n) J.L. Atwood, P.C. Junk, M.T. May, K.D. Robinson, J. Chem. Cryst. 24 (1994) 243;
(o) Yu.A. Simonov, N.F. Krasnova, A.A. Dvorkin, V.V. Yakshin, V.M. Abashkin, B.N. Laskorin, Dokl. Akad. Nauk SSSR (Russ.) (Proc. Natl. Acad. Sci. USSR) 272 (1983) 1129;
(p) V.O. Gel'mbol'dt, E.V. Ganin, L.V. Ostapchuk, A.A. Ennan, Yu.A. Simonov, V.Kh. Kravtsov, M.S. Fonari, J. Lipkowski, Russ. J. Inorg. Chem. 44 (1999) 1139;
(q) V.O. Gelmboldt, E.V. Ganin, Yu.A. Simonov, J. Lipkowski, M.S. Fonari, V.Kh. Kravtsov, Russ. J. Inorg. Chem. 40 (1995) 594;
(r) J.-P. Behr, P. Dumas, D. Moras, J. Am. Chem. Soc. 104 (1982) 4540;
(s) A. Hammerschmidt, S. Bonmann, M. Lage, B. Krebs, Z. Anorg. Allg. Chem. 630 (2004) 2035.
[20] P.C. Junk, J.L. Atwood, J. Chem. Soc., Dalton Trans. (1997) 4393.
[21] M.I. Saleh, E. Kusrini, N. Ngah, B.M. Yamin, Acta Crystallogr., Sect. E 62 (2006) o1654.
[22] A. Hammerschmidt, I. Beckmann, M. Lage, B. Krebs, Z. Anorg. Allg. Chem. 631 (2005) 393.

[23] S.P. Petrosyants, A.M. Shpirt, A.B. Ilyukhin, Russ. J. Inorg. Chem. 45 (2000) 954.
[24] J.L. Atwood, P.C. Junk, J. Coord. Chem. 51 (2000) 379.
[25] A.N. Chekhlov, Russ. J. Inorg. Chem. 51 (2006) 569.
[26] D. Braga, M. Gandolfi, M. Lusi, M. Polito, K. Rubini, F. Grepioni, Cryst. Growth Des. 7 (2007) 919.

Facility, Kochi using a VarioEL III CHNS. The room temperature magnetic susceptibility measurements were carried out in the polycrystalline state on a Vibrating Sample Magnetometer (VSM) at 5.0 kOe field strength at the Indian Institute of Technology, Roorkee, India. Infrared spectral measurements were done on an ABB Bomem FTIR instrument using KBr pellets for spectra in the region 4000–500 cm^{-1}. An Ocean Optics SD 2000 Fiber Optic spectrometer was used to measure solid-state reflectance spectra in the range 200–900 nm. NMR measurements were carried out on a Varian Mercury Plus300 NMR spectrometer using DMSO as the solvent and EPR spectral measurements were carried out on a Varian E-112 X-band spectrometer using TCNE as a standard, at the Sophisticated Analytical Instruments Facility, Indian Institute of Technology, Mumbai, India.

2.3. X-ray crystallography

Single crystal X-ray diffraction measurements were carried out on a Bruker Smart Apex CCD diffractometer equipped with a fine-focused sealed tube. The unit cell parameters were determined and the data collections were performed using a graphite-monochromated Mo Kα ($\lambda = 0.71073$ Å) radiation. The data collected were reduced using the SAINT program [29] and the empirical absorption corrections were carried out using the SADABS program [30]. The trial structure was obtained by direct methods [31] using SHELXS-97, which revealed the position of all non-hydrogen atoms, and was refined by full-matrix least squares on F^2 (SHELXL-97) [32] and the graphics tool used was DIAMOND version 3.0 [33]. All non-hydrogen atoms were refined anisotropically, while the hydrogen atoms were placed in calculated positions and refined as riding atoms.

2.4. Synthesis of ligands

The ligand HL^1 (Fig. 1) was synthesized as follows: ethanolic solutions of cyclohexyl isothiocyanate (0.706 g, 5 mmol) and hydrazine hydrate (0.250 g, 5 mmol) were mixed with constant stirring. The stirring was continued for one more hour and the white product, *N*(4)-cyclohexyl thiosemicarbazide formed was filtered, washed, dried and recrystallized from ethanol. A methanolic solution of *N*(4)-cyclohexyl thiosemicarbazide (0.519 g, 3 mmol) was then refluxed with di-2-pyridyl ketone (0.553 g, 3 mmol) in 5 ml methanol continuously for 4 h after adding a few drops of acetic acid. There was no immediate formation of the product. After refluxing for 6 h continuously, the reaction mixture was kept aside for slow evaporation at room temperature. After one week, needle shaped crystals suitable for single crystal analyses were formed, which were carefully separated. Colour: light yellow, m.p. 104 °C, yield 0.95 g (47%). ^{1}H NMR: δ (ppm) 8.78 (d, C11H), 8.57 (d, C4H), 8.11 (d, C8H and C1H), 7.91 (dt, N4H and N5H), 7.67 (m, C10H and C3H), 7.53 (m, C2H and C9H), 4.14 (m, C13H), 2.07 (m, cyH), 1.29 (m, cyH).

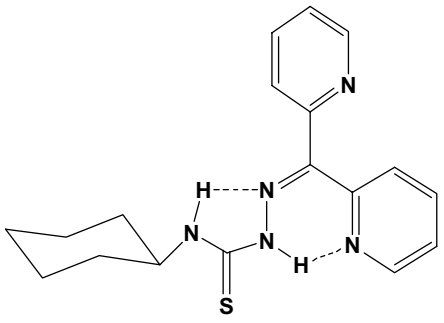


Fig. 1. Structure of the compound HL^1.

Preparation of the ligand HL^2 was done as described previously [34].

2.5. Preparation of the complexes

2.5.1. $CoL^1NCS \cdot 2H_2O$ (**1**)

$Co(OAc)_2 \cdot 4H_2O$ (0.249 g, 1 mmol) dissolved in 10 ml methanol was added to a refluxing methanolic solution of di-2-pyridyl ketone (0.184 g, 1 mmol) and 4-cyclohexyl-3-thiosemicarbazide (0.173 g, 1 mmol). Fifteen minutes later, KSCN (0.097 g, 1 mmol) dissolved in 10 ml of water was added to the reaction mixture and further refluxed for three hours. The product that separated out was collected, washed with ether and dried *in vacuo*. Colour: Brown. Yield: 0.40 g (58%), $\mu_{eff} = 3.23$ BM. Elemental *Anal.* Calc. for **1**: C, 46.43; H, 4.92; N, 17.10. Found: C, 46.31; H, 5.03; N, 17.04%.

2.5.2. $[Co(L^1)_2]ClO_4$ (**2**)

An ethanolic solution of $Co(ClO_4)_2 \cdot 6H_2O$ (0.365 g, 1 mmol) was added to a refluxing methanolic solution of di-2-pyridyl ketone (0.184 g, 1 mmol) and 4-cyclohexyl-3-thiosemicarbazide (0.173 g, 1 mmol) and further refluxed for 3 h. The resulting precipitate was washed with ether and dried over P_4O_{10} *in vacuo*. Colour: Brown. Yield: 0.35 g (49%). Elemental *Anal.* Calc. for **2**: C, 49.62; H, 5.09; N, 16.08. Found: C, 49.83; H, 4.95; N, 16.24%. ^{1}H NMR: δ (ppm) 8.76 (d, C11H), 8.54 (d, C4H), 7.88 (t, N5H), 7.81 (d, C8H and C1H), 7.72 (m, C2H, C3H, C9H and C10H), 4.23 (m, C13H), 2.01 (m, cyH), 1.25 (m, cyH).

2.5.3. $CoL^2Cl \cdot 2H_2O$ (**3**)

$CoCl_2 \cdot 6H_2O$ (0.237 g, 1 mmol) in 15 ml of ethanol was added to an ethanolic solution of HL^2 (0.317 g, 1 mmol) and refluxed for 4 h. The crystalline product that separated out was filtered and washed with ether and dried over P_4O_{10} *in vacuo*. Colour: Brown. Yield: 0.36 g (65%), $\mu_{eff} = 3.23$ BM. Elemental *Anal.* Calc. for **3**: C, 46.71; H, 3.92; N, 15.13. Found: C, 46.83; H, 4.11; N, 15.40%.

2.5.4. $[Co(L^2)_2]NO_3 \cdot 3H_2O$ (4)

A solution of $Co(NO_3)_2 \cdot 6H_2O$ (0.291 g, 1 mmol) in 10 ml of ethanol was added to HL^2 (0.317 g, 1 mmol) and refluxed for 6 h. The resulting precipitate was washed with ether and dried over P_4O_{10} *in vacuo*. Colour: Light brown. Yield: 0.32 g (52%). Elemental *Anal.* Calc. for **4**: C, 51.49; H, 4.08; N, 18.35. Found: C, 51.61; H, 3.98; N, 18.53%. ^{1}H NMR: δ (ppm) 10.65 (s, N5H), 8.72 (d, C11H), 8.50 (d, C4H), 8.29 (d, C8H and C1H), 7.80 (m, C14H and C18H), 7.68 (m, C2H, C3H, C9H and C10H), 7.46 (m, C15H and C17H), 7.26 (m, C16 H).

2.5.5. $CoL^2(NCS)_2 \cdot 3H_2O$ (5)

For the preparation of compound **5**, 1 mmol of $Co(OAc)_2 \cdot 4H_2O$ (0.249 g) dissolved in ethanol (15 ml) was added to an ethanolic solution of HL^2 (0.317 g, 1 mmol) and refluxed. An aqueous solution of KSCN (0.097 g, 1 mmol) was then added to the solution which was further refluxed for 3 h. The product that separated out was collected, washed with ether and dried *in vacuo*. Colour: Dark brown. Yield: 0.38 g (55%), Elemental *Anal.* Calc. for **5**: C, 42.78; H, 3.59; N, 17.46. Found: C, 42.89; H, 3.62; N, 16.98%. ^{1}H NMR: δ (ppm) 8.82 (d, C11H), 8.58 (d, C4H), 7.82 (m, PyH), 7.75 (t, N5H), 7.56 (m, Phenyl H).

2.5.6. $CoL^2Br_2 \cdot 4.5H_2O$ (6)

HL^2 (0.317 g, 1 mmol) was dissolved in ethanol (15 ml) and refluxed with $CoBr_2$ (0.218 g, 1 mmol) dissolved in 10 ml of hot water. The product that separated out was collected, washed with ether and dried *in vacuo*. Colour: Light brown. Yield: 0.31 g (55%). Elemental *Anal.* Calc. for **6**: C, 34.20; H, 3.67; N, 11.08. Found: C, 34.53; H, 3.51; N, 10.71%. ^{1}H NMR: δ (ppm) 10.50 (s, N5H), 8.68 (d, C11H), 8.49 (d, C4H), 7.84 (m, PyH), 7.64 (d, C14H and C18H), 7.45 (m, C15H, C16H and C17H).

3. Results and discussion

3.1. Synthesis of compounds

X-ray quality single crystals of HL^1 were isolated from a methanolic solution of the compound. In the complexes **1** and **3**, the cobalt revealed the +2 oxidation state, while in compounds **2**, **4**, **5** and **6**, it showed the +3 oxidation state. In compound **2**, the Co^{3+} nucleus appeared to be six-coordinated with two anionic ligand moieties, whereas a perchlorate ion remained outside the coordination sphere. This stoichiometry was in accordance with the elemental analyses results. The molar conductivity value was measured to be 60.23 $ohm^{-1}\,cm^2\,mol^{-1}$ in DMF, which was in the expected range for 1:1 electrolytes [35]. For compound **4**, a possible stoichiometry with two anionic ligand units coordinated to the metal centre along with a nitrate group in the outer sphere was suggested by the elemental analyses, and the molar conductivity value was measured to be 50.08 $ohm^{-1}\,cm^2\,mol^{-1}$ in DMF. Co(II) complexes **1** and **3** were observed to show a 1:1:1 ratio of metal:thiosemicarbazone:gegenion, with the general formula $Co(L)X \cdot 2H_2O$ [X = NCS when HL = HL^1 and X = Cl when HL = HL^2]. Co(III) complexes **2** and **4** possess the metal:thiosemicarbazone:gegenion ratio of 1:2:1, with the general formula $Co(L)_2X \cdot yH_2O$ [X = ClO_4, $y = 0$ when HL = HL^1 and X = NO_3 $y = 3$ when HL = HL^2], while compounds **5** and **6** revealed the metal:thiosemicarbazone:gegenion ratio as 1:1:2, with the general formula $CoL(X)_2 \cdot yH_2O$ [X = NCS, $y = 3$ when HL = HL^1 and X = Br, $y = 4.5$ when HL = HL^2].

3.2. Crystal structure of HL^1

The molecular structure of HL^1, along with the atom numbering scheme is given in Fig. 2. The crystal data and structural refinement parameters are given in Table 1 and selected bond lengths and angles are given in Table 2. The compound crystallized into a monoclinic lattice with the space group $P2_1$. The molecule exists in the *Z* conformation with respect to the C6–N3 bond. However, the S1 and N3 atoms are in the *E* conformation with respect to the N4–C12 bond, and hence the thiosemicarbazone moiety as a whole exists in the *ZE* conformation. This is contrary to the observations in 3-piperidyl and 3-hexamethyliminyl-di-2-pyridyl ketone thiosemicarbazones [27], which revealed a *ZZ* conformation for the thiosemicarbazone moiety. However, *N*4-methyl-di-2-pyridyl ketone thiosemicarbazone was observed to be in the *ZE* conformation [28]. In HL^1, the thiosemicarbazone moiety comprising of atoms N3, N4, C12, S1 and N5 is almost planar, with a maximum mean plane deviation of 0.0375(1) Å. A torsion angle of 175.21(16)° corresponding to the S1–C12–N4–N3 moiety implies a trans alignment of the thiocarbonyl S1 atom in HL^1. The azomethine bond, C6–N3 (1.297(3) Å) is in conformity with a formal C=N double bond (1.28 Å) and the C12–S1 bond distance of

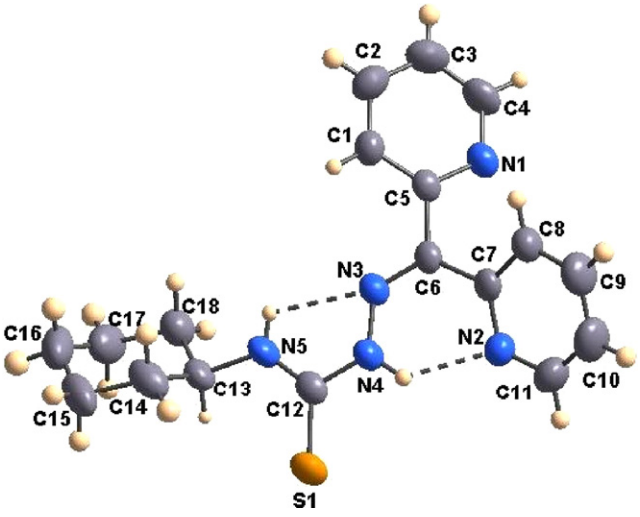


Fig. 2. Molecular structure of HL^1. Ellipsoids are drawn at 50% probability and intramolecular hydrogen bonding interactions are shown as dashed lines.

Table 1
Crystal data and structural refinement for HL^1

Parameters	HL^1
Empirical formula	$C_{18}H_{21}N_5S$
Formula weight, M	339.46
Crystal system	monoclinic
Space group	$P2_1$
Lattice constants	
a (Å)	9.9281(17)
b (Å)	8.4668(15)
c (Å)	10.9480(19)
α (°)	90.00
β (°)	101.331(3)
γ (°)	90.00
Volume V (Å^3)	902.3(3)
Z	2
D_{calc} ρ (Mg m^{-3})	1.249
Absorption coefficient, μ (mm^{-1})	0.188
$F(000)$	360
Crystal size (mm^3)	$0.66 \times 0.24 \times 0.05$
θ-Range for data collection	1.90–27.03
Limiting indices	$-12 \leqslant h \leqslant 12$, $-10 \leqslant k \leqslant 10$, $-13 \leqslant l \leqslant 13$
Reflections collected	7228
Unique reflections	3650 ($R_{int} = 0.0207$)
Completeness to θ	27.31(93.3%)
Absorption correction	multiscan
Data/restraints/parameters	3650/0/301
Goodness-of-fit on F^2	1.081
Final R indices [$I > 2\sigma(I)$]	$R_1 = 0.0440$, $wR_2 = 0.0905$
R indices (all data)	$R_1 = 0.0557$, $wR_2 = 0.0949$

1.672(2) Å, is very close to a formal C=S bond length (1.60 Å) [36]. It confirms the existence of the thiosemicarbazone in the thione form in the solid state. The N3–N4 (1.359(3)) and N4–C12 (1.372(3)) bond distances in HL^1 are intermediate between formal single or double N–N and C–N bonds, giving evidence for an extended π delocalization along the thiosemicarbazone chain. Interestingly, the hydrogen bonding interactions by N2 and the resultant increased electron density on the ring imparts slight deviations in the C–C bond distances of the corresponding atoms in the two pyridyl rings. Mean plane deviation calculations showed that the lowest deviation exists between the pyridyl ring Cg(1) comprising of atoms N1, C1, C2, C3, C4 and C5, and the thiosemicarbazone moiety (atoms N3, N4, C12, S1 and N5) with a dihedral angle of 38.34° between the planes. The intramolecular hydrogen bonding interaction, N5–H5A–N3, lead to the formation of one five-membered ring comprising of atoms N3, N4, C12, N5 and H5A. Ring puckering analyses and least square planes calculations show that the cyclohexyl ring, Cg(3), adopts a chair conformation ($Q_T = 0.5422$ Å). The molecular packing of HL^1 is shown in Fig. 3. The unit cell is viewed down the '*a*' axis. Each molecule gets repeated in a one-dimensional manner in the crystal lattice, and these one-dimensional arrays are aligned in an offset manner, which effects a two-dimensional zig-zag packing in the unit cell. The π–π, C–H–π and hydrogen bonding interactions were observed to be rather weak in the crystal lattice.

Table 2
Selected bond lengths (Å) and bond angles (°) of HL^1

Bond distance	HL^1	Bond angle	HL^1
C6–N3	1.297(3)	C7–C6–C5	119.22(18)
N3–N4	1.359(3)	C5–C6–N3	113.83(18)
N4–C12	1.372(3)	C6–N3–N4	120.05(18)
C12–S1	1.672(2)	N3–N4–C12	119.7(2)
C12–N5	1.318(3)	N4–C12–S1	118.18(18)
N5–C13	1.461(3)	N4–C12–N5	115.5(2)
C6–C7	1.478(3)	C12–N5–C13	126.9(2)
C5–C6	1.489(3)		

3.3. IR and electronic spectra

The infrared spectral data of the ligand HL^1 was observed to be in conformity with the structural results. The compound exhibits a few weak discrete bands at 3749, 3646 and 3326 cm^{-1} possibly due to the association of the thioamide groups in different molecules. The –NH stretching vibrations at $N(4)$ can also give rise to bands around 3300 cm^{-1}. The –CH stretching vibrations of the cyclohexyl moiety are observed as two sharp bands at 2929 and 2850 cm^{-1}. The absence of any bands in the 2800–2550 cm^{-1} region reveals the presence of only the thione tautomer in the solid state, due to the lack of –SH stretching absorptions in that region. The ν(C=N) vibrations are observed at 1585 cm^{-1}. The N–H bending and C–N stretching vibrations of the thioamide function give rise to weak bands at 1563 and 1547 cm^{-1} and the ν(CS) and δ(CS) vibrations are observed at 1323 and 801 cm^{-1}. In the complexes, a medium band centred around 3200 cm^{-1} is consistent with the lattice water content in the samples, while a weak band around 3050 cm^{-1} can be assigned to the ν(NH) vibration at the N(4)–H position. The cyclohexyl stretching vibrations appear as two sharp bands at 2929 and 2852 cm^{-1}. In compound **1**, a sharp band at 2067 cm^{-1} is characteristic of the N-coordinated thiocyanate group in the compound, and the unsplit attribute of the band is in accordance with the presence of a single thiocyanate species. Support for the non-coordinated nature of the perchlorate ion in compound **2** is provided by an unsplit band at 1082 cm^{-1} and a sharp band at 622 cm^{-1}, which are assigned to the $\nu_3(ClO_4)$ and $\nu_4(ClO_4)$ vibrations of the free perchlorate anion [37,38]. The IR spectrum of compound **4** reveals an unsplit sharp band at 745 cm^{-1}, a characteristic in-plane bending vibration band (ν_4) of the free nitrate ion [37]. Upon coordination, the ν_4 band is expected to split into two bands, the lack of which supports the non-coordinated nature of the nitrato ion in the compound. For compound **5**, the elemental analyses data suggest a Co^{3+} metal centre with two thiocyanate groups in the molecule. Interestingly, the IR spectrum supports this stoichiometry with a characteristic strong band split into two at 2048 and 2089 cm^{-1}, corre-

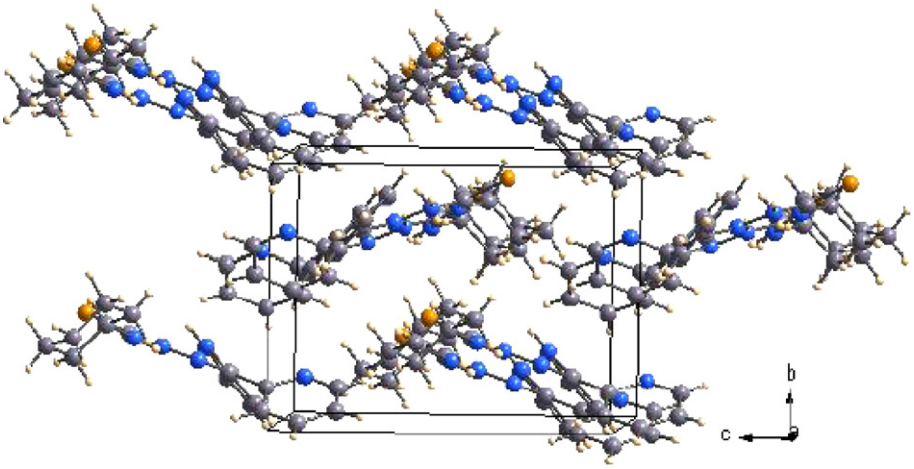


Fig. 3. Molecular packing diagram of HL^1, the unit cell is viewed down the '*a*' axis.

sponding to the possible presence of more than one thiocyanate group. Another weak split is also observed in the band at 2156 cm^{-1}. These support the proposed stoichiometry of the compound and also suggest that the thiocyanate groups are N-bonded to the metal centre, since the characteristic bands are observed near or below 2150 cm^{-1} [37]. The ν(CoBr) vibrations of the terminal bromine groups appear at 274 cm^{-1} in compound **6**. In all the complexes, the azomethine vibration bands are shifted in the range 8–40 cm^{-1} as a result of coordination. The newly formed N=C bond due to enolization of the ligands resonates near 1590 cm^{-1} in the complexes. The thiolate bending bands in the complexes are observed near 750 cm^{-1}, which are also shifted from the corresponding value in the ligand, due to coordination. The solid-state reflectance spectrum of HL^1 reveals the $\pi \rightarrow \pi^*$ transitions of the pyridyl ring and the thiosemicarbazone imine function at 263 and 291 nm. The $\pi \rightarrow \pi^*$ transitions of the thiocarbamide group and the $n \rightarrow \pi^*$ transition of the pyridine ring are observed at 364 and 384 nm respectively. In the electronic spectra of the complexes, the intraligand transitions are slightly shifted as a result of coordination. The d−d transitions are rather weak, appearing as shoulders near 500 nm. The electronic spectral details of the complexes are given in Table 3.

3.4. Nuclear magnetic resonance studies

The ^1H NMR studies of HL^1 and the diamagnetic complexes were carried out and interpreted based on the atom labelling in Figs. 2 and 4. The spectrum of HL^1 reveals two doublets at δ 8.78 and 8.57 ppm corresponding to protons at C11 and C4, respectively. The electronic effect of the adjacent pyridyl nitrogens shifts the signals to lower field and the more downfield shift of C11 H can be attributed to the increased charge density on the hydrogen bonded N2 [39]. A doublet at δ 8.11 ppm corresponds to the protons on C1 and C8, while two multiplets at δ 7.67 and 7.53 ppm belong to the other pyridyl protons. The proton resonances on the electronegative N4 and N5 atoms appear as a doublet of triplets at 7.91 ppm due to quadrupole splitting. The cyclohexyl proton C13 H is deshielded by the adjacent electronegative nitrogen, resulting in a multiplet at δ 4.14 ppm. The cyclohexyl moiety exists in the chair conformation, and the equatorial protons are observed at more downfield values ($\delta = 2.07$ ppm) compared to their axial counterparts ($\delta = 1.29$ ppm). The ^1H NMR spectra of the complexes reveal that the resonance peaks are shifted from their corresponding values in the ligand, as a result of coordination. However, the protons on the phenyl and cyclohexyl rings, which do not take part in coordination, remain more or less unchanged in the complexes, even if there are slight variations in their resonances due to the delocalisation of electron density in the system. The NMR spectra of the complexes are less resolved than that of the ligands, perhaps due to the low solubility of the complexes. For instance, the alpha proton in the pyridyl rings is clearly resolved in the spectra of the complexes, whereas some aromatic proton resonances appear as

Table 3
Electronic spectral data (nm) of the cobalt complexes

Compound	$\pi \rightarrow \pi^*$	$n \rightarrow \pi^*$	Charge transfer	d–d
$CoL^1NCS \cdot 2H_2O$ (**1**)		306 b	404	532 sh
				587 sh
$[Co(L^1)_2]ClO_4$ (**2**)	321	385	455	489
			470 b	578 b
$CoL^2Cl \cdot 2H_2O$ (**3**)	267 b		362 sh	547 sh
			445 b	579 sh
$[Co(L^2)_2]NO_3 \cdot 3H_2O$ (**4**)	277	306	458 b	529 sh
				577 sh
$CoL^2(NCS)_2 \cdot 3H_2O$ (**5**)	287	340 sh	455 sh	570 sh
		382 sh	487 b	637 sh
$CoL^2Br_2 \cdot 4.5H_2O$ (**6**)	287	317 sh	401	502 sh
			428	526 sh

b = broad, sh = shoulder.

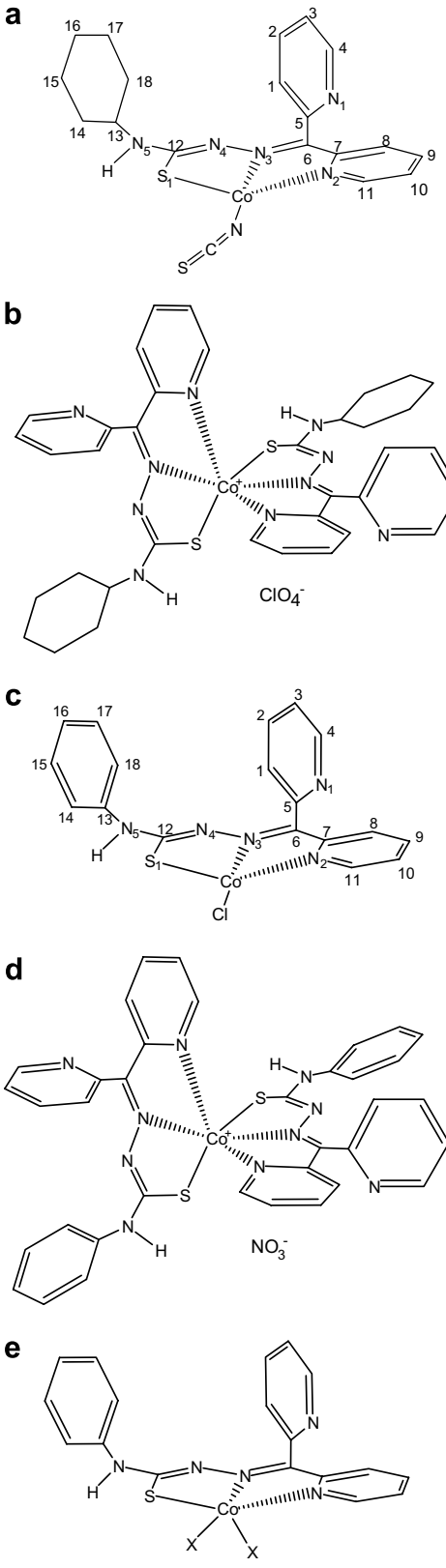


Fig. 4. Tentative structures of the complexes, omitting lattice water (a) CoL^1NCS, (b) $[Co(L^1)_2]ClO_4$, (c) CoL^2Cl, (d) $[Co(L^2)_2]NO_3$, (e) $CoL^2(NCS)_2$ (X = NCS) and CoL^2Br_2 (X = Br).

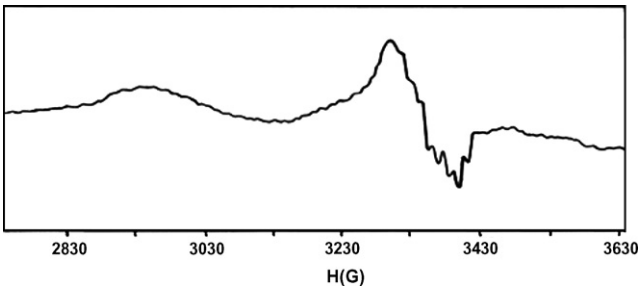


Fig. 5. EPR spectrum of $CoL^1NCS \cdot 2H_2O$ in DMF solution at 77 K.

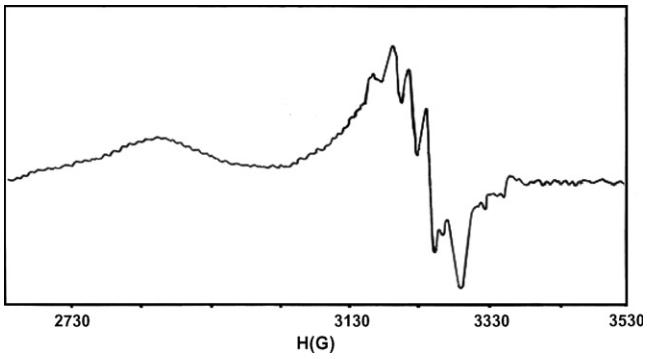


Fig. 6. EPR spectrum of $CoL^2Cl \cdot 2H_2O$ in DMF solution at 77 K.

multiplets, making it difficult to distinguish the individual proton resonances. The NMR assignments are given in Section 2.5.

3.5. Magnetic and EPR studies

Room temperature magnetic susceptibility studies reveal complexes **1** and **3** to be paramagnetic, with μ_{eff} values of 3.23 and 3.52 BM, respectively. The observed magnetic moments are much lower than that expected of four coordinate Co(II) tetrahedral complexes (4.4–4.8 BM) [40,41]. This suggests a possible tendency towards a square planar geometry in the complexes, which is further supported by the EPR studies. The X-band EPR spectrum of $CoL^1NCS \cdot 2H_2O$ (**1**) in DMSO at 77 K is given in Fig. 5. The spectrum reveals axial features with the g values, $g_{\parallel} = 2.299$ and $g_{\perp} = 1.996$. The Co(II) nucleus has a nuclear spin of 7/2 and hence eight hyperfine lines are expected in the EPR spectrum in the frozen state. The hyperfine splittings are more clearly resolved in the perpendicular region. It should be noted that the EPR spectrum at 77 K reveals that $g_{\parallel} > g_{\perp}$, which is characteristic of four coordinate square planar complexes. The magnetically dilute disposition observed in EPR spectrum denotes that the bridging interactions are weakened in the frozen state at 77 K. The EPR spectrum of the compound $CoL^2Cl \cdot 2H_2O$ (**3**) in DMSO at 77 K is given in Fig. 6, which reveals features similar to that of the compound $CoL^1NCS \cdot 2H_2O$. The spectrum appears to be axial with two g values, $g_{\parallel} = 2.282$ and $g_{\perp} = 1.994$, and it should be noted that in compound **3** also, the hyperfine splittings are more clearly resolved in the perpendicular region.

Acknowledgements

V. Suni is thankful to the Kerala State Council for Science, Technology and Environment for financial support in the form of a fellowship. M.R.P. Kurup acknowledges the Department of Science and Technology, Government of India for financial assistance. The authors also acknowledge DST IRHPA for the data collection.

Appendix A. Supplementary material

CCDC 251895 contains the supplementary crystallographic data for this paper. These data can be obtained free of charge via http://www.ccdc.cam.ac.uk/conts/retrieving.html, or from the Cambridge Crystallographic Data Centre, 12 Union Road, Cambridge CB2 1EZ, UK; fax: (+44) 1223-336-033; or e-mail: deposit@ccdc.cam.ac.uk. Supplementary data associated with this article can be found, in the online version, at doi:10.1016/j.poly.2007.07. 051.

References

[1] S. Yamada, Coord. Chem. Rev. 190–192 (1999) 537.
[2] M. Amirnasr, K.J. Schenk, A. Gorji, R. Vafazadeh, Polyhedron 20 (2001) 695.
[3] M.M. Aly, J. Coord. Chem. 43 (1998) 89.
[4] R. Cmi, S.J. Moore, L.G. Marzilli, Inorg. Chem. 37 (1998) 6890.
[5] S.M. Polson, R. Cini, C. Pifferi, L.G. Marzilli, Inorg. Chem. 36 (1997) 314.
[6] S. Hirota, E. Kosugi, L.G. Marzilli, O. Yamauchi, Inorg. Chim. Acta 275 (1998) 90.
[7] A.E. Martell, D.T. Sawyer, Oxygen Complexes and Oxygen Activation by Transition Metals, Plenum Press, New York, 1988.
[8] N.J. Henson, P.J. Hay, A. Redondo, Inorg. Chem. 38 (1999) 1618.
[9] C. Benchini, R.W. Zoeliner, Adv. Inorg. Chem. 44 (1997) 263.
[10] T. Nagata, K. Yoruzu, T. Yamada, T. Mukaiyama, Angew. Chem., Int. Ed. Engl. 34 (1995) 2145.
[11] A. Botterher, T. Takeuchi, K.I. Meade, H.B. Gray, D. Cwikel, M. Kapon, Z. Don, Inorg. Chem. 36 (1997) 2498.
[12] J. Garcia-Tojal, A. Garcia-Orad, A.A. Diaz, J.L. Serra, M.K. Urtiaga, M.I. Arriortua, T. Rojo, J. Inorg. Biochem. 84 (2001) 271.
[13] C.-Y. Duan, Z.-H. Liu, X.-Z. You, F. Xue, T.C.W. Mak, Chem. Commun. (1997) 381.
[14] V. Philip, V. Suni, M.R.P. Kurup, M. Nethaji, Polyhedron 23 (2004) 1225.
[15] V. Philip, V. Suni, M.R.P. Kurup, M. Nethaji, Polyhedron 23 (2005) 1133.
[16] V. Philip, E. Manoj, M.R.P. Kurup, M. Nethaji, Acta Crystallogr., Sect. C 61 (2005) m488.
[17] V. Philip, V. Suni, M.R.P. Kurup, M. Nethaji, Polyhedron 25 (2006) 1931.
[18] V. Philip, V. Suni, M.R.P. Kurup, M. Nethaji, Spectrochim. Acta A 64 (2006) 171.
[19] V. Suni, M.R.P. Kurup, M. Nethaji, Polyhedron 26 (2007) 3097.
[20] P. Bindu, M.R.P. Kurup, Synth. React. Inorg. Met.-Org. Chem. 30 (2000) 55.
[21] P.F. Rapheal, E. Manoj, M.R.P. Kurup, Polyhedron 26 (2007) 818.
[22] R.P. John, A. Sreekanth, M.R.P. Kurup, S.M. Mobin, Polyhedron 21 (2002) 2515.
[23] A. Sreekanth, U.L. Kala, C.R. Nayar, M.R.P. Kurup, Polyhedron 23 (2004) 41.
[24] H. Beraldo, W.F. Nacif, L.R. Teixeira, J.S. Reboucas, Transition Met. Chem. 27 (2002) 85.
[25] A.K. El-Sawaf, D.X. West, R.M. El-Bahnasawy, F.A. El-Saied, Transition Met. Chem. 23 (1998) 227.
[26] D.X. West, H. Beraldo, A.A. Nassar, F.A. El-Saied, M.I. Ayad, Transition Met. Chem. 24 (1998) 81.
[27] J.K. Swearingen, W. Kaminsky, D.X. West, Transition Met. Chem. 27 (2002) 724.
[28] J.K. Swearingen, D.X. West, Transition Met. Chem. 26 (2001) 252.
[29] Siemens, SMART and SAINT, Area Detector Control and Integration Software, Siemens Analytical X-ray Instruments Inc., Madison, WI, USA, 1996.
[30] G.M. Sheldrick, SADABS, Program for Empirical absorption correction of Area Detector Data, University of Göttingen, Göttingen, Germany, 1997.
[31] G.M. Sheldrick, SHELXS-97 Program for the Solution of Crystal Structures, University of Göttingen, Göttingen, Germany, 1997.
[32] G.M. Sheldrick, Acta Crystallogr., Sect. A 46 (1990) 467.
[33] K. Brandenburg, H. Putz, DIAMOND Version 3.0, Crystal Impact, GbR, Postfach 1251, D-53002 Bonn, Germany, 2004.
[34] V. Suni, M. Nethaji, M.R.P. Kurup, Spectrochim. Acta A 63 (2005) 174.
[35] W.J. Geary, Coord. Chem. Rev. 7 (1971) 81.
[36] G.J. Palenik, D.F. Rendle, W.S. Carter, Acta Crystallogr., Sect. B 30 (1974) 2390.
[37] K. Nakamoto, in: Infrared and Raman Spectra of Inorganic and Coordination Compounds, 4th ed., John Wiley and Sons, New York, 1986.
[38] M.R.P. Kurup, in: Stereochemical Investigations on Transition Metal Complexes of Biologically Active Substituted 2-Acetylpyridine Thiosemicarbazones, Ph.D. Thesis, University of Delhi, 1988.
[39] R.M. Silverstein, G.C. Bassler, T.C. Morrill, in: Spectrometric Identification of Organic Compounds, 4th ed., John Wiley and Sons, New York, 1981.
[40] J.R. Anacona, Gladys Da Silva, J. Chil. Chem. Soc. 50 (N 2) (2005) 447.
[41] J.C. Bailar, H.J. Emeleus, R. Nyholm, A.F. Trotman, Dickenson in Comprehensive Inorganic Chemistry, Pergamon Press, New York, 1975.

thiazoline (TnInA). The characterization of these complexes has been carried out by means of elemental analysis, IR and X-ray diffraction. The cobalt complexes have also been characterized through UV–VIS-NIR diffuse reflectance and magnetic susceptibility measurements and the zinc complexes through ^{1}H NMR and ^{13}C NMR spectroscopy.

2. Experimental

2.1. Synthesis of 2-(indazol-1-yl)-2-thiazoline (TnInA)

This ligand was synthesized according to the method described previously [9]. ^{1}H NMR (DMSO): δ 8.41 (s, 1H), 8.36 (d, $J = 8.4$ Hz, 1H), 7.88 (d, $J = 8.4$ Hz, 1H), 7.59 (t, $J = 7.7$ Hz, 1H), 7.36 (t, $J = 7.8$ Hz, 1H), 4.39 (t, $J = 8.0$ Hz, 2H), 3.48 (t, $J = 8.2$ Hz, 2H); ^{13}C NMR (DMSO): δ 158.0, 138.8, 138.4, 129.1, 125.9, 124.0, 121.8, 114.0, 62.0, 32.9. *Anal.* Calc. for $C_{10}H_9N_3S$: C, 59.09; H, 4.46; N, 20.67; S, 15.77. Found: C, 59.45; H, 4.83; N, 20.22; S, 15.43%. UV–Vis (EtOH): λ_{max}, nm; (ε, L mol^{-1} cm^{-1}) 232 (26000), 295 (9248), 306 (9585).

2.2. Synthesis of the complexes

Metal complexes were prepared by reacting an ethanol solution (1 mL) of the metal(II) salt (chloride or nitrate) (0.5 mmol) with an ethanol solution (15 mL) of the ligand (100 mg, 0.5 mmol). Upon evaporation solid precipitates were obtained. The solids were filtrated and washed with cold ether and finally air-dried.

2.2.1. $[CoCl_2(TnInA)_2]\cdot C_2H_6O$ (1)

Yield: 51.8 mg, 36.2%. X-ray quality red crystals were grown by slow evaporation from an EtOH solution. *Anal.* Calc. for $C_{20}H_{18}Cl_2CoN_6S_2\cdot C_2H_6O$: C, 45.36; H, 4.15; N, 14.43; S, 11.01. Found: C, 45.06; H, 4.22; N, 14.35; S, 10.94%.

2.2.2. $[ZnCl_2(TnInA)]$ (2)

Yield: 68.7 mg, 38.9%. ^{1}H NMR (DMSO): δ 8.40 (s, 1H), 8.34 (d, $J = 8.0$ Hz, 1H), 7.87 (d, $J = 8.0$ Hz, 1H), 7.58 (t, $J = 7.6$ Hz, 1H), 7.36 (t, $J = 7.4$ Hz, 1H), 4.38 (t, $J = 8.2$ Hz, 2H), 3.47 (t, $J = 8.4$ Hz, 2H); ^{13}C NMR (DMSO): δ 158.1, 138.9, 138.5, 129.3, 126.0, 124.1, 121.9, 114.1, 62.1, 33.0. *Anal.* Calc. for $C_{10}H_9Cl_2ZnN_3S\cdot 0.75H_2O$: C, 34.11; H, 3.01; N, 11.93; S, 9.11. Found: C, 34.14; H, 2.90; N, 11.54; S, 9.17%. UV–Vis (EtOH): λ_{max}, nm; (ε, L mol^{-1} cm^{-1}) 232 (28756), 294 (13093), 306 (10861).

2.2.3. $[Co(TnInA)_2(H_2O)_2](NO_3)_2$ (3)

Yield: 77.3 mg, 50.3%. By means of slow evaporation of the ethanol solution at room temperature, red crystals were isolated. *Anal.* Calc. for $C_{20}H_{22}CoN_8O_8S_2$: C, 38.40; H, 3.54; N, 17.92; S, 10.25. Found: C, 38.18; H, 3.37; N, 17.56; S, 9.92%.

2.2.4. $[Zn(TnInA)_2(H_2O)_2](NO_3)_2$ (4)

Yield: 53.8 mg, 34.6%. By means of slow evaporation of the ethanol solution at room temperature, colourless crystals were isolated. ^{1}H NMR (DMSO): δ 8.41 (s, 1H), 8.34 (d, $J = 8.2$ Hz, 1H), 7.88 (d, $J = 8.2$ Hz, 1H), 7.58 (t, $J = 7.7$ Hz, 1H), 7.36 (t, $J = 7.6$ Hz, 1H), 4.37 (t, $J = 7.8$ Hz, 2H), 3.47 (t, $J = 6.8$ Hz, 2H); ^{13}C NMR (DMSO): δ 158.2, 139.0, 138.6, 129.4, 126.1, 124.2, 122.0, 114.2, 62.1, 33.1. *Anal.* Calc. for $C_{20}H_{22}ZnN_8O_8S_2$: C, 38.02; H, 3.51; N, 17.73; S, 10.13. Found: C, 37.76; H, 3.62; N, 17.52; S, 10.39%. UV–Vis (EtOH): λ_{max}, nm; (ε, L mol^{-1} cm^{-1}) 232 (17276), 295 (6924), 306 (6282).

2.3. Instrumental procedures

The carbon, hydrogen, nitrogen and sulfur contents of the compounds were determined on a Leco CHNS-932 microanalyser. IR spectra were recorded on a Perkin–Elmer FT-IR 1720 spectrophotometer, from KBr pellets in the 4000–370 cm^{-1} range and on a Perkin–Elmer FT-IR 1700X spectrophotometer, from polyethylene pellets in the 500–150 cm^{-1} range. Electronic spectra in solution of the ligand and the zinc complexes were measured on a Shimadzu UV-3101 PC using a 10 mm quartz cell. Solid state electronic spectra for the cobalt complexes in the 200–1500 nm range were obtained from pellets of the samples, using a Shimadzu UV-3101 PC spectrophotometer and $BaSO_4$ as a reference. Magnetic susceptibility measurements were performed on polycrystalline samples using a magnetometer with a pendulum MANICS DSM8, equipped with a helium continuous-flow cryostat and an electromagnetometer DRUSCH EAF 16 UE. Data were corrected for temperature independent paramagnetism and diamagnetic contributions, which were estimated from the Pascal constants. ^{1}H (400 MHz) and ^{13}C NMR (100 MHz) spectra were recorded in DMSO on a Bruker AM 400 instrument.

2.4. Crystal structure determinations

Experimental details of crystal structure determinations including crystal data, data collection, structure determinations and refinement parameters for **1**, **3** and **4** are listed in Table 1. X-ray diffraction measurements were performed using a Bruker SMART CCD diffractometer equipped with graphite-monochromated Mo-Kα radiation ($\lambda = 0.71073$ Å) for **1** and **3** and an Enraf Nonius CAD4 diffractometer equipped with graphite-monochromated Cu-Kα radiation ($\lambda = 1.5418$ Å) for **4**. The intensity data were collected using the ϕ-ω scan technique (**1**, **3**) and ω-2θ scan technique (**4**). Empirical absorption corrections were applied using the SADABS [10] program for the cobalt complexes whereas semi-empirical absorption corrections were made based on the psi-scan application using the WINGX [11] package for **4**. The structures were solved by direct methods and subsequent Fourier differences using the programs SHELXS-86 [12] and SHELXS-97 [13] and refined

Table 1
Crystal data, data collection and refinement details for **1**, **3** and **4**

	1	**3**	**4**
Crystal shape	prism	prism	prism
Colour	red	red	colourless
Size (mm)	$0.31 \times 0.31 \times 0.22$	$0.70 \times 0.45 \times 0.35$	$0.80 \times 0.70 \times 0.45$
Chemical formula	$C_{22}H_{24}CoCl_2N_6OS_2$	$C_{20}H_{22}CoN_8O_8S_2$	$C_{20}H_{22}ZnN_8O_8S_2$
Formula weight	582.5	625.5	632.0
Crystal system	monoclinic	monoclinic	monoclinic
Space group	*C*2/*c*	*P*21/*c*	*P*21/*c*
Unit cell dimensions			
a (Å)	19.572(1)	10.253(1)	10.388(2)
b (Å)	10.289(1)	14.577(1)	14.648(2)
c (Å)	13.670(1)	8.683(1)	8.810(1)
β (°)	120.360(1)	106.957(1)	106.243(11)
Cell volume (Å^3)	2375.5(3)	1241.2(1)	1287.1(3)
Z	4	2	2
D_{calc} (g cm^{-3})	1.629	1.674	1.631
μ (mm^{-1})	1.153	0.924	3.396
F(000)	1196	642	648
θ Range	2.3–28.3	2.1–28.3	4.4–74.9
Index ranges	$-25 \leqslant h \leqslant 25$, $-10 \leqslant k \leqslant 13$, $-11 \leqslant l \leqslant 18$	$-10 \leqslant h \leqslant 12$, $-17 \leqslant k \leqslant 18$, $-11 \leqslant l \leqslant 11$	$-12 \leqslant h \leqslant 12$, $-18 \leqslant k \leqslant 18$, $-0 \leqslant l \leqslant 11$
Independent reflections	2723	2766	2632
Observed reflections [$F > 4.0\ \sigma(F)$]	2464	2663	2562
Data completeness	0.926	0.896	0.996
Maximum/minimum transmission	0.718/0.787	0.553/0.723	0.120/0.217
Number of refined parameters	141	186	187
R [$F > 4.0\ \sigma(F)$][a]	0.028	0.027	0.038
wR [$F > 4.0\ \sigma(F)$][b]	0.072	0.070	0.103
Goodness-of-fit[c]	1.08	1.02	1.08
ρ_{max}, ρ_{min} (e Å^{-3})	0.361,−0.232	0.383, −0.258	0.500, −0.542

[a] $R = \Sigma||F_o| - |F_c||/\Sigma|F_o|$.
[b] $R = \{\Sigma[w(F_o^2 - F_c^2)^2]/\Sigma[w(F_o^2)^2]\}^{1/2}$.
[c] The goodness-of-fit (GOF) equals $\{\Sigma[w(F_o^2 - F_c^2)^2]/(N_{reflections} - N_{params})^{1/2}\}$.

by full-matrix least-squares on F^2 with SHELXL-97 [14], included in the WINGX package [11]. All non-hydrogen atoms were refined with anisotropic displacement parameters. Hydrogen atoms attached to carbon and nitrogen atoms were positioned geometrically, with U_{iso} values derived from U_{eq} values of the corresponding carbon and nitrogen atoms. However, hydrogen atoms of the water molecules were detected by Fourier differences and were refined with fixed O–H and H–H distances (0.957(3) and 1.513(3) Å, respectively). The final electron density map for compound **1** contained various electron density peaks clustered in one region of the unit cell. These could not sensibly be resolved into a molecule and presumably represent a severely disordered solvent molecule. Despite exhaustive attempts at modelling this severely disordered solvent molecule, satisfactory solutions were not obtained and a diffuse solvent correction was applied using the SQUEEZE routine in PLATON [15]. The unit cell contains four cavities centered at (1/2, 1/7, 3/4), (0, 5/14, 1/4), (0, 9/13, 3/4) and (1/2, 6/7, 1/4), filled with disordered solvent, probably ethanol. The volume of each cavity is 82.7 Å^3, with a total of 25 electrons, corresponding to approximately one ethanol molecule per cavity.

3. Results and discussion

3.1. Crystal structure of the complex $[CoCl_2(TnInA)_2] \cdot C_2H_6O$ (1)

The X-ray study of **1** reveals that the crystals are made up of monoclinic cells, each one containing four complex molecules and four solvent ethanol molecules. Solvent molecules were disordered and included in the model using the SQUEEZE procedure [15]. A molecular view of the complex together with the atom numbering scheme is shown in Fig. 1, and selected bond lengths and angles are given in Table 2.

The complex molecule possesses a non-crystallographic C_2 symmetry, with the twofold axis being coincident with the bisector of the Cl–Co–Cl(a) angle. This arrangement results in the cis geometry.

The environment around the cobalt(II) atom may be described as a distorted octahedral geometry with the metal coordinated to two chlorine atoms [Co–Cl = 2.396(1) Å], two thiazoline nitrogen atoms [Co–N(1) = 2.184(1) Å] and two indazole nitrogen atoms [Co–N(3) = 2.119(1) Å]. The ligand–metal–ligand bite angles differ from the ideal value of 90°, varying between 74.6(1)° and 102.6(1)°.

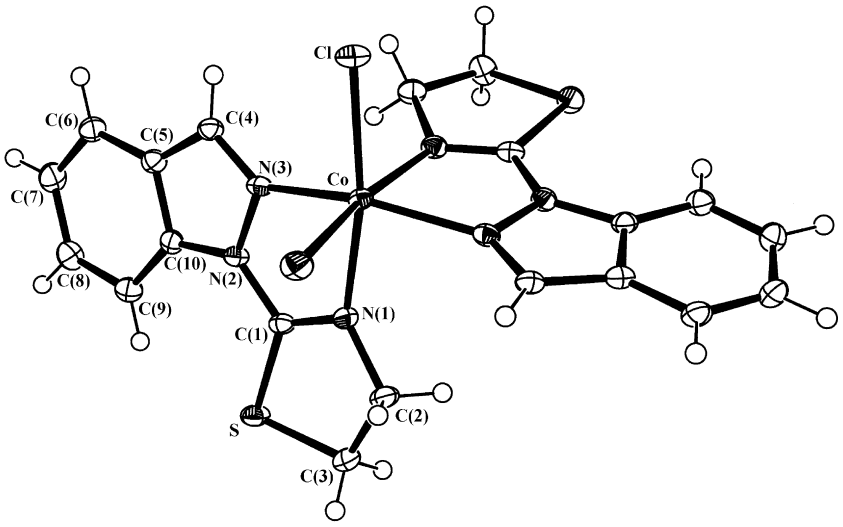


Fig. 1. Molecular structure of **1**, showing the atom-numbering scheme. The thermal ellipsoids are plotted at the 50% probability level.

Table 2
Selected bond lengths (Å), angles (°) and hydrogen-bond parameters for **1**, **3** and **4**

	1	**3**	**4**
M–Cl	2.396(1)		
M–O(1W)		2.056(1)	2.099(2)
M–NM–O(1)	2.184(1)	2.101(1)	2.085(2)
M–N(3)	2.119(1)	2.134(1)	2.185(2)
N(1)–C(1)	1.276(2)	1.276(2)	1.276(3)
N(2)–C(1)	1.386(2)	1.388(2)	1.383(2)
N(3)–N(2)	1.388(2)	1.388(2)	1.384(2)
Cl–M–Cl(a)	93.9(1)		
O(1W)–M–O(1Wa)		180	180
Cl–M–N(1)	169.6(1)		
O(1W)–M–N(1)		89.6(1)	89.6(1)
Cl–M–N(3)	95.3(1)		
O(1W)–M–N(3)		89.3(1)	88.8(1)
Cl(a)–M–N(1)	86.1(1)		
O(1Wa)–M–N(1)		90.4(1)	90.4(1)
Cl(a)–M–N(3)	102.6(1)		
O(1Wa)–M–N(3)		90.7(1)	91.2(1)
N(1)–M–N(1a)	95.7(1)	180	180
N(1)–M–N(3)	74.6(1)	76.9(1)	76.9(1)
N(3)–M–N(1a)	87.7(1)	103.1(1)	103.1(1)
N(3)–M–N(3a)	153.7(1)	180	180
C(1)–N(1)-M	115.1(1)	115.2(1)	115.7(1)
N(2)–N(3)–M	114.9(1)	111.7(1)	110.1(1)
N(1)–C(1)–N(2)	118.8(1)	119.8(1)	120.4(2)
C(1)–N(2)–N(3)	115.6(1)	116.0(1)	116.8(1)
C(1)–S–C(3)	88.9(1)	88.0(1)	88.5(1)

D–H ⋯ A	D–H (Å)	H ⋯ D (Å)	D ⋯ A (Å)	D–H ⋯ A (°)
3				
O(1W)–H(2W)⋯O(1)	0.954(5)	1.793(5)	2.718(2)	162.2(1)
O(1W)–H(1W)⋯O(2)	0.954(9)	1.839(12)	2.759(2)	161.2(1)
4				
O(1W)–H(2W)⋯O(1)	0.956(13)	1.902(19)	2.810(3)	157.9(10)
O(1W)–H(1W)⋯O(3)	0.956(6)	1.861(8)	2.780(3)	160.5(5)

The Co–Cl bond distance is comparable with the calculated average value [2.446(80) Å] for 51 six-coordinate cobalt(II) chloro-complexes with a chromophore group CoN_4Cl_2, obtained using the CONQUEST software [16] from the Cambridge Structural Database (CSD, Version v5.28, May 2007) [8]. Likewise, the Co–$N_{indazole}$ bond length is similar to those found in bis(hydrotris(indazol-1-yl)borato)-cobalt(II) chloroform solvate (1/3.5) (2.116 Å) [17], but somewhat shorter than those observed in hydrogen-tris(7-methylindazol-2-yl)borate–hydrogen-tris(3-neopentylpyrazol-1-yl) borate–cobalt (2.236 Å) [18]. The Co–$N_{thiazoline}$ bond distance is longer than that found in catena-(hexakis (μ_2-azido-*N*,*N*)-tris-2,2′-bithiazolinyl-*N*,*N*′)-tri-cobalt(II) (2.151 Å) [19], $[Co(NO_3)(PyTT)_2(H_2O)]NO_3$ (2.059 Å; 2.074 Å) [20] and $[CoCl_2(PyTn)_2]\cdot 2H_2O$ (2.097 Å) [21].

The chelate ring Co–N(1)–C(1)–N(2)–N(3) shows a conformation near to half-chair, as indicated by the parameters calculated according to Cremer and Pople [$q = 0.107$ Å; $\phi = 15.4°$] [22], with the atoms Co and N(1) deviating by −0.114 and 0.089 Å, respectively, above the plane formed by C(1), N(2) and N(3).

The thiazoline ring shows an intermediate form between envelope and half-chair with the C(2) and C(3) atoms deviating by −0.100 Å and 0.131 Å, respectively, above the plane formed by S, C(1) and N(1). This geometry is proved by the puckering parameters $q = 0.142$ Å and $\phi = 312.2°$ [22].

*3.2. Crystal structures of the complexes [(Co or Zn)(TnInA)$_2$(H$_2$O)$_2$](NO$_3$)$_2$ (**3**, **4**)*

Complex **3** crystallizes into monoclinic unit cells, each one containing two $[Co(TnInA)_2(H_2O)_2]^{2+}$ cations and four nitrate anions held by a two-dimensional hydrogen bonding network. The overall view and labelling of the atoms of the complex cation are displayed in Fig. 2. Table 2 lists the selected bond lengths, angles and hydrogen-bond parameters.

As can be observed in Fig. 2, the complex cation possesses a C_i symmetry, with an inversion centre at the cobalt atom. This arrangement results in the N(1) and N(3) atoms being cis to each other whereas the O(1W) atoms are trans. The environment around the cobalt(II) atom may be described as a distorted octahedral geometry with the ligand–metal–ligand bite angles varying between 76.9(1)° [N(1)–Co–N(3)] and 103.1(1)° [N(1a)-Co–N(3)]. The metallic atom is coordinated by two thiazoline nitrogen atoms [Co–N(1) = 2.101(1) Å], two indazole nitrogen atoms [Co–N(3) = 2.134(1) Å] and two oxygen atoms from two water molecules [Co–O(1W) = 2.056(1) Å].

The $Co–O_{water}$ bond distance is shorter than the mean value [2.099(49) Å] calculated using the data of 84 six-coordinate cobalt(II) aqua-complexes with an N_4O_2 environment in the CSD [8]. The $Co–N_{thiazoline}$ and $Co–N_{indazole}$ bond lengths are similar to those observed in complex **1**.

The chelate ring Co–N(1)–C(1)–N(2)–N(3) is essentially planar with a maximum mean plane deviation for N(1) (0.038 Å). However, the thiazoline ring shows an intermediate conformation between envelope and half-chair with the apex at C(3), deviating 0.441 Å from the mean plane formed by Co, N(1), C(1) and N(2). This geometry is proved by the puckering parameters $q = 0.278$ Å and $\phi = 321.9°$ [22].

The crystal structure presents a two-dimensional hydrogen-bonding network perpendicular to the a axis, in which oxygen atoms O(1) and O(2) from nitrate groups act as acceptors of hydrogen, whereas water molecules act as donors. A diagram showing this network is given in Fig. 3.

Complexes **3** and **4** are isostructural, crystallizing in the monoclinic system with the same space group, comparable cell dimensions and similar internal atomic coordinates. This fact is common enough among Co(II) and Zn(II) coordination compounds, as indicated in a Ref. [23]. Thus the complex cation of **4** shows a six-coordinated environment around zinc(II) with two oxygen atoms from two water molecules [Zn–O(1W) = 2.099(2) Å], two thiazoline nitrogen atoms [Zn–N(1) = 2.085(2) Å] and two indazole nitrogen atoms [Zn–N(3) = 2.185(2) Å]. The overall view and labelling of the atoms of the complex are displayed in Fig. 4. Table 2 lists the selected bond lengths, angles and hydrogen-bond parameters. The disposition of the six donor atoms is described as a distorted octahedron with a C_2 symmetry, with the twofold axis going through the zinc atom and being coincident with the Zn–O(1W) bond. The ligand–metal–ligand bite angles vary between 76.9(1)° [N(1)–Zn–N(3)] and 103.1(1)° [N(1a)–Zn–N(3)].

The $Zn–O_{water}$ bond distance is shorter than the average value [2.16(10) Å] obtained using the data of 58 six-coordinate zinc(II) complexes with an N_4O_2 environment in the CSD [8]. The $Zn–N_{indazole}$ bond length is similar to those found in bis(hydrotris(indazol-1-yl)borato)-zinc(II) dioxane solvate (1/3.5) (2.154 Å) [17]. The $Zn–N_{thiazoline}$ bond distance is similar to that found in Micacocidin A [2.050 Å] [24], [$ZnCl_2$(TdTn)] (TdTn = 2-(3,4-dichlorophenyl)imino-*N*-(2-thiazolin-2-yl)thiazolidine) [2.022 Å] [25], [$ZnCl_2$(PyTT)] (PyTT = 2-(2-pyridyl)imino-*N*-(2-thiazolin-2-yl)thiazolidine) [2.021 Å] [26] and [$ZnCl_2$(TzHy)] (TzHy = (4,5-dihydro-1,3-thiazol-2-yl)hydrazine) [2.029 Å] [27].

The chelate ring Zn–N(1)–C(1)–N(2)–N(3) is essentially planar with a maximum mean plane deviation for N(3) (0.032 Å). However, the thiazoline ring shows an intermediate conformation between envelope and half-chair with the apex at C(3), deviating 0.380 Å from the mean plane formed by Zn, N(1), C(1) and N(2). This geometry is proved by the puckering parameters $q = 0.240$ Å and $\phi = 322.7°$ [22].

The crystal structure presents a two-dimensional hydrogen-bond network perpendicular to the a axis, in which oxygen atoms O(1) and O(3) from nitrate groups act as acceptors of hydrogen, whereas water molecules act as donors. A diagram showing this network is given in Fig. 5.

Finally, it should be pointed out that the main difference in all the complexes with respect to the structure of free TnInA is due to the different degree of rotation of the thiazoline ring around the C(1)–N(2) bond, which permits coordination through N(1) [torsion angle N(1)–C(1)–N(2)–N(3) = −4.5° in **1**; −4.5° in **3**; 2.4° in **4**; −176.9° in TnInA].

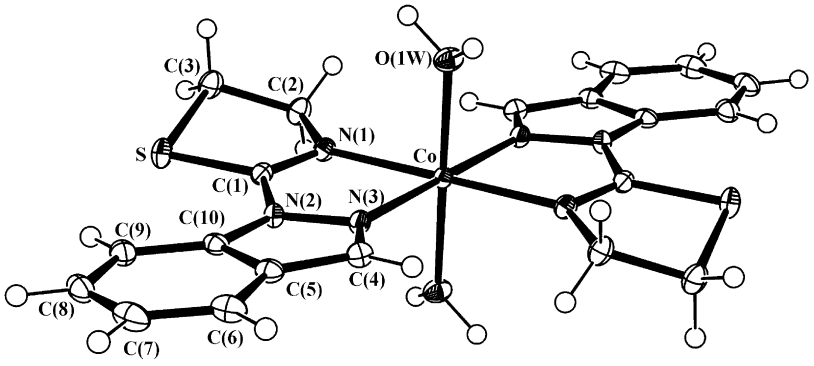


Fig. 2. Molecular structure of the cationic complex $[Co(TnInA)_2(H_2O)_2]^{2+}$ of **3**, showing the atom-numbering scheme. The thermal ellipsoids are plotted at the 50% probability level.

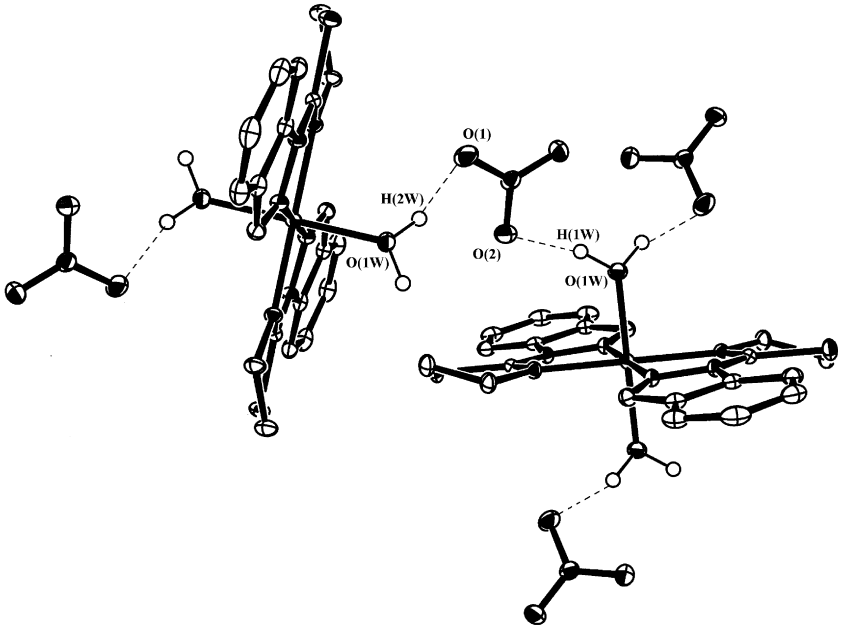


Fig. 3. View of the hydrogen bonds network of **3**.

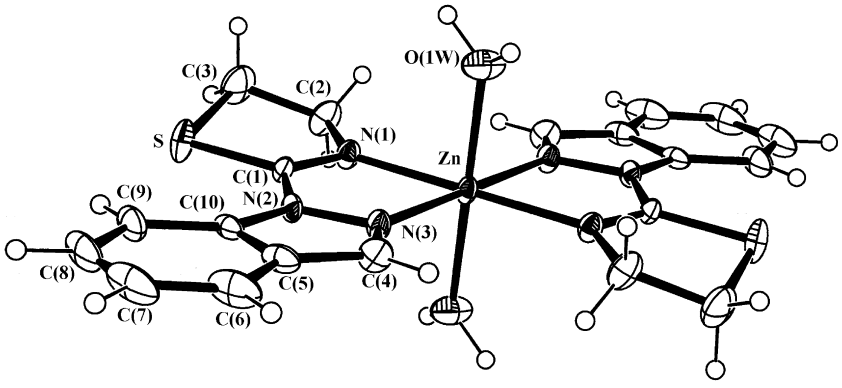


Fig. 4. Molecular structure of the cationic complex $[Zn(TnInA)_2(H_2O)_2]^{2+}$ of **4**, showing the atom-numbering scheme. The thermal ellipsoids are plotted at the 40% probability level.

3.3. Spectroscopic properties

A comparative study of the IR spectral data of the complexes with the uncomplexed ligand [9] provide meaningful information regarding the bonding sites of the primary ligand molecule. Thus, it can be observed in all the complexes that the bands assigned to the ν(C=N) vibration of the indazole ring and the in-plane stretching vibrations corresponding to ν(C=N) skeletal vibrations of the heterocyclic rings (W_1) suffer a negative shift when compared with that for the uncoordinated ligand (Table 3). This feature is indicative of coordination through the indazole and thiazoline nitrogen atoms [9,28–30].

In addition, the peaks centered at 3197 cm^{-1} in the IR spectra of complex **3**, and at 3256 cm^{-1} in the IR spectra of complex **4** are attributed to the ν(O–H) vibration of coordinated water molecules [31].

Moreover, according to the method of Lever and coll. [32], the bands registered at 1750 cm^{-1} (for **3**) and 1749 cm^{-1} (for **4**) are assigned to ($\nu_1 + \nu_4$) combination bands of the ionic nitrate group. Other bands due to the nitrate ion group are registered at 1386 cm^{-1} (ν_3), 1040 cm^{-1} (ν_1) and 829 cm^{-1} (ν_2) for **3** and at 1392 cm^{-1} (ν_3), 1041 cm^{-1} (ν_1) and 829 cm^{-1} (ν_2) for **4** [31–33].

The appearance of the new bands at low frequencies can be assigned to ν(M-ligand) modes. Tentative assignments are listed in Table 4. Thus, in the Co(II) spectra the $\nu(Co–N_{indazole})$ vibrations [34] are registered between 247 and 265 cm^{-1}, the bands in the region 212–231 cm^{-1} can be tentatively attributed to the $\nu(Co–N_{thiazoline})$ vibrations [20,21,26,35], the bands at 376 and 385 cm^{-1} in the spectrum of complex **3** are assigned to the $\nu(Co–O_{water})$ vibration [20,36–38] whereas one band due to the ν(Co–Cl) vibration [21,26,39] is found at 309 cm^{-1} for **1**. Likewise,

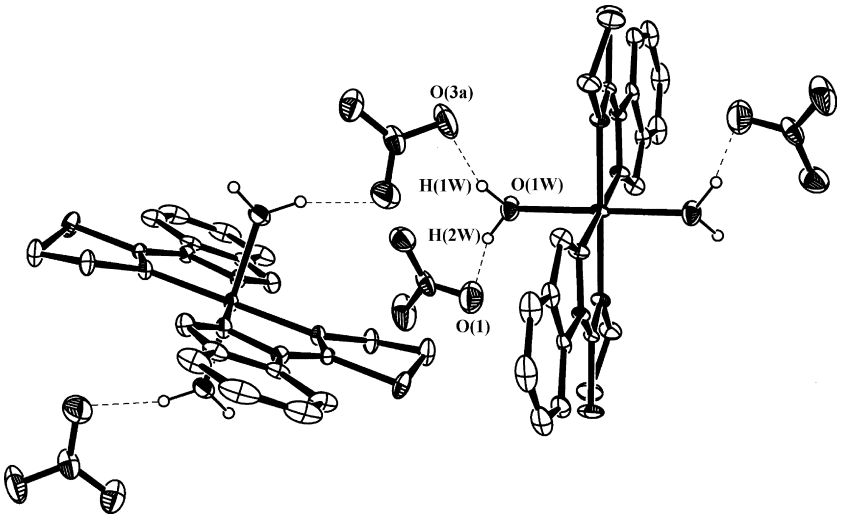


Fig. 5. View of the hydrogen bonds network of **4**.

Table 3
IR bands (cm^{-1}) with assignments for the ligand and the complexes

Compound	W_1	ν(C=N)
TnInA	1632 vs	1614 s
1	1612 vs	1612 vs
2	1608 vs	1608 vs
3	1604 vs	1604 vs
4	1608 vs	1608 vs

in the Zn(II) spectra the bands at 227–237 cm^{-1} could assigned to the $\nu(Zn–N_{indazole})$ vibrations and the band at 227 cm^{-1} to the $\nu(Zn–N_{thiazoline})$ vibrations, according to the Refs. [26,35,39–43]. Finally the band at 311 cm^{-1} in the spectrum of complex **4** is attributed to the $\nu(Zn–O_{water})$ vibration [33] and the bands at 300 and 316 cm^{-1} in the spectrum of complex **2** are assigned to the ν(Zn–Cl) vibration in accord to the literature data for this type of bond [26,35,44].

The values obtained for molar magnetic susceptibility for the cobalt(II) complexes are consistent with an octahedral environment around the metal [45]. These values were corrected for diamagnetism and temperature-independent paramagnetism to provide the fully corrected magnetic moment at room temperature ($\mu = 4.94$ BM for **1**; $\mu = 4.97$ BM for **3**).

Table 4
Far IR bands (cm^{-1}) with tentative assignments

Compound	$\nu(M–N_{thiazoline})$	$\nu(M–N_{indazole})$	ν(M–Cl)	$\nu(M–O_{water})$
1	231 s	255 s	309 m	
2	227 m	237 w	316 s 300 s	
3	225 m 212 s	265 m 247 s		385 m 376 m
4	227 s	227 s		311 s

The diffuse reflectance spectrum of **1** shows a very strong band at 32260 cm^{-1} which is assigned to the $\pi \rightarrow \pi^*$ transition of the organic ligand. Moreover, this spectrum exhibits two bands at 8870 cm^{-1} and 8050 cm^{-1} corresponding to splitting of the lowest energy transition ν_1 [$^4T_{2g}(F) \leftarrow {}^4T_{1g}(F)$] for an octahedral Co(II) complex. Therefore, the value for ν_1 has been made by calculating the baricenter of these two bands. The highest energy transition ν_3 [$^4T_{1g}(P) \leftarrow {}^4T_{1g}(F)$] is displayed at 18800 cm^{-1} in an admixture with a shoulder at 14750 cm^{-1}, which is most probably caused by a spin forbidden transition to a doublet state (^2G) [46].

The electronic spectrum of **3** gives three bands at 9190 cm^{-1}, 20240 cm^{-1} and 32680 cm^{-1}. The third of them refers to a transition of the organic ligand in a similar form to **1** whereas the first two bands are assigned to the transitions [$^4T_{2g}(F) \leftarrow {}^4T_{1g}(F)$] and [$^4T_{1g}(P) \leftarrow {}^4T_{1g}(F)$], respectively.

These results for both complexes suggest that there is an octahedral geometry around the Co(II) ion. The ligand field parameters, 10 Dq and B, were calculated using the following known relationships [47] for octahedral d^7 complexes:

$$\nu_1[{}^4T_{1g}(F) \rightarrow {}^4T_{2g}(F)] = 1/2(10Dq - 15B) + 1/2[(10Dq + 15B)^2 - 12B \cdot 10Dq]^{1/2}$$

$$\nu_3[{}^4T_{1g}(F) \rightarrow {}^4T_{1g}(P)] = [(10Dq + 15B)^2 - 12B \cdot 10Dq]^{1/2}$$

The calculated values of the ligand field parameters (10 Dq = 9547 cm^{-1} and B = 763 cm^{-1} for **1**, 10 Dq = 10376 cm^{-1} and B = 816 cm^{-1} for **3**), are in fair agreement with the predicted values for octahedral complexes of Co(II). It is also possible to notice that the position of the d–d transitions of **3** are shifted to higher energies compared to spectrum for **1** and the value obtained for 10 Dq in complex **3** is greater than that calculated for **1**. These two facts are in agreement with the chromophore groups

presents in these complexes, $[CoN_4O_2]$ for **3** and $[CoCl_2N_4]$ for **1** [20,21,37,46]. Likewise, the splitting of v_1 in **1** and the lack of splitting in **3** are in agreement with the cis and trans geometries, respectively, for these complexes [46].

4. Conclusion

In summary we have synthesized and structurally characterized Co(II) and Zn(II) complexes with 2-(indazol-1-yl)-2-thiazoline (TnInA), which acts as a bidentate ligand coordinating to the metal ion through the indazole and thiazoline nitrogen atoms. Crystallographic studies of **1**, **3** and **4** show a distorted octahedral geometry around the metal center. Elemental analysis and spectroscopic studies of **2** indicate a coordination number equal to four for a zinc(II) ion. Given that the zinc ion does not have a preferable geometry by crystal field stabilization, it can be expected that the coordination polyhedron is a tetrahedron, conditioned by steric requirements.

Finally, the results of diffuse reflectance spectroscopy for **1** and **3** are consistent with the positions in the spectrochemical series of the non-organic ligands present in both complexes (H_2O for **3** and Cl for **1**).

Acknowledgements

We thank the Junta de Extremadura (Consejería de Educación, Ciencia y Tecnología) and the FEDER [Project 2PR04A011] for financial support.

Appendix A. Supplementary material

CCDC 649504, 649505 and 649506 contain the supplementary crystallographic data for $[CoCl_2(TnInA)_2]\cdot C_2H_6O$, $[Co(TnInA)_2(H_2O)_2](NO_3)_2$ and $[Zn(TnInA)_2(H_2O)_2](NO_3)_2$. These data can be obtained free of charge via http://www.ccdc.cam.ac.uk/conts/retrieving.html, or from the Cambridge Crystallographic Data Centre, 12 Union Road, Cambridge CB2 1EZ, UK; fax: (+44) 1223 336 033; or e-mail: deposit@ccdc.cam.ac.uk. Supplementary data associated with this article can be found, in the online version, at doi:10.1016/j.poly.2007. 07.043.

References

[1] S. Bräse, C. Gil, K. Knepper, Bioorg. Med. Chem. 10 (2002) 2415.
[2] G.A. Pinna, M.A. Pirisi, J.M. Mussinu, G. Murineddu, G. Loriga, A. Pau, G.E. Grella, Farmaco 58 (2003) 749.
[3] L. Bouissane, S. El Kazzouli, S. Leonce, B. Pfeiffer, E.M. Rakib, M. Khouili, G. Guillaumet, Bioorg. Med. Chem. 14 (2006) 1078.
[4] G. Daidone, D. Raffa, B. Maggio, M.V. Raimondi, F. Plescia, D. Schillaci, Eur. J. Med. Chem. 39 (2004) 219.
[5] D.W. Robertson, W. Bloomquist, M.L. Cohen, L.R. Reid, K. Schenck, D.T. Wong, J. Med. Chem. 33 (1990) 3176.
[6] B.L. Mylari, W.J. Zembrowski, T.A. Beyer, C.E. Aldinger, T.W. Siegel, J. Med. Chem. 35 (1992) 2155.
[7] C.G. Hartinger, S. Zorbas-Seifried, M.A. Jakupec, B. Kynast, H. Zorbas, B.K. Keppler, J. Inorg. Biochem. 100 (2006) 891.
[8] I.J. Bruno, J.C. Cole, P.R. Edington, M. Kessler, C.F. Macrae, P. McCabe, J. Pearson, R. Taylor, Acta Crystallogr. Sect., B 58 (2002) 389.
[9] F.J. Barros-García, F. Luna-Giles, M.A. Maldonado-Rogado, E. Viñuelas-Zahínos, Polyhedron 25 (2006) 43.
[10] Bruker AXS Inc SADABS, version 2.03 Bruker AXS Inc., Madison, WI, 2001.
[11] L.J. Farrugia, J. Appl. Cryst. 32 (1999) 837.
[12] G.M. Sheldrick, SHELXS-86, Program for Crystal Structures Solution, University of Göttingen, Germany, 1986.
[13] M. Sheldrick, SHELXS-97, Program for Crystal Structures Solution, University of Göttingen, Germany, 1997.
[14] M. Sheldrick, SHELXL-97, Program for Crystal Structures Refinement, University of Göttingen, Germany, 1997.
[15] A.L. Spek, J. Appl. Cryst. 36 (2003) 7.
[16] F.H. Allen, Acta Crystallogr. Sect., B 58 (2002) 380.
[17] C. Janiak, S. Temizdemir, S. Dechert, W. Deck, F. Girgsdies, J. Heinze, M.J. Kolm, T.G. Scharmann, O.M. Zipffel, Eur. J. Inorg. Chem. (2000) 1229.
[18] A.L. Rheingold, B.S. Haggerty, G.P.A. Yap, S. Trofimenko, Inorg. Chem. 36 (1997) 5097.
[19] T. -Fu Liu, D. Fu, S. Gao, Y.-Z. Zhang, H.-L. Sun, G. Su, Y.-J. Liu, J. Am. Chem. Soc. 125 (2003) 13976.
[20] A. Bernalte-García, F.J. García-Barros, F.J. Higes-Rolando, F. Luna-Giles, M.M. Pacheco-Rodríguez, E. Viñuelas-Zahínos, Bioinorg. Chem. Appl. 2 (2004) 307.
[21] A. Bernalte-García, A.M. Lozano-Vila, F. Luna-Giles, R. Pedrero-Marín, Polyhedron 25 (2006) 1399.
[22] D. Cremer, J.A. Pople, J. Am. Chem. Soc. 97 (1975) 1354.
[23] D.A. Clemente, A. Marzotto, F. Benetollo, Polyhedron 21 (2002) 2161.
[24] H. Nakai, S. Kobayashi, M. Ozaki, Y. Hayase, R. Takeda, Acta Crystallogr. Sect., C 55 (1999) 54.
[25] F.J. Barros-García, A. Bernalte-García, A.M. Lozano-Vila, F. Luna-Giles, J.A. Pariente, R. Pedrero-Marín, A.B. Moratinos, J. Inorg. Biochem. 100 (2006) 1861.
[26] A. Bernalte-García, F.J. García-Barros, F.J. Higes-Rolando, F. Luna-Giles, Polyhedron 20 (2001) 3315.
[27] A. Bernalte-García, M.A. Díaz-Díez, F.J. García-Barros, F.J. Higes-Rolando, A.M. Pizarro-Galán, J.D. Martín-Ramos, C. Valenzuela-Calahorro, Polyhedron 16 (1997) 297.
[28] F.J. Barros-García, A. Bernalte-García, A.M. Lozano-Vila, F. Luna-Giles, E. Viñuelas-Zahínos, Polyhedron 24 (2005) 129.
[29] M. Shakir, S.P. Varkey, F. Firdaus, P.S. Hameed, Polyhedron 13 (1994) 2319.
[30] J. Nelson, S. Martin Nelson, W.D. Perry, J. Chem. Soc., Dalton Trans. (1976) 1282.
[31] K. Nakamoto, Infrared and Raman Spectra of Inorganic and Coordination Compounds, fifth ed., Wiley, New York, 1997.
[32] A.B.P. Lever, E. Mantovani, B.S. Ramaswamy, Can. J. Chem. 49 (1971) 1957.
[33] J.R. Ferraro, Low-Frequency Vibrations of Inorganic and Coordination Compounds, Plenum Press, New York, 1971.
[34] M. Hvastijová, R. Boča, J. Kohout, L. Jäger, I. Císařová, J. Kožíšek, Inorg. Chim. Acta 343 (2003) 217.
[35] Y.J. Weaver, J.A. Weaver, J. Inorg. Nucl. Chem. 37 (1975) 1309.
[36] R. Battistuzzi, Polyhedron 4 (1985) 993.
[37] G. Alzuet, S. Ferrer, J. Borrás, A. Castiñeiras, X. Solans, M. Font-Bardía, Polyhedron 11 (1992) 2849.
[38] J.M. Salas, C. Enrique, M.A. Romero, K. Takagi, K. Aoki, Y. Miyashita, I. Suh, Polyhedron 11 (1992) 2903.
[39] A. Chadghan, J. Pons, A. Caubet, J. Casabó, J. Ros, A. Álvarez-Larena, J.F. Piniella, Polyhedron 19 (2000) 855.
[40] A. Bernalte-García, F.J. García-Barros, F.J. Higes-Rolando, A.M. Pizarro-Galán, C. Valenzuela-Calahorro, Thermochim. Acta 339 (1999) 95.

[41] C. Preti, G. Tosi, J. Chem. Soc., Dalton Trans. (1976) 685.
[42] J. Reedijk, Inorg. Chim. Acta 3 (1969) 517.
[43] A. Cingolani, D. Martín, F. Marchetti, C. Pettinari, M. Ricciutelli, B.W. Skelton, A.H. White, Inorg. Chim. Acta 350 (2003) 641.
[44] J.A. Weaver, P. Hambright, P.T. Talbert, E. Kang, A.N. Thorpe, Inorg. Chem. 9 (1970) 268.
[45] B.N. Figgis, J. Lewis, Prog. Inorg. Chem. 6 (1967) 185.
[46] A.B.P. Lever, Inorganic Electronic Spectroscopy, Elsevier, Amsterdam, 1984.
[47] D.K. Rastogi, K.C. Sharma, S.K. Dua, M.P. Teotia, J. Inorg. Nucl. Chem. 37 (1975) 685.

2. Experimental

2.1. General procedures

The flexible ligand 1,2-bis(1,2,4-triazol-1-yl)ethane was synthesized according to the literature method [27]. All other reagents and solvents employed were commercially available and were used as received without further purification. The C, H, N microanalyses were carried out with a Perkin–Elmer 240C analyser. IR spectra were obtained for KBr pellets on a Nicolet 170SX FT-IR spectrophotometer in the 4000–400 cm^{-1} region. Thermogravimetric data were collected on a Thermal Analyst 2100 TA Instrument and SDT 2960 Simutaneous TGA-DTA Instrument in flowing dinitrogen at a heating rate 10 °C/min. Variable-temperature magnetic susceptibility measurement and field dependence of magnetization were performed with a quantum Design MPMS XL-5 SQUID system. The experimental susceptibilities were corrected for the diamagnetism of the constituent atoms (Pascal's tables).

2.2. Syntheses of $[Co(bte)_2(dca)_2]_n$ (1) and $\{[Co(bte)(dca)_2]\cdot H_2O\}_n$ (2)

A methanolic solution (15 ml) of bte (0.164 g, 1.0 mmol)was added to an aqueous solution (15 ml) of $Co(NO_3)_2\cdot 6H_2O$ (0.291 g, 1.0 mmol) and $NaN(CN)_2$ (0.178 g, 2.0 mmol) with stirring. The mixture was stirred at room temperature and the resultant solution was filtered. After the filtrate was allowed to stand in air for 3 days, light red single crystals of **1** were obtained. Standing was continued in air for the mother solution for several more days, and deep red single crystals of **2** were obtained. *Anal.* Calc. for **1** $C_{16}H_{16}CoN_{18}$: C, 37.00; H, 3.11; N, 48.55. Found: C, 36.88; H, 3.07; N, 48.52%. *Anal.* Calc. for **2** $C_{10}H_{10}CoN_{12}O$: C, 32.18; H, 2.70; N, 45.04. Found: C, 32.06; H, 2.59; N, 44.93%. IR data (cm^{-1}) for **1**: 3445w, 3125w, 2272m, 2218m, 2160s, 1532m, 1435w, 1385m, 1339m, 1285m, 1215w, 1130m, 1015w, 884w, 664 m and 529 w. IR data (cm^{-1}) for **2**: 3472w, 3113w, 2307m, 2238m, 2195s, 2164s, 1609w, 1528w, 1443w, 1385m, 1354m, 1285m, 1134m, 992w, 671w and 525w.

2.3. Crystal structure determination

All data collections were performed at a temperature of 193(2) K on a Rigaku Mercury CCD diffractometer with the ω-scan technique. The structures were solved by direct methods and refined with the full-matrix least-squares technique using the SHELXS-97 and SHELXL-97 programs [28]. Anisotropic thermal parameters were assigned to all non-hydrogen atoms. The hydrogen atoms of the bte ligands were generated geometrically (C–H 0.93 Å for triazole and 0.97 Å for ethane) and those of the water molecules were located from difference maps. Crystallographic data are listed in Table 1. Selected bond lengths and angles are listed in Table 2.

Table 1
Crystallographic data for complexes **1** and **2**

	1	**2**
Empirical formula	$C_{16}H_{16}CoN_{18}$	$C_{10}H_{10}CoN_{12}O$
Formula weight	519.40	373.23
Temperature (K)	193	193
Wavelength (Å)	0.71073	0.71073
Crystal system	monoclinic	orthorhombic
Space group	$P2_1/n$	$P2_12_12_1$
a (Å)	8.469(4)	9.625(3)
b (Å)	8.345(4)	9.641(3)
c (Å)	15.429(7)	16.634(5)
α (°)	90	90
β (°)	92.409(7)	90
γ (°)	90	90
V (Å^3)	1089.5(8)	1543.5(8)
Z	2	4
$F(000)$	530	756
ρ (Mg m^{-3})	1.583	1.606
μ (mm^{-1})	0.836	1.140
Data/restrain/parameters	2485/0/160	3519/3/225
Goodness-of-fit S	1.214	1.017
R_1 [$I > 2\sigma(I)$]	0.0566	0.0343
WR_2 (all data)	0.0960	0.0703

Table 2
Selected bond lengths (Å) and angles (°) for complexes **1** and **2**; **1** (i) $-x$, $-y$, $-z$; (ii) $-x$, $-y-1$, $-z$; (iii) x, $y+1$, z; **2** (i) $-x+1$, $y+1/2$, $-z+1/2$; (ii) $x-1/2$, $-y+1/2$, $-z$; (iii) $x-1/2$, $-y+3/2$, $-z$

1			
Co(1)–N(3)	2.124(2)	Co(1)–N(3)^{i}	2.124(2)
Co(1)–N(6)^{ii}	2.165(2)	Co(1)–N(6)^{iii}	2.165(2)
Co(1)–N(7)	2.132(3)	Co(1)–N(7)^{i}	2.132(3)
N(3)–Co(1)–N(3)^{i}	180.00(18)	N(3)–Co(1)–N(6)^{ii}	92.66(9)
N(6)^{ii}–Co(1)–N(6)^{iii}	180.0	N(7)–Co(1)–N(7)^{i}	180.00(19)
N(3)–Co(1)–N(7)	91.32(9)	N(7)–Co(1)–N(6)^{ii}	94.16(9)
2			
Co(1)–N(3)	2.139(2)	Co(1)–N(6)^{ii}	2.125(2)
Co(1)–N(7)	2.142(2)	Co(1)–N(9)^{iii}	2.145(2)
Co(1)–N(10)	2.128(2)	Co(1)–N(12)^{i}	2.090(2)
N(3)–Co(1)–N(9)^{iii}	175.92(9)	N(10)–Co(1)–N(7)	178.86(9)
N(12)^{i}–Co(1)–N(6)^{ii}	178.57(9)	N(3)–Co(1)–N(7)	88.69(9)
N(10)–Co(1)–N(3)	90.37(9)	N(7)–Co(1)–N(9)^{iii}	87.90(9)
N(10)–Co(1)–N(9)^{iii}	93.07(8)	N(6)^{ii}–Co(1)–N(3)	90.08(8)
N(6)^{ii}–Co(1)–N(7)	89.64(9)	N(6)^{ii}–Co(1)–N(9)^{iii}	87.66(8)
N(6)^{ii}–Co(1)–N(10)	90.99(8)	N(12)^{i}–Co(1)–N(3)	91.12(8)
N(12)^{i}–Co(1)–N(7)	91.16(9)	N(12)^{i}–Co(1)–N(9)^{iii}	91.19(9)
N(12)^{i}–Co(1)–N(10)	88.22(8)		

3. Results and discussion

3.1. Syntheses and characterization

The C≡N stretching vibrations of $[N(CN)_2]^-$ are 2272, 2218 and 2160 cm^{-1} in **1**, and are assigned to $\nu_{sym}+\nu_{asym}$ (C≡N), ν_{asym} (C≡N) and ν_{sym} (C≡N), respectively. The C≡N stretching vibrations of $[N(CN)_2]^-$ are 2307, 2238, 2195 and 2164 cm^{-1} in **2**, suggesting $[N(CN)_2]^-$ acts as a μ-$_{1,5}$ bridge [29].

Thermal analysis shows that polymer **1** is stable up to 211 °C, and begins to decompose above this temperature.

Polymer **2** displays that the solvent water molecule is lost in a continuous fashion (Obsd., 4.5; Calc., 4.8%) in the temperature range 84–170 °C. Then complex begins to decompose.

3.2. Crystal structure

The crystal structure of **1** is isostructural to $[Mn(bte)_2(dca)_2]_n$ [23] and $[Zn(bte)_2(dca)_2]_n$ [24], and is similar to that of the polymers $\{[Co(bte)_2(NCO)_2](H_2O)\}_n$, $[Co(bte)_2(NCS)_2]_n$ [21] and $\{[Cd(bte)_2(H_2O)_2](H_2O)_2(ClO_4)_2\}_n$ [22]. The complex molecule displays center symmetry and the cobalt(II) atom lies on an inversion center (Fig. 1). The coordination geometry of the cobalt(II) atom is a distorted compressed octahedron, and coordinates with four nitrogen atoms from the triazole rings of four symmetry-related bte ligands and two *trans*-nitrogen atoms from two symmetry-related monodentate dca ligands. The ligand bte exhibits the *gauche* conformation in **1**. The dihedral angle between the planes of the two triazole rings of one bte ligand is 57.9(1)°. The cobalt atoms are linked by bte ligands *via* the nitrogen atoms in the 4-positions of the two triazole rings. The ligand bte is twisted during coordination, and the N(1)–C(5)–C(6)–N(4) torsion angle is 58.2(3)°. Two strands of bte ligands are wrapped around one another and are held together by cobalt(II) atoms, forming an infinite double-chain structure. Each chain consists of 18-membered spiro-fused rings, in which two cobalt(II) atoms are joined *via* two bte molecules. The chains extend along the *b* axis, and all of the Co(II) atoms in one chain are on the axial line (Fig. 2). The Co···Co separation across the bridging bte ligand is equal to the *b*-axis translation, 8.345 Å.

Compound **2** crystallizes in the chiral space group $P2_12_12_1$, formed by the coordination polymer with the absolute structure parameter 0.018(14). The structure of **2** is depicted in Fig. 3. Each cobalt(II) atom has a distorted octahedral coordination geometry, and coordinates with two exodentate nitrogen atoms at the 4-position of the triazole rings of two symmetry-related bte ligands [Co(1)–N(3), 2.139(2) Å; Co(1)–N(6)^{ii}, 2.125(2) Å] and four nitrogen atoms from four symmetry-related dca ligands [Co(1)–N(7), 2.142(2) Å; Co(1)–N(9)^{iii}, 2.145(2) Å; Co(1)–N(10), 2.128(2) Å; Co(1)–N(12)^{i}, 2.090(2) Å]. The bte ligand exhibits the *gauche* conformation. The dihedral angle between the planes of the two triazole rings of one bte ligand is 121.4(1)°. The bte ligand is twisted during coordination, and the N(1)–C(5)–C(6)–N(4) torsion angle is 53.5(3)°. Each bte ligand bridges two cobalt(II) atoms *via* two 4-position nitrogen atoms of the triazole rings and each dca ligand bridges two cobalt(II) atoms in the μ-$_{1,5}$dca mode. Each cobalt atom links six adjacent cobalt(II) atoms through four μ-$_{1,5}$-dca ligands and two bridging bte ligands and a three-dimensional network is formed (Fig. 4). The adjacent Co···Co distances are 7.759 Å, 7.858 Å and 6.809 Å for Co(dca)Co of the N(7) dca ligand, Co(dca)Co of the N(10) dca ligand and Co(bte)Co, respectively. The Co···Co separation (6.809 Å) *via* the bte bridges in **2** is shorter than the corresponding value (8.345 Å) in **1**. There is a hydrogen bonding interaction between the solvent water molecule and the uncoordinated N(2) atom at the 2-position of the triazole ring of bte (O(1)···N(2) 2.922(5) Å, O(1)–HWA···N(2) 147(7)°.

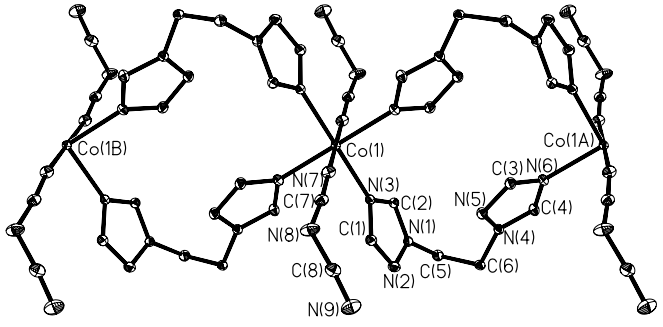


Fig. 1. The coordination environment around the cobalt(II) center in **1** with 30% thermal ellipsoids.

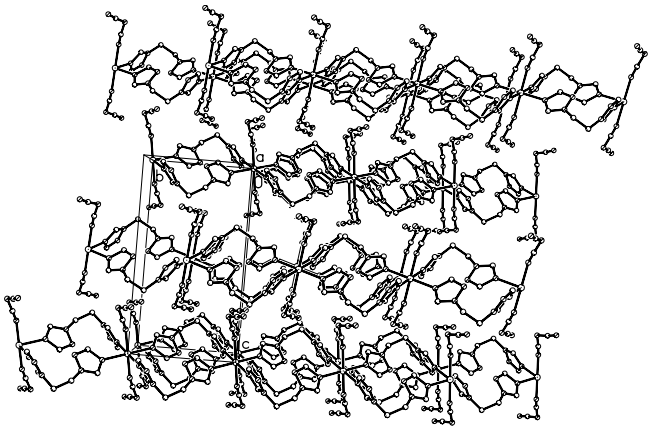


Fig. 2. The cell packing of **1** viewing along the *a* direction.

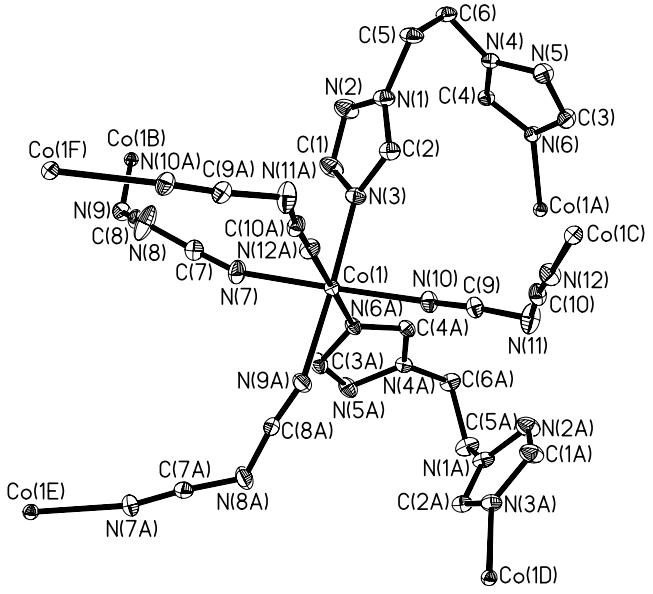


Fig. 3. The coordination environment around the cobalt(II) center in **2** with 30% thermal ellipsoids.

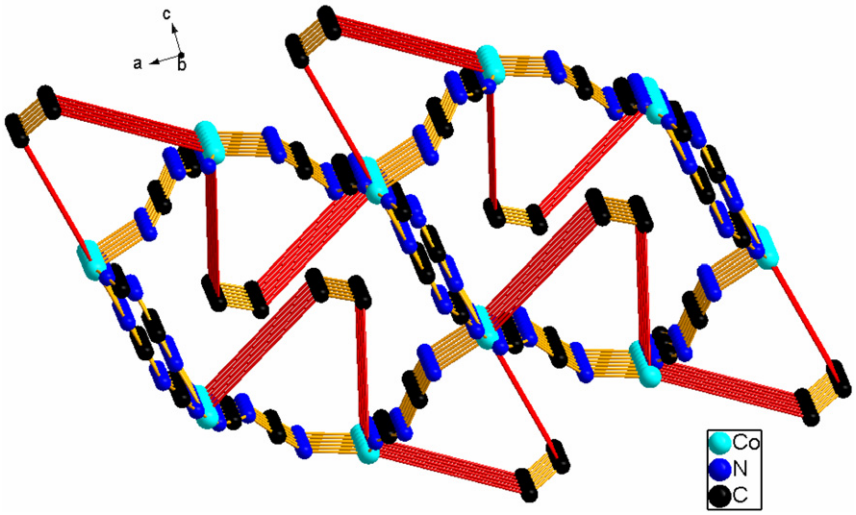


Fig. 4. Schematic view of the three-dimensional network of **1**. The representation of the bte ligands is simplified by showing the ethylene atoms.

The three-dimensional network structure of **2** is completely different from that of the similar complexes $[M(dca)_2(bpp)]_n$ (M=Co, Mn, Zn and Cd, bpp = 1,3-bis(4-pyridyl)propane) [30], in which adjacent metal ions are triply linked by two μ-1,5-dca and one bpp bridge, and a sinusoidal chain is formed. Previously we synthesized six Co-bte coordination polymers $\{[Co(bte)_2(H_2O)_2](NO_3)_2\}_n$, $\{[Co(bte)(H_2O)_2(NCO)_2](H_2O)_2\}_n$, $\{[Co(bte)_2(NCO)_2](H_2O)\}_n$, $[Co(bte)_2(NCS)_2]_n$, $\{[Co(bte)(H_2O)_2(NCS)_2][Co(bte)_2(NCS)_2]\}_n$ [21] and $[Co(bte)(NCS)_2]_n$ [20], which consist of a two-dimensional (4,4) network, single chain, double chain, double chain, a combination of single chain and double chain, and two-dimensional (4,4) network, respectively.

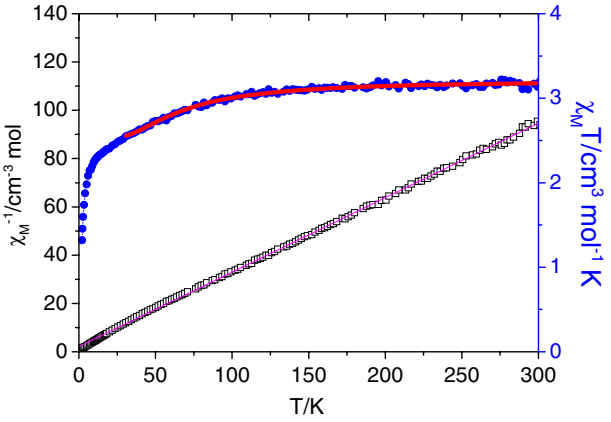


Fig. 5. Temperature dependence of $\chi_M T$ and $1/\chi_M$ for **1**.

3.3. Magnetic properties

The molar magnetic susceptibility χ_M of **1** is measured in the temperature range 2–300 K in a field of 20 KOe. The $\chi_M T$ value is 3.2 $cm^3\ mol^{-1}$ K at 300 K, which is significantly larger than the spin-only value of high-spin cobalt(II), 1.875 $cm^3\ mol^{-1}$ K, indicating a contribution of the orbital momentum typical for the $^4T_{1g}$ ground state. Upon cooling, $\chi_M T$ decreases slowly to 2.73 $cm^3\ mol^{-1}$ K at 18 K, and then decreases rapidly and reaches 1.32 $cm^3\ mol^{-1}$ K at 2 K (Fig. 5). The magnetic susceptibility obeys the Curie–Weiss law with the Weiss constant, $\theta = -0.57$ K, and the Curie constant, $C = 2.80\ cm^3\ mol^{-1}$ K. From the fitted Curie constant, C, one can deduce the g value to be about 2.45.

From the structural information, we know that the Co(II) ions are well separated, so we can treat the magnetic data by considering a mononuclear Co^{2+} with a spin–orbit coupling parameter λ ($H = -\lambda LS$) in a molecular-field approximation. The χ_{mono} for mononuclear Co^{2+} in an octahedral environment can be calculated from Eq. (1), with $x = \lambda/k_B T$ [31,32]. The parameter A gives a measure of the crystal field strength relative to the inter-electronic repulsions and it is equal to 1.5 for a weak crystal field and 1.0 for a strong field. Considering the molecular-field approach with zJ as the total exchange coupling between Co^{2+} ions, we can fit our experimental data with Eq. (2) [33].

$$\chi_{mono} = \frac{1}{T} \times \frac{\frac{7(3-A)^2x}{5} + \frac{12(2+A)^2}{25A} + \left\{\frac{2(11-2A)^2x}{45} + \frac{176(2+A)^2}{675A}\right\} \times \exp\left(\frac{-5Ax}{2}\right) + \left\{\frac{(5+A)^2x}{9} - \frac{20(2+A)^2}{27A}\right\} \exp(-4Ax)}{\frac{8x}{3}\left\{3 + 2\exp\left(\frac{-15Ax}{2}\right) + \exp(-14Ax)\right\}} \quad (1)$$

$$\chi = \frac{\chi_{mono}}{1 - (2zJ/Ng^2\beta^2)\chi_{mono}} \quad (2)$$

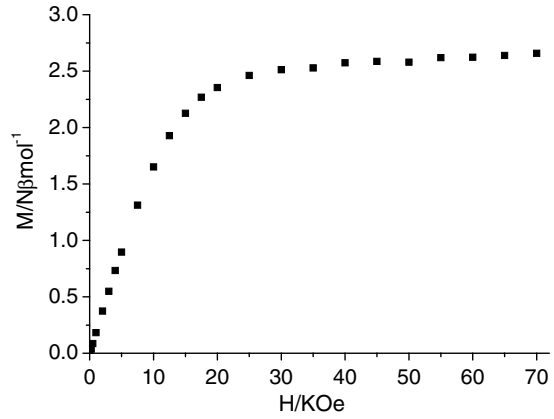


Fig. 6. Field dependence of magnetization curve from 0 to 70 k for **1** at 1.8 K.

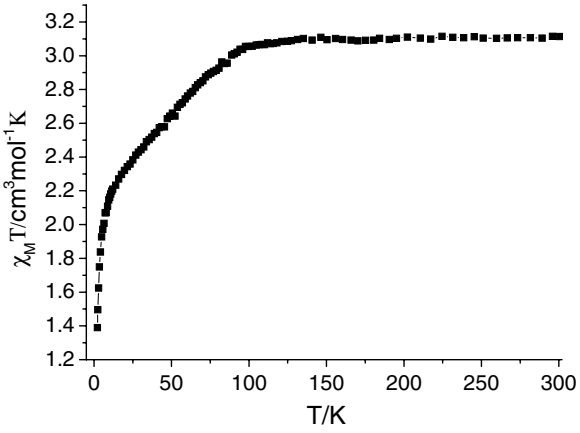


Fig. 7. Temperature dependence of $\chi_M T$ for **2**.

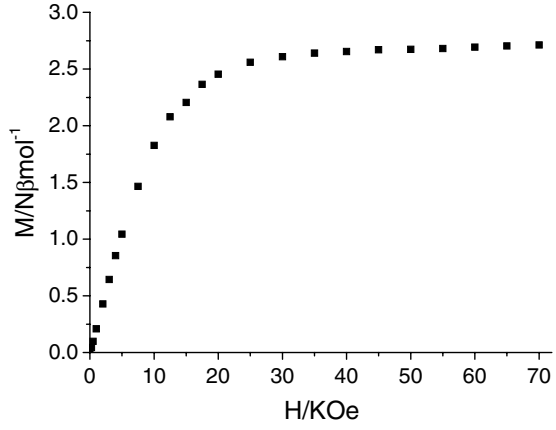


Fig. 8. Field dependence of magnetization curve from 0 to 70 k for **2** at 1.7 K.

In Eqs. (1) and (2), N, g, β, k_B and T have their usual meanings. The best fitting of the susceptibility data in the temperature range 30–300 K gives $\lambda = -104(2)\ cm^{-1}$, $A = 1.24(1)$ and $zJ = 1.33(7)\ cm^{-1}$ with $R = 4.9 \times 10^{-5}$ [$R = [\sum(\chi_{obs} - \chi_{calcd})^2 / \sum(\chi_{obs})^2]$. The field dependence of the magnetization of **1** measured at 1.8 K shows a nearly linear increase below 20 KOe and reaches a value of 2.66 $N\beta$ at 70 KOe (Fig. 6).

The molar magnetic susceptibility χ_M of **2** is measured in the temperature range 2–300 K in a field of 20 KOe. The $\chi_M T$ value remains almost constant (3.05–3.11 $cm^3\ mol^{-1}\ K$) in the temperature range 100–300 K, which is significantly larger than the spin-only value of high-spin cobalt(II), 1.875 $cm^3\ mol^{-1}\ K$, indicating a contribution of the orbital momentum typical for the $^4T_{1g}$ ground state, and decreases gradually upon cooling to 2.21 $cm^3\ mol^{-1}\ K$ at 12 K, and then decreases rapidly and reaches 1.39 $cm^3\ mol^{-1}\ K$ at 2 K (Fig. 7). The $\chi_M T$ value shows no obvious magnetic coupling between the Co(II) ions. Typically very weak antiferromagnetic coupling between the metal ions is observed for $\mu_{1,5}$-dca bridging systems [1–9,31]. The field dependence of the magnetization of **2** measured at 1.7 K shows a nearly linear increase below 20 KOe and reaches a value of 2.71 $N\beta$ at 70 KOe (Fig. 8), showing a typical paramagnetic behavior without any sign of long range ordering of **2**.

4. Conclusion

Using the anionic co-ligand dca and the flexible bis(triazole) ligand bte and Co^{2+}, we synthesized two novel cobalt(II) coordination polymers, $[Co(bte)_2(dca)_2]_n$ (**1**) and $\{[Co(bte)(dca)_2]\cdot H_2O\}_n$ (**2**). **1** is a double-chain containing metallocycles of $[Co_2(bte)_2]$. In **2**, each Co(II) center is bonded by two bridging bte ligands and four dca ligands as μ-1,5-dca in different orientations in the 3D network. The magnetic properties of these polymers were studied.

Acknowledgement

This work was supported by the Natural Science Foundation of China (No. 20671066, 20221101, 20490210), the Jiangsu Province (No. BK2006049).

Appendix A. Supplementary material

CCDC 221766 and 221767 contain the supplementary crystallographic data for **1** and **2**. These data can be obtained free of charge via http://www.ccdc.cam.ac.uk/conts/retrieving.html, or from the Cambridge Crystallographic Data Centre, 12 Union Road, Cambridge CB2 1EZ, UK; fax: (+44) 1223-336-033; or e-mail: deposit@ccdc.cam.ac.uk. Supplementary data associated with this article can be found, in the online version, at doi:10.1016/j.poly.2007.07.044.

References

[1] S.R. Batten, P. Jensen, B. Moubaraki, K.S. Murray, R. Robson, Chem. Commun. (1998) 439.
[2] P. Jensen, S.R. Batten, B. Moubaraki, K.S. Murray, Chem. Commun. (2000) 793.

[3] S.R. Marshall, C.D. Incarvito, J.L. Manson, A.L. Rheingold, J.S. Miller, Inorg. Chem. 39 (2000) 1969.
[4] T. Kusaka, T. Ishida, D. Hashizume, F. Iwasaki, T. Nogami, Chem. Lett. (2000) 1146.
[5] A. Mohamadou, G.A. van Albada, H. Kooijman, B. Wieczorek, A.L. Spek, J. Reedijk, New J. Chem. 27 (2003) 983.
[6] B.W. Sun, S. Gao, B.Q. Ma, D.Z. Niu, Z.M. Wang, J. Chem. Soc., Dalton Trans. (2000) 4187.
[7] H.L. Sun, S. Gao, B.Q. Ma, G. Su, Inorg. Chem. 42 (2003) 5399.
[8] S.C. Manna, A.K. Ghosh, J. Ribas, M.G.B. Drew, C.N. Lin, E. Zabgrando, N.R. Chaudhuri, Inorg. Chim. Acta 359 (2006) 1395.
[9] L.F. Jones, L. O'Dea, D.A. Offermann, P. Jensen, B. Moubaraki, K.S. Murray, Polyhedron 25 (2006) 360.
[10] J.G. Haasnoot, Coord. Chem. Rev. 200-202 (2000) 131.
[11] B. Ding, L. Yi, H.L. Gao, P. Cheng, D.Z. Liao, S.P. Yan, Z.H. Jiang, Inorg. Chem. Commun. 8 (2005) 102.
[12] Q.G. Zhai, X.Y. Wu, S.M. Chen, C.Z. Lu, W.B. Yang, Cryst. Growth Des. 6 (2006) 2126.
[13] J.H. Zhou, U.M. Cheng, Y. Song, Y.Z. Li, Z. Yu, X.T. Chen, Z.L. Xue, X.Z. You, Inorg. Chem. 44 (2005) 8011.
[14] W. Ouellette, M.H. Yu, C.J. O'Connor, D. Hagraman, J. Zubieta, Angew. Chem., Int. Ed. 45 (2006) 3497.
[15] J.P. Zhang, X.M. Chen, Chem. Commun. (2006) 1689.
[16] Effendy, F. Marchetti, C. Pettinari, R. Pettinari, B.W. Skelton, A.H. White, Inorg. Chem. 42 (2003) 112.
[17] L.F. Tang, Z.H. Wang, J.F. Chai, W.L. Jia, Y.M. Xu, J.T. Wang, Polyhedron 19 (2000) 1949.
[18] G.A.V. Albada, R.C. Guijt, J.G. Haasnoot, M. Lutz, A.L. Spek, J. Reedijk, Eur. J. Inorg. Chem. (2000) 121.
[19] Q.H. Zhao, H.F. Li, X.F. Wang, Z.D. Chen, New J. Chem. 26 (2002) 1709.
[20] X.Y. Wang, B.L. Li, X. Zhu, S. Gao, Eur. J. Inorg. Chem. (2005) 3277.
[21] X. Zhu, H.Y. Ge, Y.M. Zhang, B.L. Li, Y. Zhang, Polyhedron 25 (2006) 1875.
[22] B.L. Li, X. Zhu, J.H. Zhou, Y.F. Peng, Y. Zhang, Polyhedron 23 (2004) 3133.
[23] J.H. Zhou, X. Zhu, Y.N. Zhang, Y. Zhang, B.L. Li, Inorg. Chem. Commun. 7 (2004) 949.
[24] B.L. Li, B.Z. Li, X. Zhu, L.M. Zhu, Y. Zhang, Acta Crystallogr. C59 (2003) m350.
[25] B.L. Li, Y.F. Peng, B.Z. Li, Y. Zhang, Chem. Commun. (2005) 2333.
[26] Y.F. Peng, H.Y. Ge, B.Z. Li, B.L. Li, Y. Zhang, Cryst. Growth Des. 6 (2006) 994.
[27] J. Torres, J.L. Lavandera, P. Cabildo, R.M. Claramunt, J. Elguero, J. Heterocycl. Chem. 25 (1988) 771.
[28] G.M. Sheldrick, SHELX-97 and SHELXL-97, University of Göttingen, Germany, 1997.
[29] J. Kohout, L. Jäger, M. Hvastijová, J. Kožíšek, J. Coord. Chem. 51 (2000) 169.
[30] E.-Q. Gao, S.-Q. Bai, Z.-M. Wang, C.-H. Yan, J. Chem. Soc., Dalton Trans. (2003) 1759.
[31] H.L. Sun, Z.M. Wang, S. Gao, Inorg. Chem. 44 (2005) 2169.
[32] B.N. Figgis, M. Gerloch, J. Lewis, F.E. Mabbs, G.A. Webb, J. Chem. Soc. A (1968) 2086.
[33] O. Kahn, Molecular Magnetism, VCH, New York, 1993.

above studies in which the phenoxy acetic acid derivatives (**HL_1**, **HL_2** and **HL_3**) with carboxylate groups to form extended solid state structures has been explored. We reported herein the six mixed-ligand mononuclear complexes of Cu(II), Co(II), Co(III) and Mn(II).

2. Experimental

2.1. Materials and methods

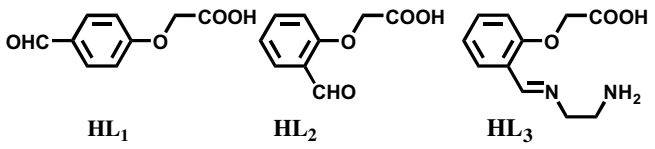
The aldehydes and the liquid olefins were distilled prior to use. Metal salts and solid olefins are used as supplied from commercial sources. All the solvents were purified prior to use by standard procedure. The IR spectra were recorded on a *Perkin–Elmer-Spectrum One* FT-IR Spectrometer with KBr disks in the range 4000–400 cm^{-1}. The thermo gravimetric analyses (TGA) of the compounds were performed by using an *SDTA 851e TGA* thermal analyzer (Mettler Toledo) with a heating rate of 2 °C per min in a N_2 atmosphere. Optical spectra were recorded in CH_3CN on a *Perkin–Elmer-Lambda 25-UV–Visible Spectrometer* at 298 K. Solid-state magnetic susceptibility of the complexes at room temperature was recorded using *Sherwood Scientific balance MSB-1*. Solution electrical conductivity measurements measured with a *Systronics Conductivity meter 306*. Elemental analyses were done using *Carlo Erba 1108* and *Perkin–Elmer series II 2400* instrument. GCMS analyses were performed using a *Perkin–Elmer Clarus* 500 gas chromatograph coupled with the *Perkin–Elmer Clarus 500* mass spectrometer.

2.2. Synthesis of ligands HL_{1-3}

Both the ligands (Scheme 1) (4-formyl-phenoxy)-acetic acid (**HL_1**) [24] and (2-formyl-phenoxy)-acetic acid (**HL_2**) [25] were synthesized following the reported procedure.

2.2.1. Synthesis of ligands HL_3

To a stirred solution of **HL_2** (111 mg, 0.5 mmol) in MeOH (10 ml) was added ethylene diamine (30 mg, 0.5 mmol) in MeOH (2 ml) at ice-cold condition. Mixture was then refluxed for 15 min and then allowed to cool to RT. Slow evaporation results the formation of yellow crystals, which was washed several times with cold MeOH. Yield 65%, m.p.: 186 °C; ESI–MS, *m/z* (%): 222 (86) $[HL_3]^+$; *Anal.* Calc. for $C_{11}H_{14}N_2O_3$: C, 59.45; H, 6.35; N, 12.60. Found: C, 59.63; H, 6.31; N 12.55%. ^1H NMR (400 MHz, $CDCl_3$, 25 °C, TMS) δ (ppm): 3.2 (*t*, 2H), 3.8 (*t*, 2H), 4.7 (*s*, 2H), 6.8–7.6 (*m*, 4H), 8.2 (*s*, 1H), ^{13}C NMR (100 MHz, $CDCl_3$, 25 °C, TMS) δ (ppm): 42.8, 58.3, 79.8, 116.8, 121.5, 123.7, 131.2, 132.6, 161.4, 165.2, 174.1. FT-IR (KBr): 3442 ν(OH); 3351 $\nu(NH_2)$; 1765 ν(C=O); 1602 ν(C=N); 1490 ν(C=C); 1164 ν(COC) cm^{-1}.



Scheme 1. The phenoxy acetic acid derivatives **HL_1**, **HL_2** and **HL_3**.

2.3. Synthesis of complexes

2.3.1. Synthesis of $[Co(L_1)_2(H_2O)_4]$ (1a)

To a stirred solution of **HL_1** (18 mg, 0.1 mmol) in MeOH (5 ml) was added $CoCl_2 \cdot 6H_2O$ (23.8 mg, 0.1 mmol) in water (5 ml) at RT. The resulting solution was continued to stir for another 30 min. Slow evaporation of the reaction mixture afforded the complex **1a** as red crystals. These were employed directly for the X-ray crystallographic study. Yield: 85%, *Anal.* Calc. for $CoC_{18}H_{22}O_{12}$: C, 44.18; H, 4.53; Co, 12.04. Found: C, 44.24; H, 4.51; Co, 12.11%. Molar conductance (in CH_3CN): 4.1 S cm^2 mol^{-1}; solid-state RT $\mu_{eff} = 5.22$ BM; UV–Vis: 456 nm (sh) $[^4A_{1g} \rightarrow {}^4A_{2g}(F)]$, 511 nm $[^4T_{1g}(F) \rightarrow {}^4T_{1g}(P)]$.

2.3.2. Synthesis of $[Mn(L_1)_2(H_2O)_4]$ (1b)

Complex **1b** was synthesized following the same procedure as **1a**, only $MnCl_2 \cdot 4H_2O$ (20 mg, 0.1 mmol) was used instead of Co-salt. A light pink colored crystal of **1b** was studied by X-ray crystallography. Yield: 78%. *Anal.* Calc. for $MnC_{18}H_{22}O_{12}$: C, 44.54; H, 4.56; Mn, 11.32. Found: C, 44.51; H, 4.52; Mn, 11.39%. Solid-state RT $\mu_{eff} = 5.91$.

2.3.3. Synthesis of $[Cu(L_1)_2(H_2O)_2]$ (1c)

Complex **1c** was synthesized following the same procedure as **1a**, only $CuCl_2 \cdot 2H_2O$ (27 mg, 0.2 mmol) was used instead of Co-salt. A blue colored crystal of **1c** was studied by X-ray crystallography. Yield: 55%. *Anal.* Calc. for $CuC_{18}H_{18}O_{10}$: C, 47.21; H, 3.96; Cu, 13.87. Found: C, 47.17; H, 3.99; Cu, 13.92%; UV–Vis: 720 nm $[^2E \rightarrow {}^2T_2]$, 900 nm (sh).

2.3.4. Synthesis of $[Cu(L_1)_2(H_2O)(Py)_2]$ (1d)

Complex **1d** was synthesized following the same procedure as **1c**, only pyridine (24 mg, 0.3 mmol) was added after addition of metal salt solution and stirring was continued for additional 45 min in a closed container at RT. Dark blue crystal of **1d** was studied by X-ray crystallography. Yield: 42%. *Anal.* Calc. for $CuC_{30}H_{26}N_2O_9$: C, 57.92; H, 4.21; N, 4.50; Cu, 10.21. Found: C, 57.96; H, 4.25; N 4.46; Cu, 10.27%.

2.3.5. Synthesis of $[Cu(L_3)(H_2O)Cl] \cdot H_2O$ (3a)

To a stirred solution of **HL_3** (11 mg, 0.05 mmol) in MeOH (3 ml) was added $CuCl_2 \cdot 2H_2O$ (7 mg, 0.05 mmol) in water (5 ml) at RT. The resulting solution was refluxed with continues stirring for another 15 min. The mixture was cooled to RT and slow evaporation of the reaction mixture afforded the complex **3a** as blue crystals. These crystals were used directly for the X-ray crystallographic study. Yield: 52%. *Anal.* Calc. for $CuC_{11}H_{18}N_2O_5Cl$: C,

36.97; H, 5.07; N, 7.84; Cu, 17.78. Found: C, 36.91; H, 5.02; N, 7.91; Cu, 17.72%.

2.3.6. Synthesis of $[Co(Sal)(H_2O)(Py)_3]\cdot 2ClO_4\cdot H_2O$ (**3b**)

To a stirred solution of **HL_3** (11 mg, 0.05 mmol) in MeOH (3 ml) was added $Co(ClO_4)_2\cdot 6H_2O$ (18.3 mg, 0.05 mmol) in water (5 ml) at RT. After 45 min of stirring at RT, excesses pyridine was added to this mixture. The resulting mixture was continued to stir for additional 45 min in a closed container at ~60 °C. Green crystal of **3b** was studied by X-ray crystallography. The perchlorate salts must be handled with care as this form potentially explosive mixtures with organic compounds. Yield: 48%. *Anal.* Calc. for $CoC_{25}H_{24}N_3O_{12}Cl_2$: C, 43.62; H, 3.51; N, 6.10; Co, 8.56. Found: C, 43.66; H, 3.54; N 6.17; Co, 8.51%; UV–Vis: 648 nm (ε 101 M^{-1} cm^{-1}) and 364 nm (ε 1420 M^{-1} cm^{-1}).

2.4. X-ray crystallography

The intensity data were collected using a Bruker SMART APEX-II CCD diffractometer, equipped with a fine focus 1.75 kW sealed tube Mo Kα radiation (λ = 0.71073 Å) at 273(3) K, with increasing ω (width of 0.3° per frame) at a scan speed of 3 s/frame. The SMART software was used for data acquisition. Data integration and reduction were undertaken with SAINT and XPREP [26] software. Multi-scan empirical absorption corrections were applied to the data using the program SADABS [27]. Structures were solved by direct methods using SHELXS-97 [28] and refined with full-matrix least squares on F^2 using SHELXL-97 [28]. All non-hydrogen atoms were refined anisotropically. Most of the hydrogen atoms were located from the difference Fourier maps and refined isotropically. While other hydrogen atoms are added in a fixed geometry. Selected crystallographic data summarized in Table 1.

3. Results and discussion

3.1. Crystal structure of $[Co(L_1)_2(H_2O)_4]$ (**1a**) and $[Mn(L_1)_2(H_2O)_4]$ (**1b**)

The complexes **1a** and **1b** were crystallized from methanol/water (1:1) mixture as red and pink colored crystals respectively. The molecular structures with atom numbering scheme of the Co(II) complex (**1a**) and Mn(II) complex

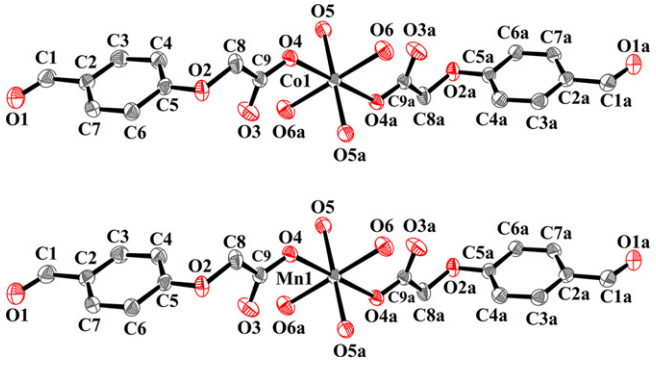


Fig. 1. ORTEP plot of complexes **1a** and **1b** with atom numbering scheme. Selected bond lengths for **1a**: Co(1)–O(4) = 2.1424(10), Co(1)–O(5) = 2.1029(14), Co(1)–O(6) = 2.0841(13); **1b**: Mn(1)–O(4) = 2.2301(9), Mn(1)–O(5) = 2.2018(12), Mn(1)–O(6) = 2.1596(12).

Table 1
Crystallographic refinement parameters of complexes **1a**–**3b**

Parameters	1a	1b	1c	1d	3a	3b
Empirical formula	$C_{18}H_{22}CoO_{12}$	$C_{18}H_{22}MnO_{12}$	$C_{18}H_{18}CuO_{10}$	$C_{28}H_{26}CuN_2O_9$	$C_{11}H_{17}ClCuN_2O_5$	$C_{22}H_{14}ClCoN_3O_8$
CCDC number	616704	616709	616707	616706	616708	616705
Fw	489.29	485.30	457.87	598.06	356.27	552.82
Temperature (K)	298(2)	298(2)	298(2)	298(2)	298(2)	298(2)
Radiation	Mo Kα	Mo Kα	Mo Kα	Mo Kα	Mo Kα	Mo Kα
Wavelength (Å)	0.71073	0.71073	0.71073	0.71073	0.71073	0.71073
Crystal system	monoclinic	monoclinic	triclinic	monoclinic	orthorhombic	monoclinic
Space group	$P2_1/c$	$P2_1/c$	$P\bar{1}$	$C2/c$	$Pbca$	$C2/c$
a (Å)	13.1134(4)	13.2560(2)	5.1099(6)	15.0747(9)	7.4235(17)	11.6418(3)
b (Å)	9.8258(3)	9.86910(10)	7.0884(9)	5.9673(3)	18.289(4)	24.3575(7)
c (Å)	8.0525(2)	8.10040(10)	13.0500(17)	30.8247(17)	21.406(5)	17.9014(5)
α (°)	90.00	90.00	80.172(3)	90.00	90.00	90.00
β (°)	106.2470(10)	106.4830(10)	87.763(3)	98.996(4)	90.00	94.838(2)
γ (°)	90.00	90.00	77.215(3)	90.00	90.00	90.00
V (Å^3)	996.13(5)	1016.18(2)	454.20(10)	2738.7(3)	2902.4(11)	5058.1(2)
Z	2	2	1	4	8	8
μ	0.932	0.709	1.260	0.849	1.698	0.827
F(000)	392	446	235	1188	1337	3248
Goodness-of-fit (S)	1.040	0.948	0.982	0.974	0.959	1.164
Final R indices	$R_1 = 0.0307$	$R_1 = 0.0301$	$R_1 = 0.0311$	$R_1 = 0.0436$	$R_1 = 0.0569$	$R_1 = 0.0551$
[$I > 2\sigma(I)$]	$wR_2 = 0.0481$	$wR_2 = 0.1071$	$wR_2 = 0.1046$	$wR_2 = 0.1117$	$wR_2 = 0.1365$	$wR_2 = 0.1660$
R indices (all data)	$R_1 = 0.0415$	$R_1 = 0.0356$	$R_1 = 0.0318$	$R_1 = 0.0788$	$R_1 = 0.0874$	$R_1 = 0.0979$
	$wR_2 = 0.493$	$wR_2 = 0.1157$	$wR_2 = 0.1057$	$wR_2 = 0.1300$	$wR_2 = 0.1607$	$wR_2 = 0.1913$

(**1b**) are shown in Fig. 1. Single-crystal X-ray analyses revealed both **1a** and **1b** are neutral and mononuclear in nature. In both the complex, metal ion is in similar coordination environment and each of them exhibits an octahedral geometry with MO_6 coordination. Bond angles and distances of mononuclear complex indicate a slightly distorted octahedral coordination with *trans*-geometry. Among the six O atoms around the metal ion, two carboxylato oxygen atoms are of ligand $\mathbf{L}_1$ and four oxygen atoms are from water molecules. Metal bound four water molecules form the equatorial planes and $\mathbf{L}_1$ is bonded in the axial positions. The little elongation of the M–O4 bond lengths agree with the bulkier nature of the ligand compared to the water molecules. The Co(II)/Mn(II) atom lies on a centre-of-inversion in the crystal structure. All the O atoms of the water and the Co or Mn atom lie exactly on the O_4 plane.

As shown in Fig. 1, carboxylate act as a uni-dentate ligand. In the crystal lattice, the coordinated water molecules are in two different environments within the 3D network. One set of water molecules has chelate type intramolecular hydrogen bonding with carbonyl group of carboxylate. The other set is hydrogen bonded to aldehyde group in the *para* position. This results in the formation of hydrogen bonded 2D tape type network along crystallographic *a* axis (see Supporting information). In the 2D tape network, the two neighboring M(II) ions show a distance of 13.113 Å (in **1a**) and 13.256 Å (in **1b**). However, the distance between benzene ring is 5.908 Å (in **1a**) and 5.945 Å (in **1b**) and they form an oval-shaped metallocycle unit. Uncoordinated O3 atom of carboxylic acid is intramolecularly hydrogen bonded to the nearest coordinated water molecule. Due to this each axial M–O4 bond is slightly tilted towards the M–O6 bond ($\angle$O(6a)–Co(1)–O(4) = 88.26 and $\angle$O(6a)–Mn(1)–O(4) = 87.92). In addition to this, both the carboxylate oxygen atoms are intermolecularly hydrogen bonded to the neighboring coordinated water molecules. Overall hydrogen bonding results the formation of staircase network viewed along crystallographic *a* axis (Fig. 2), Individual molecule is arranged in zig-zag fashion and helps to make the alternate steps of the staircase network.

The IR spectrum of complex **1a** shows typical antisymmetric and symmetric stretching bands of carboxylate groups at 1710 and 1280 cm^{-1}, respectively. The separation (Δ) between $\nu_{asym}(CO_2)$ and $\nu_{sym}(CO_2)$ is 430 cm^{-1}, indicating the presence of uni-dentate coordination modes in **1a** [29]. This result is in good agreement with the crystal structure analysis. The OH stretching for water appearing at 3571 cm^{-1} and 3483 cm^{-1} shows that there are two different types of environment for water molecules.

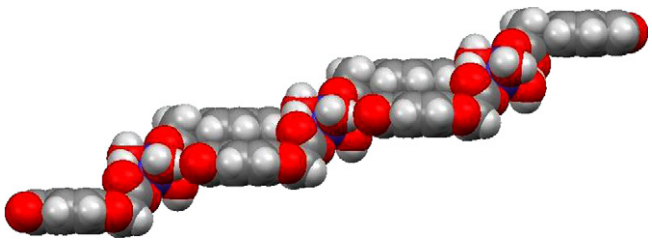


Fig. 2. Stair case network of **1a** along *a* axis.

Solid-state arrangement of complex **1b** is similar to that of **1a**, they are isostructural. The Mn–O bond distances for equatorially coordinated hetero atoms are typical for Mn(II) octahedral complexes [30,31]. It also shows the formation of similar 2D hydrogen bonded tape as well as the 3D stair case network viewed along *a* axis. The separation (Δ) between $\nu_{asym}(CO_2)$ and $\nu_{sym}(CO_2)$ is 405 cm^{-1} in the IR spectrum of **1b**, which also confirms the uni-dentate binding nature of the carboxylic acid group. In both the complex, the overall structure is stabilized by several weaker C–H···O and C–H···π interactions in addition to the stronger O–H···O hydrogen bonding (see Supporting information). Complex **1b** is very faint pink in color and have no absorption bands in the visible region, in accordance with the high-spin d^5 electronic configuration of the Mn(II) ion. This complex is very stable in spite of being based on Mn(II). They may be stored in normal laboratory atmosphere without taking any precautions for more than two months.

3.2. Crystal structure of $[Cu(L_1)_2(H_2O)_2]$ (**1c**) and $[Cu(L_1)_2(H_2O)(Py)_2]$ (**1d**)

The molecular structures with atom numbering scheme of both the Cu(II) complexes **1c** and **1d** are shown in Fig. 3.

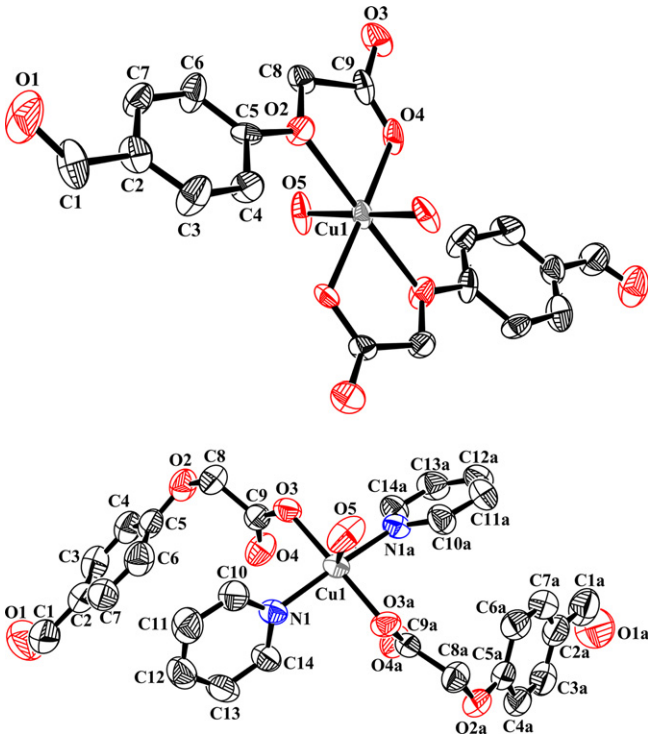


Fig. 3. ORTEP plot of complexes **1c** and **1d**. Selected bond lengths for **1c**: Cu(1)–O(2) = 2.4141(14), Cu(1)–O(4) = 1.9487(15), Cu(1)–O(5) = 1.9457(15); **1d**: Cu(1)–N(1) = 2.015(3), Cu(1)–O(3) = 1.962(2), Cu(1)–O(5) = 2.184(3).

In complex **1c** the Cu(II) atom is in the MO_6 coordination environment. It is ligated by six oxygen atoms: two carboxylato oxygen and two ether oxygen from ligand $\mathbf{L}_1$ and two oxygen from water molecules. The carboxylato oxygen atoms bonds more strongly with the Cu(II) than ether oxygen atoms. Complex **1c** has two five-membered O,O-chelate rings. Bond angles and distances of neutral, mononuclear complex indicate a slightly distorted octahedral coordination with *trans*-geometry. The bond distances and bond angles involving the metal ions are similar with the similar type of coordination environment [32,33]. The shortening of the Cu–O4 bond lengths agree with the stronger chelating ability of the carboxylate oxygen compared to ether oxygen atoms. Due to the formation of five-membered chelate rings both the axial bonds are inclined towards the carboxylate donor in the equatorial plane ($\angle$O(3)–Cu(1)–O(10) = 88.6 and $\angle$O(7)–Cu(1)–O(6) = 74.70). Carboxylate oxygen atoms and water molecules form the equatorial plane while weakly bonded ether oxygen atoms occupy the axial positions. Cu(II) atom exactly lie within the equatorial plane without any deviation from the plane. The strong O–H···O and weaker C–H···O and C–H···π type intermolecular hydrogen bonding play a major role in stabilizing the solid-state structure. Each carboxylate oxygen atom form hydrogen bond with coordinated water molecules, which result in the formation of 2D sheet of metallacycle along *b* axis (see supporting information). All the Cu atoms form linear arrays in all three directions. Shortest Cu–Cu distance in each layer of 2D sheet is 7.088 Å, while shortest Cu–Cu distance between layers is 13.050 Å. Adjacent layers run in the same direction along the *b* axis. Each aldehyde oxygen forms two C–H···O type bond which leads to the formation of 3D double-staircase network in solid-state (Fig. 4). The ν(COC) band near 1105 cm^{-1} is shifted by 35 cm^{-1} in the FT-IR spectrum of complex **1c** to a lower frequency than the free ligand, which is also confirmed form X-ray structure analysis. Carboxylic acid is uni-dentate ligand here also, which shows the separation (Δ) between $\nu_{asym}(CO_2)$ and $\nu_{sym}(CO_2)$ stretching frequency of 395 cm^{-1}. Solid-state magnetic moment of **1c** is 1.85 BM. This value is consistent with a Cu(II) complex having an octahedral coordination geometry [34,35].

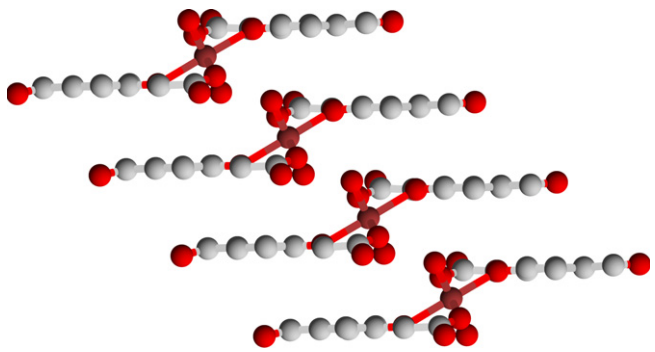


Fig. 4. Double-staircase network along *b* axis in **1c**.

Weaker coordination of the ether oxygen to the Cu(II) centre is lost, when stronger coordinating ligand pyridine is added during complex preparation. Complex **1d** crystallizes as a neutral monomer. The overall coordination environment changes from distorted octahedral to square pyramidal with *trans* geometry (Fig. 3), where the O atom of the water occupies the axial position. Square plane is formed by N_2O_2 coordination from $\mathbf{L}_1$ and pyridine molecules. In this complex also, $\mathbf{L}_1$ ligand coordinates to the copper in a uni-dentate fashion. Selected bond length and bond angels confirm the slightly distorted square pyramidal mononuclear Cu(II) complex. The equatorial Cu–O and Cu–N bond lengths are comparable with square-pyramidal CuN_2O_3 coordination spheres [36,37]. The axial Cu–O(5) bond length (2.184(3) Å) is consistent with the trend observed in other square-pyramidal Cu(II) complexes [38]. Cu(II) lies in the N_2O_2 mean plane with out any deviation. Both the ligands are bent in the opposite direction with respect to the coordinated water molecule that results in the formation of V-shape architecture. Fig. 5 shows the formation of 2D tape structure along *b* axis via formation of strong O–H···O hydrogen bond between carboxylate oxygen and water molecule. Shortest Cu–Cu distance in the same plane is 8.106 Å whereas shortest Cu–Cu distance between adjacent planes is 15.412 Å. It is also interesting to note that the pyridine molecules in the basal plane are twisted such that they are inclined at an angle of 38.93° from a common plane. This puckering brings the carbonyl group of the carboxylic acid group to the proximity of a hydrogen atom present at the 3-position of a coordinated pyridine molecule, resulting in a weak C–H···O interaction in the lattice. Due to steric crowding, two basal pyridines do not remain in the same plane. Water molecules are arranged in opposite direction on adjacent layer *i.e.* adjacent layer propagate along *b* axis in the opposite direction. Adjacent 2D tape is connected through C–H···O type

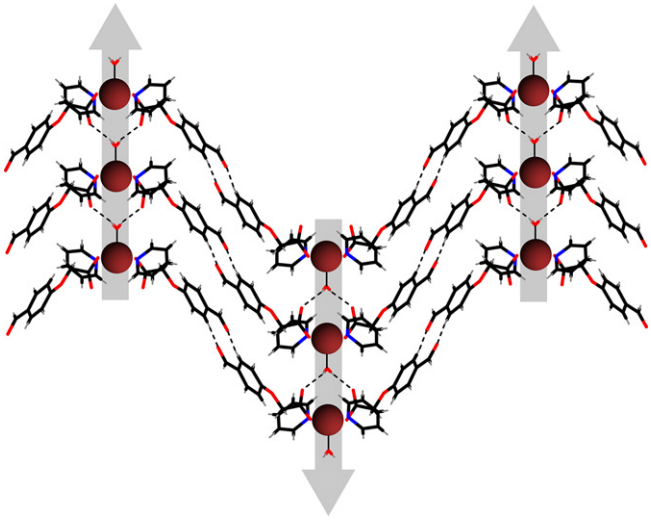


Fig. 5. Packing of **1d** along *b* axis showing O–H···O and C–H···O interactions.

hydrogen bond involving the aldehyde groups (Fig. 5), In contrast to the complex **1c**, benzene ring of the ligand in **1d** form π–π stacking interactions with another benzene ring in the adjacent layer. Upon complex formation in-pane ring deformation frequency of pyridine at 604 cm^{-1} is shifted to 643 cm^{-1} [39]. Although the electronic spectra of the copper complexes with multidentate Schiff base ligands are not in general good indicators of geometry [40], but act as supporter of it. The solid-state Nujol mull absorption spectrum for **1d** appeared at 650, 340 and 244 nm. The broad absorption band at 650 nm is attributable to a copper ion in square pyramidal chromophore CuN_2O_3 [41]. This broad visible absorption band at 650 nm is shifted slightly to a lower energy (678 nm) in acetonitrile solution, consistent with square pyramidal geometry in solution phase. The complex displays two strong absorption bands at 340 and 244 nm in solid which are clearly $\sigma(N) \rightarrow Cu(II)$ LMCT in origin and these two bands are shifted to 348 and 248 nm, respectively, in solution. The solid-state magnetic moment number for **1d** is 1.91, which is typical [42] of a discrete mononuclear Cu(II) complex.

3.3. Crystal structure of $[Cu(L_3)(H_2O)Cl] \cdot H_2O$ (**3a**)

Complex **3a** crystallizes as a neutral monomer. The molecular structures with atom numbering scheme of the Cu(II) complex is shown in Fig. 6. In the complex Cu(II) atom is in the N_2O_3Cl coordination environment. Here all six coordination site is occupied by six different coordination group. Three oxygen atoms ligate it: one carboxylato oxygen, one ether oxygen from ligand L_3 and one from water molecule. Two nitrogen atoms are from imine and primary amine groups. The carboxylato oxygen atoms bonds more strongly with the Cu(II) than ether and water oxygen atoms. The geometry of the ligand forced the ether oxygen to form a bond with the Cu(II) in more strongly nature than water molecule, which is not common to our knowledge. Complex **3a** has two five-member O,O and N,N-chelate rings along with one six-member N,O-chelate ring. Bond angles and distances of this mixed-ligand mononuclear complex indicate a slightly distorted octahedral coordination [18]. Water oxygen atom and chloride ion occupy the axial positions. Cu(II) atom exactly lie within the N_2O_2 equatorial plane without any deviation from the plane. Due to the formation two five-member and one six-member chelate rings in the same side of the complex, both the axial bonds are inclined towards the benzene ring of the donor in the equatorial plane. Uncoordinated carboxylate oxygen form hydrogen bond with neighboring coordinated water molecule. Hydrogen of NH_2 group simultaneously forms hydrogen bond with coordinated carboxylate oxygen atom and crystal water molecule.

Chloride ion form relative weaker hydrogen bond with both coordinated and uncoordinated water molecules (see Supporting information). The conventional strong O–H···O, N–H···O hydrogen bonding along with unconventional weaker C–H···O, C–H···Cl type intermolecular hydrogen bonding and π···π interactions form 3D zig-zag network (Fig. 7). All the benzene rings of the ligand form continuous π-stacking along *a* axis. Overall network is formed by 2D sheet arrangement of metallacycle along *a* axis. All the Cu atoms form rectangular boxes when viewed along *b* axis with a Cu–Cu distance of 9.347 Å and 7.848 Å, respectively. Each of the crystal water is acting as single acceptor and double donor, which stabilize the overall network.

In aqueous solution, complex has a λ_{max} value of 619 nm ($\varepsilon = 46\ M^{-1}\ cm^{-1}$) in the visible region due to a d–d transition and a λ_{max} value of 244 nm ($\varepsilon = 5055\ M^{-1}\ cm^{-1}$) in the UV region due to a LMCT transition. As these values are far from that of aqueous $CuCl_2$ at 819 nm, it is reasonable to assume that at least most of complex species of **3a** are not dissociated in solution.

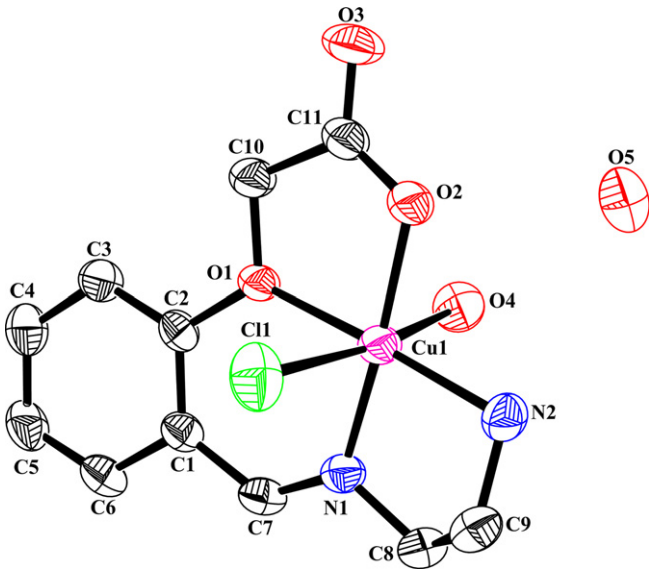


Fig. 6. ORTEP plot of Complex **3a**. Selected bond lengths are Cu(1)–O(1) = 2.051(2), Cu(1)–O(2) = 1.933(3), Cu(1)–O(4) = 2.529(3), Cu(1)–Cl(1) = 2.7102(12), Cu(1)–N(1) = 1.940(3) and Cu(1)–N(2) = 2.004(3).

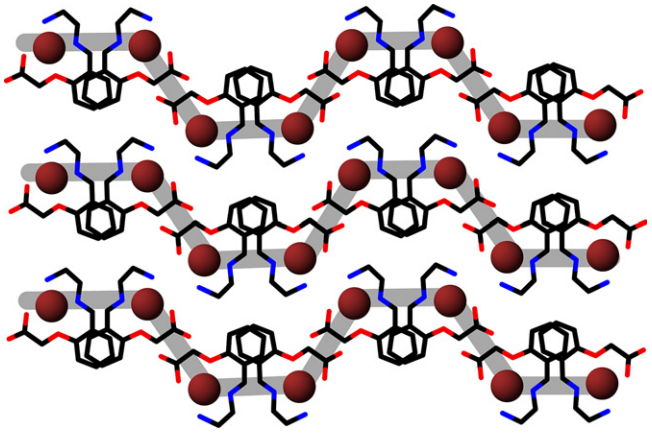


Fig. 7. Packing of **3a** along *a* axis.

3.4. Crystal structure
$[Co(Sal)(H_2O)(Py)_3]\cdot 2ClO_4\cdot H_2O$ (**3b**)

When $\mathbf{L_3}$ was treated with $Co(ClO_4)_2$ salt in open atmosphere with subsequent treatment of excesses pyridine, we got salicylaldehyde Co(III) complex **3b**. Both the Schiff base and ether linkage has been cleaved and Co(II) is oxidized to Co(III) species during complex formation in open atmospheric condition. Unit cell contains one mononuclear Co(III) complex, one water and two perchlorate ions. Fig. 8 shows the ORTEP plot of complex **3b** without the counter anions. The geometry of the complex is distorted octahedral. Three pyridine nitrogen atoms and phenolate oxygen form the equatorial plane while axial positions are occupied by aldehyde and water oxygen. Pyridine molecules in the *trans* position are almost orthogonal to each other with an torsion angle ∠C23–N4–N2–C10 = 86.10°. There is no deviation of Co(III) from N_3O basal plane. π-stacking interaction between pyridine rings forms the dimmer.

Crystal water forms hydrogen bonds with two perchlorate anions and coordinated water molecule in single acceptor–double donor way. Overall metallacycle formed 2D MOF along *ab* plane by water and perchlorate anion (Fig. 9). Overall, 3D mosaic structure is obtained via formation of different types of hydrogen bonds (see Supporting information). All the Co(III) atoms form rectangular boxes along *b* axis with a Co–Co distance of 11.642 Å and 6.819 Å, respectively.

A strong peak in FT-IR spectrum of **3b** in 1625 cm^{-1} is attributable to the η^1-bonded aldehyde (C=O) stretching vibrations. Another strong peak at 1118 cm^{-1} is attributed to the ClO_4^- ion.

3.5. Thermal and powder XRD analysis

Both **1a** and **1b** decomposed thermally in a number of steps. These complexes show successive thermal release of coordinated water molecules and the CO_2 followed by complete decomposition of the complex. The robustness of the framework is reflected in the thermo gravimetric analysis (TGA). TG analysis of complex **1a** in N_2 atmosphere shows the release of four coordinated water molecules (50–150 °C; Δm = 14.66% Calc.; 15.68% found) and two CO_2 molecules from the two coordinated carboxylate groups (230–420 °C; Δm = 21.00% Calc.; 20.93% found) (Fig. 10), which is in good agreement with the X-ray crystal structure. Complete decomposition is achieved at ~600 °C. The DSC-plot shows two endothermic peaks at 60 °C and 100 °C due to the loss of water molecules. It also shows two exothermic peaks at 260 °C and 330 °C due to the decomposition of the carboxylic acid groups. For complex **1b**, dehydration occurs at same temperature range that of **1a**, but decarboxylation occurs at 230–420 °C.

Thermal analysis of complex **1c** shows 8.69% (calculated 7.82%) weight loss in the 120–180 °C due to the removal of two coordinated water molecules. It also shows the releases of two CO_2 molecules in the temperature range of 260–320 °C associated with 21.42% weight loss (calculated 20.75%). Complete decomposition takes place at 580 °C. DSC profile shows two endothermic and one exothermic

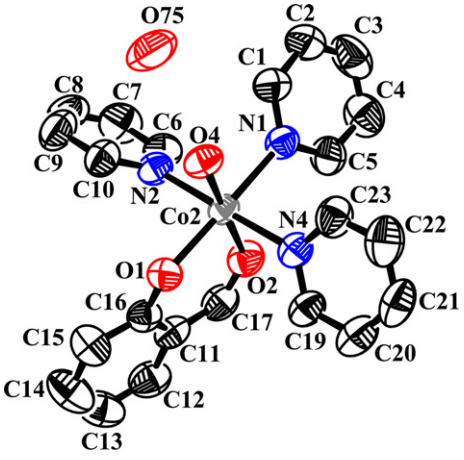


Fig. 8. ORTEP plot of complex **3b**, perchlorate anions are omitted for clarity. Selected bond lengths are Co(2)–O(1) = 2.036(2), Co(2)–O(2) = 2.055(2), Co(2)–O(4) = 2.067(3), Co(2)–N(1) = 2.124(3), Co(2)–N(2) = 2.104(3), Co(2)–N(4) = 2.105(3).

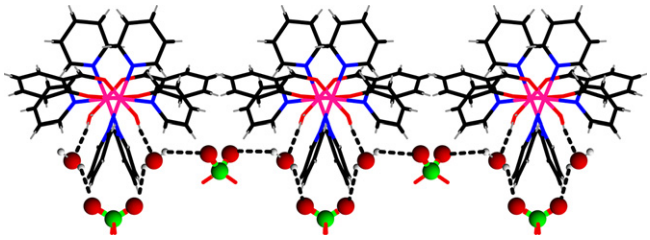


Fig. 9. Water and perchlorate assisted MOF along *ab* plane of **3b**.

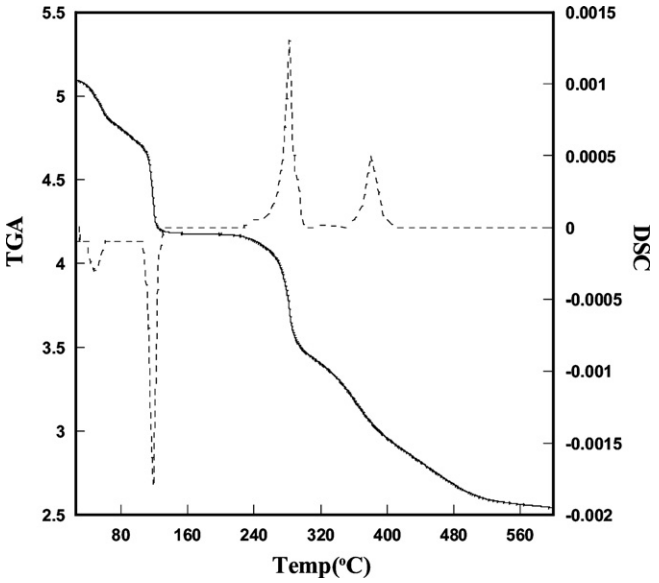


Fig. 10. TG–DSC curve of complex **1a**.

peak at 140 °C, 480 °C and 280 °C, respectively. TG analysis of **1d** exhibits a curve that corresponds to a weight loss of 28.88% (Calculated 21.17%) in the 110–190 °C range corresponds to the removal of one water, two pyridine and a further 21.42% (Calculated 20.75%) loss in the 300–490 °C temperature range, which corresponds to the release of two CO_2 molecules. DSC analysis shows one endothermic peak at 180 °C and one exothermic peak at 400 °C. Generally, a lattice water molecule is expected to be lost at a lower temperature. Thus, one would anticipate a loss of two water molecules of crystallization at a lower temperature than the coordinated water molecules in complex **3a**. TG analysis of complex **3a** in N_2 atmosphere shows the sequential release of crystal water (90–180 °C; $\Delta m = 5.05\%$ Calc.; 6.37% found) and coordinated water molecule (180–230 °C; $\Delta m = 5.32\%$ Calc.; 6.72% found). In the temperature range 300–410 °C it shows the release of chloride and one CO_2 ($\Delta m = 24.82\%$ Calc.; 36.47% found). The DSC-plot shows two endothermic peaks at 125 °C and 205 °C due to the loss of water molecules. It also shows two exothermic peaks at 470 °C and 500 °C. Thermal analysis was not performed with **3b** due to the presence of perchlorate salt.

PXRD patterns also confirm the crystalline nature of the complexes. PXRD patterns of **1a** show significant changes in the peak positions as well as intensities before and after water removal (Fig. 11). After heating the crystal of **1a** at 200 °C for 5 h in a muffle furnace, powder XRD was recorded. Loss of overall crystallinity after water removal confirms that the stability of MOF in the solid state is a result of the strong hydrogen bonding interactions involving coordinated water molecules. Similar observation was made with **1b** also. Complex **1b** was heated at 180 °C for 5 h in a muffle furnace to get rid of the coordinated water molecules. All the other complexes shows the similar type of changes in the PXRD pattern before and after the removal of water molecules (see Supporting information).

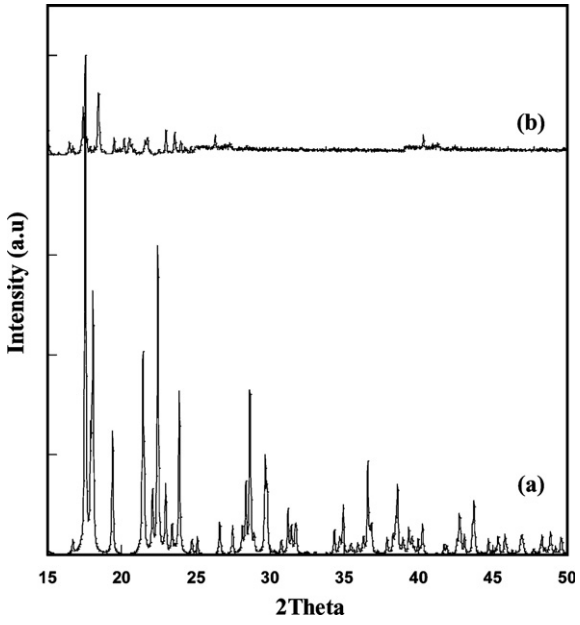


Fig. 11. Powder XRD pattern of complex **1a**. (a) Before water removal and (b) after water removal.

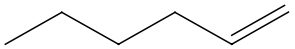
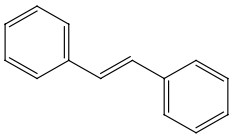
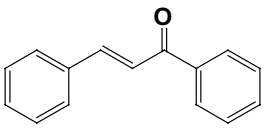
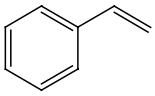
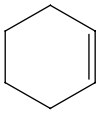
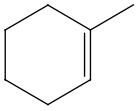
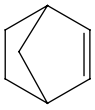
3.6. Catalytic activities of the complexes

All six water soluble complexes are tested as a catalyst in the epoxidation of linear and cyclic olefins under Mukaiyama's conditions [43]. It is found that only Co(II) complex **1a**, Cu(II) complexes **1c** and **3a** are found to be able to act as a catalyst in the epoxidation of alkenes by molecular oxygen in the presence of a sacrificial aldehyde, *i*-butyraldehyde [43–47] (Table 2). In all cases, blank tests performed in identical conditions but without metal catalyst gave negligible conversions of the substrates. It is interesting to note that the pyridine complexes (**1d**, **3b**) show very poor catalytic activity in the same reaction condition. Compared to the complexes **1a**, **1c** and **3a**, pyridine complexes required more reaction time and yielded less amount of product. In a typical experiment, a substrate (10 mmol) and *i*-butyraldehyde (20 mmol) were added to acetonitrile (15 ml) containing 5 mol% catalyst under an atmosphere of molecular oxygen at ambient pressure and temperature. TLC followed progress of the reaction. After completion or interruption of the reaction, the solid catalyst was filtered through a short plug of silica gel. The *i*-butyric acid formed is removed by washing with an aqueous $NaHCO_3$ solution. The excess of unreacted *i*-butyraldehyde is evaporated under vacuum together with the solvent. Aqueous workup followed by column chromatography afforded the corresponding epoxides. The epoxides were identified by comparison of their MS spectra and retention times in GC analysis with those of authentic samples. In absence of *i*-butyraldehyde, none of the complexes was able to cause epoxidation even if used stoichiometrically. This simple, environment friendly methodology has some drawbacks. It is not applicable to unreactive olefins. Yields are not quantitative. One has to invest stoichiometric amounts of *i*-butyraldehyde as a sacrificial reducer, whose role is that of an oxygen transfer agent. The likely mechanism is co-oxidation of the sacrificial aldehyde and the olefin. The mechanism can be compared with that of the reported in literature [47]. Detailed mechanisms of the catalytic processes are currently being investigated in our laboratory with some other acid–metal complexes, which are already published from our laboratory. A direct oxidation without using these catalysts *i.e.* the control reaction did not lead to any substantial oxidation product.

4. Conclusion

In conclusion, we reports the synthesis and crystal structure of six mononuclear mixed-ligand complexes of phenoxyacetic acid derivatives and Schiff base of Cu(II), Co(II)/(III), Mn(II). The carbonyl groups in the acetic acid

Table 2
Summary of catalyzed aerobic epoxidation of olefin

Entry	Olefin	Catalyst	Time (min)	Conversion (%)	Yield (%)
1		**1a**	45	95	58
		1c	20	98	64
		1d	480	71	33
		3a	20	98	68
		3b	300	67	28
2		**1a**	30	89	55
		1c	15	92	60
		1d	600	69	21
		3a	10	90	62
		3b	380	61	16
3		**1a**	50	94	52
		1c	30	97	68
		1d	420	66	31
		3a	15	98	65
		3b	240	70	23
4		**1a**	25	82	45
		1c	15	87	57
		1d	540	59	18
		3a	10	92	52
		3b	480	51	10
5		**1a**	20	92	48
		1c	10	96	58
		1d	360	62	26
		3a	10	98	63
		3b	240	56	17
6		**1a**	20	76	37
		1c	10	84	48
		1d	360	43	18
		3a	10	81	51
		3b	240	36	10
7		**1a**	30	94	52
		1c	25	98	63
		1d	420	58	21
		3a	20	98	71
		3b	300	47	14
8		**1a**	45	88	66
		1c	40	93	74
		1d	480	57	31
		3a	30	98	81
		3b	360	48	22

moiety provide the anchor to form two distinguishable sets of hydrogen-bonded motifs in all the complexes. It is interesting to note that carboxylic acid acts as a uni-dentate ligand in all the complexes. The Schiff base ligand has unique structure, which contains four different ligating atoms in one molecule. We have shown in the manuscript that ether oxygen can also bind to the metal center, which has very poor ligating capability. We demonstrated in the manuscript that the precise control of the coordination environment of the metal center has an effect on the formation of 3D metallo-organic framework (MOF) in the solid state. 3D MOF structure has been critically analyzed and explained based on the monomer structure. We have tested the catalytic properties of all the metal complexes. We observed that subtle change in the coordination environment changes the catalytic properties drastically. Out of six complexes, **1c** and **3a** complexes shows marginal catalytic activities in the epoxidation of olefins by molecular

oxygen in the presence of *i*-butyraldehyde under Mukaiyama's conditions. We have not been able to observe addition or insertion of oxygen into the aromatic ring with any of these complexes.

Acknowledgements

The financial support from the Council of Scientific and Industrial Research (CSIR) of India to GD (Grant No. 01(1948)/04/EMR-II) is gratefully acknowledged. A.P. thanks CSIR for JRF. We thank Central Instrument Facility, Centre for Nanotechnology and Department of Chemistry IIT Guwahati for SEM, Powder XRD and Single crystal XRD measurements.

Appendix A. Supplementary material

CCDC 616704, 616709, 616707, 616706, 616708 and 616705 contain the supplementary crystallographic data for **1a**, **1b**, **1c**, **1d**, **3a** and **3b**. These data can be obtained free of charge via http://www.ccdc.cam.ac.uk/conts/retrieving.html, or from the Cambridge Crystallographic Data Centre, 12 Union Road, Cambridge CB2 1EZ, UK; fax: (+44) 1223-336-033; or e-mail: deposit@ccdc.cam.ac.uk. Supplementary data associated with this article can be found, in the online version, at doi:10.1016/j.poly.2007.07.033.

References

[1] J.M. Lehn, Supramolecular Chemistry, Concepts and Perspectives, VCH, Weinheim, 1995.
[2] J.W. Steed, J.L. Atwood, Supramolecular Chemistry, Wiley, New York, 2000.
[3] N.L. Rosi, J. Eckert, M. Eddaoudi, D.T. Vodak, J. Kim, M. O'Keeffe, O.M. Yaghi, Science 300 (2003) 1127.
[4] C. Janlak, J. Chem. Soc., Dalton Trans. (2003) 2781.
[5] C. Benelli, D. Gatteschi, Chem. Rev. 102 (2002) 2369.
[6] J.S. Seo, D. Whang, H. Lee, S.I. Jun, J. Oh, Y.J. Jeon, K. Kim, Nature 404 (2000) 982.
[7] O.R. Evans, W. Lin, Acc. Chem. Res. 35 (2002) 511.
[8] E.Q. Gao, S.Q. Bai, Z.M. Wang, C.H. Yan, J. Am. Chem. Soc. 125 (2003) 4984.
[9] M. Shmilovits, Y. Diskin-Posner, M. Vinodu, I. Goldberg, Cryst. Growth Des. 3 (2003) 855.
[10] M. Eddaoudi, J. Kim, N. Rosi, D. Vodak, J. Wachter, M. O'Keeffee, O.M. Yaghi, Science 295 (2002) 469.
[11] R. Kitaura, K. Seki, G. Akiyama, S. Kitagawa, Angew. Chem., Int. Ed. 42 (2003) 428.
[12] P. Ayyappan, O.R. Evans, W. Lin, Inorg. Chem. 40 (2001) 4627.
[13] S.R. Batten, CrystEngComm 3 (2001) 67.
[14] G.R. Desiraju, Angew. Chem., Int. Ed. Engl. 34 (1995) 2311.
[15] A.M. Beatty, Coord. Chem. Rev. 246 (2003) 131.
[16] M. Eddaoudi, H. Li, O.M. Yaghi, J. Am. Chem. Soc. 123 (2000) 1391.
[17] D. Sun, R. Cao, Y. Liang, Q. Shi, W. Su, M. Hong, J. Chem. Soc., Dalton Trans. (2001) 2335.
[18] C.S. Hong, S.K. Son, Y.S. Lee, M.J. Jun, Y. Do, Inorg. Chem. 38 (1999) 5602.
[19] J.-R. Galán-Mascarós, J.-M. Clemente-Juan, K.R. Dunbar, J. Chem. Soc., Dalton Trans. (2002) 2710.
[20] R. Robson, J. Chem. Soc., Dalton Trans. (2000) 3735.
[21] H.W. Roesky, M. Andruh, Coord. Chem. Rev. 236 (2003) 91.
[22] H. Thakuria, G. Das, Polyhedron 26 (2007) 149.
[23] H. Thakuria, B.M. Borah, G. Das, Eur. J. Inorg. Chem. (2007) 524.
[24] Liu, H.X. Shao, M. Jia, X. Jiang, Z. Li, G. Chen, Tetrahedron 61 (2005) 8095.
[25] C.H.L. Kennard, E.J. O'Reilly, G. Smith, T.C.W. Mak, Aust. J. Chem. 38 (1985) 1381.
[26] SMART, SAINT and XPREP, Siemens Analytical X-ray Instruments Inc., Madison, Wisconsin, USA, 1995.
[27] G.M. Sheldrick, SADABS: Empirical Software for Absorption and Correction, University of Gottingen, Gottingen, Germany, 1999–2003.
[28] G.M. Sheldrick, SHELXS-97, University of Gottingen, Germany, 1997.
[29] K. Nakamoto, Infrared and Raman Spectra of Inorganic and Coordination Compounds, 5th ed., Wiley, New York, 1997.
[30] N. Reddig, D. Pursche, A. Rompel, Dalton Trans. (2004) 1474.
[31] J.A. Schlueter, U. Geiser, J.L. Manson, Acta Cryst. (2003) C59, m1.
[32] A.J. Hanss, A. Beckmann, H.-J. Kruger, Eur. J. Inorg. Chem. (1999) 163.
[33] B.L.F. Szczepura, J.G. Muller, J.G.C.A. Bessel, R.F. See, T.S. Janik, M.R. Churchill, K.J. Takeuchi, Inorg. Chem. 31 (1992) 859.
[34] S.B. Teo, S.G. Teoh, M.R. Snow, Inorg. Chim. Acta 107 (1985) 211.
[35] C.H. Ng, S.B. Teo, S.G. Teoh, J.P. Declercq, J. Coord. Chem. 55 (2002) 909.
[36] A.W. Addison, T.N. Rao, J. Reedijk, J. van Rijn, G.C. Verschoor, J. Chem. Soc., Dalton Trans. (1984) 1349.
[37] W.S. Durfee, C.G. Pierpont, Inorg. Chem. 32 (1993) 493.
[38] B.J. Hathaway, D.E. Billing, Coord. Chem. Rev. 5 (1970) 143.
[39] R.J.H. Clark, C.S. Williams, Inorg. Chem. 4 (1965) 350.
[40] M. Suzuki, A. Uehara, Bull. Chem. Soc. Jpn. 57 (1984) 3134.
[41] J.P. Costes, J.P. Laurent, J.M.M. Sanchez, J.S. Varela, M. Ahlgren, M. Sundberg, Inorg. Chem. 36 (1997) 4641.
[42] F.A. Cotton, G. Wilkinson, Advanced Inorganic Chemistry, 5th ed., Wiley, New York, 1988.
[43] T. Yamada, T. Takai, O. Rhode, T. Mukaiyama, Chem. Lett. (1991) 1.
[44] G. Das, R. Shukla, S. Mandal, R. Singh, P.K. Bharadwaj, J.V. Hall, K.H. Whitmire, Inorg. Chem. 36 (1997) 323.
[45] E. Bouhlelh, P. Laszloa, M. Levart, M.T. Montautier, G.P. Singh, Tetrahedron Lett. 34 (1993) 1123.
[46] J.M. Br'egeault, M. Vennat, L. Salles, J.Y. Piquemal, Y. Mahhaa, E. Briot, P.C. Bakala, A. Atlamsani, R. Thouvenot, J. Mol. Catal. A: Chem. 250 (2006) 177.
[47] J. Haber, T. Mlodnllka, J. Pokowicz, J. Mol. Catal. 54 (1989) 451.

and electrochemical responses to specific analytes, and they are capable of binding multiple metal ions for the development of new molecules/macrocycles [17–21].

To date, a great variety of symmetrical or pseudo-symmetrical mononuclear phthalocyanines have been comprehensively studied. Nevertheless, there have been a limited number of reports on functional phthalocyanines, mainly because of the difficulties for their preparation and purification [19–22]. In the present article, the synthesis of tetrasubstituted-phthalocyanine {M[Pc(S-$C_6H_{13}OCOC_4H_3S)_4$]} (M = 2H (**1**), Cu (**2**)) substituted with four thiophene terminated hexylsulfanyl moieties is described. Electrochemical and specific cation binding properties are also investigated.

2. Experimental

Chloroform ($CHCl_3$), tetrahydrofuran (THF), tetrabutylammonium tetrafluoroborate ($TBATBF_4$), $CuCl_2$, tetrabutylammonium perchlorate (TBAP) and dimethylsulfoxide (DMSO) were purchased from Sigma Aldrich and were used without purification. 4-Nitrophthalonitrile, 4-(6-hydroxyhexylthio)-1,2-dicyanobenzene and 6-(3,4-dicyanophenylthio)-hexylthiophene-2-carboxylate were prepared according to the literature procedure [23,24]. The purity of the products was tested in each step by TLC (SiO_2, $CHCl_3$, hexane and MeOH).

FTIR (thin solution film) were recorded on an ATI UNICOM-Mattson 1000 spectrophotometer. Chromatography was performed with silica gel (Merck grade 60 and sephadex) from Aldrich. Elemental analysis (C, H and N) was performed at the instrumental Analysis Laboratory of Marmara University. UV–Vis spectra were obtained in a quartz cuvette on a Unicom UV-2 spectrometer. ^1H NMR and ^{13}C NMR spectra were recorded on a Bruker 300 spectrometer instrument.

The cyclic voltammetry (CV), differential pulse voltammetry (DPV) and controlled potential coulometry (CPC) measurements were carried out with a Gamry Reference 600 potentiostat/galvanostat controlled by an external PC and utilizing a three-electrode configuration at 25 °C. The working electrode was a Pt plate with a surface area of 0.071 cm^2. The surface of the working electrode was polished with a diamond suspension before each run. A Pt wire served as the counter electrode. A saturated calomel electrode (SCE) was employed as the reference electrode and separated from the bulk of the solution by a double bridge. Ferrocene was used as an internal reference. Electrochemical grade tetrabutylammonium perchlorate (TBAP) in extra pure dimethylsulfoxide (DMSO) was employed as the supporting electrolyte at a concentration of 0.10 mol dm^{-3}. High purity N_2 was used for deoxygenating the solution for at least 15 min prior to each run and for maintaining a nitrogen blanket during the measurements.

During the voltammetric measurements, the reference electrode tip was moved as close as possible to the working electrode so that uncompensated resistance of the solution was a smaller fraction of the total resistance, and therefore the potential control error was low. Moreover, IR compensation was applied to the CV scans to further minimizing the potential control error.

For CPC studies, a Pt gauze working electrode (10.5 cm^2 surface area), a Pt wire counter electrode separated by a glass bridge, and a SCE as a reference electrode were used.

2.1. Maldi sample preparation

A 2,5-dihydroxybenzoic acid (DHB) (20 mg/mL in an acetonitrile–water mixture in a 1:1 ratio) matrix for compounds **1** and **2** was prepared. MALDI samples were prepared by mixing the complex (2 mg/mL in tetrahydrofuran (THF)) with the matrix solution (1:10 v/v) in a 0.5 mL Eppendorf® micro tube. Finally, 1 μL of this mixture was deposited on the sample plate, dried at room temperature and then analyzed.

2.2. Maldi mass spectrometry

Mass spectra were acquired on a Voyager-DETM PRO MALDI-TOF mass spectrometer (Applied Biosystems, USA) equipped with a nitrogen UV-Laser operating at 337 nm. Spectra were recorded in the reflectron mode with an average of 50 shots.

2.3. Synthesis

2.3.1. 2,9,16,23-Tetrakis-{6-(-thiophene-2-carboxylate)-hexylthio} metal-free pthalocyanine (*1*)

6-(3,4-Dicyanophenylthio)-hexylthiophene-2-carboxylate (0.150 g, 0.405 mmol) was heated in dry *N*,*N*′-(dimethylamino)ethanol (0.5 cm^3) in the presence of DBU (mmol) under stirring and refluxing for 48 h. After the mixture was cooled, it was treated several times with MeOH, and then with CH_3CN. Finally dark green-blue compound **1** was filtered until the filtrates were clear. The residue was then further purified by column chromatography with silica gel (eluent: $CHCl_3$/MeOH; (100:1 v/v)).

Yield: 0.025 g (16.66%). *Anal*. Calc. for $C_{76}H_{74}N_8O_8S_8$ (1482 g/mol): C, 61.53; H, 4.85; N, 7.56; S, 17.27. Found: C, 61.07; H, 4.84; N, 7.12; S, 16.59%. FTIR (KBr thin film) ν/cm^{-1}: 3284 (w, NH), 3084 (w, broad, Ar-H), 2933, 2855, 2850 (Aliph-CH_2), 1707 (–COOR thiophene, strong), 1581 (st), 1535, 1441, 1357, 1315, 1258, 1156, 1085, 1056, 970, 854, 822, 739, 721. ^1H NMR ([d_6]-DMSO) *J*/Hz δ/ppm: 7.84 (dd, 1H, *ortho* to COOR, thiophene H2), 7.82 (s, isomer, 1H, *meta* to CN and CS, Phenyl H5), 7.65 (dd, 1H, *ortho* to SR and CN, Phenyl H2), 7.70 (dd, 1H, *ortho* to CN, and Ar-H, thiophene H6), 7.58 (dd, 1H, *meta* to Ar-S, and Ar-H, thiophene H5), 7.21 (dd, 1H, *meta* to thiophene-S, and thiophene-H, thiophene H4) 4.21 (t, br, –CH_2COO Aliph. (thiophene)), 3.03 (CH_2CH_2–S–Ar), 1.65–1.78 (m, 4H, –O–CH_2CH_2–CH_2–), 1.26–1.35 (m, 4H, –$OCH_2CH_2CH_2$–CH_2–), −1.45–(−1.48) (2H, NH *inner*). UV–Vis (THF) λ_{max}/nm: 714 (Q_1), 682 (Q_2), 655

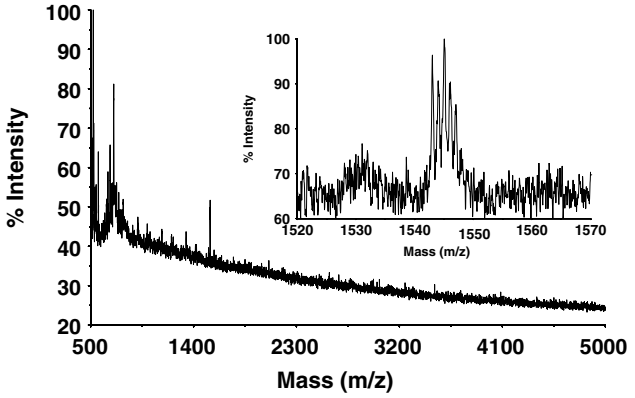


Fig. 1. Positive ion and reflectron mode MALDI-MS spectrum of **2** without metal ions was obtained in a 2,5-dihydroxybenzoic acid MALDI matrix using nitrogen laser accumulating 50 laser shots. Inset spectrum shows the expanded molecular mass region of the ligand.

(sh), 620 (sh), 344 (B), 296 (thiophene); MS (Maldi-TOF, 3-indole acrylic acid (10 mg/mL in acetonitrile as matrix)): *m*/*z* (100%): 1485 $[M+H]^+$.

2.3.2. 2,9,16,23-Tetrakis-{6-(thiophene-2-carboxylate)-hexylthio}phthalocyaninato copper(II) (2)

Compound **1** (0.150 g, 0.405 mmol), 6-(3,4-dicyanophenylthio)-hexylthiophene-2-carboxylate and anhydrous $CuCl_2$ (0.015 g, 0.107 mmol) in *n*-hexanol (~1 cm^3) were refluxed in a sealed tube under N_2 atmosphere for 6 h. The colour of the mixture turned into green-blue during the course of the reaction. After the mixture was heated for an additional 4 h, the green-blue product was cooled to room temperature. Then the mixture was diluted with petroleum ether. The crude product formed was washed several times successively, with first *i*-PrOH, and then with cold CH_3CN to remove any organic and inorganic impurities. Finally, the product was further purified by silica gel chromatography {$CHCl_3$ and then with $CHCl_3$/MeOH (20:1 v/v) and sephadex with THF/$CHCl_3$}. After the resulting oily product was washed with copious amounts of hexane, diethylether and finally with *i*-PrOH, it was dried in vacuo. The final product is soluble in THF, DMF, DMSO, pyridine and insoluble in EtOH.

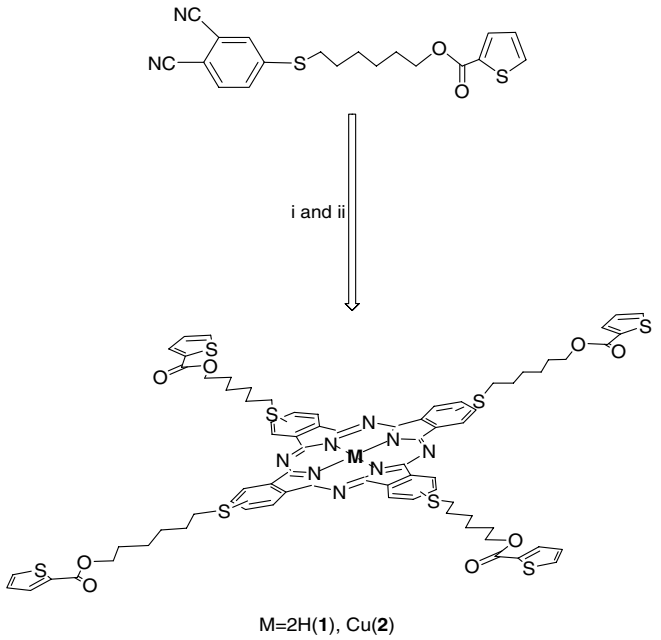
Yield: 0.029 g (18.56%). *Anal*. Calc. for $C_{76}H_{72}N_8O_8S_8Cu$ (1543.5 g/mol): C, 59.08; H, 4.66; N, 7.26; S, 16.57. Found: C, 58.77; H, 4.74; N, 7.02; S, 16.12%. FTIR (KBr, thin film) ν/cm^{-1}: 3091 (Ar-H), 2927, 2854 (Aliph-H), 1700 (COOR), 1600, 1522, 1448, 1417, 1356, 1310, 1256, 1224, 1142, 1087, 1070, 931, 897, 857, 816, 745, 718; UV–Vis (THF), λ_{max}/nm: 688 (Q), 416 (CT), 342 (B); MS (Maldi-TOF, dihydroxybenzoic acid (DHBA as matrix)): *m*/*z* (%): 1543 $[M+H]^+$, 1545 $[M+3H]^+$, 1547 $[M+4H]^+$ (Fig. 1).

3. Results and discussion

In the present work, metal ion sensor metal-free and copper phthalocyanines (**1** and **2**) bearing thiophene were prepared by heating a pulverized mixture of 6-(3,4-dicyanophenylthio)-hexylthiophene-2-carboxylate without a metal salt or with the anhydrous $CuCl_2$ salt at ca. 170–180 °C under a N_2 atmosphere in the presence of 1,8-diazabicyclo[5.4.0]undec-7-ene (DBU) (Scheme 1). The presence of isomers could be verified by a slight broadening encountered in the UV–Vis absorption bands and broadening in the ^1H NMR spectra when compared with those of octa-substituted phthalocyanines composed of a single isomer [16]. The yields of the reactions were rather low (16.65% for **1**, 18.56% for **2**). The structures of phthalocyanines **1** and **2** were verified by FTIR, ^1H NMR, UV–Vis and MALDI-TOF MS spectroscopic methods, as well as by elemental analysis. All the analytical and spectral data are consistent with the predicted structures.

Cyclotetramerization of the dinitrile derivative, 6-(3,4-dicyanophenylthio)-hexylthiophene-2-carboxylate to the phthalocyanines was confirmed by the disappearance of the sharp –C≡N vibration at 2233 cm^{-1} and the strong COOR (R = thiophene) band in compound **1** at around 1700–1710 cm^{-1} came out with a small shift. The IR spectra of the phthalocyanines are very similar with the exception of the NH stretching band at 3284 cm^{-1} due to the inner core imino group in the metal-free phthalocyanine (**1**). In the FTIR spectrum of **2**, the absence of the characteristic bands of the N–H groups also confirms the formation of compound **2**.

The ^1H NMR spectra of **1** is somewhat broader than the corresponding signals in the starting dinitrile derivative. This broadening is likely due to chemical exchange caused by an aggregation–disaggregation equilibria and the fact that the product obtained in these reactions is a mixture



Scheme 1. Synthetic route of 2,9,16,23-tetrakis-{6-(-thiophene–2-carboxylate)-hexylthio}-metallophthalocyanine {$M[Pc(S-_6H_{13}OH)_4]_2$} (M = 2H, Cu(II)); (i) *N*,*N*-dimethylaminoethanol, dbu and (ii) anhydrous $CuCl_2$, dbu.

of positional isomers which are expected to show chemical shifts that differ slightly from each other. The inner NH proton of the metal-free phthalocyanine was also identified in the ^{1}H NMR spectrum with a broad chemical shift between δ −1.45 and −1.48 ppm as a consequence of the 18 π-electron system of the planar molecule, and this signal disappears on deuterium oxide (D_2O) exchange [12]. The other resonances related to $OOCCH_2$, CH_2, SCH_2 and Ar-H protons in the ^{1}H NMR spectrum are very similar to that of the precursor compound and show the typical chemical shifts for protons of –thiophene: $–CH_2COO$ (4.21 ppm), $–CH_2$ (1.65–1.26 ppm, all CH_2) S–CH_2 (3.03 ppm) and Ar-H (7.84–7.20).

The UV–Vis spectra of the phthalocyanine complexes exhibit characteristic Q- and B-bands, one in the visible region at ca. 600–750 nm (Q-band) attributed to the π–π* transition from the HOMO to the LUMO of the Pc^{2-} ring, and the other in the UV region at ca. 300–400 nm (B-band) arising from the deeper π–π* transitions [16].

While the divalent copper phthalocyanine (**2**) gave a single Q-band of high intensity due to a single π–π* transition, as expected as a result of its D_{4h} symmetry, the metal-free phthalocyanine (**1**) gave a split Q-band as a result of D_{2h} symmetry, with shoulders at the slightly higher energy side of the Q-band in addition to B-bands in the UV region [12,16,18,21]. The Q-band absorptions in THF of the free and copper phthalocyanines (**1**–**2**) were observed at 714, 682 (Qx and Qy), and 688 nm, respectively, with shoulders at the slightly higher energy side of the Q-band for each phthalocyanine. The band between 400 and 450 nm in **2** may be due to charge transfer from the electron-rich ring to the electron-poor acceptor metal. The B-bands are broad due to the superimposition of the B1- and B2-bands in the 330–350 nm region in the case of complex **2** [25].

The aggregation behavior of compound **1** was investigated in different solvents ($CHCl_3$, DCM, DCE, chlorobenzene, benzene, CCl_4, CH_3CN and ethylacetate) at different concentrations. Compound **1** is soluble in a wide range of solvents from THF to non-polar solvents because of the amphiphilic property of the compound. Some examples of absorption spectra of compound **1** in various solvents are depicted in Fig. 4. The solvent effect on polymerization has been studied at 25.0 °C through absorption spectroscopy. The absorption bands at 682 and 714 nm (Q-band) for **1** are strongly affected by the two solvent parameters, donor number (DN) and Dimroth ET value [16,28]. Compound **1** is predominantly present as a polymer in polar solvents, such as CH_3CN and ethylacetate. As can be seen from the DN, which is an index of the donating property of the solvent, compound **1** is soluble in both less polar and non-polar solvents; that is, these peaks are very small in high DN solvents and disappear in CH_3CN and ethylacetate [16,20]. The change of the molar extinction coefficient is not quantitatively analyzed because the degree of aggregation is not unambiguous. The decrease in the peak height at 682 and 714 nm is attributed to the formation of a polymer of compound **1**. The molar extinction coefficients of compound **1** in chloroform and ethylacetate hardly change with a concentration change of the compound.

3.1. Spectroscopic metal ion binding titrations

It is known that the effect of S-substitution on the periphery for all phthalocyanines was a shift in these intense Q-bands to longer wavelengths because of the electron-donating thioether substituents when compared with those of unsubstituted, alkyl or O-substituted derivatives [17–20,26–28]. Sulfur donor atoms on the periphery of the tetra or octa substituted phthalocyanines act as a low-valent transition metals ionophore (IB and IIB) and impart a preference for coordination, especially with Ag^I and Pd^{II}, when the peripheral heteroatoms are able to interact with the metals [17–20,29], resulting in the formation of aggregates. These interactions are readily monitored by UV–Vis spectroscopy. In the aggregated state, the electronic structure of the phthalocyanine rings is perturbed, resulting in an alternation of the ground and excited state electronic structures [30,31].

In this study, titrations were carried out using a THF/MeOH solution of the Pc's (5:1, v/v) to ensure complete dissolution of the analyte salts, $AgNO_3$, Na_2PdCl_4, $CdCl_2$, $HgCl_2$ and $Pb(O_2CCH_3)_2$ dissolved in MeOH. Here the concentration of each Pc and the metal salt was ca. 10^{-5} and 10^{-3} mol dm^{-3}, respectively. The reason for the higher concentration of the metal salt was to produce negligible changes by dilution after its addition to the phthalocyanine solution.

Both **1** (H_2Pc) and **2** (CuPc) exhibit optical changes that are indicative of metal-ion binding, when they were titrated with Ag^I and Pd^{II} ions. Before the titration of the **1** with soft-metal ions, the spectrum of the compound gives a shoulder (652 nm) at the slightly higher energy side of the split Q-band. This shoulder shows aggregation of the compound in THF. Complex **2** shows similar aggregation behavior to **1**. The room temperature gradual addition (μL) of Ag^I and Pd^{II} to the THF/MeOH solution of **1** and **2** caused a decrease of these shoulders and the formation of new shoulders at the slightly higher energy side of these shoulders due to oligomeric metal-Pc complexation. A gradual color change from blue-green to dark green also supports metal-Pc complexation. Fig. 2(a–c) shows that while Ag^I, and Pd^{II} binding to the donor atoms of **1** result in pronounced effects in the spectrum of **1**, Hg^{II} has no effect. This observation is in harmony with previously reported studies [17–19,27,28]. As shown in Figs. 2 and 3, the addition of small increments of Ag^I to **1** and **2** leads to the gradual disappearance of the absorptions of monomeric species at 714, 682, 652, 425 and 345 nm, simultaneously enhancing the intensity of the oligomeric aggregated species at around 642, 298 and 241 nm for **1**, and the gradual disappearance of monomeric species absorptions for **2** at 688, 655, 414 and 346 nm, enhancing the intensity of the oligomeric aggregated species at around 629 nm. The B-bands of the complexes shift to higher

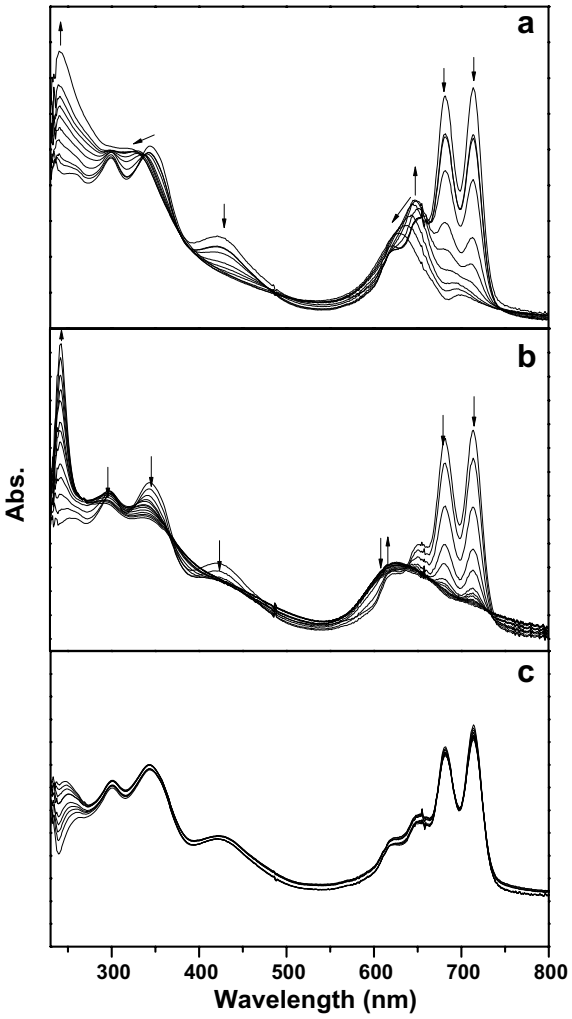


Fig. 2. UV–visible spectra of **1** in THF/MeOH during titration by Pd^{2+} (a), Ag^{+} (b) and Hg^{2+} (c) (in MeOH).

energy sides by about 5–15 nm, with a change in intensity. These spectroscopic changes indicate the coordination of Ag^{I} by the donor atoms of the phthalocyanines to form less soluble oligomeric aggregated species. At higher Ag^{I} concentration, the intensity of the absorption band of the oligomeric species decreases because of the precipitation of the aggregated species. As appeared in Fig. 2b and 3, the titrations show clear isobestic points at 734, 639, 474, 390, 365, 325 and 268 nm for **1**, and 725, 648, 614, 543, 463, 381 and 326 nm for **2**.

The titration of **1** (Fig. 2a) and **2** with Pd^{II} gives similar spectra. Addition of Pd^{II} in MeOH to the solutions of **1** and **2** in THF–MeOH (5:1, v/v) causes a decrease of the absorption of the Q-bands and increase of the absorption intensity of the aggregation shoulders with a blue shift. An immediate color change also supports the complexation of the compounds with the Pd^{II} ion. At higher Pd^{II} concentrations, the aggregation shoulders starts to decrease in intensity with a blue shift due to the precipitation of polymeric species [17–19].

Borderline-metals, such as Hg^{II}, Cd^{II} and Pb^{II} did not significantly changed the visible spectra of the Pc's upon addition of $HgCl_2$ (Fig. 2c), $CdCl_2$ and $Pb(O_2CCH_3)_2$, except for a dilution in the spectra. This lack of change in the visible spectra would be consistent with very weak or no coordination of the donor atoms on the periphery to the Hg^{II}, Cd^{II} and Pb^{II} ions [17–19,27].

3.2. Electrochemical measurements

The electrochemical behavior of the phthalocyanines was investigated by cyclic voltammetry (CV) and differential pulse voltammetry (DPV) on a platinum working electrode. The half-wave redox potential values ($E_{1/2}$) vs SCE, anodic to cathodic peak separation (ΔE_p) and peak current ratios (I_{pa}/I_{pc}) are summarized in Table 1.

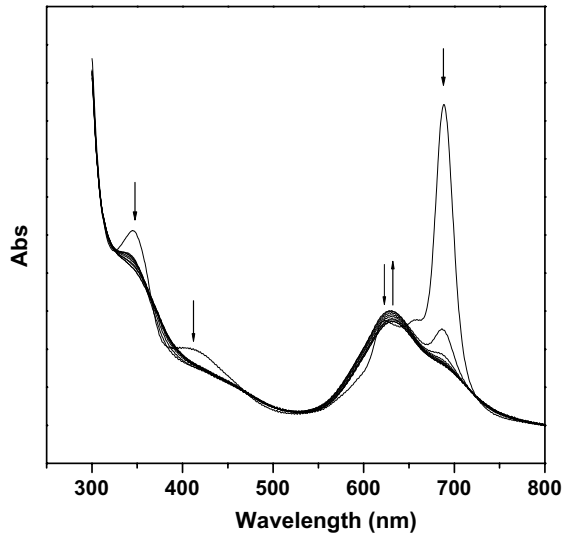


Fig. 3. UV–visible spectra of **2** in THF/MeOH during titration by Ag^{+} (in MeOH).

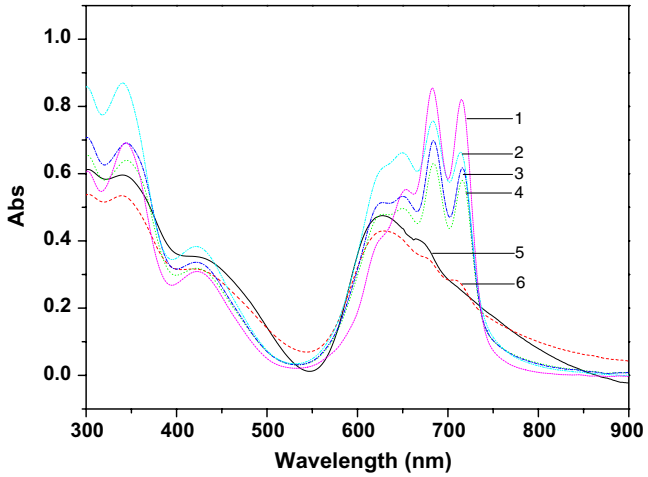


Fig. 4. Absorption spectra of **1** in various solvents. Concentration of **1** is 1.0×10^{-5} M. (1) Chloroform, (2) dichloromethane, (3) benzene, (4) carbon tetrachloride, (5) acetonitrile, (6) ethylacetate.

Table 1
Voltammetric data for the complexes (**1** and **2**)

Complexes	O_1			R_1			R_2			R_3		
	$E^a_{1/2}$ (V)	ΔE^b_p (mV)	I_{pc}/I^c_{pa}	$E^a_{1/2}$ (V)	ΔE^b_p (mV)	I_{pc}/I^c_{pa}	$E^a_{1/2}$ (V)	ΔE^b_p (mV)	I_{pc}/I^c_{pa}	$E^a_{1/2}$ (V)	ΔE^b_p (mV)	I_{pc}/I^c_{pa}
1 (H_2Pc)	0.64 (0.44[d])			−0.62	110	0.98	−0.93	100	0.90	−1.76		
2 (CuPc)	0.33	232	0.89	−0.78	73	0.95	−1.04	78	0.87			

[a] $E_{1/2} = (E_{pa} + E_{pc})/2$ at 100 mV s^{-1} scan rate vs. SCE.
[b] $\Delta E_p = E_{pa} + E_{pc}$ at 100 mV s^{-1} scan rate.
[c] I_{pa}/I_{pc} values are given for reduction and $I_{pc}/I_{pa}I_{pc}$ values are given for oxidation processes at 100 mV s^{-1} scan rate.
[d] O'_1 wave of the complex resulting from the aggregated species.

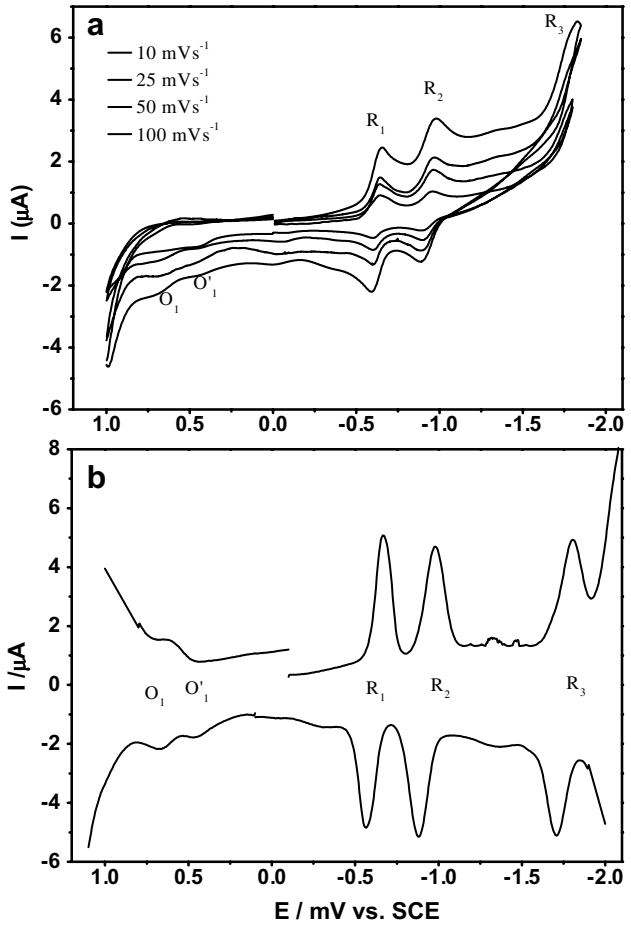


Fig. 5. Cyclic (a) and differential pulse (b) voltammograms of **1** at various scan rates on Pt in DMSO/TBAP.

Fig. 5 shows the CV and DPV of compound **1** in DMSO containing TBAP. Compound **1** gives three one-electron reduction processes labelled as R_1 at −0.62 V, R_2 at −0.93 V and R_3 at −1.76 and two one-electron irreversible oxidation processes labelled as O'_1 at 0.44 V and O_1 at 0.64 V vs. SCE at 0.100 V s^{-1} scan rate. Based on the well-known electrochemical behavior of phthalocyanine complexes, all couples in Fig. 5 are assigned to the phthalocyanine ring. The values of I_{pa}/I_{pc} for the R_1 and R_2 couples of **1** are close to unity, and the anodic to cathodic peak separation (ΔE_p) is changed from 65 to 140 mV with scan rates from 0.010 to 0.500 V s^{-1} (ΔE_p was changed from 60 to 110 mV for ferrocene), suggesting reversible electron transfer. Reversibility is illustrated by the similarity in the forward and reverse DPV scans (Fig. 5b) [32,33]. The peak currents increase linearly with the square root of the scan rates for scan rates ranging from 0.010 to 0.500 V s^{-1}, indicating the purely diffusion-controlled behaviors of the couples R_1 and R_2 [32,33]. Splitting of the oxidation processes (O_1 and O'_1) shows the aggregation of the compound during the positive potential scan, while it is present as monomeric species under negative potentials. Disappearance of O'_1 with dilution supports the aggregation processes of the compound. Peak currents of the oxidation processes are much smaller than the reduction processes for compound **1**, because during the positive potential scans the compound is aggregated. The aggregation of the complex decrease the concentration of the monomers and give a split into small peaks corresponding to the aggregated (O'_1) and monomeric species (O_1).

As is shown in Fig. 6, within the electrochemical window of TBAP/DMSO, **2** undergoes a one-electron oxidation at 0.33 V, labelled as O_1, and two one-electron reductions at −0.78 and −1.10 V at 0.100 V s^{-1} scan rate, labelled as R_1 and R_2, having reversible diffusion-controlled electron transfer characters. Because of the electro-inactive metal center of the complex, all of these processes are attributed to successive removal of electrons from, or addition of electrons to, the macrocycle orbitals. Differential pulse voltammetry of the complex confirms the recorded redox processes clearly. Reversibility is illustrated by the similarity in the forward and reverse DPV scans (inset in Figs. 6A and B). When compared with the common metallophthalocyanines, the oxidation process of **2** is recorded at a less positive potential, resulting in a significantly decreased potential difference between the first reduction and first oxidation redox processes, i.e., a decreased HOMO–LUMO gap (1.11 V) of the complex. However, the position of the reduction couples and the peak separation of the first and second reduction couples (0.38 V) are in harmony with common metallophthalocyanines [16,17,19,34–39].

CPC is used to determine the overall number of electrons in a faradic reaction. Unlike voltammetric techniques where the electrode area and diffusion coefficient of the redox species must be known, CPC can determine the overall number of electrons in the redox process without prior knowledge of the electrode area or diffusion coefficient.

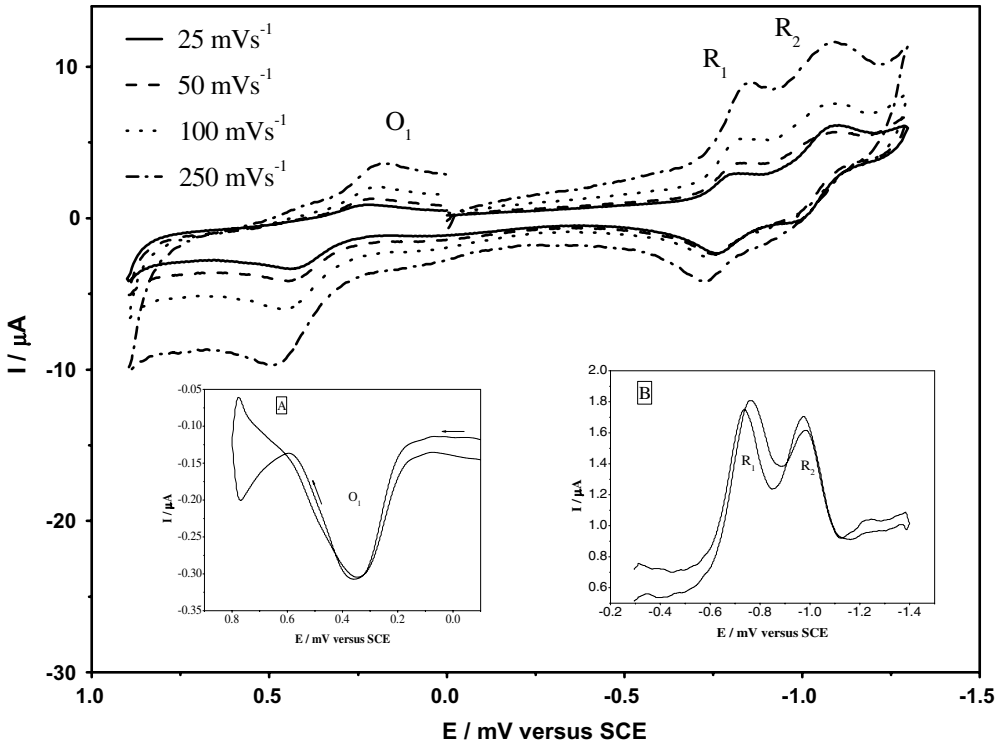


Fig. 6. Cyclic and differential pulse voltammograms of **2** (A = Oxidation) (B = Reduction) at various scan rates on Pt in DMSO/TBAP.

Applied potentials were selected approximately 50 mV higher than the reduction/oxidation peak to compensate the possible change of the peak potential due to the different cell and electrode configuration of the CPC measurement. The CPC studies indicated that the number of electrons transferred for the first reduction processes of the complexes **1** and **2** was approximately one. Since both reduction processes have very similar peak currents (except the oxidation processes of **1**), the number of electrons transferred for the remaining processes should also be one. To obtain a more accurate measurement of the redox equivalency, reduction processes were studied by DPSC. Plots of Q (charge) versus $t^{1/2}$ (time) shows a linear behavior for both first two reduction processes. Slopes with a 1:1 ratio were consistent with the involvement of one electron for R_1 and R_2 and O_1 processes of the complexes. DPSC experiments also showed the reversibility of the R_1 and R_2 processes with approximately the same slopes of the Cottrell lines representing the two potential steps of the processes.

Acknowledgements

We thank the Research Funds of Sakarya University, and DPT-2004 (Project No: 2003K120970).

References

[1] (a) A.D. Dinsmore, M.F. Hsu, M.G. Nikolaides, M. Marquez, A.R. Bausch, D.A. Weitz, Science 298 (2002) 1006;
(b) Y. Lin, H. Skaff, T. Emrick, A.D. Dinsmore, T.P. Russell, Science 299 (2003) 226;
(c) T. Joki, M. Machluf, A. Atala, J. Zhu, N.T. Seyfried, I.F. Dunn, T. Abe, R.S. Carroll, P.M. Black, Nature Biotechnol. 19 (2001) 35.
[2] (a) E. Donath, G.B. Sukhorukov, F. Caruso, S.A. Davis, H. Möhwald, Angew. Chem. 110 (1998) 2324;
(b) E. Donath, G.B. Sukhorukov, F. Caruso, S.A. Davis, H. Möhwald, Angew. Chem., Int. Ed. 37 (1998) 2201.
[3] (a) P. Bassoul, T. Toupance, J.J. Simon, Sens. Actuators B-Chem. 26 (1995) 150;
(b) Y. Sadaoka, T.A. Jones, W. Göpel, Sens. Actuators B 1 (1990) 148.
[4] L. Alagna, A. Capobianchi, A.M. Paoletti, G. Pennesi, G. Rossi, M.P. Casaletto, A. Generosi, B. Paci, V.R. Albertini, Thin Solid Films 515 (4) (2006) 2748.
[5] M. Kimura, T. Muto, H. Takimoto, K. Wada, K. Ohta, K. Hanabusa, H. Shirai, N. Kobayashi, Langmuir 16 (5) (2000) 2078.
[6] A.S. Raid, M.T. Korayem, T.G. Abdel-Malik, Physica B 270 (1999) 140.
[7] X. Li, X. He, A.C.H. Ng, D.K.P. Ng, C. Wu, Macromolecules 33 (2000) 2119.
[8] C. Zhong, M. Zhao, C. Stern, A.G.M. Barrett, B.M. Hoffman, Inorg. Chem. 44 (2005) 8272.
[9] X. Chen, C.M. Drain, Encycl. Nanosci. Nanotechol. 9 (2004) 593.
[10] M. Hanack, M. Lang, Adv. Mater. 6 (1994) 819.
[11] P. Tau, T. Nyokong, Polyhedron 25 (2006) 1802.
[12] M. Kandaz, S.L.J. Michel, B.M. Hoffman, J. Porphyrins Phthalocyanines 7 (2003) 700.
[13] R.J. Li, X.X. Zhang, P.H. Zhu, D.K.P. Ng, N. Kobayashi, J.Z. Jiang, Inorg. Chem. 45 (5) (2006) 2327.
[14] T. Kimura, T. Suzuki, Y. Takaguchi, A. Yomogita, T. Wakahara, T. Akasaka, Eur. J. Org. Chem. 27 (5) (2006) 1262.
[15] J.D. Wang, M.J. Lin, S.F. Wu, Y. Lin, J. Organomet. Chem. 691 (23) (2006) 5074.
[16] C.C. Leznoff, A.B.P. Lever, in: C.C. Leznoff, A.B.P. Lever (Eds.), Phthalocyanines: Properties and Applications, vol. 1–4, VCH, Weinheim, 1989.
[17] M. Kandaz, H.S. Çetin, A. Koca, A.R. Özkaya, Dyes Pigments 74 (2007) 298.

[18] S.L.J. Michel, A.G.M. Barrett, B.M. Hoffman, Inorg. Chem. 42 (2003) 814.
[19] M.N. Yarasir, M. Kandaz, A. Koca, B. Salih, Polyhedron 26 (2007) 1139.
[20] K. Sawada, W. Duan, K. Sekitani, K. Satoh, J. Mol. Liquids 119 (2005) 171.
[21] D.P. Goldberg, Sarah L.J. Michel, A.J.P. White, D.J. Williams, A.G.M. Barrett, B.M. Hoffman, Inorg. Chem. 37 (1998) 2100.
[22] M. Kandaz, Ö. Bekaroğlu, Chem. Ber. 135 (1997) 1833.
[23] J.G. Young, W. Onyebuagu, J. Org. Chem. 55 (1990) 2155.
[24] M.N. Yarasir, M. Kandaz, F.B. Senkal, A. Koca, B. Salih, doi:10.1016/j.dyepig.2007.02.009.
[25] A.B. Anderson, T.L. Gorden, M.E. Kenney, J. Am. Chem. Soc. 107 (1985) 192.
[26] (a) M. Kandaz, I. Yılmaz, Ö. Bekaroğlu, Polyhedron 19 (2000) 115;
(b) M. Kandaz, Ö. Bekaroğlu, J. Porphyrin Phthalocyanines 3 (1999) 339.
[27] S.J. Lange, J.W. Sibert, A.G.M. Barrett, B.M. Hoffman, Tetrahedron 56 (2000) 7371.
[28] N. Sheng, R. Li, C. Choi, W. Su, D.K.P. Ng, X. Cui, K. Yoshida, N. Kobayashi, J. Jiang, Inorg. Chem. 45 (2006) 3794.
[29] H. Holdt, J. Pure Appl. Chem. 65 (1993) 477.
[30] H. Enkelkamp, R.J.M. Nolte, J. Porphyrins Phthalocyanines 4 (2000) 454.
[31] D.D. Dominguez, A.W. Snow, J.S. Shirk, R.G.S. Pong, J. Porphyrins Phthalocyanines 5 (2001) 582.
[32] A.J. Bard, L.R. Faulkner, Electrochemical Methods: Fundamentals and Applications, second ed., Wiley, New York, 2001.
[33] P.T. Kissinger, W.R. Heineman, Laboratory Techniques in Electroanalytical Chemistry, second ed., Dekker, New York, 1996.
[34] M. Kandaz, M.N.U. Yaraşır, A. Koca, Ö. Bekaroğlu, Polyhedron 21 (2002) 255.
[35] A. Kalkan, A. Koca, Z.A. Bayır, Polyhedron 23 (2004) 3155.
[36] P. Matlaba, T. Nyokong, Polyhedron 21 (2002) 2463.
[37] A. Koca, M.K. Şener, M.B. Koçak, A. Gül, Transition Met. Chem. 30 (4) (2005) 399.
[38] A. Koca, H.A. Dinçer, M.B. Koçak, A. Gül, Russ. J. Electrochem. 41 (1) (2006) 36.
[39] J. Obirai, T. Nyokong, Electrochim. Acta 50 (2005) 3296.

denoting the axial and rhombic parts, respectively. In powder EPR spectra, the hyperfine interaction is not visible in most cases, presumably due to intermolecular dipole–dipole interactions which broaden the EPR transitions. When the manganese ion is magnetically diluted, the hyperfine interaction can be detected. In these dilute conditions, a unique feature centred around $g = 2$ is present in the EPR spectrum, corresponding to the central transition $|5/2, -1/2\rangle \rightarrow |5/2, +1/2\rangle$. This feature is split into several lines (six in the high field limit) because each electronic spin state is composed of six nuclear spin sublevels ($I = 5/2$). The transitions expected between the other Zeeman levels are not detected because they are very broad due to their dependence on the orientation of the zfs interaction. Since g-values are always close to 2.0023 because of the quasi-spherical symmetry of the fundamental spectroscopic term of the Mn(II) ion [18], the shape of the multiplet depends mainly on the magnitude of the A, D and E parameters and the microwave frequency used for the EPR experiment.

Mononuclear Mn(II) complexes display a large range of D values up to 1.21 cm^{-1} [1–13], depending on the nature and geometry of the coordination sphere of the metal ion. For mononuclear four-, five- and *trans* six-coordinate dihalide Mn(II) complexes the D values are in the range 0.9–1.2 cm^{-1} for iodo complexes, 0.5–0.7 cm^{-1} for bromo, and 0.16–0.30 cm^{-1} for chloro, whereas for *cis*-six-coordinate systems the D values are significantly lower: $|D_I| \sim 0.60\ cm^{-1}$, $|D_{Br}| \sim 0.36\ cm^{-1}$, $|D_{Cl}| \sim 0.12\ cm^{-1}$ [1–9]. Recently, we reported a HF-EPR investigation performed on the series *cis*-[Mn(tpa)X_2] (tpa = tris(2-pyridylmethyl)amine; X = I, Br, Cl) which was complemented by DFT calculations [8]. The general trend observed for Mn(II) halide complexes ($D_I > D_{Br} > D_{Cl}$) can be explained by the fact that the halide spin orbit coupling (SOC) dominates the D-value in these systems with a major contribution arising from interference terms between metal- and halide-SOC contributions which are proportional to the product of the SOC constants of Mn and X [8].

In studies of manganese sites present in metalloproteins or metalloenzymes, the samples obviously correspond to diluted conditions in which only the $|5/2, -1/2\rangle \rightarrow |5/2, +1/2\rangle$ transition can be observed. In this paper, our aim was to check the efficacy of HF-EPR for the precise determination of the electronic parameters of Mn(II) in diluted conditions over a large range of D-values. We used the corresponding Zn(II) complexes as diamagnetic hosts for the [Mn(tpa)X_2] complexes, as we have already used this strategy for the study of the [Zn(Mn)tButerpy$(N_3)_2$] (tButerpy = 4,4′,4″-tri-*tert*-butyl-2,2′:6′,2″-terpyridine) complex [9]. Only the X-ray structures of [Zn(tpa)I]·(ClO_4) [19], and [Zn(tpa)Cl]·Y (Y = BPh_4 [20]; ClO_4 [19]) have been reported in the literature. Since counter anions cannot be added during the synthesis of the Zn complexes doped with Mn, the molecular structure determined by X-ray diffraction of the neat Zn complexes [Zn(tpa)I]I (**1a**), [Zn(tpa)Br]$(ZnBr_4)_{0.5}$ (**2a**), [Zn(tpa)Cl]$(ZnCl_4)_{0.5}$ (**3a**) and [Zn(tpa)$(NCS)_2$] (**4a**) obtained under these conditions have been resolved and are presented here. The electronic properties of the [Mn(tpa)X_2] complexes doped into the corresponding Zn complexes (X = I (**1b**), Br (**2b**) and Cl (**3b**)) have been determined by HF-EPR. We use our experimental results to discuss the utility of multifrequency EPR in the interpretation of the spectra of these complexes recorded under diluted conditions with diverse D-values.

2. Results and discussion

2.1. Synthesis

The $[Zn(tpa)X]^+$ (X = I (**1a**), Br(**2a**), Cl (**3a**)) complexes were isolated from a mixture of equimolar amounts of ZnX_2 and tpa in MeOH, whereas [Zn(tpa)$(NCS)_2$] (**4a**) was isolated from the reaction of equimolar amounts of $Zn(NO_3)_2 \cdot 6H_2O$ and tpa in the presence of two equivalents of KSCN in MeOH.

The $[Zn(tpa)X]^+$ complexes doped with [Mn(tpa)X_2] (X = I (**1b**), Br (**2b**), Cl (**3b**)) were prepared in MeOH solution using a ZnX_2/MnX_2 ratio of 95/5 together with one equivalent of tpa ligand. After reflux for 30 min, the complexes were isolated by addition of diethyl ether. The Zn thiocyanate complex cannot be doped with the corresponding Mn compound since the solubility discrepancy between the Zn and the Mn complexes precludes the co-crystallization of both species.

2.2. X-ray structures

Suitable crystals for X-ray diffraction were obtained by slow diffusion of ethyl acetate into methanolic solutions of complexes **1a** and **4a**. Single crystals of complexes **2a** and **3a** were obtained similarly, but using diethyl ether. Tables 1 and 2 provide the principal crystallographic data together with selected bond distances and angles, and Fig. 1 displays the ORTEP diagrams of complexes **1a**–**4a**.

The halide complexes **1a**–**3a** are five-coordinate, whereas the thiocyanate complex **4a** is six-coordinate. There is a noticeable difference in the arrangement of the tpa ligand around the Zn cation in the latter. For compounds **1a**–**3a** the tpa ligand displays a pseudo-C_3 symmetry with N_{pyr}–Zn–N_{pyr} angles between 120° and 110°. Deviation from the theoretical 120° is due to the fact that the Zn atom is not in the N(2)–N(3)–N(4) plane. As the thiocyanate complex is six-coordinate, the pseudo-C_3 symmetry is lost and the corresponding angles approach a 90° value.

Complexes **1a**–**3a** adopt almost perfect trigonal bipyramid geometries, with τ values ranging from 0.94 to 1.04, similar to those observed in other monomeric structurally characterized transition metal complexes containing the tpa ligand [19,20]. The halide ligand is coordinated *trans* to the tertiary aliphatic nitrogen atom N(1) in all cases. Bond lengths within the chloride and iodide complexes are consistent with previously reported $[Zn(tpa)X]^+$ com-

Table 1
Principal crystallographic data and parameters for complexes **1a**–**4a**

Compound	**1a**	**2a**	**3a**	**4a**
Chemical formula	$C_{18}H_{18}I_2N_4Zn$	$C_{36}H_{36}Br_6N_8Zn_3$	$C_{36.69}H_{40.02}Cl_6N_8O_{1.32}Zn_3$	$C_{20}H_{18}N_6S_2Zn$
Formula weight	609.53	1256.30	1023.03	471.89
Crystal system	triclinic	triclinic	monoclinic	monoclinic
Space group	$P\bar{1}$	$P\bar{1}$	$P2_1/n$	$P2_1/c$
Unit cell dimensions				
a (Å)	9.624(3)	12.362(3)	14.416(2)	21.82(5)
b (Å)	14.336(5)	13.256(3)	14.159(2)	11.65(3)
c (Å)	16.858(7)	15.025(3)	21.775(3)	16.91(4)
α (°)	115.103(5)	112.896(4)	90.00	90.00
β (°)	100.328(9)	109.688(3)	105.987(3)	101.11(5)
γ (°)	91.471(6)	92.740(4)	90.00	90.00
Volume (Å^3)	2058.5(13)	2089.5(7)	4272.5(11)	4219(18)
T (K)	293(2)	223(2)	223(2)	298(2)
λ (Å)	0.71073	0.71073	0.71073	0.71073
D_{calc} (mg m^{-3})	1.967	1.997	1.590	1.486
Z	4	2	4	8
μ (mm^{-1})	4.200	7.482	2.087	1.381
F(000)	1.967	1216	2075	1936
Reflections collected	12947	13413	18370	17598
R_1[a]	0.0544	0.0350	0.0373	0.0359
wR_2[b]	0.1284	0.0820	0.0836	0.0848

[a] $R_1 = \sum\|F_o| - |F_c\|/\sum|F_o|$.

[b] $wR_2 = [(\sum w(|F_o| - |F_c|)^2/\sum wF_o^2)]^{1/2}$.

Table 2
Selected bond distances (Å) and angles (°) for the complexes **1a**–**4a**

Compound	**1a** (X = I)	**2a** (X = Br)	**3a** (X = Cl)	**4a** (X = NCS)
Zn–N(1)	2.237(5)	2.262(3)	2.264(2)	2.204(5)
Zn–N(2)	2.085(5)	2.094(3)	2.062(2)	2.126(5)
Zn–N(3)	2.096(5)	2.084(3)	2.083(2)	2.124(4)
Zn–N(4)	2.067(5)	2.087(3)	2.064(3)	2.269(5)
Zn–X	2.6397(10)	2.4078(7)	2.2744(8)	N(5) 1.990(5)
				N(6) 2.110(6)
N(1)–Zn–N(2)	77.45(19)	78.25(11)	78.11(9)	77.74(18)
N(1)–Zn–N(3)	77.4(2)	78.03(11)	77.41(9)	76.5(2)
N(1)–Zn–N(4)	77.5(2)	77.92(12)	77.64(9)	76.61(15)
N(2)–Zn–N(3)	115.0(2)	115.26(13)	110.30(9)	154.05(12)
N(2)–Zn–N(4)	117.31(19)	117.23(12)	120.57(10)	78.2(2)
N(3)–Zn–N(4)	113.9(2)	115.04(12)	115.88(10)	98.43(17)
N(1)–Zn–X	178.00(14)	179.77(8)	179.35(7)	N(5) 169.06(13)
				N(6) 92.12(14)
N(2)–Zn–X	103.58(13)	101.52(9)	101.99(6)	N(5) 103.43(19)
				N(6) 88.24(18)
N(3)–Zn–X	100.60(15)	102.06(8)	101.96(7)	N(5) 102.4(2)
				N(6) 89.93(16)
N(4)–Zn–X	103.38(15)	102.21(9)	102.83(7)	N(5) 92.91(17)
				N(6) 163.87(12)
N(5)–Zn–N(6)				98.77(16)

pounds [21,22], with distances between the Zn ion and the pyridine nitrogen atoms ranging between 2.062 and 2.096 Å, and significantly higher values for the Zn–N(1) bond (2.237–2.264 Å). As expected, the previously unreported $[Zn(tpa)Br]^+$ compound displays a Zn–Br bond length (2.4078 Å) ranging between the Zn–Cl (2.2744 Å) and the Zn–I (2.6397 Å) bond lengths in the analogous chloride and iodide complexes.

On the other hand, compound **4a** shows a pseudo-octahedral geometry where the two NCS anions are coordinated in a *cis* fashion. This complex is isostructural with its manganese parent compound [23]. As found for the Mn complex, the Zn–N bonds *trans* to the anionic ligands are significantly longer (2.204 and 2.269 Å) than the other Zn–N_{tpa} distances (2.126 and 2.124 Å). This *trans* effect has also been observed in other similar complexes [23,24].

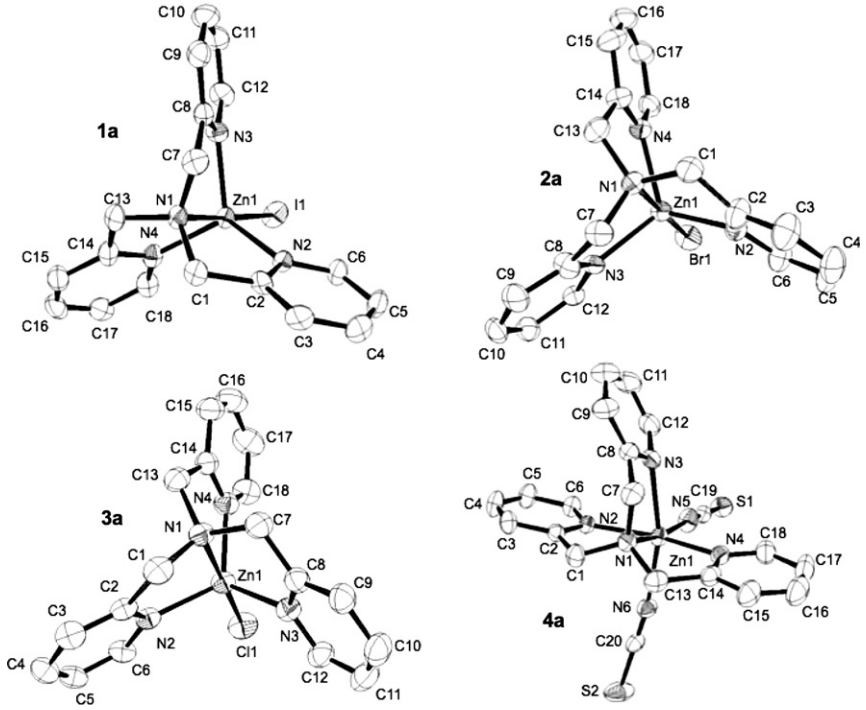


Fig. 1. ORTEP diagrams showing the molecular structures of complexes **1a**–**4a**.

2.3. Multifrequency EPR experiments

HF-EPR spectra were recorded on the magnetically diluted complexes **1b**–**3b**, at different frequencies (95–285 GHz) over the temperature range 10–50 K. The maximum intensity is found at 30 K. 285 GHz spectra recorded at 30 K are shown in Fig. 2. Features are only observed in a small field range (about 300 mT) around $g = 2.0$ due to the central $|5/2,-1/2\rangle \rightarrow |5/2,+1/2\rangle$ transition. The complexity of the spectra originates not only from the hyperfine interaction but also from the second order contribution of the zfs. Normally, six transitions are expected between the six nuclear sublevels of the two Zeeman levels ($m_s = \pm 1/2$) following the rule $\Delta m_i = 0$. However, when the second order contribution of the zfs is larger than the hyperfine interaction, other transitions are detected involving the simultaneous change in the nuclear and electronic spin state. The intensity of the latter transitions depends on the ratio between the zero field and the Zeeman interactions.

We obtained good quality spectra for the bromide and chloride complexes, but MnI_2 impurities were apparently present in the iodide complex. This causes the presence of intense lines centred at $g = 2$, which mask features belonging to compound **1b**. Fortunately, because of the large zfs parameters, the visible outer lines allow us to extract the spin Hamiltonian parameters of the system.

As can be seen in Fig. 2, the EPR spectra at the same frequency (285 GHz) become dramatically more complex as the magnitude of D increases, in accord with theoretical predictions. Whereas the EPR spectrum of the chloride compound characterized by the smallest D value is almost a sextuplet, the EPR signature of the bromide and iodide complexes is a very large multiplet. The total width of the spectra increases from complex **3b** to **1b**, being 80, 140 and 400 mT for **3b**, **2b** and **1b**, respectively. Fig. 3 shows the magnetic field effect on the complexity of the spectra. Spectra of **2b** recorded at frequencies of 95, 190 and 285 GHz reveal that the increasing magnetic field simplifies the spectra which tend toward a sextuplet at the highest field. Generally, the multifrequency character of the EPR study is of interest since at high field when a sextuplet is reached, the hyperfine coupling constant A (but not the zfs parameters) can be accurately determined. Conversely, at low field the complexity of the spectra allows a precise determination of the zfs parameters while the hyperfine coupling constant is not determined.

To determine the spin Hamiltonian parameters, the EPR spectra of **1b**–**3b** were simulated by using a full-matrix diagonalization procedure of Eq. (1). The best simulated spectra are shown in Figs. 2 and 3 and the corresponding zfs parameters are reported in Table 3 together with those obtained for the $[Mn(tpa)X_2]$ complexes.

The spin Hamiltonian parameters obtained from simulation of the HF-EPR spectra recorded on the $[Mn(tpa)X_2]$ and doped Zn complexes are essentially the same, indicating a similar environment around the Mn(II) ion in both pure and diluted lattices. The minor differences can be related to structural changes between the doped system versus the pure lattice since these two systems are not completely isostructural [8]. The A value is extracted from the magnetically diluted complexes, whereas the sign of D is obtained from the $[Mn(tpa)X_2]$ compounds.

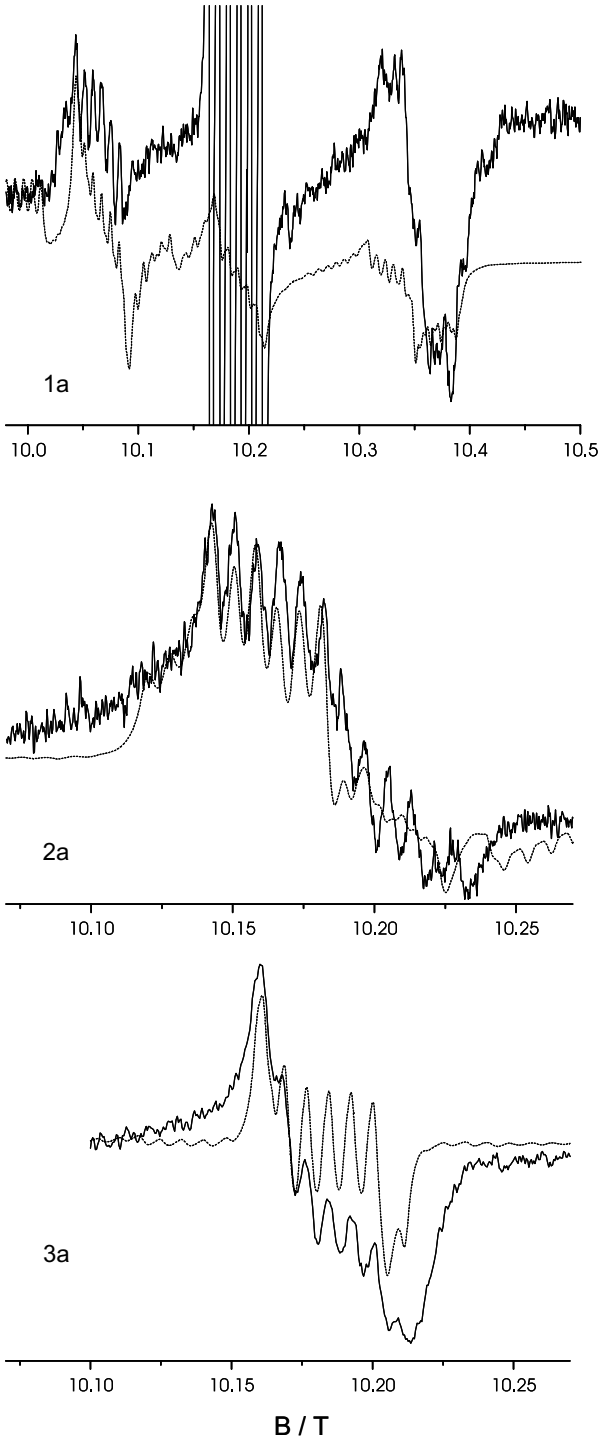


Fig. 2. Experimental (solid line) and simulated (dotted line) powder HF-EPR spectra of complexes **1b**, **2b** and **3b** at 285 GHz recorded at 30 K.

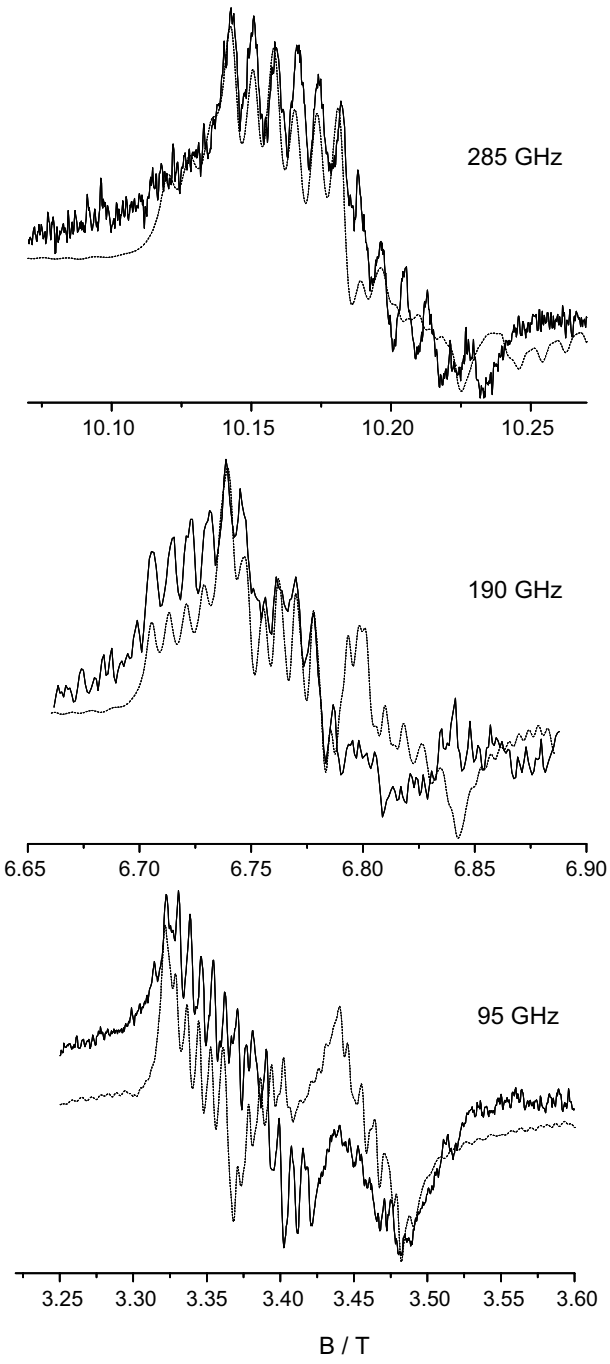


Fig. 3. Experimental (solid line) and simulated (dotted line) powder HF-EPR spectra of complex **2b** at 95, 190 and 185 GHz recorded at 30 K.

Because of the different D values of the halide complexes, this study provides a good illustration of the effect of the D parameter and the magnetic field on the shape of the multiplet observed in diluted conditions. Thus, depending on the D value of the complex and the parameters to be determined, the choice of EPR frequency becomes crucial. The accuracy of the determination of A is improved when high field conditions are reached (sextuplet) while, for the zfs parameters, a gain in precision is afforded when more complicated multiplets are obtained.

HF-EPR experiments on metalloenzymes containing a mononuclear Mn(II) site are obviously performed under diluted conditions. This study is a new example of how multifrequency HF-EPR spectroscopy can be used to explore minor changes in the environment of biological Mn(II) sites for mechanistic investigations. Furthermore,

Table 3
Electronic parameters determined by multifrequency HF-EPR on the doped **1b**–**3b** complexes and the [Mn(tpa)X_2] complexes

Complex	D (cm^{-1})	E (cm^{-1})	$\lvert E/D\rvert$	g_x, g_y, g_z	$A \times 10^{-4}$ (cm^{-1})
1b	0.635(2)	0.120(1)	0.189	2.00, 2.00, 2.00	68
2b	0.360(1)	0.069(1)	0.192	2.00, 2.00, 2.00	68
3b	0.115(2)	0.023(1)	0.200	2.00, 2.00, 2.00	68
[Mn(tpa)I_2] [8]	−0.600	0.095	0.158	1.99, 1.98, 2.00	n.d.[a]
[Mn(tpa)Br_2] [8]	−0.360	0.073	0.203	2.00, 1.98, 2.005	n.d.
[Mn(tpa)Cl_2] [8]	+0.115	0.020	0.174	1.97, 2.00, 2.00	n.d.

The sign of D is given when it can be determined.
[a] n.d. = not determined.

since the zfs parameters of the Mn(II) ion are very sensitive toward its environment (ligand exchange with halide or a change in coordination number), this ion is a good structural fingerprint and can potentially be used to substitute for other difficult to study metals in metalloenzymes.

3. Experimental

3.1. General

Reagents and solvents (analytical grade) were purchased from Aldrich and Fluka and used as received. Tris(2-pyridylmethyl)amine (tpa) was prepared according to the literature method [25]. Infrared spectra were recorded on a Perkin–Elmer Spectrum GX FTIR spectrometer.

3.2. Synthesis of the complexes

3.2.1. Synthesis of [Zn(tpa)I]I (**1a**)

To a stirred solution of tpa (50.6 mg, 0.174 mmol) in 5 mL of methanol was added a methanolic solution (2 mL) of ZnI_2 (55.6 mg, 0.174 mmol). The resulting colourless solution was stirred for 1 h and filtered. Colourless single crystals were obtained by slow diffusion of ethyl acetate into the filtrate.

Compound **1a**: Yield: 0.058 g (55%).

IR in cm^{-1} (KBr) v = 3430 (vs), 1609 (s), 1572 (m), 1482 (m), 1437 (s), 1367 (w), 1314 (m), 1270 (m), 1157 (w), 1126 (w), 1103 (m), 1053 (m), 1023 (s), 979 (w), 964 (w), 906 (w), 836 (w), 781 (s), 770 (m), 729 (w), 651 (w), 502 (w), 471 (w), 414 (w), 328 (w).

3.3. Synthesis of [Zn(tpa)Br]($ZnBr_4$)$_{0.5}$ (**2a**)

To a stirred solution of tpa (32.3 mg, 0.111 mmol) in 3 mL of methanol was added $ZnBr_2$ (25 mg, 0.111 mmol). The resulting colourless solution was stirred for half an hour. Colourless single crystals were obtained by slow diffusion of diethyl ether.

Compound **2a**: Yield: 0.016 g (34%).

IR in cm^{-1} (KBr) v = 3418 (vs), 1609 (s), 1573 (m), 1483 (m), 1439 (s), 1368 (w), 1315 (m), 1295 (w), 1270 (m), 1157 (w), 1126 (w), 1103 (m), 1053 (m), 1024 (s), 984 (w), 965 (w), 911 (w), 836 (w), 775 (s), 732 (w), 650 (m), 504 (m), 474 (w), 416 (m), 332 (w).

3.4. Synthesis of [Zn(tpa)Cl]($ZnCl_4$)$_{0.5}$ (**3a**)

To a stirred solution of tpa (54.6 mg, 0.188 mmol) in 3 mL of methanol was added a methanolic solution (3 mL) of $ZnCl_2 \cdot 6H_2O$ (25 mg, 0.188 mmol). The resulting colourless solution was stirred for half an hour. Colourless single crystals were obtained by slow diffusion of diethyl ether.

Compound **3a**: Yield: 0.028 g (44%).

IR in cm^{-1} (KBr) v = 3450 (vs), 1609 (s), 1573 (m), 1483 (m), 1438 (s), 1369 (w), 1315 (m), 1295 (w), 1269 (m), 1158 (w), 1126 (w), 1102 (m), 1054 (m), 1024 (s), 984 (w), 963 (w), 910 (w), 837 (w), 773 (s), 732 (w), 651 (m), 504 (m), 474 (w), 415 (m), 330 (w).

3.4.1. Synthesis of [Zn(tpa)($NCS)_2$] (**4a**)

To a stirred solution of tpa (62.7 mg, 0.216 mmol) and $Zn(NO_3)_2 \cdot 6H_2O$ (64.6 mg, 0.217 mmol) in 3 mL of methanol was added a methanolic solution (6 mL) of KSCN (42 mg, 0.433 mmol). The resulting colourless solution was stirred for half an hour. Colourless single crystals were obtained by slow diffusion of ethyl acetate.

Compound **4a**: Yield: 0.055 g (54%).

IR in cm^{-1} (KBr) v = 3462 (m), 3451 (w), 2918 (w), 2057 (vs), 1602 (s), 1573 (m), 1484 (m), 1435 (s), 1389 (w), 1370 (w), 1350 (w), 1351 (w), 1312 (m), 1287 (m), 1268 (m), 1220 (w), 1154 (m), 1121 (w), 1098 (m), 1052 (m), 1020 (m), 991 (w), 976 (w), 955 (w), 908 (w), 834 (w), 767 (s), 733 (w), 640 (w), 514 (w), 502 (w), 475 (w), 419 (m).

3.4.2. Synthesis of [Zn(tpa)I]I doped with [Mn(tpa)I_2] (**1b**)

To a stirred solution of tpa (120 mg, 0.413 mmol) in 2 mL of methanol was added a methanolic solution (1 mL) of MnI_2 (6.38 mg (5%), 0.021 mmol) and a methanolic solution (2 mL) of ZnI_2 (125.13 mg (95%), 0.392 mmol). The resulting colourless solution was heated to reflux for half an hour and then cooled to room temperature. Addition of diethyl ether to this solution yielded a white precipitate corresponding to **1b**. Yield: 0.176 g (70%).

IR similar as **1a**.

3.4.3. Synthesis of [Zn(tpa)Br]($ZnBr_4$)$_{0.5}$ doped with [Mn(tpa)Br_2] (**2b**)

To a stirred solution of tpa (80.9 mg, 0.279 mmol) in 2 mL of methanol was added a methanolic solution

(1 mL) of $MnBr_2$ (3.1 mg (5%), 0.014 mmol) and a methanolic solution (2 mL) of $ZnBr_2$ (60.0 mg (95%), 0.266 mmol). The resulting colourless solution was heated to reflux for half an hour and then cooled to room temperature. Addition of diethyl ether to this solution yielded a white precipitate corresponding to **2b**. Yield: 0.061 g (52%).

IR similar as **2a**.

3.4.4. Synthesis of $[Zn(tpa)Cl](ZnCl_4)_{0.5}$ doped with $[Mn(tpa)Cl_2]$ (**3b**)

To a stirred solution of tpa (81.0 mg, 0.279 mmol) in 2 mL of methanol was added a methanolic solution (1 mL) of $MnCl_2$ (0.7 mg (2%), 0.006 mmol) and a methanolic solution (2 mL) of $ZnCl_2$ (37.5 mg (98%), 0.270 mmol). The resulting colourless solution was heated to reflux for half an hour and then cooled to room temperature. Addition of diethyl ether to this solution yielded a white precipitate corresponding to **3b**. Yield: 0.044 g (46%).

IR similar as **3a**.

3.5. Physical measurements

High-frequency and high-field EPR spectra were recorded on a laboratory made spectrometer [26] using powder samples pressed in pellets to avoid preferential orientation of the crystallites in the strong magnetic field. Gunn diodes operating at 95 GHz and 115 GHz and equipped with a second- and third-harmonic generator have been used as the radiation source. The magnetic field was produced by a superconducting magnet (0–12 T). The simulation of the HF-EPR spectra was performed using the SIM program written by Weihe [2]. SIM performs a full-matrix diagonalization of the spin Hamiltonian. It is therefore adequate for spin systems with any value of the zfs parameter relative to the operating frequency. The program also takes into account the Boltzmann population factor in calculating transition intensities. Its detailed description is available on the Web site http://sophus.kiku.dk/software/epr/epr.html.

3.6. Crystal structure determination

Diffraction data were collected on a Bruker SMART diffractometer with Mo Kα radiation. Crystal of complexes of dimensions $0.50 \times 0.30 \times 0.20$ mm for **1a**, $0.40 \times 0.20 \times 0.06$ mm for **2a**, $0.50 \times 0.40 \times 0.40$ mm for **3a**, and $0.40 \times 0.20 \times 0.10$ mm for **4a** were selected. The crystallographic data are summarized in Tables 1 and 2. All calculations were effected using the SHELXTL computer program [27].

Acknowledgements

We thank Dr. H. Weihe from the Chemistry Department, University of Copenhagen, Denmark, for the simulation software. We gratefully thank the bilateral New Zealand-France Dumont D'Urville Program for financial support.

Appendix A. Supplementary material

CCDC 650220, 650221, 650364 and 650219 contain the supplementary crystallographic data for **1a**, **2a**, **3a** **4a**. These data can be obtained free of charge via http://www.ccdc.cam.ac.uk/conts/retrieving.html, or from the Cambridge Crystallographic Data Centre, 12 Union Road, Cambridge CB2 1EZ, UK; fax: (+44) 1223-336-033; or e-mail: deposit@ccdc.cam.ac.uk. The CIF files are available in the supplementary files. Supplementary data associated with this article can be found, in the online version, at doi:10.1016/j.poly.2007.07.030.

References

[1] R.B. Birdy, M. Goodgame, Inorg. Chim. Acta 50 (1981) 183.
[2] C.J.H. Jacobsen, E. Pedersen, J. Villardsen, H. Weihe, Inorg. Chem. 32 (1993) 1216.
[3] D.M.L. Goodgame, H. El Mkami, G.M. Smith, J.P. Zhao, E.J.L. McInnes, Dalton Trans. (2003) 34.
[4] W.B. Lynch, R.S. Boorse, J.H. Freed, J. Am. Chem. Soc. 115 (1993) 10909.
[5] R.M. Wood, D.M. Stucker, L.M. Jones, W.B. Lynch, S.K. Misra, J.H. Freed, Inorg. Chem. 38 (1999) 5384.
[6] C. Mantel, C. Baffert, I. Romero, A. Deronzier, J. Pecaut, M.-N. Collomb, C. Duboc, Inorg. Chem. 43 (2004) 6455.
[7] C. Duboc, V. Astier-Perret, H. Chen, J. Pecaut, R.H. Crabtree, G.W. Brudvig, M.-N. Collomb, Inorg. Chim. Acta 359 (2006) 1541.
[8] C. Duboc, T. Phoeung, S. Zein, J. Pecaut, M.-N. Collomb, F. Neese, Inorg. Chem. 46 (2007) 4905.
[9] C. Mantel, C. Philouze, M.-N. Collomb, C. Duboc, Eur. J. Inorg. Chem. (2004) 3880.
[10] S. Un, L.C. Tabares, N. Cortez, B.Y. Hiraoka, F. Yamakura, J. Am. Chem. Soc. 126 (2004) 2720.
[11] S.K. Smoukov, J. Telser, B.A. Bernat, C.L. Rife, R.N. Armstrong, B.M. Hoffman, J. Am. Chem. Soc. 124 (2002) 2318.
[12] H. Käss, F. MacMillan, B. Ludwig, T. Prisner, J. Phys. Chem. B 104 (2000) 5362.
[13] R. Kappl, K. Ranguelova, B. Koch, C. Duboc, J. Hüttermann, Magn. Reson. Chem. 43 (2005) 65.
[14] C. Mantel, A.K. Hassan, J. Pecaut, A. Deronzier, M.-N. Collomb, C. Duboc-Toia, J. Am. Chem. Soc. 125 (2003) 12337.
[15] J. Krzystek, A. Ozarowski, J. Telser, Coord. Chem. Rev. 250 (2006) 2308.
[16] P.L.W. Tregenna-Piggott, H. Weihe, A.-L. Barra, Inorg. Chem. 42 (2003) 8504.
[17] C. Duboc-Toia, H. Hummel, E. Bill, A.-L. Barra, G. Chouteau, K. Wieghardt, Angew. Chem., Int. Ed. 39 (2000) 2888.
[18] A. Abragam, B. Bleaney (Eds.), Electron Paramagnetic Resonance of Transition Ions, Clarendon Press, Oxford, 1970.
[19] A.W. Addison, T.N. Rao, J. Reedijk, J. van Rijn, G.C. Verschoor, J. Chem. Soc., Dalton Trans. (1984) 1349.
[20] A.G. Blackman, Polyhedron 24 (2005) 1.
[21] C.S. Allen, C.-L. Chuang, M. Cornebise, J.W. Canary, Inorg. Chim. Acta 239 (1995) 29.
[22] H. Adams, N.A. Bailey, D.E. Fenton, Q.-Y. He, J. Chem. Soc., Dalton Trans. (1997) 1533.
[23] H. Oshio, E. Ino, I. Mogi, T. Ito, Inorg. Chem. 32 (1993) 5697.
[24] D.F. Xiang, C.Y. Duan, X.S. Tan, Y.J. Liu, W.X. Tang, Polyhedron 17 (1998) 2647.
[25] K.D. Karlin, J.C. Hayes, J.P. Hutchinson, J. Zubieta, Inorg. Chem. 21 (1982) 4106.
[26] A.-L. Barra, L.-C. Brunel, J.B. Robert, Chem. Phys. Lett. 165 (1990) 107.
[27] G.M. Sheldrick, SHELXTL-Plus, vers. 5.1: Structure Determination Software Programs, Bruker-AXS Inc., Madison, WI, 1998.

for 6 h, the mixture was filtered and the filtrate was allowed to stand at room temperature. Colorless crystals appeared in about eight weeks. Colorless crystals suitable for X-ray diffraction analysis were obtained after the filtrate was carefully dealt with at low temperature and slowly evaporated. The filtrate of the lanthanide–amino acid complexes was reported to easily precipitate under near physiological pH conditions [7], however, no precipitate was observed in the process of crystal growth under our conditions.

Element analysis of the complexes was carried out on Elementar Aanlysensysteme GmbH Vario EL (HAMAU, Germany). Elemental *Anal.* Calc. for $[Tb_2(DL\text{-}Cys)_4(H_2O)_8]Cl_2$: C, 14.23; H, 3.83; N, 5.53. Found: C, 14.35; H, 3.65; N, 5.48%; *Anal.* Calc. for $[Eu_4(\mu_3\text{-}OH)_4(L\text{-}Asp)_2(L\text{-}HAsp)_3(H_2O)_7]Cl \cdot 11.5H_2O$: C, 14.00; H, 4.05; N, 4.11. Found: C, 14.01; H, 3.91; N, 4.08%; *Anal.* Calc. for $[Eu_8(L\text{-}HVal)_{16}(H_2O)_{32}]Cl_{24} \cdot 12.5H_2O$: C, 20.24; H, 5.59; N, 4.72. Found: C, 21.07; H, 5.56; N, 4.91%; *Anal.* Calc. for $[Tb_2(DL\text{-}HVal)_4(H_2O)_8]Cl_6 \cdot 2H_2O$: C, 20.35; H, 5.43; N, 4.75. Found: C, 22.12; H, 5.18; N, 4.87%.

2.2. X-ray diffraction determination

Single crystal X-ray data were collected on a Siemens SMART CCD diffractometer with graphite-monochromatic Mo Kα ($\lambda = 0.71073$ Å) radiation at a temperature of 298 ± 2K. The structures were solved by direct methods using the SHELXTL-97 crystallographic software package and refined by full matrix least-squares on F^2 [11]. The details of crystal data, refinement and final statistics are summarized in Table 1.

2.3. Bioassay

The various DNA oligonucleotides were synthesized by Sangon (Shanghai, China) and were used without further purification. The DNA extinction coefficient was calculated through the nearest neighbor method [12,13]. Experiments were carried out in aqueous Tris buffer (10 mM Tris, 100 mM NaCl, pH 7.1) unless stated otherwise.

Absorbance measurements were made on a JASCO V-550 UV–Vis spectrophotometer, equipped with a Peltier temperature control accessory. Fluorescence measurements and circular dichroism (CD) spectra were measured on a JASCO FP-6500 spectrofluorometer and a JASCO J-810 spectropolarimeter equipped with a temperature-controlled water-bath. The job plot was constructed from emission data [12,13]. The total concentration of the complex and DNA (in units of base) was held constant at 60 μM over the course of the titration. DNA binding constants were determined by fluorescence titration as described previously [14–17]. Titration data were fit directly by non-linear least-squares methods to get binding constants.

3. Results and discussion

X-ray structure analysis reveals a structural diversity of the complexes (Figs. 1–4), demonstrating that the cubane-like structure is one of the structures obtained under higher pH. Table 2 summarizes the bond distances for these complexes. For complex **1** (Fig. 1), a very interesting structure of the sulfur bridge is found. Complex **1** is prepared in cysteine acid, however, no separated cysteine acid can be

Table 1
Crystal data and structure refinement parameters of complexes **1**–**4**

Complex	**1**	**2**	**3**	**4**
Empirical formula	$C_{12}H_{38.80}C_{12}Tb_2N_4O_{16}S_4$	$C_{20}H_{69}ClEu_4N_5O_{42.50}$	$C_{80}H_{265}Cl_{24}Eu_8N_{16}O_{76.50}$	$C_{20}H_{64}Cl_6Tb_2N_4O_{18}$
Formula weight	1012.25	1703.09	4742.56	1179.29
Temperature (K)	293 (2)	293 (2)	293 (2)	293 (2)
Wavelength (Å)	0.71073	0.71073	0.71073	0.71073
Crystal system	orthorhombic	orthorhombic	triclinic	monoclinic
Space group	*Fddd*	$P2_12_12_1$	*P*1	*C*2/*c*
Unit cell dimensions				
a (Å)	11.462(7)	11.559(5)	14.0671(8)	26.438(3)
b (Å)	21.214(8)	20.748(9)	18.4047(11)	11.3555(14)
c (Å)	35.636(16)	23.684(10)	19.2342(12)	16.310(2)
α (°)	90	90	87.743(3)	90
β (°)	90	90	82.315(3)	115.419(2)
γ (°)	90	90	82.512(3)	90
Volume (Å^3)	8665(7)	5680(4)	4891.7(5)	4422.5(9)
Z	8	4	1	4
D_{calc} (Mg/m^3)	1.552	1.992	1.610	1.771
μ (mm^{-1})	3.605	4.509	2.931	3.600
F(000)	3958	3332	2381	2352
Crystal size (mm)	0.32 × 0.28 × 0.21	0.21 × 0.10 × 0.05	0.4 × 0.3 × 0.3	0.25 × 0.14 × 0.11
θ Range (°)	2.10–26.00	1.96–26.00	1.93–25.02	1.71–26.04
Reflections collected	2483	32108	22410	12084
Data/restraints/parameters	2047/0/103	11117/9/654	18761/5/1454	4327/4248
Goodness-of-fit on F^2	1.144	1.072	1.011	1.047
Final *R* indices	$R_1 = 0.0965$	$R_1 = 0.0315$	$R_1 = 0.0782$	$R_1 = 0.0261$
[$I > 2\sigma(I)$]	$wR_2 = 0.2197$	$wR_2 = 0.0834$	$wR_2 = 0.2024$	$wR_2 = 0.0755$

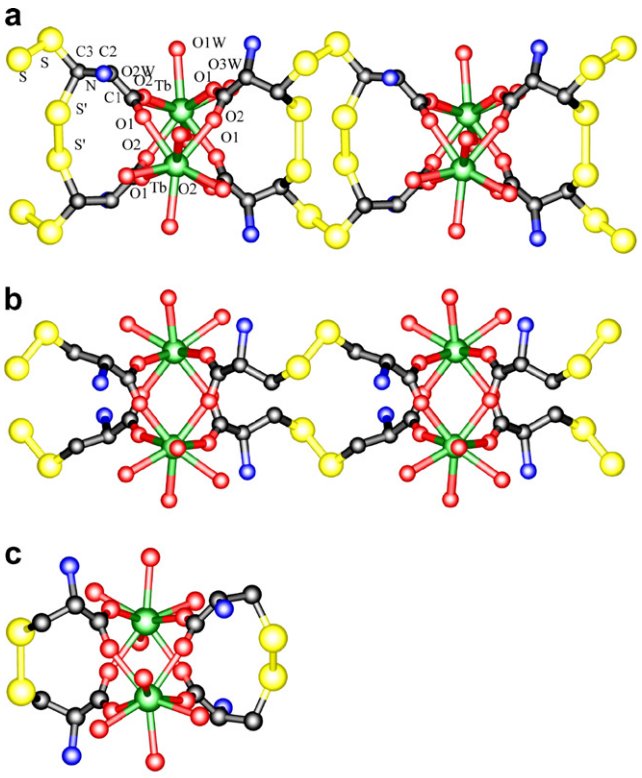


Fig. 1. Crystal structure of complex **1** (a), type 1 structure (b) and type 2 structure (c). Carbon: black; nitrogen: blue; oxygen: red; sulfur: yellow; terbium: green. Lattice water, hydrogen atoms and chloride ions are omitted for clarity. (For interpretation of the references in color in this figure legend, the reader is referred to the web version of this article.)

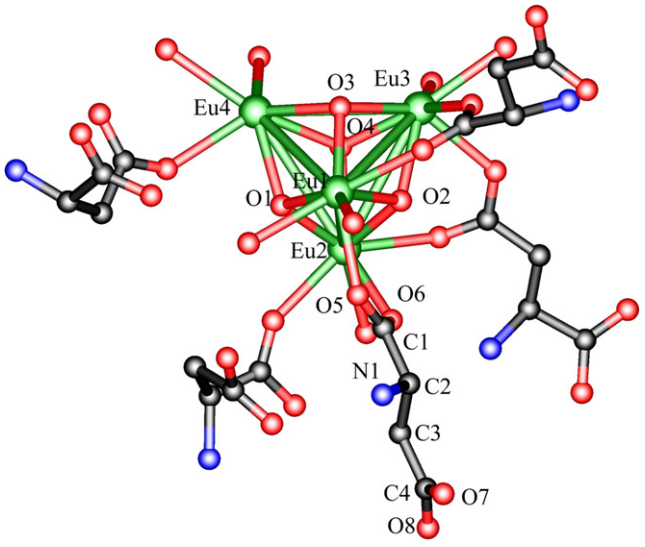


Fig. 2. Crystal structure of complex **2**. Carbon: black; nitrogen: blue; oxygen: red; europium: green. Lattice water, hydrogen atoms and chloride ions are omitted for clarity. (For interpretation of the references in color in this figure legend, the reader is referred to the web version of this article.)

found in the final product because all the cysteine acids have been connected through S–S bonds to form cystine acid. This complex consists of two types of structures. In

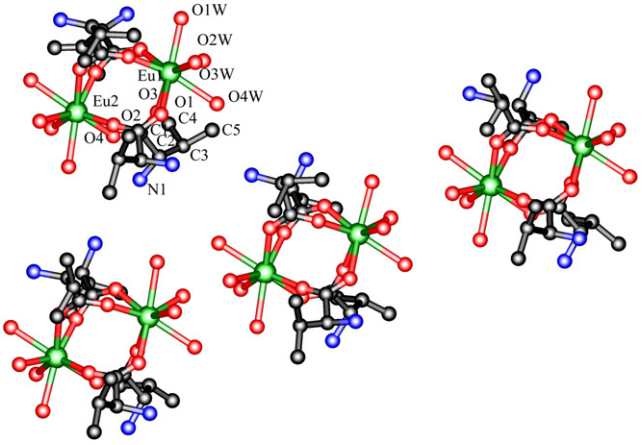


Fig. 3. Crystal structure of the four non-equivalent isolated dimers formed by complex **3**. Carbon: black; nitrogen: blue; oxygen: red; europium: green. Lattice water, hydrogen atoms and chloride ions are omitted for clarity. (For interpretation of the references in color in this figure legend, the reader is referred to the web version of this article.)

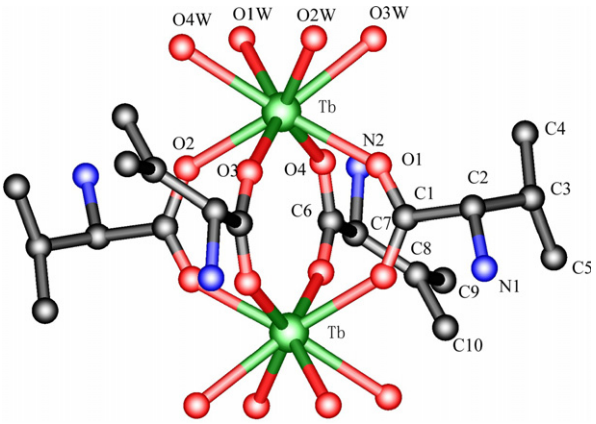


Fig. 4. Crystal structure of complex **4**. Carbon: black; nitrogen: blue; oxygen: red; terbium: green. Lattice water, hydrogen atoms and chloride ions are omitted for clarity. (For interpretation of the references in color in this figure legend, the reader is referred to the web version of this article.)

type 1 (as shown Fig. 1b), the carboxyl group from a cysteine acid connects two terbium ions forming an oxygen bridge, and the S atom connects with another S atom from the neighboring cysteine acid, which connects to an additional two terbium ions through its carboxyl group. This form constructs an infinite chain structure and 70% of complex **1** is in this form (Fig. 1). In type 2, two cysteine acids are connected to the same two terbium ions by their carboxyl groups, and a S′–S′ bond is formed. Type 2 is regarded as an independent dimer and is only 30% of the whole structure of complex **1** (Fig. 1c). The energy minimization performed under an MM+ force field using the program HyperChem 7.0 shows that type 1 is more energy favorable (106.537 kcal/mol) than type 2 (114.895 kcal/mol), which is in consistent with type 1 being predominant in the complex. The structure of lanthanide–cysteine acid has never been reported, even under extensively

Table 2
Summary of the bond distances (Å) for these four complexes

Atoms	Distance	Atoms	Distance	Atoms	Distance
Complex **1**		Eu(4)–O(11)	2.397(5)	Eu(5)–O(21)	2.312(17)
Tb–O(1)	2.363(17)	Eu(4)–O(16)	2.485(5)	Eu(5)–O(23)	2.276(17)
Tb–O(2)	2.400(14)	Eu(4)–O(17)	2.530(5)	Eu(5)–O(17)W	2.48(2)
Tb–O(1)W	2.477(14)	Eu(4)–O(6)W	2.524(6)	Eu(5)–O(18)W	2.502(17)
Tb–O(2)W	2.426(15)	Eu(4)–O(7)W	2.544(6)	Eu(5)–O(19)W	2.40(2)
				Eu(5)–O(20)W	2.451(19)
Complex **2**		*Complex* **3**		Eu(6)–O(18)	2.352(17)
Eu(1)–O(1)	2.375(5)	Eu(1)–O(1)	2.323(15)	Eu(6)–O(20)	2.308(15)
Eu(1)–O(2)	2.365(4)	Eu(1)–O(3)	2.399(16)	Eu(6)–O(22)	2.381(17)
Eu(1)–O(3)	2.368(5)	Eu(1)–O(5)	2.331(19)	Eu(6)–O(24)	2.418(17)
Eu(1)–O(5)	2.446(5)	Eu(1)–O(7)	2.376(15)	Eu(6)–O(21)W	2.474(18)
Eu(1)–O(8)	2.422(5)	Eu(1)–O(1)W	2.507(19)	Eu(6)–O(22)W	2.427(18)
Eu(1)–O(9)	2.394(5)	Eu(1)–O(2)W	2.40(2)	Eu(6)–O(23)W	2.494(17)
Eu(1)–O(1)W	2.449(6)	Eu(1)–O(3)W	2.446(15)	Eu(6)–O(24)W	2.461(17)
Eu(1)–O(2)W	2.497(6)	Eu(1)–O(4)W	2.480(18)	Eu(7)–O(25)	2.260(17)
Eu(1)–Eu(2)	3.7651(10)	Eu(2)–O(2)	2.405(17)	Eu(7)–O(27)	2.442(15)
Eu(1)–Eu(3)	3.8869(17)	Eu(2)–O(4)	2.312(16)	Eu(7)–O(29)	2.286(19)
Eu(1)–Eu(4)	3.8334(11)	Eu(2)–O(6)	2.396(16)	Eu(7)–O(31)	2.373(18)
Eu(2)–O(1)	2.380(5)	Eu(2)–O(8)	2.296(17)	Eu(7)–O(25)W	2.44(2)
Eu(2)–O(2)	2.413(4)	Eu(2)–O(5)W	2.448(15)	Eu(7)–O(26)W	2.466(17)
Eu(2)–O(4)	2.413(5)	Eu(2)–O(6)W	2.513(18)	Eu(7)–O(27)W	2.481(18)
Eu(2)–O(6)	2.410(5)	Eu(2)–O(7)W	2.350(18)	Eu(7)–O(28)W	2.47(2)
Eu(2)–O(12)	2.392(6)	Eu(2)–O(8)W	2.462(18)	Eu(8)–O(26)	2.406(18)
Eu(2)–O(13)	2.435(5)	Eu(3)–O(9)	2.295(18)	Eu(8)–O(28)	2.282(18)
Eu(2)–O(21)	2.433(7)	Eu(3)–O(11)	2.404(16)	Eu(8)–O(30)	2.429(19)
Eu(2)–O(3)W	2.520(6)	Eu(3)–O(13)	2.340(15)	Eu(8)–O(32)	2.310(17)
Eu(2)–Eu(3)	3.8023(10)	Eu(3)–O(15)	2.436(15)	Eu(8)–O(29)W	2.50(2)
Eu(2)–Eu(4)	3.9040(17)	Eu(3)–O(9)W	2.391(18)	Eu(8)–O(30)W	2.32(2)
Eu(3)–O(2)	2.387(4)	Eu(3)–O(10)W	2.51(2)	Eu(8)–O(31)W	2.444(18)
Eu(3)–O(3)	2.375(5)	Eu(3)–O(11)W	2.460(16)	Eu(8)–O(32)W	2.440(18)
Eu(3)–O(4)	2.339(5)	Eu(3)–O(12)W	2.477(15)		
Eu(3)–O(10)	2.389(5)	Eu(4)–O(10)	2.459(18)	*Complex* **4**	
Eu(3)–O(14)	2.439(5)	Eu(4)–O(12)	2.282(17)	Tb–O(1)	2.339(3)
Eu(3)–O(15)	2.417(5)	Eu(4)–O(14)	2.371(16)	Tb–O(2)	2.343(3)
Eu(3)–O(4)w	2.468(5)	Eu(4)–O(16)	2.348(17)	Tb–O(3)	2.321(3)
Eu(3)–O(5)w	2.497(5)	Eu(4)–O(13)W	2.46(2)	Tb–O(4)	2.338(3)
Eu(3)–Eu(4)	3.8390(11)	Eu(4)–O(14)W	2.442(18)	Tb–O(1)W	2.425(3)
Eu(4)–O(1)	2.408(5)	Eu(4)–O(15)W	2.442(17)	Tb–O(2)W	2.374(3)
Eu(4)–O(3)	2.447(4)	Eu(4)–O(16)W	2.48(2)	Tb–O(3)W	2.474(3)
Eu(4)–O(4)	2.447(5)	Eu(5)–O(17)	2.379(16)	Tb–O(4)W	2.480(3)
Eu(4)–O(7)	2.405(5)	Eu(5)–O(19)	2.451(16)		

investigated acid conditions, because the final product forms colloids easily. Only a Nd–Cystine complex, $(Nd_2(Cystine)_2(H_2O)_8)(ClO_4)_6 \cdot 3H_2O$, at pH 4 was reported as an infinite layer structure [18], which is different from the structure reported here.

Complex **2** forms a cubane-like structure (Fig. 2), similar to the previously reported structures of $[Dy_4(\mu_3\text{-}OH)_4(Asp)_3(H_2O)_8](ClO_4)_2 \cdot 10H_2O$ and $[Er_4(\mu_3\text{-}OH)_4(HGlu)_3(H_2O)_8](ClO_4)_5 \cdot 6H_2O$ [6,7], and is capable of forming a three-dimensional network based on the Eu_4O_4 cubane core with bridging Asp ligands. However, significant differences exist in this structure: two kinds of ligand valence (three ligands for −1 and two ligands for −2) and two europium coordination numbers (8 and 9) were observed, which was not reported in the previous cubane-like structures [6,7]. The differences can result from solution conditions and the 1:1 ratio of Ln/amino acid we used as the initial molar ratio instead of a 2:1 ratio [6,7].

For complex **3**, an unusual structure of four non-equivalent isolated dimers is found (Fig. 3). In each dimer, two europium atoms are connected by the quadruple bridge from four carboxyl groups of valine molecules. The isolated dimer structure is common, however, a structure with four non-equivalent isolated dimers has rarely been reported, and this presents another type of their structures.

For complex **4**, a simple dimeric form is obtained (Fig. 4). This structure is similar to those reported at low pH, and is consistent with the structure of a gadolinium–alanine complex obtained under near physiological pH conditions [19].

Therefore, only complex **2** is a cubane-like structure under near physiological pH conditions at a 1:1 ratio and the other three complexes show different structural characters, demonstrating the structural diversity of lanthanide–amino acid complexes. It was reported that a high reaction temperature was necessary to facilitate the hydrolytic pro-

cess [7]. Lanthanide ions prefer to form oxo-hydroxo lanthanide clusters at neutral pH under high temperature [20]. The reported structures all obtained under a high reaction temperature (80 °C) and can be regarded as amino acid oxo-hydroxo lanthanide clusters. In our experiments, at room temperature, we found that the hydrolysis of lanthanide ions can be inhibited by increasing the proportion of amino acid, and the lanthanide–amino acid complexes show structural diversity.

It should be pointed out that a Tb–cys or Tb–Val complex was formed by terbium with a 50:50 mixture of racemic amino acids, the same case in form 1 or form 2 (see Supplementary material). Lanthanide–amino acid complexes were obtained under near physiological pH conditions and have potential application in DNA detection since their fluorescence is greatly enhanced upon their binding to single-stranded DNA [1]. UV–Vis, fluorescence and circular dichroism (CD) spectroscopy were employed [14–17] to study the interactions between these complexes and five single-stranded DNA. The DNA sequences are listed in Table 3. Similar changes were observed for the terbium or europium series. Tb complex **1** and Eu complex **3** are reported in Figs. 5 and 6. Upon being complex bound, the DNA absorbance decreased and even shifted and the complex fluorescence was greatly enhanced when excited at 270 nm, showing that single-stranded DNA (ssDNA), except polydA (ssDNA 5), can transfer their excited-stated energy to the complex efficiently [1]. Typical fluorescence spectra are shown in Fig. 5a. DNA binding constants were determined by fluorescence titration as described previously [14–17]. The binding constants and F_b/F_0 (fluorescence emission intensity, $F_0 = F_{TbCys}$, $F_b = F_{TbCys\text{-}DNA}$) are summarized in Table 3 and show that the binding affinity and the fluorescence enhancement are sequence dependent, the stronger the binding affinity, the more the fluorescence enhancement. The continuous variation method was used to get the binding stoichiometry (n) of complex **1** with DNA. Typical data of complex **1** with ssDNA 5 are shown in Fig. 6. Table 3 summarizes the binding stoichiometries. The different binding stoichiometries further indicates that the complex is bound to the single-stranded DNA differently, which is also a demonstration that the difference is not from terbium ion itself but related to the property of amino acids and the structure of the complex (see Table 3), in accordance with UV–Vis and fluorescence results.

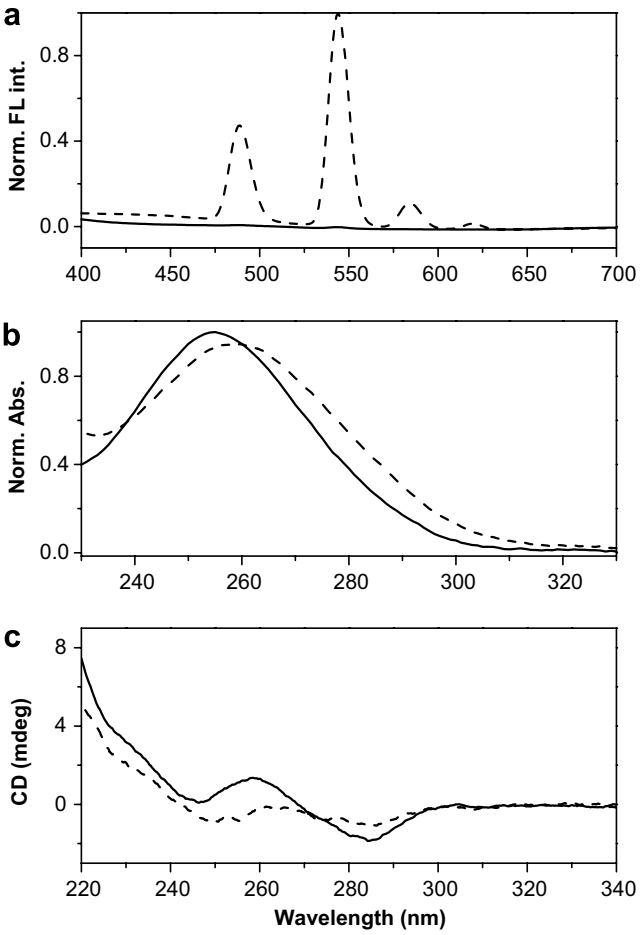


Fig. 5. (a) Fluorescence emission spectra of complex **1** in the absence (solid line) and presence (dash line) of ssDNA 4 ($\lambda_{ex} = 270$ nm). The concentration of complex **1** is 20 μM and the concentration of DNA is 40 μM. (b) UV–Vis absorbance spectra of ssDNA 4 in the absence (solid line) and presence (dash line) of complex **1**. The concentration of DNA is 20 μM and the concentration of complex **1** is 40 μM. (c) CD spectra of ssDNA 4 in the absence (solid line) and presence of complex **1** (dash line). The concentration of complex **1** is 30 μM and the DNA concentration is 60 μM. The DNA concentration is used in the base unit.

Although the UV–Vis absorption and circular dichroism spectral changes are similar, the fluorescence enhancement is different between the terbium and europium series when bound to DNA. Fig. 7 clearly shows the fluorescence enhancement for the europium complex following the order: ssDNA 1 > ssDNA 2 > ssDNA 3. SsDNA 4 and

Table 3
Summary of spectral changes and the binding parameters of complex **1** with five single-stranded DNA (ssDNA)

DNA	DNA sequence (22 mers)	K^a ($\times 10^4$)	F_b/F_0	n^b	UV maximum absorbance	CD ellipticity (mdeg)
ssDNA 1	$T_3(CCT)_4CT_6$	7.0	31	1.5	decrease	decrease (at 250 nm and 280 nm)
ssDNA 2	$T_6(CTT)_5T$	6.7	27	3.0	decrease	decrease (at 250 nm and 280 nm)
ssDNA 3	T_{22}	1.8	20	2.3	decrease	decrease (at 250 nm and 280 nm)
ssDNA 4	$A_3(GGA)_4GA_6$	8.2	38	1.0	shift 4 nm	decrease (at 260 nm and 285 nm) and shift (at 260 nm)
ssDNA 5	A_{22}				shift 3 nm	decrease (at 250 nm and 280 nm) and shift (at 280 nm)

[a] DNA binding constant. Titration data were fit directly by non-linear least-squares methods to get binding constants. The errors were within 10–15%.
[b] The binding stoichiometry ([base]/[TbCys]) which was obtained with a continuous variation method.

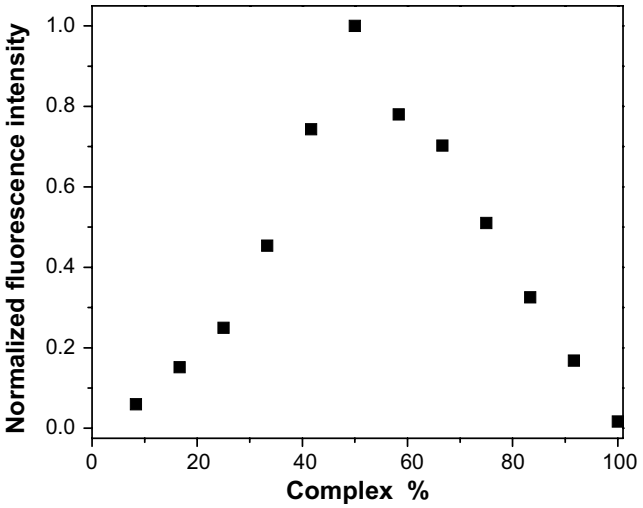


Fig. 6. Job plot of complex **1** with ssDNA 4. Total concentration of the complex and DNA (in units of base) was held constant at 60 μM over the course of the titration.

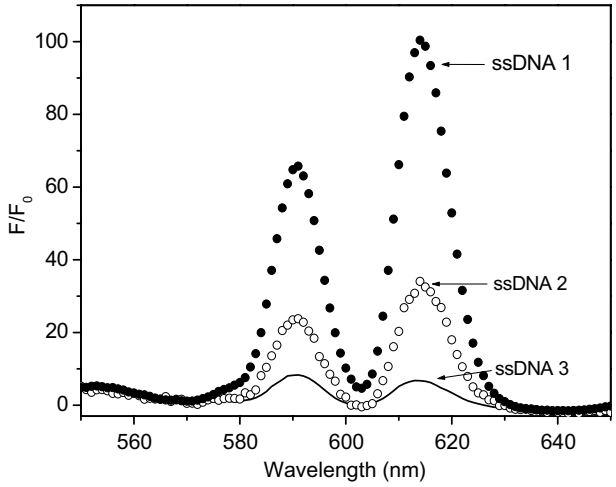


Fig. 7. Fluorescence emission spectra of complex **3** in the presence of ssDNA 1 (solid circles), ssDNA 2 (open circles) and ssDNA 3 (line). The excitation wavelength $\lambda_{ex} = 270$ nm. The emission spectra were recorded from 550 nm to 650 nm. The concentration of complex **3** is 20 μM and the concentration of DNA is 40 μM.

ssDNA 5 did not enhance the complex fluorescence but ssDNA 4 greatly increased terbium fluorescence.

Different DNA structure selectivity was found for europium amino acid complexes, such as the europium-L-aspartic acid complex [12,13]. Europium-L-aspartic acid complex is a cubane-like complex which can selectively stabilize non-B form DNA polydApolydT but destabilize polydGdCpolydGdC and polydAdTpolydAdT [12], and convert the B-form polydGdCpolydGdC to the Z-form under low salt conditions; the europium-L-valine complex can cause single-stranded polydA and polyrA to self-structure. The sigmoidal melting curve profiles indicate the transition is cooperative, similar to the cooperative melting of a duplex DNA [13]. Detailed structural studies are clearly needed to clarify their DNA selectivity.

Furthermore, the observed hypochromicity for ssDNA 1-3 and red shift for ssDNA 4-5 in the UV–Vis measurements, the different binding affinity and fluorescence enhancement, and DNA CD spectral changes indicate that the interactions between the complex and DNA are sequence dependent and are related to the structure of the complex, except for the electrostatic attraction [12,13] between the phosphate backbone and the free amino groups ($-NH_3^+$) of the amino acids and terbium ions, consistent with the DNA structural changes upon being complex bound, which was observed in circular dichroism measurements.

4. Conclusion

In summary, we have synthesized four different lanthanide–amino acid complexes under near physiological pH conditions. From the crystal structure analysis, we find they have diverse structures, and the general cubane-like structure is just one of them. The interactions of the synthesized complexes with five single-stranded DNA were studied with absorption, fluorescence and circular dichroism spectroscopy and their binding affinity was detected. We find that the recognition of DNA is sequence dependent and has some relationship with the structure of the lanthanide–amino acid complexes.

Acknowledgments

We are grateful for the referees' helpful comments on the manuscript. This project was supported by NSFC (20331020, 20325101, 20473084, 20637010), funds from the Chinese Academy of Sciences and Jilin Province.

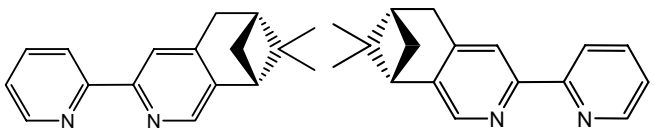
Appendix A. Supplementary material

CCDC 273462, 259959, 249478 and 273463 contain the supplementary crystallographic data for this paper. These data can be obtained free of charge via http://www.ccdc.cam.ac.uk/conts/retrieving.html, or from the Cambridge Crystallographic Data Centre, 12 Union Road, Cambridge CB2 1EZ, UK; fax: (+44) 1223-336-033; or e-mail: deposit@ccdc.cam.ac.uk. Supplementary data associated with this article can be found, in the online version, at doi:10.1016/j.poly.2007.07.052.

References

[1] C.H. Evans, Biochemistry of Lanthanides, Plenum Press, New York, 1990.
[2] A. Ma, L. Li, Y. Lin, S. Xi, J. Coord. Chem. 33 (1994) 59.
[3] J. Legendziewicz, Z. Ciunik, P. Gawryszewska, J. Sokolnicki, Polyhedron 18 (1999) 2701.
[4] E. Huskowska, I. Turowska-Tyrk, J. Legendziewicz, T. Glowiak, J. Alloys Compd. 277 (1998) 852.
[5] R. Wang, Z. Zheng, T. Jin, R.J. Staples, Angew. Chem., Int. Ed. 38 (1999) 1813.

[6] B. Ma, D. Zhang, S. Gao, T. Jin, C. Yan, G. Xu, Angew. Chem., Int. Ed. 39 (2000) 3644.
[7] R. Wang, H. Liu, M.D. Carducci, T. Jin, C. Zheng, Z. Zheng, Inorg. Chem. 40 (2001) 2743.
[8] Z. Zheng, Chem. Commun. (2001) 2521.
[9] R. Wang, H.D. Selby, H. Liu, M.D. Carducci, T. Jin, Z. Zheng, J.W. Anthis, R. Staples, Inorg. Chem. 41 (2002) 278.
[10] B. Ma, D. Zhang, S. Gao, T. Jin, C. Yan, New J. Chem. 24 (2000) 251.
[11] G.M. Sheldrick, SHELXL-97 – A Program for Crystal Structure Refinement, University of Goettingen, Germany, 1997.
[12] H. Zhang, H. Yu, J. Ren, X. Qu, Biophys. J. 90 (2006) 3203.
[13] H. Zhang, H. Yu, J. Ren, X. Qu, FEBS Lett. 580 (2006) 3726.
[14] X. Qu, J.B. Chaires, Methods Enzymol. 321 (2000) 353.
[15] X. Qu, J. Ren, P.V. Riccelli, A.S. Benight, J.B. Chaires, Biochemistry 42 (2003) 11960.
[16] X. Qu, J.O. Trent, I. Fokt, W. Priebe, J.B. Chaires, Proc. Natl. Acad. Sci. USA 97 (2000) 12032.
[17] X. Li, Y. Peng, J. Ren, X. Qu, Biochemistry 45 (2006) 13543.
[18] Q.R. Jin, X.Q. Wang, T. Jin, S. Zhang, G. Xu, J. Alloys Compd. 207 (1994) 400.
[19] J. Wang, N. Hu, K. Yang, H. Zhang, C. Niu, J. Ni, Acta Cryst. C 59 (2003) M52.
[20] R. Wang, M.D. Carducci, Z. Zheng, Inorg. Chem. 39 (2000) 1836.



Scheme 1. (−)-4,5 Pinene bipyridine (L_{RR}) (left) and (+)-4,5 pinene bipyridine (L_{SS}) (right).

representative examples are lanthanide tris-(β-diketonates) with N-containing ligands such as 2,2′-bipyridine [21,22], 1,10-phenanthroline [17,23] and their derivatives [24].

In addition, chiral ligands play an important role in the design of functional complexes showing specific physical properties, for example, second harmonic generation (SHG), ferroelectricity, etc. [25,26]. Many metal complexes with chiral ligands have had successful applications in asymmetric catalysis, enantiomerselective synthesis, chirality sensing, etc. [27–29]. However, to the best of our knowledge, there are no examples of triboluminescent lanthanide chiral complexes simultaneously showing polarizing optical activity. In this paper, using β-diketones as an efficient light-harvesting 'antennae' and introducing other chiral 2,2′-bipyridine derivative ligands, L_{SS} (+)-4,5-pinene bipyridine and L_{RR} (−)-4,5-pinene bipyridine (Scheme 1), we have successfully prepared two triboluminescent Eu(III)-based chiral complexes **1** and **2** with the formula $[Eu(DBM)_3L]$ (L_{SS} in**1**, L_{RR} in **2**, DBM = dibenzoylmethanate). Herein, we report the synthesis, crystal structures, triboluminescence and photoluminescence properties of **1** and **2**.

2. Experimental

2.1. Materials

All chemicals were purchased from commercial suppliers and were used as received. The L_{SS} and L_{RR} ligands were synthesized according to previously reported procedures [30,31] and $Eu(DBM)_3 \cdot 2H_2O$ was synthesized by a literature method [32].

2.2. Physical measurements

Elemental analyses for C, H and N were performed on a Perkin–Elmer 240C analyzer. Triboluminescence spectra, by grinding the crystals of **1** and **2** with a glass rod in a small beaker, and photoluminescence measurements were performed on an AMINCO-BOWMAN series 2 Luminescence spectrometer. The circular dichroism spectra were recorded on a JASCO J-810 Spectropolarimeter in THF (THF = tetrahydrofuran). Infrared spectra were acquired on a Vector22 Bruker spectrophotometer using the KBr pellet technique in the 400–4000 cm^{-1} region.

2.3. X-ray data collection and structure determination

The crystal structures of complexes **1** and **2** were determined on a Bruker SMART CCD diffractometer with graphite monochromated Mo Kα radiation ($\lambda = 0.71073$ Å) at room temperature using both Φ- and ω-scan modes. Intensity data were collected in the θ range of 0.996–26 for complex **1** and 0.999–26 for complex **2**; data reduction was made with the Bruker SAINT package. Absorption correction was performed using the SADABS program. The structures were solved by direct methods and refined on F^2 by full matrix least-squares using SHELXL-97 with anisotropic displacement parameters for all non-hydrogen atoms. H atoms were introduced in the calculations using the riding model. All computations were carried out using the SHELXTL-2000 program package. Crystallographic data for complexes **1** and **2** are summarized in Table 1.

2.4. Synthesis of $Eu(DBM)_3L_{SS}$ (1)

A solution of $Eu(DBM)_3 \cdot 2H_2O$ (85.1 mg, 0.1 mmol) in ethanol (10 ml) was added to a solution of the chiral 2,2′-bipyridine derivative, (+)-4,5-pinene bipyridine (25 mg, 0.1 mmol), in acetone (10 ml) with gentle stirring for 10 min. The mixture was placed undisturbed for three weeks. Yellow block crystals of **1** were obtained in 67% yield. *Anal.* Calc. for **1** ($C_{62}H_{51}N_2O_6Eu$): C, 69.41; H, 4.76; N, 2.61. Found: C, 69.67; H, 4.71; N, 2.69%. IR (KBr, cm^{-1}): ν 1601 s (C=O stretching), 1552 s (C=N stretching).

2.5. Synthesis of $Eu(DBM)_3L_{RR}$ (2)

Complex **2** was prepared as yellow block crystals by a method similar to that of **1** using (−)-4,5-pinene bipyridine instead of (+)-4,5-pinene bipyridine. Yield: 71%. *Anal.* Calc. for **2** ($C_{62}H_{51}N_2O_6Eu$): C, 69.41; H, 4.76; N, 2.61.

Table 1
Crystallographic data and details of refinement for complexes **1** and **2**

	1	**2**
Formula	$C_{62}H_{51}N_2O_6Eu$	$C_{62}H_{51}N_2O_6Eu$
F_w	1072.01	1072.01
Crystal system	monoclinic	monoclinic
Space group	$P2_1$	$P2_1$
a (Å)	9.504(3)	9.516(2)
b (Å)	20.734(7)	20.769(4)
c (Å)	12.697(4)	12.703(2)
β (°)	92.499(8)	92.524(4)
V (Å^3)	2499.6(1)	2508.2(8)
Z	2	2
D_{calc} (g/cm^{-3})	1.424	1.419
μ (Mo Kα) (mm^{-1})	1.311	1.306
Data/restraints/parameters	9376/1/642	8215/1/642
θ Range (°)	0.996–26.00	0.999–26.00
R_{int} (on F^2)	0.0610	0.0396
Goodness of fit on F^2	1.143	1.013
R_1 [$I > 2\,\delta\,(I)$][a]	0.0610	0.0488
wR_2 (all data)[b]	0.1328	0.1199

[a] $R_1 = \sum ||F_o| - |F_c|| / \sum |F_o|$.
[b] $wR_2 = [\sum w(|F_o^2| - |F_c^2|)^2 / \sum w(|F_o^2|)^2]^{1/2}$.

Found: C, 69.81; H, 4.79; N, 2.66%. IR (KBr, cm^{-1}): ν 1601 s (C=O stretching), 1552 s (C=N stretching).

3. Results and discussion

3.1. Crystal structure description of complexes *1* and *2*

X-ray single crystal analysis reveals that complexes **1** and **2** are enantiomers (Fig. 1), so only the structure of **1** is described here. Selected bond lengths and angles for **1** and **2** are listed in Tables 2 and 3. Complexes **1** and **2** crystallize in the chiral space group $P2_1$ because of introducing the chiral 2,2′-bipyridine derivative ligands. They have non-centrosymmetric structures. Complex **1** is a mononuclear neutral Eu(III)-based complex. As shown in Fig. 1, each molecule contains three β-diketonate anions, a chiral 2,2′-bipyridine derivative ligand and an eight-coordinated Eu(III) cation. Three diketonate anions each provides two donor O atoms to coordinate to the Eu(III) cation. The other two coordination sites of the Eu(III) cation are occupied by two N atoms from the chiral bipyridine derivative to complete the eight coordination environment. The O–Eu distances range from 2.2696 to 2.4431 Å, while the two N–Eu bonds are 2.570 and 2.579 Å. Eight bonds with different lengths give rise to a strongly distorted square antiprism environment around the Eu(III) cation. O3O4O5O6 (bottom plane) and O1O2N1N2 (top plane) in Fig. 2 compose the two square basic planes of the antiprism, with the mean deviations of 0.0717 and 0.1386 Å from each plane, respectively, and their dihedral angle is 2.63°. For a regular square antiprism, the two square planes are parallel to each other and one square is rotated by 45° with respect to the other. However, for **1**, relative to the bottom plane, the top plane is rotated by the smaller angle of 22.6°. So the Eu(III) cation factually has a geometrical environment intermediate between a square antiprism (SA) and a dodecahedron (D). This kind of coordination configuration around Eu(III) leads to the very low structural symmetry of **1**.

Table 2
Selected bond lengths (Å) and angles (°) for complex **1**

Bond lengths			
Eu(1)–O(1)	2.305(6)	Eu(1)–O(4)	2.356(4)
Eu(1)–O(2)	2.309(6)	Eu(1)–O(5)	2.443(7)
Eu(1)–O(3)	2.270(5)	Eu(1)–O(6)	2.344(6)
Eu(1)–N(1)	2.579(6)	Eu(1)–N(2)	2.570(6)
Bond angles			
O5–Eu1–O6	69.7(2)	O1–Eu1–O2	73.3(2)
O3–Eu1–O2	84.4(2)	O3–Eu1–O4	73.1(2)
O1–Eu1–O6	74.7(2)	O4–Eu1–O5	78.2(3)
O1–Eu1–N2	76.1(2)	N1–Eu1–N2	60.0(2)
N1–Eu1–O5	71.6(3)	N1–Eu1–O6	128.7(2)

Table 3
Selected bond lengths (Å) and angles (°) for complex **2**

Bond lengths			
Eu(1)–O(1)	2.356(5)	Eu(1)–O(4)	2.359(4)
Eu(1)–O(2)	2.373(6)	Eu(1)–O(5)	2.368(7)
Eu(1)–O(3)	2.359(5)	Eu(1)–O(6)	2.339(5)
Eu(1)–N(1)	2.616(5)	Eu(1)–N(2)	2.601(6)
Bond angles			
O5–Eu1–O6	70.7(2)	O1–Eu1–O2	72.4(2)
O3–Eu1–O2	82.6(2)	O3–Eu1–O4	72.1(2)
O1–Eu1–O6	75.2(2)	O4–Eu1–O5	81.3(3)
O1–Eu1–N2	75.9(2)	N1–Eu1–N2	61.6(2)
N1–Eu1–O5	72.5(3)	N1–Eu1–O6	131.2(3)

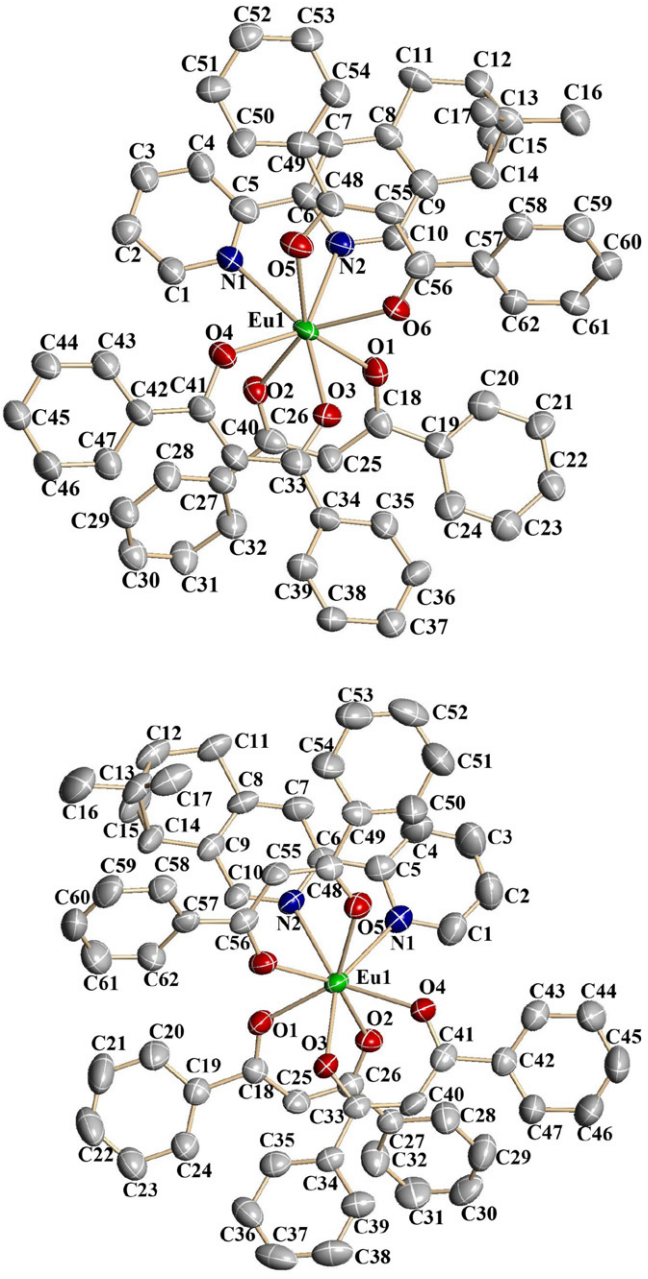


Fig. 1. The structures of **1** (top) and **2** (bottom) showing 50% probability displacement ellipsoids and the atom-numbering schemes. H atoms are omitted for clarity.

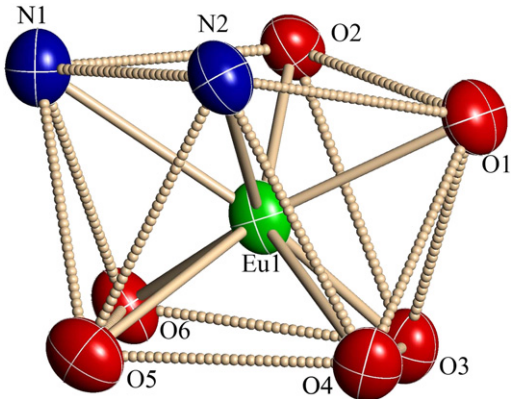


Fig. 2. Coordination geometry of **1** around the Eu(III) ion.

3.2. Optical spectroscopy

Complexes **1** and **2** are a pair of enantiomers and the circular dichroism (CD) spectra are shown in Fig. 3. Complex **1** (*SS*-isomer) shows positive Cotton effects at $\lambda = 250$ and 285 nm with a negative one at $\lambda = 225$ nm, while complex **2** (*RR*-isomer) exhibits Cotton effects with opposite sign at the same wavelength. They are mirror images in the observed CD spectra.

Additionally, the SHG (second harmonic generation) efficiency was measured for the optical activity of **1** and **2**. According to the principle proposed by Kurtz and Perry [33], we estimated the second-order non-linear optical effect of **1** and **2**. They display SHG efficiency with approximate responses of three times that of urea.

As shown in Fig. 4, the photoluminescence spectra of complexes **1** and **2** in the solid state, excited at $\lambda = 370$ nm, are measured at room temperature. The spectra of **1** and **2** are identical with the characteristic peaks of Eu(III) centered transitions from the excited state $^5D_0$ to the ground singlet state ^7F_J ($J = 0$–4) at 580, 591, 613, 650 and 702 nm. Notably, the dominant transition $^5D_0$–$^7F_2$ at $\lambda = 613$ nm is much stronger than that of $^5D_0$–$^7F_1$. This denotes that the local symmetry groups of chemical environment of the Eu(III) ion are not characterized by an inversion centre, which is consistent with the results of the single-crystal X-ray analysis for complexes of **1** and **2**.

In most cases, the intensity of triboluminescence emissions is weaker than that of photoluminescence, so only those strong emission parts of the triboluminescence, especially for centrosymmetric complexes, can be detected in the darkness [34,35]. however, for complexes **1** and **2** a brilliant red light can be observed in daylight by grinding crude crystals. As shown in Fig. 5, the position of the strongest peak (at $\lambda = 613$ nm) in their triboluminescence spectra is the same as that of photoluminescence. According to Rheingold and King's statements [35], the most intense component of triboluminescent emissions of lanthanide complexes is the characteristic photoluminescence of the

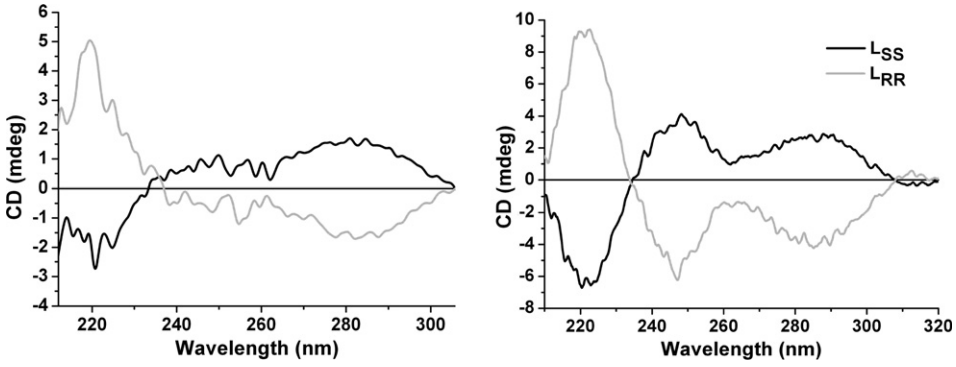


Fig. 3. The CD spectra of complexes **1** (black), **2** (grey) and ligands in THF at room temperature.

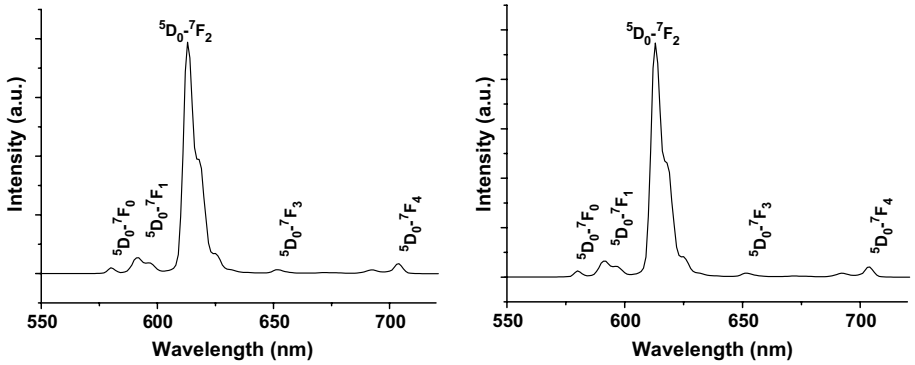


Fig. 4. The photoluminescent spectra of complexes **1** (left) and **2** (right) in the solid state under excitation at $\lambda = 370$ nm at room temperature.

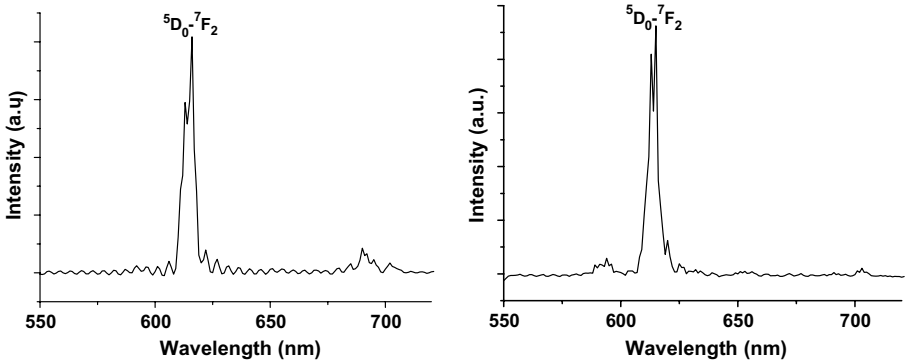


Fig. 5. The triboluminescent spectra of **1** (left) and **2** (right) at room temperature.

metallic elements. In the triboluminescence spectra of **1** and **2**, we can observe a strong peak at wavelength $\lambda = 613$ nm, being assigned to the $^5D_0$–$^7F_2$ transition of Eu(III). Therefore, we can draw the conclusion that the triboluminescence has the same exited state as that of the photoluminescence. Generally, there are two prevalent explanations to the triboluminescence mechanism. One is the discharge of nascent charged surfaces upon cleavage due to piezoelectricity when non-centrosymmetric crystals are mechanically stressed [36–38]. The other is that ionic solids and disorders in the molecular structure are responsible for the triboluminescence in centrosymmetric crystals due to the existence of an intrinsically charged plane [35,36,39]. Zink claimed that non-centrosymmetric crystals are necessary for the observation of triboluminescence [8] and estimated that the correlation of triboluminescence activity with non-centrosymmetric space groups is greater than 95%. Such materials would readily generate opposite charges on opposing surfaces of the cleavage. In our study, complexes **1** and **2** are both non-centrosymmetric structures. The discharge of nascent charged surfaces upon cleavage excites the phenyl rings (in the β-diketone) and the pyridyl rings (in the chiral pyridine derivative) of the ligands which act as 'antennae' and in turn excite the Eu(III) f states. Emission from the chelated Eu(III) provides the observed triboluminescence. It is noteworthy that we have observed the brilliant triboluminescence of **1** and **2** in daylight by grinding them. It may be due to the introduction of the chiral ligand which results in the highly asymmetric molecular structure and sequentially to be in favor of the piezoelectric role [40]. This is confirmed by another reported triboluminescent complex, $[n\text{-}Bu_4N]_2[Tb(2,6\text{-}dhb)_5\ (H_2O)]$ (2,6-Hdhb = 2,6-dihydroxybenzoic acid) [41], which also crystallizes in chiral and non-centrosymmetric space group $P2_1$.

4. Conclusions

In this study, a pair of novel Eu(III)-based enantiomers with a chiral ligand (L_{SS} and L_{RR}) were synthesized and characterized by crystal structure analysis and spectroscopic methods. When ground with a glass rod in daylight, both of them show brilliant triboluminescence which may arise from the high asymmetry of the crystal structures. This work not only presents a successful method for preparing multifunctional materials (luminescence and chirality) but also suggests that a non-centrosymmetric crystal structure is in favor of getting intense triboluminescence observed in the daylight.

Acknowledgements

This work was supported by the Major State Basic Research Development Program (Grant No. 2006CB806104) and the National Natural Science Foundation of China (Project Nos.: 20631030 and 90501002).

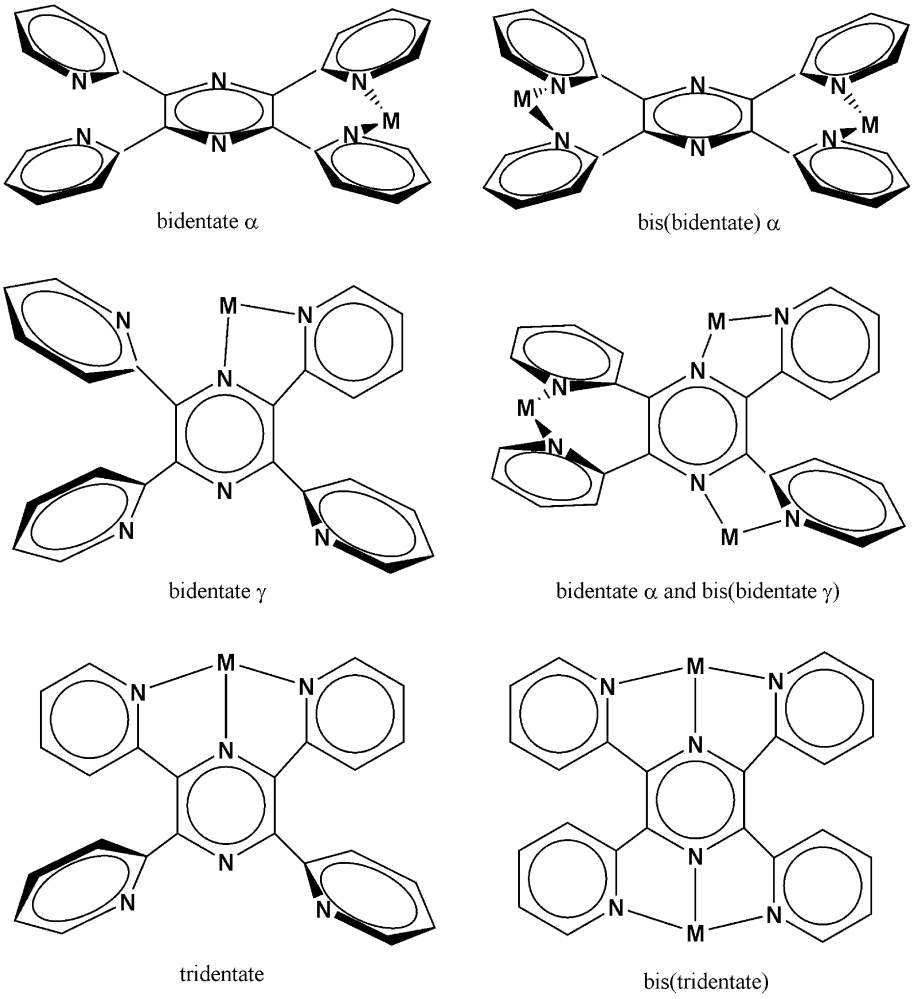
Appendix A. Supplementary material

CCDC 645347 and 645348 contain the supplementary crystallographic data for the structures reported in this paper. These data can be obtained free of charge via http://www.ccdc.cam.ac.uk/conts/retrieving.html, or from the Cambridge Crystallographic Data Centre, 12, Union Road, Cambridge CB2 1EZ, UK; fax: +44 1223 336 033; or deposit@ccdc.cam.ac.uk). Supplementary data associated with this article can be found, in the online version, at doi:10.1016/j.poly.2007.07.047.

References

[1] J.I. Zink, G.E. Hardy, J.E. Sutton, J. Phys. Chem. 80 (1976) 248.
[2] I. Sage, G. Bourhill, J. Mater. Chem. 11 (2001) 231.
[3] G. Bourhill, L.O. Palsson, I.D.W. Samuel, I.C. Sage, I.D.H. Oswald, J.P. Duignan, Chem. Phys. Lett. 336 (2001) 234.
[4] Z.P. Zheng, J.F. Wang, H. Liu, M.D. Carducci, N. Peyghambarian, G.E. Jabbourb, Acta Crystallogr. C 58 (1990) m50.
[5] I. Sage, R. Badcock, L. Humberstone, N. Geddes, M. Kemp, G. Bourhill, Smart Mater. Struct. 8 (1999) 504.
[6] L.M. Sweeting, A.L. Rheingold, J. Phys. Chem. 92 (1988) 5648.
[7] L.M. Sweeting, L.M. Cashel, M.M. Rosenblatt, J. Lumin. 52 (1992) 281.
[8] G.E. Hardy, W.C. Kaska, B.P. Chandra, J.I. Zink, J. Am. Chem. Soc. 103 (1981) 1074.
[9] M.H.V. Werts, R.H. Woudenberg, P.G. Emmerink, R.V. Gassel, J.W. Hofstraat, J.W. Verhoeven, Angew. Chem., Int. Ed. 39 (2000) 4542.

[10] T. Yamada, S. Shinoda, H. Tsukube, Chem. Commun. (2002) 1218.
[11] P. Nockemann, E. Beurer, K. Driesen, R.V. Deun, K.V. Hecke, L.V. Meervelt, et al., Chem. Commun. (2005) 4354.
[12] S. Petoud, G. Muller, E.G. Moore, J.D. Xu, J. Sokolnicki, J.P. Riehl, et al., J. Am. Chem. Soc. 129 (2007) 77.
[13] J.B. Yu, L. Zhou, H.J. Zhang, Y.X. Zheng, H.R. Li, R.P. Deng, et al., Inorg. Chem. 44 (2005) 1611.
[14] R. Pavithran, N.S.S. Kumar, S. Biju, M.L.P. Reddy, S.A. Junior, R.O. Freire, Inorg. Chem. 45 (2006) 2184.
[15] J. Kido, Y. Okamoto, Chem. Rev. 102 (2002) 2357.
[16] J.M. Lehn, Angew. Chem., Int. Ed. Engl. 29 (1990) 1304.
[17] G.F. de Sá, O.L. Malta, C. de Mello Donegá, A.M. Simas, R.L. Longo, P.A. Santa-Cruz, et al., Coord. Chem. Rev. 196 (2000) 165.
[18] C. Peng, H. Zhang, J. Yu, Q. Meng, L. Fu, H. Li, et al., J. Phys. Chem. B 109 (2005) 15278.
[19] M.D. McGehee, T. Bergstedt, C. Zhang, A.P. Saab, M.B. O'Regan, G.C. Bazan, et al., Adv. Mater. 11 (1999) 1349.
[20] G.A. Crosby, R.E. Whan, R.M. Alire, J. Chem. Phys. 34 (1961) 743.
[21] V. Bekiari, P. Lianos, Adv. Mater. 10 (1998) 1455.
[22] D.F. Mosere, L.C. Thompson, V.G.Y. Jr, J. Alloys Compd. 303–304 (2000) 121.
[23] P.C. Christidis, I.O. Tossidis, D.G. Paschalidis, L.C. Tzavellas, Acta Crystallogr. C 54 (1998) 1233.
[24] A. Bellusci, G. Barberio, A. Crispini, M. Ghedini, M.L. Deda, D. Pucci, Inorg. Chem. 44 (2005) 1818.
[25] P.G. Lacroix, R. Clément, K. Nakatani, J. Zyss, I. Ledoux, Science 263 (1994) 658.
[26] J.-F. Nicoud, Science 263 (1994) 636.
[27] H.C. Aspinall, Chem. Rev. 102 (2002) 1807.
[28] H. Tsukube, S. Shinoda, Chem. Rev. 102 (2002) 2389.
[29] T. Yamada, S. Shinoda, H. Sugimoto, J.-I. Uenishi, H. Tsukube, Inorg. Chem. 42 (2003) 7932.
[30] P. Hayoz, A.V. Zelewsky, Tetrahedron Lett. 33 (1992) 5165.
[31] P. Hayoz, A.V. Zelewsky, H. Stoeckli-evans, J. Am. Chem. Soc. 115 (1993) 5111.
[32] R.G. Charles, R.C. Ohlmann, J. Inorg. Nucl. Chem. 27 (1965) 255.
[33] S.K. Kurtz, T.T. Perry, J. Appl. Phys. 39 (1968) 3798.
[34] J.B. Yu, H.J. Zhang, R.P. Deng, L. Zhou, Z.P. Peng, L.S. Fu, J. Rare Earths 22 (2004) 126.
[35] X.-F. Chen, X.-H. Zhu, Y.H. Xu, S.S.S. Raj, S. Öztürk, H.-K. Fun, et al., J. Mater. Chem. 9 (1999) 2919.
[36] A.L. Rheingold, W. King, Inorg. Chem. 28 (1989) 1715.
[37] F.A. Cotton, L.M. Danies, P.L. Huang, Inorg. Chem. Commun. 4 (2001) 319.
[38] R.-G. Xiong, X.-Z. You, Inorg. Chem. Commun. 5 (2002) 677.
[39] L.M. Sweeting, A.L. Rheingold, J. Am. Chem. Soc. 109 (1987) 2652.
[40] X.-R. Zeng, R.-G. Xiong, X.-Z. You, K.-K. Cheung, Inorg. Chem. Commun. 3 (2000) 341.
[41] P.C.R. Soares-Santos, H.I.S. Nogueira, F.A.A. Paz, R.A.S. Ferreira, L.D. Carlos, J. Klinowski, et al., Eur. J. Inorg. Chem. (2003) 3609.



Scheme 1.

blies [4a]. In fact, in spite of the above mentioned geometric constraints, tppz is able to act as a bis-tridentate ligand generating homometallic compounds with interesting electronic and magnetic properties [5–14].

A particular emphasis has been paid to magneto-structural studies of tppz-bridged compounds of formula $[M_2(tppz)]^{2m+}$ [M = Ni(II) and Cu(II)] which were found to exhibit significant antiferromagnetic interactions between the paramagnetic metal ions involved [12a,12b, 12f–i,13b]. Additionally, the fact that the mononuclear species $[Co(tppz)_2]^{2+}$ exhibits thermally induced spin crossover behaviour from a high-spin $S_{Co} = 3/2$ at high temperatures to a low-spin $S_{Co} = 1/2$ at lower temperatures increases the interest in the tppz-containing metal complexes [13b]. Given that the ter-imine system has been found to induce a spin transition in several examples of iron(II) complexes [15], we decided to investigate the complex formation between this metal ion and tppz. Although in the initial publication concerning the preparation of tppz the authors synthesized iron(II) complexes with a 1:2 metal to tppz molar ratio [1], no crystal structure was available until 2001 when the X-ray structures of the low-spin $[Fe(tppz)_2](ClO_4)_2 \cdot CH_3CN \cdot H_2O$ and high-spin $[Fe(tppz)Cl_2]$ iron(II) species were reported [13b]. In this work, we present the preparation and structural characterization of two new tppz-containing iron(II) complexes of formula $PPh_4[Fe(tppz)(CN)_3] \cdot 7H_2O$ (**1**) and $[Fe(tppz)_2][Fe(NCS)_4]$ (**2**) where low- (**1** and **2**) and high-spin (**2**) iron(II) occur.

2. Experimental

2.1. Materials and methods

Iron(II) perchlorate hexahydrate, iron(II) chloride tetrahydrate, potassium cyanide, potassium thiocyanate and tetraphenylphosphonium chloride were purchased from commercial sources and used as received. Tppz was prepared by the reported procedure [1]. Elemental analyses (C, H, N) were performed by the Microanalytical Service of the Universidad Autónoma de Madrid. Infrared spectra were obtained on a Nicolet Avatar 320 FT-IR spectrophotometer in the 4000–400 cm^{-1} region with the samples prepared as KBr pellets. Magnetic susceptibility measurements on polycrystalline samples of **1** and **2** were carried out with a Quantum Design SQUID magnetometer at

room temperature. Diamagnetic corrections of the constituent atoms were estimated from Pascal [16] constants.

2.2. Warning

Perchlorate salts of metal complexes with organic ligands are potentially explosive. Only a small amount of compound should be prepared and it should be handled with care and without heating. The severe toxicity of cyanide and most of its compounds must be taken into account in the laboratory. Our syntheses were carried out in a hood and the samples handled with great caution.

2.3. Synthesis

$PPh_4[Fe(tppz)(CN)_3]\cdot 7H_2O$ (**1**): X-ray quality violet prisms of **1** were grown by slow evaporation of an aqueous solution (50 cm^3) containing tppz (0.1 mmol), iron(II) chloride tetrahydrate (0.1 mmol), potassium cyanide (0.3 mmol) and tetraphenylphosphonium chloride (0.1 mmol). The tppz ligand and the iron(II) salt were allowed to react in 20 cm^3 of water under continuous stirring until a deep blue solution resulted. Then, potassium cyanide dissolved in 20 cm^3 was added and the colour turned to violet. Finally, PPh_4Cl dissolved in 10 cm^3 of water was added and the solution allowed to evaporate in a hood at room temperature. Crystals were filtered off and dried on filter paper in the open air. Yield *ca.* 65%. *Anal.* Calc. for $C_{51}H_{50}FeN_9O_7P$ (**1**): C, 62.04; H, 5.06; N, 12.76. Found: C, 61.90; H, 4.94; N, 12.68%.

$[Fe(tppz)_2][Fe(NCS)_4]$ (**2**): Potassium thiocyanate (0.4 mmol) dissolved in a water/acetonitrile 1:1 v/v mixture (10 cm^3) was added to a blue acetonitrile solution of tppz (0.2 mmol) and iron(II) perchlorate hexahydrate (0.2 mmol) under continuous stirring at room temperature. Slow evaporation of the resulting violet solution yielded violet rods of **2** which were suitable for X-ray diffraction. Yield *ca.* 60%. *Anal.* Calc. for $C_{52}H_{32}N_{16}Fe_2S_4$ (**2**): C, 55.74; H, 2.86; N, 19.99. Found: C, 55.38; H, 2.79; N, 19.84%.

2.4. Crystal data collection and refinement

The diffraction data of **1** and **2** were collected with Bruker-Nonius X8 APEX CCD (**1**) and Bruker-AXS SMART 2K CCD area detector (**2**) diffractometers at 293 K and using Mo Kα radiation ($\lambda = 0.71073$ Å). Crystal parameters and refinements results are summarized in Table 1. The structures of **1** and **2** were solved by direct methods and were refined by full-matrix least-squares based on F^2, including all reflections. The water molecules in **1** were disordered over several positions and six oxygen atoms [O(5w)–O(10w)] were refined with a fixed site occupancy factor of 0.5. The remaining non-hydrogen atoms in **1** and all non-hydrogen atoms in **2** were anisotropically refined. The hydrogen atoms of the tetraphenylphosphonium cation (**1**) and the tppz ligand (**1** and **2**) were included at idealized positions and refined according to the riding model. The hydrogen atoms of the water molecules of **1** were not found. The non-optimal refinement of the structure of **1** is related to the disorder of the water molecules. In the case of **2**, the fraction of unobserved reflections were rather high at 2θ values above 50°, and hence this was chosen as the limit in data processing. The final Fourier-difference map showed maximum and minimum height peaks of 0.533 and −0.45 e $Å^{-3}$ for **1** and 0.798 and −0.406 e $Å^{-3}$ for **2**.

The diffraction data were processed through the SAINT [17a] reduction and SADABS [17b] absorption software. Structure solutions and refinements were performed with the Bruker SHELXTL system [18]. The final geometrical calculations for **1** were carried out with the PARST [19]

Table 1
Crystal data and details of structure determination

Compound	**1**	**2**
Formula	$C_{51}H_{50}FeN_9O_7P$	$C_{52}H_{32}Fe_2N_{16}S_4$
M	987.82	1120.88
Crystal system	triclinic	triclinic
Space group	$P\bar{1}$	$P\bar{1}$
a (Å)	12.258(3)	11.744(1)
b (Å)	14.254(3)	15.108(2)
c (Å)	17.139(3)	16.694(2)
α (°)	71.15(3)	72.560(3)
β (°)	69.64(3)	79.303(3)
γ (°)	79.02(3)	85.870(3)
V ($Å^3$)	2646.7(9)	2776.3(6)
Z	2	2
T (K)	293	293
ρ_{calc} (Mg m^{-3})	1.240	1.341
λ (Mo Kα) (Å)	0.71073	0.71073
μ (Mo Kα) (mm^{-1})	0.372	0.723
θ Range (°)	1.32–24.56	2.18–25.00
Index ranges	$-14 \leqslant h \leqslant 14$, $-15 \leqslant k \leqslant 16$, $-20 \leqslant l \leqslant 20$	$-13 \leqslant h \leqslant 9$, $-17 \leqslant k \leqslant 17$, $-19 \leqslant l \leqslant 19$
Data/restraints/parameters	8208/0/604	9753/0/667
Goodness-of-fit on F^2	1.068	0.870
R_1^a, wR_2^b (all data)	0.1041, 0.2431	0.1685, 0.2091
R_1^a, wR_2^b [$I > 2\sigma(I)$]	0.0807, 0.2431	0.0718, 0.181
Collected reflection	34147	17020
Independent reflection [R_{int}]	8208 [0.0378]	9753 [0.0708]

[a] $R_1 = \sum(|F_o| - |F_c|)/\sum|F_o|$.
[b] $wR_2 = \{\sum[w(F_o^2 - F_c^2)^2]/\sum[w(F_o^2)^2]\}^{1/2}$.

Table 2
Selected bond lengths (Å) and angles (°) for compound **1**

Fe(1)–N(1)	1.978(4)	Fe(1)–C(53)	1.947(5)
Fe(1)–N(2)	1.971(4)	Fe(1)–C(54)	1.940(5)
Fe(1)–N(5)	1.870(4)	Fe(1)–C(55)	1.925(6)
N(1)–Fe(1)–N(5)	82.19(16)	C(53)–Fe(1)–N(2)	89.13(17)
N(1)–Fe(1)–C(53)	90.25(17)	N(5)–Fe(1)–C(54)	90.64(17)
N(1)–Fe(1)–C(54)	88.59(17)	N(5)–Fe(1)–C(55)	177.49(18)
N(1)–Fe(1)–C(55)	97.9(2)	N(5)–Fe(1)–N(2)	80.68(15)
N(1)–Fe(1)–N(2)	162.78(16)	N(54)–Fe(1)–C(55)	86.8(2)
C(53)–Fe(1)–N(5)	93.77(17)	C(54)–Fe(1)–N(2)	93.35(17)
C(53)–Fe(1)–C(55)	88.7(2)	C(55)–Fe(1)–N(2)	99.28(19)
C(53)–Fe(1)–C(54)	175.24(19)		

Table 3
Selected bond lengths (Å) and angles (°) for compound **2**

Fe(1)–N(1)	1.960(4)	Fe(1)–N(8)	1.970(5)
Fe(1)–N(5)	1.874(4)	Fe(2)–N(13)	1.966(8)
Fe(1)–N(2)	1.964(4)	Fe(2)–N(14)	1.977(8)
Fe(1)–N(11)	1.896(4)	Fe(2)–N(15)	1.977(7)
Fe(1)–N(7)	1.962(4)	Fe(2)–N(16)	1.986(7)
N(1)–Fe(1)–N(5)	81.09(18)	N(2)–Fe(1)–N(8)	90.13(18)
N(1)–Fe(1)–N(2)	162.14(17)	N(11)–Fe(1)–N(7)	81.24(18)
N(1)–Fe(1)–N(11)	99.51(17)	N(11)–Fe(1)–N(8)	81.37(19)
N(1)–Fe(1)–N(7)	88.07(18)	N(7)–Fe(1)–N(8)	162.59(18)
N(1)–Fe(1)–N(8)	94.08(19)	N(13)–Fe(2)–N(14)	108.7(3)
N(5)–Fe(1)–N(2)	81.11(18)	N(13)–Fe(2)–N(15)	110.8(3)
N(5)–Fe(1)–N(11)	179.28(19)	N(13)–Fe(2)–N(16)	112.9(3)
N(5)–Fe(1)–N(7)	98.40(18)	N(14)–Fe(2)–N(15)	105.4(3)
N(5)–Fe(1)–N(8)	99.00(18)	N(14)–Fe(2)–N(16)	109.8(3)
N(2)–Fe(1)–N(11)	98.28(18)	N(15)–Fe(2)–N(16)	108.9(3)
N(2)–Fe(1)–N(7)	93.08(17)		
Thiocyanate ligand			
N(13)–C(49)	1.154(9)		
N(15)–C(51)	1.139(9)		
C(49)–S(1)	1.557(10)	C(51)–S(3)	1.631(9)
N(14)–C(50)	1.187(10)	N(16)–C(52)	1.153(8)
C(50)–S(2)	1.568(11)	C(52)–S(4)	1.611(9)

program. The graphical manipulations were done using the XP utility of the SHELXTL system [18b] and CRYSTALMAKER [20]. Selected bond distances and angles for **1** and **2** are listed in Tables 2 and 3, respectively.

3. Results and discussion

3.1. Description of the structure of *1*

The crystal structure of **1** consists of *mer*-[Fe(tppz)-$(CN)_3$]$^-$ anions, uncoordinated tetraphenylphosphonium cations and crystallization water molecules which are interlinked by electrostatic interactions, hydrogen bonds and van der Waals forces (Figs. 1 and 2). The cation is of meridional configuration with each iron atom being surrounded by three tppz-nitrogen and three cyanide carbon atoms in a somewhat distorted octahedral geometry.

The overall symmetry of the anion is close to C_{2v}. The main source of distortion of the metal surrounding is due to the ring strain, the chelate ring angles N(1)–Fe(1)–N(5) and N(2)–Fe(1)–N(5) are 82.19(16)° and 80.68(15)°, respectively. The Fe(1)–N(tppz) and Fe(1)–C(cyano) bond distances in **1** vary in the range 1.869(4)–1.976(4) and 1.926(5)–1.946(5) Å, respectively, and they are very close to those observed in the related diamagnetic iron(II) complex $AsPh_4$-*mer*-[Fe(terpy)$(CN)_3$]$\cdot 2H_2O$ ($AsPh_4^+$ = tetraphenylarsonium cation and terpy = 2,2′:6′,2″-terpyridine) [Fe–N(terpy) = 1.899(7)–1.979(7) Å and Fe–C(cyano) = 1.952(11)–1.986(10) Å] [21] and in the low-spin iron(III) complex PPh_4-*mer*-[Fe(bpca)$(CN)_3$]$\cdot H_2O$ [bpca$^-$ = bis(2-pyridylcarbonyl)amidate anion] [Fe–N(bpca) = 1.893(2)–1.959(2) Å and Fe–C(cyano) = 1.937(3)–1.951(3) Å] [22]. The presence of the tetraphenylphosphonium cation in **1**, the value of the magnetic moment at room temperature

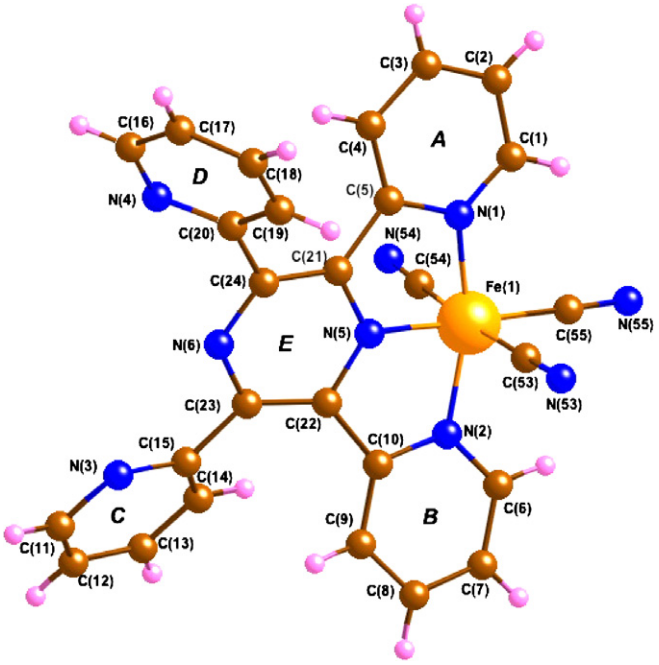


Fig. 1. Perspective view of the *mer*-[Fe(tppz)(CN_3)]$^-$ anion of **1** showing the atom numbering. The hydrogen atoms have been omitted for clarity.

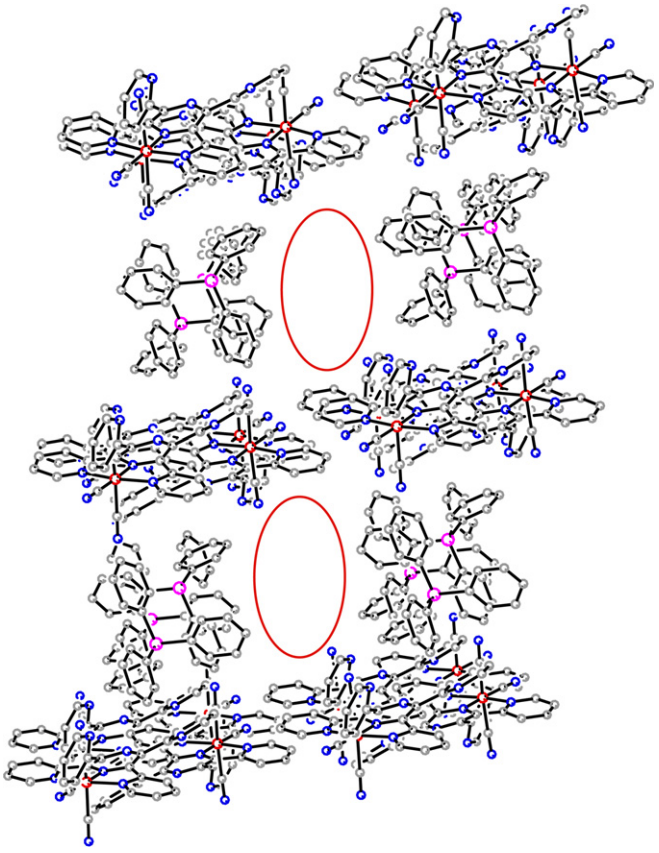


Fig. 2. View of the packing in the unit cell of **1**; red circles refer to occupation of crystallization water molecules that are omitted for clarity. (For interpretation of the references to colour in this figure legend, the reader is referred to the web version of this article.)

(*ca.* 0.6 μ_B) [23], and the cyanide stretching frequency [*ca.* 2080 cm^{-1} in **1** *versus* 2126 cm^{-1} in the bpca-containing low-spin iron(III) complex] also demonstrate the singlet spin state of the iron(II) in **1**. For the sake of comparison, the Fe–N(tppz) bond lengths in the five-coordinated mononuclear iron(II) complex [Fe(tppz)Cl_2] are somewhat longer [2.077(3)–2.107(3) Å] than in **1** as expected given the high-spin state ($S_{Fe} = 2$) of the iron(II) ion in that species [13b]. The bond lengths and angles involving the cyanide ligands are all normal [1.164(6), 1.157(6) and 1.161(7) Å for C(53)–N(53), C(54)–N(54) and C(55)–N(55), respectively]. The iron atom and each cyanide are almost linear, the values for the Fe–C–N angle ranging from 177.0(4)° to 178.7(5)°.

The pyridyl rings of the tppz molecule are planar within experimental errors but the tppz ligand as a whole is far from being planar due to the steric effects between the hydrogen atoms on the 3-pyridyl positions. Low energy conformations of tppz are predicted to have each pyridyl ring twisted from coplanarity with the pyrazine by roughly 50° [4a]. In order to describe the relevant structural features of the coordinated tppz molecule in **1** we will adopt the following convention: the pyrazine ring is noted E whereas the four pyridyl rings are labelled as A, B, C and D (see Fig. 1). It deserves to be noted that the free N(3) and N(4) pyridyl nitrogen atoms are up and down from the pyrazine ring. This E ring is considerably twisted, the value of the dihedral angle between the C(21)–N(5)–C(22) and C(23)–N(6)–C(24) planes being 7(1)°. The dihedral angle between the mean planes of the coordinated A and B pyridyl rings is 5.4(3)° whereas that between the uncoordinated C and D rings is 46.8(3)°. These different values are caused by the tridentate coordination of the tppz molecule to the iron atom through the N(1), N(2) and N(3) nitrogen atoms from the A, B and E rings.

Hydrogen bonds involving the nitrogen atoms of the terminal cyanide ligands [N(53), N(54) and N(55)] and some of the water molecules [O(9w), O(4w) and O(1w)] occur in the structure of compound **1**, the N···O_w distances varying in the range 2.80(1)–3.22(1) Å. It is noteworthy that the free nitrogen atoms of the tppz do not form any hydrogen bond. Finally, as expected for compounds with a large number of crystallization water molecules, an extended network of hydrogen bonds occurs involving all water molecules, leading to a water cluster with O···O distances varying in the range 2.66–2.98 Å. π–π type interactions involving the coordinated A [N(1)/N(1a)] and B [N(2)/N(2b)] pyridyl rings of tppz are also present with interplanar distances of *ca.* 3.34 and 3.28 Å for A and A′ and B and B′, respectively [symmetry code: (a) $1-x$, $2-y$, $1-z$; (b) $2-x$, $1-y$, $1-z$]. Considering these interactions, the anions give rise to chains with iron···iron separations of 8.706(3) and 8.249(3) Å (Fig. 2). The bulky tetraphenylphosphonium cation exhibits the expected tetrahedral shape and its bond lengths and angles are as expected. Interestingly, the PPh_4^+ cations are linked along the *a* axis by alternating off-set sextuple phenyl embrace (OSPE) and six phenyl embrace (SPE) interactions (see Fig. 3) with values of the P···P separation of 6.560(3) and 6.767(3) Å, respectively [24].

3.2. Description of the structure of **2**

The building blocks of compound **2** are the $[Fe(tppz)_2]^{2+}$ and $[Fe(NCS)_4]^{2-}$ units (Fig. 4). The tppz ligands of the cation bind to the iron atom in a tridentate fashion. Fe(1) has a distorted octahedral environment, in which the bonds to the two pyrazine nitrogen atoms [1.874(4) and 1.896(4) Å for Fe(1)–N(5) and Fe(1)–N(11), respectively] are significantly shorter than the bonds to the pyridyl nitrogen atoms ($Fe–N_{py}$ 1.960–1.970 Å), which conforms well with the situation in **1**. The same pattern of differences in the bond lengths was previously observed in the structures of the diamagnetic complexes $[Fe(tppz)_2](ClO_4)_2 \cdot CH_3CN \cdot H_2O$ [13b] and $[Fe(terpy)_2](ClO_4)_2 \cdot nH_2O$ ($n = 1$ and 1/2) [25]. The equatorial plane (with respect to the short axis) in **2** has a significant tetrahedral distortion (maximum atomic deviation 0.305 Å), the Fe(1) atom not deviating significantly from the average plane. The individual pyridyl rings are planar within experimental errors, while the two pyrazine rings are significantly puckered (maximum atomic deviation from the average plane 0.099 Å and 0.109 Å, respectively). Dihedral angles between pyridyl rings and the pyrazine ring to which they are connected, are 23.0° (A/E), 14.9° (B/E), 37.7° (C/E), 29.2° (D/E), 24.4° (F/J), 22.0° (G/J), 35.7° (H/J) and

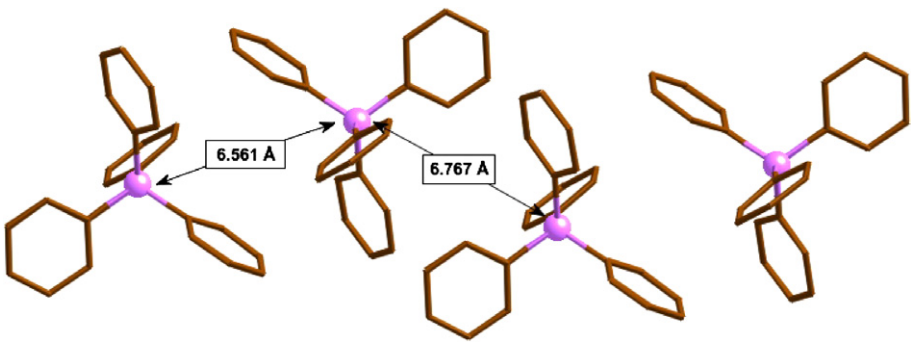


Fig. 3. A view showing the OSPE and SPE supramolecular interactions between the tetraphenylphosphonium cations in **1**.

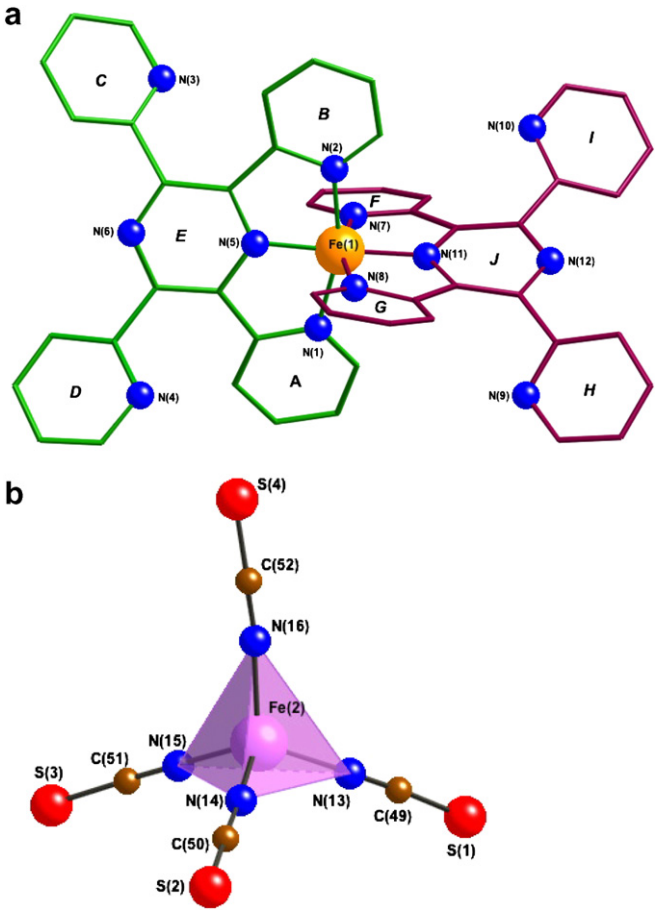


Fig. 4. Perspective view of the $[Fe(tppz)_2]^{2+}$ cation (top) and $[Fe(NCS)_4]^{2-}$ anion (bottom) in **2** with the atom numbering scheme. The hydrogen atoms have been omitted for clarity.

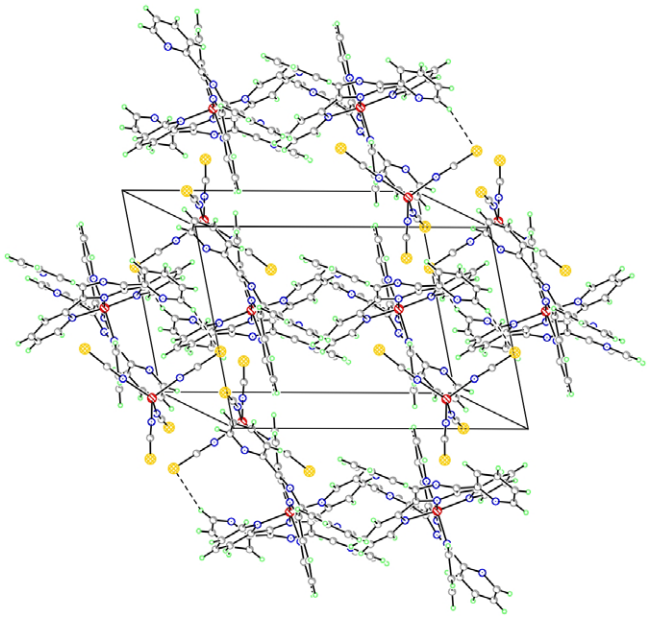


Fig. 5. A view of the crystal packing of **2**.

Table 4
S···H–C contacts[a]

S	H	C	S···H (Å)	S···C (Å)	S···H–C (°)
S(1)	H(8c)	C(8c)	3.08	3.677(8)	124
S(2)	H(35d)	C(35d)	2.91	3.724(10)	147
S(3)	H(3d)	C(3d)	3.04	3.582(7)	119
S(4)	H(1d)	C(1d)	3.04	3.709(7)	131

[a] Symmetry transformations used to generate equivalent atoms: (c) x, $y-1$, z; (d) $1+x$, y, z.

33.5° (I/J). It deserves to be noted that the nitrogen atoms of the non-coordinated pyridyl rings of the two tppz ligands in **2** are placed on the side of the ring pointing toward the metalated side of the ligand rather than on the side pointing toward the free nitrogen atom of the pyrazine ring in contrast to what occurs in **1**. These structural features of the coordinated tppz ligand in **1** and **2** would account for the tendency of this ligand to adopt either mono- or bis-chelation in its metal complexes. The iron atom of the anion, Fe(2), has a slightly distorted tetrahedral coordination sphere being bound to four thiocyanate ligands at Fe–N distances ranging from 1.966(8) to 1.986(7) Å. The presence of a strong peak at 2058 cm^{-1} in the infrared spectrum of **2** is consistent with a N-coordination of thiocyanate [26]. The thiocyanate groups in the $[Fe(NCS)_4]^{2-}$ unit display comparable classical N–C and C–S distances. They are nearly linear [values of the N–C–S angle varying in the range 175.5(10)–179.1(8)°] but the Fe–NCS groups are somewhat bent [values of the Fe–N–C angle covering the range 169.7(9)–173.9(7)°]. The value of the magnetic moment of **2** at room temperature (*ca.* 5.9 μ_B) is consistent with the occurrence of both a paramagnetic high-spin iron(II) ($S_{Fe}=2$ for $[Fe(NCS)_4]^{2-}$) species and a low-spin iron(II) ($S_{Fe}=0$ for $[Fe(tppz)_2]^{2+}$) unit. In fact, a singlet spin state was observed for the iron(II) ion in the complex $[Fe(tppz)_2](ClO_4)_2 \cdot CH_3CN \cdot H_2O$ [13b].

The crystal packing of the bulky building block units leaves cavities between the molecules (Fig. 5), voids of approximately 300 $Å^3$. The low density of the material (Table 1) reflects its open structure. Between cations stacked along the *c*-axis weak π–π interactions appear to occur between pyridyl rings. Rings involving N(3)/N(10a), N(4)/N(9b), N(8)/N(8b) and N(7)/N(7a) atoms [symmetry code: (a) $1-x$, $1-y$, $1-z$; (b) $1-x$, $1-y$, $-z$] have some overlap, the latter pair having the stronger interaction with significant overlap at an interplanar spacing of 3.42 Å. There are also several S···H–C contacts between anion and cation, the shortest of these are listed in Table 4.

4. Possibilities of metal assembling through complexes 1 and 2

Previous studies dealing with tppz-bridged metal(II) complexes have illustrated the ability of this polyatomic bridge to mediate significant magnetic interactions between the paramagnetic centres separated by distances larger than

6.5 Å [12a,12b,12f–i,13b]. Also, the mononuclear complexes of Co(II) of formula $[Co(tppz)_2]^{2+}$, where tppz adopts the tridentate coordination mode, exhibit spin crossover [13b].

The diamagnetism of the corresponding complexes with iron(II) demonstrates the strong ligand field character of tppz. Having in mind this information, it is clear that the main interest of the diamagnetic $[Fe(tppz)(CN)_3]^-$ and $[Fe(tppz)_2]^{2+}$ units from **1** and **2** is their use as ligands towards fully solvated or partially blocked metal ions in order to create new polymetallic assemblies where significant electronic and/or magnetic coupling could be involved. In the case of the $[Fe(tppz)(CN)_3]^-$ anion of **1**, its oxidation to the related iron(III) species would provide a paramagnetic low-spin iron(III) species ($S_{Fe} = 1/2$) whose potentiality as a ligand would follow the magneto-structural studies carried out with the related low-spin iron(III) complexes *mer*-$[Fe(bpca)(CN)_3]^-$ [22,27] and *fac*-$[Fe\{HB(pz)_3\}(CN)_3]^-$ [28] [$HB(pz)_3^- =$ hydrotris (1-pyrazolyl)borate] but with the advantage of having also the terminal nitrogen atoms of tppz as donors.

5. Conclusions

The combination of structural knowledge and the magnetic data at room temperature of the complexes **1** and **2** reveal the occurrence of low-spin iron(II) centres in the $[Fe(tppz)(CN)_3]^-$ anion (**1**) and $[Fe(tppz)_2]^{2+}$ cation (**2**) confirming the strong field character of the tppz ligand in its complexes with the iron(II) ion. A search in the CSD shows that complex **2** is the first structurally characterized example containing the tetrahedral iron(II) unit $[Fe(NCS)_4]^{2-}$. The occurrence of non-coordinated pyridyl and pyrazine nitrogen atoms in both the $[Fe(tppz)(CN)_3]^-$ anion (**1**) and $[Fe(tppz)_2]^{2+}$ cation (**2**) together with the free peripheral cyanide-nitrogen atoms in the former, make them suitable building blocks for metal assembling and further studies on electronic coupling.

Acknowledgement

Thanks are due the Ministero Italiano dell'Università e della Ricerca and the Ministerio Español de Ciencia y Tecnología (Project CTQ2004-03633) for financial support. One of us (L.M. Toma) acknowledges the Ministerio Español de Educación for a predoctoral fellowship.

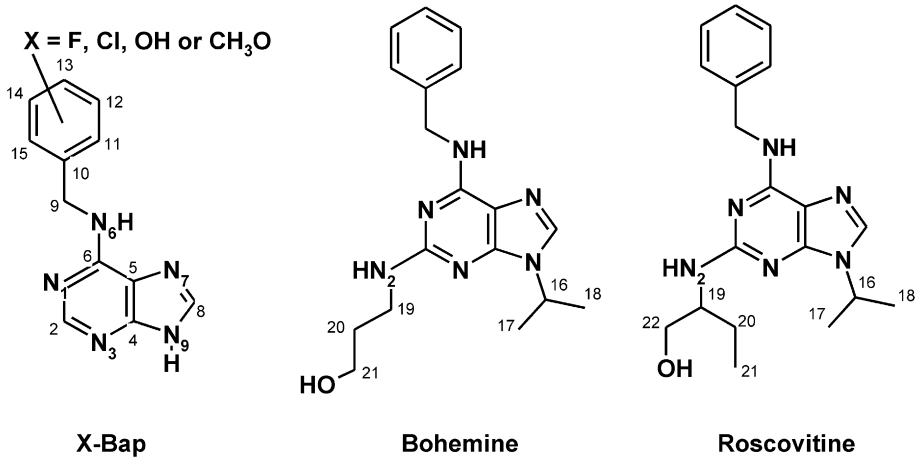
Appendix A. Supplementary material

CCDC 642856 and 642857 contain the supplementary crystallographic data for **1** and **2**. These data can be obtained free of charge via http://www.ccdc.cam.ac.uk/conts/retrieving.html, or from the Cambridge Crystallographic Data Centre, 12 Union Road, Cambridge CB2 1EZ, UK, fax: (+44) 1223-336-033, or e-mail: deposit@ccdc.cam.ac.uk.

References

[1] H.A. Goodwin, F. Lions, J. Am. Chem. Soc. 81 (1959) 6415.
[2] (a) R.T. Pflaum, C.J. Smith Jr., E.B. Buchanan, R.E. Jensen, Anal. Chim. Acta 31 (1964) 34;
(b) W.I. Stephen, Talanta 16 (1969) 939.
[3] (a) R.P. Thummel, S. Chirayil, Inorg. Chim. Acta 154 (1988) 77;
(b) R.R. Ruminski, J. Kiplinger, T. Cockroft, C. Chase, Inorg. Chem. 28 (1989) 370;
(c) R.R. Ruminski, J.L. Kiplinger, Inorg. Chem. 29 (1990) 4581;
(d) J.G. Du Preez, T.I.A. Gerkr, M.L. Gibson, R. Geyser, J. Coord. Chem. Rev. 22 (1990) 249;
(e) J.D. Petersen, L.W. Morgan, I. Hsu, M.A. Billadeau, S.E. Ronco, Coord. Chem. Rev. 111 (1991) 319;
(f) C.R. Arana, H.D. Abruña, Inorg. Chem. 32 (1993) 194;
(g) L.M. Volger, B. Scott, K.J. Brewer, Inorg. Chem. 32 (1993) 898.
[4] (a) C.W. Padgett, W.T. Pennington, T.W. Hanks, Cryst. Growth Des. 5 (2005) 737;
(b) C.W. Padgett, R.D. Walsh, G.W. Drake, T.W. Hanks, W.T. Pennington, Cryst. Growth Des. 5 (2005) 745.
[5] (a) C.M. Hartshorn, N. Daire, V. Tondreau, B. Loeb, T.J. Meyer, P.S. White, Inorg. Chem 38 (1999) 3200;
(b) N. Chanda, R.H. Laye, S. Chakraborty, R.L. Paul, J.C. Jeffery, M.D. Ward, G.K. Lahiri, J. Chem. Soc., Dalton Trans. (2002) 3496.
[6] J.K. Bera, C.S. Campos-Fernández, C. Clérac, K.R. Dunbar, Chem. Commun. (2002) 2536.
[7] M. Maekawa, T. Minematsu, H. Konaka, K. Sugimoto, T. Kuroda-Sowa, Y. Suenaga, M. Munakata, Inorg. Chim. Acta 357 (2004) 3456.
[8] Y. Yamada, Y. Miyashita, K. Fujisawa, K.I. Okamoto, Bull. Chem. Soc. Jpn. 73 (2000) 1843.
[9] L. Zhang, X.H. Zhao, Y. Zhao, Acta Crystallogr., Sect. E 61 (2005) m1760.
[10] C.J. Kuehl, R.E. Da Re, B.L. Scott, D.E. Morris, K.D. John, Chem. Commun. (2003) 2336.
[11] M. Graf, H. Stoeckli-Evans, Acta Crystallogr., Sect. C 50 (1994) 1461.
[12] (a) M. Graf, B. Greaves, H. Stoeckli-Evans, Inorg. Chim. Acta 204 (1993) 239;
(b) M. Graf, H. Stoeckli-Evans, A. Escuer, R. Vicente, Inorg. Chim. Acta 257 (1997) 89;
(c) D. Hagrman, P. Hagrman, J. Zubieta, Inorg. Chim. Acta 300–302 (2000) 212;
(d) E. Burkholder, J. Zubieta, Chem. Commun. (2001) 2056;
(e) E. Burkholder, V. Golub, C.J. O'Connor, J. Zubieta, Inorg. Chem. 42 (2003) 6729;
(f) J. Carranza, C. Brennan, J. Sletten, J.M. Clemente-Juan, F. Lloret, M. Julve, Inorg. Chem. 42 (2003) 8716;
(g) J. Carranza, J. Sletten, C. Brennan, F. Lloret, J. Cano, M. Julve, Dalton Trans. (2004) 3997;
(h) G.Y. Hsu, C.W. Chen, S.C. Cheng, S.H. Lin, H.H. Wei, C.J. Lee, Polyhedron 24 (2005) 487;
(i) H. Hzadeh, A.L. Rezvani, G.P.A. Yap, R.J. Crutchley, Inorg. Chim. Acta 385 (2005) 1289.
[13] (a) M. Koman, Z. Baloghová, D. Valigura, Acta Crystallogr., Sect. C 54 (1998) 1277;
(b) C.S. Campos-Fernández, B.W. Smucker, R. Clérac, K.R. Dunbar, Isr. J. Chem. 41 (2001) 207.
[14] E.C. Constable, A.J. Edwards, D. Phillips, P.R. Raithby, Supramol. Chem. 5 (1995) 93.
[15] H.A. Goodwin, Coord. Chim. Rev. 18 (1976) 293.
[16] A. Earnshaw, Introduction to Magnetochemistry, Academic Press, London, 1968.
[17] (a) SAINT, Versions 6.45, 6.02a, Bruker Analytical X-ray Systems Inc., Madison, WI 2003.;
(b) G.M. Sheldrick, SADABS Program for Absorption Correction, versions 2.10, 2.03, Analytical X-ray Systems, Madison, Wisconsin, USA, 2003, 2000.

[18] (a) G.M. Sheldrick, Acta Crystallogr., Sect. A 46 (1990) 467;
(b) SHELXTL, Bruker Analytical X-ray Instruments, Madison, Wisconsin, USA, 1998.
[19] M. Nardelli, Comput. Chem. 7 (1983) 95.
[20] CRYSTALMAKER, 4.2.1, Crystalmaker Software, Bicester, Oxfordshire X26 3TA, UK, 1996.
[21] R.I. Haines, D. Pieda, W. Goulding, Transit. Met. Chem. 23 (1998) 763.
[22] R. Lescouëzec, J. Vaissermann, L.M. Toma, R. Carrasco, F. Lloret, M. Julve, Inorg. Chem. 43 (2004) 2234.
[23] P. Gütlich, Struct. Bonding (Berlin) 44 (1981) 82, and references therein.
[24] I. Dance, M. Scudder, Chem. Eur. J. 2 (1996) 481.
[25] (a) A.T. Baker, H.A. Goodwin, Aust. J. Chem. 38 (1985) 207;
(b) H. Oshio, H. Spiering, V. Ksenofontov, F. Renz, P. Gütlich, Inorg. Chem. 40 (2001) 1143.
[26] J.S. Haynes, A. Kostikas, J.R. Sams, A. Simopoulos, R.C. Thompson, Inorg. Chem. 26 (1987) 2630.
[27] H.R. Wen, C.F. Wang, J.L. Zuo, Y. Song, X.R. Zeng, X.Z. You, Inorg. Chem. 45 (2006) 582.
[28] (a) R. Lescouëzec, J. Vaissermann, F. Lloret, M. Julve, M. Verdaguer, Inorg. Chem. 41 (2002) 5943;
(b) S. Wang, J.L. Zuo, S. Gao, Y. Song, H.C. Zhou, Y.Z. Zhang, X.Z. You, J. Am. Chem. Soc. 126 (2004) 8900;
(c) S. Wang, J.L. Zuo, H.C. Zhou, H.J. Choi, Y. Ke, J.R. Long, X.Z. You, Angew. Chem., Int. Ed. 43 (2004) 5940;
(d) S. Wang, J.L. Zuo, H.C. Zhou, Y. Song, S. Gao, X.Z. You, Eur. J. Inorg. Chem. (2004) 3681;
(e) J. Kim, S. Han, I.K. Cho, K.Y. Choi, M. Heu, S. Ion, B.J. Suh, Polyhedron 23 (2004) 1333;
(f) S. Wang, J.L. Zuo, H.C. Zhou, Y. Song, X.Z. You, Inorg. Chim. Acta 358 (2005) 2101;
(g) H.R. Wen, C.F. Wang, Y. Song, S. Gao, J.L. Zuo, X.Z. You, Inorg. Chem. 45 (2006) 8942;
(h) C.F. Wang, J.L. Zuo, B.M. Bartlett, Y. Song, J.R. Long, X.Z. You, J. Am. Chem. Soc. 128 (2006) 7162.



Scheme 1. Structural representations of the prepared ligands including the atom numbering scheme.

developed worldwide as drugs to block cell cycle progression at a specific point, and thus to inhibit tumour growth. Among known and potent CDK inhibitors, we have chosen *bohemine* {Boh = 2-[(3-hydroxypropyl)amino]-6-benzylamino-9-isopropylpurine} and *roscovitine* (also named as seliciclib or CYC202) {Ros = 2-(*R*)-(1-ethyl-2-hydroxyethylamino)-6-benzylamino-9-isopropylpurine} as model ligands for the preparation of platinum(IV) complexes.

The anticancer activity of platinum(IV) complexes has been noted by Rosenberg and his colleagues, and known since the 1960s [5]. Although the platinum(IV) complexes have been studied less intensively than those of platinum(II), some of them showed promising anticancer activity to enter clinical trials. The bioinorganic chemistry of platinum(IV) antitumour compounds has been reviewed by Hall and Hambley [6]. One of the conclusions of the review is the statement regarding the observations that platinum(IV) complexes can protect the more reactive platinum(II) ones on the way to the target site before reduction allowing activity within the cell.

There exists a wide number of platinum(IV) complexes prepared and X-ray structurally characterized up to now. Among these complexes, a relatively small subset is represented by those bearing a $PtNCl_5$ donor set. Moreover, there is only a limited number of octahedral pentachloroplatinum(IV) complexes involving DNA nucleobases as N-donor ligands [7]. According to the Cambridge Structural Database [8], there exists only one X-ray structurally characterized pentachloro-platinum(IV) complex with a purine derivative as a ligand of the composition $[PtCl_5(9\text{-}MeAH^+)]$ (9-MeA = 9-methyladenine), where the N1 protonated 9-methyladenine ($9\text{-}MeAH^+$) is coordinated through N7 atom of the purine moiety to platinum(IV) which adopts a distorted octahedral geometry with the $PtNCl_5$ donor set [9].

This work has been motivated not only by efforts to broaden our knowledge regarding biologically interesting Pt(IV) complexes, but also by attempts to prepare the first Pt(IV) complexes with 6-benzylaminopurine derivatives (Scheme 1). In our previous works, we have shown that the transition metal complex formation, i.e. the coordination of CKs or CDK inhibitors to a suitable metal ion (e.g. Cu, Pt and Pd) may cause significant increase in *in vitro* cytotoxicity of the formed complexes as compared to the free discussed organic molecules [10–13]. To continue our investigations in this area, herein we report the preparation, characterization and cytotoxic study of the first Pt(IV) complexes with aromatic cytokinins or CDK-inhibitors of the composition $[Pt^{IV}(LH^+)Cl_5]$ (**1**–**14**), where LH^+ stands for protonated forms of 6-benzylaminopurine derivatives (Bap), *bohemine* or *roscovitine*. The complexes have been prepared by the reaction of K_2PtCl_6 with the corresponding organic compound in 2 M HCl solution. Moreover, two X-ray crystal structures of ionic pair compounds $(BohH_2^{2+})[PtCl_6] \cdot H_2O$ (**15**) and $(RosH_2^{2+})_2[PtCl_6][Cl_2 \cdot 4H_2O$ (**16**) have been determined.

2. Experimental

2.1. Reagents and materials

All the reagents used were chemically pure and of analytical reagent grade. K_2PtCl_6 used in preparation of the complexes was purchased from Aldrich Chem. Co. All other reactants and solvents used were supplied by Merck Co., Fluka Co. and/or Fisher Scientific Co.

2.2. Physical measurements

Elemental analyses (C, H, N) of the compounds were performed on a ThermoFinnigan EA 1112 Flash Analyzer. Infrared spectra of the complexes were recorded on a ThermoNicolet NEXUS 670 FT-IR spectrometer using KBr pellets (400–4000 cm^{-1}) and polyethylene discs (150–400 cm^{-1}). Conductivity measurements were made with a WTW Cond340i/SET conductometer in DMF at 25 °C. The concentration of the complexes in solutions was 10^{-3} mol dm^{-3}. ES+ mass spectra of the complexes were

obtained using a direct probe on a Waters ZMD 2000 mass spectrometer. Full scan analyses were performed for a 10-1000 *m/z* mass range. The spectra were collected using 3.0 s cyclical scans and applying the sample cone voltage, 20, 40, 60 or 80 V, at source block temperature of 100 °C, desolvation temperature of 250 °C and desolvation gas flow rate of 400 l/h. The mass spectrometer was directly coupled to a MassLynx data system. All interpretations of *m/z* were based on ^{35}Cl and ^{194}Pt. ^{1}H, ^{13}C, ^{15}N and ^{195}Pt NMR spectra were measured on a Bruker Avance 300 spectrometer operating at 300.13 MHz (^{1}H), 75.47 MHz (^{13}C) and 64.52 MHz (^{195}Pt). The temperature of the measurements was 300 K. The samples were prepared by dissolving the compounds in DMF-d_7. Tetramethylsilane was used as an internal standard (^{1}H, ^{13}C) and $K_2[PtCl_4]$ in D_2O (−1628 ppm) as an external reference (^{195}Pt). ^{15}N NMR chemical shifts were measured relative to DMF-d_7 solvent (adjusted to 104.7 ppm), which was also used as an internal reference standard. The individual ^{1}H and ^{13}C signals were assigned and refined by means of 2D correlation experiments gs-COSY (gradient pulse sequence – correlation spectroscopy), gs-HMQC (gs-heteronuclear multiple quantum correlation) and gs-HMBC ($^{n}J_{H,C} = 7.5$ Hz) (gs-heteronuclear multiple bond correlation). ^{15}N chemical shifts for compounds Boh, Ros, **13** and **14** were obtained at natural abundance by ^{1}H–^{15}N gs-HMQC and ^{1}H–^{15}N gs-HMBC experiments and the spectra were recorded at 27 °C.

2.3. Synthesis of ligands

6-(2-Methoxybenzylamino)purine (2-MeOBap), 6-(3-methoxybenzylamino)purine (3-MeOBap), 6-(4-methoxybenzylamino)purine (4-MeOBap), 6-(2-hydroxybenzylamino)purine (2-OHBap), 6-(3-hydroxybenzylamino)purine (3-OHBap), 6-(4-hydroxybenzylamino)purine (4-OHBap), 6-(2-chlorobenzylamino)purine (2-ClBap), 6-(3-chlorobenzylamino)purine (3-ClBap), 6-(4-chlorobenzylamine)purine (4-ClBap), 6-(2-fluorobenzylamino)purine (2-FBap), 6-(3-fluorobenzylamino)purine (3-FBap) and 6-(4-fluorobenzylamino)purine (4-FBap) were synthesized using a slight modification of the previously described procedure [14]. *Bohemine* (Boh) and *roscovitine* (Ros) were obtained according to the mildly changed reported method [15]. The composition and purity of these organic molecules used as ligands were proved by elemental analysis, melting point, ^{1}H and ^{13}C NMR (for all the ligands), ^{15}N NMR (for Boh and Ros only), and thin-layer chromatography (TLC). ^{1}H and ^{13}C NMR spectral data of the ligands, except for Boh and Ros, are deposited as Supplementary material.

Boh: ^{1}H NMR (DMF-d_7, ppm): δ 7.85 (bs, 1H, N6H), 7.76 (s, 1H, C8H), 7.45 (d, $J = 7.2$ Hz, 2H, C11,15H), 7.30 (tt, $J_a = 7.2$ Hz, $J_b = 1.5$ Hz, 2H, C12,14H), 7.21 (tt, $J_a = 7.2$ Hz, $J_b = 1.5$ Hz, 1H, C13H), 6.29 (t, $J = 6.0$ Hz, 1H, N2H), 4.83 (bs, 2H, C9H), 4.72 (t, $J = 5.3$ Hz, 1H, O21H), 4.62 (sep, $J = 7.0$ Hz, 1H, C16H), 3.65 (q, $J = 5.5$ Hz, 2H, C21H), 3.51 (q, $J = 6.2$ Hz, 2H, C19H), 1.81 (qui, $J = 6.4$ Hz, 2H, C20H), 1.52 (d, $J = 6.8$ Hz, 6H, C17,18H). ^{13}C NMR (DMF-d_7, ppm): 160.49 (C2), 155.70 (C6), 151.81 (C4), 141.66 (C8), 135.61 (C10), 128.76 (C11,15), 128.19 (C12,14), 127.17 (C13), 114.80 (C5), 60.08 (C21), 46.71 (C16), 43.87 (C9), 39.32 (C19), 33.69 (C20), 22.40 (C17,18). ^{15}N NMR (DMF-d_7, ppm): 237.0 (N7), 194.2 (N1), 176.9 (N3), 172.2 (N9), 85.2 (N6), 84.4 (N2).

Ros: ^{1}H NMR (DMF-d_7, ppm): δ 7.77 (s, 1H, C8H), 7.72 (bs, 1H, N6H), 7.45 (d, $J = 7.0$ Hz, 2H, C11,15H), 7.30 (tt, $J_a = 7.0$ Hz, $J_b = 1.7$ Hz, 2H,C12,14H), 7.22 (tt, $J_a = 7.0$ Hz, $J_b = 1.7$ Hz, 1H, C13H), 5.86 (d, $J = 8.2$ Hz, 1H, N2H), 4.83 (bs, 2H, C9H), 4.79 (t, $J = 5.5$ Hz, 1H, O22H), 4.61 (sep, $J = 6.7$ Hz, 1H, C16H), 3.98 (m, 1H, C19H), 3.67 (m, 1H, $C22H_a$), 3.59 (m, 1H, $C22H_b$), 1.74 (sep, $J = 7.2$ Hz, 1H, $C20H_a$), 1.58 (sep, $J = 7.2$ Hz, 1H, $C20H_b$), 1.52 (d, $J = 6.8z$, 6H, C17,18H), 0.94 (t, $J = 7.2$ Hz, 3H, C21H). ^{13}C NMR (DMF-d_7, ppm): 160.31 (C2), 155.70 (C6), 151.86 (C4), 141.72 (C10), 135.74 (C8), 128.78 (C12,14), 128.23 (C11,15), 127.20 (C13), 114.96 (C5), 64.56 (C22), 55.33 (C19), 46.84 (C16), 43.95 (C9), 24.95 (C20), 22.38 (C17), 22.34 (C18), 11.03 (C21). ^{15}N NMR (DMF-d_7, ppm): 237.5 (N7), 194.3 (N1), 178.1(N3), 171.9 (N9), 91.7 (N2), 85.3 (N6).

2.4. Synthesis of Pt(IV) complexes (*1*–*14*): a general procedure

K_2PtCl_6 (0.24 g, 0.5 mmol), dissolved in 30 ml of 2 M HCl, was added to a solution of the corresponding ligand (0.5 mmol in 30 ml of 2 M HCl). The mixture was stirred under reflux for 2 h. A yellow precipitate formed after this time period. It was filtered off, washed with water and dried in air. All complexes were obtained in high yields (ca. 80–90%).

2.4.1. $[Pt(2\text{-}MeOBapH^+)Cl_5]$ (*1*)

Anal. Calc. for $C_{13}H_{14}Cl_5N_5OPt$: C, 24.8; H, 2.3; N, 11.1. Found: C, 24.6; H, 2.6; N, 11.2%. $\lambda_M = 37.6$ S cm^2 mol^{-1} in DMF. IR (cm^{-1}): 534s *ν*(Pt–N), 350s *ν*(Pt–Cl). ES+ MS (*m/z*): 628.4 $[Pt(L)Cl_5]^+$, 593.7 $[Pt(L)Cl_4]^+$, 522.5 $[Pt(L)Cl_2]^+$, 452.9 $[Pt(L)]^+$, 256.0 $(L)^+$. ^{1}H NMR (DMF-d_7, ppm): δ 11.10 (bs, 1H, N7H), 9.98 (bs, 1H, N6H), 8.82 (s, 1H, C8H), 8.59 (s, 1H,C2H), 7.41 (t, $J = 7.9$ Hz, 1H, C13H), 7.28 (d, $J = 7.9$ Hz, 1H, C15H), 6.99 (d, $J = 7.9$ Hz, 1H, C12H), 6.76 (t, $J = 7.9$ Hz, 1H, C14H), 5.04 (s, 2H, C9H), 3.86 (s, 3H, C16H). ^{13}C NMR (DMF-d_7, ppm): 158.64 (C11), 155.00 (C6), 153.76 (C2), 147.25 (C4), 145.47 (C8), 142.13 (C10), 130.54 (C13), 127.96 (C15), 120.98 (C14), 117.24 (C5), 111.87 (C12), 56.29 (C16), 45.42 (C9). ^{195}Pt (DMF-d_7, ppm): 99.7.

2.4.2. $[Pt(3\text{-}MeOBapH^+)Cl_5]$ (*2*)

Anal. Calc. for $C_{13}H_{14}Cl_5N_5OPt$: C, 24.8; H, 2.3; N, 11.1. Found: C, 24.4; H, 2.5; N, 10.7%. $\lambda_M = 40.1$ S cm^2 mol^{-1} in DMF. IR (cm^{-1}): 533s *ν*(Pt–N), 349s *ν*(Pt–Cl). ES+ MS (*m/z*): 628.7 $[Pt(L)Cl_5]^+$, 592.6 $[Pt(L)Cl_4]^+$, 523.0 $[Pt(L)Cl_2]^+$, 452.5 $[Pt(L)]^+$, 256.0

$(L)^+$. ^{1}H NMR (DMF-d_7, ppm): δ 11.30 (bs, 1H, N7H), 10.63 (bs, 1H, N6H), 8.82 (s, 1H, C8H), 8.58 (s, 1H, C2H), 7.30 (t, $J = 7.9$ Hz, 1H, C14H), 6.98 (s, 1H, C11H), 7.05 (d, $J = 7.9$ Hz, 1H, C15H), 6.88 (d, $J = 7.9$ Hz, 1H, C13H), 4.99 (s, 2H, C9H), 3.81 (s, 3H, C16H). ^{13}C NMR (DMF-d_7, ppm): 160.17 (C12), 154.79 (C6), 154.71 (C2), 148.27 (C4), 146.05 (C8), 141.83 (C10), 130.03 (C14), 120.91 (C15), 117.90 (C5), 114.38 (C13), 112.44 (C11), 56.21 (C16), 45.14 (C9). ^{195}Pt NMR (DMF-d_7, ppm): 102.4.

2.4.3. [Pt(4-MeOBapH$^+$)Cl$_5$] (3)

Anal. Calc. for $C_{13}H_{14}Cl_5N_5OPt$: C, 24.8; H, 2.3; N, 11.1. Found: C, 24.9; H, 2.1; N, 11.0%. $\lambda_M = 36.7$ S cm^2 mol^{-1} in DMF. IR (cm^{-1}): 530m ν(Pt–N), 351s ν(Pt–Cl). ES+ MS (m/z): 629.2 $[Pt(L)Cl_5]^+$, 593.7 $[Pt(L)Cl_4]^+$, 521.4 $[Pt(L)Cl_2]^+$, 453.1 $[Pt(L)]^+$, 256.0 $(L)^+$. ^{1}H NMR (DMF-d_7, ppm): δ 11.45 (bs, 1H, N7H), 9.41 (bs, 1H, N6H), 8.84 (s, 1H, C8H), 8.50 (s, 1H,C2H), 7.34 (d, $J = 7.7$ Hz, 2H, C12,14H), 6.90 (d, $J = 7.7$ Hz, 2H, C11,15H), 4.79 (s, 2H, C9H), 3.74 (s, 3H, C16H). ^{13}C NMR (DMF-d_7, ppm): 158.63 (C13), 154.53 (C6), 153.34 (C2), 146.91 (C4), 144.02 (C8), 131.15 (C10), 128.44 (C11,15), 117.23 (C5), 113.12 (C12,14), 54.74 (C16), 43.63 (C9). ^{195}Pt NMR (DMF-d_7, ppm): 105.2.

2.4.4. [Pt(2-OHBapH$^+$)Cl$_5$] (4)

Anal. Calc. for $C_{12}H_{12}Cl_5N_5OPt$: C, 23.5; H. 2.0; N, 11.4. Found: C, 23.1; H, 2.4; N, 11.0%. $\lambda_M = 37.9$ S cm^2 mol^{-1} in DMF. IR (cm^{-1}): 533s ν(Pt–N), 350s ν(Pt–Cl). ES+ MS (m/z): 580.4 $[Pt(L)Cl_4]^+$, 508.7 $[Pt(L)Cl_2]^+$, 479.5 $[Pt(L)Cl]^+$, 242.1 $(L)^+$. ^{1}H NMR (DMF-d_7, ppm): δ 11.65 (bs, 1H, N7H), 10.51 (bs, 1H, O1H), 8.94 (s, 1H, C8H), 8.90 (s, 1H, N6H), 8.51 (s, 1H, C2H), 7.37 (d, $J = 7.7$ Hz, 1H, C12H), 7.15 (t, $J = 7.7$ Hz, 1H,C13H), 6.89 (d, $J = 7.7$ Hz, 1H, C15H), 6.81 (t, $J = 7.7$ Hz, 1H, C14H), 4.77 (bs, 2H, C9H). ^{13}C NMR (DMF-d_7, ppm): 156.03 (C11), 153.53 (C6), 153.09 (C2), 146.91 (C4), 144.37 (C8), 128.96 (C13), 127.98 (C15), 124.74 (C10), 119.21 (C14), 116.30 (C12), 115.97 (C5), 42.27 (C9). ^{195}Pt NMR (DMF-d_7, ppm): 93.1.

2.4.5. [Pt(3-OHBapH$^+$)Cl$_5$] (5)

Anal. Calc. for $C_{12}H_{12}Cl_5N_5OPt$: C, 23.5; H. 2.0; N, 11.4. Found: C, 23.2; H, 2.1; N, 10.9%. $\lambda_M = 39.5$ S cm^2 mol^{-1} in DMF. IR (cm^{-1}): 530s ν(Pt–N), 351s ν(Pt–Cl). ES+ MS (m/z): 580.1 $[Pt(L)Cl_4]^+$, 508.5 $[Pt(L)Cl_2]^+$, 479.5 $[Pt(L)Cl]^+$, 242.1 $(L)^+$. ^{1}H NMR (DMF-d_7, ppm): δ 11.71 (bs, 1H, N7H), 9.99 (bs, 1H, O1H), 9.48 (s, 1H, N6H), 8.88 (s, 1H, C8H), 8.62 (s, 1H, C2H), 7.19 (t, $J = 7.8$ Hz, 1H, C14H), 7.08 (t, $J = 2.0$ Hz, 1H, C11H), 6.99 (d, $J = 7.8$ Hz, 1H, C13H), 6.74 (d, $J = 7.8$ Hz, 1H, C15H), 4.85 (s, 2H, C9H). ^{13}C NMR (DMF-d_7, ppm): 158.53 (C12), 155.35 (C2), 155.30 (C6), 147.93 (C4), 145.87 (C8), 141.83 (C10), 130.44 (C14), 118.96 (C15), 117.70 (C5), 115.97 (C13), 115.64 (C11), 44.91 (C9). ^{195}Pt NMR (DMF-d_7, ppm): 102.1.

2.4.6. [Pt(4-OHBapH$^+$)Cl$_5$] (6)

Anal. Calc. for $C_{12}H_{12}Cl_5N_5OPt$: C, 23.5; H. 2.0; N, 11.4. Found: C, 23.8; H, 2.2; N, 11.1%. $\lambda_M = 34.4$ S cm^2 mol^{-1} in DMF. IR (cm^{-1}): 530m ν(Pt–N), 349s ν(Pt–Cl). ES+ MS (m/z): 579.1 $[Pt(L)Cl_4]^+$, 507.5 $[Pt(L)Cl_2]^+$, 479.2 $[Pt(L)Cl]^+$, 242.0 $(L)^+$. ^{1}H NMR (DMF-d_7, ppm): δ 11.80 (bs, 1H, N7H), 9.62 (s, 1H, O1H), 8.97 (s, 1H, N6H), 8.71 (s, 1H, C8H), 8.45 (s, 1H, C2H), 7.27 (d, $J = 7.8$ Hz, 2H, C11,15H), 6.79 (d, $J = 7.8$ Hz, 2H, C12,14H), 4.78 (s, 2H, C9H). ^{13}C NMR (DMF-d_7, ppm): 155.85 (C13), 154.97 (C6), 153.70 (C2), 146.69 (C4), 143.84 (C8), 129.55 (C11,15), 129.00 (C10), 117.03 (C5), 115.60 (C12,14), 43.76 (C9). ^{195}Pt NMR (DMF-d_7, ppm): 99.0.

2.4.7. [Pt(2-FBapH$^+$)Cl$_5$] (7)

Anal. Calc. for $C_{12}H_{11}Cl_5FN_5Pt$: C, 23.4; H. 1.8; N, 11.4. Found: C, 23.9; H, 1.6; N, 11.0%. $\lambda_M = 41.4$ S cm^2 mol^{-1} in DMF. IR (cm^{-1}): 3275w ν(N–H), 3070w ν(C–H), 1657s ν(C=N), 1272m $\nu(C_{ar}–F)$. ES+ MS (m/z): 580.2 $[Pt(L)Cl_4]^+$, 545.1 $[Pt(L)Cl_3]^+$, 244.0 $(L)^+$. ^{1}H NMR (DMF-d_7, ppm): δ 11.20 (bs, 1H, N7H), 9.82 (bs, 1H, N6H), 8.99 (s, 1H, C8H), 8.72 (s, 1H, C2H), 7.60 (t, $J = 7.7$ Hz, 1H, C13H), 7.40 (q, $J = 7.7$ Hz, 1H, C15H), 7.31 (d, $J = 7.7$ Hz, 1H, C12H), 7.21 (t, $J = 7.7$ Hz, 1H, C14H), 5.08 (bs, 2H, C9H). ^{13}C NMR (DMF-d_7, ppm): 162.67, 159.23 (C11), 153.88 (C6), 155.19 (C2), 149.56 (C4), 145.62 (C8), 130.57, 130.49 (C15), 129.44, 129.35 (C13), 126.82, 126.60 (C10), 125.52 (C14), 118.27 (C5), 116.56 (C12), 39.24 (C9). ^{195}Pt NMR (DMF-d_7, ppm): 112.4.

2.4.8. [Pt(3-FBapH$^+$)Cl$_5$] (8)

Anal. Calc. for $C_{12}H_{11}Cl_5FN_5Pt$: C, 23.4; H. 1.8; N, 11.4. Found: C, 24.1; H, 1.9; N, 11.0%. $\lambda_M = 34.8$ S cm^2 mol^{-1} in DMF. IR (cm^{-1}): 3218w, 3156w ν(N–H), 3068w ν(C–H), 1661s ν(C=N), 1268m $\nu(C_{ar}–F)$, 535s ν(Pt–N), 350s ν(Pt–Cl). ES+ MS (m/z): 582.0 $[Pt(L)Cl_4]^+$, 244.3 $(L)^+$. ^{1}H NMR (DMF-d_7, ppm): δ 10.95 (bs, 1H, N7H), 9.80 (bs, H, N6H), 8.99 (s, 1H, C8H), 8.66 (s, 1H, C2H), 7.43 (q, $J = 8.2$ Hz, 1H, C14H), 7.38 (t, $J = 10.0$ Hz, 1H, C13H), 7.34 (d, $J = 8.2$ Hz, 1H, C15H), 7.16 (t, $J = 8.2$ Hz, 1H, C11H), 4.99 (s, 2H, C9H). ^{13}C NMR (DMF-d_7, ppm): 164.88, 161.48 (C12), 155.99 (C2), 154.62 (C6), 147.82 (C4), 143.79, 143.73 (C10), 145.08 (C8), 131.30, 131.25 (C14), 124.35 (C15), 118.81 (C5), 115.82, 115.30 (C13), 115.20, 114.86 (C11), 45.27 (C9). ^{195}Pt NMR (DMF-d_7, ppm): 112.8.

2.4.9. [Pt(4-FBapH$^+$)Cl$_5$] (9)

Anal. Calc. for $C_{12}H_{11}Cl_5FN_5Pt$: C, 23.4; H. 1.8; N, 11.4. Found: C, 23.5; H, 1.8; N, 11.1%. $\lambda_M = 45.7$ S cm^2 mol^{-1} in DMF. IR (cm^{-1}): 3276w, 3160w ν(N–H), 3086w ν(C–H), 1657s ν(C=N), 1272m $\nu(C_{ar}–F)$, 534s ν(Pt–N), 351s ν(Pt–Cl). ES+ MS (m/z): 616.0 $[Pt(L)Cl_5]^+$, 581.6 $[Pt(L)Cl_4]^+$, 244.3 $(L)^+$. ^{1}H NMR (DMF-d_7, ppm): δ 11.00 (bs, 1H, N7H), 9.69 (bs, 1H,

N6H), 9.04 (s, 1H, C8H), 8.72 (s, 1H, C2H), 7.59 (m, 2H, C11,15H), 7.31 (t, $J = 9.0$ Hz, 2H, C12,14H), 5.03(s, 2H, C9H). ^{13}C NMR (DMF-d_7, ppm): 163.48, 159.86 (C13), 156.18 (C2), 153.68 (C6), 148.49 (C4), 146.75 (C8), 136.27 (C10), 130.89 (C11,15), 116.82 (C5), 116.41, 116.37 (C12,14), 45.57 (C9). ^{195}Pt NMR (DMF-d_7, ppm): 128.2.

2.4.10. [Pt(2-ClBapH$^+$)Cl$_5$] (**10**)

Anal. Calc. for $C_{12}H_{11}Cl_6N_5Pt$: C, 22.8; H. 1.8; N, 11.1. Found: C, 23.0; H, 2.0; N, 10.7%. $\lambda_M = 34.9$ S cm^2 mol^{-1} in DMF. IR (cm^{-1}): 3222w, 3150w ν(N–H), 3080w ν(C–H), 1655s ν(C=N), 1121m ν(C$_{ar}$–Cl), 533s ν(Pt–N), 350s ν(Pt–Cl). ES+ MS (*m*/*z*): 563.1 [Pt(L)Cl$_3$]$^+$, 260.2 (L)$^+$. ^{1}H NMR (DMF-d_7, ppm): δ 10.70 (bs, 1H, N7H), 8.93 (bs, 1H,N6H), 8.74 (s, 1H, C8H), 8.58 (s, 1H, C2H), 7.57 (d, $J = 7.8$ Hz, 1H, C12H), 7.36 (d, $J = 7.8$ Hz, 1H, C15H), 7.34 (t, $J = 7.8$ Hz, 1H, C13H), 7.28 (t, $J = 7.8$ Hz, 1H, C14H), 4.92 (s, 2H, C9H). ^{13}C NMR (DMF-d_7, ppm): 154.11 (C6), 153.59 (C2), 146.61 (C4), 143.82 (C8), 135.87 (C10), 131.23 (C11), 129.39 (C15), 129.12 (C12), 128.96 (C13), 127.49 (C14), 117.39 (C5), 42.04 (C9). ^{195}Pt NMR (DMF-d_7, ppm): 103.2.

2.4.11. [Pt(3-ClBapH$^+$)Cl$_5$] (**11**)

Anal. Calc. for $C_{12}H_{11}Cl_6N_5Pt$: C, 22.8; H. 1.8; N, 11.1. Found: C, 23.2; H, 1.9; N, 11.2%. $\lambda_M = 40.1$ S cm^2 mol^{-1} in DMF. IR (cm^{-1}): 1657s ν(C=N), 1152m ν(C$_{ar}$–Cl), 529s ν(Pt–N), 350s ν(Pt–Cl). ES+ MS (*m*/*z*): 561.9 [Pt(L)Cl$_3$]$^+$, 525.8 [Pt(L)Cl$_2$]$^+$, 454.1 [Pt(L)]$^+$, 260.2 (L)$^+$. ^{1}H NMR (DMF-d_7, ppm): δ 10.88 (bs, 1H, N7H), 9.84 (s, 1H,N6H), 8.81 (s, 1H, C8H), 8.57 (s, 1H, C2H), 7.59 (s, 1H, C11H), 7.47 (d, $J = 7.5$ Hz, 1H, C15H), 7.42 (t, $J = 7.5$ Hz, 1H, C14H), 7.37 (d, $J = 7.5$ Hz, 1H, C13H), 5.03 (s, 2H, C9H). ^{13}C NMR (DMF-d_7, ppm): 155.97 (C2), 153.61 (C6), 145.69 (C4), 145.62 (C8), 142.46 (C10), 133.37 (C12), 131.22 (C11), 129.04 (C14), 128.38 (C13), 126.98 (C15), 116.98 (C5), 44.48 (C9). ^{195}Pt NMR (DMF-d_7, ppm): 105.3.

2.4.12. [Pt(4-ClBapH$^+$)Cl$_5$] (**12**)

Anal. Calc. for $C_{12}H_{11}Cl_6N_5Pt$: C, 22.8; H. 1.8; N, 11.1. Found: C, 23.1; H, 2.0; N, 10.6%. $\lambda_M = 39.8$ S cm^2 mol^{-1} in DMF. IR (cm^{-1}): 3223w, 3131w ν(N–H), 1660s ν(C=N), 533m ν(Pt–N), 349s ν(Pt–Cl). ES+ MS (*m*/*z*): 561.7 [Pt(L)Cl$_3$]$^+$, 260.2 (L)$^+$. ^{1}H NMR (DMF-d_7, ppm): δ 10.90 (bs, 1H, N7H), 10.17 (s, 1H, N6H), 8.85 (s, 1H, C8H), 8.74 (s, 1H, C2H), 7.55 (d, $J = 8.6$ Hz, 2H, C11, 15H), 7.48 (d, $J = 8.6$ Hz, 2H, C12, 14H), 5.00 (s, 2H, C9H). ^{13}C NMR (DMF-d_7, ppm): 155.53 (C2), 154.33 (C6), 147.10 (C4), 145.17 (C8), 139.67 (C10), 131.97 (13), 13.75 (C11, 15), 129.95 (C12, 14), 117.77 (C5), 45.36 (C9). ^{195}Pt NMR (DMF-d_7, ppm): 129.6.

2.4.13. [Pt(BohH$^+$)Cl$_5$] (**13**)

Anal. Calc. for $C_{18}H_{25}Cl_5N_6OPt$: C, 30.3; H. 3.5; N, 11.8. Found: C, 29.7; H, 3.5; N, 11.6%. $\lambda_M = 48.4$ S cm^2 mol^{-1} in DMF. IR (cm^{-1}): 3345m ν(N–H), 1640s ν(C=N). ES+ MS (*m*/*z*): 641.1 [Pt(L)Cl$_3$]$^+$, 572.6 [Pt(L)Cl]$^+$, 535.7 [Pt(L)]$^+$, 341.4 (L)$^+$. ^{1}H NMR (DMF-d_7, ppm): δ 8.81 (bs, 1H, C8H), 7.82 (bs, 1H, N2H), 8.39 (bs, 1H, N6), 7.49 (dd, $J_a = 7.2$ Hz, $J_b = 1.7$ Hz, 2H, C11,15H), 7.36 (tt, $J_a = 7.2$ Hz, $J_b = 1.7$ Hz, 2H, C12,14H), 7.29 (tt, $J_a = 7.2$ Hz, $J_b = 1.7$ Hz, 1H,C13H), 5.38 (bs, 1H, O21H), 4.94 (bs, 2H, C9H), 4.83 (m, 1H, C16H), 3.64 (t, $J = 6.0$ Hz, 2H, C21H), 3.56 (t, $J = 6.8$ Hz, 2H, C19H), 1.84 (qui, $J = 6.4$ Hz, 2H, C20H), 1.62 (d, $J = 6.8$ Hz, 6H, C17,18H). ^{13}C NMR (DMF-d_7, ppm): 159.22 (C2), 154.42 (C6), 149.69 (C4), 139.87 (C10), 138.72 (C8), 129.05 (C12,14), 128.46 (C11,15), 127.90 (C13), 107.74 (C5), 59.91 (C21), 49.39 (C16), 44.83 (C9), 39.67 (C19), 32.67 (C20), 21.98 (C17,18). ^{15}N NMR (DMF-d_7, ppm): 179.9 (N9), 163.9 (N3), 151.1 (N7), 147.0 (N1), 92.2 (N2), 27.9 (N6). ^{195}Pt NMR (DMF-d_7, ppm): 332.4.

2.4.14. [Pt(RosH$^+$)Cl$_5$] (**14**)

Anal. Calc. for $C_{19}H_{27}Cl_5N_6OPt$: C, 31.4; H. 3.7; N, 11.6. Found: C, 32.1; H, 3.7; N, 11.7%. $\lambda_M = 44.8$ S cm^2 mol^{-1} in DMF. IR (cm^{-1}): 1643s ν(C=N), 526s ν(Pt–N), 351s ν(Pt–Cl). ES+ MS (*m*/*z*): 727.7 [Pt(L)Cl$_5$]$^+$, 656.6 [Pt(L)Cl$_3$]$^+$, 621.7 [Pt(L)Cl$_2$]$^+$, 585.9 [Pt(L)Cl]$^+$, 355.4 (L)$^+$. ^{1}H NMR (DMF-d_7, ppm) δ 8.64 (bs, 1H, C8H), 8.55 (bs, 1H, N6H), 7.55 (d, $J = 7.0$ Hz, 2H, C11,15H), 7.37 (t, $J = 7.0$ Hz, 2H, C12,14H), 7.30 (t, $J = 7.0$ Hz, 1H, C13H), 6.01 (bs, 1H, N2H), 5.38 (bs, 1H, O22H), 4.94 (bs, 2H, C9H), 4.80 (t, $J = 6.7$ Hz, 1H, C16H), 4.05 (m, 1H, C19H), 3.68 (m, 1H, C22H$_a$), 3.64 (m, 1H, C22H$_b$), 1.77 (sep, $J = 7.2$ Hz, 1H, C20H$_a$), 1.66 (m, 1H, C20H$_b$), 1.62 (d, $J = 6.8$ Hz, 6H, C17,18H), 0.97 (t, $J = 7.2$ Hz, 3H, C21H). ^{13}C NMR (DMF-d_7, ppm): 158.83 (C2), 153.91 (C6), 149.95 (C4), 139.87 (C10), 139.37 (C8), 129.11 (C12,14), 128.60 (C11,15), 109.95 (C5), 63.41 (C22), 55.83 (C19), 49.41 (C16), 45.08 (C9), 24.56 (C20), 21.93 (C17,18), 10.66 (C21). ^{15}N NMR (DMF-d_7, ppm): 180.16 (N3), 179.31 (N9), 152.06 (N7), 148.45 (N1), 99.36 (N2), 27.37 (N6). ^{195}Pt NMR (DMF-d_7, ppm): 339.7.

2.4.15. ($BohH_2^{2+}$)[$PtCl_6$] · H_2O (**15**)

After two weeks, a few crystals suitable for single crystal X-ray analysis were obtained by slow evaporation of the mother liquor from the first filtrate during the preparation of **13**.

2.4.16. ($RosH_2^{2+}$)$_2$[$PtCl_6$]Cl_2 · $4H_2O$ (**16**)

A few crystals of the complex were obtained similarly as described for complex **15** but the difference is that suitable single crystals were formed after six weeks.

2.5. Single crystal X-ray crystallography

X-ray measurements on the selected crystals of compounds **15** and **16** were performed on a Kuma KM-4 four-circle κ-axis diffractometer equipped with a CCD detector and Oxford Cryostream Cooler. Mo Kα radiation

($\lambda = 0.71073$ Å) from monochromator Enhance (Oxford Diffraction) and rotation ω-scans with different κ and ϕ for covering all reciprocal sphere were used. All data collection, cell refinement, data reduction and correction procedures were performed using the CRYSALIS CCD and CRYSALIS RED software [16]. The phase problem was solved by direct methods using SHELXS-97 [17]. The program SHELXL-97 [18] was used to refine both the structures by full-matrix least-squares procedure on F^2. All non-hydrogen atoms were refined as independent atoms using anisotropic thermal parameters. The coordinates of the O-bound H atoms were refined, with the O–H distances restrained to 0.95(2) Å. All other H atoms were located in a difference map and refined using a riding model, with N–H = 0.88 Å, C–H = 0.95–1.00 Å, and $U_{iso}(H) = 1.2U_{eq}$-(C,N) or $1.5U_{eq}(CH_3)$. Crystal data and structure refinements of **15** and **16** are summarized in Table 1.

2.6. DFT calculations

Preliminary structural data were calculated on HF/6-31* level with respect to structural properties usual for complexes of studied type. Geometries of found minima were than fully optimized at the B3LYP level with the 6-311+G**/LANL2DZ and aug-cc-pVDZ/LANL2DZ basis sets, where LANL2DZ pseudo-potential was used for the Pt atom. Harmonic frequency analysis was used to verify the nature of found stationary points as the minima as well as for the calculation of zero-point vibrational energies. Calculated infrared frequencies were not scaled by any factor. All calculations were performed using the GAUSSIAN-03 program [19].

Table 1
Crystal data and structure refinements for $(BohH_2^{2+})[PtCl_6]\cdot H_2O$ (**15**) and $(RosH_2^{2+})_2[PtCl_6]Cl_2\cdot 4H_2O$ (**16**)

Compound	**15**	**16**
Empirical formula	$C_{18}H_{28}Cl_6N_6O_2Pt$	$C_{38}H_{64}Cl_8N_{12}O_6Pt$
Formula weight	768.25	1263.70
Crystal system	monoclinic	monoclinic
Space group	$P2_1/c$	$P2_1/n$
Unit cell dimensions		
a (Å)	12.9892(16)	17.8564(14)
b (Å)	16.4258(11)	6.9720(4)
c (Å)	13.4209(12)	21.353(2)
β (°)	110.439(12)	95.784(7)
Z	4	2
V (Å^3)	2683.2(5)	2644.8(4)
D_{calc} (g cm^{-3})	1.902	1.587
T (K)	120(2)	120(2)
μ (mm^{-1})	5.855	3.110
T_{max}/T_{min}	0.7314/0.1108	0.7192/0.3515
Index ranges	$-15 \leqslant h \leqslant 15$, $-19 \leqslant k \leqslant 13$, $-15 \leqslant l \leqslant 15$	$-21 \leqslant h \leqslant 21$, $-8 \leqslant k \leqslant 7$, $-19 \leqslant l \leqslant 25$
θ Range (°) for data collection	$2.99 \leqslant \theta \leqslant 25.05$	$3.32 \leqslant \theta \leqslant 25.00$
Reflection collected/unique	12885/4699	12896/4654
R_{int}	0.0399	0.0992
Data/restrains/parameters	4699/3/310	4654/24/330
Goodness-of-fit on F^2	1.231	1.183
Final R indices $[I > 2\sigma(I)]$	$R_1 = 0.0296$, $wR_2 = 0.0839$	$R_1 = 0.0689$, $wR_2 = 0.1605$
R indices (all data)	$R_1 = 0.0334$, $wR_2 = 0.0942$	$R_1 = 0.0802$, $wR_2 = 0.1676$
Largest peak and hole (e Å^{-3})	1.522 and −1.711	3.331 and −1.376

2.7. Cytotoxicity testing

The cytotoxicity of the free ligands and their platinum(IV) complexes were tested *in vitro* by a calcein AM assay against the following human cancer cell lines: malignant meloma *G361*, osteogenic sarcoma *HOS*, chronic myologenous leukemia *K562* and breast adenocarcinoma cell line *MCF7*. The cells were treated with a solution of the tested compound for 72 h at 37 °C, 5% CO_2; in the range 0.41–167 μM for **1**–**6** and 0.35–85 μM for **7**–**14.** Further details regarding the biological activity testing are detailed in [20]. The IC_{50} values are represented by arithmetic mean of three values. The measurement deviation ranges from 12% to 18%.

3. Results and discussion

3.1. General characterization

The proposed molecular formula for all the complexes **1**–**14** are in good agreement with the stoichiometric composition concluded from analytical data. The molar conductance measurements in DMF solutions indicated that the complexes behave as non-electrolytes ($\lambda_M = 34.4$–48.4 S cm^2 mol^{-1}) [21], although partial dissociation had occurred in the solvent used. Moreover, the molar conductance values showed to be time dependent and increased with time. It has been found that the values are higher by about 20–30% after 48 h as compared to the original ones. This observation can be connected with the fact that DMF belongs to a group of alkaline solvents, and thus, it may partially deprotonate the positively charged Bap derivative coordinated within the complex. This deprotonation may cause fractional decomposition of the complexes, and consequently, the conductance of the solutions can be increased. The conclusion relating to the deprotonation can be also supported by NMR spectral data where signals belonging to free organic ligands were detected in the case of solutions measured after 48 h. That is why it has been not possible to use re-crystallizations from common solvents, mainly those behaving like proton acceptors, for the preparation of single crystals of complexes **1**–**14** suitable for X-ray analysis. Thus, we have tried to prepare single crystals by slow evaporation of the solvent used during the synthesis (i.e. 2 M HCl) from the mother liquor after the first filtration. We have been successful in the case of using this method, however, crystals of compounds with different composition have been formed, i.e. complexes **15**

and **16** (see Section 3.6). Based on these findings, we have optimized the geometries of complexes **1**–**14** by means of DFT calculations (see Section 3.5).

3.2. IR spectra

The presence of the appropriate organic ligand in the complexes was indicated by IR spectra measured in the range of 400–4000 cm^{-1}. The spectra show strong peaks near 1640 cm^{-1} which are typical for ν(C=N) stretch vibration of a purine ring. The bands near 3060 and 3300 cm^{-1} can be assigned to $\nu(C_{ar}–H)$, and ν(N–H) stretching vibrations, respectively. The bands recorded in the IR spectra of the complexes **7**–**9** at ca. 1270 cm^{-1} are typical for the $\nu(C_{ar}–F)$ vibration while the peaks at 1112–1160 cm^{-1} (for complexes **10**–**12**) can be ascribed to the $\nu(C_{ar}–Cl)$ vibration [22]. The maxima attributable to ν(Pt–N) and ν(Pt–Cl) were observed at ca. 530 and 350 cm^{-1}, respectively [23].

3.3. ES+ mass spectroscopy

Dominant peaks corresponding to the protonated form of 6-benzylaminopurine ligands, LH^+, were observed in all ES+ mass spectra, i.e. complexes **1**–**3** revealed a peak at 256 *m*/*z*, complexes **4**–**6** at 242 *m*/*z*, complexes **7**–**9** at 244 *m*/*z*, the complexes **10**–**12** at 260 *m*/*z*, complex **13** at 341 *m*/*z*, and complex **14** at 355 *m*/*z*. The molecular ion peaks belonging to $[Pt(LH^+)Cl_5]^+$ were observed at 629, 616, and 728 *m*/*z* for complexes **1**–**3**, **9**, and **14**, respectively. Further fragmentation of the molecular ion peaks can be clearly seen from maxima recorded at 594 *m*/*z* (for **1**–**3**), 580 *m*/*z* (for **4**–**6**), and 582 *m*/*z* (for **7**–**9**) which correspond to $[Pt(LH^+)Cl_4]^+$. The $[Pt(LH^+)Cl_3]^+$, $[Pt(LH^+)Cl_2]^+$, $[Pt(LH^+)Cl]^+$ and $[Pt(LH^+)]^+$ fragments can be characterized by peaks at 545 (for **7**), 562 (for **10**–**12**), 641 (for **13**), and 657 *m*/*z* (for **14**), 523 (for **1**–**3**), 509 (for **4**–**6**), 526 (for **11**) and 622 *m*/*z* (for **14**), 486 (for **1**), 480 (for **4**–**6**), 573 (for **13**) and 586 *m*/*z* (for **14**), and 453 (for **1**–**3**), 437 (for **5** and **6**), 454 (for **11**) and 536 *m*/*z* (for **13**), respectively. As can be evident from the above-mentioned results, the proposed general formula $[Pt(LH^+)Cl_5]$ was clearly confirmed by ES+ mass spectroscopy for all complexes **1**–**14**.

3.4. NMR spectroscopy

^1H and ^{13}C NMR spectra of free ligands as well as the prepared complexes were measured in DMF-d_7 and their interpretation was based on differences between selected chemical shifts of the corresponding atoms in the free organic ligand and complex, where coordination chemical shifts, $\Delta\delta$, are defined as $\Delta\delta = \delta_{complex} - \delta_{ligand}$. Important ^1H, ^{13}C and ^{195}Pt NMR spectral data (δ, ppm) for the free ligand and for the complexes **1**–**14** are summarized in Table 2. Based on the analysis of chemical shifts in ^1H and ^{13}C NMR spectra (see Table 2), we assume that the coordination of CKs as ligands to platinum proceeds via the N9 atom and the ligands are N1 protonated in the case of complexes **1**–**12**. Simultaneously, the proton, originally bonded to N9 atom in the corresponding free cytokinin-derived molecule, is shifted to N7 atom. This statement can be supported by the fact that the signals corresponding to N9-H are missing in ^1H NMR spectra of the complexes **1**–**12**. On the other hand, new signals with chemical shifts of 10.70–11.80 ppm appeared in the same spectra, which can be assigned to N7-H. Most significant changes in chemical shifts were displayed in ^{13}C NMR spectra for C4 and C8 atoms, where $\Delta\delta$ ranging from −2.70 to −4.89 ppm, and 4.56 to 6.80 ppm, respectively. The situation regarding the complexes involving CDK inhibitors (**13** and **14**) is somewhat different as compared to those above-mentioned. The proton at the N9 position is substituted by an *i*-propyl chain, and thus, this site is blocked for possible coordination to platinum(IV). The changes in chemical shifts of atoms forming the adenine moiety clearly showed that the ligand is N1 protonated and coordinated to plati-

Table 2
Selected coordination chemical shifts ($\Delta\delta = \delta_{complex} - \delta_{ligand}$) in ^1H and ^{13}C NMR spectra ($\Delta\delta$, ppm) for the organic ligands and complexes and ^{195}Pt NMR spectral data (δ, ppm)

Compound	^1H NMR				^{13}C NMR						^{195}Pt
	1H,C2H	1H,C8H	1H,N6H	2H,C9	C2	C8	C5	C4	C9	C6	Pt
1	0.36	0.62	1.05	0.13	1.58	5.76	−2.11	−2.73	1.23	−0.86	99.7
2	0.34	0.63	1.68	0.13	1.56	6.50	−1.53	−2.70	1.12	−0.63	102.4
3	0.28	0.71	1.30	0.10	1.16	5.32	−1.83	−2.59	1.04	−0.44	105.2
4	0.27	0.76	0.81	0.15	1.01	4.99	−2.03	−3.15	1.03	−0.12	93.1
5	0.38	0.69	1.50	0.03	2.08	6.30	−2.18	−2.88	0.93	−0.26	102.1
6	0.23	0.58	0.88	0.12	0.89	4.63	−2.17	−3.46	0.76	0.08	99.0
7	0.46	0.76	1.73	0.11	2.06	5.58	−0.90	−2.15	1.36	−1.16	112.4
8	0.41	0.78	1.63	0.07	2.76	5.23	−1.07	−3.18	1.56	−0.77	112.8
9	0.46	0.83	1.56	0.14	2.96	6.80	−2.37	−3.15	2.06	−1.46	128.2
10	0.38	0.57	1.76	0.12	1.31	4.56	−1.01	−3.28	0.94	0.06	103.2
11	0.32	0.60	1.64	0.13	3.01	5.98	−2.46	−4.89	1.15	−1.41	105.3
12	0.50	0.66	2.06	0.12	2.30	5.47	−2.21	−3.79	1.79	−1.03	129.6
13		1.05	0.54	0.11	−1.21	3.11	−7.06	−2.12	0.96	−1.28	332.4
14		0.87	0.83	0.11	−1.48	3.63	−5.01	−1.91	1.13	−1.79	339.7

num(IV) through N7 atom. This can be deduced mainly from chemical shifts of N atoms forming the adenine moiety as determined by ^{15}N NMR spectroscopy, where the following $\Delta\delta$ were found: $\Delta\delta = -47.2$ and -45.8 ppm (for N1), 7.8 and 7.7 ppm (for N2), -13.0 and 2.1 ppm (for N3), -57.3 and -57.9 ppm (for N6), -85.9 and -85.4 ppm (for N7), 7.7 and 7.4 ppm (for N9) for **13** and **14**, respectively.

In conclusion, we can state that the results arising from ^{15}N NMR spectra correlate well with ^{1}H and ^{13}C NMR spectral data (see Table 2) in the case of both complexes **13** and **14**.

Broad signals in the range of 90.0–129.6 ppm with the half height line-widths of 150–200 Hz were found in ^{195}Pt NMR spectra of complexes **1**–**12**, while signals at 332.4 and 339.7 ppm were detected for complexes **13** and **14**, respectively. Chemical shifts for some Pt(IV) complexes with the $PtCl_5N$ chromophore have been reported recently, e.g. $\delta(^{195}Pt) = -184$ ppm for the anion $[PtCl_5(EtCN)]^-$ (in $CDCl_3$), δ (^{195}Pt) = 91 ppm for $[PtCl_5(NH_3)]^-$ (in DMSO) [24], and $\delta(^{195}Pt) = -832$ ppm $[PtCl_5(9\text{-MeAdeH}^+)]$, where 9-MeAdeH$^+$ = 9-methyladeninium cation. These types of compounds are quite uncommon and only a few ^{195}Pt NMR chemical shifts are available in the literature. However, we can deduce that the signals observed for complexes **1**–**14** may indicate the presence of an octahedral Cl_5N donor set in the vicinity of platinum(IV).

3.5. DFT analysis

In order to support conclusions regarding geometries of the complexes and the manner of the ligand coordination to platinum(IV), we have performed DFT analysis using the B3LYP hybrid functional. As model systems, $[PtCl_5(4\text{-FBapH}^+)]$ (**9**) and $[PtCl_5(RosH^+)]$ (**14**) complexes were chosen. Optimized structures are shown in Figs. 1 and 2, respectively, while the most important geometrical parameters characterizing the Pt(IV) coordination sphere are summarized in Table 3. The calculated structure of **9** has a C_s symmetry. Coordination geometry in the vicinity of the central Pt(IV) ion may be described as a slightly deformed octahedron (Fig. 1), where the Pt–N bond length is shortened by approximately 0.3–0.4 Å in comparison with lengths of the Pt–Cl bonds (for details, see Table 3). In agreement with experimental observations, the calculated infrared spectrum (B3LYP/aug-cc-pVDZ/LANL2DZ) shows maxima at 278, 288, 306 and 349 cm^{-1} which may correspond to the stretching Pt–Cl vibrations.

In the case of complex **14**, Pt(IV) ion is coordinated to N7 atom due to substitution at the N9 position. The coordination sphere also has the shape of a slightly deformed square-bipyramid (Fig. 2). Similarly to the geometry of complex **9**, the Pt–N bond length is 2.135 Å, and is shorter by approximately 0.3–0.4 Å than those of Pt–Cl bonds. The calculated geometrical parameters in the vicinity of the central atom correspond well with recently published crystallographic data for the $[PtCl_5(9\text{-MeAdeH}^+)]$ complex

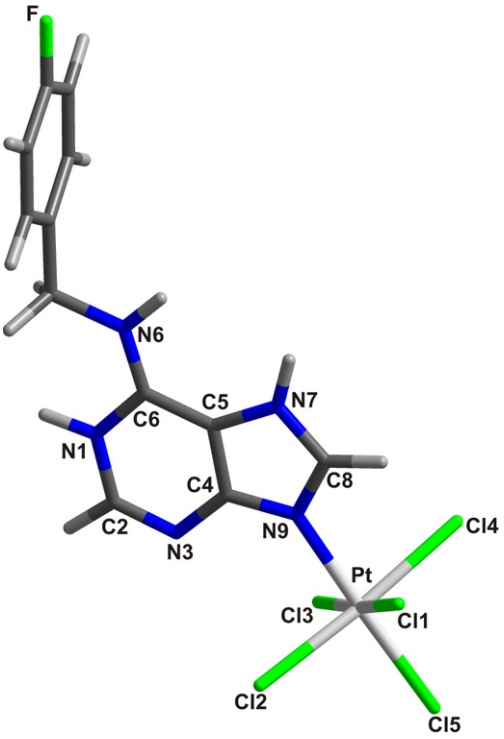


Fig. 1. The geometry of $[Pt(4\text{-FBapH}^+)Cl_5]$ (**9**) calculated on the B3LYP/aug-cc-pVDZ/LANL2DZ level.

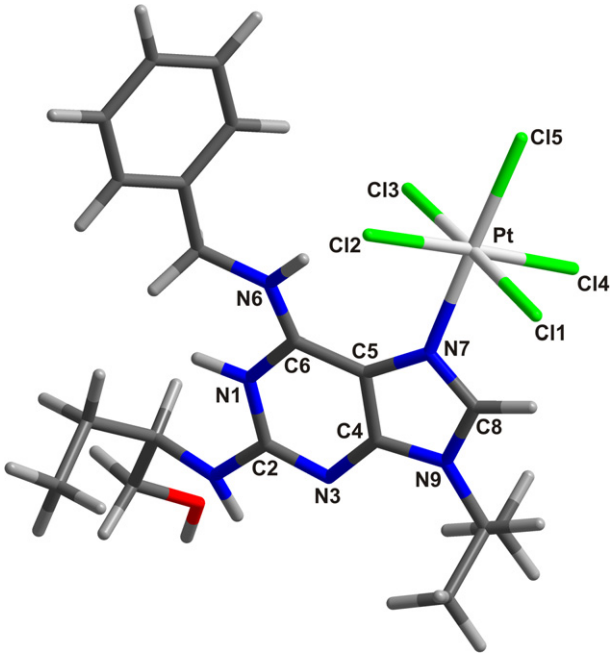


Fig. 2. The geometry of $[Pt(RosH^+)Cl_5]$ (**14**) calculated on the B3LYP/aug-cc-pVDZ/LANL2DZ level.

(Table 3). The calculated infrared spectrum (B3LYP/aug-cc-pVDZ/LANL2DZ) shows maxima at 286, 304, 308 and 342 cm^{-1} corresponding to the stretching Pt–Cl vibrations, which also indicate agreement between the calculated structure and experimental observations. Unfortunately, the maximum belonging to ν(Pt–N) cannot be assigned

Table 3
Selected bond lengths (Å) and angles (°) for complexes **9** and **14** calculated at B3LYP/6-311+G**/LANL2DZ and B3LYP/aug-cc-pVDZ/LANL2DZ levels of the theory together with their comparison with X-ray data of [Pt(MeAdeH$^+$)Cl$_5$] (MeAdeH$^+$ = 9-methyladeninium)

	9		**14**		[Pt(MeAdeH$^+$)Cl$_5$] X-ray[a]
	6-311+G**	aug-cc-pVDZ	6-311+G**	aug-cc-pVDZ	
Pt–Cl1	2.423	2.413	2.395	2.382	2.313
Pt–Cl2	2.397	2.384	2.421	2.412	2.310
Pt–Cl3	2.397	2.384	2.423	2.413	2.336
Pt–Cl4	2.425	2.413	2.392	2.378	2.319
Pt–Cl5	2.329	2.321	2.340	2.333	2.305
Pt–N7			2.135	2.116	2.073
Pt–N9	2.111	2.098			
Cl1–Pt–Cl2	89.69	89.72	89.15	89.20	89.59
Cl1–Pt–Cl3	175.93	175.95	177.32	177.32	178.41
Cl1–Pt–Cl4	89.04	89.03	89.88	89.77	88.80
Cl2–Pt–Cl3	91.31	91.27	92.41	92.29	91.49
Cl2–Pt–Cl4	175.93	175.95	178.56	178.66	178.24
Cl3–Pt–Cl4	89.69	89.72	88.51	88.71	90.10
Cl1–Pt–Cl5	92.49	92.49	91.43	91.39	90.22
Cl2–Pt–Cl5	91.44	91.41	90.45	90.23	88.71
Cl3–Pt–Cl5	91.43	91.41	90.73	90.84	88.63
Cl4–Pt–Cl5	92.49	92.49	90.63	90.65	90.58
N9(7)–Pt–Cl1	85.85	85.82	88.37	88.42	88.74
N9(7)–Pt–Cl2	90.20	90.24	90.81	91.15	92.00
N9(7)–Pt–Cl3	90.20	90.24	89.43	89.32	92.40
N9(7)–Pt–Cl4	85.85	85.82	88.10	87.97	88.69
N9(7)–Pt–Cl5	177.67	177.63	178.72	178.61	178.73

[a] Values obtained from [11].

unambiguously, although there were observed several more complex skeletal vibrations (about ca. 313 cm^{-1}) including partial contribution to the Pt–N bond vibration.

3.6. X-ray structures of $(BohH_2^{2+})[PtCl_6] \cdot H_2O$ (**15**) and $(RosH_2^{2+})_2[PtCl_6]Cl_2 \cdot 4H_2O$ (**16**)

The molecular structure of compound **15** consists of a double-protonated cation of bohemine, octahedral $[PtCl_6]^{2-}$ anion and one crystal water molecule (Fig. 3, Table 4). Most of the bond lengths and angles in bohemine can be regarded as normal in comparison with other protonated forms of similar CDK inhibitors (e.g. [25]). Atoms forming the benzene (A), pyrimidine (B) and imidazole (C) rings deviate very slightly from planarity [the greatest deviations being 0.005(5) Å for atom C10 in ring A, 0.010(5) Å for atom N(1) in ring B and 0.007(5) Å for atom C4 in ring C]. The dihedral angle between the rings B and C is 1.63(17)°, while the dihedral angle between the ring A and the purine moiety (B + C) is 86.9(2)° (DIAMOND 3.1 [26]). The torsion angles N1–C6–N6–C9, C6–N6–C9–C10 and N6–C9–C10–C11, defining the spatial arrangement of the ring A and purine moiety, are 2.5(8)°, 167.3(5)°, and 86.7(6)°, respectively. The secondary structure of the compound **15** is stabilized by extended network of intermolecular N–H···O, O–H···O, N–H···Cl and O–H···Cl hydrogen bonds (Fig. 3, Table 5).

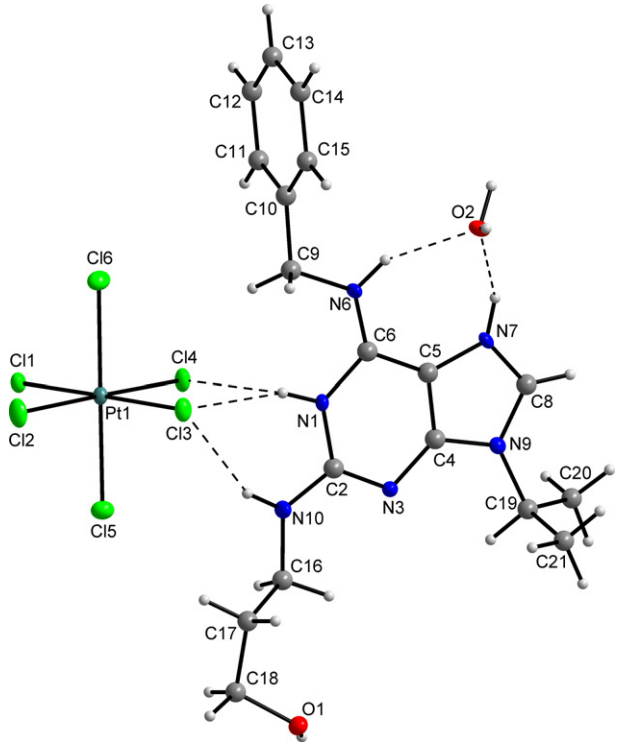


Fig. 3. The molecular structure of $(BohH_2^{2+})[PtCl_6] \cdot H_2O$ (**15**) with the atom labelling scheme. The non-H atoms are drawn as displacement ellipsoids at the 50% probability level and H atoms are shown as small spheres at arbitrary radii. Dashed lines indicate possible hydrogen bonds.

The molecular structure of compound **16** consists of two double-protonated cations of roscovitine, an centrosymmetric octahedral $[PtCl_6]^{2-}$ dianion (at special crystallographic position), two chlorine anions and four molecules of crystal water (Fig. 4, Table 4). Aromatic rings of roscovitine are almost planar, but they are more

Table 4
Selected bond lengths (Å) and angles (°) for $(BohH_2^{2+})[PtCl_6]\cdot H_2O$ (**15**) and $(RosH_2^{2+})_2[PtCl_6]Cl_2\cdot 4H_2O$ (**16**)

Compound	**15**	**16**
Pt1–Cl1	2.3196(13)	2.323(2)
Pt1–Cl2	2.3189(13)	2.333(2)
Pt1–Cl3	2.3406(13)	2.326(2)
Pt1–Cl4	2.3299(13)	
Pt1–Cl5	2.3312(14)	
Pt1–Cl6	2.3354(14)	
N1–C6	1.366(7)	1.346(10)
N1–C2	1.389(7)	1.400(11)
C2–N3	1.322(7)	1.315(12)
C2–N10	1.330(7)	1.347(11)
N3–C4	1.355(7)	1.368(11)
C4–C5	1.376(7)	1.375(12)
C4–N9	1.387(7)	1.371(11)
C5–N7	1.379(7)	1.391(11)
C5–C6	1.416(8)	1.396(12)
N6–C6	1.305(7)	1.345(11)
N6–C9	1.485(7)	1.468(11)
N7–C8	1.316(7)	1.311(12)
C8–N9	1.349(7)	1.354(11)
N9–C19	1.476(7)	
N9–C20		1.489(13)
N10–C16	1.459(7)	1.455(13)
Cl1–Pt1–Cl3	179.38(4)	89.65(8)
Cl2–Pt1–Cl4	178.85(5)	
Cl5-Pt1–Cl6	179.68(5)	
Cl2–Pt1–Cl1	89.74(5)	90.57(8)
Cl1–Pt1–Cl4	89.91(4)	
Cl1–Pt1–Cl5	89.97(5)	
Cl1–Pt1–Cl6	90.35(5)	
Cl2–Pt1–Cl3	90.22(5)	89.76(8)
Cl2–Pt1–Cl5	89.18(5)	
Cl2–Pt1–Cl6	90.86(5)	
Cl4–Pt1–Cl3	90.11(4)	
Cl5–Pt1–Cl3	89.40(5)	
Cl6–Pt1–Cl3	90.27(5)	
Cl4–Pt1–Cl5	89.72(5)	
Cl4–Pt1–Cl6	90.24(5)	
C6–N1–C2	125.1(5)	122.9(8)
N1–C6–C5	111.9(5)	114.7(8)

deformed than the rings in (**15**): the greatest deviations being 0.019(9) Å for atoms C(11) and 0.014(8) Å for atoms N(3), the dihedral angle between the two rings of purine moiety is 2.5(3)°, and the dihedral angle between benzene and pyrimidine rings is 38.1(33)° (DIAMOND 3.1), the torsion angles N1–C6–N6–C9 = 2.6(1.2)°, C6–N6–C9–C10 = 179.1(8)° and N6–C9–C10–C11 = 36.6(1.2)°. C6–N6–C9–C10 is 179.1(8)°. Similarly to **15**, the crystal structure of compound **16** is also stabilized by an extended network of intermolecular N–H···O, O–H···O, N–H···Cl and O–H···Cl hydrogen bonds (Fig. 4, Table 5).

3.7. In vitro cytotoxic activity

The cytotoxicity of the complexes **1**–**14** against *G361*, *HOS*, *K562* and *MCF7* human cancer cell lines was determined by a calcein acetoxymethyl (AM) assay. The activity was expressed as the concentration (in μM) of the compounds at which tumour cell growth showed 50% inhibi-

Table 5
Selected hydrogen bond parameters (Å, °) for **15** and **16**

D–H···A	*d*(D–H) (Å)	*d*(H···A) (Å)	*d*(D···A) (Å)	∠(DHA) (°)
*Compound **15***				
N(1)–H(1)···Cl(3)	0.88	2.45	3.272(5)	156.1
N(1)–H(1)···Cl(4)	0.88	2.75	3.215(5)	114.7
N(6)–H(6)···O(2)	0.88	2.02	2.803(6)	148.4
N(7)–H(7)···O(2)	0.88	2.01	2.731(6)	137.9
N(10)–H(10)···Cl(3)	0.88	2.57	3.388(5)	154.9
N(10)–H(10)···Cl(5)	0.88	2.97	3.612(5)	131.3
N(6)–H(6)···Cl(4)^{i}	0.88	2.90	3.338(5)	112.3
N(7)–H(7)···Cl(1)^{i}	0.88	2.67	3.249(5)	124.2
O(1)–H(1O)···Cl(5)^{ii}	0.94(2)	2.40(4)	3.255(4)	151(7)
O(1)–H(1O)···Cl(1)^{ii}	0.94(2)	2.66(7)	3.327(4)	128(6)
O(2)–H(2V)···Cl(6)^{iii}	0.94(2)	2.45(4)	3.316(4)	153(5)
O(2)–H(2W)···O(1)^{iv}	0.93(2)	1.77(3)	2.675(5)	165(6)
*Compound **16***				
N(6)–H(6)···O(3)	0.88	1.99	2.852(9)	164.7
N(7)–H(7)···O(3)	0.88	1.91	2.712(10)	150.5
O(3)–H(3W)···O(2)	0.95(2)	1.89(7)	2.745(11)	149(11)
O(2)–H(2W)···Cl(4)	0.95(2)	2.30(5)	3.212(9)	161(11)
N(1)–H(1)···Cl(4)^{v}	0.88	2.34	3.168(8)	156.2
N(10)–H(10)···Cl(4)^{v}	0.88	2.48	3.280(9)	151.6
O(3)–H(3V)···Cl(4)^{vi}	0.94(2)	2.25(6)	3.122(8)	152(10)
O(2)–H(2V)···Cl(3)^{vii}	0.95(2)	2.53(8)	3.340(8)	144(10)
O(2)–H(2V)···Cl(2)^{vii}	0.95(2)	2.76(9)	3.502(8)	136(9)

Symmetry codes: For **15**: (i) $-x+1$, $-y+1$, $-z+1$; (ii) $-x$, $-y+1$, $-z+1$; (iii) x, $-y+1/2$, $z-1/2$; (iv) $x+1$, y, z. For **16**: (v) $-x+1/2$, $y-1/2$, $-z+1/2$; (vi) x, $y-1$, z; (vii) $-x+1$, $-y+1$, $-z$.

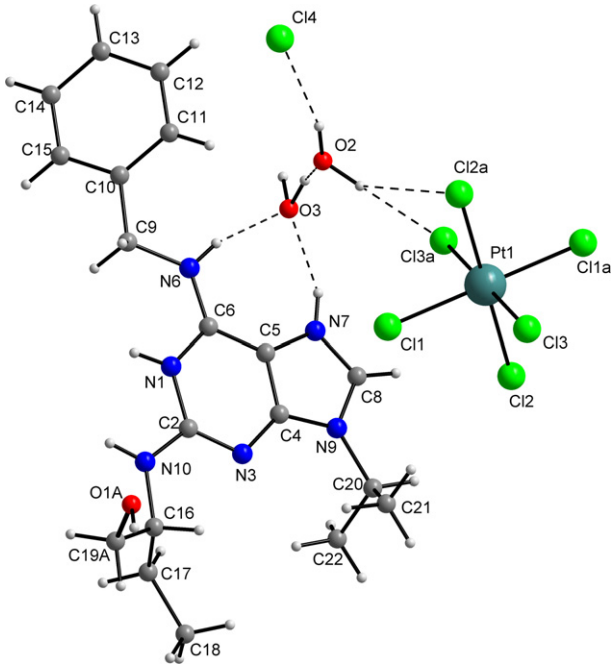


Fig. 4. A part of the crystal structure of $(RosH_2^{2+})_2[PtCl_6]Cl_2\cdot 4H_2O$ (**16**) with the atom labeling scheme. The non-H atoms are drawn as displacement ellipsoids at the 50% probability level and H atoms are shown as small spheres at arbitrary radii. Dashed lines indicate possible hydrogen bonds. One of two $RosH_2^{2+}$ cations and two of four crystal water molecules are omitted for clarity.

Table 6
The cytotoxicity of the studied compounds, expressed as IC_{50} values (μM), assessed by a calcein AM assay for several human cancer cell lines[a]

Compound		Values of IC_{50} (μM) for the complex/free ligand			
		G361	HOS	K562	MCF7
1	[Pt(2-MeOBapH$^+$)Cl$_5$]	>167/>167	>167/>167	>167/116	>167/116
2	[Pt(3-MeOBapH$^+$)Cl$_5$]	>167/125	>167/>167	>167/122	>167/158
3	[Pt(4-MeOBapH$^+$)Cl$_5$]	>167/>167	>167/>167	>167/142	>167/>167
4	[Pt(2-OHBapH$^+$)Cl$_5$]	>167/103	>167/>167	>167/117	>167/>167
5	[Pt(3-OHBapH$^+$)Cl$_5$]	>167/nt	>167/nt	>167/nt	>167/nt
6	[Pt(4-OHBapH$^+$)Cl$_5$]	>167/nt	>167/nt	>167/nt	>167/nt
7	[Pt(2-FBapH$^+$)Cl$_5$]	>85/116	>85/>167	>85/133	>85/>167
8	[Pt(3-FBapH$^+$)Cl$_5$]	>85/>167	>85/>167	>85/105	>85/163
9	[Pt(4-FBapH$^+$)Cl$_5$]	>85/>167	>85/>167	>85/>167	>85/>167
10	[Pt(2-ClBapH$^+$)Cl$_5$]	>85/57	>85/123	>85/96	>85/147
11	[Pt(3-ClBapH$^+$)Cl$_5$]	>85/149	>85/>167	>85/>167	>85/>167
12	[Pt(4-ClBapH$^+$)Cl$_5$]	>85/143	>85/>167	>85/>167	>85/>167
13	[Pt(BohH$^+$)Cl$_5$]	64/46	74/58	75/93	52/28
14	[Pt(RosH$^+$)Cl$_5$]	24/19	18/20	17/50	39/15
	K_2PtCl_6	109	56	93	>167

[a] G361, malignant melanoma; HOS, osteogenic sarcoma; K562, chronic myelogenous erythroleukemia; MCF7, breast adenocarcinoma; nt, not tested.

tion (IC_{50}). The results of the testing are summarized in Table 6. The *in vitro* cytotoxic properties can be evaluated by comparison of values found for the Pt(IV) complexes as against the starting compounds, i.e. K_2PtCl_6 and free organic molecules. As can be seen from Table 6, significant cytotoxity has been found in the case of complexes involving CDK inhibitor Bohemine or Roscovitine, i.e. complexes **13** and **14**. However, their promising IC_{50} values are probably influenced by the presence of the mentioned organic molecule in the complexes because it is cytotoxic itself. Generally, the best results have been achieved for [Pt(RosH$^+$)Cl$_5$] (**14**), and moreover, the IC_{50} value as determined against the K562 cell line is equal to 17 μM, which is ca. 3 times better value than estimated for free Roscovitine.

4. Conclusion

The paper deals with the synthesis, characterization and *in vitro* cytotoxic study of the first Pt(IV) complexes bearing 6-benzylaminopurine derivatives as ligands, i.e. organic compounds which belong to groups of plant growth hormones (cytokins) and/or cyclin-dependent kinase inhibitors. A series of octahedral Pt(IV) complexes **1**–**14** have been prepared by the reaction of K_2PtCl_6 with the appropriate organic compound in 2 M HCl. The accomplished physical and chemical studies supported complex formation with a formula of [Pt(LH$^+$)Cl$_5$]. Based mainly on multinuclear NMR spectra, it has been found that the cytokinin derivative is coordinated to platinum through N9 atom (for **1**–**12**), while the cyclin-dependent kinase inhibitor (Bohemine or Roscovitine) is bonded via N7 atom (for **13** and **14**), and moreover, organic molecules are protonated at the N1 position in all cases. Unfortunately, we have been unsuccessful with the preparation of single crystals suitable fox X-ray determination of complexes **1**–**14**. For that reason, the geometries of the complexes have been optimized by using DFT calculations. Moreover, we have obtained and determined the structures of (BohH$_2^{2+}$)[PtCl$_6$] · H$_2$O (**15**) and (RosH$_2^{2+}$)$_2$[PtCl$_6$]Cl$_2$· 4H$_2$O (**16**) which crystals have been formed as a consequence of evaporation of mother liquors during the preparation of complexes **13** and **14**, respectively. The results of the cytotoxicity testing of Pt-complexes against *G361*, *HOS*, *K562* and *MCF7* human cancer cell lines exhibited that the coordination of an organic molecule did not have substantial impact on the cytotoxicity of the Pt-complexes (**1**–**12**). However, the IC_{50} values regarding the complexes bearing cyclin-dependent kinase inhibitors (**13** and **14**) are lying in the range of 17–74 μM. It can be deduced that these significant *in vitro* cytotoxicity values are influenced by the presence of the organic molecule which is cytotoxic itself.

Acknowledgements

This research was supported by the Ministry of Education, Youth and Sports of the Czech Republic (MSM6198959218). The authors thank to Dr. Karel Doležal for obtaining of ES+ MS spectral data, Mr. Michal Šipl for help with the preparation of some ligands and Pt(IV) complexes and Mrs. Eva Hirnerová for cytotoxicity testing.

Appendix A. Supplementary material

CCDC 648384 and 648385 contain the supplementary crystallographic data for complexes (BohH$_2^{2+}$)[PtCl$_6$]· H$_2$O (**15**) and (RosH$_2^{2+}$)$_2$[PtCl$_6$]Cl$_2$ · 4H$_2$O (**16**), respectively. These data can obtained free of charge via htpp://www.ccdc.cam.ac.uk/conts/retrieving.html, or from the Cambridge Crystallographic Data Centre, 12 Union Road, Cambridge CB2 1EZ, UK; fax: (+44) 1223-336-033; or e-mail: deposit@ccdc.cam.ac.uk. ^{1}H and ^{13}C NMR spectral data of the free organic ligands used for the preparation

of complexes **1**–**12** are deposited as supplementary data. Supplementary data associated with this article can be found, in the online version, at doi:10.1016/j.poly.2007.07.026.

References

[1] D.W.S. Mok, M.C. Mok, Annu. Rev. Plant Physiol. Plant Mol. Biol. 52 (2001) 89.
[2] H. Sakakibara, Annu. Rev. Plant Biol. 57 (2006) 431.
[3] E. Zažimalová, M. Kamínek, A. Březinová, V. Motyka, in: K.R. Libbenga, M.A. Hall, P. Hooykaas (Eds.), Biochemistry and Molecular Biology of Plant Hormones, Series New Comprehensive Biochemistry, Elsevier, Amsterdam, 1999, pp. 141–160.
[4] F.I. Raynaud, S.R. Whittaker, P.M. Fischer, S. McClue, M.I. Walton, S.E. Barrie, M.D. Garrett, P. Rogers, S.J. Clarke, L.R. Kelland, M. Valenti, L. Brunton, S. Eccles, D.P. Lane, P. Workman, Clin. Cancer Res. 11 (2005) 4875.
[5] B. Rosenberg, L. Vancamp, J.E. Trosko, V.H. Mansour, Nature 222 (1969) 385.
[6] M.D. Hall, T.W. Hambley, Coord. Chem. Rev. 232 (2002) 49.
[7] A.S. Gaballa, J. Mol. Struct. 782 (2006) 204.
[8] F.H. Allen, Acta Crystallogr., Sect. B 58 (2002) 380.
[9] A. Gaballa, H. Schmidt, G. Hempel, D. Reichert, C. Wagner, E. Rusanov, D. Steinborn, J. Inorg. Biochem. 98 (2004) 439.
[10] M. Maloň, Z. Trávníček, M. Maryško, J. Marek, K. Doležal, J. Rolčík, M. Strnad, Transition Met. Chem. 27 (2002) 580.
[11] Z. Trávníček, M. Maloň, M. Zatloukal, K. Doležal, M. Strnad, J. Marek, J. Inorg. Biochem. 94 (2003) 307.
[12] M. Maloň, Z. Trávníček, R. Marek, M. Strnad, J. Inorg. Biochem. 99 (2005) 2127.
[13] Z. Trávníček, L. Szűčová, I. Popa, J. Inorg. Biochem. 101 (2007) 477.
[14] S.M. Hecht, N.J. Leonard, R.Y. Schmitz, F. Skoog, Phytochemistry 9 (1970) 1173.
[15] L. Havlicek, J. Hanus, J. Vesely, S. Leclerc, L. Meijer, G. Shaw, M. Strnad, J. Med. Chem. 40 (1997) 408.
[16] Oxford Diffraction, CRYSALIS RED and CRYSALIS CCD software (Ver. 1.171.23), Oxford Diffraction Ltd., Abingdon, Oxfordshire, England, 2003.
[17] G.M. Sheldrick, Acta Crystallogr., Sect. A 46 (1990) 467.
[18] G.M. Sheldrick, SHELXL-97: Program for Crystal Structure Refinement, University of Göttingen, Göttingen, Germany, 1997.
[19] M.J. Frisch, G.W. Trucks, H.B. Schlegel, G.E. Scuseria, M.A. Robb, J.R. Cheeseman, J.A. Montgomery Jr., T. Vreven, K.N. Kudin, J.C. Burant, J.M. Millam, S.S. Iyengar, J. Tomasi, V. Barone, B. Mennucci, M. Cossi, G. Scalmani, N. Rega, G.A. Petersson, H. Nakatsuji, M. Hada, M. Ehara, K. Toyota, R. Fukuda, J. Hasegawa, M. Ishida, T. Nakajima, Y. Honda, O. Kitao, H. Nakai, M. Klene, X. Li, J.E. Knox, H.P. Hratchian, J.B. Cross, V. Bakken, C. Adamo, J. Jaramillo, R. Gomperts, R.E. Stratmann, O. Yazyev, A.J. Austin, R. Cammi, C. Pomelli, J.W. Ochterski, P.Y. Ayala, K. Morokuma, G.A. Voth, P. Salvador, J.J. Dannenberg, V.G. Zakrzewski, S. Dapprich, A.D. Daniels, M.C. Strain, O. Farkas, D.K. Malick, A.D. Rabuck, K. Raghavachari, J.B. Foresman, J.V. Ortiz, Q. Cui, A.G. Baboul, S. Clifford, J. Cioslowski, B.B. Stefanov, G. Liu, A. Liashenko, P. Piskorz, I. Komaromi, R.L. Martin, D.J. Fox, T. Keith, M.A. Al-Laham, C.Y. Peng, A. Nanayakkara, M. Challacombe, P.M.W. Gill, B. Johnson, W. Chen, M.W. Wong, C. Gonzalez, J.A. Pople, GAUSSIAN-03, Revision C.02, Gaussian, Inc., Wallingford, CT, 2004.
[20] Z. Trávníček, M. Maloň, M. Biler, M. Hajduch, P. Brož, K. Doležal, J. Holub, V. Kryštof, M. Strnad, Transition Met. Chem. 25 (2000) 265.
[21] W.J. Geary, Coord. Chem. Rev. 7 (1971) 81.
[22] C.J. Pouchert, The Aldrich Library of Infrared Spectra, 3rd ed., Aldrich Chemical Co., Milwaukee, 1981.
[23] K. Nakamoto, Infrared and Raman Spectra of Inorganic and Coordination Compounds, Part B: Applications in Coordination, Organometallic, and Bioinorganic Chemistry, 5th ed., Wiley, New York, 1997.
[24] M.L. Kuznetsov, N.A. Bokach, V.Y. Kukushkin, T. Pakkanen, G. Wagner, A.J.L. Pombeiro, J. Chem. Soc., Dalton Trans. (2000) 4683.
[25] Z. Trávníček, V. Kryštof, Acta Crystallogr., Sect. E 60 (2004) o2324.
[26] K. Brandenburg, H. Putz, DIAMOND – Crystal and Molecular Structure Visualization Crystal Impact, Bonn, 2005.

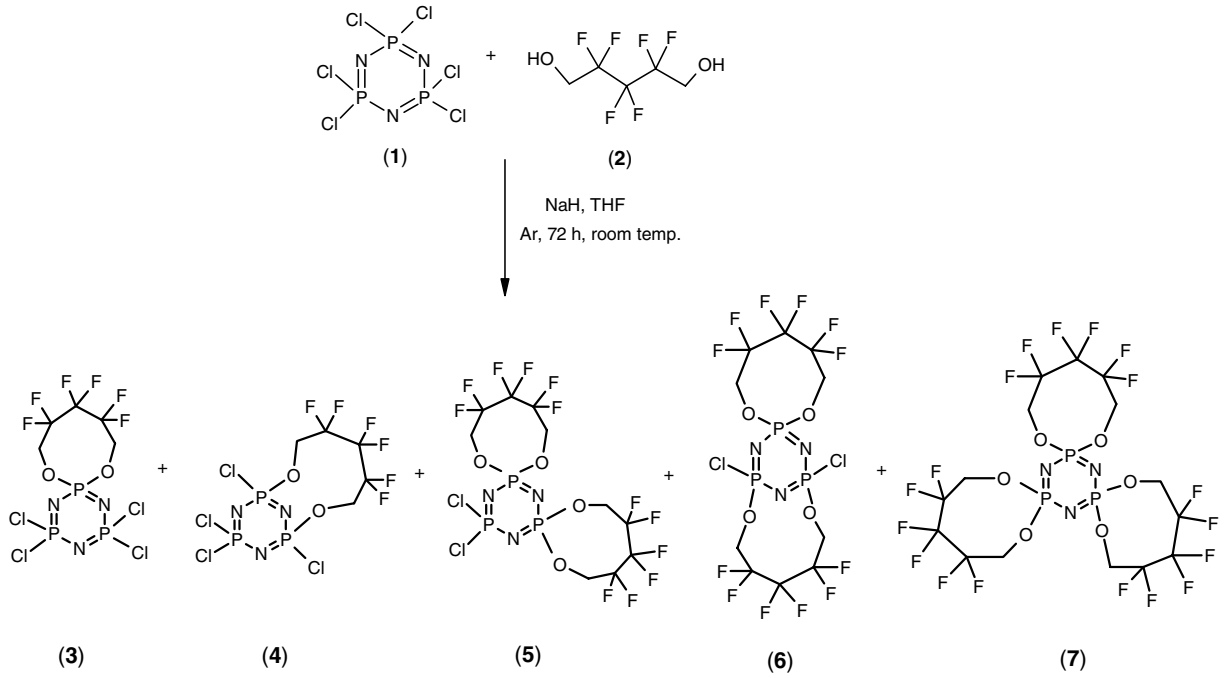
An open-chain compound and a bridged derivative were observed as minor products with 1,3-propanediol and 1,4-butanediol, indicating that chain length was a contributing factor in determining the derivative type [4]. On the other hand, for a diol with a much longer chain length, the reaction of (**1**) with the sodium derivative of tetraethylene glycol in THF gave predominantly the *cis*-ansa macrocyclic-cyclophosphazene derivative [5]. It is of interest to investigate the reaction of (**1**) with diols that are longer than 1,4-butanediol but shorter than tetraethylene glycol. In our previous work [6] on the reaction of (**1**) with the sodium derivative of 2,2,3,3-tetrafluorobutane-1,4-diol in THF we isolated six products that involved spiro and/or ansa moieties (viz. mono-spiro, mono-ansa, bis-spiro, spiro-ansa, ansa-ansa and tris-spiro). This suggests that the reaction of $N_3P_3Cl_6$ (**1**) with 2,2,3,3,4,4-hexafluoropentane-1,5-diol (**2**) under the same solution conditions would provide a good comparison for the relative importance of ring size on the formation of spiro and ansa derivatives.

In the reaction of (**1**) with 2,2,3,3-tetrafluorobutane-1,4-diol and 2,2,3,3,4,4-hexafluoropentane-1,5-diol (**2**) in toluene in the presence of triethylamine, Ratz and co-workers [7] obtained the tri-spiro derivatives, whereas the reaction of the silyl derivatives of 2,2,3,3-tetrafluorobutane-1,4-diol, $(Me_3SiOCH_2CF_2)_2$, and 2,2,3,3,4,4-hexafluoropentane-1,5-diol (**2**), $(Me_3SiOCH_2(CF_2)_3CH_2OSiMe_3)$, with $N_3P_3F_6$ afforded the mono-spiro derivatives and derivatives of the singly-bridged compound [8]. Both these sets of results contrast with those in our previous work [6] on the reaction of $N_3P_3Cl_6$ (**1**) with 2,2,3,3-tetrafluorobutane-1,4-diol in THF in the presence of NaH, where the six products isolated resulted from only spiro and/or ansa replacements. In order to assess the importance of ring size on the formation of spiro and ansa moieties we have investigated the reaction of (**1**) with the sodium derivative of 2,2,3,3,4,4-hexafluoropentane-1,5-diol (**2**) in THF and compared the results quantitatively with those obtained previously [6] for the reaction of (**1**) with 2,2,3,3-tetrafluorobutane-1,4-diol under the same solution conditions.

2. Results and discussion

*2.1. Formation of compounds (**3**)–(**7**) and characterisation by ^1H, ^{31}P and ^{19}F NMR spectroscopy*

Cyclophosphazene (**1**) was reacted with the sodium salt of 2,2,3,3,4,4-hexafluoro-1,5-pentanediol (**2**) in THF solution under the same solution conditions as those used previously for the reaction of (**1**) with 2,2,3,3-tetrafluorobutane-1,4-diol [6]. The reaction mixture was investigated by TLC and ^{31}P NMR spectroscopy, which indicated the formation of five products, compounds (**3**)–(**7**) (Scheme 1). The crude reaction mixture was filtered to remove the sodium chloride produced and any insoluble products, such as oligomers or polymers, and then re-dissolved in $CDCl_3$ for NMR measurements. The ^{31}P NMR spectrum of the soluble portion of the reaction mixture, Fig. 1a, shows that other than the five products there are only trace amounts of any other derivatives and no starting compound (**1**) remains, i.e. it is a very clean mixture, as found previously for the reaction of (**1**) with 2,2,3,3-tetrafluorobutane-1,4-diol [6]. Compounds (**3**)–(**7**) were separated by column chromatography and characterised ^1H, ^{31}P and ^{19}F NMR spectroscopy as the mono-spiro com-



Scheme 1. The reaction of hexachlorocyclotriphosphazene with 2,2,3,3,4,4-hexafluoropentane-1,5-diol and structures of the products, compounds (**3**)–(**7**).

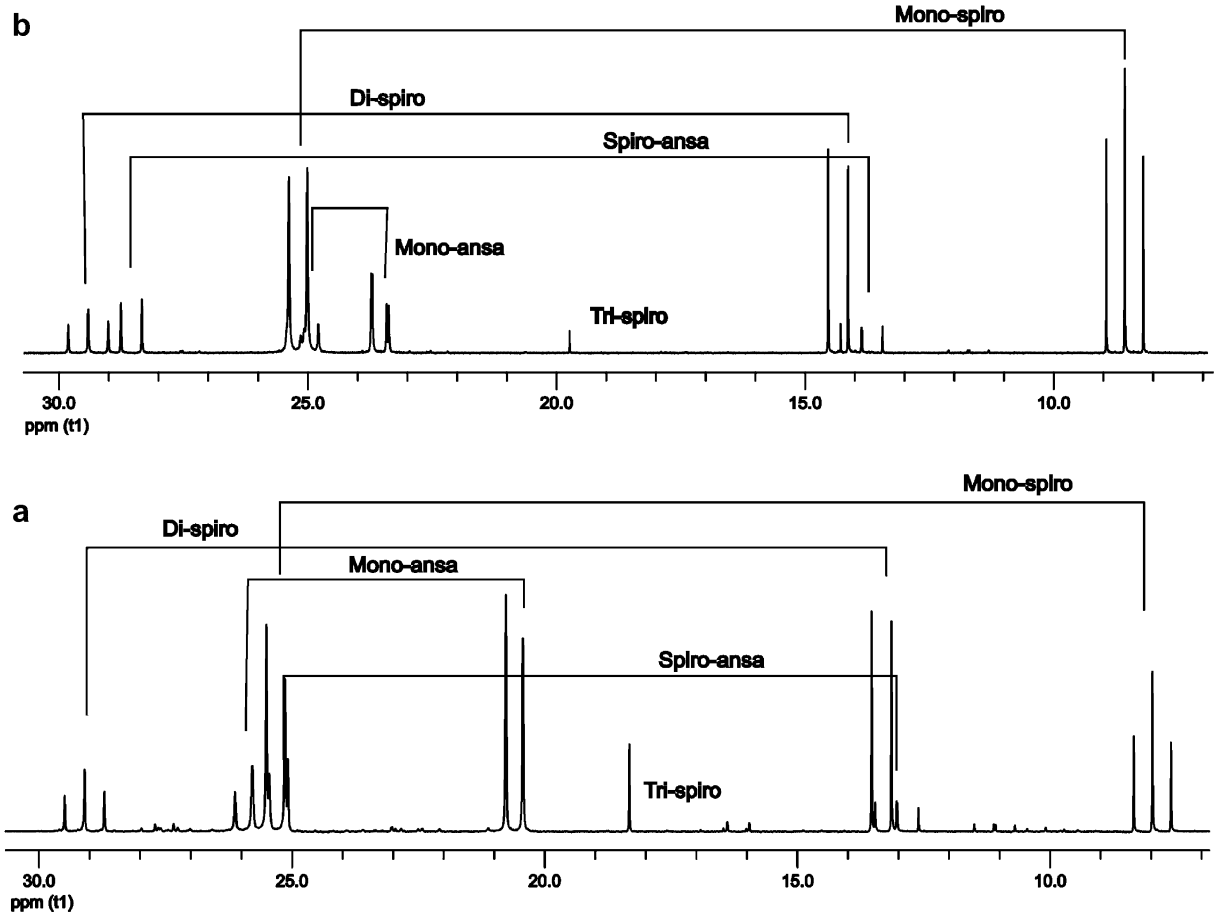


Fig. 1. ^{31}P NMR spectra of the reaction mixtures of $N_3P_3Cl_6$ (**1**) with the sodium derivatives of (a) 2,2,3,3,4,4-hexafluoro-1,5-pentanediol (**2**) and (b) 2,2,3,3-tetrafluoro-1,4-butanediol in THF solution.

pound, $N_3P_3Cl_4(OCH_2CF_2CF_2CF_2CH_2O)$ (**3**), its ansa isomer (**4**), a di-spiro derivative $N_3P_3Cl_2(OCH_2CF_2CF_2CF_2CH_2O)_2$ (**5**), its spiro-ansa isomer (**6**) and the tri-spiro compound $N_3P_3(OCH_2CF_2CF_2CF_2CH_2O)_3$ (**7**).

The ^{31}P NMR spectra of the cyclophosphazene derivatives (**3**)–(**6**), containing the spiro or ansa moieties, are observed as A_2X (or A_2B) spin systems, which can be readily assigned and analysed by comparison with their tetrafluorobutanediol analogues [6], as can the ^{31}P NMR spectrum of the tri-spiro cyclophosphazene derivative (**7**), which contains a single line. The chemical shifts and ^2J(PP) values of compounds (**3**)–(**7**) are summarised in Table 1. It can be seen that the chemical shifts reflect the number of spiro substituents in the compound, i.e. both the $\geq PCl_2$ and $\geq P(OR)_2$ chemical shifts move to high frequencies (downfield) by about 4.5–5.5 ppm per hexafluoropentanedioxy moiety, as observed for other spiro derivatives of cyclophosphazene [9]. Similarly the chemical shift of the $\geq P(OR)Cl$ group of the mono-ansa derivative (**4**) moves to a high frequency as the cyclophosphazene is further substituted with the spiro-hexafluoropentanedioxy moiety in (**6**) (Table 1).

The proton-decoupled ^{19}F NMR spectra of the spiro form of the 2,2,3,3,4,4-hexafluoro-1,5-pentanedioxy moiety of compounds (**3**), (**5**), (**6**) and (**7**) show two single signals at ca. −97.7 and −106.4 ppm, with the relative proportion of 2–1, corresponding to the $(CF_2)_2$ and (CF_2) groups, respectively. On the other hand, the proton-decoupled ^{19}F NMR spectra of the ansa ring in compounds (**4**) and (**6**) give two AB spin systems, one at ca. −93 to −96 ppm is double the intensity of the other at ca. −100 to −106 ppm, corresponding to the $(CF_2)_2$ and (CF_2) groups, respectively. The magnitudes of ^2J(FF) are in line with previous results on geminal coupling [6,10]. The ^{19}F chemical shifts and coupling constants of the products are given Table 1.

The ^{1}H NMR spectra of the ring methylene groups are observed as complex multiplets and the results are summarised with the analytical data for each compound in the section on synthesis. The ^{1}H NMR spectra of the spiro compounds (**3**), (**5**) and (**7**) have similar chemical shifts (ca. 4.5 ppm), whereas those for the mono-ansa moieties in compounds (**4**) and (**6**) are observed as two complex multiplets (ca. 4.5 and 4.9 ppm). In principle, analysis of these complex multiplets could lead to determination of the ^3J(FH) and ^3J(PH) magnitudes and so to a conformational analysis of the spiro and ansa rings, but in practice this is not feasible, partly because of the complexity of the spectra and partly because the appropriate Karplus-type

Table 1
^{31}P and ^{19}F NMR parameters of compounds (**3**)–(**7**)[a]

Cpd	Type[b]	Ring	^{31}P chemical shift (ppm)			$^{2}J_{P-P}$ (Hz)	^{19}F chemical shift (ppm)		$^{2}J_{F-F}$ (Hz)
			PCl_2	P(OR)	P(OR)Cl		$(CF_2)_2$	(CF_2)	
3	sp	Spiro	24.8	7.5		74.6	−97.7	−106.3	
4	an	Ansa	25.3		20.1	67.9	−93.3	−100.8	296.5[c]
		Ansa			20.1		−95.5	−103.4	295.6[d]
5	di-sp	Spiro	28.6	12.9		79.6	−97.7	−106.3	
6	sp-an	Spiro		12.6		86.8	−97.7	−106.5	
		Ansa			24.8		−94.1	−101.6	295.2[c]
		Ansa			24.8		−95.8	−103.8	296.6[d]
7	tri-sp	Spiro		17.8			−97.8	−106.4	

[a] 202.45 MHz ^{31}P NMR chemical shifts (ppm) in $CDCl_3$ with respect to external 85% H_3PO_4 and 470 MHz ^{19}F NMR chemical shifts (ppm) in $CDCl_3$ with respect to internal $CFCl_3$.
[b] sp = spiro, di-sp = di spiro, tri-sp = tri spiro, an = ansa and sp-an = spiro ansa.
[c] Magnitude of $^{2}J_{F-F}$ corresponds to signals at ca. −93 to −97 ppm.
[d] Magnitude of $^{2}J_{F-F}$ corresponds to signals at ca. −103 to −107 ppm.

relations for ^{3}J(FH) and ^{3}J(PH) magnitudes in such cyclophosphazene derivatives are not known. However, the conformations of the spiro and ansa rings in compounds (**3**)–(**7**) in the solid state have been characterised by X-ray crystallography.

2.2. X-ray crystallographic characterisation of compounds (*3*)–(*7*)

The X-ray crystal structures are reported for compounds (**3**)–(**7**) (Figs. 2–6), appropriate crystallographic data are summarised in Table 2 and some derived molecular parameters are summarised in Table 3.

Each structure is composed of a cyclotriphosphazene core which in all cases exhibits no unusual deviations in bond lengths and angles from either that of the parent $N_3P_3Cl_6$ structure (CSD code KAGKUY) [11] or from that observed in similar structures in the Cambridge Structural Database [12]. The cyclophosphazene rings are essentially planar, in which the deviation of individual atoms from the N_3P_3 plane in all the spiro compounds derived from hexafluoropentanediol range from 0.038 to 0.132 Å, with

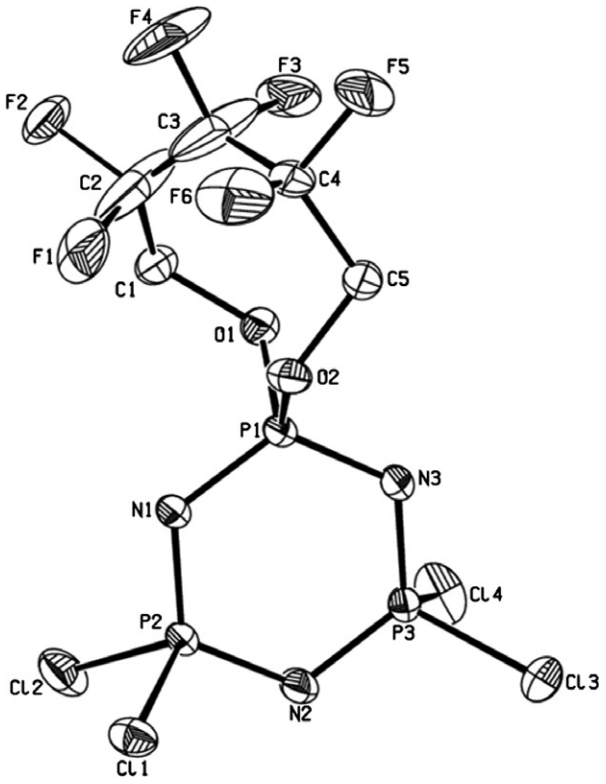


Fig. 2. X-ray crystal structure of (**3**) plotted at 50% probability. The molecular structure of (**3**) showing the atomic numbering scheme and omitting the disordered F2 atom and hydrogen atoms for clarity.

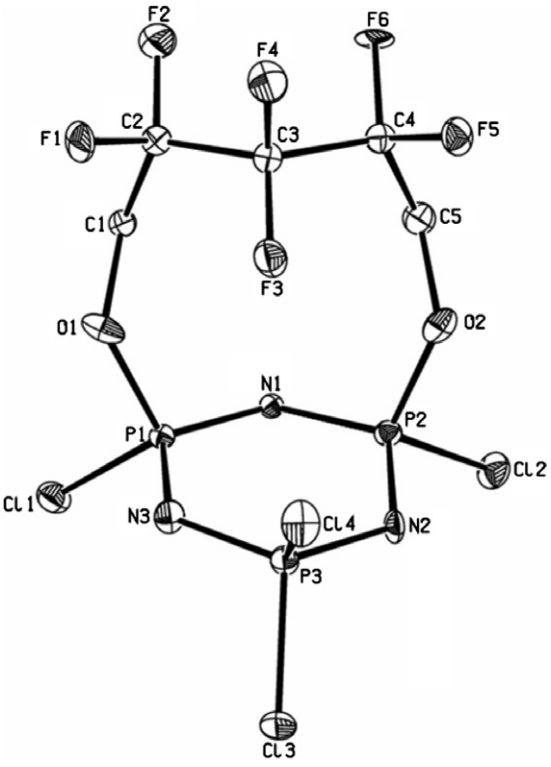


Fig. 3. X-ray crystal structure of (**4**) plotted at 50% probability. The molecular structure of (**4**) showing the atomic numbering scheme and omitting hydrogen atoms for clarity.

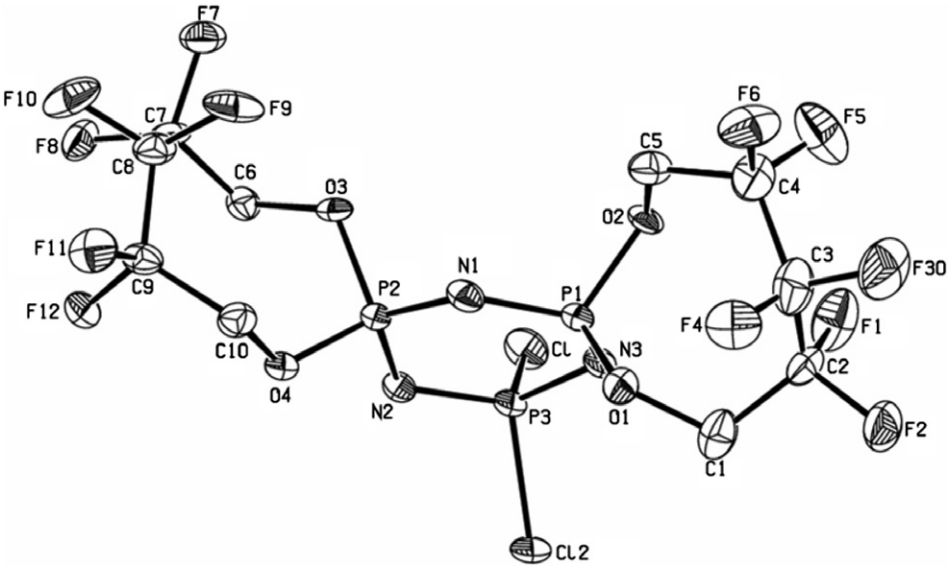


Fig. 4. X-ray crystal structure of (**5**) plotted at 50% probability. The molecular structure of (**5**) showing the atomic numbering scheme and molecular structure for one of the crystallographically independent molecules and omitting hydrogen atoms for clarity.

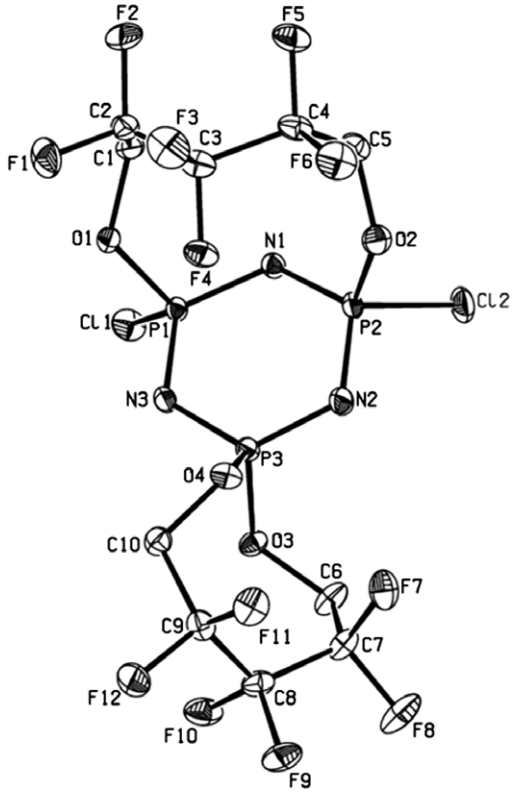


Fig. 5. X-ray crystal structure of (**6**) plotted at 50% probability. The molecular structure of (**6**) showing the atomic numbering scheme and omitting hydrogen atoms for clarity.

an average deviation of 0.092 Å (Table 3). A similar average deviation (0.107 Å) from the N_3P_3 plane was observed within experimental error for the two ansa compounds reported in Table 3. These average deviations from the N_3P_3 plane for hexafluoropentanediol derivatives are similar within experimental error to those for the analogous spiro (0.079 Å) and ansa (0.092 Å) tetrafluorobutanediol derivatives (Table 3) [6]. Unlike previous results on cyclophosphazene ansa derivatives with eight-membered rings, where the cyclophosphazene ring is strained and puckered >0.2 Å [13,14], the results summarised in Table 3 indicate that cyclophosphazene ansa derivatives with nine- and 10-membered rings are not strained and so the cyclophosphazene ring is essentially planar. The effect of different sizes of exocyclic ansa ring on the planarity of the cyclophosphazene ring is also reflected in the minimum value of the P···P distances of the cyclophosphazene ring, which is about 2.6 Å for strained eight-membered ansa compounds [13,14] but is greater than 2.7 Å for unstrained cyclophosphazene rings ([12], and Table 3). The difference in the effect of ansa compounds on the planarity of the cyclophosphazene ring is likely to reflect the higher degree of flexibility of the 16- and even the nine- and 10-membered rings compared to the eight-membered ansa ring system.

The ($OCH_2CF_2CF_2CF_2CH_2O$) moiety forms eight-membered spiro derivatives in compounds (**3**), (**5**) and (**7**), and a 10-membered ansa derivative in (**4**), whereas compound (**6**) exhibits both spiro and ansa functionality. The spiro rings in the spiro-substituted structures are all found to have similar twisted-chair conformations. It was pointed out previously [15] for 1,3-propanedioxy spiro derivatives of cyclophosphazenes that the twist of the P($OCH_2CH_2CH_2O$) spiro moiety gives a sense of chirality to the individual molecules, which has been denoted as positive (p) or negative (n) depending on the sign of the O–P–O–C dihedral angle. For such molecules the sign of the two O–P–O–C dihedral angles is the same and the magnitude of the two twist angles is very similar because the six-membered chair form is symmetrical. For the compounds measured in this work, the P($OCH_2CF_2CF_2CF_2CH_2O$) group forms an eight-membered spiro ring and it

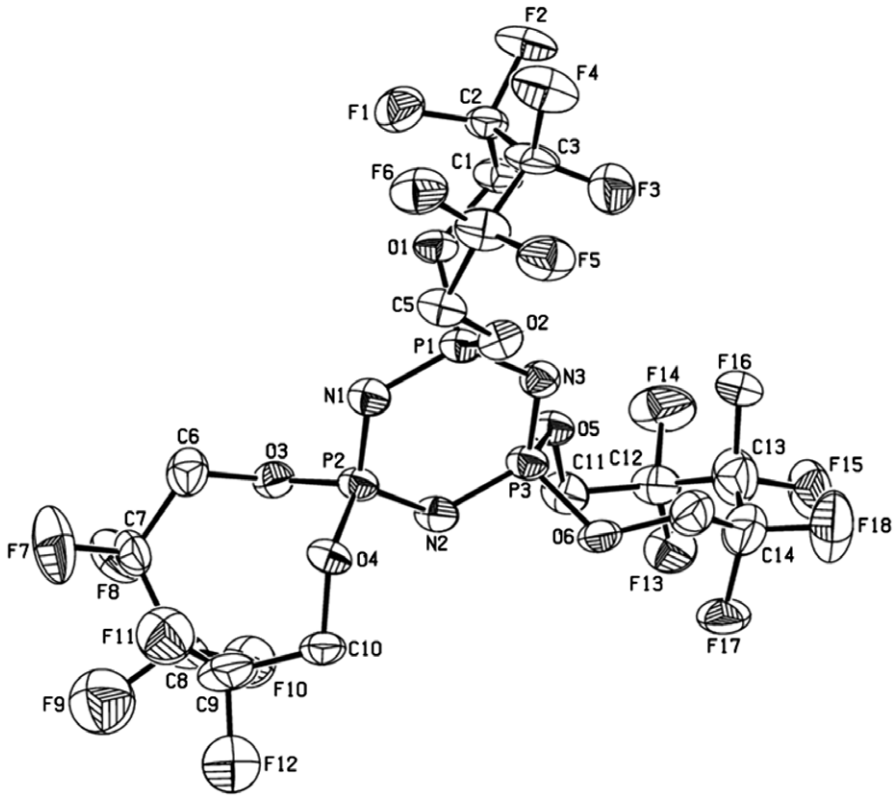


Fig. 6. X-ray crystal structure of (**7**) plotted at 50% probability. The molecular structure of (**7**) showing the atomic numbering scheme and omitting hydrogen atoms for clarity.

Table 2
X-ray crystallographic data and refinement parameters for compounds (**3**)–(**7**)

Compound number	**3**	**4**	**5**	**6**	**7**
Empirical formula	$C_5H_4Cl_4F_6N_3O_2P_3$	$C_5H_4Cl_4F_6N_3O_2P_3$	$C_{10}H_8Cl_2F_{12}N_3O_4P_3$	$C_{10}H_8Cl_2F_{12}N_3O_4P_3$	$C_{15}H_{12}F_{18}N_3O_6P_3$
Formula weight	486.82	486.82	626.00	626.00	765.19
Crystal system	monoclinic	monoclinic	monoclinic	monoclinic	triclinic
Space group	$P2_1/n$	$P2_1$	$P2_1/c$	$P2_1/n$	$P\bar{1}$
a (Å)	6.0516(3)	7.8637(8)	14.0873(16)	7.3072(5)	11.196(14)
b (Å)	19.2968(13)	12.7708(9)	21.104(2)	21.402(3)	11.454(14)
c (Å)	13.6083(7)	8.4275(10)	13.8069(16)	13.3337(11)	11.471(14)
α (°)	90	90	90	90	61.51(10)
β (°)	92.755(4)	117.467(7)	90.075(2)	96.758(8)	78.16(11)
γ (°)	90	90	90	90	78.68(9)
Volume (Å^3)	1587.29(16)	750.94(13)	4104.8(8)	2070.7(3)	1257(3)
Z	4	2	8	4	2
D_{calc} (Mg/m^3)	2.037	2.153	2.026	2.008	2.021
Absorption coefficient (mm^{-1})	1.118	1.181	0.685	0.679	0.412
$F(000)$	952	476	2464	1232	756
Crystal size (mm)	$0.40 \times 0.28 \times 0.04$	$0.60 \times 0.14 \times 0.10$	$0.08 \times 0.06 \times 0.01$	$0.50 \times 0.10 \times 0.08$	$0.14 \times 0.10 \times 0.04$
θ_{max} (°)	27.50	27.50	23.36	27.50	25.21
Reflections collected	20845	5089	29262	22033	15921
Independent reflections ($I > 2\sigma I$)	3624	3023	6830	4680	4428
R (int)	0.0358	0.0342	0.0916	0.0309	0.1298
Final R indices	$R_1 = 0.0402$	$R_1 = 0.1066$	$R_1 = 0.0744$	$R_1 = 0.0316$	$R_1 = 0.0908$
($F^2 > 2\sigma F^2$)	$wR_2 = 0.1165$	$wR_2 = 0.2947$	$wR_2 = 0.1879$	$wR_2 = 0.0775$	$wR_2 = 0.2196$
Δp max/min (e Å^{-3})	1.399/−1.301	2.641/−1.519	1.375/−0.710	0.344/−0.501	1.294/−0.814

is found that the two O–P–O–C dihedral angles have the same sign but somewhat different magnitudes (Table 3). A similar situation is found for the two O–P–O–C dihedral angles in the seven-membered P($OCH_2CF_2CF_2CH_2O$) spiro ring (Table 3) formed from the reactions of cyclophosphazene with 2,2,3,3-tetrafluorobutane-1,4-diol [6].

Table 3
Structural and conformational parameters of spiro and ansa derivatives of cyclophosphazene compounds

Compound	2,2,3,3-Tetrafluorobutane-1,4-diol[a]				2,2,3,3,4,4-Hexafluoropentane-1,5-diol			
	N_3P_3 ring		Exocyclic ring		N_3P_3 ring		Exocyclic ring	
	Maximum deviation[b]	Mean P···P (Å)	Puckering amplitude, Q	Twist angle τ[c]	Maximum deviation[a]	Mean P···P (Å)	Puckering amplitude, Q	Twist angle τ[c]
	Seven-membered spiro ring				*Eight-membered spiro ring*			
Spiro	0.094	2.743	0.797	60, 25	0.081	2.744	1.060	−72, −48
Di-spiro	0.053 0.095	2.714 2.715	0.812, 0.832, 0.814, 0.825	58, 30 53, 38 −55, −33 −59, −31	0.132, 0.117	2.743	1.153, 1.088, 1.112, 1.090	72, 55 61, 53
Spiro-ansa			0.824 sp	−48, −43			1.172 sp	80, 46
Tri-spiro	0.074	2.746	0.820, 0.836, 0.822	53, 37 −53, −38 60, 30	0.038	2.741	1.051, 0.979, 1.065	60, 57 71, 49 69, 50
Average	0.079 ± 0.016	2.730 ± 0.015	0.820 ± 0.008	|55 ± 3|, |34 ± 5|	0.092 ± 0.032	2.743 ± 0.001	1.086 ± 0.041	|69 ± 5|; |51 ± 3|
	Nine-membered ansa ring				*10-Membered ansa ring*			
Ansa	0.099	2.736	Disordered	100, −100	0.125	2.734	1.475	−94, 83
Spiro-ansa	0.085	2.746	1.187 (an)	117, −90	0.089	2.743	1.481 (an)	106, −94
Ansa-ansa	0.099	2.714	1.188, 1.188	87, −127 87, −127				
Average	0.092 ± 0.007	2.730 ± 0.016	1.188 ± 0.001	|110 ± 5|	0.107 ± 0.018	2.739 ± 0.005	1.478 ± 0.003	|94 ± 5|

[a] Data adapted from Ref. [6].
[b] Maximum deviation from the mean plane of the N_3P_3 ring.
[c] τ is the twist angle defined by (a) the C–O–P–O torsion angle for the spiro ring (Ref. [15]), and (b) the C–O–P–Cl/O torsion angle for the ansa ring.

Hence, the concept of spiro rings having positive (p) or negative (n) twist angles can be applied, so far, to six-, seven- and eight-membered spiro rings. In the present work negative twist angles are observed for the mono-spiro derivative (**3**) and positive twist angles for both spiro rings of the di-spiro compound (**5**), the spiro-ansa derivative (**6**) and all three spiro rings of the tri-spiro derivative (**7**). Puckering analysis [16] is a useful measure of ring conformation, because calculation of the mean plane and puckering parameter affords a unique quantitative descriptor, the total puckering amplitude (Q), for the ring conformation. When subjected to ring puckering analysis, the spiro-substituted structures formed from hexafluoropentanediol with eight-membered rings have a total puckering amplitude, Q, in the range 0.979–1.172, with an average value of 1.086 (Table 3), which can be compared with analogous results for spiro derivatives with seven-membered rings formed from tetrafluorobutanediol, with a total puckering amplitude, Q, in the range 0.797–0.836 and an average value of 0.820 (Table 3).

The ansa hexafluoropentanediol-substituted structures in compounds (**4**) and (**6**) adopt a similar 10-membered ring conformation, which is best described as boat–chair–boat. The total puckering amplitude [16] of the ansa rings is very similar, with an average value of 1.478, which differs from that of the analogous nine-membered ansa rings (1.188, Table 3) formed from tetrafluorobutanediol.

The crystal structure assemblies of compounds (**3**)–(**7**) are very complex, probably as a result of the molecular structure of these compounds, where there are very few classical hydrogen bond donors or acceptors. The structures of (**3**), (**6**) and (**7**) possess a single classical hydrogen bond (C–H···O), which generates a chain structure, whilst structures (**4**) and (**5**) exhibit no classical hydrogen bonds. Apart from the structure of (**4**), there are many short contacts where the separation between donor and acceptor is less than 3.2 Å. These separations are predominantly between halogen atoms and it is currently the subject of much debate (see [17] and references therein) as to whether these give rise to interactions or are simply a result of the close packing of molecules.

2.3. Quantitative analysis of the formation of spiro and ansa derivatives in the reactions of $N_3P_3Cl_6$ with tetraflurobutanediol and hexafluoropentanediol

The relative proportions of the products in the reactions of $N_3P_3Cl_6$ (**1**) with either tetrafluorobutanediol or hexafluoropentanediol under the same solution conditions (sodium alkoxides in THF at ambient temperature) have been compared in terms of both the isolation of the pure compounds and ^{31}P NMR spectra of the filtered reaction mixtures (Fig. 1). The results are summarised in Table 4 for a 1:1.2 molar ratio of (**1**) to diol. In general it can be seen that there is a similar range of spiro and ansa derivatives (mono-spiro, mono-ansa, di-spiro, spiro-ansa and tri-spiro), except that a small amount of the ansa-ansa compound was observed for the reaction of (**1**) with tetrafluorobutanediol [6]. In reactions of (**1**) with the sodium

salts of diols there is a significant proportion of ansa as well as spiro compound(s).

There are some discrepancies in the relative proportions of the compounds that have been isolated or quantified by the ^{31}P NMR spectra of the reaction mixtures (Table 4). The yields of the compounds were given as the amount of very pure product obtained. In our previous work on the reaction of (**1**) with tetrafluorobutanediol, it was found that the relative proportions of isolated products decreased in the sequence spiro > ansa > di-spiro > spiro-ansa > ansa-ansa [6], such that the spiro derivatives were more prevalent than the ansa derivatives (in a molar ratio of about 2.1:1), whereas in the reaction of (**1**) with hexafluoropentanediol in this work, it was found that the relative proportions of isolated products decreased in the sequence ansa > spiro > di-spiro > spiro-ansa > tri-spiro, such that the ansa and spiro derivatives were in about equal proportions (in a molar ratio of about 1.2:1; Table 4). The differences in relative proportions of the isolated compounds are mainly due to the proportions of the mono-spiro and mono-ansa compounds for the two diols with cyclophosphazene (Table 4), suggesting that the 10-membered ansa ring formed with hexafluoropentanediol is more stable than the nine-membered ansa ring formed with tetrafluorobutanediol. However, care should be taken in forming conclusions based on the relative proportions of the isolated compounds, unless one can account for all the products of the reaction. In the present case, the overall yield of the reaction of (**1**) with tetrafluorobutanediol is 55% [6] and it is only 39% for the reaction of (**1**) with the hexafluoropentanediol. The same sets of reactions were observed by ^{31}P NMR spectroscopy for the filtered reaction mixtures of (**1**) with both tetrafluorobutanediol and hexafluoropentanediol (Fig. 1). The ^{31}P NMR results (Table 4) show similar trends to those obtained for the isolated compounds, though the differences between the relative proportions of mono-spiro and mono-ansa compounds are not as marked, leading to a smaller difference in the ratio of spiro:ansa compounds for hexafluoropentanediol (ca. 1.3:1) compared to tetrafluorobutanediol (ca. 1.5:1). Nevertheless, the ^{31}P NMR results on the reaction mixtures also show that there is a small increase in the relative proportion of ansa compounds for the reaction of (**1**) with hexafluoropentanediol compared to tetrafluorobutanediol, which has one less CF_2 group in the chain and so forms smaller rings. The relative proportions of spiro and ansa compounds depends on the fine balance in stabilities of the different medium-sized rings in the fluorinated pentanediol (spiro, 8- and ansa, 10-membered rings) compared to the fluorinated butanediol (spiro, 7- and ansa, nine-membered rings) derivatives of cyclophosphazene.

3. Experimental section

3.1. Materials

Hexachlorocyclotriphosphazene was purified by fractional crystallisation from hexane. Sodium hydride, 60% dispersion in mineral oil (Merck) was removed by washing with dry heptane (Merck) followed by decantation. Hexane, heptane (Merck) and 2,2,3,3,4,4-hexafluoro-1,5-pentanediol (Aldrich) were used as received. THF was distilled over a sodium–potassium alloy under an atmosphere of dry argon. Silica gel (Merck 60, 0.063–0.200 mm) was used for column chromatography. All reactions were performed under a dry argon atmosphere.

3.2. Methods

Elemental analyses were obtained using a Carlo Erba 1106 Instrument. Mass spectra were recorded on a Bruker MicrOTOF LC–MS spectrometer using the electrospray ionisation (ESI) method; ^{35}Cl values were used for calculated masses. Analytical thin layer chromatography (TLC) was performed on Merck Silica gel plates (Merck 60, 0.25 mm thickness) with F_{254} indicator. Column chromatography was performed on silica gel (Merck 60, 0.063–0.200 mm; for 3 g crude mixture, 120 g silica gel was used in a column of 3 cm in diameter and 110 cm in length). ^{1}H, ^{19}F and ^{31}P NMR spectra were recorded for $CDCl_3$ solutions on a Bruker DRX 500 MHz spectrometer

Table 4
Quantitative comparison of the relative proportions (%) of spiro and ansa derivatives of the reaction of (**1**) with fluorinated diols[a]

Compound	2,2,3,3-Tetrafluorobutane-1,4-diol		2,2,3,3,4,4-Hexafluoropentane-1,5-diol	
	Isolation	^{31}P NMR[b]	Isolation	^{31}P NMR[b]
Spiro	51	45	28	29
Ansa	25	36	50	44
Di-spiro	13	8	11	13
Spiro-ansa	7	10	8	11
Ansa-ansa	4	0.6		
Tri-spiro		0.3	3	2
Spiro:ansa	2.1:1	1.5:1	1.2:1	1.3:1

[a] The diols were reacted with (**1**) in a 1.2:1 molar ratio with NaH in THF solution.
[b] The ^{31}P NMR measurements for quantisation were performed with a 45° pulse, a recycle time of 6.4 s and without NOE to allow for full relaxation of the signals.

using TMS as an internal reference for ^{1}H, $CFCl_3$ as an internal reference for ^{19}F and 85% H_3PO_4 as an external reference for ^{31}P. In order to assign the signals of some compounds both proton-coupled and proton-decoupled ^{19}F and ^{31}P NMR spectra were recorded.

3.3. Reaction of hexachlorocyclotriphosphazene (*1*) with 2,2,3,3,4,4-hexafluoro-1,5-pentanediol (*2*)

Cyclophosphazene (**1**) (3.48 g, 10 mmol) and 2,2,3,3,4,4-hexafluoro-1,5-pentanediol (**2**) (2.54 g, 12 mmol) were dissolved in 170 mL of dry THF in a 250 mL three-necked round-bottomed flask. The reaction mixture was cooled in an ice-bath and NaH (60% oil suspension, 1.1 g, 24 mmol) in 30 mL of dry THF was quickly added to the stirred solution under an argon atmosphere. The reaction mixture was stirred for 72 h at room temperature and the reaction was followed on TLC silica gel plates using hexane–DCM (4:1), giving five new products. The reaction mixture was filtered to remove the sodium chloride and any other insoluble material such as oligomeric and polymeric products. The solvent was removed at reduced pressure and the resulting colourless oil was subjected to column chromatography, using hexane–DCM (4:1) as the eluant. The first product is the mono-spiro derivative $[N_3P_3Cl_4(OCH_2CF_2CF_2CF_2CH_2O)]$ (**3**) (0.5 g, 10%, mp 70 °C). *Anal.* Calc. for $C_5H_4Cl_4F_6N_3O_2P_3$ (M, 485): C, 12.34; H, 0.83; N, 8.63. Found (M^+, 485.9): C, 12.38; H, 0.89; N, 8.57%. ^{1}H NMR, $CDCl_3$, 298 K; complex multiplet, 4.52 ppm, 4H, $(OCH_2)_2$, ^{3}J(POCH) 16.0 Hz. The second product is the mono-ansa derivative $[N_3P_3Cl_4(OCH_2CF_2CF_2CF_2CH_2O)]$, (**4**) (0.87 g, 18%, mp 152 °C). *Anal.* Calc. for $C_5H_4Cl_4F_6N_3O_2P_3$ (M, 485): C, 12.34; H, 0.83; N, 8.63. Found (M^+, 485.9): C, 12.30; H, 0.81; N, 8.59%. ^{1}H NMR, $CDCl_3$, 298 K; complex AB multiplet, 4.50 ppm, 2H, (OCH_{2A}) and 4.86 ppm, 2H, (OCH_{2B}). The third separated product is the bis-spiro derivative $[N_3P_3Cl_2(OCH_2CF_2CF_2CF_2CH_2O)_2]$ (**5**) (0.25 g, 4%, mp 87 °C). *Anal.* Calc. for $C_{10}H_8Cl_2F_{12}N_3O_4P_3$ (M, 625): C, 19.19; H, 1.29; N, 6.71. Found (M^+, 625.9): C, 19.22; H, 1.30; N, 6.68%. ^{1}H NMR, $CDCl_3$, 298 K; complex multiplet, 4.49 ppm, 8H, $2\times(OCH_2)_2$. The fourth product is the spiro-ansa derivative $[N_3P_3Cl_2(OCH_2CF_2CF_2CF_2CH_2O)_2]$ (**6**) (0.18 g, 3%, mp 110 °C). *Anal.* Calc. for $C_{10}H_8Cl_2F_{12}N_3O_4P_3$ (M, 625): C, 19.19; H, 1.29; N, 6.71. Found (M^+, 625.9): C, 19.18; H, 1.32; N, 6.75%. ^{1}H NMR, $CDCl_3$, 298 K; complex AB multiplet, 4.49 ppm, 2H, (OCH_{2A}) and 4.89 ppm, 2H, (OCH_{2B}) and complex multiplet, 4.49 ppm, 4H, spiro-$(OCH_2)_2$, ^{3}J(POCH) 16.0 Hz. The fifth product is the tri-spiro derivative $[N_3P_3(OCH_2CF_2CF_2CF_2CH_2O)_3]$ (**7**) (0.09 g, 1%, mp 245 °C); *Anal.* Calc. for $C_{15}H_{12}F_{18}N_3O_6P_3$ (M, 765): C, 23.55; H, 1.58; N, 5.49. Found (M^+, 766): C, 23.55; H, 1.50; N, 5.45%. ^{1}H NMR, $CDCl_3$, 298 K; complex multiplet, 4.46 ppm, 12H, $(OCH_2)_3$. All products were crystallised from hexane–DCM (4:1) and were obtained as white crystals.

3.4. X-ray crystallography

Intensity data were recorded on a Nonius KappaCCD diffractometer driven by COLLECT [18] and DENZO [19] software. Details of data collection and refinement are given in Table 2. X-ray crystallographic data for structure (**5**) was collected on a Bruker SMART area detector situated on the beam-line of station 9.8 at the Daresbury Synchrotron Radiation Source [20]. Structures were determined using the direct methods procedure in SHELXS-97 and refined by full-matrix least squares on F^2 using SHELXL-97 [21].

Acknowledgements

The authors would like to thank the Otsuka Chemical Co., Ltd. for gifts of $N_3P_3Cl_6$, the Gebze Institute of Technology (GIT) Research Fund for partial support (S.B. and A.K.) and the EPSRC for funding the National Crystallographic Service (Southampton, UK).

Appendix A. Supplementary material

CCDC 648540, 648541, 648542, 648543 and 648544 contain the supplementary crystallographic data for **3**, **4**, **5**, **6** and **7**. The data can be obtained free of charge via http://www.ccdc.cam.ac.uk/conts/retrieving.html, or from the Cambridge Crystallographic Data Centre, 12 Union Road, Cambridge CB2 1EZ, UK; fax: (+44) 1223-336-033; or e-mail: deposit@ccdc.cam.ac.uk. Supplementary data associated with this article can be found, in the online version, at doi:10.1016/j.poly.2007.07.050.

References

[1] (a) G. Guerch, J.F. Labarre, R. Lahana, R. Rocques, F. Sournies, J. Galy, J. Mol. Struct. 99 (1983) 275;
(b) G. Guerch, J.F. Labarre, R. Lahana, F. Sournies, J. Galy, R. Enjalbert, J. Galy, J.P. Declercq, Inorg. Chim. Acta 83 (1984) L33;
(c) R.A. Shaw, Phosphorus Sulfur Silicon 45 (1989) 103.
[2] (a) H.R. Allcock, U. Diefenbach, S.R. Pucher, Inorg. Chem. 33 (1994) 3091;
(b) A. Vij, S.J. Geib, R.L. Kirchmeier, J.M. Shreeve, Inorg. Chem. 35 (1996) 2915;
(c) V. Chandrasekhar, V. Krishnan, Adv. Inorg. Chem. 53 (2002) 159.
[3] (a) V. Chandrasekhar, S. Karthikeyan, S.S. Krishnamurthy, M. Woods, Indian J. Chem. (1985) 379;
(b) A.J. Elias, B. Twamley, J.M. Shreeve, Inorg. Chem. 40 (2001) 2120;
(c) G.A. Carriedo, L. Fernandez-Catuxo, F.J.G. Alonso, P. Gomez-Elipe, P.A. Gonzalez, Macromolecules 29 (1996) 5320.
[4] A.H. Alkubaisi, H.G. Parkes, R.A. Shaw, Heterocycles 28 (1989) 347.
[5] K. Brandt, T. Kupka, J. Drodz, J.C. Van de Grampel, A. Meetsma, A.P. Jekel, Inorg. Chim. Acta 228 (1995) 187.
[6] S. Beşli, S.J. Coles, D.B. Davies, R.J. Eaton, M.B. Hursthouse, Adem Kılıç, R.A. Shaw, Polyhedron 25 (2006) 963.
[7] R. Ratz, H. Schroder, H. Ulrich, E. Kober, C. Grundmann, J. Am. Chem. Soc. 84 (1962) 551.
[8] A.J. Elias, R.L. Kirchmeier, J.M. Shreeve, Inorg. Chem. 33 (1994) 2727.

[9] S.S. Krishnamurthy, M. Woods, Annu. Rep. NMR Spectrosc. 19 (1987) 175.
[10] J.W. Emsley, L. Phillips, V. Wary, Fluorine Coupling Constants, Pergamon Press, New York, 1977.
[11] G.J. Bullen, J. Chem. Soc. B (1971) 1450.
[12] A.G. Orpen, L. Brammer, F.H. Allen, O. Kennard, D.G. Watson, R. Taylor, International Tables for Crystallography, vol. C, 1992.
[13] (a) S.R. Contractor, M.B. Hursthouse, H.B. Parkes, L.S. Shaw (née Gözen), R.A. Shaw, H. Yılmaz, J. Chem. Soc., Chem. Commun. (1984) 675;
(b) S.R. Contractor, M.B. Hursthouse, H.B. Parkes, L.S. Shaw (née Gözen), R.A. Shaw, H. Yılmaz, Phosphorus Sulfur 28 (1986) 267.
[14] (a) K. Muralidharan, N.D. Reddy, A.J. Elias, Inorg. Chem. 39 (2000) 3988;
(b) N.D. Reddy, A.J. Elias, A. Vij, Inorg. Chem. Commun. 3 (2000) 29;
(c) K. Muralidharan, P. Venugopalan, A.J. Elias, Inorg. Chem. 42 (2003) 3176.
[15] Z. Wang, R.D. Willett, A.J. Elias, R.L. Kirchmeier, J.M. Shreeve, Acta Cryst. B52 (1996) 643.
[16] D. Cremer, J.A. Pople, J. Am. Chem. Soc. 97 (1975) 1354.
[17] K. Reichenbächer, H.I. Süss, J. Hulliger, Chem. Soc. Revs. 34 (2005) 22.
[18] R. Hooft, Collect: Data Collection Software, Nonius BV, 1998.
[19] Z. Otwinowski, W. Minor, Methods Enzymol. 276 (1997) 307.
[20] R.J. Cernik, W. Clegg, C.R.A. Catlow, G. Bushnell-Wye, J.V. Flaherty, G.N. Greaves, M. Hamichi, I. Burrows, D.J. Taylor, S.J. Teat, J. Synchotron Radiat. 4 (1997) 279.
[21] G.M. Sheldrick, SHELXS97. Programs for crystal structure solution and refinement. Univ. of Göttingen, Germany, 1997.

heated to reflux temperature while liberated H_2eg was removed by azeotropic distillation (Scheme 1a). Consequently, the reactions went on efficiently, the colourless mixtures turning rapidly purple solutions. Evaporation of toluene solvent followed by purification by column chromatography on silica gel afforded air-stable molybdenum(VI) compounds as purple solids. The reaction of H_3L^{tBu} produced complex **4b** almost quantitatively, but the reaction involving H_3L^{Me} led also to the formation of some intractable dark solids, therefore **4a** could be isolated in only a moderate yield of 37%. Both crystalline materials are soluble in toluene, ethers and chlorinated solvents though *tert*-butyl derivatives are more soluble than their methyl analogues. The NMR spectra of studied compounds show similar resonances for coordinated aminotris(phenolato) and hydrogendiolato ligands as found for analogous oxotungsten(VI) complexes $[WO(L^R)(Heg)]$ [10a]. The X-ray structure determination of **4b** confirmed that the aminotris(phenolate) has been bonded as a tetradentate, trianionic ligand, whereas the ethanediolato ligand is monoanionic and monodentate (see below).

The overall mechanism for the formation of these monooxo complexes includes an alcoholysis of one of the $Mo–O_{diolato}$ bonds as well as a condensation of one of the Mo=O bonds. Based on the literature examples [13] on the related reactions of $[MoO_2Cl_2]$, we may suggest that in the first step the ligand H_3L^R is coordinated to the $MoO_2(Heg)_2$ unit as a neutral nitrogen donor, which process is subsequently followed by an alcoholysis reaction and elimination of a H_2eg molecule. Then, the reaction proceeds via an addition of one of the remaining OH functions across the Mo=O bond to form an intermediate $MoO(OH)(Heg)(HL^R)$, which then reacts to eliminate water and produce the final product.

2.2. Preparation of alkoxide complexes $[MoO(L^{tBu})(OR')]$

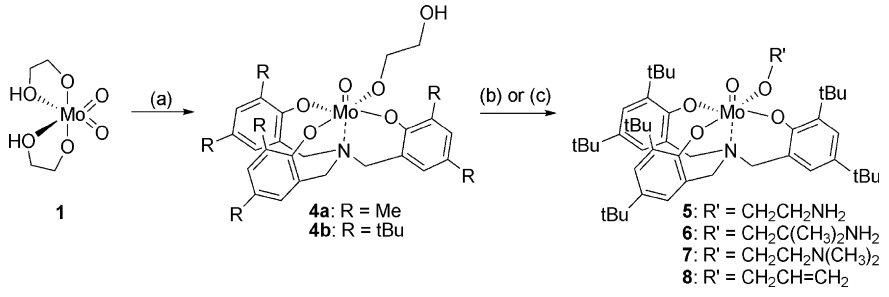
The reaction of complex **4b** with high-boiling aminoalcohols in refluxing toluene yields readily new aminoalkoxide derivatives **5**–**7**. The ligand displacement reactions were promoted using the excess of aminoalcohol, while the liberated 1,2-ethanediol was distilled out as a toluene azeotrope. These air-stable purple products are soluble in common organic solvents. All complexes can be isolated by column chromatography followed by crystallization from hot acetonitrile. Compound **8** could not be prepared similarly since allyl alcohol has a lower boiling point than H_2eg-PhMe azeotrope. However, it was formed almost quantitatively in the reaction of **4b** in neat allyl alcohol at reflux temperature.

2.3. Preparation of complexes $[MoO(L^R)Cl]$ and $[MoO(L^R)(Me)]$

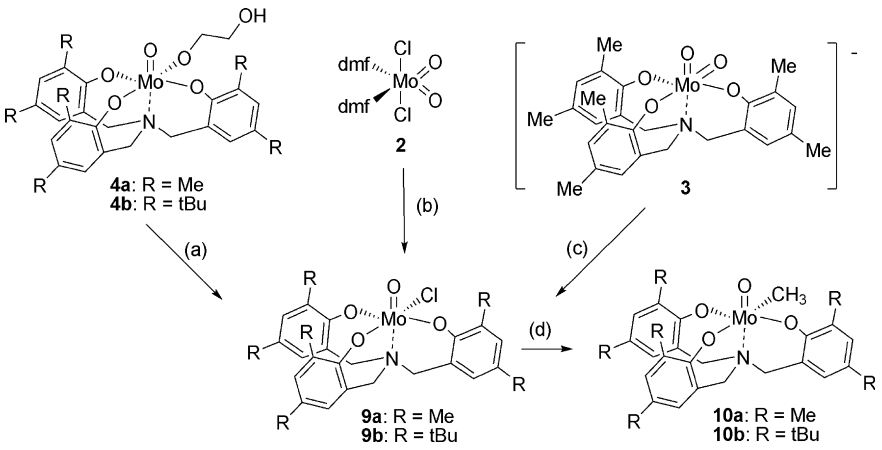
Metal alkoxide moieties can be transformed into halides by various substitution reactions [14]. In present study, Me_3SiCl was used as a chlorinating reagent. Intense blue mixtures were obtained when purple solutions of **4** in CH_2Cl_2 were treated with a five-fold excess of Me_3SiCl (Scheme 2a). As a result, complexes **9** were produced as only isolable products in nearly quantitative yields. The NMR spectra of products **9** confirmed the loss of ethanediolato group presenting typical signals for aminotris(phenol) ligands. These intense blue, air-stable solids are soluble in common organic solvents. The IR and NMR data of complexes **9** are closely similar to those recorded earlier for their tungsten analogues [10a]. The molecular structure of **9b** was also verified by X-ray diffraction (see below).

In the alternative syntheses of complexes **9**, the stirred suspensions of finely ground $[MoO_2Cl_2(dmf)_2]$ in toluene were treated with stoichiometric amounts of the ligand precursors H_3L^R (Scheme 2b), while the mixtures were heated at reflux temperature. Filtration of the reaction mixture through a short pad of silica was followed by the evaporation of toluene solvent, which afforded new molybdenum compounds **9** in nearly quantitative yields.

The silylation of Mo=O moieties with Me_3SiCl in toluene has proved a convenient procedure for the chloride-for-oxide substitution of dioxomolybdenum(VI) complexes. [15–17] Accordingly, the reaction of a yellow solid compound $H_4L^{Me}[MoO_2(L^{Me})]$ [10b] with Me_3SiCl in a toluene suspension at reflux temperature led to the formation of a dark blue solution, from which the monooxo complex **9a** was obtained (Scheme 2c). In principle, this reaction can be a direct silylation of a M=O group, but as proton sources (e.g. H_4L^{Me+} cation and traces of water)



Scheme 1. Preparation of complexes $[MoO(L^R)(Heg)]$ and $[MoO(L^{tBu})(OR')]$. Conditions: (a) H_3L^R, toluene, reflux, 4 h. (b) HOR′ (excess), toluene, reflux, 6 h (for **5**–**7**). (c) HOR′ (neat), reflux, 6 h (for **8**).



Scheme 2. Preparation of complexes [MoO(L^R)Cl] and [MoO(L^R)(Me)]. Conditions: (a) Me_3SiCl, CH_2Cl_2, reflux, 2 h. (b) H_3L^R, PhMe, reflux, 18 h. (c) Me_3SiCl, PhMe, reflux, 2 h. (d) MeMgI/Et_2O, PhMe, RT, 1 h.

are present, it is also possible that the actual reacting species is in situ generated HCl.

The methyl complexes **10** were readily prepared from corresponding chloride complexes by treating with Grignard reagent (Scheme 2d). As soon as an etheral solution of MeMgI was added to the intense blue solutions of chlorido complexes in toluene, the reaction mixtures turned rapidly purple. The products were purified by column chromatography to obtain air-stable purple-red solids, which are reasonably soluble in toluene, ether and chlorinated solvents. ^{1}H NMR spectra of methyl compounds in $CDCl_3$ show signals at 0.57 ppm (**10a**) and 0.59 ppm (**10b**) for Mo–CH_3 protons, whereas related signals in ^{13}C NMR spectra are seen at 42.78 ppm and 42.93 ppm for **10a** and **10b**, respectively. Although studied methyl derivatives are rather stable towards hydrolysis in a solid state, they seem to hydrolyse slowly in solutions, acidic impurities hastening this decomposition. When the red toluene solutions of methyl complexes were treated with gaseous HCl under non-aqueous conditions the solutions turned dark blue in two hours, since initial chlorido complexes were formed nearly quantitatively due to the chlorination of a Mo–C bond.

2.4. Structural studies

Molecular structures of complexes **4b**, **7** and **9b** were verified by X-ray diffraction analyses. Studied complexes are formed of monomeric, neutral units in which the tripodal aminotris(phenolate) group has coordinated to the cen-

Table 1
Summary of crystallographic data for **4b**, **7** and **9b** at 173(2) K

	4b	**7**	**9b**
Formula	$C_{47}H_{71}MoNO_6$	$C_{49}H_{76}MoN_2O_5$	$C_{45}H_{66}ClMoNO_4$
Crystal system	Monoclinic	Monoclinic	Orthorhombic
Space group (no.)	$P21/c$ (14)	$P21/c$ (14)	$P2_12_12_1$ (19)
a (Å)	10.5082(2)	16.1204(4)	15.1612(3)
b (Å)	19.8782(3)	11.2683(4)	15.8785(3)
c (Å)	21.8519(3)	28.0415(5)	19.8308(4)
α (°)	90	90	90
β (°)	97.9820(10)	105.570(2)	90
δ (°)	90	90	90
V (Å^3)	4520.29(13)	4906.8(2)	4774.01(16)
Z	4	4	4
μ(Mo K$_\alpha$) (cm^{-1})	3.36	3.11	3.68
Observed reflections	8857	9633	9377
R_{int}	0.0818	0.0688	0.0705
Parameters	517	540	519
R_1	0.064 (0.0445)[a]	0.1046 (0.0635)	0.1079 (0.0668)
wR_2	0.0932 (0.0863)	0.1577 (0.1401)	0.1865 (0.166)
Peak, hole (e Å^{-3})	0.399/−0.447	0.528/−0.515	1.068/−1.307

$R_1 = \sum||F_o| - |F_c||/\sum|F_o|$.
$wR_2 = \{\sum[w(F_o^2 - F_c^2)^2]/\sum[w(F_o^2)^2]\}^{1/2}$ and $w = 1/[\sigma^2(F_o^2) + (aP)^2 + (bP)]$, where $P = (2F_c^2 + F_o^2)/3$.

[a] Values in parentheses for reflections with $I > 2.0\sigma(I)$.

tral molybdenum as a tetradentate ligand through three oxygen donors and one nitrogen donor (Figs. 1–3), thus overall bonding between the metal centres and the amino-tris(phenolato) is typical for this ligand. The nitrogen donor is located *trans* to the terminal oxo group, while the sixth coordination site is occupied by a monoanionic, monodentate alcoholate ligand (**4b** and **7**) or by chlorido ligand (**9b**). The distorted octahedral MoO_5N units are

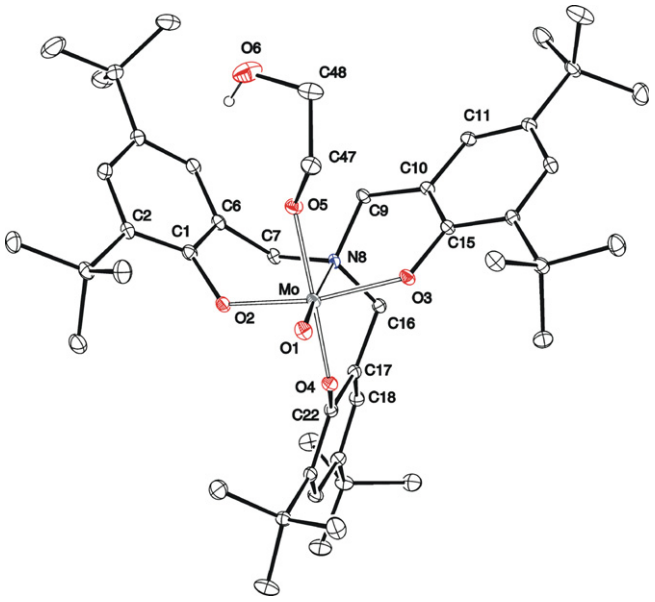


Fig. 1. Molecular structure of [MoO(L^{tBu})(Heg)] (**4b**). Thermal ellipsoids have been drawn at the 30% probability level. The hydrogen atoms are omitted for clarity.

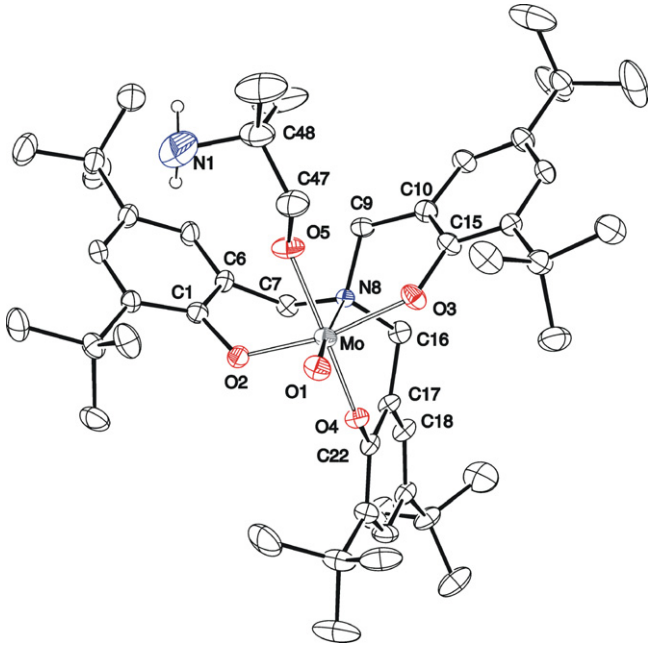


Fig. 2. Molecular structure of [MoO(L^{tBu})($OCH_2C(CH_3)_2NH_2$)] (**7**). Thermal ellipsoids have been drawn at the 30% probability level. The C–H hydrogen atoms are omitted for clarity.

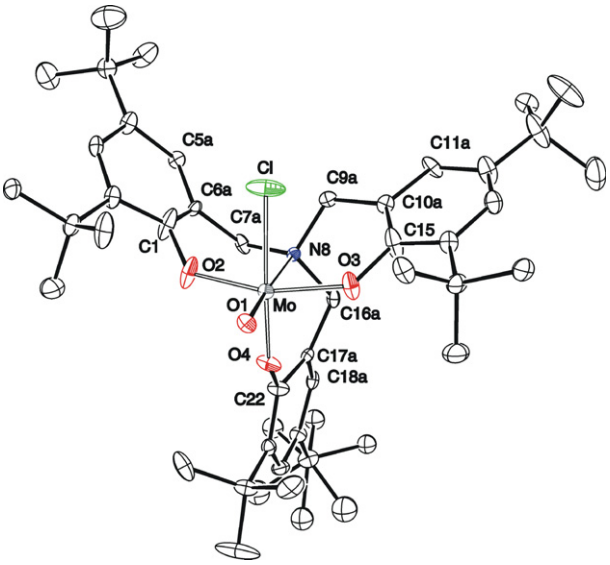


Fig. 3. Molecular structure of the main conformer of [MoO(L^{tBu})Cl] (**9b**). Thermal ellipsoids have been drawn at the 30% probability level. The hydrogen atoms are omitted for clarity. One of the *tert*-butyl groups is disorder almost in 1:1 ratio – the amount of two different rotamers is 56.6% and 43.4%, respectively.

generally similar in complexes **4b** and **7** as indicated by the bond parameters presented in Table 2, whereas Mo–$O_{phenoxide}$ bonds are clearly shorter in the chlorido derivative **9b**. In general, studied structures are closely related to the oxotungsten(VI) complexes with the very same atrane ligand [10a]. Especially **4b**, [Mo(L^{tBu})(Heg)], is isostructural with the tungsten analogue [WO(L^{tBu})(Heg)], as a result the unit cell and all bonding parameters are closely similar in these two complexes. However, the terminal Mo–O1 distances in **4b** and **7** (1.6842(18) and 1.684(3) Å, respectively) are clearly shorter than the corresponding W–O distance in [WO(L^{tBu})(Heg)] (1.706(2) Å).

Compound **9b** adopts a disorder structure in the solid state (see Supplementary material). The tris(benzyl)amino

Table 2
Selected bond lengths (Å) and angles (°) for **4b**, **7** and **9b**

	4b	7	9b
Mo–O1	1.6842(18)	1.684(3)	1.692(4)
Mo–O2	1.9433(17)	1.935(3)	1.892(5)
Mo–O3	1.9081(18)	1.907(3)	1.872(4)
Mo–O4	1.9076(18)	1.923(3)	1.873(4)
Mo–N8	2.443(2)	2.420(3)	2.438(4)
Mo–X	1.9102(19)[a]	1.914(3)[b]	2.3610(18)[c]
O1–Mo–N8	176.65(8)	175.53(13)	176.59(16)
O2–Mo–O3	158.13(8)	158.93(11)	156.4(2)
O2–Mo–O4	87.59(8)	87.69(12)	92.4(3)
O4–Mo–X	162.02(8)[a]	161.07(12)[b]	167.91(13)[c]
Mo–O2–C1	125.55(16)	126.9(2)	131.9(6)
Mo–O3–C15	138.32(16)	140.7(3)	136.5(5)
Mo–O4–C22	141.86(17)	143.8(3)	146.1(4)

[a] Mo–$O_{ethanediolate}$.
[b] Mo–$O_{aminoalcoholate}$.
[c] Mo–Cl.

fraction of the molecule can rotate around the N–Mo=O axis therefore part of the molecule can have two similar conformations in the ratio of 2:1. The Mo–$O_{phenoxide}$ distances are noticeably shorter than in analogous alkoxide complexes **4b** and **7** while the Mo–Cl bond is obviously longer than corresponding Mo–$O_{alkoxide}$ bond.

3. Conclusions

In conclusion, we have found that the dioxomolybdenum(VI) complex $[MoO_2(Heg)_2]$ (Heg = 1,2-ethanediolato monoanion) reacts in refluxing toluene solution with phenolic ligand precursors tris(2-hydroxy-3,5-dimethylbenzyl)amine (H_3L^{Me}) and tris(2-hydroxy-3,5-di-*tert*-butylbenzyl)amine (H_3L^{tBu}) to form oxomolybdenum(VI) complexes $[MoO(L^{Me})(Heg)]$ and $[MoO(L^{tBu})(Heg)]$, respectively. The labile Heg ligands can be replaced by other alcohols (i.e. 2-aminoethanol, 2-amino-2-methylpropan-1-ol, 2-(dimethylamino)ethanol or allyl alcohol) in the reaction at refluxing toluene. Complexes $[MoO(L^R)(Heg)]$ undergo chloride-for-alkoxide substitution when treated with Me_3SiCl in CH_2Cl_2, which leads to the formation of corresponding chlorido complexes $[MoO(L^{Me})Cl]$ and $[MoO(L^{tBu})Cl]$. Identical chlorido complexes can also be made by the reaction these phenolic ligand precursors with $[MoO_2Cl_2(dmf)_2]$. Chloridocomplexes $[MoO(L^R)Cl]$ can react with MeMgI to yield air-stable monomethyl derivatives $[MoO(L^R)(Me)]$.

4. Experiments

Starting compounds $[MoO_2(Heg)_2]$, $[MoO_2Cl_2(dmf)_2]$, H_4L^{Me}[$MoO_2(L^{Me})$] [12,18,10b] and ligand precursors H_3L^R [19] were synthesised and purified according to the published procedures. Other chemicals and solvents were obtained from commercial sources and used as purchased. Syntheses of organometallic compounds were done under N_2-atmosphere, other syntheses and manipulations were carried out under ambient laboratory conditions. ^1H NMR (400 MHz) and ^{13}C spectra (100 MHz) were recorded in $CDCl_3$ solutions and were referenced to the solvent residue signal.

4.1. Reaction of $[MoO_2(Heg)_2]$ with aminotris(phenol)s

Molybdenum precursor **1** (250 mg, 1.00 mmol) was heated with one equivalent of H_3L^{Me} (420 mg) or H_3L^{tBu} (672 mg) in 50 ml of toluene at reflux temperature for 4 h to form a purple solution. The H_2eg and water that formed during the reactions were removed as a toluene azeotrope. Remaining solvent was evaporated and a purple solid residue was purified by a silica column chromatography using CH_2Cl_2 as an eluent.

4.1.1. $[MoO(L^{Me})(Heg)]$ (**4a**)

Yield 218 mg (37%). IR: 3562 m, 2955 s, 1460 s, 1377 s, 1260 m, 1239 s, 1219 m, 1160 s, 1105 m, 1045 m, 1025 s (br), 974 w, 936 vs, 897 m, 856 vs, 826 m, 756 w, 730 m, 694 m, 604 s, 560 m cm^{-1}. ^1H NMR: δ 6.96 (1H, Ar*H*), 6.94 (2H, Ar*H*), 6.76 (2H, Ar*H*), 6.69 (1H, Ar*H*), 4.32 (2H, t, $J = 4.5$ Hz, Mo–O–CH_2), 3.78 (1H, N–CH_2), 3.74 (1H, N–CH_2), 3.52 (2H, N–CH_2), 3.41 (1H, N–CH_2), 3.37 (1H, N–CH_2), 3.22 (2H, t, $J = 4.5$ Hz, CH_2–OH), 2.47 (3H, Ar-CH_3), 2.29 (12H, Ar-CH_3), 2.24 (3H, Ar-CH_3). ^{13}C NMR: δ 157.31, 156.58, 132.30, 131.58, 131.04, 130.87, 129.01, 128.19, 127.96, 127.31, 125.83, 124.68, 64.06, 61.88, 60.39, 59.43, 16.57, 16.41. *Anal*. Calc. for $C_{29}H_{35}MoNO_6$: C, 59.08; H, 5.98; N, 2.38. Found: C, 58.84; H, 6.03; N, 2.68%.

4.1.2. $[MoO(L^{tBu})(Heg)]$ (**4b**)

Yield 712 mg (85%). IR: 3549 m, 2956 s, 1460 s, 1375 s, 1306 m, 1258 s, 1238 vs (br), 1205 s, 1168 vs, 1130 w, 1120 w, 1080 s, 1026 vs, 980 w, 945 vs, 915 m, 895 m, 876 m, 860 vs, 839 s, 770 m, 760 m, 694 w, 616 m, 606 m, 562 s, 490m cm^{-1}. ^1H NMR ($CDCl_3$): δ 7.36 (1H, Ar*H*), 7.28 (2H, Ar*H*), 7.05 (1H, Ar*H*), 6.98 (2H, Ar*H*), 4.26 (2H, br, Mo–O–CH_2), 3.4–3.6 (6H, overlapping broad signals, N–CH_2), 3.05 (2H, CH_2–OH), 1.62 (9H, C(CH_3)$_3$), 1.45 (18H, C(CH_3)$_3$), 1.31 (18H, C(CH_3)$_3$), 1.30 (9H, C(CH_3)$_3$). ^{13}C NMR ($CDCl_3$): δ 156.84, 145.68, 145.15, 140.20, 138.17, 128.51, 126.03, 125.03, 124.49, 124.23, 123.52, 123.27, 63.86, 60.17, 53.42, 35.41, 35.15, 34.61, 34.51, 31.57, 30.32, 30.02. *Anal*. Calc. for $C_{47}H_{71}NO_6Mo$: C, 67.04; H, 8.50; N, 1.66. Found: C, 66.71; H, 8.88; N, 1.87%.

4.2. Alcohol interchange reaction of **4b** with aminoalcohols

0.30 mmol (253 mg) of **4b** was heated with 2.0 mmol of 2-aminoethanol (120 mg, 0.12 ml), 2-amino-2-methylpropan-1-ol (180 mg, 0.19 ml) or 2-(dimethylamino)ethanol (160 mg, 0.18 ml) in 40 ml of toluene at reflux temperature for 4 h. The reaction was monitored by TLC. The liberated H_2eg was removed as a toluene azeotrope. Remaining solvents were evaporated and purple solid compounds **5**–**7** were purified by silica column chromatography using diethyl ether as an eluent.

4.2.1. $[MoO(L^{tBu})(OCH_2CH_2NH_2)]$ (**5**)

IR: 3349 m, 2955 s, 1462 s, 1378 s, 1310 m, 1260 s, 1234 s (br), 1200 s, 1166 vs, 1130 w, 1080 s, 1022 vs, 978 w, 943 vs, 915 m, 896 m, 875 m, 858 vs, 841 s, 770 m, 755 m, 694 w, 616 m, 606 m, 560 s, 490 m cm^{-1}. ^1H NMR: δ 7.37 (1H, Ar*H*), 7.32 (2H, Ar*H*), 7.10 (1H, Ar*H*), 7.06 (2H, Ar*H*), 4.30 (1H, t, $J = 4.4$ Hz, NH_2), 4.19 (2H, br, Mo–O–CH_2), 3.4–3.6 (6H, overlapping signals, *N*–CH_2), 2.66 (1H, t, $J = 4.4$ Hz, NH_2), 2.54 (2H, br, Mo–O–CH_2), 1.59 (9H, C(CH_3)$_3$), 1.43 (18H, C(CH_3)$_3$), 1.29 (18H, C(CH_3)$_3$), 1.28 (9H, C(CH_3)$_3$). ^{13}C NMR ($CDCl_3$): δ 156.81, 145.49, 144.97, 140.20, 138.09, 128.46, 126.07, 125.02, 124.23, 123.42, 123.20, 122.97, 60.77, 60.17, 44.42, 35.40, 35.14, 34.60, 34.51, 31.63, 30.33, 30.07. *Anal*. Calc. for $C_{47}H_{72}MoN_2O_5$: C, 67.12; H, 8.63; N, 3.33. Found: C, 67.43; H, 8.48; N, 3.22%.

4.2.2. [MoO(L^{tBu})($OCH_2C(CH_3)_2NH_2$)] (**6**)

IR: 3334 m, 2955 s, 1460 s, 1378 s, 1346 m, 1257 vs, 1236 vs (br), 1207 s, 1169 vs, 1127 m, 1120 w, 1050 s (br), 980 s, 945 s, 898 m, 875 m, 862 m, 840 s, 772 m, 760 m, 690 w, 667 s, 616 m, 606 m, 561 s, 490 m cm^{-1}. ^1H NMR: δ 7.37 (1H, Ar*H*), 7.28 (2H, Ar*H*), 7.07 (1H, Ar*H*), 7.00 (2H, Ar*H*), 4.16 (2H, Mo–O–*CH*$_2$), 3.9 (2H, br, N–*CH*$_2$), 3.5–3.6. (4H, overlapping signals, N–C*H*$_2$), 1.60 (9H, C(C*H*$_3$)$_3$), 1.45 (18H, C(C*H*$_3$)$_3$), 1.29 (27H, C(C*H*$_3$)$_3$), 0.46 (6H, C(C*H*$_3$)$_2$NH$_2$). ^{13}C NMR: δ 157.01, 156.75, 145.46, 145.05, 140.15, 138.03, 128.55, 126.01, 125.00, 124.17, 123.47, 123.14, 60.92, 60.43, 52.52, 35.40, 35.14, 34.59, 34.49, 31.62, 30.35, 30.14, 25.39. *Anal.* Calc. for $C_{49}H_{76}MoN_2O_5$: C, 67.72; H, 8.81; N, 3.22. Found: C, 67.66; H, 8.48; N, 3.12%.

4.2.3. [MoO(L^{tBu})($OCH_2CH_2N(CH_3)_2$)] (**7**)

IR: 2953 s, 1460 s, 1377 s, 1306 m, 1256 vs, 1240 vs (br), 1216 m, 1178 vs, 1130 w, 1120 w, 1106 m, 1060 m, 1026 vs, 980 w, 945 vs, 925 m, 895 m, 876 m, 860 vs, 839 s, 770 m, 760 m, 694 w, 616 m, 606 m, 562 s, 490 m cm^{-1}. ^1H NMR: δ 7.36 (1H, Ar*H*), 7.28 (2H, Ar*H*), 7.05 (1H, Ar*H*), 6.98 (2H, Ar*H*), 4.48 (2H, t, $J = 5.5$ Hz, Mo–O–*CH*$_2$), 3.4–4.0 (8H, overlapping broad signals, ArC*H*$_2$–N + CH$_2$–C*H*$_2$–N), 1.74 (6H, N(*CH*$_3$)$_2$), 1.60 (9H, C(C*H*$_3$)$_3$), 1.45 (18H, C(C*H*$_3$)$_3$), 1.30 (18H, C(C*H*$_3$)$_3$), 1.26 (9H, C(C*H*$_3$)$_3$). ^{13}C NMR: δ 156.73, 145.22, 144.66, 140.02, 138.04, 129.05, 128.42, 126.18, 124.93, 124.13, 123.36, 123.09, 60.91, 60.33, 44.60, 35.38, 35.29, 35.14, 34.57, 34.47, 31.65, 31.58, 30.45, 30.32, 30.22, 30.05, 21.48. *Anal.* Calc. for $C_{49}H_{76}MoN_2O_5$: C, 67.72; H, 8.81; N, 3.22. Found: C, 67.42; H, 8.57; N, 3.43%.

4.3. Reaction of **4b** with allyl alcohol

0.30 mmol (253 mg) of **4b** was dissolved in 5 ml of allyl alcohol and solution was allowed to reflux for 6 h. Volatiles were then evaporated in vacuum and purple solid residue was purified by silica column chromatography using toluene eluent.

4.3.1. [MoO(L^{tBu})(OCH_2CHCH_2)] **8**

Yield 187 mg (74%). IR: 2956 s, 1460 s, 1365 s, 1306 m, 1255 vs, 1240 vs, 1205 m, 1168 vs, 1130 w, 1112 w, 1033 s, 1006 m, 980 w, 924 vs, 915 w, 876 m, 856 s, 840 s, 811 m, 758 m, 694 w, 603 m, 564 s, 490 m cm^{-1}. ^1H NMR: δ 7.35 (1H, *ArH*), 7.26 (2H, *ArH*), 7.04 (1H, *ArH*), 6.96 (2H, *ArH*), 5.28 (1H, m, CH$_2$–C*H*=CH$_2$), 4.78 (2H, br, O–C*H*$_2$–CH), 4.44 (1H, d, $J = 11$ Hz, CH=C*H*$_2$, cis), 3.79 (1H, d, $J = 16$ Hz, CH=C*H*$_2$, trans), 3.4–3.8 (6H, overlapping broad signals, ArC*H*$_2$–N), 1.60 (9H, C(C*H*$_3$)$_3$), 1.42 (18H, C(C*H*$_3$)$_3$), 1.29 (18H, C(C*H*$_3$)$_3$), 1.28 (9H, C(C*H*$_3$)$_3$). ^{13}C NMR ($CDCl_3$): δ 154.95, 152.59, 145.28, 144.21, 140.13, 137.50, 126.69, 125.75, 124.36, 124.18, 123.80, 115.03, 63.50, 60.92, 59.95, 42.15, 31.60, 30.95, 30.30, 29.88. *Anal.* Calc. for $C_{48}H_{71}MoNO_5$: C, 68.79; H, 8.54; N, 1.67. Found: C, 68.58; H, 8.66; N, 1.57%.

4.4. Chloride-for-alkoxide substitutions of [MoO(L^R)(Heg)]

0.25 mmol of [MoO(Heg)(L^R)] was dissolved in 10 ml of CH_2Cl_2 and treated with 0.15 ml (1.2 mmol) of Me_3SiCl. The dark violet reaction mixtures were heated to reflux temperature for 2 h while the reactions were monitored by TLC. The reaction mixtures were evaporated and blue residues were dissolved in toluene, filtered through silica and re-evaporated to obtain complexes [MoOCl(L^R)] as dark blue solids.

4.4.1. [MoOCl(L^{Me})] (**9a**)

Yield: 133 mg (95%). IR: 1236 s, 1221 s, 1159 s, 1128 m, 1072 w, 949 vs, 900 w, 858 s, 841 s, 752 m, 725 w, 694 m, 563 m cm^{-1}. ^1H NMR: δ 6.85 (2H, *ArH*), 6.78 (1H, *ArH*), 6.69 (2H, *ArH*), 6.42 (1H, *ArH*), 4.14 (1H, ArC*H*$_2$–N), 4.11 (1H, ArC*H*$_2$–N), 3.37 (2H, ArC*H*$_2$–N), 3.29 (1H, ArC*H*$_2$–N), 3.25 (1H, ArC*H*$_2$–N), 2.31 (3H, Ar-*CH*$_3$), 2.24 (12H, Ar-*CH*$_3$), 2.07 (3H, Ar-*CH*$_3$). ^{13}C NMR ($CDCl_3$): δ 158.80, 158.63, 135.16, 132.89, 131.16, 130.96, 129.26, 128.45, 127.36, 127.30, 126.91, 125.52, 62.02, 59.45, 21.11, 20.81, 16.62, 16.59. *Anal.* Calc. for $C_{27}H_{30}ClMoNO_4$: C, 57.34; H, 5.35; N, 2.48. Found: C, 57.64; H, 5.03; N, 2.68%.

4.4.2. [MoOCl(L^{tBu})] (**9b**)

Yield: 183 mg (89%). IR: 1366 m, 1262 m, 1240 vs, 1204 s, 1171 vs, 1126 w, 1070 w, 954 vs, 931 s, 914 s, 874 vs, 849 vs, 806 m, 760 m, 735 w, 694 w, 601 m, 578 m, 553 m cm^{-1}. ^1H NMR ($CDCl_3$): δ 7.30 (1H, *ArH*), 7.20 (2H, *ArH*), 7.04 (1H, *ArH*), 6.90 (2H, *ArH*), 3.94–3.45 (several broad peaks, 6H, ArC*H*$_2$–N), 1.48 (9H, C(C*H*$_3$)$_3$), 1.39 (18H, C(C*H*$_3$)$_3$), 1.21 (27H, C(C*H*$_3$)$_3$). ^{13}C NMR ($CDCl_3$): δ 158.10, 147.26, 146.50, 139.89, 139.35, 128.23, 127.50, 125.21, 124.58, 123.83, 123.62, 60.58, 35.58, 34.89, 34.86, 31.74, 30.65, 30.52. *Anal.* Calc. for $C_{45}H_{66}ClMoNO_4$: C, 66.07; H, 8.14; N, 1.71. Found: C, 65.84; H, 8.03; N, 1.68%.

4.5. Reaction of $[MoO_2Cl_2(dmf)_2]$ with aminotris(phenol)s

1.00 mmol (345 mg) of milled $[MoO_2Cl_2(dmf)_2]$ and 1.00 mmol of a ligand precursor were mixed with 30 ml of PhMe and the stirred suspension was heated to the reflux temperature for 18 h. Resulting intense blue solution was filtered through a short pad of silica and evaporated to yield complexes [MoO(L^R)Cl] as dark blue solids in 535 mg (95%) and 745 mg (91%) yields for **9a** and **9b**, respectively.

4.5.1. Alternative preparation of **9a**

0.25 mmol (241 mg) of H_4L^{Me}[MoO_2(L^{Me})] was suspended in 20 ml of toluene and subsequently treated with 1.6 mmol (0.20 ml) of Me_3SiCl. The stirred reaction mixture was heated to the reflux temperature for 2 h, cooled and then filtered through a short pad of silica and evaporated to yield 90 mg (63%) of dark solid, which had identical IR and ^1H NMR spectra as described above.

4.6. Preparation of methyl complexes

To the solution of chlorido complex **9** (0.50 mmol) in 30 ml of anhydrous toluene was added a solution of freshly prepared MeMgI (ca. 1 mmol) in diethyl ether (1 ml). The reaction mixture was stirred for an hour at room temperature while the reaction was monitored by TLC. A red product that formed was purified by a silica column chromatography using a hexane–toluene mixture (1:1) as an eluent.

4.6.1. [MoO(Me)(L^{Me})] (**10a**)

Yield: 156 mg (57%). IR: 1248 s, 1238 vs, 1221 vs, 1159 s, 1076 w, 1134 w, 951 vs, 935 m, 899 w, 858 s, 843 s, 833 s, 752 m, 727 w, 694 m, 561 m cm^{-1}. ^1H NMR ($CDCl_3$): δ 6.91 (1H, *ArH*), 6.85 (2H, *ArH*), 6.71 (1H, *ArH*), 6.64 (2H, *ArH*), 3.56–3.24 (6H, overlapping broad peaks, ArCH_2–N), 2.33 (3H, Ar-CH_3), 2.20–2.15 (15H, overlapping singlets, Ar-CH_3) 0.57 (3H). ^{13}C NMR ($CDCl_3$): δ 154.74, 132.95, 131.61, 131.25, 131.07, 129.25, 129.18, 128.62, 128.44, 128.21, 127.67, 126.13, 60.62, 60.08, 42.78, 21.00, 20.96, 16.67, 16.60. *Anal.* Calc. for $C_{28}H_{33}MoNO_4$: C, 61.63; H, 6.10; N, 2.57. Found: C, 61.53; H, 5.97; N, 2.48%.

4.6.2. [MoO(Me)(L^{tBu})] (**10b**)

Yield: 220 mg (69%). IR: 1264 m, 1240 vs, 1204 s, 1170 vs, 1125 w, 1071 w, 954 vs, 912 s, 874 s, 865s, 849 vs, 807 m, 760 m, 694 w, 601 m, 578 m, 553 m cm^{-1}. ^1H NMR ($CDCl_3$): δ 7.27 (1H, *ArH*), 7.20 (2H, *ArH*), 7.00 (1H, *ArH*), 6.89 (2H, *ArH*), 3.99–2.28 (several broad peaks, 6H, ArCH_2–N), 1.47 (9H, C(CH_3)$_3$), 1.34 (18H, C(CH_3)$_3$), 1.21 (27H, C(CH_3)$_3$). ^{13}C NMR ($CDCl_3$): δ 154.94, 144.43, 140.07, 129.26, 128.66, 128.55, 128.51, 126.13, 124.90, 123.80, 123.62, 60.68, 42.93, 35.54, 35.49, 34.78, 34.74, 32.15, 31.83, 31.75, 30.46, 30.31, 29.93, 29.89, 29.59, 22.92. *Anal.* Calc. for $C_{46}H_{69}MoNO_4$: C, 69.22; H, 8.72; N, 1.76. Found: C, 68.94; H, 8.55; N, 1.48%.

4.7. Reactions of [MoO(Me)(L^R)] with HCl

0.050 mmol of complexes **10a** (27 mg) or **10b** (40 mg) were dissolved in 3.0 ml of toluene in screw cap vials and subsequently treated with gaseous HCl (bubbled slowly through the reaction mixture for 1 min). The toluene solutions were then stored at room temperature for 2 h. The blue complexes that formed were separated by silica column chromatography using a hexane–toluene mixture (70:30) as an eluent to obtain 24 mg (85%) of **9a** and 38 mg (93%) of **9b**, respectively.

4.8. X-ray crystallography

The single crystals of complexes **4b**, **7** and **9b** were obtained from acetonitrile solutions upon slow cooling. The crystal data for the compounds are summarized in Table 1. The crystallographic data were collected at 173 K on an Enraf Nonius Kappa CCD area-detector diffractometer using graphite monochromatized Mo K_α radiation ($\lambda = 0.71073$ Å). Data collection was performed using φ and ω scans and the data processed using *DENZO-SMN v0.93.0* [20]. SADABS[21] absorption correction was applied to the data of all compounds. The structures were solved by direct methods using the SHELXS-97 program [22] and full-matrix least-squares refinements on F^2 were performed using the SHELXL-97 program [22]. Compound **9b** crystallized in a chiral space group ($P2_12_12_1$ (19)), so it could be resolved as a racemic twin or as a disordered structure having two orientations of the ligand. The absolute structure given by the structural refinement seems to be correct as suggested by the Flack parameter of 0.03 (7) [23]. The structure of **9b** was finally refined using a split-atom model. For compounds **4b** and **7** the heavy atoms were refined anisotropically and for **9b** the heavy atoms were refined anisotropically and isotropically due to the disorder. The CH hydrogen atoms were included at fixed distances using fixed displacement parameters from their host atoms whilst other H atoms were refined using fixed displacement parameters. Structure figures were drawn using *Ortep-3* for *Windows* [24].

Appendix A. Supplementary material

CCDC 651324, 651325 and 632882 contain the supplementary crystallographic data for **4b**, **7** and **9b**. The data can be obtained free of charge via http://www.ccdc.cam.ac.uk/conts/retrieving.html, or from the Cambridge Crystallographic Data Centre, 12 Union Road, Cambridge CB2 1EZ, UK; fax: (+44) 1223-336-033; or e-mail: deposit@ccdc.cam.ac.uk. Supplementary data associated with this article can be found, in the online version, at doi:10.1016/j.poly.2007.07.036.

References

[1] R. Hille, Chem. Rev. 96 (1996) 2757.
[2] J.H. Enemark, J.J.A. Cooney, J.-J. Wang, R.H. Holm, Chem. Rev. 104 (2004) 1175.
[3] F.R. Fronczek, R.L. Luck, G. Wang, Inorg. Chem. Commun. 5 (2002) 384.
[4] R.R. Schrock, J. Mol. Catal. A: Chem. 213 (2004) 21.
[5] K. Most, J. Hoßbach, D. Vidovic, J. Magull, N.C. Mösch-Zanetti, Adv. Synth. Catal. 347 (2005) 463.
[6] See: I. Siewert, C. Limberg, B. Ziemer, Z. Anorg. Allg. Chem. 632 (2006) 1078, and references therein.
[7] L. Michalcczyk, S. de Gala, J.W. Bruno, Organometallics 20 (2001) 5547.
[8] Y. Kim, G.K. Jnaneshwara, J.G. Verkade, Inorg. Chem. 42 (2003) 1437.
[9] S. Groysman, S. Segal, I. Goldberg, M. Kol, Z. Goldschmidt, Inorg. Chem. Commun. 7 (2004) 938.
[10] (a) A. Lehtonen, R. Sillanpää, Organometallics 24 (2005) 2795; (b) A. Lehtonen, V.G. Kessler, Inorg. Chem. Commun. 7 (2004) 691.
[11] N.Ya. Turova, E.P. Turevskaya, V.G. Kessler, M.I. Yanovskaya, The Chemistry of Metal Alkoxides, Kluwer Academic Publishers, London, 2002, p. 26.

[12] F.A. Schröder, J. Scherle, Z. Naturfor. 28b (1973) 46.
[13] (a) T.A. Hanna, C.D. Incarvito, A.L. Rheingold, Inorg. Chem. 39 (2000) 630;
(b) T.A. Hanna, A.K. Ghosh, C. Ibarra, M.A. Mendez-Rojas, A.L. Rheingold, W.H. Watson, Inorg. Chem. 43 (2004) 1511;
(c) T.A. Hanna, A.K. Ghosh, C. Ibarra, L. Zakharov, A.L. Rheingold, W.H. Watson, Inorg. Chem. 43 (2004) 7567;
(d) L. Liu, L.N. Zakharov, J.A. Golen, A.L. Rheingold, W.H. Watson, T.A. Hanna, Inorg. Chem. 45 (2006) 4247.
[14] M.H. Chisholm, I.P. Rothwell, in: G. Wilkinson, R.D. Gillard, J.A. McCleverty (Eds.), Comprehensive Coordination Chemistry, vol. 2, Pergamon, New York, 1987, p. 335.
[15] A. Lehtonen, R. Sillanpää, Eur. J. Inorg. Chem. (2006) 2878.
[16] L. Lubin, G. Lanza, I.L. Fragalà, C.L. Stern, T.J. Marks, J. Am. Chem. Soc. 120 (1998) 3111.
[17] W.-S. Jung, H.-Y. Moon, Y.-Y. Park, Polyhedron 16 (1997) 2169.
[18] F.J. Arnaiz, R. Aguado, J. Sanz-Aparicio, M. Marinez-Ripoli, Polyhedron 13 (1994) 2745.
[19] M. Kol, M. Shamis, I. Goldberg, Z. Goldschmidt, S. Alfi, E. Hayut-Salant, Inorg. Chem. Commun. 4 (2001) 177.
[20] Z. Otwinowski, W. Minor, Methods Enzymol. 276 (1997) 307.
[21] G.M. Sheldrick, SADABS, University of Göttingen, Germany, 2002.
[22] G.M. Sheldrick, SHELXS-97 and SHELXL-97. Programs for Crystal Structure Refinement, University of Göttingen, Germany, 1997.
[23] H.D. Flack, Acta Cryst. A39 (1983) 876.
[24] L.J. Farrugia, J. Appl. Crystallogr. 32 (1999) 837.

thiohydroxamic acids are unsymmetrical bidentate ligands, *cis* (C_{2v}) and *trans* (C_{2h}) geometrical isomers are possible for square planar bis complexes [6]. Coloured complexes of thiohydroxamic acids have found application in analytical chemistry for spectrophotometric and gravimetric determination of metals [7]. *N*-Hydroxypyridine-2-thione complexes with Mn(II), Ni(II), Fe(III) and Co(III) can be used for simulation of the action of cysteinyl metalloenzymes [8], while the vanadyl VO^{2+} complexes can act as effective insulin enhancing agents [9], *N*-methylthiobenzohydroxamic acid complexes with dioxomolybdenum(VI) can be used for investigations of active redox enzymes such as xanthine oxidase and sulfide oxidase [10]. Ferric and lead complexes have been used in chelation therapy of iron overload [11] and lead poisoning [12] in humans and animals.

Several voltammetric studies of thiohydroxamic acid complexes have been described. As shown by the X-ray method in a series of mononuclear Co(II) complexes with phosphine or pyridine, the cobalt ion is in a square pyramidal environment with *trans*-oriented *N*-hydroxypyridine-2-thione ligands in the basal plane position [7]. *N*-Hydroxypyridine-2-thione complexes ML_2 and ML_3 [M = Mn(II), Ni(II), Fe(III), Co(III)] have been of interest for the simulation of cysteinyl metalloenzymes. Therefore, Co(II) complexes were investigated by cyclic voltammetry [7], showing two reversible processes following a one-electron change. The complex of Ni(II), which is unstable in air, has the nickel atom in the centre of a S_2O_2 square plane, with the two organic ligands in the *cis* configuration [7].

In this paper, we limit ourselves to bis complexes of *N*-methyl-*N*-thioformylohydroxylamine (*N*-methylthioformohydroxamic acid), customarily called thioformin. This is a bioligand that plays an important role in Fe(III) ion transport through cell membranes to cells of algae, fungi and bacteria. This function is usually carried out by hydroxamic acids, and thioformin appears to be the only thiohydroxamic acid siderophore discovered to date. *Pseudomonas fluorescens* produces two antibiotics, fluopsin C and fluopsin F, which are complexes of Cu(II) and Fe(III), respectively. These exhibit high biological activity in relation to both Gram-positive and Gram-negative bacteria. Thioformin probably acts as a siderophore, but one can presume that it transports copper ions to the cell. The kinetic lability of bis(*N*-methylthioformohydroxamato) Cu(II) and Fe(III) complexes (fluopsin C and F) precludes the isolation of *cis* and *trans* geometrical coordination isomers. As a first step in probing the mechanism of the antibiotic action of thioformin metal complexes, we began this investigation of their coordination chemistry. We have investigated the properties of the square planar complexes of *N*-methylthioformohydroxamic acid with some divalent metals. These labile complexes of thioformin display antibiotic activity against *Escherichia coli* NIHJ [13,14].

The antibiotic YC73 was found to be the cupric complex of thioformin [15], and this was named fluopsin C. Egawa et al. [14] and Shirahata et al. [16] synthesized a number of other analogues, including ones whose properties have been studied here. Fluopsin CA, N and Z are, respectively, the Ca(II), Ni(II) and Zn(II) bis complexes of thioformin. Fluopsin C, the corresponding Cu(II) complex, is also known as antibiotic YC73, or antibiotic B_1. It displays a broad-spectrum of antibiotic activity against both Gram-positive and Gram-negative bacteria and fungi [17]. This naturally occurring antibiotic has been isolated from the culture supernatant fluids of *Pseudomonas* [15,18,19] and *Streptomyces* species [20]. Table 1 summarizes the observed antimicrobial activities of the fluopsins.

In studies on metal-containing biomolecules, metal-ion selectivity, *i.e.*, the varying affinity of a ligand for different metal ions, plays a significant role. This property is often difficult to evaluate, as it is governed by subtle variations in electronic structures that modify the dominant electrostatic interactions between the ligand and the metal [2]. In this paper, we aim to use DFT to calculate the affinity of thioformin in square planar complexes for selected divalent metal ions, chosen for their importance in bio-inorganic chemistry as their metalloprotein complexes are among the most abundant.

2. Computational details

The DFT UB3LYP/6-31G(d) approach [21–23] was used for the calculations reported in this chapter. Since some of the complexes represent open shell systems (Ni(II) and Cu(II) complexes), we performed unrestricted calculations on all complexes. The geometries of all complexes were fully optimized, followed by harmonic vibrational frequency calculations. The calculated vibrational frequencies were used to confirm the nature of all stationary point structures and to account for the zero-point vibrational energy contribution, which was scaled [24] by a factor of 0.9806, and the vibrational frequencies were scaled by a factor of 0.9614. All calculations were performed with the GAUSSIAN 03W suite [25] of programs.

3. Results and discussion

3.1. Relative energies

Ca(II) is a closed-shell system (^1S), as is Zn(II), which is a d^{10} ion. For Cu(II), too, the situation is straightforward as it is a d^9 ion with a doublet ground state (^2D) in its complexes. Ni(II) (d^8) complexes, however, may exist in either the high-spin triplet or low-spin singlet states. The latter, being closed-shell, are expected to be more stable due to electron-pairing, as well as the fact that the high energy $d_{x^2-y^2}$ orbital is avoided. We investigated both multiplicities for the Ni^{2+} ion complexes, and found this to be true. Thus, the ground state is consistent with the high energy $d_{x^2-y^2}$ orbital being unoccupied for the d^8 Ni(II) complexes.

Table 2 gives the complexation energies for the *N*-methylthioformohydroxamate complexes of the four metal ions,

Table 1
Some properties of the fluopsins

Fluopsin	Crystal shape	Melting point (°C)	Antimicrobial activity		Reference
			Organism	MIC	
CA	Colourless needles	>250	*Staphylococcus aureus* FDA 209P	0.39 μg/ml	[14]
			Bacillus subtilis PCI-219	0.78 μg/ml	
N	Dark red needles	~228	*Staphylococcus aureus* FDA 209P	0.39 μg/ml	[14]
			Bacillus subtilis PCI-219	0.39 μg/ml	
C	Dark brown crystals	>182 (decomp.)	*Staphylococcus aureus* FDA 209P	0.50 M	[13]
			Escherichia coli NIHJ	5.00 M	
Z	Colourless prisms	~222 (decomp.)	*Staphylococcus aureus* FDA 209P	0.78 μg/ml	[14]
			Bacillus subtilis	1.56 μg/ml	

Table 2
Complexation energies. ΔE (kcal/mol), for the *N*-methylthioformohydroxamate bis complexes of some metal ions

Metal ion	Complex	Energy
Ca(II)	Fluopsin CA	−511.2
Ni(II) *cis*	Fluopsin N	−752.6
Ni(II) *trans*	Fluopsin N	−752.8
Cu(II) *cis*	Fluopsin C	−705.6
Cu(II) *trans*	Fluopsin C	−705.3
Zn(II)	Fluopsin Z	−684.2

Ca(II), Ni(II), Cu(II) and Zn(II), calculated from the expression

$$\Delta E = E_{\text{complex}} - E_{M^{2+}} - 2E_{\text{thioformohydroxamate}}$$

where E_{complex} is the computed energy of the complex, $E_{M^{2+}}$ is that of the metal ion and $E_{\text{thioformohydroxamate}}$ is that of the *N*-methylthioformohydroxamate anion (−606.8199802 a.u.). The computed metal ion energies are −676.866860724, −1506.99964648, −1639.2130838 and −1778.10700677 a.u., respectively, for Ca^{2+}, Ni^{2+}, Cu^{2+} and Zn^{2+}.

A large variation in complexation energies is apparent from the table. These are all negative, implying that the complexation reactions are highly exothermic. The complexation energies depend only on the metal ion and are relatively insensitive to the coordination geometry (*cis* or *trans*). The Ni(II) complexes are thermodynamically the most stable, followed by Cu(II) and Zn(II). The high-spin triplet Ni(II) complex has a much smaller value of the complexation energy (−106.8 kcal/mol) and is, therefore, much less stable. The rest of the discussion is therefore limited to the square planar low-spin complexes of Ni(II).

3.2. Structures of the complexes

Four-coordinate complexes may have either a tetrahedral or square planar coordination geometry. In protein crystal structures, zinc is tetrahedral, while Cu^{2+} bound to proteins is typically in a distorted 4-coordinate geometry, intermediate between tetrahedral and square planar [26]. As stated previously, low-spin divalent complexes of Ni(II) are also square planar. For the complexes investigated here, it was found that zinc is the only metal ion that forms a perfect tetrahedron, while the nickel complex has a square planar coordination about the metal ion. The calcium complex is a distorted tetrahedron, and the copper complexes are distorted square planar (Fig. 1).

The thiohydroxamate functional group bond lengths in the bound ligand are changed noticeably (Table 3). In the Ni(II) and Cu(II) *trans* thioformin complexes, for example, the C–N bond (−0.022 Å) is shortened and the N–O bond correspondingly lengthened (+0.037 Å), due to delocalization. However, in contrast to hydroxamates [2], in which the C=O bond is considerably lengthened (+0.025 Å), no such change is observed for the thiocarbonyl bond (−0.003 Å).

The metal–ligand bonds are relatively short (Table 4). These short bonds are presumably due to ionic contributions to the bonds. The oxygen, which is deprotonated to form the anion, carries a negative charge, −0.531. In contrast to hydroxamate systems, where both the hydroxyl oxygen and carbonyl oxygen carry large negative charges, the negative charge on sulfur is much smaller (−0.069). The optimized metal–oxygen and metal–sulfur bond lengths for the various metals are given in Table 4, along with the covalent bond orders. The latter are rather small, particularly the metal–oxygen bond orders. Thus, in the thiohydroxamate complexes, the metal–oxygen bonds are largely ionic, while the metal–sulfur bonds are largely covalent. However, the latter bonding is quite weak, while the former is stronger than in hydroxamate complexes because of the higher negative charge on oxygen.

Fig. 1 and Table 4 show that the Cu–S bond in the *trans* complex is 2.323 Å, which is much larger than the Cu–S bond distance (2.304 Å) in the *cis* complex. The metal–sulfur bond order is also much smaller in the latter. From their studies on the relationship between complex labilities and antibiotic action, Bell et al. [13] had concluded that the greater the lability, more potent is the complex. In view of this, we propose that the *trans* isomer is the more active form.

The small covalent contribution to the metal ligand bonds is apparent from the calculated covalent bond orders of 0.23 and 0.29, respectively, for Cu–O and Cu–S in the *trans* complex. The calculated metal–ligand bond orders are smaller than those calculated for Cu–O in hydroxamate

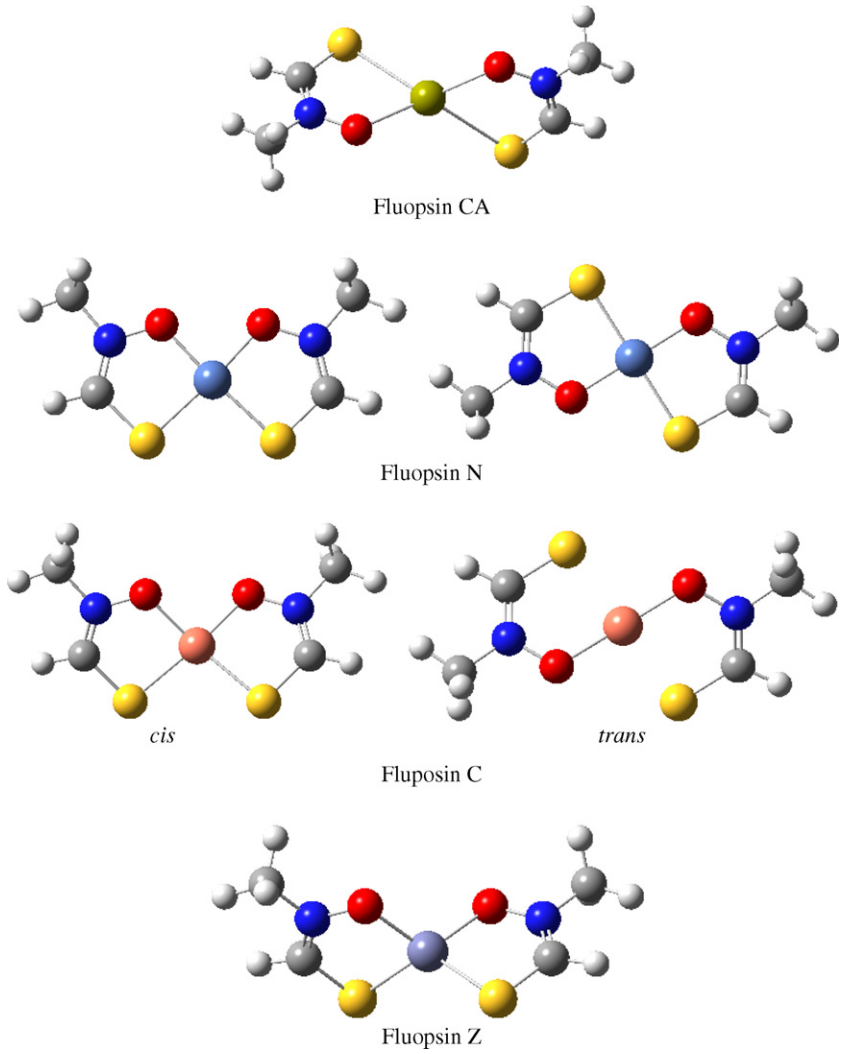


Fig. 1. Structures of Fluopsins-CA = Calcium, N = Nickel, C = Copper, Z = Zinc (Colour code: Sulfur – yellow, oxygen – red, nitrogen – blue, carbon – grey, and hydrogen – white).

Table 3
Optimized C–S, C–N and N–O bond lengths (Å) for the thioformin complexes of the metal ions

Metal (M)	C–S	C–N	N–O
Thioformin	1.706	1.333	1.304
Ca(II)	1.710	1.316	1.331
Ni(II) *cis*	1.704	1.313	1.337
Ni(II) *trans*	1.703	1.311	1.341
Cu(II) *cis*	1.709	1.316	1.330
Cu(II) *trans*	1.703	1.311	1.341
Zn(II)	1.708	1.313	1.337

Table 4
Optimized metal–ligand bond lengths (Å) and Wiberg bond orders for the thioformin complexes of the metal ions

Metal (M)	M–O		M–S	
	Length	Order	Length	Order
Ca(II)	2.277	0.092	2.842	0.132
Ni(II) *cis*	1.846	0.334	2.202	0.489
Ni(II) *trans*	1.831	0.359	2.213	0.452
Cu(II) *cis*	1.906	0.212	2.304	0.310
Cu(II) *trans*	1.894	0.228	2.323	0.285
Zn(II)	1.955	0.181	2.361	0.282

complexes, implying less charge transfer and covalency in the thiohydroxamate complexes [2].

3.3. Complexation energies

The sequence of stability constants for the complexes of various metal ions with thiohydroxamates is expected to depend on the ionic radii and electronegativities of the respective metal ions. The metal–ligand stability constants increase, in general, with increasing ionic potential (charge/radius) of the metals, since all the metal ions are bivalent. A plot of complexation energies in kcal/mol versus reciprocal of the ionic radius in Å [27] is expected to be linear for thioformin complexes. The data was fit to the empirical equation

$$E_{\text{complexation}} = A/r + B \quad (1)$$

and this yielded the regression coefficients $A = -998.4 \pm 22.5$ kcal Å/mol, $B = 447.3 \pm 25.6$ kcal/mol, and a correlation coefficient equal to -0.999. The correlation is much better than that found for formohydroxamic acid complexes [2], indicating a larger ionic component in the thiohydroxamate complexes. Table 5 indicates a good fit considering that the ionic radii pertain to high-spin octahedral complexes, while the complexation energies are for square planar/tetrahedral low-spin complexes. The standard error of the complexation energy estimate is 4.5 kcal/mol.

The complexation energies of the metal ion complexes, calculated in this work, follow the order:

$$\mathrm{Ca(II)} < \mathrm{Zn(II)} < \mathrm{Cu(II)} < \mathrm{Ni(II)}$$

This is in accord with the Irving–Williams order [28], with the exception of Ni(II), which is found to precede Cu(II). It may be noted that the Ni(II) complex is square planar, while the Cu(II) complex is tetrahedrally distorted.

3.4. Charge population analysis

Table 6 presents the partial atomic charges on the metals in the thioformin complexes, along with the electron configuration about the metal ion. The d electron population for all the complexes is consistent with the +2.0 oxidation of the metal ions. It is seen that the positive charge of the metal ion decreases in the complexes coordinating with the *N*-methylthioformohydroxamate ion, which indicates that electron transfer from the ligands to the metal ion occurs and coordination bonds form. This charge transfer is least for the closed-shell metal ion, Ca(II), but for metals containing partially filled d orbitals, particularly the d^8 system, Ni(II), in which 1.6 e electrons get transferred from the ligand to the metal ion, the charge transfer is much larger, indicating the strong covalent character of the complexes. Of the 1.6 e that get transferred in the Ni(II) complexes, only 0.4 e are accepted by the d orbitals (Table 6). Even for Zn(II), almost 1.3 e get transferred from the ligand. The thiohydroxamate ligand has both hard (oxygen) and soft (sulfur) donor atoms. While the hard oxide ion, having a negative charge, is able to form ionic bonds, the soft sulfur can facilitate complex formation through covalent bonding.

To see how the charge transfer occurs, we calculated the partial atomic charges on the ligand, *i.e.*, for the *N*-methylthioformohydroxamate anion, and the values are given in Table 7, along with those in the Cu(II) *trans* complex, which has a high magnitude of the complexation energy and in which there is substantial charge transfer. It can be seen that the atomic charge of the coordinated sulfur atom decreases on complexation. The two sulfur atoms transfer a total of 0.77 e to the metal ion, while the oxygens donate 0.12 e. However, the charge on Cu^{2+} (Table 6) demonstrates that 1.37 e transfer from the ligand to Cu(II) in the complex, suggesting that the electrons move from other parts of the ligand to the coordinated sulfur atoms, from where they are transferred to Cu(II). Surprisingly, the methyl group also has a large role to play in the charge transfer. Each donates 0.36 e to the metal ion.

Likewise, there is relocation of electron density on the nitrogen. Instead of gaining electron density in the anion, the nitrogen acquires a small positive charge. For the Cu(II) aminophenylhydroxamic acid complexes, this was traced to hyperconjugative interactions, as a result of which the nitrogen lone pair puts electron density into the carbonyl π^* orbital, weakening the carbonyl bond prior to complex formation [1]. Here too a similar situation prevails, the nitrogen lone pair donating electron density to the C=S π^* orbital. This is borne out by the calculated total Wiberg index [29] on the nitrogen in the anion (3.71), which is greater than its valency (three), while the C=S bond order is only 1.33 in the anion. The calculated bond order of the nitrogen with the sulfur is 0.18, again showing an interaction between the two in the *N*-methylthioformohydroxamate anion. Because of this, the nitrogen has a small positive charge in the anion and the complex.

The formation of the complex is therefore accompanied by a considerable decrease in the electron density at the

Table 5
Ionic radii (r) in Å and differences in complexation energies (kcal/mol) from those computed in Eq. (1) for the thioformin complexes

Metal ion	r (Å)[a]	ΔE[b]
Ca(II)	1.04	−1.5
Ni(II) *trans*	0.83	−2.8
Cu(II) *trans*	0.87	5.0
Zn(II)	0.88	−3.0

[a] From [19].
[b] $\Delta E = E$ (from Eq. (1)) − $E_{\mathrm{complexation}}$.

Table 6
The calculated Mulliken metal ion partial atomic charges in the various complexes

Metal (M)	q_M	d orbital population
Ca(II)	1.138	0.03
Ni(II) *cis*	0.435	8.40
Ni(II) *trans*	0.464	8.40
Cu(II) *cis*	0.605	9.20
Cu(II) *trans*	0.629	9.20
Zn(II)	0.728	9.93

Table 7
The calculated ligand atom partial charges in the free state, anion and in the various complexes

Atom	Acid	Anion	Ca(II)	Ni(II)		Cu(II)		Zn(II)
				cis	*trans*	*cis*	*trans*	
O	−0.499	−0.604	−0.618	−0.515	−0.531	−0.539	−0.542	−0.558
N	−0.040	0.073	0.056	0.053	0.052	0.059	0.052	0.055
C	−0.077	−0.090	−0.086	−0.117	−0.121	−0.109	−0.111	−0.106
S	−0.246	−0.534	−0.332	−0.076	−0.069	−0.146	−0.147	−0.188
CH_3	0.262	0.071	0.215	0.254	0.254	0.249	0.252	0.250
H_1(C)	0.179	0.080	0.175	0.184	0.183	0.181	0.182	0.183
H_2(O)	0.419							

carbon of the thiocarbonyl bond and the methyl group. This implies the important role of the substituent at the nitrogen in the complex formation. Recognizing this, several workers have essayed the role of the substituent at nitrogen in antibiotic action [13,14,17–20,30].

We compared the Wiberg bond orders for bonds between the ligand atoms for thioformin, its anion and in the complexes, and the results are given in Table 8. It can be seen that the O–N bond acquires double bond character on removal of the acidic proton. In the complex, the O–N bond reverts to a single bond, but the C–N bond becomes stronger. It is this π bond that is involved in the charge transfer to the metal ion, along with the oxygen and sulfur atoms.

3.5. Bonding in the complexes

As mentioned above, four coordinate ligand bonding could either be tetrahedral or square planar. We have observed that for the majority of systems, except the d^8 system (Ni(II)), where the complexes are square planar, the metal ions are tetrahedrally coordinated. In a square planar D_{4h} field, the 3d orbitals of the metal are split into four levels, which are, in order of increasing energy, $\{d_{xz}, d_{yz}\}$ $(e_g) < d_{z2}$ $(a_{1g}) < d_{xy}$ $(b_{2g}) < d_{x^2-y^2}$ (b_{1g}). The important feature of the splitting is that the $d_{x^2-y^2}$ orbital goes to a very high energy, as it is in the crowded *xy*-plane, resulting in electronic repulsion with the ligands. Therefore, the most favourable configuration for forming square planar complexes is low spin d^8 (Ni^{2+}). The d^9 case is not so favourable. According to the Valence Bond theory, the vacant $d_{x^2-y^2}$ orbital can form hybrid orbitals with 4s (a_{1g}) and two 4p orbitals $\{p_x, p_y\}$ (e_u), giving dsp^2 hybrid orbitals. These vacant orbitals can accommodate electrons from the ligand.

The electron configuration of the Zn(II) ion is $3d^{10}$. It coordinates with ligands using the 4s and 4p orbitals in sp^3 hybrid orbitals. According to the Valence Shell Electron Pair Repulsion (VSEPR) theory, tetrahedral configurations are favoured for Zn(II) four-coordination complexes, as in $[ZnCl_4]^{2-}$. In this hybridization scheme, the relatively low energy $3d_{x^2-y^2}$ orbital is replaced by a higher energy $4p_z$ orbital, and hence charge transfer from the low-lying ligand orbitals is not so facile. It is therefore not surprising that the Zn(II) thiohydroxamate complexes adopt a tetrahedral geometry. These expectations are borne out by the calculated d electron configurations about the metal ions (Table 6).

To test the hypothesis that charge transfer from the ligand to the metal ions is responsible for the stability of the complexes, we correlated the calculated complexation energies with the partial charge on the metal atom, and found a good correlation between the two. It is found that the complexation energy (kcal/mol) is related to the partial charge on the metal atom by an empirical relation,

$$E_{\text{complexation}} = Aq_{\text{M}} - B \tag{2}$$

where $A = 348.0 \pm 23.9$ kcal/mol, $B = -917.2 \pm 16.9$ kcal/mol and the correlation coefficient is −0.991 (4 degrees of freedom). The standard error of the complexation energy estimate is 13.7 kcal/mol. The positive sign of the slope indicates that as the positive charge on the metal atom increases (signifying less charge transfer from the ligand), the complexation energy becomes less negative. This is in line with expectations, since the smaller the charge transfer, the less the covalent character of the complexes. If instead of the partial charge on the metal ion, the d orbital population is taken for the correlation, the regression coefficient drops to −0.892 and the standard error of the estimate increases to 45.2 kcal/mol.

We also examined the ligand orbitals in the acid form, anion and complex. Fig. 2a gives a plot of the Highest Occupied Molecular Orbital (HOMO) of the *N*-methylthioformohydroxamate anion. This orbital has an energy of −0.224 eV. It is clear that there is charge density at the oxygen, sulfur and in the C–N bonding orbital, and this can be donated to the vacant metal orbitals.

It can be seen from the plots of the HOMOs that the ligand orbitals are retained in the HOMOs of the complexes, but the metal d orbital also becomes a part of the HOMO for the square planar Ni(II) complex, showing an interaction between the Ni(II) d orbitals and the ligand.

3.6. Vibrational spectra

The calculated vibrational spectra of the complexes are remarkably similar, and these are given as Supplementary material. The most intense band is the C–N stretching band at ~1550 cm^{-1}. This band is shifted to a slightly higher wavenumber for the square planar nickel(II) complexes. All the complexes exhibit similar spectra, *i.e.*, the number of dominating bands in the 800–1600 cm^{-1} region. Another prominent band, not reported experimentally, is a band in the 600–700 cm^{-1} region, depending on the structure of the complex (tetrahedral or *cis* or *trans* square planar), and the nature of the metal ion, and this corresponds to the O–M–O antisymmetric stretch. The C–S symmetric stretching band has a small intensity and is dwarfed by the nearby intense N–O stretching band.

In Table 9, we compare the experimental vibrational frequencies with our calculated values, and good agreement

Table 8
The calculated Wiberg bond orders in the free state, anion and in the complexes

Bond	Acid	Anion	Metal ion (M)					
			Ca	Ni		Cu		Zn(II)
				cis	*trans*	*cis*	*trans*	
O–N	1.008	1.188	1.102	1.078	1.065	1.089	1.080	1.091
C–N	1.347	1.366	1.441	1.438	1.433	1.443	1.437	1.445
C–S	1.530	1.333	1.331	1.286	1.305	1.307	1.323	1.320
N–CH_3	0.958	0.951	0.942	0.943	0.944	0.943	0.943	0.942
C–H	0.880	0.912	0.896	0.896	0.895	0.895	0.912	0.894
O–H	0.651							

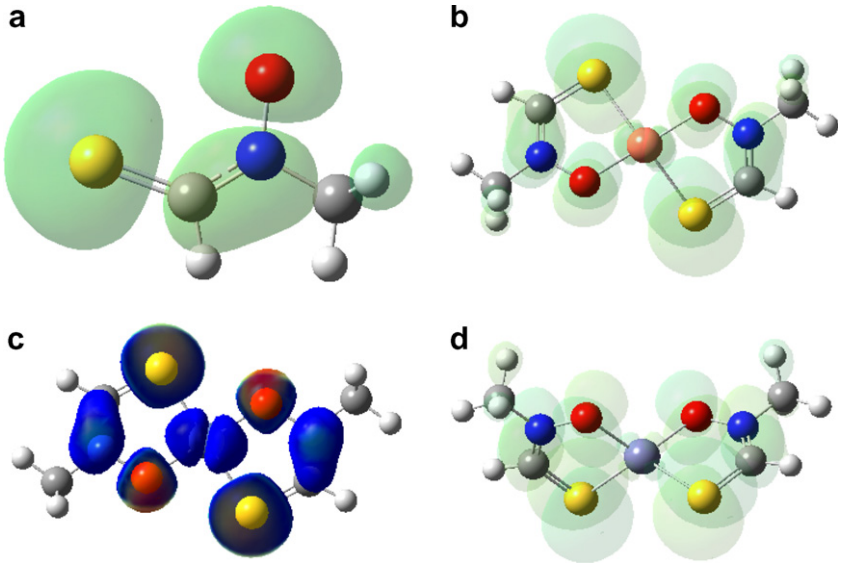


Fig. 2. Plot of the HOMOs for (a) the thioformohydroxamate anion, and the thioformin complexes of (b) Cu (II), (c) Ni(II) and (d) Zn(II) (see caption of Fig. 1 for colour codes).

Table 9
Calculated and experimental vibrational frequencies (cm^{-1})

Assignment	Fluopsin CA		Fluopsin N			Fluopsin C			Fluopsin Z	
	Calculated	Experimental[a]	*cis*	*trans*	Experimental[a]	*cis*	*trans*	Experimental[b]	Calculated	Experimental[b]
C–N str.	1555	1553	1587	1582	1590	1568	1566	1580	1560	1563
N–CH_3 str.	1154	1157	1147	1141	1153	1148	1145	1152	1149	1145
O–N str.	922	933	900	899	910	912	908	908	913	920
C–S str.	870	895	881	883	887	880	880	888	873	888

[a] From [14].
[b] From [16].

can be seen. The assignment has been made by an analysis of the normal modes. Since the complexes have 51 vibrational degrees of freedom, only the prominent bands, for which experimental data are available, are given in Table 9. The complete set of vibrational frequencies is given as Supplementary material. The C–H band is also not very intense and occurs around 3050 cm^{-1}.

4. Conclusions

In this work, we have reported calculations on *N*-methylthioformohydroxamate complexes of different metal ions. Good correlations between the calculated complexation energies and various parameters, like the reciprocal of the metal ion radius, have been obtained. We have found that the order of stabilities of various complexes is determined almost purely by the ratio of the ionic radius and transition metal ion charge (ionic contribution) and that the covalent contribution to the coordination bond (characterized by a charge transfer between the ligand and transition metal ion) does not play a significant role in determining the thermodynamic stability of the complex. This is also reflected in the calculated M–O bond orders that are quite small, in contrast to hydroxamate complexes [2], in which the covalent character is significant.

The prominent bands in the infrared spectra correspond to the C–N, N–CH_3, O–N and C–S symmetric stretching vibrations. Good agreement between the calculated and the experimental values is observed. Another prominent band in the 600–700 cm^{-1} region, corresponding to the O–M–O antisymmetric stretch, is predicted. The C–H stretching band occurs at ~3050 cm^{-1} and is not very intense.

The copper(II) and nickel(II) complexes of thioformin are almost equally potent against *S. aureus* 209P, but the Zn(II) has almost double the activity of these complexes. These complexes exhibit substitutional lability with a timescale of 6–8 h [31]. The M–O and M–S bond orders are much smaller than those calculated for the hydroxamate analogues. The metal–sulfur bond orders are smallest for the tetrahedral Ca(II) and Zn(II) complexes, and these are hence more kinetically labile. These complexes are also thermodynamically the least stable. Bell et al. [13] demonstrated that the kinetically inert Pt(II) complexes exhibit no antibiotic activity. They also showed that the observed order of potency of trivalent complexes against *S. aureus*

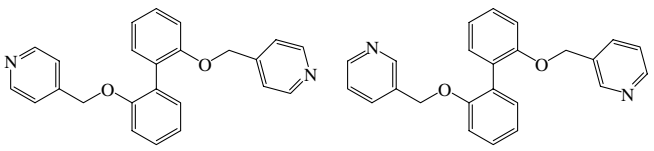
209P is also in accord with the observed order of kinetic lability [31]. They therefore concluded that kinetic lability is an important factor in determining the antimicrobial activity of a complex. It is gratifying to note that the kinetic lability, as determined by the metal–sulfur bond orders, can be correlated to the observed antimicrobial activity. However, the investigated systems are too few in number for a definite quantitative correlation to be made, so in future work, we shall report a detailed study of more such systems.

Appendix A. Supplementary material

Supplementary data associated with this article can be found, in the online version, at doi:10.1016/j.poly.2007.07.049.

References

[1] R. Kakkar, R. Grover, P. Gahlot, Polyhedron 25 (2006) 759.
[2] R. Kakkar, R. Grover, P. Gahlot, J. Mol. Struct.: THEOCHEM 767 (2006) 175.
[3] W. Walter, E. Schaumann, Synthesis 3 (1971) 111, and references cited therein.
[4] S. Mizukami, K. Nagata, Coord. Chem. Rev. 3 (1968) 267.
[5] A. Chimiak, W. Przychodzen, J. Rachon, Heteroatom Chem. 13 (2002) 169.
[6] R. Kakkar, R. Sharma, A. Dua, Spectrochim. Acta A 62 (2005) 819.
[7] B.S. Kang, Y.J. Xu, J.H. Peng, D.X. Wu, X.T. Chen, Y.H. Hu, M.C. Hong, J.X. Lu, Polyhedron 12 (1993) 871.
[8] X. Chen, Y. Hu, D. Wu, L. Weng, B. Kang, Polyhedron 10 (1991) 2651.
[9] H. Sakurai, H. Sano, T. Takino, H. Yasui, Chem. Lett. 28 (1999) 913.
[10] C.A. Cliff, G.D. Fallon, B.M. Gatehouse, K.S. Murray, P.J. Newman, Inorg. Chem. 19 (1980) 773.
[11] K. Abu-Dari, K.N. Raymond, Inorg. Chem. 30 (1991) 519.
[12] K. Abu-Dari, F.E. Hahn, K.N. Raymond, J. Am. Chem. Soc. 112 (1990) 1519.
[13] S.J. Bell, S.A. Friedman, J. Leong, Antimicrob. Agents Chemother. 15 (1979) 384.
[14] Y. Egawa, K. Umino, Y. Ito, T. Okuda, J. Antibiot. 24 (1971) 124.
[15] Y. Egawa, K. Umino, S. Awataguchi, Y. Kawano, T. Okuda, J. Antibiot. 23 (1970) 267.
[16] K. Shirahata, T. Hayashi, I. Matsubara, J. Antibiot. 24 (1971) 140.
[17] S. Itoh, K. Inuzuka, T. Suzuki, J. Antibiot. 23 (1970) 542.
[18] E. Martinez-Molina, L.A. Del Rio, J. Olivares, J. Appl. Bacteriol. 41 (1976) 69.
[19] K. Shirahata, T. Deguchi, T. Hayashi, I. Matsubara, T. Suzuki, J. Antibiot. 23 (1970) 546.
[20] S. Miyamura Japan Patent 87087; Chem. Abstr. 2 (1973) p. 189.
[21] A.D. Becke, Phys. Rev. A 38 (1988) 3098.
[22] C. Lee, W. Yang, R.G. Parr, Phys. Rev. B 37 (1988) 785.
[23] S.H. Vosko, L. Wilk, M. Nusair, Can. J. Phys. 58 (1980) 1200.
[24] A.P. Scott, L. Radom, J. Phys. Chem. 100 (1996) 16502.
[25] M.J. Frisch, G.W. Trucks, H.B. Schlegel, G.E. Scuseria, M.A. Robb, J.R. Cheeseman, J.A. Montgomery, Jr., T. Vreven, K.N. Kudin, J.C. Burant, J.M. Millam, S.S. Iyengar, J. Tomasi, V. Barone, B. Mennucci, M. Cossi, G. Scalmani, N. Rega, G.A. Petersson, H. Nakatsuji, M. Hada, M. Ehara, K. Toyota, R. Fukuda, J. Hasegawa, M. Ishida, T. Nakajima, Y. Honda, O. Kitao, H. Nakai, M. Klene, X. Li, J.E. Knox, H.P. Hratchian, J.B. Cross, C. Adamo, J. Jaramillo, R. Gomperts, R.E. Stratmann, O. Yazyev, A.J. Austin, R. Cammi, C. Pomelli, J.W. Ochterski, P.Y. Ayala, K. Morokuma, G.A. Voth, P. Salvador, J.J. Dannenberg, V.G. Zakrzewski, S. Dapprich, A.D. Daniels, M.C. Strain, O. Farkas, D.K. Malick, A.D Rabuck, K. Raghavachari, J.B. Foresman, J.V. Ortiz, Q. Cui, A.G. Baboul, S. Clifford, J. Cioslowski, B.B. Stefanov, G. Liu, A. Liashenko, P. Piskorz, I. Komaromi, R.L. Martin, D.J. Fox, T. Keith, M.A. Al-Laham, C.Y. Peng, A. Nanayakkara, M. Challacombe, P.M.W. Gill, B. Johnson, W. Chen, M.W. Wong, C. Gonzalez and J.A. Pople (2003) GAUSSIAN 03, Revision B.5, Gaussian Inc., Pittsburgh PA.
[26] J.M. Clements, R.P. Beckett, A. Brown, G. Catlin, M. Lobell, S. Palan, W. Thomas, M. Whittaker, S. Wood, S. Salama, P.J. Baker, H.F. Rodgers, V. Barynin, D.W. Rice, M.G. Hunter, Antimicrob. Agents Chemother. 45 (2001) 563.
[27] R.D. Shannon, Acta Crystallogr. Sect., A 32 (1976) 751.
[28] H. Irving, R.J.P. Williams, J. Chem. Soc. (1953) 3192.
[29] K.B. Wiberg, Tetrahedron 24 (1968) 1083.
[30] L.A. Del Rio, J. Lopez George, J. Olivares, F. Mayor, Antimicrob. Agents Chemother. 2 (1972) 189.
[31] J. Leong, S.J. Bell, Inorg. Chem. 17 (1978) 1886.



4,4'-bpp 3,3'-bpp

Scheme 1. Structure of 4,4′-bpp and 3,3′-bpp ligands.

{M–bpp} systems with the introduction of multi-carboxylate ligands. With various flexible coordination modes for carboxylate group ligands, dicarboxylate ligands can bridge two or more different metal centers and produce neutral architectures. These additional ligands could exhibit a variety of bridging abilities and have a strong tendency to form multidimensional structures, which would be markedly different from those of M–(4,4′-bpp) and M–(3,3′-bpp) complexes [11–17]. The combination of bipyridyl and dicarboxylate with d^{10}-metal ions could produce some unique frameworks with beautiful aesthetics and useful properties.

Herein, we report the syntheses, crystal structures, thermal stability and the fluorescence properties of four new complexes: $[Zn(\mu\text{-}4,4'\text{-bpp})Br_2]_n$ (**1**), $[Zn(\mu\text{-}4,4'\text{-bpp})(1,2\text{-bdc})]_n \cdot nH_2O$ (**2**), $[Zn(\mu\text{-}3,3'\text{-bpp})(1,3\text{-bdc})]_n \cdot nCH_3OH \cdot 2nH_2O$ (**3**) and $[Cd(\mu\text{-}3,3'\text{-bpp})(C_4H_2O_4)]_n \cdot 3nH_2O$ (**4**) (bdc = benzenedicarboxylate, $C_4H_4O_4$ = fumaric acid). The research results reported here are of interest with respect to the following aspects: (1) the introduction of multi-carboxylate ligands to {M–bpp} systems via the three-layer diffusion method plays an important role in the formation of fascinating metal–organic frameworks, which is significant for further exploring coordination polymer chemistry; (2) complexes **1**–**4** with flexible bipyridyl ligands present novel and unprecedented topologies such as perpendicularly linked chains, two-leg ladders and macroanionic sheets structures; (3) combination of d^{10} center metals with the conjugated aromatic or pyridine rings from both ligands provides fluorescent materials; (4) complexes such as **1** and **3**, owing to absence of inversion centers, could function for a second harmonic generation (SHG) response.

2. Experimental

2.1. General

2,2′-Biphenol and 4-picolyl chloride hydrochloride were purchased from Acros Ltd. Company and were used without further purification, the other reagents were commercially available and were used as purchased. The 4,4′-bpp and 3,3′-bpp ligands were prepared according to the literature methods [9]. The NMR spectra were recorded on a Varian Inova-500 spectrophotometer at room temperature. The mass spectra were measured on a Fisons VG platform. The IR spectra as KBr discs were recorded on a Magna 750 FT-IR spectrophotometer. C, H and N analyses were determined on an Elemental Vario ELIII elemental analyzer. Fluorescent spectra were measured on an Edinburgh Instruments analyzer model FL920. Thermal analyses were performed using a Thermal Analyst 2100 TA Instrument and a SDT 2960 Simultaneous TGA-DTA Instrument.

2.2. Synthesis of complexes

2.2.1. Synthesis of $[Zn(\mu\text{-}4,4'\text{-bpp})Br_2]_n$ (**1**)

A solution of $ZnBr_2 \cdot 4H_2O$ (0.029 g, 0.10 mmol) in H_2O (5 mL) was carefully covered by a buffer layer, prepared by mixing MeOH and water (in a 1:1 ratio). Then a solution of 4,4′-bpp (0.036 g, 0.10 mmol) in MeOH (5 mL) was slowly added above the buffer layer. Over a period of four weeks, light yellow block crystals formed on the buffer layer. Yield: 0.040 g (68%). Elementary *Anal.* Calc. for $C_{24}H_{20}Br_2N_2O_2Zn$ (593.61): C, 48.56; H, 3.40; N, 4.72. Found: C, 48.51; H, 3.43; N, 4.68%. IR (KBr, cm^{-1}): 3430 (vw), 2923 (w), 1623 (s), 1596 (w), 1505 (s), 1483 (s), 1444 (s), 1328 (m), 1269 (s), 1234 (s), 1147 (s), 1054 (m), 1029 (s), 862 (w), 751 (s), 707 (s), 492 (vw).

2.2.2. Synthesis of $[Zn(\mu\text{-}4,4'\text{-bpp})(1,2\text{-bdc})]_n \cdot nH_2O$ (**2**)

A solution of $ZnBr_2 \cdot 4H_2O$ (0.029 g, 0.10 mmol), NaOH (0.008 g, 0.20 mmol) and 1, 2-H_2bdc (0.017 g, 0.10 mmol) in H_2O (5 mL) was carefully covered by a buffer layer (MeOH:H_2O = 1:1). Then a solution of 4,4′-bpp (0.036 g, 0.10 mmol) in MeOH (5 mL) was slowly added above the buffer layer. Over a period of four weeks, light yellow block crystals of **2** formed at the buffer layer Yield: 0.051 g (83%). Elementary *Anal.* Calc. for $C_{32}H_{26}N_2O_7Zn$ (615.93): C, 62.40; H, 4.25; N, 4.55. Found: C, 62.15; H, 4.61; N, 4.50%. IR (KBr, cm^{-1}): 3435 (w), 3038 (w), 2853 (w), 1621 (w), 1595 (m), 1479 (m), 1432 (s), 1290 (w), 1231 (s), 1162 (m), 1118 (w), 1029 (m), 812 (w), 751 (s), 726 (s), 643 (w), 494 (w).

2.2.3. Synthesis of $[Zn(\mu\text{-}3,3'\text{-bpp})(1,3\text{-bdc})]_n \cdot nCH_3OH \cdot 2nH_2O$ (**3**)

A solution of $ZnBr_2 \cdot 4H_2O$ (0.029 g, 0.10 mmol), NaOH (0.008 g, 0.20 mmol) and 1,3-H_2bdc (0.017 g, 0.10 mmol) in H_2O (5 mL) was carefully covered by buffer layer (MeOH:H_2O = 1:1). Then a solution of 3,3′-bpp (0.036 g, 0.10 mmol) in MeOH (5 mL) was slowly added above the buffer layer. Light yellow block crystals were produced at the buffer layer after a few weeks. Yield: 0.048 g (72%). Elementary *Anal.* Calc. for $C_{33}H_{32}N_2O_9Zn$ (666.01): C, 59.51; H, 4.84; N, 4.21. Found: C, 59.43; H, 4.88; N, 4.16%. IR (KBr, cm^{-1}): 3065 (vw), 2927 (w), 1594 (m), 1500 (s), 1481 (s), 1444 (s), 1432 (s), 1284 (m), 1252 (s), 1227 (s), 1194 (m), 1161 (w), 1107 (s), 1050 (m), 1019 (s), 966 (vw), 871 (w), 751 (s), 701 (s), 669 (w), 616 (vw).

2.2.4. Synthesis of $[Cd(\mu\text{-}3,3'\text{-bpp})(C_4H_2O_4)]_n \cdot 3nH_2O$ (**4**)

A solution of $CdBr_2 \cdot 4H_2O$ (0.034 g, 0.10 mmol) and fumaric acid (0.012 g, 0.10 mmol) in H_2O (5 mL) was care-

fully covered by a buffer layer (MeOH:H_2O = 1:1). Then a solution of 3,3′-bpp (0.036 g, 0.10 mmol) in MeOH (5 mL) was slowly added above the buffer layer. Light yellow block crystals of **4** were obtained at the buffer layer after a few weeks. Yield: 0.048 g (75%). Elementary *Anal*. Calc. for $C_{28}H_{28}CdN_2O_9$ (648.95): C, 51.82; H, 4.35; N, 4.32. Found: C, 52.21; H, 3.99; N, 4.30%. IR (KBr, cm^{-1}): 3109 (vw), 2922 (w), 2165 (w), 1618 (w), 1595 (m), 1583 (m), 1500 (w), 1489 (m), 1453 (s), 1438 (s), 1286 (w), 1271 (s), 1241 (s), 1191 (m), 1161 (w), 1128 (s), 1049 (m), 1031 (m), 937 (vw), 911 (vw), 866 (w), 783 (m), 685 (s), 648 (w) 615 (vw), 544 (vw), 486 (vw), 454 (vw).

2.3. X-ray crystallography

Single crystals of these complexes with appropriate dimensions were mounted on a glass fiber and used for data collection. Data were collected at 293(2) K on a Siemens Smart CCD diffractometer with graphite-monochromated Mo Kα radiation ($\lambda = 0.71073$ Å). Empirical absence of the centers of symmetries meets the essential requirement of a SHG response. Absorption corrections were applied by using the SADABS program for the Siemens area detector. The structures were solved with direct methods and all calculations were performed using the SHELXTL package [18]. The structures displacement parameters were calculated for all non-hydrogen atoms. The positions of H atoms were generated geometrically and treated as riding on their parent atoms. Details of the crystal data are listed in Table 1. Selected bond lengths and angles are listed in Table 2.

3. Results and discussion

3.1. Description of crystal structures

3.1.1. $[Zn(\mu\text{-}4,4'\text{-bpp})Br_2]_n$ (1)

Single crystal X-ray diffraction analysis reveals that complex **1** is a chain structure and crystallizes in the orthorhombic space group *C*222. As depicted in Fig. 1a, complex **1** contains two independent Zn(II) centers. Each Zn(II) center has a slightly distorted tetrahedral geometry and is coordinated by two terminal bromide anions (Zn(1)–Br(1) 2.360(5) Å, Br(1)–Zn(1)–Br(1A) 117.84(3)°; and Zn(2)–Br(2) 2.348(8) Å, Br(2)–Zn(2)–Br(2A) 115.14(5)°). The remaining two coordinative sites of the Zn(II) center in each line are occupied by two nitrogen atoms from different 4,4′-bpp ligands. The bond distances between the Zn(II) center and the nitrogen donor are Zn(1)–N(1) 2.044(3), Zn(2)–N(2) 2.061(4) Å.

Because of steric exclusion, the pyridyl rings of two independent 4,4′-bpp ligands are highly twisted, the dihedral angles between the two pyridyl rings are 68.5° and 21.0°. The dihedral angles between the two phenyl rings in two 4,4′-bpp ligands are 127.6° and 71.5°. The Zn(II) centers are linked by the twisted 4,4′-bpp ligands into a zigzag chain structure. It is noteworthy that the two chains in **1** are nearly perpendicular to each other, as shown in

Table 1
Crystallographic data for complexes **1**–**4**

Complexes	**1**	**2**	**3**	**4**
Formula	$C_{24}H_{20}Br_2N_2O_2Zn$	$C_{32}H_{26}N_2O_7Zn$	$C_{33}H_{32}N_2O_9Zn$	$C_{28}H_{28}CdN_2O_9$
Formula weight	593.61	615.93	666.01	648.95
Crystal size (mm)	$0.45 \times 0.28 \times 0.22$	$0.38 \times 0.26 \times 0.20$	$0.52 \times 0.48 \times 0.40$	$0.32 \times 0.24 \times 0.41$
Crystal system	orthorhombic	triclinic	triclinic	monoclinic
Space group	*C*222	$P\bar{1}$	$P\bar{1}$	*C*2
a (Å)	12.631	10.234(3)	10.132(3)	12.9512(10)
b (Å)	14.540	11.079(3)	11.409(3)	31.835(2)
c (Å)	25.6933(10)	12.982(4)	14.038(4)	8.6952(7)
α (°)	90	90.652(2)	86.80(1)	90
β (°)	90	107.426(2)	73.84(1)	100.022(2)
γ (°)	90	102.549(4)	73.69(1)	90
V ($Å^3$)	4718.76(18)	1366.1(7)	1495.4(7)	3530.3(5)
Z	8	2	2	4
D_{calc} ($Mg\ m^{-3}$)	1.671	1.502	1.479	1.210
μ (mm^{-1})	2.460	0.953	0.882	0.663
F(000)	2352	640	692	1296
T (K)	173(2)	173(2)	173(2)	173(2)
λ (Mo Kα) (Å)	0.71073	0.71073	0.71073	0.71073
Reflections collected	16959	11240	11674	3805
Unique reflections	5341	6661	6767	1695
Parameters	141	379	414	199
Goodness-of-fit (*S*) of F^2	1.042	1.046	1.062	1.165
R_1, wR_2 [$I > 2\sigma(I)$][a]	0.0373, 0.0794	0.0353, 0.1008	0.0422, 0.1019	0.0608, 0.1686
R_1, wR_2 (all data)[b]	0.0443, 0.0824	0.0399, 0.1029	0.0471, 0.1052	0.0731, 0.1819
Maximum and minimum Δρ (e $Å^{-3}$)	0.0818 and −0.855	0.687 and −0.704	0.968 and −0.641	0.843 and −0.686

[a] $R_1 = \sum||F_o| - |F_c||/\sum|F_o|$.
[b] $wR_2=[\sum w(F_o^2 - F_c^2)^2/\sum w(F_o^4)]^{1/2}$, $w = [\sigma^2(F_o^2) + (aP)^2 + bP]^{-1}$, $P = (2F_c^2 + F_o^2)/3$.

Table 2
Selected bond lengths (Å) and angles (°) for **1**–**4**

Compound ***1***							
Zn1–Br1	2.360(5)	Zn1–N1	2.044(3)	Zn2–N2	2.061(4)	N2–Zn2–Br2A	107.17(1)
N1–Zn1–N1A	96.10(2)	N1–Zn1–Br1	112.65(1)	Zn2–Br2A	2.348(8)	N2–Zn1–Br2	113.28(1)
N1A–Zn1–Br1	107.76(1)	N1–Zn1–Br1A	107.76(1)	N2–Zn1–N2A	99.7(3)	Br2A–Zn2–Br	115.14(5)
N1A–Zn1–Br1A	112.65(1)	Br1–Zn1–Br1A	117.84(3)	N2A–Zn2–Br2A	113.28(1)	2 N2A–Zn2–Br2	107.17(1)
Compound ***2***							
Zn1–O1	1.9246(1)	Zn1–O3B	1.953(1)	Zn1–N2A	2.049(2)	Zn1–N1	2.0751(2)
O1–Zn1–O3B	111.45(6)	O3B–Zn1–N2	104.18(6)	O3B–Zn1–N1	96.90(6)	N2A–Zn(1)-N1	104.91(6)
O1–Zn1–N2A	132.34(6)	O1–Zn1–N1	101.20(6)				
Compound ***3***							
Zn1–O1	1.974(2)	Zn1–N2A	2.019(2)	Zn1–O3B	1.983(2)	Zn1–N1	2.053(2)
O1–Zn1–O3B	98.00(7)	O1–Zn1–N1	111.19(8)	O3B1–Zn1–N2A	116.61(7)	N2A–Zn1–N1	109.62(8)
O1–Zn1–N2A	110.60(7)	O3B–Zn1–N1	111.36(7)				
Compound ***4***							
Cd–N1A	2.302(8)	Cd–O1	2.416(9)	Cd–O1B	2.324(9)	Cd–O2	2.486(8)
N1A–Cd–N1	178.8(4)	Cd–O3	2.418(1)	Cd–O4	2.362(9)	N1–Cd–O2	89.6(2)
N1A–Cd–O1B	89.9(2)	N1–Cd–O3	90.57(2)	N1A–Cd–O1	89.42(2)	O1B–Cd–O2	125.5(3)
N1–Cd–O1B	89.85(2)	O1B–Cd–O3	92.6(3)	N1–Cd–O1	89.42(2)	O4–Cd–O2	87.2(4)
N1A–Cd–O4	90.43(2)	O4–Cd–O3	54.6(4)	O1B–Cd–O1	72.4(3)	O1–Cd–O2	53.1(3)
N1–Cd–O4	90.43(2)	O1–Cd–O3	165.1(3)	O4–Cd–O1	140.3(3)	O3–Cd–O2	141.9(4)
		N1A–Cd–O2	89.6(2)	N1A–Cd–O3	90.57(2)	O1B–Cd–O4	147.3(3)

Symmetry codes: For **1** A: $-x+1/2$, $-y+1/2$, B: $-x$, $-y+1$,z, C: $-x+1$, $-y+1$, z. For **2** A: $x-1$, y, z, B: $-x+1$, $-y+2$, $-z+1$. For **3** A: $-x$, $-y+2$, $-\mathbf{z}+1$, B: $x-1$, y, z. For **4** A: x, $-y$, z, B: $-x$, $-y$, $-z+1$, C: x, $-y$, $-z+2$.

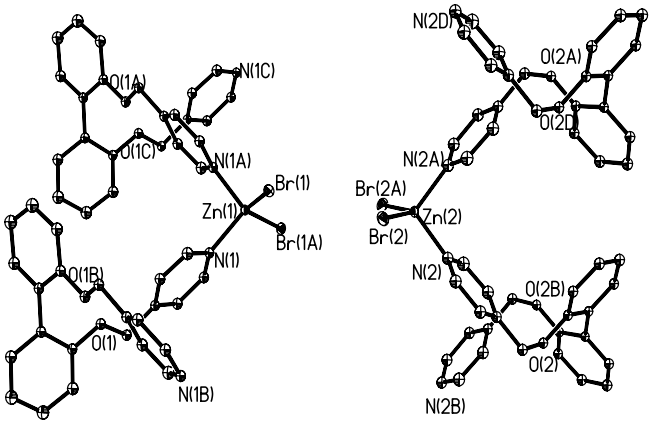


Fig. 1a. View of the coordination environment of the Zn(II) center in **1** (A: $-x+1/2$, $-y+1/2$, z; B: $-x$, $-y+1$, z; C: $-x+1$, $-y+1$; D: $x-1/2$, $y-1/2$, z).

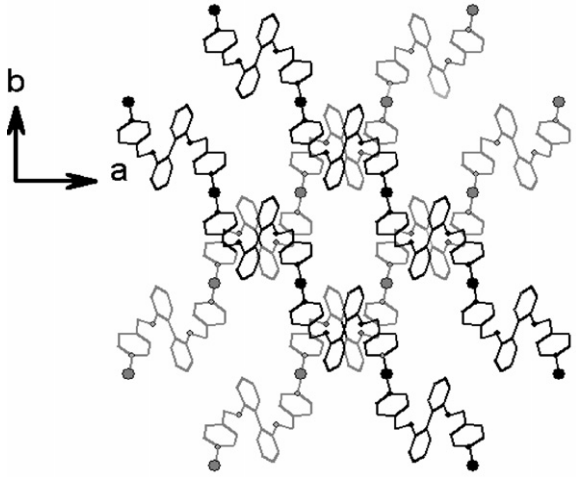


Fig. 1b. View of the vertical polymer chains in **1**.

Fig. 1b. The Zn···Zn separation in both chains is of the same distance, 9.630 Å, while the two nearest Zn(II) centers are at a distance of 11.728 Å. No guest molecules are observed within the distorted rings owing to the high distortion and flexibility of 4,4′-bpp.

3.1.2. *[Zn(μ-4,4′-bpp)(1,2-bdc)]$_n$ · nH$_2$O* (**2**)

The structure of **2** comprises a two-leg ladder running along the [0 0 1] direction. An ORTEP view of complex **2** is shown in Fig. 2a. The Zn(II) ion adopts a distorted tetrahedral coordination geometry and is coordinated by two nitrogen atoms from different 4,4′-bpp ligands (Zn(1)–N(2A) 2.0438(15), Zn(1)–N(1) 2.0751(15) Å) and two carboxyl groups from two different 1,2-bdc ligands (Zn(1)–O(1) 1.9246(13), Zn(1)–O(3B) 1.9534(13) Å, O(1)–Zn(1)–O(3B) 111.45(6)°).

The legs of such a ladder are made up of [Zn(4,4′-bpp)]$_n$ chains, in which Zn(II) ions are bridged by 4,4′-bpp ligands and each ligand acts as an *exo*-bidentate ligand. In the legs, two phenyl rings and two pyridyl rings of each 4,4′-bpp ligand are twisted more evidently than those in **1**. The dihedral angles between them are 111.5° and 51.3°, respectively. The cross rungs of the ladder are made up of 1,2-bdc ligands, where each of the carboxyl groups in a monodentate coordination mode bridges two Zn(II) ions on either side of the ladder. Interestingly, the dihedral angles between the phenyl rings and their corresponding carboxylates are 94.2° and 99.0°, respectively, indicating that the

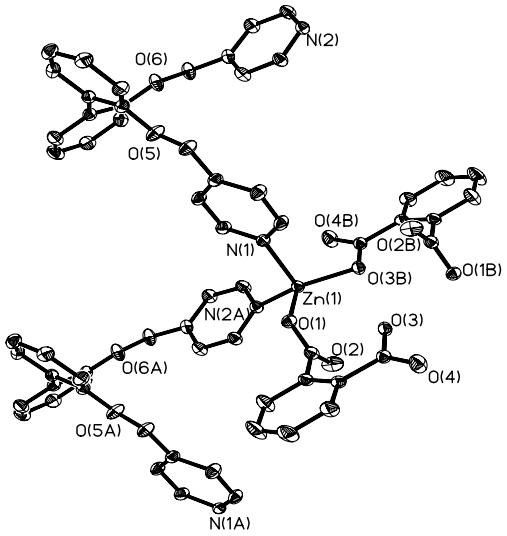


Fig. 2a. View of the coordination environment of the Zn(II) center in **2** (A: $x-1$, y, z; B: $-x+1$, $-y+2$, $-z+1$).

carboxylates are approximately perpendicular, respectively, to phenyl rings. In addition, the Zn···Zn separation among the legs of the ladder is 10.233 Å and the Zn···Zn separation in the cross rungs is 5.153 Å, as shown in Fig. 2b.

3.1.3. $[Zn(\mu\text{-}3,3'\text{-bpp})(1,3\text{-bdc})]_n \cdot nCH_3OH \cdot 2nH_2O$ (**3**)

The structure of **3** consists of neutral 1D chains through the connection of [Zn(3,3′-bpp)] units and 1,3-bdc bridging ligands (Fig. 3a). The central Zn(II) ion is coordinated tetrahedrally by two monodentate carboxylate oxygen atoms from two different 1,3-bdc ligands and two nitrogen atoms from two 3,3′-bpp ligands. The Zn–O bond lengths are 1.9721(17) and 1.9836(16) Å, in good agreement with those bond lengths found in other extended structures constructed from 1,3-bdc and Zn(II) ions, and the Zn–N bond distances are typical, with values of 2.019(0) and 2.052(7) Å. The angles O(1)–Zn(1)–O(3B) of 98.00(7)° and O(3B)–Zn(1)–N(2A) of 116.61(7)° indicate a slight distortion compared with the ideal value of 109°28′. The dihedral angle of the two pyridyl rings attaching to the Zn(II) ion is 83.2°, i.e. they are approximately perpendicular to each other. The 3,3′-bpp ligand acts as *exo*-bidentate, and its pyridyl rings are twisted out of the plane of the linking phenyl rings by 69.0° and 73.7°, while the two phenyl rings of 3,3′-bpp themselves have a drastic twisting with the dihedral angle between them being 25.6°. The combination of these twistings allows 3,3′-bpp to link two Zn(II) ions into a dimetallic ring with the Zn···Zn separation being 8.139 Å.

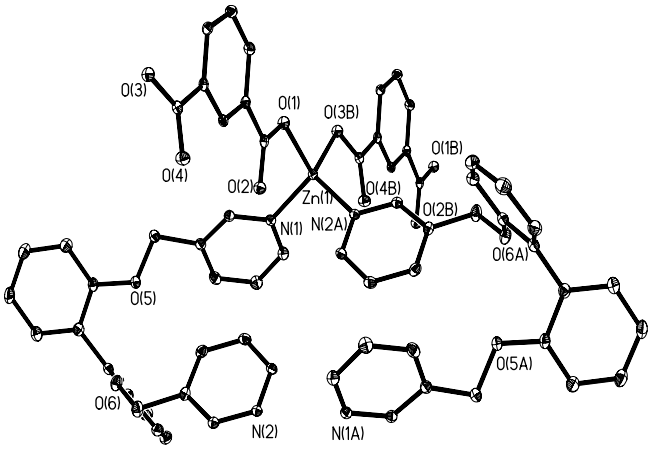


Fig. 3a. View of the coordination environment of the Zn(II) center in **3** (A: $-x$, $-y+2$, $-z+1$; B: $x-1$, y, z).

In addition, both carboxyl groups of the 1,3-bdc ligand link the metal Zn(II) ion in a monodentate fashion and they are deprotonated which is consistent with the IR data (no absorption peaks in the 1715–1680 cm^{-1} region). The Zn···Zn distance separated by 1,3-bdc is 10.132 Å. The dihedral angles between the phenyl rings and their corresponding carboxylates are 33.7° and 49.7°, indicating a slight twist between them. Thus, every two 1,3-bdc ligands, acting in the monodentate mode, connect the neighbouring

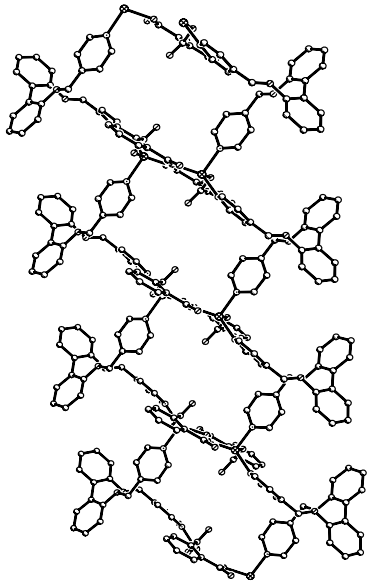


Fig. 2b. View of two-leg ladder structure in **2**.

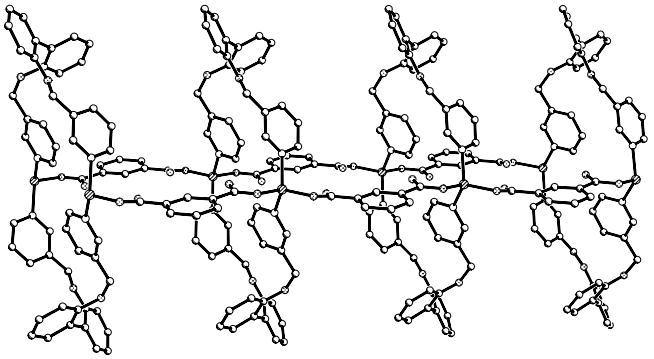


Fig. 3b. View of 1D polymeric chain with dimetallic rings of **3**.

dimetallic rings formed by the 3,3′-bpp ligand and Zn(II) centers into an interesting 1D chain structure as shown in Fig. 3b.

3.1.4. $[Cd(\mu\text{-}3,3'\text{-}bpp)(C_4H_2O_4)]_n \cdot 3nH_2O$ (4)

Complex **4** consists of anionic macrocyclic cadmium dicarboxylate sheets which are separated by 3,3′-bpp. The local coordination environment around the Cd(II) center in **4** can be described as a greatly distorted pentagonal bipyramid, as shown in Fig. 4a. Two nitrogen donors from two 3,3′-bpp ligands take up two vertexes of the coordination polyhedron to stop the layer from developing into a 3D framework (Cd–N(1) 2.302(8), Cd–N(1A) 2.302(8) Å, N(1)–Cd–N(1A) 178.8(4)°). The equatorial plane of the coordination polyhedron is composed of five oxygen atoms belonging to three fumarate ligands. Two of the three fumarate units bind the Cd(II) ions through a chelating interaction, while the remaining one exhibits a chelating/bridging bis-bidentate mode. All of five the Cd–O bond lengths are in the range of the documented Cd–$O_{(carboxy)}$ distances (2.324(9)–2.486(8) Å). The oxygen atom O(1), which participates in the chelate-bridged interaction, bridges two Cd(II) atoms to form Cd_2O_2 dimers (Cd···Cd, 3.825 Å) through the monodentate interaction, and exhibits the shortest coordination distance (Cd–O(1), 2.324(9) Å). The above binuclear Cd_2O_2 subunit is connected to four neighbouring subunits forming a network which is topologically equivalent to a (4,4) network. Thus, the binuclear subunits are inter-connected through fumarate ligands, which bridge the Cd_2O_2 to generate a parallegram-like sheet with dimensions of 16.809 × 14.288 Å, as measured from the centers of the binuclear subunits (Fig. 4b).

Moreover, every two 3,3′-bpp ligands, both in *exo*-bidentate modes, are attached to the hybrid through the Cd–N bonds to form a hybrid layer as shown in Fig. 4c. It is noteworthy that 3,3′-bpp, twisted due to the steric exclusion requirement, links two Cd(II) centers into a big

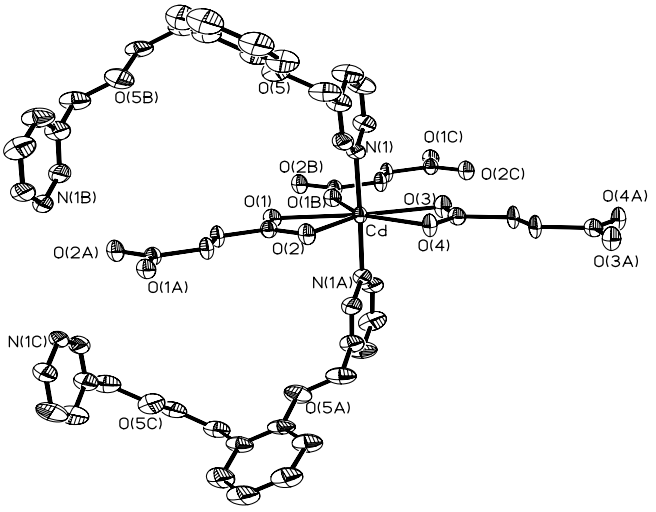


Fig. 4a. View of **4** showing the coordination environment around the Cd(II) center (A: $x, -y, z$, B: $-x, -y, -z+1$, C: $x, -y, -z+2$).

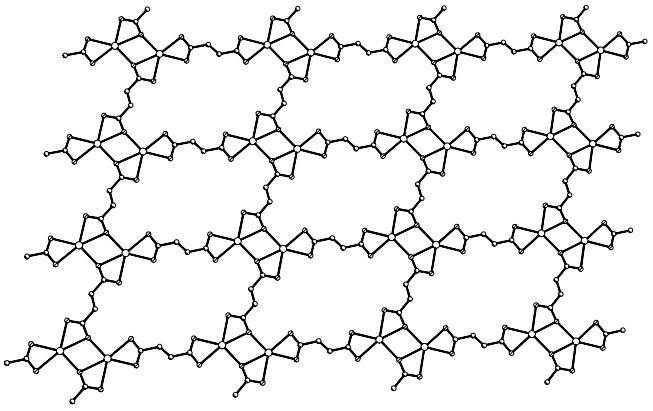


Fig. 4b. View of 2D structure of the macroanionic cadmium maleic sheets in **4**.

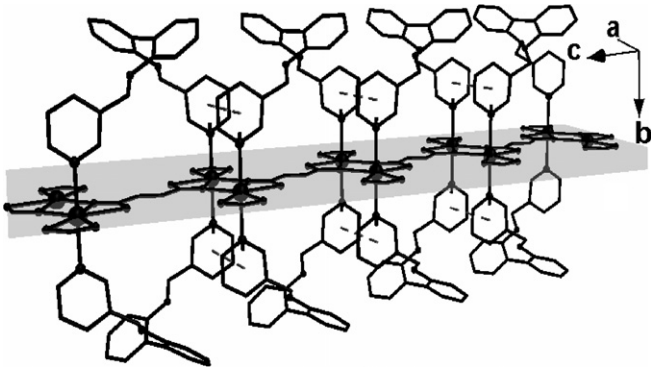


Fig. 4c. View of the hybrid layer of **4**.

dimetallic ring, where the dihedral angles between the two phenyl rings and the two pyridyl rings of the 3,3′-bpp ligand are 75.3° and 3.1°, respectively. Thus, the metal–metal layers are planar with two N atoms from the 3,3′-bpp ligand pointing above and below the plane. The layers are linked by strong π–π interactions, and the adjacent layers stacking mode can be described as the ABAB type in a staggered arrangement, as shown in Fig. 4d.

3.2. TGA results

To study the stability of the polymers, the thermogravimetric analyses (TGA) for these complexes were performed on polycrystalline samples under a nitrogen atmosphere. The TG curves showed neither weight loss nor structural change up to about 260 °C, demonstrating that the frameworks of **1**–**4** were retained up to these high temperatures. Immediately above this point, the samples began to lose ligands, the whole frameworks collapsed in a continuous fashion and finally decomposed into unidentified products.

3.3. Luminescence properties

Luminescent polynuclear d^{10} metal complexes (such as Zn(II) and Cd(II)) are of great interest because of their

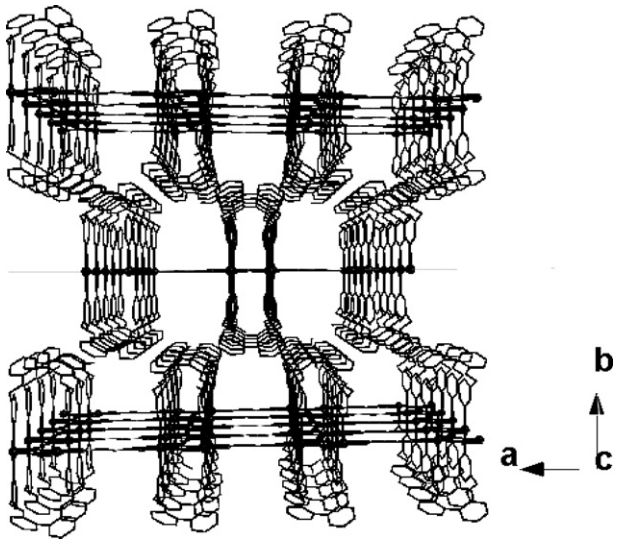


Fig. 4d. View of the layers constructed of the ···ABAB··· type for **4**.

potential application in chemical optical sensors, photosensitization and electroluminescent devices. Here, the photoluminescence of these complexes was examined and the solid-state emission spectra are shown in Fig. 5. Complex **1** exhibits a broad emission band with the maximum intensity at 502 nm upon excitation at 370 nm, while complexes **2** and **3** produce an intense pure blue sharp emission with the maximum at ca. 441 nm and a broad emission band with the maximum intensity at 457 nm, respectively, with excitation at 370 nm. For complex **4**, two broad emissions at 490 and 526 nm can be observed. For contrast, the free 4,4′-bpp and 3,3′-bpp molecules display the luminescence at around 480 nm in the solid state. Generally, the intraligand fluorescence emission wavelength is determined by the energy gap between the π and π* molecular orbitals of the free ligand, which is simply related to the extent of π conjugation in the system. As for the metal complexes, the red or blue shifted emissions of complexes **1**–**4** compared to their free ligands are not only assigned to the intramolecular π–π* and n–π* transitions of the ligands, but are also attributable to ligand-to-metal charge transfers (LMCT) [19].

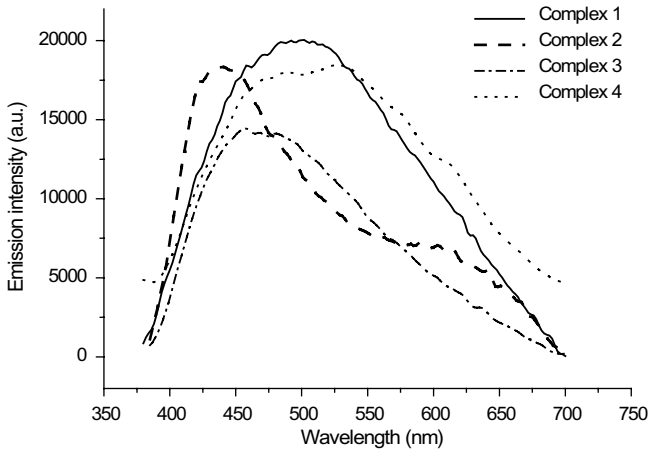


Fig. 5. The emission spectra of **1**–**4** in the solid state at room temperature.

In comparison with complex **1**, a blue-shift of 61 nm has been observed in complex **2**, partially due to the replacement of the Br^- anion by the ligand 1,3-bdc. Although complexes **2** and **3** have different structural motifs, both complexes demonstrate some similar photoluminescence behaviours. The blue-shifted emissions of **2** and **3** may originate from their larger conjugated systems for the two types of ligands as well as their similar distorted tetrahedral coordination geometries of d^{10} metal centers, where each of the Zn(II) ions is coordinated by two pyridyl N atoms and two carboxylate O atoms.

Complexes such as **1** and **3** do not have a center of symmetry, which meets the essential requirement of a SHG response. Thus, Kurtz powder SHG measurements on the acentric **1** and **3** were performed, and very weak SHG emissions were observed for both complexes. The weak SHG efficiency may be due to the following fact: the acentricities of **1** and **3** are caused by their twist of the bpp ligands and the arrangements of the individual chains result in a partial cancellation of the effective dipolar moments [20,21].

4. Conclusions

In summary, a series of novel coordination polymers with interesting structural motifs have been synthesized from the flexible bipyridyl ligands (4,4′-bpp or 3,3′-bpp) and d^{10} metal ions (Zn^{2+} or Cd^{2+}) as well as carboxylate ligands by the three-layer diffusion method. Complex **1** is a chain structure containing two unusual nearly vertical zigzag Zn(II) chains, and **2** comprises a two-leg ladder, where the legs and cross rungs are made of $[Zn(4,4'\text{-bpp})]_n$ chains and bdc ligands, respectively. In **3**, every two 1,3-bdc ligands connect the neighbouring dimetallic rings into an interesting 1D structure, while the 2D structure in **4** consists of macroanionic cadmium fumarate sheets separated by 3,3′-bpp ligands. Moreover, TGA measurements exhibit that complexes **1**–**4** have very similar thermal stability, and studies on the luminescent emissions of these obtained compounds reveal that the d^{10} metal ions cause red or blue shifts of the emissions, assigned to intramolecular π–π* and n–π* transitions of the ligands.

Acknowledgements

The authors are grateful to 973 Program (2006CB932900), the National Nature Science Foundation of China (20571074 and 20631050) and the Nature Science Foundation of Fujian province for financial support of this work.

Appendix A. Supplementary material

CCDC 268340, 268341, 292808 and 292809 contain the supplementary crystallographic data for **1**, **2**, **3** and **4**.

These data can be obtained free of charge via http://www.ccdc.cam.ac.uk/conts/retrieving.html, or from the Cambridge Crystallographic Data Centre, 12 Union Road, Cambridge CB2 1EZ, UK; fax: (+44) 1223-336-033; or e-mail: deposit@ccdc.cam.ac.uk. Supplementary data associated with this article can be found, in the online version, at doi:10.1016/j.poly.2007.07.048.

References

[1] S.A. Bourne, J.J. Lu, A. Mondal, B. Moulton, M.J. Zaworotko, Angew. Chem., Int. Ed. 40 (2001) 2111.

[2] (a) M. Munakata, L.P. Wu, T. Kuroda-Sowa, Adv. Inorg. Chem. 46 (1999) 173;
(b) S.R. Batten, R. Robson, Angew. Chem., Int. Ed. Engl. 37 (1998) 1460;
(c) S. Leininger, B. Olenyuk, P.J. Stang, Chem. Rev. 100 (2000) 853.

[3] (a) P.J. Hagrman, D. Hagrman, J. Zubieta, Angew. Chem., Int. Ed. 38 (1999) 2638;
(b) B. Moulton, M.J. Zaworotko, Chem. Rev. 101 (2001) 1629;
(c) M. Fujita, Chem. Soc. Rev. 27 (1998) 417.

[4] (a) L. Carlucci, G. Ciani, D.M. Proserpio, Coord. Chem. Rev. 246 (2003) 247;
(b) J.R. Dunbar, K.R. Galan-Mascaros, Angew. Chem., Int. Ed. 42 (2003) 2289;
(c) D.L. Caulder, K.N. Raymond, Acc. Chem. Res. 32 (1999) 975;
(d) E. Lindner, R. Zong, K. Eichele, U. Weisser, M. Strobele, Eur. J. Inorg. Chem. (2003) 705;
(e) E.J. Schelter, J.K. Bera, J. Bacsa, J.R. Galan-Mascaros, K.R. Dunbar, Inorg. Chem. 42 (2003) 4256.

[5] (a) Y. Cui, S.J. Lee, W.B. Lin, J. Am. Chem. Soc. 125 (2003) 6014;
(b) C.D. Wu, W.B. Lin, Angew. Chem., Int. Ed. 44 (2005) 1958;
(c) C.D. Wu, W.B. Lin, Inorg. Chem. 44 (2005) 1178;
(d) Y. Cui, H.L. Ngo, W.B. Lin, Chem. Commun. (2003) 1388.

[6] (a) Y. Cui, H.L. Ngo, P.S. White, W.B. Lin, Chem. Commun. (2003) 994;
(b) Y. Cui, H.L. Ngo, P.S. White, W.B. Lin, Inorg. Chem. 42 (2003) 652;
(c) H.L. Ngo, W.B. Lin, J. Am. Chem. Soc. 124 (2002) 14298.

[7] (a) Y. Cui, H.L. Ngo, P.S. White, W.B. Lin, Chem. Commun. (2002) 1666;
(b) Y. Cui, O.R. Evans, H.L. Ngo, P.S. White, W.B. Lin, Angew. Chem., Int. Ed. 41 (2002) 1159.

[8] (a) M.C. Hong, Y.J. Zhao, W.P. Su, R. Cao, M. Fujita, Z.Y. Zhou, A.S.C. Chan, J. Am. Chem. Soc. 122 (2000) 4819;
(b) M.C. Hong, Y.J. Zhao, W.P. Su, R. Cao, M. Fujita, Z.Y. Zhou, A.S.C. Chan, Angew. Chem., Int. Ed. 39 (2000) 2468;
(c) M.C. Hong, W.P. Su, R. Cao, M. Fujita, J.X. Lu, Chem. Eur. J. 6 (2000) 427.

[9] R.H. Wang, L. Han, L.J. Xu, Y.Q. Gong, Y.F. Zhou, M.C. Hong, A.S.C. Chan, Eur. J. Inorg. Chem. (2004) 3751.

[10] (a) Y.Q. Gong, R.H. Wang, Y.F. Zhou, D.Q. Yuan, M.C. Hong, J. Mol. Struct. 705 (2004) 29;
(b) Y.Q. Gong, R.H. Wang, Y.F. Zhou, Z.Z. Lin, M.C. Hong, J. Mol. Struct. 751 (2005) 121.

[11] (a) S. Belanger, J.T. Hupp, C.L. Stern, R.V. Slone, D.F. Watson, T.G. Carrell, J. Am. Chem. Soc. 121 (1999) 557;
(b) A.J. Blake, N.R. Champness, P. Hubberstey, W.S. Li, M.A. Withersby, M. Schröder, Coord. Chem. Rev. 183 (1999) 117;
(c) H.W. Roesky, M. Andruh, Coord. Chem. Rev. 236 (2003) 91.

[12] (a) R. Cao, D.F. Sun, Y.C. Liang, M.C. Hong, K. Tansumi, Q. Shi, Inorg. Chem. 41 (2002) 2087;
(b) X.J. Li, R. Cao, D.F. Sun, W.H. Bi, Y.Q. Wang, M.C. Hong, Crystal Growth Des. 4 (2004) 775;
(c) N. Hao, Y.G. Li, E.B. Wang, E.H. Shen, C.W. Hua, L. Xu, J. Mol. Struct. (2004) 6971.

[13] (a) X.J. Gu, Y.H. Chen, J. Peng, Z.Y. Shi, E.B. Wang, N.H. Hu, J. Mol. Struct. 697 (2004) 231;
(b) C. Qin, X.L. Wang, E.B. Wang, C.W. Hu, L. Xu, Inorg. Chem. Commun. 7 (2004) 788.

[14] (a) Z. Shi, S.H. Feng, Y. Sun, J. Hua, Inorg. Chem. 40 (2001) 5312;
(b) D.A. Beauchamp, S.J. Loeb, Chem. Commun. (2002) 2484;
(c) J. Tao, M.L. Tong, X.M. Chen, J. Chem. Soc., Dalton Trans. (2000) 3669.

[15] (a) S.M.F. Lo, S.S.Y. Chui, L.Y. Shek, Z. Lin, X.X. Zhang, G.H. Wen, I.D. Williams, J. Am. Chem. Soc. 122 (2000) 6293;
(b) J.Y. Lu, M.A. Lawandy, J. Li, T. Yuen, C.L. Lin, Inorg. Chem. 38 (1999) 2695.

[16] (a) S. Kitagawa, M. Kondo, Bull. Chem. Soc. Jpn. 71 (1998) 1799;
(b) D.A. McMorran, P.J. Steel, Chem. Commun. (2002) 2120.

[17] M. Maekawa, H. Konaka, Y. Suenaga, T. Kuroda-Sowa, M.J. Munakata, J. Chem. Soc., Dalton Trans. (2000) 4160.

[18] (a) G.M. Sheldrick, SADABS: Program for Empirical Absorption Correction of Area Detector Data, University of Göttingen, Göttingen, Germany, 1996;
(b) G.M. Sheldrick, SHELXS 97: Program for Crystal Structure Solution, University of Göttingen, Göttingen, Germany, 1997;
(c) G.M. Sheldrick, SHELXS 97: Program for Crystal Structure Refinement, University of Göttingen, Göttingen, Germany, 1997.

[19] M.W. Perkovic, Inorg. Chem. 39 (2000) 4962.

[20] O.R. Evans, W. Lin, Acc. Chem. Res. 35 (2002) 511.

[21] W.B. Lin, O.R. Evans, R.G. Xiong, Z.Y. Wang, J. Am. Chem. Soc. 120 (1998) 13272.

rise to polymeric structures. In this way, we present a series of nitrate and perchlorate Zn(II) complexes with different dipyridinic azamacrocycle ligands: the hexaaza 20-membered macrocycle L^1 (2,8,14,20-tetramethyl-3,7,15,19,25,26-hexaaza-tricyclo[19.3.1.1^{9,13}]hexacosa-1(24),9,11,13(26),21(25),22-hexaene), the hexaaza 18-membered ligand bearing four cyanoethyl pendant groups L^2 (3-[6,14,17-tris-(2-cyano-ethyl)-3,6,14,17,23,24-hexaaza-tricyclo[17.3.1.1^{8,12}]-tetracosa-1(23),8(24),9,11,19,21-hexaen-3-yl]-propionitrile) and the octaaza 24-membered macrocycle L^3 (3,6,9,17,20,23,29,30-octaaza-tricyclo[23.3.1.1[11,15]]triaconta-1(28),1,13,15(30),25(29),26-hexaene). The role of coordination capability of the nitrate and perchlorate counter ions and interaction between π-systems on complex structure are also studied.

2. Experimental

2.1. Chemical and starting materials

The macrocyclic ligands L^2 and L^3 were prepared following the literature methods [8,9]. 2,6-Diacetylpyridine, 1,3-diaminepropane, Ba(II) chloride dihydrated, Zn(II) hydrated nitrate and perchlorate salts were commercial products obtained from Alfa and Aldrich, and were used without further purifications. The solvents used were of reagent grade and purified by usual methods.

Caution: Although no problems were encountered during the course of this work, attention is drawn to the potentially explosive nature of perchlorates.

2.2. Synthesis of the macrocyclic ligands

The ligand L^1 was obtained following a similar method described previously [10] by a result of a barium template condensation of 2,6-diacetylpyridine and 1,3-diaminepropane. To a refluxing solution of 2,6-diacetylpyridine (0.82 g, 5 mmol) and Ba(II) chloride dihydrated (1.22 g, 5 mmol) in methanol (100 ml), a 30 ml of a methanolic solution of 1,3-diaminepropane (0.42 ml, 5 mmol) was added. The mixture was refluxed for 4 h. The solution was allowed to cool at room temperature and excess of sodium tetrahydroborate was added slowly and carefully for *in situ* reduction. The mixture was concentrated to dryness under reduced pressure and the crude solid was extracted with chloroform, concentrated to dryness to obtain a yellow oil. The oil was dissolved in small amount of methanol and bromhydric acid was added until acid pH. After isolation and characterization of the crystalline tetrahydrobromhydric salt of the ligand, it was dissolved in a small amount of water and neutralizing with NaOH. The water solution was extracted with chloroform (3×30 ml). The organic phase was dried with Na_2SO_4 anhydrous and filtered to be concentrated to dryness at reduced pressure to obtain a yellow oil, which was recrystallized in acetonitrile to give the 6*S*,10*S*,16*R*,20*R*-*meso* form L^1. It was characterized by elemental analysis, IR, LSI-MS and ^{1}H, ^{13}C, COSY, DEPT and HMQC NMR spectroscopy.

Anal. Calc. for $C_{24}H_{38}N_6$ (MW: 410): C, 65.9; H, 9.4; N, 19.2. Found: C, 66.2; H, 9.6; N, 19.3%. Yield: 57%. IR (KBr, cm^{-1}): 3291 ν(N–H), 1591, 1575, 1448 [ν(C=N)$_{py}$ and ν(C=C)]. LSI-MS (*m*/*z*): $[L^1+H]^+$ 411. ^{1}H NMR ($CDCl_3$, ppm) $\delta = 7.55$–7.40 [m, 2H, H_{py}]; 7.18–6.82 [m, 4H, H_{py}]; 3.82–3.60 [m, 4H, –CH]; 2.36–2.08 [m, 8H, –CH_2]; 1.31–1.26 [m, 12H, –CH_3]; 1.63–1.50 [m, 4H, –CH_2]. Colour: white.

2.3. Synthesis of the metal complexes – general procedure

The synthesis of metal complexes were carried out in 1:1 and 2:1 metal:ligand molar ratio. The appropriate metal salt (0.25 or 0.5 mmol) was dissolved in acetonitrile (10 ml) and added to a stirred solution of the macrocyclic ligand (0.25 mmol) in acetonitrile (20 ml). The solution was stirred for 2 h and concentrated in a rotary evaporator until *ca.* 5–6 ml. The products obtained were filtered off, dried and re-crystallized in water or acetonitrile.

2.3.1. $[ZnL^1](ClO_4)_2 \cdot H_2O$

Anal. Calc. for $C_{24}H_{40}N_6O_9Cl_2Zn$ (MW: 692.4): C, 41.6; H, 5.8; N, 12.1. Found: C, 41.3; H, 5.7; N, 12.0%. Yield: 62%. IR (KBr, cm^{-1}): 3271 [ν(NH)], 1600, 1581, 1467 [ν(C=N)$_{py}$ and ν(C=C)], 1093, 624 [ν(ClO_4^-)]. LSI-MS (*m*/*z*): 574 $[ZnL^1(ClO_4)]^+$, 474 $[ZnL^1]^+$. Λ_M/Ω^{-1} cm^2 mol^{-1} (in CH_3CN): 248 (2:1). Colour: white.

2.3.2. $[ZnL^2](NO_3)_2$

Anal. Calc. for $C_{30}H_{38}N_{12}O_6Zn$ (MW: 728.09): C, 49.5; H, 5.3; N, 23.1. Found: C, 49.2; H, 5.1; N, 23.2%. Yield: 57%. IR (KBr, cm^{-1}): 2426, 2251 [ν(C≡N)], 1612, 1582, 1472 [ν(C=N)$_{py}$ and ν(C=C)], 1383 [ν(NO_3^-)]. LSI-MS (*m*/*z*): 664 $[ZnL^2(NO_3)]^+$, 605 $[ZnL^2]^+$. Λ_M/Ω^{-1} cm^2 mol^{-1} (in CH_3CN): 230 (2:1). Colour: white.

2.3.3. $[ZnL^2](ClO_4)_2$

Anal. Calc. for $C_{30}H_{38}Cl_2N_{10}O_8Zn$ (MW: 802.98): C, 44.9; H, 4.8; N, 17.4. Found: C, 44.7; H, 5.1; N, 17.2%. Yield: 62%. IR (KBr, cm^{-1}): 2253 [ν(C≡N)], 1609, 1583, 1473 [ν(C=N)$_{py}$ and ν(C=C)], 626, 1089 [ν(ClO_4^-)]. LSI-MS (*m*/*z*): 710 $[ZnL^2(ClO_4)]^+$, 605 $[ZnL^2]^+$. Λ_M/Ω^{-1} cm^2 mol^{-1} (in CH_3CN): 242 (2:1). Colour: white.

2.3.4. $[Zn_2L^3](NO_3)_4 \cdot H_2O$

Anal. Calc. for $C_{22}H_{38}N_{12}O_{13}Zn_2$(MW: 809.38):C, 32.5; H, 4.7; N, 20.7. Found: C, 32.2; H, 4.4; N, 20.5%. Yield: 73%. IR (KBr, cm^{-1}): 3182, 3286 [ν(NH)], 1608, 1583, 1444 [ν(C=N)$_{py}$ and ν(C=C)], 1483, 1383, 1351 [ν(NO_3^-)]. LSI-MS (*m*/*z*): 664 $[Zn_2L^3(NO_3)_2]^+$. Λ_M/Ω^{-1} cm^2 mol^{-1} (in CH_3CN): 241 (2:1). Colour: white.

2.3.5. $[Zn_2L^3](ClO_4)_4 \cdot 4H_2O$

Anal. Calc. for $C_{22}H_{45}N_8O_{20.5}Cl_4Zn_2$ (MW: 1013.02): C, 25.8; H, 4.4; N, 10.9. Found: C, 24.9; H, 4.2; N, 10.9%.

Yield: 49%. IR (KBr, cm^{-1}): 1608, 1584, 1452 [$\nu(C{=}N)_{py}$ and $\nu(C{=}C)$], 3180, 3289 [$\nu(NH)$], 1143, 1120, 1088, 636, 627 [$\nu(ClO_4^-)$]. LSI-MS (m/z): 841 $[Zn_2L^3(ClO_4)_3]^+$, 741 $[Zn_2L^3(ClO_4)_2]^+$, 536 $[Zn_2L^3]^+$. $\Lambda_M/\Omega^{-1}\,cm^2\,mol^{-1}$ (in CH_3CN): 387 (4:1). Colour: white.

2.4. Physical measurements

Elemental analyses were performed in a Carlo-Erba EA microanalyser. Infra-red spectra were recorded as KBr discs on a Bruker IFS-66V spectrophotometer. LSI mass spectra were recorded using a *Micromass Autospec* spectrometer with 3-nitrobenzyl alcohol as the matrix. Conductivity measurements were carried out in 10^{-3} mol dm^{-3} acetonitrile solutions at 20 °C using a WTW LF3 conductivimeter. ^1H, ^{13}C, COSY, DEPT and HMQC NMR spectra was recorded on a Bruker 500 MHz using CD_3CN or $CDCl_3$ as solvent.

2.5. X-ray crystallographic study

The details of the X-ray crystal structure solution and refinement are given in Table 1. Measurements were made on a Bruker SMART CCD Area Detector. All data were corrected for Lorentz and polarization effects. An empirical absorption correction was also applied for all the crystal structures obtained [11]. Complex scattering factors were taken from the program package SHELXTL [12]. The structures were solved by direct methods, which revealed the position of all non-hydrogen atoms. All the structures were refined on F^2 by a full-matrix least-squares procedure using anisotropic displacement parameters for all non hydrogen atoms [13]. The hydrogen atoms were located in their calculated positions and refined using a riding model.

3. Results and discussion

The hexaaza 20-membered macrocycle L^1, was obtained by a [2 + 2] barium(II) templated cyclocondensation of 2,6-diacetylpyridine and 1,3-diaminepropane in methanol followed by an *in situ* reductive demetallation of the Schiff base macrocyclic using excess sodium borohydride, following a similar method described previously.

Reduction of the tetraiminic barium(II) complex gave an isomeric mixture of the corresponding saturated macrocycles, and by using the partial crystallization method, the

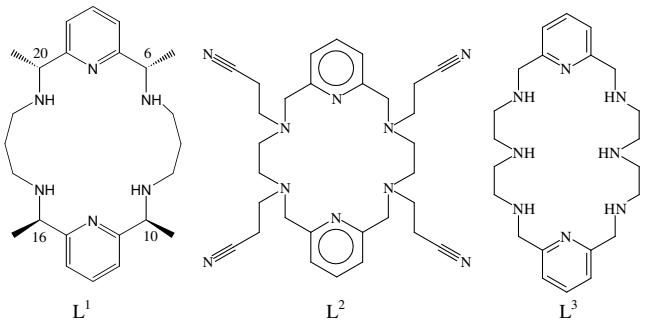
Table 1
Crystal data and structure refinement for $[ZnL^1](ClO_4)_2 \cdot H_2O$, $[ZnL^2](NO_3)_2$ and $[Zn_2L^3(NO_3)_2](NO_3)_2 \cdot H_2O$

	$[ZnL^1](ClO_4)_2 \cdot H_2O$	$[ZnL^2](NO_3)_2$	$[Zn_2L^3(NO_3)_2](NO_3)_2 \cdot H_2O$
Empirical formula	$C_{24}H_{38.5}Cl_2N_6O_{8.25}Zn$	$C_{30}H_{38}N_{12}O_6Zn$	$C_{11}H1_8N_6O_6Zn$
Formula weight	679.38	728.09	395.68
Temperature (K)	293(2)	293(2)	293(2)
Wavelength (Å)	1.54184	0.71073	0.71073
Crystal system	orthorhombic	monoclinic	monoclinic
Space group	$P2_12_12_1$	$P21/n$	P21/n
Unit cell dimensions			
a (Å)	10.250(3)	10.7906(8)	9.3510(9)
b (Å)	12.134(3)	15.3452(10)	13.7459(14)
c (Å)	25.025(5)	19.7329(13)	12.4861(13)
β (°)		92.8260(10)	92.338(2)
Volume (Å^3)	3112.5(13)	3263.5(4)	1603.6(3)
Z	4	4	4
D_{calc} (Mg/m^3)	1.450	1.482	1.639
Absorption coefficient (mm^{-1})	3.148	0.816	1.574
$F(000)$	1418	1520	816
Crystal size (mm)	$0.28 \times 0.16 \times 0.12$	$0.35 \times 0.27 \times 0.25$	$0.22 \times 0.15 \times 0.07$
θ-Range for data collection (°)	3.53–74.88	1.68–28.07	2.20–28.04
Index ranges	$0 \leqslant h \leqslant 12$, $-15 \leqslant k \leqslant 0$, $0 \leqslant l \leqslant 31$	$-14 \leqslant h \leqslant 14$, $-20 \leqslant k \leqslant 12$, $-26 \leqslant l \leqslant 25$	$-11 \leqslant h \leqslant 12$, $-17 \leqslant k \leqslant 17$, $-16 \leqslant l \leqslant 11$
Reflections collected	3632	18928	9017
Independent reflections	3603 [$R_{int} = 0.1600$]	7498 [$R_{int} = 0.0483$]	3627 [$R_{int} = 0.0710$]
Completeness to theta	100% (74.88°)	94.4% (28.07°)	93.4% (28.04°)
Absorption correction	Psi-scan	SADABS	SADABS
Maximum and minimum transmission	0.6794 and 0.5806	0.8220 and 0.7632	0.8978 and 0.7234
Refinement method	full-matrix least-squares on F^2	full-matrix least-squares on F^2	full-matrix least-squares on F^2
Data/restraints/parameters	3603/0/383	7498/0/442	3627/0/217
Goodness-of-fit on F^2	0.951	0.765	0.732
Final R indices [$I > 2\sigma(I)$]	$R_1 = 0.0634$, $wR_2 = 0.1639$	$R_1 = 0.0390$, $wR_2 = 0.0638$	$R_1 = 0.0431$, $wR_2 = 0.0540$
R indices (all data)	$R_1 = 0.1601$, $wR_2 = 0.2099$	$R_1 = 0.0988$, $wR_2 = 0.0736$	$R_1 = 0.1456$, $wR_2 = 0.0671$
Absolute structure parameter	−0.02(6)		
Largest difference in peak and hole (e Å^{-3})	0.369 and −0.358	0.317 and −0.315	0.474 and −0.330

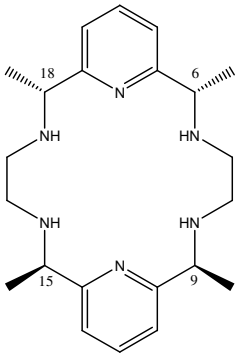
6*S*,10*S*,16*R*,20*R*-*meso* form of L^1 could be separated, as has been previously reported for the 6*S*,9*S*,15*R*,18*R*-*meso* form of the ligand L′, derived form 2,6-diacetylpyridine and ethylendiamine [14].

The elemental analysis confirms the integrity of the ligand, L^1. The IR spectrum, (KBr disc) does not show bands ascribable to carbonyl and primary amine. Also the absence of a strong band at 1620 cm^{-1} attributable to the *v*(C=N), support the reduction of the barium(II) diminic complex. Together with the band at 3300 cm^{-1} corresponding to the *v*(N–H), other absorption bands in the region of 1590–1445 cm^{-1} corresponding to *v*(C=N) and *v*(C=C) vibrations from the pyridine groups can be observed. The LSI-MS of L^1 shows the parent peak at *m*/*z* 411 further confirming the presence of the ligand. The ^1H and ^{13}C NMR data of L^1 have been recorded using $CDCl_3$ as solvent, and confirm the integrity of the ligand and its stability in solution. The assignment of the proton and carbon signals was based upon standard 2D homonuclear (COSY), DEPT-135 and HMQC measurements, using the same deuterated solvent. At room temperature the ^1H NMR spectrum shows different multiplet signals assignable to the different protons in the molecule.

The coordination ability of the L^1, L^2 and L^3 macrocyclic ligands towards hydrated nitrate and perchlorate salts of Zn(II) in 1:1 and 1:2 metal:ligand molar ratio was studied. Elemental analysis are consistent with the presence of mononuclear Zn(II) complex for L^1 and L^2 and dinuclear for L^3, independently of the metal:ligand molar ratio employed.



L^1 L^2 L^3



L'

3.1. Crystal structures

By slow concentration of acetonitrile solutions, crystals suitable for X-ray diffraction of $[ZnL^1](ClO_4)_2 \cdot H_2O$ and $[ZnL^2](NO_3)_2$ were obtained. Colourless crystals of $[Zn_2L^3(NO_3)_2](NO_3)_2 \cdot H_2O$ were obtained by slow recrystallization of the complex in water.

The details of the X-ray crystal structure solutions and refinement are given in Table 1. The molecular structure with the atomic numbering scheme adopted, together with selected bond distances and angles relating to the coordination environment of the metals are shown in Figs. 1–3.

For $[ZnL^1](ClO_4)_2 \cdot H_2O$ and $[ZnL^2](NO_3)_2$ the X-ray structure shows in both cases mononuclear endomacrocyclic complexes, with the Zn(II) ion sited in the middle of the macrocyclic cavity coordinated in a ZnN6 core by the six donor nitrogen atoms from the macrocyclic framework in a distorted octahedral geometry.

The structures show a 'twist-wrap', conformation typical of this kind of ligand, where the macrocycle adopts a helical shape with the two pyridine rings oriented 60.96° and 77.56° relative to each other for $[ZnL^1](ClO_4)_2 \cdot H_2O$ and $[ZnL^2](NO_3)_2$, respectively. The angle between the

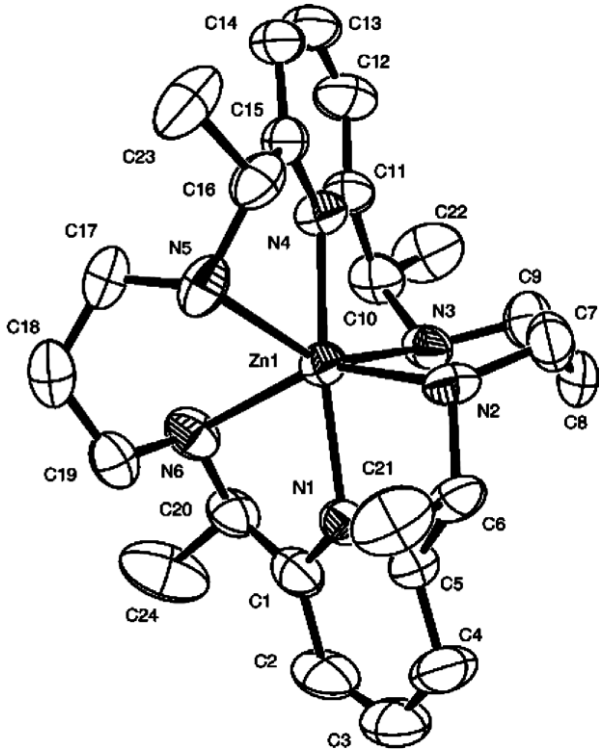


Fig. 1. Crystal structure of the cation $[ZnL^1]$, drawn with thermal ellipsoids at 50% confidence level. Hydrogen atoms, water molecule and ionic perchlorate counterions have been omitted for clarity. Selected bond lengths (Å) and angles (°): Zn(1)–N(4) 2.085(8), Zn(1)–N(1) 2.105(9), Zn(1)–N(2) 2.226(9), Zn(1)–N(6) 2.264(8), Zn(1)–N(5) 2.296(9), Zn(1)–N(3) 2.308(8), N(4)–Zn(1)–N(1) 165.2(3), N(4)–Zn(1)–N(2) 107.0(3), N(1)–Zn(1)–N(2) 76.8(3), N(4)–Zn(1)–N(6) 105.8(4), N(1)–Zn(1)–N(6) 72.7(4), N(2)–Zn(1)–N(6) 146.9(3), N(4)–Zn(1)–N(5) 74.6(4), N(1)–Zn(1)–N(5) 119.7(3), N(2)–Zn(1)–N(5) 96.5(3), N(6)–Zn(1)–N(5) 87.8(3).

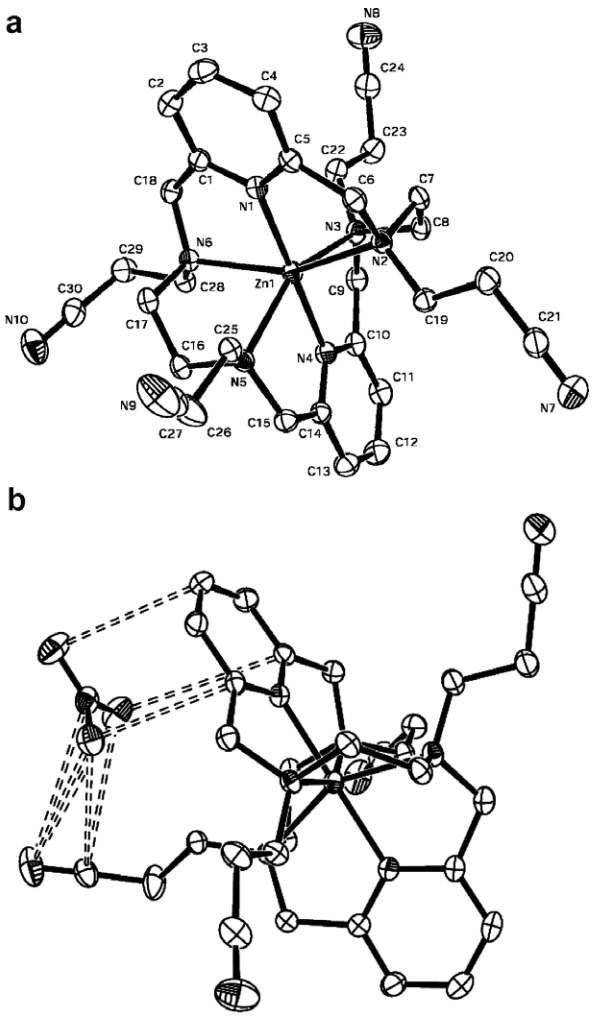


Fig. 2. (a) Crystal structure of the cation $[ZnL^2]^{2+}$, drawn with thermal ellipsoids at 50% confidence level. Nitrate anions and hydrogen atoms have been omitted for clarity. (b) Intermolecular interactions between nitrate ions, pyridine rings and nitrile groups. Selected bond lengths (Å) and angles (°): N(1)–Zn(1) 2.0556(18), N(2)–Zn(1) 2.2801(18), N(3)–Zn(1) 2.2765(18), N(4)–Zn(1) 2.0692(19), N(5)–Zn(1) 2.2822(18), N(6)–Zn(1) 2.3062(17), N(1)–Zn(1)–N(4) 179.48(8), N(1)–Zn(1)–N(3) 103.33(7), N(4)–Zn(1)–N(3) 76.73(7), N(1)–Zn(1)–N(2) 77.07(7), N(3)–Zn(1)–N(2) 82.30(7), N(3)–Zn(1)–N(5) 152.42(7), N(3)–Zn(1)–N(6) 104.82(6), N(2)–Zn(1)–N(6) 153.09(7), N(5)–Zn(1)–N(6) 82.38(6).

pyridinic nitrogen atoms and the metal ion [N(1)–Zn(1)–N(4), 165.2(3)° and 179.48(8)°, for $[ZnL^1](ClO_4)_2 \cdot H_2O$ and $[ZnL^2](NO_3)_2$, respectively], shows that the macrocycle is practically not folded.

A similar structure is observed for Zn(II) complexes with related hexaazamacrocycles [6,15,16].

The pyridine groups provides the shortest bond to the Zn atoms [Zn(1)–N(1) 2.105(9) and Zn(1)–N(4) 2.085(8) Å for $[ZnL^1](ClO_4)_2 \cdot H_2O$; N(1)–Zn(1) 2.0556(18) and N(4)–Zn(1) 2.0692(19) Å for $[ZnL^2](NO_3)_2$]. The bond lengths of the secondary amine groups vary from 2.226(9) to 2.308(8) Å for $[ZnL^1](ClO_4)_2 \cdot H_2O$ and 2.2765(18) to 2.3062(17) Å for $[ZnL^2](NO_3)_2$, not markedly different from those found in similar complexes that have been reported previously [6,15].

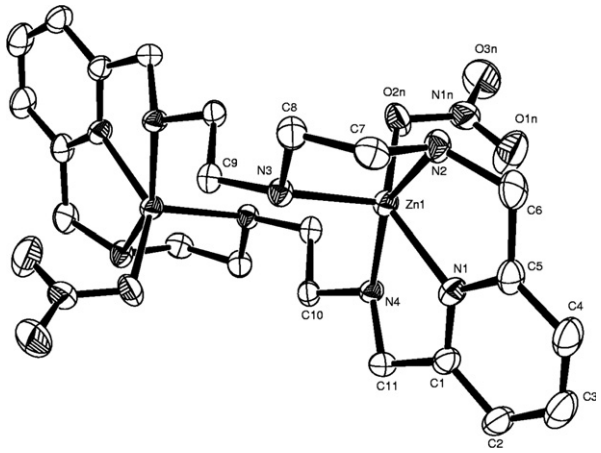


Fig. 3. Crystal structure of the cation $[Zn_2L^3(NO_3)_2]$, drawn with thermal ellipsoids at 50% confidence level. Hydrogen atoms, water molecule and ionic nitrate counterions have been omitted for clarity. Selected bond lengths (Å) and angles (°): N(1)–Zn(1) 2.035(3), N(2)–Zn(1) 2.170(3), N(3)–Zn(1) 2.069(3), N(4)–Zn(1) 2.201(3), O(2N)–Zn(1) 2.027(3), O(2N)–Zn(1)–N(1) 137.65(12), O(2N)–Zn(1)–N(3) 109.92(11), N(1)–Zn(1)–N(3) 111.75(11), O(2N)–Zn(1)–N(2) 99.63(11), N(1)–Zn(1)–N(2) 77.45(12), N(3)–Zn(1)–N(2) 84.38(11), O(2N)–Zn(1)–N(4) 97.61(10), N(1)–Zn(1)–N(4) 77.50(11), N(3)–Zn(1)–N(4) 106.67(11), N(2)–Zn(1)–N(4) 154.88(10).

In $[ZnL^2](NO_3)_2$ the donor atoms of the nitrile pendant groups are not interacting with the central ions.

The nitrate and perchlorate ions are not coordinated to the metal; they were refined with no disorder, giving bond distances and angles typical for these ions.

Inter- or intramolecular π,π-stacking interactions between the pyridine rings are not observed in the crystal structures. However, as in previous metal complexes with L^2, crystal lattice of $[ZnL^2](NO_3)_2$ contains nitrate ions close to pyridine rings and nitrile pendant groups [8]. The dihedral angle between the planes containing the nitrate counterion and the pyridine ring is 13.1°, and the distance (d_{c-N}) between the centroid of the pyridine and the N atom of the nitrate group, as analogous to the centroid-centroid distance, is 3.4 Å, commonly accepted for π,π-stacking interactions (Fig. 2b) [17]. Other nitrate ion is situated between two nitrile groups.

Interactions through hydrogen bonds have been found in the structure of $[ZnL^1](ClO_4)_2 \cdot H_2O$ (**1**) between the perchlorate counterions and amine hydrogen atoms from L^1. [N(3)–H(3N)···O(5P) 3.366 Å, 142.1°, N(3)–H(3N)···O(8P) 3.268 Å, 155.3°, N(6)–H(6N)···O(1P) 3.246 Å, 166.7°, N(6)–H(6N)···O(2P) 3.576 Å, 143.5(0.7)°, N(2)–H(2N)···O(6P)_$1 3.336 Å, 136.2°, N(2)–H(2N)···O-(7P)_$1 3.635 Å, 155.5°. $1 = x + 1, y, z$].

The crystal structure of $[Zn_2L^3(NO_3)_2](NO_3)_2 \cdot H_2O$ (Fig. 3) is consistent with the presence of the cation $[Zn_2L^3(NO_3)_2]^{2+}$, two well-separated nitrate anions and a crystallization water molecule. The cation $[Zn_2L^3(NO_3)_2]^{2+}$ shows a dinuclear endomacrocyclic complex, where both metal ions are five coordinated by one pyridinic nitrogen atom, three secondary amine groups from the macrocyclic backbone and one oxygen atom from a monodentate nitrate anion.

The largest angular difference between N(2)–Zn–N(4) and N(1)–Zn–O(2N) give rise to τ value of 0.29 confirming the distorted square pyramidal arrangement around the metal ion, with the amine nitrogen N(3) at the apical position and N(1)N(2)N(4)O(2N) as the basal plane (rms 0.2543 Å). The dihedral angle between the pyridine groups from the macrocyclic backbone is 0°, showing that the ligand is not twisted, and the planes containing the pyridinic rings are 0.15 Å away. The crystal structure also shows that there is not interaction between the metal ions, as they are 5.44 Å away.

As in the other complexes described before, the pyridine nitrogen bond length [Zn–N1 2.035(3) Å] is shorter than Zn–Namine distances, which are in the range 2.069(3)–2.201(3) Å, whilst the nitrate anion provides the shortest bond to the ion [Zn–O2N 2.027(3) Å].

Perchlorate anions interact through hydrogen bonds with the amine hydrogen atoms from the ligand. [N(4)–H(4A)···O(5N)_$1 3.03 Å, 152.5°; N(4)–H(4A)···O-(6N)_$1 3.18 Å, 128.3°; N(2)–H(2A)···O(4N)_$2 3.14 Å, 141.9°; N(2)–H(2A)···O(6N)_$2 3.11 Å, 139.2°; N(3)–H(3A)···O(4N)_$3 3.08 Å, 155.1°; N(3)–H(3A)···O-(5N)_$3 3.11 Å, 147.9°. $1 $-x+1/2$, $y-1/2$, $-z+1/2$, $2 $-x+1/2+1$, $y-1/2$, $-z+1/2$, $3 $-x+1$, $-y+1$, $-z+1$].

3.2. Spectroscopic and magnetic studies

The IR spectra of the complexes (KBr discs) show in all cases that the ν(C=N) vibration band of the pyridine groups are shifted to higher wavenumber than in the free ligand suggesting coordination to the metal atom [18]. In the case of the complexes with L^1 and L^3 the secondary amine stretches around 3300 cm^{-1} in the free ligand are split and/or shifted relative to that in the free macrocycle suggesting coordination to the metal ion. The position of the νC≡N band from the pendant groups for the perchlorate complex of L^2, is similar than in the free ligand, showing the no coordination of the nitrile groups to the metal ion. However, in the case of the nitrate complex the spectrum shows and additional band at 2426 cm^{-1} that can be related to the interaction with the nitrate ions present in the crystal lattice, as has been found previously [8]. Regarding the counterions absorptions, for $[ZnL^1](ClO_4)_2 \cdot H_2O$ and $[ZnL^2](ClO_4)_2$ the spectra feature absorptions at 1100 and 626 cm^{-1}attributable to ionic groups. The lack of splitting of this band indicates that there is no coordination of these groups to the metal centres [19,20]. However, the IR spectrum of $[Zn_2L^3](ClO_4)_4 \cdot 4H_2O$ shows the presence of several bands in the region associate with perchlorate vibrations that clearly identifies this complex as containing perchlorate coordinated groups. In the IR spectra of $[Zn_2L^3](NO_3)_4 \cdot H_2O$, the band at 1383 cm^{-1} associated with the presence of ionic nitrate is accompanied by several bands showing the presence of coordinated nitrate groups [21], but the spectrum of $[ZnL^2](NO_3)_2$ shows an intense band at 1383 cm^{-1} without splitting, suggesting the no coordination of these groups to the metal.

The LSI mass spectra of the complexes confirm the mononuclear nature of the complexes with L^1 and L^2, and the dinuclear nature for L^3 complexes.

Molar conductivity data, measured at room temperature using acetonitrile as solvent showed the presence of ionic counterions for the mononuclear complexes and the dinuclear Zn^{2+} perchlorate complex with L^3, since they are in the range reported for 2:1 electrolytes in that solvent (4:1 for the dinuclear one), whilst the conductivity data for $[Zn_2L^3](NO_3)_4 \cdot H_2O$ lies within the range reported for 2:1 electrolytes suggesting the coordination of two nitrate groups to the metal ions [22]. These values are indicative of the different coordinative capacity between perchlorate and nitrate anions. This is in agreeing with the results obtained from the IR and X-ray studies.

The ^{1}H NMR spectra of the complexes were recorded in CD_3CN. The spectrum of $[ZnL^1](ClO_4)_2 \cdot H_2O$ is quite complicated due to the low solubility of the complex in the common solvents, but it show the signals in general shifted downfield compared with the free ligands due to the complexation to the Zn(II) ion.

The ^{1}H NMR spectra of $[ZnL^2](NO_3)_2$ and $[ZnL^2](ClO_4)_2$ are similar. The spectra are more complicated than expected showing that fast interconversion of isomers in solution does not occur. The pyridinic protons appear at δ 8.25 and 7.65 ppm as a triplet and a doublet respectively. However, the aliphatic protons appear as different multiplets. The bencylic protons appear at δ 4.13–4.33, whilst the remaining aliphatic protons collapse in a multiplet at δ 2.40–3.16 ppm.

The ^{1}H NMR spectra of $[Zn_2L^3](NO_3)_4 \cdot H_2O$ and $[Zn_2L^3](ClO_4)_4 \cdot 4H_2O$ are similar. The pyridinic hydrogens appear as two multiplets at δ 8.08 an 7.48 ppm as a triplet and a doublet respectively. However, the aliphatic region is complicated, as the spectra show two broad overlapping resonances, one assigned to the bencylic protons and the other assigned to the ethylenic linkages, showing that a rapid conformational interconversion takes place in solution at this temperature.

4. Conclusion

The present work describes the synthesis and characterization of a nitrate and perchlorate Zinc(II) complexes with three different macrocyclic ligands. The different ring sizes of the ligands, the number of suitably disposed donor atoms and the presence or not of pendant-arms bearing additional potential ligating groups, give rise to complexes with different nuclearity and coordination environments. The $[ZnL^1](ClO_4)_2 \cdot H_2O$ and $[ZnL^2](NO_3)_2$ complexes present a mononuclear endomacrocyclic structure with the metal in an octahedral distorted environment coordinated by the six donor nitrogen atoms from the macrocyclic backbone. In contrast, the bigger size and number of donor atoms, let L^3 to accommodate two meal ions into

the macrocyclic cavity, and in this way, the complex $[Zn_2L^3(NO_3)_2](NO_3)_2 \cdot H_2O$ is dinuclear and both metal atoms are five coordinated by four donor nitrogen atoms from the macrocyclic framework and one oxygen atom from one monodentate nitrate anion.

In the $[ZnL^2](NO_3)_2$ complex a π interactions between a nitrate ion, a pyridine ring and a π-shell of the nitrile pendant group were found.

Acknowledgement

We thank the Xunta de Galicia (PGIDT04PXIB20901PR) for financial support.

Appendix A. Supplementary material

CCDC 652364, 652365 and 652366 contain the supplementary crystallographic data for $[ZnL^1](ClO_4)_2 \cdot H_2O$, $[ZnL^2](NO_3)_2$ and $[Zn_2L^3(NO_3)_2](NO_3)_2 \cdot H_2O$. These data can be obtained free of charge via http://www.ccdc.cam.ac.uk/conts/retrieving.html, or from the Cambridge Crystallographic Data Centre, 12 Union Road, Cambridge CB2 1EZ, UK; fax: (+44) 1223-336-033; or e-mail: deposit@ccdc.cam.ac.uk. Supplementary data associated with this article can be found, in the online version, at doi:10.1016/j.poly.2007.07.035.

References

[1] I. Bertini, C. Luchinat, W. Marek, M. Zeppezauer (Eds.), Zinc Enzymes, Birkauser, Boston, MA, 1986.
[2] C. Bazzicalupi, A. Bencini, E. Berni, A. Bianchi, P. Fornasari, C. Giorgi, B. Valtancoli, Inorg. Chem. 43 (2004) 6255.
[3] D. Kong, A.E. Martell, J. Reibenspies, Inorg. Chim. Acta 333 (2002) 7.
[4] C. Bazzicalupi, A. Bencini, E. Berni, S. Ciattini, A. Bianchi, C. Giorgi, P. Paoletti, B. Valtancoli, Inorg. Chim. Acta 317 (2001) 259.
[5] (a) R.M. Izatt, J.S. Bradshaw, S.A. Nielsen, J.D. Lamb, J.J. Christensen, D. Sen, Chem. Rev. 85 (1985) 271;
(b) K.E. Krakowiak, J.S. Bradshaw, D.J. Zamecka-Krakowiak, Chem. Rev. 89 (1989) 929.
[6] S. González, L. Valencia, R. Bastida, D.E. Fenton, A. Macías, A. Rodríguez, J. Chem. Soc., Dalton Trans. (2002) 3551.
[7] (a) L. Valencia, R. Bastida, M. Lopez-Deber, A. Macias, A. Rodríguez, M. Vicente, Z. Anorg. Allg. Chem. 629 (2) (2002) 268;
(b) L. Valencia, J. Martínez, A. Macías, R. Bastida, R.A. Carvalho, C.F.G.C. Geraldes, Inorg. Chem. 41 (20) (2002) 5300.
[8] L. Valencia, R. Bastida, M. del C. Fernández-Fernández, A. Macías, M. Vicente, Inorg. Chim. Acta 358 (9) (2005) 2618.
[9] J. Martínez-Sánchez, R. Bastida, A. Macias, P. Perez-Lourido, L. Valencia, Polyhedron 25 (2006) 3495.
[10] G.L. Rothermel, L. Miao, A.L. Hill, S.C. Jackels, Inorg. Chem. 31 (1992) 4854.
[11] G.M. Sheldrick, SADABS. Program for Empirical Absorption Correction of Area Detector Data, University of Göttingen, Germany, 1996.
[12] SHELXTL Version, An Integrated System for Solving and Refining Crystal Structures from Diffraction Data (Revision 5.1), Bruker AXS Ltd., 1996.
[13] G.M. Sheldrick, SHELXTL 97. Program for the Refinement of Crystal Structures, University of Göttingen, Germany, 1997.
[14] M. del C. Fernández-Fernández, R. Bastida, A. Macías, P. Perez-Lourido, L. Valencia, Z. Anorg. Allg. Chem. 633 (5-6) (2007) 747.
[15] R. Bastida, D.E. Fenton, M. López-Deber, A. Macías, L. Valencia, M. Vicente, Inorg. Chim. Acta 355 (2003) 292.
[16] L.H. Bryant Jr., A. Lachgar, K.S. Coates, S.C. Jackels, Inorg. Chem. 33 (2003) 2219.
[17] C. Janiak, J. Chem. Soc., Dalton Trans. (2000) 3885.
[18] N.S. Gill, R.H. Nuttall, D.E. Scaife, D.W. Sharp, J. Inorg. Nucl. Chem. 18 (1961) 79.
[19] M.F. Rosenthal, J. Chem. Educ. 50 (1973) 331.
[20] A.J. Hathaway, A.E. Underhill, J. Chem. Soc. (1961) 3091.
[21] W.T. Carnall, S. Siegel, J.R. Ferraro, B. Tani, E. Gebert, Inorg. Chem. 12 (1973) 560.
[22] W.J. Geary, Coord. Chem. Rev. 7 (1971) 81.

chemical shifts are reported in ppm. IR spectra in KBr pellets were recorded in the range of 4000–600 cm^{-1} on a Bruker Tensor 27.

2.1. Synthesis

2.1.1. [Rh(TropNMe)(CO)$_2$]

$RhCl_3 \cdot xH_2O$ (100 mg, 0.44 mmol) was dissolved in the minimum amount of DMF (ca. 3 ml) and refluxed for 30 min. until the solution turned pale yellow. The solution was treated with HTropNMe (77 mg, 0.57 mmol), precipitated with ice-water and separated by centrifuge. The complex was recrystallised from acetone (ca. 10 ml) (yield: 117 mg, 70%). ^{1}H NMR (300 MHz, $CDCl_3$, 25 °C): 7.32 (m, 2H), 7.12 (d, 1H), 6.95 (d, 1H), 6.81 (t, 1H), 1.56 (s, 3H). ^{13}C NMR (150.97 MHz, CD_2Cl_2, 25 °C): 45.8 (d, $^1J_{N-C}$ 3.6 Hz, CH_3), 118.10 (d, 1.82 Hz), 122.30 (d, 2.72 Hz), 125.07 (s), 135.51 (s), 135.87 (s), 169.41 (d, $^1J_{N-C}$ 1.73 Hz), 181.47 (s), 187.17 (d, $^1J_{Rh-C}$ 64.78 Hz), 187.90 (d, $^1J_{Rh-C}$ 71.55 Hz). IR_{KBr} (ν_{Rh-CO}) 2053, 1978 cm^{-1}, $IR_{Acetone}$ (ν_{Rh-CO}) 2070, 2000 cm^{-1}. Micro-analytical data: *Anal*. Calc. for $RhO_3C_{10}H_8N$: C, 40.98; H, 2.75; N, 4.78. Found: C, 41.53; H, 2.85; N, 4.85%.

2.1.2. [Rh(Trop)(CO)$_2$]

$RhCl_3 \cdot xH_2O$ (100 mg, 0.44 mmol) was dissolved in the minimum amount of DMF (ca. 3 ml) and refluxed for 30 min. until the solution turned pale yellow. The solution was treated with HTrop (66 mg, 0.57 mmol), precipitated with ice-water and separated by centrifuge. The complex was recrystallised from acetone (ca. 10 ml) (yield: 68 mg, 56%). ^{1}H NMR (300 MHz, $CDCl_3$, 25 °C): 7.68 (dd, 2H), 7.54 (m, 2H), 7.25 (dd, 1H). ^{13}C NMR (150.97 MHz, CD_2Cl_2, 25 °C): 128.22 (s), 130.20 (s), 138.28 (s), 184.49 (s), 184.96 (d, $^1J_{Rh-C}$ 72.74 Hz). IR_{KBr} (ν_{Rh-CO}) 2074, 2014 cm^{-1}, $IR_{Acetone}$ (ν_{Rh-CO}) 2078, 2007 cm^{-1}. Micro-analytical data: *Anal*. Calc. for $RhO_3C_{10}H_8$: C, 38.60; H, 1.80. Found: C, 38.62; H, 1.85%.

2.1.3. [Rh(TropNMe)CO(PPh$_3$)] (**1**)

[Rh(TropNMe)(CO)$_2$] (20 mg, 0.068 mmol) was dissolved in the minimum amount of warm acetone (ca. 2 ml) to which was added PPh_3 (20 mg, 0.075 mmol). The reaction mixture was allowed to evaporate and crystals suitable for X-ray crystallography were obtained as yellow blocks (yield: 20 mg, 55%). ^{1}H NMR (300 MHz, $CDCl_3$, 25 °C): 7.67 (m, 5H), 7.39 (m, 10H), 7.12 (dd, 1H), 6.95 (t, 1H), 6.88 (t, 1H), 6.63 (d, 1H), 6.51 (t, 1H). ^{13}C NMR (150.97 MHz, CD_2Cl_2, 25 °C): 45.77 (d, $^1J_{N-C}$ 3.64 Hz), 117.29 (d, 1.74 Hz), 120.04 (d, 1.63 Hz), 122.35 (d, 1.63), 128.74 (d, 9.15 Hz), 130.78 (s), 134.07 (t, 21.55, 25.35. Hz), 134.86 (d, 11.33 Hz), 168.37 (s), 181.77 (d, 5.45 Hz), 192.40 (dd, $^1J_{Rh-C}$ 76.09 Hz, $^2J_{P,C}$ 23.53 Hz). ^{31}P NMR 42.80 (d, $^1J_{Rh-P}$ 146.88 Hz). IR_{KBr} (ν_{Rh-CO}) 1943 cm^{-1}, $IR_{Acetone}$ (ν_{Rh-CO}) 1962 cm^{-1}. Micro-analytical data: *Anal*. Calc. for $RhPO_2C_{27}H_{23}N$: C, 61.49; H, 4.40; N, 2.66. Found: C, 61.94; H, 4.49; N, 2.71%.

2.1.4. [Rh(Trop)CO(PPh$_3$)] · Acetone (**2**)

[Rh(Trop)(CO)$_2$] (20 mg, 0.068 mmol) was dissolved in the minimum amount of warm acetone (ca. 2 ml) to which was added PPh_3 (20 mg, 0.075 mmol). The reaction mixture was allowed to evaporate and crystals suitable for X-ray crystallography were obtained as yellow blocks (yield: 30 mg, 78%). ^{1}H NMR (300 MHz, $CDCl_3$, 25 °C): 7.67 (m, 6H), 7.40 (m, 9H), 7.28 (m, 2H), 6.97 (m, 3H), 2.15 (s, 3H). ^{13}C NMR (150.97 MHz, CD_2Cl_2, 25 °C): 31.16 (s), 126.47 (s), 127.36 (s), 127.46 (s), 128.81 (d, 11.14 Hz), 131.08 (s), 133.43 (d, 51.21 Hz), 134.83 (d, 11.19 Hz), 137.07 (s), 137.23 (s), 184.64 (s), 185.49 (s), 190.15 (dd, $^1J_{Rh-C}$ 76.18 Hz, $^2J_{P,C}$ 25.31 Hz), 206.95 (s). ^{31}P NMR 48.80 (d, $^1J_{Rh-P}$ 173.10 Hz). IR_{KBr} (ν_{Rh-CO}) 1974 cm^{-1}, $IR_{Acetone}$ (ν_{Rh-CO}) 1978 cm^{-1}. Micro-analytical data: *Anal*. Calc. for $RhPO_4C_{28}H_{26}$: C, 60.01; H, 4.68. Found: C, 60.46; H, 4.62%.

2.2. Crystallography

The data collection was done on a Bruker Apex2 4K CCD diffractometer using Mo Kα (0.71073 Å) and ω-scans at 100(2) K. After completion the first 50 frames were repeated to check for decay, of which none was observed. All reflections were merged and integrated with SAINT-PLUS [15] and were corrected for Lorentz, polarization and absorption effects using SADABS [16]. The structures were solved by the heavy atom method and refined through full-matrix least-squares cycles using the SHELX-97 [17] package with $\sum(||F_o| - |F_c||)^2$ being minimized. All non-H atoms were refined with anisotropic displacement parameters, while H atoms were constrained to parent atom sites using a riding model (aromatic C–H = 0.93 Å; aliphatic C–H = 0.96 Å). The graphics were done with the DIAMOND [18] Visual Crystal Structure Information System software. The crystals of **2** included 0.75 acetone solvate molecule per asymmetric unit, which was disordered of two sites along the *a*-axis. The crystal structure of **2** has been reported previously, however, the authors failed to locate and describe the acetone solvate molecule [19] in the asymmetric unit. Details of the crystal data, intensity measurements and data processing are summarized in Table 1. Selected bond distances and angles are given in Table 2.

2.3. Computational data

Calculation results were obtained using the GAUSSIAN-03W [20] software package. DFT calculations were done at the B3LYP [21] level of theory; for the main group elements the 6-31G(d) [22,23] basis set were incorporated while the rhodium core was described by the LanL2DZ [24] basis set. Optimised structures were verified as a minimum through frequency analysis and from this data the stretching frequencies of the carbonyl groups were identified. The isodesmic comparisons between different isomers were calculated using the diketonato rhodium(I) dicarbonyl complexes to minimize error.

Table 1
Crystal data and structure refinement for complex **1** and **2**

Compound	**1**	**2**
Empirical formula	$C_{27}H_{23}NO_2PRh$	$C_{55}H_{40}O_7P_2Rh_2$
Formula weight	527.34	1080.63
T (K)	100(2)	100(2)
Radiation λ (Å)	0.71073	0.71073
Crystal system	triclinic	triclinic
Space group	$P\bar{1}$ (No. 2)	$P\bar{1}$ (No. 2)
Unit cell dimensions		
a (Å)	9.2395(3)	8.760(5)
b (Å)	9.7982(3)	10.388(5)
c (Å)	14.1171(5)	13.304(5)
α (°)	82.699(1)	89.256(5)
β (°)	88.676(1)	77.321(5)
γ (°)	63.557(1)	83.850(5)
V (Å^3)	1134.23(6)	1174.3(10)
Number of reflections for cell measurement	8922	3927
θ Range for cell measurement (°)	2.48–28.17	2.40–27.84
Z	2	1
D_{calc} (Mg/m^3)	1.544	1.528
Absorption coefficient (mm^{-1})	0.848	0.825
F(000)	536	546
Crystal shape/crystal colour	plate/red	cuboid/yellow
Crystal size (mm)	$0.434 \times 0.269 \times 0.065$	$175 \times 0.032 \times 0.025$
Reflections collected/unique	10 583/4945	17 585/5111
Reflections with $[I > 2\sigma(I)]$	4749	4337
Completeness to $\theta = 27°$ (%)	1	1
Absorption correction	multi-scan	multi-scan
Maximum and minimum transmission	0.758 and 0.940	0.970 and 0.981
Data/restraints/parameters	4945/0/283	5111/0/299
Goodness-of-fit on F^2	1.14	1.04
Final R indices $[I > 2\sigma(I)]$	0.020	0.037
R indices (all data)	0.021	0.048
Largest difference in peak and hole (e Å^{-3})	0.472 (0.8 Å Rh) and −1.084 (0.9 Å Rh)	1.368 (1.2 Å C41) and −0.627 (0.4 Å C41)

Table 2
Selected bond distances (Å) and angles (°) for **1** and **2**

Compound	**1**	**2**
Rh–O1	2.0365(11)	2.045(2)
Rh–N1	2.0717(14)	
Rh–O2		2.083(2)
Rh–C01	1.8038(15)	1.805(3)
Rh–P	2.2628(4)	2.2232(11)
C01–O01	1.157(2)	1.149(4)
C1–C2	1.476(2)	1.462(5)
O1–Rh–N1	77.63(5)	
O1–Rh–O2		77.90(9)
C01–Rh–O1	174.99(6)	174.03(12)
C01–Rh–N1	98.92(6)	
C01–Rh–O2		98.55(12)
C01–Rh–P	91.71(5)	87.19(11)
O1–Rh–P	91.85(3)	96.40(8)
N1–Rh–P	169.27(4)	
O2–Rh–P		174.25(6)
Rh–C01–O01	177.15(14)	176.9(3)
O1–C1–C2–N1	1.2(2)	
O1–C1–C2–O2		3.1(4)
C8–N1–C2–C1	178.23(14)	
C3–C2–C1–C7	1.6(3)	7.0(6)
C7–C6–C5–C4	2.6(3)	1.1(8)

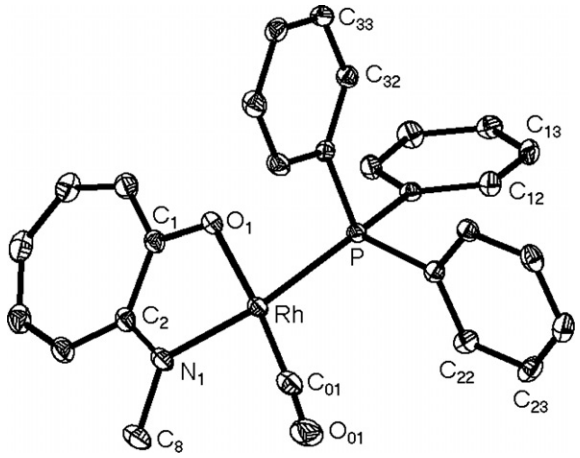


Fig. 1. Molecular diagram showing the numbering scheme and displacement ellipsoids (50% probability) in [Rh(TropNMe)(CO)(PPh$_3$)] (**1**). The first digit in the phenyl rings refers to the number of the ring, the second digit to the number of the C atom in the ring (1–6). Hydrogen atoms omitted for clarity.

3. Results and discussion

Details of the data collections and refinement parameters of [Rh(TropNMe)CO(PPh$_3$)] (**1**) and [Rh(Trop)CO(PPh$_3$)] · Acetone (**2**) are reported in Table 1 and selected geometrical parameters are summarized in Table 2. The molecular structures with thermal ellipsoids and numbering schemes for **1** and **2** are shown in Figs. 1 and 3, respectively.

3.1. Structural description

The molecular structure of [Rh(TropNMe)CO(PPh$_3$)] (**1**) is the first example of a mixed N,O-troponate complex containing carbonyl and triphenylphosphine moieties (Fig. 1). A distorted square planar geometry about the rhodium(I) metal centre can be observed as defined by the coordinated atoms. This distortion is observed as a deviation from linearity of the angle formed by O–Rh–C (carbonyl) and N–Rh–P atoms, 174.98(5)° and 169.29(4)°, respectively. The bidentate bite angle formed by O–Rh–N is close to that observed for the unfunctionalised tropolonato complexes in the order of ca. 80° [7–12]. It was expected that the Rh–N and Rh–O bond distances would differ, but in the current complex this variation is minimal. Similar trends have been observed for O,O-tropolonato

complexes [5,25,12] indicating that the seven-membered ring system reduces the effect of functionalization of the hetero-atoms.

The ordering in the solid state is significantly changed by the presence of π–π stacking between respective 2-(*N*-methylamino)troponato ligands, which is observed in the order of 3.479(7) Å, Fig. 2. The complex **1** adopts an arched configuration as defined by the dihedral angle of 8.81(3)° between the planes from the seven-membered troponato backbone with that of the Rh(I) centre and the two O-donor atoms. The rhodium(I) atom is in close proximity to a hydrogen atom of the π-stacking troponato ring, $Rh\cdots H_4$ [$1-x$, $2-y$, $1-z$], at a distance of 3.4157(1) Å.

The molecular structure of [Rh(Trop)CO(PPh_3)]·Acetone (**2**) shows the coordination of the complex to exhibit a slightly distorted square planar geometry about the rhodium(I) metal centre (Fig. 3). The deviation from planarity can be observed from the angle formed by O–Rh–C (carbonyl) and O–Rh–P atoms, 174.0(1)° and 174.25(6)°, respectively. The rhodium(I) metal centre is elevated above the four coordinating atoms by 0.0143(5) Å. The O–Rh–O bidentate bite angle is close to that observed for unfunctionalised tropolonato complexes in the order of 77.9(1)° [7–12]. The difference in *trans* directing groups (PPh_3 versus CO) does not seem to play such a significant role, as observed from the comparable Rh–O bond distances (Table 2).

The rhodium(I) metal complex co-crystallises with an acetone molecule in the asymmetric unit, exhibiting a 75% statistical disorder over two positions. No significant hydrogen bonding is found between the complex and the solvent molecule. The solvent molecule occupies voids created by the efficient packing of the metal complex. Hydrogen bonding between a tropolonato oxygen atom (O_2) and a corresponding phenyl hydrogen atom (H_{14}–C_{14}) is observed. The intermolecular hydrogen bond [2.585 Å ($O_2\cdots H_{14}$), 3.509(4) Å (O_2, C_{14}), 172.7(2)°] can be classified as a weak interaction but is enhanced by the π–π stacking in the order of 3.39(1) Å of the tropolonato moieties. The

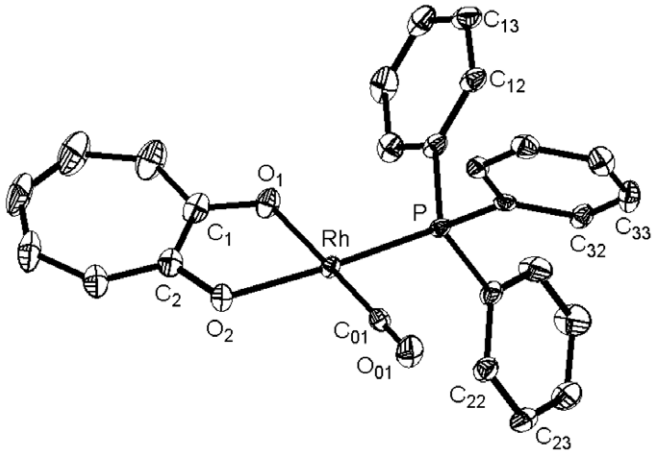


Fig. 3. Molecular diagram showing the numbering scheme and displacement ellipsoids (50% probability) in [Rh(Trop)(CO)(PPh_3)] (**2**). The first digit in the phenyl rings refers to the number of the ring, the second digit to the number of the C atom in the ring (1–6). Hydrogen atoms and disordered solvent molecule (acetone) omitted for clarity.

effect of the intermolecular hydrogen bonding and π-stacking tropolonato functionalities create a three-dimensional chain along the *b*-axis.

The change in geometrical parameters due to the introduction of a methylamino moiety on the troponoid ring system, does not seem to significantly affect the coordination to the rhodium(I) centre (Table 2). The *trans* influence of N(Me) versus O was expected to be more prominent due to the significant change observed in the infrared frequency (solid state ~30 cm^{-1}, solvent ~16 cm^{-1}). A single noteworthy difference between the two solid state structures was the observed change of the Rh–P bond distance in the order of 0.04 Å. The bite angle was also not affected by the change of hetero-atoms and is nearly constant at 77°. This relative insensitivity of functionalization of the troponoid ring might indicate that the cycloheptatriene system counterbalances the different affects of hetero group donor atoms.

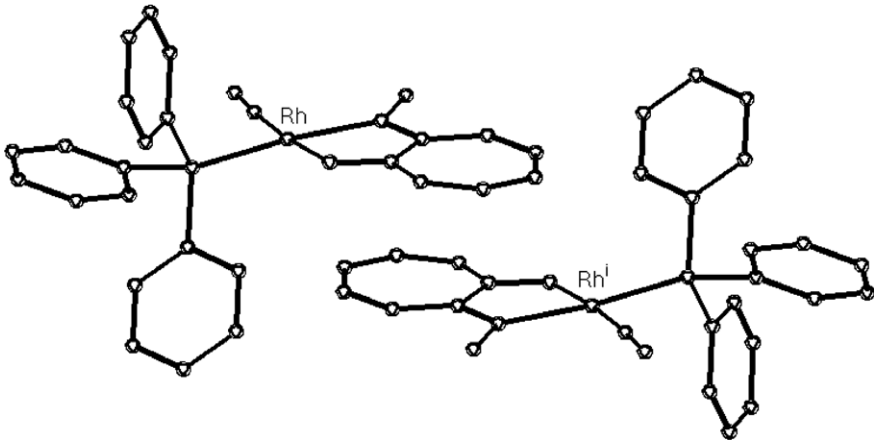


Fig. 2. Packing diagram of [Rh(TropNMe)CO(PPh_3)] (**1**) along the *ac*-plane illustrating the π–π stacking [3.479(7) Å] in the unit cell. Hydrogen atoms omitted for clarity [symmetry code: $1-x$, $2-y$, $1-z$].

3.2. Computational data

Since complexes **1** and **2** tended to behave in a similar fashion with respect to their geometrical parameters in the solid state, a theoretical study was done to determine if any significant differences could be observed at a theoretical level between these compounds. The crystallographically determined structures were first optimised and reported herein as compounds [Rh(TropNMe)CO(PPh_3)] (**I**) and [Rh(Trop)CO(PPh_3)] (**II**), respectively. Secondly, the [Rh(TropNMe)$(CO)_2$] and [Rh(Trop)$(CO)_2$] complexes were optimised to construct an isodesmic reaction scheme to compare complexes **I** and **II** relative to each other in terms of stability. Finally, the *cis*-adduct (PPh_3-*cis*-NMe) of [Rh(TropNMe)CO(PPh_3)] (**I**) was calculated to determine the structural change of the coordination sphere due to steric factors, which could indicate a preference of the *trans*-isomer over the *cis*-isomer. Calculated geometrical parameters and energies are reported in Table 3.

Geometrical results from the calculations confirmed that these two types of complexes (**I** and **II**) have similar structural parameters, Table 3. The close structural relationship between the calculated and crystallographic observed structures is best illustrated with a RMS overlay error of less than 0.376 and 0.133 Å for **1/I** and **2/II**, respectively, see Fig. 4. The increased RMS overlay error of complexes **1/I** are most probably due to solid state interactions as described below.

The calculated Rh–N and Rh–O bond distances for the 2-(*N*-methylamino)troponato complexes (**1** and **I**) do not vary by much in contrast to that observed for the solid state structure (**1**). Compared to the crystallographic data of **1**, an increase is observed in the Rh–P bond distance of ca. 0.16 Å for the optimised structure (**I**). In order to characterise the effect of functionalization, the *cis*-conformation (PPh_3-*cis*-NMe) is included and it clearly indicated a strained orientation with the Rh–N bond distance increasing significantly from the *trans*-conformation (**I**). The affect of the relative strain can also be observed from the energy difference between these two isomers which is in the order of 50 kJ/mol, indicating that isomer **I** is the preferred isomer in the solid state and solution.

Comparing the tropolonato complexes, **2** and **II**, no significant changes (less than 0.1 Å) in Rh–O or Rh–C bond distances are observed. The calculated Rh–P bond distance is slightly shorter than the reported value of 2.223 Å in the crystal structure (Table 3). The effect of rotation of the triphenylphosphine on the O–Rh–O bite angle is less than 1° and is in good agreement with the solid state structure. As an illustrative example the rotation of the triphenylphosphine moiety to its higher energy conformer (a local minimum) is only 25.2 kJ/mol. This clearly indicates that in solution the two complexes (**II** and Rotation, Table 3) are nearly in the same energetic environment.

To obtain a relative measure for the different complexes, an isodesmic reaction scheme was constructed to illustrate the energy difference profile between the 2-(*N*-methylamino)troponato (N,O; **I**) and tropolonato (O,O; **II**) complexes, Table 3. Complex **II** is ca. 26 kJ/mol lower in the energy profile than complex **I**, this is mostly from the addition of the methylamino moiety introducing strain into the five-membered chelating ring of the rhodium(I) complex. Although the energy difference is significantly large, it is still within a comparable range for the two complexes if one considers the rotation of the triphenylphosphine moiety which is only 25.2 kJ/mol.

Table 3
Selected calculated and solid state bond lengths (Å), angles and torsion angles (°) for [Rh(Trop/TropNMe)CO(PPh_3)]

	[Rh(Trop/TropNMe)$(CO)_2$]		[Rh(TropNMe)CO(PPh_3)]			[Rh(Trop)CO(PPh_3)]		
	Trop	TropNMe	*cis*-Isomer	(**I**)	(**1**) X-ray	Rotation	(**II**)	(**2**) X-ray
Rh–O	2.061	2.044	2.055	2.062	2.0365(11)	2.089	2.104	2.045(2)
Rh–O	2.061					2.085	2.09	2.083(2)
Rh–N		2.061	2.097	2.066	2.0717(14)			
Rh–C	1.873	1.866	1.857	1.835	1.8038(15)	1.837	1.84	1.805(3)
	1.873	1.895						
Rh–P			2.399	2.42	2.2628(4)	2.39	2.291	2.223(1)
O–Rh–O	78.57					77.77	76.99	77.90(9)
O–Rh–N		78.56	77.82	78.11	77.63(5)			
C–Rh–C	92.02	91.11						
C–Rh–P			90.71	93.22	91.71(5)	93.67	91.2	87.19(11)
O–Rh–C	94.71	92.15	91.04	176.29	174.99(6)	95.33	96.27	98.55(12)
O–Rh–P			178.17	90.39	91.85(3)	93.21	95.53	96.40(8)
N–Rh–C		98.18	168.84	98.27	98.92(6)			
N–Rh–P			100.45	168.45	169.27(4)			
O–C–C–O	0.01					0.71	0.53	3.1(4)
N–C–C–O		0.01	0.46	1.67	1.2(2)			
E(H)	−756.596917	−776.030176	−1364.26666	−1364.27556		−1344.84265	−1344.85225	
E_{iso} (kJ/mol)			49.49	26.12		25.20[a]	0	

[a] $E_{iso} = \{[E(\text{RhTrop}(CO)_2) + E(\text{Rh(Trop)CO}(PPh_3)^{ROT})] - [E(\text{RhTrop}(CO)_2) + E(\text{Rh(Trop)CO}(PPh_3)^{(II)})]\} \times 627.5 \times 4.184$.

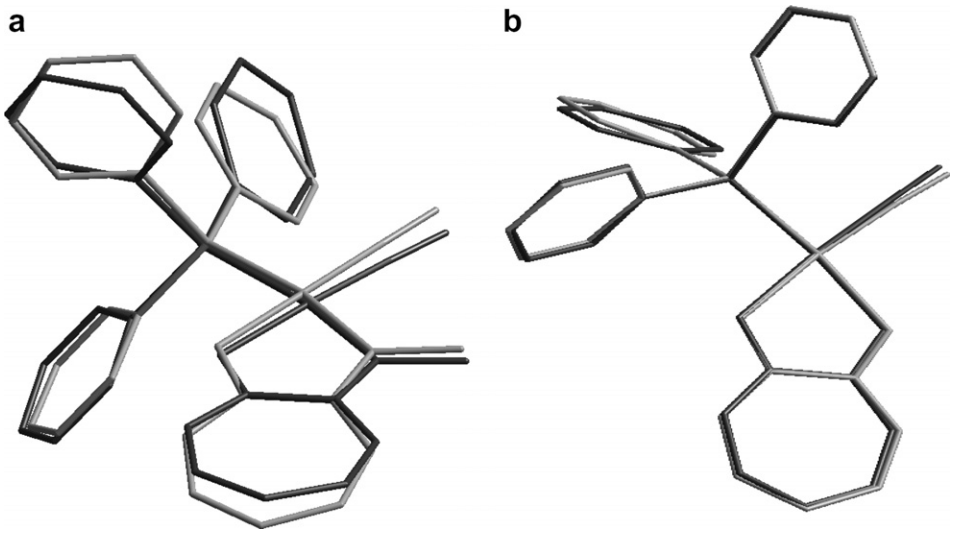


Fig. 4. Overlayed structures of the calculated (grey) and solid state (black) structures of [Rh(TropNMe)(CO)(PPh_3)] (left) and [Rh(Trop)(CO)(PPh_3)] (right). Hydrogen atoms omitted for clarity. The RMS overlay error of 0.376 and 0.133 Å does not include hydrogen atoms for the respective complexes.

4. Conclusion

The effect of substitution of a tropolonato oxygen atom with a *N*-methylamino moiety does not significantly alter the geometrical parameters of the rhodium(I) complex. The structural similarity between **1** and **2** in the solid state was confirmed by computational results. Finally, π–π stacking could be observed for both the functionalised 2-(*N*-methylamino)troponato and tropolonato rhodium(I) complexes.

Acknowledgements

I thank Prof. A. Roodt for his helpful discussions in preparation of this paper. Financial assistance from the University of the Free State is gratefully acknowledged, while Dr. A. Muller, Mr. Leo Kirsten and Mr. J.M. Janse van Rensburg are thanked for the data collections. I also express our gratitude towards SASOL and the South African National Research Foundation (SA-NRF/THRIP) for financial support of this project. Part of this material is based on work supported by the SA-NRF/THRIP under grant number GUN 2068915. Opinions, findings, conclusions or recommendations expressed in this material are those of the authors and do not necessarily reflect the views of the SA-NRF.

Appendix A. Supplementary material

CCDC 604203 and 624149 contain the supplementary crystallographic data for **1** and **2**. These data can be obtained free of charge via http://www.ccdc.cam.ac.uk/conts/retrieving.html, or from the Cambridge Crystallographic Data Centre, 12 Union Road, Cambridge CB2 1EZ, UK; fax: (+44) 1223-336-033; or e-mail: deposit@ccdc.cam.ac.uk. Supplementary data associated with this article can be found, in the online version, at doi:10.1016/j.poly.2007.07.039.

References

[1] P.L. Pauson, J. Chem. Soc. (1954) 9.
[2] M. Hashimoto, S. Ujie, A. Mori, Chem. Lett. 7 (2000) 758.
[3] P.W. Roesky, Chem. Soc. Rev. 29 (2000) 335.
[4] F. Nepveu, F. Jasanda, L. Walz, Inorg. Chim. Acta 211 (1993) 141.
[5] R. Crous, M. Datt, D. Foster, L. Bennie, C. Steenkamp, J. Huyser, L. Kirsten, G. Steyl, A. Roodt, Dalton Trans. 6 (2005) 1108.
[6] M.R. Burgstein, H. Berberich, P.W. Roesky, Organometallics 17 (1998) 1452.
[7] A. Roodt, S. Otto, G. Steyl, Coord. Chem. Rev. 245 (2003) 121.
[8] G. Steyl, A. Roodt, Acta Crystallogr., Sect. C 60 (2004) m324.
[9] G. Steyl, Acta Crystallogr., Sect. E 62 (2006) m974.
[10] G. Steyl, Acta Crystallogr., Sect. E 62 (2006) m650.
[11] G. Steyl, Acta Crystallogr., Sect. E 61 (2005) m1860.
[12] G. Steyl, S. Otto, A. Roodt, Acta Crystallogr., Sect. E 57 (2001) m352.
[13] P.W. Roesky, M.R. Burgstein, Inorg. Chem. 38 (1999) 5629.
[14] R.M. Claramunt, D. Sanz, M. Perez-Torralba, E. Pinilla, M.R. Torres, J. Elguero, Eur. J. Chem. (2004) 4452.
[15] Bruker, SAINT-PLUS (including XPREP). Version 7.12, Bruker AXS Inc., Madison, WI, 2004.
[16] Bruker, SADABS (Version 2004/1), Bruker AXS Inc., Madison, WI, 1998.
[17] G.M. Sheldrick, SHELXS-97 and SHELXL-97, University of Göttingen, Göttingen, Germany, 1997.
[18] K. Brandenburg, H. Putz, DIAMOND. Release 3.0e. Crystal Impact GbR, Postfach 1251, D-53002, Bonn, Germany, 2004.
[19] J.G. Leipoldt, L.D.C. Bok, S.S. Basson, H. Meyer, Inorg. Chim. Acta 42 (1980) 105.
[20] M.J. Frisch, G.W. Trucks, H.B. Schlegel, G.E. Scuseria, M.A. Robb, J.R. Cheeseman, J.A. Montgomery Jr., T. Vreven, K.N. Kudin, J.C. Burant, J.M. Millam, S.S. Iyengar, J. Tomasi, V. Barone, B. Mennucci, M. Cossi, G. Scalmani, N. Rega, G.A. Petersson, H. Nakatsuji, M. Hada, M. Ehara, K. Toyota, R. Fukuda, J. Hasegawa, M. Ishida, T. Nakajima, Y. Honda, O. Kitao, H. Nakai, M. Klene, X. Li, J.E. Knox, H.P. Hratchian, J.B. Cross, V. Bakken, C. Adamo, J. Jaramillo, R. Gomperts, R.E. Stratmann, O. Yazyev, A.J. Austin, R. Cammi, C. Pomelli, J.W. Ochterski, P.Y. Ayala, K. Morokuma, G.A. Voth, P. Salvador, J.J. Dannenberg, V.G. Zakrzewski, S. Dapprich,

A.D. Daniels, M.C. Strain, O. Farkas, D.K. Malick, A.D. Rabuck, K. Raghavachari, J.B. Foresman, J.V. Ortiz, Q. Cui, A.G. Baboul, S. Clifford, J. Cioslowski, B.B. Stefanov, G. Liu, A. Liashenko, P. Piskorz, I. Komaromi, R.L. Martin, D.J. Fox, T. Keith, M.A. Al-Laham, C.Y. Peng, A. Nanayakkara, M. Challacombe, P.M.W. Gill, B. Johnson, W. Chen, M.W. Wong, C. Gonzalez, J.A. Pople, GAUSSIAN-03, Revision C.01, Gaussian, Inc., Wallingford, CT, 2004.

[21] A.D. Becke, J. Chem. Phys. 98 (1993) 5648.

[22] P.C. Hariharan, J.A. Pople, Theoret. Chim. Acta 28 (1973) 213.

[23] M.M. Francl, W.J. Petro, W.J. Hehre, J.S. Binkley, M.S. Gordon, D.J. DeFree, J.A. Pople, J. Chem. Phys. 77 (1982) 3654.

[24] P.J. Hay, W.R. Wadt, J. Chem. Phys. 82 (1985) 299.

[25] G. Steyl, A. Roodt, Acta Crystallogr., Sect. E 61 (2005) m1214.

L-proline and N,N-donor heterocyclic bases as DNA groove binders. Our choice of 2,2′-bipyridine (bpy) and 1,10-phenathroline (phen) is based on their difference in DNA binding ability [13,15c]. The distinctive cyclic structure of proline's side chain gives an exceptional conformational rigidity compared to other amino acids. L-proline is essential for the synthesis of collagen, the most abundant protein in mammals [22].

Herein, we present the synthesis, structure, DNA binding and cleavage property of two ternary copper(II) complexes of formulation $[Cu(L\text{-pro})(B)(H_2O)](NO_3)$ (**1**, **2**) where B is N,N-donor heterocyclic base, *viz.* 2,2′-bipyridine (bpy, **1**) and 1,10-phenanthroline (phen, **2**) (Scheme 1). The bpy complex (**1**) has been structurally characterized by X-ray crystallography. Detailed studies have been made to elucidate the role of the DNA binder and the mechanistic pathways involved in the 'chemical nuclease' activity.

2. Experimental

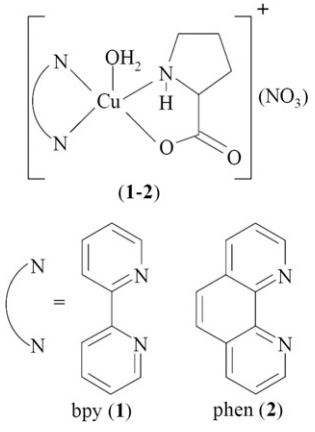
2.1. Materials

All reagents and chemicals were procured from commercial sources. Solvents used for electrochemical and spectroscopic studies were purified by standard procedures [23]. The supercoiled pUC19 DNA (cesium chloride purified) was purchased from Bangalore Genei (India). Calf thymus (CT) DNA, agarose (molecular biology grade), distamycin-A, catalase, superoxide dismutase (SOD) and ethidium bromide (EB) were obtained from Sigma (USA). Tris(hydroxymethyl)aminomethane–HCl (Tris–HCl) buffer solution was prepared by using deionized, sonicated triple distilled water.

2.2. Synthesis

*Preparation of [Cu(L-pro)(B)(H$_2$O)](NO$_3$) (**1**, **2**) (B = bpy, phen).* The complexes were prepared by following a reported [24] synthetic method with modification in which a 10 ml aqueous solution of $Cu(NO_3)_2 \cdot 3H_2O$ (0.48 g, 2.0 mmol) was reacted with L-proline (0.23 g, 2.0 mmol) treated with NaOH (0.08 g, 2.0 mmol) in water (10 ml) under magnetic stirring at room temperature. After 30 min, a 20 ml methanol solution of the heterocyclic base [bpy (0.31 g), phen (0.40 g) (2.0 mmol)] was added to the solution and the resulting mixture was stirred for 2 h at room temperature. On cooling the solution to an ambient temperature, it was filtered and the filtrate on slow concentration yielded crystalline solid of the product. The solid was isolated and washed with cold aqueous methanol and finally dried over P_4O_{10} (yield: ~70%). *Anal.* Calc. for $C_{15}H_{18}CuN_4O_6$ (**1**): C, 43.52; H, 4.38; N, 13.53. Found: C, 43.35; H, 4.18; N, 13.26%. λ_{max}, nm (ε, $M^{-1}\,cm^{-1}$) in water: 602 (50), 311 (10 820), 300 (10 790), 237sh (11 030). FT-IR, cm^{-1} (KBr disc): 3445br, 3238m, 3018m, 2946m, 2885s, 1627s, 1574w, 1448m, 1384 vs, 1287w, 1191m, 1046m, 922m, 835m, 786m, 733s, 662m, 576m, 518m, 421m (s, strong; m, medium; w, weak; br, broad; vs, very strong). μ_{eff} (solid, 298 K): 1.78 μ_B. Λ_M ($\Omega^{-1}\,cm^2\,M^{-1}$) in water at 25 °C: 128. *Anal.* Calc. for $C_{17}H_{18}CuN_4O_6$ (**2**): C, 46.61; H, 4.15; N, 12.79. Found: C, 46.35; H, 4.07; N, 12.58%. λ_{max}, nm (ε, $M^{-1}\,cm^{-1}$) in water: 612 (60), 294 (8740), 272 (29 350), 204 (38 800). FT-IR, cm^{-1} (KBr disc): 3380br, 3150br, 2884m, 1624s, 1519m, 1519m, 1387 vs, 1327w, 1148m, 1041m, 932m, 859s, 825m, 780m, 724s, 628w, 582w, 531m, 468m, 430w. μ_{eff} (solid, 298 K): 1.75 μ_B. Λ_M ($\Omega^{-1}\,cm^2\,M^{-1}$) in water at 25 °C: 190.

The complexes showed high solubility in water, good solubility in methanol and ethanol, dimethylformamide (DMF) and dimethyl sulfoxide (DMSO) and were insoluble in hydrocarbons.



Scheme 1. Complexes **1** and **2** and the heterocyclic bases.

2.3. General methods

The elemental analysis was done using a Thermo Finnigan FLASH EA 1112 CHNS analyzer. The infrared and electronic spectra were recorded on Perkin–Elmer Lambda 35 and Perkin–Elmer spectrum one 55 spectrophotometers, respectively. DNA melting experiments were carried out on a Varian Cary 300 Bio UV–Vis spectrophotometer attached to a Cary Peltier temperature controller. Magnetic susceptibility data at 298 K for the polycrystalline samples of the complexes were obtained using Model 300 Lewis-coil-force magnetometer of George Associates Inc. (Berkeley, USA) make. $Hg[Co(NCS)_4]$ was used as a standard. Experimental susceptibility data were corrected for diamagnetic contributions [25]. Molar conductivity measurements were done using a Control Dynamics (India) conductivity meter. Electrochemical measurements were made at 25 °C on an EG&G PAR model 253 VersaStat potentiostat/galvanostat with electrochemical analysis software 270 using a three electrode setup consisting of a glassy carbon working, platinum wire auxiliary and a saturated calomel reference electrode (SCE) in water containing 0.1 M KCl. The electrochemical data were uncorrected for junction potentials.

2.4. X-ray crystallographic procedures

Dark-blue single crystals of [Cu(L-pro)(bpy)-(H_2O)](NO_3) (**1**) was obtained on slow concentration of the aqueous-methanolic solution of the complex. Crystal mounting was done on glass fiber with epoxy cement. All geometric and intensity data for **1** were collected at room temperature using a Bruker SMART APEX CCD diffractometer, equipped with a fine focus 1.75 kW sealed tube Mo Kα X-ray source ($\lambda = 0.71073$ Å), with increasing ω (width of 0.3°/frame) at a scan speed of 10 s/frame. The SMART software was used for data acquisition and the SAINT software for data extraction. Absorption corrections were made using SADABS [26]. The structure was solved and refined by full-matrix least-squares method using SHELX system of programs [27]. All non-hydrogen atoms were refined anisotropically. The hydrogen atoms attached to the heteroatoms were fixed in their calculated positions and refined using a riding model.

Crystal data for **1**: Formula: $C_{15}H_{18}CuN_4O_6$; colour: blue; size: $0.32 \times 0.26 \times 0.20$ mm; $M = 413.87$; triclinic, space group $P\bar{1}$ (no. 1); $a = 7.082(3)$; $b = 10.483(5)$; $c = 11.581(5)$ Å; $\alpha = 89.700(7)$; $\beta = 83.488(8)$; $\gamma = 84.109(8)°$; $V = 849.7(7)$ Å^3; $Z = 2$; $T = 293(2)$ K; $D_c = 1.618$ g cm^{-3}; $\mu = 13.27$ cm^{-1}; $1.77 \leqslant 2\theta \leqslant 26.37$; $R(F_o) = 0.0588$; $wR = 0.1420$ for 6550 reflections with $I > 2\sigma(I)$ and 469 parameters. [$R_1(F^2) = 0.0714$ (all data)]; weighing scheme: $w = 1/[\sigma^2(F_o^2) + 0.0852P^2 + 0.0P]$, where $P = (F_o^2 + 2F_c^2)/3$. The goodness-of-fit and the largest difference peak were 1.020 and 1.080 e Å^{-3}, respectively. Perspective view of the complex was obtained by ORTEP [28].

2.5. Studies on DNA interaction

The UV absorbance at 260 and 280 nm of the CT-DNA solution in 5 mM Tris–HCl buffer (pH 7.2) gave a ratio of ~1.9, indicating the DNA was free of protein [29]. The concentration of CT DNA was measured from the band intensity at 260 nm with a known ε value (6600 M^{-1} cm^{-1}) [30]. The electronic spectra of the complexes were recorded before and after addition of CT-DNA in the 5 mM Tris–HCl/5 mM NaCl buffer (pH 7.2). The equilibrium binding constant (K_b) values for the interaction of the complexes with CT-DNA were obtained from the absorption spectral titration data using the following equation:

$$(\varepsilon_a - \varepsilon_f)/(\varepsilon_b - \varepsilon_f) = (b - (b^2 - 2K_b^2 C_t[\mathrm{DNA}]/s)^{1/2})/2K_b C_t \quad (1)$$

where $b = 1 + K_b C_t + K_b[\mathrm{DNA}]/2s$; ε_a, the extinction coefficient observed for the charge transfer absorption band at a given DNA concentration; ε_f, the extinction coefficient of the complex free in solution; ε_b, the extinction coefficient of the complex when fully bound to DNA; K_b, the equilibrium binding constant; C_t, the total metal complex concentration; [DNA], the DNA concentration in nucleotides; and s, the binding site size in base pairs [31,32].

The apparent binding constant (K_{app}) of the complexes **1** and **2** were also determined by fluorescence spectral technique using ethidium bromide (EB) bound CT DNA solution in Tris–HCl/NaCl buffer (pH 7.2). The fluorescence intensities of EB at 600 nm (546 nm excitation) with an increasing amount of the ternary complex concentration were recorded. Ethidium bromide was non-emissive in Tris-buffer medium due to fluorescence quenching of the free EB by the solvent molecules [33,34]. In the presence of DNA, EB showed enhanced emission intensity due to its intercalative binding to DNA. A competitive binding of the copper complexes to CT DNA could result in the displacement of EB or quenching of the bound EB by the paramagnetic copper(II) species decreasing its emission intensity.

DNA-melting experiments were carried out by monitoring the absorbance of CT-DNA (200 μM NP) at 260 nm with varying temperature in the absence and presence of the complexes in a 2:1 ratio of DNA and the complex with a ramp rate of 0.5 °C/min in phosphate buffer (pH 6.85) using a Peltier system attached to the UV–Vis spectrophotometer.

Viscometric titrations were performed with a Schott Gerate AVS 310 Automated Viscometer. The viscometer was thermostated at 37 °C in a constant temperature bath. The concentration of DNA was 200 μM in NP and the flow times were measured with an automated timer, and each sample was measured three times, and an average flow time was calculated. Data were presented as $(\eta/\eta_0)^{1/3}$ vs. [complex]/[DNA], where η is the viscosity of DNA in the presence of complex and η_0 that of DNA alone. Viscosity values were calculated from the observed flowing time of DNA-containing solutions (t) corrected for that of buffer alone (t_0), $\eta = (t - t_0)$.

2.6. DNA cleavage

The extent of cleavage of supercoiled (SC) DNA in the presence of the complex and reducing agent MPA was determined by agarose gel electrophoresis. In a typical reaction, supercoiled pUC19 DNA (0.2 μg), taken in 50 mM Tris–HCl buffer (pH 7.2) containing 50 mM NaCl, was treated with the complex. The extent of cleavage was measured from the intensities of the bands using UVITEC Gel Documentation System.

For mechanistic investigations, inhibition reactions were done on adding the reagents prior to the addition of the complex. The solutions were incubated for 1 h in a dark chamber at 37 °C followed by addition to the loading buffer containing 25% bromophenol blue, 0.25% xylene cyanol, and 30% glycerol (2 μL), and the solution was finally loaded on 0.8% agarose gel containing 1.0 μg/ml ethidium bromide (EB). Electrophoresis was carried out for 2 h at 60 V in tris-acetate-EDTA (TAE) buffer. Bands were visualized by UV light and photographed for analysis. Due corrections were made to the observed intensities for the low level of NC form present in the original sample of SC

DNA and for the low affinity of EB binding to SC in comparison to nicked-circular (NC) and linear forms of DNA [35].

3. Results and discussion

3.1. Synthesis and general aspects

The ternary copper(II) complexes are prepared in high yield from the reaction of $Cu(NO_3)_2 \cdot 3H_2O$ with L-proline and heterocyclic bases. The complexes are stable and soluble in water and common polar organic solvents. They are characterized from the analytical and physicochemical data (Table 1). The one-electron paramagnetic complexes display intense charge transfer (CT) band in the range of 200–320 nm that can be attributed to the $\pi \rightarrow \pi^*$ transition of the coordinated phenanthroline ligand. The d–d band is observed at ~600 nm in an aqueous medium (Fig. 1). The complexes are redox active and display a cyclic voltammetric response near 0.1 V versus SCE in water–0.1 M KCl. The redox process is assignable to the Cu(II)/Cu(I) couple. The complexes show 1:1 electrolytic behavior in solution.

3.2. Crystal structure of *1*

Complex **1** has been structurally characterized from single-crystal X-ray diffraction technique. It crystallizes in the non-centrosymmetric *P*1 space group of the triclinic crystal system having two independent molecules in the crystallographic asymmetric unit. The copper(II) ion is coordinated in a distorted square-pyramidal (4 + 1) coordination geometry through the carboxylate oxygen atom O(1) and the amino nitrogen atom N(3) of L-proline and two N-atoms of 2,2′-bipyridine and a weakly bound apical water molecule (average trigonal distortion parameter, $\tau_{av} = 0.094$) [36]. The structure resembles to the corresponding structure of reported [Cu(L-pro)(phen)(H_2O)](NO_3) complex [24]. The configuration at the proline nitrogen and the α-carbon is *S* in each complex cation. The copper atom is displaced by ~0.16 Å from the mean plane through its basal atoms in the direction towards the apical water molecule. The conformation of the five-membered ring of the proline ligand can be described as twisted. The ORTEP view of the molecule is shown in Fig. 2. Selected bond distances and angles are given in Table 2.

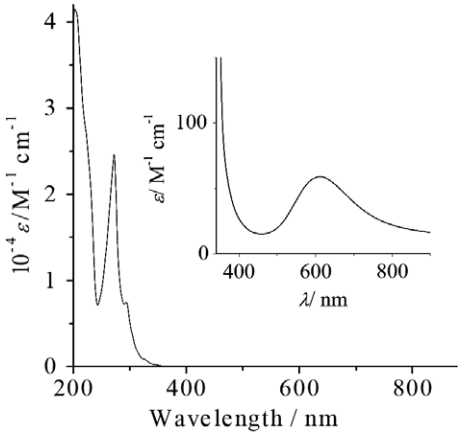


Fig. 1. Electronic spectrum of complex **2** in an aqueous medium. The inset shows the d–d band of the complex **2**.

Table 1
Physicochemical data for the ternary L-proline copper(II) complexes **1** and **2**

Complex	**1** (B = bpy)	**2** (B = phen)
IR[a]: [$\nu(NO_3^-)$/cm^{-1}]	1384	1387
d–d Band: λ_{max}/nm ($\varepsilon/M^{-1}\,cm^{-1}$)[b]	602 (50)	612 (60)
CV: $E_{1/2}$/V (ΔE_p/mV)[c]	−0.11 (470)	0.13 (330)
Λ_M[d]/$\Omega^{-1}\,cm^2\,M^{-1}$	128	190
μ_{eff}[e]/μB	1.78	1.75
K_a[f]/M^{-1}	1.8×10^3	8.28×10^5
K_b[g]/M^{-1}		$3.58\ (\pm 0.2) \times 10^5$
[*s*]		[1.53 (±0.1)]
ΔT_m[h]/°C		2.0 (±0.1)

[a] KBr phase.
[b] In aqueous medium.
[c] Cu(II)/Cu(I) couple in Tris-buffer-0.1 M KCl. $E_{1/2} = 0.5(E_{pa} + E_{pc})$, $\Delta E_p = E_{pa} - E_{pc}$, where E_{pa} and E_{pc} are the anodic and cathodic peak potentials, respectively. Scan rate: 50 mV s^{-1}.
[d] In aqueous medium.
[e] μ_{eff} for solid at 298 K.
[f] Apparent DNA binding constant from competitive binding assay by emission method.
[g] DNA binding constant from absorption spectral method.
[h] Increase in melting temperature of CT DNA.

The bpy structure shows extensive intermolecular noncovalent interactions. While one hydrogen atom of the aqua ligand in **1** is hydrogen-bonded to the oxygen atom of the lattice nitrate anion (distance 2.816 Å), the other hydrogen atom is H-bonded with the carboxylate oxygen atom of another molecule (distance = 2.696 Å). One more intermolecular hydrogen bond persists between hydrogen atom of secondary amine nitrogen of proline and oxygen

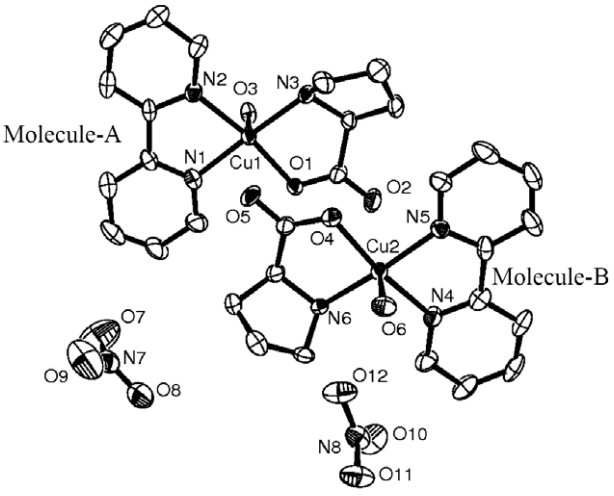


Fig. 2. ORTEP diagram of two independent molecules of complex **1** showing 50% probability thermal ellipsoids with atom labeling scheme for the metal and heteroatoms.

Table 2
Selected bond distances (Å) and angles (°) for [Cu(L-pro)(bpy)-(H_2O)](NO_3) (**1**)

Molecule-A		Molecule-B	
Cu(1)–N(1)	1.963(8)	Cu(2)–N(4)	2.023(8)
Cu(1)–N(2)	2.005(7)	Cu(2)–N(5)	2.010(7)
Cu(1)–N(3)	2.011(6)	Cu(2)–N(6)	1.994(6)
Cu(1)–O(1)	1.938(6)	Cu(2)–O(4)	1.934(6)
Cu(1)–O(3)	2.330(6)	Cu(2)–O(6)	2.271(5)
N(1)–Cu(1)–N(2)	81.2(3)	N(4)–Cu(2)–N(5)	80.3(3)
N(1)–Cu(1)–N(3)	177.2(3)	N(4)–Cu(2)–O(4)	167.9(3)
N(1)–Cu(1)–O(1)	92.8(3)	N(4)–Cu(2)–O(6)	93.0(3)
N(1)–Cu(1)–O(3)	91.2(2)	N(4)–Cu(2)–N(6)	98.9(3)
N(2)–Cu(1)–N(3)	100.6(3)	N(5)–Cu(2) –N(6)	168.7(3)
N(2)–Cu(1)–O(1)	167.2(3)	N(5)–Cu(2)–O(4)	92.9(3)
N(2)–Cu(1)–O(3)	96.9(2)	N(5)–Cu(2)–O(6)	90.0(2)
N(3)–Cu(1)–O(1)	84.8(3)	N(6)–Cu(2)–O(4)	85.8(3)
N(3)–Cu(1)–O(3)	90.7(2)	N(6)–Cu(2)–O(6)	101.2(2)
O(1)–Cu(1)–O(3)	94.6(2)	O(4)–Cu(2)–O(6)	97.1(2)

atom of lattice nitrate anion (distance 3.013 Å). The unit cell packing diagram of **1** shown in Fig. S1. The intermolecular hydrogen bonding interactions present in **1** are shown in Fig. S2.

3.3. DNA binding properties

The binding of the complexes **1** and **2** to the calf thymus (CT) DNA has been studied by electronic absorption spectral technique. The absorption spectral traces of the complex **2** with increasing concentration of CT DNA are shown in Fig. 3. We have observed minor bathochromic shift of 3 nm along with significant hypochromicity for complex **2**. The equilibrium DNA binding constants (K_b) along with binding site size (s) determination of the complexes to CT DNA are obtained by monitoring the change of the absorption intensity of the spectral bands with increasing concentration of CT DNA. The bpy complex shows weak binding to the DNA due to less extended planarity compared to phen, which is consistent with the observed trend in hypochromism. K_b and s values for the phen complex, **2** are $3.58(\pm0.2)\times10^5\ M^{-1}$ and 1.53 (±0.1), respectively. The higher binding propensity of the phen complex in comparison to its bpy analogue could be due to the presence of extended planar aromatic ring in phen. Earlier studies on bis-phen copper complex have shown that this complex binds to DNA either by partial intercalation or binding of one phen ligand to the minor groove while the other phen making favourable contacts within the groove [37–40]. The nature of binding of the phen complex is proposed to be similar as observed for the bis-phen species.

The emission spectral method is used to study the relative binding of the complexes to CT-DNA. The emission intensity of ethidium bromide (EB) is used as a spectral probe as EB shows no apparent emission intensity in buffer solution because of solvent quenching and an enhancement of the emission intensity when intercalatively bound to DNA [41]. The binding of the complexes to DNA decreases the emission intensity of EB. Relative binding propensity of the complexes to DNA is measured from the extent of reduction of the emission intensity (Fig. 4). The apparent binding constant (K_{app}) values for **1** and **2** are 1.8×10^3 and $8.28\times10^5\ M^{-1}$, respectively. The comparatively high DNA binding propensity of the phen complex in comparison to its bpy analogue could be due to the presence of extended aromatic ring in planar phen ligand facilitating non-covalent interactions with the DNA molecule. The reduction of the emission intensity of EB on increasing the complex concentration could be due to displacement of the DNA bound EB by the ternary copper(II) complexes.

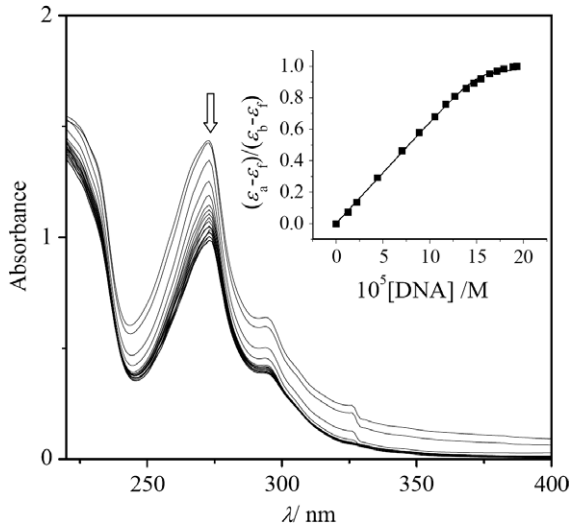


Fig. 3. Absorption spectral traces on addition of CT DNA to the solution of **2** (shown by arrow). The inset shows the best least-squares fit of $\Delta\varepsilon_{af}/\Delta\varepsilon_{bf}$ vs. [DNA].

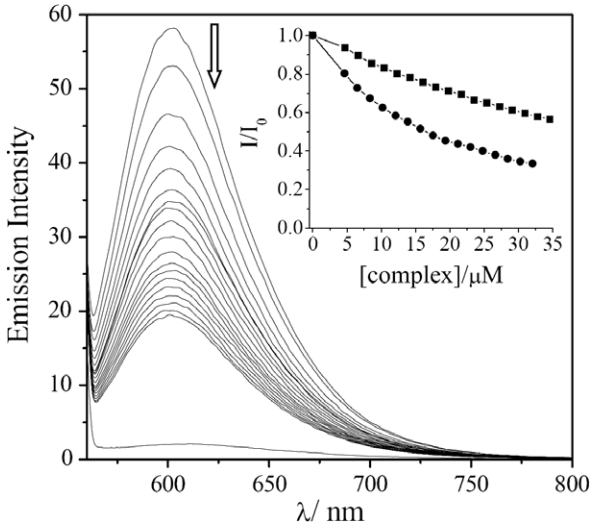


Fig. 4. Emission spectral changes on addition of [Cu(L-pro)(phen)-(H_2O)](NO_3) (**2**) to the CT-DNA bound to ethidium bromide (shown by arrow). Inset: Effect of addition of [Cu(L-pro)(B)(H_2O)](NO_3) [B = bpy (**1**, ■); phen (**2**, ●)] to the emission intensity of 300 μM CT DNA-bound ethidium bromide (1.3 μM) in a 5 mM Tris–HCl/5 mM NaCl buffer (pH 7.2) at 25 °C.

The denaturation of DNA from double-strand to single strand results in absorption hyperchromism around 260 nm. The binding of metal complexes to the double-stranded DNA usually stabilizes the duplex structure to some extent depending on the strength of interaction with nucleic acid [42]. The binding should lead to an increase in the melting temperature (T_m) of DNA as compared to DNA itself. The binding of the complex **2** results in an moderate increase (~2 °C) in the melting temperature (ΔT_m) of CT-DNA suggesting primarily electrostatic and/or groove binding nature of the complexes (Table 1, Fig. 5a).

To investigate further the binding modes of the complexes, viscosity measurements on solutions of calf thymus DNA incubated with the complexes were carried out. Because the viscosity of a DNA solution is sensitive to the addition of organic drugs and metal complexes bound by intercalation, we examined the effect on the specific relative viscosity of DNA upon addition of complexes. Since the relative specific viscosity (η/η_0), (η and η_0 are the specific viscosities of DNA in the presence and absence of the complexes, respectively) of DNA reflects the increase in contour length associated with separation of DNA base pairs caused by intercalation, a classical intercalator such as EtBr could cause a significant increase in viscosity of DNA solutions. In contrast, a partial and/or non-classical intercalation of the ligand could bend or kink DNA resulting in a decrease in its effective length with a concomitant increase in its viscosity [43,44]. The plots of relative viscosities with R = [Cu]/[DNA] are shown in Fig. 5b. The relative viscosity of DNA increases with increase in the concentration of the complex **2** but less compared to that of potential classical intercalators, e.g. ethidium bromide. This is consistent with the observed trend by other optical methods and suggesting primarily electrostatic and/or groove binding nature of the complex.

3.4. DNA cleavage studies

The oxidative DNA cleavage activity of the complexes in the presence of reducing agent 3-mercaptopropionic acid (MPA, 5 mM) is investigated by agarose gel electrophoresis using supercoiled (SC) plasmid pUC19 DNA (0.2 μg, 33.3 μM NP) in 50 mM Tris–HCl/50 mM NaCl buffer (pH 7.2) and the copper(II) complexes (Fig. 6). Selected DNA cleavage data are given in Table 3. The phen complex **2** shows efficient "chemical nuclease" activity. A 30 μM complex shows complete conversion of the SC (form I) to its nicked-circular form (NC, form II) of DNA. Control experiments with MPA or the ternary complexes alone do not show any apparent conversion of SC to its nicked-circular (NC) form. The bpy complex is cleavage inactive due to its poor binding ability to DNA. To determine the groove binding preference of **2**, control experiments have been carried out in the presence of minor groove binder distamycin-A [45,46]. Inhibition of cleavage in presence of distamycin-A for the phen complex, suggesting minor groove binding preference for the phen complex.

Mechanistic aspects of the chemical nuclease reactions are performed using various control experiments (Fig. 6). It is observed that hydroxyl radical scavengers [47] like catalase, DMSO, KI significantly inhibit the DNA cleavage activity of the complex **2** indicating the possibility of the involvement of hydroxyl radical and/or "copper-oxo" intermediate as the reactive species. Addition of superoxide dismutase (SOD) does not show any inhibitory effect on the cleavage activity suggesting the non-involvement of $O_2^{\cdot -}$ in

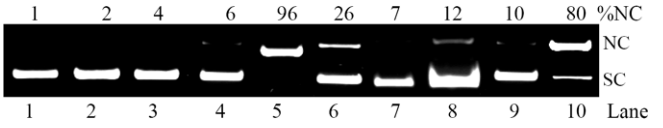


Fig. 6. Gel electrophoresis diagram showing the cleavage of SC pUC19 DNA (0.2 μg, 33.3 μM) by complexes **1** and **2** (30 μM) in 50 mM Tris–HCl/50 mM NaCl buffer (pH 7.2) in the presence of MPA (5 mM): Lane 1, DNA control; Lane 2, DNA + L-pro (30 μM) + MPA; Lane 3, DNA + **2**; Lane 4, DNA + **1** + MPA; Lane 5, DNA + **2** + MPA; Lane 6, DNA + distamycin-A (100 μM) + **2** + MPA; Lane 7, DNA + DMSO (4 μL) + **2** + MPA; Lane 8, DNA + catalase (4U) + **2** + MPA; Lane 9, DNA + KI (100 μM) + **2** + MPA; Lane 10, DNA + SOD (4U) + **2** + MPA.

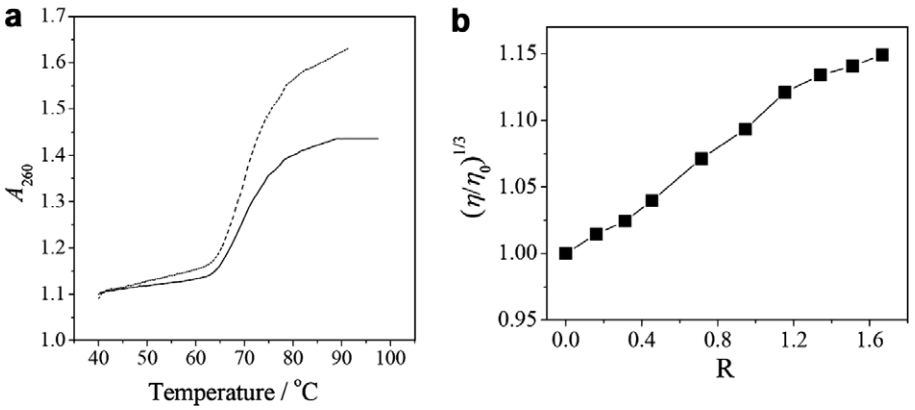
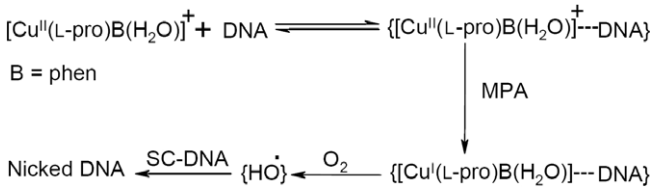


Fig. 5. (a) DNA melting curves for CT-DNA in the absence (- - -) and presence of complex **2** (—). (b) Changes in the relative viscosity of the CT DNA (200 μM) on increasing concentration of complex **2** at 37.0 (±0.1) °C in 5 mM Tris–HCl buffer (pH 7.2), R = [complex]/[DNA].

Table 3
Selected cleavage data of SC pUC19 (0.2 μg, 33.3 μM NP) by complexes **1** and **2**[a]

Sl. No.	Reaction condition	[Complex]/μM	%NC
1	DNA + MPA (5 mM)		1
2	DNA + L-proline (30 μM) + MPA		2
3	DNA + **2**	30	4
4	DNA + **1** + MPA	30	6
5	DNA + **2** + MPA	30	96
6	DNA + distamycin-A[b] + **2** + MPA	30	26
7	DNA + DMSO[c] + **2** + MPA	30	7
8	DNA + catalase[d] + **2** + MPA	30	12
9	DNA + KI[e] + **2** + MPA	30	10
10	DNA + SOD[f] + **2** + MPA	30	80

[a] NC is nicked-circular form of DNA. [MPA] = 5 mM.
[b] 100 μM.
[c] 4 μL.
[d] 4 units.
[e] 100 μM.
[f] 4 units.



Scheme 2. Proposed mechanistic pathway for the chemical nuclease activity of complex **2** in Tris-buffer medium.

the cleavage reaction. The pathways involved in the DNA cleavage reactions are believed to be analogous to those proposed by Sigman and co-workers for the chemical nuclease activity of bis(phen)copper species (Scheme 2) [1,39,40].

4. Conclusions

Two ternary copper(II) complexes having N,O-donor α-amino acid L-proline and N,N-donor heterocyclic bases are prepared and characterized. The copper(II) complex with planar phenanthroline base in CuN_3O_2 coordination geometry shows efficient DNA binding ability. The complex shows minor groove binding propensity. The study also confirms that the binding ability of the complexes is important to achieve efficient DNA cleavage activity. Significant chemical nuclease activity is observed for the phen complex **2** under physiological reaction conditions *via* a mechanistic pathway involving formation of hydroxyl radicals in presence of the MPA.

Acknowledgements

The authors gratefully acknowledge the support of Prof. Akhil R. Chakravarty, Department of Inorganic and Physical Chemistry, Indian Institute of Science, in providing facilities and useful discussions. Financial support received from the Department of Science and Technology (DST, SR/S5/BC-14/2006), Government of India, is gratefully acknowledged. R.K. is thankful to the Indian Academy of Sciences for a summer research fellowship. A.K.P. is thankful to CSIR for a fellowship. Thanks are due to the Alexander von Humboldt Foundation, Germany, for donation of an electroanalytical system; the Convener, Bioinformatics Center, Indian Institute of Science, Bangalore, for a database search; and the DST for the CCD diffractometer facility.

Appendix A. Supplementary material

CCDC 648241 contains the supplementary crystallographic data for **1**. These data can be obtained free of charge via http://www.ccdc.cam.ac.uk/conts/retrieving.html, or from the Cambridge Crystallographic Data Centre, 12 Union Road, Cambridge CB2 1EZ, UK; fax: (+44) 1223-336-033; or e-mail: deposit@ccdc.cam.ac.uk. Supplementary data associated with this article can be found, in the online version, at doi:10.1016/j.poly.2007.07.040.

References

[1] D.S. Sigman, A. Mazumder, D.M. Perrin, Chem. Rev. 93 (1993) 2295.
[2] D.S. Sigman, Acc. Chem. Res. 19 (1986) 180.
[3] B. Meunier, Chem. Rev. 92 (1992) 1411.
[4] A.M. Pyle, J.K. Barton, Prog. Inorg. Chem. 38 (1990) 413.
[5] K.E. Erkkila, D.T. Odom, J.K. Barton, Chem. Rev. 99 (1999) 2777.
[6] B. Armitage, Chem. Rev. 98 (1998) 1171.
[7] D.R. McMillin, K.M. McNett, Chem. Rev. 98 (1998) 1201.
[8] W.K. Pogozelski, T.D. Tullius, Chem. Rev. 98 (1998) 1089.
[9] H.T. Chifotides, K.R. Dunbar, Acc. Chem. Res. 38 (2005) 146.
[10] E.R. Jamieson, S.J. Lippard, Chem. Rev. 99 (1999) 2467.
[11] M. Sabat, in: A. Sigel, H. Sigel (Eds.), Metal Ions in Biological Systems, vol. 32, Marcel Dekker, New York, Basel, 1996.
[12] (a) A.R. Chakravarty, P.A.N. Reddy, B.K. Santra, A.M. Thomas, Proc. Ind. Acad. Sci. (Chem. Sci.) 114 (2002) 391;
(b) B.K. Santra, P.A.N. Reddy, G. Neelkanta, S. Mahadevan, M. Nethaji, A.R. Chakravarty, J. Inorg. Biochem. 89 (2002) 191;
(c) A.M. Thomas, G. Neelkanta, S. Mahadevan, M. Nethaji, A.R. Chakravarty, Eur. J. Inorg. Chem. (2002) 2720;
(d) A.M. Thomas, M. Nethaji, S. Mahadevan, A.R. Chakravarty, J. Inorg. Biochem. 94 (2003) 171;
(e) P.A.N. Reddy, M. Nethaji, A.R. Chakravarty, Eur. J. Inorg. Chem. (2004) 1440.
[13] S. Dhar, P.A.N. Reddy, M. Nethaji, S. Mahadevan, M.K. Saha, A.R. Chakravarty, Inorg. Chem. 41 (2002) 3469.
[14] R. Pradhan, A.M. Thomas, A. Mukherjee, S. Dhar, M. Nethaji, A.R. Chakravarty, Indian J. Chem. 44A (2005) 18.
[15] (a) A.K. Patra, S. Dhar, M. Nethaji, A.R. Chakravarty, Chem. Commun. (2003) 1562;
(b) A.K. Patra, S. Dhar, M. Nethaji, A.R. Chakravarty, Dalton Trans. (2005) 896;
(c) A.K. Patra, M. Nethaji, A.R. Chakravarty, Dalton Trans. (2005) 2798;
(d) A.K. Patra, M. Nethaji, A.R. Cakravarty, J. Inorg. Biochem. 101 (2007) 233.
[16] H. Li, X.-Y. Le, D.-W. Pang, H. Deng, Z.-H. Xu, Z.-H. Lin, J. Inorg. Biochem. 99 (2005) 2240.

[17] S. Zhang, Y. Zhu, C. Tu, H. Wei, Z. Yang, L. Lin, J. Ding, J. Zhang, Z. Guo, J. Inorg. Biochem. 98 (2004) 2099.
[18] Y. Jin, J. Cowan, J. Am. Chem. Soc. 127 (2005) 8408.
[19] F.V. Pamatong, C.A. Detmer III, R. Bocarsly, J. Am. Chem. Soc. 118 (1996) 5339.
[20] R. Ren, P. Yang, W. Zheng, Z. Hua, Inorg. Chem. 39 (2000) 5454.
[21] A. García-Raso, J.J. Fiol, B. Adrover, V. Moreno, I. Mata, E. Espinosa, E. Molins, J. Inorg. Biochem. 95 (2003) 77.
[22] A. Yaron, F. Naider, Crit. Rev. Biochem. Mol. Biol. 28 (1993) 31.
[23] D.D. Perrin, W.L.F. Armarego, D.R. Perrin, Purification of Laboratory Chemicals, Pergamon Press, Oxford, UK, 1980.
[24] (a) R. Venkatraman, J.D. Zubkowski, E.J. Valente, Acta Crystallogr., Sect. C C55 (1999) 1241;
(b) P. Sgarabotto, F. Bisceglie, G. Pelosia, L.A. Rahman, Polyhedron 18 (1999) 2505.
[25] O. Khan, Molecular Magnetism, VCH, Weinheim, 1993.
[26] G.M. Sheldrick, SADABS Version 2 Multi-Scan Absorption Correction Program, University of Göttingen, Germany, 2001.
[27] G.M. Sheldrick, SHELX 97 Programs for Crystal Structure Solution and Refinement, University of Göttingen, Göttingen Germany, 1997.
[28] M.N. Burnett, C.K. Johnson, ORTEP-III Report ORNL-6895, Oak Ridge National Laboratory, Oak Ridge, TN, 1996.
[29] J. Marmur, J. Mol. Biol. 3 (1961) 208.
[30] M.E. Reichmann, S.A. Rice, C.A. Thomas, P. Doty, J. Am. Chem. Soc. 76 (1954) 3047.
[31] J.D. McGhee, P.H. von Hippel, J. Mol. Biol. 86 (1974) 469.
[32] (a) R.B. Nair, E.S. Teng, S.L. Kirkland, C.J. Murphy, Inorg. Chem. 37 (1998) 139;
(b) M.T. Carter, M. Rodriguez, A.J. Bard, J. Am. Chem. Soc. 111 (1989) 8901;
(c) D.L. Carlson, D.H. Huchital, E.J. Mantilla, R.D. Sheardy, W.R. Murphy Jr., J. Am. Chem. Soc. 115 (1993) 6424.
[33] J.-B. LePecq, C. Paoletti, J. Mol. Biol. 27 (1967) 87.
[34] S. Neidle, Nat. Prod. Rep. 18 (2001) 291.
[35] J. Bernadou, G. Pratviel, F. Bennis, M. Girardet, B. Meunier, Biochemistry 28 (1989) 7268.
[36] A.W. Addison, T.N. Rao, J.V. Reedijk, G.C. Verschoor, J. Chem. Soc., Dalton Trans. (1984) 1349.
[37] J.M. Veal, R.L. Rill, Biochemistry 30 (1991) 132.
[38] J.M. Veal, K. Merchant, R.L. Rill, Nucleic Acids Res. 19 (1991) 3383.
[39] O. Zelenko, J. Gallagher, D.S. Sigman, Angew. Chem., Int. Ed. Engl. 36 (1997) 2776.
[40] D.S. Sigman, Biochemistry 29 (1990) 9097.
[41] J.M. Kelly, A.B. Tossi, D.J. McConnel, C. OhUigin, Nucleic Acids Res. 13 (1985) 6017.
[42] M. Lee, A.L. Rhodes, M.D. Wyatt, S. Forrow, J.A. Hartley, Biochemistry 32 (1993) 4237.
[43] S. Satyanarayana, J.C. Dabrowiak, J.B. Chaires, Biochemistry 31 (1992) 9319.
[44] T. Hirohama, Y. Kuranuki, E. Ebina, T. Sugizaki, H. Arii, M. Chikira, P.T. Selvi, M. Palaniandavar, J. Inorg. Biochem. 99 (2005) 1205.
[45] C. Bailly, J.B. Chaires, Bioconjugate Chem. 9 (1998) 513.
[46] M. Coll, C.A. Frederick, A.H.-J. Wang, A. Rich, Proc. Natl. Acad. Sci. USA 84 (1987) 8385.
[47] (a) O.I. Aruoma, B. Halliwell, M. Dizdaroglu, J. Biol. Chem. 264 (1989) 13024;
(b) S.M. Klein, G. Cohen, A.I. Cederbaum, Biochemistry 20 (1981) 6006.

such versatility as well as the steric properties of the precursors, by using the ligand framework to strategically affect the structure of the corresponding group 4 metal complex, and therefore, its reactivity in alkene polymerisation.

Our first deliberate choice was to use nitrogen precursors. Among the huge list of potential nitrogen candidates with an appropriate binding mode and the ability to be linked to a metal, 3,5-disubstituted-pyrazolato derivatives are attracting attention for a number of applied reasons. The use of 3,5-disubstituted-pyrazolato derivatives in coordination and organometallic chemistry has become conspicuous in the literature [27,28], showing the versatility of such a ligand. Excluding hydridotrispyrazolylborato derivatives [29–31] as ligands in organometallic complexes, the 3,5-disubstituted-pyrazol-1-ato moiety acting as principal ligand has been bonded to various metals either in a η^1-coordination fashion [32] (Fig. 1a) or in a chelating η^2-coordination mode (Fig. 1b), affording relatively greater stability in the monometallic system. Non-substituted-pyrazol-1-ato ligand, acting as a pyrazolato anion, can coordinate to two metals in a μ^2-coordination mode [32] (Fig. 2), which usually produces a polymetallic system. In this way, the 3,5-disubstituted-pyrazol-1-ato candidate, which appears to be structurally and electronically attractive, has moderate electron-donating properties according to Fujita's [13] recent classification, which categorised some representative oxygen, nitrogen heteroatom ligands by estimating their electron-donating properties using PM3/MNDO calculations. Some bis(3,5-di-*tert*-butylpyrazol-1-ato) dialkyl and dichloro homo- and bimetallic complexes of titanium [33–36] (alkyl = benzyl, methyl, trimethylsilylmethyl) and neutral or cationic pyrazolato cyclopentadienyl zirconium complexes [37–39] and (η^2-pyrazolato) zirconium compounds with bulky pyrazolato ligands bearing *tert*-butyl [35] indenylmethyl or fluorenylmethyl [40] substituents have been described.

Herein, we report the synthesis of some new bis(3,5-dimethylpyrazol-1-ato) zirconium complexes, the X-ray molecular structures of $[Zr(\eta^2\text{-}3,5\text{-}Me_2Pz)_2Cl_2(\eta^1\text{-}3,5\text{-}Me_2PzH)_2]\cdot(3,5\text{-}Me_2PzH)$ and $[Zr(\eta^2\text{-}3,5\text{-}Me_2Pz)_2(CH_2Ph)_2]$ (3,5-Me_2Pz = 3,5-dimethylpyrazol-1-ato) and their performance in ethylene and propylene polymerisation upon activation with MAO.

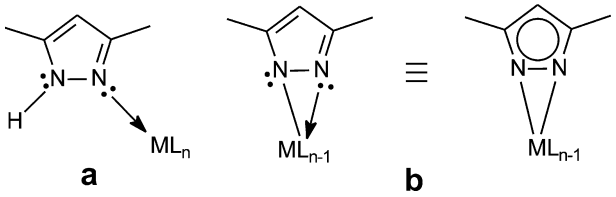


Fig. 1. Monodentate pyrazole and chelating pyrazol-1-ato coordination modes.

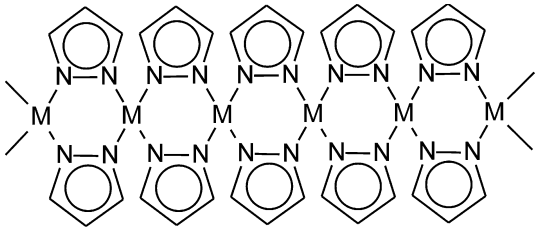


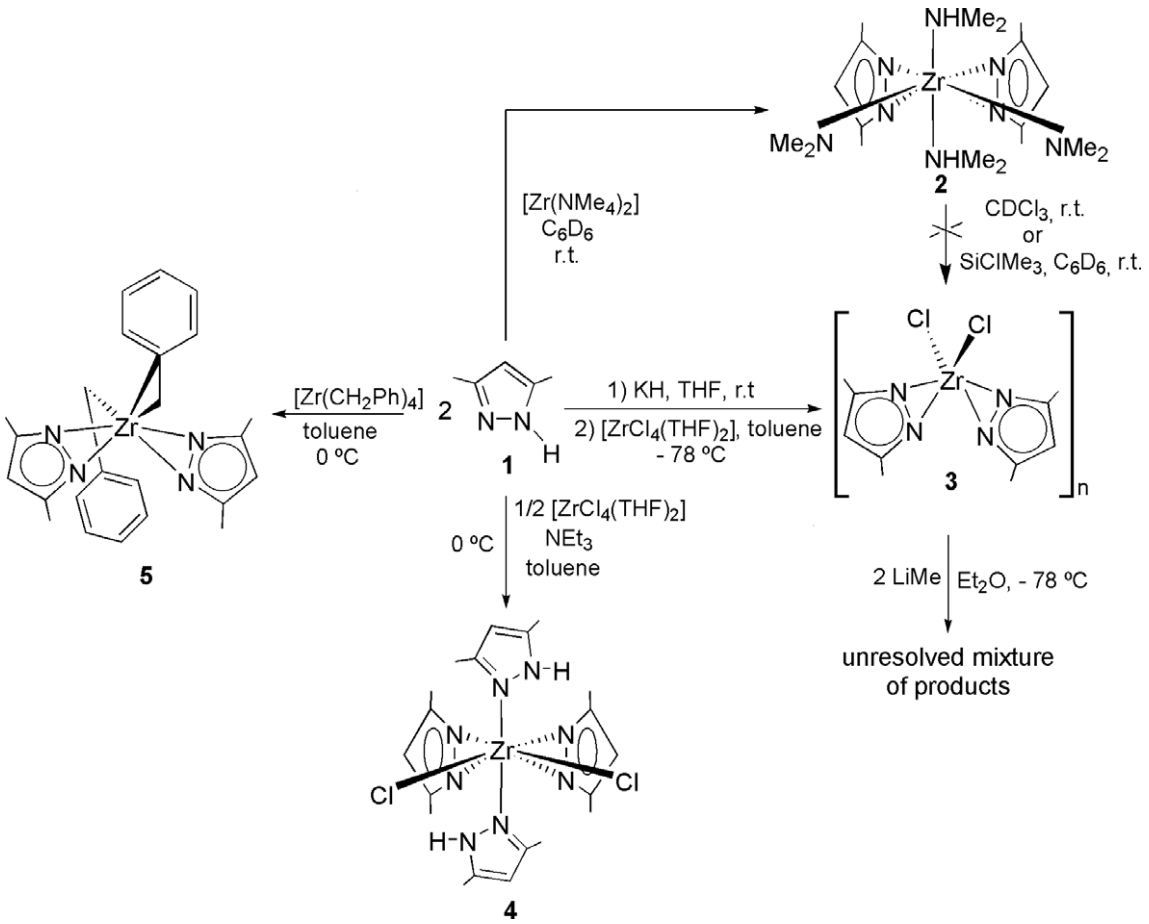
Fig. 2. Bridged pyrazol-1-ato coordination mode.

2. Results and discussion

2.1. Preparation of bis(3,5-dimethylpyrazol-1-ato) zirconium derivatives

3,5-Dimethylpyrazole (3,5-Me_2PzH) (**1**) was purchased from a commercial source or synthesised according to the literature procedure [41] and used after sublimation under high vacuum. Addition of **1** to a toluene solution of $[Zr(NMe_2)_4]$ at room temperature afforded, via amine elimination, the thermally robust bis(dimethylamido) bis(3,5-dimethylpyrazol-1-ato) zirconium(IV) complex **2**, stabilised by coordination of two molecules of the $NHMe_2$ generated. It was isolated in 95% yield as an analytically pure white solid after the solvent was completely removed under reduced pressure (Scheme 1). Compound **2** was subject to a mild chloro-solvolysis in $CDCl_3$ or treated in C_6D_6 with a slight excess of $SiClMe_3$ (2.1 equiv.) at room temperature in an attempt to access the corresponding dichloro derivative $[Zr(\eta^2\text{-}3,5\text{-}Me_2Pz)_2Cl_2]$ (**3**). The ^1H and ^{13}C NMR spectra of both resulting reaction mixtures unfortunately provide an unresolved mixture of products. To synthesise the desired dichloro zirconium complex **3**, the $[ZrCl_4(THF)_2]$ adduct was treated at −78 °C with 2 equiv. of K(3,5-Me_2Pz) [42] in a THF–toluene solution (Scheme 1). After elimination of KCl and volatiles, **3** was isolated as an analytically pure white substance in 17% yield. When the $[ZrCl_4(THF)_2]$ adduct was reacted with 4.1 equiv. of **1** in the presence of 2.1 equiv. of NEt_3 in toluene at 0 °C the zirconium complex $[Zr(\eta^2\text{-}3,5\text{-}Me_2Pz)_2Cl_2(\eta^1\text{-}3,5\text{-}Me_2PzH)_2]\cdot(3,5\text{-}Me_2PzH)$ (**4**) was exclusively produced as an analytically pure off-white solid in 46% yield after elimination of the ammonium salt (Scheme 1).

Methylation of **3** with 2 equiv. of LiMe in ether at −78 °C (Scheme 1) gave an unstable, intractable and unresolved mixture of products whose ^1H NMR spectrum was regrettably uninformative. Due to the unexpected poor behaviour of the methyl ligand to create a stable coordination environment at the zirconium centre, the use of voluminous ligands was explored to stabilise the new bis(3,5-dimethylpyrazol-1-ato) dialkyl zirconium product. The reaction of $[Zr(CH_2Ph)_4]$ with 2 equiv. of **1** in cold toluene gave, via alkane elimination, the compound $[Zr(\eta^2\text{-}3,5\text{-}Me_2Pz)_2(CH_2Ph)_2]$ (**5**) as an analytically pure white solid (98% yield) after elimination of volatiles (Scheme 1). The synthesis of dialkyl titanium compounds $[Ti(\eta^2\text{-}3,5\text{-}tBu_2Pz)_2R_2]$ (R = Me, CH_2Ph, CH_2SiMe_3) [34] has been reported following treatment of the dichloro derivative $[Ti(\eta^2\text{-}3,5\text{-}tBu_2Pz)_2Cl_2]$ [33] with the appropriate alkylating reagent.



Scheme 1.

Compounds **2**–**5** are air-sensitive but thermally stable in solution and in the solid state. They are soluble in aromatic and chlorinated solvents but poorly soluble in aliphatic hydrocarbons. Spectroscopic (^{1}H, ^{13}C NMR analyses in C_6D_6 and $CDCl_3$ solutions) and elemental analyses are in agreement with the proposed structures. The molecular structures of **4** and **5** have been determined by X-ray diffraction methods.

The 300 MHz ^{1}H NMR spectrum of **2** (C_6D_6, 20 °C) exhibits the expected pattern of resonances for the methine and methyl-substituted pyrazol-1-ato protons as singlets at δ 6.08 and 2.35, respectively. The signal at δ 3.37 is assigned to the *N*-methyl-amido protons. The resonance at δ 1.78 with a coupling constant $^3J_{HH}$ of 6.3 Hz and the multiplet signal at δ 0.31 with a 6:1 proton ratio were assigned to the methyl- and proton-amino ligand, respectively, through a ^{1}H–^{1}H-homo decoupling experiment, suggesting the evident coordination of the amino sp^3-nitrogen-donor to zirconium [43,44]. In the absence of a reliable crystal diffraction study, these spectroscopic behaviours allow us to formulate complex **2** as [Zr(η^2-3,5-Me_2Pz)$_2$(N-Me_2)$_2$(NHMe_2)$_2$], which was also confirmed by elemental analysis. According to these data and on the basis of the crystal structure analysis obtained by X-ray diffraction for the analogous dichloro compound **4**, we propose a pseudo-octahedral disposition for **2** with the pyrazolato and amido ligands in the equatorial positions and the amino groups located in a *trans* configuration (Scheme 1).

The $CDCl_3$-solution NMR spectrum of **3** displays one set of proton resonances as singlets at δ 6.04 and 2.47, showing a pattern typical for methine and methyl protons in a heterocyclic moiety. Attempts to obtain X-ray quality monocrystals with a view to corroborating this information were unfruitful. The molecular structure of the analogous bulky-substituted titanium compound [Ti(η^2-3,5-tBu$_2$Pz)$_2$Cl$_2$] [33] indicates a mononuclear disposition showing a pseudo-tetrahedral geometry around the titanium atom where the centres of the N–N bonds of the pyrazolato ligands are considered as unidentate coordination positions. Structural and chemical similarities have been established between pyrazolato and cyclopentadienyl early transition metal complexes and comparison between [Ti(η^2-3,5-tBu$_2$Pz)$_2$Cl$_2$] and [TiCp$_2$Cl$_2$] yields similar structural properties with the pyrazolato group, being a poorer donor ligand than the cyclopentadienyl ring [35]. Nevertheless, the size of the zirconium atom is larger and the zirconium complex is unsaturated. The ESI$^+$-TOF mass spectrum on a sample of **3** dissolved in a chloroform solution has showed the presence of ion peaks *m*/*z* (exact mass *m*/*z*: 964.78) superior to that expected for the mononuclear derivative **3** (exact mass

m/*z*: 349.96), although the corresponding peak for a dinuclear species was not observed. Thus, it seems very reasonable that **3** would form oligomeric species with either bridging chloro or pyrazolato ligands.

At 25 °C, the ^{1}H NMR spectrum ($CDCl_3$, 500 MHz) of **4** shows relatively uninformative broad signals. Nevertheless, it enables us to distinguish three regions of resonances. The first region has a broad signal at δ 10.77 representative of the proton N–*H* corresponding to coordinated 3,5-dimethylpyrazole. The second region features a broad signal at δ 6.08 and a singlet at δ 5.90 assigned to the methine protons of the coordinated 3,5-dimethylpyrazole and the 3,5-dimethylpyrazol-1-ato ligands, respectively. The third region at δ 2.33–2.17 contains broad signals for the methyl protons of the 3,5-dimethylpyrazol-1-ato and the coordinated 3,5-dimethylpyrazole ligands. On cooling at −40 °C, some of the signals became more defined and coalescence of the two methyl resonances of the coordinated pyrazole ligands was observed. Compared to 25 °C spectra, the amino N–*H* proton resonance appears downfield shifted at δ 11.26. Cooling at −60 °C caused a considerable sharpening and splitting of the signals and the resonance for the N–*H* proton of the coordinated 3,5-dimethylpyrazole ligand was observed at δ 11.26. The spectrum shows two singlets at δ 6.02 and 5.80 assigned to the methine protons of the coordinated 3,5-dimethylpyrazole and the 3,5-dimethylpyrazol-1-ato ligands, respectively. Two signals for the methyl protons of the coordinated pyrazole corresponding to two non-equivalent groups and a singlet for the equivalent methyl protons of the pyrazol-1-ato ligand are observed. Fluxional behaviour of **4** in $CDCl_3$ solution, corresponding to a sigmatropic displacement [45,46] of the two consecutive nitrogen of the coordinated pyrazole molecules, was apparent from this variable-temperature ^{1}H NMR study. A Gibbs activation energy $\Delta G^{\#}$(233 K) of 47.71 kJ mol^{-1} (11.4 kcal mol^{-1}) in the coalescence temperature was obtained for this process.

The 500 MHz ^{1}H NMR (C_6D_6, 25 °C) spectrum of **5** exhibits the expected pattern of resonances; two singlets at δ 6.20 and 2.14 for the methine and methyl protons of the pyrazolato ligands, respectively, and four signals, which are composed of two triplets at δ 7.06 (*meta*-C*H*), 6.88 (*para*-C*H*), a doublet at δ 6.65 (*ortho*-C*H*) with coupling constants of 7.6 Hz, 7.4 Hz, and 7.4 Hz, respectively, and a singlet at δ 2.01 (CH_2), assigned to the aromatic ring and methylene protons of the benzyl ligand, for which the pyrazolato/benzyl proton ratio is 1:1. Similar results were also observed in the ^{13}C NMR spectrum in the same conditions.

White single crystals of **4** suitable for X-ray diffraction studies grown in a saturated toluene solution at −40 °C were used to unequivocally establish the spatial arrangement of atoms in this complex (Fig. 3). Selected bond distances and angles for the structure are listed in Table 1.

The Zr atom shows a distorted octahedral geometry where the chloro ligands are mutually *cis*. The two other equatorial positions are occupied by two dimethylpyrazola-

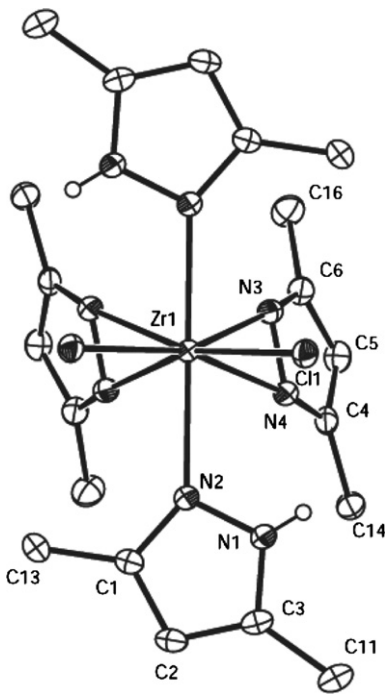


Fig. 3. X-ray ellipsoid plot of one of the independent molecules found for **4** showing the atomic numbering scheme.

to ligands coordinated by their nitrogen atoms. The centres of the N–N bonds are considered as unique coordination positions. The two dimethylpyrazole groups are placed in the apical positions in a *trans* configuration. Both nitrogen atoms of the symmetrically coordinated η^2-fashion pyrazolato ligand are nearly equidistant from the zirconium with the average Zr–N distances of 2.207 Å. The Zr–N bond distances are longer for the coordinated pyrazole groups [Zr(1)–N(2) 2.377(2) Å] than for the pyrazolato ligands [Zr(1)–N(3) 2.188(2) Å, Zr(1)–N(4) 2.226(2) Å] which show a degree of multiple bonding. All the Zr–N distances are within the range observed in similar previously reported zirconium compounds (2.306–2.369 Å for Zr–pyrazole [37] and 2.146–2.263 Å for Zr–pyrazolato [38–40]). It should be noted that only a few examples of group 4 complexes with pyrazolato and/or pyrazole ligands have been described. An intramolecular hydrogen bond with a distance of 3.142 Å for Cl(1)···N(1) and an angle of 122° for Cl(1)–H(1)–N(1) occurs in Cl(1)···H(1)–N(1) and seems to have some impact on the relative disposition of the coordinated pyrazole ligands. In contrast, the related compound [$TiCl_4(\eta^1$-3,5-$Me_2PzH)_2$] shows no such H-bond interaction [33]. Analysis of the intermolecular interactions demonstrates the presence of a weak hydrogen bond (WHB) [47] (Cl(1)···H(14)–C(14) (Cl(1)···C(14) distance of 3.687 Å and Cl(1)–H(14)–C(14) angle of 140.85°) between molecules, forming a chain arrangement in the crystal.

Further characterisation by X-ray diffraction analysis of a suitable single crystal grown from a toluene–pentane solution at −40 °C definitively revealed the structure of **5**

Table 1
Selected bond distances (Å) and angles (°) for **4** and **5**[a]

Compound	4	5
Zr(1)–N(1)		2.1469(18)
Zr(1)–N(2)	2.377(2)	2.1974(17)
Zr(1)–N(3)	2.188(2)	2.2037(17)
Zr(1)–N(4)	2.226(2)	2.1288(16)
Zr(1)–N(2)#1	2.377(2)	
Zr(1)–N(3)#1	2.188(2)	
Zr(1)–N(4)#1	2.226(2)	
Cl(1)–Zr(1)	2.5434(8)	
N(1)–N(2)	1.367(3)	1.391(3)
N(3)–N(4)	1.385(3)	1.390(3)
N(1)–C(1)		1.345(4)
N(2)–C(3)		1.335(3)
N(3)–C(6)		1.345(3)
N(4)–C(8)		1.341(3)
Zr(1)–C(11)		2.286(2)
Zr(1)–C(12)		2.8708(18)
Zr(1)–C(21)		2.280(2)
Zr(1)–C(22)		2.598(2)
N(1)–H(1)	0.75(4)	
N(1)–Zr(1)–N(2)		37.33(6)
N(1)–Zr(1)–N(3)		131.19(6)
N(2)–Zr(1)–N(3)	116.68(8)	167.74(6)
N(3)–Zr(1)–N(4)	36.55(8)	37.36(7)
N(4)–Zr(1)–N(1)		94.04(10)
N(4)–Zr(1)–N(2)	80.31(8)	
N(3)#1–Zr(1)–N(4)#1	36.55(8)	
N(2)–Zr(1)–N(2)#1	155.73(12)	
N(3)–Zr(1)–N(3)#1	86.67(13)	
N(4)–Zr(1)–N(4)#1	103.64(12)	
C(11)–Zr(1)–C(22)		92.61(7)
C(21)–Zr(1)–C(11)		126.51(8)
C(21)–Zr(1)–C(22)		34.07(7)
N(2)–Zr(1)–Cl(1)	80.95(6)	
N(3)–Zr(1)–Cl(1)	94.87(7)	
N(4)–Zr(1)–Cl(1)	85.75(6)	
N(1)–N(2)–Zr(1)		69.36(10)
N(2)–N(1)–Zr(1)		73.31(10)
N(3)–N(4)–Zr(1)	70.25(13)	73.5(2)
C(12)–C(11)–Zr(1)		97.13(12)
C(21)–C(22)–Zr(1)		60.97(11)
C(22)–C(21)–Zr(1)		84.96(12)
N(4)–N(3)–Zr(1)	73.20(14)	
Cl(1)#1–Zr(1)–Cl(1)	89.57(4)	
N(2)–N(1)–H(1)	121(3)	

Symmetric code #1 = $-x + 2$, y, $-z + 1/2$.
[a] E.s.d's are given in parentheses.

(Fig. 4). Selected bond distances and angles are listed in Table 1.

In the molecular structure, the zirconium atom is bonded to two pyrazol-1-ato and two benzyl ligands in a distorted tetrahedral geometry, considering that the two nitrogens of each pyrazol-1-ato moiety and each benzyl ligand occupy only one coordination position.

The C(11)–C(12) benzyl ligand is coordinated in a terminal η^1-mode while the C(21)–C(22) benzyl ligand coordinates in a η^2-mode with both C(21) and C(22) bonded to the Zr atom. These features in the solid state are well known and well documented elsewhere [48–57]. The distance between Zr and η^1-benzyl [Zr(1)–C(11) and Zr(1)–C(12) of 2.286(2) Å and 2.8708(18) Å, respectively] as well as between Zr and η^2-benzyl [Zr(1)–C(21) and Zr(1)–C(22) of 2.280(2) Å and 2.598(2) Å, respectively] are similar in the solid state in other analogues [48,49,51,53–57]. The benzyl ligands form Zr(1)–C(11)–C(12) and Zr(1)–C(21)–C(22) angles of 97.13(12)° and 84.96(12)°, respectively [58,59]. The two benzyl ligands are reciprocally located adopting a *chair*-type conformation.

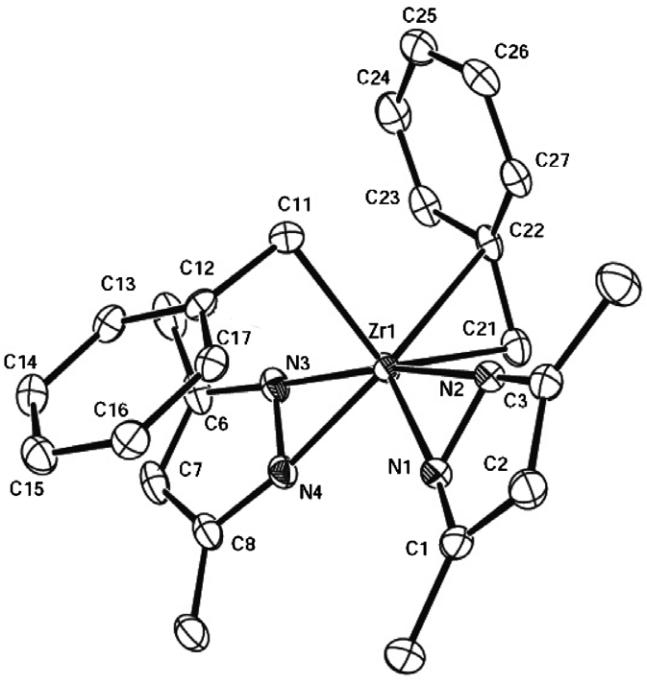


Fig. 4. X-ray ellipsoid plot of the independent molecule found for **5** showing the atomic numbering scheme.

Each pyrazol-1-ato ligand is bonded to the zirconium centre by both nitrogen atoms in a chelating η^2-coordination mode. The N(1)–N(2)-Zr(1)–N(3)–N(4) atoms lie in the same plane (mean deviation 0.026). The N(1)–N(2)–C(1)–C(2)–C(3) and N(3)–N(4)–C(6)–C(7)–C(8) rings are both bent towards the C(11)–C(17) benzyl ligand forming dihedral angles of 10.0° and 14.3°, respectively, with the N(1)–N(2)-Zr(1)–N(3)–N(4) mean plane. The pyrazolyl moieties are bonded to the Zr centre with distances Zr(1)–N(1) 2.1469(18) Å, Zr(1)–N(2) 2.1974(17) Å, Zr(1)–N(3) 2.2037(17) Å and Zr(1)–N(4) 2.1288(16) Å. The Zr–N distances are comparable with other η^2-(pyrazol-1-ato) zirconium analogues [37,40]. The distance between two consecutive nitrogens of the same pyrazol-1-ato moiety coordinated to zirconium, of about 1.391(2) Å for N(1)–N(2) and 1.390(3) Å for N(3)–N(4), is much longer than that of a simple N_{sp2}–N_{sp3} single bond type of an independent preligand **1** whose value is 1.334 Å [60].

2.2. Polymerisation studies

The strategy of searching for new olefin polymerisation catalysts [61] by making new early metal cations and new

generation of "non-metallocene" catalysts for the polymerisation of α-olefins has been recently developed based on group 4 metal complexes containing diamido ligands. These compounds exhibit a close relationship to the half-sandwich metal amido "constrained-geometry" catalyst system and to metallocene derivatives. η^2-Pyrazolato ligands act formally as three-electron donors (covalent criterion) with similar behaviour to amidinato and amido ligands. In this way, the study of the synthesised pyrazolato complexes as precatalysts in α-olefin polymerisation seems to be pertinant [38]. The zirconium complexes **3** and **5** have been preliminary examined as catalyst precursors for ethylene and propylene polymerisations upon activation with methylaluminoxane (MAO). Olefin polymerisations were investigated in toluene at 25 °C and 50 °C with 1 atm and 4 atm of olefin pressure (Al/Zr ratio ~ 1000:1). The results are summarised in Table 2. No polymerisation of propylene using either precursor **3** or **5**, at whichever operating temperature or olefin pressure, occurred. Precursor **3** remained inactive in the polymerisation of ethylene whatever the polymerisation conditions applied. This lack of activity is attributed to the non-generation of catalytically active species in solution, probably resulting from the premature decomposition of the dimethyl zirconium intermediate when the dialkylation of the corresponding dichloro derivative occurs with MAO before abstraction of the methyl ligand. This hypothesis is supported by the results of the dialkylation of **3** with 2 equiv. of LiMe already described. This is a common problem with precursors that contain N-based ligands. Polyethylene was exclusively isolated using precursor **5** (Table 2). At 1 atm of monomer pressure low activity was observed before 30 min, independent of temperature. Activity increased with time from 30 min, but was ca. twofold greater at 60 than 30 min, regardless of temperature (entries 1–4). At 4 atm and 25 °C or 50 °C, the catalytic activity of precursor **5** depends on the polymerisation time. At 25 °C, the highest activity of **5** was reached after 15 min (entry 6), which was ca. twofold greater than at 5 min. After 15 min, a continuous activity rate decrease occurred, probably due to the destruction of active sites. At 50 °C, the highest activity of **5** occurred up to 5 min (entry 9), followed by a rate decrease to roughly constant value of 4 kg of polymer/(mol Zr h atm ethylene) (entries 10–12). This decrease of activity can be explained by a thermal deactivation or by a further reduction of the group 4 transition metal by the MAO co-activator where diffusion control of the propagation reaction can also be postulated [62]. The GPC data indicate great differences in the molecular weight of the resulting polymers with M_w values in the range of 222000–690000 and the polydispersity values larger than 57, indicating the presence of different types of catalytically active species in the reaction mixture. For 1 atm at 25 °C the M_w values increased with polymerisation time, whereas, for 4 atm at 50 °C, the M_w values tend to be constant with polymerisation time. The polymers produced by this precatalyst exhibit single DSC endotherms, with melting point $T_f \approx 133$ °C. These results suggest the utility of these compounds under the used conditions in alkene polymerisation is not very promising.

Table 2
Ethylene polymerisation catalysed with **5**/MAO system[a]

Entry	P (atm)	T (°C)	t (min)	Activity[b]	M_w^c	M_n^c	M_w/M_n	T_f^d	T_c^d
1[e]	1	25	30	0.363	405000	2454	165	134	115
2[e]	1	25	60	0.727	556000	3706	150	132	119
3[e]	1	50	30	0.363	690000	4928	140	132	116
4[e]	1	50	60	0.818	222000	3894	57	131	120
5[f]	4	25	5	4.23	383000	5039	76	131	117
6[f]	4	25	15	9.51	296000	4933	60	134	116
7[f]	4	25	45	5.65	302000	2745	110	136	116
8[f]	4	25	88	1.228	425000	3863	110	133	120
9[f]	4	50	5	7.91	405000	2454	165	132	115
10[f]	4	50	22	4.06	556000	3706	150	132	117
11[f]	4	50	50	5.23	690000	4928	140	132	117
12[f]	4	50	105	3.35	222000	3894	57	132	117

[a] Conditions: 10 μmol of precatalyst, 50 mL of toluene, Al/Zr ratio ~ 1000:1.
[b] Expressed in kg polymer/(mol Zr h atm ethylene).
[c] Determined by GPC.
[d] Melting point (T_f) and crystallisation point (T_c) determined by DSC.
[e] MAO used as a 10% toluenic solution.
[f] MAO used as a $AlMe_3$-free solid dissolved in toluene.

3. Conclusions

In this report, we have provided a contribution to the synthesis and characterisation of new and somewhat unusual bis(3,5-dimethylpyrazol-1-ato) zirconium complexes supported by dimethylamido (**2**), dichloro- (**3** and **4**) and dibenzyl (**5**) ligands. We have demonstrated that **4** presented a highly fluxional behaviour in $CDCl_3$ solution, which was quantified by variable-temperature proton NMR experiments. The new complexes are interesting from basic coordination chemistry perspectives because only a few derivatives of this type are known. Initial studies of their ethylene polymerisation performance under MAO-activation conditions have been developed. Long apparent activation times, low activities, and broad molecular weight distribution are observed.

4. Experimental

4.1. General considerations

All manipulations and reactions were carried out under argon (Air Liquide N45, O_2: 1 ppm; H_2O: 3 ppm) using Schlenk and high-vacuum line techniques or in a dry argon atmosphere MBraun glovebox model MB150B-G. The solvents (Baker and SDS) were of reagent grade and were purified by distillation under argon before use by employing the appropriate drying agent. Deuterated solvents (SDS) were firstly degassed by several freeze–thaw cycles and then stored at room temperature over freshly activated 4 Å molecular sieves (10% w/v). Commercial 3,5-di-

methylpyrazole **1** (Aldrich) was used as received, otherwise prepared [41] and freshly sublimed. $SiClMe_3$, LiMe (a 1.6 M solution in Et_2O) (Aldrich) were used as received. NEt_3 (Aldrich) was treated with KOH pellets and fractionally distilled under argon over CaH_2. KH, as a 30 wt% dispersion in mineral oil (Aldrich), was washed and filtered three times with *n*-hexane, and dried until complete removing of the volatiles. K(3,5-Me_2Pz) [42], $[Zr(NMe_2)_4]$ [63], $[ZrCl_4(THF)_2]$ [64], $[Zr(CH_2Ph)_4]$ [65] were prepared by a known procedure. C, H, and N microanalyses were performed on a Perkin–Elmer 240B microanalyser. NMR spectra were recorded on Varian Mercury VX–300 and Unity^{Plus} 500 spectrometers at room temperature, otherwise as indicated. The chemical shifts δ and coupling constant J are quoted in ppm and in hertz (Hz), respectively, and are referenced with respect to residual proton and carbon resonances of the solvent ($CDCl_3$: ^{1}H: 7.25 ppm, ^{13}C: 77.1 ppm; C_6D_6: ^{1}H: 7.15 ppm, ^{13}C: 128.0 ppm), which is also referenced with respect to $SiMe_4$. Variable-temperature (VT) ^{1}H NMR experiments were recorded on the Varian Unity^{Plus} 500 spectrometer. Polymerisation grade ethylene and propylene (Air Liquide N35) were purified by passage through two columns packed with activated 4 Å molecular sieves. Methylaluminoxane (MAO) (10 wt% solution in toluene) was purchased from CROMPTON GmbH. Solid $AlMe_3$-free methylaluminoxane was obtained by drying MAO under reduced pressure at 50 °C to remove the uncoordinated $AlMe_3$ and used after washing with hexanes and dryness. Polymer melt endotherms were determined using a Perkin–Elmer DSC-4 differential scanning calorimeter at a heating rate of 10 °C min^{-1}. The GPC measurements were performed on a Polymer Laboratories PL-220 instrument, equipped with a refractive index detector. The samples were analysed in trichlorobenzene (TCB) stabilised with 0.0125% BHT on two columns of PLgelMIXED B (length 600 mm) at 160 °C with a flow rate of 1.0 mL min^{-1}. The ESI$^+$-TOF LC/MS experiment was carried out on an Agilent apparatus model 6210 using a mixture of MeOH/water (75/25, v/v) with an aqueous solution of ammonium formate (5 mM) as a mobile phase.

4.2. Synthesis of $[Zr(\eta^2\text{-}3,5\text{-}Me_2Pz)_2(NMe_2)_2(NHMe_2)_2]$ (**2**)

$[Zr(NMe_2)_4]$ (250 mg, 0.93 mmol) and **1** (180 mg, 1.87 mmol) were rapidly placed into a Teflon-valved ampoule under dry argon and toluene (5 mL) was immediately introduced. The closed ampoule was coupled with a mechanical stirrer using rubber and T-glass tubes. The ampoule was then stirred slowly at room temperature for 18 h. The solution was filtered and the volatiles were removed under reduced pressure affording 410 mg of an analytically pure white solid identified as **2** (95% yield). NMR ^{1}H (300 MHz, C_6D_6): $\delta = 6.08$ (s, 2H, C*H*), 3.37 (s, 12H, N–CH_3), 2.35 (s, 12H, CH_3-pyrazol-1-ato), 1.78 (d, $^3J_{HH} = 6.3$ Hz, 6H, HN(CH_3)$_3$), 0.31 (m, 1H, *H*N(CH$_3$)$_3$). NMR ^{13}C{^{1}H} (75 MHz, C_6D_6): $\delta = 145.1$ (*C-ipso*), 110.7 (*C*H), 46.0 (N-*C*H$_3$), 38.7 (HN(*C*H$_3$)$_3$), 13.1 (*C*H$_3$-pyrazol-1-ato). *Anal.* Calc. for $C_{18}H_{40}N_8Zr$ (459.79): C, 47.02; H, 8.76; N, 24.37. Found: C, 47.10; H, 8.69; N, 24.44%.

4.3. Synthesis of $[Zr(\eta^2\text{-}3,5\text{-}Me_2Pz)_2Cl_2]_n$ (**3**)

Compound **1** (1.17 g, 12.2 mmol) in a one portion was added to a stirred suspension of KH (490 mg, 12.22 mmol) in THF (55 mL) at room temperature, with instantaneous gas evolution. The resulting mixture was stirred for a further 1 h as soon as gas ceased to evolve. The room-temperature mixture was then slowly transferred by cannula to a solution of $[ZrCl_4(THF)_2]$ (2.3 g, 6.1 mmol) in toluene (50 mL) at −78 °C. The turbid pale yellow solution was warmed gradually with stirring overnight when volatiles were completely removed under reduced pressure and the residue was extracted into toluene (60 mL) for 2 days. The resulting precipitate was allowed to settle at 0 °C overnight, and the solution was filtered. The volatiles were completely removed under reduced pressure, yielding the desired compound as an analytically pure white solid identified as **3** (370 mg, 17% yield based on $[ZrCl_4(THF)_2]$). NMR ^{1}H (300 MHz, $CDCl_3$): $\delta = 6.04$ (s, 2H, C*H*), 2.47 (s, 12H, CH_3). NMR ^{13}C{^{1}H} (75 MHz, $CDCl_3$): $\delta = 144.7$ (*C-ipso*), 106.1 (*C*H), 11.1 (*C*H$_3$). *Anal.* Calc. for $C_{10}H_{14}Cl_2N_4Zr$ (as mononuclear: 352.37): C, 34.08; H, 4.00; N, 15.98. Found: C, 33.99; H, 4.15; N, 15.88%. ESI$^+$-TOF, exact mass *m*/*z*: 964.78.

4.4. Synthesis of $[Zr(\eta^2\text{-}3,5\text{-}Me_2Pz)_2Cl_2(\eta^1\text{-}3,5\text{-}Me_2PzH)_2]\cdot(3,5\text{-}Me_2PzH)$ (**4**)

A stirred solution of **1** (2.14 g, 22.34 mmol), and NEt_3 (1.55 mL, 11.17 mmol) in toluene (45 mL) was rapidly transferred by cannula to a stirred solution of $[ZrCl_4(THF)_2]$ (2.01 g, 5.32 mmol) in toluene (50 mL) at 0 °C. The resulting solution was warmed gradually with stirring for 21 h. The stirred mixture was cooled at 0 °C, when stirring was stopped to allow the precipitates to settle. The undesired precipitates (1.57 g) were isolated by filtration and the clean colorless solution was cooled at −40 °C to crystallise. White crystals of X-ray quality of **4** (1.38 g, 46% yield) were carefully isolated by filtration. NMR ^{1}H (500 MHz, $CDCl_3$, −60 °C): $\delta = 11.26$ (s, 2H, N*H*), 6.02 (s, 2H, C*H*-coordinated pyrazole), 5.80 (s, 2H, C*H*-pyrazolato), 2.55 (s, 6H, CH_3-coordinated pyrazole), 2.35 (s, 6H, CH_3-coordinated pyrazole), 1.79 (s, 12H, CH_3-pyrazol-1-ato). NMR ^{13}C{^{1}H} (125 MHz, $CDCl_3$, −60 °C): $\delta = 152.0$ (*C-ipso*-coordinated pyrazole), 145.6 (*C-ipso*-pyrazol-1-ato), 139.1 (*C-ipso*-coordinated pyrazole), 113.3 (*C*H-pyrazol-1-ato) 106.0 (*C*H-coordinated pyrazole), 13.8 (*C*H$_3$-coordinated pyrazole), 11.2 (*C*H$_3$-pyrazol-1-ato), 10.3 (*C*H$_3$-coordinated pyrazole). *Anal.* Calc. for $C_{20}H_{30}Cl_2N_8Zr\cdot 1/4C_5H_8N_2$ (544.64 + 24.03): C, 44.88; H, 5.67; N, 20.93. Found: C, 44.68; H, 5.73; N, 20.34%.

4.5. Synthesis of [Zr(η^2-3,5-Me_2Pz)$_2$(CH_2Ph)$_2$] (5)

A stirred solution of **1** (858 mg, 8.92 mmol) in toluene (60 mL) was added by cannula to a stirred solution of [Zr(CH_2Ph)$_4$] (2.03 g, 4.46 mmol) in toluene (60 mL) at 0 °C. The mixture was slowly warmed to room temperature with stirring and then further stirred for 19 h. The solution was filtered through a short pad of celite and the volatiles were removed under reduced pressure affording 2.03 g of an analytically pure white solid (98% yield). Suitable single crystals of **5** for X-ray diffraction analysis were collected by filtration from a toluene–pentane solution at −40 °C. NMR ^{1}H (500 MHz, C_6D_6): $\delta = 7.06$ (t, $J = 7.6$ Hz, 4H, *meta*-C*H* of phenyl ring), 6.88 (t, $J = 7.4$ Hz, 2H, *para*-C*H* of phenyl ring), 6.65 (d, $J = 7.4$ Hz, 4H, *ortho*-C*H* of phenyl ring), 6.20 (s, 2H, C*H*-pyrazol-1-ato), 2.14 (s, 12H, CH_3-pyrazol-1-ato), 2.01 (s, 4H, CH_2-benzyl). NMR ^{13}C{^{1}H} (125 MHz, C_6D_6): $\delta = 147.1$ (*ipso*-*C*-pyrazol-1-ato), 140.0 (*ipso*-*C* of phenyl ring), 129.3 (*ortho*-*C*H of phenyl ring), 128.5 (*meta*-*C*H of phenyl ring), 122.9 (*para*-*C*H of phenyl ring), 116.1 (*C*H-pyrazol-1-ato), 58.7 (*C*H$_2$-benzyl), 12.6 (*C*H$_3$-pyrazol-1-ato). *Anal.* Calc. for $C_{24}H_{28}N_4Zr$ (463.74): C, 62.16; H, 6.09; N, 12.08. Found: C, 61.89; H, 6.11; N, 12.25%.

4.6. Polymerisation procedure at 1 atm

Toluene (50 mL) was introduced under argon into the Schlenk reactor equipped with a magnetic stirrer and maintained at the desired temperature using external thermal control with vigorous stirring for 30 min. MAO (8 mL, 12.19 mmol) was then injected and the mixture stirred for 15 min. The argon was replaced by the olefin by degassing the solution under vacuum and refilling with the olefin. This procedure was repeated and the solution was finally saturated with the olefin for 15 min. As soon as the zirconium complex was injected to the mixture, polymerisation time was counted. The polymerisation was terminated by methanol injection. The polymer was precipitated with 100 mL of a 5% solution of HCl in MeOH, stirred, filtrated and washed successively with 50 mL of a 5% solution of HCl in MeOH, 100 mL of water, and 100 mL of MeOH. The polymer was finally dried under vacuum at 50 °C for 24 h to constant weight.

4.7. Polymerisation procedure at 4 atm

The sealed ampoule containing precursor **5** at the desired amount was placed into the Büchi reactor. The system, at the desired temperature, was evacuated under vacuum for 1 h. Toluene (50 mL) was introduced under argon into the reactor and MAO (8 mL, 12.19 mmol) was then injected. The mixture was stirred for 15 min. The argon was replaced by the olefin by degassing the solution under vacuum and refilling with the olefin. As soon as precursor **5** was liberated into the solution by breaking the ampoule polymerisation time was counted. The polymerisation was terminated by methanol injection. The polymer was precipitated with 100 mL of a 5% solution of HCl in MeOH, stirred, filtrated and washed successively with 50 mL of a 5% solution of HCl in MeOH, 100 mL of water, and 100 mL of MeOH. The polymer was finally dried under vacuum at 50 °C for 24 h to constant weight.

4.8. X-ray crystallographic study of [Zr(η^2-3,5-Me_2Pz)$_2$$Cl_2$($\eta^1$-3,5-$Me_2PzH$)$_2$] · (3,5-$Me_2PzH$) (4) and [Zr($\eta^2$-3,5-$Me_2Pz$)$_2$($\eta^2$-$CH_2Ph$)$_2$] (5)

Suitable crystals of **4** and **5** were selected, manipulated under perfluoropolyether, mounted on a glass fibre and the data collected on a Nonius KappaCCD diffractometer (**4**) at 200 K and a Rigaku R-Axis IIc image plate diffractometer (**5**) at 150 K. Data were processed using the DENZO/SCALEPACK programs [66]. The structure was determined by direct method routines and refined by full-matrix

Table 3
Crystal data and structure refinement details for **4** and **5**

Compound	**4**	**5**
Molecular formula	$C_{25}H_{38}Cl_2N_{10}Zr$	$C_{24}H_{28}N_4Zr$
Formula weight	640.77	463.72
Temperature (K)	200(2)	150(2)
Radiation λ (Å)	Mo Kα	Mo Kα
λ(Mo Kα) (Å)	0.71073	0.71073
Crystal system	monoclinic	monoclinic
Space group	*C*2/*c*	$P2_1/n$
Unit cell dimensions		
a (Å)	14.983(2)	10.7839(2)
b (Å)	15.631(2)	13.0955(2)
c (Å)	15.5485(11)	16.0136(2)
β (°)	116.284(12)	92.568(5)
Volume (Å^3)	3264.9(7)	2259.18(6)
Z	4	4
D_{calc} (Mg m^{-3})	1.302	1.363
Absorption coefficient (mm^{-1})	0.531	0.503
F(000)	1324	960
Color	white	pale yellow
Crystal size (mm)	0.55 × 0.33 × 0.33	0.26 × 0.26 × 0.20
θ Range for data collection (°)	3.03–27.56	3.83–27.48
Index ranges	$-19 \leqslant h \leqslant 19$, $-20 \leqslant k \leqslant 20$, $-19 \leqslant l \leqslant 20$	$-13 \leqslant h \leqslant 14$, $-17 \leqslant k \leqslant 17$, $-17 \leqslant l \leqslant 20$
Reflections collected	13685	17950
Independent reflections	3746	5148
R_{int}	0.0409	0.0417
Refinement method	full-matrix least-squares on F^2	full-matrix least-squares on F^2
Data/restraints/parameters	3746/0/188	3959/0/266
Goodness-of-fit on F^2	1.044	1.043
R_1 [$I > 2\sigma(I)$]	$R_1 = 0.0374$, $wR_2 = 0.0947$	$R_1 = 0.0318$
wR_2 (all data)	$R_1 = 0.0522$, $wR_2 = 0.1021$	$wR_2 = 0.0710$
Largest difference in peak and hole (e A^{-3})	0.687 and − 0.653	0.377 and −0.366

least-squares methods on F^2 (SHELXS and SHELXL programs) [67]. All non-hydrogen atoms were anisotropically refined. Compound **4**: hydrogen atoms were geometrically placed and left riding on their parent atoms except for H1, H2, H5, and H7 which were found in the difference map and refined isotropically. Half of a disordered molecule of free ligand appeared in the asymmetric unit. Compound **5**: methyl hydrogen atoms were refined as rigid, others riding. Relevant crystallographic data and details of the refinements for the two structures are given in Table 3.

Acknowledgements

Financial support for this research by DGICYT (Project MAT2004-02614), CAM: (Project S-0505-PPQ/0328-02) and by European Commission (Contract No. HPRN–CT2000-00004) is gratefully acknowledged. The authors would like to express the thanks to Prof. Dr. Mikhail V. Galakhov for his helpful assistance for the NMR studies and Dr. Yann Sarazin, from the Department of Prof. Dr. Manfred Bochmann, University of East Anglia for running the GPC measurements.

Appendix A. Supplementary material

CCDC 635011 and 635579 contain the supplementary crystallographic data for **4** and **5**. These data can be obtained free of charge via http://www.ccdc.cam.ac.uk/conts/retrieving.html, or from the Cambridge Crystallographic Data Centre, 12 Union Road, Cambridge CB2 1EZ, UK; fax: (+44) 1223-336-033; or e-mail: deposit@ccdc.cam.ac.uk. Supplementary data associated with this article can be found, in the online version, at doi:10.1016/j.poly.2007.08.001.

References

[1] H. Sinn, W. Kaminsky, Adv. Organomet. Chem. 18 (1980) 99.
[2] R.F. Jordan, Adv. Organomet. Chem. 32 (1991) 325.
[3] T.J. Marks, Acc. Chem. Res. 25 (1992) 57.
[4] H.H. Brintzinger, D. Fischer, R. Mülhaupt, B. Rieger, R.M. Waymouth, Angew. Chem., Int. Ed. Engl. 34 (1995) 1143.
[5] M. Bochmann, J. Chem. Soc., Dalton Trans. (1996) 255.
[6] G.G. Hlatky, Coord. Chem. Rev. 181 (1999) 243.
[7] H.A. Alt, A. Köppl, Chem. Rev. 100 (2000) 1205.
[8] L. Resconi, L. Cavallo, A. Fait, F. Piemontesi, Chem. Rev. 100 (2000) 1253.
[9] K. Angermund, G. Fink, V.R. Jensen, R. Kleinschmidt, Chem. Rev. 100 (2000) 1457.
[10] G.W. Coates, J. Chem. Soc., Dalton Trans. (2002) 467.
[11] Y. Qian, J. Huang, M.D. Bala, B. Lian, H. Zhang, H. Zhang, Chem. Rev. 103 (2003) 2633.
[12] G.J.P. Britovsek, V.C. Gibson, D.F. Wass, Angew. Chem., Int. Ed. 38 (1999) 428.
[13] H. Makio, N. Kashiwa, T. Fujita, Adv. Synth. Catal. 344 (2002) 477.
[14] V.C. Gibson, S.K. Spitzmesser, Chem. Rev. 103 (2003) 283.
[15] M. Mitani, J. Saito, S.-I. Ishii, Y. Nakayama, H. Makio, N. Matsukawa, S. Matsui, J.-I. Mohri, R. Furuyama, H. Terao, H. Bando, H. Tanaka, T. Fujita, Chem. Rec. 4 (2004) 137.
[16] S. Matsui, M. Mitani, J. Saito, Y. Tohi, H. Makio, N. Matsukawa, Y. Takagi, K. Tsuru, M. Nitabaru, T. Nakano, H. Tanaka, N. Kashiwa, T. Fujita, J. Am. Chem. Soc. 123 (2001) 6847.
[17] M. Mitani, J.-I. Mohri, Y. Yoshida, J. Saito, S. Ishii, K. Tsuru, S. Matsui, R. Furuyama, T. Nakano, H. Tanaka, S.-I. Kojoh, T. Matsugi, N. Kashiwa, T. Fujita, J. Am. Chem. Soc. 124 (2002) 3327.
[18] J. Tian, G.W. Coates, Angew. Chem., Int. Ed. 39 (2000) 3626.
[19] J. Saito, M. Onda, S. Matsui, M. Mitani, R. Furuyama, H. Tanaka, T. Fujita, Macromol. Rapid Commun. 23 (2002) 1118.
[20] R.K.J. Bott, D.L. Hughes, M. Schormann, M. Bochmann, S.J. Lancaster, J. Organomet. Chem. 665 (2003) 135.
[21] M. Lamberti, D. Pappalardo, A. Zambelli, C. Pellecchia, Macromolecules 35 (2002) 658.
[22] M. Mitani, T. Nakano, T. Fujita, Chem. Eur. J. 9 (2003) 2396.
[23] H. Bando, Y. Nakayama, Y. Sonobe, T. Fujita, Macromol. Rapid Commun. 24 (2003) 732.
[24] R. Furuyama, T. Fujita, S.F. Funaki, T. Nobori, T. Nagata, K. Fujiwara, Catal. Surv. Asia 8 (2004) 61.
[25] M. Sanz, T. Cuenca, M. Galakhov, A. Grassi, R.K.J. Bott, D.L. Hughes, S.J. Lancaster, M. Bochmann, Organometallics 23 (2004) 5324.
[26] C. Cuomo, M. Strianese, T. Cuenca, M. Sanz, A. Grassi, Macromolecules 37 (2004) 7469.
[27] S. Trofimenko, Chem. Rev. 72 (1972) 497.
[28] C. Pettinari, R. Pettinari, Coord. Chem. Rev. 249 (2005) 663.
[29] S. Trofimenko, J. Am. Chem. Soc. 89 (1967) 3170.
[30] M. Etienne, Coord. Chem. Rev. 156 (1996) 201.
[31] N. Marques, A. Sella, J. Takats, Chem. Rev. 102 (2002) 2137.
[32] W. Evans, J. Chem. Educ. 81 (2004) 1191.
[33] I.A. Guzei, C.H. Winter, Inorg. Chem. 36 (1997) 4415.
[34] C. Yélamos, M.J. Heeg, C.H. Winter, Organometallics 18 (1999) 1168.
[35] C. Yélamos, M.J. Heeg, C.H. Winter, Inorg. Chem. 38 (1999) 1871.
[36] N.C. Mosch-Zanetti, R. Kratzner, C. Lehmann, T.R. Schneider, I. Uson, Eur. J. Inorg. Chem. (2000) 13.
[37] D. Röttger, G. Erker, M. Grehl, R. Fröhlich, Organometallics 13 (1994) 3897.
[38] H. Lee, R.F. Jordan, J. Am. Chem. Soc. 127 (2005) 9384.
[39] E. Sebe, I.A. Guzei, M.J. Heeg, L.M. Liable-Sands, A.L. Rheingold, C.H. Winter, Eur. J. Inorg. Chem. (2005) 3955.
[40] J.C. Röder, F. Meyer, H. Pritzkow, Z. Naturforsch. B 57 (2002) 773.
[41] R.H. Wiley, P.E. Hexner, Org. Synth. Coll. 4 (1963) 351.
[42] C. Yélamos, M.J. Heeg, C.H. Winter, Inorg. Chem. 37 (1998) 3892.
[43] V.C. Gibson, B.S. Kimberley, A.J.P. White, D.J. Williams, P. Howard, Chem. Commun. (1998) 313.
[44] Y. Shi, C. Cao, A.L. Odom, Inorg. Chem. 43 (2004) 275.
[45] A. Wright, R. West, J. Am. Chem. Soc. 96 (1974) 3214.
[46] R. West, Adv. Organomet. Chem. 16 (1977) 1.
[47] G.R. Desiraju, T. Steiner, The Weak Hydrogen Bond in Structural Chemistry and Biology, Oxford Science Publications, Oxford, 1999.
[48] S.L. Latesky, A.K. McMullen, G.P. Niccolai, I.P. Rothwell, J.C. Huffman, Organometallics 4 (1985) 902.
[49] C. Pellecchia, A. Grassi, A. Immirzi, J. Am. Chem. Soc. 115 (1993) 1160.
[50] C. Pellecchia, A. Grassi, A. Zambelli, Organometallics 13 (1994) 298.
[51] F.G.N. Cloke, T.J. Geldbach, P.B. Hitchcock, J.B. Love, J. Organomet. Chem. 506 (1996) 343.
[52] A.D. Horton, J. de With, A.J. van der Linden, H. van de Weg, Organometallics 15 (1996) 2672.
[53] B. Qian, W.J. Scanlon IV, M.R. Smith III, D.H. Motry, Organometallics 18 (1999) 1693.
[54] J.S. Rogers, R.J. Lachicotte, G.C. Bazan, Organometallics 18 (1999) 3976.
[55] Z. Ziniuk, I. Goldberg, M. Kol, Inorg. Chem. Commun. 2 (1999) 549.
[56] R.M. Gauvin, J.A. Osborn, J. Kress, Organometallics 19 (2000) 2944.
[57] S.C.F. Kui, N. Zhu, M.C.W. Chan, Angew. Chem., Int. Ed. 42 (2003) 1628.
[58] J. Scholz, F. Rehbaum, K.H. Thiele, R. Goddard, P. Betz, C. Kruger, J. Organomet. Chem. 443 (1993) 93.

[59] F.A. Cotton, C.A. Murillo, M.A. Petrukhina, J. Organomet. Chem. 573 (1999) 78.
[60] A. Baldy, J. Elguero, R. Fawe, M. Pierrot, E.-J. Vincent, J. Am. Chem. Soc. 107 (1985) 5290.
[61] L. Resconi, in: M.P. Mingos, R.H. Crabtree (Eds.), in: M. Bochmann (Ed.), Comprehensive Organometallic Chemsitry III, vol. 4, Elsevier, London, 2006, pp. 1005–1166 (Chapter 9).
[62] G. Odian, Principles of Polymerization, 3rd ed., Wiley, New York, 1991.
[63] G.M. Diamond, R.F. Jordan, J.L. Petersen, J. Am. Chem. Soc. 118 (1996) 8024.
[64] L.E. Manzer, Inorg. Synth. 21 (1982) 135.
[65] J. Zucchini, E. Albizzati, U. Giannini, J. Organomet. Chem. 26 (1971) 357.
[66] Z. Otwinowski, W. Minor, Methods Enzymol. 276 (1997) 307.
[67] G.M. Sheldrick, SHELXL-97, Universität Göttingen, Göttingen, Germany, 1998.

antitumor activity studies *(in vitro)* of *cis* dichloride platinum(II) compounds with triazolopyrimidine ligands (HmtpO) [8], (dbtp) and (dptp; dptp -5,7-diphenyl-1,2,4-triazolo[1,5-*a*]pyrimidine) [12] indicate a moderate antiproliferative activity against the cells of rectal, breast and bladder cancer. In our earlier report the spectroscopical and biological parameters of *cis*-$PtCl_2(dbtp)_2$ [12] were presented, while in this work crystal structure has been discussed. It was demonstrated that *cis*-$PtCl_2(dbtp)_2$ exhibits high cytotoxicity against rectal adenocarcinoma SW707 and breast cancer T47D. Cytotoxicity results for this compound indicate, that *cis*-$PtCl_2(dbtp)_2$ exhibits better antitumor properties than *cis*-DDP.

In this paper, we study structural properties of platinum(II) and palladium(II) complexes with 5,7-ditertbutyl-1,2,4-triazolo[1,5-*a*]pyrimidine (dbtp): *cis*-$PtCl_2(dbtp)_2 \cdot EtOH$ (**1**) and *cis*-$PdCl_2$(dbtp)(dmso)] (**2**). It is a first report which presents the X-ray structure of mixed dichloride Pd(II) complexes with N-donor (5,7-ditertbutyl-1,2,4-triazolo[1,5-*a*]pyrimidine) and S-donor (dimethylsulfoxide) ligands.

2. Experimental

2.1. Materials

$PdCl_2$, inorganic salts and solvents of analytical grade were purchased from POCh Gliwice (Poland). Dipotassium tetrachloroplatinum(II) and 2,2,6,6-tetramethyl-3,5-heptanedione (98%), were purchased from Aldrich.

5,7-Ditertbutyl-1,2,4-triazolo[1,5-*a*]pyrimidines were prepared according to Bülow and Haas method [19] by the reaction of 3-amino-1,2,4-triazole with 2,2,6,6-tetramethyl-3,5-heptanedione [20].

2.2. Instrumentation

The contents of C, H, N was determined by elemental semi-microanalysis. IR spectra were measured with a Perkin–Elmer Spectrum-2000 FT–IR spectrometer, using KBr (400–4000 cm^{-1}) and polyethylene discs (100–400 cm^{-1}). The ^1H and ^{13}C spectra were obtained with a Bruker Avance 300 MHz spectrometer. The solvent was dmf-d_7, the concentrations of saturated solutions being *ca.* 0.01–0.05 M, temperature being 298 K. The reference standard was TMS. The ^{13}C CPMAS spectra were performed with a Bruker AMX 300 MHz spectrometer using a Bruker MASVTN500SB BL4 probe head and 4 mm zirconia rotors, at 296 K.

2.3. Preparation of complexes

The *cis*-$PdCl_2(dmso)_2$ [21] was prepared from $PdCl_2$, whereas *cis*-$PtCl_2(dbtp)_2$ was obtained by reaction of K_2PtCl_4 with dbtp in molar ratio M:L = 1:2 [12].

cis-$PtCl_2(dbtp)_2 \cdot EtOH$ (**1**): This compound was isolated by slow evaporation of *cis*-$PtCl_2(dbtp)_2$ from the mixture of ethanol and dichloromethane (1:1 v/v). Its formula and structure were determined by X-ray analysis *(vide infra)*.

cis-$PdCl_2$(dbtp)(dmso) (**2**): A suspension of *cis*-$PdCl_2(dmso)_2$ (0.051 g; 0.15 mmol) in 20 ml of dimethylsulfoxide was treated with the stoichiometric amount of dbtp (0.028 g; 0.12 mmol) in 10 ml of methanol. Reaction mixture was stirred at room temperature for 24 h. After 1 month the crystalline precipitate of this complex was obtained. The precipitate was filtered, washed with acetone, diethyl ether and dried in vacuum. 0.051 g (70%). *Anal.* Calc. for $C_{15}H_{26}Cl_2N_4OSPd$: C, 36.9; N, 11.5; H, 5.4. Found: C, 36.6; N, 11.3; H, 5.7%.

2.4. X-ray structure determination

The pale yellow crystal of *cis*-$PtCl_2(dbtp)_2 \cdot EtOH$ (**1**) was obtained by slow evaporation from the mixture of ethanol and dichloromethane (1:1 v/v) whereas the orange crystal of *cis*-$PdCl_2$(dbtp)(dmso) (**2**) was obtained from dimetylosulfoxide solution.

The X-ray data for (**1**) and (**2**) were collected at 293(2) K with an Oxford Sapphire CCD diffractometer, using Mo

Table 1
Crystal data and structure refinement for (**1**) and (**2**)

Identification code	*cis*-$PtCl_2(dbtp)_2 \cdot EtOH$ (**1**)	*cis*-$PdCl_2$(dbtp)(dmso) (**2**)
Empirical formula	$C_{28}H_{46}Cl_2N_8OPt$	$C_{15}H_{26}Cl_2N_4OSPd$
Formula weight	776.72	487.76
Temperature (K)	293(2)	293(2)
Wavelength (Å)	0.71073	0.71073
Crystal system, space group	triclinic, $P\bar{1}$	orthorhombic, *Pbca*
Unit cell dimensions		
a (Å)	10.731(1)	11.162(1)
b (Å)	11.046(1)	17.531(1)
c (Å)	14.121(1)	21.579(1)
α (°)	75.35(1)	90
β (°)	81.49(1)	90
γ (°)	79.70(1)	90
Volume ($Å^3$)	1584.0(2)	4222.6(5)
Z, D_{calc} (Mg/m^3)	2, 1.628	8, 1.534
Absorption coefficient (mm^{-1})	4.633	1.240
F(000)	780	1984
Crystal size (mm)	$0.27 \times 0.19 \times 0.05$	$0.43 \times 0.23 \times 0.12$
Θ range for data collection (°)	2.58–31.27	2.63–31.38
Limiting indices	$-15 \leqslant h \leqslant 14$, $-15 \leqslant k \leqslant 15$, $-20 \leqslant l \leqslant 18$	$-15 \leqslant h \leqslant 16$, $-22 \leqslant k \leqslant 24$, $-26 \leqslant l \leqslant 30$
Reflections collected/unique	15679/9252 ($R_{int} = 0.0408$)	39683/6569 ($R_{int} = 0.0546$)
Data/restraints/parameters	9252/0/364	6569/0/225
Goodness-of-fit on F^2	1.056	1.097
Final *R* indices [$I > 2\sigma(I)$]	$R_1 = 0.0336$, $wR_2 = 0.0700$	$R_1 = 0.0622$, $wR_2 = 0.1373$
R indices (all data)	$R_1 = 0.0454$, $wR_2 = 0.0795$	$R_1 = 0.0736$, $wR_2 = 0.1450$
Largest diffraction peak and hole (e $Å^{-3}$)	1.375 and −1.479	1.199 and −0.790

Kα radiation ($\lambda = 0.71073$ Å) and $\omega - 2\theta$ method. The shape-based numerical absorption correction was applied with the minimum and maximum transmissions of 0.3676 and 0.8014 for (**1**) and 0.6176 and 0.8654 for (**2**). The structure was solved by Patterson methods and refined with the full-matrix least-squares method on $F2$ with the use of SHELX-97 program package [22]. The data collection and refinement processes are summarized in Table 1.

3. Results and discussion

3.1. Discussion of the crystal structures of *cis*-$PtCl_2(dbtp)_2 \cdot EtOH$ (*1*)

The crystal structure of (**1**) consists of monomeric *cis*-$PtCl_2(dbtp)_2 \cdot EtOH$ units. The projection of the molecule with the atomic numbering scheme is presented in Fig. 1, whereas the selected bond distances and bond angles are listed in Table 2.

Platinum(II) ion is four-coordinated by two triazolopyrimidine nitrogen atom and two chloride ions. The two molecules of 5,7-ditertbutyl-1,2,4-triazolo[1,5-*a*]pyrimidine ligands are coordinated to platinum(II) in a monodentate manner through the nitrogen atom in position 3, which is the most frequent binding site for this type of heterocycle ligand [6,8,9,11,13,23]. The geometry of the PtN_2Cl_2 chromophore is characterized by distortion from the square-planar coordination. The angle are different from 90°: N(3)–Pt(1)–N(13) 92.87(11)°, N(13)–Pt(1)–Cl(2) 88.18(9)°, N(3)–Pt(1)–Cl(1) 88.29(8)°, Cl(2)–Pt(1)–Cl(1) 90.68(4)°. In the metal environment PtN_2Cl_2, the bond distance Pt–N and Pt–Cl *via* their nitrogen atoms N(3), the Pt(1)–N(3) distance being 2.043(3) Å and Pt(1)–N(13) 2.036(3) Å. The chloride atoms are in terminal *cis* positions resulting in Pt–Cl bond distances 2.288(1) Å and 2.297(1) Å. The Pt–N and Pt–Cl bond distances are quite comparable with these found in the related *cis*-$PtCl_2(HmtpO)_2 \cdot 2H_2O$ [8], *cis*-$PtCl_2(HmtpO)_2 \cdot 4H_2O$ [9] and *cis*-$PtCl_2(NH_3)(HmtpO)$ [9]. In addition, such a geometry of the Pt(II) coordination sphere is similar to that reported earlier for *cis*-$PtCl_2(HmtpO)_2 \cdot 2H_2O$ [8] and *cis*-$PtCl_2(HmtpO)_2 \cdot 4H_2O$ [9]. Geometry of the dbtp ligand is typical for the triazolopyrimidine ring system, and similar to those reported for dmtp [24,25].

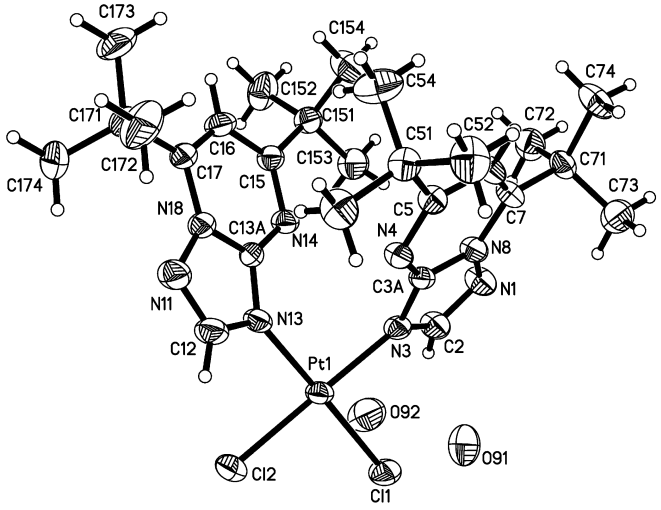


Fig. 1. The drawing of the *cis*-$PtCl_2(dbtp)_2 \cdot EtOH$ (**1**). Ellipsoids displayed at 50% probability level.

Table 2
Selected bond lengths (Å) and angles (°) for *cis*-$PtCl_2(dbtp)(dbtp)_2 \cdot EtOH$ (**1**) and *cis*-$PdCl_2(dbtp)(dmso)$ (**2**)

Bond/angle	**1** Ligand I	**1** Ligand II	**2**
Pt(1)–N(3)	2.036(3)	2.043(3)	
Pd(1)–N(3)			2.041(3)
Pd–S(1)			2.245(1)
Pt(1)–Cl(2)	2.288(1)		
Pt(1)–Cl(1)	2.297(1)		
Pd(1)–Cl(2)			2.302(1)
Pd(1)–Cl(1)			2.281(1)
C(2)–N(3)	1.355(5)	1.341(5)	1.334(5)
N(3)–C(3A)	1.334(4)	1.332(4)	1.343(4)
N(4)–C(3A)	1.341(5)	1.333(5)	1.325(4)
O(91)–O(92)#1	1.325(9)		
O(91)–O(91)#1	1.456(11)		
O(92)–O(91)#1	1.325(9)		
N(3)–Pt(1)–N(13)	92.87(11)		
N(3)–Pd–S(1)			89.11(9)
N(3)–Pt(1)–Cl(2)	178.67(9)		
N(13)–Pt(1)–Cl(2)	88.18(9)		
N(3)–Pd(1)–Cl(2)			90.07(10)
S(1)–Pd(1)–Cl(1)			89.38(4)
N(3)–Pt(1)–Cl(1)	88.29(8)		
N(3)–Pd(1)–Cl(1)			176.60(9)
N(13)–Pt(1)–Cl(1)	178.39(9)		
S(1)–Pd(1)–Cl(2)			177.32(6)
Cl(2)–Pt(1)–Cl(1)	90.68(4)		
Cl(1)–Pd(1)–Cl(2)			91.58(5)
C(3A)–N(3)–Pt(1)	130.9(2)	130.1(2)	
C(3A)–N(3)–Pd(1)			121.4(2)
C(2)–N(3)–Pt(1)	124.5(2)	124.9(3)	
C(2)–N(3)–Pd(1)			131.7(2)
O(92)#1–C(91)–C(91)#1	110.6(7)		

Both dbtp rings are planar, the r.m.s deviation from the best plane for N(11)–C(19) system is 0.0121 Å, whereas for N(21)–C(29) ring system is 0.0136 Å. The r.m.s deviation of atoms from the best plane of coordination is 0.0170 Å. The dbtp ring system planes form a dihedral angle of 52.66(9), while the angles between these planes and the PtN_2Cl_2 best plane are 39.48(9)° and 39.01(8)°. These values are much smaller than the analogous values reported for the *cis*-$PtCl_2(HmtpO)_2 \cdot 4H_2O$ [9].

The crystal packing reveals that all ring systems of the adjacent molecules are involved in the π...π stacking interactions, resulting in the formation of chains of molecules (Fig. 2). These chains are assembled into layers parallel to the crystallographic (100) by hydrophobic interactions of the tert-butyl groups. The complex molecules belonging to different layers seem to be linked by ethanol molecules interacting with the chloride ions. The details of these interactions are not discussed, since the ethanol hydrogen atoms cannot be located on the electron density maps.

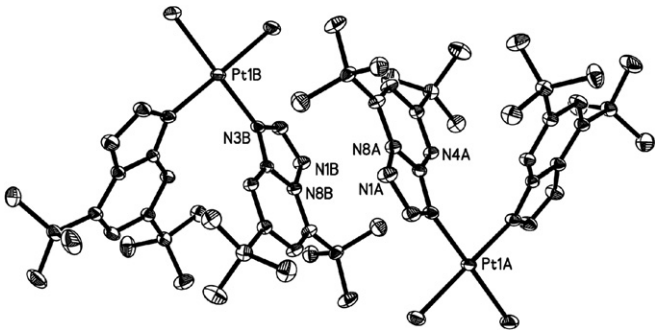


Fig. 2. The π–π interactions between the triazolopyrimidine ring systems. The symmetry codes are: A $[x, y, z]$; B $[-x, 1-y, 1-z]$.

3.2. Discussion of the crystal structures of *cis*-$PdCl_2$(dbtp)(dmso) (**2**)

The crystal structure data of *cis*-$PdCl_2$(dbtp)(dmso) (**2**) are listed in Table 1, whereas selected bond lengths and angles in Table 2. The perspective view of the molecule, with its numbering scheme is shown in Fig. 3. The structure of *cis*-$PdCl_2$(dbtp)(dmso) (**2**) is composed of square planar where the palladium atom is bound to the nitrogen atom of the dbtp (N3), sulfur atom of dimethylsulfoxide and two chloride atoms in *cis* arrangement forming a bond angle 91.58(5)°. This bond angle is smaller than those observed for dichloride palladium(II) complexes with 3-aminopyrrolidine [26], but bigger than those observed by us for *cis*-$PdCl_2$(dbtp) · $0.5C_2H_5OH$ [11]. These results seem to indicate an influence of dimethylsulfoxide molecule. The bond distances: Pd(1)–N(3) 2.041(3), Pd(1)–Cl(1) 2.281(1) and Pd(1)–Cl(2) 2.302(1) Å are similar to those described for palladium(II) compounds with N-donors ligands [26]. The angles in the coordination plane vary between 89.11(9)° and 91.58(5)°, as well as 176.60(9)° and 177.32(6)°. The Pd–S distance of 2.245(1) Å and is longer to the reported for Pt–dmso complexes [11,27–29]. The sulfur atom of the coordinated dimethylsulfoxide ligand is in an approximate tetrahedral environment although the biggest deviation has been observed for the C(11)–S(1)–C(12) 101.5(3)° and O(3)–S(1)–Pd(1) 116.03(17)° angles. Chloride ions are in *cis* position, the Pt–Cl distances being 2.302(1) and 2.281(1) Å as expected for the dichloride palladium compounds [26].

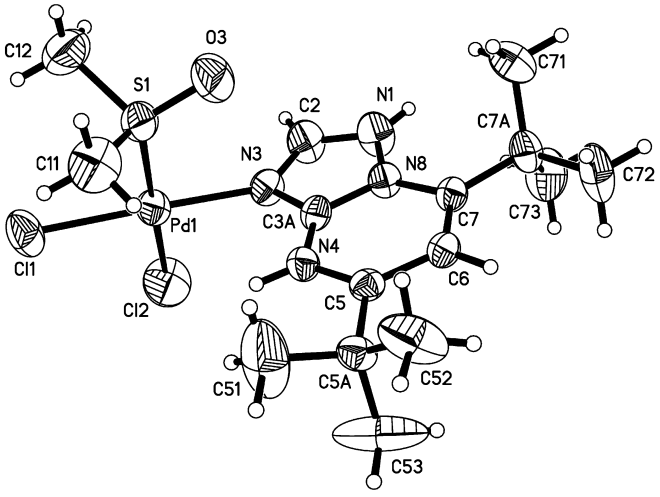


Fig. 3. The drawing of the *cis*-$PdCl_2$(dbtp)(dmso) (**2**) with the numbering scheme. The thermal ellipsoides displayed at 50% probability.

The analysis of the dbtp ligand planarity data indicates that the fused-ring system is essentially planar. The nine atoms comprising the triazolopyrimidine core have the r.m.s. deviation of 0.0147 Å from the least-squares plane. The $PdNSCl_2$ coordination sphere is also planar, the r.m.s. atomic deviation from the best plane is 0.0475 Å. The dihedral angle between the dbtp ring system plane and the $PdNSCl_2$ plane is 75.76(5)°, and is smaller than that of 88.97° reported for the HmtpO ring in the *cis*-$PtCl_2(NH_3)$(HmtpO) complex [9].

The symmetrical intermolecular interactions were found between C(2)–H group of the dbtp and Cl(1) ligand (Fig. 4) and methyl group from dmso C(12)–H and Cl(2). These are responsible for the dimerization of complex molecules related by the center of symmetry. Such interactions can be promoted by polarization of C–H group by of the adjacent heterocyclic N atoms of dbtp or S=O group of dmso.

3.3. NMR studies

The multinuclear spectral data of *cis*-$PtCl_2(dbtp)_2$ have been reported previously [12] and therefore here we presented only ^1H, ^{13}C NMR parameters for *cis*-$PdCl_2$-(dmso)(dbtp) (**2**). ^1H NMR spectrum of (**2**) exhibits signals at 0.95 and 1.53 ppm from the *tert*-butyl groups and singlets from H(2), H(6) (9.17 and 7.28 ppm), respectively. The latter chemical shifts when compared to free ligand, demonstrate deshielding of H(2) ($\Delta_{coord} = 0.53$ ppm), whereas for H(6) the opposite effect has been noted ($\Delta_{coord} = 0.01$ ppm). The deshielding of H(2) can be related to the charge density change in the heterocycle due to N(3) coordination of dbtp. The opposite effect on H(6) is much smaller due to four bonds distance in heterocylcic ring from coordinating N(3). The monodentate coordination mode of dbtp ligand *via* N(3) can be deduced from the large deshelding of H(2) proton. Thus palladium(II) binding to N(3) results in a deshelding of H(2), in a similar way to H(8) of purine bases after metal binding to N(7) [1,30]. In addition, the signals of carbons adjacent to N(3) coordination site C(2) and C(3a) are shielding (0.9–2.9 ppm), whereas: C(5), C(6) and C(7) shifted towards opposite fields (1.5–2.9 ppm). The shielding of the carbon atoms, adjacent to the coordination site N(3), as well as the deshielding of the other carbons and the protons inside the heterocyclic ring [9,11,12].

Moreover, in the ^1H NMR spectrum of (**2**) we observe also the signal of CH_3 groups of dmso molecule. The chemical shift of dmso CH_3 groups ($\delta = 3.25$ ppm), has not varied from other sulfur-bonded ligands [31–33].

The results of ^{13}C CPMAS spectra of dbtp and (**1**), (**2**) are listed in Table 3. The deshielding of aromatic carbons

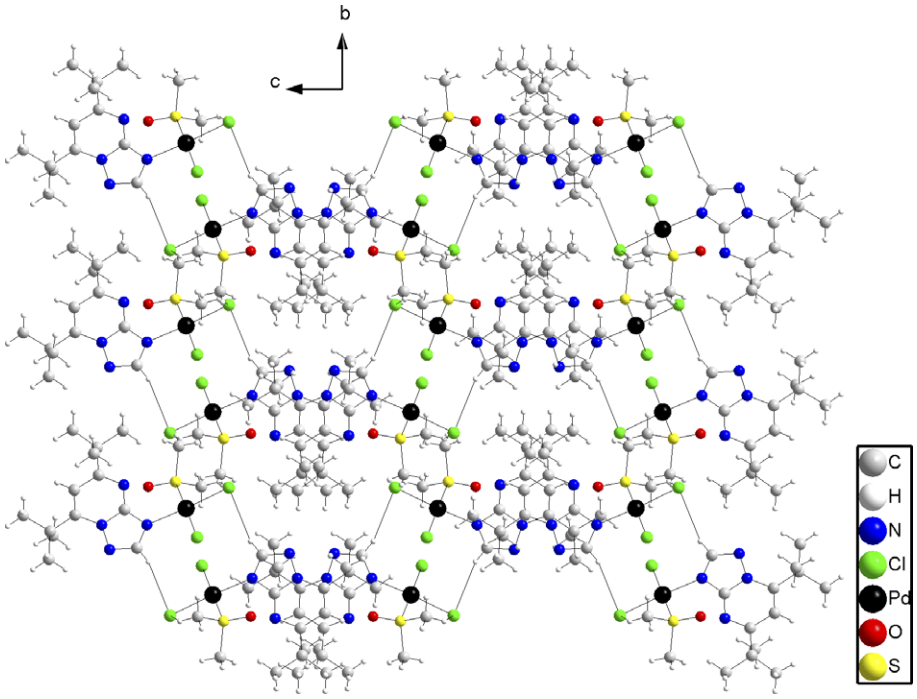


Fig. 4. View of the interaction between the C(2)–H group of the dbtp and Cl(1) ligand interaction.

Table 3
^{1}H and ^{13}C NMR chemical shifts (δ) for the platinum(II) and palladium(II) complexes (coordination shifts in parentheses)

Compound	C(2)	C(3a)	C(5)	C(6)	C(7)
dbtp in solid state	155.8	153.9	176.1	106.3	157.8
cis-$PtCl_2$(dbtp)$_2$ (**1**) in solid state	151.9 (−3.9)	153.1 (−0.8)	179.1 (+3.0)	107.9 (+2.6)	159.8 (+1.6)
cis-$PdCl_2$(dbtp)(dmso) (**2**) in solid state	151.5 (−3.9)	153.5 (−0.4)	178.2 (+2.1)	107.9 (+1.6)	158.1 (+0.3)
dbtp in dmf-d_7	155.3	156.5	175.9	104.6	157.9
cis-$PdCl_2$(dbtp)(dmso) (**2**) in dmf-d_7	154.4 (−0.9)	153.6 (−2.9)	178.8 (+2.9)	107.1 (+2.5)	159.4 (+1.5)

C(5), C(6), C(7) was observed upon complexation, except C(2) and C(3a) was detected. This suggests that the local magnetic fields are strongly influenced by the orientation or packing of the molecules in the crystal lattice present a similar pattern of the coordination shifts as observed in solution (Table 3), what indicates the same way of dbtp coordination.

3.4. Infrared spectra

Absorption bands of dbtp in the spectra of (**2**) are affected by coordination. The characteristic bands appeared at ν_{tp}(1617 cm^{-1}) and ν_{py}(1540 cm^{-1}) which are shifted *ca.* 10 cm^{-1} towards lower frequencies, upon coordination. Similar effect has been already observed by us for *cis*-$PtCl_2$(dbtp)$_2$ [12] and different transition metals complexes with triazolopyrimidine derivatives (tp, dmtp, dptp, dbtp, and HmtpO), where the N(3) coordination occurred [9,11–13,34].

In addition in the spectrum of (**2**) two new intensive absorption bands are detected at 1139 and 1033 cm^{-1}, which can be assigned to ρ_{CH_3} rocking vibrations and ν_{SO} stretching vibration, respectively [13,27,35–37]. Similar bands were noted in the spectra of alkyl sulfoxide palladium(II) complexes where S-bonded dmso was postulated [35]. Recently we have found ν_{SO} band in the spectra of $PtCl_2$(dmso)L, where L 1,2,4-triazolo[1,5-*a*]pyrimidine or its 5,7-disubstituted derivatives; thiazole, at similar frequencies (1142–1147 cm^{-1}) [14,27].

Spectrum of (**2**) in the range of metal-ligand vibrations exhibited one new strong absorption band at 321 cm^{-1}, 296 cm^{-1}, which can be assigned to Pd–Cl stretching vibrations. Similar frequency for Pd–Cl bond vibrations were detected in the spectra for other palladium(II) compounds, e.g.: *cis*-$PdCl_2(NH_3)_2$ (327, 306 cm^{-1}) [38], *cis*-$PdCl_2$(en)$_2$ (307, 296 cm^{-1}) [38], *cis*-$PdCl_2$(Him)$_2$ (335, 339 cm^{-1}) [39], *cis*-$PdCl_2$(tp)$_2$ (360, 306 cm^{-1}), *cis*-$PdCl_2$(dmtp)$_2 \cdot H_2O$ (356, 338 cm^{-1}) [11] (en – ethylenodiamine, Him – imidazole). The Pd–N stretching vibrations of the complexes can be tentatively assigned in analogy with *cis*-$PdCl_2(NH_3)_2$, *cis*-$PdCl_2$(en)$_2$ [38] and *cis*-dichloride compounds containing *N*-alkyl-3-pyridine-5-trifluoromethyl pyrazole ligands [40] to the bands appearing in the range 440–428 cm^{-1}. The presence and frequencies of the bands assignments Pd–N and Pd–Cl stretching vibrations therefore indicate coordination of the

palladium(II) *via* nitrogen atom and confirm *cis* geometry of chloride ions.

4. Conclusion

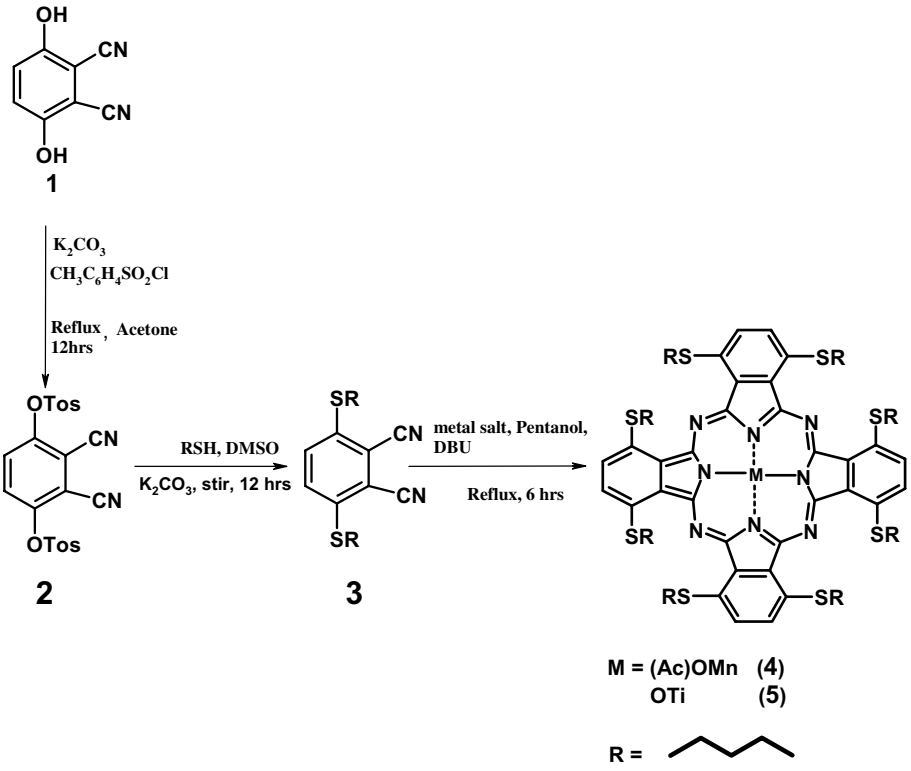
The present work displays the molecular structure of platinum(II) and palladium(II) with 5,7-ditertbutyl-1,2,4-triazolo[1,5-*a*]pyrimidine. The results described and discussed above have clearly show that in both *cis*-$PtCl_2(dbtp)_2 \cdot EtOH$ and *cis*-$PdCl_2(dbtp)(dmso)$ heterocycle ligand is coordination monodentately *via* N(3). The observed coordination mode *via* N(3) may be regarded as representative for triazolopyrimidines and analogous to N(9) complexation in purine.

5. Supplementary material

CCDC 276451 and 276450 contain the supplementary crystallographic data for (**1**) and (**2**). These data can be obtained free of charge via http://www.ccdc.cam.ac.uk/conts/retrieving.html, or from the Cambridge Crystallographic Data Centre, 12 Union Road, Cambridge CB2 1EZ, UK; fax: (+44) 1223-336-033; or e-mail: deposit@ccdc.cam.ac.uk.

References

[1] O. Renn, A. Albimati, B. Lippert, Angew. Chem., Int. Ed. Engl. 29 (1990) 84.
[2] J.M. Salas, M.A. Romero, M.P. Sanchez, M. Quiros, Coord. Chem. Rev. 193 (1999) 1119.
[3] M. Biagini-Cingi, A.M. Manotti-Lanfredi, A. Tiripicchio, J.G. Haasnoot, J. Reedijk, Inorg. Chim. Acta 72 (1983) 81.
[4] M. Biagini-Cingi, A.M. Manotti-Lanfredi, A. Tiripicchio, A. Cornelissen, J.G. Haasnoot, J. Reedijk, Inorg. Chim. Acta 129 (1987) 217.
[5] M. Abul Haj, M. Quirós, J.M. Salas, J. Chem. Soc., Dalton Trans. (2002) 4740.
[6] A.H. Velders, L. Pazderski, F. Ugozzoli, M. Biagini-Cingi, A.M. Manotti-Lanfredi, J.G. Haasnoot, J. Reedijk, Inorg. Chim. Acta 273 (1998) 259.
[7] J.A.R. Navarro, M.A. Romero, J.M. Salas, M. Quirós, Inorg. Chem. 36 (1997) 3277.
[8] J.A.R. Navarro, J.M. Salas, M.A. Romero, R. Vilaplana, F. Gonzáles-Vilchez, R. Faure, J. Med. Chem. 41 (1998) 332.
[9] I. Łakomska, A. Wojtczak, J. Sitkowski, L. Kozerski, E. Szłyk, Polyhedron 26 (2007) 803.
[10] N. Lekkas, N. Hadjiliadis, A. Garoufis, J. Kobe, P.V. Bernhardt, E.R.T. Tiekink, Inorg. Chim. Acta 359 (2006) 4297.
[11] E. Szłyk, A. Grodzicki, L. Pazderski, A. Wojtczak, J. Chatłas, G. Wrzeszcz, J. Sitkowski, B. Kamieński, J. Chem. Soc., Dalton Trans. (2000) 867.
[12] I. Łakomska, E. Szłyk, J. Sitkowski, L. Kozerski, J. Wietrzyk, M. Pełczyńska, A. Nasulewicz, A. Opolski, J. Inorg. Biochem. 98 (2004) 167.
[13] E. Szłyk, I. Łakomska, A. Surdykowski, L. Pazderski, T. Głowiak, J. Sitkowski, L. Kozerski, Inorg. Chim. Acta 333 (2002) 93.
[14] J.A.R. Navarro, M.A. Romero, J.M. Salas, M. Quirós, E.R.T. Tiekink, Inorg. Chem. 36 (1997) 4988.
[15] S. Orihuela, M.P. Sanchez, M. Quiros, D. Martin, R. Faure, Polyhedron 17 (1998) 2477.
[16] M. Abul-Haj, M. Quirós, J.M. Salas, Polyhedron 23 (2004) 2373.
[17] F. Luque, C. Fernandez-Ramos, E. Entrala, M.J. Rosales, M.C. Salas, J. Navarro, M. Sanchez-Moreno, Toxicology in Vitro 14 (2000) 487.
[18] F. Luque, C. Fernández-Ramos, E. Entrala, M.J. Rosales, J.A. Navarro, M.A. Romero, J.M. Salas, M. Sánchez-Moreno, Comparative Biochem. Physiol. 126 (2000) 39.
[19] C. Bülow, K. Haas, Berichte 42 (1909) 4638.
[20] A. Grodzicki, E. Szłyk, L. Pazderski, A. Goliński, Magn. Res. Chem. 34 (1996) 725.
[21] T.A.K. Al-Allaf, L.J. Rashan, Eur. J. Med. Chem. 33 (1998) 817.
[22] G.M. Sheldrick, T.M. Schneider, Methods Enzymol. 277B (1997) 319.
[23] M. Abul-Haj, M. Quirós, J.M. Salas, Polyhedron 23 (2004) 743.
[24] A.H. Velders, F. Ugozzoli, M. Biagini-Cingi, A.M. Manotti-Lanfredi, J.G. Haasnoot, J. Reedijk, Eur. J. Inorg. Chem. 2 (1999) 213.
[25] A. Grodzicki, E. Szłyk, A. Wojtczak, G. Wrzeszcz, L. Pazderski, T. Muzioł, Polyhedron 18 (1998) 519.
[26] X. Riera, V. Moreno, E. Freisinger, B. Lippert, Inorg. Chim. Acta 339 (2002) 253.
[27] A. Cornia, A.C. Fabretti, M. Bonivento, L. Cattalini, Inorg. Chim. Acta 255 (1997) 405.
[28] G.M. Arvanitis, Ch. E. Holmes, D.G. Johnson, M. Berardini, Acta Crystallogr., Sect. C 56 (2000) 1332.
[29] F.H. Allen, O. Kennard, R. Taylor, Acc. Chem. Res. 16 (1983) 146.
[30] B. Lippert, Prog. Inorg. Chem. 37 (1989) 1.
[31] G. Annibale, M. Bonivento, L. Cattalini, M.L. Tobe, J. Chem. Soc., Dalton Trans. (1992) 3433.
[32] C. Sacht, M.S. Datt, S. Otto, A. Roodt, J. Chem. Soc., Dalton Trans. (2000) 727.
[33] O. Clement, A.W. Roszak, E. Buncel, Inorg. Chim. Acta 253 (1996) 53.
[34] E. Szłyk, L. Pazderski, I. Łakomska, L. Kozerski, J. Sitkowski, Magn. Res. Chem. 40 (2002) 529.
[35] J.H. Price, A.S. Williamson, R.S. Schramm, B.B. Wayland, Inorg. Chem. 11 (1972) 1280.
[36] F.A. Cotton, R. Francis, W.D. Horrocks, J. Phys. Chem. 64 (1960) 1534.
[37] S.G. de Almeida, J.L. Hubbard, N. Farrell, Inorg. Chim. Acta 193 (1992) 149.
[38] J.R. Durig, R. Dayton, D.W. Sink, B.R. Mitchel, Spectrochim. Acta 21 (1965) 1367.
[39] K. Nakamoto, Infrared and Raman Spectra of Inorganic and Coordination Compounds, Wiley, New York, 1978, p. 147.
[40] V. Montoya, J. Pons, J. Garcia-Antón, X. Solans, M. Font-Bardia, J. Ros, Inorg. Chim. Acta 360 (2007) 625.



Scheme 1. Synthesis of thiol derivatised MPc complexes.

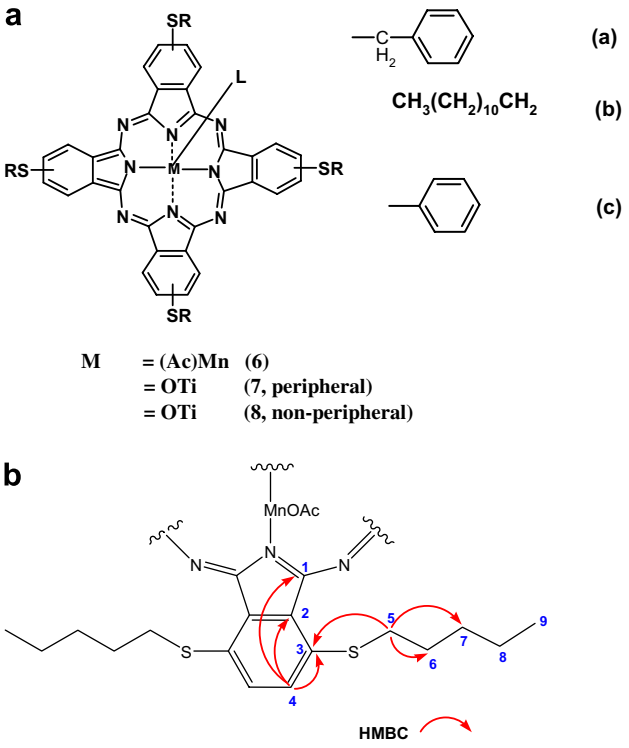


Fig. 1. (a) Molecular structures of published thiol derivatised MPc complexes. (b) Partial structure of four together with key HMBC correlations.

metal exhibits variable oxidation states ranging from Mn^{I} to Mn^{IV} [3–13]. This makes manganese phthalocyanine complexes potential catalysts for many reactions. Substituted manganese phthalocyanine complexes are still relatively few, and their electrochemistry not fully understood. For example the first reduction in $Mn^{II}Pc^{-2}$ complexes has been a subject of some controversy, with some reports proposing ring reduction to the $Mn^{II}Pc^{-3}$ species and others suggesting metal reduction to the $Mn^{I}Pc^{-2}$ species [2]. The spectra of $Mn^{II}Pc$ and $Mn^{III}Pc$ complexes is now well known. However, the spectra of $Mn^{IV}Pc$ complexes are virtually unknown. This work presents a well-defined spectrum of a $Mn^{IV}Pc^{-2}$ complex.

Titanium phthalocyanine (TiPc) also exhibits variable oxidation states. There is a growing interest in the chemistry of TiPc complexes [14–26], though their properties are relatively unexplored. Diamagnetic ions such as Zn^{2+}, Al^{3+}, Ga^{3+} and Ti^{4+} give phthalocyanine complexes comprising both high triplet yields and long triplet lifetimes [27], which are suitable for photodynamic therapy (PDT) applications, hence the need to develop new TiPc complexes. One-step two electron processes are rare but have been reported in some MPc complexes [28]. We have recently reported on TiPc complexes exhibiting overlapping reduction processes [17]. Due to the rarity of such overlapping redox processes in MPc complexes, there is a need to study the electrochemistry of more TiPc complexes in order to understand the electrochemical behaviour of these molecules.

2. Experimental

2.1. Materials

Acetone, manganese acetate, dimethylsulphoxide (DMSO), 1-pentanethiol, titanium butoxide, 1,8-diazabicyclo{5.4.0}-undec-7-ene (DBU), tetrabutylammonium tetrafluoroborate and 1-pentanol were purchased from Sigma–Aldrich. Potassium carbonate, sodium carbonate, deuterated chloroform ($CDCl_3$), 2,3-dicyanohydroquinone, *p*-toluenesulfonyl chloride, chloroform ($CHCl_3$) and dichloromethane (DCM) were procured from Merck. Solvents were dried and distilled before use. Column chromatography was performed on silica gel 60 (0.04–0.063 mm).

2.2. Electrochemical studies

Cyclic (CV) and square wave (SWV) voltammetry data were obtained with the Autolab potentiostat PGSTAT 30 (Eco Chemie, Utretch, The Netherlands) driven by the General Purpose Electrochemical Systems data processing software (GPES, software version 4.9, Eco Chemie), using a three-electrode set-up with glassy carbon electrode (GCE, 3 mm diameter) as a working electrode, platinum wire as counter electrode and Ag|AgCl wire as pseudo-reference electrode. Electrochemical experiments were performed in dry DCM containing tetrabutylammonium tetrafluoroborate ($TBABF_4$) as a supporting electrolyte. Prior to scans, the working electrode was polished with alumina paste on a Buehler felt pad, followed by washing with deionised water and rinsing with DCM. Square wave parameters were: step potential 5 mV; amplitude 20 mV at a frequency of 25 Hz. Spectroelectrochemical data were obtained using a home made optically transparent thin-layer electrochemical (OTTLE) cell which was connected to a Bioanalytical Systems (BAS) CV 27 voltammograph.

2.3. Equipment

UV/Vis spectra were recorded on a Cary 500 UV/Vis/NIR spectrophotometer. IR (KBr discs) was recorded on a Perkin–Elmer spectrum 2000 FTIR spectrometer. ^{1}H and 2-D NMR spectra were recorded using a Bruker AVANCE II+ 600 MHz spectrometer. Elemental analyses were performed at the University of Cape Town.

2.4. Synthesis

For the synthesis of phthalonitriles (**2** and **3**), a procedure similar to that reported in the literature [29–31] was employed with slight modification as follows.

2.4.1. 3,6-Bis(4′-methylphenylsulfonyloxy) phthalonitrile (*2*)

p-Toluenesulfonyl (Tos) chloride (5.2 g, 27 mmol) was added to a mixture of 2,3-dicyanohydroquinone (2 g, 13 mmol) and potassium carbonate (6.9 g, 50 mmol) in acetone (15 ml). The mixture was heated to reflux for 2 h. Thin layer chromatography (TLC) was performed to determine the consumption of compound **1**. The mixture was cooled to room temperature and poured into water (40 ml), and stirred for 1 h. The light brown product was filtered and oven dried. Yield: 4.5 g (79%). IR [(KBr) υ_{max}/cm^{-1}]: 3432, 3239, 3085, 2243, 2226(CN), 1504, 1449, 1315, 1279, 1204, 1174, 1142, 1021, 1004, 979, 934, 847, 749, 694, 638, 614.

2.4.2. 3,6-Di(pentathio)-4,5-dicyanobenzene (*3*)

1-Pentanethiol (2.4 g, 23 mmol) was dissolved in DMSO under a nitrogen atmosphere and **2** (4.3 g, 9.2 mmol) was added. The mixture was stirred for 15 min and finely ground anhydrous potassium carbonate (5.1 g, 37 mmol) was added portionwise for two hours while stirring. The mixture was stirred under a nitrogen atmosphere for 12 h. Water was added and the aqueous phase extracted using chloroform (3×50 ml). The extracts were further treated with 5% sodium carbonate solution (2×250 ml). The solution was further treated with water (2×250 ml), and the solvent evaporated off. The product was recrystallised from ethanol. Yield: 2.2 g (71.7%). IR [(KBr) υ_{max}/cm^{-1}]: 3084, 2951, 2930, 2864, 2378 (S-C), 2225 (C≡N), 1444, 1283, 1202, 1181, 1173, 1145, 877, 847, 827, 725, 547, 447. ^{1}H NMR($CDCl_3$):δ, ppm 7.49 (2H, s, Ar-H), 3.02–2.99 (4H, t, $-CH_2$), 1.71–1.63 (4H, m, $-CH_2$), 1.46–1.37 (4H, m, $-CH_2$), 1.36–1.28, (4H, m, $-CH_2$), 0.91–0.88 (6H, t, $-CH_3$).

2.4.3. 1,4,8,11,15,18,22,25-Octapentylthiophthalocyaninato manganese(III) acetate (*4*)

3,6-Dipentylthiophthalonitrile (**3**) (0.4 g, 1.2 mmol) in 1-pentanol (3.5 ml) was refluxed under a nitrogen atmosphere and manganese(III) acetate (0.069 g, 0.40 mmol) was added. After the addition of DBU (0.13 ml, 0.86 mmol), the reaction was continued for 6 h. The mixture was cooled and column chromatography over silica was done with $CHCl_3$ as eluent. Yield: 0.23 g (42%). UV/Vis (DCM): λ_{max} (nm) ($\log\varepsilon$): 285(5.0), 363(4.5), 553 (4.0), 794(4.3), 893 (4.8). IR [(KBr) υ_{max}/cm^{-1}]: 2959, 2925, 2855, 2369 (S-C), 1557, 1461, 1361, 1310, 1283, 1263, 1225, 1210, 1190, 1149, 1102, 1072, 1024, 932, 802 (υ_{Mn-O}), 750, 584, 560. ^{1}H NMR (600 MHz, $CDCl_3$): δ ppm 7.41 (8H, s, Ar-H-4), 3.01 (16H, t, $J = 7.2$, 7.2 Hz, S-H_2-5), 1.74 (16H, quintuplet, 7.2, 7.2 Hz, H_2-6), 1.46 (16H, quintuplet, 7.2, 7.2 Hz, H_2-7), 1.36 (16H, sextuplet, 7.8, 7.2, 7.2 Hz, H_2-8), 1.2 (3H, s, OAc), 0.91 (24 H, t, $J = 7.2$, 7.2 Hz, H_3-9). ^{13}C NMR (150 MHz, $CDCl_3$): δ ppm 166.6 (s, C-1), 134.7 (s, C-3), 130.3 (d, C-4), 128.0 (s, C-2), 30.7 (t, C-7), 30.5 (t, C-5), 29.2 (q, OAc), 27.7 (t, C-6), 21.8 (t, C-8), 13.5 (q, C-9). HMBC correlations: H-4/C-1, C-2, C-3; H_2-5/C-3, C-6, C-7; H_2-6/C-7, C-8; H_2-7/C-5, C-6, C-8, C-9; H_2-8/C-6, C-7, C-9; H_2-9/C-7, C-9. *Anal.* Calc. for $C_{74}H_{99}N_8S_8O_2Mn$: C, 61.55; H, 6.91; N, 7.76. Found: C, 61.72; H, 7.33; N, 7.03%.

*2.4.4. 1,4,8,11,15,18,22,25-Octapentylthiophthalocyaninato titanium(IV) oxide (**5**)*

Compound **5** was prepared as described above for compound **4**, using compound **3** (0.45 g, 1.2 mmol), titanium butoxide (0.14 ml, 0.40 mmol), DBU (0.25 ml, 1.68 mmol) and 1-pentanol (3.4 ml). The purification was done using column chromatography over silica with $CHCl_3$ as eluent. Yield: 0.12 g (22%). UV/Vis (DCM): λ_{max} (nm) ($\log\varepsilon$): 290(3.9), 352(3.5), 718(3.3), 808(3.9). IR [(KBr) υ_{max}/cm^{-1}]: 2955, 2930, 2961, 2354 (S-C), 1713, 1649, 1560, 1459, 1371, 1274, 1178, 1145, 1108, 1060, 824 (υ_{Ti-O}), 759, 643, 596, 534. ^{1}H NMR (600 MHz, $CDCl_3$): δ ppm 7.47 (8H, s, Ar-*H*), 3.00 (16H, t, $J = 7.2$, 7.2 Hz, S-*CH*$_2$), 1.67 (16H, quintuplet, 7.2, 7.2 Hz, *CH*$_2$), 1.4 (16H, m, *CH*$_2$), 1.3 (16H, sextuplet, $J = 7.8$, 7.8, 7.2 Hz *CH*$_2$–CH$_3$), 0.90 (24H, t, $J = 7.2$, 7.2 Hz, *CH*$_3$). *Anal.* Calc. for $C_{73}H_{99}N_8S_8OTi$: C, 62.04; H, 6.94; N, 8.05. Found: C, 61.74; H, 7.26; N, 7.83%.

3. Results and discussion

3.1. Synthesis and characterisation

The thiol substituted phthalonitrile was prepared via a base-catalysed (K_2CO_3) nucleophilic aromatic displacement reaction of the tosyl group with a thiol. The metallophthalocyanine complexes (**4** and **5**) were then prepared by the template reaction of thiol substituted phthalonitrile precursors with manganese acetate or titanium butoxide in the presence of DBU (Scheme 1). Yields of 42% and 22% were respectively obtained for complexes **4** and **5** after purification by column chromatography. Both MPcs were soluble in solvents such as DCM, $CHCl_3$, THF and toluene.

The new compounds were characterised by IR, UV/Vis and NMR spectroscopies, as well as elemental analysis, which were consistent with the predicted structures as shown in the experimental section. The disappearance of the sharp C≡N vibration at 2225 cm^{-1} confirmed the cyclotetramerisation of phthalonitriles **2** and **3** and typical Mn–O and Ti=O stretches appeared as medium bands at 802 cm^{-1} and 824 cm^{-1} [32], respectively, further confirming MPc formation.

The ^{1}H NMR spectra of these octa-substituted MPcs show simple spectra due to the highly symmetrical nature of the complexes. The ^{1}H NMR spectra of complexes **4** and **5** showed almost identical chemical shifts. The NMR data obtained is in accordance with the expected structures. The aromatic non-peripheral ring protons were observed as a singlet at 7.41 ppm (H-4, Fig. 1b) for complex **4** and 7.47 for complex **5**, integrating for eight protons for each complex. The methylene and methyl proton shifts belonging to the thio-alkyl side chain were clearly observed in the ^{1}H NMR spectrum. The ^{13}C NMR data proved difficult to obtain, thus chemical shifts were obtained using HSQC (Heteronuclear Single Quantum Correlations) and HMBC (Heteronuclear Multiple Bond Correlation) data. The deshielded proton resonating at δ 3.01 for **4** was attributed to the thio-methylene proton H-5, which upon analysis of the HSQC data revealed it to be attached to a carbon resonating at 30.5 ppm. The thio-methylene proton assignment was confirmed by a HMBC correlation (Fig. 1b) to an aromatic carbon resonating at 134.7 ppm (C-3). Thus a HMBC correlation to C-3 from the aromatic proton H-4 was expected, and observed, confirming its assignment. H-5 showed additional HMBC correlations to methylene carbons resonating at 27.7 and 30.7 ppm, which, together with further HMBC and HSQC studies identified them as C-6 and C-7, respectively. The ^{1}H NMR spectrum revealed a further methyl and CH_2 proton signals at δ 0.91 and 1.36 ppm, which were shown to be attached to carbons at 13.5 and 21.8 ppm, respectively. The CH_3 group was thus placed at the end of the pentylthio chain and assigned as H-9. This methyl proton showed HMBC correlations to carbons at 21.8 and 30.7 ppm. With the latter carbon shift having been assigned to C-7 previously, the carbon resonating at 21.8 ppm was attributed to the remaining methylene group C-8, thus completing the assignment of the pentylthio side chain. Finally, the aromatic proton H-4, in addition to the HMBC correlation to C-3, showed two other HMBC correlations which were observed to be aromatic quarternary carbons residing at δ 128.0 and 166.6 ppm. Based on their chemical shifts these were assigned to C-2 and C-1, respectively. Furthermore, a methyl singlet residing at 1.24 ppm in the ^{1}H NMR spectrum was shown in the HSQC spectrum to be attached to a carbon at 29.2 ppm. This methyl showed no HMBC correlations to the ring and is thus tentatively assigned to the acetate attached to the manganese metal ion. The carbonyl chemical shift belonging to acetate was not observed in the HMBC, but elemental analyses and IR spectra confirmed the presence of the acetate group.

The UV/Vis spectra of the complexes **4** and **5** are shown in Fig. 2. In DCM the spectra show typical B-bands

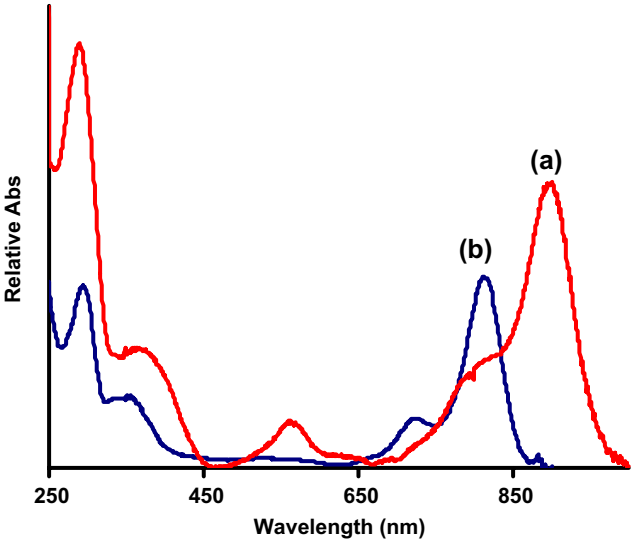


Fig. 2. UV–Vis spectrum of (a) **4** (concentration = 1.5×10^{-5} M) and (b) **5** (9×10^{-5} M) in DCM.

around 360 nm. The Q-bands are highly red-shifted for complex **4** at 893 nm and **5** at 808 nm in DCM. An additional band, typical of Mn(III)Pc [9] derivatives is observed between 450 and 650 nm. The large red shift of the Q-band is due to the electron donating properties of sulphur. In addition, substitution at the α positions enhances the red shift, making the complex **4** in particular to show a highly red-shifted Q-band compared to MPc complexes in general. The red shift for complex **5** is the longest ever reported, while for MnPc red shifts close to 900 nm are rare. The complexes did not show aggregation and Beer's law was obeyed for concentrations lower than 3×10^{-5} M.

3.2. Voltammetric and spectroelectrochemical characterisation

3.2.1. 1,4,8,11,15,18,22,25-Octapentathiophthalocyaninato manganese(III) acetate (4)

The cyclic (CV) and square wave (SWV) voltammetries of complex **4** were performed in de-aerated DCM containing $TBABF_4$ as electrolyte, Fig. 3. The half-wave potentials ($E_{1/2}$) for the complexes are summarised in Table 1. Complex **4** exhibits four main reduction processes labelled **I** ($E_{1/2} = +0.47$ V), **II** ($E_{1/2} = +0.75$ V), **III** ($E_{1/2} = -0.46$ V), and **IV** ($E_{1/2} = -1.24$ V) vs. Ag|AgCl, Table 1. All the redox processes showed both the cathodic and anodic components; however peak separations were larger than the expected 60 mV, suggesting slow electron transfer. The cathodic to anodic peak separation (ΔE) ranged from 70 to 120 mV and a ΔE value of 90 mV was obtained for ferrocene, at a scan rate of 100 mV/s.

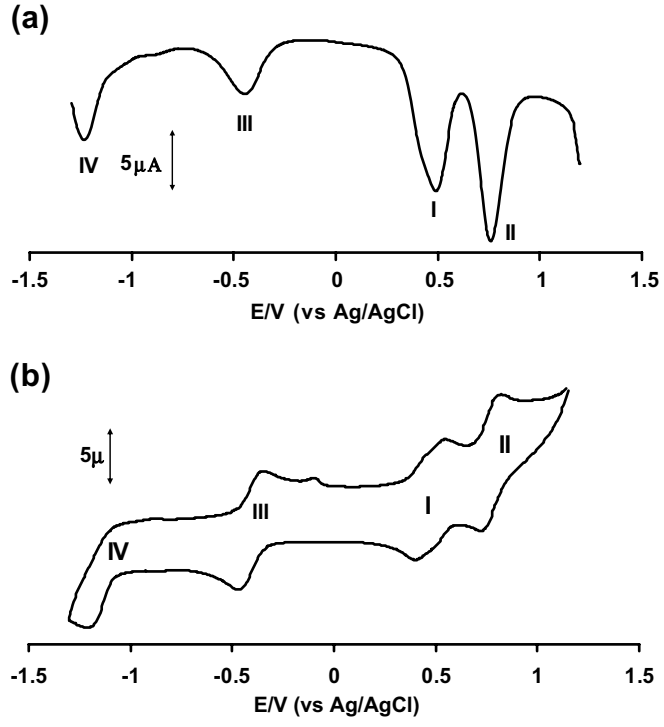


Fig. 3. Square wave (a) and cyclic (b) voltammograms for **4** in DCM containing 0.1 M $TBABF_4$. Scan rate = 100 mV s^{-1}.

The cathodic to anodic peak current ratio (I_{pc}/I_{pa}) were near unity, except for **IV** which showed a weak cathodic component. For all redox couples, plots of peak current (I_p) versus the square root of scan rate ($v^{1/2}$) were linear, thus suggesting diffusion control at the electrode surface. In comparison to other thiol substituted MnPc complexes (Table 1), process **III** may be assigned to $Mn^{III}Pc^{-2}/Mn^{II}Pc^{-2}$, though shifted to more negative potentials. The shift to more negative potentials may be due to the fact complex **4** is octa-substituted with the electron donating thiol substituents, while the rest of the complexes in Table 1 are tetrasubstituted. The plurality of the electron donating thiol groups may make the molecule more difficult to reduce. Also the ring substituents are different in the complexes. Process **IV** may either be due to $Mn^{II}Pc^{-2}/Mn^{II}Pc^{-3}$ or $Mn^{II}Pc^{-2}/Mn^{I}Pc^{-2}$. As stated in the introduction, both $Mn^{I}Pc^{-2}$ and $Mn^{II}Pc^{-3}$ species have been proposed. However, the latter species has been reported by several authors [33,34]. The first oxidation (process **I**) showed an overlap of two peaks, which were not clearly resolved even when using the more sensitive SWV. Such closely spaced redox couples may be associated with the presence of aggregates [28]. On dilution of the solution, the splitting is not evident. The last oxidation process (**II**) is in the range of ring-based processes in comparison to other MnPc complexes. The nature of the couples as well as the number of electrons transferred were confirmed by spectroelectrochemistry below. Using a narrower scan window (−1000 to +1000 mV) did not change the shape of the cyclic voltammograms.

Spectroelectrochemical studies using optically transparent thin layer electrode (OTTLE) cell gave more insight into the origin of the redox couples observed during voltammetric studies of the complexes. Fig. 4a shows the spectral changes observed during the reduction of complex **4** at potentials of process **III**. The starting spectrum in Fig. 4, is slightly more shifted to longer wavelengths compared to Fig. 2, due to the presence of an electrolyte in DCM for the former. Upon reduction, there was a blue shift in the Q-band from 908 to 795 nm with a concurrent decrease of the charge transfer bands at 571 nm, and the colour of the complex changed from purple to blue. These spectral changes occurred with clear isosbestic points at 831, 634 and 536 nm. The blue shift in the Q-band upon reduction is typical of $Mn^{III}Pc^{-2}$ to $Mn^{II}Pc^{-2}$ reduction [2]. Thus spectral changes in Fig. 4a confirmed that process **III** is due to the redox couple $Mn^{III}Pc^{-2}/Mn^{II}Pc^{-2}$. The value of n was calculated using $Q = nFCV$ (n, number of electrons involved, F, Farady's constant, C, solution concentration and V, solution volume) to be approximately 1, $n = 0.8$. Fig. 4b shows spectral changes observed on application of potentials of process **IV**. A drastic decrease in the intensity of the Q-band and the formation of new features between 500 and 700 nm is typical [34] of ring-based processes in MPc complexes. Hence the spectral changes are

Table 1
Electrochemical data of thiol derivatised MnPc and TiPc complexes. Unless otherwise stated, the data collected in DCM containing $TBABF_4$. Half-wave potential ($E_{1/2}$) as V vs. Ag|Agcl unless otherwise stated

Complex	$Mn^{II}Pc^{-2}/Mn^{II}Pc^{-3}$ (**IV**)	$Mn^{III}Pc^{-2}/Mn^{II}Pc^{-2}$ (**III**)	$Mn^{IV}Pc^{-2}/Mn^{III}Pc^{-2}$ (**I**)	$Mn^{IV}Pc^{-1}/Mn^{IV}Pc^{-2}$ (**II**)	Reference
4	−1.24	−0.46	0.47	0.75	This work
6a	−0.84	−0.08	~0.3	0.87	[35]
6b	−0.98	−0.26	~0.3	0.83	[35]
	$Ti^{III}Pc^{-2}/Ti^{II}Pc^{-2}$**(IV)**	$Ti^{IV}Pc^{-2}/Ti^{III}Pc^{-2}$**(III)**	Oxidation processes (**I**, **II** and **II′**)		
5	−1.09	−0.73	0.54 (**I**), 0.36 (**II**), 0.95 (**II′**)		This work
7a	−0.37	−0.07	No oxidation processes observed		[16][a]
7c	−0.42	−0.09	No oxidation processes observed		[16][a]
8a	−0.40	−0.09	No oxidation processes observed		[16][a]
8c	−0.46	−0.07	No oxidation processes observed		[16][a]

[a] Values recorded in DMF (dimethylformamide) containing $TBABF_4$.

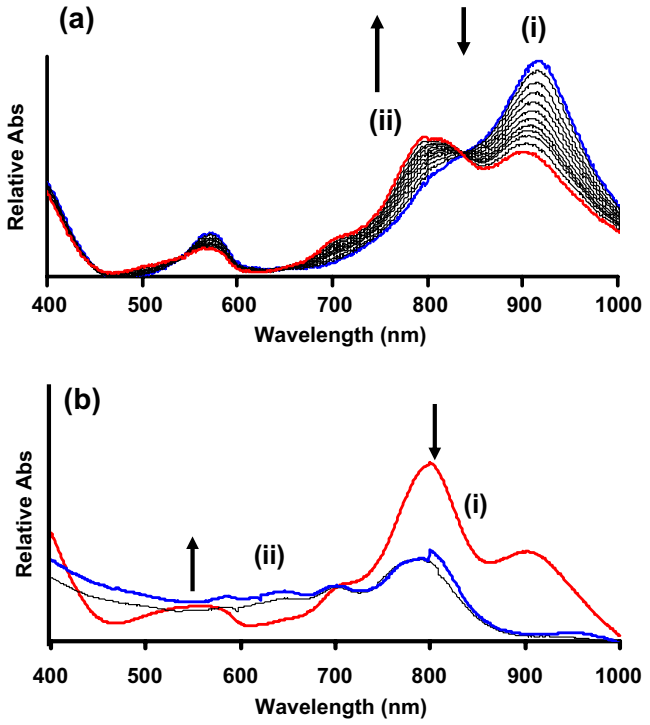


Fig. 4. UV–Vis spectral changes for **4** observed using controlled potential electrolysis at (a) −0.5 V (process **III**) and (b) −1.3 V (process **IV**). (i) Before electrolysis and (ii) at the end of electrolysis. Electrolyte = DCM containing 0.1 M $TBABF_4$. First scan in (b) same as last scan in (a).

assigned to $Mn^{II}Pc^{-2}/Mn^{II}Pc^{-3}$. As stated above, the first reduction in $Mn^{II}Pc^{-2}$ complexes has been reported to occur either at the metal to form $Mn^{I}Pc^{-2}$ species or at the ring to form $Mn^{II}Pc^{-3}$ species. The latter is observed in this work and has been reported by our group [35] and others [33].

To confirm the origin of the oxidation processes (**I** and **II**), controlled potential electrolysis was conducted. Fig. 5 shows spectral changes observed on application of potentials of process **I**. Spectral changes showed a shift in the Q-band from 908 to 920 nm, Fig. 5b. The shift in the Q-band is typical [2] of metal-based oxidation, hence the formation of a $Mn^{IV}Pc$ species. The spectrum of $Mn^{IV}Pc$ species is not well known apart from a recent report [33]. This work provides another example of a well-defined spectrum of the rare $Mn^{IV}Pc^{-2}$ species. Table 2 lists the Q-band maxima of the various oxidation states of the MnPc discussed in this work and those from the literature.

The application of potential of process **II** resulted in the collapse of the Q-band and the formation of new peaks at 809 and 720 nm with an increase in intensity at ~520 nm, Fig. 5c. The collapse of the Q-band and the formation of new less intense bands is typical [34] of ring oxidation in MPc complexes. Thus couple **II** is assigned to a $Mn^{IV}Pc^{-1}/Mn^{IV}Pc^{-2}$ process. Based on the electrochemical data above, we assign processes **I**–**IV** as follows:

$$Mn^{III}Pc^{-2} \rightarrow Mn^{IV}Pc^{-2} + e^- \quad \text{(process I)} \tag{1}$$

$$Mn^{IV}Pc^{-2} \rightarrow Mn^{IV}Pc^{-1} + e^- \quad \text{(process II)} \tag{2}$$

$$Mn^{III}Pc^{-2} + e^- \rightarrow Mn^{II}Pc^{-2} \quad \text{(process III)} \tag{3}$$

$$Mn^{II}Pc^{-2} + e^- \rightarrow Mn^{II}Pc^{-3} \quad \text{(process IV)} \tag{4}$$

*3.2.2. 1,4,8,11,15,18,22,25-Octapentathiophthalocyaninato titanium(IV) oxide (**5**)*

Detailed electrochemical characterisation of substituted OTiPcs is still under-developed. The cyclic (CV) and square wave voltammograms (OSWV) of the complex was performed in de-aerated DCM containing $TBABF_4$ as electrolyte, Fig. 6. The half-wave potentials ($E_{1/2}$) of the couples are listed in Table 1. Four main redox processes (**I**–**IV**) are observed in Fig. 6. Couples **III** (−0.73 V) and **IV** (−1.09 V) are well defined and reversible with cathodic to anodic peak separation (ΔE) of ~100 mV. The cathodic to anodic peak current ratio (I_{pc}/I_{pa}) were near unity and linear plots of I_p versus square root of the scan rate ($\upsilon^{1/2}$) were obtained for couples **III** and **IV**. Couples **III** and **IV** shifted to more positive potentials with scan number (Fig. 6) probably due to polymerisation effects discussed below.

The oxidation process showed a peculiar behaviour in that the anodic process **I** had a broad pre-peak followed by a sharp peak typical of adsorption [36,37]. It is known [36] that the adsorption of a product of the electrode reaction results in the formation of a sharp peak preceded by a more regular peak, the latter being due to the diffusion of

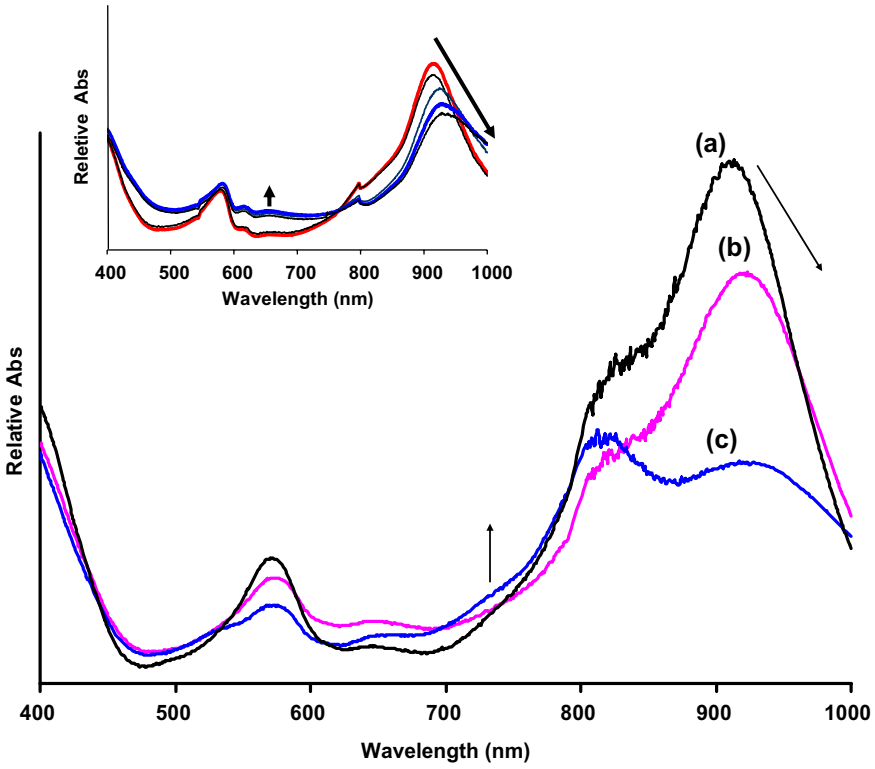


Fig. 5. UV–Vis spectral changes for **4** observed before (a) and after controlled potential electrolysis at +0.9 V (process **I**) (b) and at +1.2 (c) (process **II**). Electrolyte = DCM containing 0.1 M $TBABF_4$.

Table 2
Q-band maxima for the thiol substituted TiPc and MnPc complexes (λ, nm) in DCM unless otherwise stated

Complex	λ (nm)			Reference
	$M^{IV}Pc^{-2}$	$M^{III}Pc^{-2}$	$M^{II}Pc^{-2}$	
MnPc complexes				
4	920	908	795	This work
6a		742	701	[34]
6b		746	698	[34]
TiPc complexes[b]				
5	814	774	769	This work
7a	707 (714)	694	687	[16][a]
7c	712 (714)	703	692	[16][a]
8a	744 (745)	700	694	[16][a]
8c	744 (747)	710	706	[16][a]

[a] Values in DMF containing $TBABF_4$.
[b] Values in brackets are in DCM.

the electroactive species from solution to the electrode. During the first scan in Fig. 6, a broad peak preceding a sharp peak around 0.5 V was observed. The cathodic (return) scan of process **I** (Fig. 6) showed a sharp peak corresponding to the peak observed in the forward direction. The peak separation for couple **I** was zero confirming that the process is due to adsorption species. On subsequent scans (Fig. 6b) a sharp peak was observed at 0.36 V due to the desorption of adsorbed species. Thus, process **I** moved to less positive potentials again with a peak separation of 0 V due to adsorbed species, on second and subsequent scans. The cyclic voltammograms obtained for second and subsequent scans show more weak peaks (at ~0 V, 0.18 V and 0.79 V) most likely to the polymer formed on cycling the monomer in solution. Polymerisation is judged by the formation of new peaks (as observed in Fig. 6). Electropolymerisation of the complex onto the electrode is probably facilitated through radical polymerisation from sulphur groups, as is the case with amino groups in MPc complexes [10]. Adsorption and sharp peaks have been observed before for thiol substituted ZnPc complexes [38], and the complexes showed decomposition on oxidation. These observations suggest that the oxidation products of some thiol substituted MPc complexes are not soluble in the media and adsorb to the electrode. For process **I**, plots of scan rate versus current were linear (figure not shown) confirming adsorption of the complex. Process **II** in Fig. 6 showed regular (not sharp) anodic and cathodic currents during the first scan, probably due to diffusion of the complex from the solution. An irreversible peak (**II′**) is observed in Fig. 6 near 1 V.

We have reported [39] that depending on the ring substituents, oxidation of the TiPc complexes may or may not be observed, depending on whether the substituents result in the shift of potentials to values where oxidation can no longer be observed since they are outside the usable range of the solvent–electrolyte–electrode system employed. The thiol ligands employed in this work are expected to make oxidation easier, hence allowing the observation of the oxidation peaks. We have also reported [17] an overlap of voltammograms for tetraphenoxy

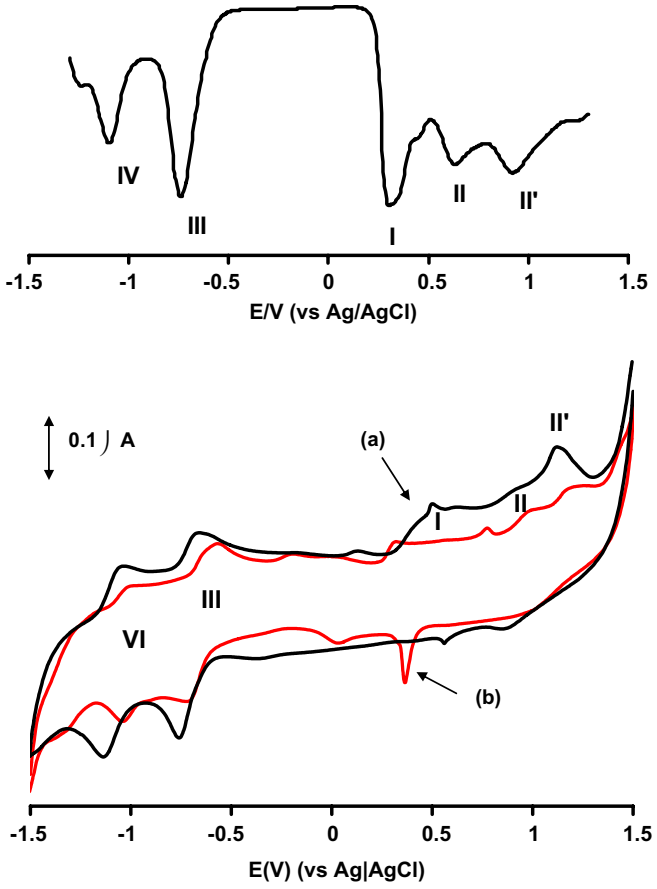


Fig. 6. Square wave (top) and cyclic (bottom) voltammograms of **5** in DCM containing 0.1 M $TBABF_4$. (a) First scan and (b) 20th Scan. The SW voltammogram is for the 10th scan. Scan rate = 100 mV s^{-1}.

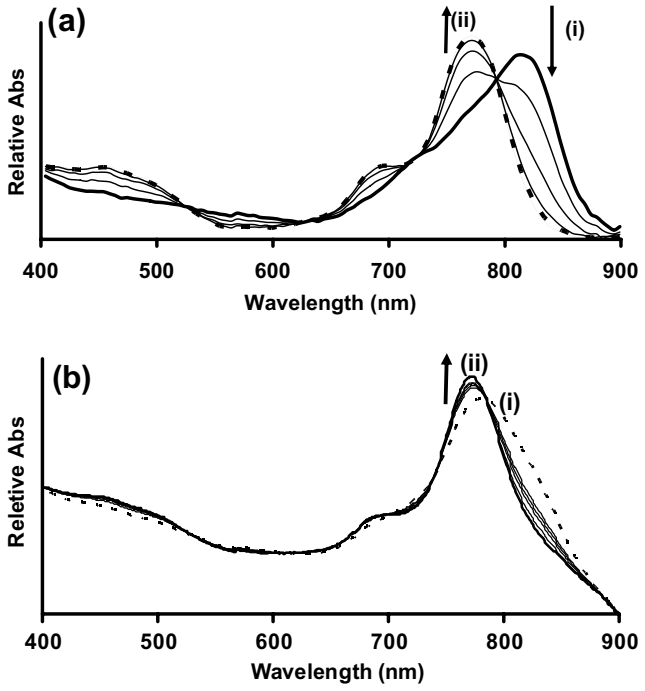


Fig. 7. UV–Vis spectral changes for **5** observed using controlled potential electrolysis at (a) −0.9 V (process **III**) and (b) −1.3 V (process **IV**). (i) Before electrolysis and (ii) at the end of electrolysis. Electrolyte = DCM containing 0.1 M $TBABF_4$.

substituted TiPc, whereby two 1-electron reductions resulted in one couple as follows:

$$Ti^{IV}Pc^{-2} + 2e^- \leftrightarrow Ti^{II}Pc^{-2} \quad \text{(process I)} \tag{5}$$

$$Ti^{II}Pc^{-2} + 2e^- \leftrightarrow Ti^{I}Pc^{-3} \quad \text{(process II)} \tag{6}$$

$$Ti^{I}Pc^{-3} + e^- \leftrightarrow Ti^{I}Pc^{-4} \quad \text{(process III)} \tag{7}$$

However, in this work, overlap of couples is not observed. Such overlap has been observed for distorted (non-planar) porphyrin complexes [40,41]. Therefore, it is possible that the TiPc complexes will show a single step multi-electron transfer process since titanyl phthalocyanine complexes have been reported to be distorted [42–45]. The distortion of MPc complexes is more pronounced when they are substituted with phenoxy groups due to the well known tilting of such groups in MPc complexes [46]. The lack of overlapping voltammogram peaks for TiPc complexes in this work could be a result of the substituents which do not distort the symmetry of the ring. Oxidation of TiPc is expected to occur only at the ring, while reduction is expected to occur at both the central metal as well as the ring. Thus the oxidation processes are due to the ring.

Spectroelectrochemistry was employed to confirm the redox processes. Fig. 7a shows the UV/Vis spectral changes observed on reduction of complex **5** at potentials of process **III**. The Q-band shifts from 814 to 774 nm with isosbestic points at 797, 719, 629, and 534 nm. The spectral changes are typical [2] of metal-based reduction in MPc complexes and are similar to those observed for thiol substituted TiPc complexes [16]. Further reduction at potentials of process **IV**, resulted in spectral changes shown in Fig. 7b and consisted of the shift in the Q-band from 774 nm to 769 nm and the formation of $Ti^{II}Pc^{-2}$ species similar to literature reports [39]. In both cases n was found to be unity confirming one electron transfer. Table 2 lists the Q-band maxima for complex **5** and reported thiol substituted TiPc complexes. Comparing complex **5** with other thiol derivatised TiPc complexes (Table 2) in the same solvent (DCM) shows the former to be more red-shifted due to differences in ring substituents, but the plurality of non-peripheral substituents in **5** will also result in shifting of the Q-band to longer wavelengths.

Attempts to oxidise complex **5** resulted in decomposition, Fig. 8. Such decomposition of oxidation of thiol MPc complexes has been reported as discussed above [38]. Based on the discussed electrochemical techniques, i.e. CV, SWV, and spectroelectrochemistry; the following mechanism for the reduction (Eqs. (8)–(10)) of the TiPc complexes is proposed for **5**:

$$Ti^{IV}Pc + e^- \rightarrow Ti^{III}Pc \tag{8}$$

$$Ti^{III}Pc + e^- \rightarrow Ti^{II}Pc \tag{9}$$

$$Ti^{IV}Pc \text{ (oxidation)} \rightarrow \text{oxidation products} \tag{10}$$

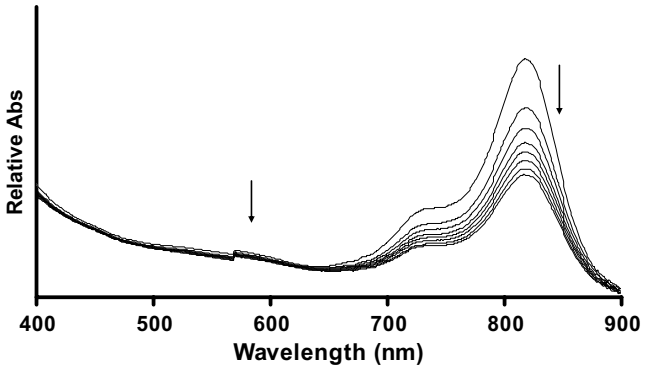


Fig. 8. UV–Vis spectral changes for **5** observed during controlled potential electrolysis at +1.0 V (process **I**), electrolyte = DCM containing 0.1 M $TBABF_4$.

The electrochemical behaviour of TiPc complexes is thus highly influenced by the nature of substituents, and the point of substitution, ie peripheral versus non-peripheral substitution.

4. Conclusions

The octapentylthiophthalocyaninato manganese (III) acetate (**4**) and octapentylthiophthalocyaninato titanium(IV) oxide (**5**) show unusual purple (**4**) and red (**5**) colouration since the Q-band is shifted to the near infra red region with Q-band maxima at 893 nm (908 nm in the presence of $TBABF_4$) and 808 nm (814 nm in the presence of $TBABF_4$) for **4** and **5** in DCM, respectively. For complex **4**, well-defined redox processes are observed and attributed to $Mn^{III}Pc^{-2}/Mn^{II}Pc^{-2}$, $Mn^{II}Pc^{-2}/Mn^{II}Pc^{-3}$, $Mn^{IV}Pc^{-2}/Mn^{III}Pc^{-2}$ and $Mn^{IV}Pc^{-1}/Mn^{IV}Pc^{-2}$. The processes were confirmed by spectroelectrochemistry. The spectrum of the rare $Mn^{IV}Pc^{-2}$ complex is reported. The reduction couples of the Ti complex **5** are assigned to $Ti^{IV}Pc^{-2}/Ti^{III}Pc^{-2}$ and $Ti^{III}Pc^{-2}/Ti^{II}Pc^{-2}$. However, oxidation processes revealed adsorption behaviour and resulted in decomposition on electrolysis using spectroelectrochemistry.

Acknowledgements

This work has been supported by the National Research Foundation of South Africa (NRF GUN = 2053657) as well as Rhodes University. G.M. thanks NRF Scarce skills for graduate scholarships. E.A. thanks the Medical Research Council of South Africa for a post-doctoral fellowship.

References

[1] T. Nyokong, H. Isago, J. Porphyr. Phthalocyan. 8 (2004) 1083.
[2] M.J. Stillman, T. Nyokong, in: C.C. Leznoff, A.B.P. Lever (Eds.), Phthalocyanines: Properties and Applications, vol. 1, VCH, New York, 1989 (Chapter 3)..
[3] N.V. Kamanina, I.Y. Denisyuk, Opt. Spectro. (Russia) 96 (2004) 77.
[4] J. Zhu, F. Gu, J. Tao, J. Zhag, Mater. Lett. 61 (2007) 1296.
[5] W. Posiuk-Bronikowska, M. Krajewska, I. Pfis-Kabulska, Polyhedron 18 (1998) 561.
[6] S. Knecht, K. Dürr, G. Schmid, L.R. Subramanian, M. Hanack, J. Porphyr. Phthalocyan. 3 (1999) 292.
[7] D.K. Rittenberg, L. Baars-Hibbe, A. Böhm, J.S. Miller, J. Mater. Chem. 10 (2000) 241.
[8] C.-L. Lin, C.-C. Lee, K.-C. Ho, J. Electroanal. Chem. 524–525 (2002) 81.
[9] J. Obirai, N.P. Rodrigues, F. Bedioui, T. Nyokong, J. Porphyr. Phthalocyan. 7 (2003) 508.
[10] J. Obirai, T. Nyokong, Electrochim. Acta 49 (2004) 1417.
[11] J. Obirai, T. Nyokong, Electrochim. Acta 50 (2005) 3296.
[12] N. Periera Rodrigues, J. Obirai, T. Nyokong, F. Bedioui, Electroanalysis 17 (2005) 186.
[13] J. Obirai, T. Nyokong, Electrochim. Acta 50 (2005) 5427.
[14] A. Muranaka, M. Okuda, N. Kobayashi, K. Somers, A. Ceulemans, J. Am. Chem. Soc. 126 (2004) 4596.
[15] A. Koca, A.R. Özkaya, Y. Arslanoğlu, E. Hamuryudan, Electrochim. Acta 52 (2007) 3216.
[16] P. Tau, T. Nyokong, Dalton Trans. (2006) 4482.
[17] P. Tau, T. Nyokong, Polyhedron 25 (2006) 1802.
[18] Y. Arslanoğlu, A.M. Sevim, E. Hamuryudan, A. Gül, Dyes Pigments 68 (2006) 129.
[19] C.G. Claessens, A. Gouloumis, M. Barthel, Y. Chen, G. Martin, F.A. Agulló-López, I. Ledoux-Rak, J. Zyss, M. Hanack, T. Torres, J. Porphyr. Phthalocyan. 7 (2003) 291.
[20] L. Lüer, H.-J. Egelhaaf, D. Oelkrug, G. Winter, M. Hanack, A. Weber, H. Bertagnolli, Synth. Met. 138 (2003) 305.
[21] D. Dini, G.Y. Yang, M. Hanack, J. Chem. Phys. 119 (2003) 4857.
[22] D. Wörhle, M. Eskes, K. Shigehara, A. Yamada, Synthesis (1993) 194.
[23] M. Barthel, D. Dini, S. Vagin, M. Hanack, Eur. J. Org. Chem. (2002) 3756.
[24] F. Henari, A. Davey, W. Blau, P. Haisch, M. Hanack, J. Porphyr. Phthalocyan. 3 (1999) 331.
[25] W.-F. Law, K.M. Lui, D.K.P. Ng, J. Mater. Chem. 7 (1997) 2063.
[26] W.-F. Law, R.C.W. Liu, J. Jiang, D.K.P. Ng, Inorg. Chem. Acta 256 (1997) 147.
[27] T. Nyokong, Coord. Chem. Rev. 251 (2007) 1707.
[28] A.B.P. Lever, E.R. Milaeva, G. Speier, in: C.C. Leznoff, A.B.P. Lever (Eds.), Phthalocyanines: Properties and Applications, vol. 3, VCH Publishers, New York, 1993, p. 1.
[29] J. Morita, H. Nakatsiju, T. Misaki, Y. Tanabe, Green Chem. 10 (2005) 711.
[30] A. Gürek, Ö. Bekaroğlu, J. Chem. Soc., Dalton Trans. (1994) 1419.
[31] A. Auger, W.J. Blau, P.M. Burnham, I. Chambrier, M.J. Cook, B. Isare, F. Nekelson, S.M. O'Flaherty, J. Mater. Chem. 13 (2003) 1042.
[32] K. Nakamoto, in: Infrared and Raman Spectra of Inorganic and Coordination Compounds, third ed., John Wiley & Sons, New York, 1978.
[33] C.C. Leznoff, L.S. Black, A. Heibert, P.W. Causey, D. Christendat, A.B.P. Lever, Inorg. Chim. Acta 359 (2006) 2690.
[34] M.J. Stillman, in: C.C. Leznoff, A.B.P. Lever (Eds.), Phthalocyanines: Properties and Applications, vol. 3, VCH Publishers, New York, 1993 (Chapter 5).
[35] B. Agboola, K. Ozoemena, P. Westbroek, T. Nyokong, Electrochim. Acta 52 (2007) 2520.
[36] P.T. Kissinger, C.R. Preddy, R.E. Shoup, W.R. Heineman, in: O.T. Kissinger, W.R. Heineman (Eds.), Laboratory Techniques in Electroanalytical Chemistry, second ed., Marcel Dekker, New York, 1996.
[37] I. Prieto, T. Martin, E. Munoz, T.L. Camacho, J. Phys. Chem. 99 (1995) 14083.
[38] K. Takahashi, M. Kawashima, Y. Tomita, M. Itoh, Inorg. Chim. Acta 232 (1995) 69.
[39] P. Tau, T. Nyokong, Electrochim. Acta 52 (2007) 3641.

[40] J.A. Hodge, H.B. Gray, M.G. Hill, Inorg. Chem. 34 (1995) 809.
[41] B. Tulythan, W.E. Geiger, J. Am. Chem. Soc. 107 (1985) 5960.
[42] V.L. Goedken, G. Dessy, C. Ercolani, V. Fares, L. Gastaldi, Inorg. Chem. 24 (1985) 991.
[43] W. Hiller, J. Strähle, Z. Kristallogr. 159 (1982) 173.
[44] P.N. Dwyer, L. Puppe, J.W. Buchler, W.R. Scheidt, Inorg. Chem. 14 (1975) 1782.
[45] R. Guilard, J. Latour, C. Lecomte, J. Marchon, J. Protas, D. Ripoll, Inorg. Chem. 17 (1978) 1228.
[46] N. Kobayashi, T. Fukuda, K. Ueno, H. Ogino, J. Am. Chem. Soc. 123 (2001) 10740.

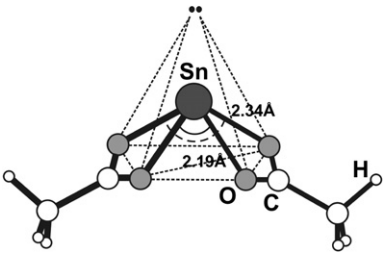


Fig. 1. Structure of the $Sn(CH_3COO)_2$ molecule in the gas phase (after Smart et al. [4]). The overall symmetry is C_2 and the molecule is viewed perpendicular to the twofold axis. The bond angles of 90° (solid line) and 121° (dashed line) are marked. The tentative SnO_4E (E – lone electron pair) trigonal bipyramid is outlined.

2. Experimental

The commercially available starting reagents SnO (''Spektrkhim'', Russia) and glacial acetic acid (Aldrich) were of analytical grade and were used as received. Elemental analysis (C, H) was performed by the Microanalytical Service of the Centre for Drug Chemistry (Moscow, Russia). IR spectra were recorded on a Perkin–Elmer 1600 FTIR spectrophotometer as Nujol and hexachlorobutadiene mulls between KBr plates in the region 4000–400 cm^{-1}. Isothermal dynamic sublimation experiments were run with samples in glass test tubes at a pressure of 10^{-2} Torr.

For the synthesis of $Sn(CH_3COO)_2 \cdot 2CH_3COOH$ the procedure described in Ref. [3] was used: a mixture of SnO (3 g, 22,2 mmol) and glacial acetic acid (11 ml, 192.3 mmol) was refluxed under stirring until the SnO was completely dissolved, and after cooling the yellowish product was collected. $Sn(CH_3COO)_2$ was formed as a white crystalline sublimate by removal of the acetic acid and sublimation at 150–160 °C and at 10^{-2} Torr. Yield ~90%. Mp 183 °C. *Anal*. Calc. for $C_4H_6O_4Sn$: C, 20.25; H, 2.53. Found: C, 19.96; H, 2.52%. IR, cm^{-1}: 661 *v* (COO sym. deformation), 930 *v* (C–C stretch), 1015 *v* (CH_3 rock), 1334 *v* (CH_3 deformation), 1395 *v* (COO sym. stretch), 1530 *v* (COO asymm. stretch). The melting temperature and IR spectra are in good agreement with the data of Donaldson et al. [3].

In spite of the good visual quality of the obtained transparent colorless needle-like crystals, it was found that every needle is composed of numerous finer needles, so that no single crystal suitable for an X-ray diffraction experiment could be selected. The structure solution was performed from X-ray powder diffraction (XRPD) data. The preliminary investigation and unit cell parameter determination were performed with a Huber G670 Guinier diffractometer (Cu $K_{\alpha 1}$-radiation, curved Ge monochromator, transmission mode, image plate). The TREOR90 program was used for indexing the XRPD pattern [5]. The data for the structure determination and Rietveld refinement were collected with a STADI-P diffractometer (Cu $K_{\alpha 1}$-radiation, curved Ge monochromator, transmission mode, linear PSD). FOX software was used for the structure solution [6]. The JANA2000 program package was used for Rietveld refinement of the crystal structure [7].

The initial experiments with matrix-assisted laser desorption/ionization mass spectroscopy (MALDI-TOF-MS) were performed with an Autoflex II (Bruker Daltonics, Germany) instrument. The spectra were recorded in a positive mode (accelerating voltage 19 kV) with a nitrogen laser (337 nm, impulse duration 1 ns). The typical procedure of sample preparation for MALDI was applied [8]. Absolutely dry THF was used as a solvent and anthracene was used as a matrix.

The chemical bonding in tin(II) acetate was analyzed using the electron localization function (ELF) [9]. The ELF distribution was determined from the results of density functional theory (DFT) calculations. A self-consistent DFT calculation was performed with the TB-LMTO-ASA program [10], and the Barth-Hedin exchange-correlation potential was applied. The ELF distribution was obtained using the intrinsic procedure of the LMTO program. The *k* mesh contained 64 points within the first Brillouin zone. The geometrical parameters for the calculation were taken from the XRPD structure refinement. The hydrogen atoms of the methyl groups were attached according to the constraints $d(C–H) = 0.98$ Å, $\angle H–C–H = \angle C–C–H = 109.4°$ typical for acetates [11]. A random mutual orientation of the $C(2)H_3$ and $C(4)H_3$ methyl groups was chosen. We assume that this choice does not influence the basic features of the ELF distribution on the Sn, C and O atoms.

3. Results and discussion

3.1. Crystal structure determination

The XRPD pattern of tin(II) acetate was indexed on a body-centered orthorhombic unit cell with the cell parameters listed in Table 1. The reflection conditions *hkl*: $h + k + l = 2n$, $0kl$, $k,l = 2n$ and $h0l$, $h,l = 2n$ correspond to the space group *Ibam* and its acentric subgroup *Iba*2. The observed unit cell parameters are similar to those reported by Donaldson et al. [2] ($a = 14.11(3)$, $b = 21.35(4)$, $c = 4.96(1)$ Å, given in the *bca* setting), although

Table 1
Crystallographic information and selected parameters from Rietveld refinement for $Sn(CH_3COO)_2$

Formula	$Sn(CH_3COO)_2$
Space group	*Iba*2
a (Å)	13.9859(4)
b (Å)	21.1870(6)
c (Å)	4.5400(1)
V (Å^3)	1345.28(6)
Z	8
D_{calc} (g cm^{-3})	2.338
Radiation	Cu $K_{\alpha 1}$, $\lambda = 1.5406$ Å
2θ Range, step (°)	5–80, 0.01
Number of reflections	243
Number of refined crystallographic parameters	12
Preferred orientation parameter and axis	0.790(2), [0 0 1]
R_I, R_P, R_{wP}	0.045, 0.037, 0.050

the latter are substantially larger (see Table 1 for comparison). Moreover, weak reflections violating the body-centering were observed on the XRPD pattern of tin(II) acetate by Donaldson et al. Careful inspection of the XRPD pattern of the tin(II) acetate prepared in the present work revealed that such forbidden reflections are definitely absent. The reason for this discrepancy is not completely clear.

Because structure solution from XRPD data is not a trivial matter, the applied procedure is explained in detail. The search for the initial structure model was performed using a Monte-Carlo based global optimization [6]. It provided the exact positions of the Sn atoms, whereas the positions of the acetate groups could not be unambiguously determined. The acetate groups were localized using a Rietveld refinement of the crystal structure. One can expect that the reliable determination of the atomic coordinates of such light scatterers as C and O will be hampered by the significant impact of the heavy scattering Sn atoms. In order to overcome this difficulty, the rigid body approximation was used to define the acetate group as a scattering unit. The geometry of the acetate group was assumed to be identical to the one determined for the structure of the $Sn(CH_3COO)_2$ molecule in the gas phase (d(C–C) = 1.51 Å, d(C–O) = 1.26 Å, ∠O–C–O = 122°) [4]. The hydrogen atoms were not taken into account. The positions of the acetate groups in the unit cell were defined by the coordinates of the C atom of the carboxyl groups and the three rotation angles. Thus six positional parameters were used for each acetate group instead of the 12 parameters in the atomic approximation.

Taking into account the assumption about a possible polymeric structure of the tin(II) acetate, the acetate groups were initially located at positions bridging the Sn atoms by the oxygen atoms of their carboxyl groups into infinite chains running along the c-axis. In such an initial model, the m_c plane of the *Ibam* space group becomes a mirror plane of the acetate groups. However, the refinement in the centrosymmetric *Ibam* space group resulted in unacceptably high reliability factors ($R_I = 0.128$, $R_P = 0.128$, $R_{wP} = 0.219$) and large atomic displacement parameters (ADPs) for the atoms of the acetate groups. A significant improvement was achieved by a transformation of the initial model into the *Iba*2 space group. In this group the positions and rotations of the acetate groups are not fixed by symmetry elements. The final refinement was performed with overall ADPs for the carbon and oxygen atoms, whereas the ADP for the Sn atom was refined independently. The preferred orientation along the [0 0 1] axis was taken into account using the March–Dollase formula. Reasonably low values of the reliability factors were achieved: $R9_I = 0.045$, $R_P = 0.037$, $R_{wP} = 0.050$. The crystallographic and atomic parameters (as calculated from the rigid body approximation) and the most relevant interatomic distances are given in Tables 1–3. Fig. 2 represents the experimental, calculated and difference XRD profiles.

Table 2
Atomic coordinates and atomic displacement parameters for $Sn(CH_3COO)_2$

Atom	Position	x/a	y/b	z/c	U_{iso} (Å^2)
Sn	8c	0.3749(1)	0.41691(7)	0	0.0375(6)
C(1)	8c	0.3839(4)	0.3185(3)	0.557(2)	0.027(2)
C(2)	8c	0.3928(4)	0.2522(3)	0.439(2)	0.027(2)
C(3)	8c	0.2116(4)	0.4215(2)	0.410(2)	0.027(2)
C(4)	8c	0.1117(4)	0.4176(2)	0.534(2)	0.027(2)
O(1)	8c	0.3396(4)	0.3274(3)	0.795(2)	0.027(2)
O(2)	8c	0.4210(4)	0.3632(3)	0.415(2)	0.027(2)
O(3)	8c	0.2795(4)	0.4364(2)	0.578(2)	0.027(2)
O(4)	8c	0.2243(4)	0.4096(2)	0.141(2)	0.027(2)

Table 3
Main interatomic distances (Å) and bond angles (°) for $Sn(CH_3COO)_2$

Sn–O(1)^2	2.170(6) × 1 [0.563]	Sn–O(3)^2	2.372(8) × 1 [0.326]
Sn–O(2)^1	2.293(7) × 1 [0.404]	Sn–O(3)^1	2.972(8) × 1 [0.064]
Sn–O(2)^2	2.961(7) × 1 [0.066]	Sn–O(4)^1	2.207(6) × 1 [0.507]
O(1)^2–Sn–O(2)^1	89.0(3)	O(2)^1–Sn–O(3)^2	155.3(2)
O(1)^2–Sn–O(3)^2	71.2(2)	O(2)^1–Sn–O(4)^1	89.7(3)
O(1)^2–Sn–O(4)^1	81.1(2)	O(3)^2–Sn–O(4)^1	73.1(3)

The impact of each Sn–O bond into BVS for the Sn atom is given in square brackets.
Symmetry codes: $^1 -x, y, z$; $^2 -x, y, z-1$.

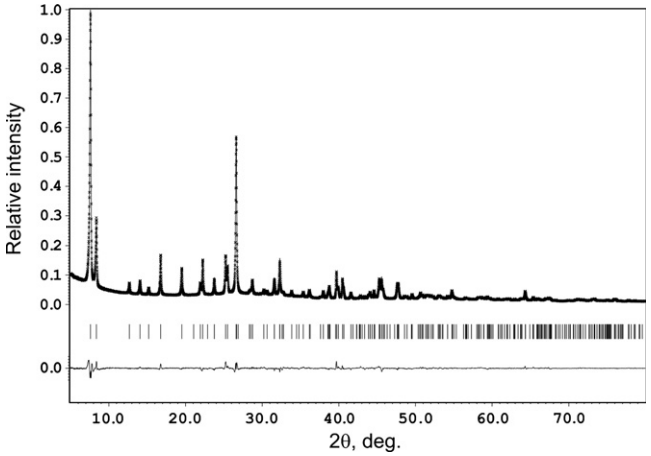


Fig. 2. Experimental, calculated and difference powder X-ray diffraction profiles for $Sn(CH_3COO)_2$.

3.2. Crystal structure discussion

The crystal structure of tin(II) acetate is shown in Fig. 3. The Sn atoms are arranged in columns oriented along the c-axis and combined in groups of four. The Sn atoms are bridged by two acetate groups along the column, coordinating the Sn atoms by the oxygen atoms of their carboxyl groups. The chains do not directly interact with each other and their packing in groups of four is caused by minimized repulsion between the methyl groups of the acetate anions and the sterical activity of the lone electron pairs (not

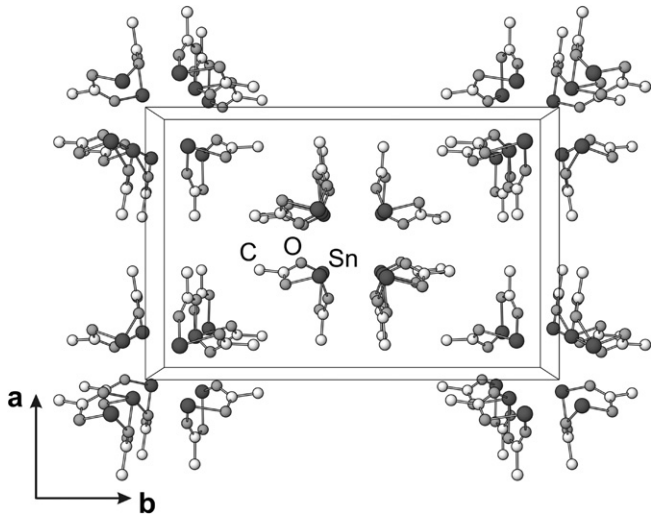


Fig. 3. The arrangement of the $Sn(CH_3COO)_2$ columns in the crystal structure of tin(II) acetate. Hydrogen atoms are not shown.

shown in Fig. 3) on the Sn atoms. The structure of the single $Sn(CH_3COO)_2$ chain is shown in Fig. 4. The experimentally observed positions of the acetate groups demonstrate a large deviation from those dictated by the *Ibam* symmetry. This causes the Sn atoms to be asymmetrically surrounded by four oxygen atoms with two short Sn–O distances (d(Sn–O(1)) = 2.170(6) Å, d(Sn–O(4)) = 2.207(6) Å) and two longer ones (d(Sn–O(2)) = 2.293(7) Å, d(Sn–O(3)) = 2.372(8) Å). The bond valence sum (BVS) for the Sn atoms, calculated using the impacts of the four Sn–O distances given above was found to be equal to 1.8, that is noticeably lower than the nominal value. Much closer agreement (BVS = 1.93) with the formal valence of +2 is achieved if two long Sn–O(2) and Sn–O(3) bonds of 2.961(7) and 2.972(8) Å are taken into account (marked by dashed lines in Fig. 4). Thus the acetate groups can be regarded as tridentate bridging ligands with some chelate character.

The ELF isosurface (Fig. 5) for tin(II) acetate reveals two types of attractors. The first one is presented by large lobes near the tin atoms. Such lobes are usually associated with sterically active (or, in other words, localized) lone pairs, although the nature of these pairs (mixed Sn 5s–5p character or mixed Sn 5s–O 2p antibonding state with empty Sn 5p orbitals) is still being discussed [12]. Attractors of the second type are located between the C atoms of the acetate groups and correspond to covalent non-polar C–C bonds. Thus, the ELF distribution confirms the basic features of the chemical bonding in tin(II) acetate: localized lone pairs on the tin atoms and covalent non-polar C–C bonds. The C–O and Sn–O bonds are polar, therefore the corresponding attractors are shifted to the oxygen atoms and are not visible in Fig. 5 due to the lower ELF values.

The first coordination sphere of the Sn atoms should be discussed considering the localization of the lone electron pair. Along with the four oxygen atoms of the acetate groups, the lone electron pair forms a strongly distorted trigonal bipyramid, SnO_4E (E is the lone electron pair), around the Sn atoms. The lone electron pair and the O(1) and O(4) atoms with the shortest d(Sn–O) = 2.17–2.21 Å distances define the equatorial plane of the trigonal bipyramid. The O(2) and O(3) atoms with longer d(Sn–O) = 2.29–2.37 Å distances are at the apical vertexes of the trigonal bipyramid. The O–Sn–O bond angles deviate significantly from their nominal values for an ideal trigonal bipyramid. The in-plane O(1)–Sn–O(4) angle is only 81.1(2)°, much smaller than its nominal value of 120°. The O(2)–Sn–O(3) angle should be straight in a perfect trigonal bipyramid, whereas its has a value of 155.3(2)° in the

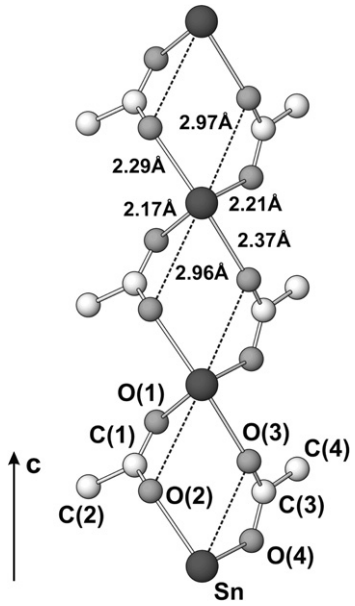


Fig. 4. Structure of the single $Sn(CH_3COO)_2$ chain. The bonding of the Sn atoms to the oxygen atoms of the second coordination sphere with d(Sn–O) = 2.96–2.97 Å is shown with dashed lines.

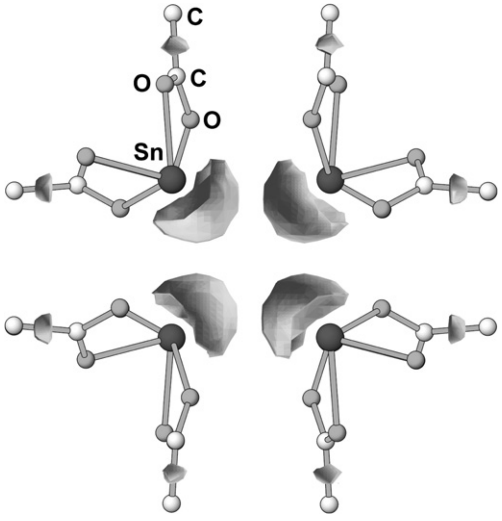


Fig. 5. ELF isosurface ($\eta = 0.85$) for $Sn(CH_3COO)_2$. The [0 0 1] projection of the four $Sn(CH_3COO)_2$ chains is shown along with the lobes of the lone electron pairs. Hydrogen atoms are not shown.

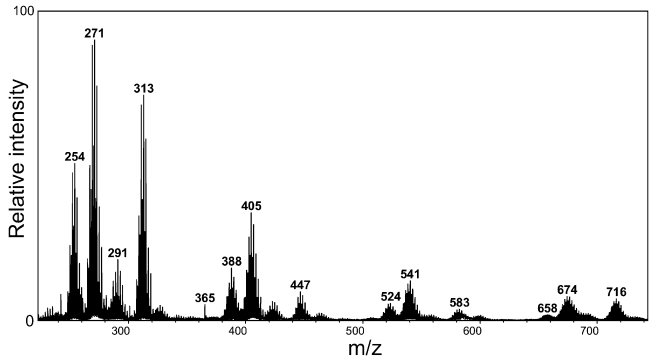


Fig. 6. MALDI-TOF mass spectrum of $Sn(CH_3COO)_2$ with anthracene as a matrix.

tin(II) acetate structure. It should be noted that in spite of the significantly different arrangement of the acetate groups around the Sn atoms in the gaseous and the solid phase, the coordination environment of Sn remains virtually the same. For the $Sn(CH_3COO)_2$ molecule in the gaseous phase (Fig. 1) the in-plane O–Sn–O bond angle (90°) and the O–Sn–O angle (121°) along the threefold axis of the SnO_4E trigonal bipyramid are also significantly smaller than their ideal values of 120° and 180° [4]. Such distortion can be accounted for by a strong repulsion between the oxygen atoms and the lone electron pair that causes the oxygen atoms to move away from the position of the lone electron pair with a decrease of the corresponding bond angles.

3.3. MALDI-TOF spectroscopy

The polymeric nature of the tin(II) acetate crystal structure was indirectly confirmed by a MALDI experiment. The MALDI-TOF spectrum of $[Sn(CH_3COO)_2]$ (Fig. 6) displays polynuclear fragments $[Sn_2O]^+$ (m/z 254.2), $[Sn_2O(CH_3COO)_2]^+$ (m/z 313.0), $[Sn_3O_2(OH)]^+$ (m/z 404.9), $[Sn_3O_2(CH_3COO)]^+$ (m/z 446.8), $[Sn_4O_3(OH)]^+$ (m/z 540.7), $[Sn_5O_4(OH)]^+$ (m/z 674.5), $[Sn_5O_4(CH_3COO)]^+$ (m/z 716.5). The characteristic isotopic abundance of tin was useful in identifying these species. Presumably, polymeric $[Sn(CH_3COO)_2]$ undergoes a deep cleavage of the acetate groups by desorption/ionization by laser irradiation but the Sn–O–Sn fragments are not destroyed so much. A similar behavior of metal–organic coordination compounds during MALDI-TOF experiments was noted in [8]. The extremely low stability of $[Sn(CH_3COO)_2]$ with respect to the UV laser (337 nm) action are in good agreement with the results by Maruyama and Morishita [13], where the deep cleavage of $[Sn(CH_3COO)_2]$ under UV irradiation was described.

4. Conclusion

The crystal structure of tin(II) acetate was solved and refined from X-ray powder diffraction data. Tin(II) acetate adopts a polymeric structure consisting of infinite $Sn(CH_3COO)_2$ chains running along the c-axis and packed into groups of four. The acetate groups bridge the Sn atoms along the chains and can be considered as tridentate bridging ligands with some chelate character. The first coordination sphere of the Sn atoms is described as a strongly distorted trigonal bipyramid, SnO_4E (E is a lone electron pair). This coordination environment is virtually identical to that in the $Sn(CH_3COO)_2$ molecule in the gaseous phase [4]. In both cases the two short Sn–O bonds and the lone electron pair are located in the equatorial plane and the two longer Sn–O bonds are directed towards the apical vertexes. The distortion of the SnO_4E trigonal bipyramid clearly demonstrates the sterical activity of the lone electron pair.

Acknowledgements

The authors thank Prof. Natalya P. Kuz'mina and Prof. Joke Hadermann for fruitful discussions.

Appendix A. Supplementary material

CCDC 653018 contains the supplementary crystallographic data for $Sn(CH_3COO)_2$. These data can be obtained free of charge via http://www.ccdc.cam.ac.uk/conts/retrieving.html, or from the Cambridge Crystallographic Data Centre, 12 Union Road, Cambridge CB2 1EZ, UK; fax: (+44) 1223-336-033; or e-mail: deposit@ccdc.cam.ac.uk. Supplementary data associated with this article can be found, in the online version, at doi:10.1016/j.poly.2007.08.010.

References

[1] A. Ditte, Ann. Chim. Phys. 27 (1882) 115.
[2] J.D. Donaldson, W. Moser, W.B. Simpson, J. Chem. Soc. (1964) 5942.
[3] J.D. Donaldson, J. F Knifton, S.D. Ross, Spectrochim. Acta 21 (1965) 275.
[4] B.A. Smart, L.E. Griffiths, C.R. Pulham, H.E. Robertson, N.W. Mitzel, D.W.H. Rankin, J. Chem. Soc., Dalton Trans. 9 (1997) 1565.
[5] P.-E. Werner, L. Eriksson, M. Westdahl, J. Appl. Crystallogr. 18 (1985) 367.
[6] V. Favre-Nicolin, R. Černy, J. Appl. Crystallogr. 35 (2002) 734.
[7] V. Petricek, M. Dusek, JANA2000: Programs for Modulated and Composite Crystals, Institute of Physics, Praha, Czech Republic, 2000.
[8] S.W. Hunsucker, R.C. Watson, B.M. Tissue, Rapid Commun. Mass Spectrom. 15 (2001) 1334.
[9] A. Savin, O. Jepsen, J. Flad, O.K. Andersen, H. Preuss, H.G. von Schnering, Angew. Chem., Int. Ed. 31 (1992) 187.
[10] G. Krier, O. Jepsen, A. Burkhart, O.K. Andersen, The TB-LMTO-ASA Program, Stuttgart, 1995.
[11] M. Schurmann, F. Huber, Acta Cryst. C 50 (1994) 1710.
[12] M.W. Stoltzfus, P.M. Woodward, R. Seshadri, J.-H. Klepeis, B. Bursten, Inorg. Chem. 46 (2007) 3839.
[13] T. Maruyama, T. Morishita, Thin Solid Films 251 (1994) 19.

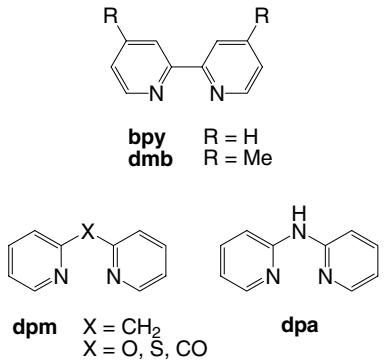
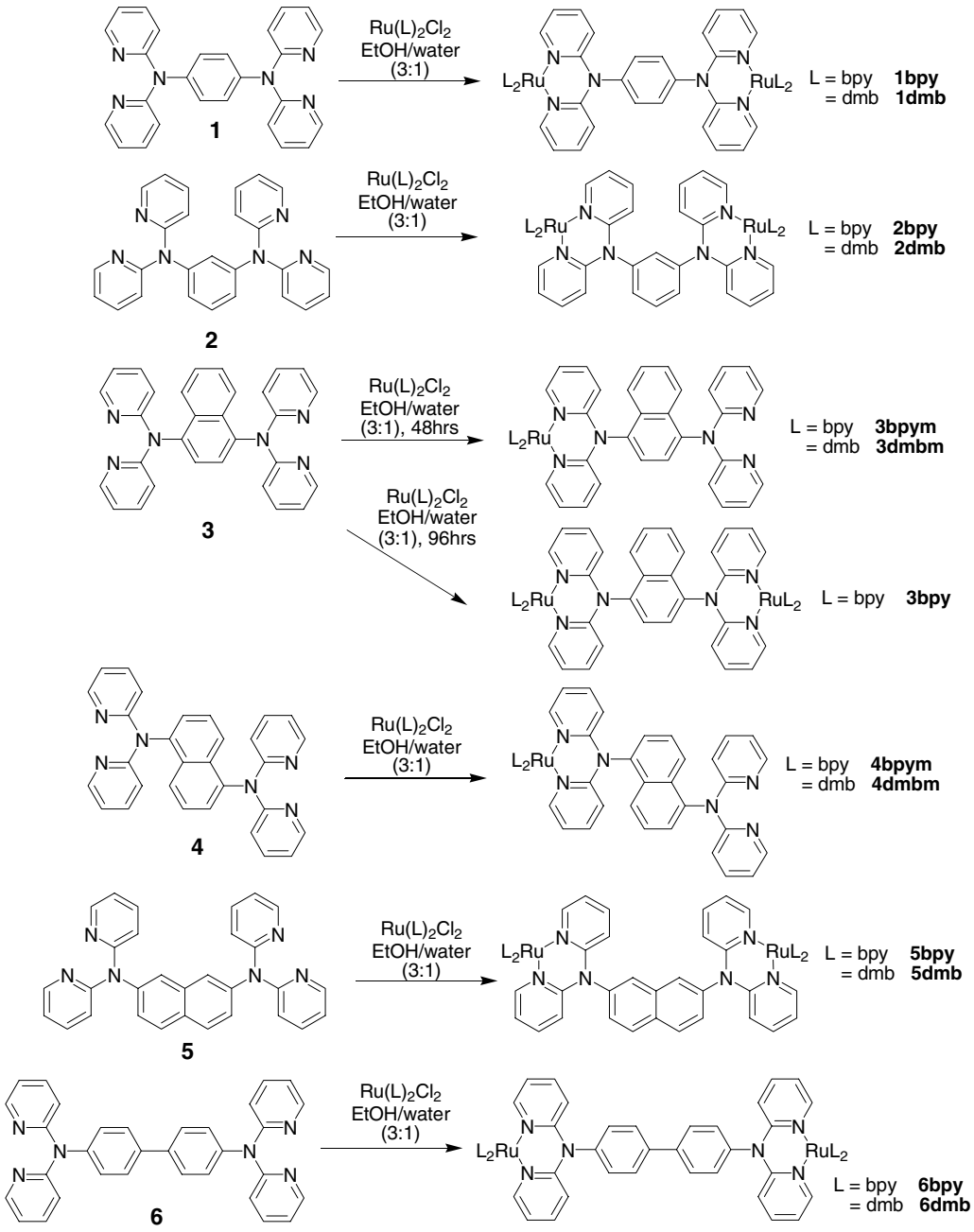


Fig. 1. Bidentate ligands that form five-membered chelate rings, **bpy** and **dmb**, and ligands that coordinate *via* six-membered chelate rings, e.g. **dpm** and **dpa**.

enhanced metal–metal interactions in complexes of bridging ligands incorporating this subunit.

In this paper we describe ruthenium complexes of six known bridging ligands **1**–**6** containing the **dpa** subunit (Scheme 1), and study the nature of the metal–ligand and metal–metal interactions within such complexes. The ligands studied are based around phenyl, naphthalenyl and biphenyl cores which have been appended with two **dpa** subunits to produce a series of potentially doubly bidentate bridging ligands. This array of ligands utilises some of the design principles outlined by us previously [4,5]; including different arene cores and substitution patterns of those cores. Ligands **1** and **6** were first studied and reported by Yang et al. [36], while we recently reported



Scheme 1.

silver(I) coordination polymers, and copper(II) and palladium(II) dinuclear complexes of ligands **1**–**5** [33].

2. Experimental

2.1. General experimental

^{1}H NMR, 1D TOCSY, 1D NOESY and ^{1}H–^{1}H COSY experiments were performed on either a Varian Mercury 300 MHz or Varian 500 MHz NMR spectrometer in CD_3CN. The ^{1}H NMR assignments for the compounds are denoted with primes to indicate the different rings of the multidentate ligands and letters to distinguish the ancillary bipyridine ligands. The different diastereoisomers of the dinuclear complexes are marked with and without an asterisk. Muliplicities are listed based on three-bond coupling only. Electrospray mass spectrometry (ES-MS) was performed on a Micromass LCT-TOF mass spectrometer. Melting points were performed on an Electrothermal melting point apparatus and are uncorrected. Elemental analyses were performed by the Campbell microanalytical laboratory at the University of Otago. Electronic spectra were recorded in acetonitrile using a Cary 5E UV/Vis or a GBC 920 UV/Vis spectrometer.

Cyclic voltammetry measurements were performed on a PAR Model 175 Universal Programmer coupled to a PAR Model 173 potentiostat, under argon. Measurements were recorded in either acetonitrile or dichloromethane/0.1 mol dm^{-3} [(n-C_4H_9)$_4$N]PF_6 solution using a glassy carbon working electrode, a platinum wire auxiliary electrode and an Ag/$AgNO_3$ (0.1 mol dm^{-3} [(n-C_4H_9)$_4$N]PF_6 in acetonitrile or dichloromethane) reference electrode. Ferrocene was added as an internal standard on completion of each experiment and tabulated potentials are given versus the saturated calomel electrode [E^0(Fc/Fc$^+$) = 310 mV versus SCE (acetonitrile)]. Cyclic voltammetry was performed with a sweep rate of 100 mV s^{-1}. Differential pulse voltammetry was recorded with a sweep rate of 4 mV s^{-1} and a pulse amplitude, width, and period of 50 mV, 60 ms and 1 s, respectively.

Unless otherwise stated reagents were obtained from commercial sources and used as received. Solvents were dried by literature procedures and freshly distilled as required. The ligands investigated in this work, **1**–**6** [33,36], bis(2,2′-bipyridine)ruthenium(II) dichloride [Ru(bpy)$_2$Cl$_2$] [40] and bis(4,4′-dimethyl-2,2′-bipyridine)ruthenium(II) dichloride [Ru(dmb)$_2$Cl$_2$] [41] were prepared by literature methods.

2.2. Syntheses of complexes

In a typical reaction, ligand (1 equiv.) was reacted with at least 2 equiv. of either [Ru(bpy)$_2$Cl$_2$] or [Ru(dmb)$_2$Cl$_2$] in 3:1 ethanol–water for a period of 48, 72 or 96 h. After cooling the solvent was removed *in vacuo* and the residue redissolved in water and filtered. The resulting red solution was treated with an excess of ammonium hexafluorophosphate to give a red precipitate of the desired ruthenium complex. Purification is as described, typically by alumina chromatography.

2.2.1. [{Ru(bpy)$_2$}$_2$(**1**)](PF$_6$)$_4$ (**1bpy**)

Ligand **1** (20 mg, 0.048 mmol) and [Ru(bpy)$_2$Cl$_2$] (59 mg, 0.12 mmol) were refluxed for 72 h. Without any chromatography, a red precipitate of **1bpy** as a 1:1 mixture of the two diastereoisomers was obtained with a yield of 81 mg (93%); m.p. 207–211 °C. *Anal*. Calc. for $C_{66}H_{52}N_{14}F_{24}P_4Ru_2 \cdot H_2O$: C, 43.05; H, 2.96; N, 10.65. Found: C, 42.71; H, 2.51; N, 10.27%. ^{1}H NMR (CD_3CN, 293 K) δ 8.61 (d, 4H, bpyH3A), 8.60 (d, 4H, bpyH3A*), 8.53 (d, 8H, bpyH3B/B*), 8.42 (d, 8H, bpyH6A/A*), 8.20 (t, 4H, bpyH4A), 8.18 (t, 4H, bpyH4A*), 8.05 (t, 8H, bpyH4B/B*), 7.95 (t, 4H, H4′), 7.93 (t, 4H, H4′*), 7.75 (d, 8H, bpyH6B/B*), 7.58 (d, 8H, H6′, H6′*), 7.53 (dd, 4H, bpyH5A), 7.52 (dd, 4H, bpyH5A*), 7.48 (d, 4H, H3′), 7.47 (d, 4H, H3′*), 7.40 (t, 8H, bpyH5B/B*), 7.11 (s, 4H, H2/H3/H5/H6), 7.09 (s, 4H, H2*/H3*/H5*/H6*), 7.06 (t, 4H, H5′), 7.05 (t, 4H, H5′*).

2.2.2. [{Ru(dmb)$_2$}$_2$(**1**)](PF$_6$)$_4$ (**1dmb**)

Ligand **1** (21.1 mg, 0.051 mmol) and [Ru(dmb)$_2$Cl$_2$] (59.6 mg, 0.110 mmol) were refluxed for 72 h. The crude product was purified on alumina eluting with 1:19 methanol–dichloromethane solution to give **1dmb** as a red solid in a 59.8 mg (61%) yield as a 1:1 mixture of the two diastereoisomers; m.p. 265–268 °C. *Anal*. Calc. for $C_{74}H_{68}N_{14}F_{24}P_4Ru_2$: C, 45.92; H, 3.54; N, 10.13. Found: C, 46.40; H, 3.66; N, 9.85%. ^{1}H NMR (CD_3CN, 293 K) δ 8.46 (s, 4H, dmbH3A), 8.45 (s, 4H, dmbH3A*), 8.37 (s, 8H, dmbH3B/B*), 8.26 (d, 8H, dmbH6A/A*), 7.89 (m, 8H, H4′, H4′*), 7.57 (m, 8H, H6′, H6′*), 7.55 (d, 8H, dmbH6B/B*), 7.43 (m, 4H, H3′, H3′*), 7.37 (m, 8H, dmbH5A/A*), 7.23 (d, 8H, dmbH5B/B*), 7.20 (s, 4H, H2/H3/H5/H6), 7.18 (s, 4H, H2*/H3*/H5*/H6*), 7.01 (t, 4H, H5′, H5′*), 2.64 (s, 12H, dmbMeA), 2.58 (s, 12H, dmbMeA*), 2.55 (s, 24H, dmbMeB/B*).

2.2.3. [{Ru(bpy)$_2$}$_2$(**2**)](PF$_6$)$_4$ (**2bpy**)

Ligand **2** (20.3 mg, 0.049 mmol) and [Ru(bpy)$_2$Cl$_2$] (51.6 mg, 0.107 mmol) were refluxed for 72 h. The crude product was purified on alumina eluting with 1:19 methanol–dichloromethane solution to give a 1:1 mixture of the two diastereoisomers of the dinuclear ruthenium complex **2bpy** as a red solid in 43.2 mg (48%) yield; m.p. 268–271 °C. *Anal*. Calc. for $C_{66}H_{52}N_{14}F_{24}P_4Ru_2$: C, 43.48; H, 2.87; N, 10.76. Found: C, 43.67; H, 3.20; N, 10.88%. ^{1}H NMR (CD_3CN, 293 K) δ 8.59 (d, 4H, bpyH3A), 8.57 (d, 4H, bpyH3A*), 8.54 (d, 8H, bpyH3B/B*), 8.31 (d, 4H, bpyH6), 8.27 (d, 4H, bpyH6*), 8.10 (t, 8H, bpyH4A/A*), 8.06 (t, 8H, bpyH4B/B*), 7.89 (t, 4H, H4′*), 7.86 (t, 4H, H4′), 7.75 (d, 4H, bpyH6B*), 7.73 (d, 4H, bpyH6B), 7.59 (d, 4H, H6′*), 7.56 (d, 4H, H6′), 7.52 (d, 4H, H3′*), 7.41 (m, 13H, bpyH5B/B*, H3′, H5), 7.34 (t, 8H, bpyH5A/A*), 7.21 (t, 1H, H5*), 7.09 (m, 8H, H5′, H5′*), 6.84 (m,

3H, H6/H4, H2*), 6.56 (dd, 2H, H6*/H4*), 6.48 (t, 1H, H2).

2.2.4. [{Ru(dmb)$_2$}$_2$(**2**)](PF$_6$)$_4$ (**2dmb**)

Ligand **2** (20.5 mg, 0.049 mmol) and [Ru(dmb)$_2$Cl$_2$] (54.6 mg, 0.101 mmol) were refluxed for 72 h. The crude product was purified on alumina eluting with 1:9 methanol–dichloromethane solution to give a 1:1 mixture of the two diastereoisomers of the dinuclear ruthenium complex **2dmb** as a red solid in 42.3 mg (45%) yield; m.p. 278–282 °C. ^{1}H NMR (CD$_3$CN, 293 K) δ 8.45 (s, 4H, dmbH3A), 8.43 (s, 4H, dmbH3A*), 8.37 (s, 8H, dmbH3B/B*), 8.12 (d, 4H, dmbH6A), 8.07 (d, 4H, dmbH6A*), 7.84 (t, 4H, H4′), 7.80 (t, 4H, H4′*), 7.57 (m, 12H, dmbH6B*, H6′, H6′*), 7.52 (d, 4H, dmbH6B), 7.44 (m, 5H, H3′, H5), 7.33 (d, 4H, H3′*), 7.23 (m, 12H, dmbH5A, dmbH5B/B*), 7.19 (m, 5H, H5, dmbH5A*), 7.09 (t, 4H, H5′), 7.03 (t, 4H, H5′*), 6.86 (t, 1H, H2), 6.81 (dd, 2H, H4/H6), 6.78 (t, 1H, H2), 6.44 (dd, 2H, H4*/H6*), 2.60 (s, 12H, dmbMeA), 2.59 (s, 12H, dmbMeA*), 2.55 (s, 12H, dmbMeB), 2.54 (s, 12H, dmbMeB*). ES-MS 1796.3 (1%, [{Ru(dmb)$_2$}$_2$(**2**)](PF$_6$)$_3^+$), 823.3 (40%, [{Ru(dmb)$_2$}$_2$(**2**)](PF$_6$)$_2^{2+}$), 500.5 (100%, [{Ru(dmb)$_2$}$_2$(**2**)](PF$_6$)$^{3+}$), 339.2 (36%, [{Ru(dmb)$_2$}$_2$(**2**)]$^{4+}$). HRMS: calc. for C$_{74}$H$_{68}$N$_{14}$F$_6$PRu$_2$ ([M−(PF$_6$)$_3$)]$^{3+}$ 500.4507; found 500.4504.

2.2.5. [{Ru(bpy)$_2$}(**3**)](PF$_6$)$_2$ (**3bpym**)

Ligand **3** (20.0 mg, 0.043 mmol) and [Ru(bpy)$_2$Cl$_2$] (52.0 mg, 0.107 mmol) were refluxed for 48 h. The crude product was purified on alumina eluting with 1:19 methanol–dichloromethane solution to give only the mononuclear ruthenium complex **3bpym** as a red solid in 29 mg (58%) yield; m.p. 234–236 °C (dec.). *Anal*. Calc. for C$_{50}$H$_{38}$N$_{10}$F$_{12}$P$_2$Ru: C, 51.33; H, 3.27; N, 11.97. Found: C, 51.09; H, 3.58; N, 12.25%. ^{1}H NMR (CD$_3$CN, 293 K) δ 8.86 (m, 3H, bpyH6B, bpyH3D, bpyH6D), 8.72 (d, 1H, bpyH3A), 8.43 (d, 1H, bpyH3B), 8.39 (t, 1H, bpyH4D), 8.32 (d, 1H, bpyH3C), 8.29 (d, 2H, H6‴), 8.22 (t, 1H, bpyH4B), 8.11 (d, 1H, H8), 8.07 (t, 1H, bpyH4A), 7.99 (t, 1H, bpyH4C), 7.95 (t, 1H, bpyH5B), 7.90 (d, 1H, H6′), 7.79 (t, 1H, bpyH5D), 7.72 (m, 5H, bpyH6C, H5, H4‴, bpyH6A), 7.58 (m, 4H, H6, H7, H4″, H6″), 7.46 (m, 3H, bpyH5C, H4′, H2), 7.30 (t, 1H, bpyH5A), 7.22 (d, 2H, H3‴), 7.18 (d, 1H, H3), 7.09 (dd, 2H, H5‴), 6.81 (t, 1H, H5′), 6.77 (t, 1H, H5″), 6.71 (d, 1H, H3″), 6.34 (d, 1H, H3′). ES-MS 1025.1 (9%, [Ru(bpy)$_2$(**3**)](PF$_6$)$^+$), 440.1 (50%, [Ru(bpy)$_2$(**3**)]$^{2+}$).

2.2.6. [{Ru(bpy)$_2$}$_2$(**3**)](PF$_6$)$_4$ (**3bpy**)

Using the same quantities and procedure as above, but with a reaction time of 96 h, a mixture of mononuclear and dinuclear compounds (as a 1:1 mixture of the two diastereoisomers) was obtained. These were separated and purified on alumina eluting with 1:19 methanol–dichloromethane solution to give two red bands. Band 1 (**3bpym**): 9.0 mg (17%); Band 2 (**3bpy**): 40.7 mg (51%); m.p. 279–283 °C. ^{1}H NMR (CD$_3$CN) δ 8.85 (m, 12H, bpyH6A, bpyH3A, bpyH6A*), 8.73 (d, 4H, bpyH3B), 8.49 (m, 4H, bpyH3A*), 8.41 (t, 4H, bpyH4A), 8.33 (m, 8H, bpyH3B*, bpyH4A*), 8.09 (t, 4H, bpyH4B), 8.02 (m, 8H, bpyH5A*, bpyH4B*), 7.94 (m, 8H, H6/H7, H6*/H7*, H6′, H6″), 7.81 (t, 4H, bpyH5A), 7.78 (d, 4H, bpyH6B*), 7.73 (m, 4H, H5/H8, H5*/H8*), 7.71 (d, 4H, bpyH6B), 7.66 (t, 2H, H4′*), 7.60 (d, 2H, H4″*), 7.57 (s, 2H, H2/H3), 7.52 (t, 2H, H4′), 7.47 (m, 8H, H2*/H3*, H4″, bpyH5B*), 7.33 (m, 4H, bpyH5B), 7.23 (t, 4H, H6′*, H6″*), 6.83 (m, 10H, H5′, H5″, H3′*, H5′*, H5″*), 6.74 (d, 2H, H3″*), 6.47 (d, 2H, H3′), 6.42 (d, 2H, H3″). ES-MS 792.2 (5%, [{Ru(bpy)$_2$}$_2$(**3**)](PF$_6$)$_2^{2+}$), 479.8 (37%, [{Ru(bpy)$_2$}$_2$(**3**)](PF$_6$)$^{3+}$), 323.6 (36%, [{Ru(bpy)$_2$}$_2$(**3**)]$^{4+}$). HRMS: calc. for C$_{70}$H$_{54}$N$_{14}$F$_6$PRu$_2$ ([M−(PF$_6$)$_3$]$^{3+}$) 479.7481; found 479.7471.

2.2.7. [{Ru(dmb)$_2$}(**3**)](PF$_6$)$_2$ (**3dmbm**)

Ligand **3** (17.0 mg, 0.036 mmol) and [Ru(dmb)$_2$Cl$_2$] (42.2 mg, 0.078 mmol) were refluxed for 72 h. The crude product was purified on alumina eluting with 1:19 methanol–dichloromethane solution to give the mononuclear ruthenium complex **3dmbm** as a red solid in 35.9 mg (81%) yield; m.p. 258–261 °C (dec.). *Anal*. Calc. for C$_{54}$H$_{46}$N$_{10}$F$_{12}$P$_2$Ru · 4H$_2$O: C, 49.97; H, 4.19; N, 10.79. Found: C, 49.97; H, 3.77; N, 10.65%. ^{1}H NMR (CD$_3$CN) δ 8.70 (s, 1H, dmbH3B), 8.69 (d, 1H, dmbH6A), 8.67 (d, 1H, dmbH6B), 8.56 (s, 1H, dmbH3C), 8.28 (m, 3H, dmbH3A, H6‴), 8.17 (s, 1H, dmbH3D), 8.11 (d, 1H, H8), 7.90 (d, 1H, H6′), 7.72 (m, 5H, H2, H5, H4‴, dmbH5A), 7.59 (m, 5H, dmbH5B, dmbH6D, H6, H7, H4″), 7.51 (d, 1H, H3), 7.45 (m, 2H, dmbH6C, H4′), 7.28 (d, 1H, dmbH5D), 7.22 (d, 2H, H3‴), 7.18 (d, 1H, H6″), 7.13 (d, 1H, dmbH5C), 7.09 (dd, 2H, H5‴), 6.79 (t, 1H, H5′), 6.74 (t, 1H, H5″), 6.67 (d, 1H, H3″), 6.31 (d, 1H, H3′), 2.79 (s, 3H, dmbMeB), 2.66 (s, 3H, dmbMeA), 2.56 (s, 3H, dmbMeC), 2.51 (s, 3H, dmbMeD).

2.2.8. [{Ru(bpy)$_2$}(**4**)](PF$_6$)$_2$ (**4bpym**)

Ligand **4** (20.0 mg, 0.044 mmol) and [Ru(bpy)$_2$Cl$_2$] (52.1 mg, 0.108 mmol) were refluxed for 48 h. The crude product was purified on alumina eluting with 1:19 methanol–dichloromethane solution to give the mononuclear ruthenium complex **4bpym** as a red solid in 10.0 mg (19%) yield. ^{1}H NMR (CD$_3$CN, 293 K) δ 8.86 (d, 1H, bpyH3A), 8.83 (d, 1H, bpyH6A), 8.79 (d, 1H, bpyH6C), 8.70 (d, 1H, bpyH3B), 8.46 (d, 1H, bpyH3C), 8.39 (t, 1H, bpyH4A), 8.33 (d, 1H, bpyH3D), 8.28 (d, 2H, H6‴), 8.25 (m, 2H, bpyH4C, H4), 8.21 (d, 1H, H8), 8.06 (t, 1H, bpyH4B), 7.99 (t, 1H, bpyH4D), 7.95 (t, 1H, bpyH5C), 7.89 (d, 1H, H6″), 7.80 (t, 1H, bpyH5A), 7.66 (m, 7H, bpyH6B, bpyH6D, H3, H7, H4′, H4‴), 7.46 (m, 2H, bpyH5D, H4″), 7.35 (d, 1H, H6), 7.29 (t, 1H, bpyH5B), 7.19 (d, 3H, H6′, H3‴), 7.13 (d, 1H, H2), 7.07 (dd, 2H, H5‴), 6.81 (t, 1H, H5″), 6.76 (t, 1H, H5′), 6.62 (d, 1H, H3′), 6.28 (d, 1H, H3″). ES-MS 1025.1 (7%, [Ru(bpy)$_2$(**4**)](PF$_6$)$^+$), 440.1 (78%, [Ru(bpy)$_2$(**4**)]$^{2+}$).

*2.2.9. [{Ru(dmb)$_2$}(**4**)](PF$_6$)$_2$ (**4dmbm**)*

Ligand **4** (10.5 mg, 0.023 mmol) and [Ru(dmb)$_2$Cl$_2$] (25.6 mg, 0.047 mmol) were refluxed for 72 h. The crude product was purified on alumina eluting with 1:19 methanol–dichloromethane solution to give the mononuclear ruthenium complex **4dmbm** as a red solid in 17.1 mg (60%) yield; m.p. 238–241 °C. ^{1}H NMR (CD$_3$CN, 293 K) δ 8.69 (s, 1H, dmbH3A), 8.64 (d, 1H, dmbH6A), 8.62 (d, 1H, dmbH6C), 8.55 (s, 1H, dmbH3B), 8.31 (s, 1H, dmbH3C), 8.28 (d, 2H, H6‴), 8.20 (m, 3H, dmbH3D, H4, H8), 7.90 (d, 1H, H6″), 7.76 (d, 1H, dmbH5C), 7.64 (m, 7H, dmbH5A, dmbH6D, H3, H7, H4′, H4‴), 7.44 (m, 4H, dmbH6B, dmbH5D, H4″,H6), 7.28 (t, 1H, H2), 7.19 (m, 3H, H6′, H3‴), 7.12 (d, 1H, dmbH5B), 7.07 (dd, 2H, H5‴), 6.79 (t, 1H, H5″), 6.73 (t, 1H, H5′), 6.58 (d, 1H, H3′), 6.26 (d, 1H, H3″), 2.79 (s, 3H, dmbMeA), 2.69 (s, 3H, dmbMeC), 2.55 (s, 3H, dmbMeB), 2.51 (s, 3H, dmbMeD). ES-MS 1080.4 (2%, [Ru(dmb)$_2$(**4**)](PF$_6$)$^+$), 468.1 (100%, [Ru(dmb)$_2$(**4**)]$^{2+}$). HRMS: calc. for C$_{54}$H$_{46}$N$_{10}$Ru ([M−(PF$_6$)$_2$]$^{2+}$) 468.1482; found 468.1491.

*2.2.10. [{Ru(bpy)$_2$}$_2$(**5**)](PF$_6$)$_4$ (**5bpy**)*

Ligand **5** (20.3 mg, 0.044 mmol) and [Ru(bpy)$_2$Cl$_2$] (45.3 mg, 0.094 mmol) were refluxed for 48 h. The crude product was purified on alumina eluting with 1:9 methanol–dichloromethane solution to give a 1:1 mixture of the two diastereoisomers of the dinuclear ruthenium complex **5bpy** as a red solid in 48.4 mg (59%) yield; m.p. 208–210 °C (dec.). ^{1}H NMR (CD$_3$CN, 293 K) δ 8.59 (d, 4H, bpyH3A), 8.56 (d, 4H, bpyH3A*), 8.52 (m, 8H, bpyH3B/B*), 8.44 (d, 4H, bpyH6A) 8.38 (d, 4H, bpyH6A*), 8.12 (t, 4H, bpyH4A), 8.05 (m, 16H, bpyH4A*, bpyH4B/B*, H4, H4*), 7.95 (t, 4H, H4′), 7.91 (t, 4H, H4′*), 7.76 (d, 8H, bpyH6/H6*), 7.60 (d, 8H, H6′, H6′*), 7.55 (d, 4H, H3′), 7.52 (d, 4H, H3′*), 7.39 (m, 10H, bpyH5/H5*, H1), 7.36 (t, 4H, bpyH5A), 7.32 (t, 4H, bpyH5A*), 7.27 (dd, 2H, H3*), 7.17 (dd, 2H, H3), 7.07 (m, 10H, H1*, H5′, H5′*). ES-MS 792.5 (6%, [{Ru(bpy)$_2$}$_2$(**5**)](PF$_6$)$_2^{2+}$), 479.8 (93%, [{Ru(bpy)$_2$}$_2$(**5**)](PF$_6$)$^{3+}$), 323.6 (100%, [{Ru(bpy)$_2$}$_2$(**5**)]$^{4+}$).

*2.2.11. [{Ru(dmb)$_2$}$_2$(**5**)](PF$_6$)$_4$ (**5dmb**)*

Ligand **5** (20.6 mg, 0.044 mmol) and [Ru(dmb)$_2$Cl$_2$] (52.3 mg, 0.097 mmol) were refluxed for 48 h. The crude product was purified on alumina eluting with 1:19 methanol–dichloromethane solution to give a 1:1 mixture of the two diastereoisomers of the dinuclear ruthenium complex **5dmb** as a red solid in 68.9 mg (78%) yield; m.p. 268–271 °C. ^{1}H NMR (CD$_3$CN, 293 K) δ 8.42 (s, 4H, dmbH3A), 8.40 (s, 4H, dmbH3A*), 8.37 (s, 4H, dmbH3B), 8.36 (s, 4H, dmbH3B*), 8.15 (m, 8H, dmbH6A/A*), 8.02 (d, 4H, H4, H4*), 7.90 (t, 8H, H4′, H4′*), 7.56 (m, 24H, dmbH6B/B*, H3′, H3′*, H6′, H6′*), 7.22 (d, 8H, dmbH5B/B*), 7.18 (m, 6H, H1, H1*, H3*), 7.14 (dd, 2H, H3), 7.07 (m, 16H, dmbH5A/A*, H5′, H5′*), 2.54 (s, 24H, dmbMeB/B*), 2.51 (s, 12H, dmbMeA), 2.49 (s, 12H, dmbMeA*). ES-MS 848.2 (2%, [{Ru(dmb)$_2$}$_2$(**5**)](PF$_6$)$_2^{2+}$), 517.1 (22%, [{Ru(dmb)$_2$}$_2$(**5**)](PF$_6$)$^{3+}$), 351.6 (20%, [{Ru(dmb)$_2$}$_2$(**5**)]$^{4+}$). HRMS: calc. for C$_{78}$H$_{70}$N$_{14}$F$_6$PRu$_2$ ([M−(PF$_6$)$_3$]$^{3+}$) 517.1222; found 517.1230.

*2.2.12. [{Ru(bpy)$_2$}$_2$(**6**)](PF$_6$)$_4$*

Ligand **6** (20.0 mg, 0.044 mmol) and [Ru(bpy)$_2$Cl$_2$] (50.0 mg, 0.103 mmol) were refluxed for 48 h. Purification on alumina eluting with 1:19 methanol–dichloromethane solution gave a red solid of **6bpy**, as a 1:1 mixture of the two diastereoisomers, in 55.7 mg (66%) yield; m.p. 234–238 °C. *Anal.* Calc. for C$_{72}$H$_{56}$N$_{14}$F$_{24}$P$_4$Ru$_2$: C, 45.53; H, 2.97; N, 10.32. Found: C, 45.84; H, 3.12; N, 9.82%. ^{1}H NMR (CD$_3$CN, 293 K) δ 8.60 (d, 4H, bpyH3A), 8.57 (d, 4H, bpyH3A*), 8.51 (m, 8H, bpyH3B/B*), 8.46 (d, 4H, bpyH6A), 8.41 (d, 4H, bpyH6A*), 8.16 (m, 8H, bpyH4A/A*), 8.04 (m, 8H, bpyH4B/B*), 7.85 (m, 12H, H4′, H4′*, H2/H6), 7.75 (m, 12H, bpyH6B/B*, H2/H6*), 7.55 (m, 8H, H6′, H6′*), 7.51 (t, 4H, bpyH5A), 7.45 (m, 12H, bpyH5A*, H6′*, H6′), 7.39 (m, 8H, bpyH5B/B*), 7.21 (d, 4H, H3/H5), 7.13 (d, 4H, H3/H5), 7.01 (m, 8H, H5′, H5′*).

*2.2.13. [{Ru(dmb)$_2$}$_2$(**6**)](PF$_6$)$_4$*

Ligand **6** (24.9 mg, 0.051 mmol) and [Ru(dmb)$_2$Cl$_2$] (56.7 mg, 0.105 mmol) were refluxed for 72 h. Eluting an alumina column of the crude product with 1:19 methanol–dichloromethane solution gave a 1:1 mixture of the two diastereoisomers of the dinuclear ruthenium complex **6dmb**, as a red solid, in 49.9 mg (50%) yield; m.p. 260–262 °C. ^{1}H NMR (CD$_3$CN, 293 K) δ 8.43 (s, 4H, dmbH3A), 8.40 (s, 4H, dmbH3A*), 8.36 (s, 4H, dmbH3B), 8.34 (s, 4H, dmbH3B*), 8.24 (d, 4H, dmbH6A), 8.16 (d, 4H, dmbH6A*), 7.84 (m, 12H, H2/H6, H4′, H4′*), 7.73 (m, 4H, H2/H6*), 7.55 (m, 16H, dmbH6B/B*, H6′, H6′*), 7.49 (d, 4H, H3′*), 7.44 (d, 4H, H3′), 7.29 (d, 4H, dmbH5A), 7.21 (m, 12H, dmbH5B/A*/B*), 7.18 (d, 4H, H3/H5), 7.08 (d, 4H, H3/H5*), 7.01 (m, 8H, H5′, H5′*), 2.63 (s, 12H, dmbMeA), 2.59 (s, 12H, dmbMeA*), 2.54 (s, 12H, dmbMeB), 2.53 (s, 12H, dmbMeB*). ES-MS 861.3 (1%, [{Ru(dmb)$_2$}$_2$(**6**)](PF$_6$)$_2^{2+}$), 525.9 (27%, [{Ru(dmb)$_2$}$_2$(**6**)](PF$_6$)$^{3+}$), 358.1 (66%, [{Ru(dmb)$_2$}$_2$(**6**)]$^{4+}$).

3. Results and discussion

3.1. Syntheses and structural characterisation of the complexes

The ruthenium complexes described in this work were prepared by reaction of the ligand with either [Ru(bpy)$_2$Cl$_2$][40] or [Ru(dmb)$_2$Cl$_2$][41] at reflux in 3:1 ethanol–water for a period of between 48 and 96 h (Scheme 1). Ligands **1**, **2**, **5**, and **6** all yielded dinuclear complexes with both ruthenium precursors that were isolated as mixtures of the *rac* and *meso* diastereoisomers [11–13]. Ligands **3** and **4** both readily yielded mononuclear complexes that were characterised by NMR spectroscopy and mass spectrometry. In the case of reaction of [Ru(bpy)$_2$Cl$_2$] and **3**, additional reaction time provided a mixture of mono- and dinuclear

ruthenium complexes that were separated by chromatography on alumina. The products of this series of reactions are summarised in Table 1, which shows the naming used for the complexes, the nature of the complex (mono- or dinuclear), the reaction time and the isolated yield.

The complexes $[\{Ru(bpy)_2\}_2(\mathbf{1})](PF_6)_4$ (**1bpy**) and $[\{Ru(dmb)_2\}_2(\mathbf{1})](PF_6)_4$ (**1dmb**) were obtained as described and characterised as dinuclear complexes by a combination of combustion analysis and ^{1}H NMR spectroscopy. The ^{1}H NMR spectrum of **1bpy** consists of 13 independent multiplets consistent with a dinuclear complex of ligand **1**. The chemical shifts for the pyridine rings of **1** and the ancillary bpy rings of the two diastereoisomers are partially resolved in some instances and overlapped in other cases consistent with slight structural differences between the two diastereoisomers. The two singlets for the protons of the benzene ring, corresponding to the two diastereoisomers, are more clearly resolved indicating there are, as expected, greater structural differences around the central benzene ring. By examination of the spin–spin coupling information and using a combination of 1D TOCSY and 1D-NOESY NMR techniques, the ^{1}H NMR spectrum of **1bpy** was assigned. The ^{1}H NMR spectrum of **1dmb** is likewise consistent with two diastereoisomers, with some multiplets that are partially resolved allowing the chemical shifts of the dmb rings of the two diastereoisomers to be differentiated. The chemical shifts for the pyridine rings of the bridging ligand in the two diastereoisomers were too close to be assigned.

The ^{1}H NMR chemical shifts for ligand **1** in acetonitrile, and for **1** in the two diastereoisomers of both **1bpy** and **1dmb**, are given in Table 2, along with the coordination-induced-shift (*cis*) values, which are given in italics. The *cis* values for the two complexes are very similar, which is consistent with the very subtle changes to the ancillary ligands of the complex. No unusual *cis* values are observed for either complex. The large negative *cis* values for the H6 protons of **1** result from inter-ligand through-space ring-anisotropy effects because, in the complexes, these protons lie over the shielding plane of adjacent bpy or dmb rings.

The crystal structure of a dinuclear copper complex of **1** was previously reported by us [33]. The square pyramidal copper(II) centres are bridged by **1** with a copper–copper separation of 11.179 Å, giving an indication of the likely M–M distance and conformation in the corresponding dinuclear ruthenium complexes of **1**.

Reaction of $[Ru(bpy)_2Cl_2]$ or $[Ru(dmb)_2Cl_2]$ with **2** gave the dinuclear complexes **2bpy** and **2dmb**, as 1:1 mixtures of the *rac* and *meso* diastereoisomers, which were isolated as their hexafluorophosphate salts. Combustion analysis, mass spectrometry and ^{1}H NMR spectroscopy were utilised to identify complexes **2bpy** and **2dmb** as $[\{Ru(bpy)_2\}_2(\mathbf{2})](PF_6)_4$ and $[\{Ru(dmb)_2\}_2(\mathbf{2})](PF_6)_4$, respectively. A dinuclear copper(II) nitrate complex was also prepared with ligand **2** in which the two copper atoms are separated by a distance of 8.785 Å [33]. This is considerably shorter than the metal–metal distance bridged by **1** in the copper complexes referred to above.

Partial separation of the diastereoisomers was achieved by alumina chromatography allowing the signals for the diastereoisomers of both complexes **2bpy** and **2dmb** to be readily assigned to individual spin systems by 1D TOCSY experiments. The different diastereoisomers of complexes **2bpy** and **2dmb** have quite different chemical shifts, in particular for the central benzene ring of the ligand. This indicates that there are significant structural differences in the two diastereoisomers above and below the plane of the central benzene ring as anticipated. The *cis* values for complexes **2bpy** and **2dmb** are shown in Table 2. While there are differences between the diastereoisomers, the general trend of the *cis* values, experienced by the pyridine rings of ligand **2** upon coordination to ruthenium, are very similar to dinuclear complexes of ligand **1**. The *cis* values for the protons of the benzene rings in these two complexes are larger than in the previous complexes with ligand **1**. For complex **2bpy**, the benzene-H2 proton of one diastereoisomer (**2bpy***) has a considerably larger negative *cis* value than the other diastereoisomer. This is also observed for complex **2dmb**, but the difference is far less dramatic. Inversely, for the equivalent H4 and H6 protons, the effect is reversed, with the other diastereoisomer experiencing larger negative *cis* values. Such differences are presumably explained by different conformations around the benzene ring.

After having prepared dinuclear complexes of ligands **1** and **2**, the ligands possessing a naphthalene core were employed to assess the effect of a more bulky arene core and in the case of ligands **4** and **5** increased metal–metal

Table 1
A summary of the synthetic work presented in the paper

Ligand	Complex	Label[a]	Time (hrs)	Yield (%)
1	$[\{Ru(bpy)_2\}_2(\mathbf{1})](PF_6)_4$	**1bpy**	72	93
	$[\{Ru(dmb)_2\}_2(\mathbf{1})](PF_6)_4$	**1dmb**	72	61
2	$[\{Ru(bpy)_2\}_2(\mathbf{2})](PF_6)_4$	**2bpy**	72	48
	$[\{Ru(dmb)_2\}_2(\mathbf{2})](PF_6)_4$	**2dmb**	72	45
3	$[Ru(bpy)_2(\mathbf{3})](PF_6)_2$	**3bpym**	48	58
	$[Ru(dmb)_2(\mathbf{3})](PF_6)_2$	**3dmbm**	72	81
	$[\{Ru(bpy)_2\}_2(\mathbf{3})](PF_6)_4$	**3bpy**[b]	96	51
4	$[Ru(bpy)_2(\mathbf{4})](PF_6)_2$	**4bpym**	48	19
	$[Ru(dmb)_2(\mathbf{4})](PF_6)_2$	**4dmbm**	72	60
5	$[\{Ru(bpy)_2\}_2(\mathbf{5})](PF_6)_4$	**5bpy**	48	59
	$[\{Ru(dmb)_2\}_2(\mathbf{5})](PF_6)_4$	**5dmb**	48	78
6	$[\{Ru(bpy)_2\}_2(\mathbf{6})](PF_6)_4$	**6bpy**	48	66
	$[\{Ru(dmb)_2\}_2(\mathbf{6})](PF_6)_4$	**6dmb**	72	50

The composition, labelling, reaction time and yield of the products are summarised.

[a] $[Ru(bpy)_2]$ complexes are named with a bpy descriptor, $[Ru(dmb)_2]$ with dmb; mononuclear complexes are designated by an '**m**'.

[b] A 17% yield of mononuclear complex **3bpym** was also obtained in this reaction.

Table 2
^{1}H NMR chemical shifts for the free ligands (**1**, **2** and **6**) in acetonitrile, the bridging ligands in the corresponding dinuclear complexes in acetonitrile, and the *cis* values ($cis = \delta_{complex} - \delta_{ligand}$) given in italics

	pyH3′	pyH4′	pyH5′	pyH6′	Φ-CH	Φ-H2	Φ-H4/H6	Φ-H5	Φ-H3/H5	Φ-H2/H6
1	7.10	7.71	7.07	8.31	7.16					
1bpy	7.48	7.95	7.06	7.58	7.11					
cis	*0.38*	*0.24*	*−0.01*	*−0.73*	*−0.05*					
1bpy*	7.47	7.93	7.05	7.58	7.09					
cis	*0.37*	*0.22*	*−0.02*	*−0.73*	*−0.07*					
1dmb/1dmb*	7.43	7.89	7.01	7.57	7.20					
cis	*0.33*	*0.18*	*−0.06*	*−0.74*	*0.04*					
2	7.06	7.66	7.02	8.28		6.90	7.37	6.95		
2bpy	7.52	7.89	7.10	7.59		6.83	6.56	7.20		
cis	*0.46*	*0.23*	*0.08*	*−0.69*		*−0.07*	*−0.81*	*0.25*		
2bpy*	7.40	7.86	7.08	7.58		6.48	6.84	7.43		
cis	*0.34*	*0.20*	*0.06*	*−0.70*		*−0.42*	*−0.53*	*0.48*		
2dmb	7.45	7.84	7.09	7.58		6.86	6.44	7.17		
cis	*0.39*	*0.18*	*0.07*	*−0.70*		*−0.04*	*−0.93*	*0.22*		
2dmb*	7.33	7.80	7.03	7.57		6.78	6.61	7.44		
cis	*0.27*	*0.14*	*0.01*	*−0.71*		*−0.12*	*−0.76*	*0.49*		
6	7.06	7.69	7.07	8.30					7.23	7.68
6bpy	7.44	7.85	7.01	7.55					7.21	7.84
cis	*0.38*	*0.26*	*−0.06*	*−0.75*					*−0.02*	*0.16*
6bpy*	7.45	7.85	7.01	7.55					7.13	7.75
cis	*0.39*	*0.26*	*−0.06*	*−0.75*					*−0.10*	*0.07*
6dmb	7.44	7.85	7.01	7.57					7.18	7.83
cis	*0.38*	*0.26*	*−0.06*	*−0.73*					*−0.05*	*0.15*
6dmb*	7.49	7.85	7.02	7.55					7.08	7.73
cis	*0.43*	*0.26*	*−0.05*	*−0.75*					*−0.13*	*0.05*

The asterisk indicates the resolved signals of one of the diastereoisomers.

separations. The 1,4-substituted naphthalene ligand, **3**, was investigated first. Reaction of either $[Ru(bpy)_2Cl_2]$ or $[Ru(dmb)_2Cl_2]$ with **3** in a 2:1 stoichiometry, using the standard reaction conditions, provided only the mononuclear complexes **3bpym** and **3dmbm**, respectively. Using a combination of combustion analysis, mass spectrometry and ^{1}H NMR spectroscopy, complexes **3bpym** and **3dmbm** were confirmed as $[Ru(bpy)_2(\mathbf{3})](PF_6)_2$ and $[Ru(dmb)_2(\mathbf{3})](PF_6)_2$, respectively. The dinuclear complex **3bpy** was prepared by undertaking the reaction for a period of 96 h as opposed to 48 h. This provided a mixture of the mononuclear and dinuclear complexes that were separated using alumina chromatography to give the mononuclear complex **3bpym** in 17% yield, and the desired dinuclear complex **3bpy** in 51% yield.

The ^{1}H NMR spectra of **3bpym** and **3dmbm** are complicated by the lower (C_1) symmetry of the complexes, which have restricted rotation about the naphthalene amine–nitrogen single bond of the chelating di-2-pyridylamine unit. Thus, the coordinated pyridine rings of the ligand are non-equivalent, but the non-coordinated pyridine rings of the other di-2-pyridylamine unit are equivalent because of free rotation about this naphthalene amine–nitrogen single bond. Employment of the 1D TOCSY experiment allowed the assignment of all chemical shifts to individual protons for both mononuclear complexes (Table 3).

cis-Values for the mononuclear complexes **3bpym** and **3dmbm** are larger and more variable than the values observed for the previously described dinuclear complexes. The two coordinated pyridine rings have quite different *cis* values, consistent with the restricted rotation of the coordinated arm of the ligand and the different environments for each ring. The naphthalene ring affects one of these coordinated pyridine rings, while the second ring has an environment, and therefore *cis* values, similar to the pyridine rings in the dinuclear complexes previously described with **1** and **2**. The former pyridine ring, denoted with a prime in the table, has a large negative *cis* value for the H3 proton because upon complexation this proton lies over the shielding region of the adjacent naphthalene ring. The non-coordinated pyridine rings are not affected by the remote coordination and the chemical shifts for these protons are relatively unchanged.

The ^{1}H NMR spectrum of **3bpy** is much simpler than the spectra for the corresponding mononuclear complex. The ^{1}H NMR spectrum of **3bpy** is, like previous spectra of other dinuclear complexes, consistent with two diastereoisomers, with some multiplets that are resolved, which allows the chemical shifts of the pyridine rings and bpy rings of the two diastereoisomers to be differentiated (Table 4). The various spin systems were not assigned to a specific diastereoisomer because there was no enrichment of any of the column fractions when the complex was purified. There are considerable similarities in the NMR spectra and the *cis* values of the mononuclear complexes of ligand **3** and the dinuclear complex **3bpy**. The latter complex has higher

Table 3
The ^{1}H NMR chemical shifts for the free naphthalene ligands (**3** and **4**) in acetonitrile, the ligands in the mononuclear naphthalene-bridged complexes (**3bpym**–**4dmbm**) in acetonitrile, and the *cis* values ($cis = \delta_{complex} - \delta_{ligand}$) given in italics

	pyH3′	pyH4′	pyH5′	pyH6′	H2	H3	H4	H5	H6	H7	H8
3	7.17	7.70	7.03	8.26	7.52	7.52		7.92	7.43	7.43	7.92
3bpym′	6.34	7.46	6.81	7.90							
cis	*−0.83*	*−0.24*	*−0.22*	*−0.36*							
3bpym″	6.71	7.61	6.77	7.59	7.18	7.46		8.11	7.59	7.57	7.72
cis	*−0.46*	*−0.09*	*−0.26*	*−0.67*	*−0.34*	*−0.06*		*0.19*	*0.16*	*0.14*	*−0.20*
3bpym‴	7.22	7.73	7.09	8.29							
cis	*0.05*	*0.03*	*0.06*	*0.03*							
3dmbm′	6.31	7.44	6.79	7.90							
cis	*−0.86*	*−0.26*	*−0.24*	*−0.36*							
3dmbm″	6.67	7.57	6.74	7.18	7.69	7.51		8.11	7.59	7.55	7.71
cis	*−0.50*	*−0.13*	*−0.29*	*−1.08*	*0.17*	*−0.01*		*0.19*	*0.16*	*0.12*	*−0.21*
3dmbm‴	7.22	7.74	7.09	8.29							
cis	*0.05*	*0.04*	*0.06*	*0.03*							
4	7.13	7.69	7.03	8.25	7.46	7.51	7.91		7.46	7.51	7.91
4bpym′	6.62	7.60	6.76	7.19							
cis	*−0.51*	*−0.09*	*−0.27*	*−1.06*							
4bpym″	6.28	7.45	6.81	7.89	7.13	7.67	8.25		7.35	7.66	8.21
cis	*−0.85*	*−0.24*	*−0.22*	*−0.36*	*−0.33*	*0.16*	*0.34*		*−0.11*	*0.15*	*0.30*
4bpym‴	7.19	7.72	7.07	8.28							
cis	*0.06*	*0.03*	*0.04*	*0.03*							
4dmbm′	6.58	7.57	6.73	7.17							
cis	*−0.55*	*−0.12*	*−0.30*	*−1.08*							
4dmbm″	6.26	7.42	6.79	7.90	7.28	7.68	8.18		7.41	7.68	8.21
cis	*−0.87*	*−0.27*	*−0.24*	*−0.35*	*−0.16*	*0.17*	*0.27*		*−0.05*	*0.17*	*0.30*
4dmbm‴	7.19	7.72	7.07	8.28							
cis	*0.06*	*0.03*	*0.04*	*0.03*							

The primes in the labels for the complexes indicate the non-equivalent pyridyl rings.

Table 4
^{1}H NMR chemical shifts for the free ligands (**3** and **5**) in acetonitrile, the bridging ligands in the corresponding dinuclear naphthalene-bridged complexes in acetonitrile, and the *cis* values ($cis = \delta_{complex} - \delta_{ligand}$) given in italics

	pyH3′	pyH4′	pyH5′	pyH6′	H2/H3	H5/H8	H6/H7	H1/H8	H3/H6	H4/H5
3	7.17	7.70	7.03	8.26	7.52	7.92	7.43			
3bpy	6.42	7.46	6.86	7.94	7.57	7.93	7.74			
cis	*−0.75*	*−0.24*	*−0.17*	*−0.32*	*0.05*	*0.01*	*0.31*			
3bpy	6.84	7.66	6.83	7.24						
cis	*−0.33*	*−0.04*	*−0.20*	*−1.02*						
3bpy*	6.47	7.52	6.87	7.95	7.49	7.93	7.74			
cis	*−0.70*	*−0.18*	*−0.16*	*−0.31*	*−0.03*	*0.01*	*0.31*			
3bpy*	6.74	7.60	6.80	7.22						
cis	*−0.43*	*−0.10*	*−0.23*	*−1.04*						
5	7.10	7.69	7.06	8.29				7.46	7.29	7.92
5bpy	7.55	7.95	7.07	7.60				7.39	7.17	8.03
cis	*0.45*	*0.26*	*0.01*	*−0.69*				*−0.07*	*−0.12*	*0.11*
5bpy*	7.52	7.92	7.08	7.60				7.09	7.27	8.04
cis	*0.42*	*0.23*	*0.02*	*−0.69*				*−0.37*	*−0.02*	*0.12*
5dmb/5dmb*	7.54	7.90	7.07	7.58				7.18	7.14	8.00
cis	*0.44*	*0.21*	*0.01*	*−0.71*				*−0.28*	*−0.15*	*0.08*
5dmb*								7.18	7.19	8.02
cis								*−0.28*	*−0.10*	*0.10*

The asterisk indicates the resolved signals of one of the diastereoisomers.

symmetry and therefore there are only two non-equivalent pyridine rings in the bridging ligand. One of the pyridine rings of each diastereoisomer is located over the naphthalene ring of the ligand and has a large negative *cis* value for the H3 proton. For both diastereoisomers, one H6 proton of a coordinated pyridine rings has quite a dramatic negative *cis* value, whereas the other has a *cis* value less than the normal value for an H6 proton of a coordinated pyridine ring in such complexes.

Ligand **4** has a 1,5-disubstituted naphthalene core with the di-2-pyridylamine units of the ligand attached to different rings of the naphthalene unit. Reaction of either

$[Ru(bpy)_2Cl_2]$ or $[Ru(dmb)_2Cl_2]$ with **4** provided only the mononuclear complexes **4bpym** and **4dmbm**, respectively. Using mass spectrometry and ^1H NMR spectroscopy, the complexes were confirmed as $[Ru(bpy)_2(\mathbf{4})](PF_6)_2$ and $[Ru(dmb)_2(\mathbf{4})](PF_6)_2$. Ligand **4** is relatively insoluble which appears to have lowered the yields of the mononuclear complexes and hindered the formation of the expected dinuclear complexes. No dinuclear complexes were observed despite repeating the reaction with longer reaction times.

The ^1H NMR spectra of **4bpym** and **4dmbm** are again, like the previous mononuclear complexes, complicated by reduced (C_1) symmetry due to restricted rotation of the coordinated arm of the ligand. The 1D TOCSY technique was used to assign the chemical shifts to individual protons for both mononuclear complexes (Table 3). The *cis* values for the mononuclear complexes **4bpym** and **4dmbm** are similar to those obtained for the previous mononuclear complexes of ligand **3**. The two coordinated pyridine rings of both complexes have quite different *cis* values, consistent with the reduced rotation of the coordinated arm of the ligand and the different environments for each ring. Again, the naphthalene ring affects one pyridine ring of each complex, which has a large negative *cis* value for the H3 proton. A second ring of each complex has an environment similar to the pyridine rings in the dinuclear complexes previously described and has a large negative *cis* value for the H6 proton. However, it also has a negative *cis* value for the H3 proton.

Reaction of $[Ru(bpy)_2Cl_2]$ or $[Ru(dmb)_2Cl_2]$ with **5** gave the dinuclear complexes **5bpy** and **5dmb**, that were confirmed by ES-MS and ^1H NMR spectroscopy as $[\{Ru(bpy)_2\}_2(\mathbf{5})](PF_6)_4$ and $[\{Ru(dmb)_2\}_2(\mathbf{5})](PF_6)_4$, respectively. The ^1H NMR spectra are consistent with a mixture of the two diastereoisomers for both complexes. The signals for both diastereoisomers of complexes **5bpy** and **5dmb** were able to be assigned to individual spin systems by 1D TOCSY experiments (Table 4). The *cis* values for the pyridine and naphthalene rings of ligand **5** upon coordination in these complexes are very similar to previous dinuclear complexes. There are subtle differences in the *cis* values for the different diastereoisomers for the H1/H8 protons of the naphthalene ring of complex **5bpy**, but interestingly not for **5dmb**.

Ligand **6** differs from ligand **1** by insertion of a second benzene ring between the two chelating domains of the ligand giving a significantly longer metal–metal separation. Reaction of $[Ru(bpy)_2Cl_2]$ or $[Ru(dmb)_2Cl_2]$ with **6** gave the dinuclear complexes **6bpy** and **6dmb** which were characterised as $[\{Ru(bpy)_2\}_2(\mathbf{6})](PF_6)_4$ and $[\{Ru(dmb)_2\}_2(\mathbf{6})](PF_6)_4$, respectively, using a combination of combustion analysis, mass spectrometry and ^1H NMR spectroscopy. The ^1H NMR chemical shifts for the ligand **6** in acetonitrile, and for the two diastereoisomers of the two dinuclear ruthenium complexes **6bpy** and **6dmb**, are given in Table 2, along with the *cis* values. An unambiguous assignment of the proton chemical shifts of each diastereoisomer of **6bpy** and **6dmb** was achieved because chromatography on alumina resulted in enrichment of some of the column fractions with one diastereoisomer.

The *cis* values for complexes **6bpy** and **6dmb** are very similar to those observed for the previous set of complexes. Again large negative *cis* values occur for the H6 protons of the coordinated pyridine rings, because they lie over the shielding region of the bpy or dmb rings. The H3 and H5 protons of the biphenyl core are more deshielded in one of the diastereoisomers than the other, which suggests a greater difference in the two structures around the biphenyl core, as expected.

3.2. Electrochemistry and UV–Vis spectroscopy

The electrochemical studies of the ruthenium complexes of the ligands **1**–**6** are potentially complicated because the ligands themselves can undergo two irreversible oxidations. Fig. 2 shows a cyclic voltammogram for the free ligand **1**, showing the two irreversible oxidation waves. These are attributed to the oxidation of the amine nitrogen atoms of the ligand and potentials for the oxidation of ligands **1** and **3** are shown in Table 5. As the results presented for the complexes below show, upon coordination, the amine nitrogen atoms of the chelating unit are no longer susceptible to oxidation, and so this feature is only a consideration for the mononuclear complexes with a non-coordinated di-2-pyridylamine subunit. In all the dinuclear complexes the oxidation waves are reversible, indicating these redox processes are metal based, whereas the amine oxidation waves observed in the free ligand are not.

The electronic absorption maxima and redox potentials, recorded in acetonitrile solution, for the mononuclear complexes **3bpym**, **3dmbm** and **4dmbm** are given in Table 5. The mononuclear complexes all have broad absorption maxima at *ca.* 430 nm, with a shoulder at *ca.* 457 nm. The MLCT transitions into the orbitals of the ligand are at a higher energy than for $[Ru(bpy)_3]^{2+}$ (452 nm) [6], while the shoulder may correspond to MLCT into the bpy ligands. The cyclic voltammograms for the mononuclear complexes, **3bpym**, **3dmbm** and **4dmbm**, all have four one electron redox processes. For complex **3bpym**, the reversible oxidation of the ruthenium centre and the irreversible oxidation of the amine on the non-coordinated arm of the ligand are

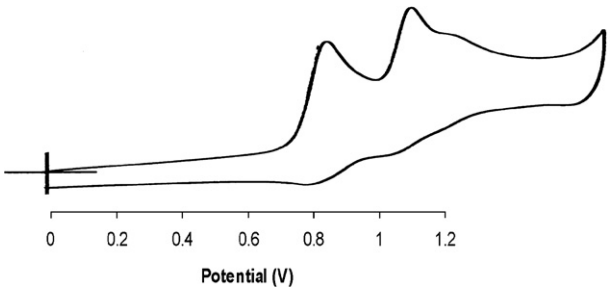


Fig. 2. A cyclic voltammogram of **1** showing the two irreversible oxidations.

Table 5
Redox potentials for ligands **1** and **3**, visible absorption maxima and redox potentials for $[Ru(bpy)_3]^{2+}$ and selected mononuclear complexes **3bpym**, **3dmbm** and **4dmbm**, and visible absorption maxima and redox potentials for dinuclear complexes

Compound	λ (nm)[a,b]	$E^{c,d}_{ox}$	$E^{c,d}_{ox(2)}$	$E^{c,d}_{red(1)}$	$E^{c,d}_{red(2)}$	$E^{c,d}_{red(3)}$
1		+0.82[e](1e)	+1.13[e](1e)			
3		+0.82[e](1e)	+1.14[e](1e)			
$[Ru(bpy)_3]^{2+}$	452	1.26(1e)		−1.33(1e)	−1.51(1e)	
3bpym	429, 457(sh)	+1.14(2e)		−1.45(1e)	−1.68(1e)	
3dmbm	431, 456(sh)	+1.02(1e)	+1.27[e](1e)	−1.56(1e)	−1.74(1e)	
4dmbm	430, 458(sh)	+1.02(1e)	+1.27[e](1e)	−1.54(1e)	−1.75(1e)	
1bpy	442	+1.13[e](1e)	+1.19[e](1e)	−1.44(2e)	−1.66(2e)	
1dmb	442	+1.05(2e)		−1.52(2e)	−1.75(2e)	
2bpy	441	+1.15[e](1e)	+1.21[e](1e)	−1.41(2e)	−1.71(2e)	−1.94[e](1e)
2dmb	440	+1.11(2e)		−1.54(2e)	−1.77[e](2e)	−2.00[e](1e)
3bpy	445	+1.13(2e)		−1.45(2e)	−1.68(2e)	
5bpy	444	+1.12(2e)		−1.45(2e)	−1.66(2e)	−1.89[e](1e)
5dmb	441	+1.07(2e)		−1.53(2e)	−1.74(2e)	−1.94[e](1e)
6bpy	443	+1.11(2e)		−1.44(2e)	−1.66(2e)	−2.01(1e)
6dmb	442	+1.01(2e)		−1.54(2e)	−1.76(2e)	−2.06(1e)

[a] The MLCT band measured in CH_3CN (±2 nm).
[b] sh = shoulder.
[c] Potentials quoted in V vs. SCE in CH_3CN/0.1 mol L^{-1} $[(n\text{-}C_4H_9)_4]PF_6$ (the ferrocene/ferrocenium couple occurred at +310 mV vs. SCE). Determined by cyclic voltammetry.
[d] Uncertainty in $E_{1/2}$ values *ca.* ± 0.01 V.
[e] Overlapped or irreversible (approximate value estimated from anodic or cathodic half-scan).

overlapped. For the dmb complexes, the ruthenium oxidation potentials are shifted *ca.* 100 mV less positive and the amine nitrogen becomes *ca.* 100 mV more difficult to oxidise. The redox potentials reveal that the ruthenium centre of the bpy complex, **3bpym**, is both easier to oxidise and more difficult to reduce than $[Ru(bpy)_3]^{2+}$ (+1.26, −1.33 V). This is consistent with the electron-rich nature of these ligands. For the dmb complex, **3dmbm**, the reduction potentials are shifted by *ca.* 100 mV related to those of the bpy complex, consistent with the electron donating effect of *ca.* 25 mV per methyl group [42].

The dinuclear ruthenium complexes all exhibit broad visible absorption maxima at *ca.* 442 nm as shown in Table 5. For all the complexes these bands can be assigned to a MLCT, as is the case for $[Ru(bpy)_3]^{2+}$. This indicates that the HOMO–LUMO energy gap in these complexes is comparable to $[Ru(bpy)_3]^{2+}$, but because of the more electron rich nature of the ligands, slightly larger than that of $[Ru(bpy)_3]^{2+}$. By comparison to the mononuclear complexes, addition of a second ruthenium centre into a complex lowers the energy gap further (the absorption maximum of **3bpym** is 429 nm, whereas the maximum occurs at 445 nm for the dinuclear complex **3bpy**).

It was postulated that the sp^2 character of the tertiary amine in the bridging ligands **1**–**6** would aid metal–metal interaction in dinuclear complexes of these ligands. This was investigated in the first instance by cyclic voltammetry. A cyclic voltammogram for complex **1bpy** is shown in Fig. 3. It shows the complex undergoes four redox processes (two partially overlapped), including two bpy-centred reductions at −1.44 and −1.66 V. The oxidation wave appears to be comprised of two redox events with a shoulder on the cathodic and anodic waves. Thus, this oxidation wave is complicated either by differences between

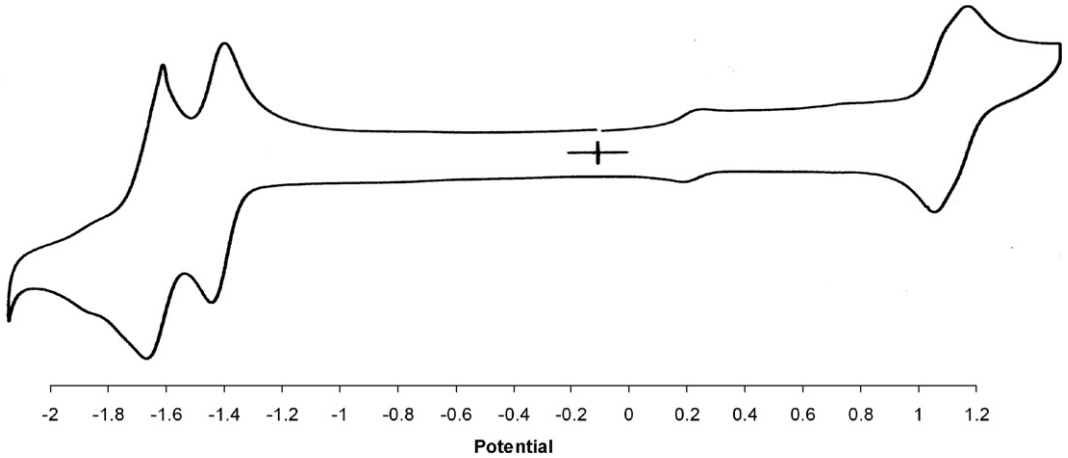


Fig. 3. The cyclic voltammogram of the dinuclear complex **1bpy**.

the two diastereoisomers, or by the interaction between the two metal centres. The flexibility of the ligand suggests that the latter possibility is more likely. Assuming full reversibility, from the cyclic voltammogram for **1bpy**, it can be calculated that these two one-electron processes are occurring *ca.* 60 mV apart. This type of behaviour was also observed for complex **2bpy**, although similar separations of the oxidation potentials for the two ruthenium atoms could not be observed in the corresponding dinuclear dmb complexes, **1dmb** and **2dmb**. Thus, ligands **1** and **2** appear to be facilitating only weak metal–metal interactions.

The differential pulse voltammograms of complex **1bpy** and **2bpy** are shown in Fig. 4, and confirm the weak interactions between metal centres in the two dinuclear complexes. For both the dinuclear bpy complexes, the differential pulse voltammograms confirm two separate, but very closely spaced processes, consistent with the observations made by cyclic voltammetry. For both complexes, the voltage separations of these two one-electron redox potentials are at the boundaries of this technique, and thus in both cases, the drop in current between the two potentials is negligible.

The cyclic voltammetry of the other dinuclear complexes revealed at least three reversible two-electron redox processes for each complex. Unlike the complexes of ligands with a benzene core, the oxidation waves of the dinuclear complexes of the biphenyl and naphthalenyl ligands are reversible two-electron waves, with a E_{ox}/E_{red} peak separation of approximately 65 mV. Thus, the metal centres are not interacting to any significant extent because of the combined effects of distance, and/or greater twisting of the chelating units out of the plane of the ligand core. This distance dependence is consistent with the assumption that the difference in oxidation potentials in **1bpy** and **2bpy** was due to metal–metal interactions and not to differences in the diastereoisomers. All the ruthenium complexes studied have oxidation potentials that are similar to but slightly harder to oxidise than the di-2-pyridylamine (**dpa**) ruthenium complex, $[Ru(bpy)(phen)(\mathbf{dpa})]^{2+}$ (+1.06 V) [6], where phen = 1,10-phenanthroline. Linking the ligands through different rings of the naphthalene core, or by a biphenyl spacer, has little effect on the redox potentials of the metal centres.

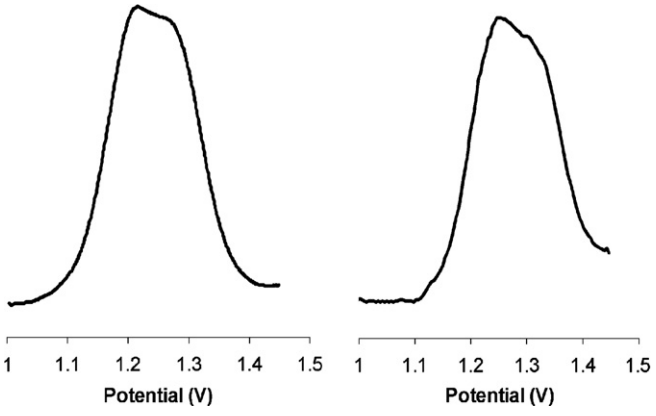


Fig. 4. The differential pulse voltammograms for complexes **1bpy** and **2bpy** (potential scale not referenced against SCE in diagrams).

The dinuclear $[Ru(bpy)_2]$ complexes all undergo ligand centred reductions at *ca.* −1.44 and −1.68 V. These are attributed to the reductions of the ancillary bpy ligands. The potentials of the dinuclear $[Ru(dmb)_2]$ complexes are shifted by *ca.* 100 mV related to those of the analogous bpy complexes, consistent with the electron donating effect of *ca*. 25 mV per methyl group [42] that was noted earlier. The di-2-pyridylamine-based ligands are very difficult to reduce, but in their $[Ru(bpy)_2]$ and $[Ru(dmb)_2]$ dinuclear complexes ligands **2**, **5** and **6** appear to undergo reductions at potentials between *ca.* −1.90 and −2.06 V.

4. Conclusion

In summary, $[Ru(bpy)_2]$ and $[Ru(dmb)_2]$ complexes of the multidentate ligands **1**–**6** have been prepared and characterised by NMR and absorption spectroscopy, electrochemistry and ES mass spectrometry or combustion analysis. Five of the ligands furnished dinuclear complexes, while only mononuclear $[Ru(bpy)_2]$ and $[Ru(dmb)_2]$ complexes of ligand **4** could be prepared. Ligands **3** and **4** were surprisingly resistant to forming dinuclear complexes; longer reaction times furnished the dinuclear complex **3bpy** but similar results could not be obtained for ligand **4**. Given the ability of ligand **3** to form both mono- and dinuclear complexes simply by variation of the reaction time, the possibility exists of using the mononuclear complex in a 'complexes as ligands' approach [43] to prepare multinuclear assemblies.

Electrochemical studies on two examples of the six multidentate ligands revealed that they are susceptible to oxidation of the amine nitrogen atoms unless the di-2-pyridylamine subunits were coordinated to a ruthenium centre. The ligands **1**–**6** are relatively electron-rich, leading to oxidation potentials for the resulting $[Ru(bpy)_2]$ or $[Ru(dmb)_2]$ complexes that are lower than the archetype complex, $[Ru(bpy)_3]^{2+}$. Furthermore, the complexes were harder to reduce than $[Ru(bpy)_3]^{2+}$, with reductions of the multidentate ligands occurring, in some cases, close to the potential limits of the solvent. The metal centres in dinuclear complexes of the ligands **1** and **2**, containing a benzene core, were shown to be weakly interacting by cyclic and differential pulse voltammetry. While the tertiary aryl amine is a potential conduit for metal–metal interactions, the di-2-pyridylamine subunits are not held in plane with the central arene because of steric factors, and thus these interactions are weak.

Acknowledgement

We thank the Royal Society of New Zealand for funding through the Marsden Fund and a James Cook Research Fellowship.

References

[1] F. Blau, Chem. Ber. 21 (1888) 1077.
[2] E.C. Constable, Adv. Inorg. Chem. 34 (1989) 1.
[3] C. Kaes, A. Katz, M.W. Hosseini, Chem. Rev. 100 (2000) 3553.
[4] P.J. Steel, Molecules 9 (2004) 440.
[5] P.J. Steel, Acc. Chem. Res. 38 (2005) 243.
[6] A. Juris, V. Balzani, F. Barigelletti, S. Campagna, P. Belser, A. von Zelewsky, Coord. Chem. Rev. 84 (1988) 85.
[7] V. Balzani, A. Juris, M. Venturi, S. Campagna, S. Serroni, Chem. Rev. 96 (1996) 759.
[8] C. Richardson, P.J. Steel, D.M. D'Alessandro, P.C. Junk, F.R. Keene, J. Chem. Soc., Dalton Trans. (2002) 2775.
[9] J.A. Zampese, F.R. Keene, P.J. Steel, Dalton Trans. (2004) 4124.
[10] J.W. Slater, D.M. D'Alessandro, F.R. Keene, P.J. Steel, Dalton Trans. (2006) 1954.
[11] F.R. Keene, Coord. Chem. Rev. 166 (1997) 121.
[12] F.R. Keene, Chem. Soc. Rev. 27 (1998) 185.
[13] D.M. D'Alessandro, F.R. Keene, Chem. Phys. 324 (2006) 8.
[14] D.M. D'Alessandro, F.R. Keene, Chem. Rev. 106 (2006) 2270.
[15] D.M. D'Alessandro, F.R. Keene, Chem. Soc. Rev. 35 (2006) 424.
[16] W.R. Browne, R. Hage, J.G. Vos, Coord. Chem. Rev. 250 (2006) 1653.
[17] W. Kaim, B. Sarkar, Coord. Chem. Rev. 251 (2007) 584.
[18] W. Kaim, G.K. Lahiri, Angew. Chem. Int. Ed. 46 (2007) 1778.
[19] E.C. Constable, P.J. Steel, Coord. Chem. Rev. 93 (1989) 205.
[20] E. Spodine, J. Manzur, M.T. Garland, J.P. Fackler Jr., R.J. Staples, B. Trzcinska-Bancroft, Inorg. Chim. Acta 203 (1993) 73.
[21] A.J. Canty, N.J. Minchin, Aust. J. Chem. 39 (1986) 1063.
[22] A.J. Canty, N. Chaichit, B.M. Gatehouse, E.E. George, G. Hayhurst, Inorg. Chem. 20 (1981) 2414.
[23] P.J. Steel, C.J. Sumby, Chem. Commun. (2002) 322.
[24] P.J. Steel, C.J. Sumby, Inorg. Chem. Commun. 5 (2002) 323.
[25] P.J. Steel, C.J. Sumby, Dalton Trans. (2003) 4505.
[26] C.J. Sumby, P.J. Steel, Inorg. Chem. Commun. 6 (2003) 127.
[27] D.M. D'Alessandro, F.R. Keene, P.J. Steel, C.J. Sumby, Aust. J. Chem. 56 (2003) 657.
[28] For example, see H. Zhu, M. Strobele, Z. Yu, Z. Wang, H.J. Meyer, X. You, Inorg. Chem. Commun. 4 (2001) 577.
[29] M.J. Plater, M.R.S.J. Foreman, J.M.S. Skakle, R.A. Howie, Inorg. Chim. Acta 332 (2002) 135.
[30] S. Youngme, N. Chaichit, C. Pakawatchai, S. Booncoon, Polyhedron 21 (2002) 1279.
[31] S. Youngme, N. Chaichit, N. Koonsaeng, Inorg. Chim. Acta 335 (2002) 36.
[32] S. Youngme, N. Chaichit, Polyhedron 21 (2002) 247.
[33] C.J. Sumby, P.J. Steel, Inorg. Chim. Acta 360 (2007) 2100.
[34] C.J. Sumby, P.J. Steel, Organometallics 22 (2003) 2358.
[35] B. Antonioli, D.J. Bray, J.K. Clegg, K. Gloe, K. Gloe, O. Kataeva, L.F. Lindoy, J.C. McMurtrie, P.J. Steel, C.J. Sumby, M. Wenzel, Dalton Trans. (2006) 4783.
[36] W.-Y. Yang, L. Chen, S. Wang, Inorg. Chem. 40 (2001) 507.
[37] J. Pang, Y. Tao, S. Freiberg, X.-P. Yang, M. D'Iorio, S. Wang, J. Mater. Chem. 12 (2002) 206.
[38] C. Seward, W.-l. Jia, R.-Y. Wang, S. Wang, Inorg. Chem. 43 (2004) 978.
[39] C. Seward, S. Wang, Comments Inorg. Chem. 26 (2005) 103.
[40] B.P. Sullivan, D.J. Salmon, T.J. Meyer, Inorg. Chem. 17 (1978) 3334.
[41] P.A. Mabrouk, M.S. Wrighton, Inorg. Chem. 25 (1986) 526.
[42] D.L. Jameson, J.K. Blaho, K.T. Kruger, K.A. Goldsby, Inorg. Chem. 28 (1989) 4312.
[43] G. Denti, S. Campagna, S. Serroni, M. Ciano, V. Balzani, J. Am. Chem. Soc. 114 (1992) 2944.

are described and discussed. Further, the luminescent properties of complexes **4**, **5** and **6** are examined and discussed.

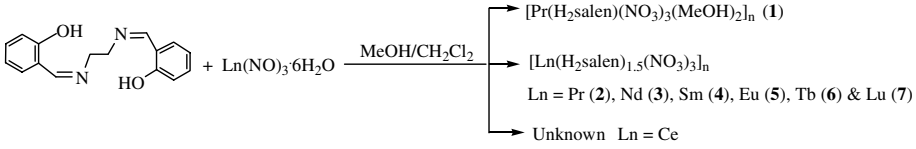
2. Results and discussion

2.1. Synthesis

Reactions of the Salen ligand with $Ln(NO_3)_3 \cdot 6H_2O$ in a molar ratio of 1:1 or 1:2 were carried out in $MeOH/CH_2Cl_2$ at ambient temperature. Methylene dichloride was employed to increase the solubility of the Salen ligand. The immediate color change of the solution upon addition of $Ln(NO_3)_3 \cdot 6H_2O$ indicates instant occurrence of the coordination reaction. Single crystals suitable for X-ray analysis were obtained by slow diffusion of diethylether into a methanol solution of the powder sample. Complexes **1**–**7** are stable in air and moderately soluble in polar organic solvents such as methanol, ethanol and DMF. X-ray crystal analyses reveal that two types of coordination complexes, $[Pr(H_2salen)(NO_3)_3(CH_3OH)_2]_n$ (**1**) and $[Ln(H_2salen)_{1.5}(NO_3)_3]_n$ (Ln = Pr (**2**), Nd (**3**), Sm (**4**), Eu (**5**), Tb (**6**) and Lu (**7**)) (Scheme 1) are isolated. Interestingly, both structures can be obtained for the Salen praseodymium(III) complex, while the other Salen lanthanide (Ln = Nd, Sm, Eu, Tb and Lu) complexes favor the composition $[Ln(H_2salen)_{1.5}(NO_3)_3]_n$. Also, initial crystal structural analysis reveals that reaction of the Salen ligand with $Ce(NO_3)_3 \cdot 6H_2O$ yields a complex which differs from complexes **1**–**7**. However, the crystal structure of the Salen cerium complex has not been solved due to the poor quality of the single crystal.

2.2. Spectroscopic analysis

The infrared spectra of complexes **1**–**7** are similar. Taking **3** as an example, the broad but weak O–H stretching vibration of the free Salen ligand at ca. 2847 cm^{-1} is replaced by a band at ca. 3398 cm^{-1} in the complexes due to the N–H vibration in $C{=}N^{+}$–H. This band indicates that the hydrogen atoms are still involved in intramolecular H-bonding with the phenolic oxygen. The C=N stretching vibration in the complexes shifts to higher wavenumber (by 20–30 cm^{-1} to about 1655 cm^{-1}). This is opposite to what was observed for the Salen nickel complex in which the strong ν(C=N) band shifts considerably towards lower wavenumber in comparison to that of the free H_2salen, indicating the coordination of an azomethine nitrogen to the transition metal ion [13]. Four bands near 1480(ν_4), 1278(ν_1), 1152(ν_2) and 816(ν_6) cm^{-1} in the infrared spectra of the complexes can be assigned to the vibrations of the coordinated nitrate group. The difference between the ν_4 and the ν_1 peak positions is ca. 200 cm^{-1}, which is typical for a bidentate nitrate group. This is identical to the lanthanide Schiff base complexes $[Ln(LH)_3(NO_3)_3]$ (LH = 4-alkoxy-*N*-alkyl-2-hydroxybenzaldimine) [14]. The UV spectrum of the free ligand consists of three main absorption maxima that are assigned to the π–π* transition of the Ar–OH chromophores and of the imine group. Accordingly, the UV spectra of the complexes **1**–**7** in methanol display a similar red shift as a result of changes in the energy levels of the ligand orbitals upon coordination. All the complexes **1**–**7** show no clear melting point before decomposing at ca 350 °C. Complex **1** loses approximately 10.43% in weight when heated to 219.8 °C. It suggests the



Scheme 1. Synthesis of the complexes.

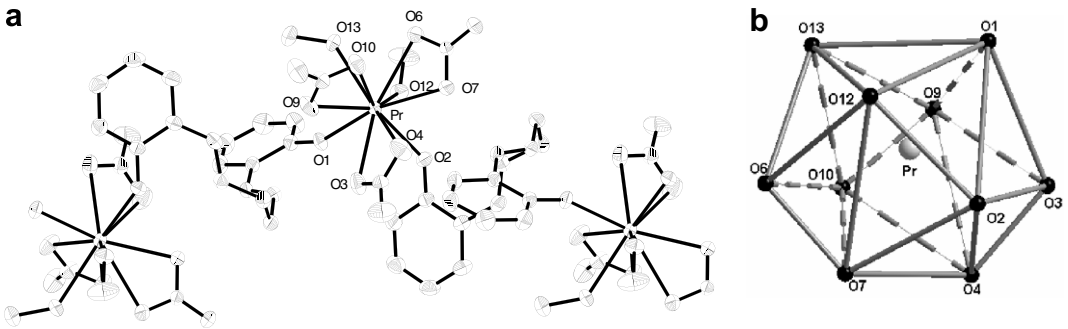


Fig. 1. (a) Ortep plot of the crystal structure for complex **1** (30% thermal ellipsoids and hydrogen atoms removed for clarity). Selected bond lengths (Å) and bond angle (°): Pr–O(1) 2.360(2), Pr–O(2) 2.394(2), Pr–O(12) 2.508(2), Pr–O(7) 2.547(2), Pr–O(13) 2.576(2), Pr–O(9) 2.581(2), Pr–O(3) 2.662(3), Pr–O(6) 2.678(2), Pr–O(10) 2.699(3), Pr–O(4) 2.703(3); O(1)–Pr–O(2) 71.2(1); (b) perspective view of coordination polyhedron for the Pr(III) ion in **1**.

presence of two moles of crystalline methanol in the empirical molar formula in the crystals.

2.3. Crystal structural analysis

Complex **1** crystallizes in the monoclinic $P2_1/n$ space group. The unit cell contains one $[Pr(H_2salen)(NO_3)_3]$ with two moles of crystalline methanol. An infinite 1D chain structure results from the bridging Salen ligand between each two Pr(III) ions through the Pr–O (hydroxyl oxygen atom) bonds (Fig. 1a). Each Pr(III) ion, showing a 10-coordinated distorted hexadecahedron (Fig. 1b), is ligated by three bidentate nitrate counterions, two methanol oxygen atoms and two oxygen atoms from different ligands. Each

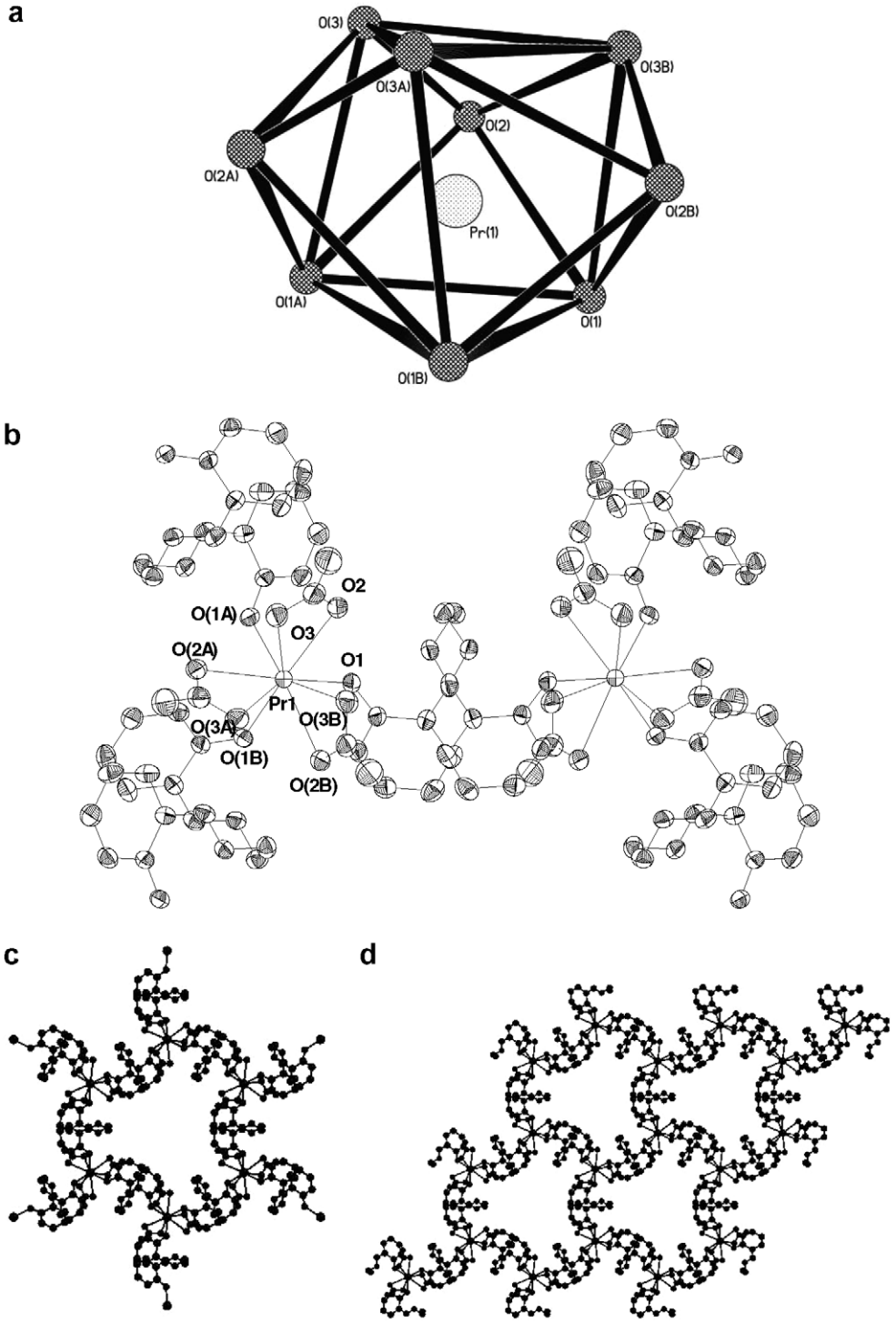


Fig. 2. (a) Perspective view of the coordination polyhedron for the Pr(III) ion in **2**. (b) Ortep plot of the crystal structure for complex **2** (30% thermal ellipsoids and hydrogen atoms removed for clarity). (c) View of a Salen bridged hexametal ring along the *c* axis in **2**. (d) View of the 2D polymeric structure along the *c* axis in **2**.

Table 1
Selected bond lengths (Å) and bond angles (°) for complexes **2**–**5** and **7**

Bond lengths/angles	Pr (**2**)	Nd (**3**)	Sm (**4**)	Eu (**5**)	Lu (**7**)
Ln(1)–O(1)/O(1A)/O(1B)	2.360(3)	2.341(3)	2.331(4)	2.309(3)	2.212(3)
Ln (1)–O(3)/O(3A)/O(3B)	2.582(4)	2.568(3)	2.543(4)	2.529(3)	2.501(3)
Ln (1)–O(2)/O(2A)/O(2B)	2.604(4)	2.593(3)	2.567(4)	2.553(3)	2.428(3)
O(1B)–Ln(1)–O(3)/O(1A)–Ln(1)–O(3B)/ O(1)–Ln(1)–O(3A)	145.4(1)	145.3(1)	145.1(1)	145.3(1)	144.2(1)
O(1)–Ln(1)–O(3)/O(1A)–Ln(1)–O(3A)/ O(1B)–Ln(1)–O(3B)	120.2(1)	120.9(1)	120.2(1)	121.6(1)	120.3(1)
O(1A)–Ln(1)–O(1B)/O(1A)–Ln(1)–O(1)/ O(1B)–Ln(1)–O(1)	93.9(1)	93.3(1)	92.7(1)	92.5(1)	91.3(1)

Salen group utilizes only one hydroxyl oxygen atom for coordination, whereas the nitrogen atoms remain uncoordinated. As a result, each H_2salen acts a bridge between two Pr(III) atoms. This is identical to the known Salen lanthanide complex $[La(H_2salen)(NO_3)_3(CH_3OH)_2]_n$ [10]. The shorter Pr–O bonds involving the deprotonated phenol oxygen atoms are in the range 2.360(1)–2.394(1) Å, while the Pr–O bonds involving the η^2 chelating nitrate ions vary from 2.547(2) to 2.703(3) Å. The O(1)–Pr–O(2) angle is 71.2(1)°. The hydrogen atoms located on the two nitrogen atoms are involved in intramolecular hydrogen bonding with the deprotonated phenol oxygen atoms, thus indicating that a proton migration occurs in the complexation reactions.

X-ray crystallographic analyses reveal that complexes **2**–**7** are isomorphic. Taking **2** as an example, complex **2** crystallizes in the trigonal $P\bar{3}C1$ space group. The unit cell contains $[Pr(H_2salen)_{1.5}(NO_3)_3]$ without a solvent molecule. Each Pr(III) ion, showing a nine-coordinated tricapped trigonal prismatic geometry (Fig. 2a), is ligated by three bidentate nitrate counterions and three independent Salen ligands that utilize only one hydroxyl oxygen atom. The distorted trigonal prism shown is composed of O(3), O(3A), O(3B), O(1), O(1A) and O(1B) atoms. The O(2), O(2A) and O(2B) atoms are at the vertices of each square pyramid. Each ligand acts as a bidentate linker bridging between two Pr(III) ions through the two hydroxy oxygen atoms (Fig. 2b). In addition, six Pr(III) ions are formed in a circular fashion through the bondings of lanthanide and deprotonated Salen linkers (Fig. 2c). The hexanuclear metal ring exhibiting C_3 symmetry acts as the building unit. Furthermore, the hexanuclear lanthanide ring is extended along the *a* and *b* axes through the bridging of Salen ligand to an infinite 2D network. This results in a uniform and porous planar sheet containing arrays of metals parallel to the *ab* plane (Fig. 2d). The Pr–O bond distances, divided into three groups, are 2.360(3), 2.582(4) and 2.604(4) Å. The O–Pr–O angles are in the range 49.3(1)–161.1(1)°. It is worth noting that the bond angles of O(salen)–Pr–O(salen), namely, O(1A)–Pr(1)–O(1B), O(1A)–Pr(1)–O(1) and O(1B)–Pr(1)–O(1) are identical, being 93.9(1)°, which is almost a right angle (90°). The bond angles O(1)–Ln(1)–O(3), O(1A)–Ln(1)–O(3A) and O(1B)–Ln(1)–O(3B) are 120.2(1)° and the angles of O(1B)–Pr(1)–O(3), O(1A)–Pr(1)–O(3B) and O(1)–Pr(1)–O(3A) are 145.4(1)°. Relevant structural parameters are gathered in Table 1.

2.4. The luminescent property of complexes *4*, *5* and *6*

Excited by the absorption band at 350 nm, the Salen ligand exhibits broad emission bands at $\lambda_{max} = 503$ nm in the solid state (the excitation and emission slit widths are 5.0 nm). Emission spectra of complexes **4** and **5** in the solid state (the excitation and emission slit widths are 5.0 nm), recorded at room temperature (Fig. 3), show characteristic metal-centered luminescence when excited at 370 and 350 nm, respectively. The fluorescence of the Salen ligand is completely quenched. It suggests that the electronic energy of the ligand is transferred to the metal ion. Energy transfer between the Salen ligand and the lanthanide(III) ion appears to follow the well-known intramolecular energy transfer mechanism exhibited by lanthanide Schiff base complexes [4b]. Complexes **4** and **5** emit red fluorescence. The emission spectrum of complex **4** exhibits a narrow band at 645 nm. Four typical emission bands of Sm(III) ion are observed, 565 nm ($^4G_{5/2} \rightarrow {}^6H_{5/2}$), 601 nm ($^4G_{5/2} \rightarrow {}^6H_{7/2}$), 645 nm ($^4G_{5/2} \rightarrow {}^6H_{9/2}$) and 712 nm ($^4G_{5/2} \rightarrow {}^6H_{11/2}$). The emission spectrum of complex **5** exhibits a single narrow band at 615 nm. Five typical emission bands of Eu(III) ion are observed, 580 nm ($^5D_0 \rightarrow {}^7F_0$), 592 nm ($^5D_0 \rightarrow {}^7F_1$), 615 nm ($^5D_0 \rightarrow {}^7F_2$), 650 nm ($^5D_0 \rightarrow {}^7F_3$) and 679 nm ($^5D_0 \rightarrow {}^7F_4$). However, for the terbium complex, the characteristic luminescence

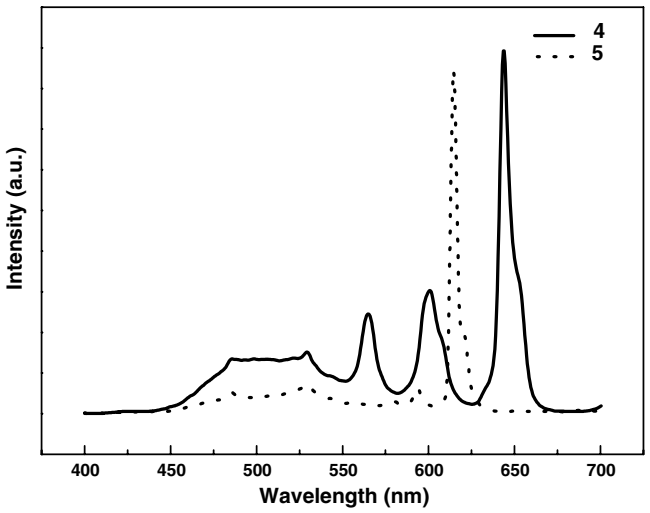


Fig. 3. Emission spectra of complexes **4** and **5**.

Table 2
Crystallographic data for complexes **1**–**5** and **7**

Crystal data	**1**	**2**	**3**	**4**	**5**	**7**
Empirical formula	$C_{18}H_{20}N_5O_{13}Pr$	$C_{24}H_{24}N_6O_{12}Pr$	$C_{24}H_{24}N_6NdO_{12}$	$C_{24}H_{24}N_6O_{12}Sm$	$C_{24}H_{24}EuN_6O_{12}$	$C_{24}H_{24}LuN_6O_{12}$
Formula weight	655.30	729.40	732.72	738.84	740.45	763.46
Temperature (K)	293(2)	291(2)	293(2)	293(2)	293(2)	291(2)
Wavelength (Å)	0.71073	0.71073	0.71073	0.71073	0.71073	0.71073
Crystal system	monoclinic	trigonal	trigonal	trigonal	trigonal	trigonal
Space group	$P2_1/n$	$P\bar{3}C1$	$P\bar{3}C1$	$P\bar{3}C1$	$P\bar{3}C1$	$P\bar{3}C1$
a (Å)	11.354(2)	16.084(2)	16.096(2)	16.029(2)	15.9869(6)	15.778(2)
b (Å)	17.014(3)	16.084(2)	16.096(2)	16.029(2)	15.9869(6)	15.778(2)
c (Å)	13.340(2)	16.348(3)	16.674(3)	16.522(5)	16.527(1)	16.855(3)
α (°)	90	90	90	90	90	90
β (°)	96.264(2)	90	90	90	90	90
γ (°)	90	120	120	120	120	120
Volume (Å^3)	2561.5(8)	3662.5(9)	3741.3(11)	3676.1(14)	3658.1(3)	3633.8(10)
Z	4	4	4	4	4	4
Calculated density (Mg/m^3)	1.699	1.323	1.301	1.335	1.344	1.396
Absorption coefficient (mm^{-1})	1.974	1.387	1.443	1.654	1.771	2.774
$F(000)$	1304	1460	1464	1472	1508	1476
Crystal size (mm)	$0.46 \times 0.26 \times 0.21$	$0.30 \times 0.25 \times 0.20$	$0.47 \times 0.25 \times 0.12$	$0.37 \times 0.21 \times 0.04$	$0.35 \times 0.24 \times 0.11$	$0.30 \times 0.19 \times 0.17$
θ-Range	1.95–25.95	3.55–27.48	2.44–26.05	1.47–26.05	1.47–26.05	6.43–54.85
Limiting indices	$-13 \leqslant h \leqslant 13$, $-15 \leqslant k \leqslant 20$, $-16 \leqslant l \leqslant 16$	$-20 \leqslant h \leqslant 20$, $-20 \leqslant k \leqslant 20$, $-21 \leqslant l \leqslant 19$	$-18 \leqslant h \leqslant 19$, $-19 \leqslant k \leqslant 19$, $-20 \leqslant l \leqslant 19$	$-15 \leqslant h \leqslant 19$, $-18 \leqslant k \leqslant 19$, $-18 \leqslant l \leqslant 20$	$-19 \leqslant h \leqslant 17$, $-15 \leqslant k \leqslant 19$, $-17 \leqslant l \leqslant 20$	$-20 \leqslant h \leqslant 20$ $-19 \leqslant k \leqslant 20$ $-21 \leqslant l \leqslant 21$
Reflections collected	14 561	32 043	20 120	19 528	19 587	31 372
Completeness to theta = 26.05°	99.5%	99.5%	99.8%	99.9%	100%	99.7%
Max. and min. transmission	0.6820 and 0.4631	0.785 and 0.658	0.8482 and 0.5479	0.784 and 0.523	0.689 and 0.451	0.4880 and 0.6484
Data/restraints/ parameters	4970/0/336	2798/7/134	2476/0/134	2435/0/134	2419/0/134	2774/0/134
Goodness-of-fit on F^2	1.065	1.040	1.109	1.120	1.131	1.101
Final R indices $[I > 2\sigma(I)]$	$R_1 = 0.0241$ $wR_2 = 0.0659$	$R_1 = 0.0461$ $wR_2 = 0.1310$	$R_1 = 0.0362$ $wR_2 = 0.1306$	$R_1 = 0.0468$ $wR_2 = 0.1241$	$R_1 = 0.0331$ $wR_2 = 0.1082$	$R_1 = 0.0471$ $wR_2 = 0.0290$
R indices (all data)	$R_1 = 0.0260$ $wR_2 = 0.0676$	$R_1 = 0.0665$ $wR_2 = 0.1428$	$R_1 = 0.0430$ $wR_2 = 0.1420$	$R_1 = 0.0769$ $wR_2 = 0.1391$	$R_1 = 0.0425$ $wR_2 = 0.1173$	$R_1 = 0.1047$ $wR_2 = 0.0969$

emission of the terbium ion is not observed either in solution or the solid state. It is probably attributed to the fact that the luminescence of lanthanide(III) chelates is correlated to the efficiency of the intramolecular energy transfer between the triple levels of the ligand and the emitting level of the ions, which depends on the energy gap between the two levels. The energy gap between the ligand triple level and the emitting level of the europium and samarium ion may be in favor of the energy transfer process. It is identical to a picrate europium complex [15]. However, this is opposite to the reported Schiff base lanthanide complexes in which the characteristic luminescent emission of europium ions was not found while that for the terbium ion was observed [12b].

3. Conclusion

In summary, the synthesis of complexes **1**–**7** demonstrates clearly that the size of lanthanide ion dominates the structures of these Salen lanthanide complexes. As a result, the Salen lanthanum(III) complex prefers a 1D chain structure, while other Salen lanthanide(III) (Ln = Nd–Lu) complexes favor to yield a unique 2D network structure. The praseodymium(III) complex can give rise to both 1D and 2D topology structures. The crystal structures of these complexes are not dependent on the stoichiometry of the reaction. Also, initial structure analysis of the cerium(III) complex indicates that the structure of Salen cerium(III) may be different from complexes **1**–**7**.

Further, the luminescence of the Salen lanthanide complexes suggests that the matching of the orbital energy level of the lanthanide ions and the Salen ligand determines the luminescence of the Salen lanthanide complexes. These results have provided valuable information for designing new lanthanide complexes with different structural chemistry and luminescent properties, as well as better understanding of the known Schiff base lanthanide complexes. Attempts to solve the structure of the Salen cerium complex and to explore the possibility of substituting the nitrate groups in mononuclear complexes with $[Fe(CN)_6]^{3-}$

and other anionic groups as well as the physical properties of these complexes are being carried out in our laboratory.

4. Experimental

4.1. General

All operations were performed in an open atmosphere. H_2salen was prepared from salicylaldehyde and 1,2-ethylenediamine by a routine method. $Ln(NO_3)\cdot 6H_2O$ was prepared according to the literature method. All other chemicals were used as purchased. Elemental (C, H and N) analyses were performed on a Perkin–Elmer 2400 analyzer. IR spectra were determined on a Perkin–Elmer 60000 spectrophotometer. UV spectra were recorded on a Shimadzu UV2240 spectrophotometer. Fluorescent spectra were taken on a LS-55 fluorescence photometer. Thermal analyses were conducted on a DTA-1700 with a heating rate of 10 °C/min in the temperature range from ambient temperature to 700 °C.

4.2. Preparation of the complexes

4.2.1. Preparation of $[Pr(H_2salen)(NO_3)_3(CH_3OH)_2]_n$ (1) and $[Pr(H_2salen)_{1.5}(NO_3)_3]$ (2)

To a solution of H_2salen (0.268 g, 1 mmol) in CH_2Cl_2 (5 mL) was slowly added $Pr(NO_3)_3\cdot 6H_2O$ (0.435 g, 1 mmol) in MeOH (6 mL) at room temperature. A yellow precipitate formed immediately. After stirring for 2 h, 0.34 g of solid was collected by filtration and washed with CH_2Cl_2. Two different crystals suitable for X-ray determination were obtained by slow diffusion of diethylether into a methanol solution of the powder sample over one week. **1**: Elemental *Anal.* Calc. for $C_{18}H_{20}N_5O_{13}Pr$ (655.30): C, 32.99; H, 3.08; N, 10.69. Found: C, 32.95; H, 3.07; N, 10.65%. IR (KBr pellet, cm^{-1}): 3580 w, 1655 vs, 1603 vs, 1523 s, 1485 s, 1432 s, 1367 s, 1324 s, 1315 s, 1288 s, 1223 s, 1150 s, 1028 s, 1002 m, 905 m, 852 m, 789 m, 762 s, 735 m, 566 s. UV–Vis spectrum in MeOH [λ_{max} (nm)]: 240, 255. m.p.: >260 °C. TG-DTA: 10.43% loss in weight (219.8 °C). **2:** Elemental *Anal.* Calc. for $C_{24}H_{24}N_6O_{12}Pr$ (729.40): C, 39.52; H, 3.32; N, 11.52. Found: C, 39.55; H, 3.37; N, 11.49%. IR (KBr pellet, cm^{-1}): 3425 w, 2972 s, 1655 vs, 1610 vs, 1539 s, 1480 s, 1344 s, 1286 s, 1218 s, 1201 s, 1198 s, 1152 s, 1032 s, 1008 m, 900 m, 817 m, 765 s, 738 s, 732 s, 576 s, 406 s. UV–Vis spectrum in MeOH [λ_{max} (nm)]: 240, 255. m.p.: >260 °C.

4.2.2. Preparation of $[Nd(H_2salen)_{1.5}(NO_3)_3]$ (3)

A mixture of H_2salen (0.268 g, 1 mmol) and $Nd(NO_3)_3\cdot 6H_2O$ (0.438 g, 1 mmol) in CH_2Cl_2/CH_3OH (5 mL/6 mL) was stirred at room temperature for 2 h. Yield: 70%. Elemental *Anal.* Calc. for $C_{24}H_{24}N_6NdO_{12}$ (732.72): C, 39.34; H, 3.30; N, 11.47. Found: C, 39.35; H, 3.27; N, 11.49%. IR (KBr pellet, cm^{-1}): 3398 w, 3058 w, 1655 vs, 1609 m, 1537 s, 1480 s, 1384 w, 1343 w, 1278 s, 1199 s, 1152 s, 1033 s, 1008 m, 948 w, 877 s, 816 m, 766 s, 735 m, 575 m, 391m. UV–Vis spectrum in MeOH [λ_{max} (nm)]: 240, 255. m.p.: >260 °C.

4.2.3. Preparation of $[Sm(H_2salen)_{1.5}(NO_3)_3]$ (4)

A mixture of H_2salen (0.268 g, 1 mmol) and $Sm(NO_3)_3\cdot 6H_2O$ (0.444 g, 1 mmol) in CH_2Cl_2/CH_3OH (5 mL/6 mL) was stirred at room temperature for 2 h. Yield: 72%. Elemental *Anal.* Calc. for $C_{24}H_{24}N_6O_{12}Sm$ (738.84): C, 39.01; H, 3.27; N, 11.37. Found: C, 39.20; H, 3.24; N, 11.40%. IR (KBr pellet, cm^{-1}): 3387 w, 3059 w, 1655 vs, 1610 m, 1538 s, 1481 s, 1384 w, 1345 w, 1279 s, 1200 s, 1152 s, 1035 s, 1008 m, 946 w, 874 s, 815 m, 763 s, 738 m, 575 m, 391 m. UV–Vis spectrum in MeOH [λ_{max} (nm)]: 240, 255. m.p.: >260 °C.

4.2.4. Preparation of $[Eu(H_2salen)_{1.5}(NO_3)_3]$ (5)

A mixture of H_2salen (0.268 g, 1 mmol) and $Eu(NO_3)_3\cdot 6H_2O$ (0.445 g, 1 mmol) in CH_2Cl_2/CH_3OH (5 mL/6 mL) was stirred at room temperature for 2 h. Yield: 69%. Elemental *Anal.* Calc. for $C_{24}H_{24}EuN_6O_{12}$ (740.44): C, 38.93; H, 3.27; N, 11.35. Found: C, 38.82; H, 3.24; N, 11.39%. IR (KBr pellet, cm^{-1}): 3400 w, 3061 w, 1655 vs, 1610 m, 1538 s, 1482 s, 1384 w, 1345 w, 1280 s, 1201 s, 1153 s, 1036 s, 1009 m, 947 w, 875 m, 815 m, 764 s, 739 m, 575 m, 393 m. UV–Vis spectrum in MeOH [λ_{max} (nm)]: 240, 255. m.p.: >260 °C.

4.2.5. Preparation of $[Tb(H_2salen)_{1.5}(NO_3)_3]$ (6)

A mixture of H_2salen (0.268 g, 1 mmol) and $Tb(NO_3)_3\cdot 6H_2O$ (0.452 g, 1 mmol) in CH_2Cl_2/CH_3OH (5 mL/6 mL) was stirred at room temperature for 2 h. Yield: 69%. Elemental *Anal.* Calc. for $C_{24}H_{24}N_6O_{12}Tb$ (747.41): C, 38.57; H, 3.24; N, 11.24. Found: C, 38.65; H, 3.27; N, 11.31%. IR (KBr pellet, cm^{-1}): 3413 w, 3070 w, 1647 vs, 1620 m, 1530 s, 1476 s, 1341 w, 1287 vs, 1206 s, 1151 vs, 1034 s, 1007 m, 945 w, 873 s, 809 m, 756 s, 737 m, 575 m, 391 m. UV–Vis spectrum in MeOH [λ_{max} (nm)]: 240, 255. m.p.: >260 °C.

4.2.6. Preparation of $[Lu(H_2salen)_{1.5}(NO_3)_3]$ (7)

A mixture of H_2salen (0.268 g, 1 mmol) and $Lu(NO_3)_3\cdot 6H_2O$ (0.464 g, 1 mmol) in CH_2Cl_2/CH_3OH (5 mL/6 mL) was stirred at room temperature for 2 h. Yield: 70%. Elemental *Anal.* Calc. for $C_{24}H_{24}LuN_6O_{12}$ (763.46): C, 37.76; H, 3.17; N, 11.01. Found: C, 37.65; H, 3.17; N, 11.09%. IR (KBr pellet, cm^{-1}): 3398 w, 3058 w, 1655 vs, 1609 m, 1537 s, 1480 s, 1384 w, 1343 w, 1278 s, 1199 s, 1152 s, 1033 s, 1008 m, 948 w, 877 s, 816 m, 766 s, 735 m, 575 m, 391 m. UV–Vis spectrum in MeOH [λ_{max} (nm)]: 240, 255. m.p.: >260 °C.

4.3. Crystallographic data collection and structure determination

X-ray crystallographic analysis: Diffraction intensity data for single crystals of the complexes were collected on a Rigaku R-AXIS RAPID imaging-plate X-ray diffractometer

at 293 K. The structures were solved by the direct method and refined by full-matrix least squares on F^2 using the SHELXTL-97 software package [16,17]. All non-hydrogen atoms were refined with anisotropic displacement parameters. Crystal data collection and refinement parameters for complexes **1**–**7** are given in Table 2.

Acknowledgements

This work is financially supported by the National Natural Science Foundation of China (Nos. 20672032 and 20572018), Heilongjiang Province (Nos. 1055HZ001, ZJG0504 and JC200605) and Heilongjiang University.

Appendix A. Supplementary material

CCDC 627129, 629928, 604348, 604349, 604351 and 627125 contain the supplementary crystallographic data for **1**, **2**, **3**, **4**, **5** and **7**. These data can be obtained free of charge via http://www.ccdc.cam.ac.uk/conts/retrieving.html, or from the Cambridge Crystallographic Data Centre, 12 Union Road, Cambridge CB2 1EZ, UK; fax: (+44) 1223-336-033; or e-mail: deposit@ccdc.cam.ac.uk.

References

[1] (a) E.M. McGarrigle, D.G. Gilheany, Chem. Rev. 105 (2005) 1563;
(b) D.A. Atwood, M.J. Harvey, Chem. Rev. 101 (2001) 37;
(c) N.S. Venkataramanan, G. Kuppuraj, S. Rajagopal, Coord. Chem. Rev. 249 (2005) 1249;
(d) A.L. Singer, D.A. Atwood, Inorg. Chim. Acta 277 (1998) 157;
(e) S. Bunce, R.J. Cross, L.J. Farrugia, S. Kunchandy, L.L. Meason, K.W. Muir, M. O'Donnell, R.D. Peacock, D. Stirling, S.J. Teat, Polyhedron 17 (1998) 4179;
(f) A.A. Khandar, K. Nejati, Polyhedron 19 (2000) 607;
(g) K. Oyaizu, E. Tsuchida, Inorg. Chim. Acta 355 (2003) 414.

[2] N.K. Dutt, K.J. Nag, Inorg. Nucl. Chem. 30 (1968) 2493.
[3] S. Afshar, J.I. Bullock, Inorg. Chim. Acta 38 (1980) 145.
[4] (a) H. Chen, R.D. Archer, Inorg. Chem. 33 (1994) 5195;
(b) R.D. Archer, H. Chen, L.C. Thompson, Inorg. Chem. 37 (1998) 2089.
[5] J.I. Bullock, H.A. Tajmir-Riahi, J. Chem. Soc., Dalton Trans. (1978) 36.
[6] A. Terzis, D. Mentzafos, H.A. Tajmir-Tiahi, Inorg. Chim. Acta 84 (1984) 187.
[7] A. Takeuchi, S. Yamada, Inorg. Chim. Acta 155 (1989) 149.
[8] W.J. Evans, C.H. Fujimoto, J.W. Ziller, Chem. Commun. (1999) 311.
[9] (a) Q.C. Liu, M.X. Ding, J. Organomet. Chem. 553 (1998) 179;
(b) Q.C. Liu, M.X. Ding, Y.H. Lin, Y. Xing, Polyhedron 17 (1998) 555.
[10] W.H. Xie, M.J. Heeg, P.G. Wang, Inorg. Chem. 38 (1999) 2541.
[11] M.T. Kaczmarek, I. Pospieszna-Markiewicz, M. Kubicki, W. Radecka-Paryzek, Inorg. Chem. Commun. 7 (2004) 1247.
[12] (a) X.P. Yang, R.A. Jones, J. Am. Chem. Soc. 127 (2005) 7686;
(b) W. Dou, J.N. Yao, W.S. Liu, Y.W. Wang, J.R. Zheng, D.Q. Wang, Inorg. Chem. Commun. 10 (2007) 105;
(c) L. Salmon, P. Thuéry, M. Ephritikhine, Polyhedron 26 (2007) 631;
(d) L. Salmon, P. Thuéry, M. Ephritikhine, Polyhedron 26 (2007) 645;
(e) Y. Luo, Y.H. Han, J. Lin, J. Lumin 122–123 (2007) 83.
[13] B.S. Garg, D.N. Kumar, Spectrochim. Acta Part A 59 (2003) 229.
[14] K. Binnemans, Y.G. Galyametdinov, R.V. Deun, D.W. Bruce, S.R. Collinson, A.P. Polishchuk, I. Bikchantaev, W. Haase, A.V. Prosvirin, L. Tinchurina, I. Litvinov, A. Gubajdullin, A. Rakhmatullin, K. Uytterhoeven, L.V. Meervelt, J. Am. Chem. Soc. 122 (2000) 4335.
[15] (a) K.Z. Tang, J. Zhang, Y. Tang, W.S. Liu, M.Y. Tan, Y.X. Sun, Inorg. Chim. Acta 359 (2006) 1207;
(b) Y. Tang, K.Z. Tang, J. Zhang, C.Y. Su, W.S. Liu, M.Y. Tan, Inorg. Chem. Commun. 8 (2005) 1018;
(c) Y.L. Guo, W. Dou, Y.W. Wang, W.S. Liu, D.Q. Wang, Polyhedron 26 (2007) 1699.
[16] G.M. Sheldrick, SHELXS 97, Program for the Solution of Crystal Structures, University of Göttingen, Germany, 1997.
[17] G.M. Sheldrick, SHELXL 97, Program for the Refinement of Crystal Structures, University of Göttingen, Germany, 1997.

As a consequence we have sought to synthesize and identify ruthenium(III)-sulfoxide (bipyridine) complexes. Thus, we report here the synthesis and reactivity of *mer*-[$RuCl_3$(DMSO)(bpy)] and *mer*-[$RuCl_3$(TMSO)(bpy)].

2. Experimental

All reagents used were analytical grade. The reagent grade solvents were dried over 4 Å molecular sieves before use. The IR spectra were measured on a JASCO 480 plus spectrophotometer with samples in compressed KBr discs. UV–Vis spectra were obtained on a JASCO V-550 spectrophotometer. Elemental analysis was performed by Atlantic Microlab, Norcross, Georgia. GC–MS (70 eV) analyses were obtained using a packed SPB-5 (30 m) capillary column. Cyclic voltammetry was carried out with a 3-electrode system comprised of a Pt counter electrode, a Pt disk working electrode, and a saturated calomel electrode (SCE) connected to the main cell compartment by a KCl salt bridge. Potential control was done with a BAS CV-50 W voltammetric analyzer used in the cyclic voltammetry mode. The supporting electrolyte was 0.100 M tetrabutylammonium hexafluorophosphate. Argon was bubbled through the solution for at least 30 min prior to and during cyclic voltammetry. Instrumental iR compensation was used when needed.

2.1. X-ray structure determination

The diffraction data were collected at low-temperature with a Nonius Kappa CCD diffractometer equipped with Mo Kα radiation ($\lambda = 0.71073$ Å), a graphite monochromator, and an Oxford Cryostream low-temperature device. For the solvate **6**. 2DMSO, one solvent molecule is ordered, while the other is disordered into two orientations which share C atom positions. Populations of the two orientations refined to 0.587(10)/0.413(10). All non-hydrogen atoms of **3**, **6**, **7** were treated anisotropically, except in the disordered solvent region of **6**. H-atoms were visible in difference mass, and were placed in calculated positions. Crystal data and details of data collection and refinement are given in Tables 1 and 2.

2.2. Computational studies

DFT computations were carried out using GAUSSIAN 03 [18]. Two possible structures of **9** were optimized and their energy determined. Infrared vibrational frequencies for the structure were also calculated. Pictures of HOMO and LUMO were obtained. The DFT method used was B3PW91 with a LANL2DZ basis set. A scaling factor of 0.9573 [19] was used in calculating the vibrational frequencies. A summary of the Cartesian coordinates, calculated

Table 2
Selected bond lengths (Å) and bond angles (°) for compounds **3**, **6** and **7**

Bond lengths	**3**	**6**	**7**
Ru–N1	2.0741(16)	2.043(3)	2.064(2)
Ru–N2	2.0788(16)	2.062(4)	2.133(2)
Ru–N3	2.085(4)		
Ru–Cl1	2.3444(5)	2.347(11)	2.4035(9)
Ru–Cl2	2.3537(5)	2.3780(11)	2.4167(9)
Ru–Cl3	2.3337(5)	2.3428(11)	
Ru–S1	2.3236(5)		2.2541(9)
Bond angles	**3**	**5**	**6**
N1–Ru–N2	78.37(6)	79.00(14)	77.93(8)
N1–RuCl2	94.99(5)	95.60(10)	87.58(6)
Cl2–RuS1	85.711(18)		178.59(3)
S1–Ru–N2	101.01(5)		92.03(6)
N2–Ru–Cl2	173.09(5)	174.18(11)	87.14(6)
N3–Ru–Cl2		86.44(10)	

Table 1
Crystal data for **3**, **6** and **7**

	3	**6**	**7**
Formula	$C_{12}H_{14}Cl_3N_2ORuS$	$C_{13}H_{12}Cl_3N_4Ru \cdot 2(C_2H_6OS)$	$C_{15}H_{16}Cl_2N_2O_2RuS$
CCDC deposit #	CCDC 622220	CCDC 622221	CCDC 622222
Formula weight	441.73	587.94	460.33
Crystal system	Monoclinic	Orthorhombic	Monoclinic
Space group	$P2_1/c$	$Pca2_1$	$P2_1/c$
T (K)	110	115	110
a (Å)	8.3967(10)	20.277(2)	8.434(2)
b (Å)	14.882(2)	6.7969(10)	15.533(4)
c (Å)	12.7157(12)	16.7675(15)	13.535(4)
β (°)	91.503(8)	90	104.150(12)
h, k, l limits	±11, ±21, ±17	±28, ±9, ±22	±12, ±23, ±20
Z	4	4	4
θ Range (°)	2.7–30.5	2.5–29.8	2.6–32.6
μ (mm^{-1})	1.618	1.228	1.353
ρ_{calc} (g cm^{-3})	1.847	1.690	1.778
Data collected	30,840	24,865	35,302
Observed/unique data	4043/4793	5299/6197	4317/6238
R	0.027	0.045	0.045
wR	0.060	0.091	0.076
Parameters	184	269	208
Residual peaks (e $Å^{-3}$)	0.77, −0.88	0.77, −0.82	0.73, −0.77

energies and electrostatic charges for structures is provided in the Supporting information.

3. Synthesis of the complexes

$[H(DMSO)_2][trans\text{-}RuCl_4(DMSO)_2]$, [20a] $[H(TMSO)][trans\text{-}RuCl_4(TMSO)_2]$ [20b] and *mer*-$[RuCl_3(TMSO)(bpy)]$ [20c] (**5**) were synthesized according to the literature procedures.

3.1. mer-[RuCl$_3$(DMSO)(bpy)] (3)

To a solution of $[H(DMSO)_2][trans\text{-}RuCl_4(DMSO)_2]$ (**1**) (0.105 g, 0.19 mmol) in ethanol (5 mL) solid 2,2′-bipyridine (0.034 g, 0.22 mmol) was added at room temperature, with constant stirring. An orange–yellow precipitate formed within a few minutes. The product was filtered, washed with chilled ethanol and diethyl ether, and vacuum dried. Yield 0.52 g (62%). *Anal*. Calc. for $C_{12}H_{14}Cl_3N_2ORuS$ (MM = 441.73): C, 32.62; H, 3.2; N, 6.34. Found: C, 32.60; H, 3.74; N, 6.30%. Selected IR absorption bands in KBr (cm^{-1}): ν_{SO} 1115 and 1019 (s)(DMSO), $\nu_{C=N}$ 1604 (ms). UV–Vis (acetone): 404 nm ($\varepsilon = 6070$ L mol^{-1} cm^{-1}) and 210 nm ($\varepsilon = 3674$ L mol^{-1} cm^{-1}).

3.2. mer-[RuCl$_3$(bpy)(im)] · 2DMSO (6)

mer-$[RuCl_3(TMSO)(bpy)]$ (0.126 g, 0.27 mmol) was dissolved in hot 1,2-dichloroethane (30 mL). To this solution, solid imidazole (0.21 g, 0.31 mmol) was added and heated at 80 °C for 3 h. During this period the color changed to brown from orange. The solution was filtered and the volume was reduced to half on a reduced pressure. The flask was kept in a refrigerator. The brown solid was filtered, washed with hexane (3 × 5 mL), and vacuum dried. Yield 0.07 g, (60.5%). *Anal*. Calc. for $C_{13}H_{12}Cl_3N_4Ru$ (MM = 431.7): C, 36.17; H, 2.8; N, 12.98. Found: C, 36.28; H, 2.68; N, 13.02%. Selected IR absorption bands in KBr (cm^{-1}): νCN 1603 (m). UV–Vis (DMSO): 384 nm ($\varepsilon = 5858$ L mol^{-1} cm^{-1}), 296 nm (vs) ($\varepsilon = 19631$ L mol^{-1} cm^{-1}) and 260 nm ($\varepsilon = 10207$ L mol^{-1} cm^{-1}). The solid was recrystallized in DMSO and acetone at −20 °C to get suitable crystals of the disolvate **6** for X-ray diffraction.

3.3. cis-[RuCl$_2$(TMSO)(CO)(bpy)] (7)

mer-$[RuCl_3(TMSO)(bpy)]$ (0.114 g, 0.24 mmol) was dissolved in 1,2-dichloroethane (50 mL), evacuated, and connected to the reservoir of carbon monoxide (1 atm) at 80 °C for 6 h with constant stirring. The yellow–orange solution gradually turned to bright red. The solution was filtered and solvent removed in vacuum. The red solid was recrystallized in dichloroethane and diethyl ether at 4 °C to get a red crystalline solid suitable for X-ray diffraction. Yield 0.06 g, (54%). *Anal*. Calc. for $C_{15}H_{16}Cl_2N_2O_2RuS$ (MM = 459.41): C, 39.44; H, 3.51; N, 6.09. Found: C, 39.50; H, 3.42; N, 6.2%. Selected IR absorption bands in KBr (cm^{-1}): νCO 2040 (vs), νCN 1602 (m), νSO 1116 and 1014 (s) (TMSO). UV–Vis (acetone): 404 nm ($\varepsilon = 6070$ L mol^{-1} cm^{-1}), 298 nm (vs) ($\varepsilon = 20652$ L mol^{-1} cm^{-1}) and 252 (vs) ($\varepsilon = 20143$ L mol^{-1} cm^{-1}).

3.4. cis-[RuCl$_2$(DMSO)(CO)(bpy)] (8)

Brown–red (0.065 g, 47%). Selected IR absorption bands in KBr (cm^{-1}): νCO 2010 (vw) and 1950 (s), νCN 1602 (w), νSO 1120 and 1073 (s) (DMSO).

3.5. K[RuCl$_3$(bpy)(SCN)] (9)

0.034 g, 0.077 mmol of *mer*-$[RuCl_3(DMSO)(bpy)]$ or *mer*-$[RuCl_3(DMSO)(bpy)]$ and KSCN (0.01 g, 0.11 mmol) were dissolved in a separate flask in acetone (6 mL) and in water (1 mL), respectively. The solutions were combined and heated at 80 °C for 4 h to get a brown–orange solution. The solvent was removed on vacuum. The product was recrystallized in the mixture of acetone/water/diethyl ether at 4 °C. Yield 0.022 g (61.5%). *Anal*. Calc. for $C_{11}H_8Cl_3N_3RuSK$ (MM = 460.80): C, 28.67; H, 1.75; N, 9.12. Found: C, 28.8; H, 2.08; N, 8.31%. Selected IR absorption bands in KBr (cm^{-1}): νNCS 2067(s), νCN 1605 (b, m).

4. Results and discussion

In an attempt to substitute bpy ligand for DMSO and/or chloride ligand, we treated **1** with 2,2′-bipyridine in equimolar amounts in ethanol. Two neutral compounds, a major unknown *mer*-$[RuCl_3(DMSO)_2(bpy)]$ (**3**) and a minor known compound *cis*-$[RuCl_2(DMSO)_4]$ (**4**) were isolated. Nonetheless when the amount of bpy was reduced to half-equivalent with respect to **1**, 40% of **3** and 60% of **4** was isolated. The **3** was characterized by spectroscopy and by X-ray diffraction. The spectroscopic measurements of **4** were compared with an authentic sample of *cis*-$[RuCl_2(DMSO)_4]$.

The IR spectra of all the complexes **3, 6, 7, 8, 9** were recorded in KBr pellets and show a weak to medium intensity sharp peak between 1589 and 1603 cm^{-1} due to C=N stretch of the bipyridine ligand [21]. After complexation, there is a distinct bathochromic shift of 4–20 cm^{-1}, which is typical for coordinated imines of this type. The peaks due to (S=O) in the coordinated DMSO for **3, 8** (1115–1022 cm^{-1}) [20b,21] and TMSO coordinated (1115–1014 cm^{-1}) [20a] for **7** are assigned to S-bonded DMSO and TMSO, respectively to ruthenium. IR spectra of **7** and **8** reveal a strong absorption at 2040 cm^{-1} and 1950 cm^{-1}, respectively. The decrease in the CO stretching band in **8** compared to **7**, is presumably due to the bonding of the DMSO ligand to metal through oxygen. Similar results have been reported [22,23]. In contrast to the **8** the electronic spectrum of **3** (acetone) shows a strong absorption band at 404 nm and a weak band at 350 nm attributed to charge transfer transition from chlorides to

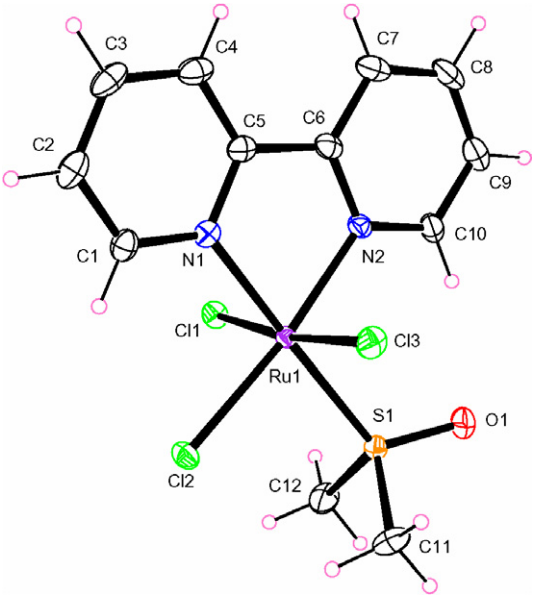


Fig. 1. Structure of mer-[$RuCl_3$(DMSO)(bpy)] **3**.

Ru(III) [24]. A sharp absorption at 210 nm is assigned to a metal-ligand charge transfer state (MLCT) [25].

5. X-ray crystal structure

5.1. *mer-[$RuCl_3$(DMSO)(bpy)] (3)*

The ruthenium (III) ion is surrounded by (Fig. 1, Table 1) six donors: S of DMSO, two nitrogens from 2,2′-bipyridine and three meridonial chloro ligands in a distorted octahedral coordination sphere. The bite angle involving coordinated bpy, N1RuN2 is 78.37(6)°, typical of a 2,2′-bipyridine coordinated to a second and third transition metal and TMSO analog, **5** [20c]. The bond angle of nonchelating ligand, S1RuCl2 is 85.711(18)°, larger than the N1RuN2 angle. The average Ru–N bond length, 2.076(16) Å is close to the distinctive bond length of 2.099 Å reported for Ru(II, III) [11,20c,21]. The average Ru–Cl bond length, 2.3439(5) Å is comparable to the TMSO analog, 2.3439 Å and other related Ru(III) complexes [10,27].

The Ru–S bond distance, 2.3236(5) Å, is near to the average value of 2.34(1) Å found for Ru(III)–S *trans* to DMSO-S in the precursor [20a,28] and slightly larger than **5** [26]. The bond angles of N1RuS1, 177.31(5)°; N2RuCl2, 173.09(5)° and Cl1RuCl3, 172.991(18)° are slightly shorter than the known values of octahedral complexes. Similarly the bond angles N1RuN1, N1RuCl2, Cl2RuS1, and S1RuN2 are varied and range from 78.37° to 101.01°. These distortions from ideal octahedral geometry are probably caused by the acute (∼78°) bite angle of the chelating bipyridine ligand [29].

6. Reactivity of 3 and 5 with imidazole, CO and KSCN

The reaction of *mer*-[$RuCl_3$(TMSO)(bpy)] **5** with imidazole and CO produced compounds **6** (substituting TMSO for imidazole) and **7** (one-electron reduction) at elevated temperature. Likewise, the DMSO analogues have also been synthesized from **3** under similar reaction conditions. Combined spectroscopic (IR, UV–Vis) and microanalysis evidence suggested that the geometry of DMSO analogues is similar to that of **6** and **7**. The reactions of **3** and **5** with KSCN, resulted in the same compound, K[$RuCl_3$-(bpy)(SCN)] **9** formed by the substitution of DMSO or TMSO in **3** and **5**.

6.1. *mer-[$RuCl_3$(bpy)(im)] · 2DMSO (6)*

The compound **6** was formed by the substitution of TMSO ligand from **5**. On recrystallization with DMSO, the compound has 2 molecules of DMSO solvate. One of the DMSO molecules exhibits disorder. As shown in Fig. 2, the coordination sphere is a distorted octahedron as can be seen from the angles subtended at the metal center. The distortion of the coordination sphere is primarily caused by the bite angle, N1RuN2, 79.00(14)° of the bipyridine ligand though the bite angle of **6** is larger than the precursor. The observed three ruthenium–nitrogen bond distances, N1Ru, 2.043(3) Å; N2Ru, 2.062(4) Å and N3–Ru, 2.085(4) fall within the range 2.049–2.085 Å as reported for $[Ru(bpy)_3]^{2+}$ [30–32]. However, the Ru–N bond distance in Ru(III)–bipyridine is slightly shorter than the reported values for Ru(II)–bipyridine complexes. The shorter Ru(III)–N bond length compared to Ru(II)–N is probably due to an increase in oxidation state [20a,33]. Also, the Ru–N bond lengths, N1Ru and N2Ru in **6** are shorter than the precursor, *mer*-[$RuCl_3$(TMSO)(bpy)], (2.0835 Å). The N3Ru bond length is significantly larger than the other two, N1Ru and N2Ru. The imidazole moiety is essentially planar and three chloride ligands occupy meridonial positions.

6.2. *cis-[$RuCl_2$(TMSO)(CO)(bpy)] (7)*

On bubbling carbon monoxide (1 atm) through the solution of **5** in dichloroethane at 80 °C, **7** was isolated. During the course of the reaction, Ru(III) is reduced to Ru(II). The coordination geometry of this complex is distorted octahedral. The coordinated bpy domain exhibits a bite angle, N1RuN2, 77.93(8)°, which falls within the typical limit of those for Ru-bpy complexes, reported earlier [34]. However, the bite angle in **7** is slightly shorter than the parent compound, 78.16 (9)° [20b]. The Ru–Cl2 bond length *trans* to S of the TMSO ligand, 2.4167(9) Å is clearly longer than Ru–Cl1 *trans* to bipyridine Ru–N1, 2.4035 (9) Å, probably due to a strong *trans* effect of the TMSO ligand. The Ru–N2 bond length *trans* to CO, 2.133(2) Å is significantly longer than Ru–N1, 2.064(2) Å *trans* to Cl1 due to the strong *trans* effect of the carbonyl ligand. The Ru(II)–N bond lengths in monodentate bipyridine ligands [12] are systematically longer (2.18–2.20 Å) than in 2,2′-bipryridine chelating complexes (2.15 Å), which in turn are much larger than the average Ru–N bond lengths (2.0985 Å) in

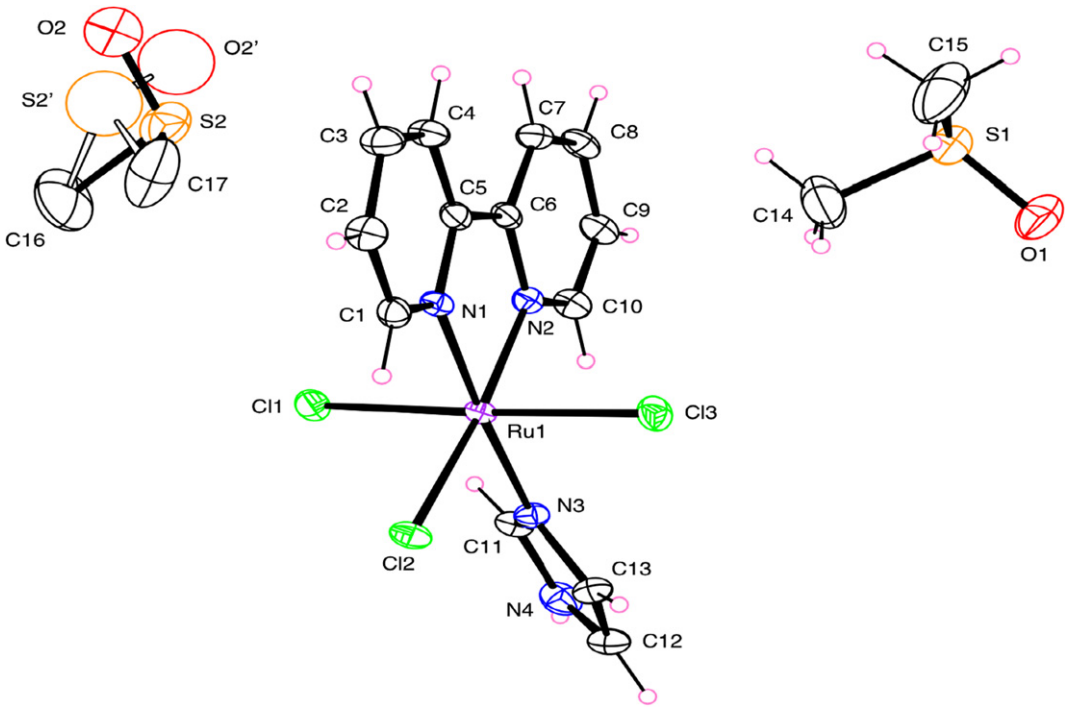


Fig. 2. Structure of *mer*-[$RuCl_3$(bpy)(im)] · 2DMSO (**6**).

complex **7**. The shortness of the Ru–N bond length in **7** is most probably related to the increased π back-bonding compared to monodentate and chelating bipyridine ligand coordination modes [12]. The Ru–C–O bond angle, 178.3(3)°, is close to linear geometry. Also, this angle is greater than the angle in [$RuCl_2(CO)_2$(bpy)], 171.1° [34a]. Similar distortion is reported for $[Ru(bpy)_2(CO)(NO_2)]^+$ and $[Ru(bpy)_2(CO)(Cl)]^+$ [35–37]. The carbonyl ligand is in a *cis* position to one of the chloride ligands and *trans* to the bipyridine nitrogen. The Ru–S bond length, 2.2541(9) Å is shorter than its precursor, *mer*-[$RuCl_3$(TMSO)(bpy)], 2.2969(8) Å (see Fig. 3).

Rather unexpectedly, the Ru–C bond length in **7**, 1.903(3) Å, is longer than in *mer*-[$RuCl_3(TMSO)_2(CO)$], 1.845(3) Å and in *cis*-[$RuCl_2(TMSO)_3(CO)$], 1.865(4) Å. While the C–O bond length in **7,** 1.090(3) Å is shorter than in [$RuCl_3(TMSO)_2(CO)$], 1.149(9) Å and *cis*-[$RuCl_2$(TMSO)$_3$(CO)], 1.132(2) Å [24,38]. It is interesting to note that during the course of synthesis of **7**, Ru(III) is reduced to Ru(II) whereas no reduction of ruthenium takes place when carbon monoxide passes through the solution of *mer*-[$RuCl_3(TMSO)_3$] under similar conditions [38].

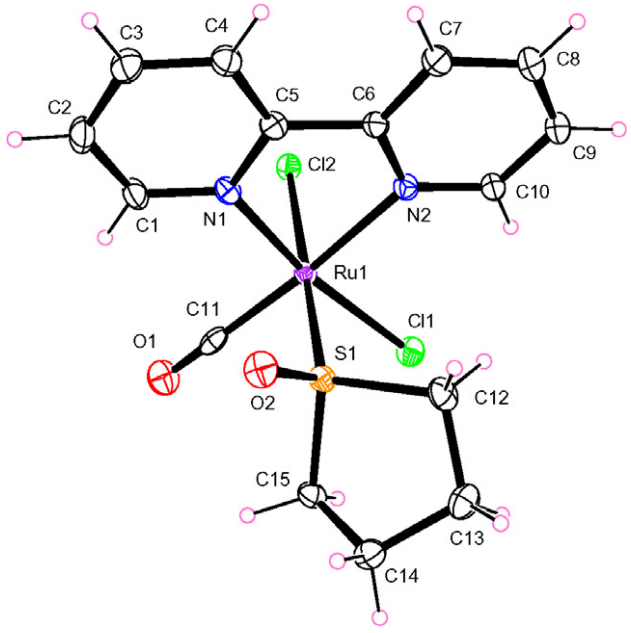


Fig. 3. Structure of *mer*-$RuCl_2$(TMSO)(CO)(bpy)] (**7**).

7. K[$RuCl_3$(bpy)(NCS)] (9)

On the basis of spectroscopic and microanalyses studies complex **9** is formulated as K[$RuCl_3$(bpy)(NCS)], which is derived either from **3** or **5**. In the absence of X-ray diffraction studies of M-thiocyanate complexes, the C–N stretching mode (ν_{SC-N}), the S–C stretching band (ν_{S-CN}), and the NCS deformation mode (δ_{SCN}) as well as the integrated intensity of ν_{SC-N} have been used as indicators of the SCN bonding mode [39]. However, ν_{S-CN} and δ_{SCN} are often weak and are masked by other absorptions, such as those of solvent or other ligands. The C–N stretching is generally at lower frequency in N-bonded complexes (around 2050 cm^{-1}) than in S-bonded complexes (around 2100 cm^{-1}), but this criterion must be applied carefully as counter examples exist [40,41]. With some exceptions *cis*

and *trans* isomers can be distinguished by IR spectroscopy: thus ν_{SC-N} usually appears as a single band in the spectrum of the *trans* isomer.

The IR spectrum of **9** shows a strong single band at 2066–2067 cm^{-1} assignable to ν_{SC-N} for N-bonded thiocyanate complexes. This is also substantiated by HSAB theory. A medium intensity frequency at 2109 cm^{-1} has been reported for the N-bonded thiocyanate complex in $[Ru(dmbpy)(CO)_2(NCS)H]$ [42]. Nonetheless electronic factors play a crucial role in the stability of metal-thiocyanate bonds [42]. In fact, decreasing electron density on the metal center has been suggested to change the bonding mode of the thiocyanate ligand from M-SCN to M-NCS.

8. Computational studies

To clarify further the role of the coordination mode of the thiocyanato ligand with ruthenium(III) in compound **9**, density functional calculations were conducted. DFT calculations of $[RuCl_3(bpy)(NCS)]^-$ and $[RuCl_3(bpy)(SCN)]^-$ were performed. The calculated energy for the former was found to be 12 kcal/mol lower than the latter, which substantiates our earlier statement. For comparing isomer energies, a DFT method had an average error of 2.8 kcal/mol in one comparative study of 45 non-transition metal isomer pairs [43]. For diastereoisomers involving transition metal compounds, accuracies within 1–2 kcal/mol are felt likely [44].

The calculated ν_{SC-N} for the former was 2069 cm^{-1} and 2019 cm^{-1} for the latter. In the ruthenium bipyridine systems, the HOMO contains ruthenium d-orbitals and the LUMO is typically π^*-orbitals of the bipyridine ring.

9. Electrochemistry

Cyclic voltammetry of **3** was carried out (acetone, 1.00 mM, Fig. 4) at sweep rates ranging from 100 to 3011 mV/s. The resulting graphs display a prominent reduction peak and corresponding oxidation peak. The difference in potential between these two peaks (ΔE_p) ranged from 71 to 102 mV. The ratio of anodic to cathodic peak current (i_a/i_c) ranged from 1.1 to 0.90. The intermediate potential of these peaks ranged from 0.026 to 0.031 V versus SCE with an average of 0.028 V versus SCE and is taken as an approximation to the formal potential $E^{\circ\prime}$. These data are consistent with the peaks being due to a nearly reversible one-electron redox couple [45] and it is assumed to be Ru(III)/Ru(II). Another redox couple seems to appear just cathodic of the Ru peaks. It is not defined enough to obtain information from it but it may be due to partial reaction of one of the ligands. Isolating the potential sweep to just this couple had little effect on its appearance.

Semi-derivative analysis [46] of the data was also done. Peak widths at half height of the semi-derivative data ranged from 98 to 118 mV for the anodic peak and 100 to 113 mV for the cathodic peak over the sweep rates used.

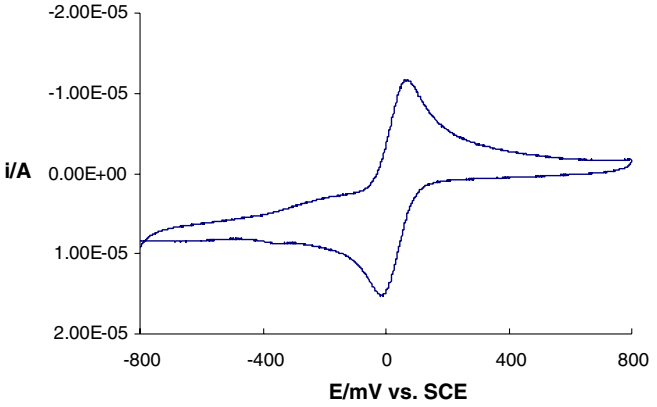


Fig. 4. Cyclic voltammetric curve of *mer*-$[RuCl_3(DMSO)(bpy)]$ (**3**) for 1.0 mM (**3**) and 0.100 M Bu_4NPF_6 in acetone at a sweep rate of 500 mV/s.

This compares to 90.7 for a one-electron reversible process. The ratio of peak heights ranged from 0.995 to 1.06. The formal potential approximated as the average of the intermediate of the anodic and cathodic peak potentials on the semi-derivative graphs was 0.028 V versus SCE.

Cyclic voltammetry of **6** (DMSO, 1.00 mM, Fig. 5) was carried out at sweep rates from 100 to 5120 mV/s. A prominent redox couple appears as a reduction peak and a corresponding oxidation peak on these graphs at an average potential of 0.276 V versus SCE as determined directly from cyclic voltammetry data as well as semi-derivative analysis. These peaks are assumed to be due to Ru(III)/Ru(II) charge transfer. ΔE_p ranged between 66 and 90 mV, indicating quasi-reversible behavior. However, i_a/i_c approached unity only at high sweep rates. Oxidation current was less than reduction current. This may be due to reaction of or mass transfer of the reduction product, an effect that would be more pronounced at lower sweep rates. Peak widths at half heights from the semi-derivative analysis ranged from 104 to 116 mV for the anodic peak and 103 to 116 for the anodic peak.

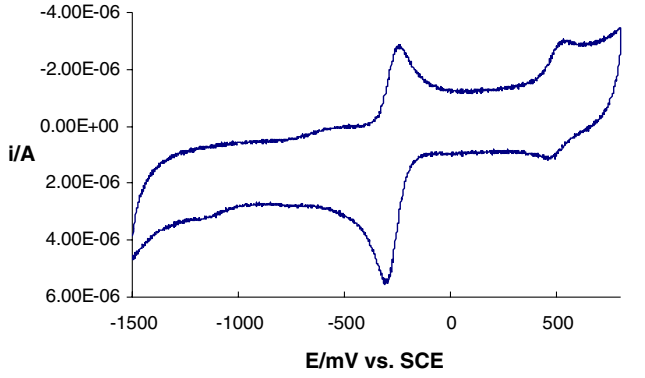


Fig. 5. Cyclic voltammetric curve of *mer*-$[RuCl_3(bpy)(im)]\cdot 2DMSO$ (**6**) for 1.0 mM (**6**) and 0.100 M Bu_4NPF_6 in DMSO at a sweep rate of 500 mV/s.

The potentials measured by us for the above two compounds compare favorably with the correlation of Lever [47] which predicts an approximate formal potential of 0.03 V for **3** and −0.32 V for **6**.

Cyclic voltammograms (acetone, 0.37 mM, Fig. 6) were obtained for **7** at sweep rates from 100 to 3011 mV/s. Three pairs of peaks were observed at all sweep rates. The largest pair is centered on an average potential of 0.447 V versus SCE both on the voltammogram and on the semi-derivative graph. i_a/i_c ranges between 1.04 and 1.17. ΔE_p ranges between 69 and 101 mV. The peak widths at half height from the semi-derivative analysis range between 94 and 125 mV. These characteristics are consistent with a quasi-reversible one-electron transfer. However, one expects to see evidence of a Ru(II)/Ru(0) couple. The data may be due to a two-electron process if this couple were not so near to reversibility. Another possibility is that the oxidation and reduction processes in the Ru(II)/Ru(0) couple occur in two consecutive one-electron processes and that the peaks for these are closely overlapping. This has been suggested previously [48]. For this situation, ΔE_p would be expected to be only slightly larger than that predicted for a one-electron reversible process.

The other two smaller pairs of peaks may be due to redox couples involving the ligands. They have average potential values of approximately 0.01 V and −0.25 V and average ΔE_p values of approximately 67 and 58 mV.

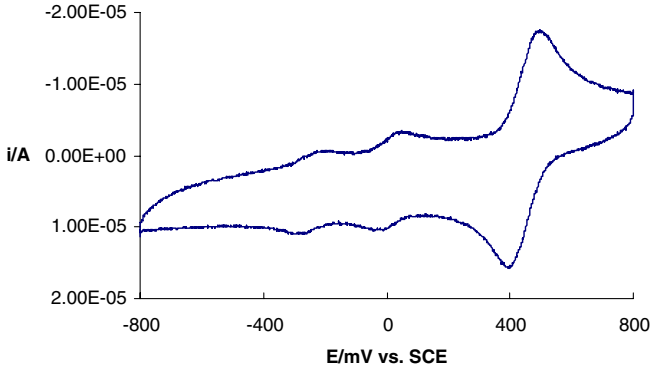
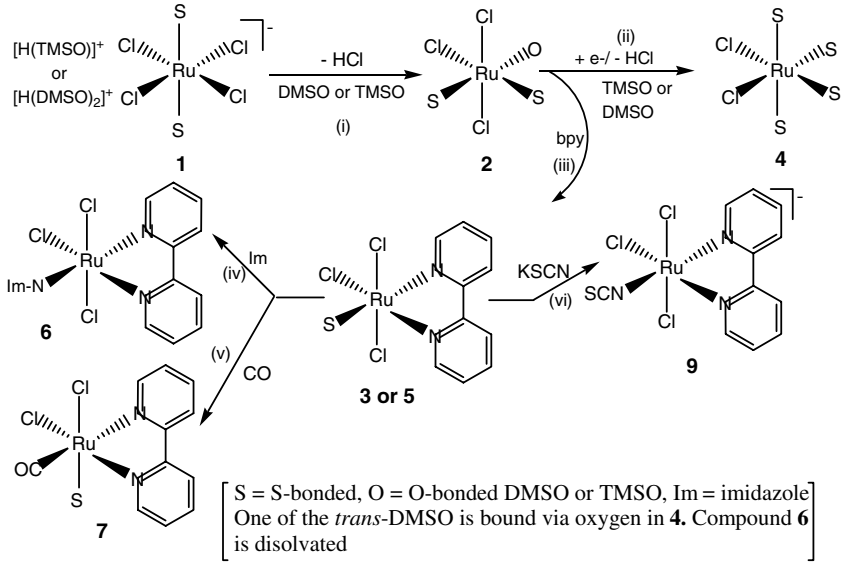


Fig. 6. Cyclic voltammetric curve of *mer*-[$RuCl_2$(TMSO)(CO)(bpy)] (**7**) for 0.37 mM (**7**) and 0.100 M Bu_4NPF_6 in acetone at a sweep rate of 3011 mV/s.

10. Formation scheme of various compounds and their reaction mechanism

On treating **1** with an equimolar amounts of 2,2′-bipyridine, **3** (major) and **4** (minor) is isolated. It is known that **2** is prepared by the reaction of **1** with DMSO/TMSO and $AgBF_4$ in boiling acetone [20b]. In view of these observations, we propose a reaction mechanism (Scheme 1), similar to the one proposed by us [20c] and Alessio earlier [20b]. To ascertain step (iii), we independently synthesized **3** by the reaction of **2** and 2,2′-bipyridine under identical reaction conditions. Thus, it is anticipated that **2** is intermediate in the formation of **3** and **4**. The identity of the reducing agent in step (ii) is ambiguous. However, we believe that sulfoxides and HCl in step (ii) are the probable reductants. In fact, the GC–MS analysis of the reaction mixture, carried out under argon, detected sulfones, substantiating the work reported earlier [20a]. Likewise, carbon monoxide acts as reductant in step (v). To probe the role of 2,2′-bipyridine in the formation of **2** and **4**, a control experiment in the absence of 2,2′-bipyridine was performed with identical conditions. The solid IR spectrum of the product was identical to **1**, suggesting that 2,2′-bipyridine is a prerequisite for the formation of **2** and **4** under present



Scheme 1. Synthetic scheme of various ruthenium complexes.

reaction conditions. Thus, 2,2′-bipyridine ligand is basic enough to pull off HCl from **1** to produce **2**, which in turn forms **3**.

Acknowledgements

We thank Dr. R. D. Braun (UL Lafayette, Chemistry Department) for editing the manuscript and making suggestions. Financial support provided by the Research Corporation (Cottrell College Science Award, #CC 6234 to RSS) and BoR, Louisiana is greatly appreciated. The purchase of the diffractometer was made possible by Grant No. LEQSF(1999–2000)-ESH-TR-13, administered by the Louisiana Board of Regents.

Appendix A. Supplementary material

CCDC 622220, 622221 and 622222 contain the supplementary crystallographic data for compounds **3**, **6** and **7**. These data can be obtained free of charge via http://www.ccdc.cam.ac.uk/conts/retrieving.html, or from the Cambridge Crystallographic Data Centre, 12 Union Road, Cambridge CB2 1EZ, UK; fax: (+44) 1223-336-033; or e-mail: deposit@ccdc.cam.ac.uk.

References

[1] E. Alessio, Chem. Rev. 104 (2004) 4203–4242.
[2] R. Cini, G. Tamasi, S. Defazio, M. Corsini, P. Zanello, L. Messori, G. Marcon, F. Picciolli, P. Orioli, Inorg. Chem. 42 (2003) 8038.
[3] P.K.L. Chan, P.K.H. Chan, D.C. Frost, B.R. James, K.A. Skov, Can. J. Chem 66 (1988) 117.
[4] P.K.L. Chan, B.R. James, D.C. Frost, P.K.H. Chan, H.-L. Hu, K.A. Skov, Can. J. Chem. 67 (1989) 508.
[5] G. Sava, E. Alessio, A. Bergamo, G. Mestroni, M.J. Clarke (Eds.), Topics in Biological Inorganic Chemistry, Metallo-pharmaceuticals, vol. 1, Springer, Berlin, 1999, p. 143.
[6] B.K. Keppler, New J. Chem. 14 (1990) 389.
[7] M.J. Clarke, V.M. Bailey, P.E. Doan, C.D. Hiller, K.J. LaChance-Galang, H. Daghlian, S. Mandal, C.M. Bastos, D. Lange, Inorg. Chem. 35 (1996) 4896.
[8] B.K. Keppler, K.G. Lipponer, B. Stenzel, F. Kratz, in: B.K. Keppler (Ed.), Metal Complexes in Cancer Therapy, VCH, Weinheim, 1993, p. 189.
[9] L.A. Huxham, E.L.S. Cheu, B.O. Patric, B.R. James, Inorg. Chim. Acta 352 (2003) 238.
[10] E. Alessio, G. Baldicci, A. Lutman, G. Mestroni, M. Calligaris, W.A. Attia, Inorg. Chim. Acta 203 (1993) 205.
[11] A. Garas, D.C. Craig, R.S. Vagg, A.T. Baker, J. Coord. Chem. 50 (2000) 79.
[12] Toni-J.J. Kinnunen, M. Haukka, E. Pesonen, T.A. Pakkanen, J. Organomet. Chem. 655 (2002) 31.
[13] B.O. ′Regan, M. Gratzel, Nature 353 (1991) 737.
[14] M.K. Nazeeruddin, A. Kay, I. Rodicio, R. Humphry-Baker, E. Muller, P. Liska, N. Vlachopoulos, M. Gratzel, J. Am. Chem. Soc. 115 (1993) 6383.
[15] M. Gratzel, Platinum Metals Rev. 38 (1994) 151.
[16] K. Murakoshi, G. Kano, Y. Wada, S. Yanagida, H. Miyazaki, M. Matsumoto, S. Murasawa, J. Electroanal. Chem. 396 (1995) 27.
[17] O. Kohle, S. Ruile, M. Gratzel, Inorg. Chem. 35 (1996) 4779.
[18] M.J. Frisch, G.W. Trucks, H.B. Schlegel, G.E. Scuseria, M.A. Robb, J.R. Cheeseman, J.A. Montgomery Jr., T. Vreven, K.N. Kudin, C. Burant, J.M. Millam, S.S. Iyengar, J. Tomasi, V. Barone, B. Mennucci, M. Cossi, G. Scalmani, N. Rega, G.A. Petersson, H. Nakatsuji, M. Hada, M. Ehara, K. Toyota, R. Fukuda, J. Hasegawa, M. Ishida, T. Nakajima, Y. Honda, O. Kitao, H. Nakai, M. Klene, X. Li, J.E. Knox, H.P. Hratchian, J.B. Cross, C. Adamo, J. Jaramillo, R. Gomperts, R.E. Stratmann, O. Yazyev, A.J. Austin, R. Cammi, C. Pomelli, J.W. Ochterski, P.Y. Ayala, K. Morokuma, G.A. Voth, P. Salvador, J.J. Dannenberg, V.G. Zakrzewski, S. Dapprich, A.D. Daniels, M.C. Strain, O. Farkas, D.K. Malick, A.D. Rabuck, K. Raghavachari, J.B. Foresman, J.V. Ortiz, Q. Cui, A.G. Baboul, S. Clifford, J. Cioslowski, B.B. Stefanov, G. Liu, A. Liashenko, P. Piskorz, I. Komaromi, R.L. Martin, D.J. Fox, T. Keith, M.A. Al-Laham, C.Y. Peng, A. Nanayakkara, M. Challacombe, P.M.W. Gill, B. Johnson, W. Chen, M.W. Wong, C. Gonzalez, J.A. Pople, GAUSSIAN 03, Revision B.05, GAUSSIAN, Inc., Pittsburgh, PA, 2003.
[19] NIST Computational Chemistry Comparison and Benchmark Database; NIST Standard Reference Database Number 101 Release 12, Aug 2005, Editor: Russell D. Johnson III http://srdata.nist.gov/cccbdb.
[20] (a) E. Alessio, G. Balducci, M. Calligaris, G. Costa, W.M. Attia, G. Mestroni, Inorg. Chem. 30 (1991) 609;
(b) E. Alessio, B. Milani, G. Mestroni, M. Calligaris, P. Faleschini, W.M. Attia, Inorg. Chim. Acta 177 (1990) 255;
(c) R.S. Srivastava, F.R. Fronsczek, Inorg. Chim. Acta 358 (2005) 854.
[21] Y. Wang, D.M. Eichhorn, N. Goswami, Q. Zhao, D.P. Rillema, J. Crystallogr. 27 (1999) 277.
[22] C.M. Duff, G.A. Heath, J. Chem. Soc. Dalton Trans. (1991) 2401.
[23] E. Alessio, B. Milani, M. Bolle, G. Mestroni, P. Faleschini, F. Todore, S. Geremia, M. Calligaris, Inorg. Chem. 34 (1995) 4722.
[24] R.S. Srivastava, F.R. Fronczek, Inorg. Chim. Acta 355 (2003) 354.
[25] R. Ziessel, V. Grosshenny, M. Hissler, C. Stroh, Inorg. Chem. 43 (2004) 4262.
[26] (a) E.C. Constable, Ad. Inorg. Chem. 34 (1989) 1;
(b) E.C. Constable, C.E. Housecroft, M. Neuberger, I. Poleschak, M. Zehnder, Polyhedron 22 (2003) 93.
[27] M. Calligaris, N. Presciani-Pahor, R.S. Srivastava, Acta Crystallogr. C49 (1993) 448.
[28] J. Jaswal, S.J. Rettig, B.R. James, Can. J. Chem. 68 (1990) 1808.
[29] S. Chakraborty, M.G. Walawalker, G.K. Lahiri, J. Chem. Soc. Dalton Trans. 16 (2000) 2875.
[30] J.M. Harrowfield, A.N. Sobolev, Aust. J. Chem. 47 (1994) 763.
[31] R.G. Gaunder, H. Taube, Inorg. Chem. 9 (1970) 2627.
[32] E. Alessio, G. Mestroni, G. Nardin, W.M. Attia, M. Calligaris, G. Sava, S. Zorzet, Inorg. Chim. 27 (1988) 4099.
[33] H.C. Stynes, J.A. Ibers, Inorg. Chem. 10 (1971) 2304.
[34] (a) M. Haukka, J. Kaviaho, M. Ahlgren, T.A. Pakkanen, Organometallics 14 (1995) 5454;
(b) M. Haukka, T. Venalainen, M. Ahlgren, T.A. Pakkanen, Inorg. Chem. 34 (1995) 2931;
(c) M. Haukka, M. Ahlgren, T.A. Pakkanen, J. Chem. Soc. Dalton Trans. (1996) 1927;
(d) D.S. Eggleston, K.A. Goldsby, D.J. Hodgson, T.J. Meyer, Inorg. Chem. 24 (1985) 4573;
(e) M.A. Greaney, C.L. Coyle, M.A. Harner, A. Jordon, E.I. Stiefel, Inorg. Chem. 28 (1989) 912.
[35] H. Tanaka, H. Nagao, K. Tanaka, Inorg. Chem. 31 (1992) 1971.
[36] H. Tanaka, B.-C. Tzeng, H. Nagao, S.-H. Peng, K. Tanaka, Organometallics 11 (1992) 3172.
[37] H. Tanaka, B.-C. Tzeng, H. Nagao, S.-H. Peng, K. Tanaka, Inorg. Chem. 32 (1993) 1508.
[38] R.S. Srivastava, F.R. Fronczek, Inorg. Chim. Acta 322 (2001) 32.
[39] G. Douglas, K.W. Muir, Acta Crystallogr. C47 (1991) 1394.
[40] M.J. Maroney, E.O. Fey, D.A. Baldwin, R.E. Stenkamp, L.H. Jensen, N.J. Rose, Inorg. Chem. 25 (1986) 1409.

[41] K. Nakamoto, Infrared and Raman Spectra of Inorganic and Coordination Compounds, Part B, fifth ed., Wiley Interscience, 1997, p. 116.
[42] P. Homanen, M. Houkka, T.A. Pakkanen, J. Pursiainen, R.H. Laitinen, Organometallics 15 (1996) 4081.
[43] W.J. Hehre, Practical strategies for electronic structure calculations, Wavefunction, 1995, in: I.L. Levine (Ed.), Quantum Chemistry, fifth ed., Prentice-Hall, 2000.
[44] S. Feldgus, C.R. Landis, J. Am. Chem. Soc. 122 (2000) 12714.
[45] J.G. Ibanez, C.-S. Choi, R.S. Becker, J. Electrochem. Soc. 134 (1987) 3083.
[46] P. Dalrymple-Alford, M. Goto, K.B. Oldham, J. Electroanal. Chem. 85 (1977) 1.
[47] A.B.P. Lever, Inorg. Chem. 29 (1990) 1271.
[48] D.O. Wipf, E.W. Kristensen, M.R. Deakin, R.M. Wightman, Anal. Chem. 60 (1988) 306.

complexes with copper(I) and mercury(II) halides, including an unusual tetrametallic complex, [{L(HgI$_2$)$_2$}$_2$]. A common feature for all the complexes is the occurrence of hydrogen bonding between the hydrazine backbone hydrogens of L and the coordinated halide ions.

2. Experimental

2.1. Materials and instrumentation

All reactions were carried out under an atmosphere of dry dinitrogen. Analytical grade solvents were purchased from standard chemical suppliers and were used without further purification. HgI_2 (M&B), $HgBr_2$ (BDH) and $HgCl_2$ (M&B) were used as received. CuCl, CuBr, CuI and (1,2-diphenylphosphino)hydrazine were prepared according to the literature [18,19,14]. ^{1}H and ^{31}P NMR spectra were recorded on a Bruker Avance 400 spectrometer. IR spectra were run as KBr discs on a Perkin–Elmer FT-IR Paragon 1000 spectrometer. Microanalyses were performed by the Campbell Microanalytical Laboratory, University of Otago.

2.2. Syntheses

2.2.1. 1,2-Bis(diphenylthioylphosphino)hydrazine (L)

To a solution of 1,2-bis(diphenylphosphino)hydrazine (2.585 g, 6.436 mmol) in toluene (20 mL) was added sulfur (0.42 g, 13.1 mmol) and the mixture was heated at reflux over 2 h. The toluene was removed on a rotary evaporator to give a cream coloured solid that was washed with cold acetone (2 × 5 mL). The solid was dissolved in hot acetone (60 mL) and slow evaporation of the solution produced a crop of white crystalline material. Yield 1.15 g (38%). ^{1}H NMR ($CDCl_3$): δ 7.81–7.76 (m, 8H, P*Ph*$_2$), 7.46 (m, 4H, P*Ph*$_2$), 7.34–7.30 (m, 8H, P*Ph*$_2$), 4.62 (m, 2H, N*H*). ^{31}P NMR ($CDCl_3$): δ 66.0 (s, 2P, P=S). ν_{PS}/cm^{-1}: 633, 615. ν_{NH}/cm^{-1}: 3222, 3158. *Anal*. Calc. for $C_{24}H_{22}N_2P_2S_2$: C, 62.05; H, 4.99; N, 6.03. Found: C, 62.18; H, 4.73; N, 6.07%. m.p. 201–204 °C (*lit.* 204 °C).

2.2.2. [{CuLCl}$_2$]

A mixture of L (0.100 g, 0.215 mmol) and CuCl (0.022 g, 0.222 mmol) in MeCN (70 mL) was heated at reflux over 7 h. The reaction mixture was filtered while hot and a white microcrystalline precipitate formed on cooling. Yield 0.105 g. An analytically pure sample and X-ray quality crystals of [{CuLCl}$_2$]·4MeCN were obtained after a second recrystallisation of a portion of the material from hot MeCN. *Anal*. Calc. for $C_{48}H_{44}Cl_2Cu_2N_4P_4S_4$: C, 51.15; H, 3.94; N, 4.97. Found: C, 51.10; H, 4.02; N, 5.01%. ν_{PS}/cm^{-1}: 620, 599. ν_{NH}/cm^{-1}: 3070. m.p. 246–250 °C (dec.).

2.2.3. [{CuLBr}$_2$]

A mixture of L (0.100 g, 0.215 mmol) and CuBr (0.032 g, 0.222 mmol) in MeCN (90 mL) was heated at reflux over 4 h. The reaction mixture was filtered while hot and a white microcrystalline precipitate formed on cooling. Yield 0.097 g. An analytically pure sample and X-ray quality crystals of [CuLBr]$_2$·2MeCN were obtained after a second recrystallisation of a portion of the material from hot MeCN. *Anal.* Calc. for $C_{48}H_{44}Br_2Cu_2N_4P_4S_4$: C, 47.41; H, 3.65; N, 4.61. Found: C,47.64; H, 3.55; N, 5.19%. ν_{PS}/cm^{-1}: 620, 601. ν_{NH}/cm^{-1}: 3075. m.p. 255–270 °C (dec.).

2.2.4. [{CuLI}$_2$]·CH$_3$CN

A mixture of L (0.100 g, 0.215 mmol) and CuI (0.041 g, 0.215 mmol) in $CHCl_3$ (5 mL) was heated at reflux over 1 h. The mixture was allowed to cool and a white precipitate was collected by filtration. Yield 0.075 g. X-ray quality crystals of [{CuLI}$_2$]·2MeCN and an analytically pure crop of the monosolvated complex were obtained by recrystallisation from hot MeCN (20 mL). *Anal.* Calc. for $C_{50}H_{47}Cu_2I_2N_5P_4S_4$: C, 44.45; H, 3.51; N, 5.18. Found: 44.11; H, 3.24; N, 5.62%. ν_{PS}/cm^{-1}: 613, 602. ν_{NH}/cm^{-1}: 3085. m.p. 255–261 °C (dec.).

2.2.5. [{L(HgI$_2$)$_2$}$_2$]

A mixture of L (0.100 g, 0.215 mmol) and HgI_2 (0.196 g, 0.431 mmol) in MeCN (20 mL) was heated at reflux over 1.5 h. The reaction mixture was filtered while hot and a pale yellow crystalline solid formed on cooling. Yield 0.217 g. *Anal.* Calc. for $C_{48}H_{44}Hg_4I_8N_4P_4S_4$: C, 20.99; H, 1.61; N, 2.04. Found: C, 21.06; H, 1.60; N, 2.09%. ν_{PS}/cm^{-1}: 620, 595. ν_{NH}/cm^{-1}: 3154, 3052. m.p. 168–200 °C (dec.).

2.2.6. [HgLCl$_2$]

A mixture of L (0.100 g, 0.215 mmol) and $HgCl_2$ (0.059 g, 0.217 mmol) in MeCN (35 mL) was heated at reflux over 5 h. The reaction mixture was allowed to cool and a white precipitate was collected by filtration. Yield 0.123 g. A small amount of material was recrystallised from hot nitromethane. *Anal.* Calc. for $C_{24}H_{22}Cl_2HgN_2P_2S_2$: C, 39.16; H, 3.01; N, 3.81. Found: C, 38.92; H, 3.04; N, 3.92%. ν_{PS}/cm^{-1}: 619, 594. ν_{NH}/cm^{-1}: 3057. m.p. 215–230 °C (dec.).

2.2.7. [HgLBr$_2$]

A mixture of L (0.100 g, 0.215 mmol) and $HgCl_2$ (0.078 g, 0.216 mmol) in MeCN (10 mL) was heated at reflux over 2 h. The reaction mixture was allowed to cool and a white precipitate was collected by filtration, washed with cold acetonitrile and air dried. Yield 0.140 g. A sample of the material was recrystallised from hot nitromethane and crystals suitable for X-ray analysis were also obtained from this solvent. *Anal.* Calc. for $C_{24}H_{22}Br_2HgN_2P_2S_2$: C, 34.94; H, 2.69; N, 3.40. Found: C, 34.88; H, 2.66; N, 3.41%. ν_{PS}/cm^{-1}: 620, 593. ν_{NH}/cm^{-1}: 3075. m.p. 210–225 °C (dec.).

2.3. Crystallography

The X-ray data were collected on a Siemens P4 four circle diffractometer, using a Siemens SMART 1K CCD area

detector. The crystals were mounted in an inert oil, transferred into the cold gas stream of the detector and irradiated with graphite monochromated Mo-Kα ($\lambda = 0.71073$ Å) X-rays. The data were collected by the SMART program and processed with SAINT to apply Lorentz and polarisation corrections to the diffraction spots (integrated 3 dimensionally). The structures were solved by direct methods and refined using the SHELXTL [20] program. The hydrogen atoms bound to the nitrogen atoms on the hydrazine backbone were located from the electron difference map and refined using a riding model. All other hydrogen atoms were calculated at ideal positions. Refinement, collection and crystal data are given on Table 1.

3. Results and discussion

3.1. Syntheses of the compounds

The free ligand L was prepared from the sulfuration of the parent phosphine, (1,2-diphenylphosphino)hydrazine in toluene. This differs from the previously reported method where it was prepared from the reaction between $Ph_2P(S)Cl$ and anhydrous hydrazine [15]. The ^{31}P NMR chemical shift of L is 66 ppm in $CDCl_3$ and downfield of phosphorus signal in (1,2-diphenylphosphino)ethane (L^1) which occurs at 44 ppm. The ligand exhibits IR bands at 3222 and 3158 cm^{-1}, (assigned to NH) and 633 and 615 cm^{-1}, (assigned to P=S) stretching frequencies, respectively.

Pure samples of copper halide complexes of stoichiometry $[\{CuLX\}_2]$ (X = I, Br or Cl) were obtained from the reactions between the ligand and the appropriate copper(I) halide followed by crystallisation from hot acetonitrile solutions. Satisfactory elemental analyses were obtained in each case. The complexes have poor solubility in common organic solvents at room temperature which precluded characterisation by NMR. In the IR spectra, both the NH and PS stretching bands are shifted to lower wave numbers when compared with the free ligand. Thus the ν(NH) stretching frequencies are observed at 3084, 3070 and 3074 cm^{-1} and the pairs of ν(PS) bands at 612 and 601, 619 and 599 and 620 and 600, respectively, for the series X = I, Cl, Br.

Similarly 1:1 mercury(II) chloride and bromide complexes, $[HgLX_2]$ (X = Cl or Br) were obtained from the reaction of equimolar ligand and mercury(II) halide in MeCN. Initially we attempted to prepare a 1:1 mercury(II) iodide complex in the same way but it was apparent that we were obtaining mixtures, with one of the components being the $[\{L(HgI_2)_2\}_2]$ species reported here. This latter complex was obtained in good yield from the reaction of the metal salt and the ligand in a 2:1 molar ration. The IR spectra for the mercury bromide and chloride complexes are similar with NH stretching frequencies at 3074 and 3056 cm^{-1} and pairs of PS stretching frequencies at 618 and 593 and 619 and 593 cm^{-1}. The tetrametallic mercury iodide complex has a different spectrum with two stretching

Table 1
Crystal and refinement data

Compound	L	$[\{CuLI\}_2]\cdot 2MeCN$	$[\{CuLBr\}_2]\cdot MeCN$	$[\{CuLCl]\}_2\cdot 4MeCN]$	$[\{L(HgI_2)_2\}_2]$	$[HgLBr_2]$
Molecular formula	$C_{24}H_{22}N_2P_2S_2$	$C_{52}H_{50}Cu_2I_2N_6P_4S_4$	$C_{50}H_{47}Br_2Cu_2N_5P_4S_4$	$C_{56}H_{56}Cl_2Cu_2N_8P_4S_4$	$C_{48}H_{44}Hg_4I_8N_3P_4S_4$	$C_{24}H_{22}Br_2HgN_2P_2S_2$
Molecular weight (M)	464.50	1391.98	1256.95	1291.19	2746.56	1649.81
T (K)	200(2)	200(2)	200(2)	200(2)	83(2)	83(2)
Crystal system	monoclinic	monoclinic	monoclinic	triclinic	triclinic	monoclinic
Space group	P2(1)	P2(1)/n	P2(1)/n	$P\bar{1}$	$P\bar{1}$	$P2(1)/n$
a (Å)	10.5252(2)	12.0932(2)	12.019(2)	10.5608(1)	10.5535(3)	8.0292(1)
b (Å)	18.2405(3)	15.4958(2)	15.559(3)	11.1659(1)	11/8678(3)	17.4989(2)
c (Å)	24.7358(1)	15.0715(3)	15.181(3)	15.1527(1)	14.8929(4)	18.9981(2)
α (°)				70.607(1)	78.697(1)	
β (°)	102.253(1)	94.648(1)	91.82(3)	72.411(1)	74.292(1)	92.535(1)
γ (°)				65.012(1)	68.929(1)	
V (Å^3)	4640.72(12)	2815.02(8)	2837.3(10)	1500.03(2)	1665.43(8)	2666.66(5)
Z	8	4	4	2	2	4
μ (MoKα) (mm^{-1})	0.381	2.155	2.455	1.088	13.154	9.062
ρ_{calc} (g cm^{-3})	1.330	1.642	1.471	1.429	2.738	2.055
2θ Maximum (°)	50.78	51.36	53.26	54.20	51.36	54.26
Number of unique reflections	15697	5329	5737	6468	6289	5862
Data/restraints/parameters	15 697/1/1081	5329/0/317	5737/0/317	6468/0/347	6289/0/325	5862/0/298
Final R indices [$I > 2\sigma(I)$]	$R_1 = 0.0279$	$R_1 = 0.0198$	$R_1 = 0.0434$	$R_1 = 0.0259$	$R_1 = 0.0224$	$R_1 = 0.0235$
	$wR_2 = 0.0642$	$wR_2 = 0.0496$	$wR_2 = 0.1275$	$wR_2 = 0.0730$	$wR_2 = 0.0523$	$wR_2 = 0.0506$
R indices (all data)	$R_1 = 0.0315$	$R_1 = 0.0220$	$R_1 = 0.0575$	$R_1 = 0.0304$	$R_1 = 0.0238$	$R_1 = 0.0306$
	$wR_2 = 0.0667$	$wR_2 = 0.0504$	$wR_2 = 0.1360$	$wR_2 = 0.0757$	$wR_2 = 0.0530$	$wR_2 = 0.0542$
Goodness of fit on F^2	1.098	1.112	1.130	1.048	1.107	1.087

frequencies assignable to NH at 3153 and 3051 cm^{-1} and a pair of PS stretching frequencies at 617 and 595 cm^{-1}. The solubilities of the mercury complexes in common organic solvents were also low.

The two P=S stretching frequencies for L at 632 and 614 cm^{-1} are both lowered by about 12–21 cm^{-1} for the complexes, consistent with metal coordination of the sulfur atoms [16]. Similarly, the two N–H stretching frequencies at 3222 and 3158 cm^{-1} for L are replaced with one band at about 3056–3084 cm^{-1} for all the complexes, apart from $[\{L(HgI_2)_2\}_2]$, which displays two bands at 3052 cm^{-1} and 3153 cm^{-1}. The lowering of these frequencies is consistent with the presence of N–H···X hydrogen bonds in the structure, rather than coordination by N–H groups in a strained four-membered ring. Moreover, the trend of the ν(NH) frequencies to lower energies increases along the series $I^- < Br^- < Cl^-$, which parallels the hydrogen-bonding ability of the anions [21].

All of the copper complexes with L remained unchanged upon recrystallization from hot CH_3CN. However, the CuCl complex of 1,2-bis(diphenylphosphino)hydrazine, after initial recrystallization from hot toluene and then left to crystallize for several months, was hydrolytically unstable with cleavage of the P–N bonds [22], and one of the products isolated was diphenylphosphinic acid. Similar reactivity has been observed for aminobis(phosphines) [23]. The polarity of the P–N bond favours attack on the phosphorus atom by the water nucleophile, and this is followed by oxidation of the P atom. This reaction is slowed down when the ligand is already oxidized as in L and does not occur when P–C bonds are present. This is the first reported cleavage reaction for a coordinated hydrazinobis(phosphine).

3.2. Description of the structures

3.2.1. 1,2-Bis(diphenylthioylphosphino)hydrazine (L)

The free ligand L crystallises from an acetone solution in the space group $P2(1)$ with four molecules in the asymmetric unit. Every independent molecule has a similar conformation in which the PNNP backbone has a torsion angle of around 16° and both pairs of N–H and P=S bonds are directed towards the same side of the mean PNNP plane. This arrangement of the sulfur atoms is similar to that observed in the structure of $Ph_2P(S)CH_2CH_2P(S)Ph_2$ (L^1) although the PCCP backbone is slightly more twisted with a torsion angle of *ca.* 25° [24]. However, molecules of L exist as hydrogen bonded dimers in the solid state with both molecules in the dimer contributing one N–H···S bond to the array (Fig. 1), whereas the sulfur atoms in L^1 are only involved in close contacts with aromatic hydrogen atoms on nearby diphenylphosphine groups. In this respect, the packing in L more resembles $Ph_2P(O)CH_2CH_2P(O)Ph_2$, in which two adjacent molecules each supply a close contact between a hydrogen atom on the $(CH_2)_2$ backbone and a P=O bond, although in this compound the P=O bonds on the same molecule are directed towards opposite sides of the PCCP mean plane [25]. Selected bond lengths and angles are given in Table 2. Structural data on hydrazinobis(phosphine) adducts is scarce although the P–N and N–N bond lengths in L (average 1.695 and 1.441 Å) are comparable with those observed in a cyclic example, 3,6-dimethoxy-1,2,4,5-tetraaza-3,6-diphosphacyclohexanedisulfide (average 1.663 and 1.435 Å) and the P–S bond lengths (average 1.945 Å) are comparable to those in L^1 (1.941 Å) [26].

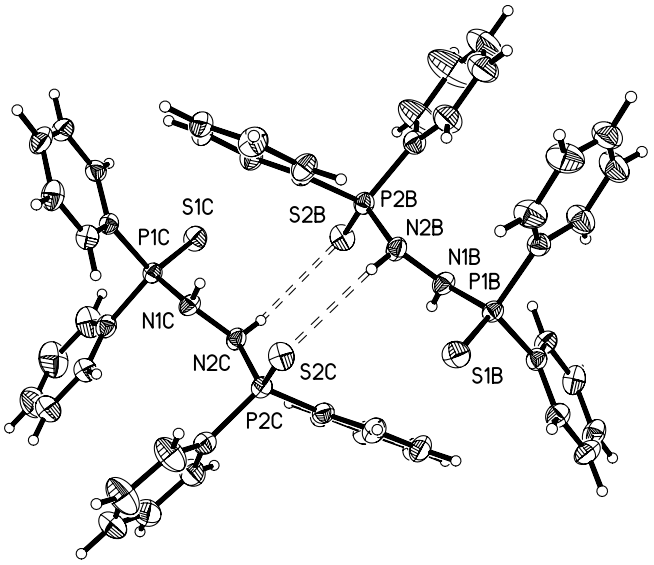


Fig. 1. Diagram of the dimeric form of L in the solid state. Thermal ellipsoids drawn at 50% probability level and most hydrogen atoms removed for clarity.

3.2.2. Copper(I) halide complexes of L

X-ray quality crystals of the copper(I) halide complexes of L were obtained in from MeCN solutions. In each case the overall structure is similar and comprises a dimetallic species of stoichiometry $[\{CuLX\}_2]$ in which L acts as a bridging ligand, bonding to separate copper centres through either sulfur atom (Fig. 2., X = I). Selected bond lengths and angles are given in Table 3.

The coordination spheres of the Cu(I) centres have 'S_2X_2' donor sets with a somewhat unusual geometry, being best described as trigonal pyramidal. The copper bonds to X1, S1 and S2 (sulfur atoms from different ligands) and X1A. The halides link the two symmetry related Cu atoms with the Cu–X1A bond lengths being around 0.5–0.65 Å longer than the Cu–X1 bonds lengths (Table 3). The X1A ion forms the apex of the trigonal pyramid. The sum of the three angles in the coordination planes formed about the copper atom by X1 and the sulfur atoms are approximately 354.7, 357.1 and 356.9°, respectively, for X1 = I, Br and Cl hence approaching an ideal trigonal geometry. The copper atom is displaced from the trigonal plane towards X1A by 0.3210, 0.2318 and 0.2360 Å, respectively, for X = I, Br and Cl.

The overall structures are comparable to the arrangement observed in $[\{CuL^1Cl\}_2]$ [27] but with some subtle dif-

Table 2
Selected bond lengths (Å) and angles (°) for L

	Molecule A	Molecule B	Molecule C	Molecule D
P1–N1	1.693(2)	1.701(2)	1.6968(19)	1.701(2)
P2–N2	1.707(2)	1.6859(19)	1.695(2)	1.683(2)
N1–N2	1.446(3)	1.435(3)	1.439(3)	1.443(3)
P1–S1	1.9507(9)	1.9397(9)	1.9399(9)	1.9415(9)
P2–S2	1.9401(9)	1.9504(9)	1.9516(9)	1.9485(9)
S1–P1–N1	116.77(7)	116.39(8)	117.05(7)	115.76(8)
S1–P1–C11	114.26(8)	114.60(8)	114.58(8)	114.55(8)
S1–P1–C21	113.68(9)	112.90(9)	113.37(9)	113.07(9)
S2–P2–N2	115.77(8)	116.81(8)	116.54(8)	117.31(8)
S2–P2–C31	113.15(10)	112.76(9)	112.28(9)	112.57(9)
S2–P2–P2–C41	115.02(9)	114.73(8)	113.93(9)	115.27(9)
P1–N1–N2	111.55(14)	110.70(14)	113.05(14)	110.59(14)
P2–N2–N1	112.66(14)	113.04(15)	111.17(14)	113.12(15)

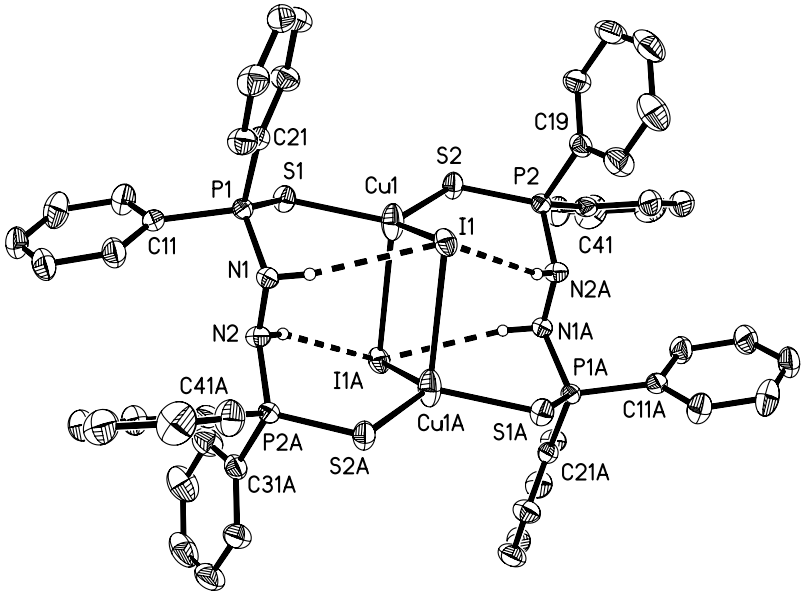


Fig. 2. Diagram of the dimetallic complex $[\{CuLI\}_2]$. Thermal ellipsoids drawn at 50% probability level and most hydrogen atoms removed for clarity.

Table 3
Selected bond lengths (Å) and angles (°) for the copper(I) complexes

	$[\{CuLI\}_2]\cdot 2MeCN$	$[\{CuLBr\}_2]\cdot MeCN$	$[\{CuLCl\}_2]\cdot 4MeCN$
Cu1–S1	2.3045(5)	2.888(12)	2.2822(4)
Cu1–S2	2.2951(5)	2.2927(12)	2.2851(4)
Cu1–X1	2.5990(3)	2.4353(8)	2.3117(4)
Cu1–X1A	3.0859(3)	3.0851(1)	2.8687(5)
P1–S1	1.9769(6)	1.9865(14)	1.9864(5)
P2–S2	1.9859(6)	1.9884(15)	1.9848(5)
N1–N2	1.444(2)	1.450(4)	1.4448(16)
S1–Cu1–S2	115.752(19)	115.15(4)	114.073(15)
S1–Cu1–X1	118.448(15)	119.41(4)	120.657(15)
S1–Cu1–X2	120.487(16)	122.53(4)	122.121(15)
S1–Cu1–X1A	94.951(15)	95.76(4)	99.79(1)
S2–Cu1–C1A	98.924(16)	98.03(4)	100.56(1)
X1–Cu1–X1A	99.130(9)	93.36(3)	87.86(1)
Cu1–X1–Cu1A	80.870(10)	86.64(3)	92.14(1)
P1–S1–Cu1	106.44(2)	105.38(5)	101.705(8)
P2–S2–Cu1	104.66(2)	102.79(5)	100.396(19)

ferences. In the three L Cu(I) complexes there are four strong intramolecular hydrogen bonds (Table 4) of the type N–H···X which have the effect of creating two pairs of fused 6-membered chelate rings. This assembly appears to have an increasing influence on the PNNP backbone as X becomes smaller and more electronegative (in each case the torsion angle for PNNP is 10, 13 and 16° for X = I, Br and Cl). In $[\{CuL^1Cl\}_2]$ the PCCP torsion angle is 4° and the intramolecular contacts from the ligand backbone are long (the relevant C–H···Cl contacts are 2.708 and 2.581 Å) compared with $[\{CuLCl\}_2]$ where N–H···Cl are 2.410 and 2.351 Å. Hence the ligand backbones in the $[\{CuLX\}_2]$ complexes remain twisted in their compression towards the Cu_2X_2 core whereas in $[\{CuL^1Cl\}_2]$ the ligand backbone is somewhat flattened. In $[\{CuLCl\}_2]$the sulfur atoms on the same ligand are further apart (5.989 *cf.* 5.846 Å) even though the phosphorus atoms are closer (4.083 *cf.* 4.424 Å). The impact of this on the coordination spheres is that in $[\{CuL^1Cl\}_2]$ the Cu···Cu separation in $[\{CuLCl\}_2]$ is longer (3.751 *cf.* 3.327 Å) and the bridging Cu–Cl distances (2.869 *cf.* 2.639 Å) are also increased.

3.2.3. $[\{L(HgI_2)_2\}_2]$

The reaction of 2 equiv of HgI_2 with L and subsequent recrystallisation from acetonitrile afforded the unusual tetrametallic complex $[\{L(HgI_2)_2\}_2]$. In this complex L is again acting as a bridging, ligand binding different Hg(II) ions through each sulfur donor with each ligand creating a moiety of stoichiometry '$L(HgI_2)_2$'. Two such moieties are linked by iodide bridges which lie about a centre of inversion to give the tetrametallic complex (Fig. 3). Selected bond lengths and angles are given in Table 5.

Hence the molecule contains two different tetrahedral 'I_3S' coordination spheres. Hg1 is bonded to I1 and I2 [2.6726(4) and 2.6919(3) Å] and is bridged to Hg2 through a slightly longer bond to I3 [3.1084(3) Å]. Hg2 is coordinated by three bridging iodine ligands I3, I4 and I4A; the bond lengths being 2.7244(4), 2.7323(3) and 3.1572(4) Å, respectively. The Hg2–S2 bond length of 2.5587(11) Å is significantly shorter than the Hg1–S1 bond length of 2.6150(11) Å although the P=S bond lengths are similar and longer than in the free ligand [1.9965(16) and 2.0012(16) Å compared to an average of 1.945 Å]. As with the dimetallic copper(I) halide structures, the NH–NH ligand backbones in $[\{L(HgI_2)_2\}_2]$ participate in strong hydrogen bonding interactions with the iodide coligands; H1···I2 is 2.91 Å and H2···I3 is 2.90 Å and the PNNP torsion angle is 17.7°.

Table 4
Hydrogen-bond lengths (Å) and angles (°) in the $[\{CuLX\}_2]$ complexes

	D–H	H···A	D···A	∠(DHA)
N1–H1···I1	0.85	2.84	3.6506(15)	160.7
N2–H2···I1A	0.86	2.75	3.5480(14)	156.4
N2–H2···Br1	0.92	2.62	3.502(3)	160.3
N1–H1···Br1	0.89	2.59	3.436(3)	158.5
N1–H1···Cl1	0.93	2.35	3.2394(12)	159.7
N2–H2···Cl1	0.89	2.41	3.2674(12)	161.7

3.2.4. $[HgLBr_2]$

From the reaction of 1 equiv of $HgBr_2$ with L, crystals of $[HgLBr_2]$ were obtained from nitromethane in which L acts as a bidentate ligand bonding through the two sulfur atoms to form a seven-membered chelate ring. The complex has a distorted tetrahedral geometry and selected bond lengths and angles are given in Table 6.

The complex (Fig. 4) is comparable with $[HgL^1Br_2]$ which has a similar donor set and distorted tetrahedral coordination geometry [8]. The ligand bite angle of 119.52(3)° in $[HgLBr_2]$ is close to that of 118.85(8)° in $[HgL^1Br_2]$. However the bond lengths in the coordination sphere of each complex are quite different. The two Hg–S bonds in $[HgLBr_2]$ are shorter at 2.5312(9) and 2.5173(9) Å compared to 2.678(2) and 2.552(2) Å in $[HgL^1Br_2]$ while the two Hg–Br

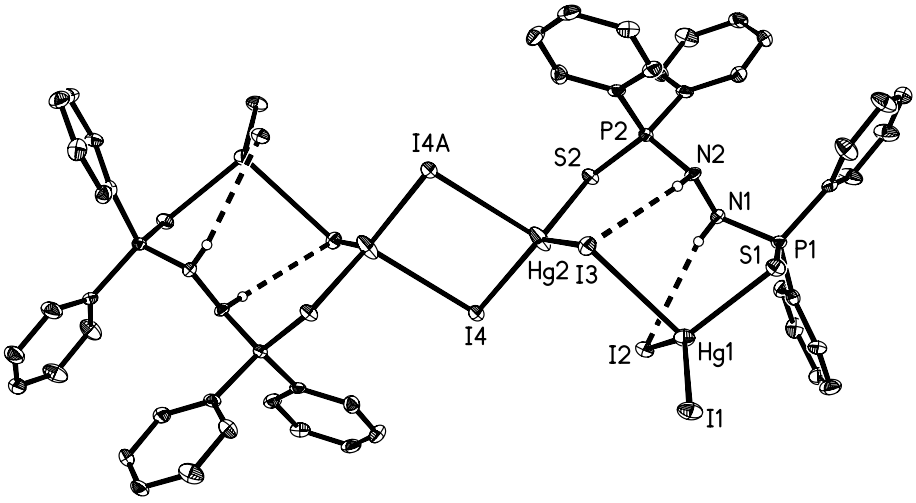


Fig. 3. Diagram of the tetrametallic complex $[\{L(HgI_2)_2\}_2]$. Thermal ellipsoids drawn at 50% probability level and most hydrogen atoms removed for clarity.

Table 5
Selected bond lengths (Å) and angles (°) for [{L(HgI$_2$)$_2$}$_2$]

Hg1–S1	2.6150(11)	Hg2–S2	2.5587(11)
Hg1–I1	2.6726(4)	Hg2–I3	2.7244(4)
Hg1–I2	2.6919(3)	Hg2–I4	2.7323(3)
Hg1–I3	3.1084(3)	Hg2–I4A	3.1752(4)
P1–S1	1.9965(16)	P2–S2	2.0012(16)
N1–N2	1.441(5)		
S1–Hg1–I1	105.26(3)	S2–Hg2–I3	115.50(3)
S1–Hg1–I2	114.88(3)	S2–Hg2–I4	111.85(3)
I1–Hg1–I2	134.101(12)	I3–Hg2–I4	128.543(12)
S1–Hg1–I3	97.27(3)	S2–Hg2–I4A	104.81(3)
I1–Hg1–I3	102.885(11)	I3–Hg2–I4A	96.727(10)
I2–Hg1–I3	93.488(10)	I4–Hg2–I4A	89.626(10)
Hg1–I3–Hg2	99.254(10)	Hg2–I4–Hg2A	90.374(10)
P1–S1–Hg1	100.80(5)	P2–S2–Hg2	103.50(6)

Table 6
Selected bond lengths (Å) and angles (°) for [HgLBr$_2$]

Hg1–S1	2.5173(9)	Hg1–S2	2.5312(9)
Hg1–Br1	2.6089(4)	Hg1–Br2	2.6078(4)
P1–S1	1.9878(12)	P2–S2	1.9979(12)
N1–N2	1.419(4)		
S1–Hg1–S2	119.52(3)	S2–Hg1–Br1	112.55(2)
S1–Hg1–Br1	98.82(2)	S2–Hg1–Br2	102.19(2)
S1–Hg1–Br2	112.98(2)	Br1–Hg1–Br2	111.107(12)
P1–S1–Hg1	107.43(4)	P2–S2–Hg2	108.36(4)

bonds are considerably longer at 2.6089(4) and 2.6078(4) Å compared to 2.5592(11) and 2.5509(11) Å.

A possible reason for this presents itself from an examination of the packing in [HgLBr$_2$]. Contrary to the conformation found in the bridging structures previously discussed, the N–H bonds on the ligand backbone of L are now directed towards the opposite side of the PNNP mean plane to the sulfur donor atoms. This allows adjacent molecules of [HgLBr$_2$] to engage in intermolecular hydrogen bonding in the crystalline state, with the distances H1···Br2A and H2···Br1A being 2.58 and 2.64 Å, respectively. It also results in a lengthening of the Hg–Br bonds along with any compensating effects due to short Hg–S bonds. The outcome is the formation of a second, seven-membered chelate-type ring *viz.* Hg1A–Br1A···H2–N2–N1–H1···Br2A in a bridging arrangement as columns of [LHgBr$_2$] stack along the *a*-axis (Fig. 5). Further

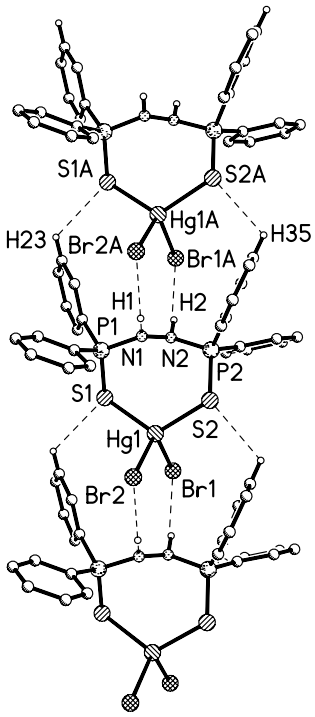


Fig. 5. A diagram showing how [HgLBr$_2$] molecules pack in columns along the *a*-axis.

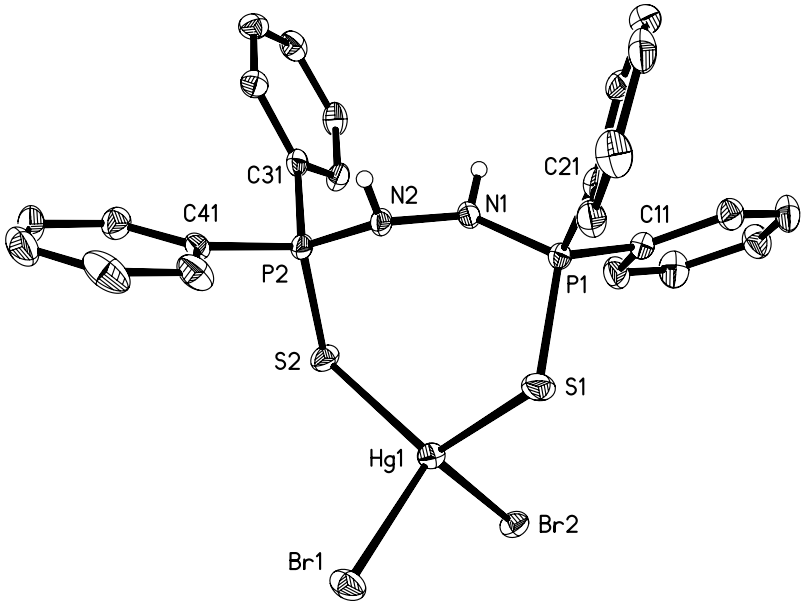


Fig. 4. Diagram of the complex [HgLBr$_2$]. Thermal ellipsoids drawn at 50% probability level and most hydrogen atoms removed for clarity.

reinforcement of the columnar array is provided by the close contacts S1A···H35 and S2B···H23 on adjacent molecules (2.916 and 2.835 Å, respectively). Interestingly, the N–N bond is significantly shorter at 1.419(4) Å than in the other structures described here [1.435(3)–1.450(4) Å] and the PNNP torsion angle is significantly larger (37.8°).

4. Conclusion

The ligand, 1,2-bis(diphenylthioylphosphino)hydrazine (L), reacts with copper(I) and mercury(II) halides affording the complexes, $[\{CuLX\}_2]$ (X = I, Br or Cl), $[HgLX_2]$ (X = Cl or Br) and the tetrametallic complex, $[\{L(HgI_2)_2\}_2]$. The complexes contain the metal in a four coordinate environment which approximates trigonal pyramidal for the copper complexes and distorted tetrahedral for the mercury complexes. In the dimetallic copper complexes L bridges the two metal atoms, with bridging halides completing the coordination sphere. The tetrametallic mercury complex, $[\{L(HgI_2)_2\}_2]$, also contains L bridging two Hg atoms but the two '$L(HgI_2)_2$' moieties are linked by coordinated iodide ions. Hydrogen bonds between the hydrazine N–H hydrogens of L and the halide ligands are an important feature in the structures of the metal complexes. This is a much more dominant effect than is observed with similar complexes of L^1, and is an interesting ligand design strategy.

Appendix A. Supplementary material

CCDC 646490–646494 contains the supplementary crystallographic data for this paper. These data can be obtained free of charge via http://www.ccdc.cam.ac.uk/conts/retrieving.html, or from the Cambridge Crystallographic Data Centre, 12 Union Road, Cambridge CB2 1EZ, UK; fax: (+44) 1223-336-033; or e-mail: deposit@ccdc.cam.ac.uk. Supplementary data associated with this article can be found, in the online version, at doi:10.1016/j.poly.2007.08.009.

References

[1] T.S. Lobana, Prog. Inorg. Chem. 37 (1989) 495.
[2] T.S. Lobana, in: F.R. Hartley (Ed.), The Chemistry of Organophosphorus Compounds, Vol. 2, Wiley, Chichester, 1992.
[3] Z. Spichal, M. Necas, J. Pinkas, J. Novosad, Inorg. Chem. 43 (2004) 2776.
[4] M.B. Hursthouse, W. Levason, R. Ratnani, G. Reid, H. Stainer, M. Webster, Polyhedron 24 (2005) 121.
[5] Z. Spichal, M. Necas, J. Pinkas, Inorg. Chem. 44 (2005) 2074.
[6] Z. Spichal, M. Necas, J. Pinkas, Z. Zdrahal, Polyhedron 25 (2006) 809.
[7] E. Subasi, O.S. Sentuerk, F.U. Sarikahya, Z. fuer Natur. B 59 (2004) 836.
[8] T.S. Lobana, R. Verma, A. Singh, M. Shikha, A. Castineiras, Polyhedron 21 (2002) 205.
[9] M. Preisenberger, A. Bauer, H. Schmidbaur, Chem. Ber./Recueil 130 (1997) 955.
[10] S. Irisli, S. Yanar, Polyhedron 25 (2006) 1333.
[11] T. Cantat, F. Jaroschik, F. Nief, L. Ricard, N. Mezailles, P. Le Floch, Chem. Commun. 41 (2005) 5178.
[12] M. Casadesus, M.P. Coogan, S. Oakley, E. Davies, L.-L. Ooi, J. Organomet. Chem. 691 (2006) 3715.
[13] A.M.J. Lees, A.W.G. Platt, Inorg. Chem. 42 (2003) 4673.
[14] R.P. Nielsden, H.H. Sisler, Inorg. Chem. 2 (1963) 753.
[15] H. Bock, G. Rudoplh, Chem. Ber. 98 (1965) 2273.
[16] R. Turpin, J. Casteran-Baumassy, P. Dagnac, J. Chem. Res. 4 (1980) 138, Synopses.
[17] G. Johannsen, O. Stelzer, E. Unger, Chem. Ber. 108 (1975) 1259.
[18] R.N. Keller, H.D. Wycoff, Inorg. Synth. 2 (1946) 1.
[19] G.B. Kauffmann, R.P. Pinnell, Inorg. Synth. 6 (1960) 3.
[20] G.M. Sheldrick, SHELXL Suite of Programs for Crystal Structure Analysis, Institüt für Anorganische Chemie der Universität, Tamanstrassse 4, Göttingen, Germany, 1998.
[21] E.W. Ainscough, A.M. Brodie, S.T. Wong, J. Chem. Soc., Dalton Trans. (1977) 915.
[22] E.W. Ainscough, A.M. Brodie, G.H. Freeman, unpublished results.
[23] S. Priya, M.S. Balakrishna, J.T. Mague, S.M. Mobin, Inorg. Chem. 42 (2003) 1272.
[24] A.L. Rheingold, G.P.A. Yap, Cambridge Structural Database, deposition code NADXZ.
[25] P. Calacagno, B.M. Kariuku, S.J. Kitchin, J.M.A. Robinson, D. Philip, K.D.M. Harris, Chem. Eur. J. 13 (2000) 2338.
[26] U. Von Englehardt, G.D. Jürgens, Acta Crystallogr. Sect., B 36 (1980) 3059.
[27] K. Brown, Acta Crystallogr. Sect., B 35 (1979) 462.

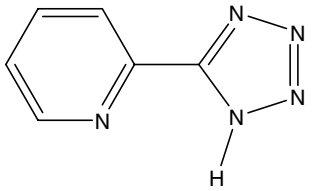


Fig. 1. Structure of 1 *H*, 5-(2′-pyridyl)tetrazole (H**pytz**).

tetrazolate ligands remains largely unexplored, with very few synthetic and structural studies appearing in the literature [11,12]. In previous work we demonstrated the possibility of using H**pytz,** whose structure is shown in Fig. 1, as a substitute for 2-picolinic acid, for the formation of hydrogels containing La^{3+} cations [12]. We showed that the formation of the gel was due to the capability of the tetrazolate ring to coordinate to the metal centre and, at the same time, form an extensive hydrogen-bonded network when water was added to the compound. These results prompted us to continue our investigation of the aqueous chemistry of different lanthanoid cations with **pytz**, focussing mainly on the structural aspects of the crystal lattices. In this work we concentrated our efforts on treating a range of lanthanoid chlorides with the tetrazolate ligands. Instead of using a 1:3 ratio, we systematically decreased the amount of ligand. This approach yielded the formation of cationic disubstituted complexes in the case of La, Gd and Ho, neutral trisubstituted for Ho, and hydroxo-bridged dimers for Y and Yb.

2. Experimental

Chemicals were obtained from Sigma–Aldrich and used as received. ^{1}H and ^{13}C NMR spectra were recorded on a Bruker AM 300 spectrometer. Chemical shifts were recorded on the δ scale and referenced to the solvent. Infrared spectra were recorded on a Perkin–Elmer 1600 Series FTIR using solid state pellets (KBr). Melting points were measured on a Stuart Scientific Melting Point Apparatus SMP3 in an open capillary. Elemental Analyses were performed by Campbell Microanalytical Laboratory, Department of Chemistry, University of Otago, Dunedin, New Zealand. For compounds **2** and **3** elemental analysis on the bulk material revealed for C, H, and N a variable amount between 1.5% and 4% lower than the calculated values. We ascribed this results to the presence of NaCl in the bulk material, which co-precipitated along with the compounds. Crystallographic data were obtained either on an Enraf-Nonius KAPPA CCD or on a Bruker X8 APEX CCD diffractometer at 123 K. All compounds were measured with Mo Kα radiation of 0.71073 Å generated by a fine-focus sealed tube using a graphite monochromator. Scans were performed in ϕ and ω and 0.5° frames. All the molecular structures were solved using the program SHELXS-97 [13]. Refinement was carried out with the program SHELXL-97 against F^2 using least-squares methods [14]. For the X-ray data refer to Tables 1 and 2.

2.1. Synthesis of *Hpytz*

The ligand was synthesised following a literature procedure [15]. HCl 33% (2.1 ml, 23 mmol) was added to toluene (50 ml). After carefully adding triethylamine (3.2 ml, 23 mmol), 2-cyanopyridine (1.9 ml, 20 mmol) and NaN_3 (1.50 g, 23 mmol), the mixture was stirred under reflux for 22 h. The organic layer was then extracted with water, and the aqueous phase acidified to pH 5 by dropwise addition of HCl 10%. The white solid formed was then filtered, washed several times with water, and dried under reduced pressure. Yield 2.10 g, 71%. Mp = 212–213 °C. ^{1}H NMR

Table 1
Summary of X-ray crystallographic data for the mononuclear compounds **1**–**4**

	1	**2**	**3**	**4**
Empirical formula	$C_{12}H_{18}LaN_{10}O_5Cl$	$C_{12}H_{18}GdN_{10}O_5Cl$	$C_{12}H_{16}HoN_{10}O_4Cl$	$C_{18}H_{22}HoN_{15}O_{6.5}$
Formula weight	556.72	575.06	564.73	714.44
Crystal system	Orthorhombic	Orthorhombic	Monoclinic	Monoclinic
Space group	*Fddd*	*Fddd*	*P*21/*n*	*P*21/*n*
Unit cell dimensions				
a (Å)	14.3814(1)	14.2351(2)	8.8460(18)	8.9640(18)
b (Å)	22.6433(1)	22.3283(2)	14.553(3)	17.720(4)
c (Å)	25.1217(1)	24.8560(3)	14.846(3)	16.698(3)
β (°)	90	90	99.79(3)	99.98(3)
Volume	8180.69(7)	7900.37(16)	1883.4(7)	2612.2(9)
Z	16	16	4	4
D_{calc} (g/cm^3)	1.808	1.934	1.992	1.824
Absorption coefficient μ (mm^{-1})	2.266	3.541	4.386	3.097
θ Range (°)	1.86–26.37	3.77–27.50	1.97–27.50	2.30–27.50
Total number of reflections	14800	10200	15817	16344
Number of unique reflections	2100	1748	4328	5992
Number of parameters	154	145	258	410
R_1, wR_2	0.0274, 0.0527	0.0313, 0.0537	0.0235, 0.0419	0.0585, 0.0841
Maximum, minimum peaks (e/Å^3)	1.439, −0.994	0.454, −0.880	1.176, −0.569	1.053, −3.594
Goodness-of-fit	1.126	0.998	1.136	1.335

Table 2
Summary of X-ray crystallographic data for the dimeric compounds **5** and **6**

	5	**6**
Empirical formula	$C_{24}H_{34}YbN_{20}O_{10}$	$C_{28}H_{42}Y_2N_{20}O_{10}$
Formula weight	1108.79	996.64
Crystal system	Triclinic	Triclinic
Space group	$P\bar{1}$	$P\bar{1}$
Unit cell dimensions		
a (Å)	8.9390(18)	9.3630(19)
b (Å)	9.3340(19)	11.567(2)
c (Å)	12.255(3)	11.696(2)
α (°)	68.75(3)	115.64(3)
β (°)	76.57(3)	91.34(3)
γ (°)	70.72(3)	113.81(3)
Volume	892.1(3)	1014.2(4)
Z	1	1
D_{calc} (g/cm^3)	2.064	1.632
Absorption coefficient (mm^{-1})	5.292	2.925
θ Range (°)	2.43–27.49	2.43–27.50
Total number of reflections	7788	19362
Number of unique reflections	4089	4637
Number of parameters	289	301
R_1, wR_2	0.0128, 0.0310	0.0901, 0.1349
Maximum, minimum peaks (e/Å^3)	0.576, −1.023	0.737, −1.457
Goodness-of-fit	1.154	1.290

(DMSO-d_6): δ 8.80 (H, ddd, $J = 4.8$, 1.7, 1.0 Hz, H6), 8.23 (H, td, $J = 7.9$, 1.0 Hz, H3), 8.08 (H, dd, $J = 7.6$, 1.7 Hz, H4), 7.63 (H, ddd, $J = 7.6$, 4.8, 1.3 Hz, H5). ^{13}C NMR (DMSO-d_6): δ 154.8 (CN_4H), 150.1 (C2), 143.7 (C6), 138.3 (C3), 126.2 (C4), 122.6 (C5).

2.2. General synthetic procedure for the preparation of the complexes

H**pytz** (1 equiv) and hydrated $LnCl_3$ (2 equiv) were added to water and heated until all the solid was completely dissolved. A NaOH solution (1 M) was then added dropwise until a persistent precipitate appeared (pH ~ 6). The solution was then filtered and left undisturbed at room temperature and block shaped crystals were then harvested after several weeks. Compounds **1**–**6** were obtained with a 25–30% yield, after which crystallisation was stopped to prevent contamination due to co-precipitation of NaCl.

2.2.1. *[La(pytz)$_2$(H$_2$O)$_5$]Cl (**1**)*

IR: ν 3300(sb), 3056(s), 1668(w), 1607(m), 1572(w), 1462(w), 1428(m), 1392(m), 1288(m), 1165(m), 1061(w), 1037(w), 1004(w), 799(w), 694(w) cm^{-1}. *Anal.* Calc. for $C_{12}H_{18}ClLaN_{10}O_5$: C, 25.89; H, 3.26; N, 25.16. Found: C, 26.08; H, 3.32; N 25.02%.

2.2.2. *[Gd(pytz)$_2$(H$_2$O)$_5$]Cl (**2**)*

IR: ν 3300(sb), 1636(w), 1605(s), 1570(w), 1461(w), 1427(s), 1386(s), 1284(s), 1248(w), 1156(w), 1099(w), 1059(w), 1035(w), 1002(w), 796(w), 750(w), 728(w) cm^{-1}. Elemental analysis revealed minor contamination of the bulk material, probably due to co-precipitation of traces of NaCl.

2.2.3. *[Ho(pytz)$_2$(H$_2$O)$_4$]Cl (**3**)*

IR: ν 3448(sb), 1681(w), 1648 (m), 1637(m), 1602(s), 1573(w), 1559(w), 1530(w), 1459(s), 1397(m), 1286(m), 1162(w), 1130(w), 1112(w), 1066(m), 993(m), 750(m), 730(m) cm^{-1}. Elemental analysis revealed minor contamination of the bulk material, probably due to co-precipitation of traces of NaCl.

2.2.4. *[Ho(pytz)$_3$(H$_2$O)$_4$] · 4H$_2$O (**4**)*

Compound **4** was obtained via recrystallisation of **3** in water. IR: ν 3448(sb), 1686(w), 1654(m), 1637(m), 1611(s), 1570(w), 1560(w), 1534(w), 1466(s), 1390(m), 1286(m), 1169(w), 1133(w), 1102(w), 1060(m), 1005(m), 750(m), 732(m) cm^{-1}. *Anal.* Calc. for $C_{18}H_{22}HoN_{15}O_5$: C, 31.18; H, 3.20; N, 30.30. Found: C, 31.77; H, 3.32; N, 30.60%.

2.2.5. *[Yb$_2$(pytz)$_4$ (μ-OH)$_2$(H$_2$O)$_4$] · 2H$_2$O (**5**)*

IR: ν 3094(sb), 1612(s), 1572(m), 1467(m), 1423(s), 1399(m), 1288(m), 1252(w), 1174(w), 1155(m), 1138(w), 1101(w), 1063(w), 1042(w), 1007(m), 903(w), 800(m), 751(s), 733(s), 634(m) cm^{-1}. *Anal.* Calc. for $C_{24}H_{34}Yb_2N_{20}O_{10}$: C, 26.00; H, 3.09; N, 25.27. Found: C, 26.08; H, 2.93; N, 24.91%.

2.2.6. *[Y$_2$(pytz)$_4$ (μ-OH)$_2$(MeOH)$_2$](H$_2$O)(MeOH) (**6**)*

Compound **6** was obtained with a different procedure: H**pytz** (0.29 g, 2 mmol) and YCl_3 (0.30 g, 1 mmol) were added to methanol (20 ml) and kept under vigorous stirring. NEt_3 (0.7 ml, 5 mmol) was then added dropwise over a period of 1 h, and the reaction was left stirring at room temperature for 36 h. The solvent was completely evaporated under reduced pressure and the residual solid mixture was washed with isopropanol to remove triethylamonium chloride. The leftover solid was then redissolved in methanol. Colourless block-shaped crystals were obtained after 3 weeks by diffusing isopropanol vapours into the solution. IR: ν 3199(sb), 1654(m), 1609(s), 1570(m), 1464(m), 1430(s), 1287(m), 1168(w), 1068(w), 1042(w), 900(w), 734(s), 634(m) cm^{-1}. *Anal.* Calc. for $C_{26}H_{38}Y_2N_{20}O_{10}$: C, 32.24; H, 3.95; N, 28.92. Found: C, 31.92; H, 3.80; N, 28.82%.

3. Results and discussion

3.1. Synthesis of the lanthanoid complexes

H**pytz** was synthesised, following a literature procedure [15], by treating 2-cyanopyridine with NaN_3 in toluene in the presence of triethylammonium chloride. The ligand, usually in its sodium salt form (generated by treatment of H**pytz** with NaOH *in situ*), was then reacted with the corresponding lanthanoid chloride. The synthesis was performed either in water or methanol as the products were insoluble in these solvents and could be easily purified from unreacted reagents by washing the precipitate after isolation. As previously reported in the literature, a stoichiometry of 1:3

metal to ligand leads to the formation of neutral trisubstituted complexes [11]. Since the tetrazolate anion can chelate forming 5-membered rings, but also bridge through the four remaining electron pairs of the N atoms, we investigated the synthesis using a deficit of ligand in the reaction mixture. Therefore $LnCl_3$ and **pytz** were mixed together in a 2:1 stoichiometric ratio. The purpose of using a lower quantity of ligand was initially to favour the formation of polynuclear compounds such as oxo/hydroxo polynuclear clusters [16]. This same procedure is known to yield such cages using carboxylates as ligands [17]. Instead, either disubstituted cationic complexes or hydroxo-bridged dimers were isolated and characterised (Scheme 1). Interestingly, in a stoichiometric ratio 2:1 metal to ligand, there is a lack of propensity to redistribute (Eq. (1)), which is a relatively common phenomenon in rare earth chemistry [18].

$$3LnL_2Cl \rightarrow 2LnL_3 + LnCl_3 \quad (1)$$

However, recrystallisation of the disubstituted compounds in hot water yielded the trisubstituted analogues, due to the fact that during the recrystallisation the metal to ligand ratio is decreased from 2:1 to 1:2. All the compounds were characterised, along with X-ray diffraction, with standard analytical techniques (IR, elemental analysis). In particular, the IR spectra show common features such as strong absorptions above 3000 cm^{-1} belonging to the water and hydroxo O–H vibration, and between 1660 and 1600 cm^{-1} for the tetrazolate C=N. All the compounds decompose around 300–310 °C.

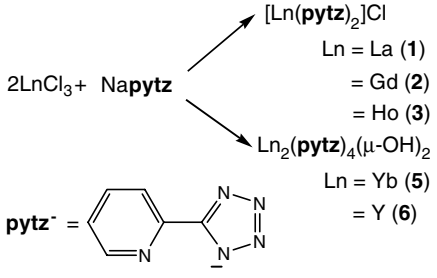
Compared with the corresponding lanthanoid carboxylates, which tend to form polymeric networks when reacted in 1:3 metal to ligand stoichiometry [19], the tetrazolate complexes are individual molecular entitites with a high tendency to interact via hydrogen bonding and π-stacking. This difference is probably due to the chelating and bridging capability of the carboxylate and the strong oxophilic nature of the lanthanoid cations.

Although we were able to grow single crystals suitable for X-ray diffraction for all the complexes, complete purification and isolation of $[Gd(\mathbf{pytz})_2(H_2O)_5]Cl$ and $[Ho(\mathbf{pytz})_2(H_2O)_4]Cl$ from the bulk material proved to be complicated, as evidenced by elemental microanalysis. This was probably due to co-precipitation of NaCl in the bulk, since cationic disubstituted complexes have a higher water solubility compared with neutral trisubstituted ones. However, since high quality single crystal X-ray data of these two complexes could be collected, we have included their solid state structural information here. Compared with previous literature studies of lanthanoid tetrazolates obtained under anhydrous conditions, in the aquo complexes only the tetrazolate nitrogen, bearing the negative charge, and the pyridine nitrogen bind the metal cations [20], thus forming a chelating five membered ring. The other three nitrogen atoms of the **pytz** ligand are involved in the hydrogen bonding network of the lattice.

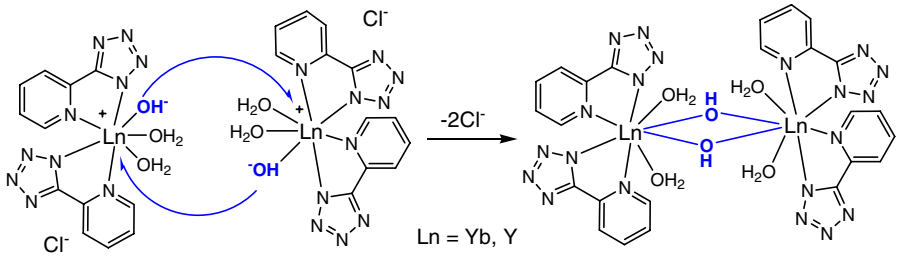
In the case of Yb^{3+} and Y^{3+}, the resulting complex is a neutral hydroxo-bridged dimer. This result can be rationalised by the increased Lewis acidity of these smaller cations, which promotes more effectively proton dissociation from the water molecules coordinated to the metal. The resulting hydroxo complex then coordinates to another metal centre displacing the chloride anion and forming the hydroxo-bridged dimers, as illustrated in Scheme 2.

3.2. X-ray crystal structures of the complexes $[Ln(pytz)_2(H_2O)_n]Cl$ Ln = La, Gd, n = 5; Ln = Ho, n = 4

Fig. 2 shows the crystal structure of $[La(\mathbf{pytz})_2(H_2O)_5]Cl$. The complex crystallises in the orthorhombic space group Fddd, with only half of the molecule belonging to the asymmetric unit. The La^{3+} cation is overall nonacoordinated by two chelating **pytz** ligands and five molecules of water. The remaining chloride anion is located outside the first coordination sphere. The two **pytz** are almost coplanar (ca. 145°) in a pseudo trans arrangement, facing each other in an antiparallel fashion with the tetrazolate ring facing the opposing pyridine ring. The five molecules of water are organised into a slightly distorted square based



Scheme 1. Synthesis of the complexes **1**–**6**.



Scheme 2. Proposed mechanism of formation of the dimeric complexes **5** and **6**.

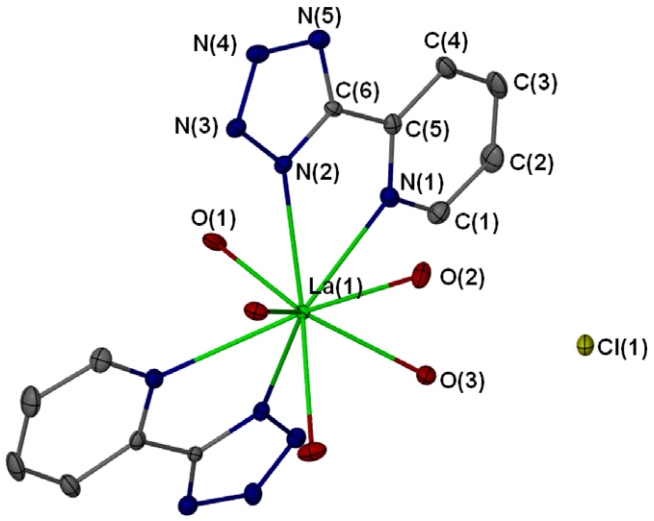


Fig. 2. X-ray crystal structure of **1** showing thermal ellipsoids at 50% probability. Hydrogen atoms are omitted for clarity.

pyramid with the apical water separated from the base by the plane of the two **pytz** ligands. All the five coordinated water molecules and the chloride counterion participate in the formation of an extended hydrogen-bonded network. The chloride anions are trapped in cavities formed between six adjacent complexes. The cavity, shown in Fig. 3a, is approximately rectangular in shape with dimensions of ca. 15.2×6.7 Å. The chloride ion is hydrogen-bonded in the centre of four La bound water molecules (O···Cl 3.1 Å). Each of the four molecules at the base of the pyramid is involved in hydrogen-bonding with Cl^-. The four remaining hydrogen atoms bind to the N3 and N4 atoms of two other ligands. The packing also reveals close contacts of the ligands via formation of π stacking, with a distance of 3.6 Å between the planes of the two **pytz** ligands. The complexes arrange themselves in a "zipper" fashion with strands parallel to the direction of the *a* axis, as shown in Fig. 3b.

$[Gd(\mathbf{pytz})_2(H_2O)_5]Cl$ is isostructural with the lanthanum analogue, with only small differences in the bond lengths between the metal and surrounding ligands and water molecules due to the smaller size of Gd^{3+} [18] (Table 3). In the case of Ho^{3+}, the structure of the disubstituted complex has one less molecule of water in the coordination sphere of the metal, $[Ho(\mathbf{pytz})_2(H_2O)_4]Cl$ (Fig. 4), presumably due to the lanthanoid contraction effect [18]. Interestingly though, this effect is not observed in the case of trisubstituted complexes, $[Ln(\mathbf{pytz})_3(H_2O)_3]$ Ln = La, Gd, Ho, Dy [11], where the solid state structure remains unchanged moving from the larger to the smaller lanthanoid cations. In fact, the crystal structure of $[Ho(\mathbf{pytz})_3(H_2O)_3]$, which was obtained via recrystallisation in hot water from $[Ho(\mathbf{pytz})_2(H_2O)_4]Cl$, is isomorphous with its homologues $[Ln(\mathbf{pytz})_3(H_2O)_3]$ Ln = La, Gd, Eu, Dy [11], with only minor variations in the Ho–O and Ho–N distances between the metal and the ligands (Table 3) due to the difference in the ionic radii [18]. $[Ho(\mathbf{pytz})_2(H_2O)_4]Cl$ crystallises in the monoclinic space group $P2_1/n$. The metal centre is octacoordinated by two ligands and four molecules of water. Compared with the structures of La and Gd, the apical water is lost, causing a closing of the angle between the two **pytz** ligands (ca. 97°). Again the two **pytz** arrange themselves in an antiparallel fashion with the tetrazole ring opposing the pyridine in a pseudo trans arrangement. The bond lengths show no significant variation from the previous two complexes (Table 3), although they are generally shorter due not only to the smaller ionic radii of Ho^{3+} compared with La^{3+} and Gd^{3+}, but also due to the less steric demand of the octacoordinated metal centre. As for the previous compounds, there is an extensive hydrogen bonding throughout the crystal lattice involving the tetrazolate rings, the coordinated water molecules and the chloride anions. The chloride anions are paired at a distance of 3.6 Å and are confined in a large cavity formed by a total of four water molecules (Fig. 5a). The cavity is approximately a rectangle of ca. 4.9×6.9 Å. Each chlorine ion is

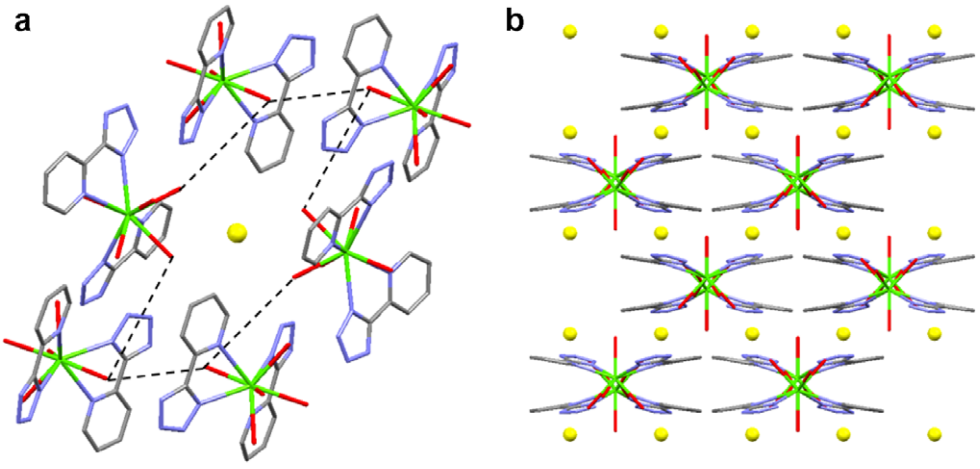


Fig. 3. (a) Position of the Cl^- anion inside the rectangular cavity formed by six complexes in **1**. The chloride anion forms hydrogen bonding with the four closest coordinated water molecules; (b) view of the "zipper" fashion arrangement and π-stacking between the **pytz** ligands in the packing of **1**.

Table 3
Selected bond lengths for the mononuclear compounds **1**–**4**

1[a]		**2**a		**3**		**4**	
La1–O1	2.528(3)	Gd1–O1	2.437(4)	Ho1–O1	2.349(2)	Ho1–O1	2.343(4)
La1–O2	2.5655(19)	Gd1–O2	2.456(2)	Ho1–O2	2.306(2)	Ho1–O2	2.377(4)
La1–O2′	2.566(2)	Gd1–O2′	2.456(2)	Ho1–O3	2.322(2)	Ho1–O3	2.378(4)
La1–O3	2.5324(19)	Gd1–O3	2.427(2)	Ho1–O4	2.352(2)	Ho1–N1	2.658(5)
La1–O3′	2.5324(19)	Gd1–O3′	2.427(2)	Ho1–N1	2.535(2)	Ho1–N2	2.550(4)
La1–N1	2.746(2)	Gd1–N1	2.644(2)	Ho1–N2	2.446(2)	Ho1–N6	2.613(5)
La1–N1′	2.746(2)	Gd1–N1′	2.644(2)	Ho1–N6	2.578(2)	Ho1–N7	2.504(4)
La1–N2	2.648(2)	Gd1–N2	2.538(3)	Ho1–N7	2.500(2)	Ho1–N12	2.624(4)
La1–N2′	2.648(2)	Gd1–N2′	2.538(3)			Ho1–N13	2.513(4)

[a] Symmetry transformation used to generate equivalent atoms: 1/4 − *x*, 1/4 − *y*, *z*.

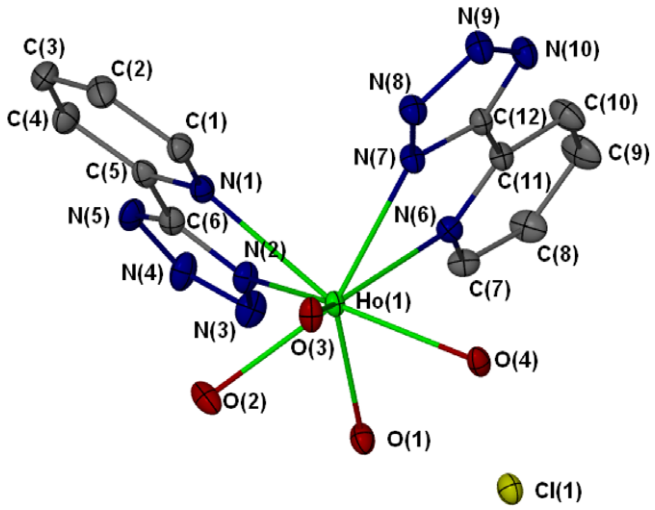


Fig. 4. X-ray crystal structure of **3** showing thermal ellipsoids at 50% probability. Hydrogen atoms are omitted for clarity.

hydrogen-bonded by three molecules of water respectively, with an average O···Cl distance of ca. 3 Å. The different arrangement of the tetrazolate favours the formation of a π stacking structure with a distance of ca. 4 Å between the planes of the two **pytz** ligands (Fig. 5b).

3.3. Crystal structures of the complexes $[Ln_2(pytz)_4(\mu\text{-}OH)_2(H_2O)_n(CH_3OH)_m]$ Ln = Yb, n = 4, m = 0; Ln = Y, n = 2, m = 2

Fig. 6 shows the crystal structure of $[Yb_2(\mathbf{pytz})_4(\mu\text{-}OH)_2(H_2O)_4]$. The hydroxo-bridged Yb dimer crystallises in the monoclinic space group centrosymmetric $P2_1/n$, and only half of the molecule belongs to the asymmetric unit. The centre of inversion is located in the middle of the parallelogram formed by the two Yb atoms and the two bridging OH groups. Both metals are octacoordinated by two chelating **pytz** ligands, two hydroxyl groups and two water molecules. Two extra water molecules are present in the lattice and are involved in the hydrogen-bonded network, along with the coordinated waters and the tetrazolate nitrogen atoms. Each of the two units forming the dimer is almost identical to the structure of the disubstituted Ho complex, with just small variations in the angles between the four oxygen and the two **pytz** ligands (Tables 3 and 4). However, in this case, not all the nitrogen atoms of the tetrazolate ligands are involved in the hydrogen-bonded network. All the four water molecules bind through the lattice, but the two bridging OH groups are not involved in any hydrogen bonding. Cavities are present in the lattice where four molecules of water are trapped (Fig. 7). Two of these are lattice waters, at two opposite

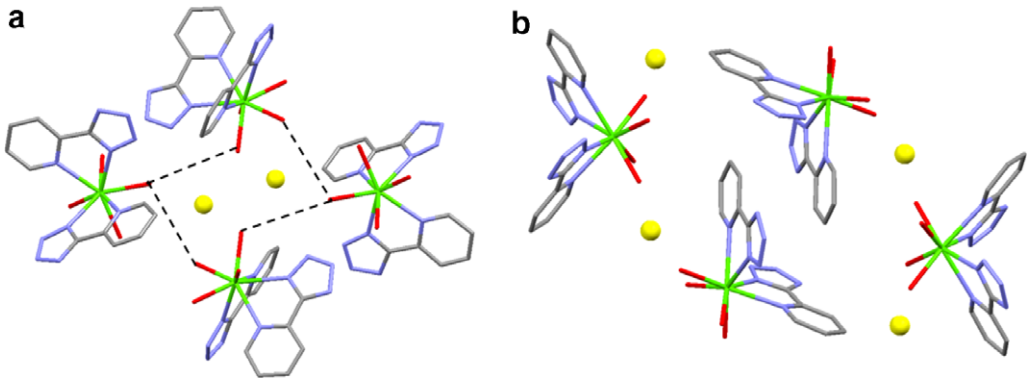


Fig. 5. (a) Position of the two Cl^- anion inside the rectangular cavity formed by four complexes in **3**. Each chloride anion forms hydrogen bonding with the three closest coordinated water molecules and (b) view of the π-stacking between the **pytz** ligands in the packing of **3**.

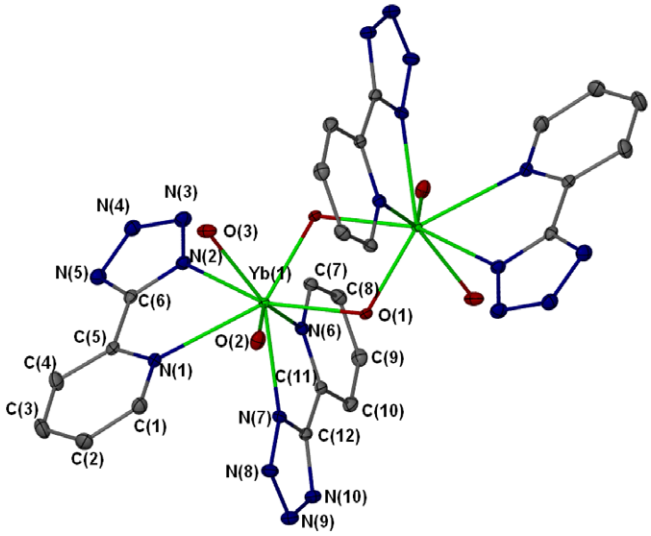


Fig. 6. X-ray crystal structure of **5** showing thermal ellipsoids at 50% probability. Hydrogen atoms are omitted for clarity.

Table 4
Selected bond lengths for the dimeric compounds **5** and **6**

5[a]		**6**[b]	
Yb1–Yb1′	3.6034(14)	Y1–Y1′	3.687(2)
Yb1–O1	2.1970(14)	Y1–O1	2.233(4)
Yb1–O1′	2.2068(16)	Y1–O1′	2.253(4)
Yb1–O2	2.3909(16)	Y1–O2	2.320(4)
Yb1–O3	2.3072(17)	Y1–O3	2.388(4)
Yb1–N1	2.6198(19)	Y1–N1	2.610(5)
Yb1–N2	2.4823(17)	Y1–N2	2.499(5)
Yb1–N6	2.5472(18)	Y1–N6	2.780(5)
Yb1–N7	2.4711(17)	Y1–N7	2.452(5)

Symmetry transformation used to generate equivalent atoms: (a) $1-x$, $2-y$, $1-z$; (b) $1-x$, $1-y$, $1-z$.

vertices of the rectangle, and they are connected to the N3 atom of a tetrazole and to the N4 atom of an adjacent **pytz** ligand. The ligands interact via an offset face to face π stacking (C···pyridine 3.46 Å).

The analogous dimeric complex of Y was obtained following a different synthetic method. We attempted to obtain tetrazolate Y oxo-hydroxo clusters with the methodology proposed by Roesky et al. [21]. Instead only the dimeric hydroxo-bridged complex was obtained (Fig. 8). The molecule crystallises in the triclinic $P\bar{1}$ space group and, as in the case of Yb, it is centrosymmetric with the centre of inversion between the metals and hydroxo groups. Both Y cations are octacoordinated by two ligands, two hydroxo, a molecule of water and a molecule of methanol. An extra molecule of water and one of methanol are present in the lattice forming the hydrogen-bonded network. The distances of the oxygen and nitrogen atoms of the first coordination sphere ligands are smaller for the Yb dimer, as expected due to its smaller ionic radius compared with Y^{3+}. Similarly to the analogous Yb dimer, all the tetrazolate ligands are involved in an offset face-to-face π stacking with an average distance of 3.36 Å between the rings.

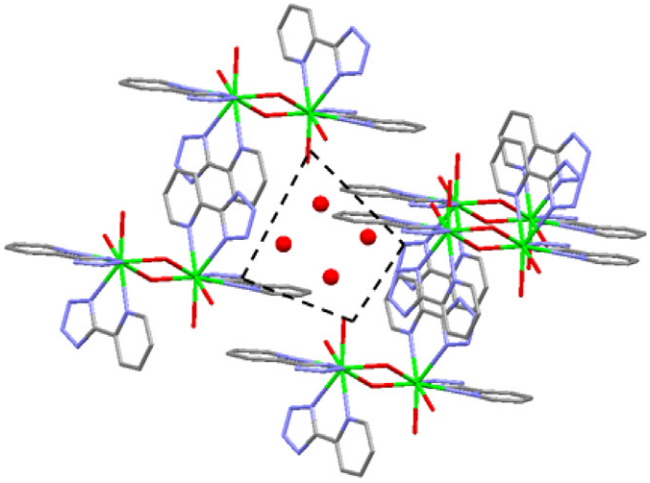


Fig. 7. View of the cavity formed by four complexes in the packing of **5** containing four hydrogen-bonded lattice water.

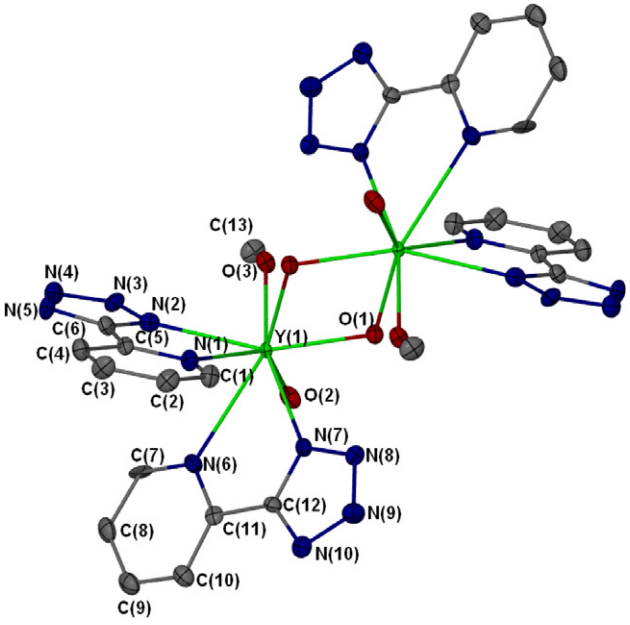


Fig. 8. X-ray crystal structure of **6** showing thermal ellipsoids at 50% probability. Hydrogen atoms are omitted for clarity.

4. Conclusions

The preparation and X-ray structural study of several new cationic disubstituted and neutral hydroxo-bridged dimeric lanthanoid tetrazolate (La, Gd, Ho, Yb, Y) has been presented in this work. Due to the intimate relationship between the crystal lattice packing and the properties of the material, we have closely investigated the intermolecular interactions of the crystal structures of all the compounds. Compared with the corresponding lanthanoid carboxylates (such as picolinic acid or benzoic acid and

its corresponding functionalised analogues [19b,19c]), which tend to form polymeric networks due to the chelating and bridging capability of the ligand and the strong oxophilic nature of the lanthanoid cations, the tetrazolate complexes are individual molecular entitites with a high propensity to interact via hydrogen bonding and π-stacking. The chemistry of the tetrazolate anion with the rare earth elements, still largely unexplored, is of potential interest for a variety of fields due to the combination of the coordinating capability of the ligand, the low toxicity of the tetrazole ring and lanthanoid complexes, and properties such as Lewis acidity, luminescence, and magnetism of the f-block elements.

Acknowledgements

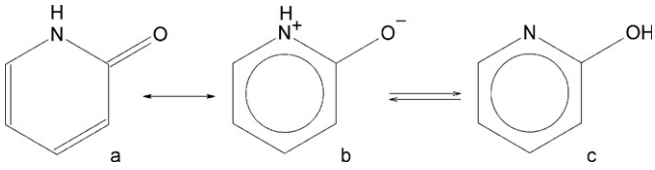
The authors thank Dr. Craig Forsyth (Monash University) for the help provided regarding the crystal structures, and the Australian Research Council for financial support. Prof. George M. Sheldrick (Fakultät für Chemie, Universität Göttingen) is also gratefully acknowledged for Tobias Beck's student exchange program at Monash University.

Appendix A. Supplementary material

CCDC 652812, 652814, 652813, 652817, 652816, and 652815 contain the supplementary crystallographic data for **1**, **2**, **3**, **4**, **5** and **6**. These data can be obtained free of charge via http://www.ccdc.cam.ac.uk/conts/retrieving.html, or from the Cambridge Crystallographic Data Centre, 12 Union Road, Cambridge CB2 1EZ, UK; fax: (+44) 1223-336-033; or e-mail: deposit@ccdc.cam.ac.uk. Supplementary data associated with this article can be found, in the online version, at doi:10.1016/j.poly.2007.08.017.

References

[1] S.T. James, Chem. Soc. Rev. 32 (2003) 276.
[2] (a) S. Stagni, A. Palazzi, S. Zacchini, B. Ballarin, C. Bruno, M. Marcaccio, F. Paolucci, M. Monari, M. Carano, J.A. Bard, Inorg. Chem. 45 (2006) 695;
(b) X.-M. Zhang, Y.-F. Zhao, H.-S. Wu, S.R. Batten, S.W. Ng, Dalton Trans. (2006) 3170;
(c) M. Dincă, A.F. Yu, J.R. Long, J. Am. Chem. Soc. 128 (2006) 8904;
(d) O.M. El-Kadri, M.J. Heeg, C.H. Winter, Dalton Trans. (2006) 4506;
(e) P. Lin, W. Clegg, R.W. Harrington, R.A. Henderson, Dalton Trans. (2005) 2388;
(f) A.J. Downward, P.J. Steel, J. Steenwijk, Aust. J. Chem. 48 (1995) 1625.
[3] (a) G.P. Ellis, G.B. West, Progress in Medicinal Chemistry, vol. 17, Elsevier/North-Holland Biomedical Press, 1980;
(b) H. Singh, A.S. Chawla, V.K. Kapoor, D. Paul, R.K. Malhotra, Prog. Med. Chem. 17 (1980) 151.
[4] (a) J.J. McGuire, C.A. Russel, W.E. Bolanowska, C.M. Freitag, C.S. Jones, T.I. Kalman, Cancer Res. 50 (1990) 1726;
(b) J.A. Zablocky, M. Miyano, N.R. Sashidhar, S. Panzer-Knodle, N. Nicholson, L. Feigen, J. Med. Chem. 35 (1992) 4914;
(c) P.L. Ornstein, M.B. Arnold, D. Evrard, J.D. Leander, D. Lodge, D.D. Shoepp, Bioorg. Med. Chem. Lett. 3 (1993) 43;
(d) R.J. Herr, Bioorg. Med. Chem. 10 (2002) 3379;
(e) Z.P. Demko, K.B. Sharpless, Org. Lett. 4 (2002) 2525.
[5] S.P. Fricker, Chem. Soc. Rev. 35 (2006) 524.
[6] L. Thunus, R. Lejeune, Coord. Chem. Rev. 184 (1999) 125.
[7] J.-C.G. Bünzli, C. Piguet, Chem. Soc. Rev. 34 (2005) 1048.
[8] (a) N. Ishikawa, M. Sugita, T. Ishikawa, S. Koshibara, Y. Kaizu, J. Am. Chem. Soc. 125 (2003) 8694;
(b) N. Ishikawa, M. Sugita, W. Wernsdorfer, J. Am. Chem. Soc. 127 (2005) 3650.
[9] (a) S.-B. Yu, A.D. Watson, Chem. Rev. 99 (1999) 2353;
(b) D.E. Reichert, J.S. Lewis, C.J. Anderson, Coord. Chem. Rev. 184 (1999) 3.
[10] J.-C. Bünzli, Acc. Chem. Res. 39 (2006) 53.
[11] A. Facchetti, A. Abbotto, L. Beverina, S. Bradamante, P. Mariani, C.L. Stern, T.J. Marks, A. Vacca, G.A. Pagani, Chem. Commun. (2004) 1770.
[12] P.C. Andrews, P.C. Junk, M. Massi, M. Silberstein, Chem. Commun. (2006) 3317.
[13] G.M. Sheldrick, SHELXS-97, Program of Crystal Structure Refinement, University of Göttingen, Germany, 1997.
[14] G.M. Sheldrick, SHELXL-9, Program of Crystal Structure Refinement, University of Göttingen, Germany, 1997.
[15] K. Koguro, T. Oga, S. Mitsui, R. Orita, Synthesis (1998) 910.
[16] Z. Zheng, Chem. Commun. (2001) 2521.
[17] (a) R. Wang, Z. Zheng, T. Jin, R.J. Staples, Angew. Chem., Int. Ed. 38 (1999) 1813;
(b) R. Wang, H. Liu, M.D. Carducci, T. Jin, C. Zheng, Z. Zheng, Inorg. Chem. 40 (2001) 2743.
[18] R.D. Shannon, Acta Crystallogr., Sect. A 32 (1976) 751.
[19] (a) D. Ang, G.B. Deacon, P.C. Junk, D.R. Turner, Polyhedron 26 (2007) 385;
(b) T. Fiedler, M. Hilder, P.C. Junk, U.H. Kynast, M.M. Lezhnina, M. Warzala, Eur. J. Inorg. Chem. (2007) 291;
(c) H. Bußkamp, G.B. Deacon, M. Hilder, P.C. Junk, U.H. Kynast, W. Lee, D.R. Turner, CrystEngComm (2007) 393.
[20] X.G. Zhou, Z.-E. Huang, R.-F. Cai, L.-X. Zhang, X.-F. Hou, X.-J. Feng, X.-Y. Huang, J. Organomet. Chem. 563 (1998) 101.
[21] P.W. Roesky, G. Canesco-Melchior, A. Zulys, Chem. Commun. (2004) 738.



Scheme 1. A tautomeric equilibrium between lactam (a and b) and lactim (c) forms of 2-pyridone (2-hydroxypyridine).

region of the X-band spectrum (9 GHz) [16,23]. On the other hand, only rare cases of H_{x1} and H_{y1} for tetracarboxylates are reported [24], next to the typical four H_{x2}, H_{y2}, H_{z1}, and H_{z2}.

In this paper, we present the structure of $[Cu_2(\mu\text{-}L)_4(HL)_2]$ (**1**) (HL = 2-pyridone) and its characterization, together with a comparison to a mixed pyridin-2-olato/methanoato analogues $[Cu_2(\mu\text{-}HCO_2)_2(\mu\text{-}L)_2(HL)_2]\cdot 2CH_3CN$ (**2**) and $[Cu_2(\mu\text{-}HCO_2)_2(\mu\text{-}L)_2(HL)_2]$ (**2a**).

2. Experimental

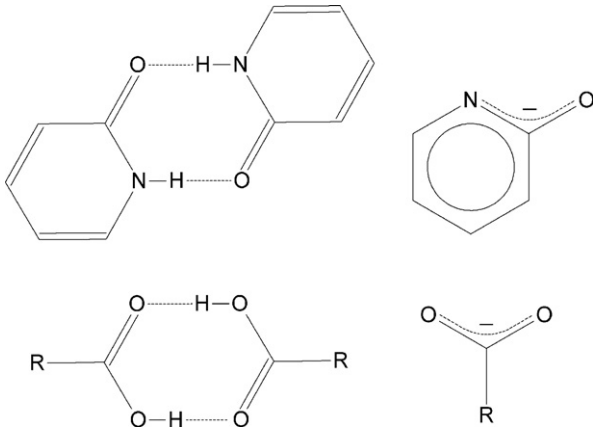
2.1. Synthesis

Compound $[Cu_2(\mu\text{-}HCO_2)_4(2\text{-mpy})_2]$ was prepared by 2-methylpyridine (75 mmol) in absolute ethanol (40 mL), adding β-$Cu(HCO_2)_2$ (4 mmol). A boiling solution was filtered, cooled down to the room temperature and than to 6 °C for 24 h. The light green product was filtered and dried over KOH for a day. β-$Cu(HCO_2)_2$ was isolated from concentrated methanoic acid (20 mL) and $Cu_2(OH)_2CO_3$ (9 mmol) at room temperature. $Cu_2(OH)_2CO_3$ was prepared from $CuSO_4\cdot 5H_2O$ (60 mmol) and $Na_2CO_3\cdot 10H_2O$ (75 mmol) in water at 65 °C. Other chemicals were readily available from commercial sources and were used as received without further purification.

*$[Cu_2(\mu\text{-}L)_4(HL)_2]$ (**1**) (HL = 2-pyridone).* The compound was prepared by a different procedure as described previously [25]. HL (0.48 g, 5.0 mmol) was dissolved in 20 mL of acetone. $[Cu_2(\mu\text{-}HCO_2)_2(\mu\text{-}L)_2(HL)_2]$ (**2a**) (0.30 g, 0.50 mmol) was added to the HL solution during heating and stirring. The temperature was stabilized below boiling point for 10 min. A dark green product (**1**) was filtered off, dried on air for 20 min and in a desiccator over KOH for 24 h. Yield: 85%. *Anal.* Calc. for $C_{30}H_{26}Cu_2N_6O_6$ ($M_r = 693.7$): C, 51.9; H, 3.8; N, 12.1; Cu, 18.3. Found: C, 50.9; H, 3.9; N, 11.7; Cu, 18.3%. IR $\bar{\nu}$, 3550–3300 ν(NH), 1656s ν(C=O), 1608s, 1582 ν_{as}(C=O) + ν(ring), 1539, 1507s, 1464, 1441, 1429s, 1349 cm^{-1}. UV/Vis λ_{max}, 300, 380(sh), 610 nm. EPR (95 K) $S = 1$: $g_x = 2.04$, $g_y = 2.05$, $g_z = 2.29$, $A_{z1} = 8.0$ mT, $D = 0.293$ cm^{-1}, $E = 0.0016$ cm^{-1}, $2J = -334$ cm^{-1}. $S = 1/2$: $g_\perp = 2.06$, $g_\parallel = 2.30$. For the powder XRD data see Table 1.

The single crystals for **1**, suitable for the X-ray analysis, were obtained by a similar procedure as described above, but $[Cu_2(\mu\text{-}HCO_2)_4(2\text{-mpy})_2]$ (2-mpy = 2-methylpyridine) was used instead of $[Cu_2(\mu\text{-}HCO_2)_2(\mu\text{-}L)_2(HL)_2]$ (**2a**) (1.52 g HL, 30 mL acetonitrile, 0.31 g $[Cu_2(\mu\text{-}HCO_2)_4(2\text{-mpy})_2]$). The boiling solution was cooled down and left at 6 °C for 24 h. Crystal data: **1**, $M_r = 693.7$ ($C_{30}H_{26}Cu_2N_6O_6$), monoclinic, $a = 8.2943(4)$ Å, $b = 12.4522(6)$ Å, $c = 13.9052(7)$ Å, $\beta = 106.389(2)°$, $V = 1377.81(12)$ $Å^3$, $T = 150(2)$ K, space group $P2_1/n$, $Z = 2$, $D_x = 1.672$ g/cm^3, $\mu = 1.602$ mm^{-1}, crystal size $0.10 \times 0.04 \times 0.02$ mm^3 (green plate), 13491 reflections measured (integrated), θ_{max} 25.03°, 2420 unique ($R_{int} = 0.06$), 1621 observed [$F^2 > 2\sigma(F^2)$], $R = 0.058$ ($R = \sum(\|F_o| - |F_c\|)/\sum|F_o|$), $wR = 0.032$ ($wR = \sum(w\|F_o| - |F_c\|)/\sum(w|F_o|)$), 199 refined parameters.

*$[Cu_2(\mu\text{-}HCO_2)_2(\mu\text{-}L)_2(HL)_2]\cdot 2CH_3CN$ (**2**), $[Cu_2(\mu\text{-}HCO_2)_2(\mu\text{-}L)_2(HL)_2]$ (**2a**) (HL = 2-pyridone).* Compound **2** was prepared as described previously [6]. HL (0.38 g, 4.0 mmol) was dissolved in 27 mL of acetonitrile during heating and stirring. This solution was slowly added to 0.31 g (0.80 mmol) of $[Cu_2(\mu\text{-}HCO_2)_4(2\text{-mpy})_2]$. The boiling solution was filtered to remove the undissolved solid particles and the obtained filtrate was cooled to the room temperature and left at 6 °C for 24 h. Green crystals of **2** were filtered off and dried on air for 20 min and in a desiccator over KOH for 24 h. During the drying, compound **2** decomposes by removal of the solvate acetonitrile, giving **2a**. All the characterization data mentioned in this paragraph are for **2a**. Yield: 60%. *Anal.* Calc. for $C_{22}H_{20}Cu_2N_4O_8$ **2a** ($M_r = 595.5$): C, 44.4; H, 3.4; N, 9.4; Cu, 21.3. Found: C, 43.6; H, 3.5; N, 9.4; Cu, 20.6%. IR $\bar{\nu}$, 3600–3300 ν(NH), 1664s ν(C=O), 1624s, 1611, 1593 ν(C=O) + ν(ring), 1578s $\nu_{as}(CO_2)$, 1541, 1480, 1444, 1430s $\nu_s(CO_2)$, 1348 cm^{-1}. UV/Vis λ_{max}, 310, 380(sh), 670 nm. EPR (95 K) $S = 1$: $g_\perp = 2.05$, $g_\parallel = 2.31$, $A_{z1} = 6.1$ mT, $D = 0.347$ cm^{-1}, $2J = -324$ cm^{-1}. $S = 1/2$: $g_\perp = 2.06$, $g_\parallel = 2.35$.



Scheme 2. A comparison between 2-pyridone and carboxylic acid and their anions. Free neutral molecules form dimeric structures, while deprotonated species enable bridges (O–C–O, N–C–O) with the delocalized double-single bonds.

2.2. Physical measurements

Metal analysis was carried out electrogravimetrically with Pt electrodes. C, H, N analysis was performed with

Table 1
Measured and calculated interplanar spacings (d/Å) with their relative intensities (I_r) for **1** [26]

d_m	9.2	8.0	6.8		6.2	5.5	4.93	4.34	4.23		3.97	3.79	3.53	3.40
(I_{rm})	(10)	(3)	(6)		(3)	(1)	(6)	(1)	(1)		(2)	(2)	(4)	(4)
d_c	9.10	7.88	6.70	6.66	6.11	5.41	4.88	4.32	4.24	4.18	3.93	3.75	3.48	3.35
(I_{rc})	(100)	(20)	(28)	(11)	(15)	(7)	(25)	(6)	(6)	(8)	(7)	(7)	(17)	(14)

a Perkin–Elmer Elemental Analyzer 2400 CHN. Powder XRD data were obtained by a Guinier Enraf Nonius FR 552 camera with Cu Kα, while the calculations $d(I)$ by 'X'Pert HighScore Plus' programme [26]. Infrared spectra were measured on mineral oil mulls, using a Perkin–Elmer FT-IR 1720X spectrometer. Electronic spectra were recorded as nujol mulls with a Perkin–Elmer UV/Vis/NIR spectrometer Lambda 19. X-band EPR spectra of powdered samples were recorded by a Bruker ESP-300 spectrometer. The values of parameters g, A, D, E and $2J$ were calculated directly from the signal positions in the spectra [27,28]. The magnetic susceptibility data of powdered polycrystalline samples were measured with a Quantum Design SQUID magnetometer, equipped with a 5 T magnet. The molar magnetic susceptibility χ_M was investigated in the temperature interval between 300 and 2 K in a magnetic field strength $H = 1000$ Oe. The data were corrected for the experimentally determined contribution of the sample holder. Corrections for the diamagnetic response of the compounds, due to the closed atomic shells as estimated from the Pascal's constants, were applied [29].

2.3. X-ray structure analysis

The diffraction data for **1** were collected on a Nonius Kappa CCD diffractometer with a graphite-monochromated Mo Kα radiation. The data were processed using DENZO [30]. A crystal structure was solved by direct methods using SIR-97 [31] and refined using Xtal 3.6 [32] by a full-matrix least-squares procedure based on F. All of the non-hydrogen atoms were refined anisotropically. The positions of the hydrogen atoms were located using difference Fourier map, while their parameters were not refined. Selected distances and angles for **1** are in Table 2.

3. Results and discussion

3.1. The crystal structure of $[Cu_2(\mu\text{-}L)_4(HL)_2]$ (1) (HL = 2-pyridone) tetrakis(μ-pyridin-2-olato-1κ^{2}O:2κ^{2}N,1κ^{2}N:2κ^{2}O)bis(2-pyridone-κO)dicopper(II)

The centrosymmetric dinuclear coordination molecule of **1** is formed by two copper atoms bridged by four pyridin-2-olato ligands, similarly as for $[Cu_2(\mu\text{-}CH_3CO_2)_4(H_2O)_2]$ type of complexes. Herein, the ligands enable N–C–O bridges in *syn–syn* mode, giving two nitrogen and two oxygen atoms around each copper at a distance (Cu–N2 2.003(5), Cu–N3 2.007(5) Å, Cu–O4 1.978(5), Cu–O11 1.964(4) Å). The square-pyramidal copper coordination sphere is completed by the apical neutral 2-pyridone molecule (Cu–O2 2.227(5) Å) (Fig. 1). Thus, a hydronated nitrogen atom of the apical ligand enables an intramolecular hydrogen bond (N1–H1···O4 2.707(8) Å, 159°) stabilizing the dinuclear molecule. These molecules are intra-connected by π–π stacking interactions via rings of the axial 2-pyridone and one of the pyridin-2-olato ligands (centroid–centroid distance 3.779(4)–3.791(4) Å, mean inter-planar separation 3.248–3.552 Å).

Compound **1** was already reported and partly characterized [25]. The herein shown crystal structure is in agreement with the predictions of the copper acetate hydrate type of complex. Structurally, several compounds show strong similarity to **1** in a form of $[Cu_2(\mu\text{-}L1)_4(L2)_2]$ (L1 = a ligand with a triatomic bridge, L2 = axial ligand), namely, $[Cu_2(\mu\text{-}CH_3CO_2)_4(HL)_2]$ [10], $[Cu_2(\mu\text{-}HCO_2)_2$-

Table 2
Selected bond distances (Å) and angles (°) for **1**

Cu–O4	1.978(5)	N1–C2	1.363(9)	C5–C6	1.334(10)
Cu–O11	1.964(4)	N1–C6	1.374(9)	C7–C8	1.420(9)
Cu–N3	2.007(5)^i	N2–C7	1.354(8)	C8–C9	1.345(11)
Cu–N2	2.003(5)^i	N2–C11	1.355(9)	C9–C10	1.392(11)
Cu–O2	2.227(5)	N3–C12	1.350(8)	C10–C11	1.359(10)
O2–C2	1.275(8)	N3–C16	1.393(9)	C12–C13	1.453(10)
O4–C7	1.293(9)	C2–C3	1.427(10)	C13–C14	1.367(11)
O11–C12	1.274(8)	C3–C4	1.369(10)	C14–C15	1.405(12)
		C4–C5	1.393(11)	C15–C16	1.361(11)
O2–Cu–O4	93.75(18)	O4–Cu–O11	88.99(17)	O11–Cu–N3^i	170.7(2)
O2–Cu–O11	91.89(18)	O4–Cu–N2^i	170.7(2)	N2^i-Cu–N3^i	89.4(2)
O2–Cu–N2^i	95.57(19)	O4–Cu–N3^i	89.11(19)	O11–Cu–N2^i	91.01(17)
O2–Cu–N3^i	97.28(18)				

Symmetry codes: (i) $2 - x$, $2 - y$, $1 - z$.

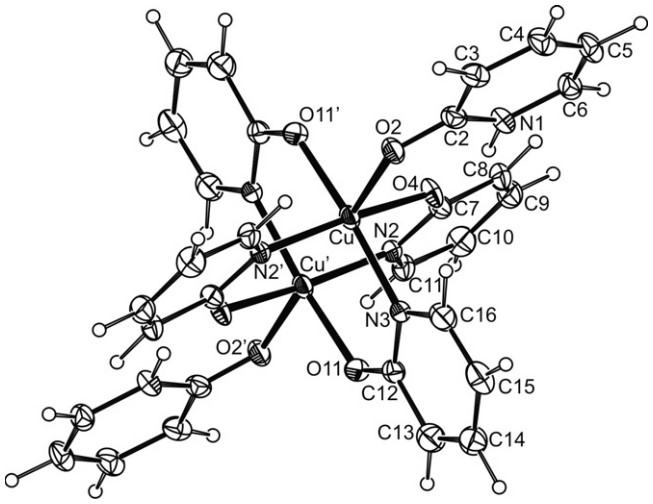


Fig. 1. The dinuclear structure of **1**, with four *paddle-wheel* bridging pyridin-2-olato and two terminal 2-pyridone ligands (Cu···Cu 2.609(1) Å). The thermal ellipsoids are drawn at the 30% probability level [33].

$(\mu\text{-L})_2(\text{HL})_2]\cdot 2CH_3CN$ (**2**) (HL = 2-pyridone) [6], and $[Cu_2(\mu\text{-3-ethyl-2-pyO})_4(DMF)_2]$ [12].

In the EPR spectra of complexes **1** and **2a**, three signals H_{z1}, $H_{\perp 2(x,y)}$ and H_{z2} for $S = 1$ are found. Additionally, a $H_{\perp 1(x,y)}$ at 100 mT is noticed in the 295 and 95 K spectra of **1** without any significant change of its relative intensity. A presence of the $H_{\perp 1}$ signal for **1** is in accordance with a relation of the axial zero-field splitting parameter D and $h\nu$ (0.293 (**1**) < 0.320 ($h\nu$) $< 0.347\ \text{cm}^{-1}$ (**2a**)). On the other hand, no $H_{\perp 1}$, but several temperature dependent signals in the 100–450 mT region are noticed for **2a** (Fig. 2). Since these broad signals are absent in the 95 K spectrum of **2a**, their origin is assumed to be due to $S = 1$ spin inter-dinuclear interactions [34–36]. This assumption is actually not in clear agreement with the shown isolated dinuclear structure of **2** [6], where direct $S = 1$ spin interactions should not be possible, due to an absence of the inter-dinucler bridges. On the other hand, the crystal structure of **2** is not an exact figure of compound **2a** (**2** unstable in air, giving **2a**), since **2** was characterized only by the XRD single crystal structure analysis, while **2a** with all the other herein described methods. The $S = 1$ EPR signals of **2a** confirm the existence of the *paddle-wheel* dinuclear structure. Thus, the inter-dinuclear interactions may take place via partly rearranged ligands (**2** → **2a**) possibly establishing new bridges, or via π–π interactions, noticed already in the structure of **2**, via rings of the apical ligands (centroid–centroid distance 3.622(1) Å, mean inter-planar separation 3.297, 3.302 Å).

A feature of the $S = 1$ system spectra with four N–C–O bridges (**1**) is almost identical to a system with four bridging carboxylate analogues. The $H_{\perp 1}$ signal in the X-band spectra is, however, more commonly observed for the N–C–O bridged complexes [16,23] than for the carboxylates (O–C–O) [24]. It seems that a substitution of oxygen with nitrogen atoms in such a triatomic bridge, plays a crucial role in the arrangement of the $S = 1$ system bands. Namely, in a 4-azabenzimidazole *paddle-wheel* complex [37] with an N–C–N bridge, the $H_{\perp 1}$ is noticed at 250 mT in the X-band spectrum showing significantly smaller axial deviation ($D = 0.124\ \text{cm}^{-1}$). Nevertheless, the rigidity of the bridge should also be taken into account.

The magnetic susceptibility $\chi_M \cdot T$ ($B_0 = 0.1$ T) of compounds **1** and **2a** gradually decreases by lowering temperature (Fig. 3), that is characteristic for the antiferromagnetic interaction typical for *paddle-wheel* dicopper complexes. The experimental data for the dinuclear compounds can be well reproduced by considering the expression of χ_M (Eq. (1)) derived from the Heisenberg Hamiltonian (Eq. (2)) [38].

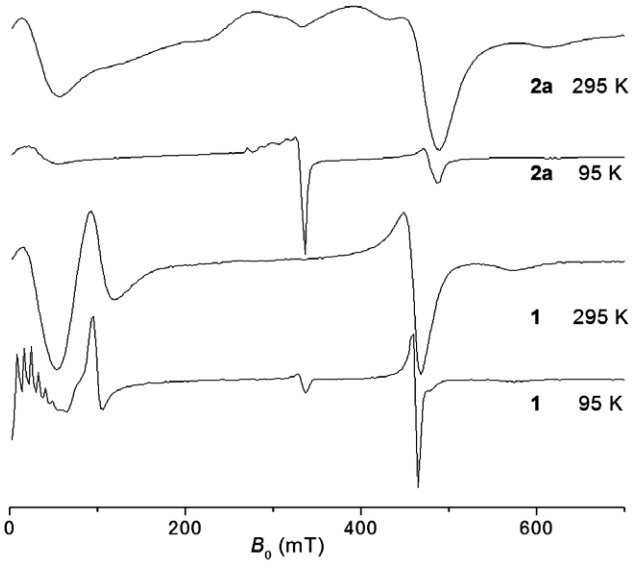


Fig. 2. EPR spectra of **1** and **2a**, respectively, with the regular $S = 1$ signals for the $[Cu_2(\mu\text{-L1})_4(L2)_2]$ type of complexes. Additionally, the $H_{\perp 1}$ signal is present in the spectra of **1**, while several broad signals only in the room temperature spectrum of **2a**.

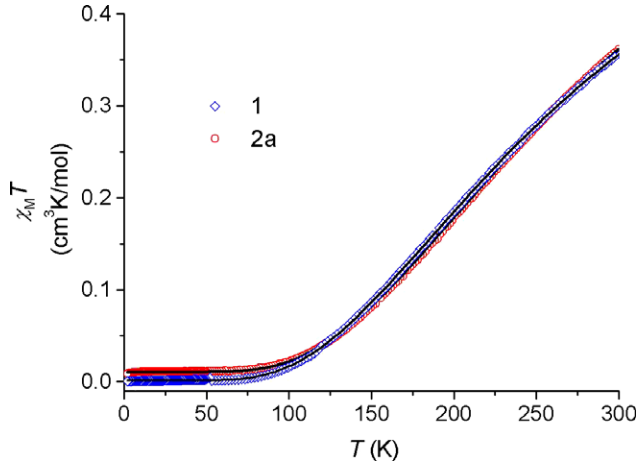


Fig. 3. A strong antiferromagnetism shown in a graph as $\chi_M \cdot T(T)$ of compounds **1** ($2J = -367\ \text{cm}^{-1}$) and **2a** ($2J = -396\ \text{cm}^{-1}$), respectively.

$$\chi_M = (1-\rho)\frac{2N_A g^2 \mu_B^2}{k_B T(3+e^{-2J/k_B T})} + \rho\frac{N_A g^2 \mu_B^2}{2k_B T} \quad (1)$$

$$\widehat{H} = -2J\widehat{S}_1 \cdot \widehat{S}_2 \quad (2)$$

The best-fit parameters give a measure of the gyromagnetic constant g, the magnetic interaction $2J$ and a yield of the non-dinuclear Cu(II) species ρ (**1**: $\rho = 0.2\%$, $g = 2.04$, $2J = -367\ cm^{-1}$; **2a**: $\rho = 1.3\%$, $g = 2.14$, $2J = -396\ cm^{-1}$). The results for **1** generally agree with the reported values $2J = -340\ cm^{-1}$ and $g = 2.10$ [25]. Relatively high amount of the non-dinuclear species noticed for **2a** ($\rho = 1.3\%$, see also Fig. 2, 330 mT signals), confirms an important change in the structure during the decomposition of **2** outside mother-liquid, though the dinuclear cage structure preserves. In relation to this, much larger deviations of $|2J|$ (cm^{-1}) values for **2a**, obtained by the two magnetically based methods are noticed (χ_M(EPR): **1** 367 (334), **2a** 396 (324)). Thus, EPR values seem more accurate in this case than χ_M due to Eq. (1) limitations.

So far we described two ways of extracting the singlet–triplet energy gap $2J$ and the gyromagnetic constant g values of the complexes **1** and **2a**, both derived from quantum mechanics. The EPR approach takes place via six 'Wasserman' equations [27], while Kahn [38–41] established the later introduced magnetic susceptibility path. Despite small differences between the results of both methods, there is clear similarity giving relatively comparable results. According to Kahn [38], it is possible to derive the expression for the magnetic interaction constant $2J$ (Eq. (3)), which relates its ferro-/antiferro-magnetic character with the spatial symmetry of magnetic orbitals.

$$2J = E_S - E_T = 2k + 4\beta s \begin{cases} >0 & (\text{ferromagnetism}, E_S > E_T) \\ <0 & (\text{antiferromagnetism}, E_S < E_T) \end{cases} \quad (3)$$

where k is the Coulomb repulsion integral for two centres >0; s is the overlap integral >0 and β is the Coulomb one electron integral – orbital energy <0.

4. Concluding remarks

The coordination compound $[Cu_2(\mu\text{-L})_4(HL)_2]$ (**1**) (HL = 2-pyridone) shows a dinuclear cage structure with four triatomic N–C–O pyridin-2-olato bridges coordinated in the *syn–syn* mode, similar as in the related copper(II) acetate hydrate type of complexes. The apical positions are fulfilled by neutral 2-pyridone ligands. The EPR spectra show six signals, as suggested for $S = 1$ spin state, although usually only four are observed. The EPR and magnetic susceptibility analysis reveal similar results for g and $2J$ values. A related mixed pyridin-2-olato/methanoato complex $[Cu_2(\mu\text{-HCO}_2)_2(\mu\text{-L})_2(HL)_2]$ (**2a**) shows similarly strong antiferromagnetic properties. Significantly larger axial zero-field splitting parameter D for **2a** than for **1** is in agreement with an appearance of the $H_{\perp 1}$ signal only for **1**. A decomposition of $[Cu_2(\mu\text{-HCO}_2)_2(\mu\text{-L})_2(HL)_2]\cdot 2CH_3CN$ (**2**) giving $[Cu_2(\mu\text{-HCO}_2)_2(\mu\text{-L})_2(HL)_2]$ (**2a**), do not have a noticeable impact on the *paddle-wheel* structure that remain preserved in **2a**, though also shows an important change in the structure, possibly by stronger inter-dinuclear associations than suggested only by the molecular structure of **2**.

Acknowledgements

Dr. M. Šentjurc, EPR centre, 'Jožef Stefan' Institute, Ljubljana (EPR spectra), and MVZT P1-0175-103 Republic of Slovenia, are gratefully acknowledged.

Appendix A. Supplementary material

CCDC 640700 contains the supplementary crystallographic data and all atom parameters for **1**. These data can be obtained free of charge via http://www.ccdc.cam.ac.uk/conts/retrieving.html, or from the Cambridge Crystallographic Data Centre, 12 Union Road, Cambridge CB2 1EZ, UK; fax: (+44) 1223-336-033; or e-mail: deposit@ccdc.cam.ac.uk. Supplementary data associated with this article can be found, in the online version, at doi:10.1016/j.poly.2007.08.019.

References

[1] J.M. Rawson, R.E.P. Winpenny, Coord. Chem. Rev. 139 (1995) 313.
[2] M.J. Cook, A.R. Katritzky, P. Linda, R.D. Tack, J. Chem. Soc., Chem. Commun. (1971) 510.
[3] J. Reedijk, Recl. Trav. Chim. Pays-Bas 88 (1969) 1139.
[4] S.K. Yeh, D.S. Liaw, S.M. Peng, Bull. Inst. Chem., Acad. Sin. 34 (1987) 49.
[5] S.R. Breeze, S.N. Wang, Inorg. Chem. 32 (1993) 5981.
[6] L. Glažar, M. Radišek, P. Šegedin, A. Golobič, Acta Crystallogr., Sect. C 61 (2005) M526.
[7] R. Obeso Rosete, D.J. Cole-Hamilton, G. Wilkinson, J. Chem. Soc., Dalton Trans. (1979) 1618.
[8] Y. Nishida, M. Masumoto, Y. Mori, Z. Naturforsch. B 44 (1989) 307.
[9] A.J. Blake, R.E.P. Winpenny, Acta Crystallogr., Sect. C 49 (1993) 799.
[10] A.J. Blake, R.O. Gould, R.E.P. Winpenny, Acta Crystallogr., Sect. C 47 (1991) 1077.
[11] D. Taylor, Aust. J. Chem. 28 (1975) 2615.
[12] Y. Nishida, S. Kida, Bull. Chem. Soc. Jpn. 58 (1985) 383.
[13] M. Ueda, M. Itou, K. Okazawa, T. Mochida, H. Mori, Polyhedron 24 (2005) 2189.
[14] L.S. Hollis, S.J. Lippard, Inorg. Chem. 22 (1983) 2600.
[15] L.S. Hollis, M.M. Roberts, S.J. Lippard, Inorg. Chem. 22 (1983) 3637.
[16] E.J.L. McInnes, F.E. Mabbs, C.M. Grant, P.E.Y. Milne, R.E.P. Winpenny, Faraday Trans. 92 (1996) 4251.
[17] S. Emori, H. Suenaga, N. Goto, Bull. Chem. Soc. Jpn. 64 (1991) 3460.
[18] A.J. Blake, R.O. Gould, P.E.Y. Milne, R.E.P. Winpenny, J. Chem. Soc., Chem. Commun. (1992) 522.
[19] A.J. Deeming, R. Peters, M.B. Hursthouse, J.D.J. Backerdirks, Dalton Trans. (1982) 1205.
[20] P. Beak, F.S. Fry, J. Lee, F. Steele, J. Am. Chem. Soc. 98 (1976) 171.
[21] B.R. Pennfold, Acta Crystallogr. 6 (1953) 591.
[22] F.H. Allen, Acta Crystallogr., Sect. B 58 (2002) 380.
[23] D.M.L. Goodgame, Y. Nishida, R.E.P. Winpenny, Bull. Chem. Soc. Jpn. 59 (1986) 344.
[24] B. Kozlevčar, D. Odlazek, A. Golobič, A. Pevec, P. Strauch, P. Šegedin, Polyhedron 25 (2006) 1161.

[25] S. Emori, I. Okano, Y. Muto, Bull. Chem. Soc. Jpn. 45 (1972) 3717.
[26] X'Pert HighScore Plus. PANalitical B. V. Almelo, The Netherlands, 2005.
[27] E. Wasserman, L.C. Snyder, W.A. Yager, J. Chem. Phys. 41 (1964) 1763.
[28] T.D. Smith, J.R. Pilbrow, Coord. Chem. Rev. 13 (1974) 173.
[29] R.L. Dutta, A. Syamal, Elements of Magnetochemistry, Affiliated East-West Pvt. Ltd., 1993, pp. 6–11.
[30] Z. Otwinowski, W. Minor, Methods Enzymol. (1997) 307.
[31] A. Altomare, M.C. Burla, M. Camalli, G. Cascarano, C. Giacovazzo, A. Guagliardi, A.G.G. Moliterni, G. Polidori, R. Spagna, J. Appl. Crystallogr. 32 (1999) 115.
[32] S.R. Hall, D.J. du Boulay, R. Olthof-Hazekamp (Eds.), Xtal3.6 System. 1999.
[33] L.J. Farrugia, J. Appl. Crystallogr. 30 (1997) 565.
[34] V.V. Gavrilov, Y.V. Yablokov, L.N. Milkova, A.V. Ablov, Phys. Status Solidi B 45 (1971) 603.
[35] J. Mrozinski, E. Heyduk, J. Coord. Chem. 13 (1984) 291.
[36] B. Kozlevčar, I. Leban, M. Petrič, S. Petriček, O. Roubeau, J. Reedijk, P. Šegedin, Inorg. Chim. Acta 357 (2004) 4220.
[37] G.A. van Albada, I. Mutikainen, U. Turpeinen, J. Reedijk, Polyhedron 25 (2006) 3278.
[38] O. Kahn, Molecular Magnetism, VCH, Weinheim, 1992, p. 26.
[39] M. Verdaguer, Polyhedron 20 (2001) 1115.
[40] O. Kahn, J. Galy, Y. Journaux, J. Jaud, I. Morgenstern-Badarau, J. Am. Chem. Soc. 104 (1982) 2165.
[41] N.W. Ashcroft, N.D. Mermin, Solid State Physics, Saunders College Publishers, Philadeiphia, PA, 1976, pp. 674–682.

amide carbonyl O atom, or only via the pyridyl N atom [10,14–16]. The neutral ligands have been used to synthesize copper(I) [14,16], copper(II) [10] and zinc(II) [15] complexes. Under basic conditions the anionic amidate form additionally coordinates via the amidate N atom, allowing a chelating/bridging coordination mode that gives rise to copper(II) monomers with HL^{SMe} [9] or copper(II) dimers and clusters with the other ligands [10,11]. Here we report the synthesis and structures of mononuclear copper(II) complexes with neutral pyridylmethylamide ligands. Specifically, we report the synthesis and structural characterization of $[Cu(HL)_2(OTf)_2]$ (**1**), $[Cu(HL^{Me})_2](ClO_4)_2$ (**2**), $[Cu(HL)_2Cl]_2[CuCl_4]$ (**3**), $[Cu(HL^{Me3})_2(THF)](OTf)_2$ (**4**), $[Cu(HL^{Me3})_2(H_2O)](ClO_4)_2$ (**5a**), $[Cu(HL^{Me3})_2(H_2O)](ClO_4)_2$ (**5b**), $[Cu(HL^{Ph3})_2(H_2O)](ClO_4)_2$ (**6**), $[Cu(HL)(2,2'\text{-bipy})(H_2O)](ClO_4)_2$ (**7**) and $[Cu(HL^{Ph})(2,2'\text{-bipy})(H_2O)](ClO_4)_2$ (**8**).

2. Experimental

2.0.1. General

All reagents were purchased from commercial sources and used without further purification. Solvents were dried and purified under nitrogen using standard methods and distilled immediately before use. ^1H NMR spectra were measured on a Varian 300 MHz spectrometer using solvent as an internal standard [^1H δ ($CHCl_3$) = 7.27 ppm; ^1H δ (CH_3OH) = 4.87 ppm; ^{13}C δ ($CHCl_3$) = 77.23 ppm]. Elemental analyses were carried out by Atlantic Microlabs (Norcross, GA). Mass spectra were recorded on a Q-TOF quadrupole time-of-flight mass spectrometer equipped with a Z-spray electrospray ionization (ESI) source (Micromass, Manchester, UK). FTIR spectra were recorded on a Nexus 470 FTIR spectrometer. X-band EPR spectra were recorded on a Bruker EMX spectrometer at 77 K as frozen solutions. The ligands *N*-(2-pyridylmethyl)acetamide (HL), 2-phenyl-*N*-(2-pyridylmethyl)acetamide (HL^{Ph}), 2,2-dimethyl-*N*-(2-pyridylmethyl)propionamide (HL^{Me3}) and 2,2,2-triphenyl-*N*-(2-pyridylmethyl)acetamide (HL^{Ph3}) were synthesized according to published procedures [10,11].

Caution: Perchlorate salts of metal complexes with organic ligands are potentially explosive. Although no problems were encountered in this work, only small amounts of material should be prepared and handled with caution.

2.1. N-(2-pyridylmethyl)propionamide (HL^{Me})

The synthesis of HL^{Me} was carried out via a modified procedure based upon an established method [29]. 2-(Aminomethyl)pyridine (1.08 g, 10 mmol) and propionic anhydride (5.50 g, 42.3 mmol) were dissolved in 3 mL of pyridine and stirred at room temperature for 24 h, after which 4 mL of water was added with stirring for another 1 h. Solvent was removed under vacuum, leaving a brown liquid. The desired product was distilled from the byproducts using a Kugelrohr distillation apparatus (170 °C, 0.1 mmHg) giving a yellow oil. Yield: 0.97 g, 60%. *Anal.* Calc. for $C_9H_{12}N_2O \cdot 0.8H_2O$: C, 60.52; H, 7.67; N, 15.68. Found: C, 60.92; H, 7.54; N, 15.65%. ^1H NMR (300 MHz, $CDCl_3$): δ 1.11 (t, 3H), 2.24 (q, 2H), 4.47 (d, 2H), 7.11 (m, 3H), 7.58 (t, 1H), 8.42 (d, 1H) ppm. FTIR (KBr): 3293 (ν_{NH}), 3065, 2977, 2038, 2890, 1653 (ν_{CO}), 1542, 1475, 1436, 1374, 1233, 1149, 1094, 1049, 997, 804, 754, 696, 620, 507, 457, 404 cm^{-1}.

2.2. $[Cu(HL)_2](OTf)_2$ (**1**)

An acetonitrile solution of HL (0.075 g, 0.5 mmol) was added dropwise to an acetonitrile solution of $Cu(OTf)_2$ (0.0904 g, 0.25 mmol) forming a light blue solution. The reaction was stirred for 3 h and vapor diffusion of diethyl ether into this solution resulted in the formation of blue crystals of **1**. Yield: 0.104 g, 56.5%. *Anal.* Calc. for $C_{18}H_{20}CuF_6N_4O_8S_2$: C, 32.66; H, 3.04; N, 8.46. Found: C, 32.09; H, 3.28; N, 8.74%. ESI-MS (CH_3CN): m/z = 363.0 $[Cu(HL)(L)]^+$; 151.1 $[H_2L]^+$. UV–Vis [CH_3CN, λ_{max}, nm (ϵ, $M^{-1}\,cm^{-1}$)]: 260 (16 700), 293 (4800), 640 (540). FTIR (KBr): 3287 (ν_{NH}), 3126, 3003, 2968, 2890, 1605 (ν_{CO}), 1492, 1443, 1381, 1365, 1244, 1162, 1116, 1070, 1032, 869, 837, 781, 759, 639, 618, 591, 573, 529, 518, 440 cm^{-1}. EPR (9.434 GHz, 0.02 mW, mod. amp. 1 G, MeOH, 77 K): $g_\parallel = 2.31$, $g_\perp = 2.06$, $A_\parallel = 146$ G.

2.3. $[Cu(HL^{Me})_2](ClO_4)_2$ (**2**)

A methanol solution of HL^{Me} (0.0834 g, 0.51 mmol) was added dropwise to a methanol solution of $Cu(ClO_4)_2 \cdot 6H_2O$ (0.0942 g, 0.25 mmol) forming a dark blue solution. The reaction was stirred overnight and vapor diffusion of diethyl ether into this solution resulted in the formation of blue crystals of **2**. Yield: 0.0999 g, 68%. *Anal.* Calc. for $C_{18}H_{24}Cl_2CuN_4O_{10}$: C, 36.59; H, 4.09; N, 9.48. Found: C, 36.36; H, 4.06; N, 9.41%. ESI-MS (CH_3CN): m/z = 490.0 $[Cu(HL^{Me})_2(ClO_4)]^+$; 390.1 $[Cu(HL^{Me})(L^{Me})]^+$; 165.1 $[H_2L^{Me}]^+$. UV–Vis [CH_3OH, λ_{max}, nm (ϵ, $M^{-1}\,cm^{-1}$)]: 208 (13 100), 261 (9300), 720 (48). FTIR (KBr): 3303 (ν_{NH}), 1598 (ν_{CO}), 1167, 1106, 1012, 975, 933 ($\nu_{ClO_4^-}$), 3853, 3118, 2995, 2949, 2890, 2458, 2362, 2334, 2019, 1491, 1469, 1448, 1390, 1364, 1342, 1325, 1295, 1255, 1233, 897, 855, 836, 804, 781, 762, 693, 655, 621, 604, 529, 476, 439, 401 cm^{-1}. EPR (9.434 GHz, 0.14 mW, mod. amp. 1 G, MeOH, 77 K): $g_\parallel = 2.31$, $g_\perp = 2.05$, $A_\parallel = 146$ G.

2.4. $[Cu(HL)_2Cl]_2[CuCl_4] \cdot 2CH_3CN$ (**3** · $2CH_3CN$)

An acetonitrile solution of HL (0.075 g, 0.5 mmol) was added dropwise to an acetonitrile solution of $CuCl_2$ (0.0672 g, 0.5 mmol) forming a dark green solution. The reaction was stirred for 13 h and vapor diffusion of diethyl ether into this solution resulted in the formation of green crystals of **3**. Yield: 0.050 g, 36.8%. *Anal.* Calc. for

$C_{36}H_{46}Cl_6Cu_3N_{10}O_4$: C, 39.81; H, 4.27; N, 12.90. Found: C, 40.11; H, 4.21; N, 12.81%. ESI-MS (CH_3CN): $m/z = 214.0$ $[CuL]^+$; 151.1 $[H_2L]^+$. UV–Vis [CH_3CN, λ_{max}, nm (ϵ, $M^{-1}\,cm^{-1}$)]: 261 (11000), 295 (4800), 460 (960), 831 (220). FTIR (KBr): 3295 (ν_{NH}), 2925, 1608 (ν_{CO}), 1551, 1486, 1444, 1374, 1360, 1301, 1226, 1156, 1114, 1062, 1031, 1015, 836, 770, 645, 618, 582, 516 cm^{-1}. EPR: no signal.

2.5. $[Cu(HL^{Me3})_2(THF)](OTf)_2$ (**4** · THF)

NaH (0.012 g, 0.5 mmol) was added to a THF solution of HL^{Me3} (0.096 g, 0.5 mmol) and the mixture was stirred for 1 h. Subsequently, this was added to a THF solution of $Cu(OTf)_2$ (0.1808 g, 0.5 mmol). The reaction mixture was stirred for 2 h, during which the color changed to dark blue. The suspension was filtered and slow evaporation of the filtrate produced crystals of **4** suitable for crystallographic characterization. Yield: 0.076 g, 37.1%. *Anal.* Calc. for $C_{28}H_{39}CuF_6N_4O_9S_2$: C, 41.15; H, 4.81; N, 6.86. Found: C, 41.27; H, 5.12; N, 6.64%. ESI-MS (CH_3CN): $m/z = 447.2$ $[Cu(HL^{Me3})(L^{Me3})]^+$; 193.1 $[H_2L^{Me3}]^+$. UV–Vis [CH_3CN, λ_{max}, nm (ϵ, $M^{-1}\,cm^{-1}$)]: 261 (22000), 205 (22700), 671 (330), 483 (150). FTIR (KBr): 3291, 3105, 2976, 2875, 1610, 1593, 1490, 1449, 1369, 1282, 1266, 1249, 1165, 1031, 992, 774, 757, 636, 575, 517 cm^{-1}. EPR (9.436 GHz, 19.9 mW, mod. amp. 1 G, CH_3CN, 77 K): $g_\parallel = 2.35$, $g_\perp = 2.07$, $A_\parallel = 150$ G.

2.6. $[Cu(HL^{Me3})_2(H_2O)](ClO_4)_2$ (**5a**)

A methanol solution of HL^{Me3} (0.06 g, 0.31 mmol) was added dropwise to a methanol solution of $Cu(ClO_4)_2 \cdot 6H_2O$ (0.058 g, 0.16 mmol) forming a dark blue solution. The reaction was stirred overnight and vapor diffusion of diethyl ether into this solution resulted in the formation of green crystals of **5a**. Yield: 0.078 g, 75%. *Anal.* Calc. for $C_{22}H_{34}Cl_2CuN_4O_{11}$: C, 39.74; H, 5.15; N, 8.43. Found: C, 39.84; H, 5.10; N, 8.36%. ESI-MS (CH_3OH): $m/z = 546.1$ $[Cu(HL^{Me3})_2(ClO_4)]^+$; 446.2 $[Cu(L^{Me3})(HL^{Me3})]^+$; 255.1 $[Cu(L^{Me3})]^+$. UV–Vis [CH_3OH, λ_{max}, nm (ϵ, M^{-1}, cm^{-1})]: 211 (9900), 261 (10600), 727 (50). FTIR (KBr): 3411 (ν_{OH}), 3375 (ν_{NH}), 2973, 1594, 1548, 1490, 1441, 1370, 1307, 1212, 1164, 1090 ($\nu_{ClO_4^-}$), 992, 932, 864, 841, 781, 625, 537, 443 cm^{-1}. EPR (9.430 GHz, 0.04 mW, mod. amp. 1 G, MeOH, 77 K): $g_\parallel = 2.311$, $g_\perp = 2.061$, $A_\parallel = 145$ G.

2.7. $[Cu(HL^{Me3})_2(H_2O)](ClO_4)_2$ (**5b** · $2CH_3OH$)

A methanol solution of HL^{Me3} (0.07 g, 0.36 mmol) was added dropwise to a methanol solution of $Cu(ClO_4)_2 \cdot 6H_2O$ (0.135 g, 0.36 mmol) resulting in the formation of an uncharacterized blue precipitate and a greenish blue filtrate. The precipitate was collected by filtration and vapor diffusion of diethyl ether into the filtrate gave rise to dark blue crystals of **5b**. Yield: 0.02 g, 16%. *Anal.* Calc. for $C_{22}H_{34}Cl_2CuN_4O_{11}$: C, 39.74; H, 5.15; N, 8.43. Found: C, 39.56; H, 5.08; N, 8.35%. ESI-MS (CH_3OH): $m/z = 546.1$ $[Cu(HL^{Me3})_2(ClO_4)]^+$; 446.2 $[Cu(L^{Me3})(HL^{Me3})]^+$; 255.1 $[Cu(L^{Me3})]^+$. UV–Vis [CH_3OH, λ_{max}, nm (ϵ, M^{-1}, cm^{-1})]: 210 (8600), 261 (8400), 728 (50). FTIR (KBr): 3439 (ν_{OH}), 3371 (ν_{NH}), 2970, 1590, 1548, 1506, 1484, 1449, 1362, 1310, 1220, 1145, 1089 ($\nu_{ClO_4^-}$), 994, 932, 864, 841, 771, 636, 626, 536, 443 cm^{-1}. EPR (9.427 GHz, 0.04 mW, mod. amp. 1 G, MeOH, 77 K): $g_\parallel = 2.32$, $g_\perp = 2.06$, $A_\parallel = 144$ G.

2.8. $[Cu(HL^{Ph3})_2(H_2O)](ClO_4)_2$ (**6**)

A methanol solution of HL^{Ph3} (0.100 g, 0.13 mmol) was added dropwise to a methanol solution of $Cu(ClO_4)_2 \cdot 6H_2O$ (0.05 g, 0.13 mmol) resulting in a clear blue solution. Slow evaporation resulted in the formation of X-ray quality crystals of **6**. Yield: 0.125 g, 91%. *Anal.* Calc. for $C_{52}H_{46}Cl_2CuN_4O_{11}$: C, 60.20; H, 4.47; N, 5.40. Found: C, 60.03; H, 4.36; N, 5.30%. ESI-MS (CH_3CN): $m/z = 918.3$, $[Cu(HL^{Ph3})_2(ClO_4)]^+$; 819.3 $[Cu(HL^{Ph3})(L^{Ph3})]^+$; 441.0 $[Cu(L^{Ph3})]^+$. UV–Vis [CH_3CN, λ_{max}, nm (ϵ, M^{-1}, cm^{-1})]: 691 (180). FTIR (KBr): 3500 (ν_{OH}), 3397 (ν_{NH}), 1969, 1814, 1603, 1525, 1491, 1444, 1352, 1269, 1254, 1190, 1102 ($\nu_{ClO_4^-}$), 970, 920, 902, 854, 765, 738, 710, 698, 673, 641, 621, 577, 533, 519, 461, 432 cm^{-1}. EPR (9.439 GHz, 20 mW, mod. amp. 1 G, CH_3CN, 77 K): $g_\parallel = 2.298$, $g_\perp = 2.05$, $A_\parallel = 135$ G.

2.9. $[Cu(HL)(2,2'\text{-bipy})(H_2O)](ClO_4)_2$ (**7**)

A 1:1 methanol solution of HL (0.025 g, 0.17 mmol) and 2,2′-bipy (0.025 g, 0.17 mmol) was added to a methanol solution of $Cu(ClO_4)_2 \cdot 6H_2O$ (0.061 g, 0.17 mmol) forming a dark blue solution with a blue precipitate. The precipitate was collected by filtration and dissolved in acetonitrile, from which vapor diffusion of diethyl ether resulted in the formation of dark blue crystals of **7**. Slow evaporation of the filtrate also resulted in the formation of dark blue crystals of **7**. Yield: 0.086 g, 87%. *Anal.* Calc. for $C_{18}H_{20}Cl_2CuN_4O_{10}$: C, 36.84; H, 3.44; N, 9.55. Found: C, 37.08; H, 3.44; N, 9.54%. UV–Vis [DMF, λ_{max}, nm (ϵ, $M^{-1}\,cm^{-1}$)]: 300 (13000), 312 (12300), 676 (70). FTIR (KBr): 3280, 3107, 1653, 1610, 1601, 1566, 1473, 1443, 1317, 1146, 1115, 1080, 1024, 1013, 775, 729, 636, 625 cm^{-1}. EPR (9.426 MHz, 2.0 mW, mod. amp. 3 G, DMF, 77 K): $g_\parallel = 2.306$, $g_\perp = 2.06$, $A_\parallel = 154$ G.

2.10. $[Cu(HL^{Ph})(2,2'\text{-bipy})(H_2O)](ClO_4)_2$ (**8** · $0.5H_2O$)

To a 1:1 methanol solution of HL^{Ph} (0.025 g, 0.11 mmol) and 2,2′-bipy (0.017 g, 0.11 mmol) was added a methanol solution of $Cu(ClO_4)_2 \cdot 6H_2O$ (0.04 g, 0.11 mmol) forming a dark blue solution with a blue precipitate. The precipitate was collected by filtration and dissolved in acetonitrile, from which vapor diffusion of diethyl ether resulted in the formation of dark blue crystals of **8**. Slow evaporation

of the filtrate also resulted in the formation of dark blue crystals of **8**. Yield: 0.068 g, 92%. *Anal.* Calc. for $C_{24}H_{24}Cl_2CuN_4O_{10}$: C, 43.48; H, 3.65; N, 8.45. Found: C, 43.72; H, 3.58; N, 8.41%. UV–Vis [DMF, λ_{max}, nm (ϵ, $M^{-1}\,cm^{-1}$)]: 301 (14200), 312 (13700), 676 (70). FTIR (KBr): 3468, 3278, 3107, 3067, 3033, 1642, 1610, 1601, 1589, 1567, 1495, 1473, 1444, 1420, 1346, 1317, 1283, 1267, 1247, 1081, 1024, 941, 905, 775, 750, 729, 702, 636, 626 cm^{-1}. EPR (9.423 MHz, 2.0 mW, mod. amp. 3 G, DMF, 77 K): $g_{\|} = 2.316$, $g_{\perp} = 2.06$, $A_{\|} = 154$ G.

2.11. X-ray crystal structure determination

Single crystals of **1**–**8** were obtained by either slow evaporation of methanol or acetonitrile solutions of the complex or by vapor diffusion of diethyl ether into solutions of the complex. Intensity data for **1**–**8** were collected on a Bruker Apex CCD area detector diffractometer with graphite-monochromated Mo Kα ($\lambda = 0.71073$ Å) radiation. Cell parameters were determined from a non-linear least-squares fit of the data. The data for the complexes were corrected for absorption by the semi-empirical method. The structures were solved by direct methods by use of the SHELXTL program, and refined by full-matrix least-squares on F^2 by use of all reflections [30,31]. Hydrogen atom positions were initially determined by geometry and refined by a riding model. Non-hydrogen atoms were refined with anisotropic displacement parameters.

The asymmetric unit in **3** contains one monocation, $(C_{16}H_{20}ClCuN_4O_2)^+$, one-half of a dianion, $[CuCl_4]^{2-}$, and a disordered acetonitrile site. The dianion was located on a 2-fold rotation axis. The acetonitrile modeled in two orientations. Note that one atom of one acetonitrile was near the 2-fold rotation axis, so both orientations were

Table 1
Crystallographic data for **1**–**3**

	1	**2**	**3** · $2CH_3CN$
Formula	$C_{18}H_{20}CuF_6N_4O_8S_2$	$C_{18}H_{24}Cl_2CuN_4O_{10}$	$C_{18}H_{23}Cl_3Cu_{1.5}N_5O_2$
Fw	662.04	590.85	543.07
Temperature (K)	87(2)	120(2)	100(2)
Space group	$P2_1/n$	$P\bar{1}$	$C2/c$
a (Å)	8.4636(14)	8.1010(4)	23.660(5)
b (Å)	17.999(3)	8.1084(4)	14.404(3)
c (Å)	8.4903(14)	9.0412(5)	15.239(3)
α (°)	90	78.230(10)	90
β (°)	107.235(7)	80.056(10)	118.514(5)
γ (°)	90	76.018(10)	90
Z	2	1	8
V (Å^3)	1235.3(4)	559.39(5)	4563.5(16)
ρ_{calc} (g/cm^3)	1.780	1.754	1.581
μ (mm^{-1})	1.551	1.280	1.786
R_1 [$I > 2\sigma(I)$]	0.0227	0.0209	0.0260
wR_2 [$I > 2\sigma(I)$]	0.0622	0.0566	0.0742
Goodness-of-fit on F^2	1.016	1.023	1.032

Table 2
Crystallographic data for **4**, **5a** and **5b**

	4 · THF	**5a**	**5b** · $2CH_3OH$
Formula	$C_{32}H_{48}CuF_6N_4O_{10}S_2$	$C_{22}H_{34}Cl_2CuN_4O_{11}$	$C_{24}H_{42}Cl_2CuN_4O_{13}$
Fw	890.40	664.97	729.06
Temperature (K)	100(2)	100(2)	100(2)
Space group	$P\bar{1}$	$P2_1/c$	$C2/c$
a (Å)	10.306(2)	19.924(4)	23.477(6)
b (Å)	11.174(2)	12.161(2)	8.847(2)
c (Å)	19.040(4)	12.225(2)	15.723(4)
α (°)	89.878(6)	90	90
β (°)	83.470(5)	104.220(5)	91.947(5)
γ (°)	68.632(5)	90	90
Z	2	4	4
V (Å^3)	2026.8(7)	2871.3(9)	3263.8(14)
ρ_{calc} (g/cm^3)	1.459	1.538	1.484
μ (mm^{-1})	0.726	1.009	0.899
R_1 [$I > 2\sigma(I)$]	0.0582	0.0359	0.0480
wR_2 [$I > 2\sigma(I)$]	0.1548	0.0979	0.1383
Goodness-of-fit on F^2	1.080	1.015	1.043

Table 3
Crystallographic data for **6–8**

	6	**7**	**8** · 0.58H_2O
Formula	$C_{52}H_{46}Cl_2CuN_4O_{11}$	$C_{18}H_{20}Cl_2CuN_4O_{10}$	$C_{24}H_{25.15}Cl_2CuN_4O_{10.57}$
Fw	1037.37	586.82	673.36
Temperature (K)	120(2)	100(2)	100(2)
Space group	$P2/n$	$P\bar{1}$	$P\bar{1}$
a (Å)	15.4058(18)	8.2507(14)	8.3994(16)
b (Å)	8.8249(10)	8.2917(14)	10.027(2)
c (Å)	18.432(2)	18.000(3)	16.470(3)
α (°)	90	85.144(5)	78.643(5)
β (°)	114.048(5)	86.372(5)	84.487(5)
γ (°)	90	65.730(5)	81.323(5)
Z	2	2	2
V (Å^3)	2288.4(4)	1118.0(3)	1341.2(4)
ρ_{calc} (g/cm^3)	1.505	1.743	1.667
μ (mm^{-1})	0.664	1.281	1.081
R_1 [$I > 2\sigma$ (I)]	0.0297	0.0267	0.0754
wR_2 [$I > 2\sigma$ (I)]	0.0879	0.0754	0.0762
Goodness-of-fit on F^2	1.058	1.035	1.003

modeled with 0.5 occupancy factors. Restraints on the positional and displacement parameters of the acetonitrile atoms were required. The anion site is disordered in the structure of **5b** and was modeled in three orientations. The occupancies for the anion refined to 0.415(4), 0.293(8), and 0.291(7) for the unprimed, primed and double-primed atoms. Restraints on the positional and displacement parameters of the anion were required.

Restraints on the O–H distances in **7** were required. Hydrogens bonded to N2 and to the water oxygen were located on a difference map and refined independently. One of the perchlorate anions in **8** was disordered and was modeled in two orientations with occupancies refined to 0.570(8) and 0.430(8). One water, that was only bound by hydrogen bonds, O(1S), had an occupancy that refined to 0.575(6). Restraints on the positional and displacement parameters of the disordered anion were required. Crystal data for **1–8** are summarized in Tables 1–3, and selected bond lengths and angles are summarized in Tables 4–6.

Table 4
Selected bond distances (Å) and bond angles (°) of complexes **1–4**

*Complex **1***			
Cu1–N1	2.0086(12)	Cu1–O1	1.9829(10)
Cu1–N1A	2.0086(12)	Cu1–O1A	1.9829(10)
O1–Cu1–O1A	180.00(3)	O1–Cu1–N1	94.73(5)
O1–Cu1–N1A	85.27(5)	O1A–Cu1–N1	85.27(5)
O1A–Cu1–N1A	94.73(5)	N1A–Cu1–N1	180.0
*Complex **2***			
Cu1–N1	1.9875(10)	Cu1–O1	1.9808(9)
Cu1–N1A	1.9875(10)	Cu1–O1A	1.9808(9)
N1–Cu1–N1A	180.00(6)	O1–Cu1–N1A	85.86(4)
O1–Cu1–N1	94.14(4)	O1A–Cu1–N1A	94.14(4)
N1–Cu1–O1A	85.86(4)	O1–Cu1–O1A	180.000(1)
*Complex **3***			
Cu1–N1A	1.997(2)	Cu1–O1B	2.1337(17)
Cu1–N1B	1.988(2)	Cu1–Cl1	2.2861(8)
Cu1–O1A	2.1085(17)		
N1B–Cu1–N1A	179.93(9)	O1A–Cu1–O1B	92.16(7)
N1B–Cu1–O1A	87.58(7)	N1B–Cu1–Cl1	89.55(6)
N1A–Cu1–O1A	92.45(7)	N1A–Cu1–Cl1	90.46(6)
N1B–Cu1–O1B	92.39(7)	O1A–Cu1–Cl1	137.83(5)
N1A–Cu1–O1B	87.55(7)	O1B–Cu1–Cl1	130.00(5)
*Complex **4***			
Cu1–N1A	1.998(3)	Cu1–O1A	1.976(3)
Cu1–N1B	1.986(4)	Cu1–O1B	1.975(3)
Cu1–O2	2.246(3)		
O1B–Cu1–O1A	177.35(13)	N1B–Cu1–N1A	173.76(15)
O1B–Cu1–N1B	93.90(14)	O1B–Cu1–O2	92.89(13)
O1A–Cu1–N1B	87.19(14)	O1A–Cu1–O2	89.42(12)
O1B–Cu1–N1A	86.44(14)	N1B–Cu1–O2	94.65(13)
O1A–Cu1–N1A	92.21(14)	N1A–Cu1–O2	91.56(13)

Table 5
Selected bond distances (Å) and bond angles (°) of complexes **5a**, **5b** and **6**

*Complex **5a***			
Cu1–N1A	1.9881(19)	Cu1–N1B	1.9874(19)
Cu1–O1A	2.0468(15)	Cu1–O1B	2.0728(15)
Cu1–O2	2.008(2)		
N1B–Cu1–O1A	88.00(7)	N1B–Cu1–N1A	175.83(7)
O2–Cu1–O1A	127.43(10)	O2–Cu1–O1B	135.38(10)
O1A–Cu1–O1B	97.18(7)	N1B–Cu1–O2	87.99(7)
N1A–Cu1–O1B	88.56(7)		
*Complex **5b***			
Cu1–N1	1.983(3)	Cu1–O1	1.977(2)
Cu1–O2	2.207(4)		
N1A–Cu1–O1	93.17(10)	N1A–Cu1–N1	165.98(17)
O1–Cu1–O1A	175.48(13)	O2–Cu1–O1	87.74(7)
O2–Cu1–O1A	87.74(7)	N1A–Cu1–O1	87.39(10)
N1A–Cu1–O2	97.01(8)		
*Complex **6***			
Cu1–N1	1.9774(13)	Cu1–O1	1.9798(10)
Cu1–O2	2.2472(17)		
N1A–Cu1–O1	87.92(5)	N1–Cu1–N1A	171.84(7)
O1–Cu1–O1A	179.06(6)	N1–Cu1–O1	92.15(5)
N1–Cu1–O2	94.08(4)	O1–Cu1–O2	89.53(3)

Table 6
Selected bond distances (Å) and bond angles (°) of complexes **7** and **8**

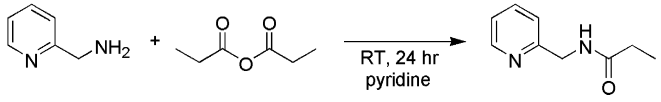
Complex 7			
Cu1–N3	1.9863(15)	Cu1–N1	1.9870(15)
Cu1–N4	2.0265(16)	Cu1–O1	1.9947(13)
Cu1–O2	2.2249(14)		
N1–Cu1–N4	95.97(6)	N1–Cu1–O2	97.83(6)
N4–Cu1–O2	91.95(6)	N3–Cu1–N1	169.46(6)
O1–Cu1–N4	170.24(5)	N3–Cu1–O1	90.44(6)
N1–Cu1–O1	91.12(6)	N3–Cu1–N4	81.38(6)
N3–Cu1–O2	92.46(6)	O1–Cu1–O2	93.72(5)
*Complex **8***			
Cu1–O10	1.9739(12)	Cu1–N18	1.9935(15)
Cu–N1	2.0021(15)	Cu–N29	2.0076(15)
Cu1–O30	2.2501(13)		
N1–Cu1–N29	169.13(6)	O10–Cu1–N1	97.99(6)
O10–Cu1–N29	170.72(6)	N18–Cu1–N29	81.62(6)
O10–Cu1–O30	88.12(5)	O10–Cu1–N18	89.37(6)
N1–Cu1–O30	93.24(6)	N29–Cu1–O30	95.20(6)
N18–Cu1–O30	97.61(5)		

3. Results and discussion

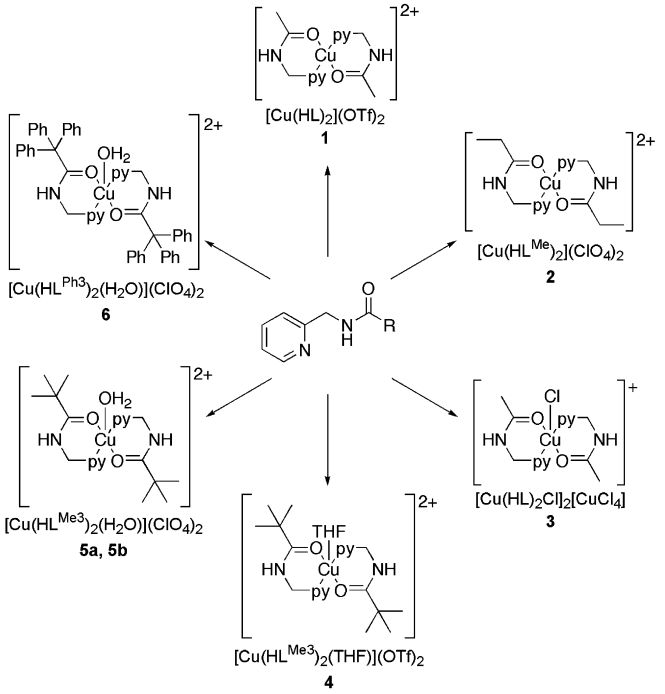
3.1. Synthesis and characterization

Our ligand design and synthesis originates from earlier reports wherein we synthesized a family of copper(I), copper(II), and zinc(II) complexes with pyridylmethylamide ligands [9–11,14–16]. Here we report the synthesis of HL^{Me}, another addition to the family of pyridylmethylamide ligands. HL^{Me} was synthesized by the reaction of 2-(aminomethyl)pyridine and propionic anhydride (Scheme 1). This ligand is nearly identical to HL, for which coordination chemistry has been thoroughly investigated [10,14–16].

Copper complexes **1**–**6**, summarized in Scheme 2, were synthesized by straightforward means via the reaction of copper(II) salts ($Cu(OTf)_2$, $Cu(ClO_4)_2 \cdot 6H_2O$ or $CuCl_2$) with a solution of the ligand in acetonitrile or methanol. They are mononuclear with two molecules of the respective ligand coordinating to the copper center. The ligands are not deprotonated so they coordinate through the carbonyl oxygen and the pyridyl nitrogen rendering them bidentate. Different metal:ligand ratios were attempted, but in all cases the complexes formed were mononuclear with a metal:ligand ratio of 1:2. Interestingly, changing the $Cu(ClO_4)_2$:HL^{Me3} reaction stoichiometry leads to two polymorphs of **5**. When a 1:2 Cu:HL^{Me3} ratio was used, trigonal-bipyramidal **5a** is formed in good yield, while when a 1:1 Cu:HL^{Me3} ratio was used, square-pyramidal **5b** formed in lower yield. Copper complexes **7** and **8** were synthesized, as shown in Scheme 3, by the reaction of a 1:1 solution of

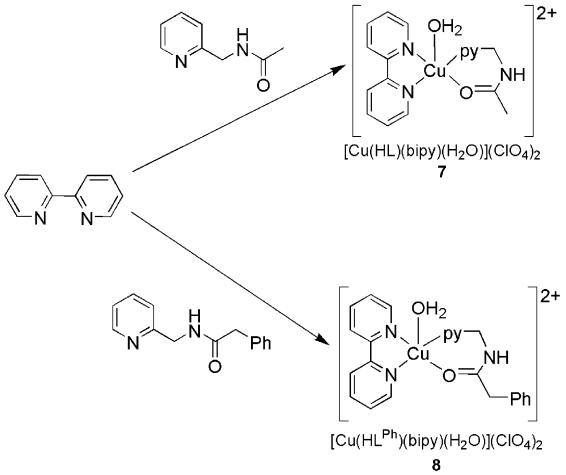


Scheme 1.



Scheme 2.

2,2′-bipyridine (bipy) and the respective ligand with a solution of $Cu(ClO_4)_2 \cdot 6H_2O$ in methanol. All complexes were characterized by elemental analysis and X-ray crystal structure determination. The spectroscopic properties of **1**–**8** are typical of mononuclear copper(II) species, consistent with their structures. All complexes exhibit intense ligand to metal charge transfer transitions (LMCT) transitions in the range of 200–315 nm. The d–d transitions are in the range of 640–690 nm for complexes **1**, **4**, **6**, **7** and **8** with geometries ranging from square-planar to square-pyramidal. For complexes **2**, **5a** and **5b**, the d–d transitions are in the range of 720–728 nm. Complex **3** with a square-pyramidal geometry has a d–d transition at 831 nm. The slight



Scheme 3.

differences in the d–d transitions is attributed to the differing geometries of the copper complexes. The X-band EPR spectra of **1**, **2**, **4**, **5b**, **6**, **7** and **8** in frozen CH_3OH or CH_3CN at 77 K are typical of mononuclear copper(II) complexes with predominantly axial character suggesting a $d_{x^2-y^2}$ ground state [32,33], consistent with the X-ray crystal structures of these complexes. Complex **3** does not exhibit any EPR signal, perhaps suggesting formation of antiferromagnetically coupled pairs in solution. Complex **5a** exhibits an EPR signal that is not typical of a trigonal-bipyramidal complex but closer to a square-pyramidal structure suggesting the possibility of interconversion in solution. This possibility is corroborated by the identical UV–Vis spectra of solutions of **5a** and **5b**.

3.2. X-ray crystal structures

3.2.1. $[Cu(HL)_2](OTf)_2$ (**1**) and $[Cu(HL^{Me})_2](ClO_4)_2$ (**2**)

The cationic portions of complexes **1** and **2** are shown in Figs. 1 and 2 respectively, and their bond parameters are listed in Table 4. Both copper centers in **1** and **2** have square-planar geometries. The similarities in the copper geometries are further supported by the τ_4 geometry index proposed by our group for four-coordinate complexes [16]. The calculated τ_4 values of 0 for complexes **1** and **2**, accurately reflect the perfect square-planar geometry of copper observed in these crystal structures. Complex **1** with triflate as the counterion is structurally very similar to its previously reported perchlorate analogue, $[Cu(HL)_2](ClO_4)_2$ [10]. The copper center has long axial interactions with the perchlorate O atoms at 2.8098(15) Å in the reported analogue. In complex **1**, when triflate is used as the counter-anion, these interactions are at 2.6221(12) Å. The four coordination sites of the copper centers are comprised of two HL ligands for **1** and two HL^{Me} ligands for **2**, via the pyridyl N atom and the carbonyl O atom. The Cu–N and Cu–O bond distances, summarized in Table 4, are typical for this type of complex. The $Cu–O_{carbonyl}$ and $Cu–N_{pyridyl}$ distances for $[Cu(HL)_2](ClO_4)_2$ are 1.9560(13) and 1.9981(15) Å [10], while they are 1.9829(10) and 2.0086(12) Å for complex **1**. These differences are trivial and can be attributed to the differences in the counter-anions, perchlorate versus triflate. For both complexes, the pyridyl rings are coplanar and the dihedral angles between the two pyridyl rings plane and the copper square plane is 46.0° for **1**, and 49.6° for **2**. The long axial interactions between copper and triflate or perchlorate O atoms in complexes **1** and **2** are 2.622 Å and 2.624 Å, respectively. The similarity of structural properties for complexes **1** and **2** indicate only trivial influences of the ethyl group in ligand HL^{Me} in **2**.

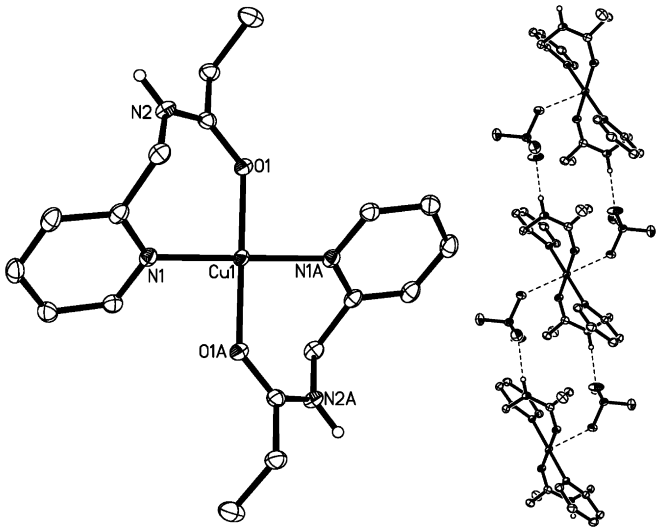


Fig. 2. X-ray crystal structure (left) and packing diagram (right) for $[Cu1(HL^{Me})_2](ClO_4)_2$ (**2**) with thermal ellipsoids at the 50% probability level. All H atoms except for the amide H atoms are omitted for clarity.

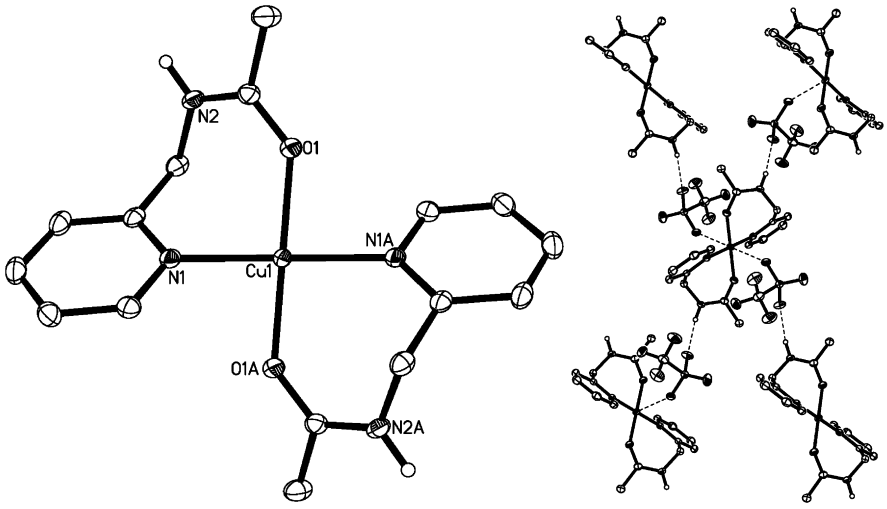


Fig. 1. X-ray crystal structure (left) and packing diagram (right) for $[Cu(HL)_2](OTf)_2$ (**1**) with thermal ellipsoids at the 50% probability level. All H atoms except for the amide H atoms are omitted for clarity.

The packing structures and hydrogen bonding interactions in **1** and **2** are quite different because of the difference in the anions present. The triflate anions in the axial positions of the copper coordination sphere of **1** form hydrogen bonds with two N–H groups from two adjacent cationic moieties (see Fig. 1). Every cationic copper complex is also hydrogen bonded via the amide NH groups to triflate anions, which are in turn loosely coordinated to another Cu to create wave-like two dimensional sheets. In the case of **2**, while the two perchlorate anions of the mononuclear unit also form two hydrogen bonds with N–H groups from two adjacent mononuclear units, these hydrogen bonding interactions extend to form a double stranded chains in the packing structure (see Fig. 2). The hydrogen bonding in $[Cu(HL)_2](ClO_4)_2$ follows the same pattern as in **2**, not surprising in light of the similarities in the structures along with the fact that both complexes are perchlorate salts [10].

3.2.2. $[Cu(HL)_2Cl]_2[CuCl_4]\cdot 2CH_3CN$ (**3**) and $[Cu(HL^{Me3})_2(THF)](OTf)_2\cdot THF$ (**4**)

Crystallographic analysis indicates that complex **3** consists of two mononuclear $[Cu(HL)_2Cl]^+$ cations and one $[CuCl_4]^{2-}$ anion (Fig. 3). The geometry of the five-coordinate copper center in the cation is slightly distorted trigonal-bipyramidal. The structural index parameter τ_5 proposed by Addison et al. has been used to describe trigonality of five-coordinate systems [32]. According to this standard, the cation $[Cu(HL)_2Cl]^+$ of complex **3** has a τ_5 value of 0.70, indicating a slight distortion from perfect trigonal-bipyramidal geometry. The pyridyl N atom and amide O atom from two HL ligands chelate to the same copper ion, and the fifth position is occupied by chloride. The two N atoms occupy the axial positions with a N1A–Cu1–N1B bond angle of 179.93(9)°. Two carbonyl O atoms and the Cl^- make up the trigonal plane. The Cu ion lies out of the equatorial plane by a distance of 0.011 Å, and the dihedral angle between the equatorial plane and axial plane formed by N1A, N1B and Cu1 is 88.4°. In the anion, the four-coordinate Cu(II) center displays a slightly distorted square-planar geometry. The four chloride ions of $[CuCl_4]^{2-}$ are involved in H-bonding interactions with the N–H groups from $[Cu(HL)_2Cl]^+$ cation units to form a H-bonding network that extends to create wave-like two dimensional sheets as shown in Fig. 3. The bond distances in **3**, summarized in Table 4, are comparable to previously reported five-coordinate Cu(II) complexes with similar N_2O_2Cl coordination environments [34,35].

The copper center of complex **4** possesses a square-pyramidal geometry. For **4**, the τ_5 value is only 0.06, which is very close to 0 for a perfect square-pyramidal structure. The four equatorial positions of the square plane are occupied by two pyridyl N atoms and two amide O atoms from two HL^{Me3} ligands, and the apical position is occupied by a THF molecule. The angles N1A–Cu1–N1B and O1A–Cu1–O1B are 173.76(15)° and 177.35(13)°, respectively, revealing slight distortion of the square-plane. The mean deviation of the N1A, N1B, O1A and O1B from the least-squares plane formed by these four atoms is only 0.0339 Å, and the copper atom lies out of the plane by a distance of 0.0743 Å. The THF molecule sits in the axial position, and the displacement of the Cu1–O2 bond from the normal to the square plane is only 2.4°. The relatively long Cu1–O2 bond distance of 2.246(3) Å is indicative of a weak interaction between the THF molecule and the copper(II). Both N–H groups of complex **4** are involved in intermolecular N–H···O hydrogen bonding interactions with two triflate anions, having an average H···O distance of around 2.08 Å and ∠N–H···F angle of around 144°.

The distinct copper center geometries of **3** and **4** are attributed to the different substituent groups on the amide side arms of HL and HL^{Me3}. The two trans pyridyl rings in **3** are nearly coplanar with a dihedral angle of 18.8°, and the two amide side arms stay on the same side of the two pyridyl rings with an O1A–Cu1–O1B angle of 92.16(7)°. However, in **4**, instead of forming a similarly small O1A–Cu1–O1B angle, the steric effect of the two *t*-butyl

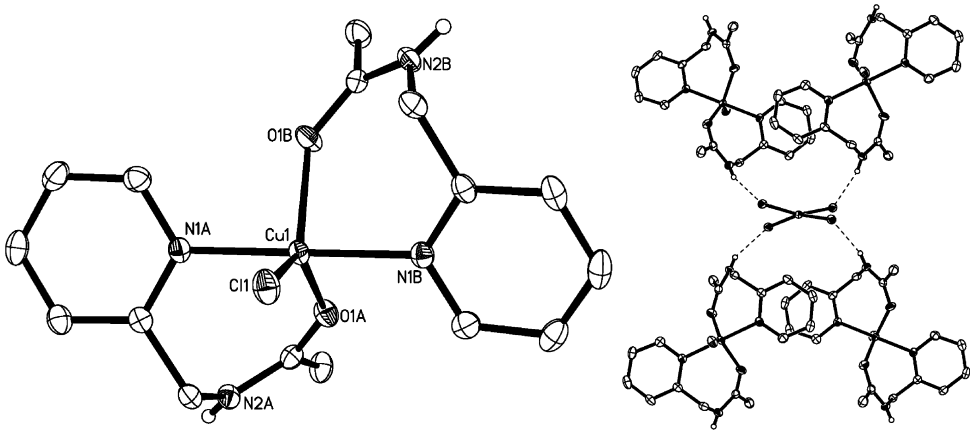


Fig. 3. X-ray crystal structure (left) for the cationic portion of **3**, $[Cu(HL)_2Cl]^+$, and packing diagram for **3** (right) with thermal ellipsoids at the 50% probability level. All H atoms except for the amide H atoms are omitted for clarity.

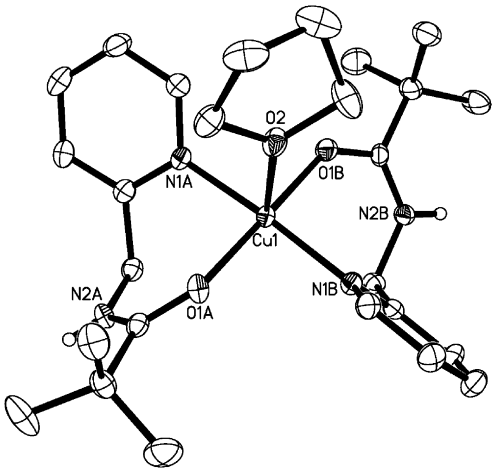


Fig. 4. X-ray crystal structure for $[Cu(HL^{Me3})_2(THF)](OTf)_2$ (**4**) with thermal ellipsoids at the 50% probability level. All H atoms except for the amide H atoms are omitted for clarity.

groups force the two side arms to stay *trans* to each other with a nearly linear O1A–Cu1–O1B angle of 177.35(13)°, which further leads to the high dihedral angle of 74.9° between the two *trans* pyridyl rings Fig. 4.

3.2.3. $[Cu(HL^{Me3})_2(H_2O)](ClO_4)_2$ (**5a** and **5b**) and $[Cu(HL^{Ph3})_2(H_2O)](ClO_4)_2$ (**6**)

The crystal structures of **5a** and **5b** are illustrated in Figs. 5 and 6, respectively. Bond distances and angles relevant to the copper coordination sphere of both compounds are listed in Table 5. Complexes **5a** and **5b** have identical ligand donor sets but are structurally different from each other. Both are coordinated by two bidentate HL ligand molecules, and a molecule of water. Complex **5a** is best described as distorted trigonal-bipyramidal with a τ_5 value of 0.67. Cu1 is coordinated to the two carbonyl oxygens (O1A and O1B) at 2.0468(15) and 2.0728(15) Å and a water molecule (O2) at 2.008(2) Å forming the equatorial plane, while the pyridyl nitrogens (N1A and N1B) are located axially. The Cu atom lies 0.01 Å out of the equatorial plane of O1A, O1B and O2. The dihedral angle between the equatorial plane formed by O1A, O1B and O2 and the axial plane formed by N1A, N1B and Cu1 is 93.8°. The pyridyl rings are located *trans* to each other

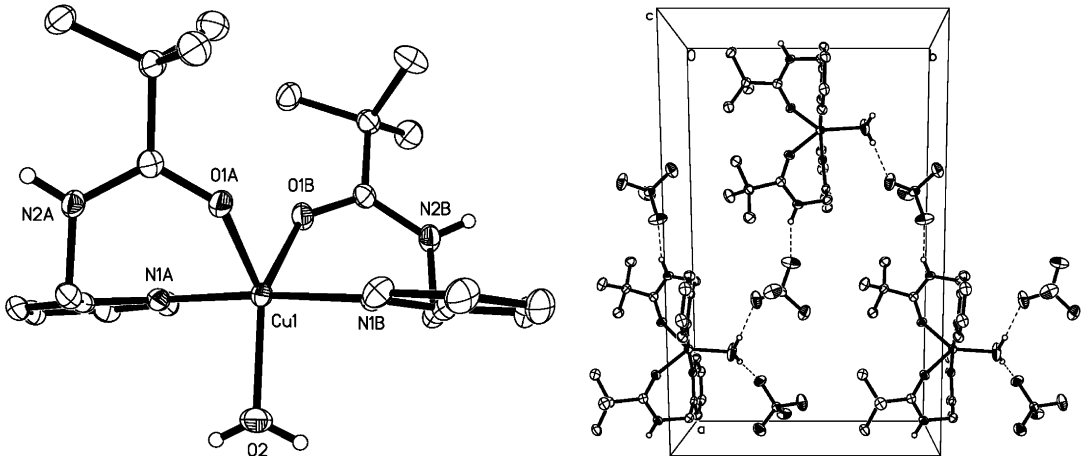


Fig. 5. X-ray crystal structure (left) and packing diagram (right) for $[Cu(HL^{Me3})_2(H_2O)](ClO_4)_2$ (**5a**) with thermal ellipsoids at the 50% probability level. All H atoms except for the amide and water H atoms are omitted for clarity.

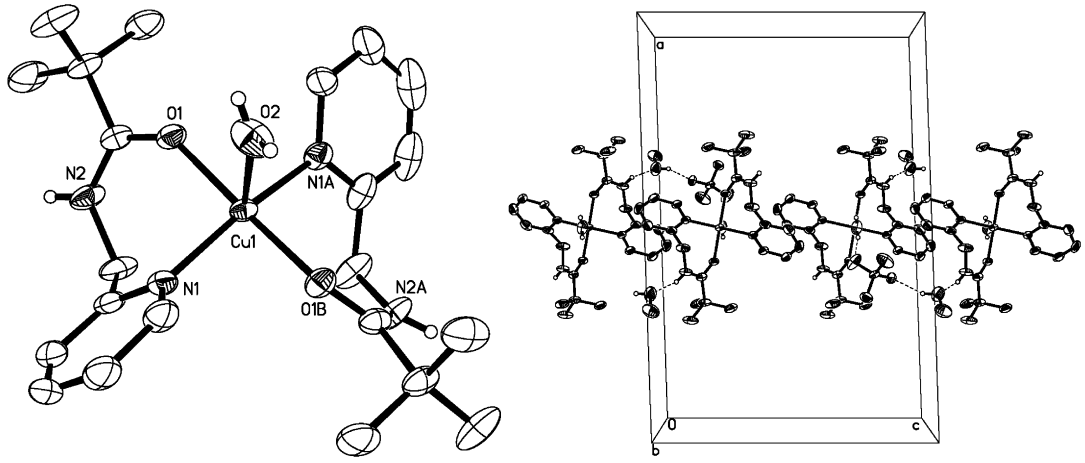


Fig. 6. X-ray crystal structure (left) and packing diagram (right) for $[Cu(HL^{Me3})_2(H_2O)](ClO_4)_2$ (**5b**) with thermal ellipsoids at the 50% probability level. All H atoms except for the amide and water H atoms are omitted for clarity.

and are nearly coplanar, with a dihedral angle of 8.6°. The coordinated water molecule (O2) hydrogen bonds to oxygens O1C and O1D of two perchlorate anions, with O2–O1C/O1D distances of 2.758(3) and 2.728(3) Å. The amide nitrogens (N2A and N2B) hydrogen bond to oxygen atoms (O2D and O3C) of adjacent perchlorate anions, with N2A–O2D and N2B–O3C distances of 2.913(3), and 2.873(3) Å.

Complex **5b** is symmetrical with a crystallographic 2-fold rotation axis passing through the metal center and dividing the molecule into two equal halves. In contrast to **5a**, **5b** has a coordination geometry closer to square-pyramidal with a τ_5 geometric index of 0.16. The basal plane of the square-pyramid is made up of two pyridyl nitrogens and two carbonyl oxygens with bond distances of 1.983(3) and 1.977(2) Å, respectively. The fifth coordination site is occupied by a water molecule located axially with a bond distance of 2.207(4) Å. With respect to **5a**, this reflects a contraction of the Cu–$O_{carbonyl}$ bonds and a lengthening of the Cu–O_{water} bond. The mean deviation of N1, N1A, O1 and O1B from the least-squares plane is 0.1597 Å. The Cu atom lies 0.0821 Å out of this plane. The pyridyl rings of the two molecules are twisted at an angle of 79.6°. The amide nitrogen (N2) is hydrogen bonded to a methanol oxygen O1S in the lattice at 2.773(4) Å. The coordinated water O2 hydrogen bonds to the perchlorate oxygens in the range 2.66–3.07 Å. The methanol oxygen O1S also hydrogen bonds to the perchlorate oxygen O2A at 3.083(11) Å and O2A and O1A in the range 2.79–3.2 Å.

The differing geometries of **5a** and **5b** are attributed to the differences in their intermolecular interactions as illustrated in their packing diagrams. In **5a**, the hydrogen bonding interactions of the coordinated water molecule with the perchlorate anions appears to pull the two anions closer to the water molecule, resulting in pushing the side arms of the two HL^{Me3} ligands on the same side of the molecule as the two pyridyl rings, and a O1A–Cu1–O1B angle of 97.18(7)°. Consequently, the two pyridyl rings are nearly coplanar with an angle of 8.6° with respect to each other. In contrast, complex **5b** has no such effect of the perchlorate anions on the water ligand, and the molecules arrange such that there are intermolecular π–π stacking interactions between pyridyl rings on adjacent molecules, and a high dihedral angle of 79.6° between the pyridyl rings *trans* to each other on the same molecule. Consequently, the two side arms are located opposite to each other with a O1–Cu–O1A angle of 175.48(13)°. The two pyridyl rings on each mononuclear unit are perfectly parallel to the pyridyl rings from adjacent mononuclear units with a mean centroid–centroid distance of 3.594 Å and a displacement angle of 21.9°. This indicates strong π–π interactions of pyridyl rings [36]. This is the driving force for the formation of the square-pyramidal geometry in complex **5b**.

The crystal structure of **6** is illustrated in Fig. 7, and bond distances and angles are summarized in Table 5. Similar to complexes **5a** and **5b**, complex **6** is also five-coordinate. The cationic portion of this complex sits on a crystallographic 2-fold rotational axis. The Cu is coordinated by two HL^{Ph3} ligands and a molecule of water in a square-pyramidal geometry. The τ_5 geometry index was calculated to be 0.12 indicating that copper(II) is closest to square-pyramidal geometry. The basal plane of the square-pyramid is made up of two equivalent pyridyl nitrogens and two equivalent carbonyl oxygens, with bond distances of 1.9774(13) and 1.9798(10) Å, respectively. The mean deviation of N1, N1A, O1 and O1B from the least-squares plane is 0.0784 Å. The Cu atom lies 0.0622 Å out of this plane. The fifth coordination site is occupied by a water molecule in the axial position at a distance of 2.2472(17) Å. The coordinated water molecule hydrogen bonds with the perchlorate oxygen O1A, with a O2–O1A distance of 2.8074(15) Å. The metrical parameters for **6** are quite similar to those of **5b**.

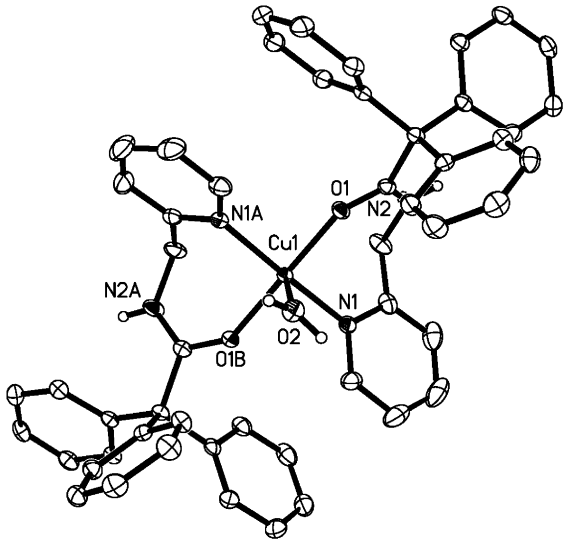


Fig. 7. X-ray crystal structure for $[Cu(HL^{Ph3})_2(H_2O)](ClO_4)_2$ (**6**) with thermal ellipsoids at the 50% probability level. All H atoms except for the amide and water H atoms are omitted for clarity.

3.2.4. $[Cu(HL)(bipy)(H_2O)](ClO_4)_2$ (7) and $[Cu(HL^{Ph})(bipy)(H_2O)](ClO_4)_2$ (8)

The crystal structures of **7** and **8** are illustrated in Figs. 8 and 9 with bond distances and angles listed in Table 6. The coordination environments for **7** and **8** are similar to **5b** and **6**, but with one HL^R ligand replaced by a bipy ligand. The Cu atoms in **7** and **8** are coordinated to the $N_{pyridyl}$ and O atoms of HL^R (HL for **7**, and HL^{Ph} for **8**), to two N atoms from bipy, and an axial water ligand. The geometry is distorted square-pyramidal with τ_5 values of 0.013 for **7** and 0.027 for **8**. In both complexes, the basal plane of the square-pyramid is comprised of the carbonyl oxygen and pyridyl nitrogen of the respective ligands and the bipy nitrogens. The mean deviation of these four atoms constituting the basal plane from the least-squares plane is 0.0364 Å for **7**, and 0.0681 Å for **8**. The Cu atom deviates from the least-squares plane by 0.1425 Å for **7**, and 0.121 Å for **8**. The pyridyl ring in **7** is at an angle of

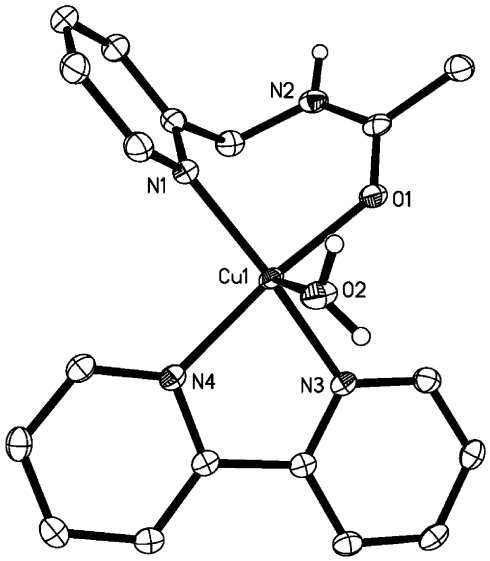


Fig. 8. X-ray crystal structure for $[Cu(HL)(bipy)(H_2O)](ClO_4)_2$ (**7**) with thermal ellipsoids at the 50% probability level. All H atoms except for the amide and water H atoms are omitted for clarity.

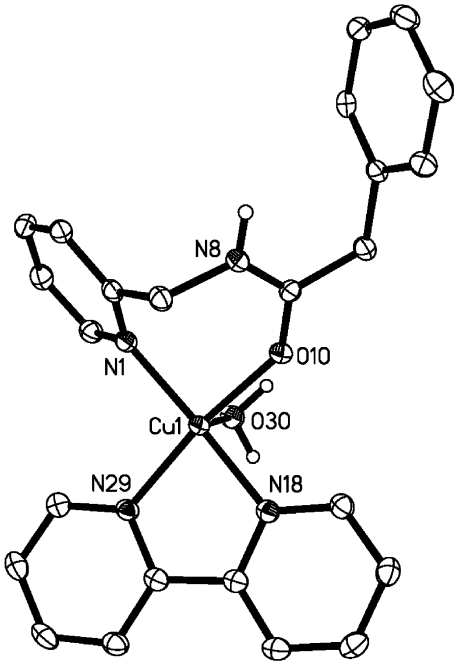


Fig. 9. X-ray crystal structure for $[Cu(HL^{Ph})(bipy)(H_2O)](ClO_4)_2$ (**8**) with thermal ellipsoids at the 50% probability level. All H atoms except for the amide and water H atoms are omitted for clarity.

63.4° with respect to the bipy plane. This angle is nearly identical in **8**, with an angle of 59.4 °. Both complexes **7** and **8** exhibit hydrogen bonding between the coordinated water and perchlorate anions. The amide NH groups in both the complexes is also involved in hydrogen bonding interactions with the perchlorate anions.

The $Cu–O_{carbonyl}$ and $Cu–N_{pyridyl}$ distances of our series of complexes have been compared with examples from the literature. A crystal structure of $[Cu(HL)_2](ClO_4)_2$, similar to **1** with perchlorate as a counter-anion instead of triflate, has been reported [10] and its bond parameters are comparable to those in **1**. Complexes **1**, **2**, **4**, **5b**, **6**, **8**, and **9** have geometries that are square-planar to square-pyramidal with $Cu–O_{carbonyl}$ distances in the range of 1.97–1.99 Å. These values are similar to distorted square-pyramidal copper complexes of the triazacyclononane ligand with amide appendages [8,37,38], and copper complexes of substituted oxamides [18,19] where the Cu–O distances are in the range of 1.98–2.01 Å. These values are slightly higher than square-pyramidal copper complexes with the substituted analogues of 2-aminoethyl pyridine, where the Cu–O distances are in the range of 1.93–1.94 Å [20]. Complexes **3** and **5b** with trigonal-bipyramidal geometries, have Cu–O distances in the range of 2.04–2.13 Å, which are similar to copper complexes with similar geometry and Cu–O distances ranging from 2.11 to 2.16 Å [35]. The $Cu–N_{pyridyl}$ distances, in the range of 1.977–2.008 Å, compare well with the literature [10,11,20]. In complexes **7** and **8**, the $Cu–O_{carbonyl}$ distances are in the range of 1.97–1.99 Å, and the $Cu–N_{pyridyl}$ distances are in the range of 1.98–2.00 Å, consistent with the literature. The $Cu–N_{bipy}$ distances are in the range of 1.98–2.02 Å, and lie in the same range as those of the literature [39–41].

4. Summary and conclusions

Copper(II) complexes **1**–**8** were synthesized with a variety of pyridylmethylamide ligands under neutral conditions. The ligands coordinate in a bidentate fashion via the pyridyl N atom and the carbonyl O atom. With the ligands HL and HL^{Me} and in the absence of strongly coordinating chloride, complexes **1** and **2** form, which are four-coordinate. With strongly coordinating chloride, copper complex **3** with HL forms, which is five-coordinate. With ligands HL^{Me3} and HL^{Ph3}, a different behavior is observed and complexes **4**–**6** are all five-coordinate. Complexes **7** and **8** are five-coordinate as well, with bipy as a co-ligand. The geometries range from square-planar to square-pyramidal to trigonal-bipyramidal. The bidentate coordination mode of pyridylmethylamide ligands under neutral conditions offers fairly limited coordination chemistry. Our laboratory continues to investigate the coordination chemistry of these ligands with copper and other transition metals under basic conditions, and will report those results elsewhere.

Acknowledgements

This work was supported by the National Science Foundation (CHE-0094079 and CHE-0616941) and the Herman Frasch Foundation. Additional support was provided by the University of Oklahoma Honors College (fellowship to L.R.W.). Finally, we thank the NSF for the purchase

of a CCD equipped X-ray diffractometer at the University of Oklahoma (CHE-0130835).

Appendix A. Supplementary material

CCDC 637902, 637903, 637904, 637905, 637906, 637907, 637908, 637909 and 637910 contain the supplementary crystallographic data for **1**, **2**, **3**, **4**, **5a**, **5b**, **6**, **7** and **8**. These data can be obtained free of charge via http://www.ccdc.cam.ac.uk/conts/retrieving.html, or from the Cambridge Crystallographic Data Centre, 12 Union Road, Cambridge CB2 1EZ, UK; fax: (+44) 1223-336-033; or e-mail: deposit@ccdc.cam.ac.uk. Supplementary data associated with this article can be found, in the online version, at doi:10.1016/j.poly.2007.08.004.

References

[1] F.T. de Oliveira, A. Chanda, D. Banerjee, X.P. Shan, S. Mondal, L. Que, E.L. Bominaar, E. Munck, T.J. Collins, Science 315 (2007) 835.
[2] J.N. Smith, J.T. Hoffman, Z. Shirin, C.J. Carrano, Inorg. Chem. 44 (2005) 2012.
[3] T.C. Harrop, M.M. Olmstead, P.K. Mascharak, Inorg. Chem. 44 (2005) 9527.
[4] K. Uemura, S. Kitagawa, K. Fukui, K. Saito, J. Am. Chem. Soc. 126 (2004) 3817.
[5] N. Niklas, F.W. Heinemann, F. Hampel, T. Clark, R. Alsfasser, Inorg. Chem. 43 (2004) 4663.
[6] J. Mrozinski, Coord. Chem. Rev. 249 (2005) 2534.
[7] S. Osa, T. Kido, N. Matsumoto, N. Re, A. Pochaba, J. Mrozinski, J. Am. Chem. Soc. 126 (2004) 420.
[8] A. Mondal, E.L. Klein, M.A. Khan, R.P. Houser, Inorg. Chem. 42 (2003) 5462.
[9] E.L. Klein, M.A. Khan, R.P. Houser, Inorg. Chem. 43 (2004) 7272.
[10] A. Mondal, Y. Li, M.A. Khan, J.H. Ross, R.P. Houser, Inorg. Chem. 43 (2004) 7075.
[11] U. Pal Chaudhuri, L.R. Whiteaker, L. Yang, R.P. Houser, Dalton Trans. (2006) 1902.
[12] L.R. Whiteaker, U. Pal Chaudhuri, D.R. Powell, R.P. Houser, Acta Crystallogr., Sect. E E62 (2006) o3337.
[13] L.R. Whiteaker, U. Pal Chaudhuri, D.R. Powell, R.P. Houser, Acta Crystallogr., Sect. E E62 (2006) o3339.
[14] L. Yang, R.P. Houser, Inorg. Chem. 45 (2006) 9416.
[15] U. Pal Chaudhuri, L.R. Whiteaker, A. Mondal, E.L. Klein, D.R. Powell, R.P. Houser, Inorg. Chim. Acta 360 (2007) 3610.
[16] L. Yang, D.R. Powell, R.P. Houser, Dalton Trans. (2007) 955.
[17] M. Nonoyama, Inorg. Chim. Acta 13 (1975) 5.
[18] F. Lloret, M. Julve, J. Faus, R. Ruiz, I. Castro, M. Mollar, M. Philochelevisalles, Inorg. Chem. 31 (1992) 784.
[19] F. Lloret, M. Julve, J.A. Real, J. Faus, R. Ruiz, M. Mollar, I. Castro, C. Bois, Inorg. Chem. 31 (1992) 2956.
[20] E.H. Alilou, E. Amadei, M. Giorgi, M. Pierrot, M. Reglier, J. Chem. Soc., Dalton Trans. (1993) 549.
[21] J.C.M. Rivas, R.T.M. de Rosales, S. Parsons, Dalton Trans. (2003) 2156.
[22] J.C.M. Rivas, E. Salvagni, R.T.M. de Rosales, S. Parsons, Dalton Trans. (2003) 3339.
[23] J.C.M. Rivas, E. Salvagni, R. Prabaharan, R.T.M. de Rosales, S. Parsons, Dalton Trans. (2004) 172.
[24] J.C.M. Rivas, E. Salvagni, S. Parsons, Dalton Trans. (2004) 4185.
[25] R.K. Afshar, A.K. Patra, M.M. Olmstead, P.K. Mascharak, Inorg. Chem. 43 (2004) 5736.
[26] H. Miyake, K. Yoshida, H. Sugimoto, H. Tsukube, J. Am. Chem. Soc. 126 (2004) 6524.
[27] H.J. Liu, Y.H. Hung, C.C. Chou, C.C. Su, Chem. Commun. (2007) 495.
[28] G.K. Ingle, M.M. Makowska-Grzyska, E. Szajna-Fuller, I. Sen, J.C. Price, A.M. Arif, L.M. Berreau, Inorg. Chem. 46 (2007) 1471.
[29] C. Li, L.S. Rittmann, A.S. Tsiftsoglou, K.K. Bhargava, A.C. Sartorelli, J. Med. Chem. 21 (1978) 874.
[30] G.M. Sheldrick, SHELXTL Version 6.10 Reference Manual, Bruker AXS Inc., Madison, WI, USA, 2000.
[31] International Tables for Crystallography, vol. C. Kluwer, Boston, 1995.
[32] A.W. Addison, T.N. Rao, J. Reedijk, J. van Rijn, G.C. Verschoor, J. Chem. Soc., Dalton Trans. (1984) 1349.
[33] A. Bencini, I. Bertini, D. Gatteschi, A. Scozzafava, Inorg. Chem. 17 (1978) 3194.
[34] J.L. Shaw, G.T. Yee, G.B. Wang, D.E. Benson, C. Gokdemir, C.J. Ziegler, Inorg. Chem. 44 (2005) 5060.
[35] M. Gupta, P. Mathur, R.J. Butcher, Inorg. Chem. 40 (2001) 878.
[36] C. Janiak, J. Chem. Soc., Dalton Trans. (2000) 3885.
[37] L.M. Berreau, J.A. Halfen, V.G. Young Jr., W.B. Tolman, Inorg. Chem. 37 (1998) 1091.
[38] H. Sigel, R.B. Martin, Chem. Rev. 82 (1982) 385.
[39] L. Cai, H.P. Xiao, L.G. Zhu, Acta Crystallogr., Sect. E 61 (2005) M2546.
[40] H.Y. Wu, Y.F. Feng, S.R. Wang, W.P. Huang, Acta Crystallogr., Sect. E 62 (2006) M1225.
[41] F.Q. Liu, Q.X. Wang, K. Jiao, F.F. Jian, G.Y. Liu, R.X. Li, Inorg. Chim. Acta 359 (2006) 1524.

redox and magnetic properties which could increase the field of possible applications [9,10]. The growing use of Pcs as advanced materials during the last decade has encouraged the synthesis of new materials [11] which differ in terms of the central metal ion and peripheral substituents [12].

The present paper reports for the first time the synthesis and characterisation of 4-nitro-2-octyloxyphenoxy substituted symmetrical and unsymmetrical MPcs. The electrical and electrochemical properties of the complexes are also presented.

2. Experimental

2.1. Synthesis and characterization

All chemicals used were of reagent grade. The solvents were dried, purified and stored over molecular sieves (4 Å). Compounds **2** and **6** were prepared by the literature methods [13,14]. Compound **1** was obtained from commercial suppliers. The progress of the reactions was monitored by TLC. Column chromotography was used for purification of the complexes. ^{1}H NMR spectra were determined with a Varian Unity Inova 500 MHz NMR spectrometer and a Varian Mercury-Vx 400 MHz NMR spectrometer. IR spectra were recorded as KBr discs in the range 400–4000 cm^{-1} on a Shimadzu FTIR-8300 infrared spectrometer. The electronic absorption spectra were measured in $CHCl_3$ with a Shimadzu UV-1601 UV/Vis spectrometer. Mass spectra were acquired on a Voyager-DE™ PRO MALDI-TOF mass spectrometer (Applied Biosystems, USA) equipped with a nitrogen UV-Laser operating at 337 nm. Spectra were recorded both in linear and reflectron modes with an average of 50 and 100 shots for linear and reflectron modes, respectively. A α-cyano-4-hydroxycinnamic acid (CHCA) MALDI matrix was used and prepared in chloroform at a concentration of 20 mg/mL for symmetrical Pcs **8** and **9**. A 3-indole acrylic acid (IAA) MALDI matrix was used for the unsymmetrical Pc **7**. The positive ion and linear mode spectrum of complex **10** could be obtained only in dithranol matrix. MALDI samples were prepared by mixing sample solutions (4 mg/mL) with the matrix solution (1:10 v/v) in a 0.5 mL eppendorf® microtube. Finally 1 μl of this mixture was deposited on the sample plate, dried at room temperature and then analyzed.

2.1.1. 3,4-Bis(3,4-dicyanophenoxy)nitrobenzene (*3*) and 4-(3,4-dicyanophenoxy)-3-hydroxynitrobenzene (*4*)

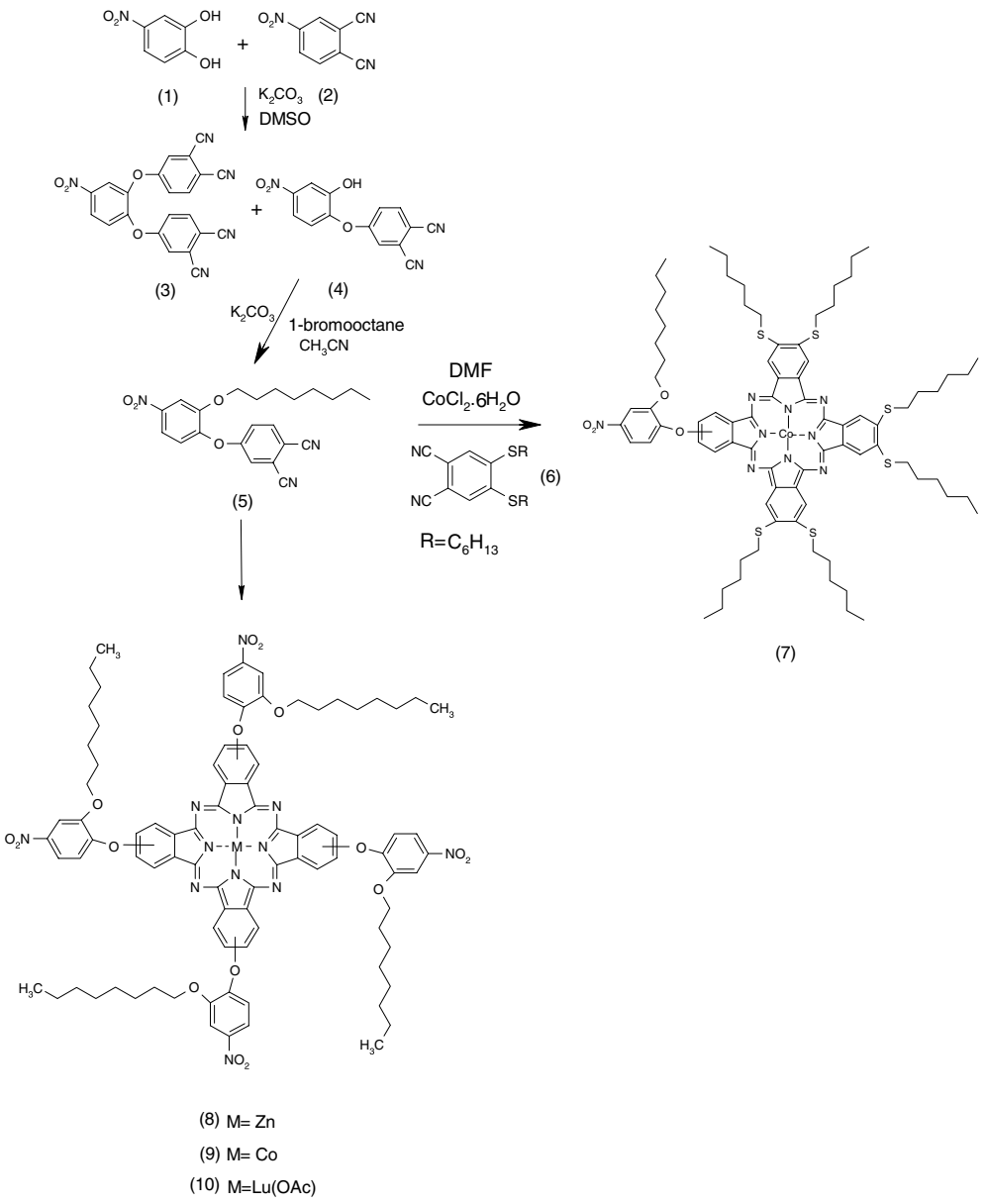
About 2 g (12.90 mmol) of **1**, 4.47 g (25.80 mmol) of **2** and 5.48 g (39.70 mmol) of K_2CO_3 in dry dimethylsulfoxide (DMSO) (30 ml) were stirred at 78–80 °C for 24 h under an argon atmosphere. Then, the reaction mixture was poured into water. The precipitate that formed was filtered, washed with cold water and dried in air. The crude compound **3** was chromatographed on a silica gel column with $CHCl_3$ as the eluent. After that, the separated filtrate was treated with hydrochloridic acid (10%) and the crude solid was filtered, washed with distilled water and ethanol. Column chromatography of this crude product on silica gel gave **4**. Products **3** and **4** were soluble in $CHCl_3$, dimethylformamide (DMF), DMSO and tetrahydrofurane (THF). Yield of **3**: 0.60 g (11%). M.p.: 193–196 °C. IR (γ_{max}/cm^{-1} KBr disc): 3083 (Ar–H), 2235 (–CN), 1588–1485 (–C=C–), 1246–1279 (Ar–O–C), 1569–1350 (–NO_2). ^{1}H NMR (δ_H ppm, 400 MHz, DMSO): 8.31 (d, $J = 2.73$, Ar–H), 8.26 (dd, $J = 2.73$, Ar–H), 8.20 (d, $J = 8.58$, Ar–H), 8.10 (d, $J = 8.58$, Ar–H), 8.06 (d, $J = 8.97$, Ar–H), 7.90 (d, $J = 2.34$, Ar–H), 7.86 (d, $J = 2.73$, Ar–H), 7.68 (dd, $J = 2.34$, Ar–H). Yield of **4**: 3.2 g (88%). M.p.: 213–215 °C. IR (γ_{max}/cm^{-1} KBr disc): 3037–3082 (Ar–H), 2223 (–CN), 1490–1598 (–C=C–), 1265–1136 (Ar–O–C), 1332–1525 (–NO_2), 3276 (Ar–OH). ^{1}H NMR (δ_H ppm, 500 MHz, DMSO): 8.14 (dd, $J = 2.44$, Ar–H), 8.09 (d, $J = 2.44$, Ar–H), 8.07 (d, $J = 8.97$, Ar–H), 7.79 (d, $J = 2.93$, Ar–H), 7.40 (dd, $J = 2.45$, Ar–H), 7.20 (d, $J = 8.79$, Ar–H), 11.6 (s, br, Ar–O–H). D_2O Exc-NMR (δ_H ppm, 500 MHz, DMSO): 8.12 (dd, $J = 2.44$, Ar–H), 8.09 (d, $J = 2.93$, Ar–H), 8.04 (d, $J = 8.79$, Ar–H), 7.72 (d, $J = 2.44$, Ar–H), 7.38 (dd, $J = 2.93$, Ar–H), 7.18 (d, $J = 9.28$, Ar–H).

2.1.2. Preparation of 4-(4-nitro-2-(octyloxy)phenoxy)phthalonitrile (*5*)

About 0.282 g (1 mmol) of **4**, 0.193 g (1 mmol) of 1-bromooctane, 0.278 g (2 mmol) of anhydrous K_2CO_3 and tetrabutylammonium bromide in dry acetonitrile (40 ml) were stirred at 80–85 °C for 48 h under an argon atmosphere. The mixture was cooled and evaporated to dryness. The product was treated with glacial-acetic acid and then flushed several times with water until the filtrate was neutral. After that it was extracted with CH_2Cl_2. Finally, pure **5** was obtained by chromatography with silica gel using $CHCl_3$. Product **5** was soluble in $CHCl_3$, CH_2Cl_2, DMF, DMSO and THF. Yield: 0.30 g (76%). M.p.: 88–92 °C (Scheme 1). IR (γ_{max}/cm^{-1} KBr disc): 3082 (Ar–H), 2234 (–CN), 1484–1606 (–C=C–), 1292–1246 (Ar–O–C), 1347 and 1512 (–NO_2), 2847–2932 (–CH_2–, –CH_3). ^{1}H NMR (δ_H ppm, 400 MHz, $CDCl_3$): 8.23 (dd, $J = 2.73$, Ar–H), 8.08 (d, $J = 2.73$, Ar–H), 7.73 (d, $J = 8.68$, Ar–H), 7.21 (dd, $J = 2.73$, Ar–H), 7.18 (d, $J = 2.34$, Ar–H), 7.10 (d, $J = 9.36$, Ar–H), 4.05 (t, $J = 6.24$, –OCH_2), 1.40 (m, –CH_2–), 0.90 (t, $J = 7.02$, –CH_3).

2.1.3. 2-[4-Nitro-2-(octyloxy)phenoxy]-9,10,16,17,23,24-hexakis(hexylthio)phthalocyaninato cobalt(II) (*7*)

Compounds **5** (0.150 g, 0.382 mmol) and **6** (0.412 g, 1.145 mmol) were dissolved in dry DMF (2–3 ml) in a tube. $CoCl_2 \cdot 6H_2O$ (90.44 mg, 0.382 mmol) was added to this solution. The mixture was heated and stirred at 160–170 °C for 24 h under nitrogen atmosphere to give an unsymmetrical substituted Pc (Scheme 1). After being cooled, the reaction mixture was poured into



Scheme 1. Summary of the synthesis of compounds **3**–**10**.

50 ml of ethanol and the dark green precipitate that formed was separated by centrifugation. The crude Pc mixture was washed with cold acetic acid, water, ethanol and methanol, and then dried in a vacuum. The purification of that aimed Pc **7** was carried out on a silica gel column with a $CHCl_3$:hexane system, changing from 10/1 to 10/2 (v/v). Compound **7** is soluble in chloroform, dichloromethane, ethyl acetate, hexane, DMF, THF and DMSO. Yield of **7**: 0.12 g (20.50%). M.p.: >300 °C. IR (γ_{max}/cm^{-1} KBr disc): 3050 (Ar–H), 1411–1595 (–C=C–), 1222–1274 (Ar–O–C), 1377 and 1517 (–NO_2), 2860–2929 (–CH_2–, –CH_3), 1072–1124 (C–S). UV–Vis λ_{max} ($CHCl_3$) (log ε/dm^{-3} mol^{-1} cm^{-1}): 697(5.4739), 629(5.0012), 424 (4.7700), 327(5.4681). MS(MALDI-TOF): *m*/*z* 1533 Da mass ($M+H^+$) and $(M-32)^+$.

*2.1.4. 2,10,16,24-Tetrakis-[4-nitro-2-(octyloxy)phenoxy]-phthalocyaninatozinc(II) (**8**)*

A mixture of compound **5** (0.168 g, 0.427 mmol), anhydrous zinc acetate (0.094 g, 0.427 mmol) and DMF (3–4 ml) was heated and stirred at 180 °C for 6 h under nitrogen atmosphere. After cooling to room temperature, methanol (5 ml) was added in order to precipitate the product. The blue product was filtered off and then washed several times, first with methanol, then with acetonitrile and acetone. The crude product was isolated by silica gel column chromatography with chloroform as the eluent. This product is soluble in $CHCl_3$, DMSO, DMF and THF. Yield: 0.020 g (11.50%). M.p.: >300 °C. IR (γ_{max}/cm^{-1} KBr disc): 3040 (Ar–H), 1514–1650 (–C=C–), 1222–1282 (Ar–O–C), 1340 and 1558 (–NO_2), 2854–2921 (–CH_2–, –CH_3). UV–Vis λ_{max} ($CHCl_3$) (log ε/dm^{-3} mol^{-1} cm^{-1}): 679 (4.16),

611 (3.47), 342 (3.98). ^{1}H NMR (δ_H ppm, 400 MHz, $CDCl_3$): 8.10 (dd, $J = 2.73$, Ar–H), 7.98 (d, $J = 2.73$, Ar–H), 7.72 (d, $J = 8.19$, Ar–H), 7.60 (dd, $J = 3.12$, Ar–H), 7.12 (d, $J = 2$, Ar–H), 6.98 (d, $J = 8.97$, Ar–H), 4.12 (t, $J = 5.86$, –OCH_2), 3.95 (t, $J = 6.44$, –CH_3), 1.25 (m, $(–CH_2)_6$). MS (MALDI-TOF): m/z 1638.0019 ($M+H^+$).

2.1.5. 2,10,16,24-Tetrakis-[4-nitro-2-(octyloxy)phenoxy]-phthalocyaninatocobalt(II) (9)

A mixture of compound **5** (0.150 g, 0.382 mmol), 90.440 mg (0.3816 mmol) $CoCl_2$ and absolute ethylene glycol (4–5 ml) was heated and stirred at 160 °C for 22 h under nitrogen atmosphere. After cooling to room temperature, the reaction mixture was treated with ethanol to precipitate the dark-blue product, which was then filtered. This product is soluble in $CHCl_3$ and THF, and partially in CH_2Cl_2 and DMF (Scheme 1). Yield 19.5 mg (12.53%). M.p.: >300 °C. IR (γ_{max}/cm^{-1} KBr disc): 3082 (Ar–H), 1467–1600 (–C=C–), 1222–1282 (Ar–O–C), 1340–1508 (–NO_2), 2854–2921 (–CH_2–, –CH_3). UV–Vis λ_{max} ($CHCl_3$) (log ε/dm^{-3} mol^{-1} cm^{-1}): 671 (4.24), 605 (3.63), 327 (4.10); MS (MALDI-TOF): m/z 1633.0136 ($M+H^+$).

2.1.6. 2,10,16,24-Tetrakis-[4-nitro-2-(octyloxy)phenoxy]-phthalocyaninato lutetium(III) acetate (10)

A mixture of $Lu(OAc)_3 \cdot nH_2O$ (0.023 g, 0.065 mmol), **5** (0.400 g, 1.018 mmol) and DBU (1.130 mg, 0.009128 mmol) in pentanol (2.5 ml) was refluxed under nitrogen atmosphere at 175–180 °C for 20 h. The dark green mixture was cooled to room temperature and then was washed with water, acetonitrile, ethanol, methanol and acetone, and then dried in vacuum. Compound **10** is soluble in acetic acid and THF, and partially in DMF and DMSO. Yield 0.155 g (36.70%). M.p.: >300 °C (Scheme 1). IR(γ_{max}/cm^{-1} KBr disc); 3066 (Ar–H), 1469–1666 (–C=C–), 1213–1276 (Ar–O–C), 1334 and 1506 (–NO_2), 2858–2925 (–CH_2–, –CH_3). UV–Vis λ_{max} (DMF) (log ε/dm^{-3} mol^{-1} cm^{-1}): 685 (4.8140), 618 (4.3802), 334 (5.0307). MS (MALDI-TOF): m/z 1808 ($M+H^+$).

2.2. Electrochemistry

The cyclic voltammetry, differential pulse voltammetry and controlled potential chronocoulometry (CPC) measurements were carried out with a Princeton Applied Research Model Versostat II potentiostat/galvanostat controlled by an external PC and utilizing a three-electrode configuration at 25 °C. The working electrode was a Pt plate with a surface area of 0.10 cm^2. The surface of the working electrode was polished with a H_2O suspension of Al_2O_3 before each run. The last polishing was done with a particle size of 50 nm. A Pt wire served as the counter electrode. A saturated calomel electrode (SCE) was employed as the reference electrode and was separated from the bulk of the solution by a double bridge. Electrochemical grade tetrabutylammonium perchlorate (TBAP) in extra pure DMSO was employed as the supporting electrolyte at a concentration of 0.10 mol dm^{-3}. High purity N_2 was used for deoxygenating the solution for at least 20 min prior to each run and to maintain a nitrogen blanket during the measurements. For CPC studies, a Pt gauze working electrode (10.5 cm^2 surface area), a Pt wire counter electrode separated by a glass bridge, and an SCE as a reference electrode were used.

2.3. Electrical measurements

For the electrical and impedance measurements, an interdigital comb structure with a 100 μm gap on glass substrate was used. Thin films of compounds were obtained by the spin-coating method. The substrate temperature was kept constant at 290 K during deposition of the materials over the electrodes. Dc conductivity and impedance spectral measurements were performed between 295 and 433 K using a Keithley 617 electrometer. Ac conductivity and impedance measurements were carried out with a Keithley 3330 LCZ meter in the frequency range 40–10^5 Hz, in the temperature range 295–433 K.

3. Results and discussion

3.1. Synthesis and characterization

Starting from **1** and **2**, a general synthetic route for the synthesis of new symmetrical and unsymmetrical Pcs is given in Scheme 1. Compounds **3** and **4** were obtained by base-catalyzed nucleophilic aromatic nitro displacement, in 10% and 88% yield, respectively. The reaction was carried out in a single step synthesis by using K_2CO_3 as the nitro-displacing base at 78–80 °C in dry DMSO under an argon atmosphere. Starting from **4** and 1-bromooctane, the general alkylation reaction gave **5** in the presence of K_2CO_3 at 80–85 °C for 48 h under an argon atmosphere in 75% yield. The symmetrical MPcs **8**, **9** and **10** were obtained from the dicyano derivative **5** and the corresponding metal salts ($Zn(OAc)_2$, $CoCl_2$, $Lu(OAc)_3 \cdot nH_2O$) in suitable anhydrous solvents under reflux in a sealed tube, in 12%, 13% and 36.7% yields, respectively. The high boiling solvents of choice for these reactions were DMF for Zn(II)Pc **8**, ethylene glycol for Co(II)Pc **9** and pentanol for Lu(III)(OAc)Pc **10**. These symmetrical MPcs were isolated by column chromatography on silica gel using $CHCl_3$ as the eluent. The unsymmetrical Co(II)Pc **7** was synthesized by $CoCl_2$-mediated statistical condensation of a 3:1 molar ratio of **5** and **6** in anhydrous DMF under reflux for 24 h. Product **7** was separated by column chromatography on silica gel using different $CHCl_3$:hexane solvent systems, changing from 10/1 to 10/2 (v/v), as the eluent. All the Pcs **7**, **8**, **9** and **10** show good solubility in common organic solvents such as chloroform, dichloromethane and tetrahydrofuran. The spectroscopic characterization of the newly synthesized compounds included ^{1}H NMR, IR, UV/Vis and mass spectral investigations, and the results are in accordance with the proposed structures.

The IR spectra of **3**, **4** and **5** indicate the presence of –C≡N groups by the intense stretching bands at 2235, 2223 and 2234 cm^{-1}, respectively. The IR spectra of **3**, **4** and **5** exhibit characteristic frequencies at 3037–3083 (Ar–H), 1485–1598 (–C=C–), 1136–1292 (Ar–O–C), 1332 and 1569 ($–NO_2$) cm^{-1}. The IR spectra of **3**, **4** and **5** are very similar, except those of **4** (Ar–OH) with vibrations at 3276 cm^{-1} and of **5** ($–CH_2–$, $–CH_3$) with vibrations at 2847–2932 cm^{-1}. Cyclotetramerization of dinitriles **5** to Pcs **7**, **8**, **9** and **10** was confirmed by the disappearance of the sharp –C≡N vibration at 2234 cm^{-1}. The IR spectra of the symmetrical Pcs **8**, **9** and **10** and the unsymmetrical Pc **7** are very similar, except for the C–S vibrations at 1072–1124 cm^{-1}. The IR spectra of **8**, **9** and **10** exhibit characteristic frequencies at 3230–3066 (Ar–H), 1467–1650 (–C=C–), 1213–1282 (Ar–O–C), 1334–1558 ($–NO_2$) and 2854–2925 ($–CH_2–$, $–CH_3$) cm^{-1}.

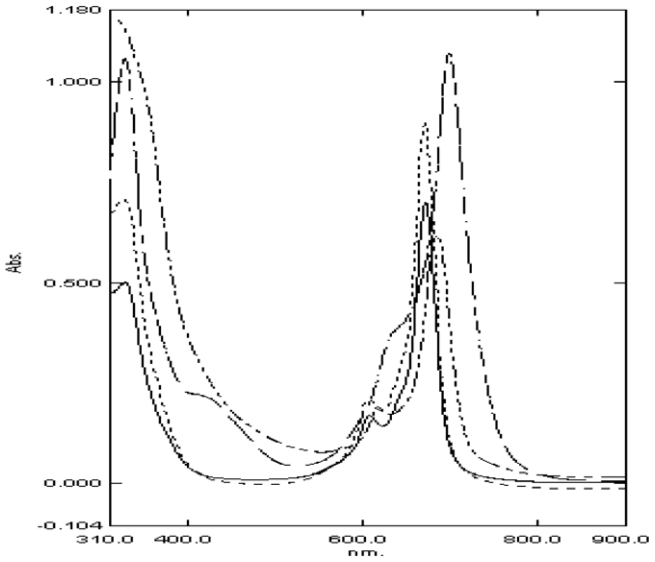


Fig. 1. UV–Vis spectra of **7**, **8**, **9** and **10** (– – – **7**, . . . **8**, — **9**, - - - **10**) (**7**, **8**, **9** in $CHCl_3$, **10** in DMF).

In the ^1H NMR spectra of **3**, **4** and **5**, the aromatic protons of the compounds appear in the low field region around 8.32–7.12 ppm. The octyl protons of **5** are observed between 0.86 and 4.07 ppm. The hydroxy proton of **4** appears at a lower field around 11.6 ppm. In the D_2O exchanged NMR spectrum of **4** this assignment was confirmed by the disappearance of the sharp hydroxy proton peak at 11.6 ppm. The ^1H NMR spectra of Zn(II)Pc **8** are almost identical. The aromatic protons of **8** appear in the low field region around 7.00–8.12 ppm. The octyl protons are observed in the range 0.70–4.14 ppm. The ^1H NMR spectra of the unsymmetrical Co(II)Pc, symmetrical Co(II)Pc and Lu(III)(OAc)Pc could not be determined because of the presence of paramagnetic cobalt and lutetium atoms.

Pcs **7**, **8**, **9** and **10** show typical electronic spectra with two strong absorption regions, one of them in the UV region at about 300–400 nm (B band) arising from the deeper π-levels → LUMO transition and the other in the visible part of the spectrum around 600–700 nm (Q band) attributed to the $\pi \rightarrow \pi^*$ transition from the highest occupied molecular orbital (HOMO) to the lowest unoccupied molecular orbital (LUMO) of the Pc^{2-}ring. Spectra of the symmetrical Zn(II) and Co(II) phthalocyanines **8** and **9** in chloroform are very similar, with intense Q bands at 679 and 671 nm due to a single $\pi \rightarrow \pi^*$ transition with shoulders at 611 and 605 nm and B bands at 342 and 327 nm, respectively. The splitting of the Q band of both compounds shows aggregation. The spectrum of **7** in chloroform shows a characteristic Q band absorption around 697 nm (with a shoulder at 629 nm) and B band absorptions around 424 and 327 nm. The spectrum of **10** in DMF indicates a Q band absorption around 685 nm and a B band absorption around 334 nm (Fig. 1). In the spectra of both compounds, besides the splitting of the Q band, a very strong of soret band indicates strong aggregation of both compounds [15].

Positive ion MALDI-MS spectra of **7**, **8**, **9** and **10** are given in Figs. 2–5, respectively. Many different MALDI matrices were tried to find an intense molecular ion peak

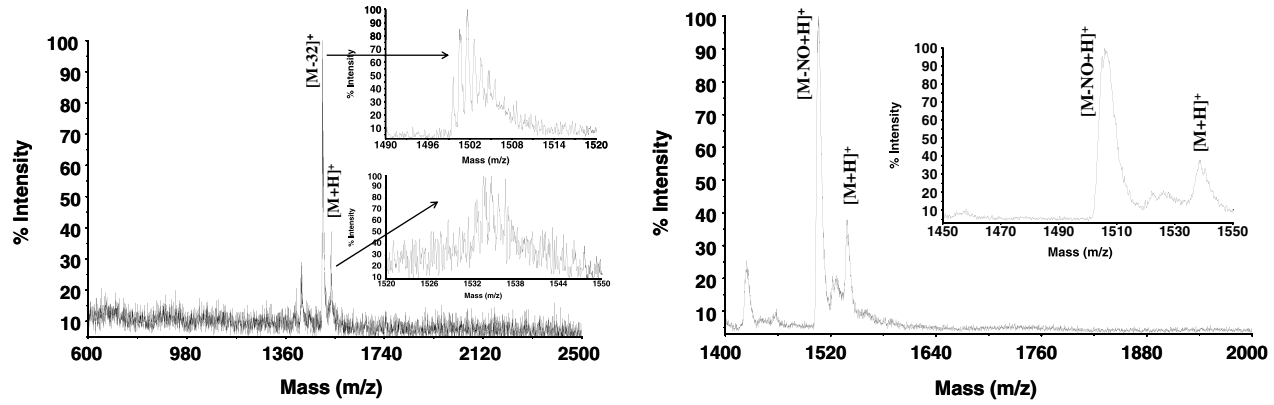


Fig. 2. MALDI-MS spectrum of the unsymmetrical Co(II)Pc **7** (left: linear mode; right: reflectron mode).

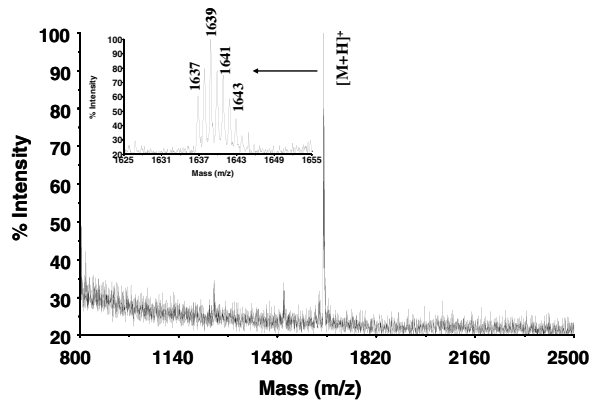


Fig. 3. MALDI-MS spectrum of the symmetrical Zn(II)Pc **8**.

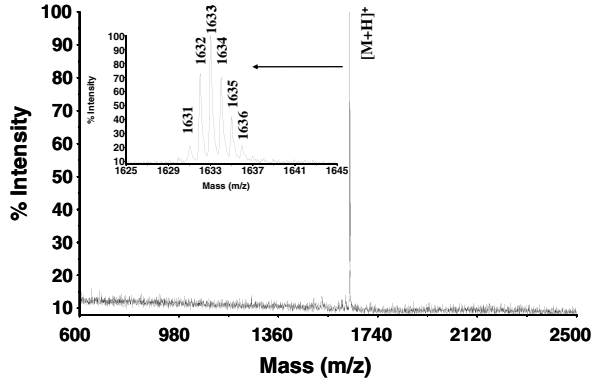


Fig. 4. MALDI-MS spectrum of the symmetrical Co(II)Pc **9**.

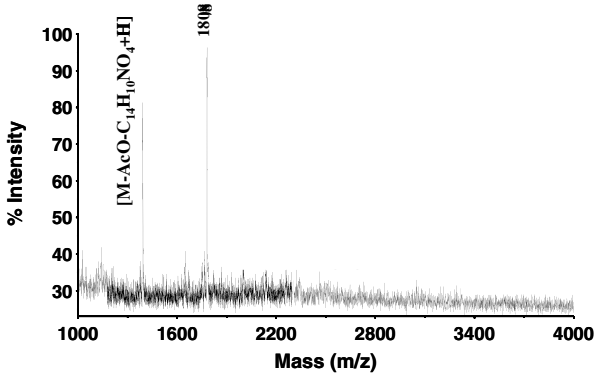


Fig. 5. MALDI-MS spectrum of the symmetrical Lu(III)(AcO)Pc **10**.

and low fragmentation under the MALDI-MS conditions for the complexes.

For complex **7**, 3-indole acrylic acid MALDI matrix yielded the best MALDI-MS spectrum. The peak group representing the protonated molecular ion of the complex was observed, starting with 1533 Da mass and finishing with 1537 Da, following each other by 1 Da mass differences. The intensity of the protonated molecular ion peak was really low when the MALDI-MS spectrum was monitored by the laser shots higher than 20. Therefore, the MALDI-MS spectrum for this complex was accumulated using 10 laser shots so as not to give high fragmentation. In this case, however, the resolution was observed at very low values of about 2500. When the number of laser shots was chosen to be between 1 and 5, more intense spectra could be obtained but the resolution was really diminished this time. Because of all these reasons, the resolution and the intensity of the protonated molecular ion peak were optimized accumulating an average of 10 laser shots for this complex. On the protonated molecular ion peak, there is an isotopic distribution resulting from ^{13}C and the isotopes of cobalt. In the positive ion MALDI-MS spectrum of **7**, beside the protonated molecular ion peak, two peaks were observed, one at high and the other at low intensity. The intense peak is because of the fragmentation of the complex. At the end of this fragmentation, the leaving group was observed as O_2, having 32 Da mass. The O_2 leaving group results from NO_2 functional groups. The second fragment peak is due to side chain elimination ($C_8H_{17}O$ leaving). This pointed out that the complex was not more stable under the MALDI matrix conditions than under the laser energy, but the positive ion MALDI-MS spectra could be carried out by MALDI-MS.

α-Cyano-4-hydroxycinnamic acid MALDI matrix yielded the best MALDI-MS spectra for **8** and **9**. The peak group representing the protonated molecular ion of **8** was observed, starting with 1637 Da mass and finishing with 1644 Da, following each other by 1 Da mass differences. This type of mass distribution resulted from the isotopic mass distribution of carbon (mainly ^{13}C) and the isotopes of zinc and cobalt in the metal complexes. The experimentally obtained isotopic mass distribution of **9** overlapped with the theoretical isotopic mass distribution calculated using isotopes of carbon and cobalt. In the MALDI-MS spectrum of **8**, besides the protonated molecular ion peak, two peaks were observed with very low intensities. These peaks are due to side chain elimination (mainly $C_8H_{17}O$) and also the other whole side chain elimination. This pointed out that the complex was very stable under the MALDI matrix conditions and also under the laser energy. The peak group representing the protonated molecular ion of **9** was observed starting with 1631 Da mass and finishing with 1636 Da, following each other by 1 Da mass differences. In the MALDI-MS spectrum of **9**, besides the protonated molecular ion peak, no fragment ion was observed. This suggests that no leaving group was available for this complex and the complex is very stable under the MALDI matrix conditions and also under the laser energy.

The positive ion and linear mode spectra of **10** could be obtained only in dithranol matrix compared to the other novel MALDI matrices. The protonated molecular ion peak of the complex was observed at 1808 Da. Beside the protonated molecular ion peak, only one another peak was observed, representing the AcO (acetate) and $C_{14}H_{20}NO_4$ groups leaving from the protonated ion peak. Limited fragmentations showed that this complex has high stability under the laser firing and MALDI-MS conditions.

The protonated molecular ion peak mass showed that a lutetium complex containing a single ligand and acetate ion was synthesized instead of the sandwich type lutetium complex. From the clean spectrum, it could be noticed that the purity of the synthesized lutetium complex was very high.

3.2. Electrochemistry

The solution redox properties of the Pc complexes (**7**–**10**) were studied using cyclic voltammetry, differential pulse voltammetry and controlled potential chronocoulometry in DMSO with a platinum electrode. Complete electrolysis of each Pc solution at the working electrode at a suitable constant potential for each redox process was achieved, and the time integration of the electrolysis current was recorded with the controlled potential coulometry studies. The charge, Q, at the end of the electrolysis was calculated using the current–time response of the solution and *Faraday*'s law was used to estimate the number of electrons transferred. The number of electrons was found to be one for all the redox processes observed in this study. Voltammetric data and the assignment of the redox couples recorded for the complexes are listed in Table 1. Fig. 6 shows typical cyclic and differential pulse voltammograms of **9** in DMSO containing TBAP.

Complex **8** gives three one-electron reduction processes labelled as R_1 at −0.67 V, R_2 at −0.98 V and R_3 at −1.76 V, and a one-electron oxidation process labelled as O_1 at 0.85 V vs. SCE at 0.100 V s^{-1} scan rate (Table 1). Voltammetric studies revealed that the redox behaviours of **8** and **10** are very similar to each other and to the metal-free Pcs [16] (Table 1). This similarity suggests that

Table 1
The electrochemical data of the Pc complexes

Complex	Redox processes	$E^{a}_{1/2}$ (V vs. SCE)	ΔE^{b}_{p} (V)	I_{pa}/I^{c}_{pc}	$\Delta E^{d}_{1/2}$ (V)
8	R1	−0.67	0.070	0.96	1.52
	R2	−0.98	0.080	0.98	
	R3	−1.76	0.160	[e]	
	O1	0.85	0.060	[e]	
9	R1	−0.37	0.100	1.00	0.82
	R2	−1.28	0.080	0.96	
	O1	0.45	0.100	0.95	
7	R1	−0.40	0.080	0.97	0.88
	R2	−1.32	0.090	0.96	
	O1	0.48	0.090	0.98	
10	R1	−0.73	0.080	0.94	1.48
	R2	−1.03	0.090	1.00	
	R3	−1.82	0.120	[e]	
	O1	0.75	0.140	0.98	

[a] $E_{1/2} = (E_{pa} + E_{pc})/2$ at 0.100 V s^{-1}.
[b] $\Delta E_p = E_{pa} - E_{pc}$ at 0.100 V s^{-1}.
[c] I_{pa}/I_{pc} for reduction, I_{pc}/I_{pa} for oxidation processes at 0.100 V s^{-1}.
[d] $\Delta E_{1/2} = E_{1/2}$(first oxidation) − $E_{1/2}$(first reduction). This value reflects the HOMO–LUMO gap for **8** and **10**, but not **7** and **9**.
[e] ΔE_p could not be determined due to an ill-defined redox wave.

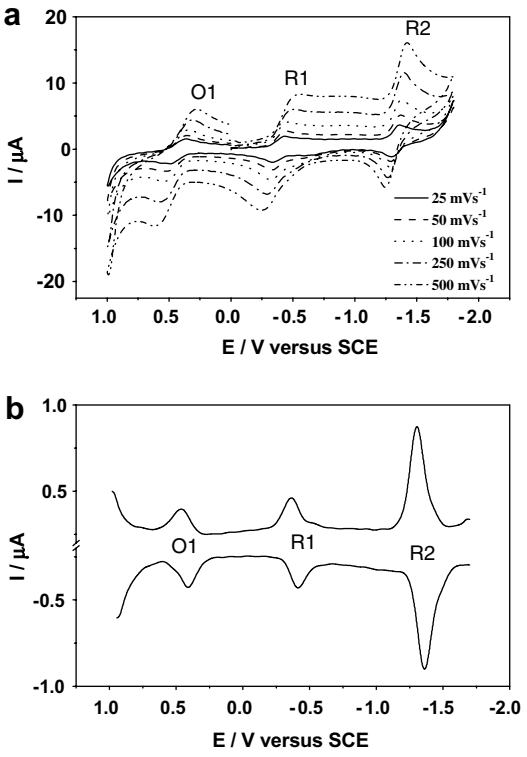


Fig. 6. Cyclic (a) and differential pulse (b) voltammograms of **9** in TBAP/DMSO.

all the one-electron redox processes of these complexes are Pc ring based. However, the redox potentials of **10** occur at potentials slightly more negative as compared to **8**. The shift in the potentials can be attributed to the difference in the polarizing effect of the metal ions. Reduction of the Pc ligand is associated with the position of the LUMO, whereas oxidation of the ligand is associated with the position of the HOMO. Thus the difference between the potentials of the first oxidation and the first reduction processes ($\Delta E_{1/2}$) reflects the HOMO–LUMO gap for metal free Pcs and it is closely related to the HOMO–LUMO gap in MPc species involving a redox inactive metal center. The $\Delta E_{1/2}$ values recorded for **8** and **10** in this study are in agreement with the values reported previously for the relevant Pcs involving a redox-inactive metal center [16]. The ratio of the anodic to the cathodic peak currents for the couples of **8** and **10** is close to unity, suggesting reversible redox processes. The anodic to cathodic peak separations (ΔE_p) changed from 0.070 to 0.140 V within the scan rates from 0.010 to 0.500 V s^{-1}(ΔE_p changed from 0.060 to 0.140 V for ferrocene), providing additional support for the reversible electron transfer. The peak currents increased linearly with the square root of the scan rates for scan rates ranging from 0.010 to 0.500 V s^{-1}, indicating purely diffusion-controlled behavior [17].

The redox potentials of **7** and **9** are considerably similar to each other, but highly different as compared to those of **8** and **10** (Table 1). Within the electrochemical window of TBAP/DMSO, compounds **7** and **9** undergo a reversible

one-electron oxidation and two reversible one-electron reductions with anodic to cathodic peak separations (ΔE_p) changing from 0.080 to 0.100 V within scan rates from 0.010 to 0.500 V s^{-1}. The peak currents increased linearly with the square root of the scan rates for scan rates ranging from 0.010 to 0.500 V s^{-1}, indicating purely diffusion-controlled behavior [17]. The difference in the voltammetric behaviour of these complexes as compared to those of **8** and **10** is due to the fact that metallo phthalocyanines, such as MnPc, CoPc and FePc, having a metal that possesses energy levels lying between the HOMO and the LUMO of the Pc ligand, in general exhibit redox processes centered on the metal [16,18–21]. Moreover, the electrochemistry of CoPc is dependent on the coordinating nature of the solvents. For CoPc complexes, the first oxidation and the first reduction processes occur on the metal center in polar coordinating solvents such as DMF and DMSO, whilst the first oxidation process occurs on the Pc ring in non-polar solvents such as DCM and THF. Therefore, the first reduction and the first oxidation processes of **7** and **9** could be assigned easily to the $[Co(II)Pc(-2)]/[Co(I)Pc(-2)]^-$ and $[Co(II)Pc(-2)]/[Co(III)Pc(-2)]^+$ redox couples and the second reduction process to the Pc ring as $[Co(I)Pc(-2)]^-/[Co(I)Pc(-3)]^{2-}$. The separation between the first oxidation and the first reduction potentials of the metal center for these Co(II) complexes (0.88 for **7** and 0.82 V for **9**) is comparable with the relevant values in the literature [15,17–20], and does not reflect the HOMO–LUMO gap. The small differences between the redox potentials of **7** and **9** can be attributed to the difference in peripheral substituents attached to the Pc core.

3.3. Electrical measurements

Arrhenius-type behavior is clearly observed from the temperature dependent conductivity measurements for all the compounds. A linear fit to $\sigma_{dc} = \sigma_0 \exp(-E_A/kT)$ is shown with different correlation coefficients. The electrical parameters corresponding to the studied compounds are shown in Table 2.

The frequency dependence of the ac conductivity, $\sigma_{ac}(\omega)$, for different values of temperatures between 295 and 433 K was investigated for all samples. The frequency dependence of the ac conductivity is shown in Fig. 7 for all compounds as a plot of $\ln \sigma_{ac}$ versus $\ln \omega$ at 373 K. The general observed frequency dependence of the ac conductivity in disordered systems, such as phthalocyanine, is that the ac conductivity obeys an empirical power law of the form $\sigma_{ac}(\omega) = A(T)\omega^s$, where $A(T)$ and s are temperature dependent parameters. To explain this type of frequency dependence of the ac conduction, two models have been used. According to the first model, which is known as the quantum mechanical tunnelling model (QMT), the conduction occurs by means of thermally assisted Quantum Mechanical Tunnelling. The other model, which is known as the Correlated Barrier Hopping (CBH) model, is based on the concept of charged defects and in this bipolarons hop between two charged defect states D^+ and D^- over the barrier separating them. In these two models, the frequency exponent s is found to have two different trends with temperature and frequency [22]. The values of the frequency exponent s were calculated from the slope of the measured $\ln \sigma_{ac}$ versus $\ln \omega$ graphs. Our results showed that s is definitely a function of temperature for all the compounds and shows a general tendency to decrease with increasing temperature. This is in agreement with the prediction of the CBH model.

Table 2
The electrical parameters of the Pc complexes

Samples	$\sigma_{290\,K}$ (Ω^{-1} cm^{-1})	E_A (eV)	$\sigma_{433\,K}$ (Ω^{-1} cm^{-1})
7	8.76×10^{-9}	0.81	1.41×10^{-4}
8	1.82×10^{-9}	0.79	1.07×10^{-4}
9	2.959×10^{-8}	0.70	1.84×10^{-4}
10	3.16×10^{-7}	0.72	2.1×10^{-4}

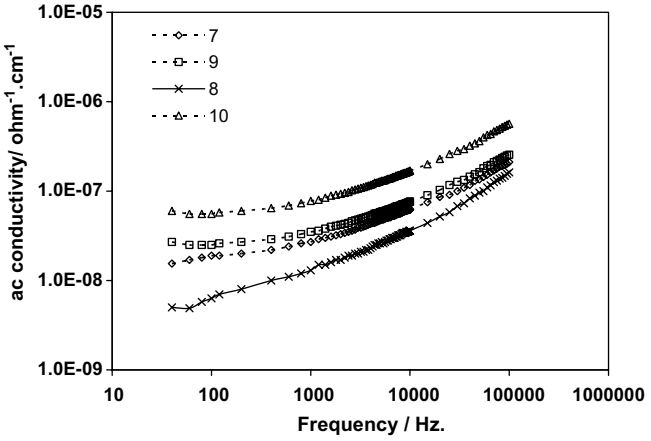


Fig. 7. The variation of the ac conductivity with frequency at 373 K.

To get more detailed information about the electrical properties of the compounds, impedance spectral measurements in the frequency range 40–10^5 Hz were also carried out on a spin coated film of the compounds. The measured impedance spectra, when plotted in a complex plane plot,

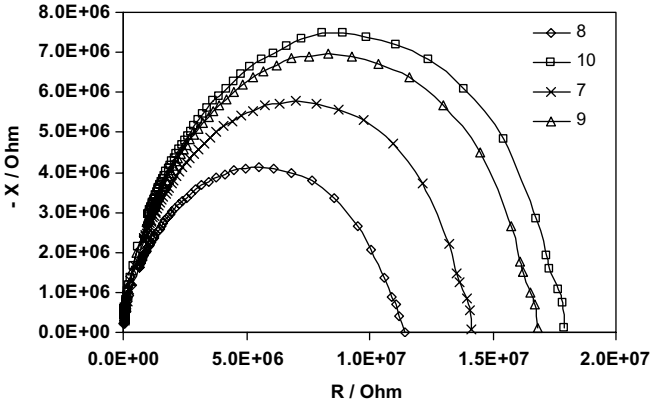


Fig. 8. Impedance spectra of the Pc films at 400 K.

appear in the form of a succession of semi-circles representing the contributions to the electrical properties due to bulk material, grain boundary effect and interfacial polarization phenomena. So, the impedance spectra technique enables us to separate the effects due to each component. At low temperatures, the impedance spectra consist of a quasi-vertical line. The existence of semicircular shaped curves in the Nyquist plot means that the impedance becomes capacitive even at relatively high frequencies. The effect of temperature on the impedance spectra of the films becomes clearly visible with a rise in the temperature. On the complex plane plot at high temperatures, only depressed semicircles with different radii were observed at higher temperatures, indicating deviation from the Debye dispersion relation (Fig. 8). In the case of a depressed semi-circle in the impedance spectra, the relaxation time is considered as a distribution of values, rather than a single relaxation time.

Acknowledgements

This work was supported in part by The Turkish Academy of Sciences (TUBA), TÜBİTAK (Project No. 106T326), The Research Fund of Marmara University (SCIENCE-YLS-290506-0124) and The State Planning Organization (DPT-2003K120810).

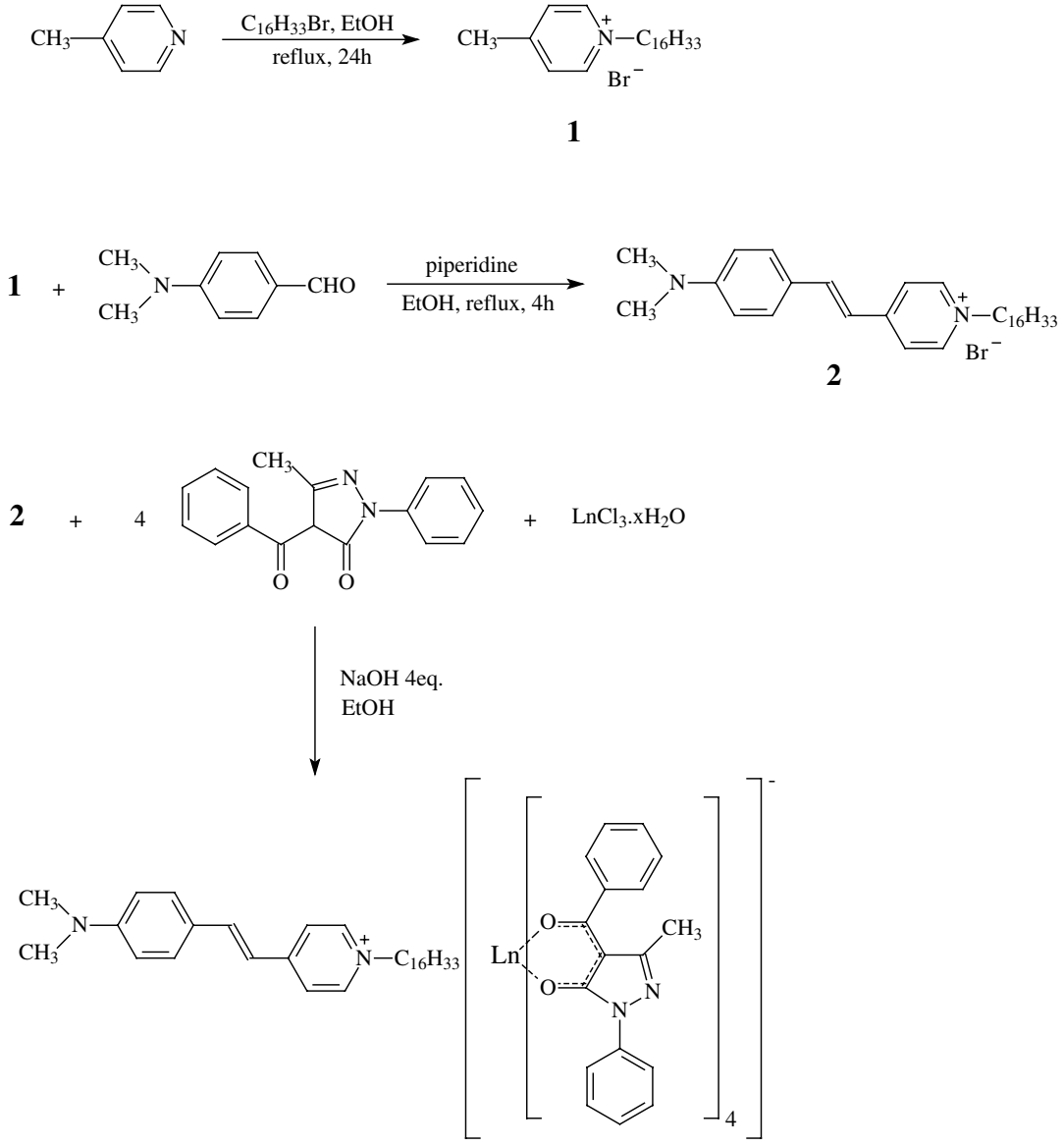
References

[1] C.C. Leznoff, A.B.P. Lever (Eds.), Phthalocyanines, Properties and Applications, vols. 1–4, VCH, New York, 1989, 1992, 1993, 1996.
[2] G. De la Torre, P. Vazquez, F. Agullo-Lopez, T. Torres, J. Mater. Chem. 8 (1998) 1671.
[3] N.B. McKeown, Phthalocyanine Materials, Cambridge University Press, Cambridge, 1998.
[4] M.J. Cook, M.F. Daniel, K.J. Harrison, N.B. McKeown, A.J. Thomson, J. Chem. Soc., Chem. Commun. (1987) 1148.
[5] M.A. Diaz-Garcia, J.M. Cabrera, F. Agulló-López, Appl. Phys. Lett. 3 (1996) 69.
[6] H. Schultz, H. Lehmann, M. Rein, M. Hanack, Struct. Bond. 74 (1991) 41.
[7] I. Rosenthal, Photochem. Photobiol. 53 (1991) 859.
[8] R. Zhou, F. Josse, W. Göpel, Z.Z. Özturk, Ö. Bekaroglu, Appl. Organomet. Chem. 10 (1996).
[9] M.J. Cook, J. Mater. Chem. 6 (1996) 677.
[10] J.C. Swarts, E.H.G. Langner, N. Kroeide-Hove, M.J. Cook, J. Mater. Chem. 11 (2001) 434.
[11] S. Abdurrahmanoglu, A. Altindal, A.R. Özkaya, M. Bulut, O. Bekaroglu, Chem. Commun. (2004) 2096.
[12] T. Ceyhan, A. Altindal, A.R. Ozkaya, M.K. Erbil, B. Salih, Ö. Bekaroglu, Chem. Commun. (2006) 320.
[13] J.G. Young, W.J. Onyebuagu, Org. Chem. 55 (1990) 2155.
[14] A.G. Gürek, Ö. Bekaroğlu, J. Chem. Soc., Dalton Trans. (1994) 1419.
[15] N. Kobayashi, Y. Niskiyama, T. Ohya, M. Sato, J. Chem. Soc., Chem. Commun. (1987) 390.
[16] A.B.P. Lever, E.R. Milaeva, G. Speier, in: C.C. Leznoff, A.B.P. Lever (Eds.), Phthalocyanines: Properties and Applications, vol. 3, VCH Publishers, New York, 1993, pp. 1–63.
[17] A.J. Bard, L.R. Faulkner, Electrochemical Methods: Fundamentals and Applications, 2nd ed., Wiley, New York, 2001.
[18] M. Özer, A. Altindal, A.R. Özkaya, M. Bulut, Ö. Bekaroglu, Polyhedron 25 (2006) 3593.
[19] A.R. Özkaya, E. Hamuryudan, Z.A. Bayır, Ö. Bekaroglu, J. Porphyr. Phthalocya. 4 (2000) 689.
[20] M. Kandaz, A.R. Özkaya, Ö. Bekaroğlu, Monatsh. Chem. 132 (2001) 1013.
[21] A. Koca, H.A. Dinçer, H. Çerlek, A. Gül, M.B. Koçak, Electrochim. Acta 52 (2006) 1199.
[22] S.R. Elliot, Adv. Phys. 36 (1987) 135.

a protective 'shell' around the rare-earth ion can lead to significant enhancement of the luminescent properties of the complex: avoiding the coordination of small but strongly quenching solvent molecules can be done by designing very bulky ligands, or by opting for a tetrakis stoichiometry instead of a tris stoichiometry [16–19].

Complexes of lanthanide ions with a hemicyanine unit have only been scarcely investigated [20–25]. Compounds with a hemicyanine chromophore are well known as dyes [26–29]. Hemicyanine dyes, having a large energy gap between the ground state and the excited states, which is beneficial for high polarisability, have been studied for their nonlinear optical (NLO) properties, e.g. in Langmuir–Blodgett films [30–32]. It was shown that combining a lanthanide complex with a hemicyanine compound enhances the film-forming properties and at the same time increases the charge separation in the chromophore, thus improving the NLO properties [33].

In this paper, we show that the hemicyanine unit in combination with the pyrazolone groups in the lanthanide complexes provide a suitable basis for sensitized near-infrared luminescence. We describe the synthesis of the hemicyanine bromide precursor as well as the final lanthanide complexes. The absorption spectrum of the complexes, as well as the luminescence spectra of the trivalent neodymium, erbium and ytterbium ions are discussed.



3 Ln = Nd (yield: 20%)
4 Ln = Er (yield: 63%)
5 Ln = Yb (yield: 52%)

Scheme 1. Synthetic procedure towards the hemicyanine counterion and the final lanthanide complexes.

2. Results and discussion

To tackle the limitations described in the introduction, we have chosen the β-diketone 1-phenyl-3-methyl-4-benzoyl-5-pyrazolone (see Scheme 1) as ligand. This molecule does not have an α-hydrogen atom, so no C–H vibrational quenching at that site is expected. At the same time, the phenyl groups provide a means of light harvesting. Finally, β-diketones are well known as ligands for rare-earth ions and easy synthetic procedures towards tetrakis complexes (with a metal-to-ligand ratio of 1:4) are available [34,35].

The synthetic procedure towards the hemicyanine counterion and the final lanthanide complexes is displayed in Scheme 1. The hemicyanine bromide was prepared in a two-step reaction: first, 4-picoline was reacted with 1-bromohexadecane. Second, the resulting 1-hexadecyl-4-methylpyridinium bromide **1** was condensed with 4-dimethylaminobenzaldehyde via a Knoevenagel-type reaction, yielding the hemicyanine bromide **2**. The lanthanide complexes **3**–**5** were synthesised by reaction of the hemicyanine bromide **2** with the β-diketone 4-benzoyl-3-methyl-1-phenyl-2-pyrazolin-5-one and the appropriate lanthanide salt. The complexes were obtained in good yields. See Section 4 for more details.

Single crystals, suitable for X-ray structure determination, were obtained of the (*E*)-*N*-dodecyl-*N*′,*N*′-dimethylamino-stilbazolium tetrakis(1-phenyl-3-methyl-4-benzoyl-5-pyrazolonato) lanthanum(III) complex. The crystal structure of the complex consists of the anionic complex molecule with four pyrazolonato ligands, a hemicyanine counterion and some water of crystallization. Fig. 1 shows the complex without the large hemicyanine counterion. The asymmetric unit contains two crystallographically independent molecules with slightly different conformations. The coordination number of the lanthanum ion is eight and the coordination polyeder of the lanthanum ion can be regarded as a slightly distorted square antiprism. No evidence of solvent coordination to the central lanthanum ion was found in the crystal structure.

Each two of the 1-phenyl pyrazolonato parts of the ligands are oriented almost parallel to each other, but with an antipodal orientation with respect to each other. The cations are situated in the cavity between two neighboring pyrazolonato ligands and exhibit weak π–π stacking interactions between the 4-benzoyl groups of the ligands and the pyridinium part of the cation (centroid-to-centroid distances range from 4.13 to 4.39 Å). This is shown in Fig. 2. Hydrogen bonding was found from the nitrogen atom of some of the pyrazolonato ligands to water molecules of crystallization with N···O distances in the range of 2.92–2.97Å. The crystal structure data are summarised in Table 1, whereas the crystal packing is shown in Fig. 3.

The complexes exhibit a strong orange-red colour, due to the charge-transfer band in the hemicyanine chromophore unit. The absorption spectrum of the neodymium complex **3** is given in Fig. 4. The peak maxima have been indicated. Whereas the maxima located at 238 and 276 nm are due to the singlet-to-singlet transitions in the pyrazolonate ligands, the broad band at 475 nm is due to the charge-transfer transition in the hemicyanine chromophore. This band is responsible for the intense orange-red colour of the complexes. Since visible excitation is a much sought-after property in NIR emitting rare-earth complexes, it was our hope that excitation of the pyrazolonato complexes in the hemicyanine band would result in

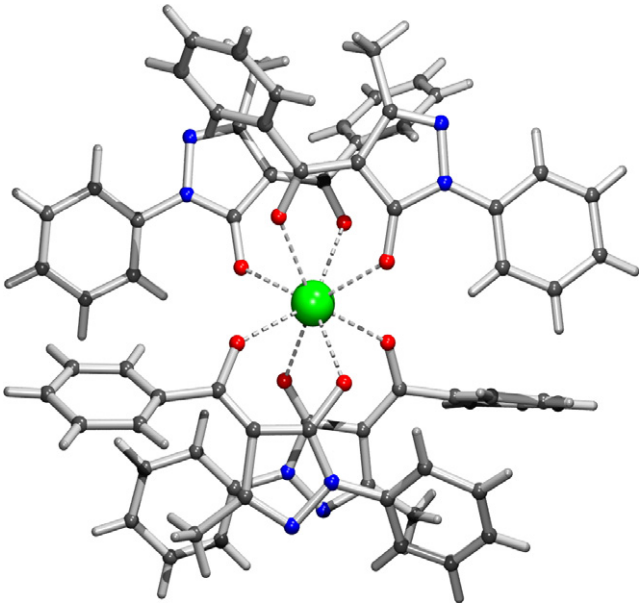


Fig. 1. Detail of the crystal structure of the (*E*)-*N*-dodecyl-*N*′,*N*′-dimethylamino-stilbazolium tetrakis(1-phenyl-3-methyl-4-benzoyl-5-pyrazolonato) lanthanum(III) complex, showing the local surrounding of the lanthanum(III) ion.

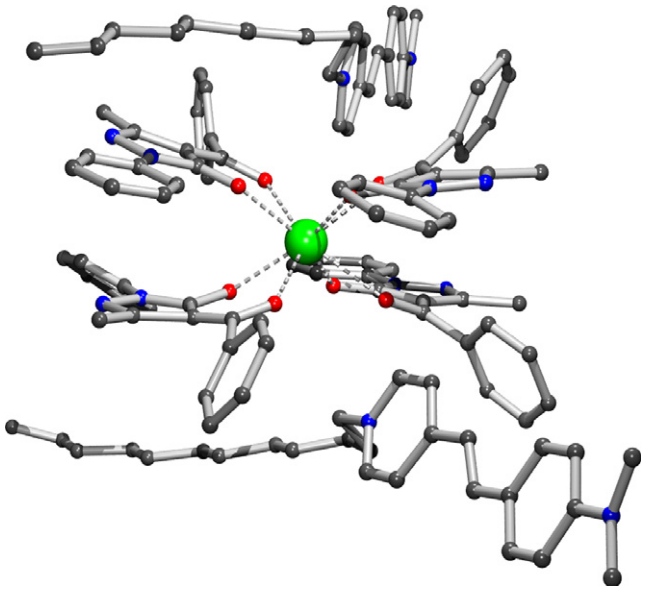


Fig. 2. Detail of the crystal structure of the (*E*)-*N*-dodecyl-*N*′,*N*′-dimethylamino-stilbazolium tetrakis(1-phenyl-3-methyl-4-benzoyl-5-pyrazolonato) lanthanum(III) complex, showing the four pyrazolonato ligands as well as the hemicyanine chromophore counterions. Hydrogen atoms have been omitted for clarity.

Table 1
Crystal structure data for the (*E*)-*N*-dodecyl-*N*′,*N*′-dimethylamino-stilbazolium tetrakis(1-phenyl-3-methyl-4-benzoyl-5-pyrazolonato) lanthanum(III) complex shown in Figs. 1–3

Formula	$C_{380}H_{372}La_4N_{40}O_{41}$
Molecular weight (g mol^{-1})	6710.83
Crystal dimensions (mm)	$0.3 \times 0.2 \times 0.1$
Crystal system	triclinic
Space group	$P\bar{1}$
a (Å)	15.545(2)
b (Å)	21.453(2)
c (Å)	28.586(2)
α (°)	68.636(4)
β (°)	75.054(4)
γ (°)	80.336(5)
V (Å^3)	8548.4(11)
Z	1
D_{calc} (g cm^{-3})	1.304
μ (Cu Kα) (mm^{-1})	4.387
Absorption correction	refined from delta-F
F(000)	3488
Measured reflections	78 888
Unique reflections	31 779
Observed reflections [$I_o > 2\sigma(I_o)$]	22 774
Parameters refined	2317
Goodness-of-fit	1.003
R_1^a	0.0653
wR_2^b	0.1680
R_1 (all data)	0.0950
wR_2 (all data)	0.1931

[a] $R_1 = \sum \| F_o | - | F_c \| / \sum | F_o |$.
[b] $wR_2 = [\sum w(F_o^2 - F_c^2)^2 / \sum w(F_o^2)^2]^{1/2}$.

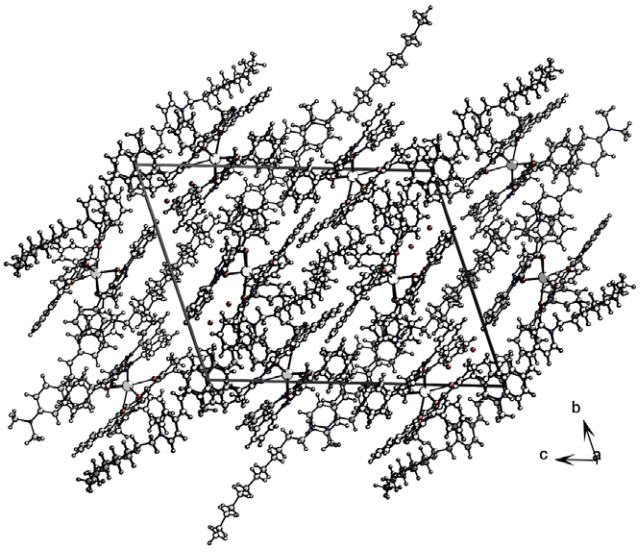


Fig. 3. Molecular crystal packing of the (*E*)-*N*-dodecyl-*N*′,*N*′-dimethylamino-stilbazolium tetrakis(1-phenyl-3-methyl-4-benzoyl-5-pyrazolonato) lanthanum(III) complex.

rare-earth centered NIR luminescence. Unfortunately, this did not turn out to be the case. Moreover, excitation of **3** in the hemicyanine chromophore at 475 nm resulted in the appearance of a strong red fluorescence band with a maximum at 630 nm. This shows that no energy is transferred from the hemicyanine moiety to the pyrazolonato ligands

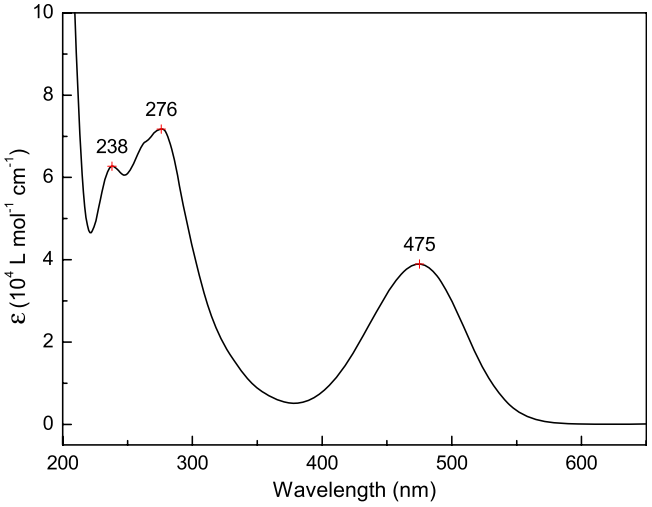


Fig. 4. Absorption spectrum of complex **3** in acetonitrile ($c = 10^{-5}$ mol L^{-1}).

or to the central neodymium ion. On the contrary, excitation of **3** at 276 nm resulted also in the appearance of this band at 630 nm, albeit less intense (about 5 times less intense) then upon excitation at 475 nm. Of course, also the neodymium(III)-centered NIR emission could be easily detected. This indicates that part of the excitation energy in the pyrazolonato ligands is transferred to the neodymium(III) ion, but another part is also transferred to the hemicyanine chromophore, which emits it as red light.

In Fig. 5, the combined emission spectra are shown of complexes **3**, **4** and **5** in acetonitrile upon excitation at 276 nm. Complex **3** shows the typical emission bands at 875 nm, 1060 nm and 1330 nm, corresponding to the $^4F_{3/2} \rightarrow {}^4I_J$ lines ($J = 9/2$, 11/2 and 13/2). The emission spectrum of **4** is shown as the dashed line and exhibits

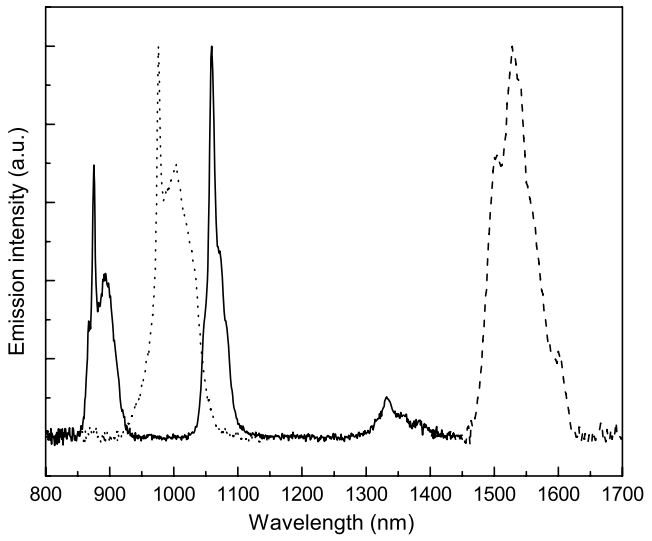


Fig. 5. Combined emission spectra of neodymium complex **3** (solid line), erbium complex **4** (dashed line) and ytterbium complex **5** (dotted line) in acetonitrile ($c = 10^{-5}$ mol L^{-1}, $\lambda_{exc} = 276$ nm, emission intensities are not to scale).

Table 2
Luminescence decay times of the Nd^{3+} ($^4F_{3/2}$), Er^{3+} ($^4I_{13/2}$) and Yb^{3+} ($^2F_{5/2}$) levels in complexes **3**, **4** and **5**, respectively[a]

Complex	Rare-earth ion	Decay time (μs)
3	Nd^{3+}	1.0
4	Er^{3+}	3.2
5	Yb^{3+}	46.4

[a] Lifetimes measured at room temperature; $\lambda_{exc} = 266$ nm; $c = 10^{-5}$ mol L^{-1}; solutions in acetonitrile.

one characteristic band at 1530 nm, corresponding to the $^4I_{13/2} \rightarrow {}^4I_{15/2}$ line. Finally, the spectrum of complex **5**, drawn as the dotted line, exhibits one emission band at 975 nm, corresponding to the $^2F_{5/2} \rightarrow {}^2F_{7/2}$ line.

In Table 2, the luminescence decay times of the Nd^{3+} ($^4F_{3/2}$), Er^{3+} ($^4I_{13/2}$) and Yb^{3+} ($^2F_{5/2}$) levels in (*E*)-*N*-hexadecyl-*N*′,*N*′-dimethylamino-stilbazolium tetrakis(1-phenyl-3-methyl-4-benzoyl-5-pyrazolonato) rare-earth(III) complexes are given. These decay times compare well to decay times of other NIR-emitting rare-earth complexes in organic solution. For example, a tetrakis (5,7-dichloro-8-oxyquinolinato) lanthanide(III) complex with a tetraethyl ammonium counterion dissolved in THF has decay time values of 0.95 μs for the neodymium(III) sample, 2.2 μs for the erbium(III) ion and 11.6 μs for the ytterbium(III) sample [36]. The hemicyanine materials presented here have comparable (neodymium(III) complex), slightly longer (erbium(III) complex) or even significantly longer (ytterbium(III) complex) luminescence decay times. On the other hand, they are not as good as the values obtained by Bassett et al. for the tetraphenylimidophosphinate complexes of NIR-emitting rare-earth ions in dry acetonitrile solution (2.6 μs for the Nd(III) complex, 6.5 μs for the Er(III) complex and 52.8 μs for the Yb(III) complex) [18]. It has to be added that the ytterbium(III) ion can be excited through an alternative redox mechanism [37]. A detailed photophysical study of the materials under investigation, however, falls outside the scope of this paper.

3. Conclusions

In conclusion, we have shown that NIR luminescence can be obtained from (*E*)-*N*-hexadecyl-*N*′,*N*′-dimethylamino-stilbazolium tetrakis(1-phenyl-3-methyl-4-benzoyl-5-pyrazolonato) rare-earth(III) complexes in acetonitrile solution. Because of the absence of the α-hydrogen atom on the pyrazolonato ligand and because of the shielding provided by the tetrakis stoichiometry of the complex, luminescence decay times could be obtained that compare well to the better behaving rare-earth complexes in solution. Nevertheless, the incorporation of the hemicyanine chromophore in the complexes did not lead to enhanced emission properties, nor did it allow visible light sensitisation of the NIR-luminescence. However, it is known from the literature that the combination of hemicyanine units with rare-earth complexes increases the film-forming properties of the hemicyanine compound, creating the possibility of developing NIR-emitting thin films based on pyrazolonato rare-earth complexes.

4. Experimental

4.1. Equipment and techniques

Absorption spectra were recorded on a Varian Cary 5000 spectrophotometer. Visible luminescence spectra were obtained with an Edinburgh Instruments F900 spectrometer, equipped with a 1800 lines/mm grating excitation monochromator and a 1800 lines/mm grating emission monochromator. A 450 W xenon lamp is used as the excitation source and a red-sensitive photomultiplier tube type S900-R is used as the detector. The steady state near-infrared luminescence spectra and the lifetime measurements were done on an Edinburgh Instruments FS920P near infrared spectrometer, with a 450 W xenon lamp as the steady state excitation source, a double excitation monochromator with 1800 lines/mm, an emission monochromator with 600 lines/mm, and a liquid nitrogen cooled Hamamatsu R5509-72 near infrared photomultiplier tube. For luminescence decay time measurements, the setup includes a Continuum Minilite Nd:YAG laser, equipped with 2nd, 3rd and 4th harmonic crystals, allowing excitation at 1064, 532, 355 and 266 nm. Repetition rate is 10 Hz, pulse width is 3–5 ns. Standard quartz 1 cm fluorescence cuvets (Hellma type QS-111) were used. Luminescence lifetime data were extracted from the decay curves using the program Origin®.

^{1}H NMR spectra have been recorded on a Bruker WM 250 spectrometer, operating at 250 MHz or a Bruker AMX 400 spectrometer, operating at 400 MHz, using deuterated chloroform ($CDCl_3$) as the solvent and tetramethylsilane (TMS) as internal standard. ^{13}C NMR spectra have been recorded on a Bruker AMX 400 spectrometer, operating at 100.6 MHz, using deuterated chloroform ($CDCl_3$) as the solvent and tetramethylsilane (TMS) as internal standard.

EI mass spectra have been obtained on a Hewlett–Packard 5989A mass spectrometer.

CHN elemental analyses have been performed on a Perkin–Elmer 2400 elemental analyser, operated by the university of Exeter (School of Chemistry) or on a CE Instruments EA-1110 elemental analyser (K.U.Leuven, Chemistry Department).

IR spectra have been recorded on a Bruker FT-IR IFS66 spectrometer, using KBr pellets.

4.2. Synthesis

The hemicyanine bromide was synthesized by a two-step reaction (Scheme 1). During the first step, 4-picoline was refluxed with *n*-bromohexadecane in ethanol. The crude 1-hexadecyl-4-methylpyridinium bromide **1** was recrystallized twice from a diethyl ether:ethanol mixture. Yield: 85% (67.8 g). ^{1}H NMR (δ_H, $CDCl_3$, 250 MHz): 0.89 (3H,

t, CH_3); 1.26 (26H, m, CH_2); 2.04 (2H, m, CH_2); 2.69 (3H, s, CH_3-aryl); 4.92 (2H, t, N^+-CH_2); 7.94 (2H, d, H-aryl, $J_0 = 6$ Hz); 9.39 (2H, d, H-aryl, $J_0 = 6$ Hz). IR (cm^{-1}, KBr): 3009 (m), 2913 (s), 2846 (s), 1639 (s), 1568 (w), 1519 (m), 1470 (s), 1383 (w), 1322 (w), 1176 (m), 1045 (w), 974 (w), 821 (m), 713 (m), 555 (w). Mass (*m*/*z*, EI, 70 eV): $M^+ = C_{22}H_{40}N^+$; 319 ($[M+1]^+$, 4); 318 (M^+, 25); 317 (M^+-1H, 97); 316 (M^+-2H, 44); 288 ($M^+-C_2H_6$, 42); 274 ($M^+-C_3H_8$, 48); 260 ($M^+-C_4H_{10}$, 55); 246 ($M^+-C_5H_{12}$, 55); 232 ($M^+-C_6H_{14}$, 51); 218 ($M^+-C_7H_{16}$, 42); 190 ($M^+-C_9H_{20}$, 40); 162 ($M^+-C_{11}H_{24}$, 40); 134 ($M^+-C_{13}H_{28}$, 72); 121 ($M^+-C_{14}H_{29}$, 53); 120 ($M^+-C_{14}H_{30}$, 61); 107 ($M^+-C_{15}H_{31}$, 100); 94 ($M^+-C_{16}H_{32}$, 52); 93 ($M^+-C_{16}H_{33}$, 36). CHN Elemental *Anal*. Calc. for $C_{22}H_{40}BrN$ (398.47 g mol^{-1}): C, 66.31; H, 10.12; N, 3.52. Found: C, 66.20; H, 10.32; N, 3.37%.

The 1-hexadecyl-4-methylpyridinium bromide **1** was then condensed with 4-dimethylaminobenzaldehyde via a Knoevenagel-type reaction. The reagents were heated in absolute ethanol with piperidine as the catalyst. The crude hemicyanine bromide **2** was recrystallized twice from an ethanol:hexane mixture. Yield: 71% (18.8 g). ^{1}H NMR (δ_H, $CDCl_3$, 400 MHz): 0.87 (3H, t, CH_3); 1.26 (26H, m, CH_2); 1.93 (2H, quintet, CH_2); 3.06 (6H, s, $(CH_3)_2N$); 4.64 (2H, t, N^+-CH_2); 6.68 (2H, d, H-aryl, $J_0 = 9$ Hz); 6.86 (1H, –CH=, $J_{trans} = 16$ Hz); 7.52 (2H, d, H-aryl, $J_0 = 9$ Hz); 7.62 (1H, –CH=, $J_{trans} = 16$ Hz); 7.88 (2H, d, H-aryl, $J_0 = 7$ Hz); 8.94 (2H, d, H-aryl, $J_0 = 7$ Hz).^{13}C NMR (δ_C, $CDCl_3$, 100.6 MHz): 14.1 (CH_3); 22.6 (CH_2); 26.1 (CH_2); 29.05 (CH_2); 29.30 (CH_2); 29.35 (CH_2); 29.50 (CH_2); 29.55 (CH_2); 29.60 (CH_2); 29.65 (CH_2); 31.6 (CH_2); 31.9 (CH_2); 40.1 ($(CH_3)_2N$); 60.2 (N^+-CH_2); 111.9; 116.3; 122.2 (quaternary C); 122.7 (alkene C); 130.6; 142.9; 152.2 (quaternary C); 154.0 (quaternary C). IR (cm^{-1}, KBr): 3000 (w), 2912 (s), 2852 (m), 1641 (m, alkene C=C), 1591 (s, aryl C=C), 1526 (s, aryl C=C), 1467 (m), 1430 (m), 1362 (m), 1330 (m), 1161 (s), 827 (w), 717 (w), 518 (w). Mass (*m*/*z*, EI, 70 eV): $M^+ = C_{31}H_{49}N_2^+$; 451 ($[M+1]^+$, 7); 450 (M^+, 5); 448 (M^+-2H, 2); 225 ($M^+-C_{16}H_{32}$, 18); 224 ($M^+-C_{16}H_{33}$, 100); 223 ($M^+-C_{16}H_{34}$, 52). CHN Elemental *Anal*. Calc. for $C_{31}H_{49}BrN_2$ (529.65 g mol^{-1}): C, 70.30; H, 9.32; N, 5.29. Found: C, 69.94; H, 9.75; N, 4.88%.

Only the *trans*-product (*E*) is formed. There was no evidence for the formation of the *cis*-isomer, probably because of steric hindrance by the aromatic groups. The 1-hexadecyl-4-methylpyridinium bromide is a white powder, whereas the hemicyanine bromide has a very intense orange-red colour.

The lanthanide complexes **3**–**5** were formed by reaction of the hemicyanine bromide **2** with the β-diketone 4-benzoyl-3-methyl-1-phenyl-2-pyrazolin-5-one and the appropriate lanthanide salt. First, the β-diketone was deprotonated by an equivalent amount of NaOH, then, the hemicyanine bromide and a lanthanide salt were added. The molar ratio β-diketone:hemicyanine bromide:lanthanide salt was 4:1:1. For the lanthanide salt, one can use the hydrated nitrate or chloride salt. All the reactions were carried out in ethanol. The complexes were recrystallized from ethanol:water (1:1). Analysis results for neodymium complex **3**: yield 20% (0.33 g). IR (cm^{-1}, KBr): 3059 (w), 2932 (m), 2849 (m), 1640 (sh, alkene C=C), 1612 (s, C=O stretching), 1595 (s, C=N), 1573 (s, aryl C=C), 1530 (m, C=C stretching), 1491 (s, C=O stretching and CH bending), 1434 (m), 1396 (m), 1361 (m), 1322 (m), 1231 (w), 1162 (m), 1053 (m), 945 (m), 837 (m), 759 (m), 703 (m), 607 (m). CHN Elemental *Anal*. Calc. for $C_{99}H_{101}N_{10}O_8Nd$ (1703.19 g mol^{-1}): C, 69.82; H, 5.98; N, 8.22. Found: C, 69.44; H, 5.91; N, 8.20%. Analysis results for erbium complex **4**: yield 63% (2.16 g). IR (cm^{-1}, KBr): 3049 (w), 2916 (m), 2847 (m), 1642 (sh, alkene C=C), 1616 (s, C=O stretching), 1593 (s, C=N), 1577 (s, aryl C=C), 1528 (m, C=C stretching), 1500 (s, C=O stretching and CH bending), 1436 (s), 1394 (m), 1371 (s), 1325 (m), 1233 (w), 1160 (s), 1057 (m), 942 (m), 835 (m), 766 (s), 694 (m), 609 (m). CHN Elemental *Anal*. Calc. for $C_{99}H_{101}N_{10}O_8Er$ (1726.21 g mol^{-1}): C, 68.88; H, 5.90; N, 8.11. Found: C, 69.02; H, 5.77; N, 8.05%. Analysis results for ytterbium complex **5**: yield 52% (1.80 g). IR (cm^{-1}, KBr): 3432 (w), 3061 (m), 2928 (w), 1644 (sh, alkene C=C), 1617 (s, C=O stretching), 1591 (s, C=N), 1573 (s, aryl C=C), 1529 (m, C=C stretching), 1498 (s, C=O stretching and CH bending), 1432 (m), 1400 (w), 1365 (m), 1321 (w), 1233 (w), 1162 (m), 1056 (w), 950 (m), 840 (m), 760 (m), 694 (m), 614 (m). CHN Elemental *Anal*. Calc. for $C_{99}H_{101}N_{10}O_8Yb$ (1731.99 g mol^{-1}): C, 68.65; H, 5.88; N, 8.09. Found: C, 68.33; H, 5.96; N, 8.00%.

4.3. Crystallography

Red single crystals of the (*E*)-*N*-dodecyl-*N*′,*N*′-dimethylamino-stilbazolium tetrakis(1-phenyl-3-methyl-4-benzoyl-5-pyrazolonato) lanthanum(III) complex were obtained by slow evaporation of diethylether into a solution of the compound in dimethylformamide. X-ray intensity data were collected on a SMART 6000 diffractometer equipped with CCD detector using Cu Kα radiation ($\lambda = 1.54178$ Å). The images were interpreted and integrated with the program SAINT from Bruker [38]. Crystal data can be found in Table 1.

The structure was solved by direct methods and refined by full-matrix least-squares on F^2 using the SHELXTL program package [39]. Non-hydrogen atoms were anisotropically refined and the hydrogen atoms in the riding mode with isotropic temperature factors fixed at 1.2 times U_{eq} of the parent atoms (1.5 times for methyl groups).

Acknowledgements

R.V.D. and T.N.P.-V. are Postdoctoral Fellows of the Fund for Scientific Research – Flanders (Belgium) (F.W.O. – Vlaanderen). Financial support by the F.W.O. – Flanders (G.0117.03) and by the K.U.Leuven (GOA 03/03) is gratefully acknowledged. R.V.D. thanks the

FWO-Flanders for a Research Grant of the Fund for Scientific Research – Flanders (FWO) (Project 1.5.099.06). The authors thank Prof. C. Görller-Walrand for providing laboratory facilities. CHN microanalyses were done by Mrs. P. Bloemen (K.U.Leuven).

Appendix A. Supplementary material

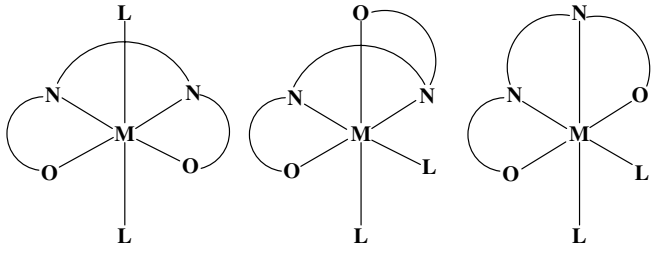
CCDC 623073 contains the supplementary crystallographic data for the (*E*)-*N*-dodecyl-*N*′,*N*′-dimethylamino-stilbazolium tetrakis(1-phenyl-3-methyl-4-benzoyl-5-pyrazolonato) lanthanum(III) complex. These data can be obtained free of charge via http://www.ccdc.cam.ac.uk/conts/retrieving.html, or from the Cambridge Crystallographic Data Centre, 12 Union Road, Cambridge CB2 1EZ, UK; fax: (+44) 1223-336-033; or e-mail: deposit @ccdc.cam.ac.uk. Supplementary data associated with this article can be found, in the online version, at doi:10.1016/j.poly.2007.08.005.

References

[1] S.I. Klink, P.O. Alink, L. Grave, F.G.A. Peters, J.W. Hofstraat, F. Geurts, F.C.J.M. van Veggel, J. Chem. Soc., Perkin Trans. (2001) 363.
[2] J.-C.G. Bünzli, C. Piguet, Chem. Soc. Rev. 34 (2005) 1048.
[3] Y. Korovin, N. Rusakova, Inorg. Chem. Rev. 21 (2001) 299.
[4] J.-C.G. Bünzli, G.R. Choppin, in: Lanthanide Probes in Life, Chemical and Earth Sciences – Theory and Practice, Elsevier, Amsterdam, 1989.
[5] M.H.V. Werts, R.H. Woudenberg, P.G. Emmerink, R. van Gassel, J.W. Hofstraat, J.W. Verhoeven, Angew. Chem., Int. Ed. 39 (2000) 4542.
[6] D. Parker, J.A.G. Williams, in: H. Sigel, A. Sigel (Eds.), Metal Ions in Biological Systems: The Lanthanides and their Interrelation with Biosystems, vol. 40, Marcel Dekker, New York, 2003, p. 233.
[7] M. Digonnet (Ed.), Rare Earth Doped Fiber Lasers and Amplifiers, 2nd ed., Marcel Dekker, New York, 2001.
[8] A. Beeby, S. Faulkner, D. Parker, J.A.G. Williams, J. Chem. Soc., Perkin Trans. 2 (2001) 1268.
[9] F. Artizzu, P. Deplano, L. Marchio, M.L. Mercuri, L. Pilia, A. Serpe, F. Quochi, R. Orru, F. Cordella, F. Meinardi, R. Tubino, A. Mura, G. Bongiovanni, Inorg. Chem. 44 (2005) 840.
[10] F. Quochi, R. Orru, F. Cordella, A. Mura, G. Bongiovanni, F. Artizzu, P. Deplano, M.L. Mercuri, L. Pilia, A. Serpe, J. Appl. Phys. 99 (2006) 053520.
[11] J. Zhang, P.D. Badger, S.J. Geib, S. Petoud, Angew. Chem.-Int. Ed. 44 (2005) 2508.
[12] M. Lezhnina, F. Laeri, L. Benmouhadi, U. Kynast, Adv. Mater. 18 (2006) 280.
[13] C. Görller-Walrand, K. Binnemans, in: K.A. GschneidnerJr., L. Eyring (Eds.), Handbook on the Physics and Chemistry of Rare Earths, vol. 25, North-Holland, Amsterdam, 1998, p. 101 (Chapter 167).
[14] N. Sabbatini, M. Guardigli, I. Manet, in: K.A. GschneidnerJr., L. Eyring (Eds.), Handbook on the Physics and Chemistry of Rare Earths, vol. 23, North-Holland, Amsterdam, 1996, p. 70 (Chapter 154).
[15] G. Stein, E. Wurzberg, J. Chem. Phys. (1975) 208.
[16] S.W. Magennis, S. Parsons, A. Corval, J.D. Woollins, Z. Pikramenou, Chem. Commun. (1999) 61.
[17] S.W. Magennis, S. Parsons, Z. Pikramenou, Chem. Eur. J. 8 (2002) 5761.
[18] A.P. Bassett, R. Van Deun, P. Nockemann, P.B. Glover, B.M. Kariuki, K. Van Hecke, L. Van Meervelt, Z. Pikramenou, Inorg. Chem. 44 (2005) 6140.
[19] P.B. Glover, A.P. Bassett, P. Nockemann, B.M. Kariuki, R. Van Deun, Z. Pikramenou, Chem. Eur. J. 13 (2007) 6308.
[20] K.Z. Wang, C.H. Huang, G.X. Xu, Q.F. Zhou, Solid State Commun. 95 (1995) 223.
[21] M.A. Pavier, M.S. Weaver, D. Lidzey, T. Richardson, T.M. Searle, D.D.C. Bradley, C.H. Huang, H. Li, D. Zhou, Thin Solid Films 285 (1996) 644.
[22] K. Binnemans, C. Bex, D.W. Bruce, Liq. Cryst. 26 (1999) 771.
[23] K. Binnemans, C. Bex, R. Van Deun, J. Incl. Phenom. Macrocycl. Chem. 35 (1999) 63.
[24] K. Binnemans, C. Bex, A. Venard, H. De Leebeeck, C. Görller-Walrand, J. Mol. Liq. 83 (1999) 283.
[25] K. Wostyn, K. Binnemans, K. Clays, A. Persoons, J. Phys. Chem. B 105 (2001) 5169.
[26] U. Narang, C.F. Zhao, J.D. Bhawalkar, F.V. Bright, P.N. Prasad, J. Phys. Chem. 100 (1996) 4521.
[27] C.F. Zhao, R. Gvishi, U. Narang, G. Ruland, P.N. Prasad, J. Phys. Chem. 100 (1996) 4526.
[28] B. Jedrzejewska, J. Kabatc, M. Pietrzak, J. Paczkowski, Dyes Pigments 58 (2003) 47.
[29] A. Mishra, G.R. Newkome, C.N. Moorefield, L.A. Godinez, Dyes Pigments 58 (2003) 227.
[30] D.J. Zhou, C.H. Huang, K.Z. Wang, G.X. Xu, X.S. Zhao, X.M. Xie, L.G. Xu, T.K. Li, Langmuir 10 (1994) 1910.
[31] K.Z. Wang, C.H. Huang, G.X. Xu, Y. Xu, Y.Q. Liu, D.B. Zhu, X.S. Zhao, X.M. Xie, N.Z. Wu, Chem. Mater. 6 (1994) 1986.
[32] C.H. Huang, K.Z. Wang, G.X. Xu, X.S. Zhao, X.M. Xie, Y. Xu, Y.Q. Liu, L.G. Xu, T.K. Li, J. Phys. Chem. 99 (1995) 14397.
[33] K. Wostyn, K. Binnemans, K. Clays, K. Persoons, Rev. Sci. Instrum. 72 (2001) 3215.
[34] K. Binnemans, in: K.A. Gschneidner, J.-C.G. Bünzli, V.K. Pecharsky (Eds.), Handbook on the Physics and Chemistry of Rare Earths, vol. 35, Elsevier, Amsterdam, 2005, p. 107 (Chapter 225).
[35] L.R. Melby, N.J. Rose, E. Abramson, J.C. Caris, J. Am. Chem. Soc. 86 (1964) 5117.
[36] P. Fias, Ph.D. Thesis, K.U.Leuven, 2005.
[37] W.D. Horrocks, J.P. Bolender, W.D. Smith, R.M. Supkowski, J. Am. Chem. Soc. 119 (1997) 5972.
[38] SAINT, Manual Version 5/6.0, Bruker Analytical X-ray Systems Inc., Madison, WI, 1997.
[39] SHELXTL-PC, Manual Version 5.1, Bruker Analytical X-ray Systems Inc., Madison, WI, 1997.

the *cis*-β-isomer, and two equatorial positions in the *cis*-α-isomer (Scheme 1). The molecule of [Rh(Salbn)Cl(py)], for example, has the Cl and pyridine ligands 90° apart with salbn twisted into a *cis*-β-conformation [17].

In continuation of our work on the synthesis and structural studies of Co(III) complexes containing Schiff base ligands [18–21], we herein report the synthesis and spectroscopic characterization of several cobalt(III) complexes of Me-salpn and Me-salbn Schiff base ligands (Scheme 2). In two representative cases, *trans*-[Co^{III}(Me-salpn)$(py)_2$]-PF_6, **1**, and *cis*-α-[Co^{III}(Me-salbn)$(4\text{-Mepy})_2$]$BPh_4 \cdot$ 4-Mepy, **4**, crystal structures have been determined to define the coordination sphere. The results of our studies on the outer coordination sphere effects, obtained by spectroscopy, cyclic voltammetry, and X-ray crystal structure determination is also discussed.



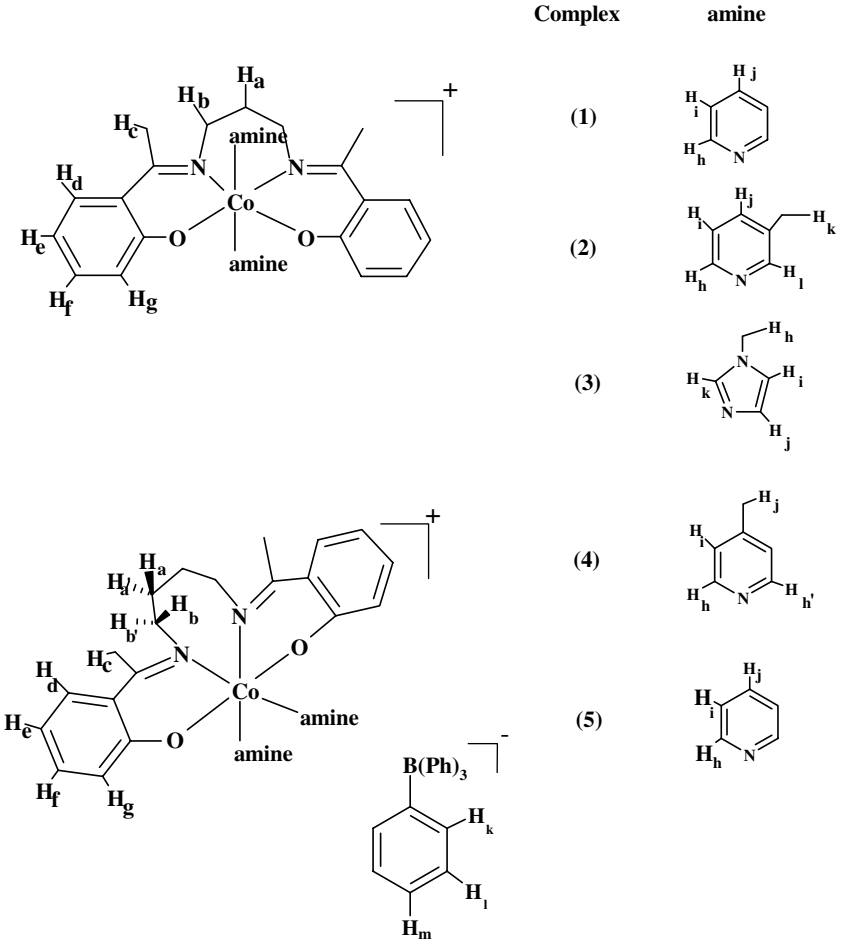
trans (**1**) *cis*-β *cis*-α (**4**)

Scheme 1.

2. Experimental

2.1. Materials and general methods

All solvents and chemicals were used as received, except for the amines which were distilled under reduced pressure prior to use. Elemental analyses were performed by using a Perkin–Elmer 2400II CHNS-O elemental analyzer. UV–Vis spectra were recorded on a JASCO V-570 spectrophotometer. Infrared spectra (KBr pellets) were obtained on a FT-IR JASCO 680 plus spectrophotometer. ^{1}H NMR spectra were obtained on a BRUKER AVANCE DR X500 (500 MHz) and DR X300 (300 MHz) spectrometer. Proton chemical shift are reported in part per million (ppm) relative to an internal standard of Me_4Si. The redox properties of the complexes were studied by cyclic voltammetry. Cyclic voltammograms were recorded by using a SAMA Research Analyzer M-500. Three electrodes were



Scheme 2.

utilized in this system, a glassy carbon working electrode, a platinum disk auxiliary electrode and Ag wire as reference electrode. The glassy carbon working electrode (Metrohm 6.1204.110) with 2.0 ± 0.1 mm diameter was manually cleaned with 1μm alumina polish prior to each scan. Tetrabutylammonium hexafluorophosphate (TBAH) was used as supporting electrolyte. Acetonitrile was dried over CaH_2. The solutions were deoxygenated by purging with Ar for 5 min. All electrochemical potentials were calibrated versus internal Fc^+/o ($E^0 = 0.40$ V versus SCE) couple under the same conditions [22].

2.2. Synthesis

2.2.1. H_2Me-salpn

H_2Me-salpn, *N*,*N*′-bis(methylsalicylidene)-1,3-propylenediamine, was prepared as reported in the literature [23] by the condensation of 1,3-propandiamine with 2-hydroxyacetophenone (1:2 mol stoichiometric ratio) in methanol at room temperature (Scheme 3), and was recrystallized from hot methanol. Yield: 95%, m.p. 122 °C. FT-IR (KBr, cm^{-1}): ν_{max} 3370–3470 (m, br, OH), 1614 (s, C=N). UV–Vis: λ_{max} (nm) (ε, L mol^{-1} cm^{-1}) ($CHCl_3$): 392 (2250), 322 (7360), 258 (23410). ^{1}H NMR ($CDCl_3$, 500 MHz): $\delta = 2.25$ (m, $2H_a$), 2.36 (s, $6H_c$), 3.75 (t, $4H_b$), 6.78 (br t, $2H_e$), 6.94 (br d, $2H_g$), 7.29 (br t, $2H_f$), 7.52 (br d, $2H_d$).

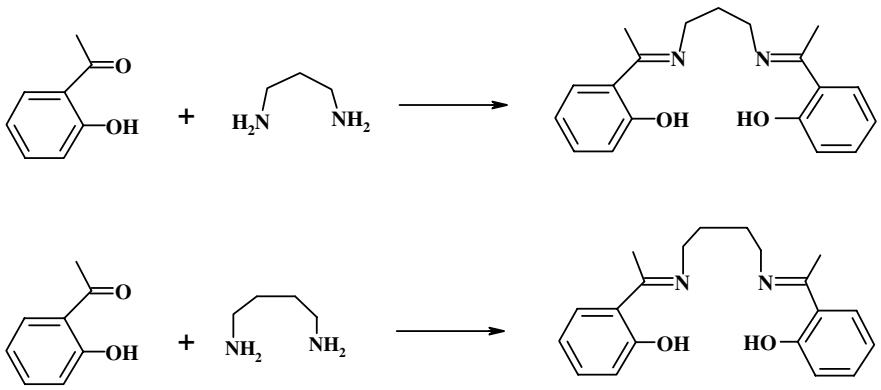
2.2.2. H_2Me-salbn

H_2Me-salbn, *N*,*N*′-bis(methylsalicylidene)-1,4-butylenediamine, was prepared by the same method as for H_2Me-salpn, using 1,4-butanediamine and 2-hydroxyacetophenone (1:2 mol stoichiometric ratio) in methanol at room temperature (Scheme 3), and was recrystallized from hot acetonitrile. Yield: 95%, m.p. 189°. *Anal.* Calc. for $C_{20}H_{24}N_2O_2$: C, 74.04; H, 7.46; N, 8.64. Found: C, 74.08; H, 7.52; N, 8.69%. FT-IR (KBr, cm^{-1}): ν_{max} 3409–3580 (w, br, OH), 1614 (s, C=N). UV–Vis: λ_{max} (nm) (ε, L mol^{-1} cm^{-1}) ($CHCl_3$): 394 (2825), 318 (8390), 251 (22660). ^{1}H NMR ($CDCl_3$, 300 MHz): $\delta = 1.96$ (m, 4H, $H_{a,a'}$), 2.36 (s, 6H, H_c), 3.64 (m, 4H, $H_{b,b'}$), 6.76 (td, 2H, H_e), 6.93 (dd, 2H, H_g), 7.29 (td, 2H, H_f), 7.51 (dd, 2H, H_d).

2.2.3. Synthesis of cobalt complexes

*2.2.3.1. Preparation of [Co^{III}(Me-salpn)(py)$_2$]PF_6 (**1**).* To a stirring solution of $Co(CH_3COO)_2 \cdot 4H_2O$ (0.125 g, 0.5 mmol) in methanol (25 ml) was added an equimolar of H_2Me-salpn (0.155 g, 0.5 mmol). The pink solution turned brown immediately upon the formation of [Co^{II}(Me-salpn)] complex. To this solution was added 4 mmol of pyridine, and air was bubbled through the reaction mixture for about 3 h. 0.5 mmol of NH_4PF_6 was then added to the resulting green brown solution and stirred for 5 min. A green microcrystalline solid was produced by slow evaporation of methanol at room temperature. The product was then recrystallized from methanol–propanol (2:1 v/v) and yellow green crystals suitable for X-ray crystallography were obtained. The crystals were filtered off and washed with a small amount of cold methanol and dried under vacuum. Yield: 62%. *Anal.* Calc. for $C_{29}H_{30}CoF_6N_4O_2P$: C, 51.95; H, 4.51; N, 8.36. Found: C, 52.0; H, 4.5; N, 8.3%. FT-IR (KBr, cm^{-1}): ν_{max} 1597 (s, C=N), 839 (s, PF_6). UV–Vis: λ_{max} (nm) (ε, L mol^{-1} cm^{-1}) ($CHCl_3$): 600 (405), 380 (6710), 265 (42585). ^{1}H NMR ($CDCl_3$, 500 MHz): $\delta = 1.5$ (m, $2H_a$), 2.63 (s, $6H_c$), 3.89 (br t, $4H_b$), 6.36 (br t, $2H_e$) 6.97 (br d, $2H_g$), 7.03 (br t, $2H_f$), 7.18 (br t, $4H_i$), 7.25 (br d, $2H_d$) 7.64 (br t, $2H_j$) 8.30 (br d, $4H_h$).

*2.2.3.2. Preparation of [Co^{III}(Me-salpn)(3-Mepy)$_2$]PF_6 (**2**).* This complex was prepared by the same method as for **1** except that 3-methylpyridine was used instead of pyridine. Recrystallization from methanol gave green crystals. The crystals were filtered off and washed with a small amount of cold methanol and dried under vacuum. Yield: 70%. *Anal.* Calc. for $C_{31}H_{34}CoF_6N_4O_2P$: C, 53.30; H, 4.91; N, 8.02. Found: C, 53.2; H, 5.0; N, 8.0%. FT-IR (KBr, cm^{-1}): ν_{max} 1596 (s, C=N), 842 (s, PF_6). UV–Vis: λ_{max} (nm) (ε, L mol^{-1} cm^{-1}) ($CHCl_3$): 598 (455), 380 (7280), 265 (43890). ^{1}H NMR ($CDCl_3$, 500 MHz): $\delta = 1.55$ (m, $2H_a$), 2.1 (s, $6H_k$), 2.61 (s, $6H_c$), 3.87 (br t, $4H_b$), 6.35 (br t, $2H_e$), 7.00 (br d, $2H_g$), 7.04 (br t, $2H_f$), 7.16 (br t, $2H_i$), 7.25 (br d, $2H_d$) 7.41 (br d, $2H_j$), 8.08 ($4H_{h,l}$).



Scheme 3.

*2.2.3.3. Preparation of [Co^{III}(Me-salpn)(1-MeIm)$_2$]PF$_6$ (**3**).* This complex was prepared by the same method as for **1** except that 1-methylimidazole was used instead of pyridine. Recrystallization from chloroform–xylene (2:1 v/v) gave green crystals. The crystals were filtered off and washed with a small amount of cold methanol and dried under vacuum. Yield: 70%. *Anal.* Calc. for $C_{27}H_{32}CoF_6N_6O_2P$: C, 47.94; H, 4.77; N, 12.42. Found: C, 47.20; H, 4.80; N, 12.20%. FT-IR (KBr, cm^{-1}): ν_{max} 1597 (s, C=N), 845 (s, PF_6). UV–Vis: λ_{max} (nm) (ε, L mol^{-1} cm^{-1}) ($CHCl_3$): 578 (384), 380 (6950), 273 (54 610). ^{1}H NMR ($CDCl_3$, 500 MHz): $\delta = 1.58$ ($2H_a$), 2.59 (s, $6H_c$), 3.59 (s, $6H_h$), 3.83 ($4H_b$), 6.38–7.45 (14H, $H_{d,e,f.g,i,j,k}$).

*2.2.3.4. Preparation of [Co^{III}(Me-salbn)(4-Mepy)$_2$]-BPh$_4$ · 4-Mepy (**4**).* To a stirring solution of $Co(CH_3COO)_2 \cdot 4H_2O$ (0.125 g, 0.5 mmol) in methanol (30 ml) was added two drops of H_2O_2 (30%). The pink solution turned green immediately and to this solution was then added a solution of equimolar H_2Me-salbn (0.162 g, 0.5 mmol) in chloroform (10 ml). Air was then bubbled through the reaction mixture for about 3 h, while adding 5 mmol of 4-methylpyridine in one h intervals. The final solution was filtered off and a solution of 0.5 mmol (0.171 g) of $NaBPh_4$ in 5 mL methanol was added drop wise to the filtrate. Red green crystals of complex **4** suitable for X-ray crystallography were obtained after one week by slow evaporation of the solvent. The crystals were filtered off and washed with a mixture of methanol–diethyl ether (1:10 v/v) and dried under vacuum. Yield: 60%. *Anal.* Calc. for $C_{62}H_{63}CoN_5O_2B$: C, 75.99; H, 6.48; N, 7.15. Found: C, 75.21; H, 6.38; N, 7.01%. FT-IR (KBr, cm^{-1}) ν_{max}: 1595 (s, C=N), UV–Vis: λ_{max} (nm) (ε, L mol^{-1} cm^{-1}) ($CHCl_3$): 648 (390), 425 (sh, 2470), 388 (5100), 260 (52600). ^{1}H NMR ($CDCl_3$, 300 MHz): $\delta = 1.58$–1.87 (m, 4H, $H_{a,a'}$), 2.22 (s, 6H, H_j), 2.38(s, H_{Me}, free 4-Mepy) 2.47 (s, 6H, H_c), 3.75–4.4 (m, 4H, $H_{b,b'}$), 6.34–8.65 (40H, ArH).

*2.2.3.5. Preparation of [Co^{III}(Me-salbn)(py)$_2$]BPh$_4$ (**5**).* This complex was prepared by the same method as for **4** except that pyridine was used instead of 4-methylpyridine and a green solid product was obtained after one week. Recrystallization from chloroform–chlorobenzene (3:1 v/v) gave red green crystals after 10 days. The crystals were filtered off and washed with a mixture of methanol–diethyl ether (1:10 v/v) and dried under vacuum. Yield: 50%. *Anal.* Calc. for $C_{54}H_{52}CoN_4O_2B$: C, 75.52; H, 6.10; N, 6.52. Found: C, 74.92; H, 6.30; N, 6.40%. FT-IR (KBr, cm^{-1}) ν_{max}: 1598 (s, C=N). UV–Vis: λ_{max} (nm) (ε, L mol^{-1} cm^{-1}) ($CHCl_3$): 646 (415), 429 (sh, 1890), 386 (4290), 257(52 510). ^{1}H NMR ($CDCl_3$, 300 MHz): $\delta = 1.62$–1.87 (m, 4H, $H_{a,a'}$), 2.47 (s, 6H, H_c), 3.76–4.41 (m, 4H, $H_{b,b'}$), 6.37–8.8 (38H, ArH).

2.3. Crystallography

2.3.1. X-ray crystallography for *1*

Yellow crystals of **1** suitable for data collection were obtained by slow evaporation of a methanol–propanol (2:1 v/v) solution of the complex. The cell and intensities were measured on a Stoe IPSD II at 120 K, using graphite monochromatized Mo Kα radiation ($\lambda = 0.71073$ Å).

A crystal-to-detector distance of 100 cm was chosen and 180 one-degree-wide images were exposed for 5 min each. Crystal data and details of the structure determination are given in Table 1. The data were corrected for Lorentz and polarization effects and a numerical absorption correction (X-RED32) was carried out [24]. The structure was solved with the help of DIRDIF-96 [25] and refined, against F^2, using SHELXL-97 [26]. Anisotropic displacement parameters were refined for all atoms, but the hydrogens were made to ride on their carrier atoms, their U-values being coupled to the latter. The measured crystal was bound by {1 0 0} and {0 1 0} pinacoids, and (0 0 1), ($\bar{1}\,\bar{1}$ 9) and ($\bar{1}$ 2 9) pedions, the latter two maybe being part of a {$\bar{1}$ 1 9} prism.

2.3.2. X-ray crystallography for *4*

Red crystals of **4** suitable for X-ray crystallography were obtained by slow evaporation of a methanol–chloroform (3:1 v/v) solution of the complex. Φ-and ω-scan were collected, at room temperature, on a Nonius Kappa CCD diffractometer (Mo Kα radiation, $\lambda = 0.71073$ Å) using the COLLECT [27] program. Cell refinement and data reduction were performed with the help of the EVALCCD [28] program. Crystal data, together with other relevant information on structure determination, are listed in Table 1. An empirical absorption correction, based on redundant intensities, was carried out using the SADABS program [29]. The structure was solved by the SIR97 program [30] and refined, against F^2, by means of the SHELXTL program [31]. Anisotropic displacement parameters were assigned to all the non-hydrogen atoms. Hydrogen atoms were placed in idealized positions and allowed to ride on their respective parent atoms, their U-values being coupled to the latter.

3. Results and discussion

3.1. Synthesis

All the cobalt(III) complexes have been prepared by the direct reaction of the corresponding ligands, H_2Me-salpn or H_2Me-salbn, and $Co(CH_3COO)_2 \cdot 4H_2O$ in the presence of the appropriate amine in aerobic conditions (Scheme 2). In the preparation of **1**–**3** complexes, a vigorous stream of air was passed through a solution of Co^{II}(Me-salpn) in methanol to which was gradually added excess amine. The air oxidation was continued for a period of 3 h, during which the color changed from brown to green. Green crystals of these complexes were obtained in good yield (60–70%). In the preparation of **4** and **5** complexes, however, the initial addition of a few drops of H_2O_2 (30%) was

Table 1
Crystal data and structure refinement for **1** and **4**

Empirical formula	$C_{29}H_{30}CoN_4O_2PF_6$ (**1**)	$C_{62}H_{63}BCoN_5O_2$ (**4**)
Formula weight	670.47	979.91
Temperature (K)	120(1)	293(2)
Radiation, wavelength (Å)	Mo Kα, 0.71073	Mo Kα, 0.71073
Crystal system, space group	monoclinic, $P2_1/c$	monoclinic, $P2_1/n$
a (Å)	12.8693(9)	9.5465(12)
b (Å)	12.3231(9)	32.262(4)
c (Å)	18.0379(12)	17.220(3)
β(°)	94.89(3)	100.883(11)
V (Å^3)	2850.2(3)	5208.3(13)
Z	4	4
D_{calc} (g cm^{-3})	1.562	1.250
Crystal color and size (mm)	yellow, $0.30\times0.29\times0.13$	red, $0.23\times0.20\times0.20$
μ (mm^{-1})	0.736	0.379
F(000)	1376	2072
θ Range (°)	2.00–29.30	4.1–24.0
Index ranges	$-16\leqslant h\leqslant 17$, $-16\leqslant k\leqslant 16$, $-22\leqslant l\leqslant 24$	$-10\leqslant h\leqslant 10$, $-36\leqslant k\leqslant 36$, $-19\leqslant l\leqslant 19$
Reflection collected	26052	45457
Independent reflections [R_{int}]	7356 [0.0519]	8112 [0.0544]
Reflections with $F^2>2\sigma$	6014	6192
Absorption correction	integration Stoe X-RED1.31	semi-empirical from equivalents
Maximum and minimum transmission	0.8992 and 0.7943	0.9179 and 0.9281
Data/restraints/parameters	7356/0/391	8112/0/645
Goodness-of-fit on F^2	1.089	1.119
Final R indices [$F^2>2\sigma(F^2)$]	$R_1=0.0470$, $wR_2=0.0994$	$R_1=0.0560$, $wR_2=0.1460$
R indices (all data)	$R_1=0.0631$, $wR_2=0.1120$	$R_1=0.0805$, $wR_2=0.1600$
Largest difference peak, hole (e Å^{-3})	0.459, −0.626	0.65, −0.57

necessary. Red green crystals of Me-salben complexes were obtained in good yield (50–60%).

3.2. Description of structures

3.2.1. Complex **1**, $[Co^{III}(Me\text{-}salpn)(py)_2]PF_6$

The structure of complex **1** consists of a mononuclear cobalt(III) unit, depicted in Fig. 1, showing very approximate C_σ symmetry with respect to Co, N(5), N(6) and C(110), but the N(11)–N(21) and O(11)–O(21) distances are quit different indeed (2.910(3) versus 2.548(2) Å). The complex can be described as a distorted octahedron (bond angles and distances are given in Table 2) involving N_2O_2 donors as the basal plane. The pyridine, salicylidene, Co,

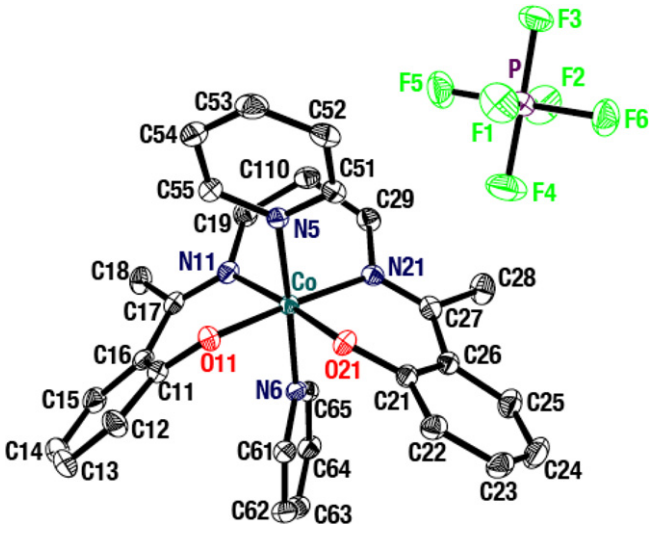


Fig. 1. ORTEP drawing of complex **1** with the atom numbering scheme. The displacement ellipsoids are drawn at the 50% probability level.

Table 2
Selected bond lengths (Å) and angles (°) for **1** and **4**

Complex	**1**		**4**
Bond lengths			
Co–O(11)	1.8839(17)	Co(1)–O(1)	1.891(2)
Co–O(21)	1.8878(17)	Co(1)–O(2)	1.882(2)
Co–N(11)	1.959(2)	Co(1)–N(4)	1.980(3)
Co–N(21)	1.966(2)	Co(1)–N(2)	1.957(3)
Co–N(5)	1.991(2)	Co(1)–N(1)	1.942(3)
Co–N(6)	1.9538(19)	Co(1)–N(3)	1.977(3)
Bond angles			
O(11)–Co–N(11)	89.20(8)	N(2)–Co(1)–O(2)	90.90(11)
O(21)–Co–N(21)	90.10(8)	N(4)–Co(1)–O(1)	90.38(11)
O(11)–Co–O(21)	85.01(8)	N(4)–Co(1)–O(2)	86.69(10)
N(11)–Co–N(21)	95.69(9)	N(2)–Co(1)–O(1)	92.02(11)
O(11)–Co–N(21)	175.10(9)	O(1)–Co(1)–O(2)	177.07(10)
O(21)–Co–N(11)	174.20(8)	N(2)–Co(1)–N(4)	177.50(12)
N(5)–Co–N(6)	173.22(9)	N(1)–Co(1)–N(3)	177.20(12)
O(11)–Co–N(5)	83.57(8)	N(1)–Co(1)–N(2)	89.37(12)
O(21)–Co–N(5)	85.57(8)	N(1)–Co(1)–N(4)	91.35(11)
N(11)–Co–N(5)	94.13(9)	N(1)–Co(1)–O(1)	89.05(11)
N(21)–Co–N(5)	96.25(8)	N(1)–Co(1)–O(2)	91.23(11)
O(11)–Co–N(6)	90.85(8)	N(3)–Co(1)–O(1)	88.33(11)
O(21)–Co–N(6)	90.13(8)	N(3)–Co(1)–O(2)	91.33(11)
N(6)–Co–N(11)	89.63(9)	N(3)–Co(1)–N(4)	87.68(11)
N(6)–Co–N(21)	88.98(8)	N(2)–Co(1)–N(3)	91.70(12)

N(11), N(21), O(11) and O(21) and N(11), C(19), C(29), N(21) planes feature RMS-values no worse than 0.038 Å, the Co atom therefore perfectly lying in the N_2O_2 plane. The two phenolic oxygen atoms and the two imine nitrogen atoms are located in *cis* positions. The angles between the imino and salicylidine planes are 20.8(1)° and 15.3(3)° for the N(11) and N(21) groups with respect to the C(11) and C(21) rings. The average Co–O distance (1.886 Å) and the O(11)–Co–O(21) angle (85.01(8)°) compare well with those reported for *trans*-[Co(salen)$(py)_2$]BPh_4 (1.884 Å and 85.8°, respectively) [32]. However, increasing the N···N distance in Me-salpn ligand has led to an elongation of the Co–N bond and the enlargement of the N–Co–N angle relative to salen. The average Co–N_{eq} distance (1.963 Å) is considerably longer than that of [Co(salen)-$(py)_2$]BPh_4 (1.888 Å) and the N(11)–Co–N(21) angle (95.69(7)°) is larger than the corresponding angle in the related salen complex (85.5(2)°) [32].

There are two pyridine molecules attached to the metal atom to fill its axial sites with a perpendicular disposition. (88.94(8)°). The N(5)-pyridine, probably for steric reasons, bends away from the six-membered diamine chelate ring N(11), N(21), C(29), C(110), C(28), Co. The axial Co–N(py) bond distances (Co–N(5) 1.991(2), Co–N(6) 1.9538(19) Å) are comparable to those found in the structure of *trans*-[Co(salen)$(py)_2$]BPh_4 (1.975(3) and 1.987(3) Å) [32], but are not equal apparently due to the stereochemical requirements of the central methylene, C(110), whose six-membered diamine chelate ring adopts the thermodynamically unfavorable boat conformation. This steric demand has some influence on the substitution of the axial pyridine ligands and the reduction potential of the cobalt complex (*vide infra*).

There are three intramolecular hydrogen bonds and two intermolecular ones providing weak stabilizing forces (normalized hydrogen bonds lie between 2.27 and 2.54 Å). The former are between the hydrogen on C(110) towards the nitrogen N(5) and between the hydrogen on C(61) towards O(11) and O(21). The latter between one of the methyl hydrogens on C(18) and C(28) towards F(3) and F(4). The intermolecular hydrogen bonds are such as to form [1 1 1] chains of complexes alternating with two hydrogen bonded PF_6 octahedra.

3.2.2. Complex 4, [Co^{III}(Me-salbn)(4-Mepy)$_2$]$BPh_4$4-Mepy

The structure of complexes **4** consist of a six coordinate mononuclear cobalt(III) unit, shown in Fig. 2, with approximate C_σ with respect to O(1)–O(2) (principle bond angles and distances are listed in Table 2). The coordination about Co is pseudo-octahedral, with angles between neighboring vertices of the octahedron varying from 86.69° to 92.02°. The tetradentate Schiff base ligand adopts a *cis*-α-configuration and the two 4-metylpyridine ligands are therefore *cis*, with an angle between them of 87.68(11)°. The Co–O distances (Co(1)–O(1) 1.891(2) Å and Co(1)–O(2) 1.882(2) Å) are similar to those found in

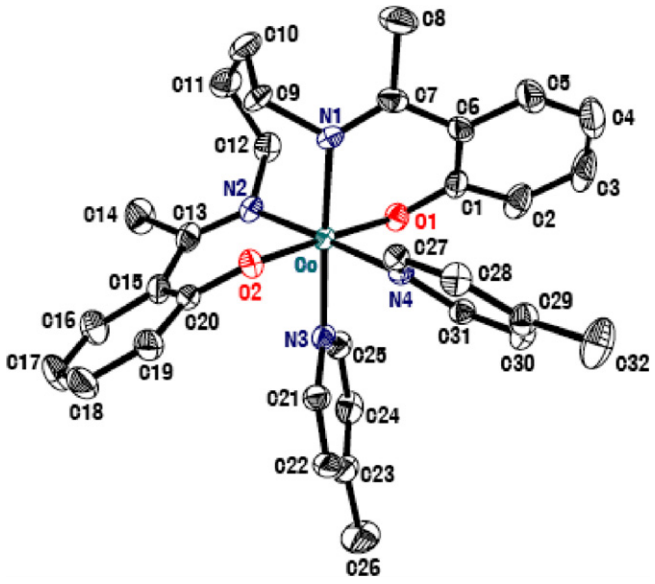


Fig. 2. ORTEP drawing of the cation of complex **4** with the atom numbering scheme. The displacement ellipsoids are drawn at the 50% probability level.

related complexes [32, complex **1**]. The Co–$N_{4\text{-Mepy}}$ distances (Co(1)–N(3) 1.977(3) and Co(1)–N(4) 1.980 (3)) are slightly longer than the Co–N_{imine} distances (Co(1)–N(1) 1.942(3) Å and Co(1)–N(2) 1.957(3)), perhaps indicating weaker coordination. The O(1)–Co(1)–O(2), N(1)–Co(1)–N(3), N(2)–Co(1)–N(4) angles of the *trans* donating atoms are between 177.07° and 177.50° and slightly less than the ideal value. The angles between the imino and the salicylidene planes are 19.0(4)° and 19.7(3)° for the N(1) and N(2) groups with respect to the C(1) and C(15) rings, thus *much more similar* than in complex **1**. The phenyl, pyridine, and salicylidene planes display RMS-values no worse than 0.024 Å (for pyridine N(3)). The coordination planes defined by Co(I) and the appropriate combinations of N(1), N(2), O(1), and O(2), feature RMS-values no worse than 0.038 Å and do contain the Co(1) atom.

As in the case of *cis*-β-[Rh(salbn)(py)(Cl)] [17], the conformation of the tetramethylene bridge in *cis*-α-[Co^{III}(Me-salbn)(4-Mepy)$_2$]$^+$ shows interesting features. While the bond lengths are all normal for C–C single bonds and very similar to that in the ethylene bridge of salen [32], C(9)–C(10)–C(11), and C(10)–C(11)–C(12) of 116.8(3)° and 116.6(3)°, respectively, are much larger than the tetrahedral angle and are closer to the trigonal angle. This suggests considerable strain in the bridge and makes it, perhaps, surprising that regular octahedral coordination is so well preserved with N(1)–Co(1)–N(2) 89.37(12)°.

There are intramolecular hydrogen bonds only in the structure of **4**. Their normalized lengths lie between 2.26 and 2.42Å, their angles between 100.6° and 119.2°. They act between C(9), C(21), and C(27) towards O(2), and between C(12) and C(25) towards O(1) and reflect the importance of the flexibility of the tetramethylene bridge.

3.3. Spectroscopic properties

A comparative study of the FT-IR spectral data of the reported complexes with those of the uncomplexed ligand gives meaningful information regarding bonding sites of the ligand molecules. Both H_2Me-salpn and H_2Me-salbn show a broad band characteristic of the OH group in the 3400–3570 cm^{-1} region. The disappearance of this band in the FT-IR spectra of the complexes is indicative of the fact that the tetradentate ligands are coordinated as dianions. The ν(C=N) band appearing at 1610 cm^{-1} in Me-salpn and 1614 cm^{-1} in Me-salbn is shifted to lower frequencies by 12–20 cm^{-1} in the corresponding cobalt complex, indicating that the ligands are coordinated to the metal ions through the nitrogen atoms of the azomethine groups [20].

The ^{1}H NMR spectral data are presented in Section 2.2. The octahedral geometry of complex **1** is evident from the X-ray structural analysis (Fig. 1). An octahedral *trans*-structure for **2** and **3** can be inferred based on the similarity of the ^{1}H NMR spectra of these complexes with that of complex **1**. The signal appearing as a singlet at ~2.60 ppm in the ^{1}H NMR spectrum of these complexes is assigned to the two CH_3 groups on Me-salpn and indicates that the equatorial coordination sites are occupied by Me-salpn ligand leading to the magnetically equivalent CH_3 protons. The signals due to the aliphatic protons of the propylene chelate ring and the methyl substituent on the axial ligands appear at $\delta = 1.5$–3.9. The aromatic protons of the phenyl rings in the coordinated Schiff base ligand appear in the appropriate region [15,33].

The two Me-salbn complexes, **4** and **5**, show similar features in their ^{1}H NMR spectra. The only noticeable difference is the additional signal at 2.22 ppm due to the methyl protons of the coordinated Mepy in **4** relative to py in **5**. In addition, the signals characteristic of the free Mepy, trapped in the crystallization process in **4**, appear in the appropriate regions. The structures of the two complexes can be considered as being similar with a *cis*-α-configuration of the Me-salbn ligand, as confirmed for complex **4** by X-ray crystallography, Fig. 2.

The electronic absorption spectrum of H_2Me-salpn in chloroform consist of two relatively intense bands centered at 258 and 322 nm, assigned to the $\pi \rightarrow \pi^*$ transitions of the benzene ring of salicylaldehyde and the azomethine group respectively, and a third band at 392 nm, corresponding to $n \rightarrow \pi^*$ which, upon coordination of the ligand, disappears from the UV–Vis spectra of cobalt complexes [33,34]. The intraligand $\pi \rightarrow \pi^*$ transition of the azomethine group is red shifted by about 60 nm in the corresponding cobalt complexes and appears at 380 nm [35]. The first d → d transition in different Me-salpn cobalt complexes (**1**–**3**) appears in the range of 578–599 nm ($\varepsilon = 384$–455).

It is interesting to note that by changing the solvent from chloroform to acetonitrile the electronic spectra of *trans*-[Co(Me-salpn)$(py)_2$]PF_6, **1**, and *trans*-[Co(Me-salpn)-$(3\text{-Mepy})_2$]PF_6, **2**, show appreciable changes with time. The existence of two well defined isosbestic points at 760 and 608 nm indicates that these complexes are presumably undergoing solvolysis and at least one of the axial ligands is substituted by acetonitrile (Fig. 3). This is not the case for *trans*-[Co(Me-salpn)$(MeIm)_2$]PF_6 **3**, however, and the transformation is very slow for this complex. These observations can be rationalized on the basis of the competition between the steric hindrance imposed by the methylene group of Me-salpn and the ligand field strength of the axial ligands.

The electronic absorption spectrum of H_2Me-salbn in chloroform shows features similar to those observed for H_2Me-salpn, consisting of two $\pi \rightarrow \pi^*$ transitions at 251 and 318 nm, and a third band at 394 nm corresponding to $n \rightarrow \pi^*$ excitation. The $n \rightarrow \pi^*$ band appears to be absent in the spectrum of the cobalt complexes. In addition, the intraligand $\pi \rightarrow \pi^*$ transition of the azomethine group is red shifted by about 70 nm, and appears to be split into two components with a well defined peak at ca. 390 and a shoulder at ca. 425 nm. This is presumably due to the change in the symmetry of the Me-salbn ligand upon coordination in a *cis*-α-configuration. The first d → d

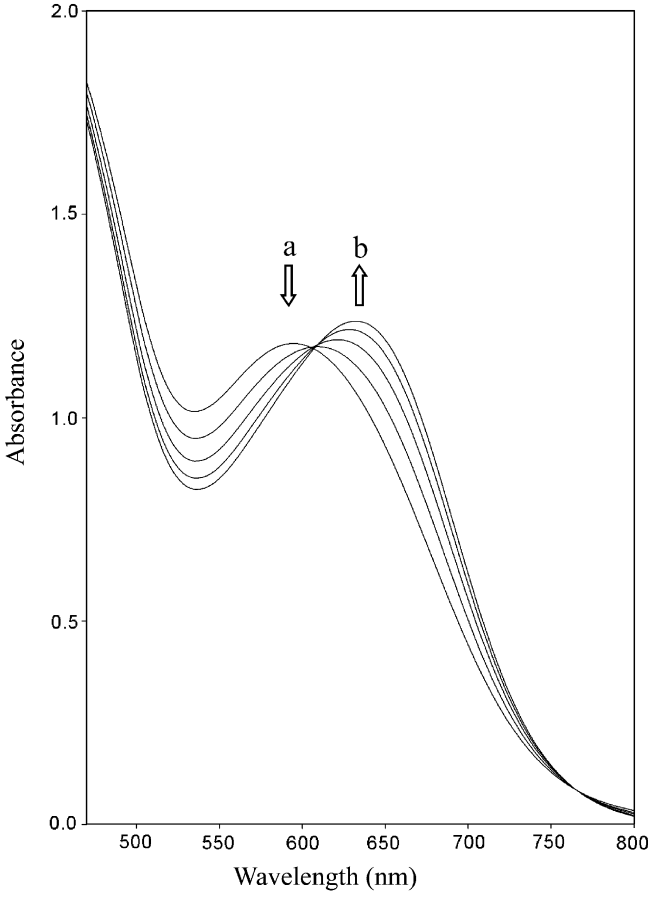


Fig. 3. Electronic absorption spectra of **1** in acetonitrile solution. $c = 2.5 \times 10^{-3}$ mol L^{-1}, time intervals: 10 min: (a) $t = 0$ min and (b) $t = 40$ min. Isosbestic points: 760, 608 nm. Reaction almost completed after 70 min.

transition in the two cobalt Me-salbn complexes (**4** and **5**) appears in the 646–650 nm rage ($\varepsilon = 390$–420). The electronic spectra of these complexes show common features in both non-coordinating and coordinating solvents which is consistent with a less sterically hindered structure for **4** and **5**, as compared to those of Me-salpn complexes (3.2.2 and Table 2).

3.4. Electrochemical studies

The cyclic voltammograms of $[Co(Me\text{-}salpn)(amine)_2]PF_6$ complexes (amine = py **1**, 3-Mepy **2**) and $[Co(Me\text{-}salbn)(amine)_2]BPh_4$ (amine = 4-Mepy **4**, py, **5**) were conducted at 25 °C under an argon atmosphere using acetonitrile solutions containing 0.1 mol dm^{-3} TBAH as supporting electrolyte and complex concentrations of about 3×10^{-3} M. The reduction potential data of cobalt complexes are summarized in Table 3. The ligands are electro-inactive over a range of +0.7 to −2.0 V. The redox properties of cobalt(III) Me-salpn complexes at the scan rates of 20–500 mV/s exhibit grossly similar features consisting of an electrochemically irreversible Co^{III}/Co^{II} reduction at ca. −0.550 V (peak separation ~ 650 mV), which is due to the process $[Co^{III}(Me\text{-}salpn)(R\text{-}py)_2]^+ + e \rightarrow [Co^{II}(Me\text{-}salpn)] + 2R\text{-}py$ [10,20]. During the experiment, the reduction potential gradually shifts to more negative values reaching a value of −0.778 V for **1**, presumably due to the concomitant substitution of the axial ligands by acetonitrile in a solvolysis reaction: $[Co^{III}(Mesalpn)(py)_2]^+ + MeCN \rightarrow [Co^{III}(Me\text{-}salpn)(py)(MeCN)]^+ + py$ (Fig. 4). This value matches the E_{pc} value of an acetonitrile solution of the complex that has been stored for 48 h to let the complete solvolysis of the complex to occur (Fig. 5). As expected, the resulting voltammogram resembles the (b) voltammogram of Fig. 4. Additional evidence comes from the observation of two well defined isosbestic points in the absorption spectra of **1** in acetonitrile solution (Fig. 3) (*vide supra*), which correlates well with the well defined isopotential point at −0.667 V in the cyclic voltammograms of this complex under the same conditions (Fig. 4). It is interesting to note that no substitution occurs in a non-coordinating solvent such as chloroform and an electrochemically irreversible reduction process occurs at −0.576 V, which is close to the initial E_{pc} value of −0.568 V for the acetonitrile solution. A similar electrochemical behavior has been observed for complex **2**, containing 3-Mepy. The Co^{III}/Co^{II} redox process remains electrochemically irreversible in the presence of excess pyridine (Fig. 6), an observation contrary to that of many cobalt Schiff base complexes [10,20].

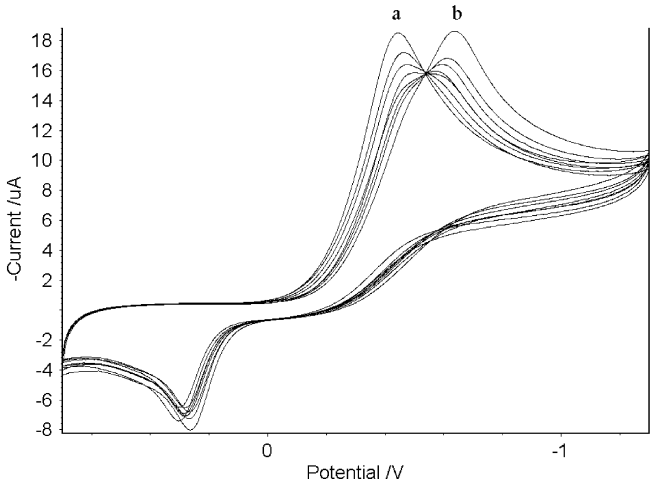


Fig. 4. Cyclic voltammograms corresponding to Co(III) → Co(II) for 4 mM $[Co(Me\text{-}salpn)(py)_2]PF_6$ in acetonitile solution at 293 K during 48 h period: (a) $t = 0$ h and (b) $t = 48$ h. Scan rate: 100 mV/s. $c = 3.2 \times 10^{-3}$.

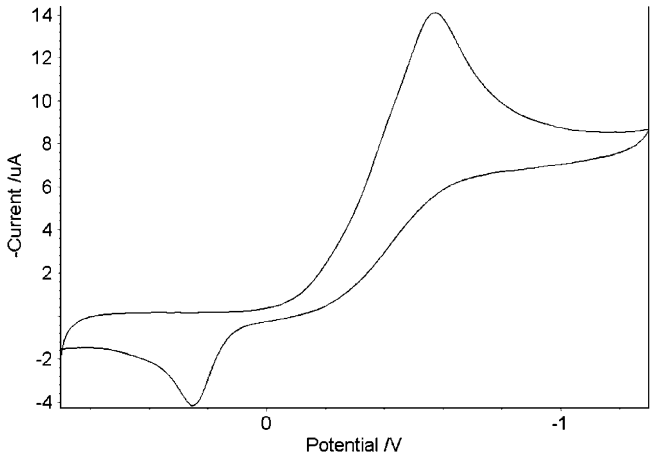


Fig. 5. Cyclic voltammogram corresponding to Co(III) → Co(II) for $[Co(Me\text{-}salpn)(py)_2]PF_6$ in acetonitrile solution stored for 48 h at 293 K. Scan rate: 100 mV/s. $c = 3.0 \times 10^{-3}$.

A similar redox process, however, occurs at −0.803 V for $[Co^{III}(Me\text{-}salbn)(py)_2]^+$, **5**, Fig. 7. It seems reasonable

Table 3
Redox potentials of cobalt complexes of Me-salpn and Me-salbn in acetonitrile[a]

Complex	E_{pc1}	E_{pa1}	E_{pc2}	E_{pa2}
$[Co(Me\text{-}salpn)(Py)_2]PF_6$ (with excess py)	−0.553	0.152	−1.909	−1.773
$[Co(Me\text{-}salpn)(Py)_2]PF_6$ (in acetonitrile solution, stored for 48 h)	−0.778	0.190	−1.914	−1.776
$[Co(Me\text{-}salpn)(3\text{-}Mepy)_2]PF_6$ (with excess 3-Mepy)	−0.546	0.083	−1.899	−1.772
$[Co(Me\text{-}salpn)(3\text{-}Mepy)_2]PF_6$ (in acetonitrile solution, stored for 48 h)	−0.677	0.158	−1.902	−1.775
$[Co(Me\text{-}salbn)(4\text{-}MePy)_2]B(Ph)_4$	−0.784	0.430	−1.884	−1.816
$[Co(Me\text{-}salbn)(Py)_2]B(Ph)_4$	−0.803	0.417	−1.807	−1.739

[a] Potentials are vs. $Fc^+/0$ in 0.1 TBAH, $T = 293$ K. Scan rate 100 mV/s. Approximate concentrations: 3×10^{-3} M.

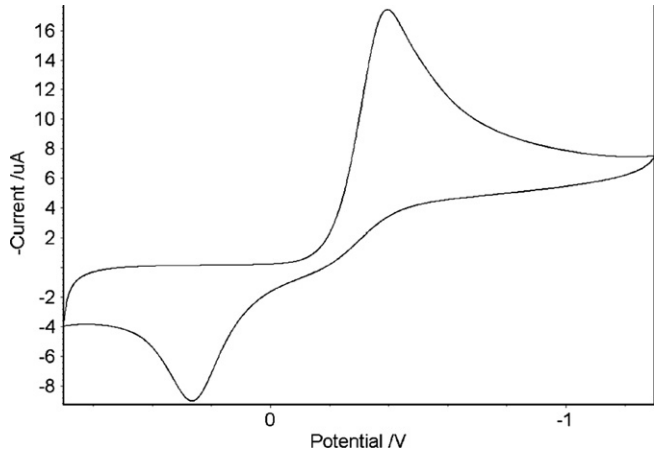


Fig. 6. Cyclic voltammogram corresponding to Co(III) → Co(II) for [Co(Me-salpn)(py)$_2$]PF$_6$ in acetonitrile solution in the presence of excess pyridine at 293 K. Scan rate: 100 mV/s. $c = 3.1 \times 10^{-3}$.

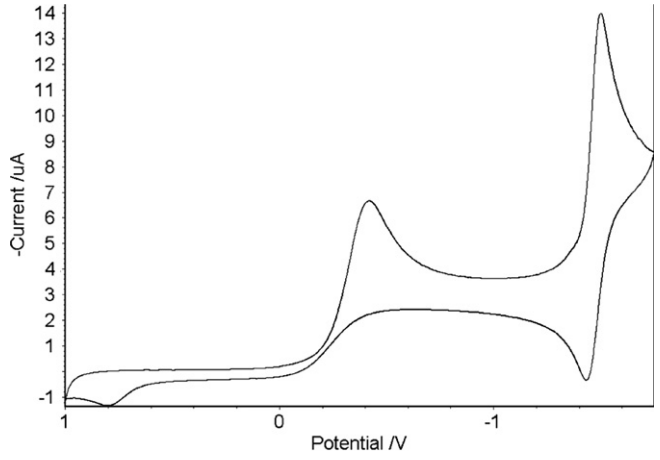


Fig. 7. Cyclic voltammogram of [Co(Me-salbn)(py)$_2$]BPh$_4$ in acetonitrile solution at 293 K. Scan rate: 100 mV/s. $c = 3.0 \times 10^{-3}$.

to assume that the Me-salpn complexes, in which one of the pyridine molecules is subject to the steric effects from the central methylene in the six-membered diamine chelate ring, are more readily reduced relative to the less sterically hindered Me-salbn complexes. Such steric interactions may tend to release the pyridine molecule and thence facilitate the reduction to cobalt(II) species. The Me-salbn, however, shows a stabilizing effect on Co(III), rendering its reduction potential to a more negative value, presumably due to a better orbital overlap leading to an increase in the electron density on cobalt atom. This speculation remains to be tested by further theoretical calculations.

Although a second well defined electrochemically reversible process at ca. −1.807 V is observed with about unit ratio of anodic to cathodic peak currents (i_{pa}/i_{pc}) and peak potential difference of 68 mV for the for [Co^{III}(Me-salbn)(py)$_2$]$^+$, **5** (Fig. 7), which corresponds to the simple one electron process [Co^{II}L] + e$^-$ → [Co^{I}L]$^-$ [10], the corresponding Co(I) salpn complex proved to be unstable, though an electrochemically irreversible Co^{II}–Co^{I} process

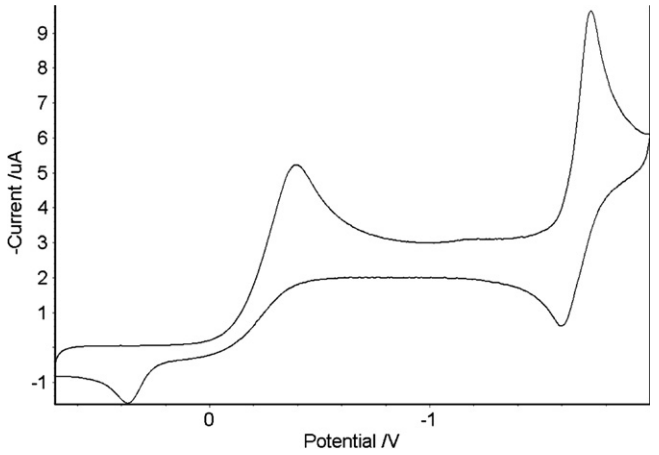


Fig. 8. Cyclic voltammogram of [Co(Me-salpn)(py)$_2$]PF$_6$ in acetonitrile solution at 293 K. Scan rate: 100 mV/s. $c = 2.9 \times 10^{-3}$.

seems to be revealed at the glassy carbon electrode with the initial E_{pc} of −1.909 V and peak potential difference of 136 mV, Fig. 8. These observations are in accord with the results reported for Co(I) complexes of tetradentate Schiff base ligands [36].

4. Conclusion

We have prepared three Co(III) complexes of Me-salpn with two ancillary ligands in the *trans*-positions, and two Co(III) complexes of Me-salbn, in which the tetradentate Schiff base ligand, Me-salbn, adopts a *cis*-α-configuration and the two ancillary ligands are therefore *cis*. In the case of Me-salpn complexes, the central methylene of the chelate ring exerts sufficient steric hindrance to remove one of the axial ligands in coordinating solvents such as acetonitrile, and shifts the Co^{III}–Co^{II} to the positive side, facilitating the reduction to cobalt(II) species. However, Me-salbn complexes with less steric demands do not undergo solvolysis in acetonitrile, and Me-salbn shows a stabilizing effect on Co(III) relative to Me-salpn. This study shows the effect of the outer coordination sphere on the coordination mode of the two Schiff base ligands and the influence on the reduction potentials of the corresponding cobalt(III) complexes.

Acknowledgements

Partial support of this work by the Isfahan University of Technology Research Council is gratefully acknowledged. Special thanks are due to Professor H. Hadadzadeh for helpful comments concerning the interpretation of electrochemical data.

Appendix A. Supplementary material

CCDC 650932 and 650931 contain the supplementary crystallographic data for **1** and **4**. These data can be obtained free of charge via http://www.ccdc.cam.ac.uk/

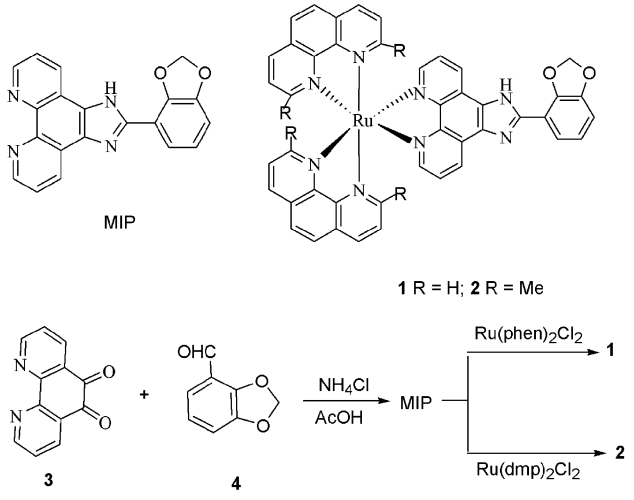
conts/retrieving.html, or from the Cambridge Crystallographic Data Centre, 12 Union Road, Cambridge CB2 1EZ, UK, fax: (+44) 1223-336-033, or e-mail: deposit@ccdc.cam.ac.uk. Supplementary data associated with this article can be found, in the online version, at doi:10.1016/j.poly.2007.08.012.

References

[1] N. Nishinaga, H. Tomita, J. Mol. Catal. 7 (1980) 178.
[2] Y.-J. Hu, X.-D. Huang, Z.-J. Yao, Y.-L. Wu, J. Org. Chem. 63 (1998) 2456.
[3] B. Speiser, H. Stahl, Angew. Chem., Int. Ed. Engl. 34 (1995) 1086.
[4] E.C. Niederhoffer, J.H. Timmons, A.E. Martell, Chem. Rev. 84 (1984) 137.
[5] N. Bresciani-Pahor, M. Forcolin, L.G. Marzilli, L. Randaccio, M.F. Summers, P.J. Toscano, Coord. Chem. Rev. 63 (1985) 1.
[6] R. Cini, S.J. Moore, L.G. Marzilli, Inorg. Chem. 37 (1998) 6890.
[7] S.M. Polson, R. Cini, C. Pifferi, L.G. Marzilli, Inorg. Chem. 36 (1997) 314.
[8] S. Hirota, E. Kosugi, L.G. Marzilli, O. Yamauchi, Inorg. Chim. Acta 275–276 (1998) 90.
[9] J.P. Collman, H. Takaya, B. Winkler, L. Libit, S.S. Sokoon, G.A. Rodley, W.T. Robinson, J. Am. Chem. Soc. 95 (1973) 1656.
[10] A. Böttcher, T. Takeuchi, K.I. Hardcastle, T.J. Meade, H.B. Gray, Inorg. Chem. 36 (1997) 2498.
[11] D. Chen, A.E. Martell, Inorg. Chem. 26 (1987) 1026.
[12] E. Kitaura, Y. Nishida, H. Okawa, S. Kida, J. Chem. Soc., Dalton Trans. 12 (1987) 3055.
[13] H. Kumita, K. Jitsukawa, H. Masuda, H. Einaga, Inorg. Chim. Acta 283 (1998) 160.
[14] S. Yamada, Coord. Chem. Rev. 190–192 (1999) 537.
[15] R. Dreos, G. Nardin, L. Randaccio, P. Siega, G. Tauzher, V. Vrdoljak, Inorg. Chim. Acta 349 (2003) 239.
[16] R.L. Lucas, M.K. Zart, J. Murkerjee, T.N. Sorrell, D.R. Powell, A.S. Borovik, J. Am. Chem. Soc. 128 (2006) 15476.
[17] B.M. Gatehouse, B.E. Reichert, B.O. West, Acta Crystallogr., Sect. B 32 (1976) 30.
[18] M. Amirnasr, K.J. Schenk, A. Gorji, R. Vafazadeh, Polyhedron 20 (2001) 695.
[19] M. Amirnasr, R. Vafazadeh, Int. J. Chem. Kinet. 34 (2002) 387.
[20] M. Amirnasr, R. Vafazadeh, A. Mahmoudkhani, Can. J. Chem. 80 (2002) 1196.
[21] M. Amirnasr, V. Langer, N. Rasouli, M. Salehi, S. Meghdadi, Can. J. Chem. 83 (2005) 2073.
[22] N.G. Connelly, W.E. Geiger, Chem. Rev. 96 (1996) 877.
[23] M. Hariharan, F.L. Urbach, Inorg. Chem. 8 (1969) 556.
[24] X-RED32, Version 1.31. Stoe & Cie GmbH, Darmstadt, Germany, 2005.
[25] P.T. Beurskens, G. Beurskens, W.P. Bosman, R. de Gelder, S. Garcia-Granda, R.O. Gould, R. Israël, M.M. Smits, The DIRDIF96 Program System, Crystallography Laboratory, Nijmegen University, The Netherlands, 1996.
[26] G.M. Sheldrick, SHELXL97, Göttingen University, Germany, 1997.
[27] Nonius, COLLECT, Nonius BV, Delft, The Netherlands, 1998.
[28] A.J.M. Duisenberg, L.M.J. Kroon-Batenburg, A.M.M. Schreurs, J. Appl. Cryst. 36 (2003) 220.
[29] G.M. Sheldrick, SADABS, Göttingen University, Germany, 2006.
[30] A. Altomare, M.C. Burla, M. Camalli, G.L. Cascarano, C. Giacovazzo, A. Guagliardi, A.G.G. Moliterni, G. Polidori, R. Spagna, J. Appl. Cryst. 32 (1999) 115.
[31] G.M. Sheldrick, SHELXTL Version 6, Bruker AXS Inc., Madison, WI, USA, 2001.
[32] X.-H. Shi, X.-Z. You, C. Li, B.-L. Song, T.-H. Li, X.-Y. Huang, Acta Crystallogr., Sect. C 51 (1995) 206.
[33] R.C. Felicio, E.T.G. Canalheiro, E.R. Dockal, Polyhedron 20 (2001) 261.
[34] S. Zolezzi, A. Decinti, E. Spodine, Polyhedron 18 (1999) 897.
[35] Y.-L. Zhang, W.-J. Ruan, X.-J. Zhao, H.-G. Wang, Z.-A. Zhu, Polyhedron 22 (2003) 1535.
[36] A. Bigotto, G. Costa, G. Mestroni, G. Pellizer, A. Puxeddu, E. Reisenhofer, L. Stefani, G. Tauzher, Inorg. Chim. Acta 4 (1970) 41.

present, various theoretical researches have been carried out in an attempt to correlate experimental results to theoretical predictions. In particular, quantum chemical studies applying the density functional theory (DFT) method in this field have been reported [16], because the DFT method can better consider electron correlation energies and obviously reduces the computation expenses and suits to compute such complexes with their ground states being a singlet state. It is well documented that the lowest energy transitions of some Ru(II) polypyridyl complexes can be assigned to a metal-to-ligand charge-transfer (MLCT) and the HOMO–LUMO (HOMO: highest occupied molecular orbital; LUMO: lowest unoccupied molecular orbital) energy difference between the corresponding complexes obtained from computations with the DFT/B3LYP method is closely correlative to $\Delta E_{1/2}$ ($E_{1/2ox} - E_{1/2red}$) [17]. The DFT calculations for the stacked DNA base-pair model with backbones have also been reported and it is well established that the energies of the HOMO and the occupied MO (the molecular orbital) near the HOMO are rather high and predominantly populated on the base pairs of DNA [18].

Herein, we report the synthesis and characterization of MIP {MIP = 2-(2,3-methylenedioxyphenyl)imidazo[4,5-*f*]1,10-phenanthroline}, a new polypyridyl ligand, and its ruthenium(II) complexes (Scheme 1) $[Ru(phen)_2(MIP)]^{2+}$ (**1**) (phen = 1,10-phenanthroline) and $[Ru(dmp)_2MIP]^{2+}$ (**2**) (dmp = 2,9-dimethyl-1,10-phenanthroline). The DNA-binding properties of the two complexes were explored by spectroscopic and viscosity measurements, and their photocleavage behavior toward pBR-322 was investigated. Theoretical calculations with the DFT method for the two complexes were also carried out and further applied to explain the obtained experimental observations. We hope that our results will aid in the understanding of DNA recognition and binding by Ru(II) complexes, as well as laying the foundation for the rational design of new photoprobes and photonucleases for DNA.



Scheme 1. Structures, syntheses of the ligand MIP and its Ru(II) complexes **1** and **2**.

2. Experimental

2.1. Materials and chemicals

The compounds 1,10-phenanthroline-5,6-dione [19], *cis*-$[Ru(phen)_2Cl_2]\cdot 2H_2O$ and *cis*-$[Ru(dmp)_2Cl_2]\cdot 2H_2O$ [20] were prepared according to literature procedures. All other materials were commercially available and of reagent grade, and were used without further purification unless otherwise noted.

2.2. Physical measurements

Microanalyses (C, H and N) were carried out on a Perkin–Elmer 240Q elemental analyzer. ^{1}H NMR spectra were recorded on an Avance-400 spectrometer with DMSO-d_6 (dimethyl sulfoxide) as the solvent at room temperature and TMS (tetramethylsilane) as the internal standard. UV–Vis (UV–visible) spectra were recorded on a Perkin–Elmer Lambda-25 spectrophotometer, and emission spectra were recorded on a Perkin–Elmer LS-55 luminescence spectrometer at room temperature. Fast atom bombardment mass spectra (FAB-MS) were recorded on a VG ZAB-HS spectrometer in a 3-nitrobenzyl alcohol matrix. Electrospray mass spectra (ES-MS) were recorded on a LQC system (Finngan MAT, USA) using CH_3CN as the mobile phase. The spray voltage, tube lens offset, capillary voltage and capillary temperature were set at 4.50 KV, 30.00 V, 23.00 V and 200 °C, respectively, and the quoted *m*/*z* values are for the major peaks in the isotope distribution. Circular dichroism (CD) spectra were measured on a JASCO-J715 spectropolarimeter.

Cyclic voltammograms measurements were performed at room temperature on a CHI 660A Electrochemical Workstation. The supporting electrolyte was 0.1 mol/L tetrabutylammonium (Nbu_4) perchlorate. All samples were purged with nitrogen prior to measurement. A standard three-electrode system comprising of a platinum microcylinder working electrode, platinum-wire auxiliary electrode and a saturated calomel reference electrode (SCE) was used. The scan rate of all voltammograms was 200 mV/s.

All spectroscopic titrations were carried out in buffer A (5 mM Tris–HCl, 50 mM NaCl, pH 7.2, *Tris* = Tris-(hydroxymethyl)methylamine) at room temperature. A solution of CT-DNA in the buffer gave a ratio of UV absorbances at 260 and 280 nm of *ca.* 1.8:1–1.9:1, indicating that the DNA was sufficiently free of protein [21]. The concentration of CT-DNA was determined spectrophotometrically ($\varepsilon_{260} = 6600\ cm^{-1}$) [22]. Stock solutions were stored at 4 °C and used within 4 days. Titration experiments were performed by using a fixed Ru(II) complex concentration (20 μM), to which CT-DNA stock solution was added. The ruthenium solutions employed were 20 μM in concentration and CT-DNA was added up to a [DNA]/[Ru] ratio of 0.75:1 and 0.25:1 for complexes **1** and **2**, respectively. The complex-DNA solutions were allowed to equilibrate for 5 min before spectra were recorded.

Viscosity measurements were carried out with an Ubbelodhe viscometer maintained at a constant temperature of 30.0 ± 0.1 °C in a thermostated bath. DNA samples of *ca.* 200-bp average length were prepared by sonication [23]. The flow time was measured with a digital stopwatch, and each sample was tested three times to get an average calculated flow time. Data were presented as $(\eta/\eta_0)^{1/3}$ versus binding ratio [24], where η is the viscosity of DNA in the presence of complex, η_0 being the viscosity of free DNA.

For the gel-electrophoresis experiments, supercoiled pBR-322 DNA (0.1 μg) was treated with **1** or **2** in buffer B (50 mM Tris-acetate, 18 mM NaCl buffer, pH 7.2). After pre-incubation of the solutions in the dark for 1 h, the samples were irradiated for 60 min inside the sample chamber of the spectrofluorimeter (λ_{ex} 400 ± 5 nm, slit-width 5 nm). The samples were then analyzed by gel-electrophoresis for 30 min at 75 V in *Tris*-acetate buffer containing 1% agarose gel. The gel was stained with ethidium bromide (EB; 1 μg/mL^{-1}) and photographed under UV light.

2.3. Synthesis

2.3.1. MIP

A mixture of 2,3-methylenedioxy-benzaldehyde (0.23 g, 1.5 mmol), 1,10-phenanthroline-5,6-dione (0.11 g, 0.5 mmol), ammonium acetate (2.31 g, 30 mmol), and glacial acetic acid (15 ml) was heated at reflux with stirring for 2 h. The cooled solution was filtered, diluted with H_2O and neutralized with concentrated aqueous ammonia. The yellow precipitate was collected and purified by column chromatography on alumina with ethanol–toluene (4:1, v/v) as the eluant to afford MIP as an amorphous yellow solid. Yield: 0.21 g, 41%. *Anal.* Calc. for $C_{20}H_{13}N_4O_{2.5}$: C, 68.75; H, 3.72; N, 16.04. (Note: half a molecule of crystal water has been assumed when calculating the elemental composition.) Found: C, 68.34; H, 3.91; N, 15.70%. FAB-MS: m/z = 341.6 [M+1].

2.3.2. [Ru(phen)$_2$(MIP)](ClO$_4$)$_2$ · 2.5H$_2$O (1)

A mixture of *cis*-[Ru(phen)$_2$(Cl)$_2$] · H_2O (151 mg, 0.25 mmol), MIP (85 mg, 0.25 mmol), and ethylene glycol (15 ml) was thoroughly deoxygenated. The purple mixture was heated for 8 h at 120 °C under Ar atmosphere. When the solution finally turned red, it was cooled to room temperature, and an equal volume of saturated aqueous sodium perchlorate solution was added under vigorous stirring. The red solid was collected and washed with small amounts of H_2O, EtOH, and Et_2O, dried under vacuum, and purified on a neutral alumina column with acetonitrile–toluene (v/v, 4:1) as the eluant. Yield: 0.19 g, 73%. *Anal.* Calc. for $C_{44}H_{33}N_8Cl_2O_{12.5}Ru$: C, 50.13; H, 3.13; N, 10.64. Found: C, 49.97; H, 3.21; N, 10.36%. λ_{max}/nm (ε/dm^3 mol^{-1} cm^{-1}, CH_3CN): 455 (16150), 264 (81350), 218(77200). ^{1}H NMR (400 MHz, DMSO-d_6 (dimethyl sulfoxide); d, doublet; s, singlet; t, triplet; m, multiplet): 9.08 (d, 2H, J = 8.5), 8.75 (d, 4H, J = 8), 8.37 (s, 4H), 8.11 (d, 2H, J = 1), 8.10 (d, 2H, J = 1), 7.90 (d, 2H, J = 5.5), 7.71–7.77 (m, 8H), 7.03 (d, 1H, J = 5.0), 6.23 (s, 2H). ES-MS (CH_3CN): m/z 900.9 ([M−ClO$_4$]$^+$), 801.3 ([M−2ClO$_4$−H]$^+$), 401.3 ([M−2ClO$_4$]$^{2+}$).

2.3.3. [Ru(dmp)$_2$(MIP)](ClO$_4$)$_2$ · 2H$_2$O (2)

Prepared analogous to **1**, but from *cis*-[Ru(2,9-Me$_2$phen)$_2$(Cl)$_2$] · 2H_2O (0.14 g, 0.25 mmol). Yield: 0.15 g, 57%. *Anal.* Calc. for $C_{48}H_{40}N_8Cl_2O_{12}Ru$: C, 52.74; H, 3.69; N, 10.26. Found: C, 52.55; H, 3.75; N, 10.13%. λ_{max}/nm (ε/dm^3 mol^{-1} cm^{-1}, CH_3CN): 463 (13810), 271 (69005), 225 (71765). ^{1}H NMR (400 MHz, DMSO-d_6): 8.88 (d, 2H, J = 8.5), 8.77 (d, 2H, J = 8), 8.41 (d, 2H, J = 8.5), 8.39 (d, 2H, J = 8.5), 8.22 (d, 2H, J = 8.5), 7.95 (d, 2H, J = 8.5), 7.22 (d, 1H, J = 9.5), 7.36 (d, 1H, J = 8.5), 7.29 (dd, 2H, J_1 = 6, J_2 = 7.5), 7.08 (d, 2H, J = 4.5), 6.87 (d, 2H, J = 7.5), 6.09 (s, 1H), 1.90 (s, 6H), 1.72 (s, 6H). ES-MS (CH_3CN): m/z 957.2 ([M−ClO$_4$]$^+$), 857.3 ([M−2ClO$_4$−H]$^+$), 429.4 ([M−2ClO$_4$]$^{2+}$).

2.4. Theoretical calculations

Each of these is complexes formed from a Ru(II) ion, one main-ligand (MIP) and two ancillary ligand (phen or dmp). All computations were performed with the G98 quantum chemistry program-package [25], and the DFT-B3LYP method [26–28] and LanL2DZ basis set [29] were adopted (Note: Due to condition limits, we were not able to carry out higher level calculations). The full geometry optimization computations for the ground states of these complexes with a singlet state were carried out. In order to vividly depict the details of the frontier molecular orbital interactions, the stereographs of some related frontier molecular orbitals of the complexes were drawn with the Molden v3.7 program [30] based on the obtained computational results.

3. Results and discussion

3.1. Synthesis and characterization

An outline of the synthesis of the Ru(II) complexes **1** and **2** with the new MIP ligand is presented in Scheme 1. The MIP ligand was prepared through the condensation of 1,10-phenanthroline-5,6-dione (**3**) with 2,3-methylenedioxy-benzaldehyde (**4**) on the basis of the method for the preparation of imidazole rings according to Steck and Day [31]. The complexes [Ru(phen)$_2$(MIP)]$^{2+}$ (**1**) and [Ru(dmp)$_2$(MIP)]$^{2+}$ (**2**) were then prepared in relatively good yield (61% and 73%, respectively) by the reaction of MIP with *cis*-[Ru(phen)$_2$Cl$_2$] · 2H_2O and *cis*-[Ru(dmp)$_2$-(Cl)$_2$] · 2H_2O, respectively, in the appropriate mole ratios, using ethylene glycol as the solvent. The desired Ru(II) complexes were isolated as the corresponding perchlorates, and were purified by column chromatography. In the ESI mass spectra of complexes **1** and **2**, ([M−ClO$_4$]$^+$),

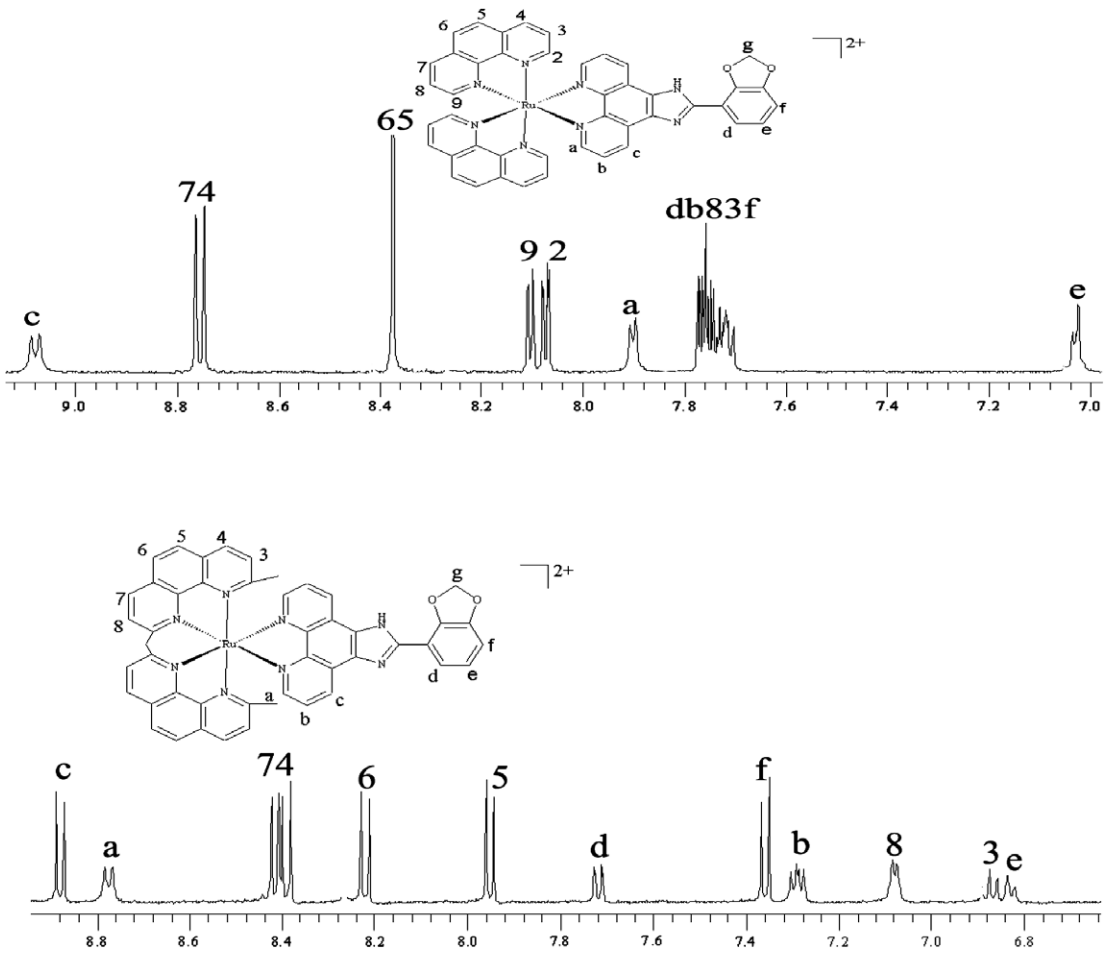


Fig. 1. ^{1}H NMR spectra of complexes **1** (top) and **2** (bottom).

($[M-2ClO_4-H]^+$) and ($[M-2ClO_4^-]^{2+}$) were observed, and the determined molecular weights were consistent with the expected values.

Both complexes **1** and **2** give well-defined ^{1}H NMR spectra (Fig. 1), permitting unambiguous identification and assessment of purity. The ^{1}H NMR chemical shifts were assigned by the aid of ^{1}H, ^{1}H–COSY experiments, and by comparison with the values of similar compounds [32–34]. Due to the shielding influences of the adjacent MIP and phen (or dmp) moieties, the phen (or dmp) H-atoms of complexes **1** and **2** exhibit two distinct sets of signals. In addition, the NH proton of MIP was not observed due to rapid H^+ exchange between the two N atoms of the imidazole ring. A similar case has been reported previously [35].

The electrochemical behaviors of the two complexes have been determined in acetonitrile. Each complex exhibits one oxidation and three reduction waves in the sweep range from −2.0 to +2.0 V (Table 1), the half-wave potentials $E_{1/2}$ being 1.61, −0.66, −1.36 and −1.54 V versus SSCE for complex **1** and 1.59, −0.76, −1.21 and −1.41 versus SSCE for complex **2**. The electrochemical behavior of the Ru(II) polypyridyl complexes have been rationalized in terms of a metal-based oxidation and a series of reductions which are ligand-based occurring in a stepwise manner for each π^* system [36]. As expected, the oxidation potentials of complexes **1** and **2** are more positive than that of $[Ru(bpy)_3]^{2+}$, in accord with the extension of the corresponding π framework. With reference to previous studies on similar systems [37,38], the first reduction, which is

Table 1
Electrochemical and absorption data of the ruthenium(II) complexes

Complex	$E_{1/2}$ (V) vs. SCE[a]				λ_{max}/nm[b] (ε/dm^3 mol^{-1} cm^{-1})
	$Ru^{II/III}$	Ligand reduction			
1	1.61	−0.66	−1.36	−1.54	455 (16150), 264 (81350), 218 (77200)
2	1.59	−0.76	−1.21	−1.41	463 (13810), 271 (69005), 225 (71765)

[a] All complexes were measured in 0.1 M NBu_4ClO_4–CH_3CN, error in potentials was ± 0.02 V; $T = 23 \pm 1$ °C; scan rate = 100 mV S^{-1}.
[b] In CH_3CN.

usually controlled by the ligand having the most lowest unoccupied molecular orbital (LUMO) [39,40], is assigned to a reduction centered on MIP, and the last reductions are characteristic of the co-ligand (phen or dmp) [41].

The UV–Vis absorption spectra of complexes **1** and **2** showed three well-resolved bands in the range 200–600 nm, characterized by intense $\pi \rightarrow \pi^*$ ligand transitions in the UV region, as well as by a metal-to-ligand charge-transfer (MLCT) transition in the VIS region (Table 1). Broad MLCT absorption bands appear at 455 and 463 nm for complexes **1** and **2**, respectively, and are attributed to Ru(dπ)→ MIP(π^*) transitions. These bands are bathochromically shifted relative to those of $[Ru(bpy)_3]^{2+}$ (452 nm) [24], in accord with the extension of the corresponding π framework. The signals below 400 nm are assigned to internal $\pi \rightarrow \pi^*$ transitions of the ligands, by comparison with the spectra of $[Ru(bpy)3]^{2+}$.

3.2. DNA-binding studies

3.2.1. Viscosity measurements

Hydrodynamic measurements sensitive to length changes, as reflected in viscosity and sedimentation, are regarded as the least ambiguous and the most-critical tests of a binding model in solution in the absence of crystallographic structural data [42]. A classical intercalation model demands that the DNA helix lengthens as base pairs are separated to accommodate the binding ligand, which, in turn, leads to an increase in the viscosity of DNA [42].

In Fig. 2, the change in viscosity on rod-like DNA is shown in the presence of complexes **1** and **2**, $[Ru(bpy)_3]^{3+}$ and ethidium bromide (EB). Whereas EB, a well-known DNA intercalator, gave rise to a strong change in DNA viscosity upon complexation, $[Ru(bpy)_3]^{2+}$, which binds by electrostatic intercalations only, exerted essentially no such effect. As can be seen from Fig. 2, upon increasing the amounts of complex **1**, the relative viscosity of DNA increases steadily, similar as in the case of EB. By contrast, on increasing the amounts of complex **2**, the relative viscosity of DNA decreases. The change in relative viscosity, expected to correlate with the compounds DNA-intercalating potential, followed the order EB > complex **1** > complex **2**. These results suggest that complex **1** binds to DNA through a classical intercalation model and complex **2** binds to DNA by the partial, non-classical intercalation model. This difference of the DNA-binding model between complexes **1** and **2** should be caused by the different ancillary ligand of the two complexes. For complex **2**, due to the steric hindrance of the methyl groups located at the 2- and 9-positions of the phen ring in the dmp ancillary ligand, the complex could not completely intercalate into DNA base pairs. The partial intercalation may act as a "wedge" to pry apart one side of a base-pair stack, as observed for Δ-$[Ru(phen)_3]^{2+}$ [43,44], but not fully separate the stack as required by the classical intercalation model. This would cause a static bend or kink in the helix and decrease the viscosity of DNA.

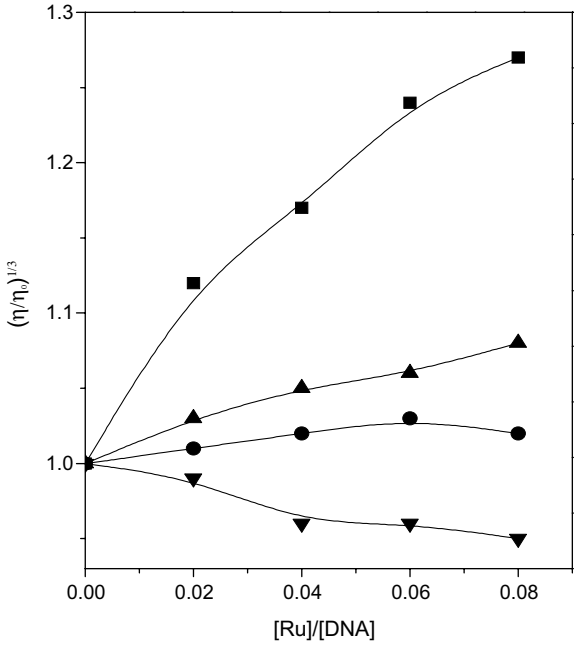


Fig. 2. Effect of increasing amounts of ethidium bromide (■), $[Ru(bpy)_3]^{2+}$ (●), **1** (▲) and **2** (▼) on the relative viscosity of CT-DNA. Total DNA concentration: 0.5 mM, $T = 30 \pm 0.1$ °C.

3.2.2. Absorption spectra studies

The application of electronic absorption spectroscopy in DNA-binding studies is one of the most useful techniques [45]. Complex binding with DNA through intercalation usually results in hypochromism and bathchromism due to the intercalative mode involving a strong stacking interaction between an aromatic chromophore and the base pairs of DNA. The extent of the hypochromism commonly parallels the intercalative binding strength.

The absorption spectra of the Ru(II) complexes **1** and **2** (at constant concentration) in the absence and presence of CT-DNA are shown in Fig. 3. As the concentration of DNA is increased, for complex **1** the hypochromism reaches about 11.4% at 267 nm with a red shift of 8 nm at a [DNA]/[Ru] ratio of 3. The MLCT band at 469 nm shows hypochromism by about 23.5% and a red shift of 2 nm under the same conditions. For complex **2**, upon addition of DNA, the IL band at 276 nm exhibits hypochromism of about 27.4% with a 4 nm red shift at a [DNA]/[Ru] ratio of 9.5. The MLCT band at 477 nm shows hypochromism by about 7.7% and a red shift of 10 nm under the same conditions. Obviously, these spectral characteristics suggest that both complexes interact with DNA most likely through a mode that involves a stacking interaction between the methylenedioxyphenyl chromophore and the base pairs of DNA.

To quantitatively compare the binding strengths of the two complexes, their intrinsic binding constants K_b were determined by UV–Vis titration. This was done by monitoring the change in absorbance at 267 nm for complex **1**

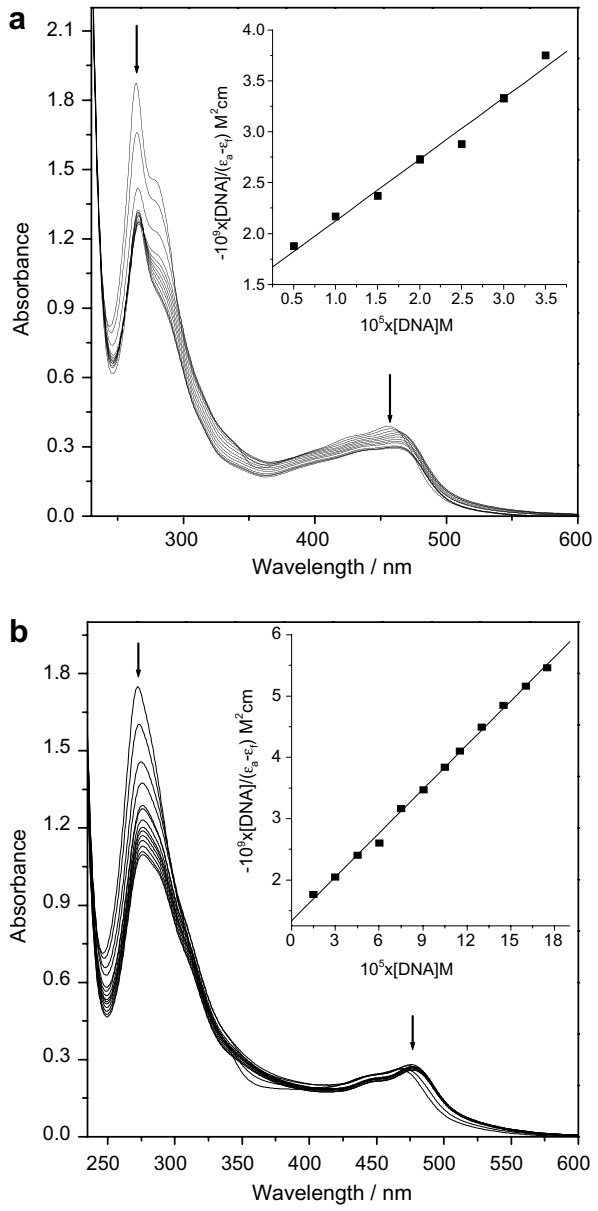


Fig. 3. Absorption spectra of complexes **1** (a) and **2** (b) in aq. Tris–HCl buffer upon addition of CT-DNA. $[Ru] = 2 \times 10^{-5}$ M, $[DNA] = (0–17.5) \times 10^{-5}$ M. Arrow shows the absorbance changes upon increasing DNA concentration. Inset: plots of $-10^9 \times [DNA]/(\varepsilon_a - \varepsilon_f)$ (in M^2 cm) vs. DNA] (in M) for the titration of DNA with the complex for the determination of the binding constant K_b.

and 276 nm for complex **2** with increasing concentration of DNA, using the following equation [46]:

$$[DNA]/(\varepsilon_a - \varepsilon_f) = [DNA]/(\varepsilon_b - \varepsilon_f) + 1/[K_b(\varepsilon_b - \varepsilon_f)]$$

Here, [DNA] is the concentration of DNA in base pairs, and ε_a, ε_f and ε_b are the extinction coefficients of the apparent, free and bound metal complexes, respectively. When plotting $[DNA]/(\varepsilon_a - \varepsilon_f)$ versus [DNA], K_b is given by the ratio of the slope to the intercept. The intrinsic binding constants K_b of complexes **1** and **2** were thus determined as $3.96 \times 10^4\ M^{-1}$ and $1.08 \times 10^4\ M^{-1}$, respectively. For comparison, the intrinsic binding constants K_b of typical 'intercalative-type' Ru(II) complexes are in the range 1.1×10^4 to $4.8 \times 10^4\ M^{-1}$ [47], whereas that of the parent complex $[Ru(phen)_3]^{2+}$ is $5.5 \times 10^3\ M^{-1}$ [47]. The intrinsic binding constants K_b of both complexes with DNA follows the order K_b (**1**) > K_b (**2**), in accord with the above viscosity studies, that is complex **1** intercalates more strongly than complex **2**. The result indicates that on going from the ancillary ligand phen to dmp, the hydrophobicity of the ancillary ligand dmp of complex **2** is greater than that of complex **1**, however, the steric hindrance of complex**2** is bigger than that of complex **1**. The later factor is not advantageous to the DNA-binding of complex **2**, in particular, in the circumstances that the ancillary ligands contain a steric hindrance group (methyl) results in lower DNA-binding affinity relative to the ancillary ligand phen. Therefore, synthetically considering these factors, the difference of the DNA-binding affinity of complexes **1** and **2** can be well understood.

3.2.3. Steady-state emission studies

In the absence of DNA, complex **1** is luminescent in *Tris* buffer at ambient temperature, with a fluorescence maximum at 591 nm. As shown in Fig. 4, upon addition of CT-DNA, the fluorescence-emission intensity increases by a factor of *ca.* 2.88 and saturates at a [DNA]/[Ru] ratio of 13.5. This indicates that complex **1** strongly interacts with DNA, which efficiently 'protects' it, since the hydrophobic environment inside the DNA helix reduces the accessibility of solvent H_2O to the complex, and because complex mobility is restricted at the binding site this results in a decrease of the vibrational modes of relaxation and thus higher emission intensity.

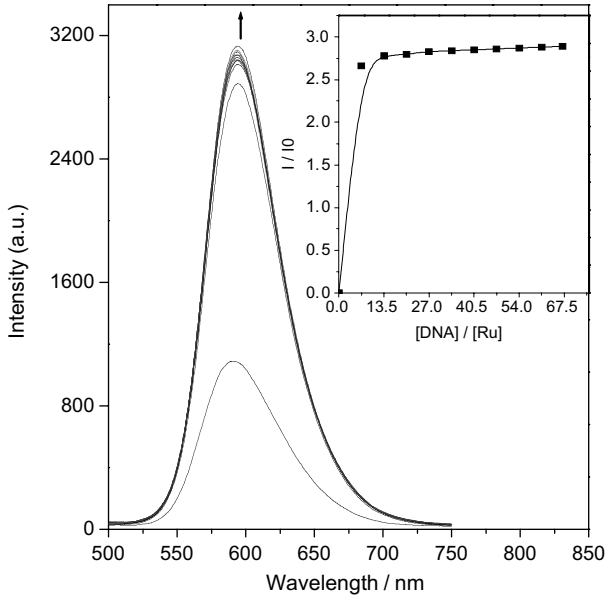


Fig. 4. Fluorescence spectra of **1** in Tris–HCl buffer at 298 K in the absence and presence of CT-DNA. Arrow shows the intensity changes upon increasing the DNA concentration. Insert: plots of relative integrated emission intensity vs. [DNA]/[Ru].

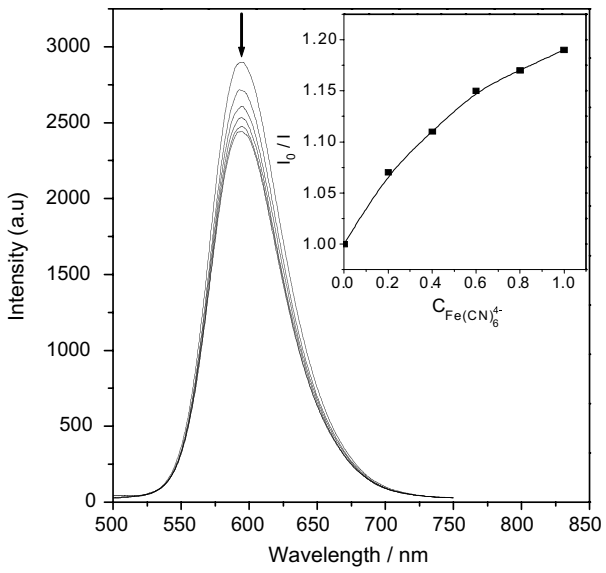


Fig. 5. Fluorescence quenching of **1** by $[Fe(CN)_6]^{4-}$. $[Ru] = 2 \times 10^{-6}$ M, $[DNA]/[Ru] = 40$), $[K^+] = 4 \times 10^{-3}$ M. $[Fe(CN)_6]^{4-} = 0$–1.0 mM. Inset: plots of I_0/I vs. $[Fe(CN)_6]^{4-}$ (in mM). Where I_0 and I are the fluorescence intensities in the absence and presence of the quencher, respectively. Insert: Fluorescence quenching curve of DNA-bound EB by complex **2**.

Steady-state fluorescence quenching experiments with $[Fe(CN)_6]^{4-}$ as a quencher can provide some information about complex binding to DNA, but they do not indicate the binding modes. We decided to perform some experiments at ambient temperature, using a similar method as that described by Satyanarayana et al. [44]. In experiments at constant ionic strength, KCl was added along with $K_4[Fe(CN)_6]$. As illustrated in Fig. 5, the fluorescence quenching curves at constant ionic strength were non-linear. The final fluorescence intensity was originally 83.3%. The result thus further confirms that complex **1** binds to DNA strongly.

For complex **2**, no emission was observed either in *Tris* buffer or in the presence of CT-DNA. It also shows no photoluminescence in any of the organic solvents examined. This could be caused by vibronic coupling between the methyl groups of dmp ligand and solvent, leading to a dissipation of energy in a non-radiative process. Similar results have been observed for this type of Ru(II) complexes [42,48]. On the other hand, this effect could also be caused by a reduced ligand field, making the excited states accessible. The reduced ligand is confirmed by the computed coordination bond lengths (Ru–N), which are 0.2126 nm (main-ligand) and 0.2156 nm (co-ligand) for complex **2**, and 0.2104 (main-ligand) and 0.2106 nm (co-ligand) for complex **1**. Some computed frontier molecular orbital energies are also given in Table 2 and Fig. 6. They show that the energy of the LUMO for complex **2** is much higher than that for complex **1**, so the excited state of complex **2** should be unstable, and can easily return to the ground state through non-radiative energy dissipation. Steady-state competitive binding experiments using complex **2** as a quencher may give further information about the binding of the complex to DNA. As we know, EB emits intense fluorescence light in the presence of DNA, due to its strong intercalation between the adjacent DNA base pairs. It was previously reported that the enhanced fluorescence could be quenched, at least partially, by the addition of a second molecule [49,50]. The extent of quenching fluorescence of EB bound to DNA is used to determine the extent of binding of the second molecule to DNA. The emission spectra of EB bound to DNA in the absence and the presence of complex **2** is shown in Fig. 7. From Fig. 7, we can see that the addition of complex **2** to DNA pretreated EB caused appreciable reduction in the emission intensity of 31.4% than that observed in the absence of complex **2** at a [Ru]/[DNA] ratio of 0.2. This indicated that complex **2** could compete with EB in binding to DNA. The fluorescence quenching curves of DNA-bound EB by complex **2** (insert in Fig. 7) illustrates that the quenching of EB bound to DNA by complex **2** is in good agreement with the linear Stern–Volmer equation. This also proves that the partial replacement of EB bound to DNA by complex **2** results in a decrease of the fluorescence intensity.

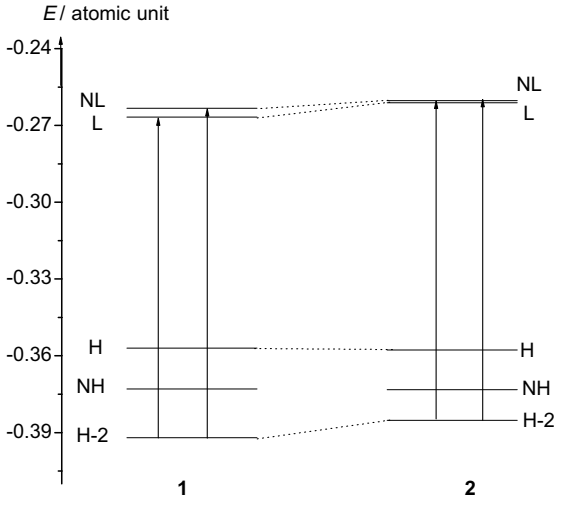


Fig. 6. Schematic diagram of energies and related ^{1}MLCT transitions of complexes **1** and **2**.

Table 2
Some frontier molecular orbital energies (ε_i/atomic unit) of complexes **1** and **2** (1 atomic unit = 27.21 eV)

Compound	Occ[a]	Occ	HOMO	LUMO	Vir[b]	Vir	$\Delta\varepsilon_{L-H}$	$\Delta\varepsilon_{L-NH}$	$\Delta\varepsilon_{L-(H-2)}$
1	−0.3920	−0.3730	−0.3570	−0.2667	−0.2633	−0.2600	0.0903	0.0937	0.1253
2	−0.3852	−0.3732	−0.3577	−0.2612	−0.2603	−0.2563	0.0965	0.0974	0.1240

[a] OCC: Occupied molecular orbital; HOMO (or H): The highest Occ.
[b] Vir: Virtual molecular ortibal; LUMO (or L): The lowest Vir.

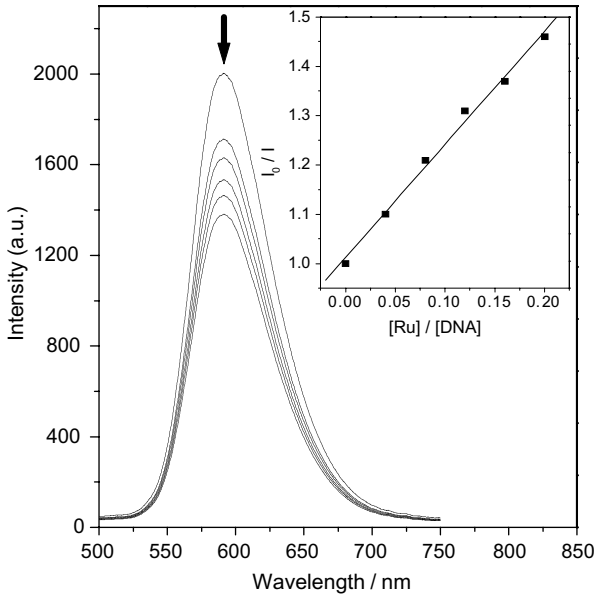


Fig. 7. Fluorescence spectra of EB bound DNA in the presence of **2**. [EB] = 20 μM, [DNA] = 100 μM, [Ru]/[DNA] = 0.04, 0.08, 0.12, 0.16 and 0.2. Arrow shows the intensity changes upon increasing the concentration of **2**. Insert: Fluorescence quenching curve of DNA-bound EB by **2**.

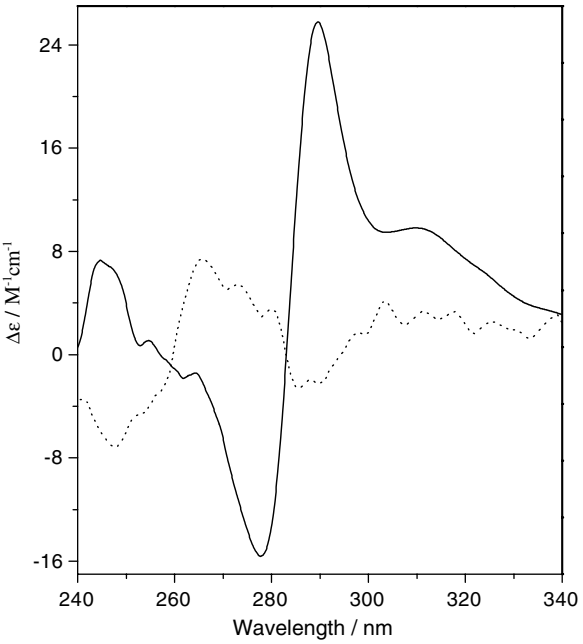


Fig. 8. CD spectra of **1** (…) and **2** (---) after 42 h of dialysis against CT-DNA in stirred aq. solution.

3.2.4. Enantioselective binding

Equilibrium dialysis experiments offer the opportunity to examine the enantioselectivity of complexes binding to DNA. According to the proposed binding model by Barton [49], the Δ enantiomer of the complex, a right-handed propeller-like structure, displays a greater affinity than the Λ enantiomer with the right-handed CT-DNA helix due to more-appropriate steric matching. Thus, complexes **1** and **2** were dialyzed against CT-DNA for 42 h and then subjected to circular dichroism (CD) analysis. In Fig. 8, the CD spectra in the UV region of the dialysates of complexes **1** and **2** are shown. The dialysate of complex **1** (dotted line) shows two CD signals with a positive peak at 265 and a negative peak at 285 nm, while complex **2** (solid line) shows strong CD signals with a positive peak at 289 nm and a negative peak at 278 nm. Furthermore, the CD signals of complex **1** are in opposition to those of complex **2**. Although neither of the complexes was resolved into the pure enantiomers and although we could not determine which enantiomer binds preferentially to CT-DNA, it is evident that both **1** and **2** interact enantioselectively with CT-DNA. The stronger CD signals of complex **2** suggest a large DNA-binding discrimination between its two antipodes. These results indicate that the ancillary ligands have a significant influence on the interaction of the enantioselectivity of Ru(II) complexes with DNA.

3.3. Photoactivated cleavage of pBR-322 DNA by Ru(II) complexes

The cleavage of plasmid DNA can be monitored by agarose–gel electrophoresis. When circular plasmid DNA is subject to electrophoresis, relatively fast migration is generally observed for the intact supercoiled form (I). When scission occurs on one strand (nicking), the supercoil relaxes to generate a slower-moving, open-circular form (II). When both strands are cleaved, a linear form (III) is generated, migrating between type-I and type-II DNA [50].

In Fig. 9, the gel electrophoresis pattern of pBR 322 DNA is shown after incubation with complex **1** or **2** and irradiation at 400 nm. No DNA cleavage was observed for negative controls (line 0). With increasing concentration of the Ru(II) complexes (lines 1–5), the amount of type-I pBR 322 DNA was gradually diminished, whereas type-II increased. At concentrations of 40 μM of complex**1** (line 5), complete conversion of DNA from type-I to type-II was observed, in contrast to complex **2**, where only partial conversion was observed at this concentration. These results indicate that complex **1** is more effective in cleaving DNA than complex **2**. Although DNA photocleavage by $[Ru(phen)_3]Cl_2$ has been reported to involve an $^1O_2$-based mechanism, [51], the nature of the reactive intermediates

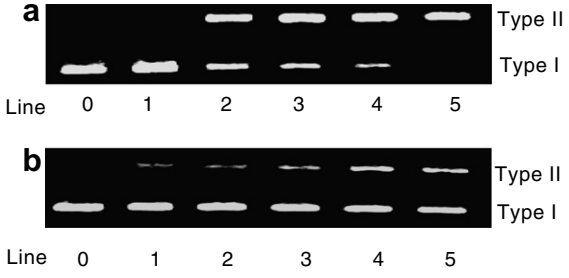


Fig. 9. Photoactivated cleavage of pBR-322 DNA in the presence of **1** (a) or **2** (b) after 60 min of irradiation at 400 nm. Lane 0, DNA alone; Lanes 1–5, at 5, 10, 15, 20 and 25 μM, Ru(II) complex, respectively.

involved in the efficient DNA photocleavage by complexes **1** and **2** observed here is not clarify. Further studies in detail are currently underway to clarify the cleavage mechanism.

3.4. Theoretical explanations of trends in DNA-binding, electrochemical and spectral properties of complexes

As is well known, there are π–π interactions in the DNA-binding of these complexes in the intercalation mode. At present, we cannot yet compute a whole supera-molecular system formed from DNA and the complex using the DFT method because such a system is too large in size to be computed, therefore, it is very important and necessary to theoretically estimate the interaction between both from their individual electronic structural characteristics.

The above-mentioned trends in DNA-binding, electrochemical and spectral properties can be explained by our theoretical computations with the DFT method and frontier molecular orbital theory [52–54]. Some computed frontier molecular energies, the schematic diagram of the max $(\lambda)^1$ MLCT transition, and the stereographs of related frontier molecular orbitals of both complexes are given in Table 2, Figs. 6 and 10 respectively. According to frontier molecular orbital theory, for a reaction controlled by orbital interactions between reactant molecules, a higher HOMO energy of one reactant molecule and a lower LUMO energy of the other are more advantageous to the reaction between the two molecules, because an electron more easily transfers from the HOMO of one reactant to the LUMO of the other in the orbital interaction. A simple and reasonable calculation model and computed results by the DFT method for stacked DNA base-pairs with backbones have been reported by Kurita and Kobayashi [18]. The reported HOMO and NHOMO energies of the DNA section model are much higher (−1.27 and −2.08 eV) [18] than our calculated LUMO and NLUMO energies (−7.07 ∼ −7.26 eV) of complexes **1** and **2**. We believe that such a trend in the relative energies should be kept in the present DNA system, because the attraction of metal complex cations with high positive charges for electrons in the frontier MOs is much stronger than that of various DNA. A lower LUMO energy of the complex in the intercalation mode should be advantageous to accept the electrons from base pairs of DNA, so that the LUMO energies of the complexes should be an important factor (but not the only one) correlating to their DNA-binding constants. The experimental results show that the trend in DNA-binding constants (K_b) is $K_b(\mathbf{1}) > K_b(\mathbf{2})$. It can be explained as follows: $K_b(\mathbf{1})$ is greater because $\varepsilon_L(\mathbf{1})$ (ε_L: energy of the LUMO) is smaller. It is why the DNA-binding constant of complex **1** is much greater than that of complex **2**, and their DNA-binding modes are also different.

The trend in electrochemical half-wave potentials of complexes **1** and **2** can be also explained by our theoretical results. From Fig. 10, we can see that the MO characterized by the metal d-orbital in the occupied frontier MO is

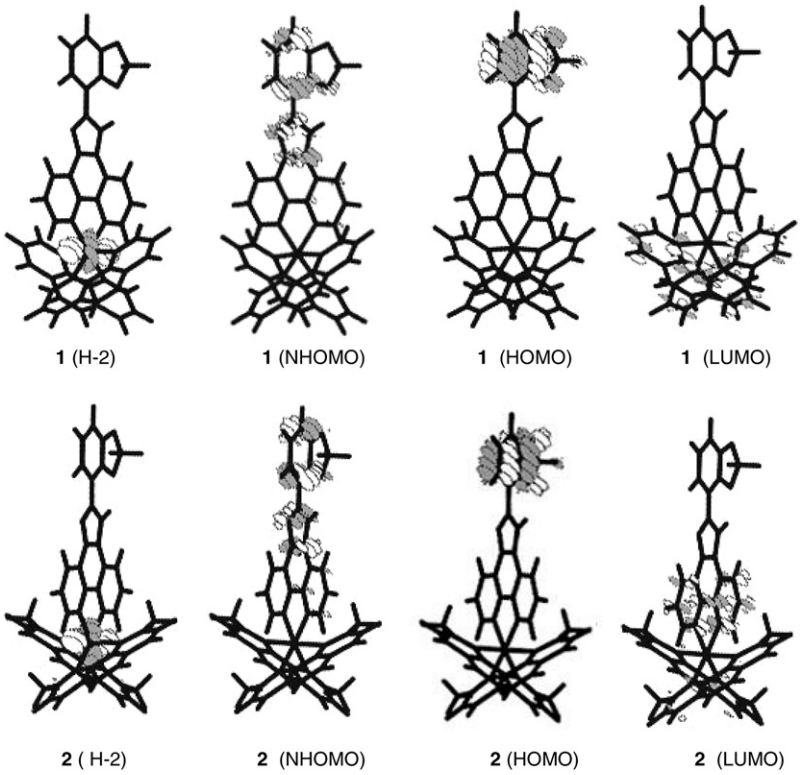


Fig. 10. Stereographs of the HOMOs and LUMOs of complexes **1** and **2**.

NHOMO-2 instead of HOMO, so that oxidation of the central metal should happen on NHOMO-2. Since the NHOMO-2 energy of complex **1** is lower than that of complex **2** (see Table 2 and Fig. 6), its oxidation potential is more positive than that of complex **2**. On the other hand, since a lower LUMO energy of the complex is advantageous for accepting the electrons offered from base-pairs of DNA, and the LUMO energy of complex **1** is also lower than that of complex **2**, the reduction potential of the former is more negative than that of the latter.

Some trends in electronic absorption spectra can also be explained by the theoretical results. From Fig. 10, we can clearly see that the lowest energy singlet metal-to-ligand charge-transfer (^{1}MLCT) bands can be assigned to the transitions from NHOMO-2 to the LUMO of the complexes. Furthermore, according to the approximate correlation of the reverse ratio of the difference between the LUMO and the HOMO energies ($\Delta\varepsilon_{L-H}$) to the experimental wavelength (λ), using the parent complex $[Ru(bpy)_3]^{2+}$ as a standard sample (experimental $\lambda = 452$ nm, $\Delta\varepsilon_{L-H} = 0.1239$ atomic unit, $\Delta\varepsilon_{L-H:}$ energy difference between the LUMO and NHOMO) [55] and $\Delta\varepsilon_{L-H}$ data of complexes **1** and **2** in Table 2, the computed max (λ)^1 MLCT absorption spectra of complexes **1** and **2** are 447 nm and 452 nm respectively, near their experimental wavelengths of 455 nm and 463 nm.

In addition, the absorption spectra also demonstrate that the corresponding energy difference between the presence and absence of DNA is small, and no special pattern changes in the absorption spectra of the complexes in the presence of DNA have been detected, except increases in hypochromism for the absorption spectra. Therefore, we can consider that there is not a great effect on the corresponding orbitals of the complexes binding to DNA (relative to the free complexes). This further suggests that the interaction between the complexes and DNA should be a weak one between the molecules, so that the properties of the ^{1}MLCT electron transition bands in the two Ru(II) complexes binding to DNA should be unchanged, in accordance with the experiments.

4. Conclusions

In summary, two novel complexes, $[Ru(phen)_2MIP]^{2+}$ (**1**) and $[Ru(dmp)_2MIP]^{2+}$ (**2**), have been synthesized and characterized. Spectroscopic studies, viscosity measurements together with equilibrium dialysis and circular dichroism spectroscopy show that complex **1** binds to CT-DNA through intercalation, and complex **2** binds to CT-DNA *via* a partial intercalative mode. Furthermore, both complexes can interact with CT-DNA enantioselectively, and complex **2** is a much better candidate as an enantioselective binder to CT-DNA than complex **1**. When irradiated at 400 nm, complex **1** was found to be a more-effective DNA-cleaving agent than complex **2**. The experimental results suggest that the ancillary ligands of Ru(II) complexes have a significant effect on the spectral properties and DNA-binding behavior of the complexes. The theoretical calculation results applying the DFT method can also be used to discuss the trend in the binding strengths or binding constants (K_b) of the complexes to DNA as well as roughly predict some of their spectral properties.

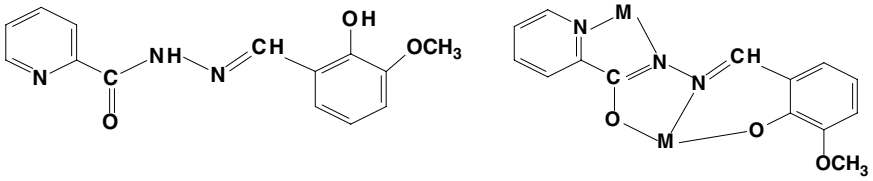
Acknowledgements

The authors thank the Provincial Natural Science Found of Hunan (06JJ5023), the Scientific Research Found of Hunan Provincial Education Department (06C828) and the Doctoral Foundation of Xiangtan University (05QDZ11) for their support of this research.

References

[1] L.N. Ji, X.H. Zou, J.G. Liu, Coord. Chem. Rev. 216–217 (2001) 513.
[2] P.P. Pelligrini, J.R. Aldrich-Wright, J. Chem. Soc., Dalton Trans. (2003) 176.
[3] C. Metcalfe, J.A. Thomas, Chem. Soc. Rev. 32 (2003) 215.
[4] J.A. Smith, J.G. Collins, B.T. Patterson, R.F. Keene, J. Chem. Soc., Dalton Trans. (2004) 1277.
[5] P.U. Maheswari, M. Palaniandavar, Inorg. Chim. Acta 357 (2004) 901.
[6] X.J. Yang, F. Drepper, B. Wu, W.H. Sun, W. Haehnel, C. Janiak, J. Chem. Soc., Dalton Trans. (2005) 256.
[7] M. Narra, P. Elliott, S. Swavey, Inorg. Chim. Acta 359 (2006) 256.
[8] D. Lawrence, V.G. Vaidyanathan, B.U. Nair, J. Inorg. Biochem. 100 (2006) 1244.
[9] D.B. Hall, R.E. Holmlin, J.K. Barton, Nature 382 (1996) 731.
[10] L. Mishra, A.K. Yadaw, S. Srivastava, A.B. Patel, New J. Chem. 24 (2000) 505.
[11] Y.J. Liu, H. Chao, Y.X. Yuan, H.J. Yu, L.N. Ji, Inorg. Chim. Acta 359 (2006) 3807.
[12] G. Yang, J.Z. Wu, L. Wang, L.N. Ji, X. Tian, J. Inorg. Biochem. 66 (1997) 141, 3807–3814.
[13] J.L. Morgan, D.P. Buck, A.G. Turley, J.G. Collins, F.R. Keene, Inorg. Chim. Acta 359 (2006) 888.
[14] L.F. Tan, H. Chao, H. Li, Y.J. Liu, B. Sun, W. Wei, L.N. Ji, J. Inorg. Biochem. 99 (2005) 513.
[15] Y. Xiong, L.N. Ji, Coord. Chem. Rev. 185–186 (1999) 711.
[16] W.J.Frisch, Æ. Frisch, Foresman, J.B. Gaussian 94 User's Reference, Gaussian Inc., Pittsburgh, PA, 1994–1995.
[17] S.R. Stoyanov, J.M. Villegas, D.P. Rillema, Inorg. Chem. 41 (2002) 2941.
[18] N. Kurita, K. Kobayashi, Compt. Chem. 24 (2000) 351.
[19] B.P. Sullivan, D.J. Salmon, T.K\J. Meyer, Inorg. Chem. 17 (1978) 3334.
[20] M. Yamada, Y. Tanaka, Y. Yoshimato, S. Kuroda, I. Shimao, Bull. Chem. Soc. Jpn. 65 (1992) 1006.
[21] J. Marmur, J. Mol. Biol. 3 (1961) 208.
[22] M.F. Reichmann, S.A. Rice, C.A. Thomas, P. Doty, J. Am. Chem. Soc. 76 (1954) 3047.
[23] J.B. Chaires, N. Dattagupta, D.M. Crothers, Biochemistry 21 (1982) 3933.
[24] G. Cohen, H. Eisenberg, Biopolymers 8 (1969) 45.
[25] M.J. Frisch, G.W. Trucks, H.B. Schlegel, G.E. Scuseria, M.A. Robb, J.R. Cheeseman, V.G. Zakrzewski, J.A. Montgomery, Jr. R.E. Stratmann, J.C. Burant, S. Dapprich, J.M. Millam, A.D. Daniels, K.N. Kudin, M.C. Strain, O. Farkas, J. Tomasi, V. Barone, M. Cossi, R. Cammi, B. Mennucci, C. Pomelli, C. Adamo, S. Clifford, J. Ochterski, G.A. Petersson, P.Y. Ayala, Q. Cui, K. Morokuma, N. Rega, P. Salvador, J.J. Dannenberg, D.K. Malick, A.D. Raghavachairi, J.B. Foresman, J. Cioslowski, J.V. Ortiz, A.G. Baboul, B.B. Stefanov, G. Liu, A. Liashenko, P. Piskorz, I. Komaromi, R.

Gomperts, R.L. Martin, D.J. Fox, T. Keith, M.A. Al-Laham, C.Y. Peng, A. Nanayakkara, M. Challacombe, P.M.W. Gill, B. Johnson, W. Chen, M.W. Wong, J.L. Andres, C. Gonzalez, M. Head-Gordon, E.S. Replogle, J.A. Pople, GAUSSIAN98, Revision A 11.4, Gaussian, Inc., Pittsburgh PA, 2002.
[26] A.D. Becke, J. Chem. Phys. 98 (1993) 1372.
[27] A. Gorling, Phys. Rev. A 54 (1996) 3912.
[28] J.B. Foresman, E. Frisch, Exploring Chemistry with Electronic Structure Methods, second ed., Gaussian Inc., Pittsburgh PA, 1996.
[29] P.J. Hay, W.R. Eadt, J. Chem. Phys. 82 (1985) 270.
[30] G. Schaftenaar, J.H. Noordik, J. Comput. Aided Mol. Des. 14 (2000) 123.
[31] E.A. Steck, A.R. Day, J. Am. Chem. Soc. 65 (1943) 452.
[32] B. Önfelt, P. Lincoln, B. Nordén, J. Am. Chem. Soc. 121 (1999) 10846.
[33] A. Ambroise, B.G. Maiya, Inorg. Chem. 39 (2000) 4256.
[34] Y. Xiong, X.F. He, X.H. Zou, J.Z. Wu, X.M. Chen, L.N. Ji, R.H. Li, J.Y. Zou, K.B. Yu, J. Chem. Soc., Dalton Trans. (1999) 19.
[35] H. Xu, K.C. Zheng, Y. Chen, Y.Z. Li, L.J. Lin, H. Li, P.X. Zhang, L.N. Ji, J. Chem. Soc., Dalton Trans (2003) 2260.
[36] S. Zails, V. Drchal, Chem. Phys. 118 (1987) 313.
[37] J.Z. Wu, B.H. Ye, L. Wang, L.N. Ji, J.Y. Zhou, R.H. Li, Z.Y. Zhou, J. Chem. Soc., Dalton Trans. (1997) 1395.
[38] H. Xu, K.C. Zheng, L.J. Lin, H. Li, Y. Gao, L.N. Ji, J. Inorg. Biochem. 98 (2004) 87.
[39] B.K. Ghosh, A. Chakraworty, Coord. Chem. Rev. 95 (1989) 239.
[40] J.E. B Johnson, R.R. Ruminski, Inorg. Chim. Acta 208 (1993) 231.
[41] A. Juris, V. Balzani, F. Barigelletti, S. Campagna, P. Belser, A. Von Zelewsky, Coord. Chem. Rev. 84 (1988) 85.
[42] J.G. Liu, Q.L. Zhang, X.F. Shi, L.N. Ji, Inorg. Chem. 40 (2001) 5045.
[43] S. Satyanarayana, J.C. Dabrowia, J.B. Chaires, Biochemistry 31 (1992) 9319.
[44] Satyanarayana, J.C. Dabrowia, J.B. Chaires, Biochemistry 32 (1993) 2573.
[45] J.K. Barton, A. Danishefsky, J. Goldberg, J. Am. Chem. Soc. 106 (1984) 2172.
[46] A. Wolf, G.H. Shimer Jr, T. Meehan, Biochemistry 26 (1987) 6392.
[47] A.M. Pyle, J.P. Rehmann, R. Meshoyrer, C.V. Kumar, N.J. Turro, J.K. Barton, J. Am. Chem. Soc. 111 (1989) 3051.
[48] J.G. Liu, Q.L. Zhang, L.N. Ji, Trans. Met. Chem. 26 (2001) 733–738.
[49] J.K. Barton, Science 233 (1986) 727.
[50] J.K. Barton, A.L. Raphael, J. Am. Chem. Soc. 106 (1984) 2466.
[51] H.Y. Mei, J.K. Barton, Proc. Natl. Acad. Sci. U.S.A. 85 (1988) 1339.
[52] K. Fukui, T. Yonezawa, H. Shingu, J. Chem. Phys. 20 (1952) 722.
[53] I. Fleming, Frontier Orbital, Organic Chemical Reaction, Wiley, New York, 1976.
[54] M. Atsumi, L. González, C. Daniel, J. Photochem. Photobiol. A: Chem. 190 (2007) 310–320.
[55] K.C. Zheng, J.P. Wang, W.L. Peng, X.W. Liu, F.C. Yun, J. Phys. Chem. A 105 (2001) 10899.



Scheme 1. The ligand H_2L and its coordinating mode in the title complexes.

material should be prepared and they should be handled with care.

2.1. Physical measurement

Elemental analyses of carbon, hydrogen and nitrogen were carried out with an Elementar Vario EL III microanalyser. Infrared spectra were recorded on a Perkin–Elmer Spectrum 2000 spectrophotometer over the frequency range 4000–400 cm^{-1} using the KBr pellet technique. Solid-state fluorescent studies were conducted at room temperature on an Edinburgh FL-FS920 TCSPC system. Variable-temperature magnetic data were obtained with a C-2000 (American CAHN Instruments Inc.) instrument in a field of 0.2 T.

2.2. Synthesis of the ligand and the complexes

2.2.1. H_2L

The synthesis and structure of H_2L (3-methoxysalicylaldehyde picoloylhydrazone) have already been reported [29].

2.2.2. $[Cu_2L(C_5H_7O_2)(H_2O)_2]ClO_4$ (**1**)

To H_2L (1 mmol) in DMF (5 mL) was added an equimolar amount of $Cu(acac)_2$ in methanol (5 mL). After stirring for 2 h, $Cu(ClO_4)_2 \cdot 6H_2O$ (0.36 g, 1 mmol) was added to the solution. The dark-green solution was stirred at room temperature for 30 min, filtered, and allowed to stand at room temperature for 3 weeks. Dark-green crystals of **1** suitable for X-ray diffraction were formed. Yield: 50%. *Anal.* Calc. for $[Cu_2(C_{14}H_{11}N_3O_3)(C_5H_7O_2)(H_2O)_2]ClO_4$: C, 36.17; H, 3.51; N, 6.66. Found: C, 35.96; H, 3.53; N, 6.88%.

2.2.3. $[Cu_4L_2(C_5H_7O_2)_2(C_5H_5N)_2](ClO_4)_2$ (**2**)

A methanol solution (5 mL) of $Cu(acac)_2$ (0.262 g, 1 mmol) was added to a stirred DMF solution (5 mL) of H_2L (1 mmol). After stirring for 2 h, $Cu(ClO_4)_2 \cdot 6H_2O$ (0.36 g, 1 mmol) and two drops of pyridine were added to the solution. Stirring was continued for 30 min at room temperature. The solution was filtered and kept for crystallization. Brown crystals of **2** suitable for X-ray diffraction were obtained after 2 weeks. Yield: 25%. *Anal.* Calc. for $[Cu_4(C_{14}H_{11}N_3O_3)_2(C_5H_7O_2)_2(C_5H_5N)_2](ClO_4)_2$: C, 42.78; H, 3.44; N, 8.31. Found: C, 42.77; H, 3.11; N, 8.25%.

2.2.4. $(VO_2)_2L_2Cu_2(acac)_2$ (**3**)

To H_2L (1 mmol) in DMF (5 mL) was added dropwise, with stirring, an equimolar amount of $VO(acac)_2$ in absolute methanol (5 mL). After stirring for 2 h, $Cu(ClO_4)_2 \cdot 6H_2O$ (0.36 g, 1 mmol) was added to the solution. The dark-green solution was stirred at room temperature for 30 min, filtered, and allowed to stand at room temperature for 3 weeks. Dark-green crystals of **3** suitable for X-ray diffraction formed. Yield: 45%. *Anal.* Calc. for $(VO_2)_2(C_{14}H_{11}N_3O_3)_2Cu_2(C_5H_7O_2)_2$: C, 44.32; H, 3.52; N, 8.16. Found: C, 44.47; H, 3.48; N, 8.15%.

2.3. X-ray crystallography

Crystals of the three title complexes of suitable size were mounted on glass fibers. Intensity data were collected on a Rigaku RAPID Weissengberg IP diffractometer with graphite-monochromated Mo Kα radiation ($\lambda = 0.71073$ Å) and the ω scan mode. The structures were solved by direct methods with SHELXS-97 [30] and refined by full-matrix least squares calculations with SHELXL-97 [31]. The high values of the thermal parameters of some oxygen atoms in the perchlorate ions for **1** and **2** suggest that oxygen atom O8 in the perchlorate ion for **1** is disordered and it has been modelled over two sites with equal occupancies of 0.5 and the four oxygen atoms in the perchlorate ion for **2** are disordered and have been modelled over two sites with unequal occupancies (0.65 and 0.35). These oxygen atoms were refined isotropically. All the other non-hydrogen atoms in the three complexes were refined anisotropically. Most of the hydrogen atoms in the three complexes were located in calculated positions or found from difference Fourier maps. Crystallographic data for complexes **1**, **2** and **3** are listed in Table 1.

3. Results and discussion

3.1. Crystal structures

3.1.1. $[Cu_2L(acac)(H_2O)_2]ClO_4$ (**1**)

As shown in Fig. 1, complex **1** consists of one binuclear $[Cu_2L(acac)(H_2O)_2]^+$ cation and one ClO_4^- anion. Selected bond distances and angles are listed in Table 2. The charge balance requires that the ligand H_2L is fully deprotonated. The two copper(II) centers in the title complex molecule **1** are in different coordination environments. Cu(1) atom has a distorted square-pyramidal geometry with the basal plane defined by the N(1) and N(2) atoms from the pentadentate L^{2-} ligand, and O(4) and O(5) atoms from the $acac^-$ group. The O(6) atom from a coordinated water molecule occupies the apical site with a long Cu(1)–O(6) distance of 2.400(3) Å. The Cu–N and Cu–O bond distances in the basal plane range from 1.904(3) to 2.029(3) Å. Cu(2)

Table 1
Crystallographic data of **1**, **2** and **3**

Compound	**1**	**2**	**3**
Formula	$Cu_2C_{19}H_{22}N_3O_{11}Cl$	$Cu_4C_{48}H_{46}N_8O_{18}Cl_2$	$Cu_2V_2C_{38}H_{36}N_6O_{14}$
Formula weight	630.93	1347.99	1029.69
Crystal size (mm)	$0.42 \times 0.40 \times 0.10$	$0.30 \times 0.25 \times 0.11$	$0.50 \times 0.35 \times 0.15$
Crystal system	monoclinic	triclinic	monoclinic
Space group	$P2_1/n$	$P\bar{1}$	$P2_1/n$
a (Å)	8.457(2)	7.335(2)	9.331(4)
b (Å)	18.710(4)	13.911(4)	13.237(4)
c (Å)	15.806(3)	14.311(5)	16.480(6)
α (°)	90	107.87(2)	90
β (°)	104.55(3)	92.96(2)	102.69(2)
γ (°)	90	94.65(2)	90
V (Å^3)	2420.7(8)	1380.7(8)	1985.7(12)
Z	4	1	2
D_{calc} (g cm^{-3})	1.731	1.621	1.722
μ (mm^{-1})	1.931	1.695	1.591
T (K)	293(2)	293(2)	293(2)
λ (Mo Kα) (Å)	0.71073	0.71073	0.71073
$F(000)$	1280	684	1044
θ_{min}, θ_{max} (°)	3.10, 27.50	2.99, 27.48	3.08, 27.48
$h_{min-max}$, $k_{min-max}$, $l_{min-max}$	$-10 \rightarrow 10$, $-24 \rightarrow 23$. $-20 \rightarrow 19$	$-9 \rightarrow 8$, $-17 \rightarrow 17$, $-18 \rightarrow 18$	$-12 \rightarrow 11$, $-17 \rightarrow 17$, $-21 \rightarrow 21$
R_{int}	0.1057	0.0957	0.0397
Number of unique data	5400	5999	4540
Number of observed	2962	2917	3234
Number of variables	331	358	284
R_1 $[I > 2\sigma(I)]$[a]	0.0710	0.0837	0.0393
WR_2 $[I > 2(I)]$[b]	0.1514	0.2335	0.0963
Goodness-of-fit	1.027	0.965	1.040
$(\Delta\rho)_{max,min}$ (e/Å^3)	0.541, −0.684	0.860, −0.962	0.930, −0.441
$(\Delta/\sigma)_{max,min}$	0.001, 0.000	0.001, 0.000	0.000, 0.000

[a] $R = \sum(|F_o| - |F_c|)/\sum|F_o|$.
[b] $wR = \{\sum[w(|F_o^2 - F_c^2|)^2]/\sum[w(F_o^2)^2]\}^{1/2}$.

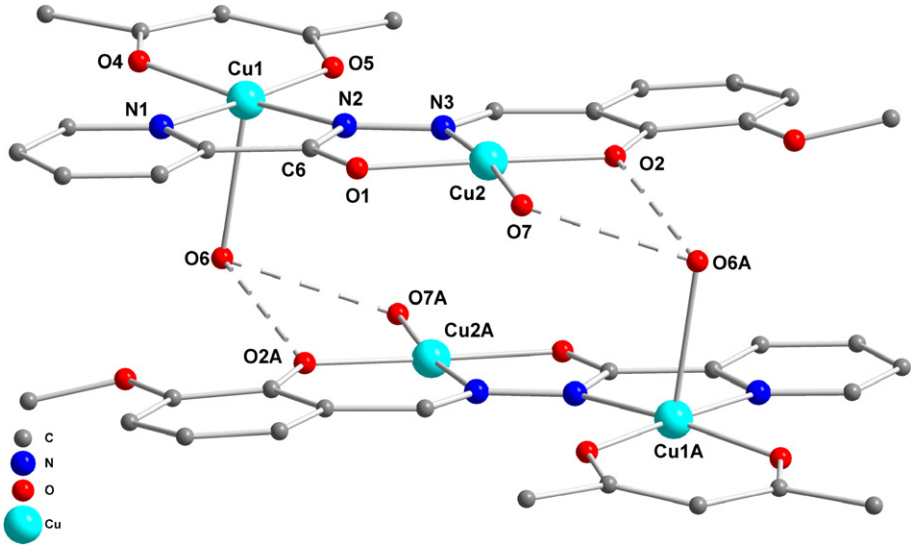


Fig. 1. Tetranuclear unit of **1** linked by hydrogen bonds. Hydrogen atoms are omitted for clarity. Symmetry code A, $-x$, $1-y$, $1-z$.

atom is coordinated by the O(1), N(3) and O(2) atoms of the ligand L^{2-} and a coordinated water molecule O(7) atom, forming a square plane. The three Cu(2)–O bond lengths are between 1.866(2) and 1.943(3) Å, and the Cu(2)–N(3) length is 1.931(3) Å. The two copper centers are bridged by single N–N bond of the pentadentate ligand L^{2-} with a Cu(1)–Cu(2) separation of 4.823(1) Å and Cu–N–N–Cu torsion angle of 179.2(2)°. The overall cation is close to a plane, with the copper basal planes coinciding with the ligand plane.

Table 2
Selected bond lengths (Å) and bond angles (°) for complex **1**

Cu(1)–O(5)	1.904(3)	Cu(1)–O(4)	1.917(2)	Cu(1)–N(1)	1.995(3)
Cu(1)–N(2)	2.029(3)	Cu(1)–O(6)	2.400(3)	Cu(2)–O(2)	1.866(2)
Cu(2)–O(1)	1.910(2)	Cu(2)–N(3)	1.931(3)	Cu(2)–O(7)	1.943(3)
O(5)–Cu(1)–O(4)	93.47(11)	O(5)–Cu(1)–N(1)	175.01(12)		
O(4)–Cu(1)–N(1)	89.30(11)	O(5)–Cu(1)–N(2)	95.61(11)		
O(4)–Cu(1)–N(2)	167.23(11)	N(1)–Cu(1)–N(2)	81.02(11)		
O(5)–Cu(1)–O(6)	95.13(10)	O(4)–Cu(1)–O(6)	89.15(10)		
N(1)–Cu(1)–O(6)	89.06(11)	N(2)–Cu(1)–O(6)	98.94(10)		
O(2)–Cu(2)–O(1)	176.45(10)	O(2)–Cu(2)–N(3)	94.66(11)		
O(1)–Cu(2)–N(3)	82.31(11)	O(2)–Cu(2)–O(7)	90.32(10)		
O(1)–Cu(2)–O(7)	92.55(10)	N(3)–Cu(2)–O(7)	173.13(12)		

There are three kinds of hydrogen bonds in **1** (see Table 3): first, O–H(H_2O)···O(H_2O) between the coordination water molecules (O(7)···O(6) = 2.637(3) Å); second, O–H(H_2O)···O(phenolic) between the coordination water molecules and phenolic oxygen atoms (O(6)···O(2) = 2.770(3) Å); third, O–H(H_2O)···O(ClO_4^-) between the coordination water molecules and the perchlorate oxygen atoms (O(6)···O(8A) = 2.810(6) Å, O(6)···O(8B) = 2.781(7) Å, O(7)···O(11) = 2.726(5) Å). The first two kinds of hydrogen bonds link two adjacent binuclear complex cations into an extended tetranuclear Cu_4 unit with a crystallographic centrosymmetry (Fig. 1). Each extended tetranuclear Cu_4 unit connects four neighboring ClO_4^- anions by hydrogen bonds O–H(H_2O)···O(ClO_4^-). Each ClO_4^- anion links two neighboring tetranuclear Cu_4 units through hydrogen bonds O–H(H_2O)···O(ClO_4^-). Therefore, an extended 2D layer is formed (Fig. 2). The Cu···Cu distances within an extended Cu_4 unit are 3.845(1), 4.589(1), 4.823(1) and 8.594(2) Å, while the shortest Cu···Cu distances between the neighboring extended Cu_4 units is 4.22(3) Å. The adjacent ligands are stacked at a distance of about 3.46 and 3.49 Å.

3.1.2. $[Cu_4L_2(acac)_2(py)_2](ClO_4)_2$ (2)

There is one tetranuclear $[Cu_4(L)_2(acac)_2(py)_2]^{2+}$ cation and two ClO_4^- anions in complex **2**. Selected bond distances and angles are illustrated in Table 4.

Fig. 3 shows the structure of a centrosymmetrically tetranuclear $[Cu_4L_2(acac)_2(py)_2]^{2+}$ cation. A diazine N–N group of the pentadentate ligand L^{2-} bridges the atoms Cu(1) and Cu(2) to form a Cu_2 pair, the Cu(1)–Cu(2) separation and Cu–N–N–Cu torsion angle being 4.822(2) Å and 165.0(1)°, respectively. Two Cu_2 pairs are connected by two phenolic oxygen atoms of two L^{2-} ligands to get a centrosymmetrically tetranuclear $[Cu_4L_2(acac)_2(py)_2]^{2+}$ cation with a (Cu–N–N–Cu–O–)$_2$ core, Cu(2)–O(2), O(2)–Cu(1A) and Cu(2)–Cu(1A) interatomic distances are 1.905(2), 2.493(2) and 3.393(1) Å, respectively. The Cu(2)–O(2)–Cu(1A) angle is 100.1(2)°.

Table 3
Intermolecular hydrogen bond distances and angles in complex **1**

X–H···Y	Symmetry transformation	X···Y (Å)	X–H (Å)	H···Y (Å)	∠(DHA)
O7–H2b···O6	$-x, 1-y, 1-z$	2.637(3)	0.84	1.94	139.4
O6–H1b···O2	$-x, 1-y, 1-z$	2.770(3)	0.92	2.08	130.7
O6–H1a···O8A	$1-x, 1-y, 1-z$	2.810(6)	0.91	1.95	158.3
O6–H1a···O8B	$1-x, 1-y, 1-z$	2.781(7)	0.91	1.88	169.8
O7–H2a···O11	$x-1/2, -y+3/2, z+1/2$	2.726(5)	0.90	1.97	141.0

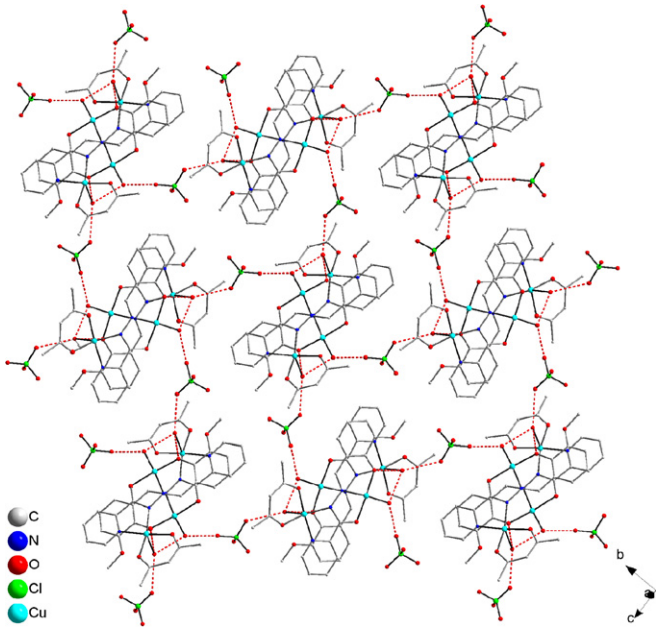


Fig. 2. Extended 2D structure of **1**. Hydrogen atoms are omitted for clarity.

The Cu(1) atom is in a distorted square-pyramidal geometry, which is completed by N(1), N(2), O(4), O(5) in the basal plane and O(2A) in the axial position. The Cu(2) atom has a distorted square-planar geometry, formed by O(1), O(2), N(3) and N(4). Except for the elongated Cu–O bond (Cu(1)–O(2A) = 2.493(2) Å), the other Cu–O and Cu–N distances fall in the ranges 1.905–1.957 and 1.953–2.020 Å, respectively. In distinction from the planar configuration of L^{2-} in **1**, neither of pentadentate ligands L^{2-} in **2** are planar.

As shown in Fig. 4, adjacent ligands within a tetranuclear unit and between the tetranuclear units are packed at a distance of *ca.* 3.60 and 3.47 Å, respectively. The aromatic ring and pyridine ring in a ligand are slightly twisted with a dihedral angle of *ca.* 18.7°. The distances between the centroids of the aromatic ring and the pyridine ring within a tetranuclear unit and between the two neighboring tetranuclear units are *ca.* 3.70 and 3.95 Å, respectively. Therefore, there is an extended 1D structure in **2** formed by weak π···π stacking interactions between the adjacent molecules. The intermolecular Cu···Cu distances are *ca.* 4.36 Å.

3.1.3. $(VO_2)_2L_2Cu_2(acac)_2$ (3)

Complex **3** is a neutral discrete heterotetranuclear molecule. The molecular structure is illustrated in Fig. 5, selected bond distances and angles are given in Table 5.

Table 4
Selected bond lengths (Å) and bond angles (°) for complex **2**

Cu(1)–O(4)	1.914(2)	Cu(1)–O(5)	1.918(2)	Cu(1)–N(1)	2.018(3)
Cu(1)–N(2)	2.020(2)	Cu(1)–O(2A)	2.493(2)	Cu(2)–O(2)	1.905(2)
Cu(2)–N(3)	1.953(2)	Cu(2)–O(1)	1.957(2)	Cu(2)–N(4)	1.998(2)

O(4)–Cu(1)–O(5)	92.53(10)	O(4)–Cu(1)–N(1)	92.14(10)
O(5)–Cu(1)–N(1)	174.99(8)	O(4)–Cu(1)–N(2)	169.24(10)
O(5)–Cu(1)–N(2)	94.93(9)	N(1)–Cu(1)–N(2)	80.20(10)
O(4)–Cu(1)–O(2A)	93.24(8)	O(5)–Cu(1)–O(2A)	89.24(8)
N(1)–Cu(1)–O(2A)	92.30(9)	N(2)–Cu(1)–O(2A)	94.59(8)
O(2)–Cu(2)–N(3)	90.20(9)	O(2)–Cu(2)–O(1)	166.31(8)
N(3)–Cu(2)–O(1)	82.82(9)	O(2)–Cu(2)–N(4)	94.00(9)
N(3)–Cu(2)–N(4)	163.90(10)	O(1)–Cu(2)–N(4)	95.93(10)
Cu(2)–O(2)–Cu(2A)	100.17(9)		

Symmetry code A: $1-x, 1-y, 1-z$.

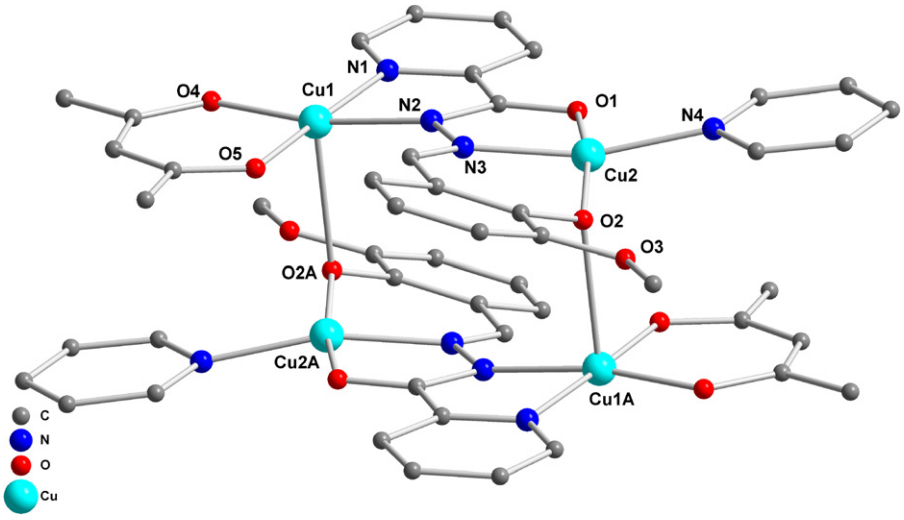


Fig. 3. Structure representation of the cation in $[Cu_4L_2(acac)_2(py)_2](ClO_4)_2$ (**2**). Hydrogen atoms are omitted for clarity.

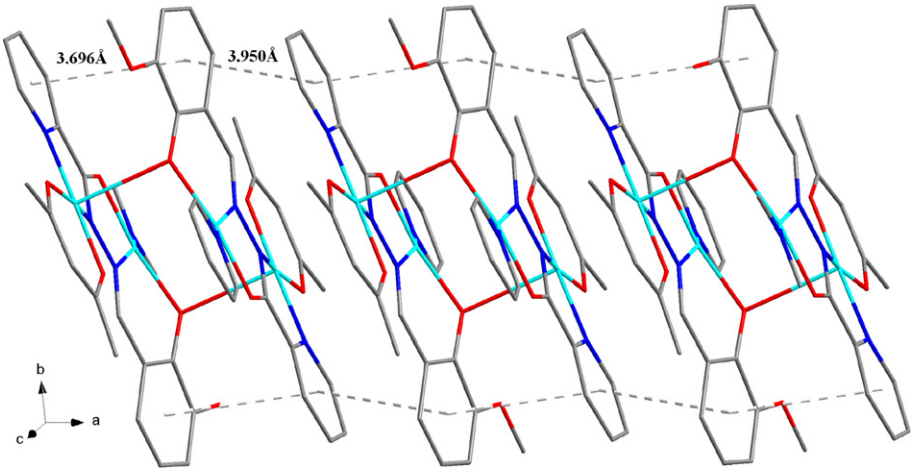


Fig. 4. Packing diagram showing π–π stacking interactions between the neighboring benzene ring and pyridine ring by dashed lines in complex **2**. Hydrogen atoms and ClO_4^- are omitted for clarity.

The V(1) atom and Cu(1) atom are bridged by a diazine N–N single bond of the pentadentate ligand L^{2-}, forming a bimetallic VO_2Cu structure unit. The torsion angle Cu(1)–N(2)–N(3)–V(1) in the VO_2Cu structure unit is 177.9(2)°. Two VO_2Cu structure units are paired by two equivalent Cu(1A)–O(6) and Cu(1)–O(6A) bonds to form a novel

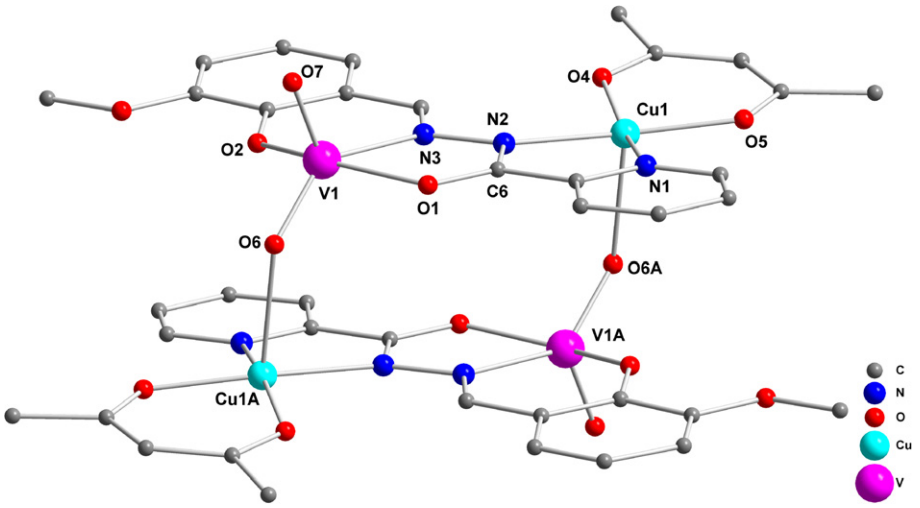


Fig. 5. Structure of the heterotetranuclear molecule $(VO_2)_2L_2Cu_2(acac)_2$ (**3**). Hydrogen atoms are omitted for clarity.

Table 5
Selected bond lengths (Å) and bond angles (°) for complex **3**

Cu(1)–O(4)	1.913(2)	Cu(1)–O(5)	1.922(2)	Cu(1)–N(1)	2.010(3)
Cu(1)–N(2)	2.049(2)	Cu(1)–O(6A)	2.293(2)	V(1)–O(7)	1.610(2)
V(1)–O(6)	1.645(2)	V(1)–O(2)	1.885(2)	V(1)–O(1)	2.016(2)
V(1)–N(3)	2.153(2)				

O(4)–Cu(1)–O(5)	92.12(8)	O(4)–Cu(1)–N(1)	166.76(10)
O(5)–Cu(1)–N(1)	88.68(9)	O(4)–Cu(1)–N(2)	97.77(8)
O(5)–Cu(1)–N(2)	167.43(9)	N(1)–Cu(1)–N(2)	79.93(9)
O(4)–Cu(1)–O(6A)	92.86(9)	O(5)–Cu(1)–O(6A)	98.21(8)
N(1)–Cu(1)–O(6A)	100.11(9)	N(2)–Cu(1)–O(6A)	89.08(8)
O(7)–V(1)–O(6)	108.51(12)	O(7)–V(1)–O(2)	101.29(11)
O(6)–V(1)–O(2)	97.86(10)	O(7)–V(1)–O(1)	96.43(10)
O(6)–V(1)–O(1)	93.35(9)	O(2)–V(1)–O(1)	154.76(8)
O(7)–V(1)–N(3)	115.19(11)	O(6)–V(1)–N(3)	135.38(9)
O(2)–V(1)–N(3)	82.49(8)	O(1)–V(1)–N(3)	73.71(8)

Symmetry code A: $1-x, 1-y, -z$.

centrosymmetrical tetranuclear molecule $(V^VO_2)_2L_2Cu_2(acac)_2$. There is a quadrangle core in the discrete tetranuclear molecule. The interatomic distances of V–Cu are 5.075(1) Å on the long sides of the quadrangle and 3.588(1) Å on the short sides of the quadrangle.

The V(1)–O(6) (oxo oxygen) and Cu(1A)–O(6) bond lengths are 1.645(2) and 2.293(2) Å, respectively, and the V(1)–O(6)–Cu(1A) bond angle is 130.5(1)°. To the best of our knowledge, complex **3** is the first example of a V^VO-Cu^{II} complex where the V^V center and Cu^{II} center are bridged by one oxo oxygen atom. Of course, many V^VO-Cu^{II} complexes have been observed in the references, but the V^V and Cu^{II} centers in those complexes are bridged by one or two oxygen atoms from a polyoxovanadate or phosphate.

The copper (II) center has a distorted square-pyramidal CuN_2O_3 environment. The basal plane is defined by N(1) and N(2) atoms from a pentadentate L^{2-}, and O(4) and O(5) atoms from the $acac^-$ group, the bond lengths of Cu–N are 2.010(3)–2.049(2) Å, the ones of Cu–O are 1.913(2)–1.922(2) Å. One oxo oxygen atom (O(6A)) is at the apical position with a bond distance of 2.293(2) Å.

The vanadium atom is coordinated by two oxo oxygen atoms (O(6) and O(7)) and three donors (O(1), N(3) and O(2)) of a pentadentate L^{2-} ligand. The coordination geometry of vanadium can be described in terms of a tetragonal pyramid, distorted towards a trigonal bipyramid. The τ value is 0.32 {[∠O(2)–V(1)–O(1)–∠O(6)–V(1)–N(3)]/60 = 0.32}, reflecting a common situation encountered with pentacoordinate oxovanadium complexes. The V–O (oxo oxygen) V(1)–O(6) and V(1)–O(7) bond distances are 1.645(2) and 1.610(2) Å, respectively, and the O(6)–V(1)–O(7) angle is *ca.* 108.5°, showing the characteristic of V=O double bonds of dioxovanadium(V) complexes [32–34].

Two L^{2-} ligands in the tetranuclear molecule are essentially planar and parallel to each other, the distance between the two ligands being *ca.* 3.41 Å. The distance between the centroids of an aromatic ring from one VO_2Cu structure unit and the pyridine ring from the other VO_2Cu structure unit in the tetranuclear molecule is *ca.* 3.92 Å.

Therefore, there exists a weak π···π contact between the two L^{2-} ligands.

3.2. Self-assembly reactions involving a bridging pentadentate ligand H_2L

First the binuclear complex **1** was synthesized by a self-assembly reaction between H_2L, $Cu(acac)_2$ and $Cu(ClO_4)_2 \cdot 6H_2O$ with solvents (DMF, methanol and water). The molecular structure of **1** shows that water molecules in the reaction medium are coordinated to the copper atoms. Taking into account that the coordinating ability of pyridine is higher than that of water for the copper atom, pyridine was added to the reaction system and the tetranuclear copper complex **2** was obtained successfully.

On replacing $Cu(acac)_2$ with $VO(acac)_2$, the novel heteronuclear oxovanadium–copper complex **3** has been synthesized, during the reaction process the valence of the vanadium was increased +4 to +5 by air oxidation. Up until now, most oxovanadium–copper complexes were synthesized by hydrothermal reactions. Complex **3** was synthesized by a solution reaction and it is the first oxovanadium–copper complex with an oxo oxygen atom as the bridging atom between the V atom and the Cu atom.

3.3. IR spectroscopic studies and fluorescent properties

The IR spectra of the ligand exhibits two bands at 3272 and 1678 cm^{-1} due to ν(NH) and ν(C=O) stretches, respectively, indicative of its ketonic nature in the solid state. The absence of these bands in the IR spectra of complexes **1**, **2** and **3** is consistent with enolization and replacement of H by the metal ion. The $\nu(C{=}N_{azomethine})$ stretch of the free ligand appears as a weak band at 1608 cm^{-1} along with the ν(C=N) stretches of the pyridine ring. A very sharp band at 1588–1601 cm^{-1} in the complexes is indicative of the coordination of the azomethine nitrogen and pyridine nitrogen atoms. Complex **3** exhibits three sharp bands in the 867–936 cm^{-1} region, corresponding to the *cis*-$[VO_2]^+$ structural unit.

The fluorescent properties of the three title complexes and the pure ligand were investigated in the solid state at room temperature (Fig. 6). The pure ligand shows an intense emission band at 548 nm (λ_{ex} = 381 nm), complex **1** and **2** have almost the same emission spectrum at 396 nm (λ_{ex} = 251 nm and 253 nm, respectively) and complex **3** shows an emission at 492 nm (λ_{ex} = 393 nm). The emission of the pure ligand may be attributed to a $\pi \rightarrow \pi$ transition, while the emission of title complexes show an obvious blue shift compared to that of pure ligand, which may originate from a LMCT [35–37].

3.4. Magnetic properties

The variable-temperature magnetic susceptibility of **1** has been measured on the crystalline samples in a field of 2 kOe. The plots of χ_M and $\chi_M T$ versus T of **1** are shown in Fig. 7, where χ_M is the magnetic susceptibility. The observed $\chi_M T$ value for **1** at 300 K is 0.62 $cm^3\ mol^{-1}$ K, which is somewhat smaller than the value (0.75 $cm^3\ mol^{-1}$ K) expected for two uncorrelated Cu(II) ($S = 1/2$) ions with $g = 2$. Upon cooling, the $\chi_M T$ of **1** is roughly unchanged in the range 300–200 K, then decreases to a minimum value of 0.02 $cm^3\ mol^{-1}$ K at 2 K. The magnetic susceptibility above 40 K obeys the Curie–Weiss law with the Curie constant $C = 0.732\ cm^3\ mol^{-1}$ K and a negative Weiss constant, $\theta = -35.7$ K, which suggests the occurrence of an antiferromagnetic interaction for **1**. This result is consistent with a trans N–N bridge connecting Cu(1) and Cu(2) [38].

The χ_M value increases with decreasing temperature, reaching a maximum value of 0.014 $cm^3\ mol^{-1}$ at around 15.2 K, and then decreases abruptly to 0.007 $cm^3\ mol^{-1}$ at 3.5 K. This is characteristic of a significant antiferromagnetic ordering (T_N = 15.2 K). The origin of the small

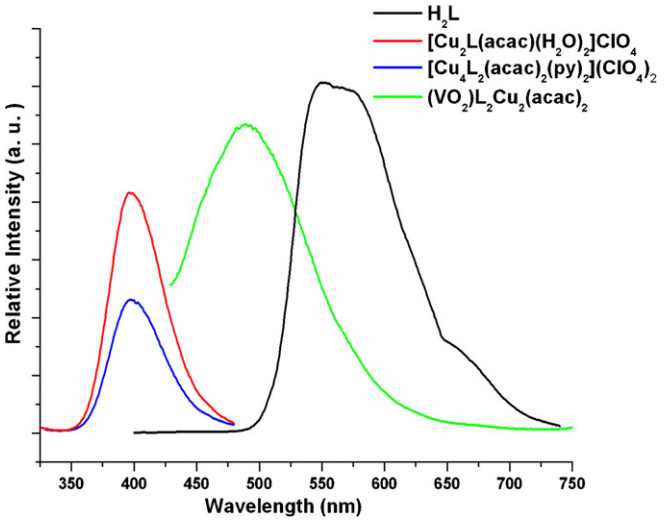


Fig. 6. The emission spectra of the title complexes and the pure ligand in the solid state at room temperature.

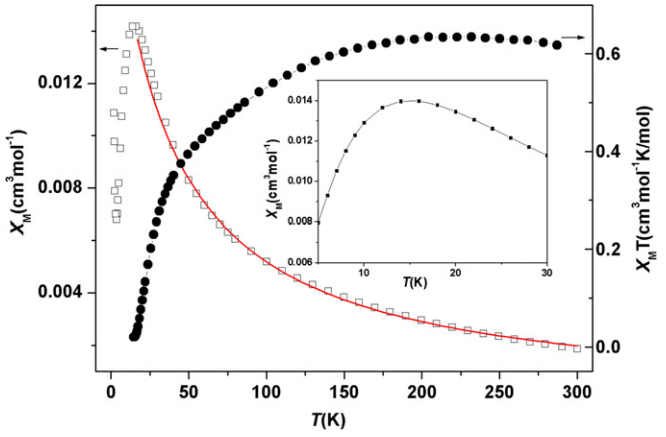


Fig. 7. Temperature dependence of χ_M and $\chi_M T$ for **1** with the solid line showing the best fit obtained through χ_M values. Inset: low temperature region of χ_M.

bump around 3 K in the χ_M versus T curve for **1** is still unclear, though the possibility of a systematic error cannot be completely excluded.

4. Conclusions

Using the same reaction system of H_2L, $Cu(acac)_2$ and $Cu(ClO_4)_2 \cdot 6H_2O$, the binuclear copper complex **1** and tetranuclear copper complex **2** have been synthesized, depending different solvents (DMF, methanol and water for **1** and DMF, methanol, water and pyridine for **2**). The different products are due to the fact that the coordinating ability of pyridine is higher than that of water for the copper atom. Replacing $Cu(acac)_2$ with $VO(acac)_2$, the novel tetranuclear oxovanadium–copper complex **3** has been synthesized. Complex **3** was synthesized by a solution reaction and is the first oxovanadium–copper complex with an oxo oxygen atom as a bridging atom between the V atom and the Cu atom.

Acknowledgements

This project was financially supported by the Natural Science Foundation of China (Nos. 20431010 and 20171012) and the Natural Science Foundation of Fujian Province, China (E0110010).

Appendix A. Supplementary material

CCDC 648498, 648499 and 648500 contain the supplementary crystallographic data for **1**, **2** and **3**. These data can be obtained free of charge via http://www.ccdc.cam.ac.uk/conts/retrieving.html, or from the Cambridge Crystallographic Data Centre, 12 Union Road, Cambridge CB2 1EZ, UK; fax: (+44) 1223-336-033; or e-mail: deposit@ccdc.cam.ac.uk. Supplementary data associated with this article can be found, in the online version, at doi:10.1016/j.poly.2007.08.031.

References

[1] L.K. Thompson, Coord. Chem. Rev. 233 (2002) 193.
[2] D. Dragancea, V.B. Arion, S. Shova, E. Rentschler, N.V. Gerbeleu, Angew. Chem., Int. Ed. 44 (2005) 7938.
[3] Z.-Q. Xu, L.K. Thompson, D.O. Miller, Chem. Commun. (2001) 1170.
[4] S.-X. Liu, S. Lin, B.-Z. Lin, C.-C. Lin, J.-Q. Huang, Angew. Chem., Int. Ed. 40 (2001) 1084.
[5] A. Fragoso, M.L. Kahn, A. Castiñeiras, J.-P. Sutter, O. Kahna, R. Cao, Chem. Commun. (2000) 1547.
[6] C.J. Matthews, K. Avery, Z.-Q. Xu, L.K. Thompson, L. Zhao, D.O. Miller, K. Biradha, K. Poirier, M.J. Zaworotko, C. Wilson, A.E. Goeta, J.A.K. Howard, Inorg. Chem. 38 (1999) 5266.
[7] S. Lin, S.-X. Liu, Z. Chen, B.-Z. Lin, S. Gao, Inorg. Chem. 43 (2004) 2222.
[8] Z.-Q. Xu, L.K. Thompson, C.G. Matthews, D.O. Miller, A.E. Goeta, J.A.K. Howard, Inorg. Chem. 40 (2001) 2446.
[9] N. Kitajima, Y. Moro-oka, Chem. Rev. 94 (1994) 737.
[10] H. Adams, D.E. Fenton, G. Minardi, E. Mura, A.M. Pistuddi, C. Solinas, Inorg. Chem. Commun. 3 (2000) 24.
[11] W.-G. Wang, J. Zhang, L.-J. Song, Z.-F. Ju, Inorg. Chem. Commun. 7 (2004) 858.
[12] M.R. Maurya, Coord. Chem. Rev. 237 (2003) 163.
[13] S. Gao, Z.-Q. Weng, S.-X. Liu, Polyhedron 17 (1998) 3595.
[14] X.-M. Zhang, M.-L. Tong, X.-M. Chen, Chem. Commun. (2000) 1817.
[15] B.-Z. Lin, S.-X. Liu, Polyhedron 19 (2000) 2521.
[16] B.-Z. Lin, S.-X. Liu, Chem. Commun. (2002) 2126.
[17] P.A. Maggard, P.D. Boyle, Inorg. Chem. 42 (2003) 4250.
[18] J.-Y. Xie, J.-G. Mao, J. Mol. Struct. 750 (2005) 186.
[19] T. Kurata, A. Uehara, Y. Hayashi, K. Isobe, Inorg. Chem. 44 (2005) 2524.
[20] G. Yucesan, N.G. Armatas, J. Zubieta, Inorg. Chim. Acta 359 (2006) 4557.
[21] R. Finn, J. Zubieta, Chem. Commun. (2000) 1321.
[22] R.C. Finn, J. Zubieta, Inorg. Chem. Commun. 3 (2000) 520.
[23] R.C. Finn, J. Zubieta, Inorg. Chim. Acta 335 (2002) 131.
[24] X.-M. Zhang, H.-S. Wu, S. Gao, X.-M. Chen, J. Solid State Chem. 176 (2003) 69.
[25] C.-M. Wang, Y.-L. Chuang, S.-T. Chuang, K.-H. Lii, J. Solid State Chem. 177 (2004) 2305.
[26] W. Ouellette, V. Golub, C.J. O'Connor, J. Zubieta, J. Chem. Soc., Dalton Trans. (2005) 291.
[27] S. Mohanta, K.K. Nanda, L.K. Thompson, U. Flörke, K. Nag, Inorg. Chem. 37 (1998) 1465.
[28] O. Kahn, J. Galy, Y. Journaux, J. Jaud, I. Morgenstern-Badarau, J. Am. Chem. Soc. 104 (1982) 2165.
[29] M.-L. Liu, J.-M. Dou, D.-Q. Wang, D.-C. Li, Acta Crystallogr. E61 (2005) o3876.
[30] G.M. Sheldrick, SHELXS SHELXS-97: Program for X-ray Crystal Structure Solution, University of Göttingen, Göttingen, Germany, 1997.
[31] G.M. Sheldrick, SHELXS SHELXS-97: Program for X-ray Crystal Structure Refinement, University of Göttingen, Göttingen, Germany, 1997.
[32] A.K. Sah, C.P. Rao, P.K. Saarenketo, E.K. Wegelius, E. Kolehmainen, K. Rissanen, Eur. J. Inorg. Chem. (2001) 2773.
[33] W. Plass, A. Pohlmann, H.P. Yozgatli, J. Inorg. Biochem. 80 (2000) 181.
[34] S.K. Dutta, S. Samanta, S. Mukhopadhyay, P. Burckel, A. Alan Pinkerton, M. Chaudhury, Inorg. Chem. 41 (2002) 2946.
[35] B. Liu, L. Xu, Inorg. Chem. Commun. 9 (2006) 364.
[36] A. Meijerink, G. Blasse, M. Glasbeek, J. Phys. Condens. Matter 2 (1990) 6303.
[37] R. Bertoncello, M. Bettinelli, M. Casarin, A. Gulino, E. Tondello, A. Vittadini, Inorg. Chem. 31 (1992) 1558.
[38] L.K. Thompson, Z.-Q. Xu, A.E. Goeta, J.A.K. Howard, H.J. Clase, D.O. Miller, Inorg. Chem. 37 (1998) 3217.

The ligation of $\mathbf{L^1}$ and $\mathbf{L^2}$ with Pd(II), Ag(I) and Cu(II) has been investigated. The single crystal structures of $[Pd(\mathbf{L^1})Cl_2]$, $[PdCl_2(\mathbf{L^2})]_2$ and $[Cu\mathbf{L^1}Br_2]$ have been solved. The results of these investigations are the subject of this paper. Both the ligands form metallamacrocyles on complexation.

2. Experimental

The ^1H and $^{13}C\{^1H\}$ NMR spectra were recorded on a Bruker Spectrospin DPX-300 NMR spectrometer at 300.13 and 75.47 MHz respectively. IR spectra in the range 4000–250 cm^{-1} were recorded on a Nicolet Protége 460 FT-IR spectrometer as KBr pellets. The C, H and N analyses were carried out with a Perkin–Elmer elemental analyzer 240C. 2-Bromopyridine, 1,2-bis(dimethylchlorosilyl)ethane, 3-bromoquinoline were obtained from Aldrich (USA) and used without further purification. The melting points determined in open capillary are reported as such.

2.1. X-ray diffraction analysis

Single crystal diffraction studies on $\mathbf{L^1}$ and **2** were carried out on a Bruker SMART CCD diffractometer at 25 °C and Bruker-Nonius Kappa CCD area detector diffractometer was used for **3**, so that ϕ and ω scans gave a complete asymmetric unit. The data for **4** was collected on Oxford Diffraction Gemini-R CCD diffractometer (one degree ϕ and ω scans were used with a 0.8 mm collimator). Table 1 lists the experimental parameters used for single crystal structure analysis. The software SADABS [12] was used for absorption correction, if required. For structure determination and refinement direct methods [13], WinGX version [14] of SHELX-97 and/or SHELXTL [15] were used. All non-hydrogen atoms were located from difference Fourier map and were refined anisotropically. The hydrogen atoms were located using geometrical constraints. The least-squares refinement cycles on F^2 were performed until the model converged.

2.2. Synthesis of 1,2-bis(dimethyl(2-pyridyl)silyl)ethane ($\mathbf{L^1}$)

To a solution of 2-bromopyridine(3.16 g, 20 mmol) made in dry diethyl ether (30 ml) was added drop wise *n*-butyllithium (20.5 mmol, 8.2 ml of 2.5 M solution in *n*-hexane) at −80 °C under nitrogen atmosphere. The mixture was stirred for 1 h. The dark reddish brown suspension thus obtained was mixed dropwise with 1,2-bis(chlorodimethylsilyl)ethane (2.15 g, 10 mmol) dissolved in dry diethyl ether (10 ml). The mixture was slowly allowed to warm to room temperature and left for 12 h. It was shaken with three aliquots (each of 50 ml) of water. The organic layer was separated each time and three aqueous extracts were

Table 1
Crystallographic data and refinements of $\mathbf{L^2}$, **1**, **3** and **4**

Compound	$\mathbf{L^2}$	**1**	**3**	**4**
Empirical formula	$C_{24}H_{28}N_2Si_2$	$C_{16}H_{24}N_2Si_2Cl_2Pd$	$C_{16}H_{24}Br_2CuN_2Si_2$	$C_{49.50}H_{57.50}Cl_{8.50}N_4Pd_2Si_4$
Formula weight	400.66	477.85	523.90	1334.98
T (K)	273(2)	120(2)	273(2)	203(2)
Wavelength (Å)	0.71073	0.71073	0.71073	0.71073
Crystal system	monoclinic	monoclinic	monoclinic	triclinic
Space group	$P2(1)/n$	$P2_1/c$	$P2(1)/c$	$P\bar{1}$
a (Å)	6.2767(9)	8.3884(1)	10.1874(11)	12.2838(17)
b (Å)	18.055(3)	15.7423(2)	13.3073(14)	15.1804(12)
c (Å)	10.2078(15)	15.2999(2)	15.9472(17)	19.249(3)
α (°)	90.00	90.00	90.00	111.951(10)
β (°)	104.144(2)	98.352(1)	94.701(2)	92.364(11)
γ (°)	90.00	90.00	90.00	106.455(10)
V ($Å^3$)	1121.8(3)	1998.97(4)	2154.6(4)	3148.9(7)
Z	2	4	4	2
D_{calc} (Mg/m^3)	1.186	1.588	1.615	1.408
Absorption coefficient (mm^{-1})	0.170	1.316	4.834	1.042
$F(000)$	428	968	1044	1350
Crystal size (mm)	$0.36 \times 0.28 \times 0.25$	$0.20 \times 0.20 \times 0.18$	$0.42 \times 0.21 \times 0.15$	$0.65 \times 0.15 \times 0.12$
θ Range (°)	2.26–23.81	3.37–27.51	2.00–25.00	4.63–32.63
Reflections collected	9507	25505	20252	45728
Independent reflections (R_{int})	1754(0.0351)	4568(0234)	3784(0.0675)	20566(0.0408)
Maximum and minimum transmission	0.959 and 0.941	0.798 and 0.779	0.470 and 0.235	1.000 and 0.690
Final R indices	$R_1 = 0.0502$	$R_1 = 0.0211$	$R_1 = 0.0593$	$R_1 = 0.0490$
$[I > 2\sigma(I)]$	$wR_2 = 0.1178$	$wR_2 = 0.0514$	$wR_2 = 0.1144$	$wR_2 = 0.1182$
Data/restraints/parameters	1754/0/129	4568/0/213	3784/0/212	20566/16/669
Goodness-of-fit on F^2	1.133	1.066	1.117	1.035
R indices (all data)	$R_1 = 0.0584$ $wR_2 = 0.1219$	$R_1 = 0.0239$, $wR_2 = 0.0526$	$R_1 = 0.0858$, $wR_2 = 0.1236$	$R_1 = 0.1047$, $wR_2 = 0.1491$
Largest difference in peak and hole (e $Å^{-3}$)	0.296 and −0.154	0.556 and −0.793	0.745 and −0.386	1.441 and −0.837

mixed. The combined aqueous layer was further extracted twice with diethyl ether (10 ml). These ether extracts were combined with the organic layer first separated. The mixture thus obtained was washed with saturated brine (10–20 ml) and dried over anhydrous Na_2SO_4. After evaporation of the solvent, yellow solid residue of $\mathbf{L^1}$ was obtained. It was purified by column chromatography on silica gel with (40% ethylacetate and 60% hexane). The $\mathbf{L^1}$ was found to be low melting solid (i.e. liquid at room temperature but sold at temperature <10 °C). Yield 1.8 g, ~60%. NMR (^{1}H, $CDCl_3$) δ (ppm), 8.77 (d, $J = 4.65$ Hz, 2H, H_7), 7.57 (t, $J = 6.25$ Hz, 2H, H_5), 7.47 (d, $J = 7.2$ Hz, 2H, H_4), 7.19 (t, $J = 6.24$ Hz, 2H, H_6), 0.77 (s, 4H, $H_1 + H_2$), 0.31 (s, 12H, Me); (^{13}C{^{1}H}, $CDCl_3$) δ (ppm), 166.1 (C_3), 148.7 (C_7), 132.4 (C_5), 127.7 (C_4), 121.3 (C_6), 5.8 (C_1, C_2), −5.3 (Me). IR (KBr, cm^{-1}): 1252, 2956, 1453, 825, 468, 410, 625.

2.3. Synthesis of 1,2-bis(dimethyl(3-quinolyl)silyl) ethane ($\mathbf{L^2}$)

The solution of 3-bromoquinoline (4.16 g, 20 mmol) was made in dry diethylether (30 ml) under nitrogen atmosphere. *n*-Butyllithium (20.5 mmol, 8.2 ml of 2.5 M solution in hexane) was added dropwise to it at −80 °C under nitrogen atmosphere. The resulting mixture was stirred for 1 h. To dark brown suspension thus obtained was added dropwise 1,2-bis(chlorodimethylsilyl)ethane (2.15 g, 10 mmol) dissolved in 10 ml of diethylether. The reaction mixture was slowly allowed to warm to room temperature and kept for 12 h. It was shaken with three aliquots of 50 ml of water and separated from the aqueous layer each time. The three aqueous layers were combined and extracted with two aliquots (10 ml) of diethyl ether. The ether extracts were combined with the organic layer separated earlier. The mixture thus obtained was washed with saturated brine (10–20 ml) and dried over anhydrous Na_2SO_4. After evaporation of the solvent, dark yellow oil was obtained, which was purified by column chromatography (silica gel; 30:70 ethyl acetate–hexane mixture). The colourless crystals of $\mathbf{L^2}$ were obtained by slow evaporation of solvents from the eluent. Yield 1.21 g, ~30%; m.p. 101 °C; *Anal.* Calc. for $Si_2C_{24}H_{28}N_2$: C, 71.97; H, 6.99; N, 6.99. Found: C, 71.79; H, 6.74; N, 6.23%. NMR: (^{1}H, $CDCl_3$) δ (ppm): 8.94 (s, 2H, H_{11}), 8.20 (s, 2H, H_4), 8.08 (d, $J = 6$ Hz, 2H, H_9), 7.77–7.69 (m, 4H, $H_8 + H_6$), 7.53 (t, $J = 7.27$ Hz, 2H, H_7), 0.77 (s, 4H, $H_1 + H_2$), 0.37 (s,12H, Me); (^{13}C{^{1}H}, $CDCl_3$) δ (ppm), 154.0 (C_{11}), 142.6 (C_4), 129.8 (C_9), 129.3 (C_8), 127.8 (C_6), 126.5 (C_7), 7.8 (C_1, C_2), −3.69 (Me). IR (KBr, cm^{-1}): 1250, 2955, 1343, 837.

2.4. Synthesis of [$PdCl_2$($\mathbf{L^1}$)] (1)

To a solution of $\mathbf{L^1}$ (0.09 g, 0.3 mmol) made in 10 ml of acetone was added $Na_2[PdCl_4]$ (0.088 g, 0.3 mmol) dissolved in 10 ml of water. The resulting mixture was stirred for 2 h at room temperature and poured into 100 ml of water. The complex was extracted into chloroform (2 × 50 ml). The extract was dried over anhydrous sodium sulfate, concentrated to ~10 ml and mixed with hexane (20 ml). The resulting red-yellow coloured compound (**1**) was filtered, washed with hexane (3 × 20 ml) and dried in vacuo. The single crystals of the complex **1** were grown from CH_2Cl_2 layered with hexane. Yield 0.11 g, ~76.9%; m.p. 160 °C; *Anal.* Calc. for $C_{16}H_{24}N_2Si_2PdCl_2$: C 40.21; H, 5.02; N, 5.86. Found: C, 39.97; H, 5.01; N, 5.45%. NMR (^{1}H, $CDCl_3$) δ (ppm): 9.06 (d, $J = 5.7$ Hz, 2H, H_7), 7.63–7.55(m, 4H, $H_5 + H_4$), 7.24(br t, 2H, H_6), 1.55 (s, 4H, $H_1 + H_2$), 0.45 (s, 12H, Me); (^{13}C{^{1}H}, $CDCl_3$) δ (ppm): 153.8 (C_7), 135.7 (C_5), 132.8 (C_4), 124.2 (C_6), 8.5 (C_1, C_2), −0.7 (Me). IR (KBr, cm^{-1}): 1249, 2954, 1468, 833, 460, 606, 727.

2.5. Synthesis of [Ag($\mathbf{L^1}$)]ClO_4 (2)

A solution of $\mathbf{L^1}$ (0.09 g, 0.3 mmol) made in acetone (5 ml) was slowly diffused into solution of $AgClO_4$ (0.06 g, 0.3 mmol) made in 3 ml of water (deionized) to give colourless crystals of **2**, which are light and air sensitive and insoluble in water. The crystals can be stored under nitrogen protected from light for several days. Yield 0.122 g, ~81.0%; m.p. 150 °C; *Anal.* Calc. for $C_{16}H_{24}N_2Si_2AgClO_4$: C, 37.90; H, 4.70; N, 5.50. Found: C, 37.21; H, 4.49; N, 5.54%. ^{1}H NMR ($CDCl_3$) δ (ppm) : 9.24 (d, 2H, H_7), 7.84 (br t, 2H, H_5), 7.74 (br, 2H, H_4), 7.50 (br, 2H, H_6), 1.30 (s, 4H, $H_1 + H_2$), 0.35 (s, 12H, Me); (^{13}C{^{1}H}, $CDCl_3$) δ (ppm): 168.1 (C_3), 154.4 (C_7), 137.0 (C_5), 132.2 (C_4), 124.9 (C_6), 6.5 (C_1, C_2), −2.11(Me). IR (KBr, cm^{-1}): 1249, 2955, 1456, 1084, 829, 627.

2.6. Synthesis of [$CuBr_2$($\mathbf{L^1}$)] (3)

The solid $CuBr_2$ (0.066 g, 0.3 mmol) was added to a solution of $\mathbf{L^1}$ (0.09 g, 0.3 mmol) made in 10 ml of methanol and the resulting mixture stirred for 15 min. A clear dark green coloured solution was formed. This solution was kept at 5 °C for 2 days. The dark green coloured crystals of **3** were obtained. Yield 0.065 g, ~41.6%; m.p. 195 °C; *Anal.* Calc. for $C_{16}H_{24}N_2Si_2AgClO_4$: C, 36.67; H, 4.58; N, 5.34. Found: C, 35.93; H, 4.03; N, 5.68%. IR (KBr, cm^{-1}): 2955, 2358, 1249, 1459, 837, 469. Its paramagnetic nature restricted us from recording its NMR data.

2.7. Synthesis of [$PdCl_2$($\mathbf{L^2}$)]$_2$ (4)

To a solution of $\mathbf{L^2}$ (0.12 g, 0.3 mmol) made in 10 ml of acetone was added $Na_2[PdCl_4]$ (0.88 g, 0.3 mmol) dissolved in 10 ml of water. The resulting mixture was stirred for 2 h at room temperature and poured into 100 ml of water. The complex was extracted into chloroform (2 × 50 ml). The extract was dried over anhydrous sodium sulfate, concentrated to ~10 ml and mixed with hexane (20 ml). The resulting red-yellow compound (**4**) was filtered, washed

with hexane (3 × 20 ml) and dried in vacuo. The single crystals of the complex **4** were grown from chloroform–acetonitrile mixture (1:1). Yield 0.241 g, ~69.65%; m.p. 190 °C; *Anal.* Calc. for $Si_2C_{24}H_{28}N_2PdCl_2$: C, 49.86; H, 4.80; N, 4.80. Found: C, 50.08; H, 4.74; N, 4.71%. NMR (^1H, $CDCl_3$) δ (ppm): 9.95 (s, 2H, H_{11}), 9.40 (s, 2H, H_4), 8.29 (br, 2H, H_9), 8.07 (br, 2H, H_8), 7.7–7.56 (m, 4H, $H_6 + H_7$), 0.90 (s, 4H, $H_1 + H_2$), 0.50 (s, 12H, Me). IR (KBr, cm^{-1}): 1257, 2954, 1411, 794, 637, 749.

2.8. Synthesis of [Ag L^2]ClO_4 (5)

A solution of $\mathbf{L^2}$ (0.12 g, 0.3 mmol) in acetone (5 ml) was slowly diffused into $AgClO_4$ (0.06 g, 0.3 mmol) dissolved in 3 ml of water (deionized) to give white powder, which is light and air sensitive and insoluble in water. The solid can be stored under nitrogen protected from light for several days. Yield 0.264 g, ~72.72%; m.p. >250 °C; *Anal.* Calc. for $Si_2C_{24}H_{28}N_2AgClO_4$: C, 47.47; H, 4.61; N, 4.61. Found: C, 47.72; H, 4.58; N, 4.70%. NMR (^1H, $CDCl_3$) δ (ppm): 9.38 (s, 2H, H_{11}), 8.49 (s, 2H, H_4), 8.20 (d, $J = 9$ Hz, 2H, H_9), 7.92–7.82 (m, 4H, $H_8 + H_6$), 7.65 (t, $J = 6$ Hz, 2H H_7), 0.92 (s, 4H, $H_1 + H2$), 0.46 (s, 12H, Me). IR (KBr, cm^{-1}): 1255, 2955, 1411, 808. ClO_4^- ion gives characteristic IR bands at 1105 and 626 cm^{-1}.

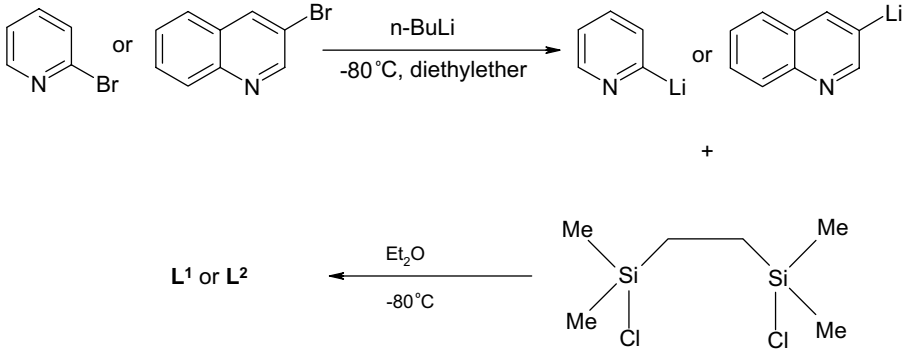
3. Results and discussion

The ligands $\mathbf{L^1}$ and $\mathbf{L^2}$ were synthesized by sequence of reactions given in Scheme 1 using Schlenk techniques. At higher temperatures the reactions of Scheme 1 were not successful. Moreover, dinitrogen atmosphere was found essential for these reactions. The $\mathbf{L^1}$ and $\mathbf{L^2}$ are air stable but $\mathbf{L^1}$ has to be stored at 4 °C. Both the ligands are highly soluble in chloroform, dichloromethane, acetone, diethylether, methanol and ethanol but only sparingly in hexane. Their reactions with metal ions Ag(I), Cu(II) and Pd(II) result in complexes [Ag($\mathbf{L^1}$/$\mathbf{L^2}$)]ClO_4 (**2** and **5**), [Cu$\mathbf{L^1}$]Br_2 (**3**), [Pd($\mathbf{L^1}$)Cl_2] (**1**) and [Pd($\mathbf{L^2}$)Cl_2]$_2$ (**4**). The complexes are stable under ambient conditions except those of Ag, which have to be protected from light as it causes their decomposition. Solubility of all the complexes was found to be good in chloroform, dichloromethane and acetonitrile. In hexane and diethyl ether they were found sparingly soluble. Pd and Cu complexes are additionally soluble in THF, acetone and benzene. Complex of $\mathbf{L^1}$ with Ag is also soluble in ethanol and methanol. The variation in the ratio M:L did not result species other than **1**–**5**.

The silver complexes of both $\mathbf{L^1}$ and $\mathbf{L^2}$ have been found to be 1:1 electrolyte [$\Lambda_M = 141/155$ S cm^2 mol^{-1} (**2**/**5**)]. IR spectra of $\mathbf{L^1}$ and $\mathbf{L^2}$ and their metal complexes were found to be characteristic. In the spectrum of **2** and **5** bands due to uncoordinated ClO_4^- were observed around 626 and 1084/1105 cm^{-1}. In the ligands and their complexes bands between 794 and 837 cm^{-1} appear due to Si–C(py/quin.) vibrations whereas Si–CH_3 vibrations appear between 1249 and 1257 cm^{-1}.

3.1. ^1H and $^{13}C\{^1H\}$ NMR spectra

The proton and carbon-13 NMR spectra of $\mathbf{L^1}$ and $\mathbf{L^2}$ are characteristic. The signals of CH_3 and CH_2 groups of $\mathbf{L^1}$ and $\mathbf{L^2}$ are marginally shielded (up to 0.06 ppm) with respect to those of their precursor halide (Scheme 1). The proton and carbon-13 NMR spectra of all the metal complexes are also characteristic. The H_6 and H_8 merge together in the ^1H NMR spectrum of $\mathbf{L^2}$. The signal of H_7 of $\mathbf{L^1}$ on complexation is deshielded by ~0.29 −0.47 ppm (with respect to that of free ligand) and deshielding is maximum in the case of Pd-complex. The signals of H_1 and H_2 exhibit deshielding in the range 0.53–0.78 ppm. The H_4, H_5 and H_6 signals of Pd-complex of $\mathbf{L^1}$ exhibit small deshielding (<0.1 ppm), however, in case of Ag-complex these signals are deshielded by 0.27 to 0.31 ppm. The signal of H_{11} of $\mathbf{L^2}$ on complex formation is deshielded ~0.44 −1.01 ppm with respect to that of free ligand. Similarly signal of H_9 on complexation is deshielded by ~0.12–0.21 ppm and that of H_4 exhibits deshielding in the range 0.29–1.20 ppm. The deshielding of H_1 and H_2 signals is in the range 0.13–0.15 ppm. The signal of H_6, H_7 and H_8 merge together in the spectrum of Pd- complex **4** but they are deshielded at least 0.17–0.30 ppm with respect to those of free ligand. In the spectrum of Ag complex **5**, H_8 and H_6 have been found merged but deshielded by ~0.15 ppm with



Scheme 1.

respect to those of free $\mathbf{L^2}$. The signal of H_7 in case of **5** shows deshielding of ~0.1 ppm.

In carbon-13 NMR spectra of metal complexes of $\mathbf{L^1}$, C_7 signal appears deshielded (~5.0–5.6 ppm). The deshielding in the case C_5 and C_4 is in the range 3.3–5.1 ppm. The signal of C_6 of $\mathbf{L^1}$on complexation is deshielded by ~2.9–3.6 ppm in all cases. In case of Ag-complex of $\mathbf{L^1}$ small deshielding (<1 ppm) is exhibited in the signals of C_1 and C_2, however, in the spectrum of Pd-complex these signals are deshielded by ~2.9 ppm. The deshielding of various protons and carbon atoms suggests that in all the complexes the ligands $\mathbf{L^1}$ and $\mathbf{L^2}$ coordinate through nitrogen of pyridine or quinoline ring. This has been further corroborated by single crystal structures of **1**, **3** and **4**.

3.2. Crystal structures

The $\mathbf{L^2}$ has been authenticated by X-ray diffraction on its single crystals. In Table 2 selected bond lengths are given and in Fig. 1 molecular structure is shown. The Si–C(alkyl) and Si–C(aryl) bond lengths (Table 2) are consistent with literature reports 1.849(4)–1.863(4) and 1.873(2) Å respectively [16]. The bond angles at Si are around 109° as expected. The bond lengths and bond angles of pyridine ring were found to be normal. The molecular structure of **1** is shown in Fig. 2 and selected bond lengths and angles are given in Table 3. The $\mathbf{L^1}$ coordinates with Pd(II) through pyridyl nitrogen atoms making a nine-membered palladamacrocyclic complex.

The Pd in **1** has a square geometry with two chloride ligands *trans* to each other. The Pd–Cl (2.3102(4)/2.3114(4) Å) bond distances of **1** (Table 3) are consistent with the literature values of 2.3110(4) Å reported [17] for Pd(II)-complex of *N*-{2-(4-methoxyphenyltelluro)ethyl} morpholine, which also has two such bonds*trans* to each other. Similarly Pd–N (2.010(1)/2.015(1) Å) bond distances of **1** are consistent with reported values, 2.095(4) Å [18] for

Table 2
Selected bond lengths (Å) and bond angles (°) for $\mathbf{L^2}$

Bond length (Å)		Bond angles (°)	
Si(1)–C(14)	1.871(2)	C(1)–Si(1)–C(15)	108.06(12)
Si(1)–C(1)	1.883(3)	C(1)–Si(1)–C(16)	109.78(12)
Si(1)–C(16)	1.858(3)	C(14)–Si(1)–C(15)	110.63(12)
Si(1)–C(15)	1.861(3)	C(14)–Si(1)–C(16)	109.34(12)
C(14)–C(14)	1.525(4)		

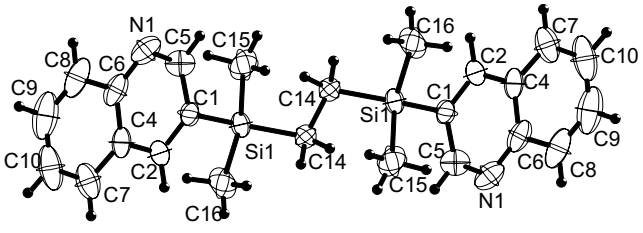


Fig. 1. Molecular structure of $\mathbf{L^2}$.

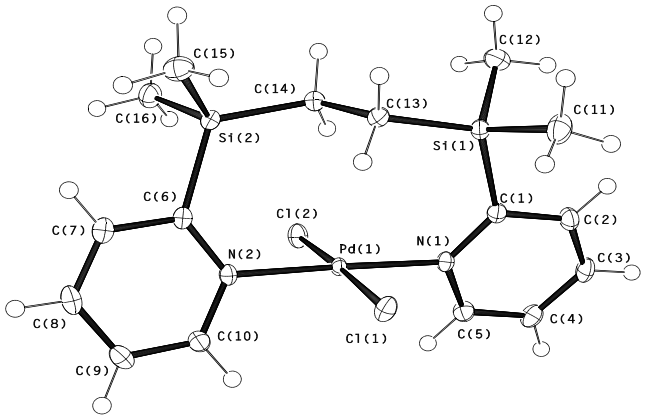


Fig. 2. Molecular structure of **1**.

Table 3
Selected bond lengths (Å) and bond angles (°) for **1**

Bond lengths (Å)		Bond angles (°)	
Si(1)–C(1)	1.921(2)	C(1)–Si(1)–C(11)	105.44(8)
Si(1)–C(13)	1.876(2)	C(1)–Si(1)–C(13)	116.78(7)
Si(2)–C(6)	1.917(2)	C(12)–Si(1)–C(13)	108.56(8)
Si(2)–C(14)	1.872(2)	C(11)–Si(1)–C(12)	111.58(9)
C(13)–C(14)	1.551(2)	C(1)–N(1)–Pd(1)	123.9(1)
N(1)–C(1)	1.354(2)	C(5)–N(1)–Pd(1)	115.4(1)
N(1)–C(5)	1.347(2)	N(1)–Pd(1)–Cl(1)	89.37(4)
N(2)–C(10)	1.349(2)	N(1)–Pd(1)–Cl(2)	90.06(4)
N(2)–C(6)	1.357(2)	N(2)–Pd(1)–Cl(2)	90.95(4)
Pd(1)–N(1)	2.010(1)	N(2)–Pd(1)–Cl(1)	89.54(4)
Pd(1)–Cl(1)	2.3102(4)	Si(1)–C(1)–N(1)	126.9(1)
Pd(1)–N(2)	2.015(1)	Si(1)–C(1)–C(2)	115.1(1)
Pd(1)–Cl(2)	2.3114(4)	C(6)–Si(2)–C(14)	117.10(8)
		C(14)–Si(2)–C(15)	109.60(9)
		C(15)–Si(2)–C(16)	111.13(9)
		C(6)–Si(2)–C(16)	103.10(8)
		C(6)–N(2)–Pd(1)	123.7(1)
		C(10)–N(2)–Pd(1)	115.8(1)
		N(2)–C(6)–Si(2)	126.9(1)
		C(7)–C(6)–Si(2)	114.9(1)

a *trans* N–Pd–N system. The bond distance (Table 3) Si–C(aryl) is greater than Si-C(alkyl) but both are consistent with the reported values [19] 1.913(3) and 1.882(3) Å for Si–C(aryl) and Si–C(alkyl) respectively. A similar observation is made in case of $\mathbf{L^2}$. The molecular structure of **3** is shown in Fig. 3 and its selected bond distances and angles are given in Table 4. The **3** is also nine-membered metallamacrocylic complex like **1**. The two Br are *trans* to each other. The Cu–Br distance 2.4137(10)/2.4172(10) Å of **3** (Table 4) is consistent with the value of 2.4151(3) Å reported for Cu(II) complex of 4,7-phenathroline [20]. Similarly Cu–N bond distances (Table 4) are in agreement with the literature values 1.983(2) Å reported for Cu(II) complex of 4,7-phenathroline [20]. The Si–C(aryl) and Si–C(alkyl) bond distances were found in case of **3** as 1.908(8)/1.895(6) Å and 1.845(6)–1.873(7) Å. They were also in agreement with the literature values mentioned above [19]. The **4** is a 22-membered metallamacrocyclic system and is the first example of this size which has ligand con-

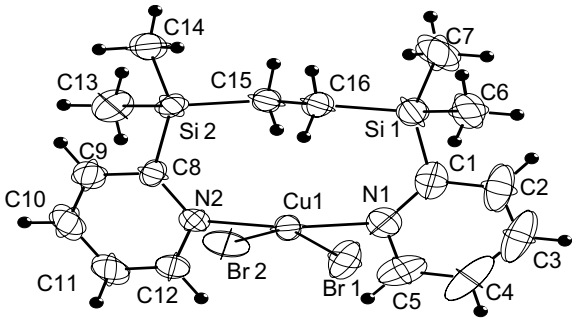


Fig. 3. Molecular structure of **3**.

Table 4
Selected bond lengths (Å) and bond angles (°) for **3**

Bond lengths (Å)		Bond angles (°)	
Si(1)–C(16)	1.848(6)	C(6)–Si(1)–C(1)	108.1(3)
Si(1)–C(1)	1.908(8)	C(6)–Si(1)–C(7)	110.9(4)
Si(2)–C(15)	1.858(6)	C(16)–Si(1)–C(1)	112.1(3)
Si(2)–C(8)	1.895(6)	C(16)–Si(1)–C(7)	109.4(3)
C(15)–C(16)	1.541(8)	C(1)–N(1)–Cu(1)	126.4(4)
N(1)–C(1)	1.345(8)	C(5)–N(1)–Cu(1)	112.8(5)
N(1)–C(5)	1.350(8)	C(15)–Si(2)–C(8)	111.9(3)
N(2)–C(8)	1.351(7)	C(14)–Si(2)–C(15)	109.8(3)
N(2)–C(12)	1.340(7)	C(14)–Si(2)–C(13)	110.2(3)
Cu(1)–N(1)	2.018(5)	C(13)–Si(2)–C(8)	107.1(3)
Cu(1)–Br(1)	2.4137(10)	C(8)–N(2)–Cu(1)	125.4(4)
Cu(1)–Br(2)	2.4172(10)	C(12)–N(2)–Cu(1)	115.1(4)
Cu(1)–N(2)	2.004(4)	Br(1)–Cu(1)–Br(2)	152.71(4)
		N(1)–Cu(1)–Br(1)	89.13(14)
		N(2)–Cu(1)–N(1)	171.2(2)
		N(2)–Cu(1)–Br(2)	89.53(14)

taining organosilicon backbone. So far the largest metallomacrocycle reported with ligands containing Si backbone is 20-membered [4]. The Si–C(aryl) and Si–C(alkyl) bond distances were found in case of **4** as 1.877(4)–1.893(4) Å and 1.852(6)–1.873(5) Å, which are little bit longer than those of free $\mathbf{L^2}$ (Table 1). The Pd–Cl distances in the case of **4**, 2.268(11)–2.3094(11) Å are somewhat shorter than those

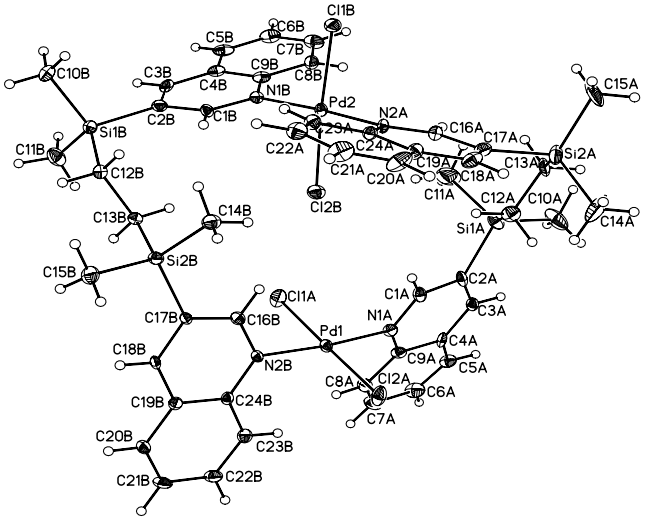


Fig. 4. Molecular structure of **4**.

Table 5
Selected bond lengths (Å) and bond angles (°) for **4**

Bond lengths (Å)		Bond angles (°)	
Pd(1)–N(2B)	2.037(2)	N(1A)–Pd(1)–Cl(1A)	88.20(9)
Pd(1)–N(1A)	2.038(3)	N(1A)–Pd(1)–Cl(2A)	91.00(9)
Pd(1)–Cl(1A)	2.2682(11)	N(2B)–Pd(1)–Cl(1A)	88.19(8)
Pd(1)–Cl(2A)	2.3099(11)	N(2B)–Pd(1)–Cl(2A)	92.57(8)
N(1A)–C(1A)	1.302(5)	Pd(1)–N(1A)–C(1A)	117.6(2)
N(1A)–C(9A)	1.380(4)	Pd(1)–N(1A)–C(9A)	122.1(2)
Si(1A)–C(2A)	1.893(4)	Si(1A)–C(2A)–C(1A)	120.4(3)
Si(1A)–C(12A)	1.862(4)	Si(1A)–C(2A)–C(3A)	122.8(2)
C(12A)–C(13A)	1.550(6)	C(2A)–Si(1A)–C(12A)	109.91(18)
Si(2A)–C(13A)	1.861(5)	C(2A)–Si(1A)–C(10A)	108.7(2)
Si(2A)–C(17A)	1.877(4)	C(10A)–Si(1A)–C(11A)	111.1(3)
N(2A)–C(16A)	1.310(4)	C(12A)–Si(1A)–C(11A)	110.0(3)
N(2A)–C(24A)	1.399(4)	C(13A)–Si(2A)–C(14A)	111.0(2)
Pd(2)–N(2A)	2.014(3)	C(13A)–Si(2A)–C(15A)	110.4(3)
Pd(2)–N(1B)	2.027(3)	C(15A)–Si(2A)–C(17A)	107.7(2)
Pd(2)–Cl(1B)	2.3063(10)	C(14A)–Si(2A)–C(17A)	108.3(3)
Pd(2)–Cl(2B)	2.3082(11)	Si(2A)–C(17A)–C(16A)	121.5(3)
N(1B)–C(1B)	1.330(4)	Si(2A)–C(17A)–C(18A)	122.9(3)
N(1B)–C(9B)	1.377(4)	Pd(2)–N(2A)–C(16A)	121.4(2)
Si(1B)–C(12B)	1.866(4)	Pd(2)–N(2A)–C(24A)	119.4(2)
C(12B)–C(13B)	1.549(5)	N(1B)–Pd(2)–Cl(1B)	91.87(8)
Si(2B)–C(13B)	1.876(4)	N(1B)–Pd(2)–Cl(2B)	89.66(8)
Si(2B)–C(17B)	1.890(3)	N(2A)–Pd(2)–Cl(1B)	90.29(9)
N(2B)–C(16B)	1.330(4)	N(2A)–Pd(2)–Cl(2B)	88.55(9)
N(2B)–C(24B)	1.364(4)	Pd(2)–N(1B)–C(1B)	116.2(2)
Si(1A)–C(10A)	1.861(5)	Pd(2)–N(1B)–C(9B)	125.0(2)
Si(1A)–C(11A)	1.869(6)	Si(1B)–C(2B)–C(3B)	123.0(3)
Si(1B)–C(10B)	1.859(4)	C(2B)–Si(1B)–C(12B)	108.59(16)
Si(1B)–C(11B)	1.873(5)	C(2B)–Si(1B)–C(10B)	109.58(19)
Si(2A)–C(14A)	1.866(6)	C(10B)–Si(1B)–C(11B)	109.5(2)
Si(2A)–C(15A)	1.852(6)	C(11B)–Si(1B)–C(12B)	110.8(2)
Si(2B)–C(15B)	1.864(4)	C(13B)–Si(2B)–C(14B)	107.95(17)
Si(1A)–C(2A)	1.893(4)	C(13B)–Si(2B)–C(15B)	111.02(19)
Si(2A)–C(17A)	1.877(4)	C(15B)–Si(2B)–C(17B)	108.00(17)
Si(2B)–C(17B)	1.890(3)	C(14B)–Si(2B)–C(17B)	111.99(17)
		Si(2B)–C(17B)–C(16B)	121.4(2)
		Si(2B)–C(17B)–C(17B)	122.2(2)
		Pd(1)–N(2B)–C(16B)	117.4(2)
		Pd(1)–N(2B)–C(24B)	122.0(2)

of **1**. Similarly Pd–N bond lengths 2.014(3)–2.038(3) are close to those of **1**. The sum of covalent radii (Å) are: Pd–N, 2.05, Pd–Cl, 2.30; Cu–N, 2.04 and Cu–Br, 2.44. On comparing these values with those of complexes **1**, **3** and **4** it appears that coordination of Pd as well as that of Cu with the ligands is strong (Fig. 4, Table 5).

4. Conclusion

Organosilicon backbone containing ligands 1,2-bis(dimethyl(2-pyridyl)silyl)ethane ($\mathbf{L^1}$) and 1,2-bis(dimethyl(3-quinolyl)silyl) ethane ($\mathbf{L^2}$), which have CH_2CH_2 spacer, have been synthesized and used to design metallamacrocyclic complexes of Pd(II) and Cu(II) having 9- or 22-membered rings. The **4** having 22-membered metallamacrocyclic is the first example containing ligand of organosilicon backbone. The geometry of Pd as well as Cu is very close to square planar in **1**, **3** and **4**. The Pd–N, Cu–N, Pd–Cl and Cu–Br bond distances are very close to sum of covalent radii indicating strong ligation of $\mathbf{L^1}$ and $\mathbf{L^2}$.

Acknowledgements

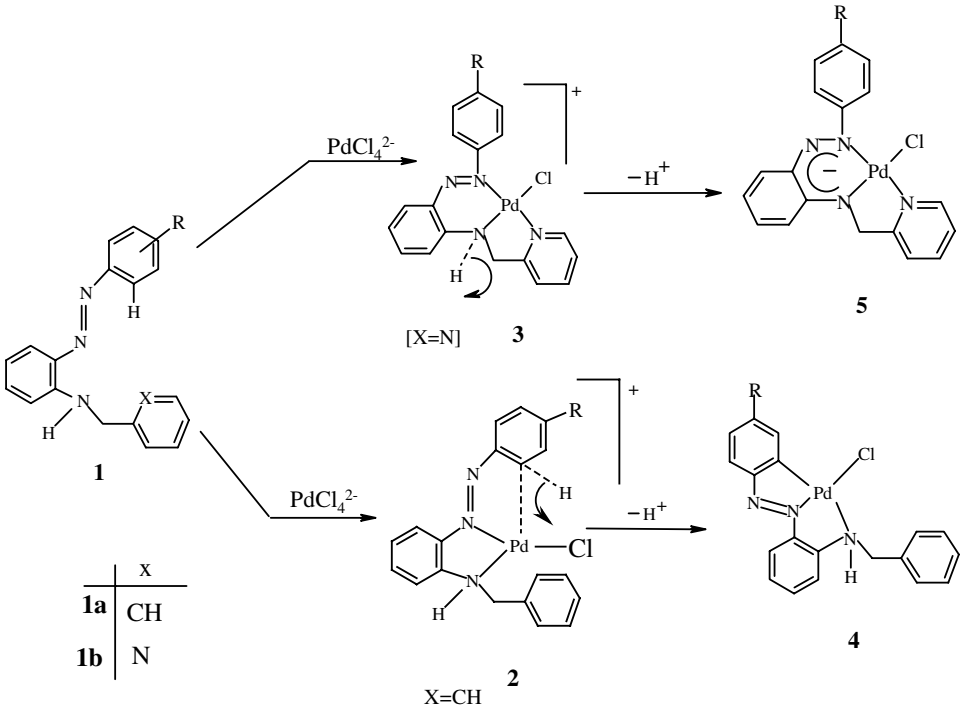
A.K.S. thanks Council of Scientific and Industrial Research (India) for Research Project No. 01(2113)07/EMR-II. N.R. thanks University Grants Commission (India) for Research Fellowship. P.S. thanks Department of Science and Technology (India) for financial support. R.J.B. wishes to acknowledge the NSR-MRI program for funds to purchase the X-ray diffractometer.

Appendix A. Supplementary material

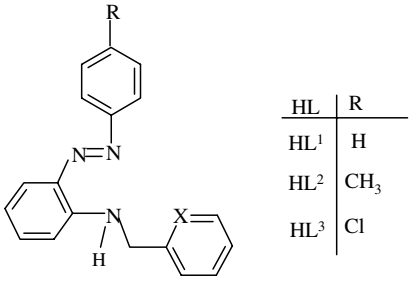
CCDC 647635, 647636, 647637 and 647638 contain the supplementary crystallographic data for L^2, **1**, **3** and **4**. These data can be obtained free of charge via http://www.ccdc.cam.ac.uk/conts/retrieving.html, or from the Cambridge Crystallographic Data Centre, 12 Union Road, Cambridge CB2 1EZ, UK; fax: (+44) 1223-336-033; or e-mail: deposit@ccdc.cam.ac.uk. Supplementary data associated with this article can be found, in the online version, at doi:10.1016/j.poly.2007.08.006.

References

[1] O.-S. Jung, Y.J. Kim, K.M. Kim, Y.A. Lee, J. Am. Chem. Soc. 124 (2002) 906.
[2] F.A. Cotton, E.V. Dikarev, M.A. Petrukhina, M. Schmitz, P.J. Stang, Inorg. Chem. 41 (2002) 2903.
[3] O.-S. Jung, Y.A. Lee, Y.J. Kim, J. Hong, Crystal Growth Des. 2 (2002) 497.
[4] M. Schmitz, S. Leininger, J. Fan, A.M. Arif, P.J. Stang, Organometallics 18 (1999) 4817.
[5] T.H. Noh, J.H. Kim, Y.-A. Lee, H. Suh, O.-S. Jung, J. Mol. Struct. 691 (2004) 165.
[6] M.E. Wright, S.A. Svejda, M.-J. Jin, M.A. Peterson, Organometallics 9 (1990) 136.
[7] M.E. Wright, Tetrahedron Lett. 28 (1987) 3233.
[8] M.E. Wright, M.-J. Jin, J. Organomet. Chem. 387 (1990) 373.
[9] O.-S. Jung, Y.A. Lee, Y.J. Kim, Chem. Lett. (2002) 1096.
[10] Y.A. Lee, K.H. Yoo, K.-M. Park, O.-S. Jung, Bull. Korean Chem. Soc. 23 (2002) 1839.
[11] O.-S. Jung, Y.J. Kim, Y.A. Lee, S.W. Kang, S.N. Choi, Crystal Growth Des. 4 (2004) 23.
[12] G.M. Sheldrick, SADABS V2.10 (2003).
[13] A. Altomare, G. Cascarano, C. Giacovazzo, A. Gualardi, J. Appl. Cryst. 26 (1993) 343.
[14] L.J. Farrugia, J. Appl. Cryst. 32 (1999) 837.
[15] G.M. Sheldrick, SHELXL 97, University of Gottingen, Germany.
[16] F. Riedmiller, A. Jockish, H. Schmidbaur, Organometallics 17 (1998) 4444.
[17] A.K. Singh, J. Sooriyakumar, S. Husebye, K.W. Tornroos, J. Organomet. Chem. 612 (2000) 46.
[18] Y. Li, Y.-H. Lai, K.F. Mok, M.G.B. Drew, Inor. Chim. Acta 279 (1998) 221.
[19] A. Asadi, A.G. Avent, M.P. Coles, C. Eaborn, P.B. Hitchcock, J.D. Smith, J. Organomet. Chem. 689 (2004) 1238.
[20] S.A. Barnett, A.J. Blake, N.R. Champness, C. Wilson, Dalton Trans. (2003) 2387.



Scheme 1.



HL	R
HL^1	H
HL^2	CH_3
HL^3	Cl

1b

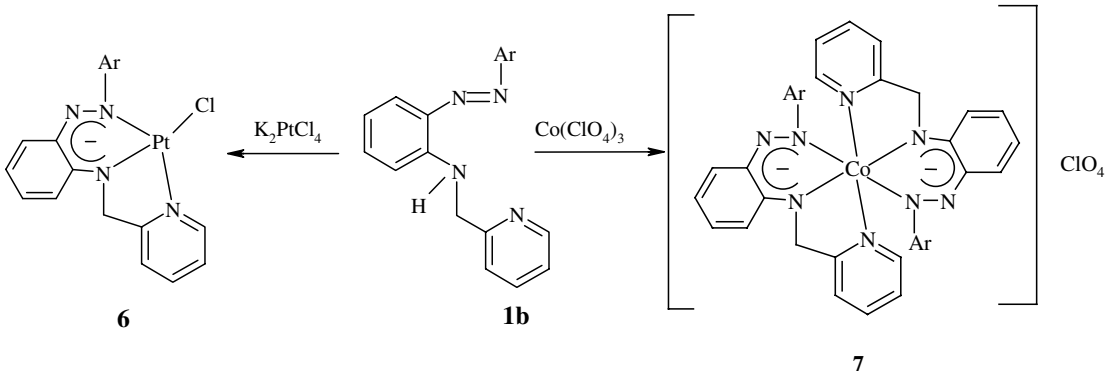
HL when X=N of **1b**

Formation of a diazoketiminato chelate, like **5**, supported our mechanistic proposal. The bis complex cation of Co(III) incorporating the tridentate diazoketimine ligand has been isolated for the first time. Synthesis, X-ray structures, redox properties and the plausible nature of the redox orbitals have been reported in this paper.

2. Results and discussion

2.1. Syntheses

The reaction of 1*N*-(2-pyridyl-2-methyl)-2-arylazo aniline, HL, with K_2PtCl_4 in methanol afforded a pink complex of platinum (II) of the composition (L)PtCl **6** incorporating the tridentate (*N*,*N*,*N*) ligand (Scheme 2). Reaction of HL **1b** with $Co(ClO_4)_3 \cdot 6H_2O$ in refluxing methanol afforded the blue-violet bis complex of the composition $[(L)_2Co]ClO_4$ **7** where L^- binds the metal in a tridentate (*N*,*N*,*N*) fashion (Scheme 2). In both cases the



Scheme 2.

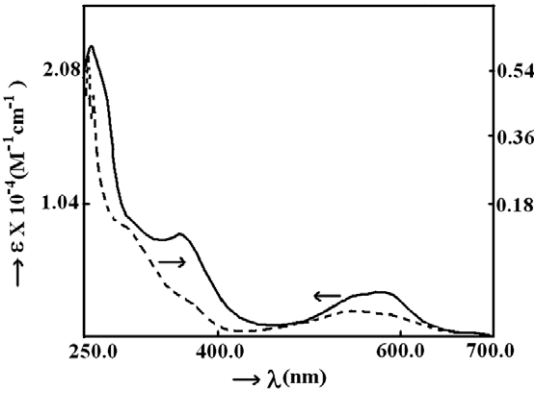


Fig. 1. UV–Vis spectra of $[(L^1)_2Co]ClO_4$ (---) and $(L^1)PtCl$ (—). The arrows indicate scales of the corresponding spectra.

deprotonated secondary amino nitrogen binds the metal forming a six-membered diazoketiminato chelate. Formation of a six-membered diazoketiminato chelate has been attributed to the delocalisation of the negative charge within the ligand backbone [14–17]. Complex **7** is diamagnetic and is consistent with a low spin t_{2g}^6 configuration.

2.2. Characterization

All the Pt(II) complexes, (L)PtCl, exhibited a characteristic low energy absorption near 580 nm which has been assigned to a MLCT transition [14–18]. The low energy absorption due to a MLCT transition for the $[(L)_2Co]ClO_4$ complexes has been observed near 570 nm. Representative UV–Vis spectra of $(L^1)PtCl$ and $[(L^1)_2Co]ClO_4$ are shown in Fig. 1. Relevant data are collected in Section 3.

The IR spectra of HL [17] displayed a sharp singlet near 3189 cm^{-1} for ν_{N-H} which was absent for both the complexes (L)PtCl and $[(L)_2Co]ClO_4$, indicating the dissociation of the amino proton upon complexation. The $\nu_{N=N}$ of the ligands (~1510 cm^{-1}) shifted to lower frequency upon complexation (1400–1410 cm^{-1}), consistent with coordination of the azo nitrogen [14–18]. The ν_{Pt-Cl} of the platinum complexes appeared at 325 cm^{-1} [19,20]. The cobalt complexes exhibited a broad absorption near 1100 cm^{-1}, characteristic of uncoordinated ClO_4^-. Relevant data are included in Section 3.

The N–H resonance of the free ligands (δ 9.37–9.55 ppm) [17] were absent in the ^1H NMR spectra of the platinum and cobalt complexes, signifying the dissociation of the N–H proton upon complexation. The resonance of the methylene protons appeared in the platinum complexes as a singlet (δ 5.29–5.48 ppm), in contrast to the doublet of the ligands (δ 4.68–4.69 ppm), indicating the lack of vicinal coupling due to the absence of the N–H proton [17]. The resonances of the pair of methylene protons in the $[(L)_2Co]^+$ ion appeared as two doublets signifying the substantial difference in chemical shielding within the pair. Resonances for the other aromatic protons are consistent with the structure as determined by X-ray studies (see below). The ^1H NMR data are collected in Section 3.

2.3. X-ray structure of $(L^3)PtCl$

Suitable crystals of $(L^3)PtCl$ were grown by the slow evaporation of a dichloromethane–methanol mixed solution. The X-ray structure of $(L^3)PtCl$ was determined and the perspective view of the molecule along with the atom numbering scheme is shown in Fig. 2. Selected bond distances and angles are collected in Table 1. The geometry about platinum is distorted square planar where the $(L^3)^-$ binds in a tridentate (*N*,*N*,*N*) fashion. A chloride ligand satisfies the tetracoordination. The three nitrogen

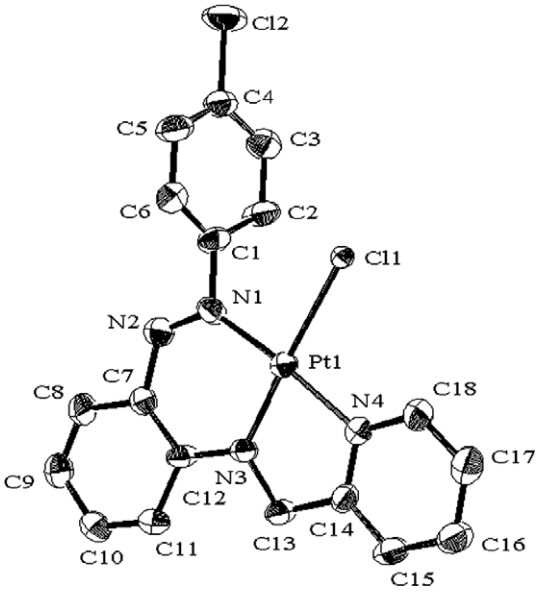


Fig. 2. Perspective view of $(L^3)PtCl$ with the atom numbering scheme. Hydrogen atoms are omitted.

Table 1
Selected bond distances (Å) and angles (°) for $(L^3)PtCl$

Bond distances			
Pt(1)–N(1)	2.004(13)	C(7)–C(12)	1.40(2)
Pt(1)–N(3)	1.957(11)	C(11)–C(12)	1.49(2)
Pt(1)–N(4)	2.054(12)	N(3)–C(13)	1.44(2)
N(1)–N(2)	1.265(19)	C(10)–C(11)	1.37(2)
N(2)–C(7)	1.44(2)	C(9)–C(10)	1.39(3)
N(1)–C(1)	1.38(2)	C(8)–C(9)	1.37(2)
N(3)–C(12)	1.345(19)	C(7)–C(8)	1.43(2)
C(13)–C(14)	1.50(2)	N(4)–C(14)	1.352(19)
Pt(1)–Cl(1)	2.540(3)		
Bond angles			
Cl(1)–Pt(1)–N(1)	92.6(4)	Cl(1)–Pt(1)–N(3)	173.5(4)
Cl(1)–Pt(1)–N(4)	93.0(3)	N(1)–Pt(1)–N(3)	92.5(5)
N(1)–Pt(1)–N(4)	174.2(5)	N(1)–C(1)–C(2)	117.3(14)
N(3)–Pt(1)–N(4)	82.0(5)	Pt(1)–N(1)–N(2)	127.7(11)
N(2)–C(7)–C(12)	127.4(13)	N(1)–N(2)–C(7)	122.5(14)
C(12)–N(3)–C(13)	117.7(12)	Pt(1)–N(3)–C(12)	125.0(10)
Pt(1)–N(4)–C(14)	113.0(9)	N(3)–C(13)–C(14)	110.1(12)

donors are azo (*N*(azo)), pyridyl (*N*(py)) and deprotonated amino (*N*(am)) nitrogens. The Pt–N(azo), Pt–N(py) and Pt–Cl lengths (2.004(13), 2.054(12) and 2.540(3) Å, respectively) are within the normal range [15,19,20]. The geometry about platinum is planar (mean deviation 0.067 Å) consistent with a dipositive oxidation state of platinum and the uninegative ligand, since the complex is non-electrolyte.

The C(12)–N(3) length (1.345(19) Å) is shorter compared to a C–N single bond (N(1)–C(1) 1.38(2) Å) in the same molecule and is similar to the imine (C=N) distance [14–17]. The effect of imine formation due to delocalisation has been reflected in the adjacent phenyl ring (C(7)–C(12)) which is distorted with two short (~1.37 Å) and four long (~1.43 Å) bonds [14–17]. Thus, the formation of a diazoketiminato chelate could be inferred from the X-ray results and the structural formula of (L^3)PtCl has been drawn accordingly in **6** of Scheme 2 (*vide supra*). All the non-hydrogen atoms of (L^3)PtCl, excluding the pendant phenyl ring (C(1)–C(6)), make a good plane (mean deviation 0.220 Å).

2.4. X-ray structure of $[(L^3)_2Co]ClO_4$

Suitable crystals of $[(L^3)_2Co]ClO_4$ were obtained from the methanolic mother liquor. The X-ray structure of $[(L^3)_2Co]ClO_4$ was determined and the perspective view of the $[(L^3)_2Co]^+$ cation along with the atom numbering scheme is shown in Fig. 3. Selected bond distances and angles are collected in Table 2. The geometry about the Co(III) centre is distorted octahedral, where the two anionic ligands, $[L^3]^-$, coordinated meridionally give rise to a CoN_6 coordination sphere. A perchlorate (ClO_4^-) ion satisfies the unipositive charge of the complex cation, $[(L^3)_2Co]^+$. The relative orientations of *N*(py), *N*(azo) and *N*(am) pairs are *cis*, *cis* and *trans*, respectively. Extensive electron delocalisation along the ligand backbone is also observed in this case. As a result, the C(12)–N(3) length (1.329(4) Å) and C(30)–N(7) length (1.343(4) Å) are shorter compared to the C–N single bonds (N(1)–C(1) 1.449(4) Å; N(5)–C(19) 1.444(5) Å) in the same molecule and are similar to the imine (C=N) distance [19–22]. The effect of imine formation due to delocalisation has also been reflected in the adjacent phenyl ring (C(7)–C(12)) which is distorted with two short (~1.35 Å) and four long (~1.42 Å) bonds, consistent with the formation of a diazoketiminato chelate [14–17,23]. The structural formula of $[(L^3)_2Co]ClO_4$ has been drawn accordingly in **7** of Scheme 2 (*vide supra*).

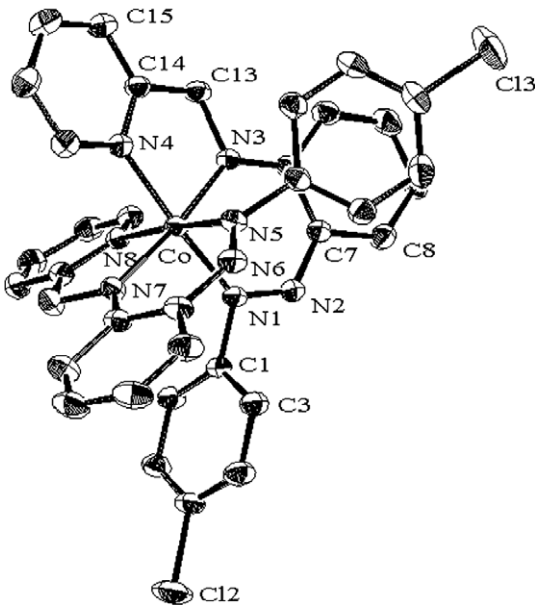


Fig. 3. Perspective view of $[(L^3)_2Co]^+$ with the atom numbering scheme. Hydrogen atoms and the perchlorate ion are omitted.

Table 2
Selected bond distances (Å) and angles (°) of $[(L^3)_2Co]ClO_4$

Bond distances			
Co–N(1)	1.919(3)	N(4)–C(18)	1.346(4)
Co–N(3)	1.910(3)	N(4)–C(14)	1.344(4)
Co–N(4)	1.980(3)	N(1)–N(2)	1.277(4)
Co–N(5)	1.924(3)	N(5)–N(6)	1.292(3)
Co–N(7)	1.915(3)	C(25)–C(26)	1.431(5)
Co–N(8)	1.977(3)	C(26)–C(27)	1.345(6)
C(7)–C(8)	1.413(5)	C(27)–C(28)	1.381(8)
C(8)–C(9)	1.347(6)	C(28)–C(29)	1.374(5)
C(9)–C(10)	1.410(6)	C(29)–C(30)	1.424(5)
C(10)–C(11)	1.355(6)	C(25)–C(30)	1.421(6)
C(11)–C(12)	1.420(5)	N(7)–C(31)	1.451(5)
C(7)–C(12)	1.452(5)	N(7)–C(30)	1.343(4)
N(3)–C(13)	1.468(4)	N(8)–C(32)	1.342(5)
N(3)–C(12)	1.329(4)	N(8)–C(36)	1.358(4)
N(1)–C(1)	1.449(4)	N(5)–C(19)	1.444(5)
Bond angles			
N(1)–Co–N(3)	91.67(11)	N(1)–N(2)–C(7)	123.7(3)
N(1)–Co–N(5)	88.09(12)	N(5)–Co–N(3)	93.19(12)
N(3)–Co–N(4)	83.37(11)	Co–N(1)–N(2)	128.30(19)
N(2)–C(7)–C(12)	126.3(3)	N(8)–Co–N(7)	83.32(12)
N(1)–Co–N(4)	175.04(11)	N(7)–Co–N(1)	93.82(11)
N(5)–N(6)–C(25)	122.5(3)	C(14)–N(4)–C(18)	118.7(3)
Co–N(3)–C(12)	127.7(2)	Co–N(4)–C(14)	114.0(2)
N(3)–Co–N(7)	172.68(14)	N(5)–Co–N(7)	91.83(12)

2.5. Redox processes and nature of redox orbitals

(L^3)PtCl and $[(L^3)_2Co]ClO_4$ displayed one and two irreversible oxidative responses, respectively, in their cyclic voltammograms (0.924 V versus SCE for the Pt(II) complex and 0.78, 1.14 V versus SCE for the Co(III) complex). To have an insight into the nature of the redox orbitals, the EHMO results have been taken into account (Supplementary material). The HOMO of (L)PtCl and $[(L)_2Co]ClO_4$ (Figs. S20 and S22) were found to be primarily ligand orbitals. Thus, the oxidative responses have been attributed to ligand oxidations as given in

$$[(L)Pt^{II}Cl] \xrightarrow{-e} [(L^{\cdot})PtCl]^+ \quad (1)$$

$$[(L)_2Co^{III}]^+ \xrightarrow{-e} [(L^-)(L^{\cdot})CO]^{2+} \xrightarrow{-e} [(L^{\cdot})(L^{\cdot})Co]^{3+} \quad (2)$$

3. Experimental

3.1. Materials

The solvents used in the reactions were of reagent grade obtained from E. Merck, Kolkata, India, and were purified and dried by reported procedures [23,24]. 2-(Arylazo) anilines and 1*N*-(2-pyridyl-2-methyl)-2-arylazoaniline were prepared according to reported procedures [14,15,17]. Chloroplatinic acid, cobalt carbonate, potassium carbonate, perchloric acid and potassium chloride were purchased from E. Merck, Kolkata, India. 2-(Chloromethyl) pyridine hydrochloride was purchased from Lancaster, England. Potassium tetrachloroplatinate was prepared by reported procedures [25]. Cobalt(III) perchlorate was prepared by oxidation of Co(II) perchlorate with H_2O_2 [26].

3.2. Syntheses of the Pt(II) complexes

The complexes $(L^1)PtCl$, $(L^2)PtCl$ and $(L^3)PtCl$ were prepared by a similar procedure. A representative example for $(L^1)PtCl$, is given below.

3.2.1. $(L^1)PtCl$

A solution of HL^1 (0.1 g, 0.35 mmol) in 10 cm^3 methanol was added to a solution of K_2PtCl_4 (0.145 g, 0.35 mmol) in 5 cm^3 water. The mixture was stirred for 15 h. The dark solid precipitate that formed was purified by washing with benzene–petroleum ether (80:20) mixed solvent. The pure solid was then dissolved in dichloromethane with a few drops of methanol and kept for crystallisation. Pure crystalline solid of $(L^1)PtCl$ was obtained. Yield: 50%. *Anal.* Calc. for $C_{18}H_{15}N_4PtCl$, $(L^1)PtCl$: C, 41.75; H, 2.92; N, 10.82. Found: C, 41.73; H, 2.90; N, 10.85%. Electronic spectrum (λ_{max}/nm (ε/dm^2 mol^{-1}), dichloromethane): 578 (2200), 359 (5000), 259 (14 260). IR (KBr pellets, cm^{-1}): $\nu_{N=N}$ 1405, ν_{Pt-Cl} 326. ^1H NMR ($CDCl_3$, ppm): δ 9.67 (d, 1H); 7.99 (d, 1H); 7.88–7.83 (m, 2H); 7.66–7.62 (m, 1H); 7.59 (d, 1H); 7.42–7.39 (m, 3H); 7.36–7.27 (m, 2H); 7.03 (d, 1H); 6.65 (t, 1H); 5.48 (s, 2H).

3.2.2. $(L^2)PtCl$ and $(L^3)PtCl$

Complexes $(L^2)PtCl$ and $(L^3)PtCl$ were prepared using the ligands HL^2 and HL^3 in place of HL^1. Yield: $(L^2)PtCl$, 50% and $(L^3)PtCl$, 55%, respectively.

Anal. Calc. for $C_{19}H_{17}N_4PtCl$, $(L^2)PtCl$: C, 42.89; H, 3.19; N, 10.53. Found: C, 42.92; H, 3.23; N, 10.50%. Electronic spectrum (λ_{max}/nm (ϵ/dm^2 mol^{-1}), dichloromethane): 579 (1230), 358 (2750), 259 (7483). IR (KBr pellets, cm^{-1}): $\nu_{N=N}$ 1402, ν_{Pt-Cl} 325. ^1H NMR ($CDCl_3$, ppm): δ 9.61 (d, 1H); 8.13 (d, 1H); 7.97–7.96 (m, 2H); 7.35–7.29 (m, 3H); 7.26–7.21 (m, 3H); 7.17–7.23 (m, 1H); 6.62 (m, 1H); 5.29 (s, 2H); 2.40 (s, 3H).

Anal. Calc. for $C_{18}H_{14}N_4PtCl_2$, $(L^3)PtCl$: C, 39.14; H, 2.56; N, 10.14. Found: C, 39.10; H, 2.60; N, 10.20%. Electronic spectrum (λ_{max}/nm (ϵ/dm^2 mol^{-1}), dichloromethane): 581 (3200), 359 (7050), 258 (18 380). IR (KBr pellets, cm^{-1}): $\nu_{N=N}$ 1400, ν_{Pt-Cl} 324. ^1H NMR ($CDCl_3$, ppm): δ 9.72 (d, 1H); 7.97 (m, 2H); 7.90 (t, 1H); 7.67 (m, 2H); 7.60 (d, 1H); 7.37–7.29 (m, 3H); 7.04 (d, 1H); 6.67 (t, 1H); 5.47 (s, 2H).

3.3. Syntheses of the Co(III) complexes

The complexes $[(L^1)_2Co]ClO_4$, $[(L^2)_2Co]ClO_4$ and $[(L^3)_2Co]ClO_4$ were prepared by a similar procedure. A representative example for $[(L^1)_2Co]ClO_4$, is given below.

3.3.1. $[(L^1)_2Co]ClO_4$

A solution of HL^1 (0.2 g, 0.70 mmol) in 10 cm^3 methanol was added to a 5 cm^3 methanolic solution of $Co(ClO_4)_3 \cdot 6H_2O$ (0.150 g, 0.35 mmol). The mixture was refluxed for 1 h. The colour of the solution became blue-violet. It was kept for five days. Pure crystalline solid of $[(L^1)_2Co]ClO_4$ was obtained. Yield: 65%. *Anal.* Calc. for $C_{36}H_{30}N_8CoClO_4$, $[(L^1)_2Co]ClO_4$: C, 58.98; H, 4.12; N, 15.28. Found: C, 59.00; H, 4.17; N, 15.25%. Electronic spectrum (λ_{max}/nm (ϵ/dm^2 mol^{-1}), dichloromethane): 552 (5000), 368 (7300), 300 (21 900). IR (KBr pellets, cm^{-1}): $\nu_{N=N}$ 1409, ν_{Cl-O} 1102. ^1H NMR ($CDCl_3$, ppm): δ 7.76 (t, 1H); 7.67 (d, 1H); 7.52–7.48 (m, 2H); 7.29–7.26 (m, 1H); 7.21–7.17 (m, 2H); 7.05 (t, 2H); 6.88 (d, 1H); 6.57 (t, 1H); 6.33 (d, 2H); 5.28 (d, 1H); 4.42 (d, 1H).

3.3.2. $[(L^2)_2Co]ClO_4$ and $[(L^3)_2Co]ClO_4$

Complexes $[(L^2)_2Co]ClO_4$ and $[(L^3)_2Co]ClO_4$ were prepared using the ligands HL^2 and HL^3 in place of HL^1, respectively. Yield: $[(L^2)_2Co]ClO_4$, 70% and $[(L^3)_2Co]ClO_4$, 60%.

Anal. Calc. for $C_{38}H_{34}N_8CoClO_4$, $[(L^2)_2Co]ClO_4$: C, 59.96; H, 4.50; N, 14.72. Found: C, 59.90; H, 4.53; N, 14.70%. Electronic spectrum (λ_{max}/nm (ϵ/dm^2 mol^{-1}), dichloromethane): 569 (6340), 368 (11 000), 310 (22 750). IR (KBr pellets, cm^{-1}): $\nu_{N=N}$ 1410, ν_{Cl-O} 1085. ^1H NMR ($CDCl_3$, ppm): δ 7.88 (t, 1H); 7.64 (d, 1H); 7.53–7.50 (m, 2H); 7.33–7.26 (m, 2H); 6.83 (d, 3H); 6.61 (t, 1H); 6.19 (d, 2H); 5.15 (d, 1H); 4.44 (d, 1H); 2.25 (s, CH_3).

Anal. Calc. for $C_{36}H_{28}N_8CoCl_2ClO_4$, $[(L^3)_2Co]ClO_4$: C, 53.91; H, 3.52; N, 13.97. Found: C, 53.88; H, 3.55; N, 13.95%. Electronic spectrum (λ_{max}/nm (ϵ/dm^2 mol^{-1}), dichloromethane): 570 (5560), 363 (10 120), 304 (21 660). IR (KBr pellets, cm^{-1}): $\nu_{N=N}$ 1408, ν_{Cl-O} 1089. ^1H NMR ($CDCl_3$, ppm): δ 7.78 (t, 1H); 7.67 (d, 1H); 7.53 (d, 1H); 7.45 (d, 1H); 7.35 (t, 1H); 7.24 (d, 1H); 7.01 (d, 2H); 6.94 (d, 1H); 6.61 (t, 1H); 6.27 (d, 2H); 5.37 (d, 1H); 4.47 (d, 1H).

3.4. Physical measurements

Microanalyses (C, H, N) were performed using a Perkin–Elmer 240C elemental analyzer. Infrared spectra were recorded on a Perkin–Elmer L120-00A FT-IR spectrometer with the samples prepared as KBr pellets. Electronic spectra were recorded on a Shimadzu UV- 2401 PC

Table 3
Crystallographic data for $(L^3)PtCl$ and $[(L^3)_2Co]ClO_4$

Chemical formula	$(C_{18}H_{14}Cl_2N_4Pt)\cdot 0.5CH_2Cl_2$	$C_{36}H_{28}Cl_2CoN_8\cdot ClO_4$
Formula weight	594.78	801.94
Crystal system	triclinic	triclinic
Space group	$P\bar{1}$ (no. 2)	$P\bar{1}$ (no. 2)
a (Å)	11.2488(4)	10.9360(7)
b (Å)	11.9115(4)	11.5597(7)
c (Å)	16.0851(5)	14.9478(14)
α (°)	89.647(2)	100.236(2)
β (°)	78.830(2)	99.415(2)
γ (°)	69.847(2)	106.886(2)
λ (Å)	0.71073	0.71073
V (Å^3)	1980.67(12)	1732.3(2)
Z	4	2
$F(000)$	1132	820
Temperature (K)	293	293
$\rho_{calc.}$ (Mg/m^3)	1.995	1.538
μ (mm^{-1})	7.499	0.781
R (all data)	0.0537	0.0493
wR_2 [$I > 2\sigma(I)$]	0.1882	0.1550
Goodness-of-fit	1.26	0.98

spectrophotometer. ^{1}H NMR spectra were obtained on Brucker Avance RPX 500 NMR spectrometers in $CDCl_3$ and in DMSO, using TMS as the internal standard. Electrochemical measurements were performed using a PAR Versastat II potentiostat, a platinum disk working electrode, a platinum wire auxiliary electrode and aqueous saturated calomel (SCE) as the reference, (0.1 M) Bu_4NClO_4 supporting electrolyte, and in acetonitrile solvent. Electrochemical measurements were carried out under a dinitrogen atmosphere at 298 K and were uncorrected for junction potentials.

3.5. Crystallography

Data for the crystals, $(L^3)PtCl$ and $[(L^3)_2Co]ClO_4$, were collected by the ω-scan technique on a Brucker smart CCD diffractometer with Mo Kα radiation monochromated by a graphite crystal. The structure solution was done by direct methods with the SHELXS-97 program. Full matrix least square refinements were performed using the SHELX-97 program (PC version). All non-hydrogen atoms were refined anisotropically using reflections $I > 2\sigma(I)$. Hydrogen atoms were included at calculated positions. The crystal data and data collection parameters are listed in Table 3. The asymmetric unit of $(L^3)PtCl$ consists of two independent molecules and a dichloromethane molecule as the solvent of crystallization. Although the bond parameters of the two molecules in the asymmetric unit were not identical, they are consistent with each other.

4. Conclusion

The general coordination mode of 1*N*-(2-pyridyl-2-methyl)-2-arylazoaniline, HL towards Pt(II) and Co(III) has been determined. Formation of diazoketiminato chelates of Co(III) have been reported for the first time. The hypothetical mechanism of reaction between HL and metal substrates has been further supported with the formation of diazoketiminato chelates of Pt(II) and Co(III). The redox properties of the complexes have been assumed to be due predominantly to ligand centered.

Acknowledgement

We are thankful to the DST (New Delhi) for funding and fellowship to J.P. under DST-SERC Project (No. SR/S1/IC-09/2003). The necessary laboratory and infrastructural facilities are provided by the Dept. of Chemistry, University of Kalyani. The support of DST under FIST program to the Department of Chemistry, University of Kalyani is acknowledged. We acknowledge Prof. Jui-Hsien Huang, National Changhua University of Education, Changhua, Taiwan for X-ray studies.

Appendix A. Supplementary material

CCDC 652204 and 652203 contain the supplementary crystallographic data for $(L^3)PtCl$ and $[(L^3)_2Co]ClO_4$. These data can be obtained free of charge via http://www.ccdc.cam.ac.uk/conts/retrieving.html, or from the Cambridge Crystallographic Data Centre, 12 Union Road, Cambridge CB2 1EZ, UK; fax: (+44) 1223-336-033; or e-mail: deposit@ccdc.cam.ac.uk. Supplementary data associated with this article can be found, in the online version, at doi:10.1016/j.poly.2007.08.029.

References

[1] L.B. Merle, M.F. Lappert, J.R. Severn, Chem. Rev. 102 (2002) 3031.
[2] T. Hirao, Coord. Chem. Rev. 226 (2002) 81.
[3] A.D. Phillips, G. Laurenczy, R. Scopelliti, P.J. Dyson, Organometallics 26 (2007) 1120.
[4] S. Yokota, Y. Tachi, S. Itoh, Inorg. Chem. 41 (2002) 1342.
[5] M.D. Ward, J.A. McCleverty, J. Chem. Soc., Dalton Trans. (2002) 275.
[6] M. Nomura, M. Fujii, K. Fukuda, T. Sugiyama, Y. Yokoyama, M. Kajitani, J. Organomet. Chem. 690 (2005) 1627.
[7] J.-Y. Cho, B. Domercq, S.C. Jones, J. Yu, X. Zhang, Z. An, M. Bishop, S. Barlow, S.R. Marder, B. Kippelen, J. Mater. Chem. 17 (2007) 2642.
[8] M. Fourmiguea, Acc. Chem. Res. 37 (2004) 179.
[9] A.M. Barthram, R.L. Cleary, R. Kowallick, M.D. Ward, Chem. Commun. (1998) 2695.
[10] A.M. Barthram, Z.R. Reeves, J.C. Jeffery, M.D. Ward, J. Chem. Soc., Dalton Trans. (2000) 3162.
[11] S. Ganguly, S. Chattopadhyay, C. Sinha, A. Chakravorty, Inorg. Chem. 39 (2000) 2954.
[12] A.P. Meacham, K.L. Druce, Z.R. Bell, M.D. Ward, J.B. Keister, A.B.P. Lever, Inorg. Chem. 42 (2003) 7887.
[13] I. Chakraborty, B.K. Panda, J. Gangopadhyay, A. Chakravorty, Inorg. Chem. 44 (2005) 1054.
[14] N. Maiti, S. Pal, S. Chattopadhyay, Inorg. Chem. 40 (2001) 2204.
[15] N. Maiti, B.K. Dirghangi, S. Chattopadhyay, Polyhedron 22 (2003) 3109.
[16] N. Maiti, S. Chattopadhyay, Indian J. Chem. 42A (2003) 2327.
[17] D. Patra, J.l. Pratihar, B. Shee, P. Pattanayak, S. Chattopadhyay, Polyhedron 25 (2006) 2637.

[18] J.l. Pratihar, N. Maiti, P. Pattanayak, S. Chattopadhyay, Polyhedron 24 (2005) 1953.
[19] K.K. Kamar, S. Das, C.-H. Hung, A. Castineiras, M.D. Kuzmin, C. Rillo, J. Bartolome, S. Goswami, Inorg. Chem. 42 (2003) 5367.
[20] M. Panda, S. Das, G. Mostafa, A. Castineiras, S. Goswami, J. Chem. Soc., Dalton Trans. (2005) 1249.
[21] A. Saha, A.K. Ghosh, P. Majumdar, K.N. Mitra, S. Mondal, K.K. Rajak, L.R. Falvello, S. Goswami, Organometallics 18 (1999) 3772.
[22] A. Saha, P. Majumdar, S. Goswami, J. Chem. Soc., Dalton Trans. (2000) 1703.
[23] P. Chattopadhyay, M.K. Nayak, S.P. Bhattacharya, C. Sinha, Polyhedron 16 (1997) 1291.
[24] F. Basuli, P. Chattopadhyay, C. Sinha, Polyhedron 15 (1996) 2439.
[25] S.E. Livingstone, Synth. React. Inorg. Met. -Org. Chem. 1 (1971) 1.
[26] B.M. Trost, T.R. Verhoeven, in: E. Abel, F.G.A. Stone, G. Wilkinson (Eds.), Comprehensive Organometallic Chemistry, vol. 8, Pergamon Press, Oxford, 1982.

Table 1
Syntheses of $R_2P–P(SiMe_3)_2$

Run no.	R	R_2PCl (mol)	Solvent (ml)	$(Me_3Si)_2PLi \cdot 2.5$ THF (mol)	Solvent (ml)	T (°C)	bp (°C)	P (Torr)	Yield (%)	Ref.
1a.1	Ph	0.029	THF 50	0.030	THF50	−40	[a,b]		56	[3,4]
1a.2	Ph	0.044	toluene 100	0.049	toluene 100	−45	[c]		83	[3,4]
1b	^{i}Pr	0.090	THF 200	0.070	THF 200	0	41–51	$2 \cdot 10^{-3}$	70	[3,6]
1c	$^i Pr_2N$	0.049	THF 120	0.049	THF 120	−35	[d]		72	[7]

[a] Crystallization from pentane (−69 °C).
[b] Formation of $Ph_2P–PPh_2$, $P(SiMe_3)_3$ and $Ph_2P–P(SiMe_3)–PPh_2$ was established and tentatively also of the phosphanophosphinidenephosphorane $Ph_2P–P{=}PPh_2Br$.
[c] Crystallization from toluene (−69 °C).
[d] Crystallization from petrol ether (−69 °C).

The reaction of $R_2P–P(SiMe_3)H$ with MH (M = Li, Na, K) was proposed by Scheer [5] as an alternative route.

In order to synthesize $R_2P–P(SiMe_3)Li$ we used the method of Fritz, which is well applicable in the case of R = ^{i}Pr [3,6] and $^i Pr_2N$ (Eq. (1)). Details of the lithiation processes are collected in Table 2.

In the case of $Ph_2P–P(SiMe_3)_2$ (**1a**) the lithiation reaction is accompanied by a significant splitting of the P–P bond in the parent diphosphane [3]. Issleib and Krech reported the cleavage of the P–P bond in $R_2P–PR_2$ in a reaction with PhLi, especially preferred for R = Ph [8], presumably due to a nucleophilic mechanism. As was reported, PhLi and LiPEt(Ph) are able to split a P–P bond in cyclic $(EtP)_n$ [9]. We have found that better results are obtained performing the lithiation of $Ph_2P–P(SiMe_3)_2$ at −70 °C in DME (run 2a.2) than in THF at −30 °C (run 2a.1) but nevertheless the isolated solid has a composition of ca. 50% of $Ph_2P–P(SiMe_3)Li \cdot 3DME$, 33% of $Ph_2P–PPh_2$ and 17% of $LiP(SiMe_3)_2 \cdot DME$. Related products $Ph_2P–PPh_2$ and $Ph_2P–P(SiMe_3)Li$ were reported in a reaction of $Ph_2P–P(SiMe_3)–PPh_2$ with BuLi in THF [3]. Thus, it seems reasonable to assume that these two side reactions proceed through the same mechanism. The formation of $Ph_2P–PPh_2$ suggests that a single electron transfer process (SET) leading to $Ph_2P\cdot$ radicals can be partially responsible for the outcomes of these reactions. To prove this suggestion we have lithiated $Ph_2P–P(SiMe_3)_2$ in THF with ^{t}BuLi at −30 °C and examined the reaction solution with ^{1}H and ^{31}P NMR. To our surprise only a small amount of $Ph_2P–PPh_2$ was detected. The main products are $^t BuPh_2P$ (17.7 ppm), $(Me_3Si)_2PLi$ and **2a**. Thus a SET mechanism leading to $Ph_2P–PPh_2$ was not favoured, instead the nucleophilic splitting of a P–P bond in **1a** is more visible (Eq. (3)).

$$Ph_2P–P(SiMe_3)_2 + {}^t BuLi \rightarrow Ph_2P^t Bu + (Me_3Si)_2PLi \quad (3)$$

The ^{31}P NMR studies of solutions of $Ph_2P–P(SiMe_3)Li$ (**2a)** in DME and in THF indicate significantly different $^1J_{P-P}$ coupling constants: −352.4 Hz in DME and −288.4 Hz in THF. This is probably due to a solvent-separated ionic form of $(Li \cdot 3DME)^+(Ph_2P–PSiMe_3)^-$ in DME and an ion-contacted (partially covalent) form of $Ph_2P–P(SiMe_3)$-$Li \cdot 3THF$ in THF solution.

The stability of $Ph_2P–P(SiMe_3)Li$ (**2a)** in DME solution is limited. It decomposes slowly giving the way to the formation of $Ph_2P–PPh_2$, $(Li \cdot 3DME)^+(Ph_2P–P–PPh_2)^-$, Ph_2PH, $LiP(SiMe_3)_2$. The solvent-separated ionic form of $Ph_2P–PLi–PPh_2 \cdot 3DME$ is suggested due to its $^{31}P\{^1H\}$ NMR data: −8.04 ppm (d), −125.6 ppm (t), $^1J_{P1-P2} = -380.4$ Hz. For $Ph_2P–PLi–PPh_2$ in THF-d_8 Fritz et al. have reported: 5.39 ppm (d), −112.06 ppm (t), $^1J_{P1-P2} = -348.3$ Hz [3].

The lithiation of $^i Pr_2P–P(SiMe_3)_2$ (**1b**) with BuLi in THF was performed at 0 °C yielding moderately stable $^i Pr_2P–$

Table 2
Syntheses of $R_2P–P(SiMe_3)Li$

Run no.	R	$R_2P–P(SiMe_3)_2$ (mol)	Solvent (ml)	BuLi (1.6 M in hexane)		T (°C)	Yield (%)	Ref.
				[ml]	[mol]			
2a.1	Ph	0.0068	THF 50	4.3	0.0069	−35	[a]	[3,4]
2a.2	Ph	0.0076	DME 40	4.7	0.0076	−70	[b]	[3,4]
2 b	^{i}Pr	0.032	THF 40	20.0	0.032	0	70[c]	[3,6]
2c	$^i Pr_2N$	0.029	THF 100	18.0	0.029	−30	66[d]	[7]

[a] In the mother liquor, side products $P(SiMe_3)_2Li$, $Ph_2P–PPh_2$, Ph_2PH, Ph_2PSiMe_3, $P(SiMe_3)_3$ and probably Ph_2PLi were found. Crystallization from 10 ml THF at −30 °C gave 1.8 g of a precipitate of composition 36% $Ph_2P–P(SiMe_3)Li \cdot 3THF$, 53% $P(SiMe_3)_2Li \cdot 3THF$, 11% $Ph_2P–PPh_2$.
[b] Crystallization from 10 ml DME at −30 °C; 1.8 g of orange precipitate of composition 50% $Ph_2P–P(SiMe_3)Li \cdot 3DME$, 33% $Ph_2P–PPh_2$ and 17% $P(SiMe_3)_2Li \cdot DME$ were isolated.
[c] Crystallization from 10 ml pentane and 1 ml THF at −30 °C; 10% of $^i Pr_2P–P(SiMe_3)H$ and a small amount of $LiP(SiMe_3)_2$ was found in the product. When the crystallization residue was stored for a few weeks, $^i Pr_2P–PLi–P^i Pr_2 \cdot 1.5THF$ was isolated as an additional product in form of colourless crystals.
[d] Crystallization from 10 ml pentane and 2 ml THF at −30 °C; 10% of $(^i Pr_2N)_2P–P(SiMe_3)H$ [6] was found in the product.

$P(SiMe_3)Li$ (**2b**) [2,3,6]. $^iPr_2P–P(SiMe_3)Li$ shows very similar ^{31}P NMR data both in DME and in THF. However the ^1H NMR spectrum of **2b** in DME differs substantially from its spectrum in THF solution. In DME solution of **2b** small amounts of $^iPr_2P–PLi–P^iPr_2$ and $LiP(SiMe_3)_2$ were established. Moreover, crystalline $^iPr_2P–PLi–P^iPr_2 \cdot 1.5THF$ [10] was isolated from the mother liquor in run 2b in THF. Thus **2b** decomposes slowly according to Eq. (4):

$$2^iPr_2P–P(SiMe_3)Li \rightarrow {}^iPr_2P–PLi–P^iPr_2 + LiP(SiMe_3)_2 \quad (4)$$

This reaction seems to be a general one. A similar chain extension was reported by Fritz et al. as a proof of the instability of $(Me_3Si)_2P–P(SiMe_3)Li$ [11]. The limited stability of **2a** in DME solution can be partially explained by such a type of reaction, too.

The lithiation of $(^iPr_2N)_2P–P(SiMe_3)_2$ (**1c**) in THF was performed at −30 °C yielding $(^iPr_2N)_2P–P(SiMe_3)Li$ (**2c**) in good yield. Repeated crystallizations did not improve the purity of **2c**. The stability of $(^iPr_2N)_2P–P(SiMe_3)Li$ in C_6D_6 or THF solution is only limited. During two months at ambient temperature we observed a formation of (probably) a phosphetane $(^iPr_2N)_2P–P(\mu_2\text{-}PN^iPr_2)_2PSiMe_3$ (**3c**) [12] and finally of the polyphosphorus compound **4c** (at least 5 P atoms) together with $LiP(SiMe_3)_2$ and $^iPr_2NH$. The initially detectable small amounts of $(^iPr_2N)_2P–P(SiMe_3)H$ disappeared.

2.2. X-ray crystallographic studies of *2a–c*

Diffraction data were recorded on a KUMA KM4 diffractometer with graphite-monochromated Mo Kα radiation using Sapphire-2 CCD detector. The apparatus was equipped with an open flow thermostat (Oxford Cryosystems) which enabled experiments at 120 K. The stream of nitrogen also prevented the specimen from contact with moisture and oxygen. The structures were solved via direct methods and refined with the SHELX97 program package [13] with the full-matrix least-squares refinement based on F^2. All non-hydrogen atoms were refined anisotropically. Hydrogen atoms were refined in geometrically idealised positions with isotropic temperature factors 1.2 times the equivalent isotropic temperature factors U_{eq} of their attached atoms (1.5 for CH_3 groups). Disorder in **2b · 3THF** in the THF molecules: C13 (*s.o.f.* 0.46(3)/0.54(3)); C19–C20 (*s.o.f.* 0.715(15)/0.285(15)); C32–C34 (*s.o.f.* 0.404(13)/0.596(13)); C37 (*s.o.f.* 0.76(3)/0.24(3)); C39–C42 (*s.o.f.* 0.40(2)/0.60(2)). Basic crystal data, description of the diffraction experiment, and details of the structure refinement are given in Table 3.

Table 3
Crystallographic data and structure refinement details for $(Li) \cdot 3DME)^+(Ph_2P–PSiMe_3)^-$ (**2a · 3DME**), $^iPr_2P–P(SiMe_3)Li \cdot 3THF$ (**2b · 3THF**) and $(iPr_2N)_2P–P(SiMe_3)Li \cdot 3THF$ (**2c · 3THF**)

	2a · 3DME	**2b · 3THF**	**2c · 3THF**
Empirical formula	$C_{27}H_{49}LiO_6P_2Si$	$C_{21}H_{47}LiO_3P_2Si$	$C_{27}H_{61}LiN_2O_3P_2Si$
M_r/g mol^{-1}	566.63	444.56	558.75
Temperature (K)	120(2)	120(2)	120(2)
Wavelength (Å) (Mo Kα)	0.71073	0.71073	0.71073
Crystal system	triclinic	monoclinic	monoclinic
Space group	$P\bar{1}$	$P2_1/c$	$P2_1/c$
a (Å)	11.5458(7)	9.0340(9)	11.045(2)
b (Å)	11.9863(7)	36.054(3)	15.027(3)
c (Å)	13.3157(8)	18.897(2)	21.453(4)
α (°)	83.219(5)		
β (°)	67.279(6)	116.569(7)	102.732(17)
γ (°)	78.304(5)		
V (Å^3)	1662.87(17)	5505.0(9)	3473.1(11)
Z	2	8	4
D_{Calc} (Mg m^{-3})	1.132	1.073	1.069
Crystal size (mm)	0.5 × 0.4 × 0.4	0.35 × 0.13 × 0.02	0.3 × 0.2 × 0.2
θ Range (°)	2.37–25.00	2.48–26.00	1.95–25.05
Limiting indices	−13 <=h <=13, −14 <=k <=13, −15 <=l <=15	−11 <=h <=10, −44 <=k <=44, −16 <=l <=23	−13 <=h <=13, −15 <=k <=17, −25 <=l <=25
Reflections collected/unique	11 022/5844 [R_{int} = 0.1009]	41 261/10 797 [R_{int} = 0.0684]	16 769/6109 [R_{int} = 0.1291]
Completeness to θ_{max} (%)	99.7	99.9	99.4
Refinement method	full-matrix least-squares on F^2	full-matrix least-squares on F_2	full-matrix least-squares on F_2
Data/restraints/parameters	5844/0/343	10 797/113/623	6109/0/324
Goodness-of-fit on F^2	1.1041	1.188	1.098
Final R indices [$I > 2\sigma(I)$] R indices (all data)	R_1 = 0.1009 wR_2 = 0.2683 R_1 = 0.1247 wR_2 = 0.2956	R_1 = 0.0885 wR_2 = 0.1804 R_1 = 0.1252 wR_2 = 0.2009	R_1 = 0.0879 wR_2 = 0.2014 R_1 = 0.1580 wR_2 = 0.2397
Largest difference peak and hole (e Å^{-3})	0.790 and −1.178	0.613 and −0.416	0.908 and −0.717

An Ortep view of **2a · 3DME** is shown in Fig. 1, of **2b · 3THF** in Fig. 2 and of **2c · 3THF** in Fig. 3. **2b · 3THF** consists of two independent molecules. Selected atom distances, bond angles and sums of bond angles around P1 and P2 are collected in Table 4.

2a · 3DME is the first known solvent-separated ionic lithium phosphinophosphide monoanion. The distance Li–P2 of 856.9 pm clearly excludes a covalent or ion-contacted P–Li bond. Some examples of anionic polyphosphides are known, *e.g.* [14]. The ionic form stabilized by crown ether was reported for (12-crown 4)$_2$LiPPh$_2$ [15].

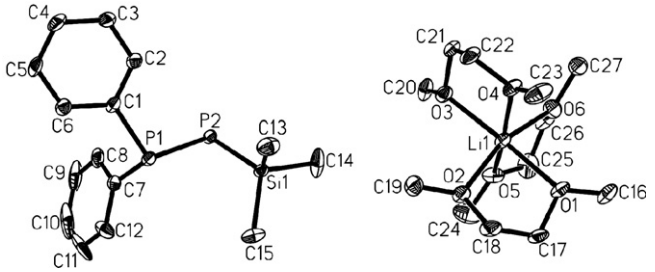


Fig. 1. Molecular structure of $(Li \cdot 3DME)^+(Ph_2P–PSiMe_3)^-$ (**2a · 3DME**). Displacement ellipsoids 30%.

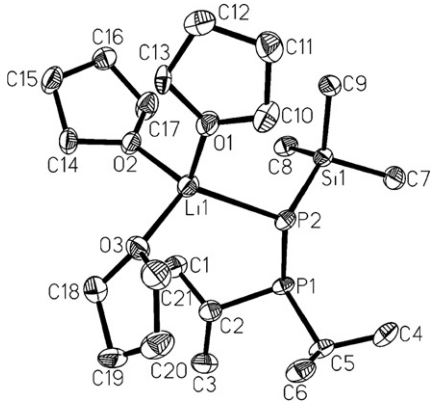


Fig. 2. Molecular structure of ^{i}Pr$_2$P–P(SiMe$_3$)Li · 3THF (**2b · 3THF**). Displacement ellipsoids 30%.

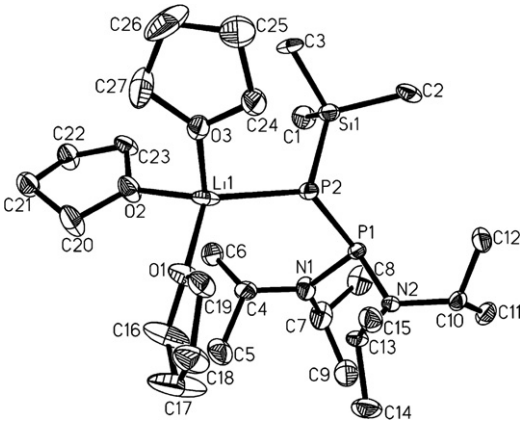


Fig. 3. Molecular structure of (^{i}Pr$_2$N)$_2$ P–P(SiMe$_3$)Li · 3THF (**2c · 3THF**). Displacement ellipsoids 30%.

To our surprise, monomeric Ph$_2$PLi · (**Me**$_2$NCH$_2$CH$_2$)$_2$NMe and dimeric Ph$_2$PLi · **Me**$_2$NCH$_2$CH$_2$NMe$_2$ in cyclic arrangement crystallized as ion-contacted compounds [16]. (Me$_3$Si)$_2$PLi in DME crystallizes as a dimer {(Me$_3$Si)$_2$PLi · **DME**}$_2$ in a cyclic arrangement [17]. However {(Ph(H)P–PPh)Li · THF}$_4$ (similar to **2a · 3DME**) crystallizes as a tetramer with an average P–Li distance of ca. 257 pm [18], and the potassium derivative {(^{t}Bu(H)P–P^{t}Bu)K · pmdeta}$_2$ crystallizes as a dimer [19]. The P2–Li distances in **2b · 3THF** and **2c · 3THF** are in the range reported previously [17–19]. These distances clearly exceed the sum of the normal covalent radii for P and for Li, thus the description of the P–Li bond as partially ionic (ion-contacted) seems to be correct. Generally, the partially anionic character of P2 increased the planarity around P2 as compared to P1. The anionic (**2a · 3DME**) or partially anionic (**2b · 3THF**, **2c · 3THF**) character of P2 in the diphosphane skeleton leads in all compounds described here to a significant shortening of the P–P distances and suggests a partial P–P multiple bond character. The P–P distance in Ph$_2$P–PPh$_2$ is 221.7 pm [20] and in (^{i}Pr$_2$N)$_2$P–P(SiMe$_3$)$_2$ it is 223.9 pm [21]. A shortening of the P–P bonds was also observed in Li derivatives of triphosphanes [22,23]. Similarly the P2–Si bonds in **2a · 3DME**, **2b · 3THF** and **2c · 3THF** are significantly shorter than in (^{i}Pr$_2$N)$_2$P–P(SiMe$_3$)$_2$ (226.9 pm) [21]. The effect of the anionic form of P2 on the distances R–P1 is negligible compared to the related compounds R$_2$P–P(SiMe$_3$)$_2$ or R$_2$P–PR$_2$, however the P1–N distances in **2c · 3THF** (ca. 172.8 pm) are slightly longer than in (^{i}Pr$_2$N)$_2$P–P(SiMe$_3$)$_2$ (170.4 pm) [21].

We have studied the effect of introducing a Li atom coordinated with 3 THF molecules on the conformational preferences of the phosphorus lone pairs measured as a torsion angle along the P–P bonds. In the anion **2a · 3DME** the lone pairs of P2 are in anticlinal conformation to the lone pair of P1 (−119.1° and +116.4°), in Ph$_2$P–PPh$_2$ the lone pairs of P1 and P2 are in antiperiplanar conformation, and in Ph$_2$P–P(N^{i}Pr$_2$)$_2$ almost in antiperiplanar position (177.4°). Thus, the anion has a significantly different lone pair conformation than the related covalent compounds with Ph$_2$P groups. In **2b · 3THF** (−115.06 and 114.30°) the lone pairs are in anticlinal conformation. In **2c · 3THF** the conformation of the lone pairs is synclinal (84.90°), similar as in (^{i}Pr$_2$N)$_2$P–P(SiMe$_3$)$_2$ (80.2°). Thus, the introduction of [Li · 3THF] in place of SiMe$_3$ exerts only a small impact on the conformational preferences in **2 · 3THF**.

3. Experimental

All manipulations were performed in flame-dried Schlenk type glassware on a vacuum line. THF and toluene were dried over Na/benzophenone and distilled under nitrogen. Petrol ether was dried over Na/benzophenone/diglyme and distilled under nitrogen. ^{31}P NMR and ^{1}H spectra were recorded on Varian 500, Bruker AMX300

Table 4
Important atom distances and bond angles of **2a · 3DME**, **2b · 3THF** and **2c · 3THF**

Compound	P1–P2 (pm)	P2–Li (pm)	P2–Si (pm)	Si–P2–P1 (degrees)	Si–P2–Li (degrees)	P1–P2–Li (degrees)	Sum ofangles around P1	Sum of angles around P2
2a · 3DME	215.5		219.5	96.35			308.59	
2b · 3THF	217.1	253.6	219.9	95.80	112.98	122.73	307.00	331.51
2c · 3THF	218.9	253.9	220.2	95.34	119.30	133.65	314.84	348.29

and Bruker Avance 400 spectrometers (external standard 85% H_3PO_4) at ambient temperature.

3.1. General description of the lithiation procedure

The solution of 1.6 M BuLi in hexane was slowly dropped to the cooled THF (DME) solution of an equimolar amount of R_2P–$P(SiMe_3)_2$. The reaction mixture was stirred at reduced temperature for 3 h and finally at ambient temperature for 20 h. The resulting solution was examined with ^{31}P NMR, then evaporated under vacuum (1 mTorr, 3 h). The residue was dissolved in THF or DME for **2a**, and in a mixture of THF and pentane for **2 b** and **2c**. The solution was stored at −30 °C yielding a precipitate of solvated R_2P–$P(SiMe_3)Li$.

The NMR data of **1a**, **1b**, **1c**, **2a**, **2b**, **2c** and some major side products (δ/ppm, J/Hz):

3.1.1. Run 1a.1 (parent liquor, only side products are listed)

$^{31}P\{^1H\}$ NMR (101.26 MHz, THF, tol-d_8): Ph_2PCl 96.92 (s); Ph_2P–PPh_2 −14.19 (s); Ph_2P1–$P2(SiMe_3)$–PPh_2 −25.13 (d, P1), −120.90 (t, P2), $^1J_{P1-P2} = -194.2$; Ph_2P1–P2═P3Ph_2Br 86.07 (dd, P3), −25.84 (dd, P1), −136.00 (dd, P2), $^1J_{P1-P2} = -215.8$, $^1J_{P2-P3} = -568.9$, $^2J_{P1-P3} = 99.0$ [3]; Ph_2P1–$P2(SiMe_3)H$ −33.85 (d, P1), −160.56 (d, P2), $^1J_{P1-P2} = -167.8$; $P(SiMe_3)_3$ −251.68 (s).

3.1.2. Ph_2P1–$P2(SiMe_3)_2$ (**1a**)

^1H NMR (500 MHz, C_6D_6): 7.87 (pst*, 7.5 Hz, $C_6\mathbf{H}_5$); 7.01 (pst, 7.4 Hz, $C_6\mathbf{H}_5$); 6.95 (psd**, 7.1 Hz, $C_6\mathbf{H}_5$); 0.13 (d, PSiC$\mathbf{H}_3$, $^3J_{PSiCH} = 4.2$); $^{31}P\{^1H\}$ NMR (202.51 MHz, C_6D_6): −28.57 (d, P1); −183.55 (d, P2); $^1J_{P1-P2} = -172.4$.

3.1.3. Ph_2P1–$P2(SiMe_3)Li \cdot 3THF$(**2a · 3THF**)

^1H NMR (500 MHz, C_6D_6): 7.81 (pst, 6.9 Hz, $C_6\mathbf{H}_5$); 7.09 (pst, 7.2 Hz, $C_6\mathbf{H}_5$); 6.94 (psd, 7.2 Hz, $C_6\mathbf{H}_5$); 3.48 (m, THF); 1.41 (m, THF); 0.51 (d, PSiC$\mathbf{H}_3$, $^3J_{PSiCH} = 3.4$); $^{31}P\{^1H\}$ NMR (202.51 MHz, C_6D_6): −5.50 (d, P1); −207.05 (d, P2); $^1J_{P1-P2} = -288.4$; contaminations: Li-$P(SiMe_3)_2$, Ph_2P–PPh_2, Ph_2PH (small amount).

3.1.4. Ph_2P1–$P2(SiMe_3)Li \cdot 3DME$(**2a · 3DME**)

^1H NMR (500 MHz, C_6D_6): 8.00 (pst, 7.1 Hz, $C_6\mathbf{H}_5$); 7.14 (pst, 7.4 Hz, $C_6\mathbf{H}_5$); 7.02 (psd, 7.5 Hz, $C_6\mathbf{H}_5$); 3.04 (s, DME), 3.00 (s, DME); 0.47 (d, PSiC$\mathbf{H}_3$, $^3J_{PSiCH} = 3.9$); $^{31}P\{^1H\}$ NMR (202.51 MHz, C_6D_6): −6.79 (d, P1); −211.41 (d, P2); $^1J_{P1-P2} = -352.4$; contaminations ^1H NMR: Ph_2P–PPh_2 7.41 (pst*, 7.0 Hz), 7.10 (pst, 7.1 Hz), 7.05 (psd, 7.1 Hz); $LiP(SiMe_3)_2$; $HP(SiMe_3)_2$ (weak) 0.27 (d, $^3J_{PSiCH} = 4.4$); $P(SiMe_3)_3$ (weak) 0.20 (d, $^3J_{PSiCH} = 4.4$); contaminations $^{31}P\{^1H\}$ NMR: Ph_2P–PPh_2 (strong) −15.30 (s); $LiP(SiMe_3)_2$ (strong); $P(SiMe_3)_3$ (weak), −251.54.

After several weeks $(Li \cdot 3DME)^+(Ph_2P$–P–$PPh_2)^-$ and Ph_2PSiMe_3 (−56.10 ppm) were additionally found. pst* – higher order spectra, pseudotriplet; psd** – higher order spectra, pseudodoublet, the "Hz" data are not coupling constants.

3.1.5. $^iPr_2P1$–$P2(SiMe_3)_2$ (**1b**) [6]

^1H NMR (500 MHz, C_6D_6): 1.99 (d, d, q, q, $^2J_{PCH} = 11.3$, $^3J_{PPCH} = 2.4$, $^3J_{HCCH} = 6.8$, $^3J_{HCCH} = 6.9$, C$\mathbf{H}$–CH_3); 1.11 (d, d, $^3J_{PCCH} = 11.8$, $^3J_{HCCH} = 6.8$, CH–C$\mathbf{H}_3$); 1.05 (d, d, $^3J_{PCCH} = 15.3$, $^3J_{HCCH} = 6.9$, CH–C$\mathbf{H}_3$); 0.29 (d, $^3J_{PSiCH} = 5.3$, PSiC$\mathbf{H}_3$); $^{31}P\{^1H\}$ NMR (202.51 MHz, C_6D_6): 10.01 (d, P1), −215.27 (d, P2), $^1J_{P1-P2} = -316.5$.

3.1.6. $^iPr_2P1$–$P2(SiMe_3)H$

^1H NMR (400 MHz, C_6D_6): 1.83 (d, d, septet, $^2J_{PCH} = 6.5$, $^3J_{PPCH} = 1.7$, $^3J_{HCCH} = 6.9$, C$\mathbf{H}$–CH_3); 1.46 (d, d, $^1J_{PH} = 184.22$, $^2J_{PPH} = 3.25$, P$\mathbf{H}$); 1.10 (d, d, $^3J_{PCCH} = 11.0$, $^3J_{HCCH} = 6.9$, CH–C$\mathbf{H}_3$); 1.06 (d, d, $^3J_{PCCH} = 14.8$, $^3J_{HCCH} = 7.0$, CH–C$\mathbf{H}_3$); 0.30 (d, d, $^3J_{PSiCH} = 4.25$, $^4J_{PPSiCH} = 0.76$, SiC$\mathbf{H}_3$); $^{31}P\{^1H\}$ NMR (202.51 MHz, THF, C_6D_6): −7.69 (d, P1); −200.69 (d, P2); $^1J_{P1-P2} = -188.5$.

3.1.7. $^iPr_2P1$–$P2(SiMe_3)Li \cdot 3THF$ (**2b · 3THF**) [6]

^1H NMR (500 MHz, THF, C_6D_6): 3.58 ppm (m, THF); 1.91 (m, C$\mathbf{H}$–CH_3); 1.34 (m, THF); 1.30 (d, $^3J_{HCCH} = 6.9$, CH–C$\mathbf{H}_3$); 1.27 (d, $^3J_{HCCH} = 6.9$, CH–C$\mathbf{H}_3$); 0.561 (br s, PSiC$\mathbf{H}_3$); $^{31}P\{^1H\}$ NMR (202.51 MHz, THF, C_6D_6): 17.35 (d, P1); −256.74 (d, P2), $^1J_{P1-P2} = -263.9$. Contaminations $LiP(SiMe_3)_2$; $^iPr_2P$–P $(SiMe_3)H$.

3.1.8. $^iPr_2P1$–$P2(SiMe_3)Li$ (**2b** in DME)

$^iPr_2P$–$P(SiMe_3)Li \cdot 3THF$ (2b) was evacuated (0.001 Torr for 6h) dissolved in DME, evacuated anew and dissolved again in DME. ^1H NMR (500 MHz, DME, C_6D_6): 3.29 (m, DME); 3.12 (m, DME); 1.42 (q, q, d, $^3J_{HCCH} = 6.9$, $^3J_{HCCH} = 6.7$, $^2J_{PCH} = 6.5$, C$\mathbf{H}$–CH_3); 0.87 (d, d, $^3J_{PCCH} = 14.0$, $^3J_{HCCH} = 6.9$, CH–C$\mathbf{H}_3$); 0.92 (d, d, $^3J_{PCCH} = 9.7$, $^3J_{HCCH} = 6.7$, CH–C$\mathbf{H}_3$); −0.05 (br d, $^3J_{P2-H} = 2.6$, PSiC$\mathbf{H}_3$); $^{31}P\{^1H\}$ NMR (202.51 MHz, DME, C_6D_6): 18.89 (d, P1); −255.19 (d, P2), $^1J_{P1-P2} = -262.6$, $^1J_{P2\text{-}29Si} = 43.8$. Contaminations $^iPr_2P$–PLi–P$^iPr_2$; $LiP(SiMe_3)_2$.

3.1.9. $^{i}Pr_2P1–P2Li–P^{i}Pr_2$ [21]

$^{31}P\{^{1}H\}$ NMR (202.51 MHz, DME, C_6D_6) 34.76 (br d, P1); −180.05 (t, P2), $^{1}J_{P1–P2} = -306.1$.

*3.1.10. $(^{i}Pr_2N)_2P1–P2(SiMe_3)_2$ (**1c**)*

^{1}H NMR (500 MHz, C_6D_6): 3.38 (d, septet, $^{3}J_{HCCH} = 6.6$, $^{3}J_{PNCH} = 11.9$, N–C**H**–CH_3); 1.26 (d, $^{3}J_{HCCH} = 6.6$, N–CH–C**H**$_3$); 1.19 (d, $^{3}J_{HCCH} = 6.6$, N–CH–C**H**$_3$); 0.44 (d, $^{3}J_{PSiCH} = 4.4$, PSiC**H**$_3$); $^{31}P\{^{1}H\}$ NMR (202.51 MHz, C_6D_6): 80.89 (d, P1); −156.09 (d, P2); $^{1}J_{P1–P2} = -470.3$.

*3.1.11. $(^{i}Pr_2N)_2P1–P2(SiMe_3)Li \cdot 3THF$ (**2c · 3THF**)*

($^{i}Pr_2N)_2P–P(SiMe_3)Li \cdot$ **3THF** (**2c**) was evacuated (0.001 Torr for 6 h) and dissolved in THF-d_8. The signals of THF are however visible. ^{1}H NMR (400 MHz, THF-d_8): 3.37 ppm (d, septet, $^{3}J_{HCCH} = 6.7$, $^{3}J_{PNCH} = 9.4$, N–C**H**–CH_3); 1.25 (d, $^{3}J_{HCCH} = 6.6$, N–CH–C**H**$_3$); 1.19 (d, $^{3}J_{HCCH} = 6.8$, N–CH–C**H**$_3$); 0.27 (d, d, $^{3}J_{PSiCH} = 3.3$, $^{4}J_{PPSiCH} = 1.1$, PSiC**H**$_3$); $^{31}P\{^{1}H\}$ NMR (161.95 MHz, C_6D_6): 86.64 (d, P1); −196.51 (d, P2); $^{1}J_{P1–P2} = -311.6$; contaminations: $^{31}P\{^{1}H\}$ NMR: ($^{i}Pr_2N)_2P1–P2(SiMe_3)H$ 56.20 (d, P1); −164.28 (d, P2); $^{1}J_{P1–P2} = -128.8$; $^{1}J_{P2–H} = 187.3$; $LiP(SiMe_3)_2$ (small amount).

After two months at ambient temperature **2c** was still present in solution, however the initially formed ($^{i}Pr_2N_2)P–P(SiMe_3)H$ disappeared, and **3c** and **4c** were additionally found: *$(^{i}Pr_2N)_2P2–P1(\mu_2\text{-}P3,4N^{i}Pr_2)_2P5\text{-}SiMe_3$* (**3c**): $^{31}P\{^{1}H\}$ NMR (161.95 MHz, THF, C_6D_6): 62.71 (m, P2); 8.52 (m, P1); −20.61 (m, P3,4); −84.80 (m, P5); $^{1}J_{P1–P2} = -186.0$; $^{1}J_{P1–P3} = -190.0$; $^{1}J_{P3–P5} = -177.0$; $^{2}J_{P2–P3} = +170.0$; $^{3}J_{P2–P5} = +36.0$; $^{2}J_{P1–P5} = +25.0$: MAB_2X [12]. **4c** (formula uncertain): 86.67 (d, d, d, P1); 75.33 (d, d, d, P2); 42.89 (d, d, d, P3); −108.84 (d, d, d, d, P4); −177.71 (d, d, t, P5); $J_{P1–P2} = 247.6$, $J_{P1–P4} = 277.2$, $J_{P1–P5} = 117.1$, $J_{P2–P3} = J_{P2–P4} = 167.4$, $J_{P2–P5} = 84.9$, $J_{P3–P4} = 51.6$, $J_{P3–P5} = J_{P4–P2} = 154.7$.

3.1.12. $(Me_3Si)_2PLi$

$^{31}P\{^{1}H\}$ NMR (161.95 MHz, THF, C_6D_6) −303.84 (s); ^{1}H NMR (400.13 MHz, THF, C_6D_6) 0.23 (d, $^{3}J_{PSiCH} = 3.3$); $^{13}C\{^{1}H\}$ NMR (100.62 MHz, THF, C_6D_6) 8.72 (d, $^{2}J_{PSiC} = 20.35$).

3.1.13. $^{i}Pr_2NH$

^{1}H NMR (400.13 MHz, THF, C_6D_6) 2.73 (d, septet, $^{3}J_{HCCH} = 6.22$, $^{3}J_{HCNH} = 6.22$, N–C**H**–CH_3), 0.87 (d, $^{2}J_{HCCH} = 6.22$, N–CH–C**H**$_3$) [24]; ^{13}C NMR (100.62 MHz, THF, C_6D_6) 45.96 (s, N–**C**H–CH_3), 24.12 (s, N–CH–**C**H_3) [25,26].

Acknowledgements

J.P. and R.G. thank the Polish State Committee of Scientific Research (Project No. 4 T09A 146 28) for financial support. W.D.-B. and J.P. thank the Polish State Committee of Scientific Research (Project No. 1 T09A 148 30) for financial support. J.P thanks Dr. L. Ponikiewski for a discussion of crystallographic data. We are especially grateful to Dr. Ilona Kovacs, Budapest, for very valuable experimental hints and for the NMR data of iPr$_2$P–P(SiMe$_3$)H.

Appendix A. Supplementary material

CCDC 634547, 634548 and 634550 contain the supplementary crystallographic data for **2c · 3THF**, **2b · 3THF** and **2a · 3DME**. These data can be obtained free of charge via http://www.ccdc.cam.ac.uk/conts/retrieving.html, or from the Cambridge Crystallographic Data Centre, 12 Union Road, Cambridge CB2 1EZ, UK; fax: (+44) 1223-336-033; or deposit@ccdc.cam.ac.uk. Supplementary data associated with this article can be found, in the online version, at doi:10.1016/j.poly.2007.08.008.

References

[1] J. Pikies, E. Baum, E. Matern, J. Chojnacki, R. Grubba, A. Robaszkiewicz, J. Chem. Soc., Chem. Commun. 2478 (2004).
[2] G. Fritz, T. Vaahs, J. Härer, Z. Anorg. Allg. Chem. 552 (1987) 11.
[3] I. Kovacs, E. Matern, G. Fritz, Z. Anorg. Allg. Chem. 622 (1996) 935.
[4] G. Fritz, W. Hölderich, Z. Anorg. Allg. Chem. 431 (1977) 76.
[5] M. Scheer, S. Gremler, E. Herrmann, M. Dargatz, H.-D. Schädler, Z. Anorg. Allg. Chem. 619 (1993) 1047.
[6] I. Kovacs, H. Krautscheid, E. Matern, G. Fritz, Z. Anorg. Allg. Chem. 620 (1994) 1369.
[7] H.R.G. Bender, E. Niecke, M. Nieger, H. Westermann, Z. Anorg. Allg. Chem. 620 (1994) 1194.
[8] K. Issleib, F. Krech, J. Organomet. Chem. 13 (1968) 283.
[9] K. Issleib, F. Krech, Z. Anorg. Allg. Chem. 385 (1971) 47.
[10] W. Domańska, K. Baranowska, J. Chojnacki, J. Pikies, in press.
[11] G. Fritz, T. Vaahs, Z. Anorg. Allg. Chem. 552 (1987) 7.
[12] R. Grubba, Ph.D. Thesis, Gdańsk University of Technology, Chemical Faculty, Gdańsk 2005.
[13] G.M. Sheldrick, SHELXS-97, SHELXL-97, Programme zur Lösung bzw. zur Verfeinerung von Kristallstrukturen, Göttingen 1997.
[14] G. Fritz, H.-W. Schneider, W. Hönle, H.G. von Schnering, Z. Naturforsch. 43b (1988) 561.
[15] H. Hope, M.M. Olmstead, P.P. Power, X. Xu, J. Am. Chem. Soc. 106 (1984) 819.
[16] R.E. Mulvey, K. Wade, D.R. Armstrong, G.T. Walker, R. Snaith, W. Clegg, D. Reed, Polyhedron 6 (1987) 987.
[17] G. Becker, H.-M. Hartmann, W. Schwarz, Z. Anorg. Allg. Chem. 577 (1989) 9.
[18] F. Garcia, S.M. Humprey, R.A. Kowenicki, M. McPartlin, D.S. Wright, J. Chem. Soc., Dalton Trans. 977 (2004).
[19] M.A. Beswick, A.D. Hopkins, L.C. Kerr, M.E.G. Mosguera, J.G. Palmer, P.R. Raitby, A. Rothenberger, D. Stalke, A. Steiner, A.E.H. Wheatley, D.S. Wright, J. Chem. Soc., Chem. Commun. 1527 (1998).
[20] A. Dashi-Mommertz, B. Neumüller, Z. Anorg. Allg. Chem. 625 (1999) 954.
[21] W. Domańska-Babul, J. Pikies, in press.
[22] I. Kovacs, H. Krautscheid, E. Matern, E. Sattler, G. Fritz, W. Hönle, H. Borrmann, H.G. von Schnering, Z. Anorg. Allg. Chem. 622 (1996) 1564.
[23] W. Domańska, J. Chojnacki, J. Pikies, Acta Crystallogr., Sect. E 61 (2005) m1114.
[24] N.D.R. Barnett, R.E. Mulvey, W. Clegg, P.A. O'Neil, J. Am. Chem. Soc. 113 (1991) 8187.
[25] K.F. Podraza, R.L. Bassfield, J. Org. Chem. 53 (1988) 2643.
[26] A.S. Galiano-Roth, D.B. Collum, J. Am. Chem. Soc. 111 (1989) 6778.

Herein, we employed pyridine-2-thionato (HPyS), 4-trifluoromethyl-2-pyrimidinthiol (4-CF_3-2-PymSH) and pyridine-2-selenolato (HPySe) as heterocyclic bidentate (N,X) ligands, X = S, Se to synthesize and characterize corresponding dinuclear μ-oxomolybdenum(V) complexes. The known compound $[Mo_2O_3(PyS)_4]$ was obtained by a different method and did crystallize in a different modification compared to the described procedure and crystal structure by Cotton et al. [10]. The catalytic oxo-transfer abilities of molybdenum(V) complexes with heterocyclic thione and selenone ligands in comparison were successfully investigated by oxo transfer reactions from DMSO to PPh_3 although compounds with the Mo_2O_3-core are often catalytically inactive with respect to the oxo transfer.

2. Experimental

2.1. General procedures

All manipulations were carried out under purified dry nitrogen atmosphere using standard Schlenk-line techniques. All solvents were purified by standard methods with subsequent distillation under nitrogen (dichloromethane over CaH_2 and methanol over $Mg(OMe)_2$), and were stored over 4-Å molecular sieves. Pyridine-2-selenolato (C_5H_4NSeH = PySeH) [11] was prepared by the reported procedure. The starting materials selenium (Aldrich), 2-bromopyridine (Aldrich), glacial acetic acid (Roth) and $NaBH_4$ (Aldrich) were used as received. $[MoO_2Cl_2(DME)]$ [12], $[MoO_2Cl_2]$ [13] and $[MoO_2(acac)_2]$ [14] were prepared according to literature procedures. 2-Pyridine-2-thionato (PySH) (Aldrich), 4-(trifluoromethyl)-2-pyrimidinthiol (4-CF_3-2-PymSH) (Aldrich) and *n*-butyllithium (2.5 M solution in hexanes, ACROS) are commercially available and were used as received.

2.2. Preparation of complexes

2.2.1. $[Mo_2O_3(PyS)_4]$ (1)

Method 1. To a −30 °C pre-cooled solution of PySH (0.222 g, 2 mmol) in 10 mL THF, *n*-BuLi (0.8 mL of a 2.5 M solution in hexane, 2 mmol) was added dropwise *via* syringe. The mixture was warmed to room temperature, stirred for 7 h, and then cooled to −30 °C. A colorless solution of $[MoO_2Cl_2(DME)]$ (0.289 g, 1 mmol) in 10 mL THF was added dropwise to this solution. The mixture was allowed to warm to room temperature and stirred overnight. The solvent was removed *in vacuo* and the obtained solid was extracted with CH_2Cl_2. The red brown solution was filtered and dried under vacuum. The complex was obtained as red brown microcrystalline solid. Yield: 0.16 g (0.235 mmol; 48%).

Method 2. Et_3N (0.30 mL, 2 mmol) was added to a methanolic solution of PySH (0.222 g, 2 mmol). The resulting solution was stirred for 1 h and a solution of $[MoO_2Cl_2]$ (0.199 g, 1 mmol) in dichloromethane was added. The reaction mixture was stirred overnight, the resulting suspension was dried under vacuum and the obtained solid was extracted with CH_3CN. The filtrate was concentrated to approx. 5 mL and left at room temperature for several days. After red brown crystals had formed they were filtered from the solution, washed thoroughly with ether and dried *in vacuo* giving 0.15 g (2.220 mmol; 44%) product.

Crystals of **1** suitable for X-ray studies were obtained by crystallization of the initial product from dichloromethane.

Mp: 215 °C. Elemental *Anal.* Calc. for $C_{20}H_{16}N_4O_3S_4Mo_2$ (680.49 g mol^{-1}): C, 35.30; H, 2.37; N, 8.23. Found: C, 35.12; H, 3.00; N, 7.66%; IR (KBr): $\tilde{\nu}$ = 3059 (m), 1615 (w), 1583 (s), 1558 (s), 1447 (s), 1425 (s), 1367 (m), 1267 (s), 1182 (w), 1151 (m), 1136 (s), 1086 (s), 1037 (s), 1017 (s), 985 (w), 963 (w), 929 (s), 897 (s), 872 (m), 801 (m), 763 (s), 754 (s), 727 (s); 645 (m), 616 (w), 484 (m), 456 (m), 446 (w), 418 (w), 405 (m), 371 (s), 329 (w), 294 (s) cm^{-1}; ^{1}H NMR ($CDCl_3$, 500 MHz): δ 8.46 (m, H_6, 4H), 7.58 (m, H_4, 4H), 7.16 (m, H_3, 4H), 6.95 (m, H_5, 4H) ppm; ^{13}C NMR ($CDCl_3$, 500 MHz): δ 167.0 (s, C_2), 125.6 (s, C_3), 139.9 (s, C_4), 119.6 (s, C_5), 145.2 (s, C_6) ppm; MS (EI): *m*/*z* (%) = 492 (15) [M^+−PyS−Py], 475 (11) [M^+−PyS−Py−O], 348 (100) [M^+−(MoO(PyS)$_2$)], 332 (55) [M^+−(MoO_2-(PyS)$_2$)], 239 (39) [M^+−(MoO(PyS)$_2$)−PyS].

2.2.2. $[Mo_2O_3(PySe)_4]$ (2)

To a −30 °C pre-cooled solution of PySeH (0.316 g, 2 mmol) in 10 mL THF, *n*-BuLi (0.8 mL of a 2.5 M solution in hexane, 2 mmol) was added dropwise *via* syringe. The mixture was allowed to warm to room temperature, stirred for 7 h, and then cooled to −30 °C. A colorless solution of $[MoO_2Cl_2(DME)]$ (0.289 g, 1 mmol) in 10 mL THF was added dropwise to this solution. The mixture was allowed to warm to room temperature and stirred overnight. The solvent was removed *in vacuo* and the obtained solid was extracted with CH_2Cl_2. The red brown solution was filtered and dried *in vacuo*. Five milliliters of CH_2Cl_2 and 30 mL hexane were added to the obtained oily residue. The product precipitated and the mixture was stored in the freezer at −30 °C overnight. The product was collected by filtration and dried under vacuum. Yield: 0.12 g (0.140 mmol; 28%).

Crystals of **2** suitable for X-ray studies were obtained by crystallization of the initial product from dichloromethane.

Mp: 240 °C. Elemental *Anal.* Calc. for $C_{20}H_{16}N_4O_3Se_4Mo_2$ (868.09 g mol^{-1}): C, 27.67; H, 1.86; N, 6.45. Found: C, 27.07; H, 1.94; N, 5.86%; IR (KBr): $\tilde{\nu}$ = 1581 (vs), 1552 (m), 1444 (s), 1421 (s), 1265 (s), 1149 (m), 1122 (s), 1079 (m), 1039 (m), 1014 (w), 939 (w), 926 (s), 892 (s), 873 (m), 804 (w), 763 (s), 753 (s), 728 (w); 701 (m), 642 (w), 468 (w), 435 (w), 418 (w), 406 (w), 364 (w), 336 (w), 296 (w), 269 (s) cm^{-1}; ^{1}H NMR ($CDCl_3$, 500 MHz): δ 8.72 (m, H_6, 4H), 7.51 (m, H_4, 4H), 7.32 (m, H_3, 4H), 6.99 (m, H_5, 4H) ppm; ^{13}C NMR ($CDCl_3$, 500 MHz): δ 159.8 (s, C_2), 129.1 (s, C_3), 139.3 (s, C_4), 120.4 (s, C_5), 147.4 (s, C_6) ppm; ^{77}Se NMR ($CDCl_3$, 500 MHz): δ 428.0 (s) ppm; MS (EI): *m*/*z* (%) = 695 (3) [M^+−PySe−O], 632

(27) [M^+−PySe−Se], 442 (70) [M^+−(MoO(PySe)$_2$)], 426 (48) [M^+−(MoO$_2$(PySe)$_2$)], 285 (100)[M^+−(MoO(PySe)$_2$)−PySe].

2.2.3. [Mo_2O_3(4-CF_3-PymS)$_4$] (3)

To a −30 °C pre-cooled solution of 4-CF_3-PymSH (0.324 g, 1.8 mmol) in 10 mL THF, *n*-BuLi (0.72 mL of a 2.5 M solution in hexane, 1.8 mmol) was added dropwise *via* syringe. The mixture was allowed to warm to room temperature, stirred overnight, and then cooled to −30 °C. A colorless solution of [MoO_2Cl_2(DME)] (0.260 g, 0.9 mmol) in 10 mL THF was added dropwise to this solution. The mixture was allowed to warm to room temperature and stirred overnight. The solvent was removed *in vacuo* and the obtained solid was extracted with CH_2Cl_2. The red brown solution was filtered, concentrated and kept at room temperature for several days. The black-purple prismatic crystals were collected by filtration and dried *in vacuo*. Yield: 0.19 g (0.200 mmol; 45%). Mp: 315 °C dec. Elemental *Anal.* Calc. for $C_{20}H_8F_{12}N_8O_3S_4Mo_2$ (956.44 g mol^{-1}): C, 25.12; H, 0.84; N, 11.72. Found: C, 25.63; H, 0.95; N, 11.90%; IR (KBr): $\tilde{\nu} = 3080$ (w), 1579 (m), 1558 (m), 1429 (m), 1361 (s), 1332 (vs), 1265 (w), 1207 (m), 1193 (m), 1149 (m), 1116 (s), 968 (m), 842 (m), 789 (w), 735 (m), 702 (w), 680 (m); 476 (w), 441 (w) cm^{-1}; ^{1}H NMR ($CDCl_3$, 300 MHz): δ 8.79 (d, 4H), 7.38 (t, 4H) ppm; MS (EI): *m/z* (%) = 818 (100) [M^+−2CF_3], 638 (89) [M^+−2CF_3-(4-CF_3-PymS)], 488 (78) [M^+−(MoO(4-CF_3-PymS)$_2$)].

2.3. Oxygen atom transfer reactions

In a sealed NMR tube a 1:10 mixture of catalyst (0.02 mmol for compounds **1** and **2**) and PPh_3 (0.20 mmol) in degassed, dry DMSO-d_6 (0.6 mL) was monitored with ^{31}P NMR spectroscopy. Only two signals were observed in both experiments: δ −6.5 ppm (PPh_3), δ 26.1 ppm ($OPPh_3$).

2.4. Other physical measurements

Melting points were obtained in sealed capillaries with a Büchi B 540 instrument and were not corrected. Elemental analyses were performed with a Heraeus CHN-O-Rapid elemental analyzer. Infrared spectra were recorded as KBr pellets with a Bio-Rad Digilab FTS-7 spectrometer from 4000 to 300 cm^{-1}. NMR spectra were recorded with a Bruker Avance 500 NMR spectrometer and referenced to the chemical shifts of the deuterated solvent. All NMR-grade solvents were dried prior to use. The chemical shifts are reported in parts per million; external reference $SiMe_4$ for ^{1}H and ^{13}C nuclei, and $SeMe_2$ for ^{77}Se nuclei. Mass spectra were obtained with a Finnigan MAT system 8230 or Varian MAT CH5 instrument by EI-MS methods.

2.5. X-ray structure determinations

Crystallographic data for compounds **1**–**3** were collected on a STOE IPDS II array detector system with four-circle instrument using graphite-monochromated Mo Kα ($\lambda = 0.71073$ Å) radiation. The data for all the compounds were collected at low temperature (for exact values see Table 1). The data reduction and space group determination were carried out using Siemens SHELXTL program [15]. All structures were solved by direct methods (SHELXS-97) [16] and refined with all data by full-matrix least-squares methods on F^2 using SHELXL-97 [17]. All non-hydrogen atoms were refined anisotropically. Hydrogen

Table 1
Crystallographic parameters

	[Mo_2O_3(PyS)$_4$] (**1**)	[Mo_2O_3(PySe)$_4$] (**2**)	[Mo_2O_3(4-CF_3-PymS)$_4$] · 2CH_2Cl_2 (**3** · 2CH_2Cl_2)
Formula	$C_{20}H_{16}Mo_2N_4O_3S_4$	$C_{20}H_{16}Mo_2N_4O_3Se_4$	$C_{22}C_{14}H_{12}F_{12}Mo_2N_8O_3S_4$
M (g/mol)	680.49	868.09	1126.32
T (K)	133(2)	133(2)	133(2)
Wavelength (Å)	0.71073	0.71073	0.71073
Crystal system	triclinic	triclinic	monoclinic
Space group	$P\bar{1}$	$P\bar{1}$	$P2_1/c$
a (Å)	8.9399(10)	7.2195(8)	14.9773(8)
b (Å)	11.3934(13)	9.0239(10)	10.5230(5)
c (Å)	13.1679(16)	10.6741(11)	12.3575(7)
α (°)	100.055(10)	73.637(8)	90
β (°)	107.432(9)	77.288(8)	106.832
γ (°)	96.812(9)	77.726(8)	90
V (Å^3)	1238.9(2)	642.40(12)	1864.18(17)
Z	2	1	2
μ (mm^{-1})	1.379	6.671	1.285
Reflections collected	13145	8007	26766
Independent reflections	4229	1893	3189
Goodness-of-fit on F^2	0.943	1.085	1.042
R_1 [$I > 2\sigma(I)$]	0.0450	0.0505	0.0289
wR_2 [$I > 2\sigma(I)$]	0.0944	0.1448	0.0697
R_1 (all data)	0.0810	0.0521	0.0332
wR_2 (all data)	0.1016	0.1474	0.0716

$R_1 = \sum\|F_o| - |F_c\|_i / \sum|F_o|$; $wR_2 = [\sum_w(F_o^2 - F_c^2)^2 / \sum wF_{oi}^4]^{1/2}$.

atoms were attached at idealized positions on carbon atoms with U_{iso} related to the U_{iso} of the parent atoms and were refined with the riding model, or by difference Fourier synthesis and refined isotropically. Parameters of the X-ray crystallography are summarized in Table 1.

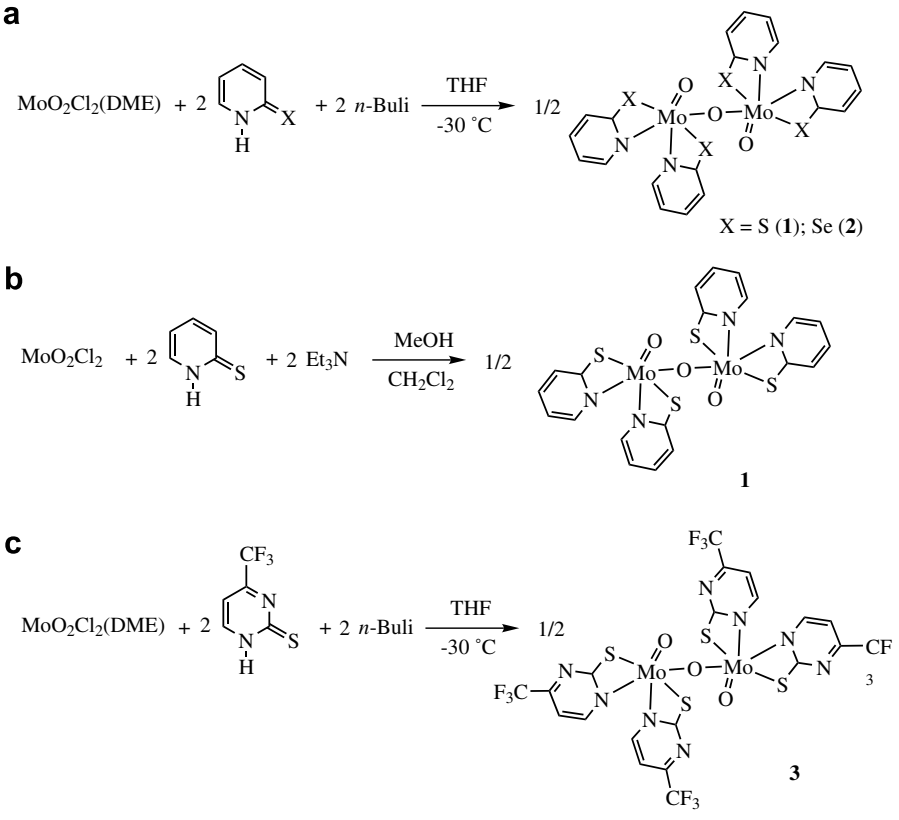
3. Results and discussion

3.1. Synthesis and characterization

The molybdenum compounds $[Mo_2O_3(PyS)_4]$ (**1**), $[Mo_2O_3(PySe)_4]$ (**2**) and $[Mo_2O_3(4\text{-}CF_3\text{-}PymS)_4]$ (**3**) were all obtained in different yields (48% for **1**, 28% for **2** and 45% for **3**) using analogous methods. At first, the nucleophilic species, lithium thionates or lithium selenate, were obtained by reaction of the corresponding pyridine-2-thiol, 2-pyrimidinthiol or pyridine-2-selenol with *n*-butyllithium in THF at −30 °C. The mixture was allowed to warm to room temperature and stirred overnight. The product was subsequently reacted with the readily available molybdenum precursor $[MoO_2Cl_2(DME)]$ [12] at −30 °C and the mixture was allowed to warm to room temperature and stirred overnight again according to the general process depicted in Scheme 1.

Different purification methods were used for the three products. Compound **1** was obtained by directly drying the filtered CH_2Cl_2 extract. Because the product of the same treatment for **2** was oily the CH_2Cl_2-filtrate of **2** was treated with hexane and stored overnight at −30 °C upon which **2** precipitated as a microcrystalline powder. Compound **3** was obtained directly by crystallizing from the initial concentrated filtered CH_2Cl_2-extract. Compound **1** can also be synthesized in 44% yield by adding a methanolic solution of the ligand and triethylamine to a stirred solution of precursor $[MoO_2Cl_2]$ [13] in dichloromethane (Scheme 1b). All compounds are intensely colored: dark red brown (**1** and **2**) or dark purple (**3**). The three obtained compounds were all dinuclear μ-oxomolybdenum(V) species which were not the initially desired unreduced mononuclear dioxomolybdenum(VI) species. Such behavior may be due to the corresponding ligands acting both as a reductant and as a ligand in the reaction and was observed previously upon the reaction of thiol ligands with Mo(VI) starting materials [18,19]. Interestingly the mononuclear species $[Mo(VI)O_2(PyS)_2]$ was prepared before by two different methods [20,21] one of which even employing the same metal precursor as was used in the here presented procedure: $[MoO_2Cl_2]$ [21]. As stated before [21] it is probable that in all these reactions the mononuclear and the reduced dinuclear species form simultaneously. The reaction medium and conditions as well as the isolation procedure determine the main product, its yield and purity. The description of the mononuclear compound $[Mo(VI)O_2(PyS)_2]$ as being dark purple [20] (contrary to the yellow color described by Arnáiz et al. [21] and to our findings as well) indeed strongly indicates that it was not pure but a mixture with the dinuclear Mo(V) compound [21].

Compound **1** was synthesized before by different methods [10,20,21] and its structure was also determined [10]



Scheme 1. Preparation of compounds **1**–**3**.

even though in a different modification than ours, the latter having a cell volume of double value and contains two molecules per cell instead of only one. By one of the synthetic routes the mononuclear dioxomolybdenum(VI) thionate was quantitatively converted into the dinuclear oxomolybdenum(V) complex by oxygen atom abstraction with common organophosphines and phosphates [20,21]. In the other route the formation of this molybdenum(V) compound from Na(PyS) and molybdenum(II) acetate was achieved with atmospheric oxygen. The preparation methods described here differ from these previous routes. To the best of our knowledge compounds **2** and **3** were unknown until now and furthermore **2** is the first oxomolybdenum complex containing pyridine-2-selenolato. Only one (non-oxo) molybdenum complex with this ligand was described before [11].

IR spectra of the complexes confirm the presence of the ligands coordinated to the metal. For example, the band attributable to the ν(N–H), which appears at 3200–3100 cm^{-1} in the free thione ligands, is absent, indicating that the ligands are in their deprotonated form. The strong ligand bands in the range of 1640–1660 cm^{-1} are caused by the presence of ν(C=N) and ν(C=C) in a non-aromatic system. In the complexes, however, these bands appear in the region of 1545–1590 cm^{-1}, which is characteristic for stretching vibrations in an aromatic group [22]. These observations confirm that the ligand is present in its complexes in the thiolate form. The IR spectrum also shows prominent absorptions in the 750–943 cm^{-1} region consistent with the presence of both terminal and bridging oxo groups.

The ^{1}H and ^{13}C NMR spectra of **1**–**3** (except for ^{13}C NMR spectra of **3** due to its poor solubility in $CDCl_3$) are consistent with their compositions. ^{1}H and ^{13}C NMR spectra of **1** are almost identical to those of **2**. A resonance signal from ^{77}Se NMR spectroscopy of compound **2** ($\delta = 428.0$ ppm) shifted to lower field relative to that of the free ligand PySeH ($\delta = 306.6$ ppm) was observed, confirming the formation of a metal–selenium bond [23].

In all cases the EI mass spectra of the compounds show peaks of the fragment ions of the molecule after partial decomposition such as the loss of heterocyclic ligands or oxo ligands. The peak cluster shows the appropriate isotope distribution.

3.2. Structural characterization

Crystals of **1**–**3** suitable for X-ray studies were obtained by the recrystallization of the initial products from dichloromethane. The crystal structures of **1**–**3** are shown in Figs. 1–3 along with the numbering schemes; solvent molecules of **3** are not shown. The selected bond lengths and angles are given in Tables 2–4.

Compounds **1** and **2** crystallize in the same space group ($P\bar{1}$) and crystal system (triclinic) but with different cell dimensions. They appear to be isostructural. Compound **3** crystallizes in the monoclinic space group $P2_1/c$. The

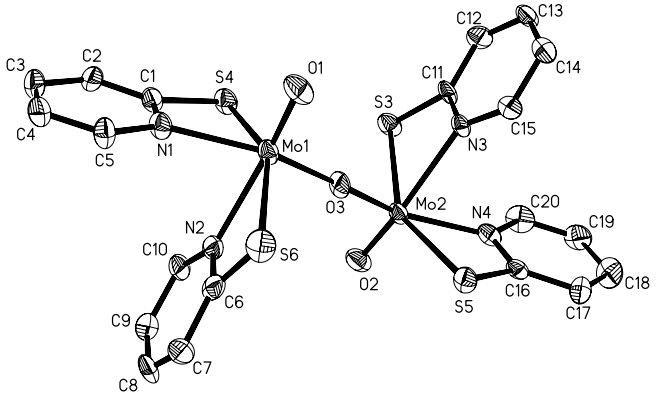


Fig. 1. Molecular structure of $[Mo_2O_3(PyS)_4]$ (**1**) without hydrogen atoms. Ellipsoids are drawn at 50% probability.

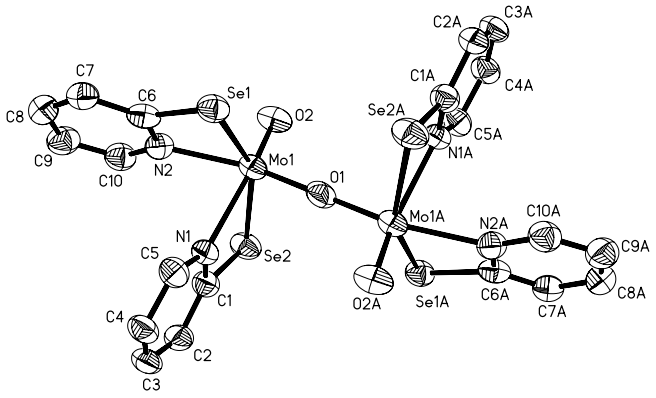


Fig. 2. Molecular structure of $[Mo_2O_3(PySe)_4]$ (**2**) without hydrogen atoms (with numbering scheme, 'A' indicating atoms at equivalent positions $(-x, -y, -z)$). Ellipsoids are drawn at 50% probability.

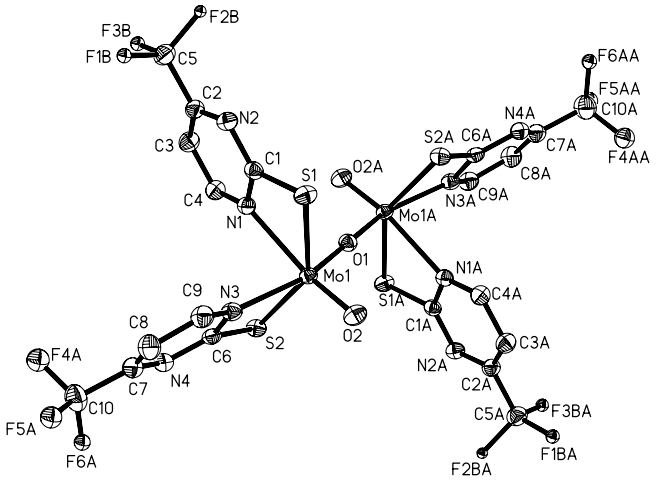


Fig. 3. Molecular structure of $[Mo_2O_3(4\text{-}CF_3\text{-}PymS)_4]\cdot 2(CH_2Cl_2)$ (**3**) without hydrogen atoms (with numbering scheme, 'A' indicating atoms at equivalent positions $(-x+1, -y, -z)$). Ellipsoids are drawn at 50% probability. For each of the disordered fluorine atoms only one out of three positions is shown. Solvent molecules are not shown.

structures of **1**–**3** are unexceptional for thiolate or selenolate complexes with the common $[Mo_2O_3]^{4+}$ core. Each molybdenum center exhibits distorted octahedral geometry

Table 2
Selected bond lengths (Å) and angles (°) for **1**

Bond lengths			
Mo(1)–O(1)	1.680(5)	Mo(1)–O(3)	1.863(5)
Mo(1)–N(1)	2.184(6)	Mo(1)–N(2)	2.308(6)
Mo(1)–S(4)	2.438(2)	Mo(1)–S(6)	2.496(2)
Bond angles			
O(1)–Mo(1)–O(3)	107.0(2)	N(1)–Mo(1)–S(4)	66.75(16)
O(1)–Mo(1)–N(1)	96.6(2)	N(2)–Mo(1)–S(4)	89.06(15)
O(3)–Mo(1)–N(1)	152.5(2)	O(1)–Mo(1)–S(6)	94.76(19)
O(1)–Mo(1)–N(2)	156.6(2)	O(3)–Mo(1)–S(6)	98.83(16)
O(3)–Mo(1)–N(2)	87.5(2)	N(1)–Mo(1)–S(6)	93.04(16)
N(1)–Mo(1)–N(2)	75.5(2)	N(2)–Mo(1)–S(6)	64.22(16)
O(1)–Mo(1)–S(4)	108.34(18)	S(4)–Mo(1)–S(6)	150.44(7)
O(3)–Mo(1)–S(4)	91.96(16)	Mo(1)–O(3)–Mo(2)	171.7(3)

Table 3
Selected bond lengths (Å) and angles (°) for **2**

Bond lengths			
Mo(1)–O(1)	1.864(1)	Mo(1)–O(2)	1.683(4)
Mo(1)–N(1)	2.314(5)	Mo(1)–N(2)	2.215(5)
Mo(1)–Se(1)	2.557(1)	Mo(1)–Se(2)	2.624(1)
Bond angles			
O(2)–Mo(1)–O(1)	106.41(18)	N(2)–Mo(1)–Se(1)	68.10(13)
O(2)–Mo(1)–N(2)	96.1(2)	N(1)–Mo(1)–Se(1)	89.87(12)
O(1)–Mo(1)–N(2)	154.57(14)	O(2)–Mo(1)–Se(2)	93.72(15)
O(2)–Mo(1)–N(1)	156.19(19)	O(1)–Mo(1)–Se(2)	97.53(3)
O(1)–Mo(1)–N(1)	87.76(12)	N(2)–Mo(1)–Se(2)	92.57(13)
N(2)–Mo(1)–N(1)	75.46(17)	N(1)–Mo(1)–Se(2)	64.98(12)
O(2)–Mo(1)–Se(1)	107.86(15)	Se(1)–Mo(1)–Se(2)	152.01(3)
O(1)–Mo(1)–Se(1)	93.32(3)	Mo(1)–O(1)–Mo(1A)	180.0

Symmetry transformations used to generate equivalent atoms: 'A' $-x, -y, -z$.

Table 4
Selected bond lengths (Å) and angles (°) for **3**

Bond lengths			
Mo(1)–O(1)	1.856(1)	Mo(1)–O(2)	1.672(2)
Mo(1)–N(1)	2.349(3)	Mo(1)–N(3)	2.193(3)
Mo(1)–S(1)	2.500(1)	Mo(1)–S(2)	2.451(1)
C(2)–C(5)	1.507(4)	C(5)–F(1A)	1.327(9)
Bond angles			
O(2)–Mo(1)–O(1)	104.22(8)	N(1)–Mo(1)–S(2)	85.56(6)
O(2)–Mo(1)–N(3)	97.78(11)	O(2)–Mo(1)–S(1)	96.63(8)
O(1)–Mo(1)–N(3)	155.15(7)	O(1)–Mo(1)–S(1)	98.64(2)
O(2)–Mo(1)–N(1)	160.12(10)	N(3)–Mo(1)–S(1)	90.05(7)
O(1)–Mo(1)–N(1)	83.16(6)	N(1)–Mo(1)–S(1)	63.76(6)
N(3)–Mo(1)–N(1)	79.90(9)	S(2)–Mo(1)–S(1)	144.74(3)
O(2)–Mo(1)–S(2)	111.83(8)	Mo(1A)–O(1)–Mo(1)	180.00(2)
O(1)–Mo(1)–S(2)	94.22(2)	F(3A)–C(5)–F(1A)	111.5(7)
N(3)–Mo(1)–S(2)	66.55(7)	F(1A)–C(5)–F(2A)	102.5(6)

Symmetry transformations used to generate equivalent atoms: 'A' $-x+1, -y, -z$.

coordinated by two chelating heterocyclic bidentate ligands, the terminal oxo group, and the bridging oxo group, which is located on a crystallographic inversion center (Figs. 1–3). Thus, the $[Mo_2O_3]^{4+}$ core exhibits a rigorously planar anti geometry. Furthermore, the three structures have a *trans* O=Mo–O–Mo=O chain with rigorous inversion symmetry, resembling previous reported compounds $Mo_2O_3[S_2P(OEt)_2]_4$ and Mo_2O_3(3-SiMe-2-SPy)$_4$ [24], while a *cis* configuration is also found for example in $Mo_2O_3[S_2CNPr_2]_4$ and Mo_2O_3(Etxan)$_4$, where Etxan represents $EtOCS_2$ [25,26]. This indicates that both the *cis* and *trans* arrangements may be of general occurrence.

In compound **2**, the distortions from the ideal octahedral geometry for each molybdenum center mainly arise from the disparate donor atom set and the restricted bite of the Py–Se ligand which subtend angles at the molybdenum center of 64.98(12)° and 68.10(13)°, respectively, considerably distorted from the octahedral limit of 90°. The Py–Se ligands are arranged so that the two selenium atoms are approximately *trans* to each other although with a grossly distorted angle of 152.01(3)°, which compels the nitrogen atoms to occupy approximate *cis*-positions (N–Mo–N, 75.46(17)°). The nitrogen donors occupy positions *trans* to the strongly π-bonding oxo groups, thus minimizing competition between the oxo groups and the weakly π-interacting selenium donors for the Mo t_{2g} orbitals. The strong *trans* influence of the terminal oxo group is evident in the Mo(1)–N(1) distance of 2.314(5) Å, as compared to the Mo(1)–N(2) distance of 2.215(5) Å for the nitrogen *trans* to the less effective bridging oxo group. The Mo–N bond lengths lie in the ranges that are observed in molybdenum complexes with the pyridine-2-selenato ligand [11] (2.247(3) and 2.206(3) Å) and the analogous pyridine-2-thiolato ligand [19,24,27] (2.157(5) [27a]–2.328(5) Å [24]). The two Mo–Se bond lengths (2.624(1) and 2.557(1) Å) which are in agreement with reported values (2.633(2)–2.661(1) Å) [11,28] are not equivalent. The four-membered rings derived from the chelating N,Se-coordination of the two 2-selenopyridines are coplanar with the adjacent pyridine rings. The distances of Mo to the terminal oxo ligand (1.683(4) Å), the bridging oxo group (1.864(1) Å) and the *cis*-O–Mo–O angle (106.41(18)°) are in the range of those reported for μ-oxomolybdenum(V) complexes (1.680(4), 1.863(1) Å and 105°, respectively) [24].

Complex **1** is isostructural to complex **2** and was described previously [10]. Since the distances and angles of our structure – though in a different modification – are almost identical to those published, we do not discuss the structure further but rather compare it with the structure of **2**. The geometrical parameters of both complexes are almost identical (see Tables 2 and 3). The main differences for bond lengths derive from the bonds containing the sulfur or the selenium atom. The differences of the corresponding Mo–Se and Mo–S bond lengths for **2** and **1** are 0.119 and 0.128 Å, and those of the bond lengths of S and Se to the carbon atom of the pyridine ring are 0.133 and 0.157 Å. All these differences can be ascribed to the different radii of both elements (van der Waals radii: 1.80 Å for S and 1.90 Å for Se) [29]. The biggest difference for the angles of **1** and **2** is within 3°. Overall both structures are similar, showing that the nature of the donor atoms in the heterocyclic ligand does not markedly influence the structure of the complex.

Complex **3** has a similar structure as **1** except for pyrimidine rings instead of pyridine rings and CF_3 groups as additional substituents in *para* position to the coordinating nitrogen. Unfortunately the CF_3 groups rotate freely and are therefore heavily disordered. Each of the fluorine atoms was found at three different positions which of course compromises the quality of the structural elucidation. The corresponding geometrical parameters for **3** and **1** are almost identical. The 4-CF_3-2-PymS ligands are also arranged in a way that the two sulfur atoms are approximately *trans* to each other (S–Mo–S, 144.74(3)°) constraining the nitrogen atoms to occupy approximate *cis*-positions (N–Mo–N, 79.90°). Both N-donor atoms occupy positions *trans* to a terminal oxo and a bridging oxo function, respectively. The *trans* influences of the two different oxo groups are responsible for the Mo–N distances being different (2.193(3) and 2.349(3) Å), which leads to different Mo–S distances (2.451(1) and 2.500(1) Å). The configuration of **3** is very close to those of **1** and **2**. Overall the electronic and steric influence of the introduced CF_3 group and an exchange of pyridine versus pyrimidine ligand is very small and does not effect the geometry of the obtained complexes. This behavior was reported for ruthenium and osmium complexes before [30].

3.3. Catalytic oxo-transfer activities

Dioxomolybdenum(VI) complexes are extensively employed as excellent catalysts for oxo transfer reactions as introduced above. A frequently used model reaction developed by Berg and Holm [31] is the oxidation of triphenylphosphine by DMSO. The formation of μ-oxo-dimers during the reduction of MoO_2 complexes is normally considered to be capable of breaking any catalytic cycle unless there is an equilibrium between the dimer and the $Mo^{VI}O_2$ and $Mo^{IV}O$ species. However, the formation of μ-oxo-bridged dimers does not necessarily exclude reversible oxo-transfer reactions. The reactivity of those dimers to catalyze oxygen atom transfer directly without conversion to the $M^{VI}O_2$ complexes was considered in some cases [32,33]. The molybdenum(V) compounds may be oxidized by a common oxidizing agent, such as DMSO, Ph_2SO and pyridine *N*-oxide. The reversibility of the oxo-transfer reactions involving dinuclear oxomolybdenum(V) complexes sometimes strongly depends on electronic features of the ligands rather than steric effects [19].

In order to assess the oxo transfer behavior of such complexes and especially comparing the influence of sulfur versus selenium coordination, oxo-transfer reactions of the molybdenum(V) compounds **1** and **2** were studied by use of PPh_3 in DMSO under analogous conditions. The experiments were performed at room temperature in dry deoxygenated DMSO-d_6 by treating the catalyst (**1** or **2**) with 10 equiv. of PPh_3 (2×10^{-4} mol) in a NMR tube. A figure showing the development of the ^{31}P NMR signals for catalyst **2** as example can be found in the Supplementary material (Fig. S1). The reactions were monitored with ^{31}P NMR spectroscopy. During the reactions only two phosphorous signals were observed: one for PPh_3 and one for $OPPh_3$. During the catalytic process for **1** as catalyst the reaction solution changed rapidly its color from deep red to yellow at the beginning of the reaction (about 7 min). Thereafter the color of the solution remained yellow and unchanged. For **2** as catalyst the color change from deep red to green yellow and finally to light brown was observed as well, but the change was slower in comparison to that for **1**. When the reaction was carried out to about 110 h, the color change stopped and the color light brown was kept to the end of the reaction. The color change for both reactions can be explained by the following assumptions (reactions (1) and (2)):

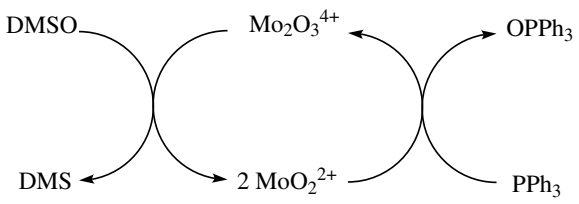
$$Mo_2^{V}O_3L_4 + DMSO \rightarrow 2Mo^{VI}O_2L_2 + DMS \quad (1)$$

$$2Mo^{VI}O_2L_2 + PPh_3 \rightarrow Mo_2^{V}O_3L_4 + OPPh_3 \quad (2)$$

First, oxidations of the oxomolybdenum(V) complexes to the mononuclear $Mo(VI)O_2$ species occur according to reaction (1). This possibility was well illustrated by previous reports [19,32,33]. It is well in accordance with the observation that the colors of the solutions for **1** and **2** in DMSO without PPh_3 also change from deep red to yellow or light brown respectively. When these solutions were monitored over time with mass spectrometry the molecule peaks for the dinuclear $Mo(V)_2O_3$ compounds decreased while the molecule peaks for the mononuclear species increased up to a total conversion from dimeric to monomeric complex. Subsequently, the reduction of the mononuclear dioxomolybdenum(VI) compounds is achieved by the reaction with PPh_3 that leads to dinuclear μ-oxomolybdenum(V) complexes (reaction (2)). This later process was observed before for the formation of **1** from $[MoO_2(PyS)_2]$ [20,21] and some other dinuclear molybdenum(V) complexes [32]. Due to a large excess of DMSO in contrast with PPh_3, the dinuclear μ-oxomolybdenum(V) complexes and PPh_3 were completely converted to mononuclear dioxomolybdenum(VI) complexes and $OPPh_3$. The similarity of the color change between the catalytic reaction mixtures and the solutions of only complexes in DMSO also provides evidence for the above assumption. The entire process is summarized in Scheme 2.

The development of the conversion of PPh_3 to $OPPh_3$ for both complexes **1** and **2** over time is shown in Fig. 4.

The functions of the reactions for **1** and **2** appear to be almost linear. A plot of $\ln c(PPh_3)$ versus the time t on the



Scheme 2.

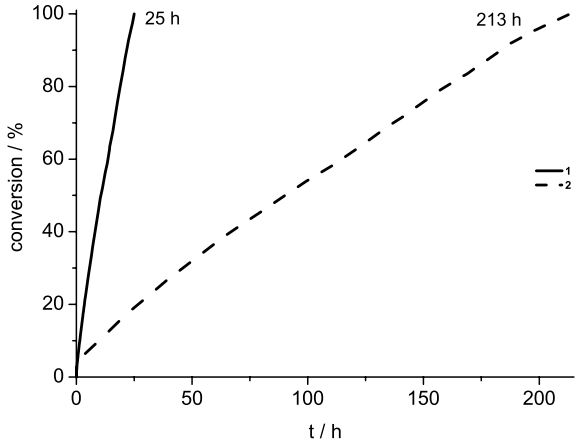


Fig. 4. Oxidation of PPh_3 to $OPPh_3$ by DMSO-d_6 at rt as a function of time for **1** and **2**.

other hand is strictly non-linear. This means the reaction cannot be described as being first order with respect to the PPh_3 concentration, which would have been expected with the large access of the second reactant DMSO. PPh_3 was completely oxidized in only 25 h (about 1 day) for **1**, which is in accordance with a previous study [21], whereas it took 213 h (nearly 9 days) for **2**. The thionato containing complex **1** shows considerably higher catalytic activity than its selenolato containing analogue **2**. This suggests that the catalytical performance of both compounds is strongly influenced by an exchanged of ligand atoms sulfur versus selenium even though no strong influence on the structures could be observed.

4. Conclusion

Molybdenum complexes with bidentate heterocyclic thiones and selenone, $[Mo_2O_3(PyS)_4]$ (**1**), $[Mo_2O_3(PySe)_4]$ (**2**) and $[Mo_2O_3(4\text{-}CF_3\text{-}PymS)_4]$ (**3**), were obtained by similar reactions of the molybdenum precursor $[MoO_2Cl_2(DME)]$ with the corresponding ligands. They all formed dinuclear μ-oxomolybdenum(V) species because the corresponding ligands are acting both as a reductant and as a ligand in the reactions. The crystal structures of **1**–**3** include the common $[Mo_2O_3]^{4+}$ core. Compounds **1** and **2** are isostructural. Through structural analysis and comparison we can conclude that the nature of the donor atoms in the heterocyclic ligand does not markedly influence the structure of the complex and the introduction of the CF_3 group on the heterocyclic ring of the ligands does not have significant influence on the structures of the complexes at least for this kind of complexes. The thionato containing complex **1** shows considerably higher catalytic activity than its selenolato containing analogue **2** for the transfer of one oxygen atom from DMSO to PPh_3. This result indicates that an exchange of ligand atoms sulfur versus selenium of the same ligand system can cause different activities of complexes even though no strong influence on other investigated properties could be observed.

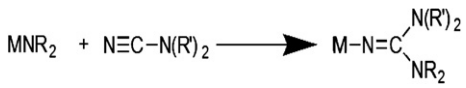
Appendix A. Supplementary material

CCDC 652135, 652136 and 652137 contain the supplementary crystallographic data for **1**, **2** and **3**. These data can be obtained free of charge via http://www.ccdc.cam.ac.uk/conts/retrieving.html, or from the Cambridge Crystallographic Data Centre, 12 Union Road, Cambridge CB2 1EZ, UK; fax: (+44) 1223-336-033; or e-mail: deposit@ccdc.cam.ac.uk. Supplementary data associated with this article can be found, in the online version, at Supplementary data associated with this article can be found, in the online version, at doi:10.1016/j.poly.2007.08.020.

References

[1] (a) E.S. Raper, Coord. Chem. Rev. 153 (1996) 199, and literature cited therein;
(b) J.A. García-Vázquez, M.L. Durán, I. Casanova, A. Sousa, J. Chem. Soc., Dalton Trans. (2003) 1379.
[2] J.H. Enemark, J.J.A. Cooney, J.-J. Wang, R.H. Holm, Chem. Rev. 104 (2004) 1175.
[3] (a) C.S. Butler, J.M. Charnock, C.D. Garner, A.J. Thomson, S.J. Ferguson, B.C. Berks, D.J. Richardson, Biochem. J. 352 (2000) 859;
(b) M. Bokranz, E. Kojoro, F. Fahrenholz, F. Lauterbach, A. Kröger, Arch. Mikrobiol. 156 (1991) 119;
(c) J.M. Dias, M.E. Than, A. Humm, R. Huber, G.P. Bourenkov, H.D. Bartunik, S. Bursakov, J. Calvete, J. Caldeira, C. Carveiro, J.J.G. Moura, I. Moura, M.J. Romão, Structure 7 (1999) 65.
[4] (a) V.N. Gladyshev, S.V. Khangulov, T.C. Stadtman, Proc. Natl. Acad. Sci. USA 91 (1994) 232;
(b) J.C. Boyington, V.N. Gladyshev, S.V. Khangulov, T.C. Stadtman, P.D. Sun, Science 275 (1997) 1305.
[5] (a) X. Ma, K. Starke, C. Schulzke, H.-G. Schmidt, M. Noltemeyer, Eur. J. Inorg. Chem. (2006) 628;
(b) X. Ma, C. Schulzke, H.-G. Schmidt, M. Noltemeyer, Dalton. Trans. (2007) 1773.
[6] (a) S. Patai, Z. Rappoport (Eds.), The Chemistry of Organic Selenium and Tellurium Compounds, J. Wiley & Sons, New York, 1986;
(b) M. Kita, H. Tamai, F. Ueta, A. Fuyuhiro, K. Yamanari, K. Nakajima, M. Kojima, K. Murata, S. Yamashita, Inorg. Chim. Acta 314 (2001) 139;
(c) S. Narayan, V.K. Jain, K. Panneerselvam, T.H. Lu, S.-F. Tung, Polyhedron 18 (1999) 1253;
(d) J. Romero, M.L. Durán, J.A. García-Vázquez, A. Castineiras, A. Sousa, L. Christiaens, J. Zubieta, Inorg. Chim. Acta 255 (1997) 307;
(e) Y. Cheng, T.J. Emge, J.G. Brennan, Inorg. Chem. 35 (1996) 7339;
(f) N. Chopra, L.C. Damude, P.A.W. Dean, J.J. Vittal, Can. J. Chem. 74 (1996) 2095.
[7] H.G. Mautner, S.-H. Chu, C.M. Lee, J. Org. Chem. 27 (1962) 3671.
[8] (a) A. Toshimitsu, H. Owada, S. Uemura, M. Okano, Tetrahedron Lett. 23 (1982) 2105;
(b) A. Toshimitsu, H. Owada, K. Terao, S. Uemura, M. Okano, J. Org. Chem. 49 (1984) 3796;
(c) A. Toshimitsu, H. Owada, K. Terao, S. Uemura, M. Okano, J. Chem. Soc., Perkin Trans. 1 (1985) 373;
(d) D.H.R. Barton, D. Crich, Tetrahedron 41 (1985) 4359;
(e) A. Toshimitsu, G. Hayashi, K. Terao, S. Uemura, J. Chem. Soc., Perkin Trans. 1 (1988) 2113.
[9] (a) H. Takaku, Y. Shimida, Y. Nakajima, T. Hata, Nucleic Acids Res. 3 (1976) 1233;
(b) H. Takaku, T. Konishi, T. Hata, Chem. Lett. 6 (1977) 655;
(c) H. Takaku, T. Yamazaki, Nucleic Acid Chem. 2 (1978) 869;
(d) H. Takaku, M. Kato, M. Yoshida, R. Yamaguchi, J. Org. Chem. 45 (1980) 3347.

[10] F.A. Cotton, P.E. Fanwick, J.W. Fitch, Inorg. Chem. 17 (1978) 3254.
[11] C.O. Kienitz, C. Thöne, P.G. Jones, Inorg. Chem. 35 (1996) 3990.
[12] T. Robin, F. Montilla, A. Galindo, C. Ruiz, J. Hartmann, Polyhedron 18 (1999) 1485.
[13] V.C. Gibson, T.P. Kee, A. Shaw, Polyhedron 7 (1988) 579.
[14] G.J.-J. Chen, J.W. McDonald, W.E. Newton, Inorg. Chem. 15 (1976) 2612.
[15] G.M. Sheldrick, SHELXTL-PLUS, Siemens X-ray Instruments, Madison, 1990.
[16] G.M. Sheldrick, Acta Crystallogr., Sect. A 46 (1990) 467.
[17] G.M. Sheldrick, SHELXL-97, Programs for Crystal Structure Refinement, University of Göttingen, Germany, 1997.
[18] C. Pickett, S. Kumar, P. Vella, J. Zubieta, Inorg. Chem. 21 (1982) 908.
[19] L. Stelzig, S. Kötte, B. Krebs, J. Chem. Soc., Dalton Trans. (1998) 2921.
[20] P.R. Traill, A.G. Wedd, E.R.T. Tiekink, Aust. J. Chem. 45 (1992) 1933.
[21] F.J. Arnáiz, R. Aguado, M.R. Pedrosa, M.A. Maestro, Polyhedron 23 (2004) 537.
[22] E. Spinner, J. Chem. Soc. (1960) 1237.
[23] E.G. Hope, W. Levason, Coord. Chem. Rev. 122 (1993) 109.
[24] E. Block, M. Gernon, H. Kang, G. Ofori-Okai, J. Zubieta, Inorg. Chem. 30 (1991) 1736.
[25] E.I. Stiefel, Prog. Inorg. Chem. 22 (1977) 1.
[26] J. Hyde, K. Venkatasubramanian, J. Zubieta, Inorg. Chem. 17 (1978) 414.
[27] (a) M.A.A.F. De C.T. Carrondo, A.R. Dias, M.H. Garcia, A. Mirpuri, M.F.M. Piedade, M.S. Salema, Polyhedron 8 (1989) 2439;
(b) P.E. Fanwick, J.-S. Qi, Y.-P. Wu, R.A. Walton, Inorg. Chim. Acta 168 (1990) 159;
(c) E. Block, H. Kang, J. Zubieta, Inorg. Chim. Acta 181 (1991) 227;
(d) E. Block, G. Ofori-Okai, H. Kang, J. Zubieta, Inorg. Chim. Acta 190 (1991) 179;
(e) E. Block, G. Ofori-Okai, J. Am. Chem. Soc. 114 (1992) 758.
[28] H. Rakoczy, M. Schollenberger, B. Nuber, M.L. Ziegler, J. Organomet. Chem. 467 (1994) 217.
[29] L. Pauling, in: The Nature of the Chemical Bond and the Structure of Molecules and Crystals, third ed., Cornell University Press, Ithaca, New York, 1960.
[30] A. Sousa-Pedrares, M.L. Durán, J. Romero, J.A. García-Vázquez, J.C. Monteagudo, A. Sousa, J.R. Dilworth, Inorg. Chim. Acta 359 (2006) 863.
[31] J.M. Berg, R.H. Holm, J. Am. Chem. Soc. 107 (1985) 925.
[32] J.A. Craig, E.W. Harlan, B.S. Snyder, M.A. Whitener, R.H. Holm, Inorg. Chem. 28 (1989) 2082.
[33] D.M. Baird, S. Falzone, J.E. Haky, Inorg. Chem. 28 (1989) 4561.



Scheme 1. The general synthesis of M(TAG).

The convenient synthesis of Li(TMG) via the reaction of lithium dimethylamide with dimethylcyanamide was first reported by Wade and co-workers [4]. Herein, we report the generalization of this reaction (Scheme 1) to cleanly generate a family of Li(TAG) precursors that are subsequently used in metathesis reactions with lithium bis- trimethylsilylamide and $ZnCl_2$ to form the corresponding hetero-ligated Zn(TAG) complex. This initial investigation utilizes dimethylamino, diethylamino, pyrrolidine, and piperidine functionalities to develop a library of structurally varied Zn(TAG) complexes. AlkylZn amides, homoleptic amides, and Zn guanidinate complexes have been reported as polymerization catalysts, as well as MOCVD and nanocrystal precursors [8]. Therefore, synthesizing, characterizing, and studying the properties of novel Zn(TAG) complexes will illuminate a new direction in metal-nitrogen chemistry while also providing a new class of low-coordinate complexes for material science applications.

2. Experimental

All syntheses were handled with rigorous exclusion of air and water using standard glove box techniques. All anhydrous solvents were stored under argon and used as received in sure seal bottles. The following chemicals were used as received from commercial suppliers: $LiNEt_2$, $LiNMe_2$, $LiN(SiMe_3)_2$, *n*-BuLi (1.6 M in hexanes), dimethylcyanamide, diethylcyanamide, pyrolidinecyanamide, piperidine, pyrrolidine and $ZnCl_2$. FT-IR data were obtained on a Bruker Tensor 27 instrument using KBr under an atmosphere of flowing nitrogen. Elemental analysis was performed on a Perkin–Elmer 2400 Series 2 CHN-S/O Elemental Analyzer. All NMR samples were prepared from dried crystalline materials that were handled and stored under an argon atmosphere and re-dissolved in C_6D_6. All solution spectra were obtained on a Bruker DRX400 spectrometer at 400.1 and 100.5 MHz for ^1H and ^{13}C experiments.

2.1. General synthesis of *1*–*6*

To a lithium dialkylamide dissolved in 15 mL of ether, an equivalent of dialkylcyanamide was added drop-wise under an inert atmosphere of argon. Subsequently, the reaction mixture was allowed to stir for 30 min completing the generation of the lithium 1,1,3,3-tetralkylguanidinate *in situ*. $LiN(SiMe_3)_2$ and $ZnCl_2$ were then added sequentially. After stirring for 24 h, LiCl was removed via centrifugation and the solution was further concentrated and cooled to −35 °C. X-ray-suitable, colorless crystals were grown in 24 h.

2.1.1. *[Zn(μ-DEDMG){N(SiMe$_3$)$_2$}]$_2$ (1)*

$LiNMe_2$ (0.15 g, 2.9 mmol); diethylcyanamide (0.29 g, 2.9 mmol); $LiN(SiMe_3)_2$ (0.50 g, 2.9 mmol); $ZnCl_2$ (0.40 g, 2.9 mmol). Yield 94% (1.0 g, 1.4 mmol). *Anal.* Calc. for $C_{13}H_{34}N_4Si_2Zn$: C, 42.43; H, 9.31; N, 15.22. Found: C, 41.88; H, 9.16; N, 14.78%. ^1H NMR (400.1 MHz, C_6D_6): δ 3.18 (t, $J_{H-H} = 7.0$ Hz, 4H, N=C(N(CH_2CH_3)$_2$)(N(CH_3)$_2$)) 2.74 (d, $J_{H-H} = 7.6$ Hz, 6H, N=C(N(CH_2CH_3)$_2$)(N(CH_3)$_2$)), 1.02 (q, $J_{H-H} = 7.0$ Hz, 6H, N=C(N(CH_2CH_3)$_2$)(N(CH_3)$_2$)), 0.28 (s, 18H, N(Si(CH_3)$_3$)$_2$). ^{13}C NMR (100.6 MHz, C_6D_6): δ 164.7 (N=*C*(N(CH_2CH_3)$_2$)(N(CH_3)$_2$)), 44.2 (N=C(N(*C*H_2CH$_3$)$_2$)(N(CH_3)$_2$)), 40.1 (N=C(N(CH_2CH_3)$_2$)(N(*C*H_3)$_2$)), 14.3 (N=C(N(CH_2*C*H_3)$_2$)(N(CH_3)$_2$)), 6.0 (N(Si(*C*H_3)$_3$)$_2$). FTIR (KBr, cm^{-1}) 2966 (s), 2895 (s), 1550 (s), 1459 (m), 1405 (m), 1380 (m), 1244 (m), 1119 (w), 1077 (w), 1006 (m), 938 (w), 879 (m), 842 (m), 749 (w), 669 (w), 633 (w), 612 (w), 561 (w), 482 (w).

2.1.2. *Zn(μ-PYRDMG){N(SiMe$_3$)$_2$}]$_2$ (2)*

Pyrrolidine (0.21 g, 2.9 mmol); 1.6 M *n*-BuLi (1.26 g, 2.9 mmol); dimethylcyanamide (0.21 g, 2.9 mmol); $LiN(SiMe_3)_2$(0.50 g, 2.9 mmol); $ZnCl_2$ (0.40 g, 2.9 mmol). Yield 64% (0.69 g, 0.93 mmol). *Anal.* Calc. for $C_{13}H_{32}N_4Si_2Zn$: C, 42.66; H, 8.81; N, 15.31. Found: C, 41.57; H, 8.18; N, 15.15%. ^1H NMR (400.1 MHz, C_6D_6): δ 3.35 (t, $J_{H-H} = 6.7$Hz,4H, N=C(N*C*H_2CH$_2$CH$_2$*C*H_2)(N(CH_3)$_2$)), 2.77 (s,6H, N=C(NCH$_2$CH$_2$CH$_2$CH$_2$)(N(*C*H_3)$_2$)), 1.63 (m,4H, N=C(NCH$_2$*C*H_2*C*H_2CH$_2$)(N(CH_3)$_2$)), 0.29 (s, 18H, N{Si(*C*H_3)$_3$}$_2$). ^{13}C NMR (100.6 MHz, C_6D_6): δ 162.8 (N=*C*(NCH$_2$CH$_2$CH$_2$CH$_2$)(N(CH_3)$_2$)), 49.4 (N=C(N*C*H$_2$CH$_2$CH$_2$*C*H$_2$)(N(CH_3)$_2$)) 40.5 (N=C(N*C*H$_2$CH$_2$CH$_2$CH$_2$)(N(*C*H_3)$_2$), 26.3 (N=C(NCH$_2$*C*H$_2$*C*H$_2$CH$_2$)(N(CH_3)$_2$), 6.0 (N{Si(*C*H_3)$_3$}$_2$) FTIR (KBr, cm^{-1}) 2950 (s), 2874 (m), 1546 (s), 1523 (s), 1476 (m), 1436 (m), 1403 (w), 1370 (m), 1346 (m), 1255 (m), 1242 (m), 1185 (w), 1140 (w), 1065 (m), 1009 (s), 938 (w), 917 (w), 879 (m), 824 (m), 769 (w), 747 (w), 669 (w), 610 (w), 495 (w).

2.1.3. *[Zn(μ-PYRDEG){N(SiMe$_3$)$_2$}]$_2$ (3)*

Pyrrolidine (0.21 g, 2.9 mmol); 1.6 M *n*-BuLi (1.26 g, 2.9 mmol); diethylcyanamide (0.29 g, 2.9 mmol); $LiN(SiMe_3)_2$-(0.50 g, 2.9 mmol); $ZnCl_2$ (0.40 g, 2.9 mmol). Yield 34% (0.38 g, 0.49 mmol). *Anal.* Calc. for $C_{15}H_{36}N_4Si_2Zn$: C, 45.72; H, 9.21; N, 14.22. Found: C, 45.10; H, 8.63; N, 14.17%. ^1H NMR (400.1 MHz, C_6D_6): δ 3.43 (t, $J_{H-H} = 6.4$ Hz,4H, N=C(NCH$_2$CH$_2$CH$_2$CH$_2$)(N(CH_2CH_3)$_2$)), 3.22 (q, $J_{H-H} =$ 7.0Hz,4H, N=C(N*C*H_2CH$_2$CH$_2$*C*H_2)(N(CH_2CH_3)$_2$)),

1.64 (t, J_{H-H} = 6.1 Hz, 4H, N=C(NCH$_2$CH$_2$CH$_2$CH$_2$)(N(CH$_2$CH$_3$)$_2$)), 1.09 (t, 6H, J_{H-H} = 7.0 Hz, N=C(NCH$_2$CH$_2$CH$_2$CH$_2$)(N(CH$_2$CH$_3$)$_2$)) 0.326 (s, 18H, N{Si(CH$_3$)$_3$}$_2$). ^{13}C NMR (100.6 MHz, C_6D_6): δ 165.6 (N=*C*(NCH$_2$CH$_2$CH$_2$CH$_2$)(N(CH$_2$CH$_3$)$_2$)', 50.5 (N=C(N*C*H$_2$CH$_2$CH$_2$CH$_2$)(N(CH$_2$CH$_3$)$_2$), 44.1 (N=C(NCH$_2$CH$_2$CH$_2$*C*H$_2$)(N(CH$_2$CH$_3$)$_2$), 26.7 (N=C(NCH$_2$CH$_2$CH$_2$CH$_2$)(N(*C*H$_2$CH$_3$)$_2$)', 14.2 (N=C(NCH$_2$*C*H$_2$CH$_2$CH$_2$)(N(CH$_2$CH$_3$)$_2$)', 6.2 (N=C(NCH$_2$CH$_2$CH$_2$CH$_2$)(N(CH$_2$*C*H$_3$)$_2$), 5.6 (N{Si(*C*H$_3$)$_3$}$_2$). FTIR (KBr, cm^{-1}) 2959 (s), 2869 (s), 1534 (s), 1512 (s), 1485 (s), 1400 (s), 1295 (w), 1254 (s), 1243 (s), 1202 (w), 1074 (w), 1017 (s), 937 (w), 878 (s), 844 (s), 823 (s), 746 (m), 671 (m), 613 (w), 596 (w), 509 (w).

2.1.4. [Zn(μ-DPYRG){N(SiMe$_3$)$_2$}]$_2$ (4)

Pyrrolidine (0.21 g, 2.9 mmol); 1.6 M *n*-BuLi (1.26 g, 2.9 mmol); pyrrolidinecyanamide (0.28 g, 2.9 mmol); LiN(SiMe$_3$)$_2$(0.50 g, 2.9 mmol); $ZnCl_2$ (0.40 g, 2.9 mmol). Yield 37% (0.43 g, 0.54 mmol). *Anal.* Calc. for $C_{15}H_{34}N_4Si_2Zn$: C, 45.96; H, 8.74; N, 14.29. Found: C, 45.75 C; H, 9.23; N, 15.03%. ^{1}H NMR (400.1 MHz, C_6D_6): δ 3.39 (t, J_{H-H} = 6.4 Hz, 8H, N=C(NC*H*$_2$CH$_2$CH$_2$C*H*$_2$)$_2$), 1.68 (m, J_{H-H} = 3.28 Hz, 8H, N=C(NCH$_2$C*H*$_2$C*H*$_2$CH$_2$)$_2$), 0.29 (s, 18H, N{Si(CH$_3$)$_3$}$_2$). ^{13}C NMR (100.6 MHz, C_6D_6): δ 160.1 (N=*C*(NCH$_2$CH$_2$CH$_2$*C*H$_2$)$_2$)', 49.6 N=C(NCH$_2$*C*H$_2$CH$_2$CH$_2$)$_2$ 26.2 (N=C(NCH$_2$CH$_2$CH$_2$CH$_2$)$_2$)', 5.8 (N{Si(*C*H$_3$)$_3$}$_2$). FTIR (KBr, cm^{-1}) 2948 (s), 2875 (s), 1508 (s), 1479 (s), 1459 (s), 1387 (s), 1353(m), 1241 (m), 1007 (m), 966 (w), 915 (w), 878(s), 825 (m), 787 (w), 767 (w), 748 (w), 670 (w), 655 (w), 543 (w).

2.1.5. [Zn(μ-PIPDMG){N(SiMe$_3$)$_2$}]$_2$ (5)

Piperidine (0.25 g, 2.9 mmol); 1.6 M *n*-BuLi (1.26 g, 2.9 mmol); dimethylcyanamide (0.21 g, 2.9 mmol); LiN(SiMe$_3$)$_2$(0.50 g, 2.9 mmol); $ZnCl_2$ (0.40 g, 2.9 mmol). Yield 12% (0.13 g, 0.17 mmol). *Anal.* Calc. for $C_{14}H_{34}N_4Si_2Zn$: C, 44.25; H, 9.02; N, 14.74. Found: C, 44.11; H, 8.51; N, 14.57%. ^{1}H NMR (400.1 MHz, C_6D_6): δ 33.38 (m, 4H, N=C(NC*H*$_2$CH$_2$CH$_2$CH$_2$C*H*$_2$)(N(CH$_3$)$_2$)) 3.20 (m, 4H, N=C(NCH$_2$CH$_2$CH$_2$CH$_2$CH$_2$)(N(C*H*$_3$)$_2$)), 1.62 (m, 2H, N=C(NCH$_2$C*H*$_2$CH$_2$C*H*$_2$CH$_2$)(N(CH$_3$)$_2$)), 1.06 (m, 2H, N=C(NCH$_2$CH$_2$C*H*$_2$CH$_2$CH$_2$)(N(CH$_3$)$_2$)), 0.28 (s, 18H, N{Si(C*H*$_3$)$_3$}$_2$). ^{13}C NMR (100.6 MHz, C_6D_6): δ 161.6 (N=*C*(NCH$_2$CH$_2$CH$_2$CH$_2$CH$_2$)(N(CH$_3$)$_2$))', 49.1 (N=C(N*C*H$_2$CH$_2$CH$_2$CH$_2$CH$_2$)(N(CH$_3$)$_2$)) 44.6 (N=C(NCH$_2$CH$_2$CH$_2$*C*H$_2$CH$_2$)(N(CH$_3$)$_2$))', 25.6 (N=C(NCH$_2$CH$_2$CH$_2$CH$_2$CH$_2$)(N(*C*H$_3$)$_2$))', 14.5 (N=C(NCH$_2$*C*H$_2$CH$_2$CH$_2$CH$_2$)(N(CH$_3$)$_2$))', 5.6 (N=C(NCH$_2$CH$_2$*C*H$_2$CH$_2$CH$_2$)(N(CH$_3$)$_2$)), 5.6 N{Si(*C*H$_3$)$_3$}$_2$. FTIR (KBr, cm^{-1}) 2991 (w), 2938 (s), 2851 (m), 1545 (s), 1530 (s), 1484 (m), 1450 (m), 1433 (m), 1365 (s), 1256 (s), 1241 (s), 1191 (m), 1120 (m), 1096 (w), 1074 (w), 1010 (s), 916 (w), 879 (s), 823 (m), 750 (w), 670 (w), 648 (w), 576 (w).

2.1.6. [Zn(μ-PIPDEG){N(SiMe$_3$)$_2$}]$_2$ (6)

Piperidine (0.25 g, 2.9 mmol); 1.6 M *n*-BuLi (1.26 g, 2.9 mmol); diethylcyanamide (0.29 g, 2.9 mmol); LiN(SiMe$_3$)$_2$(0.50 g, 2.9 mmol); $ZnCl_2$ (0.40 g, 2.9 mmol). Yield 16% (0.19 g, 0.71 mmol). *Anal.* Calc. for $C_{16}H_{38}N_4Si_2Zn$: C, 47.09; H, 9.39; N, 13.73. Found: C, 46.55; H, 8.65; N, 13.46%. ^{1}H NMR (400.1 MHz, C_6D_6): δ 3.33 (m, 4H, N=C(NC*H*$_2$CH$_2$CH$_2$CH$_2$C*H*$_2$)(N(CH$_2$CH$_3$)$_2$)) 2.27 (q, J_{H-H} = 4.7 Hz, 4H N=C(NCH$_2$CH$_2$CH$_2$CH$_2$CH$_2$)(N(C*H*$_2$CH$_3$)$_2$)), 1.47 (m, 2H, N=C(NCH$_2$CH$_2$C*H*$_2$CH$_2$CH$_2$)(N(CH$_2$CH$_3$)$_2$)), 1.41 (m, 4H, N=C(NCH$_2$CH$_2$C*H*$_2$C*H*$_2$CH$_2$)(N(CH$_2$CH$_3$)$_2$)), 1.06 (t, J_{H-H} = 7.3 Hz, 6H N=C(NCH$_2$CH$_2$CH$_2$CH$_2$CH$_2$)(N(CH$_2$C*H*$_3$)$_2$)), 0.33 (s, 18H

Table 1
Data collection parameters for **1**–**3**

Compound	**1**	**2**	**3**
Chemical formula	$C_{26}H_{68}N_8Si_4Zn_2$	$C_{26}H_{64}N_8Si_4Zn_2$	$C_{30}H_{72}N_8Si_4Zn_2$
Formula weight	735.98	731.95	788.06
Temperature (K)	100(2)	100(2)	100(2)
Crystal system	monoclinic	triclinic	monoclinic
Space group	*P*2(1)/*c*	$P\bar{1}$	*C*2/*c*
a (Å)	13.1810(8)	9.0326(6)	23.609(2)
b (Å)	22.9226(14)	13.6898(10)	8.4249(8)
c (Å)	14.9772(9)	17.2174(12)	23.474(2)
α (°)		74.0940(10)	
β (°)	113.0380(10)	81.959(2)	112.562(2)
γ (°)		75.2350(10)	
V (Å^3)	4164.3(4)	1974.3(2)	4311.7(7)
Z	4	2	4
d_{calc} (Mg/m^3)	1.174	1.231	1.214
μ, (Mo Kα) (mm^{-1})	1.293	1.363	1.253
R_1[a] (all data)	3.42 (5.14)	4.52 (9.02)	1.95 (2.15)
wR_2[b] (all data)	10.56 (12.28)	11.32 (14.77)	8.10 (8.49)

[a] $R_1 = \sum\|F_o| - |F_c\|/\sum|F_o| \times 100$.
[b] $wR_2 = [\sum w(F_o^2 - F_c^2)_2/\sum(w|F_o|^2)^2]^{1/2} \times 100$.

N{Si(CH_3)$_3$}$_2$). ^{13}C NMR (100.6 MHz, C_6D_6): δ 165.6 (N=*C*(NCH$_2$CH$_2$CH$_2$CH$_2$CH$_2$)(N(CH$_2$CH$_3$)$_2$)), 50.5 (N=C(N*C*H$_2$CH$_2$CH$_2$CH$_2$*C*H$_2$)(N(CH$_2$CH$_3$)$_2$)), 44.1 (N=C(NCH$_2$CH$_2$CH$_2$CH$_2$CH$_2$)(N(*C*H$_2$CH$_3$)$_2$)), 26.7 (N=C(NCH$_2$*C*H$_2$CH$_2$*C*H$_2$CH$_2$)(N(CH$_2$CH$_3$)$_2$)), 25.8 (N=C(NCH$_2$CH$_2$CH$_2$CH$_2$CH$_2$)(N(CH$_2$*C*H$_3$)$_2$)), 14.2 (N=C(NCH$_2$CH$_2$*C*H$_2$CH$_2$CH$_2$)(N(CH$_2$CH$_3$)$_2$)), 6.2 (N{Si(*C*H$_3$)$_3$}$_2$); FTIR (KBr, cm^{-1}) 2935 (s), 2852 (s), 1524 (s), 1467 (s), 1398 (s), 1365 (m), 1329 (m), 1254 (s), 1213 (w), 1183 (w), 1157 (w), 1130 (m), 1075 (m), 1011 (s), 938 (w), 879 (s), 827 (s), 749 (w), 669 (m), 645 (w), 623 (w), 612 (w), 583 (w), 528 (w), 452 (w), 408 (w).

Table 2
Data collection parameters for **4**–**6**

Compound	**4**	**5**	**6**
Chemical formula	$C_{30}H_{72}N_8Si_4Zn_2$	$C_{28}H_{68}N_8Si_4Zn_2$	$C_{32}H_{76}N_8Si_4Zn_2$
Formula weight	784.02	760.04	816.11
Temperature (K)	100(2)	100(2)	100(2)
Crystal sysytem	triclinic	monoclinic	monoclinic
Space group	$P\bar{1}$	$P2(1)/c$	$P2(1)/c$
a (Å)	14.5694(12)	13.4716(13)	12.5720(9)
b (Å)	14.8486(18)	14.8783(15)	18.1115(13)
c (Å)	19.729(2)	21.130(2)	20.0216(15)
α (°)	92.297(2)		
β (°)	100.618(3)	96.604(2)	90.4820(10)
γ (°)	90.477(2)		
V (Å^3)	4191.1(8)	4207.1(7)	4558.7(6)
Z	4	4	4
d_{calc} (Mg/m^3)	1.243	1.200	1.189
μ (Mo Kα) (mm^{-1})	1.289	1.282	1.187
R_1^a (all data)	4.49 (7.97)	4.14 (7.80)	2.71 (3.57)
wR_2^b (all data)	11.94 (14.52)	11.88 (15.63)	8.94 (10.07)

[a] $R_1 = \sum\|F_o\| - |F_c\|/\sum|F_o| \times 100$.
[b] $wR_2 = [\sum w(F_o^2 - F_c^2)_2/\sum(w|F_o|^2)^2]^{1/2} \times 100$.

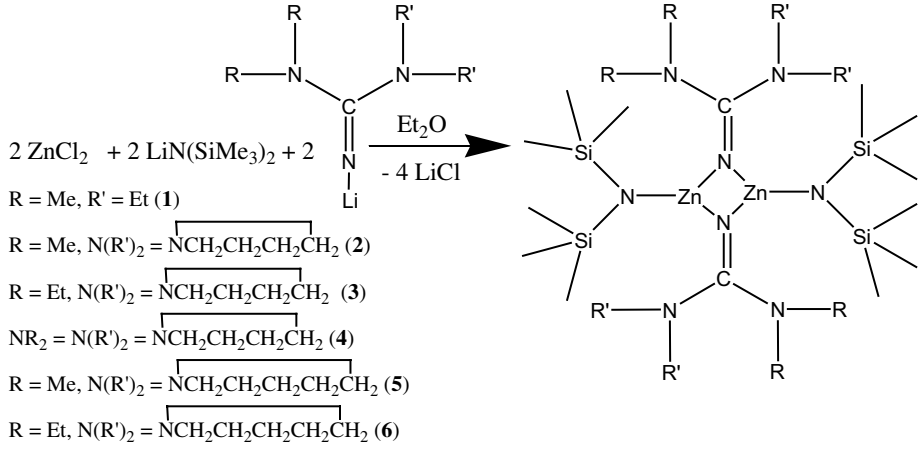
2.2. Crystallographic data

X-ray crystallography was performed by mounting each crystal onto a thin glass fiber from a pool of Fluorolube™ and immediately placing it under a 100 K N_2 stream, on a Bruker SMART APEX II diffractometer. The radiation used was graphite monochromatized Mo Kα radiation ($\lambda = 0.7107$ Å). The structures were refined by full-matrix least-squares procedures (SHELXL-97), Lorentzian and polarization corrections and absorption corrections (SADABS) were applied.

Each structure was solved using direct methods. This procedure yielded the Zn atoms, along with a number of the Si, C and N atoms. Subsequent Fourier synthesis yielded the remaining atom positions. The hydrogen atoms were fixed in positions of ideal geometry and refined within the XSHELL software. These idealized hydrogen atoms had their isotropic temperature factors fixed at 1.2 or 1.5 times the equivalent isotropic U of the C atoms to which they were bonded. The final refinement of each compound included anisotropic thermal parameters on all non-hydrogen atoms. Additional information concerning the data collection and final structural solutions of compounds **1**–**6** can be found in Tables 1 and 2.

3. Results and discussion

While undertaking a prior investigation correlating the structure and reactivity of dinuclear zinc catalysts stabilized with 1,1,3,3-tetramethylguanidine (H-TMG), it became of interest to evaluate the utility of a broader class of 1,1,3,3-tetralkylguanidine (H-TAG) ligands [9]. Unfortunately, the lack of reported examples of TAG ligands necessitated the development of a new synthetic approach. (Scheme 1) Our initial design utilizes the bulky terminal bistrimethylsilylamide, N{Si(Me$_3$)}$_2$, in conjunction with



Scheme 2. The synthesis of the complexes **1**–**6**.

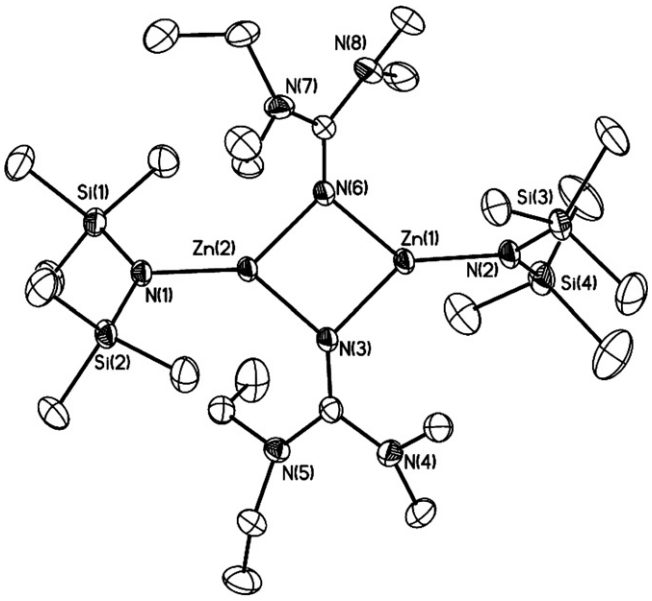


Fig. 1. Thermal ellipsoid plot of **1**. Ellipsoids are drawn at the 30% level.

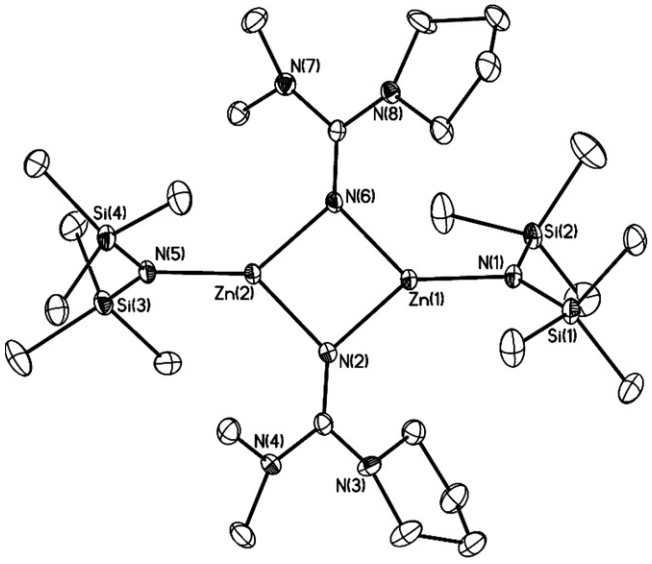


Fig. 2. Thermal ellipsoid plot of **2**. Ellipsoids are drawn at the 30% level.

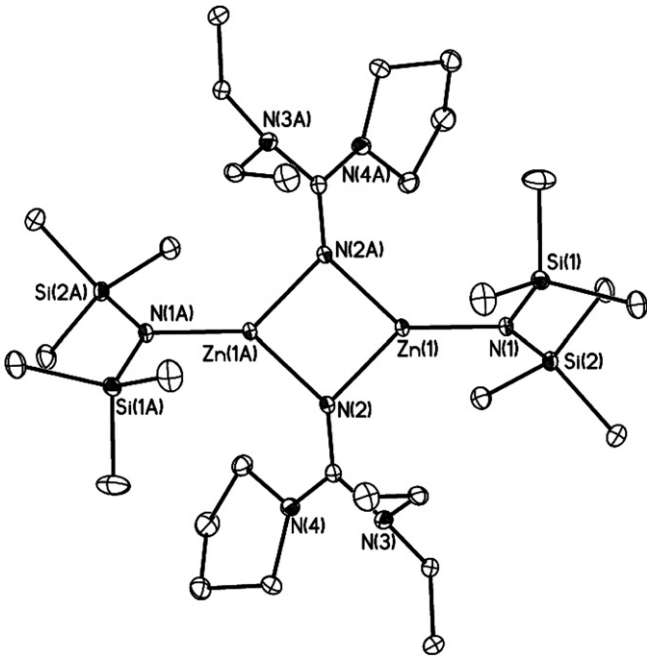


Fig. 3. Thermal ellipsoid plot of **3**. Ellipsoids are drawn at the 30% level.

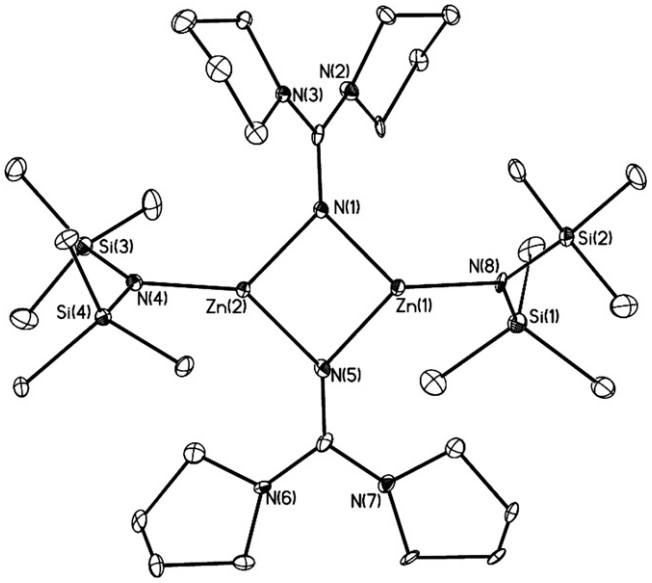


Fig. 4. Thermal ellipsoid plot of **4**. Ellipsoids are drawn at the 30% level.

a series of sterically varied TAG groups to isolate low-coordinate crystalline Zn complexes. In the following discussion, we detail the successful synthesis and characterization of six Zn complexes with the general formula, $[Zn(\mu\text{-TAG})\{N(SiMe_3)_2\}]_2$.

3.1. Synthesis

Under an argon atmosphere, metathesis reactions were performed to synthesize complexes **1**–**6**. (Scheme 2) The addition of $ZnCl_2$ to an ether solution containing one equivalent of Li(TAG) and one equivalent of $LiN(SiMe_3)_2$ generates a cloudy solution from which a white precipitate is removed via centrifugation after 24 h. Crystals suitable for X-ray structural analysis were obtained for **1**–**6** by cooling the respective saturated ether solutions at −35 °C. The isolated crystals for each complex are air-sensitive and soluble in hexanes, toluene, ether and THF.

3.2. Crystal structures

The thermal ellipsoid plots of **1**–**6** are illustrated in Figs. 1–6, respectively. For each complex, the Zn centers adopt a distorted trigonal planar geometry by utilizing the bulky

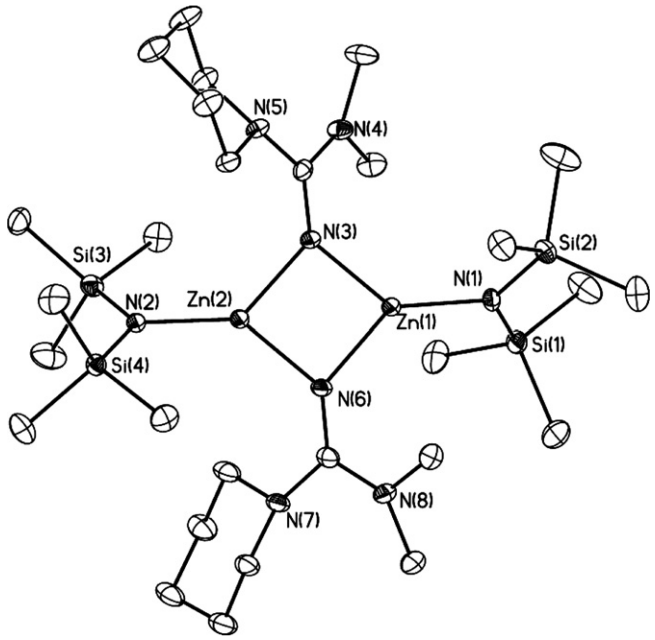


Fig. 5. Thermal ellipsoid plot of **5**. Ellipsoids are drawn at the 30% level.

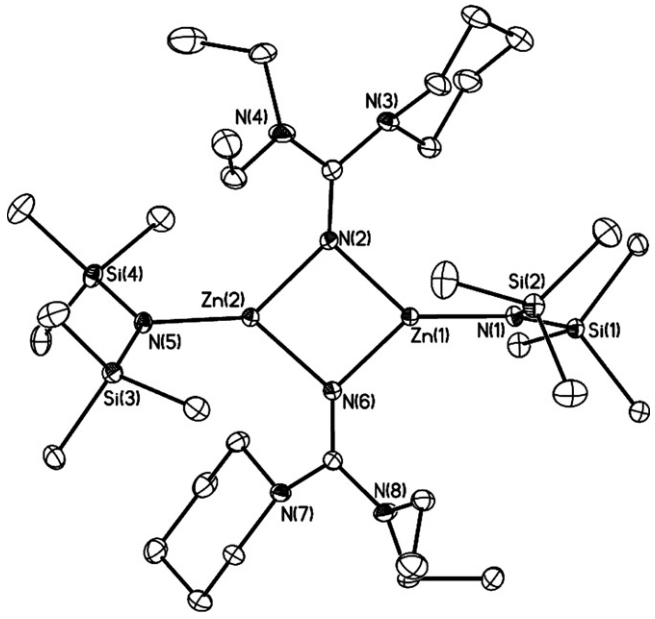


Fig. 6. Thermal ellipsoid plot of **6**. Ellipsoids are drawn at the 30% level.

Table 3
Selected inter-atomic distances (Å) and angles (°) for **1**–**3**

Complex **1**			
Zn(1)–N(2)	1.907(2)	Zn(1)–N(3)	1.976(2)
Zn(1)–N(6)	1.967(2)	Zn(2)–N(1)	1.903(2)
Zn(2)–N(6)	1.957(2)	Zn(2)–N(3)	1.973(2)
N(2)–Zn(1)–N(6)	135.74(10)	N(6)–Zn(1)–N(3)	87.67(9)
N(2)–Zn(1)–N(3)	136.59(10)	N(1)–Zn(2)–N(6)	136.29(9)
N(6)–Zn(2)–N(3)	88.03(9)	N(1)–Zn(2)–N(3)	135.57(9)
Complex **2**			
Zn(1)–N(1)	1.914(4)	Zn(1)–N(6)	1.970(4)
Zn(1)–N(2)	1.966(4)	Zn(2)–N(5)	1.901(4)
Zn(2)–N(6)	1.957(4)	Zn(2)–N(2)	1.976(4)
N(1)–Zn(1)–N(2)	138.45(16)	N(2)–Zn(1)–N(6)	88.15(15)
N(1)–Zn(1)–N(6)	132.96(16)	N(5)–Zn(2)–N(6)	137.38(16)
N(5)–Zn(2)–N(2)	134.36(16)	N(6)–Zn(2)–N(2)	88.24(15)
Complex **3**			
Zn(1)–N(4)	1.906(3)	Zn(1)–N(1)	1.965(3)
Zn(1)–N(1)	1.963(4)	Zn(1)–Zn(1)	2.7992(10)
N(4)–Zn(1)–N(1)	135.51(14)	N(1)–Zn(1)–N(2)	134.90(5)
N(2A)–Zn(1)–N(2)	89.22(5)	N(1)–Zn(1)–N(2A)	135.82(5)
Zn(1A)–N(2)–Zn(1)	90.77(5)	Si(1)–N(1)–Si(2)	129.21(7)

Table 4
Selected inter-atomic distances (Å) and angles (°) for **4**–**6**

Complex **4**			
Zn(1)–N(8)	1.914(6)	Zn(1)–N(1)	1.956(6)
Zn(2)–N(4)	1.919(6)	Zn(2)–N(1)	1.959(5)
Zn(1)–N(5)	1.967(6)	Zn(2)–N(5)	1.972(6)
N(8)–Zn(1)–N(1)	133.6(2)	N(8)–Zn(1)–N(5)	136.6(2)
N(4)–Zn(2)–N(1)	130.9(2)	N(4)–Zn(2)–N(5)	139.2(2)
N(1)–Zn(1)–N(5)	89.7(2)	N(1)–Zn(2)–N(5)	89.5(2)
Complex **5**			
Zn(2)–N(2)	1.909(3)	Zn(2)–N(6)	1.976(3)
Zn(2)–N(3)	1.967(3)	Zn(1)–N(1)	1.903(3)
Zn(1)–N(3)	1.959(3)	Zn(1)–N(6)	1.975(3)
N(2)–Zn(2)–N(3)	133.65(12)	N(1)–Zn(1)–N(3)	136.54(13)
N(3)–Zn(2)–N(6)	88.01(12)	N(1)–Zn(1)–N(6)	134.98(13)
Zn(1)–N(3)–Zn(2)	92.17(12)	N(3)–Zn(1)–N(6)	88.27(12)
Complex **6**			
Zn(1)–N(1)	1.9052(15)	Zn(1)–N(2)	1.9727(15)
Zn(1)–N(6)	1.9633(15)	Zn(2)–N(5)	1.9070(15)
Zn(2)–N(2)	1.9630(15)	Zn(2)–N(6)	1.9772(15)
N(1)–Zn(1)–N(6)	137.92(6)	N(6)–Zn(1)–N(2)	87.88(6)
N(1)–Zn(1)–N(2)	133.52(6)	N(5)–Zn(2)–N(2)	136.44(6)
N(5)–Zn(2)–N(6)	135.39(6)	N(2)–Zn(2)–N(6)	87.76(6)

hexamethydisilazide ligand as a terminal ligand while two TAG ligands act as a bridge connecting one metal to the other.

The bond distances and angles for the $N(SiMe_3)_2$ ligand in **1**–**6** (Tables 3 and 4) are consistent with previously reported $[Zn(\mu\text{-}L)\{N(SiMe_3)_2\}]_2$ compounds [10]. It is notable that the complexes with NMe_2 substituents (**1**, **2** and **5**) have an asymmetric ligand environment around each Zn center. This can tentatively be attributed to the difference in steric bulk for the NMe_2 group versus the other substituents examined in this study. Complex **4** crystallizes with two crystallographically independent, but chemically equivalent molecules per asymmetric unit. Only one of the centrosymmetric dimers is shown in Fig. 4. In this complex, each three-coordinate Zn is bridged to the adjacent Zn by two symmetric DPYRG ligands.

3.3. Bulk properties

In order to establish that the crystal structures of **1**–**6** are representative of the bulk material, FT-IR spectroscopy and elemental analysis (EA) were collected. The FT-IR

spectra of **1**–**6** show a strong diagnostic shift ranging between 1524 and 1550 cm^{-1} for the υ(C=N) band bonded to Zn. This is shifted to lower frequency than what is typically found for a neutral 1,1,3,3-tetraalkylguanidine [11]. The strong amide stretches for **1**–**6**, associated with M-NR_2, are present between 1400 and 1450 cm^{-1}. For **1**–**6**, the EA of the bulk powders were all found to be consistent with the solid state structure.

3.4. NMR studies – solution behavior

^{13}C and ^{1}H NMR spectra were collected for **1**–**6** in benzene-d_6. Retention of a zinc-bonded $N(SiMe_3)_2$ group for **1**–**6** is implied by the observation of a strong singlet ($\delta \sim 0.3$ ppm) by ^{1}H NMR spectroscopy,. Additional resonances in the ^{1}H NMR spectra could be clearly assigned for each unique TAG ligand. The ^{13}C NMR spectra for **1**–**6** have a characteristic low field resonance at ~160–165 ppm attributed to the 'CN_3' central carbon atom of the guanidinate ligand [11]. Assignment of the additional ^{13}C NMR resonances for the $N(SiMe_3)_2$ and TAG ligands for each complex was straightforward.

4. Conclusions

A novel family of dinuclear zinc guanidinate complexes has been successfully synthesized and characterized. The use of a series of structurally varied monoanionic TAG ligands in conjunction with the bulky $N(SiMe_3)_2$ ligand has demonstrated to be an effective method for generating low-coordinate Zn complexes. We envision that this approach will be amenable to isolating additional transition metal complexes. Work utilizing this approach is currently underway.

Acknowledgements

For support of this research, the authors would like to thank Kent State University.

Appendix A. Supplementary material

CCDC 648172, 648173, 648174, 648175, 648176 and 648177 contain the supplementary crystallographic data for **1**, **2**, **3**, **4**, **5** and **6**. These data can be obtained free of charge via http://www.ccdc.cam.ac.uk/conts/retrieving.html, or from the Cambridge Crystallographic Data Centre, 12 Union Road, Cambridge CB2 1EZ, UK; fax: (+44) 1223-336-033; or e-mail: deposit@ccdc.cam.ac.uk. Supplementary data associated with this article can be found, in the online version, at doi:10.1016/j.poly.2007.08.013.

References

[1] (a) T.A. Budzichowski, S.T. Chacon, M.H. Chisholm, F.J. Feher, W. Streib, J. Am. Chem. Soc. 113 (1991) 689;
(b) M.H. Chisholm, Acc. Chem. Res. 23 (1990) 419;
(c) M.H. Chisholm, K. Folting, J.C. Huffman, J.J. Koh, Polyhedron 8 (1989) 123;
(d) R.H. Cayton, M.H. Chisholm, M.J. Hampdensmith, J. Am. Chem. Soc. 110 (1988) 4438;
(e) T.P. Blatchford, M.H. Chisholm, J.C. Huffman, Inorg. Chem. 27 (1988) 2059;
(f) M.H. Chisholm, D.L. Clark, K. Folting, J.C. Huffman, M. Hampdensmith, J. Am. Chem. Soc. 109 (1987) 7750;
(g) M.H. Chisholm, C.E. Hammond, M. Hampdensmith, J.C. Huffmann, W.G. Vandersluys, Angew. Chem., Int. Ed. Engl. 26 (1987) 904.
[2] T.J. Marks, M.R. Gagne, S.P. Nolan, L.E. Schock, A.M. Seyam, D. Stern, Pure Appl. Chem. 61 (1989) 1665.
[3] (a) I. Pattison, K. Wade, B.K. Wyatt, J. Chem. Soc. A (1968) 837;
(b) W. Schneider, A. Bauer, A. Schier, H. Schmidbaur, Chemische Berichte-Recueil 130 (1997) 1417;
(c) N. Kuhn, R. Fawzi, M. Steimann, J. Wiethoff, Z. Anorg. Allg. Chem. 623 (1997) 554;
(d) N. De Vries, C.E. Costello, A.G. Jones, A. Davison, Inorg. Chem. 29 (1990) 1348;
(e) D. Stalke, M.A. Paver, D.S. Wright, Angew. Chem., Int. Ed. Engl. 32 (1993) 428;
(f) A.J. Edwards, M.A. Paver, P.R. Raithby, M.-A. Rennie, C.A. Russell, D.S. Wright, J. Chem. Soc., Dalton Trans. (1995) 1587.
[4] (a) W. Clegg, R. Snaith, H.M.M. Shearer, K. Wade, G. Whitehead, J. Chem. Soc., Dalton Trans. (1983) 1309;
(b) W. Clegg, R.E. Mulvey, R. Snaith, G.E. Toogood, K. Wade, J. Chem. Soc., Chem. Commun. (1986) 1740.
[5] (a) P.A.S. Smith, The Organic Chemistry of Open-Chain Nitrogen Compounds, vol. I, 1965.;
(b) In: S. Patai (Ed.), The Chemistry of Functional Groups: the Chemistry of Amidines and Imidates, 1975.
[6] (a) B. Kovacevic, Z.B. Maksic, Org. Lett. 3 (2001) 1523;
(b) B. Kovacevic, Z.B. Maksic, R. Vianello, M. Primorac, New J. Chem. 26 (2002) 1329;
(c) I. Novak, X. Wei, W.S. Chin, J. Phys. Chem. A 105 (2001) 1783.
[7] R. Kempe, Angew. Chem. Int. Ed. 39 (2000) 468.
[8] (a) S.D. Allen, D.R. Moore, E.B. Lobkovsky, G.W. Coates, J. Organomet. Chem. 683 (2003) 137;
(b) M. Cheng, D.R. Moore, J.J. Reczek, B.M. Chamberlain, E.B. Lobkovsky, G.W. Coates, J. Am. Chem. Soc. 123 (2001) 8738;
(c) M.P. Coles, P.B. Hitchcock, Eur. J. Inorg. Chem. (2004) 2662;
(d) J.H. Yu, J. Joo, H.M. Park, S.-I. Baik, Y.W. Kim, S.C. Kim, T. Hyeon, J. Am. Chem. Soc. 127 (2005) 5662.
[9] S.D. Bunge, J.M. Lance, J.A. Bertke, Unpublished results.
[10] (a) M. Driess, K. Merz, S. Rell, Eur. J. Inorg. Chem. (2000) 2517;
(b) S.C. Goel, M.Y. Chiang, W.E. Buhro, Inorg. Chem. 29 (1990) 4646;
(c) H. Grutzmacher, M. Steiner, H. Pritzkow, L. Zsolnai, G. Huttner, A. Sebald, Chemische Berichte-Recueil 125 (1992) 2199;
(d) M. Krieger, R.O. Gould, B. Neumuller, K. Harms, K. Dehnicke, Z. Anorg. Allg. Chem. 624 (1998) 1434.
[11] M.P. Coles, Dalton Trans. (2006) 985.

ions [14,15]. There has also been substantial interest in the rational design of novel transition metal complexes, which bind and cleave duplex DNA with high sequence and structure selectivity [16–18]. Hence, we report the synthesis and physico-chemical studies of a tetradentate Schiff base ligand, derived from 2-pyridinecarboxaldehyde and *o*-phenylenediamine, and its complexes. Although the complexes of 1,2-diaminophenyl-*N*,*N*′-bis-(2-pyridinecarboxaldimine) have been reported with Ru(III), the Schiff base was generated *in situ* and its catalytic activity was explored [19]. To add to the novelty of the work, we have successfully isolated this ligand and have screened the binding studies of its Cu (II) complex with DNA.

2. Physical measurements

Elemental analyses were obtained from the microanalytical laboratory of C.D.R.I., Lucknow, India. IR spectra (4000–200 cm^{-1}) were recorded as KBr/CsI discs on a Perkin–Elmer 621 spectrophotometer. The ^{1}H and ^{13}C NMR spectra were recorded in DMSO-d_6 using a Bruker AC 200E NMR spectrometer from B.H.U., Varanasi. Metals were estimated volumetrically [20]. The electronic spectra of the complexes in DMSO were recorded on a Pye-Unicam 8800 spectrophotometer. The electrical conductivity (10^{-3} M solution in DMSO) was obtained on a systronic type 302 conductivity bridge equilibrated at 25 ± 0.1 °C. The magnetic moment measurements (Faraday balance) were made at room temperature. Fluorescence measurements on complex **3** were performed on a Shimdzu 5301 PC spectrofluorimeter equipped with a 150 W Xenon lamp and a slit width of 5 nm. A 1.00 cm quartz cell was used for the measurements. For the determination of binding parameters, 2.5 μM of complex solution was taken in a quartz cell and increasing amounts of ct DNA solution was titrated. Fluorescence spectra were recorded at a temperature of 310 K in the range 300–500 nm upon excitation at 296 (λ_{ex} was 296 nm). The UV measurements of calf thymus DNA were recorded on a Shimadzu UV-1700 double beam spectrophotometer using a cuvette of 1 cm path length. The absorbance value of DNA in the absence and presence of complex were made in the range 200–300 nm. The DNA concentration was fixed at 0.1 mM, while the complex concentration was varied from 2.5 μM to 15 μM.

3. Experimental

3.1. Materials

All the metal salts $M(NO_3)_2 \cdot 6H_2O$ and $Cu(NO_3)_2 \cdot 3H_2O$ [where M = Co(II), Ni(II) and Zn(II)] as well as *o*-phenylenediamine and 2-pyridinecarboxaldehyde (all E. Merck) were used as received. Methanol used as solvent was of A.R. grade (E. Merck). Highly polymerized calf thymus DNA sodium salt (7% Na content) was purchased from sigma. Other chemicals were of reagent grade and were used without further purification. Calf thymus DNA was dissolved to 0.5% w/w, (12.5 mM DNA/phosphate) in 0.1 M sodium phosphate buffer (Ph 7.40) at 310 K for 24 h with occasional stirring to ensure formation of a homogeneous solution. The purity of the DNA solution was checked from the absorbance ratio A_{260}/A_{280}. Since the absorption ratio lies in the range $1.8 < A_{260}/A_{280} > 1.9$, no further deproteinization of DNA was needed. A stock solution of complex **3** with 5 mg/ml was also prepared.

4. Synthesis of 1,2-diaminophenyl-*N*,*N*′-bis-(2-pyridinecarboxaldimine) (L)

A methanolic solution of *o*-phenylenediamine (5 mmol, 0.540 g) was magnetically stirred in a three-necked round bottom flask followed by dropwise addition of 2-pyridinecarboxaldehyde (10 mmol, 0.96 ml). The reaction mixture was then refluxed for 4–5 h, resulting in a clear yellow colored solution. The resultant solution was kept for evaporation at room temperature leading to the isolation of a pale yellow microcrystalline product after a few weeks.

5. Synthesis of the complexes, $[ML(NO_3)_2]$ [M = Co(II), Ni(II), Cu(II) and Zn(II)]

A methanolic solution of Schiff base ligand **L** (5 mmol, 0.143 g) was added dropwise to a methanolic solution of the metal salt (5 mmol). The reaction mixture was refluxed for 5 h leading to the formation of a colored solid product. The product thus formed was filtered, washed with methanol and dried in vacuo.

6. Binding analysis of complex 3

To elaborate the fluorescence quenching mechanism the Stern–Volmer equation was used for data analysis [21]:

$$F_0/F = 1 + K_{SV}[Q] \quad (1)$$

where F_0 and F are the steady-state fluorescence intensities in the absence and presence of quencher, respectively. K_{SV} is the Stern–Volmer quenching constant and $[Q]$ is the concentration of quencher (DNA). The linearity of the F_0/F versus $[Q]$ (Stern–Volmer) plots for the DNA complex **3** depicts that the quenching may be static or dynamic, since the characteristic Stern–Volmer plot of combined quenching (both static and dynamic) is an upward curvature (Fig. 1). The quenching constant (K_{SV}) was calculated to be 2.91×10^3 L mol^{-1}. When ligand molecules bind independently to a set of equivalent sites on a macromolecule, the equilibrium between free and bound molecules is given by the equation [22]:

$$\log[(F_0 - F)/F] = \log K + n \log[Q] \quad (2)$$

where K and n are the binding constant and the number of binding sites, respectively. Thus, a plot of $\log(F_0-F)/F$ versus $\log[Q]$ can be used to determine K as well as n.

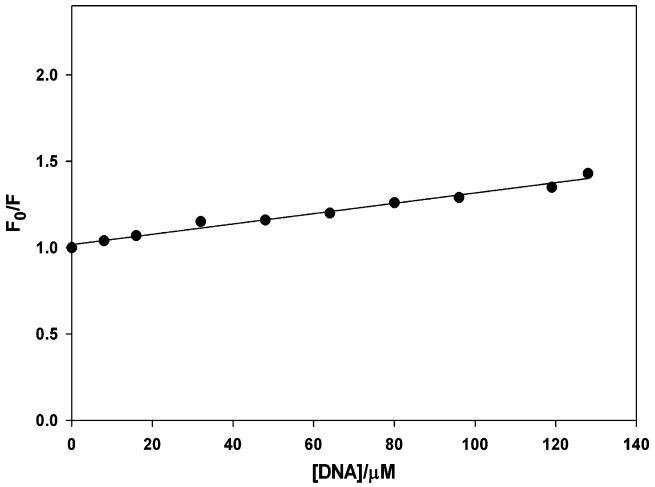
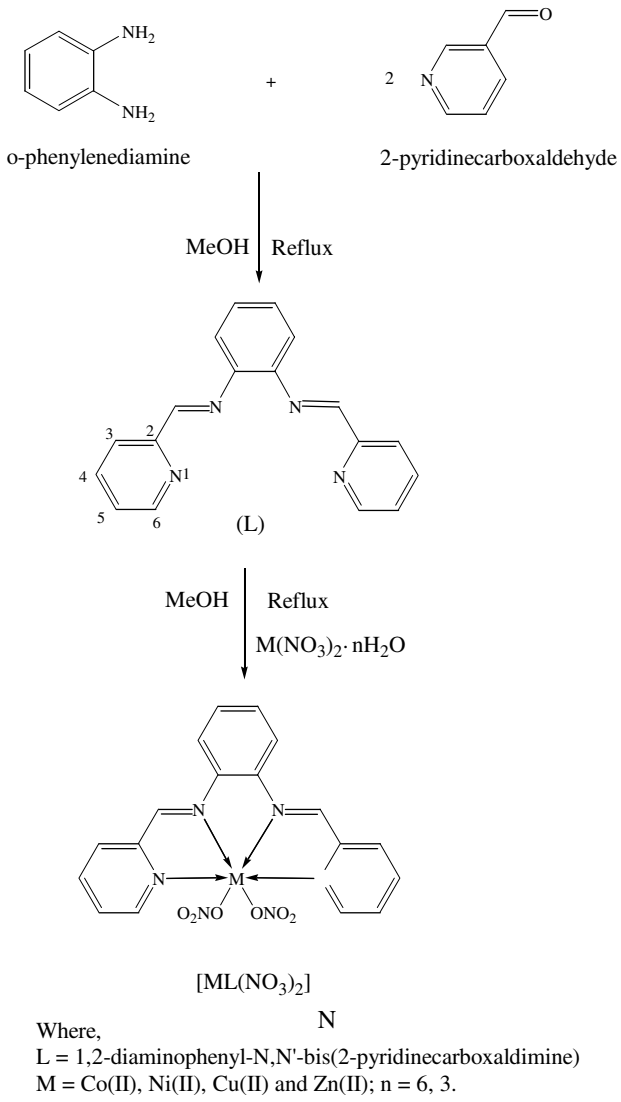


Fig. 1. Stern–Volmer plot for the binding of ct DNA with complex **3** at 298 K.

The values of K and n were found to be $(0.31 \pm 0.19) \times 10^{-3}\ M^{-1}$ and 0.75 respectively.

7. Results and discussion

The Schiff base ligand **L** has been synthesized by the condensation of *o*-phenylenediamine and 2-pyridinecarboxaldehyde in a 1:2 molar ratio in methanolic medium (Scheme 1). The level of the purity of the ligand has been checked by running TLC on a silica gel coated plate using EtOAc–MeOH (6:4 v/v) as the eluent. Complexes of the type $[ML(NO_3)_2]$ [M = Co(II), Ni(II), Cu(II) and Zn(II)] (**1**–**4**) were synthesized by the reaction of the ligand **L** and the metal salts in a 1:1 molar ratio in methanolic medium. The elemental analyses agree well with the proposed composition of the ligand and its complexes (Table 1). Formation of the Schiff base ligand (**L**) and its complexes have been inferred from the results obtained by FT-IR, ^1H and ^{13}C NMR. The geometry around the metal ion in the complexes has been deduced from the absorption bands observed in the UV–Vis spectra and magnetic moment values. All the Schiff base complexes are stable at room temperature, and are soluble in water, DMSO and methanol. The low molar conductivity values of all the complexes suggest their non-ionic nature. However, all attempts to get a single crystal of the ligand or the complexes suitable for X-ray crystallography failed.



Scheme 1. Suggested scheme of the proposed Schiff base and its complexes.

8. IR spectra

Preliminary identification regarding the formation of the Schiff base ligand and its complexes was obtained from IR spectral findings (Table 2). The absence of bands characteristic of the amino groups, $\nu(NH_2)$, of *o*-phenylenediamine and the carbonyl group, $\nu(C{=}O)$, of 2-pyridinecarboxaldehyde, and appearance of a new strong intensity band at 1630 cm^{-1} characteristic of azomethine group, $\nu(C{=}N)$, confirm that condensation between the aforesaid reactants has taken place [23]. This band undergoes a negative shift of 10–20 cm^{-1} in the complexes, which may be attributed to the coordination of the nitrogen atom of the azomethine function to the metal ion [24]. This is further confirmed by the presence of a $\nu(M–N)$ vibration in the region 440–460 cm^{-1} in all the complexes [25]. The main spectral variations of the complexes as compared to the free ligand are found in the regions 420–430 cm^{-1} (out of plane ring deformation) and 630–650 cm^{-1} (in plane ring deformation), where the absorption of the pyridine rings of 2-pyridinecarboxaldehyde occurs [26]. These vibrations are found to be positively shifted, suggesting the coordination of the pyridine nitrogen to the metal [27]. However, pyridine and phenyl ring vibrations in the higher frequency region (1560–1590 cm^{-1}) are not affected appreciably. A strong intensity band appearing in the region 260–280 cm^{-1} may reasonably be assigned to $\nu(M–N_{py})$ vibrations [27]. The IR spectra of ionic NO_3^- shows a very strong band at

Table 1
F.W., color, yield, melting point, elemental data and molar conductance values of the ligand and its complexes

Complexes	F.W.	Color	Yield (%)	Melting point (°C)	Anal. found (Calc.)%				Molar conductivity Ω^{-1} cm^2 mol^{-1}
					M	C	H	N	
L	286.33	Pale yellow	50	120–122		75.45	4.89	19.52	
(C_{18} H_{14} N_4)						(75.50)	(4.92)	(19.56)	
[CoL(NO_3)$_2$] (**1**)	469.25	Dark brown	56	>300	12.53	46.04	2.96	17.86	13.5
($C_{18}H_{14}CoN_6O_6$)					(12.55)	(46.07)	(3.00)	(17.90)	
[NiL(NO_3)$_2$] (**2**)	469.00	Brown	57	>300	12.50	46.03	2.97	17.89	12.0
($C_{18}H_{14}NiN_6O_6$)					(12.51)	(46.09)	(3.00)	(17.91)	
[CuL(NO_3)$_2$] (**3**)	473.86	Olive green	55	>300	13.39	45.57	2.93	17.69	14.0
($C_{18}H_{14}CuN_6O_6$)					(13.41)	(45.62)	(2.97)	(17.73)	
[ZnL(NO_3)$_2$] (**4**)	475.69	Yellow	53	>300	13.72	45.42	2.94	17.62	11.5
($C_{18}H_{14}ZnN_6O_6$)					(13.74)	(45.44)	(2.96)	(17.66)	

Where, L = Ligand.

Table 2
IR spectral data (cm^{-1}) of the ligand and its complexes

Complexes	ν(C=N)	ν(M–N)	Pyridine ring vibration		ν(M–N_{py})	ν(M–O) nitrate bands	
			Out of plane ring deformation	In plane ring deformation			
L	1630 s		420 m	630 s			
[CoL(NO_3)$_2$]	1615 s	440 s	425 m	645 s	265 s	235 s	1230, 1040, 860
[NiL(NO_3)$_2$]	1620 s	450 s	420 m	650 s	270 s	245 s	1235, 1045, 865
[CuL(NO_3)$_2$]	1625 s	445 s	425 m	635 s	280 s	240 s	1240, 1050, 870
[ZnL(NO_3)$_2$]	1610 s	460 s	430 m	630 s	275 s	250 s	1245, 1060, 880

Where, m – Medium.
s – Strong.
L – Ligand.

ca. 1380 cm^{-1} ν_3(A) along with sharp bands at ca. 1050 ν_1(A), 830 ν_2(E) and 720 cm^{-1} ν_4(E) [28]. The IR spectra of all the complexes exhibited three bands in the 1230–1245, 1040–1060 and 860–880 cm^{-1} regions, indicating the monodentate coordination of the nitrate moiety [29]. The presence of a band in the region 235–250 cm^{-1} may reasonably be assigned to ν[M–O] of the O–NO_2 group [30].

9. Electronic spectra and magnetic susceptibility data

The electronic spectrum (Table 3) of the Co(II) complex exhibited two spin allowed transitions at 15,300 and 19,100 cm^{-1} assignable to $^4T_{1g}(F) \rightarrow {}^4A_{2g}(F)$ and $^4T_{1g}(F) \rightarrow {}^4T_{1g}(P)$ transitions, respectively, consistent with an octahedral geometry around the Co(II) ion [31]. The observed magnetic moment of 4.60 B.M. for the [CoL(NO_3)$_2$] complex further complements the electronic spectral findings [32]. The electronic spectrum of the [NiL(NO_3)$_2$] complex exhibited three bands at 11,200, 17,000 and 28,000 cm^{-1} attributed to three spin allowed transitions, viz. $^3A_{2g}(F) \rightarrow {}^3T_{2g}(F)$, $^3A_{2g}(F) \rightarrow {}^3T_{1g}(F)$ and $^3A_{2g}(F) \rightarrow {}^3T_{1g}(P)$ respectively, corresponding to an octahedral environment for the Ni(II) complex which is further supported by its magnetic moment value of 3.12 B.M. [31,32]. A broad band at 16,710 cm^{-1} in the electronic spectrum of the Cu(II) complex, assignable to a $^2B_{1g} \rightarrow {}^2B_{2g}$ transition, and a magnetic moment of 1.83 B.M. confirms an octahedral geometry around the Cu(II) ion [31,32].

Table 3
Magnetic moment values and electronic spectral band position (cm^{-1}) with their assignments

Complexes	Magnetic moments (B.M.)	Band position cm^{-1}	Assignments
[CoL(NO_3)$_2$]	4.60	15,300	$^4T_{1g}(F) \rightarrow {}^4A_{2g}(F)$
		19,100	$^4T_{1g}(F) \rightarrow {}^4T_{1g}(P)$
[NiL(NO_3)$_2$]	3.12	11,200	$^3A_{2g}(F) \rightarrow {}^3T_{2g}$ (F)
		17,000	$^3A_{2g}(F) \rightarrow {}^3T_{1g}(F)$
		28,000	$^3A_{2g}(F) \rightarrow {}^3T_{1g}(P)$
[CuL(NO_3)$_2$]	1.83	16,710	$^2B_{1g} \rightarrow {}^2B_{2g}$

10. ^{1}H and ^{13}C NMR spectra

The ^{1}H and ^{13}C NMR spectra of the Schiff base ligand **L** and its Zn(II) complex were recorded in DMSO-d_6 at room temperature. In the ^{1}H NMR spectrum, the chemical shift values of the protons of the pyridine ring coordinated to the metal atom in the complex are noticeably different from those observed for the non-coordinated ring of the ligand (**L**). The proton resonances of the coordinated pyridine ring are observed at 8.51 (d H_3), 8.28 (t H_4), 7.39 (t H_5) and 7.67 ppm (d H_6), while the resonance of the non-coor-

dinated pyridine ring protons appear at 7.28 (d H_3), 8.16 (t H_4), 7.28 (t H_5) and 8.20 ppm (d H_6). On the basis of these data, it is possible to justify the corresponding downfield shift induced by the coordination of the pyridine nitrogen atom to the metal atom. The ^{1}H NMR spectrum of the ligand also shows a signal at 8.39–7.74 ppm attributed to the aromatic proton (m, Ar–H). However, a singlet at 9.28 ppm may be assigned to the azomethine proton (s, 2H). The Zn (II) complex shows a slight downfield shift of 0.2–0.4 ppm in the resonance peaks corresponding to the phenyl ring and the azomethine proton, which may be attributed due to the coordination of the ligand to the Zn(II) ion [33].

The ^{13}C NMR spectrum of the Zn(II) complex shows a number of sharp peaks corresponding to various carbon atoms in the proposed schiff base ligand, expected due to the non-equivalence of the various carbon atoms. The spectrum exhibits a sharp resonance signal corresponding to the azomethine carbon at 193.77 ppm and the chemical shifts of the aromatic and pyridine carbons appear at 124.52, 122.96, 121.78 and 150.29, 149.20, 137.75, 137.35, 128.49 ppm [34]. These values have been found to be downfield shifted by 1.0–1.5 ppm as compared to the free Schiff base ligand. A downfield shift of nearly 1.5 ppm has been noticed for the carbons of the phenyl ring attached to the imine nitrogen and the carbons of the imine and pyridine moieties.

11. Fluorescence measurements

11.1. Binding property of DNA to complex 3

Fluorescence spectroscopy provides insight of the changes taking place in the microenvironment of DNA-complex **3**. The interaction of complex **3** with calf thymus DNA was studied by monitoring the changes in the intrinsic fluorescence of complex **3** at varying DNA concentrations (Fig. 2). The spectra show the representative fluorescence emission spectra of complex **3** upon excitation at 296 nm. The addition of DNA causes a gradual decrease in the fluorescence emission intensity of complex **3**, with a conspicuous change in the emission spectra. It can be seen that a higher excess of DNA leads to more effective quenching of the fluorophore molecule fluorescence. The quenching of complex **3** fluorescence clearly indicates that the binding of DNA to complex **3** changes the microenvironment of fluorophore residue. The reduction in the intrinsic fluorescence of complex **3** upon interaction with DNA could be due to masking or burial of the complex **3** fluorophore upon interaction between the stacked bases within the helix and/or surface binding at the reactive nucleophilic sites on the heterocyclic nitrogenous bases of the DNA molecule.

11.2. Absorption spectroscopy

UV–Vis absorption studies were performed to further ascertain the DNA-complex **3** interaction. The UV absorbance showed an increase with the increase in drug concentration (Fig. 3). Since complex **3** does not show any peak in this region (Fig. 3), the rise in the DNA absorbance is indicative of complex formation between DNA complex **3** molecules. Complex **3** at 260 nm exhibited hyperchromism of 30% and bathchromism of 3 nm. Hypochromism and hyperchromism are both spectral features of DNA concerning of its double helix structure, hypochromism means the DNA binding mode of complex is an electrostatic effect or intercalation which can stabilize the DNA

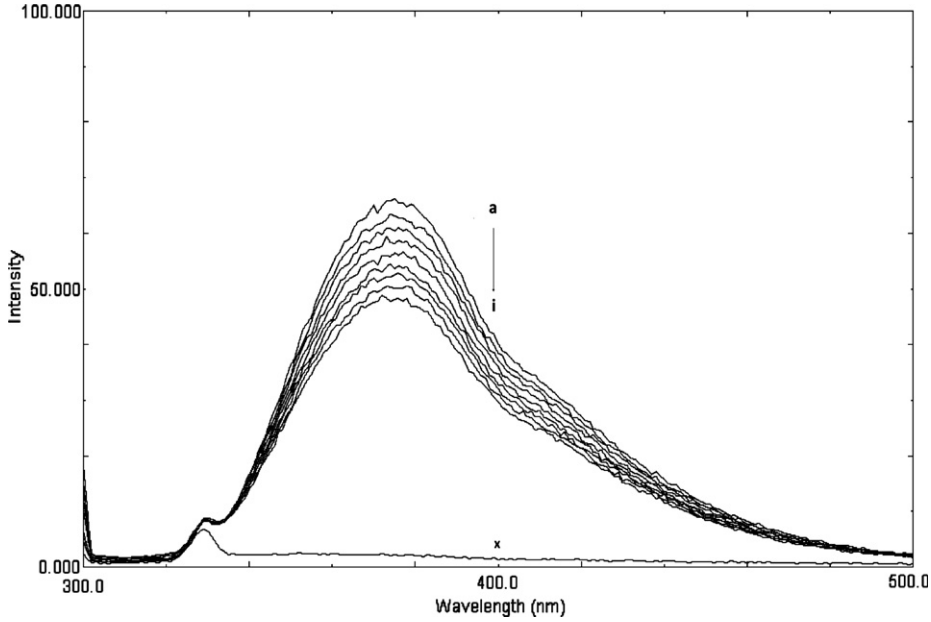


Fig. 2. Fluorescence emission spectra of complex **3** in the presence of ct DNA. The complex concentration was 12 μM (a). DNA concentration was (b) 8 μM (c) 16 μM (d) 32 μM (e) 32 μM (f) 48 μM (g) 64 μM (h) 80 μM (i) 96 μM and (x) DNA alone.

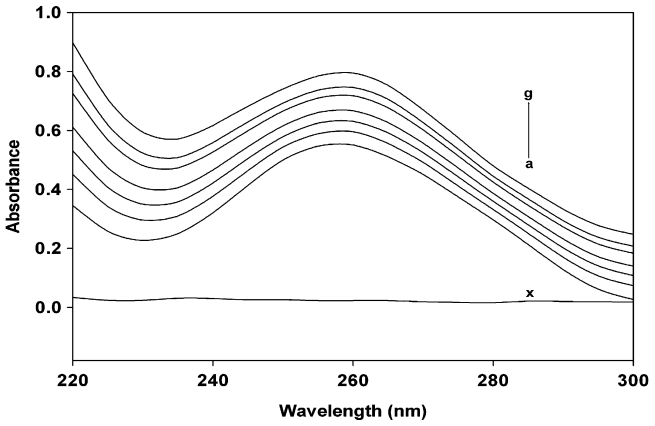


Fig. 3. Absorbance spectra of DNA, complex **3** and the DNA-complex **3** system. DNA concentration was 0.1 mM (a). Complex **3** concentration for the DNA-complex **3** system was 2.5 (b), 5.0 μM (c), 7.5 μM (d), 10 μM (e), 12.5 μM (f), 15.0 μM (g). A concentration of 2.5 μM complex **3** (x) was used for complex **3** alone.

duplex, and hyperchromism means the breakage of the secondary structure of DNA [35,36]. So we primarily speculate that complex interaction with the secondary structure of calf thymus DNA results in its breakage and perturbation. After interaction with the base pairs of DNA, the π–π^* orbital of the bound ligand can couple with the π orbital of the base pairs, due to the decreased π–π^* transition energy, which results in a bathochromic shift [37]. The above two changes are indicative of conformational alteration on complex **3** binding.

Acknowledgements

The authors acknowledge the Chairman, Department of Chemistry, Aligarh Muslim University, Aligarh for providing the necessary research facilities. The authors also thank C.D.R.I., Lucknow for providing the Elemental Analyses data and B.H.U., Varanasi for ^{1}H and ^{13}C NMR spectra.

References

[1] S.J. Coles, M.B. Hursthouse, D.G. Kelly, A.J. Toner, N.M. Walker, J. Chem. Soc., Dalton Trans. (1998) 3489.
[2] S. Yamada, Coord. Chem. Rev. 537 (1999) 190.
[3] A.A. Jarrahpour, M. Motamedifar, K. Pakshir, N. Hadi, M. Zarei, Molecules 9 (2004) 815.
[4] A.M. Mahindra, J.M. Fisher, Rabinovitz, Nature (London) 64 (1983) 303.
[5] P.R. Palet, B.T. Thaker, S. Zele, Indian J. Chem. 38 A (1999) 563.
[6] T.L. Yang, X.S. Tai, W.W. Qin, W.S. Liu, M.Y. Tan, Anal. Sci. 20 (2004) 493.
[7] J.T. Groves, in: P. Ortez de Montellano (Ed.), Cytochrome P-450: Structures, Mechanism and Biochemistry, Vol. 7, Plenum Press, New York, 1986, p. 1.
[8] T.G. Campbell, F.L. Urbach, Inorg. Chem. 12 (1973) 1836.
[9] W.C. Potter, L.T. Tay, Inorg. Chem. 15 (1976) 1329.
[10] A. Vleck Jr., Coord. Chem. Rev. 230 (2002) 225.
[11] J.G-. Tojal, T. Rojo, Polyhedron 18 (1999) 1123.
[12] J.G-. Tojal, A.G-. Orad, A.A. Diaz, J.L. Serra, M.K. Urtiaga, M.I. Arriortua, T. Rojo, J. Inorg. Biochem. 84 (2001) 271.
[13] V. Uma, V.G. Vaidyanathan, B.U. Nair, Bull. Chem. Soc. Jpn. 78 (2005) 845.
[14] W. Szczepanik, J. Ciesiolka, J. Wrzesinski, J. Skala, M. Jezowska-Bojczuk, J. Chem. Soc., Dalton Trans. (2003) 1488.
[15] R. Vijayalakshmi, M. Kanthimathi, V. Subramaniam, B.U. Nair, Biochim. Biophys. Acta 157 (2000) 1475.
[16] B.H. Geierstanger, M. Marksich, P.B. Dervan, D.E. Wemmer, Science 266 (1994) 646.
[17] C. Liu, J. Zhou, Q. Li, L. Wang, Z. Liao, H. Xu, J. Inorg. Biochem. 75 (1999) 233.
[18] G. Prativiel, J. Bernadou, B. Meunier, Angew. Chem., Int. Ed. Engl. 34 (1995) 746.
[19] D. Chatterjee, A. Mitra, J. Coord. Chem. 57 (2004) 175.
[20] A.I. Vogel, A Text Book of Quantitative Inorganic Analyses, Longman, London, 1961, p. 433.
[21] A.M. Pyle, J.P. Rehmann, R. Meshoyrer, C.V. Kumar, N.J. Turro, J.K. Barton, J. Am. Chem. Soc. 111 (1989) 3051.
[22] X.-Z. Feng, Z. Lin, L.-J. Yang, C. Wang, C.-L. Bai, Talanta 47 (1998) 1223.
[23] W.A. Welsh, G.T. Reynold, P.M. Henry, Inorg. Chem. 16 (1977) 2558.
[24] D.E. Fenton, B.P. Murphy, A.J. Leong, L.F. Lindoy, A. Bashall, M. McPartlin, J. Chem. Soc., Dalton Trans. (1987) 2543.
[25] S.K. Sahni, S.K. Sangal, S.P. Gupta, V.B. Rana, J. Inorg. Nucl. Chem. 39 (1977) 10598.
[26] N.S. Gill, R.H. Nuttall, D.E. Scarfe, D.W.A. Sharp, J. Inorg. Nucl. Chem. 18 (1961) 79.
[27] R.J.H. Clark, C.S. Williams, Inorg. Chem. 4 (1965) 350.
[28] C.C. Addison, D.W. Amos, D. Sutton, J. Chem. Soc. A (1967) 808.
[29] K. Nakamoto, Infrared and Raman Spectra of Inorganic and Coordination Compounds, fourth ed., Wiley Interscience, New York, 1986.
[30] M. Shakir, S.P. Verkey, D. Kumar, Transition Met. Chem. 19 (1994) 606.
[31] A.B.P. Lever, Inorganic Electronic Spectroscopy, second ed., Elsevier, Amsterdam, 1984.
[32] F.A. Cotton, G. Wilkinson, Advanced Inorganic Chemistry, fifth ed., Wiley, New York, 1988.
[33] R. Hage, Anouk H.J. Dijkhuis, J.G. Hassnoot, R. Prins, J. Reedijik, B.E. Buchanan, J.G. Vos, Inorg. Chem. 27 (1988) 2185.
[34] N. Raman, S. Ravichandran, C. Thangaraja, J. Chem. Sci. 116 (2004) 215.
[35] P. Yang, M.-L. Guo, B.-S. Yang, Chin. Sci. Bull. 39 (1994) 997.
[36] E.C. Long, J.K. Barton, Acc. Chem. Res. 23 (1990) 271.
[37] X.F. He, H. Chen, L. Xu, L.N. J, Polyhedron 17 (1998) 3161.

report the preparation of a new bpy ligand bearing two chiral bornyl substituents and report studies of iron(II) and ruthenium(II) complexes incorporating this species.

2. Experimental

2.1. General procedures

Commercially available chemicals were reagent grade and were used without further purification. ^{1}H and ^{13}C NMR spectra were recorded on Bruker AM 250, DRX 400 or 500 MHz or Bruker Avance 600 MHz spectrometers; chemical shifts are defined with TMS δ 0 ppm for ^{1}H and ^{13}C spectra and are measured relative to residual $CHCl_3$. Infrared spectra were recorded on Mattson Genesis or Shimadzu FTIR 8300 spectrophotometers using compressed KBr discs or on a Shimadzu FTIR-8400S spectrophotometer with neat samples on a Golden Gate diamond ATR accessory. Electronic absorption spectra were recorded on a Shimadzu UV 3101PC or Varian-Cary 5000 spectrophotometer, and luminescence spectra on a Shimadzu RF 5301PC or Perkin–Elmer LS50B spectrofluorophotometer. Electrospray (ES) mass spectra were recorded using a Finnigan MAT LCQ mass spectrometer. Microanalyses were performed with a LECO CHN-900 apparatus. CD spectra recorded on a Applied Photophysics Chirascan CD spectrometer at 298 K. Electrochemical measurements were performed with Autolab PGSTAT 20 or 30 systems using platinum or glassy-carbon working and auxiliary electrodes with an Ag/AgCl electrode as reference or a silver wire as pseudo-reference using purified MeCN as solvent and 0.1 M [^{n}Bu$_4$N][BF$_4$] as supporting electrolyte. Potentials are quoted versus the ferrocene/ferrocenium couple ($Fc/Fc^+ = 0.0$ V), and potentials were referenced to internal ferrocene added at the end of each experiment. 4,4′-Dibromo-2,2′-bipyridine [44] and [Ru(bpy)$_2$Cl$_2$] [45] were prepared by the literature methods; (+)-borneol ((1*R*,2*S*,4*R*)-1,7,7-trimethylbicyclo[2.2.1]heptan-2-ol) and (−)-borneol = ((1*S*,2*R*,4*S*)-1,7,7-trimethylbicyclo[2.2.1]heptan-2-ol) (Aldrich) were used as received.

2.2. (1*S*,2*R*,4*S*)-**1** and (1*R*,2*S*,4*R*)-**1**

(1*S*,2*R*,4*S*)-(−)-Borneol or (1*R*,2*S*,4*R*)-(+)-borneol (1.0 g, 6.5 mmol) was dissolved in DMF (50 cm^3) and NaH (60% dispersion in mineral oil, 0.26 g, 6.5 mmol) was added at room temperature. The mixture was stirred well and heated to 80 °C. After the evolution of gas had ceased, 4,4′-dibromo-2,2′-bipyridine (0.50 g, 1.6 mmol) was added in one portion and stirring was continued at this temperature for 16 h. The solvent was then evaporated and the residue dissolved in 2 M HCl after which the solution was neutralized with aqueous NaOH solution (1 M) and extracted with CH_2Cl_2 (3 × 50 cm^3). The combined organic phases were dried over $MgSO_4$ and the solvent removed *in vacuo*. The excess of borneol was sublimed from the white residue, leaving the desired ligand as white crystals (yield: (1*S*,2*R*,4*S*)-**1**, 0.47 g, 1.0 mmol, 63%; (1*R*,2*S*,4*R*)-**1**, 0.35 g, 0.76 mmol (47%). M.p. 158 °C. *Anal.* Calc. for $C_{30}H_{38}N_2O_2$: C, 78.56; H, 8.35; N, 6.11. Found: C, 78.03; H, 8.67; N, 6.10%. ^{1}H NMR (500 MHz, $CDCl_3$) δ/ppm 8.44 (d, J = 5.7 Hz, 2H, H^{A6}), 7.85 (d, J = 2.5 Hz, 2H, H^{A3}), 6.76 (dd, J = 5.7, 2.5 Hz, 2H, H^{A5}), 4.52 (m, 2H, H^2), 2.47 (m, 2H, H^{3exo}), 2.23 (m, 2H, H^{6exo}), 1.75 (m, 4H, H^{4,5exo}), 1.51 (m, 2H, H^{5endo}), 1.35 (m, 2H, H^{6endo}), 1.10 (m, 2H, H^{3endo}), 0.99 (s, 6H, H$^{8/9}$), 0.94 (s, 6H, H$^{8/9}$), 0.93 (s, 6H, H^{10}). ^{13}C{^{1}H} NMR (125 MHz, $CDCl_3$) δ/ppm 166.0 (C$^{A4/A2}$), 157.8 (C$^{A4/A2}$), 150.2 (C^{A6}), 111.2 (C^{A5}), 108.5 (C^{A3}), 83.2 (C^2), 49.5 (C$^{1/7}$), 48.0 (C$^{1/7}$), 45.1 (C^4), 36.6 (C^3), 27.9 (C^{5,6}), 26.8 (C^{5,6}), 19.7 (C$^{8/9}$), 19.1 (C$^{8/9}$), 13.7 (C^{10}). ESMS (MeCN) m/z 943 [2M+Na]$^+$, 461 [M]$^+$. UV–Vis λ_{max}/nm ($CHCl_3$) 236 (ε/dm^3 mol^{-1} cm^{-1} 104 000), 278 (65 000). $\bar{\nu}$/cm^{-1} (KBr) 2984m, 2953s, 2932s, 2884m, 1588s, 1558s, 1456s, 1289w, 1367w, 1306m, 1290s, 1232m, 1116w, 1050m, 1024s, 994w, 884m, 869w, 806m. CD ($CDCl_3$, 298 K, 5.4×10^{-5} mol dm^{-3}, nm ($\Delta\varepsilon$)) (1*R*,2*S*,4*R*)-**1**, 235 (0.9), 245 (0.6), 255 (−1.8), 270 (3.4), 280 (4.0), 294 (−2.0); (1*S*,2*R*,4*S*)-**1**, 235 (−0.9), 245 (−0.6), 255 (1.8), 270 (−3.4), 280 (−4.0), 294 (2.0). E°/V versus Fc: −2.08, −1.42 (irrev).

2.3. [Fe((1*S*,2*R*,4*S*)-**1**)$_3$][PF$_6$]$_2$

Ligand (1*S*,2*R*,4*S*)-**1** (40.1 mg, 0.0870 mmol) and $FeCl_2 \cdot 4H_2O$ (3.9 mg, 0.0196 mmol) were added to MeOH (4 cm^3) and the reaction mixture was stirred at room temperature for 17 h. Solvent was removed *in vacuo* and the residue was dissolved in MeCN (3 cm^3). The purple product was precipitated by the addition of aqueous ammonium hexafluorophosphate. It was collected by fitration, washed with water (50 cm^3) and dissolved in MeCN. Solvent was removed from the solution, and [Fe((1*S*,2*R*,4*S*)-**1**)$_3$][PF$_6$]$_2$ was isolated as a purple solid (25.0 mg, 0.0145 mmol, 74.0%). ^{1}H NMR (500 MHz, CH_3CN) δ/ppm 7.94 (br s, 6H, H^{A3}), 7.17 (two overlapping doublets, J = 7 Hz, 6H, H^{A6} diastereoisomers A + B), 6.76 (m, 6H, H^{A5}), 4.59 (m, 6H, H^2), 2.51 (m, 6H, H^{3exo}), 2.15 (m, 6H, H^{6exo}), 1.82 (m, 12H, H^{4,5exo}), 1.44 (m, 6H, H^{5endo}), 1.23 (m, 6H, H^{6endo}), 1.04 (dd, J = 13.5, 2.1 Hz, 6H, H^{3endo}), 0.99 (s, 9H, H^8 diastereoisomer A), 0.98 (s, 9H, H^8 diastereoisomer B), 0.95 (br s, 27H, H^9 diastereoisomers A + B, and H^{10} diastereoisomer A), 0.93 (s, 9H, H^{10} diastereoisomer B). ES MS (MeCN) m/z 1520 [M−PF$_6$+2MeCN]$^+$.

2.4. [Ru((1*S*,2*R*,4*S*)-**1**)$_3$][PF$_6$]$_2$

$RuCl_3 \cdot 3H_2O$ (12.5 mg, 0.0478 mmol) was combined with (1*S*,2*R*,4*S*)-**1** (66.0 mg, 0.143 mmol) in ethane-1,2-diol (5 cm^3). After the addition of two drops of *N*-ethylmorpholine, the reaction mixture was heated in a microwave oven (440 W) for 4 min. Water (25 cm^3) was added to the mixture and the mixture was then filtered. The red product was precipitated from the filtrate by adding aqueous

NH_4PF_6, was extracted with CH_2Cl_2 (25 cm^3) and was washed with water (2×25 cm^3). Solvent was removed from the combined organic phases to yield [Ru((1*S*,2*R*,4*S*)-**1**)$_3$][PF_6]$_2$ as a dark red solid (35.4 mg, 0.0200 mmol, 41.8%). ^{1}H NMR (250 MHz, CH_3CN) δ/ppm 7.88 (d, $J = 2.4$ Hz, 6H, H^{A3}), 7.49 and 7.475 (two overlapping doublets, $J = 6.5$ Hz, 6H, H^{A6} diastereoisomers A + B), 6.87 (dd, $J = 6$, 2 Hz, 6H, H^{A5}), 4.59 (m, 6H, H^2), 2.51 (m, 6H, H^{3exo}), 2.15 (m, 6H, H^{6exo}), 1.80 (m, 12H, $H^{4,5exo}$), 1.44 (m, 6H, H^{5endo}), 1.22 (m, 6H, H^{6endo}), 1.03 (m, 6H, H^{3endo}), 0.99 (s, 9H, H^8 diastereoisomer A), 0.98 (s, 9H, H^8 diastereoisomer B), 0.95 (br s, 27H, H^9 diastereoisomers A + B, and H^{10} diastereoisomer A), 0.93 (s, 9H, H^{10} diastereoisomer B). ESMS (MeCN) *m*/*z* 1628 [M−PF_6]$^+$, 1085 [M−PF_6−4bornyl]$^+$. *Anal*. Calc. for $C_{90}H_{120}F_{12}N_6O_6P_2Ru$: C, 60.97; H, 6.82; N, 4.74. Found: C, 59.95; H, 6.63; N, 4.91%. E°/V versus Fc: +0.52, −2.18, −1.81, −1.48 (irrev).

2.5. [Ru((1*S*,2*R*,4*S*)-**1**)(bpy)$_2$][PF_6]$_2$

[Ru(bpy)$_2$Cl$_2$] (0.10 g, 0.21 mmol) was combined with (1*S*,2*R*,4*S*)-**1** (95 mg, 0.21 mmol) in ethane-1,2-diol (10 cm^3). Two drops of *N*-ethylmorpholine were added, and then the mixture was heated in a microwave oven (400 W) for 4 min. After cooling to room temperature, aqueous NH_4PF_6 was added to the orange solution to precipitate the crude product. After column chromatography (silica, MeCN:H_2O:saturated aqueous KNO_3 7:0.5:0.75). [Ru((1*S*,2*R*,4*S*)-**1**)(bpy)$_2$][PF_6]$_2$ was isolated as an orange-red solid which was recrystallized from MeCN/Et_2O (148 mg, 0.127 mmol, 61%). *Anal*. Calc. for $C_{50}H_{56}F_{12}N_6O_6P_2Ru \cdot 3H_2O$: C, 49.30; H, 5.13; N, 6.90. Found: C, 49.57; H, 5.05; N, 6.91%. ^{1}H NMR (600 MHz, CH_3CN) δ/ppm 8.48 (d, $J = 8.4$ Hz, 4H, H^{B3}) and 8.47 (d, $J = 8.4$ Hz, 4H, H^{C3}), 8.04 ($J = 7.8$, 1.2 Hz, 4H, H^{B4}), 8.01 ($J = 7.8$, 1.2 Hz, 4H, H^{C4}), 7.909 and 7.915 (two overlapping d, $J = 2.6$ Hz, 2H, H^{A3} diastereoisomers A + B), 7.84 and 7.83 (two overlapping ddd, $J = 5.6$, 1.3, 0.6 Hz, 2H, H^{B6} diastereoisomers A + B), 7.7 (ddd, $J = 5.6$, 1.3, 0.6 Hz, 2H, H^{C6}), 7.429 and 7.426 (two overlapping dt, $J = 5.6$, 1.2 Hz, 2H, H^{B5} diastereoisomers A + B), 7.373 and 7.369 (two overlapping d, $J = 6.6$ Hz, 2H, H^{A6} diastereoisomers A + B), 7.35 (dt, $J = 5.6$, 1.2 Hz, 2H, H^{C5}), 6.87 and 6.86 (two overlapping dd, $J = 6.6$, 2.6 Hz, 2H, H^{A5} diastereoisomers A + B), 4.58 (m, 2H, H^2), 2.51 (m, 2H, H^{3exo}), 2.15 (m, 2H, H^{6exo}), 1.83 (m, 2H, H^{5exo}), 1.78 (m, 2H, H^4), 1.44 (m, 2H, H^{5endo}), 1.21 (m, 2H, H^{6endo}), 1.05 (dd, $J = 13.4$, 3.1 Hz, 1H, H^{3endo} diastereoisomer A), 0.99 (dd, $J = 13.4$, 3.1 Hz, 1H, H^{3endo} diastereoisomer B), 0.98 (s, 3H, H^8 diastereoisomer A), 0.97 (s, 3H, H^8 diastereoisomer B), 0.95 (s, 3H, H^{10} diastereoisomer A), 0.94 (s, 6H, H^9 diastereoisomers A + B), 0.93 (s, 3H, H^{10} diastereoisomer B). ESMS (MeCN) *m*/*z* 1019 [M−PF_6]$^+$, 437 [M−2PF_6]$^{2+}$. UV–Vis λ_{max}/nm (MeCN, 298 K) 231 (ε, dm^3 mol^{-1} cm^{-1} 73 000), 256 (40 000), 288 (105 600), 460 (19 800); fluorescence (MeCN, λ_{irr} 460 nm, 298 K) λ_{em} 631 nm; IR (KBr, cm^{-1}): 2952m, 1614m, 1553w, 1483w, 1465w, 1446w, 1316w, 1262w, 1247w, 1217w, 1049 (w), 1029w, 841s, 764w, 557m. CD ($CDCl_3$, 298 K, 4.5×10^{-5} mol dm^{-3}, nm ($\Delta\varepsilon$)) 226 (−1.9), 233 (−2.3), 244 (−0.3), 260 (−2.6), 292 (5.2). E°/V versus Fc: +0.76, −2.23, −2.00, −1.80, −1.44 (irrev). *Anal*. Calc. for $C_{50}H_{56}F_{12}N_6O_6P_2Ru \cdot 3H_2O$: C, 49.30; H, 5.13; N, 6.90. Found: C, 49.57; H, 5.05; N, 6.91%. E°/V versus Fc: +0.76, −2.23, −2.00, −1.80, −1.44 (irrev).

2.6. [Ru((1*R*,2*S*,4*R*)-**1**)(bpy)$_2$][PF_6]$_2$

The preparation was as for [Ru((1*S*,2*R*,4*S*)-**1**)(bpy)$_2$][PF_6]$_2$ and was on the same scale. [Ru((1*R*,2*S*,4*R*)-**1**)(bpy)$_2$][PF_6]$_2$ was isolated as a red solid (150 mg, 0.13 mmol, 62%). CD ($CDCl_3$, 298 K, 4.5×10^{-5} mol dm^{-3}, nm ($\Delta\varepsilon$)) 231 (3.6), 244 (0.98), 257 (1.9), 276 (−0.6), 294 (4.2).

2.7. Crystal structure determinations: general

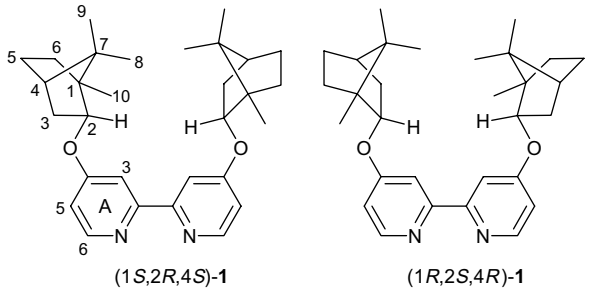
Data were collected on an Enraf Nonius Kappa CCD instrument; data reduction, solution and refinement used the programmes COLLECT [46], SIR-92 [47] and CRYSTALS [48].

2.8. Crystal data for (1*S*,2*R*,4*S*)-**1**

$C_{30}H_{40}N_2O_2$, $M = 460.66$, monoclinic, space group $P2_1$, $a = 15.1961(5)$ Å, $b = 7.3277(2)$ Å, $c = 24.1388(7)$ Å, $\beta = 107.464(2)°$; $V = 2564.0(1)$ Å^3, $Z = 4$, $D^{calc} = 1.193$ Mg m^{-3}, μ(Mo Kα) = 0.074 mm^{-1}, $T = 173$ K, 6345 reflections collected. Refinement of 4908 reflections (613 parameters) with $I > 1.0\sigma(I)$) converged at final $R_1 = 0.0906$ (0.1123 all data), $wR_2 = 0.1166$ (0.1376 all data), goodness-of-fit = 1.036.

3. Results and discussion

Ligands (1*S*,2*R*,4*S*)-**1** and (1*R*,2*S*,4*R*)-**1** (Scheme 1) were prepared by the deprotonation of the (1*S*,2*R*,4*S*)-(−)-borneol or (1*R*,2*S*,4*R*)-(+)-borneol with NaH in DMF followed by subsequent reaction with 4,4′-dibromo-2,2′-bipyridine [44]. After purification, (1*S*,2*R*,4*S*)-**1** and



Scheme 1. Structures of ligands (1*S*,2*R*,4*S*)-**1** and (1*R*,2*S*,4*R*)-**1**, and labelling scheme for NMR spectroscopic data. Ligands are drawn in the configuration in which they bind to a metal centre.

(1*R*,2*S*,4*R*)-**1** were obtained as white crystalline solids in 63% and 47% yield, respectively, and were fully characterized by spectroscopic and mass spectrometric techniques and (1*S*,2*R*,4*S*)-**1** by single crystal X-ray diffraction. The highest mass peak in the electrospray mass spectrum of the ligand appeared at *m*/*z* 943 and corresponded to $[2M+Na]^+$. The parent ion was observed at *m*/*z* 461. Both the ^1H and ^{13}C NMR spectra of the chiral ligand (1*S*,2*R*,4*S*)-**1** were consistent with the formation of a symmetrically substituted ligand. The aromatic region of the ^1H NMR spectrum exhibited three signals with the characteristic coupling patterns of a 4,4′-disubstituted 2,2′-bipyridine. Proton H^2 (see Scheme 1) appeared in the ^1H NMR spectrum at δ 4.52 ppm, well separated from the signals for the remaining bornyl protons. The ^{13}C and ^1H NMR spectra of **1** were assigned by use of COSY, HMQC and HMBC techniques, and the proton assignments were consistent with those reported for 6-{(1*S*,2*R*,4*S*)-(−)-bornyloxy}-2,2′:6′,2″-terpyridine [40]. Fig. 1 shows the CD spectra of acetonitrile solutions of (1*S*,2*R*,4*S*)-**1** and (1*R*,2*S*,4*R*)-**1**, and confirms their optical purity. Crystals (colourless plates) of (1*S*,2*R*,4*S*)-**1** suitable for X-ray diffraction were grown from an MeCN solution of (1*S*,2*R*,4*S*)-**1** layered with Et_2O. There are two crystallographically independent molecules of (1*S*,2*R*,4*S*)-**1** in the asymmetric unit, and their structures are depicted in Fig. 2a. Most bond distances and angles are unexceptional, and only selected bond parameters are listed in the figure caption. It is worth noting that the C–O–C bond angles of ≈118°, and the fact that the $C_{pyridyl}$–O is shorter than the C_{bornyl}–O bond, indicate that each O atom is sp^2 hybridized and that there is delocalization of π-electrons over each pyridyl–O unit. In both molecules, the two pyridine rings of the bpy unit are slightly twisted with respect to one another (angles between the least squares planes of the rings containing N1 and N2, and N3 and N4 are 11.7(3)° and 15.5(3)°, respectively). The most marked difference between the two independent molecules of

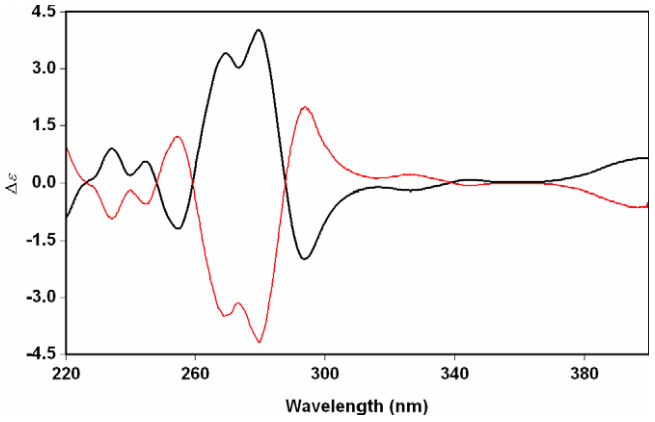


Fig. 1. CD spectra of (1*S*,2*R*,4*S*)-**1** (red line, with minimum at negative Δε) and (1*R*,2*S*,4*R*)-**1** (black line, with maximum at positive Δε) in MeCN solution at 298 K.

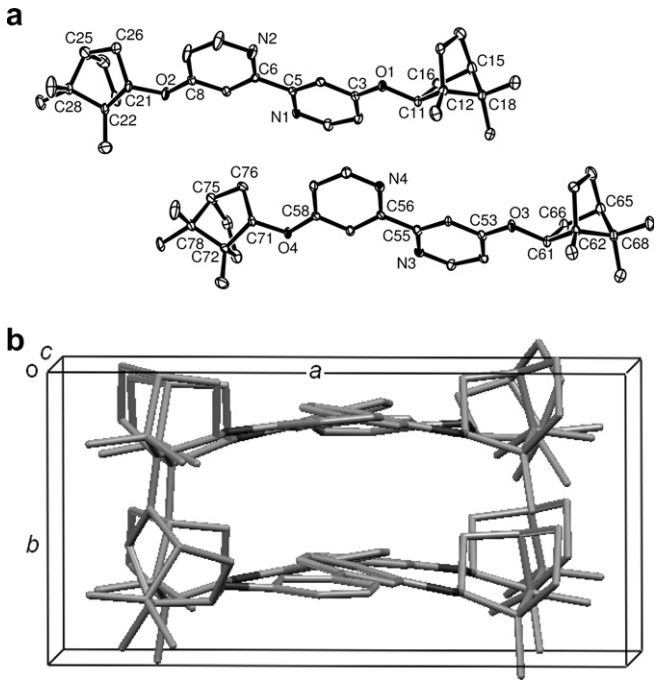
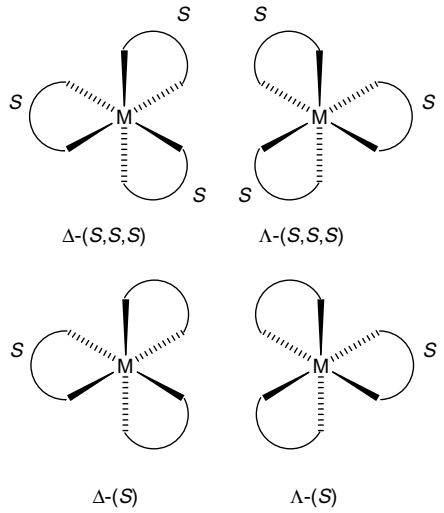


Fig. 2. (a) Molecular structure of compound (1*S*,2*R*,4*S*)-**1** with thermal ellipsoids plotted at 30% probability level. Selected bond lengths (Å) and angles (°): O1–C3 = 1.351(5), O1–C11 = 1.436(5), O2–C8 = 1.345(5), O2–C21 = 1.449(5), O3–C53 = 1.352(5), O3–C61 = 1.438(5), O4–C58 = 1.352(5), O4–C71 = 1.423(5), C5–C6 = 1.493(6), C55–C56 = 1.484(6); C3–O1–C11 = 118.7(3), C8–O2–C21 = 118.6(3), C53–O3–C61 = 118.5(3), C58–O4–C71 = 118.5(3). (b) Packing of four molecules of (1*S*,2*R*,4*S*)-**1** in the unit cell.

(1*S*,2*R*,4*S*)-**1** lies in the orientation of the bornyl substituents with respect to the pyridine ring to which they are attached. In one molecule, the angles between the least squares planes of the pyridine ring containing N1 and the plane defined by atoms C12, C11, C16 and C15 is 57.4(3)° whereas that of the pyridine ring containing N2 and the plane defined by atoms C22, C21, C26 and C25 is 49.2(4)°. In the second molecule, the corresponding angles are 56.8(3)° and 61.8(3)° for rings containing N3 and N4, respectively. Molecules of (1*S*,2*R*,4*S*)-**1** pack in rows running parallel to the *c* axis and this results in domains of bpy units, between which lie two adjacent domains of bornyl substituents (Fig. 2b). There is no face-to-face π–π stacking between bpy units.

With the enantiomerically pure ligands in hand, our next aim was to prepare a series of tris-chelate octahedral metal(II) complexes in order to investigate whether there was any preference for the formation of diastereoisomers with Δ- or Λ-stereochemistry at the metal centre. Scheme 2 shows the types of complexes studied, exemplified by $[Fe((1S,2R,4S)\text{-}\mathbf{1})_3]^{2+}$, $[Ru((1S,2R,4S)\text{-}\mathbf{1})_3]^{2+}$ and $[Ru((1S,2R,4S)\text{-}\mathbf{1})(bpy)_2]^{2+}$. The complex $[Ru((1R,2S,4R)\text{-}\mathbf{1})(bpy)_2]^{2+}$ has also been studied. $[Fe((1S,2R,4S)\text{-}\mathbf{1})_3][PF_6]_2$ was prepared by the reaction of (1*S*,2*R*,4*S*)-**1** with $FeCl_2 \cdot 4H_2O$ in methanol, and was isolated in good yield as a purple solid. The highest mass peak in the electrospray



Scheme 2. Formation of diastereoisomeric pairs of tris-chelate complexes of type $[M((1S,2R,4S)\text{-}\mathbf{1})_3]^{2+}$ and $[M((1S,2R,4S)\text{-}\mathbf{1})(bpy)_2]^{2+}$. For simplicity, the labels define the stereoechemistry at C1 only, e.g. Δ-(*S*,*S*,*S*) corresponds to three (1*S*,2*R*,4*S*)-**1** ligands, and so on.

mass spectrum of a sample injected as an acetonitrile solution was observed at *m*/*z* 1520 and corresponded to $[M-PF_6+2MeCN]^+$. The appearance of the 500 MHz ^1H NMR spectrum of the product confirmed the formation of a symmetrical species. Three signals were observed in the aromatic region at δ 7.94, 7.17 and 6.76 ppm assigned to protons H^{A3}, H^{A5} and H^{A6}, respectively (see Scheme 1). These chemical shifts are characteristic of a coordinated ligand and support the formation of $[Fe((1S,2R,4S)\text{-}\mathbf{1})_3]^{2+}$. Significantly, the signal for H^{A6} appeared as an apparent triplet ($J = 7$ Hz) instead of the expected doublet ($J \approx 7$ Hz), while the signal for H^{A5} was broader than expected. These observations can be rationalized if the Δ-(*S*,*S*,*S*) and Λ-(*S*,*S*,*S*) diastereoisomers (Scheme 2) are formed in equal amounts and are distinguishable in the ^1H NMR spectrum, i.e. two overlapping doublets of equal integrals are observed for H^{A6}. In contrast, it is not possible to distinguish the diastereoisomers of $[Fe((1S,2R,4S)\text{-}\mathbf{1})_3]^{2+}$ using protons H^{A3} and H^{A5} as probes at 500 MHz. The proton signals for the bornyl substituent were assigned using COSY and NOESY techniques. The signal for the H^{3endo} protons is informative. It appears as a pair of doublets of doublets ($J = 13.5$, 2.1 Hz), one part of which is partly obscured by a bornyl methyl signal. The splitting of the H^{3endo} signal is consistent with the H^{3endo} protons in the two diastereoisomers of $[Fe((1S,2R,4S)\text{-}\mathbf{1})_3]^{2+}$ sensing the presence of the chiral metal centre. The ^1H NMR signals that provide the best indicator of the ratio of diastereoisomers present are the bornyl methyl resonances. Four signals are observed at δ 0.99, 0.98, 0.95 and 0.93 ppm with relative integrals of 9:9:27:9. Use of the NOESY technique permits these signals to be assigned to H^8, H^8, H^{9+10} and H^{10} of the two diastereoisomers, respectively. Thus, the methyl groups (H^8 and H^{10}) which face the stereogenic metal centre sense its presence, whereas the protons H^9 of the remaining methyl group do not. The relative integrals of these signals are consistent with there being no preference for the formation of Δ- or Λ-diastereoisomers of $[Fe((1S,2R,4S)\text{-}\mathbf{1})_3]^{2+}$. Even though the complex cation $[Fe((1S,2R,4S)\text{-}\mathbf{1})_3]^{2+}$ contains 19 stereogenic centres, 18 of which are defined, the chiral auxiliaries appear to be too distant to exert any stereocontrol over the configuration at the metal centre.

The influence of the group 8 metal ion was then investigated: specifically, we were interested in the change from iron(II) which is sufficiently labile to lead to thermodynamic products to ruthenium(II) which is kinetically inert and will give kinetic products. The complex $[Ru((1S,2R,4S)\text{-}\mathbf{1})_3]^{2+}$ was prepared by treating $RuCl_3 \cdot 3H_2O$ with (1*S*,2*R*,4*S*)-**1** in ethane-1,2-diol in the presence of *N*-ethylmorpholine under microwave heating conditions. The product was isolated as the red hexafluorophosphate salt in 42% yield. In the electrospray mass spectrum, the highest mass peak (*m*/*z* 1628) corresponded to $[M-PF_6]^+$. NMR spectra for ruthenium(II) complexes are typically sharper than those of the analogous iron(II) species in which paramagnetic impurities tend to broaden the signals. Hence, a detailed study of the ^1H NMR spectrum of $[Ru((1S,2R,4S)\text{-}\mathbf{1})_3]^{2+}$ was made. The ^1H NMR spectrum of a CD_3CN solution of $[Ru((1S,2R,4S)\text{-}\mathbf{1})_3][PF_6]_2$ was recorded at both 400 and 250 MHz. A comparison of the aromatic regions of these spectra (Fig. 3a, 400 MHz, and Fig. 3b, 250 MHz) allows them to be analysed as a doublet (δ 7.88 ppm, $J = 2.4$ Hz) assigned to H^{A3}, a pair of overlapping doublets (δ 7.49 and 7.475 ppm, each $J = 6.5$ Hz, relative integrals $\approx$ 1:1) assigned to H^{A6}, and a pair of overlapping doublets of doublets (centred at δ 6.88, $J = 6$, 2 Hz) arising from H^{A5}. This is consistent with the presence of approximately equal amounts of Δ-(*S*,*S*,*S*) and Λ-(*S*,*S*,*S*) diastereoisomers of $[Ru((1S,2R,4S)\text{-}\mathbf{1})_3]^{2+}$. At 400 and 250 MHz, the H^{A6} protons in particular can be used as a probe for the stereogenic

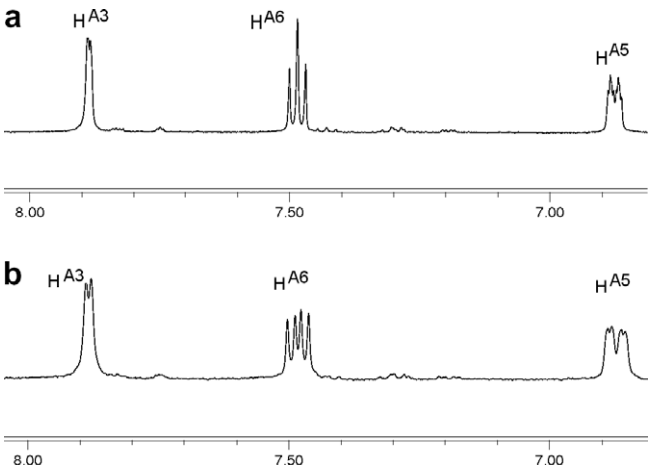
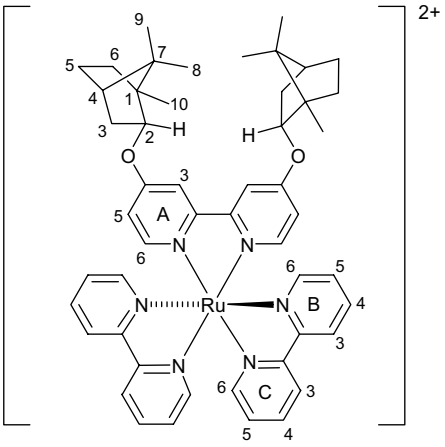


Fig. 3. The aromatic region of the ^1H NMR spectrum of $[Ru((1S,2R,4S)\text{-}\mathbf{1})_3][PF_6]_2$ in CD_3CN at (a) 400 MHz and (b) 250 MHz (chemical shifts are in δ/ppm). See Scheme 1 for atom labelling.

metal centre. The remaining resonances in the ^{1}H NMR spectrum were assigned to the bornyl protons by analogy with the spectrum of $[Fe((1S,2R,4S)\text{-}\mathbf{1})_3]^{2+}$. Among these signals, the clearest evidence for the approximately 1:1 mixture of diastereoisomers comes from the resonances arising from the methyl protons. These appear as four signals (δ 0.99, 0.98, 0.95 and 0.93 ppm) with relative integrals of 9:9:27:9 arising from the splitting of signals for the methyl groups containing H^8 and H^{10} in the two diastereoisomers. Thus, the formation of $[Ru((1S,2R,4S)\text{-}\mathbf{1})_3]^{2+}$ occurs without diastereoisomeric discrimination.

Since the formation of the homoleptic tris-chelate complexes $[M((1S,2R,4S)\text{-}\mathbf{1})_3]^{2+}$ (M = Fe or Ru) showed no preference for either Δ-(*S*,*S*,*S*) or Λ-(*S*,*S*,*S*) diastereoisomer, we turned our attention to the heteroleptic complexes $[Ru((1S,2R,4S)\text{-}\mathbf{1})(bpy)_2]^{2+}$ and $[Ru((1R,2S,4R)\text{-}\mathbf{1})(bpy)_2]^{2+}$. These were prepared by treatment of $[Ru(bpy)_2Cl_2]$ with (1*S*,2*R*,4*S*)-**1** or (1*R*,2*S*,4*R*)-**1** in ethane-1,2-diol in the presence of a small amount of the reductant *N*-ethylmorpholine under microwave heating conditions. After purification, the red-orange hexafluorophosphate salts were isolated in ≈60% yield. The number and pattern of signals observed in the ^{1}H NMR spectra of CD_3CN solutions of the two complexes confirmed the presence of coordinated bpy and (1*S*,2*R*,4*S*)-**1** or (1*R*,2*S*,4*R*)-**1** ligands in a 2:1 ratio. The most informative ^{1}H NMR spectrum was that recorded for $[Ru((1S,2R,4S)\text{-}\mathbf{1})(bpy)_2][PF_6]_2$ at 600 MHz. The ring and atom labelling are shown in Scheme 3, and signals were fully assigned by use of COSY and NOESY techniques. For protons H^{A6}, a pair of overlapping doublets ($J = 6.6$ Hz), reminiscent of those in $[Ru((1S,2R,4S)\text{-}\mathbf{1})_3]^{2+}$, was observed confirming the presence of both Δ-(*S*) and Λ-(*S*)-diastereoisomers (see Scheme 2) of $[Ru((1S,2R,4S)\text{-}\mathbf{1})(bpy)_2]^{2+}$. In the 600 MHz ^{1}H NMR spectrum, the signals for H^{A3} and H^{A5} also split and are observed as overlapping doublets ($J = 2.6$ Hz) and overlapping doublets of doublets ($J = 6.6$ and 2.6 Hz), respectively. The two pyridine rings in each bpy ligand are inequivalent (Scheme 3). Approximate inter-ligand H···H separations were determined from an optimized molecular model [49] of $[Ru((1S,2R,4S)\text{-}\mathbf{1})(bpy)_2]^{2+}$. The closest contact is between H^{A6} and H^{B6} (≈3.4 Å) with the separation of H^{A6} and H^{C6} being significantly longer (≈4.8 Å). In the NOESY spectrum, it is therefore possible to distinguish between protons H^{B6} and H^{C6}. Other assignments for the aromatic protons then follow from the COSY (Fig. 4) spectrum. The signals for the protons H^{C6} and H^{B6} are shown in Fig. 5a. Whereas the former appears as the expected doublet of doublets of doublets ($J_{B6-B5} = 5.6$, $J_{B6-B4} = 1.3$, $J_{B6-B3} = 0.6$ Hz), the latter signal responds to the presence of the Δ-(*S*) and Λ-(*S*)-diastereoisomers. This is consistent with H^{B6} being the closest bpy proton to the stereogenic ruthenium(II) centre. In the bornyl region of the ^{1}H NMR spectrum, the H^{3endo} and methyl resonances (Fig. 5b) are the best indicators of the presence of an approximately 1:1 mixture of Δ-(*S*) and Λ-(*S*)-diastereoisomers. For example, the H^{3endo} protons give rise to two doublets of doublets, each with $J = 13.4$ and 3.1 Hz; one part of one of these signals is hidden under one of the methyl resonances (Fig. 5b), but its presence is readily confirmed from the COSY spectrum (Fig. 6).

The electrochemical properties of $[Ru((1S,2R,4S)\text{-}\mathbf{1})_3]^{2+}$ and $[Ru((1S,2R,4S)\text{-}\mathbf{1})(bpy)_2]^{2+}$ were investigated using cyclic voltammetry and differential pulse voltammetry (DPV). The Ru(II) centre undergoes a well-defined one-electron oxidation at +0.52 V (versus Fc^+/Fc) in $[Ru((1S,2R,4S)\text{-}\mathbf{1})_3]^{2+}$ and +0.76 V in $[Ru((1S,2R,4S)\text{-}\mathbf{1})(bpy)_2]^{2+}$. This compares with +0.88 V in $[Ru(bpy)_3]^{2+}$ [50,51]. Thus, the replacement of a bpy ligand in $[Ru(bpy)_3]^{2+}$ by (1*S*,2*R*,4*S*)-**1** results in a 0.12 V shift per ligand to less positive potential, and this trend illustrates the increasing ease of oxidation of the Ru(II) centre and stabilization of the Ru(III) oxidation state as bpy ligands are replaced by more electron-releasing ligands. This is consistent with the Hammett σ-parameter [52,53] for a



$[Ru((1S,2R,4S)\text{-}\mathbf{1})(bpy)_2]^{2+}$

Scheme 3. $[Ru((1S,2R,4S)\text{-}\mathbf{1})(bpy)_2]^{2+}$ with ring and atom labelling for the NMR spectra.

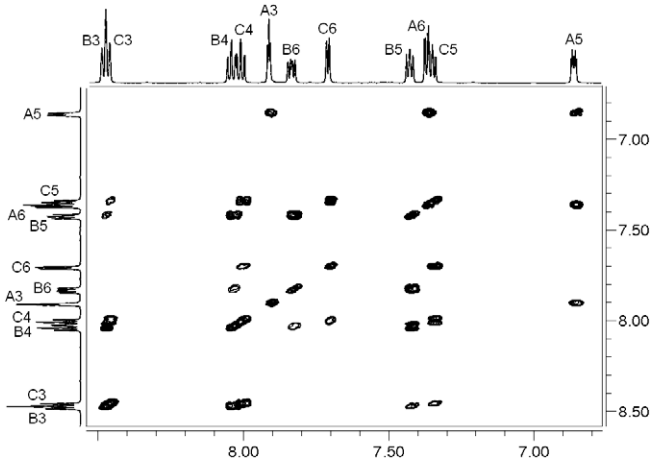


Fig. 4. 600 MHz ^{1}H COSY spectrum of the aromatic region for $[Ru((1S,2R,4S)\text{-}\mathbf{1})(bpy)_2][PF_6]_2$ (in CD_3CN); chemical shifts in δ/ppm.

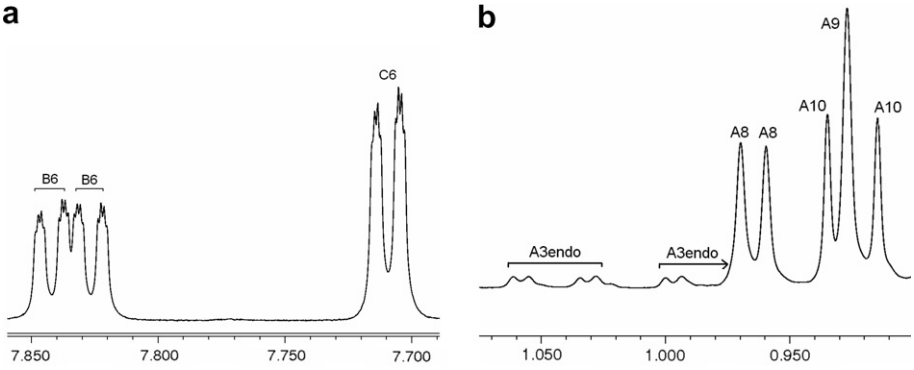


Fig. 5. (a) Part of the 600 MHz ^{1}H spectrum of [Ru((1*S*,2*R*,4*S*)-**1**)(bpy)$_2$][PF$_6$]$_2$ (in CD$_3$CN) showing the signals (δ/ppm) for the H^6 bpy protons (see Scheme 3). (b) Part of the 500 MHz ^{1}H spectrum of [Ru((1*S*,2*R*,4*S*)-**1**)(bpy)$_2$][PF$_6$]$_2$ (in CD$_3$CN) showing the signals (δ/ppm) for the bornyl methyl and H^{3endo} protons of coordinated ((1*S*,2*R*,4*S*)-**1**).

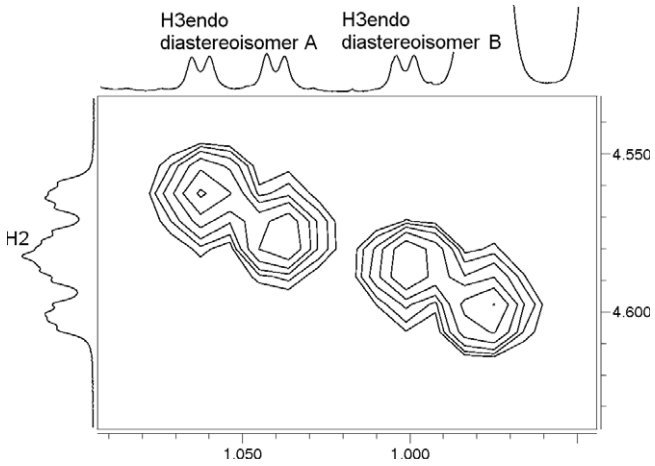


Fig. 6. Part of the 600 MHz ^{1}H COSY spectrum of [Ru((1*S*,2*R*,4*S*)-**1**)(bpy)$_2$][PF$_6$]$_2$ (in CD$_3$CN, chemical shifts in δ/ppm) showing the cross peaks for the bornyl H^2/H^{3endo} proton correlation.

para-alkoxy substituent (which is expected to have a value of about −0.3) and with our earlier observations that the redox potentials in these heteroleptic systems are described by simple additive models [54–59]. Each complex undergoes ligand-centred reduction processes. For [Ru((1*S*,2*R*,4*S*)-**1**)(bpy)$_2$]$^{2+}$, three reversible reductions at −2.23, −2.00 and −1.80 V compare with reduction potentials of −2.17, −1.96 and −1.72 V for [Ru(bpy)$_3$]$^{2+}$ [50,51]. For [Ru((1*S*,2*R*,4*S*)-**1**)$_3$]$^{2+}$, only reversible process is clearly resolved (−1.80 V).

4. Conclusions

We have prepared and fully characterized enantiomers of a 4,4′-disubstitued 2,2′-bipyridine ligand containing chiral auxiliaries. The enantiomerically pure ligands have been incorporated into homoleptic and heteroleptic complexes of type [M((1*S*,2*R*,4*S*)-**1**)$_3$]$^{2+}$ (M = Fe, Ru), [M((1*S*,2*R*,4*S*)-**1**)(bpy)$_2$]$^{2+}$ (M = Fe, Ru) and [Ru((1*R*,2*S*,4*R*)-**1**)(bpy)$_2$]$^{2+}$. ^{1}H NMR spectroscopy has been used to distinguish between the Δ and Λ-diastereoisomers of each complex. Even though complexes with up to 18 defined stereogenic centres have been prepared, no diastereoisomeric selectivity at the metal centre has been observed.

Acknowledgements

We thank the Swiss National Science Foundation and the University of Basel for general financial support and for funds enabling the purchase of a CD spectrometer under the R'Equip programme. Dr. Daniel Häussinger is thanked for recording 600 MHz ^{1}H NMR spectra, and Emma Dunphy is acknowledged for recording CD spectra.

Appendix A. Supplementary material

CCDC 651584 contains the supplementary crystallographic data including atomic coordinates, bond distances and angles for (1*S*,2*R*,4*S*)-**1**. These data can be obtained free of charge via http://www.ccdc.cam.ac.uk/conts/retrieving.html, or from the Cambridge Crystallographic Data Centre, 12 Union Road, Cambridge CB2 1EZ, UK; fax: (+44) 1223-336-033; or e-mail: deposit@ccdc.cam.ac.uk. Supplementary data associated with this article can be found, in the online version, at doi:10.1016/j.poly.2007.08.026.

References

[1] J.L. Pierre, Coord. Chem. Rev. 178 (1998) 1183.
[2] P.D. Knight, P. Scott, Coord. Chem. Rev. 242 (2003) 125.
[3] J.M. Brown, in: E.N. Jacobsen, A. Pfaltz, H. Yamamoto (Eds.), Comprehensive Asymmetric Catalysis, vol. 1, Springer, Berlin, 1999, p. 121.
[4] T. Ohkuma, M. Kitamura, R. Noyori, in: I. Ojima (Ed.), Catalytic Asymmetric Synthesis, 2nd ed., Wiley–VCH, New York, 2000, p. 1.
[5] A. Pfaltz, M. Lautens, in: E.N. Jacobsen, A. Pfaltz, H. Yamamoto (Eds.), Comprehensive Asymmetric Catalysis, vol. 2, Springer, Berlin, 1999, p. 833.
[6] B.M. Trost, C. Lee, in: I. Ojima (Ed.), Catalytic Asymmetric Synthesis, 2nd ed., Wiley–VCH, New York, 2000, p. 593.
[7] S. Gladiali, E. Alberico, Chem. Soc. Rev. 35 (2006) 226.
[8] M. Shibasaki, S. Matsunaga, Chem. Soc. Rev. 35 (2006) 269.
[9] M. Sawamura, Y. Ito, Chem. Rev. 92 (1992) 857.
[10] A. von Zelewsky, Stereochemistry of Coordination Compounds, Wiley, New York, 1996.

[11] H.U. Blaser, Chem. Rev. 92 (1992) 935.
[12] G. Casiraghi, F. Zanardi, G. Rassu, P. Spanu, Chem. Rev. 95 (1995) 1677.
[13] R.A. Sheldon, J. Chem. Technol. Biotechnol. 67 (1996) 1.
[14] C. Kaes, A. Katz, M.W. Hosseini, Chem. Rev. 100 (2000) 3553.
[15] E.C. Constable, Adv. Inorg. Chem. 34 (1989) 1.
[16] G.R. Newkome, A.K. Patri, E. Holder, U.S. Schubert, Eur. J. Org. Chem. (2004) 235.
[17] W.W. Brandt, F.P. Dwyer, E.C. Gyarfas, Chem. Rev. 54 (1954) 959.
[18] P.G. Sammes, G. Yahioglu, Chem. Soc. Rev. 23 (1994) 327.
[19] W. Sliwa, Heterocycles 12 (1979) 1207.
[20] E.C. Constable, Chem. Soc. Rev. 36 (2007) 246.
[21] U.S. Schubert, H. Hofmeier, G.R. Newkome, Modern Terpyridine Chemistry, Wiley–VCH, Weinheim, 2006.
[22] R.A. Fallahpour, Curr. Org. Synth. 3 (2006) 19.
[23] H. Hofmeier, U.S. Schubert, Chem. Soc. Rev. 33 (2004) 373.
[24] R.A. Fallahpour, Synthesis (2003) 155.
[25] A.M.W. Cargill Thompson, Coord. Chem. Rev. 160 (1997) 1.
[26] E.C. Constable, Prog. Inorg. Chem. 42 (1994) 67.
[27] E.C. Constable, Adv. Inorg. Chem. 30 (1986) 69.
[28] U. Knof, A. von Zelewsky, Angew. Chem., Int. Ed. 38 (1999) 303.
[29] H. Brunner, Angew. Chem., Int. Ed. 38 (1999) 1194.
[30] O. Mamula, A. von Zelewsky, Coord. Chem. Rev. 242 (2003) 87.
[31] G. Chelucci, R.P. Thummel, Chem. Rev. 102 (2002) 3129.
[32] T. Mizuno, M. Takeuchi, I. Hamachi, K. Nakashima, S. Shinkai, Chem. Commun. (1997) 1793.
[33] R. Annunziata, M. Benaglia, M. Cinquini, F. Cozzi, C.R. Woods, J.S. Siegel, Eur. J. Inorg. Chem. (2001) 173.
[34] S.G. Telfer, X.-J. Yang, A.F. Williams, Dalton Trans. (2004) 699.
[35] A. von Zelewsky, Coord. Chem. Rev. 192 (1999) 811.
[36] E.C. Constable, T. Kulke, M. Neuburger, M. Zehnder, New J. Chem. 21 (1997) 1091.
[37] E.C. Constable, T. Kulke, M. Neuburger, M. Zehnder, Chem. Commun. (1997) 489.
[38] E.C. Constable, T. Kulke, M. Neuburger, M. Zehnder, New J. Chem. 21 (1997) 633.
[39] G. Baum, E.C. Constable, D. Fenske, C.E. Housecroft, T. Kulke, M. Neuburger, M. Zehnder, J. Chem. Soc., Dalton Trans. (2000) 945.
[40] E.C. Constable, C.E. Housecroft, T. Kulke, C. Lazzarini, E. Schofield, Y. Zimmermann, J. Chem. Soc., Dalton Trans. (2001) 2864.
[41] E.C. Constable, R. Frantz, C.E. Housecroft, J. Lacour, A. Mahmood, Inorg. Chem. 43 (2004) 4817.
[42] T. Hasegawa, K. Matsuura, K. Kobayashi, Chem. Lett. (2000) 466.
[43] L.H. Uppadine, F.R. Keene, P.D. Beer, Dalton Trans. (2001) 2188.
[44] F.H. Case, G. Maerker, J. Am. Chem. Soc. 80 (1958) 2745.
[45] B.P. Sullivan, D.J. Salmon, T.J. Meyer, Inorg. Chem. 17 (1978) 3334.
[46] COLLECT Software, Nonius BV, 1997–2001.
[47] A. Altomare, G. Cascarano, G. Giacovazzo, A. Guagliardi, M.C. Burla, G. Polidori, M. Camalli, J. Appl. Crystallogr. 27 (1994) 435.
[48] P.W. Betteridge, J.R. Carruthers, R.I. Cooper, K. Prout, D.J. Watkin, J. Appl. Crystallogr. 36 (2003) 1487.
[49] Spartan'04, © Wavefunction Inc., 2003.
[50] E.C. Constable, E. Figgemeier, C.E. Housecroft, J. Olsson, Y.C. Zimmermann, Dalton Trans. (2004) 1918.
[51] A. Juris, V. Balzani, F. Barigelletti, S. Campagna, P. Belser, A. von Zelewsky, Coord. Chem. Rev. 84 (1988) 85.
[52] C. Hansch, A. Leo, Substituent Constants for Correlation Analysis in Chemistry and Biology, Wiley–Interscience, New York, 1979.
[53] H. Masui, A.B.P. Lever, Inorg. Chem. 32 (1993) 2199.
[54] E.C. Constable, A.M.W. Cargill Thompson, D.A. Tocher, M.A.M. Daniels, New J. Chem. 16 (1992) 855.
[55] E.C. Constable, A. Thompson, J. Chem. Soc., Dalton Trans. (1994) 1409.
[56] M. Maestri, N. Armaroli, V. Balzani, E.C. Constable, A. Thompson, Inorg. Chem. 34 (1995) 2759.
[57] E.C. Constable, P. Harverson, D.R. Smith, L. Whall, Polyhedron 16 (1997) 3615.
[58] E.C. Constable, M. Neuburger, D.R. Smith, M. Zehnder, Inorg. Chim. Acta 275–276 (1988) 359.
[59] H.S. Chow, E.C. Constable, C.E. Housecroft, M. Neuburger, S. Schaffner, Dalton Trans. (2006) 2881.

agents, those of ruthenium appear as the most promising [9], and several types of its complexes have shown high anticancer activity [10]. Substantial activity has been shown by ruthenium(II) complexes stabilized with heteroaromatic ligands, such as *cis*-[$RuCl_2(azpy)_2$] (azpy = 2-(phenylazo)pyridine) [11].

In this paper we describe the synthesis and characterization of new ruthenium(II) complexes, containing substituted quinolinediones acting as (N–O) bidentate ligands, of the type [$Ru(CO)_2Cl_2$(N–O)]. The molecular structure of [$Ru(CO)_2Cl_2$(6-methoxybenzo[*g*]quinoline-5,10-dione)] is determined by single-crystal X-ray diffraction. The electrochemical properties and the potential antitumor activities of the free ligands and ruthenium complexes are also studied.

2. Experimental

2.1. General

The ligand 4,6-dichloroquinoline-5,8-dione (**1**) was synthesized according to a literature procedure [12]. Tricarbonyldichlororuthenium(II) dimer was purchased from Aldrich and solvents (reagent grade) from Merck; both were used without further purification. Elemental analyses (C, H, N) were carried out by a Fisons EA 1108 CHNS-O microanalyzer. FTIR spectra were recorded throughout the 4000–250 cm^{-1} region, with samples prepared as KBr discs on a Bruker Vector-22 spectrophotometer. The NMR spectra were recorded on a Bruker AC-200P and Avance-400 spectrometers and the chemical shifts are reported in ppm relative to $SiMe_4$. Column chromatography was performed on silica gel Merck 60 (70–230 mesh). Thin layer chromatography separations were carried out on Merck Kieselgel 60 (70–230 mesh).

2.2. Synthesis of 6-methoxybenzo[g]quinoline-5,10-dione (*2*)

To a solution of 5-methoxynaphthalene-1,4-dione [13] (203.4 mg, 1.081 mmol) in dichloromethane (20 mL) azadiene [14] (259 mg, 2.64 mmol) was added. After stirring the reaction mixture at room temperature for 7 days silica gel was added (1 g) and the mixture stirred again for 24 h. Chloranil (800 mg. 3.24 mmol) was added and the mixture was heated at reflux for 5 h. The resulting suspension was poured into an aqueous sodium bicarbonate solution (5%) and extracted with dichloromethane (3 × 50 mL). The organic layer was washed with water and dried with magnesium sulphate. The solution was evaporated to dryness to give a solid residue, which was purified by chromatography on silica gel using a mixture of dichloromethane-ethyl acetate (8:2) as eluent. Evaporation of solvents gave a yellow solid, which was crystallized from ethanol. Yield 115 mg (45%), m.p. 218–218.5 °C (lit. [15] m.p. 218–219 °C). IR (KBr) ν cm^{-1}: 1656 (C═O). ^{1}H NMR ($CDCl_3$, 295 K): δ 4.08 (s, 3H, MeO), 7.42 (dd, 1H, $J = 1.0$ Hz, $J = 8.0$ Hz, H_7), 7.72 (dd, 1H, $J = 4.6$ Hz, $J = 8.0$ Hz, H_3), 7.79 (dd, 1H, $J = 8.0$ Hz, $J = 8.0$ Hz, H_8), 8.06 (dd, 1H, $J = 1.0$ Hz, $J = 8.0$ Hz, H_9), 8.62 (dd, 1H, $J = 1.6$ Hz, $J = 8.0$ Hz, H_4), 9.06 (dd, 1H, $J = 1.6$ Hz, $J = 4.6$ Hz, H_2). ^{13}C NMR ($CDCl_3$, 295 K): δ 56.6, 118.4, 120.5, 128.1, 131.8, 135.4, 135.6, 147.8, 154.4, 160.5, 181.6, 182.0.

2.3. General procedure for the synthesis of ruthenium(II) complexes (*3*, *4*)

A solution of tricarbonyldichlororuthenium(II) dimer (0.22 mmol) and quinolinedione ligands (**1**, **2**) (0.44 mmol) was heated under reflux in dry ethanol (5 mL). The reaction was monitored by thin layer chromatography. During the reaction time, 30–40 min, a solid complex was formed. The crude solid was filtered off and washed with ethanol.

2.3.1. [$Ru(CO)_2Cl_2$(4,6-dichloroquinoline-5,8-dione)] (*3*)

The complex was obtained by re-crystallization of the crude solid from warm ethanol. Red crystals, yield 35 mg (18%), m.p. >300 °C. *Anal.* Calc. for $C_{11}H_3Cl_4NO_4Ru$ required: C, 29.0; H, 0.7; N, 3.1. Found: C, 28.9; H, 1.0; N, 3.3%. IR (KBr) ν cm^{-1}: 2062 vs, 1992 vs (CO); 1696 s (C═O); 329 m (Ru–Cl). ^{1}H NMR (acetone-d_6, 295 K); δ 5.92 (s, 1H, H_4), 7.92 (d, 1H, $J = 6.0$ Hz, H_3), 9.06 (d, 1H, $J = 6.0$ Hz, H_2). ^{13}C NMR (acetone-d_6, 295 K); δ 125.4, 130.1, 145.6, 154.0, 157.1, 170.0, 173.9, 180.1, 180.2, 197.2 (CO), 197.9 (CO).

2.3.2. [$Ru(CO)_2Cl_2$(6-methoxybenzo[g]quinoline-5,10-dione)] (*4*)

Purified by column chromatography using a dichloromethane-ethyl acetate (1:1) mixture as eluent. Wine-red solid, yield 70 mg (34%). M.p. >300 °C. *Anal.* Calc. for $C_{16}H_9Cl_2NO_5Ru$ required: C, 41.1; H, 1.9; N, 3.0. Found: C, 40.6; H, 1.4; N, 3.1%. IR (KBr) ν cm^{-1}: 2074 vs, 2016 vs (CO); 1671 s (C═O); 343 m (Ru–Cl). ^{1}H NMR ($CDCl_3$, 295 K); δ 4.15 (s, 3H, MeO), 7.67 (dd, 1H, $J = 7.7$, H_7), 7.95 (dd, 1H, $J = 7.95$ Hz, H_8), 8.12 (dd, 1H, $J = 5.3$ Hz, $J = 8.1$ Hz, H_3), 8.30 (dd, 1H, $J = 0.8$ Hz, $J = 7.7$ Hz, H_9), 8.86 (dd, 1H, $J = 1.3$ Hz, $J = 8.1$ Hz, H_4), 9.34 (dd, 1H, $J = 1.3$ Hz, $J = 5.3$ Hz, H_2). ^{13}C NMR ($CDCl_3$, 295 K): δ 56.5, 121.7, 124.0, 128.7, 131.0, 132.5, 133.4, 135.4, 136.5, 137.8, 156.1, 160.8, 181.8, 182.2, 194.9 (CO), 196.7 (CO).

2.4. X-ray crystallography

Suitable red crystals for the X-ray study were obtained by letting a saturated ethanol solution of complex **4** stand at room temperature. A summary of crystal data and refinement parameters is reported in Table 1. Data were obtained at 100(1) K from a Bruker SMART CCD area detector diffractometer equipped with graphite-monochromated Mo-Kα radiation ($\lambda = 0.71073$ Å) using narrow frames. The SMART program package was used for data

Table 1
Crystal data and structure refinement parameters for complex **4**

Empirical formula	$C_{16}H_9Cl_2NO_5Ru$
Formula weight	467.21
Crystal system, space group	monoclinic, $P2_1/n$
a (Å)	6.1204(6)
b (Å)	13.0328(14)
c (Å)	21.172(2)
β °)	94.081(2)
V (Å^3), Z	1684.5(3), 4
D_{calc} (Mg m^{-3})	1.842
Absorption coefficient (mm^{-1})	1.275
Crystal size (mm)	$0.31 \times 0.04 \times 0.04$
Maximum and minimum transmission factor	0.951–0.692
θ Range for data collection (°)	1.84–28.85
Reflections collected	11098
Independent reflections	4038 ($R_{int} = 0.049$)
Data/restraints/parameters	4038/0/262
Goodness-of-fit on F^2	1.113
Final R indices [$I > 2\sigma(I)$]	$R_1 = 0.0525$, $wR_2 = 0.0911$
R indices (all data)	$R_1 = 0.0753$, $wR_2 = 0.0975$
Largest difference in peak and hole (e Å^{-3})	0.873 and −0.802

collection [16a]. The raw frame data were processed using SAINT [16b] and SADABS [16c]. Subsequent calculations were carried out using the SHELXTL program [16d]. The structure was solved by direct methods and refined on F^2 by full-matrix least-squares techniques. All non-hydrogen atoms were refined with isotropic and subsequent anisotropic displacement parameters. Hydrogen atoms were included in observed positions and refined as free isotropic atoms.

2.5. Electrochemical measurements

Cyclic voltammograms of ligands and complexes were obtained on a Bioanalytical Systems BAS CV-50W electrochemical analyzer. A small capacity measuring cell was equipped with a platinum disc as working electrode, a Ag/10 mM Ag^+ (CH_3CN) reference electrode for nonaqueous solvent, with a platinum wire auxiliary electrode, a mechanical mini-stirrer, and a capillary to supply an inert atmosphere with argon. A 0.1 M solution of tetrabutylammonium tetrafluoroborate in acetonitrile was used as supporting electrolyte.

2.6. Cell culture

The human leukemia cells line (HL-60) was purchased from ATCC (Rockville, USA). The cells were cultivated at 37 °C, 10% CO_2, 100% humidity in Dulbecco's modified Eagle's medium (DME), enriched with glucose and supplemented with 10% fetal bovine serum, non-essential amino acids, antibiotics (penicillin/streptomycin) and antifungals.

2.7. Cytotoxic assay

Small unilamellar liposomes of compounds **1**–**4** (12 μM) were prepared using the injection method described by Kremer et al. [17]. Typically, 0.126 mmol of compound was dissolved in 0.5 mL of ethanol solution (DPPC/ethanol = 10 mg/mL; DPPC, dipalmitoylphosphatidylcholine), which after homogenization was injected over 10 mL of DME with vigorous stirring at 55 °C.

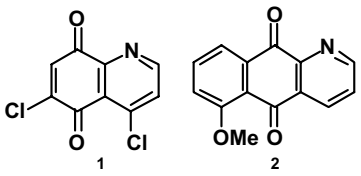
Growth inhibitory effect toward HL-60 cell line was determined by means of MTT colorimetric assay [18]. The cells were seeded into 24-well plates at 4×10^5 cells/well and 0.833 mL (12 μM) of the above solution was added. Culture medium (DME) was added until completion of 1 mL and the final concentration in each well was 10 μM. Triplicate cultures were established for all compounds and for the control drugs. The mixture was incubated at 37 °C in a humid atmosphere containing 10% CO_2 for 24 h. Cell viability was quantified after 0, 4 and 24 h by the MTT method.

3. Results and discussion

3.1. Synthesis and characterization

4,6-Chloroquinoline-5,8-dione (**1**) was prepared according to a reported synthetic method [12]. 6-Methoxybenzo[*g*]quinoline-5,10-dione (**2**) was synthesized through a Diels-Alder reaction of 5-methoxynaphthalene-1,4-dione with azadiene in dichloromethane (7 days, rt); subsequent aromatization with silica gel and chloranil gave compound **2** in 45% yield (Scheme 1).

The dimer complex $[\{Ru(CO)_3Cl_2\}_2]$ reacts in a 1:2 molar ratio with the quinolinedione ligands (**1**, **2**) in refluxing ethanol by cleavage of the chloride bridges, to give neutral mononuclear complexes of the type $[Ru(CO)_2Cl_2(N–O)]$, where N–O = 4,6-dichloroquinoline-5,8-dione (**3**) and 6-methoxybenzo[*g*]quinoline-5,10-dione (**4**). The complexes were isolated as red solids, stable in air at room temperature, and characterized by elemental analysis and NMR and IR spectroscopy. The ^{1}H NMR spectra of the complexes show very slight variations in the positions of the proton resonances of the coordinate quinolinedione ligands with respect to the free ligands. These resonances were assigned with the aid of COSY experiments and by comparison with known values for similar compounds [9,10]. The ^{13}C NMR spectra show the carbon signals of the carbonyl groups in the δ 94–198 ppm range. Their solid-state infrared spectra in KBr pellets show two strong ν(CO) vibrations in the 1990–2070 cm^{-1} range, which indicates that the carbonyl ligands are in a *cis* arrangement, together with the characteristic absorptions assigned to the quinonic



Scheme 1.

ν(C=O) and ν(Ru–Cl). Since the chloride ligands can be mutually *trans* or *cis*, two isomers with a *cis*(CO)*cis*Cl arrangement – due to the asymmetric nature of the dione ligand – or one isomer with a *cis*(CO)*cis*Cl arrangement could be expected.

To obtain an unambiguous characterization an X-ray structural determination of complex **4** was undertaken. Fig. 1 displays a molecular diagram of the complex together with the atom-numbering scheme. The most relevant bond distances and bond angles are collected in Table 2. In the complex, the ruthenium atom shows a distorted octahedral co-ordination sphere with two carbonyl groups bonded to the metal centre in relative *cis* positions [C(1)–Ru–C(2) 88.30(2)°], and two chloride atoms linked in a *trans* disposition [Cl(1)–Ru–Cl(2) 173.86(4)°]. The coordination sphere is completed with the chelating 6-methoxybenzo[*g*]quinoline-5,10-dione ligand bonded to the metal through the nitrogen and oxygen atoms, [C(1)–Ru–O(3) 174.82(17) and C(2)–Ru–N 173.77(17)°]. The quinolinedione ligand is roughly planar and is inclined 7.24(10)° with respect to the equatorial plane of the complex.

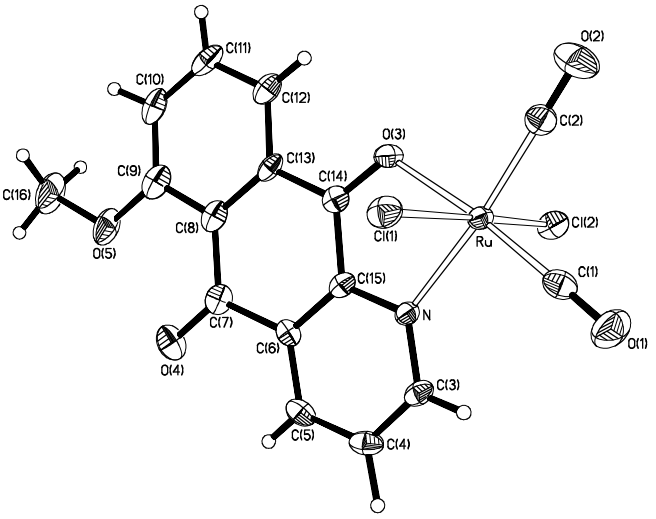


Fig. 1. Molecular structure of complex **4** with the labelling scheme used.

Table 2
Selected bond lengths (Å) and angles (°) for complex **4**

Ru–Cl(1)	2.3819(12)	Ru–Cl(2)	2.3827(12)
Ru–O(3)	2.123(3)	Ru–N	2.123(4)
Ru–C(1)	1.844(5)	Ru–C(2)	1.897(5)
C(1)–O(1)	1.135(6)	C(2)–O(2)	1.106(6)
C(7)–O(4)	1.214(5)	C(14)–O(3)	1.242(5)
Cl(1)–Ru–Cl(2)	173.86(4)	Cl(2)–Ru–C(2)	93.13(15)
Cl(1)–Ru–O(3)	86.39(9)	O(3)–Ru–N	77.28(13)
Cl(1)–Ru–N	87.96(10)	O(3)–Ru–C(1)	174.82(17)
Cl(1)–Ru–C(1)	91.76(15)	O(3)–Ru–C(2)	96.52(17)
Cl(1)–Ru–C(2)	91.08(15)	N–Ru–C(1)	97.83(17)
Cl(2)–Ru–O(3)	88.69(9)	N–Ru–C(2)	173.77(17)
Cl(2)–Ru–N	87.38(10)	C(1)–Ru–C(2)	88.30(2)
Cl(2)–Ru–C(1)	92.83(15)		
Ru–O(3)–C(14)	114.9(3)	Ru–N–C(15)	112.9(3)
Ru–C(1)–O(1)	178.9(5)	Ru–C(2)–O(2)	178.8(5)

The Ru–N [2.123(4) Å], Ru–Cl [2.3819(12) and 2.3827(12) Å] and Ru–C [1.844(5) and 1.897(5) Å] distances compare well to those found in the related ruthenium complexes *trans*(Cl)-[Ru(CO)$_2$Cl$_2$(4,4′-dimethyl-2,2′-bipyridine)] [1b] [Ru–N, average 2.1235(7); Ru–Cl *av.* 2.3975(2); Ru–C *av.* 1.8725(10) Å] and *cis*-[Ru(6,6′-dimethoxicarbonyl-2,2′-bipyridine)(CO)$_2$Cl$_2$] [7] [Ru–N, average 2.1367(14); Ru–Cl *av.* 2.41515(7); Ru–C *av.* 1.897(2) Å]. As expected, the CO quinone group bonded to the metal centre shows a larger C–O distance [1.242(5) Å] than that of the free CO [1.214(5) Å]. The Ru–O bond distance [2.123(3) Å] is identical to that of the Ru–N bond length. The mean carbonyl distances [C–O, average 1.1205(6) Å] are similar to those found in the above-mentioned ruthenium(II) complexes.

3.2. Redox behaviour

The electrochemical properties of the ligands and their ruthenium complexes were studied using acetonitrile as solvent and tetrabutylammonium tetrafluoroborate as the supporting electrolyte. Cyclic voltammograms (CV) show similar chemical redox behaviour for the free ligands. The voltammograms show two quasi-reversible electrochemical reactions [**1**: $E_{1/2} = -0.72$ ($\Delta E = 0.20$) and $E_{1/2} = -1.46$ ($\Delta E = 0.36$) V. **2** (Fig. 2A): $E_{1/2} = -0.96$ ($\Delta E = 0.98$, peak a/a') and $E_{1/2} = -1.37$ ($\Delta E = 0.12$, peak b/b') V] that correspond to the formation of semiquinolinedione $(N–O)^-$ and the dianion $(N–O)^{2-}$, respectively. Moreover, compound **2** shows a quasi-reversible oxidation maximum at $E_{1/2} = 0.84$ ($\Delta E = 0.36$, peak c/c') V that corresponds of the redox reaction of the methoxy group. The i_{pa}/i_{pc} ratio is ≈1 for the two systems, indicating that the electrogenerated semiquinolinedione and dianionic compounds are stable in acetonitrile medium.

In the CV of ruthenium complexes the Ru(II)/Ru(III) peaks were not observed. Complex **3** is slightly unstable in acetonitrile and the CV shows only the peaks of free quinolinquinone (**1**) and free chloride. Complex **4** (Fig. 2B) shows two reversible redox pairs at $E_{1/2} = -0.42$ ($\Delta E = 0.65$, peak a/a') V and $E_{1/2} = -1.20$ ($\Delta E = 0.60$, peak b/b') V. The positive potential displacement of the peaks a/a' and b/b' respect to the free ligand is in accordance with the reduction of coordinated quinolinquinone ligand in the complex. The oxidation maximum of 1.66 V (peak c) corresponds to the redox reaction of the –OMe group in the complex, while for the respective free ligand this reaction occurs at 1.02 V (Fig. 2A, peak c).

3.3. Antitumor activity

The *in vitro* antitumor activity of the free ligands (**1**, **2**) and ruthenium complexes (**3**, **4**) was evaluated against HL-60 leukemia cells (human leukemia), compared with daunorubicine and cisplatin as reference drugs. Due to the low solubility of the ruthenium complexes, the cytotoxic evaluations were carried out at a concentration of 10 μM.

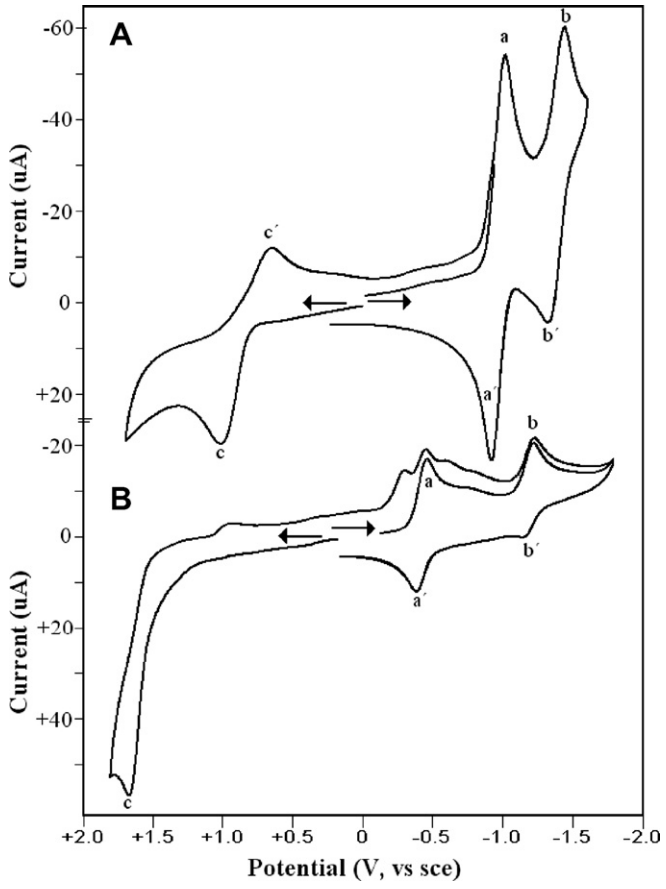


Fig. 2. Cyclic voltammograms in acetonitrile with 0.1 M TFBTBA. Scan rate 200 mV s^{-1}. Pt as working electrode: (A) ligand **2**; (B) complex **4**.

The quinolinedione compounds (**1**, **2**) exhibit cell grown inhibition comparable to that of the reference drug daunorubicine. Thus, at a 10 μM concentration, **2** is the most active with 71.6% of cell inhibition at 4 h and 100% after 24 h, compared with daunorubicine, which showed 12.4% and 99.1% at 4 and 24 h, respectively. Complex **3** shows a very low cytotoxic activity after 4 h, while complex **4** shows 8.7% of inhibition cell after 4 h, a similar value to those shown by *cis*platin (9.7%). Moreover, the cell inhibition values after 24 h decreases dramatically (to 0%), probably due to a decomposition process. In fact, the starting red colour of the solutions darkens with time.

In conclusion, the pronounced in vitro antitumoral activity shown by the quinolinedione compounds decreases after their coordination with the organometallic ruthenium(II) fragment. This effect is possibly associated to the decrease of the oxidizing capability of the quinolinedione system when it is bonded to the ruthenium centre (Fig. 2). Therefore, it seems reasonable to think that the redox cycling process is involved in the cytotoxic activity of the quinone compounds [19].

4. Conclusions

In summary, we report the synthesis of new dicarbonyldichlororuthenium(II) complexes containing quinolinediones as N,O-donor chelate ligands. The complexes were fully characterized by analytical, spectroscopic and electrochemical means. The molecular structure of complex **4** was determined by X-ray diffraction methods, indicating that the chloride ligands are bonded to the metal in relative *trans* position. The *in vitro* biological evaluation showed that the free quinolinediones exhibit a remarkable antitumoral activity against HL-60 leukemia cell lines. However, the corresponding ruthenium(II) complexes show a marginal activity, probably due to the loss of the oxidizing capability of the whole entity after co-ordination of the quinoline moiety.

Acknowledgements

We thank the "Fondo de Desarrollo Científico y Tecnológico" (FONDECYT), Chile (Project Nos. 3040053 and 1060597), and Factoria de Cristalización, CONSOLIDER INGENIO-2010 for financial support. We sincerely thank Dr. Ana María Edwards for the laboratory facilities to evaluate cytotoxic data.

Appendix A. Supplementary material

CCDC 606331 contains the supplementary crystallographic data for this paper. These data can be obtained free of charge via http://www.ccdc.cam.ac.uk/conts/retrieving.html, or from the Cambridge Crystallographic Data Centre, 12 Union Road, Cambridge CB2 1EZ, UK; fax: (+44) 1223-336-033; or e-mail: deposit@ccdc.cam.ac.uk. Supplementary data associated with this article can be found, in the online version, at doi:10.1016/j.poly.2007.08.014.

References

[1] (a) D.H. Gibson, J. Wu, M.S. Mashuta, Inorg. Chim. Acta 358 (2006) 309;
(b) P. Homanen, M. Haukka, S. Luukkanen, M. Ahlgrén, T.A. Pakkanen, Eur. J. Inorg. Chem. (1999) 101;
(c) T.B. Hadda, I. Zidane, S. Moya, H. Le Bozec, Polyhedron 15 (1996) 1571;
(d) P. Homanen, M. Haukka, M. Ahlgrén, T.A. Pakkanen, P.N.W. Baxter, R.E. Benefield, J.A. Connor, J. Organomet. Chem. 552 (1998) 205.
[2] (a) P.A. Anderson, G.F. Strouse, J.A. Treaway, F.R. Keene, T.J. Meyer, Inorg. Chem. 33 (1994) 3863;
(b) P.A. Anderson, G.B. Deacon, K.H. Haarmaan, F.R. Keene, T.J. Meyer, D.A. Reitsma, B.W. Skelton, G.F. Strouse, N.C. Thomas, J.A. Treadway, A.H. White, Inorg. Chem. 34 (1995) 6145.
[3] M. Haukka, J. Kiviaho, M. Ahlgrén, T.A. Pakkanen, Organometallics 14 (1995) 825.
[4] T.B. Hadda, I. Zidane, S.A. Moya, H. Le Bozec, Polyhedron 15 (1996) 1571.
[5] J.M. Kelly, C.M. O'Connell, J.G. Vos, Inorg. Chim. Acta 64 (1982) L75.
[6] (a) D. Mulhern, Y. Lan, S. Brooker, J.F. Gallagher, H. Görls, S. Rau, J.G. Vos, Inorg. Chim. Acta 359 (2006) 736;
(b) D. Ooyama, T. Kobayashi, K. Shiren, K. Tanaka, J. Organomet. Chem. 665 (2003) 107.
[7] P.A. Anderberg, M.M. Harding, I.J. Luck, P. Turner, Inorg. Chem. 41 (2002) 1365.

[8] (a) Z. Afrabiasi, E. Sinn, J. Chen, Y. Ma, A.L. Rheingold, L.N. Zakharov, N. Rath, S. Padhye, Inorg. Chim. Acta 357 (2004) 271;
(b) I. Gómez-Monterrey, P. Camiglia, P. Grieco, M.V. Diurno, A. Bolognese, P. La Colla, E. Novellino, Bioorg. Med. Chem. 11 (2003) 3769;
(c) T. Fryatt, H.I. Pettersson, W.P. Gardipee, K.C. Bray, S.J. Green, A.M.Z. Slawin, H.D. Beall, C.J. Moody, Bioorg. Med. Chem. 12 (2004) 1667.

[9] (a) G. Sava, S. Zorzet, T. Girardi, G. Mestroni, G. Zassinovich, Eur. J. Cancer Clin. Oncol. 20 (1984) 841;
(b) M. Clarke, Coord. Chem. Rev. 236 (2003) 209;
(c) M. Clarke, F. Zhu, D.R. Frasca, Chem. Rev. 99 (1999) 2511.

[10] (a) Z. Guo, P.J. Sadler, Angew. Chem., Int. Ed Engl. 38 (1999) 1512;
(b) S. Cauci, P. Viglino, G. Exposito, F. Quadrifoglio, J. Inorg. Biochem. 43 (1991) 739;
(c) G. Sava, Ruthenium Compounds in Cancer Chemoterapy, in: S.P. Fricher (Ed.), Chapman & Hall, London, UK, 1994;
(d) G. Sava, S. Pacor, S. Zorzet, E. Alessio, G. Mestroni, Pharmacol. Res. 21 (1989) 617.

[11] A.H. Velder, H. Kooijman, A.L. Speck, J.G. Haasnoot, D. de Vos, J. Reedijk, Inorg. Chem. 39 (2000) 2966.

[12] R.A. Tapia, Y. Prieto, F. Pautet, B. Fenet, H. Fillion, Magn. Reson. Chem. 40 (2002) 165.

[13] L.F. Tietze, C. Güntner, K.M. Gericke, I. Schuberth, G. Bunkoczi, Eur. J. Org. Chem. (2005) 2459.

[14] E. Gómez-Bengoa, A.M. Echavarren, J. Org. Chem. 56 (1991) 3497.

[15] K.T. Potts, D. Bhattacharjee, E.B. Walsh, J. Org. Chem. 5 (1986) 2011.

[16] (a) SMART Software for CCD Diffractometers, Bruker AXS, Madison, WI, 2000;
(b) SAINT Software for CCD Diffractometers, Bruker AXS, Madison, WI, 2000;
(c) G.M. Sheldrick, SADABS, Program for Corrections of Area Detector Data, University of Göttingen, Goöttingen, Germany, 1999;
(d) G.M. Sheldrick, SHELXL-97 Program for Crystal Structure Refinement, University of Göttingen, Göttingen, Germany, 1997.

[17] J.M.H. Kremer, M.W.J. v.d. Esker, C. Pathmamanoharan, P.H. Wieserma, Biochemistry 16 (1977) 3932.

[18] T. Mosmann, J. Immun. Methods 65 (1983) 55.

[19] F.C. de Abreu, P.A. de L. Ferraz, M.O.F. Goulart, J. Braz. Chem. Soc. 13 (2002) 19.

much lesser degree than squarates. Indeed, numerous lanthanide squarates [21] and squarate complexes with transition metals [22] have been reported as well as structures of all the alkaline-earth squarates [23]. On the contrary, less structure of croconate metal complexes are known. Lanthanides and actinides croconates have been reported [24] and also some complexes with transition metal ions [25] and alkalines [26] but only one alkaline-earth croconate is known [27]. These structures have demonstrated that the croconate ligand can act as a polydentate ligand and that high dimensionalities structure involving this dianion are scarce. Only two 3D frameworks have been reported in the literature involving silver and sodium ions [28] or cadmium ions [29]. The present study deals with the synthesis by soft chemistry of two new croconate complexes, $Ca(\mu_3\text{-}C_5O_5)(H_2O)_3$ (**I**) and $Ca_2(\mu_4\text{-}C_5O_5)(\mu_6\text{-}C_2O_4)(H_2O)$ (**II**), their crystal structure determination by single-crystal X-ray diffraction, their infra-red spectra and thermal behaviour. The 2D or 3D frameworks display croconates and/or oxalates connected to seven- or eightfold coordinated calcium atoms through unusual bridging and chelating modes emphasizing new rich possibilities to design open-frameworks. The thermal decomposition of mixed calcium oxalato-croconate has revealed a high thermal stability which allows to consider possible applications in catalysis.

2. Experimental

2.1. Syntheses and preliminary characterisations

All chemicals were commercially available and used as received. Crystals of calcium croconate trihydrate $Ca(C_5O_5)(H_2O)_3$ (**I**) and calcium oxalato-croconate hydrate $Ca_2(C_5O_5)(C_2O_4)(H_2O)$ (**II**) were obtained through a mild chemistry route. High purity (98%) croconic acid was purchased from Alfa Aesar and calcium nitrate from BLB (Laboratoire du Bois de Boulogne, Puteaux, France). An aqueous solution of croconic acid (0.70 mmol, 10 mL) was added dropwise to an aqueous solution of calcium nitrate (0.35 mmol, 10 mL). The evaporation of the solution at room temperature led to the formation of yellow transparent crystals after about three days. Actually, both families of crystals **I** and **II** have been indifferently obtained and the major product croconate **II** contains croconate **I** as an impurity. In spite of several repeated attempts, we were not able to prepare croconate **I** in pure form and hence, its characterization dealt only with the single-crystal structure and the infrared measurement. We can suppose that the formation of crystals **I** occurs first and then croconate decomposition into oxalate occurs rapidly leading to **II**, which is the main product. A similar decomposition process has been observed for squarate oxidized into oxalate in lanthanide oxalato-squarates due to the role of metal oxidant agent [21c]. However, the degradation of the croconate into oxalate could have been induced by the pH or dilution as already observed by Deguenon [30].

High-quality X-ray powder diffraction data of grounded crystals of **II** were collected at room temperature with a Siemens D500 diffractometer, with the parafocusing Bragg–Brentano geometry, using monochromatic Cu $K\alpha_1$ radiation ($\lambda = 1.5406$ Å) selected with an incident beam curved-crystal germanium monochromator [31]. The diffraction pattern was collected over the angular range 8–60° (2θ) with a counting time of 13 s step^{-1} and a step length of 0.02° (2θ). The extraction of the peak positions was carried out with the Socabim program PROFILE, which is a part of the DIFFRACT-AT software package supplied by Bruker AXS. Pattern indexing was performed with the program DICVOL-04 [32] and refinement of the unit-cell parameters by means of the evaluation program NBS*AIDS-83 [33].

Infrared spectra of compounds **I** and **II** have been recorded using an Equinox 55 Bruker spectrometer as KBr disks in the range 400–4000 cm^{-1}. In addition to the expected broad and intense absorptions in the 3000–3700 cm^{-1} range assigned to the OH stretching frequency of water molecules, the infrared spectra of both compounds **I** and **II** show a strong absorption centered around 1530 cm^{-1} which is the signature of the presence of the croconate ligand [17,34,35]. This vibrational mode represents a mixture of C–O and C–C stretching motions characteristic of the $(C_nO_n)^{2-}$ dianion. The presence of the oxalate group in **II** is evidenced by a medium isolated absorption at 1325 cm^{-1} which is the signature of the C–O stretching motions of the oxalate [36,37]. Finally, the coordinated carbonyl groups of croconate and oxalate are characterized by a medium absorption in the 1600–1700 cm^{-1} range [34–37].

2.2. Single-crystal data collections

Suitable single-crystals of croconates **I** and **II** were mounted on a four-circle Nonius Kappa CCD area-detector diffractometer (**I**) or an APEX II Bruker-AXS (**II**) diffractometer (Centre de Diffractométrie X, UMR CNRS 6226, Rennes), using Mo $K\alpha$ radiation ($\lambda = 0.71073$ Å). Intensities were collected by means of the program COLLECT [38] for **I** and Bruker SMART included in the APEX-2 programmes suite [39] for **II**. Reflection indexing, Lorentz-polarisation correction, peak integration and background determination were carried out with the program DENZO of the KappaCCD software package [40] for **I** and with the program Bruker SAINT [41] for **II**. Unit-cell parameters refinement and frame scaling were performed with the program SCALEPACK [40] for **I** and with Bruker SMART [39] for **II**. Numerical absorption corrections were performed using the analytical procedure [42] included in the WinGX program suite [43] for **I** and a semi-empirical absorption correction included in the program SADABS [44] for **II**. The resulting sets of hkl reflections were used for structure refinement. Crystallographic data and details on data collection are listed in Table 1.

Structure drawings were carried out with DIAMOND-2.1e, supplied by Crystal Impact [45].

2.3. Thermal analyses

Temperature-dependent X-ray diffraction (TDXD) for **II** was performed under flowing air with a powder diffractometer equipped with a curved-position-sensitive detector (INEL CPS 120) and a high-temperature attachment from Rigaku. The detector was used in a semi-focusing arrangement by reflection (Cu $K\alpha_1$ radiation) as described elsewhere [46]. With this geometry, the stationary sample is deposited on a flat sample holder located at the centre of the goniometer. An angle of 6° was selected between the incident beam and the surface of the sample. To ensure satisfactory counting statistics, a counting time of 2700 s/pattern was selected for the thermal decomposition. Decomposition was carried out in dynamic air with a heating rate of 5 °C h^{-1} between 20 and 400 °C and 25 °C h^{-1} until 600 °C. Temperature calibration was made with standard materials in the involved temperature range.

Thermogravimetric (TG) measurement for **II** was performed with a Rigaku Thermoflex instrument in dynamic air. The measurement was carried out with a heating rate of 5 °C h^{-1} between 20 and 400 °C and 25 °C h^{-1} until 1000 °C.

3. Results and discussion

3.1. Structure resolutions of compounds *I* and *II*

The diffraction lines of the powder pattern of **II** have been indexed with an orthorhombic unit cell, with the following refined parameters $a = 14.907(2)$ Å, $b = 7.2519(8)$ Å, $c = 9.363(1)$ Å, $V = 1012.2(1)$ $Å^3$ [$M_{20} = 41$, $F_{30} = 75(0.0069, 58)$]. These parameters are in agreement with those found from single-crystal X-ray diffraction (Table 1).

The structures of croconates **I** and **II** were solved in the space groups *Pbca* and *Pnma*, respectively, in agreement with the extinction conditions. The heavy atoms, as well as a part of the croconate groups, were located by direct methods with the program SIR-97 [47] for **I** and interpretation of the Patterson function with SHELXS-97 [48] for **II**. The remaining atoms, including hydrogen atoms, have been localized from successive difference Fourier maps with SHELXL-97 [49]. The positions of the hydrogen atoms were refined with soft constraints applied to the distances to their water O atoms [0.96(1) Å] and their isotropic displacement parameters were fixed equal to one and half time the U_{eq} value of their parent O atoms. Details of the final refinement are given in Table 1. The atomic coordinates, together with the equivalent displacement parameters are reported in Tables 2 and 3, and the selected bond distances and angles in Tables 4 and 5.

Table 1
Crystallographic data for $Ca(\mu_3\text{-}C_5O_5)(H_2O)_3$ (**I**) and $Ca_2(\mu_4\text{-}C_5O_5)(\mu_6\text{-}C_2O_4)(H_2O)$ (**II**)

Compound	I	II
Empirical formula	$CaC_5O_8H_6$	$Ca_2C_7O_{10}H_2$
Crystal system	orthorhombic	orthorhombic
Instrumental measurement	KCCD	APEX
Temperature (K)	293	293
Space group	*Pbca* (No. 61)	*Pnma* (No. 62)
Crystal size (mm)	$0.09 \times 0.26 \times 0.17$	$0.03 \times 0.16 \times 0.03$
a (Å)	6.4156(1)	14.9097(5)
b (Å)	15.1494(3)	7.2568(3)
c (Å)	16.2879(3)	9.3686(2)
Volume ($Å^3$)	1583.06(5)	1013.65(6)
Z	8	4
Formula weight (g mol^{-1})	234.75	326.24
ρ_{calc} (g cm^{-3})	1.965	2.138
λ (Mo Kα) (Å)	0.71073	0.71073
Absorption correction	analytical	multi-scan
θ Range (°)	2.69–27.48	2.57–27.49
Index ranges	$-7 \leqslant h \leqslant 8$, $-19 \leqslant k \leqslant 19$, $-20 \leqslant l \leqslant 21$	$-9 \leqslant h \leqslant 19$, $-9 \leqslant k \leqslant 9$, $-8 \leqslant l \leqslant 12$
Unique data	1815	1263
Observed data [$I > 2\sigma(I)$]	1591	998
R_1 [$I > 2\sigma(I)$]	0.0378	0.0344
R_1 (all data)	0.0429	0.0497
wR_2 [$I > 2\sigma(I)$]	0.0975	0.0919
wR_2 (all data)	0.1027	0.0961
Refinement method	full-matrix least-squares on $\|F^2\|$	full-matrix least-squares on $\|F^2\|$
Goodness of fit on F^2	1.113	1.093
Number of variables	146	110
Number of restraints	9	3
Largest difference map in peak and hole (e $Å^{-3}$)	0.570 and −0.597	0.394 and −0.572

Table 2
Positional and equivalent isotropic atomic displacement parameters with their standard deviations for $Ca(\mu_3\text{-}C_5O_5)(H_2O)_3$ (**I**)

Atom	*x/a*	*y/b*	*z/c*	U^{a}_{eq}/U_{iso} (Å^2)
Ca	−0.12730(6)	0.08772(2)	0.58299(2)	0.0193(2)
O1	0.2965(2)	0.31225(9)	0.29587(9)	0.0277(3)
O2	0.2746(2)	0.25679(9)	0.46318(8)	0.0266(3)
O3	0.1090(2)	0.06972(9)	0.46373(8)	0.0234(3)
O4	0.0561(2)	0.01513(8)	0.30013(8)	0.0255(3)
O5	0.1633(2)	0.16762(9)	0.18882(9)	0.0293(3)
C1	0.2339(3)	0.2387(1)	0.3182(1)	0.0208(4)
C2	0.2209(3)	0.2097(1)	0.4036(1)	0.0200(4)
C3	0.1150(3)	0.0913(1)	0.3189(1)	0.0189(4)
C4	0.1435(3)	0.1197(1)	0.4035(1)	0.0189(4)
C5	0.1680(3)	0.1654(1)	0.2648(1)	0.0203(4)
Ow1	−0.3646(2)	0.0836(1)	0.4687(1)	0.0331(4)
H11	−0.409(5)	0.031(1)	0.442(1)	0.050
H12	−0.355(4)	0.126(1)	0.425(1)	0.050
Ow2	−0.4716(2)	0.0455(1)	0.63796(9)	0.0310(4)
H21	−0.488(4)	0.024(2)	0.6922(8)	0.047
H22	−0.575(3)	0.090(1)	0.630(2)	0.047
Ow3	0.2052(2)	0.16361(9)	0.61086(9)	0.0288(3)
H31	0.249(4)	0.192(2)	0.5617(9)	0.043
H32	0.207(4)	0.207(1)	0.653(1)	0.043

[a] $U_{eq} = (1/3)\sum_i\sum_j U_{ij}a^*_i a^*_j \boldsymbol{a}_i \cdot \boldsymbol{a}_j$.

Table 3
Positional and equivalent isotropic atomic displacement parameters with their standard deviations for $Ca_2(\mu_4\text{-}C_5O_5)(\mu_6\text{-}C_2O_4)(H_2O)$ (**II**)

Atom	*x/a*	*y/b*	*z/c*	U^{a}_{eq}/U_{iso} (Å^2)
Ca1	0.68616(5)	0.7500	0.49596(7)	0.0162(2)
Ca2	0.76692(5)	0.7500	0.87337(7)	0.0138(2)
O1	0.6284(2)	0.7500	1.0281(3)	0.0310(7)
O2	0.6236(2)	0.7500	0.7283(3)	0.0191(6)
O3	0.9289(2)	0.7500	0.8627(3)	0.0283(7)
O4	0.8231(2)	0.7500	0.6164(3)	0.0202(6)
O5	0.9420(2)	0.7500	0.3579(3)	0.0388(9)
O6	0.6995(1)	1.0655(3)	0.5828(2)	0.0191(4)
O7	0.7449(1)	0.9346(3)	0.3059(2)	0.0212(4)
C1	0.5580(3)	0.7500	0.9600(4)	0.0189(8)
C2	0.5549(2)	0.7500	0.8042(4)	0.0162(8)
C3	0.9617(2)	0.7500	0.7394(4)	0.0180(8)
C4	0.9066(3)	0.7500	0.6108(4)	0.0164(8)
C5	0.9647(3)	0.7500	0.4848(4)	0.0216(9)
C6	0.7734(2)	0.8575(4)	1.1942(2)	0.0165(5)
Ow1	0.5429(2)	0.7500	0.4008(3)	0.046(1)
H11	0.495(2)	0.7500	0.468(4)	0.070
H12	0.516(3)	0.7500	0.309(2)	0.070

[a] $U_{eq} = (1/3)\sum_i\sum_j U_{ij}a^*_i a^*_j \boldsymbol{a}_i \cdot \boldsymbol{a}_j$.

3.2. Description of the structures

The crystal structure of $Ca(\mu_3\text{-}C_5O_5)(H_2O)_3$ (**I**) can be described as a 2D arrangement of eightfold coordinated Ca atoms and croconate dianions. The framework displays infinite corrugated sheets in the *ab*-plane which are piled up along the *c*-axis (Fig. 1). The sheets fit into each other through non-coordinated O5 atom of croconate group and Ow3 coordination water molecule. All the water molecules belong to the CaO_8 polyhedra, and then the intersheets are free any molecule. The cohesion of the structure is provided by hydrogen bonds. Within one sheet, two CaO_8 polyhedra are linked together by O3–O3$^{(ii)}$ shared-edge to form $[Ca_2O_{14}]$ dimers (Fig. 2). The Ca–Ca

Table 4
Bond distances (Å) and angles (°) with their standard deviations for $Ca(\mu_3\text{-}C_5O_5)(H_2O)_3$ (**I**)

Within the CaO_8 bicapped trigonal prism			
Ca–O1$^{(i)}$	2.536(1)	Ca–Ow1	2.406(2)
Ca–O3	2.479(1)	Ca–Ow3	2.465(2)
Ca–O3$^{(ii)}$	2.506(1)	Ca–O2$^{(i)}$	2.552(1)
Ca–O4$^{(ii)}$	2.502(1)	Ca–Ow2	2.468(2)
b		*c*	
O4$^{(ii)}$–O1$^{(i)}$	3.216(2)	Ow2–O3$^{(ii)}$	3.346(2)
O1$^{(i)}$–Ow3	3.052(2)	Ow2–O4$^{(ii)}$	2.994(2)
Ow3–O4$^{(ii)}$	3.499(2)	Ow2–Ow1	2.899(2)
		Ow2–O1$^{(i)}$	2.961(2)
O3$^{(ii)}$–Ow1	3.384(2)		
Ow1–O3	3.048(2)	O2$^{(i)}$–Ow3	3.246(2)
O3–O3$^{(ii)}$	2.796(3)	O2$^{(i)}$–O3	3.596(2)
		O2$^{(i)}$–Ow1	2.807(2)
h		O2$^{(i)}$–O1$^{(i)}$	2.855(2)
O3$^{(ii)}$–O4$^{(ii)}$	2.811(2)		
O3–Ow3	2.854(2)		
Ow1–O1$^{(i)}$	4.274(2)		
Angles within the square bases			
O3$^{(ii)}$–O4$^{(ii)}$–O1$^{(i)}$	105.43(5)	O3–O3$^{(ii)}$–O4$^{(ii)}$	96.77(7)
O4$^{(ii)}$–O1$^{(i)}$–Ow1	72.47(4)	O3$^{(ii)}$–O4$^{(ii)}$–Ow3	83.85(5)
O1$^{(i)}$–Ow1–O3$^{(ii)}$	80.05(5)	O4$^{(ii)}$–Ow3–O3	81.88(5)
Ow1–O3$^{(ii)}$–O4$^{(ii)}$	100.56(6)	Ow3–O3–O3$^{(ii)}$	97.46(7)
O3–Ow1–O1$^{(i)}$	78.93(4)		
Ow1–O1$^{(i)}$–Ow3	73.56(4)		
O1$^{(i)}$–Ow3–O3	106.98(6)		
Ow3–O3–Ow1	99.14(6)		
Croconate groups			
C1–C2	1.461(2)	C1–C2–C3	107.5(2)
C2–C3	1.451(3)	C2–C3–C4	108.8(2)
C3–C4	1.455(3)	C3–C4–C5	108.3(2)
C4–C5	1.467(2)	C4–C5–C1	106.7(2)
C5–C1	1.474(2)	C5–C1–C2	108.6(2)
C1–O1	1.239(2)	O1–C1–C2	124.7(2)
C2–O2	1.252(2)	O2–C2–C3	129.1(2)
C3–O3	1.259(2)	O3–C3–C4	122.5(2)
C4–O4	1.252(2)	O4–C4–C5	128.9(2)
C5–O5	1.238(2)	O5–C5–C1	125.2(2)

Possible hydrogen bonds

D–H···A	*d*(D–H) (Å)	*d*(H···A) (Å)	∠D–H···A (°)	*d*(D···A) (Å)
Ow1–H11···Ow2$^{(iii)}$	0.96(1)	1.90(1)	160(2)	2.818(2)
Ow1–H12···O5$^{(iv)}$	0.96(1)	1.97(2)	157(2)	2.870(2)
Ow2–H21···O4$^{(v)}$	0.95(1)	1.91(1)	173(2)	2.848(2)
Ow2–H22···Ow3$^{(vi)}$	0.95(1)	1.83(1)	173(3)	2.775(2)
Ow3–H31···O2	0.95(1)	1.89(1)	167(3)	2.824(2)
Ow3–H32···O5$^{(vii)}$	0.943(9)	2.01(2)	150(2)	2.867(2)

Symmetry codes: (i) $-1/2+x$, $1/2-y$, $1-z$; (ii) $-x$, $-y$, $1-z$; (iii) $-x-1$, $-y$, $-z+1$; (iv) $x-1/2$, y, $-z+1/2$; (v) $-x-1/2$, $-y$, $z+1/2$; (vi) $x-1$, y, z; (vii) x, $1/2-y$, $z+1/2$; (viii) $1/2+x$, $1/2-y$, $1-z$.

Table 5
Bond distances (Å) and angles (°) with their standard deviations for $Ca_2(\mu_4\text{-}C_5O_5)(\mu_6\text{-}C_2O_4)(H_2O)$ (**II**)

Within the Ca1O$_7$ pentagonal bipyramid			
Ca1–O7	2.394(2)	Ca1–Ow1	2.314(3)
Ca1–O6	2.438(2)	Ca1–O4	2.332(3)
Ca1–O2	2.368(2)		
Ca1–O6$^{(i)}$	2.438(2)		
Ca1–O7$^{(i)}$	2.394(2)		
Pentagonal basis			
O7–O6	2.845(2)	O7$^{(i)}$–O7–O6	109.51(5)
O6–O2	2.895(2)	O7–O6–O2	104.97(8)
O2–O6$^{(i)}$	2.895(2)	O6–O2–O6$^{(i)}$	104.6(1)
O6$^{(i)}$–O7$^{(i)}$	2.845(2)	O2–O6$^{(i)}$–O7$^{(i)}$	104.97(8)
O7$^{(i)}$–O7	2.680(4)	O6$^{(i)}$–O7$^{(i)}$–O7	109.51(5)
O7–Ow1	3.413(3)	O7–O4	3.409(3)
O6–Ow1	3.687(3)	O6–O4	2.956(2)
O2–Ow1	3.296(4)	O2–O4	3.153(4)
O6$^{(i)}$–Ow1	3.687(3)	O6$^{(i)}$–O4	2.956(2)
O7$^{(i)}$–Ow1	3.413(3)	O7$^{(i)}$–O4	3.409(3)
Ow1–Ca1–O4	173.7(1)		
Within the Ca2O$_8$ bicapped trigonal prism			
Ca2–O3	2.417(3)	Ca2–O6$^{(iii)}$	2.428(2)
Ca2–O1	2.523(3)	Ca2–O7$^{(ii)}$	2.381(2)
Ca2–O2	2.532(3)	Ca2–O4	2.549(3)
Ca2–O7$^{(iii)}$	2.381(2)	Ca2–O6$^{(ii)}$	2.428(2)
b		*c*	
O7$^{(iii)}$–O3	3.497(3)	O4–O2	3.153(4)
O3–O6$^{(iii)}$	3.115(3)	O4–O7$^{(iii)}$	3.068(2)
O6$^{(iii)}$–O7$^{(iii)}$	2.845(2)	O4–O3	2.795(4)
		O4–O7$^{(ii)}$	3.068(2)
O2–O7$^{(ii)}$	3.100(3)		
O7$^{(ii)}$–O1	3.626(3)	O6$^{(ii)}$–O6$^{(iii)}$	2.677(4)
O1–O2	2.810(4)	O6$^{(ii)}$–O1	2.939(3)
		O6$^{(ii)}$–O7$^{(ii)}$	2.845(2)
		O6$^{(ii)}$–O3	3.115(3)
h			
O2–O7$^{(iii)}$	3.100(3)		
O7$^{(ii)}$–O3	3.497(3)		
O1–O6$^{(iii)}$	2.939(3)		
Angles within the square bases			
O2–O7$^{(iii)}$–O3	91.20(7)	O2–O7$^{(iii)}$–O6$^{(iii)}$	96.76(8)
O7$^{(iii)}$–O3–O7$^{(ii)}$	81.76(9)	O7$^{(iii)}$–O6$^{(iii)}$–O1	77.61(7)
O3–O7$^{(ii)}$–O2	91.20(7)	O6$^{(iii)}$–O1–O2	101.3(1)
O7$^{(ii)}$–O2–O7$^{(iii)}$	95.2(1)	O1–O2–O7$^{(iii)}$	75.50(7)
O1–O7$^{(ii)}$–O3	83.42(6)		
O7$^{(ii)}$–O3–O6$^{(iii)}$	85.83(8)		
O3–O6$^{(iii)}$–O1	103.01(8)		
O6$^{(iii)}$–O1–O7$^{(ii)}$	86.13(8)		
Croconate groups			
C1$^{(iv)}$–C2$^{(iv)}$	1.460(5)	C1$^{(iv)}$–C2$^{(iv)}$–C3	108.2(3)
C2$^{(iv)}$–C3	1.448(5)	C2$^{(iv)}$–C3–C4	107.9(3)
C3–C4	1.458(5)	C3–C4–C5	109.4(3)
C4–C5	1.465(5)	C4–C5–C1$^{(iv)}$	105.8(3)
C5–C1$^{(iv)}$	1.485(5)	C5–C1$^{(iv)}$–C2$^{(iv)}$	108.6(3)
C1$^{(iv)}$–O1$^{(iv)}$	1.229(5)	O1$^{(iv)}$–C1$^{(iv)}$–C2$^{(iv)}$	123.1(4)
C2$^{(iv)}$–O2$^{(iv)}$	1.247(4)	O2$^{(iv)}$–C2$^{(iv)}$–C3	128.8(3)
C3–O3	1.255(4)	O3–C3–C4	122.7(3)
C4–O4	1.246(5)	O4–C4–C5	128.7(3)
C5–O5	1.236(4)	O5–C5–C1$^{(iv)}$	126.3(3)

Table 5 (*continued*)

Oxalate groups			
C6–C6$^{(i)}$	1.560(5)	O6$^{(iii)}$–C6–O7$^{(v)}$	127.1(3)
C6–O6$^{(iii)}$	1.252(3)	O6$^{(ii)}$–C6$^{(i)}$–O7$^{(vi)}$	127.1(3)
C6–O7$^{(v)}$	1.260(3)	C6$^{(i)}$–C6–O6$^{(iii)}$	116.5(2)
C6$^{(i)}$–O6$^{(ii)}$	1.252(3)	C6$^{(i)}$–C6–O7$^{(v)}$	116.4(2)
C6$^{(i)}$–O7$^{(vi)}$	1.260(3)	C6–C6$^{(i)}$–O6$^{(ii)}$	116.5(2)
		C6–C6$^{(i)}$–O7$^{(vi)}$	116.4(2)

Possible hydrogen bonds

D–H···A	*d*(D–H) (Å)	*d*(H···A) (Å)	∠D–H···A (°)	*d*(D···A) (Å)
Ow1–H11···O3$^{(vii)}$	0.95(1)	1.87(2)	163(4)	2.793(4)
Ow1–H12···O5$^{(viii)}$	0.95(1)	1.91(2)	169(4)	2.853(4)

Symmetry codes: (i) x, $3/2 - y$, z; (ii) $3/2 - x$, $-1/2 + y$, $1/2 + z$; (iii) $3/2 - x$, $2 - y$, $1/2 + z$; (iv) $1/2 + x$, $3/2 - y$, $3/2 - z$; (v) x, y, $1 + z$; (vi) x, $3/$

distance within one dimer is 4.128(1) Å which is nearly close to those reported in other binuclear calcium carboxylates [50,51]. This short Ca–Ca distance evidences the existence of weak Ca···Ca interactions. Each sheet is constituted by corrugated infinite chains, along the *b*-axis, made of CaO_8 polyhedra connected by croconate dianions. Adjacent chains are connected through common-edge of polyhedra. The resulting framework develops eight-member apertures made of four $[Ca_2O_{14}]$ dimers and four

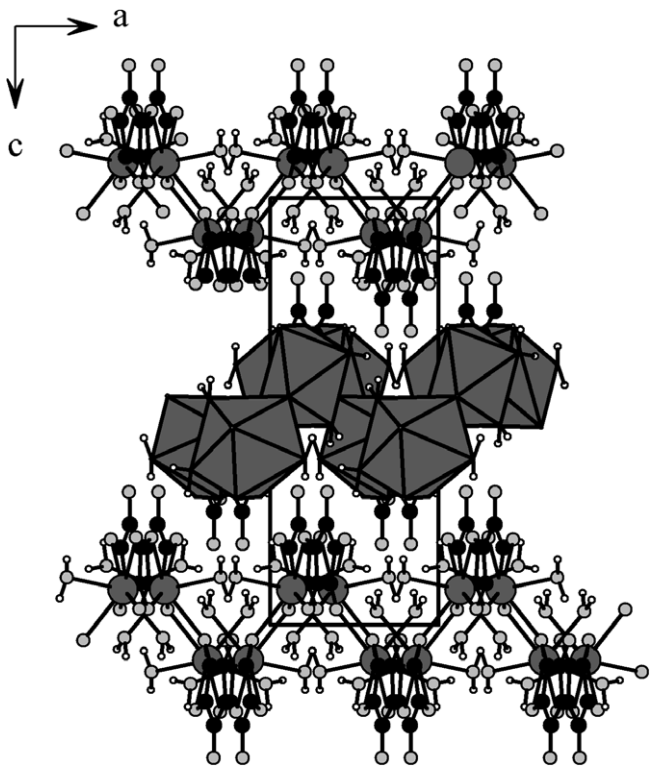


Fig. 1. Projection of the structure of $Ca(\mu_3\text{-}C_5O_5)(H_2O)_3$ (**I**) in the *ac*-plane. One sheet is illustrated by polyhedra.

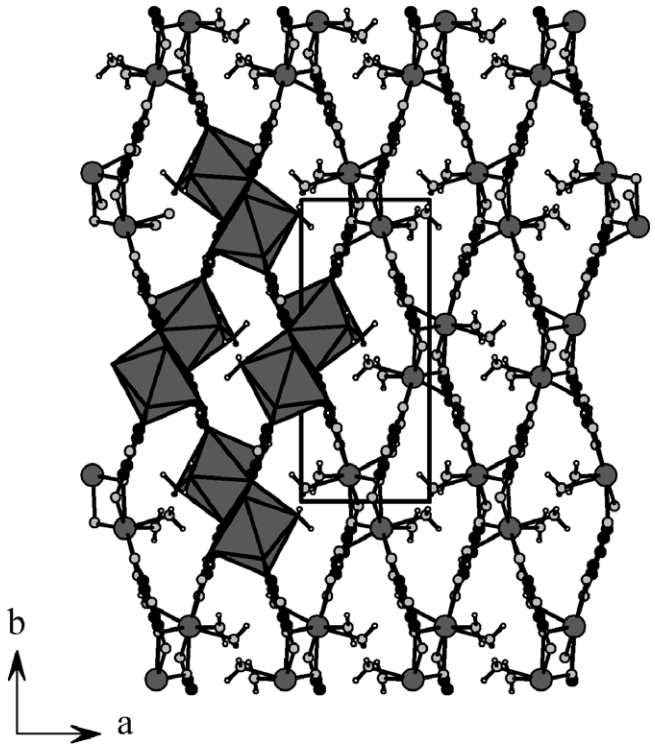


Fig. 2. View of one sheet of the structure $Ca(\mu_3\text{-}C_5O_5)(H_2O)_3$ (**I**) in the *ab*-plane showing the infinite chains and an aperture of the honeycomb pattern displayed by polyhedra.

croconate dianions. It can be described as a honeycomb pattern as already reported for numerous oxalate-based compounds [52,53] but arrangement based on dimers is original. Within a sheet, the croconate groups are exactly stacked along *a*-axis like face-to-face π–π alignment. However, the centroid–centroid distance corresponds to the *a* lattice parameter (6.416 Å) which is bigger than 4 Å preventing from π-stacking interactions [54]. Furthermore, the croconate groups are stacked between adjacent sheets in a displaced conformation but the centroid–centroid distance is again too high (~4.4 Å) to allow π-stacking interactions. The network is characterized by the presence of both intra- and inter-sheets hydrogen bonds. It is interesting to note that each coordination water molecule creates two hydrogen bonds, one between two sheets and one within the sheet. The possible hydrogen bonds, according to Desiraju and Steiner criteria [55], are reported in Table 4. Furthermore, the non-coordinated O5 atom is effectively involved in two O5···H bonds. This is simply the manifestation of the multi-chelate nature of the croconate ligand [56].

The Ca atom is surrounded by eight oxygen atoms; five of which are from two croconate dianions and three from water molecules (Fig. 3a). Eightfold coordinated Ca atoms have already been observed in numerous carboxylates in square antiprism [57], bicapped trigonal prism [51,58] or dodecahedron [14,59] configurations. The geometry of the CaO_8 polyhedron can be classified as a distorded bicapped trigonal prism [16th, 17th, 18th lowest O–Ca–O angles are 91.23(5)°, 97.21(6)°, 114.58(5)°] according to Haigh's criteria [60]. The Ca–O bond lengths are asymmetric and can be classified in two groups. The shortest distances [2.406(2) Å, 2.465(2) Å, 2.468(2) Å, 2.479(2) Å], involve Ca atom bonded to O atoms of coordination water molecules and to one atom of croconate dianion (O3) whereas the longest distances [2.502(2) Å, 2.506(2) Å, 2.535(2) Å, 2.552(2) Å] involve Ca atom bonded to only O atoms of croconate dianions. The main bond distances and angles are reported in Table 4.

One croconate group is present in the asymmetric unit. It is close to planarity, with standard deviation from the mean plane lower than 0.02 Å. The croconate dianion adopts a $\mu_3\text{-}(\eta^1{:}\eta^1{:}\eta^2{:}\eta^1)$ bis-bidentate bridging mode (Fig. 3b). To the best of our knowledge, this feature displays a new kind of coordination mode. On one side, the chelating mode is quite symmetric with similar $Ca^{(ii)}$–O3 [2.506(2) Å] and $Ca^{(ii)}$–O4 [2.502(2) Å] distances, whereas at the opposite side of the croconate group, the chelating mode is asymmetric with different $Ca^{(viii)}$–O1 [2.235(2) Å] and $Ca^{(viii)}$–O2 [2.552(2) Å] distances. This phenomenon confirms the intrinsic tendency of croconate to coordinate as an asymmetric bidentate ligand as already reported in other metal–croconate complexes [28,61]. On the other hand, one can also note that the croconate dianion acts as an asymmetric bridging ligand since the distances between O3 atom and the two Ca and $Ca^{(ii)}$ atoms are different [O3–Ca = 2.479(2) Å, O3–$Ca^{(ii)}$ = 2.506(2) Å]. Due to the inversion centre, this discrepancy is also observed for the other oxygen atom $O3^{(ii)}$ of the share-edge within the dimers (Fig. 3b). Finally, bond lengths C1–O1 [1.239(2) Å] and C5–O5 [1.238(2) Å] are shorter than the other C–O distances. The shortening of such distances results in the lengthening of the C1–C5 [1.474(2) Å] distance and thereby the inner angle C4–C5–C1 [106.7(2)°] is more acute than the others. Bond lengths and angles within the croconate group, gathered in Table 4, are in agreement with those previously reported [17,62].

The compound $Ca(\mu_3\text{-}C_5O_5)(H_2O)_3$ (**I**) is a polymorph of calcium croconate. Another phase $Ca(\mu_2\text{-}C_5O_5)(H_2O)_3$ has already been reported [27] and crystallizes in the triclinic system with the following parameters: $a = 6.642(3)$ Å, $b = 7.793(4)$ Å, $c = 8.854(5)$ Å, $\alpha = 106.97(5)°$, $\beta = 92.43(4)°$, $\gamma = 106.98(4)°$, $V = 425.1(1)$ Å^3. One can note that the *a* parameter of **I** is almost equal to that of the triclinic polymorph and that *b* and *c* parameters of **I** are twice those of the polymorph. The crystal structure of the triclinic calcium croconate consists in infinite chains of alternating CaO_7 polyhedra and croconate dianions. The Ca atom is surrounded by four O atoms of croconate dianions and three O atoms of coordination water molecules (Fig. 3c). On the contrary, in **I**, the Ca atom is surrounded by eight O atoms and five of which are from O atoms of croconate dianions (Fig. 3a). The additional eighth O atom in the Ca atom environment in **I** allows the formation of dimers $[Ca_2O_{14}]$. The coordination mode of the croconate is also different. Indeed, in the polymorphous triclinic compound,

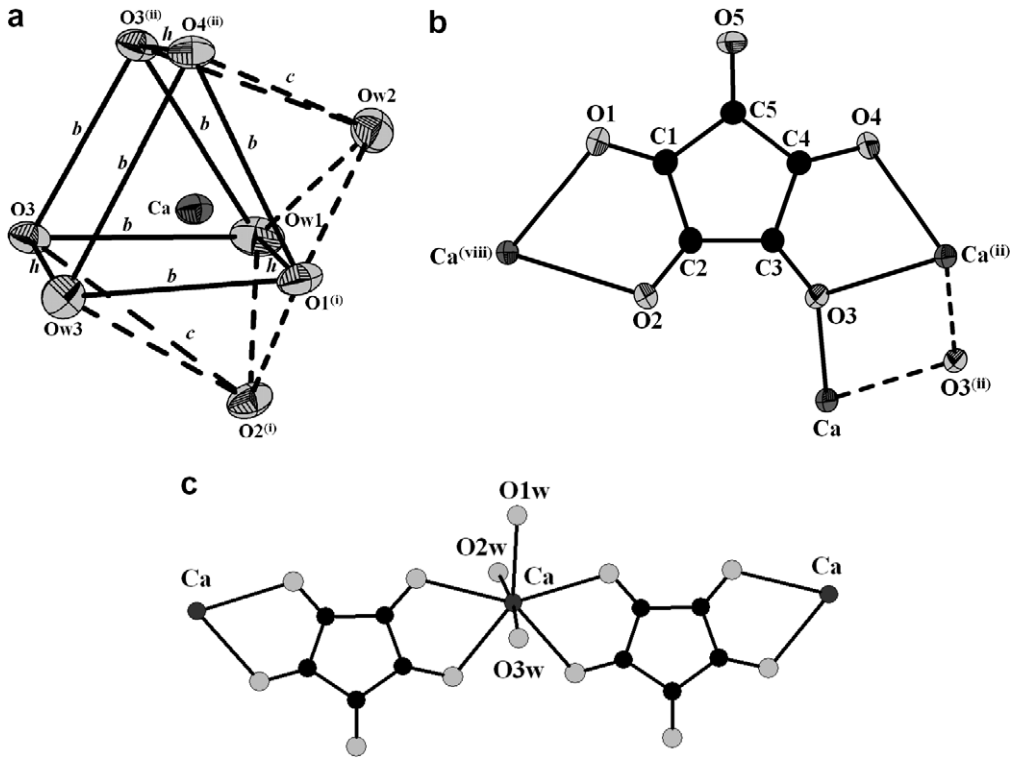


Fig. 3. (a) Eightfold environment of calcium atom in $Ca(\mu_3\text{-}C_5O_5)(H_2O)_3$ (**I**). (b) Representation of the connecting mode of the croconate group in (**I**). (c) Representation of the connecting mode of the croconate group in the triclinic polymorph of $Ca(\mu_2\text{-}C_5O_5)(H_2O)_3$ (from [27]). Atomic displacement ellipsoids are plotted at the 50% probability level.

the croconate group acts as a μ_2-(η^1:η^1:η^1:η^1) symmetric bis-bidentate ligand and connects two Ca atoms along only one direction (Fig. 3c), leading to a 1D framework. On the contrary, in **I** the croconate group connects three Ca atoms along two directions, the *a*- and *b*-axes (Fig. 3b), generating a 2D framework.

The 3D open-framework of $Ca_2(\mu_4\text{-}C_5O_5)(\mu_6\text{-}C_2O_4)(H_2O)$ (**II**) consists of layers in the *bc*-plane piled up along the *a*-axis (Fig. 4). Each layer is constituted by seven- and eightfold coordinated Ca atoms and oxalates dianions (Fig. 5). The presence of both seven- and eightfold coordination of Ca has already been observed in carboxylate-based compounds for Ca [57c,59b]. One layer contains infinite corrugated chains along the *b*-axis made of alternated $Ca1O_7$ and $Ca2O_8$ polyhedra linked together by O6–O7 shared-edge. Within this chain, the Ca1–Ca2 distance is 3.735(1) Å. This result emphasizes the tightness of the layer and indicates the existence of Ca···Ca interactions in the compound [50,51]. These chains are connected to each other along the *c*-axis by both oxalate dianion and O2–O4 shared-edge. The whole crystal structure is obtained by piling up these layers along the *a*-axis with the croconate dianion (Fig. 4). This structural arrangement provides in the *ab*-plane rectangular cavities which are free of water molecules and whose dimensions are around 3.9×6.4 Å^2. The croconate groups are stacked in opposite direction in a parallel displaced conformation in the *ac*-plane (Fig. 4) but the shift between the ring centroids is too high (~4 Å) to allow π-stacking interactions [54]. A zigzag network of hydrogen bonds is developed between the layers and the croconate dianions in the *ac*-plane (Fig. 4). These weakly bonds involve H atoms of Ow1 molecules,

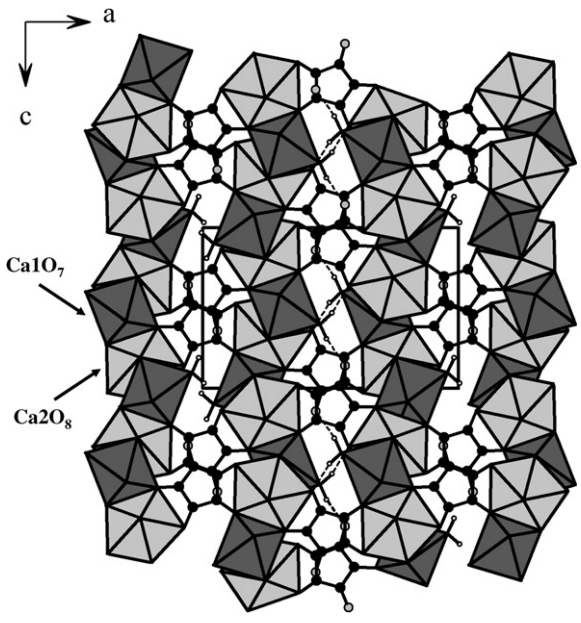


Fig. 4. Projection of the structure of $Ca_2(\mu_4\text{-}C_5O_5)(\mu_6\text{-}C_2O_4)(H_2O)$ (**II**) in the *ac*-plane showing corrugated sheets linked by croconates and hydrogen bonds in dotted lines. $Ca1O_7$ are displayed by medium grey polyhedra and $Ca2O_8$ by light grey polyhedra.

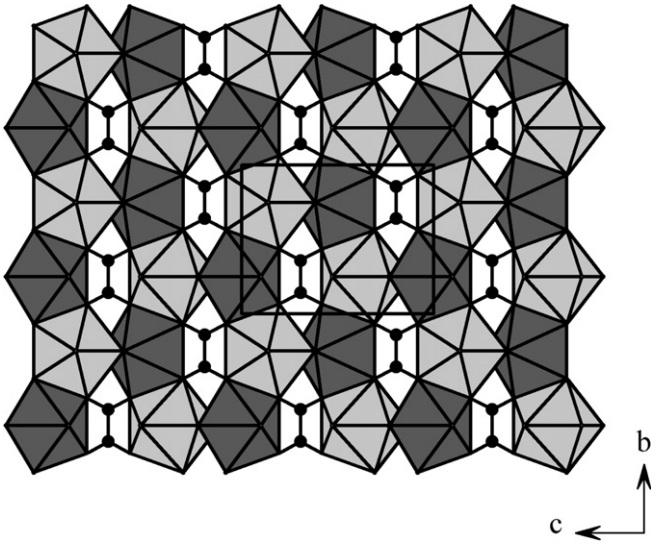


Fig. 5. Projection of one layer of $Ca_2(\mu_4\text{-}C_5O_5)(\mu_6\text{-}C_2O_4)(H_2O)$ (**II**) in the *bc*-plane. $Ca1O_7$ are displayed by medium grey polyhedra and $Ca2O_8$ by light grey polyhedra.

belonging to $Ca1O_7$ polyhedra, and O atoms from croconate dianions. The possible hydrogen bonds, according to Desiraju and Steiner criteria [55], are reported in Table 5.

The two Ca atoms have different coordination numbers and environments (Fig. 6). However, each Ca atom is bonded to the same number of croconate and oxalate dianions. Indeed, the Ca1 atom is surrounded by seven O atoms, two from two different croconate dianions (O2, O4), four from three different oxalate dianions (O6, $O6^{(i)}$, O7, $O7^{(i)}$) and one from a coordination water molecule (Ow1). All the O atoms (except Ow1) act as bridging atoms towards the Ca atom. Sevenfold coordinated Ca1 atoms have already been observed in numerous carboxylates of different structural types in pentagonal bipyramid [59b,59c,63] or capped trigonal prism [59c] configurations. The Ca2 atom is coordinated by eight O atoms: four from three different oxalate dianions ($O6^{(ii)}$, $O6^{(iii)}$, $O7^{(ii)}$, $O7^{(iii)}$) and four from two different croconate dianions (O1, O2, O3, O4). All the O atoms, except O1 and O3, act as bridging atoms towards the Ca atom.

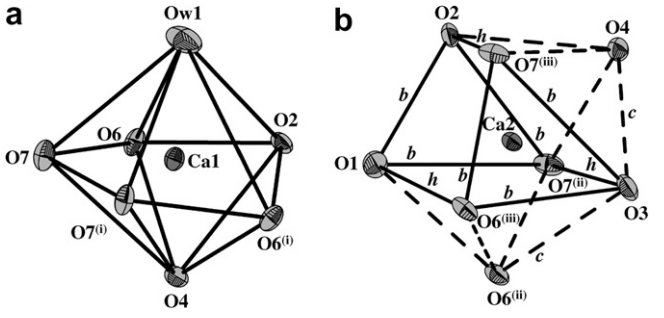


Fig. 6. (a) Sevenfold environment of Ca1 atom in (**II**); (b) eightfold environment of Ca2 atom in (**II**). Atomic displacement ellipsoids are plotted at the 50% probability level.

The geometry of the $Ca1O_7$ polyhedron can be classified as a distorted pentagonal bipyramid (Fig. 6a). The Ca1 atom and its five neighboring equatorial O atoms are approximately planar with a standard deviation from the mean plane equal to 0.2123 Å. The trans angle, involving axial O atoms, Ow1–Ca1–O4 is equal to 173.7(1)°. The Ca1–O distances are asymmetric since the equatorial bonds are longer than the axial ones. The geometry of the $Ca2O_8$ polyhedron can be classified as a bicapped trigonal prism (Fig. 6b) {16th, 17th, 18th lowest O–Ca2–O angles are 95.30(5)°, 95.30(5)°, 127.45(6)° according to Haigh's criteria [60]}. The Ca2–O distances involving oxygen atoms from oxalate groups are shorter than those from croconate dianions. The main bond distances and angles for both polyhedra are reported in Table 5.

One croconate group is present in the asymmetric binuclear unit. It is strictly plane due to the position of the croconate located in a mirror plane. The croconate dianion adopts a μ_4-(η^2:η^1:η^2:η^1) bis-bidentate and bis-bridging modes (Fig. 7a). It connects along the *a*-axis four metals (two Ca1 and two Ca2 atoms) in an original trans bis-bridging manner compared to the other tetradentate with a cis bis-bridging connection mode related in the literature [28]. On one hand, the distances Ca2–O1 [2.523(3) Å] and Ca2–O2 [2.532(2) Å] are similar whereas the distances Ca2–O3 [2.417(3) Å] and Ca2–O4 [2.549(3) Å] are different, which confirms the intrinsic tendency of croconate dianion to coordinate as an asymmetric bidentate ligand as reported for other metal–croconate complexes [28,61] and for **I**. On the other hand, one can also note that the two

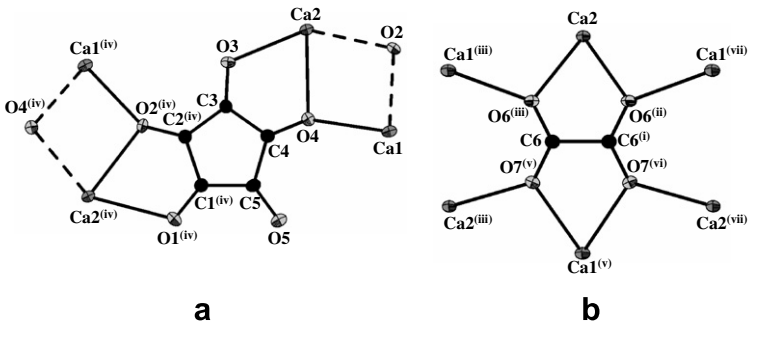


Fig. 7. Representations of the connecting modes of the croconate group (a) and of the oxalate group (b) in (**II**). Atomic displacement ellipsoids are plotted at the 50% probability level.

O2 and O4 atoms which connect the $Ca1O_7$ and $Ca2O_8$ polyhedra act as bridging atoms in an asymmetric manner. Indeed, the distances $O2^{(iv)}$–$Ca1^{(iv)}$ [2.368(2) Å] and $O2^{(iv)}$–$Ca2^{(iv)}$ [2.523(3) Å] are different as also observed for the distances O4–Ca1 [2.332(3) Å] and O4–Ca2 [2.549(3) Å]. Therefore, the croconate dianion can act as bridging and bidentate ligand through both asymmetric and symmetric manners. Finally, bond lengths $C1^{(iv)}$–$O1^{(iv)}$ [1.229(5) Å] and C5–O5 [1.236(4) Å] appear to be shorter than the other C–O distances, as observed in **I**. The shortening of such distances results in the lengthening of the $C1^{(iv)}$–C5 [1.485(5) Å] distance and thereby the inner angle C4–C5–$C1^{(iv)}$ [105.8(3)°] is more acute than the others. Bond lengths and angles within the croconate group are gathered in Table 5.

On the contrary, the oxalate group present in the structure behaves as both a bridging and a bidentate ligand which connects asymmetrically. It is close to planarity, with standard deviation from the mean plane equal to 0.004 Å. The oxalate dianion adopts a μ_6-(η^2:η^2:η^2:η^2) bis-bidentate and tetra-bridging modes (Fig. 7b). It connects along the *b*- and *c*-axes six metals (three Ca1 and three Ca2 atoms) and each O atom acts as a bridging atom. Comparing to the very usual μ_2 bis-bidentate mode, the μ_6 coordination mode has been less reported for the oxalate anion [64]. The distances within the oxalate groups (Table 5) are regular and close to the mean values reported by Hahn [65] for oxalate groups.

3.3. Thermal behaviours

The thermal decomposition of **II** can be described as two steps process. According to the TGA measurement (Fig. 8a), croconate **II** has adsorbed at ambient conditions 1.4 water molecules comparing to the formula deduced from the crystal structure resolution. This phenomenon agrees with the topology of **II** displaying rectangular cavities and demonstrates its zeolite-like behaviour. The departure of adsorbed water molecules occurs without well-defined step until ~320 °C (experimental/theoretical

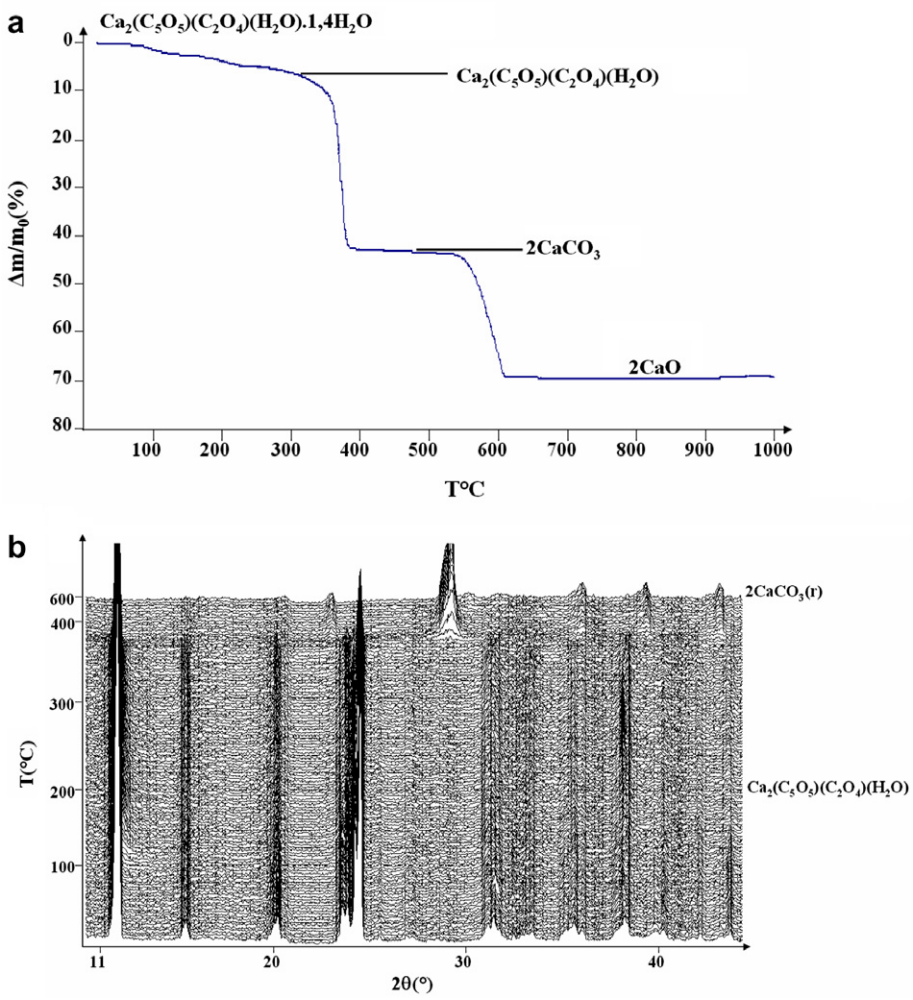


Fig. 8. (a) Thermogravimetric analysis of $Ca_2(C_5O_5)(C_2O_4)(H_2O)$ (**II**) under flowing air (heating rate: 5 °C h^{-1} between 20 and 400 °C and 25 °C h^{-1} up to 1000 °C). (b) Thermodiffractogram of $Ca_2(C_5O_5)(C_2O_4)(H_2O)$ (**II**) under flowing air (heating rate: 5 °C h^{-1} between 20 and 400 °C, then 25 °C h^{-1} up to 600 °C; counting time: 2700 s/pattern); r: rhombohedric.

weight losses: 7.4/7.1%). Then, the loss of the coordination water molecule (Ow1) and the decomposition of the organic ligands occur on one step and provide the collapse of the crystal structure. Indeed, this collapse leads to the formation of calcium carbonate [PDF2 01-0837] in the temperature range 340–390 °C. As seen on the TDXD plot (Fig. 8b), no structural change is observed until 380 °C. Consequently, the crystal structure is stable at high temperature as already observed in other structures involving croconate dianion [26–28]. This behaviour can be assigned to the delocalization of π electrons all over the ring.

Finally, nanocrystalline cubic calcium oxide (experimental/theoretical weight losses: 69.3/68.1%) is formed at about 610 °C but this step is not observed on the TDXD plot since the experiment was carried out until only 600 °C.

4. Conclusion

Attempts to synthesize with the same experimental procedures analogous structures with an alkaline-earth metal of larger radius, such strontium or barium, were successful. However, the low quality of the strontium croconate and the high electronic contrast between Ba and the other light atoms in the barium croconate did not allow to solve their crystal structures. The refined parameters for barium and strontium croconate-based complexes are: $a = 14.203(1)$ Å, $b = 8.0008(6)$ Å, $c = 11.4727(9)$ Å, $V = 1303.7(1)$ Å^3; $a = 10.7274(2)$ Å, $b = 7.7201(2)$ Å, $c = 13.7810(3)$ Å, $\beta = 93.59(2)°$, $V = 1139.06$ Å^3, respectively. These values are close to those of the calcium croconato-oxalate suggesting strong relationships between the structures.

As a conclusion, two original calcium complexes based on croconate, $Ca(\mu_3\text{-}C_5O_5)(H_2O)_3$ (**I**) and $Ca_2(\mu_4\text{-}C_5O_5)(\mu_6\text{-}C_2O_4)(H_2O)$ (**II**) have been prepared and characterized. Their structures display frameworks of high dimensionality degree. The structure of **I** is a 2D architecture which consists of corrugated sheets formed by croconate dianions and $[Ca_2O_{14}]$ dimers. The structure of **II** displays a 3D open-framework built from layers of CaO_8/CaO_7 polyhedra and oxalate dianions, connected to each other by croconate dianions. The calcium adopts different coordination polyhedra, pentagonal bipyramid in **II** and distorded bicapped trigonal prisms in **I** and **II**, pointing out the flexibility of its coordination environment. Furthermore, these polyhedra are connected by croconates and oxalates through unusual bridging and chelating coordination modes. Then, the dimensionality of the framework increases with the number of coordinated metals by the organic group. Finally, potential applications in catalysis can be expected for **II** since its open-framework structure is stable up 380 °C.

Acknowledgments

The authors thank Dr. T. Roisnel (Centre de Diffractométrie X, UMR 6226 CNRS, Rennes) and Mr. G. Marsolier (Université de Rennes 1) for their assistance in single-crystal and powder X-ray diffraction data collection, respectively, and Mr. Y. Le Gal (Université de Rennes 1) for IR spectra.

Appendix A. Supplementary material

CCDC 647655 and 647656 contain the supplementary crystallographic data for $Ca_2(\mu_4\text{-}C_5O_5)(\mu_6\text{-}C_2O_4)(H_2O)$ and $Ca(\mu_3\text{-}C_5O_5)(H_2O)_3$. These data can be obtained free of charge via http://www.ccdc.cam.ac.uk/conts/retrieving.html, or from the Cambridge Crystallographic Data Centre, 12 Union Road, Cambridge CB2 1EZ, UK; fax: (+44) 1223-336-033; or e-mail: deposit@ccdc.cam.ac.uk. Supplementary data associated with this article can be found, in the online version, at doi:10.1016/j.poly.2007.08.018.

References

[1] M. O'Keeffe, M. Eddaoudi, H. Li, T.M. Reineke, O.M. Yaghi, J. Solid State Chem. 152 (2000) 3.
[2] C.N.R. Rao, S. Natarajan, R. Vaidhyanathan, Angew. Chem., Int. Ed. 43 (2004) 1466.
[3] A. Vimont, J.-M. Goupil, J.-C. Lavalley, M. Datury, S. Surblé, C. Serre, F. Millange, G. Férey, N. Audebrand, J. Am. Chem. Soc. 128 (2006) 3218.
[4] K.C. Szeto, C. Prestipino, C. Lamberti, A. Zecchina, S. Bordiga, M. Bjorgen, M. Tilset, K.P. Lillerud, Chem. Mater. 19 (2007) 211.
[5] M. Latroche, S. Surblé, C. Serre, C. Mellot-Draznieks, P.L. Llewellyn, J.-H. Lee, J.-S. Chang, S.H. Jhung, G. Férey, Angew. Chem., Int. Ed. 45 (2006) 8227.
[6] X. Lin, J. Jia, X. Zhao, K.M. Thomas, A.J. Blake, G.S. Walker, N.R. Champness, P. Hubberstey, M. Schröder, Angew. Chem., Int. Ed. 45 (2006) 7358.
[7] O. Guillou, C. Daiguebonne, M. Camara, N. Kerbellec, Inorg. Chem. 45 (2006) 8468.
[8] C. Serre, C. Mellot-Draznieks, S. Surblé, N. Audebrand, Y. Filinchuk, G. Férey, Science 315 (2007) 1828.
[9] G. Férey, J. Solid State Chem. 152 (2000) 37.
[10] C. Mellot-Draznieks, J.M. Newsam, A.M. Gorman, C.M. Freeman, G. Férey, Angew. Chem., Int. Ed. 39 (2000) 2270.
[11] C. Mellot-Draznieks, J. Dutour, G. Férey, Angew. Chem., Int. Ed. 43 (2004) 6290.
[12] G. Férey, C. Mellot-Draznieks, C. Serre, F. Millange, J. Dutour, S. Surblé, I. Margiolaki, Science 309 (2005) 2040.
[13] M. Eddaoudi, D.B. Moler, H. Li, B. Chen, T.M. Reineke, M. O'Keeffe, O.M. Yaghi, Acc. Chem. Res. 34 (2001) 319.
[14] N. Audebrand, E. Jeanneau, T. Bataille, S. Raite, D. Louër, Solid State Sci. 6 (2004) 579.
[15] N. Mahé, N. Audebrand, Solid State Sci. 8 (2006) 988.
[16] E. Gavilan, N. Audebrand, E. Jeanneau, Solid State Sci. (2007), in press.
[17] R. West, Oxocarbons, Academic Press, New York, 1980.
[18] L. Gmelin, Ann. Phys. Chem. 4 (1825) 31.
[19] L. Gemlin, Ann. Chem. 37 (1841) 58.
[20] S. Cohen, J.R. Lacher, J.D. Park, J. Am. Chem. Soc. 81 (1959) 3480.
[21] (a) J.-F. Petit, A. Gleizes, J.-C. Trombe, Inorg. Chim. Acta 167 (1990) 51;
(b) J.-C. Trombe, J.-F. Petit, A. Gleizes, Inorg. Chim. Acta 167 (1990) 69;
(c) J.-C. Trombe, J.-F. Petit, A. Gleizes, Eur. J. Solid State Inorg. Chem. 28 (1991) 669;
(d) U. Heinl, P. Hinse, R. Mattes, Z. Anorg. Allg. Chem. 627 (2001) 2173.

[22] (a) S.C. Manna, E. Zangrando, J. Ribas, N.R. Chaudhuri, Inorg. Chim. Acta 358 (2005) 4497;
(b) M. Kurmoo, H. Kumagai, K.W. Chapman, C.J. Kepert, Chem. Commun. 24 (2005) 3012;
(c) J. Carranza, C. Brennan, J. Sletten, B. Vangdal, P. Rillema, F. Lloret, M. Julve, New J. Chem. 27 (2003) 1775;
(d) J. Greve, I. Jess, C. Näther, J. Solid State Chem. 175 (2003) 328.
[23] (a) C. Robl, D. Kinkeldey, Z. Naturforsch. B 45 (1990) 931;
(b) Z. Hulvey, A.K. Cheetham, Solid State Sci. 9 (2007) 137;
(c) C. Robl, A. Weiss, Mater. Res. Bull. 22 (1987) 373;
(d) C. Robl, V. Gnutzmann, A. Weiss, Z. Anorg. Allg. Chem. 549 (1987) 187;
(e) C. Robl, A. Weiss, Z. Naturforsch. B 41 (1986) 1485;
(f) R. Köferstein, C. Robl, Z. Anorg. Allg. Chem. 629 (2003) 371.
[24] (a) J.-C. Trombe, C. Brouca-Cabarrecq, C.R. Acad. Sci. Paris, Ser. II 310 (1990) 521;
(b) C. Brouca-Cabarrecq, J.-C. Trombe, Inorg. Chim. Acta 191 (1992) 227;
(c) C. Brouca-Cabarrecq, J.-C. Trombe, Inorg. Chim. Acta 191 (1992) 241.
[25] (a) M.D. Glick, G.L. Downs, L.F. Dahl, Inorg. Chem. 3 (1964) 1712;
(b) M.D. Glick, L.F. Dahl, Inorg. Chem. 5 (1966) 289;
(c) A. Cornia, A.C. Fabretti, A. Giusti, F. Ferraro, D. Gatteschi, Inorg. Chim. Acta 212 (1993) 87;
(d) Q. Chen, S. Liu, J. Zubieta, Inorg. Chim. Acta 175 (1990) 241;
(e) C.-C. Wang, C.-H. Yang, G.-H. Lee, Inorg. Chem. 41 (2002) 1015;
(f) S. Curreli, P. Deplano, C. Faulmann, M.L. Mercuri, L. Pilia, A. Serpe, E. Coronado, C.J. Gomez-Garcia, Inorg. Chim. Acta 359 (2006) 1177.
[26] (a) N.S. Goncalves, P.S. Santos, I. Vencato, Acta Crystallogr., Sect. C 52 (1996) 622;
(b) J.D. Dunitz, P. Seiler, W. Czechtizky, Angew. Chem., Int. Ed. 40 (2001) 1779;
(c) N.C. Baenziger, D.G. Williams, J. Am. Chem. Soc. 88 (1966) 689;
(d) D. Braga, L. Maini, F. Grepioni, Chem. Eur. J. 8 (2002) 1804;
(e) D. Braga, L. Maini, F. Grepioni, F. Mota, C. Rovira, J.J. Novoa, Chem. Eur. J. 6 (2000) 4536.
[27] M.J. Plater, M.R. St. Foreman, R.A. Howie, J. Chem. Crystallogr. 28 (1998) 653.
[28] T.K. Maji, S. Konar, G. Mostafa, E. Zangrando, T.-H. Lu, N.R. Chaudhuri, Dalton Trans. (2003) 171.
[29] C.C. Wang, C.-H. Yang, S.-M. Tseng, G.-H. Lee, Y.-P. Chiang, H.-S. Sheu, Inorg. Chem. 42 (2003) 8294.
[30] D. Deguenon, Etude des anions squarate et croconate – complexes métalliques de ces ligands, Thesis, Université P. Sabatier, Toulouse, France, 1990.
[31] D. Louër, J.I. Langford, J. Appl. Crystallogr. 21 (1988) 430.
[32] A. Boultif, D. Louër, J. Appl. Crystallogr. 37 (2004) 724.
[33] A.D. Mighell, C.R. Hubbard, J.K. Stalick, 'A FORTRAN program for crystallographic data evaluation', Nat. Bur. Stand. US Technical Note, 1141, 1980.
[34] M. Ito, R. West, J. Am. Chem. Soc. 85 (1963) 2580.
[35] R. West, H.Y. Niu, J. Am. Chem. Soc 85 (1963) 2586.
[36] H. Murata, K. Kawai, J. Chem. Phys. 25 (1956) 589.
[37] J. Fujita, K. Nakamoto, M. Kobayashi, J. Phys. Chem. (1957) 1014.
[38] Nonius, Kappa CCD Program Software for Data Collection, Nonius BV, Delft, The Netherlands, 1998.
[39] Bruker-Nonius, SMART in APEX-2 programs suite version 2.1-0. Bruker AXS Inc., Madison, WI, USA, 2006.
[40] Z. Otwinowski, W. Minor, Methods Enzymol. 276 (1997) 307.
[41] Bruker-Nonius. SAINT version 7.23A, Bruker AXS Inc., Madison, WI, USA, 2005.
[42] J. de Meulenaar, H. Tompa, Acta Crystallogr., Sect. A 19 (1965) 1014.
[43] L.J. Farrugia, J. Appl. Crystallogr. 32 (1999) 837.
[44] G.M. Sheldrick, SADABS version 2.03, Bruker AXS Inc., Madison, WI, USA, 2001.
[45] K. Brandenburg, M. Berndt, DIAMOND (version 2.1e), Crystal Impact, Bonn, 2001.
[46] J. Plévert, J.P. Auffrédic, M. Louër, D. Louër, J. Mater. Sci. 24 (1989) 1913.
[47] A. Altomare, M.C. Burla, M. Camalli, G. Cascarano, C. Giacovazzo, A. Guagliardi, A.G.G. Moliterni, G. Polidori, R. Spagna, J. Appl. Crystallogr. 32 (1999) 115.
[48] G.M. Sheldrick, Acta Crystallogr., Sect. A 46 (1990) 467.
[49] G.M. Sheldrick, SHELXL-97: Programs for Crystal Structure Refinement, University of Göttingen, Göttingen, Germany, 1997.
[50] N. Ueyama, J. Takeda, Y. Yamada, A. Onoda, T.-A. Okamura, Inorg. Chem. 38 (1999) 475.
[51] A. Karipides, J. Ault, T. Reed, Inorg. Chem. 16 (1977) 3299.
[52] E. Hansson, Acta Chem. Scand. 24 (1970) 2969.
[53] E. Hansson, Acta Chem. Scand. 27 (1973) 823.
[54] C.A. Hunter, J.K.M. Sanders, J. Am. Chem. Soc. 112 (1990) 5525.
[55] R. Desiraju, T. Steiner, The Weak Hydrogen Bond in Structural Chemistry and Biology, IUCr/OUP, 1999.
[56] H.-Y. Chen, Q. Fang, G. Xue, W.-T. Yu, Acta Crystallogr., Sect. C 61 (2005) 535.
[57] (a) C. Sterling, Science 146 (1964) 518;
(b) C. Sterling, Acta Crystallogr. 18 (1965) 917;
(c) H.-F. Zhu, Z.-H. Zhang, W.-Y. Sun, T. Okamura, N. Ueyama, Cryst. Growth Des. 5 (2005) 177.
[58] B. Chapelet-Arab, G. Nowogrocki, F. Abraham, S. Grandjean, J. Solid State Sci. 177 (2004) 4269.
[59] (a) G.K. Ambady, Acta Crystallogr., Sect. B 24 (1968) 1548;
(b) V.A. Uchtman, R.J. Jandaceck, Inorg. Chem. 19 (1980) 350;
(c) L. Pan, T. Frydel, M.B. Sander, X. Huang, J. Li, Inorg. Chem. 40 (2001) 1271.
[60] C.W. Haigh, Polyhedron 14 (1995) 2871.
[61] F. Dumestre, B. Soula, A.-M. Galibert, P.-L. Fabre, G. Bernadinelli, B. Donnadieu, P. Castan, Dalton Trans. (1998) 4131.
[62] N.C. Baenziger, J.J. Hegenbarth, J. Am. Chem. Soc. 85 (1963) 1539.
[63] R. Murugavel, V.V. Karambelkar, G. Anantharaman, M.G. Walawalkar, Inorg. Chem. 39 (2000) 1381.
[64] (a) M. Tadokoro, Y. Ozawa, M. Mitsumi, K. Toriumi, T. Ogura, Chem. Lett. 34 (2005) 236;
(b) E.V. Boldyreva, H. Ahsbahs, V.V. Chernyshev, S.N. Ivashevskaya, A.R. Oganov, Z. Kristallogr. 221 (2006) 186;
(c) D.J. Price, A.K. Powell, P.T. Wood, Polyhedron 18 (1999) 2499;
(d) A.N. Christensen, P. Norby, J.C. Hanson, Z. Kristallogr. 209 (1994) 874.
[65] T. Hahn, Z. Anorg. Allg. Chem. 109 (1957) 438.

we have synthesized a series of benzoazole palladium complexes and investigated their ability to catalyze Heck coupling reactions. The rigid backbone and the enhanced electron density of these ligands is expected to offer good stability for the active catalysts in the Heck coupling reactions and the absence of any reactive bonds in the fused benzoazole ligands is expected to minimize catalyst deactivation associated with phosphine-based catalysts. In attempts to impart different electronic and steric properties as well as improve solubility of complexes we have also developed a convenient method for the synthesis of substituted benzothiazoles by incorporating alkyl groups in both the pyridine and phenyl rings. In this contribution, we describe the synthesis of benzoazole ligands, their palladium complexes and applications as catalysts for Heck coupling of iodobenzene with butyl acrylates. The ability of the ligands to enhance the catalytic activity of palladium(II) salts when the ligands are added *in situ* in the Heck coupling reactions was also investigated.

2. Experimental

2.1. Materials and methods

Synthetic manipulations were carried out under a nitrogen atmosphere. All solvents were of analytical grade and were dried prior to use. Toluene and Et_2O were dried and distilled from sodium/benzophenone. Dichloromethane was dried and distilled from P_2O_5. Dicyclohexylcarbodiimide (DCC), 4-*tert*-butyl aniline, 4-pyrrolidnino pyridine (4-PP), 6-methyl picolinic acid, Lawesson's reagent and 2-pyridin-2-yl-1*H*-benzoimidazole (**L1**) were purchased from Sigma–Aldrich and used as received. Compounds and 2-pyridin-2-yl-benzothioazole (**L2**) [9], [Pd(COD)MeCl] [10] and $Pd(NCMe)_2Cl_2$] [11] were synthesized following the literature procedures. NMR spectra were recorded on a Varian Gemini 2000 instrument (^{1}H at 300 MHz and ^{13}C at 75 MHz) at room temperature. The chemical shifts are reported in δ (ppm) and referenced to the residual $CHCl_3$ in the NMR solvent. Coupling constants are measured in Hertz (Hz). Mass spectra were recorded on a Waters API Quattro Micro spectrometer at the University of Stellenbosch. Elemental analyses were performed by the micro analytical laboratory at the University of Cape Town, South Africa, as a service. Heck coupling products were analyzed on a Shimadzu GCMS-QP 2010 version 2 gas chromatograph fitted with flame ionization detector and column ZB1, 100% dimethylpolysiloxane with dimensions of 30 m by 0.25.

2.2. Synthesis of ligands and complexes

2.2.1. 2-tert-Butyl-pyridine-2-carboxylic acid (4-tert-butyl-phenyl)-amide (*S1*)

To a mixture of 4-*tert*-butylpicolinic acid (0.50 g, 2.80 mmol), 4-*tert*-butyl aniline (0.41 g, 2.80 mmol), DCC (0.57 g, 2.80 mmol) and 4-PP (5%) was added CH_2Cl_2 (20 mL) and the mixture stirred for 24 h at room temperature. After the reaction period the mixture was filtered and solvent removed under reduced pressure to give the crude product which was purified by column chromatography on silica gel using solvent mixtures of petroleum ether and ethylacetate (9:1). Yield = 0.75 g (85%). ^{1}H NMR ($CDCl_3$): δ 1.30 (s, 9H, ^{t}Bu, phenyl); 1.37 (s, 9H, ^{t}Bu, py); 7.39 (d, 1H, $J = 7.2$, py); 7.41 (d, 2H, $J = 8.1$, ph); 7.72 (d, 2H, $J = 5.7$, ph); 8.33 (s, 1H, py); 8.52 (d, 1H, $J = 8.1$, py); 10.04 (s, 1H, NH). ^{13}C NMR ($CDCl_3$): δ 30.4 (C-(CH_3)$_3$, ph); 31.3 (C-(CH_3)$_3$, py); 34.3 (*C*-(CH_3)$_3$, ph); 35.1 (*C*-(CH_3)$_3$, py); 119.4 (*C3*, py); 120.0 (*C2* and *C6*, ph); 123.0 (*C5*, py); 125.8 (*C5*, ph); 126.6 (*C3*-ph); 135.2 (*C2*, ph); 138.2 (*C1*, ph); 147.8 (*C4*, ph); 151.6 (*C6*, py); 157.3 (*C4*, py); 162.2 (*C*=O). HRMS (ESI) for $C_{20}H_{26}N_2O$: Calc. 310.4315. Found: 310.4322.

2.2.2. 2-tert-Butyl-pyridine-2-carbothioic acid (4-tert-butyl-phenyl)-amide (*S2*)

To a mixture of **S1** (0.80 g, 2.50 mmol) and Lawesson's reagent (0.52 g, 1.28 mmol) was added toluene (20 mL) and the solution refluxed for 48 h. The mixture was then filtered and solvent was removed under reduced pressure to afford an orange solid material which was purified by column chromatography on silica gel using solvent mixtures of petroleum ether and ethylacetate (4:1). Yield = 0.75 g (80%). ^{1}H NMR ($CDCl_3$): δ 1.32 (s, 9H, ^{t}Bu, phenyl); 1.36 (s, 9H, ^{t}Bu, py); 7.40 (d, 1H, $J = 7.8$, py); 7.43 (d, 2H, $J = 7.5$, ph); 7.97 (d, 2H, $J = 6.9$, ph); 8.45 (s, 1H, py); 8.88 (d, 1H, $J = 7.8$, and 1.8 py); 12.11 (s, 1H, NH). ^{13}C NMR ($CDCl_3$): δ 30.8 (C-(CH_3)$_3$, ph); 31.3 (C-(CH_3)$_3$, py); 34.6 (*C*-(CH_3)$_3$, ph); 35.2 (*C*-(CH_3)$_3$, py); 119.4 (*C3*, py); 122.4 (*C2* + *C6*, ph); 125.6 (*C5*, py); 128.1 (*C5*, ph); 128.9 (*C3*-ph); 137.9 (*C3*-ph); 149.6 (*C6*, ph); 150.7 (*C4*, ph); 155.5 (*C4*, py); 187.3 (*C*=S). HRMS (ESI) for $C_{20}H_{26}N_2S$: Calc. 326.5014. Found: 326.5021.

2.2.3. 2-(4-tert-Butyl pyridin-2-yl)-benzoxazole (*L3*)

To a mixture of 2-aminophenol (0.44 g, 4.00 mmol) and 2-carboxy-4-tertbutylpyridine (0.72 g, 4.00 mmol) was added to polyphosphoric acid (3.00 g). The suspension was heated at 170–180 °C. After 4 h, the reaction mixture was poured into an ice-water mixture and the pH of the resulting solution adjusted to 8 using 25% NH_4OH. The product that precipitated was filtered, washed with H_2O and dried. Yield = 0.80 (79%) ^{1}H NMR, ($CDCl_3$): δ 1.39 (s, 9 H, ^{t}Bu, py); 7.36 (m, 2H and 1H, ph, py); 7.67 (m, 1H, ph); 7.84 (m, 1H, ph); 8.37 (s, 1H, py); 8.71 (d, 1H, $J = 8.1$, py). ^{13}C NMR ($CDCl_3$): δ 30.5 (C-(CH_3)$_3$, py); 35.1 (*C*-(CH_3)$_3$, py); 111.3 (*C5*, ph); 120.5 (*C5*, py); 120.7 (*C6*, ph); 122.9 (*C2*, ph); 124.9 (*C3*, ph); 126.0 (*C4*, ph); 141.8 (*C1*, ph); 150.3 (*C6*, ph); 151.1 (*C*=N, oxazole); 161.6 (*C2*, py); 162.0 (*C4*, py). MS (ESI) *m*/*z* (%) 253 (M^+, 100). HRMS (ESI) for $C_{16}H_{17}N_2O$: Calc. 253.1341. Found: 253.1357.

*2.2.4. 2-(4-tert-Butyl pyridin-2-yl)-benzothiazole (**L4**)*

Compound **L3** was prepared following the procedure described for **L2** using 2-mercaptoaniline (0.50 g, 4.00 mmol) and 2-carboxy-4-tertbutylpyridine (0.72 g, 4.00 mmol). Yield = 0.86 g (80%). ^{1}H NMR, ($CDCl_3$): δ 1.38 (s, 9H, ^{t}Bu, py); 6.95 (d, 1H, $J = 7.8$, ph); 7.40 (m, 1H, ph); 7.54 (m, 1H, ph); 7.97 (d, 1H, $J = 9.3$, py); 8.10 (d, 1H, $J = 8.1$, ph); 8.37 (s, 1H, py); 8.60 (d, 1H, $J = 6.0$, py). ^{13}C NMR ($CDCl_3$): δ 30.4 (C-(CH_3)$_3$, py); 35.1 (*C*-(CH_3)$_3$, py); 118.1 (*C5*, py); 122.0 (*C3*, py); 123.3 (*C3* and *C6*, ph); 125.7 (*C5*, ph); 126.4 (*C4*, ph); 135.9 (*C2*, ph); 149.4 (*C6*, py); 151.0 (*C1*, ph); 154.0 (*C* = N, thiazole); 161.4 (*C2*, py); 161.9 (*C4*, py). MS (ESI) *m*/*z* (%) 291 (M^++Na^+, 20) 269 (M^+, 100). HRMS (ESI) for $C_{16}H_{17}N_2S$: Calc. 269.1112. Found: 269.1106.

*2.2.5. 6-tert-Butyl-2-(4-tert-butyl-pyridin-2-yl)-benzothiazole (**L5**)*

To a solution of **S2** (1.00 g, 3.00 mmol) in a minimum amount of ethanol was added 30% NaOH (3.20 mL, 24.00 mmol). The mixture was diluted to give 10% NaOH and stirred for about 5 min. Portions of this mixture were added at 1 min intervals to a stirred solution of $K_3[Fe(CN)_6]$ (3.95 g, 12.00 mmol) in H_2O (5.00 mL) at 85 °C. The resultant mixture was further heated at 85 °C for 1 h, solvent removed *in vacuo* and the residue extracted with CH_2Cl_2 (2 × 20 mL). The combined organic extracts was washed with H_2O (2 × 20 mL), dried over $MgSO_4$ and solvent removed to afford an orange solid. Purification by column chromatography on silica gel using solvent mixtures of petroleum ether:ethylacetate (9:1) as eluent gave **L5** as a pure compound. Yield = 0.53 g (55%). ^{1}H NMR ($CDCl_3$): δ 1.44 (s, 9H, ^{t}Bu, ph); 1.49 (s, 9H, ^{t}Bu, py); 6.90 (s, 1H, ph); 7.46 (t, 1H, ph); 7.58 (t, 1H, ph); 7.97 (d, 1H, py); 8.18 (d, 1H, ph); 8.37 (s, 1H, py); 8.50 (t, 1H, py). δ 30.4 (C-(CH_3)$_3$, py); 35.1 (*C*-(CH_3)$_3$, py); 119.1 (*C5*, py); 122.6 (*C3*, py); 123.7 (*C3* and *C6*, ph); 125.4 (*C5*, ph); 143.5 (*C4*, ph); 135.9 (*C2*, ph); 149.8 (*C6*, py); 152.1 (*C1*, ph); 155.1 (*C*═N, thiazole); 161.9 (*C2*, py); 162.4 (*C4*, py). HRMS (ESI) for $C_{20}H_{24}N_2S$: Calc. 324.4809. Found: 324.4811.

*2.2.6. {2-Pyridin-2-yl-1H-benzoimidazole}PdClMe (**1**)*

To a solution of [Pd(COD)MeCl] (0.12 g, 0.48 mmol) in Et_2O (10 mL) was added **L1** (0.10 g, 0.47 mmol) in Et_2O (10 mL) to give a light yellow compound precipitate. After stirring for 12 h, the mixture was filtered to isolate a light yellow solid. Yield = 0.12 g (71%). ^{1}H NMR (DMSO-d_6): δ 1.12 (s, 3H, Pd–Me); 7.43 (dd, 2H, $J = 7.8$, ph); 7.78 (d, 2H, $J = 8.1$, ph); 7.90 (m, 1H, py); 8.40 (m, 2H, py); 8.85 (m, 1H, py). ^{13}C NMR ($CDCl_3$): δ −5.8 (Pd-CH_3); 113.1 (*C3* and *C6*, ph); 124. 8; 126.9 (*C4* and *C5*, ph); 134.0 (*C4*, py); 139.5 (*C1* and *C2*, py); 140.8 (*C1* and *C6*, py); 148.3 (*C*═N, imidazole). MS (ESI) *m*/*z* (%) 357 (M^++NCMe, 100); 316 (30). *Anal.* Calc. for $C_{12}H_{12}N_3PdCl$: C, 44.34; H, 3.43; N, 11.97. Found: C, 44.73; H, 3.01; N, 11.67%.

*2.2.7. {2-Pyridin-2-yl-benzothiazole}PdClMe (**2**)*

This compound was prepared following the procedure described for **1** using [Pd(COD)MeCl] (0.13 g, 0.50 mmol) and **L2** (0.10 g, 0.50 mmol). Yield = 0.15 g (80%). ^{1}H NMR (DMSO-d_6): δ 1.14 (s, 3H, Pd–Me); 7.59 (d, 2H, $J = 8.1$, ph); 7.80 (d, 2H, $J = 7.8$, ph,); 8.18 (m, 1H, py); 8.31 (m, 2H, py); 8.72 (m, 1H, py). ^{13}C NMR ($CDCl_3$): δ 120.3 (*C3*, ph); 122.6 (*C6*, ph); 123.3 (*C5*, py); 126.1 (*C5*, ph); 28.4 (*C3*, py); 135.4 (*C4*, py); 137.9 (*C2*, py); 140.1 (*C1*, ph); 148.6 (*C*═N, thiazole); 149.9 (*C6*, py); (*C2*, py). MS (ESI) *m*/*z* (%) 372 (M^++NCMe, 100); 331 (40). *Anal.* Calc. for $C_{13}H_{11}N_2SPdCl$: C, 42.29; H, 3.00; N, 7.59. Found: C, 42.35; H, 3.21; N, 7.39%.

*2.2.8. {2-(4-tert-Butyl pyridin-2-yl)-benzooxazole}PdCl$_2$ (**3**)*

To a solution of [Pd(NCMe)Cl_2] (0.15 g, 0.60 mmol) in CH_2Cl_2 (20 mL) was added a solution of **L3** (0.15 g, 0.60 mmol) in CH2Cl2 (10 mL). The resultant orange solution was stirred for 24 h. The solution was then concentrated *in vacuo* and hexane (20 mL) added to precipitate a light orange solid. Yield = 0. 12 g (70%). ^{1}H NMR ($CDCl_3$): δ 1.47 (s, 9H, ^{t}Bu, py); 7.46 (t, 1H, ph); 7.60 (t, 1H, ph); 7.70 (d, 1H, $J = 7.5$, py); 7.73 (d, 1H, $J = 7.8$, ph); 8.11 (s, 1H, py); 8.68 (d, 1H, $J = 8.4$, ph); 9.15 (d, 1H, $J = 7.2$, py). ^{13}C NMR ($CDCl_3$): 31.2 (C-(CH_3)$_3$); 35.4 (*C*-(CH_3)$_3$, py); 110.9 (*C5*, ph); 111.3 (*C5*, py); 119.5 (*C6*, ph); 121.1 (*C2*, ph); 121.5 (*C3*, ph); 121.8 (*C4*, ph); 123.9 (*C1*, ph); 127.4 (*C2*, py); 131.0 (*C6*, ph); 149.4(*C*═N, oxazole); 151.6 (*C4*, py). MS (ESI) *m*/*z* (%) 436 (M^++NCMe, 50); 417 (100). *Anal.* Calc. for $C_{16}H_{16}N_2OPdCl_2$: C, 43.73; H, 3.87; N, 4.67. Found: C, 44.08; H, 3.59; N, 4.52%.

*2.2.9. {2-(4-tert-Butyl pyridin-2-yl)-benzooxazole}PdClMe (**4**)*

This compound was synthesized in a similar manner to complex **1** using **L3** (0.05 g, 0.20 mmol) and [Pd-(COD)ClMe] (0.05 g, 0.20 mmol). Yield = 0.08 g (72%). ^{1}H NMR, ($CDCl_3$): δ 1.17 (s, 3 H, CH_3, Pd–Me); 1.43 (s, 9H, ^{t}Bu, py); 7.56 (m, 2H, py); 7.64 (m, 1H, py); 8.16 (d, 2H, $J = 7.5$, ph); 8.54 (d, 1H, $J = 7.8$, py); 9.00 (d, 1H, $J = 7.5$, py). ^{13}C NMR ($CDCl_3$): −11.2 (Pd–CH_3); 30.4 (C-(CH_3)$_3$); 35.3 (*C*-(CH_3)$_3$, py); 111.0 (*C5*, ph); 111.6 (*C5*, py); 119.5 (*C6*, ph); 120.1 (*C2*, ph); 121.3 (*C3*, ph); 121.9 (*C4*, ph); 125.2 (*C1*, ph); 126.7 (*C2*, py); 127.7(*C6*, ph); 149.0 (*C*═N, oxazole); 149.4(*C4*, py). (ESI) *m*/*z* (%) 414 (M^++NCMe, 100); 253 (45). *Anal.* Calc. for $C_{17}H_{19}N_2OPdCl \cdot 0.5Et_2O$: C, 51.12; H, 5.38; N, 6.28. Found: C, 50.79; H, 5.71; N, 5.96%.

*2.2.10. {2-(4-tert-Butyl pyridin-2-yl)-benzothiazole}PdCl$_2$ (**5**)*

This compound was synthesized following the procedure described for **3** using **L4** (0.20 g, 0.80 mmol) and of [Pd(NCMe)Cl_2] (0.20 g, 0.80 mmol) to give a pale yellow

solid. Yield = 0.30 g (80%). ^{1}H NMR ($CDCl_3$): δ 1.40 (s, 9H, ^{t}Bu, py); 7.70 (m, 1H, ph); 7.90 (d, 1H, $J = 7.2$, py); 8.20 (m, 1H, ph); 8.39 (d, 1H, $J = 7.5$, ph); 8.65 (s, 1H, py); 9.03 (d, 1H, $J = 8.1$, ph); 9.54 (d, 1H, $J = 7.2$, py). ^{13}C NMR ($CDCl_3$): 30.7 (C-(CH_3)$_3$); 35.2 (*C*-(CH_3)$_3$); 111.5 (*C5*, py); 118.9 (*C3*, py); 120.8 (*C6*, ph); 121.7 (*C3*, ph); 125.6 (*C5*, ph); 127.1 (*C4*, ph); 130.6 (*C2*, ph); 149.4 (*C*=N, thiazole and *C2*, py); 150.5 (*C6*, py). MS (ESI) *m/z* (%) 446 (M^++NCMe, 100); 269 (10). *Anal.* Calc. for $C_{16}H_{16}N_2SPdCl_2 \cdot CH_2Cl_2$: C, 38.71; H, 2.44; N, 5.31. Found: C, 39.10; H, 2.60; N, 5.50%.

2.2.11. {2-(4-tert-Butyl pyridin-2-yl)-benzothiazole} PdClMe (6)

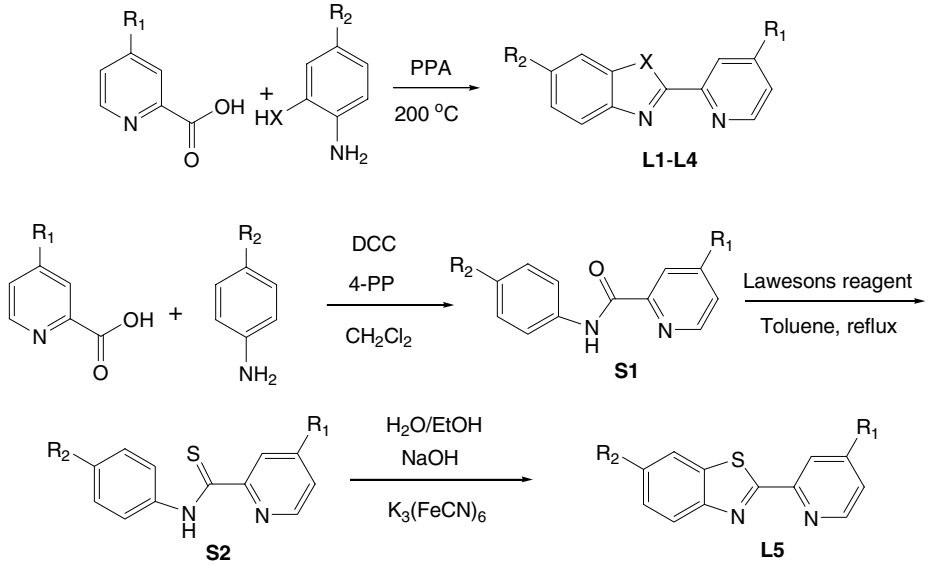
This compound was synthesised in a similar manner to complex **1** using **L4** (0.08 g, 0.20 mmol) and [Pd(COD)-ClMe] (0.07 g, 0.20 mmol). Yield = 0.09 g (82%). ^{1}H NMR ($CDCl_3$): δ 1.20 (s, 3H, CH_3, Pd–Me); 1.45 (s, 9H, ^{t}Bu, py); 7.55 (m, 2H, ph, 1H, py); 7.90 (d, 2H, $J = 8.1$, ph); 8.50 (d, 1H, $J = 7.8$, py); 9.41 (d, 1H, $J = 8.1$, py). ^{13}C NMR ($CDCl_3$): 1.3 (Pd-*C*H_3); 30.6 (C-(*C*H_3)$_3$, py); 35.3 (*C*-(CH_3)$_3$, py); 117.3 (*C3* and *C5*, py); 123.1 (*C3*, and *C6*, ph); 125.2 (*C5*, ph); 127.6 (*C4*, ph); 130.9 (*C2*, ph); 150.1 (*C*=N, thiazole and *C2*, py); 150.4 (*C6*, py). MS (ESI) *m/z* (%) 430 (M^++NCMe, 100); 269 (48). *Anal.* Calc. for $C_{17}H_{19}N_2SPdCl$: C, 48.01; H, 4.50; N, 6.59. Found: C, 47.99; H, 4.14; N, 6.45%.

2.2.12. 6-tert-Butyl-2-(4-tert-butyl-pyridin-2-yl)-benzothiazole} PdMeCl (7)

Complex **6** was prepared in a similar manner to **1** using **L5** (0.07 g, 0.21 mmol) and [Pd(COD)MeCl] (0.05 g, 0.21 mmol). Yield = 0.06 g (60%). ^{1}H NMR ($CDCl_3$): δ 1.21 (s, 3H, CH_3, Pd–Me); 1.40 (s, 9H, ^{t}Bu, ph); 1.45 (s, 9H, ^{t}Bu, py); 7.52 (d, 1H, $J = 7.8$, ph); 7.67 (d, 2H, $J = 10.5$, py); 7.86 (d, 2H, $J = 7.5$, ph); 8.47 (d, 1H, $J = 7.5$, py); 9.28 (d, 1H, $J = 9.0$, py). ^{13}C NMR ($CDCl_3$): 2.1(Pd-*C*H_3); 30.3 (C-(*C*H_3)$_3$, ph); 31.4 (C-(*C*H_3)$_3$, py); 32.9(*C*-(CH_3)$_3$, ph); 35.6 (*C*-(CH_3)$_3$, py); 117.3 (*C3* and *C5*, py) 123.4 (*C3*, ph); 124.3 (*C5*, ph); 124.9 (*C6*, ph); 126.7 (*C2*, ph); 147.8 (*C1* and *C4*, ph); 151.6 (*C1*, thiazole and *C2*, py); 163.9 (*C4*, py). MS (ESI) *m/z* (%) 486 (M^++NCMe, 100); 462 (90); 445 (10); 269 (48). *Anal.* Calc. for $C_{21}H_{27}N_2SPdCl$: C, 52.40; H, 5.65; N, 5.82. Found: C, 52.62; H, 6.03; N, 5.70%.

2.3. Typical procedure for Heck coupling reactions

In a typical experiment butylacrylate (0.06 mmol), iodobenzene (0.06 mmol) and Et_3N (0.06 mmol) were added to a



R_1	R_2	X	Ligand
H	H	N-H	**L1**
H	H	S	**L2**
^{t}Bu	H	O	**L3**
^{t}Bu	H	S	**L4**
^{t}Bu	^{t}Bu	S	**L5**

Scheme 1.

solution of the palladium catalyst (0.4%) in DMF (10 mL) at 80 °C and the reaction heated for 24 h. Samples were drawn at regular intervals and analyzed by GC to determine the percentage conversions. The coupling product was isolated by pouring the reaction mixture in water (50.00 mL) and extracted with CH_2Cl_2. The organic extract was dried over anhydrous $MgSO_4$ and the solvent was removed *in vacuo* to give a pure product as determined by ^{1}H NMR.

2.3.1. Reaction carousel experiments

For comparison and duplicate reactions, the Heck coupling reactions were also carried out in a Radley 12-place carousel on the same scale. Reaction mixtures were stirred and heated at (80 °C) heating block. Samples were drawn at regular intervals for GC analyses.

3. Results and discussion

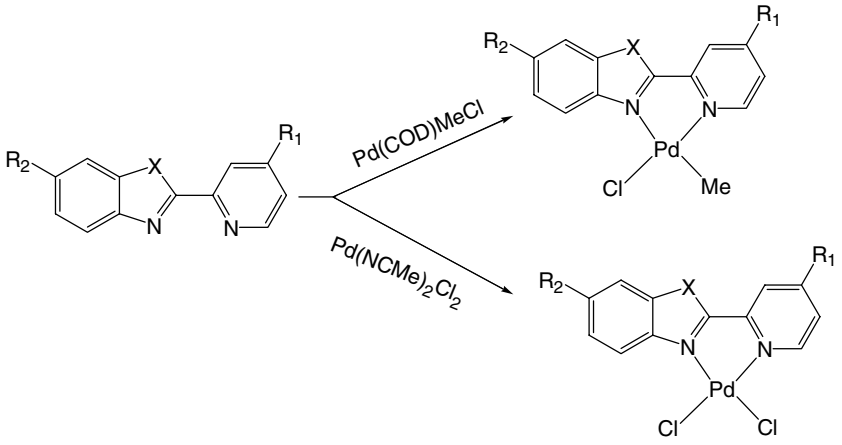
3.1. Synthesis of ligands and palladium complexes

Compounds **L1** and **L2** were prepared by the literature procedures [9] while **L3** and **L4** were prepared using a modified ring closure of 2-aminophenol and 2-aminothiophenol [9] with 4-*tert*-butylpyridine carboxylic acid, respectively (Scheme 1). Both compounds were obtained in good yields. The 4-*tert*-butylpyridine carboxylic acid was synthesized following the procedure described by Fife [12]. However, **L5** could not be synthesized by this method owing to the non-availability of substituted aminophenols or aminothiophenols. It was therefore synthesized by Jacobsen's intramolecular cyclization [13] under alkaline conditions with potassium ferricyanide (Scheme 1).

The carboxylic acid amide (**S1**) was prepared by reacting 4-*tert*-butylaniline with 4-*tert*-butylpyridine carboxylic acid and was obtained in good yields. Reactions of **S1** with 0.5 mol equivalent of Lawesson's reagent gave the corresponding carbothioic acid amide (**S2**), Scheme 1. Cyclization to give **L5** was achieved in quantitative yields by treatment of **S2** with potassium ferricyanide under basic conditions (30% NaOH). Consistent with literature reports, attempted cyclization of **S1** to give the benzooxazole analogue did not give the desired product [9].

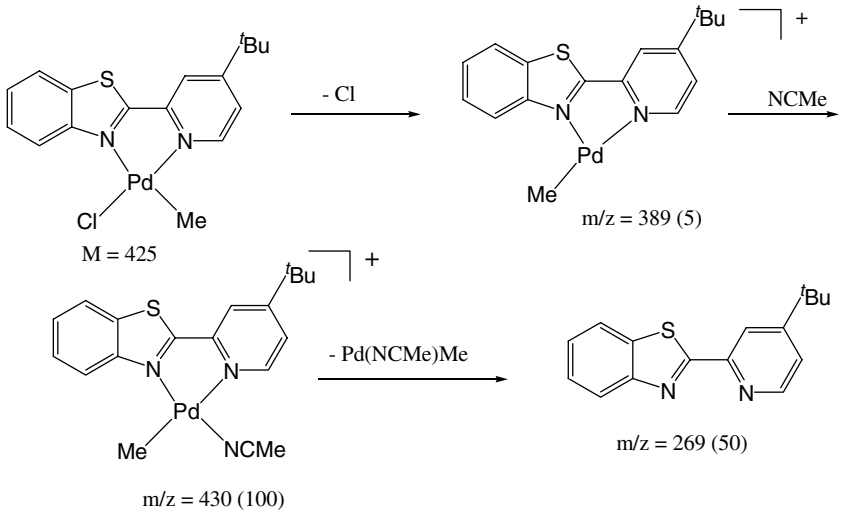
Reactions of compounds **L1**–**L5**, with either [Pd(NCMe)Cl_2] or [Pd(COD)MeCl] gave the corresponding palladium complexes (**1**–**7**) in moderate to high yields (Scheme 2). While complexes **1** and **2** showed poor solubility in most organic solvents, **3**–**6** were slightly soluble in chlorinated solvents due to the presence of the bulkier *tert*-butyl group on the pyridine ring. Complex **7**, containing *tert*-butyl groups on both the phenyl and pyridine rings, was completely soluble in chlorinated solvents.

The identities of **S1** and **S2** were established by ^{1}H NMR and ^{13}C NMR spectroscopy and high resolution



R_1	R_2	X	Complex
H	H	N-H	**1**
H	H	S	**2**
^{t}Bu	H	O	**3**
^{t}Bu	H	O	**4**
^{t}Bu	H	S	**5**
^{t}Bu	H	S	**6**
^{t}Bu	^{t}Bu	S	**7**

Scheme 2.



Scheme 3.

mass spectroscopy (HRMS). For example the N–H signal observed at 10.04 ppm (**S1**) confirmed the amide bond formation from the reaction between the pyridine carboxylic acid and the aniline, and a significant downfield shift of the N–H proton from 10.02 ppm (**S1**) to 12.11 ppm in **S2** confirmed the conversion of the C=O to C=S. Consistent with ^{1}H NMR spectra, ^{13}C NMR spectra show significant downfield shifts of the C=S (1873.3 ppm in **S2**) compared C=O (162.2 ppm in **S1**) carbon signals. HRMS spectral data for **S1** and **S2** showed *m*/*z* at 310 and *m*/*z* at 326 as the base peaks corresponding to the molecular ions of **S1** and **S2**, respectively.

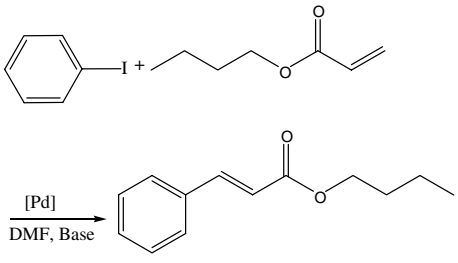
Compounds **L1**–**L5** and their complexes **1**–**7** were also characterized by a combination of ^{1}H NMR and ^{13}C NMR spectroscopy, mass spectrometry and micro-analyses. For example the intramolecular cyclization to give **L5** was evident from the disappearance of the N–H signal at 12.11 ppm and loss of symmetry in **S2** in the phenyl ring due to the formation of the C–S bond at one of the *ortho* positions of the phenyl ring. ^{1}H NMR spectra of the complexes showed significant downfield shifts of the aromatic signals in the region 7.20–9.40 ppm. For instance the shift of the *ortho* pridinyl proton from 8.60 ppm (**L4**) to 9.40 ppm in **5** indicates coordination to the palladium.

High resolution MS (ESI) mass spectra for **L3**–**L5** show *m*/*z* peaks at 253, 269 and 324 corresponding to the molecular ions of **L3**, **L4** and **L5**, respectively. The mass spectra and micro-analyses data of complexes **1**–**7** were in good agreement with the proposed structures of the complexes in Scheme 3.

All the complexes exhibited a similar mass spectral fragmentation pattern; starting with the loss of a Cl^{-} to form an unstable 14-electron cationic palladium complexes. In a typical fragmentation, **6** was found to loose a Cl^{-} to form a 14-electron fragment ($m/z = 389$), which was then stabilized by NCMe used to run the mass spectrum to give $[Pd(\mathbf{L4})(NCMe)Me]^{+}$ ($m/z = 430$) as the base peak (Scheme 3). Subsequent loss of $[Pd(NCMe)Me]^{+}$ results in the peak at $m/z = 269$ corresponding to **L4**. Fig. 1 shows the simulated and found isotopic distribution of the NCMe cationic adduct of **5**. This stabilization of the cationic species by NCMe was confirmed by isolation of the cationic adducts of **1** ($m/z = 357$) and **6** ($m/z = 430$) which were characterized by mass spectrometry.[1]

3.2. Heck coupling reactions

Complexes **1**–**7** were tested as catalysts in Heck coupling reaction of iodobenzene with butyl acrylate under different conditions. All the complexes were found to catalyze the coupling of butylacrylate with iodobenzene to form exclusively *trans*-butylcynnamate as established by ^{1}H NMR analysis.



(1)

In order to optimize the reaction conditions, the coupling reactions were performed at different conditions using catalysts **1** and **6** (Table 1). First we investigated the effect of temperature as it is well established that most Heck

[1] To a mixture of complex **6** (0.10 g, 0.24 mmol) and $NaBAr_4$ (Ar = 3,5-$(CF_3)_2C_6H_3$) was added a 1:1 mixture of CH_2Cl_2 and NCMe (20 mL) and the light yellow solution stirred for 24 h. The solvent was removed *in vacuo* to afford a light yellow solid. Yield = 0.20 g (67%). Positive MS (ESI) *m*/*z* (%) 430 (M^{+}, 50); 269 (100). Negative MS (ESI) *m*/*z* (%) 863 (M^{+}, 100). *Anal.* Calc. for $C_{52}H_{37}BF_{24}N_3PdS \cdot 0.5CH_2Cl_2$: C, 44.74; H, 2.79; N, 2.93. Found: C, 44.63; H, 2.45; N, 3.04%.

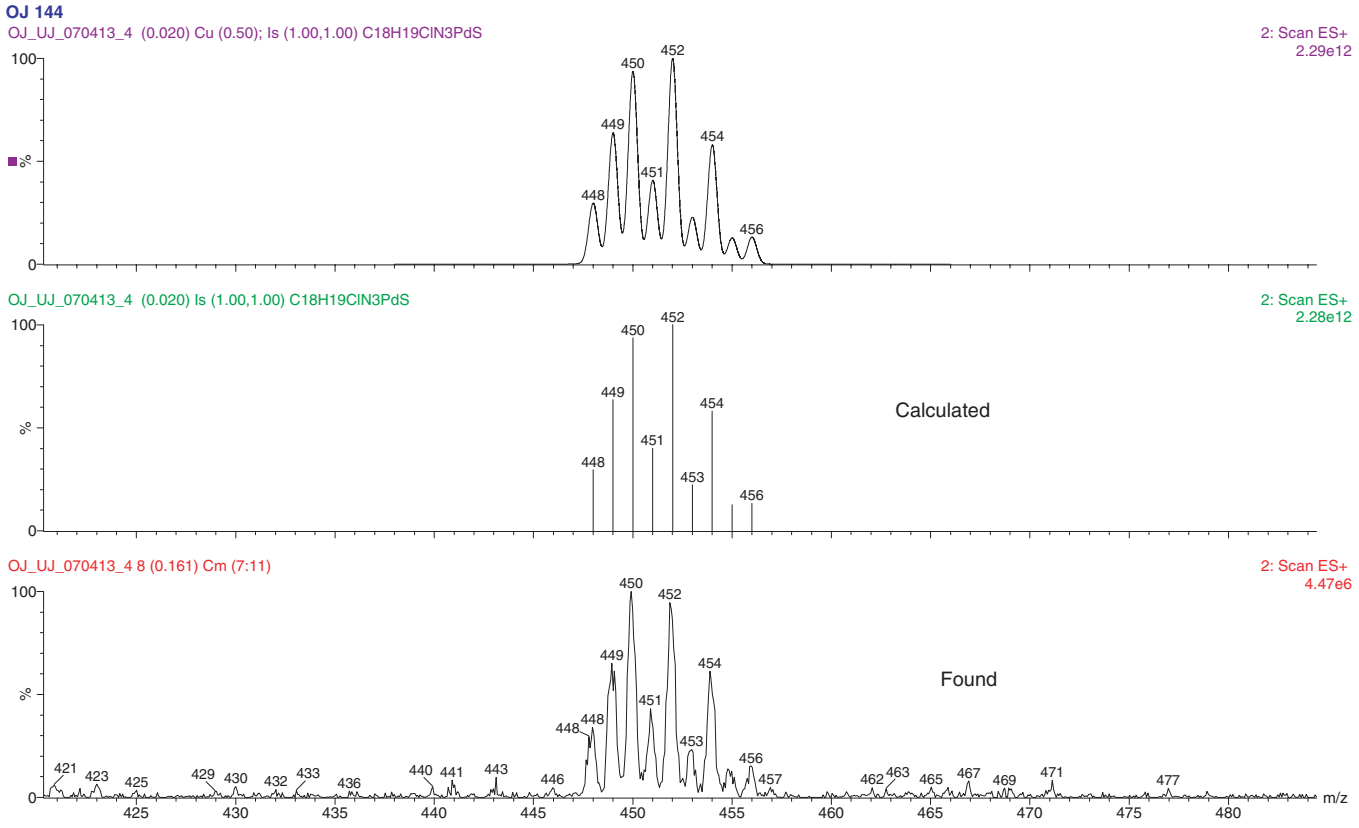


Fig. 1. Simulated and found isotopic distribution of NCMe adduct of **5**.

reactions occur at temperatures of 120–140 °C. However, literature reports also indicate catalyst deactivation at high temperatures as recently reported for the cyclopalladated imine catalysts [14]. Our catalysts are thus more stable at 120 °C than the cyclopalladated imine catalysts which are presumed to be very stable. It was evident that faster induction times were achieved at 120 °C than at 80 °C (Table 1 entries 1 and 4). After 24 h the temperature effect was less pronounced as observed from conversions of 92% at 80 °C and 98% at 120 °C.

Table 1
Effect of reaction conditions on Heck coupling reactions[a]

Entry	Catalyst	Time (h)	Temperature (°C)	[Pd] (%)	% Con[c]
1	**5**	1	120	1	94
1	**5**	4	120	1	98
3	**5**	24	120	1	98
4	**5**	1	80	1	82
5	**5**	4	80	1	90
6	**5**	8	80	1	92
7	**5**	24	80	1	92
8	**1**	1	120	1	92
9[b]	**1**	2	120	1	92
10[b]	**1**	4	120	1	92
11[b]	**1**	5	120	1	93
12[b]	**1**	24	120	1	94
13	**1**	24	120	0.8	99
14	**1**	24	120	0.4	97
15	**1**	24	120	0.2	97
16	**1**	24	120	0.1	97
17	**1**	24	120	0.05	74

[a] Conditions: amount of monomer, butylacrylate 0.06 mmol; iodobenzene, 0.06 mmol; base Et_3N solvent: DMF (10 mL).
[b] Equal amount of reactants added in situ after 1 h without addition of catalyst.
[c] Determined by GC.

To probe the stability of the active catalysts, equal amounts of the substrates and Et_3N were added at 1 h intervals to the reaction mixture using complex **1** at 120 °C. After each addition, the reaction was allowed to run for 1 h and an aliquot sampled for GC analysis. The conversions remained the same even after the fourth addition, showing that the catalyst did not deactivate with time (Table 1, entries 9–12). This observation suggests that the catalysts are "living" Heck coupling catalysts as compared to the well established phosphine-based catalysts, for example, $Pd(dippp)_2$ (dippp = 1,3-bis(diispropylphosphino)propane) that rapidly deactivate [2]. Nowotny et al. has observed diminished activity of cyclopalladated imine catalysts when a second addition of an equivalent amount of substrate and base were added, but found a total loss of activity on adding a third equivalent of substrate [14]. Our catalysts were still active even after the fourth run.

We further examined the effect of catalyst loading on the performance of the Heck reactions using catalyst **1** (Table 1, entries 8, 13–17). It is apparent that even at low catalyst loading (0.05%) there is considerable activity

with conversions of 74%. Interestingly increasing catalyst concentration to 1% resulted in reduction of activity with the optimum activity at 0.8%; though this does not differ much from the catalyst loading of 0.1–0.6%. The reduced activity at high catalyst loadings could be the result of agglomeration and thus lower the concentration of the active catalyst.

Having established the optimum catalytic conditions, **1**–**7** were screened at 80 °C to probe the effect of ligand structure on the catalysts' performance (Table 2). The low temperature of 80 °C slowed the initiation process enough to allow the reaction profiles to be established. Table 2, entries 1–6, shows how reaction with **1** gradually increased in conversion from 0% to 97% over 24 h. It is also evident from Table 2 that complexes **2**–**7** containing benzooxazole and benzothiazole exhibit almost 100% conversions within 1 h compared to the benzoimidazole complex (**1**) which showed no activity within 1 h. Thus the induction period for **1** is considerably slower compared to **2**–**7**.

As suggested by Kawano et al. [15] bidentate pyridine Pd(II) complexes catalyze Heck coupling reactions by first undergoing reduction to ligand-stabilized Pd(0). It is therefore conceivable that the electron deficient benzothiazole and benzooxazole in **2**–**7** might play a role in their rapid conversion to ligand-stabilized Pd(0), the active catalysts, as compared to the electron rich benzoimidazole in complex **1**. Bara-Behrens and co-workers [7b] have established that electron withdrawing abilities of azoles to follow the trend thiazole > oxazole > imidazole; an order that explains our observed trend in the initiation rates. We found the rates of initiation of **4** and **6** to be faster than **3** and **5** (Table 2 entries 3–6). This is consistent with earlier research findings that palladium pre-catalysts with Pd–Me show faster induction periods than the Pd-halides complexes [16]. Indeed chloromethylpalladium complexes are generally known to undergo rapid decomposition *via* reductive elimination pathway [17]. Nevertheless, the catalytic activities of all complexes after 24 h did not show any significant differences (Table 2). It is apparent that steric effect plays insignificant role in the catalytic activities of the complexes as seen in the comparable activities of complexes **2**, **6** and **7**. It is note worthy to point that complexes **2**–**7** exhibited relatively higher activity and shorter induction periods than the recently reported pyridyl-imine palladium catalysts [18] under similar conditions. For instance, while **1**–**7** display almost maximum conversion (98%) within 1 h, these palladium-imine catalysts give conversions of 35–75% within 1 h and in some cases achieve maximum conversion of 95% only after 2 h.

Table 2
Influence of catalyst system and stability on Heck coupling reactions[a]

Entry	Catalyst	Time (h)	Temperature (°C)	[Pd] (%)	Con[b] (%)
1	**1**	0.5	80	0.4	
2	**1**	1	80	0.4	
3	**1**	5	80	0.4	10
4	**1**	8	80	0.4	35
5	**1**	12	80	0.4	60
6	**1**	24	80	0.4	97
7	**2**	0.5	80	0.4	90
8	**2**	24	80	0.4	100
9	**3**	0.5	80	0.4	86
10	**3**	24	80	0.4	99
11	**4**	0.5	80	0.4	92
12	**4**	24	80	0.4	99
13	**5**	0.5	80	0.4	92
14	**5**	24	80	0.4	99
15	**6**	0.5	80	0.4	97
16	**6**	24	80	0.4	100
17	**7**	0.5	80	0.4	95
18	**7**	24	80	0.4	100

[a] Conditions: amount of monomers, butylacrylate 0.06 mmol; iodobenzene, 0.06 mmol; base, Et_3N; solvent: DMF (10 mL).
[b] Determined by GC.

Table 3
Heck coupling reactions catalyzed by in situ $Pd(OAc)_2$ and ligands **L1** and **L3**[a]

Entry	Ligand	Time (h)	[Pd] (%)[b]	Con[c] (%)
1		1	0.4	77
2		24	0.4	78
3	**L1**	1	0.4	74
4	**L1**	24	0.4	100
5	**L4**	1	0.4	98
6	**L4**	24	0.4	100

[a] Conditions: amount of monomers, butylacrylate 0.06 mmol; iodobenzene, 0.06 mmol; base, Et_3N; solvent: DMF (10 mL); temperature = 80 °C.
[b] Pd:ligand ration = 1:1.
[c] Determined by GC.

The palladium complexes, $[Pd(OAc)_2]$ and $[Pd(PPh_3)_4]$, are known to efficiently catalyze Heck coupling reactions although addition of certain ligands such as diphenylphosphino ferrocene (dppf) help in increasing their activities [1b]. In attempts to establish the comparative activities of **1**–**7** and $[Pd(OAc)_2]$, equimolar amounts of **L1** and **L4** were added to $[Pd(OAc)_2]$ and compared to the activity of $[Pd(OAc)_2]$ alone (Table 3).

We found that addition of **L1** and **L4** enhanced the activity of $[Pd(OAc)_2]$ from 78% to 100% (Table 3, entries 4–6). Consistent with the initiation rates of the corresponding complexes **1** and **6**, **L4** showed shorter induction period than **L1** (Table 3, entries 5). Amatore and Jutanda [19] have identified $[Pd(PPh_3)_2(OAc)_2]$ as the intermediate species formed when $[Pd(OAc)_2]$ and PPh_3 are used to catalyze Heck coupling reactions. The $[Pd^{(II)}(PPh_3)_2(OAc)_2]$ subsequently undergoes reduction to give $[Pd^{(0)}(PPh_3)_2(OAc)]^-$ as the active species. We expect both **L1** and **L4** to form similar palladium intermediates as suggested by Amatore and Jutanda [19] and thus the generation of the active catalysts by a similar mechanism.

4. Conclusions

In summary, this work has resulted in the identification of a convenient synthetic route to substituted

(pyridinyl)benzothiazole compounds. The ligands form mononuclear palladium complexes which catalyze Heck coupling reactions of iodobenzene with butylacrylates under mild conditions and at low catalyst loadings. The catalysts are air and moisture insensitive, thermally stable, and can be used as ''living'' Heck coupling catalysts.

Acknowledgements

The authors thank National Research Foundation, Department of Science and Technology, Centre of Excellence in Catalysis (NRF-DST, c*change) South Africa, University of Johannesburg and Chalmers University of Technology, Sweden for financial support.

References

[1] (a) I.P. Beletskaya, A.V. Cheprakov, Chem. Rev. 100 (2000) 3009;
(b) N.J. Whitcombe, S.E. Hii(Mimi) Gibson, Tetrahedron 57 (2001) 7449.
[2] (a) P. Garrou, Chem. Rev. 81 (1981) 229;
(b) R. Imbos, A.F. Minnaard, B.L. Feringa, J. Am. Chem. Soc. 124 (2002) 184.
[3] M.J. Burk, R.H. Crabtree, J. Am. Chem. Soc. 109 (1987) 8025.
[4] (a) C.M. Jensen, Chem. Commun. (1999) 2443;
(b) W.A. Hermann, C.P. Reisinger, M. Spiegler, J. Organomet. Chem. 557 (1998) 93.
[5] M.R. Buchmeiser, T. Schareina, R. Kempe, K. Wurst, J. Organomet. Chem. 634 (2001) 39.
[6] N.M. Motsoane, I.A. Guzei, J. Darkwa, Z. Naturforsch. 62b (2007) 323.
[7] (a) M.P. Fialon, N.A. Lopez, N. Barba-Behrens, R. Contreras, Heteroatom Chem. 9 (1998) 637;
(b) N.A. Lopez, A. Vazquez-Olmos, A. Ariza-Castolo, H. Tlahuex, M.P. Fialon, N. Barba-Behrens, R. Contreras, Heteroatom Chem. 9 (1997) 397;
(c) R.M.F. Batista, S.P.G. Costa, E.L. Malheiro, Tetrahedron 63 (2007) 4258;
(d) P. Hao, S. Zhang, W.-H. Sun, Q. Shi, S. Adewuyi, X. Lu, P. Li, Organometallics 26 (2007) 2437.
[8] (a) M.S. Mohlala, I.A. Guzei, J. Darkwa, S.F. Mapolie, J. Mol. Cat. A: Chem. 241 (2005) 93;
(b) S.O. Ojwach, I.A. Guzei, J. Darkwa, S.F. Mapolie, Polyhedron 26 (2007) 851.
[9] (a) R.D. Haugwitz, B.V. Maurer, G.A. Jacobs, V.N. Narayanan, L.R. Cruthers, J. Szanto, J. Med. Chem. 22 (1979) 1113;
(b) A.W. Addison, P.J. Burke, J. Heterocycl. Chem. 18 (1981) 803.
[10] D. Drew, J.R. Doyle, Inorg. Synth. 13 (1972) 47.
[11] E. Rule, I.M. Han, C.J. Elsevier, K. Vrieze, P.W.N.M. Van Leeuwen, C.F. Roobeek, M.C. Zoutberg, Y.F. Wand, C.H. Stam, Inorg. Chim. Acta 169 (1990) 5.
[12] W.K. Fife, J. Org. Chem. 48 (1983) 1375.
[13] Y. Chen, R. Chen, C. Qian, X. Dong, J. Sun, Organometallics 22 (2003) 4312.
[14] M. Nowotny, U. Hanefeld, H. Koningsveld, T. Maschmeyer, Chem. Commun. (2000) 1877.
[15] T. Kawano, T. Shinomaru, I. Ueda, Org. Lett. 4 (2002) 2545.
[16] D.S. McGuiness, M.J. Green, K.J. Cavell, B.W. Skelton, A.H. White, J. Organomet. Chem. 565 (1998) 165.
[17] M. Brookhart, B. Grant, A.F. Volpe Jr., Organometallics 11 (1992) 3920.
[18] A. Scrivanti, M. Bertoldini, U. Matteoli, V. Beghetto, S. Antonaroli, A. Marini, B. Crociani, J. Mol. Cat. A: Chem. 235 (2005) 12.
[19] C. Amatore, A. Jutanda, J. Organomet. Chem. 576 (1999) 254.

Available online at www.sciencedirect.com
ScienceDirect
Polyhedron 26 (2007) 5553
POLYHEDRON
www.elsevier.com/locate/poly

Erratum

Erratum to: "Synthesis, crystal, molecular, and electronic structure of [$ReOCl_3$(bpzm)] complex" [Polyhedron 26 (2007) 2581–2588]

B. Machura [a,*], R. Penczek [a], R. Kruszynski [b], J. Kusz [c]

[a] *Department of Inorganic and Coordination Chemistry, Institute of Chemistry, University of Silesia, 9th Szkolna Street, 40-006 Katowice, Poland*
[b] *Department of X-ray Crystallography and Crystal Chemistry, Institute of General and Ecological Chemistry, Lodz University of Technology, 16 Żeromski Street, 90-924 Łódź, Poland*
[c] *Institute of Physics, University of Silesia, 4th Uniwersytecka Street, 40-006 Katowice, Poland*

Available online 27 August 2007

The authors would like to add the following sentence to their article at the end of the first paragraph on page 2581: Recently this compound has been also obtained in the reaction [NBu_4][$ReOCl_4$] with bpzm and structurally characterized by Porchia and co-workers [M. Porchia, G.Papini, C. Santini, G.G. Lobbia, M. Pellei, F. Tisato, G. Bandoli, A. Dolmella, Inorg. Chem. 44 (2005) 4045].

DOI of original article: 10.1016/j.poly.2006.12.039.
* Corresponding author.
E-mail address: basia@ich.us.edu.pl (B. Machura).

0277-5387/$ - see front matter © 2007 Elsevier Ltd. All rights reserved.
doi:10.1016/j.poly.2007.07.011

Available online at www.sciencedirect.com
ScienceDirect
Polyhedron 26 (2007) 5554
POLYHEDRON
www.elsevier.com/locate/poly

Erratum

Erratum to "A theoretical study of a drastic structural change of bis(phthalocyaninato)lanthanide by ligand oxidation: Towards control of ligand field strength and magnetism of single-lanthanide-ionic single molecule magnet" [Polyhedron 26 (2007) 1859–1862]

Satoshi Takamatsu, Naoto Ishikawa *

Department of Applied Chemistry, Chuo University, 1-13-27 Kasusa, Tokyo, Bunkyo-ku 112-8551, Japan

Available online 27 September 2007

Page 1860, Fig. 1. There was an error in the unit for the vertical axis in the energy diagram. The correct unit is hartree, not eV.

DOI of original article: 10.1016/j.poly.2006.09.020.
* Corresponding author.
E-mail address: ishikawa@chem.chuo-u.ac.jp (N. Ishikawa).

0277-5387/$ - see front matter © 2007 Elsevier Ltd. All rights reserved.
doi:10.1016/j.poly.2007.08.028

POLYHEDRON

The International Journal for Inorganic and Organometallic Chemistry

Executive Editors

The Americas
G. Christou
Department of Chemistry, University of Florida,
Gainesville, FL 32611-7200, USA
E-mail: christou@chem.ufl.edu

Rest of the world
C.E. Housecroft
Department of Chemistry, University of Basel,
Spitalstrasse 51, CH-4056 Basel, Switzerland
E-mail: poly-chemie@unibas.ch

Associate Regional Editor for China
T.C.W. Mak
Department of Chemistry, University Science Centre,
The Chinese University of Hong Kong,
Shatin NT, Hong Kong, People's Republic of China
E-mail: tcwmak@cuhk.edu.hk

Polyhedron Reports
Editor
G. Christou *(Gainesville, FL, USA)*

Symposia-in-print
Editor
G. Parkin *(New York, NY, USA)*

Editorial Board
N.Y. Barba-Behrens *(Mexico, DF, Mexico)*
A.G. Blackman *(Dunedin, New Zealand)*
D.C. Bradley *(London, UK)*
D. Braga *(Bologna, Italy)*
A. Brodie *(Palmerston North, New Zealand)*
A. Castiñeiras *(Santiago de Compostela, Spain)*
X.-M. Chen *(Guangzhou, China)*
M.H. Chisholm *(Columbus, OH, USA)*
E.C. Constable *(Basel, Switzerland)*
E. Coronado *(Valencia, Spain)*
W.J. Evans *(Irvine, CA, USA)*
L.H. Gade *(Heidelberg, Germany)*
M.B. Hursthouse *(Southampton, UK)*
C. Kepert *(NSW, Australia)*
T. Kiss *(Szeged, Hungary)*
L. Manners *(Bristol, UK)*
S. Perlepes *(Patras, Greece)*
P.P. Power *(Davis, CA, USA)*
T.B. Rauchfuss *(Urbana, IL, USA)*
J. Reedijk *(Leiden, The Netherlands)*
A.L. Rheingold *(Newark, DE, USA)*
A.G. Sykes *(Newcastle upon Tyne, UK)*
L.K. Thompson *(St John's, NF, Canada)*
M.D. Ward *(Sheffield, UK)*
R.E.P. Winpenny *(Manchester, UK)*
M. Yamashita *(Sendai, Japan)*
M. Zaworotko *(Tampa, FL, USA)*

Aims and Scope

Polyhedron will publish original, fundamental, experimental and theoretical work of the highest quality in all the major areas of inorganic chemistry. These include synthetic chemistry, coordination chemistry, organometallic chemistry, bioinorganic chemistry, and solid-state and materials chemistry. Papers should be complete pieces of work, and the inclusion of results from spectroscopic and/or physical techniques is encouraged. Papers merely reporting the preparation and X-ray structural characterization of only a single compound will not be considered appropriate unless the compound and its structure are particularly interesting.

Similarly, papers concerned solely with stability constants determined by potentiometric titration data unsupported by other e.g. spectroscopic techniques will not be acceptable nor will solvent extraction data unless supported by other data of interest to inorganic chemists. Unnecessary fragmentation of work is not acceptable.

In addition Polyhedron publishes specially commissioned review articles (Polyhedron Reports) and collections of original research papers (Polyhedron Symposia-in-Print) of appropriate timeliness.

Publication Information: Polyhedron (ISSN 0277-5387). For 2007, volume 26 is scheduled for publication. Subscription prices are available upon request from the Publisher or from the Regional Sales Office nearest you or from this journal's website (http://www.elsevier.com/locate/poly). Further information is available on this journal and other Elsevier products through Elsevier's website (http://www.elsevier.com). Subscriptions are accepted on a prepaid basis only and are entered on a calendar year basis. Issues are sent by standard mail (surface within Europe, air delivery outside Europe). Priority rates are available upon request. Claims for missing issues should be made within six months of the date of dispatch.

Orders, Claims and Journal Enquiries

(no manuscript enquiries)

Please contact the Customer Support Department at the Regional Sales Office nearest you:

Orlando
Elsevier
Customer Service Department
6277 Sea Harbor Drive
Orlando, FL 32887-4800
USA
Tel.: (877) 8397126 or (800) 6542452 [toll free numbers for US customers];
(+1) (407) 3454020 or
(+1) (407) 3454000 [customers outside US]
Fax: (+1) (407) 3631354 or
(+1) (407) 3639661
E-mail: usjcs@elsevier.com or elspcs@elsevier.com

Amsterdam
Elsevier
Customer Service Department
P.O. Box 211
1000 AE Amsterdam
The Netherlands
Tel.: (+31) 20-485-3757
Fax: (+31) 20-485-3432
E-mail: nlinfo-f@elsevier.com

Tokyo
Elsevier K.K.
Customer Service Department
4F Higashi-Azabu, 1-Chome Bldg
1-9-15 Higashi-Azabu
Minato-ku, Tokyo 106-0044
Japan
Tel.: (+81) 3-5561-5037
Fax: (+81) 3-5561-5047
E-mail: jp.info@elsevier.com

Singapore
Elsevier
Customer Service Department
3 Killiney Road
#08-01 Winsland House 1
Singapore 239519
Tel.: (+65) 6349-0222
Fax: (+65) 6733-1510
E-mail: asiainfo@elsevier.com

USA mailing notice: *Polyhedron* (ISSN 0277-5387) is published triweekly by Elsevier Ltd. (P.O. Box 211, 1000 AE Amsterdam, The Netherlands). Annual subscription price in the USA US$ 7808.00 (valid in North, Central and South America), including air speed delivery. Periodical postage rate is paid at Jamaica, NY 11431.
USA POSTMASTER: Send change of address to *Polyhedron*, Elsevier, 6277 Sea Harbor Drive, Orlando, FL 32887-4800.
AIRFREIGHT AND MAILING in the USA by Publications Expediting Inc., 200 Meacham Avenue, Elmont, NY 11003.

Advertising Information

Advertising orders and enquiries can be sent to: **South America:** Mr Tino DeCarlo, The Advertising Department, Elsevier Inc., 360 Park Avenue South, New York, NY 10010-1710, USA; tel.: (+1) (212) 633 3815; fax: (+1) (212) 633 3820; e-mail: t.decarlo@elsevier.com. **Europe, USA, Canada and ROW:** Miss Katrina Barton, Commercial Sales, Elsevier, 84 Theobald's Road, London, WCIX 8RR, UK; phone: (+44) (0) 20 7611 4117; fax: (+44) (0) 20 7611 4463; e-mail: commercialsales@elsevier.com

POLYHEDRON

The International Journal for Inorganic and Organometallic Chemistry

Executive Editors

The Americas
G. Christou
Department of Chemistry, University of Florida,
Gainesville, FL 32611-7200, USA
E-mail: christou@chem.ufl.edu

Rest of the world
C.E. Housecroft
Department of Chemistry, University of Basel,
Spitalstrasse 51, CH-4056 Basel, Switzerland
E-mail: poly-chemie@unibas.ch

Associate Regional Editor for China
T.C.W. Mak
Department of Chemistry, University Science Centre,
The Chinese University of Hong Kong,
Shatin NT, Hong Kong, People's Republic of China
E-mail: tcwmak@cuhk.edu.hk

Polyhedron Reports
Editor
G. Christou *(Gainesville, FL, USA)*

Symposia-in-print
Editor
G. Parkin *(New York, NY, USA)*

Editorial Board

N.Y. Barba-Behrens *(Mexico, DF, Mexico)*
A.G. Blackman *(Dunedin, New Zealand)*
D.C. Bradley *(London, UK)*
D. Braga *(Bologna, Italy)*
A. Brodie *(Palmerston North, New Zealand)*
A. Castiñeiras *(Santiago de Compostela, Spain)*
X.-M. Chen *(Guangzhou, China)*
M.H. Chisholm *(Columbus, OH, USA)*
E.C. Constable *(Basel, Switzerland)*
E. Coronado *(Valencia, Spain)*
W.J. Evans *(Irvine, CA, USA)*
L.H. Gade *(Heidelberg, Germany)*
M.B. Hursthouse *(Southampton, UK)*
C. Kepert *(NSW, Australia)*
T. Kiss *(Szeged, Hungary)*
L. Manners *(Bristol, UK)*
S. Perlepes *(Patras, Greece)*
P.P. Power *(Davis, CA, USA)*
T.B. Rauchfuss *(Urbana, IL, USA)*
J. Reedijk *(Leiden, The Netherlands)*
A.L. Rheingold *(Newark, DE, USA)*
A.G. Sykes *(Newcastle upon Tyne, UK)*
L.K. Thompson *(St John's, NF, Canada)*
M.D. Ward *(Sheffield, UK)*
R.E.P. Winpenny *(Manchester, UK)*
M. Yamashita *(Sendai, Japan)*
M. Zaworotko *(Tampa, FL, USA)*

Aims and Scope

Polyhedron will publish original, fundamental, experimental and theoretical work of the highest quality in all the major areas of inorganic chemistry. These include synthetic chemistry, coordination chemistry, organometallic chemistry, bioinorganic chemistry, and solid-state and materials chemistry. Papers should be complete pieces of work, and the inclusion of results from spectroscopic and/or physical techniques is encouraged. Papers merely reporting the preparation and X-ray structural characterization of only a single compound will not be considered appropriate unless the compound and its structure are particularly interesting.

Similarly, papers concerned solely with stability constants determined by potentiometric titration data unsupported by other e.g. spectroscopic techniques will not be acceptable nor will solvent extraction data unless supported by other data of interest to inorganic chemists. Unnecessary fragmentation of work is not acceptable.

In addition Polyhedron publishes specially commissioned review articles (Polyhedron Reports) and collections of original research papers (Polyhedron Symposia-in-Print) of appropriate timeliness.

Publication Information: Polyhedron (ISSN 0277-5387). For 2007, volume 26 is scheduled for publication. Subscription prices are available upon request from the Publisher or from the Regional Sales Office nearest you or from this journal's website (http://www.elsevier.com/locate/poly). Further information is available on this journal and other Elsevier products through Elsevier's website (http://www.elsevier.com). Subscriptions are accepted on a prepaid basis only and are entered on a calendar year basis. Issues are sent by standard mail (surface within Europe, air delivery outside Europe). Priority rates are available upon request. Claims for missing issues should be made within six months of the date of dispatch.

Orders, Claims and Journal Enquiries

(no manuscript enquiries)

Please contact the Customer Support Department at the Regional Sales Office nearest you:

Orlando
Elsevier
Customer Service Department
6277 Sea Harbor Drive
Orlando, FL 32887-4800
USA
Tel.: (877) 8397126 or (800) 6542452 [toll free numbers for US customers];
(+1) (407) 3454020 or
(+1) (407) 3454000 [customers outside US]
Fax: (+1) (407) 3631354 or
(+1) (407) 3639661
E-mail: usjcs@elsevier.com or elspcs@elsevier.com

Amsterdam
Elsevier
Customer Service Department
P.O. Box 211
1000 AE Amsterdam
The Netherlands
Tel.: (+31) 20-485-3757
Fax: (+31) 20-485-3432
E-mail: nlinfo-f@elsevier.com

Tokyo
Elsevier K.K.
Customer Service Department
4F Higashi-Azabu, 1-Chome Bldg
1-9-15 Higashi-Azabu
Minato-ku, Tokyo 106-0044
Japan
Tel.: (+81) 3-5561-5037
Fax: (+81) 3-5561-5047
E-mail: jp.info@elsevier.com

Singapore
Elsevier
Customer Service Department
3 Killiney Road
#08-01 Winsland House 1
Singapore 239519
Tel.: (+65) 6349-0222
Fax: (+65) 6733-1510
E-mail: asiainfo@elsevier.com

USA mailing notice: *Polyhedron* (ISSN 0277-5387) is published triweekly by Elsevier Ltd. (P.O. Box 211, 1000 AE Amsterdam, The Netherlands). Annual subscription price in the USA US$ 7808.00 (valid in North, Central and South America), including air speed delivery. Periodical postage rate is paid at Jamaica, NY 11431.
USA POSTMASTER: Send change of address to *Polyhedron*, Elsevier, 6277 Sea Harbor Drive, Orlando, FL 32887-4800.
AIRFREIGHT AND MAILING in the USA by Publications Expediting Inc., 200 Meacham Avenue, Elmont, NY 11003.

Advertising Information

Advertising orders and enquiries can be sent to: **South America:** Mr Tino DeCarlo, The Advertising Department, Elsevier Inc., 360 Park Avenue South, New York, NY 10010-1710, USA; tel.: (+1) (212) 633 3815; fax: (+1) (212) 633 3820; e-mail: t.decarlo@elsevier.com. **Europe, USA, Canada and ROW:** Miss Katrina Barton, Commercial Sales, Elsevier, 84 Theobald's Road, London, WCIX 8RR, UK; phone: (+44) (0) 20 7611 4117; fax: (+44) (0) 20 7611 4463; e-mail: commercialsales@elsevier.com

POLYHEDRON

The International Journal for Inorganic and Organometallic Chemistry

Executive Editors

The Americas
G. Christou
Department of Chemistry, University of Florida,
Gainesville, FL 32611-7200, USA
E-mail: christou@chem.ufl.edu

Rest of the world
C.E. Housecroft
Department of Chemistry, University of Basel,
Spitalstrasse 51, CH-4056 Basel, Switzerland
E-mail: poly-chemie@unibas.ch

Associate Regional Editor for China
T.C.W. Mak
Department of Chemistry, University Science Centre,
The Chinese University of Hong Kong,
Shatin NT, Hong Kong, People's Republic of China
E-mail: tcwmak@cuhk.edu.hk

Polyhedron Reports
Editor
G. Christou *(Gainesville, FL, USA)*

Symposia-in-print
Editor
G. Parkin *(New York, NY, USA)*

Editorial Board
N.Y. Barba-Behrens *(Mexico, DF, Mexico)*
A.G. Blackman *(Dunedin, New Zealand)*
D.C. Bradley *(London, UK)*
D. Braga *(Bologna, Italy)*
A. Brodie *(Palmerston North, New Zealand)*
A. Castiñeiras *(Santiago de Compostela, Spain)*
X.-M. Chen *(Guangzhou, China)*
M.H. Chisholm *(Columbus, OH, USA)*
E.C. Constable *(Basel, Switzerland)*
E. Coronado *(Valencia, Spain)*
W.J. Evans *(Irvine, CA, USA)*
L.H. Gade *(Heidelberg, Germany)*
M.B. Hursthouse *(Southampton, UK)*
C. Kepert *(NSW, Australia)*
T. Kiss *(Szeged, Hungary)*
L. Manners *(Bristol, UK)*
S. Perlepes *(Patras, Greece)*
P.P. Power *(Davis, CA, USA)*
T.B. Rauchfuss *(Urbana, IL, USA)*
J. Reedijk *(Leiden, The Netherlands)*
A.L. Rheingold *(Newark, DE, USA)*
A.G. Sykes *(Newcastle upon Tyne, UK)*
L.K. Thompson *(St John's, NF, Canada)*
M.D. Ward *(Sheffield, UK)*
R.E.P. Winpenny *(Manchester, UK)*
M. Yamashita *(Sendai, Japan)*
M. Zaworotko *(Tampa, FL, USA)*

Aims and Scope

Polyhedron will publish original, fundamental, experimental and theoretical work of the highest quality in all the major areas of inorganic chemistry. These include synthetic chemistry, coordination chemistry, organometallic chemistry, bioinorganic chemistry, and solid-state and materials chemistry. Papers should be complete pieces of work, and the inclusion of results from spectroscopic and/or physical techniques is encouraged. Papers merely reporting the preparation and X-ray structural characterization of only a single compound will not be considered appropriate unless the compound and its structure are particularly interesting.

Similarly, papers concerned solely with stability constants determined by potentiometric titration data unsupported by other e.g. spectroscopic techniques will not be acceptable nor will solvent extraction data unless supported by other data of interest to inorganic chemists. Unnecessary fragmentation of work is not acceptable.

In addition Polyhedron publishes specially commissioned review articles (Polyhedron Reports) and collections of original research papers (Polyhedron Symposia-in-Print) of appropriate timeliness.

Publication Information: Polyhedron (ISSN 0277-5387). For 2007, volume 26 is scheduled for publication. Subscription prices are available upon request from the Publisher or from the Regional Sales Office nearest you or from this journal's website (http://www.elsevier.com/locate/poly). Further information is available on this journal and other Elsevier products through Elsevier's website (http://www.elsevier.com). Subscriptions are accepted on a prepaid basis only and are entered on a calendar year basis. Issues are sent by standard mail (surface within Europe, air delivery outside Europe). Priority rates are available upon request. Claims for missing issues should be made within six months of the date of dispatch.

Orders, Claims and Journal Enquiries

(no manuscript enquiries)
Please contact the Customer Support Department at the Regional Sales Office nearest you:

Orlando
Elsevier
Customer Service Department
6277 Sea Harbor Drive
Orlando, FL 32887-4800
USA
Tel.: (877) 8397126 or (800) 6542452 [toll free numbers for US customers];
(+1) (407) 3454020 or
(+1) (407) 3454000 [customers outside US]
Fax: (+1) (407) 3631354 or
(+1) (407) 3639661
E-mail: usjcs@elsevier.com or elspcs@elsevier.com

Amsterdam
Elsevier
Customer Service Department
P.O. Box 211
1000 AE Amsterdam
The Netherlands
Tel.: (+31) 20-485-3757
Fax: (+31) 20-485-3432
E-mail: nlinfo-f@elsevier.com

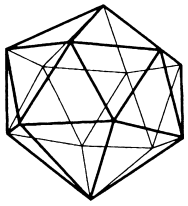
Tokyo
Elsevier K.K.
Customer Service Department
4F Higashi-Azabu, 1-Chome Bldg
1-9-15 Higashi-Azabu
Minato-ku, Tokyo 106-0044
Japan
Tel.: (+81) 3-5561-5037
Fax: (+81) 3-5561-5047
E-mail: jp.info@elsevier.com

Singapore
Elsevier
Customer Service Department
3 Killiney Road
#08-01 Winsland House 1
Singapore 239519
Tel.: (+65) 6349-0222
Fax: (+65) 6733-1510
E-mail: asiainfo@elsevier.com

USA mailing notice: *Polyhedron* (ISSN 0277-5387) is published triweekly by Elsevier Ltd. (P.O. Box 211, 1000 AE Amsterdam, The Netherlands). Annual subscription price in the USA US$ 7808.00 (valid in North, Central and South America), including air speed delivery. Periodical postage rate is paid at Jamaica, NY 11431.
USA POSTMASTER: Send change of address to *Polyhedron*, Elsevier, 6277 Sea Harbor Drive, Orlando, FL 32887-4800.
AIRFREIGHT AND MAILING in the USA by Publications Expediting Inc., 200 Meacham Avenue, Elmont, NY 11003.

Advertising Information

Advertising orders and enquiries can be sent to: **South America:** Mr Tino DeCarlo, The Advertising Department, Elsevier Inc., 360 Park Avenue South, New York, NY 10010-1710, USA; tel.: (+1) (212) 633 3815; fax: (+1) (212) 633 3820; e-mail: t.decarlo@elsevier.com. **Europe, USA, Canada and ROW:** Miss Katrina Barton, Commercial Sales, Elsevier, 84 Theobald's Road, London, WCIX 8RR, UK; phone: (+44) (0) 20 7611 4117; fax: (+44) (0) 20 7611 4463; e-mail: commercialsales@elsevier.com



POLYHEDRON

The International Journal for Inorganic and Organometallic Chemistry

Founding Editor
Sir Geoffrey Wilkinson✠

Volume 26/issue 2 (2007)

SPECIAL ISSUE
MODERN INORGANIC CHEMISTRY IN AUSTRALIA AND NEW ZEALAND

Editor
G. Christou
Department of Chemistry, University of Florida, Gainesville, FL, USA



ELSEVIER

Amsterdam – Boston – Jena – London – New York – Oxford
Paris – Philadelphia – San Diego – St Louis

POLYHEDRON

The International Journal for Inorganic and Organometallic Chemistry

Executive Editors

The Americas
G. Christou
Department of Chemistry, University of Florida,
Gainesville, FL 32611-7200, USA
E-mail: christou@chem.ufl.edu

Rest of the world
C.E. Housecroft
Department of Chemistry, University of Basel,
Spitalstrasse 51, CH-4056 Basel, Switzerland
E-mail: poly-chemie@unibas.ch

Associate Regional Editor for China
T.C.W. Mak
Department of Chemistry, University Science Centre,
The Chinese University of Hong Kong,
Shatin NT, Hong Kong, People's Republic of China
E-mail: tcwmak@cuhk.edu.hk

Polyhedron Reports
Editor
G. Christou *(Gainesville, FL, USA)*

Symposia-in-print
Editor
G. Parkin *(New York, NY, USA)*

Editorial Board
N.Y. Barba-Behrens *(Mexico, DF, Mexico)*
A.G. Blackman *(Dunedin, New Zealand)*
D.C. Bradley *(London, UK)*
D. Braga *(Bologna, Italy)*
A. Brodie *(Palmerston North, New Zealand)*
A. Castiñeiras *(Santiago de Compostela, Spain)*
X.-M. Chen *(Guangzhou, China)*
M.H. Chisholm *(Columbus, OH, USA)*
E.C. Constable *(Basel, Switzerland)*
E. Coronado *(Valencia, Spain)*
W.J. Evans *(Irvine, CA, USA)*
L.H. Gade *(Heidelberg, Germany)*
M.B. Hursthouse *(Southampton, UK)*
C. Kepert *(NSW, Australia)*
T. Kiss *(Szeged, Hungary)*
L. Manners *(Bristol, UK)*
S. Perlepes *(Patras, Greece)*
P.P. Power *(Davis, CA, USA)*
T.B. Rauchfuss *(Urbana, IL, USA)*
J. Reedijk *(Leiden, The Netherlands)*
A.L. Rheingold *(Newark, DE, USA)*
A.G. Sykes *(Newcastle upon Tyne, UK)*
L.K. Thompson *(St John's, NF, Canada)*
M.D. Ward *(Sheffield, UK)*
R.E.P. Winpenny *(Manchester, UK)*
M. Yamashita *(Sendai, Japan)*
M. Zaworotko *(Tampa, FL, USA)*

Aims and Scope

Polyhedron will publish original, fundamental, experimental and theoretical work of the highest quality in all the major areas of inorganic chemistry. These include synthetic chemistry, coordination chemistry, organometallic chemistry, bioinorganic chemistry, and solid-state and materials chemistry. Papers should be complete pieces of work, and the inclusion of results from spectroscopic and/or physical techniques is encouraged. Papers merely reporting the preparation and X-ray structural characterization of only a single compound will not be considered appropriate unless the compound and its structure are particularly interesting.
Similarly, papers concerned solely with stability constants determined by potentiometric titration data unsupported by other e.g. spectroscopic techniques will not be acceptable nor will solvent extraction data unless supported by other data of interest to inorganic chemists. Unnecessary fragmentation of work is not acceptable.
In addition Polyhedron publishes specially commissioned review articles (Polyhedron Reports) and collections of original research papers (Polyhedron Symposia-in-Print) of appropriate timeliness.

Publication Information: Polyhedron (ISSN 0277-5387). For 2007, volume 26 is scheduled for publication. Subscription prices are available upon request from the Publisher or from the Regional Sales Office nearest you or from this journal's website (http://www.elsevier.com/locate/poly). Further information is available on this journal and other Elsevier products through Elsevier's website (http://www.elsevier.com). Subscriptions are accepted on a prepaid basis only and are entered on a calendar year basis. Issues are sent by standard mail (surface within Europe, air delivery outside Europe). Priority rates are available upon request. Claims for missing issues should be made within six months of the date of dispatch.

Orders, Claims and Journal Enquiries

(no manuscript enquiries)
Please contact the Customer Support Department at the Regional Sales Office nearest you:

Orlando
Elsevier
Customer Service Department
6277 Sea Harbor Drive
Orlando, FL 32887-4800
USA
Tel.: (877) 8397126 or (800) 6542452 [toll free numbers for US customers];
(+1) (407) 3454020 or
(+1) (407) 3454000 [customers outside US]
Fax: (+1) (407) 3631354 or
(+1) (407) 3639661
E-mail: usjcs@elsevier.com or elspcs@elsevier.com

Amsterdam
Elsevier
Customer Service Department
P.O. Box 211
1000 AE Amsterdam
The Netherlands
Tel.: (+31) 20-485-3757
Fax: (+31) 20-485-3432
E-mail: nlinfo-f@elsevier.com

Tokyo
Elsevier K.K.
Customer Service Department
4F Higashi-Azabu, 1-Chome Bldg
1-9-15 Higashi-Azabu
Minato-ku, Tokyo 106-0044
Japan
Tel.: (+81) 3-5561-5037
Fax: (+81) 3-5561-5047
E-mail: jp.info@elsevier.com

Singapore
Elsevier
Customer Service Department
3 Killiney Road
#08-01 Winsland House 1
Singapore 239519
Tel.: (+65) 6349-0222
Fax: (+65) 6733-1510
E-mail: asiainfo@elsevier.com

USA mailing notice: *Polyhedron* (ISSN 0277-5387) is published triweekly by Elsevier Ltd. (P.O. Box 211, 1000 AE Amsterdam, The Netherlands). Annual subscription price in the USA US$ 7808.00 (valid in North, Central and South America), including air speed delivery. Periodical postage rate is paid at Rahway, NJ.
USA POSTMASTER: Send change of address to *Polyhedron*, Elsevier, 6277 Sea Harbor Drive, Orlando, FL 32887-4800.
AIRFREIGHT AND MAILING in the USA by Mercury International Limited, 365 Blair Road, Avenel, NJ 07001.

Advertising Information

Advertising orders and enquiries can be sent to: **South America:** Mr Tino DeCarlo, The Advertising Department, Elsevier Inc., 360 Park Avenue South, New York, NY 10010-1710, USA; tel.: (+1) (212) 633 3815; fax: (+1) (212) 633 3820; e-mail: t.decarlo@elsevier.com. **Europe, USA, Canada and ROW:** Miss Katrina Barton, Commercial Sales, Elsevier, 84 Theobald's Road, London, WCIX 8RR, UK; phone: (+44) (0) 20 7611 4117; fax: (+44) (0) 20 7611 4463; e-mail: commercialsales@elsevier.com

Funding body agreements and policies

Elsevier has established agreements and developed policies to allow authors who publish in Elsevier journals to comply with potential manuscript archiving requirements as specified as conditions of their grant awards. To learn more about existing agreements and policies please visit http://www.elsevier.com/fundingbodies

POLYHEDRON

The International Journal for Inorganic and Organometallic Chemistry

Executive Editors

The Americas
G. Christou
Department of Chemistry, University of Florida,
Gainesville, FL 32611-7200, USA
E-mail: christou@chem.ufl.edu

Rest of the world
C.E. Housecroft
Department of Chemistry, University of Basel,
Spitalstrasse 51, CH-4056 Basel, Switzerland
E-mail: poly-chemie@unibas.ch

Associate Regional Editor for China
T.C.W. Mak
Department of Chemistry, University Science Centre,
The Chinese University of Hong Kong,
Shatin NT, Hong Kong, People's Republic of China
E-mail: tcwmak@cuhk.edu.hk

Polyhedron Reports
Editor
G. Christou *(Gainesville, FL, USA)*

Symposia-in-print
Editor
G. Parkin *(New York, NY, USA)*

Editorial Board

N.Y. Barba-Behrens *(Mexico, DF, Mexico)*
A.G. Blackman *(Dunedin, New Zealand)*
D.C. Bradley *(London, UK)*
D. Braga *(Bologna, Italy)*
A. Brodie *(Palmerston North, New Zealand)*
A. Castiñeiras *(Santiago de Compostela, Spain)*
X.-M. Chen *(Guangzhou, China)*
M.H. Chisholm *(Columbus, OH, USA)*
E.C. Constable *(Basel, Switzerland)*
E. Coronado *(Valencia, Spain)*
W.J. Evans *(Irvine, CA, USA)*
L.H. Gade *(Heidelberg, Germany)*
M.B. Hursthouse *(Southampton, UK)*
C. Kepert *(NSW, Australia)*
T. Kiss *(Szeged, Hungary)*
L. Manners *(Bristol, UK)*
S. Perlepes *(Patras, Greece)*
P.P. Power *(Davis, CA, USA)*
T.B. Rauchfuss *(Urbana, IL, USA)*
J. Reedijk *(Leiden, The Netherlands)*
A.L. Rheingold *(Newark, DE, USA)*
A.G. Sykes *(Newcastle upon Tyne, UK)*
L.K. Thompson *(St John's, NF, Canada)*
M.D. Ward *(Sheffield, UK)*
R.E.P. Winpenny *(Manchester, UK)*
M. Yamashita *(Sendai, Japan)*
M. Zaworotko *(Tampa, FL, USA)*

Aims and Scope

Polyhedron will publish original, fundamental, experimental and theoretical work of the highest quality in all the major areas of inorganic chemistry. These include synthetic chemistry, coordination chemistry, organometallic chemistry, bioinorganic chemistry, and solid-state and materials chemistry. Papers should be complete pieces of work, and the inclusion of results from spectroscopic and/or physical techniques is encouraged. Papers merely reporting the preparation and X-ray structural characterization of only a single compound will not be considered appropriate unless the compound and its structure are particularly interesting.

Similarly, papers concerned solely with stability constants determined by potentiometric titration data unsupported by other e.g. spectroscopic techniques will not be acceptable nor will solvent extraction data unless supported by other data of interest to inorganic chemists. Unnecessary fragmentation of work is not acceptable.

In addition Polyhedron publishes specially commissioned review articles (Polyhedron Reports) and collections of original research papers (Polyhedron Symposia-in-Print) of appropriate timeliness.

Publication Information: Polyhedron (ISSN 0277-5387). For 2007, volume 26 is scheduled for publication. Subscription prices are available upon request from the Publisher or from the Regional Sales Office nearest you or from this journal's website (http://www.elsevier.com/locate/poly). Further information is available on this journal and other Elsevier products through Elsevier's website (http://www.elsevier.com). Subscriptions are accepted on a prepaid basis only and are entered on a calendar year basis. Issues are sent by standard mail (surface within Europe, air delivery outside Europe). Priority rates are available upon request. Claims for missing issues should be made within six months of the date of dispatch.

Orders, Claims and Journal Enquiries

(no manuscript enquiries)
Please contact the Customer Support Department at the Regional Sales Office nearest you:

Orlando
Elsevier
Customer Service Department
6277 Sea Harbor Drive
Orlando, FL 32887-4800
USA
Tel.: (877) 8397126 or (800) 6542452 [toll free numbers for US customers];
(+1) (407) 3454020 or
(+1) (407) 3454000 [customers outside US]
Fax: (+1) (407) 3631354 or
(+1) (407) 3639661
E-mail: usjcs@elsevier.com or elspcs@elsevier.com

Amsterdam
Elsevier
Customer Service Department
P.O. Box 211
1000 AE Amsterdam
The Netherlands
Tel.: (+31) 20-485-3757
Fax: (+31) 20-485-3432
E-mail: nlinfo-f@elsevier.com

Tokyo
Elsevier K.K.
Customer Service Department
4F Higashi-Azabu, 1-Chome Bldg
1-9-15 Higashi-Azabu
Minato-ku, Tokyo 106-0044
Japan
Tel.: (+81) 3-5561-5037
Fax: (+81) 3-5561-5047
E-mail: jp.info@elsevier.com

Singapore
Elsevier
Customer Service Department
3 Killiney Road
#08-01 Winsland House 1
Singapore 239519
Tel.: (+65) 6349-0222
Fax: (+65) 6733-1510
E-mail: asiainfo@elsevier.com

USA mailing notice: *Polyhedron* (ISSN 0277-5387) is published triweekly by Elsevier Ltd. (P.O. Box 211, 1000 AE Amsterdam, The Netherlands). Annual subscription price in the USA US$ 7808.00 (valid in North, Central and South America), including air speed delivery. Periodical postage rate is paid at Rahway, NJ.
USA POSTMASTER: Send change of address to *Polyhedron*, Elsevier, 6277 Sea Harbor Drive, Orlando, FL 32887-4800.
AIRFREIGHT AND MAILING in the USA by Mercury International Limited, 365 Blair Road, Avenel, NJ 07001.

Advertising Information

Advertising orders and enquiries can be sent to: **South America:** Mr Tino DeCarlo, The Advertising Department, Elsevier Inc., 360 Park Avenue South, New York, NY 10010-1710, USA; tel.: (+1) (212) 633 3815; fax: (+1) (212) 633 3820; e-mail: t.decarlo@elsevier.com. **Europe, USA, Canada and ROW:** Miss Katrina Barton, Commercial Sales, Elsevier, 84 Theobald's Road, London, WCIX 8RR, UK; phone: (+44) (0) 20 7611 4117; fax: (+44) (0) 20 7611 4463; e-mail: commercialsales@elsevier.com

Funding body agreements and policies

Elsevier has established agreements and developed policies to allow authors who publish in Elsevier journals to comply with potential manuscript archiving requirements as specified as conditions of their grant awards. To learn more about existing agreements and policies please visit http://www.elsevier.com/fundingbodies

POLYHEDRON

The International Journal for Inorganic and Organometallic Chemistry

Executive Editors

The Americas
G. Christou
Department of Chemistry, University of Florida,
Gainesville, FL 32611-7200, USA
E-mail: christou@chem.ufl.edu

Rest of the world
C.E. Housecroft
Department of Chemistry, University of Basel,
Spitalstrasse 51, CH-4056 Basel, Switzerland
E-mail: poly-chemie@unibas.ch

Associate Regional Editor for China
T.C.W. Mak
Department of Chemistry, University Science Centre,
The Chinese University of Hong Kong,
Shatin NT, Hong Kong, People's Republic of China
E-mail: tcwmak@cuhk.edu.hk

Polyhedron Reports
Editor
G. Christou *(Gainesville, FL, USA)*

Symposia-in-print
Editor
G. Parkin *(New York, NY, USA)*

Editorial Board
N.Y. Barba-Behrens *(Mexico, DF, Mexico)*
A.G. Blackman *(Dunedin, New Zealand)*
D.C. Bradley *(London, UK)*
D. Braga *(Bologna, Italy)*
A. Brodie *(Palmerston North, New Zealand)*
A. Castiñeiras *(Santiago de Compostela, Spain)*
X.-M. Chen *(Guangzhou, China)*
M.H. Chisholm *(Columbus, OH, USA)*
E.C. Constable *(Basel, Switzerland)*
E. Coronado *(Valencia, Spain)*
W.J. Evans *(Irvine, CA, USA)*
L.H. Gade *(Heidelberg, Germany)*
M.B. Hursthouse *(Southampton, UK)*
C. Kepert *(NSW, Australia)*
T. Kiss *(Szeged, Hungary)*
L. Manners *(Bristol, UK)*
S. Perlepes *(Patras, Greece)*
P.P. Power *(Davis, CA, USA)*
T.B. Rauchfuss *(Urbana, IL, USA)*
J. Reedijk *(Leiden, The Netherlands)*
A.L. Rheingold *(Newark, DE, USA)*
A.G. Sykes *(Newcastle upon Tyne, UK)*
L.K. Thompson *(St John's, NF, Canada)*
M.D. Ward *(Sheffield, UK)*
R.E.P. Winpenny *(Manchester, UK)*
M. Yamashita *(Sendai, Japan)*
M. Zaworotko *(Tampa, FL, USA)*

Aims and Scope

Polyhedron will publish original, fundamental, experimental and theoretical work of the highest quality in all the major areas of inorganic chemistry. These include synthetic chemistry, coordination chemistry, organometallic chemistry, bioinorganic chemistry, and solid-state and materials chemistry. Papers should be complete pieces of work, and the inclusion of results from spectroscopic and/or physical techniques is encouraged. Papers merely reporting the preparation and X-ray structural characterization of only a single compound will not be considered appropriate unless the compound and its structure are particularly interesting.

Similarly, papers concerned solely with stability constants determined by potentiometric titration data unsupported by other e.g. spectroscopic techniques will not be acceptable nor will solvent extraction data unless supported by other data of interest to inorganic chemists. Unnecessary fragmentation of work is not acceptable.

In addition Polyhedron publishes specially commissioned review articles (Polyhedron Reports) and collections of original research papers (Polyhedron Symposia-in-Print) of appropriate timeliness.

Publication Information: Polyhedron (ISSN 0277-5387). For 2007, volume 26 is scheduled for publication. Subscription prices are available upon request from the Publisher or from the Regional Sales Office nearest you or from this journal's website (http://www.elsevier.com/locate/poly). Further information is available on this journal and other Elsevier products through Elsevier's website (http://www.elsevier.com). Subscriptions are accepted on a prepaid basis only and are entered on a calendar year basis. Issues are sent by standard mail (surface within Europe, air delivery outside Europe). Priority rates are available upon request. Claims for missing issues should be made within six months of the date of dispatch.

Orders, Claims and Journal Enquiries

(no manuscript enquiries)
Please contact the Customer Support Department at the Regional Sales Office nearest you:

Orlando
Elsevier
Customer Service Department
6277 Sea Harbor Drive
Orlando, FL 32887-4800
USA
Tel.: (877) 8397126 or (800) 6542452 [toll free numbers for US customers];
(+1) (407) 3454020 or
(+1) (407) 3454000 [customers outside US]
Fax: (+1) (407) 3631354 or
(+1) (407) 3639661
E-mail: usjcs@elsevier.com or elspcs@elsevier.com

Amsterdam
Elsevier
Customer Service Department
P.O. Box 211
1000 AE Amsterdam
The Netherlands
Tel.: (+31) 20-485-3757
Fax: (+31) 20-485-3432
E-mail: nlinfo-f@elsevier.com

Tokyo
Elsevier K.K.
Customer Service Department
4F Higashi-Azabu, 1-Chome Bldg
1-9-15 Higashi-Azabu
Minato-ku, Tokyo 106-0044
Japan
Tel.: (+81) 3-5561-5037
Fax: (+81) 3-5561-5047
E-mail: jp.info@elsevier.com

Singapore
Elsevier
Customer Service Department
3 Killiney Road
#08-01 Winsland House 1
Singapore 239519
Tel.: (+65) 6349-0222
Fax: (+65) 6733-1510
E-mail: asiainfo@elsevier.com

USA mailing notice: *Polyhedron* (ISSN 0277-5387) is published triweekly by Elsevier Ltd. (P.O. Box 211, 1000 AE Amsterdam, The Netherlands). Annual subscription price in the USA US$ 7808.00 (valid in North, Central and South America), including air speed delivery. Periodical postage rate is paid at Rahway, NJ.
USA POSTMASTER: Send change of address to *Polyhedron*, Elsevier, 6277 Sea Harbor Drive, Orlando, FL 32887-4800.
AIRFREIGHT AND MAILING in the USA by Mercury International Limited, 365 Blair Road, Avenel, NJ 07001.

Advertising Information

Advertising orders and enquiries can be sent to: **South America:** Mr Tino DeCarlo, The Advertising Department, Elsevier Inc., 360 Park Avenue South, New York, NY 10010-1710, USA; tel.: (+1) (212) 633 3815; fax: (+1) (212) 633 3820; e-mail: t.decarlo@elsevier.com. **Europe, USA, Canada and ROW:** Miss Katrina Barton, Commercial Sales, Elsevier, 84 Theobald's Road, London, WCIX 8RR, UK; phone: (+44) (0) 20 7611 4117; fax: (+44) (0) 20 7611 4463; e-mail: commercialsales@elsevier.com

POLYHEDRON

The International Journal for Inorganic and Organometallic Chemistry

Executive Editors

The Americas
G. Christou
Department of Chemistry, University of Florida,
Gainesville, FL 32611-7200, USA
E-mail: christou@chem.ufl.edu

Rest of the world
C.E. Housecroft
Department of Chemistry, University of Basel,
Spitalstrasse 51, CH-4056 Basel, Switzerland
E-mail: poly-chemie@unibas.ch

Associate Regional Editor for China
T.C.W. Mak
Department of Chemistry, University Science Centre,
The Chinese University of Hong Kong,
Shatin NT, Hong Kong, People's Republic of China
E-mail: tcwmak@cuhk.edu.hk

Polyhedron Reports
Editor
G. Christou *(Gainesville, FL, USA)*

Symposia-in-print
Editor
G. Parkin *(New York, NY, USA)*

Editorial Board
N.Y. Barba-Behrens *(Mexico, DF, Mexico)*
A.G. Blackman *(Dunedin, New Zealand)*
D.C. Bradley *(London, UK)*
D. Braga *(Bologna, Italy)*
A. Brodie *(Palmerston North, New Zealand)*
A. Castiñeiras *(Santiago de Compostela, Spain)*
X.-M. Chen *(Guangzhou, China)*
M.H. Chisholm *(Columbus, OH, USA)*
E.C. Constable *(Basel, Switzerland)*
E. Coronado *(Valencia, Spain)*
W.J. Evans *(Irvine, CA, USA)*
L.H. Gade *(Heidelberg, Germany)*
M.B. Hursthouse *(Southampton, UK)*
C. Kepert *(NSW, Australia)*
T. Kiss *(Szeged, Hungary)*
L. Manners *(Bristol, UK)*
S. Perlepes *(Patras, Greece)*
P.P. Power *(Davis, CA, USA)*
T.B. Rauchfuss *(Urbana, IL, USA)*
J. Reedijk *(Leiden, The Netherlands)*
A.L. Rheingold *(Newark, DE, USA)*
A.G. Sykes *(Newcastle upon Tyne, UK)*
L.K. Thompson *(St John's, NF, Canada)*
M.D. Ward *(Sheffield, UK)*
R.E.P. Winpenny *(Manchester, UK)*
M. Yamashita *(Sendai, Japan)*
M. Zaworotko *(Tampa, FL, USA)*

Aims and Scope

Polyhedron will publish original, fundamental, experimental and theoretical work of the highest quality in all the major areas of inorganic chemistry. These include synthetic chemistry, coordination chemistry, organometallic chemistry, bioinorganic chemistry, and solid-state and materials chemistry. Papers should be complete pieces of work, and the inclusion of results from spectroscopic and/or physical techniques is encouraged. Papers merely reporting the preparation and X-ray structural characterization of only a single compound will not be considered appropriate unless the compound and its structure are particularly interesting.

Similarly, papers concerned solely with stability constants determined by potentiometric titration data unsupported by other e.g. spectroscopic techniques will not be acceptable nor will solvent extraction data unless supported by other data of interest to inorganic chemists. Unnecessary fragmentation of work is not acceptable.

In addition Polyhedron publishes specially commissioned review articles (Polyhedron Reports) and collections of original research papers (Polyhedron Symposia-in-Print) of appropriate timeliness.

Publication Information: Polyhedron (ISSN 0277-5387). For 2007, volume 26 is scheduled for publication. Subscription prices are available upon request from the Publisher or from the Regional Sales Office nearest you or from this journal's website (http://www.elsevier.com/locate/poly). Further information is available on this journal and other Elsevier products through Elsevier's website (http://www.elsevier.com). Subscriptions are accepted on a prepaid basis only and are entered on a calendar year basis. Issues are sent by standard mail (surface within Europe, air delivery outside Europe). Priority rates are available upon request. Claims for missing issues should be made within six months of the date of dispatch.

Orders, Claims and Journal Enquiries

(no manuscript enquiries)
Please contact the Customer Support Department at the Regional Sales Office nearest you:

Orlando
Elsevier
Customer Service Department
6277 Sea Harbor Drive
Orlando, FL 32887-4800
USA
Tel.: (877) 8397126 or (800) 6542452 [toll free numbers for US customers];
(+1) (407) 3454020 or
(+1) (407) 3454000 [customers outside US]
Fax: (+1) (407) 3631354 or
(+1) (407) 3639661
E-mail: usjcs@elsevier.com or elspcs@elsevier.com

Amsterdam
Elsevier
Customer Service Department
P.O. Box 211
1000 AE Amsterdam
The Netherlands
Tel.: (+31) 20-485-3757
Fax: (+31) 20-485-3432
E-mail: nlinfo-f@elsevier.com

Tokyo
Elsevier K.K.
Customer Service Department
4F Higashi-Azabu, 1-Chome Bldg
1-9-15 Higashi-Azabu
Minato-ku, Tokyo 106-0044
Japan
Tel.: (+81) 3-5561-5037
Fax: (+81) 3-5561-5047
E-mail: jp.info@elsevier.com

Singapore
Elsevier
Customer Service Department
3 Killiney Road
#08-01 Winsland House 1
Singapore 239519
Tel.: (+65) 6349-0222
Fax: (+65) 6733-1510
E-mail: asiainfo@elsevier.com

USA mailing notice: *Polyhedron* (ISSN 0277-5387) is published triweekly by Elsevier Ltd. (P.O. Box 211, 1000 AE Amsterdam, The Netherlands). Annual subscription price in the USA US$ 7808.00 (valid in North, Central and South America), including air speed delivery. Periodical postage rate is paid at Rahway, NJ.
USA POSTMASTER: Send change of address to *Polyhedron*, Elsevier, 6277 Sea Harbor Drive, Orlando, FL 32887-4800.
AIRFREIGHT AND MAILING in the USA by Mercury International Limited, 365 Blair Road, Avenel, NJ 07001.

Advertising Information

Advertising orders and enquiries can be sent to: **South America:** Mr Tino DeCarlo, The Advertising Department, Elsevier Inc., 360 Park Avenue South, New York, NY 10010-1710, USA; tel.: (+1) (212) 633 3815; fax: (+1) (212) 633 3820; e-mail: t.decarlo@elsevier.com. **Europe, USA, Canada and ROW:** Miss Katrina Barton, Commercial Sales, Elsevier, 84 Theobald's Road, London, WCIX 8RR, UK; phone: (+44) (0) 20 7611 4117; fax: (+44) (0) 20 7611 4463; e-mail: commercialsales@elsevier.com

POLYHEDRON

The International Journal for Inorganic and Organometallic Chemistry

Executive Editors

The Americas
G. Christou
Department of Chemistry, University of Florida,
Gainesville, FL 32611-7200, USA
E-mail: christou@chem.ufl.edu

Rest of the world
C.E. Housecroft
Department of Chemistry, University of Basel,
Spitalstrasse 51, CH-4056 Basel, Switzerland
E-mail: poly-chemie@unibas.ch

Associate Regional Editor for China
T.C.W. Mak
Department of Chemistry, University Science Centre,
The Chinese University of Hong Kong,
Shatin NT, Hong Kong, People's Republic of China
E-mail: tcwmak@cuhk.edu.hk

Polyhedron Reports
Editor
G. Christou *(Gainesville, FL, USA)*

Symposia-in-print
Editor
G. Parkin *(New York, NY, USA)*

Editorial Board

N.Y. Barba-Behrens *(Mexico, DF, Mexico)*
A.G. Blackman *(Dunedin, New Zealand)*
D.C. Bradley *(London, UK)*
D. Braga *(Bologna, Italy)*
A. Brodie *(Palmerston North, New Zealand)*
A. Castiñeiras *(Santiago de Compostela, Spain)*
X.-M. Chen *(Guangzhou, China)*
M.H. Chisholm *(Columbus, OH, USA)*
E.C. Constable *(Basel, Switzerland)*
E. Coronado *(Valencia, Spain)*
W.J. Evans *(Irvine, CA, USA)*
L.H. Gade *(Heidelberg, Germany)*
M.B. Hursthouse *(Southampton, UK)*
C. Kepert *(NSW, Australia)*
T. Kiss *(Szeged, Hungary)*
L. Manners *(Bristol, UK)*
S. Perlepes *(Patras, Greece)*
P.P. Power *(Davis, CA, USA)*
T.B. Rauchfuss *(Urbana, IL, USA)*
J. Reedijk *(Leiden, The Netherlands)*
A.L. Rheingold *(Newark, DE, USA)*
A.G. Sykes *(Newcastle upon Tyne, UK)*
L.K. Thompson *(St John's, NF, Canada)*
M.D. Ward *(Sheffield, UK)*
R.E.P. Winpenny *(Manchester, UK)*
M. Yamashita *(Sendai, Japan)*
M. Zaworotko *(Tampa, FL, USA)*

Aims and Scope

Polyhedron will publish original, fundamental, experimental and theoretical work of the highest quality in all the major areas of inorganic chemistry. These include synthetic chemistry, coordination chemistry, organometallic chemistry, bioinorganic chemistry, and solid-state and materials chemistry. Papers should be complete pieces of work, and the inclusion of results from spectroscopic and/or physical techniques is encouraged. Papers merely reporting the preparation and X-ray structural characterization of only a single compound will not be considered appropriate unless the compound and its structure are particularly interesting.

Similarly, papers concerned solely with stability constants determined by potentiometric titration data unsupported by other e.g. spectroscopic techniques will not be acceptable nor will solvent extraction data unless supported by other data of interest to inorganic chemists. Unnecessary fragmentation of work is not acceptable.

In addition Polyhedron publishes specially commissioned review articles (Polyhedron Reports) and collections of original research papers (Polyhedron Symposia-in-Print) of appropriate timeliness.

Publication Information: Polyhedron (ISSN 0277-5387). For 2007, volume 26 is scheduled for publication. Subscription prices are available upon request from the Publisher or from the Regional Sales Office nearest you or from this journal's website (http://www.elsevier.com/locate/poly). Further information is available on this journal and other Elsevier products through Elsevier's website (http://www.elsevier.com). Subscriptions are accepted on a prepaid basis only and are entered on a calendar year basis. Issues are sent by standard mail (surface within Europe, air delivery outside Europe). Priority rates are available upon request. Claims for missing issues should be made within six months of the date of dispatch.

Orders, Claims and Journal Enquiries

(no manuscript enquiries)

Please contact the Customer Support Department at the Regional Sales Office nearest you:

Orlando
Elsevier
Customer Service Department
6277 Sea Harbor Drive
Orlando, FL 32887-4800
USA
Tel.: (877) 8397126 or (800) 6542452 [toll free numbers for US customers];
(+1) (407) 3454020 or
(+1) (407) 3454000 [customers outside US]
Fax: (+1) (407) 3631354 or
(+1) (407) 3639661
E-mail: usjcs@elsevier.com or elspcs@elsevier.com

Amsterdam
Elsevier
Customer Service Department
P.O. Box 211
1000 AE Amsterdam
The Netherlands
Tel.: (+31) 20-485-3757
Fax: (+31) 20-485-3432
E-mail: nlinfo-f@elsevier.com

Tokyo
Elsevier K.K.
Customer Service Department
4F Higashi-Azabu, 1-Chome Bldg
1-9-15 Higashi-Azabu
Minato-ku, Tokyo 106-0044
Japan
Tel.: (+81) 3-5561-5037
Fax: (+81) 3-5561-5047
E-mail: jp.info@elsevier.com

Singapore
Elsevier
Customer Service Department
3 Killiney Road
#08-01 Winsland House 1
Singapore 239519
Tel.: (+65) 6349-0222
Fax: (+65) 6733-1510
E-mail: asiainfo@elsevier.com

USA mailing notice: *Polyhedron* (ISSN 0277-5387) is published triweekly by Elsevier Ltd. (P.O. Box 211, 1000 AE Amsterdam, The Netherlands). Annual subscription price in the USA US$ 7808.00 (valid in North, Central and South America), including air speed delivery. Periodical postage rate is paid at Rahway, NJ.
USA POSTMASTER: Send change of address to *Polyhedron*, Elsevier, 6277 Sea Harbor Drive, Orlando, FL 32887-4800.
AIRFREIGHT AND MAILING in the USA by Mercury International Limited, 365 Blair Road, Avenel, NJ 07001.

Advertising Information

Advertising orders and enquiries can be sent to: **South America:** Mr Tino DeCarlo, The Advertising Department, Elsevier Inc., 360 Park Avenue South, New York, NY 10010-1710, USA; tel.: (+1) (212) 633 3815; fax: (+1) (212) 633 3820; e-mail: t.decarlo@elsevier.com. **Europe, USA, Canada and ROW:** Miss Katrina Barton, Commercial Sales, Elsevier, 84 Theobald's Road, London, WCIX 8RR, UK; phone: (+44) (0) 20 7611 4117; fax: (+44) (0) 20 7611 4463; e-mail: commercialsales@elsevier.com

POLYHEDRON

The International Journal for Inorganic and Organometallic Chemistry

Executive Editors

The Americas
G. Christou
Department of Chemistry, University of Florida,
Gainesville, FL 32611-7200, USA
E-mail: christou@chem.ufl.edu

Rest of the world
C.E. Housecroft
Department of Chemistry, University of Basel,
Spitalstrasse 51, CH-4056 Basel, Switzerland
E-mail: poly-chemie@unibas.ch

Associate Regional Editor for China
T.C.W. Mak
Department of Chemistry, University Science Centre,
The Chinese University of Hong Kong,
Shatin NT, Hong Kong, People's Republic of China
E-mail: tcwmak@cuhk.edu.hk

Polyhedron Reports
Editor
G. Christou *(Gainesville, FL, USA)*

Symposia-in-print
Editor
G. Parkin *(New York, NY, USA)*

Editorial Board

N.Y. Barba-Behrens *(Mexico, DF, Mexico)*
A.G. Blackman *(Dunedin, New Zealand)*
D.C. Bradley *(London, UK)*
D. Braga *(Bologna, Italy)*
A. Brodie *(Palmerston North, New Zealand)*
A. Castiñeiras *(Santiago de Compostela, Spain)*
X.-M. Chen *(Guangzhou, China)*
M.H. Chisholm *(Columbus, OH, USA)*
E.C. Constable *(Basel, Switzerland)*
E. Coronado *(Valencia, Spain)*
W.J. Evans *(Irvine, CA, USA)*
L.H. Gade *(Heidelberg, Germany)*
M.B. Hursthouse *(Southampton, UK)*
C. Kepert *(NSW, Australia)*
T. Kiss *(Szeged, Hungary)*
L. Manners *(Bristol, UK)*
S. Perlepes *(Patras, Greece)*
P.P. Power *(Davis, CA, USA)*
T.B. Rauchfuss *(Urbana, IL, USA)*
J. Reedijk *(Leiden, The Netherlands)*
A.L. Rheingold *(Newark, DE, USA)*
A.G. Sykes *(Newcastle upon Tyne, UK)*
L.K. Thompson *(St John's, NF, Canada)*
M.D. Ward *(Sheffield, UK)*
R.E.P. Winpenny *(Manchester, UK)*
M. Yamashita *(Sendai, Japan)*
M. Zaworotko *(Tampa, FL, USA)*

Aims and Scope

Polyhedron will publish original, fundamental, experimental and theoretical work of the highest quality in all the major areas of inorganic chemistry. These include synthetic chemistry, coordination chemistry, organometallic chemistry, bioinorganic chemistry, and solid-state and materials chemistry. Papers should be complete pieces of work, and the inclusion of results from spectroscopic and/or physical techniques is encouraged. Papers merely reporting the preparation and X-ray structural characterization of only a single compound will not be considered appropriate unless the compound and its structure are particularly interesting.

Similarly, papers concerned solely with stability constants determined by potentiometric titration data unsupported by other e.g. spectroscopic techniques will not be acceptable nor will solvent extraction data unless supported by other data of interest to inorganic chemists. Unnecessary fragmentation of work is not acceptable.

In addition Polyhedron publishes specially commissioned review articles (Polyhedron Reports) and collections of original research papers (Polyhedron Symposia-in-Print) of appropriate timeliness.

Publication Information: Polyhedron (ISSN 0277-5387). For 2007, volume 26 is scheduled for publication. Subscription prices are available upon request from the Publisher or from the Regional Sales Office nearest you or from this journal's website (http://www.elsevier.com/locate/poly). Further information is available on this journal and other Elsevier products through Elsevier's website (http://www.elsevier.com). Subscriptions are accepted on a prepaid basis only and are entered on a calendar year basis. Issues are sent by standard mail (surface within Europe, air delivery outside Europe). Priority rates are available upon request. Claims for missing issues should be made within six months of the date of dispatch.

Orders, Claims and Journal Enquiries

(no manuscript enquiries)

Please contact the Customer Support Department at the Regional Sales Office nearest you:

Orlando
Elsevier
Customer Service Department
6277 Sea Harbor Drive
Orlando, FL 32887-4800
USA
Tel.: (877) 8397126 or (800) 6542452 [toll free numbers for US customers];
(+1) (407) 3454020 or
(+1) (407) 3454000 [customers outside US]
Fax: (+1) (407) 3631354 or
(+1) (407) 3639661
E-mail: usjcs@elsevier.com or elspcs@elsevier.com

Amsterdam
Elsevier
Customer Service Department
P.O. Box 211
1000 AE Amsterdam
The Netherlands
Tel.: (+31) 20-485-3757
Fax: (+31) 20-485-3432
E-mail: nlinfo-f@elsevier.com

Tokyo
Elsevier K.K.
Customer Service Department
4F Higashi-Azabu, 1-Chome Bldg
1-9-15 Higashi-Azabu
Minato-ku, Tokyo 106-0044
Japan
Tel.: (+81) 3-5561-5037
Fax: (+81) 3-5561-5047
E-mail: jp.info@elsevier.com

Singapore
Elsevier
Customer Service Department
3 Killiney Road
#08-01 Winsland House 1
Singapore 239519
Tel.: (+65) 6349-0222
Fax: (+65) 6733-1510
E-mail: asiainfo@elsevier.com

USA mailing notice: *Polyhedron* (ISSN 0277-5387) is published triweekly by Elsevier Ltd. (P.O. Box 211, 1000 AE Amsterdam, The Netherlands). Annual subscription price in the USA US$ 7808.00 (valid in North, Central and South America), including air speed delivery. Periodical postage rate is paid at Rahway, NJ.
USA POSTMASTER: Send change of address to *Polyhedron*, Elsevier, 6277 Sea Harbor Drive, Orlando, FL 32887-4800.
AIRFREIGHT AND MAILING in the USA by Mercury International Limited, 365 Blair Road, Avenel, NJ 07001.

Advertising Information

Advertising orders and enquiries can be sent to: **South America:** Mr Tino DeCarlo, The Advertising Department, Elsevier Inc., 360 Park Avenue South, New York, NY 10010-1710, USA; tel.: (+1) (212) 633 3815; fax: (+1) (212) 633 3820; e-mail: t.decarlo@elsevier.com. **Europe, USA, Canada and ROW:** Miss Katrina Barton, Commercial Sales, Elsevier, 84 Theobald's Road, London, WCIX 8RR, UK; phone: (+44) (0) 20 7611 4117; fax: (+44) (0) 20 7611 4463; e-mail: commercialsales@elsevier.com

POLYHEDRON

The International Journal for Inorganic and Organometallic Chemistry

Executive Editors

The Americas
G. Christou
Department of Chemistry, University of Florida,
Gainesville, FL 32611-7200, USA
E-mail: christou@chem.ufl.edu

Rest of the world
C.E. Housecroft
Department of Chemistry, University of Basel,
Spitalstrasse 51, CH-4056 Basel, Switzerland
E-mail: poly-chemie@unibas.ch

Associate Regional Editor for China
T.C.W. Mak
Department of Chemistry, University Science Centre,
The Chinese University of Hong Kong,
Shatin NT, Hong Kong, People's Republic of China
E-mail: tcwmak@cuhk.edu.hk

Polyhedron Reports
Editor
G. Christou *(Gainesville, FL, USA)*

Symposia-in-print
Editor
G. Parkin *(New York, NY, USA)*

Editorial Board

N.Y. Barba-Behrens *(Mexico, DF, Mexico)*
A.G. Blackman *(Dunedin, New Zealand)*
D.C. Bradley *(London, UK)*
D. Braga *(Bologna, Italy)*
A. Brodie *(Palmerston North, New Zealand)*
A. Castiñeiras *(Santiago de Compostela, Spain)*
X.-M. Chen *(Guangzhou, China)*
M.H. Chisholm *(Columbus, OH, USA)*
E.C. Constable *(Basel, Switzerland)*
E. Coronado *(Valencia, Spain)*
W.J. Evans *(Irvine, CA, USA)*
L.H. Gade *(Heidelberg, Germany)*
M.B. Hursthouse *(Southampton, UK)*
C. Kepert *(NSW, Australia)*
T. Kiss *(Szeged, Hungary)*
L. Manners *(Bristol, UK)*
S. Perlepes *(Patras, Greece)*
P.P. Power *(Davis, CA, USA)*
T.B. Rauchfuss *(Urbana, IL, USA)*
J. Reedijk *(Leiden, The Netherlands)*
A.L. Rheingold *(Newark, DE, USA)*
A.G. Sykes *(Newcastle upon Tyne, UK)*
L.K. Thompson *(St John's, NF, Canada)*
M.D. Ward *(Sheffield, UK)*
R.E.P. Winpenny *(Manchester, UK)*
M. Yamashita *(Sendai, Japan)*
M. Zaworotko *(Tampa, FL, USA)*

Aims and Scope

Polyhedron will publish original, fundamental, experimental and theoretical work of the highest quality in all the major areas of inorganic chemistry. These include synthetic chemistry, coordination chemistry, organometallic chemistry, bioinorganic chemistry, and solid-state and materials chemistry. Papers should be complete pieces of work, and the inclusion of results from spectroscopic and/or physical techniques is encouraged. Papers merely reporting the preparation and X-ray structural characterization of only a single compound will not be considered appropriate unless the compound and its structure are particularly interesting.

Similarly, papers concerned solely with stability constants determined by potentiometric titration data unsupported by other e.g. spectroscopic techniques will not be acceptable nor will solvent extraction data unless supported by other data of interest to inorganic chemists. Unnecessary fragmentation of work is not acceptable.

In addition Polyhedron publishes specially commissioned review articles (Polyhedron Reports) and collections of original research papers (Polyhedron Symposia-in-Print) of appropriate timeliness.

Publication Information: Polyhedron (ISSN 0277-5387). For 2007, volume 26 is scheduled for publication. Subscription prices are available upon request from the Publisher or from the Regional Sales Office nearest you or from this journal's website (http://www.elsevier.com/locate/poly). Further information is available on this journal and other Elsevier products through Elsevier's website (http://www.elsevier.com). Subscriptions are accepted on a prepaid basis only and are entered on a calendar year basis. Issues are sent by standard mail (surface within Europe, air delivery outside Europe). Priority rates are available upon request. Claims for missing issues should be made within six months of the date of dispatch.

Orders, Claims and Journal Enquiries

(no manuscript enquiries)

Please contact the Customer Support Department at the Regional Sales Office nearest you:

Orlando
Elsevier
Customer Service Department
6277 Sea Harbor Drive
Orlando, FL 32887-4800
USA
Tel.: (877) 8397126 or (800) 6542452 [toll free numbers for US customers];
(+1) (407) 3454020 or
(+1) (407) 3454000 [customers outside US]
Fax: (+1) (407) 3631354 or
(+1) (407) 3639661
E-mail: usjcs@elsevier.com or elspcs@elsevier.com

Amsterdam
Elsevier
Customer Service Department
P.O. Box 211
1000 AE Amsterdam
The Netherlands
Tel.: (+31) 20-485-3757
Fax: (+31) 20-485-3432
E-mail: nlinfo-f@elsevier.com

Tokyo
Elsevier K.K.
Customer Service Department
4F Higashi-Azabu, 1-Chome Bldg
1-9-15 Higashi-Azabu
Minato-ku, Tokyo 106-0044
Japan
Tel.: (+81) 3-5561-5037
Fax: (+81) 3-5561-5047
E-mail: jp.info@elsevier.com

Singapore
Elsevier
Customer Service Department
3 Killiney Road
#08-01 Winsland House 1
Singapore 239519
Tel.: (+65) 6349-0222
Fax: (+65) 6733-1510
E-mail: asiainfo@elsevier.com

USA mailing notice: *Polyhedron* (ISSN 0277-5387) is published triweekly by Elsevier Ltd. (P.O. Box 211, 1000 AE Amsterdam, The Netherlands). Annual subscription price in the USA US$ 7808.00 (valid in North, Central and South America), including air speed delivery. Periodical postage rate is paid at Rahway, NJ.

USA POSTMASTER: Send change of address to *Polyhedron*, Elsevier, 6277 Sea Harbor Drive, Orlando, FL 32887-4800.

AIRFREIGHT AND MAILING in the USA by Mercury International Limited, 365 Blair Road, Avenel, NJ 07001.

Advertising Information

Advertising orders and enquiries can be sent to: **South America:** Mr Tino DeCarlo, The Advertising Department, Elsevier Inc., 360 Park Avenue South, New York, NY 10010-1710, USA; tel.: (+1) (212) 633 3815; fax: (+1) (212) 633 3820; e-mail: t.decarlo@elsevier.com. **Europe, USA, Canada and ROW:** Miss Katrina Barton, Commercial Sales, Elsevier, 84 Theobald's Road, London, WCIX 8RR, UK; phone: (+44) (0) 20 7611 4117; fax: (+44) (0) 20 7611 4463; e-mail: commercialsales@elsevier.com

POLYHEDRON

The International Journal for Inorganic and Organometallic Chemistry

Executive Editors

The Americas
G. Christou
Department of Chemistry, University of Florida,
Gainesville, FL 32611-7200, USA
E-mail: christou@chem.ufl.edu

Rest of the world
C.E. Housecroft
Department of Chemistry, University of Basel,
Spitalstrasse 51, CH-4056 Basel, Switzerland
E-mail: poly-chemie@unibas.ch

Associate Regional Editor for China
T.C.W. Mak
Department of Chemistry, University Science Centre,
The Chinese University of Hong Kong,
Shatin NT, Hong Kong, People's Republic of China
E-mail: tcwmak@cuhk.edu.hk

Polyhedron Reports
Editor
G. Christou *(Gainesville, FL, USA)*

Symposia-in-print
Editor
G. Parkin *(New York, NY, USA)*

Editorial Board
N.Y. Barba-Behrens *(Mexico, DF, Mexico)*
A.G. Blackman *(Dunedin, New Zealand)*
D.C. Bradley *(London, UK)*
D. Braga *(Bologna, Italy)*
A. Brodie *(Palmerston North, New Zealand)*
A. Castiñeiras *(Santiago de Compostela, Spain)*
X.-M. Chen *(Guangzhou, China)*
M.H. Chisholm *(Columbus, OH, USA)*
E.C. Constable *(Basel, Switzerland)*
E. Coronado *(Valencia, Spain)*
W.J. Evans *(Irvine, CA, USA)*
L.H. Gade *(Heidelberg, Germany)*
M.B. Hursthouse *(Southampton, UK)*
C. Kepert *(NSW, Australia)*
T. Kiss *(Szeged, Hungary)*
L. Manners *(Bristol, UK)*
S. Perlepes *(Patras, Greece)*
P.P. Power *(Davis, CA, USA)*
T.B. Rauchfuss *(Urbana, IL, USA)*
J. Reedijk *(Leiden, The Netherlands)*
A.L. Rheingold *(Newark, DE, USA)*
A.G. Sykes *(Newcastle upon Tyne, UK)*
L.K. Thompson *(St John's, NF, Canada)*
M.D. Ward *(Sheffield, UK)*
R.E.P. Winpenny *(Manchester, UK)*
M. Yamashita *(Sendai, Japan)*
M. Zaworotko *(Tampa, FL, USA)*

Aims and Scope

Polyhedron will publish original, fundamental, experimental and theoretical work of the highest quality in all the major areas of inorganic chemistry. These include synthetic chemistry, coordination chemistry, organometallic chemistry, bioinorganic chemistry, and solid-state and materials chemistry. Papers should be complete pieces of work, and the inclusion of results from spectroscopic and/or physical techniques is encouraged. Papers merely reporting the preparation and X-ray structural characterization of only a single compound will not be considered appropriate unless the compound and its structure are particularly interesting.

Similarly, papers concerned solely with stability constants determined by potentiometric titration data unsupported by other e.g. spectroscopic techniques will not be acceptable nor will solvent extraction data unless supported by other data of interest to inorganic chemists. Unnecessary fragmentation of work is not acceptable.

In addition Polyhedron publishes specially commissioned review articles (Polyhedron Reports) and collections of original research papers (Polyhedron Symposia-in-Print) of appropriate timeliness.

Publication Information: Polyhedron (ISSN 0277-5387). For 2007, volume 26 is scheduled for publication. Subscription prices are available upon request from the Publisher or from the Regional Sales Office nearest you or from this journal's website (http://www.elsevier.com/locate/poly). Further information is available on this journal and other Elsevier products through Elsevier's website (http://www.elsevier.com). Subscriptions are accepted on a prepaid basis only and are entered on a calendar year basis. Issues are sent by standard mail (surface within Europe, air delivery outside Europe). Priority rates are available upon request. Claims for missing issues should be made within six months of the date of dispatch.

Orders, Claims and Journal Enquiries

(no manuscript enquiries)
Please contact the Customer Support Department at the Regional Sales Office nearest you:

Orlando
Elsevier
Customer Service Department
6277 Sea Harbor Drive
Orlando, FL 32887-4800
USA
Tel.: (877) 8397126 or (800) 6542452 [toll free numbers for US customers];
(+1) (407) 3454020 or
(+1) (407) 3454000 [customers outside US]
Fax: (+1) (407) 3631354 or
(+1) (407) 3639661
E-mail: usjcs@elsevier.com or elspcs@elsevier.com

Amsterdam
Elsevier
Customer Service Department
P.O. Box 211
1000 AE Amsterdam
The Netherlands
Tel.: (+31) 20-485-3757
Fax: (+31) 20-485-3432
E-mail: nlinfo-f@elsevier.com

Tokyo
Elsevier K.K.
Customer Service Department
4F Higashi-Azabu, 1-Chome Bldg
1-9-15 Higashi-Azabu
Minato-ku, Tokyo 106-0044
Japan
Tel.: (+81) 3-5561-5037
Fax: (+81) 3-5561-5047
E-mail: jp.info@elsevier.com

Singapore
Elsevier
Customer Service Department
3 Killiney Road
#08-01 Winsland House 1
Singapore 239519
Tel.: (+65) 6349-0222
Fax: (+65) 6733-1510
E-mail: asiainfo@elsevier.com

USA mailing notice: *Polyhedron* (ISSN 0277-5387) is published triweekly by Elsevier Ltd. (P.O. Box 211, 1000 AE Amsterdam, The Netherlands). Annual subscription price in the USA US$ 7808.00 (valid in North, Central and South America), including air speed delivery. Periodical postage rate is paid at Rahway, NJ.
USA POSTMASTER: Send change of address to *Polyhedron*, Elsevier, 6277 Sea Harbor Drive, Orlando, FL 32887-4800.
AIRFREIGHT AND MAILING in the USA by Mercury International Limited, 365 Blair Road, Avenel, NJ 07001.

Advertising Information

Advertising orders and enquiries can be sent to: **South America:** Mr Tino DeCarlo, The Advertising Department, Elsevier Inc., 360 Park Avenue South, New York, NY 10010-1710, USA; tel.: (+1) (212) 633 3815; fax: (+1) (212) 633 3820; e-mail: t.decarlo@elsevier.com. **Europe, USA, Canada and ROW:** Miss Katrina Barton, Commercial Sales, Elsevier, 84 Theobald's Road, London, WCIX 8RR, UK; phone: (+44) (0) 20 7611 4117; fax: (+44) (0) 20 7611 4463; e-mail: commercialsales@elsevier.com

POLYHEDRON

The International Journal for Inorganic and Organometallic Chemistry

Executive Editors

The Americas
G. Christou
Department of Chemistry, University of Florida,
Gainesville, FL 32611-7200, USA
E-mail: christou@chem.ufl.edu

Rest of the world
C.E. Housecroft
Department of Chemistry, University of Basel,
Spitalstrasse 51, CH-4056 Basel, Switzerland
E-mail: poly-chemie@unibas.ch

Associate Regional Editor for China
T.C.W. Mak
Department of Chemistry, University Science Centre,
The Chinese University of Hong Kong,
Shatin NT, Hong Kong, People's Republic of China
E-mail: tcwmak@cuhk.edu.hk

Polyhedron Reports
Editor
G. Christou *(Gainesville, FL, USA)*

Symposia-in-print
Editor
G. Parkin *(New York, NY, USA)*

Editorial Board
N.Y. Barba-Behrens *(Mexico, DF, Mexico)*
A.G. Blackman *(Dunedin, New Zealand)*
D.C. Bradley *(London, UK)*
D. Braga *(Bologna, Italy)*
A. Brodie *(Palmerston North, New Zealand)*
A. Castiñeiras *(Santiago de Compostela, Spain)*
X.-M. Chen *(Guangzhou, China)*
M.H. Chisholm *(Columbus, OH, USA)*
E.C. Constable *(Basel, Switzerland)*
E. Coronado *(Valencia, Spain)*
W.J. Evans *(Irvine, CA, USA)*
L.H. Gade *(Heidelberg, Germany)*
M.B. Hursthouse *(Southampton, UK)*
C. Kepert *(NSW, Australia)*
T. Kiss *(Szeged, Hungary)*
L. Manners *(Bristol, UK)*
S. Perlepes *(Patras, Greece)*
P.P. Power *(Davis, CA, USA)*
T.B. Rauchfuss *(Urbana, IL, USA)*
J. Reedijk *(Leiden, The Netherlands)*
A.L. Rheingold *(Newark, DE, USA)*
A.G. Sykes *(Newcastle upon Tyne, UK)*
L.K. Thompson *(St John's, NF, Canada)*
M.D. Ward *(Sheffield, UK)*
R.E.P. Winpenny *(Manchester, UK)*
M. Yamashita *(Sendai, Japan)*
M. Zaworotko *(Tampa, FL, USA)*

Aims and Scope

Polyhedron will publish original, fundamental, experimental and theoretical work of the highest quality in all the major areas of inorganic chemistry. These include synthetic chemistry, coordination chemistry, organometallic chemistry, bioinorganic chemistry, and solid-state and materials chemistry. Papers should be complete pieces of work, and the inclusion of results from spectroscopic and/or physical techniques is encouraged. Papers merely reporting the preparation and X-ray structural characterization of only a single compound will not be considered appropriate unless the compound and its structure are particularly interesting.

Similarly, papers concerned solely with stability constants determined by potentiometric titration data unsupported by other e.g. spectroscopic techniques will not be acceptable nor will solvent extraction data unless supported by other data of interest to inorganic chemists. Unnecessary fragmentation of work is not acceptable.

In addition Polyhedron publishes specially commissioned review articles (Polyhedron Reports) and collections of original research papers (Polyhedron Symposia-in-Print) of appropriate timeliness.

Publication Information: Polyhedron (ISSN 0277-5387). For 2007, volume 26 is scheduled for publication. Subscription prices are available upon request from the Publisher or from the Regional Sales Office nearest you or from this journal's website (http://www.elsevier.com/locate/poly). Further information is available on this journal and other Elsevier products through Elsevier's website (http://www.elsevier.com). Subscriptions are accepted on a prepaid basis only and are entered on a calendar year basis. Issues are sent by standard mail (surface within Europe, air delivery outside Europe). Priority rates are available upon request. Claims for missing issues should be made within six months of the date of dispatch.

Orders, Claims and Journal Enquiries

(no manuscript enquiries)
Please contact the Customer Support Department at the Regional Sales Office nearest you:

Orlando
Elsevier
Customer Service Department
6277 Sea Harbor Drive
Orlando, FL 32887-4800
USA
Tel.: (877) 8397126 or (800) 6542452 [toll free numbers for US customers];
(+1) (407) 3454020 or
(+1) (407) 3454000 [customers outside US]
Fax: (+1) (407) 3631354 or
(+1) (407) 3639661
E-mail: usjcs@elsevier.com or elspcs@elsevier.com

Amsterdam
Elsevier
Customer Service Department
P.O. Box 211
1000 AE Amsterdam
The Netherlands
Tel.: (+31) 20-485-3757
Fax: (+31) 20-485-3432
E-mail: nlinfo-f@elsevier.com

Tokyo
Elsevier K.K.
Customer Service Department
4F Higashi-Azabu, 1-Chome Bldg
1-9-15 Higashi-Azabu
Minato-ku, Tokyo 106-0044
Japan
Tel.: (+81) 3-5561-5037
Fax: (+81) 3-5561-5047
E-mail: jp.info@elsevier.com

Singapore
Elsevier
Customer Service Department
3 Killiney Road
#08-01 Winsland House 1
Singapore 239519
Tel.: (+65) 6349-0222
Fax: (+65) 6733-1510
E-mail: asiainfo@elsevier.com

USA mailing notice: *Polyhedron* (ISSN 0277-5387) is published triweekly by Elsevier Ltd. (P.O. Box 211, 1000 AE Amsterdam, The Netherlands). Annual subscription price in the USA US$ 7808.00 (valid in North, Central and South America), including air speed delivery. Periodical postage rate is paid at Rahway, NJ.
USA POSTMASTER: Send change of address to *Polyhedron*, Elsevier, 6277 Sea Harbor Drive, Orlando, FL 32887-4800.
AIRFREIGHT AND MAILING in the USA by Mercury International Limited, 365 Blair Road, Avenel, NJ 07001.

Advertising Information

Advertising orders and enquiries can be sent to: **South America:** Mr Tino DeCarlo, The Advertising Department, Elsevier Inc., 360 Park Avenue South, New York, NY 10010-1710, USA; tel.: (+1) (212) 633 3815; fax: (+1) (212) 633 3820; e-mail: t.decarlo@elsevier.com. **Europe, USA, Canada and ROW:** Miss Katrina Barton, Commercial Sales, Elsevier, 84 Theobald's Road, London, WCIX 8RR, UK; phone: (+44) (0) 20 7611 4117; fax: (+44) (0) 20 7611 4463; e-mail: commercialsales@elsevier.com

POLYHEDRON

The International Journal for Inorganic and Organometallic Chemistry

Executive Editors

The Americas
G. Christou
Department of Chemistry, University of Florida,
Gainesville, FL 32611-7200, USA
E-mail: christou@chem.ufl.edu

Rest of the world
C.E. Housecroft
Department of Chemistry, University of Basel,
Spitalstrasse 51, CH-4056 Basel, Switzerland
E-mail: poly-chemie@unibas.ch

Associate Regional Editor for China
T.C.W. Mak
Department of Chemistry, University Science Centre,
The Chinese University of Hong Kong,
Shatin NT, Hong Kong, People's Republic of China
E-mail: tcwmak@cuhk.edu.hk

Polyhedron Reports
Editor
G. Christou *(Gainesville, FL, USA)*

Symposia-in-print
Editor
G. Parkin *(New York, NY, USA)*

Editorial Board

N.Y. Barba-Behrens *(Mexico, DF, Mexico)*
A.G. Blackman *(Dunedin, New Zealand)*
D.C. Bradley *(London, UK)*
D. Braga *(Bologna, Italy)*
A. Brodie *(Palmerston North, New Zealand)*
A. Castiñeiras *(Santiago de Compostela, Spain)*
X.-M. Chen *(Guangzhou, China)*
M.H. Chisholm *(Columbus, OH, USA)*
E.C. Constable *(Basel, Switzerland)*
E. Coronado *(Valencia, Spain)*
W.J. Evans *(Irvine, CA, USA)*
L.H. Gade *(Heidelberg, Germany)*
M.B. Hursthouse *(Southampton, UK)*
C. Kepert *(NSW, Australia)*
T. Kiss *(Szeged, Hungary)*
L. Manners *(Bristol, UK)*
S. Perlepes *(Patras, Greece)*
P.P. Power *(Davis, CA, USA)*
T.B. Rauchfuss *(Urbana, IL, USA)*
J. Reedijk *(Leiden, The Netherlands)*
A.L. Rheingold *(Newark, DE, USA)*
A.G. Sykes *(Newcastle upon Tyne, UK)*
L.K. Thompson *(St John's, NF, Canada)*
M.D. Ward *(Sheffield, UK)*
R.E.P. Winpenny *(Manchester, UK)*
M. Yamashita *(Sendai, Japan)*
M. Zaworotko *(Tampa, FL, USA)*

Aims and Scope

Polyhedron will publish original, fundamental, experimental and theoretical work of the highest quality in all the major areas of inorganic chemistry. These include synthetic chemistry, coordination chemistry, organometallic chemistry, bioinorganic chemistry, and solid-state and materials chemistry. Papers should be complete pieces of work, and the inclusion of results from spectroscopic and/or physical techniques is encouraged. Papers merely reporting the preparation and X-ray structural characterization of only a single compound will not be considered appropriate unless the compound and its structure are particularly interesting.

Similarly, papers concerned solely with stability constants determined by potentiometric titration data unsupported by other e.g. spectroscopic techniques will not be acceptable nor will solvent extraction data unless supported by other data of interest to inorganic chemists. Unnecessary fragmentation of work is not acceptable.

In addition Polyhedron publishes specially commissioned review articles (Polyhedron Reports) and collections of original research papers (Polyhedron Symposia-in-Print) of appropriate timeliness.

Publication Information: Polyhedron (ISSN 0277-5387). For 2007, volume 26 is scheduled for publication. Subscription prices are available upon request from the Publisher or from the Regional Sales Office nearest you or from this journal's website (http://www.elsevier.com/locate/poly). Further information is available on this journal and other Elsevier products through Elsevier's website (http://www.elsevier.com). Subscriptions are accepted on a prepaid basis only and are entered on a calendar year basis. Issues are sent by standard mail (surface within Europe, air delivery outside Europe). Priority rates are available upon request. Claims for missing issues should be made within six months of the date of dispatch.

Orders, Claims and Journal Enquiries

(no manuscript enquiries)
Please contact the Customer Support Department at the Regional Sales Office nearest you:

Orlando
Elsevier
Customer Service Department
6277 Sea Harbor Drive
Orlando, FL 32887-4800
USA
Tel.: (877) 8397126 or (800) 6542452 [toll free numbers for US customers];
(+1) (407) 3454020 or
(+1) (407) 3454000 [customers outside US]
Fax: (+1) (407) 3631354 or
(+1) (407) 3639661
E-mail: usjcs@elsevier.com or elspcs@elsevier.com

Amsterdam
Elsevier
Customer Service Department
P.O. Box 211
1000 AE Amsterdam
The Netherlands
Tel.: (+31) 20-485-3757
Fax: (+31) 20-485-3432
E-mail: nlinfo-f@elsevier.com

Tokyo
Elsevier K.K.
Customer Service Department
4F Higashi-Azabu, 1-Chome Bldg
1-9-15 Higashi-Azabu
Minato-ku, Tokyo 106-0044
Japan
Tel.: (+81) 3-5561-5037
Fax: (+81) 3-5561-5047
E-mail: jp.info@elsevier.com

Singapore
Elsevier
Customer Service Department
3 Killiney Road
#08-01 Winsland House 1
Singapore 239519
Tel.: (+65) 6349-0222
Fax: (+65) 6733-1510
E-mail: asiainfo@elsevier.com

USA mailing notice: *Polyhedron* (ISSN 0277-5387) is published triweekly by Elsevier Ltd. (P.O. Box 211, 1000 AE Amsterdam, The Netherlands). Annual subscription price in the USA US$ 7808.00 (valid in North, Central and South America), including air speed delivery. Periodical postage rate is paid at Rahway, NJ.
USA POSTMASTER: Send change of address to *Polyhedron*, Elsevier, 6277 Sea Harbor Drive, Orlando, FL 32887-4800.
AIRFREIGHT AND MAILING in the USA by Mercury International Limited, 365 Blair Road, Avenel, NJ 07001.

Advertising Information

Advertising orders and enquiries can be sent to: **South America:** Mr Tino DeCarlo, The Advertising Department, Elsevier Inc., 360 Park Avenue South, New York, NY 10010-1710, USA; tel.: (+1) (212) 633 3815; fax: (+1) (212) 633 3820; e-mail: t.decarlo@elsevier.com. **Europe, USA, Canada and ROW:** Miss Katrina Barton, Commercial Sales, Elsevier, 84 Theobald's Road, London, WCIX 8RR, UK; phone: (+44) (0) 20 7611 4117; fax: (+44) (0) 20 7611 4463; e-mail: commercialsales@elsevier.com

POLYHEDRON

The International Journal for Inorganic and Organometallic Chemistry

Executive Editors

The Americas
G. Christou
Department of Chemistry, University of Florida,
Gainesville, FL 32611-7200, USA
E-mail: christou@chem.ufl.edu

Rest of the world
C.E. Housecroft
Department of Chemistry, University of Basel,
Spitalstrasse 51, CH-4056 Basel, Switzerland
E-mail: poly-chemie@unibas.ch

Associate Regional Editor for China
T.C.W. Mak
Department of Chemistry, University Science Centre,
The Chinese University of Hong Kong,
Shatin NT, Hong Kong, People's Republic of China
E-mail: tcwmak@cuhk.edu.hk

Polyhedron Reports
Editor
G. Christou *(Gainesville, FL, USA)*

Symposia-in-print
Editor
G. Parkin *(New York, NY, USA)*

Editorial Board

N.Y. Barba-Behrens *(Mexico, DF, Mexico)*
A.G. Blackman *(Dunedin, New Zealand)*
D.C. Bradley *(London, UK)*
D. Braga *(Bologna, Italy)*
A. Brodie *(Palmerston North, New Zealand)*
A. Castiñeiras *(Santiago de Compostela, Spain)*
X.-M. Chen *(Guangzhou, China)*
M.H. Chisholm *(Columbus, OH, USA)*
E.C. Constable *(Basel, Switzerland)*
E. Coronado *(Valencia, Spain)*
W.J. Evans *(Irvine, CA, USA)*
L.H. Gade *(Heidelberg, Germany)*
M.B. Hursthouse *(Southampton, UK)*
C. Kepert *(NSW, Australia)*
T. Kiss *(Szeged, Hungary)*
L. Manners *(Bristol, UK)*
S. Perlepes *(Patras, Greece)*
P.P. Power *(Davis, CA, USA)*
T.B. Rauchfuss *(Urbana, IL, USA)*
J. Reedijk *(Leiden, The Netherlands)*
A.L. Rheingold *(Newark, DE, USA)*
A.G. Sykes *(Newcastle upon Tyne, UK)*
L.K. Thompson *(St John's, NF, Canada)*
M.D. Ward *(Sheffield, UK)*
R.E.P. Winpenny *(Manchester, UK)*
M. Yamashita *(Sendai, Japan)*
M. Zaworotko *(Tampa, FL, USA)*

Aims and Scope

Polyhedron will publish original, fundamental, experimental and theoretical work of the highest quality in all the major areas of inorganic chemistry. These include synthetic chemistry, coordination chemistry, organometallic chemistry, bioinorganic chemistry, and solid-state and materials chemistry. Papers should be complete pieces of work, and the inclusion of results from spectroscopic and/or physical techniques is encouraged. Papers merely reporting the preparation and X-ray structural characterization of only a single compound will not be considered appropriate unless the compound and its structure are particularly interesting.

Similarly, papers concerned solely with stability constants determined by potentiometric titration data unsupported by other e.g. spectroscopic techniques will not be acceptable nor will solvent extraction data unless supported by other data of interest to inorganic chemists. Unnecessary fragmentation of work is not acceptable.

In addition Polyhedron publishes specially commissioned review articles (Polyhedron Reports) and collections of original research papers (Polyhedron Symposia-in-Print) of appropriate timeliness.

Publication Information: Polyhedron (ISSN 0277-5387). For 2007, volume 26 is scheduled for publication. Subscription prices are available upon request from the Publisher or from the Regional Sales Office nearest you or from this journal's website (http://www.elsevier.com/locate/poly). Further information is available on this journal and other Elsevier products through Elsevier's website (http://www.elsevier.com). Subscriptions are accepted on a prepaid basis only and are entered on a calendar year basis. Issues are sent by standard mail (surface within Europe, air delivery outside Europe). Priority rates are available upon request. Claims for missing issues should be made within six months of the date of dispatch.

Orders, Claims and Journal Enquiries

(no manuscript enquiries)
Please contact the Customer Support Department at the Regional Sales Office nearest you:

Orlando
Elsevier
Customer Service Department
6277 Sea Harbor Drive
Orlando, FL 32887-4800
USA
Tel.: (877) 8397126 or (800) 6542452 [toll free numbers for US customers];
(+1) (407) 3454020 or
(+1) (407) 3454000 [customers outside US]
Fax: (+1) (407) 3631354 or
(+1) (407) 3639661
E-mail: usjcs@elsevier.com or elspcs@elsevier.com

Amsterdam
Elsevier
Customer Service Department
P.O. Box 211
1000 AE Amsterdam
The Netherlands
Tel.: (+31) 20-485-3757
Fax: (+31) 20-485-3432
E-mail: nlinfo-f@elsevier.com

Tokyo
Elsevier K.K.
Customer Service Department
4F Higashi-Azabu, 1-Chome Bldg
1-9-15 Higashi-Azabu
Minato-ku, Tokyo 106-0044
Japan
Tel.: (+81) 3-5561-5037
Fax: (+81) 3-5561-5047
E-mail: jp.info@elsevier.com

Singapore
Elsevier
Customer Service Department
3 Killiney Road
#08-01 Winsland House 1
Singapore 239519
Tel.: (+65) 6349-0222
Fax: (+65) 6733-1510
E-mail: asiainfo@elsevier.com

USA mailing notice: *Polyhedron* (ISSN 0277-5387) is published triweekly by Elsevier Ltd. (P.O. Box 211, 1000 AE Amsterdam, The Netherlands). Annual subscription price in the USA US$ 7808.00 (valid in North, Central and South America), including air speed delivery. Periodical postage rate is paid at Rahway, NJ.
USA POSTMASTER: Send change of address to *Polyhedron*, Elsevier, 6277 Sea Harbor Drive, Orlando, FL 32887-4800.
AIRFREIGHT AND MAILING in the USA by Mercury International Limited, 365 Blair Road, Avenel, NJ 07001.

Advertising Information

Advertising orders and enquiries can be sent to: **South America:** Mr Tino DeCarlo, The Advertising Department, Elsevier Inc., 360 Park Avenue South, New York, NY 10010-1710, USA; tel.: (+1) (212) 633 3815; fax: (+1) (212) 633 3820; e-mail: t.decarlo@elsevier.com. **Europe, USA, Canada and ROW:** Miss Katrina Barton, Commercial Sales, Elsevier, 84 Theobald's Road, London, WCIX 8RR, UK; phone: (+44) (0) 20 7611 4117; fax: (+44) (0) 20 7611 4463; e-mail: commercialsales@elsevier.com

POLYHEDRON

The International Journal for Inorganic and Organometallic Chemistry

Executive Editors

The Americas
G. Christou
Department of Chemistry, University of Florida,
Gainesville, FL 32611-7200, USA
E-mail: christou@chem.ufl.edu

Rest of the world
C.E. Housecroft
Department of Chemistry, University of Basel,
Spitalstrasse 51, CH-4056 Basel, Switzerland
E-mail: poly-chemie@unibas.ch

Associate Regional Editor for China
T.C.W. Mak
Department of Chemistry, University Science Centre,
The Chinese University of Hong Kong,
Shatin NT, Hong Kong, People's Republic of China
E-mail: tcwmak@cuhk.edu.hk

Polyhedron Reports
Editor
G. Christou *(Gainesville, FL, USA)*

Symposia-in-print
Editor
G. Parkin *(New York, NY, USA)*

Editorial Board
N.Y. Barba-Behrens *(Mexico, DF, Mexico)*
A.G. Blackman *(Dunedin, New Zealand)*
D.C. Bradley *(London, UK)*
D. Braga *(Bologna, Italy)*
A. Brodie *(Palmerston North, New Zealand)*
A. Castiñeiras *(Santiago de Compostela, Spain)*
X.-M. Chen *(Guangzhou, China)*
M.H. Chisholm *(Columbus, OH, USA)*
E.C. Constable *(Basel, Switzerland)*
E. Coronado *(Valencia, Spain)*
W.J. Evans *(Irvine, CA, USA)*
L.H. Gade *(Heidelberg, Germany)*
M.B. Hursthouse *(Southampton, UK)*
C. Kepert *(NSW, Australia)*
T. Kiss *(Szeged, Hungary)*
L. Manners *(Bristol, UK)*
S. Perlepes *(Patras, Greece)*
P.P. Power *(Davis, CA, USA)*
T.B. Rauchfuss *(Urbana, IL, USA)*
J. Reedijk *(Leiden, The Netherlands)*
A.L. Rheingold *(Newark, DE, USA)*
A.G. Sykes *(Newcastle upon Tyne, UK)*
L.K. Thompson *(St John's, NF, Canada)*
M.D. Ward *(Sheffield, UK)*
R.E.P. Winpenny *(Manchester, UK)*
M. Yamashita *(Sendai, Japan)*
M. Zaworotko *(Tampa, FL, USA)*

Aims and Scope

Polyhedron will publish original, fundamental, experimental and theoretical work of the highest quality in all the major areas of inorganic chemistry. These include synthetic chemistry, coordination chemistry, organometallic chemistry, bioinorganic chemistry, and solid-state and materials chemistry. Papers should be complete pieces of work, and the inclusion of results from spectroscopic and/or physical techniques is encouraged. Papers merely reporting the preparation and X-ray structural characterization of only a single compound will not be considered appropriate unless the compound and its structure are particularly interesting.

Similarly, papers concerned solely with stability constants determined by potentiometric titration data unsupported by other e.g. spectroscopic techniques will not be acceptable nor will solvent extraction data unless supported by other data of interest to inorganic chemists. Unnecessary fragmentation of work is not acceptable.

In addition Polyhedron publishes specially commissioned review articles (Polyhedron Reports) and collections of original research papers (Polyhedron Symposia-in-Print) of appropriate timeliness.

Publication Information: Polyhedron (ISSN 0277-5387). For 2007, volume 26 is scheduled for publication. Subscription prices are available upon request from the Publisher or from the Regional Sales Office nearest you or from this journal's website (http://www.elsevier.com/locate/poly). Further information is available on this journal and other Elsevier products through Elsevier's website (http://www.elsevier.com). Subscriptions are accepted on a prepaid basis only and are entered on a calendar year basis. Issues are sent by standard mail (surface within Europe, air delivery outside Europe). Priority rates are available upon request. Claims for missing issues should be made within six months of the date of dispatch.

Orders, Claims and Journal Enquiries

(no manuscript enquiries)
Please contact the Customer Support Department at the Regional Sales Office nearest you:

Orlando
Elsevier
Customer Service Department
6277 Sea Harbor Drive
Orlando, FL 32887-4800
USA
Tel.: (877) 8397126 or (800) 6542452 [toll free numbers for US customers];
(+1) (407) 3454020 or
(+1) (407) 3454000 [customers outside US]
Fax: (+1) (407) 3631354 or
(+1) (407) 3639661
E-mail: usjcs@elsevier.com or elspcs@elsevier.com

Amsterdam
Elsevier
Customer Service Department
P.O. Box 211
1000 AE Amsterdam
The Netherlands
Tel.: (+31) 20-485-3757
Fax: (+31) 20-485-3432
E-mail: nlinfo-f@elsevier.com

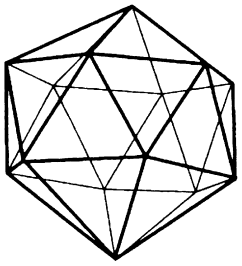
Tokyo
Elsevier K.K.
Customer Service Department
4F Higashi-Azabu, 1-Chome Bldg
1-9-15 Higashi-Azabu
Minato-ku, Tokyo 106-0044
Japan
Tel.: (+81) 3-5561-5037
Fax: (+81) 3-5561-5047
E-mail: jp.info@elsevier.com

Singapore
Elsevier
Customer Service Department
3 Killiney Road
#08-01 Winsland House 1
Singapore 239519
Tel.: (+65) 6349-0222
Fax: (+65) 6733-1510
E-mail: asiainfo@elsevier.com

USA mailing notice: *Polyhedron* (ISSN 0277-5387) is published triweekly by Elsevier Ltd. (P.O. Box 211, 1000 AE Amsterdam, The Netherlands). Annual subscription price in the USA US$ 7808.00 (valid in North, Central and South America), including air speed delivery. Periodical postage rate is paid at Rahway, NJ.
USA POSTMASTER: Send change of address to *Polyhedron*, Elsevier, 6277 Sea Harbor Drive, Orlando, FL 32887-4800.
AIRFREIGHT AND MAILING in the USA by Mercury International Limited, 365 Blair Road, Avenel, NJ 07001.

Advertising Information

Advertising orders and enquiries can be sent to: **South America:** Mr Tino DeCarlo, The Advertising Department, Elsevier Inc., 360 Park Avenue South, New York, NY 10010-1710, USA; tel.: (+1) (212) 633 3815; fax: (+1) (212) 633 3820; e-mail: t.decarlo@elsevier.com. **Europe, USA, Canada and ROW:** Miss Katrina Barton, Commercial Sales, Elsevier, 84 Theobald's Road, London, WCIX 8RR, UK; phone: (+44) (0) 20 7611 4117; fax: (+44) (0) 20 7611 4463; e-mail: commercialsales@elsevier.com



POLYHEDRON

The International Journal for Inorganic and Organometallic Chemistry

Founding Editor: **Sir Geoffrey Wilkinson**✠

Executive Editors

The Americas

G. Christou
Department of Chemistry, University of Florida, Gainesville, FL 32611-7200, USA
E-mail: christou@chem.ufl.edu

Rest of the world

C.E. Housecroft
Department of Chemistry, University of Basel, Spitalstrasse 51, CH-4056 Basel, Switzerland
E-mail: poly-chemie@unibas.ch

Associate Regional Editor for China

T.C.W. Mak
Department of Chemistry, University Science Centre, The Chinese University of Hong Kong, Shatin NT, Hong Kong, People's Republic of China
E-mail: tcwmak@cuhk.hk

Polyhedron Reports

G. Christou
Department of Chemistry, University of Florida, Gainesville, FL 32611-7200, USA
E-mail: christou@chem.ufl.edu

Symposia-in-print

G. Parkin
Department of Chemistry (Box 3115), Columbia University, 3000 Broadway, New York, NY 10027, USA
E-mail: parkin@chem.columbia.edu

Editorial Board

N.Y. Barba-Behrens *(Mexico, DF, Mexico)*
A.G. Blackman *(Dunedin, New Zealand)*
D.C. Bradley *(London, UK)*
D. Braga *(Bologna, Italy)*
A. Brodie *(Palmerston North, New Zealand)*
A. Castiñeiras *(Santiago de Compostela, Spain)*
X.-M. Chen *(Guangzhou, China)*
M.H. Chisholm *(Columbus, OH, USA)*
E.C. Constable *(Basel, Switzerland)*
E. Coronado *(Valencia, Spain)*
W.J. Evans *(Irvine, CA, USA)*
L.H. Gade *(Heidelberg, Germany)*
M.B. Hursthouse *(Southampton, UK)*
C. Kepert *(NSW, Australia)*
T. Kiss *(Szeged, Hungary)*
L. Manners *(Bristol, UK)*
S. Perlepes *(Patras, Greece)*
P.P. Power *(Davis, CA, USA)*
T.B. Rauchfuss *(Urbana, IL, USA)*
J. Reedijk *(Leiden, The Netherlands)*
A.L. Rheingold *(Newark, DE, USA)*
A.G. Sykes *(Newcastle upon Tyne, UK)*
L.K. Thompson *(St John's, NF, Canada)*
M.D. Ward *(Sheffield, UK)*
R.E.P. Winpenny *(Manchester, UK)*
M. Yamashita *(Sendai, Japan)*
M. Zaworotko *(Tampa, FL, USA)*



ELSEVIER

Amsterdam — Boston — Jena — London — New York — Oxford — Paris — Philadelphia — San Diego — St Louis

Available online at www.sciencedirect.com
ScienceDirect
Polyhedron 26, issue 7, 1 May 2007
POLYHEDRON
www.elsevier.com/locate/poly

Contents

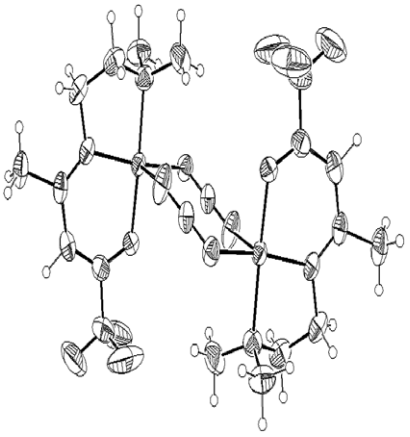
Papers

Shyamapada Shit, Pritha Talukder, Joy Chakraborty, Guillaume Pilet, M. Salah El Fallah, Joan Ribas and Samiran Mitra

Polyhedron 26 (2007) 1357

A rare ferromagnetically coupled asymmetric doubly azido bridged copper(II) dimer with an N, N, O donor Schiff base

A new end-to-end (EE) doubly azido bridged centrosymmetric dinuclear complex has been synthesized and characterized with elemental and spectroscopic techniques. In the complex, each copper atom is in a distorted square pyramidal geometry with a CuN_4O chromophore. Temperature dependent magnetic susceptibility, fitted using the Bleaney–Bowers expression indicates a ferromagnetic interaction through the double azido bridges connecting the adjacent copper(II) centers.

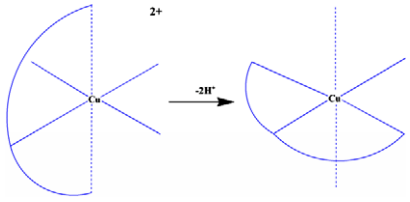


T.K. Prasad and M.V. Rajasekharan

Polyhedron 26 (2007) 1364

$[M(dipicH_2)(H_2O)_3]^{2+}, M = Ni, Cu, Zn$ (dipicH$_2$ = dipicolinic acid) – A combined crystallographic, spectroscopic and computational study

In the three isomeric crystal structures obtained with $[Ce(dipic)_3]^{2-}$ as the counter anions, the transition ions retain the structural features characteristic of their electronic configurations.

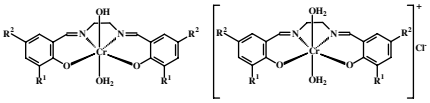


Pedro E. Aranha, Mirian P. dos Santos, Sandra Romera and Edward R. Dockal

Polyhedron 26 (2007) 1373

Synthesis, characterization, and spectroscopic studies of tetradentate Schiff base chromium(III) complexes

Eight chromium(III) complexes of tetradentate Schiff bases have been prepared and characterized by elemental analysis, m.p., IR, molar conductivity and electronic spectra. The free ligands were also characterized by ^1H and ^{13}C NMR spectra. The IR and electronic spectra of the free ligand and the complexes are compared and discussed.



R^1	R^2	L	Complexes
H	H	OH	$[Cr(L^1)(OH)(H_2O)]$
H	Br	OH	$[Cr(L^2)(OH)(H_2O)]$
H	Cl	OH	$[Cr(L^3)(OH)(H_2O)]$
H	MeO	OH	$[Cr(L^4)(OH)(H_2O)]$

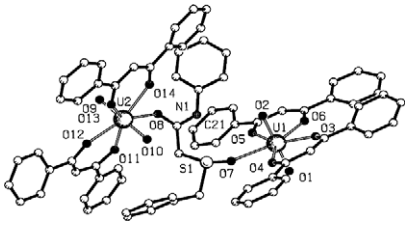
R^1	R^2	L	Complexes
H	NO_2	H_2O	$[Cr(L^5)(H_2O)_2]Cl$
Br	Br	H_2O	$[Cr(L^6)(H_2O)_2]Cl$
Cl	Cl	H_2O	$[Cr(L^7)(H_2O)_2]Cl$
I	I	H_2O	$[Cr(L^8)(H_2O)_2]Cl$

S. Kannan, K.V. Chetty, A. Usman and H.K. Fun

Polyhedron 26 (2007) 1383

Extraction and coordination studies of carbamoyl methyl sulfoxide (CMSO) with uranyl bis(β-diketonates). Synthesis and molecular structure of $[\{UO_2(DBM)_2\}_2C_6H_5CH_2SOCH_2CONHC_6H_5]$

Coordination studies of the carbamoyl methyl sulfoxide (CMSO) ligand with uranyl bis(β-diketonate) show that it acts as a monodentate ligand in 1:1 compounds and a bridging bidentate ligand in 2:1 compounds. An enhancement in the extraction for the uranyl ion from nitric acid medium is observed when a mixture of HTTA and CMSO were employed.

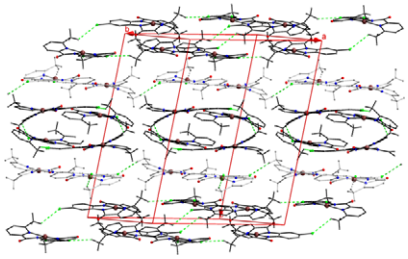


Jung Hwan Lee, Hee Jin Kim, Yun Wee Choi, Young Min Lee, Byeong Kwon Park, Cheal Kim, Sung-Jin Kim and Youngmee Kim

Polyhedron 26 (2007) 1388

Pd(II) polymeric compounds directed by intermolecular C–H···X–C interactions (X = F, Cl): Suzuki–Miyaura cross-coupling catalytic activity by a novel N4-type saturated Pd complex

New palladium polymeric compounds containing novel tetradentate halogen-substituted $6Me_2bpX^{2-}$ ligands ($6Me_2bpX^{2-}$ = 1,2-bis(6-methylpyridine-2-carboxamide) halobenzene dianion, X = F for **4**, Cl for **5**) were constructed by non-classical C–H···X–C interactions, and the novel catalyst **5** was used to carry out Suzuki coupling reactions with aryl iodides and aryl boronic acids under mild conditions.

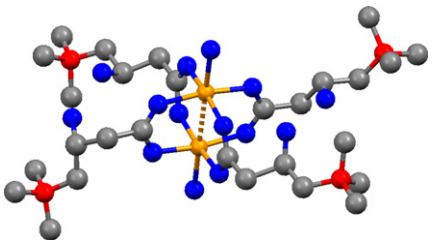


Charalambos Litos, Simon Parsons and Alexandra Karaliota

Polyhedron 26 (2007) 1397

Synthesis of two dicopper(II) complexes of L-carnitine: The first structural determination of a metal complex containing L-carnitine

The first crystal structure of a metal complex containing L-carnitine is described. Two dicopper(II) complexes with formulas $[Cu_2(L\text{-carnitine})_2Cl_2(H_2O)_2] \cdot Cl_2$ (complex **1**) and $[Cu_2(L\text{-carnitine})_4(H_2O)_2] \cdot (ClO_4)_4 \cdot H_2O \cdot CH_2Cl_2$ (complex **2**) were isolated from ethanolic and aqueous solutions, respectively. The complexes were characterized by several techniques, while the structure of complex **2** was identified by X-ray crystallography.

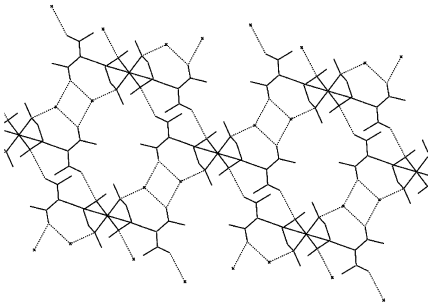


Leandros C. Tzavellas, Sofia Pachini, Chris Tsiamis and Antonis G. Hatzidimitriou

Polyhedron 26 (2007) 1404

Conformation and coordination of β-diketonates in mixed-ligand copper(II) chelates of 1,2-diamines. Theoretical approach and experimental verification. Crystal structure of [bis(*N*,*N*′-dimethyl-1,2-diaminoethane) bis(3-cyano-2,4-pentanedionate)copper(II)]dihydrate

The products of the reaction of the bis(2,4-pentanedionato)copper(II), $Cu(acac)_2$, and cognate compounds, $Cu\beta_2$, with 1,2-diaminoethane (en), and certain of its *N*-substituted derivatives have been investigated and are discussed in the light of DFT calculations. Further, the crystal structure of $[Cu(Me\text{-}en\text{-}Me)_2(NC\text{-}acac)_2] \cdot 2H_2O$ is reported.

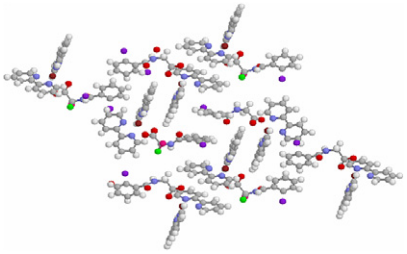


Miquel Barceló-Oliver, Angel Terrón, Angel García-Raso and Elies Molins

Polyhedron 26 (2007) 1417

Models for thyroxine: Aromatic iodine-assisted self-assemblies

Trying to understand the different recognition factors between thyroxine and its binding proteins, the chemistry of the ternary complexes between copper and *o*-iodobenzoylglycine (I-hip) [or *o*-iodobenzoylglycilglycine (B^IGG)] as simple thyroxine models were studied with 2,2′-bipyridyl as secondary ligand.

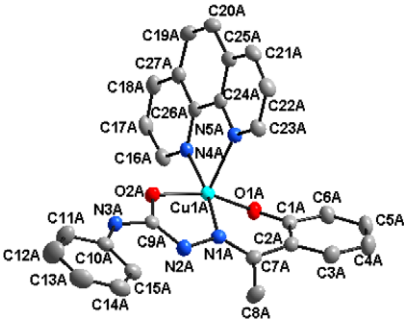


U.L. Kala, S. Suma, M.R. Prathapachandra Kurup, Suja Krishnan and Rohith P. John

Polyhedron 26 (2007) 1427

Synthesis, spectral characterization and crystal structure of copper(II) complexes of 2-hydroxyacetophenone-*N*(4)-phenyl semicarbazone

Copper(II) complexes of 2-hydroxyacetophenone-*N*(4)-phenyl semicarbazone have been synthesized and physico-chemically characterized. The tridentate character of the semicarbazone is inferred from IR spectra. The *g* values, calculated for all the complexes in frozen solution EPR, indicate the presence of the unpaired electron in the $d_{x^2-y^2}$ orbital. The metal–ligand bonding parameters evaluated showed strong in-plane σ and in-plane π-bonding. The crystal structure of CuLphen revealed a monoclinic lattice with space group symmetry $P2_1/c$. The compound adopts a distorted square pyramidal geometry with a N_2O_2 core as the base.

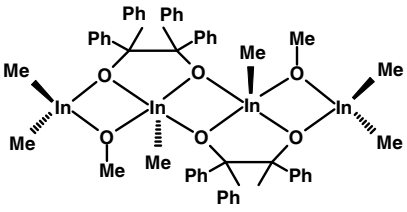


Wanda Ziemkowska, Anna Kubiak, Szymon Kucharski, Robert Woźniak and Romana Anulewicz-Ostrowska

Polyhedron 26 (2007) 1436

Reactions of benzopinacol with group 13 alkyl metals: Crystal structure of $Me_6In_4[OC(C_6H_5)_2C(C_6H_5)_2O]_2(OCH_3)_2$, a new alkylalkoxo indium diolate

$^tBu_3Al$ reacted with an equimolar amount of benzopinacol to form a monomeric complex $^tBuAl[OC(C_6H_5)_2C(C_6H_5)_2O](C_4H_8O)$ (**3**). Re-actions of Me_3Ga and Me_3In with benzopinacol afforded trinuclear complexes $Me_5M_3[OC(C_6H_5)_2C(C_6H_5)_2O]_2$ (**4** (M = Ga), **5** (M = In)). In the presence of water and alcohols, compounds **4** and **5** underwent a decomposition reaction to benzopinacol and mixtures of metalloxanes and alkoxides. An unusual methylmethoxo indium benzopinacolate $Me_6In_4[OC(C_6H_5)_2C(C_6H_5)_2O]_2(OCH_3)_2$ (**6**) was obtained in the reaction of benzopinacol with of Me_3In and Me_2InOMe in a 1:1:1 molar ratio.



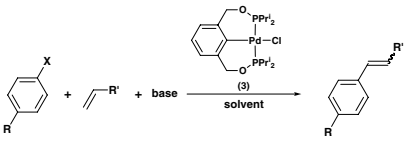
6

Ali Naghipour, S.J. Sabounchei, David Morales-Morales, Daniel Canseco-González and Craig M. Jensen

Polyhedron 26 (2007) 1445

A highly active two six-membered phosphinite palladium PCP pincer complex [PdCl{$C_6H_3(CH_2OPPr^i)_2$-2,6}]

The two six-membered phosphinite palladium PCP pincer complex [PdCl{$C_6H_3(CH_2OPPr^i)_2$-2,6}] has been synthesized and its catalytic activity for C–C coupling reactions has been investigated.

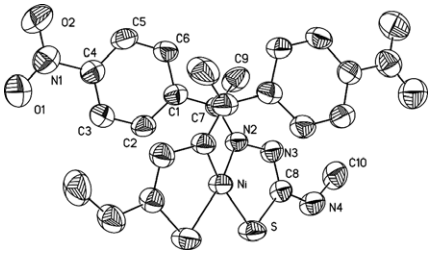


Anayive Pérez-Rebolledo, Isolda C. Mendes, Nivaldo L. Speziali, Philippe Bertani, Jarbas M. Resende, Antônio F. de Carvalho Alcântara and Heloisa Beraldo

Polyhedron 26 (2007) 1449

N(4)-Methyl-4-nitroacetophenone thiosemicarbazone and its nickel(II) complex: Experimental and theoretical structural studies

X-ray structural studies of *N*(4)-methyl-4-nitroacetophenone thiosemicarbazone, $H4NO_2Ac4M$ (**1**) and its nickel(II) complex, $[Ni(4NO_2Ac4M)_2]$ (**2**) revealed that the **1-*E*,*E*** isomer of the thiosemicarbazone and the **2-*cis*** (***E*-Ni-*E***) isomer of the complex are formed in the crystal. NMR data along with Hartree–Fock (HF) and Density Functional Theory (DFT) calculations suggest that the **1-*E*,*E*** isomer probably exists in DMSO-d_6, and the **1-*Z*,*E*** isomer in $CDCl_3$. NMR data along with HF and DFT calculations suggest the presence of **2-*cis*(*Z*-Ni-*Z*)** in DMSO-d_6 as well as in the powder, indicating **2-*cis*(*Z*-Ni-*Z*)** → **2-*cis*** (***E*-Ni-*E***) conversion during crystallization.

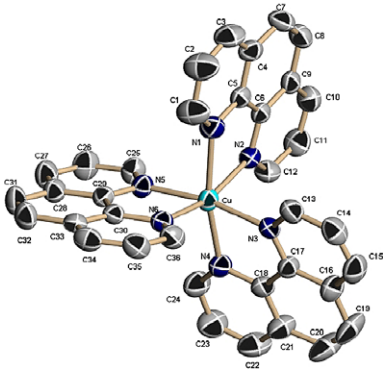


Sujittra Youngme, Nanthawat Wannarit, Chaveng Pakawatchai, Narongsak Chaichit, Eakasit Somsook, Urho Turpeinen and Ilpo Mutikainen

Polyhedron 26 (2007) 1459

Structural diversities and spectroscopic properties of bis and tris(1,10-phenanthroline)-copper(II) complexes

The crystal structures of bis and tris(1,10-phenanthroline)copper(II) complexes $[Cu(phen)_3](S_4O_6)(S_8)$ (**1**), $[Cu(phen)_3](BF_4)_2$ (**2**), $[Cu(phen)_2(OS_2O_7)]$ (**3**) and $[Cu(phen)_2(FBF_3)](BF_4)$ (**4**) have been determined by X-ray crystallography. The Cu(II) ions are octahedrally coordinated by the three phen ligands. As a consequence of the Jahn-Teller effect, the two axial Cu–N bonds are longer than the equatorial Cu–N bonds and the CuN_6 chromophores appear to be elongated rhombic octahedral with tetragonalities of 0.892 and 0.886 for **1** and **2**, respectively. Complexes **3** and **4** consist of mononuclear units, the 5-coordinate Cu(II) environment being distorted square pyramidal ($\tau = 0.31$) and distorted trigonal bipyramidal ($\tau = 0.66$), respectively. The unidentate $S_2O_8^{2-}$ anion in **3** occupies the axial position, while the unidentate BF_4^- anion in **4** is coordinated in the trigonal plane. The crystal structures and their electronic properties (IR and EPR) are discussed and compared to other relevant complexes based on the Jahn-Teller effect.

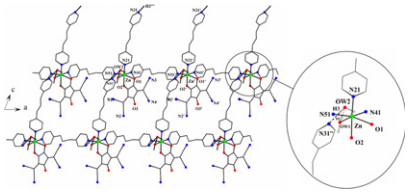


Wagner M. Teles, Regis de A. Farani, Maria Irene Yoshida, Adailton J. Bortoluzzi, Manfredo Hörner, Luiz Fernando C. de Oliveira and Flávia C. Machado

Polyhedron 26 (2007) 1469

Synthesis and crystal structure of a novel Zn(II) 2-D coordination polymer containing 1,3-bis(4-pyridyl)propane ligand and Croconate Violet dianion

Reaction between Zn(II) cation and Croconate Violet dianion (CV^{2-}) in the presence of the flexible nitrogen ligand 1,3-bis(4-pyridyl)propane (BPP) has afforded a novel neutral coordination polymer namely $\{[Zn(\mu\text{-}BPP)(BPP)(CV)(H_2O)] \cdot H_2O\}_n$ (**1**). Compound **1** was characterized by means of elemental analysis, thermogravimetric analysis and vibrational spectroscopy. The crystal structure of **1** reveals 1-D chains extended to a 2-D coordination network through hydrogen bonding.

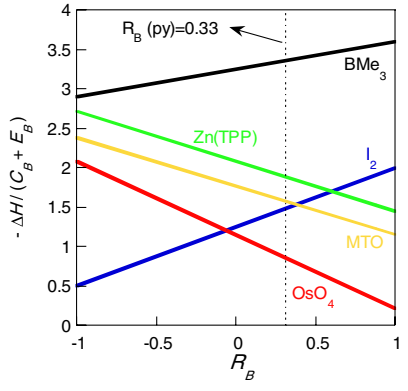


S. Masoud Nabavizadeh and Mehdi Rashidi

Polyhedron 26 (2007) 1476

Acidity of osmium tetroxide (OsO_4) towards coordination with pyridine and its derivatives

Three scales, donor ability of substituted pyridines, the Hammett reaction constant and the ECW model were used to make an acidity scale for OsO_4. The results show that the acid strength order towards pyridine is as follow: $BMe_3 > Zn(TPP) > MTO > I_2 > OsO_4$.

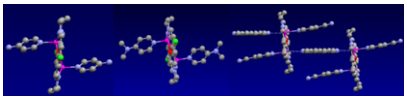


Wei Huang, Zhaolian Chu, Shaohua Gou and Takuji Ogawa

Polyhedron 26 (2007) 1483

Construction of macrocycle-based molecular stairs having pendant 4-aminopyridine, 4-dimethylaminopyridine and isonicotinonitrile groups

Self-assembly directed by dinuclear zinc(II) macrocyclic species with 4-aminopyridine, 4-dimethylaminopyridine and isonicotinonitrile produces three *trans* molecular stair elements and a 1D polymeric stair, which are stabilized by coordination bonding, H-bonding and face-to-face π–π stacking interactions. Controlled synthesis of the *cis* and *trans* isomers is achieved in the case of 4-aminopyridine, which is further verified by theoretic calculations.

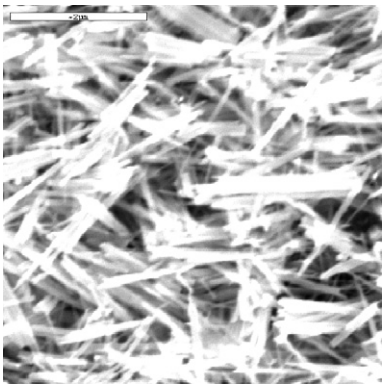


Sobia Ashraf, Russell Binions, Christopher S. Blackman and Ivan P. Parkin

Polyhedron 26 (2007) 1493

The APCVD of tungsten oxide thin films from reaction of WCl_6 with ethanol and results on their gas-sensing properties

The APCVD reaction of WCl_6 with ethanol was examined to deposit tungsten oxide on gas sensor substrates. Deposited films, which were WO_{3-x}, displayed a different morphology than those seen previously for CVD tungsten oxide. The gas-sensing properties of the deposited films were examined.

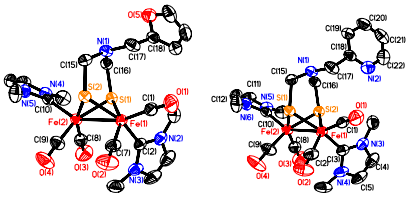


Shi Jiang, Jianhui Liu, Yu Shi, Zhen Wang, Björn Åkermark and Licheng Sun

Polyhedron 26 (2007) 1499

Preparation, characteristics and crystal structures of novel *N*-heterocyclic carbene substituted furan- and pyridine-containing azadithiolate Fe–S complexes

Two novel *N*-heterocyclic carbene di-substituted furan- and pyridine-containing azadithiolate Fe-only models have been synthesized and characterized. They show more negative reductive potential and are easier to capture a proton attributing to the strong electron-donating ligand NHC.

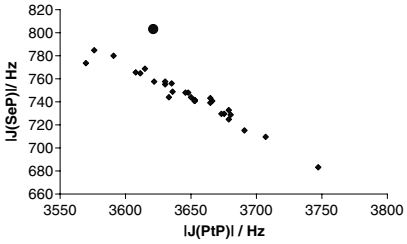


Dave J. Adams, James A. Bennett, Daniel Duncan, Eric G. Hope, Jonathan Hopewell, Alison M. Stuart and Andrew J. West

Polyhedron 26 (2007) 1505

Synthesis and characterisation of trisarylphosphine selenides: Further insight into the effect of fluoroalkylation on the electronic properties of trisarylphosphines

The electronic influence of perfluoroalkyl groups in a range of trisarylphosphines is conveniently assessed using the $^1J_{SeP}$ coupling constant of the trisarylphosphorus(V) selenides.

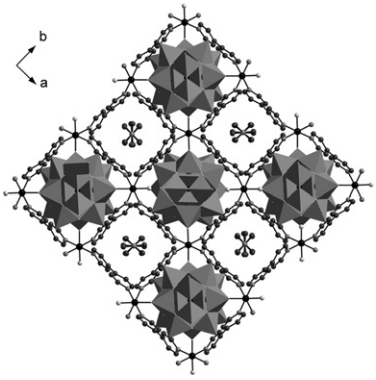


Chun-Dan Zhang, Shu-Xia Liu, Bo Gao, Chun-Yan Sun, Lin-Hua Xie, Miao Yu and Jun Peng

Polyhedron 26 (2007) 1514

Hybrid materials based on metal–organic coordination complexes and cage-like polyoxovanadate clusters: Synthesis, characterization and magnetic properties

Unique organic–inorganic hybrid compounds have been separated under hydrothermal conditions, and are constructed of metal–organic complexes and cage-like vanadium clusters. They indicate novel structures and attractive magnetic properties. Furthermore, two new clusters $[V_{16}O_{38}F]^{4-}$ and $[V_{16}O_{38}Br]^{4-}$ are reported.

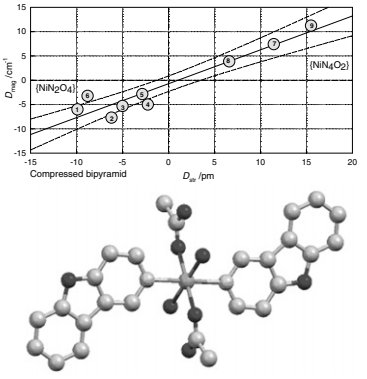


J. Titiš, R. Boča, L'. Dlháň, T. Ďurčeková, H. Fuess, R. Ivaniková, V. Mrázová, B. Papánková and I. Svoboda

Polyhedron 26 (2007) 1523

Magnetostructural correlations in heteroleptic nickel(II) complexes

Heteroleptic nickel(II) complexes with the general formula $Ni(L)_m(H_2O)_n(X)_k$ have been synthesized and structurally characterized; L stands for neutral *N*-donor ligands. The structures of the complexes $[Ni(bzfupy)_2(ac)_2(H_2O)_2]$, $[Ni(Me_2fupy)_2(H_2O)_4](ac)_2$ and $[Ni(Me_2iz)_4(H_2O)_2]Cl_2 \cdot 3H_2O$ are formed from $\{NiO_2O'_2N_2\}$, $\{NiO_4N_2\}$ and $\{NiN_4O_2\}$ chromophores, respectively. These complexes and two other previously characterized complexes were subjected to magnetochemical investigation down to 2 K (susceptibility and magnetization measurements). They show magnetic behaviour typical for zero-field splitting systems. The axial parameter of the zero-field splitting, *D*, adopts either positive or negative values and correlates with the axial distortion of the coordination polyhedra.

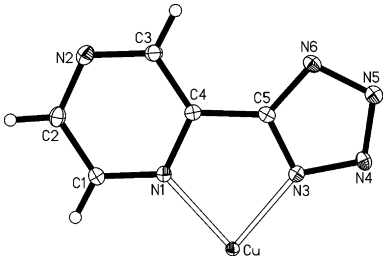


Morsy A.M. Abu-Youssef, Franz A. Mautner, Alshima'a A. Massoud and Lars Öhrström

Polyhedron 26 (2007) 1531

Synthesis, structure, network and thermal analysis of four 5-(pyrazinyl)tetrazolato copper(II) and cobalt(II) complexes

Four new copper(II) and cobalt(II) complexes with 5-(pyrazinyl)tetrazolate as chelating bidentate ligand. Hydrogen bonds connect the mononuclear units to a **3D** network structure. They can be related to the three- and six-connected rutile net (**rtl**) in $[Co(pyztz)_2(H_2O)_2]$ and the four- and six-connected **fsh**-net in $[Cu(pyztz)_2(H_2O)_2] \cdot (H_2O)$.

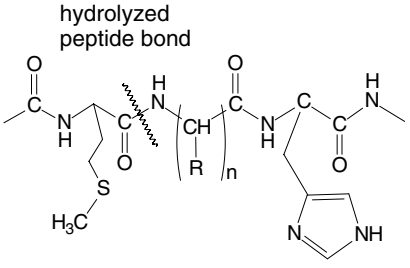


Marija D. Živković, Snežana Rajković, Urszula Rychlewska, Beata Warżajtis and Miloš I. Djuran

Polyhedron 26 (2007) 1541

A study of the reactions of methionine- and histidine-containing peptides with palladium-(II) complexes: The key role of steric crowding on palladium(II) in the selective cleavage of the peptide bond

The modes of coordination of *cis*-$[Pd(dpa)Cl_2]$ and *cis*-$[Pd(dpa)(H_2O)_2]^{2+}$ (dpa is 2,2′-dipyridylamine) in the reactions with Met-Gly and His-Gly peptides, and the regioselective cleavage of the amide bond involving the carboxylic group of methionine in the reactions of *cis*-$[Pd(dpa)(H_2O)_2]^{2+}$ with MeCOMet-Gly or MeCOHis-Gly peptides have been correlated with the steric bulk of the palladium(II) complex.

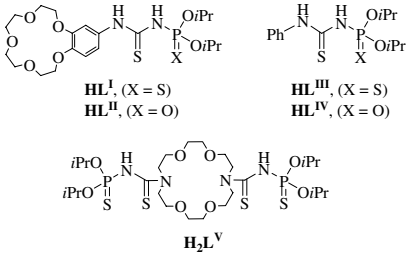


Felix D. Sokolov, Damir A. Safin, Maria G. Babashkina, Nail G. Zabirov, Vasiliy V. Brusko, Nikolay A. Mironov, Dmitry B. Krivolapov, Igor A. Litvinov, Rafael A. Cherkasov and Boris N. Solomonov

Polyhedron 26 (2007) 1550

A "sodium trap" based on benzo-15-crown-5 with an exocyclic *N*-(thiophosphoryl)thiourea moiety

For *N*-(thio)phosphorylthioureas of the common formula RC(S)NHP(X)(O*i*Pr)$_2$ **HL^{I}**, **HL^{II}**, **HL^{III}**, **HL^{IV}**, and (*N*,*N*′-bis-[C(S)NHP(S)(O*i*Pr)$_2$]$_2$-1,10-diaza-18-crown-6) **H$_2$L^{V}**, salts **LiL^{I,III,IV}**, **NaL$^{I–IV}$**, **KL$^{I–IV}$M$_2$L^{V}** (M = Li$^+$, Na$^+$, K$^+$), **Ba(L^{I,III,IV})$_2$** and **BaL^{V}** have been synthesized and investigated. Compounds **NaL^{I,II}** quantitatively drop out as a deposit in ethanol medium, allowing the separation of Na$^+$ and K$^+$ cations. This effect is not displayed for the other compounds. The crystal structure of **HL^{III}** and the solvate of the composition [**K(Me$_2$CO)L^{III}**] have been investigated by X-ray crystallography.



The Publisher encourages the submission of articles in electronic form thus saving time and avoiding rekeying errors. For detailed instructions on the preparation of manuscripts and of electronic artwork, consult the Author Gateway for Elsevier at http://authors.elsevier.com

ScienceDirect

Full text of this journal is available, on-line from **ScienceDirect**. Visit **www.sciencedirect.com** for more information.

Available online at www.sciencedirect.com
ScienceDirect
Polyhedron 26, issue 6, 11 April 2007
POLYHEDRON
www.elsevier.com/locate/poly

Contents

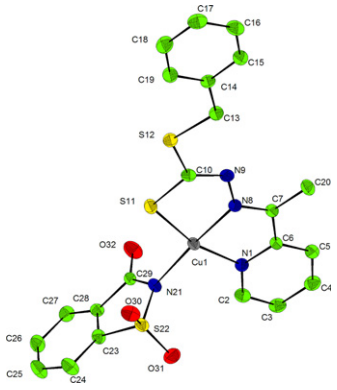
Papers

Thahira B.S.A. Ravoof, Karen A. Crouse, M. Ibrahim M. Tahir, Andrew R. Cowley, M. Akbar Ali

Polyhedron 26 (2007) 1159

Synthesis, characterization and bioactivity of mixed-ligand Cu(II) complexes containing Schiff bases derived from *S*-benzyldithiocarbazate and saccharinate ligand and the X-ray crystal structure of the copper-saccharinate complex containing *S*-benzyl-β-*N*-(acetylpyrid-2-yl)methylenedithiocarbazate

Mixed-ligand complexes of general formula, [Cu(NNS)(sac)] (NNS′ = *S*-benzyl-β-*N*-(2-acetylpyrid-2-yl)methylenedithiocarbazate, NNS″ = *S*-benzyl-β-*N*-(2-benzoylpyrid-2-yl)methylenedithiocarbazate and NNS‴ = *S*-benzyl-β-*N*-(6-methylpyrid-2-yl)methylenedithio-carbazate, sac = the saccharinate anion) have been synthesized and characterized. An X-ray crystallographic structural analysis of [Cu(NNS′)(sac)] shows that the complex has a distorted square-planar geometry with the Schiff base coordinated to the copper (II) ion as a uninegatively charged tridentate chelating agent via the pyridine nitrogen atom, the azomethine nitrogen atom and the thiolate sulphur atom while the fourth coordination position is occupied by the N-bonded saccharinate anion. The complexes have been evaluated for their biological activities against selected pathogens and cancer cell lines. They display weak activity against the bacteria and fungi. They are highly active against the leukemic cell line (HL-60) but only [Cu(NNS′)(sac)] exhibits strong cytotoxicity against the ovarian cancer cell line (Caov-3). All complexes are inactive against the breast cancer cell line (MCF-7).

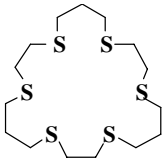


Chandrika P. Kulatilleke

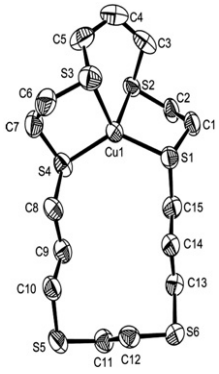
Polyhedron 26 (2007) 1166

Characterization and properties of the copper(II/I) complexes of macrocyclic hexathiaether ligand [21]aneS_6

The copper(II/I) complexes of hexathiaether macrocyclic ligand, [21]aneS_6, were synthesized, and characterized by electrochemical and spectroscopic techniques. Cu([21]aneS_6)$^{2+/+}$ forms a reversible one-electron redox couple bearing the highest formal potential 0.89 V (against SHE) reported to date for a $Cu^{2+/+}$ macrocyclic system in aqueous solution. Stability constants were also determined for the Cu(I) and Cu(II) complexes.



[21]aneS_6

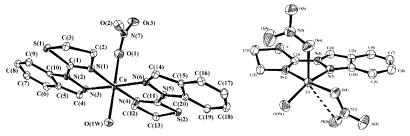


M.A. Maldonado-Rogado, E. Viñuelas-Zahínos, F. Luna-Giles, A. Bernalte-García

Polyhedron 26 (2007) 1173

Influence of heterocycles arrangement in structural isomeric ligands on coordination sphere of copper(II) complexes: Crystal structures and spectroscopic characterization

Two related copper complexes, where copper(II) ion is bonded to isomeric ligands, show significant structural variations as a result of the influence of heterocycles arrangement in isomeric ligands.

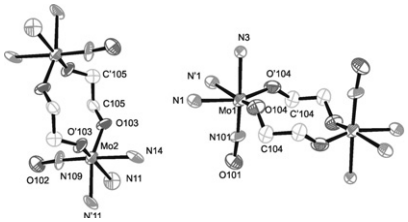


Piotr P. Romańczyk, Matylda N. Guzik, Andrzej J. Włodarczyk

Polyhedron 26 (2007) 1182

Redox activity of bimetallic complexes based on tris(3,5-dimethylpyrazolyl)borato molybdenum(II) and tungsten(II) nitrosyls. Complexes derived from ethane-1,2-diol and the crystal structure of *anti*-[Mo(NO){HB(3,5-$Me_2C_3HN_2$)$_3$}(OCH_2CH_2O)]$_2$ · 4$CHCl_3$

The bimetallic complexes [{M(NO)(Tp^{Me2})X}$_2$(OCH_2CH_2O)] [Tp^{Me2} = HB(3,5-$Me_2C_3HN_2$)$_3$; M = Mo, X = Cl, Br or I; M = W, X = Cl] have been synthesised and characterised spectroscopically and electrochemically. These species can occur as mixture of two diastereoisomers and one of them could be separated following a thermal treatment of the mixture. A direct synthesis of single diastereoisomers (M = Mo, X = I; M = W, X = Cl) is also described. The bimetallic species exhibit two one-electron reduction processes separated by a modest potential difference, $\Delta E_{1/2}$, ca. 300 mV (M = Mo, X = Cl, Br) indicating an intermediate metal–metal interaction. In the crystal structure of *anti*-[{Mo(NO)(Tp^{Me2})(OCH_2CH_2O)}$_2$] · 4$CHCl_3$ two nonequivalent dinuclear molecules (point group C_{2h}) are found, with crystallographically identical, doubly bridged {Mo(NO)(Tp^{Me2})} distorted octahedral units.

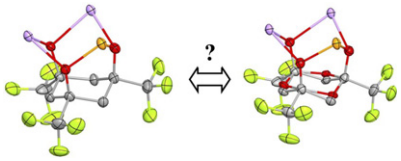


Pierre-Loic Saaidi, Erwann Jeanneau, Denis Bouchu, Jens Hasserodt

Polyhedron 26 (2007) 1191

The case of a Cd_2Cu_2 complex containing an apparently C_3-symmetric ligand: Erroneous ligand-structure assignment by X-ray diffraction data analysis

Previously reported complex **4** was resynthesized in order to have a more readily available source of cyclohexane 1. Attempts to liberate the ligand from **4** resulted in the sole formation of pyrane 2. This observation conflicts with X-ray analytical data, but could be resolved by synthetic and mass analytical results.

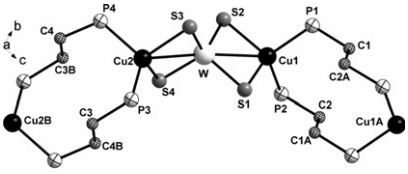


Li Song, Ping Lin, Zhi-Hua Li, Jian-Rong Li, Shao-Wu Du, Xin-Tao Wu

Polyhedron 26 (2007) 1199

W/Cu(Ag)/S complexes containing bridging diphosphine ligands: Synthesis, structures and optical properties

A tetranuclear cluster [Et_4N]$_2$[WOS_3Cu(dppe)]$_2$ · H_2O (**1**), and two polymeric complexes [WS_4Cu_2(dppe)$_2$]$_n$ (**2**) and [Et_4N]$_2$[$WEE'S_2$-Ag(dppe)]$_2$ · CH_3CN (E = 0.636S + 0.364O, E′ = 0.581O + 0.419S) (**3**) have been prepared by solution and solvothermal reactions, respectively. The W and Cu atoms in **2** form a helical chain while the anion of **3** displays a zig-zag chain structure. The optical absorption spectra and the solid-state photoluminescent properties of these complexes are also studied.



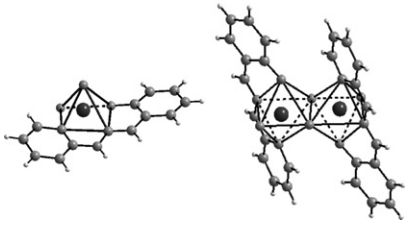
Part of the neutral polymeric chain of 2.

Anindita Sarkar, Samudranil Pal

Polyhedron 26 (2007) 1205

Dioxovanadium(V) complexes with N,N,O-donor monoanionic ligands: Synthesis, structure and properties

Synthesis and characterization of dioxovanadium(V) complexes having the general formula [VO_2(phsalR)] (HphsalR = 4-R-2-(pyridin-2-yl-hydrazonomethyl)-phenols) are described. X-ray structure of the complex with $phsal^-$ (R = H) reveals a di(μ-oxo) bridged dimeric structure due to weak association of two square-pyramidal [VO_2(phsal)] molecules. In this dimer, the metal centres are in two edge-shared N_2O_4 octahedra.

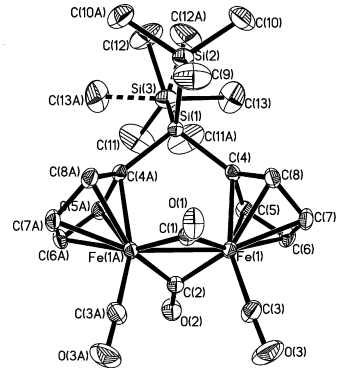


Huai-Lin Sun, Zhen-Sheng Zhang

Polyhedron 26 (2007) 1211

1,1,1,3,3,3-Hexamethyltrisilanylene-bridged bis-(cyclopentadienyl)tetracarbonyldiiron and its derivatives: Synthesis, properties and molecular structures

The title cyclic complex $[\eta^5,\eta^5\text{-}C_5H_4\text{–}Si(SiMe_3)_2\text{–}C_5H_4]Fe_2(CO)_2(\mu\text{-}CO)_2$ and its ligand substituted derivatives $[\eta^5,\eta^5\text{–}C_5H_4\text{–}Si(SiMe_3)_2\text{–}C_5H_4]Fe_2(CO)(PR_3)(\mu\text{-}CO)_2$ (R = OPh, OMe, Ph, Me) containing exocyclic Si–Si bonds attached to the bridge have been synthesized and their properties examined with emphasis on the stability of the Si–Si bonds towards the intramolecular iron centers.

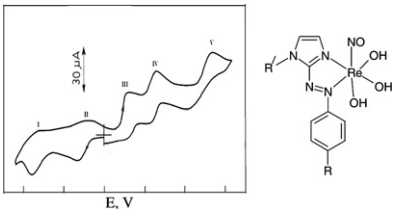


Pampa Pratihar, Anup Kumar Dasmahapatra, Chittaranjan Sinha

Polyhedron 26 (2007) 1217

Arylazoimidazole compounds of rhenium nitrosyl: Synthesis, spectral characterization and reactivity

ReO_4^- in aqueous alkaline medium has been reduced by $NH_2OH \cdot HCl$ and consequently reacted with 1-alkyl-2-(arylazo)imidazoles (RaaiR′) to synthesise $[Re(NO)(OH)_3(RaaiR')]$. The presence of $\upsilon(NO)$ at *ca.* 1700 cm^{-1} confirms the {Re–NO} motif. The complexes are ESR active. The reaction of the product with camphor in alkaline medium results in C–N bond fusion, with the synthesis of the camphorquinone monoxime complex. Cyclic voltammetry shows metal oxidation and reduction of the coordinated NO^+ and azoimine ligand.

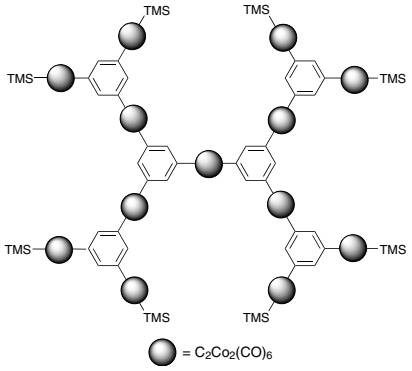


Edwin C. Constable, Deborah Gusmeroli, Catherine E. Housecroft, Markus Neuburger, Silvia Schaffner

Polyhedron 26 (2007) 1222

Nanoscale octadecacobalta- and hexacosacobaltaclusters: Synthesis and spectroscopic fingerprinting

Strategies for the construction of TMS-protected first generation star and dendritic polyynes, which can subsequently fully functionalized with $Co_2(CO)_6$-cluster units, are reported. ^{13}C NMR spectroscopy is shown to be the most valuable tool in the characterization of the cobalt cluster-decorated products.

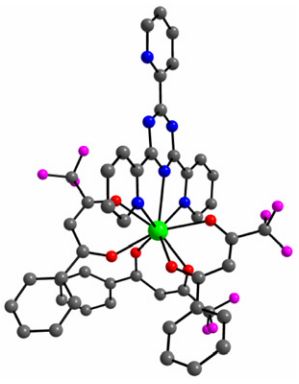


Channa R. De Silva, Jenine R. Maeyer, Alice Dawson, Zhiping Zheng

Polyhedron 26 (2007) 1229

Adducts of lanthanide β-diketonates with 2,4,6-tri(2-pyridyl)-1,3,5-triazine: Synthesis, structural characterization, and photoluminescence studies

Adducts of lanthanide β-diketonates of the general formula $LnL_3(TPTZ)$ were synthesized and structurally characterized [Ln = Eu(III), Tb(III), Er(III); L = dibenzoylmethanate (DBM), 1-benzoylacetone (BA), thenoyltrifluoroacetone (TTA), 4,4,4-trifluoro-1-phenyl-1,3-butanedione (BTFA); TPTZ = 2,4,6-tri-(2-pyridyl)-1,3,5-triazine]. Luminescence quantum yields of these complexes are significantly enhanced over their corresponding aqua analogues.

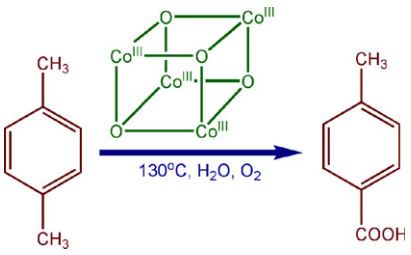


Rajesh Chakrabarty, Dipika Kalita, Birinchi K. Das

Polyhedron 26 (2007) 1239

Catalytic oxidation of *p*-xylene in water by cobalt(III) cubane cluster

A new tetrameric cubane complex $Co_4^{III}(\mu_3\text{-}O)_4(\mu\text{-}O_2CCH_3)_4(4\text{-}CNpy)_4$ has been studied as a homogeneous catalyst for the oxidation of *p*-xylene with dioxygen in aqueous media.

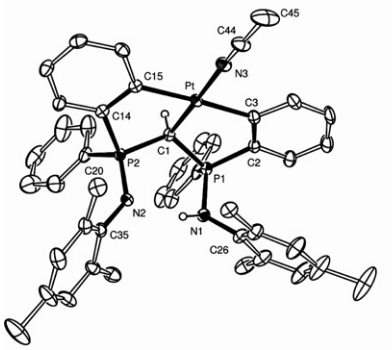


Michael S. Hill, Peter B. Hitchcock

Polyhedron 26 (2007) 1245

Reactivity of an *N*-mesityl bis(phosphinimino)-methane with group 10 metals

Reactions of an *N*-mesityl bis(phosphinimino)-methane with $[PdCl_2(MeCN)_2]$ or $[PtMe_2(COD)]$ produced bis(phosphinimino)-methanide complexes resulting from single and triple C–H activation, respectively.

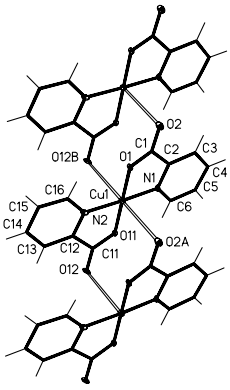


Bogumiła Żurowska, Jerzy Mroziński, Zbigniew Ciunik

Polyhedron 26 (2007) 1251

One-dimensional copper(II) compound with a double out-of-plane carboxylato-bridge – Another polymorphic form of Cu(pyridine-2-carboxylate)$_2$

The compound of the formula Cu(pyridine-2-carboxylate)$_2$ was prepared, and then characterized by infrared, ligand field, EPR spectroscopy and magnetic studies. In particular, the crystal structure was determined by X-ray methods. The structure consists of a copper atom *trans* square-planar coordinated by two picolinate anions. The weak bonding interaction between the copper and an oxygen atom of carboxylate groups of neighboring planes permits to define the structure as a one-dimensional chain with a double out-of-plane carboxylate bridge. The variable temperature (1.8–300 K) magnetic susceptibility revealed weak antiferromagnetic coupling within the chain and throughout the hydrogen bond network ($J = -0.73$, $zJ' = -0.06$ cm^{-1}, respectively).

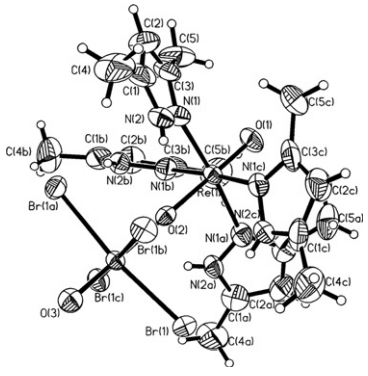


B. Machura, R. Kruszynski, J. Mroziński

Polyhedron 26 (2007) 1259

An unusual oxo-bridged rhenium complex with the Re centers in different coordination environments

The reaction of the complex $[ReOBr_3(PPh_3)_2]$ with 3,5-dimethylpyrazole (3,5-Me$_2$pzH) in acidified acetone at room temperature has been examined and a novel dinuclear oxocompound, $[\{ReOBr_4\}(\mu\text{-}O)\{ReO(3,5\text{-}Me_2pzH)_4\}]$, has been obtained. It has been studied by IR, UV–Vis spectroscopy, magnetization measurements and X-ray crystallography. The electronic structure of $[\{ReOBr_4\}(\mu\text{-}O)\{ReO(3,5\text{-}Me_2pzH)_4\}]$ has been calculated with the density functional theory (DFT) method. The spin-allowed singlet–singlet electronic transitions of $[\{ReOBr_4\}(\mu\text{-}O)\{ReO(3,5\text{-}Me_2pzH)_4\}]$ have been calculated with the time-dependent DFT method, and the UV–Vis spectrum of the title compound has been discussed on this basis.

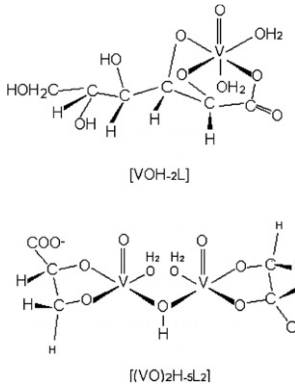


Marcela Guiotoku, Fátima Regina Mena Barreto Silva, José Carlos Azzolini, Ana Lucia Ramalho Mercê, Antônio S. Mangrich, Luis F. Sala, Bruno Szpoganicz

Polyhedron 26 (2007) 1269

Monosaccharides and the VO(IV) metal ion: Equilibrium, thermal studies and hypoglycemic effect

Protonation and complexation equilibriums of monosaccharides and the VO(IV) metal ion in aqueous solution as well as their effect on the hyperglycemia of diabetic rats were carried out. The mononuclear species formed by HGlu and VO^{2+} were confirmed by EPR. The spectra showed 8 lines ($I = 7/2$) characteristic of mononuclear VO-hexoses. A binuclear species was detected in small quantities, which was formed by coordination of two HGlu molecules and two VO^{2+} ions through a hydroxide bridge.

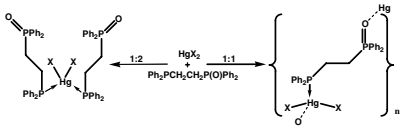


Mothi Mohamed Ebrahim, Antonia Neels, Helen Stoeckli-Evans, Krishnaswamy Panchanatheswaran

Polyhedron 26 (2007) 1277

Synthesis, crystal structures and spectra of Hg(II)-1,2-bis(diphenylphosphino)ethane monoxide complexes: Monomer and polymer formation

Mercury(II) halides react with 1,2-bis(diphenylphosphino)ethane monoxide in 1:1 and 1:2 molar ratio to form polymeric and monomeric complexes, respectively.

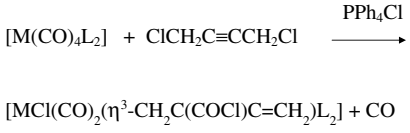


Annabelle G.W. Hodson, Simon J. Coles, Michael B. Hursthouse

Polyhedron 26 (2007) 1285

One pot synthesis of η^3-butadienyl complexes of Mo(II) or W(II): Crystal structure of $[MoCl(CO)_2(\eta^3\text{-}CH_2C(CONHCH_2C{\equiv}CH)C{=}CH_2)(2,2'\text{-bipyridine})]$

Complexes of the type $[MCl(CO)_2(\eta^3\text{-}CH_2C(COX)C{=}CH_2)L_2]$ (M = Mo, W; L_2 = 2,2′-bipy, 1,10-phen, 2,9-dimethyl-1,10-phen; X = Cl, NHR, NR_2, OR, SR) were obtained from one pot reactions of $[M(CO)_4L_2]$, 1,4-dichloro-2-butyne and Ph_4PCl in chlorinated solvents below 60 °C (Mo) or above 81 °C (W). Destabilization of X = Cl occurred at elevated temperatures to give the alternative product $[MCl_2(CO)(\eta^2\text{-}ClCH_2C{\equiv}CCH_2Cl)L_2]$.

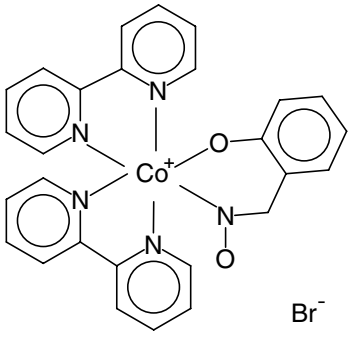


Maria Lalia-Kantouri, Christos D. Papadopoulos, Miguel Quirós, Antonios G. Hatzidimitriou

Polyhedron 26 (2007) 1292

Synthesis and characterization of new Co(III) mixed-ligand complexes, containing 2-hydroxy-aryloximes and α-diimines. Crystal and molecular structure of $[Co(saox)(bipy)_2]Br$

In the 12 novel complexes $[Co(oxime)(enR)_2]\text{-}Br \cdot 2H_2O$, with octahedral arrangement of the chromophore CoN_5O, the rare for mononuclear Co(III) complexes, bidentate dianion character of the oxime ligand is established. The theoretical investigation with GAUSSIAN-03 for the prediction of the electronic spectrum and especially the ZINDO calculations, gave good correlation with the experimental spectrum in the solid state of the complex $[Co(saox)(bipy)_2]Br$. The cyclic voltammogram study gave all the expected waves for the redox processes of the metal Co(III) and the oxime ligands, as well as for the α-diimines bipy and phen.

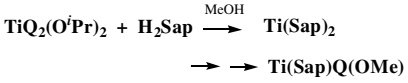


Weng Feng Zeng, Yen Hsien Chen, Michael Y. Chiang, Cheu Pyeng Cheng

Polyhedron 26 (2007) 1303

Preparations and structures of titanium(IV) complexes containing 8-hydroxyquinolinate and a Schiff-base *N*-(2-oxyphenyl)salicylideneiminate

In methanol, the reactions of $Ti(O^iPr)_4$/$TiQ_2(O^iPr)_2$ with Schiff-base *N*-(2-hydroxyphenyl)salicylideneimine (H_2Sap) in the presence/absence of 8-hydroxyquinoline (HQ) yield $Ti(Sap)_2$ initially, and Ti(Sap)Q(OMe) only after prolong standing.

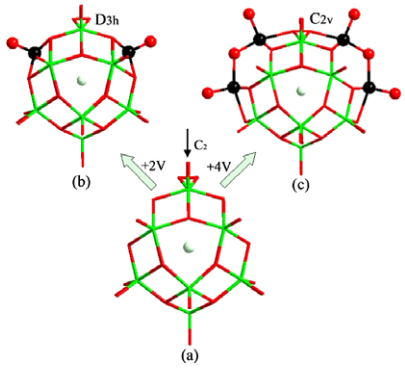


Baoxia Dong, Carlos J. Gómez-García, Jun Peng, Samia Benmansour, Jianfang Ma

Polyhedron 26 (2007) 1310

A novel oxovanadate structural type – Synthesis, single crystal structure and magnetic properties of a mixed-valence polyoxovanadate formed by $\{V_{17}O_{40}(Cl)\}$ and $\{V_{15}O_{36}(Cl)\}$ clusters

A new "hexadecavanadate", $[Ni(phen)_3]_2\{[V_{15}O_{36}(Cl)]_{0.5}[V_{17}O_{40}(Cl)]_{0.5}\} \cdot H_2O$ (phen = 1,10′-phenanthroline) (**1**), which contains two architectures of $\{V_{15}O_{36}(Cl)\}$ (b) and $\{V_{17}O_{40}(Cl)\}$ (c) has been synthesized and characterized. The $\{V_{17}O_{40}(Cl)\}$ represents a new type of framework in polyoxovanadate chemistry. The formation of the two architectures can be described as the accommodation of two or four more V atoms in a {V13} fragment (a).

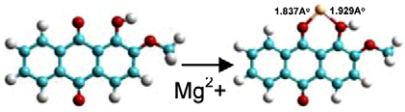


Prasenjit Kar, Moorthy Suresh, D. Krishna Kumar, D. Amilan Jose, Bishwajit Ganguly, Amitava Das

Polyhedron 26 (2007) 1317

Preferential binding of the magnesium ion by anthraquinone based chromogenic receptors

Anthraquinone based new receptor molecules have been synthesized. These chromogenic receptors show preferential binding of the Mg^{2+} ion as compared to other group IA and IIA metal ions. Ab inito calculations show the strongest binding of these receptors with the Mg^{2+} ion. An X-ray structural study reveals a right handed helical structure for one of the receptor units.

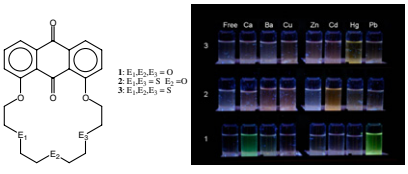


Mariappan Kadarkaraisamy, Andrew G. Sykes

Polyhedron 26 (2007) 1323

Selective luminescence detection of cadmium(II) and mercury(II) utilizing sulfur-containing anthraquinone macrocycles (part 2) and formation of an unusual Hg_2^{2+}-crown ether dimer via reduction of Hg(II) by DMF

Sulfur-containing photoinduced charge transfer (PCT) sensors 1,8-anthraquinone-18-dithiacrown-5 (**2**) and 1,8-anthraquinone-18-trithiacrown-5 (**3**) selectively detect both inorganic Cd(II) and Hg(II). Simple heteroatom substitution of the receptor combined with an integrated intraannular carbonyl oxygen fine-tunes selectivity by simple synthetic design. In addition, the high yield synthesis of mercurous ion, Hg_2^{2+}, has also been observed via the reduction of Hg(II) in the solvent dimethylformamide (DMF), which has not been previously reported. Spectroscopic and X-ray crystallographic results for Cd^{2+}, Hg_2^{2+} and Mg^{2+} complexes of oxygen and sulfur-containing derivatives of 1,8-anthraquinone-18-crown-5 are presented.

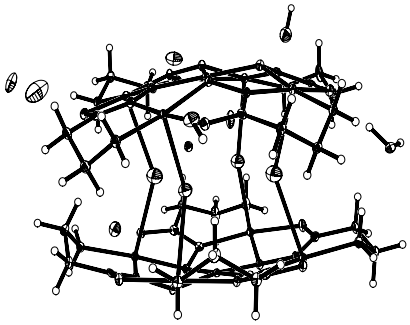


J. Legendziewicz, M. Puchalska, Z. Ciunik, W. Wojciechowski

Polyhedron 26 (2007) 1331

The new decanuclear copper(II) cluster $[Cu_5(\beta\text{-alaha})_4Cl_2]_2 \cdot 2HCl \cdot 15H_2O$, its structure, spectroscopy and magnetism

Structure, spectroscopy and magnetism of new decanuclear copper(II) cluster with β-alaninehydroxamic acid of formula $[Cu_5(\beta\text{-alaha})_4Cl_2]_2 \cdot 2HCl \cdot 15H_2O$, where β-alaha stands for β-alaninehydroxamate ($C_3H_6N_2O_2^{2-}$), are reported. The complex is composed of two pentanuclear subunits bridged by four chloride anions. Magnetic studies showed predominant antiferromagnetic interactions within Cu_5 core and weaker interactions between Cu(II) ions from two pentameric units connected through chloride bridges.

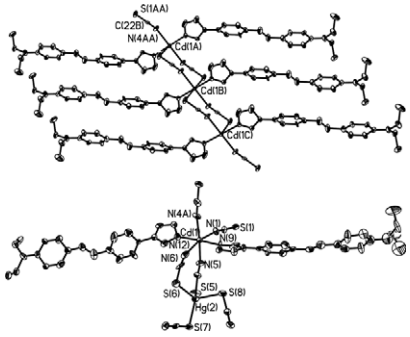


Feng Jin, Hong-Ping Zhou, Xu-Chun Wang, Zhang-Jun Hu, Jie-Ying Wu, Yu-Peng Tian, Min-Hua Jiang

Polyhedron 26 (2007) 1338

Synthesis, structures and photoluminescence of thiocyanate bridged metal-organic polymers containing functional imidazole ligand

Three new coordination polymers, $[Cd(SCN)_2L_2]_n$ (**1**), $[CdHg(SCN)_4L_2]_n$ (**2**) and $[MnHg(SCN)_4L_2]_n$ (**3**) (L is *trans*-4-imidazolyl-4′-(*N*,*N*-diethylamino)stilbene) have been prepared and the complexes have been determined by X-ray crystallography. Complex **1** is a one-dimensional chain, and complexes **2** and **3** are two-dimensional frameworks.

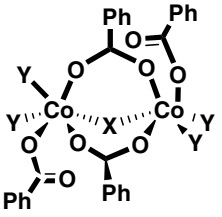


Anirban Karmakar, Rupam J. Sarma, Jubaraj B. Baruah

Polyhedron 26 (2007) 1347

Synthesis and characterisation of dinuclear and mononuclear Cobalt (II) benzoate complexes

Aqua-bridged cobalt (II) benzoate complexes are prepared through solid state synthetic route. However, synthetic route through solution resulted in mononuclear benzoate complex.



where X= H_2O; Y = pyridine

The Publisher encourages the submission of articles in electronic form thus saving time and avoiding rekeying errors. For detailed instructions on the preparation of manuscripts and of electronic artwork, consult the Author Gateway for Elsevier at http://authors.elsevier.com

ScienceDirect

Full text of this journal is available, on-line from **ScienceDirect**. Visit **www.sciencedirect.com** for more information.

Available online at www.sciencedirect.com
ScienceDirect
Polyhedron 26, issue 5, 25 March 2007
POLYHEDRON
www.elsevier.com/locate/poly

Contents

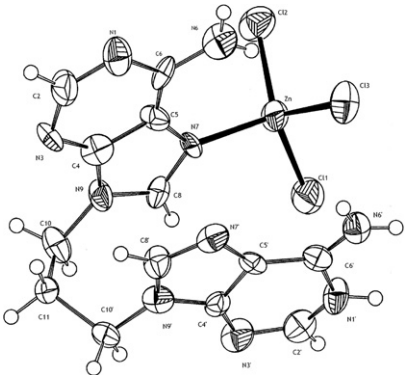
Papers

Angel García-Raso, Juan J. Fiol, Andrés Tasada, Francisca M. Albertí, Ferran Bádenas, Xavier Solans, Mercè Font-Bardia

Polyhedron 26 (2007) 949

N^9,$N^{9'}$-polymethylene-bisadenine complexes with d^{10} metal ions

The general behaviour of (tri and tetramethylene)-bisadenines with Zn(II) and Cd(II) in acidic media has been studied. The Cd(II) ion only yields outer sphere complexes with N^9,$N^{9'}$-polymethylene-bisadenines in acidic media. By a modification of the reaction conditions, it is possible to isolate the equivalent inner sphere complexes for both ligands: [H-(Ade)$_2$C$_x$(ZnCl$_3$)] (x = 3, 4).

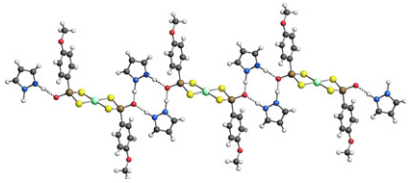


E. Alberti, G.A. Ardizzoia, S. Brenna, F. Castelli, S. Galli, A. Maspero

Polyhedron 26 (2007) 958

The synthesis of a new dithiophosphonic acid and its coordination properties toward Ni(II): A combined NMR and X-ray diffraction study

The new S-donor 4-methoxophenyldithiophosphonate ligand (L) and the corresponding *trans*-[NiL$_2$]$^{2-}$ metal complex have been investigated by combining ^{13}C and ^{31}P solution and solid state NMR techniques as well as X-ray crystallography.

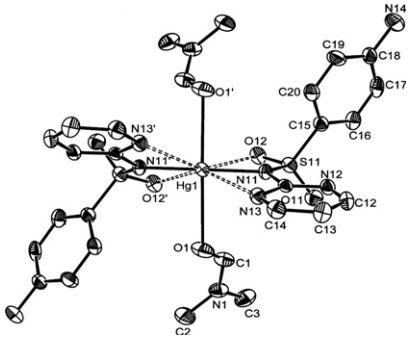


G.M. Golzar Hossain, A.J. Amoroso, A. Banu, K.M.A. Malik

Polyhedron 26 (2007) 967

Syntheses and characterisation of mercury complexes of sulfadiazine, sulfamerazine and sulfamethazine

Hg(II) complexes of sulfadiazine **1**, sulfamerazine **2** and sulfamethazine **3** were synthesised and their nature investigated by spectroscopic methods, including single crystal X-ray diffraction. In the solid state compounds **1** and **3** have eight coordinate '2+6' geometries, with two tridentate sulfonamide ions and two DMF molecules in the coordination sphere, while complex **2** has a six co-ordinate, '2+4' geometry.

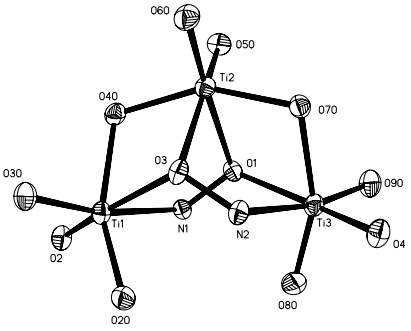


Matthew G. Davidson, Andrew L. Johnson, Matthew D. Jones, Matthew D. Lunn, Mary F. Mahon

Polyhedron 26 (2007) 975

Titanium(IV) complexes of oximes – Novel binding modes

The crystal and solution structures of four Ti(IV) oxime complexes are reported. The complexes show, for the first time, a triply bridging mode of the oxime ligands with Ti(IV) characterised via X-ray crystallography. ^{1}H and ^{13}C NMR spectroscopic studies show that the solid-state structures are maintained in solution.

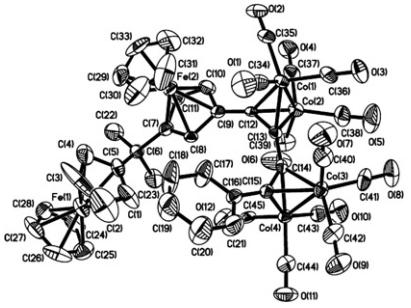


Ning Zhu, Quan-Ling Suo, Yi-Bing Wang, Li-Min Han, Yue-Guang Bai, Lin-Hong Weng

Polyhedron 26 (2007) 981

Synthesis, molecular structure and reactivity of new π-conjugated diyne with ferrocenyl and phenyl units

New clusters $FcC(CH_3)_2Fc'–C{\equiv}C–C{\equiv}C–Ph[Co_2(CO)_6]_n$ and $Fc–C{\equiv}C–C{\equiv}C–Ph[Co_2(CO)_6]_n$ (n = 1 or 2) have been synthesized by the reaction of ligands $FcC(CH_3)_2Fc'–C{\equiv}C–C{\equiv}C–Ph$ and $Fc–C{\equiv}C–C{\equiv}C–Ph$ with $Co_2(CO)_8$ respectively and the composition and structure were characterized by elemental analysis, FTIR, NMR and MS. The molecular and crystal structures of four compounds were analyzed by X-ray single crystal diffraction.

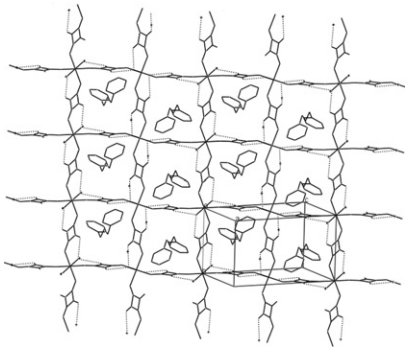


Charlane C. Corrêa, Renata Diniz, Luciano H. Chagas, Bernardo L. Rodrigues, Maria I. Yoshida, Wagner M. Teles, Flávia C. Machado, Luiz Fernando C. de Oliveira

Polyhedron 26 (2007) 989

Transition metal complexes with squarate anion and the pyridyl-donor ligand 1,3-bis-(4-pyridyl)propane (BPP): Synthesis, crystal structure and spectroscopic investigation

The synthesis, crystal structure and vibrational spectra of coordination polymers with 1,3-bis(4-pyridyl)propane (BPP) and squarate ion ligands and transition metal ions (M = Mn^{2+}, Co^{2+}, Ni^{2+}, Cu^{2+} and Zn^{2+}) are described. All compounds are isostructural, and the BPP is not coordinated to metal site since it is in cationic form due to protonation of N atoms from pyridyl rings. The metal is coordinated to two squarate ions and two water molecules in an octahedral distorted geometry.

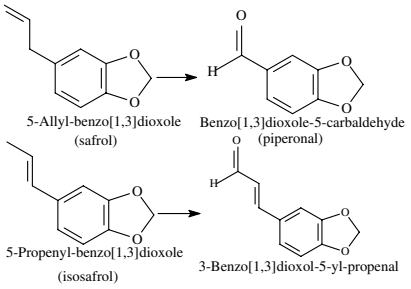


Juliana R. Steter, José O.S. Pontólio, M.I.C.F. Costa, J.R. Romero

Polyhedron 26 (2007) 996

A new polyphenol modified electrode containing an anchored ruthenium complex and its use in electrocatalytic oxidation of organic substrates

This work describes the preparation of a new modified electrode containing a ruthenium complex (*cis*-aquadimethylbipyridyltriphenylphosphineruthenium II), bonded to a stable polyphenol film. This modified electrode promotes the fast electrocatalytic oxidation of safrol (5-allyl-benzo[1,3]dioxole) and isosafrol (5-propenyl-benzo[1,3]dioxole), giving two interesting products benzo[1,3]dioxole-5-carbaldehyde (piperonal) and 3-benzo[1,3]dioxol-5-yl-propenal respectively, with good yields.

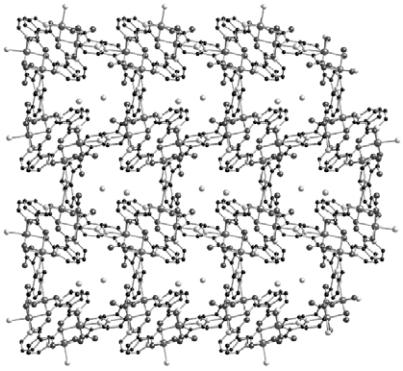


Anna E. Wasson, Robert L. LaDuca

Polyhedron 26 (2007) 1001

Hydrothermal synthesis, crystal structures, and properties of two 3-D network nickel nicotinate coordination polymers: $[Ni_4(\mu\text{-}H_2O)_2(nicotinate)_8 \cdot 2H_2O]$ and $[Ni_2(H_2O)_2\text{-}(nicotinate)_4(4,4'\text{-bpy})]$

The three-dimensional coordination polymers $[Ni_4(\mu\text{-}H_2O)_2(nic)_8 \cdot 2H_2O]$ (nic = nicotinate) (**1**) and $[Ni_2(H_2O)_2(nic)_4(4,4'\text{-bpy})]$ (**2**) were prepared via hydrothermal synthesis. The non-centrosymmetric crystal structure of **1** is constructed from binuclear $[Ni_2(\mu\text{-}H_2O)(\mu_3\text{-}nic)_2]^{2+}$ subunits joined into 3-D by μ_2-nic and μ_3-nic moieties, forming "bird"-shaped cavities. In contrast, the crystal structure of **2** is assembled from neutral $[Ni(H_2O)(\mu_2\text{-}nic)_2]$ layers, connected into 3-D via tethering 4,4′-bpy moieties. Magnetic and thermal properties are discussed.

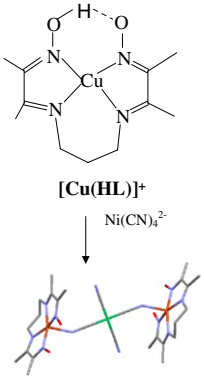


Ambarish Ray, Daipayan Dutta, Parikshit Chandra Mondal, William S. Sheldrick, H. Mayer-Figge, Mahammad Ali

Polyhedron 26 (2007) 1012

Synthesis, crystal structure, electrochemical and kinetic studies on a cyano-bridged Cu^{II}–Ni^{II}–Cu^{II} hetero-trinuclear complex

A cyano-bridged hetero-trinuclear complex, $[Cu(HL)]_2[Ni(CN)_4]$ (**2**) has been synthesized and characterized structurally. Electrochemical and chemical redox properties of $[Cu(HL)]^+$ (**1**) as well as **2** demonstrate that there is a distinct difference in behavior of **2** over **1** due to the presence of $[Ni(CN)_4]^-$ in **2**.

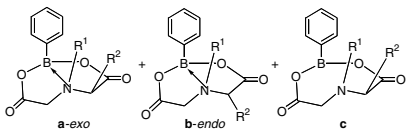


Teresa Mancilla, María de los Ángeles Calixto Romo, Lorena Amaya Delgado

Polyhedron 26 (2007) 1023

Synthesis and characterization of (N→B)-phenyl[*N*-alkyl-*N*-(2-alkyl)aminodiacetate-*O*,*O*′,*N*]boranes and phenyl[*N*-alkyl-*N*-(2-alkyl) aminodiacetate-*O*,*O*′,*N*]boranes

The reaction of boron heterocycles **1** and **2** with *n*-butyl lithium and alkyl halides led to (*N*→*B*) phenyl[*N*-alkyl-*N*-(2-alkyl)aminodiacetate-*O*,*O*′,*N*]boranes, where alkyl can be in *exo* (**a**) and/ or *endo* (**b**) position, and phenyl[*N*-alkyl-*N*-(2-alkyl)aminodiacetate-*O*,*O*′,*N*]boranes (**c**) isomers, which do not display the intramolecular *N*→*B* coordination. The existence of steric interactions between *N*-benzyl and the alkyl group at 2 position was indicated by ^1H and ^{13}C NMR, while, the $\delta(^{11}B)$ values confirm the tetrahedral and trigonal environment of the ^{11}B nucleus in these compounds. Moreover, the compounds were characterized by COSY, HETCOR and homonuclear proton decoupling experiment. The study of the intramolecular *N*→*B* coordination by dynamic NMR afforded a $\Delta G^{\ddagger}$ value of 81.09 kJ/mol for compound (*N*→*B*) phenyl[*N*-benzyl-*N*-(2-methyl)aminodiacetate-*O*,*O*′,*N*]borane.

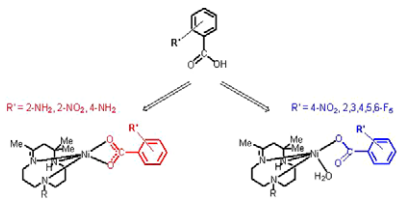


M. Dolores Santana, Gabriel García, Gregorio López, Abel Lozano, Consuelo Vicente, Luís García, José Pérez

Polyhedron 26 (2007) 1029

Preparation, crystal structures and NMR characterization of substituted-benzoate complexes Nickel(II)-N_3-macrocycles

The substituent effects upon the coordination mode of substituted benzoates have been established by X-ray diffraction. The influence of the substituents on the hyperfine shift patterns for these benzoate complexes of nickel(II) has been also studied.

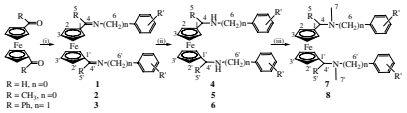


Hong-Xing Wang, Ren-Qing Gao, Xiao-Li Yang, Li Wan, Hong-Fei Wu, Feng-Ying Geng, Rong Jin

Polyhedron 26 (2007) 1037

Synthesis and characterization of 1,1′-bis[(*N*-methyl-*N*-phenyl)aminomethyl(ethyl)]ferrocenes. Crystal structures of [Fe{(η^5–C_5H_4)–C(C_6H_5)=N–$CH_2C_6H_4CH_3$-4}$_2$] and 2[Fe{(η^5–C_5H_4)–$CH_2N(CH_3)$–$C_6H_4OCH_3$-4}$_2$] · 1/4H_2O

1,1′-Bis[(*N*-methyl-*N*-phenyl)aminomethyl-(ethyl)]ferrocenes (**7**, **8**) were synthesized by reductive methylation of 1,1′-bis[(*N*-phenyl)-aminomethyl(ethyl)]ferrocenes (**4**, **5**). The latter were obtained by reduction of **1** and **2** with sodium borohydride or lithium aluminum-hydride–aluminum chloride. 1,1′-Bis[{(*N*-methyl-*N*-benzyl)amino}benzyl]ferrocenes (**9**) were not obtained, probably due to their debenzylation under the acidic conditions. The structures of **3g** and **7a** were determined by single crystal X-ray analysis.

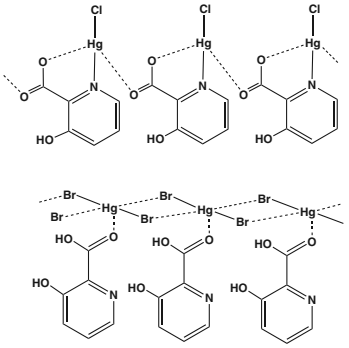


Zora Popović, Dubravka Matković-Čalogović, Jasminka Popović, Ivan Vicković, Marijana Vinković, Dražen Vikić-Topić

Polyhedron 26 (2007) 1045

Coordination modes of 3-hydroxypicolinic acid: Synthesis and structural characterization of polymeric mercury(II) complexes

Novel polymeric mercury complexes, HgCl(picOH), $HgBr_2$(HpicOH), $Hg(picOH)_2$ and $Hg(picOH)_2 \cdot H_2O$ (HpicOH = 3-hydroxypicolinic acid) were obtained. Crystal structure analysis of the halogeno-derivatives confirmed two different coordination modes of HpicOH. In DMSO solutions these complexes exist in the identical form as in the solid state.

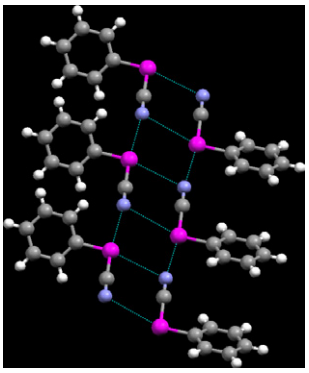


Nicholas A. Barnes, Stephen M. Godfrey, Ruth T.A. Halton, Imrana Mushtaq, Simon Parsons, Robin G. Pritchard, Mark Sadler

Polyhedron 26 (2007) 1053

A comparison of the solid-state structures of a series of phenylseleno-halogen and pseudo-halogen compounds, PhSeX (X = Cl, CN, SCN)

The solid-state structures of the series of compounds PhSeX (X = Cl, CN, SCN) have been reported. PhSeCl displays a square motif, $Ph_4Se_4Cl_4$, with four PhSeCl units linked by weak Se–Se bonds. In contrast, the pseudo-halogen derivatives PhSeCN and PhSeSCN display essentially monomeric structures, and both exhibit Se···N contacts in their extended structures which appear to be the dominant packing force in these compounds. PhSeSCN is the first crystallographically characterised example of a selenium thiocyanate compound.

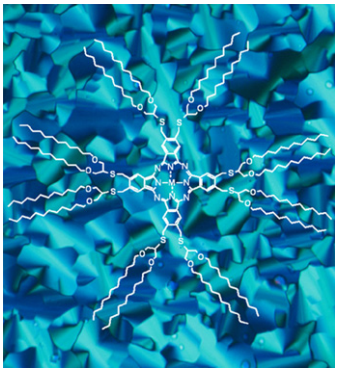


Devrim Atilla, Gökhan Aslıbay, Ayşe G. Gürek, Hatice Can, Vefa Ahsen

Polyhedron 26 (2007) 1061

Synthesis and characterization of liquid crystalline tetra- and octa-substituted novel phthalocyanines

The synthesis and characterization of methylene-bridged tetra- and octa-(13,17-dioxa nonacosane-15-sulfanyl) substituted metal free- and Ni(II) phthalocyanines were studied. The mesogenic properties of the tetra-and octa substituted phthalocyanines were described.

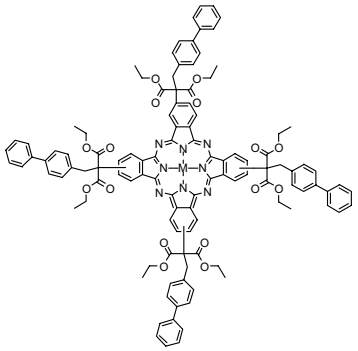


M. Kasım Şener, Atıf Koca, Ahmet Gül, Makbule Burkut Koçak

Polyhedron 26 (2007) 1070

Synthesis and electrochemical characterization of biphenyl-malonic ester substituted cobalt, copper, and palladium phthalocyanines

Phthalocyanines with four biphenyl-malonic ester groups on the periphery were synthesized by cyclotetramerization of 4-(1,1-dicarbethoxy-2-(4-biphenyl)-ethyl)-phthalonitrile. Electrochemical behaviors of novel Co(II), Cu(II), and Pd(II) phthalocyanines were investigated by cyclic voltammetry, potential differential pulse voltammetry and applied potential chronocoulometry techniques.

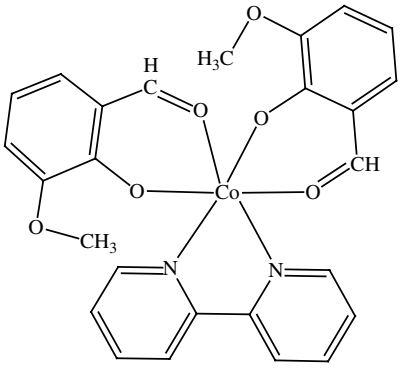


Christos D. Papadopoulos, Antonios G. Hatzidimitriou, George P. Voutsas, Maria Lalia-Kantouri

Polyhedron 26 (2007) 1077

Synthesis and characterization of new addition compounds of bis(substituted-salicylaldehydo) cobalt(II) with 2,2′-bipyridine (bipy). Crystal and molecular structures of $[Co^{II}$(3-methoxy-salicylaldehyde)$_2$(bipy)] · CH_3OH (**1**) and $[Co^{II}(bipy)_3]Br_2$ · 0.5(5-chloro-salicylaldehydeH) · $1.5CH_3OH$ (**5**)

Four noval octahedral compounds $[Co^{II}$(X-salo)$_2$bipy] were synthesized and characterized by physicochemical, spectral (IR, UV-Vis), electrochemical (cyclic voltammetry, CV) and thermal (TG-DTA) data. X-ray studies verified the existence of two different octahedral Co(II) compounds (1 and 5), coming from the same reaction. Theoretical investigations (DFT, ZINDO) with GAUSSIAN-03 for the prediction of the electronic spectra was also undertaken.

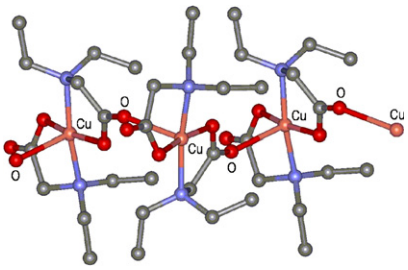


Jasmina Sabolović, Branko Kaitner

Polyhedron 26 (2007) 1087

The effects of steric aliphatic–aliphatic interactions in the coordination polymer of bis(*N*,*N*-diethylglycinato)copper(II): Experimental evidence and theoretical modeling

Discrete polymeric chains of *trans catena*-poly[(*N*,*N*-diethylglycinato-κ*O*,κ*N*)copper(II)-μ-[*N*,*N*-diethylglycinato-κO^1,κN:O^2]] were produced by axial coordinative bonding between copper(II) and carbonyl oxygen atom from adjacent asymmetric unit in the crystal structure. Steric aliphatic–aliphatic interactions between flexible ethyl chains are successfully reproduced, and conformational change of the complex upon crystallization is predicted using molecular mechanics force field.

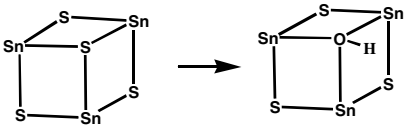


Long-Sheng Wang, Tian-Lu Sheng, Jian-Jun Zhang, Sheng-Min Hu, Rui-Biao Fu, Xin-Tao Wu, Ya-Min Li, Xi-He Huang, Sheng-Chang Xiang

Polyhedron 26 (2007) 1098

A convenient method for the conversion of $[Sn_3S_4]^{2-}$ to $[Sn_3S_3(\mu_3\text{-}OH)]^-$: Syntheses, structures and characterizations of $(Bu_4N)[Sn_3(\mu_3\text{-}OH)S_3(edt)_3]$ · DMF and $(Bu_4N)[Sn_3(\mu_3\text{-}OH)S_3(edt)_3]$ · H_2O (edt = 1,2-ethanedithiolate)

Two new trinuclear tin(IV)/oxosulfide clusters, $(Bu_4N)[Sn_3(\mu_3\text{-}OH)S_3(edt)_3]$ · DMF (**1**) and $(Bu_4N)[Sn_3(\mu_3\text{-}OH)S_3(edt)_3]$ · H_2O (**2**), containing a similar incomplete cubane-like anion cluster and different H-bond acceptors were prepared by a cluster-skeleton substitution reaction and were characterized by X-ray single crystal analysis.

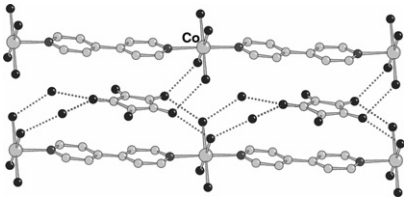


Subal Chandra Manna, Ananta Kumar Ghosh, Ennio Zangrando, Nirmalendu Ray Chaudhuri

Polyhedron 26 (2007) 1105

3D supramolecular networks of Co(II)/Fe(II) using the croconate dianion and a bipyridyl spacer: Synthesis, crystal structure and thermal study

3D supramolecular networks, $\{[Co(4,4'\text{-bipy})(H_2O)_4]\cdot(C_5O_5)\cdot(H_2O)_2\}_n$ (**1**), $\{[Fe(4,4'\text{-bipy})(H_2O)_4]\cdot(C_5O_5)\cdot(H_2O)_2\}_n$ (**2**) and $\{[Co_2(bpds)_2(C_5O_5)_2(H_2O)_4]\cdot(H_2O)_3\}_n$ (**3**) [4,4′-bipy = 4,4′-dipyridyl, bpds = 4,4′-bipyridyl disulfide, $C_5O_5^{2-}$ =croconate dianion] have been synthesized and characterized by X-ray single crystal structure determination and thermogravimetric analysis.

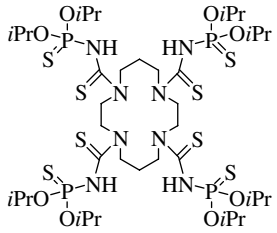


Damir A. Safin, Maria G. Babashkina, Felix D. Sokolov, Nail G. Zabirov, Joanna Galezowska, Henryk Kozlowski

Polyhedron 26 (2007) 1113

Complexes of a novel *N*-(diisopropxythiophosphoryl)thiourea derivative of 1,4,8,11-tetraazacyclotetradecane with Na^+, K^+ and $Cu(PPh_3)_2^+$ cations

We have reported a novel *N*-(diisopropxythiophosphoryl)thiourea derivative of 1,4,8,11-tetraazacyclotetradecane and its complexes with Na^+, K^+ and $Cu(PPh_3)^+$ cations. Structures of the obtained compounds were investigated by ES-MS, IR, ^1H and ^{31}P NMR spectroscopy and microanalysis. It was established that the obtained urea has a different composition in CCl_4 and $CDCl_3$, and in the solid state. The reaction of the potassium salt of thiourea with $Cu(PPh_3)_3I$ leads to the tetra-*N*-substituted cyclam. Chelating fragments C(S)NP(S) are coordinated with the copper(I) cation in a didentate mode through sulfur atoms of the thiocarbonyl and thiophosphoryl groups.

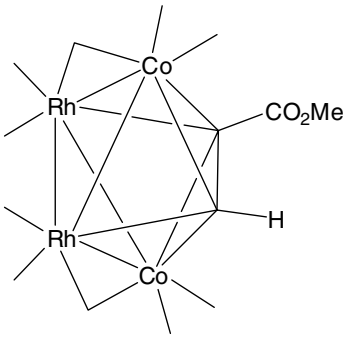


William H. Watson, Bhaskar Poola, Michael G. Richmond

Polyhedron 26 (2007) 1117

Regiospecific insertion into the Co–Co bond of the mixed-metal cluster $Co_2Rh_2(CO)_{12}$ by an electron-poor alkyne: X-ray diffraction structure of the butterfly cluster $Co_2Rh_2(CO)_{10}(\mu\text{-}HCCCO_2Me)$

Treatment of the mixed-metal cluster $Co_2Rh_2(CO)_{12}$ with the electron-poor alkyne methyl propiolate in hexane at room temperature gives a mixture of products that includes $Co_3Rh(CO)_{12}$, $Co_2Rh_2(CO)_{10}(\mu\text{-}HCCCO_2Me)$, $Co_3Rh(CO)_{10}(\mu\text{-}HCCCO_2Me)$, and $CoRh_3(CO)_9(\mu\text{-}HCCCO_2Me)_3$. The alkyne-substituted products have been characterized in solution by IR and ^1H NMR spectroscopies, and X-ray diffraction analysis in the case of $Co_2Rh_2(CO)_{10}(\mu\text{-}HCCCO_2Me)$. The observed chemistry is discussed relative to the results reported for the reaction of $Co_2Rh_2(CO)_{12}$ with other alkyne ligands.



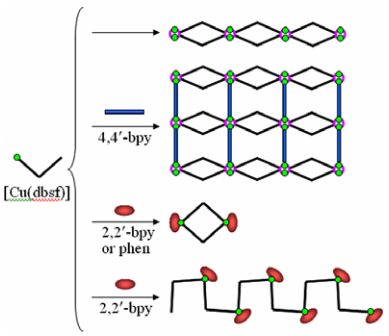
$Co_2Rh_2(CO)_{10}(HC_2CO_2Me)$

Wen-Juan Zhuang, Chang-Yan Sun, Lin-Pei Jin

Polyhedron 26 (2007) 1123

Assembly and structures of five new Cu(II) complexes based on the V-shaped building block [Cu(dbsf)]

Five new copper(II) complexes of 4,4′-dicarboxybiphenyl sulfone with auxiliary ligands are reported. All of the complexes are assembled from V-shaped building blocks of [Cu(dbsf)], showing 0D rhombic dimer, 1D chain and 2D catenane-like layer structures.

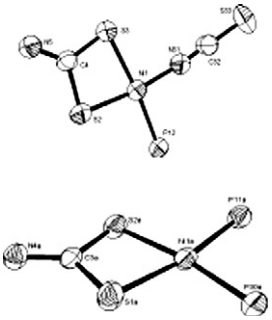


Balasubramaniyam Arul Prakasam, Kuppukkannu Ramalingam, Ramalingam Baskaran, Gabriele Bocelli, Andrea Cantoni

Polyhedron 26 (2007) 1133

Synthesis, NMR spectral and single crystal X-ray structural studies on Ni(II) dithiocarbamates with NiS_2PN, NiS_2PC, NiS_2P_2 chromophores: Crystal structures of (4-methylpiperazinecarbodithioato)(thiocyanato-*N*) (triphenylphosphine)nickel(II) and bis(triphenylphosphine) (4-methylpiperazinecarbodithioato)-nickel(II) perchlorate monohydrate

Ni(II) Dithiocarbamates with NiS_2PN, NiS_2PC, NiS_2P_2 chromophores have been synthesized. ^{13}C signals show interesting variations for the thioureide carbon signals between the neutral [**1** and **2**] and ionic complexes [**3** and **4**]. UV–Vis and XRD analyses evidence the square planar geometry around the central metal atom in all the cases.

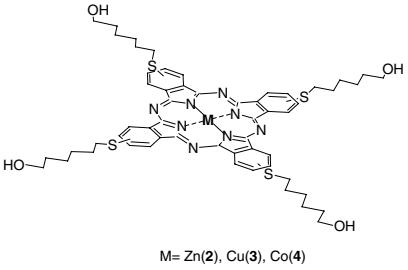


Meryem N. Yaraşir, Mehmet Kandaz, Atıf Koca, Bekir Salih

Polyhedron 26 (2007) 1139

Polytopic cation receptor functional phthalocyanines: Synthesis, characterization, electrochemistry and metal ion binding

The preparation, physical characterization and electrochemistry of 2,9,16,23-tetrakis(1-hydroxyhexylsulfanyl) phthalocyanines {$M[Pc(S–C_6H_{13}OH)_4]_2$} (M = Zn(II), Cu(II), Co(II)) were carried out.

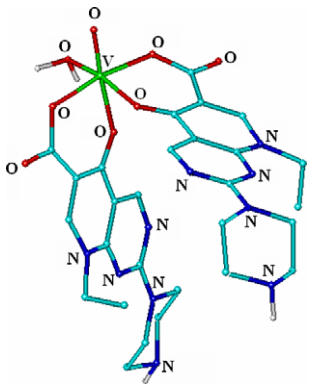


Eleni K. Efthimiadou, Yiannis Sanakis, Nikos Katsaros, Alexandra Karaliota, George Psomas

Polyhedron 26 (2007) 1148

Transition metal complexes with the quinolone antibacterial agent pipemidic acid: Synthesis, characterization and biological activity

The synthesis, characterization, antibacterial activity and interaction with calf-thymus DNA of nine new mononuclear metal complexes of the bidentate quinolone antibacterial agent pipemidic acid with VO^{2+}, Mn^{2+}, Fe^{3+}, Co^{2+}, Ni^{2+}, Zn^{2+}, MoO_2^{2+}, Cd^{2+} and UO_2^{2+} are presented.



The Publisher encourages the submission of articles in electronic form thus saving time and avoiding rekeying errors. For detailed instructions on the preparation of manuscripts and of electronic artwork, consult the Author Gateway for Elsevier at http://authors.elsevier.com

ScienceDirect

Full text of this journal is available, on-line from **ScienceDirect**. Visit **www.sciencedirect.com** for more information.

Available online at www.sciencedirect.com
ScienceDirect
Polyhedron 26, issue 3, 10 February 2007
POLYHEDRON
www.elsevier.com/locate/poly

Contents

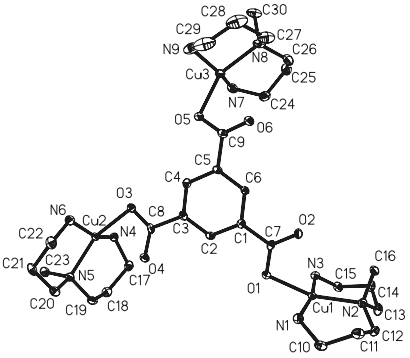
Papers

Pavel Kopel, Jiří Kameníček, Václav Petříček, Aleš Kurečka, Božena Kalinska, Jerzy Mrozinski

Polyhedron 26 (2007) 535

Syntheses and study on nickel and copper complexes with 1,3,5-benzenetricarboxylic acid. Crystal and molecular structure of $[Cu_3(mdpta)_3(btc)](ClO_4)_3 \cdot 4H_2O$

Nickel and copper complexes bridged by the 1,3,5-benzenetricarboxylate anion, with N-donor ligands or Schiff bases in the coordination sphere, were prepared and characterized. X-ray analysis of the copper trinuclear complex proved a deformed square-planar arrangement of central atoms and coordination of carboxylato groups. The complex showed a very weak antiferromagnetic interaction among the central atoms.

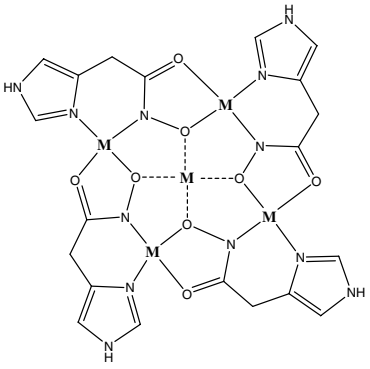


Etelka Farkas, Dávid Bátka, Edit Csapó, Péter Buglyó, Wolfgang Haase, Daniele Sanna

Polyhedron 26 (2007) 543

Synthesis and characterization of Cu^{2+}, Ni^{2+} and Zn^{2+} binding capability of some amino- and imidazole hydroxamic acids: Effects of substitution of side chain amino-N for imidazole-N or hydroxamic-N-H for -N-CH_3 on metal complexation

Solution equilibrium studies on Cu(II), Ni(II) and Zn(II) complexes of hydroxamic acids having amino or imidazole function in the side chain have been studied by pH-potentiometry, UV–Vis spectrophotometry, EPR, CD, ESI-MS and ^1H NMR methods.

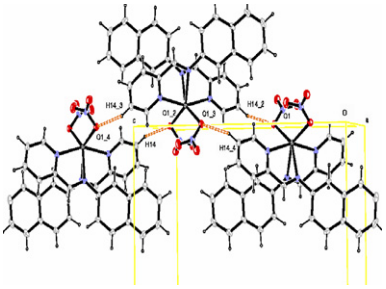


D. Das, B.G. Chand, J. Dinda, C. Sinha

Polyhedron 26 (2007) 555

Synthesis, spectral characterization and photoluminescence properties of cadmium(II) complexes of *N*-[(2-pyridyl)methyliden]-α (or β)-aminonaphthalene (α- or β-NaiPy) and comparison with the complexes of 1-alkyl-2-(naphthyl-α (or β)-azo)imidazole. Single crystal X-ray structure of $[Cd(\beta\text{-NaiPy})_2(ONO_2)_2]$

Cadmium(II) complexes of *N*-[(2-pyridyl)-methyliden]-α (or β)-aminonaphthalene (α- or β-NaiPy) are described. They have been spectroscopically characterized and structural confirmation has been carried out by an X-ray diffraction study in one case. The complexes are highly fluorescent. Naphthylazoimidazole complexes are non-fluorescent.



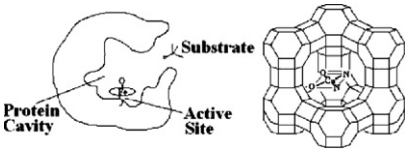
Elsevier Ltd.

Pratap Kumar Saha, Buddhadeb Dutta, Sreyashi Jana, Rajesh Bera, Sandip Saha, Ken-ichi Okamoto, Subratanath Koner

Polyhedron 26 (2007) 563

Immobilization of a copper-Schiff base complex in a Y-zeolite matrix: Preparation, chromogenic behavior and catalytic oxidation

To mimic the catalytic activity of metalloenzymes, a copper Schiff base complex has been immobilized in Y zeolite. A spectacular color change (green to red) has been observed when the complex [Cu(MeO-salen)(H_2O)] (**1**) is immobilized in a zeolitic matrix. While the prepared catalyst shows excellent catalytic activity and product selectivity, the complex itself remains virtually inactive.

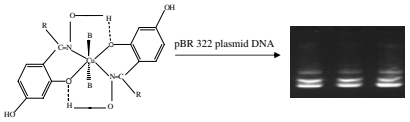


M.S. Surendra Babu, K. Hussain Reddy, Pitchika G. Krishna

Polyhedron 26 (2007) 572

Synthesis, characterization, DNA interaction and cleavage activity of new mixed ligand copper(II) complexes with heterocyclic bases

Mixed ligand complexes having the formulae $Cu(RPO)_2Py_2$, $Cu(RPO)_2Im_2$ and $Cu(DBO)_2Py_2$ [RPO = resacetophenone oxime, DBO = 2,4-dihydroxybenzophenone oxime, Py = pyridine and Im = imidazole] have been synthesized and characterized by UV–Vis, IR, ESR, cyclic voltammetry and magnetic susceptibility methods. The apparent binding constants for mixed ligand complexes are in order of 10^4–10^5 M^{-1}. Based on the data obtained in the DNA binding studies a partial intercalative mode of binding is suggested for these complexes. All the metal complexes cleaved supercoiled DNA by hydrolytic and oxidative paths. The oxidative path dominates the hydrolytic cleavage. The hydrolytic cleavage of DNA is evidenced from the control experiments showing discernable cleavage inhibition in the presence of the hydroxyl radical inhibitor DMSO or the singlet oxygen quencher azide ion.

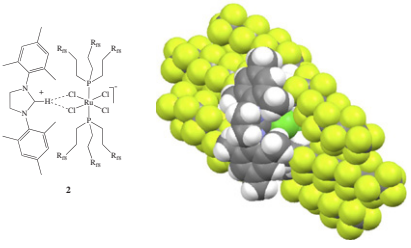


Rosenildo Corrêa da Costa, Frank Hampel, J.A. Gladysz

Polyhedron 26 (2007) 581

Crystal structure of an unusual bis(fluorous phosphine) ruthenium(III) complex derived from a fluorous Grubbs' catalyst

The title molecule **2** is obtained by air oxidation of $(H_2IMes)RuCl_2(P(CH_2CH_2R_{f8})_3)(=CHPh)$ ($R_{f8} = (CF_2)_7CF_3$). The crystal lattice exhibits fluorous and non-fluorous domains, and hydrogen bonding between the NC*H*N proton of the cation and two chloride ligands of the anion; the conformations of the ponytails are analyzed in detail.

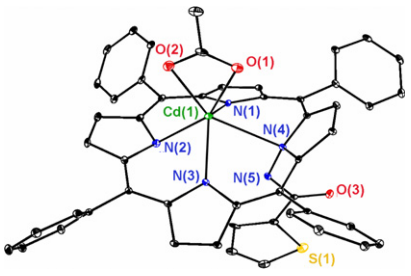


Jo-Yu Tung, Jyh-Horung Chen

Polyhedron 26 (2007) 589

Electrostatic forces that determine O,O-*trans* versus O,S-*cis* conformers in the aminated porphyrin complexes of Cd(N-NHCO-2-C_4H_3O-tpp)(OAc) and Cd(N-NHCO-2-C_4H_3S-tpp)(OAc)

An attractive electrostatic interaction between Cd^{2+} and $O(4)^-$ atoms in furan stabilizes the O,O-*trans* conformer of **3** and a repulsive electrostatic interaction between Cd^{2+} and $S(1)^+$ destabilizes the O,S-*trans* conformer of **4**.

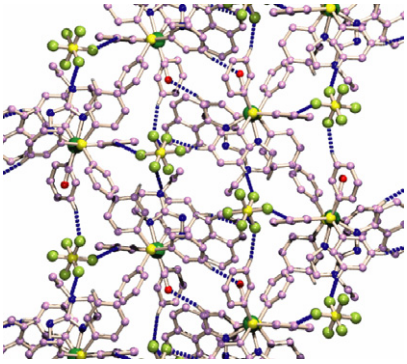


T.K. Mondal, Joydev Dinda, Alexandra M.Z. Slawin, J. Derek Woollins, C. Sinha

Polyhedron 26 (2007) 600

Osmium-carbonyl complexes of naphthylazoimidazoles. Single crystal X-ray structure of $[Os(H)(CO)(PPh_3)_2(\alpha\text{-NaiEt})](PF_6)$ {α-NaiEt = 1-ethyl-2-(naphthyl-α-azo)imidazole}

$[Os(H)(Cl)(CO)(PPh_3)_3]$ reacts with 1-alkyl-2-(naphthyl-α/β-azo)imidazole (α/β-NaiR) to prepare $[Os(H)(CO)(PPh_3)_2(\alpha/\beta\text{-NaiR})](PF_6)$. The X-ray structure of $[Os(H)(CO)(PPh_3)_2(\alpha\text{-NaiEt})](PF_6)$ shows a distorted octahedral geometry. Addition of Cl_2 in MeCN gives $[Os(Cl)(CO)(\alpha/\beta\text{-NaiR})(PPh_3)_2](PF_6)$ which were characterized spectroscopically. Cyclic voltammetry shows Os(III)/Os(II), Os(IV)/Os(III) and azo reductions.

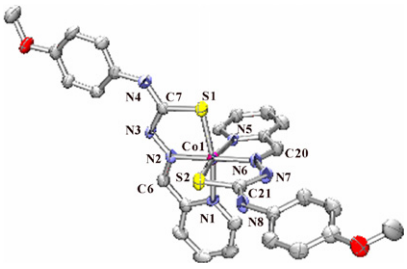


P.F. Rapheal, E. Manoj, M.R. Prathapachandra Kurup, E. Suresh

Polyhedron 26 (2007) 607

Structural and spectral studies of novel Co(III) complexes of N(4)-substituted thiosemicarbazones derived from pyridine-2-carbaldehyde

Two N(4) monosubstituted thiosemicarbazone ligands, pyridine-2-carbaldehyde-N(4)-*p*-methoxyphenyl thiosemicarbazone $[HL^1]$ and pyridine-2-carbaldehyde-N(4)-2-phenylethyl thiosemicarbazone $[HL^2]$ and a new N(4) disubstituted thiosemicarbazone ligand pyridine-2-carbaldehyde N(4)-methyl N(4)-phenyl thiosemicarbazone (HL^3) and seven of their Co(III) complexes were synthesized and characterized physico-chemically using elemental analyses, conductance measurements, electronic and IR spectroscopic methods. The complexes were given the formulae $[CoL^1_2]NO_3\cdot H_2O$ (**1**), $[CoL^1_2]Cl\cdot 2H_2O$ (**2**), $[CoL^1_2]ClO_4$ (**3**), $[CoL^2_2]NO_3$ (**4**), $[CoL^2_2]Cl\cdot 2H_2O$ (**5**), $[CoL^3_2]Br\cdot 2H_2O$ (**6**) and $[CoL^3_2]ClO_4\cdot H_2O$ (**7**). All the complexes are assigned octahedral geometries. The single crystal X-ray structures of HL_3, $[CoL^1_2]NO_3\cdot H_2O$ (**1**) and $[CoL^2_2]NO_3$ (**4**) are discussed.

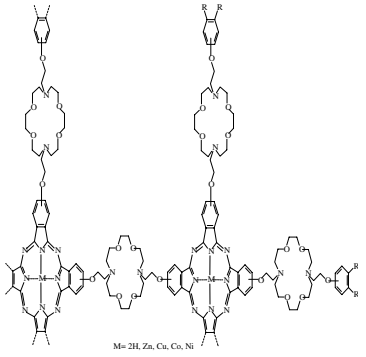


Ahmet Bilgin, Çiğdem Yağcı, Ayşegül Mendi, Ufuk Yıldız

Polyhedron 26 (2007) 617

Synthesis and characterization of new polymeric phthalocyanines substituted with diaza-18-crown-6 macrocycles through ethyleneoxy bridges

Metal-free and metallophthalocyanine polymers containing ethyleneoxy diaza-18-crown-6 units were synthesized from a tetranitrile monomer and the appropriate starting materials. Besides, their cation-binding abilities, disaggregation property, viscosities, electrical conductivities and thermal properties were evaluated. The novel compounds have been characterized by physical and spectroscopic techniques.

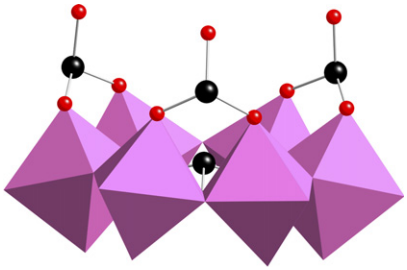


José R. Galán Mascarós, Carlos Martí-Gastaldo

Polyhedron 26 (2007) 626

Supramolecular stabilization of the phosphite-based polyoxomolybdate $[Mo_6(PO_3)(HPO_3)_3O_{18}]^{9-}$

A novel phosphite-based hetero-polyoxomolybdate, $[Mo_6(PO_3)(HPO_3)_3O_{18}]^{9-}$, has been isolated and structurally characterized. The most striking feature of this polyanion is the presence of peripheral phosphite groups linked to the MoO_6 octahedra. In the solid state, this clusture shows strong hydrogen bonding interactions that apparently play a key role in its stabilization and isolation from solution.

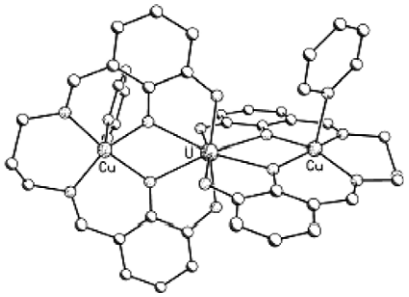


Lionel Salmon, Pierre Thuéry, Michel Ephritikhine

Polyhedron 26 (2007) 631

Trinuclear Schiff base complexes with uranium(V) and copper(II) or zinc(II) ions

Treatment of the uranium(IV) complexes $[\{ML^i(py)\}_2U]$ (M = Cu, Zn; L^i = hexadentate bicompartmental Schiff base) with silver nitrate in pyridine led to the formation of the corresponding cationic uranium(V) species.

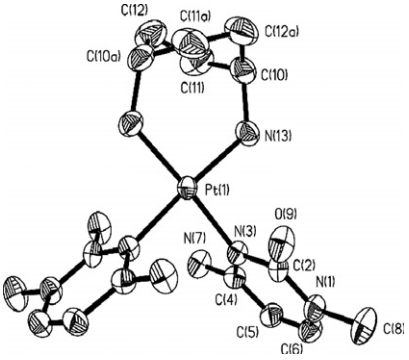


Shaikh Shamsuddin, Mohammad S. Ali, Kenton H. Whitmire, Abdul R. Khokhar

Polyhedron 26 (2007) 637

Synthesis characterization and X-ray crystal structures of *cis*-1,4-diaminocyclohexaneplatinum(II) nucleobase adducts

Synthesis, and characterization of nucleobase complexes with *cis*-1,4-DACH-Pt have been synthesized and characterized by ^1H, ^{13}C, ^{195}Pt NMR. The X-ray crystal structures of [Pt(*cis*-1,4-DACH)(9-methylguanine)$_2$]SO_4[9-methylguanine-H]$_2SO_4$ and [Pt(*cis*-1,4-DACH)-(1-methylcytosine)$_2$]$Cl_2 \cdot 6H_2O$ adducts are also reported here.

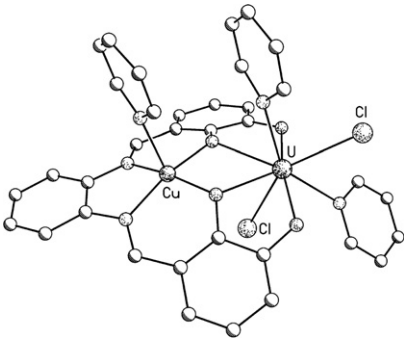


Lionel Salmon, Pierre Thuéry, Michel Ephritikhine

Polyhedron 26 (2007) 645

Strictly heterodinuclear compounds containing U^{4+} and Cu^{2+} or Ni^{2+} ions

The dinuclear complexes $[ML^i(py)UCl_2(py)_2]$ and/or $[Hpy][ML^i(py)UCl_3]$ were obtained by reactions of $[M(H_2L^i)]$ (M = Cu, Ni) with UCl_4.

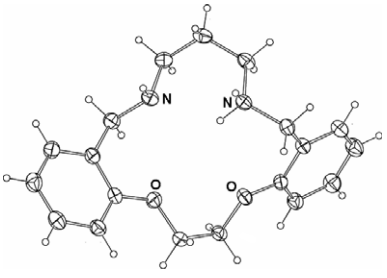


Lidia Babosa, Leonard F. Lindoy, Brian W. Skelton, Allan H. White

Polyhedron 26 (2007) 653

Structures and conformations of protonated O_2N_2- and O_2N_3-macrocyclic ligand salts

The results of an investigation of the solid state structures and hydrogen-bonding patterns present in two mixed oxygen–nitrogen donor macrocyclic salts incorporating nitrate and triflate counterions is presented.

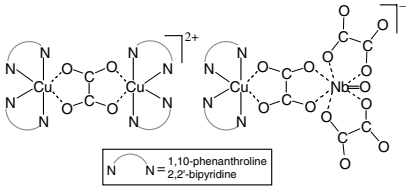


Marijana Jurić, Berislav Perić, Nevenka Brničević, Pavica Planinić, Damir Pajić, Krešo Zadro, Gerald Giester

Polyhedron 26 (2007) 659

Structure, stacking interactions and magnetism of compounds with oxalate-bridged dinuclear $Cu^{II}Cu^{II}$ and $Cu^{II}Nb^{V}$ units

The novel compounds contain dinuclear oxalate-bridged $[\{Cu(L)_2\}_2(\mu\text{-}C_2O_4)]^{2+}$ and $[Cu(L)_2(\mu\text{-}C_2O_4)NbO(C_2O_4)_2]^{-}$ (L = phen, bpy) complex ions and show ferromagnetic spin-exchange interaction between copper(II) ions within the cations.

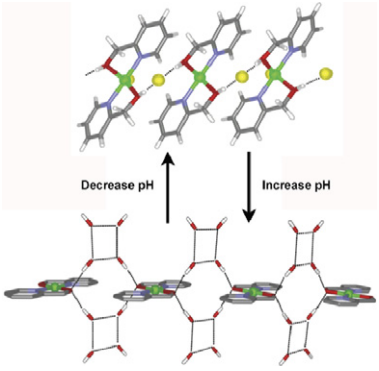


Bianca Antonioli, David J. Bray, Jack K. Clegg, Katrina A. Jolliffe, Kerstin Gloe, Karsten Gloe, Leonard F. Lindoy

Polyhedron 26 (2007) 673

Proton and anion control of framework complexity in copper(II) complex structures derived from 2-(hydroxymethyl)pyridine

The 2-(hydroxymethyl)pyridine ligand remains protonated at pH 5 when complexed to copper(II) chloride or nitrate to form 1-D and 2-D hydrogen-bonded polymeric structures while at higher pH it deprotonates to yield a more complex three-dimensional network.

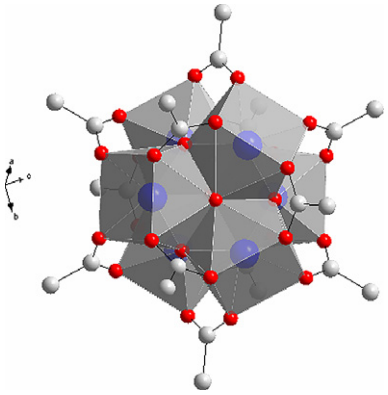


P. Piszczek, A. Radtke, A. Grodzicki, A. Wojtczak, J. Chojnacki

Polyhedron 26 (2007) 679

The new type of $[Zr_6(\mu_3\text{-}O)_4(\mu_3\text{-}OH)_4]$ cluster core: Crystal structure and spectral characterization of $[Zr_6O_4(OH)_4(OOCR)_{12}]$ (R = Bu^t, $C(CH_3)_2Et$)

Hexanuclear Zr(IV) oxo carboxylate derivatives of the general formula $[Zr_6O_4(OH)_4(OOCR')_{12}]$ (R′ = Bu^t (**1**), $C(CH_3)_2Et$ (**2**)) were synthesized from $Zr(OR)_4$ (R = Pr^i, $C(CH_3)_2Et$) and appropriate organic acids (HOOCR′, R′ = Bu^t, $C(CH_3)_2Et$) in a molar ratio 1:2. The structure of these compounds consists of hexanuclear Zr(IV) clusters formed by six zirconium atoms, linked by 4:4 system of μ_3-oxo/hydoxy bridges and stabilized by *syn–syn* carboxylate groups. Results of crystallographic and spectroscopic data suggest that in $[Zr_6(\mu_3\text{-}O_4)(\mu_3\text{-}OH)_4]$ clusters four protons migrate between eight oxide bridges. Thermal stability studies of **1** and **2** using TGA/DTA and VT IR methods have been carried out.

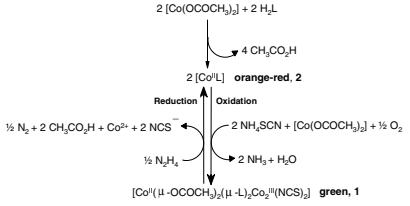


Suparna Banerjee, Jiu-Tong Chen, Can-Zhong Lu

Polyhedron 26 (2007) 686

A new trinuclear mixed-valence Co(II)–Co(III) complex stabilized by a bis(salicylidene) based ligand

Reaction of $Co(OAc)_2$ with H_2L and NH_4SCN in air afforded an octahedral mixed valent trimeric complex, **1** which was reacted with hydrazine resulting in a mononuclear Co(II) square planar complex, **2**. Compound **2** regenerates **1** on treatment with suitable reagents. **1** displayed two oxidative and one reductive response in MeCN and the electron equivalents associated with the redox couples were ascertained from coulometry and DPV. A weak antiferromagnetic interaction (=−6.39 K) is operative in **1** at low temperature. An anisotropic EPR spectrum of **1**, recorded at 4 K, suggests transitions between the ground state Kramers doublet. Synthetic strategies for **1** and other known related trimers have also been compared.

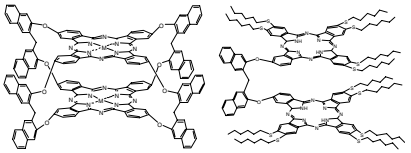


Zafer Odabaş, Ahmet Altındal, Ali Rıza Özkaya, Mustafa Bulut, Bekir Salih, Ö. Bekaroğlu

Polyhedron 26 (2007) 695

Synthesis, characterization, and electrochemical, spectroelectrochemical and electrical measurements of novel ball-type four 1,1′-methylenedinaphthalen-2-ol bridged metal-free, zinc(II) and cobalt(II), and metal-free clamshell phthalocyanines

The new binuclear ball-type bisphthalocyanines [metal-free, Zn(II) and Co(II)] and clamshell-type bisphthalocyanine (metal-free) were synthesized from the corresponding 4,4′-[1,1′-methylenebis(naphthalene-2,1-diyl)]-bis(oxy)diphthalonitrile and 4,5-bis(hexylthio)-phthalo-nitrile. The novel compounds have been characterized by elemental analysis, UV/Vis, IR, ^{1}H NMR and MALDI-TOF mass spectroscopies. The electrochemical and spectroelectrochemical measurements showed strong intramolecular interactions between the two phthalocyanine rings. The conduction properties of the compounds have been examined by d.c. and impedance spectroscopy measurements as a function of temperature and frequency.

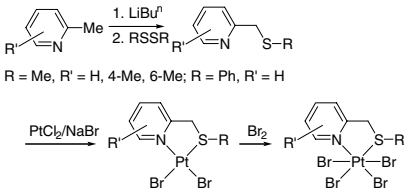


Roderick C. Jones, Brian W. Skelton, Vicki-Anne Tolhurst, Allan H. White, Adele J. Wilson, Allan J. Canty

Polyhedron 26 (2007) 708

Synthesis and solid-state structural characterisation of Pt(II,IV) bromide complexes containing bidentate organothiomethylpyridine heteroleptic ligands

Pyridyl thioether ligands are readily formed by lithiation of 2-picolines followed by reaction with diorgano disulfides, and the synthesis and structural studies of platinum(II) and platinum(IV) complexes are described.

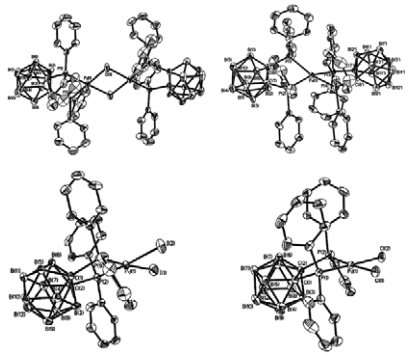


J.-M. Dou, D.-P. Zhang, D.-C. Li, D.-Q. Wang

Polyhedron 26 (2007) 719

Synthesis and crystal structure of four Pd(II) complexes containing *nido* or *closo* carborane diphosphine ligands

Three Pd(II) complexes $[Pd_2(\mu\text{-}Cl)_2\{7,8\text{-}(PPh_2)_2\text{-}7,8\text{-}C_2B_9H_{10}\}_2] \cdot 0.25CH_2Cl_2$ (**1**), $[Pd\{7,8\text{-}(PPh_2)_2\text{-}7,8\text{-}C_2B_9H_{10}\}_2] \cdot 4CHCl_3$ (**2**) and $[PdCl_2(1,2\text{-}(PPh_2)_2\text{-}1,2\text{-}C_2B_{10}H_{10})]$ (**3**) have been synthesized by the reactions of 1,2-$(PPh_2)_2$-1,2-$C_2B_{10}H_{10}$ with $PdCl_2$ in acetonitrile, cyanophenyl and dichloromethane, respectively. A fourth complex $[PdI_2(1,2\text{-}(PPh_2)_2\text{-}1,2\text{-}C_2B_{10}H_{10})]$ (**4**) was obtained by a ligand exchange reaction through substitution of $Cl^-$of complex **3** with I^-. All the four complexes have been characterized by elemental analysis, FT-IR, ^{1}H and ^{13}C NMR spectroscopy and X-ray structure determination.

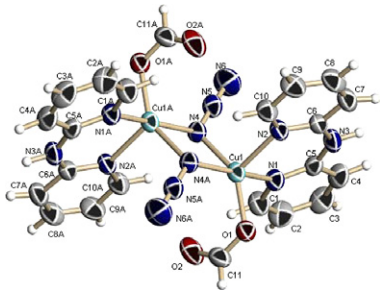


Sujittra Youngme, Thidarat Chotkhun, Somying Leelasubcharoen, Narongsak Chaichit, Chaveng Pakawatchai, Gerard A. van Albada, Jan Reedijk

Polyhedron 26 (2007) 725

Three new dinuclear bis-μ-azido-bridged Cu(II) compounds with di-2-pyridylamine as a ligand: Syntheses, X-ray structure and magnetic measurements

Three new dinuclear copper(II) compounds: $[Cu_2(dpyam)_2(\mu_{1,1}\text{-}N_3)_2(O_2CH)_2]$ (**1**), $[Cu_2(dpyam)_2(\mu_{1,1}\text{-}N_3)_2(O_2CCH_3)_2]$ (**2**) and $[Cu_2(dpyam)_2(\mu_{1,1}\text{-}N_3)_2(O_2CCH_2CH_3)_2]$ (**3**) have been synthesized in order to investigate the magnetic superexchange interaction pathway between coupled copper(II) centers. All three compounds consist of a dinuclear unit in which both Cu(II) ions are bridged by double end-on azido ligands providing a distorted square pyramidal geometry, $\tau = 0.38$, 0.48 and 0.30, with a CuN_4O chromophore. The Cu···Cu separations are 3.195, 3.200 and 3.247 Å for compounds **1**, **2** and **3**, respectively. The magnetic susceptibility measurements, measured from 5 to 300 K, revealed a medium to weak ferromagnetic exchange interactions between the copper(II) ions dominated by the bridging azido ligands, with a singlet–triplet splitting (J) of 63.3, 63.8 and 5.1 cm^{-1}, for compounds **1**, **2** and **3**, respectively. A large zero-field splitting of about 0.4 cm^{-1} is observed in the EPR for compounds **1** and **2**.

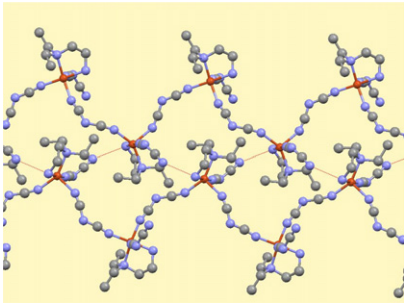


Dasarath Mal, Chandan Adhikary, Eva Rentschler, Yoshitaro Miyashita, Ken-Ichi Okamoto, Subratanath Koner

Polyhedron 26 (2007) 736

Synthesis, X-ray crystal structure and magnetic study of the 1D {[Cu(*N*,*N*-diethyl-1,2-ethanediamine)($\mu_{1,5}$-dca)(dca)]}$_n$ complex

A new infinite 1D zigzag chain compound {[CuL($\mu_{1,5}$-dca)(dca)]}$_n$ (L = *N*,*N*-diethyl-1,2-ethanediamine) has been synthesized and characterized by single crystal analysis. The magnetic interaction in this compound is found to be antiferromagnetic.

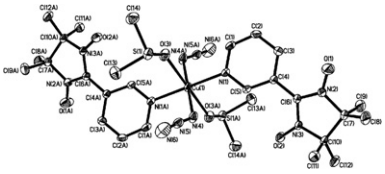


Yun-He Xu, Xiao-Ni Qu, Hai-Bin Song, Li-Cun Li, Zong-Hui Jiang, Dai-Zheng Liao

Polyhedron 26 (2007) 741

Metal–radical complexes [M(NITm-Py)$_2$-(N$_3$)$_2$(DMSO)$_2$] [M = Cu(II), Ni(II), Co(II)]: Syntheses, crystal structures and magnetic properties

Three new metal–radical complexes have been synthesized. The three complexes are three-spin complexes in which two radical ligands are coordinated to the metal ion through the nitrogen atoms of the pyridyl rings. The magnetic properties are analyzed in connection with their structures and the magnetic exchange mechanism is discussed.



The Publisher encourages the submission of articles in electronic form thus saving time and avoiding rekeying errors. For detailed instructions on the preparation of manuscripts and of electronic artwork, consult the Author Gateway for Elsevier at http://authors.elsevier.com

ScienceDirect

Full text of this journal is available, on-line from **ScienceDirect**. Visit **www.sciencedirect.com** for more information.

Available online at www.sciencedirect.com
ScienceDirect
Polyhedron 26, issue 16, 10 October 2007
POLYHEDRON
www.elsevier.com/locate/poly

Contents

Foreword: Polyhedron Symposia-in-Print, number 28 transition metal chemistry of NO, N_2O and related molecules 4619

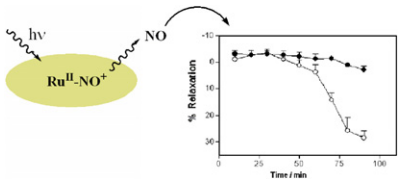
Papers

Renata Galvão de Lima, Marilia Gama Sauaia, Camila Ferezin, Iuri Muniz Pepe, Nádia Mamede José, Lusiane M. Bendhack, Zênis Novais da Rocha and Roberto Santana da Silva

Polyhedron 26 (2007) 4620

Photochemical and pharmacological aspects of nitric oxide release from some nitrosyl ruthenium complexes entrapped in sol–gel and silicone matrices

The entrapped $[Ru(terpy)(L)NO](PF_6)_3$, terpy = 2,2′:6′,2″-terpyridine and L = 2,2′-bipyridine (bpy) and 3,4-diiminebenzoic acid (NH · NHq), complexes into sol–gel and silicone matrices, shows NO release characteristics when submitted to light irradiation. The pharmacological properties of doped matrix showed vasodilator characteristics due to NO release.

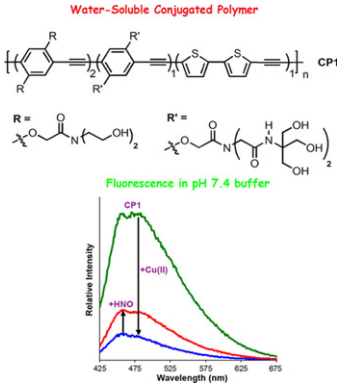


Andrew G. Tennyson, Loi Do, Rhett C. Smith and Stephen J. Lippard

Polyhedron 26 (2007) 4625

Selective fluorescence detection of nitroxyl over nitric oxide in buffered aqueous solution using a conjugated metallopolymer

A bithiophene-substituted poly(*p*-phenyleneethynylene) derivative (**CP1**) having water-solubilizing side chains was prepared and characterized. Copper(II)-induced quenching of **CP1** emission was quantified in H_2O, MeCN/H_2O, and pH 7.4 HEPES/KCl buffer. In buffer, treatment of **CP1**-Cu(II) with nitroxyl (HNO) produces an immediate 2.1-fold increase in emission, whereas exposure to NO(g) effects no fluorescence restoration.

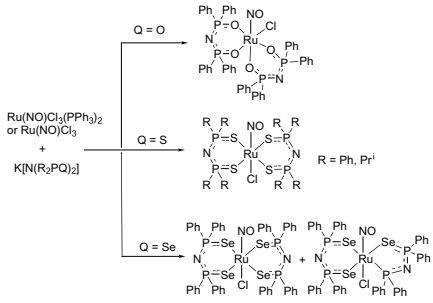


Wai-Man Cheung, Qian-Feng Zhang, Chui-Ying Lai, Ian D. Williams and Wa-Hung Leung

Polyhedron 26 (2007) 4631

Ruthenium and rhodium nitrosyl complexes containing dichalcogenoimidodiphosphinate ligands

Interaction of $[Ru(NO)Cl_3(PPh_3)_2]$ or $Ru(NO)Cl_3 \cdot xH_2O$ with $K[N(R_2PQ)_2]$ afforded *trans*-$[Ru(NO)(Cl)\{N(R_2PS)_2\}_2]$ (R = Ph, Pr^i) or *cis*-$[Ru(NO)(Cl)\{N(Ph_2PO)_2\}]$ whereas that with $K[N(Ph_2PSe)_2]$ led to a mixture of *trans*-$[Ru(NO)Cl\{N(Ph_2PSe)_2\}_2]$ and *trans*-$[Ru(NO)Cl\{N(Ph_2PSe)_2\}\{Ph_2P(Se)NPPh_2\}]$. Treatment of $[Rh(NO)Cl_2(PPh_3)_2]$ with $K[N(R_2PQ)_2]$ gave $[Rh(NO)\{N(R_2PSQ)_2\}_2]$ (R = Ph or Pr^i, Q = S or Se), in which the nitrosyl ligand is bent.

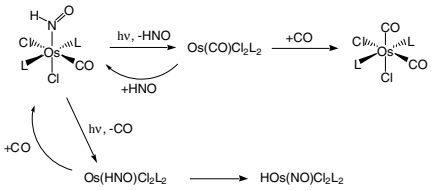


Jon Marhenke, Crisjoe A. Joseph, Marlena Z. Corliss, Tim J. Dunn and Peter C. Ford

Polyhedron 26 (2007) 4638

Thermal and photochemical reactivity of $Os(HNO)(CO)Cl_2(PPh_3)_2$: Evidence for photochemical HNO generation

Photolysis of the nitroxyl complex $Os(N(O)H)(CO)Cl_2(PPh_3)_2$ shows multiple products that are interpreted in terms of two competing, primary photoreactions, the reversible dissociation of HNO (which dimerizes to N_2O) and the dissociation of CO. The relative yields of products varied depending on whether or not excess CO was present.

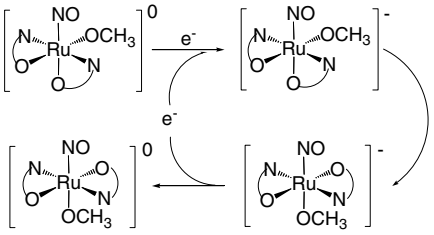


Sohei Fukui, Yoshiharu Shimamura, Yumiko Sunamoto, Tasuku Abe, Toshiyuki Hirano, Takao Oi and Hirotaka Nagao

Polyhedron 26 (2007) 4645

Cis–trans Geometrical isomerization of bis(2-pyridinecarboxylato)nitrosylruthenium complex accompanying electrochemical one-electron reduction

cis-$[Ru(NO)(CH_3CN)(pyca)_2]PF_6$ and *trans*-$[Ru(NO)(OH)(pyca)_2]$ (pyca = 2-pyridinecarboxylato) have been synthesized and characterized. Electrochemical behaviors of the two complexes in CH_3CN and the *cis-trans* geometrical change reaction occurring in the electrochemical one-electron reduction of *cis*-$[Ru(NO)(CH_3O)(pyca)_2]$ in CH_3OH–CH_3CN have been studied.

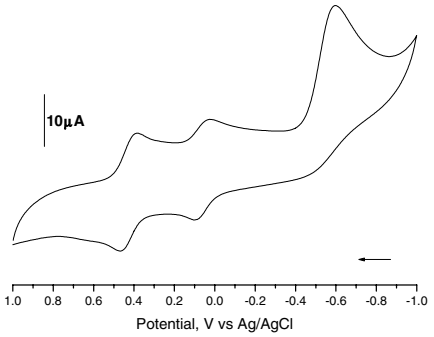


Alda K.M. Holanda, Francisco O.N. da Silva, Idalina M.M. Carvalho, Alzir A. Batista, Javier Ellena, Eduardo E. Castellano, Ícaro S. Moreira and Luiz G.F. Lopes

Polyhedron 26 (2007) 4653

Crystal structure, electrochemical and photochemical studies of the *trans*-[Fe(cyclam)(NO)Cl]Cl_2 complex (cyclam = 1,4,8,11-tetraazacyclotetradecane)

The cyclic voltammogram of the *trans*-$[Fe(cyclam)(NO)Cl]^{2+}$ complex showed three electrochemical processes at −0.70, 0.08 and 0.40 V versus Ag/AgCl. The first and last redox processes are centered at the NO ligand, whereas the second is characteristic of the residual aqua species, *trans*-$[Fe(cyclam)Cl(H_2O)]^{2+}$.

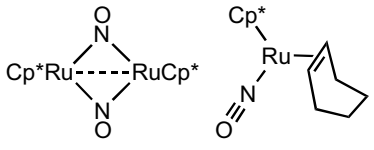


Shigeki Kuwata, Satoshi Kura and Takao Ikariya

Polyhedron 26 (2007) 4659

Hydrogenation of cyclohexene catalyzed by ruthenium nitrosyl complexes: Crystal structures of catalyst precursors $[Cp^*Ru(\mu_2\text{-}NO)_2RuCp^*]$ and $[Cp^*Ru(NO)(\eta^2\text{-}C_6H_{10})]$ (Cp^* = $\eta^5\text{-}C_5(CH_3)_5$)

We have demonstrated that the (nitrosyl)ruthenium complex $[Cp^*Ru(NO)(C_6H_5)_2]$ (**1**) serves as a catalyst precursor for hydrogenation of cyclohexene. Two nitrosyl complexes **2** and **3** have been obtained from the reaction mixture. The detailed structures of **2** and **3** have been determined by X-ray crystallography.



2 **3**

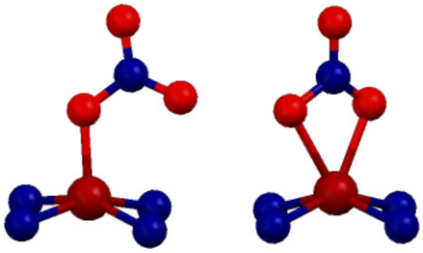
(Cp^* = $\eta^5\text{-}C_5(CH_3)_5$)

Graeme R.A. Wyllie, Orde Q. Munro, Charles E. Schulz and W. Robert Scheidt

Polyhedron 26 (2007) 4664

Structural and physical characterization of (nitrato)iron(III) porphyrinates [Fe(por)-(NO_3)] – Variable coordination of nitrate

The physical properties of high-spin nitrato-ligated iron(III) porphyrinates show differences depending on the mode of nitrate coordination.

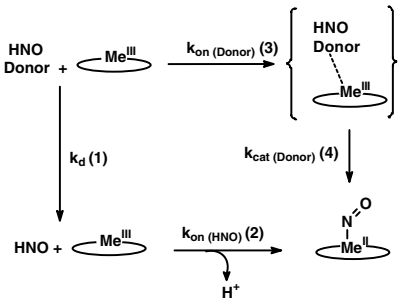


Sebastián A. Suárez, Marcelo A. Martí, Pablo M. De Biase, Darío A. Estrin, Sara E. Bari and Fabio Doctorovich

Polyhedron 26 (2007) 4673

HNO trapping and assisted decomposition of nitroxyl donors by ferric hemes

The reactions between two nitroxyl donors with MP11 and Fe^{III}TEPyP show two alternative modes of reactivity. One comprises the heme assisted decomposition of the donor enhancing its decomposition rate, while in the other the donor produces HNO which subsequently reacts with the porphyrin.

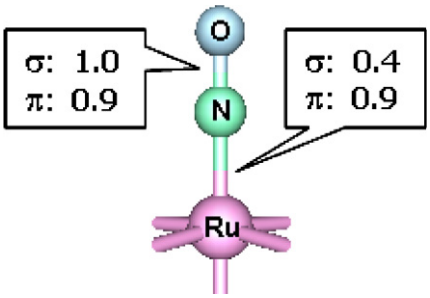


Olga V. Sizova, Alexander Yu. Sokolov, Leonid V. Skripnikov and Victor I. Baranovski

Polyhedron 26 (2007) 4680

Quantum chemical study of the bond orders in the ruthenium, diruthenium and dirhodium nitrosyl complexes

The electronic structure of the ruthenium six-coordinate nitrosyl complexes and paddle-wheel $M_2(BL)_4$ and $M_2(BL)_4(L)_2$ (M = Rh and Ru) complexes is analyzed in terms of Mayer and Wiberg bond order indices. The technique of bond order indices decomposition into σ-, π-, and δ-contributions is proposed.

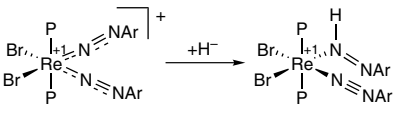


Gabriele Albertin, Stefano Antoniutti and Tiziana Donadini

Polyhedron 26 (2007) 4691

Reaction of bis(aryldiazenido) complexes of rhenium with bromine: Preparation of new diazo derivatives

The reaction of bis(aryldiazenido) $[Re(ArN_2)_2P_3]BPh_4$ complexes with Br_2 is presented. The synthesis of aryldiazene–aryldiazenido $ReBr_2(ArN_2)(ArN{=}NH)P_2$ derivatives was achieved by reacting bis-(aryldiazenido) with hydride-donor species. Protonation studies on aryldiazene complexes are also reported.

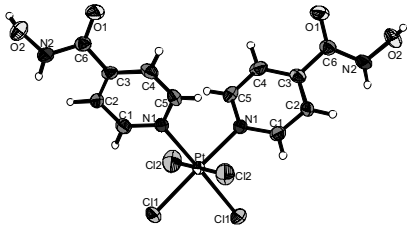


Darren Griffith, Alberta Bergamo, Sara Pin, Marta Vadori, Helge Müller-Bunz, Gianni Sava and Celine J. Marmion

Polyhedron 26 (2007) 4697

Novel platinum pyridinehydroxamic acid complexes: Synthesis, characterisation, X-ray crystallographic study and nitric oxide related properties

On the premise that there is little or no evidence in the literature of nitric oxide (NO)-releasing platinum-based compounds, the NO-releasing ability of a novel series of platinum pyridinehydroxamic acid complexes are described with a view to advancing a new class of bifunctional metallodrug with dual DNA-binding and NO-releasing properties.

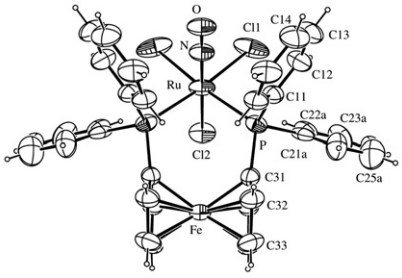


Gustavo Von Poelhsitz, André Luiz Bogado, Márcio Peres de Araujo, Heloisa S. Selistre-de-Araújo, Javier Ellena, Eduardo E. Castellano and Alzir Azevedo Batista

Polyhedron 26 (2007) 4707

Synthesis, characterization, X-ray structure and preliminary *in vitro* antitumor activity of the nitrosyl complex *fac*-[$RuCl_3$(NO)(dppf)], dppf = 1,1′-bis(diphenylphosphine)ferrocene

The reaction of $RuCl_3NO \cdot 2H_2O$ with stoichiometric amount of dppf, 1,1′-bis(diphenylphosphino)ferrocene, afforded the new neutral nitrosyl complex *fac*-[$RuCl_3$(NO)(dppf)] which was characterized by spectroscopical, electrochemical and X-ray crystallography techniques. Preliminary *in vitro* antitumor activity against the MDA-MB-231 tumor cell line was carried with the results indicating a moderate to good cytotoxicity activity (IC_{50} = 10 ± 3 μM).

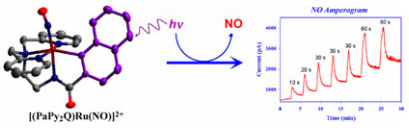


Michael J. Rose, Marilyn M. Olmstead and Pradip K. Mascharak

Polyhedron 26 (2007) 4713

Photoactive ruthenium nitrosyls derived from quinoline- and pyridine-based ligands: Accelerated photorelease of NO due to quinoline ligation

The {Ru–NO}^{6} nitrosyl [($PaPy_2Q$)Ru(NO)]-(BF_4)$_2$ exhibits greater NO photolability (as detected by NO-electrode) compared to analogous nitrosyl [($PaPy_3$)Ru(NO)](BF_4)$_2$ due to the light-harvesting quinoline moiety in the ligand frame.

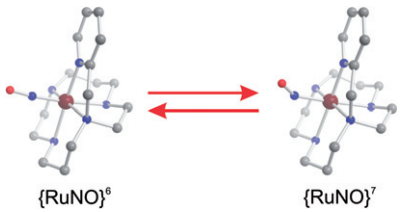


Ariel G. De Candia, Juan P. Marcolongo and Leonardo D. Slep

Polyhedron 26 (2007) 4719

A new ruthenium nitrosyl species based on a pendant-arm 1,4,8,11-tetraazacyclotetradecane (cyclam) derivative: An experimental and theoretical study

The mononuclear {RuNO}^{6} compound *cis*-[$Ru(L^{py})NO]^{3+}$ (L^{py} = *N*-(2-methylpyridyl)-1,4,8,11-tetraazacyclotetradecane) undergoes reversible one-electron reduction in solution to yield a stable {RuNO}^{7} cation.

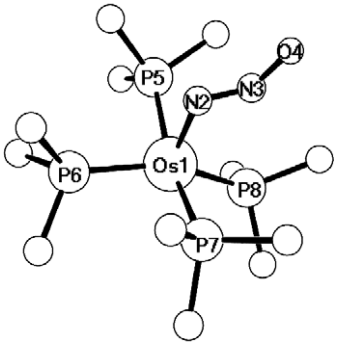


Hongjun Fan and Kenneth G. Caulton

Polyhedron 26 (2007) 4731

2-Electron reduction of N_2O yields a new ligand binding mode: *N*-Nitrosoimide

Highly reducing transition metals reduce N_2O to singly bent (at the central nitrogen) or doubly bent (at both N) forms when coordinated; the ligand is therefore properly termed an *N*-nitrosoimide, N_2O^{2-}.



Navamoney Arulsamy, D. Scott Bohle, Jerome A. Imonigie and Raecca C. Moore

Polyhedron 26 (2007) 4737

Group 8 and 10 hyponitrite and dinitrosyl complexes

Group 8 and 10 complexes bind two NO's in very different ways; either as a pair of linear dinitrosyls for group 8, or as coupled hyponitrite in the case of group 10. Thus for polynitrosyl complexes the redox state of pairs of NO ligands need to be considered in addition to their bent/linear or the metal's oxidation state.

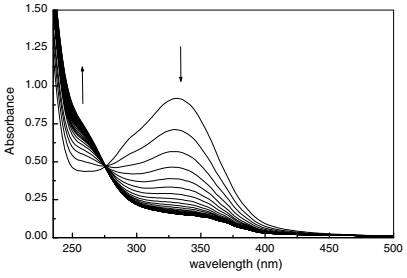


Renata Zachi de Osti and Douglas Wagner Franco

Polyhedron 26 (2007) 4746

Aspects of nitrite association with *trans*-$[Ru(NH_3)_4P(OEt)_3H_2O]^{2+}$

trans-$[Ru(NH_3)_4P(OEt)_3(H_2O)]^{2+}$ is known to reacts with nitrite ions in alkaline media (pH > 10) yielding *trans*-$[Ru(NH_3)_4P(OEt)_3(NO_2)]^+$, $K_N = (5.2 \pm 0.6) \times 10^3\ M^{-1}$ ((25 ± 0.2) °C), which releases the nitrite ligand, $k_{-N} = (1.2 \pm 0.03) \times 10^{-1}\ s^{-1}$. The nitro compound, in acid environment, undergoes quantitative conversion to the corresponding nitrosyl complex ($k_{obs} = 2.2 \times 10^{-3}\ s^{-1}$ at pH 4).

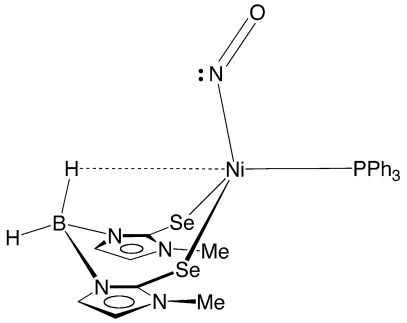


Victoria K. Landry and Gerard Parkin

Polyhedron 26 (2007) 4751

Synthesis and structural characterization of $[Bse^{Me}]Ni(PPh_3)(NO)$, a nickel complex with a bent nitrosyl ligand

The nickel nitrosyl compound $[Bse^{Me}]Ni(PPh_3)(NO)$ has been synthesized by the reaction of $Ni(PPh_3)_2(NO)Br$ with potassium *bis*(2-seleno-1-methylimidazolyl)hydroborate, $[Bse^{Me}]K$. X-ray diffraction studies demonstrate that the B–H group of the $[Bse^{Me}]$ ligand interacts with the nickel center and that the nitrosyl ligand is bent.

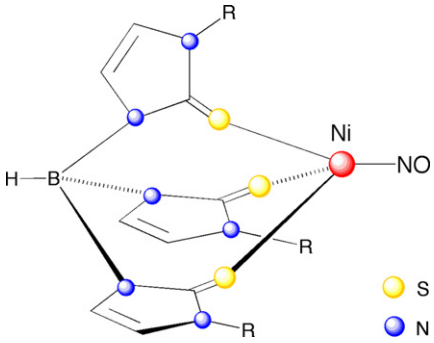


L. Summer Maffett, Kelly L. Gunter, Kevin A. Kreisel, Glenn P.A. Yap and Daniel Rabinovich

Polyhedron 26 (2007) 4758

Nickel nitrosyl complexes in a sulfur-rich environment: The first poly(mercaptoimidazolyl)borate derivatives

The first nickel nitrosyl complexes supported by bis- and tris(mercaptoimidazolyl)borate ligands, $(Bm^R)Ni(PPh_3)(NO)$ (R = Me, Bu^t) and $(Tm^R)Ni(NO)$ (R = Bu^t, *p*-Tol), have been readily prepared and fully characterized using a combination of analytical and spectroscopic techniques. Whereas the Tm^R compounds are tetrahedral and contain linear nitrosyl ligands, the Bm^R derivatives are trigonal pyramidal and display bent NO groups.

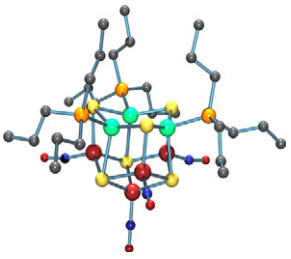


Harris Kalyvas and Dimitri Coucouvanis

Polyhedron 26 (2007) 4765

Synthesis and characterization of new heterometallic iron sulfur nitrosyl clusters

The reactivity of the $(PPN)_2[Fe_8S_6(NO)_8]$ and $(PPN)_2[Fe_6S_6(NO)_6]$ clusters is explored and new derivative clusters have been synthesized and structurally characterized. The unique $(PPN)_2Fe_4S_4(NO)_6$ "open-cubane" cluster with a chair like Fe_4S_4 core is obtained by the low temperature reaction of $[Fe_4S_3(NO)_7]^-$ with Bu_4NSH in the presence of $(PPN)_2[Fe_4(CO)_{13}]$. The mixed metal pentandite-like clusters $(PPN)_2[Mo_2Fe_6S_6(NO)_6(CO)_6]$, $(PPr_3)_2Cu_2Fe_6S_6(NO)_6$, $(PPr_3)_4Cu_4Fe_4S_6(NO)_4$, $(PPr_3)_2Ni_2Fe_6S_6(NO)_6$, $(PPr_3)_3Ni_3Fe_4S_6(NO)_4$, are obtained from the reactions of the$(PPN)_2[Fe_6S_6(NO)_6]$ prismanes with thiophilic metals.



The Publisher encourages the submission of articles in electronic form thus saving time and avoiding rekeying errors. For detailed instructions on the preparation of manuscripts and of electronic artwork, consult the Author Gateway for Elsevier at http://authors.elsevier.com

ScienceDirect

Full text of this journal is available, on-line from **ScienceDirect**. Visit **www.sciencedirect.com** for more information.

Available online at www.sciencedirect.com
ScienceDirect
Polyhedron 26, issue 8, 21 May 2007
POLYHEDRON
www.elsevier.com/locate/poly

Contents

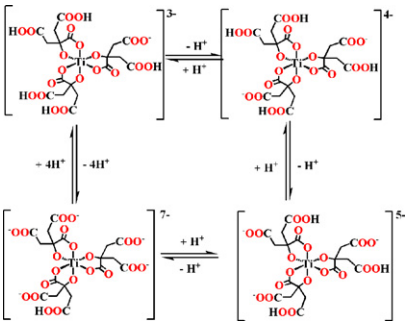
Papers

Yuan-Fu Deng, Ya-Qi Jiang, Qi-Ming Hong and Zhao-Hui Zhou

Polyhedron 26 (2007) 1561

Speciation of water-soluble titanium citrate: Synthesis, structural, spectroscopic properties and biological relevance

The pH-dependent interconversions of titanium citrate complexes and solution behavior of the titanium citrate binary system were investigated in aqueous solutions.

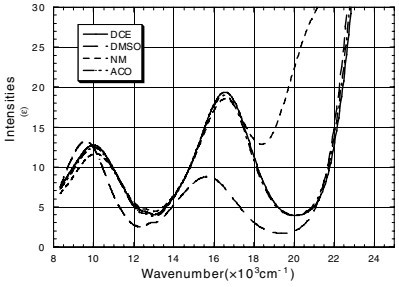


Fumiko Murata, Machiko Arakawa, Akiko Nakao, Keiichi Satoh and Yutaka Fukuda

Polyhedron 26 (2007) 1570

Syntheses, crystal structures and chromotropic properties of Nickel(II) mixed ligand complexes containing *N*-methyl-1,4-diazacycloheptane and various β-diketonates

UV–Vis absorption spectra of [Ni(medach)(bzac)NO_3] in organic solvents with different donor numbers (DN) and acceptor numbers (AN).

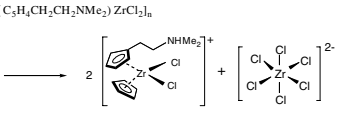


Jarosław Chojnacki, Rafał Grubba, Barbara Kugiel-Rachwalska and Jerzy Pikies

Polyhedron 26 (2007) 1579

(Cyclopentadienyl){(*N*,*N*-dimethylaminoethyl)-cyclopentadienyl} complexes of zirconium: Crystal structure of $[(\eta^5\text{-}C_5H_5)(\eta^5\text{-}C_5H_4CH_2\text{-}CH_2NHMe_2)ZrCl_2]_2[ZrCl_6]$

The reaction of the coordination polymer $[(C_6H_5)(C_5H_4CH_2CH_2NMe_2)ZrCl_2]_n$ with methanolic solution of HCl results in elimination of C_5H_5 and $C_5H_4CH_2CH_2NMe_2$ ligands from the Zr(IV) metal centre. Formation of the title compound was established by NMR spectroscopy and X-ray structural analysis.

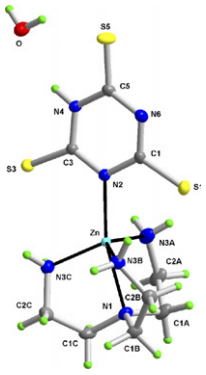


Pavel Kopel, Karel Doležal, Libor Machala and Vratislav Langer

Polyhedron 26 (2007) 1583

Synthesis, characterization and screening of biological activity of Zn(II), Fe(II) and Mn(II) complexes with trithiocyanuric acid

Mixed-ligand Zn(II), Fe(II) and Mn(II) complexes involving the trithiocyanurate anion and nitrogen-donor ligands were prepared and their in vitro antitumor and antimicrobial activities were tested. Two complexes showed good cytotoxicity against four cell lines and four complexes showed specific or extensive antimicrobial activities.

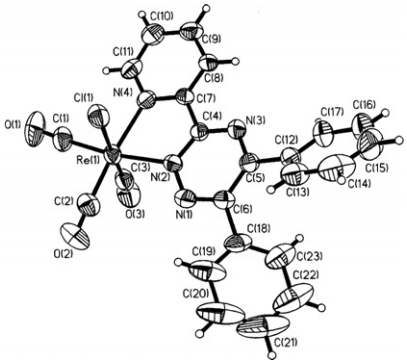


B. Machura, R. Kruszynski and J. Kusz

Polyhedron 26 (2007) 1590

X-ray structure, spectroscopic characterisation and DFT calculations of the $[Re(CO)_3(dppt)Cl]$ complex

The reaction of the complex $Re(CO)_5Cl$ with 5,6-diphenyl-3-(2-pyridyl)-1,2,4-trazine (dppt) has been examined and the $Re(CO)_3^+$ rhenium carbonyl – *fac*-$[Re(CO)_3(dppt)Cl]$ – has been obtained. The compound has been studied by IR, UV–Vis spectroscopy and X-ray crystallography. The molecular orbital diagram of the tricarbonyl has been calculated with the density functional theory (DFT) method. The spin-allowed singlet–singlet electronic transitions of $[Re(CO)_3(dppt)Cl]$ have been calculated with the time-dependent DFT method, and the UV–Vis spectrum of the title compound has been discussed on this basis.

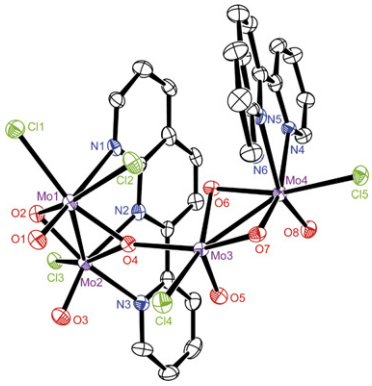


Moumita Majumdar, Sanjib K. Patra and Jitendra K. Bera

Polyhedron 26 (2007) 1597

Oxidative route to polyoxomolybdates from quadruply bonded $[Mo^{II}{\equiv}Mo^{II}]$ precursor: Structural characterization of a tetranuclear cluster $[Mo_4Cl_5O_8(pyNP)_2]$ (pyNP = (2-(2-pyridyl)1,8-naphthyridine))

Oxidation of *cis*-$[Mo_2(pyNP)_2(OAc)_2][BF_4]_2$ with $[n\text{-}Bu_4N]_2[Re_2Cl_8]$ provide the tetranuclear molybdenum cluster $[Mo_4Cl_5O_8(pyNP)_2]$ consisting of $[Mo_2^{V,V}]$ and $[Mo_2^{V,VI}]$ cores linked through a μ_3-O bridge.

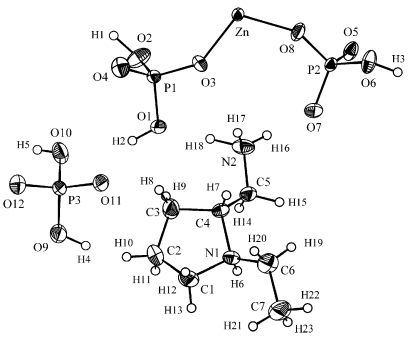


R. Kefi, C. Ben Nasr, F. Lefebvre and M. Rzaigui

Polyhedron 26 (2007) 1603

Hydrothermal synthesis and characterization of a new organic templated metallophosphate $[Zn(H_2PO_4)_2(HPO_4)][C_7H_{17}N_2]$

$$ZnO + 3H_3PO_4 + C_7H_{15}N_2 \rightarrow [Zn(H_2PO_4)_2(HPO_4)][C_7N_2H_{17}] + H_2O$$

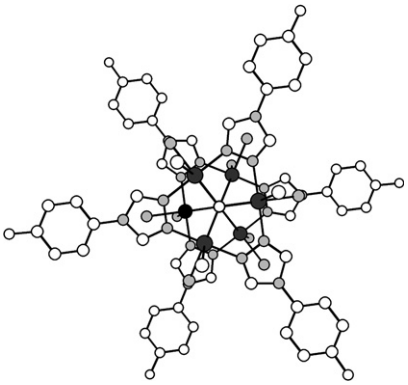


Elisaveta V. Lider, Eugenia V. Peresypkina, Anton I. Smolentsev, Valentina N. Elokhina, Tatyana I. Yaroshenko, Alexander V. Virovets, Vladimir N. Ikorskii and Ludmila G. Lavrenova

Polyhedron 26 (2007) 1612

Unusual coordination of a chloride ion to six copper ions: Synthesis and crystal structure of copper(II) complexes with 4-(4-hydroxyphenyl)-1,2,4-triazole

Novel copper(II) complexes with substituted 1,2,4-triazole, molecular and polymeric, have been prepared and characterized. The molecular complex shows interesting coordination of Cl^- to six copper ions with all six Cu–Cl bonds equal to 2.8397(3) Å. It shows mainly antiferromagnetic exchange interactions between the Cu^{2+} centers.

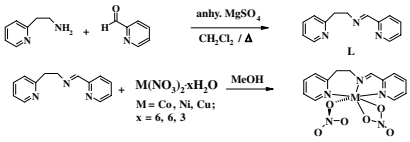


Sumanta Kumar Padhi and Vadivelu Manivannan

Polyhedron 26 (2007) 1619

Synthesis, structure and properties of $[ML(NO_3)_2]$: M = Co, Ni, Cu; **L** = *N*-(2-pyridylethyl)pyridine-2-carbaldimine

Complexes of the type $[ML(NO_3)_2]$, {M = Co(II), Ni(II), and Cu(II), **L** = *N*-(2-pyridylethyl)pyridine-2-carbaldimine} have been synthesized and characterized by spectral, magnetic, and X-ray crystallographic methods. In the cobalt (**1**), nickel (**2**), and copper (**3**) complexes, the bivalent metal ion is coordinated by the three nitrogen atoms of the tridentate **L** with two pyridine-N occupying *trans* positions. Amongst the two nitrates one coordinates in a bidentate fashion while the other coordinates in a monodentate fashion.

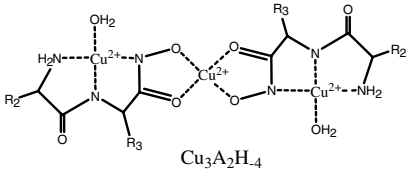


Péter Buglyó, Eszter Márta Nagy, Etelka Farkas, Imre Sóvágó, Daniele Sanna and Giovanni Micera

Polyhedron 26 (2007) 1625

New insights into the metal ion–peptide hydroxamate interactions: Metal complexes of primary hydroxamic acid derivatives of common dipeptides in aqueous solution

Hydroxamic acid derivatives of common dipeptides have been synthesized and their Fe(III), Al(III), Ni(II), Cu(II) and Zn(II) binding capabilities were studied by combined pH-potentiometric and spectroscopic techniques.



A. Kaltzoglou, P.J. Cox and P. Aslanidis

Polyhedron 26 (2007) 1634

Silver(I) bromide complexes of the rigid diphosphanes 1,2-bis(diphenylphosphano)benzene (dppbz) and 4,5-bis(diphenylphosphano)-9,9-dimethyl-xanthene (xantphos): Crystal structures of $[Ag(\mu_2\text{-}Br)(dppbz)]_2$, [AgBr(xantphos)] and [AgBr(xantphos)(py2SH)]

The behaviour of the diphos ligands 1,2-bis(diphenylphosphano)benzene (dppbz) and 4,5-bis(diphenylphosphano)-9,9-dimethylxanthene (xantphos) towards coordination of Ag(I) bromide in the presence of pyridine-2-thione has been investigated. Both diphosphanes adopt the chelating coordination mode, however two types of products have been obtained, namely a halide bridged dimer with tetrahedrally coordinated Ag^I centers for dppbz and monomeric trigonal complexes in the case of xantphos.

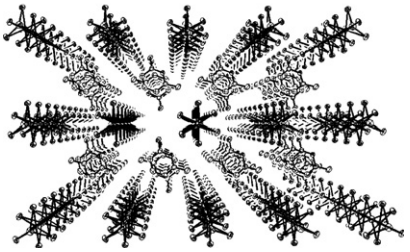


Marek Zuber and Zbigniew Ciunik

Polyhedron 26 (2007) 1643

New type of 1D coordination polymeric anions $[(MCl_3M_1Cl_3)^{2-}]_n$ (M = Rh, Ru; M_1 = Na, K). Crystal structure and IR characterization of Rh(III) and Ru(III) hexachlorometallates with 2-amino-6-methylpyridinium cations

New type of 1D coordination polymeric anions $[(MCl_3M_1Cl_3)^{2-}]_n$ (M = Rh, Ru and M_1 = Na, K) has been obtained in the reaction of $MCl_3 \cdot xH_2O$ and M_1Cl with 2-amino-6-methyl-pyridine in hydrochloric acid solution. Their X-ray structures and IR spectra are presented and discussed. Weak hydrogen bonds occur between the organic cations and inorganic polymeric anions to form layers. Organic anions form stacks because of weak π–π interactions between aromatic rings. All metals in 1D coordination polymeric anions are linked together by bridging chloride anions.

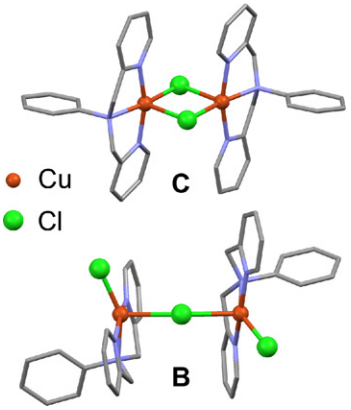


Anne Nielsen, Sune Veltzé, Andrew D. Bond and Christine J. McKenzie

Polyhedron 26 (2007) 1649

Isomerism in copper(II) chloride complexes of bis(2-pyridylmethyl)amine and *N*-substituted derivatives: Synthesis and X-ray structural characterisation

Copper(II) chloride complexes of tridentate *N*-alkylated bis(2-pyridylmethyl)amine ligands (bpa, Me-bpa and ph-bpa) form coordination oligomers with either terminal or bridging chloride. Two structural types are identified by X-ray diffraction: a mono μ-chloro bridged species (**B**) and a di-μ-chloro bridged species (**C**), both containing five-coordinate copper(II).

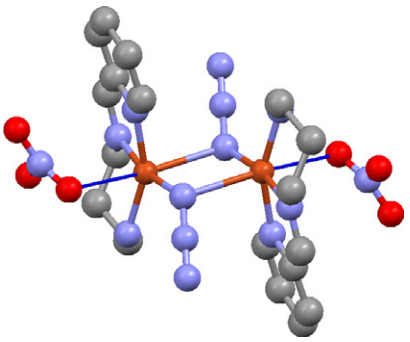


Chandan Adhikary, Dasarath Mal, Rupam Sen, Ashis Bhattacharjee, Philipp Gütlich, Siddhartha Chaudhuri and Subratanath Koner

Polyhedron 26 (2007) 1658

Synthesis, X-ray crystal structure and magnetic study of a novel μ_2-1,1-azido bridged dimeric copper(II) complex

A rare μ_2-1,1-azido bridged dimeric octahedral copper(II) complex $[Cu_2L_2(N_3)_2(NO_3)_2]$ (L = 1-(*N*-pyridylimino)-3-aminopropane) has been synthesized and characterized by single crystal analysis. Low temperature magnetic measurement shows that the interaction between the copper(II) ions in this compound is antiferromagnetic.

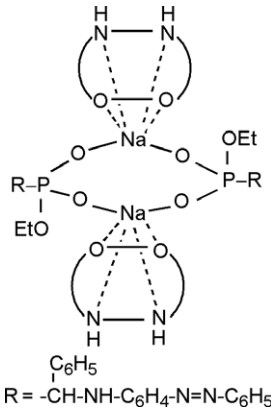


Ljerka Tušek-Božić, Ester Marotta and Pietro Traldi

Polyhedron 26 (2007) 1663

Efficient solid-state microwave-promoted complexation of a mixed dioxa-diaza macrocycle with an alkali salt. Synthesis of a sodium ethyl 4-benzeneazophosphonate complex

The simple work-up, eco-friendly microwave-promoted solid-state synthesis of an alkali complex derived from a mixed 15-membered dioxa-diaza macrocycle (L) and sodium monoethyl [4-α-(benzeneazoanilino)-*N*-benzyl]phosphonate (NaEP) has been described and compared with the syntheses carried out under conventional heating in the solid state and solution. The prepared diphosphonate bridged dinuclear complex, $[Na(L)(\mu\text{-}EP) \cdot H_2O]_2$, has been studied by IR, ^1H and ^{13}C NMR, and MS spectroscopy.

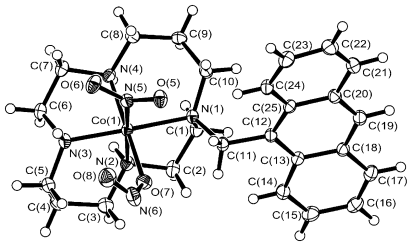


Simon Boyd, W. David McFadyen, Brendan F. Abrahams, Martin J. Grannas and Kenneth P. Ghiggino

Polyhedron 26 (2007) 1669

Synthesis and structural characterisation of a series of cobalt complexes of N-appended anthracenyl cyclam

Geometric and linkage isomerism is a feature of a series of anthracenylcyclam cobalt(III) complexes which have been synthesised for future use in photochemical studies.

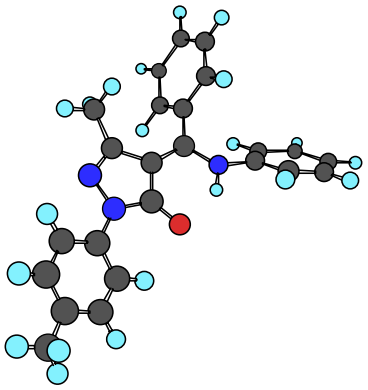


R.N. Jadeja and J.R. Shah

Polyhedron 26 (2007) 1677

Studies on some oxovanadium(IV) complexes of acyl pyrazolone analogues

A series of bidentate ligands have been synthesized by condensation of 4-benzoyl-2,4-dihydro-5-methyl-2-(4′-methylphenyl)-3*H*-pyrazol-3-one with various aromatic amines. X-ray structure determination reveals that these ligands exist in the amine-one tautomeric form. With OV(IV), these ligands form distorted octahedral complexes, $[OVL_2(H_2O)]$; TGA, μ_{eff}, electronic spectral studies of which have been carried out. *Ab initio* calculations have been performed on one of the ligand.

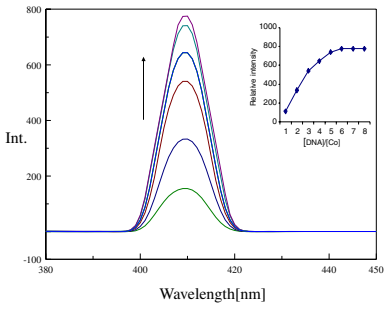


Penumaka Nagababu and S. Satyanarayana

Polyhedron 26 (2007) 1686

DNA binding and cleavage properties of certain ethylenediamine cobalt(III) complexes of modified 1,10-phenanthrolines

Two complexes of the type $[Co(en)_2IP]^{3+}$ (IP = imidazo[4,5-f][1,10]-phenanthroline) and $[Co(en)_2PIP]^{3+}$(PIP = 2-phenylimidazo[4,5-f][1,10]-phenanthroline) have been synthesized and characterized by UV–VIS, IR and ^1H NMR spectral methods. Absorption spectroscopy, emission spectroscopy, viscosity measurements and DNA melting techniques have been used to investigate the binding of these two complexes with calf thymus DNA and photocleavage studies have been used to investigate the binding of these complexes with plasmid DNA. The spectroscopic studies together with viscosity measurements and DNA melting studies support that complexes **1** and **2** bind to CT DNA(=calf thymus DNA) by an intercalation mode via IP or PIP into the base pairs of DNA. Complex **2** binds more avidly to CT DNA than **1**, which is consistent with the extended planar ring π system of PIP. Noticeably, the two complexes have been found to be efficient photosensitisers for strand scissions in plasmid DNA.

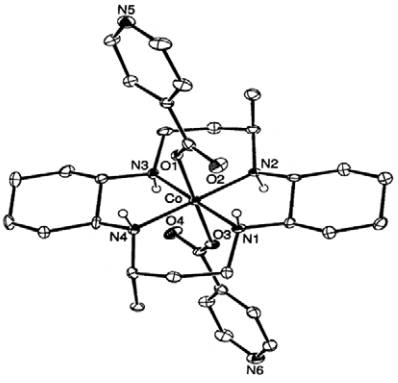


Ki-Young Choi, Hee-Kune Lee and Haiil Ryu

Polyhedron 26 (2007) 1693

Synthesis and properties of cobalt(III) complexes of 3,14-dimethyl-2,6,13,17-tetraazatricyclo[14,4,$0^{1.18}$,$0^{7.12}$]docosane

The cobalt(III) complexes $[Co(L)(int)_2]Cl \cdot 3H_2O$ (**1**), $[Co(L)(NCS)_2]NCS \cdot H_2O$ (**2**) and $[Co(L)(NCO)_2]NCO \cdot H_2O$ (**3**) have been synthesized and structurally characterized. The crystal structures of **1** and **2** show that the cobalt centers have an octahedral geometry with four secondary amines of the macrocycle and two axial ligands.

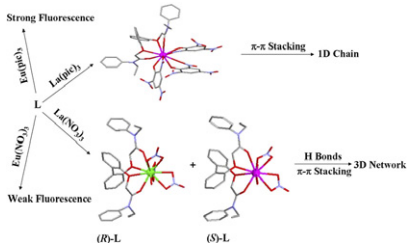


Yan-Ling Guo, Wei Dou, Ya-Wen Wang, Wei-Sheng Liu and Da-Qi Wang

Polyhedron 26 (2007) 1699

Preparation, luminescent properties of *N*-phenyl-2-{2′-[(phenyl-ethyl-carbamoyl)-methoxy]-biphenyl-2-yloxy}-*N*-ethyl-acetamide (**L**) lanthanide complexes and the supramolecular structures of $[La(pic)_3L]$ and $2[La(NO_3)_3L(H_2O)] \cdot H_2O \cdot 0.5C_2H_5OH$

Mononuclear lanthanide complexes of the tetradentate ligand *N*-phenyl-2-{2′-[(phenyl-ethyl-carbamoyl)-methoxy]-biphenyl-2-yloxy}-*N*-ethyl-acetamide (**L**) with picrate and nitrate counterions have been synthesized. The anion is seen to exert a significant influence on the supramolecular structures and luminescent properties.

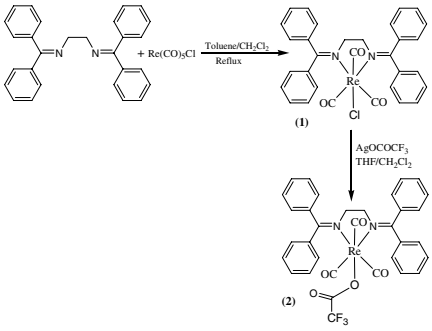


Reza Kia, Valiollah Mirkhani, Alajos Kálmán and Andrea Deák

Polyhedron 26 (2007) 1711

New chloro- and trifluoroacetato tricarbonyl-rhenium(I) complexes with a *N*,*N*′-bis(benzophenone)-1,2-diiminoethane Schiff base ligand: Spectral and structural studies

The reaction of $Re(CO)_5Cl$ with the chelating ligand *N*,*N*′-bis(benzophenone)-1,2-diiminoethane (bz_2en) afforded the neutral *fac*-$[Re(CO)_3(bz_2en)Cl]$ (**1**). Subsequent reaction with $AgOCOCF_3$ gave *fac*-$[Re(CO)_3(bz_2en)OCOCF_3]$ (**2**). Their pseudooctahedral *fac* structures have been established by FTIR, UV–Vis, ^1H, ^{13}C NMR and have been confirmed by X-ray diffraction analysis. The electrochemical behaviour of the investigated complexes has been studied by cyclic voltammetry.

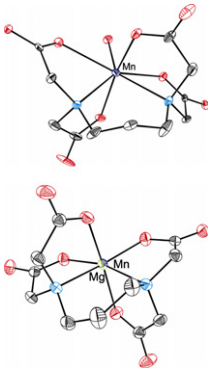


Urszula Rychlewska, Beata Warżajtis, Danica Cvetić, Dušanka D. Radanović, Dejan M. Gurešić and Miloš I. Djuran

Polyhedron 26 (2007) 1717

Two distinct manganese(II) complexes with hexadentate 1,3-propanediaminetetraacetate ligand: The ability of metal(II) complexes with 1,3-pdta ligand to form solid solutions

The preference of manganese(II) ion to form the seven-coordinated $[Mn(1,3\text{-pdta})(H_2O)]^{2-}$ complex with the hexadentate 1,3-pdta is disrupted by crystallization from a solution containing besides the $[Mn(1,3\text{-pdta})(H_2O)]^{2-}$ the $[Mg(1,3\text{-pdta})]^{2-}$ complex species, resulting in a mixed crystal inclosing the six-coordinated $[Mg(1,3\text{-pdta})]^{2-}$ and $[Mn(1,3\text{-pdta})]^{2-}$ complex anions at the same occupation site.

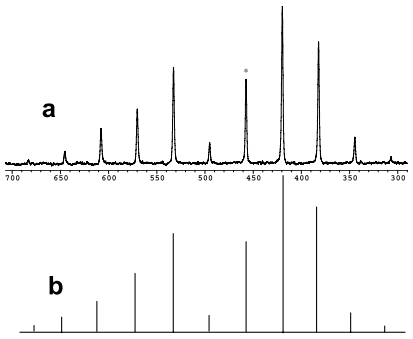


Mohammed I.M. Wazeer, Anvarhusein A. Isab and Mohammed Fettouhi

Polyhedron 26 (2007) 1725

New cadmium chloride complexes with imidazolidine-2-thione and its derivatives: X-ray structures, solid state and solution NMR and antimicrobial activity studies

Reactions of imidazolidine-2-thione (Imt), 1,3-diazinane-2-thione (Diaz) and 1,3-diazipane-2-thione (Diap) with cadmium(II) chloride in methanol result in the formation of 2:1 complexes. Both solid state and solution NMR, in addition to X-ray structures, confirm the exocyclic sulfur atom to be the donor in all cases. Cadmium shielding tensors and anisotropies were calculated from the solid-state NMR spectra. The X-ray structures of two complexes, $(NMeImt)_2CdCl_2$ and $(NEtImt)_2CdCl_2$, reveal distorted tetrahedral geometries. Antimicrobial activity studies show that the $Cd(Diap)_2Cl_2$ complex exhibits substantial antibacterial activities compared to the corresponding Zn(II) complex.

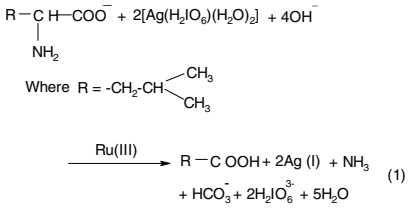


Veeresh Seregar, T.M. Veeresh and Sharanappa T. Nandibewoor

Polyhedron 26 (2007) 1731

Ruthenium(III) catalysed oxidation of L-leucine by a new oxidant, diperiodatoargentate(III) in aqueous alkaline medium

The kinetics of oxidation of L-leucine by diperiodatoargentate(III) (DPA) in the presence of micro amounts of ruthenium(III) in alkaline medium has been studied. The active species of DPA is found to be $[Ag(H_2IO_6)(H_2O)_2]$ and that of ruthenium(III) to be $[Ru(H_2O)_5OH]^{2+}$ in alkaline medium.

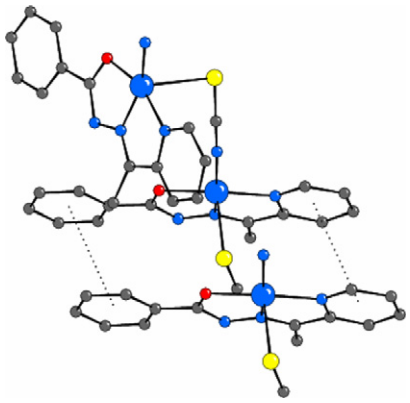


Soma Sen, Samiran Mitra, David L. Hughes, Georgina Rosair and Cédric Desplanches

Polyhedron 26 (2007) 1740

Two new pseudohalide bridged di- and polynuclear copper(II) complexes: Synthesis, crystal structures and magnetic studies

Two new pseudohalide bridged di- and polynuclear copper(II) complexes from a tridentate hydrazone ligand have been synthesised. Structures of both the complexes have been established by X-ray crystallography. Variable temperature magnetic susceptibility measurement studies indicate there is a weak ferromagnetic interaction between the two copper(II) ions in **1** ($J = +0.75$ cm^{-1}), while weak antiferromagnetic interaction is observed with J values 0.23 cm^{-1} for **2**.

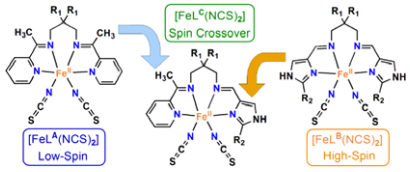


Nicolas Bréfuel, Isabelle Vang, Sergiu Shova, Françoise Dahan, Jean-Pierre Costes and Jean-Pierre Tuchagues

Polyhedron 26 (2007) 1745

Fe^{II} Spin crossover materials based on dissymmetrical N_4 Schiff bases including 2-pyridyl and 2R-imidazol-4-yl rings: Synthesis, crystal structure and magnetic and Mössbauer properties

Single-crystal X-ray structures, variable-temperature magnetic susceptibility and Mössbauer studies show that it is possible to tune the spin crossover properties in the novel $[FeL^C(NCS)_2]$ series by changing the 2-imidazole and/or C2-propylene susbtituent of the dissymmetrical tetradentate Schiff base ligands L^C containing both pyridine and imidazole rings.

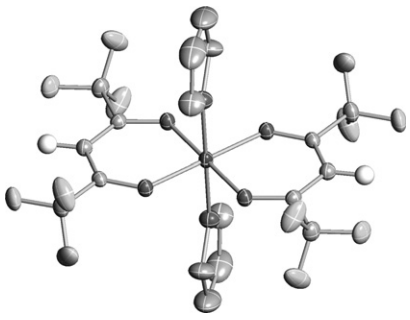


Yoshiko Harada and Gregory S. Girolami

Polyhedron 26 (2007) 1758

Synthesis and crystal structures of the chromium(II) and chromium(III) hexafluoroacetylacetonate complexes *trans*-$Cr(hfac)_2(thf)_2$ and $Cr(hfac)_3$

Treatment of $CrCl_2(thf)$ with Na(hfac), hfac = 1,1,1,5,5,5-hexafluoroacetylacetonate, affords the six-coordinate chromium(II) complex $Cr(hfac)_2(thf)_2$. The crystal structures of $Cr(hfac)_2(thf)_2$ and the chromium(III) complex $Cr(hfac)_3$ have been determined by single-crystal X-ray diffraction.



The Publisher encourages the submission of articles in electronic form thus saving time and avoiding rekeying errors. For detailed instructions on the preparation of manuscripts and of electronic artwork, consult the Author Gateway for Elsevier at http://authors.elsevier.com

ScienceDirect

Full text of this journal is available, on-line from **ScienceDirect**. Visit **www.sciencedirect.com** for more information.

Available online at www.sciencedirect.com
ScienceDirect
Polyhedron 26, issue 4, 1 March 2007
POLYHEDRON
www.elsevier.com/locate/poly

Contents

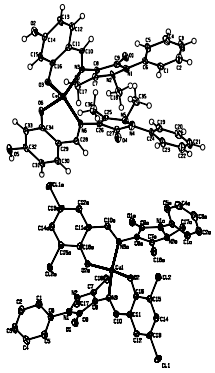
Papers

P. Mosae Selvakumar, E. Suresh, P.S. Subramanian

Polyhedron 26 (2007) 749

Synthesis, spectral characterization and structural investigation on some 4-aminoantipyrine containing Schiff base Cu(II) complexes and their molecular association

Two important antipyrine Schiff base ligands and their Cu(II) complexes have been synthesized and characterized. The single crystal X-ray structures of **1** and **2**, being the first in the series of this type of compound, explored that the mode of weak H-bonding interactions and steric effect profoundly influenced the Cu(II) geometry in **1** and **2**, rearranging from a tetrahedrally distorted square planar geometry into a distorted square planar geometry.

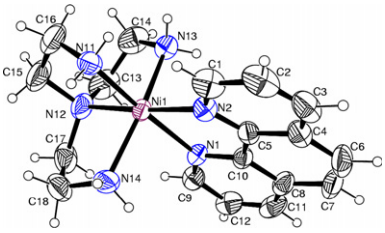


R.N. Patel, Nripendra Singh, V.L.N. Gundla

Polyhedron 26 (2007) 757

Synthesis, characterization and superoxide dismutase activity of some octahedral nickel(II) complexes

Four new octahedral Ni(II) complexes were synthesized and characterized. The crystal structures of $[Ni(tren)(phen)](ClO_4)_2$ (**1**) and $[Ni(SAA)(PMDT)] \cdot 2H_2O$ (**3**) were determined by single crystal X-ray diffraction methods. Superoxide dismutase (SOD) activity of these complexes has also been studied.

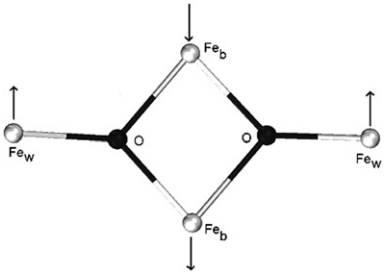


Catherine Dendrinou-Samara, Sotiris Katsamakas, Catherine Raptopoulou, Aris Terzis, Vassilis Tangoulis, Dimitris P. Kessissoglou

Polyhedron 26 (2007) 763

Interaction of Fe(III) with herbicide-carboxylato ligands – Di-, tri- and tetra-nuclear compounds: Structure and magnetic behavior

Interaction of Fe(III) with phenoxyalkanoic acids and phen leads to dinuclear neutral complexes while the absence of phen favours trinuclear cationic or tetranuclear neutral forms. The magnetic behavior of all nuclearities show antiferromagnetic exchange interaction with the ground state of the binuclear and tetranuclear compounds $S = 0$ and for the trinuclear one $S = 1/2$.

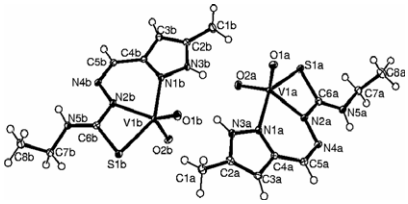


Arijit Hazra, Anil Kumar Barik, Sachindranath Pal, Samik Gupta, Somnath Roy, Ray J. Butcher, Shie-Ming Peng, G.H. Lee, Susanta Kumar Kar

Polyhedron 26 (2007) 773

Synthesis and structural studies on di-oxo-vanadium(V) complexes of *N*(4)-substituted pyrazole based thiosemicarbazones

cis-Dioxo vanadium(V) complexes (**1**–**3**) of three different tridentate thiosemicarbazone ligands synthesized from 5-methyl-3-formylpyrazole and *N*(4)-substituted thiosemicarbazides have been prepared and structurally characterized. All the three complexes have square pyramidal geometry. In **2**, two asymmetric units appreciably differ in their conformations. In **1** and **2**, the pyrazolyl N, the thioimine N (quite unusual) and the thiolato S of the corresponding tridentate ligand molecule coordinate to the vanadium atom whereas in **3**, the respective ligand utilizes the azomethine nitrogen (usual) instead of the thioimine nitrogen to coordinate the vanadium atom along with the other two donor sites.

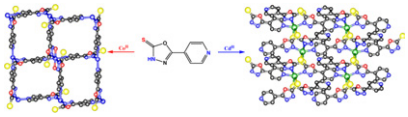


Yong-Tao Wang, Gui-Mei Tang, Wan-Yong Ma, Wen-Zhu Wan

Polyhedron 26 (2007) 782

Synthesis and characterization of two new coordination supramolecular structures from a versatile unsymmetric 5-(4-pyridyl)-1,3,4-oxadiazole-2-thione (Hpot) ligand

The rigid and unsymmetric building block 5-(4-pyridyl)-1,3,4-oxadiazole-2-thione (Hpot) is first developed as a bridging ligand and exhibits intriguing coordination modes in the process of self-assembling networks, which indicates that the versatile nature of this rigid unsymmetric ligand, together with the coordination preferences of the metal centers, plays a critical role in the construction of these novel coordination polymers or supramolecules.

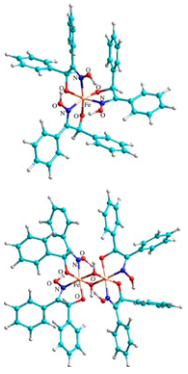


Attia S. Attia, M.F. El-Shahat

Polyhedron 26 (2007) 791

Synthesis and characterization of a monomeric and a dihydroxo-bridged dimeric complexes of iron(III) with α-benzoinoxime

A mononuclear Fe(III) complex, $Fe(HBNO)_3$ (**1**), and a dinuclear Fe(III)–Fe(III) complex, $[Fe(HBNO)_2OH]_2$ (**2**), have been synthesized and characterized. Theoretical modelling of the magnetic data indicate a weak antiferromagnetic spin exchange between the iron(III) centers of the dimeric complex ($J = -8.35$). The structural and vibrational behaviors of the two complexes have been elucidated with a quantum mechanical PM3 routine.

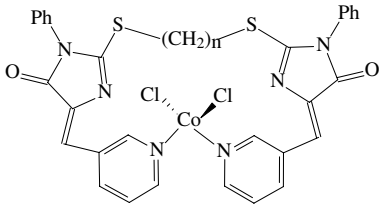


Elena K. Beloglazkina, Alexander G. Majouga, Renata B. Romashkina, Anna A. Moiseeva, Nikolai V. Zyk

Polyhedron 26 (2007) 797

The preparation, crystal structure and electrochemistry of (5*Z*,5′*Z*)-2,2′-(alkane-α,ω-diylsulfanyldiyl)bis(5-(3-pyridylmethylene)-3,5-dihydro-4*H*-imidazol-4-ones) and their complexes with cobalt(II) chloride

A series of (5*Z*,5′*Z*)-2,2′-(alkane-α,ω-diylsulfanyldiyl)bis(5-(3-pyridylmethylene)-3,5-dihydro-4*H*-imidazol-4-ones) and their complexes with $CoCl_2$ were synthesized.



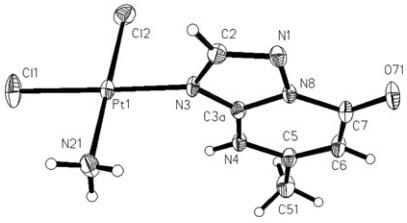
n = 2, 6, 10

Iwona Łakomska, Andrzej Wojtczak, Jerzy Sitkowski, Lech Kozerski, Edward Szłyk

Polyhedron 26 (2007) 803

X-ray structure and multinuclear NMR studies of platinum(II) complexes with 5-methyl-1,2,4-triazolo[1,5-*a*]pyrimidin-7(4*H*)-one

New dichloride platinum(II) complexes with 5-methyl-1,2,4-triazolo[1,5-*a*]pyrimidin-7(4*H*)-one (HmtpO) have been synthesized and characterized by thermal analysis, infrared and ^{1}H, ^{13}C, ^{15}N, ^{195}Pt NMR spectroscopy. X-ray crystal structures of *cis*-$PtCl_2(NH_3)$(HmtpO) (**1**) and *cis*-$PtCl_2(HmtpO)_2 \cdot 4H_2O$ (**2b**) were determined. Both complexes revealed a square-planar coordination geometry for the platinum atoms with monodentate (N3) triazolopyrimidine ligands.

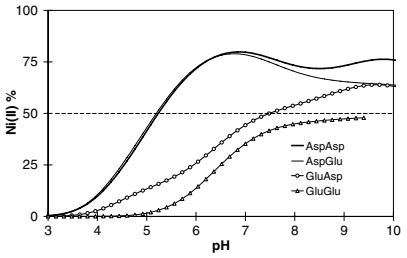


Csilla Kállay, Imre Sóvágó, Katalin Várnagy

Polyhedron 26 (2007) 811

Nickel(II) complexes of oligopeptides containing aspartyl and glutamyl residues. Potentiometric and spectroscopic studies

Metal binding affinity of dipeptides containing extra carboxylate residues follows the order: AspAsp > AspGlu > GluAsp > GluGlu. This is linked to the (NH_2,β-COO^-) coordination mode at low pH and (NH_2,N^-,β-COO^-) coordination at high pH.

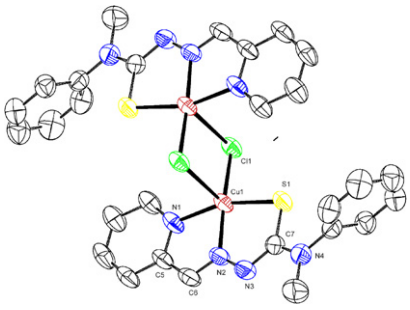


P.F. Rapheal, E. Manoj, M.R. Prathapachandra Kurup

Polyhedron 26 (2007) 818

Copper(II) complexes of *N*(4)-substituted thiosemicarbazones derived from pyridine-2-carbaldehyde: Crystal structure of a binuclear complex

Ten novel Cu(II) complexes {[CuL^1Cl] (**1**), [$CuL^1NO_3]_2$ (**2**), [$CuL^1N_3] \cdot 1/3H_2O$ (**3**), [$CuL^1]_2(ClO_4)_2 \cdot 2H_2O$ (**4**), [$CuL^2Cl]_2$ (**5**), [CuL^2N_3] (**6**), [$Cu(HL^2)SO_4] \cdot 2H_2O$ (**7**), [$Cu(HL^2)_2](ClO_4)_2 \cdot 1/2EtOH$ (**8**), [$CuL^3Cl]_2$ (**9**), [$CuL^3CNS] \cdot 1/2H_2O$ (**10**)} of three NNS thiosemicarbazone ligands {pyridine-2-carbaldehyde-*N*(4)-*p*-methoxyphenyl thiosemicarbazone [HL^1], pyridine-2-carbaldehyde-*N*(4)-2-phenylethyl thiosemicarbazone [HL^2] and pyridine-2-carbaldehyde [*N*(4)-(methyl), *N*(4)-(phenyl) thiosemicarbazone [HL^3]} were synthesized and physico-chemically characterized. The crystal structure of compound **9**, consists of two square pyramidal Cu(II) centers linked by two chlorine atoms.

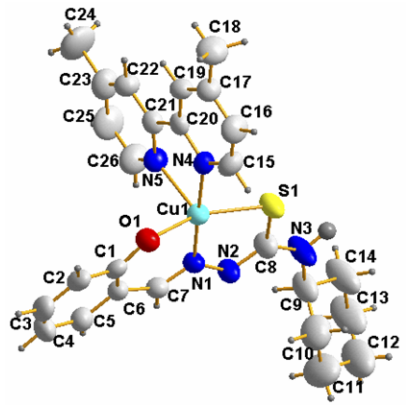


E.B. Seena, Maliyeckal R. Prathapachandra Kurup

Polyhedron 26 (2007) 829

Spectral and structural studies of mono- and binuclear copper(II) complexes of salicylaldehyde N(4)-substituted thiosemicarbazones

Three copper(II) complexes of salicylaldehyde N(4)-phenyl thiosemicarbazone (H_2L^1) an two copper(II) complexes of N(4)-cyclohexyl thiosemicarbazone (H_2L^2) have been synthesized and characterized by different physicochemical techniques like magnetic studies and electronic, infrared and EPR spectral studies. The complexes $[(CuL^1)_2] \cdot \frac{1}{2}H_2O$ (**1**) and $[(CuL^2)_2]$ (**4**) having dimeric structure. In $[Cu(HL^1)_2] \cdot H_2O$ (**2**), the ligand moieties are coordinated as monoanionic (HL^-) ones. Two of the complexes [CuL^1dmbipy] $\cdot H_2O$ (**3**) and [CuL^2dmbipy] (**5**) have been found to possess the stoichiometry [CuLB], where B = 4,4′-dimethyl-2,2′-bipyridine (dmbipy). The coordination geometry around copper(II) in **5** is trigonal bipyramidal distorted square based pyramidal (TBDSBP), as obtained by X-ray diffraction studies.

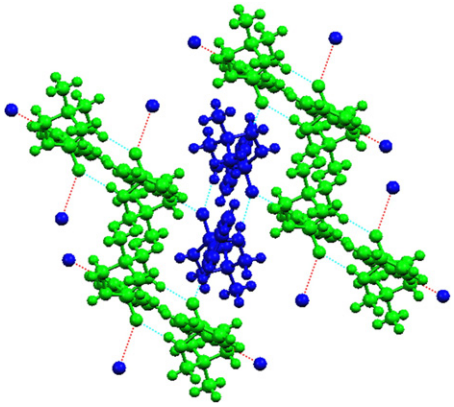


Khodayar Gholivand, Mehrdad Pourayoubi, Zahra Shariatinia

Polyhedron 26 (2007) 837

$^{2,3}J$(P,X) [X = H, C] coupling constants dependency on the ring size, hybridization and substituents in new diazaphospholes and diazaphosphorinanes, NMR and X-ray crystallography studies

New diazaphospholes and diazaphosphorinanes were synthesized and characterized by NMR, IR and mass spectroscopic methods. Effective parameters for $^{2,3}J$(P,X) [X = H, C] coupling constants are discussed. The crystal structures of four compounds were determined by X-ray crystallography.

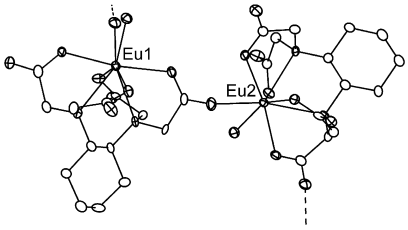


Rafał Janicki, Anna Mondry, Przemysław Starynowicz

Polyhedron 26 (2007) 845

Structural and spectroscopic investigations of the Eu^{III}–CDTA system

New polymeric structures together with spectroscopic properties of the Eu–CDTA system are presented.

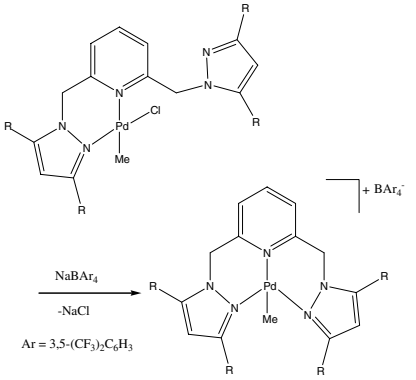


Stephen O. Ojwach, Ilia A. Guzei, James Darkwa, Selwyn F. Mapolie

Polyhedron 26 (2007) 851

Palladium complexes of multidentate pyrazolylmethyl pyridine ligands: Synthesis, structures and phenylacetylene polymerization

Bis(pyrazolylmethyl) pyridine ligands react with $[PdCl_2(NCMe)_2]$ or [Pd(COD)ClMe)] to form mononuclear palladium complexes in which the ligands bind in a bidentate fashion with a dangling pyrazolyl unit; but on removal of a chloride from these complexes the dangling arm coordinates to form tridentately bound palladium complexes. These tridentatley bound palladium complexes, however, can open up and catalyze the polymerization of phenylacetylene to polyphenylacetylene.

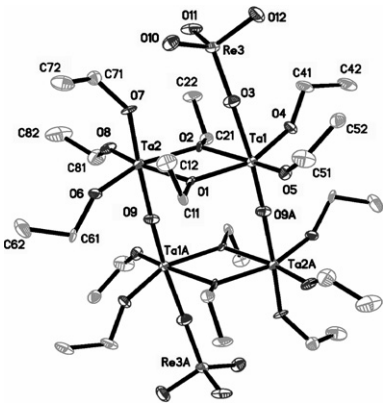


Olesya A. Nikonova, Vadim G. Kessler, Dmitrii V. Drobot, Pavel A. Shcheglov, Gulaim A. Seisenbaeva

Polyhedron 26 (2007) 862

Synthesis and X-ray single crystal study of niobium and tantalum oxo-ethoxoperrhenates, $M^V_4O_2(OEt)_{14}(ReO_4)_2$

Reproducibly soluble and solution stable oxo-alkoxo-perrhenate derivatives of niobium and tantalum, $M^V_4O_2(OEt)_{14}(ReO_4)_2$, can be obtained in high yields by interaction of $M^V(OEt)_5$ with rhenium heptoxide.

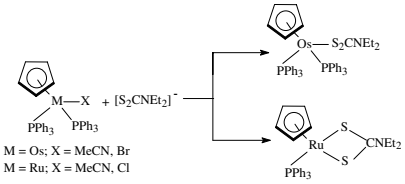


R. Lalrempuia, Hauzachin Suante, Hemant P. Yennawar, Mohan Rao Kollipara

Polyhedron 26 (2007) 867

Reactivity of the $[CpM(PPh_3)_2]^+$ (M = Ru, Os) fragment with diethyldithiocarbamate

This paper reports on the reaction of $[CpM(PPh_3)_2(L)]^{+/0}$ (Cp = η^5-C_5H_5; M = Os, L = CH_3CN, DMSO Br; M = Ru, X = Cl, CH_3CN) with diethyldithiocarbamate ($S_2CNEt_2^-$). The exceptional kinetic stability of [Os–PPh_3] compared to [Ru–PPh_3] is reflected from the isolation of a monodentate diethyldithiocarbamate complex $[CpOs(PPh_3)_2(\kappa^1\text{-}S_2CNEt_2)]$ (**3**) and bidentate diethyldithiocarbamate complex $[Cp\text{-}Ru(PPh_3)(\kappa^2\text{-}S_2CNEt_2)]$ (**5**) as the only products. The structure of $[CpOs(PPh_3)_2(CH_3CN)]BF_4$ (**2** · $\mathbf{BF_4}$) and **5** were determined by X-ray diffraction.

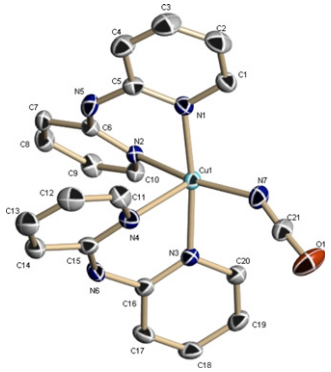


Sujittra Youngme, Jaturong Phatchimkun, Unchulee Suksangpanya, Chaveng Pakawatchai, Narongsak Chaichit, Palangpon Kongsaeree, Jurek Krzystek, Brian Murphy

Polyhedron 26 (2007) 871

Crystal structures, spectro-structural correlation and structural pathways of eight $[Cu(dpyam)_2(NCO)][Y]$ complexes (dpyam = di-2-pyridylamine), Y = Br^-, $CF_3SO_3^-$, BF_4^-·dpyam, $Cl^- \cdot 4H_2O$, NO_3^-, PF_6^-, ClO_4^- and BPh_4^-

The crystal structures and structural pathway in a series of five-coordinated complexes $[Cu(dpyam)_2(NCO)][Y]$ complexes when Y = Br^- (**1**), $CF_3SO_3^-$(**2**), $BF_4^- \cdot$dpyam (**3**), $Cl^- \cdot 4H_2O$ (**4**), NO_3^- (**5**), PF_6^- (**6**), ClO_4^- (**7**) and BPh_4^- (**8**), respectively have been studied. The distorted structures of these complexes vary from trigonal bipyramidal distorted square based pyramidal (TBDSBP) geometry to square base pyramidal distorted trigonal bipyramidal (SBPDTB) geometry with τ values of 0.09–0.76, respectively.

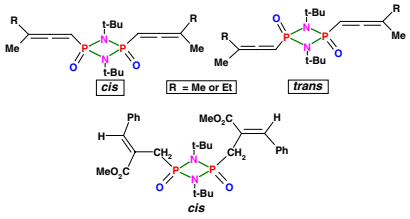


N.N. Bhuvan Kumar, K.C. Kumara Swamy

Polyhedron 26 (2007) 883

Synthesis and structures of *cis*- and *trans*-bis(allenyl)cylclodiphosph(V)azanes and a bis(allyl)cyclodiphosph(V)azane

From the reaction of *cis*-$[ClP(\mu\text{-}N\text{-}t\text{-}Bu)]_2$ (**1**) with $HOC(R)(Me)C{\equiv}CH/Et_3N$, both *cis*- and *trans*-isomers of bis-(allenyl)phosphoramidates $[((Me)RC{=}C{=}CH)(O)P(\mu\text{-}N\text{-}t\text{-}Bu)]_2$ [*R* = Me or Et] have been synthesized. No P(III) intermediate was detected. In contrast, only the *cis*-isomer of (i) *allenyl* compound $[(H_2C{=}C{=}CH)(O)P(\mu\text{-}N\text{-}t\text{-}Bu)]_2$ or (ii) *allyl* compound $[((Ph)HC{=}C(CO_2Me){-}CH_2)(O)\text{-}P(\mu\text{-}N\text{-}t\text{-}Bu)]_2$ is obtained almost exclusively by reacting **1** with $HOCH_2C{\equiv}CH$ or $PhCH(OH)C(CO_2Me){=}CH_2$, respectively.

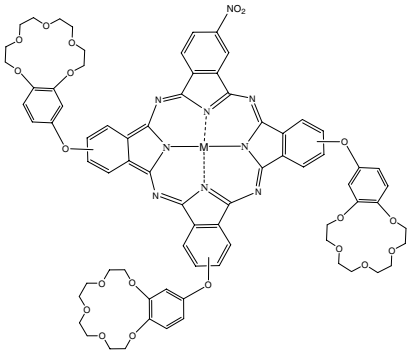


Yasin Arslanoğlu, Atıf Koca, Esin Hamuryudan

Polyhedron 26 (2007) 891

Synthesis of novel unsymmetrical phthalocyanines substituted with crown ether and nitro groups

We report on synthesis and characterization of phthalocyanines (M = Zn, Cu, Co, Ni) which carry three benzo-15-crown-5 units through oxy bridges and a nitro group.

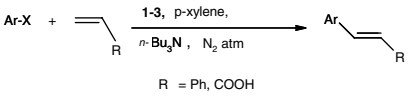


Garima Singh, Sumit Bali, Ajai K. Singh

Polyhedron 26 (2007) 897

Palladium(0) complexes of (P,P) and (P,N) ligands immobilized on silica gel as catalysts in selective Heck type carbon–carbon coupling reactions

Pd(0) complexes of Ph_2P–N–PPh_2 and (P,N) ligands anchored on silica gel (**1**–**3**) are shown to catalyze C–C coupling reactions between aryl bromides/aryl iodides, *p*-Y–C_6H_4X (where Y = NO_2, Cl; X = Br, I) and acrylic acid/styrene CH_2=CHR (R = Ph, COOH). Only the *trans* product is formed selectively. The catalysts can be reused up to 15–16 times, without significant loss of yield.

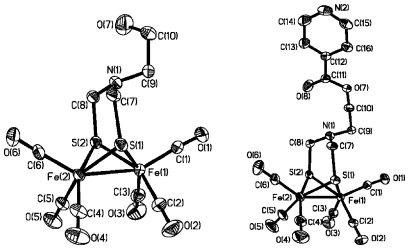


Hong-Guang Cui, Mei Wang, Wei-Bing Dong, Le-Le Duan, Ping Li, Li-Cheng Sun

Polyhedron 26 (2007) 904

Synthesis, structures and electrochemical properties of hydroxyl- and pyridyl-functionalized diiron azadithiolate complexes

Hydroxyl- and pyridyl-functionalized diiron azadithiolate complexes, [{(μ-$SCH_2)_2$N(CH_2-CH_2OH)}$Fe_2(CO)_6$] (**1**) and [{(μ-$SCH_2)_2$-N(CH_2CH_2OOCPy)}$Fe_2(CO)_6$] (**2**), were prepared and crystallographically characterized as biomimetic models of the Fe-only hydrogenase active site. A network is constructed by intermolecular H-bonds in the crystals of **1**. An S···O intermolecular contact was found in the crystals of **2**.

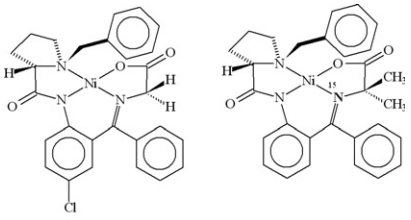


Vratislav Langer, Alexander Popkov, Milan Nádvorník, Antonín Lyčka

Polyhedron 26 (2007) 911

Two new Ni(II) Schiff base complexes: X-ray absolute structure determination, synthesis of a ^{15}N-labelled complex and full assignment of its ^{1}H NMR and ^{13}C NMR spectra

The Ni(II) complex of the Schiff base of (*S*)-*N*-(2-benzoyl-4-chlorophenyl)-1-benzylpyrrolidine-2-carboxamide and glycine (**1**) and the hemihydrate of the Ni(II) complex of the Schiff base of (*S*)-*N*-(2-benzoylphenyl)-1-benzylpyrrolidine-2-carboxamide and 2-aminoisobutiric acid (**2**) were prepared and characterized by X-ray diffraction and ^{1}H and ^{13}C NMR.



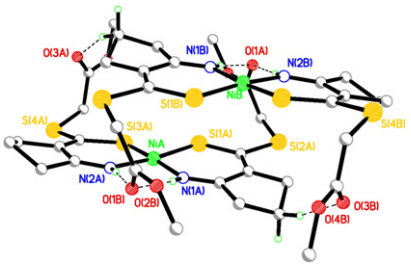
1 **2**

Jesús Morales-Juárez, Jesús Pastor-Medrano, Raymundo Cea-Olivares, Verónica García-Montalvo, R. Alfredo Toscano

Polyhedron 26 (2007) 918

Nickel(II) and cobalt(II) complexes of methyl(2-aminocyclopentene-1-dithiocarboxy)-S-acetate (ACDASAMe)

The synthesis and characterization of nickel(II) and cobalt(II) complexes of methyl(2-aminocyclopentene-1-dithiocarboxy)-S-acetate (ACDASAMe) are reported. The ligand exhibits the (S, N) coordination mode on interacting with the metal centers. The X-ray structure of Ni(II) complex exhibits a somewhat distorted NiS_2N_2 square planar geometry with the ligands showing a *cis* configuration. The dangling –CH_2COOMe arms of the ligands stay away from coordination forming dimeric association through weak intermolecular hydrogen bonding between neighboring molecules.

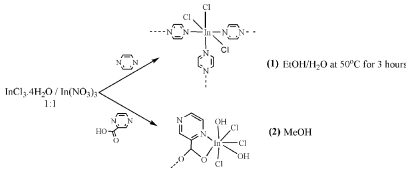


Christian R. Samanamú, Anne F. Richards

Polyhedron 26 (2007) 923

Indium(III) one-dimensional polymers with pyrazine and pyrazine, 2-carboxylic acid as the spacer molecules

The reactions of indium(III) chloride tetrahydrate with pyrazine ($C_4H_4N_2$) and pyrazine, 2-carboxylic acid afford two polymeric frameworks, the structures of which were characterized in the solid state by single crystal analysis. The former is a one-dimensional infinite structure interlinked by the pyrazine spacer, while the latter is a one-dimensional 'zigzag' polymeric structure.

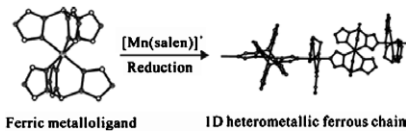


Kyoung-Tae Youm, Min Gyu Kim, Jaejung Ko, Moo-Jin Jun

Polyhedron 26 (2007) 929

1D Mn^{III}–Fe^{II} heterometallic coordination polymer built by an approach of metalloligand

1D heterometallic coordination polymer comprising of [Mn^{III}(salen)] and ferrous moiety [(Fe^{II}(**L**)$_2$)] generated by the reduction of [(Fe^{III}(**L**)$_2$)]$^+$ has been built to be a [(Fe^{II}(**L**)$_2$)(Mn^{III}(salen))(ClO_4)] (**1**) through a metalloligand approach, whether **L** stands for hydrotris(1,2,4-triazolyl)borate.

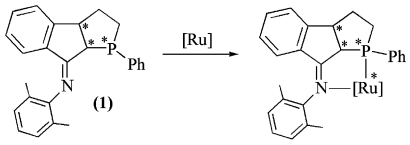


Alba E. Díaz-Álvarez, Pascale Crochet, Maria Zablocka, Victorio Cadierno, Laure Vendier, José Gimeno, Jean-Pierre Majoral

Polyhedron 26 (2007) 933

Half-sandwich ruthenium(II) complexes containing a tricyclic β-iminophosphine ligand: Catalytic activity in Diels–Alder reactions

The diastereoselective coordination of the tricyclic β-iminophosphine ligand **1** to η^6-arene and η^5-cyclopentadienyl ruthenium(II) fragments is described. Spectroscopic data, X-ray crystal structure determinations and catalytic activity in Diels–Alder reactions of the resulting complexes are presented.



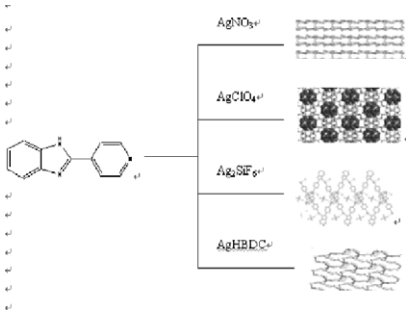
Diastereoselective coordination process

Chang-Kun Xia, Can-Zhong Lu, Xiao-Yuan Wu, Quan-Zheng Zhang, Jian-Jun Zhang, Ding-Ming Wu

Polyhedron 26 (2007) 941

Syntheses and crystal structures of four silver(I) complexes based on 2-(4-pyridyl)benzimidazole

Four silver (I) coordination polymers were prepared by the reactions of PyBIm and various silver(I) salts under different conditions. The results show that the anions play important roles in the coordination sphere of the silver(I) atoms as well as the crystal packing of the coordination polymers.



The Publisher encourages the submission of articles in electronic form thus saving time and avoiding rekeying errors. For detailed instructions on the preparation of manuscripts and of electronic artwork, consult the Author Gateway for Elsevier at http://authors.elsevier.com

ScienceDirect

Full text of this journal is available, on-line from **ScienceDirect**. Visit **www.sciencedirect.com** for more information.

Available online at www.sciencedirect.com
ScienceDirect
Polyhedron 26, issue 2, 22 January 2007
POLYHEDRON
www.elsevier.com/locate/poly

Contents

Preface 215

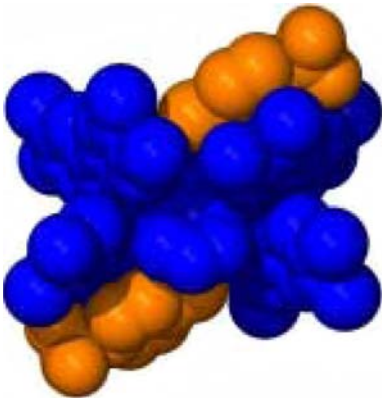
Papers

Deanna M. D'Alessandro, Fiona M. Foley, Murray S. Davies, Peter C. Junk, F. Richard Keene

Polyhedron 26 (2007) 216

Solid-state anion interactions in the diastereoisomers of dinuclear ruthenium complexes based on 2,2′-bipyrimidine

The counter-ions present in the solid-state structures of *meso*-(ΛΔ)-[{Ru(bpy)$_2$}$_2$(μ-bpm)](PF$_6$)$_4$, *meso*-(ΛΔ)-[{Ru(Me$_2$bpy)$_2$}$_2$(μ-bpm)](tos)$_4$ · 2CH$_3$OH · 4H$_2$O and *meso*-(ΛΔ)-[{Ru(Me$_4$bpy)$_2$}$_2$(μ-bpm)](tos)$_4$ · 26H$_2$O (shown) reside in the clefts above and below the plane of the bridging ligand, but show considerable variation in location compared with their known occupancy in solution.

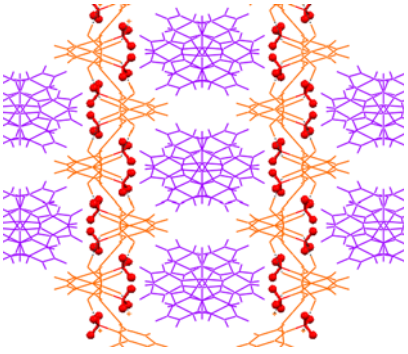


Kay Latham, Anne M. Coyle, Colin J. Rix, Alan Fowless, Jonathan M. White

Polyhedron 26 (2007) 222

Effect of ring substituents on crystal packing and H-bonding in a series of halobis(phen)-copper(II) arylphosphonic acid complexes

The effect of *ortho*-, *meta*-, and *para*-substitution of arylphosphonic acids was explored in a series of copper(II) organophosphonates. In general, the assembly strategy of 'ribbons' of [Cu^{II}(phen)$_2$Cl]$^+$ cations interleaved with H-bonded acid 'chains' was maintained. Packing was affected by substituent-position rather than type, with *para*- being the most disruptive.

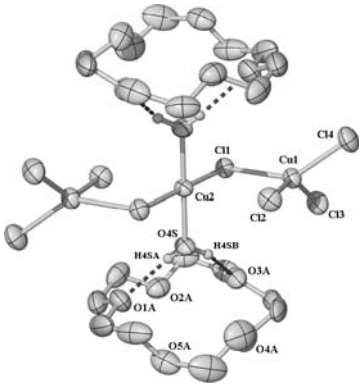


Peter C. Junk, Boujemaa Moubaraki, Keith S. Murray

Polyhedron 26 (2007) 237

Stabilisation of heterobimetallic networks by crown ethers and hydrogen-bonding in [Ni(H$_2$O)$_6$][Cu$_3$Cl$_8$(H$_2$O)$_2$] · (15-crown-5)$_2$ · 2H$_2$O: Structure and magnetism

[Ni(H$_2$O)$_6$][Cu$_3$Cl$_8$(H$_2$O)$_2$] · (15-crown-5)$_2$ · 2H$_2$O can be conveniently prepared by the interaction of NiCl$_2$ · 6H$_2$O, CuCl$_2$ · 2H$_2$O and 15-crown-5 in water and is found to display intra-trimer ferromagnetic coupling and inter-trimer antiferromagnetic interactions, the latter possibly occurring via the H-bonded [Ni(H$_2$O)$_6$]$^{2+}$ cations.

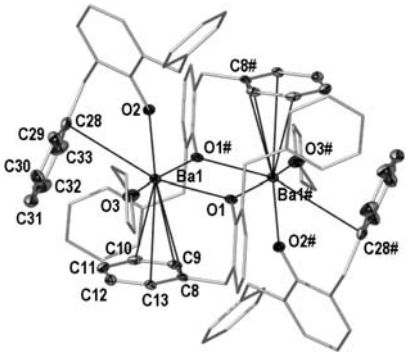


Marcus L. Cole, Glen B. Deacon, Craig M. Forsyth, Peter C. Junk, Kathryn M. Proctor, Janet L. Scott, Christopher R. Strauss

Polyhedron 26 (2007) 244

High temperature synthesis of some strontium and barium 2,6-dibenzylphenolates

The syntheses of $Sr(Odbp)_2$ and $Ba(Odbp)_2$ from the high temperature treatment of 2,6-dibenzylphenol (HOdbp) with Sr or Ba metal and the X-ray crystal structures of $[Sr_9(Odbp)_8(O_2SiMe_2)_4(OH)_2(THF)_6(OH_2)_2] \cdot 6THF$ and $[Ba(Odbp)_2(THF)]_2 \cdot 2THF$, obtained by recrystallisation of $M(Odbp)_2$ (M = Sr, Ba) from THF, are reported.

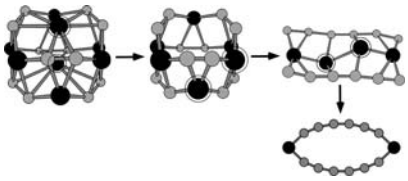


Hugh H. Harris, Ian G. Dance

Polyhedron 26 (2007) 250

Iron–carbon clusters: Geometric structures and interconversions

Possible and probable structures are reported for the experimentally observed ions $[Fe_{12}C_{12}]^+$, $[Fe_{10}C_{12}]^+$, $[Fe_8C_{12}]^+$, $[Fe_6C_{12}]^+$, $[Fe_4C_{12}]^+$, $[Fe_3C_{12}]^+$ and $[Fe_2C_{12}]^+$, together with mechanisms for the observed photodissociation of $[Fe_{12}C_{12}]^+$ to $[Fe_8C_{12}]^+$, and sequential photodissociations of $[Fe_8C_{12}]^+$ to $[Fe_2C_{12}]^+$.

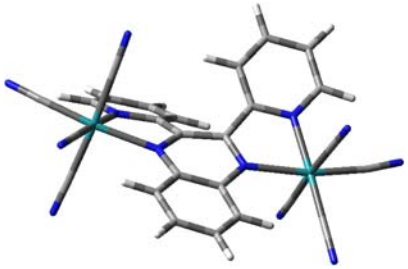


Matthew I.J. Polson, Allan G. Blackman, Keith C. Gordon

Polyhedron 26 (2007) 266

Binuclear ruthenium and osmium mixed-valence complexes containing fused and flexible polypyridyl bridging ligands

Homonuclear binuclear complexes with ligands 2,3-di-(2-pyridyl)quinoxaline and the fused dipyrido[2,3-*a*:3′,2′-*c*]phenazine and $\{Os(bpy)_2\}^{2+}$ and $\{Ru(CN)_4\}^{2-}$ have been prepared. The oxidation potentials are split consistent with the formation of mixed-valence species with comproportionation constants (K_{com}) ranging from 2.5×10^4 to 1.8×10^6. The electronic absorption spectra of the mixed-valence species reveal IVCT transitions in the near infrared region. The absorption maximum for the IVCT band ranges from 5800 to 9980 cm^{-1} and the extinction coefficients from 80 to 6300 M^{-1} cm^{-1}.

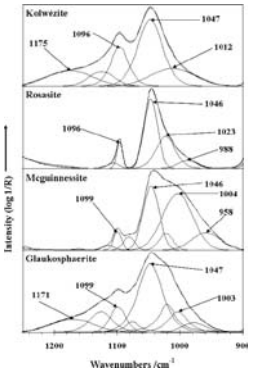


Ray L. Frost, Daria L. Wain, Wayde N. Martens, B. Jagannadha Reddy

Polyhedron 26 (2007) 275

The molecular structure of selected minerals of the rosasite group – An XRD, SEM and infrared spectroscopic study

Minerals in the rosasite mineral group rosasite, glaucosphaerite, kolwezite, mcguinnessite, have been studied by XRD, SEM and infrared spectroscopy. The spectral patterns for the minerals are similar to that of malachite implying the structure is monoclinic.

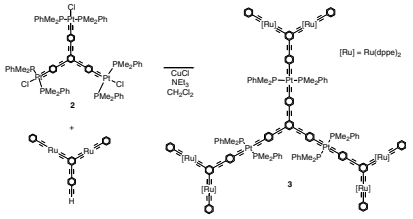


Clem E. Powell, Marie P. Cifuentes, Mark G. Humphrey, Anthony C. Willis, Joseph P. Morrall, Marek Samoc

Polyhedron 26 (2007) 284

Organometallic complexes for nonlinear optics. 37: Synthesis and third-order nonlinear optical properties of a hexaruthenium-tri-platinum dendrimer

The optical limiting merit of *trans*-[Pt(C≡CC$_6$H$_4$-4-C≡CPh)Cl(PMe$_2$Ph)$_2$] (**1**) and 1,3,5-C$_6$H$_3${C≡CC$_6$H$_4$-4-C≡C-*trans*-[PtCl(PMe$_2$Ph)$_2$]}$_3$ (**2**) has been assessed, the effective absorption cross-section for **1** being low, while that of **2** is larger. The third-order nonlinearity of 1,3,5-C$_6$H$_3$(C≡CC$_6$H$_4$-4-C≡C-*trans*-[Pt(PMe$_2$Ph)$_2$]C≡C-4-C$_6$H$_4$-3,5-C$_6$H$_3$-{C≡C-*trans*-[Ru(C≡CPh)(dppe)$_2$]}$_2$)$_3$ (**3**) is larger than that of a related Ru$_6$ dendrimer, but smaller than that of a Ru$_9$ dendrimer, suggesting that increasing metal content and electron richness is correlated to increased nonlinearity in these complexes.

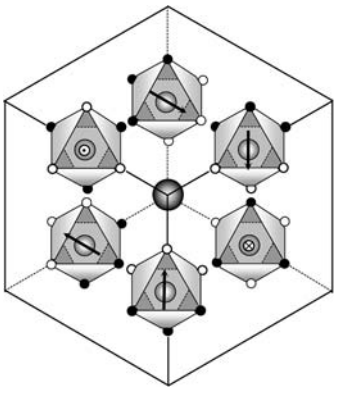


Ray L. Withers, F.J. Brink, Yun Liu, Lasse Norén

Polyhedron 26 (2007) 290

Cluster chemistry in the solid state: Structured diffuse scattering, oxide/fluoride ordering and polar behaviour in transition metal oxyfluorides

Shows one of the 8000 possible local configurations in projection along ⟨1 1 1⟩ which satisfy the local constraint that the sum of the dipole moments of the six Mo^{VI}O$_3$F$_3^{3-}$ octahedra surrounding any central *B* ion (equivalently the sum of the off-centre displacements of the Mo ions) must sum to zero. The F$^-$ ions are represented by the small dark balls while the O^{2-} ions are represented by the small open balls. The induced off-centre shifts of the metal ions are represented by the arrows.

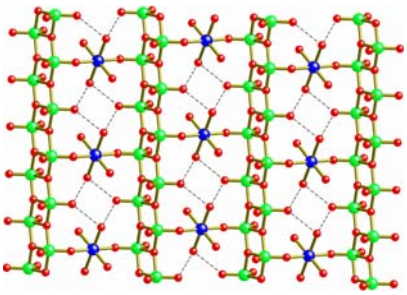


Brendan F. Abrahams, Marissa G. Haywood, Richard Robson

Polyhedron 26 (2007) 300

The structure-directing influence of guanidinium cations in the crystal structures of [C(NH$_2$)$_3$]$_2$[M^{II}(H$_2$O)$_4$(VO$_3$)$_4$] · 4H$_2$O (M = Mn, Co, Ni)

The combination of guanidinium, vanadate and the divalent transition metals Mn^{II}, Co^{II} and Ni^{II} in aqueous solution leads to the generation of crystals of formula [C(NH$_2$)$_3$]$_2$-[M^{II}(H$_2$O)$_4$(VO$_3$)$_4$] · 4H$_2$O (M = Mn, Co, Ni). The structures consist of undulating anionic [M^{II}(H$_2$O)$_4$(VO$_3$)$_4^{2-}$] sheets which stack in an ABAB fashion. Guanidinium ions bind pairs of sheets together by a combination of electrostatic attraction and hydrogen bonding to generate a 3D coordination/hydrogen-bonded network.

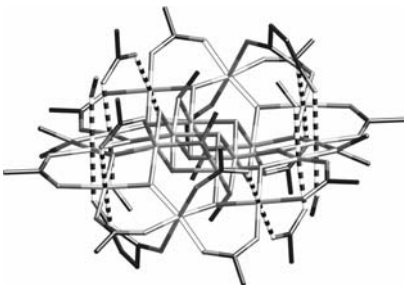


David J. Price, Stuart R. Batten, Boujemaa Moubaraki, Keith S. Murray

Polyhedron 26 (2007) 305

Synthesis, crystal structure and magnetism of a single-molecule magnet, [Mn$_{16}$O$_{16}$(OMe)$_6$-(OAc)$_{16}$(MeOH)$_3$(H$_2$O)$_3$] · 6H$_2$O, and of a mixed bridge 1D chain, [Mn(μ-OMe)-(μ-OAc)$_2$]$_n$

The Mn(III)/Mn(IV) cluster [Mn$_{16}$O$_{16}$(OMe)$_6$-(OAc)$_{16}$(MeOH)$_3$(H$_2$O)$_3$] · 6H$_2$O has an inner [Mn6IVO6(OMe)4]8+ mineral-like core structure surrounded by an outer, non-planar ring of 10 Jahn-Teller distorted Mn(III) atoms. Magnetic measurements show that it is a single-molecule magnet. A 1D Mn(III) material, [Mn(μ-OMe)(μ-OAc)$_2$]$_n$, also obtained when synthesising the Mn$_{16}$ cluster, displays antiferromagnetic coupling without long-range order.

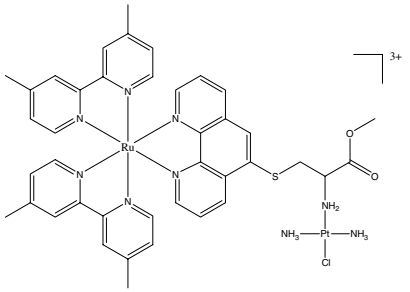


Sarah J. Yousouf, Craig R. Brodie, Nial J. Wheate, Janice R. Aldrich-Wright

Polyhedron 26 (2007) 318

Synthesis of a heterodinuclear ruthenium(II)–platinum(II) complex linked by L-cysteine methyl ester

A potential anticancer heterodinuclear ruthenium(II)–platinum(II) complex, [ruthenium(II)-(4,4′-dimethyl-2,2′-bipyridine)$_2$(5-(L-cysteine-methyl ester)-1,10-phenanthroline)-*trans*-chlorodiamineplatinum(II)] chloride, [Ru(Me$_2$-bipy)$_2$(5-(L-cysteine-Me)-phen)-*trans*-Pt(NH$_3$)$_2$-Cl]Cl$_3$, was synthesised.

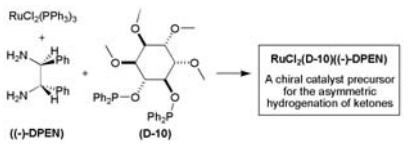


Andrew Falshaw, Graeme J. Gainsford, Cornelis Lensink, Angela T. Slade, L. James Wright

Polyhedron 26 (2007) 329

Ruthenium complexes that incorporate a *chiro*-inositol derived diphosphinite ligand as catalysts for asymmetric hydrogenation reactions

The chiral diphosphinite ligand, 1D-3,4-bis-(*O*-diphenylphosphino)-1,2,5,6-tetra-*O*-methyl-*chiro*-inositol (**D-10**), can be conveniently synthesised from 1D-*chiro*-inositol, and **L-10**, the enantiomer of **D-10**, can also be readily prepared. Ruthenium complexes of **D-10** are effective ketone hydrogenation catalysts with conversions of close to 100% and ee's up to 50% in some cases.

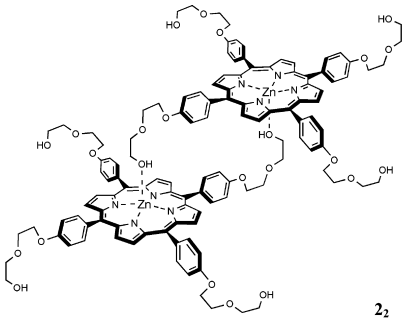


Steven J. Langford, Clint P. Woodward

Polyhedron 26 (2007) 338

Synthesis, characterisation and X-ray structure of a novel porphyrin array employing Zn–O and O–H…O bonding motifs

The crystal structure of **2** dimerises in the solid state (shown schematically) *via* an intermolecular polyether oxygen–Zn(II) interaction to form a 28-membered macrocycle. A bilayer sheeting arrangement of the dimers is achieved through cooperative hydrogen bonding of the ethoxyethanol arms to form 11-membered macrocycles containing four hydrogen bonds.

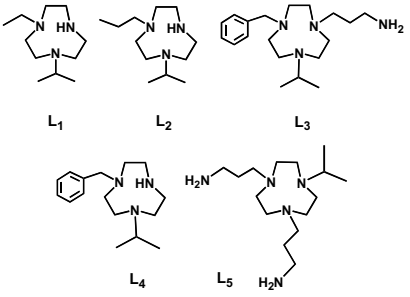


Matthew J. Belousoff, Andrew R. Battle, Bim Graham, Leone Spiccia

Polyhedron 26 (2007) 344

Syntheses, structures and hydrolytic properties of copper(II) complexes of asymmetrically *N*-functionalised 1,4,7-triazacyclononane ligands

A series of square-pyramidal copper(II) complexes of *N*-alkylated derivatives of 1,4,7-triazacyclononane (L1–L5) are reported whose ability to effectively cleave phosphate diesters decreases with the number of copper(II) coordination sites occupied by the ligand.

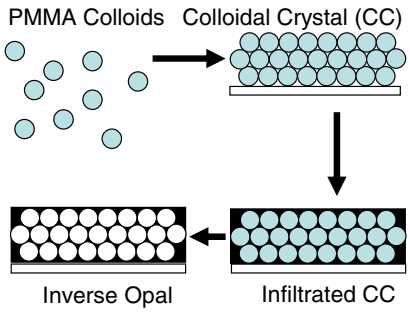


Geoffrey I.N. Waterhouse, Mark R. Waterland

Polyhedron 26 (2007) 356

Opal and inverse opal photonic crystals: Fabrication and characterization

PMMA colloidal crystals have been fabricated and used as templates for the preparation of SiO_2, TiO_2 and CeO_2 photonic crystals with inverse opal structures.

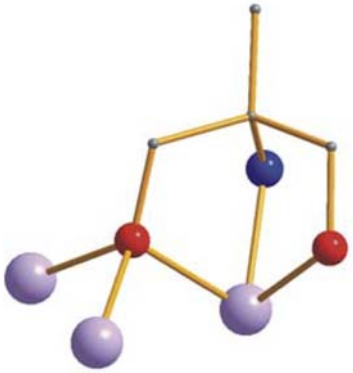


Kerwyn G. Alley, Roland Bircher, Hans U. Güdel, Boujemaa Moubaraki, Keith S. Murray, Brendan F. Abrahams, Colette Boskovic

Polyhedron 26 (2007) 369

Incorporation of a tripodal ligand with a (N,O,O)-donor set into a new family of nickel and cobalt spin clusters

Tetranuclear nickel(II) and cobalt(II) complexes of the monoanion of 2-amino-2-methyl-1,3-propanediol display related low symmetry structures based on distorted cubane units. Magnetic measurements reveal ferromagnetic exchange interactions for all complexes.

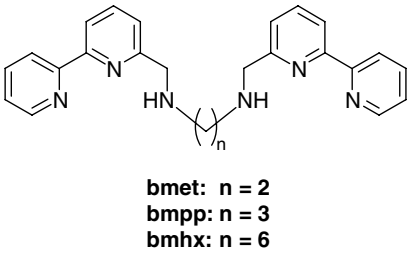


Lynton J. Baird, Cory A. Black, Allan G. Blackman

Polyhedron 26 (2007) 378

A new series of potentially hexadentate ligands derived from 2,2′-bipyridine

The syntheses and characterisation of the new, potentially hexadentate, ligands *N*,*N*′-bis(2,2′-bipyridin-6-ylmethyl)ethane-1,2-diamine (bmet), *N*,*N*′-bis(2,2′-bipyridin-6-ylmethyl)-propane-1,3-diamine (bmpp) and *N*,*N*′-bis-(2,2′-bipyridin-6-ylmethyl)hexane-1,6-diamine (bmhx) are reported and the synthesis and crystal structure of the mononuclear complex $[Co(bmet)](ClO_4)_3 \cdot H_2O$ are detailed. The first transition metal complex of 6-(aminomethyl)-2,2′-bipyridine (amb) is also described.

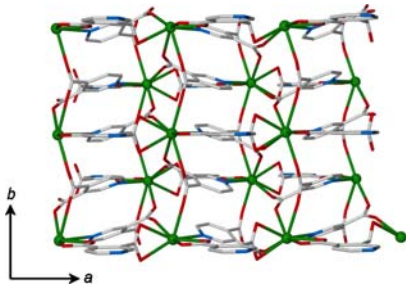


Desmond Ang, Glen B. Deacon, Peter C. Junk, David R. Turner

Polyhedron 26 (2007) 385

Synthesis and structure of the two-dimensional coordination networks $[Ln(PDC)(N\text{-}HPDC)]_\infty$ (PDC = pyridine-3,4-dicarboxylate, Ln = La, Ce, Pr)

Nine coordination of the lanthanoid invloves μ_4-η^1:η^1:η^2:η^1(*N*) coordination of a PDC^{2-} ligand and μ-η^2:η^2 coordination of the N-protonated ligand $N\text{-}HDPC^-$.

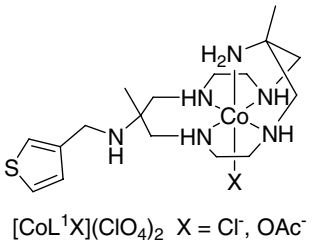


Paul V. Bernhardt, Nathan L. Kilah

Polyhedron 26 (2007) 392

Macrocyclic cobalt(III) complexes as precursors for metal-polythiophene hybrid materials

A thiophene-functionalised macrocyclic ligand (L^1) has been prepared and complexed with Co^{III}. Electro-copolymerisation of $[CoL^1Cl]Cl_2$ with 3,4-ethylenedioxythiophene (EDOT) in a 1:2 ratio on a preformed poly-3,4-ethylenedioxythiophene (PEDOT) film resulted in electroactive metal-polymer hybrid films of high quality, consistency and uniformity in appearance.



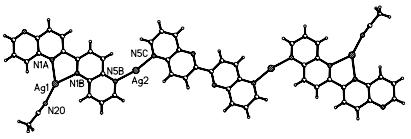
$[CoL^1X](ClO_4)_2$ X = Cl^-, OAc^-

Christopher M. Fitchett, Peter J. Steel

Polyhedron 26 (2007) 400

Synthesis and X-ray structures of two discrete metal complexes of 2,2′-bi-1,5-naphthyridine, a new ambivergent ligand

A new synthesis of 2,2′-bi-1,5-naphthyridine (**1**) is described along with its reactions with copper(II) nitrate, silver(I) tetrafluoroborate and palladium(II) chloride. X-ray crystal structures are described of a mononuclear copper complex, in which **1** acts as a convergent ligand chelating through the two internal nitrogens, and an unusual M_4L_3 silver complex containing both two- and three-coordinate silvers and with ligand **1** acting in two different bridging modes.

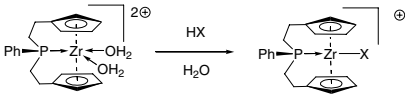


James R. Butchard, Owen J. Curnow

Polyhedron 26 (2007) 406

Aqueous chemistry of the five-coordinate zirconocene dichloride $PhP(CH_2CH_2–\eta^5C_5H_4)_2ZrCl_2$: X-ray structure of the sulfato complex $PhP(CH_2CH_2–\eta^5\text{-}C_5H_4)_2Zr(\eta^2\text{-}SO_4)$

The novel five-coordinate zirconocene(IV) dichloride complex $PhP(CH_2CH_2–\eta^5\text{-}C_5H_4)_2ZrCl_2$ contains an unusual tridentate cyclopentadienyl-phosphine ligand which stabilises the complex in aqueous solutions. Its aqueous solution chemistry has been investigated using largely ^{31}P NMR spectroscopy and ES-MS.



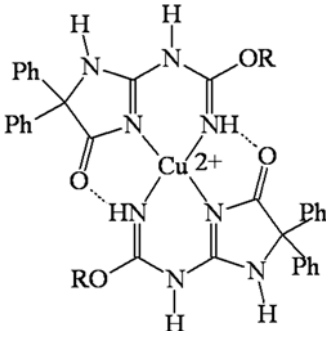
X = F, NO_3, HSO_4, HCO_3

Michael M. Bishop, Leonard F. Lindoy, Mary McPartlin, Andrew Parkin, Oliver T. Thorn-Seshold, Peter Turner

Polyhedron 26 (2007) 415

A systematic study of ligand intermolecular interactions in crystals of copper(II) complexes of bidentate guanidino derivatives

The X-ray structures of several neutral copper(II) complexes and one cationic complex incorporating bidentate alkyl *N*-(4-oxo-5,5-diphenyl-4,5-dihydro-1*H*-imidazol-2-yl)imidocarbamate ligands show extended supramolecular structures based on doublet (DA or DD) hydrogen bonding and/or phenyl embraces.

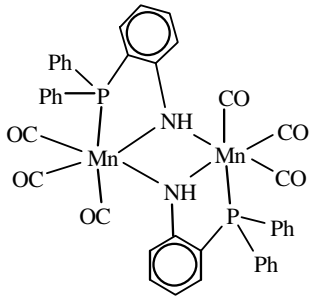


Victor D. Fester, Paul J. Houghton, Lyndsay Main, Brian K Nicholson

Polyhedron 26 (2007) 430

A manganese carbonyl complex derived from the P,N-bonding ligand (2-aminophenyl)diphenylphosphine

The first manganese carbonyl complex derived from (2-aminophenyl)diphenylphosphine is formed on reaction of the ligand with $[H_3Mn_3(CO)_{12}]$. It contains two bridging amido ligands.

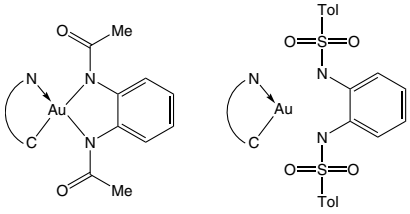


Kelly J. Kilpin, William Henderson, Brian K. Nicholson

Polyhedron 26 (2007) 434

Organogold(III) complexes containing chelating bis(amidate) ligands: Synthesis, characterisation and biological activity

A series of new auracyclic complexes containing the Au–NR–CH_2CH_2–NR (R = SO_2Tol) and Au–NR–C_6H_4–NR (R = COMe or SO_2Tol) five-membered ring systems are formed from reactions of cycloaurated gold(III) dichloride complexes with 1,2-$C_6H_4(NHCOMe)_2$, $C_2H_4(NHSO_2Tol)_2$ (Tol = *p*-tolyl) or 1,2-$C_6H_4(NHSO_2Tol)_2$ and base.

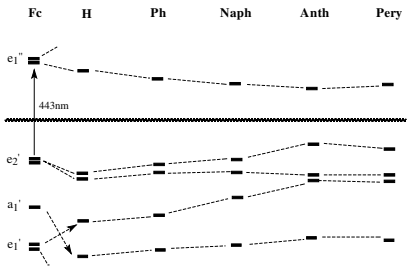


A.H. Flood, C.J. McAdam, K.C. Gordon, H.G. Kjaergaard, A.M. Manning, B.H. Robinson, J. Simpson

Polyhedron 26 (2007) 448

Electronic structure and near-IR transitions of FcC_2R and FcC_4R dyads

DFT calculations show that the frontier orbital configuration of 17e and 18e FcC_2R and FcC_4R dyads, is $(e'_2\text{-a},\pi)^2(e'_2\text{-b, metal})^2(e'_1\text{-a},\pi)^2$, $(a_1, \text{metal})^2$. A strongly solvatochromic transition in the near-IR for 17e dyads is best described as an LMCT transition.

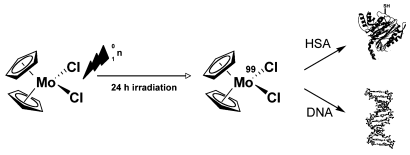


Kate S. Campbell, Carolyn T. Dillon, Suzanne V. Smith, Margaret M. Harding

Polyhedron 26 (2007) 456

Radiotracer studies of the antitumor metallocene molybdocene dichloride with biomolecules

Binding experiments with the radiotracer $Cp_2{}^{99}MoCl_2$ and the thiol containing protein human serum albumin (HSA) or calf thymus DNA, monitored for ^{99}Mo using a gamma counter, are consistent with strong preferential interaction of Cp_2MoCl_2 with thiols versus other donor sites in biomolecules including DNA.

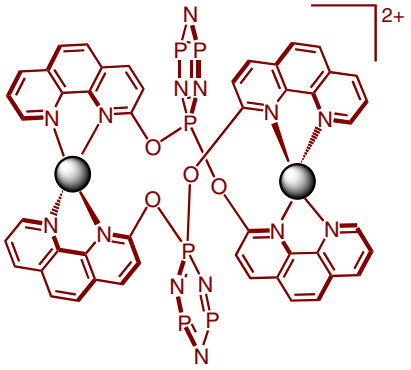


Eric W. Ainscough, Andrew M. Brodie, Geoffrey B. Jameson, Carl A. Otter

Polyhedron 26 (2007) 460

Copper complexes with 1,10-phenanthrolines tethered to a cyclotriphosphazene platform

The reaction of copper salts with 2-oxy-1,10-phenanthroline moieties tethered to a cyclotriphosphazene ring affords dimetallic copper(I) complexes with the ligand coordinating to two metal centres in a helical fashion whereas the copper(II) complexes are five-coordinate monomeric species.

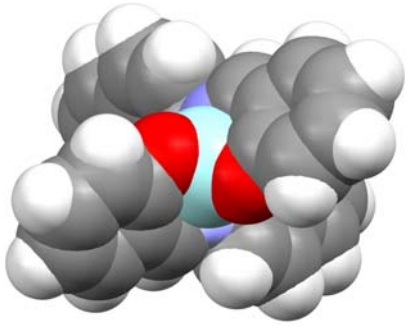


Paul G. Plieger, Kevin D. John, Anthony K. Burrell

Polyhedron 26 (2007) 472

Encapsulating beryllium – Synthesis, characterisation and modelling of a chiral binaphthyldiimine-Be(II) complex

Beryllium has been successfully incorporated into a naphthalene containing Schiff base ligand. Evidence from both experimental and calculated ^{9}Be NMR data and model compounds indicate that the ligand completely encapsulates the beryllium cation via tetradentate tetrahedral coordination using both phenol and imine donors.

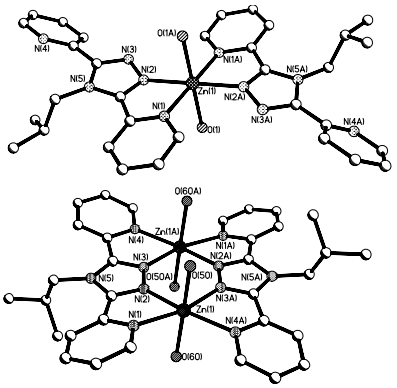


Marco H. Klingele, Andy Noble, Peter D.W. Boyd, Sally Brooker

Polyhedron 26 (2007) 479

Synthesis and X-ray crystal structures of some mononuclear and dinuclear complexes of 4-isobutyl-3,5-di(2-pyridyl)-4*H*-1,2,4-triazole

Control of the metal-to-ligand molar ratio is insufficient to completely dictate the outcome of complexation reactions of bis-bidentate ligands such as 4-isobutyl-3,5-di(2-pyridyl)-4*H*-1,2,4-triazole (ibdpt). Here we show that despite employing a 1:2 molar ratio in some cases both mononuclear $[M^{II}(ibdpt)_2(X)_2]^{y+}$ and dinuclear $[M^{II}_2(ibdpt)_2(X)_4]^{y+}$ complexes are obtained.

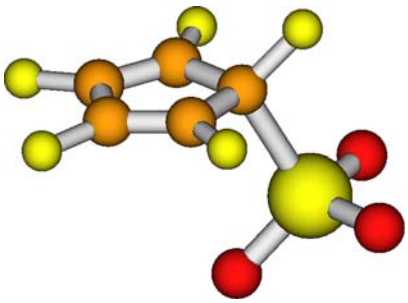


Matthias Lein, Anton Hammerl, Holger L. Hermann, Peter Schwerdtfeger

Polyhedron 26 (2007) 486

Theoretical investigations into trioxo group 7 compounds LRO_3 with perfluorated ligands

Density functional calculations show new and unusual coordination of trioxo group 7 compounds. An experimentally unknown spiecies is suggested as a viable target for synthesis.

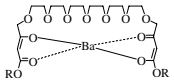


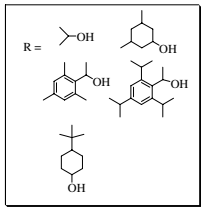
Matthew R. Hill, Jennifer J. Russell, Nicholas K. Roberts, Robert N. Lamb

Polyhedron 26 (2007) 493

Novel monomeric barium complexes as volatile precursors for chemical vapour deposition

A new range of barium complexes with single dianionic encapsulating ligands have been prepared for use in chemical vapour deposition (CVD). Preliminary testing has exhibited promising results with these prospective precursors.



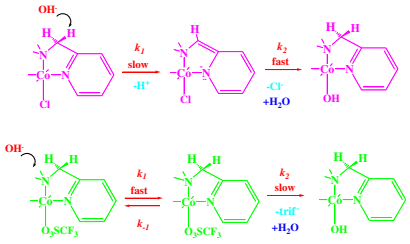


W. Gregory Jackson, Alistair Dickie, Kerrina Wells

Polyhedron 26 (2007) 508

Base catalysed substitution reactions of octahedral cobalt(III) complexes: Mechanism switching by changing the leaving group

The $[Co(pentaamine)X]^{n+}$ complexes studied bear at least one N-coordinated $–CH_2$-pyridine group. The mechanism for base catalysed hydrolysis can be switched from the classic S_N1CB to the pseudo-aminate mechanism, which involves rate limiting deprotonation, by simply changing the leaving group.



Derek W. Smith

Polyhedron 26 (2007) 519

A new approach to the relationship between bond energy and electronegativity

A modified version of Pauling's bond energy equation can be derived from intuitive expressions for homopolar and heteropolar bond energies $D_{A–A}$ and $D_{A–B}$ in terms of the quantities x and y, which are related to electronegativity and hardness/softness.

$$D_{A\text{-}A} = y_A^2 - x_A^2$$

$$D_{B\text{-}B} = y_B^2 - x_B^2$$

$$D_{A\text{-}B} = y_A y_B - x_A x_B$$

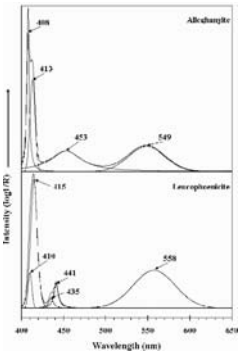
$$D_{A\text{-}B} - \tfrac{1}{2}(D_{A\text{-}A} - D_{B\text{-}B}) = \tfrac{1}{2}[(x_A - x_B)^2 - (y_A - y_B)^2]$$

Sara Palmer, B. Jagannadha Reddy, Ray L. Frost

Polyhedron 26 (2007) 524

Application of UV–Vis, near-infrared and mid-infrared spectroscopy to the study of Mn-bearing humites

The combination of electronic and vibrational spectra has been applied to correlate the spectral properties, with composition, structure and cation substitutions such as Mn, Fe, Ca and Zn for Mg in humites: norbergite, alleghanyite, leucophoenicite and sonolite with increasing number of silicate layers, 1, 2, 3 and 4.



The Publisher encourages the submission of articles in electronic form thus saving time and avoiding rekeying errors. For detailed instructions on the preparation of manuscripts and of electronic artwork, consult the Author Gateway for Elsevier at http://authors.elsevier.com

ScienceDirect

Full text of this journal is available, on-line from **ScienceDirect**. Visit **www.sciencedirect.com** for more information.

Available online at www.sciencedirect.com
ScienceDirect
Polyhedron 26, issue 18, 20 November 2007
POLYHEDRON
www.elsevier.com/locate/poly

Contents

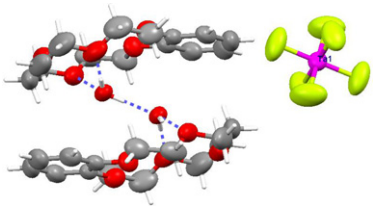
Papers

Marina S. Fonari, Yurii A. Simonov, Wen-Jwu Wang, Shang-Wei Tang, Eduard V. Ganin, Vladimir O. Gelmboldt, Tatiana S. Chernaya, Olga A. Alekseeva and Nina G. Furmanova

Polyhedron 26 (2007) 5193

Structure of oxonium hexafluoroniobate and hexafluorotantalate complexes with crown ethers of different dimensionality

Five novel complexes, $[18C6 \cdot H_3O][NbF_6]$, $[18C6 \cdot H_3O][TaF_6]$, $[15C5 \cdot H_5O_2][TaF_6]$, $[(B15C5)_2 \cdot H_5O_2][(B15C5)_2 \cdot H_3O][TaF_6]_2$ and $[(B12C4)_2 \cdot H_3O][TaF_6]$ were synthesized and identified by elemental and X-ray structural analysis.

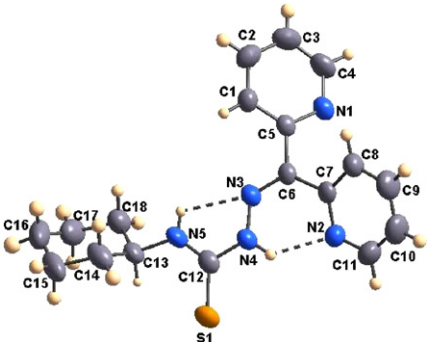


V. Suni, M.R. Prathapachandra Kurup and Munirathinam Nethaji

Polyhedron 26 (2007) 5203

Studies on Co(II) and Co(III) complexes of di-2-pyridyl ketone *N*(4)-cyclohexyl and *N*(4)-phenyl thiosemicarbazones

Six new Co(II) and Co(III) complexes (**1**–**6**) of di-2-pyridyl ketone *N*(4)-cyclohexyl thiosemicarbazone (HL^1) and di-2-pyridyl ketone *N*(4)-phenyl thiosemicarbazone (HL^2) have been synthesized and spectrochemically characterized. HL^1 is newly synthesized and has been structurally characterized by single crystal X-ray diffraction studies, while HL^2 has been previously reported. HL^1 crystallizes into a monoclinic lattice with the space group $P2_1$. The complexes are characterized by magnetic, EPR, NMR and other spectroscopic studies. The EPR spectra of the paramagnetic complexes reveal axial features with eight hyperfine lines clearly resolved in the perpendicular region.

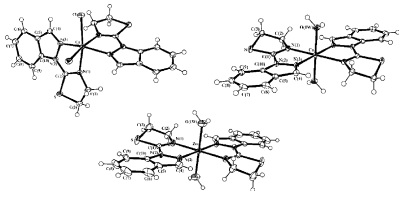


M.A. Maldonado-Rogado, E. Viñuelas-Zahínos, F. Luna-Giles and F.J. Barros-García

Polyhedron 26 (2007) 5210

Synthesis and structural characterization of cobalt(II) and zinc(II) complexes with 2-(indazol-1-yl)-2-thiazoline (TnInA). X-ray characterization of $[CoCl_2(TnInA)_2] \cdot C_2H_6O$ and $[(M)(TnInA)_2(H_2O)_2](NO_3)_2$ (M = Co, Zn)

Synthesis and characterization by physical measurements of cobalt(II) and zinc(II) complexes with a thiazoline/indazole derivative ligand. The X-ray crystal structures of $[CoCl_2(TnInA)_2] \cdot C_2H_6O$, $[Co(TnInA)_2(H_2O)_2](NO_3)_2$ and $[Zn(TnInA)_2(H_2O)_2](NO_3)_2$ have also been determined. These complexes present a distorted octahedral geometry around the metal(II) ion.

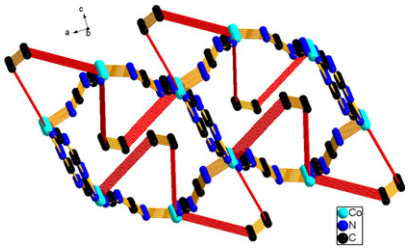


Bao-Long Li, Xin-Yi Wang, Xia Zhu, Song Gao and Yong Zhang

Polyhedron 26 (2007) 5219

Synthesis, crystal structure and magnetic behavior of two cobalt coordination polymers with 1,2-bis(1,2,4-triazol-1-yl)ethane and dicyanamide

Synthesis, crystal structure and magnetic behavior of two cobalt coordination polymers with 1,2-bis(1,2,4-triazol-1-yl)ethane and dicyanamide $[Co(bte)_2(dca)_2]_n$ (**1**) and $\{[Co(bte)(dca)_2] \cdot H_2O\}_n$ (**2**) have been synthesized and characterized by X-ray diffraction analyses and magnetic measurements. Compound **1** is a double-chain. In **2**, each Co(II) center is bonded by two bridging bte ligands and four dca ligands as μ-1,5-dca in different orientations in the 3D network.

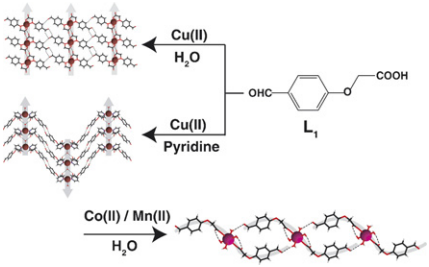


Avijit Pramanik, Srinivas Abbina and Gopal Das

Polyhedron 26 (2007) 5225

Molecular, supramolecular structure and catalytic activity of transition metal complexes of phenoxy acetic acid derivatives

Single crystal X-ray diffraction studies revealed that control on the environment of first coordination sphere of six mononuclear complexes of phenoxyacetic acid derivatives has a significant effect on the ultimate MOF structure, thermal and catalytic behaviour.

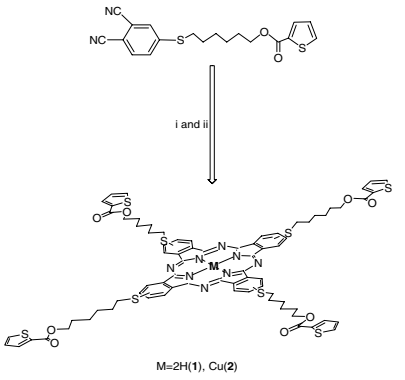


Meryem N. Yarasir, Mehmet Kandaz, B. Filiz Senkal, Atıf Koca and Bekir Salih

Polyhedron 26 (2007) 5235

Metal-ion sensing and aggregation studies on reactive phthalocyanines bearing soft-metal receptor moieties; synthesis, spectroscopy and electrochemistry

Tetrasubstituted metal-free $\{2H[Pc(S(CH_2)_6OCOC_4H_3S)_4]\}$ and copperphthalocyanine $\{Cu[Pc(S(CH_2)_6OCOC_4H_3S)_4]\}$, bearing thiophene-2-carboxylate-hexylthio moieties, have been prepared as isomeric mixtures via cyclotetramerization. Both new compounds have been characterized by elemental analysis, FTIR, ^1H and ^{13}C NMR, MS (Maldi-TOF) and UV–Vis spectral data. The cation binding abilities of the functional phthalocyanines with Ag^I, Pd^{II}, Hg^{II}, Pb^{II} and Cd^{II} are evaluated by a monomer–oligomer formation technique with UV–Vis spectroscopy.

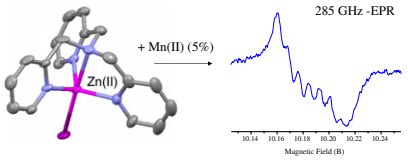


Carole Duboc, Thida Phoeung, Damien Jouvenot, Allan G. Blackman, Lisa F. McClintock, Jacques Pécaut, Alain Deronzier and Marie-Noëlle Collomb

Polyhedron 26 (2007) 5243

High-field EPR investigation of a series of mononuclear Mn(II) complexes doped into Zn(II) hosts

The mononuclear Zn(II) complexes $[Zn(tpa)X]^+$ (X = I, Br, Cl) and $[Zn(tpa)(NCS)_2]$ have been synthesized and characterized by X-ray crystallography. The electronic properties of the $[Mn(tpa)X_2]$ (X = I, Br, Cl) complexes doped into the corresponding Zn(II) complexes have been investigated by multifrequency high field EPR (HF-EPR) spectroscopy.

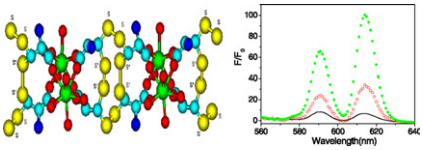


Hai-yuan Zhang, Hai-jia Yu, Hai-xia Xu, Jin-song Ren and Xiao-gang Qu

Polyhedron 26 (2007) 5250

Structural diversity of lanthanide–amino acid complexes under near physiological pH conditions and their recognition of single-stranded DNA

Four lanthanide–amino acid complexes were synthesized under near physiological pH conditions and their interactions with five single-stranded DNA were studied.

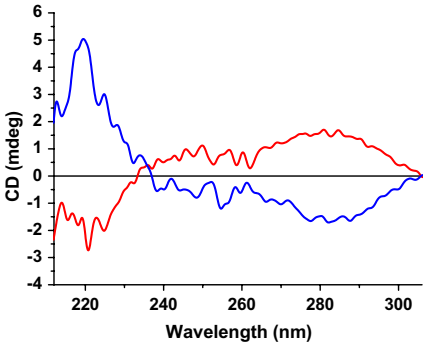


Xi-Li Li, Youxuan Zheng, Jing-Lin Zuo, You Song and Xiao-Zeng You

Polyhedron 26 (2007) 5257

Synthesis, crystal structures and triboluminescence of a pair of Eu(III)-based enantiomers

Using the chiral ligands L_{SS} (+)-4,5-pinene bipyridine and L_{RR} (−)-4,5-pinene bipyridine, two novel lanthanide enantiomers $[Eu(DBM)_3L]$ (L_{SS} in **1**, L_{RR} in **2**, DBM = dibenzoylmethanate) have been successfully synthesized and characterized by X-ray single crystal determination and spectroscopic methods. They crystallize in the chiral space group $P2_1$ of the monoclinic system. Both of them exhibit brilliant triboluminescence in daylight.

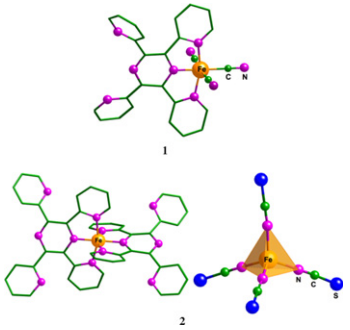


Luminita Marilena Toma, Donatella Armentano, Giovanni De Munno, Jorunn Sletten, Francesc Lloret and Miguel Julve

Polyhedron 26 (2007) 5263

2,3,5,6-Tetrakis(2-pyridyl)pyrazine (tppz)-containing iron(II) complexes: Syntheses and crystal structures

The preparation and crystal structure of two iron(II) complexes of formula PPh_4-*mer*-$[Fe(tppz)(CN)_3] \cdot 7H_2O$ (**1**) and $[Fe(tppz)_2]$-$[Fe(NCS)_4]$ (**2**) [tppz = 2,3,5,6-tetrakis(2-pyridyl)pyrazine; PPh_4^+ = tetraphenylphosphonium cation] are reported here. The structure of **1** consists of mononuclear *mer*-tricyano[2,3,5,6-tetrakis(2-pyridyl)pyrazine]ferrate(II) anions, tetraphenylphosphonium cations and crystallization water molecules. Compound **2** is an ionic salt which is made up of low-$[Fe(1)(tppz)_2]^{2+}$ six-coordinated and high-spin $[Fe(2)(NCS)_4]^{2-}$ four-coordinated iron(II) units. It is the first structurally characterized example containing the tetrahedral iron(II) unit $[Fe(NCS)_4]^{2-}$.

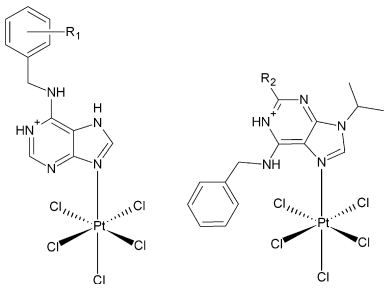


Zdeněk Trávníček, Igor Popa, Michal Čajan, Radovan Herchel and Jaromír Marek

Polyhedron 26 (2007) 5271

The first platinum(IV) complexes involving aromatic cytokinins or cyclin-dependent kinase inhibitors derived from 6-benzylaminopurine: X-ray structures of $(BohH_2^{2+})[PtCl_6] \cdot H_2O$ and $(RosH_2^{2+})_2[PtCl_6]Cl_2 \cdot 4H_2O$

A series of the first Pt(IV) complexes, involving a protonated form of cytokinin or CDK-inhibitor (Bohemine or Roscovitine) derived from 6-benzylaminopurine, of the type $[Pt^{IV}(LH^+)Cl_5]$ (**1**–**14**) {where LH^+ stands for the protonated form of the organic molecule} have been prepared and fully characterized by different physical methods.Geometries of representative complexes have been optimized by DFT calculations.The molecular structures of $(BohH_2^{2+})[PtCl_6] \cdot H_2O$ (**15**) and $(RosH_2^{2+})_2$-$[PtCl_6]Cl_2 \cdot 4H_2O$ (**16**) have been determined by a single X-ray analysis.The complexes have been also screened *in vitro* for their cytotoxicity against selected human cancer cell lines.

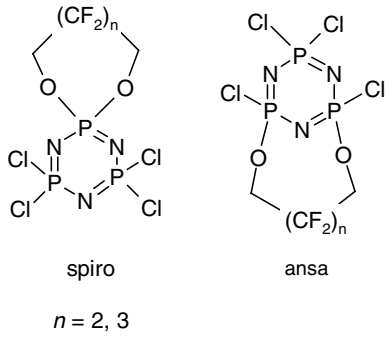


Serap Beşli, Simon J. Coles, Derya Davarcı, David B. Davies, Michael B. Hursthouse and Adem Kılıç

Polyhedron 26 (2007) 5283

Formation of spiro and ansa derivatives in the reaction of 2,2,3,3,4,4-hexafluoropentane-1,5-diol with cyclotriphosphazene: Comparison with 2,2,3,3-tetrafluorobutane-1,4-diol

The relative proportions of spiro and ansa compounds depend on the fine balance in stabilities of the different medium-sized rings formed in the reaction of cyclophosphazene with the fluorinated pentanediol (n = 3) compared to the fluorinated butanediol (n = 2).

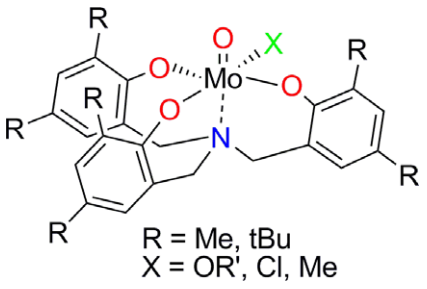


Ari Lehtonen and Reijo Sillanpää

Polyhedron 26 (2007) 5293

Alkoxo, chlorido, and methyl derivatives of oxidomolybdenum(VI) complexes with tetradentate [O_3N]-type ligands

Dioxomolybdenum(VI) complex [$MoO_2(Heg)_2$] (Heg = ethanediolato monoanion) reacts with phenolic ligand precursors tris(2-hydroxy-3,5-dialkylbenzyl)amine H_3L^R (R = Me, *tert*-Bu) to form complexes [$MoO(L^R)(Heg)$]. These compounds react further with alcohols or Me_3SiCl to form corresponding alkoxides [$MoO(L^R)(OR')$] or chlorides [$MoO(L^R)Cl$], respectively. The reaction of [$MoO(L^R)Cl$] with MeMgI yields air-stable monomethyl derivatives [$MoO(L^R)(Me)$].

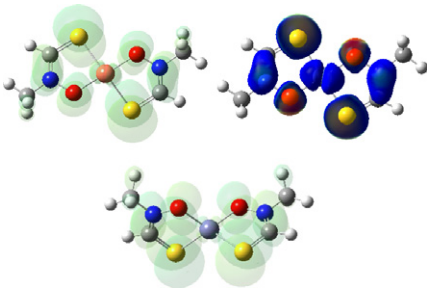


Rita Kakkar, Amita Dua and Pragya Gahlot

Polyhedron 26 (2007) 5301

Metal ion complexes of thioformin: A density functional study

Density functional calculations on a number of bis complexes of thioformin, an important siderophore belonging to the thiohydroxamic acid family, have been performed.

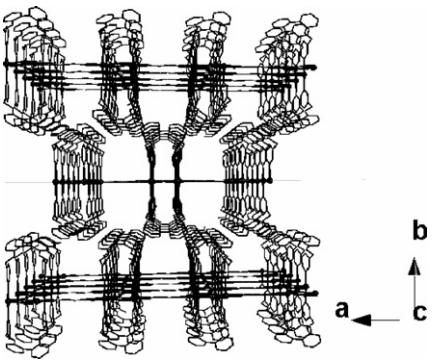


Yaqiong Gong, Ruihu Wang, Daqiang Yuan, Weiping Su, Yougui Huang, Chengyang Yue, Feilong Jiang and Maochun Hong

Polyhedron 26 (2007) 5309

Chains, ladders and sheets of d^{10} metal–organic polymers generated from the flexible bipyridyl ligands

Four novel coordination polymers, [Zn(μ-4,4′-bpp)Br_2]$_n$ (**1**), [Zn(μ-4,4′-bpp)(1,2-bdc)]$_n$ · $n$$H_2O$ (**2**), [Zn(μ-3,3′-bpp)(1,3-bdc)]$_n$ · $n$$CH_3OH$ · 2$n$$H_2O$ (**3**) and [Cd(μ-3,3′-bpp)-($C_4H_2O_4$)]$_n$ · 3$n$$H_2O$ (**4**), with interesting structural motifs have been synthesized from flexible bipyridyl, carboxylate ligands and d^{10} metal ions by the three-layer diffusion method. These d^{10} metal complexes exhibit high thermal stabilities and strong luminescence efficiencies.

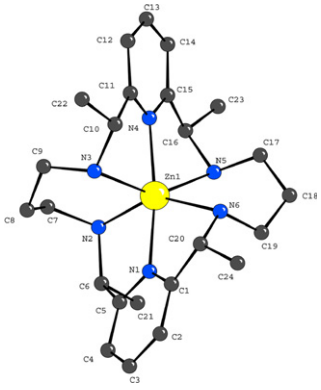


M[a] del Carmen Fernández-Fernández, Rufina Bastida, Alejandro Macías, Paulo Pérez-Lourido and Laura Valencia

Polyhedron 26 (2007) 5317

Zn(II) complexes with pyridine derived N_6 and N_8 donor azamacrocyclic ligands

A series of Zn(II) nitrate and perchlorate complexes with different pyridine derived N_6 and N_8 donor azamacrocyclic ligands were obtained. The macrocyclic ligands and zinc complexes were characterized by elemental analysis, IR, LSI-MS, conductivity measurements and ^{1}H NMR spectroscopy. Also, the crystal structure of the complexes $[ZnL](ClO_4)_2 \cdot H_2O$, $[ZnL^1](NO_3)_2$ and $[Zn_2L^2(NO_3)_2](NO_3)_2 \cdot H_2O$ were determined.

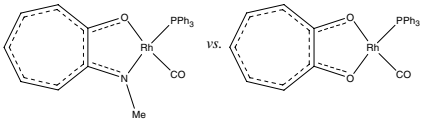


G. Steyl

Polyhedron 26 (2007) 5324

Synthesis, structure and theoretical study of two rhodium(I) complexes $[Rh(TropNMe)(CO)(PPh_3)]$ and $[Rh(Trop)(CO)(PPh_3)] \cdot$ Acetone

Rhodium(I) complexes $[Rh(TropNMe)(CO)(PPh_3)]$ (**1**) and $[Rh(Trop)(CO)(PPh_3)] \cdot$ Acetone (**2**) have been synthesized and characterized by single-crystal X-ray diffraction analysis. Substitution of an oxygen atom with a methyl functionalized nitrogen atom does not significantly alter the bond distances and angles in the rhodium(I) complex. A theoretical study is presented to clarify the solid state behaviour of these complexes.

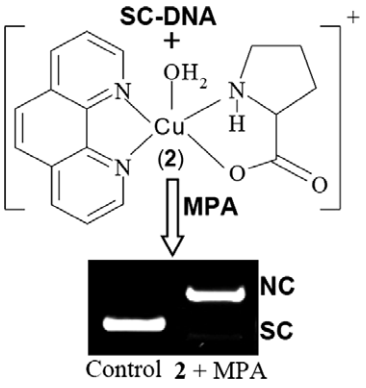


Ramakrishna Rao, Ashis K. Patra and P.R. Chetana

Polyhedron 26 (2007) 5331

DNA binding and oxidative cleavage activity of ternary (L-proline)copper(II) complexes of heterocyclic bases

The synthesis, characterization, DNA binding and "chemical nuclease" activity of a ternary copper(II) complex, $[Cu(L\text{-pro})(phen)(H_2O)](NO_3)$ containing L-proline and planar phenanthroline base are described. The complex shows efficient DNA binding and cleavage activity by hydroxyl radical pathway.

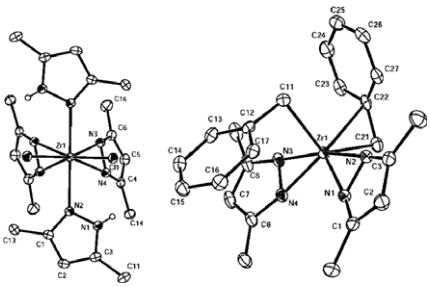


Martial Sanz, Marta E.G. Mosquera, Tomás Cuenca, Carmen Ramírez de Arellano, Mark Schormann and Manfred Bochmann

Polyhedron 26 (2007) 5339

Bis(3,5-dimethylpyrazol-1-ato) zirconium complexes as precursors for ethylene polymerisation upon activation with MAO: Syntheses, characterisation and X-ray molecular structure of $[Zr(\eta^2\text{-}3,5\text{-}Me_2Pz)_2Cl_2(\eta^1\text{-}3,5\text{-}Me_2PzH)_2] \cdot (3,5\text{-}Me_2PzH)$ and $[Zr(\eta^2\text{-}3,5\text{-}Me_2Pz)_2(CH_2Ph)_2]$ (3,5-Me_2Pz = 3,5-dimethylpyrazol-1-ato)

Bis(3,5-dimethylpyrazol-1-ato) zirconium(IV) derivatives were synthesised by various routes such as amine-, salt-, and alkane elimination. All compounds were identified by structural methods. The performance of the dichloro and dibenzyl zirconium(IV) precursors in ethylene and propylene polymerisations upon activation with MAO was evaluated.

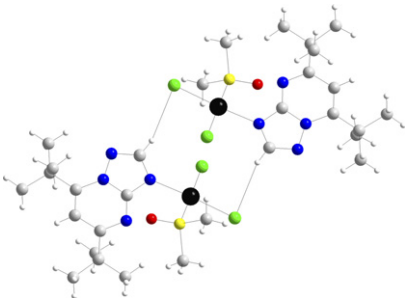


Iwona Łakomska, Magdalena Barwiołek, Andrzej Wojtczak and Edward Szłyk

Polyhedron 26 (2007) 5349

X-ray structure and multinuclear NMR studies of platinum(II) and palladium(II) complexes with 5,7-ditertbutyl-1,2,4-triazolo-[1,5-*a*]pyrimidine

Here, we described binding of 5,7-ditertbutyl-1,2,4-triazolo[1,5-*a*]pyrimidine (dbtp) to platinum(II) and palladium(II) ions. Their structures are characterized by IR, ^{1}H, ^{13}C NMR, ^{13}C CPMAS spectra and determined by X-ray. *cis*-$PdCl_2$(dbtp)(dmso) is interesting for its structural features, because it is the first report of mixed dichloride Pd(II) complexes with N-donor (triazolopyrimidine) and S-donor (dimethylsulfoxide) ligands

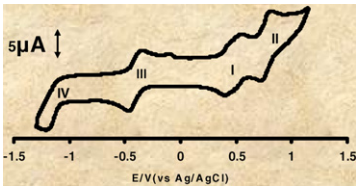


Gcineka Mbambisa, Prudence Tau, Edith Antunes and Tebello Nyokong

Polyhedron 26 (2007) 5355

Synthesis and electrochemical properties of purple manganese(III) and red titanium(IV) phthalocyanine complexes octa-substituted at non-peripheral positions with pentylthio groups

The cyclic voltammetry and spectroelectrochemistry of octapentylthio manganese(III) and titanium(IV) phthalocyanines show the following redox processes; $Mn^{III}Pc^{-2}/Mn^{II}Pc^{-2}$, $Mn^{II}Pc^{-2}/Mn^{I}\ {}^{I}Pc^{-3}$, $Mn^{IV}Pc^{-2}/Mn^{I}\ {}^{II}Pc^{-2}$ and $Mn^{IV}Pc^{-1}/Mn^{IV}Pc^{-2}$, and $Ti^{IV}Pc^{-2}/Ti^{III}Pc^{-2}$ and $Ti^{III}Pc^{-2}/Ti^{II}Pc^{-2}$.

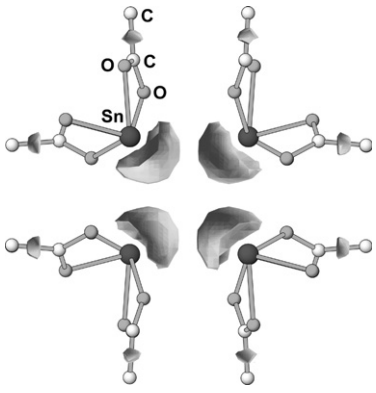


Varvara S. Stafeeva, Alexander S. Mitiaev, Artem M. Abakumov, Alexander A. Tsirlin, Artem M. Makarevich and Evgeny V. Antipov

Polyhedron 26 (2007) 5365

Crystal structure and chemical bonding in tin(II) acetate

Tin(II) acetate adopts a polymeric structure consisting of infinite $Sn(CH_3COO)_2$ chains with the acetate groups bridging the Sn atoms along the chains. The coordination environment of the Sn atoms is a strongly distorted trigonal bipyramid with a sterically active lone electron pair.

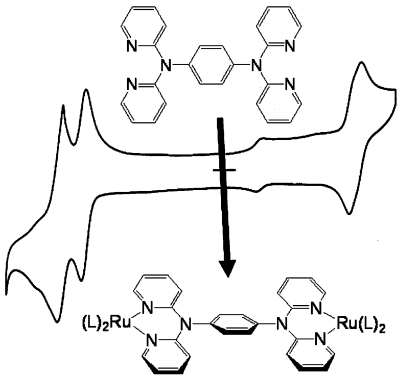


Christopher J. Sumby and Peter J. Steel

Polyhedron 26 (2007) 5370

Mono- and dinuclear ruthenium complexes of bridging ligands incorporating two di-2-pyridylamine motifs: Synthesis, spectroscopy and electrochemistry

Reaction of a series of dinucleating ligands containing two di-2-pyridylamine subunits with $[Ru(L)_2Cl_2]$ (where L = 2,2′-bipyridine or 4,4′-dimethyl-2,2′-bipyridine) gave mono- or dinuclear complexes that were characterised by NMR spectroscopy, mass spectrometry, and absorption spectroscopy, and studied by cyclic voltammetry to probe metal–metal communication.

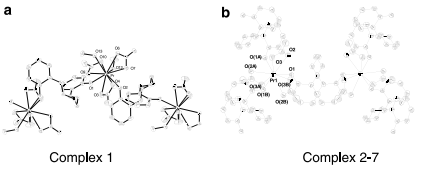


Ting Gao, Peng-Fei Yan, Guang-Ming Li, Guang-Feng Hou and Jin-Sheng Gao

Polyhedron 26 (2007) 5382

Ion size dominated 1D and 2D Salen lanthanide coordination complexes and their luminescence

Two representative structures, viz. $[Pr(H_2salen)(NO_3)_3(CH_3OH)_2]_n$ (**1**) and $[Ln(H_2salen)_{1.5}(NO_3)_3]_n$ [Ln = Pr (**2**), Nd (**3**), Sm (**4**), Eu (**5**), Tb (**6**) and Lu (**7**)] [H_2salen = *N*,*N*′-ethylenebis(salicylideneimine)] are described and discussed. Luminescent spectra of complexes **4** and **5** exhibit characteristic metal-centered fluorescence.

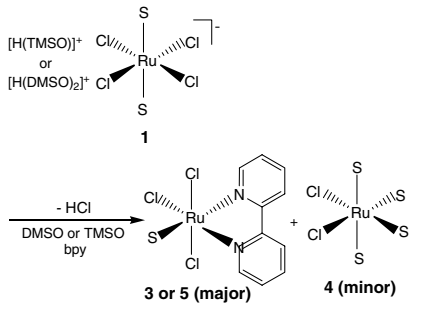


Radhey S. Srivastava, Frank R. Fronczek, Nathan R. Tarver and Richard S. Perkins

Polyhedron 26 (2007) 5389

Synthesis of *mer*-[$RuCl_3$(DMSO)(bpy)], reactivity and electrochemistry of *mer*-[$RuCl_3$-(DMSO)(bpy)] and *mer*-[$RuCl_3$(TMSO)(bpy)] complexes

The reaction of **1** with 2,2′-bipyridine in ethanol at room temperature resulted in the formation of a major compound, *mer*-[$RuCl_3$(DMSO)(bpy)] (bpy = 2,2′-bipyridine) **3**. The reaction of *mer*-$RuCl_3$(TMSO)(bpy)] **5** with imidazole, carbon monoxide and KSCN yield *mer*-[$RuCl_3$(bpy)-(im)] · 2DMSO (im = imidazole) **6** and *cis*-$RuCl_2$(TMSO)(CO)(bpy)] **7** and K[$RuCl_3$(bpy)-(SCN)] **9**, respectively. Ru-DMSO analogues are synthesized analogously. The compounds **3**, **6** and **7** are characterized by X-ray diffraction. The Compound **6** is formed by the substitution of TMSO or DMSO from*mer*-$RuCl_3$(TMSO)(bpy)] and **3**, respectively, whereas **7** and **8** are formed by unprecedented one-electron reductions of **5** and **3**. The reactions of **3** and **5** with KSCN resulted in the same compound, K[$RuCl_3$(NCS)-(bpy)] **9**. Replacing S-bonded TMSO or DMSO from **5** and **3**, respectively forms the N-bonded thiocyanate complex **9**.

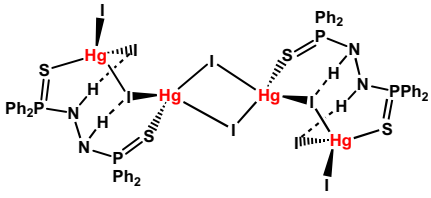


Eric W. Ainscough, Andrew M. Brodie, Andreas Derwahl, Graham H. Freeman and Carl A. Otter

Polyhedron 26 (2007) 5398

Copper(I) and mercury(II) halide complexes of 1,2-bis(diphenylthioylphosphino)hydrazine

The ligand, 1,2-bis(diphenylthioylphosphino)-hydrazine, forms dimetallic complexes with copper(I) halides, monomeric complexes with mercury(II) chloride and bromide and an unusual tetrametallic complex with mercury(II) iodide.

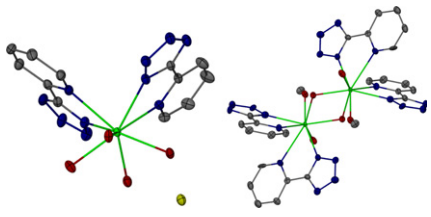


Philip C. Andrews, Tobias Beck, Benjamin H. Fraser, Peter C. Junk and Massimiliano Massi

Polyhedron 26 (2007) 5406

Synthesis and structural characterisation of cationic, neutral and hydroxo-bridged lanthanoid (La, Gd, Ho, Yb, Y) bis 5-(2-pyridyl)-tetrazolate complexes

Reaction of an excess of hydrated $LnCl_3$ (Ln = La, Gd, Ho, Yb, Y) with sodium 5-(2-pyridyl)tetrazolate in water led to the formation of either cationic disubstituted complexes (La, Gd, Ho) or neutral μ-hydroxo-bridged dimers (Y, Yb).

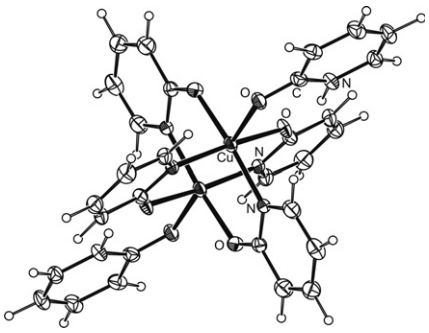


Bojan Kozlevčar, Marjeta Radišek, Zvonko Jagličić, Franci Merzel, Lea Glažar, Amalija Golobič and Primož Šegedin

Polyhedron 26 (2007) 5414

Strong antiferromagnetism in the dinuclear 2-pyridone complex with N–C–O bridges: A *paddle-wheel* analogue of the dinuclear tetracarboxylates

Compound $[Cu_2(\mu\text{-}L)_4(HL)_2]$ (**1**) (HL = 2-pyridone) shows the dinuclear cage structure with four triatomic N–C–O bridges (*paddle wheel*) and monodentate apical 2-pyridones. The EPR spectra show six signals, as suggested for $S = 1$ spin state and $D = 0.293\ cm^{-1} < h = 0.320\ cm^{-1}$. Compound **1** is compared with related mixed pyridin-2-olato/methanoato complex $[Cu_2(\mu\text{-}HCO_2)_2(\mu\text{-}L)_2(HL)_2]$ (**2a**), showing similarly strong antiferromagnetism ($2J = -334$ (**1**), $-324\ cm^{-1}$ (**2a**)).

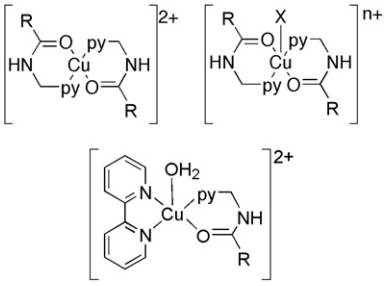


Urmila Pal Chaudhuri, Lei Yang, Laura R. Whiteaker, Arunendu Mondal, Matthew R. Fultz, Douglas R. Powell and Robert P. Houser

Polyhedron 26 (2007) 5420

Neutral pyridylmethylamide ligands and their mononuclear copper(II) complexes

Mononuclear copper(II) complexes of neutral pyridylmethylamide ligands were synthesized and characterized. X-ray structures reveal geometries ranging from four-coordinate square planar to five-coordinate square-pyramidal or trigonal-bipyramidal. The neutral ligands coordinate via the pyridyl N atom and carbonyl O atom in a bidentate fashion.

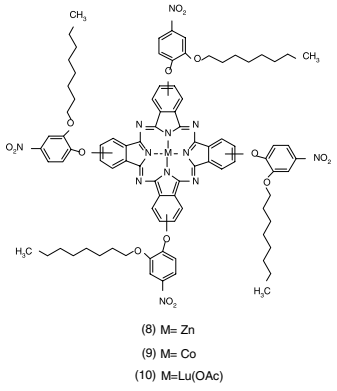


Duygu Kulaç, Mustafa Bulut, Ahmet Altındal, Ali Rıza Özkaya, Bekir Salih and Özer Bekaroğlu

Polyhedron 26 (2007) 5432

Synthesis and characterization of novel 4-nitro-2-(octyloxy)phenoxy substituted symmetrical and unsymmetrical Zn(II), Co(II) and Lu(III) phthalocyanines

Starting from 4-(3,4-dicyanophenoxy)-3-hydroxynitrobenzene (**4**) and 1-bromooctane, their alkylation reaction gave compound **5**. Zn(II) **8**, Co(II) **9**, and Lu(III) **10** complexes were synthesized by the tetramerization of compound **5**. Compound **7** was prepared by the condensation of **5** and **6**. The new compounds were characterized by FT-IR, UV/Vis, NMR and mass spectra. The electrochemical and electrical properties of the complexes were also investigated.



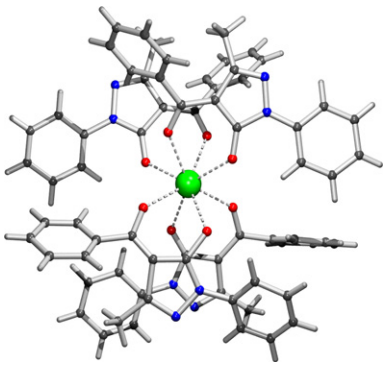
(8) M= Zn
(9) M= Co
(10) M=Lu(OAc)

Rik Van Deun, Peter Nockemann, Tatjana N. Parac-Vogt, Kristof Van Hecke, Luc Van Meervelt, Christiane Görller-Walrand and Koen Binnemans

Polyhedron 26 (2007) 5441

Near-infrared photoluminescence of lanthanide complexes containing the hemicyanine chromophore

Three (*E*)-*N*-hexadecyl-*N*′,*N*′-dimethylaminostilbazolium tetrakis(1-phenyl-3-methyl-4-benzoyl-5-pyrazolonato) lanthanide(III) complexes, containing trivalent neodymium, erbium and ytterbium, show near-infrared luminescence in acetonitrile solution upon UV irradiation. Because of the absence of an α-hydrogen atom in the pyrazolonato ligands, and because of the saturation of the coordination sphere by four bidentate ligands, the luminescence properties are enhanced when compared to, e.g. quinolinate complexes.

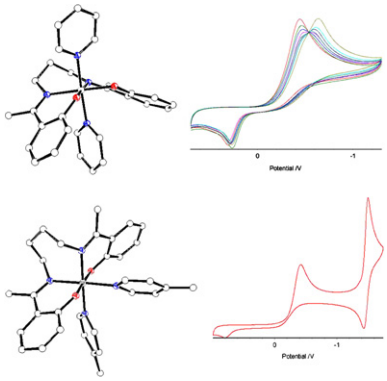


Kurt J. Schenk, Soraia Meghdadi, Mehdi Amirnasr, Mohammad H. Habibi, Ahmad Amiri, Mehdi Salehi and Abolfazl Kashi

Polyhedron 26 (2007) 5448

Co(III) complexes of Me-salpn and Me-salbn and the ring size effect on the coordination modes and electrochemical properties: The crystal structures of *trans*-[Co^{III}(Me-salpn)-$(py)_2$]PF_6 and *cis*-α-[Co^{III}(Me-salbn)$(4\text{-Mepy})_2$]-$BPh_4 \cdot$ 4-Mepy

Co(III) complexes of two tetradentate Schiff base ligands Me-salpn and Me-salbn, with two R-py ancillary ligands have been synthesized and structurally characterized. The core structures and the electrochemical properties have been studied in view of the chelate ring size. The Me-salpn forms *trans*-complexes, whereas the Me-salbn adopts a *cis*-α-configuration about Co. The Me-salpn complexes undergo sovolysis in acetonitrile and reduce at a more positive potential relative to those of Me-salbn due to the steric hindrance from the methylenic group in Me-salpn ligand.

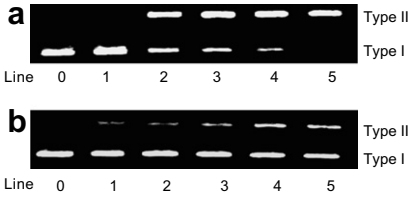


Li-Feng Tan, Hui Chao, Kang-Cheng Zhen, Jun-Jie Fei, Fang Wang, Yang-Fan Zhou and Liang-Nian Ji

Polyhedron 26 (2007) 5458

Effects of the ancillary ligands of polypyridyl ruthenium(II) complexes on the DNA-binding and photocleavage behaviors

Photoactivated cleavage of pBR-322 DNA in the presence of **1** (a) or **2** (b) after 60 min of irradiation at 400 nm. Lane 0, DNA alone; Lanes 1–5, at 5, 10, 15, 20 and 25 μM, Ru(II) complex, respectively.

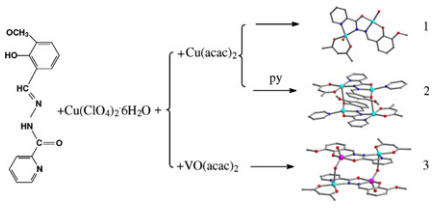


Dan Wang and Shi-Xiong Liu

Polyhedron 26 (2007) 5469

Self-assembly in dinuclear, cyclic homotetranuclear and cyclic heterotetranuclear complexes with a picolylhydrazone ligand

Reactions among $Cu(ClO_4)_2 \cdot 6H_2O$, $Cu(acac)_2$/$VO(acac)_2$ and 3-methoxysalicylaldehyde Picoloylhydrazone in different solvents give three complexes $[Cu_2L(acac)(H_2O)_2]ClO_4$ (**1**), $[Cu_4L_2(acac)_2(py)_2](ClO_4)_2$ (**2**) and $[Cu_2L_2-(acac)_2(VO_2)_2]$ (**3**) (acac = acetylacetonate and py = pyridine). There is an extended Cu_4 structure by hydrogen bonds in **1** and a cyclic tetranuclear structure in **2**. Complex **3** is an unusual cyclic heterotetranuclear complex. The solid-state photoluminescence of the four title complexes were studied. There is an antiferromagnetic interaction in **1**.

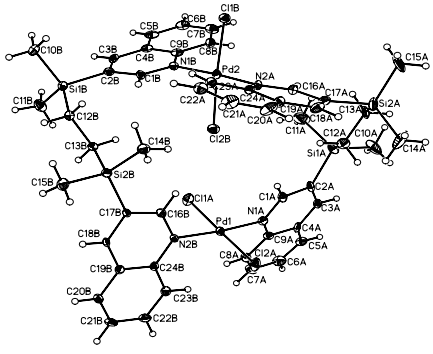


Neetu Rani, Parbati Sengupta, Ajai K. Singh and R.J. Butcher

Polyhedron 26 (2007) 5477

Organosilicon backbone containing pyridyl/quinolyl ligands: Synthesis, complexation reactions and single crystal structures of metallamacrocyclic Pd(II) and Cu(II) complexes

1,2-Bis(dimethyl(2-pyridyl)silyl)ethane ($\mathbf{L^1}$) and 1,2-bis(dimethyl(3-quinolyl)silyl)ethane ($\mathbf{L^2}$) have been synthesized and their ligation with Pd(II), Ag(I) and Cu(II) has been investigated. The single crystal structures of $\mathbf{L^2}$ and metallamacrocyclic complexes $[Pd(\mathbf{L^1})Cl_2]$ (**1**), $[Cu(\mathbf{L^1})Br_2]$ (**3**) and $[PdCl_2(\mathbf{L^2})]_2$ (**4**) have been solved. The **4** is 22-membered and the first example, which has ligand containing organosilicon backbone.

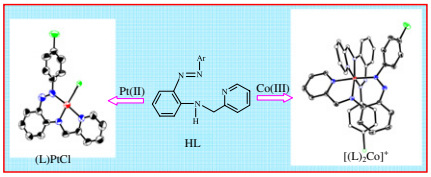


Debprasad Patra, Poulami Pattanayak, Jahar Lal Pratihar and Surajit Chattopadhyay

Polyhedron 26 (2007) 5484

Synthesis, structure and properties of delocalized transition metal chelates: Diazoketiminato chelates of Co(III) and Pt(II)

The syntheses of Pt(II) and Co(III) complexes incorporating tridentate (*N*,*N*,*N*) diazoketimine ligands give the opportunity to obtain new delocalized chelates of Pt(II) and Co(III).

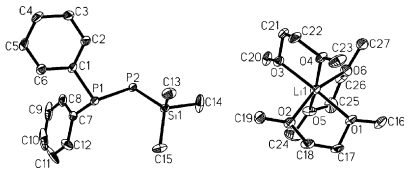


Wioleta Domańska-Babul, Katarzyna Baranowska, Rafał Grubba, Eberhard Matern and Jerzy Pikies

Polyhedron 26 (2007) 5491

Syntheses and crystal structures of lithium derivatives of diphosphanes R_2P–$P(SiMe_3)$-Li · 3L, R = Ph, ^{i}Pr and ^{i}Pr$_2$N, L = THF or DME

The first solvent-separated lithium phosphinophosphide Ph_2P–$P(SiMe_3)_2$ + BuLi + 3DME → $(Li \cdot 3DME)^+(Ph_2P–PSiMe_3)^-$ + Me_3SiBu

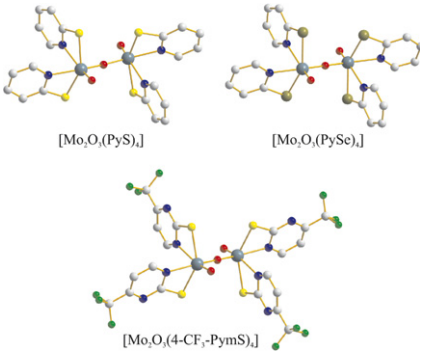


Xiaoli Ma, Carola Schulzke, Zhi Yang, Arne Ringe and Jörg Magull

Polyhedron 26 (2007) 5497

Synthesis, structures and oxygen atom transfer catalysis of oxo-bridged molybdenum(V) complexes with heterocyclic bidentate ligands (N,X) X = S, Se

The first μ-oxomolybdenum(V) pyridine-2-selenolato complex $[Mo_2O_3(PySe)_4]$ and its pyridine-2-thionato analogue $[Mo_2O_3(PyS)_4]$ as well as $[Mo_2O_3(4\text{-}CF_3\text{-}PymS)_4]$ were synthesized and structurally characterized. The oxygen atom transfer properties of the selenium and the corresponding sulfur compound are compared.

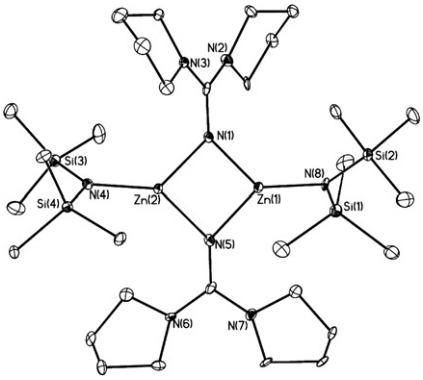


Travis L. Cleland and Scott D. Bunge

Polyhedron 26 (2007) 5506

Synthesis and characterization of a series of zinc complexes stabilized by 1,1,3,3-tetraalkylguanidinate (TAG) ligands: $[Zn(\mu\text{-}TAG)\{N(SiMe_3)_2\}]_2$

A series of novel structurally varied low-coordinate zinc complexes utilizing 1,1,3,3-tetraalkylguanidinate (TAG) ligands were synthesized and characterized. Li(TAG) and lithium bis-trimethylsilylamide, $LiN(SiMe_3)_2$, were successfully reacted with $ZnCl_2$ in a 1:1 ratio to yield the corresponding dinuclear complexes with the general formula $[Zn(\mu\text{-}TAG)\{N(SiMe_3)_2\}]_2$.

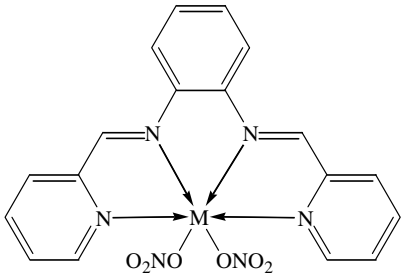


Mohammad Shakir, Mohammad Azam, Yasser Azim, Shama Parveen and Asad Ullah Khan

Polyhedron 26 (2007) 5513

Synthesis and physico-chemical studies on complexes of 1,2-diaminophenyl-*N*,*N*′-bis-(2-pyridinecarboxaldimine), (**L**): A spectroscopic approach on binding studies of DNA with the copper complex

A series of mononuclear complexes of the Schiff base ligand 1,2-diaminophenyl-*N*,*N*′-bis-(2-pyridinecarboxaldimine) has been synthesized and characterized on the basis of various spectroscopic studies. Fluorescence and absorption measurement studies on the Cu(II) complex showed an excellent binding ability to DNA.

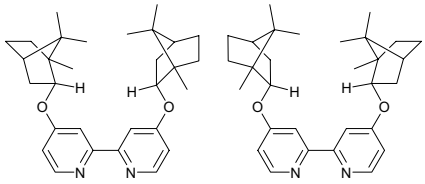


Edwin C. Constable, Catherine E. Housecroft, Valérie Jullien, Markus Neuburger, Ingo Poleschak, Sébastien Reymann, Sina Saxer and Silvia Schaffner

Polyhedron 26 (2007) 5519

Tris-chelate complexes with chiral ligands: In search of diastereoisomeric selectivity with remote stereogenic centres

The chiral ligands, 4,4′-bis{(1*S*,2*R*,4*S*)-(−)-bornyloxy}-2,2′-bipyridine, (1*S*,2*R*,4*S*)-**1**, and 4,4′-bis{(1*R*,2*S*,4*R*)-(+)-bornyloxy}-2,2′-bipyridine, (1*R*,2*S*,4*R*)-**1**, are reported; the formation of $[Fe((1S,2R,4S)\text{-}\mathbf{1})_3]^{2+}$, $[Ru((1S,2R,4S)\text{-}\mathbf{1})_3]^{2+}$, $[Ru((1S,2R,4S)\text{-}\mathbf{1})(bpy)_2]^{2+}$ and $[Ru((1R,2S,4R)\text{-}\mathbf{1})(bpy)_2]^{2+}$ proceeds without preference for either the Δ or Λ-diastereoisomers.

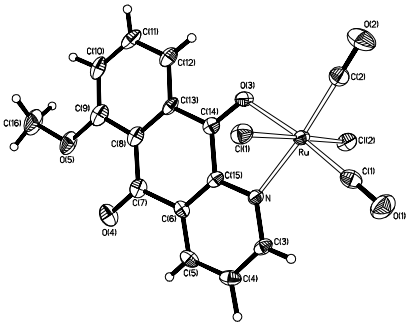


Yolanda Prieto, Marcelo Muñoz, Verónica Arancibia, Mauricio Valderrama, Fernando J. Lahoz and M. Luisa Martín

Polyhedron 26 (2007) 5527

Synthesis, structure and properties of ruthenium(II) complexes with quinolinedione derivatives as chelate ligands: Crystal structure of $[Ru(CO)_2Cl_2(6\text{-methoxybenzo}[g]\text{quinoline-}5,10\text{-dione})]$

The reaction of complex $[\{Ru(CO)_3Cl_2\}_2]$ with substituted quinolinediones in ethanol yield mononuclear complexes of the type $[Ru(CO)Cl_2(\kappa^2\text{-quinolinedione-N,O})]$. The molecular structure of complex $[Ru(CO)_2Cl_2(6\text{-methoxybenzo}[g]\text{quinoline-}5,10\text{-dione})]$ has been determined by single-crystal X-ray diffraction. The redox chemistry of ligands and complexes was investigated by cyclic voltammetry. The potential antitumor activities of free ligands and the ruthenium complexes are also evaluated.

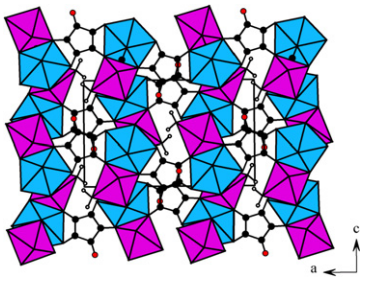


Elisabeth Gavilan and Nathalie Audebrand

Polyhedron 26 (2007) 5533

Calcium croconate and calcium oxalato-croconate complexes with 2D and 3D crystal structures

Two new calcium croconates complexes $Ca(\mu_3\text{-}C_5O_5)(H_2O)_3$ (**I**) and $Ca_2(\mu_4\text{-}C_5O_5)(\mu_6\text{-}C_2O_4)(H_2O)$ (**II**) have been prepared. The 2D framework of **I** is built from layers of $[Ca_2O_{14}]$ dimers and croconate dianions. In **II** layers made of CaO_7/CaO_8 polyhedra and oxalate dianions are connected through croconates. Oxalato-croconate **II** is stable until 380 °C.

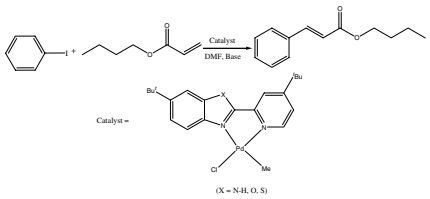


Stephen O. Ojwach, Gunnar Westman and James Darkwa

Polyhedron 26 (2007) 5544

Substituted (pyridinyl)benzoazole palladium complexes: Synthesis and application as Heck coupling catalysts

A series of (pyridinyl)benzoazole palladium complexes have been used to catalyze Heck coupling reactions of iodobenzene and butyacrylate at mild conditions. The catalysts are highly stable and can be used in more than four catalytic cycles without any signs of decomposition.



Erratum to: "Synthesis, crystal, molecular, and electronic structure of [$ReOCl_3$(bpzm)] complex" [Polyhedron 26 (2007) 2581–2588] 5553

Erratum to "A theoretical study of a drastic structural change of bis(phthalocyaninato)lanthanide by ligand oxidation: Towards control of ligand field strength and magnetism of single-lanthanide-ionic single molecule magnet" [Polyhedron 26 (2007) 1859–1862] 5554

The Publisher encourages the submission of articles in electronic form thus saving time and avoiding rekeying errors. For detailed instructions on the preparation of manuscripts and of electronic artwork, consult the Author Gateway for Elsevier at http://authors.elsevier.com

ScienceDirect

Full text of this journal is available, on-line from **ScienceDirect**. Visit **www.sciencedirect.com** for more information.

Available online at www.sciencedirect.com
ScienceDirect
Polyhedron 26, issue 17, 30 October 2007
POLYHEDRON
www.elsevier.com/locate/poly

Contents

Fred Basolo (1920–2007): A tribute from students, colleagues, and family 4779

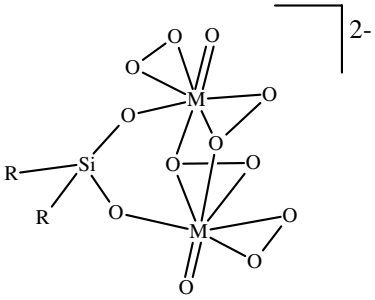
Papers

Laurent Salles, Jean-Yves Piquemal, Yahdih Mahha, Marion Gentil, Patrick Herson and Jean-Marie Brégeault

Polyhedron 26 (2007) 4786

Crystal structures of three novel dioxotetraperoxodi(molybdenum) heteropolyanions in $[PPh_4]_2[R_2SiO_2\{Mo_2O_2(\mu\text{-}O_2)_2(O_2)_2\}]$ (R_2 = $(CH_3)_2$, $(i\text{-}C_4H_9)_2$ or $(CH_3)(CH_2Cl)$) and characterization of their tungsten analogues

The reaction of MoO_3 [or "$WO_3 \cdot H_2O$"], 30 wt% aqueous H_2O_2 with $R_2Si(OR')_2$ in alkaline hydrogen peroxide–ethanol affords the dimeric title complexes. These compounds represent a type of silicon-based polyoxoperoxo species which are also obtained by grafting on silica surfaces and in the synthesis of organic/inorganic mesophases to prepare MO_x–SiO_2–MCM-41 or MO_x–SiO_2–SBA-15.



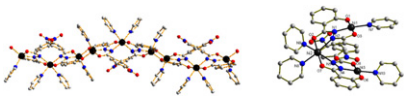
M = Mo or W
R_2 = $(CH_3)_2$, $(i\text{–}Bu)_2$ or $(CH_3)(CH_2Cl)$

Shen Lin, Ming-Xing Yang and Shi-Xiong Liu

Polyhedron 26 (2007) 4793

Three novel trinuclear zinc(II)/nickel(II) complexes with pentadentate ligands *N*-nitrobenzoylsalicylhydrazidate

Three novel trinuclear complexes $Zn_3(p\text{-nbzshz})_2(C_5H_5N)_4$ (**1**), $Ni_3(p\text{-nbzshz})_2(py)_4$ (**2**) and $Ni_3(o\text{-nbshz})_2(DMF)_2((CH_3)_2O)_2$ (**3**) have been obtained by the reaction of $Zn(OAc)_2 \cdot 4H_2O$ or $Ni(OAc)_2 \cdot H_2O$ with two new ligands, *N*-*p*-nitrobenzoylsalicylhydrazidate and *N*-*o*-nitrobenzoylsalicylhydrazidate. Complex **1** exhibits a one-dimensional wave-like chain structure resulting from the linkage of the phenolate oxygen donor atoms of the ligand between adjacent trinuclear zinc units. Complex **2** is an uncommon bent trinuclear nickel complex, whilst the three nickel atoms in complex **3** are arranged in a strictly linear fashion.

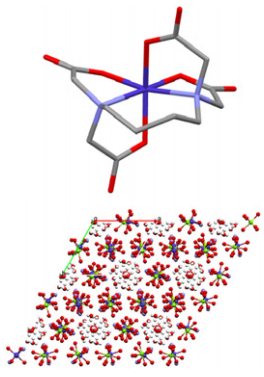


Dušanka D. Radanović, Urszula Rychlewska, Beata Warżajtis, Milica S. Cvijović, Mirjana Dj. Dimitrijević and Miloš I. Djuran

Polyhedron 26 (2007) 4799

Tuning the topologies of Co(II) and Ni(II) complexes with EDTA, 1,3-PDTA and 1,4-BDTA ligands: Synthesis and spectroscopic data of $[Mg(H_2O)_6][Co(1,4\text{-bdta})] \cdot 3H_2O$ and $[Mg(H_2O)_6][Ni(1,4\text{-bdta})] \cdot 3H_2O$ complexes, and the X-ray structure of their chiral crystals

Stereochemically labile hexadentate cobalt(II) and nickel(II) complexes with 1,4-bdta ligand, $[Mg(H_2O)_6][Co(1,4\text{-bdta})] \cdot 3H_2O$ (**a**) and $[Mg(H_2O)_6][Ni(1,4\text{-bdta})] \cdot 3H_2O$ (**b**), have been synthesized and characterized by UV–Vis spectroscopy and X-ray crystallography. These complexes have been shown to undergo a spontaneous resolution upon crystallization, an unprecedented instance with this type of ligand.



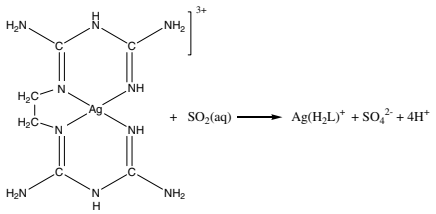
Elsevier Ltd.

Rupa Shah, Vimal Soni, Aditya Prakash and Raj N. Mehrotra

Polyhedron 26 (2007) 4809

Kinetics and mechanism of oxidation of S(IV) by the ethylenebisbiguanide Ag(III) ion

Weak intermediate are involved in the oxidation of SO_2 (aq) to SO_4^{2-} by [ethylenebis-(biguanide)]silver(II) in the acidic medium by successive one-electron transfer.

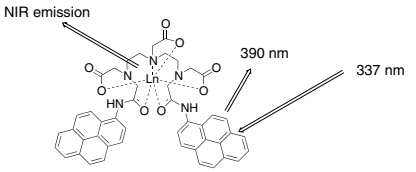


Simon J.A. Pope

Polyhedron 26 (2007) 4818

Dual-emissive complexes: Visible and near-infrared luminescence from bis-pyrenyl lanthanide(III) complexes

The syntheses and photophysical attributes of a range of dual-emissive, bis-pyrenyl lanthanide complexes based on a DTPA architecture are described. Irradiation of the pyrene chromophore results in sensitised near-IR emission from Nd^{III}, Er^{III} and Yb^{III}.

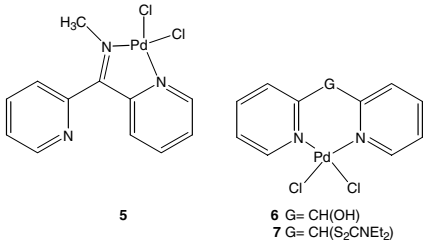


Noemí Andrade-López, José G. Alvarado-Rodríguez, Simplicio González-Montiel, María Guadalupe Rodríguez-Méndez, María Elena Páez-Hernández and Carlos Andrés Galán-Vidal

Polyhedron 26 (2007) 4825

cis-Palladium(II) complexes of derivatives of di-(2-pyridyl)methane: Study of the influence of the bridge group in the coordination mode

The synthesis and characterization by X ray diffraction, NMR and mass spectrometry of complexes $[Pd\{(C_5H_4N)_2Y\}Cl_2]$ (Y = CNMe, **5**; Y = CH(OH), **6** and Y = $CH(S_2CNEt_2)$, **7**) is described. The ligands coordinate to the palladium atom in a bidentate mode. **5** displays a five-membered ring; **6** and **7** display six membered rings.

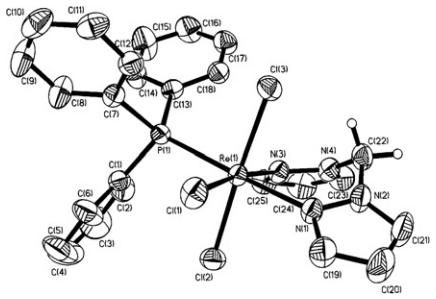


B. Machura, R. Penczek, R. Kruszynski, J. Kłak, J. Mroziński and J. Kusz

Polyhedron 26 (2007) 4833

A novel rhenium(III) complex with bis(pyrazol-1-yl)methane: X-ray structure and DFT calculations for $[ReCl_3(bpzm)(PPh_3)]$

The $[ReCl_3(MeCN)(PPh_3)_2]$ complex reacts with bis(pyrazol-1-yl)methane (bpzm) to give $[ReCl_3(bpzm)(PPh_3)]$. The compound has been studied by IR, UV-Vis spectroscopy and X-ray crystallography. The molecular orbital diagram of $[ReCl_3(bpzm)(PPh_3)]$ has been calculated with the density functional theory (DFT) method. The spin-allowed triplet–triplet electronic transitions of $[ReCl_3(bpzm)(PPh_3)]$ have been calculated with the time-dependent DFT method, and the UV–Vis spectrum of the title compound has been discussed on this basis. The magnetic behavior is characteristic of mononuclear complexes with d^4 low-spin octahedral Re(III) complexes ($^3T_{1g}$ ground state) and arise because of the large spin–orbit coupling (ζ = 2500 cm^{-1}), which gives diamagnetic ground state.

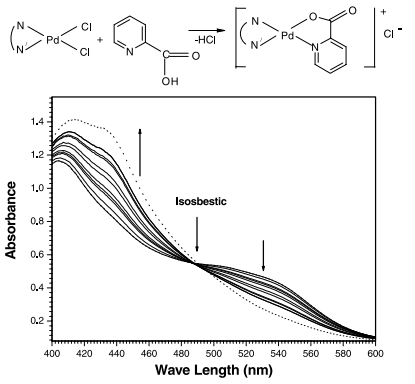


Pradip Kumar Ghosh, Sushanta Saha and Ambikesh Mahapatra

Polyhedron 26 (2007) 4841

Pd–Cl cleavage of dichloro-[1-alkyl-2-(naphthylazo)imidazole]palladium(II) complexes by picolinic acid: Kinetic and mechanistic studies

This work describes kinetics and mechanism of the reaction between picolinic acid (picH) and $[Pd(\alpha\text{-}/\beta\text{-NaiR})Cl_2]$ [α-/β-NaiR = 1-alkyl-2-(naphthyl-α/β-azo)imidazole] in acetonitrile (MeCN) medium. The product is characterized as $[Pd(\alpha/\beta\text{-NaiR})(pic)](ClO_4)$ by different spectroscopic routes. It is established that the cleavage of Pd–Cl bond is the rate-determining step. Thermodynamic parameters ($\Delta^{\ddagger}H^{\circ}$ and $\Delta^{\ddagger}S^{\circ}$) are determined from variable temperature kinetic studies.

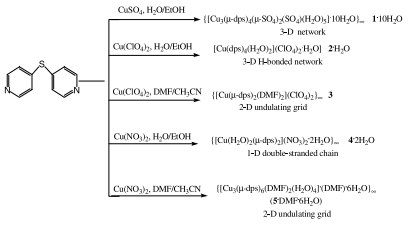


Qing-Feng Xu, Qiu-Xuan Zhou, Jian-Mei Lu, Xue-Wei Xia, Li-Hua Wang and Yong Zhang

Polyhedron 26 (2007) 4849

Synthesis, structures and NLO properties of five non-centrosymmetric coordination compounds from the copper(II)/dps system (dps = 4,4′-dipyridyl sulfide)

A series of acentric coordination frameworks constructed by Cu(II) and 4,4′-dipyridyl sulfide (dps) were synthesized. All these coordination architectures are generated from achiral building blocks without any chiral auxiliary. The influence of anion and solvent on the structural architecture is discussed. Their second-order NLO properties are also studied.

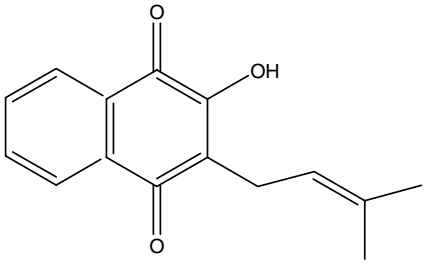


R. Hernández-Molina, I. Kalinina, P. Esparza, M. Sokolov, J. Gonzalez-Platas, A. Estévez-Braun and E. Pérez-Sacau

Polyhedron 26 (2007) 4860

Complexes of Co(II), Ni(II) and Cu(II) with lapachol

The complexes of naturally occurring hydroxynaphtho-quinone, lapachol (HL) with Co(II), Ni(II) and Cu(II) have been prepared and the crystal structures of $[CoL_2(EtOH)_2]$, $[NiL_2(EtOH)_2]$ and $[CuL_2(py)_2]$ reported. Characterisation by elemental analyses, cyclic voltammetry and FAB-MS was also performed.

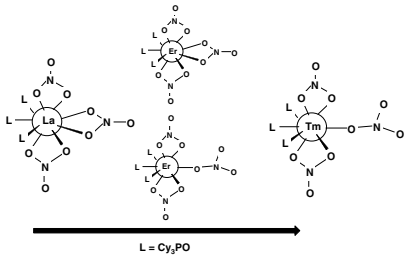


Ann P. Hunter, Anthony M.J. Lees and Andrew W.G. Platt

Polyhedron 26 (2007) 4865

Synthesis, structures and mass spectrometry of lanthanide nitrate complexes with tricyclohexylphosphine oxide

Complexes of lanthanide nitrates with tricyclolhexylphosphine oxide show variations in the nitrate coordination as the Ln^{3+} ionic radii decrease. Tandem mass spectra are simple showing loss of Cy_3PO from the complex apart for the Yb complex which undergoes more extensive fragmentation.



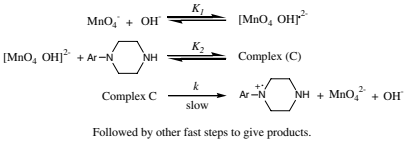
Kiran A. Thabaj, Suresh D. Kulkarni, Shivamurti A. Chimatadar and Sharanappa T. Nandibewoor

Polyhedron 26 (2007) 4877

Oxidative transformation of ciprofloxacin by alkaline permanganate – A kinetic and mechanistic study

The general scheme is proposed for oxidative transformation of ciprofloxacin, an antibacterial agent by alkaline permanganate to explore the observed experimental results. Products and intermediates were identified by LC-ESI-MS/MS technique. Derived rate law consistent with the observed kinetics is

$$\text{Rate} = \frac{kK_1K_2[\text{MnO}_4^-][\text{OH}^-][\text{CF}]}{1 + K_1[\text{OH}^-] + K_1K_2[\text{OH}^-][\text{CF}]}.$$

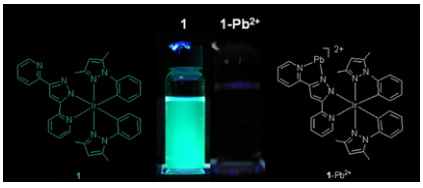


Mei-Lin Ho, Yi-Ming Cheng, Lai-Chin Wu, Pi-Tai Chou, Gene-Hsiang Lee, Fang-Chi Hsu and Yun Chi

Polyhedron 26 (2007) 4886

Probing Pb^{2+} cation via the iridium based phosphorescent dye

The emission of **1** (2×10^{-5} M in acetonitrile, left) and **1** in the presence of 4×10^{-6} M solution of Pb^{2+} excited at 365 nm (UV lamp).

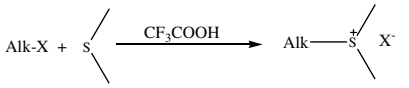


Ilia Sokka, Andreas Fischer and Lars Kloo

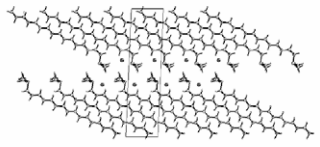
Polyhedron 26 (2007) 4893

Optimization of the synthesis of non-symmetrical alkyl dimethyl sulfonium halides

A high-yield, one-step synthesis of sulfonium halogenides with long alkyl chains is described. A polar electrophilic solvent, trifluoroacetic acid, was used as reaction medium. Dodecyl dimethyl sulfonium, hexadecyl dimethyl sulfonium bromides and chlorides of high purity were obtained and characterized. The crystal structure of hexadecyl dimethyl sulfonium bromide has been determined.



Alk = n-$CH_3(CH_2)_{10}CH_2$-, n-$CH_3(CH_2)_{14}CH_2$-
X = Cl, Br

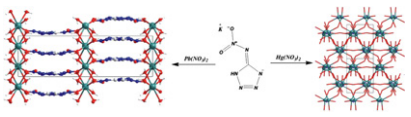


Sergey N. Semenov, Andrey Yu. Rogachev, Svetlana V. Eliseeva, Yury A. Belousov, Andrey A. Drozdov and Sergey I. Troyanov

Polyhedron 26 (2007) 4899

5-Nitroaminotetrazole as a building block for extended network structures: Syntheses and crystal structures of a number of heavy metal derivatives

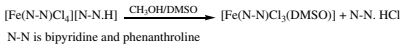
Two extended network structures with the formulas $[Pb(CHN_6O_2)_2(H_2O)_4]_n$ and $[Hg(CN_6O_2)(H_2O)_2]_n$ were obtained from 5-nitroaminotetrazole, both complexes were characterized by X-ray crystallography. The influence of chemical hardness and charge distribution on the reactivity and coordination properties of 5-nitroaminotetrazole have been estimated based on density functional calculations.



Vahid Amani, Nasser Safari, Hamid Reza Khavasi and Peiman Mirzaei

Polyhedron 26 (2007) 4908

Iron(III) mixed-ligand complexes: Synthesis, characterization and crystal structure determination of iron(III) hetero-ligand complexes containing 1,10-phenanthroline, 2,2′-bipyridine, chloride and dimethyl sulfoxide, [Fe(phen)Cl_3(DMSO)] and [Fe(bipy)Cl_3(DMSO)] [Fe(bipy)Cl_3(DMSO)] and [Fe(phen)Cl_3(DMSO)] complexes (where bipy is 2,2′-bipyridine, phen is 1,10-phenanthroline and DMSO is dimethyl sulfoxide) were prepared and characterized by elemental analysis, IR, UV–Vis and ^{1}H NMR spectroscopies and by the X-ray diffraction method.

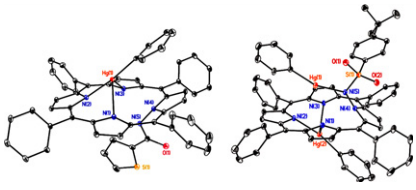


Hsi-Ying Hsieh, Ching-Wen Cheng, Fuh-An Yang, Jyh-Horung Chen, Jo-Yu Tung, Shin-Shin Wang and Lian-Pin Hwang

Polyhedron 26 (2007) 4915

The structures of (phenylato)(*N*-2-thiophenecarboxamido-*meso*-tetraphenylporphyrinato)-mercury(II) and bisphenylmercury(II) complex of 21-(4-*tert*-butyl-benzenesulfonamido)-5,10,15,20-tetraphenylporphyrin

We have investigated two new diamagnetic porphyrin complexes, namely, mononuclear mercury(II) complex of **6** · CH_2Cl_2 · 0.5C_6H_{14} and dinuclear mercury(II) complex of **7**, and their X-ray structures are established.These two porphyrins complexes are of SAT type. The tetracoordination for the Hg(1) in **6** · CH_2Cl_2 · 0.5C_6H_{14} and Hg(2) in **7** is demonstrated and a linear coordination is described for the Hg(1) in **7**.

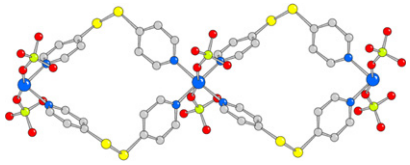


Subal Chandra Manna, Joan Ribas, Ennio Zangrando and Nirmalendu Ray Chaudhuri

Polyhedron 26 (2007) 4923

Dipyridyl bridged coordination polymers of Cu(II): Synthesis, crystal structure and magnetic study

Coordination polymers, [Cu(bpp)$(H_2O)_2$-$(ClO_4)_2]_n$ (**1**) and {[Cu(bpds)$_2$$(ClO_4)_2$] · 1.5$(H_2O)$}$_n$ (**2**) [bpp, 1,3-bis(4-pyridyl)propane and bpds, 4,4′-bipyridyl disulfide] have been synthesized and characterized by X-ray single crystal diffraction study and magnetic measurement.

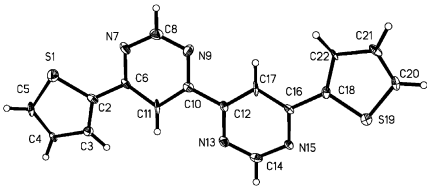


Elena Ioachim, Elaine A. Medlycott, W.G. Skene and Garry S. Hanan

Polyhedron 26 (2007) 4929

Synthesis and properties of 6,6′-dithienyl-4,4′-bipyrimidine and its hetero- and homo-leptic Ru(II) complexes

A new bis(thienyl)-bipyrimidine ligand readily forms Ru(II) complexes which emit at significantly lower energy than the parent Ru(bpy)$_3^{2+}$ complex.

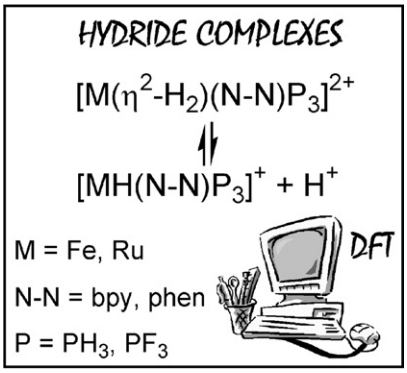


Marco Bortoluzzi, Emilio Bordignon, Gino Paolucci and Bruno Pitteri

Polyhedron 26 (2007) 4936

A computational study on mixed-ligand N_2P_3 donor-set iron(II) and ruthenium(II) classical and non-classical hydrides

The results of DFT calculations on hydride complexes of the type $[MH(N–N)P_3]^+$ and $[M(\eta^2\text{-}H_2)(N–N)P_3]^{2+}$ {M = Fe, Ru; N–N = 2,2′-bipyridine (bpy), 1,10-phenanthroline (phen); P = PH_3, PF_3}, are described. A good correlation between various computed molecular properties and experimental data reported in the literature is highlighted. The charge distributions obtained from DFT calculations allow to hypothesize that the different acidities of iron and ruthenium non-classical hydrides could be mainly justified on the basis of the difference of electronegativity of the two metal ions considered.

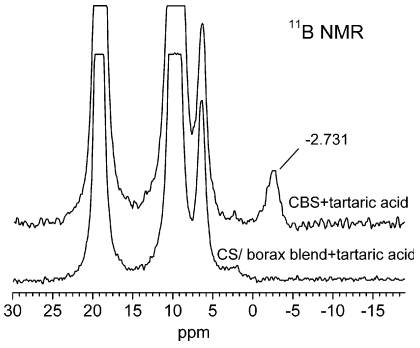


Andrei S. Zelenev, Josepha M. Fu and Bruce A. Keiser

Polyhedron 26 (2007) 4941

Establishing the difference between colloidal borosilicate and boron-modified colloidal silica via chelation of boron with catechol and DL-tartaric acid

Colloidal borosilicate and boron-modified colloidal silica sols both contain B–O–Si chemical bonds that can be detected by ^{11}B NMR. While the boron present in colloidal borosilicate is stable towards the action of catechol and tartaric acid, the boron in boron-modified silica is readily complexed by these agents.

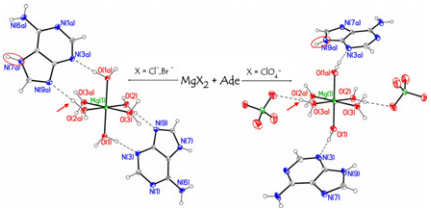


Teresa F. Mastropietro, Donatella Armentano, Nadia Marino and Giovanni De Munno

Polyhedron 26 (2007) 4945

Metal–nucleobase interactions in magnesium(II) and manganese(II) complexes with adenine: Influence of the anion on the non-covalent stabilization of 7H-adenine tautomer

The synthesis and crystal structure of the compounds $[Mg(H_2O)_6X_2 \cdot 2ade]$ (with $X = Cl^-$ (**1**), Br^- (**2**), ClO_4^- (**3**)), $[Mn(H_2O)_4 \cdot (ade)_2 \cdot (ClO_4)_2]$ (**4**), and $[Mn_2(H_2O)_6 \cdot (ade)_2 \cdot (NO_3)_4 \cdot 2H_2O]$ (**5**) (where ade = adenine) are reported. Compounds **1**–**3** consist of self-assembled hexaaquo Mg(II) ions, ade molecules and anions. Compounds **4** and **5** represent a rare example of direct Mn–N binding involving isolated nucleobases and the first one containing ade as ligand. The detailed analysis of non-covalent interactions in all the compounds prove that the anions play a crucial role in determining the non-covalent stabilization of the minor 7H-adenine tautomer.

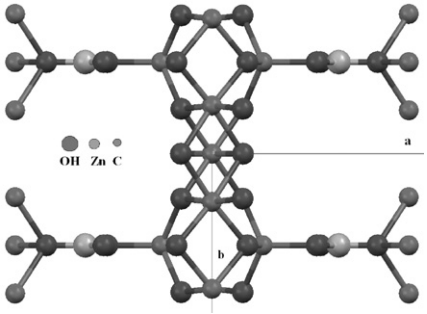


Matthew C. Hales and Ray L. Frost

Polyhedron 26 (2007) 4955

Synthesis and vibrational spectroscopic characterisation of synthetic hydrozincite and smithsonite

Hydrozincite and smithsonite were synthesised by controlling the partial pressure of CO_2 resulting from the reaction in solution of zinc chloride and sodium bicarbonate.
Raman spectroscopy complimented with infrared spectroscopy has been used to characterise the vibrational spectra of these synthesised minerals.

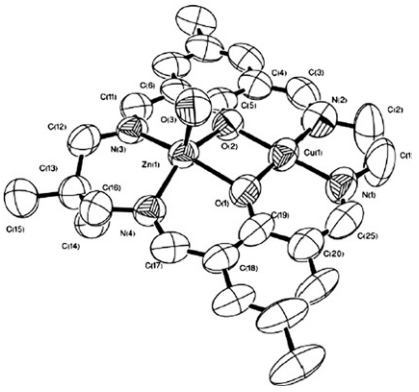


Hamid Khanmohammadi, Razyeh Arabahmadi, Mohammad H. Abnosi and Hamid R. Khavasi

Polyhedron 26 (2007) 4963

Synthesis, crystal structure, spectral and biological studies of Cu^{II}–M^{II}(M = Zn and Pb) heterodinuclear complexes of new phenol-based macrocyclic ligands

A series of heterodinuclear Cu(II)–M(II) (M = Pb and Zn) complexes of new phenol-based compartmental macrocyclic ligands, possessing contiguous (N_2O_2) and (N_xO_2) (x = 2, 3) coordination sites, was prepared and their biological activity has been tested *in vitro*. The crystal structure of [CuZn $L^3(H_2O)$]-$(ClO_4)_2$ was determined by X-ray diffraction and shows that the Zn(II) and Cu(II) centres reside in the N_2O_2 sites of the macrocyclic ligand.

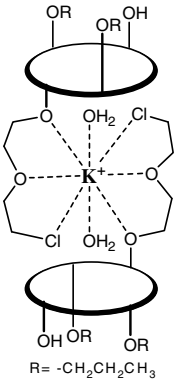


Subrata Patra, Eringathodi Suresh and Parimal Paul

Polyhedron 26 (2007) 4971

Functionalized calix[4]arene as an ionophore: Synthesis, crystal structures and complexation study with Na^+ and K^+ ions

A family of trisubstituted calix[4]arenes with a partial cone conformation has been synthesized and structurally characterized. Crystal structural analyses show that the precise shape of the molecule, and intra- and intermolecular interactions (C–H$\cdots\pi$, $\pi\cdots\pi$ and C–H$\cdots$O) of these compounds are significantly different due to the variation of the substituents. A complexation study with Na^+ and K^+ ions reveal that one of the ionophores ($\mathbf{L^3}$) selectively forms a complex with the latter ion.

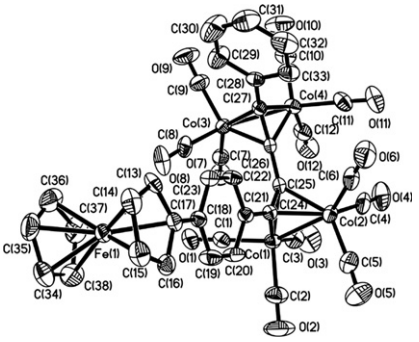


Li-Ying Wang, Quan-Ling Suo, Li-Min Han, Yi-Bing Wang and Lin-Hong Weng

Polyhedron 26 (2007) 4981

Synthesis and structural characterization of new *p*-ferrocenylphenylacetylene bridged cobalt carbonyl clusters

A new ferrocenylphenyl butadiynyl compound **L** and three new complexes **1**, **2** and **3** have been synthesized. The composition and structure of the four compounds were characterized by elemental analysis, FTIR, NMR and MS. The molecular and crystal structures of **L** and **2** were analyzed by X-ray single crystal diffraction.

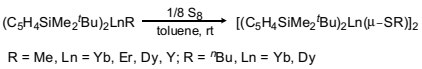


Zheng-Xing Zhang, Yan-Rong Li, Rui-Ting Liu, Zhen-Xia Chen, Lin-Hong Weng and Xi-Geng Zhou

Polyhedron 26 (2007) 4986

Insertion reaction of elemental sulfur into the Ln–C bond: Synthesis and characterization of $[(C_5H_4SiMe_2{}^tBu)_2Ln(\mu\text{-}SR)]_2$ (R = Me, Ln = Yb, Er, Dy, Y; R = ^{n}Bu, Ln = Yb, Dy)

Treatment of $(C_5H_4SiMe_2{}^tBu)_2LnR$ with elemental sulfur leads to the formation of dimeric complexes $[(C_5H_4SiMe_2{}^tBu)_2Ln(\mu\text{-}SR)]_2$ [R = Me, Ln = Yb, Er, Dy, Y; R = ^{n}Bu, Ln = Yb, Dy], providing a new route to the syntheses of lanthanocene thiolates.

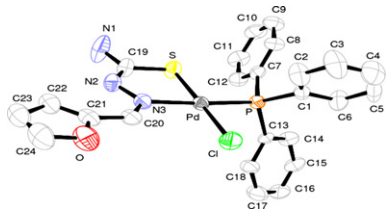


Tarlok S. Lobana, Gagandeep Bawa, Geeta Hundal, A.P.S. Pannu, Ray J. Butcher, Ben-Jie Liaw and Chen W. Liu

Polyhedron 26 (2007) 4993

The influence of substituents (R) at the C^2 carbon on bonding properties of thiosemicarbazones $\{RC^2(H)=N^3\text{-}N^2H\text{–}C^1(=S)\text{–}N^1H_2\}$ in palladium(II) complexes

Reactions of the $PdCl_2(PPh_3)_2$ precursor with furan-2-carbaldehyde thiosemicarbazone (Hftsc) and thiophene-2-carbaldehyde thiosemicarbazone (Httsc), in 1:1 molar ratios in the presence of Et_3N base, removed one Cl and one PPh_3 group from the Pd^{II} center, and yielded the complexes, $[Pd(\eta^2\text{-}N^3,S\text{-ftsc})(PPh_3)Cl]$ (**1**) and $[Pd(\eta^2\text{-}N^3,S\text{-ttsc})(PPh_3)Cl]$ (**2**), respectively, However, when a 1:2 molar ratio (M:L) was used, both the Cl and PPh_3 ligands were removed, yielding complexes, $[Pd(\eta^2\text{-}N^3,S\text{-ftsc})_2]$ (**3**) and $[Pd(\eta^2\text{-}N^3,S\text{-ttsc})_2]$ (**4**). In contrast, reactions with pyrrole-2-carbaldehyde thiosemicarbazone, (H_2ptsc) and salicylaldehyde thiosemicarbazone, (H_2stsc) in 1:1 or 1:2 molar ratios have invariably formed the complexes $[Pd(\eta^3\text{-}N^4,N^3,S\text{-ptsc})(PPh_3)]$ (**5**) and $[Pd(\eta^3\text{–}O,N^3,S\text{-stsc})(PPh_3)]$ (**6**), respectively.

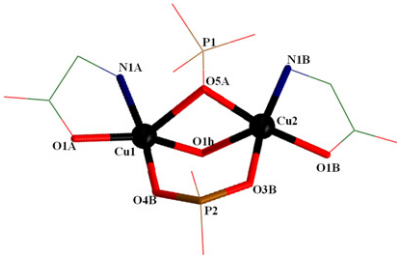


Ricardo C. Santana, Jesiel F. Carvalho, Ivo Vencato, Hamilton B. Napolitano, Adailton J. Bortoluzzi, Gastón E. Barberis, Raul E. Rapp, Mario C.G. Passeggi and Rafael Calvo

Polyhedron 26 (2007) 5001

Synthesis, crystal structure and magnetic properties of a new dinuclear copper(II) amino acid complex $[Cu_2(\text{L-arg})_2(\mu\text{-}HPO_4\text{-}O)(\mu\text{-}HPO_4\text{-}O,O')(\mu\text{-}OH)]^- \cdot (H_3O)^+ \cdot (H_2O)_6$

The synthesis, characterization and crystal structure of a novel dinuclear copper compound with L-arginine, mono and bidentate HPO_4^{2-} oxoanions and an OH^- anion are reported. The dinuclear character and bridging scheme, rare for metal–amino acid compounds, is attributed to the bonding characteristic of the phosphate anions. The magnetic properties and EPR spectra indicate an antiferromagnetic intradinuclear interaction $J/k_B = -3.7$ K and a ferromagnetic coupling between these dinuclear units of $J'/k_B \sim 0.3$ K.

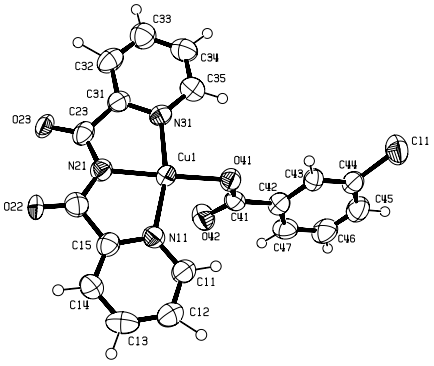


Joaquín Borrás, Gloria Alzuet, Marta González-Álvarez, Francisco Estevan, Benigno Macías, Malva Liu-González and Alfonso Castiñeiras

Polyhedron 26 (2007) 5009

Crystal structures and spectroscopic properties of copper(II)–bis(2-pyridylcarbonyl)amide–chlorobenzoate complexes

The reaction of 2,4,6-tris(pyridyl)-1,3,5-triazine (ptz) and copper(II) salts in DMF–water resulted in the hydrolysis of ptz, giving rise to the bis(2-pyridylcarbonyl)amide anion (ptO_2^-) and affording the complexes $[Cu(ptO_2)(2\text{-}Clbenz)(H_2O)]$, $[Cu(ptO_2)(3\text{-}Clbenz)]$, and $[Cu(ptO_2)(4\text{-}Clbenz)(DMF)]$. This report includes the chemical, the spectroscopic characterization and the crystal structures of all these compounds.

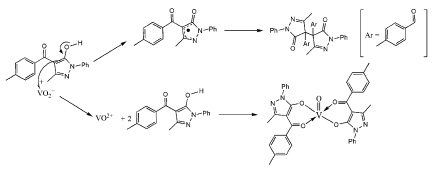


P.N. Remya, C.H. Suresh and M.L.P. Reddy

Polyhedron 26 (2007) 5016

Rapid reduction and complexation of vanadium by 1-phenyl-3-methyl-4-toluoyl-5-pyrazolone: Spectroscopic characterization and structure modelling

The reduction of vanadium(V) by 1-phenyl-3-methyl-4-toluoyl-5-pyrazolone over the pH range of 1.0–7.0 has been assessed by various spectroscopic techniques. The reaction proceeds by the transfer of one electron to vanadium(V) by the ligand *via* the formation of a free-radical intermediate, and subsequently the reduced vanadium species rapidly complexes with the available free ligand and forms vanadyl complex. These reduction reactions occur under physiological conditions and thus could be important to the reduction of vanadium(V)-containing coordination compounds used as insulin-enhancing agents for treatment of diabetics.

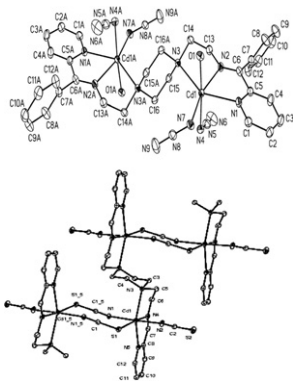


Habibar Chowdhury, Rajarshi Ghosh, Sk. Hafijur Rahaman and Barindra Kumar Ghosh

Polyhedron 26 (2007) 5023

Syntheses, X-ray structures and properties of a dinuclear cadmium(II)azido and a polymeric cadmium(II)thiocyanato compounds containing bis(tridentate) congregators

One-pot reactions of cadmium(II) perchlorate/nitrate, Schiff bases (pbap/pfap) and pseudohalides (sodium azide/ammonium thiocyanate) in a 2:1:4 molar ratio in MeOH–MeCN solvent mixtures at room temperature result in a dinuclear compound $[Cd_2(pbap)(OH_2)_2(N_3)_4]$ (**1**) [pbap = *N*-(1-pyridin-2-ylbenzylidene)-*N*-[2-(4-{2-[(1-pyridin-2-ylbenzylidene)amino]ethyl}piperazin-1-yl)ethyl]amine] and a polymeric compound $[Cd_2(pfap)(\mu_{1,3}\text{-NCS})(\mu_{1,3}\text{-SCN})(NCS)_2]_n$ (**2**) [pfap = *N*-(1-pyridin-2-ylformylidene)-*N*-[2-(4-{2-[(1-pyridin-2ylformylidene) amino]ethyl}piperazin-1-yl)ethyl]-amine]. X-ray crystal structural analyses reveal a bis (tridentate) congregation behaviour of the hexadentate blocker (pbap/pfap) encapsulating two metal centers. Both the complexes display intraligand $^1(\pi\text{–}\pi^*)$ fluorescence and intraligand $^3(\pi\text{–}\pi^*)$ phosphorescence in glassy solutions.

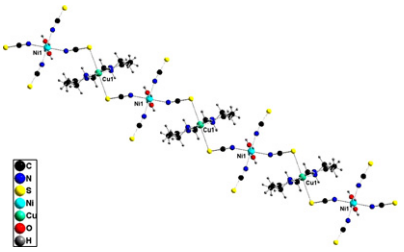


Alina Bieńko, Julia Kłak, Jerzy Mroziński, Sławomir Domagała, Bohdan Korybut-Daszkiewicz and Krzysztof Woźniak

Polyhedron 26 (2007) 5030

Magnetism and crystal structures of $Cu^{II}Mn^{II}$ and $Cu^{II}Ni^{II}$ ordered bimetallic chains

The syntheses, crystal structures and magnetic properties of the new bimetallic compounds $\{CuL_a[Ni(NCS)_4(H_2O)_2]\}$ (**1**) and $\{CuL_a[Mn(NCS)_4(H_2O)_2]\}$ (**2**), where L = *N*-dl-5,12-dimethyl-1,4,8,11-tetraazacyclotetradeca-4,11-diene, are reported. Both structures consist of well-separated and magnetically equivalent layers which are composed of thiocyanate-bridged Cu(II)–Mn(II) or Cu(II)–Ni(II) binuclear units and create infinite polymeric zig-zag-like chains in the crystal lattices. The $[Ni(NCS)_4(H_2O)_2]$ and $[Mn(NCS)_4(H_2O)_2]$ molecular fragments have a distorted octahedral symmetry. The geometry of the Cu(II) unit is octahedral with the apical positions occupied by bridging thiocyanate ligands and the basal ones by four nitrogen atoms from the macrocyclic ring. The shortest intramolecular M–M distances are: 6.342 Å (Cu–Ni) and 6.421 Å (Cu–Mn). Magnetic susceptibility and magnetization measurements for the examined compounds have been carried out over the range 1.8–300 K. The data suggest antiferromagnetic interactions through the thiocyanate bridge. Finally, the magnitudes of the Cu(II)–M(II) interactions (M = Ni and Mn) have been compared and qualitatively rationalised.

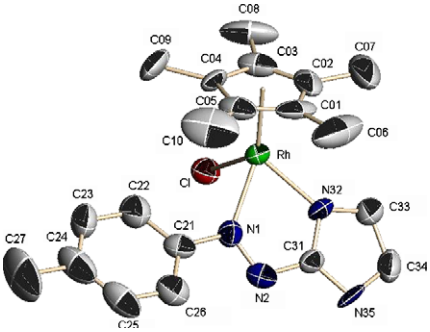


Padavattan Govindaswamy, Yurij A. Mozharivskyj and Mohan Rao Kollipara

Polyhedron 26 (2007) 5039

New pentamethylcyclopentadienyl rhodium and iridium complexes containing arylazoimidazole ligands: Crystal and molecular structure of the complex $[(\eta^5\text{-}C_5Me_5)RhCl(Me\text{–}C_6H_4\text{–}N{=}N\text{–}C_3H_3N_2)]^+$

The dimeric complexes $[\{(\eta^5\text{-}C_5Me_5)M(\mu\text{-}Cl)Cl\}_2]$ where M = Rh and Ir reacts with several arylazoimidazole (RaaiR′) ligands to give the mononuclear cationic complexes of the type $[(\eta^5\text{-}C_5Me_5)MCl(RaaiR')]^+$. The molecular structure of the complex $[(\eta^5\text{-}C_5Me_5)RhCl(Me\text{–}C_6H_4\text{–}N{=}N\text{–}C_3H_3N_2)]^+$ **4**$[PF_6]$ was established by single crystal X-ray diffraction study.

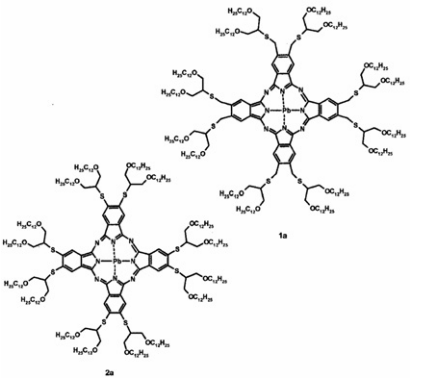


Tamara V. Basova, Ayşe G. Gürek, Devrim Atilla, Aseel K. Hassan and Vefa Ahsen

Polyhedron 26 (2007) 5045

Synthesis and characterization of new mesomorphic octakis(alkylthio)-substituted lead phthalocyanines and their films

The syntheses of new octakis (alkylthio)-substituted phthalocyanines of Pb(II) (**1a** and **2a**) are described. These phthalocyanine derivatives are liquid at room temperature and form columnar-hexagonal (Col_h) mesophases below −10 °C. Thin films of octakis(alkylthio)-substituted Pb(II) phthalocyanines **1a** and **2a** were prepared by the method of spin-coating.

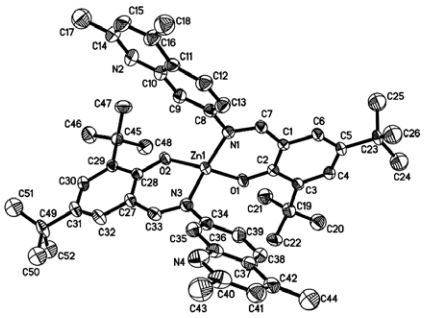


Qing Su, Qiao-Lin Wu, Guang-Hua Li, Xiao-Ming Liu and Ying Mu

Polyhedron 26 (2007) 5053

Bis-salicylaldiminato zinc complexes: Syntheses, characterization and luminescent properties

Bis-salicylaldiminato zinc complexes with four new salicylaldiminato ligands: $(Ar^1N{=}HCAr^2O)_2Zn$ (Ar^1 = 7-(2,4-Me_2)C_9H_4N, Ar^2 = C_6H_4 (**2a**); Ar^1 = 7-(2,4-Me_2)C_9H_4N, Ar^2 = 3,5-$^tBu_2C_6H_2$ (**2b**); Ar^1 = 7-(2,4-Me_2)C_9H_4N, Ar^2 = 5-BrC_6H_3 (**2c**); Ar^1 = 7-(2,4-Me_2)C_9H_4N, Ar^2 = 3,5-$Br_2C_6H_2$ (**2d**)) have been synthesized and characterized by elemental analyses, ^1H, ^{13}C NMR and IR spectroscopy.The molecular structure of complex **2b** was confirmed by X-ray crystallography, showing intermolecular π–π interactions in the solid state.These complexes produce bright fluorescence in both solution and the solid state. In addition, the emission color in solution can be tuned in the range 503–532 nm by the modification of the salicylaldiminato ligand.

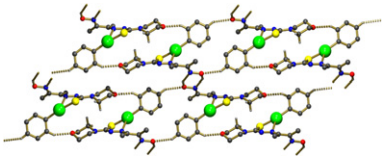


Susobhan Biswas, Saikat Sarkar, Ian M. Steele, Sougata Sarkar, Golam Mostafa, Bijali Bikash Bhaumik and Kamalendu Dey

Polyhedron 26 (2007) 5061

Two-dimensional supramolecular assembly of phenylmercury(II) and cadmium(II) complexes with a tridentate thiohydrazone NNS donor ligand: Synthesis, coordination behavior and crystal structure

The reaction of diacetylmonoxime and morpholine *N*-thiohydrazide with phenylmercury(II) acetate and cadmium(II) acetate formed the novel phenylmercury(II) complex, [PhHg(Hdammthiol)] (**1**) and the cadmium(II) complex, $[Cd(Hdammthiol)_2]$ (**2**), respectively (where H_2dammthiol is the thiol form of diacetylmonoximemorpholine *N*-thiohydrazone (Hdammth)). Both complexes form two-dimensional supramolecular sheet and a new non-conventional $CH_3\cdots O$ interaction (in cadmium complex).

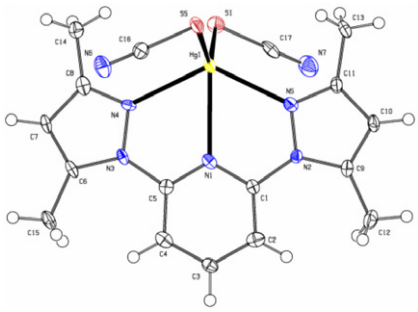


Raif Kurtaran, Sinem Odabaşıoğlu, Akin Azizoglu, Hülya Kara and Orhan Atakol

Polyhedron 26 (2007) 5069

Experimental and computational study on [2,6-bis(3,5-dimethyl-*N*-pyrazolyl)pyridine](dithiocyanato)mercury(II)

The mercury complex of 2,6-bis(3,5-dimethyl-*N*-pyrazolyl)pyridine (bdmpp) has been synthesized and characterized by X-ray diffraction, IR, UV–Vis and TGA–DTA methods. The structure consists of units in which the mercury atom is a penta-coordinated by two sulfur and three nitrogen atoms. [Hg(bdmpp)(SCN)2] has a distorted square pyramidal geometry. The optimized geometry at both PM3 and DFT methods agrees with the X-ray structure well. The infrared spectra of the title complex was studied in the 4000–400 cm^{-1} frequency range experimentally and theoretically. The experimental results are in better agreement with the DFT results at the B3LYP/LanL2DZ level than the semi-empirical results at the PM3 level.

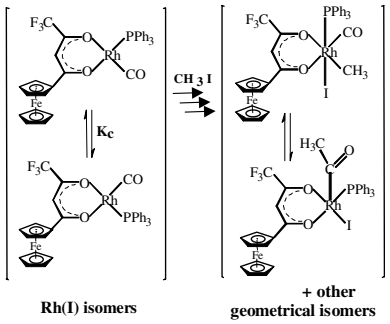


Jeanet Conradie, Gert J. Lamprecht, Andreas Roodt and Jannie C. Swarts

Polyhedron 26 (2007) 5075

Kinetic study of the oxidative addition reaction between methyl iodide and [Rh(FcCOCHCOCF$_3$)(CO)(PPh$_3$)]: Structure of [Rh(FcCOCHCOCF$_3$)(CO)(PPh$_3$)(CH$_3$)(I)]

The chemical kinetics, studied by UV/Vis, IR, ^1H and ^{31}P NMR techniques, of oxidative addition of CH_3I to [Rh(FcCOCHCOCF$_3$)(CO)(PPh$_3$)] with Fc = ferrocenyl, consist of three definite sets of reactions and involves geometrical isomers of two different Rh^{III}-alkyl and two different Rh^{III}-acyl species.

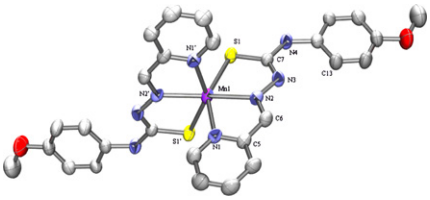


P.F. Rapheal, E. Manoj and M.R. Prathapachandra Kurup

Polyhedron 26 (2007) 5088

Syntheses and EPR spectral studies of manganese(II) complexes derived from pyridine-2-carbaldehyde based *N*(4)-substituted thiosemicarbazones: Crystal structure of one complex

Five manganese(II) complexes {$[MnL^1_2]\cdot H_2O \cdot EtOH$, $[Mn(L^1)(HL^1)]OAc$, $[MnL^1_2]\cdot 3H_2O$, $[MnL^1_2]\cdot 3H_2O$ and $[Mn(HL^3)_2](SCN)_2 \cdot MeOH$} of three NNS donor *N*(4)-substituted thiosemicarbazone ligands {pyridine-2-carbaldehyde *N*(4)-*p*-methoxyphenyl thiosemicarbazone [HL^1], pyridine-2-carbaldehyde *N*(4)-2-phenethylthiosemicarbazone [HL^2] and pyridine-2-carbaldehyde *N*(4)-methyl, *N*(4)-phenyl thiosemicarbazone [HL^3]} were synthesized and physico-chemically characterized. The crystal structure of the compound $[MnL^1_2]\cdot H_2O$ has been determined by X-ray diffraction studies. It is found to have a distorted octahedral geometry. EPR spectra in DMF solutions at 77 K show hyperfine sextets with low intensity forbidden lines lying between each of the two main hyperfine lines.

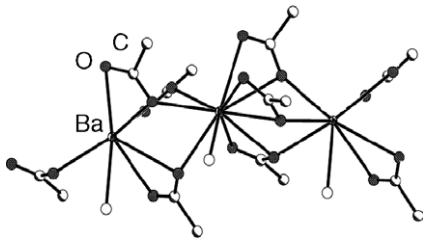


Timothy J. Boyle, Harry D. Pratt III, Todd M. Alam, Mark A. Rodriguez and Paul G. Clem

Polyhedron 26 (2007) 5095

Synthesis and characterization of solvated trifluoroacetate alkaline earth derivatives

A series of alkaline earth trifluoracetic acid (TFA) derivatives were crystallographically characterized as: $Mg(TFA)_2(py)_4$ (**1**), $\{[Ca_2(\mu\text{-}TFA)_3(THF)_4](\mu\text{-}TFA)\}_n$ (**2**), $\{[(\mu\text{-}TFA)_2\text{-}Sr(\mu_c\text{-}TFA)][H\text{-}py]py\}_n$(**3**); and $\{[Ba(\mu_c\text{-}TFA)_2\text{-}(\mu_c\text{-}TFA)(py)][H\text{-}py]\}_n$ (**4**) (shown). Elemental analyses, solid-state, and solution multinuclear NMR, and FTIR data confirms the bulk powders were consistent with the X-ray structures.

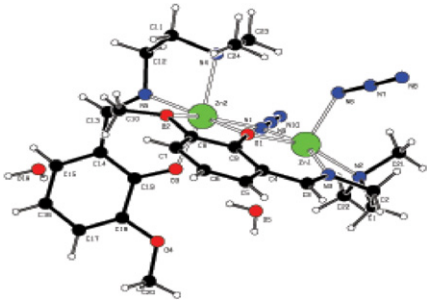


Subhra Basak, Soma Sen, Sambuddha Banerjee, Samiran Mitra, Georgina Rosair and M.T. Garland Rodriguez

Polyhedron 26 (2007) 5104

Three new pseudohalide bridged dinuclear Zn(II) Schiff base complexes: Synthesis, crystal structures and fluorescence studies

Three new dinuclear Zn(II) complexes $[Zn(L)(\mu_{1,1}\text{-}N_3)Zn(L)(N_3)]\cdot 1.5H_2O$ (**1**), $[Zn(L)(\mu_{1,1}\text{-}NCO)Zn(L)(NCO)]\cdot 1.5H_2O$ (**2**) and $[Zn(L)(\mu_{1,1}\text{-}NCS)Zn(L)(NCS)(OH_2)]$ (**3**) of the Schiff base ligand **LH** [**LH** = $(O\text{-}CH_3)(OH)C_6H_3CHN(CH_2)_2N(CH_3)_2$] have been synthesized and characterized by elemental analysis, IR, ^1H NMR spectroscopy, TGA, fluorescence and single crystal X-ray diffraction studies. All the synthesized complexes display intraligand $^1(\pi\text{–}\pi^*)$ fluorescence and can serve as potential photoactive materials.

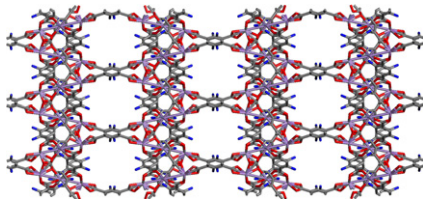


Kjell Ove Kongshaug and Helmer Fjellvåg

Polyhedron 26 (2007) 5113

Syntheses, structures and magnetic properties of Mn(II) containing 3D polymeric networks

Two novel coordination polymers based on Mn(II) have been prepared, and their crystal structures have been solved by single crystal X-ray diffraction. Thermal and magnetic properties are discussed.

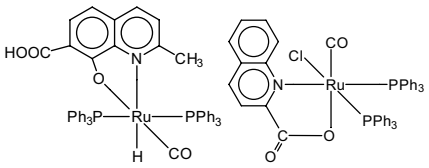


J.G. Małecki, R. Kruszyński, D. Tabak and J. Kusz

Polyhedron 26 (2007) 5120

The reactions between $[RuHCl(CO)(PPh_3)_3]$ and quinoline carboxylic acids

The reactions of $[RuHCl(CO)(PPh_3)_3]$ with 8-hydroxy-2-methyl-quinoline-7-carboxylic acid and quinoline-2-carboxylic acid have been examined, and two novel ruthenium(II) complexes – $[(PPh_3)_2RuH(CO)(C_{10}H_8NO_3)]$ and $[(PPh_3)_2RuCl(CO)(C_9H_6O_2)]$ – have been obtained. The compounds have been studied by IR and UV–Vis spectroscopy, and X-ray crystallography. The molecular orbital diagrams of the complexes have been calculated with the density functional theory (DFT) method. The spin-allowed singlet–singlet electronic transitions of the compounds have been calculated with the time-dependent DFT method, and the UV–Vis spectra of the compounds have been discussed on this basis.

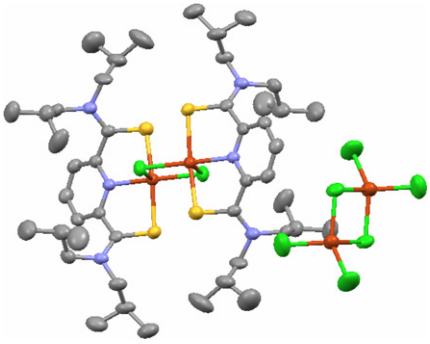


Ramesh Kapoor, Ashok Kataria, Pratibha Kapoor, Ajay Pal Singh Pannu, Maninder Singh Hundal and Montserrat Corbella

Polyhedron 26 (2007) 5131

Synthesis, X-ray structure and magnetic studies of Cu(II) complexes of tridentate SNS ligands (S-dbpt, *N*,*N*,*N*′,*N*′-tetraisobutylpyridine-2,6-dithiocarboxamide; S-dppt, *N*,*N*,*N*′,*N*′-tetraisopropylpyridine-2,6-dithiocarboxamide): Role of steric factors on the geometry around Cu(II)

Two new tetranuclear copper(II) complexes, each formed by a cationic and an anionic dinuclear species are reported. Both of them, characterized by X-ray diffraction, show the same anionic complex $[\{CuCl_2\}_2(\mu\text{-}Cl)_2]^{2-}$ which shows weak antiferromagnetic coupling. The dinuclear cationic species $[\{Cu(S\text{-}dbpt)\}_2(\mu\text{-}Cl)_2]^{2+}$ shows ferromagnetic behaviour.

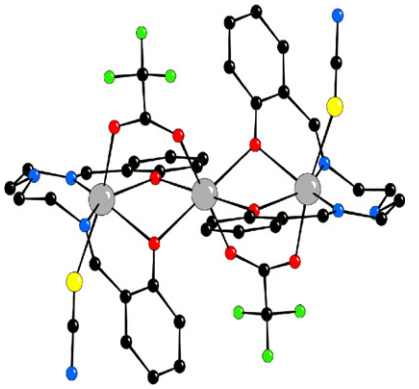


Joy Chakraborty, Santarupa Thakurta, Brajagopal Samanta, Aurkie Ray, G. Pilet, Stuart R. Batten, Paul Jensen and Samiran Mitra

Polyhedron 26 (2007) 5139

Synthesis, characterisation and crystal structures of three trinuclear cadmium(II) complexes with multidentate Schiff base ligands

Three novel trimeric Cd(II) complexes have been prepared from two different symmetrical Schiff bases. Crystal structures of all the complexes have been established by single crystal X-ray diffraction methods. The ligands and their metal complexes have been characterised by analytical and spectroscopic techniques. Among the three complexes, **1** and **3** are linear whereas **2** is a cyclic trimer. In **1** and **3**, all the doubly phenoxo bridged Cd(II) metal centres have a distorted octahedral environment. In the complex **2**, two out of the three Cd(II) centres reside in a distorted octahedral environment and the remaining one enjoys a monocapped octahedral geometry. Altogether a variety in the bridging mode of two new salen-type ligands has been established.

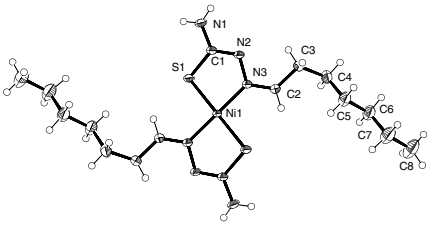


Marisa Belicchi-Ferrari, Franco Bisceglie, Giorgio Pelosi, Silvana Pinelli and Pieralberto Tarasconi

Polyhedron 26 (2007) 5150

Synthesis, characterization, crystal structure and antiproliferative *in vitro* activity of long-chain aliphatic thiosemicarbazones and their Ni(II) complexes

Nine long-chain aliphatic thiosemicarbazones and their nickel complexes were prepared and characterized by spectroscopic methods and for five of the complexes also by X-ray crystallography diffraction analysis. Heptanal thiosemicarbazone and the corresponding nickel complex were chosen after a solubility/stability test to carry out preliminary experiments *in vitro* on human leukemia cell line U937. The complex possesses a remarkable biological activity in inhibiting cell growth and in inducing apoptosis.

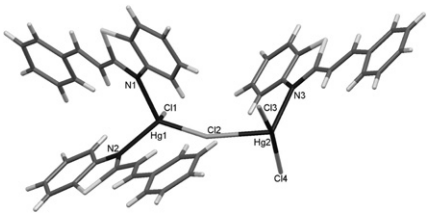


Gordana Pavlović, Željka Soldin, Zora Popović and Vesna Tralić-Kulenović

Polyhedron 26 (2007) 5162

Synthesis and characterization of mercury(II) complexes with 2-styryl-1,3-benzothiazole (sb). Presence of two differently coordinated Hg(II) ions in the dinuclear complex $Hg_2Cl_4(sb)_3$. Structural characterization of 2-styryl-1,3-benzothiazole and some of its derivatives

Mercury(II) chloride and bromide form two novel complexes **2** and **5** with 2-styryl-1,3-benzothiazole (sb). Compounds with different nuclearities were obtained under identical reaction conditions (ethanol medium, 1:2 molar ratio). The structure of **2** consists of dinuclear $Hg_2Cl_4(sb)_3$ units and compound **5** of monomeric $HgBr_2(sb)_2$ units.

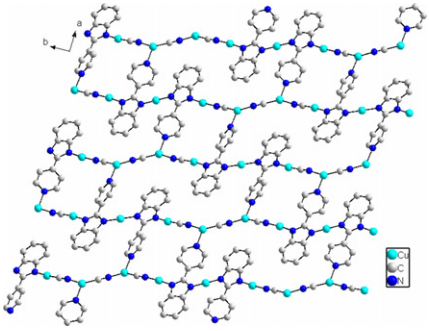


Hui Wang, Ming-Xing Li, Min Shao and Xiang He

Polyhedron 26 (2007) 5171

Syntheses, structures and luminescent properties of four copper(I) cyanide coordination polymers based on 2-(*n*-pyridyl)benzimidazole ligands (*n* = 2,3,4)

Four copper(I) cyanide coordination polymers containing 2-(*n*-pyridyl)benzimidazole ligands were synthesized. They possess one-dimensional linear chain, ladder-like double chain, saddle-shaped helical chain, and two-dimensional layer polymeric structures.

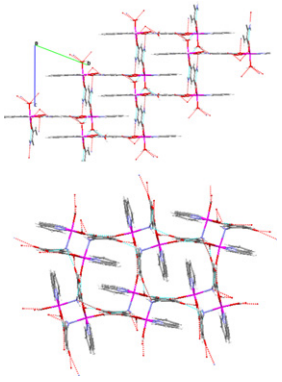


Kou-Lin Zhang, Hong-Yan Gao, Zi-Cai Pan, Wei Liang and Guo-Wang Diao

Polyhedron 26 (2007) 5177

Preparation and characterization of two three-dimensional metal–organic photoluminescent supramolecular networks

Two novel photoluminescent coordination compounds of the formula $[Cd(atpt)phen(H_2O)] \cdot H_2O$ (**1**) and $[Zn_2(atpt)_2(bipy)_2(H_2O)_2]$ (**2**) (H_2atpt = 2-aminoterephthalic acid, bipy = 2,2′-bipyridine and phen = 1,10-phenanthroline) were synthesized through the self-assembly of H_2atpt and N-containing ligands (bipy for **1** and phen for **2**) with metal(II) ions in the presence of NaOH, and characterized by FT-IR spectroscopy, thermogravimetric analysis (TG), X-ray analysis and photoluminescence spectra in the solid state. The coordination mode of the atpt ligand in **2** is novel and is first reported in this presentation. Compound **1** shows a 1D architecture and further assembles into a 3D supramolecular network *via* interchain hydrogen bonds and π–π stacking interactions. Compound **2** exhibits a binuclear structure with intramolecular π–π stacking interactions, which is further extended into a 3D supramolecular framework *via* intermolecular hydrogen bonds and C–H···π interactions. Compounds **1** and **2** exhibit green photoluminescence in the solid state at room temperature.

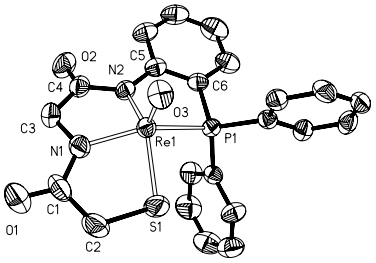


Laure Latapie, Julien Le Gal, Bassem Hamaoui, Joël Jaud, Marie Gressier and Eric Benoist

Polyhedron 26 (2007) 5185

First examples of neutral rhenium(V) complexes with a novel semi-rigid ligand containing a P,N,N,S donor atom set: Synthesis, characterisation and crystal structure

The synthesis of a novel PN_2S-tetradentate ligand [Ph-P(Ph_2)N_2S(Trt)] (**2**) and its metal complexation with Re^V precursors have been studied. Whilst the reaction of **2** with $ReOCl_3(PPh_3)_2$ gave the expected stable complex [ReO{Ph-P(Ph_2)N_2S}] (**4**), an unexpected neutral and diamagnetic species, [ReN{Ph-P(Ph_2)N_2S(Trt)}] (**5**), has been isolated during the complexation of **2** with $ReNCl_2(PPh_3)_2$.



Corrigendum to "Structural diversities and spectroscopic properties of bis and tris (1,10-phenanthroline)copper(II) complexes" [Polyhedron 26 (2007) 1459–1468] 5191

The Publisher encourages the submission of articles in electronic form thus saving time and avoiding rekeying errors. For detailed instructions on the preparation of manuscripts and of electronic artwork, consult the Author Gateway for Elsevier at http://authors.elsevier.com



Full text of this journal is available, on-line from **ScienceDirect**. Visit **www.sciencedirect.com** for more information.

Available online at www.sciencedirect.com
ScienceDirect
Polyhedron 26, issue 14, 31 August 2007
POLYHEDRON
www.elsevier.com/locate/poly

Contents

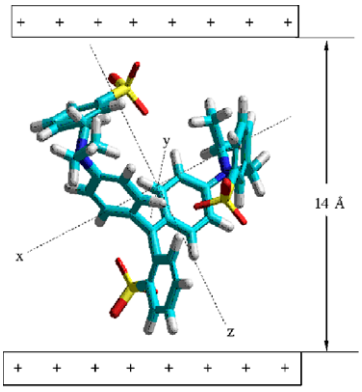
Papers

Anthony R. Auxilio, Philip C. Andrews, Peter C. Junk, Leone Spiccia, Daniel Neumann, Warwick Raverty and Nafty Vanderhoek

Polyhedron 26 (2007) 3479

Adsorption and intercalation of Acid Blue 9 on Mg–Al layered double hydroxides of variable metal composition

The surface dye adsorption and intercalation properties of Mg–Al–LDH have been greatly enhanced by fine tuning of the Mg/Al molar ratio; intercalation (interlamellar anionic exchange) of Acid Blue 9 was achieved with the aid of glycerol in low loading (5:1 (v/v) H_2O:glycerol).

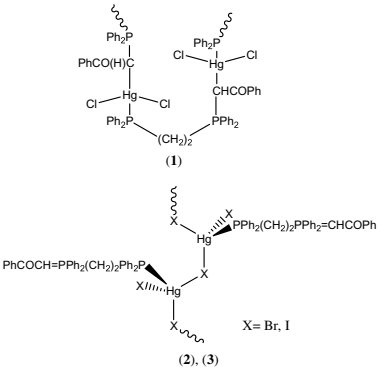


Mothi Mohamed Ebrahim, Helen Stoeckli-Evans and Krishnaswamy Panchanatheswaran

Polyhedron 26 (2007) 3491

Reactivity of mercury(II) halides with the unsymmetrical phosphorus ylide Ph_2PCH_2-CH_2PPh_2=C(H)C(O)Ph: Crystal structure of $\{HgI_2[PPh_2CH_2CH_2PPh_2$=C(H)C(O)Ph$]\}_n$

The title ylide and Hg(II) halides react to form polymeric complexes, $\{HgX_2[PPh_2CH_2CH_2$ $PPh_2C(H)C(O)Ph]\}_n$, where X = Cl (**1**), Br (**2**), I (**3**). The ylide in complex **1** exhibits P, C-bridging mode of coordination. The products **2** and **3** are halo bridged complexes involving P-coordination with the dangling ylide.

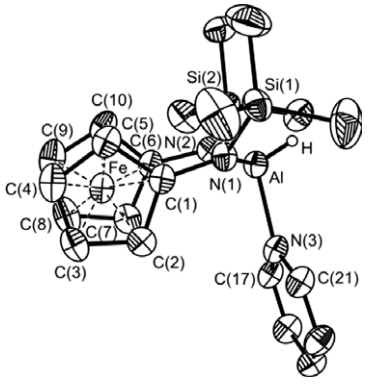


Bernd Wrackmeyer, Elena V. Klimkina and Wolfgang Milius

Polyhedron 26 (2007) 3496

Novel diaminoaluminum halides and a diaminoaluminum hydride: 1,3,2-Diazaalumina-[3]-ferrocenophanes

1,1′-Bis(lithio-trimethylsilylamino)ferrocene reacts with the pyridine adducts of the aluminum trihalides AlX_3 (X = Cl, Br, I) to give the respective 1,3,2-diazaalumina-[3]ferrocenophanes as pyridine adducts. The fluoride and the hydride have been prepared by different routes. The molecular structures of the pyridine adducts were determined by X-ray analysis in the solid state and by multinuclear dynamic NMR spectroscopy in solution.

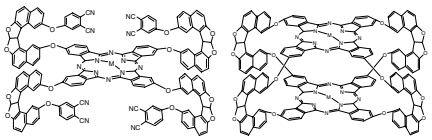


Zafer Odabaş, Ahmet Altındal, Ali Rıza Özkaya, Mustafa Bulut, Bekir Salih and Özer Bekaroğlu

Polyhedron 26 (2007) 3505

Synthesis, characterization, and electrochemical and electrical properties of novel mononuclear and binuclear ball-type Zn(II) and Co(II) phthalocyanines substituted with 1a, 8b-dihydronaphtho[*b*]naphthofuro-[3,2-*d*]furan-7,10-diyl

New mononuclear phthalocyanines {Zn(II) and Co(II)} and ball-type bisphthalocyanines {Zn(II) and Co(II)} have been synthesized from the corresponding 4,4′-(1a,8b-dihydronaphtho[*b*]naphthofuro[3,2-*d*]furan-7,10-diyl)-bis(oxy)diphthalonitrile, which can be obtained by the reaction of 4-nitrophthalonitrile with 1a,8b-dihydronaphtho[*b*]naphthofuro[3,2-*d*]furan-7,10-diol. The novel compounds have been characterized by elemental analysis, UV/Vis, IR, ^{1}H NMR and MASS spectroscopy.

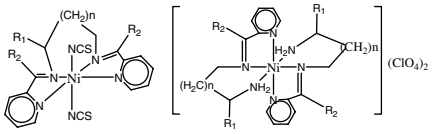


Shouvik Chattopadhyay, Michael G.B. Drew and Ashutosh Ghosh

Polyhedron 26 (2007) 3513

Anion directed templated synthesis of mono- and di-Schiff base complexes of Ni(II)

Reaction of Schiff base ligands derived from diamine (1,2-propanediamine or 1,3-propanediamine) and carbonyl compounds (2-acetylpyridine or pyridine-2-carboxaldehyde) separately with Ni(II) perchlorate and Ni(II) thiocyanate reveals that the perchlorate salt yields the bis-complexes of mono-condensed terdentate ligands having general formula $[NiL_2](ClO_4)_2$ whereas the thiocyanate salt results in the formation of tetradentate Schiff base complexes, $[NiL](SCN)_2$. Formation of the complexes has been explained by anion modulation of cation templating effect.

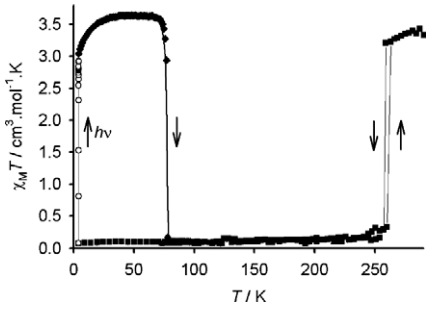


Malcolm A. Halcrow

Polyhedron 26 (2007) 3523

The spin-states and spin-transitions of mononuclear iron(II) complexes of nitrogen-donor ligands

A survey of mononuclear iron(II) complexes with heterocyclic N-donor ligation is presented. Thermal spin-transitions and low-temperature spin-trapping behaviour undergone by several of these compounds are described.

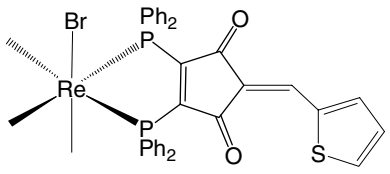


William H. Watson, David Wiedenfeld, Aparna Pingali, Bhaskar Poola and Michael G. Richmond

Polyhedron 26 (2007) 3577

Synthesis, electrochemistry, MO properties, and X-ray diffraction structures of the new redox-active diphosphine ligand 2-(2-thienylidene)-4,5-bis(diphenylphosphino)-4-cyclopenten-1,3-dione (tbpcd) and the rhenium compound *fac*-BrRe(CO)$_3$(tbpcd)

The new diphosphine ligand 2-(2-thienylidene)-4,5-bis(diphenylphosphino)-4-cyclopenten-1,3-dione (tbpcd) has been prepared from 4,5-bis(diphenylphosphino)-4-cyclopenten-1,3-dione (bpcd) and thiophene-2-carboxaldehyde. The reaction of the tbpcd ligand with BrRe(CO)$_5$ or BrRe(CO)$_3$(THF)$_2$ yields *fac*-BrRe(CO)$_3$(tbpcd) in high yield. The ligand and its rhenium complex have been fully characterized in solution and their solid-structures determined by X-ray crystallography. The cyclic voltammetric behavior, emission photophysics, and MO properties of these new compounds have also investigated and the results discussed relative to the parent diphosphine ligand bpcd and *fac*-BrRe(CO)$_3$(bpcd).



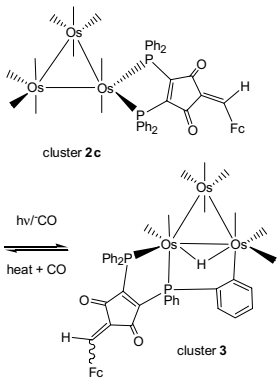
fac-BrRe(CO)$_3$(tbpcd)

William H. Watson, Bhaskar Poola and Michael G. Richmond

Polyhedron 26 (2007) 3585

Synthesis and reactivity studies of the diphosphine ligand 2-(ferrocenylidene)-4,5-bis(diphenylphosphino)-4-cyclopenten-1,3-dione (fbpcd): Bridge-to-chelate ligand isomerization kinetics in $Os_3(CO)_{10}$(fbpcd) and X-ray diffraction structure of the *ortho*-metalated cluster $HOs_3(CO)_9[\mu\text{-}PhP(C_6H_4)C{=}C(PPh_2)C(O)C{=}CH(C_5H_4FeCp)C(O)]$

The synthesis of the new diphosphine ligand 2-(ferrocenylidene)-4,5-bis(diphenylphosphino)-4-cyclopenten-1,3-dione (fbpcd) is described. The fbpcd ligand reacts with 1,2-$Os_3(CO)_{10}(MeCN)_2$ to give the diphosphine-bridged cluster 1,2-$Os_3(CO)_{10}$(fbpcd) (**2b**) as the principal product (>80%). Thermolysis of **2b** promotes the isomerization of the fbpcd ligand and formation of the chelating isomer 1,1-$Os_3(CO)_{10}$(fbpcd) (**2c**). Near-UV photolysis of **2c** leads to the formation of the hydride-bridged cluster $HOs_3(CO)_9[\mu\text{-}PhP(C_6H_4)C{=}C(PPh_2)C(O)C{=}CH(C_5H_4FeCp)C(O)]$ (**3**). All new compounds have been isolated and fully characterized by IR and NMR spectroscopies and X-ray diffraction analysis in the case of cluster **3**.

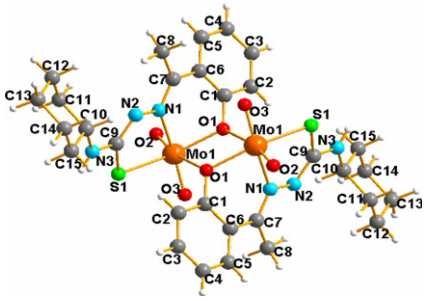


E.B. Seena and M.R. Prathapachandra Kurup

Polyhedron 26 (2007) 3595

Synthesis of mono- and binuclear dioxomolybdenum(VI) complexes derived from N(4)-substituted thiosemicarbazones: X-ray crystal structures of $[(MoO_2L^1)_2]$, $[MoO_2L^1py]$ and $[MoO_2L^2py]$

Four molybdenum(VI) thiosemicarbazonato complexes have been synthesized and characterized. The dinuclear complexes $[(MoO_2L^1)_2]$ (**1**) and $[(MoO_2L^2)_2]$ (**3**) have been prepared by the reaction of $[MoO_2(acac)_2]$ with 2-hydroxyacetophenone N(4)-cyclohexyl (H_2L^1) and N(4)-phenyl (H_2L^2) thiosemicarbazones in alcoholic medium. Mononuclear dioxomolybdenum(VI) complexes of the type $[MoO_2L^1py]$ (**2**) and $[MoO_2L^2py]$ (**4**) have been prepared by the reaction of **1** or **3** with pyridine (py) in alcoholic medium. In all the complexes, molybdenum is coordinated by two terminal oxo-oxygen atoms, (O_t), oxygen, nitrogen and sulfur atoms from the principal ligand and by an oxygen atom from the second unit in **1**, and by a nitrogen atom from pyridine in complexes **2** and **4**. All complexes have been spectroscopically characterized. The molecular structures of complexes **1**, **2** and **4** have been determined by the single crystal X-ray diffraction method.

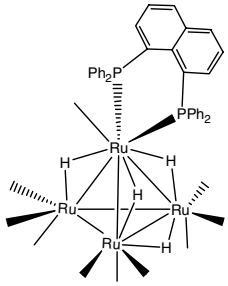


Vladimir N. Nesterov, William H. Watson, Srikanth Kandala and Michael G. Richmond

Polyhedron 26 (2007) 3602

CO substitution in $H_4Ru_4(CO)_{12}$ by the diphosphine ligands 1,2-bis(diphenylphosphino)benzene (dppbz) and 1,8-bis(diphenylphosphino)naphthalene (dppn): X-ray diffraction structures of the diphosphine-chelated clusters 1,1-$H_4Ru_4(CO)_{10}$(dppbz) and 1,1-$H_4Ru_4(CO)_{10}$(dppn)

The reaction of the tetraruthenium cluster $H_4Ru_4(CO)_{12}$ (**1**) with the unsaturated diphosphine ligands 1,2-bis(diphenylphosphino)-benzene (dppbz) and 1,8-bis(diphenylphosphino)naphthalene (dppn) under thermolysis and Me_3NO activation affords the diphosphine-chelated clusters 1,1-$H_4Ru_4(CO)_{10}$(dppbz) (**2**) and 1,1-$H_4Ru_4(CO)_{10}$(dppn) (**3**), respectively, as the only isolable products. Compounds **2** and **3** have been isolated and fully characterized by IR and NMR spectroscopies and X-ray diffraction analyses. The robust stability of **2** and **3** are discussed with respect to the other ruthenium clusters containing these diphosphine ligands.

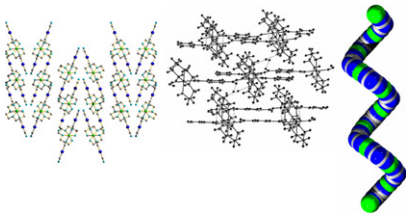


Jishnunil Chakraborty, Partha Roy, Heike Mayer-Figge, William S. Sheldrick and Pradyot Banerjee

Polyhedron 26 (2007) 3609

Synthesis, crystal structures and magnetic properties of three Ni(II) complexes having NiN_4 core with argentocyanide, terephthalate and dicyanamide ions: From discrete molecule to a helical network

Three Ni(II) complexes $[Ni(3,2,3\text{-tet})\{Ag(CN)_2\}_2]$ (**1**), $[Ni(3,2,3\text{-tet})(\mu\text{-tp})]_n \cdot 1.5nH_2O$ (**2**) and $\{[Ni(3,2,3\text{-tet})(\mu_{1,5}\text{-dca})](ClO_4)\}_n$ (**3**) where 3,2,3-tet = *N*,*N*′-bis(3-aminopropyl)-1,2-ethylenediamine, tp = terephthalate and dca = dicyanamide, have been synthesized and structurally characterized. Complex **1** is a discrete molecule whereas complexes **2** and **3** form terephthalate and dicyanamide bridged polymeric networks respectively. Complex **3** forms a novel helical 1D network.

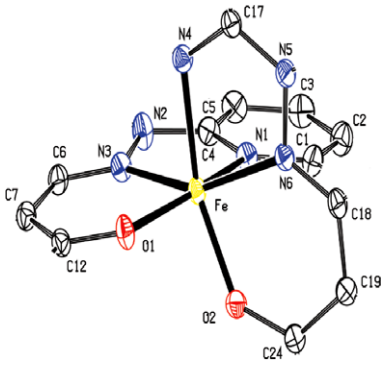


Chandrama Basu, Santanu Chowdhury, Rajat Banerjee, Helen Stoeckli Evans and Soma Mukherjee

Polyhedron 26 (2007) 3617

A novel blue luminescent high-spin iron(III) complex with interlayer O–H···Cl bridging: Synthesis, structure and spectroscopic studies

The acyclic tridentate salicyl-2-pyridyl hydrazone afforded a blue luminescent high-spin iron(III) complex (s = 5/2, λ_{ex} = 390 nm, λ_{em} = 449 nm) with interesting interlayer O–H···Cl bridging. Deprotonation and insertion of a nucleophile in the ligand frame significantly modulates the photophysical and chemical properties of the complex. Moreover, the ligand and its iron(III) complex undergo photoinduced intramolecular azo-imine tautomerism.

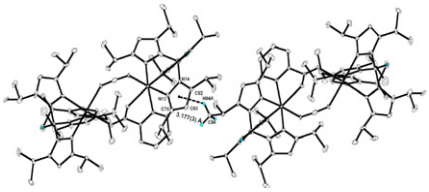


Udai P. Singh, Pooja Tyagi and Shailesh Upreti

Polyhedron 26 (2007) 3625

Manganese complexes as models for manganese-containing pseudocatalase enzymes: Synthesis, structural and catalytic activity studies

Some manganese complexes having $Tp^{Ph,Me}$ and Tp^{ipr2} as supporting ligands have been synthesized and structurally characterized. Since the coordination geometry of the manganese ions in complex **9** are very similar to the active site structure of manganese-containing pseudocatalase, we have tested the catalytic activity of the same towards the disproportionation of hydrogen peroxide.

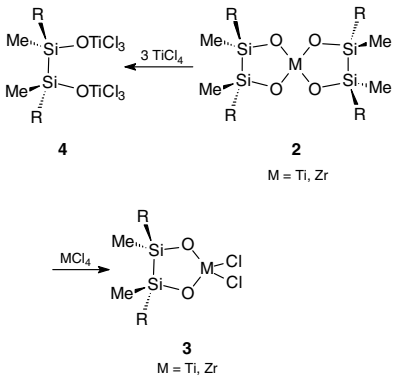


C. Krempner, H. Reinke and K. Weichert

Polyhedron 26 (2007) 3633

Synthesis and structure of titanium and zirconium disilane-1,2-diolates

The synthesis and structure of (*E*)-[Me(Me$_3$Si)$_3$SiSiO]$_2$M (**2**), where M is titanium and zirconium, are reported. Both compounds react with $TiCl_4$ and $ZrCl_4$, respectively, to yield the complexes (*E*)-[Me(Me$_3$Si)$_3$SiSiO]$_2$MCl$_2$ (**3**). Upon treatment with 3 equiv. of $TiCl_4$, the titanium compound **2** readily undergoes a ring opening reaction to produce the dinuclear complex a (*E*)-[Me(Me$_3$Si)$_3$SiSiO]$_2$Ti$_2$Cl$_6$ (**4**).

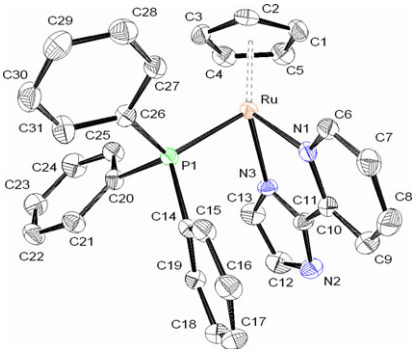


Khenglawt Pachhunga, Bruno Therrien, Kevin A. Kreisel, Glenn P.A. Yap and Mohan Rao Kollipara

Polyhedron 26 (2007) 3638

Reactivity studies of cyclopentadienyl ruthenium(II), osmium(II) and pentamethylcyclopentadienyl iridium(III) complexes towards 2-(2′-pyridyl)imidazole derivatives

The reactions of [CpRu(PPh$_3$)$_2$Cl], [CpOs(PPh$_3$)$_2$Br] and [Cp*Ir(μ-Cl)Cl]$_2$ with chelating 2-(2′-pyridyl)imidazole (N ∩ N) ligands and NH_4PF_6 yields cationic complexes of the type [CpM(N ∩ N)(PPh$_3$)]PF$_6$ and [Cp*Ir(N ∩ N)Cl]PF$_6$, respectively in good yield. These complexes were characterized with spectral and single-crystal X-ray study.

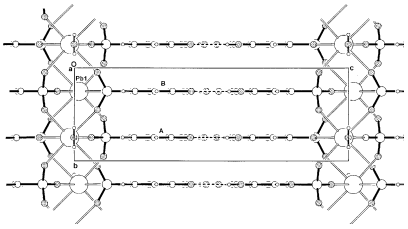


Graham Smith, Urs D. Wermuth, David J. Young and Jonathan M. White

Polyhedron 26 (2007) 3645

Polymeric structures in the metal complexes of 5-sulfosalicylic acid: The rubidium(I), caesium(I) and lead(II) analogues

Three-dimensional coordination polymers are found the structures of the complexes of 5-sulfosalicylic acid with rubidium(I): a tetrahydrate having both mono- and dianionic ligand species, and lead(II): a monohydrate which has a helical substructure with hydrogen-bonding peripheral extensions giving a layered structure.

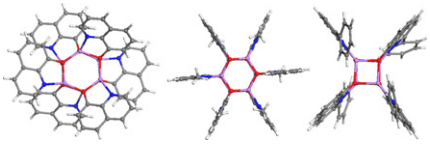


Manju Rajeswaran, William J. Begley, Leif P. Olson and Shouquan Huo

Polyhedron 26 (2007) 3653

Steric effects of substituted quinolines on lithium coordination geometry

Comparison of the solid-state structures of Li complexes, Liq, MeLiq, and PhLiq, illustrates steric effects on the coordination chemistry of lithium. Just by replacing the hydrogen in a quinoline ring with a methyl or phenyl changes the structure from a doubly stacked trimer to a paddle-wheel hexamer to a tetramer.

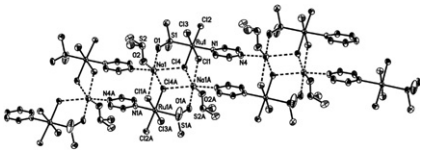


Craig M. Anderson, Amnon Herman and Fernande D. Rochon

Polyhedron 26 (2007) 3661

Synthesis and characterization of ionic Ru(III) complexes containing dimethylsulfoxide and dinitrogen heterocyclic ligands

Several new Ru(III) compounds containing both DMSO and a heterocyclic dinitrogen ligand were synthesized. The crystal structures of the *trans*-$[Ru(DMSO)(pz)Cl_4]^-$ (pz = pyrazine) monoanion, an analogue to the anticancer complex NAMI, with two different cations, tetraphenylphosphonium and Na show very different architectures. The Na complex has an interesting extended structure, while the PPh_4 complex shows discrete ions.

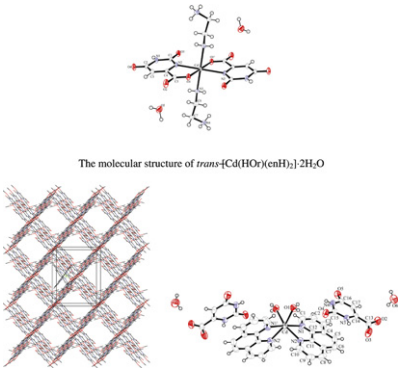


Okan Zafer Yeşilel, Halis Ölmez and Cengiz Arici

Polyhedron 26 (2007) 3669

The first bis(orotato-*N*,*O*) cadmium complex with monodentate protonated ethylenediamine ligands: Synthesis, spectrothermal properties of a cadmium(II)-orotato complex with ethylenediamine – Crystal structure of *trans*-$[Cd(HOr)_2(enH)_2] \cdot 2H_2O$ and *cis*-$[Cd(H_2O)_2(phen)_2](H_2Or)_2 \cdot 2H_2O$

In this study, we describe the synthesis, spectroscopic, thermal characterization and crystal structure of the first bis(orotato)cadmium(II) complex with monodentate protonated ethylenediamine ligands, *trans*-$[Cd(HOr)(enH)_2] \cdot 2H_2O$, and the crystal structure of the diaquabis(1,10-phenanthroline)cadmium(II) complex with an ororate counter ion, *cis*-$[Cd(H_2O)_2(phen)_2](H_2Or)_2 \cdot 2H_2O$.

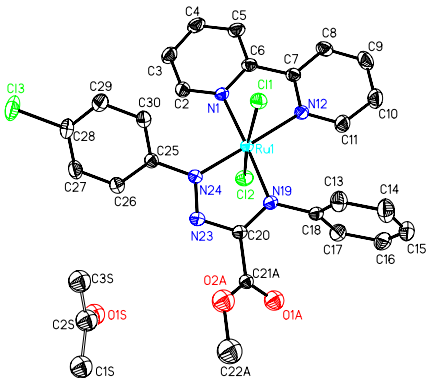


Mousa Z. Al-Noaimi, Haytham Saadeh, Salim F. Haddad, Musa I. El-Barghouthi, Mohammad El-khateeb and Robert J. Crutchley

Polyhedron 26 (2007) 3675

Syntheses, crystallography and spectroelectrochemical studies of ruthenium azomethine complexes

Complexes of the type $[Ru^{II}(bpy)(L)(Cl_2)]$, where **L** is an azomethine ligand, have been synthesized and characterized by IR, ^{1}H-NMR and UV-vis spectroscopies, elemental analysis, X-ray crystallography and cyclic voltammetry. Crystallographic, electrochemical and electronic spectral data and time-dependent DFT calculations are all consistent with azomethine ligands possessing strong p-acceptor properties. These p-acceptor properties can be "tuned" by a judicious choice of substituents on the azomethine ligand.

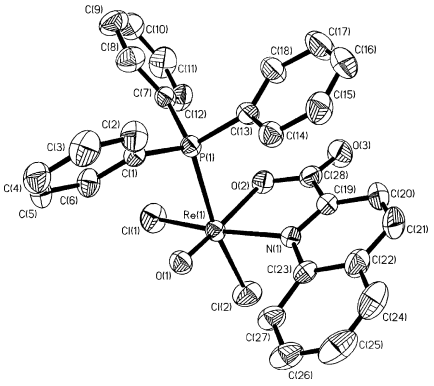


B. Machura and R. Kruszynski

Polyhedron 26 (2007) 3686

Oxorhenium(V) complexes with quinoline-2-carboxylate ligand. X-ray structure of $[ReOCl_2(quin\text{-}2\text{-}c)(PPh_3)]$ and $[ReOBr_2(quin\text{-}2\text{-}c)(AsPh_3)]$ complexes: DFT and TD-DFT calculations for $[ReOCl_2(quin\text{-}2\text{-}c)(PPh_3)]$

Novel $[ReOX_2(quin\text{-}2\text{-}c)(EPh_3)]$ complexes (X = Cl, Br; E = As, P; quin-2-c = quinoline-2-carboxylate ion) have been prepared by treatment of $[ReOX_3(EPh_3)_2]$ with quinoline-2-carboxylic acid in acetone at room temperature. All the complexes were characterised by IR, UV–Vis spectroscopy and elemental analysis. The crystal and molecular structures have been determined for $[ReOCl_2(qiun\text{-}2c)(PPh_3)]$ (**1**) and $[ReOBr_2(qiun\text{-}2c)(AsPh_3)]$ (**4**). The electronic structure of **1** has been calculated with the density functional theory (DFT) method. The spin-allowed electronic transitions of **1** have been calculated with the time-dependent DFT method.

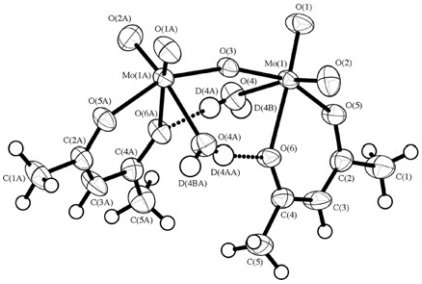


María R. Pedrosa, Jaime Escribano, Rafael Aguado, Virginia Díez, Roberto Sanz and Francisco J. Arnáiz

Polyhedron 26 (2007) 3695

Dinuclear oxomolybdenum(VI) acetylacetonates: Crystal and molecular structure of $Mo_2O_5(acac)_2L_2$ (L = D_2O, DMF)

The behavior of $MoO_2(acac)_2$ towards representative amines, amides, sulfoxides and phosphine oxides in common solvents has been examined. Compounds of the composition $Mo_2O_5(acac)_2L_2$, derived from the partial hydrolysis of $MoO_2(acac)_2$, can be readily isolated. The crystal and molecular structures of $Mo_2O_5(acac)_2L_2$ (L = D_2O, DMF) have been established by X-ray diffraction analysis.

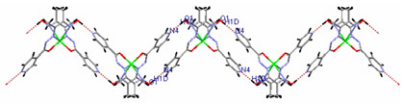


Subhendu Naskar, Dipankar Mishra, Ray J. Butcher and Shyamal Kumar Chattopadhyay

Polyhedron 26 (2007) 3703

Crystal engineering with aroyl hydrazones of diacetyl monooxime – Molecular and supramolecular structures of two Ni(II) and two Zn(II) complexes

Four new Schiff bases of aroyl hydrazides with diacetyl monooxime have been prepared and Ni(II) and Zn(II) complexes of these ligands have been synthesized. Two Ni(II) and two Zn(II) complexes have been characterized by X-ray crystallography. The aroyl hydrazone ligands were designed in such a way that there is a systematic variation in the H-bond forming abilities of their aroyl moiety, e,g. both H-bond acceptor and donor (salicyloyl), only H-bond donor (anthraniloyl), only H-bond acceptor (isonicotinoyl). It is shown in this work that such a variation in the H-bond donor acceptor properties of the ligands leads to considerable diversity in their supramolecular architecture.

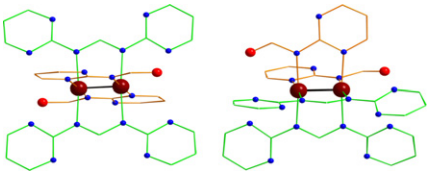


Zhi-Kai Chan, Tsun-Ren Chen, Yow-Fu Tsai, Jhy-Der Chen and Ju-Chun Wang

Polyhedron 26 (2007) 3715

Dimolybdenum complexes containing anions of *N*,*N*′-bis(pyrimidine-2-yl)formamidine and *N*-(2-pyrimidinyl)formamide

The reactions of $Mo_2(O_2CCH_3)$ with different equivalents of *N*,*N*′-bis(pyrimidine-2-yl)formamidine (H**L1**) and *N*-(2-pyrimidnyl)-formamide (H**L2**) afforded complexes of the types $Mo_2(O_2CCH_3)$(**L1**)$_2$ (**L2**) (**1**) *trans*-Mo_2(**L1**)$_2$ (**L2**)$_2$ (**2**) *cis*-Mo_2(**L1**)$_2$ (**L2**)$_2$ (**3**) and Mo_2(**L2**)$_4$ (**4**). Complexes **2** and **3** establish the first pair of *cis* and *trans* forms of dimolybdenum complexes containing formamidinate ligands. The Mo–Mo distances of complexes **1**–**3**, which contain both Mo···N and Mo···O axial interactions, are slightly longer than those of complex **4** which has only Mo···O interactions.

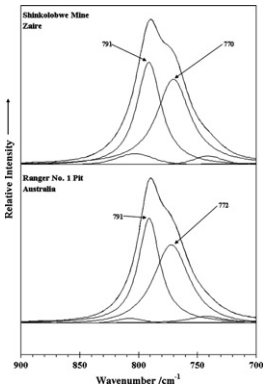


Ray L. Frost, Jiří Čejka, Godwin A. Ayoko and Matt L. Weier

Polyhedron 26 (2007) 3724

Vibrational spectroscopic study of hydrated uranyl oxide: Curite

Observed Raman bands of curite are attributed to the $(UO_2)^{2+}$ stretching and bending vibrations, U–OH bending vibrations, H_2O and $(OH)^-$ stretching, bending and libration modes. U–O bond lengths in uranyls and O–H…O bond lengths are calculated from the wavenumbers assigned to the stretching vibrations.

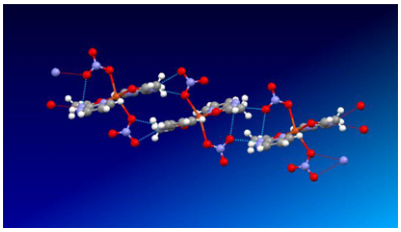


Gerard A. van Albada, Isja Dominicus, Ilpo Mutikainen, Urho Turpeinen and Jan Reedijk

Polyhedron 26 (2007) 3731

Synthesis, X-ray crystal structures, spectroscopic properties and magnetism of copper(II) compounds of formula *trans*-Cu(LL)$_2$(anion)$_2$, with *N*-(pyridin-2-yl)acetamide and *N*-(pyrimidin-2-yl)acetamide as ligands: Unexpected absence of hydrogen bonding to the non-coordinating nitrogen atom of the ligand

The bifunctional ligands Haap and Haapm generate chains of coordination units, organized by hydrogen bonds between the semi-coordinating counter anions and the NH group of the amide.

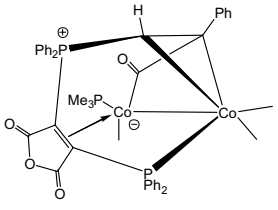


Simon G. Bott, Kaiyuan Yang and Michael G. Richmond

Polyhedron 26 (2007) 3737

PMe_3-induced CO insertion and CO deinsertion in the zwitterionic hydrocarbyl complex $Co_2(CO)_4$[μ-PhC═C(H)PPh_2C═C(PPh_2)C(O)OC(O)]: Syntheses and X-ray structures of $Co_2(CO)_3(PMe_3)$[μ-PhC(CO)═C(H)PPh_2C═C(PPh_2)C(O)OC(O)] and $Co_2(CO)_3(PMe_3)$[μ-PhC═C(H)PPh_2C═C(PPh_2)C(O)OC(O)]

The zwitterionic hydrocarbyl compound $Co_2(CO)_4$[μ-PhC═C(H)PPh_2C═C(PPh_2)C(O)OC(O)] (**1**) reacts with PMe_3 to afford the acyl species $Co_2(CO)_3(PMe_3)$[μ-PhC(CO)═C(H)PPh_2C═C(PPh_2)C(O)OC(O)] (**2**). Decarbonylation of **2** is observed on thermolysis and furnishes a mixture containing the PMe_3-substituted compound $Co_2(CO)_3(PMe_3)$[μ-PhC═C(H)PPh_2C═C(PPh_2)C(O)OC(O)] (**3**) and **1**. Compounds **2** and **3** have been isolated and fully characterized by IR and NMR spectroscopies and X-ray diffraction analyses.



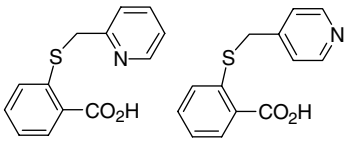
$Co_2(CO)_3(PMe_3)$[μ-PhC(CO)═C(H)PPh_2C═C(PPh_2)C(O)OC(O)] (**2**)

Xiao-Yan Zhang, Hai-Bin Song, Qing-Shan Li, Xiu-Feng Liu and Liang-Fu Tang

Polyhedron 26 (2007) 3743

Synthesis, structure and biological activity of organotin derivatives with pyridylmethylthiobenzoic acid

A series of organotin pyridylmethylthiobenzoates have been synthesized by the reaction of pyridylmethylthiobenzoic acid with R_2SnO (R = Et or ^{n}Bu) and $(Ph_3Sn)_2O$, and their fungicidal activity has been tested *in vitro*.

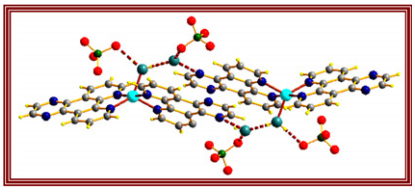


Meenakshi Ghosh, Papu Biswas and Ulrich Flörke

Polyhedron 26 (2007) 3750

Structural, spectroscopic and redox properties of transition metal complexes of dipyrido-[3,2-*f*:2′,3′-*h*]-quinoxaline (dpq)

First row transition metal complexes of dipyrido[3,2-*f*:2′,3′-*h*]-quinoxaline have been synthesized and their structural, spectroscopic and electrochemical behaviour have been studied thoroughly.

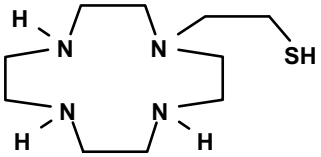


Sara Lacerda, Maria Paula Campello, Isabel C. Santos, Isabel Santos and Rita Delgado

Polyhedron 26 (2007) 3763

Study of the cyclen derivative 2-[1,4,7,10-tetraazacyclododecan-1-yl]-ethanethiol and its complexation behaviour towards d-transition metal ions

The compound 2-[1,4,7,10-tetraazacyclododecan-1-yl]-ethanethiol (**L2**) has been synthesized and fully characterized. The protonation constants of **L2** as well as its stability constants with Cu^{2+}, Zn^{2+} and Cd^{2+} were determined by potentiometric methods. Zn(II)/**L2** and Cu(II)/**L2** complexes were studied by NMR, UV–Vis, and EPR spectroscopies. The pM values calculated for the metal complexes of **L2**, at physiological pH, are higher than the pM values found for the corresponding complexes with cyclen or cyclam, but **L2** is less selective for copper.



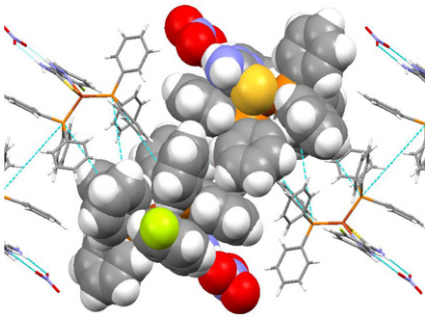
L2

Marisa Belicchi-Ferrari, Franco Bisceglie, Chiara Cavalieri, Giorgio Pelosi and Pieralberto Tarasconi

Polyhedron 26 (2007) 3774

Bis(triphenylphosphine)4-fluorobenzaldehyde thiosemicarbazone copper(I): Forcing chelation through oxoanions

Six 4-fluorobenzaldehyde thiosemicarbazone and 4-fluoro-4*N*-methylthiosemicarbazone bis-(triphenylphosphine) copper(I) complexes with different oxoanions were synthesized and characterized, for three of them the crystal structure was determined. The structures are the first reported in the literature in which a thiosemicarbazone binds as chelate on a bis-(triphenylphosphine)copper(I). The role of the oxoanions is determinant in stabilizing the *Z* configuration without competing as ligands.

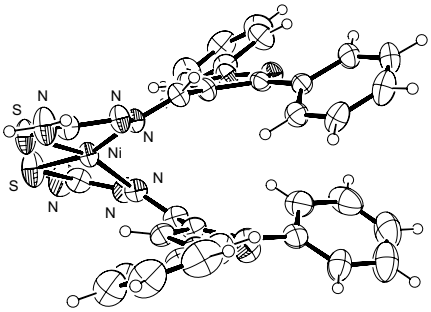


Vukadin M. Leovac, Slaana B. Novaković, Goran A. Bogdanović, Milan D. Joksović, Katalin Mészáros Szécsényi and Valerija I. Češljević

Polyhedron 26 (2007) 3783

Transition metal complexes with thiosemicarbazide-based ligands. Part LVI: Nickel(II) complex with 1,3-diphenylpyrazole-4-carboxaldehyde thiosemicarbazone and unusually deformed coordination geometry

The synthesis, crystal, and molecular structure of 1,3-diphenylpyrazole-4-carboxaldehyde thiosemicarbazone (Ph_2PzTSC) ligand and its markedly distorted diamagnetic *cis*-square-planar nickel(II) complex, [Ni(Ph_2PzTSC-H)$_2$] is described. The ligand has NS coordination in its thioenolato form.

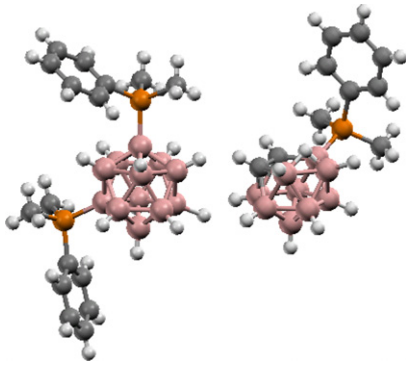


Steve A. Jasper Jr., John Mattern, John C. Huffman and Lee J. Todd

Polyhedron 26 (2007) 3793

Palladium-mediated substitution of the *closo*-$B_{12}H_{12}(-2)$ and *nido*-7,8-$C_2B_9H_{12}(-1)$ ions by PMe_2Ph: The single-crystal structure studies of 1,7-$(PMe_2Ph)_2$-*closo*-$B_{12}H_{10}$ and 9-PMe_2Ph-*nido*-7,8-$C_2B_9H_{11}$

Palladium-mediated phosphine derivatization of borane anions was demonstrated using the reagent $(PMe_2Ph)_2PdCl_2$ (**1**). Treatment of icosahedral borane anion [*closo*-$B_{12}H_{12}]^{2-}$ with (**1**) formed three phosphine derivatives: [(PMe_2Ph)-*closo*-$B_{12}H_{11}]^-$, 1,7-$(PMe_2Ph)_2$-*closo*-$B_{12}H_{10}$, and 1,12-$(PMe_2Ph)_2$-*closo*$B_{12}H_{10}$, in moderate yield. Reaction of [*nido*7,8-$C_2B_9H_{12}]^-$ with **1** similarly formed two phosphine derivatives: 9-PMe_2Ph-*nido*-7,8-$C_2B_9H_{11}$ and 10-PMe_2Ph-*nido*-7,8-$C_2B_9H_{11}$, in overall good yield.

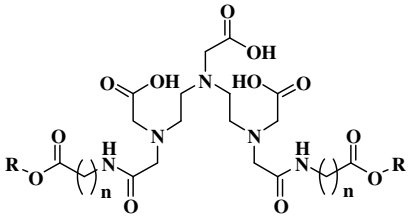


Sujit Dutta, Suk-Kyung Kim, Daksha B. Patel, Tae-Jeong Kim and Yongmin Chang

Polyhedron 26 (2007) 3799

Some new DTPA-*N*,*N*″-bis(amides) functionalized by alkyl carboxylates: Synthesis, complexation and stability properties

A new series of DTPA-bis(amides) (**1a**–**1l**) significantly enhance thermodynamic stabilities of the corresponding Gd(III) complexes as compared with related DTPA-BMA. Yet, the relaxivities (R_1 and R_2) drop significantly in an aqueous solution, whereas they increase by 6–10 fold in aqueous hydroxypropyl-β-cyclodextrin solutions.

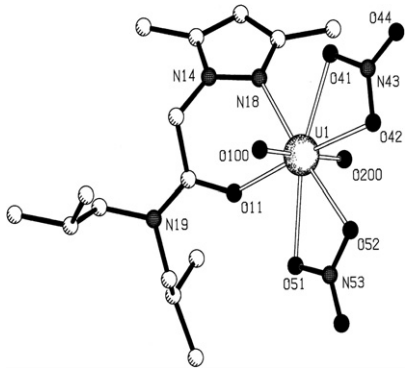


S. Kannan, J.S. Gamare, K.V. Chetty and M.G.B. Drew

Polyhedron 26 (2007) 3810

Coordination and extraction studies of an unexplored bi-functional ligand, carbamoyl methyl pyrazole (CMPz) with uranium(VI), lanthanum(III) and cerium(III) nitrates

Coordination studies of an unexplored bi-functional ligand carbamoyl methyl pyrazole (CMPz) with uranium(VI), plutonium(IV), lanthanum(III) and cerium(III) nitrates show that it acts as a bidentate chelating ligand in all these compounds. The extraction studies show an appreciable extractions for uranium(VI) and plutonium(VI) from nitric acid medium.

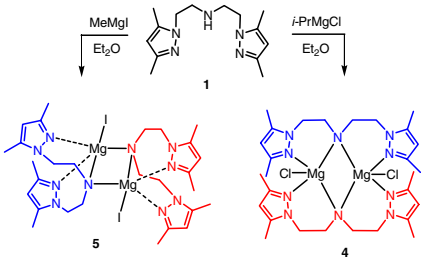


Bing Lian, Christophe M. Thomas, Osvaldo L. Casagrande Jr., Thierry Roisnel and Jean-François Carpentier

Polyhedron 26 (2007) 3817

Magnesium complexes based on an amido-bis(pyrazolyl) ligand: Synthesis, crystal structures, and use in lactide polymerization

Monomeric diamido bis(ligand) and dimeric amido-halide magnesium complexes based on a tridentate *NNN* ligand are respectively shown to be active in lactide polymerization and to feature a different coordination mode of the *NNN* ligand according to the nature of the halide ion.

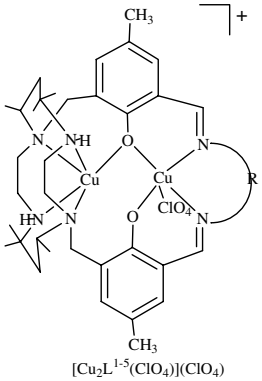


N. Sengottuvelan, D. Saravanakumar and M. Kandaswamy

Polyhedron 26 (2007) 3825

Electrochemical, magnetic, catalytic and DNA cleavage studies of binuclear copper(II) complexes derived from pendant substituted tetraaza macrobicyclic compartmental ligands

Novel *N*-difunctionalised tetraaza macrocyclic ligands and their binuclear copper(II) complexes have been synthesized and characterized. Electrochemical studies indicate that the copper(II) complexes show two irreversible one-electron reduction processes. Catechol oxidation, phosphate hydrolysis and DNA cleavage studies show that the distorted complex has a higher catalytic activity than the other rigid complexes.

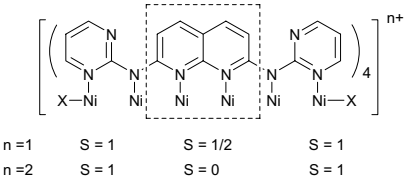


Ting-Bin Tsao, Shang-Shih Lo, Chen-Yu Yeh, Gene-Hsiang Lee and Shie-Ming Peng

Polyhedron 26 (2007) 3833

Novel multi-spin-state linear hexanickel complexes Ni_6^{11+} and their singly oxidized products Ni_6^{12+} with 1,8-naphthyridine-based ligands: Tuning the redox properties of the metal string

A series of hexanickel complexes (Ni_6^{12+}) and their corresponding one-electron reduction forms (Ni_6^{11+}) have been synthesized and structurally characterized. In the Ni_6^{12+} complexes, there is no metal–metal bonding between the adjacent nickel ions. In contrast, the central dinickel unit shows partial metal–metal bonding for the Ni_6^{11+} complexes.

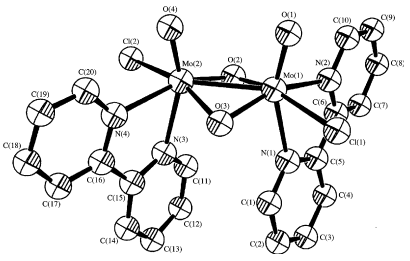


Rafael Aguado, Jaime Escribano, María R. Pedrosa, André De Cian, Roberto Sanz and Francisco J. Arnáiz

Polyhedron 26 (2007) 3842

Binuclear oxomolybdenum(V) chlorides: Molecular structure of $Mo_2O_4Cl_2(DMF)_4$ and $Mo_2O_4Cl_2(bipy)_2 \cdot DMF$

Reduction of $MoO_2Cl_2(DMF)_2$ (DMF = dimethylformamide) with PPh_3 in mild conditions afforded the dinuclear species $Mo_2O_3Cl_4(DMF)_4$. Related compounds could be prepared by substitution of DMF with stronger bases. The molecular structures of $Mo_2O_4Cl_2(DMF)_4$, and $Mo_2O_4Cl_2(bipy)_2$ (bipy = 2,2′-bipyridine) have been established by X-ray diffraction analysis.

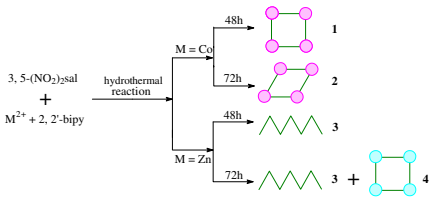


De-Cai Wen, Shi-Xiong Liu and Joan Ribas

Polyhedron 26 (2007) 3849

Hydrothermal syntheses, structures and properties of three cyclic tetranuclear complexes and one 1D chain complex with 3,5-dinitrosalicylate

Hydrothermal reactions of $Co(OAc)_2 \cdot 4H_2O$/$Zn(NO_3)_2 \cdot 6H_2O$, 3,5-dinitrosalicylate (3,5-$(NO_2)_2$sal) and 2,2′-bipyridine (2,2′-bipy) with different reaction times give three cyclic tetranuclear complexes (**1**, **2** and **4**) and complex **3** with a 1D structure. The cobalt complexes **1** and **2** are polymorphic, and the zinc complexes **3** and **4** are polymorphic too. Compounds **1** and **4** form an isomorphous pair.

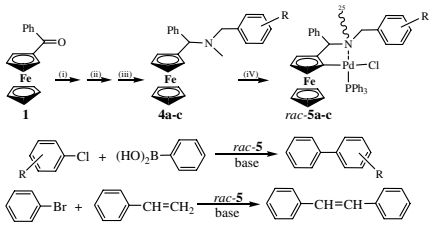


Hong-Xing Wang, Hong-Fei Wu, Xiao-Li Yang, Nan Ma and Li Wan

Polyhedron 26 (2007) 3857

Highly active ferrocenylamine-derived palladacycles for carbon–carbon cross-coupling reactions

{[(*N*-Methyl-*N*-*p*-R-benzyl)amino]benzyl}ferrocenes**4a**–**c** were synthesized from *sec*-amines **3a**–**c** and CH_3I. Treatment of **4a**–**c** with Na_2PdCl_4 produced a pair of palladacycles σ-Pd[(η^5-C_5H_5)Fe(η^5-C_5H_3CH(C_6H_5)N(CH_3)-CH_2-C_6H_4-R)]Cl(PPh_3) **5a**–**c**, consisting of R_NR_P and S_NS_P configurations. High catalytic activities of **5a**–**c** for the Suzuki coupling of aryl chlorides with phenylboronic acid and for the Heck reaction of bromobenzene with styrene were observed.

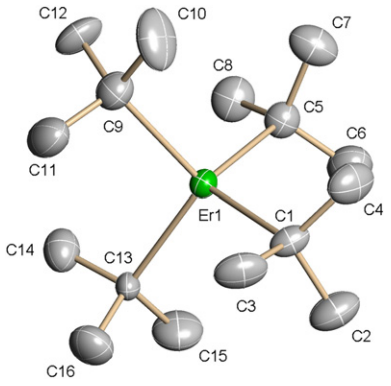


Wontae Noh and Gregory S. Girolami

Polyhedron 26 (2007) 3865

X-ray crystal structure of the tetra(*tert*-butyl)erbate anion and attempts to prepare tetravalent organolanthanide complexes

The new [$Li(DME)_3^+$] salt of the previously-known tetra(*tert*-butyl)erbate(III) anion [Er-(*t*-$Bu)_4^-$] has been prepared and structurally characterized. The erbium(III) center is ligated by four *tert*-butyl groups in an approximately tetrahedral arrangement. Attempts to oxidize the analogous terbate complex [$Li(DME)_3$]-[Tb(*t*-$Bu)_4$] to electrically neutral tetra(alkyl)-lanthanide(IV) compounds are described.

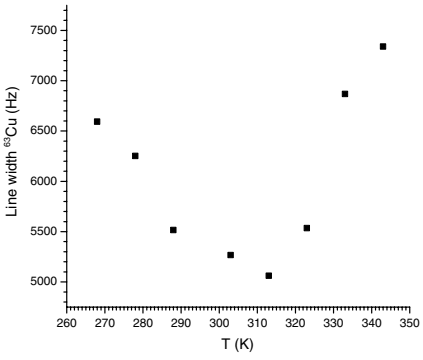


Viviane A.S. Falcomer, Sebastião S. Lemos, Guilherme B.C. Martins, Gleison A. Casagrande, Robert A. Burrow and Ernesto S. Lang

Polyhedron 26 (2007) 3871

Synthesis, structural characterization and reactivity of copper(I)-nitrile complexes: Crystal and molecular structure of [$Cu(BzCN)_4$][BF_4]

The [CuL_4][BF_4] (L = benzonitrile – PhCN **2** or phenylacetonitrile – BzCN **3**) complexes have been prepared and their structure evaluated both in solution and in the solid-state by ^{63}Cu NMR spectroscopy and by X-ray crystallography.

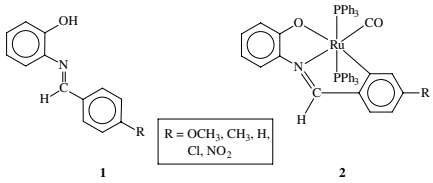


Chhandasi GuhaRoy, Sakya Singha Sen, Swati Dutta, Golam Mostafa and Samaresh Bhattacharya

Polyhedron 26 (2007) 3876

Synthesis, structure and electrochemical properties of a family of organoruthenium complexes

Reaction of a group of *N*-(2′-hydroxyphenyl)benzaldimines (**1**) with $[Ru(PPh_3)_2(CO)_2Cl_2]$ in refluxing 2-methoxyethanol in the presence of a triethylamine afforded a family of organoruthenium complexes (**2**) in which the benzaldimine ligands are coordinated to the metal center, via C–H activation, as dianionic tridentate C,N,O-donors.

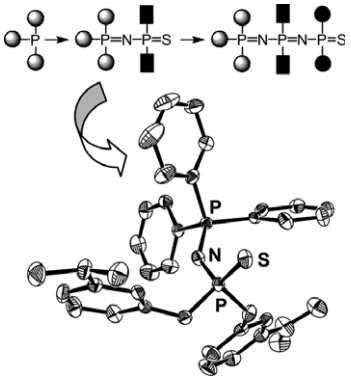


Germinal Magro, Bruno Donnadieu, Grégory Spataro, Anne-Marie Caminade and Jean-Pierre Majoral

Polyhedron 26 (2007) 3885

Step-by-step synthesis of multifunctionalized linear oligophosphazenes: X-ray crystal structures of compounds issued from the first steps

An inorganic oligomeric chain constituted of P=N linkages is synthesized step-by-step. Such methodology allows the selective grafting of different selected functional groups to the inorganic backbone. The structure of a compound possessing a P=N—P=S linkage and two types of side groups was determined by X-ray crystallography.

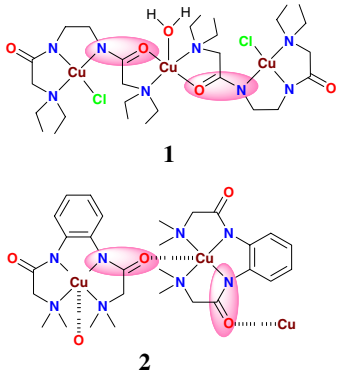


Jyoti Singh, Geeta Hundal, Montserrat Corbella and Rajeev Gupta

Polyhedron 26 (2007) 3893

Synthesis, characterization and structures of copper(II) complexes with amide-based ligands: Unusual formation of a linear trimer and a zig-zag chain and their contrast magnetic behaviour

Novel copper(II) complexes of amide-based ligands are reported having linear trimeric (**1**) and one-dimensional zig-zag chain (**2**) structures. The copper centers bridged by the amidic NCO group (highlighted in pink shade) show interesting but contrast magnetic properties. The complex **1** shows antiferromagnetic coupling ($J = -110\ cm^{-1}$) while **2** shows a weak ferromagnetic interaction ($J = +3\ cm^{-1}$).

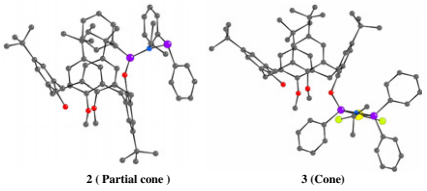


Arindam Sarkar, Munirathinam Nethaji and Setharampattu S. Krishnamurthy

Polyhedron 26 (2007) 3904

Structure and solution dynamics of a "P–N–P" ligand attached to calix[4]arene scaffold and its palladium dichloride complex

Synthesis, solid-state structure analysis and solution NMR study of a new calixarene-phosphorus ligand, $Ph_2PN(CHMe_2)P(Ph)$-{1,3-dimethoxycalix[4]arene} (**2**), incorporating a "P–N–P" unit and its $PdCl_2$ complex (**3**), are reported.



Xiao-Ju Li, Rong Cao, Zhen-Gang Guo, Ya-Feng Li and Xian-Dong Zhu

Polyhedron 26 (2007) 3911

Conformational isomerism of 1,2-bis(imidazol-1′-yl)ethane in five-coordination polymers: Influence of metal ions and *m*-isophthalate ligands bearing different substituents

The solvothermal reactions of 1,2-bis(imidazol-1′-yl)ethane (bime), *m*-isophthalic acid (H_2bdc) or its derivatives 5-hydroxylisophthalic acid (HO-H_2bdc) and 5-nitroisophthalic acid (O_2N-H_2bdc) with different metal ions gave rise to five novel coordination polymers, $\{[Zn(gauche\text{-bime})(bdc)] \cdot 0.5H_2O\}_n$ (**1**), $\{[Zn(anti\text{-bime})(HO\text{-bdc})] \cdot 2.5H_2O\}_n$ (**2**), $\{[Zn(anti\text{-bime})(O_2N\text{-bdc})] \cdot H_2O\}_n$ (**3**), $[Cu(gauche\text{-bime})_{0.5}(anti\text{-bime})_{0.5}(O_2N\text{-bdc})]_n$ (**4**) and $[Ni_2(gauche\text{-bime})(anti\text{-bime})(O_2N\text{-bdc})_2(H_2O)_2]_n$ (**5**). The presence of coexistent electron-donating and electron-withdrawing groups in dicarboxylate ligands and different metal ions play crucial roles on the conformational preference of bime in the five structures.

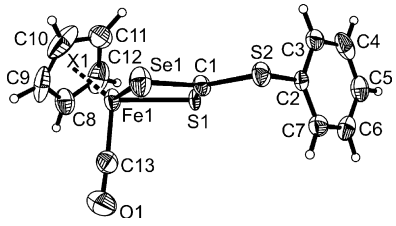
Solvothermal reaction	Compound	Comoformational isomer of bime
bime + H_2bdc + $Zn(NO_3)_2{\cdot}6H_2O$	**1**	*gauche*
bime + HO-H_2bdc + $Zn(NO_3)_2{\cdot}6H_2O$	**2**	*anti*
bime + O_2N-H_2bdc + $Zn(NO_3)_2{\cdot}6H_2O$	**3**	*anti*
bime + O_2N-H_2bdc + $Cu(NO_3)_2{\cdot}3H_2O$	**4**	*gauche* : *anti* = 1 : 1
bime + O_2N-H_2bdc + $Ni(NO_3)_2{\cdot}6H_2O$	**5**	*gauche* : *anti* = 1 : 1

Mohammad El-khateeb and Alexander Roller

Polyhedron 26 (2007) 3920

Synthesis and structures of $CpFe(CO)_2(\kappa E\text{-}ECS_2Ph)$ and $[CpFe(CO)(\kappa^2 S,E\text{-}ECS_2Ph)]$ (E = S, Se)

The complexes $CpFe(CO)_2(\kappa E\text{-}SCS_2Ph)$ (**1a**) and $CpFe(CO)_2(\kappa Se\text{-}SeCS_2Ph)$ (**1b**) were generated by room temperature reactions of $(\mu\text{-}E_x)[CpFe(CO)_2]_2$ (E = S; *x* = 2, 3. E = Se; *x* = 1) with PhSC(S)Cl. These compounds can be converted into the complexes $CpFe(CO)(\kappa^2 E,S\text{-}ECS_2Ph)$ [E = S (**2a**), Se (**2b**)], under photolytic conditions. All products have been characterized by elemental analyses, IR and ^{1}H NMR spectroscopies. The X-ray crystal structures of **1a**, **1b** and **2b** are determined.

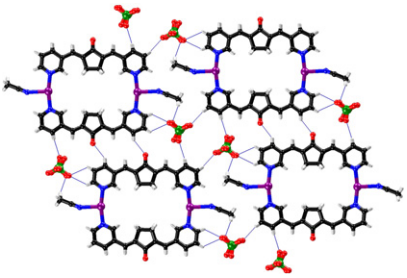


Aref A.M. Aly, Sergey Z. Vatsadze, Aleksey V. Chernikov, Bernhard Walfort, Tobias Rüffer and Heinrich Lang

Polyhedron 26 (2007) 3925

A binuclear silver(I) perchlorate macrocycle based on 2,5-bis[(*E*)-(3-pyridyl)methylene]cyclopentanone: Crystal structure and solution behavior

In the solid state, a 26-membered disilver macrocycle is formed. The coordination sites at the silver metal center are occupied by two nitrogen donor atoms of the ligands, one nitrogen donor atom of an acetonitrile solvent molecule and an oxygen donor atom from a weakly-coordinated $OClO_3$ counter-anion.

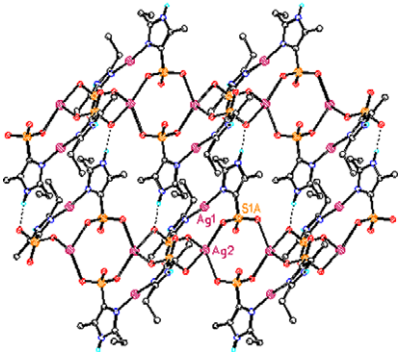


Andrew P. Purdy, Richard Gilardi, Justin Luther and Raymond J. Butcher

Polyhedron 26 (2007) 3930

Synthesis, crystal structure, and reactivity of alkali and silver salts of sulfonated imidazoles

The synthesis and crystal structures of 2-methylimidazole-5-sulfonic acid, 2-ethyl-4-methylimidazole-5-sulfonic acid, and the Li, Ag, and bis(trimethylsilyl) derivatives of the latter are described. Silver 2-ethyl-4-methylimidazole-5-sulfonate (pictured) is a three-dimensional network in the crystal assembled by bonds between 2-coordinate Ag and N, 4-coordinate Ag and O, and by hydrogen bonding.

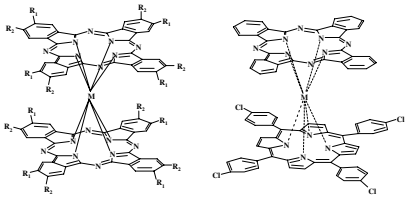


Fan-Li Lu

Polyhedron 26 (2007) 3939

The effects of substituents, molecular symmetry, ionic radius of the rare earth metal, and macrocycle on the electronic absorption spectra characteristics of sandwich-type bis(phthalocyaninato) and mixed (phthalocyaninato)-(porphyrinato) rare earth complexes

In this paper, the influence of the symmetry of macrocycle rare earth molecules, the effects of ionic radius of the rare earth metal and the influence of substituent species (*tert*-butyl and octyloxy groups) in the peripheral benzene rings on the electronic absorption characteristics of sandwich-type compounds have also been tentatively studied in detail.

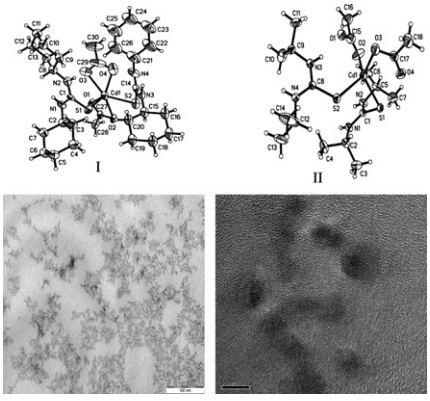


N. Moloto, N. Revaprasadu, M.J. Moloto, P. O'Brien and M. Helliwell

Polyhedron 26 (2007) 3947

N,*N*′-Diisopropyl- and *N*,*N*′-dicyclohexylthiourea cadmium(II) complexes as precursors for the synthesis of CdS nanoparticles

The two complexes $[Cd(CH_3COO)_2(SC(NHC_6H_{11})_2)_2]$ (**I**) and $[Cd(CH_3COO)_2(SC(NHC_3H_7)_2)_2]$ (**II**), were characterized by crystallography and indicate bonding through sulphur from the alkylthiourea ligands and also the acetate binding through oxygen atoms. Upon thermolysis of these complexes in HDA (hexadecylamine), CdS nanoparticles were obtained, which showed quantum confinement in their optical spectra, broadening of peaks in the XRD and the TEM images confirms particles in the nanosized region.

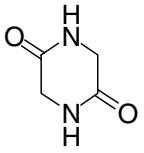


Mohamed E. Mahmoud, Sawsan S. Haggag and Tarek M. Abdel-Fattah

Polyhedron 26 (2007) 3956

Synthesis, characterization and metal chelating properties of silica-physisorbed and chemisorbed-2,5-dioxypiperazine

2,5-Dioxypiperazine, also known as piperazine-2,5-dione or glycine anhydride is used as a chelating compound to incorporate some chelating characters onto the surface of silica via chemisorption and physisorption approaches. The modified chelating silicas were characterized and studied by evaluation of the metal chelating properties for a series of toxic and non-toxic metals.

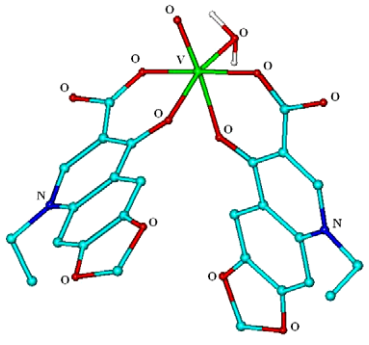


Alketa Tarushi, Petros Christofis and George Psomas

Polyhedron 26 (2007) 3963

Synthesis, characterization and interaction with DNA of mononuclear metal complexes with oxolinic acid

The synthesis, the characterization and the structure of the neutral mononuclear complexes of the bidentate quinolone antibacterial agent oxolinic acid with VO^{2+}, Mn^{2+}, Fe^{3+}, Co^{2+}, Ni^{2+}, Zn^{2+} and Cd^{2+}as well the study of the interaction of the resulting complexes with calf-thymus DNA are presented.

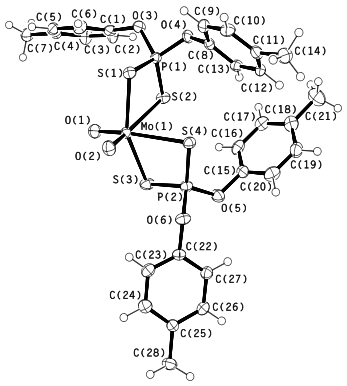


Lalit Awwal, John E. Drake, Michael B. Hursthouse, Ravindra Kumar, Mark E. Light, Raju Ratnani and Keerti Saraswat

Polyhedron 26 (2007) 3973

Synthesis and characterization of binuclear oxomolybdenum(V) and dioxomolybdenum(VI) *O*,*O*′-ditolyl dithiophosphate complexes

Binuclear oxomolybdenum(V) and Dioxomolybdenum(VI) *O*,*O*′-ditolyl dithiophosphate complexes were synthesized. These synthesized complexes were characterized by elements analysis and IR, ^{1}H and ^{31}P NMR spectroscopy and, in three cases, by X-ray crystallography. $Mo_2O_3[S_2P(OC_6H_4Me\text{-}o)_2]_4$ and $Mo_2O_3[S_2P(OC_6H_4Me\text{-}m)_2]_4$, the environment around each molybdenum atom can be described as the expected distorted octahedral. The geometry around the Mo atom in $MoO_2[S_2P(OC_6H_4Me\text{-}p)_2]_2$ is again distorted octahedral.

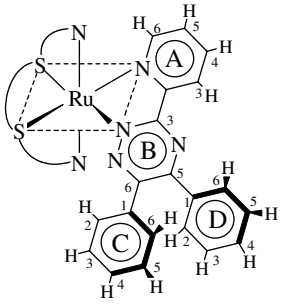


Mariappan Murali and Mallayan Palaniandavar

Polyhedron 26 (2007) 3980

Synthesis, spectral and electrochemical properties of mixed-ligand ruthenium(II) complexes of bis(pyrid-2-yl)- and bis(benzimidazol-2-yl)-dithioether ligands: Effect of an asymmetric diimine co-ligand

The synthesis, spectral and redox behaviour of two new mixed-ligand ruthenium(II) complexes of N_2S_2 and asymmetric diimine ligands are described. The NMR spectral studies reveal the exclusive formation of an isomer in which the N_2S_2 ligands are coordinated *cis*-α to ruthenium and with the involvement in coordination of both the triazine N2 and pyridine nitrogen atoms of the diimine.

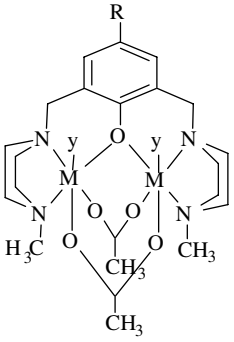


K. Shanmuga Bharathi, S. Sreedaran, A. Kalilur Rahiman, K. Rajesh and V. Narayanan

Polyhedron 26 (2007) 3993

Synthesis, spectral, magnetic, electrochemical and kinetic studies of copper(II), nickel(II) and zinc(II) acetate complexes derived from phenol based 'end-off' ligands: Effect of *p*-substituents

A new class of symmetric, end-off, *N*-methyl piperazine armed binucleating ligands 2,6-bis(4-methyl piperazin-1-yl-methyl)-4-acetyl phenol (HL^1) and 2,6-bis[(4-methyl piperazin-1-yl-methyl)]-(4-methylcarboxy) phenol (HL^2) were synthesized by the Mannich reaction. Their mononuclear and binuclear Cu(II), Ni(II) and Zn(II) complexes were prepared. The effect of the *p*-substituent of the phenolic ring of the complexes on the LMCT charge transfer band, magnetic moment, reduction behaviour and oxidation of catechol is clearly explained.

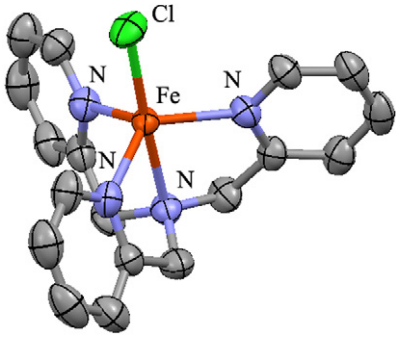


Mihyang Kim, Yong-Ung Kim and Jaehong Han

Polyhedron 26 (2007) 4003

X-ray crystallographic structure and physical properties of the pentacoordinated $[TPAFeCl]^+$ complex

A new pentacoordinated ferrous compound $[TPAFeCl]^+$ (TPA = tris(2-pyridylmethyl)-amine) was synthesized from the reaction between $H_3TPA(ClO_4)_3$ and $Fe(P^nPr_3)_2Cl_2$ in MeCN. The trigonal bipyramidal $[TPAFeCl]^+$ complex was characterized as a $S = 2$ high spin complex.

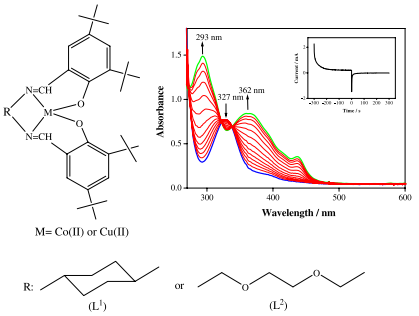


Ahmet Kilic, Esref Tas, Bedriye Deveci and Ismail Yilmaz

Polyhedron 26 (2007) 4009

Synthesis, electrochemical and *in situ* spectroelectrochemical studies of new transition metal complexes with two new Schiff-bases containing N_2O_2/N_2O_4 donor groups

New Schiff-base copper and cobalt complexes, [Cu(L^1)], [Cu(L^2)], and [Co(L^1)], [Co(L^2)] (where L^1 = *N*-*N*′-bis(3,5-di-*tert*-butylsalicylaldimine)-1,4-cyclohexane bis(methylamine) and L^2 = *N*-*N*′-bis(3,5-di-*tert*-butylsalicylaldimine)-1,8-diamino-3,6-dioxaoctane), were synthesized and characterized, and their electro-spectrochemical properties were investigated using cyclic voltammetric (CV) and thin-layer spectroelectrochemical techniques in a dichloromethane solution (CH_2Cl_2).

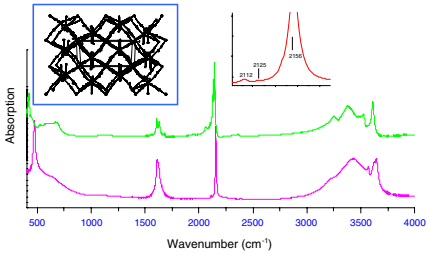


Lin-Ping Zhang, Xian-ju Zhou, Thomas C.W. Mak and Peter A. Tanner

Polyhedron 26 (2007) 4019

Reassignment of the crystal space group of crystalline Pr[M(CN)$_6$] · 5H$_2$O (M = Cr, Fe, Co)

Refinement of the X-ray crystal structures of Pr[M(CN)$_6$] · 5H$_2$O (M = Cr,Fe,Co) enables their space group to be revised from $P6_3/m$ to $P6_3/mmc$. Spectral characteristics are reported for M = Cr.



The Publisher encourages the submission of articles in electronic form thus saving time and avoiding rekeying errors. For detailed instructions on the preparation of manuscripts and of electronic artwork, consult the Author Gateway for Elsevier at http://authors.elsevier.com

ScienceDirect

Full text of this journal is available, on-line from **ScienceDirect**. Visit **www.sciencedirect.com** for more information.

Available online at www.sciencedirect.com
ScienceDirect
Polyhedron 26, issue 15, 20 September 2007
POLYHEDRON
www.elsevier.com/locate/poly

Contents

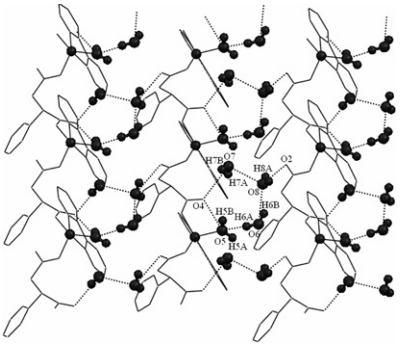
Papers

Jie Zhou, Chang-Yan Sun and Lin-Pei Jin

Polyhedron 26 (2007) 4025

Solvothermal syntheses and crystal structures of new Cu(II) complexes with phenylsuccinic acid

Five Cu(II) complexes with phenylsuccinic acid and diamine-like ligands were obtained under solvothermal conditions, and complexes **2** and **3** were obtained in one-pot reaction. Complexes **1**–**3** and **5** are composed of $[psa]^{2-}$ and terminal ligands phen, 2bpy, and N_3^- resulting in 2D and 3D supramolecular networks, and complex **4** forms a 3D metal–organic framework by bridging ligands $[psa]^{2-}$ and 4bpy.

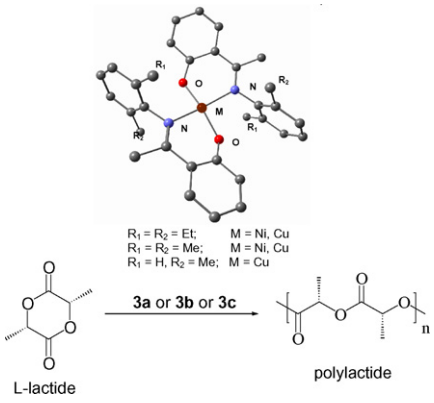


Alex John, Vimal Katiyar, Keliang Pang, Mobin M. Shaikh, Hemant Nanavati and Prasenjit Ghosh

Polyhedron 26 (2007) 4033

Ni(II) and Cu(II) complexes of phenoxyketimine ligands: Synthesis, structures and their utility in bulk ring-opening polymerization (ROP) of L-lactide

The Ni(II) and Cu(II) complexes of phenoxyketimine ligands have been synthesized and structurally characterized. Interestingly, the Cu(II) complexes were found to be efficient catalysts for the ring-opening polymerization (ROP) of L-lactide producing polylactide polymer of moderate molecular weights and narrow molecular weight distributions under solvent-free melt conditions.

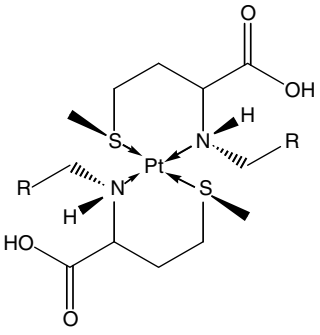


Erika Ferrari, Romano Grandi, Sandra Lazzari, Gaetano Marverti, Maria Cecilia Rossi and Monica Saladini

Polyhedron 26 (2007) 4045

^1H, ^{13}C, ^{195}Pt NMR study on platinum(II) interaction with sulphur containing Amadori compounds

^1H, ^{13}C, ^{195}Pt NMR study on platinum(II) interaction with sulphur containing Amadori compounds is performed. The Amadori compounds are derived from the reaction of β-D-glucose with L-cystine leading to *N*,*N*′-di-(1-deoxy-β-fructos-1-yl)-L-cystine [FruCyscys], and with L-methionine leading to *N*-(1-deoxy-β-fructos-1-yl)-L-methionine [FruMet]. The reaction of FruMet with Pt(II) forms the *trans* complex $[Pt(FruMet\text{-}N,S)_2]Cl_2$.

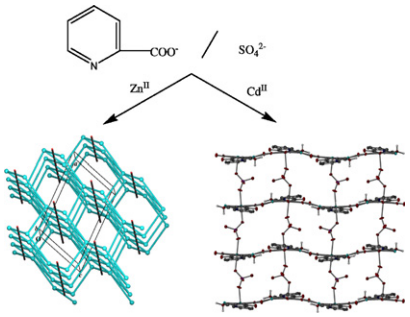


Constantina Papatriantafyllopoulou, Catherine P. Raptopoulou, Aris Terzis, Jozef F. Janssens, Evy Manessi-Zoupa, Spyros P. Perlepes and John C. Plakatouras

Polyhedron 26 (2007) 4053

Assembly of a helical zinc(II) chain and a two-dimensional cadmium(II) coordination polymer using picolinate and sulfate anions as bridging ligands

The simultaneous employment of the picolinate and sulfate ligands in zinc(II) and cadmium(II) chemistry leads to a helical chain complex and a 2D coordination polymer, respectively; the two complexes have interesting molecular and supramolecular structures.

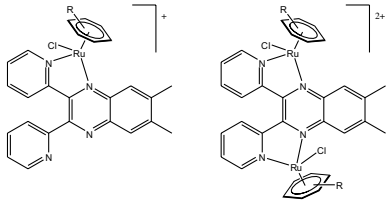


Bruno Therrien, Georg Süss-Fink, Padavattan Govindaswamy and Cynthia Saïd-Mohamed

Polyhedron 26 (2007) 4065

Mono and dinuclear arene ruthenium complexes containing 6,7-dimethyl-2,3-di(pyridine-2-yl)quinoxaline as chelating ligand: Synthesis and molecular structure

The reaction of $[(\eta^6\text{-arene})Ru(\mu\text{-}Cl)Cl]_2$ (arene = C_6H_6; C_6H_5Me; *p*-$Pr^iC_6H_4Me$; C_6Me_6) with 6,7-dimethyl-2,3-di(pyridine-2-yl)-quinoxaline ($dpqMe_2$) in methanol yields cationic mononuclear and dinuclear complexes with a chelating $dpqMe_2$ ligand. On the basis of a structural characterisation, the catalytic potential of these complexes for transfer hydrogenation reactions has been studied.

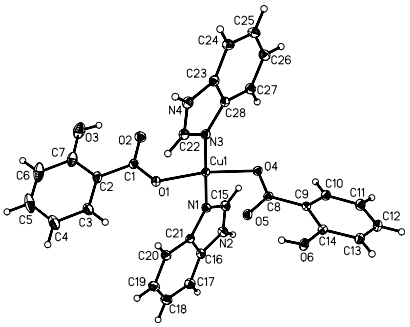


Michael Devereux, Denis O'Shea, Mark O'Connor, Helen Grehan, Gavin Connor, Malachy McCann, Georgina Rosair, Fiona Lyng, Andrew Kellett, Maureen Walsh, Denise Egan and Bhumika Thati

Polyhedron 26 (2007) 4073

Synthesis, catalase, superoxide dismutase and antitumour activities of copper(II) carboxylate complexes incorporating benzimidazole, 1,10-phenanthroline and bipyridine ligands: X-ray crystal structures of $[Cu(BZA)_2(bipy)(H_2O)]$, $[Cu(SalH)_2(BZDH)_2]$ and $[Cu(CH_3COO)_2(5,6\text{-}DMBZDH)_2]$ ($SalH_2$ = salicylic acid; BZAH = benzoic acid; BZDH = benzimidazole and 5,6-DMBZDH = 5,6-dimethylbenzimidazole)

Eight Cu(II)carboxylate complexes containing phen, bipy or benzimidazole ligands have been prepared. Crystal structures for three of the complexes are presented. They are poor catalase mimics but they all exhibit excellent SOD activity. Five of the complexes exhibit significant in vitro cytotoxicity against human hepatic, renal and lung cancer cell lines.

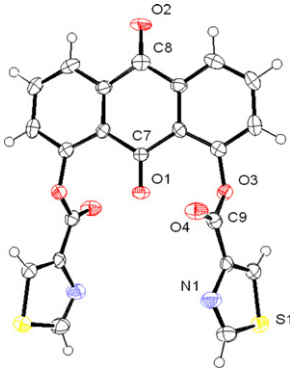


Mariappan Kadarkaraisamy, Debdutta Mukherjee, Chin Chen Soh and Andrew G. Sykes

Polyhedron 26 (2007) 4085

Complexation, crystallography, and electrochemistry of new chelating nicotinyl and thiazolyl anthraquinone ligands

Chelating anthraquinone ligands that contain nicotinyl and thiazolyl binding units have been synthesized, and the complexation chemistry with cadmium(II), lead(II), and ruthenium(II) has been explored. Both crystallographic and electrochemical data indicate that interaction between the intraannular carbonyl group and the neighboring metal centers within these complexes is not observed.

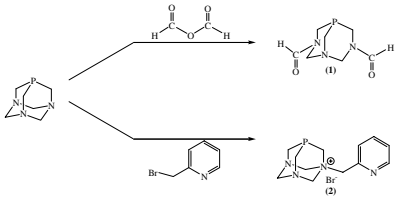


Donald Alan Krogstad, Gordon S. Ellis, Andrew K. Gunderson, Alyssa J. Hammrich, Joseph W. Rudolf and Jason A. Halfen

Polyhedron 26 (2007) 4093

Two new water-soluble derivatives of 1,3,5-triaza-7-phosphaadamantane (PTA): Synthesis, characterization, X-ray analysis and solubility studies of 3,7-diformyl-1,3,7-triaza-5-phosphabicyclo[3.3.1]nonane and 1-pyridylmethyl-3,5-diaza-1-azonia-7-phosphatricyclo-[3.3.1.1]decane bromide

Two water-soluble phosphines, 3,7-diformyl-1,3,7-triaza-5-phosphabicyclo[3.3.1]nonane (**1**, DFPTA) and 1-pyridylmethyl-3,5-diaza-1-azonia-7-phosphatricyclo[3.3.1.1]decane bromide (**2**, [pymePTA]Br), have been prepared by respectively, reacting 1,3,5-triaza-7-phosphaadamantane (PTA) with formic anhydride and bromomethylpyridine. Compound **1** is only the second acyl derivative of PTA to be prepared while **2** is only the second derivative of PTA that contains an aromatic appendage.

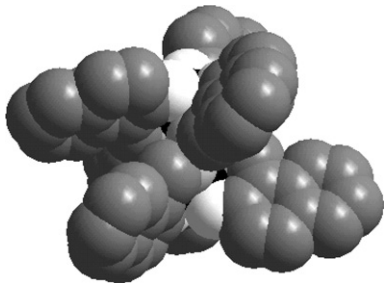


Subramanya Gupta Sreerama, Abhik Mukhopadhyay and Samudranil Pal

Polyhedron 26 (2007) 4101

Dinuclear triple helical Mn(III), Fe(III) and Co(III) complexes

Synthesis and characterization of dinuclear triple helical complexes of general formula $[M_2(\mu\text{-}L)_3]$ (M = Mn, Fe and Co) with a diazine ligand (L^{2-}) are described. X-ray structures of the diiron(III) and the dicobalt(III) complexes are determined. Cryomagnetic data reveal a weak antiferromagnetic interaction between the metal centres in both dimanganese(III) and diiron(III) complexes.

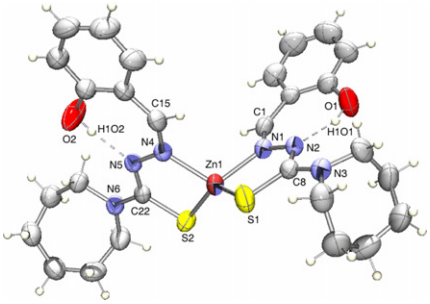


Leji Latheef, E. Manoj and M.R. Prathapachandra Kurup

Polyhedron 26 (2007) 4107

Synthesis and spectral characterization of zinc(II) complexes of N(4)-substituted thiosemicarbazone derived from salicylaldehyde: Structural study of a novel –OH free Zn(II) complex

Five novel zinc(II) complexes of salicylaldehyde 3-hexamethyleneiminyl thiosemicarbazone were synthesized and physico-chemically characterized. The complexes were given the formulae $[Zn(HL)_2]$ (**1**), [Zn(L)py] (**2**), [Zn(L)bipy] · $3.5H_2O$ (**3**), [Zn(L)phen] · H_2O (**4**) and [Zn(L)γ-pic] (**5**). The thiosemicarbazone binds the metal as a dianionic ONS donor ligand in all the complexes, except in **1**. Compound **1** is a homoleptic complex with zinc occupying the center of a distorted tetrahedral environment and being coordinated by two azomethine nitrogen and two thiolate sulfur atoms.

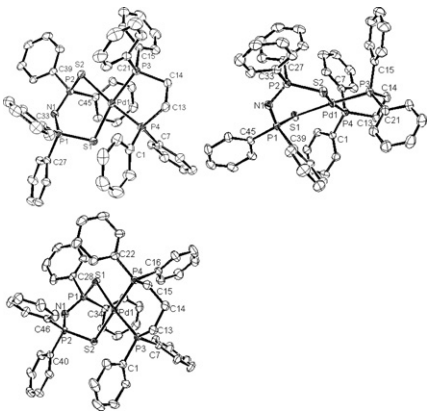


Selmin Yanar, Sevil İrişli and Orhan Büyükgüngör

Polyhedron 26 (2007) 4114

Preparation and crystallographic characterization of Pd(II) complexes containing imidobis-(diphenylthiophosphinato) ligand

The reactions of $PdCI_2$(L-L) [L-L = $Ph_2PCH_2PPh_2$(dppm), $Ph_2PCH_2CH_2PPh_2$(dppe) and $Ph_2PCH_2CH_2CH_2PPh_2$ (dppp)] with an equivalent amount of $(Ph_2P(S)NHP(S)Ph_2)$-(dppaS_2) gave the complexes [Pd(L-L)(dppaS_2-H)]ClO_4 [L-L = dppm (**1**), dppe (**2**), dppp (**3**)]. The different synthetic route was used for complex **2** by using of Pd(dppe)Cl_2 and $K[N(PSPh_2)_2]$ as starting materials (**2a**). The complexes **2**, **2a** and **3** were crystallographically characterized.

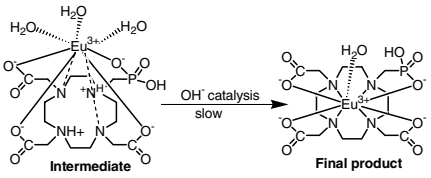


Petr Táborský, Ivona Svobodová, Přemysl Lubal, Zbigniew Hnatejko, Stefan Lis and Petr Hermann

Polyhedron 26 (2007) 4119

Formation and dissociation kinetics of Eu(III) complexes with H_5do3ap and similar dota-like ligands

The complexation and dissociation kinetics of europium(III) complexes of H_3do3a, H_4dota and H_4dota-like ligands having one methylphosphonic (H_5do3ap) or one phosphinic acid pendant arm with a propionate side chain (H_5do3ap^{PrA}) were studied by means of UV/VIS absorption spectroscopy and time-resolved laser-induced fluorescence spectroscopy (TRLIFS). The advantages and disadvantages of the TRLIFS methodology for the study of reaction mechanisms are discussed.

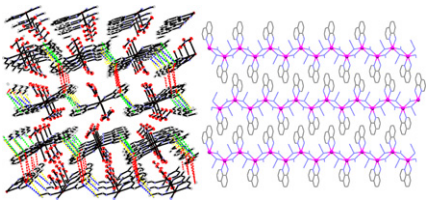


M.K. Paira, J. Dinda, T.-H. Lu, A.R. Paital and C. Sinha

Polyhedron 26 (2007) 4131

Zn(II), Cd(II) and Hg(II) complexes of 8-aminoquinoline. Structure, spectra and photoluminescence property

8-Aminoquinoline (8-aq) reacts with Group 12 salts, and different complexes have been synthesised. The presence of N_3^- forms an end-on bridging polymer. The complexes show potential emissions. The X-ray structure of some of the complexes exhibit CH–π, and π–π interactions.

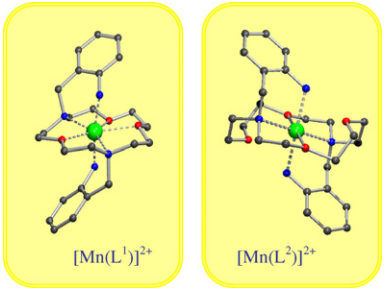


Lea Vaiana, David Esteban-Gómez, Carlos Platas-Iglesias, Marta Mato-Iglesias, Fernando Avecilla, Andrés de Blas and Teresa Rodríguez-Blas

Polyhedron 26 (2007) 4141

Synthesis and crystal structure of manganese(II) complexes with high-denticity ligands derived from azacrowns

Herein we describe the synthesis and structure of Mn(II) complexes with the heptadentate and octadentate receptors derived from azacrowns, *N*,*N*′-bis(2-aminobenzyl)-1,10-diaza-15-crown-5 (**L**^{1}) and *N*,*N*′-bis(2-aminobenzyl)-1,10-diaza-18-crown-6 (**L**^{2}), with which only mononuclear complexes are formed. **L**^{1} imposes a pentagonal bipyramidal coordination geometry on the Mn(II) guest, while **L**^{2} forms mononuclear complexes with the Mn(II) ion in a distorted octahedral coordination environment.

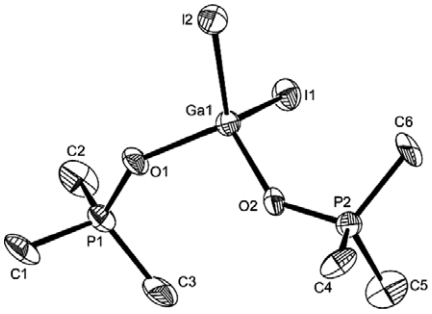


Fei Cheng, Hannah L. Codgbrook, Andrew L. Hector, William Levason, Gillian Reid, Michael Webster and Wenjian Zhang

Polyhedron 26 (2007) 4147

Gallium(III) halide complexes with phosphines, arsines and phosphine oxides – a comparative study

Phosphine oxide and phosphine complexes of GaX_3 (X = Cl, Br or I) are reported and their spectroscopic and structural properties show that the Lewis acidity of GaX_3 towards phosphinoyl ligands decreases with heavier halogen; competitive NMR studies show that Ga(III) binds the hard R_3PO in preference to phosphine/arsine ligands, while hydrolysis of $[GaX_3(R_3P)]$ gives $[R_3PH][GaX_4]$.

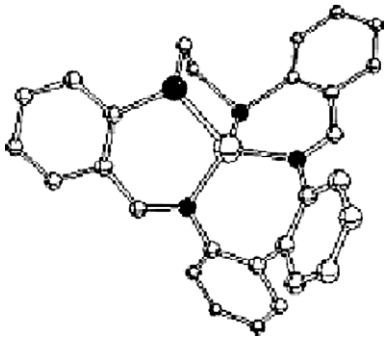


Martin Breza and Pavel Májek

Polyhedron 26 (2007) 4156

DFT studies of copper complexes with biphenyldiimino dithioether. Part III: AIM analysis

The electronic structure of tetrabenz[*a*,*e*,*g*,*k*]-15,18-dithia-9,24-diaza-cyclohexadeca-9,23-diene (bite), as well as of its quasi-tetrahedral and quasi-planar Cu(bite)^q complexes (q = +1 or +2), has been investigated at the MP2/6-31G level of theory in terms of atoms-in-molecule (AIM) topological analysis of electron density.

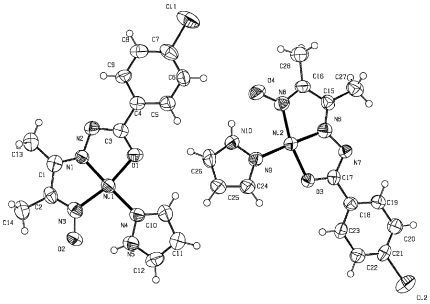


Nahed M.H. Salem, L. El-Sayed, Sabine Foro, Wolfgang Haase and Magdi F. Iskander

Polyhedron 26 (2007) 4161

Metal complexes derived from hydrazoneoxime ligands: III – Synthesis, characterization and electrospray ionization mass spectra of some nickel(II) complexes with aroylhydrazoneoximes

Three types of nickel(II) complexes namely [{Ni(L-R)}$_2$], [Ni(HL-R)$_2$] and [Ni(L-R)HPyr], where H_2L-R and HPyr refer to diacetylmonooxime aroylhydrazone and Pyrazole respectively, were prepared and characterized. The molecular and supramolecular structures of [Ni(L-H)HPyr], [Ni(L-CH_3O)HPyr] and [Ni(L-Cl)HPyr] were determined by single crystal X-ray analysis.

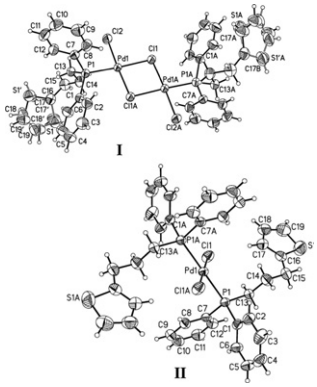


Khalifah A. Salmeia, Rawhi H. Al-Far and Hamdallah A. Hodali

Polyhedron 26 (2007) 4173

Synthesis and crystal structure of palladium-(II) complexes with 2-[3-(diphenylphosphino)-propyl]thiophene

The palladium complexes: *trans*-[Pd(μ-Cl)-Cl(P-S3)]$_2$ (**I**) and *trans*-[PdCl$_2$(P-S3)$_2$] (**II**) were isolated from the reaction of 2-[3-(diphenylphosphino)propyl]thiophene (**P-S3**) with [PdCl$_2$(PhCN)$_2$]. Single crystal X-ray structures of **I** and **II** have been determined.

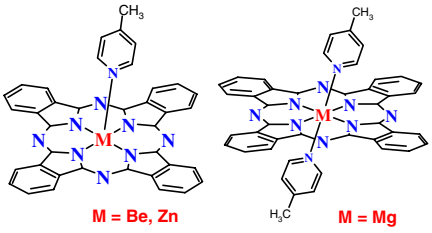


R. Kubiak, J. Janczak, M. Śledź and E. Bukowska

Polyhedron 26 (2007) 4179

Comparative study of beryllium, magnesium and zinc phthalocyanine complexes with 4-picoline

BePc and ZnPc in 4-Mepy solution form 4 + 1 coordinated complexes, while the 4-Mepy molecules biaxially ligate MgPc. The axial M(II)–N(4-Mepy) bond is longer than the four equatorial M(II)–N$_{iso}$ bonds in the Mg and Zn phthalocyaninato complexes, while in the Be complex the opposite relationship is observed. The thermogravimetric analysis for all these compounds shows only one slope down, responsible for the loss of the 4-Mepy molecules.

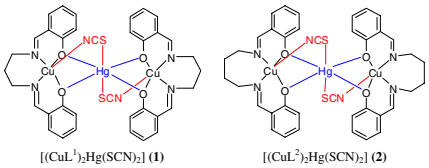


L.T. Yıldırım, R. Kurtaran, H. Namli, A.D. Azaz and O. Atakol

Polyhedron 26 (2007) 4187

Synthesis, crystal structure and biological activity of two new heterotrinuclear thiocyanato bridged Cu(II)–Hg(II)–Cu(II) complexes

The mononuclear copper(II) complexes CuL^1 and CuL^2 have been prepared with two tetradentate Schiff base ligands, abbr. L^1H_2 = *N*,*N*′-bis(salicylidene)-1,3-diaminopropane and L^2H_2 = *N*,*N*′-bis(salicylidene)-1,4-butanediamine, and then transformed into the heterotrinuclear complexes, $[(CuL^1)_2Hg(SCN)_2]$ and $[(CuL^2)_2Hg(SCN)_2]$, in the presence of the $Hg(SCN)_2$ salt. Both heterotrinuclear complexes have been characterized by means of elemental analyses, IR and electronic spectra, and their structures determined by X-ray analysis. The ligands and the complexes were screened for antibacterial and antifungal activities by the disc diffusion and microtiter plate techniques using DMF as the solvent. The minimum inhibitory concentration (MIC) values were calculated. It has been found that antimicrobial activities of the complexes are higher than those of the free ligands.



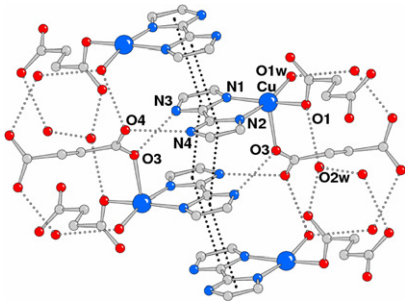
$[(CuL^1)_2Hg(SCN)_2]$ (**1**) $[(CuL^2)_2Hg(SCN)_2]$ (**2**)

Ananta Kumar Ghosh, Debajyoti Ghoshal, Ennio Zangrando and Nirmalendu Ray Chaudhuri

Polyhedron 26 (2007) 4195

Synthesis, crystal structure and thermal analysis of supramolecular architectures of copper(II)(2,2′-biimidazole) complexes using dicarboxylate as a coligand

Two new copper(II) complexes have been synthesized and characterization, and they show extended structural dimensionality through supramolecular interactions. In this way the biimidazole present in these complexes nicely recognizes the dicarboxylate group.

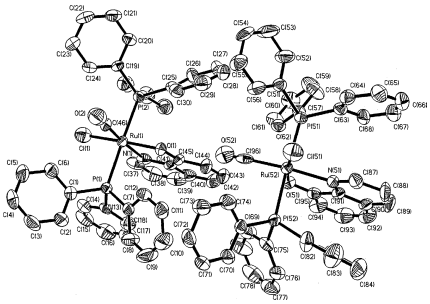


J.G. Małecki, R. Kruszynski and Z. Mazurak

Polyhedron 26 (2007) 4201

The reactions of 8-hydroxyquinoline with $[RuHCl(CO)(PPh_3)_3]$: A new ruthenium(II) carbonyl complex with a N-donor ligand

The reaction of $[RuHCl(CO)(PPh_3)_3]$ with 8-hydroxyquinoline has been examined and a novel ruthenium(II) complex – $[RuCl(CO)(PPh_3)_2(C_9H_6NO)]$ – has been obtained. This compound has been studied by IR, UV–Vis (absorption and emission), ^1H and ^{31}P NMR spectroscopy, and X-ray crystallography. The molecular orbital diagram of the complex has been calculated with the density functional theory (DFT) method. The spin-allowed singlet–singlet electronic transitions of the complex have been calculated with the time-dependent DFT method, and the UV–Vis spectrum of the compound has been discussed on this basis.

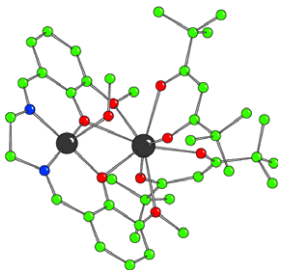


Fatima Zohra Chiboub Fellah, Jean-Pierre Costes, Françoise Dahan, Carine Duhayon and Jean-Pierre Tuchagues

Polyhedron 26 (2007) 4209

Varying the metal/metal ratio in related Cu–Ca complexes

Copper complexes derived from compartmental Schiff base ligands react with calcium ions to yield trinuclear Cu–Ca–Cu entities while dinuclear Cu–Ca complexes can also be isolated with use of auxiliary ligands such as diketones; the trinuclear Cu–Ca–Cu entities do not allow to synthesize the corresponding trinuclear Cu–Ln–Cu complexes.



Jianmin Dou, Daopeng Zhang, Yuehua Zhu, Dacheng Li and Daqi Wang

Polyhedron 26 (2007) 4216

Synthesis and characterization of two types of skeleton heterobimetallic trinuclear Mo(W)–Cu–S clusters containing 1,2-bis(diphenylphosphino)-1,2-dicarba-*closo*-dodecaborane

A carborane skeleton was introduced into heterometallic sulfide cluster cores and five heterobimetallic trinuclear Mo(W)–Cu–S clusters with linear or butterfly-shaped skeletons containing 1,2-bis(diphenylphosphino)-1,2-dicarba-*closo*-dodecaborane have been synthesized by the reactions of $(NH_4)_2MS_4$ or $(NH_4)_2MOS_3$ (M = Mo, W) with CuSCN and 1,2-$(PPh_2)_2$-1,2-$C_2B_{10}H_{10}$ (L) in dichloromethane. The products have been characterized by elemental analysis, FT-IR, UV/Visible, ^1H and ^{13}C NMR spectroscopy and X-ray structure determination.

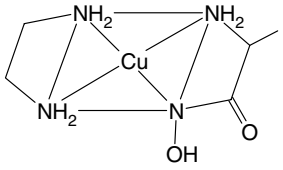


Barbara Kurzak, Anna Kamecka, Katarzyna Bogusz and Julia Jezierska

Polyhedron 26 (2007) 4223

Coordination modes of histidine- or methioninehydroxamic acids in copper(II) mixed-ligand complexes with ethylenediamine in aqueous solution

Equilibrium studies of the mixed-ligand complexes of the copper(II) ion with ethylenediamine and methionine- or histidinehydroxamic acid show that the mixed-ligand species is formed in the basic solution. Their absorption and EPR spectra indicate 4N coordination – both amine and hydoxamic nitrogens of aminohydroxamic acid and two amine nitrogens of ethylenediamine in the equatorial plane. The weak interactions between thioether sulfur of methioninehydroxamic acid or imidazole ring of histidinehydroxamic acid and copper(II) ion are suggested.

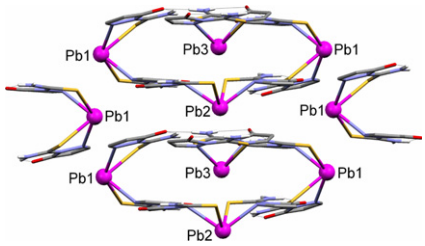


José S. Casas, Eduardo E. Castellano, Javier Ellena, María S. García-Tasende, Agustín Sánchez, José Sordo, Ángeles Touceda and Saulo Vázquez Rodríguez

Polyhedron 26 (2007) 4228

New lead(II) complexes with N,S-ligands, including a lead pyrazolonate with unusual packing flexibility

New lead(II) complexes with N,S-ligands including a lead pyrazolonate with unusual packing flexibility Lead(II) pyrazolonate complexes obtained from thiosemicarbazone ligands are reported. An X-ray study on a lead(II) pyrazolonate complex suggests that the crystal packing forces can decisively influence the primary and secondary metal–ligand interactions.

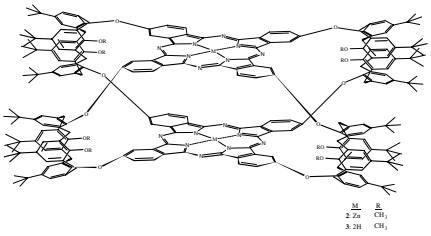


T. Ceyhan, A. Altındal, A.R. Özkaya, Ö. Çelikbıçak, B. Salih, M. Kemal Erbil and Ö. Bekaroğlu

Polyhedron 26 (2007) 4239

Synthesis, characterization and electrochemical properties of novel metal free and zinc(II) phthalocyanines of ball and clamshell types

The tetramerization of compound **1** gave a binuclear zinc(II) phthalocyanine and a metal-free phthalocyanine of the ball type, **2** and **3**, respectively. Its condensation with 4,5-bis-(hexylthio)phthalonitrile results in a binuclear phthalocyanine of the clamshell type **4**. The newly synthesized compounds were characterized by elemental analysis, UV/VIS, IR, MS and ^1H NMR spectra.

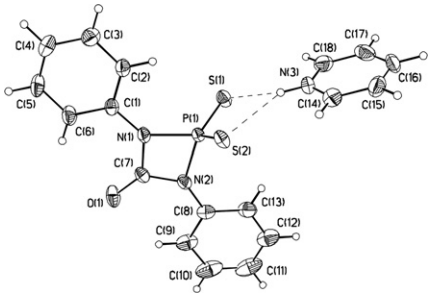


Lenka Dastychová, Marie Sotolářová, Dalibor Dastych, Jan Taraba, Marek Nečas and Jiří Příhoda

Polyhedron 26 (2007) 4250

Reactions of P_4S_{10} and $pyPS_2Cl$ with *N*,*N*′-diphenylurea and *N*,*N*′-diphenylthiourea

Two new heterocyclic compounds, the pyridinium salts of 1,3-diphenyl-2-sulfido-2-thioxo-1,3-diaza-2λ^5-phosphetidine (with a P–N–C–N cycle) and 1,4-diphenyl-2,5-disulfido-2,5-dithioxo-1,4-dithiadiaza-2λ^5,5λ^5-diphosphinane (containing a $(P–S–N)_2$ cycle), were prepared in the reaction of P_4S_{10} with *N*,*N*′-diphenylurea $(PhNH)_2CO$ (**2**). The cyclic thiophosphates $[pyH]_2[P_2S_8]$, $[pyH]_2[P_2S_7]$ and $[pyH]_3[P_3S_9]$ were also formed.

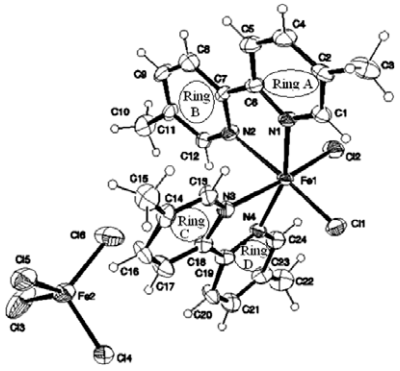


Vahid Amani, Nasser Safari and Hamid Reza Khavasi

Polyhedron 26 (2007) 4257

Synthesis, characterization and crystal structure determination of iron(III) hetero-ligand complexes containing 2,2′-bipyridine, 5,5′-dimethyl-2,2′-bipyridine and chloride, $[Fe(bipy)Cl_4][bipy{\cdot}H]$ and $[Fe(dmbipy)_2Cl_2][FeCl_4]$

The complex $[Fe(bipy)Cl_4][bipy{\cdot}H]$ (**1**) (bipy is 2,2′-bipyridine) was prepared from the reaction of $FeCl_3 \cdot 6H_2O$ with 2,2′-bipyridine in a 0.1 M aqueous solution of HCl. The same method was employed to make $[Fe(dmbipy)_2Cl_2][FeCl_4]$ (**2**) (dmbipy is 5,5′-dimethyl-2,2′-bipyridine). Both complexes were characterized by IR, UV–Vis and ^1H NMR spectroscopies and single-crystal X-ray diffraction.



Hossein Dehghani and Ali Reza Ansari Sardrood

Polyhedron 26 (2007) 4263

Molecular complexation of free base *meso*-tetraarylporphyrins with antimony(III) chloride in free solvent media

Mixing of *meso*-tetraarylporphyrins ($H_2t(Xp)p$) and $SbCl_3$ under free solvent conditions leads to the formation of $[(H_2t(Xp)p)_2Sb_2Cl_6]$ complexes, where two nitrogen atoms of pyrrolenine in the porphyrin core act as electron donors to an antimony center, and so there is a $(\mu\text{-}Cl)_2$ bridge between two antimony atoms. The molecular complexes exhibit no hydrogen bonding but show a large downfield shift for the NH signals (~3 ppm).

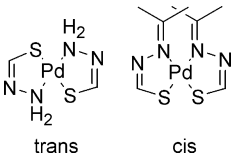
$$2H_2t(Xp)p + 2SbCl_3 \longrightarrow [Sb_2Cl_4(\mu\text{-}Cl)_2\ (H_2t(Xp)p)_2]$$

Konstantinos Tampouris, Silverio Coco, Athanasios Yannopoulos and Spyros Koinis

Polyhedron 26 (2007) 4269

Palladium(II) complexes with *S*-benzyl dithiocarbazate and *S*-benzyl-*N*-isopropylidenedithiocarbazate: Synthesis, spectroscopic properties and X-ray crystal structures

Bis(*S*-benzyl dithiocarbazato)palladium(II) (**1**) and bis(*S*-benzyl-*N*-isopropylidenedithiocarbazato)palladium(II) (**2**) have been prepared and characterized using single-crystal X-ray diffraction and spectroscopic (electronic, IR and NMR) techniques. Complex **1** has a perfectly square planar *trans* configuration (point group C_i), while complex **2** has a distorted square planar *cis* configuration.

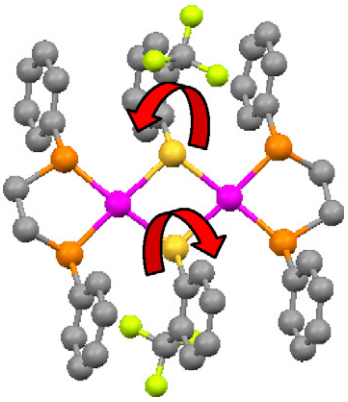


Guillermina Rivera, Sylvain Bernès and Hugo Torrens

Polyhedron 26 (2007) 4276

Mono- and bimetallic platinum(II) and palladium(II) complexes containing fluorinated benzothiolates

Fluxional bimetallic complexes, $[M_2(\mu\text{-}SRf)_2(dppe)_2](SO_3CF_3)_2$ M = Pd, Rf = *p*-$C_6F_4(CF_3)$ **3a**, C_6F_5 **3b**, *p*-C_6HF_4 **3c**, *o*-$C_6H_4(CF_3)$ **3d**; M = Pt, Rf = *p*-$C_6F_4(CF_3)$ **4a**, C_6F_5 **4b**, *p*-C_6HF_4 **4c** and *o*-$C_6H_4(CF_3)$ **4d**, obtained from metalloligands –[M(SRf)$_2$(dppe)]– and "[M(dppe)]" moieties, have been studied by variable temperature ^{19}F NMR. Crystal and molecular structures of $[Pd(p\text{-}SC_6HF_4)_2(dppe)]$, $[Pt(SC_6F_5)_2(dppe)]$, $[Pt(o\text{-}SC_6H_4(CF_3))_2(dppe)]$, and $[Pt_2(\mu\text{-}o\text{-}SC_6H_4(CF_3))_2(dppe)_2](SO_3CF_3)^2$ have been solved.

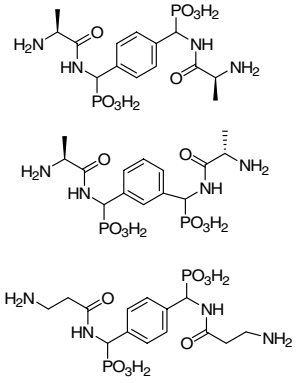


Joanna Gałęzowska, Łukasz Szyrwiel, Piotr Młynarz, Sylwia Śliwińska, Paweł Kafarski and Henryk Kozłowski

Polyhedron 26 (2007) 4287

Coordination abilities of difunctional, diaminophosphonic acid and its dipeptides towards Cu(II) ions

Aminophosphonates and their peptidic analogues are systematically investicated compounds as the receptors for biomolecules. We have synthesized a potential receptor, 1,4-phenylene-di(*N*-L-alanylaminomethyl-phosphonate) able to form ionic-pairs with lysine and arginine in methanol and aqueous solutions. The binding abilities toward Cu(II) ions of this ligand as well as its analogues are presented in this paper.

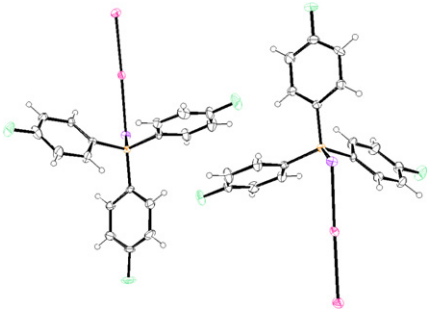


Nicholas A. Barnes, Stephen M. Godfrey, Ruth T.A. Halton, Rana Z. Khan, Sheena L. Jackson and Robin G. Pritchard

Polyhedron 26 (2007) 4294

The reaction of $(p\text{-}FC_6H_4)_3PE$ (E = Se, S) with diiodine: The single crystal X-ray structures of $(p\text{-}FC_6H_4)_3PSe$, $(p\text{-}FC_6H_4)_3PS$, $(p\text{-}FC_6H_4)_3PSeI_2$, and $(p\text{-}FC_6H_4)_3PSI_2$

The tertiary phosphine chalcogenides $(p\text{-}FC_6H_4)_3PE$ (E = Se and S) react with I_2 to form 1:1 charge transfer adducts $(p\text{-}FC_6H_4)_3PEI_2$ (E = Se and S). The I–I bonds in these spoke adducts are relatively short, reflecting the weak donating nature of $(p\text{-}FC_6H_4)_3PE$.

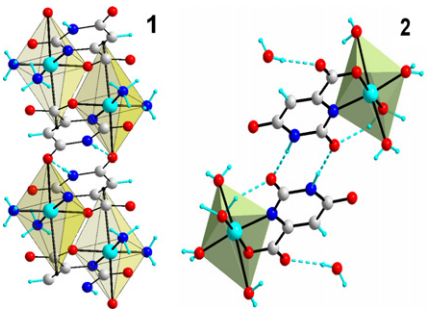


Danuta Michalska, Katarzyna Hernik, Rafał Wysokiński, Barbara Morzyk-Ociepa and Adam Pietraszko

Polyhedron 26 (2007) 4303

Copper(II)–π interaction in *cis*-$[Cu(orotato)(NH_3)_2]$ and the crystal structure of $[Cu(orotato)(H_2O)_4] \cdot H_2O$: X-ray, vibrational spectroscopy and density functional study

Evidence is presented that complex **1** exhibits a Cu–π interaction between the chelated Cu^{2+} cation and the axial C=C bond of a neighboring orotate ligand. This weak interaction is very important in stabilizing the columnar, polymeric structure of **1**. In the novel complex **2**, the coordination geometry around copper(II) can be described as an elongated octahedron. It is suggested that the non-covalent Cu–π interaction of the chelated Cu^{2+} ion can play a significant role in the active sites of copper enzymes.

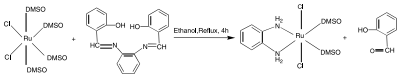


Duraiswamy Sukanya, Michael R. Evans, Matthias Zeller and Karuppannan Natarajan

Polyhedron 26 (2007) 4314

Hydrolytic cleavage of Schiff bases by $[RuCl_2(DMSO)_4]$

New hexa-coordinated Ru(II) complexes of the type $[RuCl_2(DMSO)_2(diamine)]$ (diamine = *o*-phenylenediamine and ethylenediamine) have been prepared by reacting *cis*-$[RuCl_2(DMSO)_4]$ with Schiff bases (H_2sal-en, **1**; H_2nap-en, **2**; H_2sal-*o*-pdn, **3**; H_2nap-*o*-pdn, **4**) in a 1:1 ratio. The ligands, which were expected to act as tetradentate (N_2O_2) chelates under the normal reaction conditions, were found to undergo hydrolytic cleavage to form the diamine and the corresponding aldehyde. All the complexes have been characterized by analytical and spectroscopic (IR, electronic and ^{1}H NMR) data. Single-crystal X-ray analysis of the complex $[RuCl_2(DMSO)_2$-(*o*-pndn)] revealed that the coordination environment around the ruthenium metal consists of a $N_2S_2Cl_2$ octahedron.

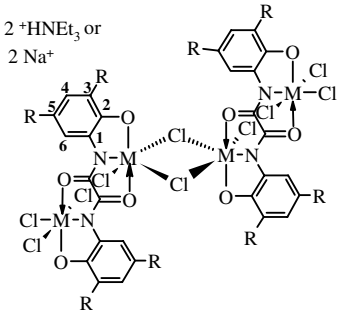


Marisol Güizado-Rodríguez, Víctor M. Jiménez-Pérez, Jesús E. Hernández-Rivera, J.M. Domínguez, Rosalinda Contreras and Raúl Quijada

Polyhedron 26 (2007) 4321

Synthesis, characterization and ethylene polymerization activity of titanium, zirconium and hafnium compounds derivatives from symmetric oxamide

In this article, we discuss synthesis, characterization and the polimerization activity of titanium, zirconium and hafnium heterocycles complexes derived from 1,2-bis(3,5-di-*tert*-butyl-2-hydroxyphenyl)oxamide. The catalytic activity and polymer mass were measured under several polymerization conditions. The zirconium catalyst exhibits the highest activity and produces high density linear polymers.



R = *t*-Bu M = Ti (**4**), Zr, (**5**), Hf (**6**).

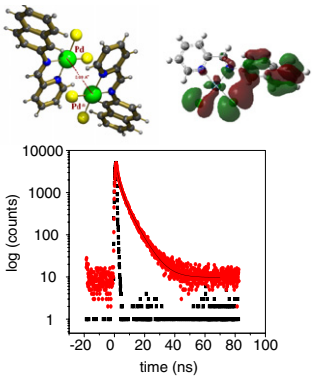
solvating molecules = i (Et_3N), ii (CH_3OH), iii (THF).

P. Pratihar, S. Jha, T.K. Mondal, G. Mostafa and C. Sinha

Polyhedron 26 (2007) 4328

Palladium(II) complexes of *N*-[(2-pyridyl)-methyliden]-α(or β)-aminonaphthalene: Single crystal X-ray structure of di-chloro-*N*-[{(2-pyridyl)methyliden}-β-aminonaphthalene]-palladium(II), Pd(β-NaiPy)Cl_2, spectra and DFT, TD-DFT study

(*N*-[(2-Pyridyl)methyliden]-α(and β)-aminonaphthalene (α/β-NaiPy)) are used to prepare palladium(II) complexes. The structures of the complexes are established by spectroscopic (FTIR, UV–Vis, NMR) studies and in one case by the single crystal X-ray diffraction technique. Ligands and complexes are photoluminescent. They exhibit decay following a bi-exponential route and lifetime in ns units.

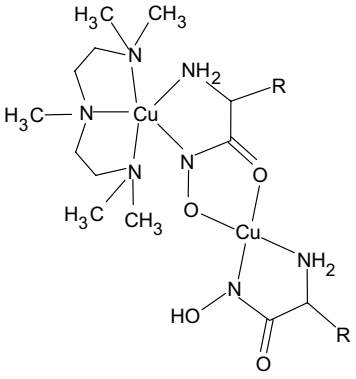


Barbara Kurzak, Anna Kamecka, Katarzyna Bogusz and Julia Jezierska

Polyhedron 26 (2007) 4345

Unexpected formation of the copper(II) dinuclear mixed-ligand species in the ternary system of *N*,*N*,*N*′,*N*″,*N*″-pentamethyldiethylenetriamine with methionine- or histidinehydroxamic acids in aqueous solution

Equilibrium studies of the mixed-ligand complexes of the copper(II) ion with the tridentate amine as a primary ligand and methionine- or histidinehydroxamic acid as a secondary ligand. In these ternary systems the dinuclear $[Cu_2(Me_5dien)L_2H_{-1}]^+$ species is formed as a predominant one in the basic solution. The monomeric $[Cu(Me_5dien)L]^+$ species is formed in low concentration. The geometry of mixed-ligand five-coordinate complexes is strongly distorted towards trigonal-bipyramidal.

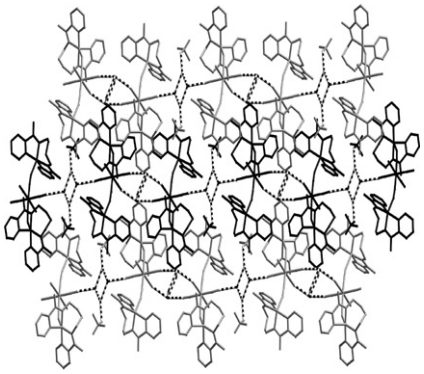


Brajagopal Samanta, Joy Chakraborty, R.K. Bhubon Singh, Manas K. Saha, Stuart R. Batten, Paul Jensen, M. Salah El. Fallah and Samiran Mitra

Polyhedron 26 (2007) 4354

Hexacyanometallate anions as precursors of two new trinuclear heterobimetallic assemblies: Syntheses, structures and cryomagnetic properties

Two new cyano bridged Cu–Co and Cu–Fe trinuclear bimetallic assemblies, [(CuL)[Co(CN)$_6$](CuL)]ClO$_4$ · 3.5H$_2$O (**1**) and [(CuL)-[Fe(CN)$_6$](CuL)] · 13H$_2$O (**2**) [where L = *N*,*N*′-bis(2-pyridylmethylene)butane-1,4-diamine] have been prepared using cyanometallates as anion precursors, and they have been characterised by elemental analyses, spectroscopic studies and single crystal X-ray diffraction. Cryomagnetic susceptibility measurements exhibit weak anti-ferromagnetic interactions with $J = -0.81$ and -0.73 cm^{-1} for **1** and **2**, respectively.

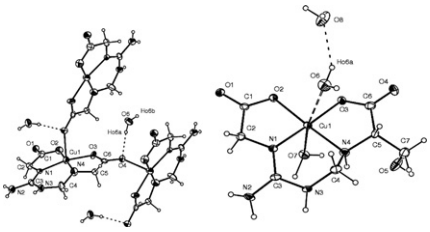


O. Versiane, B.L. Rodrigues, J.L. de Miranda, Joanna Maria Ramos, Claudio A. Téllez S and J. Felcman

Polyhedron 26 (2007) 4363

A methylenic group binds guanidinoacetic acid to glycine and serine in two novel copper(II) complexes: Synthesis, X-ray structure and spectroscopic characterization

This paper reports two new condensed amino acids that were observed in two Cu(II) complexes, both involving guanidinoacetic acid (GAA). The copper(II) complexes, **1** and **2**, were synthesized and characterized by X-ray crystallography and infrared spectroscopy. Vibrational assignments were carried out with the aid of density functional theory (DFT) calculations. Both complexes present an elongation of the carbon chain of the starting amino acid, GAA.

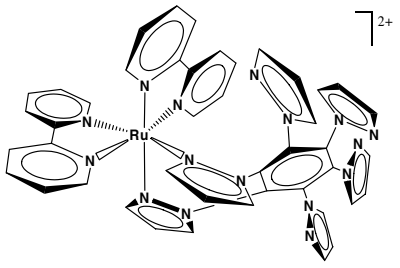


Blanca R. Manzano, Félix A. Jalón, Gustavo Espino, Ana Guerrero, Rosa M. Claramunt, Consuelo Escolástico, José Elguero and M. Aránzazu Heras

Polyhedron 26 (2007) 4373

Synthesis, spectral characterization and cytotoxicity of Ru–bipyridyl complexes containing hexakis(pyrazol-1-yl)benzene (hpzb) as a co-ligand

The new derivative [Ru(bpy)$_2$(hpzb)](PF$_6$)$_2$ (**1**) (hpzb = hexakis(pyrazol-1-yl)benzene) was obtained selectively in the reaction between [Ru(bpy)$_2$Cl$_2$], hpzb and NH$_4$PF$_6$. A complete assignment of all the proton and carbon NMR signals was carried out. The orientation of the free pyrazolyl groups is discussed. The anticancer activity of **1** has been tested.

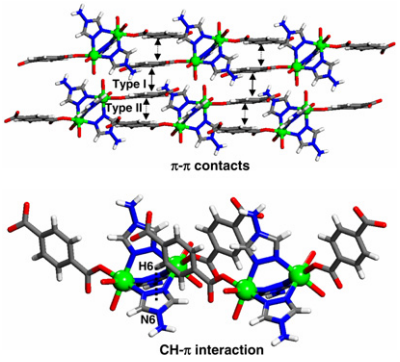


Houng Sik Yoo, Jeong Hak Lim, Jun Sung Kang, Eui Kwan Koh and Chang Seop Hong

Polyhedron 26 (2007) 4383

Triazole-bridged magnetic M(II) assemblies (M = Co, Ni) capped with the end-on terephthalate dianion involving multi-intermolecular contacts

Two dimeric complexes [M$_2$(atrz)$_3$(H$_2$O)$_4$-(tp)$_2$] · 11H$_2$O [M = Co(**1** · 11H$_2$O), Ni(**2** · 11-H$_2$O); tp = terephthalate, atrz = 4-amino-triazole] were constructed by triply-bridged triazole ligands and terminal tp groups. Among the dinuclear assemblies, three types of intermolecular interactions (hydrogen bond, face-to-face π–π and edge-to-face CH–π contacts) as well as intramolecular hydrogen bonding are involved, eventually leading to the formation of a 3D network. Magnetic data show that moderate antiferromagnetic interactions between two metal centers communicate through triazole groups and non-negligible interdimer antiferromagnetic couplings are also involved in this system.

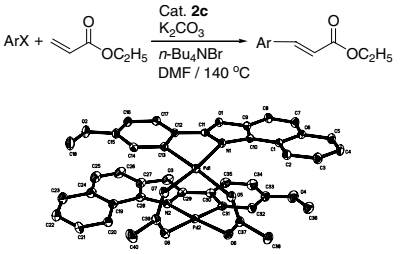


Hong Li, Yang-Jie Wu, Chen Xu and Rong-Qiang Tian

Polyhedron 26 (2007) 4389

2-Arylnaphthoxazole-derived palladium(II) complexes as phosphine-free catalysts for Heck reactions

Four air- and moisture-stable palladium(II) complexes have been synthesized from 2-arylnaphthoxazoles and shown to function as efficient phosphine-free catalysts for the Heck reaction with aryl bromides and ethyl acrylate.



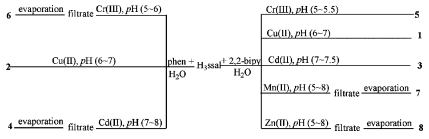
2c

Jiang-Feng Song, Yan Chen, Zhi-Gang Li, Rui-Sha Zhou, Xiao-Yu Xu, Ji-Qing Xu and Tie-Gang Wang

Polyhedron 26 (2007) 4397

Syntheses, supramolecular structures and properties of six coordination complexes based on 5-sulfosalicylic acid and bipyridyl-like chelates

Six new complexes constructed by 5-sulfosalicylic acid and bipyridyl-like ligands, namely, $[Cu_4(OH)_2(ssal)_2(phen)_4 \cdot 7H_2O]$ **1**, $[Cu_4(OH)_2(ssal)_2(bipy)_4 \cdot 2H_2O]$ **2**, [Cd(Hssal)(bipy)] **3**, $[Cd(HL)_2(phen)_2]$ **4**, $[Cr(ssal)(bipy)(H_2O)_2 \cdot 2H_2O]$ **5** and $[Cr(ssal)(phen)_2]$ **6**, were prepared under hydrothermal conditions. The results of magnetic determination show that ferromagnetic interactions exist in complex **1**, however, antiferromagnetic interactions exist in **2**. Complexes **3** and **4** exhibit intense green and blue photoluminescence, respectively.

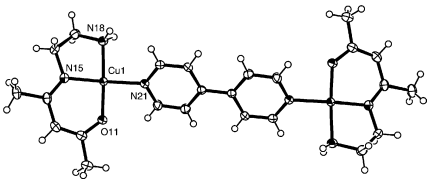


Chaitali Biswas, Shouvik Chattopadhyay, Michael G.B. Drew and Ashutosh Ghosh

Polyhedron 26 (2007) 4411

Synthesis, crystal structure and hydrolysis of a dinuclear copper(II) complex constructed by N_2O donor Schiff base and 4,4′-bipyridine: Discrete supra-molecular ensembles vs. oligomers

The tridentate Schiff base ligand, 7-amino-4-methyl-5-aza-3-hepten-2-one (HAMAH), prepared by the mono-condensation of 1,2-diaminoethane and acetylacetone, reacts with $Cu(BF_4)_2 \cdot 6H_2O$ to produce initially a dinuclear Cu(II) complex, $[\{Cu(AMAH)\}_2(\mu\text{-}4,4'\text{-bipy})](BF_4)_2$ (**1**) which undergoes hydrolysis in the reaction mixture and finally produces a linear polymeric chain compound, $[Cu(acac)_2(\mu\text{-}4,4'\text{-bipy})]_n$ (**2**). On the other hand, the ligand HAMAH reacts with $Cu(ClO_4)_2 \cdot 6H_2O$ to yield a polymeric zigzag chain, $[\{Cu(acac)(CH_3OH)(\mu\text{-}4,4'\text{-bipy})\}(ClO_4)]_n$ (**3**).

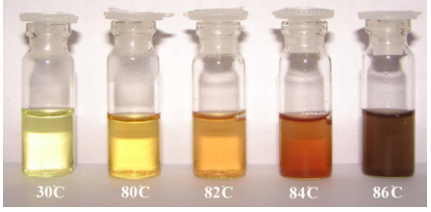


Sougata Sarkar, Atish Dipankar Jana, Samir Kumar Samanta and Golam Mostafa

Polyhedron 26 (2007) 4419

Facile synthesis of silver nano particles with highly efficient anti-microbial property

Tollen's reaction in presence of an anionic surfactant SDS has been employed for the facile syntheses of higher dimensional silver nano-structures in the temperature range 80–86 °C. Anti-microbial activity of the nano particles was established against seven bacterial strains.

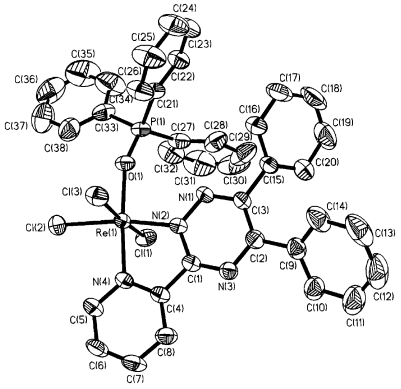


B. Machura, R. Kruszynski, J. Kusz, J. Kłak and J. Mroziński

Polyhedron 26 (2007) 4427

Novel rhenium(III) complexes with 5,6-diphenyl-3-(2-pyridyl)-1,2,4-trazine: X-ray structures and DFT calculations for [$ReCl_3(OPPh_3)$(dppt)] and [$ReCl_3(PPh_3)$(dppt)] complexes

The reaction of [$ReOCl_3(PPh_3)_2$] with 5,6-diphenyl-3-(2-pyridyl)-1,2,4-trazine (dppt) has been examined and [$ReCl_3(OPPh_3)$(dppt)] has been obtained. The triphenylphosphine oxide can be easily replaced by PPh_3 in the reaction of [$ReCl_3(OPPh_3)$(dppt)] with an excess of triphenylphosphine. The [$ReCl_3(OPPh_3)$-(dppt)] and [$ReCl_3(PPh_3)$(dppt)] complexes have been structurally and spectroscopically characterized. Their molecular orbital diagrams have been calculated with the density functional theory (DFT) method, and their electronic spectra have been discussed on the basis of time-dependent DFT calculations. The compound [$ReCl_3(OPPh_3)$(dppt)] has been studied additionally by magnetic measurement.

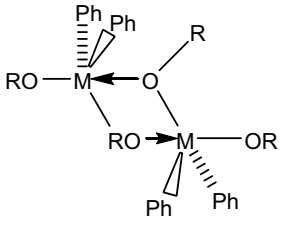


Malcolm H. Chisholm, Judith C. Gallucci and Clemens Krempner

Polyhedron 26 (2007) 4436

Ring-opening polymerization of L-lactide by organotin(IV)alkoxides, $R_2Sn(OPr^i)_2$: Estimation of the activation parameters

Studies of the ring-opening polymerization of L-lactide by $R_LSn(OPr^i)_2$ compounds where R = Bu^n and *p*-XC_6H_4 (X = CF_3, F, H, Me and OMe) over a temperature range in benzene reveals activation parameters $\Delta H^{\neq}$ = 11 ± 2 Kcal mol^{-1} and $\Delta S^{\neq}$ = − 50 ± 5 eu. The consistently large and negative value of $\Delta S^{\neq}$ is taken to imply a highly ordered transition state for the ring-opening (enchainment) event.

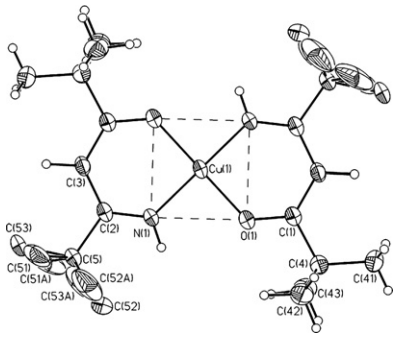


P.A. Stabnikov, G.I. Zharkova, I.A. Baidina, S.V. Tkachev, V.V. Krisyuk and I.K. Igumenov

Polyhedron 26 (2007) 4445

Synthesis and properties of a new ketoiminate derivative of the 2,2,6,6-tetramethylheptane-3,5-dionate ligand to prepare volatile CVD precursors

The β-aminoketone $(CH_3)_3CC(NH_2)CHC(O)C(CH_3)_3$ was synthesized by amination of the relative β-diketone with dry ammonia in the presence of $TiCl_4$. ^1H and ^{13}C NMR spectroscopy of the solution and a single-crystal X-ray diffraction study shows that the structure of **1** is the ketone form. The reaction of **1** with copper(II) and nickel(II) salts in solution gave ketoiminate metal chelates: Cu[$(CH_3)_3$-$CC(NH)CHC(O)C(CH_3)_3]_2$ (**2**) and Ni-[$(CH_3)_3CC(NH)CHC(O)C(CH_3)_3]_2$ (**3**). These complexes are volatile and sublimate at 180–190 °C at 10^{-2} Torr. An X-ray diffraction study reveals that these metal complexes are monomeric and isostructural in the solid state.

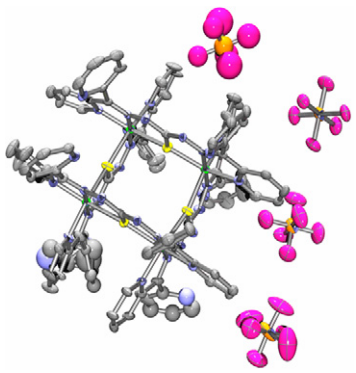


E. Manoj, M.R. Prathapachandra Kurup, H.-K. Fun and Alex Punnoose

Polyhedron 26 (2007) 4451

Self-assembled macrocyclic molecular squares of Ni(II) derived from carbohydrazones and thiocarbohydrazones: Structural and magnetic studies

Four novel molecular square grids were achieved by self-assembly using the flexible ligands bis(di-2-pyridyl ketone) thiocarbohydrazone (H_2L^1), bis(quinoline-2-carbaldehyde) thiocarbohydrazone (H_2L^2), bis(di-2-pyridyl ketone) carbohydrazone (H_2L^3) and bis(2-benzoyl pyridine) carbohydrazone (H_2L^4). Three complexes were given a general formula of [$Ni(HL)]_4[PF_6]_4 \cdot nH_2O$ and one [$Ni_2(HL^2)$-$L^2]_2(PF_6)_2 \cdot 7H_2O$. The MALDI-MS spectra reveal the formation of tetranuclear molecular squares. The square grid of the Ni(II) centers in all the complexes were organized by deprotonated ligands. The complex [$Ni(HL^1)]_4$-$[PF_6]_4 \cdot 11H_2O$ crystallized as [$Ni(HL^1)]_4$-$(PF_6)_4 \cdot 0.5\ CH_3CH_2OH \cdot 2.8H_2O$ and X-ray study revealed octahedral geometries around the Ni(II) centers. Variable temperature magnetic studies suggest intramolecular antiferromagnetic coupling between the Ni(II) electrons by a super exchange mechanism through intervening sulfur/oxygen atoms.

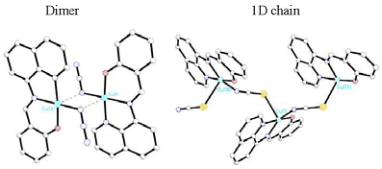


Heng Xu, Cheng He, Yuan-Xia Sui, Xiao-Ming Ren, Li-Min Guo, Yuan-Guang Zhang, Sadafumi Nishihara and Yuko Hosokoshi

Polyhedron 26 (2007) 4463

Self-assembled molecular magnets from discrete dimer to one-dimensional helical chain: Syntheses, crystal structures and magnetic properties

The tectons of CuL^+ (L = deprotonated tridentate *N*-(8-quinolyl)salicylaldimine) with different counter anions (ClO_4^-, Ac^-, N_3^- and SCN^-) form discrete dimers in **1**–**3** and a 1D chiral chain in **4**.

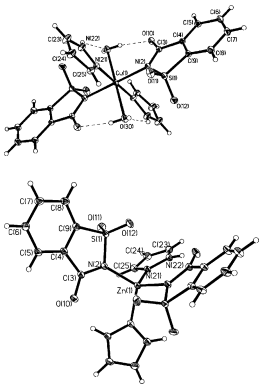


Grettel Valle-Bourrouet, Leslie W. Pineda, Larry R. Falvello, Rosa Lusar and Thomas Weyhermueller

Polyhedron 26 (2007) 4470

Synthesis, structure and spectroscopic characterization of Ni(II), Co(II), Cu(II) and Zn(II) complexes with saccharinate and pyrazole

Mixed-ligand complexes: $[M(sac)_2(pz)_2(H_2O)_2]$, M = Co; Ni, Cu and $[Zn(sac)_2(pz)_2]$ were synthesized and characterized. Thermal decomposition of the complexes in a nitrogen atmosphere resulted in removal of the water molecules and pyrazole ligands at relatively low temperature and formation of stable metal saccharinates as intermediates, which also decomposed at higher temperatures, about 300 °C.

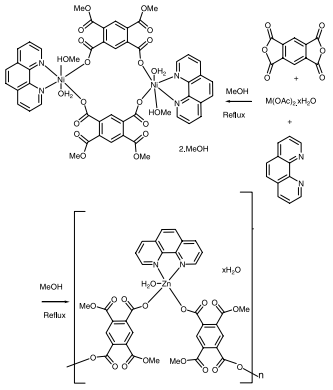


Abhilasha M. Baruah, Anirban Karmakar and Jubaraj B. Baruah

Polyhedron 26 (2007) 4479

Ring opening reactions of pyromellitic dianhydride for the synthesis of first row transition metal dicarboxylate complexes

The ring opening reaction of pyromellitic dianhydride by methanol is an effective method to prepare first row transition metal carboxylate complexes. The reactions of different first row transition metal salts with pyromellitic dianhydride in the presence of nitrogen donating bidentate ligands such as 1,10-phenanthroline and 2,2′-bipyridine gives different compositions depending on the ligand and the metal salts used.

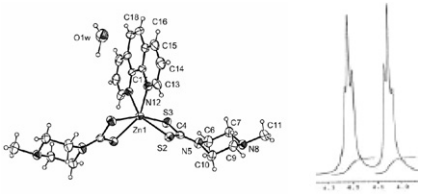


Balasubramaniyam Arul Prakasam, Kuppukkannu Ramalingam, Gabriele Bocelli and Andrea Cantoni

Polyhedron 26 (2007) 4489

NMR and fluorescence spectral studies on bisdithiocarbamates of divalent Zn, Cd and their nitrogenous adducts: Single crystal X-ray structure of (1,10-phenanthroline)bis(4-methylpiperazinecarbodithioato) zinc(II)

Six complexes with the MS_4N_2 (M = Zn or Cd) chromophore have been synthesized. IR spectra of the complexes show the contribution of the thioureide form to the structures. NMR and fluorescence spectra of the complexes show interesting properties. Single crystal X-ray structural analysis of one of the complexes showed the zinc atom to be in a highly distorted octahedral environment with the MS_4N_2 chromophore.

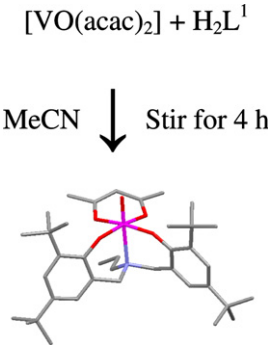


Dipankar Maity, Md. Mijanuddin, Michael G.B. Drew, Jaromir Marek, Parikshit Chandra Mondal, Bholanath Pahari and Mahammad Ali

Polyhedron 26 (2007) 4494

Oxovanadium(V) complexes of bis(phenolate) ligands with acetylacetone as co-ligand: Synthesis, crystal structure, electrochemical and kinetics studies on the oxidation of ascorbic acid

Two octahedral vanadium(V) complexes, $[VO(L^1)](acac)]$ (**1**) and $[VO(L^2)(acac)]$ (**2**), have been synthesized and characterized by single crystal X-ray studies. The kinetics of oxidation of ascorbic acid by complex **1** was found to proceed by the formation of a H-bonded intermediate with $Q = 63 \pm 7\ M^{-1}$.

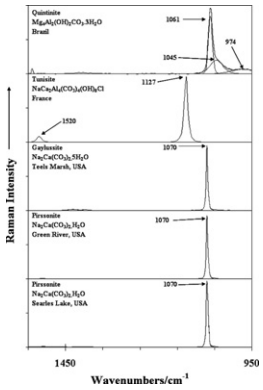


Ray L. Frost and Marilla Dickfos

Polyhedron 26 (2007) 4503

Hydrated double carbonates – A Raman and infrared spectroscopic study

The Raman spectra of selected double carbonates including pirssonite, gaylussite, tunisite, shortite and quintinite complemented with infrared spectra have been used to characterise the structure of these carbonate minerals. By using a Libowitzky type function hydrogen bond distances for these minerals of 2.669–2.766 Å are estimated.

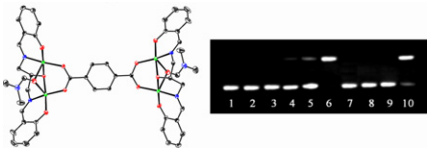


Koushik Dhara, Partha Roy, Jagnyeswar Ratha, Mario Manassero and Pradyot Banerjee

Polyhedron 26 (2007) 4509

Synthesis, crystal structure, magnetic property and DNA cleavage activity of a new terephthalate-bridged tetranuclear copper(II) complex

A new ferromagnetic ($2J = 18.70\ cm^{-1}$) terephthalate-bridged tetranuclear copper(II) complex has been synthesized and structurally characterized by X-ray crystallography: $[Cu_4(L)_2(tp)(dmf)_2]$ (**1**) (H_3L = 1,3-bis(salicylideneamino)propan-2-ol, tp = terephthalate and dmf = *N*,*N*′-dimethylformamide). **1** binds to double-stranded CT (calf-thymus) DNA giving a K_{app} value of $1.25 \times 10^7\ M^{-1}$ and displays efficient cleavage of supercoiled pUC19 DNA in the presence of H_2O_2 following a hydroxyl radical pathway.

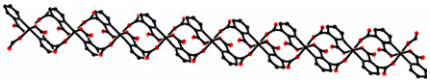


Abhilasha M. Baruah, Anirban Karmakar and Jubaraj B. Baruah

Polyhedron 26 (2007) 4518

Hydrolytic ring opening reactions of anhydrides for first row transition metal dicarboxylate complexes

Ring opening reactions of 2,3-pyridine dicarboxylic anhydride were studied with hydrated cobalt, nickel and zinc salts. Hydrated metal salts preferentially hydrolyze 2,3-pyridine dicarboxylic anhydride over the esterification reaction in alcoholic medium. The bonding and the nature of the metal carboxylate complexes formed in these reactions are dependent on the type of metal as well as on the anion and nitrogen donor ligands.

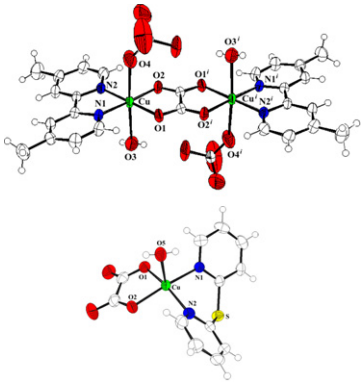


Daniella M. de Faria, Maria Irene Yoshida, Carlos B. Pinheiro, Kassílio José Guedes, Klaus Krambrock, Renata Diniz, Luiz Fernando C. de Oliveira and Flávia C. Machado

Polyhedron 26 (2007) 4525

Preparation, crystal structures and spectroscopic characterization of oxalate copper(II) complexes containing the nitrogen ligands 4,4′-dimethyl-2,2′-bipyridine and di(2-pyridyl)-sulfide

The preparation, crystal structures and spectroscopic characterization of four oxalate copper(II) complexes containing the 4,4′-dimethyl-2,2′-bipyridine (Mebpy) or di(2-pyridyl)sulfide (DPS) nitrogen ligands namely $[\mu\text{-}(ox)\{Cu(Mebpy)(NO_3)(H_2O)\}_2]$ (**1**), $[\mu\text{-}(ox)\{Cu(Mebpy)(ClO_4)(H_2O)\}_2]$ (**2**), $[\mu\text{-}(ox)\{Cu(DPS)(H_2O)\}_2](ClO_4)_2$ (**3**) and $[Cu(DPS)(ox)(H_2O)] \cdot 2H_2O$ (**4**) are described. The complexes **1**–**3** are binuclear while the complex (**4**) is mononuclear and all of them can be used as molecular building blocks for coordination polymers construction.

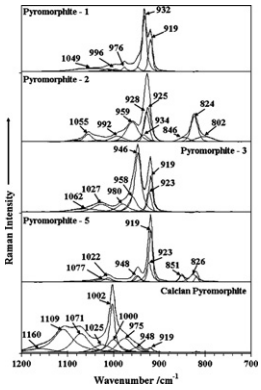


Ray L. Frost and Sara J. Palmer

Polyhedron 26 (2007) 4533

A Raman spectroscopic study of the phosphate mineral pyromorphite $Pb_5(PO_4)_3Cl$

A comparison of Raman spectra of pyromorphites with published infrared and Raman data of similar minerals has been made. Crystals of the pyromorphite–mimetite series are chemically zoned, resulting in changes in the crystal structure with the isomorphic replacement of phosphate by arsenate with the consequential change in crystal structure from monoclinic to hexagonal. Such dimorphic relationships are exemplified by the shift in the Raman spectral band positions of phosphate with increasing arsenate substitution.

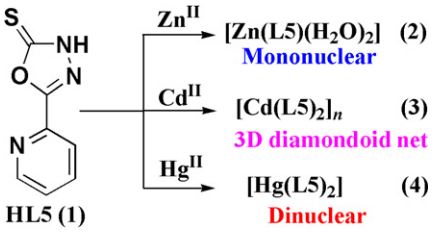


Yong-Tao Wang, Gui-Mei Tang and Zhen-Wei Qiang

Polyhedron 26 (2007) 4542

Radius-dependent assembly of complexes with the rigid unsymmetric ligand 5-(2-pyridyl)-1,3,4-oxadiazole-2-thione: Syntheses, structures and luminescence properties

The radius and coordination preferences of the metal centers based on the versatile nature of the rigid unsymmetric ligand 5-(2-pyridyl)-1,3,4-oxadiazole-2-thione (**HL5**) obviously affect the structures and luminescent properties of the coordination complexes.

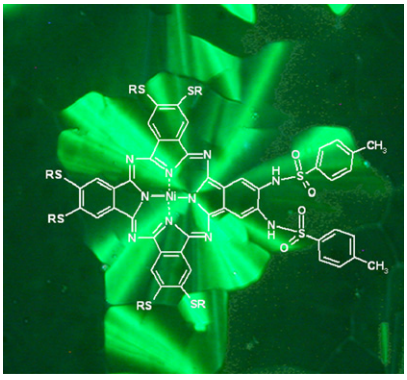


Fatma Yuksel, Devrim Atilla and Vefa Ahsen

Polyhedron 26 (2007) 4551

Synthesis and characterization of liquid crystalline unsymmetrically substituted phthalocyanines

The synthesis and characterization of unsymmetrically substituted phthalocyanines bearing two *p*-tolyl-sulfonyl (tosyl)amido and six alkylthio moieties were studied. The mesogenic properties of these new materials were described.

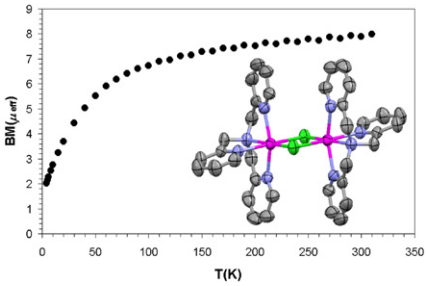


Bok-Kyu Shin, Youngmee Kim, Mihyang Kim and Jaehong Han

Polyhedron 26 (2007) 4557

Synthesis, structure and catalase activity of the $[TPA_2Mn_2(\mu\text{-}Cl)_2]^{2+}$ complex

The dinuclear Mn complex $(Et_3NH)_2[TPA_2Mn_2(\mu\text{-}Cl)_2](ClO_4)_4$ (**I**) was synthesized and characterized. The $[Mn_2(\mu\text{-}Cl)_2]^{2+}$ core, with a Mn–Mn distance of 3.521(2) Å, is similar to the active site found in chloride-inhibited Mn catalase. EPR and temperature-dependent magnetic susceptibility measurements of complex **I** showed an antiferromagnetic interaction between the two $S = 5/2$ Mn centers.

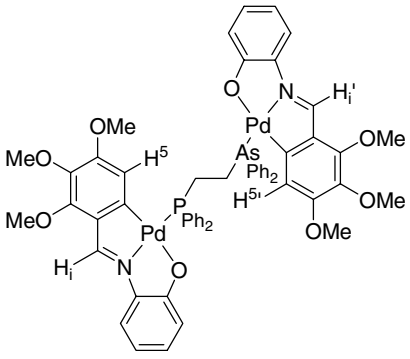


Jesús J. Fernández, Alberto Fernández, Digna Vázquez-García, Margarita López-Torres, Antonio Suárez and José M. Vila

Polyhedron 26 (2007) 4567

Reactivity of tetranuclear complexes of Pd(II) with potentially homo- and heterobidentate ligands

Schiff base ligands derived from 2-aminophenols bind tightly to the metal centre yielding cyclometallated palladium(II) species, and leaving only one coordination site available for further bonding to group 15 donor atom ligands.

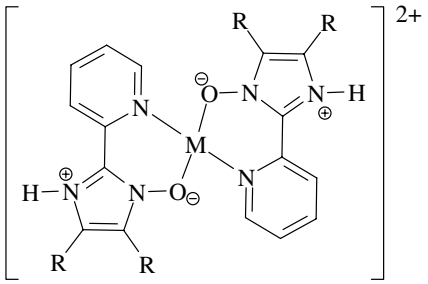


Suaad Abuskhuna, Malachy McCann, John Briody, Michael Devereux, Kevin Kavanagh, Nijhuma Kayal and Vickie McKee

Polyhedron 26 (2007) 4573

Synthesis and structure of metal complexes containing zwitterionic *N*-hydroxyimidazole ligands

Cu(II) and Zn(II) complexes of *N*-hydroxyimidazoles formulate with a metal:ligand ratio of 1:2. The two *trans*, *N*-hydroxyimidazole ligands form six-membered, chelate rings with the metal. Both of the NO chelating, neutral *N*-hydroxyimidazole ligands are in the zwitterion form, with the uncoordinated imidazole imine N atom being protonated and the oxime O atom deprotonated.

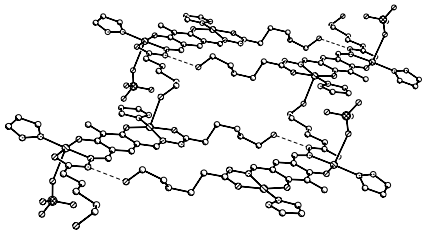


Daniel Plaul, Axel Buchholz, Helmar Görls and Winfried Plass

Polyhedron 26 (2007) 4581

meta-Phenylene-bridged double Schiff base copper(II) complexes as building blocks for 1D coordination polymers: Synthesis, crystal structure and magnetic properties

The X-ray structural characterization as well as the magnetic properties of three novel Cu(II) 1D coordination polymers derived from dinuclear resorcinol-bridged schiff base complexes linked over the hydroxyalkyl ligand side chains are reported. The resulting cationic coordination chains are further linked by hydrogen bonding with the perchlorate counterions forming 3D or 2D supramolecular networks.

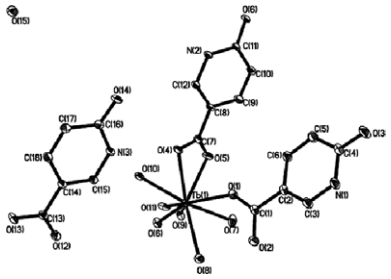


Yi-Shan Song, Bing Yan and Lin-Hong Weng

Polyhedron 26 (2007) 4591

Four distinctive 1-D lanthanide carboxylate coordination polymers: Synthesis, crystal structures and spectral properties

Four new lanthanide carboxylate complexes have been synthesized. Single crystal X-ray diffraction analyses reveal that all the complexes form 1-D molecular structures. Especially, complexes **1** and **2** have seven-coordinated centers; in the structures of the isomorphous complexes **3** and **4**, there exist three types of 6-OHnicH ligands: a bridging $Onic^{2-}$ anion, a chelating $HOnic^{-}$ anion and a neutral H_2Onic molecule.

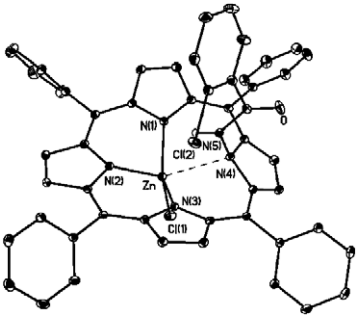


Chun-Yi Chen, Hua-Yu Hsieh, Jyh-Horung Chen, Shin-Shin Wang, Jo-Yu Tung and Lian-Pin Hwang

Polyhedron 26 (2007) 4602

Two-stage formation of chloro (*N*-*o*-chlorobenzamido-*meso*-tetraphenylporphyrinato) zinc(II) methylene chloride solvate: Zn(*N*-NHCO(*o*-Cl)C_6H_4-tpp)Cl · CH_2Cl_2

The new complex Zn(*N*-NHCO(*o*-Cl)C_6H_4-tpp)Cl (**13**) was synthesized by the reaction of Zn(*N*-NCO(*o*-Cl)C_6H_4-tpp)(MeOH) (**12**) with acid and the coordination sphere around Zn^{2+} in **13** is described as a square-based pyramid in which the apical site is occupied by Cl(1) atom.

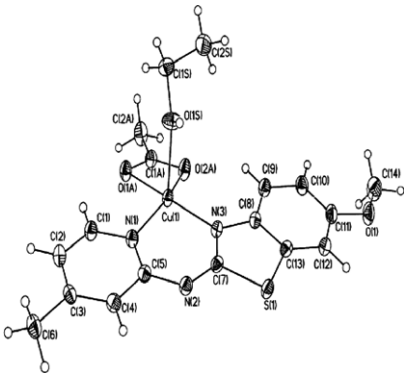


Azadeh Tadjarodi, Forough Adhami, Younes Hanifehpour, Maryam Yazdi, Zohreh Moghaddamfard and Guido Kickelbick

Polyhedron 26 (2007) 4609

Structural characterization of a copper(II) complex containing oxidative cyclization of *N*-2-(4-picolyl)-*N*′-(4-methoxyphenyl)thiourea, new ligands of 4-picolylthiourea derivatives and the precursor molecular structure of oxidative cyclization of *N*-(2-pyridyl)-*N*′-(4-methoxyphenyl)thiourea

Some aryl thiourea derivatives, such as *N*-2-pyridine-*N*′-arylthioureas, are able to be oxidized in the presence of a suitable oxidant, but this chemical change depends on the different groups in the aryl ring. Respectively, electron donating and withdrawing groups support and prevent this reaction. The product can also act as a ligand.



The Publisher encourages the submission of articles in electronic form thus saving time and avoiding rekeying errors. For detailed instructions on the preparation of manuscripts and of electronic artwork, consult the Author Gateway for Elsevier at http://authors.elsevier.com

ScienceDirect

Full text of this journal is available, on-line from **ScienceDirect**. Visit **www.sciencedirect.com** for more information.

Available online at www.sciencedirect.com
ScienceDirect
Polyhedron 26, issue 13, 6 August 2007
POLYHEDRON
www.elsevier.com/locate/poly

Contents

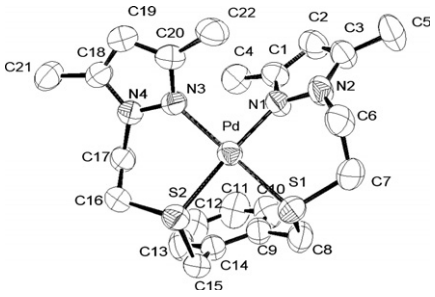
Papers

Antonio de León, Josefina Pons, Jordi García-Antón, Xavier Solans, Mercè Font-Bardia and Josep Ros

Polyhedron 26 (2007) 2921

Preparation, NMR studies and crystal structure of mononuclear and dinuclear Pd(II) and Pt(II) complexes that contain 1,2-bis[3-(3,5-dimethyl-1-pyrazolyl)-2-thiapropyl]benzene

The reactivity of 1,2-bis[3-(3,5-dimethyl-1-pyrazolyl)-2-thiapropyl]benzene (**bddf**) towards Pd(II) and Pt(II) has been tested. The synthesis, characterisation and X-ray crystal structure of $[Pd(bddf)](BF_4)_2 \cdot H_2O$ is reported.

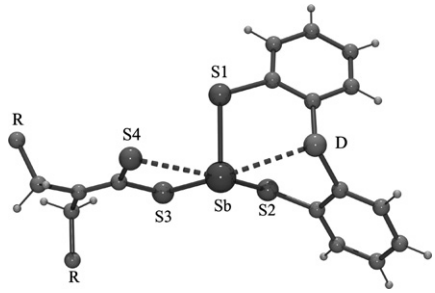


José G. Alvarado-Rodríguez, Simplicio González-Montiel, Noemí Andrade-López and Liliana B. López-Feliciano

Polyhedron 26 (2007) 2929

Pentacoordination at antimony in dibenzostibocines via D–Sb transannular interactions (D = O, S): A structural study

The synthesis of the $D(C_6H_4S)_2SbS_2CN(CH_2R)_2$ (D = O, R = Me, **1**; D = S, R = Me, **2**; R = Ph, **3**) complexes containing two different types of dithioligands is described. The antimony acceptor atom in complexes **1**–**3** expands its coordination number from three to five and displays a skew trapezoidal local geometry via an intramolecular transannular D → Sb interaction.

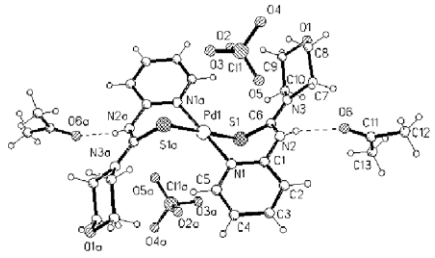


Vladimir V. Bon, Svetlana I. Orysyk, Vasilii I. Pekhnyo, Viktor V. Orysyk and Sergei V. Volkov

Polyhedron 26 (2007) 2935

Synthesis and spectroscopic investigations of Rh(III) and Pd(II) complex compounds with *N*-(pyridine-2-yl)morpholine-4-carbothioamide

The present paper describes the synthesis and spectral properties of Rh(III) and Pd(II) coordination compounds with *N*-(pyridine-2-yl)-morpholine-4-carbothioamide (PMCTA). It has been shown that PMCTA behaves as a bidentate (N,S)-ligand. The molecular structure of the Pd(II) complex with PMCTA (M:L = 1:2) was determined by single-crystal X-ray diffraction.

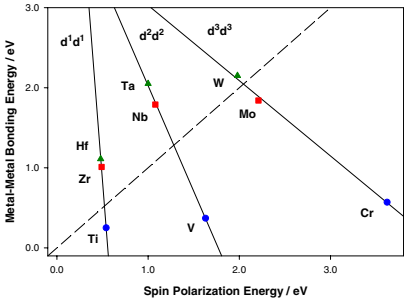


Germán Cavigliasso, Chung-Yen Yu and Robert Stranger

Polyhedron 26 (2007) 2942

Periodic trends in metal–metal bonding in edge-shared $[M_2Cl_{10}]^{4-}$ systems

Periodic trends in metal–metal interactions in edge-shared $[M_2Cl_{10}]^{4-}$ systems, involving the transition metals from groups 4 through 8 and electronic configurations ranging from d^1d^1 through d^5d^5, have been investigated using density functional theory and the results are compared with earlier work on the analogous face-shared $[M_2Cl_9]^{3-}$ complexes.

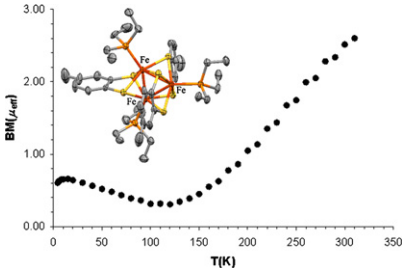


Mihyang Kim and Jaehong Han

Polyhedron 26 (2007) 2949

Synthesis, structure and physical properties of trinuclear $M_3tdt_3(PEt_3)_3$ (M = Fe^{II}, Co^{II}) clusters containing metal–metal bonds

Trinuclear $M_3tdt_3(PEt_3)_3$ (M = Fe^{II} for **I**, Co^{II} for **II**) clusters have been synthesized and characterized. The isosceles triangular clusters with short M–M distances, comparable to the extensive M–M frameworks found in the FeMo-cofactor, show unique physical properties.

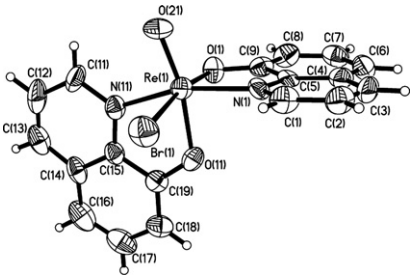


B. Machura and R. Kruszynski

Polyhedron 26 (2007) 2957

New oxorhenium complexes with the 8-quinolinolato ligand: X-ray structure and DFT calculations for $[ReOBr(hqn)_2]$

The reactions of $[ReO(OEt)X_2(PPh_3)_2]$ (X = Cl or Br) with 8-hydroxyquinoline (Hhqn) have been examined and the $[ReOX(hqn)_2]$ complexes have been obtained. The crystal and molecular structures of $[ReOBr(hqn)_2]$ have been determined. The electronic structure of $[ReOBr(hqn)_2]$ has been calculated with the density functional theory (DFT) method, and additional information about binding in the ReO^{3+} unit has been obtained by NBO analysis. The spin-allowed electronic transitions of $[ReOBr(hqn)_2]$ have been calculated with the time-dependent DFT method, and the UV–Vis spectra of the $[ReOX(hqn)_2]$ compounds have been discussed on this basis.

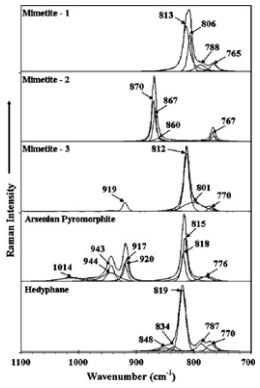


Ray L. Frost, Jocelyne M. Bouzaid and Sara Palmer

Polyhedron 26 (2007) 2964

The structure of mimetite, arsenian pyromorphite and hedyphane – A Raman spectroscopic study

A comparison of Raman spectra of mimetites with published infrared and Raman data of similar minerals has been made. Crystals of the mimetite–pyromorphite series are chemically zoned, resulting in changes in the crystal structure with the isomorphic replacement of arsenate by phosphate with the consequential change in crystal structure from hexagonal to monoclinic. Such dimorphic relationships are exemplified by the shift in the Raman spectral band positions of arsenate with increasing phosphate substitution.

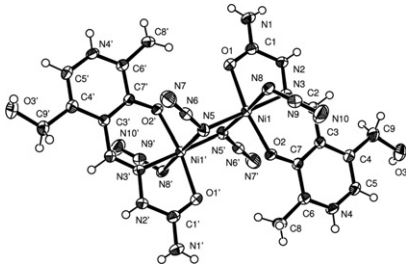


Vukadin M. Leovac, Ljiljana S. Jovanović, Violeta S. Jevtović, Giorgio Pelosi and Franco Bisceglie

Polyhedron 26 (2007) 2971

Transition metal complexes with thiosemicarbazide-based ligand – Part LV: Synthesis and X-ray structural study of novel Ni(II) complexes with pyridoxal semicarbazone and pyridoxal thiosemicarbazone

The syntheses and physico-chemical characteristcs of Ni(II) complexes of pyridoxal semicarbazone (PLSC) and pyridoxal thiosemicarbazone (PLTSC), obtained in the presence (**1**–**3**)/absence (**4**) of NaN_3, viz. $[Ni_2(PLSC)_2(\mu_{1,1}\text{-}N_3)_2(N_3)_2] \cdot 2H_2O$ (**1**), $[Ni(PLSC–H)_2] \cdot 2H_2O$ (**2**), $[Ni(PLTSC–H)N_3] \cdot H_2O$ (**3**) and $[Ni(PLTSC)_2](NO_3)_2 \cdot H_2O$ (**4**) are described. The octahedral complexes **1**, **2** and **4** are characterized also by X-ray monocrystal diffraction method.

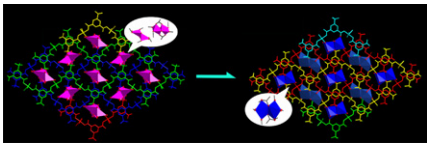


Jian Lü, Feng Li, Da-Qiang Yuan and Rong Cao

Polyhedron 26 (2007) 2979

Assembly of two novel three-dimensional networks driven by Alkali metals with an irreversible structural conversion

Two new three-dimensional (3-D) heterometallic networks containing dinuclear p-block metal–oxygen clusters and an irreversible structural conversion controlled by alkali metals are reported.

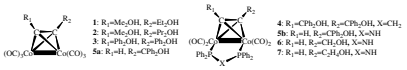


Jian-Cheng Lee, Yu-Chang Chang, Yi-Jung Ho, Kang-Ming Chu, Hsueh-Liang Chen and Fung-E Hong

Polyhedron 26 (2007) 2987

Preparation and characterization of cobalt-containing alcohols and diols

Several $PPh_2CH_2PPh_2$- or PPh_2NHPPh_2-bridged cobalt-containing alcohols and diols, **1**–**7**, were prepared and characterized. Intramolecular hydrogen bonding between two hydroxyl groups was observed for diols. Compounds **5b**, **6** and **7** are the first reported examples of PPh_2NHPPh_2-bridged dicobalt complexes.

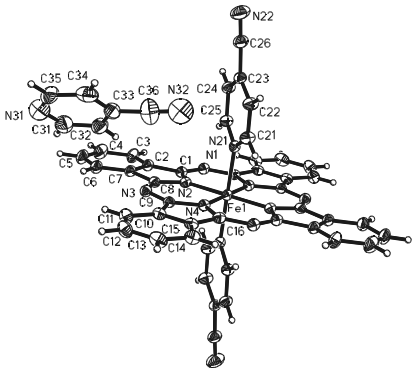


Jan Janczak and Ryszard Kubiak

Polyhedron 26 (2007) 2997

Synthesis, thermal stability and structural characterisation of iron(II) phthalocyanine complex with 4-cyanopyridine

New complex of bis-axailly coordinated iron(II) phthalocyanine by 4-cyanopyridine (4-CNpy) has been obtained in crystalline form as a adduct with two 4-CNpy molecules. Ligation of the intermediate-spin iron(II) phthalocyanine by 4-CNpy molecules leads to the low spin Fe(II) complex. The coordination polyhedron around the Fe(II) atom approximates to a tetragonal by-pyramid. The thermal analysis of the crystals of $[FePc(4\text{-}CN)_2] \cdot 2(4\text{-}CNpy)$ shows two steps responsible for the lose of solvated (~170 °C) and coordinated (~235 °C) 4-CNpy molecules.

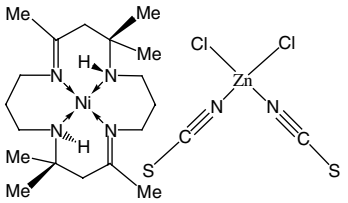


Neil F. Curtis, Rebekah Pawley and Ward T. Robinson

Polyhedron 26 (2007) 3003

The structure of *N-meso*-(6,8,8,14,16,16-hexamethyl-1,5,9,13-tetraazacyclohexadeca-5,13-diene)nickel(II) chloro(isothiocyanato)zincate(II)

The yellow crystals formed when (6,8,8,14,16,16-hexamethyl-1,5,9,13-tetraazacyclohexadeca-5,13-diene)bis(isothiocyanato)nickel(II) reacts with aqueous zinc(II) chloride have a structure with *N-meso* cations with *trans* imine groups. One anion is $[ZnCl_2(NCS)_2]^{2-}$, the other is disordered $[ZnCl_2(NCS)_2]^{2-}/[ZnCl_3(NCS)]^{2-}$ with the overall composition [Ni(*trans*-Me_6[16]diene)][$ZnCl_{1.91}(NCS)_{2.09}$].

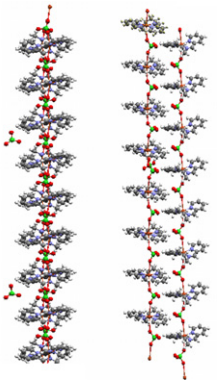


Varadarajan Uma, Alfonso Castineiras and Balachandran Unni Nair

Polyhedron 26 (2007) 3008

Copper(II) complexes of N_4 tetradentate ligands with flexible alkyl spacers: Crystal structure, DNA binding and cleavage studies

A series of copper(II) complexes (**1**, **2** and **3**) of homologous N_4 tetradentate ligands have been synthesized and compound **1** has been crystallographically characterized. The complexes exhibit minor groove binding and oxidatively cleave DNA in the presence of ascorbic acid.

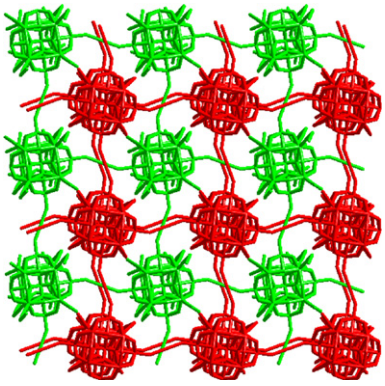


Chun-Ling Wang, Shu-Xia Liu, Lin-Hua Xie, Yuan-Hang Ren, Da-Dong Liang, Chun-Yan Sun and Hai-Yan Cheng

Polyhedron 26 (2007) 3017

New 3D two-fold interpenetrating polyoxometallate compounds built up of dititanium-substituted Keggin polyoxotungstates and transition metals

The structural features of **1** along the crystallographic *c* axis. Wire or stick schematic representation of the 3D two fold interpenetrating inorganic framework of **1**. The clusters of building units $[\alpha\text{-}PTi_2W_{10}O_{40}]^{7-}$ fragments are replaced by red and green nodes of the net.

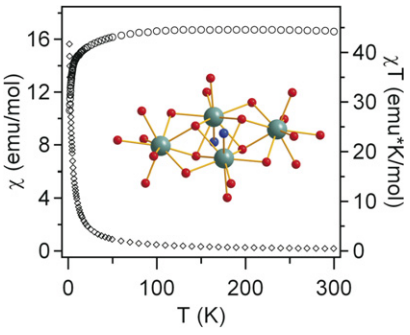


Roland Bircher, Brendan F. Abrahams, Hans U. Güdel and Colette Boskovic

Polyhedron 26 (2007) 3023

Synthesis, structure and magnetic properties of a novel Tb_4 spin cluster and synthesis of a Tb chain

The syntheses of a tetranuclear terbium complex incorporating the ligand 2-((2-hydroxybenzylidene)-amino)-2-hydroxy-methyl-propane-1,3-diol and of a linear terbium chain are reported. The magnetic properties of the tetranuclear complex were investigated by variable temperature magnetic susceptibility and magnetization measurements.

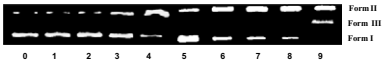


Li-Feng Tan, Hui Chao, Yang-Fan Zhou and Liang-Nian Ji

Polyhedron 26 (2007) 3029

Synthesis, characterization, DNA-binding and DNA-photocleavage studies of $[Ru(bpy)_2(BPIP)]^{2+}$ and $[Ru(phen)_2(BPIP)]^{2+}$ (BPIP = 2-(4′-biphenyl)imidazo[4,5-*f*][1,10]phenanthroline)

Photoactivated cleavage of pBR 322 DNA in the presence of Ru(II) complexes, light after 60 min irradiation at 365 nm. Lane 0 and Lane 5, DNA alone; Lanes 1–4, in the different concentrations of complex **1**: (1) 20; (2) 40; (3) 60; (4) 80 μM; Lanes 6–9, in the different concentrations of complex **2**: (6) 20; (7) 40; (8) 60; (9) 80 μM.

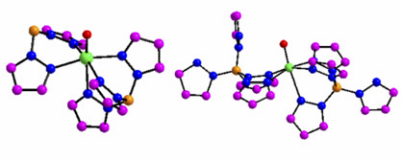


Yong-Heng Xing, Bao-Li Zhang, Yuan-Hong Zhang, Hou-Qun Yuan, Zheng Sun and Mao-Fa Ge

Polyhedron 26 (2007) 3037

Insulin-like model complexes: Synthesis, spectra characterization and crystal structure of two novel oxovanadium complexes with poly(pyrazolyl)borate ligands $VO(HB(pz)_3)(H_2B(pz)_2)$ and $VO(B(pz)_4)_2$

In this paper, two oxo-vanadium complexes with poly(pyrazolylborate) as ligand have been synthesized, and they are characterized by spectra characterization, crystal structure, thermal decomposition and quantum chemistry calculation.

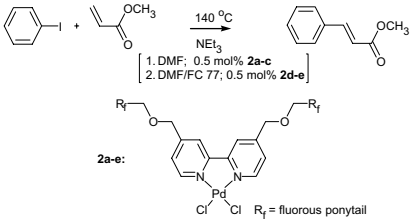


Norman Lu, Yan-Chou Lin, Jeng-Yung Chen, Tsung-Chi Chen, Shih-Chieh Chen, Yuh-Sheng Wen and Ling-Kang Liu

Polyhedron 26 (2007) 3045

Synthesis, structure and reactivity of novel palladiumdichloride-2,2′-bipyridine with 4,4′-bis(fluorous-ponytail)

The TGA curves of fluorous-ponytailed 4,4′-bis($R_fCH_2OCH_2$)-2,2′-bpy **1a**–**e** and the corresponding Pd complexes [$PdCl_2$(4,4′-bis($R_fCH_2OCH_2$)-2,2′-bpy)] **2a**–**e**, where R_f = *n*-C_3F_7 (**a**), $HCF_2(CF_2)_3$ (**b**), $HCF_2(CF_2)_7$ (**c**), *n*-C_8F_{17} (**d**), *n*-$C_{10}F_{21}$ (**e**), indicated that the Pd complexes are thermally more stable than the corresponding ligands. With the highest fluorine content in the series, Pd complex **2e** was successfully applied in the Heck reaction, using the fluorous biphasic catalysis strategy.

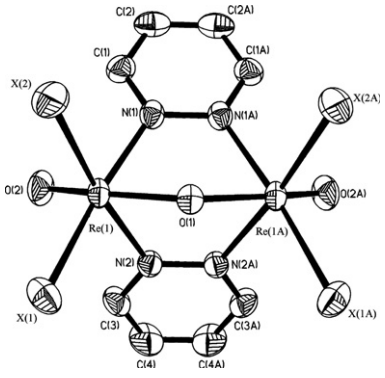


B. Machura, R. Kruszynski and J. Kusz

Polyhedron 26 (2007) 3054

Reactivity of $[ReOX_3(PPh_3)_2]$ complexes towards pyridazine. X-ray structures of $[\{ReOCl_2\}_2(\mu\text{-}O)(\mu\text{-}pyd)_2] \cdot C_6H_6$ and $[\{ReOBr_2\}_2(\mu\text{-}O)(\mu\text{-}pyd)_2] \cdot CH_3CN$, and DFT calculations for $[\{ReOCl_2\}_2(\mu\text{-}O)(\mu\text{-}pyd)_2]$

The reactions of the $[ReOX_3(PPh_3)_2]$ (X = Cl, Br) complexes with pyridazine (pyd) have been examined and $[\{ReOX_2\}_2(\mu\text{-}O)(\mu\text{-}pyd)_2]$ dinuclear oxocomplexes with a bent $Re_2O_3^{4+}$ core have been obtained. The X-ray structures of $[\{ReOCl_2\}_2(\mu\text{-}O)(\mu\text{-}pyd)_2] \cdot C_6H_6$ (**1** · C_6H_6) and $[\{ReOBr_2\}_2(\mu\text{-}O)(\mu\text{-}pyd)_2] \cdot CH_3CN$ (**2** · CH_3CN) have been determined. The electronic structure of **1** has been calculated with the density functional theory (DFT) method, and additional information about binding in the $Re_2O_3^{4+}$ unit has been obtained by NBO analysis. The spin-allowed electronic transitions of **1** have been calculated with the time-dependent DFT method, and the UV–Vis spectrum of $[\{ReOCl_2\}_2(\mu\text{-}O)(\mu\text{-}pyd)_2]$ has been discussed on this basis.

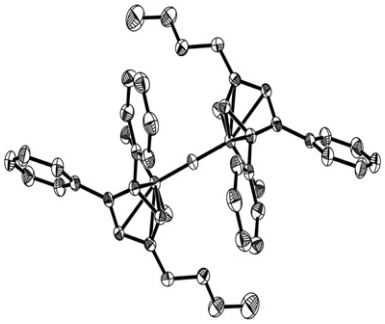


Qiao-Lin Wu, Guang-Hua Li, Ling Ye, Wei Gao and Ying Mu

Polyhedron 26 (2007) 3063

Synthesis, structures and catalytic properties of stable oxo-bridged half-sandwich titanium complexes

The oxo-bridged monocyclopentadienyl titanium complexes (1,2-Ph_2-4-R-$CpTiCl_2)_2(\mu$-O) (R = Me (**3**), *n*-Bu (**4**)), have been synthesized and structurally characterized. Both complexes show moderate catalytic activity for ethylene polymerization when activated with $Al(^iBu)_3$ and $Ph_3C^+B(C_6F_5)_4^-$, and those catalyst systems produces polyethylenes with moderate molecular weights and melting transition temperatures. The **3** or **4**/MAO systems also show good catalytic performance for styrene polymerization in terms of catalytic activity and syndiotacticity.

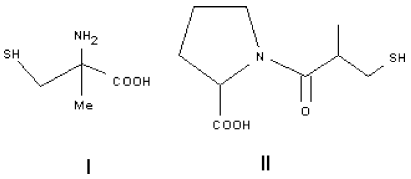


Rana N. Zahdeh, Ribhi A. Zaru and Hamdallah A. Hodali

Polyhedron 26 (2007) 3069

Kinetics of oxidation of cysteine and captopril via $Cs_3[Mo(CN)_8]$ and $Cs_3[W(CN)_8]$

Kinetics of the oxidation of cysteine (**I**) and captopril (**II**) by octacyanomolybdate(V) and octacyanotungstate(V) to their corresponding disulfide have been studied. The activation parameters and a proposed mechanism for the above oxidation processes have been given.



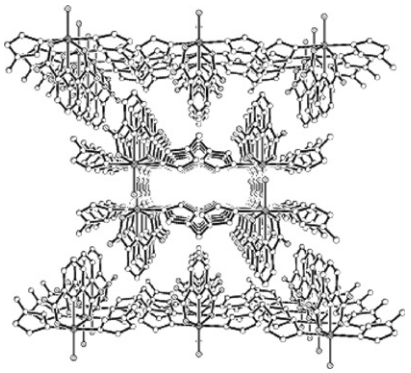
I II

Shou-Wen Jin and Wan-Zhi Chen

Polyhedron 26 (2007) 3074

Synthesis and characterization of Cu(II), Co(II) and Ni(II) coordination polymers containing bis(imidazolyl) ligands

A series of novel coordination polymers with different structures have been synthesized by reacting Cu(II), Co(II) and Ni(II) salts of aliphatic/aromatic dicarboxylic acids with flexible bisimidazole derivatives. The dicarboxylates can adopt chelating μ_2, bridging μ_2 and chelating-bridging μ_3 coordination modes, or act as uncoordinated counter anions. The coordination polymers exhibit 1D single chain, ladder, 2D sheet and 3D network structures.

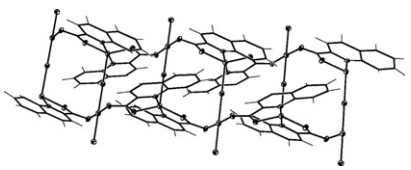


Bogumiła Żurowska, Jerzy Mroziński and Zbigniew Ciunik

Polyhedron 26 (2007) 3085

Structure and magnetic properties of a copper(II) compound with *syn–anti* carboxylato- and linear Cu–Cl–Cu chloro-bridges

The copper(II) polymer Cu(2-qic)Cl (2-qic = quinoline-2-carboxylate) was synthesized and characterized by X-ray crystal structure determination, spectroscopic and magnetic studies. The copper ions are sequentially bridged by the carboxylate groups in a *syn–anti* conformation to form an infinite a one-dimensional zigzag chain with two alternating non-equivalent copper(II) chromophores. The chloride atom acts as single chloro-bridge link to an adjacent chain forming a ribbon type structure. The magnetic behaviour is interpreted on the basis of the structural data.

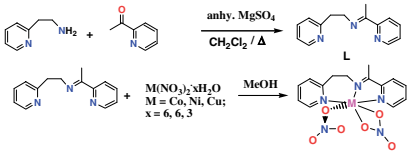


Sumanta Kumar Padhi and Vadivelu Manivannan

Polyhedron 26 (2007) 3092

Synthesis, spectral, and structural investigation of $[ML(NO_3)_2]$: M = Co, Ni, Cu; **L** = *N*-(2-pyridylethyl)pyridine-2-methylketimine

Synthesis and structural characterization of distorted pentagonal bipyramidal Co(II), pseudo-octahedral Ni(II) and Cu(II) complexes of the type $[ML(NO_3)_2]$, {**L** = *N*-(2-pyridylethyl)pyridine-2-methylketimine} are reported. Characterization includes elemental analysis, spectral, magnetism, and X-ray crystallographic studies.

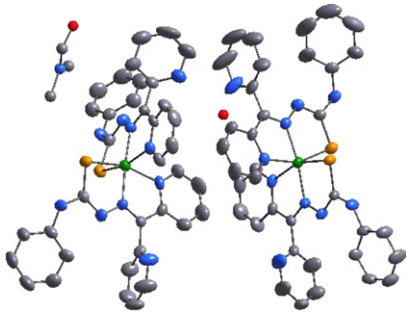


V. Suni, Maliyeckal R. Prathapachandra Kurup and Munirathinam Nethaji

Polyhedron 26 (2007) 3097

Structural and spectral investigations on some new Ni(II) complexes of di-2-pyridyl ketone *N*(4)-phenylthiosemicarbazone

Ni(II) complexes (**1**–**5**) of di-2-pyridyl ketone *N*(4)-phenylthiosemicarbazone, HL have been synthesized spectrochemically characterized. The elemental analyses revealed a $NiL_2 \cdot 2H_2O$ stoichiometry for the compound **1**. However, the single crystals isolated revealed a composition $NiL_2 \cdot 0.5(H_2O)0.5(DMF)$. The compound crystallizes into a monoclinic lattice with space group $P2_1/n$.

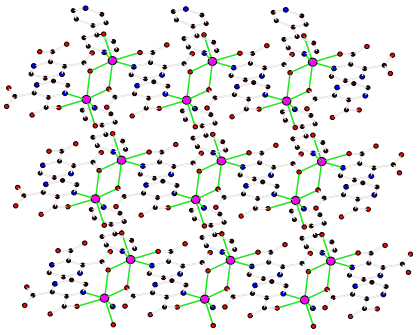


Hua Yin and Shi-Xiong Liu

Polyhedron 26 (2007) 3103

Syntheses, crystal structures and photoluminescence of three coordination polymers with 2,3-pyrazinedicarboxylic acid and N-donor ligands

The reactions between $Cd(OAc)_2/Cu(NO_3)_2$ and mixed ligands (2,3-pyrazinedicarboxylic acid (pzdc) and N-donor ligands) under different reaction conditions give the three title complexes **1**, **2** and **3**. There is a (4,8) net 2D network structure and a rectangular grid network structure in the cadmium complexes $[Cd(pzdc)(phen)] \cdot H_2O$ (**1**) and $Cd_2(pzdc)_2(4,4'\text{-bpy})(H_2O)_2$ (**2**), respectively. The complex $[Cu_4(pzdc)_4(phen)_2(H_2O)_4] \cdot 10H_2O$ (**3**) has a 1D zigzag chain structure. The influences of coordination modes of the pzdc ligand and N-donor ligands on the superstructural diversity have been discussed. Complexes **1** and **2** exhibit strong fluorescent emission bands in the solid state at room temperature.

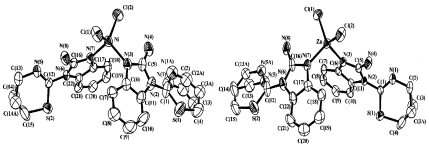


M.A. Maldonado-Rogado, E. Viñuelas-Zahínos, F. Luna-Giles and A. Bernalte-García

Polyhedron 26 (2007) 3112

Nickel(II) and zinc(II) complexes with *N*-(5,6-dihydro-4H-1,3-thiazin-2-yl)-2-aminobenzimidazole (BzTz): Synthesis, spectral and structural characterization

Some thiazine/2-aminobenzimidazole derivative nickel(II) and zinc(II) complexes were synthesized and characterized by physical measurements. The X-ray crystal structures of $[NiCl_2(BzTz)_2]$ and $[ZnCl_2(BzTz)_2]$ have also been determined. The geometry around the metallic atoms can be described as a distorted tetrahedron.

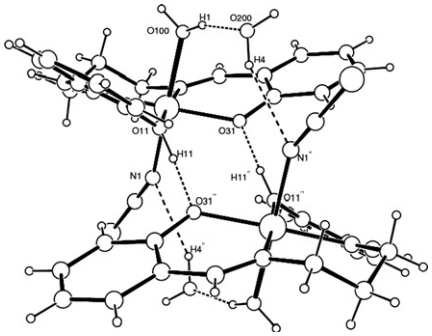


Pampa Mukherjee, Chaitali Biswas, Michael G.B. Drew and Ashutosh Ghosh

Polyhedron 26 (2007) 3121

Structural variations in Ni(II) complexes of salen type di-Schiff base ligands

The different ligating behavior of three very similar Schiff-base ligands, *N*,*N*′- bis(salicylidene)-1,3-propanediamine, *N*,*N*′-bis(salicylidene)-1,3-pentanediamine and *N*,*N*′-bis(salicylidine)-ethylenediamine with Ni(SCN)$_2 \cdot 4H_2O$ results in the formation of mononuclear [Ni(HSalpn)(NCS)(H_2O)] $\cdot$ H_2O (**1a**) and trinuclear [{Ni(Salpen)}$_2$Ni(NCS)$_2$] (**2b**) and trinuclear [Ni(Salen)]$_2$[Ni(NCS)$_2$] (**3**) complexes respectively. In **1**, one of the oxygen atoms of the Schiff base is protonated and it is involved in a very strong hydrogen bond with a neighboring unit to form a centrosymmetric dimmer.

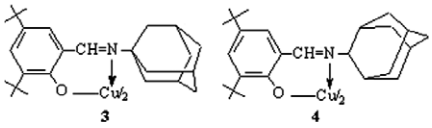


Veli T. Kasumov, Ali İ. Öztürk and Fevzi Köksal

Polyhedron 26 (2007) 3129

Synthesis, characterization and redox behavior of bis(*N*-1-adamantanyl- and *N*-2-adamantanyl-3,5-^{t}Bu$_2$-salicylaldiminato)copper(II) complexes

The synthesis, spectroscopic (^{1}H NMR, IR, UV/Vis, EPR), chemical and electrochemical redox behaviors of two new bis(*N*-1-adamantanyl and 2-adamantanyl-3,5-^{t}Bu$_2$-salicylaldiminato)copper(II) complexes (**3** and **4**) are described. EPR and UV/Vis results suggest that the chemical oxidation of the ligands and their complexes with $(NH_4)_2Ce(NO_3)_6$ results in the generation of the free phenoxyl and Cu(II)-phenoxyl radicals. The more tetrahedrally distorted **3** was reduced at a more negative potential than the less distorted **4**.

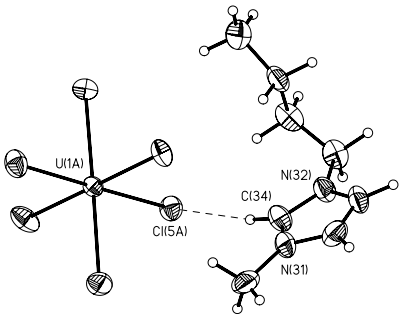


Sergey I. Nikitenko, Christoph Hennig, Mikhail S. Grigoriev, Claire Le Naour, Celine Cannes, Didier Trubert, Emilie Bossé, Claude Berthon and Philippe Moisy

Polyhedron 26 (2007) 3136

Structural and spectroscopic studies of the complex [BuMeIm]$_2$[UCl$_6$] in the solid state and in hydrophobic room temperature ionic liquid [BuMeIm][Tf$_2$N]

Single-crystal XRD data of the complex [BuMeIm]$_2$[UCl$_6$] reveal the existence of a hydrogen bond between the most acidic H atom of the imidazolium ring (C2) and the chloride anion of the UCl_6^{2-} octahedron, with the shortest Cl$\cdots$H(C2) distance equal to 2.57 Å. Visible absorption spectroscopy and ^{1}H NMR spectroscopy confirm the existence of hydrogen bonding in RTIL [BuMeIm][Tf$_2$N] solution, similar to that in the solid state.

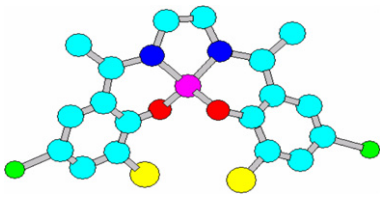


Aurel Pui and Jean-Pierre Mahy

Polyhedron 26 (2007) 3143

Synthesis, characterization and catalytic activity of halo-methyl-bis(salicylaldehyde)ethylenediamine cobalt(II) complexes

Some halo-methyl-salen derivatives and their cobalt(II) complexes were prepared. Their properties were investigated by UV–VIS, IR, ESMS spectroscopy and cyclic voltammetry. A good correlation between their redox behavior and catalytic activity was found.

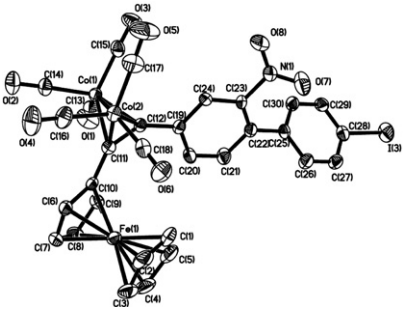


Quan-Ling Suo, Yue-Guang Bai, Yi-Bing Wang, Li-Min Han and Lin-Hong Weng

Polyhedron 26 (2007) 3153

Studies on the synthesis, characterization and reactivity of new ferrocenylacetylenylbiphenyl derivatives

Six new ferrocenylacetylenylbiphenyl derivatives and seven relevant cobalt complexes have been synthesized.The compositions and structures of 14 compounds were characterized by elemental analysis, FTIR, NMR and MS, and the molecular and crystal structures of five compounds were analyzed by X-ray single crystal diffraction.

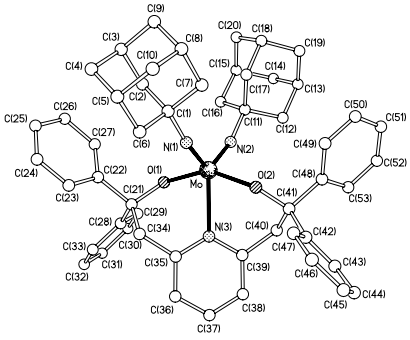


Vernon C. Gibson, Carl Redshaw, William Clegg and Mark R.J. Elsegood

Polyhedron 26 (2007) 3161

'Electronic bending' of imido ligands and the effect on the coordination mode of a tridentate ancillary ligand

The synthesis and structural characterisation of [Mo(N*t*-Bu)(NC_6F_5)(L)] (**1**) and [Mo(N-Ad)$_2$(L)] (**2**) are reported, which possess aea and eee coordination geometries for L, respectively, where LH_2 is 2,6-bis(2-hydroxy-2,2-diphenylethyl)pyridine. Complex **1** has one of the largest deviations from linearity for an M–N–C angle recorded to-date [135.98(16)°]. The structure of the trace product [MoCl-(NAd)$_2$(L_{dehyd})] (**3**) is also reported.

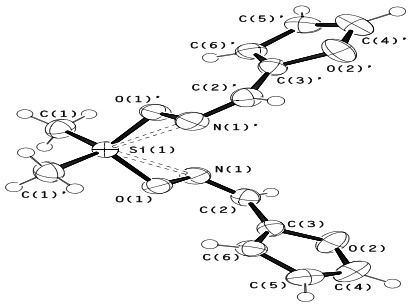


Veena Dhayal, Nikita Sharma, Vinita Sharma, Rakesh Bohra, John E. Drake and Charles L.B. MacDonald

Polyhedron 26 (2007) 3168

Synthesis and characterization of some dimethylsilicon(IV) complexes with internally functionalized oximes: Crystal and molecular structure of [$Me_2Si\{ON{=}C(H)C_4H_3O\text{-}2\}_2$]. Formation of mesoporous materials by the hydrolytic study of [$Me_2Si\{ON{=}C(CH_3)\text{-}C_4H_3O\text{-}2\}_2$] in the presence of Al(OPr^i)$_3$

Dimethylsilicon(IV) complexes, [$Me_2Si\{ON{=}C(R)Ar\}_2$], have been prepared and characterized. The X-ray structure (R = H, Ar = 2-C_4H_3O) confirms the presence of a distorted tetrahedral environment around silicon. Formation of a mesoporous material has been observed on hydrolysis of the complex (R = CH_3, Ar = 2-C_4H_3O) in the presence of Al(OPr^i)$_3$.

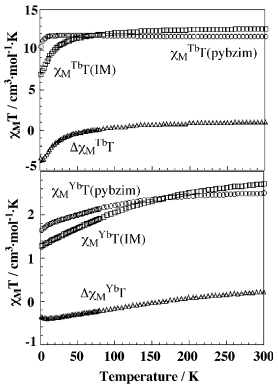


Toshiaki Tsukuda, Takayoshi Suzuki and Sumio Kaizaki

Polyhedron 26 (2007) 3175

Magnetic interactions in a series of paramagnetic Ln(III) complexes with a chelated imino nitroxide radical

Examination of the magnetic properties in a new series of isostructural complexes, [Ln(hfac)$_3$(IM2py)] (Ln = Gd–Yb), reveals that the magnetic interaction is completely reverse to the previous cases for a series of the Ln–NIT radical complexes by comparing the corresponding [Ln(hfac)$_3$(pybzim)] complexes with the diamagnetic pybzim ligand; antiferromagnetic for 4f^7 to 4f^{13}. This reverse nature substantiates the experimental Kahn's approach for a series of spin-coupled Ln(III) complexes.

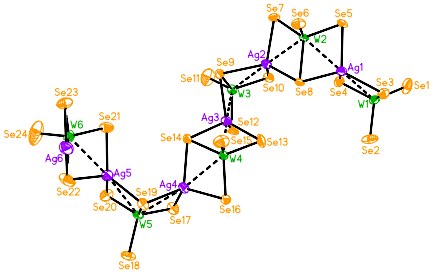


Ji-Xiang Dai, Qian-Feng Zhang, Yinglin Song, Wai-Yeung Wong, Alexander Rothenberger and Wa-Hung Leung

Polyhedron 26 (2007) 3182

Syntheses, structures, and optical properties of heteroselenometallic W–Se–Ag polymer compounds $\{[Et_4N][(\mu\text{-}WSe_4)Ag]\}_n$ and $\{[Ln(Me_2SO)_8][(\mu_3\text{-}WSe_4)_3Ag_3]\}_n$ (Ln = Pr, Er)

The heteroselenometallic W–Se–Ag one-dimensional linear polymer $\{[Et_4N][(\mu\text{-}WSe_4)Ag]\}_n$ and helical polymers $\{[Ln(Me_2SO)_8][(\mu_3\text{-}WSe_4)_3Ag_3]\}_n$ (Ln = Pr, Er) were synthesized and structurally characterized. Their optical properties were investigated by third-order optical non-linearities and UV–Vis solid-state absorption spectra.

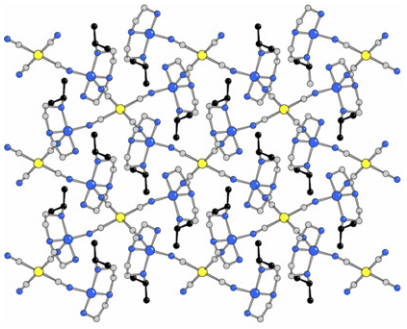


Subal Chandra Manna, Joan Ribas, Ennio Zangrando and Nirmalendu Ray Chaudhuri

Polyhedron 26 (2007) 3189

Hetero-metallic frameworks of $[Pd(CN)_4]^{2-}$ and Cu(II) with triamines: A rare example of a tetracyanometallate bridged 2D coordination polymer

Cu(II)–Pd(II) heterometallic complexes, $[Cu(dpt)Pd(CN)_4]_n$ (**1**), $\{[Cu_2(medpt)_2Pd(CN)_4](ClO_4)_2 \cdot 3H_2O\}_n$ (**2**), $\{[Cu_2(dien)_2Pd(CN)_4](ClO_4)_2 \cdot 2CH_3OH\}_n$ (**3**) and $\{[Cu_2(i\text{Prdien})_2Pd(CN)_4](ClO_4)_2 \cdot 2H_2O\}_n$ (**4**) [dpt = 3,3′-imino bispropylamine; medpt = 3,3′-diamino-*N*-methyldipropylamine; dien = diethylenetriamine and *i*prdien = *N*′-isopropyldiethylenetriamine] have been synthesized and characterized by single crystal X-ray diffraction analysis, magnetic measurement and thermal study. Complex **4** is a rare example of a tetracyanometallate bridged 2D coordination polymer.

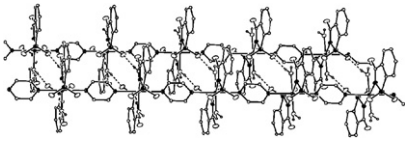


Veysel T. Yilmaz, Evrim Senel and Canan Kazak

Polyhedron 26 (2007) 3199

One-dimensional pyrazine bridged M(II)-saccharinato coordination polymers: Synthesis, characterization, crystal structures and thermal studies

The reaction of $[M(sac)_2(H_2O)_4] \cdot 2H_2O$, where M is Mn(II), Fe(II), and Co(II), and sac is the saccharinate anion, with pyrazine (pyz) result in the formation of the corresponding coordination polymers $[M(sac)_2(\mu\text{-}pyz)(H_2O)_2]_n$. The pyz ligands bridge the metal centers leading to an one-dimensional linear chain. The chains are linked into 2D layers by hydrogen bonds and the 2D layers are further arranged into three-dimensional supramolecular networks by weak $\pi\cdots\pi$ and $CH\cdots\pi$ interactions.

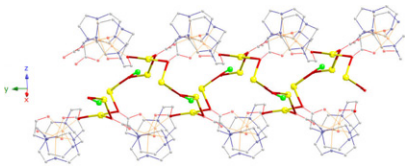


Ute Kreher, Milton T.W. Hearn, Boujemaa Moubaraki, Keith S. Murray and Leone Spiccia

Polyhedron 26 (2007) 3205

Coordination chemistry of 1,4-bis(carboxymethyl)-1,4,7-triazacyclononane: Synthesis and characterization of mononuclear and binuclear μ-oxo-bridged iron(III) complexes, and a 1D-helical copper(II) chain

A pentadentate derivative of 1,4,7-triazacyclononane has been used to prepare a carboxylate bridged copper(II) 1D-chain, a mononuclear iron(III) complex and an antiferromagnetic oxo-bridged binuclear iron(III) complex; the binuclear complex co-crystallized with three molecules of sodium perchlorate which form 1D-chains along the *y* axis.

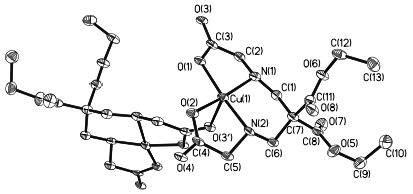


Subrahmanian Supriya, Aravamudhan Raghavan, V.R. Vijayaraghavan, Kandasamy Chinnakali, Hoong-Kun Fun and J. Subramanian

Polyhedron 26 (2007) 3217

Mannich aminomethylation reactions of a series of bis(α-amino acidato)metal(II) complexes with formaldehyde and diethylmalonate: Crystal structure of (5,5-dicarboxyethyl-3,7-diazanonanedioato)copper(II) monohydrate

Mannich aminomethylation reaction of chelated amino acid complexes with formaldehyde and diethylmalonate produces carboxylate appended systems and one of the synthesized products was found to be catalytically active in the hydrogen peroxide induced degradation of pyrocatechol violet dye.

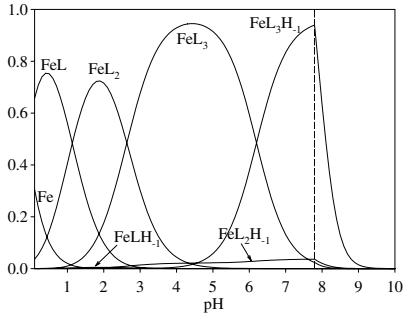


Valerio B. Di Marco, Annalisa Dean, Robert A. Yokel, Haitao Li and G. Giorgio Bombi

Polyhedron 26 (2007) 3227

Evaluation of 1-methyl-3,4-hydroxypyridinecarboxylic acids as possible bidentate chelating agents for iron(III): Metal–ligand solution chemistry

The aqueous solution chemistry of Fe(III)/1-methyl-3-hydroxy-4-pyridinecarboxylic acid and Fe(III)/1-methyl-4-hydroxy-3-pyridinecarboxylic acid was studied by potentiometry and UV–Vis. Thermodynamic results were supplemented by chelation efficiency measurements. The two ligands show a lower efficiency with Fe(III) than that of available chelators, but higher than that of their non-methylated analogs 3-hydroxy-4-pyridinecarboxylic acid and 4-hydroxy-3-pyridinecarboxylic acid.

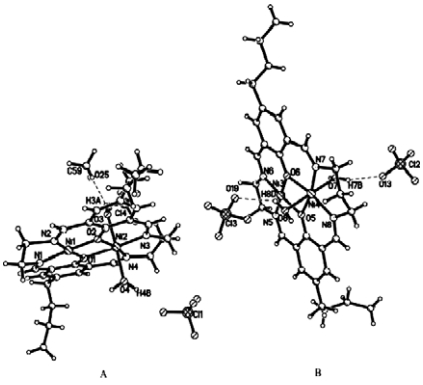


H. Zhou, Z.-H. Peng, Z.-Q. Pan, Y. Song, Q.-M. Huang and X.-L. Hu

Polyhedron 26 (2007) 3233

Synthesis, crystal structure, electrochemical, EPR and magnetic properties of dinuclear complexes with an Okawa-style unsymmetrical diphenolato Schiff base macrocyclic ligand

Three unsymmetrical dinuclear macrocyclic complexes have been synthesized. One structure was determined by X-ray diffraction. Each complex undergoes a stepwise reduction process, e.g.$[Ni_2L]^{2+}$ with $E^1_{1/2} = -0.862$ V and $E^2_{1/2} = -1.20$ V. Magnetic measurements in the 2–300 K range indicate weak antiferromagnetism for the dinuclear nickel(II) complex with the exchange constant $J = -0.90$ cm^{-1}.

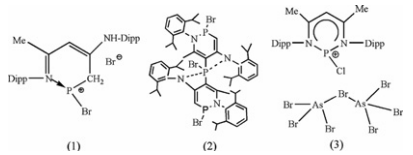


Leslie A. Lesikar, William D. Woodul and Anne F. Richards

Polyhedron 26 (2007) 3242

The reactions of phosphorus(III) halides with β-diketiminato ligands

Reactions of the lithium or sodium salt, $[HC(CMeNDipp)_2]M$ (Dipp = 2,6-diisopropylbenzene, M = Li or Na), with PBr_3 or PCl_3 affords a series of phosphenium cations that were characterized in the solid state by X-ray crystallography. Solid-state analysis reveals that for compounds **1** and **2**, C–H activation of the ligand occurs and the phosphorus is bound to a nitrogen and carbon atom of the ligand. Compound **3** exhibits the more traditional nitrogen chelation of the ligand to the phosphorus atom.

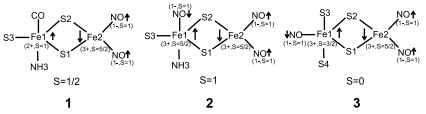


Maria Jaworska

Polyhedron 26 (2007) 3247

Electronic structure of dinuclear iron nitrosyl complexes with different ligands at two iron centers

Electronic structure of three dinuclear iron complexes was determined with the DFT method. In the lowest energy states of these complexes iron atoms possess spin $S = 1$, 3/2 or 5/2. Nitrosyl is coordinated as NO^- antiferromagnetically coupled to iron, and two iron units are antiferromagnetically coupled to each other.

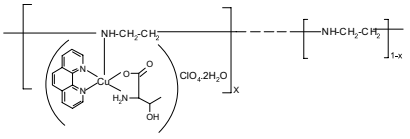


R. Senthil Kumar and S. Arunachalam

Polyhedron 26 (2007) 3255

DNA binding and antimicrobial studies of some polyethyleneimine-copper(II) complex samples containing 1,10-phenanthroline and L-theronine as co-ligands

Some polymer–copper(II) complex samples (containing both 1,10-phenanthroline and L-theronine ligands) with varying amount of copper(II) complex content in the polymer chain were prepared and characterized. DNA binding properties of these complex samples have been carried out using different physico-chemical methods. A sample of this polymer–copper(II) complex was tested for its antibacterial and antifungal activity and it was found to have good antibacterial and antifungal activities.

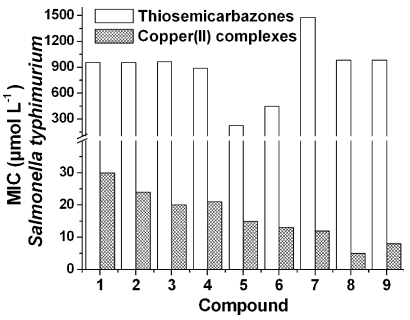


Isolda C. Mendes, Juliana P. Moreira, Antonio S. Mangrich, Solange P. Balena, Bernardo L. Rodrigues and Heloisa Beraldo

Polyhedron 26 (2007) 3263

Coordination to copper(II) strongly enhances the *in vitro* antimicrobial activity of pyridine-derived *N*(4)-tolyl thiosemicarbazones

Copper(II) complexes with *N*(4)-*ortho*, *N*(4)-*meta* and *N*(4)-*para*-tolyl thiosemicarbazones derived from 2-formyl and 2-acetylpyridine were obtained. The crystal structures of *N*(4)-*meta*-tolyl-2-acetylpyridine thiosemicarbazone (H2Ac4mT) and its complex [Cu(2Ac4mT)Cl] were determined. Upon coordination a substantial decrease in the minimum inhibitory concentration was observed against the growth of *Salmonella typhimurium*, from 225 to 1478 μmol L^{-1} for the thiosemicarbazones to 5–30 μmol L^{-1} for the complexes, and against the growth of *Candida albicans*, from 0.7–26 to 0.3–7 μmol L^{-1}, suggesting that complexation to copper(II) could be an interesting strategy of dose reduction.

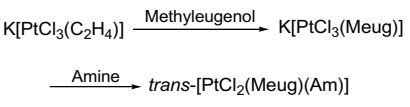


Tran Thi Da, Nguyen Thi Tuyet Minh, Nguyen Thi Thanh Chi and Nguyen Huu Dinh

Polyhedron 26 (2007) 3271

Synthesis and spectral characterization of some complexes of platinum(II) containing η^2-methyleugenol

$$K[Pt(C_2H_4)Cl_3] \overset{\text{Methyleugenol}}{\rightarrow} K[Pt(Meug)Cl_3] \overset{\text{Amine}}{\rightarrow} \textit{trans}\text{-}[Pt(Meug)(Am)Cl_2]$$

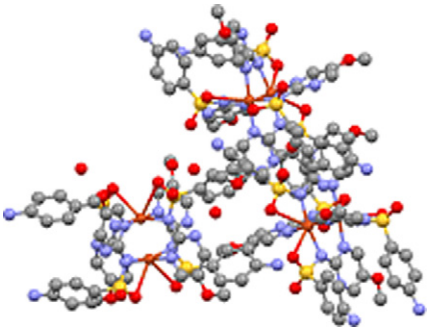


J. Ellena, E. Kremer, G. Facchin, E.J. Baran, O.R. Nascimento, A.J. Costa-Filho and M.H. Torre

Polyhedron 26 (2007) 3277

X-ray structure and EPR behavior of a new dimeric copper(II) complex with 4-amino-*N*-(5-methoxy-2-pyrimidinyl)benzenesulfonamide

A new complex, $[Cu_2(sulfameter)_4]_3 \cdot 2.5H_2O$ (sulfameter = 4-amino-*N*-(5-methoxy-2-pyrimidinyl)benzenesulfonamide), has been synthesized. The structure presented three different dimeric units in the unit cell and the EPR spectra, characteristic of antiferromagnetically coupled dimers, revealed two magnetically different dimeric environments.

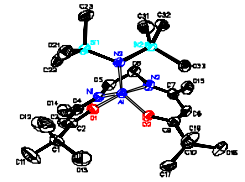


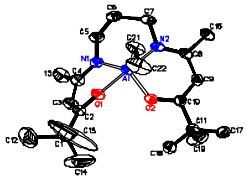
C.R. Wade, B.J. Lamprecht, V.W. Day and J.A. Belot

Polyhedron 26 (2007) 3286

Synthesis and structural characterization of two five coordinate aluminum alkyl and bis(trimethylsilyl)amino complexes bearing acyclic tetradentate Schiff bases

The synthesis and characterization of two acyclic Schiff base aluminum complexes are presented. The complexes adopt five coordinate trigonal bipyramidal geometry and can be activated with MeOH to polymerize *rac*-lactide.



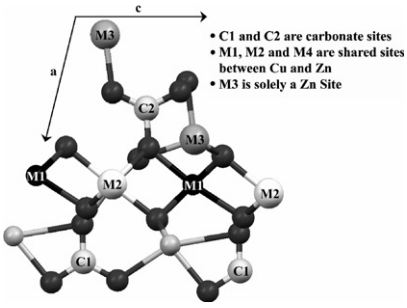


Ray L. Frost, Matt C. Hales and B. Jagannadha Reddy

Polyhedron 26 (2007) 3291

Aurichalcite – An SEM and Raman spectroscopic study

Raman spectroscopy complimented with supplementary infrared spectroscopy has been used to characterise the vibrational spectrum of aurichalcite a zinc/copper hydroxy carbonate $(Zn,Cu^{2+})_5(CO_3)_2(OH)_6$.

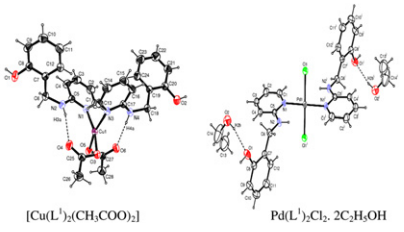


Bahattin Yalçın, Perizad A. Fatullayeva, Orhan Büyükgüngör, Başak Koşar, Sülin Taşcıoğlu, Akif I. Israfilov, Zaur D. Ibayev, Ajdar A. Medjidov and Adnan Aydın

Polyhedron 26 (2007) 3301

Cu(II) and Pd(II) complexes of *N*-(2-hydroxybenzyl)aminopyridines

N-(2-hydroxybenzyl)aminopyridines (L^i) react with Cu(II) and Pd(II) ions as neutral monodentate ligands which coordinate through pyridinic nitrogen. Cu(II) complex of N-(2-hydroxybenzyl)-2-aminopyridine (L^1), $[Cu(L^1)_2(CH_3COO)_2]$ has slightly distorted square planar *cis*-mononuclear structure. The complexes $[Cu(L^2)_2(CH_3COO)_2 \cdot 2H_2O]$ and $[Cu(L^3)_2(CH_3COO)_2 \cdot 4H_2O]$ where L^2 and L^3 are N (2-hydroxybenzyl)-3- or 4-aminopyridines are in mononuclear octahedric structure. XRD data of $[Pd(L^1)_2Cl_2 \cdot 2C_2H_5OH]$ shows square planar environment around Pd (II) ion. The spectral data indicate structural similarity in the Pd complexes of both L^2 and L^3.

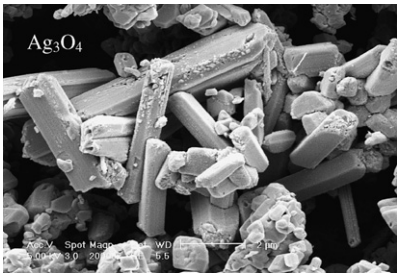


Geoffrey I.N. Waterhouse, James B. Metson and Graham A. Bowmaker

Polyhedron 26 (2007) 3310

Synthesis, vibrational spectra and thermal stability of Ag_3O_4 and related Ag_7O_8X salts ($X = NO_3, ClO_4^-, HSO_4^-$)

Ag_3O_4 and several related Ag_7O_8X salts ($X = NO_3^-, ClO_4^-, HSO_4^-$) were synthesized by ozonolysis of aqueous solutions of different Ag(I) salts at 273–298 K. Spectroscopic studies show that all of these compounds exhibit remarkable metallic character at 298 K, due to overlap between valence and conduction bands in their electronic structure.

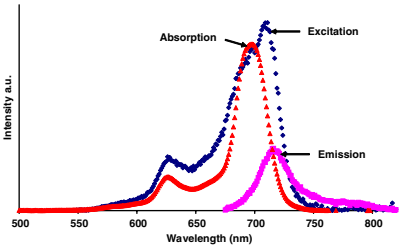


Mahmut Durmuş and Tebello Nyokong

Polyhedron 26 (2007) 3323

Synthesis, photophysical and photochemical properties of tetra- and octa-substituted gallium and indium phthalocyanines

The fluorescence studies of tetra- and octa-[4-(benzyloxyphenoxy)] substituted gallium(III) and indium(III) phthalocyanines show that for the indium phthalocyanine complexes **7b**, **8b** and **9b**, the shape of excitation spectra was different from the absorption spectra due the larger indium metal being more displaced from the core of the phthalocyanine ring.

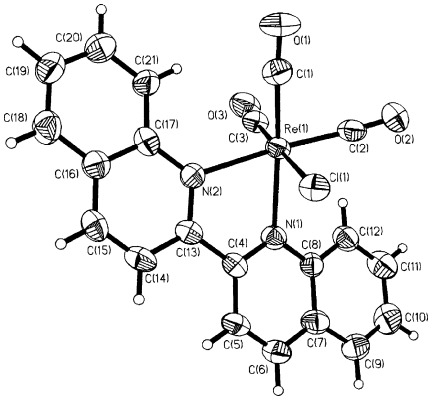


B. Machura and R. Kruszynski

Polyhedron 26 (2007) 3336

X-ray structure, spectroscopic characterisation and DFT calculations of the [Re(CO)$_3$(2,2′-biquinoline)Cl] complex

The *fac*-[Re(CO)$_3$(2,2′-biquinoline)Cl] complex has been obtained in reaction of Re(CO)$_5$Cl with 2,2′-biquinoline. The compound has been studied by IR, UV–Vis spectroscopy and X-ray crystallography. The molecular orbital diagram of the tricarbonyl has been calculated with the density functional theory (DFT) method. The spin-allowed singlet–singlet electronic transitions of [Re(CO)$_3$(2,2′-biquinoline)Cl] have been calculated with the time-dependent DFT method, and the UV–Vis spectrum of the title compound has been discussed on this basis.

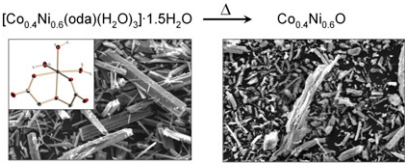


Abdessamad Grirrane, Antonio Pastor, Eleuterio Álvarez, Manuel González and Agustín Galindo

Polyhedron 26 (2007) 3343

Synthesis of mixed cobalt–nickel oxydiacetate compounds: The X-ray characterization of $[Co_{0.4}Ni_{0.6}(oda)(H_2O)_3] \cdot 1.5H_2O$

Compound $[Co_{0.4}Ni_{0.6}(oda)(H_2O)_3] \cdot 1.5H_2O$ (**1**) (oda = $O(CH_2COO)_2^{2-}$), a representative example of several synthesized mixed cobalt–nickel oxydiacetate compounds, was characterized by single-crystal X-ray analysis. Complex **1** is a co-crystallization of $[Ni(oda)(H_2O)_3] \cdot 1.5H_2O$ and $[Co(oda)(H_2O)_3] \cdot 1.5H_2O$, the latter species being a new hydrated form of cobalt oxydiacetate that shows a *fac*-coordination for the oda ligand. Thermal decomposition of **1**, carried out under nitrogen atmosphere, produces essentially $Co_{0.4}Ni_{0.6}O$ oxide.

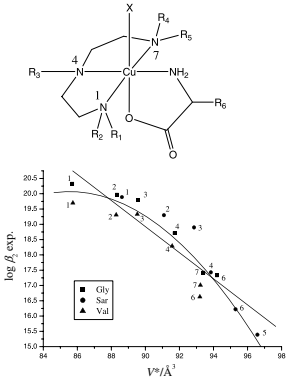


Ante Miličević and Nenad Raos

Polyhedron 26 (2007) 3350

Estimation of stability constants of copper(II) chelates with triamines and their mixed complexes with amino acids by using topological indices and the overlapping spheres method

Stability constants of Cu(II) chelates with ethylenediamines and diethylenetriamines, and their mixed complexes with amino acids were calculated from their connectivity indices, $^3\chi^v$, and OS volumes, V^*, by using calibration models developed on the same or different classes of compounds.

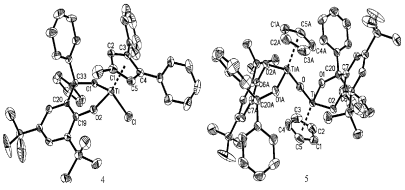


Tie-Qi Xu, Wei Gao, Ying Mu and Ling Ye

Polyhedron 26 (2007) 3357

Titanium(IV) complexes with monocyclopentadienyl and phenoxy-alkoxo ligands: Synthesis, structures and catalytic properties for ethylene polymerization

Three monochlorotitanium complexes with monocyclopentadienyl and phenoxy-alkoxo ligands [Cp′Ti(2,4-^{t}Bu$_2$-6-(CPh$_2$O)C$_6$H$_2$O)] (Cp′ = η^5-C$_5$H$_5$ (**2**), η^5-C$_5$(CH$_3$)$_5$ (**3**), η^5-C$_5$H$_2$Ph$_2$CH$_3$ (**4**)) have been synthesized and characterized. Complexes **2**, **3** and **4** have been studied as catalysts for ethylene polymerization in the presence of $[Ph_3C]^+[B(C_6F_5)_4]^-$ and Al^{i}Bu$_3$ as co-catalyst and good activities were observed. Addition of excess water to complex **2** gave the oxo-bridged complex [Ti(η^5-C$_5$H$_5$)(2,4-^{t}Bu$_2$-6-(CPh$_2$O)C$_6$H$_2$O)]$_2$O (**5**).

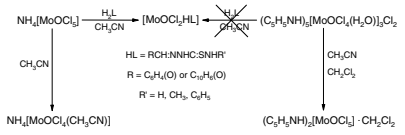


Višnja Vrdoljak, Dalibor Milić, Marina Cindrić, Dubravka Matković-Čalogović and Dominik Cinčić

Polyhedron 26 (2007) 3363

Synthesis of novel molybdenum(V) complexes: Structural characterization of two thiosemicarbazonato complexes [MoOCl$_2${C$_6$H$_4$(O)-CH:NNHC:SNHC$_6$H$_5$}] and [MoOCl$_2$-{C$_{10}$H$_6$(O)CH:NNHC:SNHC$_6$H$_5$}] · CH$_3$CN, and two oxohalomolybdates NH$_4$[MoOCl$_4$-(CH$_3$CN)] and [C$_5$H$_5$NH]$_2$[MoOCl$_5$] · CH$_2$Cl$_2$

Eight mononuclear oxomolybdenum(V) complexes were prepared. All the complexes were characterized by chemical analysis, IR spectroscopy, thermogravimetry and four of them, [MoOCl$_2${C$_6$H$_4$(O)CH:NNHC:SNHC$_6$H$_5$}], [MoOCl$_2${C$_{10}$H$_6$(O)CH:NNHC:SNHC$_6$H$_5$}] · CH$_3$CN, NH$_4$[MoOCl$_4$(CH$_3$CN)] and (C$_5$H$_5$NH)$_2$[MoOCl$_5$] · CH$_2$Cl$_2$, by single-crystal X-ray structural analysis.

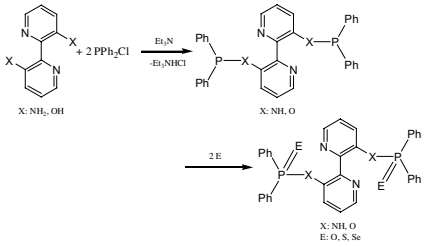


Akın Baysal, Murat Aydemir, Feyyaz Durap, Bahattin Gümgüm, Saim Özkar and Leyla Tatar Yıldırım

Polyhedron 26 (2007) 3373

Synthesis and characterizations of 3,3′-bis-(diphenylphosphinoamine)-2,2′-bipyridine and 3,3′-bis(diphenylphosphinite)-2,2′-bipyridine and their chalcogenides

3,3′-Bis(diphenylaminophosphine)-2,2′-bipyridine, 3,3′-bis(diphenylphosphinite)-2,2′-bipyridine and their chalcogenides were prepared and characterized.

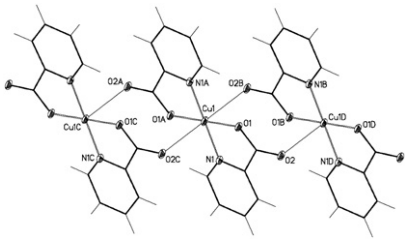


Bogumila Żurowska, Jerzy Mroziński and Katarzyna Ślepokura

Polyhedron 26 (2007) 3379

Structure and magnetic properties of a double out-of-plane carboxylato-bridged Cu(II) compound with pyridine-2-carboxylate

A double of out-of-plane carboxylato-bridged linear polynuclear copper(II) compound of the formula $Cu(2\text{-pca})_2$, (2-pca = pyridine-2-carboxylate ion) has been characterized by X-ray crystallography and magnetic susceptibility measurements. Two key factors control the crystal structure of the compound, the bridging coordination and the C–H···O interchain hydrogen bonds. The magnetic behaviour of the complex can be explained as a result of magnetic exchange within the chain through long Cu–O axial bonds ($J = -1.04$ cm^{-1}) and a superexchange pathway through the hydrogen bond network between adjacent molecules ($zJ' = 0.34$ cm^{-1}).

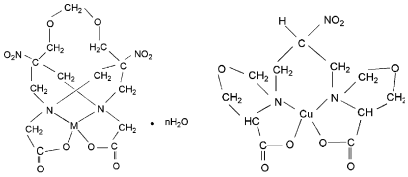


Subrahmanian Supriya, Aravamudhan Raghavan, V.R. Vijayaraghavan and J. Subramanian

Polyhedron 26 (2007) 3388

Syntheses, characterization and catalytic activity of Mannich aminomethylation products of bis(glycinato)metal(II) complexes

Reactions of chelated glycine complexes with formaldehyde and nitromethane yielded different Mannich aminomethylation products under acidic and alkaline conditions. The synthesized bridged complexes have been characterized by suitable spectroscopic and analytical techniques. One of the synthesized products, tested for its catalytic activity, has been found to be effective in the hydrogen peroxide induced degradation of pyrocatechol violet dye.



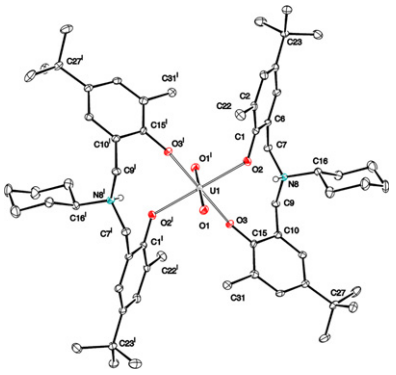
Proposed structure for the complexes

Harri Sopo, Kamal Goljahanpoor and Reijo Sillanpää

Polyhedron 26 (2007) 3397

Aminoalkylbis(phenolate) [O,N,O] donor ligands for uranyl(VI) ion coordination: Syntheses, structures, and extraction studies

The syntheses of five new aminoalkylbis(phenolate) ligands (as hydrochlorides) and their uranyl complexes are described. The reaction between uranyl nitrate hexahydrate and phenolic ligand precursor [(*N*,*N*-bis(2-hydroxy-5-*tert*-butyl-3-methylbenzyl)-aminoalkyl) · HCl], (alkyl = propyl, butyl, hexyl, cyclohexyl or benzyl) (H_2L1–H_2L5), in acetonitrile in presence of a base affords the mononuclear, neutral complexes $[UO_2(HL)_2] \cdot x$S ($x = 0$, 1 or 2 and S = acetonitrile or methanol). Extraction studies of the uranyl ion from water to dichloromethane with these new ligands (H_2L1–H_2L5) are also presented and the ligands $H_2L2 \cdot HCl$ and $H_2L4 \cdot HCl$ are the most effective ones.

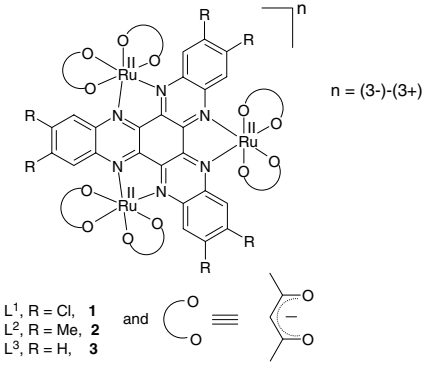


Sandeep Ghumaan, Biprajit Sarkar, Mahendra P. Patil, Jan Fiedler, Raghavan B. Sunoj, Wolfgang Kaim and Goutam Kumar Lahiri

Polyhedron 26 (2007) 3409

Multiple one-electron oxidation and reduction of trinuclear bis(2,4-pentanedionato)ruthenium complexes with substituted diquinoxalino[2,3-*a*:2′,3′-*c*]phenazine ligands

Three reversible oxidation steps and at least three reversible reduction processes were found for the title complexes. Analysis via EPR and UV–Vis–NIR spectroelectrochemistry revealed metal-centered oxidation to form mixed-valent intermediates without conspicuous IVCT absorptions in the infrared. Reduction occurs on the bridging ligands with very little participation from ruthenium.



L^1, R = Cl, **1**
L^2, R = Me, **2**
L^3, R = H, **3**

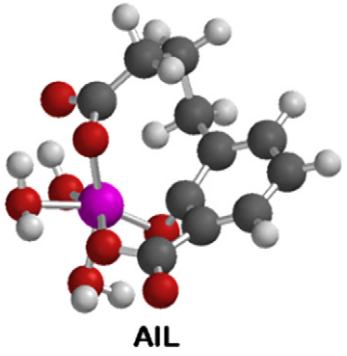
and

G. Giorgio Bombi, Valerio B. Di Marco, Daniele Marton, Stefano Moro, Aikebaier Reheman, Andrea Tapparo and Lisa Viero

Polyhedron 26 (2007) 3419

2-Hydroxy-3-carboxy-dihydrocinnamic acid: Complexation properties towards aluminium-(III) and iron(III)

Number, stoichiometry and stability constants of the complexes formed in aqueous (Na)Cl 0.6 m solution by 2-hydroxy-3-carboxy-dihydrocinnamic acid with Al(III) and Fe(III) were obtained at 25 °C by potentiometric titrations, UV–Vis and NMR measurements. Most of the Al(III) and Fe(III) species are either bidentate or mixed ligand-hydroxo complexes. The tridentate chelation is displayed in the AlL species. Molecular modeling confirmed experimental results.

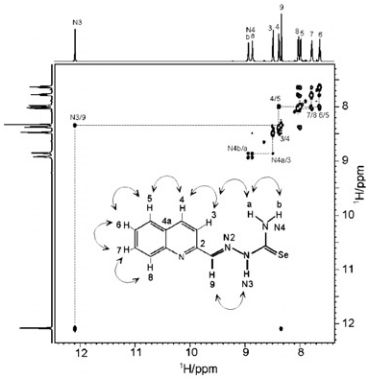


Tamara R. Todorović, Alessia Bacchi, Nenad O. Juranić, Dušan M. Sladić, Giancarlo Pelizzi, Tatjana T. Božić, Nenad R. Filipović and Katarina K. Anelković

Polyhedron 26 (2007) 3428

Synthesis and characterization of novel Cd(II), Zn(II) and Ni(II) complexes with 2-quinolinecarboxaldehyde selenosemicarbazone. Crystal structure of bis(2-quinolinecarboxaldehyde selenosemicarbazonato)nickel(II)

A ligand 2-quinolinecarboxaldehyde selenosemicarbazone (Hqasesc) was synthesized and coordinated with Zn(II), Cd(II) and Ni(II). Single crystal X-ray analysis shows that the Ni(II) coordinates two deprotonated qasesc$^-$ ligands giving the octahedral bischelate complex. NMR study showed a difference in structures of Cd(II) and Zn(II) complexes in solid state and in solution. Preliminary results of cytotoxic activity determination showed that the complexes are more active than the ligand.

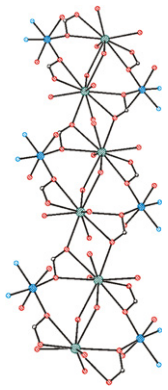


S. Grubišić, D.D. Radanović, U. Rychlewska, B. Warżajtis, N.S. Drašković, M.I. Djuran and S.R. Niketić

Polyhedron 26 (2007) 3437

Conformational study of Co(II), Ni(II), and Cr(III) complexes of the edta-type: Crystal structure of 1D polymeric *trans*(O^6)-Ba[Co(1,3-pddadp)] · $8H_2O$ complex stabilized by infinite water tapes

MM calculations indicate that for the [M-(1,3-pddadp)]$^{n-}$ system [where 1,3-pddadp represents the 1,3-propanediamine-*N*,*N*′-diacetate-*N*,*N*′-di-3-propionate ion, and M = Co(III), Cr(III), Rh(III), Ni(II), and Co(II)], the *trans*(O^5O^6) isomer is of the lowest energy. The least energetically favored *trans*($O)^6$ [Co(1,3-pddadp)]$^{2-}$ complex anion possesses unusual geometry and conformation of the β-alaninate rings, and forms, in a crystal, polymeric chains glued by infinite water tapes.

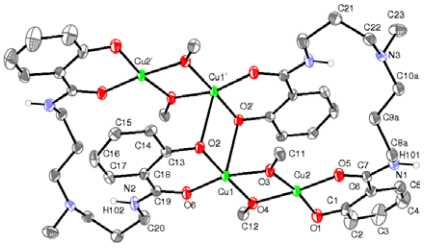


Samira Louhibi, Aicha Yacouta Nour, Laure Vendier, Jean-Pierre Costes and Jean-Pierre Tuchagues

Polyhedron 26 (2007) 3448

Polynuclear 3d complexes based on potentially tetra-anionic heptadentate ligands including amido, amino and phenoxo donors: Synthesis, crystal structure and magnetic properties

The diamide ligands H_4L^1 and H_4L^2, including seven potential donor atoms, do not wrap around the metal ions and do not act as common dinucleating ligands. They respectively yield a 14-membered metalla-macrocycle in the dinuclear $[HL^1Mn(DMSO)]_2$ complex and a 32-membered metalla-macrocycle in the tetranuclear $[H_2L^2Cu_2(MeO)_2]_2$ complex.

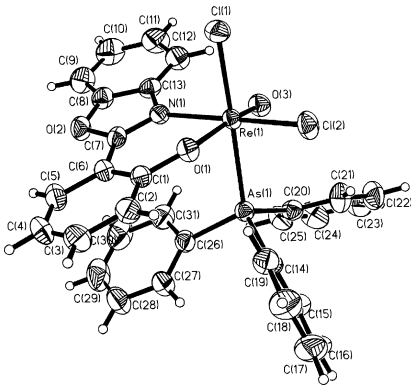


B. Machura, R. Kruszynski and J. Kusz

Polyhedron 26 (2007) 3455

New oxorhenium complexes with 2-(2′-hydroxyphenyl)-2-benzoxazolinato ligand. X-ray structure and DFT calculations for $[ReOX_2(hbo)(AsPh_3)]$ and $[ReOX_2(hbo)(PPh_3)]$ complexes

The reactions of $[ReOX_3(AsPh_3)_2]$ and $[ReOX_3(PPh_3)_2]$ with 2-(2′-hydroxyphenyl)-2-benzoxazoline (Hhbo) have been examined and $[ReOX_2(hbo)(AsPh_3)]$ and $[ReOX_2(hbo)(PPh_3)]$ (X = Cl, Br) complexes have been obtained. The crystal and molecular structures of $[ReOCl_2(hbo)(AsPh_3)]$ (**1**) and $[ReOBr_2(hbo)(PPh_3)]$ (**4**) have been determined. The electronic structures of **1** and **4** have been calculated with the density functional theory (DFT) method. The spin-allowed electronic transitions of **1** and **4** have been calculated with the time-dependent DFT method, and the UV–Vis spectra of these complexes have been discussed.

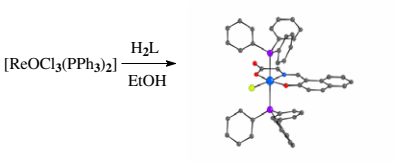


Sucharita Basak, Amrita Mondal, Deepak Chopra and Kajal Krishna Rajak

Polyhedron 26 (2007) 3465

Synthesis and structural characterisation of new Re(III) complexes using aldimines of α-amino acids as coligands

The reaction of $[ReOCl_3(PPh_3)_2]$ with the imines of α-amino acids (glycine, L-alanine, L-valine, L-phenylalanine) derived from salicylaldehyde and naphthaldehyde in ethanol afforded orange-red coloured complexes of the general formula $[Re^{III}(L)Cl(PPh_3)_2]$. The crystal structure of one complex has been determined. Their solution properties were deduced from spectroscopic measurements.



Mary S. Thomas, Marilé Landman, Simon Lotz and Elizabeth M. van der Merwe

Polyhedron 26 (2007) 3471

The synthesis, characterization and melting properties of thiophene-containing dithiocarboxylate complexes of nickel(II)

The reactions of a series of 5-alkyl-2-thiophenedithiocarboxylates with nickel(II) chloride afforded two types of complexes, blue nickel(II) complexes with two terminal dithiocarboxylate ligands and violet nickel(II) complexes with perthio- and dithiocarboxylate ligands. Liquid-crystalline properties of these complexes were examined by DSC and POM and the violet complexes with C_8 and C_{12} alkyl chains showed liquid-crystalline properties.



The Publisher encourages the submission of articles in electronic form thus saving time and avoiding rekeying errors. For detailed instructions on the preparation of manuscripts and of electronic artwork, consult the Author Gateway for Elsevier at http://authors.elsevier.com

ScienceDirect

Full text of this journal is available, on-line from **ScienceDirect**. Visit **www.sciencedirect.com** for more information.

Available online at www.sciencedirect.com
ScienceDirect
Polyhedron 26, issue 12, 23 July 2007
POLYHEDRON
www.elsevier.com/locate/poly

Contents

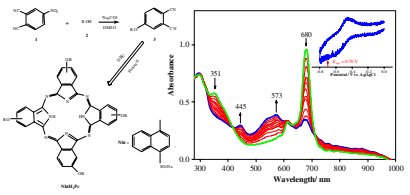
Papers

Sonmez Arslan and Ismail Yilmaz

Polyhedron 26 (2007) 2387

A new water-soluble metal-free phthalocyanine substituted with naphthoxy-4-sulfonic acid sodium salt. Synthesis, aggregation, electrochemistry and in situ spectroelectrochemistry

A new water-soluble metal-free phthalocyanine, 2,9,16,23-tetrakis(4-(1-naphthoxy-4-sulfonic acid sodium salt))phthalocyanine **$NhtH_2Pc$**, was synthesized and its electrochemical and spectroelectrochemical properties were investigated in DMSO solution. The aggregation study of **$NhtH_2Pc$** shows that **$NhtH_2Pc$** exhibits the characteristic monomeric UV–Vis absorption of phthalocyanine in methanol and DMSO. **$NhtH_2Pc$** displays three reversible one-electron reductions waves assigned to Pc^{3-}/Pc^{2-}, Pc^{4-}/Pc^{3-} and Pc^{4-}/Pc^{5-} couples, respectively. The well-defined UV–Vis spectrum of the electro-reduced species **$[NhtH_2Pc]^-$** was obtained with an applied potential (E_{app} = −0.70 V) in a thin-layer cell.

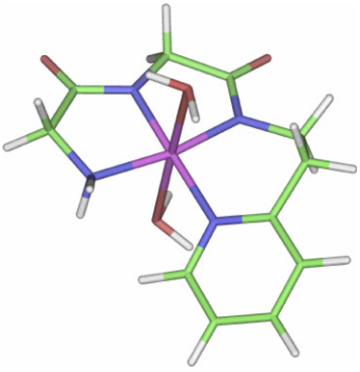


John N. Zvimba and Graham E. Jackson

Polyhedron 26 (2007) 2395

Thermodynamic and spectroscopic study of the interaction of Cu(II), Ni(II), Zn(II) and Ca(II) ions with 2-amino-*N*-(2-oxo-2-(2-(pyridin-2-yl)ethyl amino)ethyl)acetamide, a pseudo-mimic of human serum albumin

Solution speciation of Cu(II), Ca(II), Zn(II) and Ni(II) complexes of a mixed amino/amido/pyridyl ligand is reported. The ligand is able to promote dermal absorption and mobilize Cu(II) *in vivo*.

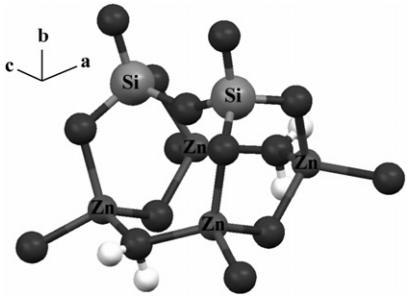


Ray L. Frost, Jocelyn M. Bouzaid and B. Jagannadha Reddy

Polyhedron 26 (2007) 2405

Vibrational spectroscopy of the sorosilicate mineral hemimorphite $Zn_4(OH)_2Si_2O_7 \cdot H_2O$

Raman spectroscopy complimented by infrared spectroscopy of the mineral hemimorphite from different origins shows OH bands providing hydrogen bond distances of 2.910, 2.825, 2.762 and 2.716 Å.

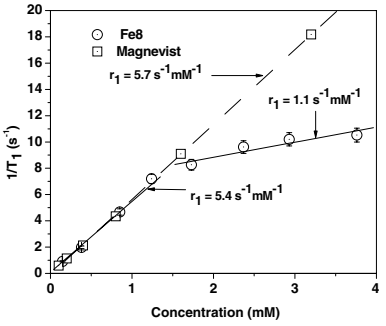


Brant Cage, Stephen E. Russek, Richard Shoemaker, Alex J. Barker, Conrad Stoldt, Vasanth Ramachandaran and Naresh S. Dalal

Polyhedron 26 (2007) 2413

The utility of the single-molecule magnet Fe_8 as a magnetic resonance imaging contrast agent over a broad range of concentration

The inverse proton longitudinal relaxation time T_1^{-1} of Fe_8 and Magnevist aqueous solutions as a function of concentration. While the Magnevist data are monotonic over the entire concentration range, the Fe_8 data exhibits two distinct linear regions. These results indicate the magnetic behavior of Fe_8 aqueous is highly concentration dependent.

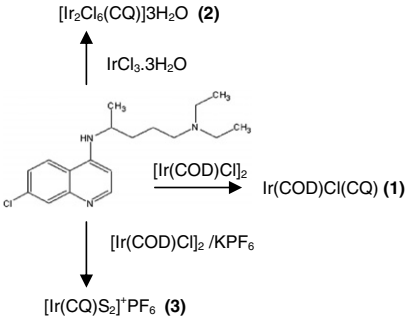


Maribel Navarro, Sara Pekerar and Hilda A. Pérez

Polyhedron 26 (2007) 2420

Synthesis, characterization and antimalarial activity of new iridium–chloroquine complexes

Three new iridium–chloroquine complexes Ir(CQ)Cl(COD) (**1**), $Ir_2Cl_6(CQ) \cdot 3H_2O$ (**2**) and $[Ir(CQ)(Solv)_2]PF_6$ (**3**) were synthesized and testing in vitro against *Plasmodium berghei*. Comparison of the IC_{50} values obtained for complexes (**1**–**3**) versus parental drug indicated a higher activity for complex **1**, while complexes **2** and **3** showed a similar and lower activity, respectively.

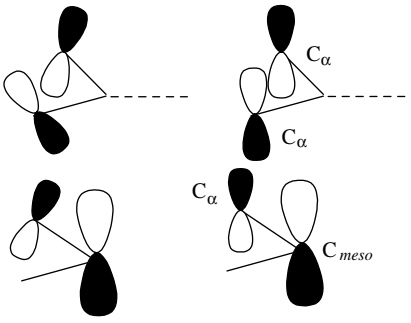


Saeed Zakavi and Nasrin Gholami Gharab

Polyhedron 26 (2007) 2425

Interaction of *para*-substituted *meso*-tetraphenylporphyrins and *meso*-tetra(*n*-propyl)porphyrin with weak and strong carboxylic acids: A UV–Vis spectroscopic study

Porphyrins may be protonated using weak and strong carboxylic acids. The formation of these weak complexes is accompanied by a shift of the Soret and Q(0,0) bands which may be explained on the basis of decreased C_α–C_α and C_α–C_{meso} antibonding interactions upon the saddling of the macrocycle, the enhanced coplanarity of the aryl groups with the porphyrin mean plane which lead to an interaction between the HOMOs of the porphyrin core with the proper orbitals of the aryl substituents, and the protonation of the pyrrolenine nitrogen atoms.

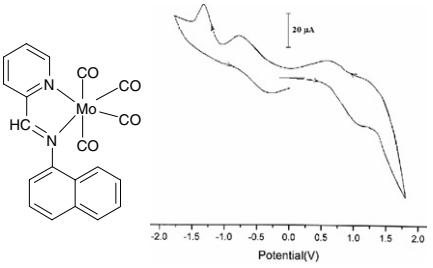


P. Datta and C. Sinha

Polyhedron 26 (2007) 2433

Group 6 tetracarbonyl complexes of *N*-[(2-pyridyl)methyliden]-α (or β)-aminonaphthalene: Spectral characterization, electrochemistry, solvatochromism and photophysical studies

Cis-$[M(CO)_4(\alpha/\beta\text{-NaiPy})]$ (M = Cr(0), Mo(0), W(0) and α/β-NaiPy = *N*-[(2-pyridyl)methyliden]-α (or β)-aminonaphthalene) are described in this work. Fluorescence shows a high quantum yield π–π^* emission. Cyclic voltammetry gives a metal centred oxidation, M^+/M^0 and two ligand centred reductions.

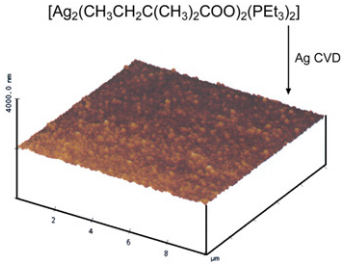


I. Szymańska, P. Piszczek, R. Szczęsny and E. Szłyk

Polyhedron 26 (2007) 2440

Thermal and MS studies of silver(I) 2,2-dimethylbutyrate complexes with tertiary phosphines and their application for CVD of silver films

$[Ag_2(CH_3CH_2C(CH_3)_2COO)_2]$, $[Ag_2(CH_3CH_2C(CH_3)_2COO)_2(PMe_3)_2]$ and $[Ag_2(CH_3CH_2C(CH_3)_2COO)_2(PEt_3)_2]$ were prepared and characterized. Silver layers were produced from $[Ag_2(CH_3CH_2C(CH_3)_2COO)_2(PEt_3)_2]$ in *hot-wall* CVD experiments, between 200 and 280 °C, under a pressure of 2.0 mbar, using argon as a carrier gas. Thin films obtained on Si(1 1 1) at moderate temperature (220–250 °C) revealed a thickness below 50 nm, and were whitish colored and slightly matt.

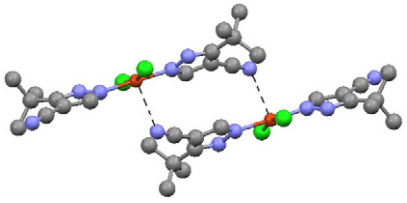


Ningfeng Zhao, Michael J. Van Stipdonk and David M. Eichhorn

Polyhedron 26 (2007) 2449

Syntheses and crystal structures of 3-*tert*-butyl-4-cyano pyrazole and its complexes with cobalt(II), manganese(II), and copper(II)

The syntheses and crystal structures of 3-*tert*-butyl-4-cyano pyrazole ($Hpz^{t\text{-}Bu,4CN}$), $Co(Hpz^{t\text{-}Bu,4CN})_4(H_2O)_2$, $Mn(Hpz^{t\text{-}Bu,4CN})_2(H_2O)_2(OTf)_2$, and $Cu(Hpz^{t\text{-}Bu,4CN})_2Cl_2$ are reported. $Hpz^{t\text{-}Bu,4CN}$ forms a cyclic hydrogen-bound dimer. Hydrogen bonding in the Mn complex results in a linear double chain. The Cu complex has a slightly distorted square-planar geometry, with a long bond to the cyano N atom of a neighboring Cu complex, forming a pseudodimer.

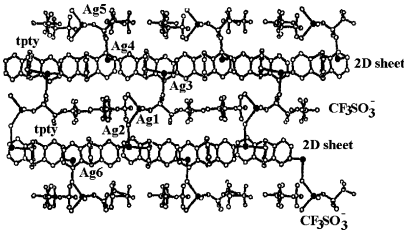


Ming Wen, Megumu Munakata, Yi-Zhi Li, Yusaku Suenaga, Takayoshi Kuroda-Sowa, Masahiko Maekawa and Manabu Anahata

Polyhedron 26 (2007) 2455

1D Chain and 3D framework of silver(I) organo-metallic polymers self-assembled with triptycene

Two silver(I) organometallic polymer self-assemblies with triptycene, $[Ag(tpty)(THF)_2](ClO_4)$ (**1**) and $[Ag_6(tpty)_4(CF_3SO_3)_2(H_2O)_6](CF_3SO_3)_4$ (**2**) have been synthesized and structurally determined by single-crystal X-ray diffraction. Silver(I) ions exhibit unprecedented μ–η^1–η^1–η^1, μ–η^1–η^1–η^2 or μ–η^1–η^2–η^2 coordination modes with triptycene, and generate an interesting array of organometallic compounds with 1D chain and 3D porous frameworks.

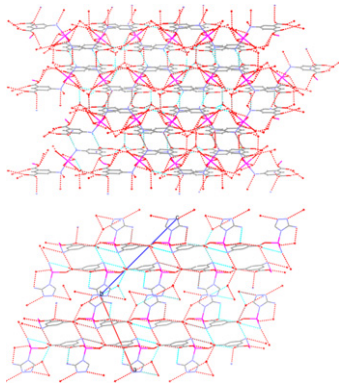


Kou-Lin Zhang, Na Qiao, Hong-Yan Gao, Fang Zhou and Ming Zhang

Polyhedron 26 (2007) 2461

Self assembly of two novel three-dimensional supramolecular networks with blue photoluminescence

Two novel coordination polymers $[Cd(Haip)_2(H_2O)_2] \cdot 2H_2O$ (**1**) and $[Zn(aip)(atz)] \cdot 3H_2O$ (**2**) (H_2aip = 5-aminoisophthalic acid) with blue photoluminescence have been synthesized through the self-assembly of metal(II) ions with H_2aip and N-containing ligands [2-amino-5-mercapto-1,3,4-thiadiazole for **1** and atz (3-amino-1,2,4-triazole) for **2**]. **1** is a first example where only one carboxylate group of H_2aip ligand coordinates with the metal(II) ion and exhibits a 2D framework, which further assembles into a 3D supramolecular network *via* interlayer π–π stacking interaction and hydrogen bonds. **2** exhibits a 2D porous architecture. The hydrogen bonds and interlayer π–π stacking interactions in **2** lead to the formation of a 3D supramolecular network.

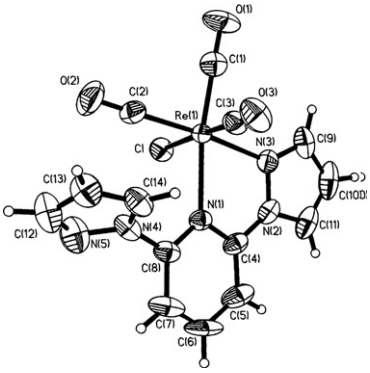


B. Machura, R. Penczek and R. Kruszynski

Polyhedron 26 (2007) 2470

A novel tricarbonyl rhenium complex of 2,6-bis(pyrazo-1-yl)-pyridine – X-ray structure, spectroscopic characterization and DFT calculations

The reaction of $Re(CO)_5Cl$ with 2,6-bis(pyrazo-1-yl)-pyridine (bpzpy) has been examined and a novel $Re(CO)_3^+$ tricarbonyl – *fac*-[$Re(CO)_3$(bpzpy)Cl] – has been obtained. The compound has been studied by IR, UV–Vis spectroscopy and X-ray crystallography. The molecular orbital diagram of the tricarbonyl has been calculated with the density functional theory (DFT) method. The spin-allowed singlet–singlet electronic transitions of [$Re(CO)_3$(bpzpy)Cl] have been calculated with the time-dependent DFT method, and the UV–Vis spectrum of the title compound has been discussed on this basis.

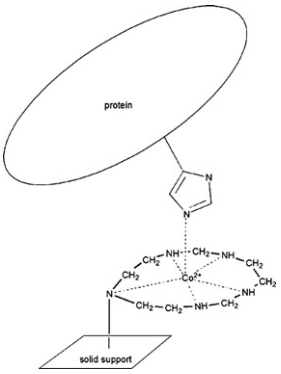


Bartosz Trzaskowski, Roberto Guzman and Ludwik Adamowicz

Polyhedron 26 (2007) 2477

Cyclododecane and cyclotridecane complexes with cobalt as potent histidine chelators: A theoretical study

Density functional calculations have been performed for novel cyclotridecane complexes with cobalt. The results suggest that these systems are good candidates for chromatography systems due to their high affinity toward histidine.

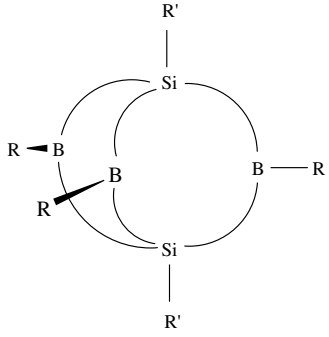


George Ferguson, Simon E. Lawrence, Lorraine A. Neville, Brian J. O'Leary and Trevor R. Spalding

Polyhedron 26 (2007) 2482

Synthetic and X-ray diffraction studies of borosiloxane cages [$R'Si(ORBO)_3SiR'$] and the adducts of [$Bu^tSi\{O(PhB)O\}_3SiBu^t$] with pyridine or *N*,*N*,*N*′,*N*′-tetramethylethylenediamine

Eleven borosilicate compounds [$R'Si\{O(RB)O\}_3SiR'$] were synthesized and five were characterized with X-ray methods. The "spherical" borosilicate $Si\{OBO\}_3Si$ core structures are remarkably similar irrespective of the groups attached at boron. The products of reactions of [$Bu^tSi\{O(PhB)O\}_3SiBu^t$] with pyridine and *N*,*N*,*N*′,*N*′-TMEDA are reported and the structure of the pyridine adduct was determined with X-ray methods.

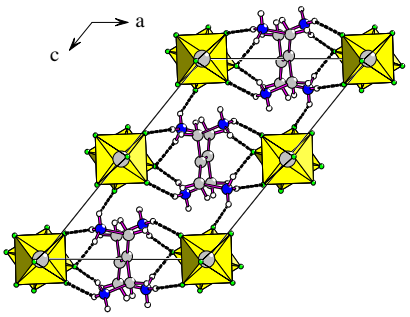


Karim Adil, Armel Le Bail, Gilles Dujardin and Vincent Maisonneuve

Polyhedron 26 (2007) 2493

A new 1D hybrid fluoroaluminate templated by an original tetramine

A new hybrid fluoroaluminate [H_4*ten*] · $(AlF_5)_2$ templated by 2,3 di-2-aminomethyl 1,4 diaminobut-2-ene (*ten*).

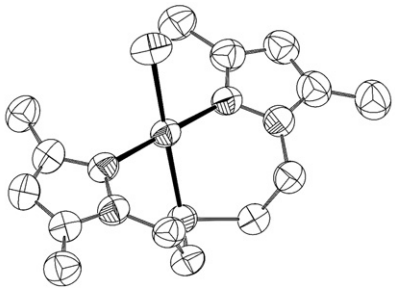


Antonio de Leon, Josefina Pons, Jordi García-Antón, Xavier Solans, Mercè Font-Bardia and Josep Ros

Polyhedron 26 (2007) 2498

New Pt(II) complexes containing hemilabile thioether-pyrazole ligands. Structural analysis by ^{1}H, $^{13}C\{^{1}H\}$ and $^{195}Pt\{^{1}H\}$ NMR spectroscopy and crystal structure of [PtCl(bdtp)](BPh$_4$) [bdtp = 1,5-bis(3,5-dimethyl-1-pyrazolyl)-3-thiapentane]

The reactivity of 1,5-bis(3,5-dimethyl-1-pyrazolyl)-3-thiapentane (bdtp) with several platinum compounds has been tested and compared to the Pd(II) complexes with the same ligand. The synthesis, characterisation and X-ray crystal structure of [PtCl(bdtp)](BPh$_4$) are reported.

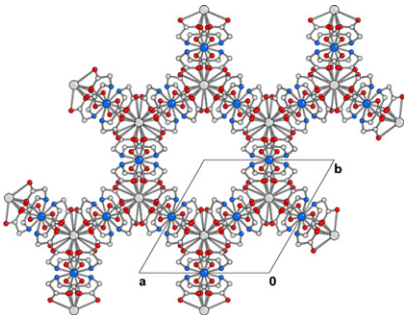


Subal Chandra Manna, Sanjit Konar, Ennio Zangrando, Joan Ribas and Nirmalendu Ray Chaudhuri

Polyhedron 26 (2007) 2507

3D Heterometallic (3d–4f) coordination polymers: A ferromagnetic interaction in a Gd(III)–Cu(II) couple

Ln(III)–Cu(II) (Ln = Gd, Nd, Sm) coordination polymers have been synthesized and characterized by single crystal structure and low temperature magnetic studies. There is a ferromagnetic interaction in the Gd(III)–Cu(II) couple, it being impossible to know if there is any magnetic interaction in the remaining couples.

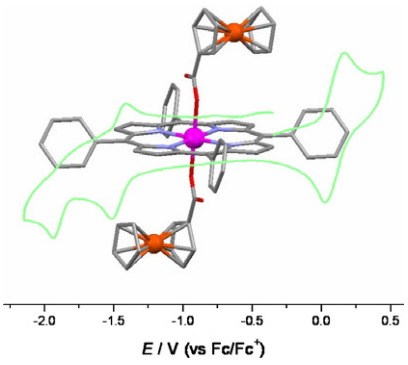


Hee Jung Kim, Woo Sung Jeon, Jeong Hak Lim, Chang Seop Hong and Hee-Joon Kim

Polyhedron 26 (2007) 2517

Synthesis, X-ray crystal structure, and electrochemistry of *trans*-bis(ferrocenecarboxylato)-(tetraphenylporphyrinato)tin(IV)

The crystal structure of bis(ferrocenecarboxylato)(tetraphenylporphyrinato)tin(IV) reveals that the tin center is octahedrally coordinated by the porphyrin occupying square base and axial coordination of two ferrocenecarboxylato ligands in an *anti* orientation. The cyclic voltammogram of the complex exhibits three redox couples consisting of one oxidative and two reductive waves due to the ferrocenecarboxylato ligands and the porphyrin ring, respectively.

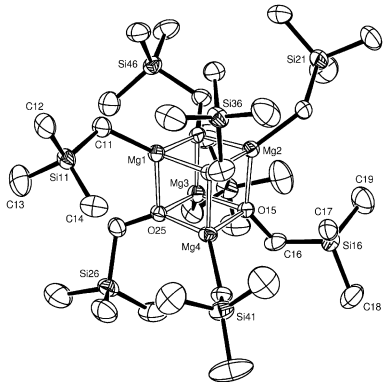


Carlos Alonso Moreno, David L. Hughes and Manfred Bochmann

Polyhedron 26 (2007) 2523

Synthesis and molecular structure of [Mg(CH$_2$SiMe$_3$)(μ^3-OCH$_2$SiMe$_3$)]$_4$

The reaction of traces of oxygen with ClMgCH$_2$SiMe$_3$ gave crystalline [Mg(CH$_2$SiMe$_3$)(μ^3-OCH$_2$SiMe$_3$)]$_4$ containing a Mg$_4$O$_4$ cubane core.

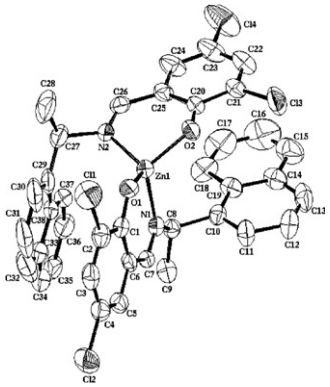


Takashiro Akitsu

Polyhedron 26 (2007) 2527

Photofunctional supramolecular solution systems of chiral Schiff base nickel(II), copper(II), and zinc(II) complexes and photochromic azobenzenes

We present preparations, crystal structures, electronic and CD spectra of chiral Schiff base complexes, bis(*N*-*R*-1-naphthylethyl-3,5-dichlorosalicydenaminato)nickel(II), copper(II), and zinc(II), and investigate their conformational changes induced by photoisomerization of azobenzenes via intermolecular interactions in solutions.

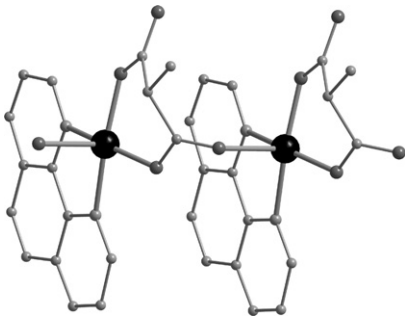


Catherine Gkioni, Athanassios K. Boudalis, Yiannis Sanakis and Catherine P. Raptopoulou

Polyhedron 26 (2007) 2536

Weak ferromagnetism in 1D coordination polymers: Syntheses, crystal structures, spectroscopic and magnetic properties of $[Cu(L)(Memal)]_n$ ($Memal^{2-}$ = the dianion of methylmalonic acid, L = 1,10-phenanthroline, 2,2′-bipyridine)

Two analogous 1D coordination polymers, presenting the [Cu(L)(Memal)]($Memal^{2-}$ = the dianion of methylmalonic acid, L = 1,10-phen or 2,2′ = bpy) repeating unit have been structurally characterized; their magnetic and EPR properties have been also studied. Both compounds exhibit weak ferromagnetic intrachain interactions attributed to the *syn–anti* bridging mode of the carboxylato groups of the $Memal^{2-}$ ligand.

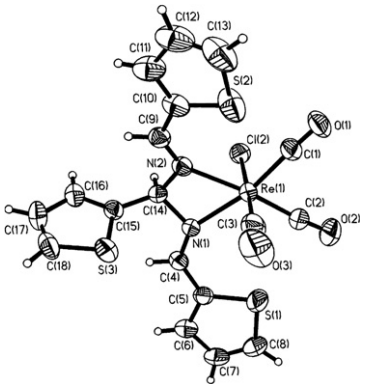


B. Machura, R. Kruszynski and J. Kusz

Polyhedron 26 (2007) 2543

A novel tricarbonyl rhenium complex of 2-thienyl-*N*,*N*-bis(2-thienylmethylene)methanediamine – X-ray structure, spectroscopic characterisation and DFT calculations

The reaction of $Re(CO)_5Cl$ with 2-thienyl-*N*,*N*-bis(2-thienylmethylene)methanediamine (tbtmma) has been examined and a novel $Re(CO)_3^+$ tricarbonyl – *fac*-[$Re(CO)_3$(tbtmma)-Cl] – has been obtained. The compound has been studied by IR, UV–Vis spectroscopy and X-ray crystallography. The molecular orbital diagram of the tricarbonyl has been calculated with the density functional theory (DFT) method. The spin-allowed singlet–singlet electronic transitions of [$Re(CO)_3$(tbtmma)Cl] have been calculated with the time-dependent DFT method, and the UV–Vis spectrum of the title compound has been discussed on this basis.

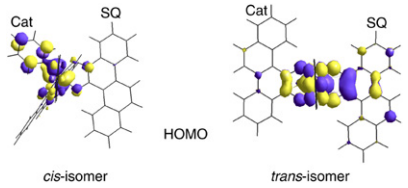


Attia S. Attia

Polyhedron 26 (2007) 2550

cis- and *trans*-Bis(pyridine)chromium(III) complexes containing mixed-valence chrysene-semiquinonate–chrysenecatecholate ligands: Synthesis, characterization and interpretation of the electronic absorption spectra using ZINDO/S method

Two new geometrical isomers of $[Cr(py)_2$(chrySQ) (chryCat)] were synthesized by two different synthetic procedures. The structures of the two isomers have been modeled using parameterized PM3 semiempirical method. Theoretical harmonic vibrational frequencies of the *cis*- and *trans*-isomers have been computed and compared well with the experimental vibrational frequencies. Theoretical modeling of the magnetic data indicated strong antiferromagnetic exchange interaction between Cr^{III} (S = 3/2) and chrySQ (S = 1/2) with $J = -365 \pm 6$ and -395 ± 4 cm^{-1} for the *cis*- and *trans*-isomers, respectively. The electrochemical behavior of *cis*- and *trans*-[$Cr(py)_2$(chrySQ)(chryCat)] complexes were studied by cyclic voltammetry in acetonitrile solvent. The electronic spectra of the two isomers were dominated by charge-transfer (LMCT, MLCT and ILCT) transitions. In addition, a low-energy intervalence charge-transfer (IVCT) transition was observed for the *cis*-isomer at 1085 nm. Theoretical studies of the electronic spectra by ZINDO/S-CI method were useful in interpreting the observed electronic transitions.

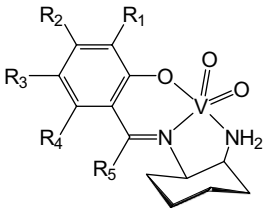


Edmund Kwiatkowski, Grzegorz Romanowski, Waldemar Nowicki, Marek Kwiatkowski and Kinga Suwińska

Polyhedron 26 (2007) 2559

Chiral dioxovanadium(V) complexes with single condensation products of 1,2-diaminocyclohexane and aromatic *o*-hydroxycarbonyl compounds: Synthesis, characterization, catalytic properties and structure

Eighteen new chiral VO_2L complexes where L is the deprotonated product of single condensation of *RR*(−)-1,2-diaminocyclohexane or of *SS*(+)-1,2-diaminocyclohexane with aromatic hydroxyaldehyde or ketone, were synthesized and characterized by various spectroscopic methods. Crystal structure of the complex derived from 1-hydroxy-2-acetylonaphtalene and *RR*(−)-1,2-diaminocyclohexane was determined. Complexes bearing methoxy substituent in position 3 or 5 of the aryl group act as catalyst in the oxidation of prochiral methyl phenyl sulfide to the corresponding sulfoxide.

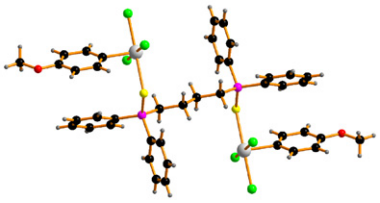


Veronika Matulova, Stanislav Man and Marek Necas

Polyhedron 26 (2007) 2569

Binuclear complexes of 4-methoxyphenyltellurium trichloride with variably linked diphosphine disulfide ligands

Four binuclear complexes of 4-$MeOC_6H_4$-$TeCl_3$ with different diphosphine disulfide ligands were prepared and characterized by X-ray crystallography. The coordination around Te is pseudo-octahedral with aryl group and the lone electron pair in axial positions relative to the $TeCl_3S$ equatorial plane. One compound shows weak secondary Te···Cl bond completing the distorted octahedral coordination around the central atom.

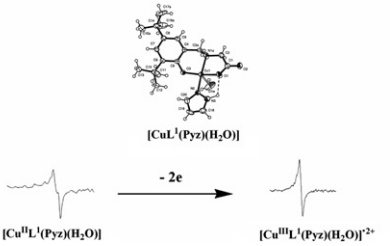


Sohaham Dasgupta, Snehadrinarayan Khatua, Valerio Bertolasi and Manish Bhattacharjee

Polyhedron 26 (2007) 2574

Synthesis and characterization of copper(II) complexes containing tridentate modified amino acid ligands, $[CuL(H_2O)(Pyz)]$ [L = {(3,5-di-*tert*-butyl-2 hydroxybenzyl)amino}acetic acid and *S*(−)2-(3,5-di-*tert*-butyl-2-hydroxybenzylamino)-3-methyl-butyric acid; Pyz = pyrazole] and their oxidation to a copper(III) coordinated phenoxyl radical

Two modified amino acid ligands and their ternary copper(II) complexes have been synthesized and characterized. On chemical oxidation these complexes generate copper(III) coordinated phenoxyl radicals. The oxidized species have been characterized by EPR and UV–visible spectroscopy.

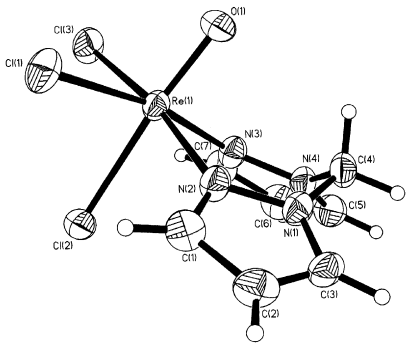


B. Machura, R. Penczek, R. Kruszynski and J. Kusz

Polyhedron 26 (2007) 2581

Synthesis, crystal, molecular, and electronic structure of $[ReOCl_3(bpzm)]$ complex

The $[ReOCl_3(OAsPh_3)(AsPh_3)]$ and $[ReOCl_3(PPh_3)_2]$ complexes react with bis(pyrazol-1-yl)methane (bpzm) to give $[ReOCl_3(bpzm)]$. The $[ReOCl_3(bpzm)]$ compound has been studied by IR, UV–Vis spectroscopy, and X-ray crystallography. The molecular orbital diagram of the oxocomplex has been calculated with the density functional theory (DFT) method. The spin-allowed singlet–singlet electronic transitions of $[ReOCl_3(bpzm)]$ have been calculated with the time-dependent DFT method, and the UV–Vis spectrum of the title compound has been discussed on this basis.

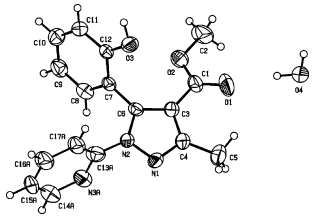


Aleksander Kufelnicki, Magdalena Woźniczka, Lilianna Chęcińska, Magdalena Miernicka and Elżbieta Budzisz

Polyhedron 26 (2007) 2589

Synthesis and structure of novel copper(II) complexes with pyrazole derived ligands and metal–ligand interaction in solution

The synthesis of two new chelating ligands has been presented. These ligands form solid complexes with $CuCl_2 \cdot 2H_2O$ salt. The X-ray structure of ligand **2** has been determined.

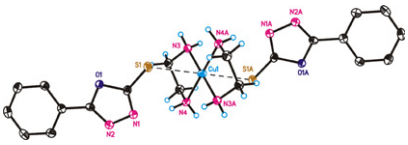


Pratibha Tripathi, Aritra Pal, Vojtech Jancik, A.K. Pandey, J. Singh and N.K. Singh

Polyhedron 26 (2007) 2597

Metal-assisted transformation of *N*-benzoyldithiocarbazate to 5-phenyl-1,3,4-oxadiazole-2-thiol in the presence of ethylenediamine, and its first row transition metal complexes

The potassium salt of *N*-benzoyldithiocarbazate (H_2L) generates 5-phenyl,1,3,4-oxadiazole-2-thiol(pot^-) in an alkaline medium by an internal ring closer reaction *via* desulfurization. The molecular structure of $[Cu(en)_2](pot)_2$ has been determined by a single crystal X-ray diffraction study. Weak interaction studies on the complex reveal the presence of a hydrogen-bonded network in the molecule involving non-coordinating donor atoms of the pot anion with en, resulting in the formation of an extended three-dimensional network.

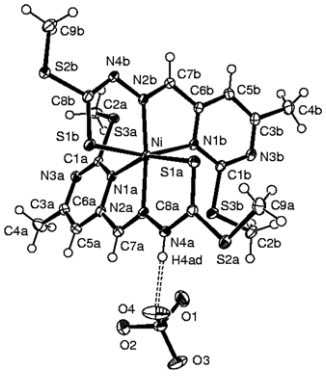


Somnath Roy, Tarak Nath Mandal, Anil Kumar Barik, Sachindranath Pal, Samik Gupta, Arijit Hazra, Ray J. Butcher, Allen D. Hunter, Matthias Zeller and Susanta Kumar Kar

Polyhedron 26 (2007) 2603

Metal complexes of pyrimidine derived ligands – Syntheses, characterization and X-ray crystal structures of Ni(II), Co(III) and Fe(III) complexes of Schiff base ligands derived from *S*-methyl/*S*-benzyl dithiocarbazate and 2-*S*-methylmercapto-6-methylpyrimidine-4-carbaldehyde

Ni(II), Co(III) and Fe(III) complexes (**1**–**3**) of two similar tridentate Schiff base ligands synthesized from 2-*S*-methylmercapto-6-methylpyrimidine-4-carbaldehyde and *S*-methyl/*S*-benzyl dithiocarbazate have been prepared and structurally characterized. All the three complexes have gross octahedral geometries with a N_4S_2 chromophore. In **1**, one ligand molecule binds the Ni(II) center as a uninegative tridentate and other ligand molecule functions as a neutral tridentate, whereas in **2** and **3** each of the ligand molecules acts as a uninegative tridentate.

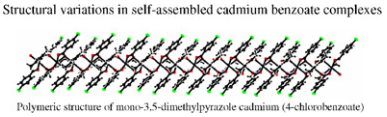


Kusum Bania, Nilotpal Barooah and Jubaraj B. Baruah

Polyhedron 26 (2007) 2612

Structural variations in self-assembled cadmium benzoate complexes

A series of mixed ligand cadmium(II) complexes having 3,5-dimethylpyrazole and aromatic carboxylate are structurally characterized. Mononuclear complexes are obtained from composition $[Cd(L)_2(L^a)_2]$ where L_a = 3,5-dimethylpyrazole L = R–C_6H_4COO– [R = H (**1**), 2-Cl (**2**), 4-OH (**3**), 2-OH (**4**)]. The cadmium complex (**5**) having composition $[Cd(L)_2(L_a)(H_2O)]$ (L = 2-NO_2–C_6H_4COO–) is tetra nuclear. Cadmium complexes having composition $[Cd(L)_2(L_a)]$ such as R = 4-NO_2 (**6**), 4-Cl (**7**), and 1-naphthoate complex (**8**) are co-ordination polymers with seven co-ordination geometry around cadmium.

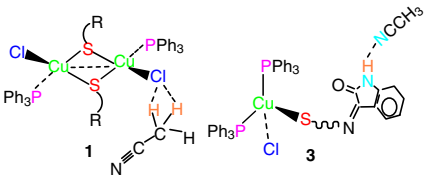


Tarlok S. Lobana, Rekha, A.P.S. Pannu, Geeta Hundal, Ray J. Butcher and A. Castineiras

Polyhedron 26 (2007) 2621

Synthesis and structures of monomeric [chloro-(isatin-3-thiosemicarbazone)bis(triphenylphosphine)]copper(I) and dimeric [dichloro-bis-(thiophene-2-carbaldehyde thiosemicarbazone) bis(triphenylphosphine)]dicopper(I)] complexes

Acetonitrile-chlorine hydrogen bonding stabilises sulfur bridging in the reaction of copper(I) chloride with thiophene-2-carbaldehyde thiosemicarbazone (**1**). Acetonitrile forms a hydrogen bond with the ring of isatin in monomer (**3**).

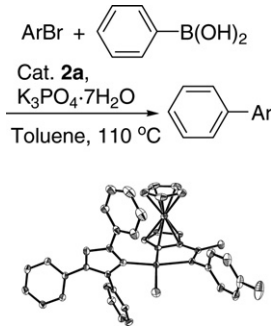


Jing-Ya Li, A-Juan Yu, Yang-Jie Wu, Yu Zhu, Chen-Xia Du and Hua-Wei Yang

Polyhedron 26 (2007) 2629

N-Heterocyclic carbene adducts of cyclopalladated ferrocenylimines: Synthesis, characterization and catalytic activity for the Suzuki–Miyaura reaction

A series of novel air-stable carbene adducts of cyclopalladated ferrocenylimines have been synthesized and characterized. The structures of these complexes were determined by single-crystal X-ray analysis. These adducts have been successfully applied to the Suzuki–Miyaura coupling reaction under aerobic conditions. Good to excellent yields were obtained.

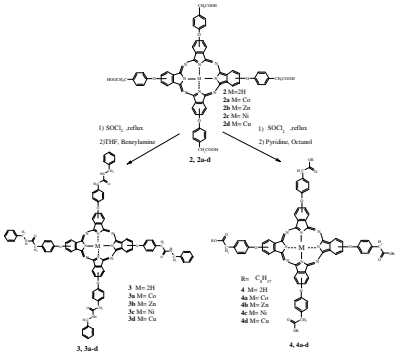


Meryem Çamur, Ali Rıza Özkaya and Mustafa Bulut

Polyhedron 26 (2007) 2638

Novel phthalocyanines bearing four 4-phenyloxyacetic acid functionalities

A metal-free phthalocyanine was synthesized from *p*-(3,4-dicyanophenoxy)phenylacetic acid. The metallo derivatives were prepared by its treatment with metal salts. Further reactions of these products with thionylchloride and then benzylamine and octanol gave amide and ester derivatives, respectively. The compounds were characterized and cyclic voltammetry of these compounds was also presented.

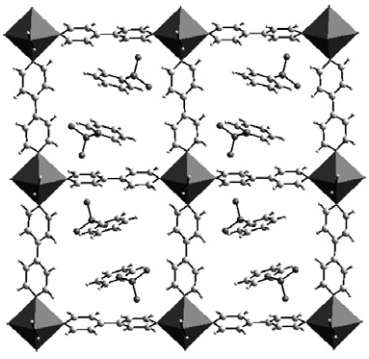


Zhao-Xun Lian, Jiwen Cai and Cai-Hong Chen

Polyhedron 26 (2007) 2647

A series of metal-organic frameworks constructed with arenesulfonates and 4,4′-bipy ligands

Five transition metal compounds containing arenesulfonates and 4,4′-bipy ligands were obtained via hydrothermal or aqueous reactions, and their structures determined by single crystal structural analyses.

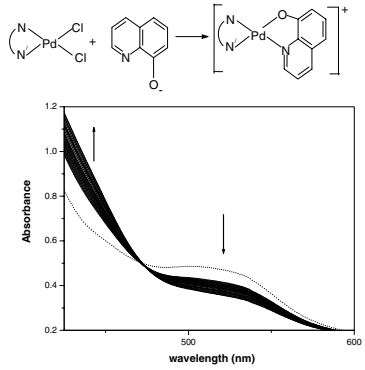


Pradip Kumar Ghosh, Sushanta Saha and Ambikesh Mahapatra

Polyhedron 26 (2007) 2655

Mechanistic studies on the Pd–Cl cleavage of dichloro-[1-alkyl-2-(naphthylazo)imidazole]-palladium(II) complexes by 8-quinolinol

This work describes the kinetics and the mechanism of the reaction between 8-quinolinol (HQ) and [Pd(α-/β-NaiR)Cl_2] [α-/β-NaiR = 1-alkyl-2-(naphthyl-α-/β-azo)imidazole] in acetonitrile (MeCN) medium. The product is characterized as [Pd(α-/β-NaiR)(Q)](ClO_4) by different spectroscopic routes. It is established that cleavage of the Pd–Cl bond is the rate-determining step. Thermodynamic parameters ($\Delta^{\ddagger}H^{\circ}$ and $\Delta^{\ddagger}S^{\circ}$) are determined from variable temperature kinetic studies.

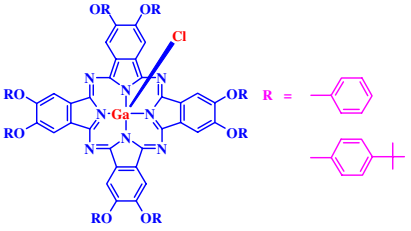


Vongani Chauke, Abimbola Ogunsipe, Mahmut Durmus and Tebello Nyokong

Polyhedron 26 (2007) 2663

Novel gallium(III) phthalocyanine derivatives – Synthesis, photophysics and photochemistry

The triplet and singlet oxygen quantum yields for gallium(III) phthalocyanine derivatives are higher than reported in the literature for other GaPc complexes, making these complexes excellent candidates for use as photosensitizers.

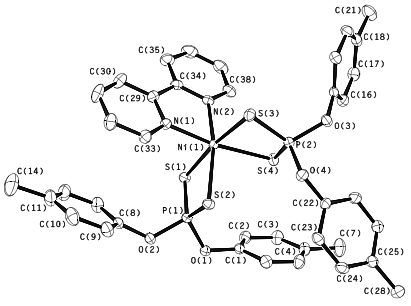


Ann L. Bingham, John E. Drake, Michael B. Hursthouse, Mark E. Light, Manisha Nirwan and Raju Ratnani

Polyhedron 26 (2007) 2672

Synthesis, characterization and spectral studies of nitrogen base adducts of bis(*O*,*O*′-ditolyldithiophosphato)nickel(II). Crystal structures of Ni[S_2P(OC_6H_4Me-*p*)$_2$]$_2$ · $C_{10}H_8N_2$ and Ni[S_2P(OC_6H_4Me-*o*)$_2$]$_2$ · $C_{14}H_{12}N_2$ · C_6H_6

Reactions of Ni[S_2P(OR)$_2$]$_2$(R = *o*-, *m*- and *p*-C_6H_4Me) with pyridine, 2,2′-bipyridyl and 2,9-dimethyl-1,10-phenanthroline were carried out to yield green paramagnetic solids. These adducts were characterized by UV–visible, IR spectroscopy, magnetic measurements and X-ray crystallography in two cases. The molecular structures of 2,2′-bipyridylbis{*O*,*O*′-di(*p*-tolyl) dithiophosphate}nickel(II), Ni[S_2P(OC_6H_4Me-*p*)$_2$]$_2$ · $C_{10}H_8N_2$ and 2,9-dimethyl-1,10-phenanthrolinebis {*O*,*O*′-di(*o*-tolyl) dithiophosphate}nickel(II), Ni[S_2P(OC_6H_4Me-*o*)$_2$]$_2$ · $C_{14}H_{12}N_2$ · C_6H_6 are described.

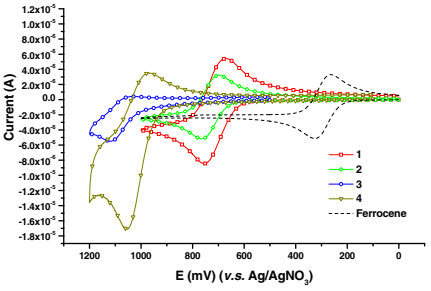


Li-Lan Wu, I-Wen Sun and Cheng-Hsien Yang

Polyhedron 26 (2007) 2679

Photophysical and electrochemical properties of heteroleptic tris-cyclometallated Ir(III) complexes

Novel heteroleptic tris-cyclometallated iridium(III) complexes have been synthesized and fully characterized. The photophysical and electrochemical properties of these iridium complexes have been investigated. Although bis(1-phenylpyrazolato-*N*,$C^{2'}$)iridium(III)[5-(2′-pyridyl)tetrazolate] (**3**) and bis(3-methyl-1-phenylpyrazolato-*N*,$C^{2'}$)iridium(III)[5-(2′-pyridyl)tetrazolate] (**4**) undergo a quasi-reversible oxidation, they show excellent quantum yields at room temperature.

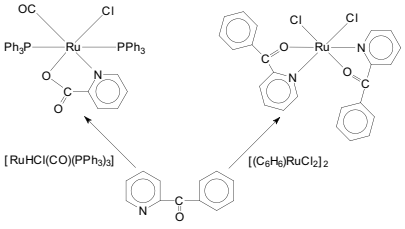


J.G. Małecki and R. Kruszynski

Polyhedron 26 (2007) 2686

The reactions of 2-benzoylpyridine with $[RuHCl(CO)(PPh_3)_3]$ and $[(C_6H_6)RuCl_2]_2$

The reactions of $[RuHCl(CO)(PPh_3)_3]$ and $[(C_6H_6)RuCl_2]_2$ with 2-benzoylpyridine have been examined and two novel ruthenium(II) complexes – $[RuCl(CO)(PPh_3)_2(C_5H_4NCOO)]$ and $[RuCl_2(C_{12}H_9NO)_2]$ – have been obtained. The compounds have been studied by IR, UV–Vis spectroscopy and X-ray crystallography. The molecular orbital diagrams of the complexes have been calculated with the density functional theory (DFT) method. The spin-allowed singlet–singlet electronic transitions of the compounds have been calculated with the time-dependent DFT method, and the UV–Vis spectra of the compounds have been discussed on this basis.

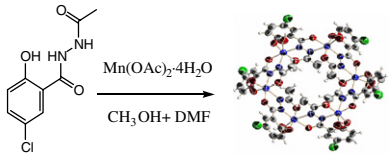


Feng-Ping Xiao, Long-Fei Jin, Gong-Zhen Cheng and Zhen-Ping Ji

Polyhedron 26 (2007) 2695

Two novel 18-metallacrown-6 complexes: Synthesis, structural characterization and bioactivity

Two new 18-metallacrown-6 complexes, $[Mn_6(acshz)_6(H_2O)_6] \cdot 18H_2O$ (**1**) and $[Fe_6(acshz)_6(CH_3OH)_6] \cdot 6CH_3OH \cdot 6H_2O$ (**2**), have been prepared using *N*-acetyl-5-chlorosalicylhydrazidate ($acshz^{3-}$) and characterized. The integrity and stability of the metallacrown in methanol has been confirmed by ESI-MS and UV–Vis spectroscopy. Antibacterial screening data showed that the iron metallacrown **2** has strong antimicrobial activity against *Bacillus subtilis*.

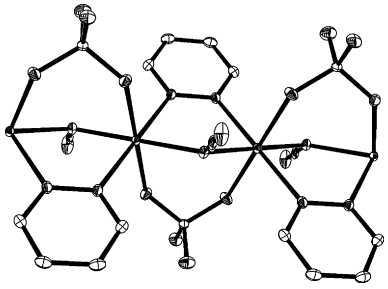


Franz A. Mautner, Mohamed A.S. Goher, Hanna'a E. Moustafa, Morsy A.M. Abu-Youssef and Lars Öhrström

Polyhedron 26 (2007) 2703

1D and 3D coordination polymers with the $M(\mu_1,\mu_1\text{-}X)_2M$ motif (M = Na, Zn, Cd): Observation of a linear $[Na(H_2O)_4]_n^{n+}$ cation and a five-connected **sqp**-net

Three polymeric complexes $[Zn(pydz)(N_3)(SO_4)]_n[Na(H_2O)_4]_n(H_2O)_{4n}$, $[Cd(3\text{-ampy})(N_3)Cl]_n$, and $[Cd(DENA)Cl_2(H_2O)]$, (pydz = pyridazine or 1,2-diazine, 3-ampy = 3-aminopyridine, DENA = *N*,*N*-diethylnicotineamide) have been synthesized and characterized by spectral and structural methods and their network topologies analysed.

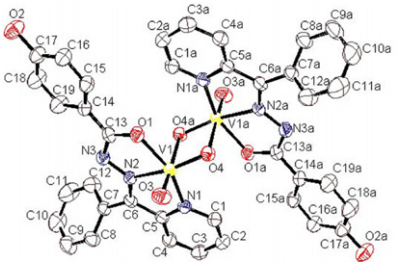


Mini Kuriakose, M.R. Prathapachandra Kurup and E. Suresh

Polyhedron 26 (2007) 2713

Synthesis, spectroscopic studies and crystal structures of two new vanadium complexes of 2-benzoylpyridine containing hydrazone ligands

A new aroylhydrazone ligand and two oxovanadium complexes are synthesized and characterized. The ligand exists in keto form in the solid state. The tridentate ligand effectively coordinates through two nitrogens and one oxygen, thus undergoing enolization. Crystal studies of VO_2L^1 and $[VO(HL^2)(\mu_2\text{-}O)]_2$ reveals a distorted square pyramid and dimeric structure with oxobridging resulting in a distorted octahedral structure, respectively.

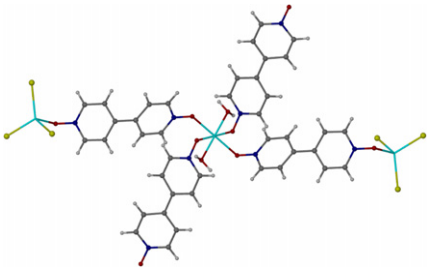


Susan A. Bourne and Lesego J. Moitsheki

Polyhedron 26 (2007) 2719

Monomer, dimer, tetramer and salt: Structural variations in Zn(II) complexes of 4,4′-bipyridine-*N*,*N*′-dioxide

Reaction of 4,4′-bipyridine-*N*,*N*′-dioxide with $ZnBr_2$ under different crystallisation conditions allows formation of three different complexes. These, and a similar complex formed from $Zn(NCS)_2$ have been characterised by crystallographic methods.

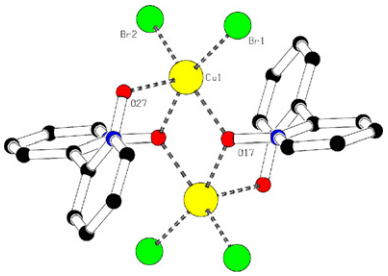


Gerard A. van Albada, Ilpo Mutikainen, Urho Turpeinen and Jan Reedijk

Polyhedron 26 (2007) 2728

Crystal structure, spectroscopy and magnetism of a dinuclear strongly antiferromagnetically coupled *N*-oxido-bridged Cu(II) compound with 2,2′-bipyridine-1,1′-dioxide (bpdo) as a ligand; $[Cu_2(bpdo)_2Br_4]$

The compound $[Cu_2(2,2'\text{-Bipyridine-}1,1'\text{-dioxide})_2Br_4]$ has been synthesized and characterized. Each copper(II) ion has a distorted square pyramidal geometry. The magnetic susceptibility measurements agree with a very strong antiferromagnetic interaction ($J = -905\ cm^{-1}$).

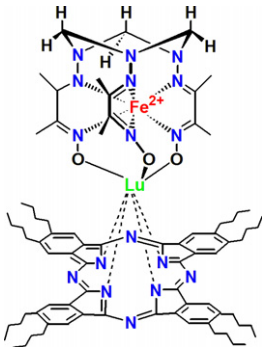


Yan Z. Voloshin, Oleg A. Varzatskii, Larisa G. Tomilova, Marya O. Breusova, Tatiana V. Magdesieva, Yurii N. Bubnov and Roland Krämer

Polyhedron 26 (2007) 2733

First hybrid oximehydrazonate phthalocyaninoclathrochelates: The synthesis and properties of lutetium phthalocyanine-capped cage iron(II) complexes

Ditopic oximehydrazonate iron(II) phthalocyaninoclathrochelates were synthesized by a transmetallation reaction of the labile triethylantimony-capped clathrochelate iron(II) oximehydrazonates with lutetium(III) phthalocyanine. Encapsulated iron(II) ion was found to be in a low-spin state. The cyclic voltammograms show oxidation and reduction waves assignable to $Fe^{2+/3+}$ couples of macrobicyclic framework and to phthalocyanine macrocycles.

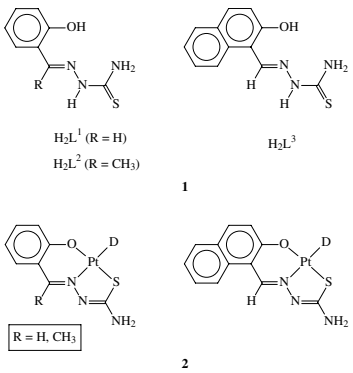


Sarmistha Halder, Ray J. Butcher and Samaresh Bhattacharya

Polyhedron 26 (2007) 2741

Synthesis, structure and spectroscopic properties of some thiosemicarbazone complexes of platinum

Reaction of salicyldehyde thiosemicarbazone (H_2L^1), 2-hydroxyacetophenone thiosemicarbazone (H_2L^2) and 2-hydroxynapthaldehyde thiosemicarbazone (H_2L^3) (**1**) with $K_2[PtCl_4]$ afforded a family of polymeric complexes of the type $[\{Pt(L)\}_n]$, which upon reaction with two monodentate ligands (D), viz. triphenylphosphine (PPh_3) and 4-picoline (pic), yielded complexes of the type [Pt(L)(D)] (**2**).

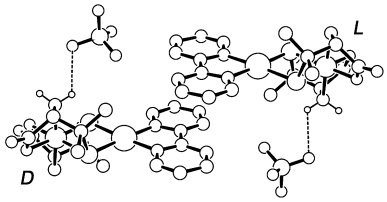


Yasunori Yamada, Masahiko Inoue, Yoshitaro Miyashita, Ken-ichi Okamoto, Masayuki Koikawa and Tadashi Tokii

Polyhedron 26 (2007) 2749

Effects of counter anions on stereospecific interactions through π-conjugated systems of sulfur-bridged dinuclear cobalt(III)–platinum(II) complexes with optically active penicillaminates: Synthetic, structural, and spectroscopic studies

The racemic crystals containing two enantiomers, $[Pt(bpy)Co(D\text{-}pen)_2]^+$ (***D***) and $[Pt(bpy)Co(L\text{-}pen)_2]^+$ (***L***), can be obtained when their aqueous solutions are mixed in equimolar amounts. Depending on the nature of the counter anion in these crystals, dimers or linear-chains are established by the stereospecific interactions of the electronic systems between a pair of enantiomers, ***D*** and ***L***.

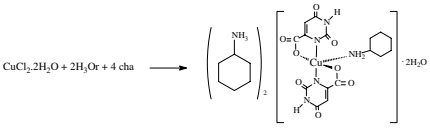


Okan Zafer Yeşilel, Hümeyra Paşaoğlu, Kamber Akdağ and Orhan Büyükgüngör

Polyhedron 26 (2007) 2761

The first bis(orotato–*N*,*O*) complex: Synthesis, crystal structure, spectroscopic and thermal characterization of $(chaH)_2[Cu(HOr\text{–}N,O)_2(cha)] \cdot 2H_2O$ (cha = cyclohexylamine and HOr = orotate(2−))

To the best of our knowledge, a bis(orotato–*N*,*O*) complex has not been reported so far although there are many metal complexes of orotic acid.

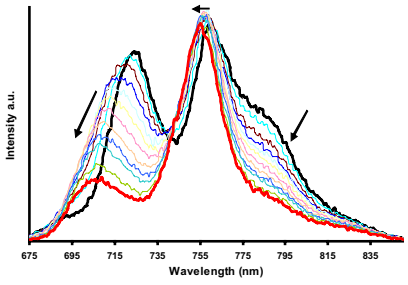


Mahmut Durmuş and Tebello Nyokong

Polyhedron 26 (2007) 2767

Synthesis and solvent effects on the electronic absorption and fluorescence spectral properties of substituted zinc phthalocyanines

The syntheses of tetra- and octa-substituted aryloxy zinc(II) phthalocyanine complexes are reported; the non-peripherally tetra substituted complexes show protonation in methanol and dichloromethane, whereas peripherally substituted derivatives do not.

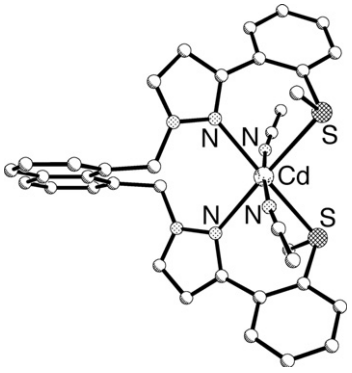


Tanya K. Ronson, Harry Adams, Lindsay P. Harding, Ross W. Harrington, William Clegg and Michael D. Ward

Polyhedron 26 (2007) 2777

Synthesis and structures of cadmium(II) complexes of a series of multinucleating N/S donor ligands

Cd(II) complexes of a series of bis-bidentate ligands, containing two N,S-chelating binding sites, have been prepared and structurally characterised and display structural types including a mononuclear complex, Cd_2L_2 mesocates, and an infinite coordination polymer.

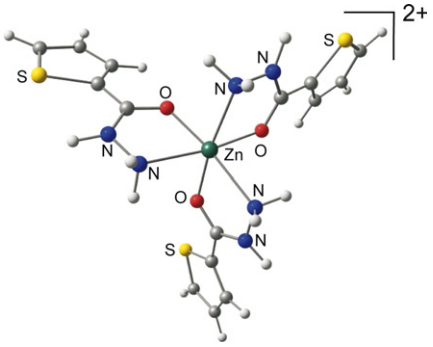


Anna Hołtra, Piotr Drożdżewski and Maria Kubiak

Polyhedron 26 (2007) 2786

Reinvestigation of zinc(II) complexation by 2-thiophenecarboxylic hydrazide: X-ray structure of tris(2-thiophenecarboxyhydrazide)zinc(II) tetrachlorozincate(II) di(ethanol) and vibrational spectroscopy of its decomposition product

The reaction of $ZnCl_2$ with 2-thiophenecarboxylic hydrazide in ethanolic solution affords a salt with complexed metal present in the cation and anion. This compound has been characterized by single-crystal X-ray diffraction and by IR and Raman spectroscopy. The complex cation has a distorted octahedral environment around zinc(II) with a fac-orientation of the bidentate organic ligands. The cation is accompanied by a typical tetrachlorozincate(II) anion.

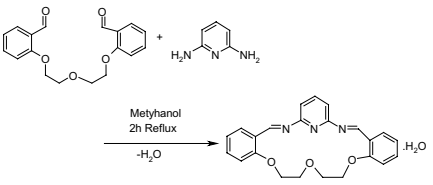


Salih Ilhan, Hamdi Temel, Ismail Yilmaz and Memet Şekerci

Polyhedron 26 (2007) 2795

Synthesis and characterization of new macrocyclic Schiff base derived from 2,6-diaminopyridine and 1,7-bis(2-formylphenyl)-1,4,7-trioxaheptane and its Cu(II), Ni(II), Pb(II), Co(III) and La(III) complexes

A new macrocyclic ligand and its complexes were synthesized, and characterized by elemental analysis, IR, ^1H and ^{13}C NMR, UV–Vis spectra, magnetic susceptibility, thermal gravimetric analysis, conductivity measurements, mass spectra and cyclic voltammetry.

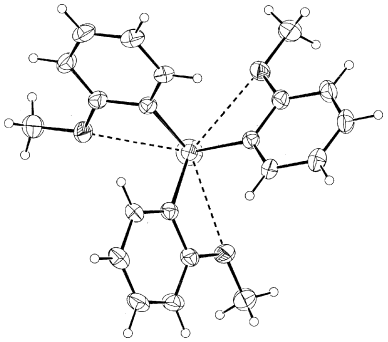


Raymond C. Bott, Peter C. Healy and Graham Smith

Polyhedron 26 (2007) 2803

Structural studies of two-coordinate complexes of tris(2-methoxylphenyl)phosphine and tris(4-methoxyphenyl)phosphine with gold(I) halides

In the series of crystallographically characterized two-coordinate complexes of gold(I) of the type $[AuP(anis)_3X]$ [where anis = tris(*o*-methoxyphenyl)phosphine and tris(*p*-methoxyphenyl)phosphine, and X = Cl, Br, I], significant Au···O interactions are present in the *ortho*-substituted isomers, most significant with tris interaction in the isomorphous pair (X = Br, I) which have perfect C_3 symmetry.

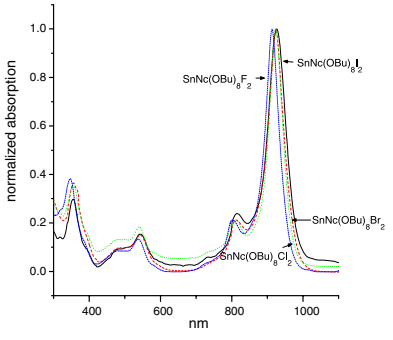


Cheolbeom Bae, Gwanghoon Kwag and Malcolm E. Kenney

Polyhedron 26 (2007) 2810

Synthesis and characterization of near-infrared absorption tin octabutoxy naphthalocyanines

A series of tin octabutoxy naphthalocyanines is presented, which shows near infrared absorptions (900–930 nm) with a high extinction coefficient (*ca.* 1×10^5 M^{-1} cm^{-1}). The position of the Q-band is more shifted the heavier the halogen, which is corresponded to the HOMO–LUMO gaps calculated with density functional theory (0.932, 0.911, 0.905, 0.893 eV).

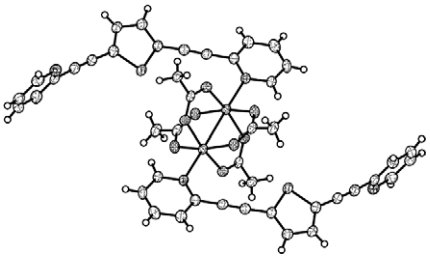


Salomé Delgado, Agustín Molina-Ontoria, Manuela E. Medina, Cesar J. Pastor, Reyes Jiménez-Aparicio and José L. Priego

Polyhedron 26 (2007) 2817

Structural diversity of copper complexes with angular and linear dipyridyl ligands

New compounds generated from the reactions of 2,5-bis(2-pyridylethynyl) thiophene (L_1), 2,2′-dipyridyldisulfide (L_2) and 4,4′-dipyridyldisulfide (L_3) with copper acetate have been synthesized, structurally characterized by X-ray diffraction and your magnetic properties studied. The observed structures in these compounds based on dipyridyl ligands in 2,2′ and 4,4′-positions, illustrate as the positional orientation of pyridyl nitrogen atoms affect to structure during the self-assembly process.

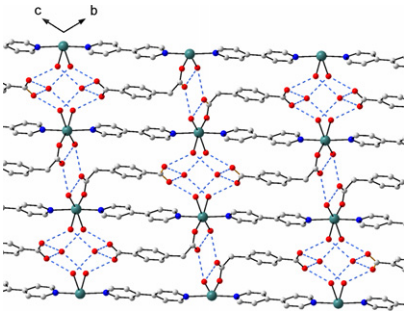


Zheng-Fang Tian, Yang Su, Jian-Guo Lin and Qing-Jin Meng

Polyhedron 26 (2007) 2829

From discrete entity to three-dimensional architecture: Syntheses, crystal structures and optical properties of a series of transition metal complexes constructed from 4-carboxymethylbenzoic acid and 4,4′-bipyidine

Quadrangles and six-membered rings formed by hydrogen-bonds are essential to the three-dimensional supramolecular architecture.

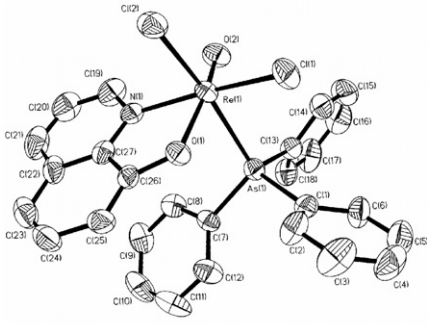


B. Machura, S. Michalik, R. Kruszynski and J. Kusz

Polyhedron 26 (2007) 2837

Oxorhenium complexes with the 8-quinolinolato ligand. X-ray structure and DFT calculations for $[ReOX_2(hqn)(AsPh_3)]$ and $[ReOX_2(hqn)(PPh_3)]$ complexes

The reactions of $[ReOX_3(AsPh_3)_2]$ and $[ReOX_3(PPh_3)_2]$ with 8-hydroxyquinoline (Hhqn) have been examined and $[ReOX_2(hqn)(AsPh_3)]$ and $[ReOX_2(hqn)(PPh_3)]$ (X = Cl, Br) complexes have been obtained, respectively. The crystal and molecular structures of $[ReOCl_2(hqn)(AsPh_3)]$ (**1**) and $[ReOBr_2(hqn)(PPh_3)]$ (**4**) have been determined. The electronic structure of **1** has been calculated with the density functional theory (DFT) method. The spin-allowed electronic transitions of **1** have been calculated with the time-dependent DFT method, and the UV–Vis spectrum of $[ReOCl_2(hqn)(AsPh_3)]$ has been discussed on this basis.

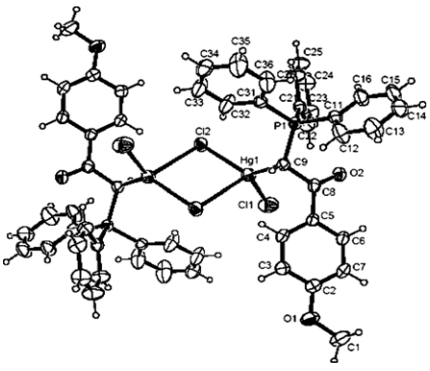


Seyyed Javad Sabounchei, Vida Jodaian and Hamid Reza Khavasi

Polyhedron 26 (2007) 2845

Synthesis, spectroscopic and X-ray structural studies of mercury(II) halide complexes of 4-methoxybenzoylmethylenetriphenylphosphorane

The reaction of a phosphorus ylide, 4-methoxybenzoylmethylenetriphenylphosphorane, $\{(Ph)_3PCHCOC_6H_4OCH_3\}$, with mercury(II) halides yielded dimeric complexes of the form $[\{(Ph)_3PCHCOC_6H_4OCH_3\}(HgX_2)]_2$ (where X = Cl, Br or I). Single crystal X-ray analysis of the chloride and bromide complexes reveals the presence of a centrosymmetric dimeric structure.

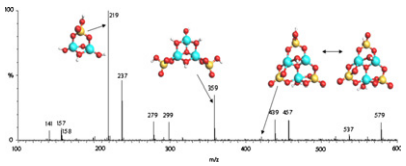


Arja Sarpola, Heikki Hellman, Vesa Hietapelto, Jorma Jalonen, Jukka Jokela, Jaakko Rämö and Jaakko Saukkoriipi

Polyhedron 26 (2007) 2851

Hydrolysis products of water treatment chemical aluminium sulfate octadecahydrate by electrospray ionization mass spectrometry

Hydrolysis and speciation of $Al_2(SO_4)_3{\cdot}18H_2O$ was studied by ESI TOF MS. Several polymeric species, whose compositions mimic those of stable mineral forms, were determined.

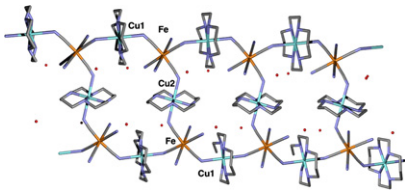


Antonio Rodríguez-Diéguez and Enrique Colacio

Polyhedron 26 (2007) 2859

Crystal structure and magnetic properties of $[\{Cu(cyclam)\}_3\{Fe(CN)_6\}_2] \cdot 6H_2O$, a cyano-bridged assembly with a rope-ladder chain structure

The title complex is made up of centrosymmetric S-shaped pentanuclear $[\{Cu(cyclam)\}_3\{Fe(CN)_6\}_2]$ units, held together by two weak and complementary Fe–CN···Cu bonds to form a rope-ladder chain. Interestingly enough, the ferromagnetic interaction between Cu(II) and Fe(III) ions through the long Cu–N axial bonds is not so weak as is usually assumed.

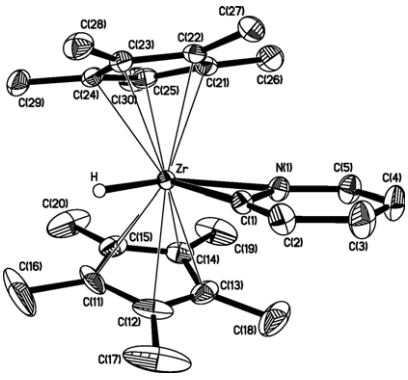


Dmitrii P. Kruťko, Roman S. Kirsanov, Sergey A. Belov, Maxim V. Borzov, Andrei V. Churakov and Judith A.K. Howard

Polyhedron 26 (2007) 2864

Reduction-induced *o*-C–H bond activation of pyridine with decamethylzirconocene dichloride

Treatment of decamethylzirconocene dichloride $(\eta^5\text{-}Cp^*)_2ZrCl_2$ with amalgamated magnesium in pyridine results in the formation of the *o*-C–H bond activation product $[\eta^5\text{-}C_5Me_5]_2ZrH[\eta^2\text{-}\kappa C,N\text{-}C_5H_4N]$ with the lateral positioning of the nitrogen atom. At elevated temperatures, this complex smoothly rearranges into its isomer with a medial positioning of the N-atom.

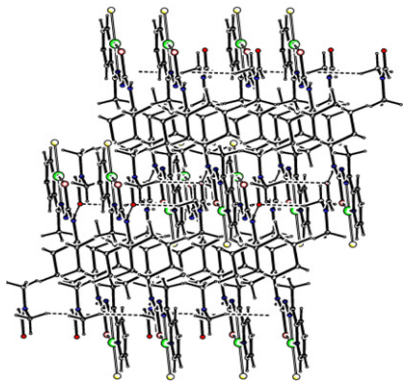


Dimitra Kovala-Demertzi, Anastasia Galani, Nikolaos Kourkoumelis, John R. Miller and Mavroudis A. Demertzis

Polyhedron 26 (2007) 2871

Synthesis, characterization, crystal structure and antiproliferative activity of platinum(II) complexes with 2-acetylpyridine-4-cyclohexyl-thiosemicarbazone

New platinum complexes have been synthesized by the reaction of Na_2PtCl_4 with 2-acetylpyridine-4-cyclohexyl-thiosemicarbazone, HAc4CyclHexyl (**1**). The new complexes [Pt(Ac4CyclHexyl)Cl] (**2**) and [Pt(Ac4CyclHexyl)$_2$] (**3**) have been characterized by elemental analyses, spectroscopic studies and the crystal structure of the complex [Pt(Ac4CyclHexyl)Cl] · DMF has been solved by single-crystal X-ray diffraction. The results of the cytotoxic activity of **1**–**3** have been evaluated for antiproliferative activity in vitro against the cells of three human cancer cell lines: MCF-7, T24 (bladder cancer cell line), A-549 and a mouse L-929. The compounds **1**–**3** display IC_{50} values in a μM range better than that of the antitumor drug cisplatin and are considered as agents with potential antitumor activity candidates for further stages of screening in vitro and/or in vivo.

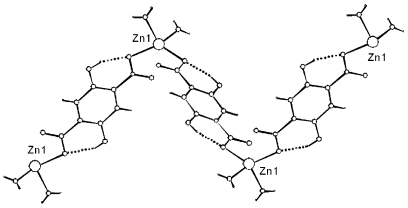


Nour Eddine Ghermani, Georges Morgant, Jean d'Angelo, Didier Desmaële, Bernard Fraisse, François Bonhomme, Emma Dichi and Mehrez Sgahier

Polyhedron 26 (2007) 2880

Covalently bonded infinite zigzag chain structure in a novel Zn(II) complex of 2,5-dihydroxy-1,6-benzenedicarboxylic acid

A new type of Zn(II) complex of 2,5-dihydroxy-1,6-benzenedicarboxylic acid (DHBDC) was formed by mixing aqueous solutions of the disodium salt of DHBDC and of zinc sulfate at room temperature. The individual units of this complex $[Zn(H_2O)_2(DHBDC)]$ are covalently linked, forming infinite zigzag chains, the ZnO_4 tetrahedra being at the vertices of the zigzag (shown). These chains, in turn, are further engaged in two-dimensional hydrogen bonding, yielding a 3D supramolecular architecture.

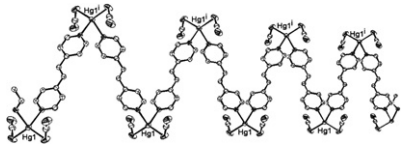


Ghodrat Mahmoudi, Ali Morsali and Long-Guan Zhu

Polyhedron 26 (2007) 2885

Mercury thiocyanate coordination polymers generated from rigid or flexible organic nitrogen donor-based ligands

A series of new mercury(II)–organic polymeric complexes, $[Hg(4,4\text{-bipy})(SCN)_2]_n$ (**1**), $[Hg(bpa)(SCN)_2]_n$ (**2**), $[Hg(bpe)(SCN)_2]_n$ (**3**), $[Hg\text{-}(bpp)(SCN)_2]_n$ (**4**) {4,4-bipy = 4,4′-bipyridine, bpa = 1,2-bis(4-pyridyl)ethane, bpe = 1,2-bis(4-pyridyl)ethene and bpp = 1,3-di(4-pyridyl)propane} was prepared from reactions of mercury(II) thiocyanate with four rigid and flexible organic nitrogen donor-based ligands under thermal gradient conditions, brunched tube method. All these compounds were structurally determined by X-ray single-crystal diffraction. The thermal stabilities of compounds **1**–**4** were studied by thermal gravimetric (TG) and differential thermal analyses (DTA). Solid state luminescent spectra of compounds **1** and **3** indicate intense fluorescent emissions at ca. 430 and 468 nm, respectively.

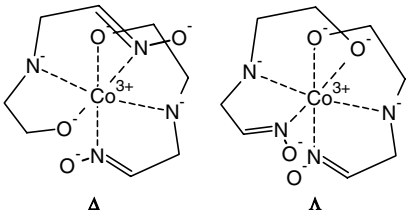


Aleksander Kufelnicki, Igor O. Fritsky, Tatiana Yu. Sliva, Inna F. Golovaneva and Rostislav D. Lampeka

Polyhedron 26 (2007) 2894

Stereoselective synthesis of cobalt(III) anionic complexes with chiral pyruvylaminoacid oximes and metal–ligand interactions in aqueous solution

A series of Co(III) anionic complexes with hydroxyiminoanalogs of dipeptides has been synthesized and investigated. For Met and Phe a significant discrimination of the $S(C_2)$ isomer is observed in comparison with $R(C_2)$. Equilibria in solution have been studied.

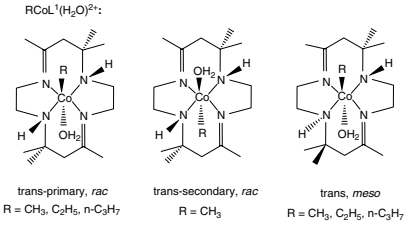


Shaoyung Lee and Tsung Yao Ku

Polyhedron 26 (2007) 2901

Bimolecular homolytic reactions of alkylcobalt complexes

The reactions of $RCoL(H_2O)^{2+}$ (R = CH_3, C_2H_5 and n-C_3H_7; L^1 = 5,7,7,12,14,14-hexamethyl-1,4,8,11-tetraazacyclotetradeca-4,11-diene, L^2 = 1,4,8,11-tetraazacyclotetradecane) with Cr^{2+} in aqueous solution were studied. The reactivity is clearly dependent on the size of the alkyl group, the ligand and the configuration of the complex.

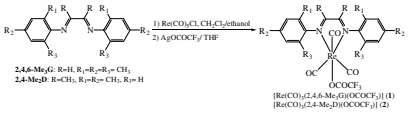


Reza Kia, Valiollah Mirkhani, Alajos Kálmán and Andrea Deák

Polyhedron 26 (2007) 2906

Re(I)(tricarbonyl)(carboxylate) complexes with the [*N*,*N*′-*bis*(2,4,6-trimethylbenzene)-1,4-diazabutadiene] (2,4,6-Me_3G) and [*N*,*N*′-*bis*(2,4-dimethylbenzene)-2,3-dimethyl-1,4-diazabutadiene] (2,4-Me_2D) ligands – Syntheses and spectroscopic studies. The crystal structure of [$Re(CO)_3$(2,4,6-Me_3G)($OCOCF_3$)]

Two new carboxylato complexes, [$Re(CO)_3$(DAB)($OCOCF_3$)] (DAB = substituted diazabutadiene ligands), were prepared by the reaction of [$Re(CO)_5Cl$] with the DAB ligands, and the subsequent reaction with $AgOCOCF_3$ gave the related carboxylate complexes. Their pseudooctahedral *fac* structure has been established by FTIR, UV–Vis and NMR spectroscopies, and has been confirmed by X-ray diffraction analysis. Electrochemical behaviour of the investigated complexes has been studied by cyclic voltammetry.

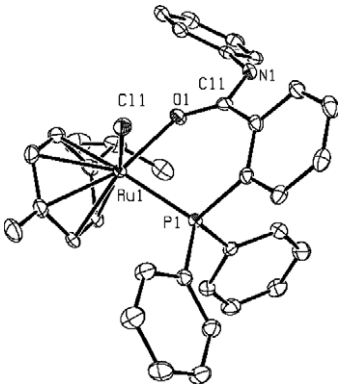


Gregorio Sánchez, Joaquín García, Juan J. Ayllón, José L. Serrano, Luis García, José Pérez and Gregorio López

Polyhedron 26 (2007) 2911

Synthesis, crystal structure and spectroscopic characterization of new neutral and cationic (η^6-*p*-cymene)–ruthenium(II) complexes with phosphine–amide ligands

The coordination properties of phosphinoamide ligands *o*-$Ph_2PC_6H_4CONHR$ [R = ^{i}Pr (**a**), Ph (**b**), 4-MeC_6H_4 (**c**), 4-FC_6H_4 (**d**)] have been studied by synthesizing and characterizing several (η^6-*p*-cymene)–ruthenium(II) complexes in which P,N- or P,O-bidentate coordination modes are displayed. The strong P,O-chelating ability towards ruthenium shown by these ligands prevent the preparation of complexes with ligands acting as P-monodentate and any hemilabile behaviour. The crystal structures of three new complexes have been determined.



Erratum to: "Lanthanide complexes of 2 + 2 meso-type macrocycle derive from *trans*-1,2-diaminocyclohexane and 2,6-diformylpyridine: X-ray crystal structures of La(III) and Sm(III) complexes" [Polyhedron 25 (2006) 2745–2754] 2919

The Publisher encourages the submission of articles in electronic form thus saving time and avoiding rekeying errors. For detailed instructions on the preparation of manuscripts and of electronic artwork, consult the Author Gateway for Elsevier at http://authors.elsevier.com

ScienceDirect

Full text of this journal is available, on-line from **ScienceDirect**. Visit **www.sciencedirect.com** for more information.

Available online at www.sciencedirect.com
ScienceDirect
Polyhedron 26, issue 1, 2 January 2007
POLYHEDRON
www.elsevier.com/locate/poly

Contents

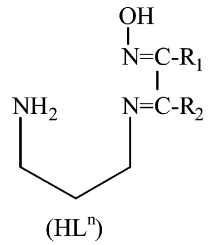
Papers

Mohamed A.-Z. Eltayeb, Yousif Sulfab

Polyhedron 26 (2007) 1

Stabilization of the trivalent oxidation state of copper by tridentate imine–oxime–amine ligands

Two tridentate imine–oxime–amine ligands HL^1 and HL^2 and their corresponding Cu^{II} complexes were synthesized. These complexes are readily oxidized to give diamagnetic d^8Cu^{III} complexes.



(HL^n)

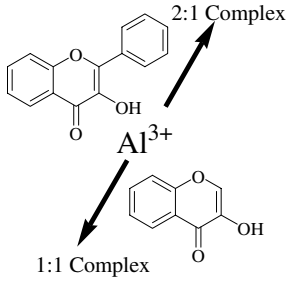
n	R_1	R_2
1	CH_3	CH_3
2	$CH(CH_3)_2$	CH_3

Nursen Binbuga, William P. Henry, Tor P. Schultz

Polyhedron 26 (2007) 6

Binding of hydroxychromones with Al^{3+} in methanol

The coordination of 3-hydroxychromone and 5-hydroxychromones with Al^{3+} in methanol was studied spectrophotometrically. A comparison with the corresponding flavones gives comparable binding for the 5-hydroxy derivatives. However, where the 3-hydroxyflavone binds in a 2:1 ratio, the 3-hydroxychromone forms a 1:1 complex.

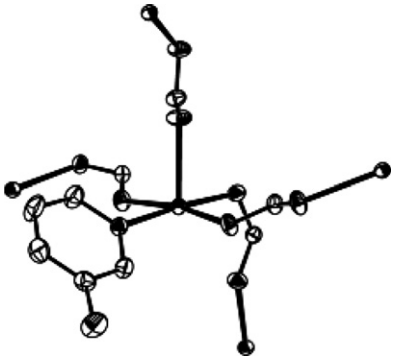


Bojan Kozlevčar, Lea Glažar, Gordana Pirc, Zvonko Jagličić, Amalija Golobič, Primož Šegedin

Polyhedron 26 (2007) 11

Diverse coordination of two ligands in ferromagnetic $[Cu(\mu\text{-}HCO_2)_2(3\text{-}pyOH)]_n$ and $[Cu_2(\mu\text{-}HCO_2)_2(\mu\text{-}3\text{-}pyOH)_2(3\text{-}pyOH)_2(HCO_2)_2]_n$

The polynuclear complex $[Cu(\mu\text{-}HCO_2)_2(3\text{-}pyOH)]_n$ (**1**) shows triatomic methanoate bridges of *anti–anti* and *syn–anti* modes, on the other hand $[Cu_2(\mu\text{-}HCO_2)_2(\mu\text{-}3\text{-}pyOH)_2(3\text{-}pyOH)_2(HCO_2)_2]_n$ (**2**) reveals only monoatomic methanoate coordination inside the dinuclear moiety and 3-hydroxypyridine connecting these units by semi-coordination. A ferromagnetic interaction is found in both complexes, however it is significantly important only for **1** ($2J = 9.2\ cm^{-1}$). This interaction takes place via the *syn–anti* methanoates, due to the magnetic Cu(II) $d_{x^2-y^2}$ orbitals on both sides of the bridge. In all the other bridging cases in **1** and **2**, the nonmagnetic d_{z^2} orbital is always involved.



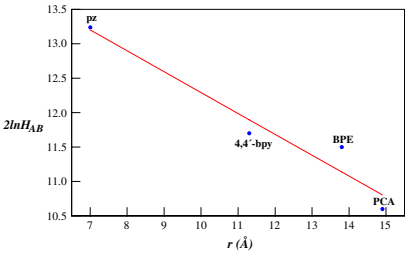
Elsevier Ltd.

Florencia Fagalde, Mónica E. García Posse, Mónica M. Vergara, Mauricio Cattaneo, Néstor E. Katz, Isabel Romero, Teodor Parella, Antoni Llobet

Polyhedron 26 (2007) 17

Increasing transmission of electronic interaction in dinuclear unsymmetric mixed-valent ruthenium complexes

New dinuclear complexes of general formula $[(tpm)(bpy)Ru^{II}(L)Ru^{II/III}(NH_3)_5]^{4+/5+}$, with bpy = 2,2′-bipyridine; tpm = tris(1-pyrazolyl)-methane; L = pz (pyrazine), 4,4′-bpy (4,4′-bi-pyridine), BPE (*trans*-1,2-bis(4-pyridyl)-ethylene) and PCA (4-pyridinecarboxaldehyde azine), have been prepared and characterized. Increased transmission of the metal-to-metal electronic interaction is induced in the mixed-valent species by using tpm as a spectator ligand.

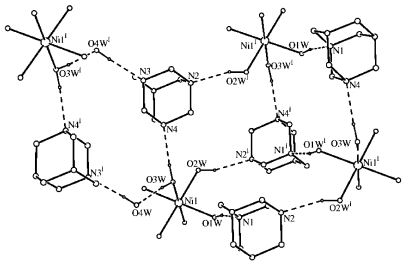


Suparna Banerjee, Angshuman Roy Choudhury, T.N. Guru Row, Siddhartha Chaudhuri, Ashutosh Ghosh

Polyhedron 26 (2007) 24

Three-dimensional supramolecular H-bonding network in the compounds containing hexamethylenetetramine and aquated Ni(II) or Cd(II) salts

The supramolecular H-bonded structures of three compounds, $[Ni(H_2O)_6](ClO_4)_2 \cdot 2\{(CH_2)_6N_4\} \cdot 2H_2O$ (**1**), $[Ni(H_2O)_6]Cl_2 \cdot 2\{(CH_2)_6N_4\} \cdot 4H_2O$ (**2**) and $[Cd(H_2O)_4\{(CH_2)_6N_4\}_2](ClO_4)_2 \cdot 2H_2O$ (**3**) (where $(CH_2)_6N_4$ = hexamethylenetetramine) have been described. Compounds **1** and **2** show R44(16) motif linking the cationic moieties with hexamine which are in turn interwoven with anionic moieties via water molecules whereas the supramolecular structure of **3** shows $R_2^2(12)$ motif.

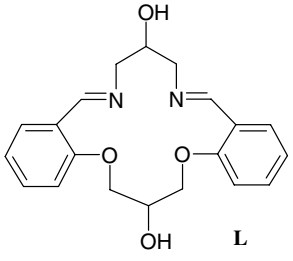


Ali Akbar Khandar, Seyed Abolfazl Hosseini-Yazdi, Masomeh Khatamian, Patrick McArdle, Seyed Amir Zarei

Polyhedron 26 (2007) 33

Synthesis, characterization and structure of nickel(II) complexes of a 16-membered mixed-donor macrocyclic Schiff base ligand, potentially hexadentate, bearing two pendant alcohol functions

Nickel(II) complexes of the potentially hexadentate, two alcohol pendant-arms macrocyclic Schiff base ligand with 16-member mixed N_2O_4 donors, containing different counter ions, were synthesized and characterized by a variety of physico-chemical techniques in both solid and solution states. In all the complexes, the ligand **L** behaves as a pentadentate ligand.

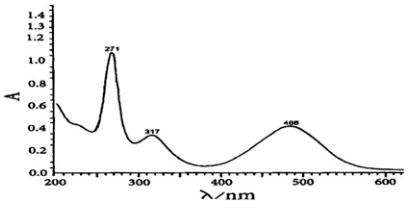


Mohamed A. Eltayeb, Yousif Sulfab

Polyhedron 26 (2007) 39

Synthesis and characterization of silver(III) complexes with tetradentate and tridentate ligands with imine-oxime groups

Silver(I) in the presence of tetradentate and tridentate ligands having imine-oxime groups are readily oxidized to the corresponding silver(III) complexes. The isolated complexes are diamagnetic and their cyclic voltammograms are electrochemically irreversible. The complexes have high molar absorption in the visible region that may be attributed to ligand to metal charge transfer (LMCT).

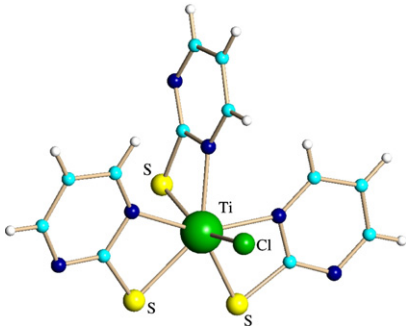


Claire J. Carmalt, Emily S. Peters, Ivan P. Parkin, Derek A. Tocher

Polyhedron 26 (2007) 43

Synthesis and characterisation of titanium pyridine- and pyrimidine-thiolates and their application as precursors to titanium disulfide

Low pressure chemical vapour deposition (LPCVD) of $[TiCl(SC_5H_4N)_3]$ forms thin films of TiS_2 at 600 °C and TiS_2/TiO_2 films at 500 °C. LPCVD of $[TiCl(SC_4H_3N_2)_3]$ resulted in TiS_2 films contaminated with Cl, C and N.

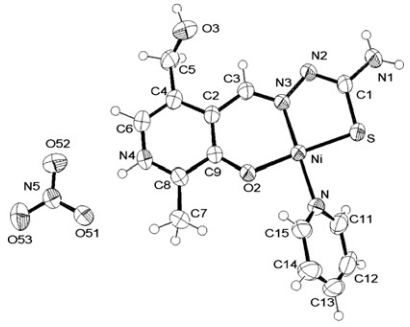


Vukadin M. Leovac, Ljiljana S. Jovanović, Vladimir Divjaković, Andrej Pevec, Ivan Leban, Thomas Armbruster

Polyhedron 26 (2007) 49

Transition metal complexes with thiosemicarbazide-based ligands. Part LIV. Nickel(II) complexes with pyridoxal semi- (PLSC) and thiosemicarbazone (PLTSC). Crystal and molecular structure of $[Ni(PLSC)(H_2O)_3](NO_3)_2$ and $[Ni(PLTSC\text{-}H)py]NO_3$

The syntheses of the first Ni(II) complexes with pyridoxal semicarbazone (PLSC): $Ni(PLSC)Cl_2 \cdot 3.5H_2O$ (**1**), $[Ni(PLSC)(H_2O)_3](NO_3)_2$ (**2**), $Ni(PLSC)(NCS)_2 \cdot 4H_2O$ (**3**), $[Ni(PLSC\text{-}2H)NH_3] \cdot 1.5H_2O$ (**4**), and two new complexes with pyridoxal thiosemicarbazone (PLTSC): $[Ni(PLTSC\text{-}H)py]NO_3$ (**5**) and [Ni(PLTSC-H)NCS] (**6**) are described. Complexes **1**–**3** are paramagnetic with an octahedral structure and complexes **4**–**6** are diamagnetic and have a square-planar geometry.

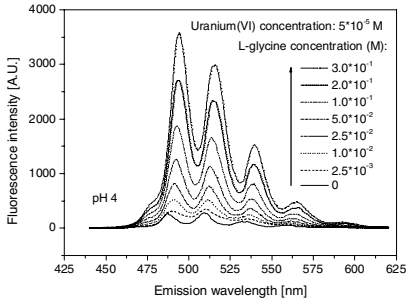


A. Günther, G. Geipel, G. Bernhard

Polyhedron 26 (2007) 59

Complex formation of uranium(VI) with the amino acids L-glycine and L-cysteine: A fluorescence emission and UV–Vis absorption study

The complex formation of uranium(VI) with L-glycine and L-cysteine was studied at low pH values by use of time-resolved laser-induced fluorescence spectroscopy and UV–Vis spectroscopy. Differences in the fluorescence emission and UV absorption properties between free UO_2^{2+} and the several formed uranyl amino acid species were detected.

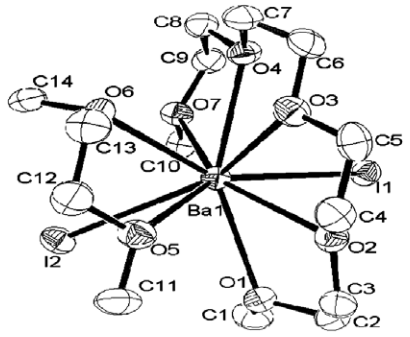


Shashank Mishra, Liliane G. Hubert Pfalzgraf, Erwann Jeanneau

Polyhedron 26 (2007) 66

Redistribution reactions of heteroleptic barium iodide derivatives: Synthesis and structures of *trans*-BaI_2(DME)(triglyme), *cis*-BaI_2-(DME)(tetraglyme) and $[Ba(tetraglyme)_2]I_2 \cdot C_7H_8$

The reactions between $BaI_2 \cdot 2H_2O$ and sodium hexafluoroisopropoxide or sodium trifluoroacetate in a 1:1 stoichiometry lead to heterometallic Na–Ba compounds. These undergo redistribution reactions in the presence of O-donor ligands affording barium iodide adducts such as *trans*-BaI_2(DME)(triglyme), *cis*–BaI_2(DME)(tetraglyme) and $[Ba(tetraglyme)_2]I_2 \cdot C_7H_8$ which were characterized by analysis, FT-IR, NMR and X-ray diffraction.

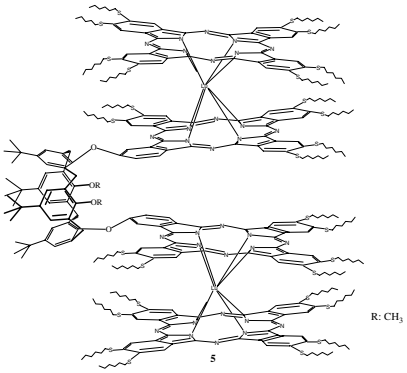


Tanju Ceyhan, Ahmet Altındal, Ali Rıza Özkaya, Mehmet K. Erbil, Özer Bekaroğlu

Polyhedron 26 (2007) 73

Synthesis, characterization, and electrochemical, electrical and gas sensing properties of a novel *tert*-butylcalix[4]arene bridged bis double-decker lutetium(III) phthalocyanine

A novel *tert*-butylcalix[arene] bridged bis double-decker lutetium(III) phthalocyanine (Lu_2Pc_4) (**5**) has been synthesized by the reaction of dimeric lutetium(III) phthalocyanine (**4**) with two equiv. of dilithium octakis hexylthiophthalocyanine in amyl alcohol. Distinctive differences between the voltametric behaviour of the double decker Lu and precursor Pc were detected. Detailed d.c. and a.c. conductivity and gas sensing measurements all of the Pcs synthesized in this work have been carried out.

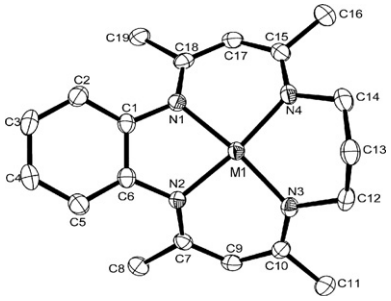


E.H. Kim, D.I. Kim, H.S. Lee, H.G. Na, J.C. Byun, J.H. Choi, Y.C. Park

Polyhedron 26 (2007) 85

Synthesis, structures, electrochemistry and catalytic activities of copper(II) and palladium(II) complexes with asymmetric tetraazacycloannulenes

The copper(II) and palladium(II) complexes with 15-membered asymmetric 5,9-dihydro-2,4,10,12-tetramethyl-1,5,9,13-monobenzotetraazacyclo[15]tetradecine have been synthesized and characterized by electrochemical behavior and catalytic activities. The structures of the 15-membered copper(II) and palladium(II) complexes were determined using the X-ray diffraction method.

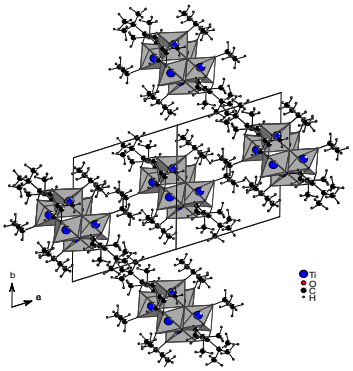


P. Piszczek

Polyhedron 26 (2007) 93

Thermal behaviour of hexanuclear titanium(IV) oxo isopropoxide carboxylates, and their usability as a single-source TiO_2 CVD precursors

Hexanuclear oxo titanium(IV) isopropoxide carboxylates, of the general formula $[Ti_6O_6(OPr^i)_6(O_2CR)_6]$ (R = Bu^t (**1**), CH_2Bu^t (**2**)) and $[Ti_6O_6(OPr^i)_6(O_2CC(CH_3)_2Et)_6] \cdot 0.5(C_7H_8)$ (**3**), have been synthesized as polycrystalline powders in order to study their thermal properties and usability as TiO_2 CVD precursors. Analysis of thermogravimetric and variable temperature (VT-IR) data shows that the thermal stability of the synthesized complexes decreases as follows **3** > **2** > **1**. Composition of vapors formed during thermolysis of **1**–**3** were qualitatively analysed with VT-IR methods and mass spectrometry (MS-EI).

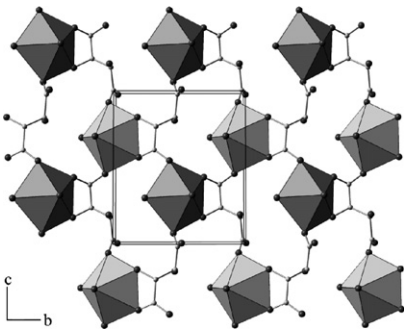


Pierre Thuéry

Polyhedron 26 (2007) 101

Reaction of uranyl nitrate with carboxylic diacids under hydrothermal conditions. Crystal structure of complexes with L(+)-tartaric and oxalic acids

Reaction of uranyl nitrate with L(+)-tartaric acid in the presence of KOH under mild hydrothermal conditions permitted to obtain the first uranyl tartrate complex to be crystallographically characterized. Prolonged heating resulted in oxidative cleavage of tartaric acid and formation of a mixed uranyl/sodium oxalate complex which crystallizes as a three-dimensional assemblage.

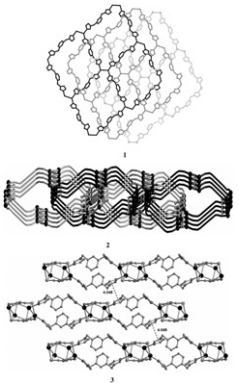


Jian-Di Lin, Zhi-Hua Li, Jian-Rong Li, Shao-Wu Du

Polyhedron 26 (2007) 107

Synthesis and crystal structures of three novel coordination polymers generated from AgCN and AgSCN with flexible N-donor ligands

The solvothermal reactions of AgX (X = CN, SCN) with mbix [mbix = 1,3-bis(imidazole-l-yl-methyl)benzene] or bix [bix = 1,4-bis-(imidazole-l-yl-methyl)benzene] afforded $[AgCN(mbix)]_n$ (**1**), $[(AgCN)_4(bix)_2]_n$ (**2**) and $[(AgSCN)_2(mbix)]_n$ (**3**). The structure of **1** contains 3-fold-interpenetrated 2D networks, while that of **2** exhibits 2-fold parallel interpenetration. There is no interpenetration observed in **3**. These three polymers all contain $\pi \cdots \pi$ interactions.

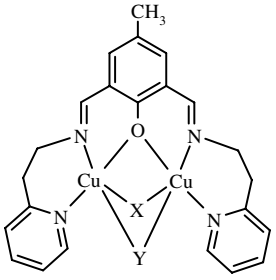


Jorge Manzur, Ana María García, Andrés Vega, Andrés Ibañez

Polyhedron 26 (2007) 115

Synthesis and structure of copper (II) complexes with L–OH (L–OH = 2,6-bis-[*N*-(2-pyridylethyl)-formidoyl]-4-methyl-phenol)

The synthesis and molecular structure of three new copper (II) complexes: $[Cu_2(L–O)(\mu\text{-}OH)(\mu\text{-}ClO_4)](ClO_4)$ (**I**), $[Cu_2(L–O)(\mu\text{-}Cl)_2][Cu_2Cl_6]_{0.5}$ (**II**) and $[Cu_2(L–O)(\mu\text{-}OH)(CH_3OH)]_2[Cu(CAT\text{-}O_2)_2]_{0.5}(ClO_4)_2$ (**III**), with the ligand 2,6-bis-[*N*-(2-pyridylethyl)-formidoyl]-4-methyl phenol (L–OH) is reported. Compound **I** shows a very poor catecholase activity. Compounds **II** and **III** show very uncommon anions: a hexachloro dicuprate (II) and a bis-catecholate cuprate (II) moieties, respectively.



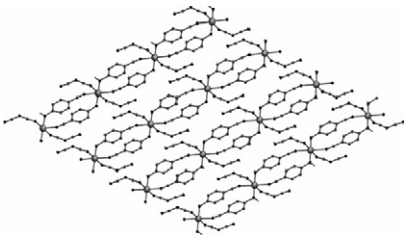
I: $X = OH^-$; $Y = ClO_4^-$
II: $X = Y = Cl^-$
III: $X = OH^-$

Moumita Biswas, Georgina M. Rosair, Guillaume Pilet, M. Salah El Fallah, Joan Ribas, Samiran Mitra

Polyhedron 26 (2007) 123

Synthesis, crystal structures and magnetic properties of five new metal(II) compounds constructed with isomers of aminobenzonitrile and dicyanamide ligands

Five new metal(II) compounds with isomers of aminobenzonitrile and dicyanamido ligands have been synthesized and characterized by structural and low temperature (2–300 K) magnetic properties. This work contains the first example of Cu–ABN compounds. The structural analyses revealed that all the compounds extended their geometry to 2D or 3D networks through hydrogen bonding interactions. The variable temperature magnetic susceptibility measurements show that weak antiferromagnetic interactions propagate through the bridging ligands.

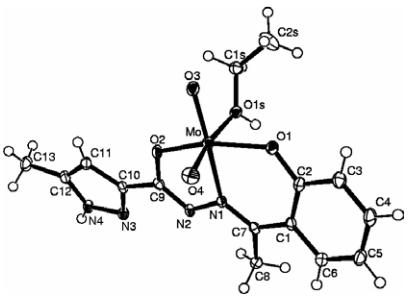


Samik Gupta, Anil Kumar Barik, Sachindranath Pal, Arijit Hazra, Somnath Roy, Ray J. Butcher, Susanta Kumar Kar

Polyhedron 26 (2007) 133

Oxomolybdenum(VI) and (IV) complexes of pyrazole derived ONO donor ligands – synthesis, crystal structure studies and spectroelectrochemical correlation

A few *cis*-dioxomolybdenum(VI) complexes have been prepared with pyrazole derived Schiff base ligands. One of these complexes has been subjected to oxo-transfer reaction with PPh_3 to produce the corresponding oxomolybdenum(IV) complex. A comparative account of the Mo(VI) complexes regarding the redox stability and spectral behavior has been correlated with the variation of electron donating properties of the ligands.

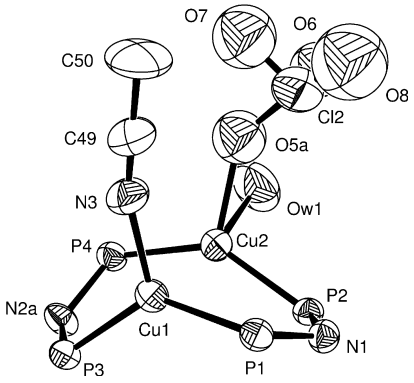


Ritu Ahuja, M. Nethaji, A.G. Samuelson

Polyhedron 26 (2007) 142

Mitigating repulsions in close quarters: Copper tells us how!

Destabilization due to d^{10}–d^{10} repulsion in structurally characterized copper(I) diphosphinoamine $(PPh_2)_2N(R)$ (R = H; dppa, R = ^{i}Pr; dppipa) dimers such as $[Cu_2(dppa)_2(CH_3CN)(H_2O)(OClO_3)]ClO_4$ (**1**), is mitigated by charge transfer interaction promoted by unsymmetrical coordination. Cambridge Structural Database studies support the proposition.

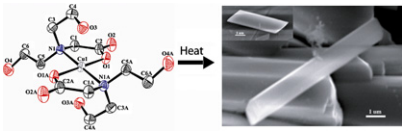


Harjyoti Thakuria, Gopal Das

Polyhedron 26 (2007) 149

CuO micro plates from a 3D metallo-organic framework (MOF) of a binary copper(II) complex of *N*,*N*-bis(2-hydroxyethyl)glycine

The blue colored mononuclear binary complex $[Cu(Bic)_2]$ (**1**) (Bic^- = *N*,*N*-bis(2-hydroxyethyl) glycinate), on heating at 500 °C for 6 h resulted in the formation of black CuO (Tenorite) micro plates

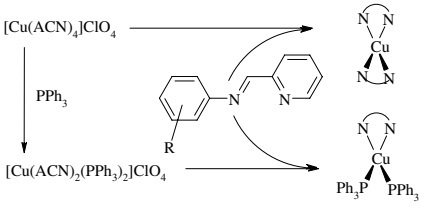


Saeed Dehghanpour, Nouri Bouslimani, Richard Welter, Fresia Mojahed

Polyhedron 26 (2007) 154

Synthesis, spectral characterization, properties and structures of copper(I) complexes containing novel bidentate iminopyridine ligands

The copper(I) complexes $[Cu(LL)_2]ClO_4$ $Cu(LL)(PPh_3)_2]ClO_4$, where LL is iminopyridine derivatives, have been synthesized and characterized by CHN analyses, ^1H, ^{13}C-NMR, IR, and UV–Vis spectroscopy. The crystal structures of some complexes have been determined. The redox behavior of the complexes has been studied.

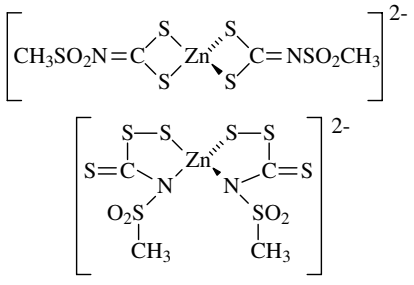


Marcelo R.L. Oliveira, Genivaldo J. Perpétuo, Jan Janczak, Mayura M.M. Rubinger

Polyhedron 26 (2007) 163

Synthesis, structural and spectroscopic characterization of novel zinc(II) complexes with *N*-methylsulfonyldithiocarbimato and *N*-methylsulfonyltrithiocarbimato ligands

A new *N*-*R*-sulfonyldithiocarbimato–zinc(II) complex with the formula $(Ph_4P)_2[Zn(CH_3SO_2NCS_2)_2]$ (**1**) has been obtained by the reaction of potassium *N*-methylsulfonyldithiocarbimate, zinc(II) acetate and tetraphenylphosphonium chloride. A secondary product with the formula $(Ph_4P)_2[Zn(CH_3SO_2N{=}CS_3)_2]$ (**2**) was also obtained. Compounds **1** and **2** were characterized by X-ray diffraction and by IR and NMR spectroscopies.

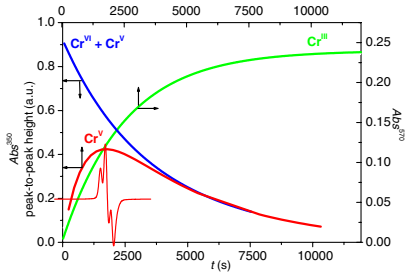


Mabel Santoro, Evangelina Caffaratti, Juan Manuel Salas-Peregrin, Laszlo Korecz, Antal Rockenbauer, Luis F. Sala, Sandra Signorella

Polyhedron 26 (2007) 169

Kinetics and mechanism of the chromic oxidation of *myo*-inositol

The redox reaction of *myo*-inositol with Cr^{VI} yields the inosose and Cr^{III} as final redox products. The reaction occurs through a mechanism that combines $Cr^{VI} \rightarrow Cr^{IV} \rightarrow Cr^{II}$ and $Cr^{VI} \rightarrow Cr^{IV} \rightarrow Cr^{III}$ pathways.

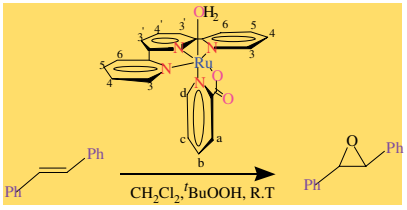


Debabrata Chatterjee, Ayon Sengupta, Anannya Mitra

Polyhedron 26 (2007) 178

Synthesis, characterization and reactivity of a novel ruthenium(II) complex containing polypyridyl ligand

$[Ru^{II}(trpy)(pic)(H_2O)]^+$ complex catalyzes the epoxidation of stilbenes in presence *t*-BuOOH in dichloromethane at room temperature. Formation of a radicaloid [Ru–O(*t*-Bu)–O]˙ type intermediate is proposed for the catalytic process.

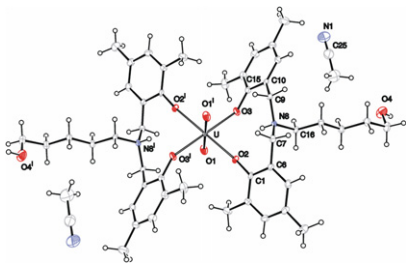


Harri Sopo, Ari Väisänen, Reijo Sillanpää

Polyhedron 26 (2007) 184

Uranyl ion complexes with long chain amino-alcoholbis(phenolate) [O,N,O,O′] donor ligands

The reaction between uranyl nitrate hexahydrate and phenolic ligand precursors *N*,*N*-bis(2-hydroxy-3-methyl-5-alkylbenzyl)-4-aminobutanol (alkyl = methyl or *t*-butyl), *N*,*N*-bis-(2-hydroxy-3-methyl-5-alkylbenzyl)-5-aminopentanol (alkyl = methyl or *t*-butyl) and *N*,*N*-bis(2-hydroxy-3-methyl-5-alkylbenzyl)-6-aminohexanol (alkyl = *t*-butyl) (H_3L1–H_3L5) or their hydrochlorides in acetonitrile in presence of the base affords the mononuclear, neutral complexes $[UO_2(H_2L)_2] \cdot xCH_3CN$ (x = 0, 1 or 2). Extraction studies of the uranyl ion from water to dichloromethane with these new ligands (H_3L1–H_3L5) are also presented.

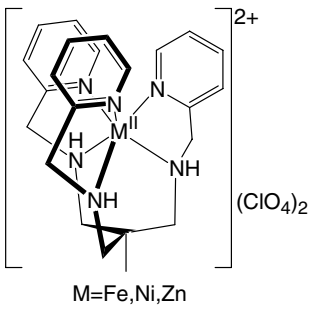


Daniel P. Kennedy, Antonio G. DiPasquale, Arnold L. Rheingold, Roy P. Planalp

Polyhedron 26 (2007) 197

Ni(II)-mediated synthesis of the novel tripodal aminopyridyl ligand *tamepyr*: Coordination geometry and rigidity of complexes with the divalent 3d metals Fe–Zn and with In(III)

The synthesis of the novel tripodal chelator 'tamepyr' (*N*,*N*′,*N*″-tris(2-pyridylmethyl)-1,1,1-tris(aminomethyl)ethane) and complexation of the ligand with Fe(II) and Zn(II) has been studied. The Ni(II) complex of tamepyr was prepared cleanly by a template reaction of the 1,1,1-tris(aminomethyl)ethane framework with 2-pyridinecarboxaldehyde and $Ni(ClO_4)_2 \cdot 6H_2O$ followed by a sodium borohydride reduction to afford the desired material (>40% yield). Treating the Ni(II) complex with excess sodium cyanide liberated the free ligand. A Zn(II) and low-spin Fe(II) complex form readily from free tamepyr.

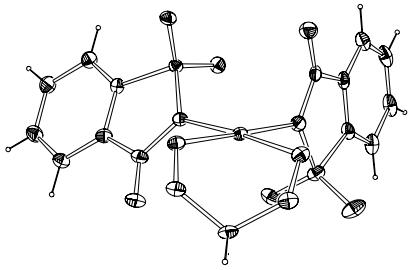


Kelly J. Kilpin, William Henderson, Brian K. Nicholson

Polyhedron 26 (2007) 204

Synthesis, characterisation and biological activity of cycloaurated organogold(III) complexes with imidate ligands

The synthesis, characterisation and biological activities of a range of gold(III) imidate complexes of saccharin, phthalimide and isatin, containing ancillary cycloaurated benzylpyridine or *N*,*N*-dimethylbenzylamine ligands is reported.



The Publisher encourages the submission of articles in electronic form thus saving time and avoiding rekeying errors. For detailed instructions on the preparation of manuscripts and of electronic artwork, consult the Author Gateway for Elsevier at http://authors.elsevier.com

ScienceDirect

Full text of this journal is available, on-line from **ScienceDirect**. Visit **www.sciencedirect.com** for more information.

Available online at www.sciencedirect.com
ScienceDirect
Polyhedron 26, issues 9–11, 15 June 2007
POLYHEDRON
www.elsevier.com/locate/poly

Contents

Preface 1763

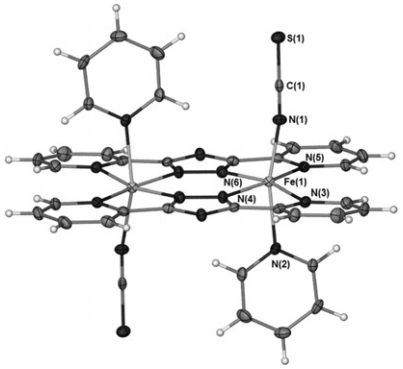
Papers

Caspar J. Schneider, John D. Cashion, Boujemaa Moubaraki, Suzanne M. Neville, Stuart R. Batten, David R. Turner and Keith S. Murray

Polyhedron 26 (2007) 1764

The magnetic and structural elucidation of 3,5-bis(2-pyridyl)-1,2,4-triazolate-bridged dinuclear iron(II) spin crossover compounds

The structurally similar families of dinuclear iron(II) complexes of type $[Fe(NCX)(py)]_2(\mu\text{-}L)_2$, where L^- is a bridging pyrazolate or triazolate dinucleating ligand, and X = S, Se, BH_3, display different spin-crossover behaviour that is fundamentally related to the different ligand field strengths provided by the bridging azolate and apical NCX^- ligands.

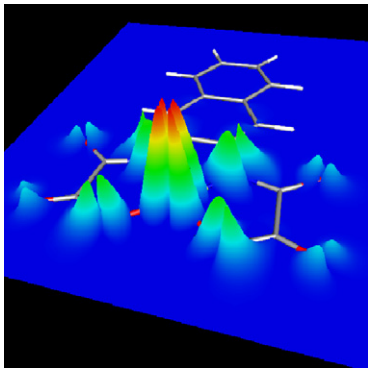


Björn Bräuer, Tobias Rüffer, Reinhard Kirmse, Jan Griebel, Florian Weigend and Georgeta Salvan

Polyhedron 26 (2007) 1773

Spin density distribution in oxamato-type transition metal complexes

The spin density distribution of a paramagnetic Cu-oxamato complex has been derived from angular dependent electron paramagnetic resonance measurements at room temperature. The results indicate a noticeable spin density transfer from the central metal to the coordinated atoms. Quantum chemical studies using density functional theory reinforce the results.

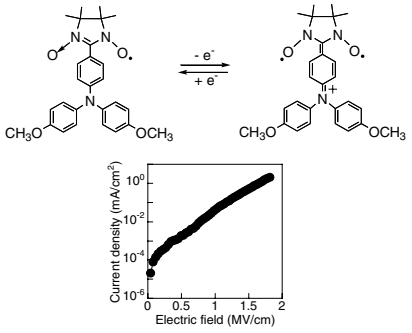


Takashi Kurata, Kenichiroh Koshika, Fumiaki Kato, Junji Kido and Hiroyuki Nishide

Polyhedron 26 (2007) 1776

Triarylamine-combined nitronyl nitroxide and its hole-transporting property

A durable nitronyl nitroxide molecule combined with the triarylamine moiety was prepared as a new hole-transporting molecule. Electrochemical measurements and photoelectron spectroscopy of the radical molecule showed a reversible redox with the ionization potential of −5.4 eV. The hole-transporting property was proved by current density–electric field plots for the single-layer device.



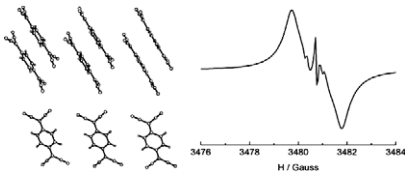
Elsevier Ltd.

Y.C. Chen, G.X. Liu, P.F. Wang, H. Xu, X.M. Ren, Y. Song and Y.X. Sui

Polyhedron 26 (2007) 1781

Mixed-valence molecular magnets based on $[TCNQ]_3^{2-}$ building block: Structures, magnetic properties and DFT analyses

Crystals of two radical compounds, based on $[TCNQ_3]^{2-}$ ions, posses two independent TCNQ moieties and exhibit mixed-valence feature, which were identified by IR, EPR spectra and DFT calculations.

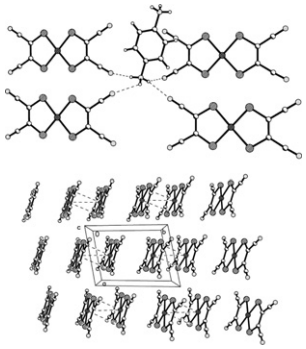


X.M. Ren, S. Nishihara, S. Noro, T. Akutagawa and T. Nakamura

Polyhedron 26 (2007) 1787

2D H-bonding molecular magnets based on $[Ni(mnt)_2]^-$ monoanion: Syntheses, crystal structures and magnetic properties

Two new H-bonding molecular magnets were designed. In their crystals, magnetic $[Ni(mnt)_2]^-$ monoanions form the π-stacked sheets and the neighboring anionic sheets are held together via H-bonding interactions between -NH groups of cations and CN groups of mnt^{2-} ligands.

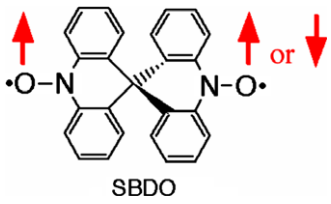


Takayuki Ishida, Motohiro Ooishi, Norio Ishii, Hironori Mori and Takashi Nogami

Polyhedron 26 (2007) 1793

Mono- and dinitroxide radicals from 9,9′(10*H*,10′*H*)-spirobiacridine: An approach to a D_{2d} triplet biradical

Is the ground state of a title biradical (**SBDO**) molecule triplet or singlet? The X-ray crystallographic analysis revealed the orthogonality between the two π-spin systems. Although the magnetic measurements on a polycrystalline sample of **SBDO** revealed the presence of antiferromagnetic interaction, the diluted ESR experiments and the DFT calculation on a single **SBDO** molecule indicated the ground triplet state.

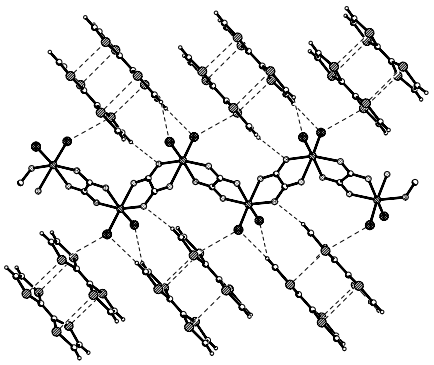


Bin Zhang, Zheming Wang, Yan Zhang, Hayao Kobayashi, Mohamedally Kurmoo, Takehiko Mori, Francis L. Pratt, Katsuya Inoue and Daoben Zhu

Polyhedron 26 (2007) 1800

Dual-function molecular crystal containing the magnetic chain anion $[Fe^{III}(C_2O_4)Cl_2^-]_n$

We report on the structural, optical, electrical and magnetic properties of the charge-transfer salts of TTF (TTF = tetrathiafulvalene) and BETS (BETS = bis(ethylenedithio)tetraselenafulvalene) with the magnetic chain anion $[Fe^{III}(C_2O_4)Cl_2^-]_n$. They have been synthesized by diffusion and electrocrystallization, respectively. The structures from single-crystal X-ray diffraction reveal one-dimensional anions separated by either dimers of TTF^+ or κ-type layers of $BETS^{0.5+}$. Infrared reflectivity and electrical conductivity measurements on single crystals are in good agreement with those of an insulator for TTF and a metal for BETS, as the calculated band-structures predict. Interestingly, the former exhibits π–d interaction leading to a long-range Néel state below 20 K with a small canting of the moments. Similar anomaly is seen below 5 K for the BETS salt which is metallic to 2 K, thus a weak-ferromagnetic conductor.

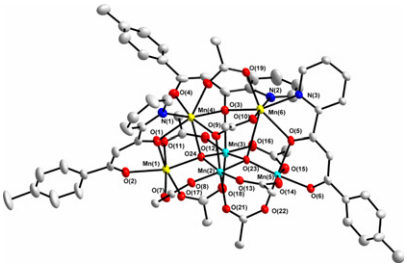


Chen-I Yang, Yu-Jhe Tsai, George Chung, Ting-Shen Kuo, Minghuey Shieh and Hui-Lien Tsai

Polyhedron 26 (2007) 1805

Synthesis, structure, and magnetic properties of a hexanuclear manganese complex

A mixed-valence $Mn^{II}_3Mn^{III}_3$ hexanuclear $[Mn_6O_2(O_2CPh)_8L_3]$ (**1**) complex has been synthesized by the reaction of 1-(2-pyridyl)-3-(*p*-tolyl)propane-1,3-dione (HL) with $[Mn_3O(O_2CPh)_6(H_2O)(py)_2]$ in CH_2Cl_2. The magnetic data indicate that complex **1** has an $S = 7/2$ with the D value of $-0.46\ cm^{-1}$ and slow magnetic relaxation below 2.5 K.

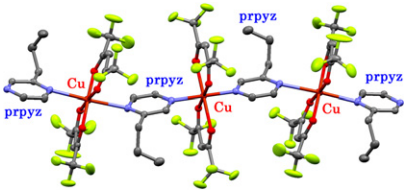


Tamizo Kogane, Nobumasa Koyama, Takayuki Ishida and Takashi Nogami

Polyhedron 26 (2007) 1811

Structures and magnetic properties of one-dimensional copper(II) complexes bridged with diazaaromatic rings

Seven kinds of polynuclear complexes of $[Cu(hfac)_2]$ (Hhfac = 1,1,1,5,5,5-hexafluoropentane-2,4-dione) with diazaaromatic rings have been prepared. The crystal structures of $[\{Cu(hfac)_2(\mu\text{-}L)\}_n]$ (L = 2,5- and 2,6-dimethylpyrazines, propylpyrazine (prpyz), quinoxaline, phenazine, 4,6-dimethylpyrimidine, and 1,6-naphthyridine) have been determined. These complexes consist of a one-dimensional chain structure, and the geometry around the copper ion is approximately an octahedral structure. The relations between the magnetic properties and coordination structure were discussed from the magnetic measurements.

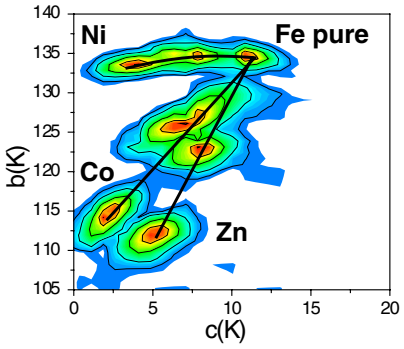


Radu Tanasa, Cristian Enachescu, Alexandru Stancu, François Varret, Jorge Linares and Epiphane Codjovi

Polyhedron 26 (2007) 1820

Study of impurities effect in spin crossover compounds using first order reversal curves (FORC) method

The distribution of the switching temperatures obtained for $[Fe_xM_{1-x}(btr)_2(NCS)_2] \cdot H_2O$ where M are impurities, respectively, Zn, Ni, Co using first order reversal curve technique is converted in the coercivity and bias (c, b) plane for direct reading of the physical information from the diagram.

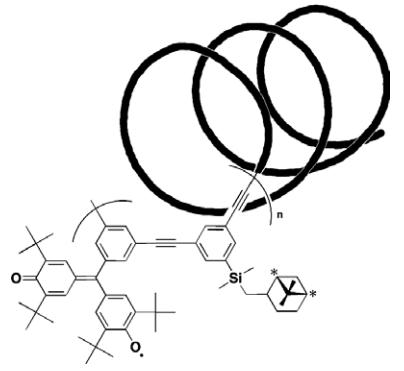


Takashi Kaneko, Shota Yoshimoto, Shingo Hadano, Masahiro Teraguchi and Toshiki Aoki

Polyhedron 26 (2007) 1825

Synthesis of an optically active helical poly(1,3-phenyleneethynylene) bearing stable radicals and its chiroptical and magnetic properties

An optically active poly(1,3-phenyleneethynylene) bearing galvinoxyl units and dimethyl(10-(1*S*)-pinanyl)silyl groups was synthesized via condensation polymerization of (3,5-dihalogenophenyl)hydrogalvinoxyl and 1,3-diethynyl-5-[dimethyl(10-(1*S*)-pinanyl)silyl]benzene using $Pd(PPh_3)_4$ catalyst.

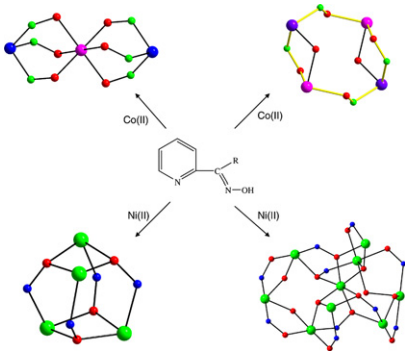


Theocharis C. Stamatatos, Constantina Papatriantafyllopoulou, Eugenia Katsoulakou, Catherine P. Raptopoulou and Spyros P. Perlepes

Polyhedron 26 (2007) 1830

2-Pyridyloximate clusters of cobalt and nickel

The use of 2-pyridyloximes, (py)C(R)NOH, in reactions with Co(II) and Ni(II) sources has led to four families of structurally interesting complexes which have been magnetically characterized.

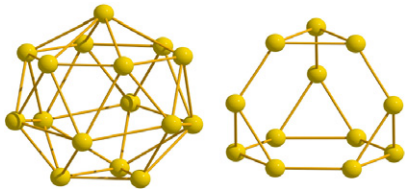


Ian A. Gass, Constantinos J. Milios, Marco Evangelisti, Sarah L. Heath, David Collison, Simon Parsons and Euan K. Brechin

Polyhedron 26 (2007) 1835

Synthesis and magnetic properties of heptadecametallic Fe(III) clusters

A family of Fe_{17} complexes whose structures are based on magnetite is reported. Magnetic studies show all to possess $S = 35/2$ spin ground states.

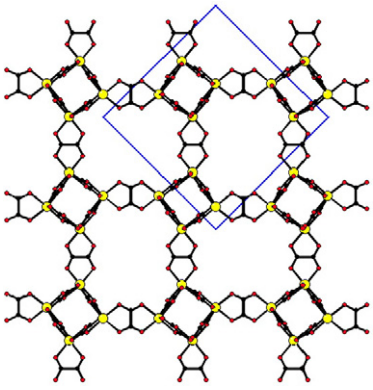


Eugenio Coronado, José R. Galán Mascarós, Mari Carmen Giménez-López, Manuel Almeida and João C. Waerenborgh

Polyhedron 26 (2007) 1838

Spin crossover Fe^{II} complexes as templates for bimetallic oxalate-based 3D magnets

Achiral 3D oxalate-bridge bimetallic extended networks have been prepared using as template a Fe^{II} spin crossover complex. Ferromagnetic ordering is observed below 3 K. No cooperative spin transition has been detected.

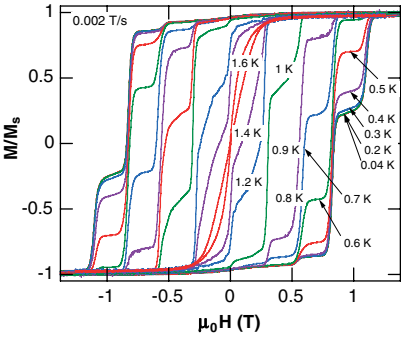


Muralee Murugesu, Wolfgang Wernsdorfer, George Christou and Euan K. Brechin

Polyhedron 26 (2007) 1845

New derivatives of an enneanuclear Mn SMM

The syntheses, structures and magnetic properties of a family of Mn_9 SMMs are discussed.

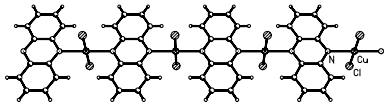


Ryan T. Schneider, Christopher P. Landee, Mark M. Turnbull, Firas F. Awwadi and Brendan Twamley

Polyhedron 26 (2007) 1849

Copper azine compounds: Synthesis, structure and magnetic analyses of Cu(phenazine)Cl_2, (phenazinium)$_2CuCl_4 \cdot H_2O$, and [Cu(phenazine)$Cl_2 \cdot H_2O$]$_2$

Three compounds composed of phenazine and copper chloride have been prepared and studied by infrared spectroscopy, X-ray diffraction, and variable temperature magnetization. The compounds synthesized and studied are: Cu(phenazine)Cl_2 (**1**), (phenazinium)$_2CuCl_4 \cdot H_2O$ (**2**), and [Cu(phenazine)$Cl_2 \cdot H_2O$]$_2$ (**3**). Compounds **1** and **2** are described as antiferromagnetic Heisenberg chains with exchange constants $|J|/k_B$ = 33.8 K and 8.6 K, respectively.

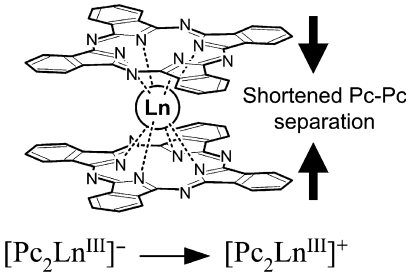


Satoshi Takamatsu and Naoto Ishikawa

Polyhedron 26 (2007) 1859

A theoretical study of a drastic structural change of bis(phthalocyaninato)lanthanide by ligand oxidation: Towards control of ligand field strength and magnetism of single-lanthanide-ionic single molecule magnet

A density functional theory (DFT) study on bis(phthalocyaninato)lanthanides showed that removal of two electrons from the anionic complex shortens significantly the separation between phthalocyaninato (Pc) ligands. This suggests that $[Pc_2Y]^+$, which is generated from a previously reported $[Pc_2Tb]^-$ SMM, can have significantly larger ligand field splitting than the anionic form.

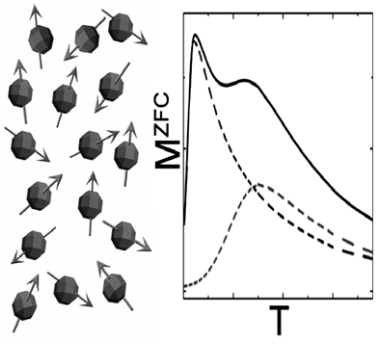


Simon Trudel and Ross H. Hill

Polyhedron 26 (2007) 1863

Magnetic properties of binary mixtures of metal oxide nanoparticles

The magnetic properties of mixtures of nanoparticles with similar size distribution but distinct superparamagnetic characteristics were investigated by SQUID magnetometry. The magnetic behaviour of the mixtures can be described as the sum of the superparamagnetic contributions. The presence of weak interparticle interactions was indicated.

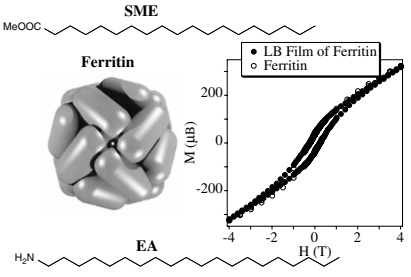


M. Clemente-León, E. Coronado, A. Soriano-Portillo, M.T. Martín-Romero, M. Pérez-Morales, J.M. Domínguez-Vera and N. Gálvez

Polyhedron 26 (2007) 1871

Langmuir monolayers and Langmuir–Blodgett films of ferritin prepared by using a surfactant mixture of eicosylamine (EA) and methyl stearate (SME)

Magnetic LB films of ferritin have been prepared by using a 1/4 mixed monolayer of EA and SME. BAM images show a homogeneous distribution of ferritin at the air–water interface. UV–Vis spectroscopy measurements reveal that the amount of ferritin has been increased with respect to the previous DODA/SME LB films. Magnetic measurements confirm a superparamagnetic behavior.

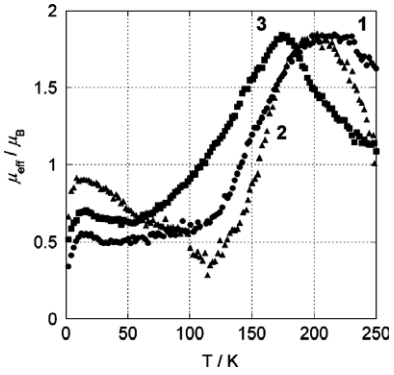


Chihiro Kachi-Terajima, Takamasa Akatsuka, Masa-aki Kohbara and Satoshi Takamizawa

Polyhedron 26 (2007) 1876

Magnetic properties of nitric oxide adsorbed within channel crystals

The adsorption properties of nitric oxide were investigated on the crystalline one-dimensional compounds, $[M_2(bza)_4(pyz)]_n$ (bza = benzoate; pyz = pyrazine; M = Cu^{II} (**1**)) and $[M_2(bza)_4(2\text{-mpyz})]_n$ (2-mpyz = 2-methylpyrazine; M = Rh^{II} (**2**), Cu^{II} (**3**)). Magnetic susceptibility measurements revealed the antiferromagnetic interactions between included NO molecules in these hosts.

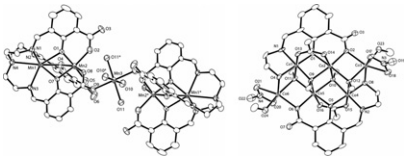


Takuya Shiga and Hiroki Oshio

Polyhedron 26 (2007) 1881

Syntheses, structures and magnetic properties of mixed-valence pentanuclear $[Mn_3^{II}Mn_2^{III}]$ and hexanuclear $[Co_4^{II}Co_2^{III}]$ complexes derived from 3-formylsalicylic acid

Mixed-valence pentanuclear manganese complex and hexanuclear cobalt complex with Schiff-base ligand derived from 3-formylsalicylic acid have been prepared. Structures and magnetic properties of these compounds are reported.

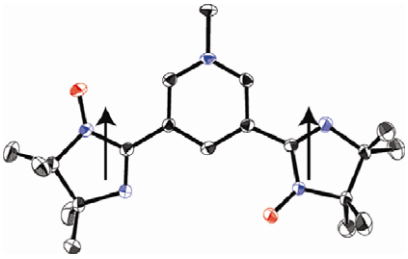


Kenichi Hayakawa, Tomoaki Ise, Daisuke Shiomi, Kazunobu Sato and Takeji Takui

Polyhedron 26 (2007) 1885

Stable iminonitroxide biradicals: Building blocks for organic heterospin, heteromolecular complexes

A salt of radical-substituted pyridinium triflate $\mathbf{2}^+ \cdot TfO^-$ has been synthesized. The cationic biradical $\mathbf{2}^+$ has been found to have a triplet ground state from magnetic susceptibility measurements. The ground-state triplet biradical serves as a building block for molecule-based magnets of $S > 1/2$ based on intermolecular noncovalent bonding architecture.

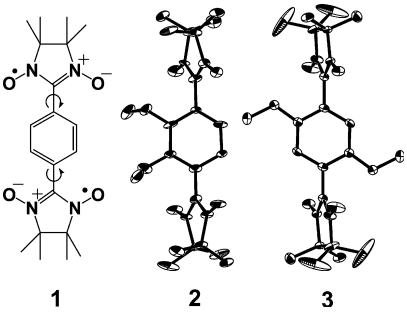


Yuki Kanzaki, Daisuke Shiomi, Tomoaki Ise, Kazunobu Sato and Takeji Takui

Polyhedron 26 (2007) 1890

Magnetic interactions in *p*-phenylene-bis-(nitronyl nitroxide) biradicals with large torsion angles

New *p*-phenylene-based biradicals of nitronyl nitroxide **2** and **3** have been synthesized. The bulky methoxy substituents give rise to large inter-ring torsion angles of about 70°, which weakens the intramolecular exchange interaction to $2J/k_B \sim -6$ K, about 6% of that for the parent biradical **1**.

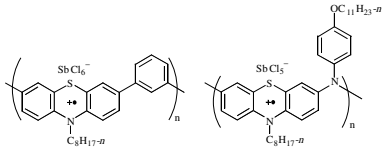


Hiroyuki Oka, Masaki Terane, Yasushi Kiyohara and Hitoshi Tanaka

Polyhedron 26 (2007) 1895

Synthesis and magnetic behavior of stable organic open-shell polymers containing phenothiazine cation radicals as spin resources

Two types of organic open-shell polymer containing phenothiazine cation radicals as spin resources were synthesized and the magnetic behaviors were investigated. The one is the 1,3-phenylene-linked polymer, and the other is the arylamine nitrogen-linked polymer. The magnetic behavior of 1,3-phenylene-linked polymer was intramolecularly ferromagnetic, but intermolecularly antiferromagnetic. Whereas, the arylamine nitrogen-linked polymer was in the $S = 1$ spin state in spite of low spin concentration.

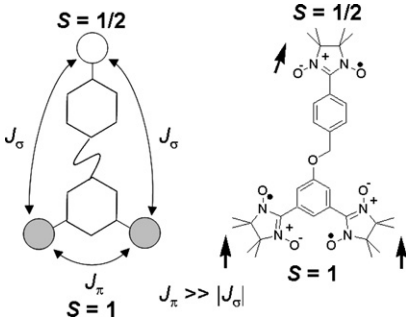


Yuki Kanzaki, Daisuke Shiomi, Tomoaki Ise, Kazunobu Sato and Takeji Takui

Polyhedron 26 (2007) 1901

Benzyl-phenyl ether derivatives of nitronyl nitroxide triradicals as a model for single-component organic molecule-based ferrimagnetics

As a model compound for single-component molecule-based ferrimagnetics, a nitronyl nitroxide triradical **1** has been synthesized. From the analysis of X-ray crystal structure and magnetic susceptibility measurements, the triradical molecules are found to form exchange-coupled systems composed of six $S = 1/2$ spins in the crystal.

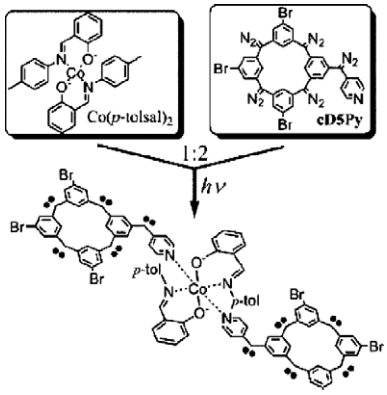


Hiroyuki Tobinaga, Madoka Suehiro, Tetsuji Ito, Guangyuan Zhou, Satoru Karasawa and Noboru Koga

Polyhedron 26 (2007) 1905

Magnetic property of 1:2 mixture of Co(*p*-tolsal)$_2$; *p*-tolsal = *N*-*p*-tolylsalicylideniminato, and cyclic pentacarbene–pyridine with $S = 10/2$ in dilute frozen solution

A cyclic pentadiazo-pyridine derivative, **cD5py**, was prepared. The 1:2 complex of Co(*p*-tolsal)$_2$ with **cD5py** in frozen solution after irradiation functions as the single-molecule magnet with $U_{eff} = 72$ K and $\tau_0 = 2.0 \times 10^{-9}$ s. A hysteresis loop with $H_c = 7.1$ kOe at 1.9 K was also observed.

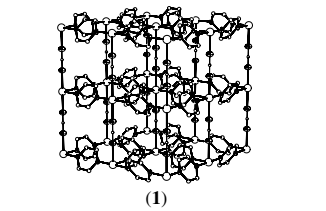


Jamie L. Manson, Marianne M. Conner, John A. Schlueter and Kylee A. Hyzer

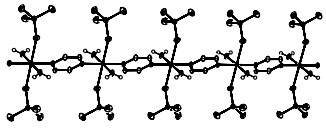
Polyhedron 26 (2007) 1912

Structural and magnetic properties of quasi-1 and 2D pyrazine-containing spin-1/2 antiferromagnets

Two new copper(II) coordination polymers are reported. $[Cu(HF_2)(pyz)_2]BF_4$ (**1**) consists of a novel 3D framework in which Cu^{2+} centers are linked by pyrazine and bifluoride ligands. Long-range magnetic ordering occurs below 1.54 K. The second compound, $Cu(ReO_4)_2(H_2O)_2(pyz)$ (**2**) has a linear chain structure and shows a broad maximum in the magnetic susceptibility at 7.7 K while LRO was not observed above 2 K.



(**1**)



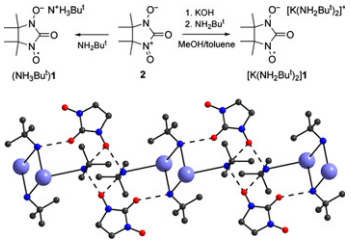
(**2**)

Eugene Tretyakov, Sergey Fokin, Galina Romanenko, Vladimir Ikorskii and Victor Ovcharenko

Polyhedron 26 (2007) 1917

Structure and magnetic properties of 3-oxyl-4,4,5,5-tetramethyl-2-oxoimidazolidin-1-olates

The paramagnetic salts (NH_3Bu^t)**1** and $[K(NH_2Bu^t)_2]$**1**, where **1** is the 3-oxyl-4,4,5,5-tetramethyl-2-oxoimidazolidin-1-olate anion, were isolated. The crystal structure of $[K(NH_2Bu^t)_2]$**1** involves polymer chains formed by hydrogen bonding between anions **1** and $[K_2(NH_2Bu^t)_4]^{2+}$ cation dimer fragments. The magnetic properties of $[K(NH_2Bu^t)_2]$**1** are well described by the quasi-isolated dimer model with spins S = 1/2 coupled by weak exchange interactions via $[K_2(NH_2Bu^t)_4]^2$ fragments in polymer chains.

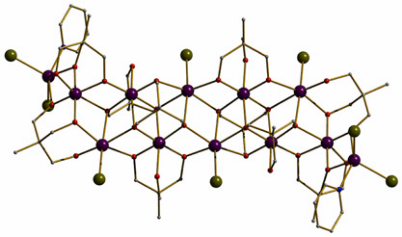


Maria Manoli, Constantinos J. Milios, Abhudaya Mishra, George Christou and Euan K. Brechin

Polyhedron 26 (2007) 1923

New octa- and dodecametallic mixed-valent Mn rods

The combination of $MnBr_2 \cdot 4H_2O$ with tripodal alcohols results in the formation of new octa- and dodecametallic $[Mn_4^{III}Mn_4^{II}]$ and $[Mn_6^{III}Mn_6^{II}]$ clusters. Their structures describe 'one-dimensional' rod-like arrays of six and ten edge-sharing triangles, respectively. Both complexes display $S \approx 0$ spin ground states.

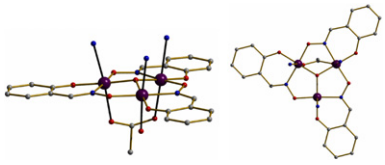


Constantinos J. Millos, A. Gavin Whittaker and Euan K. Brechin

Polyhedron 26 (2007) 1927

Microwave heating – A new synthetic tool for cluster synthesis

Microwave heating is a new and extremely attractive method for synthesizing polymetallic clusters of paramagnetic transition metal ions. Here we give a brief overview of some of the complexes we have made so far, highlighting the enormous potential of the technique.

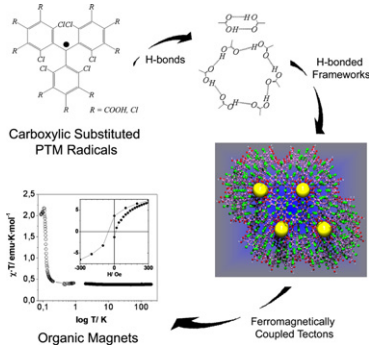


Nans Roques, Daniel Maspoch, Angela Datcu, Klaus Wurst, Daniel Ruiz-Molina, Concepció Rovira and Jaume Veciana

Polyhedron 26 (2007) 1934

Self-assembly of carboxylic substituted PTM radicals: From weak ferromagnetic interactions to robust porous magnets

In this short review, the work that have been developed over the last six years in our group on the use of polychlorotriphenylmetyl radicals (PTM) functionalized by carboxylic groups to access to purely organic/molecular magnetic materials is reported. Starting from the seminal work on the monocarboxylic PTM, we will then report the self-assembly of PTM radicals functionalized with two and three carboxylic groups. In those cases, the self-assembly of the paramagnetic units yield robust and porous magnetic 2D-structures. The last part of the review will present the latest results obtained with the idea to increase both the structural and magnetic dimensionality in purely organic PTM-based materials using a PTM radical functionalized by six carboxylic groups.

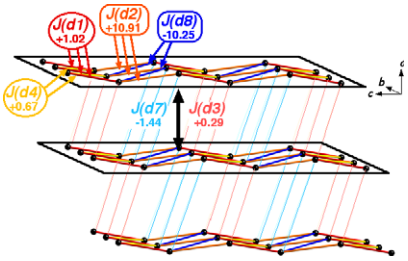


M. Deumal, S. LeRoux, J.M. Rawson, M.A. Robb and J.J. Novoa

Polyhedron 26 (2007) 1949

A theoretical study of the magnetism of the α-*p*-cyano-tetrafluorophenyl-dithiadiazolyl radical using a first principles *bottom-up* procedure

A first-principles *bottom-up* theoretical study of this polymorph indicates that there are six non-negligible magnetic interactions, two of them (+10.91 and −10.25 cm^{-1}) dominating. The magnetic topology (figure) presents a complex 3D topology that explains the experimental *bulk* antiferromagnetic properties. The computed magnetic susceptibility curve reproduces well the experimental one.

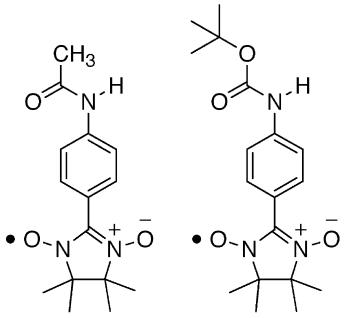


Safo Aboaku and Paul M. Lahti

Polyhedron 26 (2007) 1959

Crystallography and magnetism of 2-amido-4,4,5,5-tetramethyl-4,5-dihydro-1*H*-imidazole-3-oxide-1-oxyls

Nitronylnitroxides **pAPNN** and **pBPNN** were synthesized, and studied by crystallography and magnetism. **pAPNN** forms hydrogen bonded dyads and nitroxide–nitroxide stacks (the latter give spin pairing exchange behavior), while **pBPNN** lacks strong hydrogen-bonding crystallographic motifs.

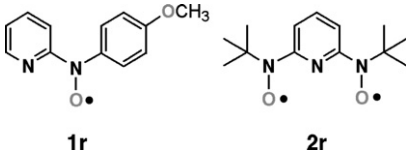


Atsushi Okazawa, Takashi Nogami and Takayuki Ishida

Polyhedron 26 (2007) 1965

Preparation, structures, and magnetic properties of precursors for chelating compounds of 2-pyridyl nitroxide derivatives

We synthesized and characterized two precursors for paramagnetic chelating ligands, *N*-*p*-anisyl-*N*-2-pyridylhydroxylamine and 2,6-bis(*N*-*t*-butylhydroxylamino)pyridine. The oxidation with silver(I) oxide gave radicals (**1r** and **2r**) showing typical nitroxide ESR signals. Theoretical DFT calculation indicated the ground triplet state for **2r**.

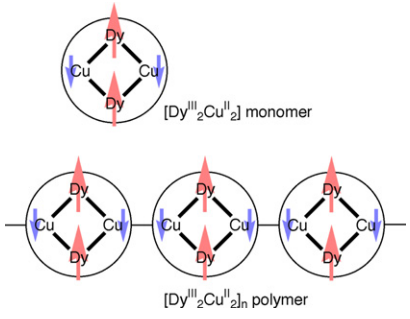


Sohei Ueki, Atsushi Okazawa, Takayuki Ishida, Takashi Nogami and Hiroyuki Nojiri

Polyhedron 26 (2007) 1970

Tetranuclear heterometallic cycle Dy_2Cu_2 and the corresponding polymer showing slow relaxation of magnetization reorientation

Ac magnetic susceptibility measurements of monomeric $[Dy_2Cu_2]$ and polymeric $[Dy_2Cu_2]_n$ exhibited a χ'_{ac} (in-phase) decrease and a concomitant χ_{ac} (out-of-phase) increase with an increase of frequency. Low-temperature magnetization measurements on $[Dy_2Cu_2]_n$ exhibited hysteresis with magnetization jumps. This behavior is characteristic of single-chain magnets.

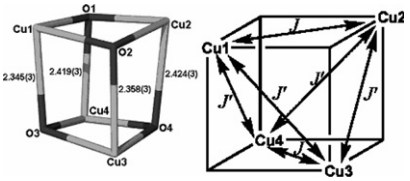


Leigh F. Jones, Colin A. Kilner and Malcolm A. Halcrow

Polyhedron 26 (2007) 1977

Variable temperature structural and magnetic characterisation of the cubane cluster $[Cu_4(\mu_3\text{-}OH)_4(L)_4][ClO_4]_4$ (L = 5-*tert*-butyl-3-(pyrid-2-yl)-1*H*-pyrazole)

We present the structural and magnetic data of a rare μ_3-OH^- bridged tetranuclear cubane cluster $[Cu_4(\mu_3\text{-}OH)_4(L)_4](ClO_4)_4 \cdot xCH_2Cl_2$ (**1** $\cdot$ xCH_2Cl_2 x = 1–2) containing the ditopic ligand 5-*tert*butyl-3-(pyrid-2-yl)-1*H*-pyrazole ('L'). Fitting of the magnetic susceptibility data above 30 K using the Bleaney Bowers equation for two dicopper(II) dimers gives rise to Spin-Hamiltonian parameters $J = -5.2$ cm^{-1}, $J' = 0$ (fixed) and $g = 2.15$.

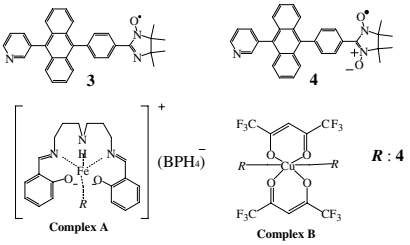


Hirotaka Tamekuni and Yoshio Teki

Polyhedron 26 (2007) 1984

Design, synthesis and physical properties of the metal complexes using π-radical with photo-excited high-spin state as a ligand

3-Pyridinyl substituted iminonitroxide (**3**), nitronylnitroxide (**4**) and two metal complexes, $[Fe(III)(L)(\mathbf{4})] \cdot (BPh_4)$ (LH_2 = *N*,*N*′-bis(1-hydroxy-2-benzyliden)-1,7-diamino-4-azaheptane) and $[Cu(II)(hfac)_2(\mathbf{4})_2]$ were prepared. Their magnetic behaviors were clarified in the ground states, showing weak antiferromagnetic interactions between the paramagnetic centers of the metal ions and the π-radical. The lowest photo-excited quartet high-spin states of **3** and **4** have been clarified by time-resolved ESR.

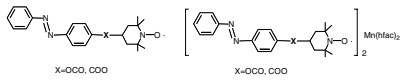


Masahiro Fujino, Satoko Hasegawa, Hiroki Akutsu, Jun-ichi Yamada and Shin'ichi Nakatsuji

Polyhedron 26 (2007) 1989

Radical compounds and metal complexes with azobenzene chromophore

A couple of *trans*-azobenzene derivatives with an ester unit and a TEMPO group showed photo-isomerizations by irradiation in solution and the changes of solid state magnetic properties of the photo-isomers were clarified, while the corresponding $Mn(hfac)_2$ complexes were found to be reluctant to the photo-isomerization.

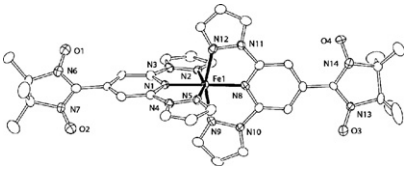


Masayuki Nihei, Tadashi Maeshima, Yuka Kose and Hiroki Oshio

Polyhedron 26 (2007) 1993

Synthesis, structure and magnetic properties of an iron(II) complex with nitronyl nitroxides

An iron(II) complex with nitronyl nitroxide radicals was synthesized and structure and magnetic properties were presented. The central iron(II) ion was coordinated by two tridentate ligands with nitronyl nitroxide radicals. In a magnetic susceptibility measurement, **1** showed thermally and light induced spin transitions.

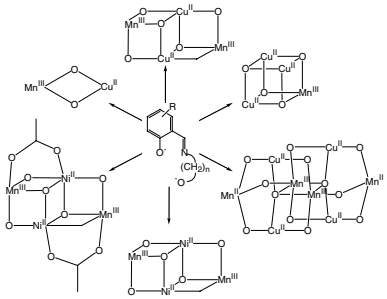


Masayuki Nihei, Ayano Yoshida, Satoshi Koizumi and Hiroki Oshio

Polyhedron 26 (2007) 1997

Hetero-metal Mn–Cu and Mn–Ni clusters with tridentate Schiff-base ligands

Novel Mn–Cu and Mn–Ni multi-nuclear hetero-metal clusters were synthesized by simple one-pot reactions of multidentate Schiff base ligands with metal sources.All clusters were selectively obtained by changing reaction conditions, suitable co-ligands, and slight modification of ligand structures.The structures and magnetic properties of these hetero-metal clusters were presented.

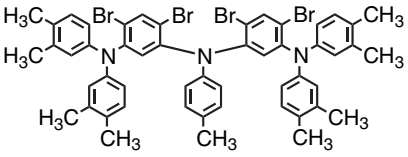


Masafumi Yano, Akira Fujiwara, Masakazu Tatsumi, Munetaka Oyama, Kazunobu Sato and Takeji Takui

Polyhedron 26 (2007) 2008

Amine-based organic high-spin systems: Synthesis, electrochemical and spectroscopic studies of polyalkylated one-dimensional oligoaryl triamines

A polyalkylated oligoaryl triamine was designed and synthesized as a precursor of positively charged high-spin systems. The electrochemical and spectroscopic properties were examined.

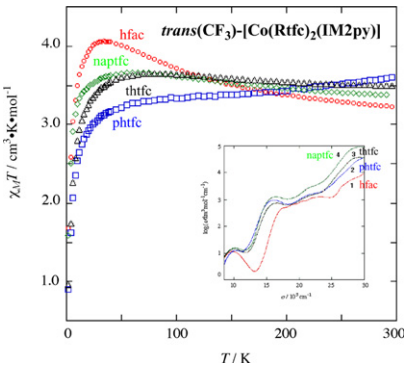


Terukazu Ishida, Keiichi Adachi, Satoshi Kawata, Takayoshi Suzuki, Akira Fuyuhiro and Sumio Kaizaki

Polyhedron 26 (2007) 2013

Synthesis and magneto-optical properties of a series of bis(β-diketonato) Co(II) complexes with imino nitroxide radical chelate

For a series of the stereospecifically formed bis(β-diketonato)(IM2py) Co(II) complexes, *trans*(CF_3)-[$Co(Rtfc)_2$(IM2py)] both the magnetic interaction and MLCT band is affected by the substituents of the β-diketonates, which is elucidated in consideration of the inversion of the $d_\pi(t_{2g})$ orbital levels leading to the orbital orthogonality or overlap with the SOMO of IM2py in terms of AOM parametrization.

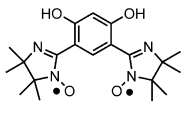


Koichiro Tanaka, Kimiaki Furuichi, Masatoshi Kozaki, Shuichi Suzuki, Daisuke Shiomi, Kazunobu Sato, Takeji Takui and Keiji Okada

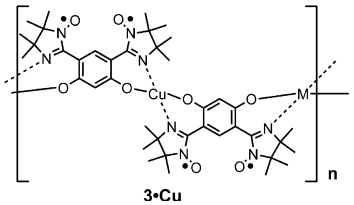
Polyhedron 26 (2007) 2021

Preparation and magnetic properties of 4,6-bis(imino nitroxide)-substituted resorcinol and its Cu-complex

A spin-ligand, **3H**, was prepared. **3H** showed an intramolecular ferromagnetic (J/k_B = +5 K) and a weaker intermolecular antiferromagnetic (J/k_B = −0.9 K) interactions. The reaction of **3H** with copper acetate gave a hardly soluble complex of the type **3 · Cu** showing ferromagnetic interaction in relatively high temperatures.



3H



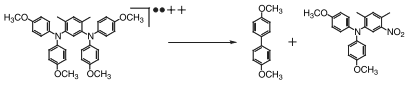
3•Cu

Masafumi Yano, Kengo Kitagawa, Masakazu Tatsumi, Kazunobu Sato and Takeji Takui

Polyhedron 26 (2007) 2027

m-Phenylenediamine-based high-spin dication diradicals: Analysis of the decomposed products

A tetraaryl-*m*-phenylenediamine dication diradical, which exhibits ground-state triplet, was chemically generated and decomposed in preparative scale. A nitro compound and a biaryl were formed as main products, indicating the cleavage of pi-system.

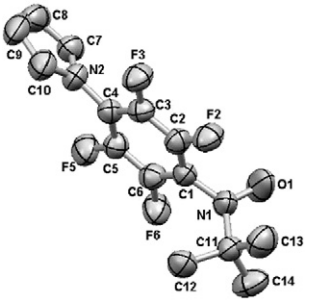


Zeynep Delen and Paul M. Lahti

Polyhedron 26 (2007) 2031

Crystallography and magnetism of 1-(4-[*N*-*tert*-butylaminoxyl]-2,3,5,6-tetrafluorophenyl)-pyrrole

The title compound is a stable, highly ring-fluorinated aryl *tert*-butylnitroxide, the first of this type made by a preparative synthesis. It exhibits chain-like crystal packing motifs, but has magnetic behavior in better accord with spin pairing exchange.

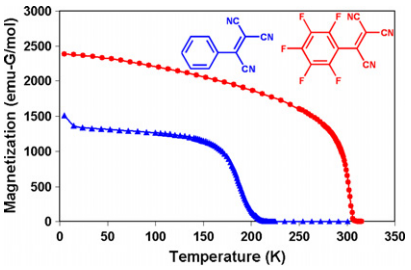


Mark D. Harvey, Josephine T. Pace and Gordon T. Yee

Polyhedron 26 (2007) 2037

A room temperature ferrimagnet, vanadium-[pentafluorophenyltricyanoethylene]$_2$

Analogs of the V[TCNE]$_2$ ferrimagnet were synthesized by replacing the TCNE with H_5PTCE and F_5PTCE in order to gain insight as to the reason why small changes in structure give different ordering temperatures. These molecule-based magnets, V[H_5PTCE]$_2$ and V[F_5PTCE]$_2$, exhibit T_cs of around 215 K and 307 K, respectively.

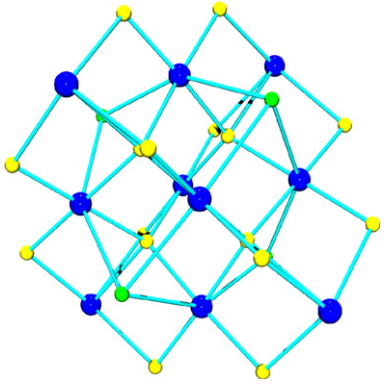


Theocharis C. Stamatatos, Khalil A. Abboud, Wolfgang Wernsdorfer and George Christou

Polyhedron 26 (2007) 2042

Ferromagnetically-coupled decanuclear, mixed-valence $[Mn_{10}O_4(N_3)_4(hmp)_{12}]^{2+}$ [hmpH = 2-(hydroxymethyl)pyridine] clusters with rare *T* symmetry and an *S* = 22 ground state

The combined use of 2-(hydroxymethyl)-pyridine and azido ligands in reactions with simple Mn^{II} sources has given two $Mn^{II}_4Mn^{III}_6$ clusters with a beautiful, high-symmetry structure. The Mn_{10} cation (see structure: Mn blue, O yellow, N green) is completely ferromagnetically coupled and possesses an *S* = 22 ground state, one of the highest ever reported.

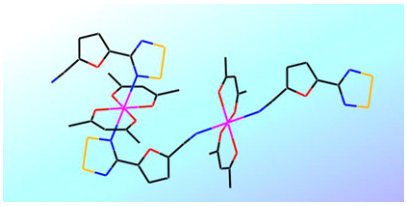


Nigel G.R. Hearns, Kevin D. Hesp, Michael Jennings, Jasmine L. Korčok, Kathryn E. Preuss and Chad S. Smithson

Polyhedron 26 (2007) 2047

Monodentate N-coordination of a 1,2,3,5-dithiadiazolyl to Mn(II), Co(II) and Ni(II): A new coordination mode

Coordination of neutral radical 4-(2′-cyanofuryl-5′)-1,2,3,5-dithiadiazolyl with bis(hexafluoroacetylacetonato)-manganese(II), -cobalt(II) or nickel(II) generates chain-like structures in the crystalline state. There are two metal coordination environments, one involving the nitrogen atoms of two nitrile groups and the other involving one nitrogen atom each of two dithiadiazolyl rings. This is the first evidence that monodentate N-coordination of a dithiadiazolyl ring can be achieved.

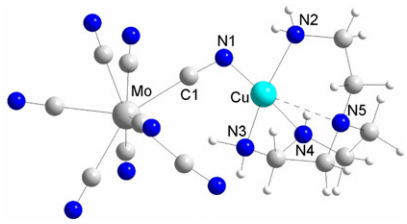


Bingwu Wang, Mingwei Wang and Zhida Chen

Polyhedron 26 (2007) 2054

Theoretical study on photoinduced magnetization process: Possible meta-stable molecular structure for a photomagnetic high-spin molecule $[Mo^{IV}(CN)_2(CN\text{-}CuL)_6]^{8+}$

The local structure and magnetic exchange properties of the possible intermediate in photoinduced magnetization process for the photomagnetic high-spin molecule $[Mo^{IV}(CN)_2(CN\text{-}CuL)_6]^{8+}$ are studied by theoretical calculations

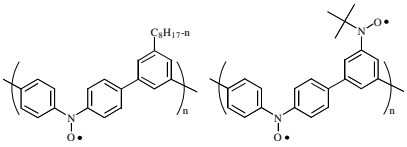


Hiroyuki Oka, Yasushi Kiyohara, Hiroshi Kouno and Hitoshi Tanaka

Polyhedron 26 (2007) 2059

Intramolecular spin interaction of 1,3-phenylene linked polyradicals bearing nitroxides in the π-conjugated polymeric main and side chains

Stable 1,3-phenylene linked polyradicals bearing nitroxides in the π-conjugated main and side chains were synthesized and the intramolecular spin interaction was investigated. The *S* values numerically calculated based on the degree of polymerization and the spin concentration of polyradicals were in good agreement with the experimental values. This showed that the spin defect intercepts the intramolecular spin interaction in the polyradicals bearing nitroxides only in the π-conjugated main chain, whereas, in the polyradical bearing another nitroxide in the side chain, there is the intramolecular spin interaction across the spin defect.

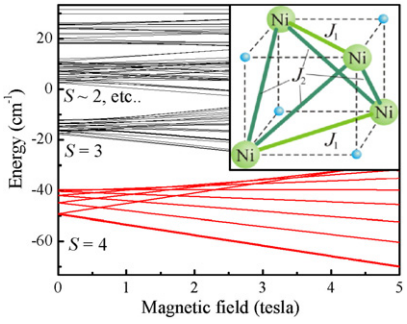


Anthony Wilson, En-Che Yang, David N. Hendrickson and Stephen Hill

Polyhedron 26 (2007) 2065

On the validity of the giant spin approximation and its application to single-molecule magnets

Numerical analysis of the Single-Molecule Magnet, $[Ni(hmp)(dmb)Cl]_4$, compares the giant spin approximation to a four-particle model. Higher order giant spin terms appear as a consequence of exchange coupling within the molecule convoluting physical interpretation of a giant spin Hamiltonian.



Marilena Ferbinteanu, Takashi Kajiwara, Fanica Cimpoesu, Kensuke Katagiri and Masahiro Yamashita

Polyhedron 26 (2007) 2069

The magnetic anisotropy and assembling of the lanthanide coordination units in $[Fe(bpca)_2]$-$[Er(NO_3)_3(H_2O)_4]NO_3$

The magnetic properties of the title compound are discussed in correlation with the molecular and crystal structure. The $[Er(NO_3)_3(H_2O)_4]$ units are connected via hydrogen bonds. Static and dynamic magnetic properties are reported. The ab initio calculations and subsequent modeling revealed the lobes of the easy magnetization axes.

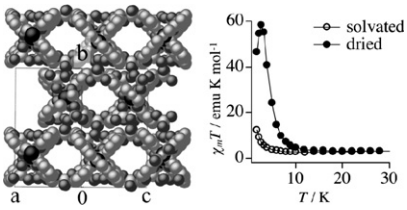


Yukihiro Kaneko, Takashi Kajiwara, Hisanori Yamane and Masahiro Yamashita

Polyhedron 26 (2007) 2074

Solvent induced reversible change of magnetic properties in a Fe(II)–Fe(III) single chain magnet

Crystals of single chain magnet (SCM), *catena*-$[Fe^{II}(ClO_4)_2\{Fe^{III}(bpca)_2\}]ClO_4$ (**1**), include CH_3NO_2 molecules as crystallized solvent, which can be released or reabsorbed accompanied by a reversible changing of SCM behavior during this process. Compound **1** is the first nano-magnet which shows the solvent induced reversible change of magnetic properties.

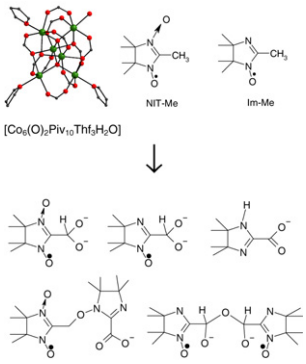


Elena Fursova, Olga Kuznetsova, Victor Ovcharenko, Galina Romanenko, Vladimir Ikorskii, Igor Eremenko and Alexey Sidorov

Polyhedron 26 (2007) 2079

Simultaneous transformation of a polynuclear complex and nitroxide in the reaction of the $\{Co_6(O)_2Piv_{10}\}$ cluster with 2,4,4,5,5-pentamethyl-4,5-dihydro-1*H*-imidazolyl-(3-oxide)-1-oxyl

New group of heterospin complexes based on polynuclear cobalt pivalates with nitroxides have been synthesized and characterized by X-ray crystallography.

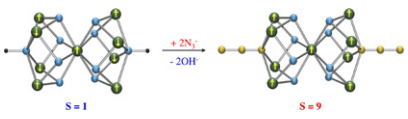


Giannis S. Papaefstathiou, Athanassios K. Boudalis, Theocharis C. Stamatatos, Constantinos J. Milios, Constantinos G. Efthymiou, Catherine P. Raptopoulou, Aris Terzis, Vassilis Psycharis, Yiannis Sanakis, Ramon Vicente, Albert Escuer, Jean-Pierre Tuchagues and Spyros P. Perlepes

Polyhedron 26 (2007) 2089

A general synthetic route for the preparation of high-spin molecules: Replacement of bridging hydroxo ligands in molecular clusters by end-on azido ligands

Incorporation of end-on N_3^- ligands, instead of OH^- ligands, or replacement of OH^- bridges by end-on N_3^- bridges through rational reactivity chemistry can be considered as a general synthetic route of increasing the ground-state total spin value of a 3d-metal cluster.

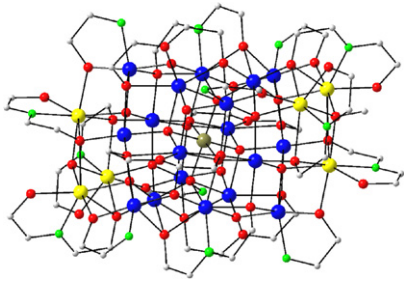


Theocharis C. Stamatatos, Khalil A. Abboud, Wolfgang Wernsdorfer and George Christou

Polyhedron 26 (2007) 2095

A new Mn_{25} single-molecule magnet with an $S = 61/2$ ground state arising from ligand-induced 'spin-tweaking' in a high-spin molecule

The replacement of the 12 azide groups in $[Mn_{25}O_{18}(OH)_2(N_3)_{12}(pdm)_6(pdmH)_6]^{2+}$ with 6 $\eta^1{:}\eta^2{:}\mu_2$ hmp^- groups in MeCN/MeOH gives $[Mn_{25}O_{18}(OH)(OMe)(hmp)_6(pdm)_6(pdmH)_6]^{8+}$. The resulting small perturbations to the structure and exchange parameters cause a change to the ground state from $S = 51/2$ to $S = 61/2$. Hysteresis studies below ~1.0 K show the new compound to also be a single-molecule magnet.

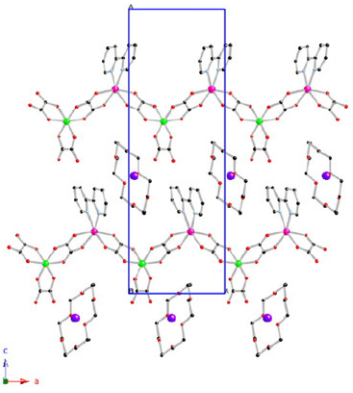


Eugenio Coronado, José R. Galán Mascarós and Carlos Martí-Gastaldo

Polyhedron 26 (2007) 2101

Controlling the dimensionality of oxalate-based bimetallic complexes: The ferromagnetic chain $\{[K(18\text{-crown-6})][Mn(bpy)Cr(ox)_3]\}_\infty$ (18-crown-6 = $C_{12}H_{24}O_6$, ox = $C_2O_4^{2-}$, bpy = $C_{10}H_8N_2$)

The bimetallic ferromagnetic chain $\{[K(18\text{-crown-6})][Mn(bpy)Cr(ox)_3]\}_\infty$ (**1**) has been synthesized and characterized. The magnetic exchange within the anionic $[Mn(bpy)Cr(ox)_3]^-$ 1D chains is ferromagnetic. In the solid state, the ferromagnetic chains are well isolated magnetically and no long range magnetic ordering has been observed above 2 K.

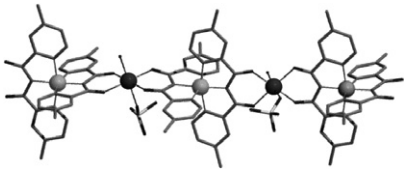


Hiroki Tanaka, Takashi Kajiwara, Yukihiro Kaneko, Shinya Takaishi and Masahiro Yamashita

Polyhedron 26 (2007) 2105

Synthesis, structure, and magnetic property of a new Fe(II)–Fe(III) alternating single-chain magnet constructed with a methyl-substituted $bpca^-$ ligand

A new Fe(II)–Fe(III) alternating single chain magnet, *catena*-$[Fe^{II}(ClO_4)(H_2O)\{Fe^{III}(bmpca)_2\}](ClO_4)_2$, was synthesized using methyl-substituted $bpca^-$ ligand, $bmpca^-$ (Hbpca and Hbmpca denote bis(2-pyridylcarbonyl)amine and bis(4-methyl-2-pyridylcarbonyl)amine, respectively).

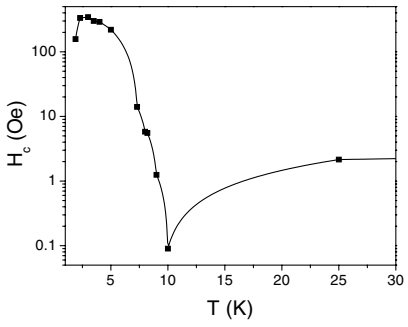


M. Bremer, J. Sandstrom, P. Jeppson, B. Anderson, M. Kaderbhai, Orhan Kizilkaya, S. Zinoveva, Shengming Liu, D.L. Schulz and A.N. Caruso

Polyhedron 26 (2007) 2110

The low temperature magnetic response of a layered manganese acetate benzoate complex

The low temperature magnetic properties of a manganese carboxylate complex are reported. The magnetic conclusions involve multiple low temperature and applied field transitions including regions of frustration and metamagnetism. A model to qualitatively measure interlayer exchange is proposed by measurement of the exchange anisotropy.

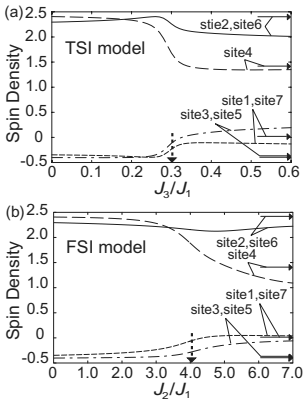


Shun Tonooka, Koichi Kusakabe, Hiroki Nakano and Naoshi Suzuki

Polyhedron 26 (2007) 2117

Determination of the effective spin Hamiltonian of Mn_6R_6 referring to the spin density functional theory

An *ab-initio* calculation determines the effective spin model of Mn_6R_6. The model including the three-spin interactions (TSI model) shows inconsistency in the spatial configuration of the spin density (Fig. a). The best fit of the spin-density configuration is achieved by the frustrated spin interaction model (FSI model) (Fig. b).

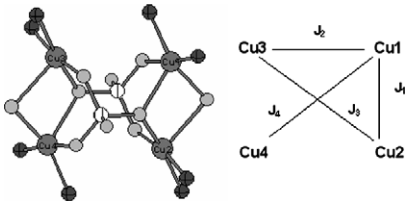


E. Spodine, D. Venegas-Yazigi, S. Ushak, V. Paredes-García, M. Saldias, E. Le Fur and J.Y. Pivan

Polyhedron 26 (2007) 2121

Magnetic properties of hybrid organo-inorganic copper(II) oxovanadate(V) phosphate and phosphonate bridged systems

The hybrid organo-inorganic compounds $[Cu_4(bipy)_4V_4O_{11}(PO_4)_2]nH_2O(n \sim 5)$ (**1**), $[Cu_2(phen)_2(PO_4)(H_2PO_4)_2(VO_2) \cdot 2H_2O]$ (**2**) and $[Cu_2(phen)_2(O_3PCH_2PO_3)(V_2O_5)(H_2O)]$-$H_2O$ (**3**) which present different bridging forms of the phosphate/phosphonate group, show different bulk magnetic properties. We also report a theoretical study for compound (**1**) assuming four different magnetic exchange pathways between the copper centres present in the tetranuclear unit.

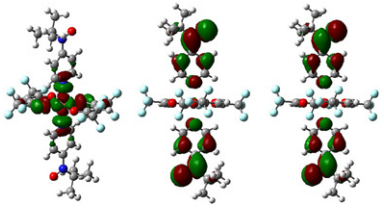


Zhe An, Jingping Zhang, Rongshun Wang and Noboru Koga

Polyhedron 26 (2007) 2126

DFT investigation for 1:2 complexes of bis(hexafluoroacetylacetonato)copper(II) coordinated with 4-(*N*-*tert*-butyl-*N*-oxyamino)-pyridine

With the aim to explore the nature of interaction between organic radicals and paramagnetic ion, various functionals and basis sets have been performed on the 1:2 complexes of bis(hexafluoroacetylacetonato)copper coordinated with 4-(*N*-*tert*-butyl-*N*-oxyamino)-pyridine. The proper chemical models for the magnetic orbitals of investigated system are RO-B3LYP, RO-BLYP, RO-PBE, and RO-PBE0.

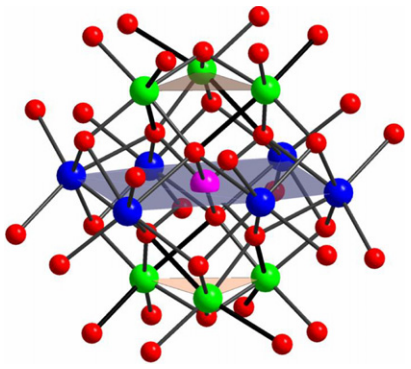


Christos Lampropoulos, Muralee Murugesu, Khalil A. Abboud and George Christou

Polyhedron 26 (2007) 2129

A family of mixed-valent $Mn^{IV}Mn^{III}_6Mn^{II}_6$ tridecanuclear clusters, and their magnetostructural correlation

Three mixed-valent ($Mn^{IV}Mn^{III}_6Mn^{II}_6$) complexes $[Mn_{13}O_8(OH)_6(ndc)_6]$ (**1**), $[Mn_{13}O_8(EtO)_{5.5}(OH)_{0.5}(ndc)_6]$ (**2**), and $[Mn_{13}O_8(O_2CPh)_{12}(EtO)_6]$ (**3**) have been synthesized and studied. Complexes **1**, **2**, and **3** have $S = 9/2$, 11/2, and 11/2 ground states, respectively. A qualitative magnetostructural correlation allows insights as to the structural origin of the differences in magnetic properties.

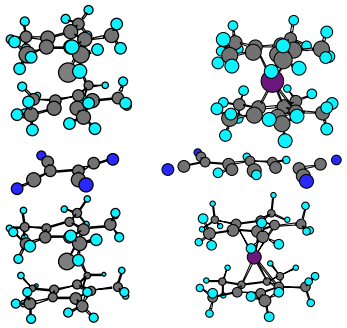


Kenichi Koizumi, Mitsuo Shoji, Yasutaka Kitagawa, Ryo Takeda, Shusuke Yamanaka, Takashi Kawakami, Mitsutaka Okumura and Kizashi Yamaguchi

Polyhedron 26 (2007) 2135

Theoretical studies on ferromagnetic behavior of $[Cr(C_5(CH_3)_5)_2]^+[TCNE]^-$ and $[Mn(C_5(CH_3)_5)_2]^+[TCNQ]^-$

By using broken-symmetry hybrid-DFT (UB3LYP and UB2LYP) calculation, *J* values of $[Cr(C_5(CH_3)_5)_2]^+[TCNE]^-[Cr(C_5(CH_3)_5)_2]^+$ and $[Mn(C_5(CH_3)_5)_2]^+[TCNQ]^-[Mn(C_5(CH_3)_5)_2]^+$ were determined theoretically. Our results supported the so-called McConnell I mechanism. Natural orbital analysis made it clear that orbital overlap between SOMO on metals and SOMO on TCNE or TCNQ cations was nearly zero.



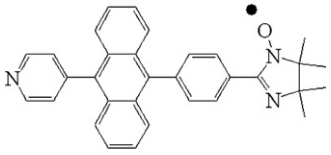
Models

Naoaki Mihara and Yoshio Teki

Polyhedron 26 (2007) 2142

The metal complexes using organic ligands with photo-excited high-spin states

4-Pyridinyl substituted phenyl-anthracene-iminonitroxide radical **2**, the metal complexes $Cu(II)(hfac)_2(\mathbf{2})_2$ and $Mn(II)(hfac)_2(\mathbf{2})_2$ were synthesized. The photo-excited quartet high-spin state of **2** was proved by time-resolved ESR. The magnetic properties and molecular structures of the metal complexes in the ground states were also investigated by magnetic susceptibility measurements and X-ray analysis.



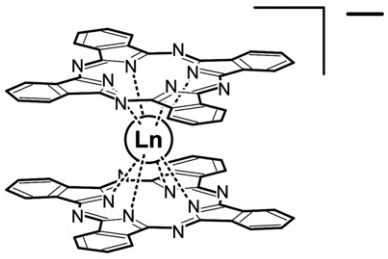
2

Naoto Ishikawa

Polyhedron 26 (2007) 2147

Single molecule magnet with single lanthanide ion

The single molecule magnet behavior of metal complexes containing a single magnetic ion was first reported for phthalocyaninato–lanthanide complexes with a "double-decker" structure. In this paper, recent attempts by the author and coworkers at revealing the magnetism and electronic structures of the mononuclear and dinuclear lanthanide complexes with phthalocyaninato ligands are reviewed.



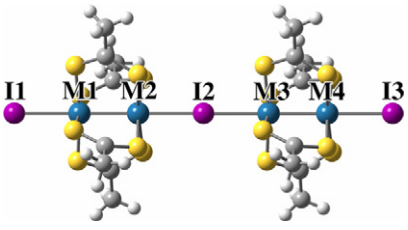
$[Pc_2Ln^{III}]^-$

Y. Kitagawa, M. Shoji, K. Koizumi, T. Kawakami, M. Okumura and K. Yamaguchi

Polyhedron 26 (2007) 2154

Theoretical studies on relation among structures, electric structures and magnetic interactions in MMX complexes

The electronic structures of $Ni_2(dta)_4I$ and $Pt_2(dta)_2I$ complexes were examined by using UB3LYP calculations. In order to explain a variety of structural phases in those complexes, potential and J_{ab} surfaces were also investigated. The calculated potential surfaces explained experimental results of the complexes.

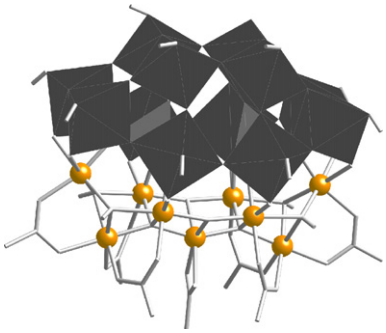


Eliseo Ruiz, Joan Cano, Santiago Alvarez, Pierre Gouzerh and Michel Verdaguer

Polyhedron 26 (2007) 2161

Theoretical study of the exchange coupling interactions in a polyoxometalate Fe_9W_{12} complex

The exchange coupling interactions in a Fe_9W_{12} polyoxometallate complex have been studied using theoretical methods based on Density Functional Theory.

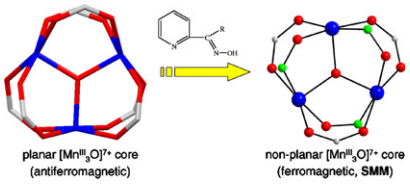


Theocharis C. Stamatatos, Dolos Foguet-Albiol, Constantinos C. Stoumpos, Catherine P. Raptopoulou, Aris Terzis, Wolfgang Wernsdorfer, Spyros P. Perlepes and George Christou

Polyhedron 26 (2007) 2165

New Mn_3 structural motifs in manganese single-molecule magnetism from the use of 2-pyridyloximate ligands

The distortion imposed on two $[Mn_3(\mu_3\text{-}O)]^{7+}$ members of the well known and well studied class of triangular, oxide-centered $[Mn_3O(O_2CR)_6(py)_3]^+$ complexes by methyl or phenyl 2-pyridyl ketone oxime (L'H) switches the exchange interactions to ferromagnetic and makes the $[Mn_3O(O_2CR)_3L'_3]^+$ products the first examples of triangular single-molecule magnets.

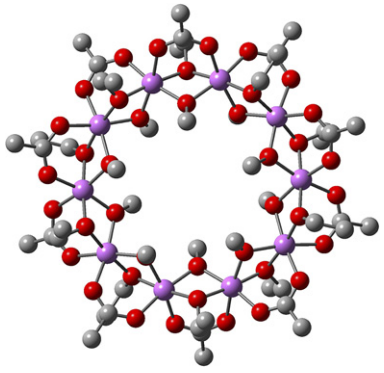


Le Sun, Jingping Zhang and Shuxin Cui

Polyhedron 26 (2007) 2169

Solvothermal synthesis, structure, and magnetic property for nano-'chromic wheels' $[Cr_{10}(\mu\text{-}O_2CMe)_{10}(\mu\text{-}OMe)_{10}(\mu\text{-}OEt)_{10}]$

Nano-decanuclear cyclic Cr(III) complex, $[Cr_{10}(\mu\text{-}O_2CMe)_{10}(\mu\text{-}OMe)_{10}(\mu\text{-}OEt)_{10}]$, has been synthesized. The Cr_{10} rings are close to planar, with ethoxide and acetato ligands pointing outside of the "wheel" and methoxide ligands pointing to inside of the "wheel". Magnetic susceptibility studies reveal very weak anti-ferromagnetic Cr···Cr exchange.

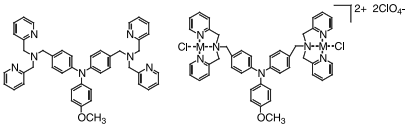


Masafumi Yano, Masayuki Fujita, Masaya Miyake, Masakazu Tatsumi, Tatsuo Yajima, Osamu Yamauchi, Munetaka Oyama, Kazunobu Sato and Takeji Takui

Polyhedron 26 (2007) 2174

Synthesis and properties of a redox active ligand with bispicorylamino groups and its dinuclear complex

A novel ligand with a redox active triarylamine unit and its dinuclear palladium and copper complexes were designed and synthesized. Electrochemical and spectroscopic propertise of the complexes were examined.

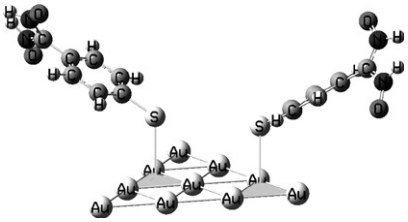


Mitsutaka Okumura, Yasutaka Kitagawa, Takashi Kawakami and Kizashi Yamaguchi

Polyhedron 26 (2007) 2179

Theoretical studies of magnetic interaction of organic π-radicals on gold cluster surface

In order to elucidate the magnetic interaction in gold nanoparticles chemisorbed by alkanethiol systems, small slab gold cluster, such as Au_{10}, and π-radical hybrid model systems were examined using the hybrid DFT method.

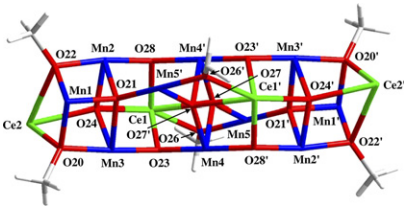


Anastasios J. Tasiopoulos, Abhudaya Mishra and George Christou

Polyhedron 26 (2007) 2183

Synthetic routes to a family of Mn–Ce heterometallic clusters

A synthetic method that involves addition to Mn salts or preformed clusters of Ce^{IV} and has resulted in the synthesis of several mixed metal Mn–Ce clusters is described.

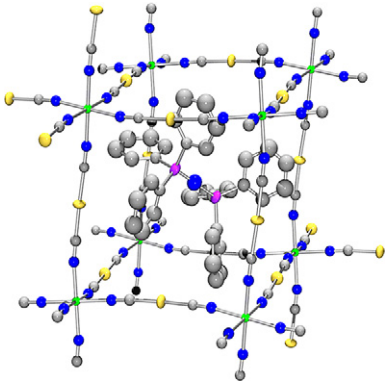


Julie Lefebvre, Daniel Chartrand and Daniel B. Leznoff

Polyhedron 26 (2007) 2189

Synthesis, structure and magnetic properties of 2-D and 3-D [cation]{$M[Au(CN)_2]_3$} (M = Ni, Co) coordination polymers

Studies on the templating effect of the cation and the resulting impact on the magnetic properties were conducted on a series of [cation]{$M[Au(CN)_2]_3$} coordination polymers. Despite the high-dimensionality structures, no significant magnetic coupling was observed, suggesting that the $[Au(CN)_2]$ bridging unit behaves as a poor mediator of magnetic exchange in these systems.

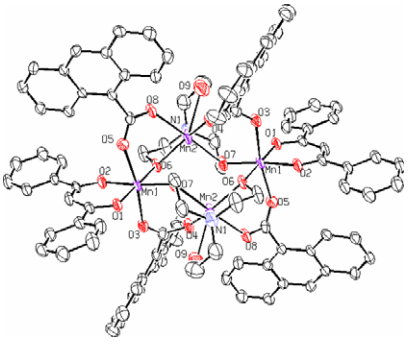


Christopher C. Beedle, Katie J. Heroux, Motohiro Nakano, Antonio G. DiPasquale, Arnold L. Rheingold and David N. Hendrickson

Polyhedron 26 (2007) 2200

Antiferromagnetic tetranuclear manganese complex: Wheel or dicubane?

Magnetic susceptibility data are presented for $[Mn_4(anca)_4(Htea)_2(dbm)_2] \cdot 2.5Et_2O$ and analyzed with theoretical fits employing the Kambe approach, and by fitting the data employing a full matrix diagonalization approach which includes terms for Heisenberg isotropic exchange, single-ion zero-field and Zeeman interactions.

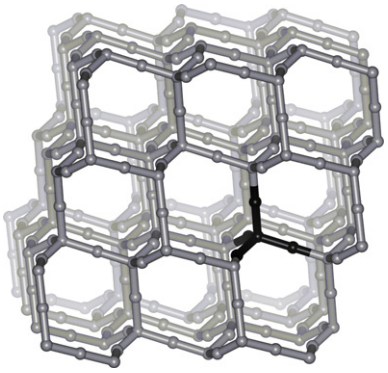


Zheming Wang, Bin Zhang, Yanjuan Zhang, Mohamedally Kurmoo, Tao Liu, Song Gao and Hayao Kobayashi

Polyhedron 26 (2007) 2207

A family of porous magnets, $[M_3(HCOO)_6]$ (M = Mn, Fe, Co and Ni)

A family of porous magnets of $[M_3(HCOO)_6]$ (M = divalent Mn, Fe, Co and Ni), with open diamond framework based on M-centred MM_4 tetrahedron, prepared by conventional solution chemistry method, displays permanent porosity, stability for thermal treatment, guest removal, guest inclusion for a wide spectrum of guests of different size, 3D long-range magnetic ordering and guest-modulated magnetic properties. The mixed-metal porous $[Fe_xZn_{3-x}(HCOO)_6]$ series shows gradual evolution from 3D long-range ordering to spin glass then superparamagnet and finally paramagnet upon magnetic dilution.

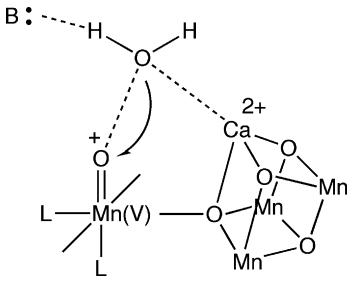


K. Yamaguchi, S. Yamanaka, H. Isobe, M. Shoji, K. Koizumi, Y. Kitagawa, T. Kawakami and M. Okumura

Polyhedron 26 (2007) 2216

Theory of chemical bonds in metalloenzymes VI: Manganese–oxo bonds in the photosynthesis II system

Electronic structures of high-valent manganese–oxo bonds in the photosynthesis II system (oxygen evolving center) and manganese–oxo porphyrine artificial system are investigated by the use of spin polarized hybrid DFT method. Possibility of the SE_2, ^{1}O- and ^{3}O-models for oxygenation reactions by metaloxo species is discussed.

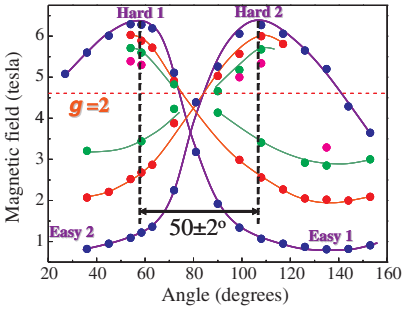


Sheng-Chiang Lee, Theocharis C. Stamatatos, Stephen Hill, Spyros P. Perlepes and George Christou

Polyhedron 26 (2007) 2225

High-frequency EPR characterization of a triangular Mn_3 single-molecule magnet

The results of a multi-high-frequency single-crystal EPR study of a recently discovered triangular trinuclear Mn complex, $[Mn_3O(O_2CMe)_3(mpko)_3](ClO_4) \cdot 3CH_2Cl_2$, are presented. The obtained data confirm the findings of earlier magnetic measurements, which suggested that this complex is a single-molecule magnet with a spin ground state of $S = 6$. The zero-field splitting parameters obtained from the present EPR study are: $D = -0.3\ cm^{-1}$, $B_4^0 = -3 \times 10^{-5}\ cm^{-1}$ and $g = 2.00$.

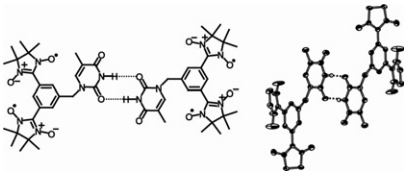


Hiroyuki Tanaka, Daisuke Shiomi, Tomoaki Ise, Kazunobu Sato and Takeji Takui

Polyhedron 26 (2007) 2230

Thymine-substituted nitronyl nitroxide biradical as a triplet ($S = 1$) component for bio-inspired molecule-based magnets

As a building block of bio-inspired molecule-based magnets, a thymine-substituted biradical **1** has been synthesized. The biradical **1** has a triplet ground state with $2J/k_B = 21.4$ K. In the crystalline solid state, **1** forms hydrogen-bonded aggregates, in which the thymine moiety plays a primary role in the molecular packing.

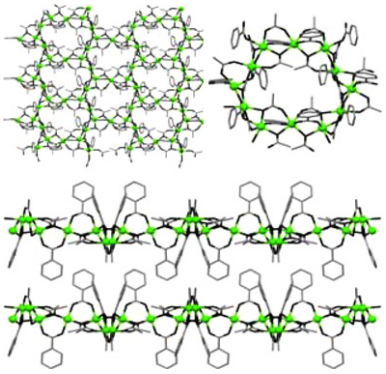


Shengming Liu, Pamela Jeppson, Joseph Sandstrom, A.N. Caruso and D.L. Schulz

Polyhedron 26 (2007) 2235

Synthesis, structure and magnetic properties of $\{Mn_5(OC(O)CH_3)_6(OC(O)C_6H_5)_4\}_\infty$

A new layered manganese (II) mixed-carboxylate complex is reported. The structure of $\{Mn_5(OC(O)CH_3)_6(OC(O)C_6H_5)_4\}_\infty$ is described as edge-shared Mn_{12} loops arranged in a honeycomb-like 2D sheet. A sideview of the sheets shows the acetate ligands slightly displaced out of the plane and an intersheet spacing of 12 Å is reported.

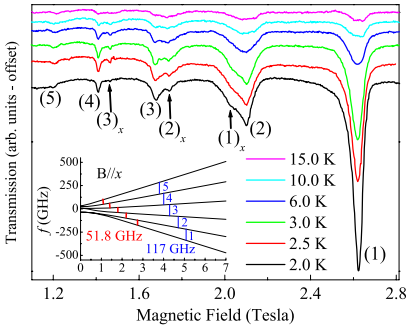


Saiti Datta, Amalia Betancur-Rodriguez, Sheng-Chiang Lee, Stephen Hill, Dolos Foguet-Albiol, Rashmi Bagai and George Christou

Polyhedron 26 (2007) 2243

EPR characterization of half-integer-spin iron molecule-based magnets

The results of high frequency single crystal EPR studies of two recently discovered half-integer Fe_7 complexes: $[Fe_7O_3(O_2CBu^t)_9(mda)_3(H_2O)_3]$ (**1**) and $[Fe_7O_4(O_2CPh)_{11}(dmem)_2]$ (**2**) are presented. The obtained spectra confirm spin $S = 5/2$ ground states for both complexes. Detailed frequency and field orientation dependent studies showed complex **1** is a single-molecule magnet (uniaxial zero-field-splitting parameter, $D < 0$) while complex **2** is not ($D > 0$). The EPR linewidth for complex **1** is considerably narrower in comparison to spectra obtained for other single-molecule magnets.

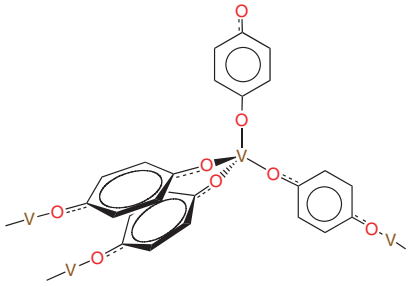


Mathew S. Thorum, Michelle L. Taliaferro, Kil Sik Min and Joel S. Miller

Polyhedron 26 (2007) 2247

The quest for magnets composed of vanadium and 1,4-benzoquinones

Reaction of $V^o(CO)_6$ and benzoquinone, chloranil, 2,3-dicyano-1,4-naphthoquinone, and dihydroxy-1,4-benzoquinone), form materials of $V(qunione)_2 \cdot zCH_2Cl_2$ ($z < 0.1$) composition, which exhibits antiferromagnetic coupling and do not magnetically order above 5 K.

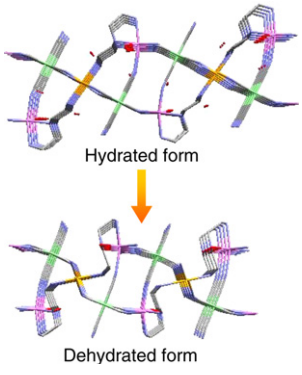


Wakako Kaneko, Susumu Kitagawa and Masaaki Ohba

Polyhedron 26 (2007) 2252

A unique 2-D hollow sheet structure and magnetic behavior of a cyanide- and triamine-bridged $Mn^{II}Cr^{III}$ ferrimagnet

A two-dimensional cyanide- and triamine-bridged $Mn^{II}Cr^{III}$ ferrimagnet, $[Mn_3(dien)_2(H_2O)_2][Cr(CN)_6]_2 \cdot 4H_2O$, has been prepared and characterized its structural and magnetic changes associated with dehydration. This compound irreversibly changed to a dehydrated form and the hydrated and the dehydrated forms show an unusual long-range ferrimagnetic ordering with multiple magnetic phase changes reflecting a unique 2-D hollow sheet structure.

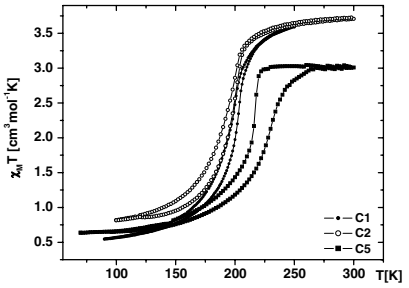


Marinela M. Dîrtu, Yann Garcia, Mihai Nica, Aurelian Rotaru, Jorge Linares and François Varret

Polyhedron 26 (2007) 2259

Iron(II) spin transition 1,2,4-triazole chain compounds with novel inorganic fluorinated counteranions

$\chi_M T$ versus T on cooling and warming modes for $[Fe(NH_2trz)_3]TiF_6 \cdot nH_2O$ ($n = 0.5$ (●); $n = 1$ (○)) and $[Fe(NH_2trz)_3]SnF_6 \cdot 0.5H_2O$ (■).

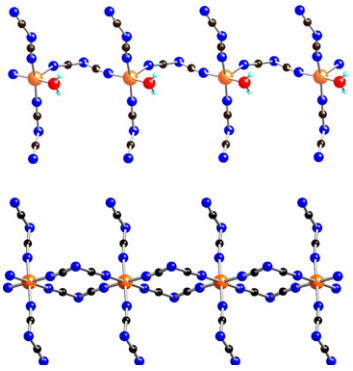


John A. Schlueter, Jamie L. Manson, Kylee A. Hyzer and Urs Geiser

Polyhedron 26 (2007) 2264

Novel anionic dicyanamidocuprate(II) structural motifs through cation templation

Two new anionic dicyanamidocuprate(II) coordination polymers, $(PPh_4)Cu(dca)_3H_2O$ and $(PPh_3Bu)_2Cu(dca)_4$, have been crystallized. The singly bridged $\mu_{1,5}$-dicyanamide chains in the former are linked into a two-dimensional array through hydrogen bonding, while in the latter, doubly bridged $\mu_{1,5}$-dicyanamide chains are formed. Long range magnetic order has not been observed in either compound.

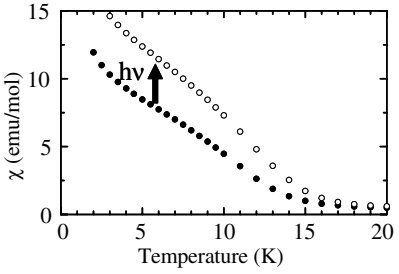


Franz A. Frye, Daniel M. Pajerowski, Norman E. Anderson, Jerome Long, Ju-Hyun Park, Mark W. Meisel and Daniel R. Talham

Polyhedron 26 (2007) 2273

Photoinduced magnetism in rubidium cobalt hexacyanoferrate Prussian blue analogue nanoparticles

Nanoparticles (10 nm ± 2 nm) of rubidium cobalt hexacyanoferrate ($Rb_{1.8}Co_4[Fe(CN)_6]_{3.2}$) were synthesized. The nanoparticles show ferrimagnetic ordering in DC magnetization below $T_C \sim 15$ K. Upon illumination with white light at 5 K, the field-cooled DC magnetization of these particles increased.

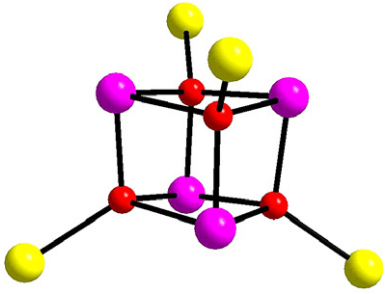


Antonio Masello, Muralee Murugesu, Khalil A. Abboud and George Christou

Polyhedron 26 (2007) 2276

A family of ferrocene-rich Mn_7, Mn_8 and Mn_{13} clusters

The reactions of ferrocene-1,1′-dicarboxylic acid with Mn reagents have led to the preparation of Mn_7, Mn_8 and Mn_{13} clusters. The crystal structures and magnetic properties of these complexes are reported, which establishes that they possess $S = 2$, 5 and 9/2, respectively.

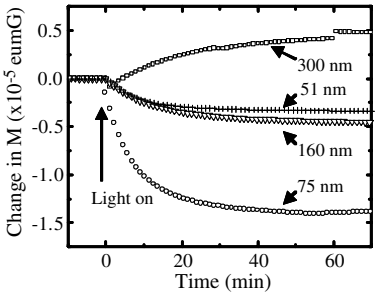


Franz A. Frye, Daniel M. Pajerowski, Sarah M. Lane, Norman E. Anderson, Ju-Hyun Park, Mark W. Meisel and Daniel R. Talham

Polyhedron 26 (2007) 2281

Effect of film thickness on the photoinduced decrease in magnetism for thin films of the cobalt iron Prussian blue analogue $Rb_{0.7}Co_4[Fe(CN)_6]_{3.0}$

The photomagnetic behavior of thin films of the Co–Fe Prussian blue analogue is investigated as the films transition from a quasi-two-dimensional system to a three-dimensional system with increasing thickness. A quasi-two-dimensional film with thickness less than ~200 nm is needed to observe the photoinduced decrease in magnetization unique to thin films of this material.

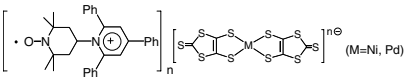


Bilkish Rahman, Ken-ichi Kanbara, Hiroki Akutsu, Jun-ichi Yamada and Shin'ichi Nakatsuji

Polyhedron 26 (2007) 2287

Radical salts derived from TEMPO-substituted 2,4,6-triphenylpyridinium

Magnetic radical salts consisting of a TEMPO-substituted 2,4,6-triphenyl pyridinium with $Ni(dmit)_2$, $Pd(dmit)_2$ or $Ni(mnt)_2$ counter anions have been prepared and the oxidized salts of the $Ni(dmit)_2$ as well as $Pd(dmit)_2$ complexes show semi-conducting properties with relatively high conductivities and low activation energies.

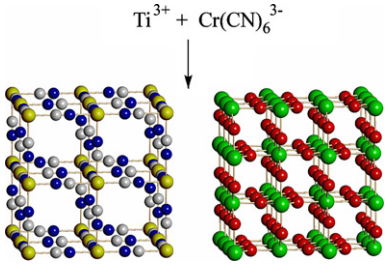


Stephen M. Holmes, Amy S. Whelpley and Gregory S. Girolami

Polyhedron 26 (2007) 2291

Nanocomposite of a chromium Prussian blue with TiO_2. Redox reactions and the synthesis of Prussian blue molecule-based magnets

The reaction of $[NEt_4]_3[Cr(CN)_6]$ with titanium(III) *p*-toluenesulfonate affords a gray solid that appeared to be a Prussian blue of stoichiometry "$Ti^{III}[Cr^{III}(CN)_6] \cdot H_2O$" but is actually a nanocomposite of $Cr^{II}[Cr^{III}(CN)_6]_{0.67} \cdot xH_2O$ and $TiO_2 \cdot nH_2O$, an amorphous form of rutile. Evidently, Ti^{III} reduces some of the $[Cr^{III}(CN)_6]^{3-}$ ions to generate Ti^{IV} and Cr^{II}; subsequent reactions generate the observed products.

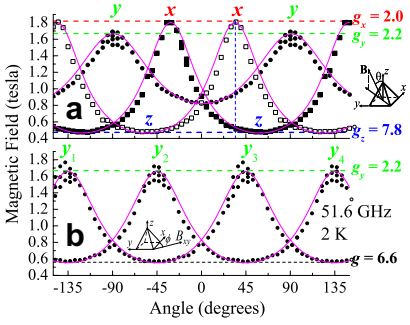


Jon Lawrence, Chris C. Beedle, En-Che Yang, James Ma, Stephen Hill and David N. Hendrickson

Polyhedron 26 (2007) 2299

High frequency electron paramagnetic resonance (HFEPR) study of a high spin Co(II) complex

Variable high-frequency electron paramagnetic resonance data are presented for a single crystal of $[Zn(hmp)(dmb)Cl]_4$ doped with a small quantity of high spin Co(II). Data obtained for various field orientations, frequencies, and temperatures indicate the ground state of the Co^{2+} ions to be an effective spin $S' = 1/2$ Kramers' doublet with a highly anisotropic *g*-tensor. The anisotropy is of the easy-axis type, with the single-ion easy axis directions tilted away from the crystallographic *c* direction by 58°.

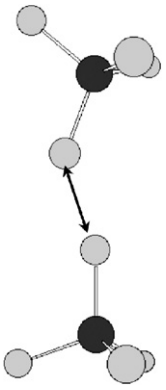


Mao Takenaka, Youhei Nishimura, Takashi Kawakami, Yasutaka Kitagawa, Mitsutaka Okumura and Kizashi Yamaguchi

Polyhedron 26 (2007) 2304

Theoretical studies of *d–d* magnetic interaction in organic superconductors

To investigate all the magnetic interactions between neighboring two $FeCl_4^-$ anions, various spatial conformation of dimers were assumed and studied. For variety of configurations of $FeCl_4^-$ anion dimers, the values of effective exchange integral (J) in the Heisenberg spin model were calculated by using *ab initio* MO methods.

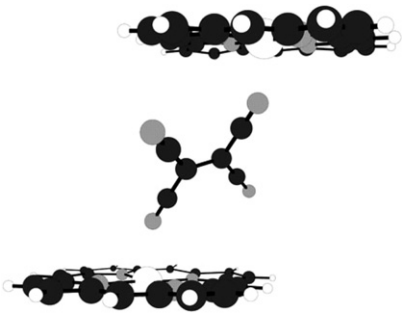


Ryo Takeda, K. Koizumi, M. Shoji, H. Nitta, S. Yamanaka, M. Okumura and K. Yamaguchi

Polyhedron 26 (2007) 2309

Ab initio studies on the zero-field splitting parameters of manganese porphyrin complexes

The magnetic property of a one-dimensional magnetic chain, 5,10,15,20-tetrakis(4-bromophenyl)porphyrinatomanganese(III) tetracyanoethenide ($[MnTBrPP]^+[TCNE]^-$), is investigated by using model complexes and density functional calculations. In these models, MnTBrPP is reduced to a manganese porphyrin complex (MnP). It found that the TCNE coordination hardly affects the magnetic anisotropy of MnP.

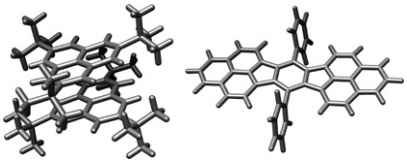


T. Ukai, K. Nakata, S. Yamanaka, T. Kubo, Y. Morita, T. Takada and K. Yamaguchi

Polyhedron 26 (2007) 2313

CASCI-DFT study of the phenalenyl radical system

We present ab initio complete-active-space density functional theory (DFT) study of the phenalenyl radical dimeric compounds. The calculated magnetic interactions and excited spectra are compared with those of Hartree-Fock, hybrid DFT, and the experimental ones.

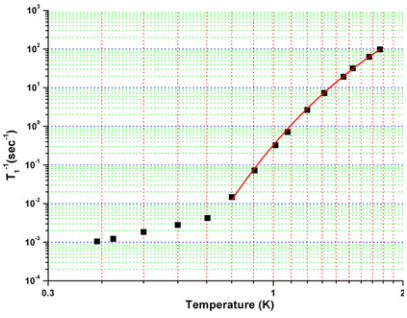


A.G. Harter, C. Lampropoulos, M. Murugesu, P. Kuhns, A. Reyes, G. Christou and N.S. Dalal

Polyhedron 26 (2007) 2320

^{55}Mn nuclear spin relaxation in the truly axial single-molecule magnet Mn_{12}-*t*-butylacetate thermally-activated down to 400 mK

Inverse T_1 of the Mn(1) peak of Mn_{12}-*t*-Bu single crystal. Below 0.8 K, temperature-independent behavior is not present, suggesting that quantum tunneling of the magnetization is not responsible for the relaxation of the nuclei in this temperature range.

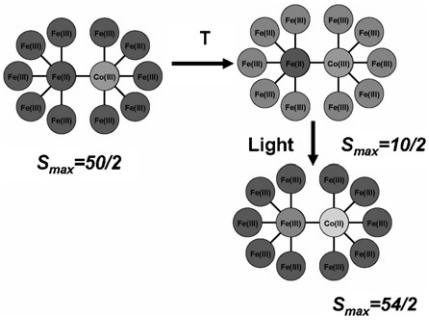


F. Renz, D. Hill, M. Klein and J. Hefner

Polyhedron 26 (2007) 2325

Unprecedented multistability in dodecanuclear complex compound observed by Mössbauer spectroscopy

The pentadentate ligand precursors [Fe(III)LCl] yield in synthesis with the bridging unit $[(NC)_5Fe(II)\text{-}CN\text{-}Co(III)(CN)_5]^{6-}$ a star-shaped dodecanuclear compound. They are high-spin systems with 50 unpaired electrons at room temperature. Some of them change sequentially between multiple electronical states on cooling while light irradiation favours a concerted reaction mechanism.

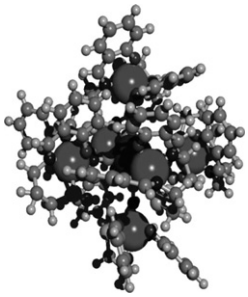


F. Renz, J. Hefner, D. Hill and M. Klein

Polyhedron 26 (2007) 2330

Heptanuclear high-spin complex compounds based on S-donors

Pentadentate ligands with S,N,O-donors were prepared to synthesize the precursors [Fe(III)LCl]. In combination with $[M(CN)_6]$-salts some heptanuclear complexes have been synthesized. They are high-spin systems with 40 unpaired electrons at room temperature. Some of them change sequentially between different high spin state on cooling.

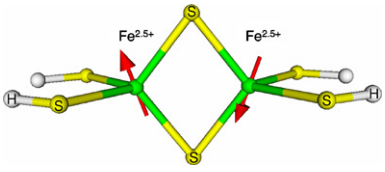


Mitsuo Shoji, Kenichi Koizumi, Ryo Takeda, Yasutaka Kitagawa, Shusuke Yamanaka, Mitsutaka Okumura and Kizashi Yamaguchi

Polyhedron 26 (2007) 2335

A GSO–HDFT study of noncollinear spin structures of [2Fe–2S] cluster

The generalized spin orbital (GSO) DFT calculations were carried out in order to investigate the noncollinear spin structures of a [2Fe–2S] complex, $Fe_2S_2(SH)_4^{3-}$. Natural orbital (NO) clearly showed the difference between the mixed-valence (MV) state and the trapped valence (TV) state.

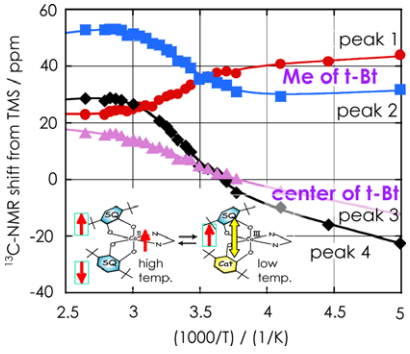


Yusuke Kadohashi, Goro Maruta and Sadamu Takeda

Polyhedron 26 (2007) 2342

Spin and charge fluctuation occurring in valence tautomerism and cooperative effects in the solid-state

Spin and charge fluctuations associated with valence tautomeric conversion were characterized for [Co (3,6-di-*t*-butyl-1,2-benzoquinone)$_2$(2,2′-bipyridine)] in the solid-state by solid-state high-resolution ^{13}C NMR, magnetic susceptibility, and dielectric measurements. The conversion occurs with a cooperative effect, which can be explained by a domain model.

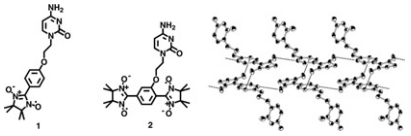


Kensuke Maekawa, Tomoaki Ise, Daisuke Shiomi, Kazunobu Sato and Takeji Takui

Polyhedron 26 (2007) 2347

Cytosine-substituted nitronyl nitroxide radicals as building blocks for generalized ferrimagnetic system

A cytosine-substituted nitronyl nitroxide monoradical **1** and a biradical **2** with a singlet ground state have been synthesized and characterized from X-ray crystallographic analyses and magnetic susceptibility measurements. The radicals **1** and **2** are building blocks for generalized ferrimagnets based on hydrogen-bonded Watson–Crick base pairing in a crystalline solid state.

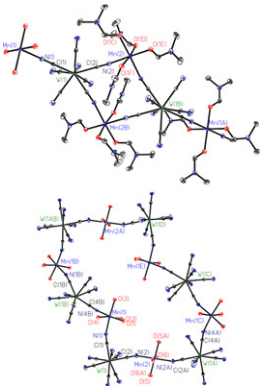


Jeffrey R. Withers, Dongfeng Li, Jeremy Triplet, Chad Ruschman, Sean Parkin, Guangbin Wang, Gordon T. Yee and Stephen M. Holmes

Polyhedron 26 (2007) 2353

Synthesis and characterization of one- and two-dimensional octacyanometalate(V) networks: $\{[trans\text{-}M^{II}(DMF)_4][cis\text{-}M^{II}(DMF)_4]_2[M^{V}(CN)_8]_2\}_n$ (M^{II} = Mn, Fe, Ni; M^{V} = Mo, W)

A series of one- and two-dimensional octacyanometalate(V) networks of $\{[M^{II}(DMF)_4]_3[M^{V}(CN)_8]_2\}_n$ (M^{II} = Mn, **5**, **6**; Fe, **10**; Ni; **7**, **8**; M^{V} = Mo, W) stoichiometry have been prepared and characterized via structural, spectroscopic, and magnetic methods. Magnetic measurements indicate that **6** is a ferrimagnet (T_N = 8 K) that exhibits frequency-dependent behavior in χ'' that is qualitatively similar to 1- and 2-D lattices reported by Tang and Holmes, respectively; additional magnetic measurements suggest that **5**, **7**, and **8** exhibit incipient magnetic ordering. Conversion of **5**–**6** requires the presence of counterions and appears to be favored when using wet DMF. The experimental evidence suggests that coordinated DMF ligands are labile and the $M^{II}(\mu\text{-NC})M^{V}$ linkages are susceptible to fragmentation.

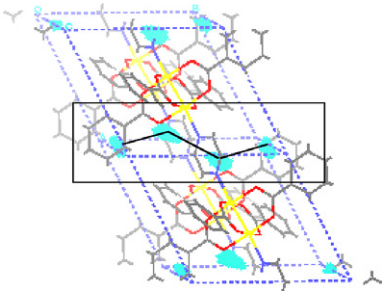


Takashi Kawakami, Satoshi Takamizawa, Mao Takenaka, Yohei Nishimura, Yasutaka Kitagawa, Mitsutaka Okumura, Wasuke Mori and Kizashi Yamaguchi

Polyhedron 26 (2007) 2367

Theoretical studies of radical spin arrangements in the cavity of nano-porous complexes

Adsorption properties of magnetic species in nano-porous crystals were studied theoretically. The crystal $[Rh_2bza_4pyz]_n$ (host) and oxygen molecules (guest) were employed. From the results by our MO calculations, weak magnetic interactions between O_2 molecules in cavities existed. Cloud of mass densities of O_2 molecules by our MD simulation showed stacking styles in nano-pores. Number of adsorbed gas was estimated to be 3.00 molecules/unit.

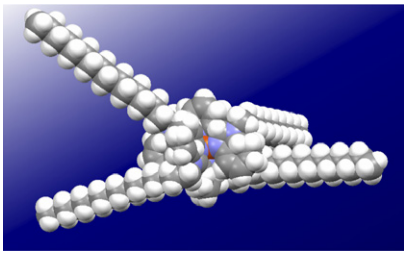


Shinya Hayami, Natsuko Motokawa, Aya Shuto, Reiko Moriyama, Naoji Masuhara, Katsuya Inoue and Yonezo Maeda

Polyhedron 26 (2007) 2375

Spin-crossover iron(II) compounds with liquid-crystal properties

The iron(II) compounds $[Fe(1C16\text{-}O\text{-}bzimpy)_2](BF_4)_2$ (**1**) and $[Fe(2C16\text{-}bzimpy)_2](BF_4)_2$ (**2**) were synthesized and their properties were characterized. Both of the compounds **1** and **2** have exhibited crystal-liquid crystal transition. The compound **1** exhibits spin-crossover behavior and photo-induced spin transition, and the compound **2** is in the low-spin state.

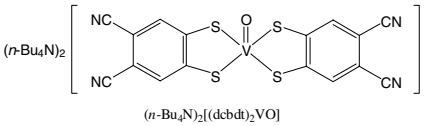


Kazumasa Ueda and Masahiro Utsumi

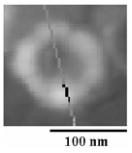
Polyhedron 26 (2007) 2381

Dithiolene vanadium complexes based regulated domain arrangement by colloidal lithography

We have successfully fabricated nanometer-sized ring structures of paramagnetic metal complex of $(n\text{-}Bu_4N)_2[(dcbdt)_2VO]$, (dcbdt) = 4,5-dicyanobenzene-1,2-dithiolato a on glass substrates using a colloidal lithography technique. Obtained nano-scale rings has around 130 nm outer diameter and around 10 nm height on a surface of the substrate reflecting the position of particle templates.



$(n\text{-}Bu_4N)_2[(dcbdt)_2VO]$



AFM image of the $(n\text{-}Bu_4N)_2[(dcbdt)_2VO]$ ring

The Publisher encourages the submission of articles in electronic form thus saving time and avoiding rekeying errors. For detailed instructions on the preparation of manuscripts and of electronic artwork, consult the Author Gateway for Elsevier at http://authors.elsevier.com

ScienceDirect

Full text of this journal is available, on-line from **ScienceDirect**. Visit **www.sciencedirect.com** for more information.